PROCEEDINGS OF THE
10TH INTERNATIONAL CHEMICAL AND
BIOLOGICAL ENGINEERING CONFERENCE
CHEMPOR 2008

PROCEEDINGS OF THE
10TH INTERNATIONAL CHEMICAL AND BIOLOGICAL ENGINEERING CONFERENCE - CHEMPOR 2008

4-6 SEPTEMBER 2008, BRAGA, PORTUGAL

ORGANIZED BY

UNIVERSIDADE DO MINHO

ORDEM DOS ENGENHEIROS

INSTITUTE FOR BIOTECHNOLOGY AND BIOENGINEERING

SUPPORT

SOCIEDADE PORTUGUESA DE QUÍMICA

SOCIEDADE PORTUGUESA DE BIOTECNOLOGIA

EDITED BY

EUGÉNIO C. FERREIRA

MANUEL MOTA

UNIVERSIDADE DO MINHO, DEPARTAMENT OF BIOLOGICAL ENGINEERING

BRAGA, PORTUGAL

This volume contains full papers presented at the 10th International Chemical and Biological Engineering Conference - CHEMPOR 2008, held in Braga, Portugal, between September 4th and 6th, 2008.

Title: **Proceedings of the 10th International Chemical and Biological Engineering Conference - CHEMPOR 2008 (CD-ROM)**

Edited by **Eugénio C. Ferreira** and **Manuel Mota**

First edition August 2008

ISBN: 978-972-97810-3-2

Tiragem: 1000 exemplares

CD-ROM cover design: Helena Martins www. helenamartinsdesign.com

Publisher:

Universidade do Minho, Departamento de Engenharia Biológica

Campus de Gualtar, 4700 Braga, Portugal

Printed by:

MediaPromo - www.mediapromo.com

This publication was sponsored by:

FCT Fundação para a Ciência e a Tecnologia

MINISTÉRIO DA CIÊNCIA, TECNOLOGIA E ENSINO SUPERIOR

Foreword

This digital book contains the full papers presented at the 10th International Chemical and Biological Engineering Conference - CHEMPOR 2008, held in Braga, Portugal, over 3 days, from the 4th to the 6th of September, 2008. Previous editions took place in Lisboa (1975, 1889, 1998), Braga (1978), Póvoa de Varzim (1981), Coimbra (1985, 2005), Porto (1993), and Aveiro (2001).

The conference was jointly organized by the University of Minho, "Ordem dos Engenheiros", and the IBB - Institute for Biotechnology and Bioengineering with the usual support of the "Sociedade Portuguesa de Química" and, by the first time, of the "Sociedade Portuguesa de Biotecnologia".

Thirty years elapsed since CHEMPOR was held at the University of Minho, organized by T.R. Bott, D. Allen, A. Bridgwater, J.J.B. Romero, L.J.S. Soares and J.D.R.S. Pinheiro. We are fortunate to have Profs. Bott, Soares and Pinheiro in the Honor Committee of this 10th edition, under the high Patronage of his Excellency the President of the Portuguese Republic, Prof. Aníbal Cavaco Silva. The opening ceremony will confer Prof. Bott with a "Long Term Achievement" award acknowledging the important contribution Prof. Bott brought along more than 30 years to the development of the Chemical Engineering Science, to the launch of CHEMPOR series and specially to the University of Minho. Prof. Bott's inaugural lecture will address the importance of effective energy management in processing operations, particularly in the effectiveness of heat recovery and the associated reduction in greenhouse gas emission from combustion processes.
The CHEMPOR series traditionally brings together both young and established researchers and end users to discuss recent developments in different areas of Chemical Engineering. The scope of this edition is broadening out by including the Biological Engineering research. One of the major core areas of the conference program is life quality, due to the importance that Chemical and Biological Engineering plays in this area. "Integration of Life Sciences & Engineering" and "Sustainable Process-Product Development through Green Chemistry" are two of the leading themes with papers addressing such important issues. This is complemented with additional leading themes including "Advancing the Chemical and Biological Engineering Fundamentals", "Multi-Scale and/or Multi-Disciplinary Approach to Process-Product Innovation", "Systematic Methods and Tools for Managing the Complexity", and "Educating Chemical and Biological Engineers for Coming Challenges" which define the full papers arrangements along this book.

A total of 516 extended abstracts are included in the Abstract Book, consisting of 7 invited lecturers, 15 keynote, 105 short oral presentations given in 5 parallel sessions, along with 6 slots for viewing 389 poster presentations. This companion CD-ROM contains the Proceedings with 384 full papers. All extended abstracts have been reviewed and we are grateful to the members of scientific and organizing committees for their evaluations. It was an intensive task since 610 submitted abstracts from 45 countries were received.

It has been an honor for us to contribute to setting up CHEMPOR 2008 during almost two years. We wish to thank the authors who have contributed to yield a high scientific standard to the program. We are thankful to the sponsors who have contributed decisively to this event. We also extend our gratefulness to all those who, through their dedicated efforts, have assisted us in this task.

On behalf of the Scientific and Organizing Committees we wish you that together with an interesting reading, the scientific program and the social moments organized will be memorable for all.

Braga, September 2008

Eugénio C. Ferreira

Manuel Mota

Committee Members

Honor Committee:
Under the high Patronage of his Excellency the President of the Portuguese Republic, Prof. Aníbal Cavaco Silva.

Members:
Ministro da Ciência, Tecnologia e Ensino Superior, Prof. Doutor José Mariano Gago
Secretário de Estado Adjunto, da Indústria e da Inovação, Prof. Doutor António Castro Guerra
Bastonário da Ordem dos Engenheiros, Engº Fernando Santo
Reitor da Universidade do Minho, Prof. Doutor António Guimarães Rodrigues
Presidente da Câmara Municipal de Braga, Engº Francisco Mesquita Machado
Governador Civil do Distrito de Braga, Dr. Fernando Moniz
Presidente da Fundação para a Ciência e a Tecnologia, Prof. Doutor João Sentieiro
Presidente da Sociedade Portuguesa de Química, Prof. Doutor José Luís Figueiredo
Presidente da Sociedade Portuguesa de Biotecnologia, Prof. Doutor F. Xavier Malcata
Presidente da Escola de Engenharia da Universidade do Minho, Prof. Doutor António Cunha
Prof. Doutor T. Reg. Bott (Univ. Birmingham)
Prof. Doutor João de Deus Pinheiro (Univ. Minho)
Prof. Doutor Luís J. Soares (Univ. Minho)

Scientific Committee:
President: Manuel Mota (Univ. Minho)

Members:
C. Bernardo (Univ. Minho)
J.C. Bordado (IST-UTL)
M. Carrondo (UNL)
C. Costa (Univ. Porto)
J. Coutinho (Univ. Aveiro)
J. P. G. Crespo (UNL)
J. J. C. Cruz Pinto (Univ. Aveiro)
E. C. Ferreira (Univ. Minho)
S. Feyo de Azevedo (Univ. Porto)
M. M. Figueiredo (Univ. Coimbra)
M. H. Gil (Univ. Coimbra)
J. Lafuente (Univ. Aut. Barcelona)
J. Lema (Univ. Santiago de Compostela)
F. Lemos (IST-UTL)
L. Q. Lobo (Univ. Coimbra)
F.X. Malcata (Univ. Católica)
L. Melo (Univ. Porto)
A. Q. Novais (INETI)
M. Nunes da Ponte (UNL)
R. Oliveira (Univ. Minho)
C. Pedro Nunes (IST-UTL)
F. Ramôa Ribeiro (IST-UTL)
A. E. Rodrigues (Univ. Porto)
R. Salcedo (Univ. Porto)
J. Sampaio Cabral (IST-UTL)
P. Saraiva (Univ. Coimbra)
R. Simões (UBI)
L. Sousa Lobo (UNL)
J. A. Teixeira (Univ. Minho)

Organizing Committee:
President: Eugénio C. Ferreira (Univ. Minho & Ordem dos Engenheiros)

Members:
M. Alves (Univ. Minho)
J. Azeredo (Univ. Minho)
I. Belo (Univ. Minho)
J. C. Bordado (Ordem dos Engenheiros)
J. M. Costa Reis (Soc. Portuguesa Química)
L. Domingues (Univ. Minho)
C. Gaudêncio (Ordem dos Engenheiros)
M. Henriques (Univ. Minho)
A. S. Pinheiro (Ordem dos Engenheiros)
I. Rocha (Univ. Minho)
L. Rodrigues (Univ. Minho)
T. Tavares (Univ. Minho)
A. Venâncio (Univ. Minho)
A. Vicente (Univ. Minho)

Contents

T. REG. BOTT: Meeting the challenge 1
HENRIQUE J.O. PINHO, RUI SANTANA, SEBASTIÃO S. ALVES: Gas-liquid mass transfer in gas-liquid-liquid dispersions in a stirred tank: effect of spreading coefficient 8
GUILLERMO QUIJANO, FRÉDÉRIC THALASSO: Oxygen transfer characterization in three-phase reactors using silicone oil as vector 13
WIJITHA SENADEERA: Fluidization behaviour of different shaped large particulate food materials: effect of moisture and shape 19
JOANA T. CARNEIRO, ROB BERGER, JACOB A. MOULIJN, GUIDO MUL: Modeling of a novel photoreactor for multiphase applications 25
MARCEL O. CERRI, JULIANA C. BALDACIN, ANTONIO J. G. CRUZ, CARLOS O. HOKKA, ALBERTO C. BADINO: Prediction of mean bubble size in three scales of internal loop airlift reactor 31
A.J. QUEIMADA, F.L. MOTA, S.P. PINHO, E.A. MACEDO: Solubility of multifunctional associating molecules: measurements and thermodynamic modeling 37
CHUN-LI WONG, MENG-HUI LI: Diffusion coefficients and conductivities of 1-butyl-3-methylimidazolium-based ionic liquids 43
CRISTIANA LOUREIRO, FÁTIMA FARELO, LURDES SERRANO, MANUEL PEREIRA: Inhibitor effect of selected anionic surfactants on the dissolution of calcium sulfate in aqueous brines 49
JÚLIO PAIVA, ROMUALDO SALCEDO, PAULO ARAÚJO: Particle agglomeration in cyclones 56
MANUEL MOTA, ALEXANDER YELSHIN: Extending Kozeny-Carman permeability model to highly porous media 61
NAOTO OHMURA, NAMI NISHIOKA, ALATENGTUYA, MOHAMED N. NOUI-MEHIDI, JIE WU, NORIHISA KUMAGAI, TEIJI TAKIGAWA: Observation of inertial particle motion in laminar flow in a stirred vessel 67
PATRÍCIA A.M.H. SOARES, VÍTOR GERALDES, CRISTINA FERNANDES, PAULO CAMEIRA DOS SANTOS, MARIA NORBERTA DE PINHO: Assessment of the tartaric stability of wines deionised by electrodialysis 73
PATRÍCIA F. LITO, SARA B. BARROS, JOÃO ROCHA, ZHI LIN, CARLOS M. SILVA: Characterization of a microporous titanosilicate AM-3 membrane – pure gas permeation 79
FÁTIMA L. MOTA, ANTÓNIO J. QUEIMADA, SIMÃO P. PINHO, EUGÉNIA A. MACEDO: Pure solvent solubility of some pharmaceutical molecules 84
JUNJIANG ZHU, JOSÉ L. FIGUEIREDO, JOAQUIM L. FARIA: Basicity promotion and mechanism aspect of liquid selective oxidation of alcohols on Au/Actived-Carbon catalyst 90
A. TOMÁS, A., M.G. RASTEIRO, L. FERREIRA, S. FIGUEIREDO: PVC paste rheology: polymer properties and viscoelastic behaviour 96
IVONE M.R. TRIGO, MIGUEL A.D. GONÇALVES, ROLANDO C.S. DIAS, MÁRIO RUI P.F.N. COSTA: SEC/MALLS measurement of the branched structure of methyl methacrylate + ethylene glycol dimethacrylate copolymers synthesized by atom transfer radical polymerization 102
ANABELA COELHO, LUÍS COSTA, MARIA DAS MERCÊS MARQUES, ISABEL FONSECA, MARIA AMÉLIA LEMOS, FRANCISCO LEMOS: Thermal degradation kinetics of polyethylene in dynamic conditions using simultaneous DSC/TG analysis 108
S.F. REBOCHO, A.S. RIBEIRO, O. FERREIRA, M.V. OLIVEIRA, P. VIDINHA, S. BARREIROS, E.A. MACEDO, J.M. LOUREIRO: Decyl acetate synthesis by enzyme catalysis in scCO2 114
MIGUEL TEIXEIRA, MIGUEL MADEIRA, JOSÉ SOUSA, ADÉLIO MENDES: Improving propylene streams purity using catalytic membrane reactors 120
JORGE VICENTE, JAVIER EREÑA, ALAITZ ATUTXA, ANA G. GAYUBO, JAVIER BILBAO: Improvement by alkaline treatment of HZSM-5 zeolite performance in DME steam reforming 126
MARIANA B. OLIVEIRA, FÁTIMA R. VARANDA, MARIA JORGE MELO, ISABEL M. MARRUCHO, ANTÓNIO JOSÉ QUEIMADA, JOÃO A.P. COUTINHO: Application of a group contribution CPA EoS to the modeling of biodiesel production 132
ADRIÁN FERRARI, EVARISTO C. BISCAIA JR., PRIAMO A. MELO: Sequential batch reactor and plug flow reactor network comparison under dynamic conditions for wastewater treatment 138
RICARDO MORALES-RODRÍGUEZ, RAFIQUL GANI: Systematic modelling framework in product-process design and development 147
MARCO S. REIS: Combining predictions at multiple scales for process modelling 153
MARIANA SOUSA COSTA, A.R. SAMPAIO DE SOUSA, ANA RITA C. DUARTE, M. MARGARIDA CARDOSO, CATARINA M.M. DUARTE: Integration of traditional and supercritical fluid techniques to design drug delivery systems 159
ANNA KARPINSKA, JOANA P. PEREIRA, MADALENA M. DIAS, RICARDO J. SANTOS: CFD simulation of an oxidation ditch 165
RODRIGO J.G. LOPES, ROSA QUINTA-FERREIRA: CFD modelling of trickle-bed reactor in the catalytic wet air oxidation of syringic acid 171
YASUYUKI KONISHI, MASAYOSHI KOBAYASHI AND KOU-ICHI MIURA: Characterization of water species revealed in the drying operation of squid by using water proton NMR analysis 177
C. ALLEGRE, E. CARRETIER, P. MOULIN: Cholesterol removal by nanofiltration in organic solution 183
MARGARIDA CATARINO, LUÍS M. MADEIRA, ANTÓNIO FERREIRA, ADÉLIO MENDES: Beer aroma recovery by pervaporation 189
FANNY SPRINGER, RÉMY GHIDOSSI, EMILIE CARRETIER, DAMIEN VEYRET, DIDIER DHALER AND PHILIPPE MOULIN: Determination of the wall shear stress by numerical simulation: membrane process applications 195

M. Ashar Sultan, Ertugrul Erkoç, Ricardo J. Santos, Madalena M. Dias, José Carlos B. Lopes,: Active mixing strategies for confined impinging jets 201
Ani Alupului, V. Lavric: Ultrasound – assisted extraction of active principles from Arctium lappa L. (Burdock) roots, Stevia rebaudiana Bert. leaves and Cynara scolymus L. (Artichoke) leaves 207
Luís Costa, Vânia Brissos, Francisco Lemos, Fernando Ramôa Ribeiro, Joaquim M.S. Cabral: Monitoring multi-component liquid reaction systems containing highly dispersible heterogeneous catalysts using in situ diode array spectrophotometry and band-fitting techniques 213
Zsanett Herseczki, Gyula Marton: Synthesis of triproprionin from crude glycerol the by-product of biodiesel production 219
Renato H. Carvalho, Luís R. Vilela de Matos: The future sustainability of biodiesel 225
Carolina Cateto, Filomena Barreiro, Alírio E. Rodrigues, Naceur Belgacem: Lignin-based polyurethane materials 231
M.E. Suárez-Ojeda, J. Lafuente, J. Font and J. Carrera: Catalytic wet air oxidation plus biological treatment to deal with a high-strength o-cresol wastewater 237
L.J. Nogueira Duarte, J.P. Canselier: Two-aqueous phase extraction for the removal of organic pollutants and metal ions 243
Figueiredo, H., Silva, B., Quintelas, C., Neves, I.C., Tavares, T.: Biosorption of CrVI supported on mordenite zeolite 248
A. Sánchez Sánchez, Sonia Barros, Ramón Méndez, J.M. Garrido: Phosphorus removal from an industrial wastewater by struvite crystallization into an airlift reactor 253
Marta Herva, Amaya Franco, Eugenio F. Carrasco, Enrique Roca: EcoDesign through a multi-criteria environmental decision tool based on fuzzy logic 259
Ana Carvalho, Rafiqul Gani, Henrique Matos: Design of sustainable processes: Systematic generation and evaluation of alternatives 265
Gergo Mezohegyi, Christophe Bengoa, Frank Stuber, Josep Font, Agustí Fortuny, Azael Fabregat: Modeling of Orange II advanced biodecolourisation in upflow stirred packed-bed reactor 271
C. Águia, Francesc X. Llabrés i Xamena, Esther Dominguez, Hermenegildo García, L.M. Madeira, A. Mendes: Photocatalytic paint production for the abatement of nitrogen oxides 277
Etel Kameda, Rafael F. de Mesquita, Marta A. P. Langone, João C. de Queiroz Neto, Maria Alice Zarur Coelho: Starch filter-cake enzymatic degradation 283
Carlos Garcia, Francisco Molina, Eugenio Carrasco, Enrique Roca, Juan M. Lema: Robust multi-objective cascade controller for an anaerobic digester 289
Xavier Bernat, Agustí Fortuny, Christophe Bengoa, Frank Stüber, Azael Fabregat, Josep Font: Fenton's treatment of aqueous phenol effluents in presence of anionic surfactants 295
Ysrael M. Vera, Roberto J. Carvalho, Mauricio L. Torem: Electrochemical ozone production for in situ atrazine degradation in aquifer 301
Patrícia C.C. Faria, José J.M. Órfão, Manuel F. R. Pereira: Catalytic ozonation applied to the treatment of coloured effluents 306
A.R. Ricardo, R. Oliveira, S. Velizarov, M.A.M. Reis, J. G. Crespo: Ion exchange membrane bioreactor modelling for removal of anionic micropollutants from drinking water supplies 312
Cátia M. Augusto, Margarida J. Quina, Licínio M. Gando-Ferreira: Performance comparison of biological and Fenton processes for treatment of urban landfill leachates 318
Pedro Sá Gomes, Michal Zabka, Mirjana Minceva and Alírio E. Rodrigues: Design and Construction of a Lab-Scale Simulated Moving Bed Unit. The FlexSMB-LSRE – from Theory to Practice 324
Joana Afonso, Cláudia P. Passos, Carlos M. Silva, Manuel A. Coimbra, Patrício Soares-da-Silva: Inhibitory effect of phenolic compounds on the activity of Angiotensin I converting enzyme 330
Isabel Fernandes, Filomena Barreiro, Mário Rui Costa: A novel view of the manufacture of polyurethane-polyurea aqueous dispersions 336
Samantha C. Burnham and Mark J. Willis: Constructing chemical reaction networks through decoupling, regression and rationalisation 342
Tânia Rute Pinto Ana Paula Barbósa-Póvoa and Augusto Q. Novais: A multi-objective optimization for the design and periodic scheduling of multipurpose facilities 348
Ana C. S. Amaro, Ana P. Barbosa-Póvoa: The influence of products' portfolio demand on the optimal supply chain planning 354
Nuno M.R. Batalha, Pedro M.C. Oliveira, João M.A. Silva, Carla I.C. Pinheiro: Nonlinear dynamic modeling of a real pilot scale continuous distillation column for fault tolerant control purposes 360
Dulce C.M. Silva, Rui M. Bastos, Nuno M.C. Oliveira: Applications of model based design of polymer products 366
Jose A. Egea, María-Sonia G. García, Eva Balsa-Canto, Julio R. Banga: Global dynamic optimization of chemical and bio-processes using the Scatter Search metaheuristic 372
Silvia Ochoa, Jens-Uwe Repke, Günter Wozny: Integrating real-time optimization and control for optimal operation: Application to the bio-ethanol process 378
João Dias, Filipa Pardelha, Mário Eusébio, Maria A.M. Reis, Rui Oliveira: On-Line adaptive metabolic flux analysis: Application to PHB production by mixed microbial cultures 384

CLAUDIA F. GALINHA, CARLA PORTUGAL, GILDA CARVALHO, GIUSEPPE GUGLIELMI, DANIELE CHIARANI, GIANNI ANDREOTTOLA, RUI OLIVEIRA, MARIA A.M. REIS, JOÃO G. CRESPO: Modelling of membrane bioreactors for wastewater treatment incorporating 2D-fluorescence monitoring data 390

RUI M. FILIPE, HENRIQUE A. MATOS, AUGUSTO Q. NOVAIS: Performance indicators for reactive distillation design 394

PEDRO SÁ GOMES, MIRJANA MINCEVA AND ALÍRIO E. RODRIGUES: The importance of models and practical integration in process development. Cases from the simulated moving bed technology 400

JOSÉ CARLOS COSTA, M. MADALENA ALVES, EUGÉNIO C. FERREIRA: A chemometric tool to monitor high-rate anaerobic granular sludge reactors during load and toxic disturbances 406

MANUELA S. LEITE, FLÁVIO V. SILVA, TATIANA L. FUJIKI, ANA M. F. FILETI: Control of bromelain recovery process through conventional and fuzzy controllers 412

KANYALUK AO-EKKASIT, SLITA NUSONG, SOORATHEP KHEAWHOM: Optimal cleaning schedule for heat exchangers in a heat exchanger network based on continuous time approach 418

JOÃO TELES, PEDRO M. CASTRO, HENRIQUE A. MATOS: Optimal design of water using networks 424

M. SORIN, E. AYOTTE-SAUVÉ AND F. RHEAULT: A Shortcut Design Method for Hybrid Separation Processes 430

MARÍA RODRÍGUEZ-FERNÁNDEZ, JULIO R. BANGA: Methods and tools for global sensitivity analysis of dynamic models of biological systems 436

ANTÓNIO ROLDÃO, MANUEL J.T. CARRONDO, PAULA M. ALVES AND R. OLIVEIRA: Stochastic modelling of the baculovirus/insect cells system: prediction of recombinant protein expression 442

L. DEWASME, X. HULHOVEN, A. VANDE WOUWER: Scaling-up control of yeast fed-batch cultures 448

L. DEWASME, A. VANDE WOUWER, M. PERRIER: Adaptive extremum-seeking control of yeast fed-batch cultures 454

NUNO CARINHAS; VICENTE BERNAL; ADRIANA Y. YOKOMIZO; TIAGO VICENTE; MANUEL J. T. CARRONDO,; RUI OLIVEIRA,; PAULA M. ALVES: Improvement of baculovirus vectors production based on the metabolic characterization and modelling of Sf-9 cultures 460

PEDRO M.R. GUIMARÃES, JOSÉ A. TEIXEIRA, LUCÍLIA DOMINGUES: Lactose fermentation by recombinant Saccharomyces cerevisiae strains 465

DRAGANA P. C. DE BARROS, SUSANA M.S.A. BERNARDINO, PEDRO FERNANDES, JOAQUIM M. S. CABRAL, LUÍS P. FONSECA: Studies on fed-batch operation mode on biosynthesis of short chain ethyl esters catalyzed by cutinase 471

ANDREA BALASSY, ARON NEMETH, BELA SEVELLA: New enzymatical process for glycerol utilization 477

BRUNA SILVA, HUGO FIGUEIREDO, CRISTINA QUINTELAS, ISABEL C. NEVES, TERESA TAVARES: Biosorption of hexavalent chromium by Arthrobacter viscosus 483

CÁTIA V.T. MENDES, JORGE M.S. ROCHA, CRISTINA M.S.G. BAPTISTA, M. GRAÇA V.S. CARVALHO: Treatment of wood hydrolysates for bioethanol production by fermentation 489

FILOMENA FREITAS, VITOR D. ALVES, JOANA PAIS, NUNO COSTA, MÓNICA CARVALHEIRA, RUI OLIVEIRA, M. A. M. REIS: Biopolymers production by microbial fermentation on glycerol-rich product 495

JUAN P. MAESTRE, ROGER ROVIRA, XAVIER GAMISANS, KERRY A. KINNEY, MARY J. KIRISITS, JAVIER LAFUENTE, DAVID GABRIEL: Bacterial community ctructure in a biotrickling filter treating H2S by Terminal Restriction Fragment Length Polymorphism (T-RFLP) 500

MARIA F. MATOS, CLÁUDIA F. ALVES, ANTÓNIO G. BRITO, REGINA B. NOGUEIRA: Biofilm technology: from support design to reactor operation 506

MATJAŽ KUNAVER, EDITA JASIUKAITYTE, VESNA TIŠLER, SERGEJ MEDVED: Lignocellulosic materials as a feedstock for polymer synthesis 512

TAKANORI TANINO, CHIAKI OGINO, NORIHISA KUMAGAI, NAOTO OHMURA: Bioethanol production from sugars by yeast having sugar uptake ability by expression of sugar transporter 518

CÁTIA V.T. MENDES, JORGE M.S. ROCHA, CRISTINA M.S.G. BAPTISTA, M. GRAÇA V.S. CARVALHO: Treatment of wood hydrolysates for bioethanol production by fermentation 522

ANABELA S. ANTUNES, JORGE M.S. ROCHA: Integration of bioprocesses in polyesters microbial synthesis 528

ANA P. TEIXEIRA, PAULA ALVES, MJT CARRONDO AND RUI OLIVEIRA: Macroscopic control of intracellular regulation: application to mammalian cell cultures 534

ZITA I.T.A. SOONS, MATHIEU STREEFLAND, ANTON J.B. VAN BOXTEL: Towards PAT bioprocess monitoring and control: near infrared and software sensor 540

SÍLVIA S. ROSA, PEDRO A. BARATA, JOSÉ M. MARTINS, JOSÉ CARDOSO MENEZES: Near-infrared reflectance spectroscopy as a process analytical technology tool in pharmaceutical industry 546

M.G. RASTEIRO, L.M. GANDO-FERREIRA, J.C.TEIXEIRA, F.P. BERNARDO, M.G. CARVALHO, A.G. FERREIRA, R.M. QUINTA-FERREIRA, F.P. GARCIA, C.G. BAPTISTA, N.C. OLIVEIRA, M.J. QUINA, L.O. SANTOS, P.A. SARAIVA, A.M. MENDES, F.M. MAGALHÃES, J. GRANJO, R. BASTOS, M. AS: Enhancing engineering education in the area of chemical processes through a virtual platform (LABVIRTUAL) 550

FERNANDO G. MARTINS, M.I.M.S. CRUZ, DOMINGOS BARBOSA: Add-ins for shortcut design and sizing of distillation columns 556

CARLOS M. SILVA, RAQUEL V. VAZ, TIAGO M.F. CANHOTO, PATRÍCIA F. LITO, ANA S. SANTIAGO: Continuous and batch distillation in an oldershaw tray column 562

S. MEYSAM HASHEMNEJAD, MATIN PARVARI: Regeneration of sulfur poisoned nickel based catalysts for steam reforming catalysts in Razi petrochemical complex 568

V. P. Santos, M. F. R. Pereira, J. J. M. Órfão, J. L. Figueiredo: Total oxidation of ethyl acetate over TiO2 supported noble metals catalysts 574
Sonia Bocanegra, Alberto Castro, Osvaldo Scelza, Sergio de Miguel: Incidence of the preparation method of the support on the behavior in the n-butane dehydrogenation of Pt/MgAl2O4, PtSn/ MgAl2O4 y PtPb/ MgAl2O4 catalysts 580
Tatiana V. Franco, Cícero N. Ávila-Neto, Lucienne L. Romanielo, Carla E. Hori, Adilson J. Assis: Hydrogen production from methane reforming: thermodynamic assessment 586
Sandra C. Dantas, Fabiano de A. Silva, Carla E. Hori, Adilson J. de Assis: Hydrogen production from methane autothermal reforming: mathematical modeling and parametric optimization 592
Renata de Aquino B. Lima and Maria C. Ferreira: Fluid-dynamics of fluidized beds operating with flat particles 598
João P. F. Simão, Cristina M. S. G. Baptista, M. Graça Carvalho: Heterogeneous model for mass transfer of dissolved lignin during kraft pulping of Eucalyptus globulus 604
Brandão, M.M. and Góis, L.M.N.: Axial mixing in extractor column liquid-liquid, without mechanical agitation 610
Marcela K. Silva, Renato Dionísio, Marcos A. d'Ávila, Milton Mori: Three-dimensional simulation of bubbly flow: influence of break up and coalescence models 617
Lucas M. Policarpo, Marcel O. Cerri, Antonio J. G. Cruz, Carlos O. Hokka, Alberto C. Badino: Mass transfer coefficient in three airlift reactors with internal loop using Newtonian fluid 623
Paulo Jardel P. Araújo, Teresa M. K. Ravagnani: Evaluation of parameters and process conditions of the ethylbenzene dehydrogenation in a fixed bed reactor wrapped with permselective membrane 629
Fukuji Yamashita and Megumi Nakajima: Effect of kinds of gas on gas holdup in bubble columns 635
Fukuji Yamashita ✻, Tomoyuki Suzuki, Haruki, Kobayashi: Simulation of dynamic performance of ozonation treatment of surfactants in a semi-batch bubble column reactor by CFX 641
J.C.S.C. Bastos, R.K. Decker, M. Mori, U. Fritsching: Particle interaction with coherent structures in a confined two-phase jet 647
P. Neto, A.M. Ribeiro, C. Pinho: Heat transfer in the freeboard of a bubbling fluidized bed 653
Ulrich M. Scheven, Rob Harris, Mike L. Johns: Dispersion in packed beds 659
Dolginun V.N., Ivanov O.O., Klimov A.M. and Ukolov Al-dr. A.: Operating the segregated flows of particulate materials as a principle of technological process organization 665
Manuel Mota, Alexander Yelshin: Hindered motion in highly porous media: steric and fractal approaches 671
Patrícia F. Lito, Carlos M. Silva: Maxwell-Stefan based model for ion exchange in microporous materials 677
R.L. Wu, M.F. Cuel, C.O. Hokka, M. Barboza, W.H. Kwong: A sequencing method applied to the solution of a linear model of an adsorption column 683
Irene Sierra, Andrés T. Aguayo, Javier Ereña, Ana G. Gayubo, Javier Bilbao: Study of the adsorption process of methanol and water over a SAPO-18 catalyst by means of pulse techniques 689
António E. Ribeiro, Nuno S. Graça, Luís S. Pais, Alírio E. Rodrigues: Optimization of mobile phase composition for preparative separation of profens enantiomers by chiral liquid chromatography 695
Ana B.N. Brito, Sandra G.R. Azevedo , Edison Ricco Jr, José R. Coury, Mônica L. Aguiar: Gas filtration at high pressure 701
Alicia G. Abuín, Diego Gómez-Díaz, José M. Navaza, Isabel Vidal: Kinetics of carbon dioxide absorption with chemical reaction in piperidine aqueous solutions 707
Estrella Álvarez, Diego Gómez-Díaz, M. Dolores La Rubia, José M. Navaza, Lourdes C. Quintáns-Riveiro: Absorption of carbon dioxide by MDEA aqueous solutions in a bubble column reactor 713
Paulo Brito, Licínio M. Gando-Ferreira, António Portugal: Simulation of membrane separations using a modified Maxwell-Stefan model 720
Marta C. Campo, Tymen Visser, Kitty Nymeijer, Matthias Wessling, Fernão D. Magalhães, Adélio M. Mendes: Influence of pyrolysis parameters on the performance of CMSM 726
E. L. Galvão, J. A. C. Barros, A. V. B. Moreira, H. N. M. Oliveira, E. M. B. D. Sousa: Influence of pressure on the yield of supercritical CO2 extraction of linseed (Linum usitatissimum l.) oil and investigation of its antioxidant potential 732
C P. Passos, R.M. Silva, F.A. da Silva, M.A. Coimbra, C.M. Silva,: Supercritical fluid extraction of grape seed oil using an enzymatic pre-treatment 738
A. Tenorio, M. D. Gordillo, C. M. Pereyra and E. J. Martínez de la Ossa: Supercritical antisolvent process applied to the pharmaceutical industry 744
M. Reis, L. Moreira, R. E. Leitão, F. Martins: Solvent effects on ionic association of 2,6-lutidinium chloride salt at 60.00 ºC: A QSPR study 749
A.A. Leopold, A. Fortuny, M.T. Coll, N.S. Rathore and A.M. Sastre: Modelling of the solvent extraction equilibrium of cadmium (II) in neutral chloride medium using Cyanex 923 755
Alicia G. Abuín, Diego Gómez-Díaz, José M. Navaza, Isabel Vidal: Models to correlate the surface tension of solvent mixtures 761
Alicia G. Abuín, Antonio Blanco, Diego Gómez-Díaz, José M. Navaza, Isabel Vidal: Thermodynamic analysis of surface tension in water / pyrrolidone system 767
Nelson Nunes, Filomena Martins, Lídia Pinheiro, Ruben E. Leitão: Volumetric properties for the ternary mixture methanol-formamide-acetonitrile 772

ADRIAN BONILLA-PETRICIOLET, GUSTAVO A. IGLESIAS-SILVA, JOSE ENRIQUE JAIME-LEAL: An effective method for calculation of homogeneous azeotropes in reactive and nonreactive mixtures 778
JOANA C. VIEIRA, MIGUEL A. MESQUITA, FRANCISCO A. DA SILVA: A portable library for equilibrium and thermodynamics properties calculations based on object oriented paradigms 784
FILIPA A.M.M. GONÇALVES, ABEL G.M. FERREIRA, ISABEL M.A. FONSECA J. PONMOZHI, MÓNICA S.A.O. CORREIA, SUBRAMANI KANAGARAJ: Thermophysical properties of aqueous solutions of CNTs in the temperature range (298.15-343.15) K 789
H.F. COSTA, I. JOHNSON, F.M. GONÇALVES, ABEL G.M. FERREIRA, ISABEL M.A. FONSECA: Liquid-liquid equilibria, surface and interfacial tension for water+n-butyl acetate+1-propanol at 323.15 K 795
MÓNICA ROSAS, VALENTINA DOMINGUES, TERESA OLIVA-TELES, PAULO SILVA, ANTÓNIO CRISPIM: Thermodinamic analysis of leather tanned with different tanning agents 801
KHOSRAVANIPOUR MOSTAFAZADEH, M. R. RAHIMPOUR, A. SHARIATI: Effect of isooctane on vapor-liquid equilibria of water and TEG solution 807
CARLOS E.C. LAGINHAS, A.J. PALACE CARVALHO, J.P. PRATES RAMALHO, LUÍS F.G. MARTINS: Optimized force fields for predicting vapour-liquid equilibria of binary mixtures involving alkanes and xenon at low temperatures 813
R. MOREIRA, F. CHENLO, D. LE GALL: Kinematic viscosity of ternary solutions of ethanol, glycerol and water from 293.1 to 318.1 K 819
CATARINA M. S. S. NEVES, SÓNIA M. P. VENTURA, MARA G. FREIRE, MARIA ALICE Z. COELHO, ISABEL M. MARRUCHO AND JOÃO A. P. COUTINHO: Aqueous biphasic systems with ionic liquids 825
CATARINA M. S. S. NEVES, MARA G. FREIRE, LUÍS M. N. B. F. SANTOS, ISABEL M. MARRUCHO, JOÃO OLIVEIRA AND JOÃO A. P. COUTINHO: Hydrophobic ionic liquids and water mutual solubilities 829
PEDRO J. CARVALHO, JOSÉ J. B. MACHADO, JÉRÔME PAULY, JEAN-LUC DARIDON, ISABEL M. MARRUCHO, JOÃO A. P. COUTINHO: Carbon dioxide solubilities in [Cnmim][Tf2N] ionic liquids at high-pressure 834
ISABEL MOUTINHO, MARGARIDA FIGUEIREDO, PAULO FERREIRA: Physicochemical characterization of surface sized paper surfaces 842
CARMENCITA MATEESCU, MIHAELA MIHAI, RALUCA ISOPESCU, IRINELA CHILIBON, FLORINA BRANZOI: Sub-micron size aragonite synthesis by double-jet precipitation 848
E. ÁLVAREZ, M.A. CANCELA, N. DELGADO-BASTIDAS, R. MACEIRAS: Change on rheological properties of mushroom cream due to freezing process 854
S. MOHAMMADI, M. ALAVI, M.R. MOGHBELI: The effect of operating conditions on styrene bulk polymerization in a spinning disk reactor 860
TOMÁS, A., GIL, M.H., BORDADO, J.C., GONÇALVES, P., RODRIGUES, P.: Synthesis of crosslinked poly(vinyl chloride): Study of polymer properties 866
MIGUEL A.D. GONÇALVES, ROLANDO C.S. DIAS, MÁRIO RUI P.F.N. COSTA: Experimental study of the TEMPO mediated copolymerization of styrene with divinylbenzene 872
S. MOHAMMADI, M.R. MOGHBELI, M. ALAVI: The effect of shear on styrene polymerization 878
BRUNO MIGUEL REIS, SIMON BIGGS: Novel stimulus responsive coating for polystyrene particles 884
LIDIANA BARREIRA, ELIZABETH CAMARINHA, PATRÍCIA F. LITO, JOÃO ROCHA, ZHI LIN, ARMANDO C. DUARTE, EDUARDA PEREIRA, CARLOS M. SILVA: Cadmium (II) removal from aqueous solution using microporous titanosilicate ETS-4 and ETS-10 890
JOSÉ E. CASTANHEIRO, ISABEL M. FONSECA, ANA M. RAMOS, JOAQUIM VITAL: Poly(vinyl alcohol) with sulfonic acid groups as catalyst for the alpha-pinene alkoxylation 895
B.F. MACHADO, S. MORALES-TORRES, H.T. GOMES, A.F. PÉREZ-CADENAS, F.J. MALDONADO-HÓDAR, F. CARRASCO-MARÍN, J.L. FIGUEIREDO, J.L. FARIA: Carbon aerogel supported platinum catalysts for selective hydrogenation of cinnamaldehyde 901
S. MEYSAM HASHEMNEJAD, MATIN PARVARI: Extraction of nickel from spent nickel catalyst with inorganic acid 907
SÍLVIA M.C. SANTOS, ANA E. FERREIRA, RITA C. FIGUEIREDO, MARIA. J.N. CORREIA, MARIA T.A. REIS, MARIA R.C. ISMAEL, REMÍGIO M. MACHADO, JORGE M.R. CARVALHO: Oxidation of Fe(II) in sulphuric medium 912
H. ALTZIBAR, G. LOPEZ, J. BILBAO, M. OLAZAR: Influence of temperature and internal devices on the drying of fine particles in a conical spouted bed 918
RAQUEL O. CRISTÓVÃO, ANA P.M. TAVARES, JOSÉ M. LOUREIRO, RUI R. BOAVENTURA, EUGÉNIA A. MACEDO: Decolourization of reactive red 180 by laccase: optimization by response surface methodology 924
J. HERNEY RAMIREZ, FILIPA DUARTE, FERNANDO G. MARTINS, CARLOS A. COSTA AND LUIS M. MADEIRA: Modeling orange II azo dye degradation by Fenton's reagent 930
ANDREIA AMARO DE LIMA , KRISHNASWAMY RAJAGOPAL , MARCO ANTONIO FARAH: Viscosity of heavy oil and distillation residues with diluents 936
R. ISOPESCU, V. LAVRIC: Solving population balance models in precipitation using orthogonal collocation and stochastic optimization 942
BRENER A.M., TAUASAROV B.R.: Analyzing regimes in chemical reactors with allowing for the multistage kinetics and non-perfection of a system 948
ANA RITA A. SEITA, RUI ALVES, M. MERCEDES ESQUÍVEL: Optimisation of a package production process for the implementation of a "Total Productive Maintenance" 954
ÁLVARO F. C. VAZ, ANDREIA C.S. FIAL, ANA P. R. GOMES, ROGÉRIO M. S. SIMÕES: Rheological and thermodynamic study on a biodiesel production process 960

M. Teresa García, Silvia Bolado, Gerardo González, Israel López, Isabel Catalina: Comparison of ozonolysis and steam explosion of wheat straw to obtain bioethanol 964
Ana Rita B. Mancelos Beirão, M. Gabriela Bernardo-Gil, Humberto E. Ferreira: The vegetative cycle of Lavandula luisieri – influence on essential oils and antioxidants 970
Cláudia L. Munhoz, Eliana J.Sanjinez-Argandoña, Manoel S. Soares Júnior: Pectin extraction from guavas using response surface methodology 976
Paulo M. Castro, Eliana J. Sanjinez-Argandoña, Iriani R. Maldonade: Study on caqui (Diospyrus Kaki L) fruit osmotic dehydration treatments 982
Ana L. Magalhães, Cláudia P. Passos, Jorge A. Saraiva, Manuel A. Coimbra, Carlos M. Silva: High pressure treatment of grape seed to enhance the yield of oil extraction 988
M. Mercedes Esquível, M. Albertina Ribeiro, M. G. Bernardo-Gil: Relations between oxidative stability and antioxidant content in vegetable oils using an accelerated oxidation test –Rancimat 994
R. Moreira, F. Chenlo, M.D. Torres, N. Vallejo: Experimental sorption isotherms of loquat and quince fruits in the range from 20 to 65 ºC. 1000
R. Moreira, F. Chenlo, L. Chaguri: The Influence of sucrose osmotic pretreatment on the kinetics of rehydrated dried chestnuts 1006
Maria do Rosário Freixo, Amin Karmali, José Maria Arteiro: Production of polygalacturonase from Coriolus versicolor grown on tomato pomace and its chromatographic behaviour on immobilized metal chelates 1012
Susana C. Ribeiro, Ana Xavier, Inês Portugal, Filipe Centeno: Biological deacidification of wine – must 1018
Ana C. Pereira, Marco S. Reis, Pedro M. Saraiva, José C. Marques: Using GC-MS and multivariate statistics to safeguard the identity of Madeira wine: a preliminary study 1024
Giovani B.M. Carvalho, Daniel P. Silva, António A. Vicente, Maria das Graças A. Felipe, José A. Teixeira, João B. Almeida e Silva: A new strategy for using banana as an ingredient in the brewing process 1030
David F.M. Neri, Victor M. Balcão, Rafael S. Costa, Eugénio C. Ferreira, Duarte P.M. Torres, Lígia R. Rodrigues, Luiz B. Carvalho Jr, José A. Teixeira: β-Galactosidase from Aspergillus oryzae immobilized onto different magnetic supports: A comparative experimental and modeling study of the galactooligosaccharides production 1036
Marco S. Reis: Multivariate analysis of DNA microarrays 1042
Kelly A. Silva, Maria H. Rocha-Leão, Maria A.Z. Coelho: Evaluation of olive oil-lemon juice emulsion stability through digital image analysis 1048
Ana C. Fonseca, Susana Jarmelo , Rui A. Carvalho, Rui Fausto, Maria H. Gil, Pedro Simões: Looking toward new biomolecules: IR and 1H NMR spectroscopies and DFT calculations on Nα-benzoyl-L-Arginine ethyl ester hydrochloride 1054
Filipa Carneiro, Vasco Gama Ribeiro, José C.F. Teixeira, Senhorinha F.C.F Teixeira: CFD analysis of blood rheology 1060
N.Masoumi, D. Bastani, S.Najarian, F.Framanzad, A.S.Seddighi: Study of cerebrospinal fluid dynamics in a computational model of stenosed aqueduct 1066
Sofia Abreu, Luís F. Silva, Henedina Antunes, Senhorinha F. C. F. Teixeira: Multiphase flow inside the Volumatic® spacer: a CFD approach 1072
João B. Fernandes, Pedro C. Simões, José P.B. Mota, Esteban Saatdjian: Application of CFD in the study of supercritical fluid extraction with structured packing – pressure drop calculations 1081
Rosa, L.M., Bastos, J.C.S.C , Mori, M., Martignoni, W.P.: Application of CFD techniques in a high-flux riser-reactor flow prediction 1087
M. Simcik, L. Kulaviak, J. Havlica, M. C. Ruzicka, J. Drahoš, J. Teixeira: Gas holdup in laboratory scale bubble column: CFD simulations vs. measurements 1093
Conceição Granja, Adélio Mendes, Paulo Cruz: Healthcare Decision Support System 1099
João F. P. Gomes, Cristina C. Granadeiro, Miguel A. Silva, Milton Hoyos, Rodrigo D. Silva, Filipe Antunes, José E. Amaral, Teresa Vieira: Optimization of hydroxyapatite synthesis 1105
Adriano G. Fisch, Nilo S.M. Cardozo, Argimiro R. Secchi, Nadya P. da Silveira, João H.Z. dos Santos: Investigation of Silica Particle Structure Containing Metallocene Immobilized by a Sol-Gel Method 1112
Mihaela-Doina Ghiga, Laurentiu Filipescu, Ion Ion, Zoltan Ecsedi, Marian Crudu: Studies on developing the red mud capability of binding the tannery residual chromium 1118
Eugenia Panturu, Rozalia Radulescu, Antoneta Filcenco Olteanu: Statistics model and optimization of uranium extraction in ultrasounds field in sulphuric acid medium 1124
María J. San José, Sonia Alvarez, Alvaro Ortiz de Salazar, Alberto Morales: Stability of binary mixtures in a novel combustor conical spouted bed with a draft tube of different length 1130
Eduardo L. G. Oliveira, Carlos A. Grande, Alirio E. Rodrigues: Production of hydrogen by methane steam reforming coupled with CO2 sorption 1136
P. Oliveira, P. Borges, R. Ramos Pinto, M.A.N.D.A. Lemos, F. Lemos, F. Ramôa Ribeiro: Modelling of light olefin transformation over ZSM-5 zeolites with different acid strengths 1141
José A. Pacífico, Ana C. Cabral, Nelson M.L. Filho, Augusto Knoechelmann, César A.M. Abreu: Carbon dioxide reforming of methane over Ni-/Al2O3 in fluidized-bed ractor 1147
Joana Tudella, Maria Rosário Ribeiro, Henri Cramail and Alain Deffieux: New polystyrene-based polymers as supports for ethylene polymerisation 1152

LIZANDRO S. SANTOS, ROGÉRIO L. PAGANO, VERÔNICA M.A. CALADO, EVARISTO C. BISCAIA JR.: Cure of a fiberglass-vinyl ester I beam composite: a new heating strategy 1158
CARVALHO, A., VIEIRA, R. AND GIL, M. H.: Preparation of polymeric hydrogel microparticles for textile applications ... 1164
CLÁUDIA G. SILVA, JOAQUIM L. FARIA: Photocatalytic oxidation of clofibric acid using nanocrystalline sol-gel TiO2 under visible irradiation 1169
N. FONSECA, S. LAFORGE, P. MAGNOUX, F. LEMOS, F. RAMÔA RIBEIRO: Catalytic cracking of n-decane as model molecule of Fisher-Tropsch synthesis 1175
LUÍS A.S.B. MARTINS, CELINA P. LEÃO, ANGELA M. SILVA, MANUEL L. NUNES, SENHORINHA F.C.F. TEIXEIRA: Optimization tools and economical issues in the design of a residential cogeneration system 1181
FLORINDA MARTINS, CARLOS COSTA: Environmental performance assessment in process design 1187
ROSA A. RODRIGUEZ, CARLOS PALACIOS, SUSANA ACOSTA, STELLA M. UDAQUIOLA: Environmental perfomance of the wine industry. opportunities for uptake cleaner production 1193
VIORICA DESELNICU, F. PLATON, L. ALBU, M. CRUDU: Reducing the pollution of leather manufacturing process 1199
MARIAN CRUDU, V. DESELNICU, I. ROSCA , D. SUTIMAN, A. CAILEAN, M. GHIGA, V. BOCU, N. BOCA, D. CAPAC: Eco-friendly tanning agents to be used in leather manufacture 1204
LUÍS RAMOS, RUI FERNANDES, ANTÓNIO CRISPIM RIBEIRO, ELISA RAMALHO, NÍDIA S. CAETANO, PAULA SILVA: Biodiesel production from leather industry wastes 1210
ALEXANDRA NICOLAU, PEDRO FELIZARDO, NUNO CANHA, JOSÉ CARDOSO MENEZES, M. JOANA N. CORREIA: Influence of feedstocks and operation conditions in biodiesel production 1215
PEDRO FELIZARDO, JOÃO MACHADO, DANIEL VERGUEIRO, M. JOANA N. CORREIA, JOÃO MOURA BORDADO: High free fatty acids oils for biodiesel production 1220
JOANA M. DIAS, MARIA C. M. ALVIM-FERRAZ, AND MANUEL F. ALMEIDA: Comparison between biodiesel produced from sunflower oil and waste frying oil 1226
JAIME F. PUNA, JOÃO F. GOMES, J.C. BORDADO, MARIA J. CORREIA: Development of heterogeneous catalysts for transesterification of triglycerides in biodiesel 1232
G.F. SILVA, F.A.S. MOTA, J.S. MENDES, L.B.R. GONÇALVES, A.L.O. FERREIRA: Modeling and simulation of process continuous production of biodiesel from soybean oil using immobilized Candida antarctica in fluidized bed bioreactor ... 1238
JOSÉ F.O. GRANJO, NUNO M.C. OLIVEIRA: Kinetic models for the homogeneous alkaline and acid catalysis in biodiesel production 1244
MARCELLE FERNANDA CARULO, MARINA AYALA CARULO, LÍLIAN CALEFO RODER, FLÁVIO VASCONCELOS DA SILVA E ANA MARIA FRATTINI FILETI: Online monitoring of the transesterification reaction 1250
F. LÓPEZ, JUAN C. GARCÍA, A. PÉREZ, G. GARROTE: Exploitation of agroindustrial biomass by fractionation of its components. Characterization of hemicelluloses, celluloses and other fractionation products 1256
ANA I. S. BRÍGIDA, LUCIANA R. B. GONÇALVES, MARIA ALICE Z. COELHO: Influence of different chemical treatments in lipase immobilization in a lignocellulosic support 1262
ARKADIY M. BESSARABOV, ALEXEY A. ALYAKIN, ALEXEY L. KOCHETIGOV: Information CALS-model of the innovation technology of biologically active additives of a new generation 1268
F.J. HERNÁNDEZ-FERNÁNDEZ, A.P. DE LOS RÍOS, F. TOMÁS-ALONSO, D. GÓMEZ, M.RUBIO, G. VÍLLORA: Stability of hydrolase enzymes in ionic liquids 1273
SOLANGE I. MUSSATTO, GIULIANO DRAGONE, JOSÉ A. TEIXEIRA: Fructooligosaccharides production using immobilized cells of Aspergillus japonicus 1279
ANA RITA BARBOSA AND AMIN KARMALI: Development of a biosensor based on ion-selective electrode for urea in milk by using immobilized amidase from Pseudomonas aeruginosa 1285
LÍVIA MARIA DA COSTA SILVA, ANDRÉA MEDEIROS SALGADO, MARIA ALICE ZARUR COELHO: Characterization of the fungi tissue of Agaricus bisporus for its future use as a component of a biosensor for phenolic compounds determination .. 1291
CRISTINA ROCHA, LOÏC HILLIOU, JOSÉ A. TEIXEIRA, MARIA PILAR GONÇALVES: Influence of the concentration of locust bean gum on the gelling ability of whey peptic hydrolysates 1296
V. A. MUKHIN, V. YU. NOVIKOV, K. S. RYSAKOVA: Enzymatic agent from red king crab hepatopancreas and its applications 1302
V. YU. NOVIKOV, I. N. KONOVALOVA: Alkaline hydrolysis of chitin and chitosan 1308
J GRYZELDA POŹNIAK, RYSZARD POŹNIAK, KAZIMIERA A. WILK: Application of surfactants to membrane separation processes 1314
FERREIRA C., PEREIRA M. C., BASTOS M.M.S.M., NUNES O.C., COELHO M. AND MELO L. F.: Functionalized nano-microstructures to combat biofilms 1319
ANTONETA FILCENCO- OLTEANU, ROZALIA RADULESCU, EUGENIA PANTURU: Synthesis and characterization of organic phase gold nanoparticles obtained through chloroaurate ions reduction with sodium citrate 1326
LUÍSA DURÃES, SOFIA NOGUEIRA, ANA SANTOS, JESSICA HERNANDEZ, ANTÓNIO PORTUGAL: Flexible silica based xerogels and aerogels for spatial applications 1331
O. BENITO, S. LUCAS, E. ALONSO: Effect of operating conditions on the extraction of β-glucans from barley 1337
DINA A. S. MARQUES, CRISTINA M. S. G. BAPTISTA, M. H. GIL: Alternative route to poly(lactic acid) synthesis 1343
MARTINA KOPCILOVA, JAROMIR HOFFMANN, MIROSLAVA TOMALOVA, PAVOL ALEXY, MARKETA JULINOVA AND ANNA NAHALKOVA: Biodegradability of mixed plastics containing PVAL/Gellan and PVAL/Xanthan in soil environment 1349

PAULO A. N. DIAS; MARCO S. REIS; MARIA H. GIL; JOSÉ C. ALVES: Development of semi-transparent wood polymer composites 1355
JESUSA RINCÓN, ISAAC ASENCIO, RAFAEL CAMARILLO AND ALICIA MARTÍN: Solubility of some sulphates in supercritical water 1361
LUIS PADRELA, MIGUEL RODRIGUES, SITARAM VELAGA, HENRIQUE A. MATOS, EDMUNDO G. AZEVEDO: Generation of pharmaceutical cocrystals using supercritical fluid technology 1366
JOSEFA FERNÁNDEZ, FERNANDO GONZÁLEZ, CARMEN PESQUERA, CARMEN BLANCO AND Mª JOSEFINA RENEDO: CO2 capture with CaO / MCM-41 materials 1372
CLARA SANTOS, ANGELA MARTINS, RUBEN ELVAS LEITÃO, JOÃO PIRES, CRISTINA FREIRE, ANA PAULA CARVALHO: Preparation of mesoporous carbons using a porous clay heterostructured as template 1378
OLÍVIA SALOMÉ G. P. SOARES, JOSÉ J. M. ÓRFÃO, MANUEL F. R. PEREIRA: Influence of the preparation methodologies in the performance of Pd-Cu/AC and Pt-Cu/AC catalysts for nitrate reduction with hydrogen 1384
VIVIANA PAIXÃO, ANA PAULA CARVALHO, ANGELA MARTINS: Modification of zeolite porosity by alkaline treatments 1390
SILVIO V. ALBUQUERQUE, CAROLINY G. OLIVEIRA, GIOVANILTON F. SILVA, ANDREA L.O. FERREIRA, RICARDO E.F.Q. NOGUEIRA: The kinetics of ampicillin release from hydroxyapatite porous for bones regeneration 1396
IDALINO MANUEL COSTA FAÍSCA, M. GABRIELA BERNARDO-GIL, JOSÉ ABECASSIS EMPIS, M. JOÃO CEBOLA, PAULA GOMES PEREIRA: Solvent effect on the antioxidant activity of extracts of Myrtus communis L. leaves 1402
MÓNICA COCA, M. TERESA GARCÍA, SILVIA MATO, GERARDO GONZÁLEZ: Selection of a suitable adsorbent for decoloring sugar solutions from beet industry with ion exchange resins 1408
PEDRO E.G. LOUREIRO, DMITRY V. EVTUGUIN, M. GRAÇA V.S. CARVALHO: Kinetics of Kraft pulp brightening with hydrogen peroxide in a final ECF stage 1413
ISABEL M.B. PEREIRA, M. TERESA SENA ESTEVES, VITORINO M. BELEZA, FERNANDO MARTINS: A case study of an absorption process for flue gas treatment 1419
SOFIA I.V. SOUSA, MARIA C. PEREIRA, FERNANDO G. MARTINS, MARIA C.M. ALVIM-FERRAZ: Influence of nitrogen oxides on ozone concentrations at urban and remote areas 1425
KLARA SLEZAKOVA, MARIA C. PEREIRA, MARIA C. ALVIM-FERRAZ: Influence of tobacco smoke on carcinogenic content of indoor particulate matter 1431
LILIANA R. SANTOS, M. CONCEIÇÃO PAIVA, ANA V. MACHADO, M. TERESA CARVALHO: Mechanized separation of plastics from municipal solid waste: evaluation of the separation efficiency by selective dissolution and infrared spectroscopy 1436
JOSÉ RICARDO CARNEIRO, INÊS MARIA VALENTE, PAULO JOAQUIM ALMEIDA, MARIA DE LURDES LOPES: Photo-degradation studies of polypropylene geotextiles 1442
J.F. ORTUÑO, V. MESEGUER, N. MURCIA, M.I. AGUILAR, M. LLORÉNS, J. SÁEZ, A.B. PÉREZ-MARÍN: Biosorption kinetic of Orange II dye with non living leaves of Posidonia oceanica 1448
V. MESEGUER, J.F. ORTUÑO, S. CALVO, M.I. AGUILAR, M. LLORÉNS, J. SÁEZ, A.B. PÉREZ-MARÍN: Continuous biosorption of methylene blue in packed bed of Posidonia oceanica leaves 1454
ANDELIB AYDIN, NURAN DEVECI AKSOY, BAYRAM ANDAK: Optimization of chromium adsorption upon chitosan by surface response analysis 1459
LUÍSA ANDRADE, SHAIK M. ZAKEERUDDIN, MOHAMMED K. NAZEERUDDIN, MICHAEL GRAETZEL, HELENA AGUILAR RIBEIRO, ADÉLIO MENDES: Influence of different cations of N3 dyes on their photovoltaic performance and stability 1465
XAVIER BERNAT, FRANK STÜBER, AGUSTÍ FORTUNY, CHRISTOPHE BENGOA, AZAEL FABREGAT, JOSEP FONT: Membrane charge effects on the recovery of Fe-EDTA species in aqueous solution by nanofiltration 1471
VÂNIA DIAS, DMITRY EVTUGUIN, INÊS PORTUGAL: Sorption Isotherms of organic-inorganic hybrids 1477
MAGNA A.S.B. SOUSA, ANDRÉA O. NUNES, MATHEUS C. BORGES, HENIO N.S. MELO, JOSETTE L.S. MELO: Evaporation solar produced water and fresh water in trays of Teflon 1483
A.B. PÉREZ MARÍN, M. LLORÉNS, J. SÁEZ, J.F. ORTUÑO, V.F. MESEGUER, M.I. AGUILAR: An innovative biological system to treat wastewater: A year of operation of the first wastewater treatment plant in real scale 1487
SUSANA CORTEZ, PILAR TEIXEIRA, ROSÁRIO OLIVEIRA, MANUEL MOTA: Denitrification in an anoxic rotating biological contactor under two carbon/nitrogen ratios 1493
SASSANO, F.C.N.; MORAES, J.E.F.,; NASCIMENTO, C.A.O.,: Integration of advanced and biological oxidation processes: Enhancing biodegradability of phenol solutions 1498
ADRIANA V. RIBEIRO, MAGALI C. CAMMAROTA, MARIA ALICE Z. COELHO: Impact of Operational Parameters in Activated Sludge System treating Persistent Industrial Wastewater 1505
M. T. SANTOS, L. M. AMARAL, J. V. PRATA: Influence of the reactor contents recirculation on methane production - anaerobic digestion of fruits, vegetables and grass waste feedstocks 1511
CARLOS GARCIA, FRANCISCO MOLINA, EUGENIO CARRASCO, ENRIQUE ROCA, JUAN M. LEMA: Comparison of different control cascade strategies for anaerobic digesters using ADM1 1517
ADŽAMIĆ TAMARA, JUKIĆ ANTE, SERTIĆ-BIONDA KATICA, VEDRANKA BOBIĆ: Treatment of waters contaminated with diesel fuel by electrocoagulation 1523
FRANCIELE R. FURLAN, LAÍS G. M. DA SILVA, ANTÔNIO A. ULSON DE SOUZA, AYRES F. MORGADO, SELENE M. A. GUELLI ULSON DE SOUZA: Application of coagulation systems coupled with adsorption on powdered activated carbon to textile wastewater treatment 1529

M. M. Barmaki, M. R. Rahimpour, A. Jahanmiri: Treatment of wastewater polluted with urea by counter-current thermal hydrolysis in an industrial urea plant 1535
D.B. Luiz, H.J. José, R.F.P.M. Moreira: Tertiary treatment of slaughterhouse wastewater using ferric coagulation followed by UV or UV/H2O2 processes 1541
José L. Tambosi, Rênnio F. Sena, Wilhelm Gebhardt, Regina F.P.M. Moreira, Humberto J. José and Horst Fr. Schröder: Membrane bioreactor and advanced oxidation processes applied to wastewater containing non-steroidal anti-inflammatory drugs (NSAIDs)..... 1547
M. L., Ávila, C. F. Farinha, S. A. Figueiredo: Basic dyestuffs removal from textile wastewaters using almond hulls: Equilibrium and kinetic studies..... 1553
Marcio B. Rodrigues; João V.B. Souza; Érica S. Silva; Flávio T. Silva; Teresa C.B. Paiva: Integration of emergent processes for the treatment of wastewater from nitrocellulose indutry: treatment with Aspergillus 2BNL1 fungus and TIO2/UV 1559
Rui C. Martins, Nádia Costa, Cátia M. Augusto, Margarida J. Quina, Licínio M. Gando-Ferreira and Rosa M. Quinta-Ferreira: Olive mill effluents treatment by physical-chemical integrated processes 1565
Shiva Agarwal, Ana E. Ferreira, Licínio M. Ferreira, M. Teresa A. Reis, Remígio M. Machado, Jorge M. R. Carvalho: Removal of formaldehyde by oxidation from phenolic resin plant effluents 1571
Ana C. Morelli, Erika C. Cren, Antonio J. Meirelles: Removal of linoleic acid from ethanolic solutions with ion exchange resins..... 1577
Natália P. Macedo, Erika C. Cren, Antonio J. Meirelles: Breakthrough curves for oleic acid adsorption in ion exchange resin 1582
Dina M.R. Mateus, Ângela Leonardo, Filipe Pequeno, Henrique J.O. Pinho: Chromium removal by constructed wetlands: evaluating the effects of chromium rich industrial effluents..... 1588
Gryzelda Poźniak, Ryszard Poźniak, Kazimiera A. Wilk: Recovery of heavy metals by hybrid membrane processes.... 1592
Andressa R. Vasques , Letícia Weissenberg, Selene M. Guelli U. de Souza, José A. B. Valle, Antônio A. Ulson de Souza: Removal of dyes from the textile industry by adsorption in fixed bed columns – A sustainable process 1597
Maretva Baricot, Geoffrey Fowler, Agustí Fortuny, Frank Stüber, Christophe Bengoa, Azael Fabregat and José Font: Activated carbon from coconut shells as catalyst in the CWAO of phenol in a trickle bed reactor 1603
A.B. Pérez Marín, J.F. Ortuño, M.I. Aguilar, V.F. Meseguer, J. Sáez, M. Lloréns: Use of chemical modification to determine the binding of Cd(II), Zn(II) and Cr(III) ions by orange waste..... 1609
Cláudia B. Lopes, Marta Otero, Zhi Lin, Carlos M. Silva, João Rocha, Eduarda Pereira Armando C. Duarte: Comparative mercury removal by ETS-4 and activated carbon from low contaminated solutions 1615
Susana M. Paixão, Maria C. SàÁgua, Lina Baeta-Hall, Carlos Nogueira, Paula Sá-Pereira, José C. Duarte, Ana M. Anselmo: Selection of indigenous acidophilic bacteria for the bioleaching of two SOMINCOR concentrates 1621
Marco S. Lucas, Joaquín R. Domínguez, José A. Peres: Kinetic constants of phenolic compounds oxidation by Fenton's reagent..... 1626
Teodora Miteva, Nadja Hvala, Rodrigo Alvarez, Dolores Kukanja: Model-based optimization of a semi-batch industrial polymerization process..... 1632
Chernykh I.G., Stoyanovskaya O.P., Zasypkina O.A.,: Reacting media models building optimization..... 1638
Paula A. G. Portugal, Marco S. Reis, Cristina M. S. G. Baptista: Multiobjective optimization of the benzene nitration process..... 1641
Patrícia C. S. Borges, Adriene A. Pfeifer, Fran Sérgio Lobato, Eloízio J. Ribeiro, Valéria V. Murata: Dynamic optimization of fed-batch alcoholic fermentation 1647
Mojgan Ebrahiminejad and Reza Eslamloueyan: Selection of controlled variables for an industrial distillation column with heat pump 1653
Belmiro P.M. Duarte, Nuno M.C. Oliveira, João F.M. Gândara,: An SPC inspired MPC formulation for quality variables 1658
Fernando G. Martins, Marta I. M. S. Cruz, Manuel L. Tavares, Manuel A. N. Coelho: The Importance of the simulation in refinery processes..... 1664
Greer T., Bedelbayev, A., Igreja, J.M., Gomes, J. F., Anastácio, P, B. Lie: Dynamic simulation of CO2 absorption from post combustion gases 1670
Fábio Marini, Maria G. E. Silva, Milton Mori: Three-dimensional gas-solid fluidized bed simulation based on kinetic theory of granular flow 1676
Eduardo L.T. Conceição, Antônio A.T.G. Portugal: Writing a software package for simulation of the three-dimensional structure of paper..... 1682
Ângela M. Silva, Senhorinha F.C.F. Teixeira, José C.F. Teixeira: 3D simulation of multiphase flow in large-scale venturi scrubbers 1688
Carlos M. Silva, Claudia P. Passos, Manuel A. Coimbra, Francisco A. Da Silva: Numerical simulation of supercritical extraction processes..... 1694
Raquel D. Moita, Henrique A. Matos, Cristina Fernandes, Clemente P. Nunes, Mário J. Pinho: Influence of a heated brine spray system on the dynamic model of an integrated recrystallization industrial process 1700
Pablo M. Aballay, Gustavo J.E. Scaglia, Martha D. Vallejo Oscar A. Ortiz: Non isothermal phenomenological model of an enological fermentation: modelling and performance analysis..... 1706

ZUZANA GOGOVÁ, JIŘÍ HANIKA: Model aided design of gas-lift reactor for oxidation reaction with fast reversible catalyst deactivation 1712
M. VON STOSCH, R. OLIVEIRA, J. PERES, S. FEYO DE AZEVEDO: A new hybrid modeling methodology based on delayed differential equations: application to antibody expression by Pichia pastoris 1718
JUAN CARLOS SERRATO B., JONATAN GÓMEZ P., LUIS A. CAICEDO M.: Adaptive evolutionary design of extractants for the separation of organic compounds from aqueous streams by liquid extraction 1724
JOSÉ A.V. OLIVEIRA: Heuristic methods to scheduling operations in parallel machines 1730
SUSANA RELVAS, ANA PAULA F.D. BARBOSA-PÓVOA, HENRIQUE A. MATOS JOÃO FIALHO: Multiproduct pipeline with inventory management: the CLC's case study 1736
PATRICIA OLIVER, ROSA A. RODRIGUEZ, STELLA M. UDAQUIOLA: Water use optimization in wine industry. Design of the water and the wastewater treatment network 1742
M.A.S.S. RAVAGNANI, A.P. SILVA, E.C. BISCAIA JR. AND J.A. CABALLERO: Optimal heat exchanger network synthesis including the detailed equipment design using particle swarm optimization 1748
R. ESLAMLOUEYAN AND E. HOSSEINZADEH: Neural network control for riser- slugging suppression 1754
CLEBER GUSTAVO DIAS, JOSÉ CARLOS CURVELO SANTANA, , SANTANA; ROBERTO RODRIGUES DE SOUZA, ELIAS BASILE TAMBOURGI: Use of Kohonen neural network in the sensorial analysis of Malpighia glabra L. wines 1760
MARIANA A.N. MOREIRA, HELENA M.M. CAMPOS, SÓNIA C.F. SANTOS, ANA R. MARQUES, MANUEL L.C. TAVARES, PAULA C. P. SILVA, LUÍSA A.C.N.GOMES: Study of aromatic recovery by extractive distillation 1766
RIBEIRO M. M. M., GOMES E.F.G. , BRÁS, L.M.R., GUIMARÃES M. M. L.,: Drop distribution determination in a liquid-liquid dispersion by image processing 1772
D.P. MESQUITA, O. DIAS, A.L. AMARAL, E.C. FERREIRA: Bright field versus phase contrast microscopy in activated sludge image acquisition methodologies 1778
PAULA SÁ-PEREIRA, SUSANA M. PAIXÃO, LINA BAETA-HALL, MARIA C. SÀÁGUA, ANA M. ANSELMO, JOSÉ C. DUARTE: Functional screening of a metagenomic library obtained from soils and water of S. Domingo's mine 1784
LICÍNIO M. GANDO-FERREIRA, MARGARIDA M. QUINA AND ROSA QUINTA-FERREIRA: Equilibrium and kinetics modelling of separation of Cr(III)/Cu by a chelating resin from industrial effluents 1789
LEANDRO C. SILVA, CARLA E. HORI, ADILSON J. ASSIS: Hydrogen production from methane steam reforming: parametric optimization of a membrane reactor 1795
JOSÉ C.M. PIRES, FERNANDO G. MARTINS, MARIA C.M. ALVIM-FERRAZ, MARIA C. PEREIRA: Evaluation of redundant measurements on the air quality monitoring network of Lisbon and Tagus Valley 1801
ANDREA C. FARIAS, RICARDO G. DURAISKI, ARGIMIRO R. SECCHI: Comparison of dynamic data reconciliation estimators and gross errors detection strategies 1807
MILLIC GIL, MARTA HERVA, AMAYA FRANCO, ENRIQUE ROCA: Risk estimation of compost application in agriculture: evaluating metal accumulation and biotransfer 1813
CARLOS LOPES, PATRÍCIA CORREIA, CARLA RAMINHOS, JOÃO LOURENÇO: In what way may recent laws on chemical substances promote scientific research 1819
M. ÇETIN KOÇAK: Simulation optimizes feedback control on the temperature of a heterogeneous batch reactor 1826
PATRÍCIA AP. SANTIAGO, CLÁUDIO A.T. SUAZO, ROBERTO C. GIORDANO: Study of volumetric oxygen transfer coefficient in a Taylor vortex flow bioreactor 1832
L.C.G. DOMINGUES, J.C. TEODORO, C.O. HOKKA, A.C. BADINO-JUNIOR, M.L.G.C. ARAUJO: Studies on synthetic medium composition for continuous production of clavulanic acid by Streptomyces clavuligerus 1838
L.M. BRITES, J. H. OLIVEIRA, C.O. HOKKA, M. BARBOZA: Effect of physicochemical properties of solvents on clavulanic acid extraction from fermentation broth 1843
JUAN S. HERNÁNDEZ-RIVERA, ANTONIO F. AGUILERA-CARBO, RAUL RODRÍGUEZ-HERRERA, JOSE L. HERNÁNDEZ AND CRISTOBAL N. AGUILAR: Kinetic production of the antioxidant ellagic acid by solid state culture 1849
ANA S.N. PONTES, MARIANA F. CORREIA, ANA M.R.B.XAVIER, DMITRY EVTYUGIN, ANTÓNIO PRATES: Biorefinary of pulp and paper hardwood spent sulfite liquor 1855
ARIELA V. PAULA, GISELE F. M. NUNES, JOSIANE L. SILVA, HEIZIR F. CASTRO, JÚLIO C. SANTOS: Enzymatic interesterification of milkfat with soybean oil using lipases of different sources immobilized in polysiloxane–polyvinyl alcohol hybrid matrix 1861
BERNARDO DIAS RIBEIRO, MARIA ALICE Z. COELHO, DANIEL W. BARRETO: Enzymatic hydrolysis of Buriti (Mauritia vinifera) oil for obtainment of beta-carotene 1867
PEDRO FERNANDES, STEFANO CATTORINI, JOAQUIM M.S. CABRAL: Enzymatic inulin hydrolysis using PVA-base matrices 1873
RAFAELLA F. NASCIMENTO, ANA I. S. BRÍGIDA, CARLA C. C. M. SILVA; MARIA HELENA ROCHA-LEÃO, LUCIANA R. B. GONÇALVES, MARIA A. Z. COELHO, SUELY P. FREITAS: Kinetic study of enzymatic biodiesel production from macauba acid oil using Candida antarctica B lipase immobilized in coconut fiber 1879
CARLOS M. MONTEIRO, NUNO M. T. LOURENÇO, CARLOS A. M. AFONSO: Enzymatic resolution and separation of sec-alcohols based on sustainable acylating agents 1885
ARSHAD JAWED, K. L. DIKSHIT, DEBENDRA K. SAHOO: Enhanced production of recombinant staphylokinase: An experimental design approach 1890
MAGDA C. SEMEDO, AMIN KARMALI, PATRÍCIA D. BARATA AND JOSÉ V. PRATA: Biocataysis in organic media by using calixarene-myoglobin complex with pseudoactivity of peroxidase 1896

KAREN M. GONÇALVES, IVELIZE BABICZ, INGRID C. R. COSTA, RODRIGO O. M. A. DE SOUZA, OCTAVIO A. C. ANTUNES: Immobilization of Lecitase ® Ultra in XAD-2 and XAD-4 under ultrasound irradiation 1902
ROGER ROVIRA, JUAN P MAESTRE, XAVIER GAMISANS, JAVIER LAFUENTE, JORDI MAS, DAVID GABRIEL: Use of molecular biology techniques to compare the bacterial community diversity of a lab-scale biofilter and an industrial biofilter treating high loads of H2S..... 1907
MARIA DO ROSÁRIO FREIXO, AMIN KARMALI, JOSÉ MARIA ARTEIRO: Production and chromatographic behaviour of polygalacturonase from Pleurotus ostreatus on immobilized metal chelates..... 1913
CLÁUDIA P. PASSOS, SUSANA M. CARDOSO, ANTÓNIO S. BARROS, CARLOS M. SILVA, MANUEL A. COIMBRA: Procyanidin Average Degree of Polymerization 1919
MAGDA SEMEDO, AMIN KARMALI, PATRÍCIA D. BARATA AND JOSÉ V. PRATA: One-step purification of hemoglobin from human erythrocytes by using a novel chromatographic matrix based on polymer-bound calix[6]arenes..... 1925
MICHIAKI MATSUMOTO, TAKASHI SUGIMOTO, NAOYA WADA AND KAZUO KONDO: Kinetic resolution of 1,2-epoxyhexane by whole cells of Rhodotorula glutinis in a two-liquid phase system..... 1931
P. FERNANDES, STEFANO CATTORINI, FILIPE CARVALHO, MARCO P.C. MARQUES, SUSANA BERNARDINO, FILIPA MADURO, SARA BADENES, DRAGANA BARROS, CARLA C.C.R. CARVALHO, LUIS P. FONSECA, JOAQUIM M.S. CABRAL: A multipurpose hydrogel system for biocatalyst immobilization..... 1935
ALTAN GÜVENÇ, BEYHAN HACIOĞLU: The effects of operation parameters on the electrodialysis recovery of citric acid from dilute solutions..... 1941
CAROLINA ARNAU, RAMÓN RAMÓN AND FRANCISCO VALERO: Influence of operational fed-batch strategies on heterologous Rhizopus oryzae lipase production in Pichia pastoris system using mixed substrates 1947
FILIPE ATAÍDE, ANA R. FERREIRA, JOÃO J. CLEMENTE, ANTÓNIO E. CUNHA, RUI OLIVEIRA: Adaptive control of glycerol and methanol feeding in recombinant Pichia pastoris cultures: Impact on antibody titre..... 1953
ROBERTA R. RIBEIRO, TATIANA F. FERREIRA, PRISCILLA F.F. AMARAL, MARIA ALICE Z. COELHO, MARIA HELENA M. ROCHA-LEÃO: Yarrowia lipolytica as biocatalyst for crude oil degradation 1959
MARLENE LOPES, NELMA GOMES, MANUEL MOTA, ISABEL BELO: Hyperbaric bioreactors use with Yarrowia lipolytica cultures: cellular adaptation to hyperbaric conditions..... 1965
NELMA GOMES, CRISTIANA GONÇALVES, MARLENE LOPES, MÁRIO AGUEDO, JOSÉ A. TEIXEIRA, MANUEL MOTA, ISABEL BELO: Development of bioprocesses based in biphasic media involving the yeast Yarrowia lipolytica..... 1971
ANDRÉ A. C. DE OLIVEIRA, PRISCILLA F.F. AMARAL, MARIA ALICE Z. COELHO, OFELIA Q.F. ARAÚJO: Image analysis to investigate electrochemical stress in lipase production by Yarrowia lipolytica 1977
PRISCILA GAVA MAZZOLA, ANGELA FAUSTINO JOZALA, PÉROLA DE OLIVEIRA MAGALHÃES, ADALBERTO PESSOA JR. , THEREZA CHRISTINA VESSONI PENNA: Liquid-liquid extraction in the presence of electrolytes of nisin and green fluorescent protein (GFPuv) 1983
PATRÍCIA A.T. BORGES, RITA PACHECO, AMIN KARMALI: Analysis of production of recombinant wild-type amidase from Pseudomonas aeruginosa in Escherichia coli..... 1989
RAFAEL S. COSTA, I. ROCHA AND EUGÉNIO C. FERREIRA: Mathematical modeling of recombinant Escherichia coli aerobic batch fermentations 1995
JOSÉ M. SANTOS ARTEIRO, M. ROSÁRIO MARTINS, CÁTIA SALVADOR, FÁTIMA B. CANDEIAS, SÓNIA MARTINS, AMIN KARMALI, A. TERESA CALDEIRA,: Overproduction of protein-bound polysaccharides from a Coriolus versicolor strain by submerged fermentation..... 2001
S. SILVA, S. MARTINS AND A. KARMALI: Production, purification and partial characterization of protein – bound polysaccharides from Pleurotus ostreatus and Lentinula edodes 2007
MARGARIDA MARTINS, MARIANA HENRIQUES, JOANA AZEREDO, ROSÁRIO OLIVEIRA: Headspace - SPME as a screening system for yeast metabolic compounds - A case study..... 2013
CRISTALDI M. GRAU R. AND MARTINEZ E.: Model-based iterative design of dynamic experiments imodeling for optimization of a bioprocess for a recombinant protein production 2019
PATRICIA C.S. BORGES, FRAN S. LOBATO, ELOÍZIO J. RIBEIRO, VALÉRIA V. MURATA: Kinetic models evaluation for fed-batch alcoholic fermentation..... 2025
HECTOR GUTIERREZ-MURILLO, GABRIELA MAGAÑA, ARTURO SANCHE: Production costs of wheat straw-based ethanol in Mexico. A parametric analysis 2031
S. FARIA, M.M. RESENDE, E. J. RIBEIRO, F. P. DE FRANÇA AND V.L. CARDOSO: Optimization of process variables and kinetics of the xanthan gum biosynthesis using sugar cane broth..... 2037
MICHELE MICHELIN, MARIA DE LOURDES T. M. POLIZELI, DENISE S. RUZENE, DANIEL P. SILVA, ANTÓNIO A. VICENTE, JOÃO A. JORGE, HÉCTOR F. TERENZI, JOSÉ A. TEIXEIRA: A new strategy for xylanase production using wheat straw autohydrolysis liquor as substrate..... 2043
JOSÉ CARLOS CURVELO-SANTANA, ANDRÉ FELIPE H. LIBRANTZ, ELIAS BASILE TAMBOURGI: Approach model for simulation of the starch hydrolysis by α- amylase and alcohol production from manioc root starch 2049
JOANA PAULA MENEZES BIAZUS, TAÍS RAMAIANA SILVA GUIMARÃES, JOSÉ CARLOS CURVELO SANTANA, , SANTANA; ROBERTO RODRIGUES DE SOUZA, ELIAS BASILE TAMBOURGI: RSM optimization of fractional precipitation and characterizing of amylase from maize malt 2055
DENISE S. RUZENE, ELIF YAGIZ, , DILEK MARANGOZ, , DANIEL P. SILVA,: Hydrothermal treatments of corn cob and hemicelluloses extraction 2060

BEATA ABRAHAM, ALEXANDRU SZEP, ILDIKO MIKLOSSY, EMESE BOTH, MARIA PALFI, SZABOLCS LANYI: Bioconversion of xylose from lignocellulose wastes in raw materials for biochemical syntheses 2065
GIULIANO DRAGONE, SOLANGE I. MUSSATTO, JOÃO B. ALMEIDA E SILVA, JOSÉ A. TEIXEIRA: Optimization of ethanol production from cheese whey powder by Kluyveromyces fragilis using factorial design and response surface methodology 2071
OTONIEL CORZO, NELSON BRACHO, CARLOS ALVAREZ: Application of normalized Weibull model for describing the air drying of mango slices at different maturity stages..... 2077
OTONIEL CORZO, NELSON BRACHO, CARLOS ALVAREZ: Determination of suitable thin layer model for air drying of mango slices 2082
R. MOREIRA, F. CHENLO, L. CHAGURI: Analysis of cellular tissue of chestnuts during drying and rehydration process... 2088
A. TERESA CALDEIRA, CÁTIA SALVADOR, FÁTIMA PINTO, JOSÉ M. ARTEIRO, M. ROSÁRIO MARTINS,: Molecular biomarkers to characterize Amanita ponderosa mushrooms..... 2094
ANA FRAGOSO, RITA PACHECO AND AMIN KARMALI: Structural and kinetics effects of amidase from Pseudomonas aeruginosa encapsulated in reversed micelles 2100
ROSA MARIA RODRIGUEZ JASSO, JOSÉ A. TEIXEIRA, CRISTOBAL AGUILAR GONZALEZ, LORENZO PASTRANA: Identification and evaluation of fungal strains with fucoidan degradation potential..... 2106
DÉBORA JUNG LUVIZETTO FACCIN, IVANA MARTINS, NILO SÉRGIO MEDEIROS CARDOZO, ROSANE RECH, MARCO ANTÔNIO ZÁCHIA AYUB, TITO LÍVIO MOITINHO ALVES, ROSSANO GAMBETTA, ARGIMIRO RESENDE SECCHI: Modeling and experimental evaluation of poly(3-hydroxybutyrate) production in Bacillus megaterium..... 2110
AZAM NAJAFLOO, MOHAMMAD H. SARRAFZADEH,ABBAS GERAMI: Statistical analysis of oxygen effect on the culture of Bacillus thuringiensis 2116
CRISTIANA GONÇALVES, JOÃO P. FERREIRA, MARLENE LOPES, SORAIA FALCÃO, ANTÓNIO M. PERES, SUSANA M. CARDOSO, ISABEL BELO: Characterization of phenolic compounds of OMW: toxicity and degrability by yeasts 2121
FERNANDA R. PINHATI, EDUARDO M. DEL AGUILA, ALINE F. VIERO, ANA PAULA R. TORRES, JOAB T. SILVA, VÂNIA M. F. PASCHOALIN: Changes in the wastewater bacterial community of oil refinery during phenol shock loadings 2127
PALMA, C., CONTRERAS, E., SEPÚLVEDA, L., CARVAJAL, A.: Degradation of acid, basic and reactive dye mixture in a continuous bioreactor 2133
EDGAR SILVEIRA, PETRUS P. MARQUES, JOSÉ L. LIMA-FILHO, ANA L.F. PORTO, ELIAS B. TAMBOURGI: Optimization of industrial textile dye colour removal by Pseudomonas oleovorans 2139
M. OLIVEIRA, J.M. NOBREGA, A. V. MACHADO, R. NOGUEIRA: Phosphorus removal from water by polyolefins activated with Al2O3 2145
CRISTINA QUINTELAS, ZÉLIA ROCHA, BRUNA SILVA, BRUNA FONSECA, HUGO FIGUEIREDO AND TERESATAVARES: Application of an E. coli biofilm supported on kaolin to the removal of Cd(II), Cr(VI), Fe(III) and Ni(II) from aqueous solutions 2151
ISABEL TORRES, ANA GUIMARÃES, VALENTINA M.F. DOMINGUES, CRISTINA M.F. DELERUE-MATOS: Reactive dyestuff removal by cork residues..... 2156
J.T. ALBERGARIA, C.M. DELERUE-MATOS, M.C.M. ALVIM FERRAZ: Influence of airflow rate on soil remediation using soil vapour extraction 2162
SARA C. SILVÉRIO, PEDRO P. MADEIRA, OSCAR RODRÍGUEZ, JOSÉ A. TEIXEIRA, EUGÉNIA A. MACEDO: Relative hydrophobicity of (PEG or Ucon)-salt ATPSs..... 2168
MARIA ALICE G. DE ANDRADE LIMA, SARA H. DE OLIVEIRA, LÍVIA A. SANTOS, GLÓRIA Mª VINHAS, SEVERINO L. URTIGA F., ALICE ALEXSANDRA S. VIEIRA, MITSUE M. NAKAZAWA, FRANCISCA PESSOA DE FRANÇA: Biofilms formation and biocorrosion in coupons exposed in marine environment 2172
LÚCIA C. SIMÕES, MANUEL SIMÕES, MARIA J. VIEIRA: Drinking water biofilm monitoring by Propella™ and Flow Cell bioreactors under different operating conditions 2178
MARTA H.F. HENRIQUES, ANA I.C. SILVA, SARA H.N. VICENTE, JORGE M.S. ROCHA: Environmental conditions in Nannochloropsis gaditana cultivation for effective aquaculture live feed 2184
EDSON R. NUCCI, VANESSA R. SOUZA, ROSINEIDE G. SILVA, RAQUEL L.C. GIORDANO, ROBERTO C. GIORDANO, ANTONIO J.G. CRUZ: On-line monitoring of penicillin G acylase production using a fuzzy logic algorithm 2190
DÁLIA M.D.BARBOSA, TERESA ALVES, LARA RIBEIRO, JOAQUIM P.QUEIROGA, JOSÉ C. MENEZES: Monitoring by HPLC-PDA impurities generated by forced degradation conditions on an active pharmaceutical ingredient..... 2196
O. PREISNER, R. GUIOMAR, J. MACHADO, J.C. MENEZES, J.A. LOPES: FT-IR spectroscopy and chemometrics in clinical microbiology 2202
ANA M. QUINTO, PEDRO A. BARATA, JOSÉ M. MARTINS, JOSÉ C. MENEZES: Risk quantification of microbiological contamination in aseptic processes..... 2206
VALERY P. NESTERENKO: Novel method for accelerated analytical control of biological (bacteriological) agents 2212
M. HERNÁNDEZ, M. PEÑA MIRANDA, G. GONZÁLEZ BENITO: Influence of phosphate and maltose concentrations in the dextransucrose production by Leuconostoc m. B-512-f 2217
FERNANDO G. MARTINS, M.I.M.S. CRUZ , DOMINGOS BARBOSA: A software tool for design of evaporator systems 2222
ALICE M. DE LIMA, ADILSON J. DE ASSIS: Process synthesis for hydrogen production from glucose: bioreactor design and scale-up and downstream process 2228
S. LUCAS, M.T. GARCÍA-CUBERO, A. CARTÓN, S. BOLADO, P.A. GARCÍA-ENCINA, G. GONZÁLEZ-BENITO, M-A. URUEÑA: Teaching and learning strategies to improve the development of student skills in Chemical Engineering degree 2234

DOLGINUN V.N., KUDY A.N., KLIMOV A.M. AND IVANOV O.O.: Another basic segregation mechanism in aerated gravity flows of particulate solids 2240
T. REG. BOTT: Biofouling Control in Cooling Water 2246
M.T.M. SENA ESTEVES, I.M.B. PEREIRA, M.N.M. COELHO PINHEIRO, A.M.F.R. PINTO: Comparison of Hydrodynamic Parameters between an Internal and an External Airlift Column..... 2251

Proceedings of the 10th International Chemical and
Biological Engineering Conference - CHEMPOR 2008
Braga, Portugal, September 4-6, 2008
E.C. Ferreira and M. Mota (Eds.)

Meeting the Challenge

T. Reg. Bott
School of Chemical Engineering, University of Birmingham, Edgbaston,
Birmingham B15 2TT, U.K.

Keywords: Chemical Engineering, Food, Water, Waste, Energy, Biofuels, Hydrogen.
Topic: Invited Lecture

Abstract

The first Chempor Conference held in Lisbon in 1975 under the auspices of the Calouste Gulbenkian Foundation, heralded a regular wide-ranging review of research and development in Portugal and the U.K. Progressively in later years the Conferences have attracted contributions from other European countries and indeed further afield. There is an increasing awareness of the problems for the environment, notably global warming, brought about by human activities. Recent predictions about the future are dire, particularly regarding food and water for a rapidly growing world population. They represent a substantial challenge to the scientific and technical fraternity. In response to that challenge it is important to keep up to date with technical developments, to meet and keep in touch with co - workers in associated fields, and to cooperate wherever possible. The papers presented at the Chempor and other conferences have made and continue to make, a significant contribution to that objective of meeting the challenge.

1 Introduction

For thousands of years humanity has had to cope and come to terms with the challenges of starvation, disease and conflict. There have been some useful developments over the years in food production (particularly the so called “Green Revolution” in the ‘60s) and in medicine. Sadly though the establishment of universal peace seems as distant as ever. Despite the strides in agriculture and disease control, the basic needs have not been made for a large proportion of the world population. With the anticipated dramatic rise in the world population in the coming decades, estimated to be at around eleven billion in 2050, the problems of food production and medical care will become even more intense, unless effective action is taken. The provision of clean water for human consumption is also of vital importance in the suppression of disease. Technology has a responsive role to play in meeting this challenge.

In addition to these basic needs of humanity, energy has played an important part in the lives of many members of the human family since the Industrial Revolution, not least in food production but also in aspects of disease control and particularly in the field of transportation. In previous millennia, energy primarily required for food production, was provided either by human or animal power. The phenomenal growth in energy usage generally provided by the heat of combustion of fossil fuels (coal and oil) or other combustible, usually carbonaceous, material, has led to the discharge of vast quantities of products from the combustion process, notably carbon dioxide. Although there are dissenters, it is believed by the majority of the informed, that the random discharge of these so-called greenhouse gases to the atmosphere is leading to the phenomenon of global warming, bringing in turn changes to the climate. Additional problems associated with industrialisation and a higher standard of living is waste disposal and satisfactory sanitation.

In a U.K. government document (a summary of a White Paper) entitled, “This Common Inheritance” (HMSO, 1990) the following points were made; Mankind long believed that, whatever we did, the earth would remain much the same. We now know that this

is untrue. The ways we produce everything and the rate at which we multiply, use natural resources and produce waste, threatens to make fundamental changes in the world environment. Nature is under threat. We have a moral duty to look after our planet and hand it on in good order for future generations. That does not mean trying to halt economic growth. We need growth to give the opportunity to live better and healthier lives.

In recent years, though, the issue of climate change has been paramount in the United Nations, the European Union and individual nations, and various summit gatherings. The Kyoto agreement in 1997 pledged to cut the emission of greenhouse gases principally CO_2 by 12.5 % (based on 1990 levels) by 2010. At a recent G8 summit (July 2008) a target of achieving 50% reduction in global emissions by 2050 was suggested. In December, 2007, 15,000 people flew to Bali to discuss climate change (Campbell, 2008). It was the intention to build on the achievements of the Kyoto agreement and it was considered to be a success with a continuation of the dialogue begun at Kyoto.

The European Union environmental legislation (Integrated Pollution Prevention and Control – IPPC) applies separately to different aspects of the natural environment – air, water, waste and so on. Porteous (2008) states that the IPPC Directive, based mainly on U.K. law, requires major industrial installations to be licensed in an integrated way for controlling emissions to air and water and the management of waste to protect the environment as a whole. The approach encourages industrialists to think about the whole process adopting cleaner technology rather than just adding “end of pipe” controls

2 Food Production

One of the major problems of attempting to increase food production to satisfy the growing world population is land use, and land availability. Tropical rainforests are constantly burnt and wetlands drained to provide land for agriculture – growing crops and rearing animals as sources of food. The use of land for raising sheep and cattle for food however, is not considered by many as an efficient use of that land. The opportunity of growing two crops per year of edible foods is much more attractive in the light of the growing number of mouths to feed in the world. Together with pollution of water courses and overfishing, many species of wild plants and creatures are being driven to extinction. As a result valuable sources of food and medicine are lost. The alternative is to improve the output from existing agricultural land, which may be substantially achieved by the application of artificial fertilisers and use of herbicides and insecticides with special safeguards. A recent discourse (McClafferty and Islam, 2008) emphasised that billions of people worldwide suffer from “hidden hunger”, an insidious form of malnutrition, that can leave children stunted, immune systems compromised and adults unable to work effectively. The condition results from micronutrient malnutrition caused by their lack in the diet. The poor in developing countries who live mostly in rural areas, depend largely on locally grown staple foods like rice,wheat and corn to satisfy hunger but provide insufficient nutrition. A world wide organisation “Harvestplus” is dedicated to the development of micronutrient rich staple foods that rural populations can grow and consume. In order to provide the necessary content of iron, zinc and vitimin A suitable low cost fertilisers will be required on a large scale.

3 Water

As important as food if not more important in many ways, is the availability of clean water. Water supplies around the world are heading towards crisis point. Experts are predicting large-scale water shortages over the next 25 years. It is anticipated that two out of three people on the planet will face regular depletion of water supplies. Population increase and rising standards of living, together with pollution, are rapidly diminishing the availability of naturally occurring sources of clean water. Water related

diseases, such as diarrhoea, cholera, tachoma, hepatitis and intestinal worms afflict millions of people worldwide. Approximately 1.8 million people die each year from diarrhoeal diseases alone,90% of whom are children under the age of five (Laursen,W., 2007). Many pathogens excreted by humans and animals can cause these diseases when they are ingested via faeces-contaminated drinking water. These pathogens, and other contaminants can be physically removed by filtering, adsorption or sedimentation, and they can be rendered innocuous by chemical, heat or u.v treatment.

In developed countries the potable water supply is carefully protected from contamination. In the E.U. for instance,there are stringent requirements for water quality to safeguard the health of people in respect of micro organisms and toxic substances. The water origin is usually rivers or it may be obtained from boreholes in suitable locations tapping into aquifers. In addtion to serving the public, water has many industrial uses such as a medium for conveyance of wastes, slurries.and wood pulp, as a solvent and as a heat transfer medium principally through vapour (steam), or cooling

Where sea water is available, desalination becomes a possiblity. In multi-stage evaporation there are implications for energy use and its associations with global warming. An alternative is the application of reverse osmosis. Kowtsakos(2008) states that there are not enough chemical engineers employed in this industry.

The disposal of waste water from public sewage systems and industrial use, also requires stringent controls, since it is often returned to its source. It has been said that the water in the River Thames is used ten times over in its journey from its source to the sea! In the methods available for the treatment of water the application of physical forces predominate, (well known to chemical engineers). In general terms there are three stages. In the treatment of waste water particularly, the primary treatment involves physical operations such as screening and sedimentation that are used to remove the floating and settleable solids from the water. Secondary treatment involves biological and chemical processes to remove organic matter. A final treatment is applied to remove any trace constituants that still remain in the water.

Filtration is widely used for the preparation of public water supplies - including traditional sand filtration and membrane fitration, that have application outside the water industry such as solvent recovery and the production of potable water from sea water. Papers presented at the Chempor Conference in 1975, described the disinfection of water in the 1974 epidemic of cholera (Lobato de Faria) and water demineralisation (Rodriques and Tondeur).

4 Waste Disposal

Substantial industrialisation and improved standards of living, have given rise to the production of waste materials of one sort or another, from manufacturing to domestic and retail outlets. It is usual to classify waste disposal into three categories; landfill. incineration and recycling. Landfill is subject to tight scrutiny because of the risks to public health.through the contamination of ground water.Disposal at sea, consisting of long term persistent noxious substances with a lowering of the amenity of an area due to smell visual degradation and possibly noise, is also not readily acceptable. Flamable waste incineration particularly domestic waste, has been practiced for many years. Because of the problem of emissions notably CO_2 , the technique has come under critical assessment.

The best option is to recycle but this is no easy option because there is likely to be a mixture of components that may need separation,which can be labour intensive.In order to overcome some of these difficulties it might be possible to recycle in a different way; by the incorporation of say,plastics and broken bottles in building materials for

instance. At the first Chempor Conference in 1975, Bridgewater presented a paper entitled “Plastic waste-disposal or recovery?”

5 Energy

Increased industrialisation and improved living standards that have been achieved in many parts of the world have been largely based on the availability of energy, one sort or another.The traditional acquisation of energy going back over countless generations has been through combustion to provide heat. Combustion is still an important component in the scheme of things,and is likely to remain so, but the associated technology has become more complex, due to the concern for the effects of the associated emissions on the climate, already discussed.

The first priority in achieving minimum output of greenhouse gases is effective energy management. Chemical engineering technology is uniquely placed to make a substantial contribution to effective management to maximise energy efficiency. A basic requirement is effective design, not only in respect of the combustion process itself, but in achieving maximum heat transfer. A recent simplified study (Casanueva-Robles and Bott, 2005) of the water-cooled steam condensers on a 550 MW coal fired power station,demonstrated that a 1mm thick biofilm on the condensers resulted in an increase of the CO_2 .discharged to atmosphere of 6.2 tonnes/h. Although this may be considered to be a large additional CO_2 discharge, it represents only a relatively small proportion of the total emission. Nevertheless,if the biofilm formation could be reduced or even eliminated altogether, it would make a significant contribution to the aim of reducing the effects of emissions.

Effective control of the accumulation of microbial biofilms can be achieved by the use of biocides. Chlorine has been the preferred biocide for many years on account of its availability and relativly low cost. Chlorine however represents an environmentally unacceptable pollutant when the water is discharged back to its source. Cooling water is usually taken from a natural source such as a river, lake or the sea. Under these circumstances the residual chlorine is a danger to living plants and creatures in the water. Furthermore chlorine reacts with organic material to form carcinogenic compounds that are clearly a danger to humans who may come incontact with the water and particularly if it is used for drinking purposes. As a result, alternative, environmentally friendly biocides are available that are continually being improved. The method of dosing e.g. continuous or intermittent, may affect the overal effectiveness of biocide application

Similarly heat exchangers that recover the heat from hot combustion gases can become fouled with deposits of mineral matter originally contained in the fuel. If steps are not taken to reduce or eliminate these unwanted deposits,the efficiency of heat recovery will be jeopardised, so for a given heat requirement the fuel consumption will increase and the production of CO_2.will also increase.

The reduction of surface fouling in heat exchangers, by good design and suitable control techniques,can make a substantial contribution to a reduction of greenhouse gas discharged to atmosphere.from combustion based systems.Tackling the problem of heat exchanger surface fouling has been a top technological priority in recent years, particularly since the so called “oil crisis” in the early 1970s. Improvements to heat exchanger design in respect of fluid velocity and temperature distribution,have made significant contributions to energy conservation. The use of helical baffles in shell and tube heat exchangers (Boxma, 2000) and the use of inserts in the tubes (Wills et al, 2000), to improve the opportunity to remove deposits are examples of technical advances in design. The material from which a heat exchanger is made and its quality in terms of roughness, have also come under the designers’ scrutiny.

Attention to operational managemement to ensure that the design requirements such as flow velocity and temperature distribution, are maintained is also an effective tool in maximising energy transfer. The use of modified surfaces and coatings to prevent or reduce surface fouling is also a possibility, although cost and durability have to be carefully considered. The use of additives, as with cooling water, is an option but its presence may not be acceptable in certain products as it may be considered an impurity. This is of particular significance in the processing of food.

In addition to these aspects of energy management, it is possible to reduce emissions by capturing the CO_2 and storing it, usually below ground in deep disused mines and the like. An underground carbon storage facility has recently opened in Australia (Anon. 2008). The CO_2 originates from a natural gas well, not from a combustion process, but the principal is identical. The storage facility consists of rock formations 2km below the surface with an estimated capacity of 10,000 tonnes of greenhouse gas. Such a capacity would not be sufficient for a large 1,000 MW coal fired power station that could have around 8 Mt/year CO_2 emission.

The process is most cost effective when applied to large stationary sources of CO_2, such as power stations, refining furnaces and metal smelting, which account for more than half of all man-made CO_2 emissions. Techniques for capturing CO_2 include absorption,adsorption and membrane filtration. At the first Chempor Conference in1975, a paper was presented by Carter et al entitled " The adsorption of carbon dioxide by deep beds of molecular sieve adsorption". Although this paper was principally concerned with a gas coolant purification system for a high temperature nuclear power reactor, it did herald the concept of CO_2 capture for storage underground.

Fossil fuels particularly oil, are running out - with associated higher costs that have recently been in evidence, so that alternative sources of energy will be required. The combustion of waste, particularly domestic waste, can be a source of energy for power generation, but the emissions that include greenhouse gases, may also contain other unwanted compounds, that could be difficult to handle. Preliminary work on the use of hydrogen as an alternative source of energy is a possibility since it does not give rise to greenhouse gas emission from combustion. It may also be used in fuel cells that convert chemical energy directly into electrical energy without combustion. Research is being carried out to investigate their use for powering vehicles. The source of hydrogen in the quantities that will be needed and the fact that it is a gas at atmospheric pressure will create major problems. At the present time hydrogen is largely produced by the electrolysis of water; the source of that power may have come from a conventional power station! Research is being carried out on the posibility of using solar thermo-chemical cycles to produce hydrogen without producing CO_2 (Sattler et al 2007).There are however technical problems still to be overcome . An interesting application for industrially generated CO_2. resulting from hydrogen generation is for use in actual greenhouses, to encourage plant growth and capture of CO_2 (Anon 2007). Other sources of electrical energy that do not generate greenhouse gases include wind power, solar power, river and tidal barriers, sea wave motion and geothermal energy.

A developing industry, considered to be a replacement for the combustion of fossil fuels, is the production of "biofuel", It is a fuel as the name implies, which is biological in origin, such as methane, biogas and biodiesel, seen as sustainable supplements to petrol and diesel.These can be a means of reducing carbon emissions

Biodiesel refers to a diesel type fluid originating in biological sources such as vegetable oils or animal fats. The manufacturing process produces methyl esters (biodiesel) and a valuable biproduct - glycerine, that has many potential uses. Apart from use in vehicle engines there are other applications such as domestic heating oil to reduce or

eliminate the dependence on fossil fuel. Such an application would be of advatage in rural areas where there is no access to domestic gas supplies.

Although combustion generates greenhouse gas emissions, it is argued that since it is plant derived, the CO_2 produced is taken up in subsequent plant growth so that the actual pollution, when this is taken into account, is zero, i.e. carbon neutral. An alternative is biomass produced from organic materials directly from plants or from industrial processes. Woody biomass refers to wood type material or less dense material such as straw and tall grass. Non-woody biomass as the name implies, includes waste from industrial and food processes and specially grown crops such as sugar cane and maize.

Another alternative is biogas, formed by anaerobic digestion of organic materials, generally waste materials such as sewage sludge and waste from food production. The biogas produced is generally a mixture of methane and carbon dioxide with a ratio of approximately 2:1 respectively. It is possible, with suitable modification to use it in internal combustion engines or to generate electricity by the usual method of combustion to raise steam to operate turbines.

In an assessment of the potential for biofuels Bourne (2007) quoting a U.N. report, concludes that although the benefits from biofuels are large, an extensive use of biofuels could jeopodise the security of food supplies, with an increase in food prices. At the present time it is estimated that 25,000 people die from starvation each day! In the light of these kinds of data it is unfortunate that in some parts of the world rain forests and natural habitats are destroyed to provide areas for the production of crops, not for human consuption, but to provide biofuel of one sort or another. Sugar is a typical example. It is fermented to produce alcohol as a liquid fuel to replace petrol in specially adapted internal combustion engines.

A compromise that might go some way to meeting this concern about biofuel and food, is to utilise the waste produced in food production and agriculture generally, rather than using the food substance itself for the production of biofuel. Sugar production from cane is a good example of this approach. For many years waste material from cane sugar refining (bagasse) has been used as a fuel for combustion to produce steam and electricity for the refining process, and the surplus electricity has been made available for the local community. In addtion there is waste associated with the harvesting of the cane on the plantation currently often burnt in situ. This could also be used as a source of energy.It is anticipated that improvements could make the whole process carbon neutral since the equivalent $C0_2$ emission will be absorbed by the next year's growth.

Green algae, waterborne micro organisms, imbibe CO_2 and provided there is sufficient light available they will rapidly multiply to form a substantial mass of growth. They have often been regarded as a nuisance in reservoirs and in places where there are leisure activities.The Chinese authorities for instance, had to clear vast amounts of algae in preparation for some of the boating competitions at the Olympic Games. It has been suggested that algae might be a good source of biofuel since it is easy to grow and removes greenhouse gas from the environment.

Boyle (2008) reports that a company (Ineos) in the U.K.is proposing to prodce bioethanol fuel from municipal solid waste, agricultural waste and organic commercial waste. It is claimed that 400 litres of ethanol could be produced from one tonne of waste. It is pointed out that unlike other biofuels there is no choice to be made between food or fuel with this technology.

6 Concluding remarks

Humanity is facing a huge challenge in respect of the provision of food and clean water to sustain a rapidly increasing world population. In addition there is the availability of energy to satisfy the needs of the growing population in terms of standard of living and manufacturing industry. The examples cited illustrate the tremendous unique opportunity and indeed the moral obligation for chemical engineers, to apply their skills to meeting this challenge. It is in a spirit of optimism and dedication and the cooperation of governments and industrial entrepreneurs, that will ensure success. The whole process will continue to be facilitated by the exchange of ideas that results from conferences such as Chempor.

References

Anon, (2007), *IEA GHG Meetings in The Netherlands,* Greenhouse Issues, No. 86, 3.
Anon, (2008), *CCS:Saviour or Smokescreen?* The Chem. Engr. Issue No 803, 3.

Bourne, J.K., (2007), *Green Dreams,* Nat. Georaphic Magazine, No 4, Vol. 212.

Boyle, C.,(2008), *Rubbish Idea That Could Make Driving Cheaper*, The Times, 21st. July, London.

Boxma,B.(2000), *Helical Baffles in Shell and Tube Heat Exchangers,* 2nd. Int. Conf., Petroleum Phase Behaviour and Fouling, Copenhagen, 2000, Paper No.53.

Campbell,N.,(2008) *Postcard from Bali*, The Chem. Engr. Issue No. 801, 30.

Casanueva-Robles,T.and Bott, T.R. (2005), *The Environmental Effect of Heat Exchanger Fouling- A Case Study,* ECI Symposium Series, Vol. RP2, Proc. 6th. Int. Conf. Heat Exchanger Fouling and Cleaning, Eds., Muller-Steinhagen H., et al, Eng.Conf.Int., Kloster- Irsee

HMSO (1990), *The Common Heritage,* HMSO Publications Centre, London, SW8 5DT.

Koutsakos, E. (2008),*Thirsting for Chemical Engineers,* The Chem. Engr. Issue No. 804, 26

Laursen, W.,(2007), *Potters for Peace-Filters for Life,* The Chem. Engr., June, 31.

McCafferty, B. and Islam,Y. (2008) *Fighting Hidden Hunger*. The Chem. Engr. Issue 800, 26.

Porteous, A. (2008), *Environmental Science and Technology,* 4th. Edition, 369, John Wiley and Son, Chichester.

Sattler,C., Roeb, M. and Muller-Steinhagen, H., (2007), *The Sun + Water = Hydrogen,* The Chem. Engr. Issue No. 796, 46.

Wills, A., Bott T.R. and Gibbard, I.J., (2000) *The Control of Biofilms in Tubes using Wire- Wound Inserts,* Can. J. Chem. Eng. 78, 3, 43.

Proceedings of the 10th International Chemical and
Biological Engineering Conference - CHEMPOR 2008
Braga, Portugal, September 4-6, 2008
E.C. Ferreira and M. Mota (Eds.)

Gas-liquid mass transfer in gas-liquid-liquid dispersions in a stirred tank: effect of spreading coefficient.

Henrique J.O. Pinho[1,2], Rui Santana[3], Sebastião S. Alves[1*]
[1] IBB-Institute for Biotechnology and Bioengineering, Centre for Biological and Chemical Engineering, Instituto Superior Técnico, Av. Rovisco Pais, 1049-001 Lisboa, Portugal.
[2] Escola Superior de Tecnologia de Tomar, IPT, Estrada da Serra, Quinta do Contador, 2300-313 Tomar, Portugal
[3]Rolear-Automatizações, Estudos e Representações, S.A., Parque Rolear, Sítio do Areal Gordo, Apartado 530, 8001-906 Faro, Portugal

Keywords: mass transfer, gas-liquid-liquid, spreading coefficient, phase equilibria, multiphase reactors.
Topic: Advancing the chemical engineering fundamentals.

Abstract

Gas-liquid mass transfer in an aerated stirred tank containing two liquid phases was investigated by measuring the saturation of an organic solute in the gas phase. The purpose of this work was to provide experimental evidence for the mechanisms at play. Gas-liquid-liquid mass transfer is studied by measuring evaporation of an organic liquid from an aerated stirred tank 0.232 m in diameter. The continuous liquid phase consisted of tap water, while the dispersed organic phase consisted of n-heptane, n-dodecane or solutions thereof. Exhaust air was sampled using 125 ml sampling bulbs and analysed by gas chromatography. Change in outlet gas saturation (saturation in the transferred organic solute) as a function of organic phase composition in this system unequivocally shows that organic phase spreading coefficient is an extremely important factor in mass transfer rate in gas-liquid-liquid systems. Once the spreading coefficient of the organic solution changes from negative to positive, the outlet gas becomes saturated, corresponding to a several-fold increase in mass transfer coefficient.

1 Introduction

Interest in gas-liquid-liquid systems has recently been increasing due to its application in homogeneous catalysis systems [Cents 2001, Dumont 2003] and in the bioprocess industry. Aerobic fermentations [Nielsen 2003, Galaction 2004], VOC biodegradation [Daugulis 2003] and biotransformations using a gaseous substrate [Tecelão 2001] are examples of such bioprocesses involving an organic liquid finely dispersed in the aqueous medium.

In all these processes, mass transfer of one or more gases/vapours into/from the liquid-liquid emulsion occurs and is often rate determining. It is known that the presence of the second liquid phase dispersed in the continuous aqueous phase affects the gas-liquid mass transfer rate. An extensive review [Dumont 2003] of gas-liquid mass transfer to “oil-in water” systems reveals that, while most authors have found mass transfer enhancement due to the presence of the organic phase, both the extent of this enhancement and the mechanism by which it is achieved are not agreed upon by researchers. Gaps and contradictions in the experimental data do not allow definite choice between mathematical (and/or conceptual) models proposed for the phenomena involved.

The pathways for mass transfer between dispersed organic and dispersed gas phases may involve either (i) direct gas/organic contact or (ii) indirect mass transfer through the

* Corresponding author. Tel + 351-218417188. E-mail: salves@alfa.ist.utl.pt

intermediate continuous aqueous phase. Both mechanisms may coexist leading to a series/parallel set of pathways.

The effect of adding a second liquid phase may thus be expected to be different depending on the spreading coefficient *S*, defined as:

$$S = \sigma_{WG} - (\sigma_{OG} + \sigma_{OW}) \quad (1)$$

where σ_{WG}, σ_{OG} and σ_{OW} are the water-gas, organic-gas and organic-water interfacial tensions, respectively. If the spreading coefficient is positive, the dispersed organic phase tends to spread on the bubbles. Direct contact is thus likely and very high mass transfer coefficients are expected.

If the spreading coefficient is negative, on the other hand, such an organic film is not thermodynamically stable. Even so, gas-liquid mass transfer enhancement may occur due to the presence of organic droplets (which are much smaller than the bubbles) in the bubble boundary layer: they may either improve the concentration gradient due to a shuttle effect [Rols 1991] or improve boundary layer mixing.

In this paper, gas-liquid mass transfer effectiveness is quantified in a gas-liquid-liquid system in an aerated stirred tank, with organic phases of variable spreading coefficients, to elucidate the effect of spreading coefficient on gas-liquid mass transfer.

2 Materials and methods

The experimental set-up consisted of a 0.232 m diameter, flat-bottomed, fully baffled glass vessel with steel bottom. Liquid level was kept equal to tank diameter. Agitation was provided by a 0.090 m diameter Rushton turbine placed 0.118 m above the tank base. Temperature was not controlled. It was measured both in the liquid and in the gas above.
The continuous liquid phase consisted of tap water, while the dispersed organic phase consisted of n-heptane (anhydrous, 99%, Aldrich), n-dodecane (Reagent Plus, > 99%, Aldrich), or solutions thereof.
Air was introduced through a ring distributor placed below the turbine. Air flow rate was measured using a rotameter.
Exhaust air was sampled using 125 mL sampling bulbs and analysed for the relevant organic compound(s) by gas chromatography in a Hewllet-Packard 8690 II, equipped with a HT5 capillary column.

3 Theory and calculations

A simple measure of mass transfer effectiveness is the approach to equilibrium of the exit gas, i.e. the Murphree efficiency, *E*. In the present work, since there are no volatile organics in the inlet air, this is given by

$$E = \frac{p_{Gout}}{p_G^*} \quad (2)$$

where p_{Gout} is the partial pressure of the relevant organic compound at gas outlet, and p_G^* is its equilibrium partial pressure, which may be calculated assuming Raoult's law for the liquid organic phase. The advantage of *E* is its simplicity and the fact that no gas phase mixing assumptions are required for its calculation. Thus, although mass transfer coefficients may be calculated from *E* under the aforementioned assumptions, the simpler concept of *E* is enough to draw conclusions from the data obtained in this work and will thus be used.
The relationship between *E* and mass transfer coefficients may be established through mass balance:

$$Q_V \cdot \rho_{mol} \cdot dy = Q_V \cdot \rho_{mol} \cdot \frac{dp_G}{P} = K_G a\left(p_G^* - p_G\right)dV \qquad (3)$$

where K_G is the gas overall mass transfer coefficient between the gas and the organic liquid, a is the specific gas-liquid interfacial area, V is the liquid volume, P is pressure, Q_V is the gas volumetric flow rate and ρ_{mol} is the gas molar density.

Integration depends on the degree of backmixing of the gas, which lies between the two limiting conditions of its being well mixed and following plug flow. Assuming plug flow:

$$K_G a = -\frac{Q_V \rho_{mol}}{VP} \ln\left(1 - E\right) \qquad (4)$$

And assuming a well-mixed gas phase:

$$K_G a = -\frac{Q_V \rho_{mol}}{VP} \left(\frac{E}{1 - E}\right) \qquad (5)$$

4 Results and discussion

Figures 1 and 2 present the % saturation (= E x 100) of heptane in the outlet gas as a function of heptane % mol fraction in the organic liquid for an organic holdup of 2%, 2 different gas flow rates.

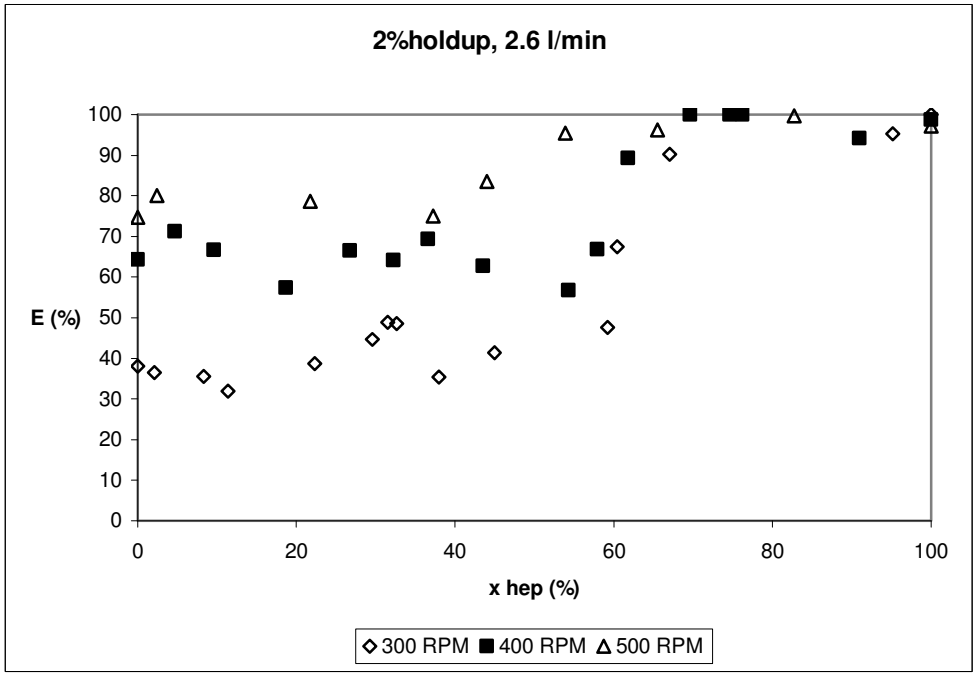

Figure 1 - % saturation (= *E*.100) vs. mol % heptane in the organic phase for Q_v=2.6 l/min and 2% organic holdup, at varying stirrer speeds.

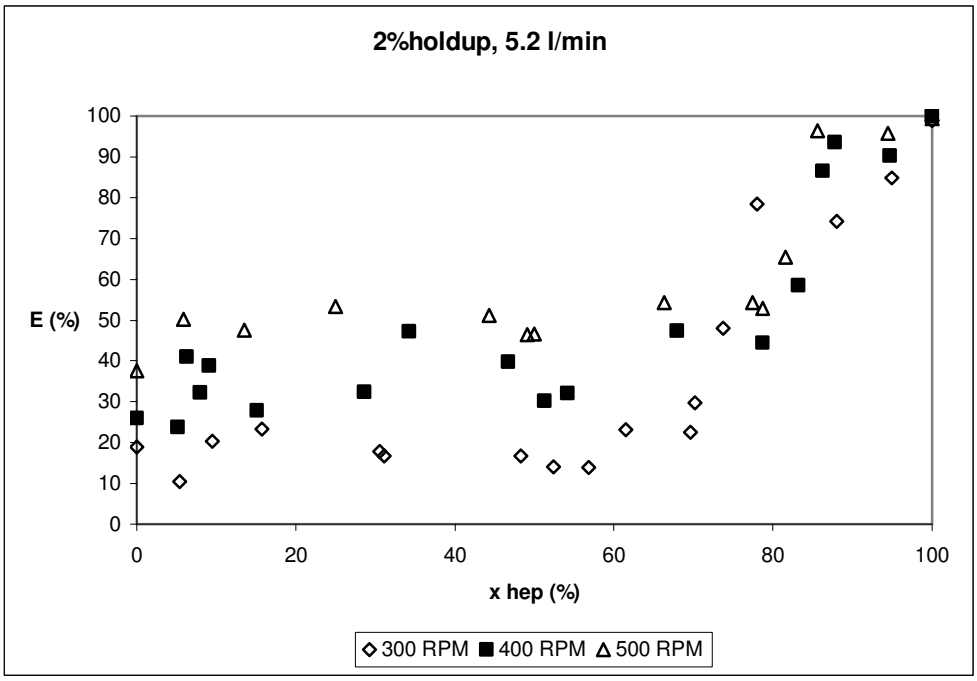

Figure 2 - % saturation (= *E*.100) vs. mol % heptane in the organic phase for Q_v=5.2 l/min and 2% organic holdup, at varying stirrer speeds.

The most striking features that we can see in these figures are the following:

(i) For any given set of conditions (constant N, constant Q_v) % saturation of heptane in the outlet gas is low at low concentrations of heptane in the organic liquid, high for high concentrations. In fact there appear to be two plateaus of approximately constant % saturation in the gas separated by a steep change at between 50% and 80% heptane in the liquid.

(ii) Above this transition-concentration the gas leaves almost saturated in heptane. The exception is when N = 300 rpm and Q_v = 5.2 l/min, which corresponds to the lowest agitation power.

(iii) Stirrer speed, as expected increases outlet percentage saturation, due to increased mass transfer coefficient.

The transition concentration happens to coincide roughly with the concentration of heptane at which the spreading coefficient of the organic solution changes from negative to positive. The spreading coefficient at 25ºC is 2.4 for heptane, and -5.5 for dodecane [Drelich 1999]. Assuming that surface tension varies approximately linearly with mole fraction [Tahery 2005] so will the spreading coefficient, in which case the transition composition is $x_{heptane}$ = 0.70. It may therefore be concluded that there are two mechanisms of mass transfer, depending on the spreading properties of the organic phase.

4 Conclusions

Change in outlet gas saturation (saturation in the transferred organic solute) as a function of organic phase composition in a gas-liquid-liquid system unequivocally shows that organic phase spreading coefficient is an extremely important factor in mass transfer rate in gas-liquid-liquid systems.

Acknowledgments
This work was supported by FCT - Fundação para a Ciência e a Tecnologia and Program FEDER (Project POCI/EQU 59782/2004). An FCT PhD grant (Nº SFRH/BD/37480/2007) to one of the authors (Henrique J.O. Pinho) is also acknowledged.

References

Cents, A. H. G., Brilman, D. W. F., Versteeg, G. F. (2001). Gas absorption in an agitated gas-liquid-liquid system. *Chemical Engineering Science*, 56, 1075-1083.

Daugulis, A.J., Boudreau, N.G. (2003). Removal and destruction of high concentrations of gaseous toluene in a two-phase partitioning bioreactor by *Alcaligenes xylosoxydans. Biotechnology Letters*, 25, 1421-1424.

Drelich, J., Miller, J.D. (1999/2000). Spreading kinetics for low viscosity n-alkanes on a water surface as recorded by a high-speed video system. *Annales Universitatis Mariae-Slodowska,* vol. LIV/LV, sectio AA, 105-113.

Dumont, E., Delmas, H. (2003). Mass transfer enhancement of gas absorption in oil-in-water systems, *Chemical Engineering and Processing*, 42, 419-438.

Galaction, A.-I., Cascaval, D., Oniscu, C., Turnea, M. (2004). Enhancement of oxygen mass transfer in stirred bioreactors using oxygen-vectors. 1. Simulated fermentation broths. *Bioprocess and Biosystems Engineering*, 26, 231-238.

Nielsen, D.R., Daugulis, A.J., McLellan, P.J. (2003). A novel method of simulating oxygen mass transfer in two-phase partitioning bioreactors. *Biotechnology and Bioengineering*, 83, 735-742.

Rols, J.L., Condoret, J.S, Fonade, C., Goma, G. (1991). Modeling of oxygen transfer in water through emulsified organic liquids. *Chemical Engineering Science*, 46 (7), 1869-1873.

Tahery, R., Modarress, H., Satherley, J. (2005). Surface tension prediction and thermodynamic analysis of the surface for binary solutions, *Chemical Engineering Science*, 60 (17), 4935-4952.

Tecelão, C.S.R., van Keulen, F., Fonseca, M.M.R. (2001). Development of a Reaction System for Selective Conversion of (-)-trans-carveol to (-)-Carvone with Whole Cells of *Rhodococcus erythropolis* DCL14, *Journal of Molecular catalysis B: Enzymatic*, 11, 719-724.

Proceedings of the 10th International Chemical and
Biological Engineering Conference - CHEMPOR 2008
Braga, Portugal, September 4-6, 2008
E.C. Ferreira and M. Mota (Eds.)

Oxygen transfer characterization in three-phase reactors using silicone oil as vector

Guillermo Quijano, Frédéric Thalasso*

Centro de Investigación y de Estudios Avanzados del IPN, Departamento de Biotecnología y Bioingeniería, Apdo. Postal 14-740, México D. F. 07360, México.

Keywords: vectors, transfer pathway, transfer enhancement, OTR
Topic: Advancing the chemical engineering fundamentals

Abstract

This paper presents the quantification of the air/vector and the air/vector/water oxygen transfer in three-phase reactors. A mathematical model was developed and used to characterize mass transfer in an airlift (AL) and a stirred-tank (ST) reactors containing from 0 to 50% of silicone oil as vector. A positive effect of the vector on oxygen transfer was observed. In both reactors, the optimum oxygen transfer was observed with 10% vector. Under these conditions, a transfer increase of 65 and 84% for the AL and ST respectively was observed, compared to reactors operated without silicone oil. It was also observed that the overall transfer enhancement was mainly due to a better air/water transfer. With 10% vector, the air/water transfer contribution to the overall oxygen transfer was 94.7 and 93.0% for the AL and ST, respectively.

1. Introduction

Transfer of poorly water-soluble compounds is a key issue in numerous biotechnological processes. Several methods have been proposed to overcome mass transfer limitations. Among these, the use of vectors has been explored for more than 30 years (Deziel et al., 1999). The use of vectors is based on the addition of an immiscible liquid with high affinity towards the target compound (Muñoz et al., 2007). An additional gas/vector/water transfer pathway is established. Numerous liquids have been used as vectors, including perfluorocarbons, silicone oil and long-chain alkanes. Despite numerous published works, no agreement on the positive or negative effect of vectors on mass transfer has been reached (Dumont and Delmas, 2003).

The effect of vectors on mass transfer has been traditionally assessed by the determination of the overall transfer rate. Due to the difficulty to characterize the vector phase under real operational conditions, a common simplification made in the literature is to assume that water and vector constitute a single homogeneous phase (Cesario et al., 1997). This simplification, adopted by many authors (Clarke and Correia, 2008), does not allow a separate estimation of the partial transfer rates (i.e. gas/vector, vector/water and gas/water transfers). To our knowledge, no report on partial mass transfer in three phase reactors has been made. The aim of this work was the quantification of the partial transfer rates of oxygen in an air/silicone-oil/water system. These oxygen transfer rates were estimated in an airlift (AL) and a stirred tank (ST) lab-scale reactor.

2. Mathematical model development

This work considers air and silicone oil (vector) dispersed in an aqueous sulfite solution (called water for simplification). Sulfite oxidation simulates oxygen uptake as occurring in biological processes. In this system two assumptions were made; (*i*) oxygen is transferred from air to water directly or through the vector and (*ii*) oxygen uptake occurs only in water.

* Corresponding author. Tel +5255-5061-3320; fax: +5255-5061-3313. E-mail: thalasso@cinvestav.mx

According to these assumptions, oxygen is transferred directly from air to water, and indirectly, from air to vector and then from vector to water. Mass transfer was characterized by two transfer rates; the actual transfer rate (OTR_{ij}) and the maximum transfer rate also called oxygen transfer capacity (OTC_{ij}). Subscripts *i* and *j* refer to the origin and the target phases; *g*, *v* and *w* for gas, vector and water respectively. Both OTR_{ij} and OTC_{ij} were expressed per unit of reactor volume to allow comparison. OTC_{ij} are the OTR_{ij} observed when the maximal gradient concentration is reached between the i^{th} and j^{th} phases. Thus OTR_{ij} can be expressed as a fraction of OTC_{ij} as follows;

$$OTR_{gv} = OTC_{gv}\left(1 - \frac{C_v}{C_v^*}\right) \quad (1)$$

$$OTR_{vw} = OTC_{vw}\left(1 - \frac{C_w}{C_w^*}\right)\left(\frac{C_v}{C_v^*}\right) \quad (2)$$

$$OTR_{gw} = OTC_{gw}\left(1 - \frac{C_w}{C_w^*}\right) \quad (3)$$

In these equations, C_i and C^*_i represent the actual and the saturation concentration of oxygen in the i^{th} phase. In presence of sodium sulfite, oxygen mass balance in vector and water can be written as follows;

$$\frac{dC_v}{dt} = \left[OTR_{gv} - OTR_{vw}\right]\frac{V_r}{V_v} \quad (4)$$

$$\frac{dC_w}{dt} = \left[OTR_{gw} + OTR_{vw} - q\right]\frac{V_r}{V_w} \quad (5)$$

In Equations 4-5, V_r, V_v and V_w represent the reactor, vector and water volume respectively; *q* is the oxygen consumption rate due to sulfite oxidation. In Equations 4 and 5, OTR_{ij} can be substituted by Equations 1-3. Additionally, the presence of sulfite ensures that C_w equal zero, giving Equations 6 and 7. Equation 8 gives the sulfite oxidation rate in which $Y_{SO_3^{2-}/O_2}$ is the sulfite /oxygen yield.

$$\frac{dC_v}{dt} = \left[OTC_{gv}\left(1 - \frac{C_v}{C_v^*}\right) - OTC_{vw}\left(\frac{C_v}{C_v^*}\right)\right]\frac{V_r}{V_v} \quad (6)$$

$$\frac{dC_w}{dt} = \left[OTC_{gw} + OTC_{vw}\left(\frac{C_v}{C_v^*}\right) - q\right]\frac{V_r}{V_w} \quad (7)$$

$$\frac{dSO_3^{2-}}{dt} = -\left(Y_{SO_3^{2-}/O_2} \cdot q\right)\frac{V_r}{V_w} \quad (8)$$

2.1 Model Solution

In order to estimate OTC_{gw}, OTC_{gv} and OTC_{vw}, Equations 6 to 8 were solved simultaneously and adjusted to experimental data obtained during mass transfer experiments as described below. A fitting procedure based on Runge-Kutta method with Marquardt optimization was

used. Once OTC_{ij} were determined, OTR_{ij} values were obtained from Equations 1-3. Model solution and statistic analyses were performed with Model Maker (Cherwell Scientific Publishing, 1993) and NCSS (Jerry Hintze, 2001), respectively.

3. Experimental

3.1 Setup and operating conditions

The AL reactor was a glass column (0.12 m inner diameter, 0.57 m height, 6.4 L total volume, 5 L working volume) with a concentric tube (0.075 m inner diameter, 0.35 m height) located at 0.05 m of the bottom of reactor. A porous plate (0.05 m diameter) was used for air supply. The ST reactor was a glass reactor (0.133 m inner diameter, 0.55 m height, 7.6 L total volume, 5 L working volume), mixed with a double Rushton turbine operated at 300 rpm. A perforated ring (orifice diameter of $1x10^{-3}$ m) was used for air supply. In both reactors, the air flow-rate was maintained at 1 vvm and controlled with a variable area flow-meter (Cole Parmer, Mexico) previously calibrated with a mass flow controller (GFC171S, Aalborg). Experiments were performed at 23 ± 2 °C. Reactors were operated with 0 to 50% v/v silicone oil (polydimethylsiloxane 200R, Dow Corning. México), characterized at 25ºC, by kinematic viscosity of 20 cSt, specific gravity of 0.95 and surface tension of 20.6 din cm^{-1} (Ascon-Cabrera and Lebeault, 1993).

3.2 Mass transfer experiments

Mass transfer was characterized in both reactors operated with air, sulfite solution (2.6×10^{-2} M) and silicone oil. Before mass transfer measurements, the reactor was operated until vector and water saturation was reached; this typically lasted about 10 minutes. Then cobalt sulfate, as sulfite oxidation catalyser, was added to the reactor (final cobalt concentration of 2.5×10^{-4} M) and measurements of C_w, C_v and sulfite concentration were immediately started. Experiments were made in triplicate for each tested condition.

3.3 Measurements techniques

Sulfite concentration and C_v were measured from time to time as follows: aeration and mixing were interrupted, then vector and water started to separate immediately. Samples of water were taken at the bottom of reactor and samples of the vector were taken from the top of the reactor. After sampling, the aeration and/or mixing were resumed. For data interpretation time scale was corrected to discard times during which aeration and mixing were interrupted. Sulfite concentration in water was measured by iodometric back-titration according to Zhao et al. (1999). The samples of vector were transferred to serological bottles with inert atmosphere (N_2, 99.97% purity) containing an aqueous sulfite solution of known concentration. Bottles were maintained at 23° C and 160 rpm during 24 h. Final sulfite concentration was then measured and C_v was assumed to be the amount of oxygen consumed by sulfite per volume of vector sampled. C^*_v was measured by the same procedure using a sample of vector aerated for 2 hours. C_w and C^*_w were measured with a dissolved oxygen probe (Hannah Instrument HI 2400, Mexico). The total gas holdup was measured by height differences according to Vandu et al. (2004).

4. Results and discussion

4.1 Validation of the sampling methods

The method used in this work was based on mixing and aeration interruption. It was therefore important to confirm that (*i*) the successive interruption did not affect the overall oxygen transfer and (*ii*) that C_v measurements were not affected significantly due to aeration and mixing interruption. To guarantee that the successive interruption did not affect the overall oxygen transfer, overall transfer rates with and without successive aeration and mixing interruptions were compared. No significant difference (p<0.05) were observed between both experimental conditions (data not shown). The second experiment to confirm

the validity of the vector sampling method was to measure C_v after aeration and mixing interruption. Vector samples were taken immediately after aeration and mixing interruption and up to 9 minutes later. Figure 1 shows an example of the results observed in the ST reactor, operated with 20% vector. No significant difference ($p<0.05$) was observed between C_v measured at several time after aeration and mixing interruption. Similar results were observed in all experimental conditions. It was concluded that mixing and aeration interruption did not affect significantly C_v determinations.

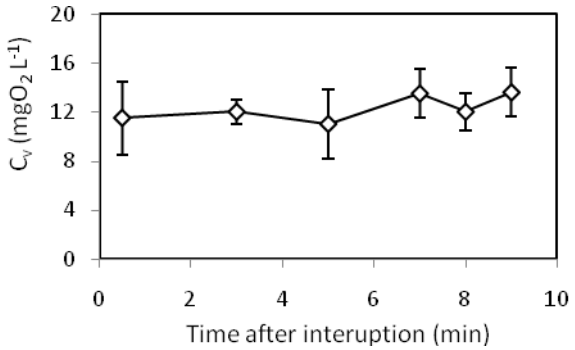

Figure 1. C_v trends after aeration and mixing interruption.

4.2 Mass transfer estimation

Figure 2 presents an example of experimental data fitting using Equations 6-8. These experimental data were obtained in the AL reactor operated with 10% vector. The model fitted correctly the experimental sulfite concentration, C_v and C_w. The goodness of fit was estimated by weighted sum of squares calculation after running the model against experimental data (intrinsic Model Maker tool). The coefficient of determination, r^2, was systematically over 0.97 (maximum, 0.999; minimum, 0.947; average, 0.978; Std. Deviation, 0.018).

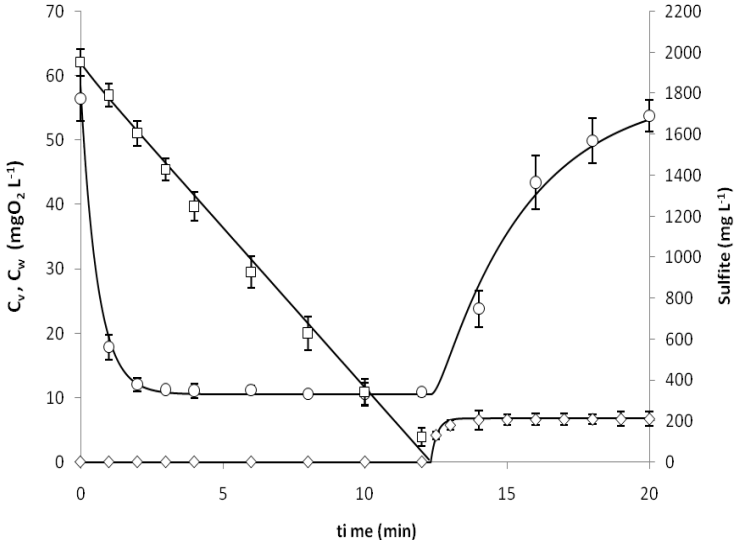

Figure 2. C_v (○), C_w (◊) and sulfite concentration (□) trends observed in the ALR operated with 10% vector versus model solution (solid lines).

Figure 2 shows that C_v rapidly reached a pseudo-steady state. During this pseudo-steady state, both OTR_{gv} and OTR_{vw} are equal (Equation 6). Thus, the indirect air/vector/water transfer rate can be represented by the global parameter OTR_{gvw}. Figure 3 presents the values of the direct transfer rate (OTR_{gw}) and the indirect transfer rate (OTR_{gvw}) observed in the AL (A) and the ST (B) reactors. It was observed that the vector had a positive effect on

the overall oxygen transfer rates in all tested vector percentages. In both reactor designs the optimum overall transfer rates was observed with 10% vector. Under these conditions, the overall transfer rates was 65% and 84% superior to the transfer rate observed with no vector, for the AL and the ST reactor, respectively. This result is in accordance to the Literature. According to the Clarke and Correia (2008) literature review, 10% is the tested percentage for which most of the authors have observed the optimum effect of vector on mass transfer. Figure 2 also shows the contribution of the direct air/water transfer to the overall transfer. With 10% vector, it was observed that the direct air/water transfer accounted for 94.7 and 93.0% of the overall transfer rate, in the AL and the ST reactors, respectively.

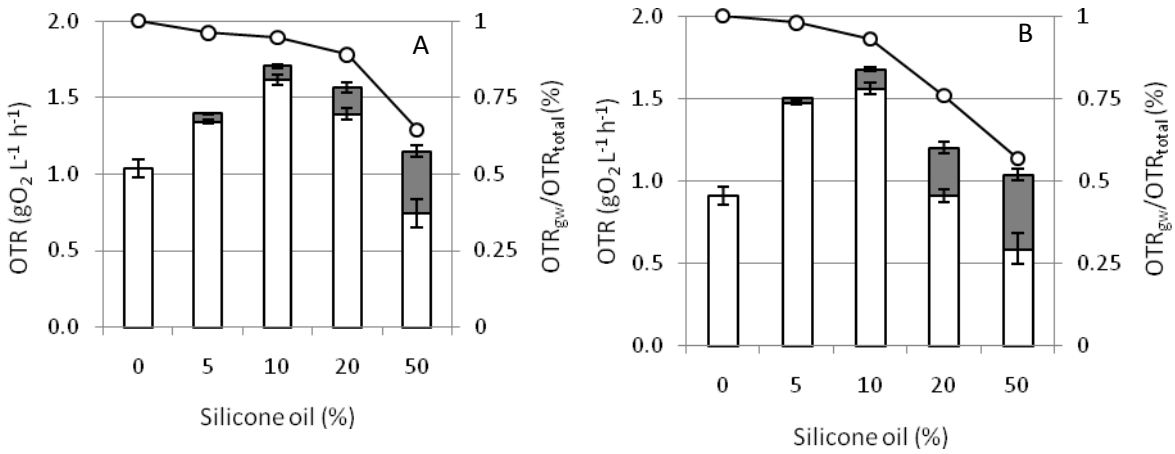

Figure 3. OTR_{gw} (□), OTR_{gvw} (■) and the OTR_{gw} contribution to the overall oxygen transfer (○), observed in the AL (A) and the ST (B) reactors.

According to these results, the presence of vector had a positive effect on the direct air/water transfer rates which could be explained by a better gas/water dispersion. Indeed, Galindo et al. (2000) reported that the presence of vector (castor oil) in a three-phase reactor decreased the bubble mean diameter and consequently increased the gas/water interfacial area. To evaluate the effect of vector on gas/liquid dispersion, the gas holdup (ε_G) was measured. Figure 4 shows the ε_G values observed at different vector percentages. It was observed that ε_G increased significantly in the AL reactor. Furthermore, in the ST reactor, practically no change in ε_G was observed. These results suggest that the vector had an indirect effect on air/water interface. Interfacial modification or complex hydrodynamic phenomena are probably involved.

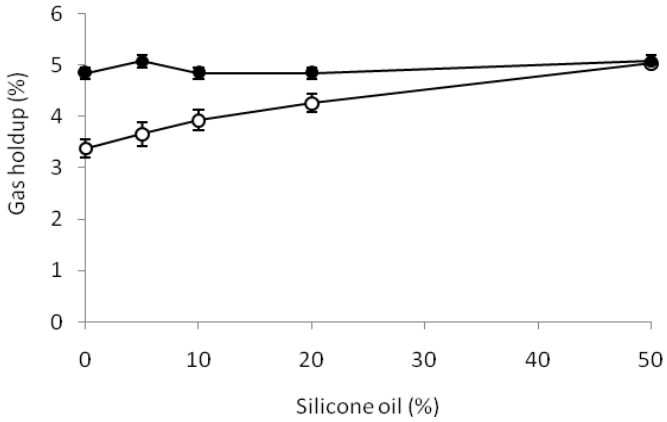

Figure 4. Gas holdup observed in the AL (○) and ST (●) reactors.

5. Conclusion

The mathematical model and the experimental method developed in this work allowed the characterization of direct and indirect oxygen transfer pathways in three-phase reactors. The results obtained confirm that the presence of vector has a positive effect on the overall oxygen mass transfer. In both AL and ST reactor designs, the optimum transfer rate was obtained with 10% vector. Under these conditions, the improvement of the overall oxygen transfer was 65 and 84% for the AL and the ST respectively, compared to reactors operated without vector. It was clearly observed that the presence of vector had mainly a positive impact on the direct air/water transfer. These results differ to what commonly considered by the literature. The positive effect of vector is not due to the creation of an additional air/vector/water pathway or to improved overall oxygen solubility. The effect of the vector on the direct air/water transfer has not been elucidated yet. Additional research is required to understand the effect of vector on the reactors hydrodynamics and gas/liquid interface. The model and the method developed allowed a better understanding of three-phase reactors. This method has been applied so far to two lab-scale reactor designs operated under single mixing and aeration conditions. Further researches are needed and particularly with other reactor design, more extended operational conditions and larger scale.

References

Ascon-Cabrera, M., Lebeault J.M. (1993). Selection of xenobiotic-degrading microorganisms in a biphasic aqueous-organic system. *Applied and Environmental Microbiology*, 59, 1717-1724.

Cesario, M.T., Beverloo, W.A., Tramper, J., Beeftink, H.H. (1997). Enhancement of gas-liquid mass transfer rate of apolar pollutants in the biological waste gas treatment by a dispersed organic solvent. *Enzyme and Microbial Technology*, 21, 578-588.

Clarke, K.G., Correia, L.D.C. (2008). Oxygen transfer in hydrocarbon–aqueous dispersions and its applicability to alkane bioprocesses: A review. *Biochemical Engineering Journal,* 39, 405-429.

Deziel, E., Comeau, Y., Villemur, R. (1999). Two-liquid-phase bioreactors for enhanced biodegradation of hydrophobic/toxic compounds. *Biodegradation,* 10, 219-233.

Dumont, E., Delmas, H. (2003). Mass transfer enhancement of gas absorption in oil-in-water systems: a review. Chemical Engineering and Processing, 42, 419-438.

Galindo, E., Pacek, A.W., Nienow, A.W. (2000). Study of drop and bubble sizes in a simulated mycelial fermentation broth of up to four phases. *Biotechnology and Bioengineering*, 69, 213-221.

Muñoz, R., Villaverde, S., Guieysse, B., Revah, S. (2007). Two partitioning bioreactors for treatment of volatile organic compounds. *Biotechnology Advances*, 25, 410-422.

Vandu, C.O., Koop, K., Krishna, R. (2004). Volumetric mass transfer coefficient in a slurry bubble column operating in the heterogeneous flow regime. *Chemical Engineering Science*, 59, 5417-5423.

Zhao, S., Kuttuva, S.G., Ju, L.K. (1999). Oxygen transfer characteristics of multiple-phase dispersions simulating water-in-oil xanthan fermentations. *Bioprocess Engineering*, 20, 313-323.

Proceedings of the 10th International Chemical and
Biological Engineering Conference - CHEMPOR 2008
Braga, Portugal, September 4-6, 2008
E.C. Ferreira and M. Mota (Eds.)

Fluidization Behaviour of Food Materials: Effect of Moisture and Shape

Wijitha Senadeera
School of Engineering Systems, Queensland University of Technology
2 George Street GPO Box 2434, Brisbane QLD 4001
Australia
w3.senadeera@qut.edu.au

Key words: fluidisation, large particulates, physical properties
Topic: Advancing the chemical and biological engineering fundamentals

Abstract
Changes in fluidization behaviour of three geometrical shaped food particulates, cylindrical (beans), parallelepiped (potato) and spherical (green peas) with change in moisture content during drying were investigated using a fluidized bed dryer. Fluidization behaviour was characterised for cylindrical shape particles with three length diameter-ratios; 1:1, 2:1 and 3:1, parallelepiped particles with three aspect ratios, 1:1, 2:1 and 3:1 and spherical particles. All drying experiments were conducted at 50^0C and 15 % RH using a heat pump dehumidifier system. Fluidization experiments were undertaken for the bed heights of 100, 80, 60 and 40 mm and at 10 moisture content levels.

An empirical relationship of the form $\mathbf{U_{mf} = A + B\, e^{-Cm}}$ was developed for change of minimum fluidization velocity with moisture content for cylindrical shapes and for spherical shapes a linear model of $\mathbf{U_{mf} = A + B\, m}$. Due to irregularities in shape minimum fluidisation velocity of parallelepiped particulates (potato) could not fitted to any empirical model. Also a generalized equation was used to predict minimum fluidization velocity.

Introduction

Fluidized bed drying is recognized as a gentle, uniform drying, down to very low *residual moisture* content, with a high degree of efficiency (Borgotte et al., 1981). The application of this technique is best suited to smaller and spherical particles. The disadvantages of this method include entrainment of friable solids by the gas and limited application to larger and poorly fluidized materials. Simultaneous moisture removal, shrinkage and structural changes during drying operations, affect physical properties of the agro-food materials and hence influence fluidization behaviour (Senadeera et al., 1998)

The Ergun equation (Ergun, 1952) is the widely accepted model to determine *minimum fluidization velocity* of a fluid to fluidize the particle (Kunii and Levenspiel, 1977).The Ergun equation (Equation 1) is used to calculate minimum fluidization velocity of peas (Rios et al., 1984) and diced potato and potato strips (Vazquez and Calvelo, 1980; 1982). The values obtained by the Ergun equation are mostly reliable for spherical and relatively small particles. Most agro-food particulates however comprise of various shapes and sizes, and consist of larger particles. Therefore, the minimum fluidization values obtained from Ergun equation do not conform to the experimental values (Mclain and McKay, 1980, 1981; McKay et al., 1987)

$$(1-\varepsilon_{mf})(\rho_s-\rho_f)\,g = 150\frac{(1-\varepsilon_{mf})^2}{\varepsilon_{mf}^{\,3}}\frac{\mu u_{mf}}{(\phi d_p)^2} + 1.75\frac{(1-\varepsilon_{mf})}{\varepsilon_{mf}^{\,3}}\frac{\rho_f u_{mf}^{\,2}}{\phi d_p} \qquad (1)$$

where ε_{mf} – bed porosity at minimum fluidization velocity, ρ_s – particle density (kg/m^3), ρ_f – fluid density (kg/m^3), μ - viscosity (N s/m^2), u_{mf} – minimum fluidization velocity (m/s), d_p – particle equivalent diameter (m), ϕ - sphericity

The Ergun equation consists of *viscous* and *kinetic energy* terms. In the case of larger particles at higher Reynolds numbers (Re > 1000) the fluidization behaviour is mainly governed by the kinetic energy term in the Ergun equation. Hence the Ergun equation can be simplified for (Kunii and Levenspiel, 1977) a wide variety of systems and a generalized equation can be applied to predict minimum fludisation velocity for larger particles when Reynolds number > 1000 using some modification.

$$u^2_{mf} = \frac{\phi\, d_p{}^2}{1.75} \frac{(\rho_s - \rho_f)}{\rho_f}\, g\, \varepsilon^3_{mf} \qquad (2)$$

where, ε_{mf} – bed porosity at minimum fluidization velocity, ρ_s – particle density (kg/m^3), ρ_f – fluid density (kg/m^3), u_{mf} – minimum fluidization velocity (m/s), d_p – particle equivalent diameter (m), ϕ - sphericity, g - acceleration due to gravity (m/s^2)

For wide variety of systems it was found that value $\frac{1}{\phi\, \varepsilon_{mf}{}^3} \cong 14$ (Wen and Yu, 1966) and a generalized equation can be applied to predict u_{mf} for larger particles when Re > 1000.

$$u^2_{mf} = \frac{d_p(\rho_s - \rho_f)}{24.5\, \rho_f}\, g \qquad (3)$$

where, ρ_s – particle density (kg/m^3), ρ_f – fluid density (kg/m^3), u_{mf} – minimum fluidization velocity (m/s), d_p – particle equivalent diameter (m), Re – Reynolds number

It is important to understand changes in fluidisation behaviour, so that the air-flow during drying can be controlled to achieve an optimum fluidization. The objective of this study is to study the continuous change in minimum fluidization velocity for a given shape of food material during drying and relate this to moisture content by a suitable model, and compare with the generalized model.

Material and Methods

Fresh green beans *Phaseolus vulgaris* of Labrador variety with consistence diameter 10 $\pm$ 1 mm was used for producing cylindrical particles. Samples were prepared at three length to diameter ratios of 1:1, 2:1 and 3:1, respectively. Potato *Solanum tuberosum* of the variety Sebago was used to make parallelepipeds in a Dicing Machine (Hobart, Australia), by incorporating a cutter which makes 6.5mm X 6.5mm square cross-section and lengths of 19.5, 13 and 6.5 mm to obtain aspect ratios of 3:1, 2:1 and 1:1, respectively. Fresh green peas *Pisum sativum* of the variety Bounty were shelled by hand and graded using a wire mesh. Those with average diameter 10$\pm$1 mm were selected.

Particle density was obtained measuring the volume of the weighed particles by the liquid displacement method using liquid paraffin (SG = 0.8787 at 30^o C) as the medium (Zogsas, 1994). The vacuum oven was used to measure the moisture content of the particles according to the AOAC method 934.06 (1995).

First, fluidisation characteristics of the un dried samples were measured in the fluidizing column (Figure 1) with the prepared samples. After that samples were dried on a fixed bed in a heat pump dehumidifier system (Intertherm P/L, Brisbane, Australia) and withdrawn at nine pre-determined time intervals during drying and used for measurement of minimum fluidisation velocity at four bed heights of 100, 80, 60, and 40 mm in same fluidized bed column.

Graphs of bed pressure drop versus velocity of fluidising air were constructed to determine the minimum fluidisation velocity at different moisture contents. This was also confirmed with the visual observation of the bed, such as expansion and movement.

Figure 1 Fluidisation column connected to the heat pump dryer

Analysis of experimental data and modelling procedure

The data were analysed for the analysis of variance (ANOVA) to evaluate differences, and, linear and non-linear regression to obtain suitable models. The coefficients were estimated using SAS (1985) least squares routine on a personal computer. Model validity was tested using measures of coefficient of determination (R^2) and mean absolute error percentage (MAE%).

Results and Discussion

Fluidisation behaviour of cylindrical food particulates - beans

Slugging and channelling were a common phenomena at higher moisture contents for every L:D ratio. It was difficult to achieve good fluidisation at initial moisture levels. This was more evident as the L:D ratio increased. As moisture was reduced, the quality of fluidisation improved, with reduced slugging and channelling.

Modelling the minimum fluidisation velocity with change in moisture content

The data were best fitted to the model $u_{mf} = A + B\, e^{-C\, m}$ and its parameters are shown in the Table1 for L:D = 1:1 and Table 2 for 2:1 for different bed heights.

Table 1 Parameters for Equation $u_{mf} = A + B\, e^{-Cm}$ for L:D = 1:1

Bed height (mm)	A	B	C	R^2	MAE%
100	2.3541	-0.8825	0.0017	0.91	3.89
80	2.2990	-0.8514	0.0015	0.91	4.07
60	2.0793	-0.7097	0.0019	0.86	4.62
40	2.1202	-0.7691	0.0016	0.86	4.52

Table 2 Parameters for Equation $u_{mf} = A + B\, e^{-Cm}$ for L:D = 2:1

Bed height(mm)	A	B	C	R^2	MAE%
100 mm	2.3632	-0.7446	0.0021	0.73	11.23
80 mm	2.3409	-0.7480	0.0025	0.72	11.54
60 mm	2.1965	-0.6884	0.0020	0.76	11.23
40 mm	2.1204	-0.6532	0.0032	0.79	9.58

This model adequately described the fluidisation behaviour of beans at L:D = 1:1. The model for L:D = 2:1 and 3:1 gave poor correlation coefficients and higher mean absolute error percentage values, could be due to irregular variation of the minimum fluidisation velocity.

Calculation of minimum fluidisation velocity based on dimensional changes during drying

The Generalized model (Equation 3) was used to calculate the predicted values of minimum fluidisation velocity. For all three L:D ratios (Table 3).

Table 3 Mean Absolute Error % for predicted versus observed minimum fluidisation values in the generalized model

L:D ratio/ Bed height	MAE%			
	100mm	80mm	60mm	40mm
1:1	9.54	3.81	1.61	3.18
2:1	7.66	1.83	6.13	2.74
3:1	5.32	1.62	0.36	4.03

Fluidisation behaviour of parallelepiped particles - potato

Good fluidisation was impossible at higher values of moisture at all aspect ratios. Decreasing the moisture resulted in a bed which was fluidised, but was accompanied by channelling and slugging. At lower moisture levels quality of fluidisation improved. An increase in minimum fluidisation velocity was attributed to the increase in particle density and interlocking of particles in the bed (Figure 2).

Modelling of minimum fluidisation velocity with change in moisture content

Fluidisation behaviour of potato particles could not be modelled due to the irregular trend of change of minimum fluidisation velocity with moisture content for all aspect ratios.

Minimum fluidisation velocity calculation based on the generalized equation

The Generalized model was used to calculate the predicted values of minimum fluidisation velocity. For all three aspect ratios, this generalized model value was compared with the experimental value. The mean absolute error percentage value is more than 10% for the aspect ratio 3:1, for the bed heights of 100, 80 and 60 mm (Table 4).

Table 4. Mean absolute error percentage (MAE%) of observed and predicted values of potato based on the generalized model

Aspect ratio	MAE%			
	100mm	80mm	60mm	40mm
1:1	8.83	4.09	2.75	2.03
2:1	7.55	6.26	1.03	1.02
3:1	13.46	12.98	10.80	3.68

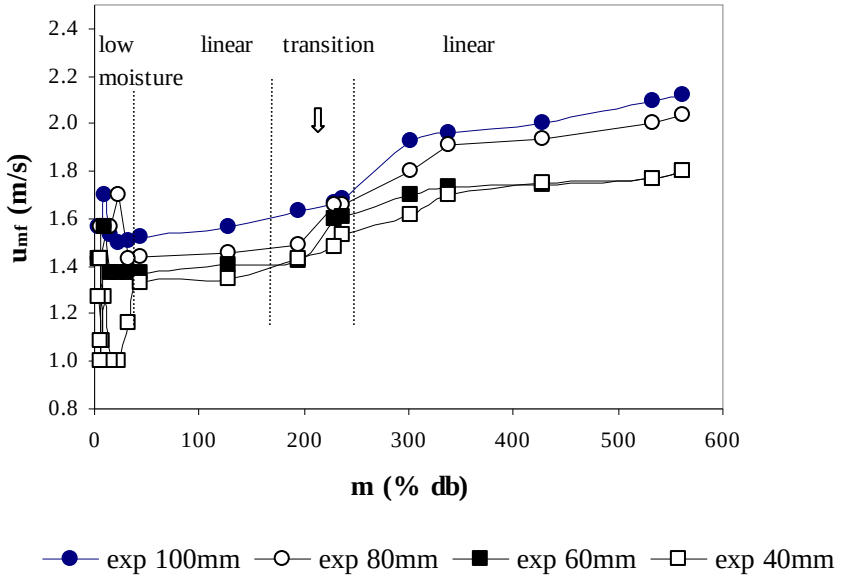

FIGURE 2 Fluidisation behaviour of potato L:D = 1:1

Fluidisation behaviour of spherical particles -green peas

In the case of peas, fluidisation was possible even at the higher moisture contents. Minimum fluidisation velocity decreased as drying proceeded. Slugging, and channeling phenomena was less than in the case of beans and potato due to good packing and spherical shape of the material in the bed.

Modelling of minimum fluidisation velocity with change in moisture content

The change in minimum fluidisation velocity was modelled linearly with the moisture content of the form $u_{mf} = A + B\ m$ for all bed heights. Model parameters are given in Table 5. MAE% lower than 10% indicating that the model equations can be used to predict the fluidisation behaviour reasonably.

Table 5. Coefficients for green pea models at different bed heights

Bed height (mm)	A	B	R^2	MAE%
100	1.5589	0.025	0.88	3.93
80	1.4786	0.0023	0.88	4.20
60	1.3853	0.0022	0.87	4.69
40	1.2685	0.0023	0.81	7.07

Minimum fluidisation velocity calculation based on the Generalized equation

The Generalized model (Equation 2) was used to calculate the predicted values of minimum fluidisation velocity of peas, and found that it can be used to predict minimum fluidisation velocity accurately for all bed heights and all moistures.

Table 6. Mean absolute error percentage (MAE%) for different bed heights of

peas for Generalised model

Bed height (mm)	MAE %
100	7.24
80	1.75
60	4.76
40	9.51

Conclusion

This work showed effect of moisture and shape on fluidisation behaviour of three real food materials. Fluidisation behaviour was modelled into empirical equations for cylindrical (beans) and spherical (peas) with moisture and could not be for parallelepiped (potato) particles due to its irregular nature. Generalised equation predicts the minimum fluidisation with a reasonable accuracy for all particle shapes. If sphericity changes during drying is measured an accurate predictions of minimum fluidisation velocity could be obtained using Ergun Equation.

References

AOAC, (1995). Official methods of analysis, 16th edition, Association of Official analytical Chemists, Washington DC.

Borgolte, G. and Simon, E. J. (1981). Fluid bed processes in the manufacture of snack products, CEB review for chocolate, *Confectionary and Bakery*. 6(2),7-8,10.

Ergun, S. (1952). Fluid flow through packed columns. *Chemical Engineering Progresses*. 48(2), 89 110.

Kunii, D. and Levenspiel, O. (1977). *Fluidization Engineering*. (Second Edition) Butterworth - Heinemann, Sydney, Australia.

McLain, H. D. and McKay, G. (1980). The fluidization of cuboid particles, *Trans.I ChemE*. 58(4), 107 - 115.

McLain, H. D. and McKay, G. (1981). The fluidization of potato chips. *Journal of Food Technology*. 16, 59 - 66.

McKay, G., Murphy, W. R. and Jodieri-Dabbaghzadeh, S. (1987). Fluidisation and hydraulic transport of carrot pieces. *Journal of Food Engineering*. 6, 377 - 399.

Rios, G. M., Marin, M. and Gibert, H. (1984). New developments of fluidization in the IQF food area. In Engineering and Food, Vol 2: Processing Applications. B. M. McKenna eds) pp. 669 - 667, Elsevier Applied Science Publishers. London.

Senadeera, W.,Bhandari, B. R., Young, G. and Wijesinghe, B. (1998). Change of physical propeties of green beans during drying and its influence on fluidisation. In '*Drying'98* Volume B-Proceedings of the 11th International Drying Symposium, Halkidiki, Greece, Eds. C. B. Akitidis, D. Marinos-Kouris and G. D. Saravakos, Ziti Editions, thesssaloniki, Greece: 1139-1146.

Shilton, N. C. and Niranjan, K.(1993). Fluidization and its Applications to food processing,*Food Structure*, 12,199- 215.

SAS. (1985). User's Guide, Statistics, 5th edition, SAS Institute Inc., Cary., NC.

Vazquez, A. and Calvelo, A. (1983). Gas-particle heat transfer coefficient for the fluidization of different shaped foods, *Journal of Food Science*. 48, 114 - 118.

Vazquez, A. and Calvelo, A. (1980). Gas particle heat transfer coefficient in fluidized pea beds, *Journal of Food Process Engineering*, 4, 53 - 70.

Wen, C. Y. and Hu Y. H. (1966). A generalized method for predicting the minimum fluidization velocity. *AIchE Journal*. 12, 610- 612.

Proceedings of the 10th International Chemical and
Biological Engineering Conference - CHEMPOR 2008
Braga, Portugal, September 4-6, 2008
E.C. Ferreira and M. Mota (Eds.)

Modeling of a novel photoreactor for multiphase applications

Joana T. Carneiro[1*], Rob Berger[2], Jacob A. Moulijn[1], Guido Mul[1]
[1] DelftChemTech, Catalysis Engineering, Delft University of Technology,
Julianalaan 136, Delft, 2628 BL, The Netherlands
[2] Anaproc, Julianalaan 136, Delft, 2628 BL, The Netherlands

Keywords: Photoreactor, Monolith, Optical Fiber, Model, Kinetics
Topic: Advancing the chemical and biological engineering fundamentals

Introduction

Photocatalytic synthetic processes using selective oxidation are currently not industrially applied, partially due to the lack of a proper design of multiphase photo-reactors. Currently photo-reactors for liquid phase oxidation are typically based on slurry systems i.e., the solid phase is dispersed within the liquid in the reactor. Although this design offers ease of construction and high catalyst loading, it has clearly drawbacks, such as the difficulty of separation of catalyst particles from the reaction mixture, and low light utilization efficiencies due to the scattering and shielding of light by the reaction medium and catalyst particles.
Various attempts have been made to amend the aforementioned light distribution problem with immobilized photocatalytic systems (de Lasa et al. 2005; Schiavello 1997). One approach was to employ optical fibers as light distributing guides and support for photocatalysts, the so-called Optical Fiber Reactors (OFR's). Light propagates through the fiber core, whilst certain amount of photons is refracted into the coated titania layer. By this means, the optical fibers enable the remote delivery of photon energy to the reactive sites of the photocatalyst. Ollis and Marinangeli were the first to conduct studies on an optical fiber reactor (OFR) (Ollis and Al-Ekabi 1993).The most recent example is the development of an optical fiber monolith reactor, as reported by Lin and Valsaraj (Ollis and Al-Ekabi 1993; Lin and Valsaraj 2005). They used the monolith for photocatalytic wastewater treatment with the channels of the monolith completely filled with flowing liquid. The monolith structure was used merely as the distributor of the optical fibers, while the benefits of monoliths, such as low pressure drop and excellent mass transfer characteristics for gas/liquid systems in certain hydrodynamic regimes, were not fully exploited to optimize the photocatalytic oxidation reaction (Kreutzer et al. 2005). Later in our group we developed the Internally Illuminated Monolith Reactor (IIMR), (Du et al. 2008). This reactor system is based on a modified design of the abovementioned combination of side light emitting fibers and ceramic monoliths. The 'side-light fibers' are evenly distributed inside a ceramic monolith structure, on the inner walls of which titania photocatalyst is coated. The reaction system is so constructed that the hydrodynamic regimes of Taylor flow and film flow can be realized. Because no catalyst is coated on the fibers, the emitted light can reach the catalyst-reactant interface without being strongly attenuated by the catalyst coating. Compared with conventional OFR's, this unique configuration provides extra design flexibilities, because the light propagation process from the source to the catalyst-reactant interface is decoupled from the physical properties of the catalyst. Furthermore, the fibers used in this reactor were tip-coated with a reflective material which introduced a new design flexibility since the length of the fiber where light intensity emitted from the sides of the fiber is sufficient to drive the reaction is no longer limited to 10 cm. To investigate the potential of the IIMR in organic synthesis, the selective photo-oxidation of cyclohexane was chosen as the model reaction, a reaction we previously investigated using conventional slurry reactors (Du et al. 2006). The photonic efficiency achieved with the IIMR reactor in the selective photo-oxidation of

* Corresponding author. Tel + 31-15-2784396. E-mail:j.t.carneiro@tudelft.nl

cyclohexane (0.062) was less than obtained with a top illumination reactor, slurry type (0,151). It was concluded that the value for the IIMR could be improved by reducing the TiO_2 layer thickness, which was acting like a “sponge” for the strongly adsorbed product, limiting the amount detected in the recirculated liquid.

With the objective to validate our photoreactor design, a model was developed to compare the Top Illumination Reactor and the IIMR. The difference between these two reactors is mostly in the way the light is guided to the catalyst surface. For the IIMR, the following model has been developed to determine the light intensity that reaches the catalyst particles deposited on the walls of each channel.

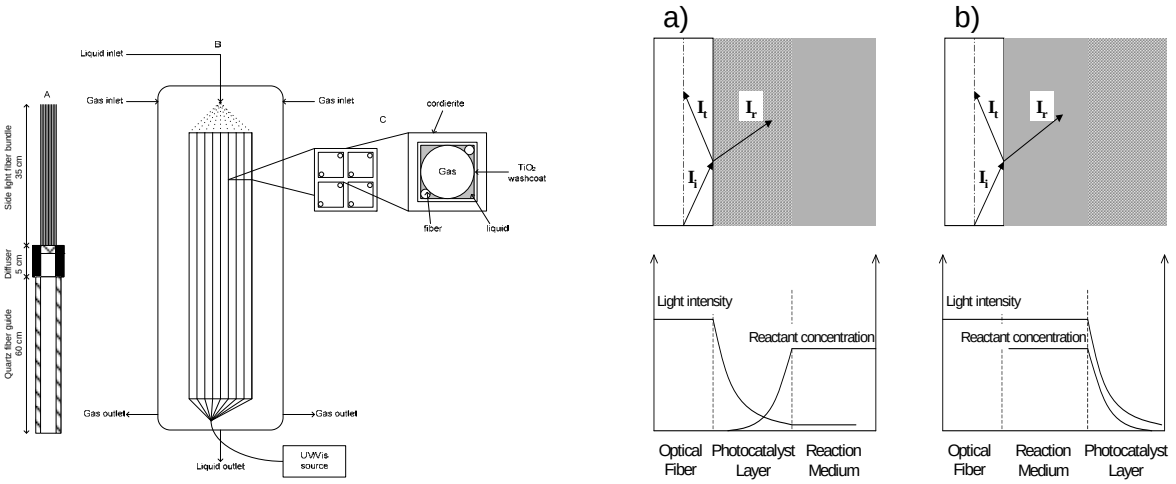

Fig. 1. Left side figure: scheme of the IIMR and optical fiber bundle used. Right side figure: comparison of the catalytic activation mechanism a) OFR’s, b) IIMR.

Light intensity in a square monolith channel illuminated by two light fibers

Light intensity, light position and light profiles play an important role in modeling the performance of photocatalytic reactors. An optimized photocatalytic process requires light of sufficient intensity to be present at all locations where there is catalyst. The design equations for the reaction rate of the slurry type top illumination reactor (TIR) and the IIMR reactor are shown in Eq 1 and 2, respectively.

• TIR $$r_1 = k_1 \left(I_0^{''} \right)^m \left(C_A \right)^n C_{sites} \quad (1)$$

• IIMR $$r_1 = gt\, k_1 \left(I_0^{''} \right)^m \left(C_A \right)^n C_{sites} \quad (2)$$

The rate depends on the initial intensity of the light entering the reactor ($I_0^{''}$), the proportionality power of the light intensity (*m*), the reaction order (*n*), and the concentrations of the reactant (C_A) and the concentration of the catalytically active sites in the coating (C_{sites}). For the IIMR an additional factor is added, the geometric term (*gt*), which will be explained later.

The initial light intensity ($I_0^{''}$) is, in the TIR, the light entering the reactor through a pyrex window and in the IIMR corresponds to the light irradiated from the side light fibers. The value of $I_0^{''}$ can be determined, using a calibrated spectrophotometer S-2000 (Avantes) equipped with a cosine collector. The output generated by this equipment consists of the spectral irradiance, I_λ, in $J.s^{-1}.m^{-1}.nm^{-1}$, which can be converted into an $I_0^{''}$ in $Einstein.m^{-2}$ (Du et al. 2008). For the IIMR this intensity depends on the distance of the catalytic site to the light fiber (L_i), the incident angle (α) and the depth in the coating. Fig. 2 shows our

approach to estimate the light intensity at 21 wall sections of the monolithic channels. In each channel two fibers are located in diagonally opposite corners. It is assumed that the light is emitted from two point sources on each fiber. It is also assumed that the liquid in the corners where the fibers are located is stagnant, indicated by section p in Fig. 2, causing the light emitted from the two point sources located against the wall to be lost. These two point sources are therefore omitted in Fig. 2. and it also shows the lengths of the wall segments considered.

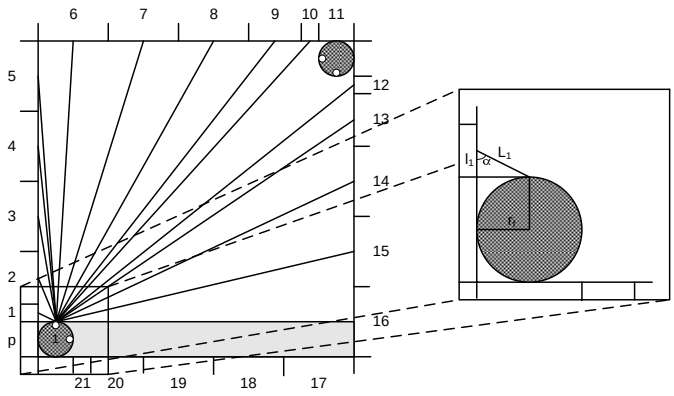

Segment	l_s (m)
1/10/12	$2.5.10^{-4}$
2/9/13	6.10^{-4}
3/8/14	1.10^{-3}
4/7/15	1.10^{-3}
5/6/16	1.10^{-3}
P	$4.5.10^{-4}$

Fig. 2. Light directions in a monolith channel illuminated by two side-light fibers and length of the segments considered in the monolith walls.

The light intensity for each point source, with radius r_p is obtained by Eq. (3) where I is the incident light flux at z = 0 and r_f the fiber radius. For each point source it is considered that 50% total of light is lost in the wall of the corner behind the fibers. As shown in the Fig. 1, segment p is not illuminated by light source 1. The same procedure is followed for the other point sources.

$$I_p^{"} = \frac{1}{4} I_0^{"} \frac{r_f}{r_p} \tag{3}$$

Fig. 2 shows that each light beam forms a right triangle. Considering point source 1, the incident light flux at the surface of each segment (in this case 1 to 15), $I_s^{"}$, can be estimated with Eq. 4. Here L_i is the distance between the light point source and the surface in segment 1, as calculated by using Eq. 5. In this equation l_i is the distance as indicated in Fig. 2.

$$I_s^{"} = \frac{I_0^{"} r_f}{4} \frac{\sin(\alpha)}{L_i} \tag{4}$$

$$L_i = \sqrt{\left(r_f\right)^2 + \left(\frac{l_i}{2}\right)^2} \tag{5}$$

Since the total amount of light irradiated must be equal to the total amount of light received at all the segments, Eq. 6, a correction factor is introduced given by Eq. 7. The recalculation of the local light at the catalyst external surface becomes Eq. 8.

$$\frac{I_0^{"} 2\pi r_f}{4} = c_f \frac{I_0^{"} r_f}{4} \sum_{i=1}^{15} \left(l_i \frac{\sin(\alpha)}{L_i} \right) \tag{6}$$

$$c_f = \frac{2\pi}{\sum_{i=1}^{15} \left(l_i \frac{\sin(\alpha)}{L_i} \right)} \tag{7}$$

$$I_s^{"} = c_f \frac{I_0^{"} r_f}{4} \frac{\sin(\alpha)}{L_i} \tag{8}$$

From the surface to a certain depth (x) into the catalyst layer in a perpendicular direction, the intensity will be attenuated according to a Lambert-Beer law type of equation, Eq. 9.

$$I_x^{"} = I_s^{"} e^{\frac{-bx}{\sin(\alpha)}} \tag{9}$$

The effective surface reaction rate for point source 1, i.e. the rate per unit area of external coating surface, is obtained by integration of the reaction rate over the depth of the coating using the linear absorption coefficient *b* and assuming the chemical reaction rate to be proportional with the light intensity to the power *m* yielding Eq. 10. The rate depends on the intensity of the light reaching the wall section ($I_s^{"}$), the incident angle (α), the linear absorption coefficient (b), the proportionality power of the light intensity (m), the reaction order (n), and the concentrations of the reactant (C_A) and the concentration of the active sites in the coating (C_{sites}). Since there is no significant diffusion limitation inside the porous walls, the total activity follows from integration over the depth (i.e. C_A and C_{sites} are independent of x), that yields Eq. 11 for the case where the layer thickness is much higher than the penetration depth.

$$r_i = \left(I_s^{"} \right)^m e^{\frac{-mbx}{\sin(\alpha)}} k_i C_A^n C_{sites} \tag{10}$$

$$\int_0^x \left(\left(I_s^{"} \right)^m e^{\frac{-mbx}{\sin(\alpha)}} \right) dx = \left(I_s^{"} \right)^m \left(\frac{\sin(\alpha)}{mb} \left(1 - e^{\frac{-mbx}{\sin(\alpha)}} \right) \right) \approx \left(I_s^{"} \right)^m \left(\frac{\sin(\alpha)}{mb} \right) \tag{11}$$

Thus, the reaction rate multiplied with the depth for the 4 light sources considered is given by Eq. 12 in the case of 1 segment.

$$xr_i = \sum_{i=1}^{4} \left\{ \left(c_f \frac{r_f}{4} \frac{\sin(\alpha)}{L_i} \right)^m \frac{\sin(\alpha)}{mb} \right\} \left(I_0^{"} \right) k_i C_A^n C_{sites} \tag{12}$$

To finalize, this geometric term takes into account the 5 segments at the 3 walls that each light source can illuminate.

Results and discussion

The model developed has been validated. Results showed that, intrinsically, and only comparing the TIR and the IIMR for a range of light intensities, the IIMR results in a higher conversion for a first order reaction, Fig.3. For each photoreaction considered this model has to be adapted since a reaction may be limited by the *photo-physical properties of the catalyst* (interaction of the semiconducting material with light) or by the *surface chemistry* (formation of radicals/active sites on the surface). Modeling results will be presented for a specific photoreaction.

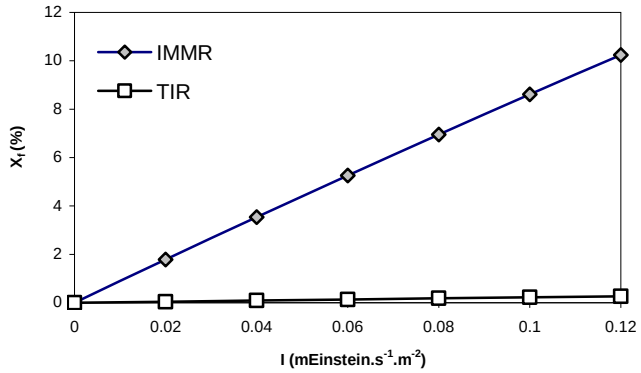

Fig. 3. Model results for the conversion vs light intensity for the two photoreactors in study.

With the reaction studied by our group, the cyclohexane selective photo-oxidation, several drawbacks make a comparison between the experimental values and the model values difficult. The reaction mechanism is not fully developed yet, and slow product desorption doesn't allow full quantification of the product formed (Du et al. 2008). Furthermore, catalyst deactivation is extensive. We observed that the values delivered by the model were higher for both reactors, when compared with the experimental ones, which was expected. Furthermore this model offers a very flexible design since it is possible to change the dimensions of the reactors and lamps in order to adapt to each situation. The dimensions of the reactors can be modified for the slurry system and the IIMR maintaining the principle of each photoreactor.

Future work will consist of evaluation of the model with a simple photocatalytic reaction (in water, limiting catalyst deactivation), and study of the effect of hydrodynamics on reactor preformance.

Conclusions

A model for a novel multiphase photoreactor was developed. The light distribution inside each monolith channel was described. The model predicts that for the same initial light intensity and a first order reaction, the IMMR results in a higher conversion as compared to the TIR. Furthermore the reaction performed for validating the model (cyclohexane oxidation) has several intrinsic drawbacks, leading to significant differences between experimental and theoretical values for the conversion. We propose to perform a simple photocatalytic reaction to further validate the model, such as the photocatalytic decomposition of formic acid.

References

de Lasa,H., Serrano,M., and Salaices,M. 2005. *Photocatalytic Reaction Engineering*, Springer, New York.

Du,P., Cameiro,J.T., Moulijn,J.A., and Mul,G. 2008. A novel photocatalytic monolith reactor for multiphase heterogeneous photocatalysis, *Applied Catalysis A-General* 334: 119-128.

Du,P., Moulijn,J.A., and Mul,G. 2006. Selective photo(catalytic)-oxidation of cyclohexane: Effect of wavelength and TiO2 structure on product yields, *Journal of Catalysis* 238: 342-352.

Kreutzer,M.T., Kapteijn,F., Moulijn,J.A., and Heiszwolf,J.J. 2005. Multiphase monolith reactors: Chemical reaction engineering of segmented flow in microchannels, *Chemical Engineering Science* 60: 5895-5916.

Lin,H.F. and Valsaraj,K.T. 2005. Development of an optical fiber monolith reactor for photocatalytic wastewater Treatment, *Journal of Applied Electrochemistry* 35: 699-708.

Ollis,D.F. and Al-Ekabi,H.E. 1993. *Photocatalytic purification and treatment of water and air*, Elsevier,Amsterdam.

Schiavello,M. 1997. *Heterogeneous Photocatalysis*, Wiley, Chichester.

Proceedings of the 10th International Chemical and
Biological Engineering Conference - CHEMPOR 2008
Braga, Portugal, September 4-6, 2008
E.C. Ferreira and M. Mota (Eds.)

Prediction of mean bubble size in three scales of internal loop airlift reactor

Marcel O. Cerri[1], Juliana C. Baldacin[1], Antonio J. G. Cruz[1], Carlos O. Hokka[1], Alberto C. Badino[1]
[1]DEQ-UFSCar - Department of Chemical Engineering, Federal University of São Carlos, P.O. Box 676, Post Code 13565-905, São Carlos, SP, Brazil

Keywords: airlift reactor, hold-up, bubble size, Higbie´s penetration theory, volumetric oxygen transfer coefficient.
Topic: Advancing the chemical engineering fundamentals.

Abstract

In the present work a new methodology to estimate a mean bubble size (d_B) in internal-loop airlift reactor (ALR) is proposed. The semi-theoretical method is based on Higbie´s penetration theory and uses for the estimative of d_B the experimental data of gas hold-up (ε) and volumetric mass transfer coefficient (k_La) obtained in three scales of internal-loop ALR of 2, 5 and 10 dm^3. Mean bubble size (d_B) and convective oxygen transfer coefficient (k_L) showed it is not dependent on the superficial gas velocity (U_{GR}) for all scales in the experimental range studied. The results indicate the k_La is a function only of the gas-liquid interfacial area of the bubbles (a) and therefore of the gas hold-up (ε).

1. Introduction

Internal-loop airlift reactors (ALR) are a special class of pneumatic reactors. This type of reactor is attractive for chemical and biological reactions due to their inexpensive and simple construction without moving mechanisms and low energy costs, when compared to stirred tank reactors (Blažej *et al*., 2004a).

One of the most significant parameters in the design of such airlift reactors is the volumetric mass transfer coefficient (k_La) commonly used to evaluate the capacity of oxygen transfer in bioreactors. This quantity depends on the system geometry and fluid properties which are related to several other parameters (Ruen-gnam *et al*., 2008). Most investigations performed on aerobic systems are limited to the determination of the k_La. Unfortunately, this parameter is global and insufficient to provide an understanding of the mass transfer mechanisms. Normally, the influence of each parameter, convective oxygen transfer coefficient (k_L) and interfacial area of the bubbles (a), in the oxygen mass transfer rate are not clear. Therefore, the separation of the parameters k_L and should be considered for a better comprehension of gas-liquid mass transfer mechanisms (Bouaifi, *et al* 2000). The interfacial area (a) can be determined from the fractional gas hold-up and the mean bubble diameter (d_B), which is a very important parameter in gas liquid reactor design and a good criterion for evaluating the efficiency of gas liquid contactor. Small bubbles and a uniform distribution over the cross section of the equipment are desired to maximize the interfacial area, hence improving transport phenomena.

Many authors have studied the influence of the bubble size in the mass transfer phenomena; most of the bubble size measurements were taken using photographic techniques. Tung *et al.* (1998) compared the bubble size and hydrodynamic behavior in airlift and bubble column reactors. They noticed that the circulation velocity did not have a significant effect on bubble size, however it had a large influence on the bubble frequency. Wongsuchoto *et al.* (2003) investigated the effect of various designs and operating parameters on bubble size distribution in annulus sparged airlift contactors. It was found that the interfacial area, rather than the mass transfer coefficient, played a more significant role in controlling the overall oxygen transfer rate in the system. At high superficial air velocity (U_G), the bubble size was smaller and uniform. In the range of U_G from 0 to 0.08 $m.s^{-1}$, the average bubble diameter was found to be between 3 and 8 mm. Ruen-gnam *et al.* (2008) investigated the effect of

salinity on the performance of an ALR. The bubble mean diameter appeared to be smaller in saline water than in fresh water. For fresh water, the average bubble diameter was found to be between 5 and 8 mm in the range of U_{GR} from 0 to 0.06 $m.s^{-1}$.

Mass transfer by convection involves the transport of material between a boundary surface and a moving fluid or between two relatively immiscible moving fluids. The determination of the mass transfer coefficient is not a simple undertaking. It is not related to the physical properties of the fluid, to the dynamic characteristics of the flowing fluid and the geometry of the system. It is the reason for expecting an analytical treatment to estimate k_L. At constant temperature, any improvement in the k_L, and therefore k_La, may be achieved only by changes in the liquid film thickness (two-film theory), the exposure time (penetration theory) or surface renewal rate (surface renewal theory), depending on the mass transfer hypothesis that is chosen (Cerri *et al*., 2008). The oxygen transfer rate depends not only on the gas hold-up and bubble size but also on the value of k_L. The liquid side mass transfer coefficient k_L depends on the diffusivity coefficient and turbulence created in the liquid phase (Bouaifi, *et al* 2000). According to the results of Wangsuchoto *et al.* (2003), the k_L to pure water in an ALR is constant in the range of U_{GR} from 0 to 0.08 $m.s^{-1}$. Ruen-ngam *et al*. (2008) found that this system with water provided a higher level of k_L than saline solutions.

In the literature review there are many works where the bubble size measurement in pneumatic reactors is conducted by experimental methods, but none of them present a correlation to estimate the bubble size. Therefore, the aim of this work proposes a methodology to predict the convective oxygen transfer coefficient (k_L) and the mean bubble diameter (d_B) from experimental values of volumetric oxygen transfer coefficient (k_La) and gas hold-up (ε) in three scales of internal-loop ALR (2, 5 and 10 dm^3) with similar geometric configurations using water as the liquid phase.

2. Materials and Methods

Fluids: Distilled water at 28 ºC was used as Newtonian fluid.

Equipments: concentric-tube airlift reactors (ALR) with 2, 5 and 10 dm^3 total working volumes were used in this study. The external tube was made of glass, but the bottom and top plates, the draft tube, the gas sparger, and the condenser were made of stainless steel. The temperature of the reactor was controlled by the circulation of water through the hollow draft tube. Geometrical characteristics, relationships between distances are shown in Table 1 for the three different scales of airlift bioreactor. The holes of the cross-piece type sparger are 0.5 mm diameter and are spaced at 5 mm (Badino *et al.*, 2006).

Volumetric oxygen transfer coefficient (k_La): the volumetric oxygen transfer coefficient ((k_La) was determined by the dynamic pressure-step method (Blažej et al. 2004b). In this experimental method, the pressure in the vessel is changed abruptly by approximately 15 kPa, and an increase in the dissolved oxygen concentration (C_e) in the bubble dispersion occurs regardless of the gas flow pattern. Equation 1 was fitted to the experimental data (C_e as a function of time) and k_La values were estimated through the procedure that uses the least squares non-linear regression.

$$C_e = C_{e0} \cdot e^{-k_e \cdot (t-t_0)} + C_{es} \cdot (1 - e^{-k_e \cdot (t-t_0)}) + \frac{k_e \cdot (C_{es} - C_{e0})}{k_e - k_L a} \cdot (e^{-k_e \cdot (t-t_0)} - e^{-k_L a \cdot (t-t_0)}) \qquad (1)$$

In Equation 1, C_{e0} is the signal of the electrode in the initial condition when $t = t_0$; C_{es} is the signal of the electrode or the dissolved oxygen concentration in the liquid phase in the saturation with air, and k_e is the time constant of the oxygen probe calculated from the inverse of the response time (τ_e). The response to a unit step function, in triplicate, allowed the calculation of k_e = 0.125 s^{-1} assuming the "first order response". The dissolved oxygen concentration was measured by means of a sterilizable amperometric electrode (Mettler-Toledo, model InPro 6800) bearing a Teflon membrane (Mettler-Toledo, model InPro T96). Values of k_La were obtained in duplicate for Newtonian and non-Newtonian systems with the superficial gas velocity (U_{GR}) for the three scales of airlift bioreactor.

Gas hold-up (ε): The gas holdup was determined by measuring the increase in height of the dispersion upon aeration as follows (Chisti, 1989):

$$\varepsilon = \frac{h_D - h_L}{h_D} \tag{2}$$

where h_D is the height of the gas-liquid dispersion and h_L is the height of gas free liquid.

Table 1. Geometric characteristics of the three scales of concentric-tube internal-loop ALR

Liquid volume (dm^3)	2.0	5.0	10.0
H1 (m)	0.032	0.045	0.055
H2 (m)	0.033	0.055	0.045
H3 (m)	0.262	0.350	0.450
H4 (m)	0.327	0.450	0.550
H5 (m)	0.450	0.600	0.700
De2 (m)	0.100	0.135	0.170
H4/De1	3.63	3.60	3.44
A_D/A_R	1.68	1.78	1.84
D_{i2}/De1	0.61	0.60	0.59

Theory: the prediction of the convective oxygen transfer coefficient (k_L) in the ALR was made according to a theoretical mass transfer model based on Higbie´s penetration theory.

$$k_L = \frac{2}{\sqrt{\pi}} \cdot \sqrt{\frac{D_L}{\theta}} \tag{3}$$

where D_L is the oxygen diffusivity and θ is the surface renewal time, which is defined in terms of the mean diameter of the bubbles (d_B) and the bubble liquid slip velocity (u_S) by Shamlou *et al.* (1995) as follows:

$$\theta = \frac{d_B}{u_S} \tag{4}$$

The bubble liquid slip velocity (u_S) is proposed by Ruen-ngam *et al.* (2008) as follows:

$$u_S = \frac{u_\infty}{(1-\varepsilon)} \tag{5}$$

Talaia (2008) proposed a new model to determine the terminal velocity of bubble (u_∞):

$$u_\infty = 0.694 \cdot \left(\frac{g \cdot d_B \cdot \Delta\rho}{\rho_L} \right)^{1/2} \tag{6}$$

The relationship between k_L and d_B (ψ) was proposed by Chisti (1989), where ψ can be obtained experimentally using k_La and gas hold-up (ε).

$$\frac{k_L}{d_B} = \psi = \frac{k_L a \cdot (1-\varepsilon)}{6 \cdot \varepsilon} \tag{7}$$

Substituting equation 6, 5 and 4 into equation 3 and rearranging it, results in semi-empiric (or semi-theoretical) correlation to calculate the d_B from experimental values of k_La and ε. Values of k_L can be calculated from equation 7.

$$d_B = \left(\frac{4 \cdot D_L \cdot 0.694}{\pi \cdot (1-\varepsilon) \cdot \psi^2} \right)^{\frac{2}{5}} \cdot \left(\frac{g \cdot \Delta\rho}{\rho_L} \right)^{1/5} \tag{8}$$

3. Results and Discussion

From experimental data of k_La and gas hold-up (ε), the values of d_B for the three scales of ALR were estimated by equation 8 and are presented in Figure 1 as function of the superficial gas velocity in the riser region (U_{GR}). The results of d_B obtained by the proposed

method are in excellent agreement with the experimental values found in recent literatures (Wongsuchoto *et al.*, 2003 and Ruen-ngam *et al.*, 2008). It can be observed in Figure 1 that d_B changed with U_{GR} in a close range between 3 and 5.5 mm for three scales of the bioreactor studied. These results are in agreement with those of Wangsushoto *et al*. (2003) that observed a d_B range from 3 to 8 mm. Tung *et al.* (1998) also observed that U_{GR} has a weak influence on the mean bubble diameter (d_B), but a strong influence on bubble frequency (number).

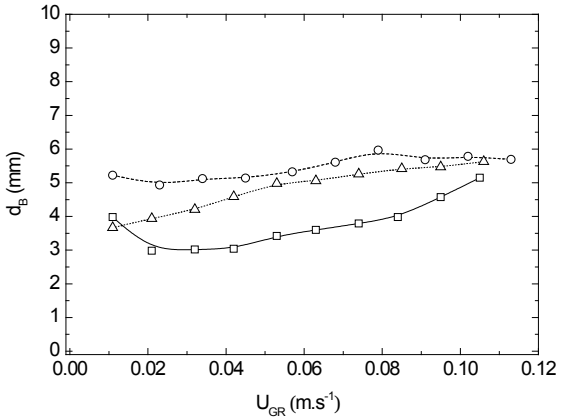

Figure 1: Mean bubble diameter (d_B) as a function of U_{GR}. (□) 2 dm^3, (○) 5 dm^3, (Δ) 10 dm^3.

The results of gas hold-up (ε) and interfacial area (a) as a function of the superficial gas velocity (U_{GR}) are illustrated in Figure 2. It can be observed in Figure 2a that ε increases with the increase of U_{GR} in the experimental range investigated and the ε values are very close to the three scales of ALR. A similar behavior is observed in Figure 2b for interfacial area (a). As the d_B is practically constant with U_{GR}, "a" is a direct function of the gas hold-up (ε) according to equation 9. Therefore, the gas hold-up is the main factor which influences the interfacial area of the bubbles.

$$a = \frac{6 \cdot \varepsilon}{d_B \cdot (1 - \varepsilon)} \tag{9}$$

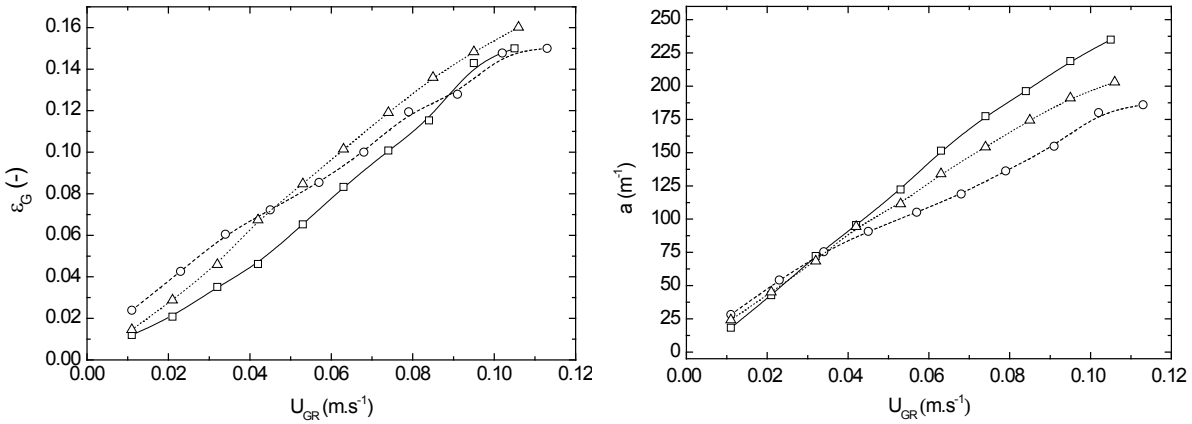

(a) (b)

Figure 2. Effects of superficial gas velocity (U_{GR}) in (a) gas hold-up (ε) and (b) interfacial area (a) for three scales of ALR: (□) 2 dm^3, (○) 5 dm^3, (Δ) 10 dm^3.

The volumetric oxygen mass transfer (k_La) is a product of the liquid-film convective oxygen transfer coefficient (k_L) and the interfacial area (a). Figure 3 shows the dependence of k_L, calculated by equation 3, with the superficial gas velocity (U_{GR}).

It can be observed in Figure 3 that for all ranges of U_{GR} (0.01 - 0.11 $m.s^{-1}$) the value of k_L remained nearly constant for the three scales of ALR studied.

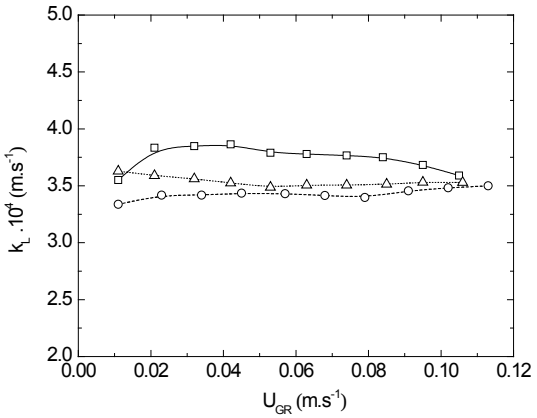

Figure 3. Convective oxygen transfer coefficient (k_L) as a function of U_{GR} for three scales of ALR: (□) 2 dm^3, (○) 5 dm^3, (Δ) 10 dm^3.

This demonstrates that the increase in the values of k_La with an increase of U_{GR} is due to the gas-liquid interfacial area (a) and not to the convective oxygen transfer coefficient (k_L). As demonstrated before, "a" is a direct function of the gas hold-up (ε). It shows that k_La depends solely on the gas hold-up (ε). Therefore, this observation should be considered in the design of ALRs. In a recent work, Ruen-ngam *et al*. (2008) investigated the effect of salinity on k_L in a 17 dm^3 internal-loop ALR using water and salt solutions as liquid phase. The results revealed that k_L only became significantly different at high values of U_{GR}. For low values of U_{GR}, the convective oxygen transfer coefficient remains practically constant. In Figure 4, k_La is plotted as a function of $6\cdot\varepsilon/(1-\varepsilon)$. Equation 7 was fitted to the experimental data for three scales of ALR. The slopes of the curves ($k_L/d_B=\Psi$) were obtained as follows:

2 dm^3: $\Psi=0.065\ s^{-1}$ ($R^2=0.98$)

5 dm^3: $\Psi=0.060\ s^{-1}$ ($R^2=0.993$)

10 dm^3: $\Psi=0.059\ s^{-1}$ ($R^2=0.998$)

The excellent fitting can be noted between the calculated and experimental data. The values of $k_L/d_B=\Psi$ were very close among each other and when compared to those of the literature (Mirón *et al.*, 2000). The fact that the relation $k_L/d_B=\Psi$ is constant demonstrates the non-dependence of k_L and d_B with operational conditions as previously discussed.

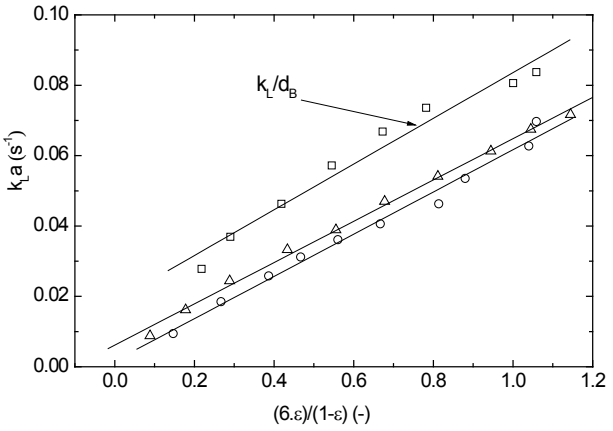

Figure 4. Volumetric oxygen transfer coefficient (k_La) as a function of $6\cdot\varepsilon/(1-\varepsilon)$ for three scales of ALR: (□) 2 dm^3, (○) 5 dm^3, (Δ) 10 dm^3.

4. Conclusions

This work proposed a simple methodology for evaluating the mean bubble size in internal-loop ALR using an air-water system. The results showed that the variable responsible for the increase of the bubbles' interfacial area is the gas hold-up, because the mean bubble-size value was independent of the superficial gas velocity (U_{GR}). The convective oxygen transfer coefficient (k_L) was dependent on the physical properties of fluid and on the mean bubble size, remaining practically constant for any values of U_{GR}. The fact that the relation $k_L/d_B=\Psi$ is constant demonstrated the non-dependence of k_L and d_B with operational conditions. It is an important conclusion for the design of bioreactors, indicating that the gas hold-up is the principal variable to increase the volumetric oxygen transfer coefficient (k_La), excluding the operational conditions and should be taken into account for the scale-up of this type of bioreactor.

Acknowledgements

The authors thank the financial support provided by the Brazilian foundations FAPESP (Grant Procs. 03/11722-5 and 05/55079-4) and CAPES.

5.References

Badino, A. C.; Hokka, C. O.; Cerri M. O. (2004), Pneumatic reactor with an inner and a transparent outer cylinder gas injection for circulation and temperature control of the enclosed reaction mixture, Braz. Pat. (PI 0404703-6).

Blažej, M., Juraščík M., J. A. J. M. (2004b), Measurement of mass transfer coefficient in an airlift reactor with internal loop using coalescent and non-coalescent liquid media, *Journal of Chemical Technology and Biotechnology* 79, 1405 - 1411.

Blažej, M.; Annus, J. & Markos, J. (2004a), Comparison of gassing-out and pressure-step dynamic methods for k(L)a measurement in an airlift reactor with internal loop, *Chemical Engineering Research & Design* 82(A10), 1375--1382.

Boauifi, M.; Hebrard, G.; Bastoul, D.; Roustan, M.; (2000), A comparative study of gas hold-up, bubble size, interfacial area and mass tranfer coefficients in stirred gas-liquid reactor and bubble columns.Chemical Engineering and Processing, V. 40, p. 97-111.

Cerri, M. O.; Futiwaki, L.; Jesus, C. D. F.; Cruz, A. J. F. & Badino, A. C. (2008), Average shear rate for non-Newtonian fluids in a concentric-tube airlift bioreactor, *Biochemical Engineering Journal* 39(1), 51-57.

Chisti, M.Y. (1989). Air-Lift Bioreactors, Elsevier, New York.

Mirón, A. S.; Camacho, F. G.; Gomez, A. C.; Grima, E. M. & Chisti, Y. (2000), Bubble-column and airlift photobioreactors for algal culture, *Aiche Journal* 46(9), 1872-1887.

Ruen-gnam, D. *et al.* (2008), Influence of salinity on bubble size distribuition and gas-liquid mass transfer in airlift contactors, Chemical Engineering Journal, doi:10.1016/j.cej.2007.12.024.

Shamlou, P.A., Pollard, D.J., Ison, A.P. (1995) Volumetric mass transfer coefficient in concentric-tube airlift bioreactors, Chemical Engineering Science, 50, 1579-1590.

Tung, H.L.; Tu, C.C.; Wu, W.T. (1998), Bubble characteristics and mass transfer in an airlift reactor with multiple net draft tubes. Bioprocess Engineering, V. 18, p. 323-328.

Wongsuchoto, P., Charinpaitkul, T., Pavasant, P., (2003) Bubble size distribuition and gas-liquid mass transfer in airlift contactors, Chemical Engineering Journal, 92, 81-90.

Proceedings of the 10th International Chemical and
Biological Engineering Conference - CHEMPOR 2008
Braga, Portugal, September 4-6, 2008
E.C. Ferreira and M. Mota (Eds.)

Solubility of Multifunctional Associating Molecules: Measurements and Thermodynamic Modeling

A. J. Queimada[1,*], F. L. Mota[1], S. P. Pinho[2], E. A. Macedo[1]

[1] LSRE/LCM – Laboratory of Separation and Reaction Engineering, Faculdade de Engenharia da Universidade do Porto, Rua Dr. Roberto Frias, 4200-465 Porto, Portugal.

[2] LSRE/LCM – Laboratory of Separation and Reaction Engineering, Escola Superior de Tecnologia e Gestão, Instituto Politécnico de Bragança, Campus de Santa Apolónia, 5301-857 Bragança, Portugal.

Keywords: CPA EoS, Modeling, Phenolic compounds, Solubility, UNIQUAC
Topic: Advancing the chemical and biological engineering fundamentals

Abstract

In this work, the aqueous solubilities of four hydroxybenzoic acids and four phenilpropenoic acids were measured as function of temperature (between 288.15 and 323.15 K), using the shake-flask method, followed by compositional analysis by spectrophotometry. In the modeling, two approaches were used: the modified UNIQUAC model and the Cubic-plus-Association equation of state. CPA is used with a new methodology that explicitly takes into account the number and nature of the associating sites and predicting the pure component parameters only from molecular structure. Both approaches show to be appropriate to represent the water solubility of these molecules.

1. Introduction

Numerous molecules in the pharmaceutical, food and chemical industries present complex chemical structures with different functional group substitutions. Many of these groups such as amine, carboxyl and hydroxyl can form hydrogen bonds. To adequately describe the phase equilibria of these complex chemicals, models able to take into account association effects are required. Still, for model development and evaluation, experimental data on some representative systems are needed. In this work, new experimental measurements and literature data were combined to develop a methodology to model the phase equilibria of phenolic acids using the Cubic-plus-Association (CPA) equation of state (Mota et al., 2008). A comparison with the modified UNIQUAC activity coefficient model (Peres and Macedo, 1996) is also presented.

Within the different classes of multifunctional associating molecules, phenolic compounds, due to their chemical and biological importance, are among the most important, having properties like antioxidant, chelating, free-radical scavenging, anti-inflammatory, antialergic, antimicrobial, antiviral, anticarcinogenic, chemopreventive and Uv filtering properties. Fruits, vegetables, spices and aromatic herbs are a natural source of these compounds. Apart from being starting materials for many chemical synthesis, such as some drugs, cosmetics, antioxidants, antiseptics and flavors, they can be used in the preparation of resins, plasticizers, dyes, inks and pharmaceutical products. There is also huge evidence that some phenolic compounds have beneficial effects on human health. Perhaps the oldest medical application of phenolic compounds is the use of phenol as antiseptic (Vermerris and Nicholson, 2006). Another very common use of these compounds is in sunscreens. Because their hydrogen-bonding ability and aromaticity, they can frequently act as free-radical scavengers, forming aryloxyl radicals. The stabilization of these radicals by other functional groups enhances the antioxidant activity (Chen and Ho, 1997). They also have ability to scavenge the oxidative radicals that are caused by cumulative and prolonged exposure to Uv

* Corresponding author. Tel +351 225 081 686. E-mail:ajq@fe.up.pt

radiation, which has been recognized to induce harmful reactions in human skin (Saija et al., 2000). Also, the low incidence of coronary heart disease, artherosclerosis and some types of cancer has been correlated by several authors with the phenolic content of olive oil (de Lorgeril et al., 1999).

Although the importance of these molecules is well known, very few solubility data are available and comprehensive experimental studies combining solubility with melting properties and acidity constants are clearly lacking in literature. In this work, aqueous solubilities of the hydroxybenzoic acids, salicylic, gallic, protocatechuic and syringic, and the phenilpropenoic acids, cinnamic, ferulic, coumaric and caffeic, were addressed. The work is part of a project concerning the solubility of natural phenolic compounds in water and organic solvents. Its final aim is to understand and predict their solubility in different solvents and to adequately understand the fate and separation processes of these molecules.

2. Experimental

Solid-liquid equilibria of hydroxybenzoic acids such as gallic, salicylic, syringic and protocatechuic acids and phenilpropenoic acids such as trans-cinnamic, ferulic, o-coumaric and caffeic acids were measured from 288 K up to 323 K using the analytical shake-flask method. Particular attention was given to aqueous solubilities. Constant-temperature jacketed glass cells were used to prepare the saturated solutions, where excess solute and solvent were mixed and stirred in a plate stirrer. Temperature was maintained constant with a constant-temperature circulating water bath and monitored with platinum resistance probes placed in the thermostatic jackets connected to a data acquisition unit. Some phenilpropenoic acids were reported to suffer photodegradation with daylight, and to prevent that, the cells were isolated with aluminum foil. When the equilibrium was attained, the agitation was stopped and then the solution was kept still, to allow undissolved solid to settle. Samples were taken from the liquid phase using plastic syringes coupled with syringe filters previously thermostatized at the equilibrium temperature and analyzed by spectrophotometry. The corresponding pHs of the saturated aqueous solutions were determined by potentiometry with a glass electrode. To verify the accuracy of the spectrophotometric method, some measurements were performed using the gravimetric method.

Besides solubility data, the melting properties (fusion enthalpies and temperatures) were also determined by DSC. Because phenolic compounds are organic acids, their acid dissociation constants (pKa) were obtained by potentiometric titration of aqueous solutions with aqueous NaOH solutions.

3. Modeling

The scarcity of literature data increases the importance of the development of correlation and prediction models. Different approaches can be used for modeling the solid solubility. In this work, an activity coefficient model, the modified UNIQUAC (Peres and Macedo, 1996) and an equation of state, the CPA EoS (Mota et al., 2008) were evaluated for modeling the measured data, neglecting the heat capacity term in the general solid-liquid equilibria equation (Prausnitz et al., 1999).

As both the solute and the solvent can associate (self and cross-association is present in these mixtures), the CPA EoS was adopted in this work. In terms of compressibility factor (Z), this equation can be expressed as the sum of two contributions: one accounting for physical interactions (in this work the Soave-Redlich-Kwong-EoS is used), and another accounting for the association contributions (the Wertheim association term).

$$Z = Z^{phys.} + Z^{assoc.} = \frac{1}{1-b\rho} - \frac{a\rho}{RT(1+b\rho)} - \frac{1}{2}\left(1+\rho\frac{\partial \ln g}{\partial \rho}\right)\sum_i x_i \sum_{A_i}(1-X_{Ai}) \quad (1)$$

where *a* is the energy parameter, *b* is the co-volume parameter, ρ the density, *g* a simplified hard-sphere radial distribution function, X_{Ai} the mole fraction of pure component *i* not bonded at site A, x_i the mole fraction of component *i*, *R* the ideal gas constant and *T* the absolute temperature. The pure component energy parameter is obtained from:

$$a(T) = a_0\left[1+c_1\left(1-\sqrt{T_r}\right)\right]^2 \quad (2)$$

where a_0 and c_1 are constants and T_r is the reduced temperature. The mixture *a* and *b* parameters are obtained through the classical mixing and combining rules, with a single, temperature-independent binary interaction parameter being used in the cross-energy parameter (a_{ij}):

$$a_{ij} = \sqrt{a_i a_j}\left(1-k_{ij}\right) \quad (3)$$

X_{Ai} is related to the association strength $\Delta^{A_iB_j}$ between two sites belonging to two different molecules and is calculated by solving the equation:

$$X_{Ai} = \frac{1}{1+\rho\sum_j x_j \sum_{B_j} X_{Bj}\Delta^{A_iB_j}} \quad (4)$$

For self-associating molecules,

$$\Delta^{A_iB_i} = g(\rho)\left[\exp\left(\frac{\varepsilon^{A_iB_i}}{RT}\right)-1\right]b_{ii}\beta^{A_iB_i} \quad (5)$$

where $\varepsilon^{A_iB_i}$ and $\beta^{A_iB_i}$ are the association energy and the association volume, respectively, and g(ρ) is a radial distribution function. For sites that belong to two different associating molecules, the Elliot combining rule is used:

$$\Delta^{A_iB_j} = \sqrt{\Delta^{A_iB_i}\times\Delta^{A_jB_j}} \quad (6)$$

As the studied phenolic acids are multifunctional associating molecules, a new methodology is proposed to take into account the different associating groups as well as their repetitions and ring positions in the chemical structure. Values for the associating energies and volumes of these groups are proposed. Additionally, to effectively model their water solubility, the acid dissociation must also be considered (Mota et al., 2008). Different results will be used to demonstrate the reliability of the proposed model.

Following a more classic approach, the UNIQUAC equation is also applied. It consists of two terms: a combinatorial one that attempts to describe the dominant entropic contribution (that depends on the composition, sizes and shapes of the molecules), and a residual one that is due mainly to the intermolecular forces responsible for the enthalpy of mixing. Peres and Macedo (1996) proposed a modified version of this model, that turned to be very successful in the representation of highly associating mixtures.

4. Discussion

Among the hydroxybenzoic acids, protocatechuic and gallic acids present higher solubilities due to the higher number of hydroxyl groups, leading to increased association interactions with water. When possible, our results were compared with the literature data. For gallic acid, our results, were compared with published data (Lu and Lu, 2007), showing a slight disagreement at lower temperatures. Our results for gallic, protocatechuic and syringic acids were compared to the results obtained by Noubigh et al. (2007), but their data do not

increase significantly with temperature, which is contrary to what would be expected. For salicylic acid, our results are in good agreement with previous works (Apelblat and Manzurola, 1989; Nördstrom and Rasmuson, 2006; Peña et al., 2004), as can be seen from Figure 1. In the phenilpropenoic series, higher solubilities were found for caffeic, followed by ferulic, coumaric and cinnamic acid. This order follows the extent of hydrogen bonding of each molecule with water. For ferulic acid, our results are very different from those obtained by Noubigh et al. (2007), but the equilibrium time reported by these authors are very different from ours: while we had equilibrium times between 64h and 84h, depending on the working temperature, these authors had always equilibrium times of 3 hours. Ferulic acid is reported to have two polymorphic forms that are obtained by recrystallization from various solvents (Sohn and Oh, 2003). Thus, we may be comparing different crystalline structures of the same compound, which may explain the different results. For cinnamic acid, our value compare well with the value given in the *Merck Index* (O'Neil and Budavari, 2001).

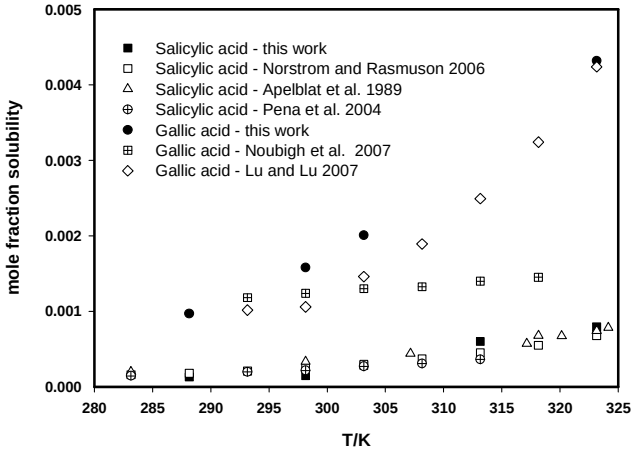

Figure 1. Solubility of hydroxybenzoic, gallic and salicylic acids in water, as function of temperature.

Another important fact about solubilization of solids in liquids is related to the fusion enthalpies and melting temperatures. From the results found so far, it can be concluded that the extent of hydrogen bonding with water is certainly more important than the fusion process for determining the degree of solubilization. Also, the results for the acid dissociation constants lead to the conclusion that acid dissociation is not so important in the solubilization process of these molecules (Mota et al., 2008).

CPA parameters are frequently obtained from pure-component vapor-pressure and liquid-density data. In the particular case of the phenolics studied in this work, these data are only available for salicylic and cinnamic acids. Another drawback is the presence of different associating groups on the same molecule, some of them repeated in different positions. Thus, it is appropriate to individually assign association energies and volumes for each group and to consider multiple group substitution, either or not with the same association parameters. These parameters were obtained using the critical temperatures, pressures and van der Waals volumes (Mota et al., 2008), obtained from Marrero and Gani (2001) and Bondi (1964) group-contribution approaches. As can be seen from Figures 2 (a) and (b), a good description can be achieved with the CPA-EoS, but a small k_{ij} value was always required to obtain smaller deviations. Still, in all cases, only a single, temperature-independent k_{ij} value was sufficient. Maximum absolute average deviations of 59% were obtained for salicylic acid and 53% for ferulic acid, while for the other phenolics the average deviations did not exceed 30%.

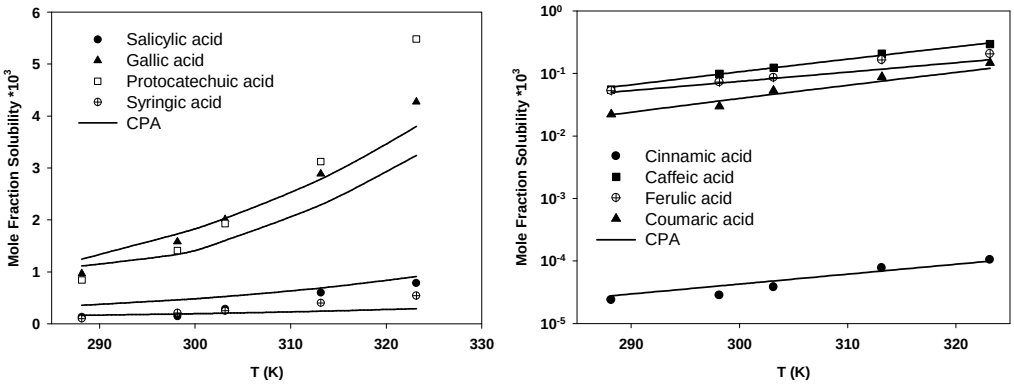

(a) **(b)**

Figure 2. Experimental solubility data and modeling results by CPA for (a) hydroxybenzoic acids (b) phenilpropenoic acids. Modeling results: gallic acid, k_{ij} = -0.13; salicylic acid, k_{ij} = -0.06; protocatechuic acid, k_{ij} = -0.10; syringic acid, k_{ij} = -0.17; *trans*-cinnamic acid, k_{ij} = -0.05; caffeic acid, k_{ij} = -0.10; ferulic acid, k_{ij} = -0.13; and coumaric acid, k_{ij} = -0.05.

For the modified UNIQUAC model, the residual term binary interaction parameters were fitted to the measured data. Two temperature independent interaction parameters were regressed per binary water + phenolic system. In the next figures, the experimental and calculated solubilities are compared, with an excellent description being obtained. The root mean square deviations (RMSD) are smaller than 5% and the absolute average deviations (AAD) smaller than 9% for the correlation of all studied systems.

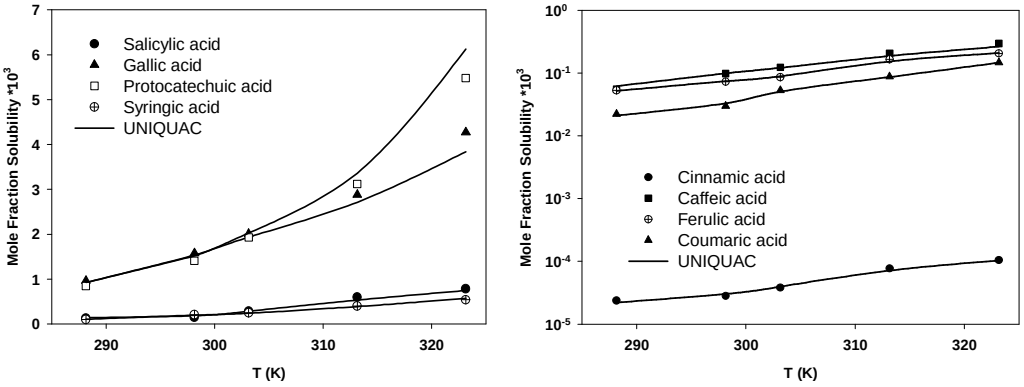

(a) **(b)**

Figure 3. Experimental solubility data and modeling results by modified UNIQUAC model for (a) hydroxybenzoic acids (b) phenilpropenoic acids.

5. Conclusions

In this work, aqueous solubility data were measured for some phenolic compounds, in the temperature range from 288 K to 323 K, using the shake-flask method, coupled with spectrophotometric analysis. For all compounds under study, the solubility follows the general increasing trend with temperature. Besides solubility, melting data and apparent acid dissociation constants were also determined, providing a broader knowledge about the solubilization processes of these molecules. From the measured data, it can be concluded that the extent of hydrogen bonding with water is the dominant effect in determining the degree of solubilization.

The CPA EoS was used with different association energies and volumes for the different associating groups. A methodology to obtain the pure-component parameters without requiring experimental data was developed, and the results indicate that CPA is an adequate tool to correlate the water solubility of these molecules. The modified UNIQUAC model, with two adjustable parameters from solubility data, showed and excellent description of solubilities of these phenolics compounds.

References

Apelblat, A., Manzurola, E., (1989). Solubility of Ascorbic, 2-Furancarboxylic, Glutaric, Pimelic, Salicyclic, and O-Phthalic Acids in Water from 279.15-K to 342.15-K, and Apparent Molar Volumes of Ascorbic, Glutaric, And Pimelic Acids in Water at 298.15-K. *Journal of Chemical Thermodynamics*, 21, 1005-1008.

Bondi, A., (1964). Van der Waals Volumes + Radii. *Journal of Physical Chemistry*, 68, 441-451.

Chen, J.H., Ho, C.T., (1997). Antioxidant activities of caffeic acid and its related hydroxycinnamic acid compounds. *Journal of Agricultural and Food Chemistry*, 45, 2374-2378.

de Lorgeril, M., Salen, P., Martin, J.L., Monjaud, I., Delaye, J., Mamelle, N., (1999). Mediterranean diet, traditional risk factors, and the rate of cardiovascular complications after myocardial infarction - Final report of the Lyon Diet Heart Study. *Circulation*, 99, 779-785.

Lu, L.L., Lu, X.Y., (2007). Solubilities of gallic acid and its esters in water. *Journal of Chemical and Engineering Data*, 52, 37-39.

Marrero, J., Gani, R., (2001). Group-contribution based estimation of pure component properties. *Fluid Phase Equilibria*, 183, 183-208.

Mota, F.L., Queimada, A.J., Pinho, S.P., Macedo, E.A., (2008). Aqueous solubility of some natural phenolic compounds. *Industrial & Engineering Chemistry Research*, (accepted).

Nördstrom, F.L., Rasmuson, A.C., (2006). Solubility and melting properties of salicylic acid. *Journal of Chemical and Engineering Data*, 51, 1668-1671.

O'Neil, M.J., Budavari, S. (2001) The Merck Index: an Encyclopedia of Chemicals, Drugs and Biologicals. In Co. M ed., Whitehouse Station, N.J.

Peña, M.A., Bustamante, P., Escalera, B., Reillo, A., Bosque-Sendra, J.M., (2004). Solubility and phase separation of benzocaine and salicyclic acid in 1,4-dioxane-water mixtures at several temperatures. *Journal of Pharmaceutical and Biomedical Analysis*, 36, 571-578.

Peres, A.M., Macedo, E.A., (1996). Thermodynamic properties of sugars in aqueous solutions: Correlation and prediction using a modified UNIQUAC model. *Fluid Phase Equilibria*, 123, 71-95.

Prausnitz, J.M., Lichtenthaler, R.N., Azevedo, E.G., (1999). *Molecular Thermodynamics of Fluid-Phase Equilibria*, 3rd ed., Prentice Hall PTR, Upper Saddle River, N.J.

Saija, A., Tomaino, A., Trombetta, D., De Pasquale, A., Uccella, N., Barbuzzi, T., Paolino, D., Bonina, F., (2000). In vitro and in vivo evaluation of caffeic and ferulic acids as topical photoprotective agents. *International Journal of Pharmaceutics*, 199, 39-47.

Sohn, Y.T., Oh, J.H., (2003). Characterization of physicochemical properties of ferulic acid. *Archives of Pharmacal Research*, 26, 1002-1008.

Vermerris, W., Nicholson, R., (2006). *Phenolic Compound Biochemistry*, Springer, Dordretcht.

Acknowledgements

The authors thank the support provided by *Fundação para a Ciência e a* Tecnologia (FCT) by LSRE financing FEDER/POCI/2010. Fátima L. Mota acknowledges her FCT Ph.D. scholarship SFRH/BD/32372/2006 and A. J. Queimada acknowledges financial support from POCI/N010/2006.

Proceedings of the 10th International Chemical and
Biological Engineering Conference - CHEMPOR 2008
Braga, Portugal, September 4-6, 2008
E.C. Ferreira and M. Mota (Eds.)

Diffusion coefficients and conductivities of some ionic liquids

Chun-Li Wong, Allan N. Soriano, Meng-Hui Li*
R&D Center for Membrane Technology and Department of Chemical Engineering, Chung Yuan Christian University, Chung Li, TAIWAN, 32023, R.O.C.

Keywords: Diffusion coefficient, conductivity, ionic liquid, Taylor dispersion technique
Topic: Suitable conference topic — Advancing the chemical engineering fundamentals, ionic liquids

Abstract

In this study, the mutual diffusion coefficients of some ionic liquids (ILs) in water at infinite dilution for temperatures (303.2 to 323.2) K were measured using the Taylor dispersion technique. The investigated ILs were as follows: 1-ethyl-3-methylimidazolium dicyanamide [Emim][C_2N_3], 1-ethyl-3-methylimidazolium tetrafluoroborate [Emim][BF_4], 1-ethyl-3-methylimidazolium ethylsulfate [Emim][$EtSO_4$], 1-ethyl-3-methylimidazolium trifluoromethanesulfonate [Emim][CF_3SO_3], and 1-ethyl-3-methylimidazolium 2-(2-methoxyethoxy) ethylsulfate [Emim][$MDEGSO_4$]. The present diffusion coefficients data were correlated using two different approaches: (a) the diffusing component was treated as an organic solute using the Wilke–Chang equation and (b) as an electrolyte solute using the Nernst–Haskell equation. The Wilke–Chang equation underestimated the present data of diffusion coefficients, thus, it was modified by introducing temperature-dependent empirical parameters and the results were satisfactory. The Nernst–Haskell equation requires infinite dilution conductances of ions and to this end, the molar conductivities of several infinitely dilute concentrations of aqueous ionic solutions for the temperatures (303.2 to 323.2) K were also measured using a commercial conductivity meter. Considering the experimental error involved and that no adjustable parameter was used, the predictions using the Nernst–Haskell equation are reasonably accurate.

Introduction

Since the vapor pressure of ILs is very small, the most likely way for them to pollute the environment is in the waste water stream. To predict the behavior of a chemical substance in the waste water stream, it is important to know such physical properties as partition and sorption coefficients and solubility in water. For several imidazolium-based ILs, Ropel *et al.* (2005), reported the partition coefficients (index of bioaccumulation in an aquatic environment)

to the mixture of 1-octanol and water. The study of Wong *et al.* (2002) reported the solubility of [emim][PF_6] and [bmim][PF_6] in water.

Aside from the previously mentioned properties, another important property that can be used to determine the ability of IL to spread in the environmental stream (water) is the diffusion coefficients. In the past years, a number of measurements of diffusion coefficient for different species such as carbon dioxide and several hydrofluorocarbons, in ILs were reported by different research groups (Every *et al.*, 2000; Every *et al.*, 2004; Morgan *et al.*, 2005; Shiflett and Yokozeki, 2005; Shiflett and Yokozeki, 2006). However, there were few data of diffusion coefficients of ILs in solvents, even in water. Richter et al. (2003) reported the diffusion coefficient measurements of molten salts and ionic liquids in methanol using digital image holography. Su et al. (2007) reported diffusion coefficient measurements of alkylimidazolium tetrafluoroborates and hexafluorophosphates in water at 303.2 K using Taylor dispersion experiment.

Thus, in this present work, we reported the measurements of diffusion coefficients of five [Emim]-based ILs for the temperatures ranging from (303.2 to 323.2) K using Taylor dispersion method. The studied ILs were [Emim][C_2N_3], [Emim][BF_4], [Emim][$EtSO_4$], [Emim][CF_3SO_3], and [Emim][$MDEGSO_4$]. The present diffusion coefficients data were correlated using two different approaches: (a) the diffusing component was treated as an organic solute using the Wilke–Chang equation (Wilke and Chang, 1955) and (b) as an electrolyte solute using the Nernst–Haskell equation (Robinson and Stokes, 1965). In the prediction of diffusion coefficients using Wilke–Chang equation, the density values of the solute (IL) and viscosity of the solvent (water) were needed, so the densities and viscosities at the studied isotherms, (303.2 to 323.2) K, were also determined. The densities of ILs were measured while the viscosities of water were calculated from a reliable correlation (Hsu and Li, 1997). The use of Nernst–Haskell equation requires an infinite dilution conductance of individual cations and anions, thus, the molar conductivities of the investigated ILs in water at various concentrations were also measured.

Materials and methods

All ILs used in this work were supplied by TCI Co. with minimum purity of 97 %. The ILs were used without further purification. A water purification system supplied by Barnstead Thermodyne (model Easy Pure 1052) was used to provide Type I reagent-grade water with a resistivity of 18.3 (M·Ωcm) and with a total organic carbon content of less than 15 ppb. The infinitely dilute concentration aqueous solutions were prepared by mass, with a weighing accuracy of $\pm 1 \times 10^{-4}$ g.

The Taylor dispersion apparatus used in this study was described previously by Kao and Li (2006). In this work, the mutual diffusion coefficients of the investigated ionic liquids in water were measured at infinite dilution. The samples of dilute solutions of ionic liquids in water

were injected into a carrier fluid of pure deionized water. The concentration of the solution greatly affects the diffusion coefficient. To this end, the concentration of the injected samples were kept as dilute as possible so that the measured diffusion coefficients were not influenced by concentrations of the samples, but still a steady detectable signal could be obtained.

The molar conductivity Λ was measured using a commercial electrical conductivity meter (model SC-170) manufactured by Suntex. The uncertainty of the conductivity measurement was $\pm$0.001 (mS·cm^{-1}) for readings below 50 (mS·cm^{-1}). The temperature was monitored using digital thermometer (model 3002) from CROPICO, with an uncertainty of $\pm$0.01 K.

The densities of IL (solute) were measured using a viscometer from Anton Paar Stabinger (model SVM 3000). The density was measured by the integrated density measuring cell, which used the principle of the oscillating U-tube. The repeatability of the density measurement was ±0.0002 (g·cm^{-3}). The estimated uncertainty of temperature was ±0.002 K. The estimated uncertainty of the density was ±0.0004 (g·cm^{-3}).

The viscosities of water at various temperatures were calculated using a correlation used in the study of Hsu and Li (1997) and is given by the expression

$$\ln \eta = a_1 + \frac{a_2}{T + a_3} \tag{1}$$

Results and discussion

The present experimental results of diffusion coefficient measurements for the studied [Emim]-based ILs in water at infinite dilution are presented in Table 1 and also shown in Fig. 1. Among the studied ILs, [Emim][BF_4] has the highest value of diffusion coefficients while [Emim][$MDEGSO_4$] has the lowest value of diffusion coefficients. The most common correlation used for estimating diffusion coefficient of organic molecules in a solvent is the Wilke-Chang equation (Wilke and Chang, 1955) where the diffusing component is treated as an organic solute and the diffusion of solute A in solvent B is represented by Eq. (2)

$$D_{\mathrm{AB}}^{0} = 7.4\times10^{-12}\frac{\left(\psi M_{\mathrm{B}}\right)^{0.5} T}{\eta_{\mathrm{B}} V_{\mathrm{A}}^{0.6}} \tag{2}$$

As shown in Table 1, the Wilke–Chang equation underestimated the present measurements of diffusion coefficient. To this end, the Wilke–Chang equation was modified by introducing a temperature–dependent correction factor which is expressed as

$$F_{\mathrm{C}} = b_1 + b_2 T \tag{3}$$

Where F_c is the temperature–dependent correction factor, T the absolute temperature in K, and b_i, the empirical parameters. The modified Wilke–Chang equation are then rewritten as

$$D_{\mathrm{AB}}^{0} = F_{\mathrm{C}}\left[\frac{7.4\times10^{-12}\left(\psi M_{\mathrm{B}}\right)^{0.5} T}{\eta_{\mathrm{B}} V_{\mathrm{A}}^{0.6}}\right] \tag{4}$$

The modified Wilke–Chang equation correlated well the present experimental results with an overall AAD % of 1.62.

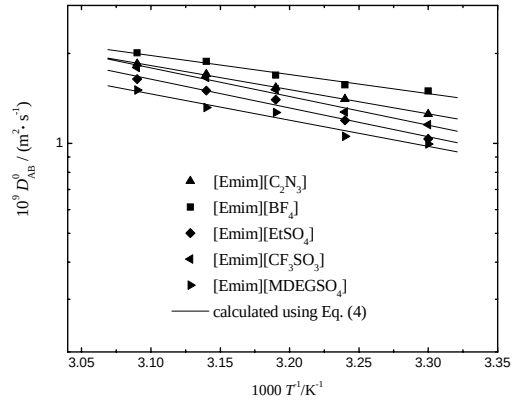

Fig. 1. Diffusion coefficient of the studied ILs

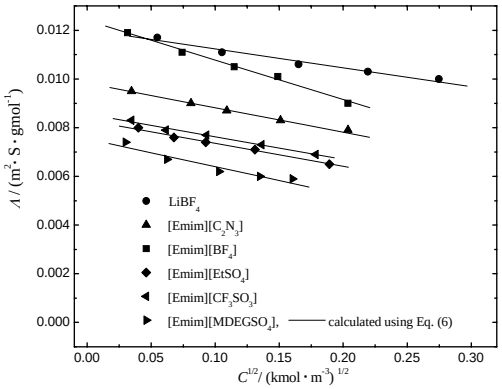

Fig. 2. Molar conductivity of the studied systems

Table 1. Comparison of diffusion coefficients for the studied ionic liquids

	Experimental	Wilke-Chang eqn.	Modified W-C Wilke-Chang eqn.	Nernst-Haskell eqn.
T / K	$10^9 D_{AB}^0$ / $\left(m^2 \cdot s^{-1}\right)$, [Emim][$C_2N_3$]			
303.2	1.253	0.844	1.258	1.324
313.2	1.407	0.946	1.399	1.449
323.2	1.538	1.054	1.546	1.590
333.2	1.706	1.167	1.697	1.802
343.2	1.849	1.285	1.853	1.975
T / K	$10^9 D_{AB}^0$ / $\left(m^2 \cdot s^{-1}\right)$, [Emim][$BF_4$]			
303.2	1.499	0.861	1.459	1.603
313.2	1.571	0.966	1.595	1.788
323.2	1.692	1.076	1.732	1.979
333.2	1.882	1.191	1.867	2.158
343.2	2.011	1.312	2.001	2.374
T / K	$10^9 D_{AB}^0$ / $\left(m^2 \cdot s^{-1}\right)$, [Emim][$C_2H_5SO_4$]			
303.2	1.036	0.758	1.065	1.092
313.2	1.195	0.850	1.202	1.219
323.2	1.401	0.947	1.347	1.305
333.2	1.504	1.048	1.501	1.460

343.2	1.641	1.155	1.664	1.638
T / K	$10^9 D_{AB}^0$ / $\left(m^2 \cdot s^{-1}\right)$, [Emim][$CF_3SO_3$]			
303.2	1.156	0.764	1.159	1.135
313.2	1.274	0.857	1.310	1.291
323.2	1.514	0.955	1.471	1.413
333.2	1.661	1.057	1.641	1.581
343.2	1.797	1.164	1.821	1.741
T / K	$10^9 D_{AB}^0$ / $\left(m^2 \cdot s^{-1}\right)$, [Emim][$MDEGSO_4$]			
303.2	0.995	0.611	0.977	0.931
313.2	1.056	0.685	1.097	1.045
323.2	1.270	0.763	1.223	1.138
333.2	1.318	0.845	1.356	1.326
343.2	1.508	0.931	1.494	1.446

Diffusion coefficients of electrolytes are related to infinite dilution conductance via the Nernst–Haskell equation (Robinson and Stokes, 1965):

$$D_{AB}^0 = \frac{RT}{F^2}\frac{|z_+|+|z_-|}{|z_+ z_-|}\frac{\Lambda_+^0 \Lambda_-^0}{\Lambda_+^0 + \Lambda_-^0} \tag{5}$$

Figure 2 shows the conductivity of $LiBF_4$ (reference substance) and the investigated ionic liquids. The conductivity varies linearly with the square root of concentration:

$$\Lambda = \Lambda^0 + \left(d_1 \Lambda^0 + d_2\right) C^{1/2} \tag{6}$$

The infinite dilution conductance Λ^0 can be obtained by fitting the experimental data using Eq. (6). The relation between the infinite dilution conductivity of an electrolyte and the infinite dilution conductances of the ions is given by:

$$\Lambda^0 = z_+ \Lambda_+^0 + z_- \Lambda_-^0 \tag{7}$$

From Eq. (7) and the infinite dilution conductivity of the ionic liquids, the infinite dilution conductances of the ions were determined. As shown in Table 1, the Nernst–Haskell equation (Robinson and Stokes, 1965) can be used to predict the diffusivities of ionic liquids, the average absolute error of 6% was found. Considering the experimental error involved and that no adjustable parameter was used, the predictions are reasonably accurate.

Conclusions

The diffusion coefficients of five [Emim]-based ionic liquids in water at infinite dilution were measured using Taylor dispersion method from temperatures of (303.2 to 323.2) K. The

diffusion coefficients were well correlated by a modified Wilke–Chang equation in which a temperature-dependent correction factor was introduced to the Wilke–Chang correlation. The molar conductivities of the investigated ionic liquids were also measured to predict the diffusion coefficient using the infinite dilution conductances of the ions via the Nernst–Haskell equation. The results of the calculation of diffusion coefficients using the Nernst–Haskell equation were reasonably accurate.

References

Every, H., Bishop, A.G., Forsyth, M., MacFarlane, D.R. (2000). Ion Diffusion in Molten Salt Mixtures. *Electrochim. Acta*, 45, 1279-1284.

Every, H., Bishop, A.G., MacFarlane, D.R., Oradd, G., Forsyth, M. (2004). Transport Properties in a Family of Dialkylimidazolium Ionic Liquids. *Phys. Chem. Chem. Phys.*, 6, 1758-1765.

Hsu, C.-H., Li, M.-H. (1997). Viscosities of Aqueous Blended Amines. *J. Chem. Eng. Data*, 42, 714-720.

Kao, C.-Z., Li, M.-H. (2006). Diffusion Coefficients of Aqueous N,N-Diethylethanolamine, N,N-Dimethylethanolamine, Monoisopropanolamine, Piperazine, and Sulfolane Solutions. *J. Chin. Inst. Chem. Eng.*, 37, 341-353.

Morgan, D., Ferguson, L., Scovazzo, P. (2005). Diffusivities of Gases in Room-Temperature Ionic Liquids: Data and Correlations Obtained Using a Lag-Time Technique. *Ind. Eng. Chem. Res.*, 44, 4815-4823.

Richter, J., Leuchter, N., Grosser, N. (2003). Digital Image Holography for Diffusion Measurements in Molten Salts and Ionic Liquids - Method and First Results. *J. Mol. Liq.*, 103, 359-370.

Robinson, R.A., Stokes, R.H. (1965). *Electrolyte Solutions*, Butterworths, London.

Ropel, L., Belveze, L.S., Aki, S.N.V.K., Stadtherr, M.A., Brennecke, J.F. (2005). Octanol-Water Partition Coefficients of Imidazolium-based Ionic Liquids. *Green Chem.*, 7, 83-90.

Shiflett, M.B., Yokozeki, A. (2005). Solubilities and Diffusivities of Carbon Dioxide in Ionic Liquids: [bmim][PF_6] and [bmim][BF_4]. *Ind. Eng. Chem. Res.*, 44, 4453-4464.

Shiflett, M.B., Yokozeki, A. (2006). Solubility and Diffusivity of Hydrofluorocarbons in Room-Temperature Ionic Liquids. *AIChE J.*, 52, 1205-1219.

Su, W.C., Chou, C.H., Wong, D.S.H., Li, M.-H. (2007). Diffusion Coefficients and Conductivities of Alkylimidazolium Tetrafluoroborates and Hexafluorophosphates. *Fluid Phase Equilib.*, 252, 74-78.

Wilke, C.R., Chang, P. (1955). Correlation of Diffusion Coefficients in Dilute Solutions *AIChE J.*, 1, 264-270.

Wong, D.S.H., Chen, J.P., Chang, J.M., Chou, C.H. (2002). Phase Equilibria of Water and Ionic Liquids [emim][PF_6] and [bmim][PF_6]. *Fluid Phase Equilib.*, 194, 1089-1095.

Proceedings of the 10th International Chemical and
Biological Engineering Conference - CHEMPOR 2008
Braga, Portugal, September 4-6, 2008
E.C. Ferreira and M. Mota (Eds.)

Inhibitor effect of selected anionic surfactants on the dissolution of calcium sulfate in aqueous brines

Cristiana Loureiro[1]; Fátima Farelo[1*]; Lurdes Serrano[1]; Manuel Pereira[2]
[1]Centre for Chemical Processes, IST, Technical University of Lisbon, Portugal
[2]CEPGIST, IST, Technical University of Lisbon, Portugal

Keywords: Calcium sulfate, Dissolution, Surfactants
Topic: Advancing the chemical and biological engineering fundamentals

Leaching of halite from mineral deposits by solution mining is a technology with worldwide application. For the salt industry, only the valuable components in the mineral deposit must be dissolved and removed to the surface for further processing. Inevitably, several minor impurities, such as calcium sulfate minerals, are also leached and the outgoing contaminated brine must be subject to costly purification treatments. Therefore, the inhibition of the dissolution of calcium minerals is a subject with scientific interest and potential economic impact. The dissolution of anhydrite in saturated brines of sodium chloride may be inhibited by the presence of water-soluble macromolecules, being the effectiveness of the inhibitor evaluated from the degree of coverage of the target surface and the desorption resistance. The ideal macromolecule, besides being selective towards anhydrite, should not harm the morphologic characteristics of the main salt in downstream crystallizations.

In this study, the influence of some selected anionic surfactants on the solubility of gypsum, anhydrite and anhydrite-rich sediments in concentrated brines was investigated.

Introduction

Although the prevention of calcium sulfate scale formation has received a lot of attention from industry and research, studies concerning the inhibition of dissolution of calcium minerals in aqueous brines are scarce. Effective inhibitors are usually good sequestering agents for the lattice cations and it is generally accepted that they exert their action through adsorption at cationic sites on the solid surfaces. Additives may also adsorb upon crystal faces, reducing the rate of dissolution. Since the molecular interactions at the inorganic/organic interfaces depend on the size, ionic charge and structure of the admixture, Nancollas and Zawacki (1984), small molecules with high charge density will interact with charged solids. The concentration and size of the inhibitor molecule are important parameters because the inhibition of dissolution requires a considerable coverage of the surfaces. Anionic surfactants with negative charged head groups seem to have a strong blocking effect upon the dissolution of calcium minerals, according to Mahmoud et al. (2004). The effectiveness of adsorption is inversely proportional to the minimum area demand per molecule, thus making of single-chained surfactants potential good inhibitors. It is not clear however, to what extent the salts present in the solution affect the inhibitor performance.

Within the scope of this study, the effect of some selected anionic benzene sulfonate surfactants on the dissolution of different forms of calcium sulfate are here reported. Because the length of the chain determines the physicochemical behavior of surfactants in solution, representatives of C_8, C_{12} and C_{12}/C_{13} anionic surfactants were studied. Both the acid and the sodium salt forms of the polar head group were considered for some of these surfactants.

Materials and methods

Three different forms of calcium sulfate were used in the study. The samples of anhydrite-rich sediments, $CaSO_4 \geq 42\%$ (w/w), from three salt dissolution caverns under leaching,

* Corresponding author. Tel + 351 218417335. E-mail:fatima.farelo@ist.utl.pt

belonging to the Porto de Mós diapir (Hetangian formation), were kindly provided by REN, Portugal. Gypsum and anhydrite were commercial products with particle mean size < 10 μm and BET surface area of 1.9 and 1.7 m^2/g, respectively. Four anionic surfactants with hydrophilic head group of the benzene sulfonate (BS) type were used. OBS (Na, octyl BS), DBS (Na, dodecyl-BS) and ADBS (dodecyl-BS acid) were purchased from Sigma-Aldrich. A commercial acid surfactant, a mixture of branched and straight chained alkyl, mainly C_{12} and C_{13}, here referred to as D550, was kindly supplied by InChemica, Portugal. Analytical grade sodium chloride, Riedel-de Haën (> 99.8 %), and deionized water were used to prepare the brines by mass to ± 0.01 g. The maximum overall uncertainty in the concentration of the surfactants' stock solutions was ± 0.3 mg L^{-1}.

Anhydrite-rich sediments from 3 different salt caverns under leaching, hereafter referred to as S1, S2, and S3, were used in the experiments. Prior to use the sediments were air-dried, homogenized and sieved. The mean superficial diameter of the solids, calculated from the size distributions, was 52 μm for S1 and S3, and 74 μm for S2, being the BET surface areas 0.4 and 0.2 m^2/g, respectively. Zeta potential measurements showed that all the sediments are negatively charged, ca. – 11 mV.

The mineralogical composition of the sediments was confirmed by X-ray diffraction and FTIR spectroscopy (4000-400 cm^{-1}) and stereo and polarizing microscopy showing the presence of halite, anhydrite, low quartz, carbonate minerals (dolomite, ankerite) and minor contents of clay (clinochlore), organic and inorganic carbon, gypsum, muscovite and pyrite.

Samples of about 6 to 17 g/L of three forms of solid calcium sulfate, gypsum, anhydrite and anhydrite-rich sediments, together with sodium chloride were equilibrated in aqueous solutions with a surfactant concentration ranging from 0 to 73 mg/kg of saturated brine. Although an excess of solid halite was used in most of the runs to mimic the salt caverns environment, the influence of the degree of saturation of the leaching agent was also evaluated. The plastic flasks were shaken for 7 to 14 days in an orbital shaker, at room temperature. Periodically, the solutions were sampled for analysis. After a settling period of about 3 h, liquid samples were collected with a syringe, equipped with a 0.45-μm filter, and aliquots of the liquid were analyzed for calcium content (S.M. 3500-Ca B. "EDTA Titrimetric Method"). The reported concentrations are the mean values of duplicate analyses on each sample. The content of sulfate ion in the samples was also regularly determined (S.M. 4500 SO42- E. "Turbidimetric Method"), as a cross check for the calcium analysis. At the end of each run, the slurry was filtered and the solids air-dried and weighed. The residual solutions and solids were subsequently analyzed for the content of surfactants (MBAS standard method). Blank runs were carried out to account for the natural variability of sediments composition and for the dependence of calcium sulfate solubility on temperature and NaCl content in the brines. In each series of experiments the effect of the surfactants on the dissolution of the calcium salt was assessed against the corresponding control run.

In order to interpret the behavior of the selected surfactants, the surface tension of concentrated NaCl brines (300 g/kg_{water}), with and without admixtures, was determined with a Du-Noüy tensiometer equipped with a Pt ring. All measurements were performed after a 30-min period of equilibration at constant temperature. The tensiometer was previously calibrated against water and NaCl solutions (up to ≈ 6 m), at 298 K.

Results and Discussion

Figure 1 presents the change of calcium sulfate concentration in saturated brines as a function of time, for the three forms of salt studied. The reported rates of dissolution, measured in the presence of solid halite, represent the average values of at least duplicate measurements.

For sediments S1 and S3, Figure 1a, the saturation concentration was reached after one week, whereas for the pure forms of calcium sulfate, Figure 1b, this value was attained in about 24 h. Sediments S2, the coarser of the solids tested, were the slower to dissolve. The

results show that both the availability of the calcium salt in the solid and the size of the particles play an important role on rate of dissolution of the calcium mineral.

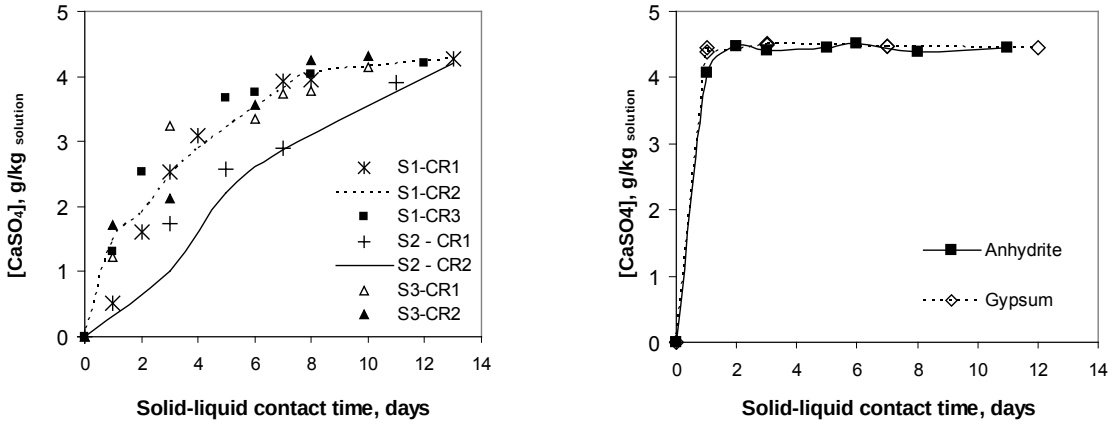

(a) (b)

Figure 1- Rate of dissolution of different forms of calcium sulfate in saturated brines

In order to determine how the selected C_8, C_{12} and C_{12}/C_{13} anionic benzene sulfonate surfactants influence the dissolution of calcium sulfate, a total of 76 independent runs were carried out. The decrease of the content of calcium sulfate in solution was evaluated by the relative solubility calculated, for each data point, as the ratio of calcium content in the solution and in the parallel blank run.

Figure 2a illustrates the effect of the type and concentration of the selected anionic surfactants on the calcium sulfate content, after 14 days of curing in slurries of sediments and halite. The chain's length of the organic molecule clearly determines the admixture effectiveness, as a dissolution inhibitor for the calcium mineral, being the effect of the C_8 surfactant, OBS, almost negligible. The type of the head group of the linear C_{12}-BS surfactants (acid for ADBS and sodium salt for DBS) had no significant influence on the solubility reduction. The curves also indicate that, independent of the C_{12}-surfactant type, the maximum reduction in dissolution ($\cong$ 70%) was obtained in slurries containing an initial concentration of about 40 $mg/kg_{solution}$ of the admixtures. For higher contents, the blocking effect of the surfactants decreases. Oppositely, Figure 2b shows that the tested surfactants had no effect whatsoever on the dissolution of either the hydrate or the non-hydrate calcium sulfate. This behavior stems most probably from a very different order of magnitude between the rates of dissolution and of solid shielding by the surfactants.

The inhibitor effect of the C_{12} and C_{12}/C_{13} surfactants becomes more apparent as the residence time increases, as shown in Figure 3 for DBS and D550. The dissolution of calcium sulfate in the blank run continues up to saturation, whereas in the presence of the surfactants the process is effectively blocked, resulting in a decrease of the relative solubility.

The rate of leaching of the salt caverns determines the concentration of the outgoing brine. The injected water containing the added admixtures is gradually enriched in sodium chloride as the residence time increases, becoming saturated if enough time is allowed. Therefore, to examine the influence of the NaCl content in the admixed solutions upon the rate of the dissolution of the sediments, a series of experiments was carried out using as leaching agents aqueous solutions of DBS and near-saturated NaCl brines (350 g/kg water) containing the same surfactant or its acid form (ADBS).

The results thus obtained are compared in Figure 4 with the relative solubility of calcium sulfate measured in the presence of solid halite. It is clear that the leaching agent, water+surfactant, does no hinder the dissolution of the anhydrite-rich sediments before it becomes enriched in sodium chloride. In near-saturated brines even small concentrations of the admixtures are effective in blocking the dissolution of anhydrite, the equilibrium calcium

content in the solution representing 20 to 30% of the blank run concentration. However, it is worth noting that in the presence of solid halite - a more realistic approach to a salt cavern environment - the hindering effect is less pronounced, a fact that might be explained by the existence of a much larger solid surface area to which the organic molecules will indistinctly adhere.

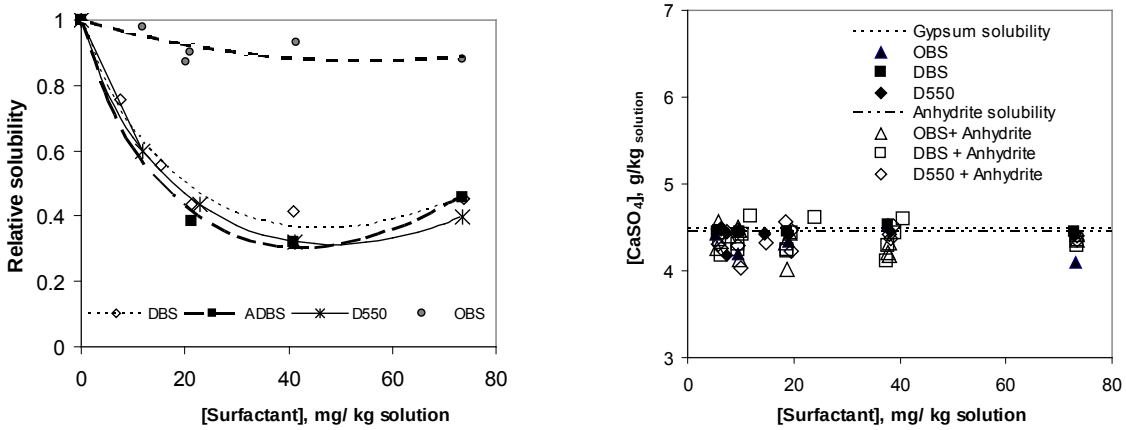

(a) Sediments (b) Gypsum and anhydrite

Figure 2 - Effect of the type and concentration of OBS, DBS, ADBS and D550 on the dissolution of calcium sulfate after 14 days of curing

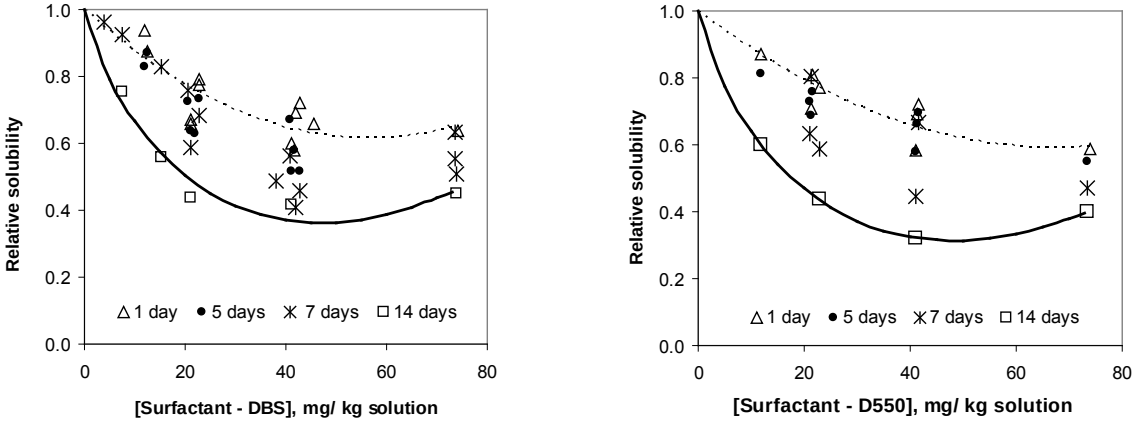

Figure 3 – Influence of the solid-liquid contact time on the dissolution of sediments S3 for several initial contents of two C_{12}BS surfactants

In order to get a better understanding of the observed phenomena, the surface tension of the near-saturated brines containing the studied surfactants was measured at 298 K. Minute amounts of the admixtures originated a sharp reduction in the solution surface tension, but beyond a limiting concentration, which coincided with the appearance of solution opalescence, no further change in this quantity was detected. This surge of turbidity, which represents the onset of a macroscopic phase separation, occurred at concentrations of 0.9, 0.8, 1.4 and 2.3 mg/L for OBS, D550, ADBS and DBS, respectively. It can, therefore, be inferred from these results that during the equilibration of the sediments+halite solid mixtures in the leaching solutions a phase separation will occur, as soon as a high ionic strength is reached. As a consequence of the rejection of the organic phase, the content of the monomers in the leaching solution will remain nearly identical to the clouding concentrations measured. The rejected phase will tend to adhere to the solid surfaces existing in the slurries, thus acting as an organic barrier to the solids' dissolution.

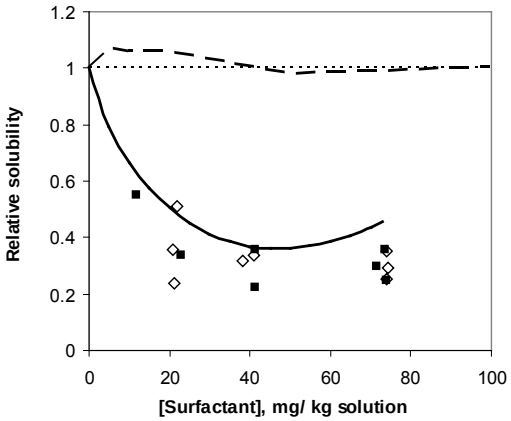

Figure 4- Influence of salt concentration on the solubility reduction of calcium sulfate after 14 days of contact. Lines: broken - DBS in water. Solid - DBS in brines with solid halite. Symbols. Surfactants In near-saturated brines: ■ ADBS; ◇ DBS.

The surfactant contents in the saturated solutions equilibrated during 7 days with anhydrite-rich sediments, shown in Figure 5a, were found to be slightly lower than the corresponding clouding concentrations measured in pure NaCl solutions. These results may indicate that some precipitation of calcium or sodium salts of the benzene sulfonate detergents occurred in the saturated brines. The amount of additives adhering to the anhydrite-rich sediments, Figure 5b, was nearly independent of the type of C_{12}BS surfactants, as well as of the substrata. Due to the negative charge of sediments, electrostatic interactions between the negatively charged head groups and the solid surfaces were ruled out as a possible explanation for the high contents of the admixtures adhering to the sediments.

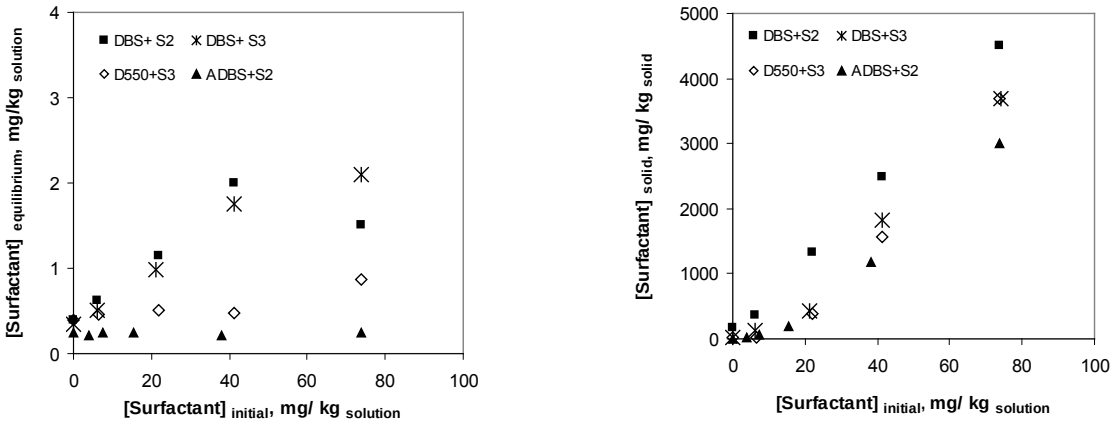

(a) (b)

Figure 5 – Surfactants concentrations in the (a) liquid and (b) solid phases at equilibrium after 7 days of curing.

As expected, the surfactants are also retained by the halite crystals, Figure 6, although in a much lesser extent than by the sediments. The coverage of the salt, and the consequent decrease in its equilibrium concentration, may help explaining the apparent loss of effectiveness of the surfactants for a content of 73 mg/$kg_{solution}$. Because the equilibrium concentration of calcium sulfate varies inversely with the content of sodium chloride at elevated concentrations of the latter salt, the relative solubility of $CaSO_4$, used as the evaluation tool for the surfactant performance, will increase only because the reference blank run is not affected by the same phenomenon.

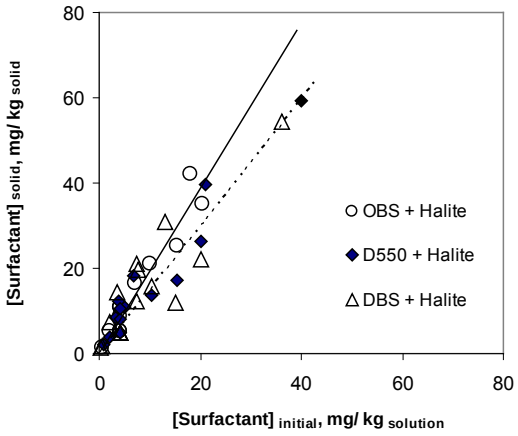

Figure 6 – Surfactants retention in halite crystals after 7 days of solid-liquid contact

Conclusions

Leaching of anhydrite-rich sediments with aqueous solutions of anionic C_{12}-benzene sulfonate surfactants reduces significantly the solubility of calcium sulfate. A maximum reduction of ≅70% was observed in the presence of halite, using brines containing about 40 mg/kg solution of the additives. The type of the surfactant head group (acid or sodium salt) does not influence the detergent performance, but the chain's length of the organic molecule is relevant to the hindering of calcium sulfate dissolution. The availability of the calcium salt in the solid, as well as the size of the "insoluble" debris within the cavern, play an important role on rate of dissolution of the calcium mineral and, therefore, on the contamination of the outgoing brine.

The reduction of the calcium sulfate equilibrium concentration from the negatively charged sediments cannot be attributed to electrostatic interactions between the solid surfaces and the charged head groups of the anionic surfactants. However, the behavior of the C_{12}BS surfactants may be interpreted in terms of the balance between the electrostatic repulsive forces of polar head groups and the attractive forces due to hydrophobic interaction. Aggregation of surface-active molecules stems from the insolubility of the non-polar moiety of the surfactant in the solution. The opposing hydrophilic interactions between polar head groups must be strong enough to ensure the self-assembly of the amphiphile. However, above a certain ionic strength threshold, the hydrophilic interactions are shielded, the driving force to expel the hydrophobic groups from solution augments and macroscopic phase separation occurs, Jönsson et al (1998). It can, therefore, be inferred from the results here obtained that for the examined surfactants a phase separation occurred in the saturated brines. The expelled organic phase, by adhering to the solid surfaces in the slurries, acts as a barrier to the dissolution of the mineral impurities.

References

Nancollas, G.H. and Zawacki, S.J. (1984) Inhibitors of crystallization and dissolution, *Industrial Crystallization 84*, 51-59.

Mahmoud, M.H.H., Rashad, M.M., Ibrahim, I.A. and Abdel-Aal, E.A. (2004). Crystal modification of calcium sulfate dihydrate in the presence of some surface-active agents, *J. of Colloid and Interface Science*, 270, 99-105.

Jönsson, B.; Lindman, B.; Holmberg, K. and Kronberg, B. (1998). *Surfactants and Polymers in Aqueous Solutions*, John Wiley & Sons, Chichester.

Acknowledgment

The financial support of Fundação para a Ciência e a Tecnologia, Portugal, for POCTI/QUE/59829/2004 is gratefully acknowledged.

Proceedings of the 10th International Chemical and
Biological Engineering Conference - CHEMPOR 2008
Braga, Portugal, September 4-6, 2008
E.C. Ferreira and M. Mota (Eds.)

Particle Agglomeration in Cyclones

Júlio Paiva[1], **Romualdo Salcedo**[1]*, **Paulo Araújo**[2]
[1]LEPAE, Departamento de Engenharia Química
Faculdade de Engenharia da Universidade do Porto
Rua Dr. Roberto Frias, s/n 4200-465 Porto, Portugal
[2] CUF - Químicos Industriais,
Quinta da Industria, 3860-680 Estarreja, Portugal

July 14, 2008

Keywords: Optimised Cyclones; Recirculation; Turbulent Dispersion; Particle Agglomeration
Topic: Advancing the chemical engineering fundamentals

Abstract

The purpose of this work is to build a model to predict in a more realistic way the collection efficiency of a gas cyclone recirculating system [Chibante et al., 2007; Salcedo et al., 2007]. These systems consist in an optimised reverse-flow cyclone combined with partial recirculation of uncaptured particles via a straight-through cyclone concentrator, with very high collection efficiencies (η > 90 %) for very fine particles.

The model starts by solving the particle trajectory in a turbulent flow field, and by fixing a set of parameters, it determines if a collision or an agglomeration occurs. In case of agglomeration, the initial particles will have a dynamic behaviour inside the gas-cyclone as a newly formed agglomerate. So the effective collection efficiency of the particles will be different from that proposed by current models, and will in fact increase. This can be observed in various experimental results, and usually referred as "hook-like" grade-efficiency curves.

The hypothesis of particle agglomeration within the cyclone turbulent flow seems a sound justification for the higher than predicted collection efficiencies observed for smaller particles inside a gas-cyclone.

1 Introduction

Collection efficiency models currently developed for gas cyclones, such as the Mothes and Löffer's model [Mothes and Loffler, 1988], can predict with high accuracy the collection efficiencies of particles with diameters above 3-4 μm.

Experimentally, it was observed at laboratory, pilot and industrial-scales that cyclone systems with or without recirculation can have complete collection below about 250 nm, viz the grade-efficiency curves have a very pronounced hook-like shape, showing a minimum in collection at an intermediate particle size (from about 0.8 to 2 μm). However, no model, to the authors' knowledge, can correctly predict this behaviour. Muschelknautz's model [Hoffman and Stein, 2002] predicts, at high solid loadings, a fairly constant value of collection efficiency for the smaller particles, since it is postulated that a portion of the feed is separated unclassified, but it does not predict the abnormal high collection for very fine particles at low loadings.

This abnormal behaviour for very fine particles is attributed to agglomeration within the cyclone turbulent flow field [Salcedo et al., 2007], much as it happens in recirculating fluidised beds [Mao et al., 2002; Sommerfeld, 2001]. Thus, this work concentrates on modelling this phenomena, by considering the particles' trajectories inside the cyclone and the probability of interparticle collisions. If some of

*Corresponding author. E-mail: rsalcedo@fe.up.pt., Phone +351-22-5081644, Fax +351-22-5081449

these collisions result in effective particle agglomeration, then one of the direct implications is that the particle size distribution actually processed by the gas cyclone differs from the feed size distribution to the cyclone.

In fact, upon agglomeration of fine particles by larger ones, the smaller particles will be captured as much larger particles, viz. with a much higher collection efficiency than that predicted by any of the currently available models. If the cyclone is highly efficient above about 4-5 μm, as it indeed happens with high efficiency cyclone systems, then the finest particles will also be collected with these extremely high efficiencies, and this could explain the minima observed in the grade-efficiency curves.

2 Modelling

A model was developed to predict the agglomeration inside a gas-cyclone, which has a fully-developed turbulent flow field. Afterwards, the model can reconstruct the path in terms of agglomeration of each particle, and take that history into account to rebuild the effective efficiencies of the initial (unagglomerated) particles.

Therefore the proposed model was obtained by combining the Mothes and Loffler [1988] model which predicts collection efficiencies in reverse-flow gas-cyclones, the Salcedo et al. [2007] model which is an extension to the Mothes and Loffler [1988] model to recirculating reverse-flow gas-cyclones and the Sommerfeld [2001] model which predicts the agglomeration of particles in turbulent flows.

2.1 Particle behaviour in turbulent flow

In this work, agglomeration was estimated using a stochastic Lagrangian approach of the inter-particle collisions in a turbulent field as proposed by Sommerfeld [2001] and Ho and Sommerfeld [2002]. This is a complex method to predict the evolution of each particle inside a control volume, hence, its simplified structure is presented in Figure 1.

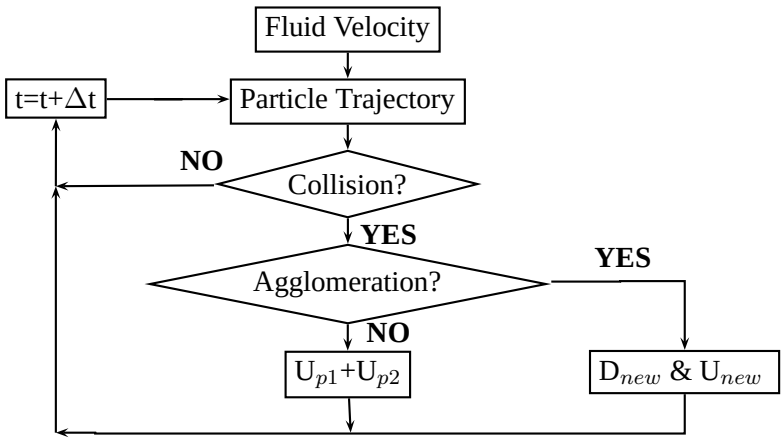

Figure 1: Scheme of the agglomeration model

Inducing a primary flow field in the control volume, we calculate the particles trajectories by integrating the following system of equations.

$$\frac{dx_{p,i}^N}{dt} = u_{p,i}^N \qquad i = 1\ldots3 \quad \wedge \quad N = 1\ldots N_{particles} \quad (1)$$

$$\frac{du_{p,i}^N}{dt} = \frac{3\,\rho_F c_D}{4\,\rho_p D_p^N}\left(u_{F,i} - u_{p,i}^N\right)\left|\overrightarrow{u_F} - \overrightarrow{u_p^N}\right| + g_i \qquad i = 1\ldots3 \quad \wedge \quad N = 1\ldots N_{particles} \quad (2)$$

Equation 1 solves the particle trajectory explicitly while Equation 2 calculates the particle velocity. This is directly related to some physical parameters such as the fluid and particle specific gravities and mainly of the relative velocity between the particle and the fluid.

Solving these equations in a predetermined flow field leads each particle to have a deterministic behaviour in the control volume. Therefore, to introduce turbulence into the system, the fluid velocity is changed, in consecutive time steps and at the same position, according to Equation 3.

$$u_{F,i}^{n+1} = u_{F,i}^{n} R_p + \left|u_{F,i}^{n}\right| \sqrt{1 - R_p^2} \times N\left(0,1\right) \tag{3}$$

The parameters associated with turbulence are taken into account in the variable R_p which is bounded to $[0, 1]$. As a short explanation of the impact of this variable in the final fluid velocity field, if R_p has a value near one, the velocity of the fluid in the next step has a strong correlation to the previous step, so the turbulence is low and the fluid velocity has almost a deterministic behaviour. However, if R_p has as value near zero, the velocity of the fluid in the next step has almost no correlation to the previous step, implying a strong turbulent flow and consequent almost random behaviour of the fluid velocity between consecutive time steps.

After obtaining the particles' trajectories in turbulent flow, a statistical criteria proposed by Sommerfeld [2001] is used to determine if a collision occurs between two particles or not. In the case where a collision occurs, using a momentum criteria the decision is made whether the result of the collision is an agglomerate or how the collision affects the velocities of the two particles. The formation of an agglomerate is determined by a number of parameters but has high dependency on the relative velocities of each particle. The process repeats itself, analysing all the binary interactions, until the final time of interaction is reached. No simultaneous three-particle or higher level interactions are considered.

The results of this part of the model are the final number distribution, which has stored the resulting number of particles after interaction (in their respective original class diameter), and the particle agglomeration history, which contains the time evolution of each resulting diameter.

2.2 Final particle decomposition

After obtaining the final number distribution the purpose is to follow the time dependent history of each of the resulting particles and/or agglomerates, taking in account that each agglomerate is a result of at least two particles, in order to build the particle size distribution that the cyclone actually "sees".

By using the information on the constitution of each new particle and of the final number of particles, an information matrix can be obtained, which allows to follow the path of each initial particle until the final agglomerates, and to calculate (backtrack) the effective efficiency of each class of initial particles.

Equation 4 presents the new class efficiency using the information matrix which is obtained from the final number distribution. This matrix (referred as **INFO**) has dimensions $N_{classes} \times N_{diameters}$ and each $N_{diameters}$ has a corresponding efficiency η_j calculated by the Mothes and Loffler [1988] model for the cyclone or by the Salcedo et al. [2007] model for the recirculating system, whatever is the case.

$$\eta_i^{new} = \frac{\sum_j \mathbf{INFO_{ij}} \times \eta_j}{\sum_j n_{ij}}, \qquad i = 1 \ldots N_{classes} \quad \wedge \quad j = 1 \ldots N_{diameters} \tag{4}$$

3 Results

In this section we present some results obtained using the proposed model. All the results were obtained with the cyclone geometry proposed by Salcedo and Candido [2001], with internal diameter = 447 mm and inlet mean velocity of 30 m/s, without partial recirculation of gases and particles. The trajectories of some particles in a turbulent flow are first presented followed by the effect of the agglomeration in terms of the number and mass distribution, ending with the presentation of a sensitivity analysis of some parameters of the model.

By solving Equations 1, 2 and 3 to obtain the trajectories of each particle and using this information, their behaviour is calculated inside the control volume. Figure 2 presents some of the basic steps of the model as an example of two intersecting trajectories and the corresponding generation of an agglomerate.

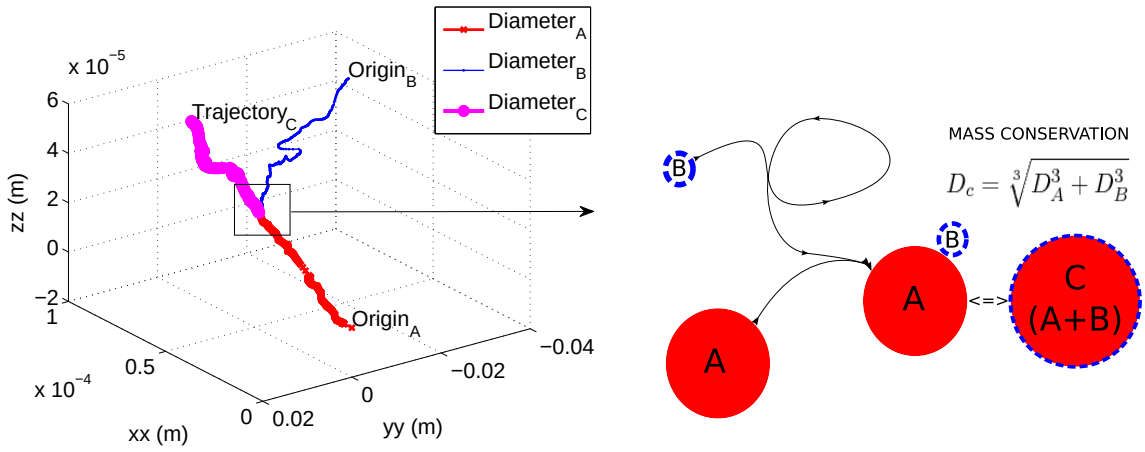

(a) Trajectories of two colliding particles and of generated agglomerate

(b) Diagram of formation of a new particle with mass conservation

Figure 2: Trajectories and agglomeration effect in two particles

Figure 2a presents the trajectories of two particles with different diameters. The larger particle has a more deterministic trajectory while the smaller particle has a more random trajectory, which is a direct result of solving the system of equations presented by Equations 1 and 2. In this case, the particles collide in their trajectories and the result is a formation of a new agglomerate. The trajectory of this new agglomerate is calculated solving the momentum equations, and the resulting particle has a tendency to follow the trajectory of the larger particle.

To better understand the process of formation of new particles, we present in Figure 2b one scheme to illustrate the calculation of the new diameter of the agglomerate. This calculation takes into account the mass conservation of the particles.

The mass distribution is an input to the model. After some pretreatment, the model converts the information stored in this distribution to a number distribution. After completing the part of the model presented in Section 2.1, the model calculates the final number distribution and recalculates the corresponding mass distribution. Figure 3 shows the initial and final number and mass distributions before and after particle interaction/agglomeration.

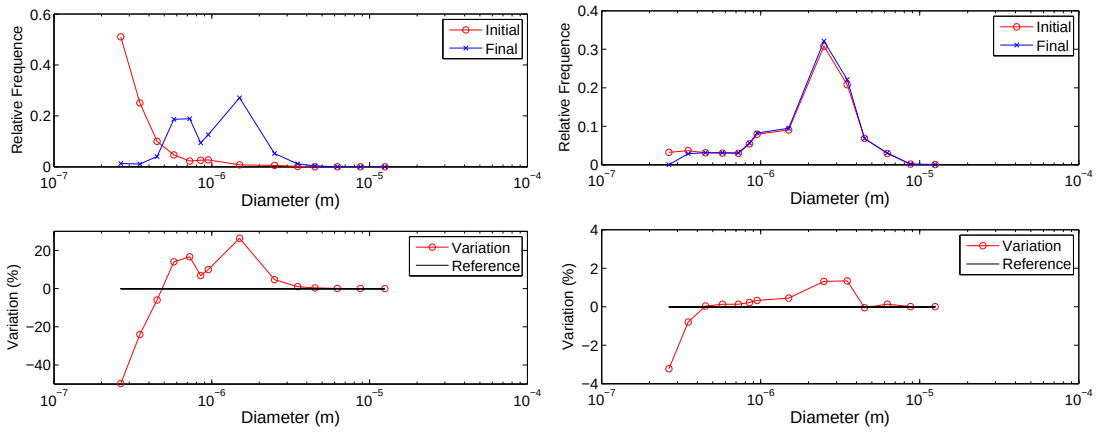

(a) Number Distribution

(b) Mass Distribution

Figure 3: Changes in the each distribution

Figure 3a shows that the modal class in the beginning corresponds to the first class (corresponding to a

diameter around 0.3 μm). Analysing the result of the model, there is a displacement of the finer particles towards diameters both below and above 1 μm. This proves that the smaller particles are disappearing (the variation of the first three classes is negative) and indicates that there is formation of larger particles (the variation of the next five classes is positive).

Figure 3b shows the corresponding implications for the initial and final volume (mass) distributions. The reduction in the mass of the smaller particles and the increase in the mass of the particles above 1 μm is clearly seen.

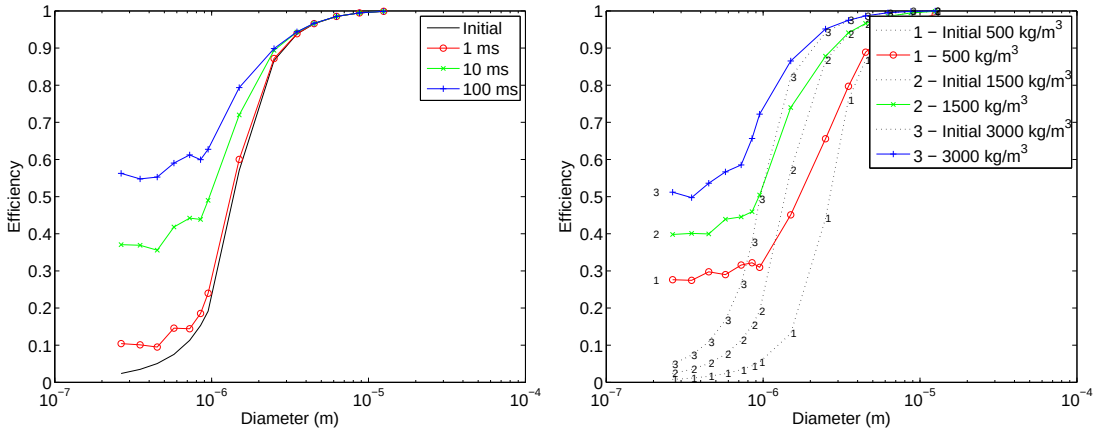

(a) Time of interaction: 6 μm, 1500 kg/m^3, 700 mg/m^3 **(b)** Specific Gravity: 10 ms, 6 μm, 700 mg/m^3

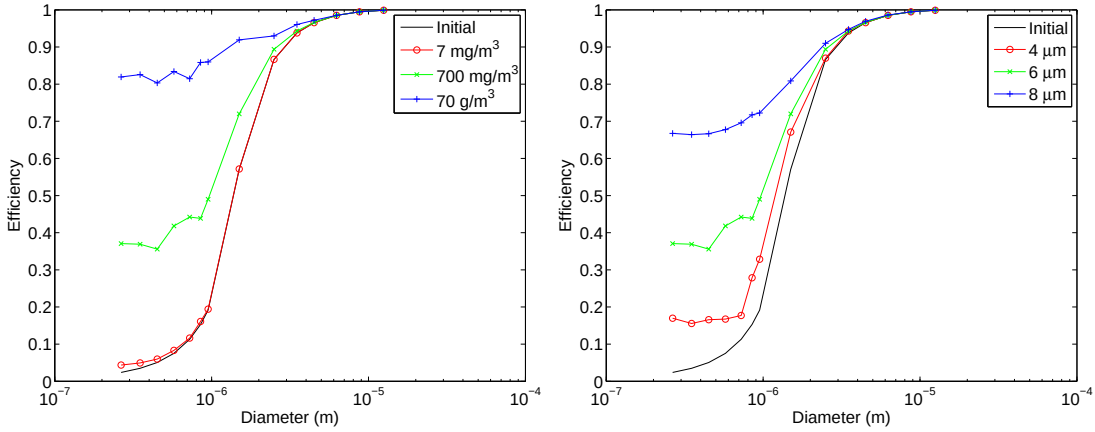

(c) Concentration: 10 ms, 1500 kg/m^3, 6 μm **(d)** Cut-Diameter: 10 ms, 1500 kg/m^3, 700 mg/m^3

Figure 4: Sensitivity analysis of some of the parameters of the model

Figure 4 shows the grade-efficiency curves and the sensitivity to some model parameters. The chosen parameters were the time of interaction, the particle specific gravity, the particle concentration and the cut-diameter of the initial distribution, viz, the maximum allowable particle present in the original distribution. In each situation, the reference case has the following values: time of interaction (**10** ms), particle specific gravity (**1500** kg/m^3), cut-diameter (**6** μm), concentration (**700** mg/m^3).

Synthesising the information obtained in the sensitivity analysis of the model, we can observe that as the time of simulation increases (Figure 4a), higher efficiencies are obtained for the smaller particles.

Figure 4b presents the initial efficiency without agglomeration varying the particle specific gravity. The prediction of the Mothes and Loffler [1988] model increases as expected, as we increase the particle specific gravity. In terms of agglomeration, the agglomeration model leads to higher efficiencies as we increase this parameter, due to the initially higher theoretical efficiency for all the diameters.

Another important parameter of the model is the particle concentration, and Figure 4c gives the effect of this parameter. If the concentration is very low, the collision and consequent agglomeration will be two phenomena with almost no significance due to the small number of particles present in the control

volume. Therefore, as expected with low concentration, the results after agglomeration are almost those initially predicted by Mothes and Loffler [1988]. On the other hand, for the higher concentrations, the agglomeration phenomena has increasing relevance, so the final efficiency of the smaller particles increases substantially over the base-case.

Figure 4d shows the influence of the cut-diameter on the initial distribution. This parameter determines directly the initial highest diameter available for collision and as this parameter increases, higher efficiencies are obtained for the smaller particles. This is justified by the fact that, as we increase the cut-diameter, we have more larger particles to interact, and injecting more quantity of larger particles implies that there are more particles available with collection efficiencies around 100 % to collect the smaller ones. In this case we can observe that the results are also much smoother, which may simply mean that the "noise" of the results has been reduced by injecting more particles in the control volume.

4 Conclusions

The agglomeration model presented in this work has yet some parameters which must be further studied, like the collision properties or the influence of the material under study, but at the present moment, the model can predict in qualitative manner the increase of the efficiencies of the smaller particles observed experimentally.

The agglomeration phenomena seems to be a good justification of the larger observed collection efficiencies obtained experimentally for fine particles using cyclones. After an initial sensitivity analysis, we conclude that this model may lead to results closer to reality.

This model is an improvement of the existing models developed to predict grade-efficiency curves in gas-cyclones being expected that, after further studying the parameters of the model, theoretical results qualitatively nearer to the experimental ones may be obtained, allowing a more correct optimisation of the design of gas-cyclones.

5 Acknowledgements

The authors would like to thank to FCT (Fundação para a Ciência e Tecnologia) for the grant BDE/15628/2006 and for the Co-financing of the industrial partner CUF-Químicos Industriais S.A..

References

Chibante, V., et al. Dry scrubbing of acid gases in recirculating cyclones. *Journal Of Hazardous Materials*, 144(3):682–686, 2007.

Ho, C. A. and Sommerfeld, M. Modelling of micro-particle agglomeration in turbulent flows. *Chemical Engineering Science*, 57(15):3073–3084, 2002.

Hoffman, A. C. and Stein, L. E. *Gas Cyclones and Swirl Tubes - Principles, Design and Operation*. Springer, second edition, 2002.

Mao, D., et al. A model for fine particle agglomeration in circulating fluidized bed absorbers. *Heat Mass Transference*, 38:379, 2002.

Mothes, H. and Loffler, F. Prediction of particle removal in cyclones separators. *International Chemical Engineering*, 28:231, 1988.

Salcedo, R. L. R. and Candido, M. G. Global optimization of reverse-flow gas cyclones: application to small-scale cyclone design. *Separation Science and Technology*, 36(12):2707–2731, 2001.

Salcedo, R. L. R., et al. Fine particle capture in biomass boilers with recirculating gas cyclones: Theory and practice. *Powder Technology*, 172(2):89–98, 2007.

Sommerfeld, M. Validation of a stochastic lagrangian modelling approach for inter-particle collisions in homogeneous isotropic turbulence. *International Journal Of Multiphase Flow*, 27(10):1829–1858, 2001.

Proceedings of the 10th International Chemical and
Biological Engineering Conference - CHEMPOR 2008
Braga, Portugal, September 4-6, 2008
E.C. Ferreira and M. Mota (Eds.)

Extending Kozeny-Carman permeability model to highly porous media

Manuel Mota*, Alexander Yelshin
IBB – Institute for Biotechnology and Bioengineering, Centre of Biological Engineering, University of Minho, Campus de Gualtar, 4710–057 Braga, Portugal.

Keywords: Permeability, Porosity, Tortuosity, Shape factor, Model
Topic: Advancing the chemical and biological engineering fundamentals.

Abstract

Anomalous normalised permeability as a ratio of permeability to square of particle size for snow, diatomite, kieselgel was considered using Kozeny-Carman model and tortuosity factor defined as the square of average tortuosity pathway. Since the Kozeny-Carman model is based on the geometrical models of a capillary tube, the model adopted for high porous media with shaped particles (often with fractal properties) becomes complex. To show how the problem of permeability may be complex, two types of particles are analysed in porous media: snowflakes and diatomite and kieselguhrs. Snowflakes are typical fractal particles, whereas diatomite and kieselguhr can form pores with fractal tortuosity. Based on theoretical investigation a model including fractal measurements for void and solid phases and dependence of tortuosity on packing porosity is proposed. The obtained results show that within the developed model we can describe a wide range of porous media with different fractality and tortuosity. Based on presented numerous examples it was concluded that further experimental investigation should be useful to improve the model and validate the application range.

1. Introduction

Highly porous media play a significant role in many practical applications including nanotechnology, biomedicine, fuel cells, catalysis etc. However, the interpretation of experimental permeability data is difficult whenever the particle shape or particle arrangement becomes significantly different of conventional granular packing.

In this case conventional Kozeny-Carman model (1) does not satisfy experimental conditions

$$k = \frac{\varepsilon^3}{K_0 \tau^2 (1-\varepsilon)^2 S^2} = \frac{d^2 \varepsilon^3}{36 K_0 \tau^2 (1-\varepsilon)^2} = \frac{d^2 \varepsilon^3}{72 \tau^2 (1-\varepsilon)^2} \quad (1)$$

where k is the permeability, 1/m; S is the specific surface area based on the solid volume; $d = 6/S$ is the equivalent spherical particle size; ε is the porosity; $K_0 \tau^2$ includes tortuosity τ (ratio of average pathway to the porous medium thickness) and K_0 - a coefficient dependent on the pore cross-section shape (for cylindrical pores K_0 = 2). In particular cases model (1) may be used in the form

$$k = (d^2 \varepsilon^3) / [180(1-\varepsilon)^2] \quad (1a)$$

As Kozeny-Carman model is based on the geometrical models of a capillary tube, then the model adopted for high porous media with shaped particles (often with fractal properties) becomes complex (see Figs. 1 - 2).

In some cases porous media with fractal wall surface do not have a fractal tortuosity of pore channels, as in Fig. 1 (a-b) or, in contrary, display a fractal dimension dependent

* Corresponding author. Tel + 351-25360-1191. E-mail: MMota@reitoria.uminho.pt

on a channel topology, as in Fig. 1 (c-e). In theses examples two fractal curves with different fractal dimension were used to built the pore channels: (a) von Koch snowflake curve, fractal dimension 1.26, has 4 levels of structure, each level with tortuosity τ_i = 4/3, and the overall tortuosity of the curve is $\tau \approx$ 3.16, Fig. 1a; the (b) curve has fractal dimension 1.5, 3 levels of structure, each level with a tortuosity τ_i = 2, and overall tortuosity of the curve is τ = 8, Fig. 1b. The case in Fig. 1 (a-b) corresponds to the symmetrical pore channel with fractal perimeter (contour) where a centreline geometrical tortuosity is equal to 1.

In the case of non-symmetrical pore channels, Fig. 1 (c) and (d), built by fractal curves of types (a) and (b), they have a centreline tortuosity of τ = 1.97 and 2.62 with a fractal dimension of 1.01 and 1.03. In turn, in case (e), tortuosity is much higher, τ = 8, and the fractal dimension of pore channel walls is 1.5. Moreover, the porous medium fractal dimension is dependent on porosity and on the particle shape.

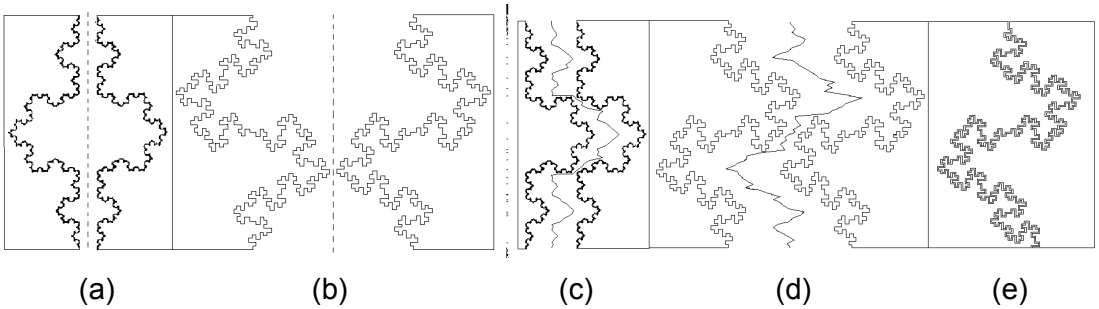

Figure 1. Two symmetrical pore channels built by fractal curves (See text) having the average geometrical tortuosity τ = 1.0, case (a) and (b). Non-symmetrical pore channels built by fractal curves, cases (c-d).

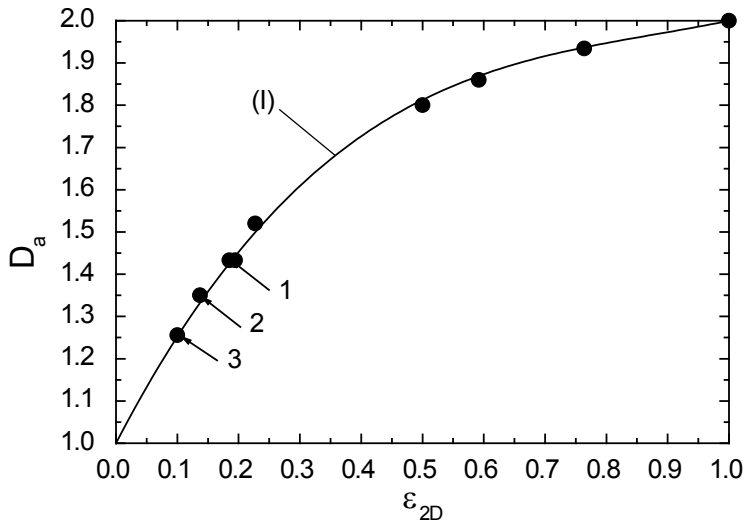

Figure 2. Fractal dimension D_a vs. ε_{2D} for regular packing of discs: 1 – square packing; 2 – hexagonal packing; 3 – discs square arrangement of two sizes (space between large size square packing filled by inscribed discs). I – correlation function.

Porous media porosity is one of the most important characteristics involved in all models of mass and heat transfer. Dependence of the 2D porous media fractal properties on porosity (ε_{2D}) is shown in Fig. 2, where a disc type porous structures are presented. Increasing porous media complexity (the structure deviates from uniformity)

renders the topological properties of the system (fractal dimension) dominant.

As can be seen, porosity and tortuosity are interrelated and both connected with fractal properties of porous media and properties interplay gives different results. For instance, a carbon felt (*Le Carbone Lorraine*, RVC 4002) for electrodes has the porosity 0.98 and tortuosity 5 – 6, (González-Garcia et al., 1999); α-alumina catalyst pellet, ε = 0.68, average tortuosity 4.0,(Dogu et al. ,1989); iron-based Fischer-Tropsch catalyst, ε = 0.628, tortuosity ~ 6.0, (Eaton et al. , 1995); mica (powdered) and vermiculite at porosity 0.85 – 0.9 have tortuosity over 2.0, (Currie ,1960).

2. Theoretical background

To show how the problem may be complex, two types of particles are considered below: snowflake and diatomite/kieselguhr.

Jordan et al. (1999) summarised and analysed published and own experimental data on snow permeability by using Kozeny-Carman model in the form (1a) and an approach of the form

$$k = 0.077 d^2 \exp(-0.0078 \rho_i (1-\varepsilon)) \qquad (2)$$

where ρ_i = 917 is ice density, kg/m^3.

Normalised experimental snow permeability k/d^2 together with models (1a) and (2) are shown in Fig. 3, where some data for low-density snow are below theoretical predictions for a granular bed (curve 1) as well as for a model (2), curve 2.

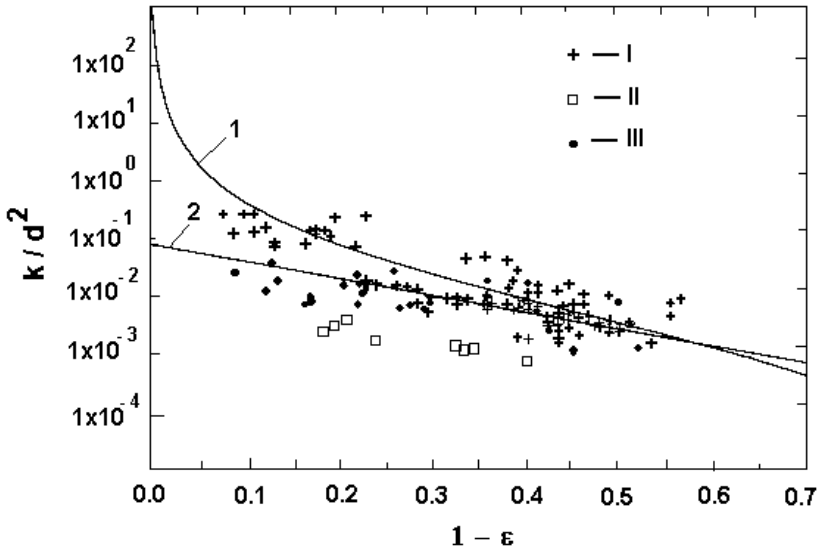

Figure 3. Reduced permeability k/d^2 vs. ice fraction $\phi = 1-\varepsilon$ as presented by Jordan (1999) in fig. 7. I – Shimizu, Ishido and Shimizu data; II – Sommerfeild and Rocchio data; III - Jordan data. 1 – granular bed model, equation (1a); 2 – approach, equation (2).

According to snow classification by solid fraction and permeability (Jordan , 1999), the main part of snow samples which does not fit to the above mentioned models belong to wind-packed (dense) and new snow (low density) which leads to consider particle shape as an important parameter of the permeability behaviour. However, in (2) we can speculate that $(1-\varepsilon)$ is accounted for in fractal properties as well.

For non-spherical particle the model (1) may be partially corrected by introducing a sphericity factor Φ of a particle as the ratio of the surface area of a sphere S (with the same volume as the given particle) to the surface area of the particle S_p, $\Phi = S/S_p$, hence, $d_p = 6/S_p = 6\Phi/S = \Phi d$. In this case, fractal behaviour may affect all or part

of variables (Xu and Yu, 2008): pore space (ε), solid ($1-\varepsilon$) or ratio $\varepsilon/(1-\varepsilon)$, and tortuosity ($\tau$).

In general, the tortuosity depends on porosity and may be presented in the form $\tau = a/\varepsilon^n$ ($n \geq 0$; $a \geq 1$, conventionally a = 1). By substituting τ and Φ in (1) and introducing the normalised permeability we have the following $k/d^2 = (\Phi^2/K_0)[\varepsilon^3/(36\cdot(a/\varepsilon^n)^2(1-\varepsilon)^2)]$. The value of K_0 depends on a pore cross-section configuration that, in turn, reflects the particles shape. Since the exact relations between Φ, K_0 and ε are unknown, complex $\Phi^2/(K_0 a^2)$ can be considered as the fitting coefficient $1/A$.

If we assume that in porous media structure particles are generated from sub-units of smallest scale, as shown in Fig. 4, then external and internal factors may yield substantial particle transformation. In the case of snow, primary snowflake melting results in porous media compaction and in structural degradation, with loss of fractal properties and an approach to granular packing.

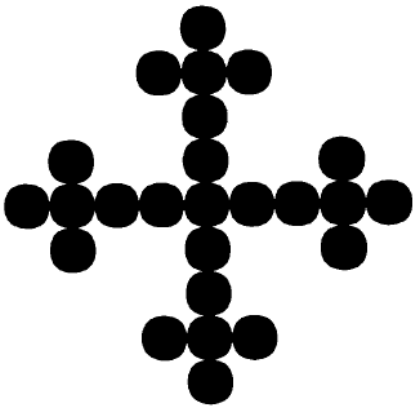

Figure 4. Simplified representation of a complex primary particle structure build by sub-units.

Structural properties based upon fractal analysis must be introduced in normalised permeability under the form of ΔD and $\Delta_1 D\cdot\varphi(\varepsilon)$ as fractal measures for void and solid phases, where $0 \leq \Delta D \leq 1$, $0 \leq \Delta_1 D \leq 1$, and $\varphi(\varepsilon)$ is a function accounting for deviation of porous media from granular packing. Finally, dependence of normalised permeability on porosity becomes

$$k/d^2 = \frac{\varepsilon^{3\Delta D}}{36A(1/\varepsilon^n)^2(1-\varepsilon)^{2\Delta_1 D\cdot\varphi(\varepsilon)}} = \frac{\varepsilon^{3\Delta D+2n}}{36A(1-\varepsilon)^{2\Delta_1 D\cdot\varphi(\varepsilon)}} \qquad (3)$$

3. Discussion

Two types of particles are presented in Fig. 5: snowflakes (shaded area occupied by data of Jordan et al. (1999)), diatomite (I), from Yoon et al. (1992) and kieselguhrs (II), Mota et al. (2000, 2003). Snow represents fractal particles, whereas diatomite and kieselguhr can form pores with a significant fractal tortuosity.

Application of relation (1a) and model (2) as proposed for the snow layer (Fig. 5), gives rise to curves 1 and 2, respectively. Ignoring dependence of τ on ε does not allow covering the whole region of experimental data. Conventional model (1) has as upper limit τ = 1.0 and curve 1′ is far from the experimental bounds.

The model (3) was accepted and deviation from granular packing $\varphi(\varepsilon)$ was assumed

to be $\varphi(\varepsilon) = 1 + \varepsilon_0 - \varepsilon$. The function $\varphi(\varepsilon)$ = 1 when $\varepsilon = \varepsilon_0$ where ε_0 has a value in the range 0.3 – 0.45 and is defined as a fitting parameter.

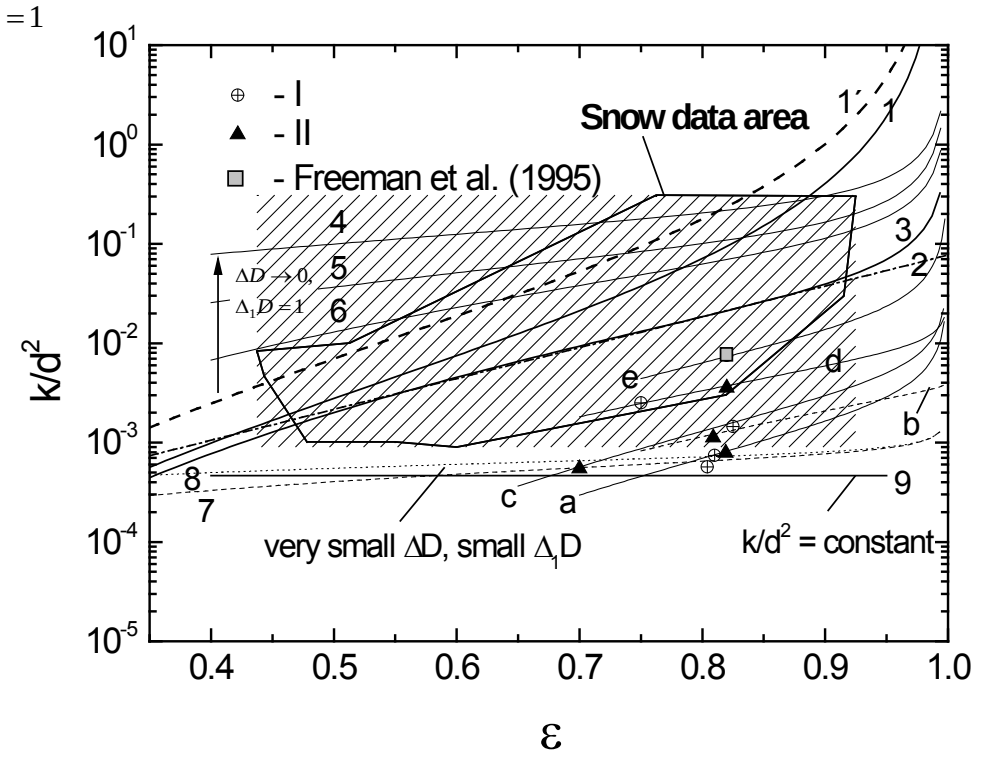

Fig. 5. Normalised permeability k/d^2 vs. porous media porosity. Shaded area is occupied by snow data of Jordan et al. (1999). 1 – equation (1a); 1´ – case (1) when τ = 1; 2 – relation (2); 3 – fitting relation (2) by model (3). Curves a – e are fitting data of mineral porous media: a - Kieselguhr fine; b – Kieselgel; c - Radiolite 600; d - Dialite UND; e – Kieselguhr. For curves 4 – 9 see the text.

Table 1. Coefficients of model (3) for curves presented in Figure 5

Curve	ΔD	$\Delta_1 D$	n	ε_0	A
4	0	1	0	0.42	1
5	0.1	1	0.1	0.45	2
6	0.3	1	0.5	0.4	2
3	0.69	1	0.6	0.4	5
Granular packing	1	1	0.4-0.5	$\varepsilon_0 = \varepsilon$	2
e	1	1	0.5	0.35	10.54
d	1	0.35	0.5	0.35	6.36
b	1	0.05	1	0.3	8.64
c	1	0.78	1	0.35	27.8
a	1	0.8	1	0.38	58.4
7	0.05	0.25	0.25	0.4	60
8	0.05	0.25	0.025	0.4	60
9	0	0	0	--	60

The obtained results show that within model (3) we can describe a wide range of porous media. In particular for snow, correlation (2), curve 2, is well fitted by model 3 (curve 3) with the following parameters: ΔD = 0.69, n = 0.6, A = 5, and ε_0 = 0.4. For new snow, in particular, a tendency (Fig. 5, arrow) to increase the permeability was found, when

$\Delta D \to 0$ and $\Delta_1 D = 1$. Curve 4 corresponds to the case $\Delta D = 0$, $\tau = 1$, when A = 1: $k/d^2 = 1/[36(1-\varepsilon)^{2(1.42-\varepsilon)}]$. Moreover, model (3) at $\varepsilon \to$ 1 gives $k/d^2 \to \infty$, whereas correlation (2) gives finite normalised permeability value. Examples of fitting data of mineral porous media by (3) are given by curves a – e and are also presented in Table 1: a - Kieselguhr fine; b – Kieselgel; c - Radiolite 600; d - Dialite UND; e – Kieselguhr.

Dependences 7 – 9 are hypothetic and simulate cases of very small ΔD. With decreasing ΔD and $\Delta_1 D$ we observe insignificant linear changes in k/d^2 and in limited case of ΔD and $\Delta_1 D$ equal zero dependence (3) becomes constant $k/d^2 = 1/(36A)$, as seen in Fig 5, bottom, curve 9. Even in the hypothetic case of A = 60 and a = 1 for Φ = 0.5 we have K_0 = 15. Assuming a = 1.5, K_0 becomes 6.7 and at a = 2 K_0 = 3.75. Formally, this situation is related with the degradation of porous media structure when tortuosity weakly depends on porosity, which is typical for non-granular porous media. For instance, when porous media contain homogeneous pores similar in length the porosity totally depends on number of pores on unit area of porous medium. Fractality behaviour of such systems is not enough investigated.

Model (3) allows simulating and predicting permeability or other parameters when experimental data are scarce.

4. Conclusion

Obtained results form the modified Kozeny-Carman model show that application of the fractal approach to the porous media void space as well as to solid phase enables to extend the model to highly porous media. The obtained results show that within the developed model we can describe a wide range of porous media with different fractality and tortuosity. In spite of the numerous examples presented, further experimental investigation will be useful to improve the model and validate its application range.

References

González-Garcia, J., Bonete, P.B., Expósito, E., Montiel, V., et al. (1999). *J. Mater. Chem.*, 9, 419-426.

Dogu, G., Pekediz, A., Dogu, T. (1989). *AIChE Journal*. 35, 1370-1375.

Eaton, A., Bukur, D.B., Akgerman, A. (1995). *J. Chem. Eng. Data.* 40, 1293-1297.

Currie, J.A. (1960). *Brit. J. Appl. Phys.* 11, 318-324.

Jordan, R.E., Hardy, J.P., Perron, F.E., Fisk, Jr.J., et al. (1999). *Hydrological Processes*, 13, 1733-1753.

Xu, P., Yu, B. (2008). *Advances in Water Resources*, 31, 74–81.

Yoon, S.-H., Murase, T., Iritani, E. (1992). *Int. Chem. Eng.*, 32, 172-180.

Mota, M., Teixeira, J. A., Bowen, R., Yelshin, A. (2000). *Proc. 8-th World Filtration Congress, 3-7 April 2000*, Volume 1, Filtration Society, Brighton, UK, 57-60.

Mota, M., Teixeira, J. A., Bowen, R., Yelshin, A. (2003). *Minerals Engineering*. 16, 135-144.

Freeman, G.J., Mckechnie, M.T., Smedley, S.M., Hammond, R.V., et al. (1995). *Trans. IChemE*, 73, 157-164.

Proceedings of the 10th International Chemical and
Biological Engineering Conference - CHEMPOR 2008
Braga, Portugal, September 4-6, 2008
E.C. Ferreira and M. Mota (Eds.)

Observation of Inertial Particle Motion in Laminar Flow in a Stirred Vessel

Naoto Ohmura[1*], Nami Nishioka[1], Alatengtuya[1], Mohamed N. Noui-Mehidi[2], Jie Wu[2], Norihisa Kumagai[1], Teiji Takigawa[3]

[1]Graduate School of Engineering, Department of Chemical Science and Engineering, Kobe University, 1-1 Rokkodai, Nada-ku, Kobe 657-8501, Japan.

[2]Manufacturing and Material Technology, CSIRO, 37 Graham Road, Highette, Vic. 3190, Australia

[3]Process Research Laboratories, Kashima Plant, Eisai Co. Ltd., 22 Sunayama, Hasaki-machi, Kashima, Ibaraki 314-0255, Japan

Keywords: Stirred Vessel, Laminar Flow, Particle Motion, Solid-Liquid Flow, Nonlinear Dynamics,
Topic: Multiphase Flow.

Abstract

Inertial particle motion in a stirred vessel with no baffle plate was observed experimentally and numerically at low Reynolds numbers. Several particles were captured on a torus orbit within one of the IMRs and kept traveling around the impeller. The particles captured in the IMRs enhance the exchange of material with the outside active mixing region.The primary and secondary circulation flow directions were defined ϕ- and θ-direction respectively. Initially, particle orbit obtained by Poincaré section showed that the particle motion covered the full surface of the torus orbit and the ratio of the period for one round of a particle in ϕ-direction to that in θ-direction, P_θ / P_ϕ, was irrational, while after a long time, the circular orbit on the Poincaré section converges on three discrete points and P_θ / P_ϕ was rational. Numerical simulation revealed that even after a particle seemed to have almost settled on a final orbit, the diameter of secondary circulation was not constant. After a particle has been captured, the drag force frequently works on the surface of the particle since the particle always exists near the impeller.

1 Introduction

Mixing is one of the most important unit operations in chemical and biochemical industries. Stirred vessels commercially available in a wide variety of sizes and impeller configurations are the most frequently used to homogenize different substances, to conduct chemical reactions and to enhance mass transfer between different phases. Owing to their versatility, stirred vessels can be operated under a wide range of conditions. Although turbulent flow is efficient for mixing, some situations require laminar mixing, e.g. for high viscosity fluids and shear-sensitive materials. Koiranen *et al.* (1995) proposed specific principles for effective mixing in laminar flow mixing regimes for highly viscous liquids or shear-sensitive materials. In the laminar flow mixing regimes, however, global mixing is inefficient due to the existence of isolated mixing regions (IMRs). Much attention has been paid to how to eliminate IMRs at low Reynolds numbers. Lamberto *et al.* (1996) and Yao *et al.* (1998) demonstrated that IMRs could be eliminated by using an unsteady rotation method.

The authors (Nishioka *et al.*; 2007) found that particles released at the liquid surface were captured by the recirculation of IMRs. This phenomenon may conceivably affect laminar mixing characteristics in a stirred vessel. Futhermore, solid-liquid two-phase flows in stirred vessels are often encountered in industrial processes.The present work, therefore, observed inertial particle motion in a stirred vessel with no baffle plate experimentally and numerically at low Reynolds numbers.

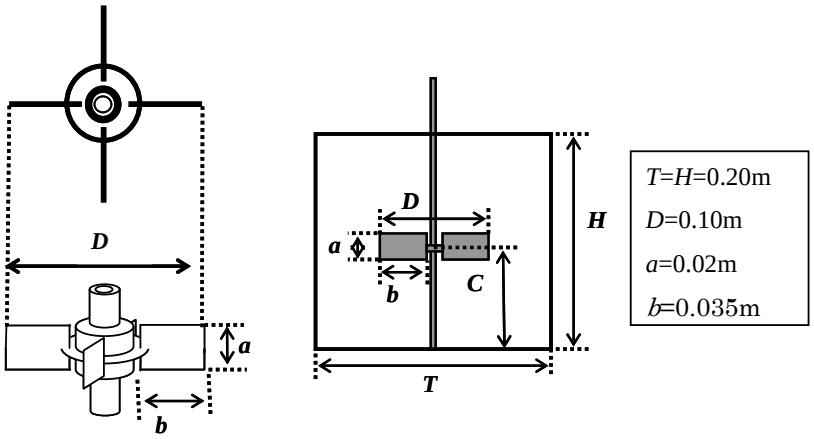

Fig. 1 Schematic of stirred vessel

2 Experiment and Numerical Simulation

In this study, inertial particle motion in a stirred vessel was investigated experimentally and numerically at low Reynolds numbers (*Re* = 10, 30). The mixing system consists of a cylindrical flat-bottom vessel without baffle and a 4-bladed Rushton turbine, as shown in Figure 1. In order to reduce photographic distortion, the cylindrical vessel was immersed in a square vessel of acrylic resin filled with the same glycerine solution. The ratio of impeller off-bottom clearance to the tank diameter *C*/*T* was 0.5. The working fluid was glycerine (ρ = 1260 kg/m^3, μ = 1.4 Pa·s).

Fluorescent pH-sensitive neutrally-buoyant green dye was used as a passive tracer to observe the mixing process. The working fluid was initially made basic by a small amount of basic solution consisting of 0.5 N NaOH and glycerine. After the turbine reached a certain rotational speed, a small amount of acidic solution consisting of 0.5 N HCl and glycerine was carefully added at the top of the vessel so as to decolorize the green dye by a neutralization reaction.The trajectories of resin particles having the density of 1377–1663 kg/m^3 and the diameter of 5 mm were analyzed using image processing. After a steady state was achieved, 10 particles were released on the upper surface at 1 or 5 cm away from the impeller axis.

The commercial CFD code RFLOW (Rflow Co, LTD) was used for the simulation of the motion of a particle. This numerical code is based on the finite volume method and makes it possible to simulate particle motion by a particle tracking method. All numerical conditions except particle size and particle density were the same as those for the experiment. The number of computational mesh is 60×60×60 in radial, circumferential and axial directions, respectively. Particle size and particle density were changed from 1.0×10^{-6} to 1.0×10^{-3} m and from 1200 to 1300 kg/m^3, respectively. Each particle was generated at the top of the device. At the first step, flow fields were obtained by solving the three-dimensional Navier-Stokes equations and the mass conservation for incompressible fluid in cylindrical coordinates, as shown in Eqs (1) –(4).

$$\rho\left(\frac{\partial v_r}{\partial t}+v_r\frac{\partial v_r}{\partial r}+\frac{v_\theta}{r}\frac{\partial v_r}{\partial \theta}-\frac{v_\theta^2}{r}+v_z\frac{\partial v_r}{\partial z}\right)=-\frac{\partial P}{\partial r}+\mu\left[\frac{\partial}{\partial r}\left\{\frac{1}{r}\frac{\partial}{\partial r}(rv_r)+\frac{1}{r^2}\frac{\partial^2 v_r}{\partial \theta^2}-\frac{2}{r^2}\frac{\partial v_\theta}{\partial \theta}+\frac{\partial^2 v_r}{\partial z^2}\right\}\right]+\rho g_r \quad (1)$$

$$\rho\left(\frac{\partial v_\theta}{\partial t}+v_r\frac{\partial v_\theta}{\partial r}+\frac{v_\theta}{r}\frac{\partial v_\theta}{\partial \theta}+\frac{v_r v_\vartheta}{r}+v_z\frac{\partial v_\theta}{\partial z}\right)=-\frac{1}{r}\frac{\partial P}{\partial \theta}+\mu\left[\frac{\partial}{\partial r}\left\{\frac{1}{r}\frac{\partial}{\partial r}(rv_\theta)+\frac{1}{r^2}\frac{\partial^2 v_\theta}{\partial \theta^2}+\frac{2}{r^2}\frac{\partial v_\theta}{\partial \theta}+\frac{\partial^2 v_r}{\partial z^2}\right\}\right]+\rho g_\theta \quad (2)$$

$$\rho\left(\frac{\partial v_z}{\partial t}+v_r\frac{\partial v_z}{\partial r}+\frac{v_\theta}{r}\frac{\partial v_z}{\partial \theta}+v_z\frac{\partial v_z}{\partial z}\right)=-\frac{\partial P}{\partial z}+\mu\left\{\frac{1}{r}\frac{\partial}{\partial r}\left(r\frac{\partial v_z}{\partial r}\right)+\frac{1}{r^2}\frac{\partial^2 v_z}{\partial \theta^2}+\frac{\partial^2 v_z}{\partial z^2}\right\}+\rho g_z \quad (3)$$

$$\frac{1}{r}\frac{\partial(rv_r)}{\partial r}+\frac{1}{r}\frac{\partial v_\theta}{\partial \theta}+\frac{\partial v_z}{\partial z}=0 \tag{4}$$

Then the particles were tracked by solving Eq. (5),

$$\rho_p\frac{d\mathbf{V}_p}{dt}=\frac{3}{4d_p}C_D\rho_f\left|\mathbf{V}-\mathbf{V}_p\right|\left(\mathbf{V}-\mathbf{V}_p\right)+\rho_f\frac{D\mathbf{V}}{Dt}+\frac{1}{2}\rho_f\left(\frac{D\mathbf{V}}{Dt}-\frac{D\mathbf{V}_p}{Dt}\right)+\left(\rho_p-\rho_f\right)\mathbf{g} \tag{5}$$

where $\mathbf{V}_p$ is the velocity of the particle, $\mathbf{V}$ is the velocity field of the fluid, d_p is the particle diameter, ρ_p is particle density, ρ_f is fluid density, $\mathbf{g}$ is gravitational acceleration and C_D is the drag coefficient. The Basset history force, which is important in the initial motion of a particle starting from rest under certain conditions, was neglected.

3 Results and Discussion

As shown in Figure 2, when particles were released on the surface at 1.0 cm away from the impeller, several particles were captured on a torus orbit within the lower IMR and kept traveling around the impeller, while the rest of the particles sunk to the bottom of the vessel. On the other hand, when particles were released on the surface at 5.0 cm away from the impeller, several particles were captured on a torus orbit within the upper IMR (not shown in Figure 2). Initially, two IMRs clearly can be seen in Figure 2 a), After 18 h, the upper IMR is still visible, while the lower IMR is decolorized as shown in Figure 2b). This result indicates that particles caputured in the IMRs enhance the exchange of material with the outside active mixing region.

In our previous works (Ohmura *et al.*, 2003; Nishioka *et al.*, 2007), the primary and secondary circulation flow directions were defined as ϕ- and θ-direction respectively and the period for one round of a particle in ϕ-and θ-direction were also defined as P_ϕ and P_θ. This work also followed the above manner and investigated the relation between P_θ and P_ϕ of the particle captured in the IMRs. In order to clarify particle orbit within IMR, this work constructed Poincaré sections corresponding to an arbitrary plane cutting a torus orbit transversally in the manner of nonlinear dynamics. Particle orbit obtained by Poincaré section obtained particle obit initially shows that the particle motion covers the full surface of the torus orbit and P_θ/P_ϕ of the particle is irrational, as shown in Figure 3 a).

a) b)

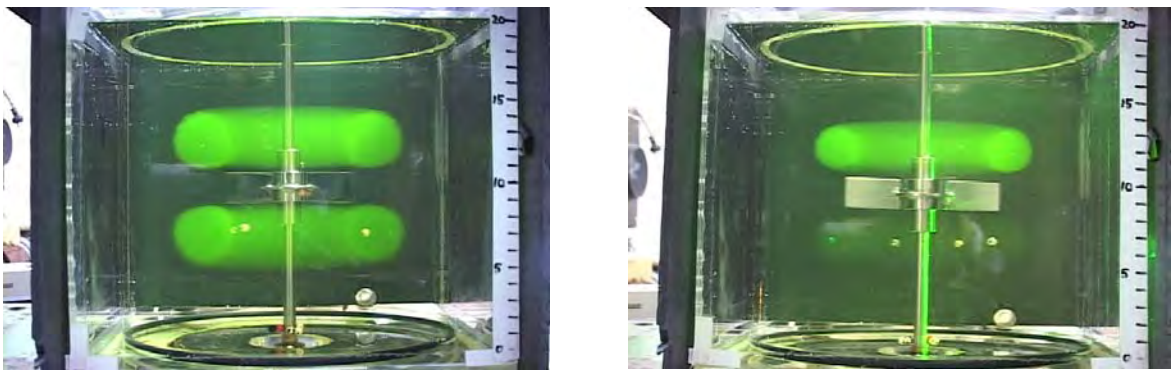

Fig. 2 Flow visualization of IMRs in a stirred vessel: a) initial state and b) 18 h later (*Re* = 10)

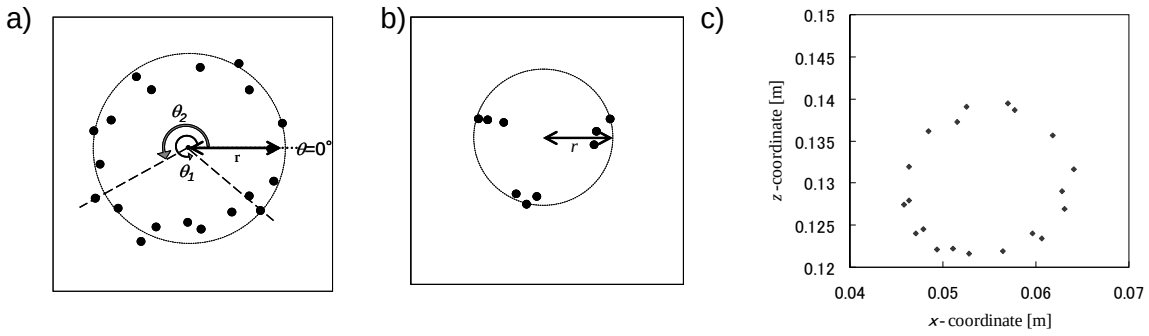

Fig. 3 Poincaré sections of particle orbit; a) experimental (30 min), b) experimental (120 min) and c) numerical (30 min)

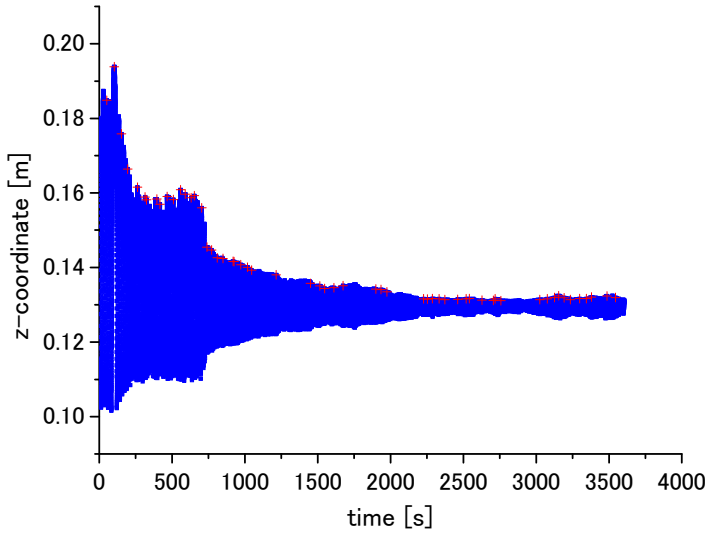

Fig. 4 Numerically obtained time trace of particle position in *z*-component (Re = 10, d_p = 8 mm, ρ_p = 1200 kg/m^3)

On the other hand, a circular orbit on the Poincaré section converges on three discrete points as shown in Figure 3b).This indicates that P_θ / P_ϕ is rational and the particle motion becomes phase-locked on the torus. Ohmura *et al*. (2003) revealed that the ratio of the time period for one round of a filament around the core IMR in θ-direction to the time for one round of a tracer particle in the filament in ϕ-direction is rational. It can thererfore be considered that particles initially move on the surface of the core torus and finally move in a filament within IMR. The particle trajectories obtained by numerical simulation show good agreement with the results of the experiment, as shown in Figure 3 c). However, no phase-locked orbit could be observed in numerical simulations so far.

Figure 4 shows numerically obtained time trace of particle position in *z*-component. This figure shows that the diameter of particle rotation orbit decreases stepwise with time. As can be seen during 250 and 750 s, even once a particle has settled on a certain orbit, the diameter flactuates. Furthermore, even after a particle seems to have almost settled on a final orbit (after 2000 s), the diameter is not constant. This particle motion may contribute to enhancement of material exchange with the outside active mixing region, as previously shown in Figure 2 b). The effects of particle diameter and particle density on particle motions were investigated by extracting local maximum values of particle position in *z*-component.

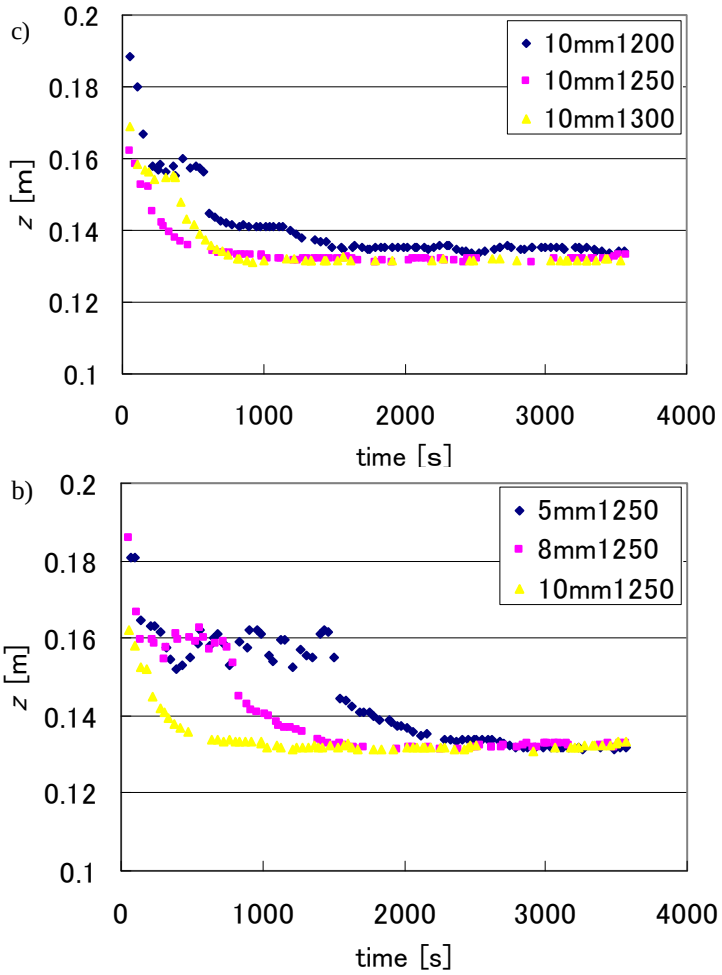

Figure 5 local maximum values of particle position in z-component against time

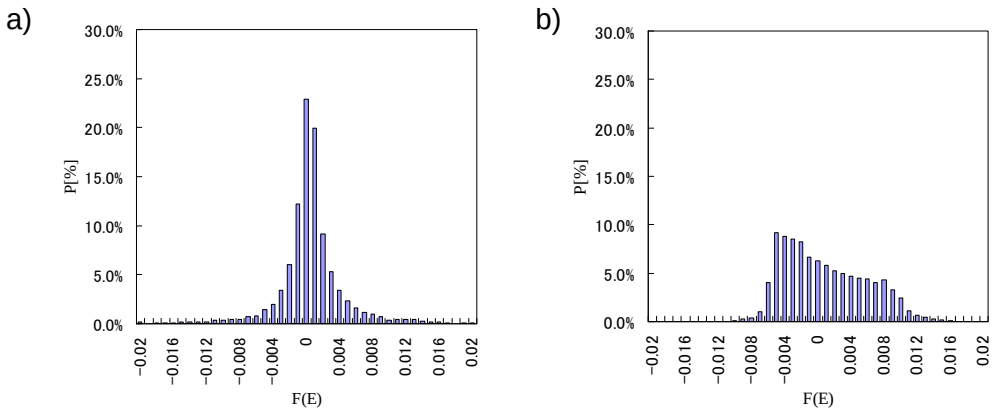

Fig. 6 Distribution of drag force on particle in *r*-direction; a) 0–25 min (before the convergence) and b) 25–60 min (after the convergence)

Figure 5 shows the tendency that the larger and heavier the particle is, the faster it converges. When the diameter is 5 mm, however, the heavier particle does not always converge faster.

Figure 6 shows that the drag force on particle in *r*-direction has drastically changed after particles are captured by the recirculation of IMRs. The drag force arises from the velocity difference between fluid and particles. Before a particle has been captured, it circulates through the whole region in the vessel. While the particle circulates through a tank apart from the impeller, the particle hardly receives the influence of accelerating flow discharged from the impeller. This means that the drag force does not work on the particle during this circulation. On the other hand, after the particle has been captured, the flow around the particle is repeatedly accelerated and decelerated by the impeller, because the particle always exists near the impeller. This indicates that the drag force frequently works on the surface of particle. The term of drag force on the particle is closely related to the mass transfer between partcle and liquid. Hence, mass transfer might be enhanced when a particle is within an IMR. In future work, the authors will investigate mass transfer between paticle and liquid in IMRs.

4 Conclusion

In this study, inertial particle motion in a stirred vessel with no baffle plate was observed experimentally and numerically at low Reynolds numbers (*Re* = 10, 30). Several particles were captured on a torus orbit within one of the IMRs and kept traveling around the impeller. Which IMR particles are captured depends on the position of particles when released. Initially, particle orbit obtained by Poincaré section showed that the particle motion covered the full surface of the torus orbit and P_θ / P_ϕ of the particle was irrational, while after a long time, the circular orbit on the Poincaré section converged on three discrete points. This indicates that P_θ / P_ϕ is rational and the particle motion becomes phase-locked on the torus. Numerical simulation revealed that even after a particle seemed to have almost settled on a final orbit (after 2000 s), the diameter of secondary circulation was not constant. This particle motion may contribute to enhancement of material exchange with the outside active mixing region. After a particle has been caputured, the drag force frequently works on the surface of the particle since the particle always exists near the impeller and the flow around the particle is repeatedly accelerated and decelerated by the impeller. This effect may enhance mass transfer between particle and liquid in IMRs.

Acknowledgement
This research was financially supported by a Grant-in-Aid for Scientific Research (A) (No. 20246115) from the Japan Society for the Promotion of Science (JSPS).

References

Koiranen, T., Kraslawski, A., Nyström, L. (1995). Knowledge-based system for the preliminary design of mixing equipment. *Industrial & Engineering of Chemistry Research*, 34, 3059-3067.

Lamberto, D. J., Muzzio, F. J., Swanson, P. D., Tonkovich, A. L. (1996). Using Time-Dependent RPM to Enhance Mixing in Stirred Vessels. *Chemical Engineering Science*, 51, 733-741.

Nishioka, N., Tago, Y., Takigawa, T., Noui-Mehidi, M. N., Wu, J., Ohmura, N. (2007). Partcle migration in a stirred vessel at low Reynolds numbers. *AIDIC Conference Series: Selected Papers of the Eight Italian Conference on Chemical and Process Engineering,* 8, 243-247.

Ohmura, N., Makino, T., Kaise, T., Kataoka, K. (2003). Transition of organized flow structure in a stirred vessel at low Reynolds numbers. *Journal of Chemical Engineering of Japan*, 36, 1458-146

Yao, W. G., Sato, H., Takahashi, K. Koyama, K. (1998). Mixing Performance Experiments in Impeller Stirred Tanks Subjected to Unsteady Rotational Speeds. *Journal of Chemical Engineering of Japan*, 53, 3031-3040.

Proceedings of the 10th International Chemical and
Biological Engineering Conference - CHEMPOR 2008
Braga, Portugal, September 4-6, 2008
E.C. Ferreira and M. Mota (Eds.)

Assessment of the tartaric stability of wines treated by electrodialysis

Patrícia A.M.H. Soares[1], Vítor Geraldes[1*], Cristina Fernandes[1], Paulo Cameira dos Santos[2] and Maria Norberta de Pinho[1]

[1]Technical University of Lisbon, Instituto Superior Técnico, Department of Chemical and Biological Engineering, Av. Rovisco Pais, 1, 1049-001 Lisbon, Portugal

[2]INIAP, Estação Agronómica Nacional, DTPA, Quinta do Marquês, 2784-505 Oeiras, Portugal

[*]Corresponding author. Tel.: +351218417511; fax: +351218499242. E-mail address: vitor.geraldes@ist.utl.pt

Key words: wine, tartaric stability, saturation temperature; mini-contact test

Topic: Sustainable process-product development through green chemistry.

Abbreviations: ED: electrodialysis; MCT: mini-contact test; DD: deionization degree; KHT: potassium hydrogen tartrate; RT: refrigerator test; T_{Sat}: saturation temperature.

Abstract

The development of electrodialysis (ED) as a robust industrial technology for wine tartaric stabilization is interlinked to the mini-contact test (MCT) as a mean of predicting the correct deionisation degree (DD) that should be carried out to guarantee the treated wine tartaric stability. The objective of this work is to quantify, for different type of wines, the influence of the key-parameters of the MCT - running time and granulometry of the seeding KHT crystals on the predicted DD and to determine the best values of these parameters that ensure that the ED treated wine is stable according to the refrigerator test (RT), which is widely used in the wine industry. The ED experiments were carried out in a bench scale ED apparatus using white, rosé, red and liqueur wines in batch mode. The DD varied from 0 to 30%. The MCT was performed for each wine during a maximum running time of 65 h. The tartaric stability of the raw and partially deionised wines was assessed by the RT and by the saturation temperature (T_{sat}). For the type of wines investigated, the MCT predicts a DD required for stabilizing the wine that is strongly dependent on the running time of the test. The RT exhibited a very good reliability for the wines tested. The MCT can predict an accurate DD that ensures the tartaric stability of the ED treated wine, provided its key-parameters (e.g. running time) are adjusted empirically for each type of wine.

1. Introduction

In winemaking it is usually necessary to reduce the concentration of potassium hydrogen tartrate (KHT) of the wine, to avoid the precipitation of this salt in the bottles, which adversely affects the percepted quality of the product. The conventional process for the tartaric stabilization of wine does not allow a precise control of the final KHT concentration and may also decrease the wine quality due to the simultaneous precipitation of polysaccharides and polyphenols together with the KHT salts (Maujean 1994, Moutounet et al. 1997, Ribereau-Gayon et al. 1998, Benítez et al. 2003).

A more recent process developed to overcome the previous drawbacks in tartaric stabilization is electrodialysis (ED) (Strathman 1986, Moutounet et al 1994, Gonçalves et al 2003). With this process and under an applied electric potential, the KHT is transferred from the wine to an aqueous solution that is separated from the wine by ion exchange membrane.

The degree of deionization (DD) (defined by the relative decrease of the wine conductivity) required to stabilize a wine by ED, must be determined with accuracy before the wine treatment. The DD has been determined with recourse to the mini-contact test (MCT), (Ribéreau-Gayon et al. 2006, Benítez et al. 2004). The difference between conductivity at the beginning and at the end of the time period gives an estimative of the DD required to stabilize a wine by ED. It is crucial, for the widespread of this more recent technology, to confirm experimentally for different types of wines if the DD predicted by the MCT if sufficient to ensure that the treated wine passes the common quality control tests that are used to monitor the tartaric stability of the wine.

The traditional method to verify if a wine is stable, which is widely used by many wine producers is the refrigerator test (RT). The method, basically, consists in verifying if crystalline sediments appear in a sample stored at low temperature, for red wines, and bellow the freezing temperature, for other types of wines. At best of our knowledge, there are no established standard protocols for this test and each wine producer uses its own. The stability of wines has been assessed also by the measurement of the saturation temperature (T_{Sat}) (Würdig et al. 1982). At the T_{Sat}, the wine attains the equilibrium concentration of KHT and, for this reason, T_{Sat} is a good indicator of the wine saturation level in KHT (Santos et al. 2002).

The development of ED as a robust industrial technology for wine tartaric stabilization is interlinked to the MCT as a mean of predicting the correct DD that should be carried out to guarantee the treated wine tartaric stability.

The aim of this work is to quantify, for different type of wines, the influence of the key-parameters of the MCT – running time and granulometry of the seeding KHT crystals – on the predicted DD and to determine the best values of these parameters that ensure that the ED treated wine is stable according to the RT.

2. Material and methods

2.1 Wine Samples. The ED experiments were carried out with wine samples that were supplied by José Maria da Fonseca Vinhos SA, Azeitão, Portugal. The white, rosé, red and liqueur wines were produced from grapes harvested in 2006, 2006, 2005, and 2001, respectively. The summary analysis of the wines used is presented in Table 1.

Table 1 Physico-chemical characterization of the wines.

Parameter	Red wine	White wine	Rose wine	Liqueur wine
pH	3.48	3.20	3.11	3.41
Conductivity (20ºC) ($\mu S.cm^{-1}$)	2040	1920	2140	878
Ethanol (%v/v)	13.4	12.0	10.4	17.4

2.2 Analytical methods. The ethanol concentration was determined by the reference method of the Office International de la Vigne et du Vin, 1990. The wine conductivity was measured with a conductivity meter, model GPL32 from CRISON (Barcelona, Spain), using a conductivity cell with a constant of 1 cm^{-1}.

2.3 ED experiments. The several wines were processed by the bench scale ED unit EUR2C-7P18 from Eurodia Industrie, S.A, France. The ion exchange membranes were supplied by TOKUYAMA SODA, Japan and the ED stack had seven cells constituted by 7 anionic membranes (type CMXSb) and 9 cationic membranes (type CMXSb). Each membrane had an effective area of 2 dm^2. A sample of 3.0 L of wine was processed at room temperature using a constant electric potential difference of 1.5 Volt/cell, corresponding to the maximum value recommended by the equipment manufacturer. The concentrate compartment was initially filled with 3.0 L of an aqueous solution of 0.2 mol/L of KHT (pro analysis grade from Riedel-de Haën) acidified at pH 3 with nitric acid (65% from Panreac). The electrodes were rinsed with 3.0 L of an aqueous solution of 0.2 mol/L of K_2SO_4 (pro analysis grade, from Scharlau, Germany). The flowrate of the concentrate, diluate and electrode rinsing solution were 180 L/h, 250 L/h and 400 L/h, respectively. Both the conductivity and pH of the wine were measured during the experiments.

2.4 Mini-contact test. The conductivity of a wine sample of 100 mL with 4 g/L of very fine KHT crystals seeds, was measured and registered in a computer during 65 hours. The wine sample was continuously agitated with a magnetic stirrer at 700 RPM and the wine temperature was controlled at -4º for white, rose and red wines and at -8ºC for liqueur wine. The required degree of deionization (DD) was estimated by the relative variation of the wine conductivity after a given running time.

2.5 Saturation Temperature (T_{Sat}). The experimental saturation temperature of a wine was determined by measuring electrical conductivity in a two-step experiment, using a set-up described elsewhere (Santos et al. 2002). In the first experiment, the wine was brought to 0ºC in a thermostat-controlled bath equipped with sources of heat and cold. The temperature was then raised to 30ºC with 0.5ºC/min increments and the wine's conductivity measured continuously. In the second experiment, the same wine was brought to 0ºC, 4.0 g/L of KHT crystals were added and the temperature was once again raised to 30ºC in 0.5ºC/min increments. In both experiments the wine was agitated continuously with a magnetic stirrer at 700 rpm and its conductivity was measured every second. The T_{sat} of any wine is given by the intersection of the two experimental curves of the variation of the conductivity versus temperature. KHT pro analysis grade from Riedel-de Haën was used in this test.

2.6 Refrigerator Test. Before the refrigeration, the wine samples were first filtrated to remove suspended mater. The filtration was performed with 2.5 μm Whatman Paper filter number 22, with a pre-coating of filter aid Fibroklar L (Reinhardt Kellereibedarf, Germany), to assured that particles that may act as crystallisation seeds are kept to a minimum value for all the wines in order to increase the reproducibility of the test. For the case of the white, rose and liqueur wines, 100 mL glass screw cap bottles from ISOLAB (Germany) were filled with wine and then were placed in a refrigerator at -20 ºC until the wine freeze. After that, the glass bottles were placed in room temperature water to unfreeze the wine and, as soon as there was sufficient liquid wine, the bottoms of the bottles were inspected at naked eye to determine if crystals had precipitated. The wine was considered unstable if crystal were detected and stable, otherwise. For the case of the red wine, and following the same practice used by some wine producers in Portugal, the visual inspection of the existence of KHT crystal was performed after maintaining 100 mL of a wine sample at -4 ºC during 6 h without stirring.

3. Results and discussion

3.1 Mini-contact test. The DD for the different wines predicted by the MCT depends strongly on the running time of the test, as shown in Table 2 for all the types of wine. These results indicate that the running time of the MCT must be optimised in order to predict accurately the DD required stabilizing the wine.

Table 2. Deionization degree predicted by the mini-contact test at different running times.

	DD (%) for running time of			
Wine type	18 min	4h	24h	65h
White	6.98	13.7	17.8	20.1
Rose	19.0	23.8	26.7	28.1
Red	0.00	0.23	3.66	7.09
Liqueur	3.46	11.9	17.7	20.8

3.2 Tartaric stability analysis of the wines deionised by ED. The tartaric stability of the different wines deionised by ED was accessed by the RT for different DD, ranging from 0 to 30%, and the results are displayed in Table 3. According to this test, the untreated red and liqueur wines were already stable, but the white and the rosé wines were only stable after a DD of 5% and 30%, respectively. It has been claimed (Ribéreau-Gayon et al. 2006, Benítez et al. 2004) that the RT suffers from poor reproducibility and is not always reliable, nor easily repeatable due to the complex phenomenon of spontaneous, non-induced crystallization. Nevertheless, with the protocol used in the present work, the RT exhibited a very good reliability for the wines tested.

Table 3. Tartaric stability state[1] of the different wines vs. the DD, according to the refrigerator test.

		Wine tartaric stability state of			
	DD (%)	Red wine	White wine	Rose wine	Liqueur wine
wine samples filtered with 2.5 μm paper filter + Fibroklar L	0	S	U	U	S
	10	S	U	U	S
	15	S	U	U	S
	20	S	U	U	S
	25	S	S	U	S
	30	S	S	S	S

[1)] S - stable wine; U - unstable wine

In fact, as it can be seen in Table 4, the RT gave always the same result below and above the required value of the DD, for all the different of wines tested. For the different DD, Table 4 displays also the tartaric stability state of the different wines predicted by the MCT for running times of 18 min, 4 h, 24 h and 65 h. With this test, a wine is considered stable if the predicted DD of the MCT is lower that the real DD of the wine. It is noteworthy to observe that both the RT and the MCT, at a running time of 65 h, predict the same tartaric stability state for the white, rosé and red wines, for all the values of DD, except for the red wine without deionization. For the liqueur wine, the MCT is in agreement with the RT only for a running time of 18 min. This wine exhibits a good tartaric stability at low DD values, despite of the fact of being thermodynamically unstable.

For the white and rosé wines, the discrepancies between the predictions of the RT and the ones of the MCT, increase when the running time of the MCT decreases. For a running time of 4 h, the MCT strongly under-predicts the DD required for stabilizing the wine. When the running time increases to 24 h, the under-prediction is not higher than 5%. If an error of this magnitude is considered acceptable for the DD imposed to the ED of the wine, the time required to perform the MCT may be reduced from 65 h to 24 h. Further reduction of the running time to 4 h must be done with caution and taking into account that the true DD required for wine stabilization may be substantially higher that the predicted value.

Table 4 Tartaric stability state[a] predicted by different methods and saturation temperature for the different wines vs. the DD.

Wine type	DD (%)	Wine tartaric stability state according to					
		Refrigerator test	mini-contact test at				
			18 min	4 h	24 h	65 h	T_{Sat}
White	0	U	U	U	U	U	19.0
	10	U	S	U	U	U	15.0
	15	U	S	S	U	U	13.7
	20	U	S	S	S	U	11.2
	25	S	S	S	S	S	9.0
	30	S	S	S	S	S	6.2
Rose	0	U	U	U	U	U	20.0
	10	U	U	U	U	U	15.4
	15	U	U	U	U	U	10.9
	20	U	S	U	U	U	9.6
	25	U	S	S	U	U	7.6
	30	S	S	S	S	S	2.7
Red	0	S	S [b)]	S [b)]	S [b)]	U	25.0
	10	S	S	S	S	S	23.1
	15	S	S	S	S	S	20.3
	20	S	S	S	S	S	17.9
	25	S	S	S	S	S	17.5
	30	S	S	S	S	S	[c)]
Liqueur	0	S	S [b)]	U	U	U	19.0
	10	S	S	S	U	U	14.6
	15	S	S	S	U	U	14.0
	20	S	S	S	S	U	[c)]
	25	S	S	S	S	S	[c)]
	30	S	S	S	S	S	[c)]

[a)] S - stable wine, U - unstable wine.

[b)] The wine was considered stable because the predicted DD was not higher than 5%.

[c)] The test was irreproducible.

The T_{Sat} of the different wine samples is also displayed in Table 4. For the white and rosé wines, the T_{Sat} decreases almost linearly with the DD in a similar way as observed already in a previous work for the other type of wines (Gonçalves et al. 2003). For the white wine with a DD of 25%, which is considered stable by the RT and by the MCT at 65 h, the T_{Sat} is 9.0 ºC.

According to Maujean et al. (1985, 1986), for white and rosé wines with alcohol content of about 11%v/v, the spontaneous crystallization temperature is equal to the T_{Sat} minus 15ºC. With this criterion, the white wine with a DD equal to or higher than 25% is stable at the temperature of the MCT, which is -4 ºC. In the case of the rosé wine, and using the Maujean criterion, the rosé wine is stable for a DD equal to or higher than 15%. These results show that the Maujean criterion gives results compatible with the RT for the white wine, but not for the rosé wine. For the case of the red and liqueur wines, the Maujean criterion is not applicable by default, due to their higher alcohol content.

4. Concluding remarks.

For the type of wines investigated, the MCT predicts a DD required stabilizing the wine that is strongly dependent on the running time of the test. With the protocol used is present work, the RT exhibited a very good reproducibility for the wines tested. Both the RT and the MCT, at a running time of 65 h, predict the same tartaric stability state for the white, rosé and red wines, for all the values of DD, except for the red wine without deionization. For the liqueur wine, the MCT is in agreement with the RT only for a running time of 18 min. This indicates that the MCT at 65 h is a very robust method to predict a DD that ensures that the ED treated wine is always stable. The MCT can predict a less severe and more precise DD that ensures the tartaric stability of the ED treated wine, provided its key parameters (e.g. running time) are adjusted empirically for each type of wine. The fine-tuning of the MCT key-parameters for different types of wines contributes to increase the ED reliability and robustness for wine tartaric stabilization.

Acknowledgments: Financial support was provided by the Portuguese National Innovation Agency, through the project DemTec STABVINHO, no. 70/00226, and by the wine company José Maria da Fonseca Vinhos S.A..

Literature cited

Benítez, J.G., Macías, V.M.P., Gorostiaga, P.S., López, R.V. and Rodríguez, L.P. 2003. Comparison of electrodialysis and cold treatment on an industrial scale for tartrate stabilization of sherry wines. Journal of Food Engineering, 58, pp. 373-378.

Gonçalves, F., Fernandes, C., Santos, Paulo and de Pinho, M.N. 2003. Wine tartaric stabilization by electrodialysis and its assessment by the saturation temperature. Journal of Food Engineering, 59, pp. 229-235.

Maujean, A. 1994. Traitement par le froid artificiel dês vins en relation avec leur stabilisation vis-à-vis des troubles cristallins tartriques. In Les acquisitions récents dans les traitments physiques du vin, pp. 81-101. Lavoisier Tec & Doc., Paris.

Moutounet, M., Escudier, J.L. and Saint-Pierre, B. 1994. L'Électrodialyse, adaptation à la stabilisation tartrique des vins. In acquisitions récentes dans les traitements physiques des vins. Lavoissier Tec & Doc. Paris. pp. 103-114.

Office International de la Vigne et du Vin, 1990. Recueil des méthodes internationales d'analyse des vins et des moûts. OIV, Paris.

Ribéreau-Gayon, P., Glories, Y., Maujean, A. and Dubourdieu, D. 2006. The chemistry of wine and stabilization and treatments. Handbook of Enology, Volume 2, pp.3-37, John Wiley & Sons, Ltd.

Santos, P.C., Gonçalves, F. and de Pinho, M.N. 2002. Optimisation of the method for determination of the temperature of saturation in wines. Analytica Chimica Acta, 458, pp. 257-261.

Strathman, H. 1986. Electrodialysis. In P.M. Bungay, H.K. Lonsdale & M.N. Pinho (Eds.). Synthetic Membranes: Science, Engineering and Applications. NATO Asi Series C Mathematics and Chemical Science. Reidel Publishing Company.

Wurdig, G., Muller, T. & Trèves, G. 1982. Méthode pour caractériser la stabilité du vin vis-à-vis du tartre par determination de la temperature de saturation. Bulletin of de l'OIV, 613, pp. 220-229.

Proceedings of the 10th International Chemical and
Biological Engineering Conference - CHEMPOR 2008
Braga, Portugal, September 4-6, 2008
E.C. Ferreira and M. Mota (Eds.)

Characterization of a Microporous Titanosilicate AM-3 Membrane – Pure gas permeation

Patrícia F. Lito, Sara B. Barros, Chunfang Zhou, João Rocha, Zhi Lin, Carlos M. Silva[1]

University of Aveiro, Department of Chemistry, CICECO, 3810-193 Aveiro, Portugal

Keywords: AM-3, Titanosilicates, Microporous Membranes, Gas permeation.
Topic: Advancing the chemical and biological engineering fundamentals.

Abstract

In this work, two microporous AM-3 membranes were studied. Thin AM-3 films were hydrothermally crystallized on porous α-alumina supports by seeded hydrothermal technique, and were subsequently characterized by measuring pure N_2 permeation flux. The enhancement in the N_2 fluxes observed after an heating/cooling cycle confirms the hydrophilic character of AM-3 crystals. The flux of N_2 in both membranes depends linearly on the transmembrane pressure drop, evidencing the absence of viscous flow. Permeances found were 6.84×10^{-7} mol/(m^2sPa) and 8.42×10^{-7} mol/(m^2sPa) for one membrane, and 1.03×10^{-7} mol/(m^2sPa) and 1.23×10^{-7} mol/(m^2sPa) for the second membrane, which are well inside typical values for microporous membranes. Accordingly, results suggest that good quality membranes were obtained.

1. Introduction

Membrane processes are very attractive methods to separate a variety of gas mixtures due to their relatively low energetic consumption and high selectivities observed in comparison with more conventional processes (Xomeritakis and Tsapatsis, 2001). Accordingly, the interest in the application of membrane technology in gas separation and purification processes has been intensified.

Microporous inorganic membranes are promising materials due to their high thermal and chemical stability, and resistance to high pressure differences. Among them, a variety of zeolite membranes have been successfully synthesized and applied in the separation of different mixtures, including azeotropic and other difficult ones (Kita et al., 1995; Coronas et al., 1997; Giroir-Fendler et al., 1996; Xomeritakis et al., 2001).

Titanosilicate membranes belong to the microporous inorganic group. Similarly to zeolites, these materials exhibit a crystalline structure with molecular dimensions and are able to separate mixtures based on differences in affinity and sieving effect (Poshusta et al., 1998). In addition, they comprise benefits over more classical zeolite membranes (Lin et al., 2004), namely: they can be synthesized without organic templates, avoiding subsequent calcination treatments which often causes irreversible defects and/or loss of active surface groups; they are prepared under moderate pH conditions, reducing chemical attack of the support surfaces; and they exhibit novel possibilities of isomorphous framework substitution, allowing for fine-tuning of catalytic and adsorption properties.

Only a small number of microporous titanosilicate membranes have been recently synthesized and characterized, mainly reporting to ETS-4 (Guan et al., 2001; Braunbarth et al., 2000; Guan et al., 2002). Preparation of ETS-4 films on porous alumina and titania supports by secondary growth method was described by Yilmaz et al. (2006), however only crystals orientation were investigated. Hetero-epitaxial growth of ETS-10 on ETS-4 has been

[1] Corresponding author. Tel +351 234 401549. E-mail:carlos.manuel@ua.pt

accomplished, but no permeation or separation results have also been published (Jeong et al., 2002). Preparation and characterization of ETS-10 membranes were presented for the first time by Lin et al. (Lin et al., 2004) and subsequently by Tiscornia et al. (2005, 2007). Sebastían et al. (2005, 2006) reported the synthesis, characterization, and separation properties of a Ti-Silicate umbite membrane (AM-2) by seeded hydrothermal synthesis. Reported results suggest the potential of titanosilicate membranes for water/organic compounds, and gas mixtures separations.

AM-3 is a synthetic microporous titanosilicate analogue of mineral penkvilksite $Na_4Ti_2Si_8O_{22}.5H_2O$ (Lin et al., 1997, 2006; Rocha and Anderson, 2000). Its structure consists of SiO_4 tetrahedra connected by individual TiO_6 octahedra forming a three-dimensional framework of 6-ring channels (Lin et al., 2006), and contrarily to most titanosilicates, it does not contain Ti–O–Ti linkages. In a previous work (Lin et al., 1997) it was shown that AM (Aveiro-Manchester) materials adsorb water in relatively large amounts. In addition, AM-3 was demonstrated to be stable up to ca. 600 ºC, loosing water and rehydrating back after being kept in air for a few hours at room temperature. A detailed morphological characterization of AM-3 was reported first by Lin et al. (1997) and later by Rocha and Anderson (2000). At the moment, no publications have been presented concerning the preparation and characterization of AM-3 membranes. Only its ability to sorb radioactive cobalt-60 using an ion-exchange batch-type method has been studied (Koudsi and Dyer, 2001).

Membranes characterization is a fundamental test before their use in a mixture separation. In addition to its structure determination, it is essential to study permeation properties, which are directly related to the density and size of defects. With this information, ideal preparation and operation conditions can be established in order to obtain a defect-free membrane, and so a good quality membrane. Permeation of certain molecules, such as nitrogen, can be used to detect the presence of rough defects in the zeolite structure. Accordingly, over enhanced N_2 permeances evidence the presence of defects.

In the present work, two thin AM-3 films were hydrothermally crystallized outside a porous α-alumina support by seeded hydrothermal technique (Lovallo and Tsapatsis, 1996). Subsequently, the existence of rough defects or cracks in both membranes was investigated by means of single N_2 permeation runs.

2. Experimental Section

The experimental set-up used for the permeation measurements is shown below in Figures 1a and 1b. Membrane features of both synthesized AM-3 membranes may be found in Table 1.The presence of adsorbed compounds, like water from air humidity, affects the results; therefore a previous heating/cooling cycle up to ca 200ºC was performed before the permeation measurements. Experiments were conducted with a transmembrane pressure difference providing the driving force for permeating and no sweep gas was used.

A stainless-steel module containing the membrane was placed inside an oven with temperature control (TC). Viton o-rings were used to seal the membrane inside the module. The flow rate of feed gas was fixed by means of a mass flow controller (MFC) and the permeate flow rate was measured by a mass flow meter (MFM) until the equilibrium be reached. The permeate side was kept at atmospheric pressure; the feed side pressure was measured in this work with a back pressure regulator (BPR). During the experiments the feed flow rate was varied between 10 and 300 cm^3(PTN)/min and the temperature was kept at 298 K.

Table 1: Features of AM-3 membrane.

Membrane material	AM-3
Support material	α-alumina
Membrane pore diameter, 10^{-9}m	direction a: 0.3x0.3 direction b: 0.4x0.25
Support pore diameter, 10^{-9}m	3000
Membrane diameter, 10^{-2}m	1.0
Membrane length,10^{-2}m	5.6

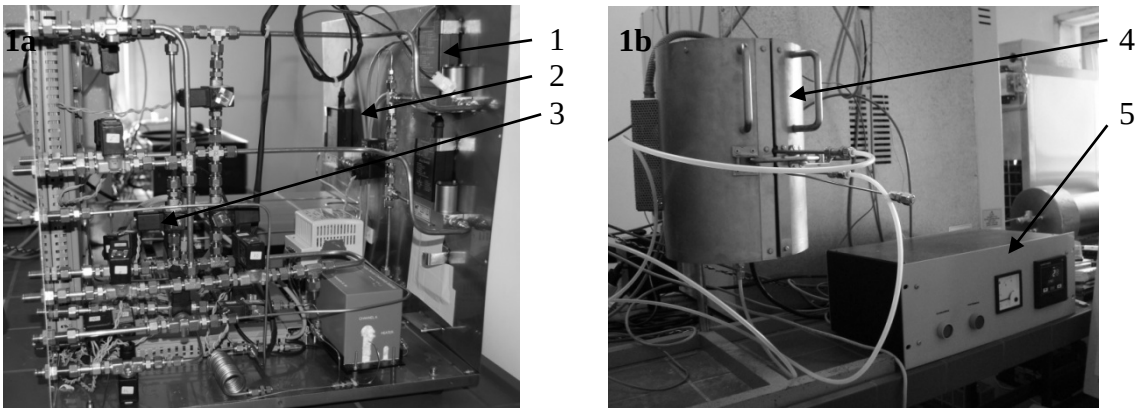

Figures 1a and 1b – Experimental set-up used for permeation measurements. Legend: 1 – MFM; 2 – BPR; 3 – MFM; 4 – Oven; 5 – TC.

3. Results and discussion

Figure 2 shows nitrogen permeation flux as function of transmembrane pressure drop for both synthesised membranes, before and after the heating/cooling cycle; calculated permeances, corresponding to the slop of linear fittings to the experimental data, are also included in the figure. Permeances found were 6.84×10^{-7} mol/(m^2sPa) and 8.42×10^{-7} mol/(m^2sPa), for one membrane, and 1.03×10^{-7} mol/(m^2sPa) and 1.23×10^{-7} mol/(m^2sPa), for the other one. Generally, single N_2 permeances in microporous membranes have values in the range of 1×10^{-7} and 1×10^{-6} mol/(m^2.s.Pa); over-enhanced values denunciate the existence of rough defects in the membrane. Accordingly, results suggest good quality membranes. It is important to note that permeances depend on the membrane thickness, which explains the difference observed in the permeance values of both membranes.

As may be observed, the N_2 fluxes are enhanced after the heating/cooling cycle; such behaviour supports the hydrophilic character of AM-3 crystals. Besides, the flux of N_2 in both membranes depends linearly on the transmembrane pressure drop, which evidences that viscous flow may be neglected. In fact, for non-adsorbable gases the permeation flux in micro and mesopores is directly proportional to the pressure gradient. Therefore, it may be anticipated that our synthesized membranes do not exhibit macropores or other rough defects.

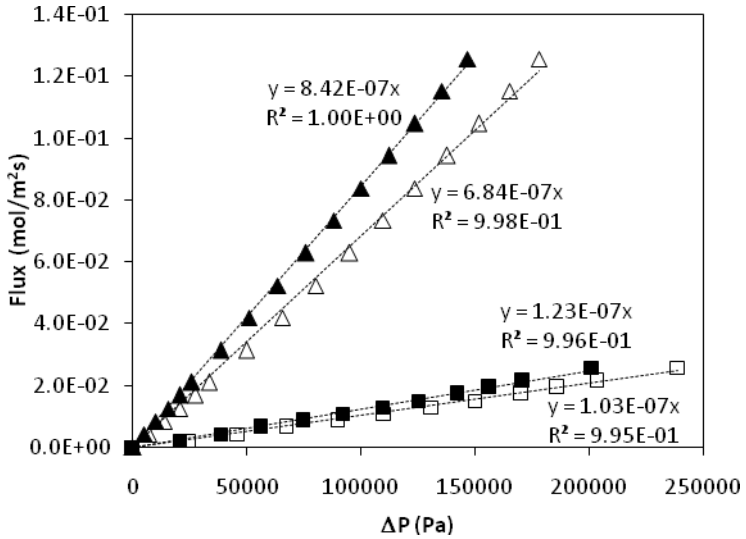

Figure 2: N_2 permeation flux plotted as function of transmembrane pressure. Symbols: ▲ and △: membrane 1; ■ and □: membrane 2. Open and full symbols: before and after the heating/cooling cycle, respectively. Lines: correlations.

3. Conclusions

In this work two microporous AM-3 membranes were characterized by measuring pure N_2 permeation flux. The enhancement of the N_2 fluxes observed after the heating/cooling cycle confirms the hydrophilic character of AM-3 crystals. The flux of N_2 in both membranes depends linearly on the transmembrane pressure drop, evidencing negligible viscous flow contribution. Furthermore, permeances found are well inside typical values for microporous membranes. In the whole, results suggest that good quality membranes were obtained.

Acknowledgments

Patrícia F. Lito wishes to express her gratitude to Fundação para a Ciência e Tecnologia (Portugal) for the PhD grant provided (SFRH/BD/25580/2005).

References

Braunbarth, C.M., Boudreau, L.C., Tsapatsis, M., (2002). Synthesis of ETS-4/TiO_2 composite membranes and their pervaporation performance. *Journal of Membrane Science,* 174, 31-42.

Coronas, J., Falconer, J.L., Noble, R.D., (1997). Characterization and permeation properties ZSM-5 tubular membranes. *AIChE Jornal*, 43, 1797-1812.

Giroir-Fendler, A., Peureux, J., Mozzanega, H., Dalmon, I.A., (1996). Characterization of a zeolite membrane for catalytic membrane reactor application. *Studies in Surface Science and Catalysis*, 111, 127-136.

Guan, G., Katsuki, K., Morooka, S., (2001). Synthesis and permeation properties of ion-exchanged ETS-4 tubular membranes. *Microporous and Mesoporous Materials,* 50, 109-120.

Guan, G., Katsuki,K., Morooka,S., (2002). Separation of nitrogen from oxygen using a titanosilicate membrane prepared on a porous α-alumina support tube**.** *Separation Science and Technology*, 37, 1031-1039.

Horii, H.K., Ohtoshi, Y., Okamoto, K., (1995). Synthesis of a zeolite NaA membrane for pervaporation of water/organic liquid mixtures. *Journal of Materials Science Letters*, 14, 206-208.

Jeong, H.K., Krohn, J., Sujaoti, K., Tsapatsis, M., (2002). Oriented Molecular Sieve Membranes by Heteroepitaxial Growth. *Journal of the American Chemical Society*, 124, 12966-12968.

Koudsi, Y., Dyer, A., (2001). Sorption of ^{60}Co on a synthetic titanosilicate analogue of the mineral penkvilksite-2O and antimonysilicate. *Journal of Radioanalytical and Nuclear Chemistry*, 247(1), 209-219.

Lin, Z., Rainho, J.P., Rocha, J., Carlos, L.D., (2006). Preparation of Photoluminescent materials from a Lanthanide-Doped Microporous Titanosilicate Precursor. *Materials Science Forum*, 514-516, 123-127.

Lin, Z., Rocha, J., Brandão, P., Ferreira, A., Escultas, A.P., Pedrosa de Jesus, J.D., (1997). Synthesis and Structural Characterization of Microporous Umbite, Penkvilksite, and Other Titanosilicates. *Journal of Chemical Physics B*, 101, 7114-7120.

Lin, Z., Rocha, J., Navajas, A., Téllez, C., Coronas, J., Santamaría, J., (2004). Synthesis and characterisation of titanosilicate ETS-10 membranes. *Microporous and Mesoporous Materials*, 67, 79-86.

Lovallo, M.C., Tsapatsis, M. (1996). Preferentially Oriented Submicron Silicalite Membranes, *AIChE Journal*, 42, 3020-3029.

Poshusta, J.C., Tuan, V.A., Falconer, J.L., Noble, R.D., (1998). Synthesis and Permeation Properties of SAPO-34 Tubular Membranes. *Industrial and Engineering Chemistry Research*, 37, 3924-3929.

Rocha, J., Anderson, M. (2000). Microporous Titanosilicates and other Novel Mixed Octahedral-Tetrahedral Framework Oxides, *European Journal of Inorganic Chemistry*, 801-818.

Sebastián, V., Lin, Z., Rocha, J., Téllez, C., Santamaría, J., Coronas, J., (2005). A new titanosilicate umbite membrane for the separation of H_2. *Chemical Communications*, 3036-3037.

Sebastián, V., Lin, Z., Rocha, J., Téllez, C., Santamaría, J., Coronas, J., (2006). Synthesis, Characterization, and Separation Properties of Sn- and Ti-Silicate Umbite Membranes. *Chemistry of Materials*, 18, 2472-2479.

Tiscornia, I., Irusta, S., Prádanos, P., Téllez, C., Coronas, J., Santamaría, J., (2007). Preparation and Characterization of Titanosilicate Ag-ETS-10 for Propylene and Propane Adsorption. *Journal of Physical Chemistry C*, 111, 4702-4709.

Tiscornia, I., Lin, Z., Rocha, J., Téllez, C., Coronas, J., Santamaría, J., (2005). Preparation of titanosilicate ETS-10 and vanadosilicate AM-6 Membranes. *Studies in Surface Science and Catalysis*, 158(1), 423-430.

Xomeritakis, G., Lai, Z., Tsapatsis, M., (2001). Separation of xylene isomer vapors with oriented MFI membranes made by secondary growth. *Industrial and Engineering Chemistry Research*, 40, 544-552.

Yilmaz, B., Shattuck, K.G., Warzywoda, J., Sacco JR, A., (2006). Controlling crystal orientation in microporous titanosilicate ETS-4 films by secondary growth method. *Journal of Materials Science*, 41, 3135-3138.

Proceedings of the 10th International Chemical and
Biological Engineering Conference - CHEMPOR 2008
Braga, Portugal, September 4-6, 2008
E.C. Ferreira and M. Mota (Eds.)

Pure Solvent Solubility of Some Pharmaceutical Molecules

Fátima L. Mota[1], António J. Queimada[1], Simão P. Pinho[2], Eugénia A. Macedo[1,*]
[1] LSRE/LCM – Laboratory of Separation and Reaction Engineering, Faculdade de Engenharia da Universidade do Porto, Rua Dr. Roberto Frias, 4200-465 Porto, Portugal.
[2] LSRE/LCM – Laboratory of Separation and Reaction Engineering, Escola Superior de Tecnologia e Gestão, Instituto Politécnico de Bragança, Campus de Santa Apolónia, 5301-857 Bragança, Portugal.

Keywords: Solubility, Drugs, Pure solvents, Modeling.
Topic: Advancing the chemical and biological engineering fundamentals.

Abstract

In this work, solubilities in pure solvents of some drugs measured in the temperature range from 298.2 K to 315.2 K are presented. Measurements were performed using the standard shake-flask method, followed by compositional analysis by HPLC. Theoretical work was essentially focused on the application of the NRTL-SAC model, with a very satisfactory agreement between experimental data and predicted values. The *reference solvent approach* was also addressed but the results were worst, although still fair.

1. Introduction

New drugs are always under development during the establishment of new therapies. Solubility is important both for drug production and in its therapeutic use. Many separation processes in the pharmaceutical industry are based on the solubilities in different solvents, while solvation is important in each stage of drug transport and delivery. Properties like lipophilicity, hydrophilicity, the ability to establish hydrogen bonds and other interactions of the molecules with the surrounding media play an important role in the solvation process. Although some thermodynamic tools can be used to predict drug solubility, the availability of experimental data is still fundamental for appropriate model development and evaluation. However, there are inherent complexities with experimental measurements: accuracy and reliability are difficult to achieve, and experiments are time consuming. So, efficient methods to predict solubilities are a main research subject, with high value for drug design.

In spite of drugs being so complex molecules, with several functional groups, having different structures or isomers, or even different solid structures, a few methods were proposed to represent their solubility. In this work, two approaches are addressed. The Nonrandom Two Liquid–Segment Activity Coefficient (NRTL-SAC) model (Chen and Song, 2004) which is a modification of the original NRTL model (Prausnitz et al., 1999), and has been widely applied to correlate and predict phase equilibria of highly nonideal systems. It is, in fact, one of the most successful models for the representation of drug solubility. Alternatively, Abildskov and O'Connell (Abildskov and O'Connell, 2003) proposed the *reference solvent approach* to predict the changes of solubilities with solvent composition. This methodology is also focused in this work.

In this study, solubilities of some drugs, such as paracetamol, budesonide, furosemide and allopurinol, were measured in the temperature range from 298.2 K to 315.2 K, in water, and in a set of organic solvents (ethanol, acetone, n-hexane, ethyl acetate and carbon tetrachloride), at 298.2 and 310.2 K. Measurements were performed using the shake-flask method for generating the saturated solutions, followed by compositional analysis by HPLC or gravimetry. Concerning the theoretical work, it was possible to find a very satisfactory agreement for correlation of the solubility data measured.

* Corresponding author. Tel + 351-22-508 1653. E-mail: eamacedo@fe.up.pt

2. Experimental

All the solubility experiments were carried out using the isothermal saturation shake-flask method. The aqueous solubilities were measured at five different temperatures 298.2, 303.2, 310.2, 313.2 and 315.2 K, while for the other solvents (ethanol, acetone, ethyl acetate, carbon tetrachloride and n-hexane), the solubilities were only obtained at 298.2 and 313.2 K. Saturated solutions were prepared mixing an excess of solute and solvent, stirring for 2 days and then allowing to settle for 1 day. The temperature was maintained constant by a circulating water bath and with an air bath (composed by an acrylic box, a resistance, an electric fan and a temperature controller) and monitored by platinum resistance probes connected to a data acquisition unit. Samples from the saturated liquid phase were removed with isothermal syringe filtration and the drug composition determined from liquid chromatography (HPLC). To verify the accuracy of the chromatographic method, some measurements were also done by the gravimetric method.

Melting data (melting temperature and enthalpy of fusion) of the pure drugs were obtained by differential scanning calorimetry (DSC) to provide a broader understanding of the solubilization process, as well as for modeling purposes.

3. Modeling

Considering that the heat capacity difference between the liquid and the solid phases is negligible (Prausnitz et al., 1999), the temperature dependence of solubility can be described by the following general equation:

$$\ln x_2 = -\frac{\Delta_{fus}H}{R}\left(\frac{1}{T}-\frac{1}{T_m}\right)-\ln\gamma_2 \tag{1}$$

where x_2 is the mole fraction of the solute, $\Delta_{fus}H$ is its enthalpy of fusion, R the ideal gas constant, T the absolute temperature, T_m the melting temperature, and γ_2 is the solute activity coefficient.

The NRTL-SAC model (Chen and Crafts, 2006; Chen and Song, 2004) is a modification of the original NRTL equation, where the combinatorial term (γ_I^C) is calculated from the Flory-Huggins approximation for the combinatorial entropy of mixing. The residual term (γ_I^R) is set equal to the sum of the local composition interaction contributions for each segment:

$$\ln\gamma_I = \ln\gamma_I^C + \ln\gamma_I^R \tag{2}$$

$$\ln\gamma_I^C = \ln\frac{\phi_I}{x_I} + 1 - r_I\sum_J\frac{\phi_J}{r_J} \tag{3}$$

with

$$r_I = \sum_i r_{i,I} \tag{4}$$

$$\phi_I = \frac{r_I x_I}{\sum_J r_J x_J} \tag{5}$$

$$\ln\gamma_I^R = \ln\gamma_I^{lc} = \sum_m r_{m,I}\left[\ln\Gamma_m^{lc} - \ln\Gamma_m^{lc,I}\right] \tag{6}$$

$$\ln \Gamma_m^{lc} = \frac{\sum_j x_j G_{jm} \tau_{jm}}{\sum_k x_k G_{km}} + \sum_{m'} \frac{x_{m'} G_{mm'}}{\sum_k x_k G_{km'}} \left(\tau_{mm'} - \frac{\sum_j x_j G_{jm'} \tau_{jm'}}{\sum_k x_k G_{km'}} \right) \quad (7)$$

$$\ln \Gamma_m^{lc,I} = \frac{\sum_j x_{j,I} G_{jm} \tau_{jm}}{\sum_k x_{k,I} G_{km}} + \sum_{m'} \frac{x_{m',I} G_{mm'}}{\sum_k x_{k,I} G_{km'}} \left(\tau_{mm'} - \frac{\sum_j x_{j,I} G_{jm'} \tau_{jm'}}{\sum_k x_{k,I} G_{km'}} \right) \quad (8)$$

with

$$x_j = \frac{\sum_J x_J r_{j,J}}{\sum_I \sum_i x_I r_{i,I}} \quad \text{and} \quad x_{j,I} = \frac{r_{j,J}}{\sum_i r_{i,I}} \quad (9) \text{ and } (10)$$

where I and J are the component indices, while i, j, k, m and m' are the segment based species indices, r_I is the total segment number, ϕ_I is the segment mole fraction, x_j is the segment based mole fraction of segment species j, x_J is the mole fraction of component J, $r_{m,I}$ is the number of segment species m contained in component I, Γ_m^{lc} is the activity coefficient of segment species m and $\Gamma_m^{lc,I}$ is the activity coefficient of segment species m contained only in component I. G and τ are local binary quantities related to each other by the NRTL nonrandomness parameter α:

$$G = \exp(-\alpha\tau) \quad (11)$$

To account for several interactions, predefined conceptual segments were proposed, along with their corresponding segment-segment binary parameters: one hydrophobic that represents the molecular surface area unlike to form hydrogen bonds; two polar (one repulsive and one attractive) that represent the surface area with interactions characteristic of an electron donor or acceptor; and one hydrophilic that represents the area with interactions characteristic of a hydrogen-bond donor or acceptor. The essence of this model consists on the use of these conceptual segments, which is different, for example, from group-contribution approaches which build molecules from a large set of predefined functional groups based in their chemical structure. Since for most of the solvents used in the pharmaceutical industry the parameters are already available (Chen and Crafts, 2006), the experimental data measured here are useful to estimate the solute parameters. After, the model can be applied to predict solute solubility in other solvent systems.

The *reference solvent approach*, proposed by Abildskov and O'Connell (2003, 2004, 2005), is a simplified methodology that allows the prediction of differences in solubilities of sparingly soluble chemicals when the solvent is changed, based on a limited set of experimental data. The method can not be applied if there are phase transitions in the solid phase, as long as, some compounds can have more than one metastable solid forms. If we have an activity coefficient model and know the solubility of the solute in one pure solvent *j*, the solubility in another pure solvent *i* can then be directly calculated according to:

$$\ln x_{2i} = \ln x_{2j} + \ln \gamma_{2j} - \ln \gamma_{2i} \quad (12)$$

where *i* and *j* are subscripts refering to the solvents and 2 to the solute. This equation is useful because no pure solute properties are needed. However, it requires the selection of a reference solvent *j*. The optimal reference solvent is one for which: (Abildskov and O'Connell, 2005, 2004, 2003)

$$\ln x_{2j} + \ln \hat{\gamma}_{2j} = \sum_{i=data} \frac{\ln x_{2i} + \ln \hat{\gamma}_{2i}}{N} \quad (13)$$

where the circunflex denotes a calculated value and the mole fractions are experimental solubility data of solute 2 in solvent *j* and *N* are the number of experimental solubility data points.

4. Results and Discussion

Among the studied drugs, only for paracetamol data are available in the literature (Bustamante et al., 1998; Granberg and Rasmuson, 2000, 1999; Hojjati and Rohani, 2006). In general, the agreement between the data measured in this work and that published in the literature is good, showing the adequacy of the experimental method for drug solubility measurements.

The melting properties have an important role in the solubilization of solids in liquids, and are also necessary for modeling purposes. Furosemide decomposes at melting, and like that, its melting properties had to be calculated by a group-contribution method (Marrero and Gani, 2001). For all the other drugs, DSC measurements were carried out, but only for paracetamol it was possible to find literature data (NIST Chemistry Webbook, 2007) to compare, showing a very good agreement.

To apply the NRTL-SAC model, the selection of the solubility measurements to be carried out for solute parameter regression involves the careful choice of solvents to cover the four types of distinctive surface interaction characteristics. Alkanes are hydrophobic compounds; ketones and esters are polar molecules with varying degrees of hydrophobicity; alcohols are hybrids of hydrophobic and hydrophilic segments. In this way, n-hexane, carbon tetrachloride, acetone, ethyl acetate and ethanol were used as representative solvents, with distinctive surface interaction characteristics. The solute model parameters were regressed using the solubility data in these pure solvents, melting data and the solvent parameters (Chen and Crafts, 2006). Once these model parameters were regressed, the model can be used to predict the solubility of the same solute in different solvents. Experimental and modeling results for the drugs solubility in water are presented in Figure 1. It can be seen that NRTL-SAC is an appropriate tool for the solubility modeling of aqueous solutions of these complex molecules.

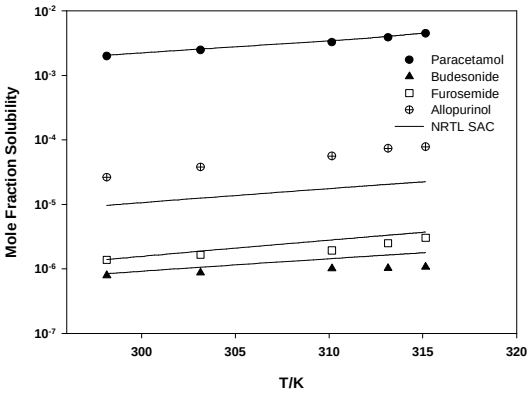

Figure 1. Experimental and NRTL-SAC calculated aqueous solubilities of the studied pharmaceuticals.

The model parameters based on the pure solvents regression can also be used to predict the solubility of these solutes in some mixed solvent systems. For paracetamol, data available in the literature for mixtures of water/acetone (Granberg and Rasmuson, 2000), ethanol/water and ethanol/ethyl acetate (Romero et al., 1996) were checked, and the prediction results showed to be very satisfactory. For the other studied drugs, no data were available. Thus, the solubilities of allopurinol and budesonide, at 298.2 K, in the extremely non-ideal system acetic acid/1-butanol; and the solubility of furosemide, at 298.2 K, in a binary mixture methyl

acetate/methanol were measured. These solvents are not included in the database for solute parameter estimation, even though the alcohol group and the ester groups were considered. The results were very satisfactory. For allopurinol a good prediction was obtained, with a root mean square deviation (RMSD), in the logarithm of mole fraction, of 0.191; for budesonide, the model overpredicted the solubility (RMSD of 0.561); and for furosemide, the prediction values were lower than the experimental values (RMSD of 0.697). Figure 2 shows the experimental data against the predicted results for allopurinol in the mixed system acetic acid/1-butanol, at 298.2 K.

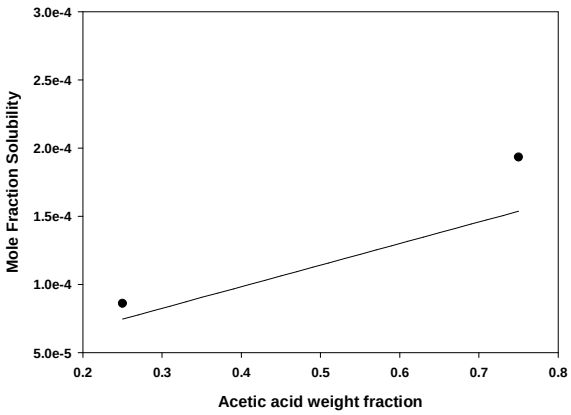

Figure 2. Measured and predicted (NRTL-SAC) allopurinol solubility in the mixed system acetic acid/1-butanol (acetic acid weight fraction in allopurinol free basis).

To apply the *reference solvent approach*, the NRTL-SAC model was used (Chen and Crafts, 2006) to calculate the activity coefficients. The solute parameters used were those obtained from the previous correlation. The reference solvents found were: water for paracetamol and furosemide, and carbon tetrachloride for allopurinol and budesonide. For paracetamol and budesonide, the prediction results were very satisfactory (RMSD of 3.075 and 2.875), but for the other two compounds the results presented considerable scattering. The results for all compounds can be observed from Figure 3.

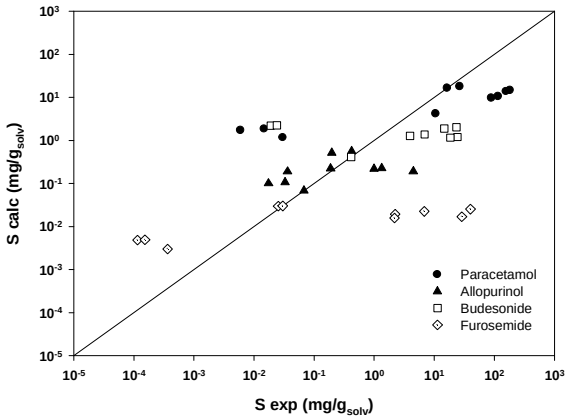

Figure 3. Measured and predicted (*reference solvent approach*) drug solubility in pure solvents.

5. Conclusions

Solubilities of some pharmaceutical compounds in pure water were measured, at five different temperatures, ranging from 298.2 to 315.2 K, and in other organic solvents (ethanol, acetone, carbon tetrachloride, ethyl acetate and n-hexane) at 298.2 K and 310.2 K, using the shake-flask method coupled with HPLC analysis. The aqueous solubility follows the general

increasing trend with temperature. Besides solubility data, melting temperatures and enthalpies of fusion were also measured, providing a broader knowledge about the solubilization process of these molecules. The NRTL-SAC model and the reference solvent approach were applied to calculate solubilities. For the NRTL-SAC, the solubility data in pure solvents were used to estimate the solute parameters which were used in the prediction of the solubility of these compounds in pure water as a function of temperature and also in mixed solvent systems. This model showed to be an appropriate tool to represent the solubility of these molecules. With the reference solvent approach, the predicted results were very scattered. This methodology was used with the NRTL-SAC model to obtain the solute activity coefficients. To improve the results, further studies should be accomplished such as the use of another activity coefficient model, explicitly considering other specific interactions.

References

Abildskov, J., O'Connell, J.P., (2005). Thermodynamic method for obtaining the solubilities of complex medium-sized chemicals in pure and mixed solvents. *Fluid Phase Equilibria*, 228, 395-400.

Abildskov, J., O'Connell, J.P., (2004). Prediction of solubilities of complex medium-sized chemicals. II. Solutes in mixed solvents. *Molecular Simulation*, 30, 367-378.

Abildskov, J., O'Connell, J.P., (2003). Predicting the solubilities of complex chemicals I. Solutes in different solvents. *Industrial & Engineering Chemistry Research*, 42, 5622-5634.

Bustamante, P., Romero, S., Peña, A., Escalera, B., Reillo, A., (1998). Enthalpy-entropy compensation for the solubility of drugs in solvent mixtures: Paracetamol, acetanilide, and nalidixic acid in dioxane-water. *Journal of Pharmaceutical Sciences*, 87, 1590-1596.

Chen, C.C., Crafts, P.A., (2006). Correlation and prediction of drug molecule solubility in mixed solvent systems with the Nonrandom Two-Liquid Segment Activity Coefficient (NRTL-SAC) model. *Industrial & Engineering Chemistry Research*, 45, 4816-4824.

Chen, C.C., Song, Y.H., (2004). Solubility modeling with a nonrandom two-liquid segment activity coefficient model. *Industrial & Engineering Chemistry Research*, 43, 8354-8362.

Granberg, R.A., Rasmuson, A.C., (2000). Solubility of paracetamol in binary and ternary mixtures of water plus acetone plus toluene. *Journal of Chemical and Engineering Data*, 45, 478-483.

Granberg, R.A., Rasmuson, A.C., (1999). Solubility of paracetamol in pure solvents. *Journal of Chemical and Engineering Data*, 44, 1391-1395.

Hojjati, H., Rohani, S., (2006). Measurement and prediction of solubility of paracetamol in water-isopropanol solution. Part 1. Measurement and data analysis. *Organic Process Research & Development*, 10, 1101-1109.

Marrero, J., Gani, R., (2001). Group-contribution based estimation of pure component properties. *Fluid Phase Equilibria*, 183, 183-208.

NIST Chemistry Webbook, (2007). http://webbooknistgov/chemistry/,

Prausnitz, J.M., Lichtenthaler, R.N., Azevedo, E.G., (1999). *Molecular Thermodynamics of Fluid-Phase Equilibria*. Third ed. New Jersey, Prentice Hall PTR.

Romero, S., Reillo, A., Escalera, B., Bustamante, P., (1996). The behavior of paracetamol in mixtures of amphiprotic and amphiprotic-aprotic solvents. Relationship of solubility curves to specific and nonspecific interactions. *Chemical & Pharmaceutical Bulletin*, 44, 1061-1064.

Ackowledgments

The authors thank the support provided by *Fundação para a Ciência e a* Tecnologia (FCT) by LSRE financing FEDER/POCI/2010. Fátima Mota acknowledges her Ph.D. scholarship from FCT SFRH/BD/32372/2006. The authors are grateful to *BIAL* for kindly providing the drugs used in this work.

Proceedings of the 10th International Chemical and
Biological Engineering Conference - CHEMPOR 2008
Braga, Portugal, September 4-6, 2008
E.C. Ferreira and M. Mota (Eds.)

Basicity promotion and mechanism aspect of liquid selective oxidation of alcohols on Au/Actived-Carbon catalyst

Junjiang Zhu*, José L. Figueiredo, Joaquim L. Faria
Laboratório de Catálise e Materiais (LCM), Laboratório Associado (LSRE/LCM),
Departamento de Engenharia Química, Universidade do Porto, Porto, Portugal.

Keywords: Selective Oxidation, alcohols, Molecular Oxygen, Au/AC, Alkali
Topic: Sustainable process-product development through green chemistry

Abstract

Gold catalysts supported on activated carbon (Au/AC) are investigated for the liquid phase oxidation of alcohols with molecular oxygen under atmospheric pressure. This work focus on two issues: 1) The role of basicity in the reaction; and 2) the way by which molecular oxygen participates in the reaction. The first issue was investigated by changing the initial reaction conditions and by using promoters with different basicity. The results suggest that promoters with strong basicity favor the reaction, and their role is to supply OH^- anions to Au, to form Au-OH^- active sites where H-abstraction from alcohol takes place. The second issue was addressed by comparing the catalytic performance of gold catalysts on carbon supports with different amounts of oxygen-containing functional groups. The results indicate that the amount of oxygen-containing species relates closely to the catalyst activity, and increases largely after the reaction, suggesting that an interaction between molecular oxygen and the carbon support occurs, so that molecular oxygen participates in the reaction via the carbon support. The unchanged oxidation state of gold (detected by XPS) before and after reaction suggested that the interaction between gold and molecular oxygen did not occur, supporting the above proposal.

1 Introduction

The liquid phase oxidation of alcohols with molecular oxygen is an attractive route for the synthesis of fine chemicals. Carbon supported metal catalysts are particularly useful in this context, since carbon materials are stable in acidic and basic media (Figueiredo et al., 1999; Rodriguez-Reinoso, 1998), while gold seems to be a more promising catalyst than other noble metals (such as Pt and Pd), as it is more resistant to deactivation (Biella et al., 2002; Comotti et al., 2005; Prati and Porta, 2005). As a result, gold supported on carbon received much attention in this field and many interesting results have been obtained (Mallat and Baiker, 2004). It is generally accepted that the dehydrogenation of alcohol is the first step of reaction and proceeds on the interface of noble metals, see reaction (1) and (2), followed the removal of hydrogen by oxidation with molecular oxygen and the regeneration of the catalyst (Beltowsk-Brzezinska et al., 1997; Dijkgraaf et al., 1988).

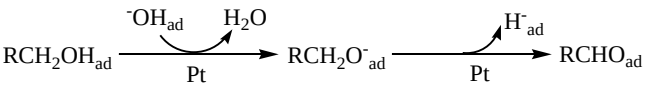

(1)

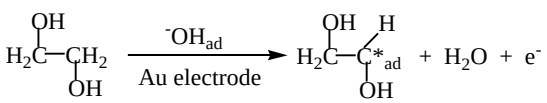

(2)

However, it is surprising to find that no work regarding the actual role of basicity (OH^-) or the way by which oxygen participates in the reaction has been reported. All the published reports

* Corresponding author. Tel + 351-225-081663. E-mail:feupzjj@fe.up.pt

just mention that the presence of basicity is necessary (especially for gold catalysts) and that the role of oxygen is to remove the adsorbed hydrogen, while no evidence and sound explanation for this assumption is normally given.

Thus, the aim of our work is to investigate the role of basicity and how molecular oxygen participates in the reaction, in order to provide better insight about the reaction mechanism. Herein, we used 1wt. % Au/AC as catalyst and benzyl alcohol as substrate, and NaOH as promoter for investigation.

2 Experimental

2.1 Materials

$HAuCl_4 \cdot 3H_2O$ (99.99% ACS, Au ≥ 49.5%) was purchased from Alfa Aesar, Polyvinyl alcohol (PVA) (> 99%), $NaBH_4$, NaOH, benzyl alcohol from Sigma-Aldrich, Decane from Fluka, Toluene from Panreac and Activated Carbon Aerosorb LR4 (BET: 875 m^2/g) from Degussa.

2.2 Modification of carbon supports

The original activated carbon (AC0) was first treated by 5% O_2/N_2 at 400 ºC for 10 h (denoted as: AC5), subsequently treated in inert atmosphere (N_2) at 650, 735, 820 and 910 ºC for 1 h, respectively. The obtained carbon supports were, accordingly, denoted as AC5_T (T = 650, 735, 820 and 910).

2.3 Preparation of catalyst

Gold supported on activated carbon (loading: 1wt. %) catalysts were prepared by gold sol method similar to that reported by Onal et al (2004). Here, $HAuCl_4 \cdot 3H_2O$ was used as the gold precursor; PVA and $NaBH_4$ were used as the protective and reductive agent, respectively. The samples obtained were finally treated by N_2 at 350 ºC for 3h, followed by reduction with H_2 at 350 ºC for 3h. According to the treatment temperature of the carbon supports, the gold catalysts were named as: Cat0, Cat5 and Cat5_T (T = 650, 735, 820 and 910).

2.4 TPD experiments

The TPD profiles were obtained with an Altamira equipment (AMI-200). The helium carrier gas was passed over 0.1 g sample at a flow rate of 25 cm^3/min, with a heating rate of 5 ºC/min. The amounts of CO and CO_2 desorbed from the carbon samples were monitored with a quadrupole mass spectrometer. For the analysis of samples after reaction, the samples were first filtered, washed with water several times, and dried in an oven at 100 ºC for 2h before the experiment.

2.5 Oxidation procedure

Alcohol oxidation was carried out at atmospheric pressure and 80 ºC, in a 30 mL, three-necked batch reactor fitted with a reflux condenser, oil bath, thermocouple and magnetic stirrer. A mixture of 40 µL NaOH, 20 µL benzyl alcohol, 10 µL decane (used as internal standard) and 0.05 g catalyst in toluene (20 mL) was prepared. The flask was then heated to 80 ºC and flushed with O_2 (or O_2/N_2) at a rate of 50 cm^3 min^{-1} , under vigorous stirring. The products of reaction were analyzed by GC (DANI 1000) with a flame ionization detector, using a CP-Sil 8 CB column and N_2 as carrier gas.

3 Results and discussion

3.1 Role of Basicity

It is generally accepted that basicity is necessary to increase the activity of supported gold catalyst in selective alcohol oxidation (Biella et al., 2003; Carrettin et al., 2003). Conversion was rather modest in the absence of any promoter (Zheng and Stucky, 2007). To better understand the role of each intervening species (O_2, catalyst and NaOH), we performed a series of exploratory experiments as described in Fig. 1: (a) with catalyst (Cat0) and O_2; (b) with catalyst (Cat0) and NaOH; (c) with O_2 and NaOH (homogeneous reaction); and (d) with (Cat0), O_2 and NaOH (Zhu et al., 2008a). At point (a), where NaOH was not added, only a

very low yield was obtained, indicating that the reaction is difficult to proceed in the absence of alkali. The selectivity increased abruptly when NaOH was added, no matter there is O_2 or not – points (b) and (c) – suggesting that basicity is necessary for benzyl alcohol oxidation. Only low conversion was observed at point (b), since O_2 was not bubbled into the reaction to oxidize benzyl alcohol. This indicates that it is not a stoichiometric reaction between benzyl alcohol and NaOH, and O_2 must take part in the oxidation process. (Activity at this point derives from the residual O_2 in toluene, the free space of the flask before reaction or the oxygen in the oxygen-containing species on the carbon support). Interestingly, a moderate conversion was observed at point (c), where catalyst was not present. It means that a homogeneous reaction occurs in the presence of NaOH. In all, these results indicate that the presence of either O_2, NaOH or Au/AC are beneficial for the reaction, but only two of these factors are not enough for the reaction to be carried out with satisfying results. Expectably, a significant improvement both in selectivity and conversion was achieved when all of them were presented – point (d). Comparing the results at points (a) and (d), one can easily conclude that basicity is necessary and is crucial in promoting the activity of Au/AC catalyst for the selective oxidation of benzyl alcohol.

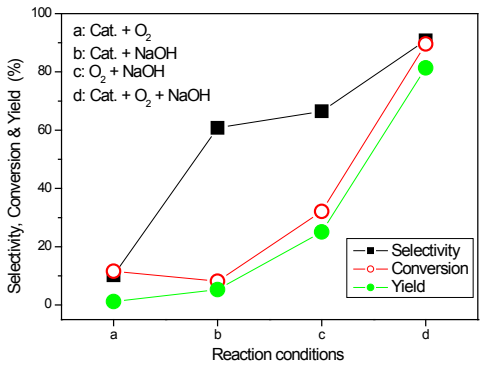

Fig.1: Benzyl alcohol oxidation on 1wt.%Au/AC under different initial conditions (NaOH/alcohol = 1 except for (a)) (Zhu et al., 2008a)

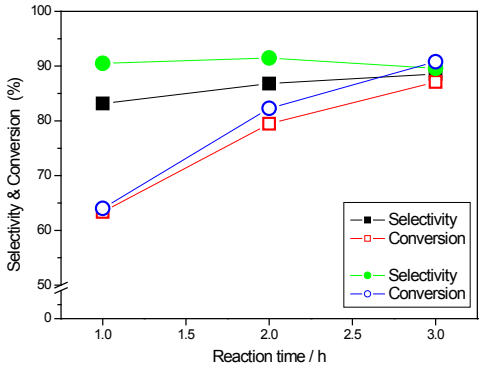

Fig.2 Benzyl alcohol oxidation on 1wt.%Au/AC: 1) OH^- physical loading (squares) and 2) adding NaOH solution (circles) (Zhu et al., 2008a)

To investigate whether the promotion of activity is caused by the basicity, we compared the effect of promoters with different basicity (neutral, weak and strong basicity) on the activity, and the results are listed in Table 1 (entries 1-3, 7). It is obvious that the activity is in sequence of $NaNO_3$ < Na_2CO_3 < NaOH ≈ KOH, which suggests that the promotion is indeed caused by basicity. For neutral $NaNO_3$, both the conversion and the selectivity are low, indicating it is not a suitable promoter. For alkalescent Na_2CO_3, which has the possibility to produce OH^- anion, the increase is small in conversion but is large in selectivity. This shows that weak basicity can improve selectivity satisfactorily, but not the conversion (Note: because the solubility of Na_2CO_3 is low, a 5 M solution cannot be prepared at room temperature, so we used a concentration of 2.5 M and a volume of 2x40 μL). As expected, addition of strongly basic NaOH/KOH improves greatly both the conversion and the selectivity, indicating that basicity indeed plays an important role in the reaction.

Optimizing the NaOH amount was then performed and the results are also listed in Table 1 (entries 4-8). Obviously, the conversion increases with NaOH amount up to a molar ratio of NaOH:alcohol equal to 1:1. We recall that this is not a stoichiometric reaction between $C_6H_5CH_2OH$ and NaOH, as explained above (see point (b)). Moreover, when we used solid NaOH in the reaction, we observed that there was still a large mass of NaOH remaining after the reaction (with ~80% conversion), indicating that it is indeed not a stoichiometric reaction and NaOH will not be dissolved in toluene. So, we advance the idea that NaOH supplies OH^- to Au, in order to form an Au-OH^- active site where H-abstraction from alcohol takes place, which is difficult to be accomplished by gold alone.

Furthermore, when we used a catalyst washed with a 5M NaOH solution and filtered (to physically load OH^- on Au surface); it showed similar activity to that of adding NaOH solution

(see Fig.2). This supports the idea that the addition of NaOH is indeed to form the Au-OH^- site required for H-abstraction from alcohol. When the NaOH amount was further increased (NaOH/alcohol = 1.5), the activity was a little lower than that measured at NaOH/alcohol = 1, indicating that the optimum value is at molar ratio of NaOH/alcohol = 1.

Table 1: Selective oxidation of benzyl alcohol using different (amount of) promoters [a] (Zhu et al., 2008a)

Entry	Promoter	P/A [b]	Conv. / %	Sel. / %
1	$NaNO_3$	1.0	7.6	49.2
2	Na_2CO_3	1.0	18.9	72.2
3	KOH	1.0	89.4	89.0
4	NaOH	0	11.6	10.2
5	NaOH	0.25	42.8	95.9
6	NaOH	0.5	60.5	96.2
7	NaOH	1.0	90.8	89.6
8	NaOH	1.25	80.2	94.9

[a] Catalyst used: 1wt. %Au/AC
[b] Ratio of promoter to alcohol

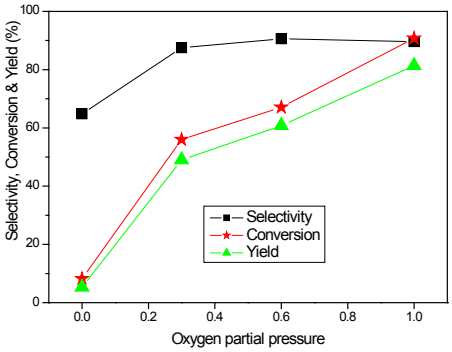

Fig.3 Effect of oxygen partial pressure on the reaction (P/A = 1.0)

3.2 Oxygen pathway

In subsequent experiments, it was found that the oxygen partial pressure affects greatly the reaction (Fig.3), which prompted us to study how oxygen participates in the reaction.

In a previous work (Figueiredo et al., 1999), it was shown that gas phase oxidation changes both the texture and surface chemistry of carbon materials (i.e. AC0 vs. AC5), while thermal treatments under inert atmosphere do not produce significant textural changes with respect to the parent materials (i.e. AC5 vs. AC5_T). So, this section is based on the catalytic performances of Cat5 and Cat5_T, in which the texture of the carbon supports is similar, and the major difference is the type and amount of oxygen-containing species on their surfaces.

Fig.4 shows the TPD results of AC5 and AC5_T. it is seen that the total amount of oxygen-containing species decreased with increasing treatment temperature. For CO desorption, a significant decrease was observed when the treatment temperature increased from 735 to 820 ºC, and only a very small CO desorption peak was observed for sample AC5_910. For CO_2 desorption, the area also decreased with increasing temperature, no CO_2 signal being observed for samples AC5_820 and AC5_910.

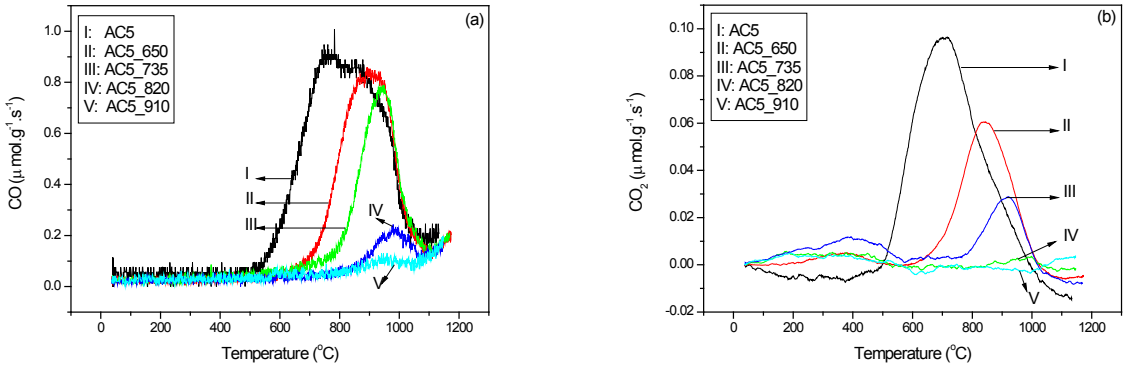

Fig.4 TPD spectra of AC5 and AC5_T: (a) CO evolution; (b) CO_2 evolution (Note: the CO_2 desorption profiles were smoothed due to the strong noise generated). (Zhu et al., 2008b)

Fig.5 shows the alcohol conversion observed with Cat5 and Cat5_T. It is seen that the conversion decreased with the increase in the carbon support treatment temperature, i.e., Cat5 > Cat5_650 > Cat5_735 > Cat5_820 > Cat5_910, which is the same sequence as the amount of oxygen-containing species of the carbon supports (see Fig.4). This means that the conversion has a close relation to the amount of oxygen-containing species in the catalyst. It may be possible that the carbon support has some activity of its own due to the presence of some type of oxygen functional group, such as observed in the oxidative dehydrogenation of ethylbenzene, where quinone groups were identified as the active sites (Pereira et al., 1999).

We do not exclude this possibility. However, the present results show that the activity decreases irrespective of the type of oxygen-containing species being removed. On the other hand, as it is known that the alcohol dehydrogenation step proceeds on the surface of the active phase (i.e. Au) and oxygen dissociation on gold surface is difficult, we propose that the contribution of oxygen-containing species is to offer a place for oxygen adsorption and dissociation (O_2 → 2O), which subsequently reacts with the hydrogen left on the gold surface to regenerate the OH^- anion ($H + O + e^- \rightarrow OH^-$)

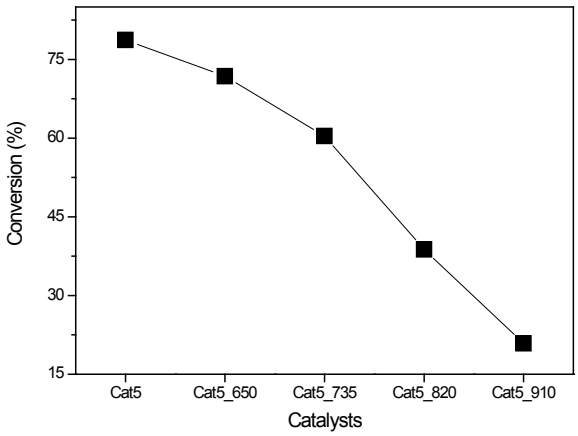

Fig.5 Alcohol conversion tested from Cat5 and Cat5_T (T = 650, 735, 820 and 910) (Zhu et al., 2008b)

In order to support the above idea that an interaction between molecular oxygen and oxygen-containing species occurs during the reaction, TPD experiments for Cat5 before and after reaction were carried out. The results in Fig.6 indicate that the amount of oxygen-containing species increased greatly after reaction, suggesting that an interaction between oxygen and the carbon support has indeed occurred, some of the oxygen entering the carbon support as a new oxygen-containing species.

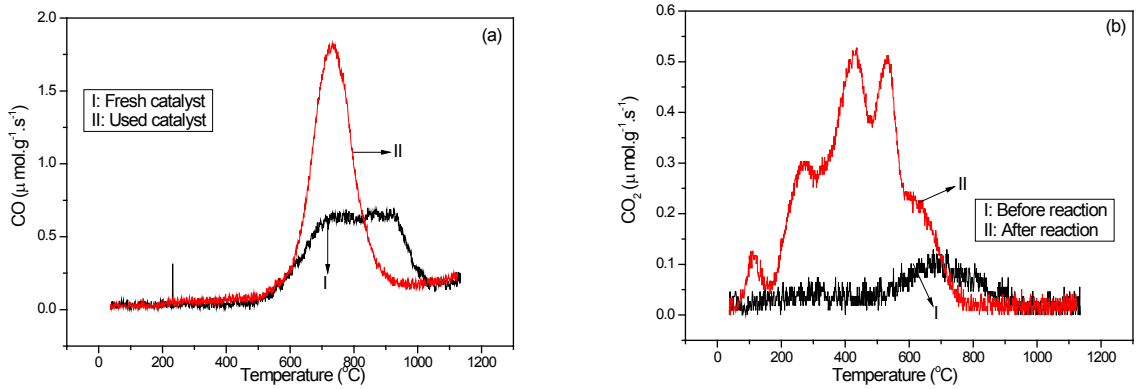

Fig.6 TPD spectra of fresh and used Cat5: (a) CO evolution; (b) CO_2 evolution (Zhu et al., 2008b)

On the other hand, according to previous results (Figueiredo et al., 1999), we propose that, for the catalyst after reaction, the CO_2 desorption (T < 600 ºC) results from carboxylic or lactone groups, while CO desorption (T = ~720 ºC) is from carbonyl or quinone groups, all of them containing a C=O group. Based on this result and the fact that it is difficult to adsorb and dissociate oxygen on the gold surface (XPS results, which were not shown here, indicate that the oxidation state of gold before and after reaction is zero), we therefore propose that the pathway for oxygen participating in the reaction is through the carbon support, as shown in Scheme 1.

Scheme 1: Suggested pathway for molecular oxygen participation in the reaction (Zhu et al., 2008b)

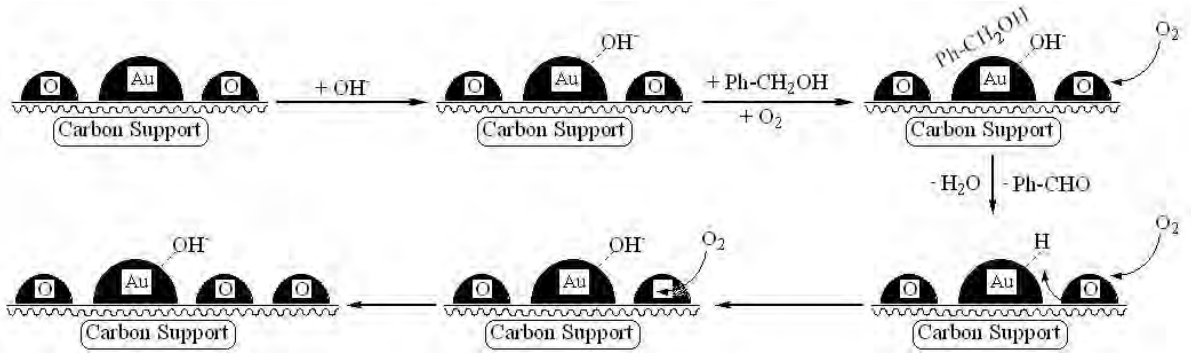

Because molecular oxygen cannot react directly with hydrogen, it must be dissociated into atomic oxygen before participating in the reaction. This may occur by interaction with the carbon support, since oxygen dissociation on gold is difficult. However, as the carbon support, unlike metal oxides, does not have oxygen vacancies (sites for oxygen dissociation), we thus suggest that the carbon support should be activated (interaction between H and O in Scheme 1) before oxygen dissociation proceeds. After activation (i.e. removal of initial oxygen), a site for molecular oxygen adsorption is created, on which the oxygen dissociation proceeds, accompanied by the oxidation of an adjacent carbon atom (the amount of oxygen-containing species increased after the reaction, see Fig.6).

4 Conclusion

In summary, this work suggested 1) the role of basicity in gold catalyzed alcohol oxidation is to supply OH^- to the gold surface, to form an Au-OH^- active site, where H-abstraction takes place; 2) molecular oxygen participates in the reaction through the carbon support, by exchanging oxygen with the oxygen-containing species on surface.

Acknowledgement

Financial support was provided by FCT (SFRH/BPD/28390/2006 and POCI/EQU/58252/2004), with contribution from FEDER.

References

Beltowsk-Brzezinska, M., Luczak, T., Holze, R. (1997). Electrocatalytic oxidation of mono- and polyhydric alcohols on gold and platinum. *J. Appl. Electrochem.*, 27, 999-1011.

Biella, S., Prati, L., Rossi, M. (2002). Selective oxidation of D-glucose on gold catalyst. *J Catal*, 206, 242-247.

Biella, S., Prati, L., Rossi, M. (2003). Selectivity control in the oxidation of phenylethane-1,2-diol with gold catalyst. *Inorg Chim Acta*, 349, 253-257.

Carrettin, S., McMorn, P., Johnston, P., Griffin, K., Kiely, C.J., Hutchings, G.J. (2003). Oxidation of glycerol using supported Pt, Pd and Au catalysts. *Phys Chem Chem Phys*, 5, 1329-1336.

Comotti, M., Della Pina, C., Matarrese, R., Rossi, M., Siani, A. (2005). Oxidation of alcohols and sugars using Au/C catalysts - Part 2. Sugars. *Appl Catal A-gen*, 291, 204-209.

Dijkgraaf, P.J.M., Rijk, M.J.M., Meuldijk, J., Vanderwiele, K. (1988). Deactivation of Platinum Catalysts by Oxygen .1. Kinetics of the Catalyst Deactivation. *J Catal*, 112, 329-336.

Figueiredo, J.L., Pereira, M.F.R., Freitas, M.M.A., Orfao, J.J.M. (1999). Modification of the surface chemistry of activated carbons. *Carbon*, 37, 1379-1389.

Mallat, T., Baiker, A. (2004). Oxidation of alcohols with molecular oxygen on solid catalysts. *Chem Rev*, 104, 3037-3058.

Onal, Y., Schimpf, S., Claus, P. (2004). Structure sensitivity and kinetics of D-glucose oxidation to D-gluconic acid over carbon-supported gold catalysts. *J Catal*, 223, 122-133.

Pereira, M.F.R., Orfao, J.J.M., Figueiredo, J.L. (1999). Oxidative dehydrogenation of ethylbenzene on activated carbon catalysts. I. Influence of surface chemical groups. *Appl Catal A-gen*, 184, 153-160.

Prati, L., Porta, F. (2005). Oxidation of alcohols and sugars using Au/C catalysts - Part 1. Alcohols. *Appl Catal A-gen*, 291, 199-203.

Rodriguez-Reinoso, F. (1998). The role of carbon materials in heterogeneous catalysis. *Carbon*, 36, 159-175.

Zheng, N.F., Stucky, G.D. (2007). Promoting gold nanocatalysts in solvent-free selective aerobic oxidation of alcohols. *Chem Commun*, 3862-3864.

Zhu, J.J., Figueiredo, J.L., Faria, J.L. (2008a). Au/activated-carbon catalysts for selective oxidation of alcohols with molecular oxygen under atmospheric pressure: Role of basicity. *Catal Commun*, In press.

Zhu, J.J., Figueiredo, J.L., Faria, J.L. (2008b). How does the molecular oxygen paticipates in the selective alcohol oxidation reaction catalyzed by Au/AC catalyst? In preparation.

Proceedings of the 10th International Chemical and
Biological Engineering Conference - CHEMPOR 2008
Braga, Portugal, September 4-6, 2008
E.C. Ferreira and M. Mota (Eds.)

PVC Paste Rheology: Polymer Properties and Viscoelastic Behaviour

Tomás[1], A., Rasteiro[2], M.G., Ferreira[2], L., Figueiredo[2], S.
[1] Companhia Industrial de Resinas Sintéticas, CIRES, S.A., Estarreja, Portugal
[2] Chemical Engineering Department, Coimbra University, Coimbra, Portugal

Keywords: PVC plastisol, rheology, viscosity aging, particle size, surfactant.
Topic: Advancing the Chemical and Biological Engineering Fundamentals

Abstract

A plastisol is a dispersion (suspension) of fine particles of poly(vinyl chloride) with a plasticizer that is normally applied over a substrate, by spreading or coating, The selection of the type of emulsion polymer to obtain the desired rheology and the quality of the final product plays a major importance. Although several factors can affect the rheological properties, this work is concerned with the particular impact of different anionic surfactants that are used during the polymerization reaction. Namely, the effect over the aging period and, additionally, their physical properties correlated with the final viscosity level of the plastisol.

Introduction

Considering the several types of poly(ethylene), poly(vinyl chloride) (PVC) is the second world consumed thermoplastic. Although the vast majority of homopolymer and copolymer products are produced in a suspension system, a particular type is produced by the emulsion or microsuspension processes, making the so called dispersion grades (Saeki and Emura, 2002). These types of PVC products are normally fine powders of spherical particles (0.1-15 μm) that are mixed with a plasticizer to produce a dispersion (suspension), normally referred as paste or plastisol. Industrially, the said dispersion is applied over a substrate, by spreading, coating or molding, before the gelification and fusion into the final commercial products, such as: films, sheets, paper coatings, mats, flooring, life preservers and roof tops (Sarvetnick, 1972; Nakajima and Harrel, 2001).

Depending on each application type, the shear stress applied over the plastisol during the production stage makes the study of the paste's rheological behaviour a very important factor to determine and fine tune all process conditions and formulations (Marcilla *et al*, 1997). Also, in the particular case of the emulsion PVC polymers, the conditions during the free radical polymerization, as well as the process conditions of the industrial spray-dryer and the subsequent milling of the powder, can have a great influence over the final properties (Nakajima and Harrel, 2001).

The emulsion polymers are normally made up in the presence of a surfactant and a free radical initiator, to produce a polymer that can have different particle sizes and surface characteristics. Also, depending on the production process, an aggregation effect is normally observed, affecting the size and size distribution of the final powder. Nevertheless, during the plastisol formation, these agglomerated particles are not sufficiently strong to resist to the high shearing mixing conditions, together with the solvating plasticizer effect over the polymer. This effect is normally translated by an increase of the plastisol viscosity with time, in a process normally called "viscosity aging" (Nakajima and Harrel, 2005). The aging rate and the rheological behaviour of the plastisols are also sensitive to the type of surfactants used during the polymerization process, type and quantity of plasticizer and to other

* Corresponding author. Tel + 351-234-811212. E-mail: arnaldo.tomas@cires.pt

additives used in the final formulation, such as fillers, pigments and thermal stabilizers (Sarvetnick, 1972, Alsopp and Vianello, 2003).

Considering the final application of the plastisol, the applied surfactant during the polymerization can play a fundamental role on the product characteristics, namely, for distinct applications of vinyl foams or films and sheets (Sarvetnick, 1972). Thus, the surfactant should be carefully selected for the final application which, normally, undergoes several trials to get sufficient knowledge of the type and quality of the obtained final product. Although the rheology of the plastisols has been quite studied, the effect of the surfactants, over the type of the particles aggregates and the correspondent effect in the viscosity aging, are normally kept within the know-how of the industrial producers and their product developers.

The application of a developed laser diffraction spectroscopy's technique (LDS) to evaluate the particle size distribution of the initial polymer's powder, as well as its evolution on the plastisols, allows very significant information of the aggregates dimension during the aging period, correlating with the paste's viscoelastic response (Rasteiro and Antunes, 2005).

The present study was aimed at identifying the effect of three selected anionic surfactants on the rheological behaviour of the pastes. For that we have fixed the plastisol formulation, having varied the main surfactant type during the emulsion polymerization.

Experimental

Materials

Emulsion PVC samples from *Companhia Industrial de Resinas Sintéticas, CIRES, S.A.:* produced in a 5L pilot reactor according to a standard emulsion polymerization recipe using the same dosage of different types of main surfactants. The free radical initiator used was ammonium persulphate. All standard procedures for the reaction are described in the literature (Burgess, 1982; Butters, 1982).

Surfactants: commercial grades of Sodium Lauryl (C_{12}-C_{14}) Sulphate (SLS) and Sodium n-Alkyl (C_{10}-C_{13}) Benzene Sulfonate (SABS) from Cognis Iberia. Sodium Alkyl (C_{15}) Sulfonate (SAS) from Leuna Tenside GmbH.

Plasticizer: Di-isodecyl Phtalate (DIDP), trade name Palatinol® 10P from BASF GmbH.

Thermal stabilizer: Mark BZ505 (Barium-Zinc) from Crompton Vinyl Additives GmbH.

Organic solvent: n-Heptane (commercial grade).

Plastisol samples preparation

Commercial formulations of 70 phr (parts of plasticizer per hundred parts of polymer) of DIDP were considered, with a common heat stability additive (Barium-Zinc) (2 phr) and the emulsion PVC samples. The preparation of the plastisols was carried out in a planetary mixer during 15 min to obtain a homogeneous final paste. While ageing proceeded, the paste was kept in a closed chamber at constant temperature (23ºC) and relative humidity (≈35%).

Particle Size Distribution

Laser diffraction spectroscopy technique (LDS): Mastersizer 2000, Malvern Instruments, UK.

LDS was used to measure the particle size distribution of the dry PVC powder in a diluted dispersion with n-heptane. Regarding the plastisol samples, according to the already published method by Rasteiro and Antunes (2005), the dilution procedure was made with n-heptane.

Rheology Measurements:

Rheological measurements: Controlled stress rheometer, Model RS1, Haake.

The rheological tests were carried out in a controlled stress rheometer, with a sensor system Z34 DIN that comprises one rotor and one beaker, with a connected thermocontroller (constant temperature 23ºC). The spindle used had 20,00 mm (radius) at a clearance to bottom 7,2 mm. For the plastisol samples, flow and dynamic tests were performed.

Zeta Potential
Zetasizer NanoZS, Malvern Instruments.
The Zeta potential is normally applied to access the charge stability of colloidal systems. In practice, the Zeta potential of the dispersion is measured by applying an electric field across the mixture. Particles, within the referred dispersion, will migrate toward the electrode of opposite charge with a velocity proportional to the magnitude of the zeta potential. A higher zeta potential will confer stability, i.e. the dispersion will keep original properties. In the particular case of the PVC powder, the Zeta potential will give an indication of the degree of packing of the particles within the aggregates.

Results and Discussion

Polymer Properties

The emulsion PVC samples are listed on table 1, including the known type of main surfactant used during polymerization, average molecular weight, polydispersity and commercial K value (inherent viscosity method ISO 1628-2). The main physical properties of the plasticizer DIDP used in the plastisol formulations are also given in Table 1.

Table 1: Main physical properties of all PVC samples and DIDP.

PVC sample	Surfactant	Mn Da	Mw Da	Polydispersity Mw/Mn	Inherent viscosity ml.g-1	K value
E-PVC 1	SLS	49223	94079	1.91	102.28	72.3
E-PVC 2	SABS	51069	92566	1.81	104.06	73.0
E-PVC 3	SAS	49752	93646	1.88	102.79	72.5
DIDP	Molecular weight (g/mol)		Density (kg/cm^3)		Viscosity 20ºC (mPa s)	
	446		962		120	

Considering the data from table 1, with the exception of the surfactant type, there is no significant difference in the polymer properties from the free radical polymerization. Also, from the dilute viscosity method (inherent viscosity method ISO 1628-2), it is possible to calculate the Fikentscher “K value”, normally used for industrial purposes.

Table 2 shows the main properties of the powder samples, namely the zeta potential and the particle size distribution (PSD), including the median size (d_{50}), the distribution ratios d_{90}/d_{10} and $(d_{90}-d_{10})/d_{50}$.

Table 2: PVC powder properties

PVC sample	Zeta (mV)	d_{50} (µm)	d_{90}/d_{10}	$(d_{90}-d_{10})/d_{50}$
E-PVC 1	-53.2	31.22	4.7	1.8
E-PVC 2	-52.1	24.72	4.5	1.6
E-PVC 3	-54.1	28.52	4.0	1.4

Considering all the samples, there is only a slight difference in all the PSD parameters, although E-PVC 3 has the lowest ratio d_{90}/d_{10} and $(d_{90}-d_{10})/d_{50}$, which corresponds to a lower fraction of aggregates and a narrower distribution. E-PVC 1 has the highest d_{50} and a broader PSD type.
The Zeta potential of the powder gives an indication of the effect of each surfactant over the packing stability of the aggregates. In fact, it is possible to access some differences between

the three samples, namely the higher value of E-PVC 2, which induces a stable behavior of the aggregates.

Plastisol's PSD Properties During Aging

Considering the stated experimental procedure, table 3 summarizes the PSD distribution of the plastisols during the aging time from 1h to 168h (7 days) after preparation.

Table 3: Particle size distributions of Plastisols during aging.

	d_{50} (µm)						d_{90}/d_{10}						$(d_{90}-d_{10})/d_{50}$					
Plastisol	1h	3h	24h	48h	120h	168h	1h	3h	24h	48h	120h	168h	1h	3h	24h	48h	120h	168h
P1	18,72	19,15	18,17	18,29	18,49	18,43	10,8	9,7	8,6	8,6	8,2	8,8	3,1	3,0	2,7	2,7	2,6	2,8
P2	17,37	19,61	18,49	19,58	18,67	18,64	11,9	11,6	10,5	11,1	10,9	10,6	2,8	2,6	2,5	2,5	2,6	2,6
P3	17,49	16,73	16,66	16,69	16,61	16,40	7,5	6,8	7,4	8,3	8,5	8,1	2,3	2,2	2,5	2,7	2,8	2,7

Comparing with the PSD results from the powder samples (Table 2), there is a general decrease on d_{50} just 1h after the plastisol's preparation. This fact is directly correlated with the plasticizer solvent effect over the particle's aggregates during the aging period. Also, for all samples, the ratio d_{90}/d_{10} decreases from 1 to 24h, indicating the destruction of the loose agglomerates in an earlier stage.
The size distribution, analysing the ratio $(d_{90}-d_{10})/d_{50}$, indicates a constant relative width of each sample through the aging period. With the exception of P3, there is a general decrease in that item, in tune with the justification made to d_{90}/d_{10}.

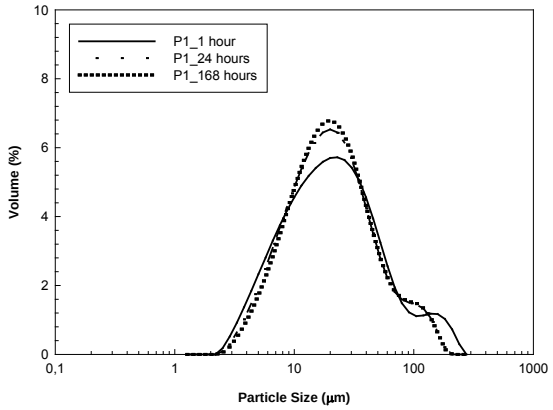

a) P1_1, 24 and 168h

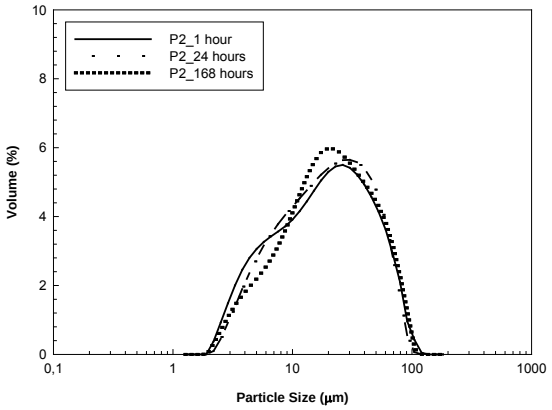

b) P2_1, 24 and 168h

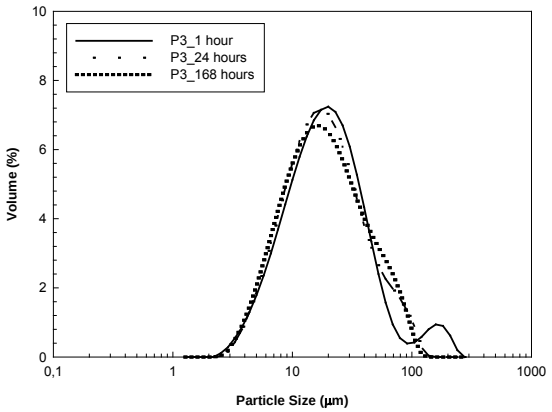

c) P3_1, 24 and 168h

Figure 1: PSD distributions (from LDS) of plastisol's samples P1, P2 and P3 at 1, 24 and 168h.

Adding to the data shown in table 3, in fig. 1 it is possible to analyse the PSD evolution (from 1 to 168h) in all plastisol samples. Again, more clearly, the early destruction of the large aggregates of P1 and P3 (fig. 1a),b)) and the almost stable behaviour of P2 (fig. 1c). This fact is consistent with the findings from the zeta potential analysis of the powder samples.

Plastisol's Flow Properties During Aging

The viscosity *vs* shear rate of all plastisol samples are shown in Fig. 2. Considering the aging period at 1, 24 and 168h over the applied shear rate, there are significant differences between the samples. With the respect to the rheological behaviour, all plastisols have a markedly pseudoplastic behaviour, although P2 (fig. 2b) has a significant lower viscosity for the same shear rate (mainly for the lower shear rates) and a lower yield stress. P3 (fig. 2c) exhibits a tyxotropic effect at low shear rate followed by a steady decrease in viscosity. The aging effect is observed in P1 and P3. Nevertheless, for P2 the viscosity level tends to decrease slightly through the aging period. This unusual behaviour can only be explained by the difference in the used surfactant nature. Considering some possibilities advanced by Collins and Hoffmann (1979), the effect of the interparticle repulsion can decrease with the progressive swelling of the plasticizer by the polymer particles, suppressing the normal aging profile. Also, for low shear rates, the applied stress can not overcome the electrical and van der Waals forces between the particles layers, inducing an abrupt increase in viscosity. This effect is slightly observed in P2 and markedly in P3, inducing the reported tyxotropic behaviour in the initial stage.

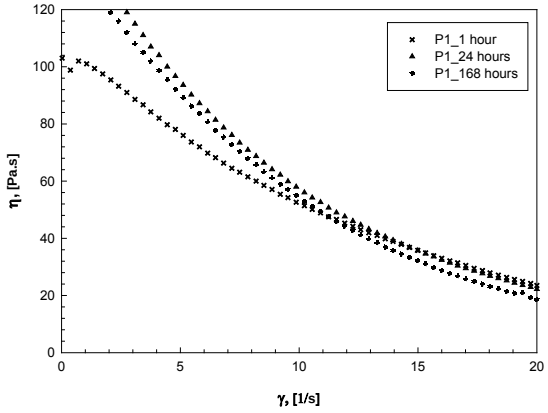

a) P1_1, 24 and 168h

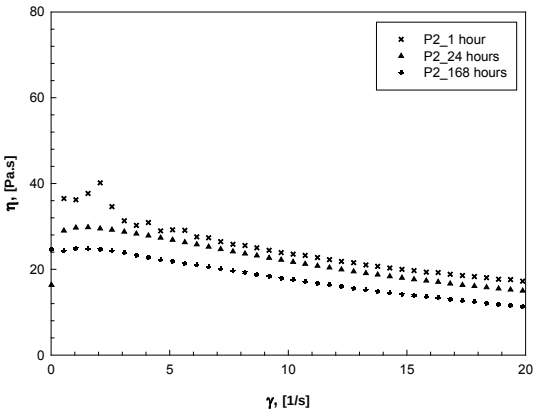

b) P2_1, 24 and 168h

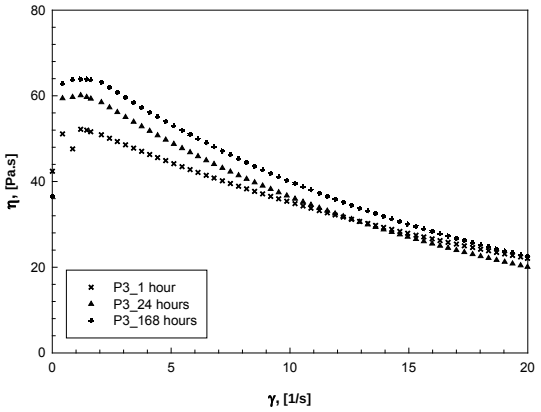

c) P3_1, 24 and 168h

Figure 2: Viscosity (η) *vs* shear rate (γ) of plastisol's samples P1, P2 and P3 at 1, 24 and 168h.

Besides the small changes in the PSD curves (see fig. 1), the narrower PSD of P3 agreeing with the higher viscosity values observed, the major differences in the flow properties can be only justified by the different surfactant on the surface of the particles. Thus, for a control shear rate of 5 s^{-1}, the overall viscosity tends to decrease from P1>P3>P2. Therefore, for the considered formulation, the anionic surfactant SABS, present in E-PVC 2, provides a lower viscosity level together with a steady decrease through the aging period. Besides the given general theories, other properties of surfactants can be correlated, namely the critical micelle concentration (cmc), deeply linked to the alkyl chain and anionic nature (Myers, 2006). Thus, SLS has a cmc of 0,38 $g.L^{-1}$ (E-PVC 1), SAS has 0,50 $g.L^{-1}$ (E-PVC 2) and SABS has 1,00 $g.L^{-1}$ (E-PVC 3) (Myers, 2006). That is, for the tested conditions, it becomes quite acceptable that a higher cmc value induces a lower plastisol viscosity.

Conclusions

The effect of the particle size and size distribution of the dispersion PVC grades have been quite studied and, generally, elected as the most important factor for controlling the flow behaviour of the commercial plastisol formulations. However, it becomes clear that the surfactant type used during the emulsion polymerization plays a crucial role in the plastisol rheology and in the aging characteristics.

From the differences in the plastisol rheology from the tested surfactants, it is possible to achieve a low viscosity level with SABS that can, for instance, lead to a further decrease in the plasticizer concentration or other improvement in the formulation.

Furthermore, upon the results, it seems that the cmc data can be correlated with the achieved plastisol viscosity. Nevertheless, due to the low number of tested surfactants, further confirmation studies are required to have a deeper understanding of the interaction mechanism associated with the surfactant type over the (inter)particles surface layer and the plasticizer.

Aknowledgment

We want to acknowledge the financial support from FCT, contract nr.POCI/EQU/47024/2002.

References

Saeki, Y, Emura, T. (2002). Technical progresses for PVC production. *Progress Polymer. Science*, 27, 2055–2131.

Sarvetnick, H.A. (1972). Plastisols e Organosols. Van Nostrand Reinhold Company, New York, USA.

Nakajima, N., Harrell, E.R. (2001). Rheology of PVC Plastisol: Particle size Distribution and Viscoelastic Properties, *Journal of Colloid and Interface Science*, 238, 105–115.

Nakajima, N., Harrel, E.R. (2001), Rheology of PVC Plastisol: Formation of Immobilized layer in pseudoplastic flow, Journal of Colloid and Interface Science, 238: 116–124.

Marcilla, A., García, J.C., Beltrán, M. (1997). Study of the Flow Properties and the Aging Process in PVC Plastisols from Commercial PVC Resins. *European Polym. Journal*, 5, 753-759.

Nakajima, N., Harrell, E.R. (2005). Viscosity Aging of Poly(vinyl Chloride) Plastisol: The Effect of the Resin Type and Plasticizer Type. *Journal of Applied Polymer Science*, 9, 448-464.

Alsopp, M, Vianello, G. (2003). *In* Vinyl Chloride Polymers, *Encyclopedia of Polymer Science and Technology 3rd Ed*., Volume 8, 437-476, John Wiley & Sons, New Jersey, USA.

Rasteiro, M.G., Antunes, E. (2005). *Correlating the Rheology of PVC-Based Pastes with Particle Characteristics*, *Particulate Science and Technology*, 23, 361–375.

Collins, E.A., Hoffmann, D.J., Soni, P.L. (1979), Rheology of PVC Dispersions- I. Effect of Particle Size and Particle Size Distribution. *Journal of Colloid and Interface Science*, 71-1, 21-29.

Myers, D. (2006), Surfactant Science and Technology, 3rd Ed. John Wiley & Sons, Inc., New Jersey, USA.

Proceedings of the 10th International Chemical and
Biological Engineering Conference - CHEMPOR 2008
Braga, Portugal, September 4-6, 2008
E.C. Ferreira and M. Mota (Eds.)

SEC/MALLS Measurement of the Branched Structure of Methyl Methacrylate + Ethylene Glycol Dimethacrylate Copolymers Synthesized by Atom Transfer Radical Polymerization

Ivone M.R. Trigo[1], **Miguel A.D. Gonçalves**[1], **Rolando C.S. Dias**[1,*], **Mário Rui P.F.N. Costa**[2]
[1]LSRE-Instituto Politécnico de Bragança
Quinta de Santa Apolónia, 5300 Bragança, Portugal.
[2] LSRE-Faculdade de Engenharia da Universidade do Porto
Rua Roberto Frias s/n, 4200-465 Porto, Portugal.

Keywords: Branching, Crosslinking, Atom-Transfer, Molecular Weight, Radius of Gyration.
Topic: Advancing the chemical engineering fundamentals.

Introduction

In the last few years, atom transfer radical polymerization (ATRP) of acrylate and methacrylate monomers in the presence of a small amount of cross-linker has been investigated in order to produce branched polymers and gels with applications in microelectronics, coatings industries or biomedicine (Wang and Zhu, 2005; Gao et al., 2007). In this context, it is being explored the production by ATRP of branched/crosslinked polymers with a lower degree of heterogeneity than that obtained by conventional free radical polymerization (FRP). This work reports an experimental study on the ATRP of methyl methacrylate (MMA) + ethylene glycol dimethacrylate (EGDMA) initiated by MBPA (methyl α-bromophenylacetate) and mediated by copper bromide (CuBr) ligated with HMTETA (1,1,4,7,10,10-hexamethyltriethylenetetramine). The synthesized copolymers were analyzed by size exclusion chromatography (SEC) with simultaneous detection of refractive index (RI) and multi-angle laser light scattering (MALLS) signals. Important details of the molecular architecture of these materials can therefore be measured, namely absolute molecular weights and *z*-average radius of gyration. Different experimental runs were performed in order to investigate the influence of the operating conditions (e.g. temperature and initial molar ratios MMA/EGDMA/MBPA/CuBr/HMTETA) on the structure of the products.

In conventional radical polymerization (FRP), the expected life time of a radical t_l is very short (of the order of 1 s) owing to the termination reaction according to Eq. (1):

$$t_l = \frac{R}{r_t} \simeq \frac{1}{2k_t R} \tag{1}$$

In this equation, R represents the concentration of radicals, r_t the rate of termination and k_t the correspondent rate coefficient. However, with ATRP the expected life time of a radical can attain several hours, since it is determined by the dynamic equilibrium between activated and deactivated states according to

* Corresponding author. Tel. +351-273-303088. E-mail: rdias@ipb.pt.

Eq. (2):

$$-\mathrm{P}^{\bullet} + \mathrm{X} - \mathrm{M}_{\mathrm{t}}^{\mathrm{n}+1} - \mathrm{Y/Ligand} \underset{k_{act}}{\overset{k_{deact}}{\rightleftharpoons}} -\mathrm{P} - \mathrm{X} + \mathrm{M}_{\mathrm{t}}^{\mathrm{n}} - \mathrm{Y/Ligand} \tag{2}$$

Here, $-\mathrm{P}^{\bullet}$ represents a radical in a polymer molecule, $\mathrm{X} - \mathrm{M}_{\mathrm{t}}^{\mathrm{n}} - \mathrm{Y/Ligand}$ a transition metal complex (e.g. $\mathrm{Cu(I)Br/HMTETA}$), $\mathrm{X} - \mathrm{M}_{\mathrm{t}}^{\mathrm{n}+1} - \mathrm{Y/Ligand}$ the correspondent oxidized metal complex (g. $\mathrm{Cu(II)Br_2/HMTETA}$) and $-\mathrm{P} - \mathrm{X}$ a dormant radical. This intermittent exchange reduces the concentration of growing radicals and therefore minimizes the termination reactions (usually less than 5% of the total polymer chains undergoes termination in ATRP). The more usual applications of the almost "living" character of ATRP are the synthesis of low polydispersity linear polymers and of block copolymers. Nevertheless, it will be shown next that it is also useful for the controlled production of well defined hyperbranched polymers and comparatively much more homogeneous networks than those achieved by conventional radical polymerization, as the effect of intramolecular reactions is decreased.

Experimental Part

Polymerization runs were carried our using a $2.5\ \mathrm{dm}^3$ maximum capacity stainless steel reactor (Gonçalves et al., 2007). Anisole at 99% purity, N,N-dimethylformamide at 99.8% purity, toluene at 99.7% purity, MBPA at 97% purity, HMTETA at 97% purity, Cu(I)Br at 98% purity, MMA stabilized with 10 to 100 ppm monomethyl ether hydroquinone at 99% purity and EGDMA stabilized with 100 ppm monomethyl ether hydroquinone at 98% purity have been purchased from Sigma Aldrich and used as received. MMA, EGDMA, solvent(s), CuBr and HMTETA were premixed at 60 °C for at least 30 min in a volumetric flask. This mixture was charged to the reactor (previously purged with argon) and brought up to the desired temperature. The initiator (MBPA) was rapidly added to the system and its introduction is used to define the zero reaction time $t = 0$. Argon was bubbled in the reactor during the whole polymerization. At prescribed polymerization times, samples of polymer were withdrawn from the reactor and analyzed by SEC/RI/MALLS. A poor solubility of copper species in the polymerization system was observed when toluene was used as solvent. This difficulty was not eliminated by extending the mixing period, increasing the temperature or using a higher initial molar ratio HMTETA/CuBr. Better results could be obtained by excluding toluene (therefore using bulk MMA) or adding DMF as a solvent (Pascual et al., 1999) even in a small amount (10%). Good solubility could also be achieved by using anisole (Xia and Matyjaszewski, 1997) + DMF as a co-solvent.

Kinetic Modeling

As described in previous works (Costa and Dias, 2007, 2005; Dias and Costa, 2007, 2006), it is possible to obtain the generating functions (GF) of molecular size distributions (MSD) of the rate equations of formation of polymer species by chemical reactions ($G_{\mathcal{R}_P}$, $G_{\mathcal{R}_S}$ and $G_{\mathcal{R}_{H_n}}$). The insertion of these GF in the population balance equations (PBE) of a non-steady state perfectly mixed continuous stirred tank reactor (CSTR) yields PBE in terms of the GF of size distributions of mole concentrations of polymer degrees of polymerization, sequences and pendant chains, $G(\mathbf{s})$, $U(\mathbf{s})$ and $G_n^H(\mathbf{s}^-, \mathbf{s}^+)$, respectively:

$$\frac{\partial G}{\partial t} = G_{\mathcal{R}_P} + \frac{G_F(t) - G}{\tau} - \mathcal{R}_v G; \qquad G_{|t=0} = G_0\left[\mathbf{s_0}(t, \mathbf{s})\right] \tag{3}$$

$$\frac{\partial U}{\partial t} = G_{\mathcal{R}_S} + \frac{U_F(t) - U}{\tau} - \mathcal{R}_v U; \qquad U_{|t=0} = U_0\left[\mathbf{s}_0(t, \mathbf{s})\right] \tag{4}$$

$$\frac{\partial G_n^H}{\partial t} = G_{\mathcal{R}_{H_n}} + \frac{G_{n\ F}^H(t) - G_n^H}{\tau} - \mathcal{R}_v G_n^H; \qquad G_{n\ |t=0}^H = G_{n\ 0}^H \left[\mathbf{s_0}^-(t,\mathbf{s}^-), \mathbf{s_0}^+(t,\mathbf{s}^+)\right] \qquad (5)$$

Eqs. (3)-(5) are non-linear first order partial differential equations solvable by the method of the characteristics. These master equations allow the prediction of the MSD, SSD (sequence size distribution) and RG (radius of gyration) distributions for general irreversible non-linear polymerizations. For the present chemical system, modeling studies were carried out considering a kinetic scheme comprising a total of 22 species and 44 different chemical reactions, as summarized in Table 1. Due to its generality, this method can be applied to different chemical systems and reactors (e.g. semi-batch), as recently shown for conventional (Gonçalves et al., 2007) and nitroxide-mediated non-linear radical copolymerizations.

Table 1: Chemical groups and kinetic scheme considered in the modeling of ATRP of MMA/EGDMA.

Chemical Groups	Chemical Reactions
Three monomers: MMA, EGDMA	Activation/deactivation of initiator and radicals.
and pendant double bonds (PDB).	Initiations of monomers and PDB.
Three polymer growing radicals.	Propagations of monomers and PDB.
Three polymer dormant radicals.	Chain transfers to monomers and solvent.
Initiator and radical from initiator.	Combination and disproportionation.
Complex metal/ligand and deactivator.	
Solvent and correspondent primary radical.	

Results and Discussion

Figure 1(a) compares experimental observations and predictions for monomer conversion in ATRP copolymerizations of MMA/EGDMA at different temperatures. A good agreement between predictions and measurements is observed using kinetic parameters available in literature for linear polymerizations (e.g. Al-Harthi et al. (2007), Zhang and Ray (2002) and references therein). Notice that the reactivity of pendant double bonds of EGDMA have a minor impact in the global monomer conversion but strongly affects the gelation phenomenon, as will be discussed below. Figure 1(b) compares experimental measurements and predictions of $\overline{M}_n$ and $\overline{M}_w$ in linear ATRP polymerizations of MMA at different temperatures. Good agreements are also observed at low temperatures but major deviations are identified at 90 °C possibly due to side reactions and loss of termination control which is known to occur in ATRP at high temperatures.

Figure 1(c) shows the RI chromatograms of ATRP synthesized polimethylmethacrylate (PMMA) samples at different polymerization times. The living character of this polymerization is confirmed by the observed growth of the molecular weight (MW) without a concomitant raise of polydispersity index (PDI). Figure 1(d) shows the good control of the molecular architecture achieved with ATRP for linear polymerization systems.

Predicted and observed time evolution of $\overline{M}_w$ in linear and crosslinked polymers obtained in the ATRP copolymerization of MMA/EGMDA are compared in Figure 1(e). Here a system with a mole fraction of EGDMA of 0.5% was considered. From Figure 1(e) it is clear the influence of a small amount of crosslinker in the properties of the resulting materials, namely in comparison with the linear analogs. It is also shown the possibility of synthesize soluble hyperbranched polymers (without gelation) using living polymerization instead of conventional radical polymerization (FRP). A good agreement is also observed between predictions and measurements of $\overline{M}_w$ in the non-linear polymerization system. Nevertheless, it should be mentioned that the most important kinetic parameter governing the crosslinking process is the

reactivity of the pendant double bonds (PDB) of EGDMA. In the present work this parameter was used to fit the experimental data and the reactivity ratio between PDB of EGDMA and MMA double bonds, $r = k_p^*/k_{p11} = 0.45$ was estimated. The decrease in the reactivity of PDB here estimated is consistent with other measurements neglecting the effect of intramolecular cyclizations in diluted systems (see for instance Gonçalves et al. (2007) and references therein) but is not in agreement with findings for bulk polymerizations stating the equal reactivity of PDB and double bonds of monovinyl monomers (Ide and Fukuda, 1997). This means that the reactivity ratio here estimated is likely an apparent value affected by the neglected influence of intramolecular cyclizations which may become appreciable already for the 50 % dilution used in our experiments. Similar findings about the importance of cyclizations have been recently reported by Matyjaszewski group in the synthesis of polyacrylate networks by ATRP (Gao et al., 2008). Complementary studies concerning reaction runs in bulk should yield a more complete assessment on the possibilities of this synthetic method to prepare well defined hyperbranched polymers and networks devoid of intramolecular loops.

Figure 1(f) shows the predicted and experimentally observed influence of the temperature on the *z*-average radius of gyration ($\overline{R}_g$) in ATRP copolymerizations of MMA/EGDMA with constant mole fraction of crosslinker ($y_{EGDMA} = 0.5\%$). Predictions were obtained with the same set of kinetic parameters used for the computation of molecular weights. The good agreement between experimental measurements and predictions confirms the ability of the proposed kinetic approach to obtain some details of the molecular architecture of non-linear polymers.

Figure 2(a) shows bimodal chromatograms due to the formation of a polymer population at a low concentration but high molecular weight in ATRP of MMA/EGDMA. Notice that this observation is only possible using a SEC/RI/MALLS system. Time evolutions of the molecular architectures of highly branched samples are compared in Figure 2(b). In this figure it is possible to observe the gradual shift of the molecular architecture of branched copolymers away from the one of linear polymers. It is also possible to conclude that erroneous interpretations of chromatograms of non-linear polymers will result from using molecular weight calibrations based upon linear polymers, as before shown in the framework of FRP systems (Gonçalves et al., 2007).

Conclusions

It is shown that important features of the molecular architecture of ATRP synthesized MMA/EGDMA branched copolymers can be measured using a SEC/MALLS system. A general kinetic approach was also used to predict some structural properties of these materials, namely their *z*-average radius of gyration. The experimental results of this work agree with those found in a comparable research on polyacrylate networks (Gao et al., 2007, 2008) which have also detected the effect of intramolecular cyclizations at a comparable dilution ratio. Reaction runs in bulk are planned to be carried out at a short term and they should yield a more complete assessment on the possibilities of this synthetic method to prepare well defined hyperbranched polymers and networks with few intramolecular loops. The interest of such polymers as building blocks for advanced materials with applications in electronics and in biomedicine/pharmacy is one of the main driving forces for such efforts. The availability of the computing tools to predict the formation and final structure of these complex materials (such as the radius of gyration in sol) despite the huge number of reactions strongly enhances the possibilities of better design of the involved products and processes.

Acknowledgments

Financial support by Fundação para a Ciência e a Tecnologia (FCT), Ministry of Science and Technology of Portugal and European Community through FEDER (projects POCI/EQU/44784/2002 and POCI/EQU/60483/2004 - PPCDT/EQU/60483/2004) is gratefully acknowledged.

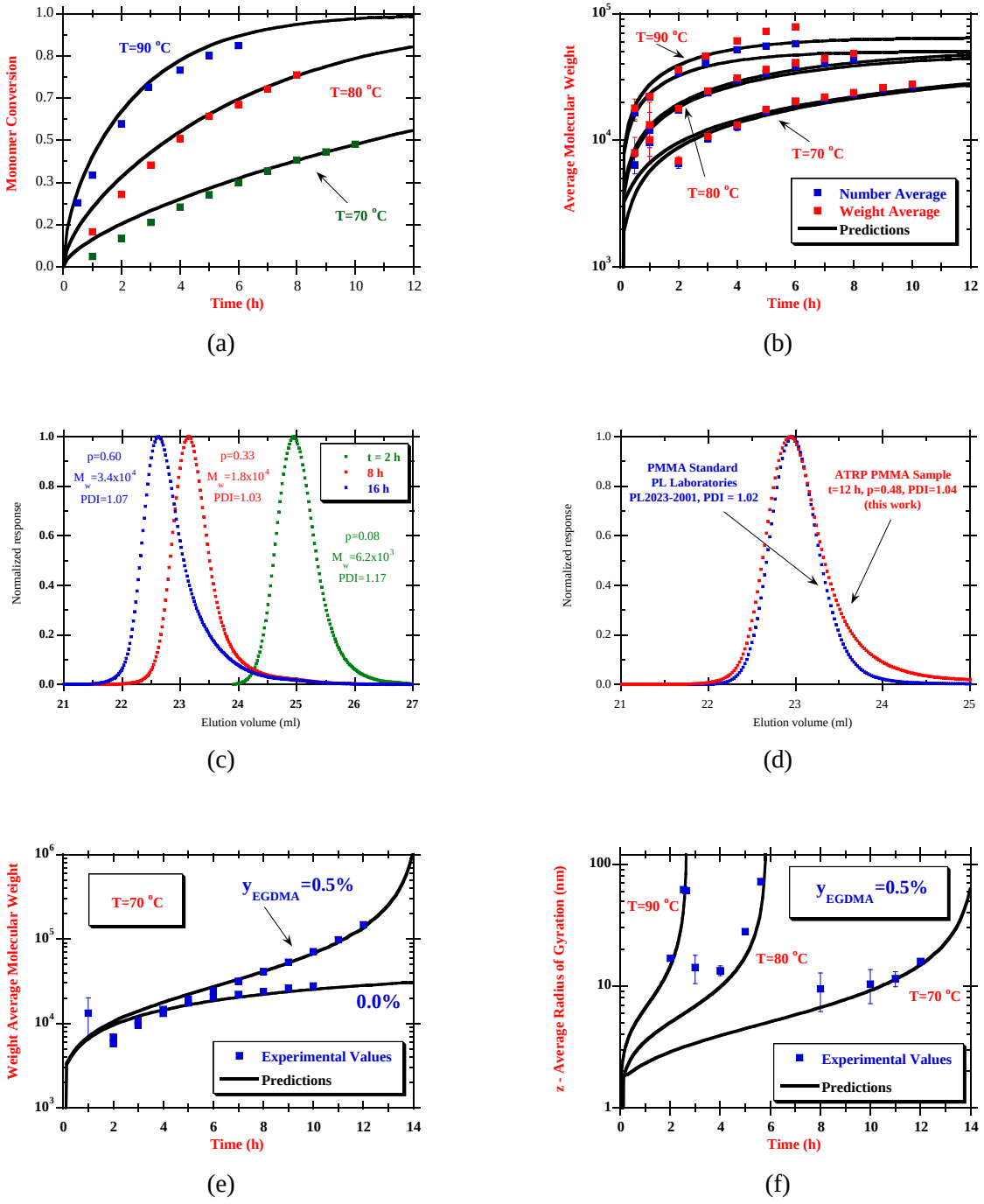

Figure 1: (a) Predictions and experimental observations for monomer conversion in ATRP copolymerizations of MMA/EGDMA at different temperatures. Initial molar ratio MBPA/CuBr/HMTETA=1/1/1 in all runs. (b) Predictions and experimental observations of $\overline{M}_n$ and $\overline{M}_w$ in linear ATRP polymerizations of MMA ($y_{EGDMA} = 0.0\%$) at different temperatures. Experiments at 50 % dilution. (c) RI chromatograms of ATRP synthesized PMMA at 80 °C . Samples with different times of polymerization showing the living character of the polymerization (increase of molecular weight MW without a concomitant increase of PDI). Polymerizations in MMA/Toluene solution (35 % v/v) with initial molar ratios MMA/MBPA=500 and MBPA/CuBr/HMTETA=1/1/1. (d) Comparison of the RI chromatograms of PMMA samples: commercial standard and ATRP synthesized. (e) Predicted and observed time evolution of $\overline{M}_w$ in linear and crosslinked polymers obtained in the ATRP copolymerization of MMA/EGMDA at 70 ° C. (f) Predicted and experimentally observed influence of the temperature on $\overline{R}_g$ in ATRP copolymerizations of MMA/EGDMA with constant mole fraction of crosslinker ($y_{EGDMA} = 0.5\%$). Experiments at 50 % dilution.

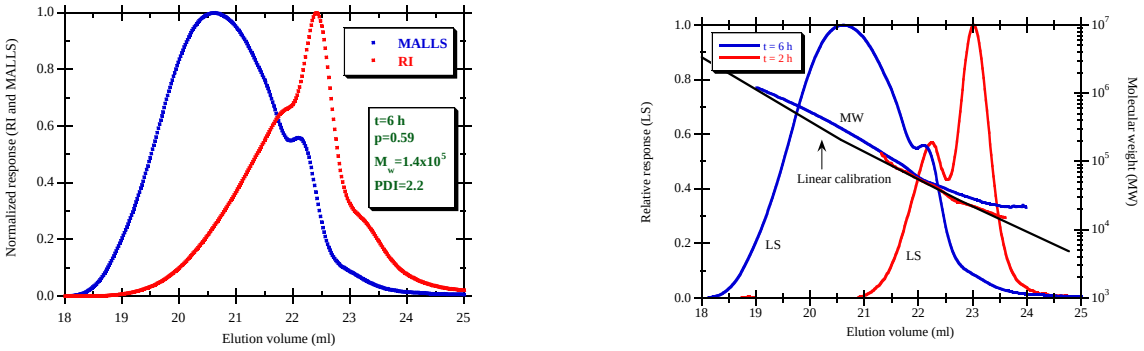

(a) (b)

Figure 2: (a) MALLS and RI chromatograms of MMA/EGDMA sample synthesized using ATRP at 90 °C . Copolymerization MMA/EGDMA was performed with 0.5% mole fraction of EGDMA. (b) Molecular weight along SEC chromatogram of MMA/EGDMA samples synthesized using ATRP at 90 °C .

References

Al-Harthi, M., Soares, J.B.P., Simon, L.C. (2007). Mathematical Modeling of Atom-Transfer Radical Copolymerization, *Macromol. React. Eng.*, 1, 468–479.

Costa, M.R.P.F.N., Dias, R.C.S. (2005). An Improved General Kinetic Analysis of Non-Linear Irreversible Polymerizations, *Chem. Eng. Sci.*, 60, 423–446.

Costa, M.R.P.F.N., Dias, R.C.S. (2007). Prediction of Mean-Square Radius of Gyration of Tree-Like Polymers by a General Kinetic Approach, *Polymer*, 48, 1785–1801.

Dias, R.C.S., Costa, M.R.P.F.N. (2006). A general kinetic method to predict sequence length distributions for non-linear irreversible multicomponent polymerizations, *Polymer*, 47, 6895–6913.

Dias, R.C.S., Costa, M.R.P.F.N. (2007). Branching and Cross-Linking in Coordination Terpolymerizations, *Macromol. React. Eng.*, 1, 440–467.

Gao, H., Min, K., Matyjaszewski, K. (2007). Determination of Gel Point during Atom Transfer Radical Copolymerization with Cross-Linker, *Macromolecules*, 40, 7763–7770.

Gao, H., Li, W., Matyjaszewski, K. (2008). Synthesis of Polyacrylate Networks by ATRP: Parameters Influencing Experimental Gel Points, *Macromolecules*, 41, 2335–2340.

Gonçalves, M.A.D., Dias, R.C.S., Costa, M.R.P.F.N. (2007). Time programmed feed of semi-batch reactors with non-linear radical copolymerizations: an experimental study of the system styrene+divinylbenzene using SEC/MALLS, *Macromol. Symp.*, 259, 124–134.

Ide, N., Fukuda, T. (1997). Nitroxide-Controlled Free-Radical Copolymerization of Vinyl and Divinyl Monomers. Evaluation of Pendant-Vinyl Reactivity, *Macromolecules*, 30, 4268–4271.

Pascual, S., Coutin, B., Tardi, M., Polton, A., Vairon, J.-P. (1999). Homogeneous Atom Transfer Radical Polymerization of Styrene Initiated by 1-Chloro-1-phenylethane/Copper(I) Chloride/Bipyridine in the Presence of Dimethylformamide, *Macromolecules*, 32, 1432–1437.

Wang, A.R., Zhu, S. (2005). Branching and Gelation in Atom Transfer Radical Polymerization of Methyl Methacrylate and Ethylene Glycol Dimethacrylate, *Polym. Engng. Sci.*, 45, 720–727.

Xia, J., Matyjaszewski, K. (1997). Controlled/"Living" Radical Polymerization. Atom Transfer Radical Polymerization Using Multidentate Amine Ligands, *Macromolecules*, 30, 7697–7700.

Zhang, M., Ray, W.H. (2002). Modeling of "Living" Free-Radical Polymerization Process. I. Batch, Semibatch, and Continuous Tank Reactors, *J. Appl. Polym. Sci.*, 86, 1630–1662.

Proceedings of the 10th International Chemical and
Biological Engineering Conference - CHEMPOR 2008
Braga, Portugal, September 4-6, 2008
E.C. Ferreira and M. Mota (Eds.)

Thermal Degradation Kinetics of Polyethylene in Dynamic Conditions using simultaneous DSC/TG analysis

Anabela Coelho[1,2], Luís Costa[1], Maria das Mercês Marques[3], Isabel Fonseca[2], Maria Amélia Lemos[1], Francisco Lemos[1] *

[1] IBB – Institute for Biotechnology and Bioengineering, Centre for Biological and Chemical Engineering, Instituto Superior Técnico, Av. Rovisco Pais, 1049-001 Lisboa, Portugal.
[2] REQUIMTE-CQFB, Universidade Nova de Lisboa, Faculdade de Ciências e Tecnologia, Campus da Caparica, 2829 Caparica, Portugal.
[3] CQE – Centro de Química Estrutural, Instituto Superior Técnico, Av. Rovisco Pais, 1049-001 Lisboa, Portugal.

Keywords: Polyethylene, Kinetic modeling, thermal degradation, differential scanning calorimetry (DSC), thermogravimetry (TG)
Topic: Sustainable process-product development through green chemistry Suitable conference — Environmental engineering & management.

Abstract

Thermal degradation of high and low density polyethylene (LDPE) (HDPE) in an inert atmosphere was studied using simultaneous thermogravimetry (TG) and differential scanning calorimetry (DSC) at four different heating rates: 5, 10 ,20 and 40ºC/min. The products obtained in depolymerisation reaction were analyzed by gas chromatography. In this work a kinetic model has been developed that allows a simultaneous correlation of the signals obtained from TG and DSC, under dynamic conditions at different heating rates and allows further insight into the chemical process that is taking place. Fitting this model to the all experimental results made possible to estimate several kinetic parameters. It was also shown that the simultaneous use of TG and DSC information allows the measurement of the reaction rate before any gas-phase products can be observed.

1 Introduction

The consumption of plastic materials has been growing progressively. Consequently, increase amounts of waste plastics are causing serious pollution problems. Reduction of polymer waste is important both from environmental and energetic aspects. In this way, pyrolysis can be considered as a sustainable solution for urban waste polymer recycling (Aguado et al. 2007). During this process, the polymers are heated in an inert atmosphere, leading to cracking of their backone (Dong et al 2007 and Demirbas et al. 2004). The light hydrocarbons formed can be used either as fuels or as feed stock in the petrochemical and chemical production (Demirbas et al. 2004). Polyethylene is the most commonly used plastic worldwide which explains why many studies on the pyrolysis of polyethylene have appeared in literature in the last few years

Thermal behaviour of polymers can be improved by the knowledge of their thermal degradation kinetics and this can be done using dynamic techniques, such as TG/DSC, coupled with gas phase products analysis. Different techniques have been considered to investigate the reaction, but due to the nature of the process, thermogravimetric analysis (TGA) is widely considered as a useful technique to study polymers decomposition processes, including their kinetics (Kayacan et al. 2008, Ceamanos et al. 2002 and H. Bockhorn et al. 1999). Kinetic models used to describe the pyrolysis of polymers are basically based on the analysis of weight loss curves obtained during thermal gravimetric analysis of the polymeric samples. However, with this technique the reaction will only be

* Corresponding author. Tel + 351-239-798700. E-mail: francisco.lemos@ist.utl.pt

detect after it has occurred, when the products became sufficiently small to evaporate into the gas phase thus leading to the decrease of the observed polymer mass. Nevertheless, it is possible to follow the reaction from the very start, by measuring the heat involved in the breaking of the polymer bonds, for example using DSC. In this work, we have developped a model that makes use of the combination of the DSC and TG signal to give a more complete picture of the reaction.

2 Experimental

Polymers Investigated

The polymers studied in this work were pure, high density and low density polyethylenes used without any type of additivation. The high density polyethylene samples (HDPE) show an average molecular weight Mw~300 000 (Mw/Mn~20) and the low density polyethylene ones (LDPE) a Mw~390 000 (Mw/Mn~21).

Degradation of PE

All TG/DSC experiments were carried out in a TA Instruments SDT 2960 simultaneous DSC-TGA apparatus. The PE samples were placed in an alumina TG pan and their thermal degradation was analyzed. The initial sample mass was about 10 mg. The run was performed under nitrogen, with a continuous flow rate of 80 ml/min, and heating rates of 5,10,20 and 40 ºC/min temperature increase rate from room temperature up to 600 ºC; this temperature was maintained for an additional 10 min. At the end of each run, the oven was cooled and a second run was performed with the same pan arrangement to obtain the baselines, particularly for the DSC signal, which is very sensitive to the layout of the pans inside the oven. The gas phase products of the thermal and catalytic degradation of the polymers were collected and analysed by GC Shimadzu GC-9A chromatograph equipaded with a flame ionization detector (FID) and a capillary KCl/Al_2O_3 PLOT column.

3 Results and Discussion

DSC and TG Analysis

As shown in Figures 1b and 2b, there is a displacement of the maximum of the heat-flow curves to higher temperatures with increasing heating rate, due to the kinetics of the process itself and to dynamic effects of the equipment being used. For lower heating rates the time taken to heat up to a certain temperature is longer that at higher heating rates and, thus, the conditions for the appearance of the maximum occur at lower temperatures. The effect of heat transfer also becomes more important as the heating rates increase and the dynamics of the equipment itself may also become important for very high heating rates (Conesa et al 1996). From table 1, it is possible verify that the degradation temperature increased as the increasing heating rate.

The same table also shows that the thermal degradation of LDPE tends to occur at lower temperatures than that observed for HDPE.

Table 1. Degradation temperatures for the polymer samples obtained from TGA/DSC results.

Sample	$T_{degrad.}$ (ºC)
HDPE 5ºC/min	470.9
HDPE 10ºC/min	483.2
HDPE 20ºC/min	493.2
HDPE 40ºC/min	511.7
LDPE 5ºC/min	459.7
LDPE 10ºC/min	475.3
LDPE 20ºC/min	494.8
LDPE 40ºC/min	511.0

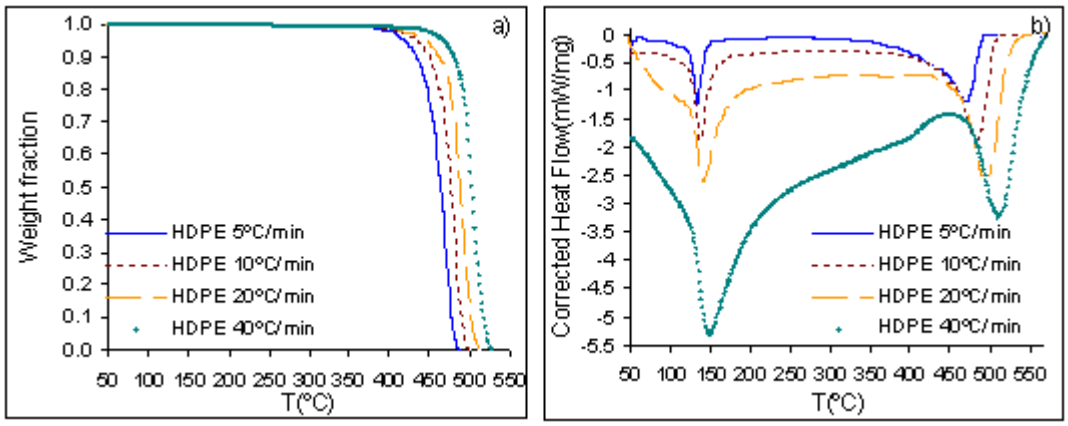

Fig. 1.TG (a) and Heat Flow (b) curves obtained in the degradation of HDPE at different heating rates.

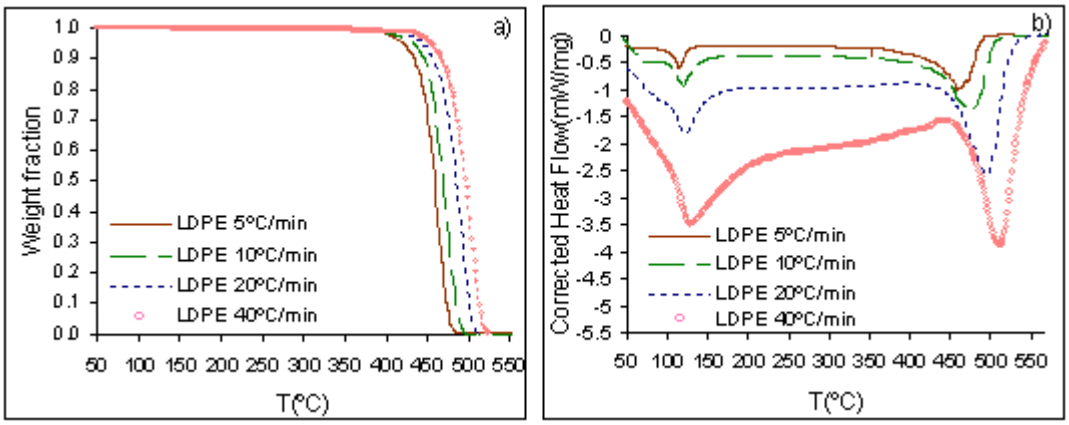

Fig. 2.TG (a) and Heat Flow (b) curves obtained in the degradation of LDPE at different heating rates.

Kinetic Model

The degradation process takes place by a succession of bond breakages. For each bond broken, a certain amount of energy is required and this should be seen directly in the heat flow signal. On the other hand, the TG signal only registers mass losses and not all the bond breakages are accompanied by losses of mass. In fact only when relatively small molecules are formed they will leave the system in the gas flow and a mass loss will be detected. The initial bond breakages will lead to quite large molecules which will not be volatile. Only the combination of TG and DSC analysis will be able to describe adequately the degradation processes.

The kinetic model developed was based on the material balance in respect to the number of bonds in the sample at each time, coupled with the energy balance. If we assume that the polymer molecules are very long chains of alkanes, the number of C-C bonds per unit mass, N, will be given, for a very large n, by the limit of the expression

$$N = \frac{n-1}{14n+2} = \frac{1}{14} \qquad \text{(Eq. 1)}$$

where n is the number of carbon atoms in the molecule. When n is very large, the number of C-C bonds will be close to 1/14 and we assume that this is the bond density at the beginning of the run. As mentioned above, C-C bonds will be lost in two ways: the first one will be due to the cracking reactions, either thermally induced or promoted by a catalyst, if present; however, when relatively small molecules are formed they will evaporate into the gas phase, carrying with them a certain number of unbroken bonds; this corresponds to the second way that bonds will be lost from the sample. We will note the average number of bonds lost to the gas phase, per unit mass of evaporated material, at a given moment, by α. Thus, the balance to the number of bonds in the sample will be:

$$\frac{dN}{dt} = -k(T)N + \frac{dm}{dt}\alpha \qquad \text{(Eq. 2)}$$

where dm/dt is the rate of mass loss. We assumed that the bond breaking process is first-order in relation to bond concentration and k(T) is the corresponding temperature-dependent rate constant, which will be taken as being described by the Arrhenius law.

$$k(T) = k_{ref}\, e^{-\frac{E_a}{R}\left(\frac{1}{T}-\frac{1}{T_{ref}}\right)} \qquad \text{(Eq. 3)}$$

where T_{ref} is a reference temperature chosen within the range of significant weight loss (573 K in this case), E_a is the activation energy of reaction and k_{ref} is the kinetic constant at the reference temperature (T_{ref}). With this information,it will now be possible to estimate the heat flow that will be measured by the apparatus, by performing an energy balance to the pan:

$$\text{Heat Flow} = -mCp\frac{dT}{dt} - k(T)N\Delta H_{\text{C-C}} + \Delta H_{vap}\frac{dm}{dt} \qquad \text{(Eq. 4)}$$

where m is the weight of the sample at any given time, Cp is the average heat capacity, $\Delta H_{C\text{-}C}$ is the average C-C bond enthalpy and ΔH_{vap} is the average vaporization enthalpy per unit mass.

This model was fitted, within the range of temperatures where degradation occurs, to the experimental Heat Flow curve. The average number of bonds in the evaporated material, α, was taken as independent of time. In addition to these equations, we had to assume that the response time of the heat flow sensor was finite and a first order dynamics was assumed for the sensor, for which the corresponding time constant was also estimated in the fitting procedure.

The differential Equation 2 was solved numerically, using the Euler method, for each run, and the model parameters were obtained by a least-squares procedure, using the sum of the squares of the residues on the heat flow as the objective function (O.F.) to be minimized:

$$\text{O.F} = \sum_{\text{all data points}} \left[\left(\text{Heat Flow}\right)_{\text{exp}} - \left(\text{Heat Flow}\right)_{\text{computed}}\right]^2 \qquad \text{(Eq. 5)}$$

The optimization procedure was carried out using the “Solver” tool in an Excel (© Windows) spreadsheet.

Table 2. Model parameters obtained by fitting the kinetic model for the thermal degradation of HDPE and LDPE at different heating rates

Polymer	Heating Rates (ºC/min)	k_{ref} (min^{-1})	E_a ($kJ.mol^{-1}$)	$\Delta H_{C\text{-}C}$ ($kJ.mol^{-1}$)	ΔH_{vap} ($J.g^{-1}$)	α (Bond $mole.g^{-1}$)	C_p ($J.g^{-1}.K^{-1}$)
HDPE	5	7.01×10^{-4}	131	4.41	410	0.0092	1.86
	10	2.18×10^{-4}	143	4.77	284	0.0343	1.86
	20	3.32×10^{-5}	188	3.12	203	0.0421	1.87
	40	5.40×10^{-6}	202	7.49	114	0.0628	1.86
LDPE	5	8.42×10^{-4}	123	4.21	297	0.0139	2.21
	10	4.90×10^{-4}	138	2.79	222	0.0206	2.28
	20	7.83×10^{-5}	144	8.53	223	0.0582	2.25
	40	6.06×10^{-6}	189	5.13	202	0.0630	2.19

The values obtained for some of the parameters can be compared with estimates obtained from tabled data. Averaging tabled data for olefins from C2 to C10 (Lide, 2004-2005), we estimated ΔH_{vap} as being around 360 $J.g^{-1}$ and C_p as 2.18 $J.g^{-1}.K^{-1}$. Although the values estimated from the experimental data show some variation, they are in reasonable agreement with the average values thus computed.

Average bond and vaporization enthalpies are similar for the two polymers and the same can be said in relation to C_P values, which are averaged to 1.9 and 2.2 $J.g^{-1}.K^{-1}$ to the HDPE and LDPE, respectively.

In this work, the values of estimated apparent activation energies are consistent with other authors (Ceamanos et al. 2002). If we compare the results obtained for thermal processes of the HDPE and LDPE at four different heating rates, we can see that the estimated apparent activation energy for the process increases as the heating rates increase. Conversely the specific reaction rate at the reference temperature decreases with increasing heating rates.

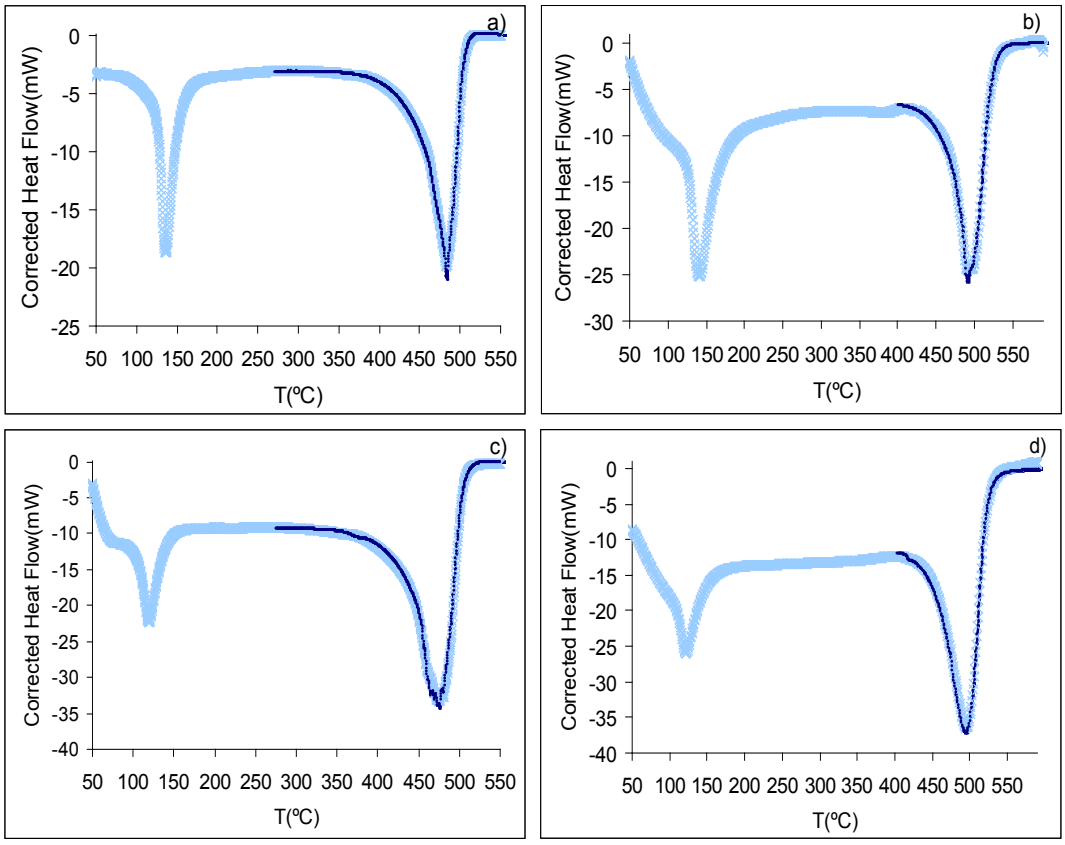

Fig. 3. Experimental (×) and calculated (—) heat flow curves - (a) HDPE 10ºC/min; (b) HDPE 20ºC/min; (c) LDPE 10ºC/min; (d) LDPE 20ºC/min.

Analysis of products

The products distributions (%molar) obtained in the thermal degradation of polyethylene at four different heating rates are shown in fig.5 (HDPE) and fig.6 (LDPE). Either for degradation of HDPE or for degradation of LDPE the products were mainly C2 (ethane, ethylene), C3 (propane, propylene) and C4 (butane, iso-butane, butene,…). As a general observation the amount of lighter products increases as the heating rate increases

This is likely to occur since the contribution of the reaction occurring at higher temperatures increases as the heating rate is increased and, thus, reactions with higher activation energy are favoured by this increase in the heating rate, justifying the observed increase in the estimated apparent activation energy (see table 2).

The use of lower heating rates leads to an increase in the production of the gasoline fraction whilst higher heating rates will tend to produce lighter fractions.

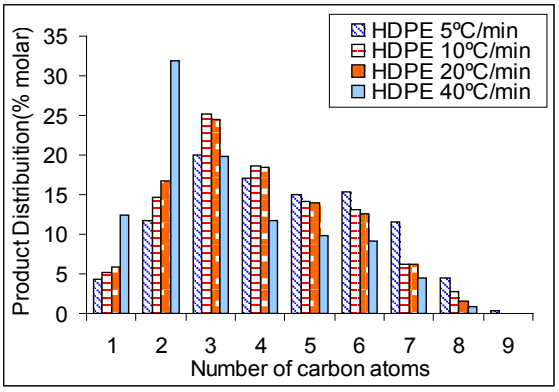

Fig. 5. Distribution of evolved products as a function of carbon number at different different heating rates with HDPE

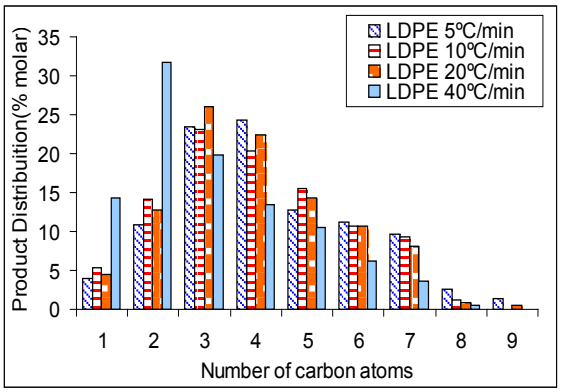

Fig. 6. Distribution of evolved products as a function of carbon number at different different heating rates with LDPE

Conclusions

The simultaneous use of DSC/TG together to GC analysis allowed us to have a clearer picture of the thermal degradation process. The model developed provides quite good fittings to the experimental data, and despite their simplicity allowed us to estimate kinetic and thermodynamic parameters, such as: bond energies, vaporization enthalpies and specific heat capacities wich are in accordance with published and calculated values.
The results also show that the product distribution depends on the heating rates.
In this way an increase in the heating rate leads to an increase of the amount of lighter products in accordance with the observed estimated apparent activation energy

Acknowledgements

The authors wish to thank Borealis for the HDPE and LDPE sample used in this work.

References

Aguado, J., Serrano, D.P., San Miguel, G., Castro, M.C., Madrid, S. (2007). Feedstock recycling of polyethylene in a two-step thermo-catalytic reaction system. *Journal of Analytical and Applied Pyrolysis*, 79, 415-423.

Dong, C., Yang, Y., Jin, B., Horio, M. (2007). The pyrolysis of sawdust and polyethylene in TG and U-shape tube reactor. *Waste Management*, 27, 1557–1561.

Bockhorn, H., Hornung, A., Hornung, U., Jakobstroer, P. (1999). Modelling of isothermal and dynamics Pyrolysis of plastics considering non-homogeneous temperature distribution and detailed degradation mechanism. *Journal of Analytical and Applied Pyrolysis,*49, 53–74.

Demirbas, A. (2004). Pyrolysis of municipal plastic wastes for recovery of gasoline-range hydrocarbons. *Journal of Analytical and Applied Pyrolysis*, 72, 97-102.

Kayacan, İ, Doğan, Ö.M. (2008). Pyrolysis of Low and High Density Polyethylene. Part I: Non-isothermal Pyrolysis Kinetics. *Energy Sources, Part A*, 30, 385–391

Ceamanos, J., Mastral, J.F., Millera, A., Aldeã, M.E. (2002). Kinetics of pyrolysis of high density polyethylene. Comparison of isothermal and dynamic experiments. *Journal of Analytical and Applied Pyrolysis*, 65 , 93–110.

Conesa, J.A., Marcilla, A., Font, R., Caballero, J.A. (1996). Thermogravimetric studies on the thermal decomposition of polyethylene. *Journal of Analytical and Applied Pyrolysis*, 36 , 1-15.

Lide, D.R., Editor-in-Chief. (2004-2005). CRC *Handbook of Chemistry. and Physics*, 85. th. Edition. CRC Press, Boca Raton, London, New York, Washington

Proceedings of the 10th International Chemical and
Biological Engineering Conference - CHEMPOR 2008
Braga, Portugal, September 4-6, 2008
E.C. Ferreira and M. Mota (Eds.)

Decyl acetate synthesis by enzyme catalysis in sc-CO_2

S. F. Rebocho[1], A. S. Ribeiro[1], O. Ferreira[2], M. V. Oliveira[1], P. Vidinha[3], S. Barreiros[3], E. A. Macedo[1], J. M. Loureiro[1*]

[1] LSRE/LCM – Laboratory of Separation and Reaction Engineering, Faculdade de Engenharia da Universidade do Porto, Rua Dr. Roberto Frias, 4200-465 Porto, Portugal

[2] LSRE/LCM – Laboratory of Separation and Reaction Engineering, Escola Superior de Tecnologia e Gestão, Instituto Politécnico de Bragança, Campus de Santa Apolónia, 5301-857 Bragança, Portugal

[3] REQUIMTE/CQFB – Departamento de Química, Faculdade de Ciências e Tecnologia, Universidade Nova de Lisboa, 2825–516 Caparica, Portugal

Keywords: Supercritical CO_2; immobilized lipase B of *Candida antarctica*; Transesterification; Ping-pong bi-bi mechanism; Decyl acetate.

Topic: Advancing the chemical and biological engineering fundamentals

Abstract

The synthesis of decyl acetate, from the transesterification of vinyl acetate with decanol, was studied in a high-pressure experimental set-up, equipped with a variable volume batch reactor, operating isothermally at 35 ºC and 100 bar, using CO_2 in supercritical conditions as solvent, and *Candida antarctica* lipase B (CALB), immobilized on the macroporous resin Lewatit B (Novozym 435®), as catalyst. The enzymatic content was determined for each particle size of the catalyst. It was shown that the smallest particles have a larger specific amount of enzyme, and the results indicate that the enzyme is located in an external shell of the particle, following an "egg-shell" model type, with a thickness of ca. 60 μm (assuming a homogeneous distribution), independent of the particle size. Both external and internal mass transfer resistances were evaluated. External resistances were easily eliminated by stirring and internal diffusional limitations can be considered as negligible. The effect of the feed concentration of substrates on the initial reaction rate was also studied. It was observed that, above a certain concentration of decanol in excess relatively to vinyl acetate, the reaction is inhibited by the alcohol. On the contrary, the reaction is favoured when the reactor is fed with excess of vinyl acetate, with a significant enhancement of its initial rate. These results are consistent with a Ping-pong bi-bi type mechanism with competitive inhibition by the alcohol, commonly used in the description of enzymatic reactions of esterification/ transesterification.

1 Introduction

The growing interest in industrial biocatalysis and in the research concerning enzymatic catalysis opened a wide range of applications in the field of pharmaceuticals, (fine-) chemicals and intermediates, leading to an increasing number of industrial biotransformations (Rozzell, 1999). Simultaneously, increased concern for the environment led to awareness for environmental friendly production methods. In this field, supercritical (sc) fluids may play a major role as they can be used for the reduction of organic waste, with the additional benefit that separation after reaction is relatively simple, which offers several process advantages. Another useful characteristic of sc-fluids is their adjustable solvation ability and properties that facilitate mass transfer. Among the four most extensively studied sc-fluids (CO_2, ethane, ethene and water), there is a wide interest in the use of sc-CO_2 since it has several advantages like non-toxicity, non-flammability, availability in high purity and solubilities of solutes can be tuned by changing temperature and pressure. As sc-CO_2 has

* Corresponding author. Tel + 351-225081672. E-mail: loureiro@fe.up.pt

the GRAS (generally regarded as safe) status, it can be used in food and pharmaceutical processes without major regulatory issues. The possibility to combine two sustainable technologies – biocatalysis and supercritical technology using green/natural solvents – allows to establish processes without environmental costs, and whose products are considered natural, resulting in a significant increase of their market value due to the present trends of such products.

In this work, the production of decyl acetate was studied. It is an ester with applications in the industry of fragrances where its floral odour is greatly appreciated. Since it mainly appears in nature in expensive oils, enzyme catalysis in a green solvent, such as CO_2, can be a valuable process for production of natural decyl acetate. The reaction studied was the transesterification of vinyl acetate with decanol, obtaining decyl acetate as the main product. *Candida antarctica* lipase B (CALB), immobilized on the macroporous resin Lewatit B (Novozym 435®), was chosen as the catalyst.

2 Materials and Methods

Catalyst. Novozym 435® (Candida antarctica lipase B (CALB) immobilized on the macroporous resin Lewatit B) was gently provided by Novozymes (Denmark). The catalyst particles were sieved in four size groups: >598, 425–500, 297–350 and 250–297 μm. The enzyme content of the Novozym 435® particles was determined by a modified Lowry method (Lowry et al., 1951). Measurements were made for each size group.

Chemicals. The reactor was fed with 1-decanol (>99 wt%, Aldrich), vinyl acetate (>99 wt%, Aldrich), n-decane (> 98 wt%, Fluka) and carbon dioxide (N45, Air Liquide). For GC calibration solutions, decyl acetate (> 98 wt%, Alfa Aesar) and n-hexane (> 99 wt%, Riedel – de Haën) were also used. For the modified Lowry method the following chemicals were used: sodium carbonate anhydrous (> 99.5 wt%, Fluka), potassium sodium tartrate (> 99 wt%, Riedel-de Haën), copper (II) sulphate pentahydrate (> 99 wt%, Riedel-de Haën), sodium hydroxide (Pronolab), Folin-Ciocalteau reagent (Merck) and Bovine Serum Albumin (SigmaDiagnostics).

Apparatus. A variable-volume stainless steel batch reactor equipped with a sapphire window and with loading and sampling valves was used. Details of the high-pressure apparatus and experimental technique have been given elsewhere (Fontes et al., 2001). All experiments were performed with a reaction mixture volume of ca. 22 mL.

Sample Analysis. The samples were analysed on a gas chromatograph (Trace 2000 series, Unicam) equipped with a flame ionization detector (FID) and an autosampler. The compounds were separated in a chiral capillary column with 30 m length, 0.25 mm inner diameter and 0.25 μm film thickness (BGB – 178, BGB Analytik AG). Helium N50 (2 mL/min) was used as the carrier gas. The injector and detector temperatures were set at 250 ºC. The oven temperature program was set as follows: 80-150 ºC ramp at 4 ºC/min, 150-170 ºC ramp at 6 ºC/min. n-decane (20 mM) was used as internal standard for GC analysis.

3 Results and Discussion

Enzyme distribution on the catalyst particles. The results of the specific enzyme content for the different size groups of the Novozym 435® particles are shown in Table 1.The values obtained for the enzyme content show that the specific enzyme loading (mass of enzyme/mass of particle) depends on the particle size and smaller particles have a higher specific enzyme loading than the larger ones. Garcia-Alles and Gotor (1998) already presented some experimental evidence suggesting that the specific enzyme loading varies with the particle size, being larger for smaller particles. A similar correlation was reported by van Roon et al. (2003) for immobilized Penicilin-G Acylase and such dependence of the specific enzyme loading with the particle size could be related to internal mass transfer limitations during the enzyme immobilization process. This is supported by the results

obtained more recently by Chen et al. (2007) with experimental evidence that, although the maximum attainable enzyme loading (saturation) is independent of the particle size, smaller particles will saturate with enzyme faster. Mei et al. (2003) studied the internal distribution of Novozym 435® using synchrotron infrared microspectroscopy, showing that for a particle size around 600 μm there is only an 80-100 μm thick enzyme layer in the outer portion of the particle, distributed heterogeneously. Several modeling studies were done in the eighties (Clark et al., 1985; Hossain et al., 1986) that associated this kind of intraparticle distribution with restricted diffusion conditions during the immobilization process since, as the immobilization proceeds, the pore size will be reduced by the adsorbed enzyme. More recently, Mei et al. (2003) suggested that restricted diffusion during the immobilization process is unlikely in the case of Novozym 435® since the enzyme molecules are ten times smaller than the average pore size of the support. Moreover, in their studies to regulate the thickness of the enzyme outer shell, these authors found that, by increasing the time for diffusion and the concentration of CALB, it was possible to obtain particles containing protein distributed throughout.

Table 1: Enzymatic content for each particle size group of Novozym 435®.

Particle diameter (μm)	Enzymatic content (mg enzyme/g particle)
> 598	54.09
425-500	61.94
297-350	84.13
250-297	89.18

The results obtained in this work also suggest that Novozym 435® has an egg-shell intraparticle distribution. Assuming a homogeneous distribution of the enzyme on the outer shell (i.e., the ratio volume of the outer shell/mass of enzyme is constant in each particle), the enzyme thickness should be independent of the particle size, since all of them are exposed to the same time for diffusion. In fact, we obtained an enzyme outer shell thickness of 60 μm, with an average error of ca. 3%. This thickness is less than the reported by Mei et al. (2003), as should be expected, since our calculation considers a homogeneous distribution of the enzyme.

In order to correctly account for the different specific enzyme loadings, care must be taken to express the reaction rate in terms of the mass of enzyme instead of the total mass of the catalyst particles, since when using the same amount of catalyst particles we are actually performing the reactions with different amounts of enzyme. As the particle size decreases, the amount of enzyme in the reactors will be higher, contributing to an enhancement in the reaction rate that is not directly related to the reduction of diffusion limitations.

External mass transfer studies. When working with immobilized enzymes, as with any other supported catalysts, in order to reach the enzyme molecules, the reactants must firstly diffuse from the bulk liquid to the surface of the particles, across a stagnant layer of fluid, and then inside its pores, where the enzyme is immobilized. When working with a batch reactor, the thickness of the stagnant film can generally be reduced by stirring the reaction mixture, minimizing, if not eliminating, the influence of this transport phenomenon in the overall reaction process. To ensure the absence of external diffusion limitations in all experiments, the stirring was gradually increased until it had no influence in the evolution of the observed concentrations of the reacting components, which occurred around 950 rpm. These experiments were performed keeping all the other conditions constant (temperature, pressure, amount of enzyme, particle size, initial substrate concentrations).

Internal mass transfer studies. The influence of internal mass transfer in a given heterogeneous catalytic process can be minimized by reducing the particle size and hence, shortening the diffusion path. If catalyst particles of different sizes are available, they can be used to assess the relative influence of internal diffusion in the overall process. Whenever internal diffusion limitations are present, a reduction in the particle size, usually leads to an enhancement of the reaction rate; when reducing the particle size has no further influence in

the reaction rate, internal diffusion is fast enough to be considered negligible and the process is controlled by the reaction. In order to assess the influence of internal diffusion, several reactions were performed using different particle sizes, but with the same amount of enzyme, the same initial substrate concentrations, the same stirring speed, temperature and pressure. The results obtained, in terms of the reactants conversion as a function of time and in terms of initial reaction rate (R^0), are presented in Figure 1a and 1b, respectively, and show that the size of the catalyst particles does not have a significant effect on the initial reaction rate (maximum relative difference of 4.5% between R^0). Therefore, the internal diffusional limitations can be considered negligible, and any size group of particles can be used without considering mass transfer resistances inside the particles. As mentioned previously, amongst the usually stated advantages of supercritical fluids as solvents for reaction processes are the reduction of mass transport resistances that arise from the high gas-like diffusivities.

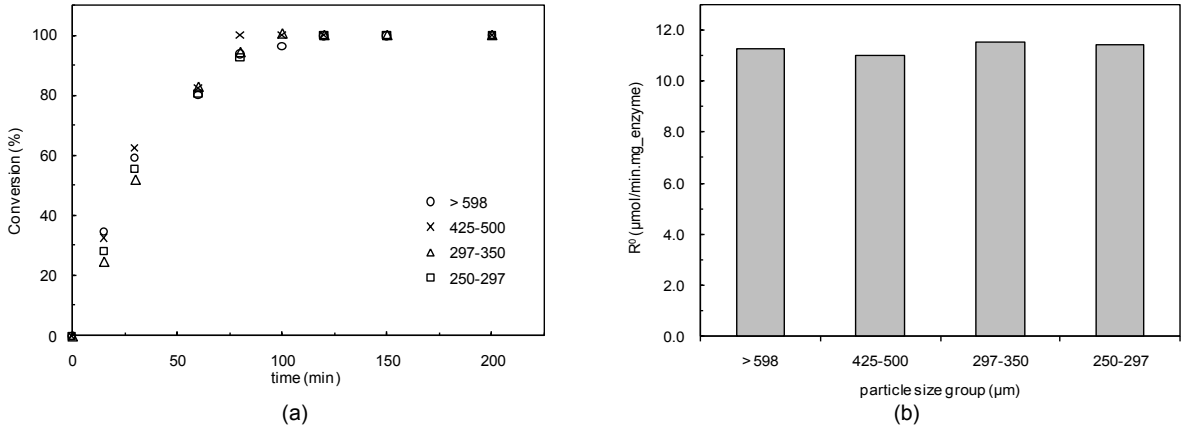

Figure 1: Effect of particle diameter on the: (a) reactants conversion as a function of time; (b) initial reaction rate. Equimolar feed (50 mM), 2.2 mg of enzyme, 35 ºC and 100 bar for all assays.

Effect of feed concentration. The effect of the feed concentration of substrates on the initial reaction rate was also studied. The Ping-pong bi-bi model is widely used to describe the kinetics of transesterification reactions (Yadav and Devi, 2004; Zhang et al., 2005). According to this ordered mechanism, the ester firstly binds to the active site of the enzyme, and the first product is released (bi-product), leading to the formation of a substrate altered enzyme complex. The alcohol then binds to this complex and the second product (main product) is formed and released, returning the enzyme to its native state. When vinyl acetate is used as a reactant, the first product formed is vinyl alcohol that quickly tautomerizes to acetaldehyde, making the overall transesterification irreversible, which is consistent with our experimental results where full conversions were always obtained. The Ping-pong bi-bi reaction rate equation can be simplified if the enzyme has a significantly higher affinity for some of the components or if there are large differences in their concentrations. When the affinity of the enzyme for the substrates is much higher than the affinity for the products, and if the concentration of the reactants is much higher than the concentration of the products, i.e. in the beginning of the reaction, the initial reaction rate can be described as:

$$R^0 = \frac{V_{max}}{\frac{K_{MA}}{[A]} + \frac{K_{MB}}{[B]} + 1} \quad (1)$$

where V_{max} is the maximum reaction rate, [A] is the concentration of vinyl acetate and [B] the concentration of decanol; K_{Mi} represents the Michaelis constant for component i. For transesterifications (and esterifications) reactions, an additional competitive inhibition step is usually added to the Ping-pong bi-bi kinetic mechanism since the alcohol can also compete with the ester (or acid) in binding to the enzyme in its native state but no product is formed:

$$R^0 = \frac{V_{max}}{\frac{K_{MA}}{[A]}\left(1+\frac{[B]}{K_I}\right)+\frac{K_{MB}}{[B]}+1} \quad (2)$$

where K_I represents the competitive inhibition constant.

Equation (2) can be further simplified by raising the concentration of one of the reactants, eliminating the influence of the other substrate:

$$R^0 = \frac{V_{max}}{\frac{K_{MB}}{[B]}+1} \text{ for } [A]>>[B], \qquad R^0 = \frac{V_{max}}{\frac{K_{MA}}{[A]}+\frac{K_{MA}}{K_I}\frac{[B]}{[A]}+1} \text{ for } [B]>>[A] \quad (3a, 3b)$$

From Equation (3a), provided that the concentration of vinyl acetate is sufficiently larger than the concentration of decanol, the initial reaction rate becomes independent of the concentration of the reacting ester. On the opposite end, if the concentration of decanol is much larger than the concentration of vinyl acetate (Equation 3b), unless inhibition by decanol is negligible, the initial reaction rate will still depend on the concentration of both reactants.

The experimental results obtained while varying the concentration of each reactant individually (Figure 2a and Figure 2b) were qualitatively consistent with this model: (i) the reaction is enhanced by higher concentrations of vinyl acetate ([A] ≥ 100 mM); (ii) the reaction is inhibited by larger concentrations of the alcohol ([B] ≥ 100 mM). When fixing the concentration of decanol and increasing the concentration of vinyl acetate, R^0 increased ca. 83% (Figure 2a). Moreover, the concentration of vinyl acetate no longer influenced the initial reaction rate, as predicted by Equation (3a). As a result of the competitive inhibition by decanol, fixing the concentration of vinyl acetate and increasing decanol has an adverse effect in the initial reaction rate; in this case, as predicted by Equation (3b), the initial reaction rate remains a function of the concentration of decanol: R^0 decreased ca. 18%, relatively to the equimolar feed, for [B]=100 mM, and ca. 49% for [B]=150 mM (Figure 2b).

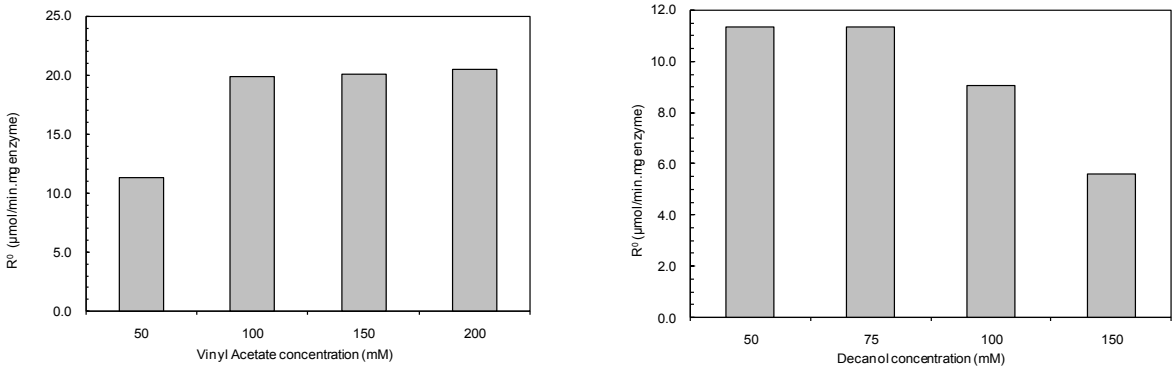

(a) (b)

Figure 2: Effect of the feed concentration of substrates on the initial reaction rate: (a) excess of vinyl acetate ([B]=50 mM, 35 ºC and 100 bar for all assays; 2.2 mg of enzyme for [A]=50 and 100 mM, 1.1 mg of enzyme for [A]=150 and 200 mM); (b) excess of decanol ([A]=50 mM, 2.2 mg of enzyme, 35 ºC and 100 bar for all assays).

4 Conclusions

The transesterification of vinyl acetate and decanol in sc-CO_2 by Novozym 435® was studied, with particular emphasis on the influence of enzyme distribution, internal diffusion and feed concentration of substrates. It was shown that the specific enzyme loading increases as the particle size decreases. As a consequence, care should be taken to ensure that this does not affect mass transfer studies by using the same enzyme amount instead of the same mass of catalyst particles. It was also shown that the enzyme is located in an external shell of the particle, following an “egg-shell” model type, with a thickness of ca. 60

μm (assuming a homogeneous distribution in this outer shell), independent of the particle size. Diffusion limitations were shown to be negligible. Finally, the experimental results obtained while varying the concentration of each reactant individually were qualitatively consistent with the Ping-pong bi-bi kinetic model with competitive inhibition by the alcohol: the reaction was enhanced by concentrations of vinyl acetate ≥ 100 mM, and inhibited by concentrations of decanol ≥ 100 mM.

References

Chen, B., Miller, E.M., Miller, L., Maikner, J.J., Gross, R.A. (2007). Effects of macroporous resin size on Candida Antarctica lipase B adsorption, fraction of active molecules, and catalytic activity for polyester synthesis. *Langmuir*, 23, 1381-1387.

Clark, D.S., Bailey, J.E., Do, D.D. (1985). Mathematical model for restricted diffusion effects on macromolecule impregnation in porous supports. *Biotechnology and Bioengineering*, 27, 208-213.

Fontes, N., Almeida, M.C., Barreiros, S. (2001). Biotransformations in supercritical fluids. *Enzymes in Nonaqueous Solvents. Methods and Protocols; Methods in Biotechnology*, Volume 15, Vulfson, E.N., Halling, P.J., Holland, H.L., Eds.; Humana Press: Totowa, New Jersey, pp. 565-573.

Garcia-Alles, L.F., Gotor, V. (1998). Lipase-catalyzed transesterification in organic media: Solvent effects on equilibrium and individual rate constants. *Biotechnology and Bioengineering*, 59, 684-694.

Hossain, M.M., Do, D.D., Bailey, J.E. (1986). Immobilization of enzymes in porous solids under restricted diffusion conditions. *AIChE Journal*, 32, 1088-1098.

Lowry, O.H., Rosenbrough, N.J., Farr, L., Randal, R. (1951). Protein measurement with Folin phenol reagent. *Journal of Biological Chemistry*, 193, 265-275.

Mei, Y., Miller, L., Gao, W., Gross, R. (2003). Imaging the distribution and secondary structure of immobilized enzymes using infrared microspectroscopy. *Biomacromolecules*, 4, 70-74.

Rozzel, J.D. (1999). Commercial scale biocatalysis: myths and realities. *Bioorganic & Medicinal Chemistry,* 7, 2253-2261.

van Roon, J.L., Joerink, M., Rijkers, M.P.W.M., Tramper, J., Schroen, C.G.P.H., Beeftink, H.H. (2003). Enzyme distribution derived from macroscopic particle behavior of an industrial immobilized penicillin-G acylase. *Biotechnology Progress*, 19, 1510-1518.

Yadav, G.D., Devi, K.M. (2004). Immobilized lipase-catalyzed esterification and transesterification reactions in non-aqueous media for the synthesis of tetrahydrofurfuryl butyrate: comparision and kinetic modeling. *Chemical Engineering Science,* 59, 373-383.

Zhang, T., Yang, L., Zhu, Z. (2005). Determination of internal diffusion limitation and its macroscopic kinetics of the transesterification of CPB alcohol catalyzed by immobilized lipase in organic media. *Enzyme and Microbial Technology*, 36, 203-209.

Acknowlegments

Financial support for this work was in part provided by national research grant POCI/EQU/56732/2004 and by LSRE financing by FEDER/POCI/2010, for which the authors are thankful. A.S.Ribeiro and P.Vidinha acknowledge their Ph.D. scholarship by FCT (SFRH/BD/13084/2003 and SFRH/BD/13787/2003).

Proceedings of the 10th International Chemical and
Biological Engineering Conference - CHEMPOR 2008
Braga, Portugal, September 4-6, 2008
E.C. Ferreira and M. Mota (Eds.)

Improving Propylene Streams Purity Using Catalytic Membrane Reactors

Miguel Teixeira[1], Luís M. Madeira[1], José Sousa[*1,2], Adélio Mendes[1]

[1] LEPAE - Department of Chemical Engineering, Faculty of Engineering at the University of Porto, Rua Dr. Roberto Frias, 4200-465 Porto, Portugal

[2] Department of Chemistry, University of Trás-os-Montes e Alto Douro, 5001-911 Vila-Real, Portugal

Keywords: catalytic membrane reactors, hydrogenation, propylene purification

Topic: Advancing the chemical and biological engineering fundamentals

Abstract

The purification of propylene is a very energy demanding industrial separation. The present work analyses theoretically the performance of various Catalytic Membrane Reactor (CMR) arrangements with perfect mixing flow pattern. It is concluded that the best arrangement consists of two CMR in series. This arrangement allows reaching the same results as a conventional reactor, though with a lower Damköhler number.

1. Introduction

For the synthesis of polypropylene, the feed (propylene) stream should contain less than 10 ppm of propadiene and 5 ppm of propyne (Liu *et al*., 1997). However, typical industrial propylene produced by steam cracking contains about 2-5 % (mol) of alkynes and dienes (Liu *et al*., 1997, Fajardo *et al*., 1996). The traditional purification process consists in the selective hydrogenation of such impurities (Fajardo *et al*., 1996), carried out in a fixed-bed catalytic reactor (Liu *et al*., 1997). In this process, however, the over-hydrogenation of propylene to propane is a drawback to be avoided, beyond the high cost of the catalysts.

An alternative approach for propylene purification is the use of membranes, such as carbon molecular sieves or zeolites (Steel and Koros, 2003, Stoitsas *et al*., 2005). When functionalized, these membranes are highly selective towards propyne and propadiene (Padin *et al*., 2000).

The objective of this work is to perform a theoretical study combining the separation selectivity of membrane-based processes with the catalytic hydrogenation selectivity in a single process unit, showing synergetic performance. Indeed, it is expectable that using a selective hydrogenation catalyst, placed on the permeate side, one can increase the driving force and selectivity. For comparison purposes, we consider that the results obtained in a membrane reactor operating in the total flow-through configuration (total permeation condition, TPC, or no retentate stream) are equivalent to the ones obtained in a conventional catalytic reactor. “Conventional”, in the context of this work, means a catalytic gas-phase reactor with perfectly mixed flow pattern (CSTR) fed with the same stream, with the same reactions taking place at the catalyst surface and described by equivalent kinetic equations.

[*] Corresponding author. Tel + 351-225081695. E-mail:jmsousa@fe.up.pt

2. Model Development

The catalytic membrane reactor considered in this study has the general features of the one depicted in Figure 1. It consists of retentate and permeate perfectly mixed chambers with constant pressure, separated by a flat hypothetical composite membrane, highly selective towards alkynes, and supporting a catalytic layer on the permeate side. The hydrocarbon mixture (propyne and propylene) is fed at a higher pressure to the retentate chamber, while a low-pressure hydrogen stream is fed to the permeate side.

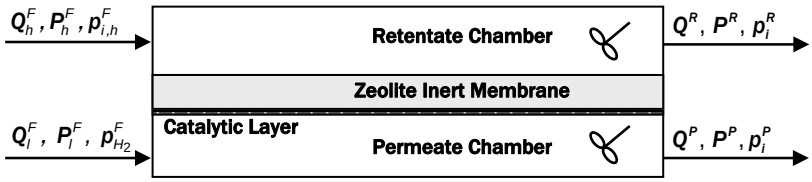

Figure 1 – Schematic diagram of the catalytic membrane reactor (CMR).

The model proposed for this reactor is based on the following main assumptions: (1) steady-state, ideal gas behavior and isothermal conditions; (2) the transport through the membrane is considered to be described by an “overall” permeability coefficient, constant for all the operating conditions; (3) homogeneous distribution of the catalytic nanoparticles throughout the catalytic layer, which is considered to be part of the permeate chamber. (4) the kinetic equations are considered valid for all the operating conditions.

The reaction considered is of the consecutive-parallel and irreversible type, describing the hydrogenation of propyne, $C_3H_4 + H_2 \rightarrow C_3H_6$, and propylene, $C_3H_6 + H_2 \rightarrow C_3H_8$. To describe the reaction kinetics, power-law type equations were considered, which simplifies the problem without compromising the main conclusions. In fact, some works report that simple power-law type rate equations represent well the experimental results for hydrocarbon catalytic hydrogenation reactions, sometimes even better than the Langmuir-Hinshelwood/Hougen-Watson models (Fajardo *et al*. 1996, Groschel *et al*., 2005). Based on a literature review (Brandão *et al*., 2007; Groschel *et al*, 2005; Bond and Sheridan, 1952; Bond and Wells, 1965), the following reaction rate equations were considered:

$$r_1 = k_1 p_{H_2} \left(p_{C_3H_4}\right)^{-0.25} \quad \text{(propyne hydrogenation)} \tag{1}$$

$$r_2 = k_2 p_{H_2} p_{C_3H_6} \quad \text{(propylene hydrogenation)} \tag{2}$$

The steady state mass balances are presented in the following sections in their dimensionless form. The variables were made dimensionless with respect to the feed conditions (Q_h^F , P_h^F) and to propylene species ($L_{C_3H_6}$).

2.1 Partial and Total Mass Balances for the Retentate Side

$$Q_h^{F*} p_{i,h}^{F\,*} = Q^{R*} p_i^{R*} + \Gamma L_i^* \left(p_i^{R*} - p_i^{P*}\right) \tag{3}$$

$$Q_h^{F*} P_h^{F*} = Q^{R*} P^{R*} + \Gamma \sum_i L_i^* \left(p_i^{R*} - p_i^{P*}\right) \tag{4}$$

2.2 Partial and Total Mass Balances for the Permeate Side

$$Q_l^{F*} p_{i,l}^{F\,*} = Q^{P*} p_i^{P*} - \Gamma L_i^* \left(p_i^{R*} - p_i^{P*}\right) + Da\left(\nu_{i,1} f_1\left(p_i^*\right) + \nu_{i,2} R_r f_2\left(p_i^*\right)\right) \tag{5}$$

$$Q_l^{F*} P_l^{F*} = Q^{P*} P^{P*} - \Gamma \sum_i L_i^* \left(p_i^{R*} - p_i^{P*}\right) + Da \sum_i \left(\nu_{i,1} f_1\left(p_i^*\right) + \nu_{i,2} R_r f_2\left(p_i^*\right)\right) \tag{6}$$

Where $f_1\left(p_i^*\right) = p_{H_2}^* \left(p_{C_3H_4}^*\right)^{-0.25}$, $f_2\left(p_i^*\right) = p_{H_2}^* p_{C_3H_6}^*$, $Da = \frac{k_1 \Re T P_{ref}^{-0.25}}{Q_{ref}}$, $\Gamma = \frac{A \Re T L_{ref}}{\delta Q_{ref}}$, $R_r = \frac{k_2}{k_1} P_{ref}^{0.25}$

i refers to the i^{th} component (C_3H_4, C_3H_6, C_3H_8, H_2); the superscripts *F*, *R* and *P* refer to feed, retentate and permeate conditions, respectively; the subscripts *h* and *l* refer to high (retentate) and low (permeate) pressure sides, respectively; L_i^* is the dimensionless permeability coefficient of the membrane (L_i/L_{ref}), p_i^* is the dimensionless partial pressure (p_i/P_{ref}) and Q^* is the dimensionless volumetric flow rate (Q_i/Q_{ref}). *Da* is the Damköhler number (based on the propyne hydrogenation reaction), Γ is the dimensionless contact time (ratio between the maximum possible flux across the membrane for the reference component, that is, permeation of pure species against null permeate pressure, and its molar feed flow rate) and R_r is the ratio of the reaction rate constants. ν is the stoichiometric coefficient, taken negative for reactants, positive for reaction products, and null for the components that do not take part in the reaction, *A* is the membrane surface area, *T* is the temperature, $\Re$ is the ideal gas constant and δ is the membrane thickness. It should be emphasized that the reaction rate constants include the catalyst amount.

3. Results and Discussion

The ranges of values for the model parameters are listed in Table 1. It is assumed that the permeability value for propyne is much higher than for the other components (which are considered all with the same value). The permeability range listed is based on several published reports (Steel and Koros, 2003, Padin *et al*. 2000, Olson *et al*., 2004). The volumetric feed flow rate of hydrogen (Q_l^{F*}) was set to a value so that its molar flow rate would be equal to propyne's molar flow rate. R_r values were chosen in accordance to some reported results (Groschel *et al*., 2005). Reference pressure was considered to be 1 atm.

Table 1 – Parameter ranges used in the simulations.

P^{P*}	0.005	Γ	0.01-TPC
Q_l^{F*}	4	*Da*	$1 - 10^5$
$L_{C_3H_4}^*$	$10 - 10^4$	R_r	0.001 – 0.1
$L_{C_3H_6}^*$, $L_{C_3H_8}^*$, $L_{H_2}^*$	1	$y_{C_3H_4}^F$	0.02

The catalytic membrane reactor (CMR) was compared with a conventional reactor and with an equivalent membrane system without catalyst, in terms of the outlet propyne concentration. It was assumed that a CMR operating in the total flow-through configuration (total permeation condition – TPC) with a nonpermselective membrane is loosely equivalent to the conventional catalytic reactor described above. This equivalence is discussed elsewhere (Sousa and Mendes, 2006). From this point on, this equivalent CMR will be named "ECSTR".

3.1 Equivalent Conventional Reactor (ECSTR)

Figure 2 shows the simulation results for the ECSTR. As it can be seen, this reactor is able to achieve the desired product purity with a reaction rate ratio (R_r) equal to or below 0.01. Propylene's overall yield (defined as the moles of propylene produced per mole of propyne fed) is very close to 1, so there is no deeper hydrogenation of propylene to propane, for this set of kinetic parameters. The minimum *Da* for this separation, when R_r is 0.01, is very high (around 20 000), which constitutes a downfall for the traditional approach.

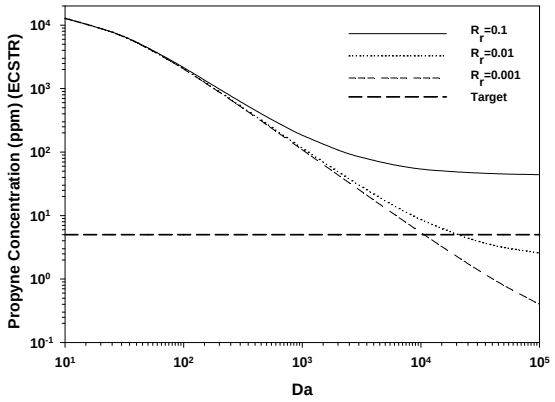

Figure 2 - Propyne outlet concentration (in ppm) as a function of the Damkhöler number, for different reaction rate ratios in a CMR ($L_i^* = 1, \Gamma = \Gamma_{TPC}$). The other parameters have the values reported in Table 1.

3.2 Membrane and Catalytic Membrane Reactor (CMR)

Figures 3 shows the results obtained for a membrane-based separation system (A), *i.e*., the CMR here considered with $Da = 0$ and for the CMR (B). In the second case the overall yield of propylene is again approximately 1.

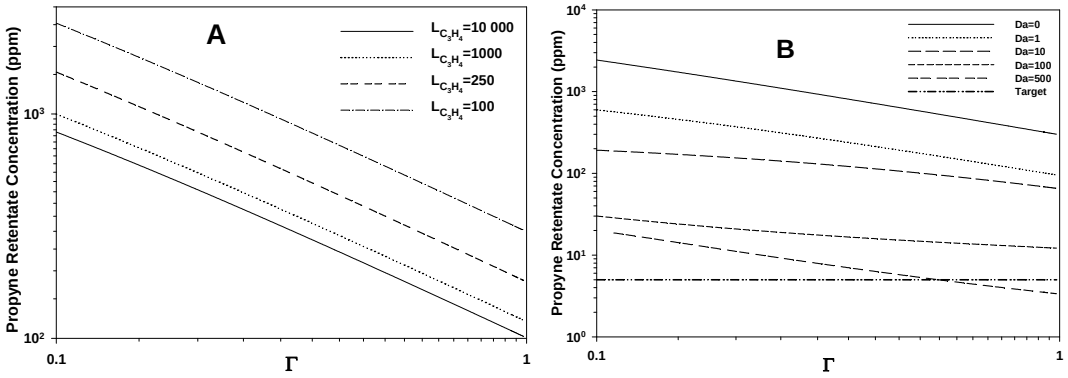

Figure 3 – Propyne outlet concentration as a function of the dimensionless contact time. (A) - membrane; (B) – CMR with $L^*_{C_3H_4}$=10 000 and R_r=0.01)

Figure 3A shows a decrease in the propyne outlet concentration when increasing the dimensionless contact time; an increase of Γ increases the stage-cut ratio (ratio between the flux across the membrane and feed flow rate), leading to retentate streams poorer on the most permeable components (which is the case of propyne, cf. Table 1). A membrane is unable to perform the desired separation (conc. < 5 ppm) even with very high membrane selectivities.

Figure 3B shows that a CMR achieves the desired product purity at relatively low Damkhöler values when compared with the ECSTR (Fig. 2), meaning that, for example, lower catalytic activity (lower mass of catalyst) is required. However, it requires very high membrane selectivities (a CMR with selectivity for propyne of 1000 is unable to meet the outlet stream concentration requirements) and high dimensionless contact time values (high membrane area requirements or low feed flow rates, for example).

3.3 Two Separation Units in Series (Membrane/CMR; CMR/CMR)

A CMR's advantage over a membrane is the enhancement on the driving force for propyne caused by its hydrogenation on the permeate side. This driving force enhancement is more significant when feeding a less concentrate stream. Placing a separation unit before the CMR in order to decrease the propyne concentration would then optimize the latter's performance. Two different strategies of combined separation

units were then tested: Membrane-based separation/CMR and CMR/CMR (Membrane/Membrane strategies require very high contact times). The first unit's retentate stream enters the feed/retentate chamber of the second unit, from where the final stream exits. For the case of two CMRs in series, the unreacted hydrogen from the first unit is fed to the second one. The hydrogen flow rate on the second unit was set so that its molar flow rate would equal propyne's molar flow rate entering the unit.

A qualitative optimization of the results was made. Reasonable membrane selectivies were used (100-1000) and the final retentate flow rate was maximized, for a maximum propyne concentration of 5 ppm. The combined separation units met the requirements for propyne concentration with a low catalytic activity of the catalyst, when compared to the ECSTR.

Figure 4 shows the results obtained with the Membrane/CMR and CMR/CMR assemblies at the exit of the first unit. A membrane or a CMR decreases significantly the propyne concentration, even at very low Γ values (feed value is 20 000 ppm). It is worth noting that as the membrane selectivity increases, the difference in performance between a membrane and a CMR is accentuated.

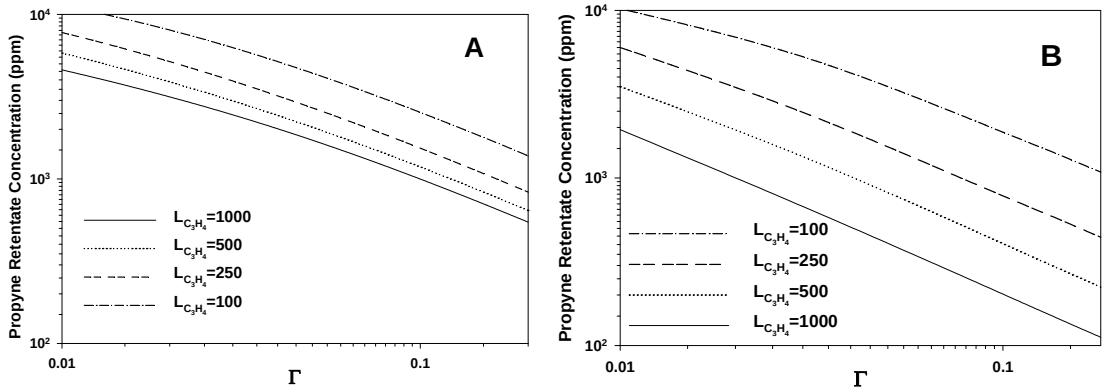

Figure 4 – Propyne retentate concentration at the exit of the first unit as a function of the dimensionless contact time. (A) – membrane; (B) – CMR. CMR results are for optimum Damkhöler values for each pair of Γ and membrane selectivity (*Da* ranges from 1 to 200).

Results at the exit of the second unit for both strategies are summarized in Table 2. In general, two membrane reactors in series generate better results than a membrane followed by a CMR; indeed, while the flow rate at the exit of the second unit is much higher in the case of the CMR/CMR configuration, there is little difference in the Damkhöler number. To obtain high flow rate recoveries ($\geq$ 75 %), membrane selectivity must be at least 500.

Table 2 – Set of conditions that maximize the production retentate flow rate for both strategies. $ProdFR_1$ (%) and $ProdFR_2$ (%) represents the flow rate percentage relative to the initial feed flow rate for units 1 and 2, respectively. Da_1 and Da_2 are the optimum Damkhöler values for units 1 and 2, for each pair of Γ and membrane selectivity.

System	$L^*_{C_3H_4}$	Da_1	$ProdFR_1$ (%)	Da_2	$ProdFR_2$ (%)
Membrane/CMR	500	-	75%	50	58%
CMR/CMR	500	75	85%	15	75%
CMR/CMR	250	100	75%	45	54%

4. Conclusions

Alternative methods to the typical fixed bed reactor were considered for propyne hydrogenation. The use of a low-pressure hydrogen feed on the permeate side of a catalytic membrane reactor (CMR) greatly increases propyne's driving force for transport across the membrane as it is selectively hydrogenated therein. A CMR with

such a design decreases propyne concentration to the desired levels with low Damkhöler number (low catalyst amount, for example), but very high selective membranes towards propyne are required. An alternative two-step approach consisting of a membrane-based separation and a CMR or two CMRs in series was analyzed. In the latter configuration, higher flow rate streams were obtained with low propyne contents, low Damkhöler numbers and with relatively high selective membranes.

Acknowledgments

Miguel Teixeira is grateful to the Portuguese Foundation for Science and Technology (FCT) for his doctoral grant (reference: SFRH/BD/24768/2005). The authors also acknowledge financing from FCT through the projects POCTI/EQU/59344/2004 and POCTI/EQU/59345/2004.

References

Brandão, L., Madeira, L.M., Mendes, A., (2007) *Propyne hydrogenation in a continuous polymeric catalytic membrane reactor*. Chemical Engineering Science 62, 6768 – 6776

Bond, G.C., Sheridan, J., (1952) *Studies in heterogeneous catalysis. Part 1. The hydrogenation of methylacetylene*. Transactions of the Faraday Society 48, 651–658.

Bond, G.C., Wells, P.B., (1965) *The hydrogenation of acetylene. II. The reaction of acetylene with hydrogen catalyzed by alumina-supported palladium*. Journal of Catalysis 5, 65–73.

Fajardo, J. C., Godínez, C., Cabanes, A. L., Víllora, G. (1996) *Kinetic analysis of rate data for propylene and methylacetylene hydrogenation*. Chemical Engineering and Processing, 35 (3), 203-211.

Groschel, L., Haidar, R., Beyer, A.,Colfen, H., Frank, B., Schomacker, R., *Hydrogenation of Propyne in Palladium-Containing Polyacrylic Acid Membranes and Its Characterization (2005).,* Industrial and Engineering Chemistry Research, 44, 9064-9070

Liu, C., Xu, Y., Liao, S.; Yu, D., Zhao, Y., Fan, Y. (1997) *Selective hydrogenation of propadiene and propyne in propene with catalytic polymeric hollow-fibre reactor*. Journal Membrane Science, 137, 139-144.

Olson, D. H., Yang, X., Camblor, M., (2004) *ITQ-12: A zeolite having temperature dependent adsorption selectivity and potential for propene separation*. Journal of Physical Chemistry B, 108, 11044-11048

Padin, J., Rege, S. U., Yang, R. T., Cheng, L. S. (2000) *Molecular sieve sorbents for kinetic separation of propane/propylene*. Chemical Engineering Science 55, 4525-4535.

Sousa, J.M., Mendes, A., (2006) *Consecutive-Parallel Reactions in Nonisothermal Polymeric Catalytic Membrane Reactors*. Industrial and Engineering Chemistry Research 45, *2094-2107*

Steel, K.M., Koros, W.J. (2003) *Investigation of porosity of carbon materials and related effects on gas separation properties*. Carbon, 41, 253-266.

Stoitsas, K. A., Gotzias, A., Kikkinides, E. S., Steriotis, T. A., Kanellopoulos, N.K., Stoukides, M., Zaspalis, V. T., (2005) *Porous ceramic membranes for propane-propylene separation via the pi-complexation mechanism: unsupported systems*. Microporous and Mesoporous Materials 78, 235-243.

Proceedings of the 10th International Chemical and
Biological Engineering Conference - CHEMPOR 2008
Braga, Portugal, September 4-6, 2008
E.C. Ferreira and M. Mota (Eds.)

Improvement by alkaline treatment of HZSM-5 zeolite performance in DME steam reforming

Jorge Vicente*, Javier Ereña, Alaitz Atutxa, Ana G. Gayubo, Javier Bilbao
Dpto. Ingeniería Química, Universidad País Vasco, Apartado 644, 48080 Bilbao, Spain

Keywords: dimethyl ether, steam reforming, HZSM-5 zeolite, alkaline treatment
Topic: Advancing the chemical and biological engineering fundamentals

Abstract

Dimethyl ether (DME) steam reforming to produce hydrogen has been studied over a bifunctional catalyst prepared by (wet) physical mixture of a metallic function (a commercial $Cu/ZnO/Al_2O_3$ catalyst for methanol steam reforming) and an acidic function of HZSM-5 zeolite modified by alkaline treatment. The alkaline treatment affects the porous structure of the zeolite (leading to an increase in the mesoporous surface and a decrease in microporous volume and BET surface area) and its acidic properties (attenuating both total acidity and acidic strength). The attenuation in acidity lowers the formation of undesired hydrocarbons from oxygenates (methanol + DME) over the acidic function in DME steam reforming. Consequently, a moderate alkaline treatment (with a 0.2M NaH solution for 300 min) improves the kinetic behavior of the bifunctional catalyst as it enables to obtain high selectivity and yield of H_2 at temperatures (< 300 ºC) which are low enough to minimize the formation of byproducts (hydrocarbons) and CO and deactivation by Cu sintering.

1. Introduction

Hydrogen fuel cells are presented as an efficient and environmentally friendly power generator applicable to both mobile and stationary use (Funagnawakj et al., 2007). Although hydrogen has a high fuel density, it is difficult to handle. Therefore it is necessary to use a hydrogen vector like ethanol, gasoline, diesel and methane. However, the reforming of these fuels requires high temperature, which means that carbon deposit formation and catalyst poisoning by sulphur must be borne in mind (Semelsberger et al., 2005).

Over the last few years, there has been significant interest in methanol steam reforming. However, dimethyl ether (DME) steam reforming is a more promising alternative for hydrogen production than methanol steam reforming, given that DME synthesis from syngas is more profitable and, moreover, CO_2 can be added in the feed together with the syngas (Aguayo et al., 2007). Furthermore, DME is relatively inert, non-corrosive, non-carcinogenic and can be stored and handled as LPGs. DME has also attracted increased attention as a clean fuel. An interesting review of the advantages of DME has been published recently (Semelsberger et al., 2006).

Steam reforming of DME consists of two steps in series (Tanaka et al., 2005): DME hydrolysis (Eq. (1)) upon an acid function, and methanol steam reforming (Eq. (2)) upon a metallic function.

$$(CH_3)_2O + H_2O \leftrightarrow 2CH_3OH \quad (1)$$

$$CH_3OH + H_2O \leftrightarrow 3H_2 + CO_2 \quad (2)$$

$$(CH_3)_2O + 3H_2O \leftrightarrow 6H_2 + 2CO_2 \quad (3)$$

Besides DME SR, reverse water gas shift reaction (r-WGSR) (Eq. (4)) generally takes place over metallic catalysts in the reforming process. In addition, methane is also

* Corresponding author. Tel + 34-94-6015361. E-mail: jvicente003@ikasle.ehu.es

generated via DME decomposition (Eq. (5)) when strong acidic catalyst or high reforming temperatures are used (Faungnawakij et al., 2007).

$$CO_2+H_2 \leftrightarrow H_2O + CO \quad (4)$$

$$(CH_3)_2O \rightarrow CH_4 + H_2 + CO \quad (5)$$

Finally, conversion of methanol and dimethyl ether to hydrocarbons (MTG process) (Eq. (6)) can take place at temperatures above 300 ºC over strong acid sites (Semelsberger et al., 2005), and a significant coking may occur on the catalyst surface due to dehydrogenation of the hydrocarbons formed (Eq. (6)) (Kawabata et al., 2006).

$$\text{Oxygenate} \rightarrow \text{hydrocarbons} \rightarrow \text{coke} \quad (6)$$

Consequently, suitable metallic and acid functions are required for attaining high DME conversion and high H_2 selectivity. Cu based catalysts are well known for their high activity for DME steam reforming (Badmaev and Snytnikov, 2008) and a commercial $Cu/Zn/Al_2O_3$ catalyst has been widely used as metallic function. Another important characteristic is the contact mode of the metallic and acid functions. Kawabata et al. (2006) reported that composite materials showed better activity than separate loading and mechanically mixed loading of acid and metallic functions.

The selection of the acid function is essential for the development of catalysts for DME steam reforming, given that hydrolysis is the process limiting step and MTG reactions must be avoided. γ-Al_2O_3 is the more commonly used acid function in the literature for DME steam reforming (Takeishi and Suzuki, 2004), but due to its very low acidity, high temperatures (> 400 ºC) are required for attaining high conversion, and sintering of the metallic function based on Cu may be considerable at these temperatures. As an alternative, the use of zeolites such as ZSM-5 has been proposed (Semelsberger et al., 2006), but due to their excessive acidity, they give way to hydrocarbon formation.

In this paper, a HZSM-5 zeolite has been subjected to an alkaline treatment in order to moderate its acidity (Alonso et al., 2007), with the aim of minimizing the formation of hydrocarbons in DME steam reforming. The severity of the treatment with alkali for maximizing the selectivity and yield of hydrogen has been determined.

2. Experimental

The bifunctional catalysts have been prepared by (wet) physical mixture of equal mass proportions of the metallic function $Cu/ZnO/Al_2O_3$ (a commercial catalyst for methanol steam reforming supplied by Süd-Chemie) and different acid functions; pure HZSM-5 zeolite (SiO_2/Al_2O_3=30 supplied by Zeolyst) and zeolites modified by different alkaline treatments. The homogeneous mixture obtained was dried in air for 12 h, pressed, crashed and sieved to a particle size between 0.15-0.25 mm.

The alkaline treatments have consisted of mixing at 80 ºC the ammonium ZSM-5 zeolite with a NaOH solution of different concentration (0.2 or 0.4 M) for different times (10 or 300 min). The sodium ZSM-5 zeolites obtained have been ion-exchanged with ammonium nitrate solution, and subsequently washed and dried in air for 24h. All the zeolites have been calcined at 575 ºC for 2 h. The parent zeolite has been called Z30 and the treated zeolites A02T10, A02T300 and A04T300, where the number following A refers to the concentration of the NaOH solution and the number following T denotes the duration of the treatment.

The porous structure of the zeolites has been measured by N_2 adsorption using a Micromiretics ASAP 2010 instrument. Before the measurements, samples were degasified under vacuum at 150 ºC for 10h.

Total acidity and the acid strength distribution of the zeolites have been measured by calorimetric measurements of differential adsorption of ammonia and subsequent temperature programmed desorption (TPD) of NH_3, which have been carried out in a Setaram TG-DSC 111 calorimeter connected on-line to a Balzers Omnistar mass

spectrometer. After degasing the zeolite sample (1h in He stream at 500 ºC), it has been cooled to 150 ºC, an ammonia stream (10 μl/min) has been introduced by means of a syringe until saturation of the sample and finally the sample has been swept with He at 150 ºC in order to desorb physisorbed ammonia. The ratio between the continuous signals corresponding to heat flow and to weight change obtained during the ammonia adsorption step provides a measurement of the acid strength distribution, whereas the total amount of chemically retained base corresponds to the total acidity of the sample. Subsequently the TPD of ammonia has been carried out by heating the sample at 5 ºC min^{-1} to 550 ºC and the mass corresponding to desorbed ammonia has been registered in the mass spectrometer.

The nature of the sites (Bronsted or Lewis) has been determined by FTIR spectroscopy (Nicolet 6700 spectrometer provided with a Specac catalytic chamber) of adsorbed pyridine. After subjecting the finely ground sample to high vacuum at 400 ºC for 30 min temperature has been stabilized at 150 ºC and successive pyridine pulses have been injected until saturation of the sample, which has been subsequently subjected to vacuum at 150 ºC for 1 h to eliminate physisorbed pyridine, and the corresponding spectrum has been recorded. Brosnsted/Lewis ratio has been determined by integration of the bands at 1545 and 1450 cm^{-1} and taking into account the molar extinction coefficients of both adsorption bands (Emeis, 1993).

The kinetic runs have been carried out in automated reaction equipment provided with an isothermal fluidized-bed reactor with 22 mm of internal diameter connected on-line to a MicroGC Agilent 3000 for product analysis. The hydrodynamic properties of the bed have been improved by mixing the catalyst (particle size between 150 and 250 μm) with inert alumina (particle size between 60 and 90 μm) in a catalyst/inert ratio of 1/4. The operating conditions were: atmospheric pressure, steam/DME/He ratio= 3/1/0.85, space time up to 0.60 $g_{catalyst}h/g_{DME}$, temperature between 225-325 ºC. Prior to the catalytic runs, the catalyst was reduced using 10% H_2 in He at 300 ºC for 2 h with a total flow rate of 60 ml min^{-1}.

DME conversion and selectivity and yield of H_2 and CO have been calculated as follows:

$$X_{DME} = \frac{F_{DME,0} - F_{DME}}{F_{DME,0}} \quad (7)$$

$$S_i = \frac{F_i \cdot \upsilon_i^{-1}}{F_{DME,0}} \quad (8)$$

$$Y_i = X_{DME} \cdot S_i \quad (9)$$

where F_i is the molar flow of component i, which is evaluated from its molar fraction (calculated from chromatographic results) and the total molar flow (determined by atomic balances of H, C and O), υ is the stechiometric coeficient of the component i produced in DME SR, and the subscript 0 denotes the initial molar flow.

3. Results and discussion

3.1. Characterization of the zeolites

Table 1 shows the BET surface area, total pore volume, micropore volume and mean pore diameter of the acid functions. All the zeolites have high surface area due to their microporosity. However, increasing the severity of the alkaline treatment the surface area and the micropore volume are reduced, whereas the pore volume and the mean pore diameter are increased. Therefore, the alkaline treatment affects the porous structure of the zeolite leading to an increase in the mesoporous surface area.

Table 1 also shows the B/L ratio of the zeolites. As observed, a moderate alkaline treatment increases the B/L ratio, which is evidence that alkali attacks Lewis sites to a greater extent than Bronsted sites. Furthermore, a severe treatment lowers the B/L

ratio, which is a consequence that, under severe conditions, weak Bronsted sites (together with strong sites) are also affected by the alkali.

Table 1. Physic properties of the zeolites and B/L ratio.

	Z30	A02T10	A02T300	A04T300
BET surface area ($m^2\ g_{cat}^{-1}$)	430	387	413	358
Micropore volume ($cm^3\ g_{cat}^{-1}$)	0.134	0.118	0.121	0.093
Pore volume ($cm^3\ g_{cat}^{-1}$)	0.258	0.317	0.412	0.585
Mean pore diameter (nm)	40.8	67.6	71.9	103.6
$B/L^{150ºC}$	1.83	2.23	1.93	1.44

Figure 1 illustrates the effect of the alkaline treatment on the acid strength and total acidity of the zeolites. Graph (a) shows the acid strength distribution and total acidity obtained in the differential adsorption of NH_3 at 150 ºC, whereas graph (b) corresponds to the results of TPD of NH_3. It is observed that the alkaline treatment attenuates both total number of acid sites (which decreases from 0.92 mmol of NH_3/(g of zeolite) for the parent zeolite to 0.68 mmol of NH_3/(g of zeolite) for the catalyst that has been more severely treated with alkali). This treatment also affects the acid strength of the sites (which has a predominant value of 135 kJ/(mol of NH_3) for the untreated zeolite and decreases to 115 kJ/(mol of NH_3) for the more severely treated catalyst). The results of TPD show that the strong acid sites (desorption peak at 420 ºC) are the more affected by a moderate alkaline treatment, whereas a severe treatment affects both strong and weak sites (desorption peak at 250 ºC), with strong sites being affected to a greater extent.

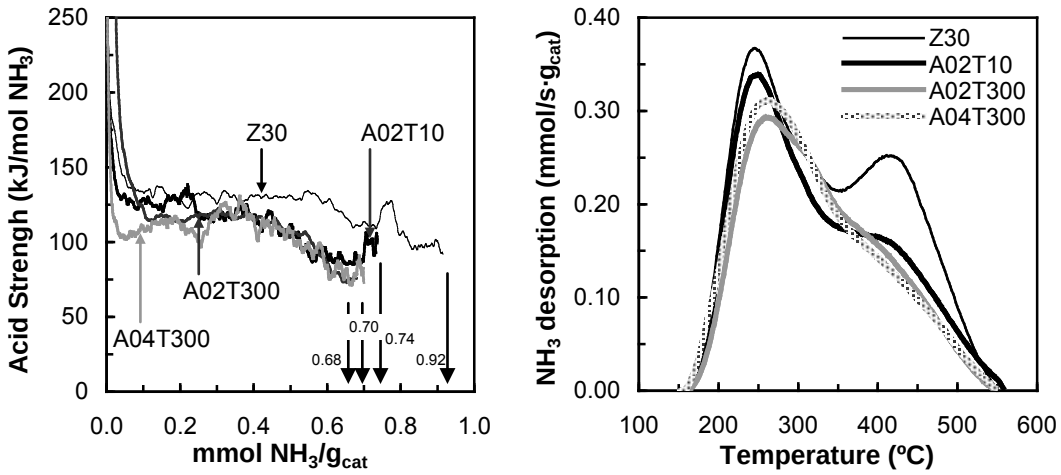

Figure 1. Acidic strength distribution and total acidity (a) and TPD of ammonia (b) for the parent HZSM-5 zeolite and for zeolites subjected to alkaline treatment

3.2. The effect of the acid function in the DME steam reforming

Figure 2 shows the results of initial DME conversion (left) and yields of hydrogen and CO (right) for different operating conditions at zero time-on-stream. The conversion and yield of H_2 with the Z30 zeolite catalyst are slightly higher than with the treated zeolites, as would be expected taking into account its higher acidity. Nevertheless, the yield of CO with this catalyst is significantly higher than with the modified zeolites.

For the catalysts of pure zeolite or zeolite subjected to a moderated alkali treatment (A02T10 or A02T300), the maximum yield of H_2 is obtained at 300 ºC, and the subsequent decrease in H_2 production at 325 ºC is due to the rapid formation of hydrocarbons from methanol and DME (MTG process).

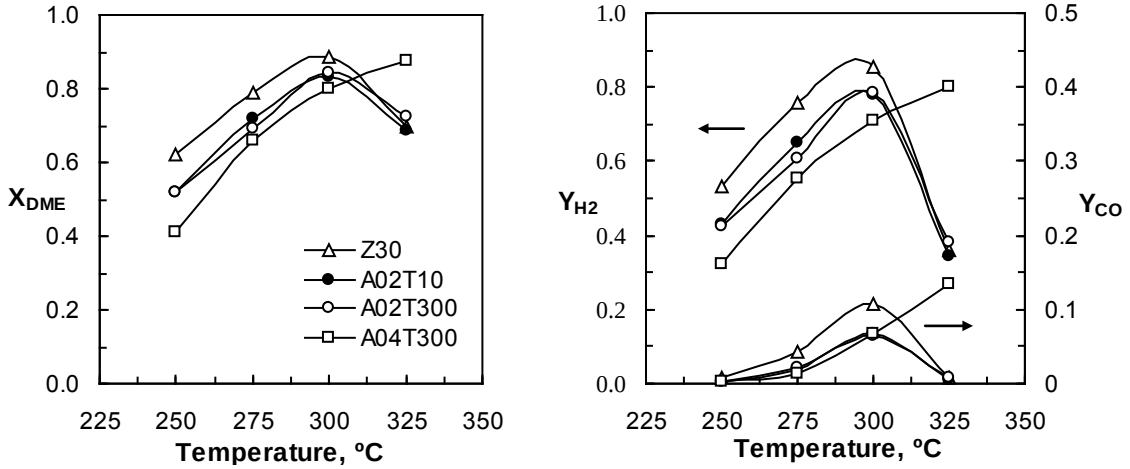

Figure 2. Conversion of DME (left) and yield of H_2 and CO (right) in DME steam reforming for the catalysts prepared with the different acid functions. Space time= 0.60 $g_{catalyst}h/g_{DME}$; steam/DME= 3/1; 1 atm.

In order to explain more clearly the differences in the kinetic behaviour above 300 ºC, Figure 3 shows the evolution with time of the molar fraction of byproducts (hydrocarbons) at different temperatures. None of the catalysts based on zeolites favours the MTG reactions under 300ºC. At 300 ºC this reaction only takes place with the catalyst based on Z30, although an induction period is needed (Aguayo et al., 2005). At 325 ºC the formation of hydrocarbons is fast for the catalyst based on Z30, but requieres an induction period for the catalysts based on treated zeolites, whose duration significantly increases with alkaline treatment severity (consistent with the decrease in acidity). The catalyst based on A04T300 zeolite (severe alkaline treatment), avoids hydrocarbons formation in the whole range of temperature studied. Nevertheless, the higher temperature required for attaining high DME conversion using A04T300 catalyst favours a higher formation of CO by reverse water-gas shift reaction.

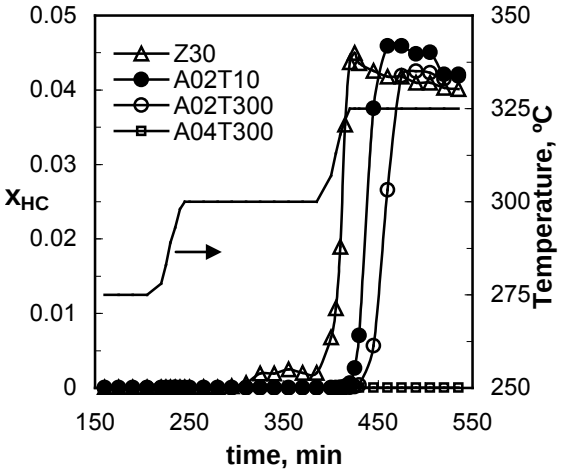

Figure 3: Evolution with time and temperature of the molar fractions of the hydrocarbons produced from oxygenates in DME SR.

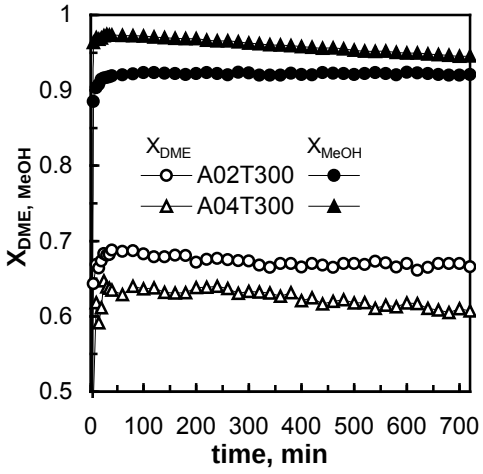

Figure 4. Evolution with time of DME and methanol conversion during DME steam reforming over catalysts A02T300 at 300 ºC and A04T300 at 325 ºC.

Moreover, catalyst deactivation by Cu sintering will also be higher due to the higher temperature required for obtaining high DME conversion with A04T300 catalyst. Thus, in a long duration run (Figure 4) carried out with a space time of 0.30 $g_{catalyst}h/g_{DME}$ at

300 ºC with A02T300 catalyst, DME conversion decreased from 0.687 to 0.666 subsequent to 12 h, whereas the conversion of DME decreased from 0.643 to 0.608 in the same period of time when the run was carried out with the same value of space time at 325 ºC and using A04T300 catalyst.

4. Conclusions

A moderate alkaline treatment (with a 0.2 M NaOH solution during 300 min) is suitable for modifying the HZSM-5 zeolite in order to use as an acid function for DME steam reforming. This moderate alkaline treatment slightly moderates the acidity of the zeolite, which allows for obtaining high H_2 selectivity and yield at temperatures that are low enough to minimize the formation of byproducts (hydrocarbons) and CO and deactivation by Cu sintering.

Acknowledgements

This work was carried out with the financial support of the Ministry of Science and Technology of the Spanish Government (Project PPQ2006-12006).

References

Aguayo, A.T., Ereña, J., Mier, D., Arandes, J.M., Olazar, M., Bilbao, J. (2007). Kinetic modeling of dimethyl ether synthesis in a single step on a CuO-ZnO-Al_2O_3/gamma-Al_2O_3 catalyst. *Industrial & Engineering Chemistry Research*, 46, 5522-5530.

Aguayo, A.T., Gayubo, A.G., Vivanco, R., Alonso, A, Bilbao, J. (2005). Initiation Step and Reactive Intermediates in the Transformation of Methanol into Olefins over SAPO-18 Catalyst. *Industrial & Engineering Chemistry Research*, 44, 7279-7286.

Alonso, A., Valle, B., Atutxa, A., Gayubo, A.G., Aguayo, A.T. (2007). Development of Alternative Catalysts Based on HZSM-5 Zeolite for the BTO Process. *Int. J. Chem. Reac. Eng.*, 5, Article A61.

Badmaev S.D., Snytnikov P.V. (2008), Hydrogen production from dimethyl ether and bioethanol for fuel cell applications. *International Journal of Hydrogen Energy*, 33, 3026-3030.

Emeis C.A. (1993) Determination of Integrated Molar Extinction Coefficients for Infrared Absorption Bands of Pyridine Adsorbed on Solid Acid Catalysts. *Journal of Catalysis*, 141, 347.

Faungnawakij K., Tanaka Y., Shimoda N., Fukunaga T., Kikuchi R., Eguchi K. (2007). Hydrogen production from dimethyl ether steam reforming over composite catalyst of copper ferrite spinel and alumina. *Applied Catalysis B*, 74, 144-151.

Kawabata T., Matsuoka H., Shisido T., Li D., Tian Y., Sano T., Takehira K. (2006). Steam reforming of dimethyl ether over ZSM-5 coupled with Cu/ZnO/Al_2O_3 catalyst prepared by homogeneous precipitation. *Applied Catalysis A*, 308, 82-90.

Semelsberger, T.A., Borup, R.L., Greene, H.L., (2006). Dimethyl ether as an alternative fuel. *Applied. Catalysis A*, 156, 497-511.

Semelsberger, T.A., Ott, K.C., Borup, R.L., Greene, H.L., (2005). Role of the acidity on the hydrolisis of dimethyl ether to methanol. *Applied Catalysis A*, 61, 281-287.

Semelsberger, T.A., Ott, K.C., Borup, R.L., Greene, H.L., (2006). Generating hydrogen-rich fuel-cell feeds from dimethyl ether using Cu/Zn supported on various soli-acid substrates. *Applied Catalysis A*, 309, 210-223.

Takeishi, K., Suzuki, H. (2004). Steam reforming of dimethyl ether. *Applied Catalysis A*, 260, 111-117.

Tanaka, Y., Kikuchi, R. Takeguchi, T., Eguchi, K. (2005). Steam reforming of dimethyl ether over composite catalyst of γ-Al_2O_3 and Cu-based spinel. *Applied Catalysis B*, 57, 211-222.

Proceedings of the 10th International Chemical and
Biological Engineering Conference - CHEMPOR 2008
Braga, Portugal, September 4-6, 2008
E.C. Ferreira and M. Mota (Eds.)

Application of a group contribution CPA EoS to the modelling of biodiesel production

Mariana B. Oliveira[1], Fatima R. Varanda[1], Maria Jorge Melo[1], Isabel M. Marrucho[1], António José Queimada[2], João A.P. Coutinho[1*]

[1]CICECO, Chemistry Department, University of Aveiro, 3810-193 Aveiro, Portugal

[2]LSRE - Laboratory of Separation and Reaction Engineering, Faculdade de Engenharia, Universidade do Porto, Rua do Doutor Roberto Frias, 4200 - 465 Porto, Portugal

Keywords: Biodiesel, Group contribution method, CPA EoS, Water solubility
Topic: Systematic methods and tools for managing the complexity.

Abstract

Due to the continuous increase in crude oil prices, limited resources of fossil energies and environmental concerns, biodiesel (a blend of fatty acid esters) is being considered as a good alternative to conventional diesel for road transportation.

During biodiesel production several aspects need to be considered to insure fuel quality. One of the most important is the water content. Up to now, little information was available about the water solubility in esters and commercial biodiesels. To overcome this lack of data, solubility measurements were carried out for 11 esters and 6 biodiesels. Simultaneously, mutual solubility measurements were made for 6 fatty acid (C_5-C_{10}) + water systems. This new experimental data was used to support the development of a group contribution version of the Cubic plus Association (CPA) equation of state, that can adequately predict water solubility in fatty acids, esters and biodiesel mixtures, required for a correct design of the biodiesel washing and purification processes.

1 Introduction

The most commonly used method to produce biodiesel is the transesterification of vegetable oils and animals fats with monohydric alcohols, using a homogeneous basic catalyst such as NaOH. As, chemically, biodiesel is different from conventional diesel, the European Committee for Standardization (CEN) developed quality standards specifying minimum requirements and test methods for biodiesel to be used in diesel engines and for heating purposes, in order to increase the biodiesel quality and its acceptance. One of these quality values is the water content, that the DIN EN 14214:2003 limits below 0.05% (w/w).

Water is introduced into biodiesel during production and may remain in it if the drying procedure is not efficient. It can also be absorbed during storage, since fatty acid esters are hygroscopic, making biodiesel much more hydrophilic than regular diesel. Water in biodiesel affects its calorific value and, above all, the shelf life of the fuel (lower oxidation stability).

During biodiesel production the fatty esters rich current leaving the reactor is saturated with glycerol, alcohol, catalyst and unreacted soaps. This current is washed in a liquid-liquid extractor in counter current with acidified water to neutralize the catalyst and to convert soaps to free fatty acids. The raffinate current is composed of water saturated biodiesel while the extract is a low pH aqueous solution containing the polar compounds. The design and optimization of the purification of biodiesel with water thus requires a model that can describe this phase equilibria.

To overcome the inability to apply equations of state in the absence of pure component data

* Corresponding author. Tel +351 234401507. E-mail:jcoutinho@ua.pt

and to reduce the amount of experimental work and related costs, it is useful to develop predictive thermodynamic models based on group contributions.

When water is involved, association equations of state are needed, since the general cubic equations of state such as SRK and PR EoS are not able to take into account the association between molecules of water and alcohol or the solvation between esters and water. Among these associating equations there is the Cubic plus Association equation of state (CPA EoS) that combines the SRK cubic contribution for describing the physical interactions with the association contribution proposed by Wertheim. CPA has previously shown to be able to provide an accurate description of the phase equilibria of aqueous mixtures with n-alkanes, aromatics, fluorocarbons, alcohols and glycols.

One of the goals of this work is to create a new group contribution model for the Cubic plus Association equation of state (CPA EoS), combining the good description of this equation to represent associating systems with the predictive character of a group contribution method.

2 Experimental Section

Water solubility measurements were carried out at 288.15 - 323.15 K and atmospheric pressure. The organic and water phases were agitated and allowed to reach equilibrium by the separation of both phases in 20 mL glass vials for at least 48 h. This period proved to be the minimum to guarantee a complete separation and no further variations in solubilities.

Temperature was maintained by keeping the vials inside an aluminium block, placed in an isolated air bath (± 0.01 K). Temperature control was achieved with a PID controller driven by a calibrated Pt100 sensor. To reach temperatures below room temperature, a Julabo circulator, model F25-HD, was coupled to the overall oven system.

Water solubilities in the ester or acid rich phases were determined using a Metrohm 831 Karl Fischer (KF) coulometer.

The organic phase was sampled at each temperature from the equilibrium vials using glass syringes maintained dry and at the same temperature of the measurement. Samples of 0.1 to 0.2 g were taken and injected directly into the KF coulometric titrator.

For pentanoic and hexanoic acids, measurements of the phase envelope for the two phase region were made by turbidimetry. Several samples covering the entire concentration range were prepared. The mixture was heated inside a closed glass tube in a thermostatic bath up to the one phase region. On slowly cooling, the phase separation temperature was registered. The temperature assigned to the phase envelope is an average of five measurements.

3 Model

The CPA equation of state, in terms of the compressibility factor, is given by:

$$Z = Z^{phys.} + Z^{assoc.} = \frac{1}{1-b\rho} - \frac{a\rho}{RT(1+b\rho)} - \frac{1}{2}\left(1+\rho\frac{\partial \ln g}{\partial \rho}\right)\sum_i x_i \sum_{A_i}(1-X_{Ai}) \quad (1)$$

where a is the energy parameter, b the co-volume parameter, ρ is the density, g a simplified hard-sphere radial distribution function, X_{Ai} the mole fraction of pure component i not bonded at site A and x_i is the mole fraction of component i.

X_{Ai} is related to the association strength Δ^{AiBj} between sites belonging to two different

molecules and is calculated by solving the following set of equations (2):

$$X_{Ai} = \frac{1}{1+\rho\sum_j x_j \sum_{B_j} X_{Bj}\Delta^{A_iB_j}} \quad (2) \qquad \Delta^{A_iB_j} = g(\rho)\left[\exp\left(\frac{\varepsilon^{A_iB_j}}{RT}\right)-1\right]b_{ij}\beta^{A_iB_j} \quad (3)$$

where ε^{AiBj} and β^{AiBj} are the association energy and the association volume, respectively.

For non-associating components, such as n-esters, CPA has three pure component parameters (a_0, c_1 and b) while for associating components like water and organic acids it has five (a_0, c_1, b, ε, β). These parameters are estimated by a simultaneous regression of vapour pressure and liquid density data. To overcome the inability to apply this approach in the absence of density and vapour pressure data, a group contribution method was developed (Oliveira et al. (2008)). This method may be applied as a predictive tool for the following families: n-alkanes, n-alcohols, saturated and unsaturated fatty acid esters and fatty acids.

The development of the group contribution scheme started with the definition of the groups. The chemical groups adopted as suitable for the description of these compounds were: (CH_3), (CH_2), (OH), (COO), (HCOO), (COOH), and (CH=).

The CPA pure component parameters are thus calculated from the following relations:

$$a_0 = k_1 \times \left(\ln\left(k_2 + \sum_{i=1}^{n_{groups}} n_i a_{0i}\right)\right)^{k_3} \quad (4) \qquad c_1 = k_1 \times \left(\ln\left(k_2 + \sum_{i=1}^{n_{groups}} n_i c_{1i}\right)\right)^{k_3} \quad (5)$$

$$b = \sum_{i=1}^{n_{groups}} n_i b_i \quad (6) \qquad \beta = k_1 + k_2 \exp(-k_3 \sum_{i=1}^{n_{groups}} n_i \beta_i) \quad (7) \qquad \varepsilon = \sum_{i=1}^{n_{groups}} n_i \varepsilon_i \quad (8)$$

In these equations, subscript i refers to a specific structural group, n_i is the number of structural groups of type i, and n_{groups} is the total number of structural groups in the molecule. The parameters a_{0i}, c_{1i}, b_i , ε_i, and β_i are the values of the parameter related to each group i. These values, along with the constants for each equation, are reported in **Table 1**.

Table 1. Group contribution parameters for the CPA EoS and constant values for equations 4, 5 and 7.

	Group Parameters									
Parameter	**CH_3**	**CH_2**	**OH**	**HCOO**	**COO**	**C=**	**COOH**	**k_1**	**k_2**	**k_3**
a_o	13.787	6.884	13.218	16.8781	11.025	8.443875	27.124	1.69E-04	-3.349	6.953
c_1	0.418	0.157	0.365	0.895	0.635	-0.424*	0.697	0.846	1.337	1.294
b	1.81E-05	1.81E-05	7.59E-06	2.40E-05	2.49E-05	1.46E-05	3.02E-05			
ε	14996.3	782.3	3977				18713.1			
β	-0.373	0.652	1.595				2.738	5.06E-05	7.75E-02	1.038

∗For the unsaturated methyl esters with more than one double bound, a correction factor should be added when calculating c_1:

$$k_1 \times \left(\ln\left(k_2 + \sum_{i=1}^{n_{groups}} n_i c_{1i} + 1.269\right)\right)^{k_3}$$

4 Results and discussion

In order to compare the performance of the proposed group contribution approach, CPA parameters were initially regressed for compounds for which there were vapor pressure and liquid density data. This will be hereafter callled the “usual approach”.

While using the “usual approach” for obtaining the pure component parameters, an excellent description of vapour pressure and liquid densities was achieved for 42 esters and 20 organic acids, covering the range of reduced temperatures from 0.45-0.85, with global average deviations of about 2% for both properties. Although the GC parameters were very similar to the “usual approach” ones, generally, the quality of the pure component vapour pressure estimates was significantly decreased, while in terms of liquid densities, a minor decrease in the description quality was observed.

Having the pure compound parameters, it was possible to model binary mixtures of water with several methyl, ethyl and propyl esters, and fatty acids. Solubility calculations were performed using both set of parameters: from the “usual approach” and from the group contribution model.

The cross-association (solvation) between the ester group and water was taken into account as previously done for aromatic hydrocarbons. Using this approach, both the binary interaction k_{ij} and the cross-association volume (β_{ij}) parameters are fitted to solubility data. As cross-association between water and esters will always occur between water and the ester group, the β_{ij} value was fixed to 0.20 for all ester + water systems, and the binary interaction parameters were then regressed using this value.

To obtain a good description of the mutual solubilities of water + fatty acids, the fitting of the k_{ij} parameter was also required. Calculations for fatty acids were performed initially using two different combining rules (CR-2 and CR-4), but it was found that for long chain esters the CR-4 combining rule gave the best results, as can be seen from **Table 2**.

A generalized linear correlation for the k_{ij} parameter was found with the chain length of the ester and the acid, C_n, when using the “usual approach” and the group contribution parameters, described, respectively by equations 9-12.

Usual approach Acids (CR-4)	$k_{ij} = -0.0142 \times C_n + 0.0020$	(9)
Usual approach Esters	$k_{ij} = 0.0136 \times C_n - 0.3322$	(10)
GC approach Acids (CR-4)	$k_{ij} = -0.0106 \times C_n - 0.040$	(11)
GC approach Esters	$k_{ij} = 0.0154 \times C_n - 0.3458$	(12)

With this single value of k_{ij} for each system, it was possible to describe the water solubility in fatty acid esters with a global average deviation of 7.0 % for both the “usual approach” and the group contribution approach parameters. For fatty acid + water systems, global average deviations lower than 30 % were obtained for the water solubility and lower than 6% for the acid solubility, with both approaches.

Values for the binary interaction parameters and average deviations are presented in **Tables 2** and **3**. Water solubility in two fatty acid esters and mutual solubilities for three fatty acid + water systems are presented, as examples, in **Figures 1** and **2**.

The proposed GC approach, while producing worst estimates for pure component vapour pressure, is as accurate as the approach with fitted parameters for the estimation of water solubilities in ester systems, and mutual solubilities of acid + water systems, and may even present lower global average deviations.

Using the group contribution approach and the linear correlation for the binary interaction parameters, the proposed model can be used as a predictive tool for more complex mixtures

such as biodiesels. Good results were obtained for the water solublity in biodiesels with both approaches with global average deviations of 15.5 % and 14.9 %, respectively, for the usual and the GC approach. Water solubility in one of the studied commercial biodiesels is depicted in **Figure 2**.

Table 2. CPA modelling results for the mutual solubilities of fatty acid + water systems and binary interactions parameters.

Regressed CPA parameters						
	CR-2			**CR-4**		
		AAD %			**AAD %**	
n.º Carbons	k_{ij}	**acid rich phase**	**water rich phase**	k_{ij}	**acid rich phase**	**water rich phase**
5	-0.0903	39.01	10.4	-0.0951	56.17	9.19
6	-0.0833	11.87	4.24	-0.0894	42.4	4.67
7	-0.0918	21.14	2.70	-0.0987	29.51	2.08
8	-0.0967	40.49	2.38	-0.1033	24.78	2.63
9	-0.1151	84.39	6.93	-0.1217	11.14	8.11
10	-0.1333	78.5	8.83	-0.143	9.05	3.88
AAD Global %		**45.9**	**5.92**		**28.84**	**5.09**
GC CPA parameters						
5	-0.1099	36.22	10.12	-0.1147	60.09	9.64
6	-0.1044	10.47	4.73	-0.1096	40.82	5.63
7	-0.1067	23.10	2.95	-0.1100	28.05	4.04
8	-0.1123	43.10	2.58	-0.1190	22.72	2.86
9	-0.1255	87.30	7.48	-0.1314	9.85	9.77
10	-0.1462	79.63	2.85	-0.1543	9.39	5.24
AAD Global %		**46.64**	**5.12**		**28.48**	**6.20**

Table 3. CPA modelling results for the water solubilities in fatty acid esters and binary interactions parameters.

		Regressed CPA parameters		***GC CPA parameters***	
n.º Carbons	**Compounds**	k_{ij}	**AAD %**	k_{ij}	**AAD %**
6	**Ethyl butanoate**	-0.254	7.42	-0.2602	7.02
7	**Propyl butanoate**	-0.238	6.97	-0.2371	6.89
7	**Methyl hexanoate**	-0.234	7.38	-0.2370	7.32
8	**Methyl heptanoate**	-0.221	6.00	-0.2239	4.84
9	**Methyl octanoate**	-0.210	7.52	-0.2034	6.51
12	**Ethyl decanoate**	-0.166	6.40	-0.1576	6.44
13	**Methyl dodecanoate**	-0.150	7.39	-0.1444	7.12
15	**Methyl tetradecanoate**	-0.123	6.44	-0.1103	5.91
17	**Methyl hexadecanoate**	-0.092	9.35	-0.0840	7.96
19	**Methyl octadecanoate**	-0.075	3.10	-0.0586	5.83
19	**Methyl oleate**	-0.100	4.27	-0.1028	4.53
	AAD Global %		**6.57**		**6.40**

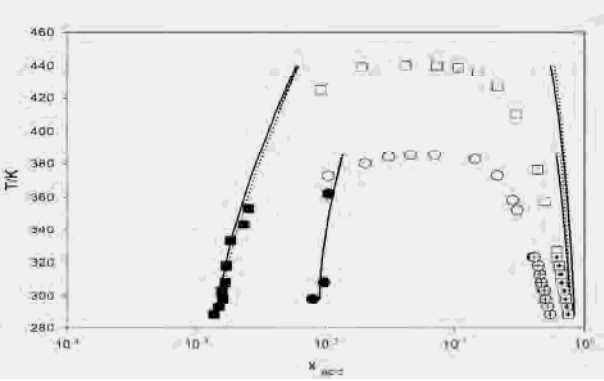

Figure 1. LLE for two water + acid systems. Experimental values for pentanoic acid (○, turbidimetry; ⊕, Karl Fisher; •, literature data) and for hexanoic acid (□, turbidimetry; ⊠, Karl Fisher; ■, literature data), and CPA results (—, regressed CPA parameters; ···, GC CPA parameters).

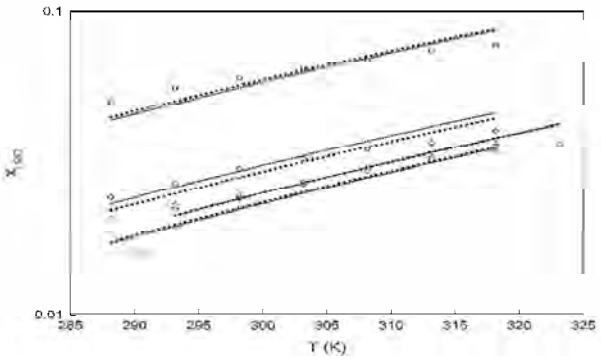

Figure 2. Experimental water solubility (□, in ethyl butanoate; o, in methyl tetradecanoate; ◊, in ethyl decanoate; Δ, in Biodiesel F), and CPA results (—, regressed parameters; ···, GC parameters).

5 Conclusions

Using an equation of state for phase equilibria requires parameters that in the absence of pure component data are not possible to determine. In this work, a new group contribution method for the estimation of the pure compound parameters of the CPA EoS was developed. This new method was used to describe the water solubility in ester systems and the mutual solubilities of fatty acid + water systems and compared with the "usual approach" where these parameters are regressed from vapour pressure and liquid density data.

For both approaches a single, small, and temperature-independent k_{ij} was sufficient. The binary interaction parameters are chain length dependent making the model predictive.

It was possible to conclude that the proposed GC approach may lead to poorer vapour pressure estimates, but is as accurate as the "usual approach" for the estimation of water solubilities in ester systems, and mutual solubilities of fatty acids and water systems. For the majority of the binary mixtures, the results provided by GC parameters are even better than those with the parameters adjusted from vapour pressure and density data. Therefore, it is possible to conclude that the group contribution parameters take more information into account than the adjusted parameters, leading to improved liquid-liquid equilibria results.

The proposed model thus seems to be a promising tool for the biodiesel industry and future work will focus in extending this approach to other phase equilibria and systems of interest for biodiesel production and purification.

References

1.Oliveira, M.B., Varanda, F.R., Marrucho, I.M., Queimada, A.J., Coutinho, J.A.P. (2008). *Prediction of water solubility in biodiesel with the CPA Equation of State*. *Industrial and Engineering Chemistry Research*, 47, 4278-4285.

Proceedings of the 10th International Chemical and
Biological Engineering Conference - CHEMPOR 2008
Braga, Portugal, September 4-6, 2008
E.C. Ferreira and M. Mota (Eds.)

Sequential Batch Reactor and Plug Flow Reactor Network Comparison under Dynamic Conditions for Wastewater Treatment

Adrián Ferrari[1*], Evaristo C. Biscaia Jr.[2], Priamo A. Melo[2]
[1] IIQ – Reactors Engineering Department, Chemical Engineering Institute, Engineering School, Oriental Republic of Uruguay University, J. H. y Reissig 565 Montevideo, Uruguay.
[2] LMSCP/PEQ/COPPE/UFRJ, Rio de Janeiro, Brasil.

Keywords: SBR, PFR, Reactor Network, Wastewater Modeling and Simulation, Dynamic Modeling and Simulation, Wastewater Treatment.
Suitable Topics: Process Systems Engineering, Wastewater Modeling and Simulation, Environmental Engineering.

Abstract

A single Plug Flow Reactor Network (PFRN) approach to modeling continuous wastewater treatment plants based on Sequential Batch Reactors (SBR) was developed. The simplified structure of PFRN makes this representation more suitable for stationary analysis and design purposes. New insights were obtained through the comparison of transient responses to typical industrial disturbances from both models (SBR and PFRN). Despite the different nature of SBR (lumped) and PFRN (distributed) models, they presented quite similar qualitative dynamic evolutions, and even their quantitative values were not so different. The similarities of the transient responses encourage the use of PFRN models to describe confidently the stationary as well as the dynamic behavior of real SBR plants, since the PFRN structure is considerably easier.

Introduction

The Sequential Batch Reactor (SBR) technology is widely used for biological wastewater (WW) treatments with carbon and nutrients removal purposes. This kind of technology can be applied to aerobic, anoxic, as well as to anaerobic processes (Artan and Orhon, 2005; Benitez et al., 2006). Figure 1 shows an example of a classic SBR process.

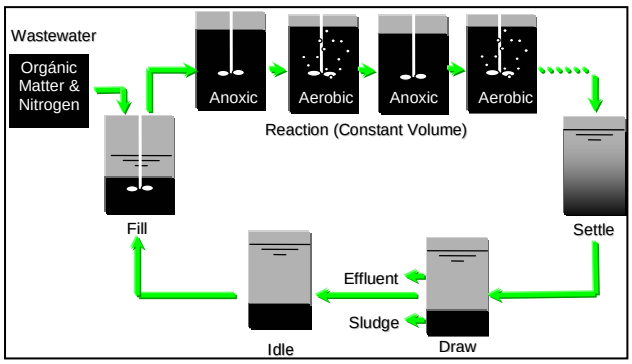

Figure 1: Typical SBR Configuration for Carbon and Nitrogen Removal

This process can be partitioned by two main role patterns: a Batch Reactor Network ("sequencing"), and a Feeding Pattern ("wastewater management"), as presented in Figure 2(a). Under steady state conditions, SBR compositions at the beginning and at the final of cycled operations are equal, and wastewater composition and flow rate are both maintained constant.

The main purpose of this contribution is to compare two models of a real multiple parallel SBR plant (applied to a continuous WW treatment): (i) Batch Reactor Network/Feeding

Pattern; (ii) Plug Flow Reactor Network (PFRN) (Artan and Orhon, 2005). Diagrams of the structures of both models are presented in Figure 2.

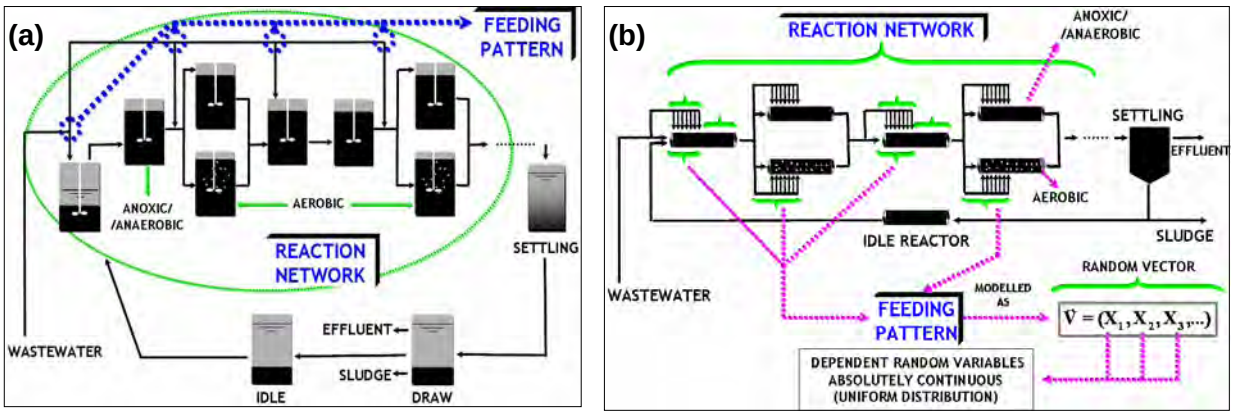

Figure 2: SBR representations: Batch Reactor Network/Feeding Pattern (a) and PFRN (b)

The simplified structure of the PFRN, in comparison with the multiple parallel SBR representation, makes this model more adequate for design purposes and stationary analysis. New insights of both approaches can be obtained comparing their dynamic simulations. Very few papers related with the dynamic behavior of this kind of equipment can be found in the open literature.

A comparison of dynamic responses of SBR and PFRN structures, when submitted to step changes in feed wastewater flowrate and composition, is presented in this paper. This kind of perturbation occurs typically in real industrial processes.

Mathematical Modeling and Applied Numerical Methods

SBR Model

The dimensionless transient component *i* mass balance (incompressible fluid) applied to the multiple parallel SBR representation is presented below:

$$\frac{dc_i(t)}{dt} = Fe_{SBR} \cdot \frac{q(t)}{v(t)} \cdot \left[c_{f,i}(t) - c_i(t) \right] - Da_i \cdot r_i \left[\mathbf{c}(t) \right]$$

Where:

- c_i: Dimensionless component *i* concentration;
- $c_{f,i}$: Dimensionless component *i* feed concentration;
- t : Dimensionless time variable;
- q: Dimensionless wastewater flow rate;
- v: Dimensionless reactor volume;
- r_i: Dimensionless component *i* consumption rate;
- Da_i : Damköhler number (dimensionless) for component *i*;
- Fe_{SBR} : Dimensionless feeding number;
- $\mathbf{c}$: Column vector of the dimensionless concentration of all components.

The lumped nature of SBR process model is characterized by the ordinary form of the differential equation system above.

PFRN Model

The dimensionless transient component *i* mass balance (incompressible fluid) applied to the plug flow reactor network (PFRN) is presented below:

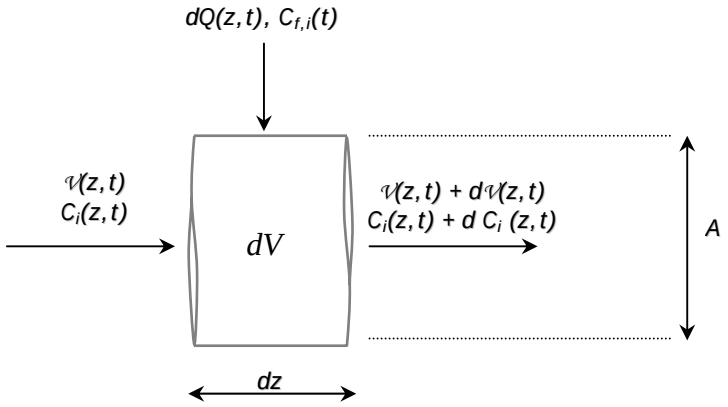

Figure 3: PFRN Control Volume

$$\frac{\partial c_i(z,t)}{\partial t} + v(z,t)\frac{\partial c_i(z,t)}{\partial z} = Fe_{PFRN} \cdot q(z,t) \cdot \left[c_{f,i}(t) - c_i(z,t)\right] - Da_i \cdot r_i\left[\boldsymbol{c}(z,t)\right]$$

Where:

- c_i: Dimensionless component *i* concentration;
- $c_{f,i}$: Dimensionless component *i* feed concentration;
- z : Dimensionless axial space variable;
- t : Dimensionless time variable;
- q: Dimensionless wastewater flow rate;
- v : Dimensionless interstitial flow rate;
- r_i: Dimensionless component *i* consumption rate;
- Da_i : Damköhler number (dimensionless) for component *i*;
- Fe_{PFRN} : Dimensionless feeding number;
- $\boldsymbol{c}$: Column vector of the dimensionless concentration of all components.

The distributed nature of PFRN process model is characterized by the partial form of the differential equation system above. This equation was spatially discretized by an implicit finite difference method resulting in the system of *N* ordinary differential equations:

$$\frac{dc_i^{(j)}(t)}{dt} + \upsilon^{(j)}(t)\frac{c_i^{(j)}(t) - c_i^{(j-1)}(t)}{\Delta z} = Fe_{PFRN}.q^{(j)}(t).\left[c_{f,i}(t) - c_i^{(j)}(t)\right] - Da_i.r_i\left[c^{(j)}(t)\right]$$

Where:

- $c_i^{(j)}(t) = c_i(z_j, t)$: Dimensionless component *i* concentration at z_j;
- $c^{(j)}(t) = c(z_j, t)$: Column vector of the dimensionless concentration of all components at z_j;
- z_j : Dimensionless value of the axial space variable at node *j* (*j* = 1, 2,…*N*).

Numerical Methods

The ordinary differential equations of both mathematical models were solved using an adaptive 4th order Runge-Kutta method.

Operational Conditions and Simulation Parameters

The Table 1 summarizes the plant conditions adopted in our simulations. These conditions were obtained from a typical real dairy SBR plant (milk powder plant).

Table 1: Operational data and simulation parameters for the dairy SBR plant

WW Steady State Composition & Flow Rate	3000 mgChemical Oxygen Demand(COD_{Total})/L - 100mgTotal Kjeldhal Nitrogen(TKN)/L - 100mgN-NO_3^-/L & 1500 m^3/d (Buitron et al., 2008)		
Effluent Steady State Composition	2.5 mg$COD_{Soluble}$/L – 0 mgTKN/L – 0.9 mgN-NO_3^-/L		
SBR's in Parallel // Cycle Period // Total Cycles by Day	2 // 24 hs. // 2		
SBR Sequencing (each cycle) (Idle Time ~ 0)	Stage 1: Anoxic Fill 5.5hs	Stage 2: Aerobic Fill 2hs	Stage 3: Anoxic Fill 4.5hs
	Stage 4: Aerobic 1.7hs	Stage 5: Settling 9.3 hs	Stage 6: Draw (effluent & sludge) 1 h
Initial // Maximum Volume (each SBR)	4000 m^3 // 4750 m^3		
Initial Biomass Content // Biomass Residence Time	3000 mgVolatile Suspended Solids (VSS)/L // 18 days		
Dissolved Oxygen (DO) Content	Not limiting (DO > 3 mgO_2/L)		
Kinetic Modelling	Based on ASM1 Model [Aerobic Carbon Removal & Denitrification Processes] (Orhon and Artan, 1994; Buitron et al., 2008)		
Dynamic Test 1: WW Composition Step Change to:	6000mgCOD_{Total}/L - 200mgTKN/L - 200mgN-NO_3^-/L		
Dynamic Test 2: WW Flow Rate Step Change to:	3000 m^3/d		

The kinetic modelling description considered in the simulations is summarized in Appendix 1. Autotrophic processes extent in the system (nitrification) is neglected due to the high wastewater COD_T/TKN ratio.

The effluent steady state composition, the initial reactor volume (analogy with the interstitial flow rate in PFRN) and the initial biomass content showed in Table 1 represent the initial (SBR) and boundary (PFRN) conditions employed for the steady state simulations.

Results and Discussion

Dimensionless Numbers

The Feeding and Damköhler number calculations for both developed structures are shown in Table 2.

Table 2. Dimensionless Number Values

Parameter	Name	Value
Fe	Feeding	0.312
Da_{Sc}	Damköhler for Organic Matter	1.67
Da_{SNO}	Damköhler for Nitrate	4.04
Da_{XH}	Damköhler for Biomass	0.65

It must be pointed out that same values of dimensionless parameters were considered in SBR and PFRN models. This has been done to reinforce the existing analogy between the models.

Steady State Simulations

Figure 4 shows the stationary composition profiles obtained for SBR and PFRN structures considering the values listed in Table 1. The results presented show that the stationary composition profiles of both models are quite similar. However, comparing SBR and PFRN responses, larger profile difference occurs for nitrate profile, during the initial stage of the process (low time/position values). As can be verified in Table 2, nitrate Damköhler number is larger than organic matter and biomass Damköhler numbers. This fact is a possible explanation to the nitrate profiles difference. Regardless of this, it must be pointed out that these differences are unimportant from an industrial point of view. Besides, the final effluent composition results at draw stage (the most important quality parameter of the system) in both models are practically the same.

The results obtained confirm the analogy between SBR and PFRN models during steady state conditions.

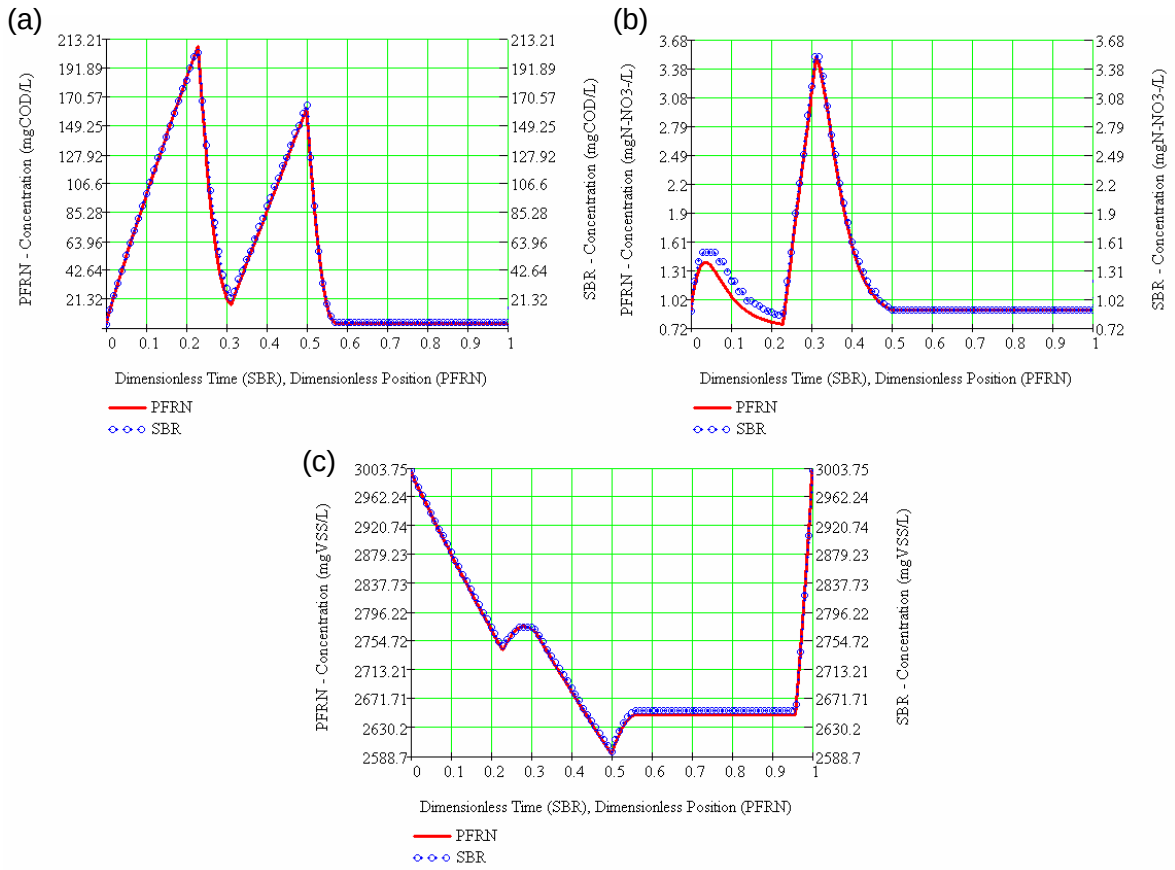

Figure 4: SBR and PFRN Steady State Results: Organic Matter (a), Nitrate (b) and Biomass (c) profiles

Dynamic Simulations

The dynamic response profiles for effluent composition for both models (Table 1) are shown in Figure 5 and Figure 6. All the simulations were made during a real total transient time of eight days. This value was adopted considering a realistic time scale of industry processes. Further details related with the dynamic simulations are presented in Appendix 2.

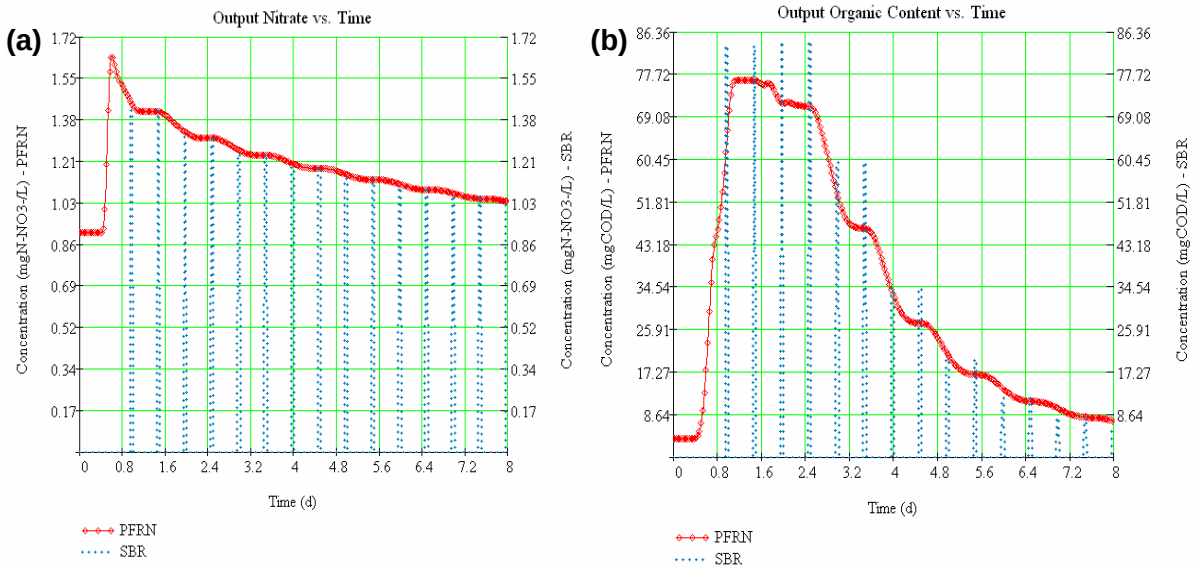

Figure 5: Simulation results for effluent composition during Test 1: Nitrate (a) and Organic Content (b) evolution

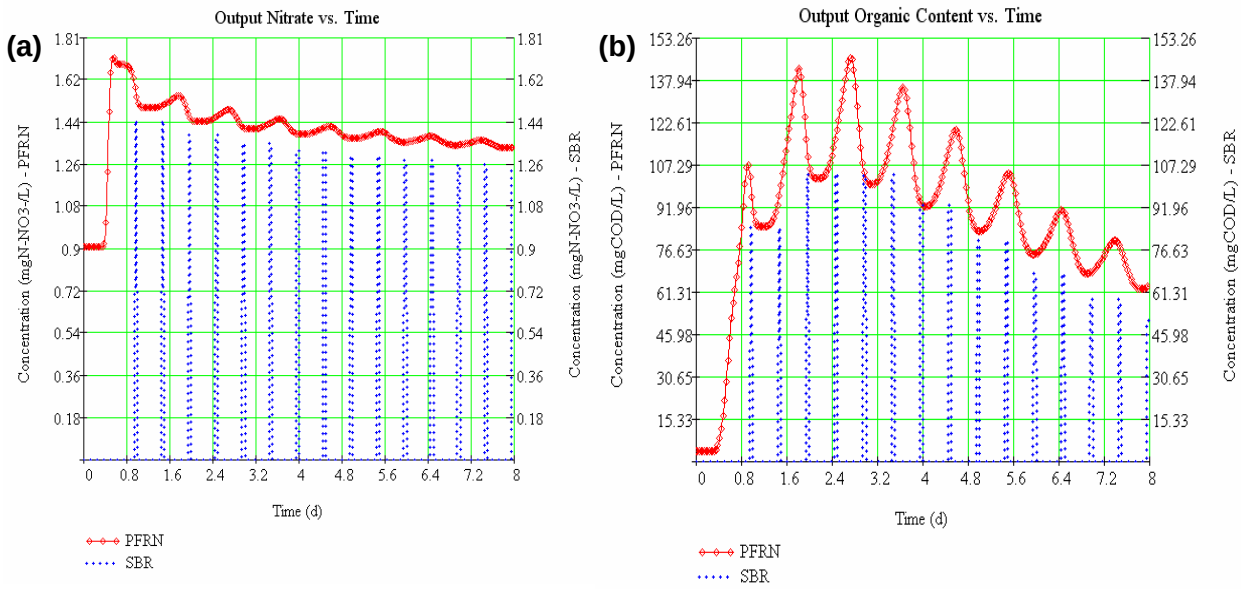

Figure 6: Simulation results for effluent composition during Test 2: Nitrate (a) and Organic Content (b) evolution

These results show that, despite the different nature of SBR (lumped) and PFRN (distributed) dynamic models, the qualitative dynamic evolutions are quite similar, and even their quantitative values are not so different if they compare with the corresponding WW composition (Table 1).

These observations can be very useful for industrial purposes, because, despite PFRN represents an easier handling model than SBR (multiple parallel plants), in real WW treatment processes high accuracy is not normally of special interest.

Conclusions

The well known analogy of the SBR and PFRN stationary models were also verified in this contribution. New insights were obtained through the comparison of transient responses to typical industrial perturbations of both models. Qualitative and quantitative aspects of both dynamic responses were analysed. The similitudes of the dynamic responses encourage the use of PFRN models to describe confidently the stationary and dynamic behavior of real SBR plants (industrial scale). Dynamic optimization of real SBR plants using the PFRN approach is a work in progress by the authors.

References

Artan, N., Orhon, D. (2005). *Mechanism and Design of Sequencing Batch Reactors for Nutrient Removal.* Scientific and Technical Report No. 19, IWA Publishing.

Benítez, A.; Ferrari, A.; Gutiérrez, S.; Canetti, R.; Cabezas, A.; Travers, D.; Menes, J.; Etchebehere, C. (2006). Sequential Batch Reactor as a Post – Treatment of Anaerobically Treated Dairy Effluent. *Water Science and Technology*, 54(2), 199 - 206.

Buitrón, G.; Canziani, R.; Torrijos, M.; Gutiérrez, S.; Moreno-Andrade, I.; Mazouni, D.; Fiocchi, N.; Ficara, E.; Moreno, G.; Benitez, A.; Pérez, J.; Ferrari, A. (2008). Experiments for Modelling the Biodegradation of Wastewater in Sequencing Batch Reactors. *Mathematical and Computer Modelling of Dynamical Systems,* 14(1), 3-15.

Orhon, D., Artan, N. (1994). *Modelling of Activated Sludge Systems.* Technomic Publishing Company Inc.

* Corresponding author. Tel + 541-2-7114478/int.102. E-mail:aferrari@fing.edu.uy

Appendix 1: Kinetic Description (Based on ASM1 Model)

Anoxic Reaction (Denitrification)

$$r_{X_H} = (\mu_{hN} - kd_{hN}).X_H \qquad \mu_{hN} = \mu_{hNmax} \cdot \left(\frac{S_C}{K_{C1} + S_C}\right)\left(\frac{S_{NO}}{K_{NO} + S_{NO}}\right)$$

$$r_{S_C} = -\frac{1}{Y_{hN}}.\mu_{hN}.X_H \qquad r_{S_{NO}} = \frac{1}{Y_{\frac{X}{N}}}.\mu_{hN}.X_H + kd_{hN}.X_H.f_{\frac{N}{X}}.\left(\frac{S_{NO}}{K_{NO} + S_{NO}}\right)$$

Aerobic Carbon Removal

$$r_{X_H} = (\mu_h - kd_h).X_H \qquad r_{S_C} = \frac{1}{Y_H}.\mu_h.X_H \qquad \mu_h = \mu_{hmax} \cdot \left(\frac{S_C}{K_{Ch} + S_C}\right)\left(\frac{S_O}{K_O + S_O}\right)$$

Table A1. Nomenclature description for kinetic expressions

Symbol Components	Name	Adopted Value	Dimension
S_C	Soluble Chemical Oxygen Demand ($COD_{Soluble}$)	-	$gCOD.m^{-3}$
S_{NO}	Nitrate Concentration (NO_3^-)	-	$gN.m^{-3}$
S_O	Dissolved Oxygen (DO)	-	$gO_2.m^{-3}$
X_H	Heterotrophic Biomass Concentration	-	$gVSS.m^{-3}$
Kinetic Parameters			
μ_{hmax}	Maximum Specific Aerobic Growth Rate for X_H	1	d^{-1}
μ_h	Specific Aerobic Growth Rate for X_H	-	d^{-1}
K_{Ch}	Aerobic Saturation Constant for S_C	75	$gCOD.m^{-3}$
K_O	Saturation Constant for S_O	~ 0	$gO_2.m^{-3}$
kd_h	Aerobic Decay Coefficient for X_H	0.05	d^{-1}
μ_{hNmax}	Maximum Specific Anoxic Growth Rate for X_H	0.5	d^{-1}
μ_{hN}	Specific Anoxic Growth Rate for X_H	-	d^{-1}
K_{C1}	Anoxic Saturation Constant for S_C	75	$gCOD.m^{-3}$
K_{NO}	Saturation Constant for S_{NO}	15	$gN.m^{-3}$
kd_{hN}	Anoxic Decay Coefficient for X_H	0.05	d^{-1}
Stoichiometry Parameters			
Y_H	Aerobic Heterotrophic Biomass Yield Coefficient	0.42	$gVSS.gCOD^{-1}$
Y_{hN}	Anoxic Heterotrophic Biomass Yield Coefficient	0.42	$gVSS.gCOD^{-1}$
$Y_{X/N}$		1.67	$gVSS.gN\text{-}NO_3^{-1}$
$f_{N/X}$	Chemical Nitrate Demand for X_H (applicable for anoxic endogenous respiration)	0.36	$gN\text{-}NO_3.gVSS^{-1}$
Reaction Rates			
r_{XH}	Growth Rate for X_H		$gVSS.m^{-3}.d^{-1}$
r_{SC}	Removal Rate for S_C		$gCOD.m^{-3}.d^{-1}$
r_{SNO}	Removal Rate for S_{NO}		$gN\text{-}NO_3^-.m^{-3}.d^{-1}$

Appendix 2: Dynamic Simulations

SBR

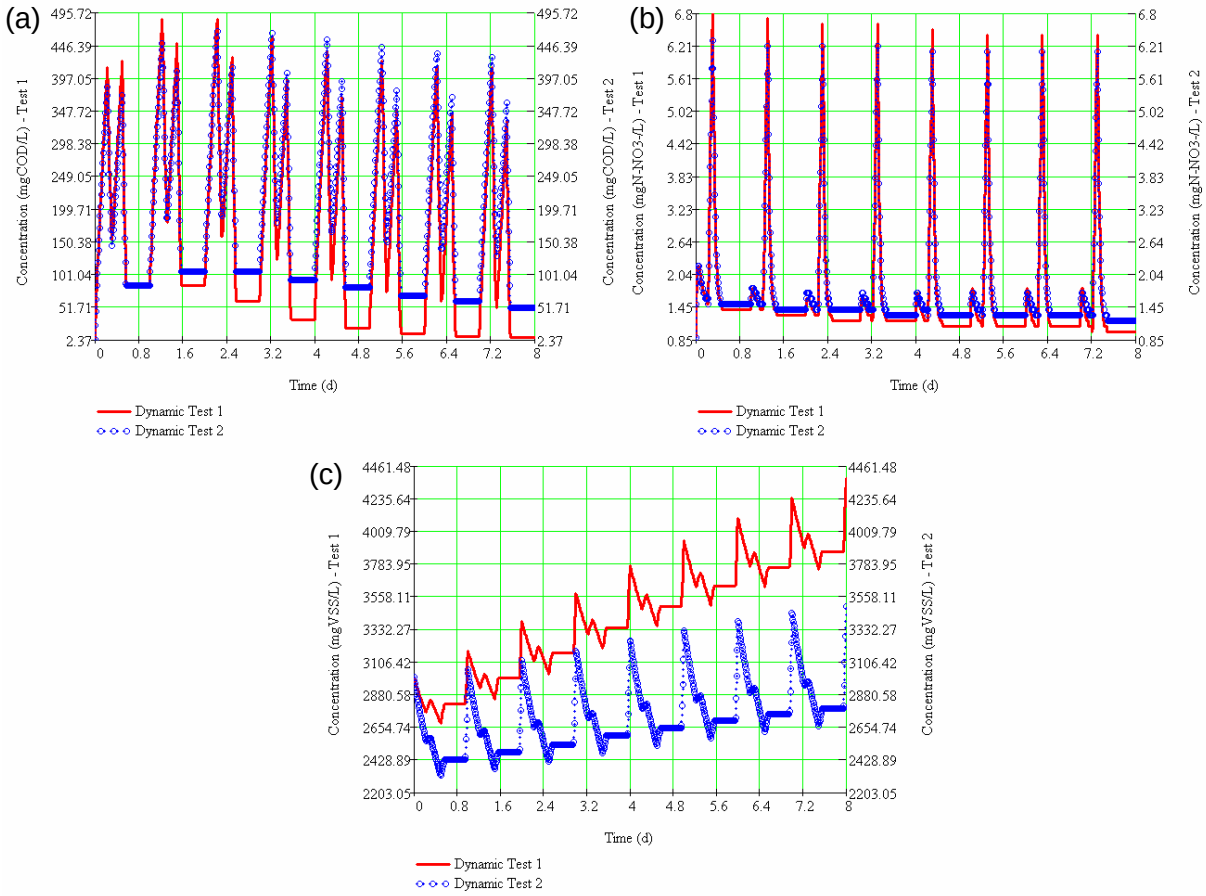

Figure A1: Dynamic simulation results for both tests: Organic Matter (a), Nitrate (b) and Biomass (c) evolution

PFRN

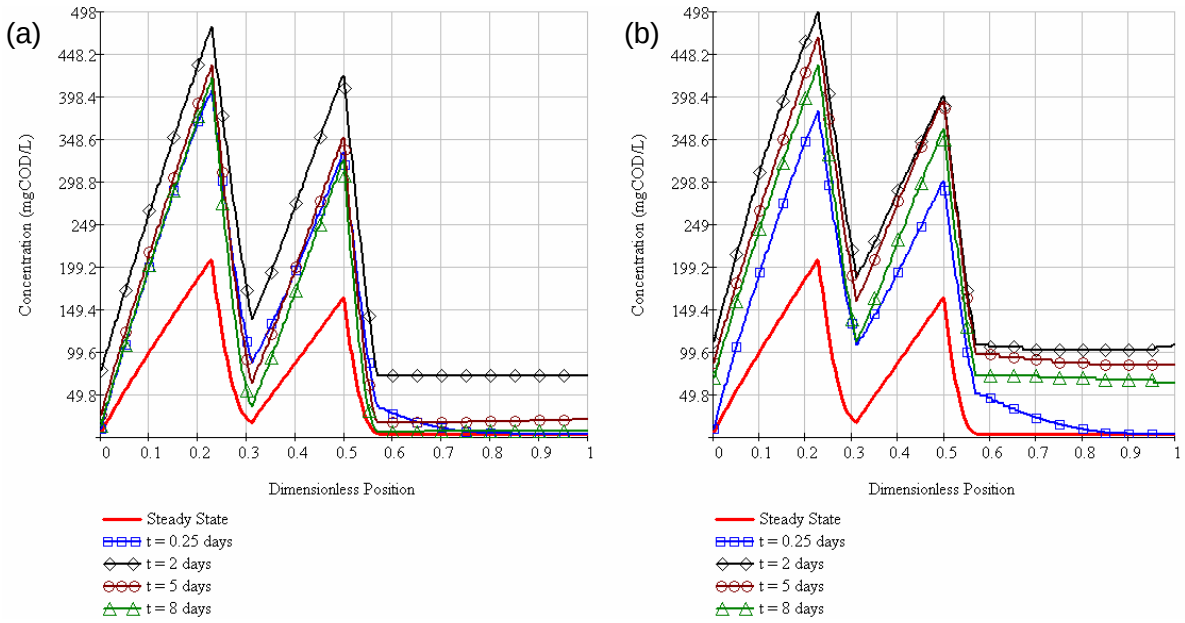

Figure A2: Dynamic simulation results for Organic Matter profiles: Test 1 (a) and Test 2 (b)

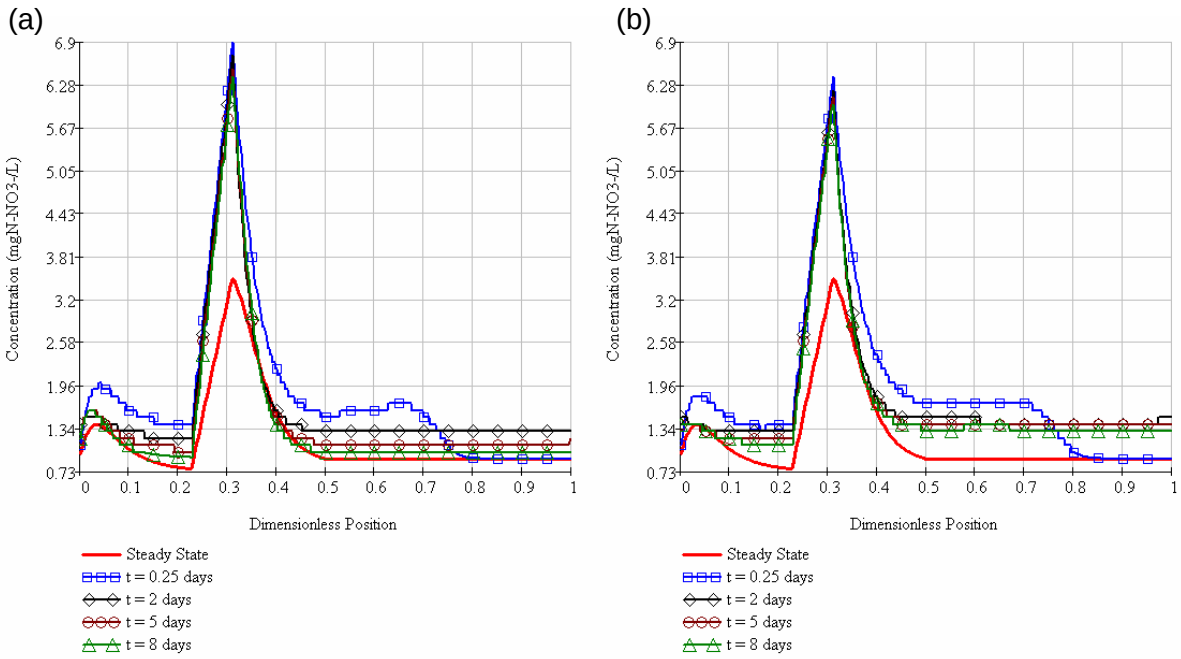

Figure A3: Dynamic simulation results for Nitrate profiles: Test 1 (a) and Test 2 (b)

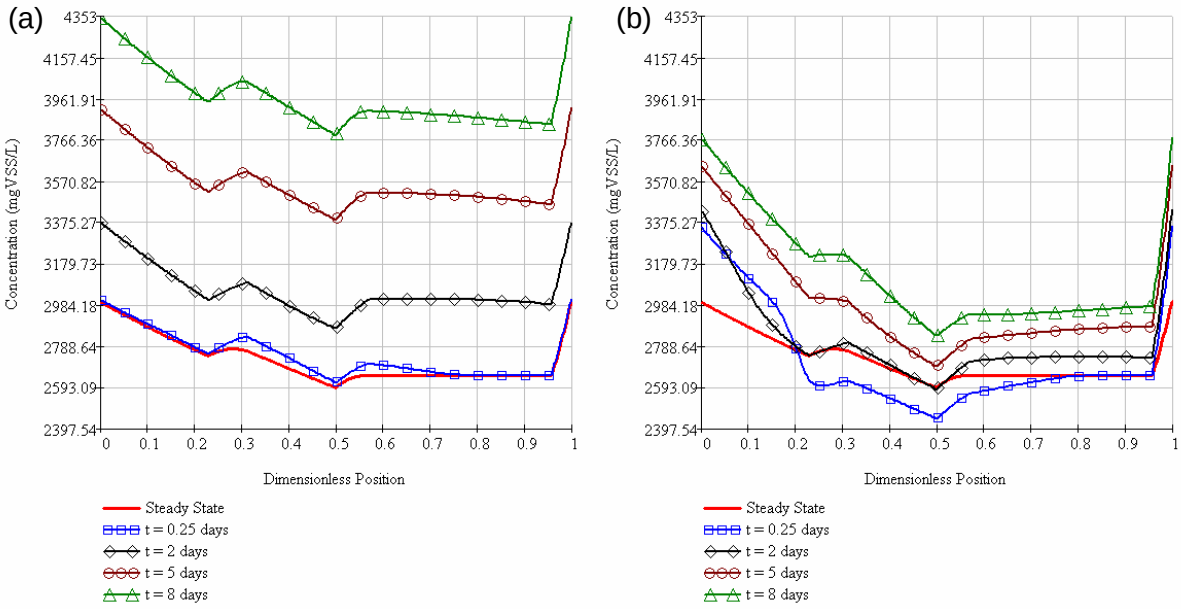

Figure A4: Dynamic simulation results for Biomass profiles: Test 1 (a) and Test 2 (b)

Proceedings of the 10th International Chemical and
Biological Engineering Conference - CHEMPOR 2008
Braga, Portugal, September 4-6, 2008
E.C. Ferreira and M. Mota (Eds.)

Systematic Modelling Framework in Product-Process Design and Development

Ricardo Morales-Rodríguez[1], Rafiqul Gani[1*]
[1] CAPEC-Department of Chemical and Biochemical Engineering, Technical University of Denmark, DK-2800 Lyngby, Denmark.

Keywords: Product Design, process design, work-flow, multi-scale modelling.
Topic: Systematic methods and tools for managing the complexity — see Process synthesis & design.

Abstract

One way to achieve success in product-process design/development is first to identify the end-use properties of a product and then to match product quality by controlling the structure, shape, odor, color, etc, of the chemical species. Usually, many repetitions of experiments need to be performed with asociated high expenses of time and material resources to find an acceptable design. A computer-aided modelling framework for product-process design is proposed as an alternative, where some of the tasks related to product-process design can be performed efficiently and systematically through an integrated set of computational tools. The application of a model-based framework specially developed for product-process design is illustrated through a case study involving the design and evaluation of a microcapsule for controlled release of active ingredients.

1 Introduction

The design, development and manufacture of a product and its process need to be consistent with the end-use characteristics of the desired product. One of the common ways to achieve the desired characteristics of the product-process is through trial and error based experiments. Although it is the most commonly used practice, it can be expensive and time consuming. An alternative approach is the introduction of a systematic model-based framework consisting of established work-flows in product-process design. In this way, some of the time consuming and/or repetitive experimental steps can be replaced with the use of reliable computational tools.

The appropriate set of models and the model-based framework for product-process design need to have multi-scale modelling features as the properties defining the chemical structure and end-use characteristics of the product are dependent on parameters of different size and time scale. The advantages of the use of multi-scale modelling approach is that the design, development and/or manufacturing of a product-process can be described at different scales of length and time, providing thereby the knowledge of the applied phenomena at diverse degrees of abstractions and details. Charpentier (2002), Gani (2004), Klatt and Marquardt (2007) and Charpentier (2007) have highlighted the importance of the multi-scale and multidiciplinary approach in product-process design and identified design issues related to different scales of size, time and complexity.

In this paper, the development and use of a model-based a framework for systematic product-process design using established work-flows is proposed. This framework will allow the design of the product-process through a set of computer-aided modelling tools by guiding

* Corresponding author. Tel + 45-4525-2882. E-mail: Rag@kt.dtu.dk

the user through the calculation steps to determine the desired product-process. Although the method and tools are generic, their application is highlighted in this paper to a class of formulated chemical products. The performance of the model-based framework, the associated models and the work-flow for a specific product-process design is illustrated through a case study involving the modelling and design of the release of a formulated pesticide product through a polymeric microcapsule. Product design, in this case, involves the design of the microcapsule and its contents (the active compound, the membrane used for the microcapsule, solvents, additives, release medium, etc.). Process design and modelling, in this case, involves the the simulation of the release of the active ingredient through the microcapsule, that is, evaluation of the product performance.

2 Development of Framework for product-process design

The framework for chemical product-process design is shown in figure 1 where chemical product-process design pathway has four main section embedded within the model-based framework:

i) Problem Definition
ii) Product Design
iii) Product-Process Modelling
iv) Product-Process Evaluation

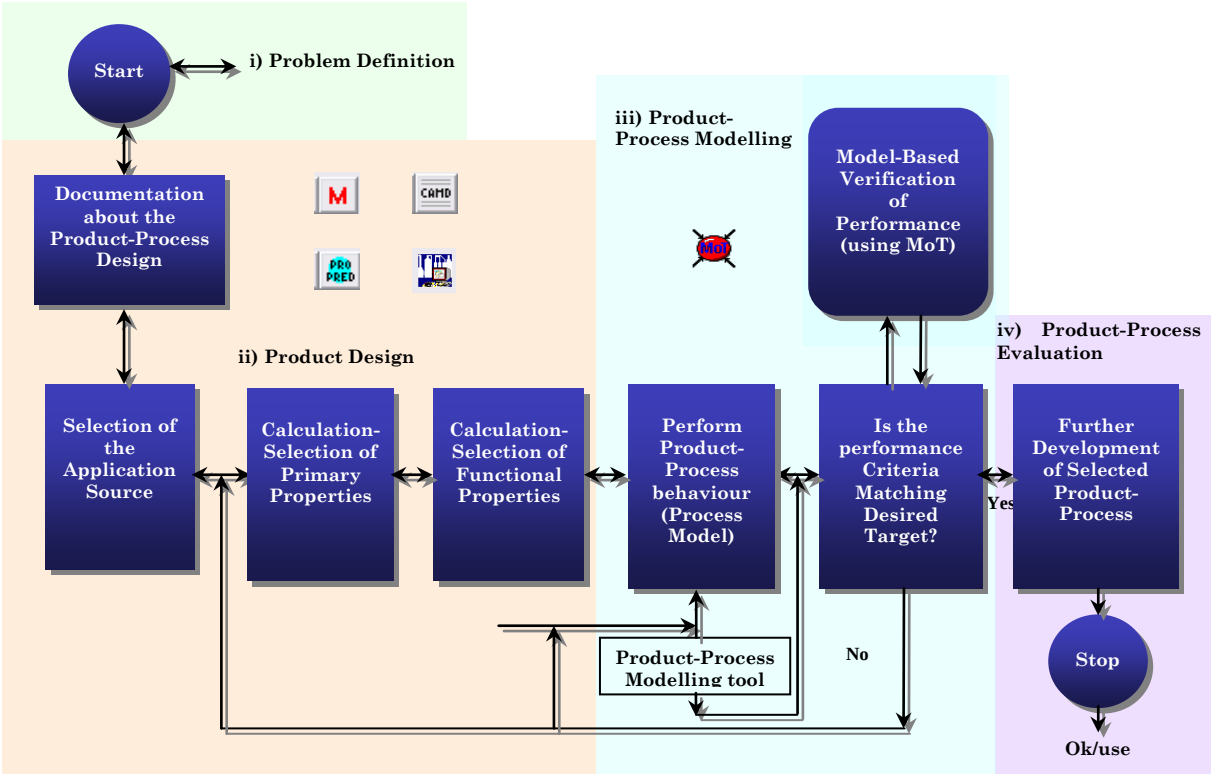

Figure 1. Systematic modelling Framework for chemical product-process design

For any chemical product-process design problem, the model-based framework guides the user though a conceptual problem definition steps, which concerns the definitions of desired characteristics of the products, its properties, its needs, and its qualities. This is true for a new product or an existing product that needs an improvement.

The product design step consists of sub-steps for design and/or selection of product alternatives; a sub-step to generate data/knowledge related to the modelling needs for product-process behaviour and evaluation; and a sub-step for product design problem definition in terms of property targets.

In the next product-process modelling step, prediction/verification of the product behaviour is performed through the use of different computer-aided tools whitin the model-based framework. Also, a comparison of the results from the current process analysis and desired target is carried out to validate the quality of the designed product.

Further developments of the product-process is evaluated in the last step of the model-based framework for chemical product-process design before the production/manufacture of the designed product.

The model-based framework to be useful for chemical product-process design, different computer-aided modelling tools are necessary. For instance; modelling tools (ICAS-MoT), model-based libraries, databases (database manager), property prediction package (ProPred), solvent selections and molecular design software (CAMD), etc. where, the use of the methods and tools are related in accordance with the different products and phenomenon behaviour. All these software suites are available in the Integrated Computer Aided Software (ICAS) developed by Computer Aided Process Engineering Center (CAPEC) at Technical University of Denmark (DTU).

Work-flows, their corresponding data-flows as well as methods/tools needed for the different calculaion steps are usually associated with the product to be designed. That is, the amount of “knowledge” (data-flows) and the needed sequence of steps (work-flow) are related to the kind of product that is to be created. For example, after the problem definition and the generation of relevant documentation, the next step is to select-calculate the design properties (such as, application source, active ingredients, additives, solvents, etc. are the main steps in product design). Here, documentation, databases and search engines (for data retrieval) play an important role in the model-based framework as these tools are useful to verify some properties and available information during the creation and development of the product. Therefore, product design consists in the selection of the material of the product, the main ingredient, solvent/additives in the product, etc., as well as the calculation of the necessary product properties. In the analysis of the behaviour of the product as, thermodynamic properties, physical properties, etc.; frequently, the lack of information to perform the behaviour of the product is found; so as to overcome those gaps of information, computer-aided methods and tools can be applied to address this issue. The properties calculated in this part of the product-process design framework, for instance, diffusion coefficients, partition coefficients, viscosities of compounds and/or mixture, mass and heat transfer coefficients and so on, are transferred (data-flow) to the product-process modeling tools to carried out the calculation of the product-process behaviour.

Once, the complete information and characteristics about the product have been chosen; product behaviour and performance can be carried out. Here, modelling tools can assist in the simulation, generation of alternatives and verification of the formulation properties through the use of ICAS-MoT, that basically is a modelling tool able to perform the generation/analysis/simulation of mathematical models without extra programming effort; at this point, the values of target variables are calculated based in the information obtained from

property model section.

Subsequently, simulation results of product behaviour is compared with the desired targets established at the beginning and decide if the targets have been matched? If, “No”, new design of the product is started, or, an adjustement or analysis of the mathematical model is made to repeat the subsequent steps; if, “Yes”, before starting the production of the product; product-process performance verification is performed through the use of the modelling tools (for instances, ICAS-MoT). Furthermore, a sustainability analysis may also be carried out in order to evaluate the environmental impact of the production and performance of the product.

The work-flow for any specific product-process design is different and therefore, the corresponding data (knowledge), models, methods and tools needed for the various calculation steps in the work-flow need to be identified, However, in general terms, the following main steps are followed in many formulated chemical product design:

- Define product-needs in terms of target (design) properties
- Generate product (molecule, mixture, formulation, etc.) alternatives
- Determine if process considerations are important
- If yes, define the process design problem and solve/create it
- If no, go directly to the product evaluation (analysis) step
- Analyse the product-process in terms of a defined set of performance criteria

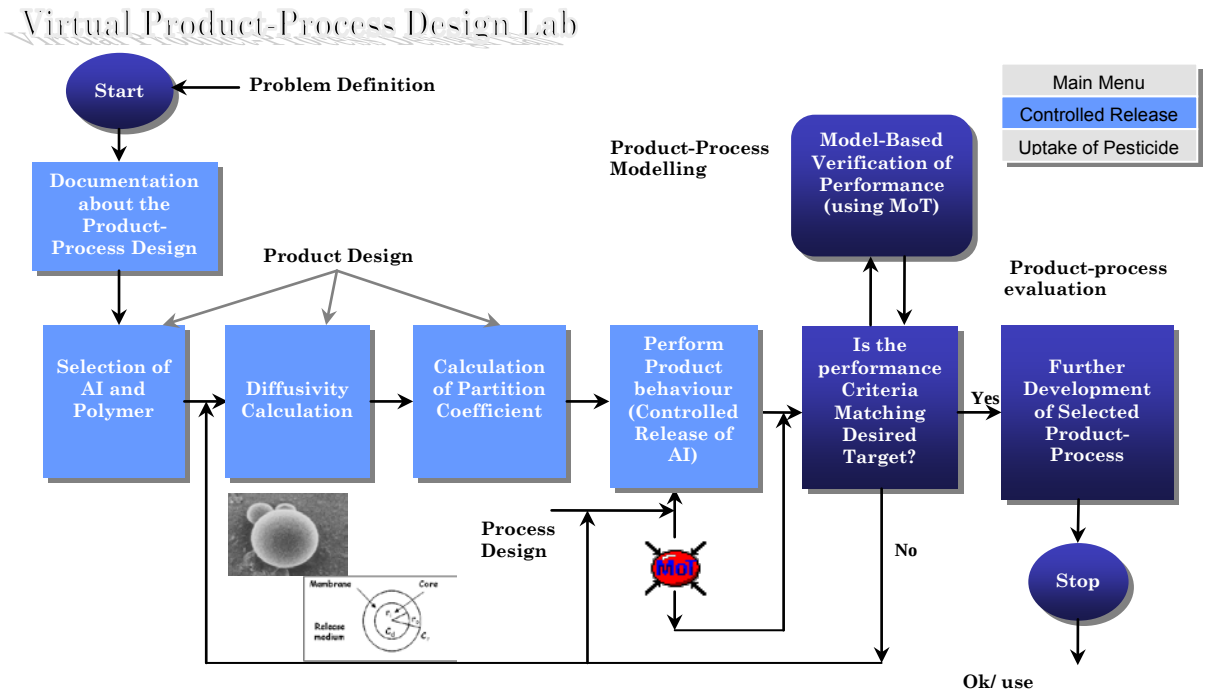

Figure 2. Virtual product-process design lab

A framework (see fig. 1) is neccesary to allow the work-flow to function by producing the different needs for each calculation step. From an analysis of the model and data used through this framework for any specific work-flow, it is easy to observe that product-process design problems are by nature, multidisciplinary and multi-scale and the gaps among the different disciplines/scales need to be bridged for efficient methods of solution. Also, this

model-based framework requires the interaction between human and computer, where human is handling and controlling the work-flow while the computer is carrying out the calculations in the work-flow and most of the tasks in the data-flow. It is important to highlight that the performance of this computer-aided system will depend on the availability of appropriate models and the ability to quickly generate them.

3 Design of a controlled release for microcapsule through the use of the systematic modelling framework for Product-Process Design.

A software called the "Virtual Product-Process Design Lab" has been developed by implementing the model–based framework for chemical product-process design. Currently, the software contains model-based libraries for design/analysis of controlled release and pesticide uptake. Figure 2 illustrates the work-flow related to design for controlled release though microcapsules.

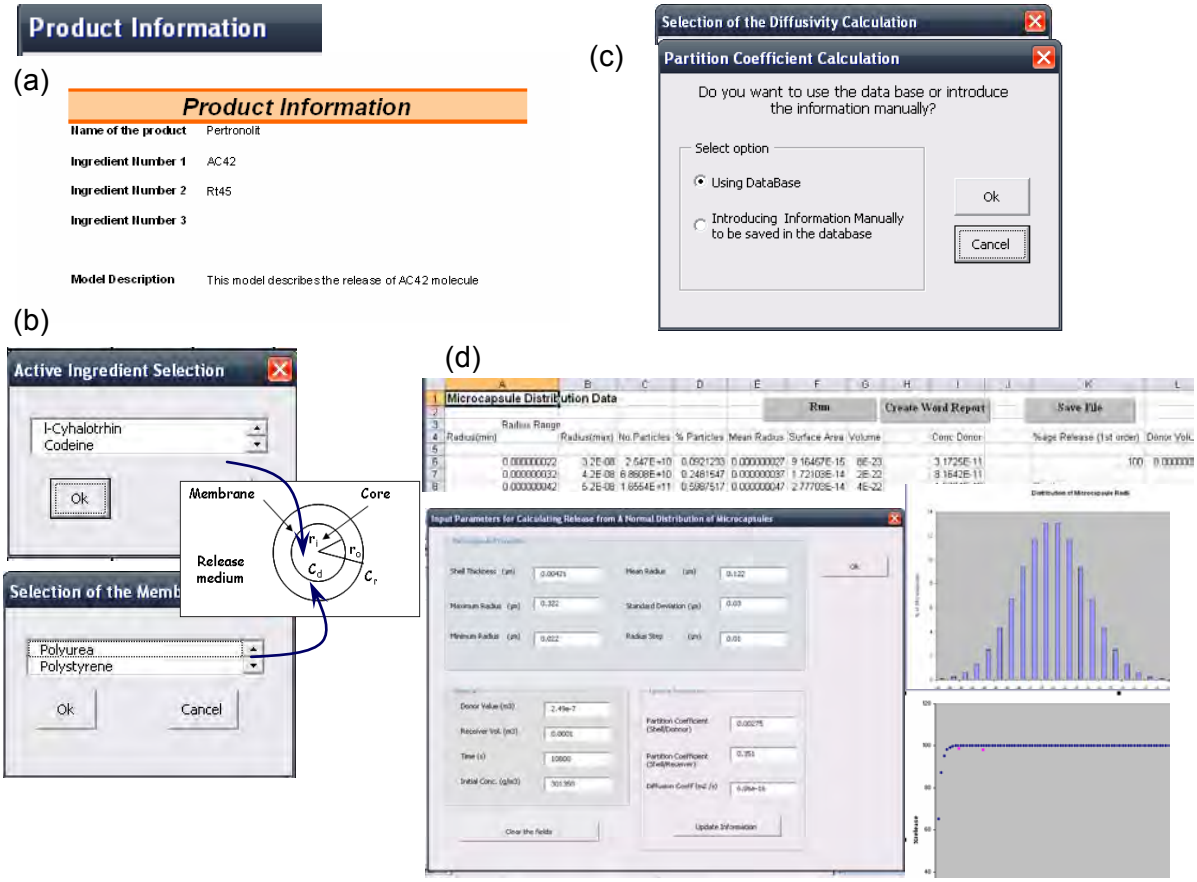

Figure 3. Design of the microcapsule controlled release

Figures 3a-3d illustrate the different steps of the work-flow for design/analysis of controlled release through microcapsules. Figure 3a shows the first step involving the generation of the documentation for the new product, where information related to model assumptions, ingredients of the product, etc., are given and saved in a documentation file. Figure 3b highlights the selection of the active ingredient and the polymer to be used for the microcapsule. Figure 3c highlights the calculation of the diffusivity and partition coefficients using the mathematical models proposed by Muro-Sune (2005), which are necessary for the microcapsule design calculations. Figure 3d highlights the performance simulation step. That is, once, all the information about the ingredients and polymers (specifically diffusion partition

coefficients) have been generated/obtained; an excel interface using the model for controlled release through a microcapsule is used in order to predict the product behaviour. Here, plots of the distribution of microcapsules according to size and number and the percent release of the active ingredient as a function of time are highlighted. At this point, it is possible to ask whether the performance criteria have matched the desired target, if “Yes” a new product alternative has been found. Otherwise, it is possible to return to the product design steps and try with other options until the target criteria are reached.

4 Conclusions

A model-based framework for systematic product-process design has been developed and its application illustrated through the design/analysis of controlled release of a pesticide active ingredient through a microcapsule. This important aspect has been demonstrated for virtual design of new products with the desired end-used characteristics without the use of a trial and error experimental-based approach but recommending the use of experiments only to verify the final product selection.

Finally, for the virtual product-process design lab to succeed, reliable models must be available in a model-library and used through an appropriate model-based framework, that can also help to generate models, when they are not available.

The framework provides the architecture needed for a software to implement specific work-flows of product-process design and defines the integration issues related to multi-scale models, methods, tools and data from various sources.

References

Charpentier, J.C. (2002). The Triplet “molecular processes-product-process” engineering: the future of chemical engineering?. *Computers and Chemical Engineering*, 57, 4667-4690.

Charpentier, J.C. (2007). Among the trends for a modern chemical engineering: CAPE an efficient tool for process intensification and product design and engineering. In V. Plesu & P.S. Agachi (Eds.), ESCAPE-17: Vol. CACE 24 (pp. 11-18). The Netherlands: Elsevier.

Gani, R. (2004). Chemical product design: challenges and opportunities. *Computers and Chemical Engineering*, 28, 2441-2457.

Klatt, K.U., Marquardt, W. (2007). Perspectives for Process systems Engineering – a Personal View from Academy and Industry. In V. Plesu & P.S. Agachi (Eds.), ESCAPE-17: Vol. CACE 24 (pp. 19-32). The Netherlands: Elsevier.

Muro-Sune, N. (2005). Prediction of solubility and diffusion properties of pesticides polymers, *PhD Thesis*, Technical University of Denmark.

Proceedings of the 10th International Chemical and
Biological Engineering Conference - CHEMPOR 2008
Braga, Portugal, September 4-6, 2008
E.C. Ferreira and M. Mota (Eds.)

Combining Predictions at Multiple Scales for Process Modelling

Marco S. Reis *
Department of Chemical Engineering, University of Coimbra
Rua Sílvio Lima, 3030-790, Coimbra, Portugal

Keywords: Multiscale modelling, Wavelets, Data-driven modelling, Time series
Topic: Multiscale modelling

Abstract

An inductive data-driven multiscale framework for empirical process modelling is presented. This approach essentially consists of combining independently estimated models for the different scales of data representation obtained with the wavelet decomposition. Such transformation is performed over a receding horizon moving window of data, with dyadic length, that always includes the last observation, in order to enable the on-line application of the proposed procedure. The scales, whose models will be combined, are selected on the basis of their prediction accuracy, and those not showing good prediction performance during the preliminary assessment, that essentially consist of unstructured variation, are discarded from the analysis. An illustrative example, consisting of a non-isothermal dynamic CSTR under feedback control shows the method's potentialities when compared to their single-scale counterparts, in particular when addressing prediction problems when the output variable has most of its energy concentrated in intermediate or higher (coarser) time-scales, i.e., when the focus of prediction is not strictly at the finest scale.

1 Introduction

Process modelling plays a central role in Chemical Engineering, as virtually any activity in this field requires a simplified description of reality, i.e., a model. Multiscale modelling, is a class of modelling approaches that has recently gained momentum with new and relevant applications emerging in engineering, where the phenomena to be simultaneously addressed appear spread through different scales of length and operating at different scales of time. In fact, this is not a new problem for chemical engineers. For instance, the dynamic analysis of fixed bed catalytic reactors does require the simultaneous modelling of phenomena going on in the catalytic particle and in the bulk phases of the reactor. However, such traditional analysis usually led, after some simplifications, to modelling at a single scale, with appropriate boundary conditions linking phenomena at different scales. Current applications are however more demanding in the way the vertical integration of all relevant scales for the problem at hand is accomplished. For instance, as we move down to the micro- and nano-scales, in order to analyze, design, control and monitor systems and operations at such fine scales, the whole hierarchy of phenomena occurring at the different, intermediate scales of length and time must be necessarily addressed and properly combined. It is also becoming increasingly evident that some class of systems do exhibit very well defined scale dependent associations and dynamics, notably biologic complex systems (Butts et al., 2007; de la Rocha et al., 2007; Henzler-Wildman et al., 2007).

Significant advances have been achieved in modelling multiscale systems, using first principles approaches (Braatz et al., 2004; Charpentier and McKenna, 2004; Li and Kwauk, 2003; Li and Christofides, 2005). However, another paradigm of multiscale modelling should also be developed, in order to properly address those situations where large amounts of data are available, that are generated from phenomena occurring at different scales, but where fundamental knowledge of the underlying mechanisms is incomplete or even inexistent. Such data-driven multiscale modelling of systems, is therefore an area demanding for new

* Corresponding author. Tel + 351-239-798700. E-mail:marco@eq.uc.pt

developments, to keep the pace of the challenges raised by modern science, namely by the large amounts of information currently being made available with the recently developed measurement techniques, that now require proper processing and integration in order to generate useful information about the systems.

In this communication, we present an approach for data-driven modelling, where predictions computed from models estimated at different scales are properly combined, after a preliminary stage of scale selection. Such an approach is focused on prediction ability and is implemented according to a well defined and coherent sequence of steps, which can be performed quite efficiently, leading to potential improvements in the time and efforts spent in complex system identification tasks.

2 Methods

The multiscale data-driven modelling approach essentially consists on independently estimating models at different scales, using the wavelet transform coefficients of a receding horizon sliding window that always includes the last measured values, in order to make the resulting model adequate for on-line use (Figure 1).

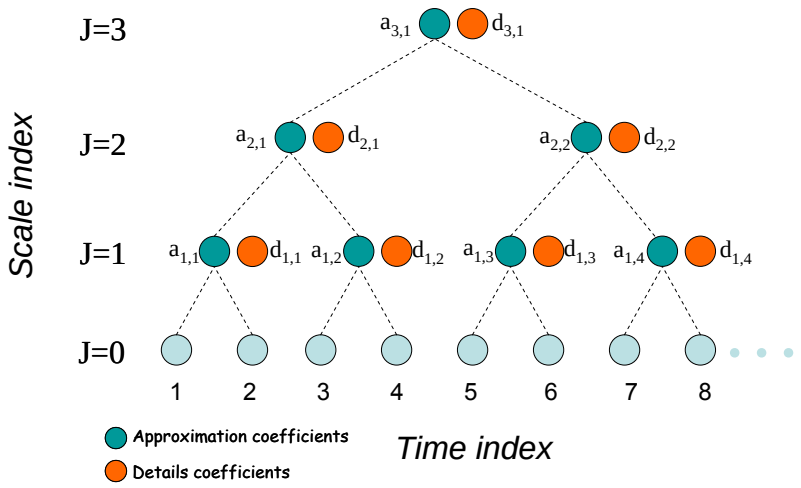

Figure 1. Scheme illustrating the computation of wavelet coefficients, starting from the finest scale representation of data, at scale $j = 0$, and recursively proceeding to coarser scales. In this case, the decomposition depth used was three ($J_{dec} = 3$), and the recursive relationship linking coefficients at different scales is the one for the Haar wavelet transform. In the proposed framework, this window of data is successively shifted in order to always include the last measured value.

The procedure is essentially based on a well defined sequence of steps (Figure 2). Simple models are first estimated at each scale in order to infer their prediction ability. The use of simple models in this task is a direct consequence of the decorrelation ability of the wavelet transform, that approximately diagonalise the variables' autocorrelation matrix, meaning, in practice, that simpler model structures are enough for capturing the dynamic behaviour at each scale (Dijkerman and Mazumdar, 1994; Golden, 1991). Analyzing these results, the relevant scales to include in such a multiscale modelling can be selected (those with predictive information power), after which the final model structure is again re-estimated and fine tuned.

The final model will consist of a set of models at different scales, that provide independent estimates for any value to be estimated. Such estimates, arising from different scales, are

then combined upon application of the inverse wavelet transform (using only the selected scales) in order to get the desired estimated value at the finest scale.

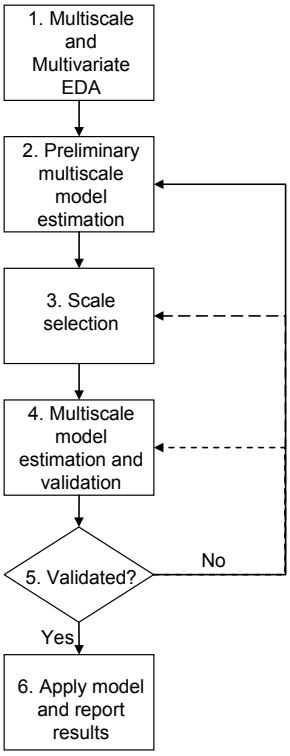

Figure 2. Basic sequence of steps for conducting the proposed multiscale data-driven system identification methodology.

3 Illustrative Example

In this section we illustrate the application of the proposed procedure for multiscale combination of predictions. In order to have the complete knowledge about the true values of the output variables, necessary for properly assessing and comparing our methodology with its single-scale counterparts, it was applied to a system which is complex enough to exhibit most of the features of complex processes, namely multiscale dynamics, but whose true values are known, for the sake of computing accurate prediction performance metrics. The system consists of a simulated industrial non-isothermal CSTR operating under feedback control, where an irreversible and exothermic first order reaction (A→B) takes place (Luyben, 1990; Reis and Saraiva, 2006). There are 10 variables involved in this process, collected every 10s, and the main purpose is to identify and estimate a proper model for predicting the composition of reactant A (CA) in the outlet stream, using all variables available (i.e., the goal is essentially to develop a soft sensor for CA). The data set used for the estimation tasks is composed by 10000 observations (~28h of continuous operation), while a second group of data, also with 10000 observations, constitutes a test set, based on which the prediction performance relative to each model structure is computed.

Following the procedure presented in Figure 1, after a preliminary stage of exploratory data analysis, simple models were estimated at each scale. The predictions thus obtained as a function of the respective measured values, are presented in Figure 3, where it is possible to see that some scales do present good prediction ability regarding CA for the phenomena contained in their frequency range (those relative to the three plots in the lower row of

graphics), whereas others do not (see plots in the upper row) and therefore should be removed from the analysis.

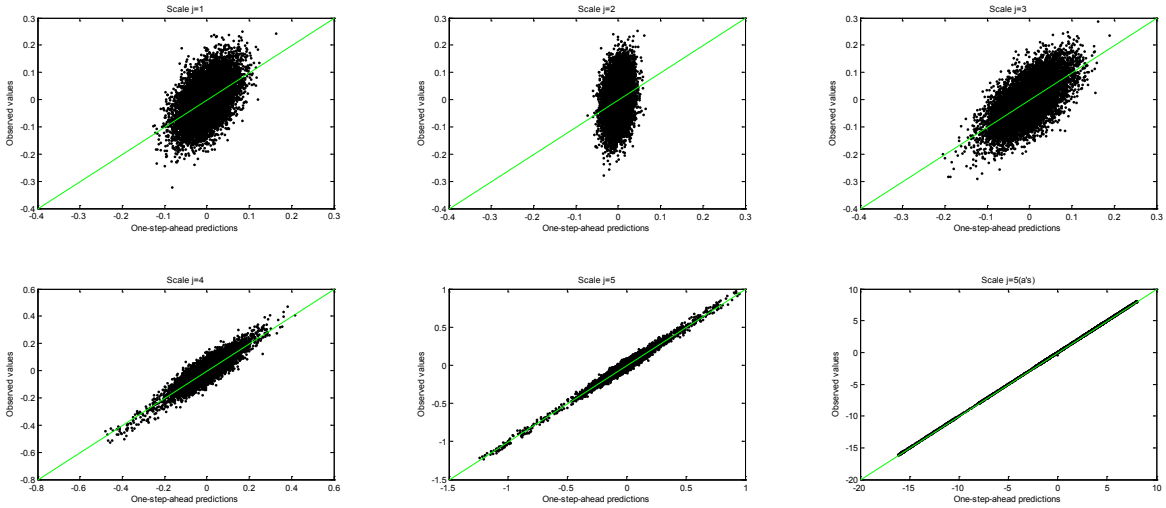

Figure 3. Plots of predicted versus observed values for CA at each scale, using independent ARX(1,1) model structures (Box et al., 1994).

Selecting the relevant scales in this way (namely, j=4, 5 and the approximation coefficients for scale j=5), and apply the estimated multiscale model to perform one-step-ahead predictions over the test set, the results presented in Table 1 were obtained, where RMSEP stands for the root mean square error of prediction, computed using both the real values of CA as a reference (since we are using a simulates system) and the observed values as reference (the true values plus additive noise). Such results do show the superiority of the proposed approach regarding the single-scale counterparts.

Table 1. Prediction results obtained (RMSEP).

RMSEP	***MS-ARX(1,1)***	***ARX(1,1)***	**ARX(2,2)**
Observed	0.0820	0.1065	0.0900
Real	0.0422	0.0806	0.0570

Figure 4 provides a graphical picture of the performance achieved with the multiscale method, where it can be seen that this method has an inherent ability to simultaneously perform prediction and filtering activities, being quite insensible to noise present in data. This observation arises from the preliminary elimination of scales containing mostly unstructured variation, focusing the modeling and predictions efforts only on those scales that really carry information about the output variable.

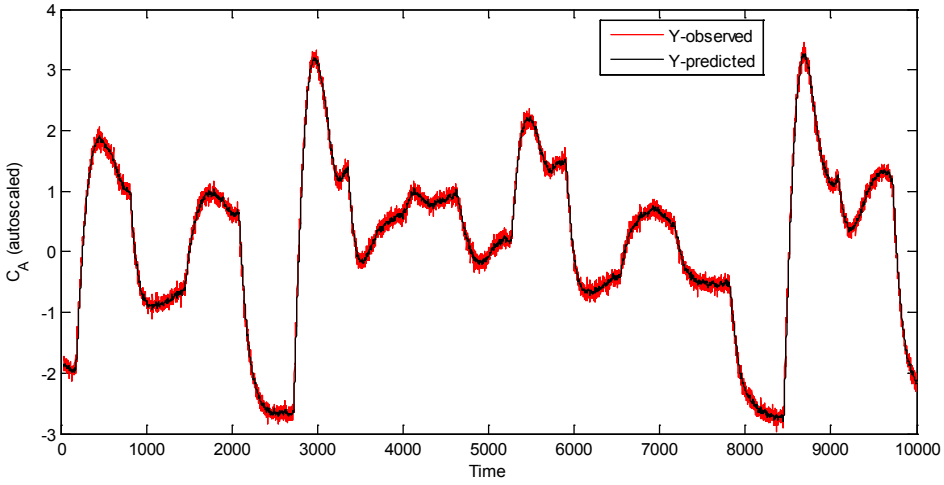

Figure 4. One-step-ahead predictions for CA (at the original scale), using the multiscale model structure with independent ARX(1,1) models at scales 4 and 5.

4 Conclusions

A model structure consisting of assemblies of black-box models describing system evolution at different scales of time (or frequency bands) is proposed, the result of which, once combined by the inverse wavelet transform, give rise to the predicted response at the finest scale. In the illustrative example presented, better predictive results were obtained when comparing to the classical single-scale approaches. The proposed systematic methodology also allows for an effective reduction in the analysis time of complex data sets, as well as brings important concepts to the core of the analysis, such as those leading to the selection of scales with predictive power, something that is absent from other current approaches. Such a multiscale approach can bring new added value to the analysis of problems where the output variable has most of its energy concentrated in intermediate or higher (coarser) time-scales, i.e., when the focus of prediction is not strictly at the finest scale.

References

Box, G.E.P., Jenkins, G.M., Reinsel, G.C. (1994). Time Series Analysis - Forecasting and Control. Prentice Hall, Upper Saddle River, NJ.

Braatz, R.D., Alkire, R.C., Rusli, E., Drews, T.O. (2004). Multiscale Systems Engineering with Application to Chemical Reaction Processes. *Chemical Engineering Science*, 59, 5623-5628.

Butts, D.A., Weng, C., Jin, J., Yeh, C.-I., Lesica, N.A., Alonso, J.-A., Stanley, G.B. (2007). Temporal Precision in the Neural Code and the Timescales of Natural Vision. *Nature*, 449, 92-95.

Charpentier, J.C., McKenna, T.F. (2004). Managing Complex Systems: Some Trends for the Future of Chemical and Process Engineering. *Chemical Engineering Science*, 59, 1617-1640.

de la Rocha, J., Doiron, B., Shea-Brown, E., Josić, K., Reyes, A. (2007). Correlation Between Neural Spike Trains Increases with Firing Rate. *Nature*, 448, 802-806.

Dijkerman, R.W., Mazumdar, R.R. (1994). Wavelet Representations of Stochastic Processes and Multiresolution Stochastic Models. *IEEE Transactions on Signal Processing*, 42(7), 1640-1652.

Golden, S.A. (1991). Identifying Multiscale Statistical Models Using the Wavelet Transform. MSc. Thesis, MIT.

Henzler-Wildman, K.A., Lei, M., Thai, V., Kerns, S.J., Karplus, M., Kern, D. (2007). A Hierarchy of Timescales in Protein Dynamics is Linked to Enzyme Catalysis. *Nature*, 450, 913-916.

Li, J., Kwauk, M. (2003). Exploring Complex Systems in Chemical Engineering - The Multi-Scale Methodology. *Chemical Engineering Science*, 58, 521-535.

Li, M., Christofides, P.D. (2005). Multi-Scale Modeling and Analysis of an Industrial HVOF Thermal Spray Process. *Chemical Engineering Science*, 60, 3649-3669.

Luyben, W.L. (1990). Process Modeling, Simulation and Control for Chemical Engineering. McGraw-Hill, New York.

Reis, M.S., Saraiva, P.M. (2006). Multiscale Statistical Process Control with Multiresolution Data. *AIChE Journal*, 52(6), 2107-2119.

Proceedings of the 10th International Chemical and
Biological Engineering Conference - CHEMPOR 2008
Braga, Portugal, September 4-6, 2008
E.C. Ferreira and M. Mota (Eds.)

Active mixing strategies for Confined Impinging Jets

M. Ashar Sultan[1], Ertugrul Erkoç[1], Ricardo J. Santos[1], Madalena M. Dias[1], José Carlos B. Lopes[1,2*]

[1] LSRE– Laboratory of Separation and Reaction Engineering
Faculdade de Engenharia da Universidade do Porto, Dept. Eng. Química
Dr. Roberto Frias, 4200-465 Porto, Portugal
[2]Fluidinova, Engenharia de Fluidos, S.A.,
TECMAIA, Rua Engº Frederico Ulrich, 2650
4470-605 Moreira da Maia - Portugal

Abstract

The effect of the feed streams pulsation on the flow dynamics in a Confined Impinging Jets (CIJ) reactor was studied in this work. Different frequencies and amplitudes are studied. The out phase pulsation of the opposed jets with frequency close to natural oscillation frequencies enhances the order of the system, yielding a well defined vortices street. The results showed that the amplitude of the jets oscillations has a strong effect on the flow dynamics, up to the extreme case where the imposed pulsation completely drives the dynamics of the system.

Introduction

Confined impinging jets (CIJ), where two opposed jet streams impinge each other in a confined mixing chamber have a wide range of applications, mainly for the production of polyurethanes in Reaction Injection Molding, RIM, and in precipitators. The flow regime in the mixing chamber can be oscillatory or self sustainable chaotic. In self sustainable chaotic flow regimes, the jet streams engulf each other in evolving vortices throughout the mixing chamber, see Figure 1 for $Re = 150$. In oscillatory flow regimes both streams flow segregatedly throughout the mixing chamber, see Figure 1 for $Re = 100$. In self sustainable chaotic flow regimes the vortices formation is associated with strong oscillations of the jets' impingement (Teixeira et al., 2005) that present frequencies around typical values, while the oscillatory flow regimes present low amplitude oscillations with very well defined frequency. Erkoç et al.(2007) reported the usage of dynamic measurements of static differential pressure signal between the two impinging jets for the determination of oscillations typical frequencies at both flow regimes.

The flow field structures occurring at self sustainable chaotic flow regimes are the main mixing mechanisms in the RIM process and other CIJ mixers, as shown in Santos et al. (2005). The efficiency of mixing in such kind of processes is critical for the quality of the product as shown from the polymerization works of Kolodziej et al. (1982 and 1986). When fast reactions are present and short mixing times are required it is of outmost importance to operate the CIJ mixers at self sustainable chaotic flow regimes. In case of RIM the process wide spreading has been seriously compromised due to failure of operation at chaotic flow regimes, either self-sustained or imposed.

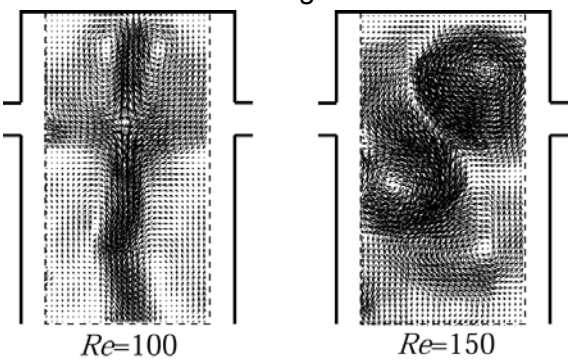

Fig. 1. Vector maps from PIV measurements at Re=100 and 150.

* Corresponding author. Tel + 351-22 -508 16 69. E-mail:lopes@fe.up.pt

From the very early works on RIM of Malguarnera and Suh (1977) it was reported that to establish a self sustainable chaotic flow regime, the Reynolds number has to be above a certain value and the momentum ratio of the jets has to be equal to one. Erkoç et. al. (2007) showed that even if these conditions are satisfied, the continuous operation of RIM at self sustainable chaotic regime is not assured, as for the same conditions, both oscillatory or self sustainable chaotic regime can be observed.

On way to assure mixing is to modulate/pulsate the jets' flowrate. The process of enhancing mixing through modulation/pulsation of the inlet flow streams is called active mixing. Bierdel and Piesche (2001) were the only authors to discuss the pulsation of jets and test the effect of pumps flow pulsation on the beginning of convective mixing in RIM. Active mixing in other CIJ reactors was studied by Deshmukh et al. (2000 and 2001), Zhongliang et al. (2002), Ito et al.(2006), although only its effect on mass transfer was analysed.

In this study, mixing is not engaged from the pulsation, since the flow field in the mixing chamber at the Reynolds number value of 300 here studied has natural advective chaotic pattern. The purpose here is to scrutinise the interaction between the flow natural oscillations and the imposed jets oscillations, namely its effect on the flow dynamics and on the shape and evolution of the natural advective chaotic patterns formed downstream the opposed jets impingement point.

CFD Model

The flow field was simulated with Fluent™ using a 2D model of the mixing chamber introduced and validated previously by Erkoç et al. (2007). Detailed results from the 2D model CFD simulations have been previously presented (Santos 2003,Santos et al.,2002 and Santos et al.,2005). Here the injectors averaged Reynolds number, Re, is defined for the 2D geometry as

$$Re = \frac{\rho \overline{v}_{inj} w}{\mu} \qquad \text{eq1}$$

where w is the injector width, which is 1.5 mm, μ is the viscosity that here is $20\text{mPa}\cdot\text{s}$, ρ is the density that here is 1200kg/m^3 and $\overline{v_{inj}} = 3.333\text{m/s}$ is the time and space average fluid velocity at the injectors. The chamber width is 10mm and the chamber height is 50mm, the injectors are locate at 5mm from the close top of the mixing chamber. The boundary conditions were set as no slip in the walls, and the liquid leaves the chamber from a pressure outlet set at atmospheric conditions. The dynamic simulations were always started from a steady state solution of the flow field for $Re = 300$. The pulsation of the jets is performed according to the following equations:

on the left injector $$v_{inj}(t)_l = \overline{v_{inj}} + A_l \overline{v_{inj}} \sin(2\pi f t) \qquad \text{eq2}$$

on the right injector $$v_{inj}(t)_r = \overline{v_{inj}} + A_r \overline{v_{inj}} \sin(2\pi f t + \varphi) \qquad \text{eq3}$$

where A_l and A_r are the left and right pulsation amplitudes, respectively, f the pulsation frequency and φ the phase displacement between the right and left injector pulsation.

Results

The previous studies of Erkoç et al. (2007) reported that in CIJ the jets impingement point oscillates with a natural oscillation frequency, ϕ. The jets impingement point oscillation frequency is around $\phi = 200\text{Hz}$ for a fluid with $\mu = 20\text{mPa}\cdot\text{s}$ in the defined 2D geometry at $Re = 300$. The tested jets flow rate oscillation frequencies are $f = \phi/2 = 100\text{Hz}$, $f = \phi = 200\text{Hz}$, and $f = 2\phi = 400\text{Hz}$ z. The simulated cases are all at $Re = 300$ and summarized in Table 1. All simulations were performed dynamically using a fixed time step of

10^{-4} s. The x component velocity, v_x, was recorded in the axis of the chamber at a distance of $z = 5$mm from the top (at the jets impingement point: P1).

Table 1 Summary of simulated active mixing strategies

Case Number	Pulsation Strategy	Amplitude and Frequency
1	No Pulsation	$A = 0$
2	Only one jet is pulsed	$A_l = 0.50, f = \phi$
3	On-Phase	$A_l = A_r = 0.50, f = \phi, \varphi = 0$
4	Out-of-Phase	$A_l = A_r = 0.25, f = \phi, \varphi = \pi$
5	Out-of-Phase	$A_l = A_r = 0.50, f = \phi, \varphi = \pi$
6	Out-of-Phase	$A_l = A_r = 1.00, f = \phi, \varphi = \pi$
7	Out-of-Phase	$A_l = A_r = 0.50, f = 2\phi, \varphi = \pi$
8	Out-of-Phase	$A_l = A_r = 0.50, f = \phi/2, \varphi = \pi$

Figure 2 shows the streamlines, at some selected time instants, of the dynamic simulations of the eight defined cases. The same flow behaviour previously reported in Santos *et al*.of the formation of a vortex street downstream the jets impingement point is observed for the eight cases. Some differences are yet observable between the flow fields:

- The vortices in Cases 2 and 3, corresponding to one side oscillation and on-phase oscillation, are more distorted, less rounded, than the case of no pulsation.
- The cases with out-of-phase pulsation present greater regularity of the vortex street, namely Cases 4, 5, 6 and 8 except for Case 7, where pulsation frequency is 2ϕ.

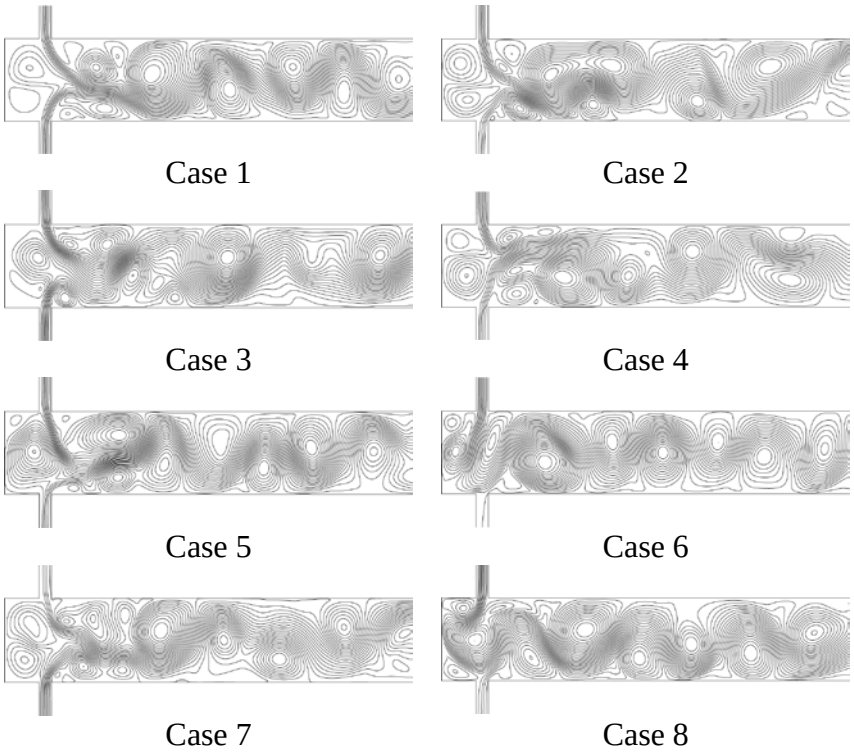

Fig. 2. Streamlines of flow field in the mixing chamber from the dynamic simulations at average *Re*=300, using different pulsation strategies.

For a clear image of the pulsation effect on flow dynamics, in Figure 3 it is presented the power spectra of the velocity time histories at the impingement point, P1, for the simulated

cases. The highest spectral energy values obtained from the spectra are listed in Table 2.

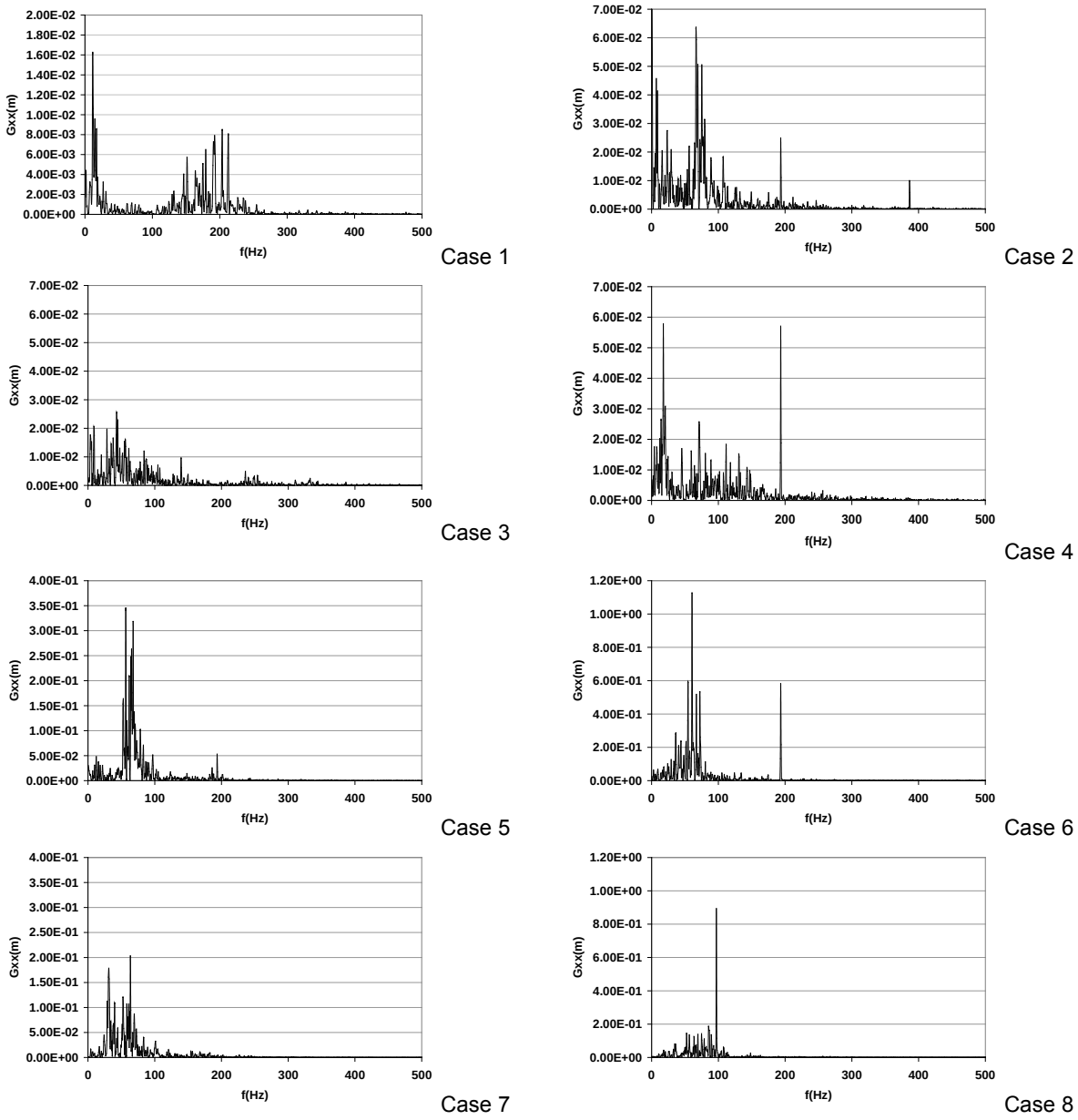

Fig. 3. Power spectra at the impingement point from the dynamic simulations at average Re=300 using different pulsation strategies.

For Case 1, where there is no pulsation applied to the system, typical frequency of the jets oscillations is $\phi = 200\text{Hz}$. The energy of the jets oscillation is much smaller than for the cases with forced pulsation as seen from Table 2, where the maximum energy value is seen to be almost one order of magnitude less than from the out-of-phase pulsation cases with $f = \phi$.

When only one of the jets is pulsed, the appearance of a lower frequency peak, between 50 and 100Hz, is observed, as can be seen in Figure 3 for Case 2. The on-phase pulsation, Case 3, presents the lowest energy peaks, since both jets are pulsated simultaneously, their strengths keep balanced and there is no significant disturbance of the jets oscillation. When a jet loses its strength, it is not compensated by the opposed jet, which is also retracted, and on the other hand when a jet increases its strength it is matched-up by the opposed jet.

Table 2 Maximum energy levels from the power spectra of v_x around f=200Hz, at the impingement point.

Case Number	Max Energy, m
1	0.00843
2	0.0247
3	0.00168
4	0.0571
5	0.0530
6	0.583
7	0.000921
8	0.894 *

The cases promoting the highest dynamics of the jets oscillations are the ones with out-of-phase perturbations, mostly the ones with the highest amplitudes. At $A_l = A_r = 1.00$, the jets oscillations are mainly determined from the imposed pulsation.

On the other cases, $A_l = A_r = 0.50$ there is a strong interaction between the flow field natural oscillations and imposed oscillations by pulsation. The resulting power spectrum, see Figure 3, shows both the influence of the natural flow oscillation, Case 1, and of the imposed jets oscillation. This result suggest that the flow field somehow preserves its own dynamics up to pulsation values of 50% of the inlet flow rate.

For Cases 4 to 6, streamline maps of Figure 2 show the earlier appearance of fully developed vortices, and when $A_l = A_r = 1.00$ the vortices are generated at the jets inlet region, which is the reason for the increase of the energy peaks in the range of 50 to 100Hz. For the double frequency oscillations, where $f = 2\phi$, Case 7, the natural flow oscillations and the imposed oscillations interact in a complex fashion cancelling the high energy peaks above 100 Hz.

The highest energy peak is obtained with a pulsation frequency of $\phi/2$, which is close to the flow oscillation frequency at the vortex street region. The pulsation frequencies probably set the whole system into resonance. From the streamlines in Figure 2, the earlier formation of the fully developed vortices at the impingement point occupying the entire mixing chamber width and evolving in perfect order to the outlet is clearly observed for Case 8.

Conclusion

In summary we studied the effect of opposed jets pulsation on the mixing dynamics and vortex formation on flow field dynamics inside the CIJ reactor. The flow dynamics had a strong effect from the pulsation frequency:

- With values close to the natural jets oscillation frequencies, ϕ, pulsation enhances the regularity of the system which results in a clear oscillatory behaviour of the jets at the impingement point.
- With values close to the natural frequency of the fully developed vortices, $\phi/2$, pulsation can force the frequency of the fully developed vortices passage and make it more orderly.

It was observed that the amplitude of the pulsation also has a strong effect on the flow field:

- Lower amplitudes can not impose to the system dynamics.
- Higher amplitudes, close to 100% of the flow rate, can completely dominate the dynamics of the flow field.

The other studied parameter was the impact of the pulsation strategy, which has shown that the strategies consisting of out-of-phase jets pulsation impose more clearly its dynamics to the system, since the displacement of the jets impingement point is completely determined

from the pulsation. One side oscillation and on-phase oscillation were not able to impose a clear influence on the flow field.

Acknowledgements

Financial support for this work was in part provided by national research grants FCT/POCTI/EQU/345115/2000, PTDC/CTM/72595/2006 and by LSRE financing by FEDER/POCI/2010, for which the authors are thankful. Ertugrul Erkoc¸ acknowledges his Ph.D./scholarship by FCT (SFRH/BD/18901/2004). Ricardo J. Santos acknowledges financial support from POCI/N010/2006.

References

Bierdel, M. and Piesche, M., CFD - Simulation and Experimental Investigation of Impingement Mixing in Reaction Injection Molding (RIM), 3rd European Congress of Chemical Engineering, (2001).

Deshmukh, A.A., Liepmann, D. and Pisano, A., *Characterization of a micro-mixing, pumping, and valving system*, Proceedings of the 11th International Conference on Solid-State Sensors and Actuators, 779-782 (2001).

Deshmukh, A.A., Liepmann, D. and Pisano, A., *Continuous micromixer with pulsatile micropumps*, Technical Digest of the IEEE Solid State Sensor and Actuator Workshop, 73-76 (2000).

Erkoç, E., Santos, R.J., Nunes, M.I., Dias, M.M., Lopes, J.C.B., *Mixing dynamics control in RIM machines*, Chemical Engineering Science, 62, 5276-5281 (2007).

Ito, Y. and Komori, S., A vibration technique for promoting liquid mixing and reaction in a microchannel, AIChE Journal, 52, 3011-3017 (2006).

Kolodziej, P., Macosko, C.W. and Ranz, W.E., *The Influence of Impingement Mixing on Striation Thickness Distribution and Properties in Fast Polyurethane Polymerisation*, Polymer Engineering and Science, 22, 388-392 (1982).

Kolodziej, P., Yang, W.P., Macosko, C.W. and Wellinghoff, S.T., *Impingement Mixing and its Effect on the Microstructure of RIM Polyurethanes*, Journal of Polymer Science, 25, 2359-2377 (1986).

Macosko CW. *RIM Fundamentals of Reaction Injection Molding*, Munich, Germany: Hanser; 1989.

Malguarnera, S.C. and Suh, N.P., *Liquid Injection Molding I. An Investigation of Impingement Mixing*, Polymer Engineering and Science, 17, 111-115 (1977).

Santos, R.J., *Mixing Mechanisms in Reaction Injection Moulding – RIM. An LDA/PIV Experimental Study and CDF Simulation*, Ph.D. Thesis in Chemical Engineering, Universidade do Porto (2003).

Santos, R.J., Teixeira, A.M., Costa, M.R.P.F.N., Lopes, J.C.B., *Operational and Design Study of RIM Machines*, International Polymer Processing Journal, 17, 387-394 (2002).

Santos, R.J., Teixeira, A.M., Lopes, J.C.B., *Study of Mixing and Chemical Reaction in RIM*, Chemical Engineering Science, 60, 2381 – 2398 (2005).

Teixeira, A.M. *Escoamento na Cabeça de Mistura de uma Máquina RIM (Flow in a RIM Machine Mixing Head)*, Ph.D. Thesis in Chemical Engineering, Universidade do Porto (2000).

Teixeira, A.M., Santos, R.J., Costa, M.R.P.F.N., Lopes, J.C.B., *Hydrodynamics in the Mixing Head of a RIM Machine: Flow Field Characterization by LDA*, AIChE Journal, 51, 1608-1619 (2005).

Zhongliang, T., Seungbae, H., Djordje, D., Vijay, M., Alan, C.W., James, Y. and Richard, M.O., *Electrokinetic flow control for composition modulation in a microchannel*, Journal of Micromechanics and Microengineering, 12, 870 (2002).

Proceedings of the 10th International Chemical and
Biological Engineering Conference - CHEMPOR 2008
Braga, Portugal, September 4-6, 2008
E.C. Ferreira and M. Mota (Eds.)

CFD simulation of an oxidation ditch

Anna Karpinska, Joana P. Pereira, Madalena M. Dias, Ricardo J. Santos*
LSRE – Laboratory of Separation and Reaction Engineering
Faculdade de Engenharia da Universidade do Porto, Dept. Eng. Química
Rua do Dr. Roberto Frias s/n, 4200-465 Porto, Portugal.

Keywords: Activated Sludge, CFD, Oxidation Ditch
Topic: Integration of life sciences & engineering

Abstract

An oxidation ditch is a modified activated sludge biological process for wastewater treatment. The oxidation ditch process, although being widespread, was rarely studied. In this work Computational Fluid Dynamics (CFD) simulations are used to make a detailed analysis of the overall transport mechanisms in the oxidation ditch: macromixing. The impact of the chosen turbulence model for the CFD simulations is also assessed. The Residence Time Distributions, i.e. macromixing, are computed for the different turbulence models. It is shown that for mixing studies the flow dynamics should always be simulated, if computationally possible. The effect of macromixing in the yield of an Activated Sludge process is computed from an ideal reactor model: Plug Flow Reactor with Recirculation. The macromixing is shown to have a determinant role in the reactor efficiency.

1 Introduction

The oxidation ditch technology was developed in Netherlands by A. Pasveer in 1950s (Pasveer, 1962) and the first full scale plant was set working in Voorschooten at Holland, in 1954 (EPA, 2000). Nowadays, oxidation ditches found application in USA in over 9200 wastewater treatment plants (EPA, 2000). The process is also commonly used in Portugal (Vila Nova de Gaia - Febros, Viana do Castelo – Areosa, Golegã...). A survey of 14 activated sludge (AS) processes in USA showed that oxidation ditches have more robust and reliable operation than other AS processes (Benefield et al., 1980), particularly in enduring unfavorable temperature conditions and with regard to nutrient removal. An oxidation ditch is a modified activated sludge biological treatment process used in Wastewater Treatment Plants having a ditch system with a single or multi-channel configuration, within a ring-, oval- or horseshoe-shaped basin, equipped with aeration and mixing devices, generally surface brush aerators. The process runs with long cell residence times resulting in high Biological Oxygen Demand (BOD) removal efficiency, average 75% – 95% up to 99% (Benefield et al., 1980; EPA, 2000). The oxidation ditches, besides BOD removal, can also perform denitrification, due to presence of zones with high and low dissolved oxygen concentration. The oxidation ditches are usually regarded as complete mix systems (EPA, 2000), although this process is still scarcely studied mainly in what regards to the flow regime.

Simulation for AS has been mostly based on ideal reactor models: Continuous Stirred Tank Reactor (CSTR) or in a cascade of CSTRs. This approach is not based in any hydrodynamics studies, but on the assumption that the reactor yield is not determined from the flow regime (mixing) because the reactions are typically slow. Most of the effort in AS simulations has then been focused on modeling the microbiology of the process (Gernay et al., 2004). One of the aims of this study is to determine the mixing behaviour in oxidation ditches from the computation of the Residence Time Distribution (RTD). The RTD is computed from Computational Fluid Dynamics (CFD) simulations of the oxidation ditch. The effect of the hydrodynamic models used in the CFD simulations will also be assessed.

* Corresponding author. Tel + 351-22 -508 14 89. E-mail:rsantos@fe.up.pt

2 CFD Model and Boundary Conditions

Geometry and boundary conditions

The CFD studies of the oxidation ditch, were conducted using Fluent™ commercial software, considering a 3D model of a scaled, oval-shaped tank with the design shown in Figure 1. The tank volume is around 30m^3. Several simulations were made to determine the grid density that would render the simulation results independent of it. The oxidation ditch system consists of an oval tank and a jet aeration device (hydrojets) that simultaneously forces the fluid circulation throughout the ditch and injects a stream saturated with oxygen. Here, the hydrojets are two slot inlets with 0.1m height extending from one side to the other and positioned at middle height of the tank. The surfaces of the inlet and outlet (0.25mx1.38m) of the ditch are placed in the top of the tank – where usually the piping system is placed. Hydrojets, inlet and outlet are opposite-sided and distant from each other for half of the length of the ditch.

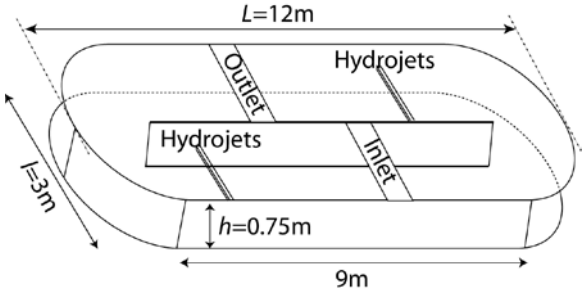

Figure 1 Drawing of the simulated geometry and boudary conditions.

Water was defined as the working fluid. Inlet of the oxidation ditch has a velocity magnitude of 0.006m/s. The hydrojets were set as momentum sources guarantying a fluid velocity of 0.3m/s, typical of oxidation ditches aerated by conventional devices, such as surface brush-type aerators.

Turbulence models

The fluid flow inside the oxidation ditch is simulated using the Reynolds Averaged Navier-Stokes (RANS), and Unsteady Reynolds Averaged Navier-Stokes (URANS) with the $k-\varepsilon$ turbulence model, and using the Large Eddy Simulation (LES) with the Smagorinsky's subgrid scale model.

RTD computing

The RTD was computed from the residence times of particles injected through the inlet in a very short period, 10^{-3}s. The particles trajectories were integrated over the flow field with Fluent™, and the flux of particles out of the tank through the outlet recorded. The physical characteristics of the particles were chosen in order to make them adjust to the flow as much as possible (Le Moullec et al., 2008). Their density is identical to the density of the water (998kg/m^3) and they are spherical having a diameter of 10^{-6}m.

3 Results and discussion

CFD results

The velocity vectors in a vertical plane of the oxidation ditch are presented in Figure 1. The same overall distribution of velocity vectors were observed within the tank for RANS and URANS simulations. The velocity vectors obtained from LES simulation distinctly differs from the others, by the appearance of vortices and of a sinuous path of the jets.

From the vector maps it is clearly seen that the hydrojets create an average flow with great stratification inside the oxidation ditch, with very few vertical transport. However from LES results it is seen that there are transient patterns that mix flow from top to bottom layers.

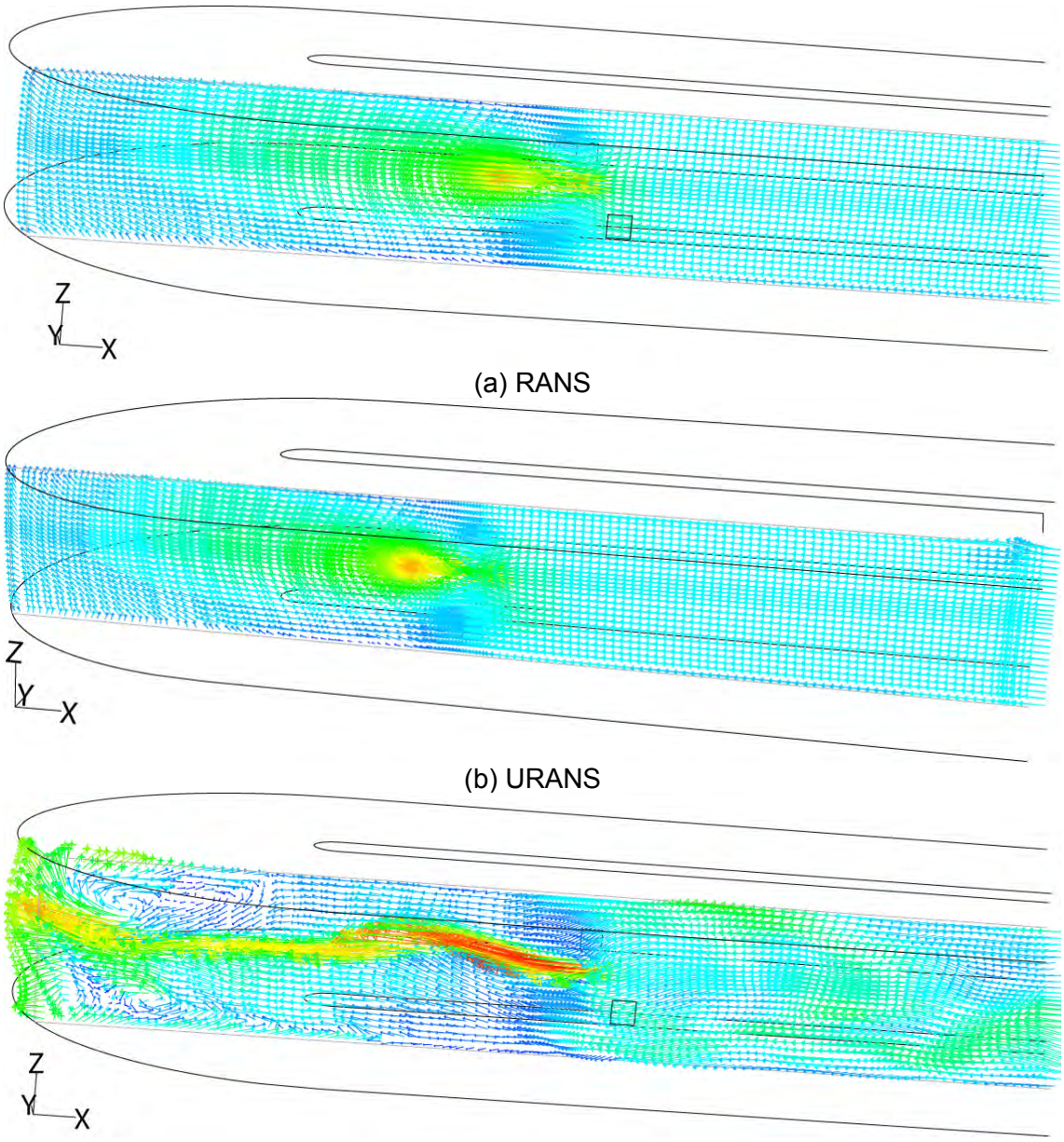

Figure 2 Maps of vectors of velocity magnitude from CFD simulations of the oxidation ditch with (a) RANS, (b) URANS, and (c) LES.

In Figure 3 are shown the RTD functions, $E(t)$, where t is time, for the simulations using the three different turbulence models: RANS, URANS and LES. Although the mean residence time of fluid in the tank is 4h=14400s, in Figure 3 plots only the first 1500s are shown, and LES was only made until 800s, due to the high computational times involved. Since the mean travel time of the flow across the entire ditch is approximately 200s, the average number of turns of fluid particles within the ditch before exiting is around 70.

For RANS and URANS there is a considerable amount of particles exiting in the first two turns, as can be seen from the peaks of the RTD around 150s and 350s. This is due to the high stratification of the flow obtained in RANS and URANS, as can be seen in Figure 2. Since particles are not being transported to lower regions of the ditch in the first turns, only a small percentage of the volume is used. The particles that go to the lower part of the ditch will be trapped there for long time, yielding a long tail in the RTD.

The results with RANS and URANS suggest that the hydrojets caused an intense vertical segregation of the flow, rendering only a part of the ditch for the actual wastewater treatment.

Although, as seen from the LES results in Figure 2, the vertical mixing mechanisms can be accounted if models that simulate the flow dynamics are used.

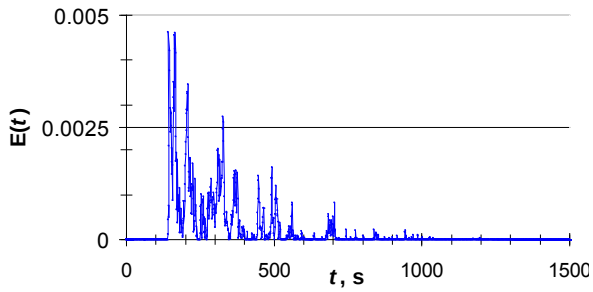

(a) RANS

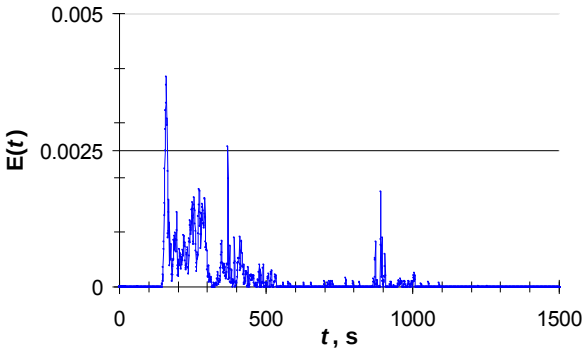

(b) URANS

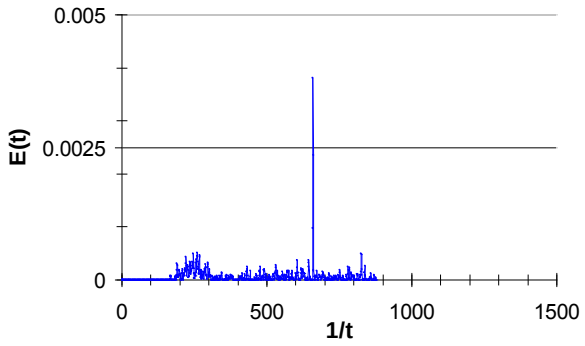

(c) LES

Figure 3 RTD from CFD simulations with (a) RANS, (b) URANS, and (c) LES.

The RTD obtained with LES does not show the peaks related with huge amounts of particles exiting in the first turns. This is due to the convective patterns observed in LES, see Figure 2, that promote transport to the lower regions of the ditch, and thus a greater fraction of the ditch volume is used.

The comparison of results from the different turbulence models is clear when the percentage of total injected particles exiting during the first 800s is considered:

- 30% for RANS;
- 20% for URANS;
- 5% for LES.

As seen from these figures the turbulence model used has a strong impact in the advection patterns took by the particles in the oxidation ditch.

Although from the RANS and URANS simulations the reactor seems to present a high percentage of dead volumes, or strong channeling from inlet to outlet, this is only due to the fact that with these models an average flow is simulated. The computation of macromixing (RTD) based on the average flow field may lead to errors. The flow dynamics underlies mixing at all its scales, both macro and micro, and thus it must always be accounted.

The differences between the turbulence models are clear from the dynamic presentation of the particles advection in the ditch, which is not possible to make on paper. The dynamic visualization of the results will be shown in the oral session at the conference.

ASM1 results

The effect of macromixing on the reactor efficiency/yield is here assessed from the Activated Sludge Model Nº 1 - ASM1, (Henze et al., 1987). The ASM1 was implemented in an ideal reactor closely approaching an oxidation ditch, a Plug Flow Reactor with Recirculation - PFRR (Pereira et al., 2008). The macromixing was changed by varying the internal circulation in the ditch. For a PFRR the RTD is given by

$$E(t) = \sum_{i=1}^{n} \delta\left(t = i \times \frac{s}{\upsilon}\right) \frac{1}{\beta + (i-1)(1+\alpha)} \qquad \text{eq. 1}$$

where δ is the Dirac function, t is the time, υ is the space velocity at the ditch cross section, s is the is the oxidation ditch length, α is the recirculation ratio from the secondary settler to the ditch, and β is the internal recirculation ratio in the ditch. The PFRR RTD is a Dirac comb with peaks spaced by s/υ having coefficients that decay at a ratio of $1+\alpha$ per fluid internal circulation. The macromixing in the PFRR is thus easily changed from the ditch length, s, and the internal circulation ratio, β.

Figure 4 shows the effect of the internal circulation parameter, β, and the cells residence time on the reactor yield in terms of substrate (BOD) and nitrate. The cells residence time is defined as

$$\tau_c(t) = \frac{1}{QX_W}\int_0^V X\, dV \qquad \text{eq. 2}$$

where QX_W is the mass flux of cells wasted from the system, X is the cells concentration and V is the reactor volume.

The ASM1 simulations were made considering the same mean residence time has in the CFD study, 4h, and using the bio-kinetics parameters of Henze et al. (1987). Complete description of the model is made in Pereira et al. (2008).

The macromixing, i.e. β, has a strong effect in the reactor yield, namely for lower values of β. For higher values of β the system tends to the case of a perfectly mixed reactor. Although the reactions in ASM1 are slow, since there are several reaction steps involved, mixing plays a relevant role in the final reactor yield. On the effect of both macro and micromixing on an oxidation ditch see Pereira et al. (2008).

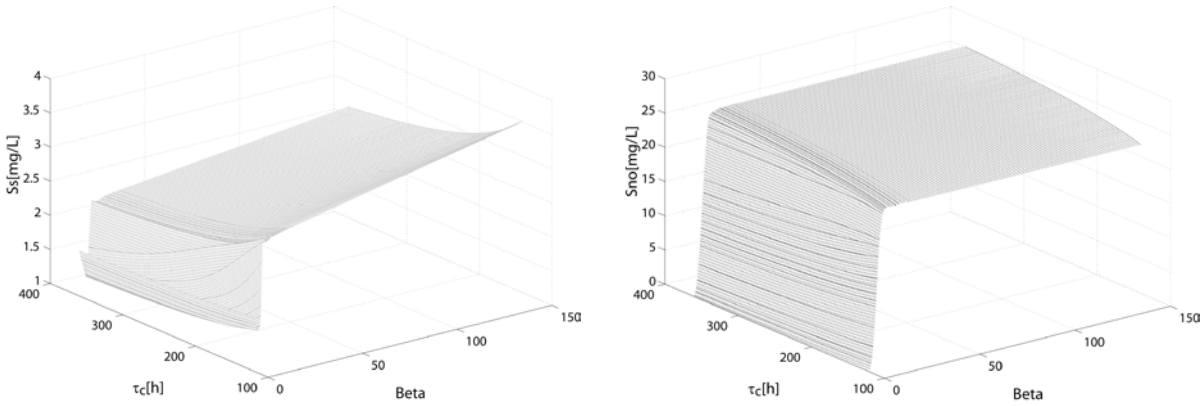

(a) (b)

Figure 4. Oxidation ditch outlet concentrations of (a) substrate and (b) nitrate for several internal circulation values (β) and cells residence time (τ_c).

4. Conclusions and future studies

In North America models such as the ASM1 are regularly used in AS processes design, while in Europe those models are more often used to set the operation parameters of running processes. Mixing is playing a key role in the AS process, but in both sides of the Atlantic it is usually regarded as secondary in comparison with bio-kinetic models.

Here it is shown the relevant role of mixing in the reactor yield. Furthermore, it is shown that the turbulence models used in reactor simulations have a strong impact in the mixing results. From the turbulence models that simulate the average flows, RANS and URANS, mixing is underestimated, as expected. The results of these models may lead to decisions such as introducing baffles to eliminate flow vertical segregation, which can reveal being useless, as seen from the results of LES.

Acknowledgements

Financial support for this work was in part provided by national research grant FCT PTDC/AMB/65983/2006 and by LSRE financing by FEDER/POCI/2010, for which the authors are thankful. Ricardo J. Santos acknowledges financial support from POCI/N010/2006.

References

Benefield, L.D., Randall, C.W. (1980). *Biological Process Design for Wastewater Treatment*. Series in Environmental Sciencies, Prentice Hall, Inc.

EPA (2000), *Wastewater Technology Fact Sheet. Oxidation Ditches*, United States Environmental Protection Agency.

Gernaey KV, Loosdrecht MCM, Henze M, Lind M, Jørgensen SB. (2004). Activated sludge wastewater treatment plant modelling and simulation: state of the art. *Environmental Modelling & Software*, **19**, 763-783.

Henze, M., Grady, C.P.L., Jr., Gujer, W., Marais, G.v.R., Matsuo, T. (1987). *Activated Sludge Model nº 1*, IWAPRC Scientific and Technical Report Nº1, London

Le Moullec Y, Potier O, Gentric C, Leclerc JP. (2008) Flow field and residence time distribution simulation of a cross-flow gas-liquid wastewater treatment reactor using CFD. *Chemical Engineering Science*.**63**, 2436-2449.

Pasveer, A. (1962). *Verfahren und Anlage zum Reinigen von Abwasser* (Process and Device for the Purification of the Sewage). Switzerland, Pasvavant Werke.

Pereira, J.P., Karpinska, A., Martins, A.A., Dias, M.M., Santos, R.J., (2008) Study of Mixing Effects on Simulation Results for ASM. *1st IWA/WEF Wastewater Treatment Modelling Seminar*. Québec, Canada.

Proceedings of the 10th International Chemical and
Biological Engineering Conference - CHEMPOR 2008
Braga, Portugal, September 4-6, 2008
E.C. Ferreira and M. Mota (Eds.)

CFD Modelling of Trickle-bed reactor in the Catalytic Wet Air Oxidation of Syringic Acid

Rodrigo J.G. Lopes, Rosa Quinta-Ferreira*
GERSE – Group on Environmental, Reaction and Separation Engineering
Department of Chemical Engineering, University of Coimbra
Rua Sílvio Lima, Polo II – Pinhal de Marrocos, 3030-790 Coimbra, Portugal

Keywords: Computational Fluid Dynamics, Multiphase flow, Trickle-bed reactor.
Topic: Multi-scale and multi-disciplinary approach to process-product innovation: CFD & Chemical Engineering.

Abstract

A computational fluid dynamic (CFD) model based on Euler-Euler multiphase approach is presented for a trickle-bed reactor (TBR). The hydrodynamic model is developed with the integration of interphase momentum exchange terms between gas, liquid and solid phases. The interphase coupling parameters are assembled in the momentum balance by means of interstitial velocities and phase volume fractions. A case study comprising the catalytic wet air oxidation (CWAO) of a phenolic acid pollutant is considered at different liquid superficial velocities and operating pressures.

Total organic carbon (TOC) conversion profiles are evaluated radially at different bed heights. Poor radial mixing is remarkable mainly for high liquid flow rates whereas operating pressure at the same liquid superficial velocity only has a minor effect in the radial TOC depletion rate. Afterwards, the Eulerian model was used to probe the interaction of hydrodynamic parameters and chemical reaction. Different catalyst wetting levels were detected which reflect the existence of certain gas-liquid flow maldistribution and local temperature variation.

1 Introduction

Multiphase flows are often encountered in environmental reaction engineering and the knowledge of computational transport phenomena models for the practical analysis of such complex chemical processes is far from being complete. In fact, three-phase systems related with CWAO in the treatment of liquid effluents containing a high content of organic matter are emerging as a new application of trickle-bed reactors (Bhargava *et al*., 2006), specifically in the olive oil mill processing industries that generate a large amount of highly contaminated wastewaters in Mediterranean countries (Paraskeva and Diamadopoulos, 2006).

TBR models reported in the literature considered isothermal operation and used either a pseudo-homogeneous approach or a heterogeneous model with plug-flow for gas and liquid phase whereas others accounted for liquid flow non-uniformity and maldistribution by using an axial dispersion model (Dudukovic *et al*., 2002; Al-Dahhan *et al.*, 1997). To improve the capability of multiphase reactor models, one has to solve the complete multidimensional flow equations coupled with chemical species transport, reaction kinetics and mass and heat transport phenomena. Therefore, multicomponent reacting flows in which kinetic models are experimentally determined have to be modeled with additional phase interaction terms. This study aims to assess an Eulerian multiphase CFD model in order to investigate the phases interaction coupled with turbulence models to make use of large-scale CFD computations that can be helpful in pointing out the cause of incomplete catalyst utilization in particle-scale level.

* Corresponding author. Tel + 351-239-798723. E-mail:rosaqf@eq.uc.pt, rodrigo@eq.uc.pt

2 Mathematical Model

Taking into account the numerical power available nowadays to address complex chemical process operational and design issues, our case study outlines an alternative CFD modeling method to investigate the oxidation behaviour of a TBR in terms of total organic carbon concentration profiles taking into account the kinetic expressions obtained elsewhere (Lopes *et al.*, 2007a). Transport phenomena such as mass and heat transfer are integrated in an Eulerian *k*-fluid model, resulting from the volume averaging of the continuity and momentum equations and solved for a 3D representation of the bed at unsteady state. In the Euler-Euler mathematical approach, both the continuous and dispersed phases are considered as interpenetrating continuous media (Jiang *et al*., 2002). These models incorporate two-way coupling, which is specially important for high voidage flows. The interfacial momentum transfer between the liquid and the gas includes a number of force contributions, form and viscous drag, mass force as an inertial force caused by relative acceleration, the effect of turbulent fluctuations on the effective momentum transfer, and the lift force which denotes the transverse force caused by rotational strain, velocity gradients, or the presence of walls. The CFD model equations were implemented in commercial software FLUENT (of Fluent Inc., USA) using user defined routines. Only the main conservation equations are presented. The continuity and momentum balances for phase *q* are written in Eqs. (1) and (2), respectively:

$$\frac{\partial}{\partial t}(\alpha_q \rho_q) + \nabla \cdot (\alpha_q \rho_q \vec{v}_q) = \sum_{p=1}^{n} (\dot{m}_{pq} - \dot{m}_{pq}) + S_q \tag{1}$$

$$\frac{\partial}{\partial t}(\alpha_q \rho_q \vec{v}_q) + \nabla \cdot (\alpha_q \rho_q \vec{v}_q \vec{v}_q) = -\alpha_q \nabla p + \nabla \cdot \bar{\bar{\tau}}_q + \alpha_q \rho_q \vec{g} + \sum_{p=1}^{n} (\vec{R}_{pq} + \dot{m}_{pq} \vec{v}_{pq} - \dot{m}_{qp} \vec{v}_{qp}) + (\vec{F}_q + \vec{F}_{lift,q} + \vec{F}_{vm,q}) \tag{2}$$

$\vec{R}_{pq}$ represents the interphase force and depends on the friction, pressure, cohesion, and other effects, and is subject to the conditions that $\vec{R}_{pq} = -\vec{R}_{qp}$ and $\vec{R}_{qq} = 0$. The momentum balance equation is closed with interphase exchange terms assuming individually the form of a simple phase interaction term given by Eq. (3):

$$\sum_{p=1}^{n} \vec{R}_{pq} = \sum_{p=1}^{n} K_{pq} (\vec{v}_p - \vec{v}_q) \tag{3}$$

where $K_{pq} = K_{qp}$ is the interphase momentum exchange coefficient which is expressed based on the model developed by Attou and Ferschneider, 1999. The interphase coupling terms are written in terms of interstitial velocities and phase volume fractions for gas-liquid, gas-solid and liquid-solid momentum exchange forms as expressed in Eqs (4-6):

$$K_{GL} = \varepsilon_G \left(\frac{E_1 \mu_G (1-\varepsilon_G)^2}{\varepsilon_G^2 d_p^2} \left[\frac{\varepsilon_S}{1-\varepsilon_G} \right]^{2/3} + \frac{E_2 \rho_G (u_G - u_L)(1-\varepsilon_G)}{\varepsilon_G d_p} \left[\frac{\varepsilon_S}{1-\varepsilon_G} \right]^{1/3} \right) \tag{4}$$

$$K_{GS} = \varepsilon_G \left(\frac{E_1 \mu_G (1-\varepsilon_G)^2}{\varepsilon_G^2 d_p^2} \left[\frac{\varepsilon_S}{1-\varepsilon_G} \right]^{2/3} + \frac{E_2 \rho_G u_G (1-\varepsilon_G)}{\varepsilon_G d_p} \left[\frac{\varepsilon_S}{1-\varepsilon_G} \right]^{1/3} \right) \tag{5}$$

$$K_{LS} = \varepsilon_L \left(\frac{E_1 \mu_L \varepsilon_S^{\ 2}}{\varepsilon_L^2 d_p^2} + \frac{E_2 \rho_L u_G \varepsilon_S}{\varepsilon_L d_p} \right) \tag{6}$$

The energy conservation balance for multiphase flow is described by a separate enthalpy equation for each phase as shown in Eq. (7):

$$\frac{\partial}{\partial t}(\alpha_q \rho_q h_q) + \nabla \cdot (\alpha_q \rho_q \vec{u}_q h_q) =$$
$$-\alpha_q \frac{\partial p_q}{\partial t} + \overline{\overline{\tau}}_q : \nabla \vec{u}_q - \nabla \cdot \vec{q}_q + S_q + \sum_{p=1}^{n} (\vec{Q}_{pq} + \dot{m}_{pq} h_{pq} - \dot{m}_{qp} h_{qp}) \tag{7}$$

Turbulent flows are characterized by fluctuating velocity fields mixing transported quantities such as momentum, energy and species concentration, and cause the transported quantities to fluctuate as well. It was used the *k*-**ε** mixture model which is a semi-empirical model based on model transport equations for the turbulence kinetic energy (*k*) and its dissipation rate (ε) as described for the liquid phase in Eqs. (8-9), respectively.

$$\frac{\partial}{\partial t}(\rho_L \alpha_L k_L) + \nabla \cdot (\rho_L \alpha_L \vec{u}_L k_L) = \nabla \cdot \left(\alpha_L \frac{\mu_{t,L}}{\sigma_k} \nabla k_L \right) + \alpha_L G_{k,L} - \alpha_L \rho_L \varepsilon_L + \alpha_L \rho_L \Pi_{kL} \tag{8}$$

$$\frac{\partial}{\partial t}(\rho_L \alpha_L \varepsilon_L) + \nabla \cdot (\rho_L \alpha_L \vec{u}_L \varepsilon_L) = \nabla \cdot \left(\alpha_L \frac{\mu_{t,L}}{\sigma_\varepsilon} \nabla \varepsilon_L \right) + \alpha_L \frac{\varepsilon_L}{k_L} \times (C_{1\varepsilon} G_{k,L} + C_{2\varepsilon} \rho_L \varepsilon_L) + \alpha_L \rho_L \Pi_{\varepsilon L} \tag{9}$$

The representative computational grid for the experimental system investigated in this work is shown in Fig. 1. It consists of a cylindrical vessel with 5 cm internal diameter and 1 m bed height packed with catalyst spherical particles 2 mm diameter. The catalytic bed is meshed in tetrahedral cells by means of the FLUENT preprocessor GAMBIT 2. The mesh quality was analyzed using the skewness criteria and the results were made to be grid independent. Numerical simulations were compared previously to experimental data in order to validate the predicted hydrodynamic parameters pressure drop and liquid holdup. The simulated operating conditions were 10-30 bar pressure and temperatures from 290 to 500 K. Gas and liquid mass flow rates were in the range 0.10 – 0.70 and 0.05 – 15 kg/m^{2}s, respectively.

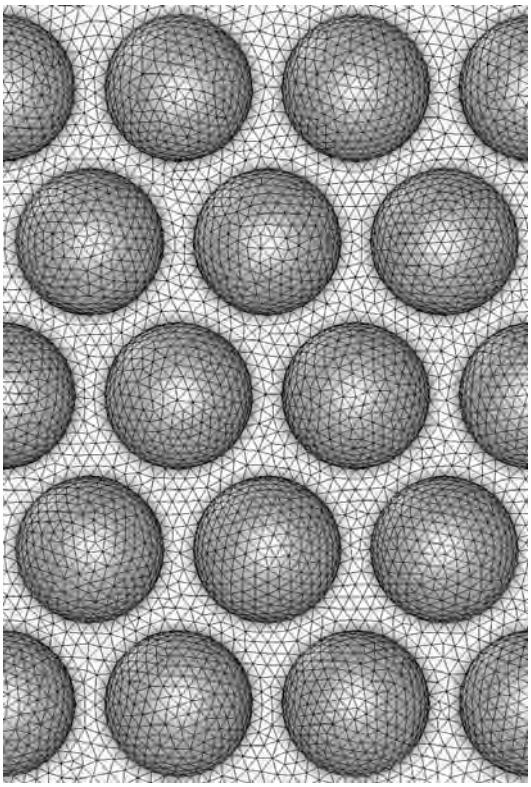

The system domain is discretized by an unstructured finite volume method using the CFD solver FLUENT 6.1. The gas flow rate at the distributor is defined via inlet-velocity-type boundary condition with gas volume fraction charging according to the specifications made in the simulations. The flow model is based on solving Navier-Stokes equations for the Eulerian-Eulerian multiphase model along with multiphase *k*-**ε** turbulence model. The governing differential equations are solved using iterative solution to the discrete form of the mathematical model using a PISO algorithm for pressure-velocity coupling with first order implicit formulation for unsteady integration and first order upwind scheme discretization for spatial derivatives. The gas and liquid are described as interpenetrating continua and equations for conservation of mass and momentum are solved for each phase. The transient calculations were made for two-phase flow starting with different time steps and the converged solution is assumed when the scaled residuals of all variables were smaller than 10^{-4}.

Fig.1 – Tetrahedral mesh used in TBR simulations

3 Results and Discussion

Figure 2 shows the TOC concentration profiles predicted by the CFD model at different relative heights ($z^* = z/H$) for two liquid superficial velocities (u_L) at P = 10 and 30 bar, when the catalytic wet air oxidation is simulated at 200 ºC. Comparing TOC radial profiles at z^* = 1/3, CFD predictions showed that TOC conversion is higher with low liquid superficial velocities (Fig. 2a), as expected. In fact, high liquid velocities correspond to low residence times for the pollutant to be oxidized in the catalyst surface leading to poor decontamination efficiencies in terms of organic carbon removal (Fig. 2b). At the same column height, a ten time increase for the liquid phase shifted the TOC conversion from 71.2 to 60.4% at 10 bar in the reactor centre. At 30 bar, the related shift is from 72.9 to 64.5% of TOC degradation. Therefore, the effect of liquid flow rate seems to have more significance in the TOC conversion rather than the operating pressure. Indeed, at $u_L = 1\times10^{-4}$ m/s, the radial profile for the TOC concentration is more pronounced than with low liquid superficial velocities so that we have a TOC conversion difference of 6.2 and 8.5% at 10 bar between the reactor centre and the wall; at 30 bar this conversion difference became 7.4 and 9.3%.

At the same operating pressures and liquid superficial velocities, TOC concentration profiles are plotted now at z^* = 2/3 in Figs. 2c) and d). According to these plots, the radial TOC concentration was likely to dissipate as we move forward along the packed bed. At $u_L = 1\times10^{-5}$ m/s, the TOC conversion is 90.1 and 90.5% at 10 and 30 bar. As one can conclude, the effect of operating pressure is also vanishing but if we increase the liquid superficial velocity up to 1×10^{-4} m/s, the TOC conversions are 82.9 and 84.9% for 10 and 30 bar, respectively. Hence, the outcome of liquid superficial velocity is still remarkable even at z^* = 2/3. Nevertheless, the conversion difference attained for the reactor centre and the wall is almost insignificant having a minor magnitude of 2.1 and 2.0% for the lowest liquid flow rate and at 10 and 30 bar, whereas at $u_L = 1\times10^{-4}$ m/s the computed differences were 4.2 and 4.9%, respectively.

At the trickle-bed reactor exit (z^* = 1), Figs. 2e) and f) compare the TOC concentration profiles for the bulk phase at the same liquid superficial velocities and operating pressures. As soon as we reach the reactor outlet, the effect of pressure can now be disregarded so that we have roughly the same TOC conversions at 10 and 30 bar, specifically 96.9 and 97.0% at $u_L = 1\times10^{-5}$ m/s, respectively. If we operate at $u_L = 1\times10^{-4}$ m/s, its influence is also negligible being the corresponding TOC conversions of 90.2 and 91.0% at 10 and 30 bar. Moreover, the radial TOC concentration profile obtained at $u_L = 1\times10^{-5}$ m/s for z^* = 1 showed that we have closely no conversion differences between the centre and the reactor wall: 0.6 and 0.7% TOC for 10 and 30 bar. As a matter of fact, only 2.2 and 2.4% of TOC conversion difference was computed for 10 and 30 bar between the reactor wall and centre when operated at the highest liquid superficial velocity, $u_L = 1\times10^{-4}$ m/s.

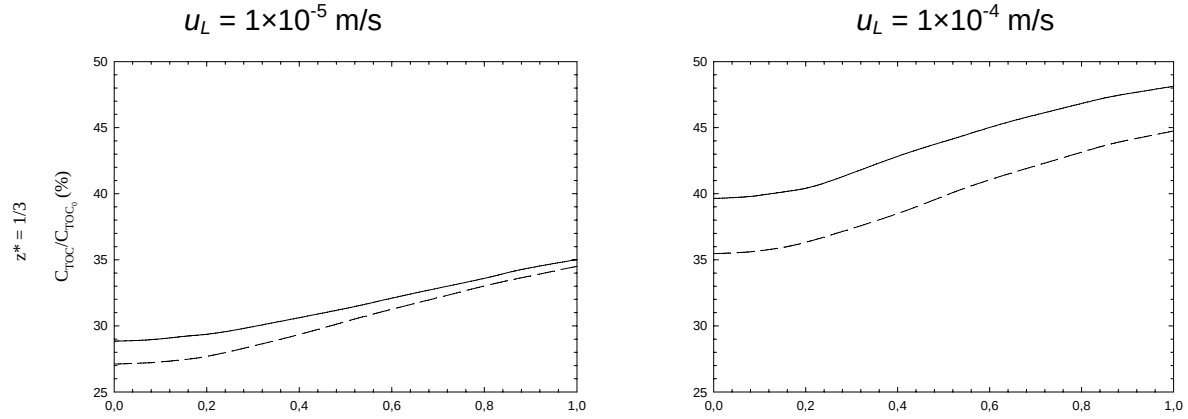

a) b)

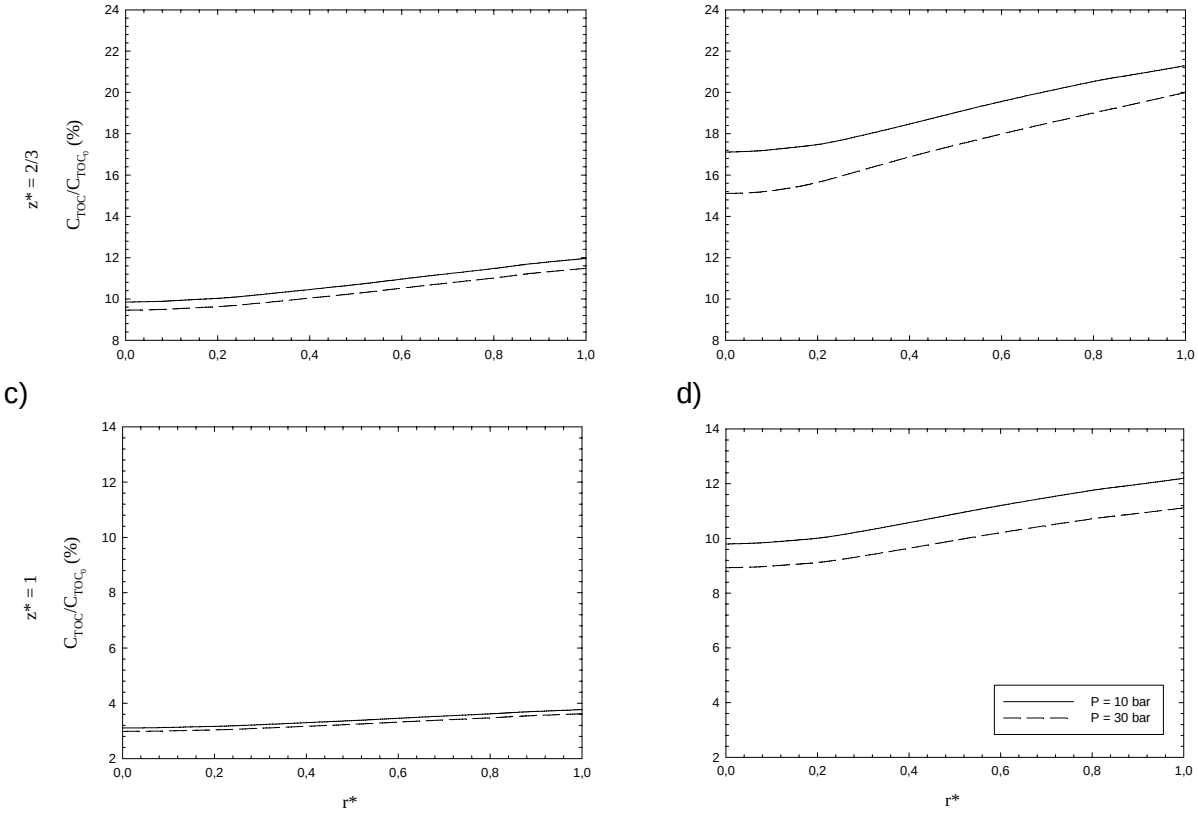

Fig. 2 – Radial profiles of dimensionless Total Organic Carbon concentration at different bed heights for different liquid flow superficial velocities and isobaric operating conditions (*T* = 200 ºC)

In Fig. 3 it is shown the TOC degradation in steady-state for an isometric view of twenty-five catalytic layers, radially.

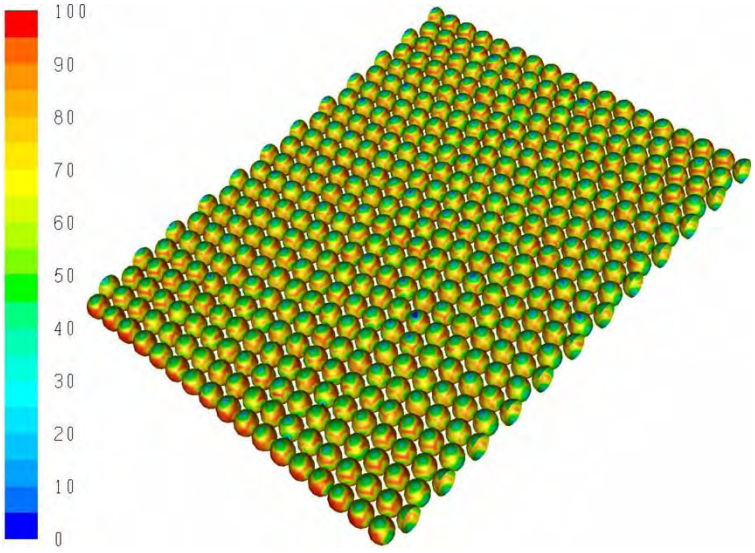

Fig. 3 – Total Organic Carbon degradation map for 25 catalytic layers in steady-state

According to Fig. 3, it is possible to detect different TOC concentration profiles in the catalyst surface corresponding to different oxidation rates. This fact is related to the liquid holdup distribution achieved in the trickle-flow regime so that different wetting levels can be detected, which can cause insufficient reactant or pollutant feeding to the catalyst surface. This fact can be further evaluated in terms of liquid and gas distribution with interface

tracking methods. In a broad range of gas and liquid flows studied at different operation conditions, CFD demonstrated the considerable effect of temperature, pressure, gas-liquid flows in the catalytic wet air oxidation of phenolic wastwaters (Lopes and Quinta-Ferreira, 2007b) evaluating the ultimate axial TOC conversion attained for the trickle-bed reactor.

Therefore, the Euler-Euler multiphase model is a promising tool and a rational choice for flow simulation in packed beds, if good closures for fluid/fluid and fluid/particle interactions are incorporated in the hydrodynamic model. The CFD approach can state that external catalyst wetting can be investigated in downflow flow mode performing a benchmark of reaction parameters encountered in the commercial-scale TBR deployment for CWAO technology.

4 Conclusions

This work is devoted to the performance evaluation of trickle-bed reactor designed for advanced wastewater treatment. A computational flow model based on Euler-Euler two-fluid treatment was developed for the simulation of catalytic wet air oxidation in the multiphase flow reactor. Interphase coupling exchange terms were integrated in the momentum balance equation providing a hydrodynamic model for the computation of total organic carbon concentration profiles at different bed heights.

CFD predictions demonstrated considerable radial profiles mainly at low axial coordinates. The model was used to investigate the effect of operating pressure and liquid superficial velocities in the organic carbon removal of a simulated phenolic wastewater. Several computational runs showed that operating pressure had small influence when compared with different liquid flow rates in the TOC degradation of syringic acid. Moreover, the operating pressure is only relevant for low axial coordinates whilst the liquid flow rate effect is always responsible for significant differences of TOC removal efficiencies and extensive radial profiles.

Finally, the Eulerian model was used to investigate the catalyst wetting efficiency reported indirectly by different TOC degradation rates. The catalyst surface map revealed likely the existence of trickling flow conditions under unsteady-state operation mode.

References

Bhargava, S. K., Tardio, J., Prasad, J., Foger, K., Akolekar, D. B. and Grocott, S. C. (2006) Wet Oxidation and Catalytic Wet Oxidation. *Industrial and Engineering Chemistry Research* 45 (4); 1221-1258.

Paraskeva, P., Diamadopoulos, E. (2006) Technologies for olive mill wastewater (OMW) treatment: a review. *Journal of Chemical Technology & Biotechnology* 81, 1475-1485.

Dudukovic, M.P., Larachi, F., Mills, P.L. (2002) Multiphase catalytic reactors: A perspective on current knowledge and future trends, *Catalysis Reviews. Science and Engineering*, 44 (1) 123-246.

Al-Dahhan, M. H., Larachi, F., Dudukovic, M. P., Laurent, A. (1997). High pressure trickle-bed reactors: A Review. *Industrial and Engineering Chemical Research* 36 (8), 3292-3314.

Lopes, R.J.G., Silva, A.M.T., Quinta-Ferreira, R.M. (2007a). Screening of catalysts and effect of temperature for kinetic degradation studies of aromatic compounds during wet oxidation. *Applied Catalysis B: Environmental,* 73 (1), 193-202.

Jiang, Y., Khadilkar, M.R., Al-Dahhan, M.H., Dudukovic, M.P. (2002) CFD modeling of multiphase in packed bed reactors: results and applications. *A.I.Ch.E. Journal* 48, 716-730.

Attou, A., Ferschneider, G.A. (1999) Two-fluid model for flow regime transition in gas–liquid trickle-bed reactors. *Chemical Engineering Science* 54 (21), 5031-5037.

Lopes, R.J.G., Quinta-Ferreira, R.M. 2007b. Trickle-Bed CFD Studies in the Catalytic Wet Oxidation of Phenolic Acids, *Chemical Engineering Science* 62 (24) 7045-7052.

Proceedings of the 10th International Chemical and
Biological Engineering Conference - CHEMPOR 2008
Braga, Portugal, September 4-6, 2008
E.C. Ferreira and M. Mota (Eds.)

Characterization of Water Species Revealed in the Drying Operation of Squid by Using Water Proton NMR Analysis

Yasuyuki Konishi[1*], Masayoshi Kobayashi[2] and Kou-ichi Miura[3]
[1]Hokkaido Industrial Technology Center, 379 Kikyo-cho, Hakodate, Hakodate, 041-0801, Japan
[2]Advanced Technology Institute of Northern Resources, 8-6 Tonden 2Jo 2chome, Kitaku, Sapporo, Hokkaido, 002-0852, Japan
[3]Department of Biotechnology and Environmental Chemistry, Kitami Institute of Technology, 165 Koencho, Kitami, Hokkaido, 090-8507, Japan

Keywords: water species-A_1 and -A_2, reproducibility of the water species, correlation time, effective moisture diffusivity(*De*), activation energy of *De*
Topic: Integration of life sciences & engineering

Abstract

For the discrimination of water molecules during the drying process of a squid, multifunctional water molecules were separately characterized by water proton-NMR and moisture diffusivity (*De*) analysis methods as a function of the moisture content (W_0). The proton-NMR spectrum showed the appearance of three peaks at the specified chemical shifts with different ppm's, indicating three different species (species-A, -B, and -C) distributed in the squid muscle, each of which had a characteristic behavior of the correlation time (τ_C) as a function of the W_0. The modified moisture content linearly increased in the whole range of W_0 for species-A suggesting that it can be attributed to water species. Species-C showed no change without depending on W_0, indicating a characteristic species different from the water species. Species-B was difficult to be assigned to any species without a presumption as some hydrogen species binding with protein molecules.

The τ_C of species-A was drastically varied at W_0 = 120%-d.b., indicating two further categories, i.e., species-A_1 and -A_2, depending on the dehydration degree. For species-A_1 at W_0 > 120%-d.b. (region I), the τ_C was 4.8×10^{-9}s independently of the W_0, whereas, for species-A_2 at W_0 < 120%-d.b. (region II), the τ_C decreased from 1.2×10^{-7} to 1.0×10^{-8} s with increasing the W_0. Species-A_1 and -A_2 were further examined by *De* analysis. For species-A_1, *De* and the activation energy of moisture diffusivity (E_D), respectively, indicated identical values of 1.8×10^{-6} m^2/h and 17 kJ/mol, without depending on the W_0 in the range of W_0 =120 ~ 360%-d.b. (region I). For species-A_2, the two parameters clearly varied as $De = 1.7\times10^{-6}$ ~ 0.6×10^{-6} m^2/h and E_D = 25 ~ 35 kJ/mol, with decreasing the W_0 from 120 to 30%-d.b. (region II). Species-A_1 and -A_2 were assigned as free water and slightly restricted water, respectively.

Species-C was accurately assigned as a lipid by relating to the spectra of proton NMR spectroscopy of squid-liver lipid.

1 Introduction

Many researchers have attempted to evaluate multifunctional water species in biomaterials. Various results have been reported so far because of the dynamic variation of water species depending on the kind of biomaterials and the experimental conditions, especially with regard to their dehydration degree. To evaluate the states of water molecules, physicochemical analysis has generally been applied for various biomaterials. Caurie (1971) and Rockland and Nishi (1980) classified the water species of food products into physisorbed and chemisorbed water by the model of adsorption isotherms. Lichfield and Okos (1992)

* Corresponding author. Tel + 81-138-34-2600. E-mail:konishi@techakodate.or.jp

reported gaseous water and liquid water in pasta based on the variation of diffusivity (*De*). In previous papers by our group (Konishi *et al.* 2001; Konishi & Kobayashi 2003), two water species were demonstrated as weakly restricted and strongly restricted water by using the dynamic behavior of *De* .

For a more direct identification of the water species, the ^{1}H-NMR method has frequently been used (Yoshikawa & Ohsaka 1980). Bodurka *et al.* (1996) demonstrated free water and bound water in the rabbit lenses based on the relaxation time difference of the water species. Miedziejko *et al.* (1996) distinguished free water and bound water in a triticale seed cell based on the time assessment of ^{1}H-NMR spin-spin relaxation. Almost all results reported have been under static conditions, even though the water species dynamically shift depending on the moisture contents and situation. For a further identification of the water species, a dynamic analysis under a dehydration operation should be conducted.

In the present study, by using the dynamic analysis of the ^{1}H-NMR with effective diffusivity (*De)* analysis, the objectives sought were (1) to quantitatively discriminate the water species by the ^{1}H-NMR method in a wide range of moisture contents (W_0) and to reconfirm the reproducibility due to the dehydration and hydration operations; and (2) to additionally classify the water species by the dynamic behaviour of *De*.

2. Experimental

A Japanese common squid (50mm square and 8±1.5mm in thickness, initial moisture content of 300 ~ 360%-d.b. (dry base, W_D)) was used as a model sample. Drying air with a flow rate of 0.7m/s was introduced into a drying room passing through a rectifiable compartment without regulating the humidity. The drying temperature was electrically controlled within ±2ºC at given temperatures. The sample was placed in a stainless steel net basket (10 meshes) that was mechanically hung from a strain gage transducer in the dryer. During the drying process, a poultice-up process (designated as PUP) was operated to keep the moisture distribution in the squid sample uniform. For the PUP, the samples were stored in an incubator for 36h, the temperature of which was regulated at 2°C. The PUP was operated at a given moisture content (W_0) in the range of 15 ~ 285%-d.b. The sample weight was continuously recorded by the output of a strain-gage transducer using a data-logger. Thirty, 40, and 50°C were chosen as the drying temperatures (T_D). In the present drying conditions, it was previously reconfirmed that all the drying operations for the squid were within a falling-rate period. The diffusivity (*De*) of a sample at given moisture content was evaluated by

$$\frac{W - We}{W_D - We} = \left(\frac{8}{\pi^2}\right)^3 exp\left(\frac{-\pi^2 \cdot De \cdot t}{4} \cdot \left(L_a^{-2} + L_b^{-2} + L_c^{-2}\right)\right) \cdots (1)$$

where W is the moisture content at the drying time t, We is the equilibrium moisture content, W_D is the initial moisture content of a drying fresh sample, t is the drying time, and L_a, L_b, and L_c are the half-distances of the sample width.

For the characterization of the moisture species in the squid, a nuclear magnetic resonance (NMR) technique was used to measure the ^{1}H-NMR spectra and a spin-spin relaxation time (T_2) of water protons. Squid samples cut into 2×2×10mm pieces were inserted into an NMR sample tube (4mm in inner diameter and 180mm in length). ^{1}H-NMR spectra were obtained using a JEOL A-500 FT-NMR spectrometer operating at 500MHz for protons. The observed frequency width was 20 kHz. The 90º pulse width was 12.5 *μs*, and the number of pulse repetitions was 8. The proton chemical shifts were measured by using a slight amount of water containing deuterium oxide as an external reference. All the NMR measurements were performed at 23.5±0.5ºC. The spin-spin relaxation times, T_2, were obtained by the CPMG method and from the obtained T_2, the correlation time of a water

proton, τ_C , was evaluated.

For the readsoption of water, the dried sample was stored into a humidifier for a given time; the temperature and humidity of the humidifier were regulated at 23.5±0.5ºC and 90±5% respectively. The W_0 for the water-readsorbed sample was controlled by the storage time in the humidifier.

Further detailed experimental procedures and the evaluation details of *De* have been presented elsewhere (Konishi *et al*. 2001).

3. Results and Discussion

3.1. Dynamic Multiplicity of Water Species Distinguished by the ^{1}H-NMR Method

3.1.1. Dynamic Behavior of the Spectra of Proton NMR Spectroscopy for Fresh Squid Muscle

As has been demonstrated by many researchers (Miwa *et al*. 2003; Lechert 1981; Barara *et al.* 1999; Labbé *et al.* 2002), water species in solid materials are classified into various restricted strengths based on physicochemical data, indicating physisorbed, chemisorbed, strongly restricted, and weakly restricted water. In a previous study (Konishi *et al*. 2001), two different types of water species were distinguished in a fish paste sausage. One was a strongly restricted water species characterized by a lower *De*, and the other was a weakly restricted water species with a higher *De*. Our attention is focused on a more direct identification of water species retained in foods by using the ^{1}H-NMR method.

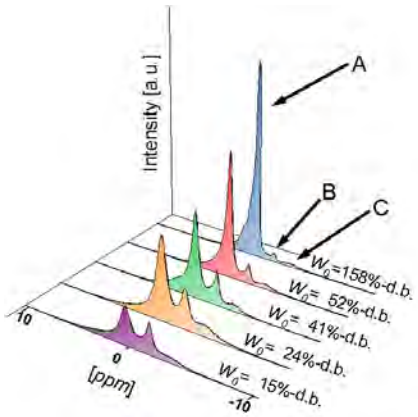

Fig.1 Dynamic behavior of ^{1}H-NMR spectra for species-A, -B, and -C in the squid muscle in the course of a drying operation

Figure 1 is an illustration of a typical example for the ^{1}H-NMR spectrum of the squid muscle with W_0 = 41%-d.b. Three peaks can be clearly recognized, indicating three different proton species, named species-A, -B, and -C, each of which has a different ppm value, 0.42, -1.43, and -3.14ppm, respectively. Our interest focuses on a characterization of the three species based on the dynamic behavior of each species in the course of a drying operation. The peak height of species-A drastically decreased, and that of species-B gradually decreased with the progress of dehydration, whereas species-C indicated no change. The individual behavior strongly indicates that the three species have their own characteristics with different natures and states, as demonstrated in the following sections.

3.1.2. Characterization of Species-C

For the assignment of species-C, two additional experiments were conducted. First, the ^{1}H-NMR spectra of squid liver lipid were effectively used. Figure 2(A) illustrates the dynamic behavior of ^{1}H-NMR spectra influenced by the squid liver lipid. The peak at the chemical shift of -3.37ppm clearly increased with increasing the dipping time into the lipid. Second, ^{1}H-NMR spectra of

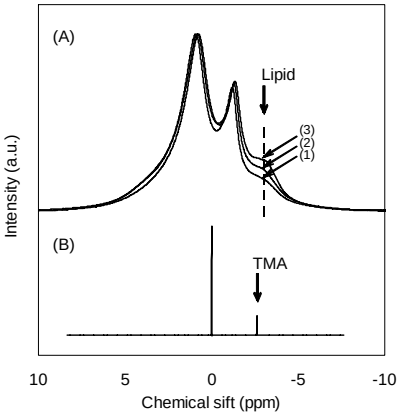

Fig.2(A)NMR spectra of squid muscle influenced by dipping into the squid liver lipid for (1) zero, (2) 1 and (3) 24 hrs, (B)Spectrum of proton NMR spectroscopy of the 30% TMA solution.

trimethylamine (TMA) were compared, as shown in Fig. 2(B). The peak of TMA exactly indicated that the chemical shift of -2.62ppm different from that of species-C. This chemical shift was consistent with the results proposed by Toussaint *et al.* and Howell *et al.* (Toussaint *et al.* 2002; Howell *et al.* 1996). These two pieces of evidence strongly demonstrate that species-C can be attributed to a lipid and not TMA.

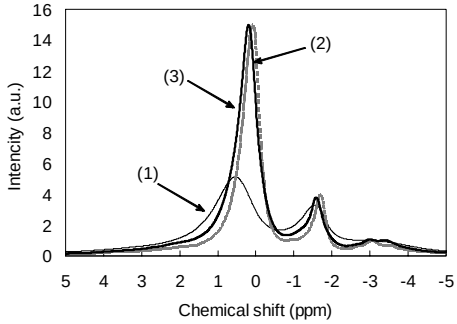

Fig.3 Reproduced dynamic behavior of ^{1}H-NMR spectra for species-A, -B and -C in the squid muscle derived from a dehydration and water re-hydration operations: (1)under the drying operation at W_0 = 18%-d.b., (2) after the re-hydration of water for sample (1) up to W_0 = 45%-d.b. and (3) under the drying operation at W_0 = 45%-d.b.

3.1.3. Reproduced Dynamic Behavior of Species-A Due to the Readsorption of Water

The reproducibility of species-A due to the removal and readsoption of water moisture is important evidence to reconfirm whether or not species-A result from dehydration and water addition. Figure 3 is an illustration of the dynamic behavior of the ^{1}H-NMR spectra for the species-A due to the repeated operation of dehydration up to W_0 = 18%-d.b. (curve (1)) and re-hydration from W_0 = 18%-d.b. up to W_0 = 45%-d.b. (curve (2)). Curve (3) is obtained in a continuous drying operation. Comparing curves (1) and (2) with curve (3), the exact reproducibility of the species-A can be appreciated, suggesting that species-A is the result of the water moisture retained in the squid muscle.

The reproducibility of species-A can be recognized again by further evidence, namely, the τ_C-dynamic behavior due to the repeated operation of dehydration and water readsorption. Figure 4 is an illustration of the dynamic behavior of τ_C for species-A as a function of the W_0 due to the readsorption of water in comparison with a continuous drying operation (broken curve (a)). All the readsorption curves (solid lines) nearly follow the continuous dehydration curves (broken line). All the readsorption data fall on a continuous drying curve of the broken line. The good reproducibility obtained again demonstrates that species-A is due to water moisture retained in the squid muscle.

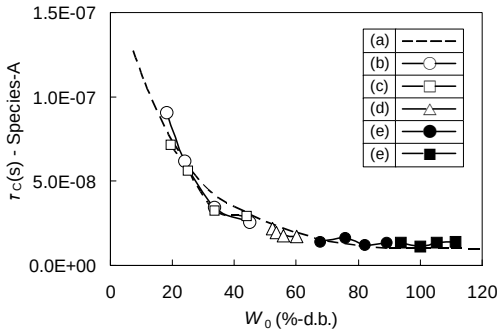

Fig.4 Reproducibility of τ_C(species-A) observed between the dehydration and the water-readsorption operations: (a) under the continuous drying operation from W_0 = 120%-d.b. to 10%-d.b., (b) after the gradual readsorption of water from W_0 = 18%-d.b. to W_0 = 45%-d.b., (c) from W_0 = 20%-d.b. to W_0 = 44%-d.b., (d) from W_0 = 50%-d.b. to W_0 =60%-d.b., (e) from W_0 = 68%-d.b. to W_0 = 89%-d.b. and (f) from W_0 = 94%-d.b. to W_0 = 111%-d.b.

3.2. Further Discrimination of the Water Species

3.2.1. Discrimination of Water Species-A by τ_C

As pointed out in Fig.3, species-A has a good reproducibility due to the dehydration and the readsorption of moisture. Based on this characteristic behaviour, it could be assumed that species-A should mainly contribute to the dehydration of squid muscle. Focusing on whether or not species-A consists of one species of water molecule, a further discrimination of species-A can be attempted. Figure 5 illustrates the τ_C as a function of the W_0. The τ_C-W_0 curve obtained

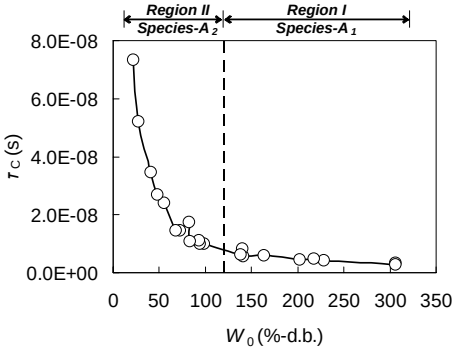

Fig.5 Discrimination of species-A_1 and -A_2 recognized by τ_C-W_0 dependency

is clearly divided into two regions, I and II, at W_0 = 120%-d.b., a slight decrease for region I at W_0 >120%-d.b. and a steep decrease for region II at W_0 <120%-d.b. This characteristic difference between regions I and II strongly indicates, at least, two different water species, species-A_1 and -A_2, respectively. Since a higher τ_C means a larger restriction strength, species-A_1 may be assumed to be a free-water species and species-A_2, a weakly restricted-water species.

3.2.2. Discrimination of Water Species-A by Moisture Diffusivity (De)

For further discrimination of species-A_1 and -A_2, the moisture diffusivity (*De*) during the drying operation can be proposed as a possible parameter for water moisture mobility. Figure 6 is an illustration of the *De* as a function of the W_0. Two regions can again be recognized, indicating a constant *De* as $1.8\pm0.1\times10^{-6}$m^2/h at W_0 >120%-d.b. for region I and a steep increase of *De* from 0.6×10^{-6} to 1.7×10^{-6}m^2/h at W_0 <120%-d.b. for region II. Thus, two species can be recognized as species-A_1 and -A_2 based on the moisture mobility evaluated by *De*. Species-A_1 gives identical mobility without depending on the W_0, whereas species-A_2 indicates a linear increase of *De* with increasing the W_0.

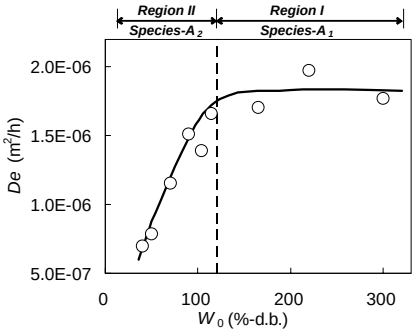

Fig.6 Discrimination of species-A_1 and -A_2 recognized by *De*-W_0 dependency

From the viewpoint of the mobile energy of diffusion water molecules, the activation energy (E_D) for the moisture diffusivity can be considered. Figure 7 is an illustration of the E_D as a function of the W_0. Again, the result indicates two regions, I and II. In region I, the moisture diffusivity has an identical activation energy, E_D = 17±0.2 kJ/mol, whereas region II exhibits a steep increase of E_D from 25 to 35 kJ/mol with decreasing the W_0. Again, species-A_1 and -A_2 can be recognized as corresponding to regions I and II, respectively. The diffusion activation energy of species-A_2 steeply increases with the progress of dehydration. Taking this result into account with the steep decrease of *De* in Fig. 6, the diffusion difficulty of species-A_2 is dynamically accelerated by the decrease in the W_0.

The question of how the obtained water moisture mobility can be related to the water molecules evaluated by the ^{1}H-NMR method is intriguing. Focusing the τ_C as a function of the E_D. using Figs.5 and 7, one may understand that species-A_1 gives identical E_D = 17±0.2 kJ/mol and $\tau_C = 4.8\pm1.5\times10^{-9}$ s, whereas species-A_2 indicates a linear increase of the τ_C with increasing the E_D. From these results, it is evident that species-A_1 has an identical τ_C and E_D in region I and that species-A_2 exhibits a linear increase of E_D and τ_C with the progress of dehydration in region II. In conclusion, the higher τ_C (higher restriction) contributes to the higher mobile energy.

Based on the large number of data obtained for *De*, E_D and τ_C and their reproducibility, two different states may be reasonably proposed, namely, free water (species-A_1) and weakly restricted water (species-A_2). Further identification of the two species, however, is hardly warranted by the present experimental data.

On the characterization of species-B, we have no any evidences to evaluate physicochemical nature except some presumption as a proton species retained by protein molecules.

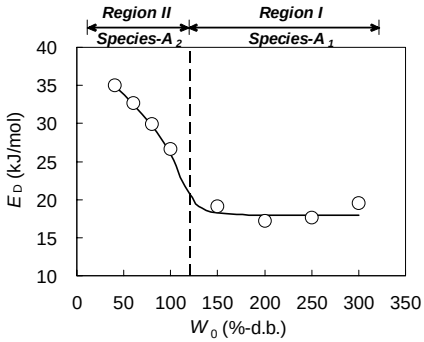

Fig.7 Discrimination of species-A_1 and -A_2 recognized by E_D-W_0 dependency

4. Conclusions

The dynamic behavior of water moisture retained in squid muscle under a drying operation was characterized in detail by the correlation time (τ_C) of the ^{1}H-NMR method accompanied with the dynamic change of the moisture diffusivity (*De*) and the activation energy (E_D) of the diffusivity, as a function of moisture content (W_0). The water species was clearly classified into two different species, i.e., species-A_1 and -A_2. The two species were characterized as follows: (1) species-A_1 has identical *De*, E_D,and τ_C and is named as free water at W_0 >120%-d.b., (2) species-A_2 shows a steep increase of E_D, T_P, and τ_C, at W_0 <120%-d.b., in contrast to the steep decrease of *De* with decreasing the W_0, and is classified as weakly restricted water.

References

Barara, G., Matteo, P. Di, Lamanna, R., Limone, G., Osséo L. Sesti and Vittoria, V. (1999). Water-polysaccharides interaction during apples drying process. *Macromol. Symp.*, 138, 237-243.

Bodurka, J., Buntkowsky, G., Olechnowicz, R., Gutsze, A. and Limbach, H-H. (1996). Investigation of water in normal and dehydration rabbit lenses by ^{1}H NMR and calorimetric measurements. *Colloids Surf. A*, 115, 55-62.

Caurie, M. (1971). A single layer moisture adsorption theory as a basis for the stability and availability of moisture in dehydration foods. *J. Food Technol.*, 6, 193-201.

Howell, N., Shavila, Y., Grootveld, M. and Williams, S. (1996). High-Resolution NMR and Magnetic Resonance Imaging (MRI) Studies on Fresh and Frozen Cod (Gadus morhua) and Haddock (Melanogrammus aeglefinus). *J. Sci. Food Agric.*, 72(1), 49-56.

Konishi, Y., Horiuchi, Y. and Kobayashi, M. (2001). Dynamic evaluation of the dehydration response curves of foods characterized by a poultice-up process using a fish-paste sausage.(I. Determination of the mechanism for moisture transfer). *Drying Technol.*, 19(7), 1253-1270.

Konishi, Y. and Kobayashi, M., (2003). Characteristic innovation of a food drying process revealed by the physicochemical analysis of dehydration dynamics. *J. Food Engin.* 59, 277-283.

Labbé, N., Jéso, B. De, Lartigue, J-C., Daudé, G., Pétraud, M. and Ratier, M. (2002). Moisture content and extractive materials in maritime pine wood by low field ^{1}H NMR. Holzforschung, 56, 25-31.

Lechert, H. T. (1981). Water binding on starch (NMR studies on native and gelatinized starch). In *Water Activity : Influences on Food Quality*, ed. L.B.Rockland and G.F.Stewart, Academic Press, New York. pp223-245

Litchfield, J. B. and Okos, M.R. (1992). Moisture diffusivity in pasta during drying. *J. Food Engng.*, 17, 117-142.

Miedziejko, E. M., Plenzler, G. B., Napierala, D. M. and Narozna, A. T. (1996). 1H-NMR spin-spin relaxation times assessment of the reflection coefficient of the Triticale seed cell wall-plasmalemma barrier. *Plant Cell Environ*, 19(12), 1443-1448.

Miwa, Y., Tanaka, T., Oshiyama, H. and Mochizuki, A. (2003). Study on structure of water in poly (2-methoxyethylacrylate) (PMEA) and poly (2-hydroxyethylmethacrylate) (PHEMA) by 2H solid-state NMR. *Journal of Japanese Society for Biomaterials*, 21-2, 143-148.

Rockland, L. B. and Nishi, S. K. (1980). Influence of water activity on food product quality and stability. *Food Technol.*, 34(4), 42-59.

Toussaint, C. A., Davenel, A., Fauconneau, B., Haffray, P. and Akoka, S. (2002). Determination of the lipid content in fish muscle by a self-calibrated NMR relaxometry method: comparison with classical chemical extraction methods. *J. Sci. Food Agric.*, 82(2), 173-178.

Yoshikawa, K. and Ohsaka, A. (1980). ^{1}H and ^{13}C NMR spectroscopic study of rat organs. *Physiol. Chem. & Physics.*, 12, 515-5.

Proceedings of the 10th International Chemical and
Biological Engineering Conference - CHEMPOR 2008
Braga, Portugal, September 4-6, 2008
E.C. Ferreira and M. Mota (Eds.)

Cholesterol removal by nanofiltration in organic solution

C. Allegre, E. Carretier* et P. Moulin
UMR 6181; CNRS, Aix-Marseille Université, Département en Procédés Propres et Environnement; Europôle de l'Arbois, BP. 80, Bâtiment Laennec, Hall C, 13545 Aix en Provence Cedex 04, France

Keywords: Cholesterol; Triacylglycerides; Phospholipids; Nanofiltration
Topic: Advancing the chemical and biological engineering fundamentals

Abstract

Three components of the egg yolk which are extracted in ethanolic solution are interesting in the field of the nutritional supplements. These three components are triacylglycerides (65%, w/w), glycerophospholipids (28%, w/w) and cholesterol (5%, w/w). This work is in relation with the separation of interesting components using membrane processing. The first components to be separated is the cholesterol because of its relationship with cardiovascular disease. This has been done by nanofiltration which is a technique able to separate compounds which molecular weights range between 200 to 2000 $g.mol^{-1}$. Differents nanofiltration membranes have been tested, with different cut off. Only a little influence on the separation has been notices with these different membranes. Then, the best separation conditions have been determined with the best membrane.

1 Introduction

The lipids contained in egg yolk are principally triacylglycerides (65%, w/w), glycerophospholipids (28%, w/w) and cholesterol (5%, w/w). The structure of these compounds are presented in figure 1. A more or less selective extraction of these lipids can be performed using various organic solvents such as diethyl ether, methyl chloride, ethyl acetate, propane/butane, hexane, benzene, ethanol (Tokarska and Clandinin, 1985) or supercritical CO_2 in the presence or the absence of ethanol (Rossi et al., 1990). In our case, after extraction, these products were recovered in 95% ethanol. The lipid concentration in ethanol ranged from 3 to 15%, w/w. The lipids present in the ethanol were glycerophospholipids (760 $g.mol^{-1}$), 80%, and a mixture of cholesterol (386.7 $g.mol^{-1}$) and triacylglycerides (860 $g.mol^{-1}$), 20%.

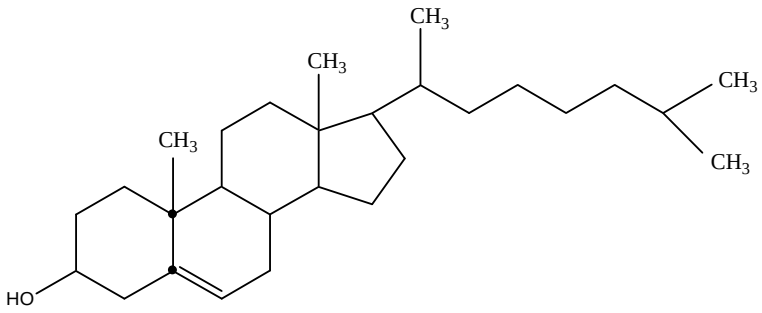

CHOLESTEROL

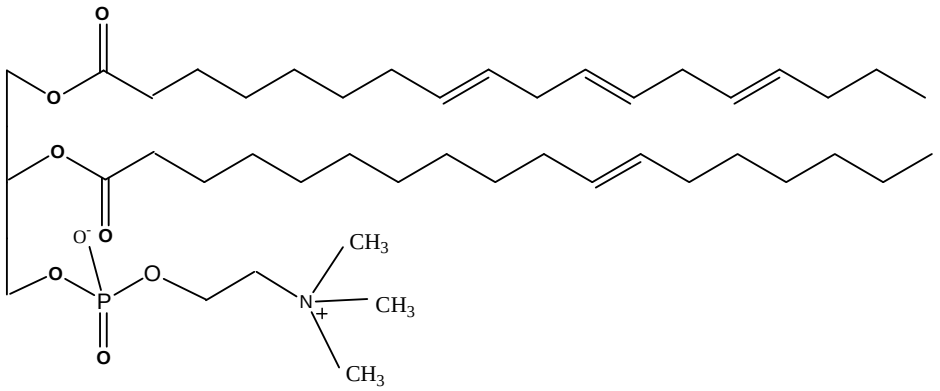

PHOSPHOLIPIDS

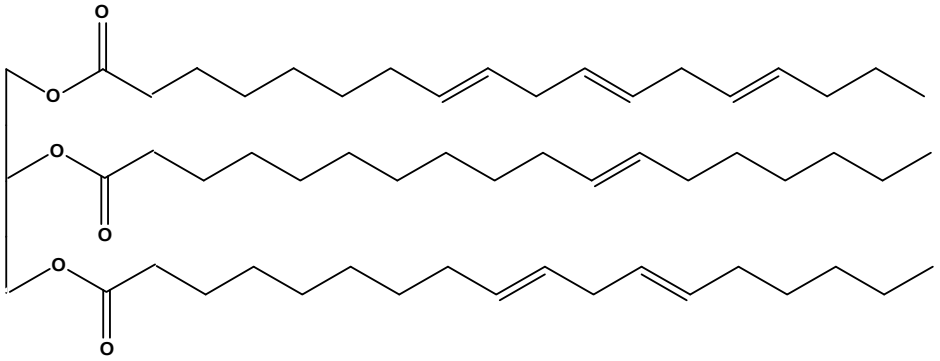

TRIACYLGLYCERIDES

Figure 1: Compounds structures

Glycerophospholipids contain fatty acids that can be highly polyunsaturated. They can thus be considered as a source of essential fatty acids in C18 or conditionally essential fatty acids in C20 or C22 for the families of ω6 (molecules composed of a polyunsaturated carbon chain with two or more double bonds, the first double bond being located on the 6th carbon atom from the terminal methyl) and ω3 (the first double bond is located on the 3rd carbon atom). Thanks to their surface-active properties, glycerophospholipids, once completely purified, can be used in the preparation of emulsions of lipids in water used in the fabrication of food additives or even pharmaceuticals. For these applications, the amount of cholesterol in egg yolk is a problem. Cholesterol ingestion can increase cholesterol concentration in the blood, which is a marker linked to the risk of arteriosclerosis and coronary diseases. It is therefore of interest to eliminate the cholesterol from the lipids extracted from egg yolk.

2 Material and methods

The solutions to treat results from ethanolic extraction of the egg yolk lipids contained in egg yolk powder. The solution are purified by filtration. These real solutions have been used for separation of cholestorerol because synthetic solutions can have some different behaviour due to the variety of compounds in the real solutions.

The pilot plant we used (Figure 2) allowed us to work on membranes with an industrial elementary surface and to collect results for easy scaling up. The installation consists of a 25 L metapolyacrylate tank (A) containing the feed solution. This tank is connected to the membrane module D by a feed line 2 made of stainless steel and its temperature is regulated by a heat exchanger. This feed line consists of a high-pressure pump B equipped with a variator. The retentate is recovered through circuit 3. On its way back to tank A, it passes

through a regulating valve E. In order to keep the initial solution volume constant and to prevent possible fouling of the membrane, ethanol may be added to tank A at a flow rate equal to that of the permeate flux (diafiltration step). This ethanol is taken from tank G and is maintained at the same temperature T as that of the fluid circulating in 2. It is fed into tank A by means of a pump F through circuit 4 in which two pressure detectors P1 and P2 allow measurement of the pressure drop (ΔP = P1 - P2) and transmembrane pressure (TMP = (P1 + P2)/2). The diafiltration step (addition of ethanol from tank G) is stopped when the concentration of cholesterol in tank A reaches a value corresponding to the minimum concentration of cholesterol desired and the filtration operation goes on, which is expressed by the variation of triacylglyceride and phospholipid concentrations in the retentate A. When the dead volume of the plant is reached (0.5 L), the nanofiltration operation is stopped. After every operation the membrane is rinsed with ethanol.

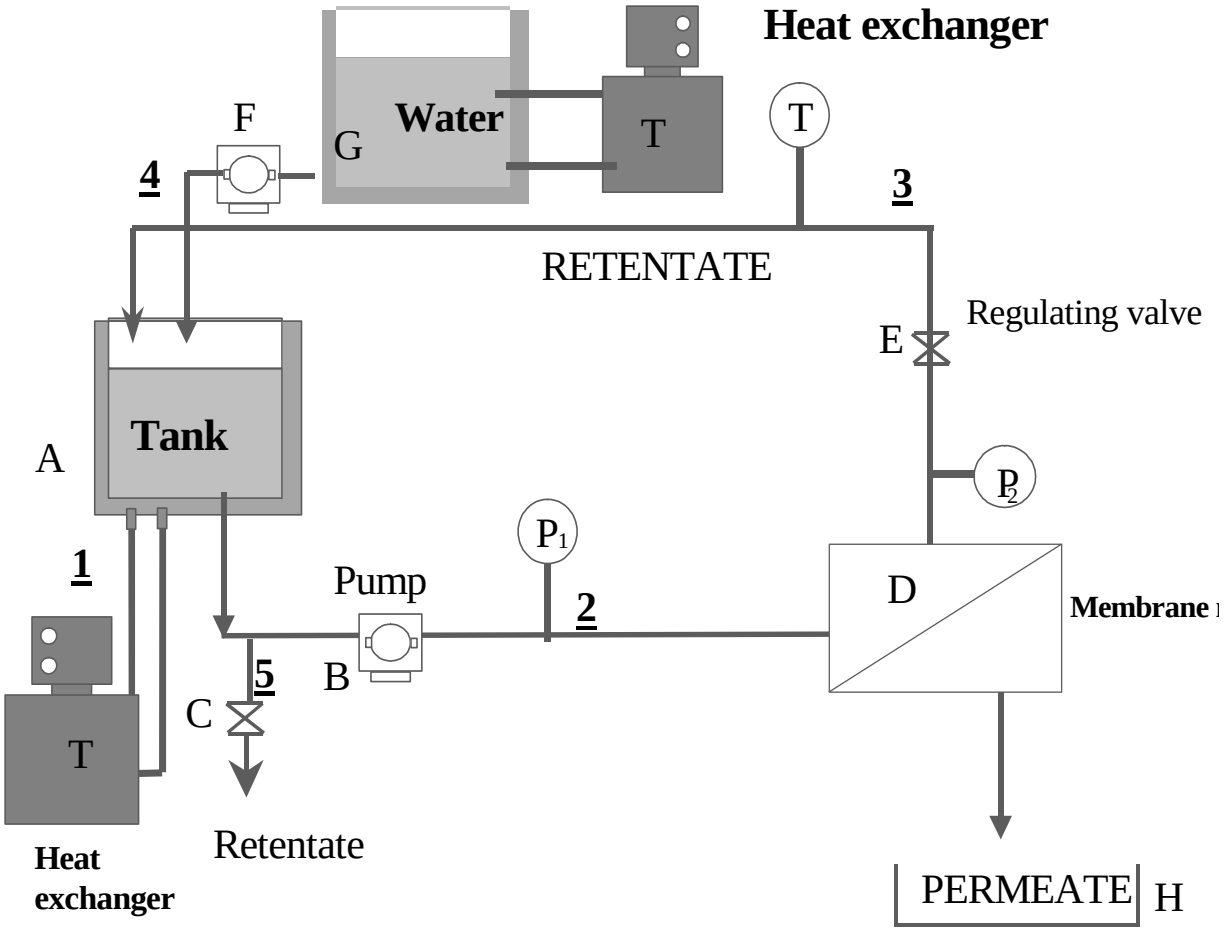

Figure 2: Pilot plant

For each separation (different membranes and operating conditions) samples of permeate and retentate are simultaneously collected for analysis. The retention factor RF of each compound was calculated from the analysis following the relation (1):

$$RF = (1-Cp/Cr) \times 100 \qquad (1)$$

with RF the retention factor (%), Cp the concentration in the permeate ($g.L^{-1}$) and Cr the concentration in the retentate ($g.L^{-1}$) at the same time.

3 Results and discussion

No information was found in the literature that would help estimate the performances of filtration or even of membrane processes for the separation of this type of mixture. In view of the size of the compounds, we decided to use a process of nanofiltration. However, the initial mixture was complex and the treatment was made difficult by the following: (i) The molecular weights of the compounds were quite similar: 386.7 $g.mol^{-1}$ for cholesterol, between 850 and 1020 $g.mol^{-1}$ for triacylglycerides and between 760 and 878 $g.mol^{-1}$ for phospholipids, (ii) The solution was ethanolic. The stability of a membrane in an organic solvent such as ethanol depends on the physicochemical characteristics of the solvent and of the membrane. The membrane-solvent interaction may result in swelling, plasticization or dissolution of the membrane material and subsequent loosening of the membrane structure, leading to modified separation properties and/or loss of mechanical strength under pressure. Besides, the cut-off of a membrane determined in aqueous solutions (e.g., as provided by the manufacturer) is insufficient to characterize its Molecular Weight Cut Off ($g.mol^{-1}$) (MWCO) in organic solutions. The MWCO of a membrane varies depending on the solute and the solvent. Tsui et al. (2004) reported that low lipid rejection could be due to lipid-membrane interactions that cause plasticization of the polymer, leading to membrane swelling and reduced lipid rejection.

The aim of this work was the fractionation of a complex and real ethanolic solution. The membrane cut-off could not be taken as the main criterion for the selection of the best membrane, and this for several reasons: the molecular weights of the different compounds were similar and the membrane cut-offs were defined by each manufacturer according to a specific protocol. Moreover even if these cut-offs had been more precisely defined, extrapolating to organic solutions would have been hazardous. It is very difficult to take into account the effects of the electric charges in an ethanolic medium, and no information is available concerning the membrane behaviour with regard to an alcoholic medium. However, we clearly showed that fractionation was possible with a cellulose acetate membrane. We selected a cellulose triacetate membrane (CK 2540 F 30D, from the firm Osmonics), with an area of 2.5 m2 and a cut-off of 350 Da for an industrial experiment. This membrane was selected because cellulose acetate is a hydrogen bond acceptor and cholesterol is the only one of the three compounds to contain a hydrogen bond.

We studied the influence of some operating parameters on the permeate flux and defined the optimum conditions of transmembrane pressure and flow rate (figure 3): for a constant TMP, if the flow rate decreases, the permeate flow rate decreases. The membrane is well regenerated after each experiment with a simple wash with pure ethanol. The variation of the retention coefficient as a function of the concentration leads us to consider that the upstream solution has a kind of “organisation” which constitutes an important resistance to mass transfer. The cholesterol being the problem, the possibility to separate this compound by an appropriate membrane is an important breakthrough in the domain of nutraceutics and nutritional supplements.

The cholesterol has been removed from the ternary mixture as it is shown in figure 4. The permeation of cholesterol compared to phospholipids is better for low concentration (during the diafiltration step, figure 5). So by having a longer diafiltration step, the removal of cholesterol will be achieved and the losses in phospholipids (5%) were limited. However, in view of the results obtained, increasing the diafiltration time will enable us to reach our objective of 80% of cholesterol removal. Actually, the diafiltration time should be 5 times the space time if the retentate is well mixed which is not our case. On the other hand a too long diafiltration will drives to important losses in phospholipids. Some experiments have to be done to have the optimal time and conditions for the diafiltration step.

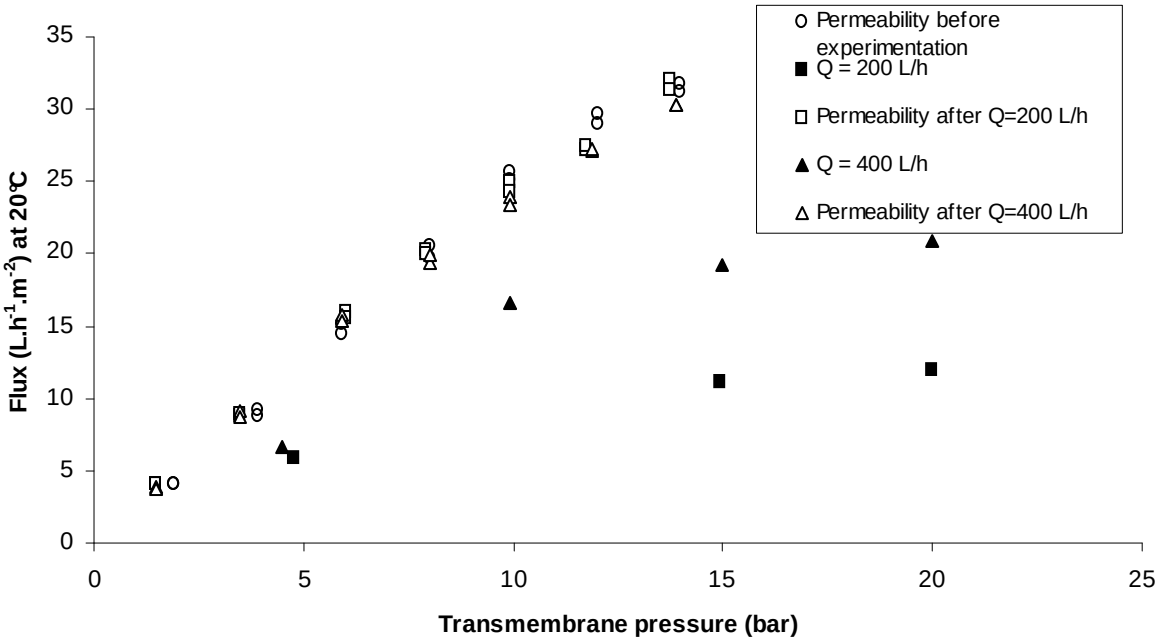

Figure 3: Variation of the permeate flux as a function of the transmembrane pressure for different flow rates (T_{ave} = 20°C, V_0 = 5 L)

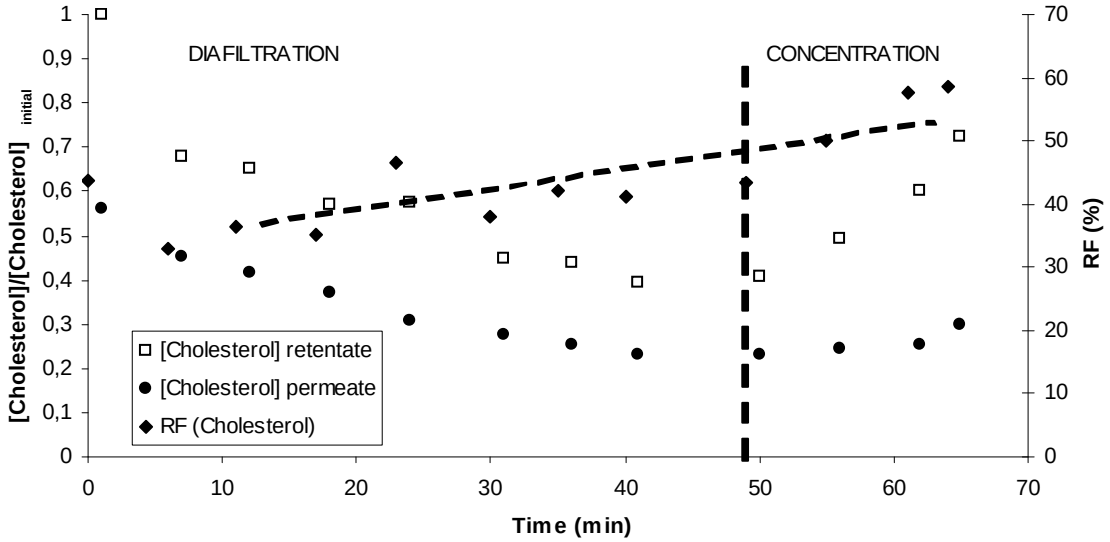

Figure 4: Variation of the cholesterol concentration and retention factor versus time (T_{ave} = 20°C, TMP = 15 bar, Q= 300-350 L.h^{-1}, V_0 = 15 L)

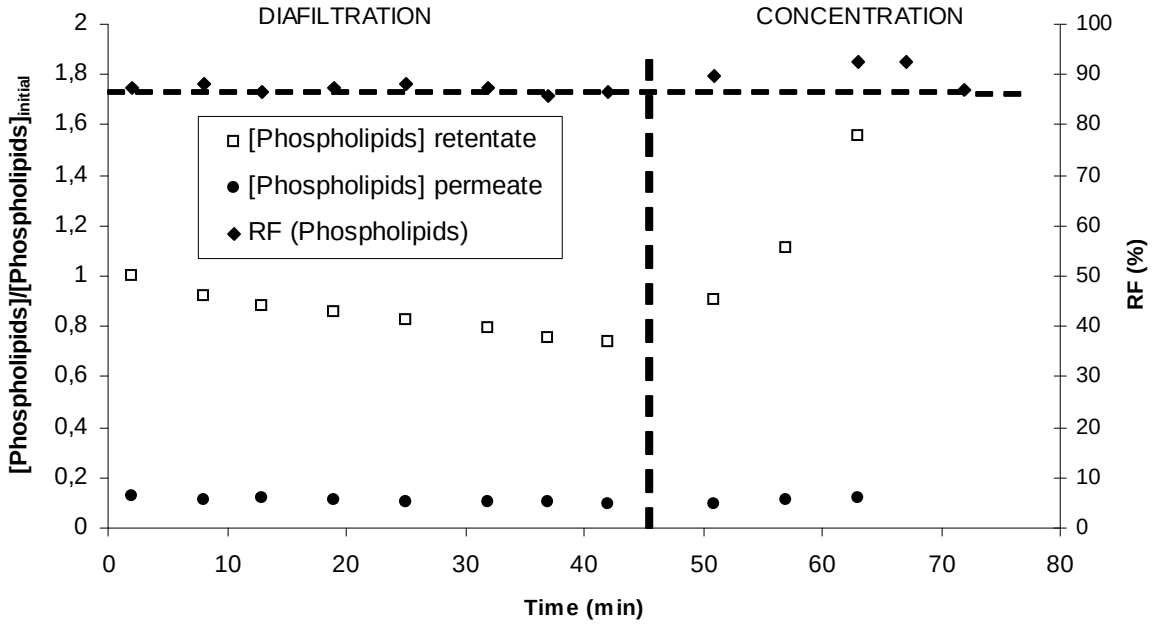

Figure 5: Variation of the phospholipids concentration and retention factor versus time (T_{ave} = 20°C, TMP = 15 bar, Q = 300-350 $L.h^{-1}$, V_0 = 15 L)

Conclusion

The nanofiltration has been tested in this study to eliminate cholesterol from egg yolk in ethanolic solution in order to make nutritional supplements. This method was efficient because the cholesterol has been removed and the losses of other products of interest have been limited. This separation technique is also very interesting for this industry area because of the safety of these processes. This process can be used for a lot of other separations in paraphamaceutical or pharmaceutical industries. It could be used to eliminated an unwished or dangerous product, as in our case, but it also could be used to recycle active substance. Going further in the field of nanofiltration in organic solvent, it will be necessary to test others solvents than ethanol and to understand in deep the interactions solvent membranes.

References

[1] Tokarska, B., M.T. Clandinin. Extraction of egg yolk oil of reduced cholesterol content. Can. Inst. Food Sci. Tech. J., 18 (1985) 256-258.

[2] Rossi M., A. Schiraldi and E. Spedicato. Supercritical fluid extraction of cholesterol and its oxidized products from eggs: premiminary experiments. Developments in Food Science, 24 (1990) 855-863.

[3] Tsui, E.M. and M. Cheryan. Characteristics of nanofiltration membranes in aqueous ethanol. J. Memb. Sci, 237 (2004) 61-69.

Proceedings of the 10th International Chemical and
Biological Engineering Conference - CHEMPOR 2008
Braga, Portugal, September 4-6, 2008
E.C. Ferreira and M. Mota (Eds.)

Beer aroma recovery by pervaporation

Margarida Catarino[1], Luis M. Madeira[1], António Ferreira[2], Adélio Mendes[1*]
[1] LEPAE, Chemical Engineering Department, Faculty of Engineering, University of Porto, Rua Roberto Frias, 4200-465 Porto, Portugal
[2] Unicer Bebidas S.A., Via Norte, Leça do Balio, Matosinhos, Apartado 1044, 4466-955 S. Mamede de Infesta, Portugal

Keywords: Beer, Aroma Compounds, Pervaporation, Response Surface Methods
Topic: Advancing the chemical and biological engineering fundamentals

Abstract

In this work, the extraction of beer aroma compounds by pervaporation was studied, using polyoctylmethylsiloxane/polyetherimide (POMS/PEI) composite asymmetric membranes. A design of experiments, using a response surface methodology (RSM), was applied to obtain the hyper-surface of the process responses. The process factors or independent variables selected were the feed temperature, feed velocity and permeate pressure, while the process responses were the permeate flux, the selectivity towards selected aroma compounds (high alcohols and esters) and the relationship between the concentration of these class of aromas in the permeate. RSM methods generate polynomial models that relate the operation conditions and the process responses, which are thus useful for predicting purposes or for processes optimization. A good agreement between the experimental results and the predicted values was observed, therefore allowing process optimization that was experimentally validated.

1 Introduction

Beer aroma profile is constituted by many volatile organic compounds at very low concentration (ppm level), which are responsible for its flavour. Compounds from several chemical groups, such as alcohols, esters, aldehydes, lactones, carboxylic acids, phenols and ethers, can be found on beer composition, imparting it a particular flavour. For instance, esters are responsible for sweet and fruity flavours, while aldehydes are associated to the beverage freshness. Alcohols, which are the major group of aroma compounds in this beverage (ethanol is the compound in highest quantity), confer an alcoholic, fruity and immature flavour to the beer (Catarino et al., 2007).

Beer treatment processes, such as pasteurization or dealcoholization, submit it to extreme conditions (namely high temperatures) that cause the loss of important aroma components. The aroma recovery from beverages is therefore becoming a critical food processing operation (Karlsson and Trägårdh, 1997).

In order to overcome the beer aroma loss, particularly in processes aiming non-alcoholic beer production, it is possible to extract the aroma compounds before submitting the beverage to the heat processing (Mendes et al., 2007). Nowadays there is observed an increasingly offer in processes for aroma extraction, being membrane-based processes most promising. Pervaporation gained an important role on this area due to its high selectivity and the possibility of being carried out at low temperatures, which is advantageous for removing thermosensitive compounds (Karlsson and Trägårdh, 1997).

The main goal of this study was the extraction of beer aroma compound by means of pervaporation. A response surface methodology (RSM) with a central composite design

* Corresponding author. Tel + 351-22-5081695. E-mail:mendes@fe.up.pt

(CCD) was used to analyze the effect of critical operation conditions on the process performance and to select the operation conditions that optimize the process responses.

2 Experimental

In all experimental runs a regular alcoholic beer, from the same batch, was used as feed solution; membranes made of POMS/PEI, gently provided by GKSS (Geesthacht, Germany), were applied.

Pervaporation experiments were carried out using a semi-batch lab unit (Mendes et al., 2007). The laboratorial set-up is illustrated in Figure 1.

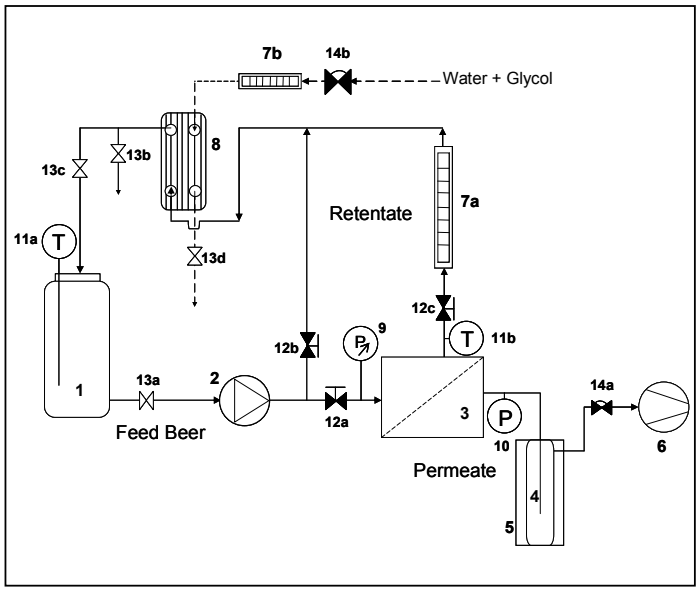

Figure 1. Pervaporation lab set-up.

Beer stored in the feed tank (1 – cf. Figure 1) was circulated with a centrifuge pump (2, Efacec, Model E-JETMA/A100) through the membrane cell (3) which membrane effective area is 107.46 cm^2. Part of the feed returned back to the tank through a plate heat exchanger (8, Arsopi, Model FH00-HJ-15, with 0.20 m^2 transfer area) and the rest as retentate stream. In the membrane cell, the feed aroma compounds permeate through the membrane, due to the vacuum applied to the downstream side by means of a vacuum pump (6, Boc Edwards, RV5). Once the aroma compounds leave the membrane as vapour, a condensation system was connected before the vacuum pump in order to condense the permeate. The condensation system consisted in a stainless steel cold trap (4), which was immersed in liquid nitrogen at -196 ºC, stored in a dewar flask (5). Three needle valves (12a, 12b and 12c) regulated the feed pressure and the flowrate of feed and retentate streams. A manometer (9) measured the feed pressure while the downstream pressure was determined by a pressure sensor (10, Druck, PMP 4010), which was regulated by a diaphragm valve (14a) placed at the vacuum pump inlet. The feed and membrane cell temperatures were read using two thermocouples (11a – C.L.V. PT100, 11b – Eurotherm, PR12-K-15-200) and they were adjusted by tuning the refrigerated fluid flow rate in a diaphragm valve (14b). Two rotameters (7a and 7b) measure the retentate and cooling water flowrate.

The operating conditions selected in the design of experiments analysis were the feed temperature, feed velocity and permeate pressure because preliminary runs showed that feed pressure has almost no effect on the responses considered. According to the CCD, implemented using JMP5.1, SAS software, the levels of the process factors are those depicted in Table 1. Note that axial value (α) is equal to the unity, because it was aimed to perform experiments considering only operation conditions within the factor's levels, in order to explore the entire region of operation/interest.

Table 1. CCD factors and respective levels.

Factor	Symbol	Level				
		-α	-1	0	+1	+α
T_f (ºC)	x_1	5.0	5.0	10.0	15.0	15.0
v_f (m·s^{-1})	x_2	0.1	0.1	0.3	0.5	0.5
P_l (mbara)	x_3	1.0	1.0	10.5	20.0	20.0

The process responses considered were the permeate flux, the selectivity towards selected aroma compounds and the relationship between the aromas concentration in the permeate. The most important beer aroma compounds are high alcohols and esters. The chosen selected aroma compounds for quality control were ethyl acetate - EA and isoamyl acetate - iAA (esters) and propanol - Pr, isobutanol - iB and amyl alcohols - AA (high alcohols).

The permeate flux, J_p (kg·m^{-2}·s^{-1}), the selectivity towards aromas against ethanol, $\alpha_{i/E}$, and the high alcohols/esters ratio, *A/E*, were evaluated by the following equations:

$$J_p = \frac{m_p}{a\,t} \quad (1) \quad ; \quad \alpha_{i/E} = \frac{w_{p,i}/w_{p,E}}{w_{b,i}/w_{b,E}} \quad (2) \quad \text{and} \quad A/E = \frac{C_{high\ alcohols}}{C_{esters}} \quad (3)$$

were m_p is the mass of condensed permeate, *a* is the effective membrane area, *t* is the permeation time, and w_p and w_b stand for the mass fractions on the condensed permeate and on the feed bulk, respectively. Subscripts "*i*" and "*E*" denote the aroma compound and ethanol, respectively. $C_{high\ alcohols}$ and C_{esters} are the concentrations of high alcohols and esters, respectively.

Aromas concentrations were analyzed using a gas chromatograph (Varian Star 3400) and the ethanol content was determined using and an Alcolyzer Plus (Anton Paar) meter.

3 Results and discussion

Using the experimental results of all the 17 CCD runs (data not shown), second order polynomial models were fitted, which describe the influence of the main operation conditions on the pervaporation responses. The significance of the models was verified based on the analysis of variance (ANOVA) of the results (Montgomery, 2001). The relation between process responses and process factors is described by the following equations:

$$J_p \times 10^5 = 3.781 + 1.560X_1 + 0.311X_2 - 1.869X_3 - 0.329X_1X_3 + 0.918X_3^2 \quad (4)$$

$$\alpha_{Pr/E} = 1.272 + 0.027X_1 + 0.004X_2 - 0.150X_3 + 0.043X_1X_2 \quad (5)$$

$$\alpha_{iB/E} = 2.460 + 0.073X_1 + 0.073X_2 - 0.345X_3 + 0.095X_3^2 \quad (6)$$

$$\alpha_{AA/E} = 2.599 + 0.174X_1 + 0.072X_2 - 0.600X_3 + 0.243X_3^2 \quad (7)$$

$$\alpha_{EA/E} = 18.619 - 2.910X_1 + 2.057X_2 + 1.838X_3 - 0.920X_1X_3 - 1.612X_2^2 \quad (8)$$

$$\alpha_{iAA/E} = 24.292 - 4.612X_1 + 3.678X_2 + 4.138X_3 - 1.881X_1X_3 - 1.841X_2^2 - 0.881X_3^2 \quad (9)$$

$$A/E = 0.719 + 0.196X_1 - 0.105X_2 - 0.259X_3 - 0.046X_1X_2 - 0.024X_1X_3 + 0.061X_2X_3 + 0.052X_2^2 + 0.142X_3^2 \quad (10)$$

were X_1, X_2 and X_3 are the coded process parameters (cf. Table 1), which are determined from the real factor values (and their null points and variation intervals) as follows:

$$X_1 = \frac{x_1 - 10}{5}; \quad X_2 = \frac{x_2 - 0.3}{0.2}; \quad X_3 = \frac{x_3 - 10.5}{9.5} \quad (11)$$

A comparison between experimental results and predicted values, obtained by Equations 4 to 10, is represented in the parity plots shown in Figure 2.

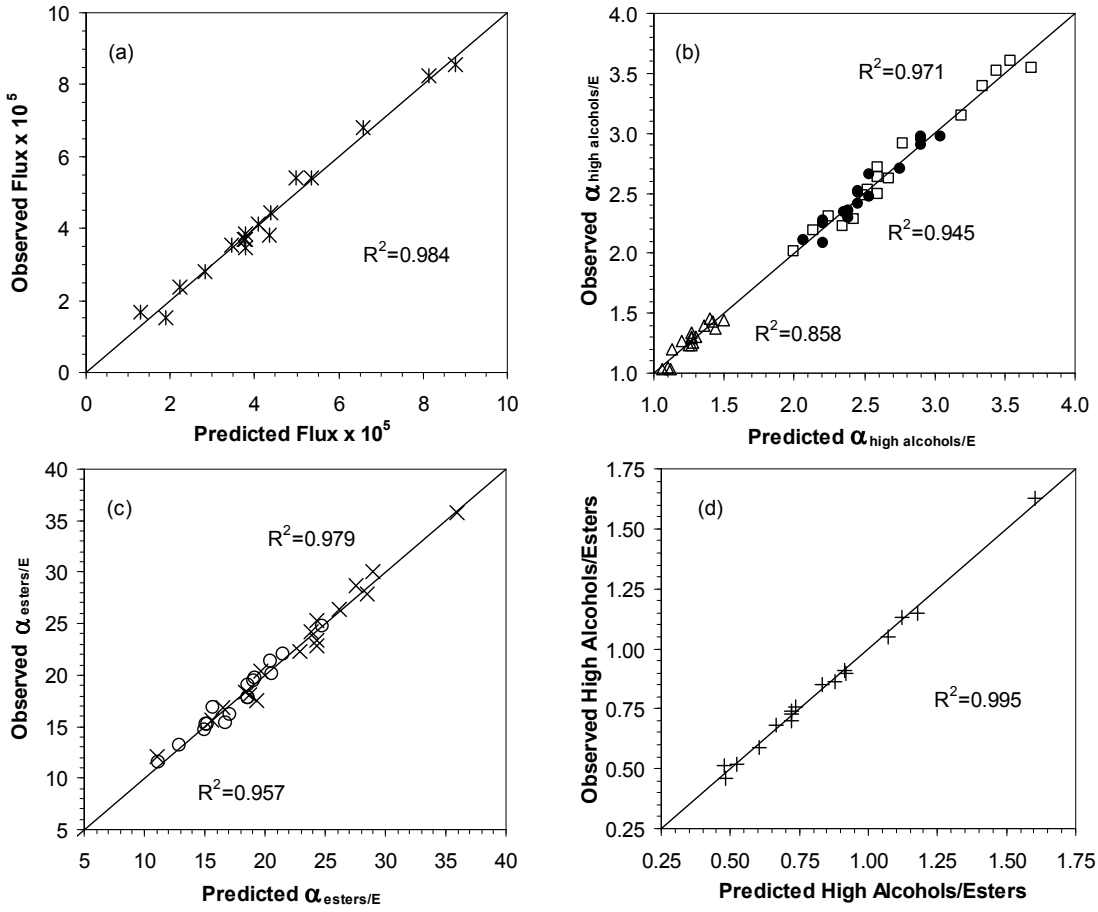

Figure 2. Comparison between predicted values and experimental results for: (a) permeate flux ($kg \cdot m^{-2} \cdot s^{-1}$); (b) high alcohols selectivity (△ propanol, ● isobutanol, □ amyl alcohols); (c) esters selectivity (○ ethyl acetate and × isoamyl acetate); and (d) high alcohols/esters ratio.

Figure 2 shows a good agreement between observed and predicted values (values very close to the plot's diagonals), meaning that the residuals are vey low. On the other hand, coefficient of determination (R^2) varied from 0.858 to 0.995, which is reasonably acceptable.

From these results, it is verified that esters show higher selectivities than high alcohols, according to the following order: isoamyl acetate > ethyl acetate > amyl alcohols > isobutanol > propanol. These results are consistent with the ones found by Börjesson et al. (1996).

The developed models can be used to predict the effect of the operation variables on process responses. Figures 3 and 4 show the surface response plots of the permeate flux and of the ratio between high alcohols and esters concentrations as a function of the independent variables, respectively. One can observe that permeate flux increases with temperature due to the increase of membrane permeability with such variable (Arrhenius dependence) and that it also slightly increases with the feed velocity (Figure 3a). On the other hand, the higher the permeate pressure the lower the membrane flux, due to the decrease of the process driving force, according to the solution-diffusion model (Karlsson et al., 1995). The effect of the operation conditions on the aromas selectivity's assumes different trends according to the compounds nature. In general, high alcohols selectivity increases with temperature (X_1), due to their transport activation energy being higher than that of water. High alcohols selectivity also slightly increases with feed velocity (X_2), meaning that they are affected by concentration polarization, and finally it decreases with permeate pressure (X_3), due to their low volatilities (cf. Eqs. 5, 6 and 7). On the other hand, esters selectivity decreases with temperature. It increases strongly with feed velocity, since they are the most permeable compounds and consequently, they are highly affected by concentration polarization. Esters selectivity also increases with permeate pressure due to their high

volatilities (cf. Eqs. 8 and 9). As a result, the ratio between high alcohols and esters concentrations increases with temperature but decreases with feed velocity and permeate pressure (cf. Figure 4 and Eq. 10). These results are also in agreement with other studies previously reported (Lipnizki et al., 2002; Karlsson et al., 1995).

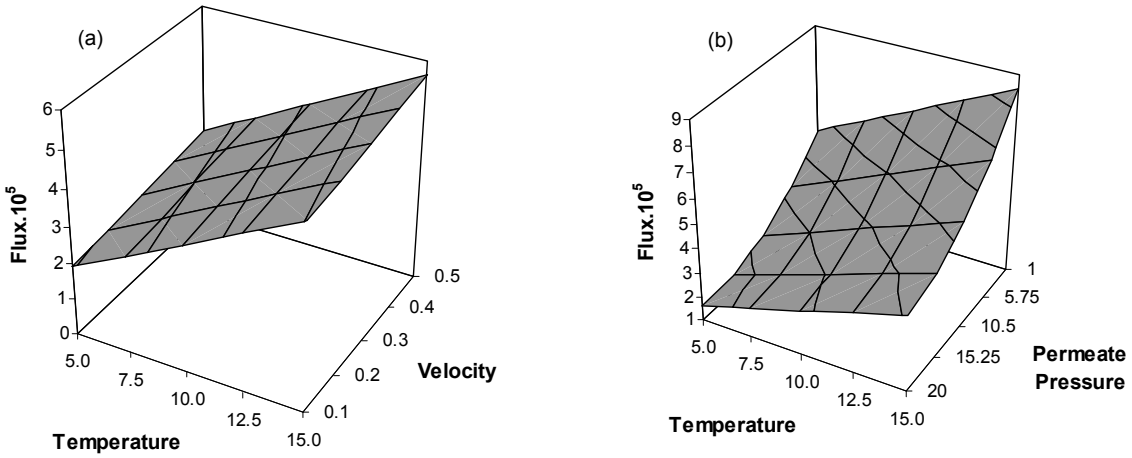

Figure 3. Influence of process variables on the permeate flux: (a) feed temperature and feed velocity, keeping permeate pressure at middle point (10.5 mbara); (b) feed temperature and permeate pressure, keeping feed velocity at middle point (0.3 $m \cdot s^{-1}$).

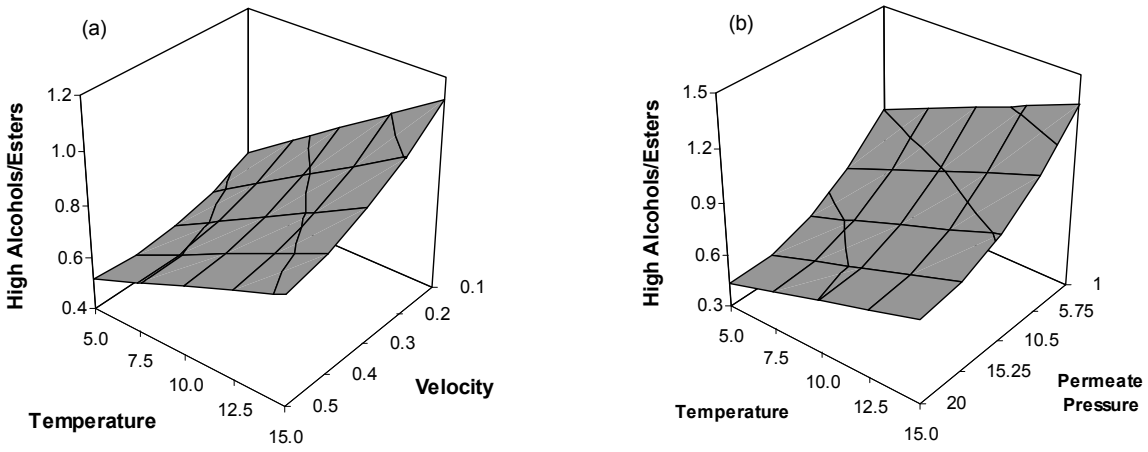

Figure 4. Influence of process variables on the high alcohols/esters ratio: (a) feed temperature and feed velocity, keeping permeate pressure at middle point (10.5 mbara); (b) feed temperature and permeate pressure, keeping feed velocity at middle point (0.3 $m \cdot s^{-1}$).

In order to optimize all the responses simultaneously (maximization of permeate flux,aroma selectivity's and high alcohols/esters ratio), the desirability fuction was applied (JMP5.1, SAS), giving the same importance (weight = 1) to all the responses The optimal operation conditions found were the following: 12.4 ºC for feed temperature (x_1), 0.45 $m \cdot s^{-1}$ for feed velocity (x_2) and 1.00 mbara for permeate pressure (x_3). For these conditions, the predicted responses and intervals of variation are given in Table 2, along with the experimental values, which were performed to validate the adequacy of the models. From Table 2 it is observed that observed process responses lie whithin the predicted range of confidence, except for amyl alcohols selectivity and high alcohols/esters ratio, although they show acceptable values. Hence, it can be said that the developed models were reasonably valid and thus useful for process optimization.

Table 2. Results of optimization conditions and confirmation runs.

	$J_p \times 10^5$ ($kg \cdot m^{-2} \cdot s^{-1}$)	$\alpha_{Pr/E}$	$\alpha_{iB/E}$	$\alpha_{AA/E}$	$\alpha_{EA/E}$	$\alpha_{iAA/E}$	*A/E*
Min predicted	7.26	1.31	2.87	3.39	14.46	17.10	1.07
Target	7.82	1.44	3.01	3.59	15.97	19.06	1.12
Max predicted	8.38	1.56	3.14	3.78	17.48	21.03	1.17
Observed	8.15	1.53	3.11	3.89	15.50	18.31	1.26

4 Conclusions

RSM was used for studying the extraction of beer aroma compounds by pervaporation and analyzing the effect of operation conditions on the process responses. The responses which were aimed to optimize were the permeate flux, beer aroma compounds selectivity's and high alcohols to esters ratio on the permeate.

Analysis of variance and surface plots revealed that permeate flux increases with temperature and feed velocity, whereas it decreases with permeate pressure. In contrast, these factors have different significances and influences on the aromas selectivity's, depending on their nature. High alcohols selectivity's increases with temperature and feed velocity while it decreases with permeate pressure; esters selectivity is negatively affected by temperature and is positively affected by velocity and permeate pressure. Consequently, high alcohols/esters ratio increases with temperature and decreases with feed velocity and permeate pressure.

Since process variables have different/opposite effects on the responses, the Desirability function was used for optimizing the trade-off between multiple responses. The responses in the optimum conditions were experimentally confirmed, meaning that the developed models were reasonably accurate.

Acknowledgements

M. Catarino acknowledge the Portuguese Foundation for Science and Technology (FCT) for the PhD grant (SFRH/BDE/15564/2005). The authors are grateful to GKSS research group for the kind supply of the pervaporation membranes.

References

Börjesson, J., Karlsson, H.O.E., Trägårdh, G (1996). Pervaporation of a model apple juice aroma solution: comparison of membrane performance. Journal of Membrane Science, 119, 229–239

Catarino, M., Mendes, A., Madeira, L.M., Ferreira, A. (2007). Alcohol Removal From Beer by Reverse Osmosis. *Separation Science and Technology,* 42, 3011-3027.

Karlsson, H.O.E., Loureiro, S., Trägårdh, G. (1995). Aroma compound recovery with pervaporation – temperature effects during pervaporation of a muscat wine. Journal of Food Engineering, 26, 177–191

Karlsson, H.O.E., Trägårdh, G. (1997). Aroma Recovery During Beverage Processing. *Journal of Food Engineering,* 34, 159-178.

Lipnizki, F., Olsson, J., Trägårdh, G. (2002). Scale-up of pervaporation for the recovery of natural aroma compounds in the food industry. Part 1: Simulation and Performance. Journal of Food Engineering, 54, 183–195.

Mendes, A., Madeira, L.M., Catarino, M. (2007). Process for Enriching the Aroma Profile of a Beverage Obtained by Dealcoholization. PT103657.

Montgomery, D.C. (2001). Design and Analysis of Experiments, 5th Edition, John Wiley & Sons, New York.

Proceedings of the 10th International Chemical and
Biological Engineering Conference - CHEMPOR 2008
Braga, Portugal, September 4-6, 2008
E.C. Ferreira and M. Mota (Eds.)

Determination of the wall shear stress by numerical simulation: membrane process applications

Fanny Springer[1], Rémy Ghidossi[2], Emilie Carretier[1], Damien Veyret[2], Didier Dhaler[3] and Philippe Moulin [1*]

[1] Université Paul Cézanne Aix Marseille (M2P2, CNRS-UMR 6181), Europôle de l'Arbois, Bâtiment Laennec, Hall C, 13545 Aix en Provence Cedex 4, France
[2] POLYTECH Marseille, (CNRS-UMR 6595) Technopôle de Château-Gombert, 5 rue Enrico Fermi, 13453 Marseille Cedex 3, France
[3] NOVASEP – APPLEXION SAS Site Saint Maurice de Beynost 5 Chemin du Pilon 01708 Miribel, France

Keywords: Computational fluids dynamics, wall shear stress, channel, geometry, ceramic membrane, fouling
Topic: CFD & Chemical Engineering

Abstract

Membrane processes have been intensely developing during the last decades, and mainly in dairy industries. Considering the feed effluent complexity, concentration polarization (CP) phenomenon and fouling are accentuated limitations for the development of membrane dairy filtration processes. Knowledge of the wall shear stress developed at the membrane science is fundamental to reduce those phenomena. In our work, we studied the repartition of the wall shear stress on cylindrical, square, triangular and hybrid channels by numerical simulation for various operating parameters. We aimed at establishing predictions for different commercial ceramic membranes and predict the geometry that tends to enhance mass transport characteristics by enhancing hydrodynamics conditions. Numerical simulations are performed over a typical range of Reynolds numbers inside different channel geometry under laminar and turbulent conditions. Consequently, this paper intended to enhance the performances of these processes by maximizing the average wall shear stress on the membrane surface by numerical simulation. A comparison with experimental results has been realized and a good agreement is obtained. Given those conclusions, we designed a new membrane according to the whole CFD results consistent with experimental results.

1 Introduction

In dairy industries, microfiltration is more and more used for milk sterilizing and casein separation. Ultrafiltration is currently the most used process for applications as protein separations or milk composition standardization. Considering the feed effluent complexity, concentration polarization (CP) phenomenon and fouling are accentuated limitations for the development of membrane dairy filtration processes. The accumulation of materials near the membrane, with the deposition of colloids and suspended solids triggers the reduction of its performances. Fouling strongly depends on the wall shear stress that occurs from radial velocity gradient during the filtration step. So, better knowing the wall shear stress is fundamental to reduce the fouling phenomena. Enhancing turbulence to the membrane surface: Dean vortices (Moulin et al., 1999), dynamic filtration (Koutsou et al., 2004) and unsteady flows (Krstic et al., 2002) enables indeed to increase the mass transfer coefficient and sweep the deposition at the surface (Noriatsu et al., 2001).

* Corresponding author. Tel (+ 33) 4 42 90 85 01. E-mail:philippe.moulin@univ-cezanne.fr

It was shown, in previous works on various effluents filtrations, that the limiting permeate flux was linked to the wall shear stress by a phenomenological relation $J_{lim} = A\tau^n$ with J_{lim} the limit permeate flux ($m.s^{-1}$) and τ the wall shear stress (Pa) (Manno et al.,1998 ; Moll et al., 2007). The simplified approach considered for our work was "the higher the shear stress, the higher the permeate flux". No mass transfer model was used. So, our work aimed at finding the channel geometry that shows the optimal wall shear stress to reduce uttermost the fouling. We also determined the influence of the channel section and the membrane process parameters (transmembrane pressure (TMP), flow rate…) on the wall shear stress characteristics. Given these results, the final purpose was to design the most appropriate membrane for the intended application.

2 Materials and methods

For this aim, numerical modelling tool appears as the most appropriate (Ghidossi et al. 2006). It permits to better apprehend complex mechanics and to reduce experiments number. Computational Fluid Dynamics (CFD) has become an effective tool to attain these objectives more quickly and cost effectively.
Numerical simulations were made for high Reynolds numbers in complex geometries. A large range of MF and UF cases was studied in this work for a more accuracy prediction of the wall shear stress. The problem was studied in 3D. The grid was refined near the wall with the intention of resolving the laminar sub-layer. We used RNG k-ε model for it appears in literature as preferentially used in turbulent flow. We consider the wall as impermeable. This assumption could be validated: (i) in ceramic membrane, the permeate flow is often lower than 2% of the circulating flow; (ii) it was shown that the wall shear stress can be calculated in permeable tube with the value obtained in no permeable tube and the value of permeate flow (Moll et al. 2007).

3 Results and discussion

3.1 Influence of the membrane channel geometry

The raw simulation results enable to obtain the variation of the wall shear stress according to the section of the channel for different flow velocities. On Figure 1 are represented the caracteristics of the wall shear stress for the different geometries studied. A logical and periodic variation of wall shear stresses according to the perimeter is obtained for all inlet velocities and simulated geometries. As expected, the cylindrical geometry develops a constant wall shear stress. For the other geometries, the results obtained by numerical simulation prove that the distribution of wall shear stress presents a maximum which is located in the middle of the side and a minimal value at the angle of the square for any rate of flow (laminar or turbulent flow).
The variation of the wall shear stress on the triangular geometry has many analogies with those observed on the square geometry. Indeed, a maximum of wall shear stress is observed in the middle of each edge which decreases progressively until reaching a minimal value on the corner for a constant section. Considering only the maximal values of the wall shear stress, the optimal configuration is the triangular one and secondly the square and cylinder geometries.
The simulations showed that there is no influence of the velocity on the ratio τ_{local}/τ_{max}. Only the geometry has an influence on this ratio and the importance of the dead zones created. The Figure 2 synthesizes simulated results and represents the variation of the average wall shear stresses for different geometries. It appears that the wall shear stress reduces with an increasing channel section. The cylindrical geometry offers the highest values in term of wall shear stress for the smallest section (4.0 mm^2). For the largest sections, the triangular geometry is more advantageous. The square geometry shows lower performances.

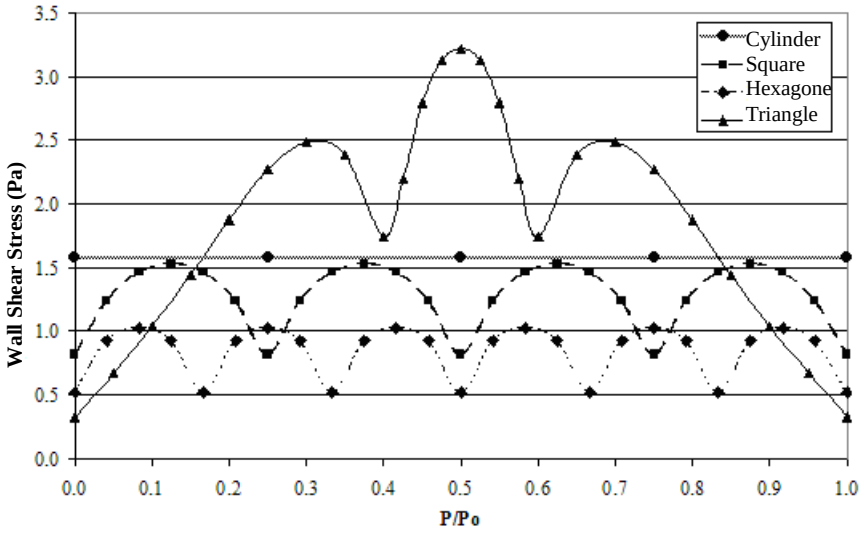

Figure 1. Variation of the wall shear stress vs. perimeter position for different channel geometries(Re = 1128, S = 4 mm^2)

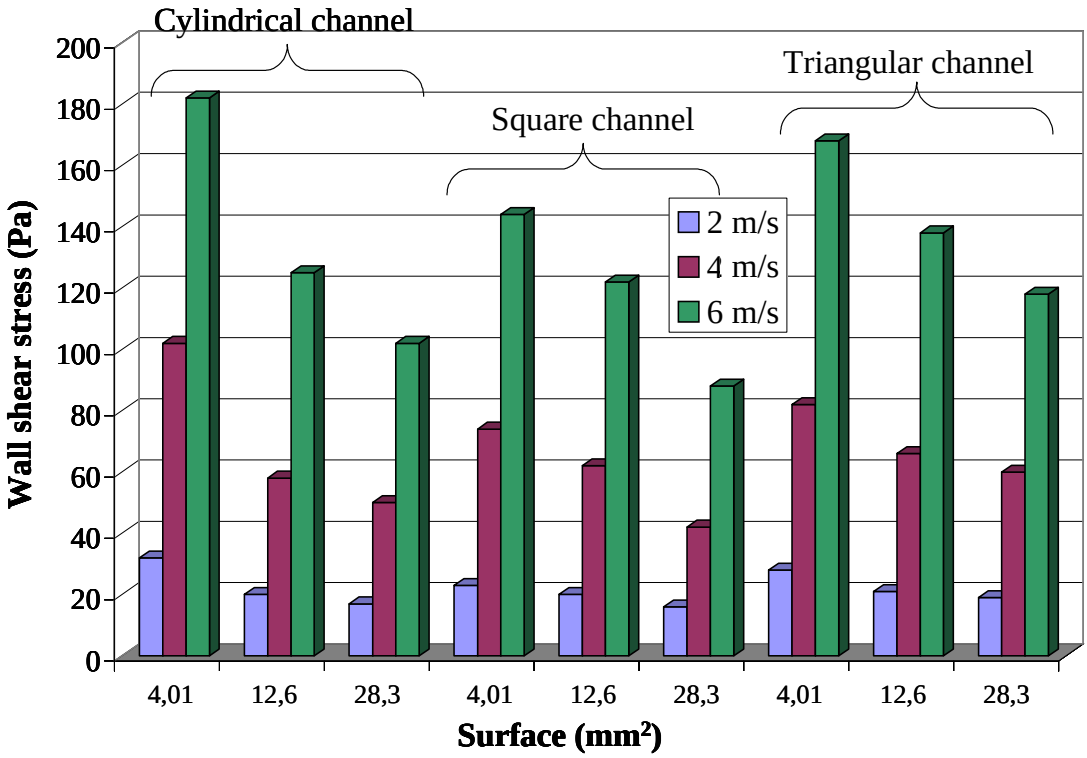

Figure 2. Variation of average wall shear stresses vs. channel surfaces for different geometries and different velocities

It is possible to obtain the local values of the wall shear stress by numerical simulations and to calculate an average value with the perimeter. Given those studies, we can design a new membrane prototype more appropriate for the complex filtration process when it comes to dairy effluents. The Evolution prototype has a hybrid form channel. Considering the effluent of milk, which is strongly fouling and pressure losses triggering, large channel sections were chosen for industrial productivity reasons. The choice of the channel shape is justified by the efficiency of the triangular geometry for high values of channel sections. Nevertheless, the angles are subjected to a rapid fouling, which affects the process performances during the filtration step and the regeneration step. We chose to round the corners so as to obtain a

heart-like channel shape, as shown on Figure 3, more likely to satisfy industrial objectives.

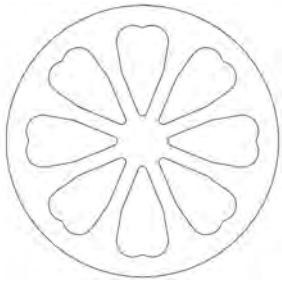

Figure 3. Hybrid shape of the Evolution membrane

The advantage of our simplified approach is the global view of the system Disadvantage is: predicting permeate flux is impossible and only comparisons are acceptable. An experimental campaign was necessary to validate this approach.

3.2 Validation of the modeling results and comparison of commercial membrane performances

The results of milk ultrafiltration campaigns are presented on Figure 4. The milk characteristics are given in Table 1. The reversible resistance was experimentally measured after rinsing the membrane after the filtration process, for different commercial ceramic membranes (15 KDa) with various geometries and sections. This characteristic shows how the wall shear stress influences the reversible resistance whatever the membrane geometry or section considered.

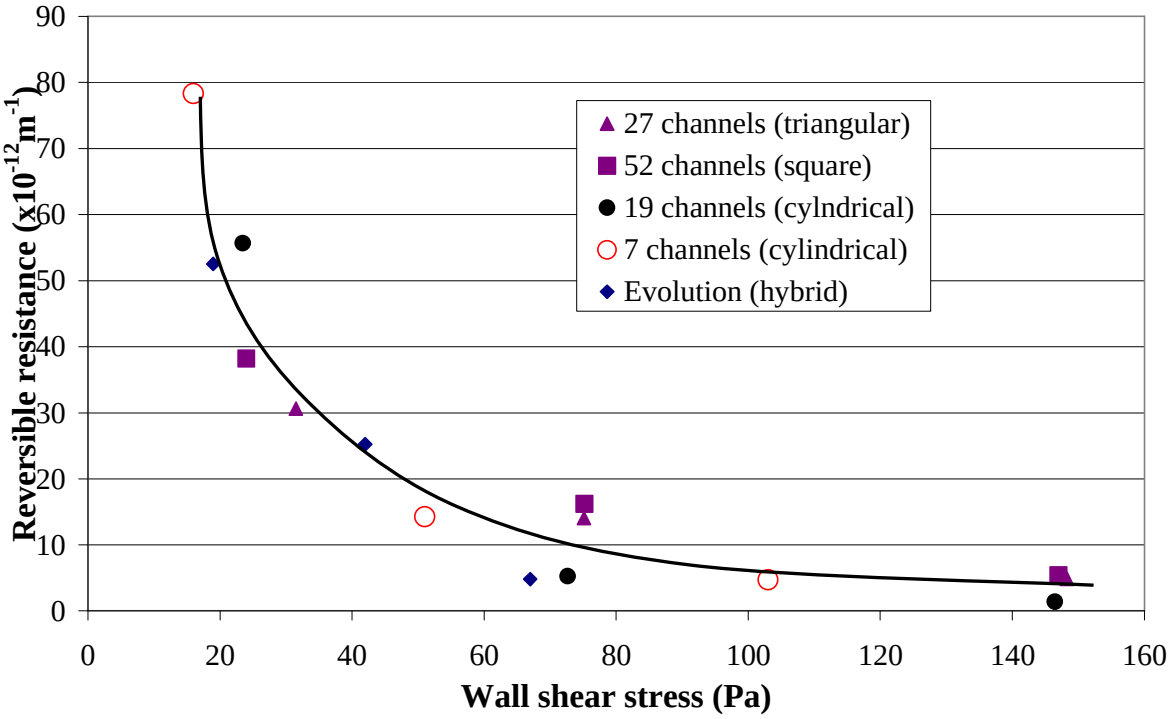

Figure 4. Variation of the reversible resistance vs. wall shear stress for different membranes

For all geometries, irreversible fouling also decreases with an increasing wall shear stress, so our simplified approach is validated.

Table 1. UHT milk composition

Compounds	Concentration ($g.L^{-1}$)
Glucids	49
Grease matter	39
Casein	25,6
Lactose	46
Calcium	1,2
Salt	9
Water	900
Density	1030

Moreover this figure shows an identical behaviour of the reversible resistance according to the wall shear stress values given by simulations, whatever the membrane considered: this validates our simulations results. Furthermore, beyond a value of ≈70 Pa for the wall shear stress, the reversible resistance remains very low, so it is of high interest to privilege geometries that enable to reach such an average value of wall shear stress.
The ultrafiltration experimental campaign enabled us to compare the commercial membrane performances. The results are shown on Figure 5 that represents the membrane production in term of permeate flux ($m^3.h^{-1}$) as a function of the process tangential velocity.

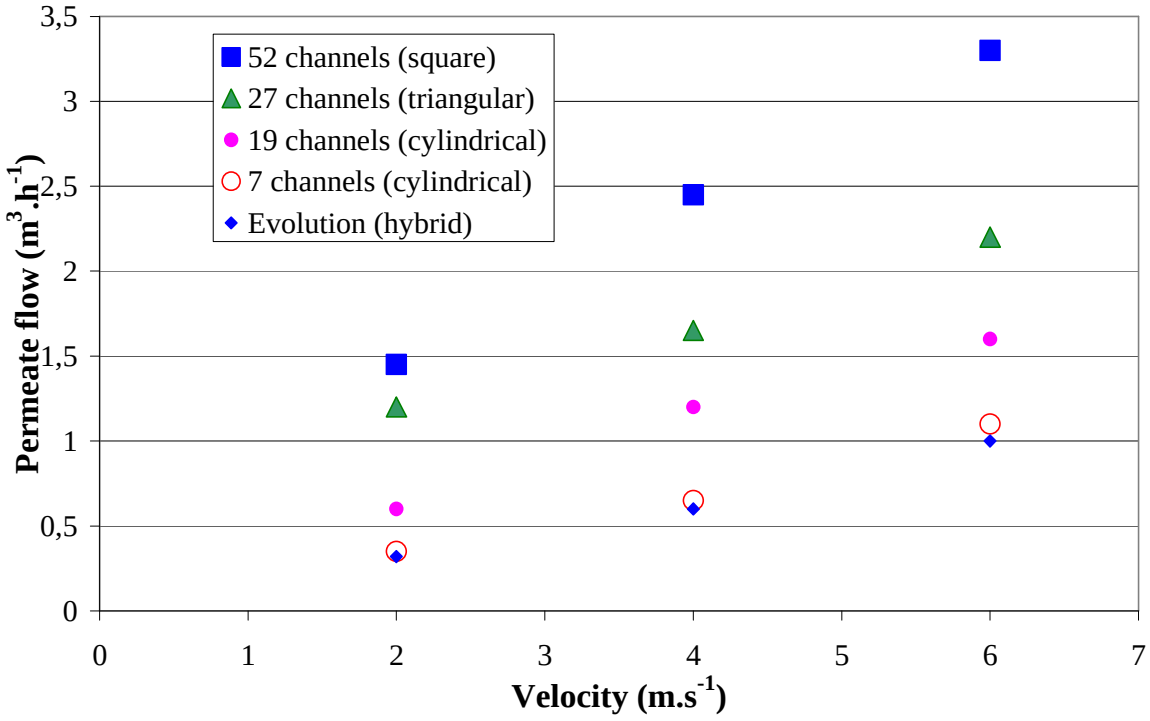

Figure 5. Variation of the permeate flow vs. tangential velocities for different membranes (TMP 2 bars)

Considering those results, the 52 channels membrane shows the most interesting performances and presents the real advantage to offer a surface definitely more important than the other geometries considered (0.50 m²). So, the production in term of permeate flux is expected to be more important than the other membranes. The 27 channels membrane with large channels (0.35 m²) section appears as interesting configuration. The choice of this geometry is coherent to permit an optimization. Nevertheless, the drawbacks previously developed of such geometries must be taken into account: the problem given by the corners in square and triangular geometry facilitates fouling what presents a weak point for the industrialization. Following the performances hierarchy, 7 channels (0.15 m²) or 19 channels

(0.25 m^2) membranes present larger sections and give high and similar performances. Considering fouling issues, the cylindrical geometry can show advantages that could counterbalance the lower production rate. Finally, the Evolution prototype shows interesting performances. The permeate flux produced is similar to the 7 channels cylindrical membrane performances.

4 Conclusion

This modeling work relies on the simplified approach: “the higher the shear stress is, the more satisfactory the permeate flux will be”. So, our simulation results enabled us to obtain the variation of the wall shear stress according to the section of the channel for different flow velocities under laminar and turbulent conditions. We compared the influence of different parameters such as the channel geometry, the channel section and the operating parameters on the process performances. The channel geometry was then optimized by maximizing the average wall shear stress on the membrane surface. A comparison with experimental results obtained during milk ultrafiltration campaigns has been realised and a good agreement is obtained. Moreover an identical behaviour of the reversible resistance according to the wall shear stress values given by simulations, whatever the membrane considered is showed. This shows our simulation results and modelling approach are validated. So, this methodology is relevant to design new membrane geometries intended to specialized applications. In this study, we concentrated on the complex and fouling effluent of milk and dairy co-products. Finally, a compromise between membrane area, channel geometry and energy consumption must be taken into account for optimizing those processes.

References

Ghidossi R., D. Veyret and P. Moulin, (2006) Computational fluid dynamics applied to membranes: State of the art and opportunities, *Chem. Eng. Pro.*, 45: 437-454.

Koutsou C.P., S.G. Yiantsios and A.J. Karabelas, (2004) Numerical simulation of the flow in a plane-channel containing a periodic array of cylindrical turbulence promoters, *J. Membr. Sci.*, 231:81-90.

Krstic D.M., M.N. Tekic, M.D. Caric and S.D. Milanovic, (2002) The effect of turbulence promoter on cross-flow microfiltration of skim milk, *J. Membr. Sci.*, 208: 303-314.

Manno P, Moulin P, Rouch JC, Clifton M and Aptel P (1998). Mass transfer improvement in helically wound hollow fiber ultrafiltration modules: Yeast suspensions. *Sep. Pur. Tech.*, 14, Issues 1-3:175-182.

Moll R, Veyret D, Charbit F, Moulin P. (2007). Dean vortices applied to membrane process. Part II. Numerical approach. *J. Membr. Sci.*, 288:321-335.

Moulin P., P. Manno, J. C. Rouch, C. Serra, M. J. Clifton and P. Aptel, (1999) Flux improvement by Dean vortices: ultrafiltration of colloidal suspensions and macromolecular solutions, *J. Membr. Sci.*, 156: 109-130.

Noriatsu O. and K. Yamamoto, (2001) Hydraulic effects on sludge accumulation on membrane surface in crossflow filtration, *Water Research,* 35: 3137-3146.

Proceedings of the 10th International Chemical and
Biological Engineering Conference - CHEMPOR 2008
Braga, Portugal, September 4-6, 2008
E.C. Ferreira and M. Mota (Eds.)

Active mixing strategies for Confined Impinging Jets

M. Ashar Sultan[1], Ertugrul Erkoç[1], Ricardo J. Santos[1], Madalena M. Dias[1], José Carlos B. Lopes[1,2*]

[1] LSRE– Laboratory of Separation and Reaction Engineering
Faculdade de Engenharia da Universidade do Porto, Dept. Eng. Química
Dr. Roberto Frias, 4200-465 Porto, Portugal
[2]Fluidinova, Engenharia de Fluidos, S.A.,
TECMAIA, Rua Engº Frederico Ulrich, 2650
4470-605 Moreira da Maia - Portugal

Abstract

The effect of the feed streams pulsation on the flow dynamics in a Confined Impinging Jets (CIJ) reactor was studied in this work. Different frequencies and amplitudes are studied. The out phase pulsation of the opposed jets with frequency close to natural oscillation frequencies enhances the order of the system, yielding a well defined vortices street. The results showed that the amplitude of the jets oscillations has a strong effect on the flow dynamics, up to the extreme case where the imposed pulsation completely drives the dynamics of the system.

Introduction

Confined impinging jets (CIJ), where two opposed jet streams impinge each other in a confined mixing chamber have a wide range of applications, mainly for the production of polyurethanes in Reaction Injection Molding, RIM, and in precipitators. The flow regime in the mixing chamber can be oscillatory or self sustainable chaotic. In self sustainable chaotic flow regimes, the jet streams engulf each other in evolving vortices throughout the mixing chamber, see Figure 1 for $Re = 150$. In oscillatory flow regimes both streams flow segregatedly throughout the mixing chamber, see Figure 1 for $Re = 100$. In self sustainable chaotic flow regimes the vortices formation is associated with strong oscillations of the jets' impingement (Teixeira et al., 2005) that present frequencies around typical values, while the oscillatory flow regimes present low amplitude oscillations with very well defined frequency. Erkoç et al.(2007) reported the usage of dynamic measurements of static differential pressure signal between the two impinging jets for the determination of oscillations typical frequencies at both flow regimes.

The flow field structures occurring at self sustainable chaotic flow regimes are the main mixing mechanisms in the RIM process and other CIJ mixers, as shown in Santos et al. (2005). The efficiency of mixing in such kind of processes is critical for the quality of the product as shown from the polymerization works of Kolodziej et al. (1982 and 1986). When fast reactions are present and short mixing times are required it is of outmost importance to operate the CIJ mixers at self sustainable chaotic flow regimes. In case of RIM the process wide spreading has been seriously compromised due to failure of operation at chaotic flow regimes, either self-sustained or imposed.

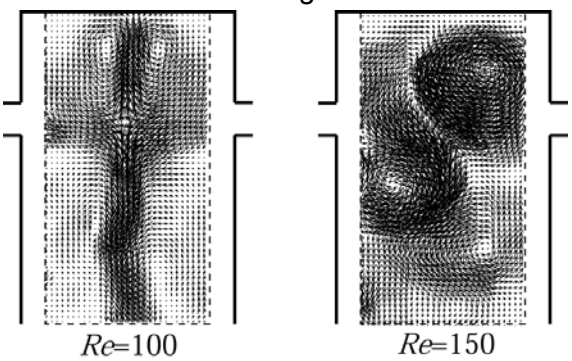

Fig. 1. Vector maps from PIV measurements at Re=100 and 150.

* Corresponding author. Tel + 351-22 -508 16 69. E-mail:lopes@fe.up.pt

From the very early works on RIM of Malguarnera and Suh (1977) it was reported that to establish a self sustainable chaotic flow regime, the Reynolds number has to be above a certain value and the momentum ratio of the jets has to be equal to one. Erkoç et. al. (2007) showed that even if these conditions are satisfied, the continuous operation of RIM at self sustainable chaotic regime is not assured, as for the same conditions, both oscillatory or self sustainable chaotic regime can be observed.

On way to assure mixing is to modulate/pulsate the jets' flowrate. The process of enhancing mixing through modulation/pulsation of the inlet flow streams is called active mixing. Bierdel and Piesche (2001) were the only authors to discuss the pulsation of jets and test the effect of pumps flow pulsation on the beginning of convective mixing in RIM. Active mixing in other CIJ reactors was studied by Deshmukh et al. (2000 and 2001), Zhongliang et al. (2002), Ito et al.(2006), although only its effect on mass transfer was analysed.

In this study, mixing is not engaged from the pulsation, since the flow field in the mixing chamber at the Reynolds number value of 300 here studied has natural advective chaotic pattern. The purpose here is to scrutinise the interaction between the flow natural oscillations and the imposed jets oscillations, namely its effect on the flow dynamics and on the shape and evolution of the natural advective chaotic patterns formed downstream the opposed jets impingement point.

CFD Model

The flow field was simulated with Fluent™ using a 2D model of the mixing chamber introduced and validated previously by Erkoç et al. (2007). Detailed results from the 2D model CFD simulations have been previously presented (Santos 2003,Santos et al.,2002 and Santos et al.,2005). Here the injectors averaged Reynolds number, Re, is defined for the 2D geometry as

$$Re = \frac{\rho \overline{v}_{inj} w}{\mu} \qquad \text{eq1}$$

where w is the injector width, which is 1.5 mm, μ is the viscosity that here is $20\text{mPa}\cdot\text{s}$, ρ is the density that here is 1200kg/m^3 and $\overline{v_{inj}} = 3.333\text{m/s}$ is the time and space average fluid velocity at the injectors. The chamber width is 10mm and the chamber height is 50mm, the injectors are locate at 5mm from the close top of the mixing chamber. The boundary conditions were set as no slip in the walls, and the liquid leaves the chamber from a pressure outlet set at atmospheric conditions. The dynamic simulations were always started from a steady state solution of the flow field for $Re = 300$. The pulsation of the jets is performed according to the following equations:

on the left injector $$v_{inj}(t)_l = \overline{v_{inj}} + A_l \overline{v_{inj}} \sin(2\pi f t) \qquad \text{eq2}$$

on the right injector $$v_{inj}(t)_r = \overline{v_{inj}} + A_r \overline{v_{inj}} \sin(2\pi f t + \varphi) \qquad \text{eq3}$$

where A_l and A_r are the left and right pulsation amplitudes, respectively, f the pulsation frequency and φ the phase displacement between the right and left injector pulsation.

Results

The previous studies of Erkoç et al. (2007) reported that in CIJ the jets impingement point oscillates with a natural oscillation frequency, ϕ. The jets impingement point oscillation frequency is around $\phi = 200\text{Hz}$ for a fluid with $\mu = 20\text{mPa}\cdot\text{s}$ in the defined 2D geometry at $Re = 300$. The tested jets flow rate oscillation frequencies are $f = \phi/2 = 100\text{Hz}$, $f = \phi = 200\text{Hz}$, and $f = 2\phi = 400\text{Hz}$ z. The simulated cases are all at $Re = 300$ and summarized in Table 1. All simulations were performed dynamically using a fixed time step of

10^{-4} s. The x component velocity, v_x, was recorded in the axis of the chamber at a distance of $z = 5$mm from the top (at the jets impingement point: P1).

Table 1 Summary of simulated active mixing strategies

Case Number	Pulsation Strategy	Amplitude and Frequency
1	No Pulsation	$A = 0$
2	Only one jet is pulsed	$A_l = 0.50$, $f = \phi$
3	On-Phase	$A_l = A_r = 0.50$, $f = \phi$, $\varphi = 0$
4	Out-of-Phase	$A_l = A_r = 0.25$, $f = \phi$, $\varphi = \pi$
5	Out-of-Phase	$A_l = A_r = 0.50$, $f = \phi$, $\varphi = \pi$
6	Out-of-Phase	$A_l = A_r = 1.00$, $f = \phi$, $\varphi = \pi$
7	Out-of-Phase	$A_l = A_r = 0.50$, $f = 2\phi$, $\varphi = \pi$
8	Out-of-Phase	$A_l = A_r = 0.50$, $f = \phi/2$, $\varphi = \pi$

Figure 2 shows the streamlines, at some selected time instants, of the dynamic simulations of the eight defined cases. The same flow behaviour previously reported in Santos *et al*.of the formation of a vortex street downstream the jets impingement point is observed for the eight cases. Some differences are yet observable between the flow fields:

- The vortices in Cases 2 and 3, corresponding to one side oscillation and on-phase oscillation, are more distorted, less rounded, than the case of no pulsation.
- The cases with out-of-phase pulsation present greater regularity of the vortex street, namely Cases 4, 5, 6 and 8 except for Case 7, where pulsation frequency is 2ϕ.

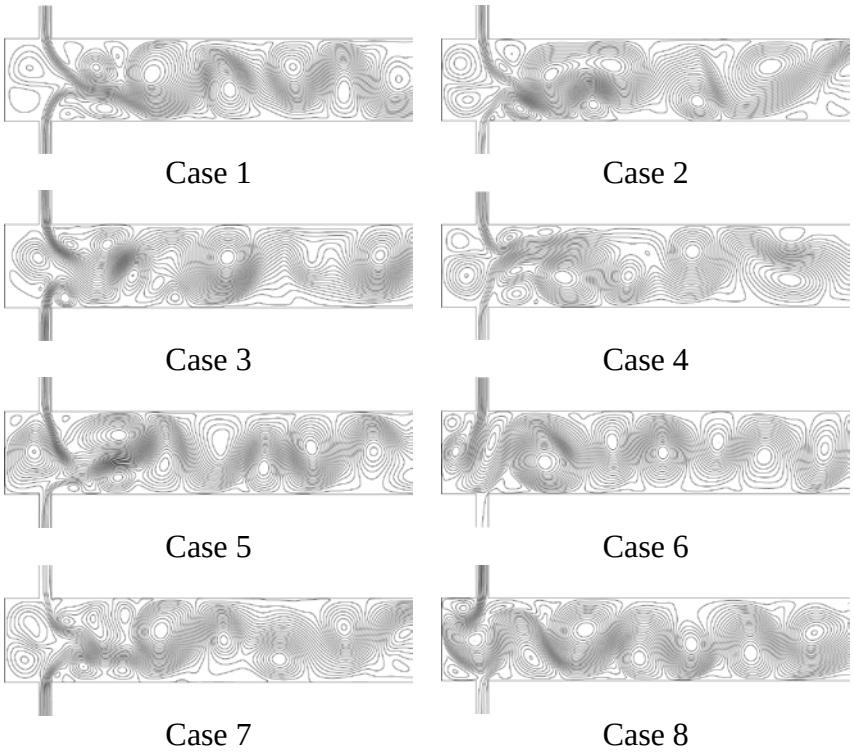

Fig. 2. Streamlines of flow field in the mixing chamber from the dynamic simulations at average *Re*=300, using different pulsation strategies.

For a clear image of the pulsation effect on flow dynamics, in Figure 3 it is presented the power spectra of the velocity time histories at the impingement point, P1, for the simulated

cases. The highest spectral energy values obtained from the spectra are listed in Table 2.

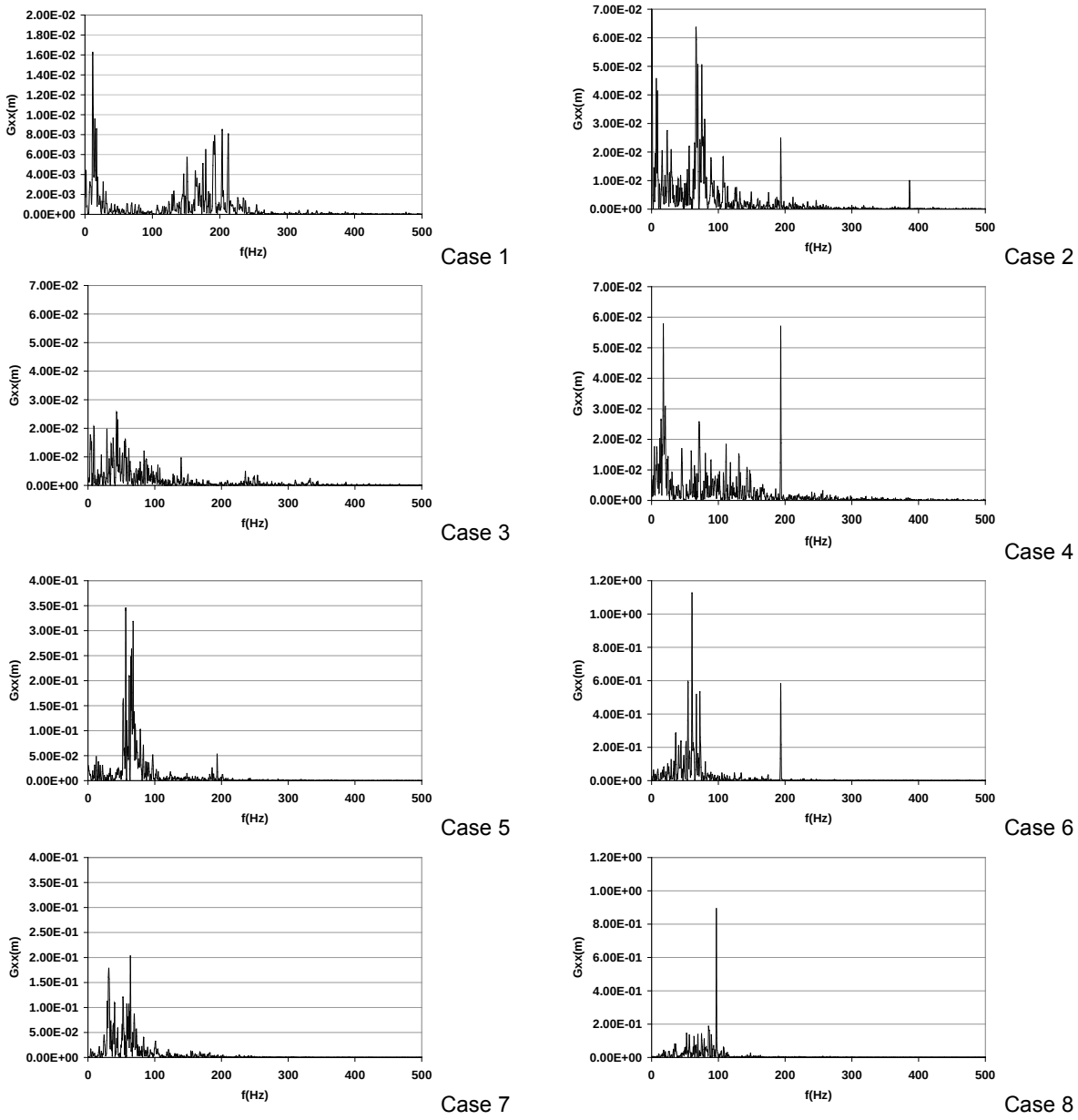

Fig. 3. Power spectra at the impingement point from the dynamic simulations at average Re=300 using different pulsation strategies.

For Case 1, where there is no pulsation applied to the system, typical frequency of the jets oscillations is $\phi = 200\text{Hz}$. The energy of the jets oscillation is much smaller than for the cases with forced pulsation as seen from Table 2, where the maximum energy value is seen to be almost one order of magnitude less than from the out-of-phase pulsation cases with $f = \phi$.

When only one of the jets is pulsed, the appearance of a lower frequency peak, between 50 and 100Hz, is observed, as can be seen in Figure 3 for Case 2. The on-phase pulsation, Case 3, presents the lowest energy peaks, since both jets are pulsated simultaneously, their strengths keep balanced and there is no significant disturbance of the jets oscillation. When a jet loses its strength, it is not compensated by the opposed jet, which is also retracted, and on the other hand when a jet increases its strength it is matched-up by the opposed jet.

Table 2 Maximum energy levels from the power spectra of v_x around f=200Hz, at the impingement point.

Case Number	Max Energy, m
1	0.00843
2	0.0247
3	0.00168
4	0.0571
5	0.0530
6	0.583
7	0.000921
8	0.894 *

The cases promoting the highest dynamics of the jets oscillations are the ones with out-of-phase perturbations, mostly the ones with the highest amplitudes. At $A_l = A_r = 1.00$, the jets oscillations are mainly determined from the imposed pulsation.

On the other cases, $A_l = A_r = 0.50$ there is a strong interaction between the flow field natural oscillations and imposed oscillations by pulsation. The resulting power spectrum, see Figure 3, shows both the influence of the natural flow oscillation, Case 1, and of the imposed jets oscillation. This result suggest that the flow field somehow preserves its own dynamics up to pulsation values of 50% of the inlet flow rate.

For Cases 4 to 6, streamline maps of Figure 2 show the earlier appearance of fully developed vortices, and when $A_l = A_r = 1.00$ the vortices are generated at the jets inlet region, which is the reason for the increase of the energy peaks in the range of 50 to 100Hz. For the double frequency oscillations, where $f = 2\phi$, Case 7, the natural flow oscillations and the imposed oscillations interact in a complex fashion cancelling the high energy peaks above 100 Hz.

The highest energy peak is obtained with a pulsation frequency of $\phi/2$, which is close to the flow oscillation frequency at the vortex street region. The pulsation frequencies probably set the whole system into resonance. From the streamlines in Figure 2, the earlier formation of the fully developed vortices at the impingement point occupying the entire mixing chamber width and evolving in perfect order to the outlet is clearly observed for Case 8.

Conclusion

In summary we studied the effect of opposed jets pulsation on the mixing dynamics and vortex formation on flow field dynamics inside the CIJ reactor. The flow dynamics had a strong effect from the pulsation frequency:

- With values close to the natural jets oscillation frequencies, ϕ, pulsation enhances the regularity of the system which results in a clear oscillatory behaviour of the jets at the impingement point.
- With values close to the natural frequency of the fully developed vortices, $\phi/2$, pulsation can force the frequency of the fully developed vortices passage and make it more orderly.

It was observed that the amplitude of the pulsation also has a strong effect on the flow field:

- Lower amplitudes can not impose to the system dynamics.
- Higher amplitudes, close to 100% of the flow rate, can completely dominate the dynamics of the flow field.

The other studied parameter was the impact of the pulsation strategy, which has shown that the strategies consisting of out-of-phase jets pulsation impose more clearly its dynamics to the system, since the displacement of the jets impingement point is completely determined

from the pulsation. One side oscillation and on-phase oscillation were not able to impose a clear influence on the flow field.

Acknowledgements

Financial support for this work was in part provided by national research grants FCT/POCTI/EQU/345115/2000, PTDC/CTM/72595/2006 and by LSRE financing by FEDER/POCI/2010, for which the authors are thankful. Ertugrul Erkoc¸ acknowledges his Ph.D./scholarship by FCT (SFRH/BD/18901/2004). Ricardo J. Santos acknowledges financial support from POCI/N010/2006.

References

Bierdel, M. and Piesche, M., CFD - Simulation and Experimental Investigation of Impingement Mixing in Reaction Injection Molding (RIM), 3rd European Congress of Chemical Engineering, (2001).

Deshmukh, A.A., Liepmann, D. and Pisano, A., *Characterization of a micro-mixing, pumping, and valving system*, Proceedings of the 11th International Conference on Solid-State Sensors and Actuators, 779-782 (2001).

Deshmukh, A.A., Liepmann, D. and Pisano, A., *Continuous micromixer with pulsatile micropumps*, Technical Digest of the IEEE Solid State Sensor and Actuator Workshop, 73-76 (2000).

Erkoç, E., Santos, R.J., Nunes, M.I., Dias, M.M., Lopes, J.C.B., *Mixing dynamics control in RIM machines*, Chemical Engineering Science, 62, 5276-5281 (2007).

Ito, Y. and Komori, S., A vibration technique for promoting liquid mixing and reaction in a microchannel, AIChE Journal, 52, 3011-3017 (2006).

Kolodziej, P., Macosko, C.W. and Ranz, W.E., *The Influence of Impingement Mixing on Striation Thickness Distribution and Properties in Fast Polyurethane Polymerisation*, Polymer Engineering and Science, 22, 388-392 (1982).

Kolodziej, P., Yang, W.P., Macosko, C.W. and Wellinghoff, S.T., *Impingement Mixing and its Effect on the Microstructure of RIM Polyurethanes*, Journal of Polymer Science, 25, 2359-2377 (1986).

Macosko CW. *RIM Fundamentals of Reaction Injection Molding*, Munich, Germany: Hanser; 1989.

Malguarnera, S.C. and Suh, N.P., *Liquid Injection Molding I. An Investigation of Impingement Mixing*, Polymer Engineering and Science, 17, 111-115 (1977).

Santos, R.J., *Mixing Mechanisms in Reaction Injection Moulding – RIM. An LDA/PIV Experimental Study and CDF Simulation*, Ph.D. Thesis in Chemical Engineering, Universidade do Porto (2003).

Santos, R.J., Teixeira, A.M., Costa, M.R.P.F.N., Lopes, J.C.B., *Operational and Design Study of RIM Machines*, International Polymer Processing Journal, 17, 387-394 (2002).

Santos, R.J., Teixeira, A.M., Lopes, J.C.B., *Study of Mixing and Chemical Reaction in RIM*, Chemical Engineering Science, 60, 2381 – 2398 (2005).

Teixeira, A.M. *Escoamento na Cabeça de Mistura de uma Máquina RIM (Flow in a RIM Machine Mixing Head)*, Ph.D. Thesis in Chemical Engineering, Universidade do Porto (2000).

Teixeira, A.M., Santos, R.J., Costa, M.R.P.F.N., Lopes, J.C.B., *Hydrodynamics in the Mixing Head of a RIM Machine: Flow Field Characterization by LDA*, AIChE Journal, 51, 1608-1619 (2005).

Zhongliang, T., Seungbae, H., Djordje, D., Vijay, M., Alan, C.W., James, Y. and Richard, M.O., *Electrokinetic flow control for composition modulation in a microchannel*, Journal of Micromechanics and Microengineering, 12, 870 (2002).

Proceedings of the 10th International Chemical and
Biological Engineering Conference - CHEMPOR 2008
Braga, Portugal, September 4-6, 2008
E.C. Ferreira and M. Mota (Eds.)

Ultrasound – assisted extraction of active principles from *Arctium lappa L.* (Burdock) roots, *Stevia rebaudiana Bert.* leaves and *Cynara scolymus L.* (Artichoke) leaves

Ani Alupului*, V. Lavric
University Politehnica of Bucharest, Chemical Engineering Department
RO-011061, Polizu 1-7, Bucharest, Romania

Keywords: Polyphenolic acids, Flavonoids, Stevioside, Ultrasound – assisted extraction, HPLC
Topic: Integration of life science & engineering

Abstract

The intensification of the extraction process in ultrasonic fields is addressed, emphasizing its advantages in obtaining hypoglycemic extracts with great economical potential from medicinal plants: flavonoids and polyphenol acids from *Cynara scolymus L.* (artichoke) leaves and *Arctium lappa L.* (burdock) roots and sweet diterpenic glycosides from *Stevia rebaudiana Bert.* leaves.

The objective of this work was to isolate favourable extraction conditions for a fast and reliable protocol of ultrasound-assisted extraction (UAE). Compared with classic methods like maceration, heat and/or stirred extraction, the UAE has higher productivity, defined as the quantity of the extracted product with respect to time and volume of mixture. The efficiency of the classic extraction was investigated with respect to the solvent used, the ratio of sample quantity to solvent volume, the plant material granulation size and the time of extraction.

The quantification of flavonoids and polyphenolic acids from autochthonous medicinal plants was performed with a spectrophotometric method, while the diterpenic glycosides of Paraguayan plant were measured by HPLC.

1 Introduction

Plants containing large amounts of flavonoids and polyphenolic acids have been used in the traditional medicine of many different cultures. Recent papers have focused attention to the biological activity and therapeutic potential of these compounds. These properties give them a prime role in the prevention of various diseases associated with oxidative stress, such as cancer and cardiovascular and neurodegenerative diseases, metabolic diseases (Sharaf-Eldin et al., 2007).

Extracts of leaves of the plant *Stevia rebaudiana Bertoni*, have been used for many years in traditional treatment of diabetes in South America. Stevia leaves contain diterpene glycosides, stevioside and rebaudioside as the most abundant. Recently, it was demonstrated that stevioside stimulates the insulin secretion both *in vitro* and *in vivo* (Gregersen et al., 2004).

The mechanical effects of ultrasound (formation and destruction of small cavities in the solvent) induce a greater penetration of solvent into cellular materials and improve mass transfer. Ultrasounds can also disrupt biological cell walls, facilitating the release of its contents. In contrast to conventional extraction, where there is no external field in which the fluid is placed, plant extracts diffuse across cell walls since the ultrasounds cause cell rupture over a short period Ultrasound can increase extraction kinetics and even improve the quality of extracts. Use of ultrasound-assisted extraction is recommended for thermo-labile compounds, whose properties may be altered under thermal extraction due to temperature beyond critical

* Corresponding author. Tel + 40726-209-800. E-mail:alupului_ani@yahoo.com

point. Ultrasound-assisted extraction was proved to be an efficient method for extracting polyphenolic acids and flavonoids, steroids and triterpenoids (Vinatoru, 2001).

2 Materials and Methods

2.1 Reagents and plant material

Stevioside (S3572, assay ≥98% - HPLC - form: solid , colour: white, free soluble in water and ethanol, solubility H_2O: >20 mg/mL, storage temperature: 2-8°C, chemical name: 4α-13-[(2-O-β-D-Glucopyranosyl-β-D-glucopyranosyl)oxy]kaur-16-en-18-oic acid β-D-glucopyranosyl ester, chemical formula: C38H60O18, molecular weight: 804.87) was used as standard chemical for HPLC analysis. Gallic acid and Rutoside were used as standard chemicals for spectrophotometric analysis.

Chromatographic grade – double distilled water, HPLC grade acetonitrile, aqueous ethanol and distilled water were used as extraction solvents and mobile phase.

Folin-Ciocalteu reactive, sodium carbonate 10%, sodium acetate 100 g/L and aluminium trichloride 25g/L were used as regents in spectrophotometric analysis.

The plant material consists of dried leaves of *Stevia rebaudiana* purchased from the Paraguay Medicine Market, harvested in 2007, dried leaves of *Cynara scolymus* (artichoke) and dried roorts of *Arctium lappa* (burdock), harvested in 2007, both from Romania. They were stored in dark ermeti tight bags to protect them from humidity and light and, before each bunch of experiments, they were cut into pieces of the appropriate equivalent diameter.

2.1 Experimental setup

Three ultrasonic baths (T420 Elma, T460 Elma, and T570) working at 35 kHz frequency and an output power of 70 W, 170 W and 320 W respectively were used during the experiments. For stirring and heating a TK-22 Magnetic stirrer with heating was used. For chromatographic measurements, a HPLC system Agilent Technologies 1200 series model with UV-VIS detector was used. The filtrate was separated from the residual plant material by vacuum pump filtration irrespectiv of the extraction process used get it.

2.2 Ultrasound assisted extraction

Samples of 10 g of dry leaves from *Stevia rebaudiana* and *Cynara scolymus* and dry roots from *Arctium lappa* with particles sizes of 0.315 mm equivalent diameter were mixed with distilled water for *Stevia* leaves and water/ethanol mixture of 55% for *Artichoke* leaves and *Burdock* roots, using 1/5 (w/v) sample weight to solvent volume ratios. Then these mixtures were placed into the ultrasound assisted extractors at room temperature.

The ultrasonic baths were filled with liquid water into which glasses with samples were placed and sonicated from 30 seconds up to 15 minutes at 70 W, 170 W and 320 W output power respectively.

2.3 Dry residue analysis. Extractive values

According to the Romanian Pharmacopoeia (10th edition) approximately 2 g (2 ml) of extract was placed into a flat-bottomed glass dish (36 mm diameter and 28 mm height) covered to prevent evaporation of solvent before weighting. After weighting, the extract was dried in oven at 103^0C for 3 h. The content of extractive substances in the plant material was calculated from the mass of dry extract and the initial mass of plant subject to experiment. The concentration of extractive substances in the liquid extract was calculated from the mass of dry extract and the volume of liquid extract. The extractive value of the soluble compounds from the extract was calculated as a mass percentage of dry residue (g/100 g extract).

2.4 Determination of steviol glycosides percentages using HPLC

Standard solution (2.2 mg/5 mL) of stevioside was prepared in the mobile phase consisting of mix HPLC grade acetonitrile and bi-distilled water (80:20, v/v). Standard series in the concentration range of 100-1000 µg/mL were obtained from the stock solution. The mobile

phase was used as solvent for all HPLC studies. The HPLC analysis conditions were performed by isocratic elution at 40^0C column temperature with a flow rate of 0.4 mL/min, separations being carried out using Supelcosil LC-NH2 or equivalent (length: 15 - 30 cm; inner diameter: 3.9 - 4.6 mm). All solvents were filtered through a 0.22 µm Millipore filter. Volumes of 5 µL extracts prepared from each sample were directly injected into HPLC then the peak areas at the characteristic wavelength of the steviol glycosides were measured. The UV-VIS detector was set to 210 nm and peak areas were integrated automatically using Agilent software. The instrument was calibrated pumping mobile phase through it until a drift-free baseline was obtained. The Agilent software recorded the chromatograms of the sample standard solution.

All the computations concerning the quantitative analysis were performed with external standardization of the measured peak areas. The results were obtained as the mean value of three separate injections. Using the measured peak areas of stevioside from the sample solution and of the standard solution, the percentage of the extracted stevioside was computed as: % stevioside = [Ws/W] x [Aa/As] x 100, where Ws is the mass of stevioside in the standard solution (mg), W is the mass of sample (mg), As and Aa are the peak area of stevioside from standard and sample solutions.

2.5 Determination of flavonoids and polyphenolic acids percentages using spectrophotometer

Determination of the phenolic acids and flavonoids content was performed according with the methods presented in Romanian Pharmacopeia (10^{th} edition).

The method was implemented using a Spekol 1000 Series spectrophotometer with VIS detector.

All the calculations concerning the quantitative analysis were performed with external standardization by measurement of absorbance of a specific wavelength of light.

Stock solutions of gallic acid (0,1g/L) and rutoside (0,1 g/L) were prepared in distilled water (v/v). Standard series in the concentration range of 25- 200 µg/mL for flavonoids and 4-16 µg/mL for polyphenols acid were obtained from the stock solution.

Volumes of 2 mL solution prepared from each sample were placed into quartz cuvettes into the spectrophotometer and analised.

The total content of polyphenols was determined with Folin-Ciocalteu reactive and Na2CO3 10%, the maximum of absorption of thr obtained coloration, with respect to the calibration curve. The polyphenols are expressed in mg/g gallic acid correspondents at a final set concentration of 16 µg/mL.

The total content in flavonoids was measured with ethanol solution of aluminium trichloride 25g/L and sodium acetate 100 g/L, throughout the evaluation of the maximum of absorption of obtained coloration, relatwith respect to the calibration curve. The total content of flavonoids is expressed in mg/g rutoside correspondents related to a final set concentration of 200 µg/mL.

The blank solutions were prepared in the same conditions as the samples and are used for all spectrophotometric experimental studies.

Quantification was realized by measuring the absorbance at the wavelength 430 nm for flavonoids and 765 nm for polyphenolic acids to determine the concentration of a known solute in a given solution by the application of the Beer-Lambert law, which states that the concentration of a solute is proportional to the absorbance. Optical density, or OD, is the absorbance per unit length, although it is sometimes used as a synonym for the absorbance with a base-10 logarithm. The results were obtained as a mean value of three separate samples.

3 Results and Discussions

3.1. Results

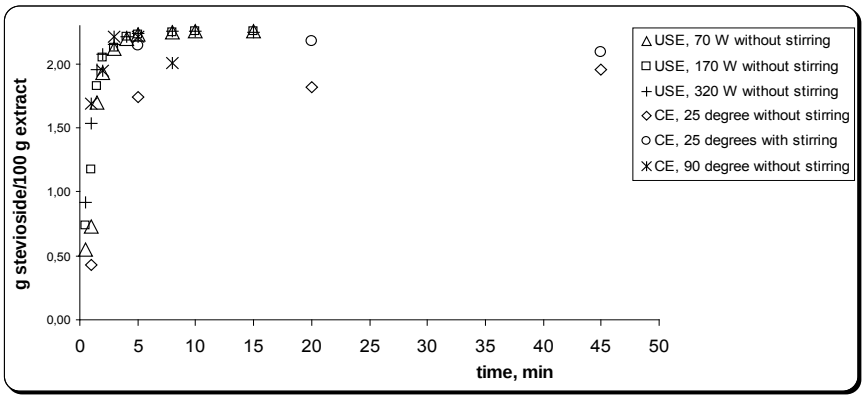

Figure 2. Time profiles of ultrasound-assisted extracted stevioside from Stevia rebaudiana (ultrasonic bath). Influence of the output ultrasound power on the extraction yield (70 W, 170 W and 320 W respectively)

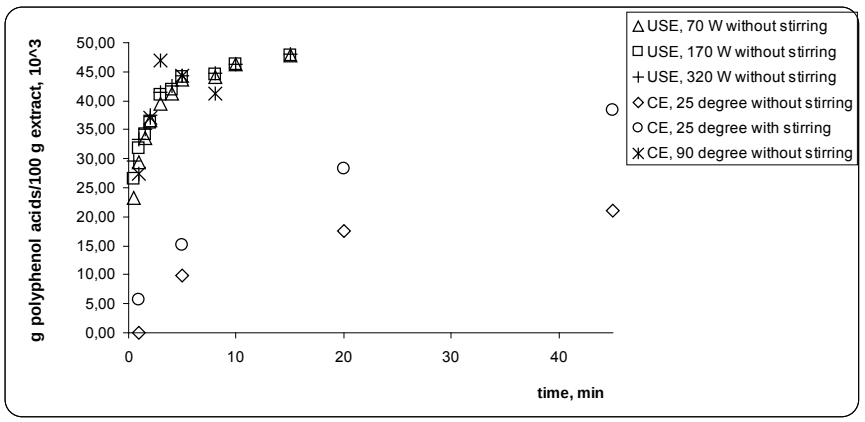

Figure 3. Time profiles of ultrasound-assisted extracted phenolyc acids from Cynara scolymus (ultrasonic bath) – the rest is the same as in Figure 2

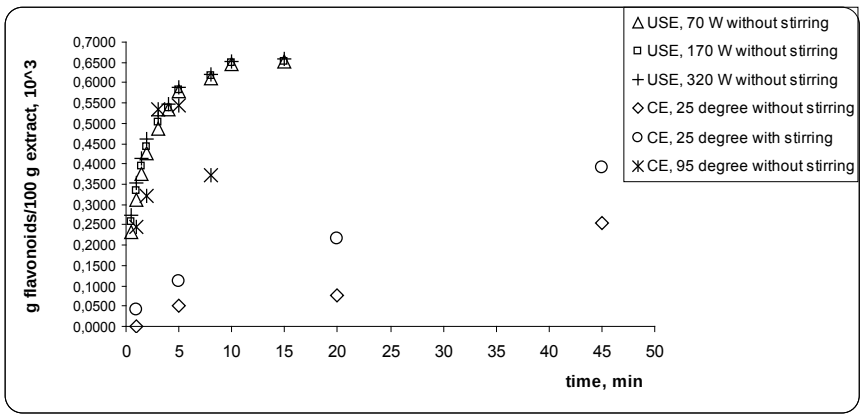

Figure 4. Time profiles of ultrasound-assisted extracted flavonoids from Cynara scolymus (ultrasonic bath) – the rest is the same as in Figure 2

The results of the ultrasound assisted extractions are presented, *per see* or compared with the classical extractions, in Figures 2 to 6. We used the results for classical extraction, presented already in details in two papers (Alupului and Lavric, 2008 a&b) as reference for comparison with the ultrasound-assisted extraction.

The influence of the equivalent diameter of dry leaves and of the solvent nature upon the ultrasound assisted extraction yields has been already presented in the paper (Alupului and Lavric, 2008 a).

Further on, we will present the results of ultrasound assisted extraction protocol in comparison with the classic extraction findings.

Figure 2 depicts the extracted stevioside time profiles sing three crescent output power for the ultrasonic fieled. It is worth mention that these are not the absobded powers, but still could give a hint about the rate at which the extraction ceases. A comparison with maceration is done presenting the time profiles of the extracted stevioside with or

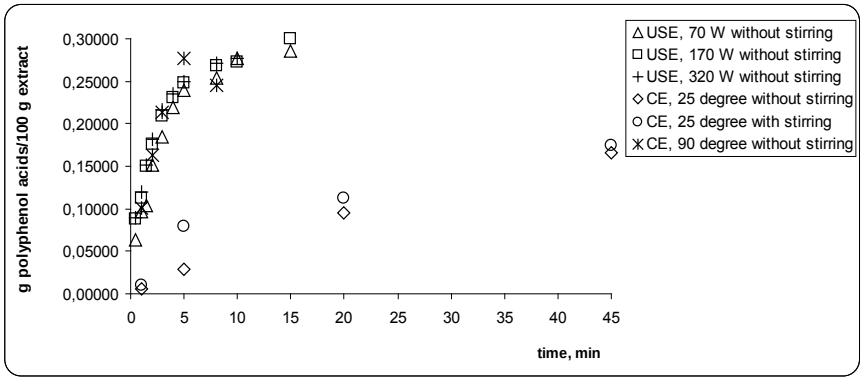

Figure 5. Time profiles of ultrasound-assisted extracted phenolyc acids from Arctium lappa (ultrasonic bath) – the rest is the same as in Figure 2

without agitation and, also, with decoction.

The same, but this time for phenolyc acids from *Cynara scolymus* is done in Figure 4, while in Figure 5 the time profiles are for flavonoids from *Cynara scolymus*. Figure 6 shows the results of the extraction process in ultrasonic fields or classically for the flavonoids from *Arctium lappa.*

3.2. Discussions

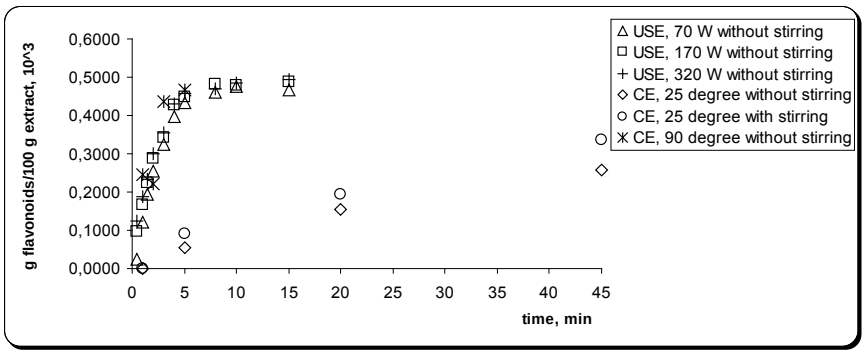

Figure 6. Time profiles of ultrasound-assisted extracted flavonoids from Arctium lappa (ultrasonic bath) – the rest is the same as in Figure 2

Generally speaking, like any other process governed by thermodynamic equilibrium, the extraction of active principles from plant parts is an asymptotic process, vanishing when the driving force becomes zero. One efficient way to improve the extraction rate is to increase the kinetic energy of the contacting fluid. When this supplemental kinetic energy was introduced from outside into the liquid phase through heating and/or stirring, the process rate was increased and the extraction process becomes faster, as can be observed for all experiments. Although it helps the diffusion process, stirring is not as efficient as heating, though thermal degradation of the valuable compounds starts manifesting when, at the extraction temperature of 90°C as in the present study, the contact time is too long.

When using ultrasound waves as intensification technique, the extraction rate increases dramatically, due to the direct transfer of the kinetic energy from the field to the liquid throughout the formation and destruction of very small cavities. There are at least two side effects o this kinetic energy transfer: the local disruption o the cell wall, with beneficial effect upon releasing the active principles in the liquid phase and rapid temperature increase, due to the violent friction and, consequently, mechanical energy dissipations.

When the extraction develops in the presence of an ultrasonic field, the stevioside concentration attains its maximum value after less than ten minutes (see Figure 2 for details). Good results for flavonoids and polyphenolic acids from *Cynara solymus* and *Arctium lappa* were obtained also, less than 15 minutes being necessary for the process to complete (see Figures 3 to 6 for details). This is the effect of the sharp increase of the local turbulences, which increase the mass transfer and also boost mixing of the liquid, thus maintaining the highest possible driving force. Increasing the power of the ultrasonic field hasn't an observable effect, since there is a rate of energy absorption into the liquid which attains a maximum for a satu-

ration level of output ultrasonic power lower than 70 W. This saturation level should be in connection with the liquid mass implied in the extraction process. Due to these side effects, mainly to the local temperature increases but also to the sudden local kinetic energy changes, ultrasounds are detrimental when the mixture is overexposed, as can be seen in Figures 2, 4 and 6.

Compared to maceration, ultrasound assisted extraction increased the productivity and decreasing the time of completion. With respect to hot extraction, whose performance is by far better than maceration, ultrasound assisted extraction has the main advantage of working at ambient temperatures, thus avoiding the thermal overexposure.

Like hot extraction, ultrasound assisted intensification needs special equipment to be functional, which means higher investments, and electricity to produce the ultrasonic waves, which means higher operating costs than maceration. So, a soundly economic analysis should be done, in order to choose the best extraction procedure.

4 Conclusions

Ultrasound assisted extraction (UAE), as a new extraction method, was used to extract stevioside, polyphenolic acids and flavonoids from *Stevia rebaudiana* leaves, *Cynara scolymus* leaves and *Arctium lappa* roots.

Comparing with other extraction methods, UAE has excellent advantages, such as shorter extraction time and higher yield extraction. Compared with classical extraction methods like maceration and hot extraction, the ultrasound assisted extraction proved to be a simpler but more effective procedure to obtain active compounds from medicinal plants; it works at lower temperatures, avoiding thermal degradation and higher rates, a very important asset for industry.

UAE is expected to offer a new way for the production and analyses of the plant extractions, and the modernization of pharmaceutical engineering herbal medicine.

Acknowledgments

The authors would like to thank ing. Anton Perescu of National Institute of Research and Development for Biological Sciences and Prof. Dr. Ioan Burzo of University of Agronomical Sciences and Veterinary Medicine of Bucharest for their kind support.

References

Albu, S., Joyce, E., Paniwnyk, L., Lorimer, J. P., Mason, T. J. (2004). Potential for the use of ultrasound in the extraction of antioxidants from Rosmarinus officinalis for the food and pharmaceutical industry, *Ultrasonics Sonochemistry*, **11**, 261–265.

Alupului, Ani, Lavric, V., (2008a). Ultrasound Extraction of Active Principles with Hypoglycaemic Activity from Medicinal Plants, *Chem. Eng. Transactions,* **14**, 83-90.

Alupului, Ani, Lavric, V., (2008b). Obtaining and Characterization of *Cynara scolymus L.* (Artichoke) leaves and *Arctium lappa L.* (Burdock) roots flavonoids and polyphenolic acids, *Scientific Works USAMVB*. Bothany and physihology, **LI**, 541-544.

Gregersen, S., Jeppesen, P.B., Holst, J.J., Hermansen, K. (2004). Antihyperglycemic effects of stevioside in type 2 diabetic subjects. *Metabolism*, **53**(1), 73-76.

Schinor, E.C., Salvador, M.J., Turatti, I.C.C. (2004). Comparison of classical and ultrasound-assisted extractions of steroids and triterpenoids from three *Chresta spp.*, *Ultrasonics Sonochemistry*, **11**, 415.

Sharaf-Eldin, M.A., Schnitzler, W.H., Nitz, G., Razin, A.M. (2007). The effect of gibberellic acid (GA3) on some phenolic substances in globe artichoke (*Cynara cardunculus var. scolymus* (L.) Fiori), *Scientia Horticulturae*, **111** (4), 326-329.

Vinatoru, M. (2001). An overview of the ultrasonically assisted extraction of bioactive principles from herbs, *Ultrasonics Sonochemistry*, **8** (3), 303.

Proceedings of the 10th International Chemical and
Biological Engineering Conference - CHEMPOR 2008
Braga, Portugal, September 4-6, 2008
E.C. Ferreira and M. Mota (Eds.)

Monitoring multi-component liquid reaction systems containing highly dispersible heterogeneous catalysts using in situ diode array spectrophotometry and band-fitting techniques

Luís Costa, Vânia Brissos, Francisco Lemos*, Fernando Ramôa Ribeiro, Joaquim M.S. Cabral

IBB – Institute for Biotechnology and Bioengineering, Centre for Biological and Chemical Engineering, Instituto Superior Técnico, Av. Rovisco Pais, 1049-001 Lisboa, Portugal.

Keywords: Diode array spectrophotometry, band-fitting, kinetic modelling, zeolite NaY, cutinase
Topic: Systematic methods and tools for managing the complexity - PAT.

Abstract

The kinetic behaviour of the reaction system during the hydrolysis of *p*-nitrophenyl butyrate (PNPB) catalysed by a single-site mutant of *Fusarium solani pisi* cutinase immobilized on zeolite NaY was followed using UV/Vis *in situ* diode array spectrophotometry.

Spectral band-fitting techniques allowed the use of this spectroscopic technique to obtain quantitative data on the concentrations of the various species present in an aqueous reaction medium with solid catalyst particles. This methodology overcame the problems arising from the variable light scattering produced by the catalyst particles. Kinetic modelling of the reaction system was used to estimate the reaction rate constants involved.

1 Introduction

Process analytical technologies may provide outstanding contributions for the quality control of various production processes, namely in the food and pharmaceutical industries (Lopes et al., 2004) and they will also have a significant impact in laboratory experimental data interpretation.

Herein, the reaction kinetics of the hydrolysis of PNPB catalysed by a single-site mutant of *F. solani pisi* cutinase, supported on zeolite NaY, was followed using *in situ* UV/Vis diode array spectrophotometry. PNPB is an ester whose hydrolysis is commonly employed to characterize the activity of lipases (Almeida et al., 2004). To exploit the benefits of a heterogeneous catalyst, both in terms of ease of separation from the reaction medium and in terms of stability of the biocatalyst, the enzyme was supported on zeolite NaY by physical adsorption.

In aqueous media, the highly dispersible solid catalyst particles produce very significant interference

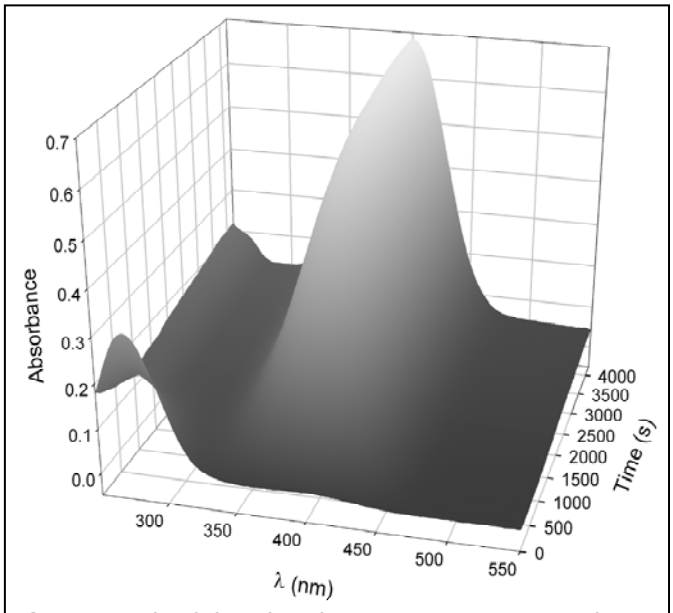

Fig. 1 Graph of the absorbance spectra captured over the course of the hydrolysis of PNPB catalyzed by cutinase T179C immobilized on zeolite NaY.

* Corresponding author. E-mail: francisco.lemos@ist.utl.pt

with the absorption measurements. This effect is further aggravated by the dynamic behaviour of the light scattering phenomena caused by the random breakdown of catalyst particle aggregates over the course of the reaction. Combining a high-throughput data acquisition technique, such as diode array spectrophotometry, with spectral band-fitting methods allowed the retrieval of quantitative data on the concentrations of the various species present in the reaction medium, thus enabling us to perform a kinetic analysis of the reaction.

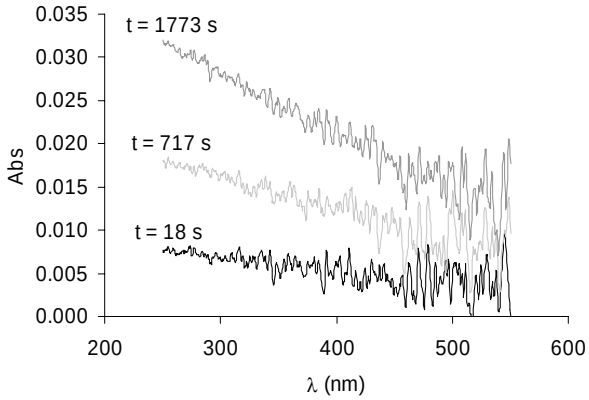

Fig. 2 Evolution of the absorbance during a blank (NaY in buffer) PNPB hydrolysis assay due to the presence of the zeolite

2 Experimental

A *F. solani pisi* cutinase single site mutant T179C was selected from a complete saturation mutagenesis library (Brissos et al., 2008). Zeolite NaY (Union Carbide, Si:Al = 2.5) was used as a support after calcination and the enzyme was immobilized by adding 400 $mg_{zeo}.mL^{-1}$ to a 20 $mg_{enz}.mL^{-1}$ solution in 50 mM potassium phosphate buffer pH 8.5 for 30 min, subsequently washed and vacuum dried for 6 h.

The hydrolysis of PNPB was followed *in situ* using an Ocean Optics USB2000® UV/Vis diode array spectrophotometer equipped with a Mikropack® DH-2000-BAL deuterium-halogen light source and a computer running the Spectra Suite® software. The reactions took place in a cell with a reaction volume of 1 mL, at 30 ºC and with magnetic stirring. A stock solution of PNPB (Sigma, 98 %) 3.5 mM in acetonitrile (Merck, HPLC grade) was prepared and kept at 0 ºC. For each assay, 0.25 mg of catalyst and 990 μL of phosphate buffer were placed in the cell and the reaction was started by the addition of 10 μL of the PNPB solution.

Reference spectra (molar absorptivities, ε) in the 250<λ<550 nm range were obtained from an orthogonal calibration set (Brereton, 2000) prepared with standard solutions of PNPB and its product *p*-nitrophenol (PNP). No absorption was detected with the other product, butyric acid. A reference spectrum of the zeolite suspension was obtained with a weighed average of the spectra collected during a blank assay.

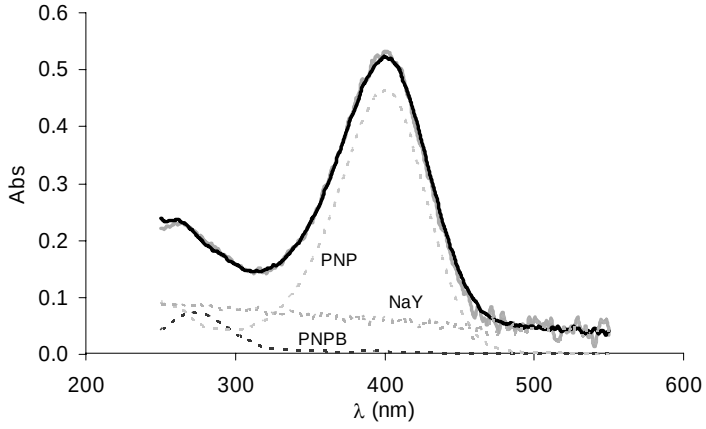

Fig. 3 Band-fitting procedure used to determine the concentration of the species present in the reaction medium during the hydrolysis of PNPB catalyzed by 0.25 mg of zeolite NaY-supported cutinase T179C at a reaction time of 2513 s. The absorbance contributions from PNPB, PNP and the solid catalyst are added to calculate the total simulated absorbance (—), which is then fitted to the experimental absorbance (—) by a least-squares method using the concentrations as the fitting parameters

3 Results and discussion

Throughout each assay, the spectrophotometer collected light intensity spectra that were converted to absorbance using the dark and reference spectra (Eq. 1). A 3D graph showing the evolution of the spectra with the reaction time is depicted in Fig. 1.

$$Abs = log_{10}\left(\frac{I - I_{dark}}{I_{reference} - I_{dark}}\right) \quad \text{(Eq. 1)}$$

From this graph, focusing on the λ_{max} values for PNPB (273.52 nm) and PNP (402.06 nm), it can be seen that the absorbance of both species increases simultaneously after ~2000 s. However, according to the stoichiometry of the reaction (1:1), the sum of PNPB and PNP concentrations was expected to remain constant throughout the assay.

To clarify this observation, an experiment was performed under the same conditions, in the presence of NaY, but without enzyme or PNPB (blank). The results presented in Fig. 2 show that the absorbance increased over time for all wavelengths. This effect is most likely the result of the breakdown of zeolite particle clusters caused by stirring in the reaction cell and by the interaction between the hydrophilic zeolite crystallites and the aqueous reaction medium. Thus, the particles in suspension become progressively finer, intensifying the light scattering effects over time. This change in the aggregation state of the catalyst seems to depend on several factors, including the initial aggregation state, which is very difficult to control.

Realizing that the presence of the zeolite would affect the measurements by contributing to the absorbance value, it became necessary to determine the concentrations of PNPB and PNP over time not only considering $\varepsilon_{PNPB}(\lambda)$ and $\varepsilon_{PNP}(\lambda)$, but also an "$\varepsilon_{NaY}(\lambda)$" to account for the variable light scattering effect caused by the zeolite. This "artificial" NaY absorptivity was determined by a weighed average of the spectra acquired during the NaY assay. The NaY absorptivity has an associated virtual NaY concentration, which can be roughly seen as the concentration of light scattering particles and is

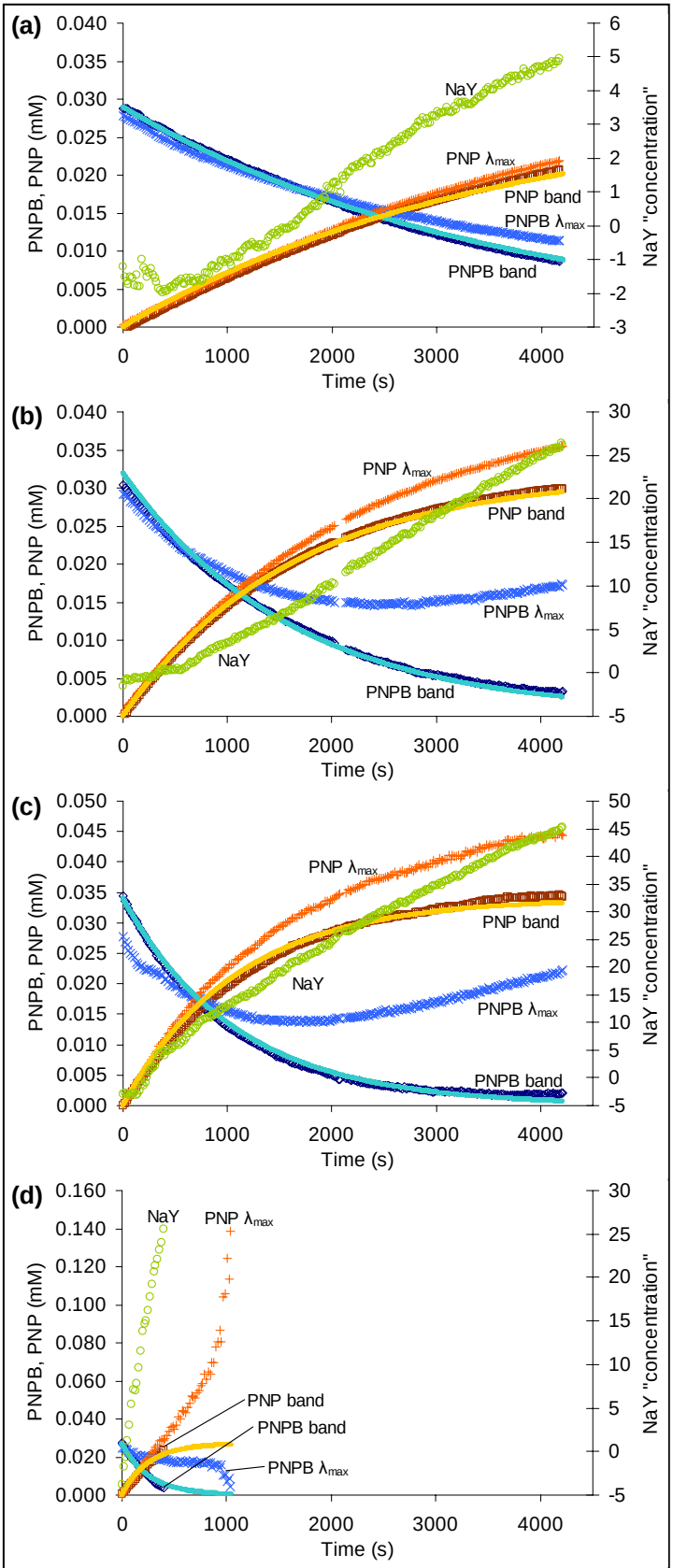

Fig. 4 Hydrolysis of PNPB catalysed by **(a)** 0.10, **(b)** 0.25, **(c)** 0.50 and **(d)** 1.0 mg.mL^{-1} of NaY-supported cutinase T179C. Concentrations determined with $\varepsilon(\lambda_{max})$ (PNPB ×, PNP +) and by band-fitting, using $\varepsilon(\lambda)$ and accounting for the NaY effect (PNPB ◊, PNP □, "NaY" ○). The lines are the result of kinetic modeling.

expected to increase with time due to the change in the aggregation state of the solid catalyst.

The concentration profiles of the various species were determined by decomposing each spectrum (at a fixed reaction time) into a linear combination of the previously recorded standard spectra (represented by the absorptivities as a function of λ), as illustrated in Eq. 2.

$$Abs_{simulated}(\lambda,t) = \varepsilon_{PNPB}(\lambda)\times C_{PNPB}(t) + \varepsilon_{PNP}(\lambda)\times C_{PNP}(t) + " \varepsilon_{NaY}"(\lambda)\times "C_{NaY}"(t) \qquad \text{(Eq. 2)}$$

An example of this band-fitting procedure for a single reaction time is shown in Fig. 3.

The graphs in Fig. 4 present a comparison between the profiles obtained by band-fitting and the concentrations calculated by simply using the conventional spectrophotometric method: applying Beer's law to the data obtained at the maximum absorption wavelengths, $\varepsilon_{PNPB}(\lambda_{max})$ and $\varepsilon_{PNP}(\lambda_{max})$, and not considering the effect of the zeolite. Four biocatalyst concentrations were assayed in the hydrolysis of PNPB, so as to determine the influence of this variable on the reaction kinetics and on the monitoring technique itself.

Accounting for the presence of the zeolite and introducing this information into the spectral decomposition notably improved the concentration profiles obtained. Indeed, the concentrations of both PNPB and PNP now stabilize at the end of the assay, as expected.

The zeolite "concentration" curves determined for each case are different not only in magnitude but also in shape, suggesting that the aggregation state of the catalyst at the starting point and over the course of each assay is difficult to control.

Estimates of the typical error values of the band-fitting procedure were computed by a standard bootstrapping methodology (Manly, 2006) with 20 simulations for a single time point of an experiment. So, choosing for example a catalyst concentration of 0.25 mg.mL^{-1} (Fig. 4b), at t = 376 s, yielded values of the half-width of the confidence intervals (significance level, α, of 0.05) for C_{PNPB}, C_{PNP} and "C_{NaY}" of, respectively, 0.04 %, 0.06 % and 7.2 %. This was considered acceptable, given that "C_{NaY}" contributes the least to the final spectrum composition (Fig. 3).

For a catalyst concentration of 1.0 mg.mL^{-1} (Fig. 4d), after approximately 1000 s no more absorbance measurements could be made because the zeolite particles in solution disperse the light beam to such a large extent that it caused the detector to receive a lower light intensity than the dark spectrum acquired at the start of the experiment, which results in error when using Eq. 1. The light intensity of the reference minus the dark spectra for each catalyst concentration used is displayed in Fig. 5. When 1.0 mg.mL^{-1} of catalyst is used, the light intensity reaching the detector is very low from the very start of the experiment, and this situation is aggravated over time as a result of the increase in light dispersion caused by the particle breakdown. This constitutes a clear limitation of the technique presented herein.

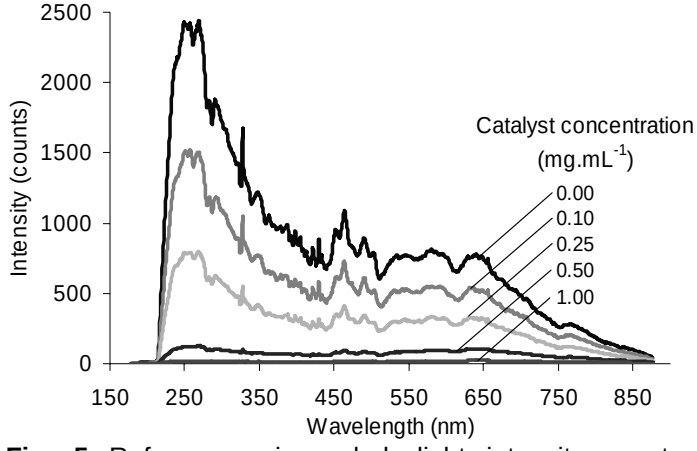

Fig. 5 Reference minus dark light intensity spectra obtained at the start of the PNPB hydrolysis experiments with several zeolite NaY-supported cutinase T179C concentrations

Kinetic modelling

Kinetic modelling was performed using the concentration profiles data

for each catalyst concentration. For the assay with 1.0 mg.mL^{-1} of catalyst, only the initial fraction of experimental data was selected. The reaction was considered first order, reversible and with a large excess of water (pseudo-first order), so the system was described according to the scheme displayed in Fig. 6 and the resulting material balances (Eq. 3).

$$\frac{dPNPB}{dt} = -\frac{dPNP}{dt} = -\frac{dHBut}{dt} = -k_1.PNPB + k_{-1}.PNP.HBut \qquad \text{(Eq. 3)}$$

The equations corresponding to the material balances of the relevant species (PNPB, PNP, HBut) were solved using Euler's method and the model was fitted to the experimental results by a least squares method. The initial concentrations of PNP and butyric acid were both assumed to be 0 and k_1, k_{-1} and $PNPB_{init}$ were used as fitting parameters. The resulting model curves (Fig. 4) provided a reasonably accurate description of the experimental data after band-fitting, but not for a simple application of Beer's law.

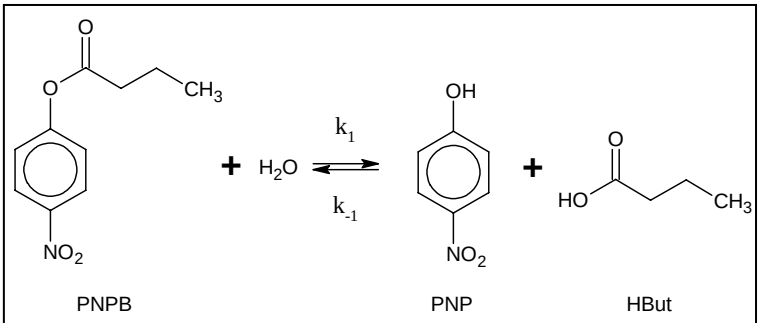

Fig. 6 Reaction scheme for the hydrolysis of PNPB

The forward reaction kinetic constant, k_1, obtained from the model fitting was plotted against the respective catalyst concentration (Fig. 7). The kinetic constant k_1 varies linearly with the catalyst concentration up to 0.50 mg.mL^{-1}. It can be observed that at 1.0 mg.mL^{-1} of zeolite, the value obtained by modelling is significantly higher, probably as a result of the absorbance measurement difficulties previously discussed. The bootstrapping technique described earlier was employed to obtain an estimate of the error of the parameters fitted during the kinetic modelling process. The half-widths of the confidence intervals (α = 0.05) for k_1, k_{-1} and $PNPB_{init}$ were, respectively, 0.2 %, 3.9 % and 0.2 %, as averaged from the 4 fittings shown in Fig. 4.

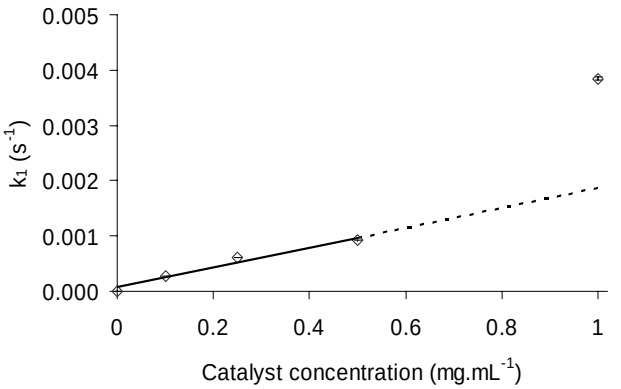

Fig. 7 Modelling results obtained for the kinetic constant k_1 with each catalyst concentration. The line represents a linear regression (R^2 = 0.96)

4 Conclusions

In the work described herein, spectral band-fitting techniques based on *in situ* diode array spectrophotometry allowed quantitative measurements in a liquid reaction medium containing a highly dispersible heterogeneous catalyst, despite its non-predictable interference pattern. However, this method can only be used with catalyst concentration values below a certain limit, which is dependent on the properties of the solid being used, *e.g.* hydrophilicity. Above this value, the particles completely block the beam pathway and no light reaches the detector. In the present case, we were able to apply this technique to catalyst concentrations up to 0.50 mg.mL^{-1}.

Acknowledgments

L. Costa and V. Brissos acknowledge PhD grants (SFRH/BD/19108/2004 and SFRH/BD/9019/2002) from Fundação para a Ciência e Tecnologia.

References

Lopes, J.A., Costa, P.F., Alves, T.P., Menezes, J.C. (2004). Chemometrics in bioprocess engineering: process analytical technology (PAT) applications. *Chemometrics and Intelligent Laboratory Systems*, 74, 269-275.

Almeida, C.F., Cabral, J.M.S., Fonseca, L.P. (2004). Flow injection analysis system for on-line cutinase activity assay. *Analytica Chimica Acta*, 502, 115-124.

Brissos, V., Eggert, T., Cabral, J.M.S., Jaeger, K.E. (2008). Improving activity and stability of cutinase towards the anionic detergent AOT by complete saturation mutagenesis. *Protein Engineering Design and Selection*, 21, 387-393.

Brereton, R.G. (2000). Introduction to multivariate calibration in analytical chemistry. *The Analyst*, 125, 2125-2154.

Manly, B.F.J. (2006). *Randomization, Bootstrap and Monte Carlo Methods in Biology*, 3rd ed., Chapman & Hall/CRC, Boca Raton, p. 42.

Proceedings of the 10th International Chemical and
Biological Engineering Conference - CHEMPOR 2008
Braga, Portugal, September 4-6, 2008
E.C. Ferreira and M. Mota (Eds.)

Synthesis of tripropionin from crude glycerol the by-product of biodiesel production

Zsanett Herseczki, Gyula Marton
Cooperative Research Centre for Environmental and Information Technology, University of Pannonia, H-8200 Veszprem, Hungary

Keywords: glycerol, tripropionin, fuel additives
Topic: Advancing the chemical and biological engineering fundamentals or Sustainable process-product development through green chemistry

Abstract

Glycerol is a by-product obtained during the production of biodiesel. An increase in biodiesel production would decrease the market price of glycerol. The objective of this study is to investigate glycerol purification and esterification. Crude glycerol from a Hungarian biodiesel factory was partly refined, soaps, water, methanol and pigments were removed and glycerol containing salts was used for certain esterification reactions. The best result of glycerol esterification by propionic acid at 100% conversion of glycerol with selectivity to tripropionin larger than 94% was obtained in case of H_2SO_4 catalyst using continuously water removal. Ion exchange resins were also investigated. A potential process for utilization of crude glycerol was created, which can be applied not only for tripropionin production but production of other glycerol esters like glyceryl triacetate, glyceryl tributyrate. Effect of tripropionin blending on engine performance characteristics and environmental repercussions were studied.

1 Introduction

Biodiesel has high potential as liquid transportation fuel because of its environmental benefits such as minimal emission of CO_2 when compared to regular diesel fuel. Biodiesel is produced from vegetable sources (soybean, sunflower, canola, cotton seed, rapeseed and palm oil) and animal fats using the processes such as micro emulsions, thermal cracking (pyrolysis) and transesterification. Of the several methods available for producing biodiesel, transesterification of natural oils and fats is the most common method. Transesterification is the reaction of fat or oil with an alcohol to form esters known as biodiesel and glycerol using a catalyst. Approximately 10% of the converted feedstock is released as crude glycerol. Hungarian government has planned to produce 150 000 t of biodiesel by 2010, it means that 15 000 t/year glycerol is expected from biodiesel production. This product fraction comprises several impurities, e.g. residues of vegetable oil and esters, salts, different alkaline catalysts and water. Although biofuels such as biodiesel and bioethanol represent a secure, renewable and environmentally safe alternative to fossil fuels, their economic viability is a major concern. The implementation of biorefineries that co-produce higher value products along with biofuels has been proposed as a solution to this problem. The biorefinery model would be especially advantageous if the conversion of byproducts or waste streams generated during biofuel production were considered. Glycerol-rich streams generated in large amounts by the biofuels industry, especially during the production of biodiesel, present an excellent opportunity to establish biorefineries. Once considered a valuable ‘co-product’, crude glycerol is rapidly becoming a ‘waste product’ with a disposal cost attributed to it.
As glycerol is a nontoxic, edible, biodegradable compound, it will provide important environmental benefits to the new platform products. Lower cost glycerol could open significant markets in polymers, ethers, esters and other compounds. From a technical standpoint, glycerol’s multifunctional structure can be exploited by several different means.

One alternative is to esterify glycerol with organic acids (e.g. acetic acid) or anhydrides (e.g. acetic anhydride) and produce oxygen-containing components, which could have suitable properties for use for example in fuels or solvents.
Our aim was to study esterification of glycerol by propionic acid and investigate the field of application of the product.

2 Experimental

Catalyst and chemicals

The commercial strong acid ion-exchange resins Amberlysts (A15 and 36) from Sigma-Aldrich were used as esterification catalysts. Wet ion-exchange resin (A36) was washed with methanol and dried to remove water and impurities from the catalyst pores. A15 in a dry form was used directly. Pure glycerol (99,5%), activated-carbon and calcium-hydroxide were obtained from Spektrum-3D Ltd. (Hungary). Pure glycerol was used for the initial baseline reactions. Crude glycerol was obtained from Öko-Line Hungary Ltd. (Hungary). Propionic acid (>99%), methyl isobutyl ketone (>98,5%), n-hexane (>96%), phosphoric acid and sulfuric acid were obtained from Sigma-Aldrich.

Apparatus and procedure

Due to the fact that composition of crude glycerol obtained from Hungarian biodiesel factory (1. Table) differs from composition offered by Mc Ketta (soaps, more water and salt), a new purification process had to be developed.

Table 1: Composition of G-phases obtained from Hungarian biodiesel factories

Material	**Composition (wt %)**
Glycerol	45-50
Water, methanol	10-15
Salt	10-15
Soaps	30

According to references, the following views were accepted during our purification process:

Due to the high viscosity of the crude glycerol all purification steps were carried out at elevated temperature. In this way we were able to decrease the load of agitators. It is not practical to eliminate the methanol from crude glycerol at the beginning of technology, because it has a favorable advantage of diluting the mixture. It is advisable to dilute the crude glycerol with water to reduce the viscosity.

First step of our refining process was acid treatment. Phosphoric acid was used to reach pH=3 and mixture was stirred at 80 °C, for 1 hour. After the treatment free fatty acid derived from soaps were separated from crude glycerol by simple phase separation.
Next step was neutralization to separate applied acid in excess. Calcium-hydroxide was used for precipitation, optimal pH of neutralization was found to be around 4,8. Formed $Ca_3(PO4)_2$ was eliminated by simple filtration. Filtrate coming from neutralization step is yellow or light brown, if it is necessary, pigments and odor can be eliminated by adsorption on activated-carbon (2 wt%/ crude glycerol). Bleached solution contains only water, methanol and salt. Removal of whole amount of water can be achieved only by distillation at 80°C under vacuum (~ 3kPa). Unfortunately, normal boiling point of glycerol is rather high (290°C) and glycerol oligomerization starts over 200°C, so extremely deep vacuum should be used to distill glycerol from heavies (inorganic salt). Specific use of chemicals depends on the composition of crude glycerol.
The esterification reactions were carried out in a glass flask (500 ml) with magnetic stirring.
Propionic acid was used in excess to shift reaction equilibrium towards the product. Reaction were carried out by straight – forward distillation in absence of entraining solvents and by

help of entraining solvent (MIBK or n-hexane) to remove water azeotropically. The unreacted propionic acid and residual water were distilled off at 80-100°C under reduced pressure (3 kPa). The most difficult problem in connection with crude glycerol refining is removal of salt which is formed during neutralization of the catalyst (KOH, NaOH). Due to the fact that presence of salt does not disturb the reaction and it is insoluble in tripropionin, this problem can be solved by simple filtration.
In a typical run, 46 g (0,5 mol) of glycerol and 222 g (3 mol) propionic acid were used. 2 ml was used from H_2SO_4 and 10 g A15 and 12 g A36 were used in a typical run. Reactions were stopped at the end of water formation.

Analysis

The samples of reaction products were analyzed with a HP 5890 Series II gas chromatograph equipped with a Restek Rtx-5MS column (30m x 0,25 mm x 0,25 µm) and a HP 5971 MSD detector. Analyses were carried out with temperature program from 60 to 240°C (with a slope of 10°C min^{-1}) and 240°C for 2 min isothermally.

3 Results and discussion

The aim of this work was to study the influence of catalyst and the quality of raw material on esterification of glycerol with propionic acid.
The esterification of glycerol (G) with propionic acid (PA) is a complex of three acid catalyzed consecutive equilibrium reactions with formation of monopropionin (MP), dipropionin (DP) and tripropionin (TP). Summary of reaction is shown in Figure 1.

$$G + PA \leftrightarrow MP + H_2O$$
$$MA + PA \leftrightarrow DP + H_2O$$
$$DA + PA \leftrightarrow TP + H_2O$$

Conversion (X) is generally a good indicator of reaction progress. Conversion in the context of these reactions can be based on either glycerol or propionic acid. Glycerol reacts to form the stepwise ester products. However, since reacted glycerol may result in a mono-, di-, or tri-ester of glycerol, conversion is not a good indicator of the extent of reaction. Due to this fact selectivity (S) and yield (Y) were determined.

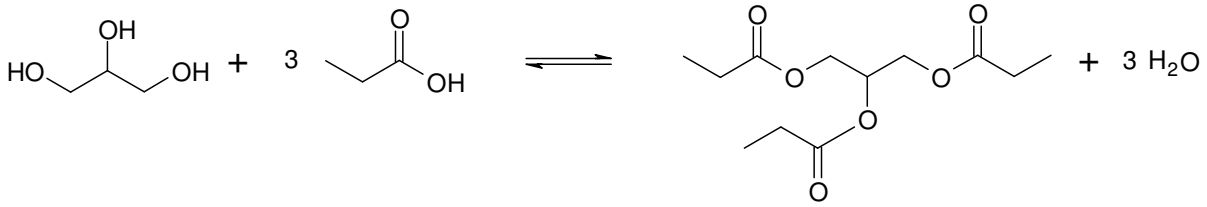

Figure 1: Reaction scheme for esterification of glycerol with acetic acid

As first step, reaction was carried out in presence of sulfuric acid. Forming water was removed by straight – forward distillation in absence of entraining solvents. The best result, 100 % conversion, 94 % selectivity and 94 % yield was received in presence of H_2SO_4 catalyst in case of pure glycerol as raw material. When glycerol containing salt was the raw material, the yield of tripropionin was ~ 83 % (Table 2). Due to the fact that amount of propionic acid decreases during the reaction quickly because it leaves with water, utilization of a structured packed tower to separate water or entraining solvent to remove water azeotropically at lower temperature is reasonable.
Homogeneous catalysts, although effective, lead to serious contamination problems that make essential the implementation of good separation and product purification protocols, which translate into higher production costs. The appropriate solid catalysts could be easily incorporated into a packed bed continuous flow reactor, simplifying product separation and purification and reducing waste generation.
Currently, the esterification of acids with alcohols is commercially achieved using liquid

catalysts, such as sulfuric acid, hydrofluoric acid, and p-toluene-sulfonic acid. The scientific literature contains a good number of reports about the use of heterogeneous acid catalysts for esterification. For instance, esterification has been carried out using ion-exchange resins such as Amberlyst-15 and Nafion with good results. In general, when using organic resins, the catalytic activity strongly depends on their swelling properties. Resin swelling capacity is fundamental since it controls substrate accessibility to the acid sites and, therefore, affects its overall reactivity. Once swelled, the resin pores usually become macropores. This means that big molecules with long hydrocarbon chains show no diffusion limitations and can readily access the acid sites in the bulk.

Table 2: Comparison of catalysts and quality of raw materials for esterification of glycerol

Raw material	Catalyst	Procedure	Reaction Time (min)	Distribution of products wt%				X_G %	S_{TP} %	Y_{TP} %
				Glycerol	MP	DP	TP			
Pure glycerol	H_2SO_4	Raschig r. tower distillation	155	0	0	5,1	94,8	**100**	**94**	**94**
Glycerol cont. salt	H_2SO_4	Raschig r. tower distillation	210	0	0	13,7	86,8	**100**	**83**	**83**
Pure glycerol	A15	Raschig r. tower distillation + n-hexane	660	0	0	11,9	88,4	**100**	**85**	**85**
Glycerol cont. salt	A15	Raschig r. tower distillation + n-hexane	715	0	0	74,8	25,2	**100**	**21**	**21**
Pure glycerol	A36	Raschig r. tower distillation + n-hexane	455	0	0	42,3	57,7	**100**	**52**	**52**
Glycerol cont. salt	A36	Raschig r. tower distillation + n-hexane	575	0	0	72,7	7,7	**100**	**7,6**	**7,6**
Pure glycerol	A15	Raschig r. tower distillation + MIBK	380	0	8,7	10,1	81,8	**100**	**74**	**74**
Pure glycerol	A36	Raschig r. tower distillation + MIBK	455	0	5,1	10,9	84,1	**100**	**79**	**79**

Despite of the fact that most ion-exchange resins are not stable at temperatures above 140 °C, which prohibits their application to reactions that require higher temperatures and inorganic acid catalysts are generally more suitable, Amberlyst 15 and 36 were investigated.
Due to the fact that the maximal operating temperature is 120°C in case of A15 and 150°C in case of A36 further improvement had to be achieved to decrease the reaction temperature, so the temperature of water-removal. A solvent had to be found which does not form an azeotrop with propionic acid and is able to remove water at lower temperature. Methyl isobutyl ketone (MIBK) and n-hexane are potential entraining solvents to remove water azeotropically. Boiling point of MIBK-water azeotrop is 87,9°C and it contains 24,3 wt%

water. After water-MIBK phase separation MIBK was recycled back to the reactor.
As it can be seen from Table 2 relatively high yield can be reached when raw material is pure glycerol. When raw material is glycerol containing salt reaction product contains mainly dipropionin.
There are not any information about boiling point of monopropionin and dipropionin in the literature, so it is difficult to estimate the possibility of tripropionin separation by distillation. Due to this fact further experiments need to be done to improve synthesis of tripropionin to receive ~100% yield and investigate the potential of mono-, di- and tripropionin separation.
Figure 2 shows a potential process for utilization of crude glycerol. This scheme can be applied to produce other glycerol esters like glyceryl triacetate, glyceryl tributyrate.
If esters of glycerol are produced from crude glycerol, some purification steps can be eliminated like previous distillation of water because water is removed azeotropically during ester formation. Preceding activated-carbon treatment is not necessary because esters of glycerol need to be likely decolorized at the end of the process.

Engine performance

Effect of tripropionin blending on engine performance characteristics and environmental repercussions were studied (Table 3). VW-AUDI 1.9 TDI engine was used for the measurements. Blended fuel contained 5 wt% tripropionin.

Table 3. Comparison of reference fuel and blended fuel

	Reference fuel	**Blended fuel**	**Change [%]**
THC [ppm]	35,6	37	**+3,9**
NO_X	767	768	**+0,1**
CO (V/V%)	0,0174	0,0163	**-6,3**
Smoke [FSN]	1,48	1,29	**-12,8**
Specific fuel consumption [g/kWh]	251	260	**+3,6**
$T_{exhaust}$ [°C]	524	520	**-0,8**

An increase of total unburned hydrocarbons (THC) in blended fuel was observed which must be in connection with the inadequate burnout of tripropionin. Due to the high oxygen content of tripropionin a decrease of CO, smoke and exhaust temperature was observed. Specific fuel consumption increased which can be explained by the measured lower maximal motor torque.

According to the engine performance characteristics and environmental repercussions tripropionin represents a promising material, which can be used as fuel additive. Further studies need to be done to find the optimal ratio of tripropionin in Diesel oil.

4 Conclusion

Crude glycerol is a considerable by-product of biodiesel production for which new uses are being sought. Purification of G-phase and esterification of glycerol with propionic acid using sulfuric acid and strong acid ion-exchance resins Amberlyst type were studied. The best result of glycerol esterification by propionic acid at 100% conversion of glycerol with selectivity to tripropionin larger than 94% was obtained in case of H_2SO_4 catalyst using continuously water removal. Homogeneous catalysts (H_2SO_4), although effective, lead to serious contamination problems. The appropriate solid catalysts could be easily incorporated into a packed bed continuous flow reactor, simplifying product separation and purification and reducing waste generation.
A potential process for utilization of crude glycerol was created, which can be applied not

only for tripropionin production but production of other glycerol esters like glyceryl triacetate, glyceryl tributyrate.
Tripropionin represents a promising material, which can be used as fuel additive to improve engine performance characteristics and environmental repercussions. Further studies need to be done to find the optimal ratio of tripropionin in Diesel oil and to examine other fields of application of this relatively new product.

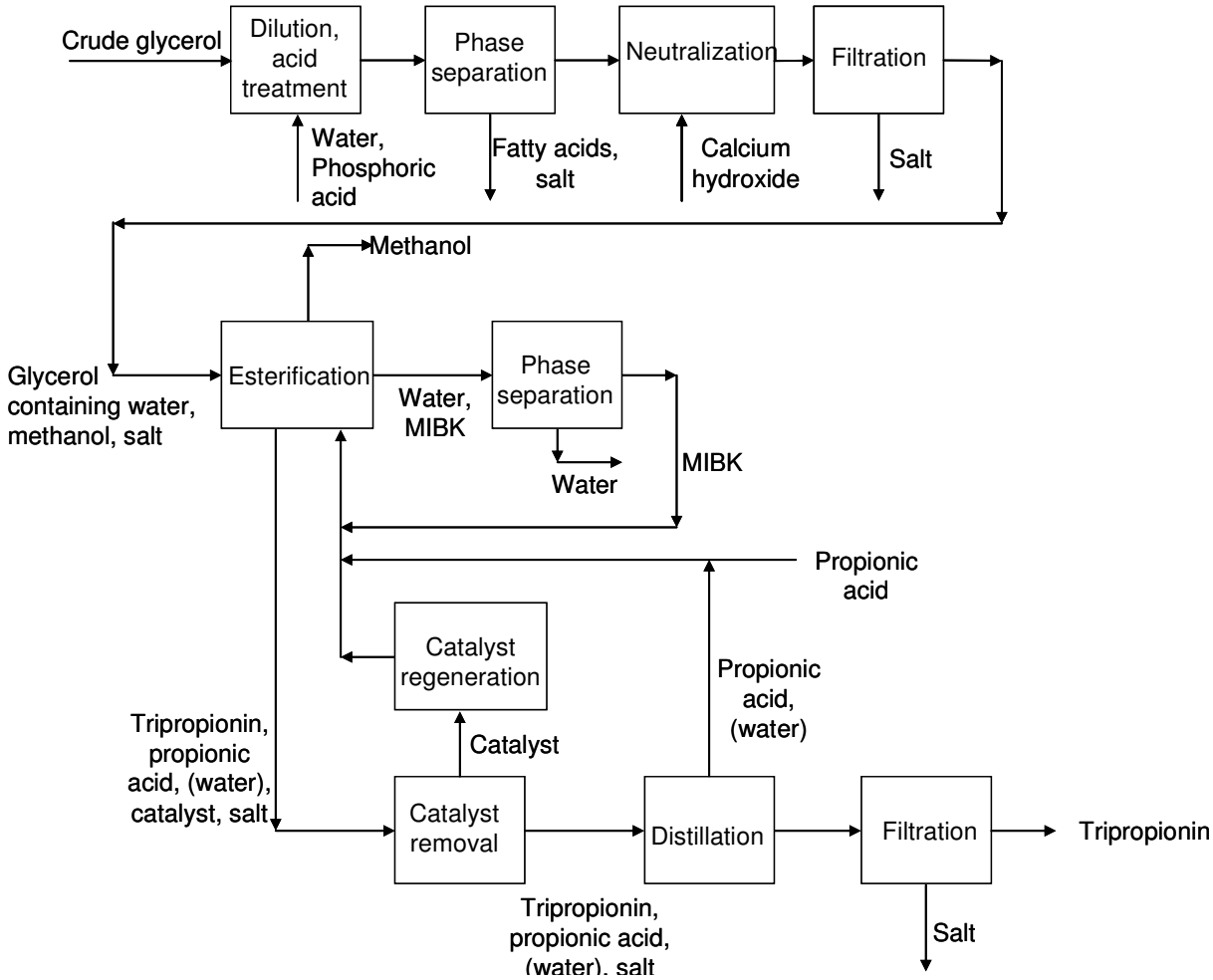

Figure 2: Scheme for production of tripropionin from crude glycerol

References

T. Valliyappan, N.N. Bakhshi, A.K. Dalai (2008). *Bioresource Technology,* 994476-4483

J. Van Gerpen, B. Shanks, R. Pruszko (2002-2004), Biodiesel Production Technology Subcontractor Report, National Renewable Energy Laboratory

J.J. Mc Ketta (1986). Encycl. of Chem. Proc. and Des. Vol. 24, 387.

Chen, X.; Xu, Z.; Okuhara, T. (1999). Liquid-phase esterification of acrylic acid with 1-butanol catalyzed by solid acid catalysts. *Appl. Catal., A*, *18*0, 261-269.

Heidekum, A.; Harmer, M. A.; Hoelderich, W. F. (1999). Addition of carboxylic acids to cyclic olefins catalyzed by strong acidic ion-exchange resins. *J. Catal.*, *18*1, 217-222.

Zhang, Z. Y.; Hidajat, K.; Ray, A. K. (2001). Determination of adsorption and kinetic parameters for methyl *tert*-butyl ether synthesis from *tert*-butyl alcohol and methanol. *J. Catal.*, *20*0, 209-221.

L. H. Horsley (1952). Azeotropic data, *American Chemical Society*, Washington D.C.

Proceedings of the 10th International Chemical and
Biological Engineering Conference - CHEMPOR 2008
Braga, Portugal, September 4-6, 2008
E.C. Ferreira and M. Mota (Eds.)

The future sustainability of biodiesel

Renato H. Carvalho[1]*, Luís R. Vilela de Matos[1]
[1] Iberol – Sociedade Ibérica de Biocombustíveis e Oleaginosas, S.A., Technological Development Department, Quinta da Hortinha - Alhandra, 2601–908 Vila Franca de Xira, Portugal.

Keywords: Biodiesel, Soybean oil, Non-edible oil, Renewable Energy, CO_2 Reduction
Topic: Multi-scale and/or multi-disciplinary approach to process-product innovation (Energy and environment).

Abstract

This paper shows Iberol perspective in what concerns to the future sustainability of biodiesel.

The significant imposed tax gap between gasoil and gasoline, resulted in a transportation fleet based on the first one. As an effort to decrease the gasoil dependence and at the same time, reduce the CO_2 emissions, biodiesel has become the most important biofuel in European Union (EU).

The biodiesel has to be considered as a complement to push ahead, the end of fossil diesel in a medium term, and never a total substitute. The competitiveness between biodiesel and fossil petrodiesel can only be equalised if the non-edible raw materials are used.

We are sure that soybean oil is in short time the answer since most protein comes from this proteoleaginous, increasing meal for the food chain in which results a by-product that can be considered as a non-edible oil and can be used to decrease the fossil fuels, producing biodiesel.

The by-products from the biodiesel production have a paramount importance in this type of market, having an enormous potential as feedstoks for other chemical products, such as, epichlorohydrin and propylene glycol, among others.

Biodiesel can be produced by a sustainable way, only if the right policies and attitudes are taken in a short term.

1 Introduction

The use of biofuels in the European Union is playing an increasingly important role. Both political issues such as, EU legislation, Kyoto protocol, Bali agreement, and market issues such as, economic opportunities, responsible business, encourage their use. Part of the raw-materials need to be imported from the outside of EU and, although biofuels have a green image, an increasing concern arises about the sustainability of the produced raw-materials (including impacts on biodiversity, displacement of food production and effectiveness in the greenhouse gas reduction).

The name biofuels can be generally defined as solid, liquid, or gas fuel derived from new biological material, distinguishing itself from the fossil fuels (long time dead biological materials under extreme conditions). However, for the transport sector, only two are considered due to the available quantities in the world, biodiesel and bioethanol. If we evaluate the macro-structure of these two, bioethanol has importance in south and north America, because the demand of gasoline is very high, and the availability of raw-materials such as sugarcane are abundant (Brazil). In contrast, bioethanol in Europe should not be produced since exists a large excess of gasoline that is exported. Another important point is

* Corresponding author. Tel +351 219 519 400. E-mail: Renato.Carvalho.Iberol@Sortico.pt

that edaphoclimatic conditions are not adequate for the production of economic raw-materials (sugarcane). This biofuel in Europe is produced from corn (maize), a raw-material that interferes with the food chain, as it happens in the USA.

Corn ethanol produced in the USA shows that one unit of fossil-fuel energy is required to create 1.3 energy units from the resulting ethanol. The energy balance for sugarcane ethanol produced in Brazil is 1:8 and the biodiesel energy balance is 1:2.5. Another indicative balance is the cellulosic bioethanol biofuel, known as second generation bioethanol, which has an energy balance of 1:2-36. Second generation bioethanol is produced from feedstock containing cellulosic biomass such as the stalks, leaves, and husks of corn plants, wood chips, and sawdust. This biofuel has an index between 2 and 36, depending of the production process; however, these are experimental values because these methods are not economically feasible and thus, they are not industrially implemented so far (National Geographic Portugal, 2007). As it can be seen, the production of biodiesel in Europe is the reasonable choice at short term.

One hundred years ago, Rudolf Diesel tested vegetable oil (peanut oil) as fuel for his engine, however, with the advent of cheap petroleum and optimisation of the crude oil fractions to produce gasoil and gasoline, only on emergency times it was used vegetable oil. Today, this kind of emergency situation has arrives once again in our lives and the consideration of biomass use has become more than necessary, not only from an economic point of view, but also because of environmental protection.

EU imports more than 20 million tonnes of biodiesel, so must be by far the biggest and most important biofuel, representing more than 80% of total biofuels production. The EU is the worldwide leader in biodiesel production, both in terms of biodiesel capacities and production. In 2006 it was produced 77% of world-wide biodiesel production and in 2007 produced 5.7 million tonnes. An alternative fuel like biodiesel can be technically feasible, environmentally acceptable and readily available but it is not until now economically competitive, due to the price of raw-materials as it can be seen in Figure 1 (EBB, 2006).

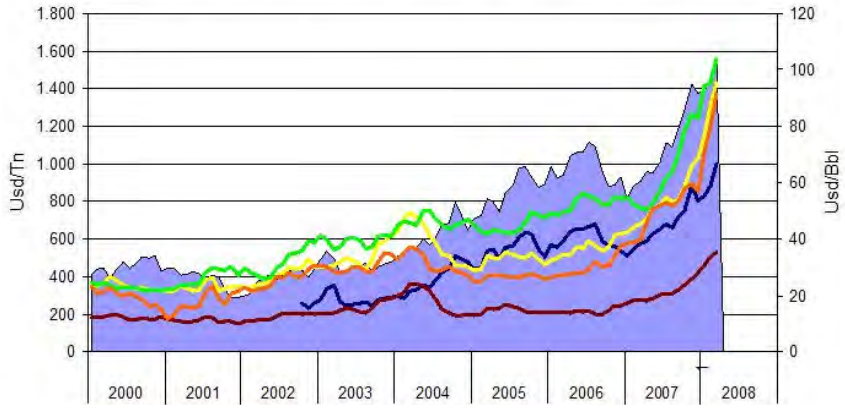

Figure 1- International commodities prices for petroleum, diesel, soybean, soybean oil, rapeseed oil, palm olein (Reuters, 2008).

The cost of biodiesel varies depending on base stock, geographic area, variability in crop production from season to season, the price of the crude oil and other independent factors such as speculation in trade markets. The high price of biodiesel is in large part due to the feedstocks.

Since the economic growth is always accompanied by commensurate increase in the transports sector, this type of energy is gaining more and more importance due to the depleting of fossil fuel resources and also to avoid the monopoly of some oil-exporting countries. As a consequence of this depletion, the fuel price grows exponentially and the vegetable oils prices follow it. It is a mistake to think that biodiesel will be competitive in comparison with petrofuels. Methanol is also dependent today of a fossil fuel, since it is

produced from natural gas. Moreover, the limited oleaginous production implies limitations in vegetable oils production and thus, the demand is higher than the offer. The raw-materials are strongly dependent of the fossil fuels and speculations of prices.

Because of these mentioned situations, the biodiesel has to be considered as a complement, or adjuvant to push ahead, the end of fossil diesel in a medium term, and never a total substitute.

But what is biodiesel? The biodiesel is a renewable fuel that is produced by transesterification, in which a vegetable oil (edible and non-edible) or animal fat reacts with a short-chain alcohol in the presence of a catalyst, to form esters and glycerol (Marchetti et al., 2007). The major components of vegetable oils and animal fats are triacylglycerols (TAG; often also called triglycerides). This biofuel is biodegradable, non-toxic, sulphur-free and has low emission profiles as compared to petroleum diesel.

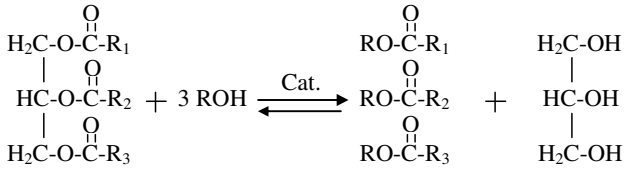

Other processes such as hydrotreating (NExBTL: catalytic hydrogenation of vegetable oils is not economically feasible) or even the second-generation fuel to blend with gasoil (Biomass To Liquid) that could replace biodiesel, are not well developed so far.

Because the growing of plants consumes CO_2, biodiesel has a closed carbon cycle dramatically reducing the CO_2. This allied with the desire to reduce dependence on foreign energy sources, manifesting itself through a variety of public policies over the years, have served to increase biodiesel use in the European Union (EU) (Knothe et al., 2005).

Industrially, the biodiesel is made mostly with rapeseed oil, palm olein, soybean oil and in small cases with animal fats. The parameters given by the specific European norm (EN 14214) are very restricted since they were based mostly on a biodiesel produced with rapeseed oil, thus it is not possible to produce an extreme biodiesel with only one type of oil/fat other than rapeseed oil of the referred ones.

In a global macro-economic point of view, the selection of the vegetable oil is very important, not only because of its cost but also due to the repercussions that this selection has in the world food structure. The competitiveness between biodiesel and fossil diesel can only be equalised if the non-edible raw materials are used.

Non-edible oil as raw materials, with enormous potential but still in development production, are obtained from plant species such as Jatropha curcas (Sarin et al., 2007), Pongamia pinnata (Meher et al., 2006) or microalgaes. Nevertheless, extreme biodiesel produced with these oils could not also fulfil totally the necessary specification of the EN 14214. These are indeed the expected raw material for the future biodiesel production, with enormous potentials due to the yield/crop and content of oil of the oleaginous. However, their massive production for the biodiesel industry is under development and thus cannot be at short term the answer to the biodiesel demand.

From all the mentioned above, only the soybean oil is each time more a non-edible oil (less than 5% is used in human alimentation). We can consider that in this case the principal product of the oil extraction is the soybean meal, very rich in proteins (44%), that is used in every animal feedstock, since soybean is considered a proteoleaginous. In addition, the soybean oil utilisation in human feed has very limitations. Given its economic value and availability, the soybean oil is nowadays a preferential raw material in the manufacture of biodiesel. However, as it was mentioned before, for example, the soybean oil presents an iodine index between 128 and 132, too high to meet the European specification of biodiesel in this parameter (equal to 120). Because of this fact, it is not currently possible in all EU

countries that have transposed these specifications, manufacture biodiesel entirely from soybean oil, it becomes necessary to incorporate other vegetable oils of higher costs, such as rapeseed oil from north of Europe and palm olein from tropical countries.

The European Mediterranean region has the appropriate edaphoclimatic conditions to produce soybean, which could have a significant contribution as endogenous production, not only oil, but mainly protein, in a similar comparison with the north appropriate edaphoclimatic conditions to produce rapeseed.

It can be conclude that soybean oil is in short term the answer since most protein comes from this proteoleaginous, increasing meal for the food chain in which results a by-product that can be used to decrease the fossil fuels, producing biodiesel.

Other way to promote the biodiesel and its future viability is the creation of conditions by governments to impose the biodiesel blending in every diesel, as well as, the removal of biofuels subsidies with the concomitant increasing of the diesel cost (a 5% biodiesel blending would increase ± 1 Euro cent on the diesel final cost).

Commercial production and consumption of glycerol were generally considered a reasonable indicator of industrial activity since it enters into such a large number of industrial processes. With the arrival of biodiesel, this biofuel industry has become practically a large consumer of methyl esters as the detergent industry and thus, resulted in a major production of glycerine (10% of the biodiesel production) that changed this market dynamic. The by-product nature of glycerol production leads to quite volatile price oscillations in the marketplace due to the stimulation or restrictions of the demand, to meet the available supply which is determined by factors outside the glycerol market. However, glycerine is a by-product with an enormous potential to substitute part of petrochemical feedstocks. The increasing abundance of glycerine, its renewability, and attractive pricing, make glycerol an appealing platform chemical to derive a family of commercially valued compounds (Figure 2).

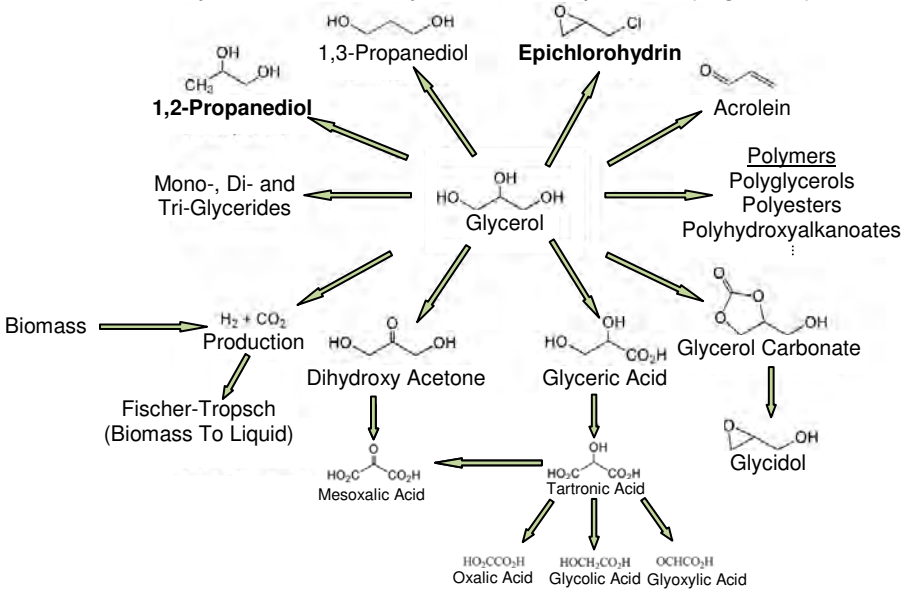

Figure 2- Platform chemical resulted from glycerol (Pagliaro et al., 2007).

The replacement of propylene from fossil origin by glycerine, that is a renewable and low-cost raw-material (Figure 3), has become very attractive to industry for the production of valued added chemicals, such as propylene glycol (1,2-propanediol) and epichlorohydrin.

Propylene glycol: the hydration of propylene oxide that is derived from propylene is then replaced by a liquid and vapour phase hydrogenation of the glycerine over a metal catalyst. Dow, Cargill, Archer Daniels Midland and Huntsman have recently announced plants to produce propylene glycol from glycerine.

Epichlorohydrin: a reaction of propylene with chlorine gas produces the allyl chloride which is further reacted to give dichloropropanol. This process can be replaced by the Solvay patent *Epicerol*, in which the glycerine reacts with hydrochloric acid over a catalyst that directly results in the dichloropropanol. This dichloropropanol in both processes is dehydrochlorinated with NaOH to give the final epichlorohydrin product. Hydrochloric acid is inexpensive and much safer in comparison with chlorine gas. Solvay started a 10.000 tonnes/year plant in France from glycerol and plan to start up a 100.000 tonnes/year plant in Thailand in 2009, due to the fast increasing demand for epichlorohydrin.

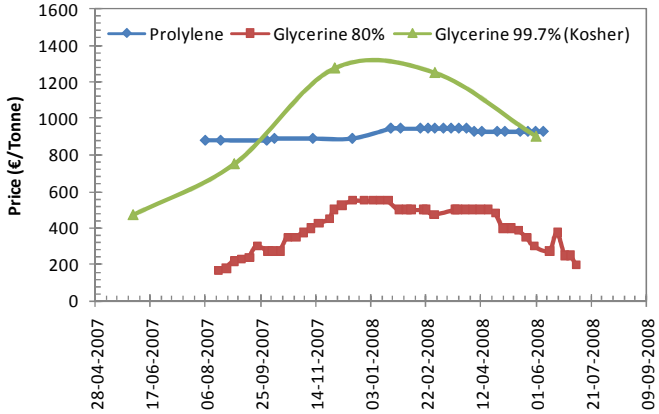

Figure 3- Prices of chemical compounds in Europe (Reuters, 2008 and ICIS, 2008).

In which respect to the international context, the EU market is disturbed by the continuing negative effects of "B99" (blending 1 part of diesel and 99 of biodiesel) from United States (US) with an export subsidy. With this unfair scheme the US producers can access the EU markets with a remarkable advantage, selling the biodiesel at the same or even at a lower price than the cost of EU industry's raw materials (EuropaBio, 2007).

The European parliament and council are creating a document with proposals for a Renewable Energy Directive (RED), which sets an overall binding target for the European Union of 20% renewable energy sources in energy consumption and a 10% minimum target for biofuels in transport by 2020 (Commission of the European Communities, 2008). The RED proposal introduces strict environmental sustainability criteria for the production of biofuels which gives the guidelines to each country transpose for their legislations, the sustainability criteria for the biodiesel production. Most importantly, the RED directive should provide a comprehensive set of sustainability criteria and calculation mechanisms for biofuels.

One of the major issues is the greenhouse gas balance biofuels that should assessed in a pragmatic and realistic way, both in terms of threshold and methodology. If the methodology is very restrictive, the 10% target of the threshold incorporation in 2020 will be very difficult to accomplish. This enforces the urgent need to establish a neutral set of criteria for assessing the GHG performances biofuels.

Another point of discussion is the understanding of the real influence of biodiesel in the food market. Some bad publicity is being made for the protection of individual interest and lobbies from specific markets that are indirectly involved. For example, EU biodiesel industry uses less than 3% of all imported palm oil. Before the implementation of biodiesel industry in the world economy, the lack of food for the poorest people was evident, however, with the development of the emergent countries like China, India, Indonesia and others, the fuel consumption and demand also increased. This led to the necessity for better human conditions and consumptions, resulting in a major demand of food and energy for these countries. There are a lot more causes than the biofuels production that increase the price of food and it is unreasonable to blame biodiesel for the major part of it. As it was said before, we have to distinguish between the good biofuels that are produced with non-edible raw-material and the bad biofuels that can interfere with the food market.

In the EU, biodiesel production can be done in accordance with sustainability principles and without endangering the food supply. The EU has to raise the oilseeds production from 23 million tonnes to the expected 35 million tonnes. Additionally, biodiesel production development will improve the EU self-sufficiency in terms of vegetable proteins as it was mentioned in relation to soybean. Today, the EU has currently a deficit in protein meals for animal feed. The development of biodiesel industry increases in 3 million tonnes this product since 2002 and the expected production should provide an additional 8 million tonnes by 2015-2020, thus increasing the EU self-sufficiency ratio from 20% to 30%. Europe still has available large Set-Aside areas that can be prepared and cultivated for these purposes.

2 Conclusions

The biofuels are not the ultimate solution of energy for the transport sector but is the short and medium term solution, pushing ahead the lifetime of petrofuels.

The main engines of increasing food costs worldwide include high crude oil prices, growing food demand in developing countries, droughts that have hurt crops globally, commodity speculators, the US dollar crisis and in the end, biofuels.

The right way to produce biodiesel it is indeed doing it with non-edible raw-material, in which the soybean oil has the major advantage of being a by-product of the seeds extraction process.

Europe has to increase its endogenous crops, not only to be more self-sufficiently in proteins, but also as consequence, by producing biodiesel, more self-sufficiently in fuels.

The by-products, such as glycerine, have an enormous effect and influence in the future sustainability of biodiesel.

Short term directives and legislation for sustainability criteria are mandatory to end the insecurity of the biofuels market and the enforced incorporation of biodiesel in petrodiesel is an important measure to take.

References

EBB - European Biodiesel Board (2006). 2006-07 production statistics confirm a strong growth in the EU, but legislative and fair trade improvements are urgently needed to confirm expansion. *PRESS RELEASE*.

EuropaBio - The European Association of Bioindustries (2007). *EuropaBio position and specific recommendations.*

Knothe, G., Gerpen, J.V., Krahl, J. (2005). *The Biodiesel Handbook,* AOCS Press, Champaign, Illinois.

Marchetti, J.M., Miguel, V.U., Errazu, A.F. (2007). Possible methods for biodiesel production. *Renewable and Sustainable Energy Reviews*, 11, 1300-1311.

Meher, L.C., Dharmagadda, V.S.S., Naik, S.N. (2006). Optimization of alkali-catalyzed transesterification of *Pongamia pinnata* oil for production of biodiesel. *Bioresource Technology*, 97, 1392-1397.

Sarin, R., Sharma, M., Sinharay, S., Malhotra, R.K. (2007). Jatropha-Palm biodiesel blends: An optimum mix for Asia. *Fuel,* 86, 1365-1371.

Commission of the European Communities, 2008. Proposal for a DIRECTIVE OF THE EUROPEAN PARLIAMENT AND OF THE COUNCIL on the promotion of the use of energy from renewable sources.

Reuters, 2008. Data information consulted in June 2008 on http://www.reuters.com/.

ICIS, 2008. Periodicals entry of ICISChemicalBusiness from August 2007 to June 2008.

National Geographic Portugal (2007). Biocombustíveis. Prós e contras de uma nova energia. Número 80, 1-31.

Pagliaro, M., Ciriminna, R., Kimura, H., Rossi, M., Pina, C.D. (2007). From glycerol to value-added products. *Angewandte Chemie International Edition*, 46, 4434-4440.

Proceedings of the 10th International Chemical and
Biological Engineering Conference - CHEMPOR 2008
Braga, Portugal, September 4-6, 2008
E.C. Ferreira and M. Mota (Eds.)

Lignin-based polyurethane materials

Carolina Cateto[1,2,3], Filomena Barreiro[1], Alírio Rodrigues[2], Naceur Belgacem[3]
1. LSRE - Laboratory of Separation and Reaction Engineering, Instituto Politécnico de Bragança, Campus de Santa Apolónia, Ap 1134, 5301-857 Bragança, Portugal
2. LSRE - Laboratory of Separation and Reaction Engineering, Faculdade de Engenharia da Universidade do Porto, Rua Dr. Roberto Frias, 4200-465 Porto, Portugal
3. LGP2, École Française de Papeterie et des Industries Graphiques (EFPG-INPG), BP 65, 38402 St. Martin d´Hères, France

Keywords: Lignin, Polyurethanes, Bio-based, Added-value
Topic: Sustainable process–product development through green chemistry

Abstract

Four technical lignins (Alcell, Indulin AT, Sarkanda and Curan 27-11P) were used as macro-monomers in the synthesis of polyurethane materials following two global approaches. In the first one Alcell and Indulin AT lignins were used directly as co-monomers in combination with a linear polycaprolactone (PCL) in order to produce polyurethane elastomers where lignin content varied between 10 and 25% (w/w) with respect to polyol mixture (PCL+lignin). The thermomechanical properties of the resulting materials were determined by dynamical mechanical analysis (DMA), differential scanning calorimetry (DSC) and swelling tests. In lignin-based elastomers Indulin AT showed to be more efficiently incorporated in the polyurethane network compared with Alcell lignin. Elastomers prepared with Indulin AT lignin exhibited a cross-linking density and storage modulus (rubbery plateau) higher than those of Alcell lignin-based counterpart and a lower soluble fraction. For both Alcell and Indulin AT based elastomers the glass transition temperature increased and extended over a wide temperature range with the increase of lignin content.
The second approach consisted of producing rigid polyurethane foams (RPU) using lignin-based polyols obtained after chemical modification by an oxypropylation procedure. Two polyol formulations (20/80 and 30/70, in what concerns the weight ratios between lignin and propylene oxide, PO), were used in RPU formulations and their content varied from 0 to 100% (w/w with respect to a commercial polyol, used as a reference). The resulting RPU foams were characterized in terms of density, mechanical properties, conductivity and morphology. The prepared RPU foams with lignin-based polyols presented properties, very similar to those obtained from conventional commercial polyols. RPU foams prepared with 30/70 polyols exhibited improved properties comparatively to those arising from 20/80 formulations. Exceptions were however detected in RPU foams prepared with all Sarkanda lignin based polyols and Curan 27-11P 30/70 formulation, which were found to be inadequate for RPU formulation.

1 Introduction

Polyurethanes are considered as one of the most versatile polymeric materials offering a wide range of products with various applications in diverse sectors. Rigid polyurethane (RPU) foams and elastomers belong to this class of products. Nowadays, due to economical and environmental concerns, the utilization and development of low-cost polyols from abundant and renewable biomass resources has gained an increasing attention in polyurethane industry. Lignin belongs to these biomass resources, and its application as a macro-monomer in polyurethane synthesis, has been the subject of several studies (Yoshida et al., 1990; Thring et al., 1998; Gandini et al., 2000).
Lignin is defined as a random, amorphous three-dimensional polymeric network, which does not possess a uniform, homogenous, well defined structure with well established repeating

units. Commercially available lignins are, most often, Kraft or lignosulfonates associated to the corresponding most commonly used industrial processes for wood delignification and fibres isolation (Kraft and sulphite, respectively). These lignins are largely used in dispersing and binding applications and a small part is employed in the production of specialty chemicals like vanillin and dimethylsulfoxide (Gosselink et al., 2004). Recently, sulphur-free lignins are becoming an emerging class of lignin products, partly motivated by environmental policies, but also, by less capital intensive associated technologies (Lora and Glasser, 2002).
The utilization of lignin as a macromonomer in polyurethane synthesis often follows two global approaches: (i) the direct utilization of lignin without any preliminary chemical modification, alone or in combination with other polyols (Yoshida et al., 1990, Evtuguin et al., 1998, Cateto et al., 2008) or, (ii) by making hydroxyl functions more readily accessible by chemical modification, such as esterification and etherification reactions (Glasser, 1989, Gandini et al., 2002, Nadji et al., 2005).
In this work, the two approaches were studied. Four technical lignins (Alcell, Sarkanda, Indulin AT and Curan 27-11P) representing softwood and non-wood lignin types and three pulp processes: Kraft, soda and organosolv (properties shown in table 1) have been used. In the first approach Alcell and Indulin AT were used directly as a co-monomer in combination with a linear PCL. PCL was introduced into the formulation to provide flexibility and enable polymerization in bulk. In the second approach the four lignin samples were oxypropylated and the resulting liquid polyols incorporated into RPU foams, alone or in combination with other commercial polyether-polyol.

Table 1. Properties of the technical lignins used in this work

Lignin Sample	Total OH (mmol/g)	Phenolic OH (mmol/g)	COOH (mmol/g)	Ash content (% w/w)
Alcell	5.26	3.81	0.23	0.05
Sarkanda	5.26	2.41	0.62	3.26
Indulin AT	6.99	3.95	0.39	3.06
Curan 27-11P	6.21	3.63	0.47	17.0

2 Material and Methods

2.1 Rigid polyurethane foams

Materials The lignin-based polyols used in this work were obtained from the oxypropylation of four technical lignins (Alcell, Indulin AT, Curan 27-11P and Sarkanda) as described elsewhere (Cateto et al., 2007). The following terminology will be used to identify the polyol formulations used in this work: L/PO/C (ratio between lignin, PO and catalyst content). The commercial polyether polyol (Lupranol® 3323), polymeric MDI (PMDI with a functionality of 2.7), silicone surfactant (SR-321 NIAX) and the catalysts NIAX and DMCHA were kindly supplied by Elastogran-BASF (France). Glycerol and *n*-pentane were obtained commercially.

Foam Preparation Polyurethane foams were prepared by mixing, during 1 minute, the polyol or polyol mixture in combination with glycerol (10%, w/w), surfactant (2%, w/w), water (2%, w/w) and a catalyst combination (2%, w/w of a mixture with equal amounts of DMCHA and NIAX). Thereafter, *n*-pentane was added (20%, w/w) and the mixture was stirred during 30 s. Finally, the polymeric isocyanate was added and the resulting mixture vigorously stirred until the foam started to grow. Foams were left to cure during 24 hours at room temperature. The weight percentage of glycerol, surfactant, water, catalysts and, *n*-pentane are given relatively to total weight of polyol. The isocyanate/hydroxyl ratio (NCO/OH) chosen was of 1.1.

Foam Characterization For density and compression tests, foams were cut into cube specimens of 50×50×50 mm^3 dimensions and thereafter conditioned during 40 hours at 23ºC and 50% of humidity. The densities of the foams were determined according to ASTM D1622 standard method. The specimens were weighted and its dimensions measured. Density was calculated by dividing the mass and volume obtained for each specimen. Compression tests were conducted according to ASTM D1621 standard. Measurements were performed using a tensile instrument (Instrom model 4501) in the direction perpendicular to foam growth. A load

was applied at a crosshead speed of 5 mm/min until the specimen was compressed to approximately 15% of its original thickness. Conductivity measurements were conducted according to ASTM C177 standard. Specimens with a diameter of 90 mm and thickness of 4 mm were cut and placed in an apparatus developed to measure the thermal conductivity of insulating materials. This apparatus is composed of two plates maintained with a temperature differential. The thermal conductivity of the samples was determined when the thermal equilibrium was reached and a uniform temperature gradient thought the sample was attained. Morphology analysis of RPU foams was performed on a Quanta 200 FEI field emission scanning electron microscope (SEM). The samples were cut and gold coated before scanning. The used accelerating voltage was of 12.5 Kv and the sample was observed both in the free-rise and free-rise perpendicular directions.

2.2 Polyurethane elastomers

Materials and Formulations The lignin-based polyurethanes were prepared starting with 4,4'-methylene-diphenylene diisocyanate (MDI), policaprolactonediol (PCL) with an average molecular weight of 750 (PCL750) and two different technical lignins, Indulin AT from Meadwestvaco (South Carolina, USA) and Alcell from Repap, with different weight contents (10, 15, 20 and 25%). PCL was kindly supplied by Solvay Interox (Cheshire, UK) and MDI was commercially obtained from Aldrich.

Elastomers Preparation Lignin and PCL were degassed overnight under vacuum at 60 ºC. MDI (Aldrich) was purified by heating at 60 ºC and filtered through a heated filter just prior use. Lignin and PCL were weighed in an analytical balance in the desired proportions and the mixture homogenised by stirring during 1 hour at 80 ºC. Then, molten MDI was added and the reaction mixture thoroughly stirred during 30 s and rapidly transferred into a Teflon mould. The obtained films were left to cure during 24 hours at 80 ºC.

Elastomers Characterization Differential Scanning Calorimetry (DSC) experiments were performed using a DSC Q100 differential calorimeter (TA Instruments) working in modulated mode. Analyses were carried out from -60 to 200 ºC with a heating rate of 5 ºC/min. The oscillation period and the amplitude were 60 s and ± 1 ºC, respectively. Dynamical Mechanical Analysis (DMA) of lignin-based elastomers was carried out using a RSA3 (TA Instruments) equipment working in tensile mode. The measurements were performed at a constant frequency of 1 Hz, strain amplitude of 0.03% and a distance between the jaws of 10 mm. The heating rate was 5°C.min^{-1} and the temperature ranged from -100 to 200 ºC. The width of the samples varied from 3 to 5 mm.

3 Results and Discussion

3.1 Rigid polyurethane foams from lignin- based polyols

Oxypropylated lignin was incorporated into RPU foams formulations without performing any purification concerning the homopolymer and catalyst (KOH) contents removal. Thus, several RPU foams were prepared by varying the lignin-based polyol content from 0 to 100% (w/w). Additionally, for the 20/80/5 based formulation a more detailed study was performed. RPU foams with 25, 50, 75 and 100% (w/w) of lignin-based polyol were prepared. For the 30/70/2 formulations only foams containing 50 and 100% (w/w) of lignin-based polyol were produced. Table 2 summarizes some of the data obtained for the lignin based RPU foams produced with 20/80/5 and 30/70/2 polyols. The properties of the RPU foams produced with the commercial polyol are also shown as a reference.

The produced lignin-based RPU foams (particularly those based on 20/80/5 polyols) exhibit lower mechanical properties and density to compare with reference foams (those obtained from the commercial polyol). Additionally, it was also observed that RPU foams based on Alcell and Indulin AT polyols showed higher mechanical properties and density values to compare with those produced with Sarkanda and Curan 27-11P polyols. In fact, RPU foams prepared with 20/80/5 Sarkanda based polyols were found to be brittle presenting quite large cells, as observed in SEM micrographs (Figures not shown). For Sarkanda lignin 30/70/2

polyol, the generated mixtures were so heterogeneous that the production of RPU foams was not possible, probably because of the complex rheological properties of this polyol.
Foams produced with 30/70/2 Curan 27-11P based polyol also showed some brittleness. For RPU foam samples including 100% (w/w) Curan 27-11P based polyol no defined cells were observed by SEM. For those including 50% (w/w) irregular size and deteriorated cells were observed. In conclusion, the studied Sarkanda based polyols and the 20/80/5 Curan 27-11P seems to be unsuitable for RPU formulations.

Table 2. Density, thermal conductivity and compressive modulus of lignin based RPU foams.

L/PO/C (w/v/(%w/w))	Lignin sample/ % Lignin polyol (w/w)	Density (Kg/m^3)	Conductivity (mW/mK)	Compressive Modulus (MPa)
30/70/2	Alcell/100	22.3	25.7	3.1
	Alcell/50	25.1	26.9	3.0
	Indulin AT/100	23.1	27.4	4.0
	Indulin AT/50	23.7	29.1	3.6
20/80/5	Alcell/100	20.9	26.7	2.5
	Alcell/50	23.9	30.5	3.3
	Indulin AT/100	19.2	26.8	2.6
	Indulin AT/50	22.4	32.9	2.4
	Curan 27-11P/100	18.4	28.5	2.3
	Curan 27-11P/50	19.4	31.3	2.7
Reference Foam (100% commercial polyol)		31.1	30.3	4.6

For thermal conductivity it was observed that RPU foams produced with 100% (w/w) lignin-based polyols present the lowest conductivity values. RPU foams prepared with 20/80/5 based formulations presented cells with an elongate hexagonal well defined shape and a quite homogeneous size distribution. For comparison, foams prepared with different lignin based polyols contents, are presented in Figure 1. The observed elongate form can explain the low density and compressive modulus obtained for these RPU foam formulations. As a consequence of lower density, mechanical properties are influenced (anisotropy effect) (Hawkins et al., 2005). In fact, SEM micrographs showed that with the increase of commercial polyol content, the cells tend to become smaller and less elongate, thus explaining the observed increase of density and compressive modulus. For the studied lignin-based RPU foams, cells with very large size are often detected thus contributing to less homogeneous structures. This heterogeneity can justify the reason why no relation was found between RPU foam lignin content and the conductivity. Nonetheless, compressive modulus and density were found to correlate relatively well.
Foams produced with 30/70/2 formulations presented cells with smaller size (approximately 370 µm instead of 550 µm obtained with 20/80/5 based RPU foams) and with a more pronounced spherical form comparatively to those produced with 20/80/5 based polyols (see Figure 2). This can explain the higher density and the improved thermal conductivity and mechanical properties of the latter formulations (20/80/5 lignin-based polyols). Also, this could be associated with higher hydroxyl number and lignin content and a decrease of KOH and homopolymer contents in the final 30/70/2 polyol mixture.

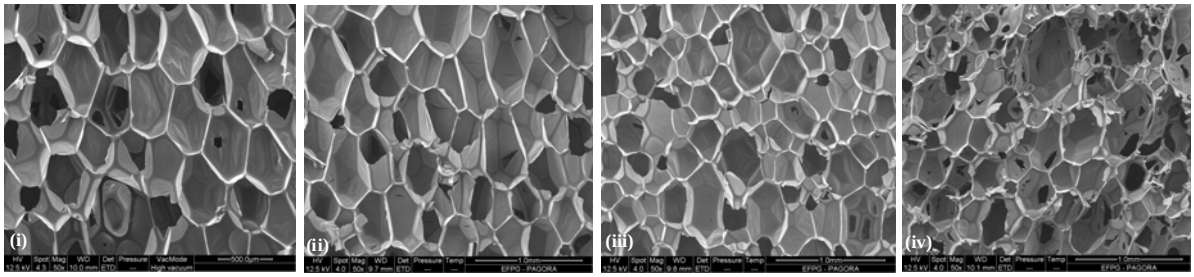

Figure 1 Scanning electron micrographs obtained for RPU foams containing 100% (w/w) for (i), (ii) 20/80/5 and (iii),(iv) 30/70/2 for Alcell and Indulin AT based polyol, respectively (free-rise direction).

3.2 Lignin-based elastomers polyurethanes

The obtained data showed that Alcell and Indulin AT produced elastomers with quite distinct properties. Figure 2 shows the effect of Alcell and Indulin AT content on the storage modulus (E´) and loss tangent (tan δ) with temperature. As can be observed for both Alcell and Indulin based elastomers, the maximum of tan δ shifts towards higher temperatures and the peak become broader as the lignin content increased. This trend was also confirmed by DSC analysis. Thus, glass transition temperature (Tg) increases with the increase of lignin content and the associated transition temperature range also increases with the increase of lignin content. Yoshida et al. (1990) pointed out that the increase of the transition temperature range may reflect structural heterogeneities in the network structure, e.g., a broad distribution of molecular weights between cross-linking points may exist. Also, the shift observed for Tg with the increase of lignin content must be due to an increasing of lignin incorporation. It is well know that increasing of cross-linking density introduces restrictions on the molecular motion thereby increasing the Tg value.

The dependence of storage modulus with temperature observed for lignin-based elastomers corresponded to that obtained for typical cross-linked polymers. For Alcell lignin elastomers the E´ in the rubbery region remained approximately constant with the increase of lignin content. Cross-linking density, determined from DMA data and soluble fraction also exhibit the same trend, i.e., the increase of lignin content did not yield significant modification neither concerning the cross-linking density nor that related to soluble fraction with. Soluble fraction and cross-linking density values were found to be approximately 0.085 and 0.28 × 10^{-3} mol/cm^3, respectively.

The E´ (rubbery region) of Indulin AT based elastomers increased with the lignin content until a value of 20% (w/w). Among the prepared materials incorporating 20 and 25% (w/w) no significant difference was noticed. The same trend was observed for cross-linking density, which increases from 0.6 × 10^{-3} to 1.0 × 10^{-3} mol/cm^3, as the lignin content increases. Regarding the soluble fraction a slight linear increment was observed from 4.4 to 7.5% (expressed in w/w %). Nevertheless, for a given lignin content the percentage of the soluble fraction was always lower than those obtained for Alcell based elastomers. This indicates that the incorporation of Indulin AT lignin in the polymer network was more effective than that of Alcell counterpart. The increase of cross-linking density and E´, for Indulin AT-based samples, can reflect more effective reactions between lignin hydroxyl groups and isocyanate functions. In fact, in comparison with Alcell, Indulin AT lignin presents higher hydroxyl group content, particularly, a higher aliphatic hydroxyl content (known to be more reactive with isocyanates to compare with phenolic ones). Also, Yoshida et al. (Yoshida et al., 1990) found that medium and high molecular lignin fractions act as cross-linking points, whereas low molecular weight fractions act more like a chain extender. This can also explain the different properties observed with Alcell and Indulin AT based elastomers since Alcell lignin has a weight average molar mass (M_W) much lower that that of Indulin AT homologue, i.e., 7281 and 13979 g/mol (determined from DMF/LiBr solutions using a GPC and based on polystyrene calibration), respectively.

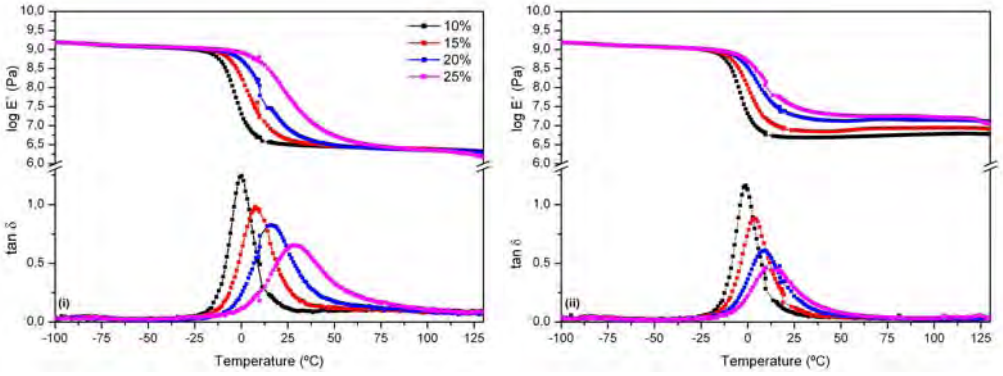

Figure 2 Storage modulus and tan δ as a function of temperature for elastomers containing 10, 15, 20 and 25% (w/w) of (i) Alcell and (ii) Indulin AT lignin.

4 Conclusions

This study provides irrefutable evidence about the possibility to incorporate lignin in polyurethane materials. A wide range of polyurethane materials presenting properties which depended on the lignin type and content introduced. Moreover, both approaches of using lignin (as such or after chemical modification, oxypropylation) yielded materials with very promising properties. In most cases, these materials exhibit properties similar to those of conventional ones, thus presenting a viable option to rationally valorise an abundant renewable industrial by- product.

Acknowledgements

The authors wish to thank Meadwestvaco, Borregaard LignoTech and Granite SA for kindly providing Indulin AT, Curan 27-11P and Sarkanda samples, respectively. Alcell lignin of Repap Enterprises Inc. was offered by Dr. Jairo Lora, to whom we are indebted. Financial support from the Portuguese Foundation for Science and Technology (grant SFRH/BD/18415/2004) and French-Portuguese Scientific Cooperation Programme (action F-32/08) are also acknowledged.

References

Yoshida, H., Mörck, R., Kringstad, K.P., Hatakeyama, H., (1990). Kraft lignin in polyurethanes. II. Effects of the molecular weight of kraft lignin on the properties of polyurethanes from a kraft lignin-polyether triol-polymeric MDI system, *J. Appl. Polym. Sci.* 40, 1819-1832.

Thring, R.W., Vanderlaan, M.N., Griffing, S.L. (1998). Polyurethanes from Alcell®. *Biomass and Bionergy,* 13, 125-132.

Gandini, A., Belgacem M.N., Guo, Zhao-Xio and Montanari, S., (2002). Lignins as a macomonomers for polyester and polyurethanes*.* In: Hu, Thomas Q. (Ed.), Chemical Modification, Properties and Usage of Lignin, Kluwer Academic/Plenum Publishers, 57-80.

Hatakeyama, H., (2002). Polyurethanes containing lignin. In: Hu, Thomas Q. (Ed.), Chemical Modification, Properties and Usage of Lignin, Kluwer Academic/Plenum Publishers, 41-56.

Gosselink, R.J.A., Jong, E. de, Guran, B. and Abächerli, A., (2004). Co-ordination network for lignin—standardisation, production and applications adapted to market requirements (EUROLIGNIN)*, Ind. Crops and Prod*. 20, 121-129.

Lora, J.H. and Glasser, W.G., (2002). Recent Industrial Applications of Lignin: A Sustainable Alternative to Nonrenewable Materials, Journal of Polymers and the Environment. 10, 39-48.

Evtuguin, D.V., Andreolety, J.P. and Gandini, A., (1998). Polyurethanes Based on Oxygen-Organosolv Lignin, *Eur. Polym. J.,* 34, 1163-1169.

Cateto, C.A., Barreiro, M.F., Rodrigues, A.E., (2008). Monitoring of lignin-based polyurethane synthesis by FTIR-ATR. Ind. Crops and Prod*.,* 27, 168-174.

Glasser, W.G., (1989). Novel structural materials from lignin. In: Kennedy, J.F., Phillips, G.O., Williams, P.A. (Eds), Wood Processing and Utilization. Ellis Hordwood Limited Publishers, Chichester, 163-173.

Nadji, H., Bruzzèse, C., Belgacem, M.N., Benaboura, A., Gandini, A., (2005). Oxypropylation of Lignins and Preparation of Rigid Polyurethane Foams from the Ensuing Polyols, *Macromol. Mater. Eng.*, 209, 1009-1016.

Cateto, C.A., Barreiro M.F., Rodrigues, A.E., Belgacem, M.N., (2007). Oxypropylation of lignins and characterization of the ensuing polyols. *Proceedings of* 8th *ILI Forum*, p. 115-119.

Hawkins, M.C., O´Toole, B., Jackovich, D., (2005). *Cell* Morphology and Mechanical Properties of Rigid Polyurethane Foam, Journal of Cellular Plastic, 41, 267-285.

Proceedings of the 10th International Chemical and
Biological Engineering Conference - CHEMPOR 2008
Braga, Portugal, September 4-6, 2008
E.C. Ferreira and M. Mota (Eds.)

Catalytic Wet Air Oxidation plus Biological Treatment to deal with a high-strength o-cresol wastewater

M.E. Suárez-Ojeda[1*], J. Lafuente[1], A. Fabregat[2], J. Font[2] and J. Carrera[1]
[1] Departament d'Enginyeria Química, Universitat Autònoma de Barcelona, Edifici Q-ETSE, 08193 Bellaterra (Barcelona), Catalunya, Spain
[2] Departament d'Enginyeria Química, Universitat Rovira i Virgili, Av. dels Països Catalans 26, 43007 Tarragona, Catalunya, Spain

Keywords: Activated carbon, catalytic wet air oxidation, biodegradability enhancement, respirometry, biological treatment, inhibition and toxicity
Topic: Sustainable process-product development through green chemistry.

Abstract

This study examines the feasibility of coupling a Catalytic Wet Air Oxidation (CWAO), with activated carbon (AC) as catalyst, and an aerobic biological treatment to treat a high strength o-cresol wastewater. Two goals are pursued: a) To determine the effect of the main AC/CWAO intermediates on the activated sludge of a municipal WasteWater Treatment Plant (WWTP) and b) To demonstrate the feasibility of coupling the AC/CWAO effluent as a part of the influent of a municipal WWTP. Also, it is established the AC/CWAO intermediates distribution and the biodegradability enhancement. The main challenge in the coupling is to achieve the right balance between the oxidation deepness (economic cost) and the effluent biodegradability (distribution of oxidation products) after the oxidation step, which ensures the success of a subsequent biological treatment.

First of all, several CWAO tests were completed (140ºC-160ºC, 2-9 bar of oxygen partial pressure, at a space time of 0.12 h) for a high-strength o-cresol wastewater. All the experiments were done in a fixed bed reactor, operating in trickle flow regime, and using AC as catalyst. The results of this part (Suárez-Ojeda et al., 2007a) show that o-cresol disappearance, chemical oxygen demand (COD) removal and total organic carbon (TOC) abatement are very sensible to temperature change but almost independent of oxygen partial pressure.

Secondly, biological parameters were measured using respirometric tests that were completed before and after CWAO and independently, for each one of the identified intermediates (Suárez-Ojeda et al., 2007a). In the case of CWAO effluents, these tests have enabled the determination of the biodegradability, toxicity and inhibition over a non-acclimated activated sludge. Taking into account these results, it was possible to establish whether or not the CWAO effluents are suitable for a non adapted sludge and to develop suitable acclimatisation procedures to couple the CWAO step with a biological pilot plant.

Finally, the results of coupling the AC/CWAO effluent as a part of the influent of a municipal WWTP are presented (Suárez-Ojeda et al. 2007b). For instance, using 30%, as COD, of AC/CWAO effluent in the inlet to the pilot scale WWTP, the integrated AC/CWAO-biological treatment achieved a 98% of total COD removal and, particularly, a 91% of AC/CWAO effluent COD removal without any undesirable effect on the biomass.

The whole study shows a promising way for the development of efficient coupled processes for the treatment of wastewater containing toxic or biologically non-degradable compounds.

* Corresponding author: Tel: ++34 935814792, e-mail: mariaeugenia.suarez@uab.es

1 Introduction

Wastewater reduction and treatment is one of the challenges faced by our society. As an example, in the EU, 2700 tons/year of phenolic compounds in wastewater are released having both, toxic and bactericide effect (EPER, 2008). Several technologies have shown their potential for treating a wide variety of wastewater. Nearly all of them are based on the oxidation of the organic pollutants, which are converted into carbon dioxide and water or into harmless intermediate products, more suitable for a biological treatment (Bhargava et al., 2006). Therefore, Catalytic Wet Air Oxidation (CWAO), H_2O_2 promoted CWAO and Fenton process have become attractive techniques to efficiently treat organic wastewater that is either too concentrated or toxic to be biologically restored.

However, complete mineralisation of pollutants is extremely costly and the bactericide effect of some often found pollutants prevents industrial wastewater from being directly treated in a biological wastewater treatment plant (WWTP). Coupling of an initial oxidative step with a biological treatment can solve these pollution problems in a rational and less expensive way (Mantzavinos et al., 1999 and Patterson et al., 2002).

Hence, this study examines the feasibility of coupling a Catalytic Wet Air Oxidation (CWAO), with activated carbon (AC) as catalyst, and an aerobic biological treatment to deal with a high strength o-cresol wastewater. Two goals are pursued: a) To determine the effect of the main AC/CWAO intermediates on the activated sludge of a municipal WWTP and b) To demonstrate the feasibility of coupling the AC/CWAO effluent as a part of the influent of a municipal WWTP. Also, it is established the AC/CWAO intermediates distribution and the biodegradability enhancement. The main challenge in the coupling is to achieve the right balance between the oxidation deepness (economic cost) and the effluent biodegradability (distribution of oxidation products) after the oxidation step, which ensures the success of a subsequent biological treatment.

2. Experimental

2.1. Materials

Aldrich provided analytical grade o-cresol. Feed concentration was always 5 g l^{-1}. However, in terms of COD concentration, the initial concentration was 9.5 g COD l^{-1}. The AC used as catalyst was supplied by Merck (reference #102518) in the form of 2.5 mm pellets. Prior to use, AC was crushed and sieved. Then, the chosen particle size was in the range 0.7-0.3 mm in order to minimise mass transfer limitations according to Stüber et al. (2001). The characteristics of this AC, prior to use, can be found elsewhere (Suárez-Ojeda et al. 2005).

2.2. Experimental set-up and procedures for CWAO experiments

A complete scheme of the CWAO experimental apparatus as well as a more detailed description of the procedures can be found elsewhere (Suárez-Ojeda et al. 2005).

Several CWAO experiments were carried out (140ºC-160ºC, 2-9 bar of oxygen partial pressure, at a space time of 0.12 h) for a high-strength o-cresol wastewater. All the experiments were done in a fixed bed reactor, operating in trickle flow regime, and using AC as catalyst. Liquid samples were periodically withdrawn and analysed to determine target compound destruction (X), COD reduction (X_{COD}), TOC abatement (X_{TOC}), distribution of partial oxidation products, and biodegradability enhancement, measured as $\%COD_{RB}$.

2.3. Experimental set-up for respirometric experiments.

A complete scheme of the respirometric experiments as well as a more detailed description of the procedures can be found elsewhere (Suárez-Ojeda et al. 2007b). The respirometer used for the biodegradability screening tests corresponds to a LFS type, in which dissolved oxygen concentration (S_O) is measured in the liquid-phase (L), which is static (S) and continuously aerated (F). The pH was maintained at 7.5±0.5 and the temperature was set at 31±0.5ºC. The biomass used as seed culture came from a municipal biological WWTP (Tarragona, Catalonia, Spain). The biomass was starved overnight to ensure endogenous

conditions before each respirometric experiment. The presence of 20 mg l^{-1} of 1-allyl-2-thiourea (ATU) avoided nitrification interference. The average concentration of volatile suspended solids (VSS) in the respirometric tests was 3400±300 mg VSS l^{-1}.

To assess the biodegradability of the treated and non-treated effluents, a 20 mg COD l^{-1} (COD_{added}) pulse of either the CWAO effluent or o-cresol solution was added inside the respirometer. Then, the Oxygen Uptake Rate (OUR) profile and the Oxygen Consumption (OC) are obtained solving the S_O balance in the liquid phase of the respirometer. More information about the OUR and OC calculation can be found elsewhere (Spanjers et al., 1998).Once the OC is obtained from the respirometric tests, the readily biodegradable COD (COD_{RB}) can be calculated using the heterotrophic yield coefficient (YH) as follows:

$$COD_{RB} = \frac{OC}{1 - Y_H} \qquad \text{Equation 1}$$

The biological COD removal is a process where part of the substrate is directly used for new biomass growth and the rest is oxidized for energy production. In this context, Y_H represents the fraction of substrate used for production of new biomass. The COD_{RB} fraction of CWAO effluents is then calculated according to:

$$\%COD_{RB} = \frac{COD_{RB}}{COD_{added}} \cdot 100 \qquad \text{Equation 2}$$

2.4. Experimental set-up for the aerobic biological treatment

A pilot scale municipal WWTP was constructed by scaling down the Tarragona municipal WWTP. The bioreactor of the pilot plant is a 20 l aerated CSTR where the S_O is ranged from 2 to 5 mg l^{-1}. The bioreactor has S_O and pH probes that are connected to probe indicators-controllers. pH is left uncontrolled whereas S_O is controlled through manipulation of the pneumatic valve using an on/off control. The pilot plant was located inside a laboratory where the temperature was maintained at 25±1ºC through the air conditioning system.

The pilot plant was inoculated with sludge from the Tarragona municipal WWTP and its main operational parameters (a sludge retention time (SRT) of 8 d, an average organic loading rate (OLR) of 0.35 g COD g^{-1} VSS d^{-1} and VSS concentration of 4000 mg VSS l^{-1}) were maintained at similar values than those of the Tarragona WWTP.

The pilot plant began with an adaptation period to a synthetic municipal wastewater, which is similar to the original influent of the Tarragona WWTP. This period covered the first 10 d of operation. Later, the pilot plant behaviour in front of increasing loads of the o-cresol AC/CWAO effluent was studied. The parameters used to monitor the pilot plant were: COD effluent concentration, OLR, VSS concentration in the reactor and SVI. Analyses of TSS, VSS and COD were done as described in Standard Methods (APHA, 1999). The most relevant AC/CWAO intermediates were analysed using the methodology described in Suarez-Ojeda et al. (2007a).

3. Results and Discussion

The steady-state conversions (X, X_{COD} and X_{TOC}) and AC mass change (M_{AC}) are listed in Table 1. As expected, temperature has a strong influence on the conversions. For o-cresol, at 2 bar, X goes from 33% to 83%, X_{COD} from 15% to 53% and X_{TOC} from 14% to 47% as temperature increases from 140 to 160ºC. In turn, P_{O2} has a weaker effect on the overall conversions.

The M_{AC} was calculated as the relative difference between the final and the original mass of the loaded AC dried at 400ºC and serves to quantify if oxidative coupling or AC oxidation prevails, as oxidative coupling renders a gain in M_{AC} whereas AC oxidation/burning results in a decrease of M_{AC}. In the less severe CWAO conditions, the M_{AC} was always positive. But, for the most severe oxidative condition, 160ºC –and 9 bar, the M_{AC} was always negative.

Table 1. Final conversions for o-cresol and M_{AC} in CWAO tests.

		140ºC				160ºC			
Compound	P_{O2} (bar)	X (%)	X_{COD} (%)	X_{TOC} (%)	M_{AC}(%)	X (%)	X_{COD} (%)	X_{TOC} (%)	M_{AC}(%)
o-cresol	9 bar	97	42	40	19.3	90	64	46	-62.3
	2 bar	33	15	14	17.0	83	53	47	54.2

Regarding to the reaction intermediates, the theoretical chemical oxygen demand (COD_{Th}) of each effluent was calculated from the obtained HPLC concentrations. The partial oxidation products have been grouped into carboxylic acids, quinone-like products, condensation products, non-identified products and, remaining target compound. Later, the contribution of each group was compared to the total experimental COD analytically measured. The results are summarised in Figure 1.

For o-cresol, at 140-9 and 160-2, the products distribution are similar, indicating that these reaction conditions were severe enough to oxidize the o-cresol but not sufficient to yield significant changes in the selectivity towards carboxylic acids. At 140-2 bar, the reaction conditions were not sufficient to transform o-cresol into more suitable intermediates.

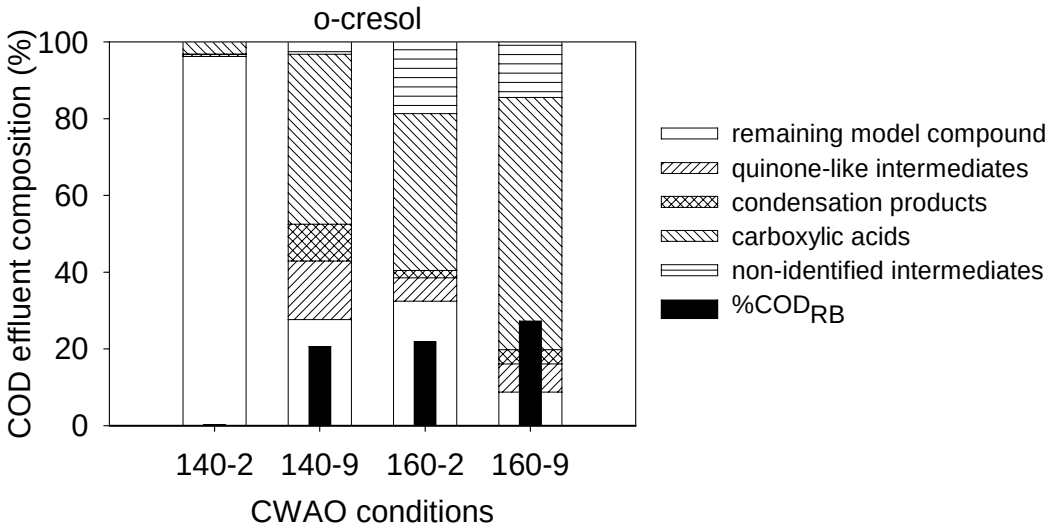

Figure 1. Intermediates distribution and $\%COD_{RB}$ obtained by respirometric test for each o-cresol CWAO effluent.

Figure 1 also shows the $\%COD_{RB}$ of each CWAO effluents for o-cresol. The measured $\%COD_{RB}$ of the initial o-cresol solution was 0%. There was no biodegradability at 140-2 because the remaining o-cresol concentration was the highest and the carboxylic acids concentration was almost negligible. For the rest of conditions, the $\%COD_{RB}$ was very similar, being 160-9 the condition which had the highest proportion of carboxylic acids and consequently the highest biodegradability, as reflected by the maximum $\%COD_{RB}$ (27%).

Three different features should be considered when selecting the most suitable CWAO condition: the maximum COD conversion obtained in the CWAO, the maximum $\%COD_{RB}$ and the catalyst preservation. In general, it could be concluded that the best CWAO condition for o-cresol is 160-2. At this condition, the X_{COD} was higher and the catalyst preservation was clearly better at 2 bar than at 9 bar of P_{O2}. Finally, the $\%COD_{RB}$ was 23% very similar to the obtained at 160-9 (27%).

The biological treatment study is divided into three periods according to the percentage of the total influent COD coming from the AC/CWAO effluent (5, 15 or 30%). Figure 2 shows the pilot plant evolution. Total influent and effluent COD concentrations and SVI were monitored during 125 d. Also, the TSS and VSS were measured during the study and the average values of biomass concentration and VSS/TSS ratio were 4400±300 mg VSS l^{-1} and 80±10% mg VSS l^{-1}, respectively.

Figure 2 shows that the total effluent COD concentration never surpassed the COD discharge limit fixed by the EU Directive, i.e. 125 mg COD l^{-1} (ECC, 1991), although the pilot scale WWTP worked in the range of the typical OLR for municipal WWTP (WEF, 1992). Moreover, the most relevant components of the effluents of periods 2 and 3 were analysed. This analysis showed that the COD of these effluents was basically in form of: phenol (13 mg COD l^{-1} in period 2 and 32 mg COD l^{-1} in period 3), o-cresol (9 and 18 mg COD l^{-1}) and malonic acid (2 and 7 mg COD l^{-1}). The rest of intermediates were completely biodegraded. The removal of COD in form of phenol was 48% in period 2 and 64% in period 3. The removal of COD in form of o-cresol was 87% in period 2 and 92% in period 3. The removal of both phenolic compounds was quite high and it was probably due to their co-metabolic biodegradation with readily biodegradable compounds. The increase in the removal of phenolic compounds between period 2 and 3 could be due to the progressive acclimatisation of the pilot plant sludge to phenolic compounds.

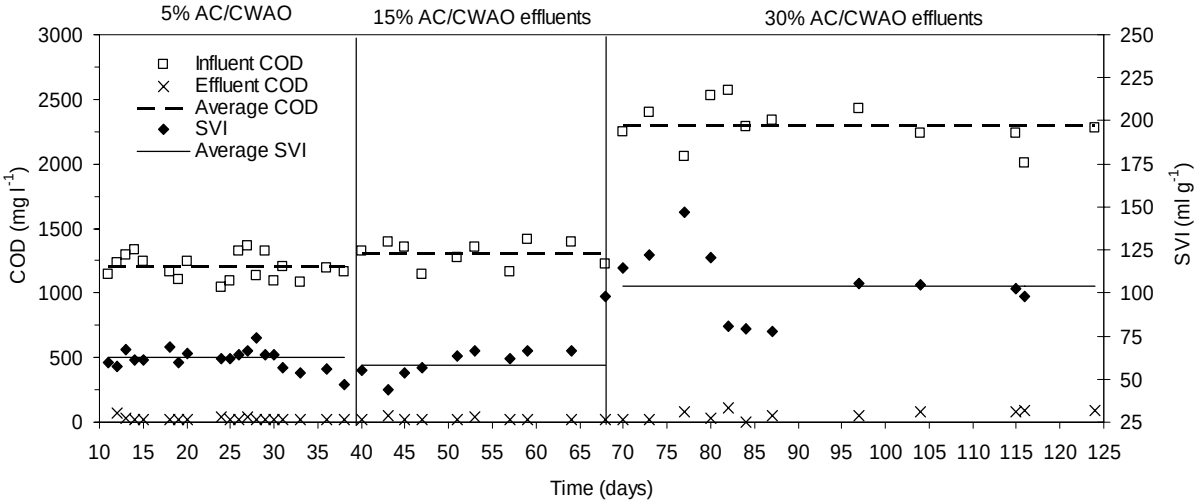

Figure 2. Evolution of pilot scale municipal WWTP parameters during the 125 days of continuous operation with o-cresol AC/CWAO effluent as a part of the total influent

Moreover, Figure 2 shows that the SVI was not affected by the presence of 5% (period 1) or 15% (period 2) of COD in form of AC/CWAO effluent in the influent of the pilot plant. After the increase of the COD coming from the AC/CWAO effluent to 30% (period 3), the SVI increased considerably. This increase could be due to some toxic effect on the biomass. Therefore the sludge purge was reduced 50% until the system recovered and returned to normal operation being the average SVI of 104 ml g^{-1}. In any case, the system never exceeded the SVI value of 150 ml g^{-1}, which is considered the threshold of poor settleability (WEF, 1992).

4. Conclusions

In the context of integrated management of high-strength o-cresol wastewater, for 30% of the total influent COD from the AC/CWAO effluent, the results show more than 99% in overall COD removal from the initial o-cresol: from 9500 mg l^{-1} to just only 64 mg l^{-1}. In terms of o-cresol removal, the integrated process is capable of passing from 5000 mg l^{-1} to only 7 mg l^{-1} that is 99.9% o-cresol removal (Figure 3).

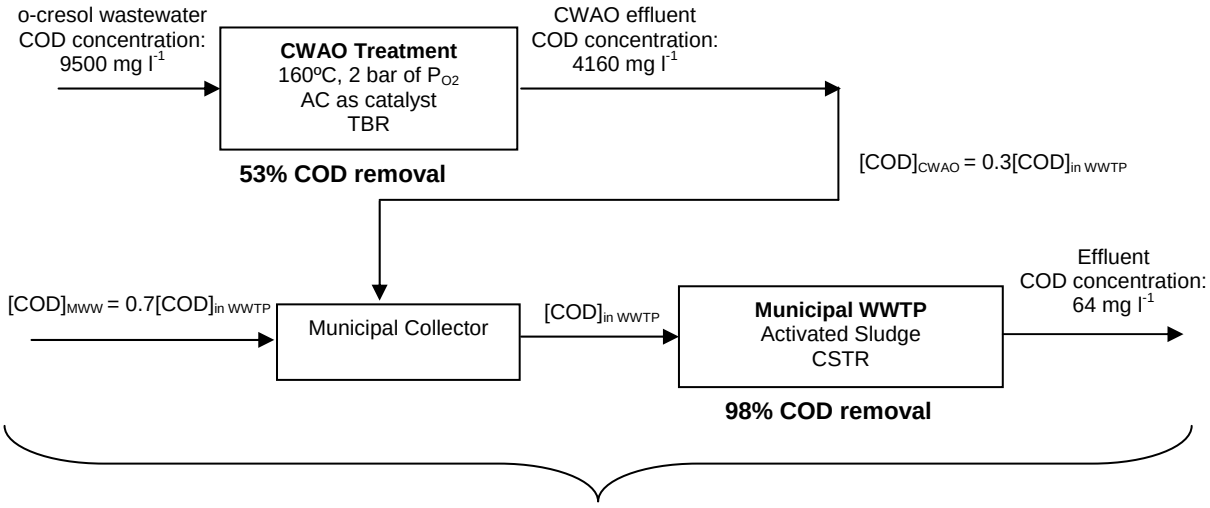

Figure 3. Schematic view of an integrated treatment of high strength o-cresol wastewater

References

American Public Health Association (APHA), 1999. Standard methods for the examination of water and wastewater. American Water Association (Ed.). Washington, DC.

Bhargava, S.K., Tardio, J., Prasad, J., Folger, K., Akolekar, D.B., and Grocott, S.C. (2006). Wet Oxidation and Catalytic Wet Oxidation. Ind. Eng. Chem. Res.; 45, 1221-1258

European Pollutant Emission Register, http://eper.ec.europa.eu/eper/default.asp, 2001 data (accessed May 2008).

ECC., 1991. Directive 1991/271/EEC of 30.05. Official Journal of the European Communities, 13.02.2003, L 135, pp. 40-52.

Mantzavinos, D., Sahinzada,M., Livingston, A. G., Metcalfe, I. S. and Hellgardt, K. (1999). Wastewater treatment: wet air oxidation as a precursor to biological treatment. Catal. Today; 53, 93-106.

Patterson, D. A., Metcalfe, I. S., Xiong, F. and Livingston, A. G. (2002). Biodegradability of linear alkylbenzene sulfonates subjected to wet air oxidation. J. Chem. Technol. Biot.; 77, 1039-1049.

Spanjers, H.; Varolleghem, P.; Olsson, G.; Dold, P. L. Respirometry in control of the activated sludge process: Principles. International Association on Water Quality, London, England, 1998.

Stüber, F.; Polaert, I.; Delmas, H.; Font, J.; Fortuny, A.; Fabregat, A. Catalytic wet air oxidation of phenol using active carbon: performance of discontinuous and continuous reactors, J Chem. Technol. Biotechnol., 76 (2001), 743-751.

Suárez-Ojeda, M.E.; Stüber, F.; Fortuny, A.; Fabregat, A.; Carrera, J.; Font, J. Catalytic wet air oxidation of substituted phenols using activated carbon as catalyst. Appl. Catal. B, 58 (2005), 105-114

Suárez-Ojeda, M.E., Fabregat, A., Stüber, F., Fortuny, A., Carrera, J. and Font, J. (2007a). Catalytic Wet Air Oxidation of Substituted phenols: Temperature and Pressure effect on the Substrate Removal, the Catalyst Preservation and the Biodegradability Enhancement. Chem. Eng. J.; 132, 105-115

Suárez-Ojeda, M.E., Guisasola, A., Baeza, J.A., Fabregat, A., Stüber, F., Fortuny, A., Font, J. and Carrera, J. (2007b). Integrated catalytic wet air oxidation and aerobic biological treatment in a municipal WWTP of a high-strength o-cresol wastewater. Chemosphere; 66, 2096–2105.

Water Environment Federation (WEF), 1992. Design of Municipal Wastewater Treatment Plants. Vol I. Alexandria, USA.

Proceedings of the 10th International Chemical and
Biological Engineering Conference - CHEMPOR 2008
Braga, Portugal, September 4-6, 2008
E.C. Ferreira and M. Mota (Eds.)

Two-aqueous Phase Extraction for the Removal of Organic Pollutants and Metal Ions

[1]L.J. Nogueira Duarte, [2]J.P. Canselier*
[1]Centro Federal de Educação Tecnológica da Bahia (CEFET-BA)
Via Universitária, s/n, Pitanguinhas, Simões Filho, BA - Cep: 43.700-000
[2]Laboratoire de Génie Chimique (UMR CNRS 5503, ENSIACET- INPT/UPS) BP 1301,
F31106 Toulouse Cedex 01, France

Keywords: Cloud point extraction, polyethoxylated alcohols, metal or organic pollutants.

Abstract

Above a temperature called "cloud point" (T_c), the aqueous solutions of most polyethoxylated non-ionic surfactants separate into two equilibrium phases: a surfactant-rich one (coacervate) and a dilute one. Micellar solubilization allows two-aqueous phase extraction and concentration of hydrophobic or amphiphilic compounds into the small volume of coacervate. For electrolytes (*e.g.* heavy metal salts), the use of ionic/non-ionic mixed micelles makes a chelating agent unnecessary. Such a cloud point extraction may be applied to the decontamination of industrial effluents containing metal or organic compounds (soluble or dispersed pollution) or to the concentration or even the separation of high value-added substances. This is therefore a "Green Chemistry" process, *i.e.* environmentally-friendly and energy-saving. Cloud point extraction of metal ions (Ni^{2+}, Cd^{2+}, Pb^{2+}, Cr^{3+}) with mixed micelles of polyethoxylated alcohols (C_iE_j) and anionic surfactants (sodium dodecylsulfate "SDS" or dodecylbenzenesulfonates "SDBS") is achieved from model solutions of metal nitrates, possibly mixed with organics. The results are promising, due to extraction percentages lying between 50 and 90% and small volume fractions of coacervate, the best performances being obtained for Pb^{2+}, whose hydration enthalpy is the lowest. Moreover, the ability of those mixed micelles to extract both organic (phenol and 2,4-dimethylaniline) and heavy metal pollutants from model solutions is shown.

1. Introduction

The respect of environment is nowadays a worldwide requirement which implies the development of new curative processes and the design of intrinsically clean processes. Among others, these processes apply to wastewater treatment (water polluted by organics or heavy metals). The criteria of water quality (compliance with regulations) and economy are decisive; in order to take into account the physical and chemical specificities of the effluents, tests with real wastewaters are necessary.

Surfactant adsorption at interfaces makes them useful auxiliaries in several types of extraction processes. On the other hand, volatile organic solvents, commonly used in liquid-liquid extraction, are subject to more and more severe regulations, due to their toxicity and/or ecotoxicity. Since the phase diagrams of many polyethoxylated surfactant/water binary systems show a lower consolute point curve, the existence of the corresponding two-phase region can be turned to account to extract metal ions, small organic molecules or biological macromolecules from their dilute aqueous solutions. This operation, known as liquid-coacervate or cloud-point extraction (CPE), consists of two steps: (1) organic solute or metal-chelate complex solubilization into the extractant (aqueous solution of non-ionic surfactant) and (2) cloud-point phase separation of this solution into a dilute phase and a surfactant-rich one, called coacervate. Whether the dilute phase or the coacervate is of interest, two main

Corresponding author. Tel. 33 (0) 5 34 61 52 54. E-mail: JeanPaul.Canselier@ensiacet.fr

types of applications may be considered: removal of pollutants from aqueous effluents and concentration, recovery and, possibly, separation of high added-value substances [1-6].

Since the CPE technique has been proposed, a lot of applications in wastewater treatment have been published. However, previous studies on the removal of dissolved contaminants by CPE were mainly based on the use of single surfactant systems and restricted to some types of organic solutes [4-8]. Few studies have been conducted on the applications of mixed surfactants on the simultaneous removal of metal ions and organic solutes in a CPE process [9]. One of the most important properties of these organized structures is their good capacity to solubilise solutes of different character and nature. These solutes may interact with surfactant aggregates electrostatically, hydrophobically or by a combination of both effects.

This work involves the extraction of soluble electrolytes (Ni^{2+}, Cd^{2+}, Pb^{2+}, Cr^{3+}), from model solutions with polyethoxylated alcohols (C_iE_j) mixed with anionic surfactants (sodium dodecylsulfate "SDS" or dodecylbenzenesulfonates "SDBS"). The non-ionic surfactant, along with its cloud point property, is responsible for phase separation; the anionic species plays the role of a complexing agent. The CPE technique thus offers a convenient alternative to conventional liquid-liquid extraction that uses organic solvents, with another major interest: the absence of classical but expensive chelating agents for metal ions.

2. Experimental

Materials

The two anionic surfactants used were sodium dodecylsulfate (SDS 98,5% purity, Aldrich) and sodium dodecylbenzenesulfonates (SDBS 97,5% purity, kindly supplied by Rhodia France). The non-ionic surfactant was an oxo-alcohol (Oxo-$C_{10}E_3$). About 20% of the oxo-alcohol chains are branched. This sample was kindly supplied by SEPPIC (Castres, France). The Oxo-$C_{10}E_3$ sample was freed from residual polyols by washing with water at 95°C. The inorganic salts used were: $Pb(NO_3)_2.4H_2O$ (99%, Aldrich), $Cd(NO_3)_2.4H_2O$ (99%, Aldrich), $Ni(NO_3)_2.6H_2O$ (99%, Aldrich) and $Cr(NO_3)_3.9H_2O$ (99%, Aldrich). Reagent grade phenol, C_6H_5OH, and 2,4-Dimethylaniline, $(CH_3)_2C_6H_3NH_2$, from Aldrich, were used as received. The water was distilled and deionised.

Procedure

The concentrations of phenol and 2,4-dimethylaniline were measured by a reversed-phase HPLC system consisting of one SpectraSystem P-1000-XR pump, an AS-1000-XR auto injector, a RP18 (ODS) column, and a SpectraSystem UV-2000. The conditions used for the determination of aromatic solute concentrations were as follows: column temperature, 25°C; pressure, 80 bar; flow rate 1 mL/min of 67/37 (v/v) of H_2O/CH_3CN eluant. Phenol and 2,4-dimethylaniline concentrations were obtained from data processed with the Chromquest 3.0 software.

Inductively coupled plasma - ICP (Jobin Yvon – Ultima 2R) was used to measure the concentration of metal ions in the following conditions: plasma temperature, 8000 °C; air flow rate 20 mL/min; nebulizer pressure, 3.10 bar. The concentration of heavy metal was measured by UV absorption at the relevant wavelength (λ, nm): λ_{Pb} = 220.353; λ_{Cd} = 228.802; λ_{Ni} = 221.647; λ_{Cr} = 283.563.

The polluted aqueous phase and the surfactant solution were mixed together and separated at room temperature or after heating, according to the cloud point curve of the surfactant [10].

3. Results and discussion

Figure 1 represents the ratio, E%, of metal ions (Ni^{2+}, Cd^{2+}, Pb^{2+}, Cr^{3+}) extracted as a function of anionic surfactant (SDS and SDBS) concentration. From zero for pure non-ionic micelles, this ratio increases with anionic surfactant concentration. Only for Cr^{3+} is the

Corresponding author. Tel. 33 (0) 5 34 61 52 54. E-mail: JeanPaul.Canselier@ensiacet.fr

variation linear in the concentration range studied. The incorporation of an anionic surfactant into non-ionic micelles involves Coulombic interactions with metal ions. In other words, the negatively charged micelles cause the cations to bind or adsorb onto the micelle surface, however, the coacervate volume fraction, ϕ_C, increases with surfactant concentration. The main issue is to obtain the best compromise between E% (maximum) and ϕ_C (minimum).

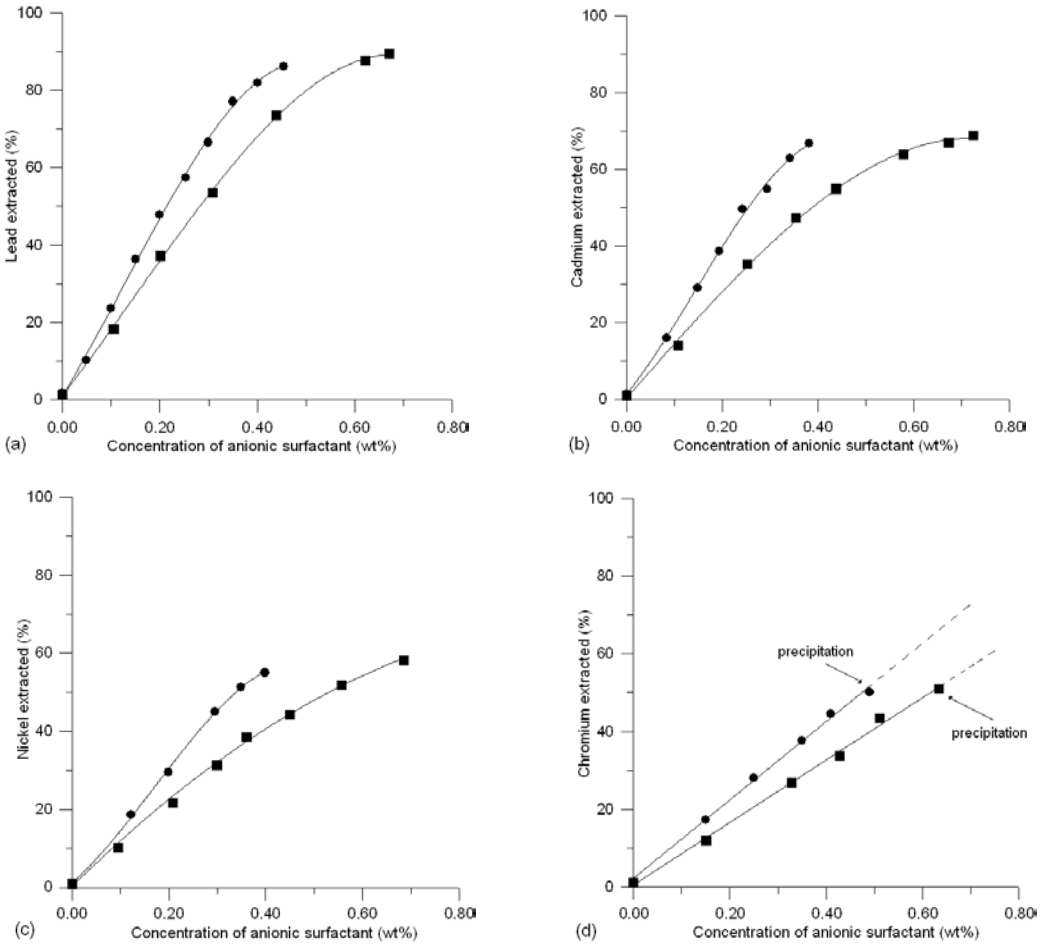

Figure 1. Effect of anionic surfactant concentration on heavy metal pollutants recovery.
(•) SDS, (■) SDBS ; oxo-$C_{10}E_3$ = 2,0% ; $[M^{n+}]$ = 1,5 g/L ; t = 45°C
(a) Pb^{2+}, (b) Cd^{2+}, (c) Ni^{2+}, (d) Cr^{3+}

The maximum extraction ratios are summarized in Table 1. Extraction efficiency increases in the following order: $E\%_{Pb} > E\%_{Cd} > E\%_{Ni} > E\%_{Cr}$. This order seems to be correlated with those of ionic radii, RI_M ($RI_{Pb} > RI_{Cd} > RI_{Ni} > RI_{Cr}$), hydration enthalpies, Δ_hH_M and hydration radii, RH_M ($\Delta_hH_{Pb} < \Delta_hH_{Cd} < \Delta_hH_{Ni} < \Delta_hH_{Cr}$; $RH_{Pb} < RH_{Cd} < RH_{Ni} < RH_{Cr}$).

Table 1. E% maximum for the metal ions.

Anionic surfactant	E% (M^{n+})			
	Pb^{2+}	Cd^{2+}	Ni^{2+}	Cr^{3+}
SDS	86	68	55	49
SDBS	90	70	59	51

The case of Cr^{3+}, a trivalent cation, is slightly different from those of the other three metal cations and it makes sense that, although the attraction of Cr^{+3} ions towards the micelle surface is strong, for a given density of micellar charge, Cr^{+3} extraction is less efficient, probably due to the reduction of the charged micelle binding sites for Cr^{+3} to be adsorbed

Corresponding author. Tel. 33 (0) 5 34 61 52 54. E-mail: JeanPaul.Canselier@ensiacet.fr

onto the micelle surface. So, to obtain the same performance as with the divalent cations, it is likely that a mixed micelle richer in anionic species should be required. In fact, at least with Oxo-$C_{10}E_3$, the use of higher ratios of anionic surfactant comes up against the precipitation of chromium dodecylsulfate or dodecylbenzenesulfonates.

Figure 2 shows that the recoveries of phenol and 2,4-dimethylaniline are strongly improved when the non-ionic surfactant (Oxo-$C_{10}E_3$) concentration increases. Thus, in a 8 wt.% Oxo-$C_{10}E_3$ solution, the extents of phenol and 2,4-dimethylaniline recovery are about 90% and 86%, respectively. However, for lead, the effect of the non-ionic surfactant concentration is relatively insignificant. The recovery of lead is about 80% in a 4 wt.% surfactant solution.

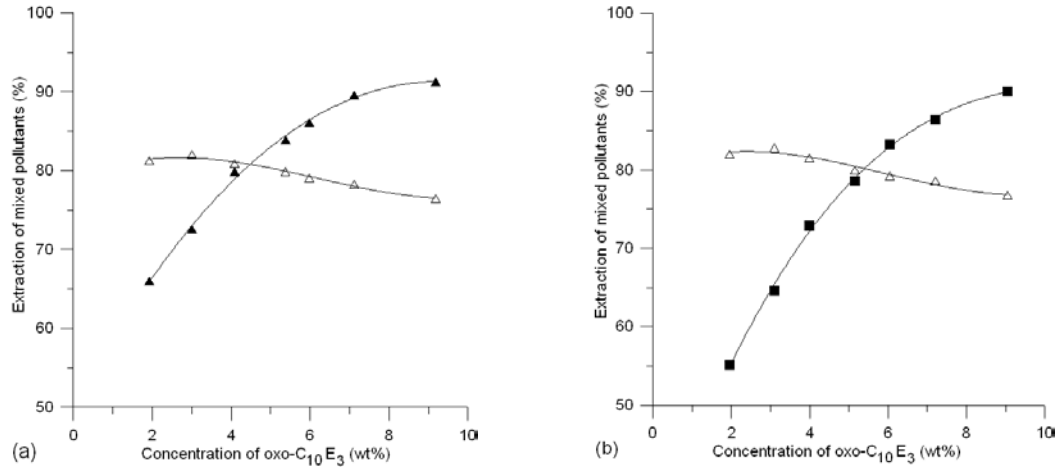

Figure 2. Effect of surfactant concentration on organic and heavy metal pollutants recovery. SDS = 0,38 %, SDBS = 0,60 %, [Pb^{2+}] = 1,5 g/L, [Ph] = 2,0 g/L, [DMA] = 1,3 g/L, T = 45°C
(▲) Phenol, (■) DMA, (∆) lead,
(a) SDS, (b) SDBS

These results suggest that mixed micelles can form hydrogen bonds between hydroxyl or amino groups and the most available ether oxygen atoms of the polyoxyethylene chain (reducing surfactant solubility)[11]. The rate of recovery in such systems can be correlated to the log P (octanol/H_2O partition coefficient) of the aromatic solutes but not to their aqueous solubility [12]. On the other hand, metal ions bind to the negatively charged surface of anionic surfactant micelles by Coulombic interactions. In summary, metal ions bind or adsorb on the surface of oppositely charged micelles, while organic solutes are solubilised within the micelles.

4. Conclusions

A new possibility for the application of CPE involves the use of mixed surfactants as extractants. The combination of the surfactant capacity to solubilise different species can be applied to the extraction of organic and heavy metal pollutants from model solutions. The results are promising, due to extraction percentages lying between 50 and 90%, the best performances being obtained for Pb^{2+}, whose hydration enthalpy is the lowest. Moreover, the ability of those mixed micelles to extract both organic (*e.g.* phenol and 2,4-dimethylaniline) and heavy metal pollutants from model solutions is shown. Further studies on the extraction of metals under anionic form or both cationic and anionic forms are currently in progress, affording encouraging results. A compromise is always to be found between E% (maximum) and coacervate volume fraction (minimum). These results let predict a possible treatment of more complex media. In addition, CPE offers the benefit of low cost, easy handling and reduced toxic effects. Finally, a continuous, multi-stage process should be developed rather soon.

Corresponding author. Tel. 33 (0) 5 34 61 52 54. E-mail: JeanPaul.Canselier@ensiacet.fr

Acknowledgments

One of the authors (L.J.N. Duarte) gratefully acknowledges financial support from the CNPq - Brazil.

References

1. Quina, F.H., Hinze, W.L. (1999). Surfactant-Mediated Cloud Point Extractions: An Environmentally-Benign Alternative Separation Approach. *Ind. Eng. Chem. Res*., 38, 4150-4168.
2. Ferrera, Z.S., Sanz, C.P., Santana, C.M., Rodriguez, J.J.S. (2004). The Use of Micellar Systems in the Extraction and Pre-concentration of Organic Pollutants in Environmental Samples. *Trends Anal. Chem.,* 23(7), 479-489.
3. Kimchuwanit, W., Osuwan, S., Scamehorn, J.F., Harwell, J.H., Haller, K.J. (2000). Use of a Micellar-Rich Coacervate Phase to Extract Trichloroethylene from Water. *Sep. Sci. Technol*., 35(13), 1991-2002.
4. Sakulwongyai, S., Trakultamupatam, P., Scamehorn, J.F., Osuwan, S., Christian, S.D. (2000). Use of Surfactant Coacervate Phase to Extract Chlorinated Aliphatic Compounds from Water: Extraction of Chlorinated Ethanes and Quantitative Comparison to Solubilization in Micelles. *Langmuir*, 16, 8226-8230.
5. Trakultamupatam, P., Scamehorn, J.F., Osuwan, S. (2002). Removal of Volatile Aromatic Contaminants from Wastewater by Cloud Point Extraction. *Sep. Sci. Technol*., 37(6), 1291-1305.
6. Carabias-Martinez, R., Rodriguez-Gonzalo, E., Dominguez-Alvarez, J., Garcia-Pinto, C., Hernandez-Mendez, J. (2003). Prediction of the Behavior of Organic Pollutants Using Cloud Point Extraction. *J. Chromatogr*. A, 1005, 23-34.
7. Haddou, B., Canselier, J.P., Gourdon, C. (2003). Purification of Effluents by Two-Aqueous Phase Extraction, *Trans IChemE (Chem. Eng. Res. Des*.), 81A, 1185-1192.
8. Haddou, B., Canselier, J.P., Gourdon, C. (2006). Cloud Point Extraction of Phenol and Benzyl Alcohol from Aqueous Stream, *Sep. Purif. Technol*., 50(1), 114-121.
9. Gotlieb, L. Bozzelli, J.W., Gotlieb, E. (1993). Soil and water decontamination by extraction with surfactants, *Sep. Sci. Technol*., 28(1-3), 793-204.
10. Duarte, L.J.N., Canselier, J.P. (2005). Oxo-alcohol Ethoxylates: Surface and Thermodynamic Properties and Effect of Various Additives on the Cloud Point, *Tenside Surf. Deterg*., 42(5), 299-306.
11. Bai, D., Li, J., Chen, S.B., Chen, B.H. (2001). A Novel Cloud-Point Extraction Process for Preconcentrating Selected Polycyclic Aromatic Hydrocarbons in Aqueous Solution. *Environ*. *Sci. Technol*., 35, 3936-3940.
12. Duarte, L.J.N., Canselier, J.P. (2005). Extração de Compostos Orgânicos Homólogos e Isômeros em um Sistema de Duas Fases Aquosas, *Quím. Nova*, 28(3), 426-432.

Corresponding author. Tel. 33 (0) 5 34 61 52 54. E-mail: JeanPaul.Canselier@ensiacet.fr

Proceedings of the 10th International Chemical and
Biological Engineering Conference - CHEMPOR 2008
Braga, Portugal, September 4-6, 2008
E.C. Ferreira and M. Mota (Eds.)

Biosorption of Cr^{VI} supported on mordenite zeolite

Figueiredo. H.[1*], Silva. B.[1], Quintelas. C.[1], Neves. I.C.[2], Tavares. T.[1]
[1] IBB – Instituto de Biotecnologia e Bioengenharia, Centro de Engenharia Biológica, Universidade do Minho, Campus de Gualtar, 4710-057 Braga, Portugal.
[2] Departamento de Química, Centro de Química, Universidade do Minho, Campus de Gualtar, 4710-057 Braga, Portugal.

Keywords: Zeolite, Chromium, Biosorption, Mordenite
Topic: Integration of Life Sciences and Engineering.

Abstract

This work reports the usage of a combined zeolite-biosorbent system for the removal and recovery of aqueous Cr^{VI}. The biosorption system consisted of a bacterium, *Arthrobacter viscosus*, supported on two mordenite (MOR) type zeolites with different Si/Al ratio, HMOR (Si/Al = 10) and NaMOR (Si/Al = 6.5). The results show that the biofilm of *A. viscosus* supported on MOR zeolite is able to recover chromium from dilute solutions. For both biosorption-MOR systems, the maximum removal was obtained for initial concentration of 20 mg_{Cr}/L. However, the best results were obtained for HMOR-system with a removal of 52.1 % for the diluted concentration and the best uptake, 3.3 $mg_{Cr^{VI}}/g_{zeolite}$, was achieved for the initial concentration of 100 mg_{Cr}/L. The Langmuir isotherm model was applied with good fitting to the experimental data.

1 Introduction

The emission of organic and inorganic pollutants from industrial sources into the environment is a well known risk factor. Pollution of the aquatic environment is mainly caused by the discharge of industrial effluents. The contamination with heavy metals is of great concern, where industries such as tanneries, electroplating and mining are found present. The continuous increase in emission of heavy metals into the environment poses a threat to human health, as the ingestion of several metals beyond admissible concentrations causes chronic disorders (Demir et al., 2007). Chromium is a metal of widespread industrial usage and is a common pollutant found in wastewaters. It is considered carcinogenic to humans in its Cr^{VI} oxidation state, whereas the Cr^{III} oxidation state is considered less dangerous.

From the different technologies available for the remediation of wastewaters containing heavy metals, biosorption has received considerable attention. The usage of microbial biomass for the removal of metals has been widely studied in recent years (Gavrilescu, 2004). Some studies refer that biosorbents require an adequate support to enhance good performance (Kratochvil et al., 1998). The employment of zeolites as supports for biosorbents has been reported (Figueiredo et al., 2006 and Tavares et al., 2006). Zeolites are widely known to be versatile materials, having found industrial application in various fields such as catalysis, adsorption, molecular sieving and ion exchange. In pollution control, the adsorption and ion exchange capacities have been exploited in the treatment of industrial effluents. The use of zeolites for the removal of heavy metals found in wastewaters has been proposed as a low-cost technique (Babel et al., 2003). However, zeolites can only be used as ionic exchangers for the removal of cationic species, due to the proprieties of the negatively charged aluminosilicate framework. While most metal species in water are cationic, aqueous Cr^{VI} is found in the anion form as chromate or dichromate ions. The repulsion between these ions and the zeolite framework avoids direct removal of Cr^{VI} by zeolite.

* Corresponding author. Tel +(351)-253604400. E-mail: hsfigueiredo@deb.uminho.pt

The different method for the removal of Cr^{VI} from effluents proposed (Figueiredo et al., 2006; Tavares et al., 2006 and Silva et al., 2008) combines the biosorption capabilities of the *A. viscosus* bacteria with a robust support of faujasite (FAU) zeolite. The bacterium reduces Cr^{VI} to the cationic Cr^{III} species which are exchanged by the charge-balancing cations in the zeolite structure. The combined technology enables Cr recovery from contaminated effluents in a solid matrix that can be easily recovered from solution and reused as catalysts for several reactions. The oxidation of 1,2-dichlorobenzene in gas phase with Cr containing NaY and NaX zeolites recovered from biosorption essays was reported by Figueiredo et al. (2006).

As there are various zeolitic structures available, it is possible to draw a series of catalysts with recovered metals by simply changing the support for biosorption. The present work reports the usage of mordenite (MOR) type zeolites as supports for the *A. viscosus* bacteria. MOR zeolite differs from FAU zeolite as its structure has channels in a single axis orientation, whereas FAU zeolite has channels in all three axes (Čejka et al., 2005). FAU zeolite also has large supercages, unlike the tubular structure of MOR. Both zeolites present large 12-ring pore opening. MOR zeolites have been studied as catalysts for several reactions and it is common to find them associated to different transition metals. Yim et al. (2000) studied the oxidation of perchloroethylene over chromium supported on mordenite in gas phase, while catalysis in liquid phase reactions was also studied with these zeolites, as described by Kostrab et al. (2006).

This work presents the usage of a different zeolitic structure, mordenite type zeolite as support for the biosorption of Cr^{VI}. Two MOR zeolites, H-form (HMOR) and Na-form (NaMOR) were tested as supports for the biosorption of aqueous Cr^{VI} species.

2 Materials and Methods

a) *Preparation of the zeolitic supports*

Powder samples of HMOR (CBV 21A, Si/Al = 10, surface area of 500 m^2/g) and NaMOR (CBV 10A, Si/Al = 6.5, surface area of 425 m^2/g) were obtained from Zeolyst International and were previously calcined at 500 ºC during 8 h under dry air flow prior to use.

b) *Preparation of the A. viscosus*

A. viscosus was obtained from the Spanish Type-Culture Collection of the University of Valencia. The culture medium is composed by glucose (10 g/L), peptone (5 g/L), yeast extract (3 g/L) and malt extract (3 g/L). The medium is sterilized at 121 ºC, cooled to room temperature, inoculated with the bacteria and it is grown for 24 h at 28 ºC in an incubator prior to use in the Cr^{VI} removal essays.

c) *Cr^{VI} removal essays*

The removal of Cr^{VI} from aqueous solutions was performed in batch conditions: 1 g of either NaMOR or HMOR zeolite was transferred to 250 mL Erlenmeyer flasks, where 15 mL of the grown culture medium and 150 mL of each chromium solution were added. A total of 6 different Cr solutions were tested, with initial concentrations ranging from 20 to 120 mg_{Cr}/L, and were prepared by dilution of $K_2Cr_2O_7$ (Panreac. p.a.) in deionized water. All concentrations were tested in triplicate. The flasks were kept in an incubator at 28 ºC with moderate agitation for 8 days, for both zeolites. Samples were taken at a daily basis, centrifuged and the supernatant was analyzed for Cr^{VI} using the 1,5-diphenylcarbazide colorimetric method (Eaton et al., 1995).

3 Results

Cr^{VI} removal was observed for both NaMOR and HMOR based biosorption systems. Figure 1 presents the Cr^{VI} removal for both supports and the results are detailed in table 1:

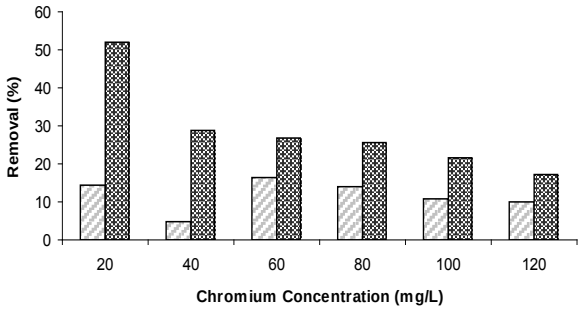

Figure 1: Cr^{VI} removal for NaMOR (light grey) and HMOR (dark grey), for the different chromium concentrations.

Table 1: Cr^{VI} removal and uptakes for both systems tested.

Support	NaMOR		HMOR	
Initial Cr^{VI} concentration (mg/L)	Removal (%)	Uptake ($mg_{Cr^{VI}}/g_{zeolite}$)	Removal (%)	Uptake ($mg_{Cr^{VI}}/g_{zeolite}$)
20	14.6	0.4	52.1	1.5
40	4.7	0.3	28.9	1.6
60	16.3	1.5	26.7	2.4
80	13.9	1.7	25.5	3.1
100	10.9	1.7	21.5	3.3
120	10.1	1.8	17.3	3.1

The best performance in terms of Cr^{VI} removal and uptake was achieved with the HMOR-*A. viscosus* system in all tested solutions with different Cr^{VI} concentrations. With this system, the best removal was obtained for diluted solutions and the uptake increased steadily up to the initial concentration of 80 mg_{Cr}/L and remained stable for the more concentrated solutions. For the NaMOR-based system, the removal appears to be better at the intermediate concentration solutions (40 to 60 mg_{Cr}/L), although the uptake progressed similarly to the HMOR-based system.

The efficiency of Cr^{VI} removal is related to the reduction performed by the *A. viscosus* bacterium (Silva et al., 2008). The ability of several bacteria to bio-reduce Cr^{VI} has been thoroughly studied. Namely, several *Arthrobacter* species are known to perform the reduction of Cr^{VI} (Tsibakhashvili et al., 2004. and Lin et al., 2006) and the reaction takes place in the electron-donor functional groups present in the polysaccharide chains. This reaction is pH-sensitive, as reported in the studies of Cr^{VI} removal by microbial biomass by Park et al. (2005, 2008), which suggest that acidic conditions favor the reduction of Cr^{VI}. Higher pH values limit the reduction capacity and the removal of Cr^{VI} species is performed by retention in the surface of the biomass. The pH values of the solutions were measured at the initial and final experimental time and the results are presented in table 2:

Table 2: Measured pH values for the different solutions

Solution	Initial Cr^{VI} solution	HMOR		NaMOR	
		Initial	Final	Initial	Final
20	5.21	3.60	3.35	7.03	7.85
40	5.20	3.52	3.27	6.31	8.19
60	4.30	3.53	3.21	6.22	7.83
80	5.02	3.29	3.10	6.08	5.41
100	4.83	3.39	3.11	6.12	5.18
120	4.72	3.31	3.07	6.09	5.34

The initial shift in the pH is related to the rapid ion exchange between the zeolite and the residual protons and potassium ions present in the aqueous media (K^+ originates from the chromium salt employed). For the biosorption-NaMOR, the system increases pH at the initial stages, with this effect being more notorious in the lower Cr^{VI} concentration solutions which have a lower K^+ concentration. In fact, this support has 6.5 % of Na_2O and most likely protons co-exchanged with Na^+ ions from the zeolite. For the biosorption-HMOR system the behavior is different. The principal charge balancing cation in its framework is the proton due to the absence of sodium (Na_2O = 0.05%). Charge compensation by co-exchange of protons and potassium leads to some residual acidity in the zeolite, so the shift in the pH of the solutions is towards a more acidic region. Therefore, the biosorption-HMOR system is more adequate to the reduction of Cr^{VI} by the *A. viscosus* bacterium and the differences in the uptake are related to this fact. It is expected that the HMOR zeolite recovered from solution will present a higher Cr loading when compared to the NaMOR.

The Langmuir adsorption isotherm model was applied to the experimental data obtained for the biosorption-MOR systems. The data was plotted (figure 2) and the parameter values were calculated and are presented in table 3:

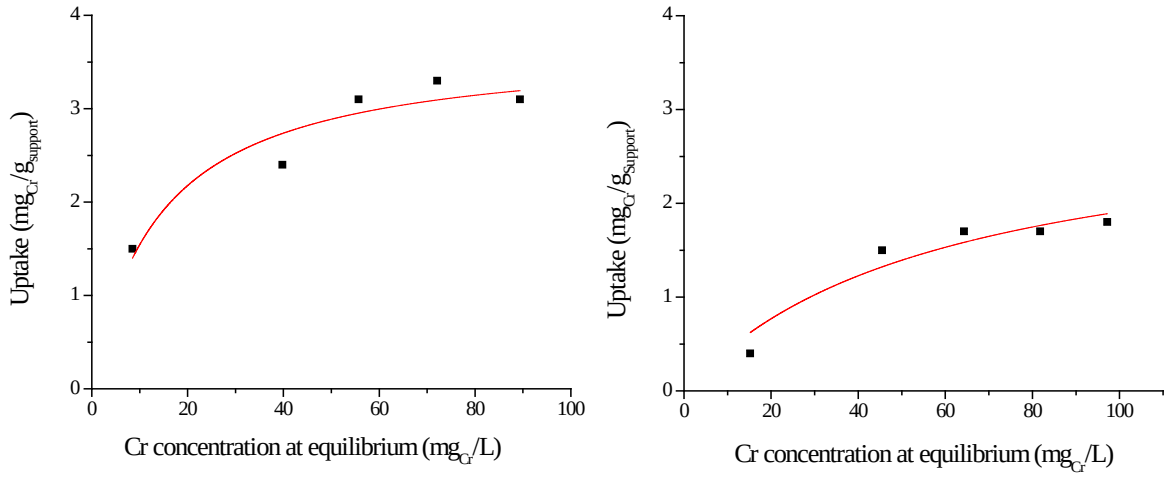

Figure 2: Uptake vs. equilibrium concentration for HMOR – bacteria (left) and NaMOR – bacteria (right), with plotted Langmuir fitting to experimental data for both systems.

Table 3: Langmuir model parameters

System	Parameters	
HMOR	q_{max}	3.5 $mg_{Cr}/g_{support}$
	b	0.37 $mg^{-1}.L$
NaMOR	q_{max}	2.0 $mg_{Cr}/g_{support}$
	b	0.33 $mg^{-1}.L$

The Langmuir adsorption model presented good fitting to experimental data for both systems, indicating that the Cr^{VI} removal performed by both systems is similar to an adsorption process. The calculated maximum uptakes (q_{max}) are similar to the obtained experimentally.

4 Conclusions

Both biosorption HMOR and NaMOR systems were able to recover Cr^{VI} from solution, with the biosorption-HMOR system being more efficient for all tested chromium solutions. The removal is higher for the lower concentration solutions. The pH regulation performed by the HMOR support increases the amount of Cr^{VI} reduced by the *A. viscosus* bacterium, whereas the pH shift into higher values performed by the NaMOR support hinders the reduction and therefore limits Cr^{VI} removal and uptake.

The Langmuir adsorption model was successfully applied to the experimental data making possible the modeling of the Cr^{VI} removal process by the combined *A. viscosus* - mordenite zeolite.

Acknowledgements

H.Figueiredo and B.Silva are thankful to FCT – Fundação para a Ciência e Tecnologia – for the concession of their PhD grants. C.Quintelas would like to thank the same institution for the concession of a Pos-Doc grant.

References

Babel, S., Kurniawan, T.A. (2003). Low-cost adsorbents for heavy metals uptake from contaminated water: a review. *Journal of Hazardous Materials*, B97, 219-243.

Čejka, J., van Bekkum, H. (2005). Zeolites and Ordered Mesoporous Materials: Progress and Prospects. *Studies in surface science and catalysis*¸vol 157, Elsevier.

Demir, A., Arisoy, M. (2007). Biological and chemical removal of Cr(VI) from waste water: Cost and benefit analysis. *Journal of Hazardous Materials*, 147, 275-280.

Eaton, D., Clesceri, L.S., Greenberg, A.E. (1995). *Standard methods for the examination of water and wastewater*, American Public Health Association (APHA), Washington.

Figueiredo, H., Neves, I.C., Quintelas, C., Tavares, T., Taralunga, M., Mijoin, J., Magnoux, P. (2006). Oxidation catalysts prepared from biosorbents supported on zeolites. *Applied Catalysis B: Environmental*, 66, 274-280.

Gavrilescu, M., (2004). Removal of Heavy Metals from the Environment by Biosorption. *Engineering in Life Sciences*, 4, 219-232.

Kostrab, G., Mravec, D., Bajus, M., Janotka, I., Sugi, Y., Cho, S.J., Kim, J.H. (2006). *Tert*-Butylation of toluene over mordenite and cerium-modified mordenite catalysts. *Applied Catalysis A: General*, 299, 122-130.

Kratochvil, D., Volesky, B. (1998). Advances in the biosorption of heavy metals. *Trends in Biotechnology*, 16, 291-300.

Lin, Z., Zhu, Y., Kalabegishvili, T.L., Tsibakhashvili, N.Y., Holman, H.-Y. (2006). Effect of chromate action on morphology of basalt-inhabiting bacteria. *Materials Science & Engineering*, C26, 610-612.

Park, D., Yun. Y.-S., Jo, J.H., Park, J.M. (2005). Mechanism of hexavalent chromium removal by dead fungal biomass of *Aspergillus niger*. *Water Research*¸39, 533-540.

Park, D., Yun. Y.-S., Kim, J.-Y., Park, J.M. (2008). How to study Cr(VI) biosorption: Use of fermentation waste for detoxifying Cr(VI) in aqueous solution. *Chemical Engineering Journal*, 136, 173-179.

Silva, B., Figueiredo, H., Quintelas, C., Neves, I.C., Tavares, T. (2008). Zeolites as supports for the biorecovery of hexavalent and trivalent chromium. *Microporous and Mesoporous Materials*, Elsevier, doi:10.1016/j.micromeso.2008.05.015.

Tavares, M.T., Quintelas, C., Figueiredo, H., Neves, I. (2006). Comparative study between natural and artificial zeolites as supports for biosorption systems. *Advanced Materials Forum III*, 2006, 1294-1298.

Tsibakhashvili., N.Y., Mosulishvili, L.M., Kalabegishvili, T.L., Kirkesali, E.I., Frontasyeva, M.V., Pomyakushina, E.V., Pavlov, S.S., Holman, H.-Y.N. (2004). ENAA studies of chromium uptake by *Arthrobacter oxydans*. *Journal of Radioanalytical and Nuclear Chemistry*, 259, 527-531.

Yim, S.D., Chang, K-H., Koh, D.J., Nam, I-S., Kim, Y.G. (2000). Catalytic removal of perchloroethylene (PCE) over supported chromium oxide catalysts. *Catalysis Today*¸ 63, 215-222.

Proceedings of the 10th International Chemical and
Biological Engineering Conference - CHEMPOR 2008
Braga, Portugal, September 4-6, 2008
E.C. Ferreira and M. Mota (Eds.)

Phosphorus removal from an industrial wastewater by struvite crystallization into an airlift reactor

A. Sánchez Sánchez[1], Sonia Barros[2], Ramón Méndez[1], J.M. Garrido[1]
[1]Chemical Engineering Department
School of Engineering, University of Santiago de Compostela
Campus Sur, E-15782 Santiago de Compostela, Spain
[2]3R Ingeniería Ambiental, Vía Ptolomeo 3, E-15890, Santiago de Compostela, Spain.

Keywords: Crystallization, Phosphorus recovery, Struvite, Airlift reactor.

Topic: Sustainable process-product development through green chemistry

Abstract

Crystallization of struvite in an airlift reactor was achieved with different phosphorus or magnesium sources. Struvite was precipitated from either a secondary treated industrial wastewater from the frozen seafood sector, or from a synthetic wastewater with high phosphate concentration. Seawater and a magnesium chloride solution were used as magnesium source for struvite precipitation. Struvite precipitation was not influenced by either the nature of the phosphorus or magnesium source used. The main parameter that could affect the phosphorus removal was pH. The treated effluent with the lower phosphorus concentration was obtained when pH was above 8.5 and close to 9.

Amorphous calcium precipitation was also observed during the period in which seawater was used as magnesium source. The formation of calcium phosphate had two different effects, one positive as acts as glue that promotes the agglomeration of the struvite crystals, and one negative as some fraction of this phosphate was washed out with the effluent. Seawater was found to be a reliable and inexpensive magnesium source for MAP crystallization, especially for those facilities located near the seashore.

1 Introduction

Phosphorus removal from wastewaters is currently achieved by precipitation with Fe and Al salts or lime. These precipitation processes are widely used for removing phosphorus during the treatment of wastewater from diluted wastewaters. However the precipitation could be disadvantageous when the concentration of phosphorus is very high as occurs for some industrial wastewaters. For these wastewaters a high amount of precipitates are generated and the cost of the chemicals required could be a drawback that could made uneconomic the precipitation of phosphates. Additionally considering sustainability, the phosphorus recovery process from these precipitates is very difficult and expensive. Due to the above mentioned drawbacks, the precipitation of phosphate by crystallization of struvite (magnesium ammonium phosphate, MAP, $NH_4MgPO_4 \cdot 6H_20$) could be an alternative for the sustainable and economical recovery of this compound from concentrated wastewaters.

Struvite is a white, crystalline substance of distinctive orthorhombic crystal structure (Abbona et al., 1984). Its density is 1710 kg/m^3. The crystallization of struvite represents an interesting technique to recover this element from wastewater. The product recovered, struvite, is easy to hand and free of sludge-handling problems. Struvite crystallization has been demonstrated to be an economical way to remove phosphorous of wastewater effluents, especially at high phosphorous concentrations. Additionally, struvite has a commercial value as a fertiliser, so is supposed to be really beneficial in all senses for

nutrient recovery (Ghosh et al 1996). Struvite usually precipitates as stable white orthorhombic crystals in a 1:1:1 molar ratio according to equation 1:

$$Mg^{2+} + NH_4^+ + H_nPO_4^{n-3} + 6H_2O \leftrightarrow MgNH_4PO_4{\cdot}6H_2O + nH^+ \quad (1)$$

Struvite has a solubility product, Ksp, around $5.37 \cdot 10^{-14}$ (Ohlinger 1998). As suggested by equation 1, struvite solubility is conditioned by the pH of the solution. It is highly soluble at acid pH and highly insoluble at alkaline pH environment. Thus, its precipitation could be controlled by pH adjustment, as well as by alteration of the concentration of the ions indicated in equation 1. The pH range within which struvite may precipitate is between 7 and 11. This is closely related to the decrease in struvite's solubility when pH increases (Battistoni et al., 1997; Matynia et al., 2002).

Struvite crystallization may be achieved with different plant configurations: Complete Stirred Tank Reactors (Regy et al. 2001) and either Two-phase (Bhuiyan et al. 2008) or Three-phase Fluidized bed reactors (Battistoni et al. 1997; Matsumiya et al. 2000). The main aim of this research was to study the performance of a three-phase airlift reactor for recovering MAP from industrial wastewaters with a high phosphorus concentration. Wastewaters were generated in a frozen seafood factory located near the seashore. Magnesium concentration in the wastewater is low, and thus should be externally added in order to precipitate struvite in the reactor.

2 Materials and methods.

A 2.7 L volume airlift reactor with a three-phase separator at the top of the system was used during the experiments of MAP crystallization (Figure 1). An external settler was coupled in series to the airlift reactor in order to avoid the outflow of fine particles with the effluent. Two different influents were fed to the reacto to study and compare the efficiency of the MAP crystallization with either a synthetic solution or with the real wastewater in the airlift system:

i.- A synthetic wastewater with a phosphate concentration similar to that observed in the industrial wastewater (average 630 mg P-PO_4^{3-}/L), that was prepared by diluting sodium phosphate in tap water.

ii.- An industrial wastewater, generated in a frozen seafood factory located in Galicia (NW Spain) with very high phosphate concentration was used. This wastewater was previously secondary treated in an aerobic biological pilot plant in order to reduce the COD concentration and hydrolyse organic P and polyphosphates present in the raw influent.

Additionally, the precipitation of struvite was assayed by using two different magnesium sources: a concentrated magnesium chloride solution and seawater. The seawater used was collected near the industrial facility and contained around 1250 mg/L of Mg and 400 mg/L Ca. The reactor was operated during 128 days and the operation could be divided in three different stages:

Stage I: Days 0 to 34, Start up period: The Airlift reactor was fed continuously during 6 hours per day, feeding it with the synthetic medium. Ammonium chloride and magnesium chloride solutions were used Mg and NH_4^+ sources. During the operation the "Hydraulic Retention Time" (HRT) of the reactor was fixed in 6 h.

Stage II: Days 43 to 91, Operation with industrial wastewaters: During this period the reactor was operated continuously. The secondary treated industrial wastewater was fed to the reactor and the two concentrated media with ammonia and magnesium salts. HRT ranged between 1.1 and 6 h.

Stage III: Days 103 to 128, Synthetic wastewater and the concentrated ammonia media were fed continuously again. Nevertheless, in this case, seawater was used as magnesium source. HRT was maintained in 1.1 h.

The determination of orthophosphate and ammonium concentrations Most of the analyses were done accordingly to the Standard Methods. Phosphate and ammonia concentration, Suspended solids, Conductivity, alkalinity, TOC, IC and were measured in the influent and effluent from the reactor. Mg and Ca were punctually determined in the effluent. Suspended solids concentration, temperature and pH were determined in the reactor. X-ray fluorescence and ICP-OES were used for determine the elemental composition of the precipitates and the effluent, respectively. Samples of struvite crystals were taken in the reactor or the settler for observation by using SEM with Energy Dispersive X-ray analysis (SEM-EDS) and to identify the nature of the crystals by using X-ray diffraction (XRD).

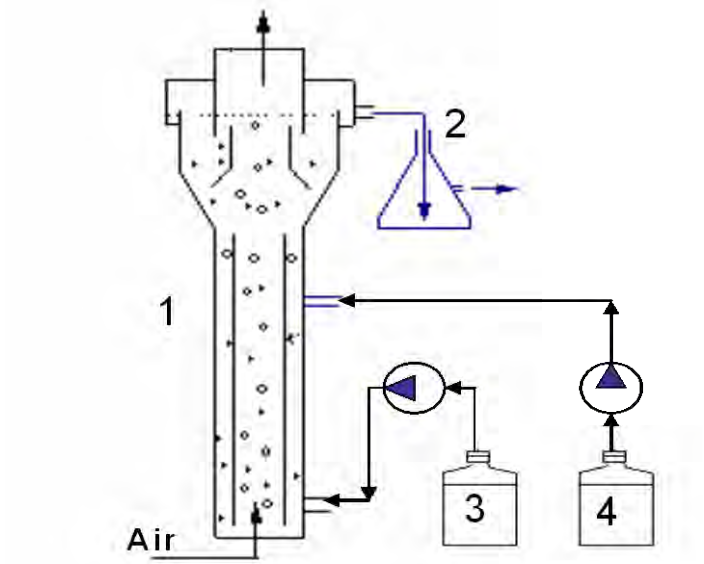

Figure 1. Schematic diagram of the Lab-scale airlift reactor for struvite crystallization. **(1)** Airlift reactor; **(2)** Secondary settler; **(3)** wastewater **(4)** Magnesium source.

3 Results and discussion

Figure 5 shows pH evolution all over the operation time. Reactor pH was controlled by using a NaOH solution, in order to maintain it above 7.5. The efficiency of the reactor depended on the pH of operation; in fact the best results in terms of low fine particles outflow and phosphate concentration in the effluent were achieved when pH values were between 8.5 and 9.0, independently of either the magnesium or phosphate source. This pH was achieved either by adding NaOH into the reactor. Other authors referred optimum pH for MAP crystallization of 9.0 (Wang et al. 2006) or even at 10 if seawater is used as magnesium source (Lee et al. 2003). Stripping of a fraction of the inorganic carbon present in the influent was observed. This was especially observed during period II in which the secondary treated wastewater was fed.

Struvite formation can be inhibited by the interaction of calcium and magnesium, depending on their relative concentrations (Battistoni et al., 1997). It has been concluded that the precipitation of the calcium phosphate apatite occurs at pH values above 9.5 whereas struvite precipitation takes place at pH values of 8 and above. In fact, when

seawater was employed as magnesium source, the calcium forms an amorphous precipitate of $Ca_3(PO_4)_2$, at pH values below 8,5 (Figures 4A and 4B).

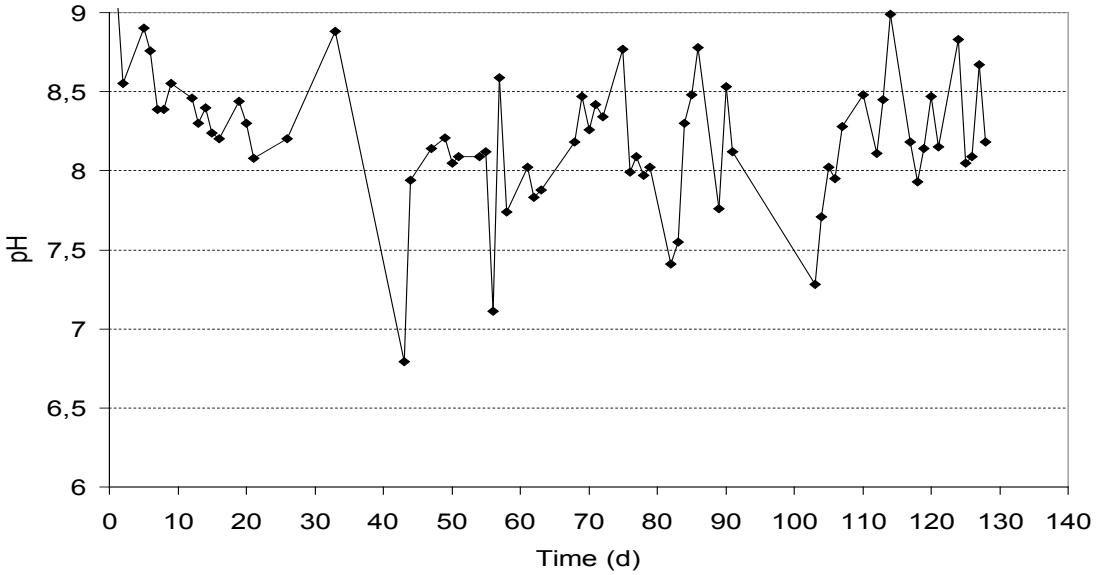

Figure 2. pH evolution in the airlift reactor during the experiments.

Phosphorus recovery, through struvite precipitation, from either synthetic or real wastewater was achieved during the three experimental periods in which the reactor was fed with different sources of phosphate and magnesium. Primary nucleation (crystal birth) was induced during the first experimental of the stage I, by raising the pH of the reactor, and later secondary nucleation (crystal growth) was observed. MAP crystals concentration in the reactor ranged from 20 to 90 g/L during the operation.

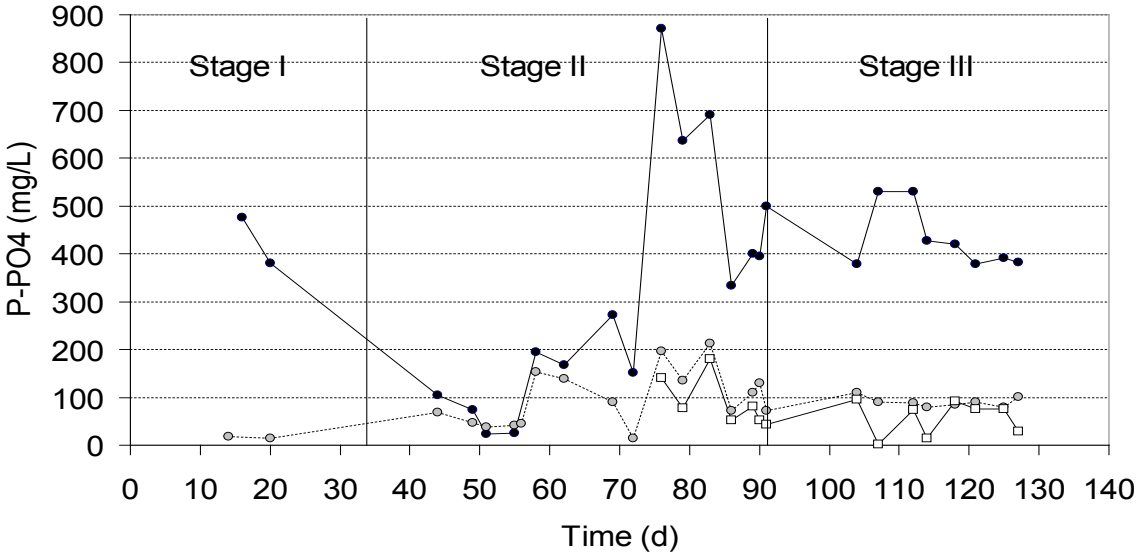

Figure 3. Evolution of orthophosphate concentration in the influent (●), soluble orthophosphate in the effluent (□) and total phosphate in the effluent (●) of the airlift reactor.

Microscopical observations of precipitates using SEM showed different kinds of precipitates depending on the period of operation (Figure 4). Obviously, the best results

were obtained during the first operating period, with HRT of 6 h. Nevertheless, a high phosphate separation was also achieved under different feeding conditions, even with HRT of 1.1 h, by maintaining an adequate range of pH. Recovery efficiency (Phosphate precipitates that were retained into the reactor) was above 80%.

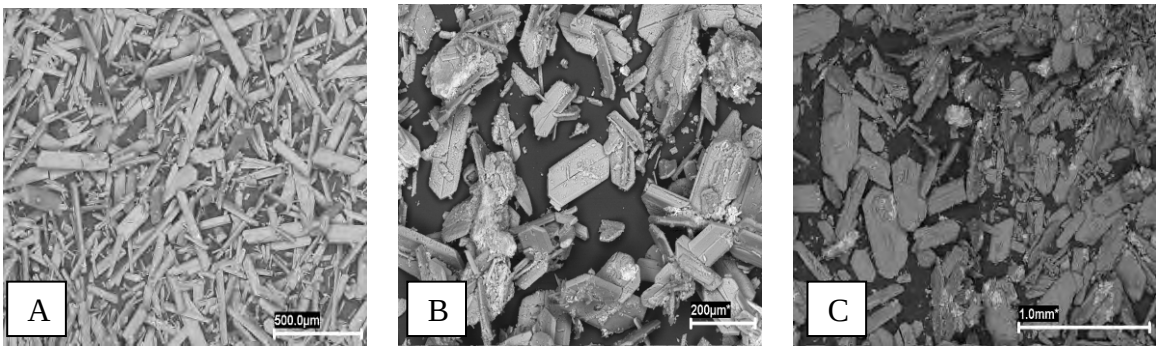

Figure 4. Microphotography of the struvite crystals on stages 1 (A), 2, (B) and 3 (C).

During the first operation period (feeding synthetic wastewater), small amounts of fine particles was detected in the effluent. Needle-form struvite crystals grew as monocrystrals, not agglomerated. Kinetics studies demonstrated that during this period magnesium excess was not a key factor in the formation of struvite, as the P efficiency was similar at molar ratios higher than 1:1 of Mg and P.

The precipitation of a amorphous calcium phosphate was also observed, during the third operation periods in which seawater was used as magnesium source. Used seawater contained around 400 mg/L Ca. XRD analysis demonstrated the amorphous nature of this precipitate. Calcium phosphate [$Ca_3(PO_4)_2$] also acts like a glue for the struvite crystals, The presence of agglomerates of struvite with amorphous calcium was observed by using XRD and SEM-EDS. Le Corre el al. (2005) also observed an increase of the struvite particle size formed, that was caused by the addition of Ca during batch assays. In this sense Ca had a positive effect, as promote the growth of aggregates and promotes the P precipitation. Nevertheless, the addition of seawater also had a negative effect on P efficiency.

The main inconvenient observed during the operation with seawater was the increment of fines that was observed in the effluent. These fines caused a certain loss on the phosphate efficiency of the system and were principally composed by amorphous precipitates of $Ca_3(PO_4)_2$ on stage 3 (Figure 5B).

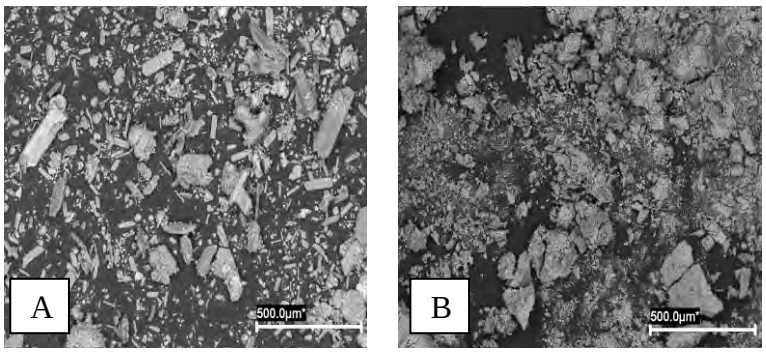

Figure 5. Microphotography of the particle fines washed out from the reactor with the effluent but retained in the secondary settler during operating stages 2 (A) and 3 (B).

Phosphate concentration in the effluent was influenced more by the operation pH than for the magnesium source. In this sense, seawater provides inexhaustible and inexpensive source for MAP precipitation in facilities near the seashore. In this sense, the cost of adding a magnesium salts could be a major economic constrain to application of MAP crystallization for nutrient recovery.

4 Conclusions

Crystallization of struvite was observed during the three periods studied and was not influenced by either the nature of the phosphorus or magnesium source used. The main parameter that could affect the phosphorus removal was pH. pH also affected the formation of fine particles that were washed out of the airlift reactor. Regardless of the feed synthetic or real wastewater, best periods of operation took place when pH is above 8.5 and close to 9. pH may be controlled by adding NaOH or other suitable alkali.

Amorphous calcium formation was observed during the period in which seawater is used as magnesium source. The formation of calcium phosphate had two different effects, one positive as acts as glue that promotes the agglomeration of struvite crystals, and one negative as some fraction of this phosphate was washed out with the effluent. Seawater, for those facilities located near the seashore, is a reliable and inexpensive magnesium source for MAP crystallization.

Acknowledgements: To the Ministry of Education and Science through the Novedar-Consolider project (CSD2007-00055) and to the Consellería de Innovación e Industria, Xunta de Galicia (PGIDIT06TAM008E) that funded this project.

References

Abbona F. et al. (1982). Journal of Crystal Growth 57, 6-14.

Battistoni P. et al. (1997). Water Research 31 (11), 2925-2929.

Bhuiyan M.I.H., et al. (2008) Water Science and Technology 57(2), 175-181.

Ghosh G.K. et al. (1996). Nutrient Cycling in Agroecosystems 46, 71-79.

Lee S.I. (2003) Chemosphere 51, 265-271.

Matsumiya Y. (2000) Journal of the Chartered Institution of Water and Environmental Management 14, 291-296.

Matynia A. et al. (2006). Chemical Engineering 193, 160-176.

Ohlinger K.N. et al. (1998). Water Research 32, 3607-3614.

Regy S. et al (2001) Phosphate Recovery by struvite precipitation in a stirred reactor. CEEP-LAGEP report.

Wang J. (2006) Chemosphere 65, 1182-1187.

Proceedings of the 10th International Chemical and
Biological Engineering Conference - CHEMPOR 2008
Braga, Portugal, September 4-6, 2008
E.C. Ferreira and M. Mota (Eds.)

EcoDesign through a Multi-criteria Environmental Decision Tool based on Fuzzy Logic

Marta Herva[1*], Amaya Franco[2], Eugenio F. Carrasco[1], Enrique Roca[1]
[1] Dept. of Chemical Engineering, School of Engineering, University of Santiago de Compostela, Campus Sur, 15782 Santiago de Compostela, Spain.
[2] Process Engineering Group, Marine Research Institute IIM-CSIC Eduardo Cabello, 6 - 36208 Vigo, Spain.

Keywords: Ecological Footprint, Life Cycle Assessment, Environmental Risk Assessment, Fuzzy Logic, Ecodesign Tool
Topic: Sustainable process – product development through green chemistry.

Abstract

The ecodesign of a product implies that different potential environmental problems of diverse nature must be considered, apart from the general design criteria. In this sense, an ecodesign tool integrating the criteria provided by three environmental evaluation methodologies, i.e., Ecological Footprint (EF), Life Cycle Assessment (LCA) and Environmental Risk Assessment (ERA), has been constructed on the basis of fuzzy logic reasoning and features. This idea enabled the decision making at process level taking into account the values of the different indicators at a time. The relative importance of each of them has been established through the definition of membership functions as inputs to the fuzzy inference reasoning procedure in the case of a specific product. As a result, a Fuzzy EcoDesign Index (FEcoDI) was obtained. A well known case study was used to test the tool. Different packaging materials for a beverage bottle were considered to identify the most environmentally friendly option.

1 Introduction

Ecodesign may be defined as the systematic introduction of environmental concerns during product design and development (AENOR, 2003). This means to bear in mind the environmental impacts at all stages of the product life cycle from the designing and development phases. The identification and valorization of the environmental burdens requires the application of evaluation tools. There are different options when deciding which supporting tools to use. Some traditional tools used in ecodesign are qualitative and subjective like the Life Cycle Design Strategies (LiDS) Wheel, or semi-quantitative like the Materials Energy Toxicity (MET) Matrix. On the other side, the more developed ones, like the Ecoindicators or the Life Cycle Assessment (LCA), include objective criteria and quantitative evaluation of the environmental impact (Rieradevall and Vinyets, 1999).

The different kinds of tools can highlight different potential environmental problems (Byggeth and Hochschorner, 2006). Consequently, none of them can be believed to offer a totally comprehensive evaluation. In some cases the limitations stem from the application of a single approach can be assumed, but in other situations an integrative proposal needs to be considered. Ecological Footprint (EF), Life Cycle Assessment (LCA) and Environmental Risk Assessment (ERA) are considered as examples of objective and quantitative ecodesign tools. Besides, they provide complementary information about environmental performance of processes and products. The EF gives valuable information about the degree of sustainability of a particular process since this indicator especially accounts for resources and energy consumption, as well as for waste generation. However, some limitations were

* Corresponding author. Tel + 34-981-563100 Ext. 16800. E-mail: marta.herva@usc.es

acknowledged for this methodology (Kitzes et al, 2007), and for this reason it results interesting to complement EF studies through a simplified LCA (Herva et al, 2008a). In addition to using LCA to assess aspects excluded from EF estimates (e.g. emissions different from CO_2 or hazardous wastes), its application was proposed when a more in depth analysis was required for a particular functional unit, thus helping to identify more sustainable solutions or best available technologies (Azapagic, 1999). The existence of a relation between EF and LCA has been identified by Huijbregts et al (2007) when the Ecoindicator 99 was employed. Regarding CO_2 emissions, another concept becoming popular because of its relation with the Kyoto Protocol is the Carbon Footprint (CF). This indicator, which is part of the total EF estimate, is employed to measure the total greenhouse emissions.

Although LCA is claimed to offer an integrative assessment of a process, the information provided regarding human and ecosystem toxicity, for example, is more incomplete than desirable. This means that it has a limited capacity to predict toxicity effects. ERA provides an established methodology based on the assessment of different scenarios, exposure pathways, duration and frequency that allows for a more rigorous and exhaustive evaluation. Therefore, LCA and ERA are complementary tools (Leet and Geibig, 2006) that can be integrated (Huijbregts et al, 2000). ERA is used to estimate a risk index associated to certain hazardous substances that raw materials may contain (organic compounds, heavy metals…) and that would affect the final consumers or factory employees (Franco et al, 2007).

In the present work, a framework based on the integration of EF, LCA and ERA is proposed. This approach was built on the basis of Fuzzy Logic (FL) reasoning and features. The usefulness of FL based methods to address uncertainty and subjectivity in environmental problems has already been stated (Carrasco et al, 2002). The established objective was to obtain a final Fuzzy EcoDesign Index that could help to distinguish the best option from an environmental point of view. To test the tool, different packaging materials for a beverage bottle were considered to identify the most environmentally friendly option.

2 Materials and methods

2.1. Case study

A 2 litre bottle of drinking water has been studied. Two kind of plastic materials were proposed: PET and PVC. Based on the life cycle inventory of these products (Feijoo and Roca, 2005), EF and complementary LCA were estimated. For ERA, particular acknowledged risk problems were taken into account, like the migration of bisphenol A and aldehydes in PET (Le et al, 2008; Dabrowska et al, 2003), or vinyl chloride monomer in PVC (Fayad et al, 1997).

2.2 Ecodesign tools methodologies

The methodology employed for the EF assessment was based on the fundamentals of yield and equivalence factors stated by the creators of this concept (Monfreda et al, 2004). In particular, EF estimates were done with the adaptation carried out by Herva et al (2008b) to assess the sustainability of a production process. This indicator was employed to evaluate the energy and materials consumption in the production process of the product.

Emissions released during the manufacture were evaluated via LCA. In this case, the methodology established in the ISO 14040 standards was used. During the life cycle impact assessment, only the compulsory characterization phase was carried out. However, normalization phase was also conducted in order to obtain environmental impacts prioritization criteria. Characterization and normalization factors from the Dutch Institute of Environmental Sciences (CML, 2000) were applied in equations [1] and [2], respectively. Global Warming Potential (GWP) and Acidification Potential (AP) impact categories were incorporated to the EF estimate using absorption factors (Herva et al, 2008a). In the GWP case, this would constitute the Carbon Footprint (CF).

$$C_j = \sum_i C_{ij} = \sum_i A_i \cdot W_{ij} \qquad [1] \qquad C_{j,N} = C_j / N_j \qquad [2]$$

where A_i is the amount of emission *i* released, W_{ij} is the characterization factor for the emission *i* within the category *j*, C_{ij} is the contribution of the emission *i* to the category *j*, C_j is the characterized value of the category *j*, N_j is the normalization factor of the category *j* and $C_{j,N}$ is the category *j* normalized. C_j units depend on the category considered, whereas $C_{j,N}$ is dimensionless.

For the environmental risk estimates, migration rates from bottle to water and final concentrations in water for the compounds considered (bisphenol A, vinyl chloride monomer and aldehydes) were found in the literature (Table 1).

Table 1. Data used for the risk characterization.

Compound	Material	Migration rate / Concentration in water			RfDs[(a)] (mg kg^{-1} day^{-1})	SF[(a)] (kg day mg^{-1})
		Value	Units	Source		
Bisphenol A	PET	0.19±0.13	ng/h[(b)]	Le et al, 2008	$5.00 \cdot 10^{-2}$	-
Vinyl monomer	PVC	0.6	µg/l	Fayad et al, 1997	$3.00 \cdot 10^{-3}$	1.50
Acetaldehyde	PET	60.0±6.0	µg/l	Dabrowska, 2003	-	-
Formaldehyde	PET	78.1±7.8	µg/l	Dabrowska, 2003	$2.00 \cdot 10^{-1}$	-

[(a)] US-EPA, 2007 [(b)] A six-month storage period considered.

The concentration of these compounds in water stored depended mainly on initial concentrations in the bottle material, as well as in temperature and time of storage. Thus, estimations were made under the worst case scenario conditions. Final concentrations achieved in the beverage were multiplied by a human water intake factor of $2.5 \cdot 10^{-2}$ l/(kg·d) (Clark et al, 2003) during the exposition evaluation phase. Thus, only the oral pathway was considered. For the risk characterization, reference doses (RfDs) for non carcinogenic effects, and slope factors (SF) for carcinogenic effects, were used in order to calculate the Hazard Quotient (HQ) and the Cancer Risk factor (CR) as stated in equations [3] and [4].

$$HQ = Dose / RfDs \qquad [3] \qquad CR = Dose \cdot SF \qquad [4]$$

HQ and CR values calculated for the different compounds must be summed up for each material. The result must keep under maximum acceptable levels of 1 and 10^{-4}, respectively.

2.3. Fuzzy logic structure

The use of FL techniques allows us to mesh a quantitative approach using a qualitative representation (Carrasco et al, 2002). Membership functions were defined for each methodology as inputs to a fuzzy inference reasoning procedure in the case of a specific product, a 2 litre water bottle. Since in this case the most important LCA environmental impacts were GWP and AP (obtained in the normalization phase), and they could be integrated in the EF value, membership functions were defined for CR, HQ and EF. The EF contribution to the ecodesign indicator was measured in terms of EF variation (ΔEF) in relation to a base case; that is to say, the higher the decrease in the EF value, the better.

As output to the inference engine, a Fuzzy EcoDesign Index (FEcoDI) was obtained, which collected the different criteria given by the tools used. Thus, each considered alternative was evaluated and the FEcoDI obtained. The Matlab® Fuzzy Logic Toolbox was used and the Mamdani inference system selected. The best option, from an overall environmental point of view, will be the one with the highest FEcoDI (Figure 1).

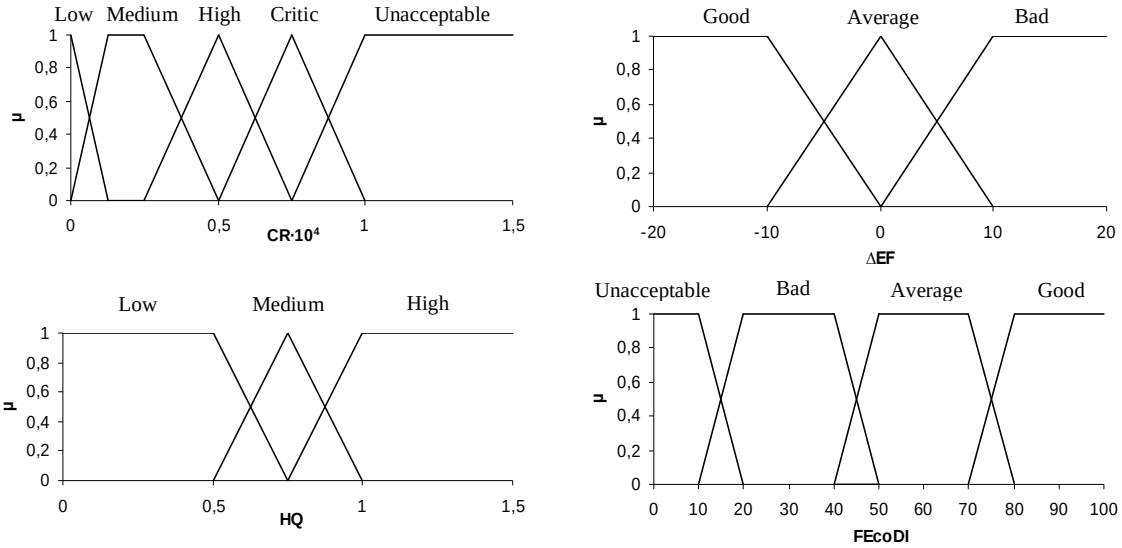

Figure 1. Membership functions for input variables (CR, HQ, EF) and for the output FEcoDI.

3 Results and discussion

On the basis of the inventoried data for the manufacture of a 2 litre bottle of these materials, the EF and ACV were calculated, the former accounting for materials and energy consumption, and the latter for atmospheric and aquatic emissions. LCA results for the characterization and normalization phase are shown in Table 2 and Figure 2, respectively. Observing the major influence of GWP and AP categories, the other ones were discarded from the study. After the integration of these two into EF estimates, the total amount of productive land required resulted in 2.27 m^2/bottle for PVC and 2.43 m^2/bottle for PET. Since in the fuzzy structure EF is measured in terms of variance with respect to a base case, the lowest value of the two (the correspondent to PVC) was taken as reference level. Consequently, the input for the PET bottle would correspond to a 7% increase in relation to the PVC bottle EF.

Table 2. Characterization phase for PVC and PET bottle.

Impact category	Units	PVC	PET
GWP	g CO_2	61.5	55.0
AP	g SO_2	0.75	0.90
ODP	g CFC	$1.44 \cdot 10^{-5}$	$2.16 \cdot 10^{-5}$
EP	g PO_4	$6.96 \cdot 10^{-2}$	$6.60 \cdot 10^{-2}$

GWP = Global Warming Potential AP = Acidification Potential
ODP = Ozone Depletion Potential EP = Eutrophization Potential

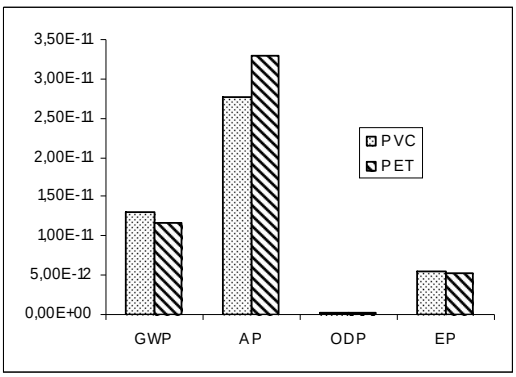

Figure 2. Normalization phase for PVC and PET bottle.

Results from ERA are collected in Table 3. Although acetaldehyde and formaldehyde have the R40 risk phrase associated (ESIS, 2008), what means that there is limited evidence of a carcinogenic effect (they are catalogue as carcinogenic type 3), at the moment there is no slope factor available recognised by and international organisation for these substances. Furthermore, acetaldehyde has neither RfDs nor SF; thus, it was not possible to assess the potential environmental risk contribution of this compound. The HQ and CR are below the safety limits stated by the US-EPA in all cases. It must be noticed that in the case of PET the risk contribution of two compounds was considered, while for the PVC only the potential risk

derived from the vinyl monomer migration was assessed. This was made according to main risk problems acknowledged in literature, and taking into account that the purpose of the analysis was to test the tool, not to present definite results on the evaluation of the two materials.

The results obtained with each methodology were introduced in the ecodesign tool. As a result, a FEcoDI of 30.0 for the PVC bottle was obtained, while a value of 66.6 was estimated for the PET bottle. Consequently, this would lead to select the PET bottle as the best option from an environmental point of view.

Table 3. Results for the Environmental Risk Assessment.

Material	Compound	HQ	CR
PET	Bisphenol A	$2.05 \cdot 10^{-4}$	-
	Formaldehyde	$9.76 \cdot 10^{-3}$	-
	Total	$9.97 \cdot 10^{-3}$	-
PVC	Vinyl monomer	$5.00 \cdot 10^{-3}$	$2.25 \cdot 10^{-5}$

The main difference between the two materials studied was the existence of a carcinogenic slope factor for the vinyl monomer. In the definition of membership functions, the universe of discourse for CR was divided into more categories than for the other variables. The CR has a probabilistic nature; this means that if it has a value different from zero, a risk of someone suffering from cancer will exist. However, in the case of HQ there will be effects on exposed population only if the reference dose is exceeded. As a result, fewer precautions were taken for HQ values lower than 1, while for the CR a more strict characterization was considered necessary. The tool seemed to be sensitive to changes in the EF only when CR and HQ were low enough. This may be because of the way the decision tree was constructed, first evaluating the CR and then the HQ, and only allowing the EF appraisal of those products that had passed the first barriers. Therefore, materials that may cause carcinogenic effects will receive a bad evaluation from the tool. In this case, the PET bottle obtained a better FEcoDI in spite of having a higher EF and HQ. The revision of this imbalanced weight for the input variables may lead to variations in the structure of the decision tree in the fuzzy reasoning. Besides, it was observed in this case study that even if different HQ values were calculated for the two materials evaluated, no changes in the FEcoDI were obtained.

4 Conclusions

A first approach of a tool based on EF, LCA and ERA was built on the basis of fuzzy logic reasoning and features. The output obtained was a Fuzzy EcoDesign Indicator (FEcoDI) that could range between 0 and 100, and that collected the criteria offered by the different environmental evaluation methods. In general terms, the constructed tool seemed to work properly. However, when testing it with real cases some limitations were detected and further development is proposed. The following steps may be considered: a.- Integration of more LCA impact categories that may be significant in the evaluation of other products; b.- A refinement of the decision tree in the fuzzy reasoning; and c.- A revision in the number of categories defined in the universe of discourse of HQ.

Acknowledgements
This work has been supported by the Galician Government (Dirección Xeral de I+D+i) through the Project PGIDIT 07MDS050E.

References

AENOR. (2003). Environmental Management of Design and Development Process. Design for Environment. UNE 150301. (In spanish).

Azapagic, A. (1999). Life cycle assessment and its application to process selection, design and optimisation. *Chemical Engineering Journal,* 73, 1-21.

Byggeth, S., Hochschorner, E. (2006). Handling trade-offs in Ecodesign tools for sustainable product development and procurement. *Journal of Clearner Production*, 14, 1420-1430.

Carrasco, E.F., Rodríguez, J., Puñal, A., Roca, E., Lema, J.M. (2002). Rule-based diagnosis and supervision of a pilot-scale wastewater treatment plant using fuzzy logic techniques. *Expert Systems with Applications,* 22, 11-20.

Clark, K., Cousins, I.T., Mackay, D. Assessment of critical exposure pathways. In: C.A. Staples, Editor, The handbook of environmental chemistry vol. 3, part Q, Springer, Berlin, Germany (2003), pp. 227–262.

CML (Institute of Environmental Sciences). 2000. CML 2 baseline 2000 V2.3.

Dabrowska, A., Borcz, A., Nawrocki, J. (2003). Aldehyde contamination of mineral water stored in PET bottles. *Food additives and contaminants*, 20(12), 1170-1177.

ESIS. (2008). European chemical Substances Information System. http://ecb.jrc.it/esis/.

Fayad, N.M., Sheikheldin, S.Y., AlMalack, M.H., ElMubarak, A.H., Khaja, N. (1997). Migration of vinyl chloride monomer (VCM) and additives into PVC bottled drinking water. *Journal of Environmental Science and Health Part A, Environmental Science and Engineering*, 32, 1065–1083.

Feijoo, G., Roca, E. (2005). Chapter 11. Environmental Technologies. In *Galicia Ecology, Volume XLVII: Environmental Science and Technology I. Part II: Technology for environmental protection*, 403-427. Hercules de Ediciones, A Coruña, Spain (in Spanish).

Franco, A., Costoya, M.A., Roca, E. (2007). Estimating Risk During Showering Exposure to VOCs of Workers in a Metal-Degreasing Facility. *Journal of Toxicology and Environmental Health*, Part A, 70, 627–637.

Herva, M., Franco, A., Álvarez, A., Ferreiro, S., Roca, E. (2008a). Combined use of EF and LCA to assess environmental impact in the textile sector. Proceedings 2nd International Conference on Engineering for Waste Valorisation (CD). June 3-5, Patras, Greece.

Herva, M., Franco, A., Ferreiro, S., Álvarez, A., Roca, E. (2008b). An approach for the application of the ecological footprint as environmental indicator in the textile sector. *Journal of Hazardous Materials*, 156, 478-87.

Huijbregts, M.A.J., Thissen, U., Guinèe, J.B., Jager, T., Kalf, D., van de Meent D., Ragas, A.M.J., Wegener Sleeswijk, A., Reijnders, L. (2000). Priority assessment of toxic substances in life cycle assessment. Part I: Calculation of toxicity potentials for 181 substances with the nested multi-media fate, exposure and effects model USES-LCA. *Chemosphere,* 41, 541-573.

Huijbregts, M., Hellweg, S., Frischknecht, R., Hungerbühler, K., Hendriks, A. (2007). Ecological Footprint Accounting in the Life Cycle Assessment of Products. *Ecological Economics*, 64, 798-807.

Kitzes, J., Peller, A., Goldfinger, S., Wackernagel, M. (2007).Current methods for calculating National Ecological Footprint Accounts. Science for Environ & Sustain Society, 4(1), 1-9.

Le, H.H., Carlson, E.M., Chua, J.P., Belcher, S.M. (2008). Bisphenol A is released from polycarbonate drinking bottles and mimics the neurotoxic actions of estrogen in developing cerebellar neurons. *Toxicology Letters*, 176, 149-156.

Leet Socolof, M., Geibig, J.R. (2006). Evaluating Human and Ecological Impacts of a Product Life Cycle: The Complementary Roles of Life-Cycle Assessment and Risk Assessment. *Human and Ecological Risk Assessment,* 12, 510-527.

Monfreda, C., Wackernagel, M., Deumling, D., 2004. Establishing national natural capital accounts based on detailed ecological footprint and biological capacity assessments. Land Use Policy 21, 231-246.

Rieradevall, J., Vinyets, J. (1999). Ecodesign and ecoproducts. Ed. Rubes, Barcelona, Spain (in Spanish).

US-EPA. (2007). Risk Assessment Information System (RAIS).

Proceedings of the 10th International Chemical and
Biological Engineering Conference - CHEMPOR 2008
Braga, Portugal, September 4-6, 2008
E.C. Ferreira and M. Mota (Eds.)

Design of sustainable processes: Systematic generation & evaluation of alternatives

Ana Carvalho[1,2], Rafiqul Gani[1], Henrique A. Matos[2]
1: CAPEC, Dept of Chem Eng, Tech Univ of Denmark, DK-2800, Lyngby, Denmark
2: CPQ, Dept of Chem & Bio Eng, IST, Av. Rovisco Pais, 1049-001, Lisboa, Portugal

Keywords: Process design, Sustainability metrics, Mass and Energy Indicators, Safety indices
Topic: Systematic methods and tools for managing the complexity

Abstract

In this paper presents a methodology able to generate, screen and then identify sustainable alternatives in any chemical process by locating the operational, environmental, economical and safety related bottlenecks in the process. New alternatives were identified through a set of indicators and then evaluated through performance criteria, which includes a set of Sustainability Metrics and Safety indices. The methodology was already described for continuous processes and has now been extended to handle also batch operations. The methodology is described for both continuous and batch processes highlighting the differences among them. The main features/advantages of the software called SustainPro, which includes the indicator-based methodology, is presented. Through a batch case study (Insulin Process) the important features of the methodology and its application for sustainable process design are highlight through the use of SustainPro.

Introduction

Nowadays the concerns about the human future are growing everyday and consequently the need for improving the industrial plant operation and design is also increasing. The use of green compounds and the operability at sustainable conditions are two factors among many others that should be taken into account in the retrofitting of the already existing processes. Important questions to ask in this respect are - How should we improve an existing process (that is generate retrofit alternatives) without too much effort? What should be done in order to make the process more sustainable? Which are the process points that are going to significantly improve the plant performance? In order to address all the previous issues, it is useful to develop systematic methods and tools, which enable the generation of more sustainable alternatives and also improve the ability to adapt to the future needs.

Many methodologies have been proposed in order to determine new design alternatives of a chemical process with respect to improvement of the process. The indicator-based methodology proposed by Uerdigen et al., (2003) is considered in this paper. This methodology is based on mass and energy indicators, which are able to identify and screen processes operating in the continuous mode, however in this methodology there is no performance evaluation between the new design alternative for a given process with the "reference" design. Jensen et al., (2003) further extended this methodology where the previously defined indicators were retained but the choice of the best alternative was obtained using new parameters related to economic, safety and environmental factors.

Recently, Carvalho et al., (2007) presented a new generic and systematic methodology, which combines the previous versions, incorporates new features, as well as extend the application range to a while spectrum of chemical process. This was achieved through improvements in the flowsheet decomposition technique combine with flow-path identification, selection of target indicators as well as generation of new feasible alternatives. Recently the methodology has also been extended to batch processes.

Some work has also being developed in the batch process improvements. Houghton et al.

(1996) presented a hierarchical design procedure with potential strategies for reducing waste generation in a batch plant. This was done by listing a series of heuristic solutions that is directed at each decision level of the hierarchical design procedure. Halim and Srinivasan, (2006) presented an intelligent system to guide the non-expert in waste minimization assessment of batch processes (BATCHENVOP*Expert*).
In this paper a methodology to screen and identify the critical points in a batch process will be presented. As done for the continuous processes an evaluation in terms of economical, environmental and safety will be performed for the batch process. A batch case study will be described step by step in order to illustrate the methodology.

Methodology

The methodology has been developed for the continuous processes (Carvalho *et al*., 2007) and now it has been extended to batch processes. The following figure shows a diagram with the methodology description.

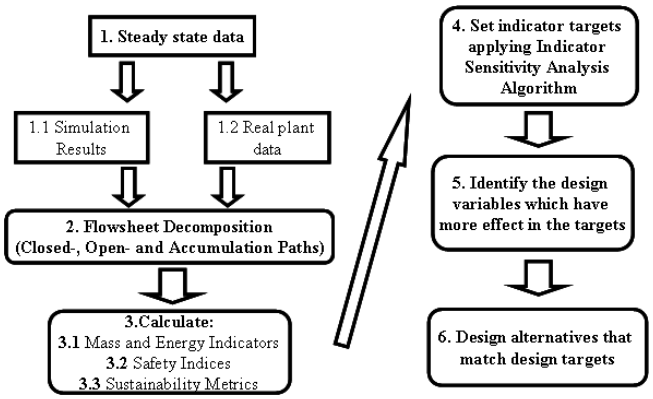

Figure 1: Flow-diagram of the indicator-based methodology

A brief description about both approaches is given below.

Step 1: Collect the steady state data
Process data needed to apply the methodology is collected. In the continuous processes, steady state data related to the mass and the energy balance is needed. In the batch processes the information required is the time of each operation, the equipment volume, the initial and the final mass for each compound in each operation and the energy used in each operation. The purchase and sale prices for each compound as well as the treatment costs are also included in the initial data. This data can be provided from the real plant data or through model-based simulations.

Step 2: Flowsheet decomposition
The flowsheet decomposition for continuous processes is performed to identify all the open- and closed-paths for each compound in the process flowsheet. In the batch processes, although the same decomposition takes place, in this case the accumulation paths (AP) are also determined. These paths (AP) correspond to the accumulation in a given operation.
It is important to mention the difference between the flowsheets for the continuous and batch modes. In the continuous processes the flowsheet is represented as a sequence of equipments, however in the batch processes the flowsheet is represented as a sequence of operations. Initially the flowsheet decomposition is performed in the same way for both continuous and batch processes, the only difference is the addition of accumulation paths for the batch processes.

Step 3: Calculate the indicators, the sustainability and the safety parameters
There is a set of 5 mass indicators and 3 energy indicators, which were defined for the

continuous processes analysis but that, can also be applied to batch processes. In this step the entire mass and energy indicators are calculated for all open- and closed-paths determined in step 2 for both batch and continuous processes. Two new set of indicators for batch processes have been developed: The Operation Indicator (compares the operation performance) and the Compound Indicator (indicate for each operation which compound is most likely to cause operational problems). These two set of indicators are applied to the batch processes analysis.
Operation Indicators were already described in Carvalho et. al, 2008. In table 1 a summary of the Compound Indicators is presented.

Table 1- Summary of compound indicators expressions

Indicator	Description	Operation	Definition
FVF	Free Volume Fraction	All	$FVF = \frac{V_{equi} - \sum_{i}^{I} \frac{F_{AP}^{i}}{\rho^{i}(t)}}{V_{equi}}$
TF	Time Factor	Mixer	$TF_{j,i} = \frac{1}{\frac{F_{AP}^{i}}{\sum_{AP}^{CO} F_{AP}^{i-1}}} \times \frac{t_j}{t_{total}}$
		Reactor	$TF_{j,i} = x\left(\frac{1}{\frac{F_{AP}^{i}}{\rho^{i}}} \times \frac{t_j}{t_{total}}\right) + (1-x)\left((1-z)\frac{1}{\frac{F_{AP}^{i}}{\rho^{i}}} \times \frac{t_j}{t_{total}}\right)$
		Heat Exchanger	$TF_{j,i} = \frac{F_{AP}^{i} \times cp^{i}}{\sum_{AP}^{CO} F_{AP}^{i-1} \times cp^{i-1}} \times \frac{t_j}{t_{total}}$
		Separation	$TF_{j,i} = \frac{F_{AP}^{i}}{\lvert Property^{c} - Property^{c} \rvert} \times \frac{t_j}{t_{total}}$
EF	Energy Factor	Mixer	$EF_{j,i} = \frac{F_{AP}^{i} \sum_{k}^{n} \Delta p_k^{i}}{\sum_{AP}^{n} F_{AP}^{i} \sum_{k}^{n} \Delta p_k^{i}} \times \frac{E_j}{\sum_j E_j}$
		Reactor	$EF_{j,i} = F_{AP}^{i} \times \Delta H_f \left[y \times \left(x \times \frac{\Delta H_f}{\sum_{AP}^{CO} \Delta H_f^{i-1}} + (1-x)\left(1 - \frac{\Delta H_f}{\sum_{AP}^{CO} \Delta H_f^{i-1}}\right)\right) + (1-y)\left(x \times \frac{\Delta H_f}{\sum_{AP}^{CO} \Delta H_f^{i-1}} \left(1 - \frac{\Delta H_f}{\sum_{AP}^{CO} \Delta H_f^{i-1}}\right) + (1-x)\frac{\Delta H_f}{\sum_{AP}^{CO} \Delta H_f^{i-1}}\right)\right] \times \frac{E_j}{\sum_j E_j}$
		Heat Exchanger	$EF_{j,i} = \frac{F_{AP}^{i} \times cp^{i}}{\sum_{AP}^{CO} F_{AP}^{i-1} \times cp^{i-1}} \times \frac{E_j}{\sum_j E_j}$
		Separation	$EF_{j,i} = \frac{F_{AP}^{i} \times Property^{i}}{\sum_{AP}^{CO} F_{AP}^{i-1} \times Property^{i-1}} \times \frac{E_j}{\sum_j E_j}$

In the previous table V_{equi} is the volume of the equipment, F_{AP} is the accumulation-path flowrate, ρ is the density, t is the time, υ is the stoichiometric coefficient, c_p is the heat capacity, E is the energy consumed and ΔHf is the heat of formation. The entire set of indicators show high potential for improvement when they present high values. The indicators values show the compounds responsible for the high energy consumption, the time used in a given operation or the volume occupancy. Summarizing, once this indicators are applied to each compound, those presenting high values compared with the others should be reduced in order to improve the process performance.
Through the values obtained for all indicators it is possible to identify the locations within the process where the mass/energy “paths” face “barriers” with respect to costs, benefits, or accumulation problems. These critical points “indicate” high potential for process improvements. The process impact analysis is carried out through the calculation of a set of sustainability metrics and/or the LCA analysis. The safety of the process is measured by the use of a set of safety indices. These two set of metrics are used in the evaluation of the new alternative when compared to the “base” process.

Step 4: Indicator Sensitivity Analysis (ISA) algorithm
In this step the target indicators are determined using the ISA algorithm. To apply this algorithm the indicators having the highest potential for process improvement with respect to sustainability and other criteria are first identified. Then an objective function such as gross-profit or process total cost is specified. Through a sensitive analysis the indicators that allow the best improvements in the objective function among the selected indicators are determined. The ones with the best improvements will be the design targets for the new

process design alternative.

Step 5: Process Sensitivity Analysis
A process sensitivity analysis with respect to the operational (parameters) variables, which influence the target indicators, is performed. The analysis identifies the operational variables that need to be changed to improve the process in the desired direction.

Step 6: Generation of new design alternatives
New alternatives are generated using a systematic analysis where a collection of synthesis algorithm can be used. This collection combines three different algorithms for process-product synthesis Jaksland and Gani, (1996), Harper, (2000) and D'Anterroches and Gani, (2005) into one integrated method.

Sustain-Pro
Based on the above methodology, a software (Sustain-Pro) has been developed to allow an easy application of the methodology for generation of more sustainable design alternatives. The inputs for Sustain-Pro are the mass and the energy balance data as well as the prices of the compounds present in the process. Sustain-Pro follows all the steps of the methodology, allowing thereby, the creation/evaluation of new alternatives strategy to any chemical process.

Insulin Production-Case Study
The insulin process is divided into four sections: 1) Fermentation, 2) Primary Recovery, 3) Reactions, and 4) Final Purification. In this paper the process analysis will be done exclusively to the fermentation part in order to illustrate the methodology potential. The flowsheet for the fermentation section is presented in the following figure.

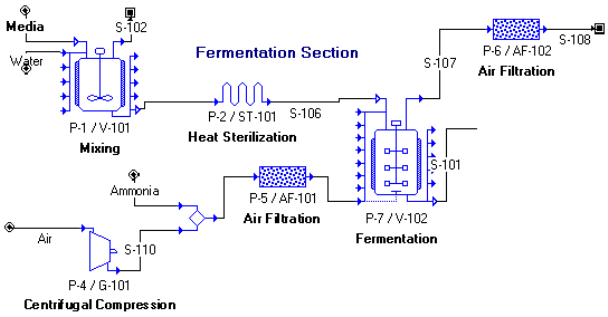

Figure 2: Fermentation section flowsheet

Step 1: Collect the steady state data
A *SuperPro Designer* simulation model of insulin synthesis plant was used as an example of the batch methodology's extension. The flowsheet of the process can be found in case studies provided by *SuperPro Designer* software package. The prices and costs are also specified by the *SuperPro Designer*.

Step 2: Flowsheet decomposition
The process involves 21 streams, 14 operations and 8 compounds. The flowsheet for the sequence of operations is represented in the following figure.

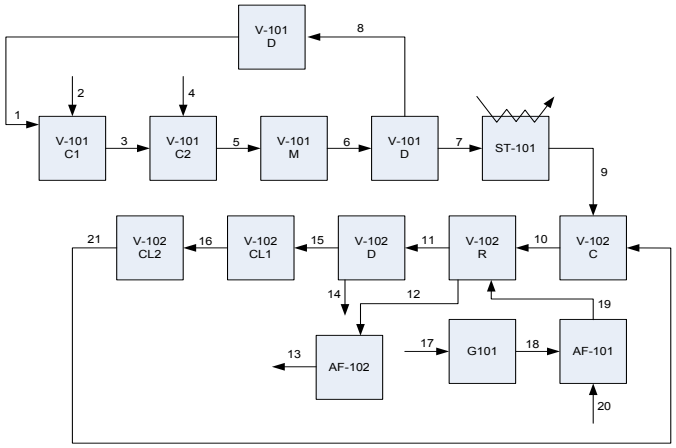

Figure 3: Insulin operations diagram

For this case study the operations diagram decomposition generated 16 closed-paths, 27 open-paths having flowrates greater than zero and 80 accumulation-paths (Sustain-Pro).

Step 3: Calculate the indicators, the sustainability and the safety metrics
For the entire set of flow-paths, the full-set of indicators were calculated and only the most sensitive indicators were selected. The sustainability metrics as well as the safety index were also calculated. For this case study the most sensitive indicators were the MVA – Material Value Added, for OP 7 and OP10 (see table 2). They presented very negative values, which mean that a lot of money was being spent with the entrance and the exit of glucose and salts respectively. The value of the target indicators should be increased. Regarding the batch indicators, TF in AP51 for Glucose was the most sensitive indicator and its value should be reduced in order to have a lower operational time.

Table 2- MVA values for the insulin process

Open Path	Compound	MVA (10^3\$/y)
OP7	Glucose	-7233
OP10	Salts	-1757

Step 4: Indicator Sensitivity Analysis (ISA) algorithm
Through the ISA algorithm it was found out that among the two selected indicators the MVA indicator related with OP7 was the most sensitive and consequently the one that should be primarily improved.

Step 5: Process sensitivity Analysis
Making a sensitivity analysis to the operational parameters influencing the target indicators it was verified that the most significant parameter was the reduction of the flowrate for OP7.

Step 6: Generation of new design alternatives
To reduce the OP7 flowrate, the recycle of the glucose needs to be considered. To recycle glucose a separation needs to be inserted in order to separate/recover the raw material. Through the use of the synthesis method to identify new separation processes, Jaksland and Gani, (1996), it was verified that a filter and an evaporation unit need to be inserted in order to recover the glucose.
Regarding the compound indicators for the batch operations, the TF presented some problems in the reaction operation for the glucose, once its value was higher than the other values. This means that the glucose was limiting the rate of the reaction. Consequently, it would be better to operate with a greater excess of glucose.
Summarizing, the new design alternative consisted of recycling the glucose. With this new alternative the profit increased 1.04%, the water and the energy metrics per value added

improved by 1.03% and finally the material metrics improved by 2.55% and 3.26 respectively per kg of final product and per value added. All the other parameters remained constant. The target indicators improved by 100%.

Conclusions and Future Work

The development of a systematic and generic indicator-based methodology for continuous and batch process analysis and for generating sustainable processes improvements has been presented and highlighted. With the development of corresponding software (Sustain-Pro), the application of the methodology to continuous processes has become easier and wide. This methodology has been applied to a number of case studies involving well known processes such as the HDA-process, MTBE, VCM, ammonia production, natural gas purification plant and many more (details of these case studies can be obtained from the authors). Current and future work will further develop the methodology to incorporate more features to handle various types of batch and continuous processes as well as the corresponding software (Sustain-Pro). There will be also collaboration with the Institute of Chemical and Engineering Sciences to join two softwares, SustainPro and ENVOPExpert, (Halim and Srinivasan, 2002) in order to generate a more powerful tool, which generates optimal sustainable new design alternatives.

Acknowledgment

The authors gratefully acknowledge financial support from Fundação para a Ciência e a Tecnologia (under Grant No. SFRH/BD/24470/2005).

References

Carvalho, A., Matos, H. A., Gani. R., 2007, Process Safety and Environmental Protection, accepted to publication

Carvalho, A., Matos, H.A., Gani, R., 2008, Systematic Methodology for Continuous/ batch processes: analysis and generation of sustainable alternatives, *Procedings of Foundations of Computer-Aided Process Operations*

D'Anterroches, L., Gani, R., 2005, The Reverse Approach for Synthesis and Design of Chemical Products & Processes, *Procedings of 7th WCCE*

Harper, P.M. Gani, R., 2000, A Multi-Step and Multi-Level Approach for Computer Aided Molecular Design, *Comput. Chem. Eng*, 24, 2-7, 677-683.

Jaksland, C., Gani, R. and Lien, K., 1996, An integrated approach to process/product design and synthesis based on properties-process relationship, *Comput. Chem. Eng*, 20: 151-156.

Jensen, N.; Coll, N.; Gani, R., 2003, An integrated computer-aided system for generation and evaluation of sustainable process alternatives, Clean Techn Environ Policy, 5: 209–225.

Halim, I. and Srinivasan, R., 2002, An Integrated Decision Support System for Waste Minimization Analysis in Chemical Processes, Environmental Science and Technology, 36: 1640-1648

Halim, I. and Srinivasan, R., 2006, Systematic Waste Minimization in Chemical Processes: Part III. Batch Operations, Industrial and Engineering Chemistry Research, 45: 4693-4705.

Houghton, C., Sowerby, B. and Crittenden, B., 1996, Clean Design of Batch Processes, in Case Studies in Environmental Technology, Sharratt, P. and Sparshott, M. (eds) (Institution of Chemical Engineers, Rugby, Warwickshire, UK), pp 59-71.

Uerdingen, E., Gani, R., Fischer, U., Hungerbühler, K., 2003, A New Screening Methodology for the Identification of Economically Beneficial Retrofit Options in Chemical Processes, AIChE J., 49: 2400-2418.

Proceedings of the 10th International Chemical and
Biological Engineering Conference - CHEMPOR 2008
Braga, Portugal, September 4-6, 2008
E.C. Ferreira and M. Mota (Eds.)

Modeling of Orange II advanced biodecolourisation in upflow stirred packed-bed reactor

Gergo Mezohegyi[1], Christophe Bengoa[1], Frank Stuber[1], Josep Font[1], Agustí Fortuny[2], Azael Fabregat[1]*

[1] CREPI Group, Departament d'Enginyeria Química, ETSEQ, Universitat Rovira i Virgili, Av. Països Catalans 26, 43007 Tarragona, Catalunya, Spain.

[2] Departament d'Enginyeria Química, EPSEVG, Universitat Politécnica de Catalunya, Av. Víctor Balaguer s/n, 08800 Vilanova i la Geltrú, Catalunya, Spain.

Keywords: Azo dye, biological activated carbon, packed-bed reactor, reduction
Topic: Catalysis and reaction engineering

Abstract

The anaerobic decolourisation of azo dye Orange II (O-II) was studied in a continuous upflow stirred packed-bed reactor (USPBR) filled with biological activated carbon (BAC). A model was developed involving both heterogeneous catalysis and biological decolourisation. First-order, autocatalytic and Michaelis–Menten kinetics were found to describe the decolourisation process rather well at lower initial dye concentration. O-II showed significant inhibition effect to biomass beyond inlet dye concentrations of 300 mg L^{-1}. Expanding Michaelis–Menten kinetics by a substrate inhibition factor resulted in a model giving good fitting to experimental points, independently on the initial colourant concentration. Processing at very low hydraulic residence time together with higher initial dye concentration resulted in toxicity to bacteria.

1 Introduction

A typical drawback of azo dye colouration – mainly occuring in textile industry – is that large amounts of the dyestuff are directly spilt to wastewater. Discharging dyes into the hydrosphere can cause environmental damage as they give water undesirable color and reduce sunlight penetration (Al-Degs et al., 2008), with some dyes and their degradation products also being toxic or carcinogenic. Considering both the volume generated and the effluent composition, textile industry wastewater is rated as the most polluting amongst all industrial sectors (Sandhya and Swaminathan, 2006). Relevant factories have deficiencies of treating efficiently these effluents on industrial scale, particularly at higher dye concentrations and at lower energy consumptions.

Bioremediation-based technologies for treating azo dye wastewater have attracted interest since they are both economic and environmentally friendly. One possible strategy for efficient biomineralisation of these azo compounds is a sequential anaerobic–aerobic process (Kalyuzhnyi and Sklyar, 2000). However, the unspecific anaerobic reduction of many azo dyes usually proceeds rather slowly. To overcome this problem, by using redox mediators, such as quinoid compounds (Rau et al., 2002) during the reduction, anaerobic biodegradation can be enhanced resulting much higher removal rates. By immobilizing the electron mediator in the bioreactor, the problem of continuous dosing of the redox compound can be avoided resulting lower process costs. Activated carbon as a possible solid redox mediator containing surface quinonic structures, was reported to be enable to accelerate azo dye reduction (Van der Zee et al., 2003; Mezohegyi et al., 2007a).

To our knowledge, packed bed-type reactors using biological activated carbon (BAC) system have never been applied for anaerobic azo dye decolourisation by other authors. In our previous study (Mezohegyi et al., 2007a) the results cleared that comparing to other continuous and biological processes treating azo dyes, continuous

* Corresponding author. Tel + 34-977-559643. E-mail:afabrega@urv.cat

upflow packed-bed reactor (UPBR) with BAC seemed to be one of the most effective systems for anaerobic azo dye biodegradation. It was also found (Mezohegyi et al., 2007b) that the application of special stirring in the carbon bed resulted in an increase of azo dye bioconversion compared to unstirred reactor system with ensuring high dye degradation rates at very short space times/hydraulic residence times. In recent study, the anaerobic decolourisation of an acid azo dye in continuous upflow stirred packed-bed reactor (USPBR) was investigated. Different decolourisation models were compared and the effects of initial dye concentration on biodegradation were discussed.

2 Materials and methods

2.1 Chemicals

The azo dye Orange II (O-II) sodium salt (dye content 99%, Sigma, ref. O8126) was selected as the model colourant. Sodium acetate (99%, Aldrich, ref. 11019-1) was used as co-substrate being both the carbon source for sludge and electron donor for azo reduction. Activated carbon (Merck, granules of 2.5 mm, ref. 1.02518.1000) was used as catalytic support material in the upflow stirred packed-bed reactor. Activated carbon was crushed and granules of 25-50 mesh size were separated, washed with distilled water, dried at 104°C for 15 h and stored under normal conditions. The basal media containing microelements accorded with the one used in our previous study (Mezohegyi et al., 2007a).

2.2 Upflow stirred packed-bed reactor setup

Figure 1 shows schematically the continuous and anaerobic experimental system. The upflow stirred packed-bed reactor has a diameter of 15 mm with a volume of 10 mL. It is filled with the mixture of 10 g of carborundum granules as inert and 250 mg of activated carbon (AC) with size of 25-50 mesh. The packed-bed porosity is about 0.3. Two filters were placed into the top and bottom of the reactor to prevent washing out of AC. The temperature was kept constant at 35°C. The entering feed was 100 mg L^{-1} azo dye solution containing 200 mg L^{-1} sodium acetate and the basal media. The flow rate of the feed was varied between 25 and 350 mL h^{-1} and was ensured by a micro pump (Bio-chem Valve Inc., ref. 120SP2420-4TV). The anaerobic condition in the feeding bottle (5 L) was maintained by both cooling of the solution (at 5°C) and bubbling of helium. The redox potential was continuously monitored (measured where the outlet immediately left the USPBR) and remained below -500 mV (referred to Ag^{+}/AgCl electrode). The reactor was built together with a stirring system that makes possible to apply a very fine and slow agitation (1 revolution per hour) in the biological activated carbon bed that was established in the same way as described in (Mezohegyi et al., 2007a).

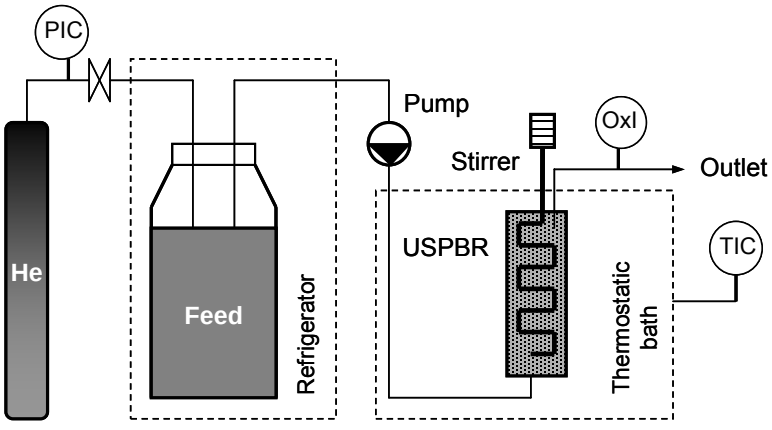

Figure 1. Anaerobic upflow stirred packed-bed reactor setup.

2.3 Analytical methods

Quantitative determination of Orange II and acetate in the outlets was done by HPLC on a C_{18} Hypersil ODS column in a gradient of methanol–water mobile phase with a flow rate of 1 mL min^{-1}. O-II was determined at 487 nm and acetate at 210 nm.

3 Results and discussion

3.1 Modeling O-II anaerobic biodegradation in USPBR

3.1.1 Determination of reaction rate

Kinetic models with a specified reaction rate were developed involving both heterogeneous catalysis and biological decolourisation in the reactor. The mole balance for the packed-bed reactor is given by (eq. 1):

$$\frac{dF_{AZO}}{dm_C} = -r'_{AZO} = \frac{d(c_{AZO} \cdot F_V)}{d(\tau \cdot F_V \cdot \rho)} \quad (1)$$

where F_{AZO} (mmol min^{-1}) is the molar flow of azo dye solution, m_C (g) is the mass of catalyst in the reactor, r'_{AZO} (mmol min^{-1} g^{-1}) is the rate of the reaction, c_{AZO} (mmol L^{-1}) is the dye concentration, F_V (L min^{-1}) is the volumetric flow, τ (min) is the space time and ρ (g L^{-1}) is the density of solution. If the flow rate of azo dye solution is kept constant and the density difference between the dye solution and water is neglected, the reaction rate r_{AZO} (mmol min^{-1} L^{-1}) will finally be (eq. 2):

$$\frac{dc_{AZO}}{d\tau} = -r_{AZO} \quad (2)$$

3.1.2 Kinetic models

The upflow stirred packed-bed reactor provided reproducible data to make kinetic modeling of O-II biodegradation possible. More than one kinetic model was found to describe rather well Orange II anaerobic biodegradation, namely, first-order model, Michaelis–Menten (MM) model and a second-order autocatalytic model (Van der Zee et al., 2000). Table 1 shows the kinetic parameters encountered for these models. The simple first-order model and the second-order autocatalytic model fit well the experimental points (data not shown). Latter one can be proved by the autocatalytic nature of 1-amino-2-naphthol, being one of the anaerobic degradation products of Orange II. On the other hand, Michaelis–Menten model is expected to describe O-II biodecolourisation since it is a biological process and, also, the amount of consumed acetate by bacteria – providing the electrons to azo reduction – is directly proportional to dye conversion. Indeed, MM kinetics seems to be applicable for modeling Orange II degradation in our reactor system (Fig. 2). According to the very good fitting of all models, the reaction rate predicted by all then should be similar. This is accomplished when comparing the first-order and autocatalytic model, since the first-order constants are similar and the second part of the autocatalytic model gives relatively small values because of the second-power function of the small dye concentration used. The reaction rates of the first-order and MM model are similar as well, since the first-order constants are similar and the Michaelis-constant is rather big relatively to the outlet dye concentrations, thus MM reduces to first-order model in this case.

One of the most frequent models having been found to describe dye biodegradation in different reactor systems are Monod-types and some further include dye adsorption onto biologically activated carbon (Walker and Weatherley, 1997). On the other hand,

many azo dyes may have strong adsorption affinity to activated carbons depending on the surface chemistry of the carbon (Pereira et al., 2003). It can be interesting to mention that the so-called Langmuir–Hinshelwood equation – describing the rate law for surface catalysed reactions where the overall reaction rate is proportional to the surface coverage of the substrate over the catalyst – is analogous with the MM model and differences only are between the kinetic constants. Hereby, the former equation may also be used to describe our system suggesting that strong adsorption capacity of the carbon for O-II can play an important role during this complex biological decolourisation process.

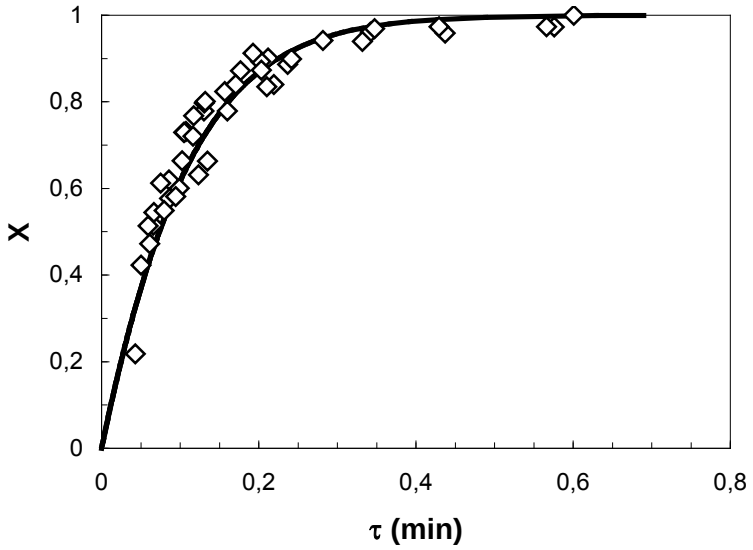

Figure 2. Kinetic modeling of Orange II anaerobic biodegradation in upflow stirred packed-bed reactor: Orange II conversion (X) in the function of space time (τ, min); line shows the fitting to Michaelis–Menten model.

3.2 Substrate inhibition and toxicity effects

50 days after measuring experimental points in USPBR, the reproducibility of the reactor system was checked by measuring O-II conversions again, at certain space times. The previously determined Michaelis–Menten model fitted still well the newly measured points. After that, the inlet dye concentration was increased from 100 mg L^{-1} to 300 mg L^{-1} to check if higher O-II concentrations may have inhibition or toxicity effects to the biomass. Figure 3 shows that the MM model set before shows significant deviation from experimental points at initial concentration of 300 mg L^{-1}. This suggests that O-II possesses concentration-dependent inhibition effects for bacteria in the reactor. For this, MM model was expanded by an inhibition factor and this model with 3 kinetic constants describes well the degradation process, independently on the initial dye concentrations (Fig. 3). The substrate inhibition was found to be significant since the value of the constant ratio k_i/k_2 is less than 10. Table 1 also shows the standard deviation value associated to experimental points involving both initial dye concentrations of 100 and 300 mg L^{-1}. However, the recalculated kinetic constants – including both inlet concentrations – differ from the former ones. This can be explained by having not only inhibition but also toxicity effects to the biomass at higher inlet dye concentrations. Indeed, using very high flow rate in the reactor at 300 mg L^{-1} of initial dye concentration resulted toxicity, i.e. the redox potential was increased from -485 mV up to -180 mV in 3 hours after changing the flow of solution from 150 to 260 mL h^{-1}. Then, to avoid the irreversible deactivation of microbes, the flow was set back to 55 mL h^{-1} and, in addition, after 2 days the initial O-II concentration was changed back to 100 mg L^{-1}. After 5 more days, the redox potential decreased back to -486 mV and O-II conversion nearly returned to the value as it was before the toxicity to biomass (Fig. 3).

Table 1
Kinetic data of models used for anaerobic Orange II degradation

model type	model equation	kinetic constants	SD[a]
first-order	$r_{AO7} = -k \cdot c_{AO7}$	$k = 10.1\ min^{-1}$	0.048
autocatalytic	$r_{AO7} = -k_1 \cdot c_{AO7} - k_2 \cdot c_{AO7} \cdot (c_0 - c_{AO7})$	$k_1 = 10.8\ min^{-1}$ $k_2 = 1.05\ L\ mmol^{-1}\ min^{-1}$	0.047
Michaelis–Menten	$r_{AO7} = -\frac{k_1 \cdot c_{AO7}}{k_2 + c_{AO7}}$	$k_1 = 10.8\ mmol\ L^{-1}\ min^{-1}$ $k_2 = 0.94\ mmol\ L^{-1}$	0.054
Michaelis–Menten with substrate inhibition	$r_{AO7} = -\frac{k_1 \cdot c_{AO7}}{k_2 + c_{AO7} + \frac{{c_{AO7}}^2}{k_i}}$	$k_1 = 11.7\ mmol\ L^{-1}\ min^{-1}$ $k_2 = 1.15\ mmol\ L^{-1}$ $k_i = 4.38\ mmol\ L^{-1}$	0.048
		$k_1' = 6.18\ mmol\ L^{-1}\ min^{-1}$ $k_2' = 0.55\ mmol\ L^{-1}$ $k_i' = 0.09\ mmol\ L^{-1}$	0.056[b]

[a] Standard deviation associated to the model fitting: $SD = \sqrt{\Sigma\left(X - X^{MOD}\right)^2 / (n-1)}$ where n is the number of experimental points.

[b] Standard deviation associated to k' values calculated from experimental points involving both initial dye concentrations of 0.286 and 0.857 mmol L^{-1} (100 and 300 mg L^{-1}, respectively).

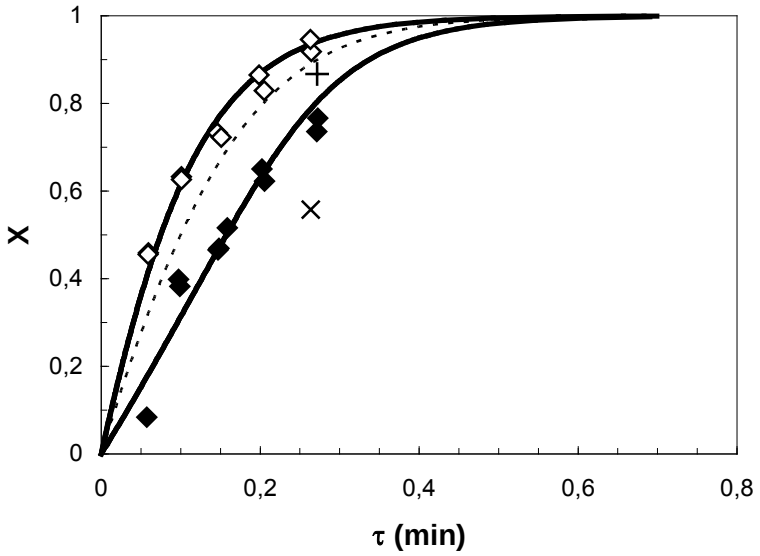

Figure 3. Substrate inhibition and toxicity effects during Orange II decolourisation in upflow stirred packed-bed reactor: (◇) shows repeated experimental points with initial O-II concentration of 100 mg L^{-1}; (◆) shows experimental points with initial O-II concentration of 300 mg L^{-1}; (×) shows O-II conversion, 1 day after biomass toxicity; (+) shows O-II conversion, 6 days after biomass toxicity; dotted line represents the Michaelis–Menten model at initial Orange II concentration of 300 mg L^{-1} supposing no substrate inhibition; continuous lines show the fitting to Michaelis–Menten model with substrate inhibition at initial O-II concentrations of 100 and 300 mg L^{-1}.

4 Conclusions

To the best of our knowledge, a continuous upflow stirred packed-bed reactor with biological activated carbon was applied for the first time for anaerobic azo dye decolourisation. The USPBR provided reproducible data to make kinetic modeling of O-II biodegradation possible. First-order, autocatalytic and Michaelis–Menten models were all found to give good fittings to experimental points of dye conversion at lower inlet dye concentration. On the other hand, O-II showed significant inhibition effects to

the biomass at higher initial concentration and, also, processing at very low hydraulic residence times together with high initial dye concentration resulted in toxicity to bacteria. It can be assumed that a general model, describing the anaerobic biodegradation of diverse azo dyes in USPBR-BAC system, will be made up of the combination of dye inhibition and possible autocatalytic effects together with Michaelis–Menten kinetics.

Acknowledgements

The authors gratefully acknowledge the fellowship from Universitat Rovira i Virgili, the financial support provided by the Spanish Ministry of Science and Education (CTM2005-01873) and by the Catalan government (2007ITT-00008).

References

Al-Degs, Y.S., El-Barghouthi, M.I., El-Sheikh, A.H., Walker, G.M. (2008). Effect of solution pH, ionic strength, and temperature on adsorption behavior of reactive dyes on activated carbon. *Dyes and Pigments*, 77, 16-23.

Kalyuzhnyi, S., Sklyar, V. (2000). Biomineralisation of azo dyes and their breakdown products in anaerobic-aerobic hybrid and UASB reactors. *Water Science and Technology,* 41 (12), 23-30.

Mezohegyi, G., Kolodkin, A., Castro, U.I., Bengoa, C., Stuber, F., Font, J., Fabregat, A., Fortuny, A. (2007a). Effective anaerobic decolorization of azo dye Acid Orange 7 in continuous upflow packed-bed reactor using biological activated carbon system. *Industrial & Engineering Chemistry Research,* 46, 6788-6792.

Mezohegyi, G., Bengoa, C., Stuber, F., Font, J., Fabregat, A., Fortuny, A. (2007b). Innovative reactor design for anaerobic decolorization of azo dyes. *Proceedings of 10th International Conference on Environmental Science and Technology,* A970-977.

Pereira, M.F.R., Soares, S.F., J.J.M. Órfão, J.J.M., Figueiredo, J.L. (2003). Adsorption of dyes on activated carbons: influence of surface chemical groups. *Carbon*, 41, 811-821.

Rau, J., Knackmuss, H-J., Stolz, A. (2002). Effects of different quinoid redox mediators on the anaerobic reduction of azo dyes by bacteria. *Environmental Science & Technology,* 36, 1497-1504.

Sandhya, S., Swaminathan, K. (2006). Kinetic analysis of treatment of textile wastewater in hybrid column upflow anaerobic fixed bed reactor. *Chemical Engineering Journal*, 122, 87-92.

Van der Zee, F.P., Lettinga, G., Field, J.A. (2000). The role of (auto)catalysis in the mechanism of an anaerobic azo reduction. *Water Science and Technology*, 42 (5-6), 301-308.

Van der Zee, F.P., Bisschops, I.A.E., Lettinga, G., Field, J.A. (2003). Activated carbon as an electron acceptor and redox mediator during the anaerobic biotransformation of azo dyes. *Environmental Science & Technology,* 37, 402-408.

Walker, G.M., Weatherley, L.R. (1997). A simplified predictive model for biologically activated carbon fixed beds. *Process Biochemistry*, 32 (4), 327-335.

Proceedings of the 10th International Chemical and
Biological Engineering Conference - CHEMPOR 2008
Braga, Portugal, September 4-6, 2008
E.C. Ferreira and M. Mota (Eds.)

Photocatalytic Paint Production for the Abatement of Nitrogen Oxides

C. Águia[1], Francesc X. Llabrés i Xamena[2], Esther Dominguez[2], Hermenegildo García[2], L. M. Madeira[1], A. Mendes[1*]

[1] LEPAE – Departamento de Engenharia Química, Faculdade de Engenharia - Universidade do Porto, Rua Dr. Roberto Frias s/n, Porto, 4200-465, Portugal

[2] Instituto de Tecnología Química CSIC-UPV, Universidad Politécnica de Valencia, Camino de Vera s/n, 46022 Valencia, Spain

Keywords: Nitrogen oxides, photocatalysis, TiO_2, photocatalytic paint
Topic: Sustainable process-product, development through green chemistry.

Abstract

In the present paper it is compared the performance of most of the commercially available photocatalysts (based on titanium dioxide), as well as synthesized new ones (TiO_2 encapsulated in adsorbents), on photooxidizing NO. Commercial samples are also tested when incorporated in a water-base paint coating. Lower NO conversions achieved with the encapsulated photocatalytic TiO_2 materials (TiO_2 content about 1 wt.% except for zeolite Y with two exchanges steps) than with the commercial ones suggest the possible influence of the intrinsic characteristics of the encapsulated materials on the photo-activity. It is observed a strong synergetic effect between the adsorbent, such as zeolite Y, and the TiO_2, in mechanical mixtures. In fact, a film produced from mixtures of P25 and zeolite Y, with only 15 wt.% in P25, originated approximately the same values of NO conversion (55 %) and ionic selectivity (35 %) than a film with 100 wt.% of P25. It is also concluded that by using a paint with a pigment volume concentration (PVC) above the critical value, hosting 10 wt.% of photocatalyst, it is possible to photo oxidize approximately 50 % of NO with approximately 30 % of ionic selectivity, in operating conditions close to those suggested in standard ISO 22197-1:2007(E).

1. Introduction

NOx is a precursor for urban smog and tropospheric ozone formation that are related with healthy damages (EPA, 1998). Therefore, improvements in de-NOx technologies are needed.

Photocatalysis has been tested at lab scale in the NOx abatement and photocatalytic construction materials, such as paints, have been pointed as a possible solution to help in the de-NOx of the environment (e.g. Strini *et al*., 2005). However, for successful application of this technology it is important to protect the constituents of these construction materials towards the photocatalytic process occurring in its matrix. In this line some studies have been performed and basically two strategies can be identified in the literature: i) decrease the amount of incorporated photocatalytic TiO_2 and select constituents with higher chemical stability (Motohashi and Inukai, 2007); and ii) use of encapsulated TiO_2 particles (Cosa *et al.*, 2002). Encapsulating TiO_2's particles shows other attractive advantages, such as concentrate the target compounds to abate, over the product ones, by adsorption, increasing therefore the reaction rate (Corma and García, 2004).

At our lab, it is aimed to produce a photocatalytic paint with chemical stability towards

* Corresponding author. Tel + 351-225-081-695. E-mail:mendes@fe.up.pt

photooxidation and obeying to the parameters of the paint industry regarding its properties. With this and the above-mentioned issues in mind, TiO_2 was incorporated inside the porous structure of zeolites Y and USY (*zeolyst Inc*.) and montmorillonite K-10 (*Sigma-Aldrich*). The photo-activity of these composite materials was tested in powder pressed films and discussed taking into account some of their intrinsic characteristics. Comparison was made with the photo-activity of commercial photocatalytic TiO_2 samples. These commercial materials were also tested when incorporated in an exterior high quality paint above the critical Pigment Volume Concentration (CPVC).

2. Experimental procedure

2.1. Encapsulated photocatalysts, synthesis and characterization

The experiments described below aim at testing the photo-activity of encapsulated TiO_2 on various adsorbent materials (hereafter named as encapsulated "photocatalytic" TiO_2) and compare their performance with that of commercial photocatalytic TiO_2, which are plain, mostly anatase, TiO_2 particles. The encapsulated photocatalytic materials were produced by ion exchange using $(Ti{=}O)K_2(C_2O_4)\cdot H_2O$ as TiO_2 precursor, as described by Cosa *et al*. (2002). The adsorbents used as support were montmorillonite k-10 (mK-10) from *Sigma-Aldrich* and Zeolites Y and USY from *Zeolyst Inc*. These materials were exchanged once or twice. The first exchange was performed with a 0.2 M solution in TiO_2 precursor and the second with a 0.6 M solution. The encapsulated photocatalyic TiO_2 obtained by one or two ion exchanges were denoted as TiO_2@support and $(TiO_2)_2$@support, respectively, with "support" being USY, Y or mk-10. "(P25+Y)_15 wt.% TiO_2" refers to the material produced from the mechanical mixture of zeolite Y and P25 TiO_2 (15 wt.% in P25).

Elemental analysis was performed by ICP using a Varian 715-ES instrument. The surface area and porosity was studied by nitrogen adsorption at 77 K using a Micromeritics ASAP 2010. RAMAN analyses were performed with a Renishaw instrument in order to investigate the anatase and rutile-related bands. Diffuse reflectance UV-Vis spectroscopy (Varian Cary 5) was also performed targeting to evaluate the light absorption spectrum and to measure the related optical band-gap.

Commercial photocatalytic TiO_2 here used for comparison are the following: P25, from *Degussa;* PC500, from *Millennium;* VLP7000, from *Kronos;* UV100, from *Sachtleben; and* AMT100, from *Tayca.*

2.2. Photocatalytic films application

Powder pressed films and paint films were tested in the setup described below. Powder pressed films were produced by pressing the powder to the base of the reactor, applying 20 bar for 7 min. Two film sizes were used, 10 x 5 cm^2 and 6 x 5 cm^2, depending on the available amount of sample. The name of the experimental run indicates the area used (see section 3.2). Paint films were produced using a draw down bar. It was used an exterior water-base paint above CPVC and produced accordingly to the formulation kindly supplied by CIN, S.A. The original formulation was modified by replacing a portion of the TiO_2 used for opacity (which it is not photoactive), by the photocatalytic one, in order to produce a photocatalytic paint with ca. 10 wt.% of photocatalytic TiO_2.

2.3. Setup and photocatalytic experiments

The operating conditions and construction of the setup were inspired on standard ISO 22197-1:2007(E). Basically it comprehends a thermostatic cabinet where the reactor and the feed system are assembled. In the rectangular base of the reactor it is applied the photocatalytic film to be tested. A photoluminescent NO and NO_2 analyser (*Thermoelectron*

42C) is used to read the concentration of these species. The irradiance, relative humidity (RH), NO concentration at the inlet of the reactor (NO_{in}) and temperature were set to 10 $W \cdot m^{-2}$ (UV BLB lamp 365 nm – *Vilbert Lourmat*), 50 %, 1 ppmv (in ArK), and 25 ºC, respectively. Total gas flow rate used was 0.7 $L_N \cdot min^{-1}$.

3. Results and discussion

Photocatalysis of NOx can proceed as reduction and/or as oxidation. However, photo-reduction is not probable to occur in the presence of water and oxygen. Also, it is not referred the formation of N_2O in similar systems (Devahasdin *et al.*, 2003). NO photooxidation should then proceed to NO_2 and then to NO_2^- or NO_3^-. NO conversion (X_{NO}) and selectivity towards NO_2^- and NO_3^- (hereafter referred as ionic selectivity - S_{ionic}) were calculated using the following equations:

$$X_{NO} = \left(\frac{NO_{in} - NO_{out}}{NO_{in}} \right) \times 100 \qquad S_{ionic} = \left(\frac{(NO_{in} - NO_{out}) - NO_{2_{out}}}{NO_{in} - NO_{out}} \right) \times 100$$

where NO_{in} stands for the concentration of NO at the inlet of the reactor and NO_{out} and $NO_{2,out}$ to the NO and NO_2 outlet concentrations, respectively.

3.1. Characterization of the photocatalysts

Raman studies were performed in order to identify the typical rutile or anatase structures of TiO_2. However, typical peaks, as detected for P25, were not observed for the encapsulated materials. X-ray diffraction also did not allow the identification of typical peaks of crystal structures of TiO_2. Such fact does not mean that a crystalline structure does not exist; actually, a photocatalytic activity was detected, as shown later on. The analysis of the diffractogram of zeolite Y with one and two exchanges (Fig. 1a) reveals complete loss of crystallinity. Diffuse reflectance was performed and has also shown the light absorption characteristic of TiO_2. However, due to a low signal to noise ratio it was impossible to calculate the band-gap.

Table 1 presents the weight percentage of Ti in each sample, and the BET surface area, obtained by ICP and nitrogen adsorption isotherms performed at 77 K, respectively. Results of $(TiO_2)_2$@Y show a very large amount of incorporated Ti, which can be the cause of the loss of crystallinity shown in Fig. 1a. Such loss produces a strong decrease in the BET surface area of zeolite Y from the first to the second ion exchange steps (Table 1 and Fig. 1b). A decrease was also noticed in the other supports tested, however much less pronounced than with zeolite Y.

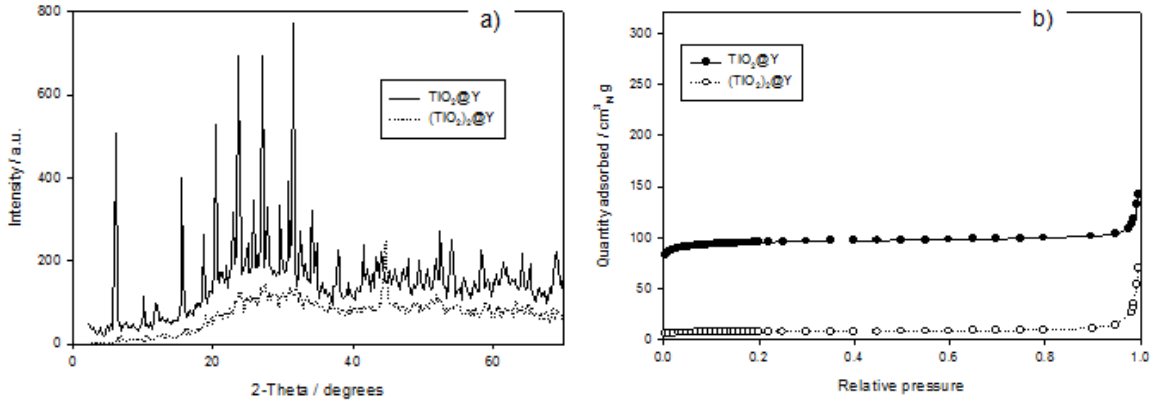

Figure 1 – X-ray diffraction patterns (a) and nitrogen adsorption isotherms performed at 77 K (b) for the encapsulated photocatalysts into zeolite Y.

Table 1 – Results of elemental analysis performed by ICP, and BET surface areas obtained by nitrogen adsorption isotherms performed at 77 K.

	TiO_2@Y	$(TiO_2)_2$@Y	USY	$(TiO_2)_2$@USY	mK-10	TiO_2@mK-10	$(TiO_2)_2$@mK-10
Ti (wt.%)	0.96	10.68	0.07	1.12	0.28	0.60	0.89
BET surface area (m^2 g^{-1})	311	25	558	519	269	264	259

3.2. Photocatalytic experiments

Table 2 presents the mass of each photocatalytic material used. The names of the experiments code the material tested and the area of the film. For example, the first test in Table 2 was made with PC500 titania in a film of 10 x 5 cm^2. In the case of the photocatalyst P25, three replicates were performed with different masses ("P25_10x5_exp1" and two following experiments). The masses of TiO_2 employed in powder pressed films were obtained by direct weighting, in the case of commercial photocatalysts, and were estimated, taking into account the amount of Ti exchanged, in the case of the encapsulated materials.

Figure 2 summarizes the NO conversions and ionic selectivities (taken at steady state). Experiments with paint films are denoted with the suffix "paint".

From Table 2 one can see that there is a relatively large variation in the photocatalytic masses from experiment to experiment, due to the associated difficulties on its control. However, experiments "P25_10x5_exp1", "P25_10x5_exp2" and "P25_10x5_exp3" show that for the mass range used this variable has little influence on the performance of the photocatalyst (cf. Fig. 2). Actually, the mass increments on these tests were achieved by increasing the thickness of the same film, meaning that there is a critical photocatalytic thickness beyond which no further improvements are achievable. The photocatalyst film effective area is, on the other hand, a very important variable. Figure 2 highlights this issue by comparison of experiments "P25_10x5_exp1" with "P25_6x5", which films have the same thickness but different areas; the later shows a NO conversion of 50 % vs. 80 % in the first one. Figure 2 puts into evidence that commercial titania samples provide, when used alone (pressed powder films) NO conversions above 50 %, except for the P25_6x5 film, due to the reasons just mentioned (smaller area). It is thus worth of noting that although the film area is the same as in the experiment where it is mechanically mixed with zeolite Y - "(P25 + Y)_15 wt.% TiO_2_6x5" (Table 2), the latter exhibits a similar NO conversion (Fig. 2), in spite of its much lower photocatalyst surface that is possibly exposed to radiation (as a consequence of a TiO_2 load of only 15 wt.%). This indicates that the adsorbent is playing a significant role on the photoactivity, an issue that needs however to be further investigated.

Regarding encapsulated materials, it is possible to see that the increase in the number of ion exchange cycles leads to better performances (Fig. 2). This can be related with either the increase in the Ti content of the samples (Table 1) or with the TiO_2 particles size (thus decreasing the so-called quantum size effect – blue shift) (Corma and García, 2004). Indeed, for zeolite Y only after a second exchange step some activity is noticed, which can be ascribed to the particle diameter increase leading to absorption of radiation in the wavelength range of the UV lamp used (> 300 nm), and being responsible for the structure destruction above-mentioned (Fig 1a). However, further investigation must be performed in order to confirm such fact. In general, performances reached with the encapsulated materials are quite low. Even so, it must be noticed the lower masses of TiO_2 per surface area of film when compared with the powder pressed films of commercial TiO_2 (Table 2). Comparing with the performance of paint films (with commercial TiO_2) it is possible to see that either the environment of the TiO_2 and/or the photocatalytic particle properties play an important role. Nevertheless, encapsulated materials are promising as long as one can still increase the Ti content (case of the mK-10 support) and the radiation absorption spectra by means of

sensitizing/doping.

Table 2 – Photocatalytic materials and estimated TiO_2's mass in each experiment.

		Powder pressed films		Paint films
	Experiment	**Mass of powder pressed (g)**	**Estimated mass of TiO_2 (g cm^{-2})**	**Estimated mass of TiO_2 (g cm^{-2})**
Commercial TiO_2	PC500_10x5	3.02	0.0604	0.0012
	UV100_10x5	3.29	0.0658	0.0012
	VLP7000_10x5	2.89	0.0578	0.0017
	AMT100_10x5	3.35	0.0670	0.0013
	P25_10x5_exp1	0.67	0.0134	0.0012
	P25_10x5_exp2	0.92	0.0184	n.p.
	P25_10x5_exp3	1.18	0.0236	n.p.
	P25_6x5	0.44	0.0147	n.p.
	(P25+Y)_15 wt.% TiO_2_6x5	1.00	0.0050	n.p.
Encapsulated photocatalytic TiO_2	$(TiO_2)_2$@Y_6x5	1.60	0.0097	n.p.
	TiO_2@Y_6x5	1.61	0.0010	n.p.
	$(TiO_2)_2$@USY_6x5	1.32	0.0010	n.p.
	$(TiO_2)_2$@mK-10_6x5	1.23	0.0007	n.p.
	TiO_2@mK-10_6x5	1.78	0.0007	n.p.

(n.p. – not-performed)

Paint films have lower photocatalytic activity than the corresponding powder films (Fig. 2). However it must be noticed the lower mass of TiO_2 per surface area exposed to the light. NO conversions were approximately 45-55 % and ionic selectivities around 40 % (with exception for paint films loaded with VLP7000 and AMT100, which originate ionic selectivities of only ca. 20 %). The performances reached with most paint films are worth mentioning, being thus promising for further studies.

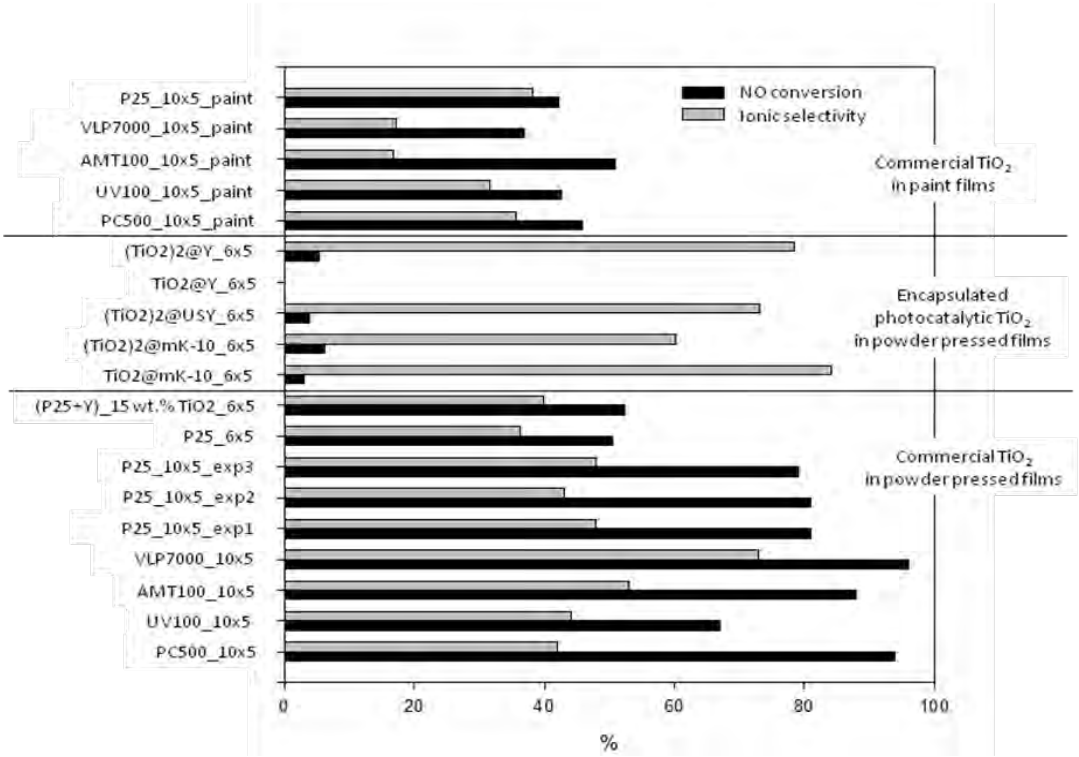

Figure 2 – NO conversion and ionic selectivity at steady state for all tested films of Table 2.

4. Conclusions

Among all the experiments performed, best NO conversions were obtained with powder pressed films of commercial TiO_2. The highest performance was achieved with VLP7000 from *Kronos* (96 %). Mixtures of commercial P25 with zeolite Y showed the same performance of a film with only P25, revealing the importance of the surroundings of the TiO_2 photocatalyst in its activity.

The mass content of TiO_2 in adsorbents, among other properties, seem to play an important role on the photo-activity. In this way, in future works efforts must be directed to analyse these properties and their correlation with the photo-activity.

Paint films produce a NO conversion of approximately 45 %, which is higher than the performance obtained with the encapsulated materials in powder pressed films.

Acknowledgments

César Águia is grateful to the Portuguese Foundation for Science and Techonology (FCT) for his PhD grant (SFRH/BD/23263/2005). The authors also acknowledge financial support by FCT through the project POCI/EQU/60366/2004, CRUP (Integrated Action, ref. AI-E/07 No. E-28/08) and Spanish DGI (CTQ06-06859). The authors are also grateful to the companies for supplying the commercial photocatalytic TiO_2 samples.

References

Corma, A., García, H. (2004). Zeolite-based photocatalysts, Chem. Commun., 2004, 1443.

Cosa, G., Galletero, M., Fernández, L., Márquez, F., García, H., Scaiano, J. (2002). Tuning the photocatalytic activity of titanium dioxide by encapsulation inside zeolites exemplified by the cases of thianthrene photooxygenation and horse radish peroxidase photodeactivation, New J. Chem., 26, 1448-1455.

Devahasdin, S., Fan Jr., C., Li, K., Chen, D. (2003). TiO2 photocatalytic oxidation of nitric oxide: transient behavior and reaction kinetics, Journal of Photochemistry and Photobiology A: Chemistry 156 161–170.

Motohashi, K., Inukai, T. (2007). Self-cleaning performance evaluation of commercial photocatalyst coting materials trough 5 years outdoor exposure, International RILEM symposium on photocatalyst, environment and construction materials, 8-9 October, Florence, Italy - Istituto degli Innocenti,80 - 86.

Strini, A., Cassese, S., Schiavi, L. (2005). Measurement of benzene, toluene, ethylbenzene and o-xylene gas phase photodegradation by titanium dioxide dispersed in cementitious materials using a mixed flow reactor, *Applied Catalysis B: Environmental*, 61, 90–97.

US Environmental Protection Agency (1998). *NOx: How nitrogen oxides affect the way we live and breathe*, Office of Air Quality Planning and Standards Research Triangle Park, NC 27711.

Proceedings of the 10th International Chemical and
Biological Engineering Conference - CHEMPOR 2008
Braga, Portugal, September 4-6, 2008
E.C. Ferreira and M. Mota (Eds.)

Design and Construction of a Lab-Scale Simulated Moving Bed Unit: The FlexSMB-LSRE® – from Theory to Practice

Pedro Sá Gomes, Michal Zabka, Mirjana Minceva and Alírio E. Rodrigues*
Laboratory of Separation and Reaction Engineering, Associate Laboratory LSRE/LCM
Department of Chemical Engineering, Faculty of Engineering, University of Porto
Rua Dr. Roberto Frias, 4200-465 Porto, Portugal

Keywords: Simulated Moving Bed, Chromatography, Adsorption, Sustainable technology, Separations, Equipment development and Process intensification
Topic: Sustainable process-product development through green chemistry

Introduction

Nowadays, it is widely accepted that process innovation should be based not only on the challenges, problems, and needs but also on the social, political, and cultural conditions prevailing in the prospective market. Concepts such as Sustainability or Sustainable Development (Brundtland report [1]), the problematic of resources depletion and eco-efficient techniques have to be taken into account. The reduction or renouncement of organic solvents represents not only the trend of the so-called green chemistry but also a sustainable and environmentally friendly production of chemical products that accounts for the economical as security (social) aspects.

The use of continuous chromatographic counter current operation modes maximizes the mass transfer driving force, providing a better utilization of the adsorbent as solvent consumption than the traditional batch mode. Nevertheless, in this counter current operation (so-called TMB-True Moving Bed), it is necessary to circulate not only the fluid phase but also the solid. The solid motion has some disadvantages (attrition, lack of efficiency, fluid velocity limited by fluidization phenomena, etc.) and from a technical point of view, is not easy to implement. The solution to this major problem was first proposed through an inventive way by Broughton and Gerhold (1961) [2]; using simple fixed bed columns the solid movement is simulated by a synchronous shift of all inlet and outlet ports in the direction of the fluid flow. This simulated solid motion lead to the Simulated Moving Bed (SMB) concept firstly implemented by the UOP Inc, Figure 1.

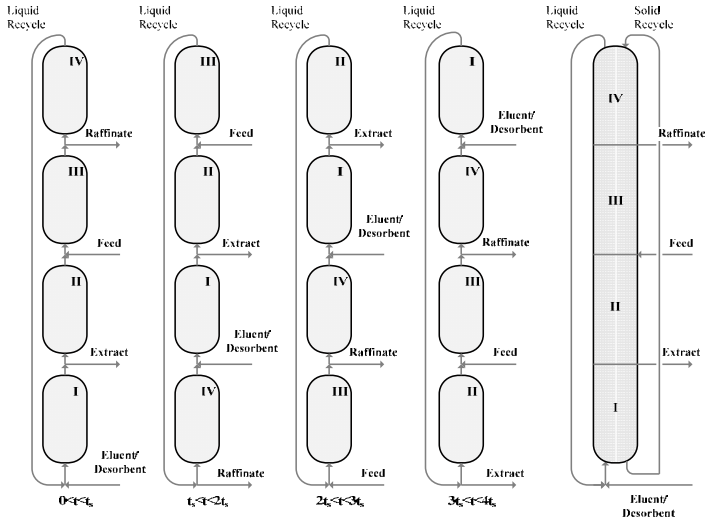

(a) (b) (c)

* Corresponding author. Tel + 351-225-081671. E-mail:arodrig@fe.up.pt

Figure 1 - Schematic representation of a 4 columns SMB unit operating over a complete cycle, from 0 to $4t_s$ (with t_s representing the ports switch time); (a) period of the first switch; (b) period of the second switch and an equivalent 4 "columns length" TMB unit (c).

Until the 90s the major implementation of the SMB technology continued to be in the petrochemical separation field with more than 100 industrial plants. Nevertheless, the application of the SMB concept to HPLC chromatographic separations in the earlier 90s, led to the second "boom" on the SMB technology applied now to the fine chemistry separations [3].

This late demand on the SMB technique has been the cause and consequence of an also emergent interest in the study and research on this particular matter, leading to the formulation of quite singular/different operation modes since the original patent. Non conventional strategies as the introduction of non synchronous inlet/outlet shifts (the Varicol process [4,5]) or the variable flux with/or variable composition in the inlet/outlet streams (the PowerFeed process [6,7]) and Modicon ([8,9]), as well as the utilization of multiple feed or distributed feed (the Two Feeds SMB in [10,11]) and the Outlet Streams Swing (OSS) [11], have increased the potential of this technique for a vast range on binary the separation field.

The practical application of the so-called "non conventional modes of operation" in Simulated Moving Bed (SMB) units is per itself a challenge. Generally an SMB unit, industrial, pilot of laboratory-scale, is limited to one or two modes of operation and to implement a new operating mode is necessary to contact the supplier, do adjustments, even to reformulate the entire unit if not to acquire a new one. Therefore, flexibility is seen as one of the more relevant qualities for this kind of equipment [12], principally for laboratory-scale usage in technology demonstration stage, as for the separation low quantities in the fine chemical area, Figure 2.

Figure 2 – Positioning of the FlexSMB-LSRE® unit as pilot/lab scale unit in the "R&D flow sheet".

This aspect was the main reason that led to the design and construction of a 6 columns unit at LSRE, the FlexSMB-LSRE®, here by presented.

FlexSMB-LSRE – from theory to practice

As mentioned before, there is a considerable number of different operation techniques related with SMB, namely the asynchronous SMB, Modicon, Powerfeed, Multifeed, OSS, Pseudo SMB etc… Classified by: binary or multicomponent separation; the number of zones and number of rings etc… However, with the assemblage of new units the classification takes into account the number and type of valves and pumps, dead volumes fraction and principally its flexibility, i.e., its capacity of operating different modes with the same unit, and therefore to extend its own performance and operability.

In the FlexSMB-LSRE® unit it was chosen to operate with two SD (dead end slow path) valves per stream in the extract and raffinate current and one SD per stream in the feed and eluent/desorbent currents and a two way valve per column, Figure 3.

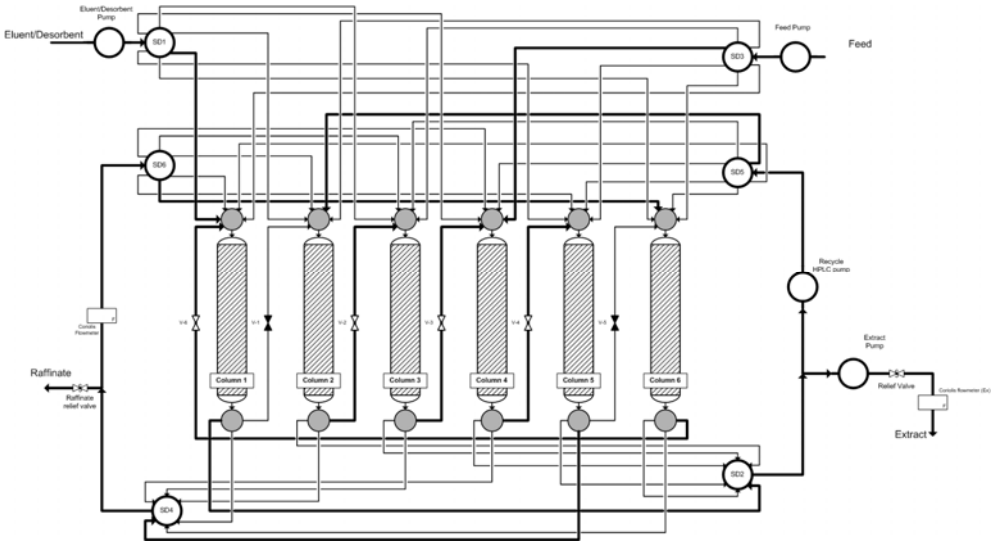

Figure 3 - Flexible SMB valves Scheme, during the first step, 6 columns operating a [1 2 2 1] classic SMB, bold lines the active connections, thick lines stagnated volumes.

It is possible to operate most of the different SMB modes, with simple adjustments and columns re-configuration. From Figure 3, it can be observed that stream from the zone I exit, in this case, from column 1, is fully withdrawn by valve SD2. Part of this stream leaves as the extract and the remaining is pumped to valve SD5 which returns the stream to the inlet of column 2. Similarly, valve SD4 withdraws the complete stream from column 5, splits part of it into the raffinate outlet and pumps the remaining to valve SD6 which returns the stream to the inlet of column 6. The inlet flows to column 1 by means of SD3 valve and the eluent/desorbent current with valve SD1. Each valve, each HPLC pump and flowmeter are computer controlled, and fully automated. The LabView platform was chosen for the automation and control of the FlexSMB-LSRE® unit, Figure 4.

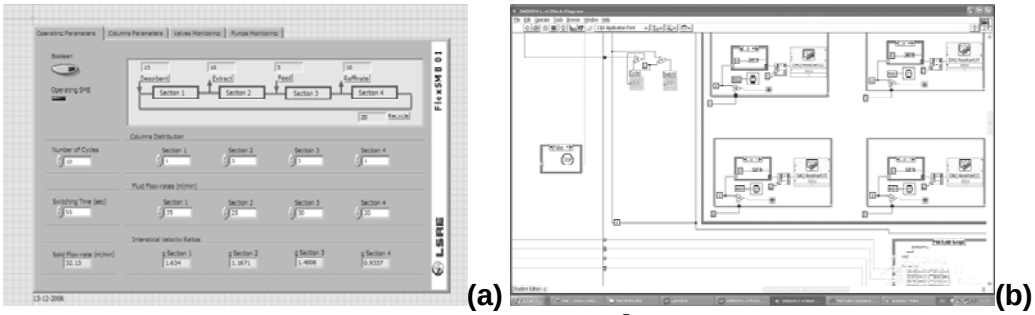

Figure 4 – LabView front Panel of the FlexSMB-LSRE® automation routines, (a) Operation Parameters, and (b) code.

The LabView automation routines are user friendly and also allow to acquire pressure as flow rate measurements for different streams in the SMB unit.

Test and Operation

An SMB unit is usually assembled with similar columns, and packing material, as the ones used in the batch systems. In this unit, 6 columns with 10.0 cm of length and diameter of 2.0 cm, in stainless steel were used. For each column a slurry of approx. 18.5 g of Chiral AD 20 μm in approx. 36 ml of 2-propanol was prepared (pure 2-propanol was chosen as slurry solvent taking into account its physical proprieties, namely its viscosity), and packed by means of an Analytical Slurry Packer from Alltech Associates Inc.

In the case of SMB operation, the main consequences associated with columns packing fluctuations remain in the heterogeneity of the retention factors and asymmetrical pressure drops. The columns should present similar retention factors for a given species. Therefore,

one Column (0) was tested for HETP (Height Equivalent to the Theoretical Plate) numbers, Figure 5, and for comparison, tracer experiments were performed to the remaining columns, Figure 6.

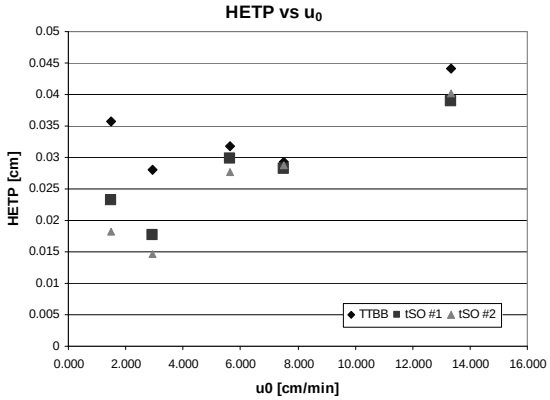

Figure 5 – HETP experiences for Column 0, (TTBB: 1,3,5 – TriTert ButyBenzol; TSO: Trans – Stilbene Oxide).

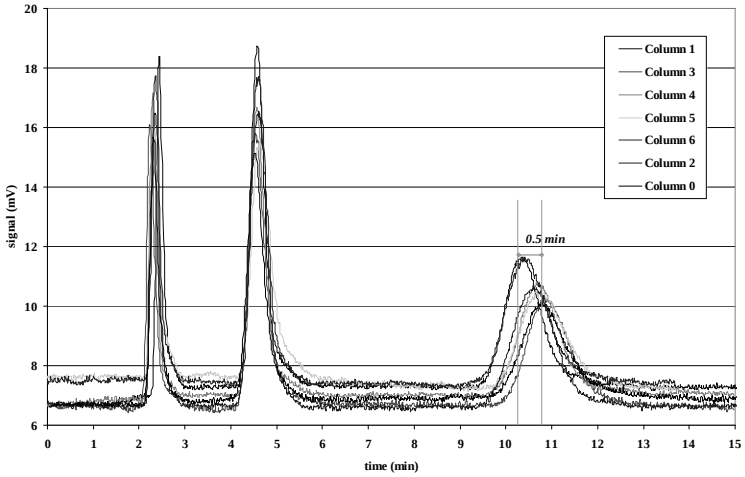

Figure 6 – Tracer experiences for the 7 columns, first peak TTBB, second and third the racemic mixture of TSO.

Then a first experiment was performed for the separation of a racemic mixture, (R,S)-α-Tetralol ((S,R)-(±)-1,2,3,4 Tetrahydro-1-naphthol) studied before by Zabka and Rodrigues [13-14], racemate concentration of 1.0 $g.l^{-1}$ in a heptane-2propanol solvent (95 %+5 % volumic fraccion, respectively), and the operating conditions as mentioned in Table 1.

Table 3 – FlexSMB-LSRE® operanting parameters.

SMB Operating Conditions	
C_R^F=0.50 $g.l^{-1}$;	C_S^F=0.5 $g.l^{-1}$
t_c=3.05 min;	
Q_{Eluent}=6.0 $ml.min^{-1}$;	$Q_{Extract}$=4.3 $ml.min^{-1}$;
Q_{Feed}=1.0 $ml.min^{-1}$;	$Q_{Raffinate}$=2.7 $ml.min^{-1}$;
Q_{IV}^*=23.0 $ml.min^{-1}$	

In the cyclic steady state (cycle 27) it was possible to obtain the following concentration profiles within the column, Figure 7.

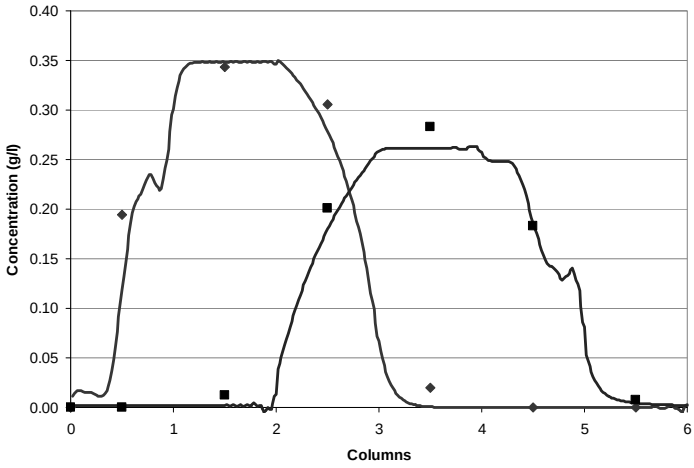

Figure 7 – Concentration profiles obtained from cycle 24 to 28, diamonds R tetralol and squares the S tetralol, lines the theoretical profiles obtained from a dead volumes approach.

And the concentration of each enantiomers in the respective outlet current, as shown in Figure 8.

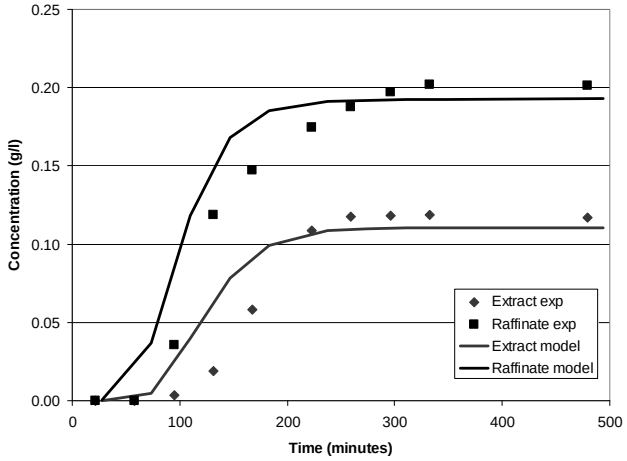

Figure 8 – History of the average concentration on more retained product on the extract and the less retained species in the raffinate current over a cycle, namely, cycle: 2; 4; 6; 8; 10; 13; 15; 17; 19; 27, each pure, diamonds R tetralol and squares the S tetralol, lines the theoretical profiles obtained from a dead volumes approach.

Taking into account of the major objectives of this unit, its flexibility, it was developed the asynchronous SMB mode of operation for the inner columns, i.e., section 2 and 3 with variable number of columns per switch. This routine has been tested and will soon be implemented for a racemic mixture separation.

Conclusion

Throughout the years LSRE developed a considerable know how related with design, simulation and optimization of Simulated Moving Bed units for petrochemical, and specially, fine chemical separation and reaction fields. These skills were now complemented with the full design and construction of a flexible SMB unit, able to operate most of the non conventional SMB modes. Years of intangible assets can now be put into practice.

This unit was already tested for a classic SMB separation for a racemic mixture of (R,S)-α-Tetralol, in columns packed with Chiral AD 20 μm, and operated for asynchronous SMB. The tests to different separations will now continue demonstrating all the potential of this Flexible Unit.

References:

[1]. Brundtland, G.H. et al., (1987) Report of the World Commission on Environment and Development – "Our Common Future", General Assembly of United Nations 42th session item 83(e).

[2]. Broughton, D. B.; Gerhold, C. G. (1961) Continuous Sorption Process Employing Fixed Bed of Sorbent and Moving Inlets and outlets. U.S. Patent No 2,985,589.

[3]. Sá Gomes, P.; Minceva, M.; Rodrigues A. E.; (2006) Simulated Moving Bed: Old and New, Adsorption, 12:375-392.

[4]. Adam, P. R.; Nicoud, M.; Bailly, M.; Ludemann-Hombourger, O. U.S. Patent No 6,136,198, 2000.

[5]. Ludemman-Hombouger, O.; Nicoud, R.; Bailly, M. (2000) The "Varicol" Process: a New Multicolumn Continuous Chromatographic Process. Sep. Sci. Tech., 35(12), 1829-1862.

[6]. Morbidelli, M.; Mazzotti, M. (2002) Advances in Simulated Moving bed Chromatography. In: *PREP, 15th International Symposium, Exhibit Workshops on Preparative/Process Chromatography Ion Exchange, Adsorption/Desorption Processes & related Separation Techniques,* Lecture 201 Washington DC, USA, 53-54.

[7]. Zhang, Z.; Mazzotti, M.; Morbidelli, M. PowerFeed (2003) Operation of Simulated Moving bed Units: Changing the Flow-rates During the Switching Interval. Journal of Chromatography A, 87-99.

[8]. Schramm, H.; Kaspereit, M.; Kienle, A.; Seidel-Morgenstern, A. (2002) Improving Simulated Moving Bed Processes by Cyclic modulation of the Feed Concentration. Che. Eng. Tech. , 25(12), 1151-1155.

[9]. Schramm, H.; Kaspereit, M.; Kienle, A.; Seidel-Morgenstern, A. (2003) Simulated Moving Bed Process with a Cyclic Modulation of the Feed Concentration. Journal of Chromatography A 1006, 77-86.

[10]. Kim, J. K.; Abunasser, N.; Wankat, P. C. (2005) Use of Two feeds in Simulated Moving Beds for Binary Separation. Korean J. Chem Eng. 22(4), 619-627.

[11]. Sá Gomes, P.; Rodrigues, A. E.; (2007) Outlet Stream Swing (OSS) and MultiFeed (MF) Operation of Simulate Moving Beds, Separation Science and Technology, 42: 223-252.

[12]. Ching, C. Y. and N.-H. L. Wang, (2004) Simulated Moving Bed Equipment Designs Separation and Purification Reviews, 33: 77–155.

[13]. Zabka, M. and A. E. Rodrigues, (2007) Thermodynamic and Kinetic Study of Adsorption of R,S- -Tetralol Enantiomers on the Chiral Adsorbent CHIRALPAK AD, Sep. Sci. And Tech., 42, 739-768.

[14]. Zabka, M. and A. E. Rodrigues, (2007) Measurement of pore diffusivity of R, S-α-Tetralol enantiomers in chiral adsorbent CHIRALPAK AD by zero length column method, accepetd on Sep. Pur. Tech.

Proceedings of the 10th International Chemical and
Biological Engineering Conference - CHEMPOR 2008
Braga, Portugal, September 4-6, 2008
E.C. Ferreira and M. Mota (Eds.)

Robust multi-objective cascade controller for an anaerobic digester

Carlos Garcia Dieguez[1*], Francisco Molina[2], Eugenio F. Carrasco[1], J. M. Lema[1], Enrique Roca[1]

[1] USC - University of Santiago de Compostela, Department of Chemical Engineering/School of Engineering. Rua Lope Gomez de Marzoa s/n, 15782 Santiago de Compostela, Spain.
[2] Faculty of Engineering, University of Antioquia, A.A. 1226, Medellin, Colombia.

Keywords: Advanced control; anaerobic digestion; cascade control; multi-objective control.
Topic: Systematic methods and tools for managing the complexity — Process control & operations.

Abstract

A new multi-objective control strategy based on volatile fatty acids (VFA) and methane flow rate (Q_{CH4}) is derived for an Upflow Sludge Bed-Filter (USBF) reactor, which is used for the anaerobic treatment of industrial wine distillery wastewater. The approach presented here is novel in the sense that (i) considers two operational objectives, the control on the effluent quality and the control on the maximum production rate of methane; (ii) takes advantage of the difference between the dynamics of the liquid and gas phase, using variables of both phases. The control system includes a cascade controller with a reference signal for methane flow rate. The control system computes the feed flow rate for adjusting the organic load applied to the reactor. The performance of the proposed control scheme is illustrated via numerical simulations and parameter optimization with the Anaerobic Digestion Model no.1 (ADM1) respect of influent perturbations.

1 Introduction

Anaerobic digestion processes consist of a set of conversions of organic matter into methane and carbon dioxide, occurring in absence of oxygen. The use of methane as an energy source, the low growth of sludge and its ability to treating wastewater with medium to high organic loads are some of the reasons that contributed to increase the popularity of anaerobic wastewater treatment (AWT) in the last few decades. However, the AWT has classically been regarded as a difficult process to be controlled and managed. In this sense, the ideal control system must fulfill different characteristics for assuring altogether: (a) high quality of effluent; (b) maximum methane production; (c) general stability criterion; and (d) applicability to different types of wastewaters.

In the literature different process variables and promising controllers have been proposed using different control schemes and techniques. In this sense, the advances in the development and increasing availability of the on-line sensors (Vanrolleghem & Lee, 2003; Spanjers & van Lier, 2006) together with a better knowledge of involved biological phenomena (Batstone et al., 2002) allowed to design new controllers in the last years. Recently, in the European project TELEMAC (Bernard, 2005) a number of controllers for anaerobic wastewater treatment were developed. However, they only consider effluent quality as an operational criterion. Other controllers (Steyer et al., 1999; Liu et al., 2004) were designed to achieve the maximum organic loading rate and the greater production of methane.

In this contribution, a new robust multi-objective controller is derived for an Upflow Sludge Bed-Filter (USBF) reactor. The approach is novel in the sense that considers the main operational criteria in the same control structure. Moreover, this controller takes advantage of

* Corresponding author. Tel +34 981-563100 Ext.: 16742. E-mail:carlos.garcia.dieguez@usc.es

the difference in the dynamics of the liquid phase and the gas phase through a cascade structure with a reference signal.

2 Model description and problem statement

2.1. *IWA Anaerobic Digestion Model no. 1 (ADM1)*

ADM1 (Batstone et al., 2002) is a complex model of the multistep anaerobic process transformations. This tool is adequate for predictions of enough accuracy to be useful in process development, optimization, and control. It is a standard benchmark for developing operational strategies and evaluating controllers (Batstone & Steyer, 2007). ADM1 incorporates processes such as hydrolysis of particulates, acidogenesis, acetogenesis, and methanogenesis, and it includes 26 dynamic state concentration variables, 19 biochemical kinetic processes, 3 gas-liquid transfer kinetic processes, and 8 implicit algebraic variables per liquid vessel. A modified version of the ADM1 incorporating ethanol degradation pathways and calibrated for a USBF reactor (Ruiz-Filippi et al., 2004) was used. In the modified version used, an additional group of ethanol degraders was included as well as a new state variable for ethanol. The extension for ethanol not only considers the hydrogen and acetate pathways but also takes into account other controller design volatile fatty acids (VFA) pathways (propionate and butyrate) by means of the stoichiometry. Thus, VFAs are suitably predicted, including overloads or transitions between steady states.

2.2. *Controller Objectives*

Many authors had used Haldane kinetic model for describing the behavior of the anaerobic digesters (Bastin & Dochain, 1990). In this case, Haldane model supplies a simple way to explain the controller objectives as well. Haldane kinetics has an obvious wash-out equilibrium point and two operational equilibrium points that have different dynamical properties in terms of stability. The latter two equilibrium points enable to distinguish two regions, a stable region and an unstable region (Figure 1). A controller always must keep the AWT system in the stable region; this is the main objective of any controller for AWT plants. Additionally other objectives can be established. In general, the biological wastewater treatment attempts decompose the organic compounds contained into the wastewater and fulfill with the environmental regulations. However, in the case of AWT other objective could be the maximum recovery of energy in methane form.

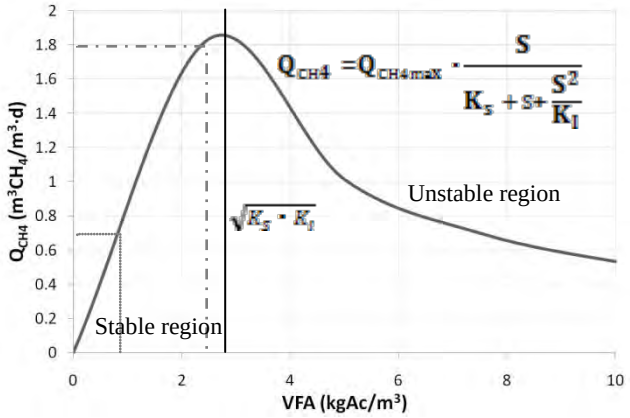

Figure 1. Haldane kinetic for an anaerobic digester. (- - -) Operational point with objective methane flow rate. (.....) Operational point with objective fulfill environmental regulation.

Therefore, the development of a controller able to integrate both objectives and provide a robust regulation of the process in a same single structure is of great interest for such wastewater treatment systems. Different control structures could be considered for this task, however a cascade framework was preferred in this case.

3 Controller design

3.1. *Selection of control variables*

Different combinations of variables were studied for establishing the most appropriate combination of them that permit the best control regulation in a cascade structure. When two variables for process state identifications are considered for winery wastewater, there are several combinations of pairs of these variables that accomplish complete classification of states (Castellano et al., 2007). A similar behavior had been observed with other types of wastewaters using experimental data and the same statistical technique. Variables in the liquid phase are supposed to present higher response times than the gas phase variables. Therefore, with this criterion an inner control loop with a secondary variable in the liquid phase doesn't seem to be the most appropriate. In addition with the same criterion, a combination between variables in the gas and in the liquid phase will allow us take advantage of the difference between the dynamics of both phases. Taking into account the above, a variable of the liquid phase, due to its slower response, should be used as a control variable in the external loop, and against a variable in the gas phase, which has a rapid response, should be used as a control variable in the inner loop. From the point of view of technical, economical and dynamical criteria, we decided flow rate of methane (Q_{CH4}) as inner-loop variable because a combination between this variable together with volatile fatty acids (VFA) allow us to detect a situation of imbalance in the AWT process. Furthermore; Q_{CH4} has a better relationship with the objective of maximize the methane production and the VFA with the environmental regulations. Currently, VFA can be determined by means of titrimetric methods to relatively low cost, per example with the AnaSense® analyzer (Ruiz-Filippi et al., 2005). In addition, accumulation of VFA can be very dangerous for the biological and structural stability to long-term of the anaerobic sludge.

3.2. *Methane productivity – Inner control loop*

The scheme of methane productivity control mode is depicted in Figure 2. This is an auto-setting controller system, having a methane reference signal (Q_{CH4} reference). Note that Q_{CH4} reference provides the set-point to the inner controller. The inner controller was implemented as PID controller. After a parameter adjustment, the conclusion is that integral and derivative terms are negligible. Therefore the equation of this controller can be expressed as: $Q(t) = Q_0 + K_p\ \Delta Q_{CH4}(t)$, where Q is the feed flow rate of the reactor or controller output, Q_0 is the controller output bias, K_P is the proportional gain, and ΔQ_{CH4} is the error between the Q_{CH4} actual value and the reference signal. We considered sampling interval of 15 min for the methane flowrate (Q_{CH4}) and the same interval of time for controller actions. This time is appropriate taking into account the scale of industrial anaerobic bioreactors and the slow dynamic of this process.

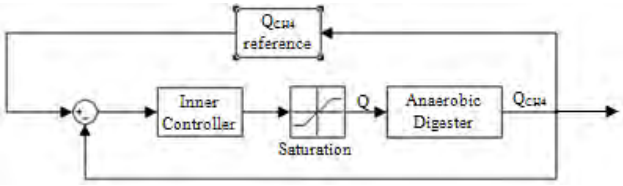

Figure 2. Block diagram of the methane productivity controller (inner-loop).

The controller operating in this mode was designed to maintain the process near to the maximum methane production ($Q_{CH4\ max}$) and push the system to higher OLR values, still avoiding overload and unstable operations.

3.3. *Tracking methane reference*

The methane reference signal (Q_{CH4} reference) is established in function of the chemical oxygen demand in the influent (COD_{in}) through an empirical correlation. The correlation is different for each control objective. It is obtained in this case by means of simulations. In the case of cascade controller, the simulations consist in optimize in pseudo steady-state the methane feed flow rate for different concentrations of COD_{in} that accomplished the

requirement of spillage (150 mg Ac/l). And in the case of inner loop controller, the simulation consist in obtain the maximum methane flow rate vs COD_{in}.

For a future closep-loop implementation in a pilot plant, a neuro-fuzzy system, that combines the advantages of artificial neural networks (ANN) and fuzzy inference system (FIS), was development in order to estimate COD_{in} (not measured in the plant). Any other technique of observation could be implemented for obtain this variable. Normally, COD_{in} presents high frequency noise, therefore in closep-loop implementation could be very useful the use of dead bands.

3.4. *Effluent quality control – cascade scheme*

A single-loop provides good performance when the dynamics are fast, the fraction dead time is small and disturbances are small and slow, like in the case of methane productivity controller. However, a single-loop for controlling VFA is insufficient because it lacks the characteristics described before. In this case a control cascade structure presents itself as an alternative. The cascade structure proposed for this task is shown in Figure 3.

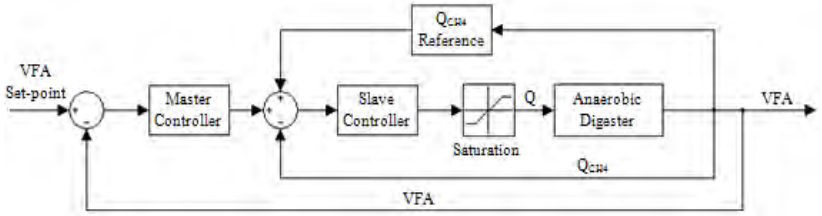

Figure 3. Block diagram of the cascade controller. Note that QCH4 reference signal provides the set-point to the inner controller and modifies this one in the cascade scheme.

Some considerations must be taken into account on this controller:

Assumption 1. The process behavior is linear in a range of values close to the set-point. This is more or less true while not occur inhibition episodes.

Assumption 2. The inlet compositions are piecewise constant, bounded and uncertain functions (organic load disturbances).

Assumption 3. The feed flow rate (Q) is constrained by a saturation function (according to physical restrictions on manipulated variable). Clearly, the minimum feed flow rate ($\underline{Q}$) is zero and the maximum feed flow rate ($\overline{Q}$) was established using the criterion of minimum hydraulic retention time (HRT) of 9 hours for prevent undesired wash-out of biomass.

$$sat(Q) = \begin{cases} \overline{Q}, & Q \geq \overline{Q} \\ Q, & \underline{Q} < Q < \overline{Q} \\ \underline{Q}, & \leq \underline{Q} \end{cases}$$

Furthermore, the speed with which increases or decreases the feed flow rate (ΔQ) was limited to 0.5 l/h each 15 minutes.

4 Results and discussion

4.1. *Optimization of the parameters*

In order to improve the controller settings, a tuning by means parameter optimization was computed using ADM1. The optimization of the controller parameters was made using a multiobjective optimization function “fminimax” in Matlab®. This function uses a sequential quadratic programming (SQP) method.

The parameters turned out to be very similar for the range of concentration studied, from 7 to 16 g/l in the CODin. This range is characteristic of this type of wastewater (wastewater containing ethanol).

Parameters	Slave	Master
K_c	0.0172	0,38
K_I	$7.2 \cdot 10^{-7}$	0
K_d	0,0006	0

Table 1. Parameters of the controllers

4.1. *Validation using ADM1*

The developed cascade controller system was tested using data generated by simulation with the modified ADM1, previously commented, under different operational situations: automatic restart-up, after short stops; organic overloads and organic underloads. In the Figure 4 the different simulations are shown. The initial conditions for the simulations were obtained for a medium value of OLR during a large period of time in order to ensure that a steady state was reached.

Restart-up of AWT plants after a short stop is often carried out in industrial applications. Automatic control systems can help to minimize the period for restarting the AWT plants. The cascade controller (see Figure 4a) restart-up the AWT plant in 3 days with a very small initial value for feed flow rate (5 l/h) and a COD_{in} of 10 g/l. However, the wished set-point was achieved in only two days.

As it can be seen in Figure 4b, the controller was able to maintaining stable the process after of a severe increment of COD_{in}, from 10 g/l to 15 g/l (50% of increment in the organic load). In a similar way, the controller responds to a decrease of a 30% in the organic load increasing the feed flow rate and handles accurately the organic underload. These perturbations without automatic control would cause a failure in the treatment system. In these cases a minimum variation of the volatile fatty acids was detected. In all the cases, the pH was kept stable near a neutral value and the IA/TA ratio was lower than 0.2, an adequate value lower than the 0.3 recommended limit value (results not shown here).

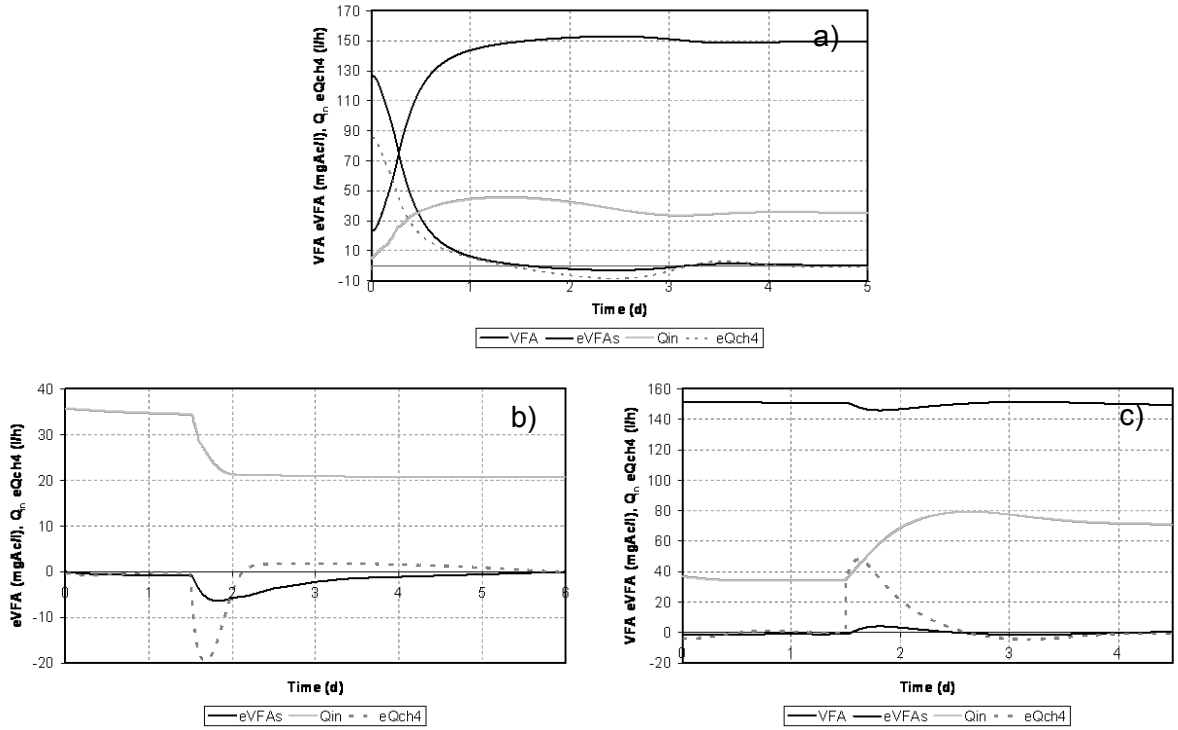

Figure 4. Simulations with ADM1. a) Restart-up, b) Organic overload, c) Organic underload.

Other few authors have successfully used cascade configurations for controlling anaerobic digesters. Alvarez-Ramirez et al. (2002) have shown that direct feedback control using linear controllers in a cascade configuration has potential application for optimal operation of AWT

plants. However, these authors used VFA and COD as process variables, both variables belong to the liquid phase which would delay the response of the controller system. Another interesting application in cascade for the monitoring of pH and biogas flow rate was developed by Liu et al. (2004). In this case good control performances were achieved in closed-loop during operation in a lab scale digester. Nevertheless, the quality of the effluent was not taking into account. Moreover, we consider that the pH in the inner loop is not a variable that allows us to act with fast enough, if there is not a good control on the addition of alkalinity especially in a full scale reactor.

5 Conclusions

In this paper, a new multi-objective cascade control for regulating anaerobic wastewater treatment was developed, optimized and validated by simulations carry out with an ADM1 virtual plant. This controller provided good performance against severe perturbations, supplying an adequate control action to achieve the desired set point as well as to manage sudden changes in the influent, and it is able to restart-up the AWT plant in a short period of time.

The relatively low cost of the measurement devices required, makes this controller very interesting for industrial application. Further closed-loop tests in a pilot plant are needed to assure the controller robustness in an industrial environment.

Acknowledgements

Authors wish to acknowledge to Spanish National R&D Program and European Regional Development Fund (ERDF) for the Project ANACOM CTQ2004-07811-C02-01.

References

Alvarez-Ramirez,J., Meraz,M., Monroy,O., and Velasco,A. (2002) Feedback control design for an anaerobic digestion process. *Journal of Chemical Technology and Biotechnology* 77 (6), 725-734.

Batstone, D. J., Keller, J., Angelidaki, I., Kalyuzhny, S., Pavlostathis, S. G., Rozzi, A., Sanders, W., Siegrist, H., and Vavilin, V. A. Anaerobic Digestion Model No. 1 (ADM1). Report No. 13]. 2002. London, IWA Publishing.

Batstone,D.J. and Steyer,J.P. (2007) Use of modelling to evaluate best control practice for winery-type wastewaters. *Water Science and Technology* 56 (2), 147-152.

Bernard,O. (2005) An integrated system to remote monitor and control anaerobic wastewater treatment plants through the internet. *Water Science and Technology* 52 (1/2), 457-464.

Castellano,M., Ruiz-Filippi,G., Gonzalez,W., Roca,E., and Lema,J.M. (2007) Selection of variables using factorial discriminant analysis for the state identification of an anaerobic UASB-UAF hybrid pilot plant, fed with winery effluents. *Water Science and Technology* 56 (2), 139-145.

Liu,J., Olsson,G., and Mattiasson,B. (2004) Monitoring and Control of an Anaerobic Upflow Fixed-Bed Reactor for High-Loading-Rate Operation and Rejection of Disturbances. *Biotechnology and Bioengineering* 87 (1), 43-53.

Ruiz-Filippi, G., Molina, F., Steyer, J. P., Vanrolleghem, P., Zaher, U., Roca, E., and Lema, J. M. Industrial scale validation of a new titrimetric sensor for anaerobic digestion processes: Comparison of methodologies. 133. 2005. Busan, Korea, IWA publishing. 2nd IWA Conference on Instrumentation, Control and Automation for Water and Wastewater Treatment and Transport System (ICA 2005). 29-5-2005.

Ruiz-Filippi, G., Rodriguez, J., Roca, E., and Lema, J. M. Modification of the IWA-ADM1 for application to anaerobic treatment of ethanolic wastewater from wine factories. 1341-1344. 2004. Anaerobic Digestion 10th World Congress Anaerobic Bioconversion for Sustainability. 29-8-2004.

Spanjers,H. and van Lier,J. (2006) Instrumentation in anaerobic treatment-research and practice. *Water Science and Technology* 53 (4-5), 63-76.

Vanrolleghem,P. and Lee,D.S. (2003) On-line monitoring equipment for wastewater treatment processes: state of the art. *Water Science and Technology* 47 (2), 1-34.

Proceedings of the 10th International Chemical and
Biological Engineering Conference - CHEMPOR 2008
Braga, Portugal, September 4-6, 2008
E.C. Ferreira and M. Mota (Eds.)

Fenton's treatment of aqueous phenol effluents in presence of anionic surfactants

Xavier Bernat[1], Agustí Fortuny[2], Christophe Bengoa[1], Frank Stüber[1], Azael Fabregat[1], Josep Font[1]*

[1] Departament d'Enginyeria Química, ETSEQ, Universitat Rovira i Virgili, Av. Països Catalans 26, 43007 Tarragona, Catalunya, Spain

[2] Departament d'Enginyeria Química, EPSEVG, Universitat Politècnica de Catalunya, Av. Víctor Balaguer s/n, 08800 Vilanova i la Geltrú, Barcelona, Catalunya, Spain

Keywords: Fenton process, phenol, anionic surfactants, micelles, wastewater treatment
Topic: Advancing the chemical engineering fundamentals — Catalysis & reaction Engineering.

Abstract

The Fenton process is an adequate oxidation treatment for the partial-abatement of industrial effluents contaminated with organic pollutants, such as phenol, which are refractory towards biological treatments. The efficiency of the Fenton process depends on the wastewater composition as well as on the oxidation conditions, but also on the presence of other compounds, e.g. surfactants, that can interfere the oxidation. In this study, the effect of the oxidation conditions (catalyst and oxidant concentrations) is presented for phenolic wastewater in presence of an anionic surfactant. The results show that, selecting the appropriate amounts of catalyst and oxidant (40 mg/L and 12500 mg/L, respectively), the process is able to almost totally degrade phenol and phenol+anionic surfactant (sodium dodecylsulfate) solutions. The study also demonstrates that, when dealing with phenol+surfactant solutions, the efficiency of the process is decreased at low catalyst concentration. In addition, an increase of the surfactant concentration up to its critical micelar concentration causes a decrease of the phenol conversion. However, a further surfactant concentration increase does not change the phenol elimination achieved. It is believed that the morphology of the surfactant present in the polluted solutions has a crucial role on the degradation of phenol as it hosts phenol molecules in the interior of the micelles, worsening the interactions between the OH• radicals produced in the bulk phase by the Fenton's reaction and the phenol molecules, thus decreasing the degradation obtained.

1 Introduction

Chemical process industry produces large amounts of polluted waters which need to be treated before being released to the nature or re-used. Typically, biological treatments are preferred as they achieve adequate abatement of organic compounds at low cost. Nevertheless, many organic contaminants, such as phenol, are refractory to biological treatments. Thus, phenolic effluents cannot be directly treated in a conventional municipal wastewater treatment plant. In such a case, an effective pre-treatment step has to be applied prior to the biological treatment. Anyway, it is not appropriated to totally destroy the biorefractory organic contaminants because the associated cost would be unacceptably high. Hence, an effluent needs to be treated just for providing enough biodegradability to allow the subsequent biological treatment to successfully perform.

Physical methods, such as adsorption (Mukherjee et al., 2007), nanofiltration (Van der Bruggen et al., 1999), emulsion liquid membranes (Park et al., 2006) among many others can be employed as effective pre-treatments for removing phenol from wastewaters.

* Corresponding author. Tel + 34 977559646. E-mail:jose.font@urv.cat

However, physical methods only transfer the organic contaminant from one effluent to a secondary liquid or solid waste. In addition, physical methods often need regeneration or cleaning cycles. Thus, the environmental problem still remains after the physical methods.

Chemical pre-treatments, such as oxidation processes, are being designed for achieving a partial mineralisation of phenolic compounds. The biodegradability of the partially-treated effluent can be controlled as the formed oxidation intermediates and their concentrations depend on the operating conditions. Thus, the pair oxidation-biological treatment is an attractive and feasible option for dealing with phenolic effluents (Suárez-Ojeda et al., 2007).

Advanced Oxidation Processes (AOP's) are a group of chemical pre-treatments whose common characteristic is that a very powerful and non-selective radical, the hydroxyl radical (OH•), is formed. Among them, Fenton process is able to effectively degrade phenolic compounds at room temperature and atmospheric pressure (Chamarro et al., 2001) using the well-known Fenton liquor, i.e. ferrous ions (soluble salts) and hydrogen peroxide. The fast interaction between these two species leads to the formation of hydroxyl radicals, which then attack organic contaminants at different extent.

The Fenton process has also been used for the partial treatment of other organic pollutants such as dyes (Lodha and Chaudhari, 2007), chelating agents (Ghiselli et al., 2004), pharmaceuticals (Esplugas et al., 2007) and so on. However, no attention has been paid in the effect of the presence of a secondary organic product on the degradation efficiency of an easy-to-degrade organic contaminant, such as phenol.

The aim of this work is to study the effect of an anionic surfactant (sodium dodecylsulfate, SDS) on the degradation of phenol by the Fenton process. In all the tests, carried out in a batch reactor, the initial concentration of phenol was 2500 mg/L and the solution pH was not adjusted. The effect of the catalyst and the oxidant concentration on the degradation of phenol was explored in both absence and presence of SDS. As surfactants are molecules having a hydrophobic head and a hydrophilic tail, they group forming micelles above its critical micelar concentration (cmc). All the experiments showing the effect of the catalyst and the oxidant concentration in presence of SDS were performed at a SDS concentration equal to its cmc. On the other hand, to test the effect of the morphology of the SDS (micelar or monomeric form), experiments at several SDS concentrations (from 577 to 3170 mg/L) were also conducted.

2 Materials and methods

The oxidation experiments were conducted in batch mode in a 500-mL jacketed glass reactor. The reactor was stirred at 300 rpm with a magnetic stirrer (Selecta, model Agimatic REV-S). All the experiments were performed at 30 ºC, controlled by means of a thermostatic bath (Haake S, model Fisous). A typical experiment started by placing in the reactor 250 mL of solution containing phenol (phenol crystallised; Panreac, purity 99%) and iron sulfate (iron sulfate heptahydrate (Riedel de-Haën, purity 99%) at the desired concentration. In the experiments where the effect of the presence of SDS on the phenol conversion had to be tested, SDS (sodium dodecylsulfate; Fluka, purity 96%) was also dissolved in the solution together with the phenol and iron sulfate. After this, 10-mL sample were withdrawn and kept in the fridge for further iron analysis (Atomic absorption spectrometry; Perkin Elmer, model 3110) and phenol (HPLC; Agilent Technologies, model 1100). The details of the used HPLC method can be found elsewhere (Suárez-Ojeda et al., 2005). Then, the stirring and the thermostatic bath were switched on and when the reactor temperature was 30 ºC, the desired amount of hydrogen peroxide (hydrogen peroxide 30% w./v.; Panreac) was added. At this point, the Fenton's reaction started. Several samples (5 mL each) were periodically withdrawn from the reactor and stored in glass vials containing 100 μL of NaOH 6N. The basification of the samples was done in order to instantaneously stop the Fenton's reaction in the vials. The samples were stored in the fridge for at least 24 h. Then, samples were

centrifuged (Ortodiresa, model Digicen 20) at 10000 rpm for 10 min. Phenol was analysed as the initial solution.

3 Results

3.1 Hydrogen peroxide concentration and SDS presence effects

In this section, the effect of the oxidant (hydrogen peroxide) and catalyst (iron sulfate) concentrations on the phenol conversion is presented. The initial concentrations of phenol and SDS (when present) were 2500 mg/L and 2307 mg/L (equal to cmc), respectively. The catalyst concentration was constant and equal to 7.0 mg/L in this set of experiments. The hydrogen peroxide concentration ranged between 2500 and 15000 mg/L. These hydrogen peroxide concentrations represent 0.2 and 1.2 times the theoretical stoichiometric amount of hydrogen peroxide needed to totally mineralize 2500 mg/L of phenol. Figure 1 shows the effect of the oxidant concentration on the phenol conversion both in absence and presence of SDS.

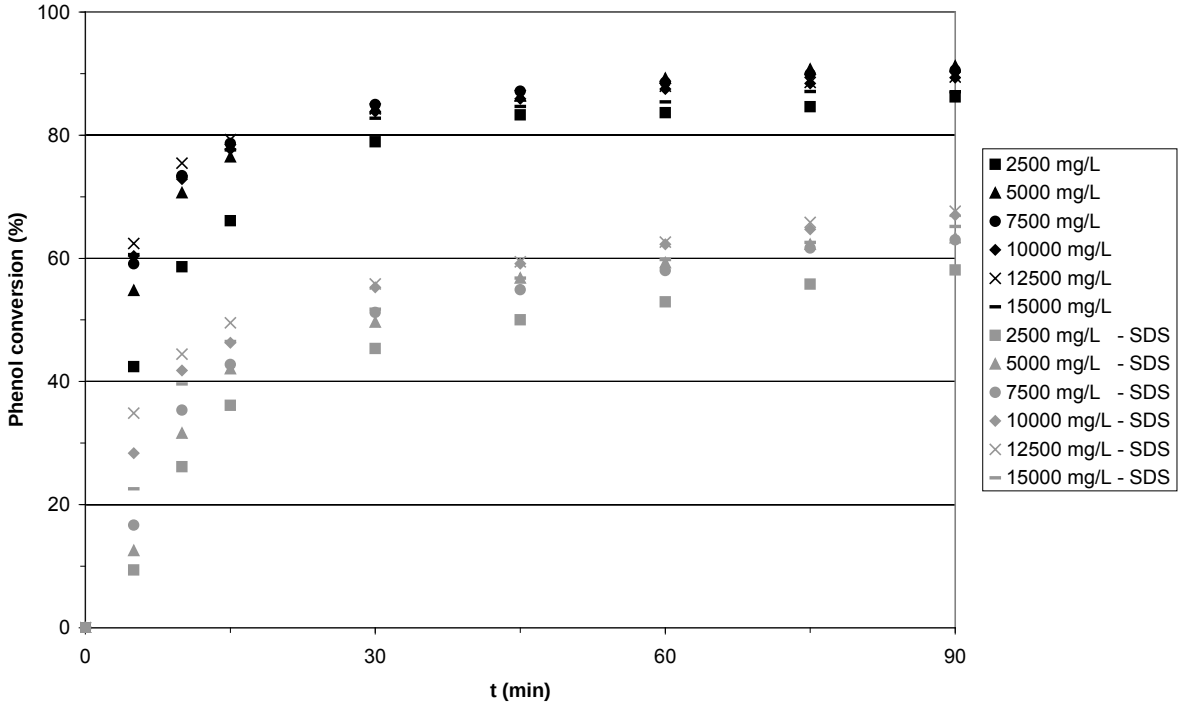

Figure 1. Effect of the oxidant concentration on the phenol conversion in absence (black symbols) and presence (grey symbols) of SDS. 2500 mg/L phenol; 7 mg/L Fe (II); 2307 mg/L SDS (when present).

As it can be seen, when no SDS was present, an increase in the oxidant concentration did not cause an important enhancement on the phenol conversion. Even when increasing the oxidant concentration beyond 12500 mg/L the phenol conversion decreased. This effect could be caused by its possible self-consumption at high concentrations, as previously reported (Cobra Guimaraes et al., 2008). At the same oxidation conditions but with the presence of SDS at its cmc, the phenol conversions decreased by a 20% compared to those obtained when no SDS was present. This may indicate that surfactant molecules are also attacked by the hydroxyl radicals. However, it could also occur that, as SDS micelles host phenol molecules due to their hydrophobic internal nature, it may be more difficult for OH• radicals to arrive to the interior of the micelles and attack the phenol molecules. It is worth mentioning that both possibilities may occur, decreasing the phenol conversion.

3.2 Iron (II) concentration and SDS presence effects

As with hydrogen peroxide, iron (II) concentration may have a strong effect on the phenol conversion as it is involved in the production of OH• radicals from the oxidant. Thus, in this section, the effect of the catalyst concentration on the phenol conversion is presented. As in the section 3.1, the effect of the presence of SDS is tested at a concentration equal to its cmc. The hydrogen peroxide concentration in these experiments was 12500 mg/L. Figure 2 shows the phenol conversion after 90 min of treatment as function of the iron concentration. As shown in Figure 2, the presence of SDS decreases the achieved phenol conversion at low iron concentrations. These results can be explained by the difficulty for the hydroxyl radicals to arrive to the micelar interior and/or the codegradation of SDS micelles, as when exploring the effect of the oxidant concentration.

As it can be deducted from Figure 2, the iron content has an important effect on the phenol conversion as an almost complete oxidation of phenol of almost 100% can be attained at high catalyst doses, both in absence and presence of SDS at its cmc. It is important to note that an almost complete degradation does not mean a total mineralisation of the effluent as oxidation intermediates may appear in the effluent from the Fenton process. These results could indicate that as the concentration of catalyst increases, the amount of produced OH• radicals may increase, causing a higher degradation of SDS molecules. This would release the phenol molecules from the micelles, enhancing the phenol degradation. Besides, it could also occur that, as the amount of OH• radicals is higher at elevate Fe concentrations, there are more OH• radicals available, which cross the micelles and attack the phenol molecules inside the micelles. As aforesaid, both possibilities could occur at the same time.

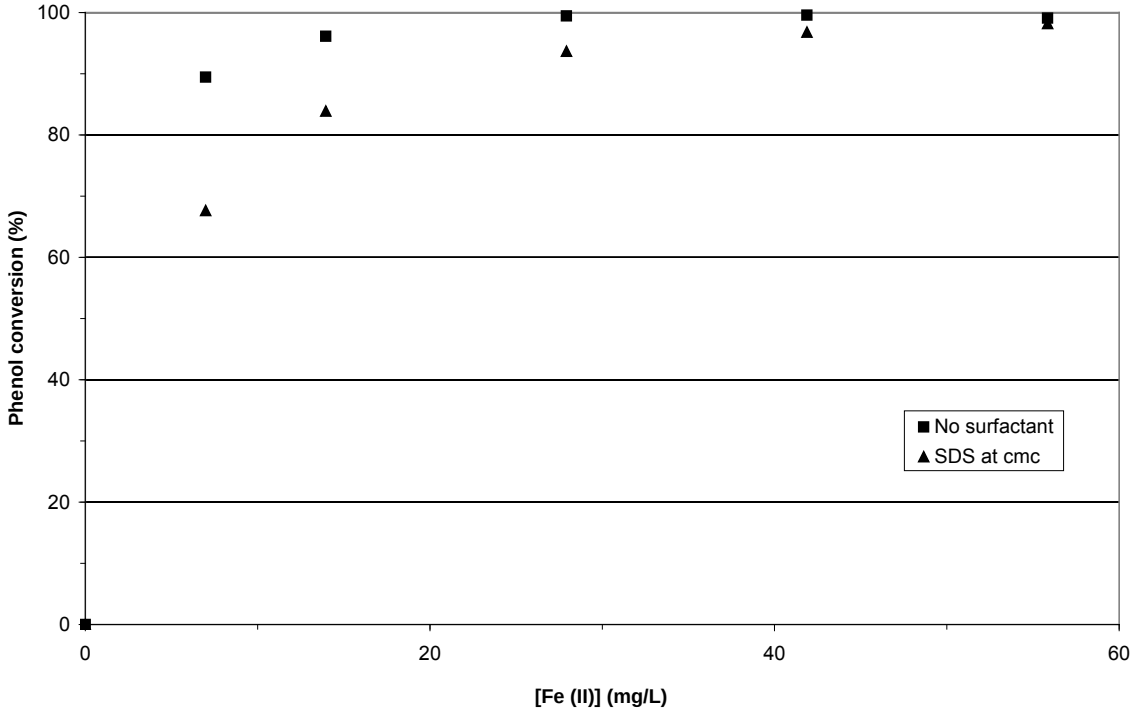

Figure 2. Effect of the iron concentration on the phenol conversion in the absence/presence of SDS at its cmc after 90 min. 2500 mg/L phenol; 12500 mg/L H_2O_2; 2307 mg/L SDS (when present).

3.3 SDS morphology effect

The effect of the SDS concentration on the phenol conversion is discussed in this section as it can affect both on its degradation as well as on that of the phenol. The iron and hydrogen peroxide concentrations in these experiments were 7 and 12500 mg/L, respectively. Figure 3

shows the effect of the SDS concentration on the phenol conversion along the time. As it can be observed, an increase of the SDS concentration, up to its cmc (2307 mg/L), results in a phenol conversion decrease. However, any further increase on the SDS beyond its cmc does not change the phenol conversion. Thus, it is clear that the morphology of the surfactant molecules plays a key role on the phenol degradation efficiency. As the oxidation conditions (iron and hydrogen peroxide concentrations) remain unchanged in the experiments of this section, the amount of produced OH• radicals is assumed to be the same in all cases. Thus, any increase on the SDS concentration would result in higher SDS degradation (if occurring), therefore in a lower phenol degradation, if the degradation of SDS is seen as a parallel reaction competing for the radicals. As the results do not show this tendency, it can be deducted that the decrease on the phenol conversion when SDS is present in solution is mainly due to the fact that phenol molecules are hosted in the interior of surfactant micelles, decreasing their availability to be oxidised by the OH• radicals produced in the bulk solution.

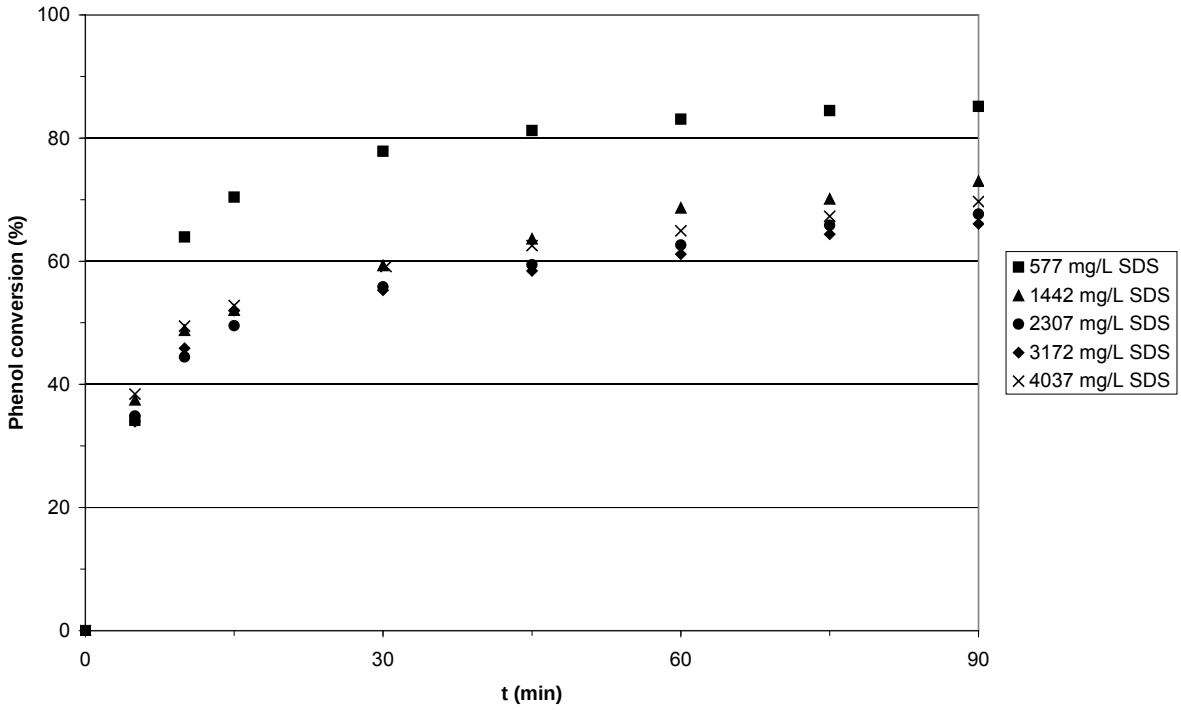

Figure 3. Effect of the SDS concentration on the phenol conversion. 2500 mg/L phenol; 12500 mg/L H_2O_2; 7 mg/L Fe (II).

4 Conclusions

The Fenton process is an adequate oxidation process for dealing with aqueous phenol solutions. However, at the same oxidation conditions, when SDS is present in the phenolic solution, the phenol conversion is lower at low iron (II) concentrations (below around 40 mg/L) than when no SDS is present in the solutions to be treated. Nevertheless, increasing the Fe (II) concentration, an almost complete oxidation of the phenol can be achieved even when SDS is present in the polluted solution at a concentration equal to its cmc. The effect of the concentration of hydrogen peroxide is not a crucial parameter as it does not enhance the oxidation efficiency at the tested conditions. On the contrary, when working at high oxidant concentrations, the phenol conversion decreases (in absence/presence of SDS) owing to its self-consumption.

A possible codegradation of the SDS molecules as well as the fact that phenol molecules are hosted in the SDS micelles interior, thus decreasing their availability to be attacked by the hydroxyl radicals involved in the process, may be the reason of the decrease of phenol

degradation when SDS is present at its cmc concentration. The results obtained at variable SDS concentrations demonstrate that the morphology of the SDS in solution is crucial for the decrease of the oxidation efficiency. At SDS concentrations lower than the cmc, an increase on the SDS concentration causes a decrease on the phenol conversion. However, beyond the cmc, any further increase on the SDS concentration does not render any change on the phenol conversion. These experimental findings seem to indicate that the main phenomenon responsible of the phenol conversion decrease is the presence of SDS in micelar form. These micelles host phenol molecules in their interior, which are more difficult to be attacked by the OH• radicals produced in the bulk solution. Although the previous hypothesis seems to be the most likely for describing the presented results, a possible codegradation of the SDS cannot be completely rejected as the OH• radicals involved in the Fenton's reaction are non-selective radicals and might also attack the SDS molecules.

Acknowledgements

This work was funded by the Spanish Ministry of Education and Science (research grant CTM2005-01873/TECNO). We are also indebted to the Rovira i Virgili University for providing a fellowship to one of the authors.

References

Chamarro, E., Marco, A., Esplugas, S. (2001). Use of Fenton reagent to improve organic chemical biodegradability. *Water Research,* 35, 1047-1051.

Cobra Guimaraes, O.L., Villela Filho, D.N., Siqueira, A.F., Izário Filho, H.J., Borges Silva, M. (2008). Optimization of the AZO dyes decoloration process through neural networks: Determination of the H_2O_2 addition critical point. *Chemical Engineering Journal,* 141, 35-41.

Esplugas, S., Bila, D.M., Krause, L.G.T., Dezotti, M. (2007). Ozonation and advanced oxidation technologies to remove endocrine disrupting chemicals (EDCs) and pharmaceuticals and personal care products (PPCPs) in water effluents. *Journal of Hazardous Materials,* 149, 631-642.

Ghiselli, G., Jardim, W.F., Litter, M.I., Mansilla, H.D. (2004). Destruction of EDTA using Fenton and photo-Fenton-like reactions under UV-A irradiation. *Journal of Photochemistry and Photobiology A: Chemistry,* 167, 59-67.

Lodha, B., Chaudhari, S. (2007). Optimization of Fenton-biological treatment scheme for the treatment of aqueous dye solutions. *Journal of Hazardous Materials,* 148, 459-466.

Mukherjee, S., Kumar, S., Misra, A.K., Fan, M. (2007). Removal of phenols from water environment by activated carbon, bagasse ash and wood charcoal. *Chemical Engineering Journal,* 129, 133-142.

Park, Y., Skelland, A.H.P., Forney, L.J., Kim, J.-H. (2006). Removal of phenol and substituted phenols by newly developed emulsion liquid membrane process. *Water Research,* 40, 1763-1772.

Suárez-Ojeda, M.E., Stüber, F., Fortuny, A., Fabregat, A., Carrera, J., Font, J. (2005). Catalytic wet air oxidation of substituted phenols using activated carbon as catalyst. *Applied Catalysis B: Envioronmental,* 58, 105-114.

Suárez-Ojeda, M.E., Guisasola, A., Baeza, J.A., Fabregat, A., Stüber, F., Fortuny, A., Font, J., Carrera, J. (2007). Integrated catalytic wet air oxidation and aerobic biological treatment in a municipal WWTP of a high-strength o-cresol wastewater. *Chemosphere,* 66, 2096-2105.

Van der Bruggen, B., Schaep, J., Wilms, D., Vandecasteele, C. (1999). Influence of molecular size, polarity and charge on the retention of organic molecules by nanofiltration. *Journal of Membrane Science,* 156, 29-41.

Proceedings of the 10th International Chemical and
Biological Engineering Conference - CHEMPOR 2008
Braga, Portugal, September 4-6, 2008
E.C. Ferreira and M. Mota (Eds.)

Electrochemical ozone production for *in situ* atrazine degradation in aquifers – a laboratory study

Ysrael M.Vera[1], Roberto J. Carvalho[1], Mauricio L. Torem[1]
[1] PUC-Rio – Department of Materials Science and Metallurgy.
Pontifícia Universidade Católica de Rio de Janeiro
225, Gávea - Rio de Janeiro, RJ - Brasil - 22453-900

Keywords: groundwater, remediation, electrooxidation, ozone, atrazine
Topic: Sustainable process-product development through green chemistry (Sustainable & clean technologies).

Introduction

The impact of pesticides on the quality of groundwaters has been subject of scientific and public health concerns in the entire planet, especially in the areas where groundwaters are mainly used for human consumption. The intensive use of pesticides in agriculture and the high persistence of several of these chemicals has required a rigorous control of possible environmental contaminations, especially of drinking water sources.

Atrazine (2-chlorine-4-etil-6-isopropil-1,3,5-triazin), is a herbicide that is still used extensively in Brazilian agriculture, specifically for corn, cotton, sorghum and sugar-cane. It is one of the largest pollutants of groundwater in many countries (Dörfler et al., 1997) and was selected for study because of its widespread use.

Atrazine is frequently detected in natural waters, and has been known to affect reproduction of aquatic flora and fauna, which in turn impacts on the community structure as a whole (Graymore et al., 2001).

The *in situ* chemical oxidation technology uses chemical oxidants that directly destroy dissolved contaminants in a subsurface medium. Because the process is *in situ*, no surface treatment system for the contaminants is needed and there is no treated groundwater to be discharged.

Ozone is a powerful oxidant (e^0 = 1,51 V *vs* Standard Hydrogen Electrode Potential) that does not produce toxic byproducts when decomposed and has been used in degradation of organic compounds present in soils and aquifers.

The technology of permeable reactive barriers (PRBs) is one of the remediation alternatives of greater acceptance. This technique has some advantages, such as: it is an *in situ* method; it is adequate to treat persistent pollutants in aquifers; it does not produce important physical and chemical alterations to the ground.

A new technology uses groups of electrodes as active reactive medium of the PRB to treat contaminated underground waters (e-barriers) (Wani et al., 2006). This technology can be used in situ in combination with the advanced chemical oxidation technology for the treatment of pollutants. An oxidant (ozone) is electrochemically produced in one of the electrodes that is part of the electrochemical barrier. Pollutants of interest would be transformed by the generated ozone instead of directly on the surface of the electrode. This creates an in situ degradation system constituted by an electrochemical cell that generates an oxidant substance which will transform the pollutants present in underground waters.

A study on the evaluation of the effectiveness, in a laboratory scale, of this in situ new treatment technique for atrazine was conducted. The work is divided in three main stages: 1) electrochemical ozone production in an electrochemical cell at different values of applied current as well as the determination of the dissolved ozone

concentration; 2) degradation of the atrazine in aqueous solution in order to obtain depletion curves of contaminants at different electrolysis current; 3) degradation of the atrazine in horizontally mounted column packed with cleaned sand. The results of the study are presented in this work.

Materials and methods

The Ti plates (De Nora Brazil) were polished with sand paper. The plates were degreased in 40% NaOH solution for 2 hours at 313K, pretreated by etching in boiling 10% oxalic acid for 2 hours until TiO_2 was thoroughly dissolved, and a reddish-brown titanium oxalate was produced, and conserved in an aqueous solution of 1% oxalic acid to avoid the re-formation of TiO_2 (Liu and Liu, 2008).

β-PbO_2 electrodes were prepared by electrodeposition on Ti plates a solution of $Pb(NO_3)_2$ (0.2 mol L^{-1}; pH 2; T=60 ^oC). β-PbO2 deposition was done at constant anodic current (20 mA cm^{-2}; t=20 min). The β-PbO_2 coating was deposited on top of an intermediate platinum interlayer obtained by electrodeposition at 30 mA cm^{-2} (t=5 min) from H_2PtCl_6 solution (0.002 mol L^{-1}).

The electrochemical ozone production for different current densities (50, 100 and 150 mA cm^{-2}) was achieved in a divided cell comprising one β-PbO_2 coated titanium anode and one ruthenium oxide-coated titanium cathode. Each compartment has a volume of around 500 mL.The geometric area of the electrodes was 15 cm^2. A phosphate buffer solution 0.1 M (pH=7) was used. Nitrogen gas was passed through both side of the cell and the gas exiting the anode was bubbled through a solution of 20g L^{-1} KI. The iodine formed from the oxidation of iodide with ozone was determined by titration with sodium thiosulphate. Starch solution was used as indicator (Gordon et al., 1989).

Determination of dissolved ozone is made in a one-compartment cell. The electrolysis cell is cooled by tap water circulating around it. The electrodes and electrolytic solution are the same as above. The volume of solution was 400 mL. The dissolved ozone concentration was measured by the indigo method (Bader and Hoigné, 1981).

The degradation of a 400 mL of a phosphate buffered (0.1 M, pH=7) solution containing an atrazine concentration of 1 mgL^{-1} by electrochemically produced ozone has been studied by applying three different current densities (50, 100 and 150 mA cm^{-2}). The atrazine depletion concentration in solution was determined by HPLC analytical method.

The acrylic column (25 cm x 4 cm ID) contained a single set of electrodes. Two expanded titanium mesh coated with β-PbO_2 and RuO_2 (De Nora Brazil) served as anode and cathode, respectively. The surface area of a single electrode was approximately 15 cm^2. The electrodes were mounted at 12.6 cm (anode) and 13.4 cm (cathode) from the inlet to the e-barrier column. The inter-electrode space was filled with a 6 mm layer of glass beads. The remainder of the column was packed with cleaned sand intended to approximate the aquifer material. A reference electrode of Ag/AgCl/Cl^-(saturated) was installed in the vicinity of the anode to measure the electrode potential.

A solution with a concentration close to 1 mg L^{-1} was pumped through the column using a peristaltic pump at a flow around 0.5 ml min^{-1}. After the reactor was completely filled with the pesticide solution, a constant current was applied to the electrodes in two steps, 400 mA for 4.5 hours followed by 1.5 hours at 600 mA (26.7 and 40 mA cm^{-2}, respectively).

Three glass sample ports allow for the collection of aqueous samples for bed profile analysis. One sampling port was positioned in the middle of the electrodes and the others upstream and downstream of the electrodes.

A tracer test was performed to evaluate the hydrodynamic properties of the sand pack in the column. Tracer test was performed by adding chloride at a 1000 mg L^{-1} and sampling the effluent periodically to develop a breakthrough curve. An advection-dispersion model was fitted to the data to determine dispersivity and bed porosity.

Results

The obtained results show that the ozone production increases with incrementing the current density. The rate of ozone production during the electrolysis was 4.8, 18.0 and 38.6 mg h^{-1} for current densities of 50, 100 and 150 $mAcm^{-2}$, respectively.

In addition, for all density current values considered in the dissolved ozone experiments (0.5 x 10^3, 1 x 10^3 and 1.5 x 10^3 Am^{-2}), the dissolved ozone concentration increases with time, remaining constant beyond a certain time (around 50 minutes). The dissolved ozone concentration for current densities of 100 and 150 $mAcm^{-2}$ was higher than for a current density of 50 $mAcm^{-2}$. The rate of ozone production at 150 $mAcm^{-2}$ was two times the rate at 100 $mAcm^{-2}$, however the dissolved ozone concentration in solution during the experiments was very similar at these two current densities as shown in Figure 1.

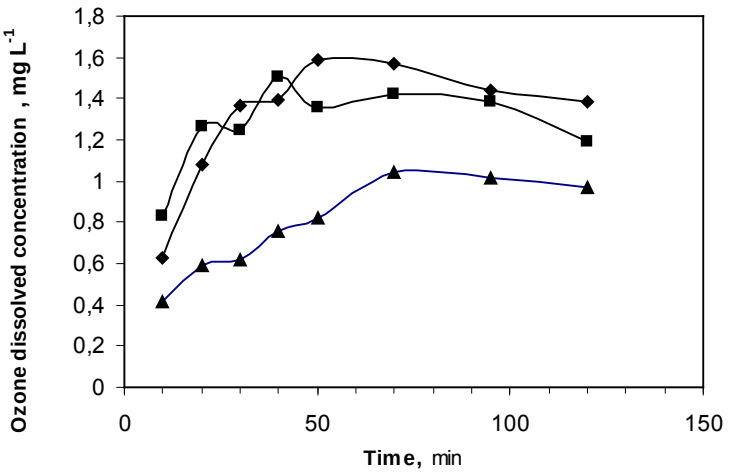

Fig. 1. Effect of current density on ozone dissolved concentration with β-PbO_2 anode (electrolyte, 0.1M phosphate buffer; pH 7): (▲) 50$mAcm^{-2}$, (■) 100$mAcm^{-2}$, and (♦) 150$mAcm^{-2}$.

In the experiments of atrazine degradation by electrochemically generated ozone a difference in atrazine degradation was found when the applied current density was varied, as shown in Figure 2. The results show that electrolytic transformation of atrazine occurred under different rates that depend upon current density. This is indicative of a greater oxidation ability of the anode with increasing the current applied due to the production of more electrogenerated active oxidant (O_3). The extent of O_3 generation can be controlled by a proper choice of current, thus it is quite possible to obtain the higher degradation efficiency.

The kinetic analysis of the above results related to different reaction orders gave good linear correlations, when the data was fitted with a pseudo first-order reaction rate equation. The straight lines thus obtained for three different current densities with an initial concentration of 1 mg L^{-1}, are presented as an inset in Figure 2. The pseudo first-order rate constants obtained are 6.2×10^{-3}, 9.7×10^{-3}, and 1.21×10^{-2} s^{-1} for 50, 100, and 150$mAcm^{-2}$, respectively.

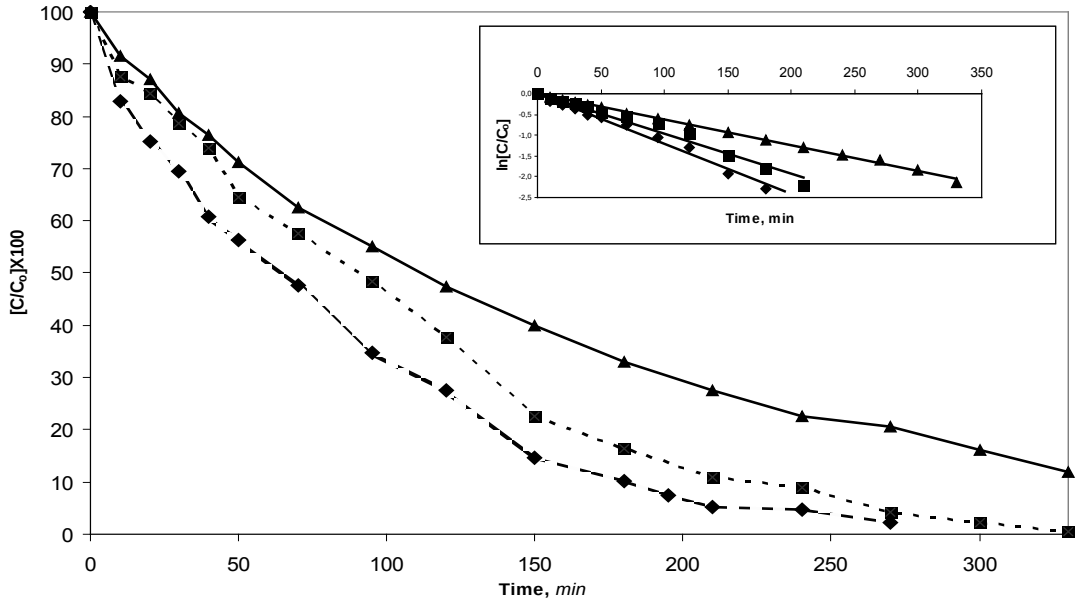

Fig. 2. Effect of current density on atrazine degradation with β-PbO_2 anode (atrazine, 1mgL^{-1}; electrolyte, 0.1M phosphate buffer; pH 7): (▲) 50mAcm^{-2}, (■) 100mAcm^{-2}, and (♦) 150mAcm^{-2}. *Inset*: Corresponding kinetic analysis assuming a pseudo first-order reaction for atrazine decay.

The results of tracer tests revealed that the e-barrier column packing material has an effective porosity of 0.15 and dispersivity of 0.24 cm.

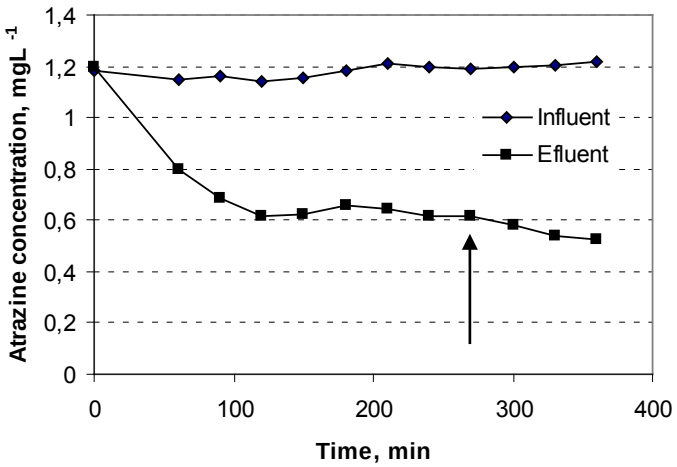

Fig. 3. Atrazine concentration, in the influent and effluent to column, as a function of time. Arrow indicates the time when the current applied was augmented from 400 mA to 600 mA.

Atrazine concentrations in the influent and effluent streams from the e-barrier column were monitored over time and are shown in the Figure 3. The increase in current results in increased transformation of atrazine. Atrazine inlet concentrations of ~1.2 mg L^{-1} were reduced to about 0.52 mg L^{-1}.

Conclusion

The column study reported herein demonstrated that approximately 56% of influent atrazine concentrations can be transformed. These results confirm the potential applicability of this type of groundwater plume control strategy. Based on the results of this study, it is expected that in a field application more than one set of electrodes would be required to completely transform atrazine to environmentally benign products.

References

Bader, H. and Hoigné, J. (1981). Determination of ozone in water by the indigo method. *Water Research*, 15, 449-456.

Dörfler, U., Feicht, E.A., Scheunert, I. (1997). S-Triazine residues in groundwater. *Chemosphere,* 35, 99-106.

Gordon, G.,Rakness, K., Vomehm, D., Wood, D. ILimitations of the Iodometric Determination of Ozone. *Journal American Water Works Association*, 81, 72-76.

Graymore, M., Stagnitti, F., Allinson, G. (2001). Impacts of atrazine in aquatic ecosystems. *Environment International*, 26, 483-495*.*

Liu, Y. and Liu, H. (2008). Comparative studies on the electrocatalytic properties of modified PbO2 anodes. *Electrochimica Acta*, 53, 5077–5083.

Wani, A.H., O'Neal, B.R., Gilbert, D.M., Gent, D.B., Davis, J.L. (2006). Electrolytic transformation of ordinance relate compounds in groundwater: Laboratory mass balance studies. *Chemosphere*, 62, 689-698.

Proceedings of the 10th International Chemical and
Biological Engineering Conference - CHEMPOR 2008
Braga, Portugal, September 4-6, 2008
E.C. Ferreira and M. Mota (Eds.)

Catalytic ozonation applied to the treatment of coloured effluents

Patrícia C.C. Faria, José J.M. Órfão, Manuel F. R. Pereira*
Laboratório de Catálise e Materiais (LCM), Laboratório Associado LSRE/LCM,
Departamento de Engenharia Química, Faculdade de Engenharia, Universidade do Porto,
Rua Dr. Roberto Frias, 4200-465 Porto, Portugal

Keywords: ozonation, catalysis, activated carbon, cerium oxide, textile dyes
Topic: Advancing the chemical and biological engineering fundamentals

Abstract

The present work reports data on the catalytic ozonation of three commercial dyes from different chemical classes. One acid azo dye, CI Acid Blue 113, and two reactive dyes, CI Reactive Yellow 3 and CI Reactive Blue 5, with azo and anthraquinone chromophores, respectively, were used as representative textile dyes. The catalytic activities of activated carbon, cerium oxide and a ceria-activated carbon composite were evaluated in the mineralisation of the selected dyes. In all cases, complete decolourisation was achieved by single ozonation. The ceria-activated carbon composite allowed the highest removal of total organic carbon. For the lower dye concentrations, total mineralisation was achieved with the composite after two hours of reaction. The activity of the catalyst containing cerium was affected by the presence of carbonate and bicarbonate ions due to their scavenging effect towards hydroxyl radicals. All the catalytic systems were evaluated in the treatment of a textile effluent, collected after conventional biological treatment. Catalytic ozonation was proven to be effective when used as tertiary treatment for bio-treated effluents.

1 Introduction

Intense colour is one of the main characteristics of textile wastewater originated from spent dye baths and dye rinsing operations. Besides the undesirable aesthetic impact caused by such effluents in receiving natural water courses, the persisting colour and the non-biodegradable nature of most of the textile dyes represent serious problems to the environment. Conventional aerobic biological treatments have proven insufficient to completely remove colour from textile plant effluents (Marmagne and Coste 1996; Vandevivere et al. 1998). Although there are several physical-chemical methods applied for colour removal, such as adsorption, membrane processes or physico-chemical treatments, chemical oxidation has become the method of choice due to its high efficiency and ease of operation. Owing to its extremely high redox potential, ozone is one of the most effective oxidant agents used for this purpose. The oxidation of dyes and chemical auxiliaries present in textile effluents lead to the formation of intermediates that are frequently resistant to ozone attack. Such compounds of low reactivity towards ozone may be efficiently removed by oxidation via $HO^{\bullet}$ radicals (Hoigné and Bader 1983). Presently, advanced oxidation processes and catalytic oxidation are the main emerging routes for the removal of such compounds. Heterogeneous catalytic ozonation aims to enhance the removal of more refractory compounds by the transformation of ozone into more reactive species and/or by adsorption and reaction of the pollutants on the surface of the catalyst (Legube and Leitner 1999). Oxides of transition metals are trendy catalysts in ozonation processes, and activated carbon is also an attractive and promising alternative to the treatment of wastewater containing dyes or other organic contaminants (Lin and Lai 2000; Rivera-Utrilla and Sánchez-Polo 2002; Faria et al. 2005; Beltrán et al. 2006; Faria et al. 2008a). The

* Corresponding author. Tel + 351-225-081-468. E-mail: fpereira@fe.up.pt

development of highly effective catalysts for the application in ozonation processes, and the understanding of the inherent mechanisms are of great relevance.

2 Material and Methods

Three commercial textile dyes from different classes (CI Reactive Blue 5, CI Reactive Yellow 3 and CI Acid Blue 113), with known molecular structure, were selected for this study. The experiments were carried out at the natural pH of the solutions. The concentration of each dye in solution was followed by UV/Vis spectrophotometry. The mineralisation of the solutions was followed by measuring the total organic carbon (TOC).

Cerium oxide (Ce-O) was prepared by precipitation from the corresponding nitrate aqueous solution ($Ce(NO_3)_3.6H_2O$) (Imamura et al. 1985). A composite of activated carbon/cerium oxide (AC_0-Ce-O) was prepared by a similar procedure used for the preparation of sample Ce-O, where a given amount of activated carbon (AC_0) was dispersed in the cerium nitrate solution before precipitation. The textural characterization of the materials was based on the corresponding N_2 equilibrium adsorption isotherms. Cerium containing samples were characterized by XRD, XPS and SEM. Thermal analysis of sample AC_0-Ce-O, carried out under a flow of air, revealed a cerium oxide average content of 45% wt. Samples Ce-O and AC_0-Ce-O have BET surface areas of 72 and 583 m^2/g, respectively. The selected activated carbon has a BET surface area of 909 m^2/g, and its complete characterization is reported elsewhere (Faria et al. 2006). According to the XRD results, the dominant diffraction peaks observed for both samples are those characteristic of cerianite (CeO_2). The presence of the Ce (IV)/Ce (III) redox couple on the surface of the prepared ceria containing catalysts was evidenced by XPS analysis. Additional detailed information on the characterization of the ceria materials is reported elsewhere (Faria et al. 2008b)

3 Results and Discussion

The mineralisation of the AB113, RY3, and RB5 solutions with an initial concentration of 50 mg/L was carried out by ozonation catalysed by AC_0, Ce-O and AC_0-Ce-O. Experimental data corresponding to the decolourisation kinetics of AB113, RY3 and RB5 by non-catalytic ozonation and adsorption on AC_0 are depicted in Figure 1, in order to allow the comparison of the performance of the different dyes towards activated carbon adsorption and ozone attack.

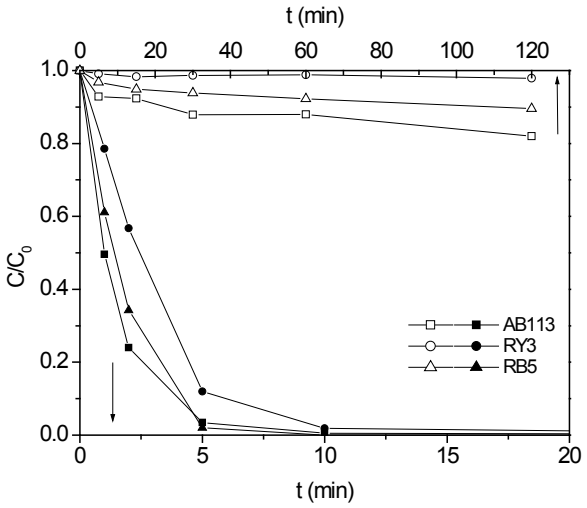

Figure 1 Kinetics of the non-catalytic ozonation (filled symbols) and adsorption on AC_0 (open symbols) of AB113, RY3 and RB5 at the natural pH of the solutions (C_0 = 50mg/L, AC_0 = 0.5 g/L).

Under the experimental conditions used in this work, the adsorption of the selected dyes is rather limited, as shown in Figure 1. In fact, the RY3 dye has a very low affinity towards activated carbon. After 120 min, the removal of AB113 and RB5 by adsorption on AC_0 was ca. 18% and 11%, respectively. The presented data show that adsorption is not effective for the decolourisation of these solutions. On the other hand, single ozonation allows a fast colour removal in short reaction times (less than 10 min).

Even though the decolourisation of the synthetic coloured solutions was not visibly enhanced by the studied catalytic systems, entirely different results were observed when analyzing the extent of the mineralisation achieved during catalytic ozonation. The kinetic data corresponding to the evolution of TOC during the catalytic ozonation of RY3 and RB5 are presented in Figure 2.

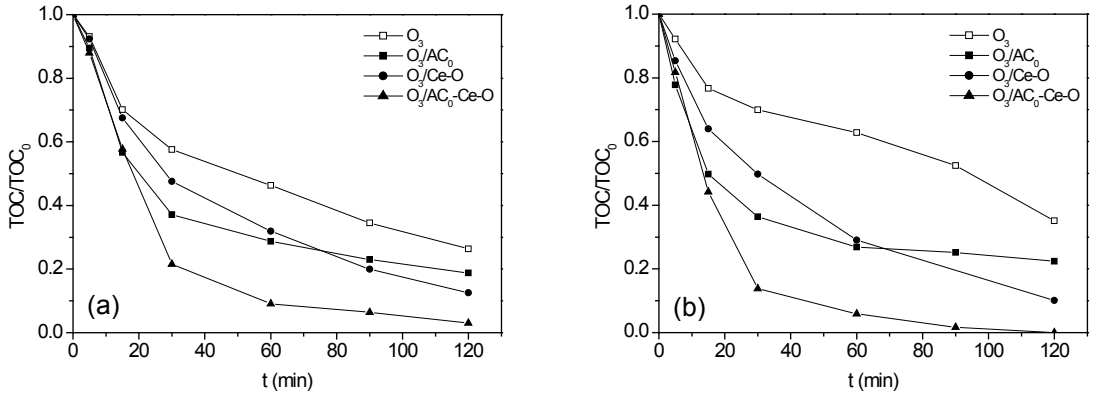

Figure 2 Evolution of dimensionless TOC during non-catalytic and catalytic ozonation of (a) RY3 (C_0 = 50 mg/L, pHi = 5.8) and (b) RB5 (C_0 = 50 mg/L, pHi = 5.6).

A very similar trend was observed for all the studied dyes. In the case of RY3 the simultaneous use of ozone and activated carbon led to an enhanced TOC removal when compared to single ozonation (Figure 2a). As previously shown, RY3 has very little affinity towards activated carbon; therefore, the enhanced results may be attributed to the catalytic effect of activated carbon mainly in the oxidation of intermediate products. Comparatively to non-catalytic ozonation, the simultaneous use of ozone and activated carbon increased the removal of TOC from 42% to 63%, after 30 min. The highest mineralisation extent was obtained with the activated carbon-ceria composite. After 30 min of reaction, the TOC removal achieved was 78% against 42% obtained by single ozonation. Sample AC_0-Ce-O allowed nearly total mineralisation of the solution after a longer reaction period.

The reactive blue dye RB5 was shown to be the most refractory towards single ozonation and the biggest difference between non-catalytic and catalytic ozonation was observed in this case (Figure 2b). After 30 minutes of reaction, the mineralisation extent obtained in non-catalytic ozonation was only about 30%, but the addition of the activated carbon to the process approximately doubled the percentage of TOC removed. A remarkable enhancement in the mineralisation degree was obtained during the ozonation catalysed by the composite AC_0-Ce-O. After 30 min, less than 14% of the initial TOC is present in solution and total mineralisation is achieved in less than 2 h of reaction.

In all cases, cerium oxide was found to be an efficient ozonation catalyst and higher mineralisation degrees were achieved comparatively to the performance of activated carbon, but only for longer reaction periods (higher than ca. 60 min). Superior initial reaction rates are observed for the TOC removal during ozonation catalysed by both AC_0 and AC_0-Ce-O. This observation suggests a reaction mechanism distinct from that of cerium oxide catalytic ozonation. The latter is dependent of the formation of $HO^{\bullet}$ radicals (Faria et al. 2008b), while the former namely comprises surface reactions on the activated carbon, as reported in a

previous work (Faria et al. 2008a). It was suggested that cerium oxide promotes the decomposition of ozone into $HO^{\bullet}$ radicals, which are the main oxidant species responsible for the oxidation of the compounds in the liquid phase. A strong synergic effect was observed between activated carbon and cerium oxide in the AC_0-Ce-O composite. The reaction mechanism is believed to comprise both surface reactions, similar to what occurs with activated carbon promoted ozonation and also liquid bulk reactions involving $HO^{\bullet}$ radicals. It was assumed that the existence of delocalized electrons on the basal planes of the activated carbon contributes to the formation of Ce (III) species, which are thought to be necessary for promoting the decomposition of O_3 into $HO^{\cdot}$ radicals by redox reactions on the catalyst surface involving the pair Ce(III)/Ce(IV).

Generally, in addition to dyes, reactive dye baths involve the use of several auxiliary chemicals, such as sodium chloride (NaCl), sodium carbonate (Na_2CO_3), and sequestering agents. The main role of the Na_2CO_3 is to increase and buffer the pH of the dye bath, favouring the reaction between the reactive group of the dye and the -OH groups of cellulose. The influence of the addition of Na_2CO_3 in the catalytic ozonation of dye solutions was also assessed. The simulated effluent containing 300 mg/L of RB5 and 1 g/L of Na_2CO_3 was treated by catalytic and non-catalytic ozonation. After 15 min of reaction, the colour removal achieved lies between 97% and 98% for all the catalytic systems and the time required for nearly total decolourisation was less than 30 minutes. The effect of the addition of sodium carbonate was mostly noticeable in the extent of the mineralisation of the solution. Experimental data referring to the TOC removal in the studied catalytic systems is depicted in Figure 3.

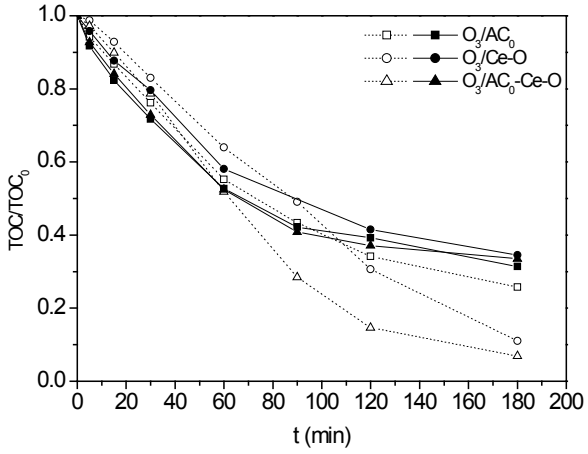

Figure 3 Effect of the presence of HCO_3^-/ CO_3^{2-} (filled symbols) on the evolution of dimensionless TOC during catalytic ozonation of RB5 C_0 = 300 mg/L.

The presence of HCO_3^-/ CO_3^{2-} was found to significantly affect the activity of Ce-O for the mineralisation of RB5. A similar effect was observed for the composite AC_0-Ce-O. On the contrary, the catalytic action of AC_0 is only slightly affected, if compared with the results obtained in the absence of Na_2CO_3. As previously mentioned, the addition of Na_2CO_3 increases the solution pH and alkalinity. The mineralisation of organic compounds, achieved by ozonation, is usually favoured at higher pH values, due to the participation of $HO^{\bullet}$ radicals in the reaction mechanism. However, the scavenging effect of both of HCO_3^- and CO_3^{2-} species decrease the amount of $HO^{\bullet}$ radicals available for reaction with the organic compounds, therefore partially inhibiting the mineralisation process. In a previous work (Faria et al. 2008b), cerium oxide was shown to catalyse the ozonation of carboxylic acids manly through reactions involving $HO^{\bullet}$ radicals. In this work, the inhibiting effect of the HCO_3^-/ CO_3^{2-} confirms that the mineralisation of the intermediates of the process also occurs by a radical

mediated reaction mechanism. Nevertheless, Ce-O still has a significant catalytic activity, as higher mineralisation is attained when compared to single ozonation. In the case of the composite, the results obtained up to 60 minutes of reaction are not noticeably affected by the presence of sodium carbonate (see Figure 3). After this period, a significant reduction in the catalyst activity was observed. The removal of TOC obtained after 120 min of reaction was 63% contrasting with the 85% obtained in the absence of carbonates.

The similarity of the performance of AC_0 and AC_0-Ce-O in the mineralisation of the CI RB5 should be pointed out. Apparently, the presence of the scavenger has very little effect on the activity of the activated carbon, since only a slight reduction in the removal of TOC was observed for longer reaction period comparatively to the results obtained in the absence of the carbonates. This observation suggests that the contribution to the production of $HO^{\bullet}$ radicals is not the only role of activated carbon. It is thought that activated carbon also promotes the decomposition of dissolved ozone that may originate surface oxygen-containing radical species, which participate in the oxidation of the organic compounds. In this way, activated carbon seems to be a good catalyst for practical purposes, as its activity is not significantly affected by the presence of $HO^{\bullet}$ scavenging species.

Catalytic ozonation is a powerful chemical oxidation process that can be applied to the treatment of a vast range of organic pollutants, and it has been shown to be a promising technique to the treatment of wastewater from the textile industry. In order to evaluate the efficiency of the selected catalysts in the ozonation of real wastewater samples, a mixed textile effluent collected after biological treatment was used as a case study. Despite the strong visible colour of the effluent, complete decolourisation was achieved by single ozonation shortly after 5 minutes, confirming the strong decolourisation potential of ozone.

A higher mineralisation degree was achieved with catalytic ozonation, being AC_0 and AC_0-Ce-O the catalysts leading to the best results. In the presence of activated carbon, the removal of TOC achieved after 30 min was approximately 57%, which is significantly higher when compared to the 30% TOC removal achieved in non-catalytic ozonation. Unlike what was observed for all the studied dye solutions, no major differences were observed between activated carbon and the composite. Additionally, sample Ce-O was visibly less active. The performance observed during the catalytic ozonation of the bio-treated effluent was attributed to the presence of HCO_3^- and CO_3^{2-}, which, as explained in the previous section, act as radical scavengers, therefore inhibiting the mineralisation of the organic compounds via $HO^{\bullet}$ oxidation. AC_0 and AC_0-Ce-O have similar catalytic activities, which may be explained by the contribution of the surface reactions that are believed to occur preferentially on the activated carbon, therefore not involving $HO^{\bullet}$ radicals in solution.

The application of ozone processes as post-treatment for a refined depuration of wastewater is of great interest. In the case of liquid effluents from the textile industry, ozone has proven to be highly effective for an extensive elimination of colour. Concerning the removal of recalcitrant compounds, which cannot be eliminated in biological processes, catalytic ozonation emerges as a feasible solution to significantly enhance the mineralisation of such effluents.

4. Conclusions

Ozonation is a powerful oxidation process for fast and total decolourisation of both synthetic dye solutions and real textile effluents.

The combination of activated carbon with ozone enhanced the mineralisation levels of both the dye solutions and the textile effluents. The results obtained in this study show that cerium oxide is an effective ozonation catalyst for the mineralisation of textile dye solutions. Comparatively to the performance of the commercial activated carbon, an enhanced mineralisation extent was achieved, which is explained by a higher ability to catalyse the decomposition of ozone into $HO^{\bullet}$ radicals. A strong synergic effect was observed between activated carbon and cerium oxide in the prepared composite, leading to enhanced

mineralisation degrees for all the studied dye solutions. The mechanism of the ozonation catalysed by the ceria-activated carbon composite is believed to comprise both surface reactions, similar to what occurs with activated carbon promoted ozonation, and also liquid bulk reactions involving $HO^{\bullet}$ radicals, resultant from the catalytic decomposition of ozone on the surface of the catalyst, mainly in the presence of cerium oxide.

The presence of bicarbonate and carbonate ions in solution was shown to partially inhibit the mineralisation of the CI Reactive Blue 5 dye. The negative impact on both Ce-O and AC_0-Ce-O activities is supposed to be related to the scavenging effect of those inorganic ions on the $HO^{\bullet}$ radicals formed. The presence of high concentrations of inorganic ions with scavenging properties may restrain the results obtained in wastewater treatment by advanced oxidation processes. Activated carbon catalysts also promote surface oxidation reactions that do not involve $HO^{\bullet}$ radicals in solution; therefore their activity is not severely affected by the presence of scavenger species. This was confirmed by testing the efficiency of these catalytic systems in the mineralisation of a bio-treated textile effluent.

References

Beltrán, F. J., García-Araya, J. F., Giráldez, I. (2006). Gallic acid water ozonation using activated carbon. *Applied Catalysis B: Environmental*, 63, 249-259.

Faria, P. C. C., Órfão, J. J. M., Pereira, M. F. R. (2005). Mineralisation of coloured aqueous solutions by ozonation in the presence of activated carbon. *Water Research*, 39, 1461-1470.

Faria, P. C. C., Órfão, J. J. M., Pereira, M. F. R. (2006). Ozone decomposition in water catalyzed by activated carbon: Influence of chemical and textural properties. *Industrial & Engineering Chemistry Research*, 45, 2715-2721.

Faria, P. C. C., Órfão, J. J. M., Pereira, M. F. R. (2008a). Activated carbon catalytic ozonation of oxamic and oxalic acids. *Applied Catalysis B: Environmental*, 79, 237-243.

Faria, P. C. C., Órfão, J. J. M., Pereira, M. F. R. (2008b). A novel ceria-activated carbon composite for the catalytic ozonation of carboxylic acids. *Catalysis Communications*, 9, 2121-2126.

Hoigné, J., Bader, H. (1983). Rate constants of reactions of ozone with organic and inorganic compounds in water - II Dissociating organic compounds. *Water Research*, 17, 185-194.

Imamura, S., Doi, A., Ishida, S. (1985). Wet oxidation of ammonia catalyzed by cerium-based composite oxides. *Industrial & Engineering Chemistry Product Research and Development*, 24, 75-80.

Legube, B., Leitner, N. K. V. (1999). Catalytic ozonation: a promising advanced oxidation technology for water treatment. *Catalysis Today*, 53, 61-72.

Lin, S. H., Lai, C. L. (2000). Kinetic characteristics of textile wastewater ozonation in fluidized and fixed activated carbon beds. *Water Research*, 34, 763-772.

Marmagne, O., Coste, C. (1996). Color removal from textile plant effluents. *American Dyestuff Reporter*, 15-21.

Rivera-Utrilla, J., Sánchez-Polo, M. (2002). Ozonation of 1,3,6-naphthalenetrisulphonic acid catalysed by activated carbon in aqueous phase. *Applied Catalysis B: Environmental*, 39, 319-329.

Vandevivere, P. C., Bianchi, R., Verstraete, W. (1998). Treatment and reuse of wastewater from the textile wet-processing industry: Review of emerging technologies. *Journal of Chemical Technology and Biotechnology*, 72, 289-302.

Acknowledgments: This work was carried out with the support of Fundação para a Ciência e a Tecnologia (FCT) – (POCTI/1181) and research fellowship BD/18169/2004.

Proceedings of the 10th International Chemical and
Biological Engineering Conference - CHEMPOR 2008
Braga, Portugal, September 4-6, 2008
E.C. Ferreira and M. Mota (Eds.)

ION EXCHANGE MEMBRANE BIOREACTOR MODELLING FOR REMOVAL OF ANIONIC MICROPOLLUTANTS FROM DRINKING WATER SUPPLIES

Ana Rita Ricardo, Rui Oliveira, Svetlozar Velizarov, Maria Reis, João Crespo*
REQUIMTE / CQFB, Department of Chemistry, FCT, Universidade Nova de Lisboa,
P-2829-516 Caparica, Portugal

Keywords: Ion exchange membrane bioreactor, Donnan dialysis, Water treatment, Anionic micropollutants, Modelling
Topic: Sustainable process-product development through green chemistry

Abstract

This paper gives an overview of our most recent studies on the Ion Exchange Membrane Bioreactor concept for treating drinking water streams polluted with anionic micropollutants such as nitrate, perchlorate and bromate. Special focus is put on the process modelling strategies, including mechanistic, non-parametric as well as hybrid models, in order to allow for covering a broader range of possible polluted water treatment scenarios and operating conditions. A recent modification of the IEMB concept to situations, in which biotransformation is not an advantageous solution (e.g. arsenate) is also mentioned briefly.

1 Introduction

A general limitation of using ion exchange membranes for removal of micropollutants from water is the formation of a toxic brine stream, which has to be treated before disposal. Oppositely, biological treatment processes are able to degrade the pollutants transforming them into harmless products. However, biodegradation may induce secondary contamination of the treated water by microbial cells, nutrients and metabolic by-products. Therefore, integrated and eco-efficient process solutions are highly desirable.

The ion exchange membrane bioreactor (IEMB) (Velizarov et al., 2000/2001; Crespo and Reis, 2003) combines the transport of charged pollutants through a dense ion exchange membrane with their simultaneous biodegradation by an anoxic microbial culture in a separated compartment (biological compartment) as schematically illustrated in Figure 1. The membrane is positively charged, thus allowing the passage of anions like nitrate, perchlorate, bromate, etc. Once in the biological compartment these anions are reduced to innocuous species, such as nitrogen, chloride, bromide respectively. Using this technology, no toxic brine is produced and, due to a physical separation of the water and the biological compartment, no secondary contamination of the treated water occurs. The transport across the membrane is governed by the Donnan dialysis principles, using chloride as the driving counter-ion. Therefore, the transport of target anions can be improved using an excess of chloride in the biological compartment.

Besides exploring the IEMB concept for the removal of cationic micropollutants such as heavy metals (e.g. Hg^{2+}, Velizarov et al., 2008), we are presently focusing on the impact of the membrane choice (lower cost common anion exchange membranes versus mono-anion selective anion exchange membranes) on the process performance and on optimizing the IEMB process regarding the biomedium composition and biocompartment operating conditions.

* Corresponding author. Tel + 351-212-948385. E-mail:jgc@dq.fct.unl.pt

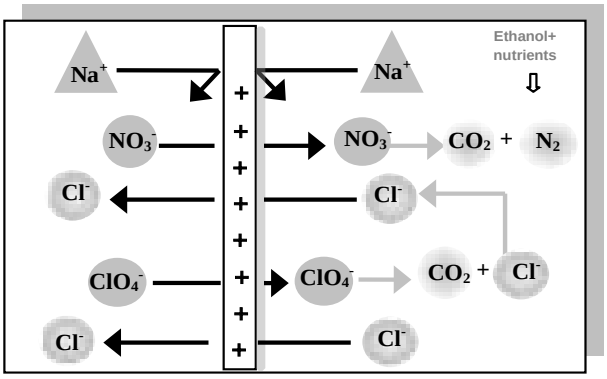

Figure 1. Shematic diagram of target polluting anions (NO_3^- and ClO_4^-) transport and bioreduction in the IEMB. Driving anion: Cl^-. Electron donor and carbon source: Ethanol.

2 Materials and methods

Two different membranes were used, an anion exchange membrane, Excellion™ I-200, produced by SnowPure (USA) and a mono-anion selective membrane Neosepta ACS, manufactured by Tokuyama Soda (Japan). The IEMB set-up was composed by a membrane module with two identical rectangular channels separated by the membrane under study, with an effective working area of 39 cm^2. One of the channels was connected through a gear pump to an external loop, where water supplemented with nitrate and perchlorate was recirculated at a flow rate of 97.2 l/h, corresponding to a Reynolds number of 3000. This compartment, referred to as water compartment, was continuously fed with the polluted water at different flow rates per membrane area (F/A), depending on the objective of the experiment. The other module channel was connected to a stirred vessel through another recirculation loop, also kept at a Reynolds number of 3000. This vessel was inoculated with 100 ml of an enriched microbial culture and continuously fed at a flow rate of 0.0048 l/h with a mineral medium composed of 1 g/l of K_2HPO_4, 0.592 g/l of KH_2PO_4, 0.5 g/l of NaH_2PO_4, 0.233 g/l of NH_4Cl, 0.1 g/l of $MgSO_4.7H_2O$ and 5.84 g/l of NaCl and of 280 to 560 mg/l of ethanol as a carbon source, depending on the experiment. This compartment was operated at an hydraulic retention time (HRT) of 5 days. The IEMB was operated using the Excellion membrane and compared to control trials performed with the Neosepta ACS. All experiments were run for at least one week and samples were taken periodically from the polluted water feed, treated water outlet, biomedium feed and biocompartment. These samples were used for conductivity measurements as well as for determination of the concentration of ions, ethanol and cells. All experiments were performed at a temperature of 23 ± 1 ºC in an air-conditioned room.

Anion concentrations, were determined as recently described (Matos et al., 2008) using a Dionex ion exchange chromatography system constituted by an ED 50 electrochemical detector, suitable analytical columns and an Anion Suppressor-ULTRA (4 mm). For the ClO_4^- analyses, a Ionpac AG16 Guard and Analytical AS16 (4 mm) columns were used. For the analysis of ClO_4^- in the samples taken from the water compartment, the detection limit was 1 ppb (injecting 1 ml of sample).

3 Results and discussion

Mechanistic modelling

With the objective of predicting the flux a target pollutant in the IEMB process at steady state, a mechanistic resistances-in-series trace counter-ion transport model was elaborated:

$$J_i = \frac{\frac{C_{i,1}}{C_{a,1}^{\ z}} - \frac{C_{i,2}}{C_{a,2}^{\ z}}}{\frac{L}{P_{i,m} \times \left(\frac{Q}{a}\right)^z} + \frac{\delta_1}{D_{i,w} \times C_{a,1}^{\ z}} + \frac{\delta_2}{D_{i,w} \times C_{a,2}^{\ z}}} \qquad (1)$$

where $C_{i,1}$ and $C_{i,2}$ are the concentrations of the polluting anion *i* in the water and the receiving compartment (biocompartment), respectively noted as 1 and 2; $C_{a,1}$ and $C_{a,2}$ are the major driving counter-ion concentrations in each compartment (e. g. chloride); *z* represents the ratio between the valence of the target ion (*i*) and the valence of the major counter-ion (*a*); δ_1, δ_2 are the thickness of the corresponding boundary layers next to the membrane surfaces at the water and biomedium sides, respectively; *L* is the membrane thickness; $P_{i,m}$ is the membrane permeability to the target counter-ion; *Q* is the ion exchange capacity of the membrane and $D_{i,w}$ is the diffusion coefficient of the target counter-ion *i* in water. Equation 1 shows that the flux is proportional to the difference between the ratios of the target counter-ion (NO_3^-, ClO_4^- or BrO_3^-) to the major counter-ion (in this case, Cl^-) concentration in the two compartments. This difference is the process driving force. The second term in the driving force can usually be neglected because the target counter-ions are bio-reduced to very low concentrations in the biocompartment and the major counter-ion is kept at a relatively higher concentration in this compartment, in order to enhance the transport of the polluting anions from the water stream to the biocompartment. The overall transport resistance is given by three resistances in series: a resistance associated with the transport through the membrane, expressed by the first term in the denominator, while the second and the third terms represent the resistances due to the corresponding liquid phase boundary layers at the two membrane surfaces. This steady state mass transport model can only be applied after a bi-ionic approximation and in case of an effective Donnan exclusion of the co-ions by the membrane, if the ion exchange kinetics is considered not rate-controlling, and if the water flux due to osmosis can be neglected (Velizarov et al., 2003).

The performance of the IEMB system was evaluated for different concentration scenarios of pollutants (nitrate and perchlorate) in the water, using the Excellion membrane. Three experiments were performed at a water flow rate per membrane area ratio (F/A) of 3.1 l/(m^2h) at different anion concentrations. The accuracy of the transport model to predict the IEMB behaviour at steady state was evaluated. The target anion fluxes were calculated based on the corresponding mass balances while some of the required membrane properties were determined through independent experiments (Table 1).

Table 1. Membrane characteristics experimentally determined in this study

Parameter	Excellion I-200	Neosepta ACS
Ion Exchange capacity (meq/ g dry membrane, Cl^- form)	1.24 ± 0.06	1.42 ± 0.20
Density (g/cm^3 wet membrane, Cl^- form)	0.70 ± 0.02	1.13 ± 0.02
Water content (%)	42 – 44	24 – 29
Thickness (mm)	0.330 ± 0.001	0.130 ± 0.001

Figure 2 shows that the fluxes calculated by Equation 1 (the straight lines), using pre-determined values of P_m, are comparable with those obtained experimentally. This result confirms the applicability of the mechanistic model within this concentration range.

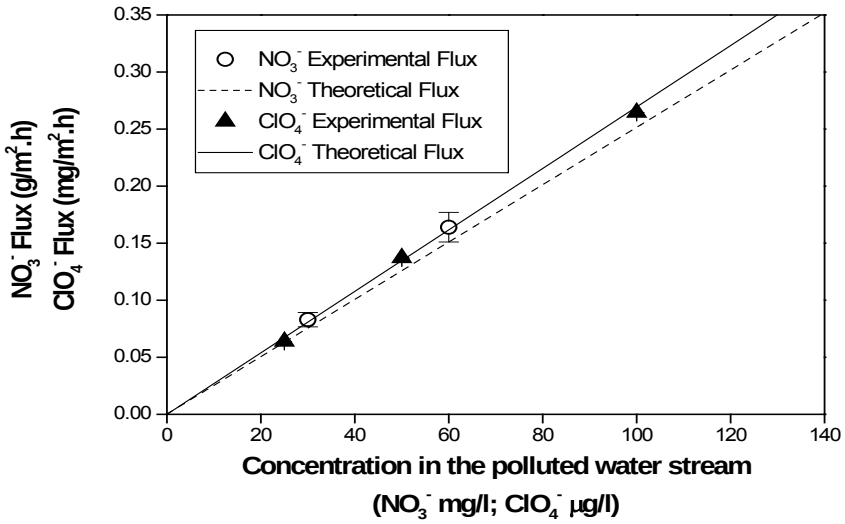

Figure 2. Effect of the pollutant concentration on the experimental and theoretical fluxes (predicted by Equation 1) of target anionic pollutants for an IEMB operation at an F/A ratio of 3.1 l/(m^2h), using the Excellion membrane (Matos et al. 2008).

Besides for treating polluted drinking water, the applicability of the IEMB process and the mechanistic model for the removal of nitrate from closed marine systems was also demonstrated. The IEMB process was able to remove naturally accumulated nitrate at concentrations of 251 mg/L and 380 mg/L to below 27 mg/L from water taken from the Lisbon oceanarium. Thus, the IEMB proved to be a selective technology for nitrate removal, while preserving the original composition of the water with respect to other ions. This is an advantage of the IEMB concept, since it allows for the reutilisation of the treated water by the aquarium, thus decreasing the need for water renewal and the frequency of wastewater discharge.

Hybrid modelling

For situations, in which the mass transfer assumptions used in developing the mechanistic transport model (Equation 1) are not satisfied, or in which the biological reaction controls the IEMB process, due to intrinsic metabolic complexity and to non-linear kinetics of the biological activity and transport phenomena, the modelling of the IEMB can be extremely difficult.

Process optimization aims at increasing the economical viability and minimizing the biomass produced. To fulfil this aim, the main variables affecting the biological compartment were identified. Seven factors were selected and, in order to design a proper number of experiments, a statistical design of experiments was used. The Plackett-Burman design is selected for screening proposes since it uses an orthogonal matrix in order to decrease the number of experiments to be performed.

The results obtained cover a wide range of conditions under which the mechanistic model was not able to correctly predict the transport fluxes of the target pollutants. Therefore, the data obtained in these experiments were further analyzed by chemometric techniques, which use mathematical and statistical methods to obtain relations between data sets. A hybrid semi-parametric model (Teixeira et al., 2006) was also adopted that combines mechanistic and black-box models according to the structure shown in Figure 3. In this strategy, two phases of the process are modelled, the transport across the membrane and the consumption in the biocompartment. For the membrane transport, a black-box model (BB1) compensates for the mechanistic model inaccuracies. A second black-box model (BB2) is used to identify the

biological reaction kinetics.

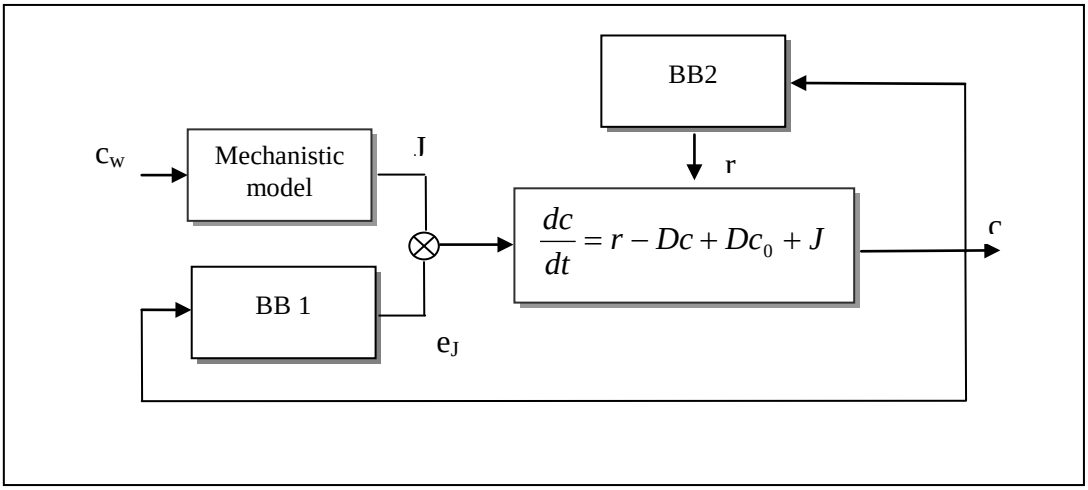

Figure 3: Hybrid model structure (c_w: ion concentration in water, e_j: transport kinetics residual).

This approach, based on hybrid structure, has the advantage of requiring less data than purely black-box models. The back-bone of the hybrid model consists of the dynamic material balance equations of the biological compartment, which account for the biological reaction kinetics (r), transport kinetics (J) and dilution terms (Dc_0-Dc). This global model is expected to predict the system performance over a broader range of operating conditions, and can be used for operational parameters optimization in the two compartments of the IEMB.

Removal of arsenic

Arsenic is generally present in polluted drinking water sources as negatively charged arsenate ($H_2AsO_4^-$) or arsenite ($H_2AsO_3^-$). However, contrary to the cases of nitrate, perchlorate and bromate, biodegradation of arsenate/arsenite to a harmless by-product(s) is not feasible. Therefore a modification to the IEMB concept was developed replacing the usual application of a mixed microbial culture by co-precipitation with iron as a means of achieving cost-effective arsenic removal in the stripping solution (Figure 4).

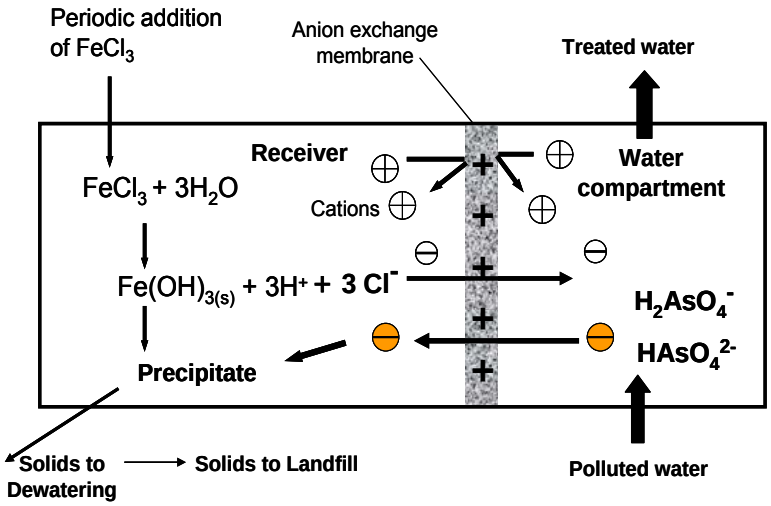

Figure 4. Integrated Ion Exchange Membrane process for removal of negatively charged arsenic-containing species from polluted drinking water streams.

The co-precipitation process with $FeCl_3$ is usually considered as one of the most feasible and economically adequate since this chemical is easily available and cheap. The disadvantages are mainly related to the need for its direct addition to the water, thus leading to residual levels of iron as well as to increased levels of chloride, which is not beneficial. The process is also sensitive to pH and requires its adjustment in some cases. Therefore its integration with an anion exchange membrane transport of the pollutant (in a way similar to the IEMB concept) but using a physicochemical process (instead of a bioprocess) could solve these problems.

In preliminary experiments performed with the integrated system with a naturally polluted groundwater, taken from the region of Ponte de Sôr, Portugal, and under conditions, in which the stripping solution was totally recirculated in a closed stripping compartment, it was clear that the addition of a precipitation agent ($FeCl_3$) to the stripping compartment improved the degree of arsenic removal from the water compartment, This can be attributed to the higher driving force for arsenic transport due to its precipitation by $FeCl_3$. In this case, $FeCl_3$ is completely utilized as a chemical precipitant (i.e. Fe^{3+}) and as a source of counter-ions for arsenate transport (i.e. Cl^-), simultaneously achieving both purposes with the addition of only one chemical (Figure 4). Process optimisation is currently in progress, where factors such as the hydrodynamic conditions in the water compartment, the effect of pH of the stripping solution and possible transport competition through the anion exchange membrane by other anions present in water are being tested.

Acknowledgments

Ana Rita Ricardo acknowledges FCT for the PhD scholarship SFRH/BD/25275/2005. Fundação para a Ciência e a Tecnologia (FCT) is acknowledged for Project POCI/AMB/57356/2004. Dr. A. Oehmen, S. Serra and J. Fradinho have been actively participating in this project. Eng. P. Fernandes from the Municipality of Ponte de Sôr is acknowledged for his kind assistance in collecting the arsenic-polluted groundwater samples.

References

Crespo, J.G., Reis, A.M. (2003). Treatment of aqueous media containing electrically charged compounds, WO 01/40118 A1.

Crespo, J.G., Velizarov, S., Reis, A.M. (2004). Membrane bioreactors for the removal of anionic micropollutants from drinking water. *Current Opinion in Biotechnology,* 15, 463-468.

Matos, C. T., Fortunato, R., Velizarov, S., Reis, M. A. M., Crespo, J. G. (2008). Removal of monovalent oxyanions from water in an ion exchange membrane bioreactor: Influence of membrane permselectivity. *Water Research,* 42, 1785 – 1795.

Teixeira, A., Clemente, J.J., Cunha, A.E., Carrondo, M.J.T., Oliveira, R. (2006). Bioprocess Iterative Batch-to-batch optimization based on hybrid parametric/nonparametric models, *Biotechnology Progress*, 22, 247-258.

Velizarov, S., Rodrigues, C.M., Reis, A.M., Crespo, J.G. (2000/2001). Mechanism of charged pollutants removal in an ion exchange membrane bioreactor: Drinking water denitrification. *Biotechnology and Bioengineering,* 71, 245-254.

Velizarov, S., Reis, A.M., Crespo, J.G. (2003). Removal of trace mono-valent inorganic pollutants in an ion exchange membrane bioreactor: analysis of transport rate in a denitrification process, *Journal of Membrane Science*, 217, 269-284.

Velizarov, S., Matos, C., Oehmen, A., Serra, S., Reis, A.M., Crespo, J.G. (2008). Removal of inorganic charged micropollutants from drinking water supplies by hybrid ion exchange membrane processes. *Desalination,* 223, 85–90.

Proceedings of the 10th International Chemical and
Biological Engineering Conference - CHEMPOR 2008
Braga, Portugal, September 4-6, 2008
E.C. Ferreira and M. Mota (Eds.)

Performance comparison of biological and Fenton processes for COD degradation of urban landfill leachates

Cátia M. Augusto, Margarida J. Quina, Licínio M. Gando-Ferreira[1*]

GERSE – Group on Environmental, Reaction and Separation Engineering, Department of Chemical Engineering, University of Coimbra, Pólo II, Rua Sílvio Lima, 3030-790 Coimbra, Portugal.

Keywords: Biological treatment, Fenton process, landfill leachate, COD degradation
Topic: Advancing the chemical and biological engineering fundamentals

Abstract

The urban landfill leachate is usually considered as a refractory effluent, mainly due to the presence of specific substances (e.g., xenobiotic organics compounds). Currently, the landfill leachate is usually treated by biological aerobic processes, since they reveal high efficiency and low cost. However, when the landfill leachate is produced in old sites, the presence of toxic or refractory components requires other alternatives such as Advanced Oxidation Processes (AOP).

In this study, the biological and Fenton processes were tested for the landfill leachate treatment in which the effluent degradation was evaluated mainly through Chemical Oxygen Demand (COD) removal. Leachate samples collected in an urban sanitary landfill from the centre region of Portugal were used for both processes. The characterization of these leachate samples entails the evaluation of pH, COD, BOD_5, the ratio BOD_5 to COD, TSS and VSS. By comparing the performance of both treatment processes one may notice that the largest COD removal occurred for the biological treatment (70% reduction at maximum) against 27%, for the Fenton process. For the leachate in analysis, the integration of both processes (biological followed by fenton) may be an attractive solution.

1 Introduction

The Urban landfill leachates are liquids generated by infiltration of water from externals sources that percolates through the mass of waste and by the biological decomposition of organic material within the municipal solid waste (MSW). A set of physical, chemical and microbiological transformations promote the transference of the pollutants from the waste to the water. With the increase of the landfill age, the disposed material undergoes several phases of decomposition, producing leachates with different physical-chemical characteristics, as a consequence of the transformation processes within the landfill (Duggan, 2005 and Slack*, et al*., 2005). The composition and the amount of leachate vary with the state of degradation, the decomposition of the MSW and the movement of the water in landfill (Öman and Junestedt, 2007). The pollutants observed in landfill leachates can be associated in four groups: dissolved organic matter, inorganic macro components, heavy metals and xenobiotic organics components (XOC) (Öman and Junestedt, 2007; Christensen *et al*., 1998). The hazardous characteristics of this type of effluent are attributed not only to the presence of toxics components, but mainly to the synergic effect between different substances of the leachate.
In the recent literature, some studies indicate new methods for the treatment of landfill leachate (Laconi *et al*., 2006; Kurniawan *et al*., 2006; Sarasa *et al*., 2006). However, the process often used in full scale still is the aerobic biological treatment, which usually leads to

* Corresponding author. Tel + 351-239-798700. E-mail:lferreira@eq.uc.pt

satisfactory results. The objectives of the biological treatment deal with the stabilization of organic matter and the removal of solids (Laconi *et al*., 2006; Metcalf & Eddy, 1991). The activated-sludge processes are largely used worldwide, once they required reduced installation areas and lead to high quality of the final effluent. Usually, this process includes a biological reactor and a sedimentation tank with recirculation of sludge (Metcalf & Eddy, 1991). Some physicochemical treatments are associated to aid the biological process, but they should not interfere with the microbiology. The biomass growth reflects the state of the biological treatment, and thus requires stable environmental conditions such as pH, temperature, nutrients, dissolved oxygen and time of contact between biomass and substrate (Metcalf & Eddy, 1991).

The Advanced Oxidation Processes (AOP) come out as a promising alternative due to the high removal percentages of toxic pollutants and bio-recalcitrant chemical species. The AOP were defined in 1994 by Glaze as processes that generate hydroxyl radicals (HO) which are known to have high oxidant power (2.33 V) reacting with several organic and inorganic species at high kinetic constants values. Generally, the goal is to obtain total mineralization of the organic matter into water and carbon dioxide, however for economical reasons it may be favourable to achieve partial oxidation of the organic compounds into biological degradable matter (Morais and Zamora, 2005).

The Fenton process remained without importance for a few years ago. Currently, this process had been demonstrated significant oxidizing potential for organic compounds. The Fenton reagent is a suitable process in acidic conditions, where a combination of an iron salt with hydrogen peroxide occurs, leading to the generation of hydroxyl radicals (HO·).The radical acts in the decomposition of organic compounds (RH), as oxidizing agent, and promote radical oxidation reactions. It should be noted that the Fenton reagent converts complex and toxic compounds, but fails in some cases such as small chlorinate alkenes, paraffines and small carboxylic acids (Zhang *et al*., 2005).

2 Experimental Procedures

The effluent considered in this study was municipal landfill leachate collected in an urban sanitary landfill located near to Coimbra. The samples were characterized and treated.

Characterization

Seven samples of leachate were collected, transported to the laboratory and immediately preserved at a temperature lower than 4ºC. The characterizations of the samples involved pH, Chemical Oxygen Demand (COD), Biochemical Oxygen Demand (BOD), BOD_5/COD ratio, Total Suspended Solids (TSS) and Volatile Suspended Solids (VSS). The COD was measured with photometer (WTW CR3000) using commercial kits containing an oxidant mixture of potassium dichromate under acidic conditions (sulphuric acid) and using silver sulphate as catalyst. The BOD was determined according to Standard Methods (1985) measuring the dissolved oxygen in the initial diluted sample and after 5 days of incubation (BOD_5) at 20 ºC. The TSS and VSS were determined by gravimetry, being the solids separated using a 0.45 µm pore filter, according to Standard Methods (1985). The pH was measured by potentiometry (WTW pH-electrode SenTix 21).

Biological treatment

For the assessment of the biological treatment, the organic matter degradation of six samples (S1-S6) of leachate was investigated. The treatment was carried out by using a reactor of 1 L with bottom aeration. The oxygen concentration in the liquid phase was continuously monitored using an adequate sensor. The system was agitated by a magnetic stirrer to provide homogenization and ensure uniform distribution of the oxygen and nutrients. In general, 20% (v/v) of inoculum was mixed with 80% (v/v) of the leached solution. The inoculum was previously obtained in an acclimation phase that ensures active biomass for

the treatment. The temperature, pH and dissolved oxygen (OD) was recorded along the time. The Mixed Liquid Volatile Suspended Solids (MLVSS) were determined as a measure of the biomass growing. At the end of treatment also the COD was evaluated to assess the degradation of the organic matter of effluent.

Fenton Treatment

The Fenton process was employed for only one sample (S7), but in this case a design of experiments was used for testing the influence of 3 factors: initial concentration of H_2O_2, initial concentration of Fe, and initial pH. In practice, the 3 factors were tested according to a full factorial design (2^k). Thus, 8 experiments were performed (2^3), involving 3 factors (k=3) at 2 levels. Fenton experiments were carried out in batch mode using a Jarr-test system, providing a 200 rpm stirring speed with baffles paddles. When necessary, sulphuric acid was added to 300 mL of effluent for pH adjustment. After the samples for analysis were collected, the oxidation reaction must be stopped to avoid its interference into COD measurements, and for this a sodium hydroxide solution was added. During the Fenton treatment, the COD was measured for evaluating the organic matter degradation at different times.

3 Results and Discussion

This study is related with the urban landfill leachates and the main objective was the characterization and the evaluation of the performance of Biological and Fenton treatments.

3.1 Characterization of the landfill leachate

It is well known that the landfill leachate may be characterized by a significant variability. The parameters determined in this study were the pH, COD, BOD_5, the ratio BOD_5 to COD, TSS and VSS, and the obtained values are indicated in Table 1. The different samples analysed (S1 to S7) were characterized by pH values in the range between of 7 to 8; The COD of the leachate are within 630-2780 mg O_2/L, reflecting a significant amount of organic matter. As expected, the BOD_5 is lower than COD for all samples and the determined amounts were in the range of 525 to 2510 mg O_2/L; the observed ratio for BOD_5 to COD was 0.76 to 0.90, which correspond to values of high biodegradability. Regarding the TSS and VSS parameters, significant variability was observed (114-2690 mg/L), which causes difficulties during the treatment of the effluent.

Table 1 – Characterization of leachate samples (S1-S7).

Parameters	S1	S2	S3	S4	S5	S6	S7
pH	7.42	7.73	7.72	7.64	7.56	7.54	7.90
COD (mg/L)	1000	2000	2780	1380	630	1940	2350
BOD_5 (mg/L)	(a)	1673	2510	1150	525	1470	1560
BOD_5/COD	(a)	0.84	0.90	0.83	0.83	0.76	0.70
TSS (mg/L)	730	114	1440	620	445	334	2690
VSS (mg/L)	690	127	1010	580	200	260	(a)

(a)- Values not determined.

3.2 Biological treatment of the landfill leachate

For monitoring the biological treatment several parameters were evaluated along time. Figure 1 shows the evolution of MLVSS of the leachate suspension for six samples in analysis (S1-S6), characterized by initial concentrations of 630 to 2780 mg/L of COD. These

analyses allowed the monitoring of biomass growth, being possible to conclude that the concentration of microrganisms increases along the time in all experiments. As an example, in Figure 2, the parameter MLVSS and MLTSS are represented for the sample S4, and as expected, one may use both of them for following biomass in the biological reactor. To ensure suitable operating conditions, the temperature, pH and Dissolved Oxygen (DO) were monitored during the biological degradation, and Figure 2 shows that these parameters were almost constant over the time of operation.

The initial concentration of substrate had some influence in the biological suspension characteristics. In fact, in sample S3, a higher concentration of microrganisms was achieved, being reached values 25000 mg/L of MLVSS. On the other hand, lower growth efficiency was observed for sample S5, since in this case the initial substrate concentration may be a limiting factor.

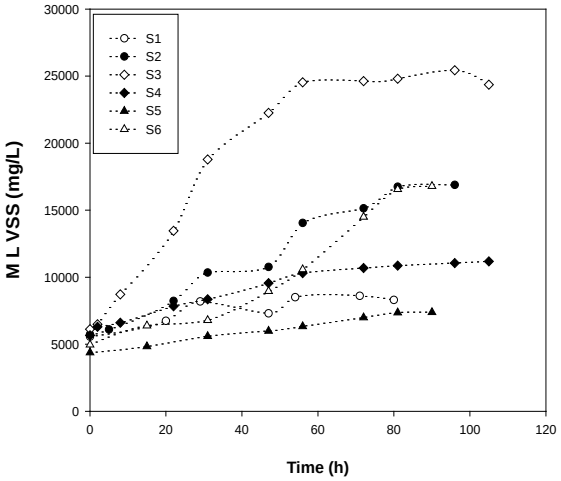

Figure 1 – Evolution along time of MLVSS for samples S1 to S6.

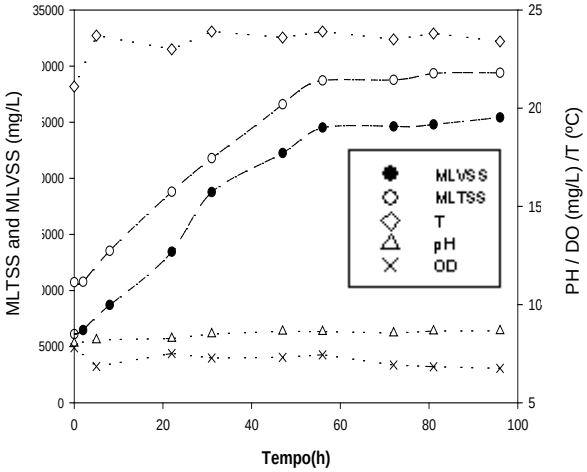

Figure 2 – Evolution along time of MLVSS, MLTSS, Temperature, pH and OD for sample S4.

3.3 Fenton treatment of landfill leachate

The most important variables whose initial values determine the Fenton process performance are: pH, amount of iron and hydrogen peroxide concentration. For evaluating the importance of these 3 factors, a design of experiments was tested according to a full factorial strategy at 2 levels (Table 2). Therefore, the number of experiments tested was 2^3=8. The minimum and maximum values tested for each variable were selected according to literature. Thus, pH was tested at 3.0 and 7.9; the H_2O_2 concentration at 7 and 14 g/L; and the iron concentration at 0 and 1.5 g/L .

The Fenton treatment was monitored for 120 minutes. However, for all conditions tested less than 30 minutes seems to be enough for reaching steady state conditions (Figure 3). The results show that the greater degradation occurred in F1 experiment (14 g H_2O_2 /L; 1.5 g Fe^{2+} /L; pH = 7.9). However, the faster reduction of COD was observed for the experiment F5. The worst results were observed for lower concentration of H_2O_2, higher concentration of iron and higher pH (F7 experiment). In fact, the analyse of the outputs obtained from the design of experiments enabled to conclude that among the parameters tested, only the H_2O_2 initial concentration should be considered as a relevant main factor from the statistical point of view. Moreover, none interaction between factors was statistically significant.

Table 2 – Design of Experiment condition tested for Fenton Process.

Experiments	H_2O_2(g/L)	Fe^{2+}(g/L)	pH
F1	14	1.5	7.9
F2	7.0	0.0	3.0
F3	7.0	1.5	3.0
F4	14	0.0	3.0
F5	14	1.5	3.0
F6	7.0	1.5	7.9
F7	7.0	0.0	7.9
F8	14	0.0	7.9

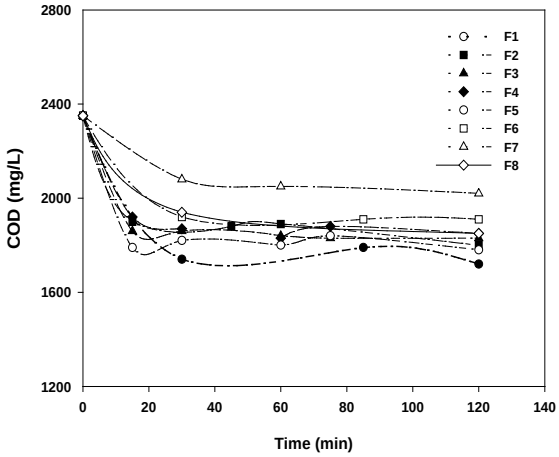

Figure 3 – Evolution along time of COD for sample S7 at condition F1 to F8 (Table 2).

3.4 Biological and Fenton treatments

For comparing both treatments, the initial and final COD, at the end of each treatment, were represented in Figure 4 and 5, where the percentage values indicate a reduction in these parameters. From these Figures, it is noticeable that the largest removal occurred for the biological treatment (70% reduction maximum) against 27% for Fenton process. However, the reaction time is much longer in biological treatment (order of days) while for Fenton process only a few minutes are required for partial chemical oxidation. These results were expected taking into account the characterization of landfill leachate tested. In fact, the effluent is characterized by high biodegradability (high BOD_5/COD), and thus one may conclude that the biological process is suitable for the treatment of this effluent. In this case, the Fenton process may be used in an integrated approach. At industrial level, the efficiency of the system of activated sludges is not enough for discharging the effluent into the environment. From our study, it seems that the Fenton process may be used after the leachate to be pre-treated by the biological process.

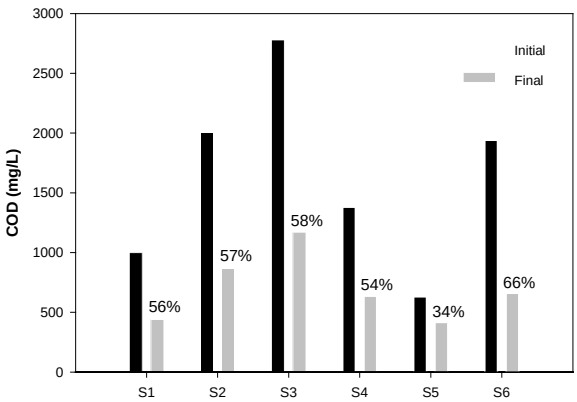

Figure 4 – COD removal for sapmles S1 to S6.

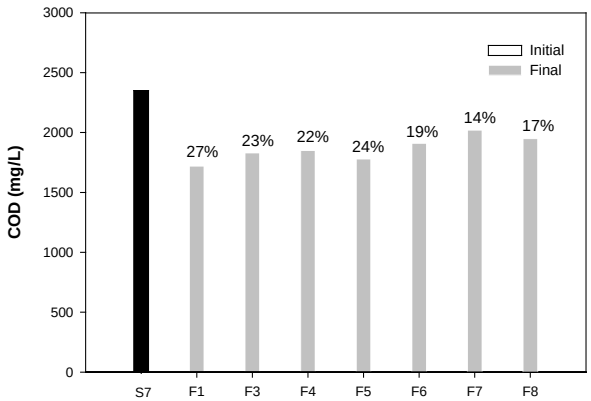

Figure 5 – COD removal for sample S7 and for experiments F1 to F8.

4 Conclusions

The main objective of this work was to compare the performance of the biological treatment with Fenton process for landfill leachate. Once the tested effluent is characterized by high biodegradability (high CBO_5/COD), the biological treatment leads to better results than the process of Fenton. However, the biological process needs a long period for degradation. Contrarily, Fenton process is fast for COD removal, being necessary only a few minutes (15 - 30 min). Moreover, the analyse of the outputs obtained from the design of experiments enabled to conclude that among the parameters tested and for the system under study, only the H_2O_2 initial concentration should be considered as a relevant main factor from the statistical point of view. Since at industrial scale, the biological treatment is not enough to achieve the compliance with regulatory limits, one may suggest the integration of biological treatment followed by Fenton.

References

Christensen, J. B., Jensen, D. L., Gron C., Fili, Z., Christensen, T. H., 1998. Characterization of the dissolved organic carbon in landfill leachate- polluted groundwater. Water Research 32, 125-135.

Duggan, J., 2005. The potential for landfill leachate treatment using willows in the UK – A critical review. Resources, Conservation and Recycling 45, 97-113.

Kurniawan, T.A., Lo, W.H., Chan, G. Y.S., 2006. Radicals-catalysed oxidation reactions for degradation of recalcitrant compounds from landfill leachate. Chemical Engineering Journal 125, 35-57.

Laconi, C.D., Ramadori, R., Lopez, A., 2006. Combined biological and chemical degradation for treating a mature municipal landfill leachate. Biochemical Engineering Journal 31, 118–124.

Metcalf & Eddy, 1991. Wastewater Engineering: Treatment Disposal and Reuse, third ed. McGraw-Hill International Editions, California.

Morais, J. L., Zamora, P. P., 2005. Use of advanced oxidation processes to improve the biodegradability of mature landfill leachates Journal of Hazardous Materials B123, 181–186.

Öman, C. B., Junestedt, C., 2007. Chemical characterization of landfill leachates – 400 parameters and compounds. Waste Management (In press) doi:10.1016/j.wasman. 2007.06.018.

Sarasa, J., Llabrés, T., Ormad, P., Mosteo, R., Ovelleiro, J. L., 2006. Characterization and photo-Fenton treatment of used tires leachate. Journal of Hazardous Materials B136, 874–881.

Slack, R.J., Gronow, J.R., Voulvoulis N., 2005. Household hazardous waste in municipal landfills:contaminants in leachate. Science of the Total Environmental 337, 119-137.

Zhang H., Choi, H. J., Huang, C-P., 2005. Optimization of Fenton process for the treatment of landfill leachate Journal of Hazardous Materials B125, 166–174.

Proceedings of the 10th International Chemical and
Biological Engineering Conference - CHEMPOR 2008
Braga, Portugal, September 4-6, 2008
E.C. Ferreira and M. Mota (Eds.)

Starch filter-cake enzymatic degradation

Etel Kameda[1], Rafael F. de Mesquita[1], Marta A. P. Langone[2], João C. de Queiroz Neto[3], Maria Alice Zarur Coelho[1*]

[1]Escola de Química – Universidade Federal do Rio de Janeiro - Centro de Tecnologia, Bloco E, Lab. 103, Cidade Universitária – 21949-900, Rio de Janeiro - RJ, Brazil.
[2]Instituto de Química – Universidade Estadual do Estado do Rio de Janeiro - Rua São Francisco Xavier, 524 – PHLC/IQ sala 310, Rio de Janeiro - RJ, Brazil.
[3]CENPES – PETROBRAS, Rio de Janeiro, Brazil.

Keywords: starch filter-cake removal, openhole conditions, well completion
Topic: Sustainable process-product development through green chemistry.

Abstract

Drill-in fluid systems usually comprise natural polymers like starch as the main component. During the drilling operation, the polymer deposit as a filter-cake on the wellbore wall in permeable formations due to its filtration into the rock pores. Before prodution or injetion could start, filter-cake removal is a demand. The application of acids or strong oxidative solutions is a traditional approach to well clean-up. However, these compounds are non-specific and can react with species that are acid soluble or oxidizable, including formation walls, lines, hydrocarbons, etc. Thus, enzymatic preparations are an alternative to filter-cake removal. Enzymes are very specific catalysts, inherent environmental friendly and can be used to hydrolyse filter-cake main polymer, as starch. In this work, a kinetic study of a filter-cake enzymatic breaker and a commercial α-amylase were investigated face to their starch hydrolysis capability at 65 and 80^{o}C in brine solution. Their kinetic parameters (Km and Vmax) were obtained under well operational conditions. In brine solution ocurred a mixed-type inhibition. Synthetic unconsolidated sandstone samples were used to simulate a natural formation reservoir from typical deep oil field at Campos Basin (Rio de Janeiro-RJ, Brazil) in filtration tests carried in HPHT (high pressure high temperature) cell, with a 5% (w/v) enzymatic fluid at 65^{o}C. Both enzymatic products were able to hydrolyse starch in the internal filter-cake, leading glucose and maltose as main reaction products. Filtration rates were measured and the filter-cake enzymatic breaker presented a higher filtration rate mostly due to the emulsification activity (28.57%) detected, indicating that the enzymatic breaker probably attained a better self-diffusion into the filter-cake.

1 Introduction

Horizontal wells are increasingly used to maximize well productivity due to its higher efficiency and cost effective in draining hydrocarbons from the underground. Drilling fluids are used in field operations for cooling the drilling head, transporting stone and control well pressure. Most drilling fluids are designed to build up a filter-cake on the boreole wall formation production or injection zone to ensure fluid loss. Initialy a filter-cake is needed to limit the leak-off of drilling fluid and fitrate into the formation. In many well completions, before production or injection operations can start, filter-cake must be removed and it can be done by mechanical and/or chemical procedures. When the filter-cake is not properly cleaned-up, it causes formation damage reducing the productivity (Hanssen *et al.*, 1999). Thus, the filter-cake removal process reduces significantly the formation damage and improves the oil production. Drill-in fluids systems are usually comprised of starch, xanthan gum and calcim carbonete in a base brine solution. Starch is the main component in many drilling fluids and consequently in filter-cake. Thus, starch degradation improves significantly filter-cake removal (Queiroz, 2006).

* Corresponding author. Tel +5521 25627622. E-mail: alice@eq.ufrj.br

The application of acids or strong oxidative solutions is a traditional approach to well clean-up. However, these compounds are non-specific and can cause permeability damage by re-precipitation of dissolved components (Hanssen *et al.*, 1999). Considering such problems, enzymatic preparations are presented as an alternative to filter-cake removal. First applications in oil industry were as blends of few generic hydrolytic enzymes. Enzymes are very specific catalysts, inherent environmental friendly and can be used to hydrolyse filter-cake main polymer, as starch (Batttistel *et al.*, 2005). Although downhole conditions may limit enzyme activity, many wells operate within the range 65-80^{o}C, as Brazilian ones, and some biocatalysts may tolerate well environmental conditions of pressure and temperature. (Kameda *et al.*,2007).

The main motivation for this work was to investigate starch degradation under openhole operation conditions for a commercial α-amylase and a filter-cake enzymatic breaker through a kinetic analysis. Filtration tests to evaluate stach degradation on filter-cake were taken as well.

2 Materials and Methods

Materials

Commercial amylase (Termamyl) from *Bacillus licheniformis* was gently provided by Novozyme A/S (Paraná, Brazil) and a commercial enzymatic filter-cake breaker (CENPES/PETROBRAS, Brazil) were used for comparative studies. CENPES/PETROBRAS also gently provided a completion fluid, i.e. a brine solution 9.4 ppg (pounds per gallon) / 203.57g/L NaCl, and drilling fluid comprising starch (8g), xantam gum (1.5g), NaCl (9g), $CaCO_3$ (35g) glutaraldehyde (1mL), MgO (1g) and distilled water (350mL).

Amylolytic activity

The enzymatic activity was measured by the increase of reducing sugars content as a result of starch hydrolysis, spectrophotometrically quantified according to modified dinitrosalicylic acid (DNSA) method (Miller, 1959). α-amylase activity was assayed by incubating 0.5mL of enzyme solution within 0.5mL soluble starch (1%, w/v) prepared in 0.02M sodium phosphate buffer (pH 6.9 and NaCl 0.05M). After 5min incubation at 30^{o}C the reaction was stopped by the addition of 1mL of DNSA solution and the resultant mixture was immediately heated at 100^{o}C for 10 minutes. The reducing sugars released were quantified at 540nm in a Hach DR/4000UV spectrophotometer. One activity unit (U) was defined as the amount of enzyme which releases 1 µmol of reducing end groups per minute in 0.02 M sodium phosphate buffer (pH 6.9) with 1.0% (w/v) soluble starch as substrate at 30^{o}C.

Emulsification index (EI)

The emulsification index was determined according to Iqbal *et al.* (1995) with a modification. The EI was determined by adding 1 ml of hexadecane to the same amount of sample, vortex-mixing for 2 min and leaving to stand for 24 hours. The sample EI is given as percentage of height of emulsified layer (cm) divided by total height of the liquid column (cm).

Determination of kinetics parameters

The enzyme kinetic parameters (Km and Vmax) were obtained at 65 and 80^{o}C. A sample of enzymatic product was incubated in a soluble starch solution (concentration ranging from 1.25 to 8.75mg/mL) prepared in 0.02 M sodium phosphate buffer (pH 6.9 and NaCl 0.05) or completion fluid (brine solution). The amount of reducing end groups formed was measured according to modified dinitrosalicylic acid (DNS) method (Miller, 1959) as previously described.

Filtration tests

The filtercake was build on the top of synthetic unconsolidated sandstone plugs (Figure 1) in a HPHT (high pressure high temperature) filter press working at 65°C with 500 psi (34,47 bar) overpressure for 2 hours. External filtercake was mechanically removed by a spatula. The plug with internal filter-cake was inserted into a HPHT cell and soaked with a 5% (v/v) enzymatic fluid (enzyme product in the brine solution) at 65°C. A overpressure range of 0 to 22psi was gently applied to enzymatic fluid pass through the plug and internal filter-cake, taking care to degrade filter-cake in the plug by enzymatic fluid while do not disturbing it mechanically. Fluid filtration through the plug was measured determining the filtrate fluid mass (Figure 2) along the assay. Internal filter-cake degradation was evaluated by the amount of reducing end groups formed in filtrate fluid. Control assays were also carried out by soaking internal filter-cake in brine solution without enzymatic products.

Figure 1.Synthetic unconsolidated sandstone plug

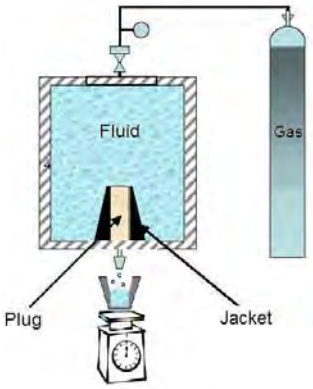

Figure 2. HPHT filtration system

3 Results and Discussion

Kinetic parameters

In previous work, Kameda *et al.* (2007) demonstrated that a commercial α-amylase solution were thermostable under certain completion conditions (65°C in brine solution - NaCl 3.5M or 203.57g/L), but at 80°C some reduction in amylolytic activity occurred and at 95°C no activity remained. A filter-cake enzymatic breaker catalysis was herein investigated under identical conditions (65 or 80°C in brine and in buffer solutions) and its performance was compared to the previously reported commercial α-amylase, through a kinetic study of both products. The results demonstrated that both were able to hydrolize starch in the assay conditions.

Commercial α-amylase seems to behave according to Michaelis-Menten kinetics in buffer solution (Figure 3) as expected (Li *et al.*, 2007, Toledo *et al.*, 2007, Lopez *et al.*, 2006) and in brine solution as well. Enzymatic breaker seems also to follow Michaelis-Menten kinetics in buffer and brine solution (Figure 4). However reaction velocity clearly decline in brine solution for both products assays.

Kinetic parameters (Km and Vmax) for both products were determinated by Lineaweaver-Burk plot for all conditions tested (Table 1). At 65°C (Figures 5 and 6) and 80°C (Figures 7 and 8) as well, a mixed-type inhibition in brine solution can be considered affecting both Km and Vmax values of the enzyme formulations (Segel, 1993). Higher Km values of commercial α-amylase suggest lower affinity in brine solution at both temperatures tested (Table 1). Identical behavior occurred also with enzymatic breaker.

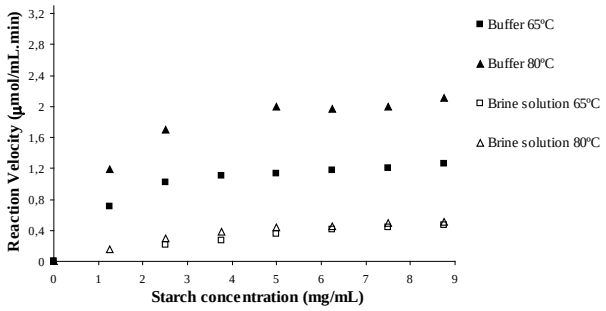

Figure 3. Stach hydrolysis kinetics by commercial α-amylase at 65 and 80°C in phosphate buffer and brine solution

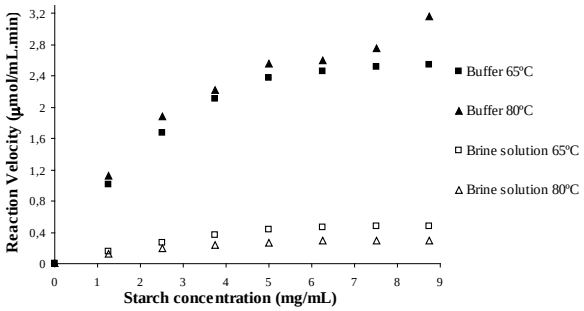

Figure 4. Stach hydrolysis kinetics by enzymatic breaker at 65 and 80°C in phosphate buffer and brine solution

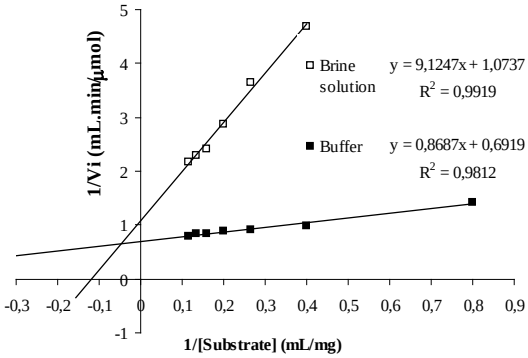

Figure 5. Lineweaver-Burk plot for 65°C reaction in buffer and brine solution of commercial α-amylase

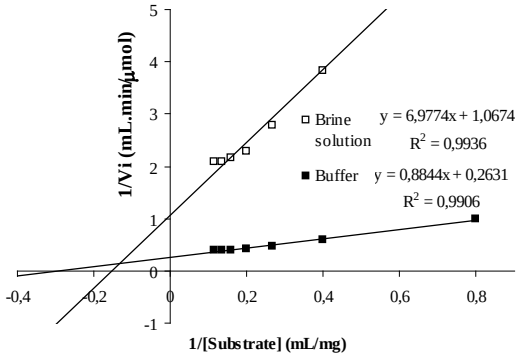

Figure 6. Lineweaver-Burk plot for 65°C reaction in buffer and brine solution of enzymatic breaker

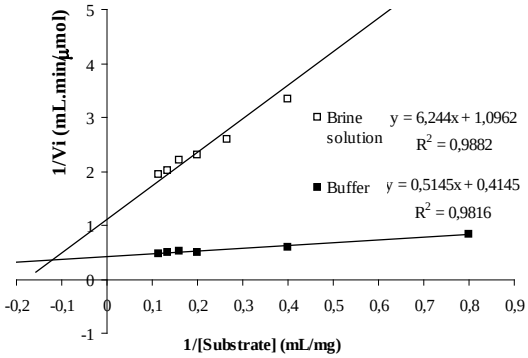

Figure 7. Lineweaver-Burk plot for 80°C reaction in buffer and brine solution of commercial α-amylase

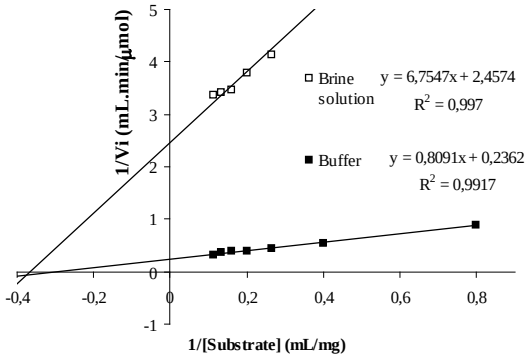

Figure 8. Lineweaver-Burk plot for 80°C reaction in buffer and brine solution of enzymatic breaker

Table 1. Kinetic parameters of commercial α-amylase and enzymatic braker in starch hidrolisis reaction under assay conditions.

	Temperature (°C)	Media	Km (mg/mL)	Vmax (µmol/mL.min)	R^2
α-Amylase	65ºC	Buffer solution	1,26	1,45	0,98
		Brine solution	8,50	0,93	0,99
	80ºC	Buffer solution	1,24	2,41	0,98
		Brine solution	5,70	0,91	0,99
Enzymatic breaker	65ºC	Buffer solution	3,36	3,80	0,99
		Brine solution	6,54	0,94	0,99
	80ºC	Buffer solution	3,42	4,23	0,99
		Brine solution	2,75	0,41	0,99

Filtration tests

Synthetic unconsolidated sandstone samples (Figure 1) were prepared appropriately accordding the method described by Queiroz (2006) to simulate a natural formation reservoir from typical deep oil field at Campos Basin (Rio de Janeiro-RJ, Brazil). Resultant filtrate mass was measured and the filtration rate was determinated (Table 2). Battistel *et al.* (2005); Al-Otaibi *et al.* (2004) and, Hanssen *et al.* (1999) reported higher overpressure range (100 – 500psi) compared to the values herein reported. However, these authors used ceramic discs as filtration medium that present lower permeability than the synthetic unconsolidated sandstone samples herein used.

Table 2. Filtration rates of enzymatic fluids at 65°C through internal filter-cake in synthetic unconsolidated sandstone samples.

Fluid	Filtration rate (g/min)	Δt (t_{final}-$t_{initial}$) (min)	Overpressure range (psi)	R^2
Brine solution (blank test)	3,8047 (±0,15)	19	20 - 22	0,99
α-Amylase	7,2431 (±0,93)	20	22 - 22	0,99
Enzymatic breaker	30,317 (±7,51)	10	17 - 20	0,99

1 bar ≅ 14,5 psi

Filtrations tests results showed that enzymatic fluids enhance filtrations rates (Table 2). Enzymatic fluid should contact the polymer into the filtercake to clean-up the rock pore. This contact could be established by enzyme flowing into the filter-cake with the help of additives that can act as a surfactant. Since the enzymatic breaker fluid showed higher filtration rate than commercial α-amylase (Table 2), assays for emulsification activity were carried and the former product presented emulsification activity (EI=28.57%) while the commercial α-amylase does not. Such result indicates that probably the enzymatic breaker attained a better self-diffusion into the filtercake, leading to such higher filtration rate.

Filter-cake degradation was evaluated by quantifying reducing sugars in the filtrate. As shown in Table 3, both enzymatic products were able to hydrolyse starch in the internal filter-cake being glucose and maltose detected as the main reaction products by high performance liquid chromatography (HPLC – data not shown). These results showed that both products could produce almost same reducing sugar quantity.

Table 3. Reducing sugar concentration in resultant fluid from filtration tests.

Fluid	Reducing sugar in resultant fluid (μmoles/mL)
Brine solution (blank test)	0,28
α-Amylase	2,89
Enzymatic breaker	3,16

4 Conclusions

Commercial α-amylase and filter-cake enzymatic breaker were able to hydrolise starch in completion operation conditions in all assays tested. Kinetics parameters values were affected in brine solution for both products, leading to a mixed-type inhibition in this latter condition.

On filtration tests, filter-cake enzymatic breaker presented higher filtration rate most probably due to the emulsification activity detected improving enzymatic breaker filtration rate, since both products produced almost same quantity of reducing sugar in the resultant fluid.

5 Acknowledgements

The authors gratefully acknowledge the financial support given by CNPq, FAPERJ, FINEP as well as the collaboration with CENPES/PETROBRAS and Novozyme A/S. Marta A.P. Langone thanks to Prociência/UERJ.

6 References

Al-Otaibi, M. B.; Nasr-El-Din, H. A.; Siddiqui, M. A. (2004) Chemical treatment to enhance productivity of horizontal and multilateral wells: lab studies and case histories. SPE 89467 *Fourteenth Symposium on Improved Oil Recovery*, Tulsa, USA.

Battistel, E., Bianchi, D., Fornaroli, M., Guglielmetti, G., Europa, P., Cobianco, S. (2005) Enzyme breakers for chemically modified starches. SPE 94702. *European Formation Damage Conference,* Sheveningen, Netherlands.

Hanssen, J.E., Høst, H., Jiang, P., Jørgensen, J.F. (1999). New enzyme process for downhole cleanup of reservoir drilling fluid filtercake SPE 50709 *International Symposium on Oilfield Chemistry,* Houston, USA.

Iqbal, S.; Khalid Z. M; Malik K. A. (1995) Enhanced biodegradation and emulsification of crude oil and hyperproduction of biosurfactants by gamma ray-induced mutant of Pseudomonas aeruginosa. *Letters in Applied Microbiology,* 21, 176-179.

Kameda, E. Queiroz Neto, J.C. de, Langone, M.A.P., Coelho, M.A.Z. (2007) Removal of polymeric filter cake in petroleum wells: A study of commercial amylase stability *Journal of Petroleum Science and Engineering,* 59, 263-270.

Li, H.; Chi, Z.; Wang, X.; Duan, X.; Ma, L.; Gao, L. (2007) Purification and characterization of extracellular amylase from marine yeast Aureobasidium pullulans N13d and its raws potato starch digestion. *Enzyme Microbial Technology* 40, 1006-1012.

Lopez, C.; Torrado, A.; Fuciños, P.; Guerra, N. P.; Pastrana, L. (2006) Enzymatic inhibition and thermal inativation in hydrolysis of chestnut purée with an amylase mixture. *Enzyme Microbial Technology,* 39, 252-258.

Miller, G. L. (1959) Use of dinitrosalicylic acid reagent for determination of reducing sugar. *Analytical Chemistry,* 31, 426-428.

Queiroz, J. C de (2006) Redução na pressão de rompimento da torta de filtração através de melhorias na composição do fluido de perfuração à base de polímeros. Tese de Doutorado, *COPPE, Universidade Federal do Rio de Janeiro*, Rio de Janeiro, Brasil.

Segel, H. (1993) *Enzyme Kinetics: Behavior and Analysis of Rapid Equilibrium and Steady-State Enzyme Systems*, Wiley–Interscience, New York.

Toledo, A. L.; Severo Jr., J. B.; Souza, R .R.; Campos, E. S.; Santana, J. C. C.; Tambourgi, E. B. (2007) Purification by expanded bed adsorption and characterization of an a-amylase FORILASE NTL from *A. niger. Journal of Cromatography B,* 846, 51-56.

Proceedings of the 10th International Chemical and
Biological Engineering Conference - CHEMPOR 2008
Braga, Portugal, September 4-6, 2008
E.C. Ferreira and M. Mota (Eds.)

Inhibitory effect of phenolic compounds on the activity of Angiotensin I Converting Enzyme

Joana Afonso[1,2*], Cláudia P. Passos[2], Carlos M. Silva[2], Manuel A. Coimbra[3], Patrício Soares-da-Silva[1]

[1]Institute of Pharmacology and Therapeutics, Faculty of Medicine, 4200-319 Porto, Portugal
[2]CICECO, Department of Chemistry, University of Aveiro, 3810-193 Aveiro, Portugal
[3]QOPNA, Department of Chemistry, University of Aveiro, 3810-193 Aveiro, Portugal

Keywords: angiotensin converting enzyme; ACE inhibitor; polyphenols; grape seeds; hypertension
Topic: Integration of life sciences & engineering.

Abstract

Inhibition of angiotensin converting enzyme (ACE) has proved to have beneficial effects in the treatment of several cardiovascular disorders. The aim of this study was to evaluate ACE inhibitory potential of phenolic compounds. Isolated compounds and white grape seeds polyphenolic extracts were studied. A fluorometric method was used to detect the formation of histidyl-leucine, after hydrolyses of hippuryl-histidyl-leucine by ACE action, in the presence and absence of polyphenolic compounds. Phenolic extracts from grape seeds are endowed with higher inhibitory power of ACE than the pure monomers. A synergetisc effect of different compounds, longer polymerization degree in the extracts composition, associated with the view that the structure and hydroxyl groups can define inhibitory effect, may explain these unexpected findings.

1. Introduction

Several epidemiological studies have shown associations between the regular consumption of flavonoid-rich foods and a decreased risk for cardiovascular disease (Middleton et al., 2000; Nijveldt et al., 2001; Hung et al. 2004). Angiotensin II is a very potent agent that causes the muscles surrounding blood vessels to contract and thereby decreases blood flow. The angiotensin-induced constriction of blood vessels increases the pressure within the vessels and can cause hypertension. Angiotensin II is formed from angiotensin I in the blood by an enzyme, the Angiotensin I Converting Enzyme (ACE).

ACE is a glycoprotein peptidyldipeptide hydrolase, that cleaves angiotensin-I to produce angiotensin-II and also hydrolyzes and inactivates the vasodilator peptide, bradykinin to inactive peptides (Actis-Goretta, et al., 2003, 2006).

ACE inhibition is considered to be an important therapeutic approach in the treatment of high blood pressure, and the intake of certain synthetic inhibitors provides definitive positive health effects ((Middleton et al., 2000; Nijveldt et al., 2001; Hung et al. 2004). However, as ACE inhibitors are pharmacological drugs their use in healthy or low-risk populations is not advisable. The finding that certain flavonoid-rich foods can reduce blood pressure and inhibit ACE activity, opens up the possibility that consumption of select flavonoid-rich foods may

* Corresponding Author: Tel.: +351 225 513 642; E-mail: jafonso@med.up.pt

mimic synthetic ACE inhibitors and provide health benefits, but without adverse side effects (Actis-Goretta, et al., 2003, 2006).

Grape seed (*Vitis vinifera*) is a well known oilseed crop containing typically between 5-10% of phenolic compounds, and may be obtained by solid-liquid extraction with methanol and acetone/water. Subsequent fractionation may be carried out by graded methanol/chloroform precipitation, producing a broad range of extracts with decreasing average degree of polymerization (DPn)

Our research team accomplished previous tasks and characterized such fractions by ESI-MS/MS (Passos et al., 2007) and thiolysis (pre-treatment) followed by HPLC-UV detection, from which the corresponding DPn values were determined. The same extracts have been also characterized by FT-IR spectroscopy within the region of 1300-800 cm^{-1} (Passos et al., 2008).

The main objective of this work is the evaluation of the impact such natural phenolic extracts have upon ACE activity. This study started with monomers (+)-catechin, (-)-epicatechin, catechin-*O*-gallate and epigallocatechin. Afterwards, fractions of natural extracts of grape seed have been also evaluated. A comparison is accomplished with captopril, a synthetic compound commonly used for the treatment of hypertension and some types of congestive heart failure.

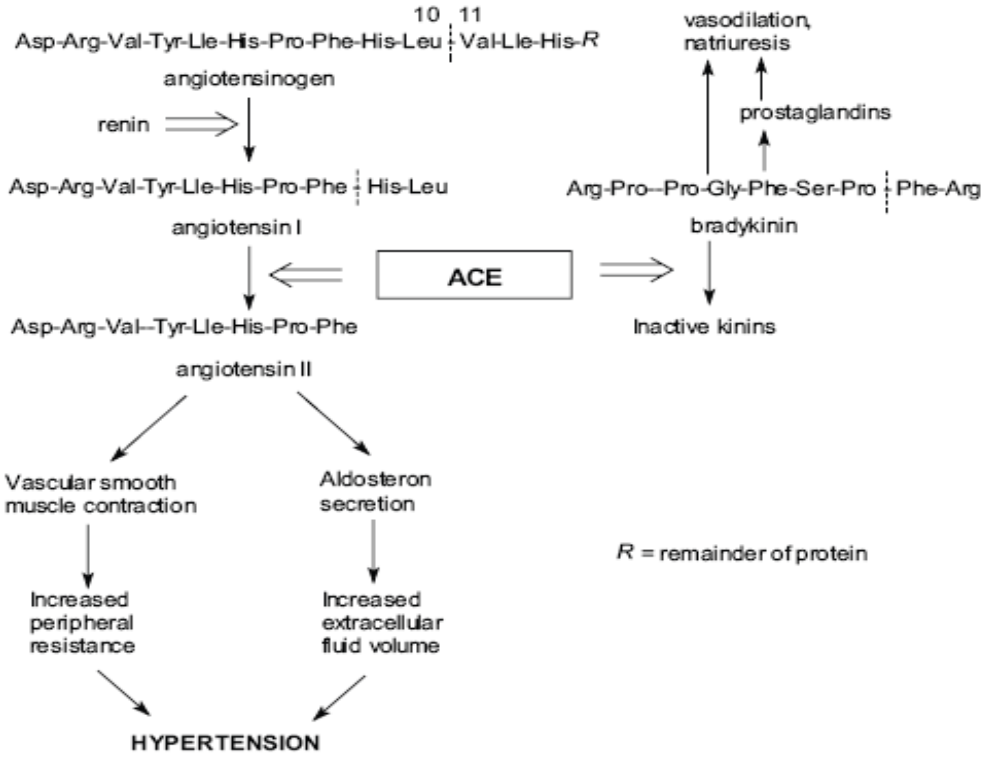

Figure 1 – The suggested hypertensive mechanism of Angiotensin (Hansen et al., 1995; Barbosa-Filho et al., 2006).

2. Materials and Methods

2.1 Extraction/fractionation of procyanidins crude extract (PCE) from grape seed

Detailed experimental procedure may be found elsewhere (Passos et al., 2008). In the following the main guidelines are presented.

Seeds were immersed into liquid nitrogen, milled in a domestic coffee mill and sieved (pore size<0.75 mm diameter). Extraction procedure was adapted from Guyot, Marnet, and Drileau (2001). A pre-treatment of three times extraction using n-hexane was applied to the seed powder to remove the lipids. Phenolic compounds were then extracted with a three times treatment with methanol containing 5% acetic acid (100 g seed powder/L MeOH). The acetic acid avoids the oxidation of compounds during extraction. The phenolic extracts were combined and filtered through, first a G1 and then a G3 sintered glass filter, and concentrated under vacuum at 40ºC, with several additions of water to assure the complete removal of methanol and acetic acid. Further, the see powder product of methanol extraction is treated with a mixture of acetone:water (2:3) and 5% acetic acid. The extraction with acetone: water mixture was repeated three times and the phenolic extract was treated in the same procedure as phenolic extract from methanol. Both methanol and acetone:water extracts were fractionated according to the methanol/chloroform graded precipitation proposed by Saucier et al (2001).

2.2 Inhibition of purified ACE activity

The ACE activity was assayed by fluorometric determination of the amount of histidyl-leucine (His-Leu) released from a substrate, hippuryl-histidyl-leucine (Hip-His-Leu), in the present of ACE. For the determination of ACE activity, 0,7 mM Hip-His-Leu substrate, in a reaction medium of 100 mM HEPES buffer (pH 8.3) containing 300 mM NaC1, was used to initiate all reactions after pre-incubation of ACE (0.75mU) at 37°C, for 3 min. When ACE activity was determined in the presence of inhibitor, the inhibitor was pre-incubated for 15 min with the enzyme before adding the substrate. The enzyme reaction was carried out at 37°C, for 30 min and then terminated with 1N sodium hydroxide. The His-Leu product in the reaction mixture was estimated following o-phthalaldehyde (0,2% in methanol) treatment, during 15 min, in the dark at 0ºC followed by neutralization with 1.5M phosphoric acid. The fluorescence of the o-phthalaldehyde condensation product of His-Leu was determined with a spectrophotofluorometer Spectramax Gemini (Molecular Devices, Sunnyvale, CA, USA) (360nm excitation, 480nm emission wavelength, cutoff of 420 nm). Different inhibitors were used. A first assay with pure phenolic compounds as inhibitors: catechin, epicatechin, catechin-O-gallate, epigallocatechin (0-100 uM) was tested. A second assay using different fractions of grape seeds extract was carried (0-30 mg extract/L).

3. Results and Discussion

Captopril was used as a positive control of ACE activity assay and shows a strongly effect on ACE inhibition in the nanomolar range (see Figure 2). Pure phenolic compounds were also tested: catechin, epicatechin, catechin-*O*-gallate and epigallocatechin. Catechin and catechin-*O*-gallate (100uM) decrease the ACE activity to 20.6 and 20.3%, respectively; epigallocatechin was able to decrease it in 35.5%; epicatechin performed in between.

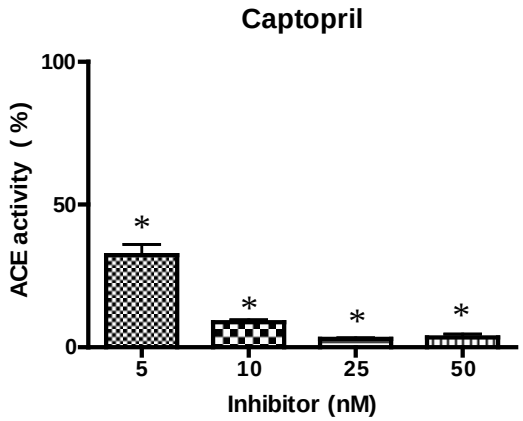

Figure 2 – Positive control of ACE activity assay. Captopril was incubated with ACE for 15 min, at 37ºC, previously the addition of substrate, HHL.

Phenolic extracts from white grape seeds were use to evaluate their capability to inhibit the ACE activity. The phenolic-grape seeds extracts used in this work were previously characterized (Passos et al., 2008). Extracts are constituted essentially by flavan-3-ols, a group with monomeric fractions of catechin, epicatechin, epicatechin-*O*-gallate units and polymerized molecules, the procyanidins. The three different fractions tested, WM-F2.2, WM-F2.6 and WA-F2.2, have different degrees of polymerization (DPn); WM stands for "white grape seed extracted with methanol", WA means "white grape seed extracted with a mixture acetone/water", and Fm.n identifies "fraction m.n" in the original work by Passos et al. (2007, 2008).

WM-F2.2 has the higher average DPn and WM-F2.6 the lower of the 3 extracts (8 and 6, respectively). The extract WM-F2.2 seems to a have highly inhibition effect on ACE activity, showing almost complete inhibition for 3 mg extract/L, whereas WM-F2.6 originates approximately 47% for the same concentration (see Figure 3).

WA-F2.2 has an average degree of polymerization DP_n=7, and produced inhibitory effects upon ACE well between those by WM-F2.2 and WM-F2.6.

The number of monomer units could define the extent and specificity of ACE inhibition. Studies evaluating the effect of albumin in the inhibitory action of procyanidins (since albumin has the ability to bind procyanidins) reveled that smaller oligomeric compounds (dimers and tetramers) were not affected in their inhibitory action on ACE while inhibitory action of hexamers were highly reduced. These results strengthen the view that larger procyanidins tend to exert broader interactions on protein surfaces. (Ottaviani, 2006). Moreover, kinetic analysis suggest that flavan-3-ols and procyanidins compete with the substrate for the active sites and indicating that larger molecules can inhibit both C- and N-active sites to a similar extent while monomers seem to inhibit preferentially the N-active site (Actis-Goretta, 2003).

However, the number of monomers appears not to define by itself the specificity of interaction with ACE. The way that monomers units are bound should also be considered, epicatechin dimers with different linkage bound structure had completely different effects in the activity of ACE (Ottaviani, 2006). Furthermore, when using an isolated enzyme, possible interactions with other cell structures by the higher procyanidins, are not taken in consideration. The number of hydroxyl groups on the procyanidins could also be related with

the interaction of procyanidins with the enzyme, since hydroxyl groups appear to determine the capability to adsorb to membrane surface (Actis-Goretta, 2003).

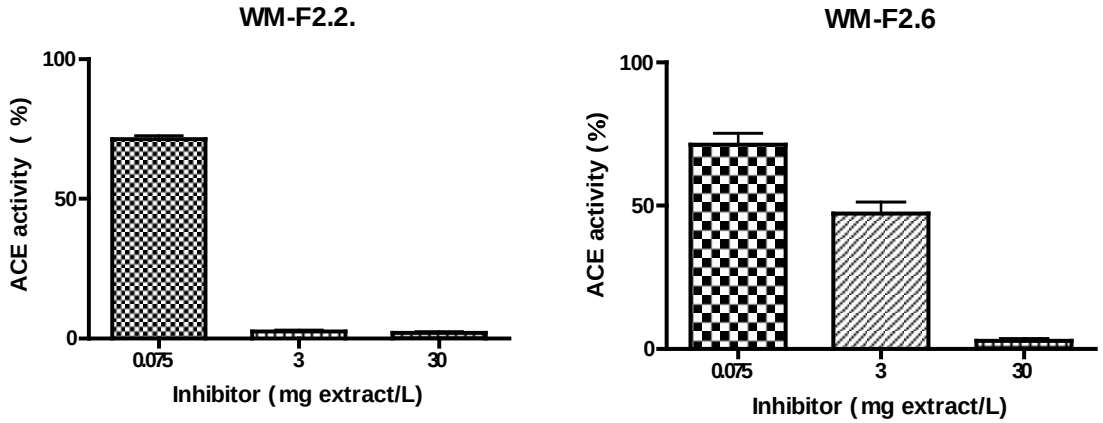

Figure 3 – ACE activity in the presence of different concentrations of white grape seed extracts obtained with methanol: WM-F2.2 and WM-F2.6.

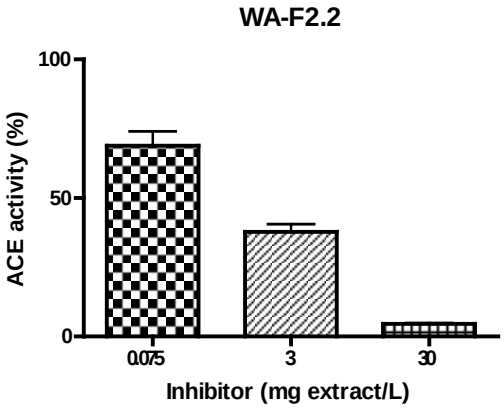

Figure 4 - ACE activity in the presence of different concentrations of the white grape seed extract obtained with a mixture of Acetone/Water: WA-F2.2.

4. Conclusions

Pure monomeric phenolic compounds were use to evaluate their capability to inhibit the ACE activity. Catechin, epicatechin, catechin-*O*-gallate, and epigallocatechin 100 μM decreased ACE activity to 20 to 35%.

Phenolic extracts from white grape seeds were also used to evaluate their inhibitory performance. A stronger effect has been clearly observed in comparison to the isolated monomers, suggesting that the longer degree of polymerization and perhaps a synergetic effect is achieved with such extracts. The differences found between different extracts indicate that the structure of procyanidins can define inhibitory effect in ACE as well hydroxyl group units.

References

Middleton, E. J.; Kandaswami, C.; Theoharides, T. C. (2000). The effects of plant flavonoids on mammalian cells: Implications for inflammation, heart disease, and cancer. *Pharmacol. Rev.*, *52*, 673-751.

Nijveldt, R. J.; Van Nood, E.; Van Hoorn, D. E.; Boelens, P. G.; Van Norren, K.; Van Leeuwen, P. A. (2001). Flavonoids: a review of probable mechanisms of action and potential applications. *Am. J. Clin. Nutr.*, *74*, 418-425.

Hung, H. C.; Joshipura, K. J.; Jiang, R.; Hu, F. B.; Hunter, D.;Smith-Warner, S. A.; Colditz, G. A.; Rosner, B.; Spiegelman, D.; Willett, W. C. (2004). Fruit and vegetable intake and risk of major chronic disease. *J. Natl. Cancer Inst.*, *96*, 1577-84.

Actis-Goretta, L.; Ottaviani, J.I.; Keen, C.L.; Fraga, C. G. (2003). Inhibition of angiotensin converting enzyme (ACE) activity by flavan-3-ols and procyanidins. *FEBS Lett.*, 555, 597-600.

Actis-Goretta, L; Ottaviani, J.I.; Keen, C.L.; Fraga, C. G. (2006) Inhibition of angiotensin converting enzyme activity by flavanol-rich foods. *J. Agri. Food Chem*., 54, 229-234.

Barbosa-Filho, J. M., Matins, V.K.M., Rabelo, L.A., Moura, M.D., Silva, M.S., Cunha, E.V.L., Souza, M.F.V., Almeida, R.N., Medeiros, I.A. (2006). Natural products inhibitors of the angiotensin converting enzyme (ACE). A review between 1980-2000. *Brazilian Journal of Pharmacognosy*, 16, 421-446.

Hansen K, Nyman U, Smitt UW, Adsersen A, Gudiksen L, Rajasekharan S, Pushpangadan P. (1995). In vitro screening of traditional medicines for anti-hypertensive effect based on inhibition of the angiotensin converting enzyme (ACE). *J. Ethnopharmacol*, 48, 43-51.

Passos, C.P.; Cardoso, S.M.; Domingues, M.R.M.; Domingues, P.; Silva, C.M.; Coimbra, M.A.: Evidence for galloylated type-A procyanidins in grape seeds. Food Chem., 2007, 105, 1457-1467.

Passos, C.P., Cardoso, S.M., Barros, A.S., Silva, C.M., Coimbra, M.A. (2008, to submit). Procyanidin Average Degree of Polymerization using FT-IR Spectroscopy and O-PLS/PLS1 Regression.

Ottaviani, J.I., Actis-Goretta, L., Villordo, J.J., Fraga, C.G. (2006). Procyanidin structure defines the extent and specificity of angiotensin I converting enzyme inhibition, *Biochimie*, 88, 359-365.

Saucier, C.; Mirabel, M.; Daviaud, F.; Longieras, A.; Glories, Y. (2001). Rapid Fractionation of Grape Seed Proanthocyanidins. *J. Agric. Food Chem*., 2001, 49, 5732-5735.

Proceedings of the 10th International Chemical and
Biological Engineering Conference - CHEMPOR 2008
Braga, Portugal, September 4-6, 2008
E.C. Ferreira and M. Mota (Eds.)

A novel view of the manufacture of polyurethane-polyurea aqueous dispersions

Isabel Fernandes[1], Filomena Barreiro[1*], Mário Rui Costa[2],
1. LSRE - Laboratory of Separation and Reaction Engineering, Instituto Politécnico de Bragança, Campus de Santa Apolónia, Ap 1134, 5301-857 Bragança, Portugal
2. LSRE - Laboratory of Separation and Reaction Engineering, Faculdade de Engenharia da Universidade do Porto, Rua Dr. Roberto Frias, 4200-465 Porto, Portugal

Keywords: Polyurethanes**,** Aqueous dispersions, Solvent-free
Topic: Sustainable process–product development through green chemistry

Abstract

Over the past few decades, polyurethane-polyurea aqueous dispersions (PUDs) have developed a solid reputation for high performance applications, particularly in the field of adhesives and coatings. PUDs are mostly environmentally compatible products; they are totally devoid or contain only low amounts of volatile organic compounds (VOC). This is an important feature in view of the present environmental policies where governments and internal agencies are placing emphasis on developing sustainable processes, improving work conditions and reducing emissions of toxic and polluting substances into the atmosphere. Moreover, polyurethanes are known as “tailor-made” products with properties resulting from a wide diversity of raw-materials which can be combined in different ways during the synthesis.

In recent years, our research group has been involved in the development of polyurethane-polyurea aqueous dispersions for various applications. With this work we intend to review this theme and describe the most recent developments. Characterization of industrial dispersions will be presented and examples of synthesis will be described.

1 Synthesis of aqueous polyurethane dispersions: general concepts

The industrial production of PUDs is nowadays a well established technology. There are two main synthetic routes to produce PUDs: the acetone process (a former process developed by Bayer AG) and the pre-polymer process (developed as an alternative response to the patented acetone process). A schematic representation of the two processes, putting into evidence their similarities and differences, is shown in Figure 1.

The acetone process can be described as comprising five main stages: (1) formation, in bulk, of an isocyanate terminated pre-polymer from the reaction of a diisocyanate (aromatic or aliphatic) and a macrodiol (usually a polyester or polyether α,ω-diol); (2) pre-polymer dilution in acetone in order to suppress any viscosity constraints and also to dissolve the hydrophilic diamine; (3) chain extension. In this step, the hydrophilising diamine assumes a double role, i.e., it acts simultaneously as an internal emulsifier and a chain extender; (4) dispersion. Phase inversion is promoted by adding water to the previously generated polymer acetone solution; and (5) acetone removal to achieve a solvent-free product.

The described acetone process presents some advantages; it avoids viscosity constraints by using a low boiling point solvent, acetone, which will be easily removed at the end of the synthesis and can be further recycled and reused in the process. Moreover, it is described as a reproducible process yielding final products with good performance. The main drawback of this process is related to the associated costs. Owing to the use of large amounts of acetone,

* Corresponding author. Tel + 351-273 303 089. E-mail: barreiro@ipb.pt

it requires a high reactor volume and, in general, explosion-proof equipment. Moreover, acetone needs to be distilled and dried before recycling (Dieterich, 1981; Gertzmann et al., 2007).

The pre-polymer process can be described as comprising four main stages: (1) formation, in bulk, of an isocyanate terminated pre-polymer from the reaction of a diisocyanate (aliphatic), a macrodiol (usually a polyester or polyether α,ω-diol) and a hydrophilising diol. Since the hydrophilising diol is not soluble, neither in the pre-polymer mixture nor in acetone, it requires other co-solvents which are in general highly polar and low volatility components. In general, the co-solvent will remain in the final product; (2) neutralization of the internal emulsifier acid groups using a tertiary amine; (3) dispersion. Phase inversion is promoted by adding water to the previously produced pre-polymer and (4) chain extension, usually using a short diamine. If viscosity constraints are encountered during the process, acetone is added to dilute the medium. If so, the last stage will correspond to its removal. These steps (dilution and acetone removal) can be viewed as optional and are directly related to the chemical system used. As an example, polyester based formulations have higher viscosity than the counterpart polyether based formulations.

Comparatively to the acetone process, the pre-polymer process has one major advantage, i.e., it requires none or only small amounts of acetone. As main disadvantages, it uses other co-solvents that might be difficult to remove and will remain in the final product. Chain extension is carried out in heterogeneous medium in opposition to the acetone process that uses a homogeneous medium (acetone solution before dispersion). This could lead to incomplete isocyanate conversion (inaccessible isocyantes entrapped inside polymer particles) and consequently to a lower final molecular weight polymer (Dieterich, 1981).

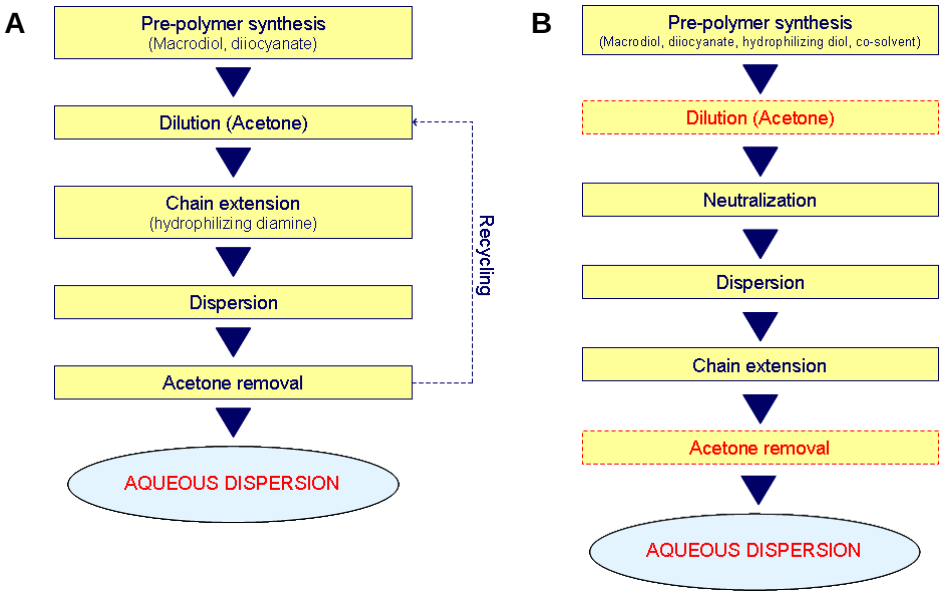

Figure 1 Schematic drawing of the acetone (A) and prepolymer (B) processes.

The chemical system associated to the pre-polymer process is rather complex and it involves polyols (mainly a polyester or polyether α,ω-diol), aliphatic diisocyanates to hinder isocyanate consumption due to water reactivity, hydrophilising diols that will act as internal emulsifiers, co-solvents to dissolve the hydrophilising diol and suppress process viscosity constraints, neutralizing agents to activate the ionic groups present in the internal emulsifier, chain extenders (mainly di- or tri- amines) to increment the molecular weight. Moreover catalysts are also added during pre-polymer synthesis.

Table 1 shows a set of typical chemical components used in the pre-polymer process and Table 2 presents a basic recipe for the synthesis of a polyurethane dispersion adapted from Kim Jung Hyun 's group research work (Cheong et al., 2002). This recipe uses a typical NCO/OH ratio of 1.7, a relative degree of neutralization of 100% and a chain extension degree of 100%. Typical used process temperature conditions are: 70 – 90 ºC during pre-polymer synthesis, 35 – 50 ºC during the neutralizing stage and 25 – 35 ºC during dispersion phase. The extension reaction is usually performed atroom temperature (around 25 ºC).

Our laboratory set-up for aqueous polyurethane production is shown in Figure 2. It comprises a reaction vessel of 500 ml, a mechanical stirrer, a silicone bath, a nitrogen inlet and controlled feed addition. Reaction temperature is controlled inside the reactive mixture by means of a thermocouple.

Table 1 Examples of typical chemical components used in the pre-polymer process

Component	Examples
Polyol	*Polyesters:* polyadipates, polycaprolactones (PCL) *Polyethers:* Polypropylene glycol (PPG), Polyethylene glycol (PEG), Polytetramethylene ether glycol (PTMG) *Others:* Polycarbonates (PC), acrylics
Isocyanates	*Aliphatic diisocyanates:* Dicyclohexylmethane Diisocyanate (HMDI), Isophorone Diisocyanate (IPDI), Tetramethylxylylene Diisocyanate (TMXDI)
hydrophilising diol	Dimethylol propionic acid (DMPA)
Co-solvents	*hydrophilising diol dissolution medium*: N-metil-2- pyrrolidone (NMP) *Viscosity control:* Acetone
Neutralizing agent	Triethylamine (TEA)
Chain extenders	Diethylene triamine (DETA), Hydrazine Monohydrate (HYD), Ethylenediamine (EDA)
Catalysts	Dibutyltin Dilaurate

Table 2 Basic recipe for the synthesis of polyurethane dispersions (*in Cheong et al*.)

Component	Amount (mol/g)
Polyhexamethylene adipate (polyol)	0.065 (130.0)
IPDI	0.176 (39.2)
DMPA	0.039 (5.2)
NMP	0.079 (7.8)
TEA	0.039 (3.9)
EDA	0.073 (4.4)

2 Considerations about the pre-polymer process face to the present environmental policies

The pre-polymer process, at present, is being forced to readapt due to ongoing developments, partly motivated by process constraints, raw materials restrictions and the need to obtain a true solvent-free product. Allied to this fact it is worth mentioning the upcoming of European REACH legislation, which is expected to have a considerable influence on the PUD industry. Most of the industrially produced PUDs use dimethylol propionic acid (DMPA) as the internal emulsifier. DMPA is sparingly soluble in the reactive mixture and needs to be previously dissolved in an organic solvent. The chosen solvent must fulfil a series of criterions: dissolve DMPA, be inert towards isocyanates and be miscible in water. Additionally it must present low odour and low cost. Alternatives to the traditionally

used option (N-methyl-2-pyrrolidone, NMP) include ketones, cyclic ethers, amines and amides.

NMP has one major problem; it has a high boiling point, near 200 ºC, and thus remains in the final product. The upcoming product restrictions refer that all products containing more than 5% (w/w) of NMP will be considered toxic from June 2009 onwards (Mestach and Goossen, 2007) and at present almost all commercially available PUDs have NMP contents from 5-15 %. In this context, the NMP-free concept is gaining a growing importance, particularly for PUD industry which uses the pre-polymer process.

1. Silicone bath
2. Reactor vessel with lid including thermocoulple, condenser, nitrogen and feed inlets
3. Mechanical stirrer
4. Peristaltic and vacuum pumps
5. Condenser for acetone recover
6. Computer for control and data registration

Figure 2 Bench scale set-up for preparing aqueous polyurethane dispersions.

Some new markets for PUD, where restrictions are even more specific, such as adhesives for food contact, are justifying also additional studies. In this case, besides the absence of solvents, the raw materials must be carefully chosen to avoid toxicity, component migration and noticeable smell. Moreover, there is a lack of protocols to characterize these issues (Petrie, 2007).

In USA, Food and Drug Administration (FDA) regularizes the allowed reactants through the elaboration of positive lists. Reactants allowed to be incorporated in the synthesis of PUD adhesives for indirect food contact are catalogued in the 21CFR 175.105 positive list. In the European Union (EU) context, since 1989 the legislation has been harmonized and the main restrictions were assembled in one directive: the “Plastics Directive”, 2002/72/EC. It is worth to mention that adhesives are not yet treated as an individual regulated group (Petrie, 2007). A summary of the existing limitations considering PUD production in general using the EU directive 2002/72/CE and FDA positive list 21CFR 175.105 are shown in Table 3.

3. New challenges to PUD formulators

Owing to the described restrictions PUD formulators are obliged to readapt and test alternatives to the traditional pre-polymer process:

NMP free concept. Presently, there are some alternatives to achieve the NMP-free concept. Among them we may refer the direct NMP replacement by an equivalent solvent, DMPA replacement by an equivalent hydrophilising diol but with better solubility in the reactive mixture, and replacement of the macrodiol by one of the commercially available new macrodiols with incorporated ionic groups in the molecular backbone (Gertzman et al., 2007).

NMP direct replacement. For direct NMP replacement some alternatives could be envisaged, namely, using dimethylsulfoxide (DMSO) or N-ethyl-2-pyrrolidone (NEP). DMSO has one major disadvantage related to the presence of strong odour that intensifies as a result of exothermic decomposition (formation of dimethylsulfide). NEP was been recently

commercially announced as a directly obvious alternative to NMP. Nevertheless it presents as a drawback the fact of being a new product, which is at present too expensive and insufficiently studied. Other possible NMP substitutes are ketones (acetone or methyl ethyl ketone (MEK)). Ketones have an additional benefit: their low boiling point allows an easy removal by vacuum distillation from the final product. However, DMPA presents low solubility in ketones and its incorporation will require large volumes of solvent. As a reference, 1 g of DMPA needs 250 ml acetone to solubilise.

DMPA replacement. Another alternative will be the direct DMPA replacement by an equivalent hydrophilising diol but with higher solubility in the reactive mixture, such as dimethylolbutanoic acid (DMBA). DMBA is more soluble both in acetone and in the relevant macrodiols than DMPA (Gertzmann, et al., 2007). Even so, DMBA has two main problems; it is a relatively new product, more expensive and the properties imparted to the developped products, which are still under study, may often not be better.

Macrodiols with incorporated ionic groups. It is also feasible to replace DMPA by macrodiols with incorporated ionic groups in the molecular backbone (Gertzman et al., 2007). These products are already available in the market. However, two major disadvantages are their high viscosity and high cost.

DBTDL replacement. Another important question in PUD industry is the changing of hazard classifications now labelling tin catalysts as toxic instead of harmful. This issue will have a great impact in PUD industry since the most applied catalyst is a tin based one (dibutyltin dilaurate, DBTDL). DBTDL is used worldwide mainly because it presents excellent catalytic effect and is selective towards hydroxyl reaction with isocyanates. A direct alternative is the use of amines, but the recent established restrictions also pose limits to these compounds. New alternatives are being made available in the market, among them the most effective to PUD synthesis are zinc and bismuth carboxylates and zirconium complexes. But again, there is a lack of studies about their catalytic performance in PUD synthesis. Comparatively to the presently used catalysts they are rather expensive (Extance, 2007).

Table 3. PUD component limitations face to EU directive 2002/72/CE and FDA positive list 21CFR 175.105

Component		Directive 2002/72/CE	FDA
Diisocyanate	Dicyclohexylmethane Diisocyanate	QM(T)=1mg/Kg (free NCO)	21CFR 175.105
	Isophorone Diisocyanate		21CFR 175.105
	Tetramethylxylylene Diisocyanate		
Poliol	Polycaprolactone	Without limitations	NR
	Polypropylene glycol		21CFR 175.105
	Polyethylene glycol		
	Polytetramethylene ether glycol		
Catalyst	Dibutyltin Dilaurate	NR	Only allowed as Polyurethane catalyst
Internal Emulsifier	Dimethylol propionic acid	QM(A)=0.05 mg/6dm^2 (free DMPA)	21CFR 175.105
	Dimethylolbutanoic acid	NR	21CFR 175.105
Neutralizing Agent	Triethylamine (TEA)	NR	21CFR 175.105
Chain Extender	Diethylene triamine	LME=5 mg/Kg	21CFR 175.105
	Hydrazine Monohydrate	NR	NR
	Ethylenediamine	LME=12 mg/Kg	21CFR 175.105
Co-Solvent	N-ethyl-2-pyrrolidone	NR	NR
	Dimethyl sulfoxide	NR	NR
	Acetone	Without limitations	21CFR 175.105
	N-metil-2- pyrrolidone (NMP)	NR	NR

NR- not referred, QM(T)- Maximum total amount, QM(A)- Maximum amount allowed, LME- Specific Migration Limit

4 Examples of PUD characterization – typical technical data

The characterized PUDs were kindly supplied by Bayer Material Science and Alberdingk Boley GMB. The relevant properties according to the characterization presented in the technical data sheet were performed and shown in Table 4.

PUDs were described in terms of solids content and pH, viscosity (measured with a Visco Star Fungilab viscometer of concentric cylinders, equipped with an Electro Temp heating/refrigerating bath) and Mean Particle Size and Particle Size Distribution (analyzed by laser dispersion using a Coulter LS230 instrument).

Table 4 Characterization of a commercial PUD

Properties	**Sample**			
	PUD1	PUD2	PUD3	PUD4
Solid Content (%, w/w)	50.5	41.0	40.8	36.6
Viscosity (mPa.s)	46.5	24.4	17.1	61.6
pH	7.0	7.6	7.4	7.7
Mean Particle Size (nm)				
Volume distribution	113	107	115	107
Number distribution	56	103	110	103

PUD 1 (Dispercoll U56), PUD2 (Alberdingk U3251), PUD3 Dispercoll XP2578) and PUD4 (Bayhydrol XP2593/1)

5 Conclusions

Over the past few decades, polyurethane-polyurea aqueous dispersions (PUDs) have developed a solid reputation for high performance applications, particularly in the field of adhesives and coatings. The industrial production of PUDs is nowadays a well established technology. There are two main synthetic routes to produce PUDs: the acetone process (a former process developed by Bayer AG) and the pre-polymer process (developed as an alternative response to the patented acetone process).

PUD industry in general and the pre-polymer process in particular, are facing some challenges due to the emerging new markets and environmental restrictions. According to FDA and EU legislation, substitutes for some of the traditionally used raw materials need to be found and implemented. A strong effort should be done in terms of both the optimization of the systems already implemented and the search for new ones. This will be achieved by means of basic, technological and economical research.

References

Cheong, I.W., Kong, H.C., Shin, J.S., Kim, J.H. (2002). Kinetic aspects of chain extension reaction using water-soluble diamines in aqueous polyurethane dispersion, *Journal of dispersion Science and Technology*, 23 (4), 511-518.

Dieterich, D., (1981). *Aqueous* Emulsions, Dispersions and Solutions of Polyurethanes; Synthesis and Properties, *Progress in Organic Coatings,* 9, 281-340.

Extance, A. (2007), Implications of changing hazard classifications for tin catalysts, www.specialchem4adhesives.com (July, 2008)

Gertzmann, R., Irle, C., Schmitt, P. (2007). Waterborne Polyurethane Coatings for Wood Floor-The Next Generation, *Bayer MaterialScience AG technical information*, Leverkusen, Germany

Mestach, D., Goossen, J., (2007). *New* Approaches for Solvent-Free Waterborne Polyurethanes, *Polyurethane Magazine International*, 5, 313-318.

Petrie, E. M. (2007), Food contact adhesives, www.specialchem4adhesives.com (July, 2008)

Proceedings of the 10th International Chemical and
Biological Engineering Conference - CHEMPOR 2008
Braga, Portugal, September 4-6, 2008
E.C. Ferreira and M. Mota (Eds.)

Constructing Chemical Reaction Networks Through Decoupling, Regression and Rationalisation

Samantha C. Burnham[1], Mark J. Willis[2] and Moses O. Tadé[1]
[1]Department of Chemical Engineering, Curtin University of Technology, Bentley Campus, Bentley, Perth, 6102, Australia
[2]School of Chemical Engineering and Advanced Materials, Newcastle University, Newcastle-upon-Tyne, NE1 7RU, UK.

Keywords: Chemical Reaction Network, Regression, Stoichiometry.
Topic: Systematic methods and tools for managing the complexity.

Abstract

The aim of this work is a move towards the automated determination of chemical reaction networks, from batch process data. In this paper it is demonstrated how, in principal, this may be achieved using simple systematic mathematical and statistical analyses of the process data. Initially a global ordinary differential equation (ODE) model structure, capable of representing an entire set of possible chemical reactions, is specified and decoupled. Regression analyses are then used to reduce the ODE model structure to a subset of reactions. Rationalisation procedures that exploit the basic rules of reaction chemistry and a number of mathematical principals, often employed in biological systems theory (BST), are incorporated to ensure consistent chemical reaction networks are obtained. The methods are demonstrated using a simulated case study. It is concluded that it is possible to successfully determine chemical reaction networks, and their associated rate constants, from batch process data.

Introduction

The primary objective of this paper is to present an incremental approach to network identification. The method is based upon the use of composition and the rate of heat evolution ($\mathbf{q_R}$) data. Where $\mathbf{q_R}$ data may readily be obtained from a reaction calorimeter. During early process development in the fine chemical industry reaction calorimeters are used for systematic and quick characterization of the relevant kinetic and thermodynamic reaction parameters. $\mathbf{q_R}$ represents the sum of individual heats of reaction multiplied by the rates of reaction and may therefore be used to obtain kinetic data (see Wright *et al*, 1993 and Zogg *et al*, 2004).

This paper is split into seven stages a) the kinetic models are specified as decoupled ODEs, b) simulated batch process data is generated to demonstrate the techniques, c) singular value decomposition (SVD) is used to estimate the number of reactions occurring, (N_R), d) given N_R and the $\mathbf{q_R}$ data, regression procedures are applied to reduce the number of concentration terms to a subset of N_R terms, e) multiple linear regression (MLR), based on the composition data, is then used to obtain parameter estimates, thus, determine the concentration terms that are influential on the individual ODEs, f) as each ODE is considered separately a rationalisation procedure is applied to ensure consistent chemical reaction network equations are obtained that preserve system stoichiometry and g) the isothermal rate constants are estimated and the network is constructed.

As opposed to the rationalisation strategy described in Burnham *et al* (2008), the strategy here is to use topological features of the reaction network that may be obtained from the elemental matrix (particularly the atomic matrix). These topological features provide mathematical constraints that may be used to determine whether the estimated model parameters (and stoichiometries) are consistent with the atomic matrix and, given the event that they are not, constrain them to be. It is also possible to check that the (constrained) estimated model parameters (and stoichiometries) are consistent with the process data.

Kinetic models

Assuming batch, isothermal, operation, the (1 x N_R) vector of reaction step rates (RSRs) at any specified time instant, t, $\mathbf{r_r}$, may be defined by (1).

$$\mathbf{r_r} = \mathbf{Kr} \tag{1}$$

Where **K** is a diagonal matrix of the rate constants, **r** is a (1 x N_R) vector of relevant concentration terms, at the same specified time point. Assuming mass action kinetics and elementary reactions the concentration terms may be specified as the products of the concentrations of the reacting species, in the respective reaction, raised to a power equal to their order of reaction. For example, consider the Van de Vusse reaction scheme (Van de Vusse, 1964) involving three reactions and four chemical species, (2). Thus, **r** would be given by (3).

$$x_1 + x_1 \rightarrow x_2 \qquad x_1 \rightarrow x_3 \rightarrow x_4 \tag{2}$$

$$\mathbf{r} = \begin{bmatrix} x_1^2 & x_1 & x_3 \end{bmatrix} \tag{3}$$

Further, the species rate expression (SRE), which defines the rate of change of concentration of the species i due to reaction, can be expressed as the sum of the RSRs that are associated with the reaction steps in which species i is involved, multiplied by the stoichiometric coefficient of species i in that reaction step. Thus, for n species, a (1 x n) vector of the SREs, $\mathbf{r_s}$, may be defined by (4).

$$\mathbf{r_s} = \mathbf{VKr} \tag{4}$$

The (n x N_R) stoichiometric matrix **V** describes the topology of a chemical reaction network. The stoichiometries of the chemical species in the reactions, which make up the network, provide the entries of the stoichiometric matrix. For a network with n species and N_R chemical reactions, the stoichiometric relationships, which are assumed to be time invariant, are given by (5a). Where $v_{i,l}$, i = 1, …, n, l = 1, …, N_R, are the stoichiometric coefficients for the i^{th} species in the l^{th} reaction. For the reaction scheme given by (2), the stoichiometric matrix is then given by (5b).

$$\mathbf{V} = \begin{bmatrix} v_{1,1} & v_{1,N_R} \\ & \\ v_{n,1} & v_{n,N_R} \end{bmatrix} \qquad \mathbf{V} = \begin{bmatrix} -2 & -1 & 0 \\ 1 & 0 & 0 \\ 0 & 1 & -1 \\ 0 & 0 & 1 \end{bmatrix} \tag{5}$$

For any reaction step it can be noted that $v_{i,l} > 0$ represents a product formed by that reaction step, $v_{i,l} < 0$ represents a reactant consumed by that reaction step. $v_{i,l} = 0$ may represent either a catalyst or a species not involved in that reaction step.

For a batch, isothermal reactor, the total rate of heat evolution due to reaction per unit volume is $\mathbf{q_R}$, this may be equated to the sum of individual heats of reaction multiplied by the rates of reaction (7) where **h** (1 x N_R) is a vector of the individual heats of reaction, and for the reaction scheme given by (2) these are arbitrarily assigned in (8).

$$\mathbf{q_R} = \mathbf{hKr} \tag{7}$$

$$\mathbf{h} = \begin{bmatrix} -8e^4 & -1e^4 & -1e^5 \end{bmatrix} \tag{8}$$

It is possible to specify a set of possible concentration terms that may be used to define the structure of the RSRs/SREs. If it is assumed that a) the reactions are at most the result of bimolecular collisions and the total reaction order is no greater than two, b) the concentration terms are of integer order with respect to each species concentration and c) there are no terms consisting of purely zero order elements. Then, given the n species, a set of all of the possible concentration terms that may appear in the RSRs, S_C, are given by (9).

$$S_C = \left\{ [x_h],\ [x_h][x_j] \right\}, \quad h = 1,\cdots,n;\ \ j = h,\cdots,n \tag{9}$$

Where the total number of possible concentration terms, n_c, is given by (10).

$$n_c = 2n + \frac{n(n-1)}{2} \tag{10}$$

Thus, the vector **r** may become $\hat{\mathbf{r}}$, (11), which is a vector of all of the possible concentration

terms defined by (9).

$$\hat{\mathbf{r}} = \begin{bmatrix} [x_1] & [x_2] & \cdots & [x_n] & [x_1]^2 & [x_1][x_2] & \cdots & [x_n]^2 \end{bmatrix} \quad (11)$$

For the reaction scheme given by (2), $\hat{\mathbf{r}}$ may be defined as (12).

$$\hat{\mathbf{r}} = \begin{bmatrix} [x_1] & [x_2] & \cdots & [x_4] & [x_1]^2 & [x_1][x_2] & \cdots & [x_4]^2 \end{bmatrix} \quad (12)$$

Parameter estimates are obtained for each possible concentration term (term in $\hat{\mathbf{r}}$) for each SRE in (4). Therefore, a (n x n_c) matrix $\boldsymbol{\Theta}$ of parameters may be defined, where $\boldsymbol{\Theta}$ is an estimate of **VK** and, for $\hat{\mathbf{r}}$ defined as (12), is given by (13).

$$\boldsymbol{\Theta} = \begin{bmatrix} \theta_{0,1,1} & \theta_{0,2,1} & \cdots & \theta_{1,1,1} & \cdots & \theta_{4,4,1} \\ \vdots & & & & & \vdots \\ \theta_{0,1,4} & \theta_{0,2,4} & \cdots & \theta_{1,1,4} & \cdots & \theta_{4,4,4} \end{bmatrix} \quad (13)$$

As the SREs represent the rate of change of species concentration, (4) may be rewritten as (14), a general set of ODEs which represents the entire set of possible chemical reactions. Where $\dot{\mathbf{x}}$ is a vector of the rates of change of species concentrations at a specified time instant. It should be noted that for the reaction scheme given by (2), ideal parameter estimation would give the non zero estimates $\theta_{0,1,1}$= -k_2, $\theta_{1,1,1}$= -2k_1, $\theta_{1,1,2}$= +k_1, $\theta_{0,1,3}$= +k_2 $\theta_{0,3,3}$= -k_3 and $\theta_{0,3,4}$= +k_3.

$$\dot{\mathbf{x}} = \boldsymbol{\Theta}\hat{\mathbf{r}} \quad (14)$$

Further the rate of heat evolution (7) may be rewritten as (15), where correct parameter estimation would provide the estimates $\varphi_{0,1}$=$\Delta H_{R2}k_2$, $\varphi_{0,3}$= ΔH_{R3},k_3 $\varphi_{1,1}$=$\Delta H_{R1}k_1$.

$$\mathbf{q_R} = \boldsymbol{\Phi}\hat{\mathbf{r}} \quad (15)$$

Generating process data

For reaction scheme (2), it was assumed that it was only possible to alter the initial concentrations of the reactant x_1. Four simulated batch experiments were performed, where the levels of initial concentration of x_1 were chosen to be equidistant between 0.25 and 1.00 moldm^{-3}. Note that the volume of each batch is specified as 1 litre and that the reactions take place in an inert solvent. The kinetic rate constants were specified as k_1 = 0.00100 min^{-1}mol^{-1}dm^3, k_2 = 0.00685 min^{-1} and k_3 = 0.00248 min^{-1}. Eleven concentration measurements of each species were generated, for each simulated batch experiment, by numerical integration of the true system ODEs, that represent the SREs, using the initial reactant concentrations specified above. The total simulation period was specified as 1200 mins and measurements of all species were recorded every 120 mins. In this case no simulated measurement error was added to the signals. For the last batch (initial concentration of x_1 at 1.0 moldm^{-3}), the simulated concentration data and the fits of this data are given by figure 1. The rate of heat evolution data, $\mathbf{q_R}$, was also generated, using (7) given (8), at the same sampling times, refer to figure 2.

Estimating the number of reactions

It is known that $\mathbf{r}$ may be estimated as $\hat{\mathbf{r}}$, (11) but only N_R of the set of n_c concentration terms in $\hat{\mathbf{r}}$ are relevant. Methods to calculate the actual number of reaction steps from measured process data have been suggested in the literature e.g.Hamer (1989) and Bonvin and Rippin (1990) have demonstrated that the number of reactions may be obtained from a SVD analysis (Lawson and Hanson, 1974) of the matrix of the process data.

Based on the work of Burnham *et al* (2008), the fist derivatives of the concentration profiles were calculated and compiled to give the matrix $\dot{\mathbf{X}}$ which represents the rate of change of concentration of all species at all measured time points. $\dot{\mathbf{X}}$ was decomposed using SVD, to obtain the eigenvalues of $\dot{\mathbf{X}}$. The cumulative percentage variance represented by each eigenvalue was found, and the number of largest eigenvalues which represent a summed

variance larger than a fixed threshold of 95% was then determined. This corresponded to the first three eigenvalues which accounted for 98.78% of the variation, hence $\hat{N}_R$ is three.

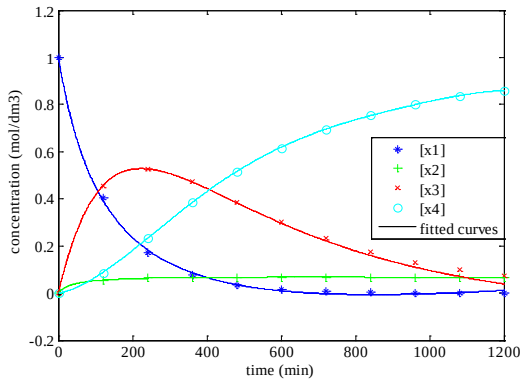

Fig. 1: Measured concentration values for the last batch of data

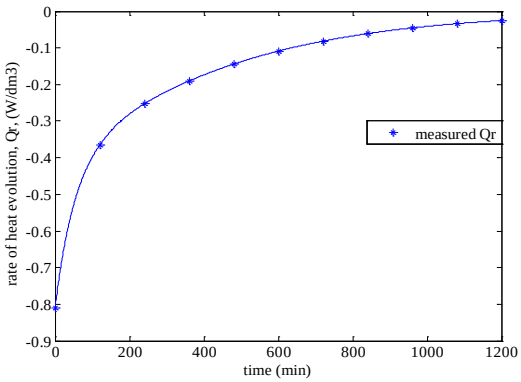

Fig. 2: Simulated rate of heat evolution measurements

Determining the concentration terms

From (7) it is known that $\mathbf{q_R}$ is proportional to all of the relevant N_R concentration terms. Thus, it is believed that the $\mathbf{q_R}$ data will be helpful in determining the relevant N_R concentration terms through regression analysis. Best subsets regression allows a number of models containing different predictors (and different numbers of predictors) to be compared. Hence, it is possible to compare the models comprised of all possible combinations of $\hat{N}_R$ terms from the set of n_c concentration terms, regressed against the $\mathbf{q_R}$ data. It is usually not feasible to model each combination of predictors individually; alternatively, a statistical algorithm is used to produce summary statistics for the possible combinations of predictors. Hence, this procedure does not produce a regression equation but identifies the best combination of $\hat{N}_R$ concentration terms that describe the variability in the $\mathbf{q_R}$ expression.

To determine the best set of predictors, commonly, the adjusted R^2 value and Mallows' *C-p* statistic (Mallows, 1973) are used. Given, that $\hat{N}_R$ was estimated to be three, the number of predictors for the regression models was specified as three. Best subsets regression of all combinations of three of the fourteen concentration terms defined by (12) against the $\mathbf{q_R}$ experimental data were generated. Based on the adjusted R^2 value and the Mallows' *C-p* statistic, $\mathbf{q_R}$ was taken to be proportional to the set of terms, $[x_1]^2$, $[x_1]$, $[x_3]$. Thus $\hat{\mathbf{r}}$ is given by (16).

$$\hat{\mathbf{r}} = \begin{bmatrix}[x_1]^2 & [x_1] & [x_3]\end{bmatrix}^{\mathsf{T}} \tag{16}$$

Obtaining estimates for the coefficients of Θ

Multiple linear regression (MLR) of the three concentration terms against $\dot{\mathbf{X}}$ was executed, in order to estimate $\boldsymbol{\Theta}$, thus, obtain estimates for $\mathbf{V}$ and $\mathbf{K}$. With use of the t-statistics and p-values it was possible to identify that a number terms were insignificant at the 95% level with p-values ≥ 0.05. These were removed from the models and the models were again regressed. This was repeated until only terms significant at the 95% level (p-values ≤ 0.05) remained. This gave an estimate for $\boldsymbol{\Theta}$ shown by (17), along with adjusted R^2 values for the respective SRE models.

$$\hat{\boldsymbol{\Theta}} = \begin{bmatrix} -0.00162 & -0.00699 & 0.00000 \\ 0.00092 & 0.00000 & 0.00000 \\ 0.00000 & 0.00676 & -0.00244 \\ 0.00000 & 0.00000 & 0.00248 \end{bmatrix} \quad \begin{aligned} adjR^2 &= 100\% \\ adjR^2 &= 99.1\% \\ adjR^2 &= 100\% \\ adjR^2 &= 100\% \end{aligned} \tag{17}$$

A posteriori application of mass conservation for rationalisation

If all the chemical species involved in a chemical reaction network have been characterised they may be expressed in terms of an atomic matrix, **A**, (18a). The n columns represent the reacting species and the rows represent the N_A distinct atoms (or molecular groups) in the chemical system ($a_{f,i}$, f = 1, …,N_A, i = 1, …n, $a_{f,i}$ is the number of atoms of the f^{th} type in the i^{th} chemical species). For reaction scheme (2), for example, the atomic matrix may be arbitrarily chosen to be (18b). In the case where it is not possible to characterise all chemical species it is possible to replace the atomic matrix, **A**, with a (1 x n) vector of the species' relative molecular masses (RMMs) if these are known.

$$\mathbf{A} = \begin{bmatrix} a_{1,1} & \cdots & a_{1,n} \\ \vdots & \ddots & \vdots \\ a_{N_A,1} & \cdots & a_{N_A,n} \end{bmatrix} \qquad \mathbf{A} = \begin{bmatrix} 2 & 4 & 2 & 2 \\ 6 & 12 & 6 & 6 \\ 1 & 2 & 1 & 1 \\ 1 & 2 & 1 & 1 \end{bmatrix} \tag{18}$$

As atoms are conserved during a chemical reaction, any composition change must obey (19).

$$\mathbf{AV} = \mathbf{0} \tag{19}$$

Therefore if $\hat{\mathbf{\Theta}}$ is correctly identified, (20) is true.

$$\mathbf{A}\hat{\mathbf{\Theta}} = \mathbf{0} \tag{20}$$

Thus it is possible to check whether the $\hat{\mathbf{\Theta}}$ (17) provides a mass balanced solution, consistent with **A** (18b). The magnitude of the values obtained was comparable to that of the specified rate constants. Thus it is still somewhat ambiguous as to whether (or not) $\hat{\mathbf{\Theta}}$ in (17) provides a mass balanced solution. It is possible to calculate an improved estimate for $\hat{\mathbf{\Theta}}$, which adheres to the constraint given by (20). This is achieved by projecting $\hat{\mathbf{\Theta}}$ onto the null space of **A**, through a projection matrix, $\mathbf{P_A}$ size (n x n), associated with the null space of **A.** $\mathbf{P_A}$ is given by (21), where **I** is an identity matrix size (n x n). Refer to Lawson and Hanson (1974). Given (21) an improved estimate for $\hat{\mathbf{\Theta}}$, $\hat{\mathbf{\Theta}}_{\mathbf{P_A}}$, which adheres to the constraint given by (20) may be calculated, (22).

$$\mathbf{P_A} = \mathbf{I} - \mathbf{A}^{+}\mathbf{A} \tag{21}$$

$$\hat{\mathbf{\Theta}}_{\mathbf{P_A}} = \mathbf{P_A}\mathbf{A} = \begin{bmatrix} -0.0018 & -0.0070 & 0.0000 \\ 0.0009 & 0.0001 & 0.0000 \\ 0.0000 & 0.0068 & -0.0025 \\ 0.0000 & 0.0000 & 0.0025 \end{bmatrix} \tag{22}$$

Also, it is possible to perform target factor testing, Bonvin and Rippin (1990), on each of the estimated stoichiometries from $\hat{\mathbf{\Theta}}_{\mathbf{P_A}}$ to test whether (or not) it is consistent with the measured data.

Obtaining the chemical reaction network

Given that it may be assumed that $\hat{\mathbf{\Theta}}_{\mathbf{P_A}}$ is an accurate estimate, therefore, from $\hat{\mathbf{\Theta}}_{\mathbf{P_A}}\mathbf{r}$ it may be deduced that species x_1 reacts with itself to form x_2, that species x_1 rearranges to form x_3 and that species x_3 in turn rearranges to form x_4. This gives the chemical reaction network defined by (23).

$$x_1 + x_1 \rightarrow C_1 x_2 \qquad x_1 \rightarrow C_2 x_3 \qquad x_3 \rightarrow C_3 x_4 \tag{23}$$

Also given that $\hat{\mathbf{\Theta}}$ has been projected onto the null space of **A**, it is possible to identify the stoichiometry of the products of each reaction step (each column in (22) was standardised). This suggests that C_1 = C_2 = C_3 = 1, leading to correct estimation of the stoichiometric matrix. It is then possible to accurately estimate the kinetic rate constants, achieved by the repeated simulation (numerical integration) of the ODEs that represent the SREs whilst adjusting the kinetic parameters using an optimisation algorithm, until the simulation closely

matches the experimental data. The BatchCAD software package (1995-2004) was used to fit the kinetic rate constants and heats of reaction (24).

$$\hat{K} = \begin{bmatrix} 0.00101 & 0 & 0 \\ 0 & 0.00679 & 0 \\ 0 & 0 & 0.00246 \end{bmatrix} \qquad \hat{\mathbf{h}} = \begin{bmatrix} -8e^4 & -1e^4 & -1e^5 \end{bmatrix} \qquad (24)$$

The correct stoichiometric matrix, the actual individual heats of reaction specified for simulation and accurate estimates for **K** with percentage errors of 0.99%, 0.88% and 0.81% respectively, have been obtained.

Conclusion

This paper proposes a method for the determination of chemical reaction networks, their associated rate constants and heats of reaction. This is achieved through an incremental strategy to analyse composition and heat of heat evolution data. The procedure is demonstrated to be successful, through a worked example of the Van de Vusse chemical reaction network, consisting of four chemical species and three reaction steps, Van de Vusse (1964).

The majority of methods in the literature, are based on system perturbations around stationary states, thus do not lend themselves to batch experimentation often performed in chemical laboratories. In comparison the techniques proposed here are based solely on the analysis of process data obtained from batch reactors. Another advantage of the method proposed is that it is not necessary to have any prior knowledge about the reaction stoichiometry; in fact, given that a number of kinetic assumptions are valid, the stoichiometries may be deduced from the estimated models. Furthermore. the presented analyses are relatively simple from a mathematical viewpoint and use concepts and tools that will be familiar to most researchers and engineers, for example curve fitting and regression analysis.

The use of the rate of heat evolution data for determining reaction networks should be applied with caution as one or more of the reaction step(s) may not exhibit any heat evolution ($\Delta H_{Rl} = 0$) or the heat evolution of one reaction step may be significantly less than that of another ($\Delta H_{Rl} << \Delta H_{Rl+1}$). Therefore it may not be possible to obtain all of the relevant concentration terms from analysis of the rate of heat evolution data.

References

Bonvin, D. and Rippin, D. W. T. (1990). Target factor analysis for the identification of stoichiometric models, *Chemical Engineering Science*, 44, 3417-3426.

Burnham, S. C., Searson, D. P., Willis, M. J. and Wright, A. R. (2008). Inference of chemical reaction networks, *Chemical Engineering Science*, 63, 4, 862-873.

Hamer, J. W. (1989). Stoichiometric interpretation of multireaction data: application to fed-batch fermentation, *Chemical Engineering Science*, 44, 2363-2374.

Lawson, C. L. and Hanson, R. L. (1974). *Solving Least Squares Problems*, Prentice-Hall, New Jersey.

Mallows, C. L. (1973). Some Comments on Cp, *Technometrics*, 15, 661-675.

Van de Vusse J.G. (1964). Plug-flow Type Reactor Versus Tank Reactor, *Chemical Engineering Science*, 19, 994-997.

Wright, A. R., Bramfitt, V. J., Wright, A. W. and Zollinger, J. (1993). Kinetic fitting using RC1 data, *RC User Forum, Zermatt.*

Zogg, A., Stoessel, F., Fischer, U. and Hungerbühler, K. (2004). Isothermal reaction calorimetry as a tool for kinetic analysis. *Thermochimica Acta*, 419, 1-17.

Proceedings of the 10th International Chemical and
Biological Engineering Conference - CHEMPOR 2008
Braga, Portugal, September 4-6, 2008
E.C. Ferreira and M. Mota (Eds.)

A Multi-objective Optimization for the Design and Periodic Scheduling of Multipurpose Facilities

Tânia Rute Pinto[1,2] Ana Paula Barbosa-Póvoa[2*] and Augusto Q. Novais[1]
[1]Dep. de Modelação e Simulação, INETI, Lisboa, Portugal
[2]Centro de Estudos de Gestão do IST, CEG-IST, Lisboa, Portugal

Keywords: Design, scheduling, batch, multi-objective, RTN
Topic: Systematic methods and tools for managing complexity.

Abstract

Like most real-world problems, the design of multipurpose batch facilities involves multiple objectives, however the existing literature on the subject has been mainly centered on mono-criterion objectives (Barbosa-Povoa, 2007). Therefore, the multi-objective optimisation is a modeling approach that requires further study when applied to such facilities. The best way to deal with various goals simultaneously is to define the efficient frontier which offers the optimal solutions found by multi-objective optimization. The inspection of the efficient frontier allows the decision maker to select the most satisfactory solution depending on the relative worthiness of each objective. In this work, the detailed design of multipurpose batch facilities with periodic mode of operation, as proposed by Pinto et al. (2005), is extended with the incorporation of economic aspects, which are targeted as multi-objectives within an optimization approach. This allows the identification of a range of plant topologies, design facilities and storage policies that minimize the total cost of the system, while maximizing production, subject to total product demands and operational restrictions. The ε-constraint method is employed to handle the multi-objective optimization, which has as its major advantage the fact that it can be used for any arbitrary problem with either convex or non convex objective space. An example, where different situations are evaluated, is solved to test the model applicability.

1 Introduction

In multipurpose batch facilities, a wide variety of products can be produced via different processing recipes by sharing all available resources, such as equipment, raw material, intermediates and utilities. Sometimes this type of facilities operates under conditions of relatively stable production demands, over extended periods of time. In such situations it is profitable to establish a regular periodic operating schedule, in which the same sequence of operations is carried out repeatedly, thus simplifying the operation and control of such facilities. The periodic mode of operation applied to the design/schedule of multipurpose-batch plants has been so far centered on mono-criterion objectives (Barbosa Povoa, 2007). Some published work is next reviewed.

Fuchino et al. (1994, 1995) studied the design problem of multipurpose batch plants under a periodic operation through an evolutionary design method. Voudouris and Grossmann (1996) proposed a method for integrating scheduling and design for a special class of multipurpose batch processes. A novel representation for periodic schedules is proposed that has the effect of aggregating the number of batches for each product. Heo et al. (2003) addressed the periodic scheduling, planning and design of batch plants. A non linear model is proposed

* To whom correspondence should be addressed. Tel.: +351-214233507. Fax: +351-214233568 e-mail: apovoa@ist.utl.pt

that was linearized using a separable programming method. Finally, Castro et al. (2005) presented a continuous general mathematical formulation based on the RTN process representation. A periodic operation is assumed where the cycle time value is optimized simultaneously with the rest of the design variables.

The existing literature does not explore the application of the multi-objective optimization to the design of multipurpose facilities. Frequently, real-world problems involve multiple objectives and the multi-objective approach is a form of modeling such realistic situations conferring the resulting models characteristics that will allow them to act as potentially powerful decision making tools. On the basis of the Pareto-optimum surface, decision makers will be able to select any given solution depending on the relative worth of each objective.

In the present paper the work of Pinto et al. (2005) is generalized so as to account for a multi-objective decision context where more than one economic objective is considered. This early work presents a generic and detailed formulation for the optimal design and retrofit of multipurpose batch facilities operating in a periodic mode for a single mono-criterion objective. A multi-objective approach based on the ε-constraint is now explored. This method has the advantage of suiting any arbitrary problem, i.e. with either convex or non convex objective spaces. The final results allows the identification of a range of plant topologies, facilities design and storage policies associated with a scheduling operating mode that minimizes the total cost of the system, while maximizing the production, subject to total product demands and operational restrictions.

An example is solved to test the model applicability where different situations are evaluated.

2 Design Problem

The optimal plant design can be obtained by solving the following problem:

Given:

- Process description, through a RTN representation;
- The maximal amount of each type of resource available, its characteristics and costs;
- Time horizon of planning and cycle time;
- Demand over the time horizon (production range);
- Task and resources operating cost data;
- Equipment and connection suitability;

Determine:

- The amount of each resource used;
- The process scheduling;
- The optimal plant topology as well as the associated design for all equipment and connectivity required.

Mixed storage policies, shared intermediated states, material recycles and multipurpose batch plant equipment units with continuous sizes, are allowed. In terms of operation mode, a periodic operation is considered where the concept of cycle time T is used. This is taken as the shortest interval of time at which a cycle is repeated, where the cycle represents a sequence of operations involving the production of all desired products and the utilization of all available resources.

Since all cycles are equal, the problem is formulated over a single cycle where it is guaranteed that the operation of the plant is the same at the beginning and at the end of the cycle. The execution of a task is allowed to overlap successive cycles and, since a cycle is repeated over the time of planning, its execution is modeled by wrapping around to the beginning of the same cycle. To do so, the wrap-around operator as defined by Shah et al. (1993) is used:

$$\Omega(t) = \begin{cases} t & if\ t \geq 1 \\ \Omega(t+T) & if\ t \leq 0 \end{cases}$$

When this is applied, for instance to the variable $N_{k,\Omega(t-\theta)}$ for t–θ ≤ 0, it leads to an identical equipment resource allocation which will start at time t–θ +T.

In terms of modeling, a discretization of time is used, where the cycle time is divided into T intervals of equal duration. The start of the cycle is defined as time t=1, and the end as t=T+1. The latter coincides with the starting point of the next cycle. A planning horizon (H) is assumed which is divided into n equal cycles of duration (T). A cycle is divided into a number of elementary time steps of fixed duration (δ), as shown in Figure 1.

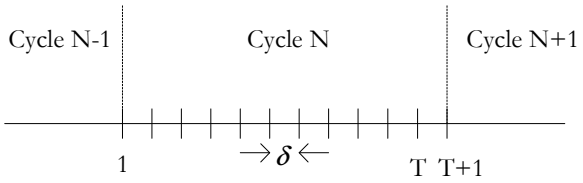

Figure 1-Time discretization for a single cycle

Based on the above problem description and considering the discretization of time, a model was developed using the RTN representation.

3 Multi-objective Optimization

In general those models requiring a single objective, have a clear, quantitative way to compare alternative feasible solutions. In many applications a single objective is sufficient to model realistically the actual decision process. However, decisions become much more problematical when dealing with complex engineering designs, where more than one objective is at stake. For such cases, as referred above, a multi-objective optimization model is required to capture all the possible perspectives. This is the case of batch plants design, addressed in this work, where two objectives are under consideration – maximization of revenue (that is, production) and minimization of cost. Contrary to common practice, where these are usually assigned equal weights and merged into a single index such as profit, revenue and cost are now handled separately since the desired trade-off between them is meant to be open to the decision maker. The multi-objective optimization can be generically represented as:

$$\begin{aligned} &Maximize\ f_m(x) && m = 1,2,...,M; \\ &s.t. \\ &\quad g_j(x) \leq 0 && j = 1,2,...J; \\ &\quad h_k(x) = 0 && k = 1,2,...,K; \\ &\quad x_i^{(L)} \leq x_i \leq x_i^{(U)} && i = 1,2,...,n. \end{aligned}$$

where M identifies the objective function $f(x) = (f_1(x), f_2(x),\ldots,f_m(x))^T$ and J and K are, respectively, the number of inequality and equality constraints. A solution will be given by a vector X of n decision variables: $X=(x_1, x_2,\ldots, x_{n-1}, x_n)^T$

However, no solution vector X exists that maximizes all objective functions simultaneously. A feasible vector X is called an optimal solution if there is no other feasible vector that increases one objective function without causing a reduction in at least one of the others. It is up to the decision maker to select the best compromising solution among a number of optimal solutions in the efficient frontier. There are several methods to define this frontier, but one of the most popular methods is the ε-constraint, which is very useful since it overcomes duality gaps in convex sets.

Using the ε-constraint, the above formulation becomes:

$$
\begin{aligned}
&Maximize\ f_u(x)\\
&s.t. \quad f_m(x) \le \varepsilon_m \quad m = 1,2,...,M \ and\ m \ne u\\
&\qquad g_j(x) \le 0 \quad j = 1,2,....;\\
&\qquad h_k(x) = 0 \quad k = 1,2,...,K;\\
&\qquad x_i^{(L)} \le x_i \le x_i^{(U)}
\end{aligned}
$$

where ε_m represents an upper bound of the value of f_m. This technique suggests handling one of the objectives and restricting the others within user-specified values. First the upper and lower bounds are determined by the maximization of the total revenue and minimization of the cost, respectively. Next, varying ε, the optimization problem (maximization) is implemented with the objective function being the total revenue and the cost being a constraint varying between its lower and upper bounds.
Once obtained, the efficient frontier allows the decision maker to select any solution depending on the relative worthiness of each objective.

4 Example

The presented method is applied to the design of a multipurpose batch plant that must produce [0; 170] tons of products S5, [0; 166] tons of S9 and S10, [0; 270] tons of products S6 and [0; 143] tons of products S11. Three raw materials, S1, S2 and S7, are used over the horizon of 24 h. The products S5 and S6 are both intermediate and final products. There are six main reactors available (R1 to R6), and nine dedicated vessels. In terms of equipment suitability, only reactors R1 and R2 may carry out two processing tasks, T1 and T2, while each storage vessel and reactors R3, R4, R5 and R6 are only dedicated to a single state/task. Task T1 may process S1 during 2 hours in R1 or R2; task T2 may process S2 during 2 hours in R1 or R2; task T3 may process during 4 hours in R3; task T4 processes during 2 hours in R4; task T5 may process S6 during 1 hour to produce the final product 0.3 of S11 and 0.7 of S8 in R5, and finally task T6 processes during 1 hour S8 in reactor R6 to produce the final products S9 and S10. The connections capacity range from 0 to 200 [m.u./m^2] at a fix/variable cost of 0.1/ 0.01 [10^3c.u.]. The capacity of R1, R2, R5 and R6 range from 0 to 150 [m.u./m^2] while the others range from 0 to 200 [m.u./m^2] (where m.u. and c.u. are, respectively, mass and currency units).

The problem described is solved and the obtained efficient frontier shown in figure 2, which forms the boundary of the feasibility region defined by the values of the two objectives. Every efficient point lies along the depicted boundary because no further progress is possible in one objective function without degrading the other. This is an alternative way to plot solutions of multi-objective models. For the case under study the objective value space is represented with cost and revenue axes. In the efficient frontier are visible some optimal plant topologies. A, B, F and G represent points where there is a topology change caused by the addition or replacement of one or more main equipment units in relation to the previous topology. In figure 2 are shown these different topologies and the corresponding final products. In table 1 are presented, for each point assigned, the final products and their quantities. Table 2 presents the main equipment optimal design, in terms of capacities, for points A to G. For point G, the optimal scheduling is shown in figure 3. It is visible the multi-task nature of equipment R1, since it performs not only T1 but also T2. All the other processing equipment units are single-task dedicated.

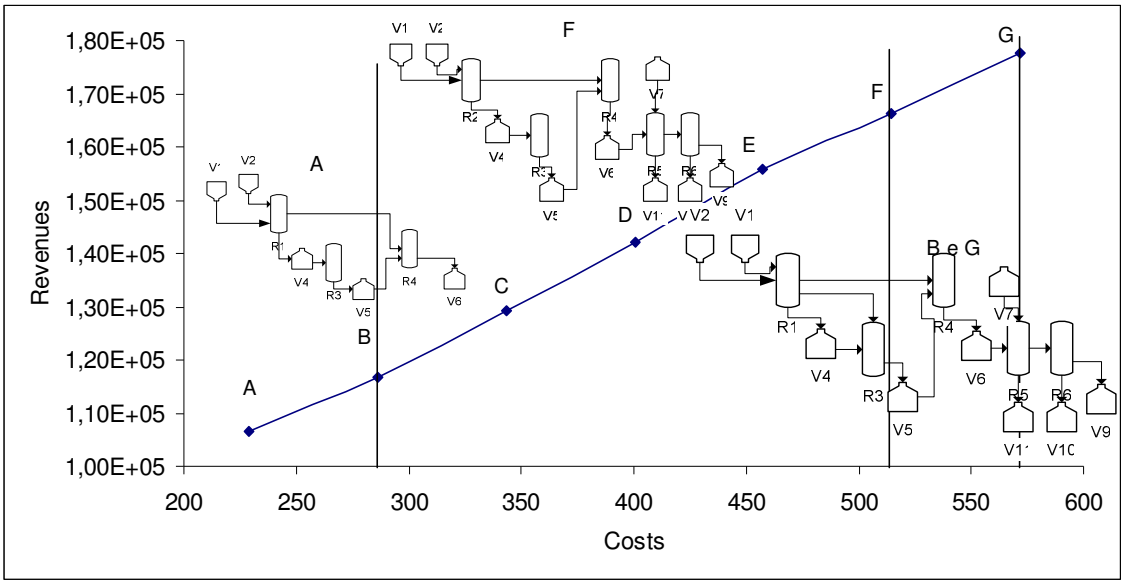

Figure 2 – Efficient frontier for the optimal design of the multipurpose batch plant.

Table 1 – Quantities produced for each final product.

	A	B	C	D	E	F	G
S5	170	170	170	170	170	170	170
S6	270	270	270	270	270	270	270
S9/S11	-	24.15	52.97	83.4	115.12	139.56	166
S11	-	20.70	45.41	71.5	98.67	119.63	142.3

Table 2 – The optimal design for the main equipment.

	A	B	C	D	E	F	G
R1	71.75	72.95	77.07	65.13	68.76	-	124.3
R2	-	-	-	-	-	71.55	-
R3	69.50	58.36	61.65	54.28	68.76	59.63	103.52
R4	90.00	101.50	115.23	97.28	108.61	117.34	126.79
R5	-	34.50	50.45	79.42	82.23	99.69	118.57
R6	-	24.15	35.32	55.59	57.56	69.78	83

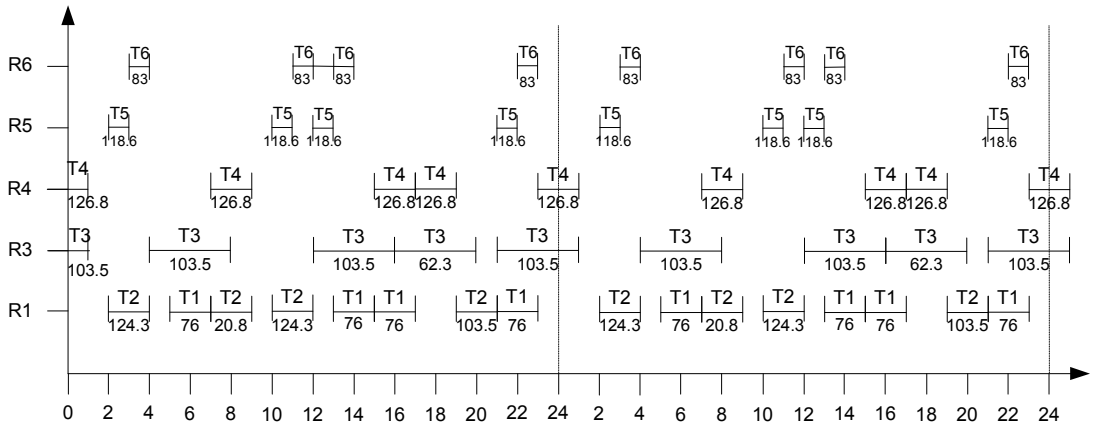

Figure 3 – Optimal scheduling for the plant topology at point G.

5 Conclusions

The plant topology, equipment design, scheduling and storage policies of multipurpose batch plants are addressed in this paper, considering simultaneously production maximization and cost minimization - a multi-objective optimization. The model was developed as a MILP and the multi-objective method used was the ε-constraint. The obtained efficient frontier defined the optimal solutions, allowing the identification of a range of plant topologies, facilities design and storage policies that minimize the total cost of the system, while maximizing production, subject to total product demands and operational restrictions. The proposed methodology allows the decision makers to evaluate the relationship between revenue and cost of given batch facilities, thus enabling them to develop an adequate business strategy.

References

Barbosa-Póvoa, A.P.F.D.(2007), A Critical review on the design and retrofit of batch plants, *Computers and Chemical Engineering*, 31,833-855.

Castro, P. M., Barbosa-Povoa, A. P., & Novais, A. Q. (2005). Simultaneous design and scheduling of multipurpose plants using resource task network based continuous-time formulations, *Industrial & Engineering Chemistry Research*, 44(2), 343-357.

Fuchino, T., Muraki, M., & Hayakawa, T. (1994). Scheduling Method in Design of Multipurpose Batch Plants with Constrained Resources, *Journal of Chemical Engineering of Japan*, 27(3), 363-368.

Fuchino, T., Muraki, M., & Hayakawa, T. (1995). Design of Multipurpose Batch Plants with Multiple Production Plans Based on Cyclic Production, *Journal of Chemical Engineering of Japan*, 28(5), 541-550.

Heo, S. K., Lee, K. H., Lee, H. K., Lee, I. B., & Park, J. H. (2003). A new algorithm for cyclic scheduling and design of multipurpose batch plants, *Industrial & Engineering Chemistry Research*, 42(4), 836-846.

Pinto, T., A.P.F.D. Barbosa-Póvoa e A.Q. Novais (2005), Optimal design and retrofit of batch plants with a periodic mode of operation, *Computers and Chemical Engineering*, 29, 1293-1303.

Shah, N., C.C. Pantelides and R.W.H. Sargent (1993), Optimal Periodic Scheduling of Multipurpose Batch Plants, *Annals of Operations Research*, 42, 193-228.

Voudouris, V. T., & Grossmann, I. E. (1996). MILP model for scheduling and design of a special class of multipurpose batch plants, *Computers & Chemical Engineering*, 20(11), 1335-1360.

Proceedings of the 10th International Chemical and
Biological Engineering Conference - CHEMPOR 2008
Braga, Portugal, September 4-6, 2008
E.C. Ferreira and M. Mota (Eds.)

The Influence of Products' Portfolio Demand on the Optimal Supply Chain Planning

Ana C.S. Amaro[1] and Ana P.F.D. Barbosa-Póvoa[2*]
[1] ISCAC, IPC, Qt.ª Agrícola, 3060-316 Coimbra, Portugal
[2]CEG-IST, UTL, Av. Rovisco Pais, 1049-001 Lisbon, Portugal

Keywords: Supply chain management, optimal planning, uncertainty
Topic: Systematic methods and tools for managing the complexity

Abstract

In this paper, we study the supply chain planning decisions under uncertainty on product portfolios demand and prices. A supply chain centralized managing strategy is adopted for the multi-period planning problem, where the supply chain operational decisions, at the actual period, take into consideration both contracted and uncertain products' demand and/or prices. The operational decisions on supply, production, transportation, and distribution are evaluated in face of a defined supply chain economical performance objective (e.g. global operating costs/ profit realized) for different demand and price behaviours.

A general model, based on the work of Amaro and Barbosa-Póvoa (2008), is proposed that considers the supply chain topology, operability and market demand/price uncertainty while accounting for product recovery through the integration of reverse material flows and remanufacturing operations. A Mixed Integer Linear Programming formulation (MILP) is developed for each planning scenario and the optimal solution is reached using a standard Branch and Bound (B&B) procedure. The final results provide details on the supply chain partners production, transportation and inventory at each planning period while accounting for demand/price uncertainties.

The model applicability was tested on a real industrial case involving a pharmaceutical supply chain.

1 Introduction

Nowadays enterprises face important economical challenges. The trade-off between quality, price and service levels is definitively a key to success in a worldwide scale. Thus, enterprises need to provide high quality products around the world at the right time, in the right quantity and at the lowest prices. Supply chain structures have, in this area, an important role in the fulfilment of such goals in global markets (Varma et al, 2007). Therefore, the supply chain planning is one of the areas that needs a special care and should be optimized so as to enhance the desired operational efficiency.

Planning problems involve usually medium to large time horizons and accordingly, decisions on future events are frequently taken based on more or less accurate forecasts. Therefore, uncertainties regarding product demands and prices, amongst other supply chain conditions, need to be accounted for in planning decisions (Guillen *et al*, 2007).These sources of uncertainty depend on the products demand pattern and are at least partially explained by the demand to price dependency.

Moreover, customers' demand behaviour is influenced by distinct sources of uncertainty other than price forecasts. Different contributions have been proposed so far to enhance different uncertainty aspects (Guillen et al., 2006). Almost all the proposed methodologies

* Corresponding author. Tel + 351-239-798700. E-mail:user1@eq.uc.pt

agree on the fact that the complex demand behaviour can not be fully explained by deterministic measures and therefore some stochastic parameters are required to explain customers' subjective nature as well as some market patterns'.

In the present work, the demand behaviour is characterized by a set of polynomial functions representing the demand to price dependencies, according to the products considered. The demand uncertainty induced by price changes (i.e. different probabilistic price forecasts) is modelled through a set of planning scenarios with a probability of occurrence corresponding to the price forecasts. In each one of these scenarios the demand uncertainty is considered through the demand to price elasticity coefficient. The influence of market scores over the optimal planning solution is also considered. The elasticity to price coefficient observed for each product family, at each market place, is analysed and mutually compared in order to identify the embedded market characteristics.

On the other hand, the economical flows raised at each planning period are converted to a common time point, in order to be comparable. This conversation corresponds to the actualization of the economical flows based on a defined average market rate (Gupta et al, 2004). In fact, the strategy implemented to actualize economical flows is an actual and largely discussed subject, although it is not the scope of this study. Some literature contributions as the one of Gupta et al. (2004) based on real option values (ROV), or the corporate value evaluations proposed by Puigjanner (2008), promise important advantages against the commonly used net profit value (NPV) methodology. The major difference in between is essentially due to the market rate considerations and to the entailed financial assumptions. Our approach considers regular *cash-flows* (i.e. resulting from equally spaced periods) subject to an actualization, defined by a 2% constant market rate, done to each planning period and economical flow. The actualized planning profit (APP) is considered as the problem economical goal.

2 Problem Characterisation and Modelling Approach

The proposed contribution considers a close-loop supply chain, SC, with a centralized managing strategy defined over a multi-period. The supply chain decisions, at each period, take into consideration the supply chain topology, its operability and market demand/price uncertainty, while accounting for product recovery through the integration of reverse material flows and remanufacturing operations (see figure 1).

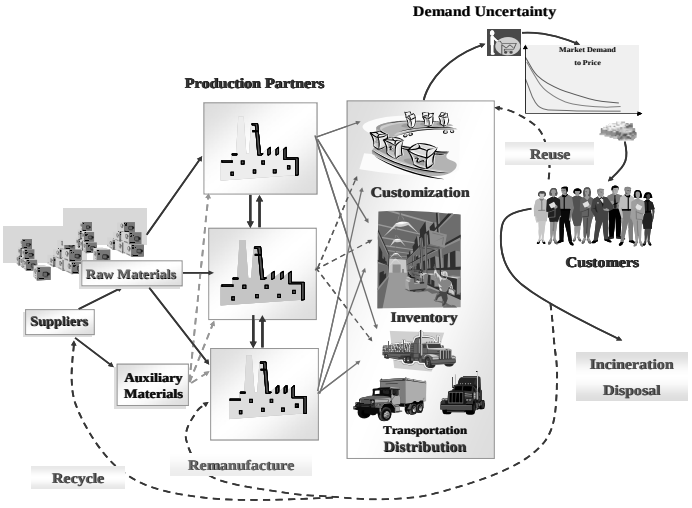

Figure 1.- Closed loop supply chain, SC.

Under an uncertainty environment this contribution studies how medicine portfolios' and marketplaces influence the SC economical performance. A general formulation is develop

and the final results provide details on the supply chain partners production, transportation and inventory levels, at each planning period, while accounting for demand/price uncertainties. The supply chain planning problem can be stated as follows:

Given the supply chain:

- planning horizon;
- topology structure (i.e. partners geographical location; suitability to process, store, receive and deliver products; the corresponding capacities and processing times);
- connectivity network (i.e. transportation capacities, suitability and transportation times);
- materials' network (i.e. available materials and SC location) and the recovery policy (i.e. products' recycling and remanufacture capacities and suitability);
- markets network (i.e. market locations and scoring; demands and prices; demand to price elasticity to each suitable product and marketplace);
- Price forecasts to each final product and its probability of occurrence during each planning period and the actualization rate of economical flows during the planning horizon or per planning period;

Determine:

- the optimal allocation of products production, recovery, transportation, delivering, receipts and storage and the associated timings;
- the economical performance of the supply chain as well as of each SC partner under each demand and price uncertainty scenario;

So as to: Maximize the actualized Global Planning Profit, APP, under a defined partnership structure subject to demand and price uncertainty.

Modelling Consideration

The proposed SC planning formulation is summarized in table 1. A discrete time approach of the planning horizon is considered. The model is based on the works of Amaro and Barbosa (2007, 2008) and considers the following assumptions:

- the profit at each planning period is actualized based on a fixed market rate;
- Products demand patterns' follow a polynomial form $\hat{D}_{st} = \hat{D}_s^0 \left(\hat{p}_{st} \right)^k$, where *k* represents the constant elasticity to price coefficient (i.e. logarithmic derivative of demand to price) and $\hat{D}_s^0$ represents the demand value observed for each product s, when it is sold at the lowest suitable market price $\left(\text{i.e.} \quad \hat{D}_s^0 = \hat{D}_{st}\big|_{Min_t(\hat{p}_{st})}, \quad \forall s \right)$. This represents a demand upper bound for all products, s, with a demand to price elasticity less than 1 (i.e. having a negative k value); and a demand lower bound to all products having an elasticity coefficient greater than 1.
- a price forecast is considered for each final product and planning period;
- the price of final products is considered unchanged till the planning period where forecasts indicate a given probability of price changes (defined as a percentage of the current price);
- the probabilistic occurrences of products price variations' are independent events modelled as a scenario approach with a defined probability of occurrence: three scenarios are considered as representative of both optimistic, pessimistic and unchanged price situations within a risk analysis strategy (Tsikaris et al. (2001). This can however be generalised for a N, number of scenarios;

- demand uncertainty is represented according to the price elasticity coefficient defined for each medicine family.

Table 1. Summary of SC Planning Formulation.

Objective Function: Actualized Planning Profit,
$APP\left(u(\hat{D});PS\right)=\sum_{ip}\xi(ip)\quad\sum_{Sc}\Upsilon(Sc)\left(\sum_{t=1}^{H_p}\frac{GPP_t}{(1+\overline{r})^{t-1}}\right)$
Scenarios: $\left(\Upsilon(Sc_1),-x\%p\right);\left(\Upsilon(Sc_2),0\%p\right);\left(\Upsilon(Sc_3),+x\,p\%\right)$ with $\sum_i\Upsilon(Sc_i)=1$ Constraints: Processing and Recovery Transportation; Supply; Deliver; Store, to all or some SC partners;
Variables: Integer – assignment of tasks and flows to resources; Continuous – capacities, demands, supplies.

Case Study

A real pharmaceutical SC is studied (figure 2). This involves three industrial plants (I1 and I2, located in Portugal and I3 in Spain) with a distribution channel supported by five warehouses (WH1, WH2 and WH3 in Portugal and WSH1 and WSH2 in Spain) involving seven distribution points (i.e. warehouses, airport AP and seaport SP).

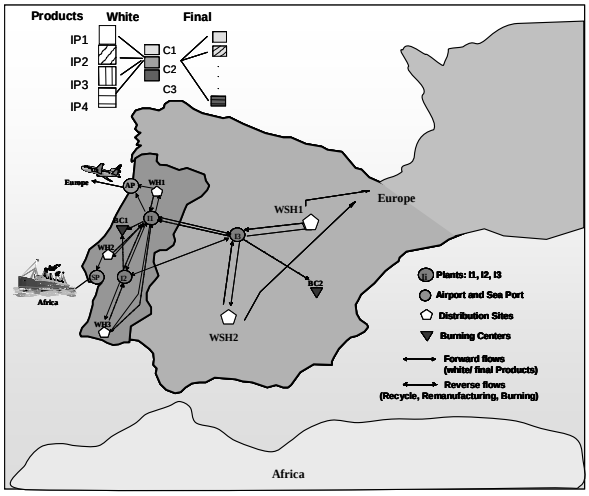

Reference Case (Rc) O.F = 7219359 m.u.

Single (m.u.):

Case EC_{u1}: O.F.= 7985559;	ΔEC_{u1}-Rc= 766200
EC_{u2}: O.F.= 6740293;	ΔEC_{u2}-Rc= -479066
Case SP_{u1}: O.F.= 7980251;	ΔSP_{u1}-Rc= 760892
SP_{u2}: O.F.= 6609859;	ΔSP_{u2}-Rc=-609500
Case PG_{u1}: O.F.= 7961304;	ΔPG_{u1}-Rc= 741945
PG_{u2}: O.F.= 6688652;	ΔPG_{u2}-Rc=-530707

Combined (m.u.):

Case IB_{u1}: O.F.= 7979675;	ΔIB_{u1}-Rc= 760317
IB_{u2}: O.F.= 6641879;	ΔIB_{u2}-Rc=-577480
Case GL_{u1}: O.F.= 7996629;	ΔGL_{u1}-Rc=777270
GL_{u2}: O.F.= 6666910;	ΔGL_{u2}-Rc=-552449

Figure 2.- Pharmaceutical supply chain and results on the uncertainty scenarios studied.

The pharmaceutical chain supplies the European and African markets with three manufactured product families: injection, soft-table and oral suspension medicines. These involve the formulation of four intermediate medicines that are subject to three types of customizations, resulting into eleven final product medicines. The medicines distribution is ensured by three transportation structures, with different capacities and number of transportation resources. The SC planning problem was solved for a three months horizon of planning with weekly periods (12th periods).

As referred above, the developed study comprises two major scopes: i) the effect of demand uncertainty due to price; and ii) the influence, under an uncertain scenario, of market scores on the optimal products portfolios'. To illustrate each one of these model developments a set of operational scenarios was defined. Firstly, the optimal planning solution, without demand uncertainty was determined (i.e. reference case, Rc) and the actualized planning profit obtained. This is compared with those resulting from the integration of a demand pattern

submitted to price uncertainties (i.e. u1 and u2 cases). A set of cases was studied using two price scenarios denoted by *u1 (represent 80% probability of a 5% increase on the actual medicines price, 20% probability of a 5% decrease on products price and a null probability of a constant price) and *u2 (20% probability of a 5% price increase, 80% probability of a 5% products price decrease and again a null probability of unchanged price values). Due to the lack of space, only the results achieved to soft-tablet medicines are shown. These consider both probabilistic behaviours occurring at the 8th period, till the end of the planning horizon.

Moreover, the SC structure comprises ten geographical positions covering three customer markets': Portuguese (PG) and Spanish (SP), as country-side for production partners; other EC markets (EC) and the African positions. Having these market specificities the goal is to identify the behaviour of the SC planning profit for: **i)** each single market; and **ii)** the combined effect of uncertainty due to its simultaneous occurrence at more than a market place. In cases EC, PG and SP, two different uncertain conditions, (EC_{u1},EC_{u2}); (PG_{u1},PG_{u2}); (SP_{u1},SP_{u2}), are analysed for price uncertainties occurring at a single and specific market (i.e. EC, SP and PG markets). Finally, cases IB and GL comprise uncertainty scenarios for the Iberian (IB) market (i.e. Portugal and Spain) and for the whole European market (GL).

As it can be observed in figure 2 the demand reduction caused by a highly probable price increase, scenarios u1 for EC, PG and SP cases, is covered by the unitary profit change. This is partially explained by the increment on stock existences and since the time frame to the end of planning horizon is small the storage costs does not have a significant contribution. On the other hand, for scenario u2, the demand increase caused by the price reduction is not enough to overcome the income decrease and a global profit reduction is observed when compared to u1, having as reference the Rc case. It is also important to note that soft-tablet medicines have an elasticity coefficient higher than the one observed for injection and oral suspensions, but these are not the top of the demanded medicines.

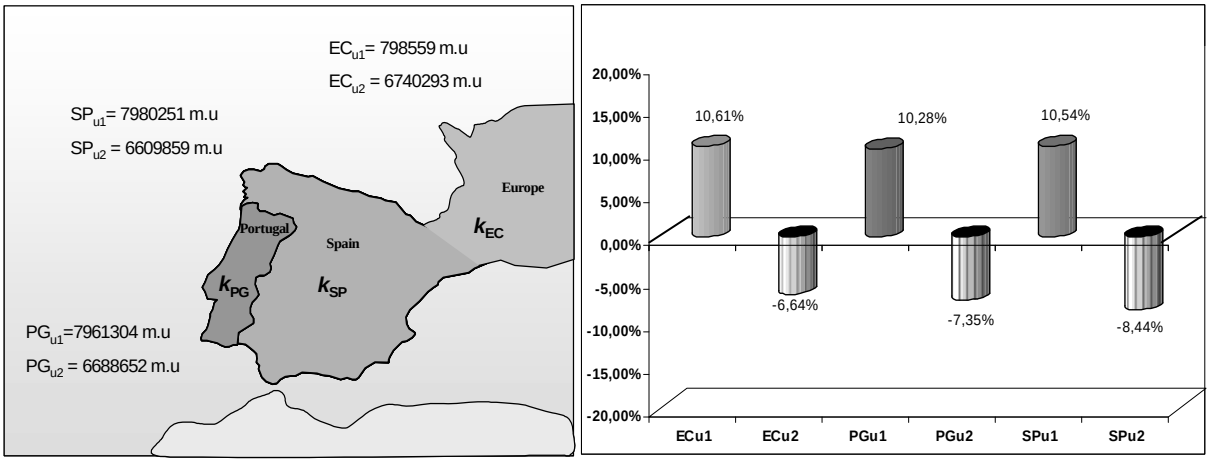

Figure 2 – Planning results for both uncertainty scenarios at EC, PG and EC markets.

Although, the effect of the same type of uncertainty is not the same for all the markets considered. For the uncertainty scenario due to a most probable price reduction almost all markets behave similarly, but the less profitable (PG) is also the less sensitive to price increase since it presents the lower percentage deviation (-6.64% at scenario u2) from the constant demand behaviour (i.e. scenario Rc). Concerning the profitable cases (EC and SP) these have lower demand to price elasticity coefficients than the PG case and larger medicine demands. Thus, their performance is less sensitive to price reduction than to the demand reductions. The later increases the level of handled stocks and a globally less profitable solution is raised.

The influence of market scores on the chain global planning profit under an uncertain environment was also explored. The uncertainty conditions defined above are assumed.

When analyzing figures (3a) and (3b) it can be seen that the effect of price uncertainties influences differently the optimal planning profit, as above, and the combined effect of market's uncertainties is also more visible for u1. This is explained essentially by the increase of handled medicine inventories' and to the cumulative effect of demand reduction.

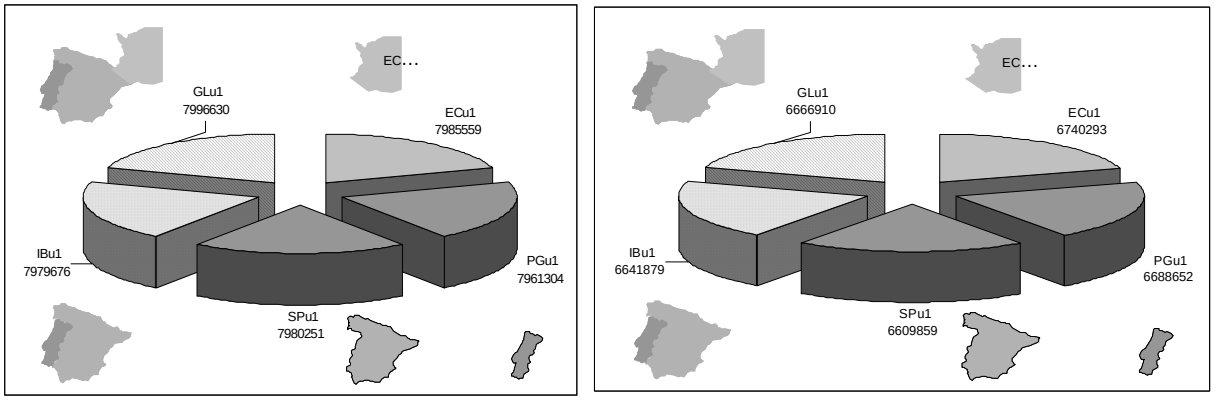

Figure 3- Global planning analysis for (a) u1 and (b) u2 uncertainty scenarios.

The model was implemented in GAMS/CPLEX on a Pentium III. The statistics of the model involve 22275 continuous variables, 8856 integer/binary variables and 44512 equations. The problems were solved on average after 8000 CPU seconds for a relative gap of 2.5%.

Conclusions

This paper presents the optimal planning of a generic supply chain where detailed aspects involving the supply chain production, storage and transportation are considered. The planning is performed under market demand/price uncertainty while accounting for product recovery through the integration of reverse material flows and remanufacturing operations. An actualized profit is considered as well as demand and price uncertainties related to each product, by the elasticity to price coefficient. The influence of market scores on the allocation of product portfolios' and supply chain operations was studied.

The formulation applicability was tested on a real industrial case involving a pharmaceutical supply chain. Some interesting results where achieved but improvements should be further explored. Namely, the relation among demand to price elasticity coefficients, products and markets can be extended. Also, price uncertainties should be explored to larger planning horizons with different periods of occurrence in order to capture the cumulative effect of demand uncertainties induced by price changes.

References

Amaro, A.C.S., Barbosa-Póvoa, A. P. F. D. (2008), Planning and Scheduling of Industrial Supply Chains with Reverse Flows: A real pharmaceutical case-study, in publication in *Comp.Chem. Eng*.

Amaro, A.C.S., Barbosa-Póvoa, A. P. F. D. (2008), The effect of Uncertainty on the optimal Supply Chain planning under different partnerships structure, Foundations on Computer Aided Process Operations, Boston, USA, 481-484, Edição CD-ROM

Guillén, G., Mele, F.D., Bagajewicz, M.J., Espuña, A. and Puigjaner, L. (2005), Multiobjective supply chain design under uncertainty, *Comp. Eng. Science*, 60, 1535.

Gupta, A., Maranas, C.D. (2004), Real-Options-Based Planning Strategies under Uncertainty, *Ind. Eng. Chem. Res*., 43, 3870.

Varma, V.A., Reklaitis, G.V., Blau, G.E. and Pekny, J.F. (2007), Enterprise-wide modeling & optimization-An overview of emerging research challenges and opportunities, *Comp. Chem. Eng*., 31, 692-711.

Proceedings of the 10th International Chemical and
Biological Engineering Conference - CHEMPOR 2008
Braga, Portugal, September 4-6, 2008
E.C. Ferreira and M. Mota (Eds.)

Nonlinear dynamic modelling of a real pilot scale continuous distillation column for fault tolerant control purposes

Pedro M.C. Oliveira[1], Nuno M.R. Batalha[1], Carla I.C. Pinheiro[1*], José Borges[2], João M.A. Silva[3]

[1] IBB – Institute for Biotechnology and Bioengineering, Centre for Biological and Chemical Engineering, Instituto Superior Técnico, Av. Rovisco Pais, 1049-001 Lisboa, Portugal.

[2] IDMEC, Instituto Superior Técnico, Av. Rovisco Pais, 1049-001 Lisboa, Portugal.

[3] Chemical Engineering Department, Instituto Superior de Engenharia de Lisboa, Av. Conselheiro Emídio Navarro, 1959-007 Lisboa, Portugal

Keywords: continuous distillation column, nonlinear dynamics, dynamic modelling, fundamental models, fault tolerant control
Topic: Systematic methods and tools for managing the complexity.

Abstract

The aim of the present work is to develop and validate a nonlinear dynamic model of a pilot-scale continuous distillation process for the simulation of the dynamic behaviour of a real continuous distillation plant at the Chemical Engineering Department of ISEL, in the absence and in the presence of faults. The model of the overall pilot scale distillation plant is derived from fundamental principles including mass and energy balances for the individual systems such as the distillation column sections, the condenser, the heated reboiler, the feed pre-heater, the reflux valve, the bottom product control valve and the PID regulatory level controller. The complete dynamic model for the separation of a non-ideal binary liquid mixture of ethanol/water was developed within Matlab®/Simulink environment and was validated against experimental data collected from the plant under normal operating conditions in the absence and in the presence of faults showing a good agreement with the experimental results. Thus, this non-linear dynamic model is well-suited to be used for the implementation of Fault-Tolerant Control strategies in real time.

1 Introduction

Distillation columns are probably among the most common process units within the chemical industry (Kister, 1990). Industrial distillation columns are complex systems which exhibit nonlinear dynamic behaviour, so the development of models for control strategies is usually based on nonlinear models (Abdullah et al., 2007). In recent years, one of the major challenges in developing an effective model based control strategy is to generate a dynamic model which is used to describe the process under consideration. At present, most industrial controllers use a linear process model such as first-order-plus-time-delay models, and the linear model is applied to the estimation of the linearity for the dynamic range of the process (Abdullah et al., 2007). Satisfactory performance of these linear models is generally achieved over a narrow operating range, so the development of nonlinear process models is tremendously essential for the design of controllers that are capable of dealing with the unavoidable nonlinearity and complexity of nonlinear processes.

* Corresponding author. Tel + 351-21 8417887. E-mail:carla.pinheiro@ist.utl.pt

The steady-state analysis is not sufficient for the development and testing of control schemes. Nevertheless, very few dynamic modelling and simulation studies have been carried out and validated on real distillation columns (Can et al., 2002).

Many sophisticated model based control algorithms have been developed under the assumption that all system components will not fail. Once a failure occurs, the system performance will degrade and may lead to divergence, generating dangerous situations, particularly when the failure occurs in the control loops.

The demand for increased efficiency, in various branches of industry, such as chemical industry leads to an increased degree of automation of the production process. In order to meet this demand, while at the same time maintaining or improving the quality and safety, it is necessary that the (complex) control system is fault tolerant. This means that the effects of failures, such as component failures, actuator or sensor failures, on the quality and safety of the production process are minimized.

An important class of approaches to design fault tolerant control systems, includes the so-called Model Based Fault Detection and Isolation part (Calado et al., 2001) and a Controller Reconfiguration part. A key step in designing these two parts is the development of a mathematical model for the system.

It is well known that the ultimate judgment of the model quality is through model validation under normal operating conditions. However, the literature has been relatively sparse on studies concerned with model validation using process data under normal operating conditions.

In this work, a nonlinear dynamic model of a pilot-scale continuous distillation process is developed for the simulation of the dynamic behaviour of an experimental continuous distillation column at the Chemical Engineering Department of ISEL. This model is valide in both the absence and the presence of system faults. The complete model includes mass and energy balances for the individual systems such as the distillation column sections, the condenser, the heated reboiler, the feed pre-heater, the reflux valve, the bottom product control valve, and the PID regulatory level controller. The complete dynamic model is developed within Matlab®/Simulink environment and is validated against experimental data collected from the plant under normal operating conditions, in the absence and in the presence of faults, for the separation of a binary liquid mixture of ethanol/water.

2 Experimental Distillation Process

A photograph and a schematic overview of the pilot scale continuous distillation column are presented in Figure 1. This continuous distillation column is used to separate a liquid binary mixture of water and ethanol (10-20%) into a distillate product with ethanol (75-88%) and bottom product with (92-98%) water (mole fractions).

The column structure is made of several glass sections supported by an external steel framework. The glass is enfolded with proper isolation material to guarantee minimal heat loss into the surroundings. The column internals used for distillation are two structured packing sections (type 1900) with 1000 mm height and 4.3 mm inside diameter. Each structured packing is equivalent to a number of 30 equilibrium stages.

The liquid feed mixture is pre-heated using a 1200 W ON/OFF electrical heater element, which is actuated by an automatic controller, and enters the column at the feed stage with volumetric flow rate (Fv), ethanol molar fraction (xF) and temperature (TF). Ethanol evaporates along the distillation process, going upwards throughout the column section above the feeding point. Distillate ethanol leaves the top section of the column with a molar fraction (xD) and flow rate (D) into a water cooled condenser. A fraction of the condensed distillate is fed back into the top of the column at a rate determined by the actuation of a solenoid valve (freflux). The liquid mixture travels

downwards through the section below the feed into the reboiler. Here part of the mixture changes phase from liquid to vapour upon the action of two 2000 W electrical ON/OFF heater elements, which are controlled by an automatic controller. The water rich mixture leaves the bottom section of the column with a molar fraction (xB) at flow rate (B) and goes through a condenser before being stored in the product tank.

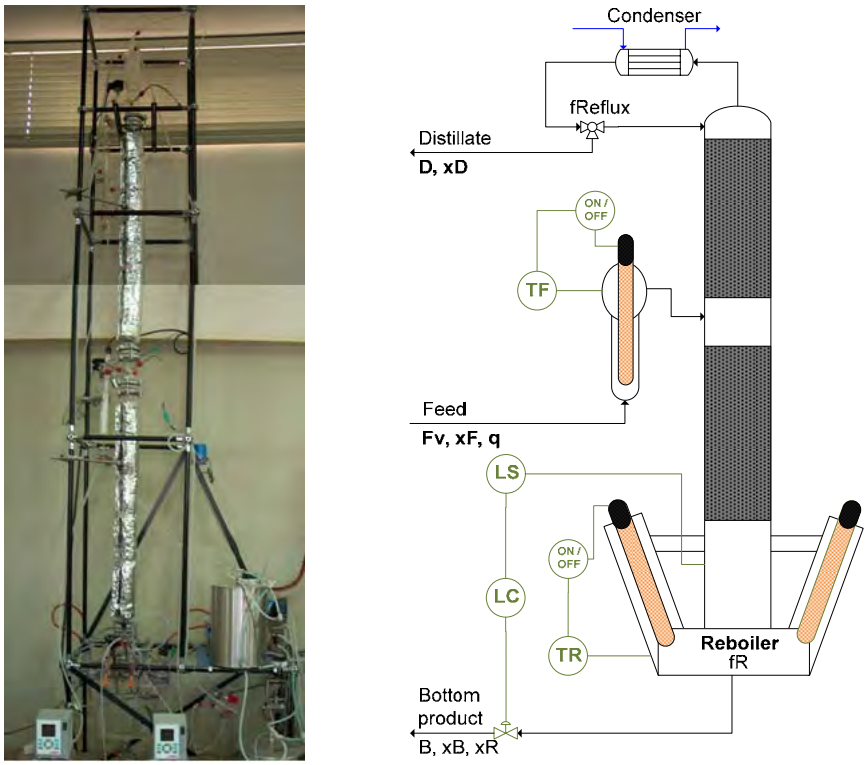

Figure 1 – Pilot scale distillation column at Chemical Engineering Department – ISEL.

The column measurement instrumentation consists of two types of sensors: temperature thermopars type Kv (e.g.TF or TR), and pressure sensors (e.g. LS). These sensors gather the online information about temperature and pressures at different points in the column. The measured signals are fed into the digital controller in real time using the National Instruments FieldPoint 2000 system. All the signal conditioning operations and the network communications are carried on using this modular distributed I/O system. The actuators consist of: heater elements, valves and peristaltic pumps. These devices are operated by an automatic digital control system, which interfaces with the actuators through the FieldPoint I/O bus. This system handles the network communications and the device actuation in the control process. The digital controllers were designed and run over LabView software. An automatic level control (LC) system was implemented at the reboiler.

3 Mathematical Model and implementation

Mathematical model

The mathematical model developed for the pilot scale distillation column includes global and component transient mass balances along the column trays, and is based on the well established simplifying assumptions and steady-state behaviour of both trayed and packed columns, which can be modelled using a staged equilibrium model (Skogestad, 1997). Several modifications were considered to develop the model according to the characteristics of the pilot scale distillation unit and of the non-ideal binary mixture (Skogestad, 2003). The set of ordinary differential equations obtained

was solved numerically using “ode15s” Matlab® solver. The heat lost along the column is taken into account as parameter HL (heat loss), which corresponds to the fraction of vapour condensed in each tray. With the introduction of this parameter in the model, liquid (L) and vapour (V) flows are allowed to change along the column influencing tray efficiencies. So, by using L/V ratio, the tray efficiency (Ef_i) is defined by the following equation:

$$Ef_i = \left(1 - \frac{1}{\left(L/V\right)_i + 1}\right)^{ef}$$

where $\left(L/V\right)_i$ is the liquid and vapour ratio in tray *i* and *ef* its influence in tray efficiency.

By including parameter Ef_i, the number of theoretical stages are fixed to the number indicated by the column manufacturer (60). The feed tray is considered the middle (31) tray, since the column has two equal sections, as described above. With this approach, instead of adjusting the real number of theoretical plates and feed position, the efficiency of the column is allowed to vary when dynamic changes occur without the need of changing other parameters.

It is important to note that the binary mixture used (ethanol-water) is highly non-ideal, which means that the relative volatility cannot be used. Therefore, vapour-liquid activity coefficients are used.

Model Inputs

Since the main objective is to simulate the dynamic behaviour of the real distillation column described above, the Matlab®/Simulink model inputs are the same used in the real column: the volumetric feed flow rate (Fv), the ethanol molar fraction of the feed (xF) and its temperature (TF), the time fraction that Reboiler is turned on at maximum power (fR) and the fraction of time that reflux valve is fully open (fReflux). These five variables are converted into the following variables: refluxed liquid (Lr), vapor generated in the reboiler (Vs), distillate flow rate (D), bottom flow rate (B), molar feed flow rate (F) and the liquid fraction in the feed (q).

Model implementation

The dynamic model was implemented in Matlab®/Simulink. The Simulink diagram is shown in Figure 2. With this model it is easy to implement perturbations/faults in the input variables and also to implement control loops or model-based control strategies. The Simulink diagram includes three main blocks (Figure 2). In the first and second blocks the inputs are processed and converted into the input variables used in the block of the column nonlinear model implemented in Matlab. This block has three outputs: distillate (xD) and bottom (xB) ethanol compositions and reboiler holdup. As in the real distillation column, a level control loop is also implemented in the model to keep the reboiler holdup constant when dynamic changes occur in the column.

4 Model validation

The developed model has three parameters for the fitting of the column steady states and other four parameters for adjusting the dynamic behaviour. These parameters were tuned by fitting the model to experimental data that resulted from 12 different steady states and 5 dynamic responses to step disturbances in the inputs. The quality of the fittings can be evaluated by the parity plot obtained for the different steady states in the column. The inputs supplied to the experimental column were designed as a series of persistently exciting steps that drive the column in transient regime. Some examples of dynamic responses are shown in Figure 3.

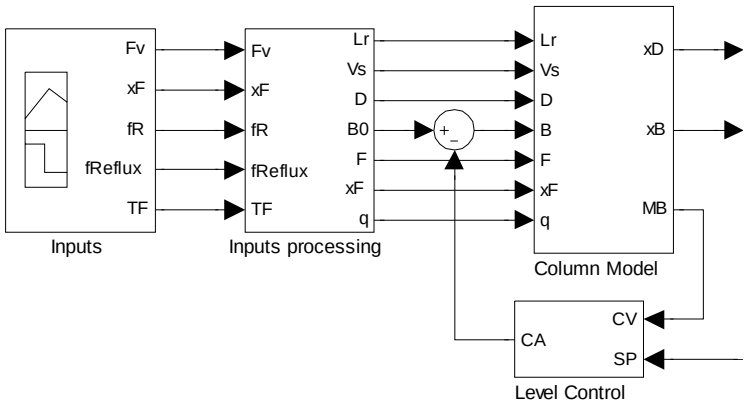

Figure 2 – Simulink diagram for the distillation column nonlinear model.

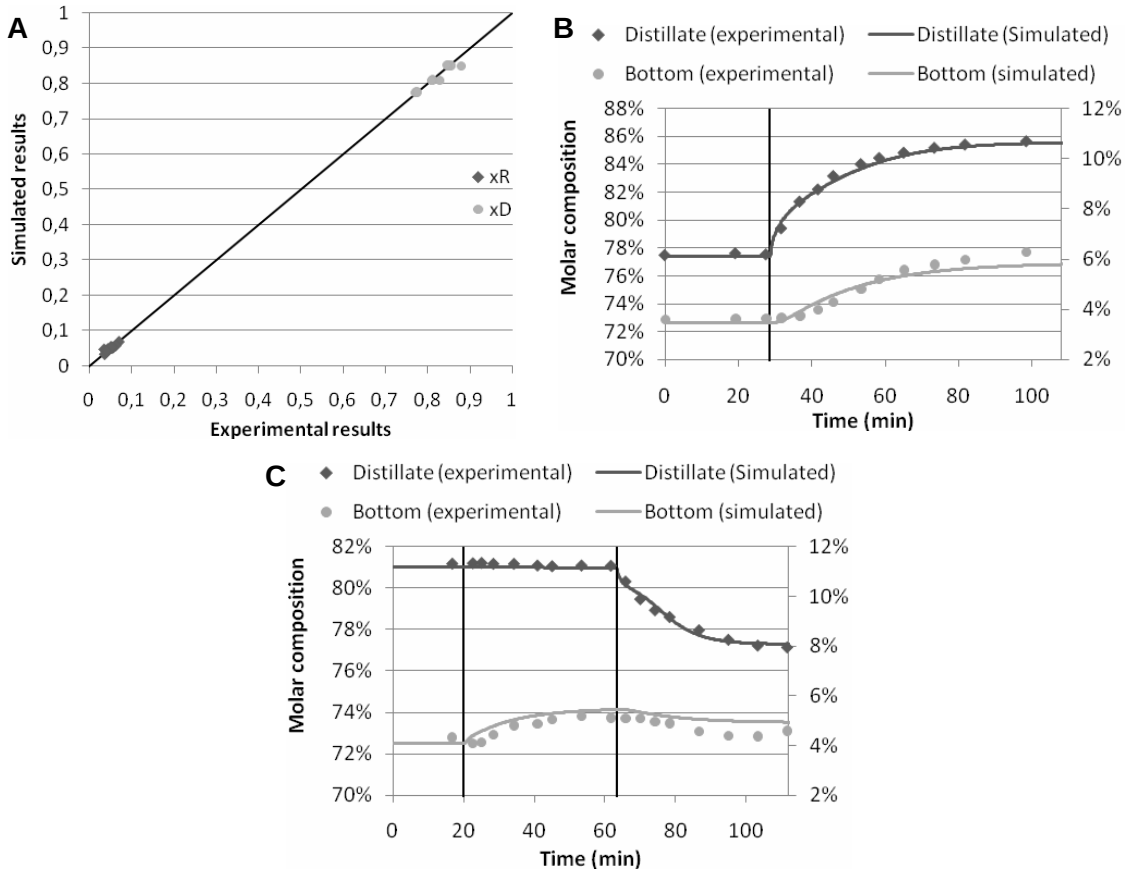

Figure 3 – A) Parity plot for the distillate (xD) and bottom (xR) ethanol compositions. B) Dynamic response of the column to a step abrupt change in reflux ratio (+600%). C) Dynamic response of the column to a step abrupt change in the feed rate (+50% at t=20 min) followed by a step change in reflux ratio (-60% at t=65 min).

5 Results and Discussion

From the results presented in Section 4, we can conclude that the model is capable of describing both the steady states and the dynamic behaviour of this real distillation column. Further, since the online measurements available experimentally are some tray temperatures and not the compositions, we added to the model the conversion between the predicted compositions and certain stage temperatures. Figure 4, also shows a good agreement between the experimental temperatures and those predicted by the model.

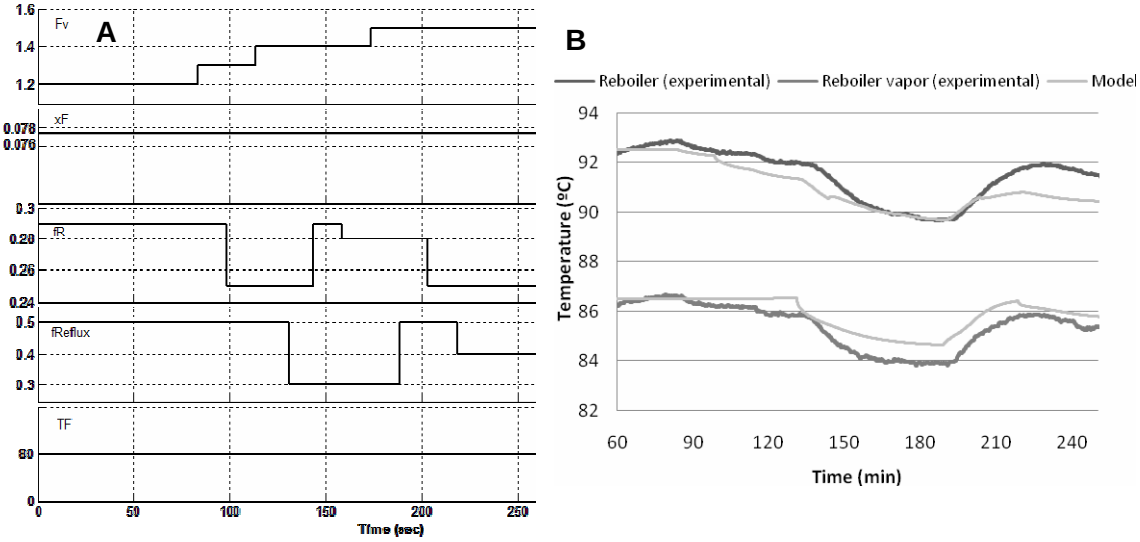

Figure 4 – A) Sequence of multiple steps in the model inputs that were designed to drive the column in transient regime. B) Simulated and real temperatures obtained for the Figure 4A inputs.

6 Conclusions

A simulator for a real a pilot scale continuous distillation process was developed, which implements a detailed nonlinear mathematical model in Matlab®/Simulink simulation environment. This simulator can predict both the steady-state and the dynamic behaviour of this pilot scale distillation column at the Chemical Engineering Department of ISEL, for the separation of a non-ideal binary liquid mixture of ethanol/water, in the absence and in the presence of faults. The model developed was validated against data collected from the plant for the separation of a non-ideal binary liquid mixture of ethanol/water, showing a good agreement with the experimental results.

Thus, this dynamic model is well-suited to be used as a reference model for the implementation of Fault-Tolerant Control strategies in real time.

Aknowledgments

The authors thank the financial support of the project POCI/EME/59522/2004 from FCT granted by the program Programa Operacional Ciência e Inovação 2010 (POCI 2010) with the co participation of the communitarian European fund FEDER.

References

Abdullah, Z., Aziz, N., Ahmad, Z. (2007). Nonlinear Modelling Application in Distillation Column. *Chemical Product and Process Modeling*, 2 (3), Article 12.

Calado, J.M.F., Korbicz, J., Patan, K., Patton, R.J., and Sá da Costa, J.M.G.S. (2001). Softcomputing approaches to fault diagnosis for dynamic systems. *European Journal of Control*, 7, 248-286.

Can, U., Jimoh, M., Steinbach, J. & Wozny, G. (2002). Simulation and experimental analysis of operational failures in a distillation column. *Separation and Purification Technology*, 29, 163-170.

Kister, H.Z. (1990). *Distillation Operation*. McGraw Hill, New York.

Skogestad, S. (1997), Dynamics and control of distillation columns— A tutorial introduction, *Trans IChemE*, 75(Part A): 539–562.

Skogestad, S. (2003). Distillation research and models. Retrieved June 2006, from Web site: http://www.nt.ntnu.no/users/skoge/distillation/.

Proceedings of the 10th International Chemical and
Biological Engineering Conference - CHEMPOR 2008
Braga, Portugal, September 4-6, 2008
E.C. Ferreira and M. Mota (Eds.)

Applications of Model Based Design of Polymer Products

Dulce C. M. Silva[1], Rui M. Bastos[1], Nuno M. C. Oliveira[1*]
[1]GEPSI — PSE Group, Department of Chemical Engineering, University of Coimbra
Rua Sílvio Lima – Pólo II, 3030–790 Coimbra, Portugal.

Keywords: Dynamic optimization, Product Design, Polymerization.
Topic: Multi−scale and/or multi−disciplinary approach to process – product innovation.

Abstract

Previous work (**Silva, 2006; Silva and Oliveira, 2007**) described a systematic methodology for the design of free-radical polymer products based on discontinuous operation. This design problem is characterized by considerable complexity, high dimensionality, nonlinear behaviour of the physical models, and multi-objective nature. To avoid most of these limitations, a two-step methodology was introduced, where the problem is initially reformulated in terms of the decision variables used. Here, additional aspects of the application of the methodology to particular cases are considered, and modifications proposed to enhance its practical application. A particular problem addressed is the residual amount of initiators present is the final product. The application is demonstrated with the batch suspension polymerization of vinyl chloride, one of the most used thermoplastics.

1 Introduction

Previous work in the optimization of polymeric materials addressed the search of operating conditions that improve productivity, resulting from minimum time formulations (**Silva and Oliveira, 2002**) and the effects of constraining the variance of the chain length distribution of the final product (**Silva, 2006**). In a systematic approach to polymer design, additional aspects need also to be considered; namely, it must be possible to rigorously control the size distributions (moments and shape) and to completely determine the operating conditions (*e.g.* temperature, concentrations), processing agents, such as suitable initiators (which ones, how many, in what concentrations, when to add) and other additives like suspension or chain transfer agents.

The resulting design problem is characterized by considerable complexity, high dimensionality, highly nonlinear behaviour of the physical models, multi-objective nature and the need to perform discrete design decisions. To tackle most of these limitations, a two-step methodology was recently introduced (**Silva, 2006; Silva and Oliveira, 2007**). Initially the problem is reformulated in terms of the decision variables used, namely the reaction temperature and the initiation reaction rates, aiming to seek an extreme of a performance criterion (e.g., minimize the reaction time). Given that the initiation reaction rate profile is independent of the set of initiators used, the choice of suitable initiators may be considered in a second step, and formulated as an algebraic MILP problem. This later step leads to the set of initiators and their respective addition policies, which minimize the cost of obtaining the initiation profile obtained in the first step of the methodology. As demonstrated previously, this sequential approach significantly diminishes the overall problem complexity, and allows the systematic optimization of the major aspects related to the batch production of free-radical polymer products.

* Corresponding author. Tel + 351-239-798700. E-mail:nuno@eq.uc.pt

2 Improving the base methodology

A relevant aspect in the industrial practice of free-radical polymerization is the control of the residual amounts of initiators that are present in the final product, after the end of the operation. This must be considered not only due to the potential extra costs incurred, but also because of a number of additional criteria, including product quality, health and environmental factors.

During the application of the first step of the methodology previously presented the maximum concentrations of initiators cannot be directly constrained, since the decision variables used are still independent from a particular choice of initiators. Therefore, to assure that excessive residual concentrations of initiators are not obtained at the end of the operation, both steps of the methodology need to be simultaneously considered.

2.1 Problem statement

In some of the previously studied cases, a swift rise in the initiation reaction rate was observed at the end of the operation, while applying the first step of the methodology (**Figure 1**). This is due to the fact that the design problem was formulated as a minimum time problem. This objective is decreased when, at the final stage of the operation, we are able to increase the initiation reaction rate while also increasing the probability of the occurrence of termination of the active chains.

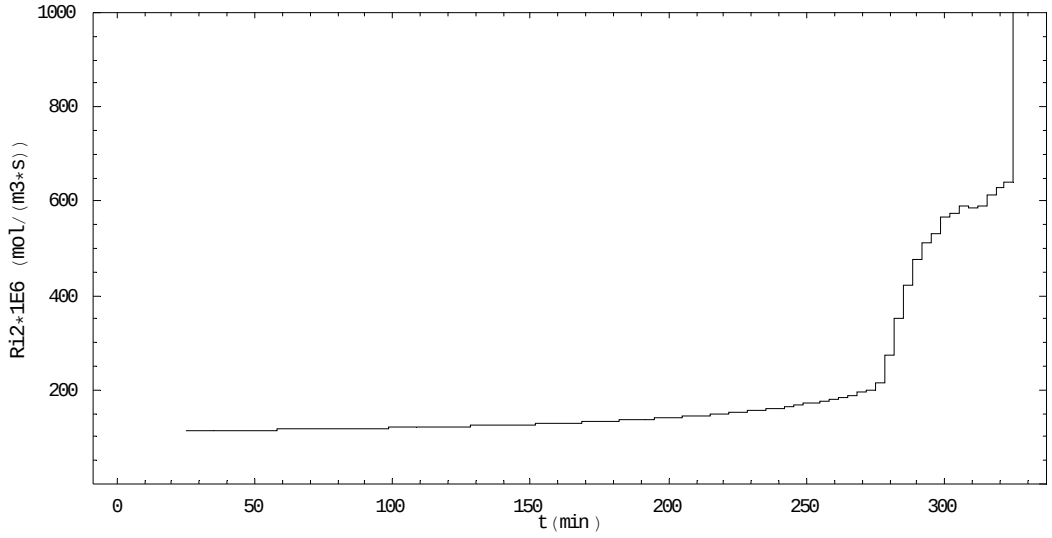

Figure 1 – Graphical representation of the initiation reaction rate profile in the polymer rich phase, with constraints only in the $\overline{M}_n$ (Initial case).

However, an increase in the initiation reaction rate during the final stages of the operation, such as the one observed in **Figure 1**, may lead to undesirable situations from a practical standpoint. If the temperature is kept approximately constant, excessive quantities of initiators might need to be added in the later stages of the operation, causing higher residual concentrations of these species. Additionally, it might be necessary to use excessive quantities of fast initiators, with the subsequent increase of operational costs. In a practical application, the temperature profile can also be changed during the last operational phase to mitigate this problem, but this effect might not be sufficient. Therefore, a more direct control of the residual concentration of the initiators is required, to enhance the applicability of the systematic design methodology.

2.2 Problem solution

Considering the particular application to the batch suspension polymerization of vinyl chloride, we started by comparing different initiation reaction rate profiles obtained close to standard operation conditions, in order to infer the typical values relative to this product. For this purpose, an optimization problem was prepared, where the objective function was the minimization of the final time (t_f), in case study I, with two typical initiators specified (one fast and the other slow).

Case Study I: Preliminary runs

This case study consists in the minimization of t_f, selecting the concentrations of two initiators at the beginning of operation and the addition policies of these species. The only constraints imposed were the desired numeric average molecular weight, $\overline{M}_n$ (in all situations presented in this work, the constraint $0.98 \leq \overline{M}_n \leq 1.02$, was used, with normalized values). **Figure 2** presents the addition profiles determined this way.

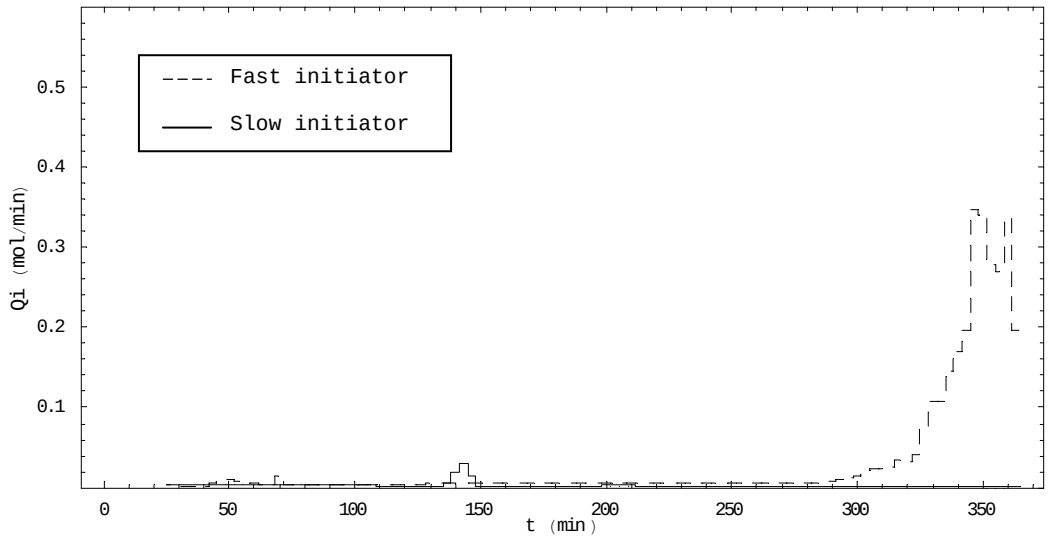

Figure 2 – Graphical representation of the addition profiles of initiators determined in case study I.

The solution of this problem also produced the values of 0.10 x 10^{-3} mol/kg_{VCM} for the fast initiator and 2.38 x 10^{-3} mol/kg_{VCM} for the slow one, as quantities of the initiators to be added at the beginning; the residual concentrations of initiators added to a total value of 1.15 x 10^{-3} mol/kg_{VCM}. This last value is close to the one obtained in typical operation, considering just the initial addition of initiators (10^{-3} mol/kg_{VCM}). **Figure 3** presents the initiation reaction rate calculated from the above results. Here, a slight rise in the initiation reaction rate when the operation is close to its end is visible. This means that if upper limits in the initiation rate, with linear shape and small slope, are imposed on the initiation reaction rate profile during the first optimization phase, then low (i.e., acceptable) residual concentrations of initiators may be expected at the end of operation. This can be easily specified in the first step of the systematic design methodology for polymer design.

Case Study II: Application of the first step of the design methodology

The objective in this case study is the minimization of t_f having as decision variable the initiation reaction rate profile (the temperature is maintained constant and equal to 55ºC). The previous constraint is applied regarding the final value of $\overline{M}_n$. After the critical

conversion (i.e., when the monomer rich phase is depleted) the initiation reaction rate now has as an upper limit corresponding to a straight-line with a specified slope (0.1, 0.05 and 0.01 mol / (m^3.s.min)). **Figure 4** shows the initiation reaction rate profiles determined in each situation. As can be observed, with successively lower slopes the duration of the operation presented increases slightly; this is in agreement with the initial observations. Applying the restriction with slope 0.01 resulted in the largest increase in operation time (6.4%). With these scenarios, we proceed to the following step of the methodology.

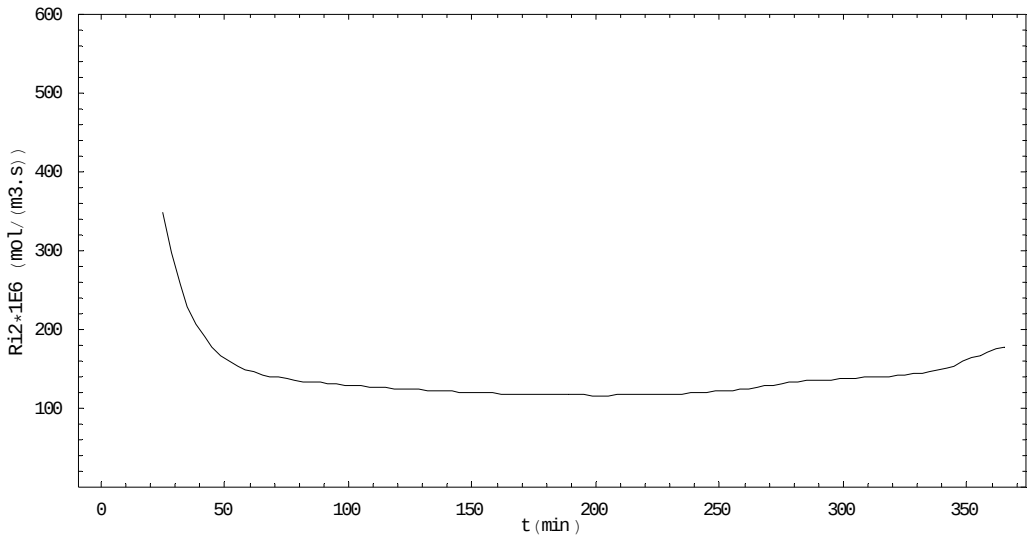

Figure 3 – Graphical representation of the initiation reaction rate profile determined in case study I.

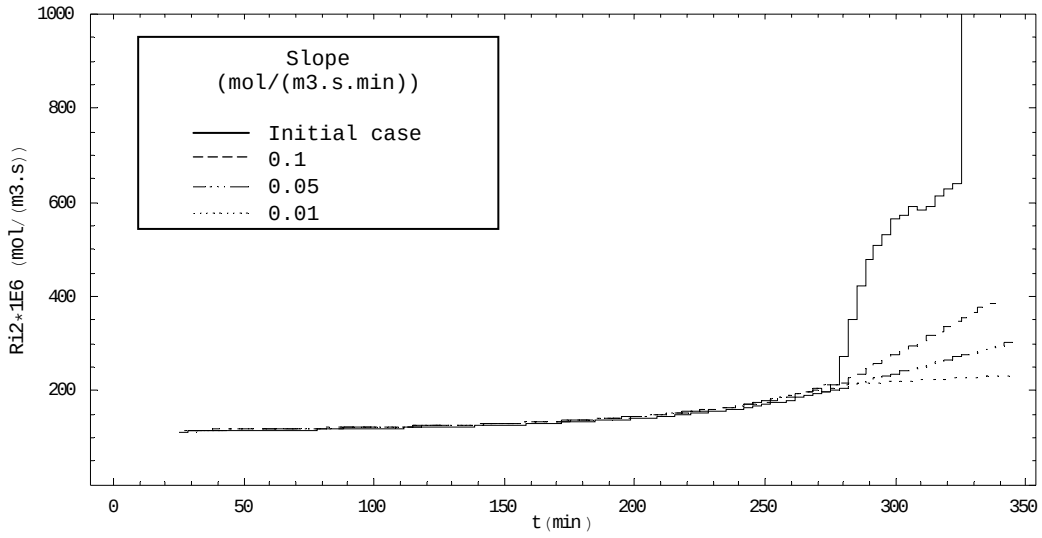

Figure 4 – Graphical representation of the initiation reaction rate profiles for case study II.

Case Study III: Second step of the design methodology

The objective in the second step of the methodology is to minimize the costs associated with the initiators used, considering the set of species and their addition policies as decision variables. Additionally, a good fit between the initiation reaction rate profiles of this and the first step of the methodology was imposed. Table 2 presents the relative costs and dissociation constants of the set of initiators made available to the optimization framework.

With this data (which will be referred to as set *A*), the optimization problem determined the results presented in **Table 3**.

Table 2 – Relative costs and inititation reaction rate constants of the set of initiators available (**Sanches e Myers, 1996; Akzo Nobel Chemicals BV, 2000**).

Initiator	*Cost* (m.c.u.* / mol)	$kd_{(T=55\ ºC)}$ (1/min)	*Initiator*	*Cost* (m.c.u./mol)	$kd_{(T=55\ ºC)}$ (1/min)
i1	1.73	1.37×10^{-2}	i11	3.8	6.82×10^{-3}
i2	0.9	5.28×10^{-5}	i12	0.7	1.10×10^{-3}
i3	0.8	3.13×10^{-4}	i13	3.7	6.39×10^{-4}
i4	0.8	3.38×10^{-4}	i14	0.8	2.75×10^{-3}
i5	1	2.54×10^{-3}	i15	0.5	9.02×10^{-4}
i6	3.4	2.07×10^{-3}	i16	1.1	1.55×10^{-3}
i7	3.8	3.46×10^{-4}	i17	1.51	8.81×10^{-2}
i8	4.2	1.23×10^{-2}			
i9	3.6	7.49×10^{-3}			
i10	1.6	9.08×10^{-3}			

* monetary cost units.

Table 3 – Results obtained by applying the second step of the methodology.

Initiator data cost	*Slope* (mol/(m^3.s.min))	*Total cost* (m.c.u.)	*Residual concentration of initiators* (mol/kg_{VCM})	*Initiators selected*
A	Initial case	24.58	2.81×10^{-4}	i17
	0.1	21.96	9.40×10^{-5}	i17
	0.05	21.65	7.26×10^{-5}	i17
	0.01	21.41	5.81×10^{-5}	i17
B	Initial case	36.90	1.60×10^{-3}	i10, i14, i17
	0.1	26.67	1.44×10^{-3}	i10, i14, i17
	0.05	25.65	1.34×10^{-3}	i10, i14, i17
	0.01	24.71	1.41×10^{-3}	i10, i14, i17

When smaller slopes were used as upper limits, a reduction in the residual concentration of initiators was observed, together with a smaller total cost associated (a decrease of 13.8% in the total cost was observed with slope 0.01, compared to the initial case). This is due to the fact that in situations with higher slopes greater quantities of initiator must be added during the operation. As the slope of the constraint is decreased, the residual quantities of initiators at the end of the operation also tend to present lower values.

From the available set of initiators, the program initially chose only i17. In **Table 2** it can be noticed that not only is this the fastest initiator, but that also it presents a relative low cost. Therefore initiator i17 becomes the natural choice. To assess the ability of the methodology to produce alternative solutions, a second analysis was performed, penalizing this time the choice of fast, low cost, initiators (set *B*). In this situation the solution is different (**Table 3**). The total cost also decreases with the slope (39.6% for the restriction with slope 0.01, relative to the initial case). This is due to the additional penalization that fast initiators have in this scenario. Although the residual concentrations have slightly increased in this situation, they are still reduced, when compared the situations with an upper limit to the initial case, and in the acceptable range.

With the cost data set *A*, in all scenarios, a substantial decrease in the initiators residual concentrations can be observed, when compared to the base case (10^{-3} mol/kg_{VCM}).This demonstrates the capacity of the methodology to make careful choices of the initiators, in the presence of diverse sets of objectives and constraints. Likewise, the residual concentrations regarding situation *B* are similar to the value considered to be acceptable (10^{-3} mol/kg_{VCM}), and can be reduced even further, if necessary. Thus, it is possible to state that the systematic optimization methodology for polymeric materials design applied is sufficiently flexible to accommodate the generality of objectives and restrictions found in the industrial production of this category of polymers.

3 Conclusions

With this work we aimed at improving a systematic methodology for polymeric material optimization. Namely, it was intended to consider the residual concentrations of initiators. The path followed was searching for aspects of the methodology that could be readily changed by the user, while trying to achieve residual concentrations suited to the case studies. Here, the temperature was kept constant, in order to study independently the behaviour of the initiator addition policies.

A possible way of reducing the initiator residual concentrations was identified. This is based on imposing an upper limit to the initiation reaction rate profile, in the later stages of operation, during the first step of the methodology. From this procedure, a reduction in the residual concentration of initiators will also occur. This is obtained while reduced costs with initiators are also verified, when compared to the situations without restrictions on the initiation reaction rate profiles. Smaller slopes in the upper limit will result in larger operation times, which need to be verified, but have usually small effects, in industrial applications.

References

Akzo Nobel Chemicals BV (2000). Initiators for High Polymers, Amersfoort, Holland.

Sanches, J., Myers, T.N. (1996). Peroxide Initiators (Overview), in J.C. Salamone (Ed.), *Polymeric Materials Encyclopedia*, Volume 7 (pp. 4927–4938). CRC Press, New York, NY, EUA.

Silva, D.C.M., N.M.C. Oliveira (2002). Optimization and Nonlinear Model Predictive Control of Batch Polymerization Systems, *Computers and Chemical Engineering*, 26, 649-658.

Silva, D.C.M. (2005). Controlo Predictivo Não-Linear de Processos Químicos – Aplicação a Sistemas de Polimerização Descontínuos, *PhD Thesis*, Universidade de Coimbra, Portugal.

Silva, D.C.M., N.M.C. Oliveira (2007). Model Based Design of Polymer Products, em V. Plesu, P.S. Agachi (Eds.), *Proceedings of the 17th European Symposium on Computer Aided Process Engineering* (pp. 583-588). Elsevier, Amsterdam, Holland.

Proceedings of the 10th International Chemical and
Biological Engineering Conference - CHEMPOR 2008
Braga, Portugal, September 4-6, 2008
E.C. Ferreira and M. Mota (Eds.)

Global dynamic optimization of chemical and bio-processes using the scatter search metaheuristic

Jose A. Egea, María-Sonia G. García, Eva Balsa-Canto, Julio R. Banga*
Process Engineering Group, Instituto de Investigaciones Marinas (IIM-CSIC)
c/ Eduardo Cabello, 6, 36208 Vigo, Spain.

Keywords: dynamic optimization, chemical engineering, global optimization, scatter search, metaheuristics.
Topic: Advances in computational & numerical methods, Process control & operations.

Abstract

A scatter search-based algorithm for global dynamic optimization in chemical engineering is presented. It is designed to overcome typical difficulties of non-linear dynamic systems optimization such as noise, flat areas, non-smoothness and/or discontinuities. It balances between intensification and diversification by coupling a local search procedure with a global search and makes use of memory to avoid simulations in previously explored areas. Its application to three dynamic optimization case studies proves its efficiency and robustness, showing also a very good scalability.

1 Introduction

Dynamic optimization appears in many industrial applications to optimize a pre-defined performance index (e.g., profitability) subject to some specifications over a time interval. Objective functions and/or constraints formulated from mathematical models describing industrial processes are usually highly nonlinear, which often causes non-convexity. Besides, non-smoothness and discontinuities can be present, thus the use of global optimization methods is needed for many dynamic optimization problems (Banga et al., 2005). In recent years, a special class of stochastic global optimization methods called metaheuristics have appeared as efficient optimization techniques.

Scatter search is a population-based metaheuristic introduced by Glover (1977) which combines a global phase with an intensification method, usually a local search (Laguna and Martí, 2003). Our scatter search-based algorithm has been written in Matlab under the name *SSm*. This study goes beyond a simple exercise of applying scatter search to dynamic optimization problems, but presents innovative mechanisms to obtain a good balance between intensification and diversification in a short-term search horizon. In many instances, dynamic optimization problems are non-convex and multimodal, thus the use of global optimization techniques becomes crucial for solving them (Banga et al., 2005). The application of our algorithm for solving nonlinear optimization problems arising from chemical and biological systems has provided excellent results (Egea et al., 2007; Rodríguez-Fernández et al., 2006).

This paper is organized as follows: Section 2 states the problem of dynamic optimization. Our algorithm is depicted in Section 3. Section 4 presents the three case studies used in this paper for our experiments as well as the results obtained. The paper finishes with some conclusions.

2 Dynamic Optimization: Problem Statement

The general dynamic optimization problem has the following mathematical form:

*Corresponding author. Tel. +34-986-214473. E-mail: julio@iim.csic.es

$$\min_{\mathbf{u}(t),\mathbf{v},t_f} C\left(\mathbf{x}(t_f),\mathbf{z}(t_f),\mathbf{u}(t_f),\mathbf{v},t_f\right) \tag{1}$$

subject to the system dynamics:

$$\mathbf{F}\left(\dot{\mathbf{x}}(t),\mathbf{x}(t),\mathbf{z}(t),\mathbf{u}(t),\mathbf{v},\mathbf{t}\right)=\mathbf{0} \tag{2}$$

$$\mathbf{x}(0)=\mathbf{x}_0,\mathbf{u}(0)=\mathbf{u}_0,\mathbf{z}(0)=\mathbf{z}_0 \tag{3}$$

where $\mathbf{x}(t)\in\mathbf{X}\subset\mathbb{R}^n$ and $\mathbf{z}(t)\in\mathbf{Z}\subset\mathbb{R}^m$ are the vectors of differential and algebraic states respectively; $\mathbf{u}(t)\in\mathbf{U}\subset\mathbb{R}^p$ is the vector of control (input) variables; $\mathbf{v}\in\mathbf{V}\subset\mathbb{R}^q$ are time invariant parameters; t is the time (and t_f is the final time); C is a functional to be minimized; $\mathbf{F}$ is the set of differential-algebraic equations describing the systems dynamics; finally, $\mathbf{x}_0$, $\mathbf{z}_0$, and $\mathbf{u}_0$ are the values of the respective vectors at the initial time t_0. Equality and inequality constraints may be imposed. Some of them must be satisfied over the whole process time (path constraints), while others must be only satisfied at the end of the process (endpoint constraints). The control variables and/or the time-invariant parameters may be subject to lower and upper bounds.

In this work we will consider the CVP approach (Vassiliadis et al., 1994) using the Piecewise Constant approximation, PC (i.e., zero order polynomial) with fixed-length time intervals. Different number of intervals will be used for each problem in order to check the scalability of the different optimization methods.

3 Scatter search algorithm for dynamic optimization of chemical and bio-processes

***Diversification Generation Method*:** *SSm* begins by generating an initial set of diverse vectors in the search space. The method makes use of memory taking into account the number of times that every decision variable appears in different parts of the search space (Glover et al., 2003).

Initial *RefSet* formation: For building the initial *RefSet*, after generating the set of diverse solutions, a subset of high quality and diverse points is selected. The first step consists in evaluating all diverse vectors and select some of them in terms of quality. The *RefSet* is completed with the remaining diverse vectors by maximizing the minimum Euclidean distance to the included vectors in the *RefSet*.

***Subset Generation* and *Solution Combination* methods:** After the initial *RefSet* is built, its solutions are sorted according to their quality and we apply the *Subset Generation Method*. In our implementation, it consists in selecting all pairs of solutions in the *Refset* to combine them. To avoid repeating combinations with the same pair of solutions, we use a memory term which keeps track of the pairs previously combined. Regarding the *Solution Combination Method*, we use a type of combination based on hyper-rectangles (Ugray et al., 2005), which enhances the diversification. Depending on their position in the *RefSet* every pair of combined solutions may generate from two up to four new solutions.

Updating the *RefSet*: As recommended by Laguna and Martí (2005), we update the *RefSet* considering the quality of the elements. This strategy may cause convergence to sub-optimal solutions or stagnation of the search in flat areas. To avoid these effects, we have implemented two filters (Egea et al., 2007) which restrict the incorporation of solutions that contribute only slight diversity to the *RefSet*

***Improvement Method*:** The *Improvement Method* consists in a local search, selecting the initial points by means of different filters. In this work, we have considered a gradient-based method (Exler and Schittkowski, 2007) and a direct-search method (Lagarias et al., 1999). In applications related to chemical and bioprocess engineering, we often face time-consuming evaluation problems or complex topologies which can make the local search inefficient. This implies that the application of the *Improvement Method* should be restricted to a low number of promising solutions. Here we use merit and distance heuristic filters introduced by Ugray et al. (2005) to avoid performing local searches from poor quality solutions or from solutions which are likely to provide already found local minima.

***RefSet* Rebuilding:** Due to the memory term which avoids combinations between *RefSet* members previously combined, the optimization procedure may stop if no new solutions enter the *RefSet* in a given iteration. Advanced scatter search designs overcome this problem by resorting a mechanism to partially rebuild the *RefSet*. The method is usually the same as that used to create the initial *RefSet*, in the sense that it uses the max-min distance criterion for selecting diverse solutions. We propose an alternative strategy to maximize the number of search directions. In this strategy, the vectors refilling the *RefSet* are chosen to maximize the number of relative directions defined by them and the existing vectors in the *RefSet* (Egea et al., 2007).

Intensification strategies: One of the filters mentioned above may prevent the search from focusing on intensification, especially during the first iterations. To allow combinations between high quality solutions (which do not apply to enter the *RefSet* because of the distance filter) and *RefSet* members, we store the solutions which can not enter the *RefSet* but have a better function value than the second *RefSet* member. These stored solutions are then combined with the best *RefSet* solution, increasing the probability of obtaining high quality solutions by combination in early stages of the search (Egea et al., 2007). Another advanced strategy (the *go beyond* strategy) to enhance the intensification of the search has been implemented in our algorithm. It consists in exploiting promising directions (Egea, 2008).

4 Computational experiments

In this section, a set of bioprocess dynamic optimization problems will be used as case studies to test the performance of the algorithm proposed in this work. A set of different state-of-the-art global optimization methods has been selected to compare their results with those obtained with the algorithm proposed in this study: *CMAES* (Hansen et al., 2003), *DE* (Storn and Price, 1997), *SRES* (Runarsson and Yao, 2000), *DIRECT* (Jones, 2001) and *OQNLP* (Laguna and Martí, 2002). Regarding stochastic solvers, a total number of 10 runs were performed for each problem.

4.1 Case studies

4.1.1 Fed-batch reactor for ethanol production

This system is a fed-batch bioreactor for the production of ethanol (Banga et al., 1997). The objective is to find the feed rate which maximizes the yield of ethanol. Table 1 presents results for every solver with the different levels of discretization considered. Table 2 compares the best result obtained by our algorithm for this problem with those found in the literature. Figure 1 presents the optimal control profile for the highest level of discretization.

4.1.2 Fed-batch fermenter for penicillin production

This problem deals with the dynamic optimization of a fed-batch fermenter for the production of penicillin (Banga et al., 1997). The optimal control problem is to maximize the total amount of penicillin

		CMAES	DE	glcDirect	OQNLP	SRES	SSm
$\rho = 10$	**Best**	**20316.11**	**20316.08**	20203.74	**20316.11**	20305.96	**20316.11**
	Mean	19889.67	20100.72	-	-	20093.14	20291.38
	Worst	18996.02	19672.46	-	-	19554.01	20192.48
$\rho = 20$	**Best**	**20412.14**	20404.36	19738.01	**20412.19**	20327.11	**20412.19**
	Mean	20273.76	20383.95	-	-	20237.58	20412.19
	Worst	19953.39	20341.29	-	-	20095.71	20412.19
$\rho = 40$	**Best**	20430.84	20375.32	19544.88	**20444.47**	20214.40	**20444.86**
	Mean	20360.73	20239.27	-	-	19726.07	20444.86
	Worst	20110.08	19902.08	-	-	19466.64	20444.86

Table 1: Results for the ethanol production problem

Ref.	Method	ρ/Approach	f_{opt}
Luus (1993a)	DP	N/A	20430
Banga et al. (1997)	CVP-*ICRS*	8/PCL-VI	20423
Present study	CVP-*SSm*	40/PC-FI	20445

Table 2: Comparison of results for the ethanol production problem

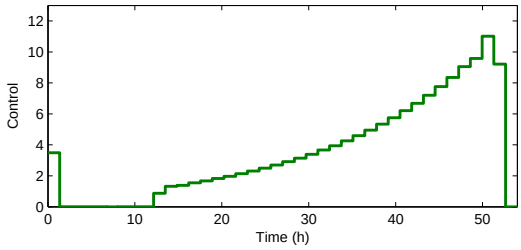

Figure 1: Optimal control profile for the ethanol production problem ($\rho = 40$)

produced using the feed rate of substrate as the control variable. In our experiments, *SSm* provided the best solution for the levels of discretization $\rho = 10, 40$. Table 3 compares the best result obtained by our algorithm for this problem with those found in the literature

Ref.	Method	ρ/Approach	f_{opt}
Luus (1993b)	IDP	N/A	87.95
Banga et al. (2005)	TPH	$\geq$ 4/PCL-VI	87.99
Present study	CVP-*SSm*	40/PC-FI	88.00

Table 3: Comparison of results for the penicillin production problem

4.1.3 Drying operation

In this section we consider a food convective drying problem, similar to the one formulated by Banga and Singh (1994). The aim is to dry a cellulose slab maximizing the retention of a nutrient. The dynamic optimization problem associated with the process consists of finding the dry bulb temperature along the time to maximize the nutrient retention at the final time. Table 4 presents results for every solver with the different levels of discretization.

4.2 Executive summary of results

In this section we provide a summary of the results obtained in this work by making use of the performance profiles methodology (Dolan and Moré, 2002). Following Auger and Hansen (2005), we define the success performance FE for a solver on a specific problem by:

		CMAES	DE	glcDirect	OQNLP	SRES	SSm
$\rho = 10$	**Best**	**0.20002**	**0.20003**	0.19979	0.19875	0.20001	**0.20003**
	Mean	0.19710	0.19683	-	-	0.19894	0.19694
	Worst	0.19108	0.18939	-	-	0.19579	0.18742
$\rho = 20$	**Best**	0.19997	0.19913	0.19329	0.15483	0.19989	**0.20010**
	Mean	0.19696	0.19608	-	-	0.19878	0.19687
	Worst	0.19298	0.19185	-	-	0.19728	0.19326
$\rho = 40$	**Best**	**0.19952**	0.19859	0.18848	0.15102	0.19001	0.19788
	Mean	0.19751	0.19442	-	-	0.18796	0.19618
	Worst	0.19522	0.19103	-	-	0.18623	0.19311

Table 4: Results for the drying process problem

$$\mathsf{FE} = eval_{mean} \cdot \frac{\#\text{all runs}(10)}{\#\text{successful runs}} \tag{4}$$

where a run is considered successful if it obtained the optimal solution with a relative error $\leq 0.1\%$ (in our problems, we consider it as the best solution found by any of the solvers). With this definition the best success performance FEbest is given by the lowest value of FE for every problem. Figure 2 shows the empirical distribution function of the success performance FE/FEbest over all the problems.

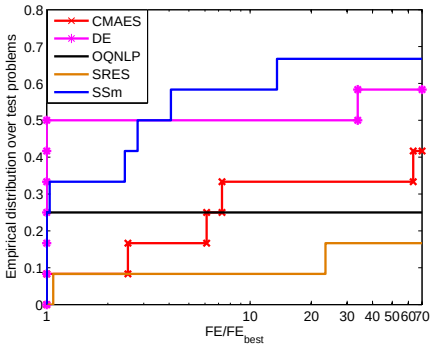

Figure 2: Performance profiles

As shown in the performance profiles, *SSm* solves the highest percentage of problems compared with the rest of solvers tested.

Conclusions

We have developed a scatter search-based methodology which intends to be effective for solving global optimization problems from the biotechnological and food industries. The procedure treats the objective function as a black box, making the search algorithm context-independent. We have expanded and advanced knowledge associated with the implementation of scatter search procedures. We have tested the proposed methodology over a set of dynamic optimization problems from the biotechnological and food industries. In order to have an idea about their efficiency, they have been compared with other state-of-the-art global optimization methods. The results obtained showed that the proposed methodology is adequate for the kind of problems intended to solve. In all cases our algorithm was competitive, providing the best solution among the tested solvers in many of the examples. It is to note that the algorithm's behavior is not affected by the problem size since it provides excellent results for every level of discretization considered in this study.

References

Auger, A., Hansen, N. (2005) Performance evaluation of an advanced local search evolutionary algorithm. *IEEE Congress on Evolutionary Computation, IEEE CEC 2005*, pages 1777–1784.

Banga, J. R., Alonso, A. A., Singh, R. P. (1997). Stochastic dynamic optimization of batch and semicontinuous bioprocesses. *Biotechnology Progress*, 13(3), 326–335.

Banga, J. R., Balsa-Canto, E., Moles, C. G., Alonso, A. A. (2005). Dynamic optimization of bioprocesses: Efficient and robust numerical strategies. *Journal of Biotechnology*, 117(4), 407–419.

Banga, J. R., Singh, R. P. (1994). Optimization of air drying of foods. *Journal of Food Engineering*, 23(2), 189–211.

Dolan, E. D., Moré, J. J. (2002). Benchmarking optimization software with performance profiles. *Mathematical Programming*, 91(2), 201–213.

Egea, J. A. (2008). *New Heuristics for Global Optimization of Complex Bioprocesses*. PhD thesis, University of Vigo, Spain.

Egea, J. A., Rodríguez-Fernández, M., Banga, J. R., Martí, R. (2007). Scatter search for chemical and bio-process optimization. *Journal of Global Optimization*, 37(3), 481–503.

Exler, O., Schittkowski, K. (2007). A trust region SQP algorithm for mixed-integer nonlinear programming. *Optimization Letters*, 1(3), 269–280.

Glover, F. (1977). Heuristics for integer programming using surrogate constraints. *Decision Sci.*, 8, 156–166.

Glover, F., Laguna, M., Martí, R. (2003). Scatter search. In Ghosh, A., Tsutsui, S., editors, *Advances in Evolutionary Computation: Theory and Applications*, pages 519–537. Springer-Verlag, New York.

Hansen, N., Müller, S. D., Koumoutsakos, P. (2003). Reducing the time complexity of the derandomized evolution strategy with covariance matrix adaptation (CMA-ES). *Evolutionary Computation*, 11(1), 1–18.

Jones, D. R. (2001). DIRECT global optimization algorithm. In Floudas, C. A., Pardalos, P. M., editors, *Encyclopedia of optimization*, pages 431–440. Kluwer Academic Publishers, Dordrecht.

Lagarias, J. C., Reeds, J. A., Wright, M. H., Wright, P. E. (1999). Convergence properties of the nelder-mead simplex method in low dimensions. *SIAM Journal on Optimization*, 9(1), 112–147.

Laguna, M., Martí, R. (2002). The OptQuest callable library. In Voss, S., Woodruff, D. L., editors, *Optimization Software Class Libraries*. Kluwer Academic Publishers, Boston.

Laguna, M., Martí, R. (2003). *Scatter Search: Methodology and Implementations in C*. Kluwer Academic Publishers, Boston.

Laguna, M., Martí, R. (2005). Experimental testing of advanced scatter search designs for global optimization of multimodal functions. *Journal of Global Optimization*, 33(2), 235–255.

Luus, R. (1993a). Application of dynamic programming to differential-algebraic process systems. *Computers & Chemical Engineering*, 17, 373–377.

Luus, R. (1993b). Optimization of fed-batch fermentors by Iterative Dynamic Programming. *Biotechnology and Bioengineering*, 41, 599–602.

Rodríguez-Fernández, M., Egea, J. A., Banga, J. R. (2006). Novel metaheuristic for parameter estimation in nonlinear dynamic biological systems. *BMC Bioinformatics*, 7, 483+.

Runarsson, T. P., Yao, X. (2000). Stochastic ranking for constrained evolutionary optimization. *IEEE Transactions on Evolutionary Computation*, 4, 284–294.

Storn, R., Price, K. (1997). Differential evolution - a simple and efficient heuristic for global optimization over continuous spaces. *Journal of Global Optimization*, 11, 341–359.

Ugray, Z., Lasdon, L., Plummer, J., Glover, F., Kelly, J., Martí, R. (2005). A multistart scatter search heuristic for smooth NLP and MINLP problems. In Rego, C., Alidaee, B., editors, *Adaptive Memory and Evolution: Tabu Search and Scatter Search*, pages 25–58. Kluwer Academic Publishers.

Vassiliadis, V. S., Sargent, R. W. H., Pantelides, C. C. (1994). Solution of a class of multistage dynamic optimization problems. 1. problems without path constraints. *Industrial & Engineering Chemistry Research*, 33(9), 2111–2122.

Proceedings of the 10th International Chemical and
Biological Engineering Conference - CHEMPOR 2008
Braga, Portugal, September 4-6, 2008
E.C. Ferreira and M. Mota (Eds.)

Integrating Real-Time Optimization and Control for Optimal Operation: Application to the Bio-ethanol Process

Silvia Ochoa[1,2,*], Jens-Uwe Repke[1], Günter Wozny[1]

[1] Chair of Process Dynamics and Operation, Berlin Institute of Technology, Sekr. KWT9, Strasse 17. Juni. 135, Berlin 10623, Germany.

[2] Research Group on Modelling and Control (GIMOC), University of Antioquia, Colombia

Keywords: Bio-ethanol process, direct optimizing control, NMPC.
Topic: Systematic methods and tools for managing the complexity.

Abstract

In this work, the integration of real-time optimization and control for optimal operation of a continuous bio-ethanol process is investigated, providing a first insight into a plantwide control methodology for bioprocess applications. The results obtained are compared to the open loop behavior of the process, showing the importance of incorporating an optimization-based control strategy to the traditional pH and temperature control.

1 Introduction

During the last years, significant improvements have been done in the bio-ethanol industry in order to make it economically more competitive. However, the economical feasibility of the bio-ethanol industry is still questioned, and therefore much effort should be oriented to the optimization and control of the process. In the same way, as argued by Engell (2007) for chemical processes, the purpose of control should be to achieve optimal process operation despite the presence of uncertainties. Thus, optimization and control are not considered anymore as isolated tasks but as tasks that should be combined in order to operate the chemical or biochemical process at maximal productivity, which is the real purpose of any production plant. In the last years, many works related to the real-time dynamic optimization of chemical processes coupling dynamic optimization and Nonlinear Model Predictive Control, have been reported in chemical process applications (Engell., 2007; Manenti and Rovaglio, 2007). However, to the authors' knowledge no applications on the bio-ethanol process taking into account more than one process unit have been presented. On the other hand, the problem of optimal process operation should be addressed from a plantwide perspective. Independently of the kind of process (chemical or biochemical), it is clear that the interactions between different operating units affect the dynamic behavior of the whole process (and therefore the productivity), and that in real operation these interactions cannot be neglected especially if the process contains recycle loops. Specifically for bioprocesses, optimal operation is a compromise between several facts: i) a proper environment for the microorganisms should be guaranteed; ii) the production of the main metabolite should be maximized; iii) inhibition factors should be avoided or minimized. In this work, the real-time dynamic optimization problem for the bio-ethanol process (including saccharification, fermentation, cells recycle and a first separation step) is addressed from two perspectives: direct finite horizon optimizing control (Engell, 2007) and dynamic optimization involving real time optimization coupled with NMPC (Kadam et al 2003).

2 Description of the Process

The process shown in Figure 1 corresponds to the so called extractive alcoholic fermentation studied by Costa et al (2001). The raw material entering into the process is liquefied starch, which is broken down into monosaccharides (glucose) by means of enzymatic action. The

* Corresponding author. Tel + 49-30-31426905. E-mail: ochoa@mailbox.tu-berlin.de

output stream of the saccharificator is fed into a fermentor in which ethanol production is carried out by the action of *Saccharomyces cerevisiae*. After the fermentation stage, stream F_4 is fed into a filter in which all the yeast are retained to be recycled into the fermentor through stream F_9. The yeast-free stream F_6 is mainly a mixture of starch, glucose, ethanol, water and some CO_2. This stream is fed into a flash vessel which operates under vacuum conditions to separate in the top a mixture of CO_2, ethanol and water. After that, the mixture is fed into a condenser in which all the remaining CO_2 is released. The condensate (F_{16}) is a mixture ethanol – water that is mixed with a portion of the liquid leaving the bottom of the flash resulting the stream F_{17}, which will be used as feed for the purification stage (distillation and molecular sieves).The process has been simulated using Simulink, assuming that pH, temperature and the liquid volumes on the tanks are regulated by means of internal control loops. Besides, it is considered that the dynamics on the yeast filter, the flash vessel and the condenser are much faster than the dynamics on the saccharification and fermentor tanks, and therefore they were simulated by using a steady state model. The saccharification and fermentation stages were modeled by unstructured non-linear dynamic models obtained from the corresponding mass balances for starch, glucose, enzymes, ethanol, cells, and CO_2.

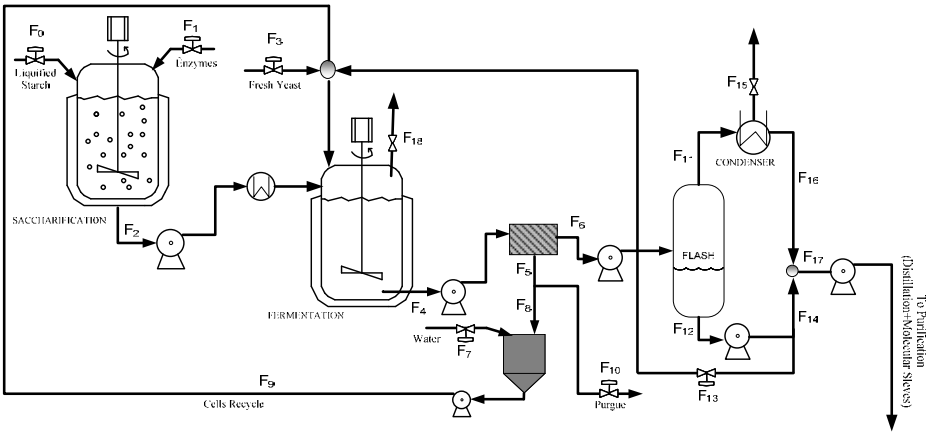

Figure 1. Bio-ethanol Process: Saccharification- Fermentation- Cells Recycle- First Purification step.

3 Optimization-based Control: Two-layer Integrated Dynamic Optimization and Control Vs Direct finite Horizon Dynamic Optimization

The challenge of controlling a plant for reaching optimal operation has been addressed from two main frameworks. The first one is the two-layer integrated optimization and control framework (two-layer approach) and the second corresponds to the direct optimizing framework (one-layer approach). Figure 2 shows the structure of these two approaches.

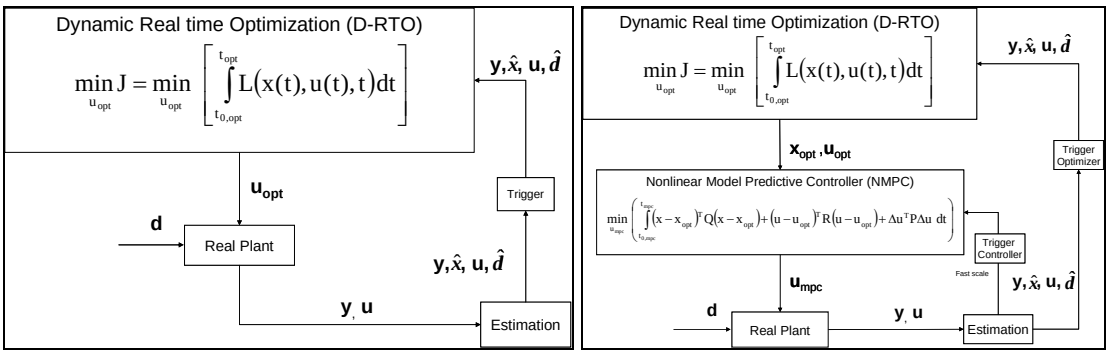

Figure 2. Dynamic Optimization based Control: One-layer (left) vs. Two-layer (right) approach.

As can be seen in Figure 2, the approaches have very much in common, actually the only different aspect is that in the one-layer approach, the input variables applied to the real plant (u_{opt}), are given by the optimization layer; whereas for the two-layer framework, the inputs applied to the real plant (u_{mpc}) are calculated by a control layer (usually containing a NMPC

controller); that uses as set points, the optimal values of the states given by the optimization layer (x_{opt}). In the following a description of each block presented in Figure 2 is given:

- D-RTO layer: This layer consists on a dynamic real time optimization problem in which the objective function is usually an economical function that should be maximized. The decision variables of the optimization problem are the manipulated variables (u_{opt}). Although the Bio-ethanol process shown in Figure 1 has six available manipulated variables (F_0, F_1, F_3, F_7, F_{10}, F_{13}) for controlling the plant, only three of these variables (F_0, F_1, F_{13}) are taken as decision variables during the optimization problem, because the remaining are used in an internal control loop proposed in Section 4.1.
- Real Plant: For the case of the bio-ethanol process considered in this paper, the real plant is the Simulink model mentioned before; in which the main disturbance (d) considered is the starch input concentration to the process (S_0).
- Estimation Block: In order to find the optimal operating point at each time, it is necessary to estimate the main state variables ($\hat{\boldsymbol{x}}$) that cannot be measured directly on the process; this can be done by using software sensors which employ the information of the available measurement variables (y). In this work, we assume that all the state variables and the disturbances ($\hat{\boldsymbol{d}}$) are known at every sample time during the process.
- Trigger: This block acts like a switch for re-calling the optimization layer. A trigger can work based on a time criteria (that means that the optimization is called periodically at a predetermined frequency) or based on the disturbance dynamics. A controller trigger is also used in the two-layer approach for re-calling the control-layer, whose re-calling frequency should be faster than that of the optimization-trigger. Due to the slow dynamics on the process, and after making a balance between performance and computational time, for the example presented in this work, it is used a re-calling frequency of 0.5h for the optimization-trigger and 0.2h for the controller-trigger.
- Control layer: This layer usually consists on a NMPC, in which the optimal values given by the optimization layer are used as set points for the controller. The NMPC solves an optimization problem, in which the objective function is usually composed of three terms: a penalization of the deviation of the main state variables from their set points (x_{opt}), a term that prevents large changes on the manipulated variables from one sample time to the next, and a term that constraints the manipulated variables to a small envelope around the reference trajectories (optimal values for the manipulated variables, u_{opt}, given by the optimization layer). In the present work, the cost functional of the NMPC considers the deviation of the ethanol concentration in the fermentor (E_4) from its optimal value calculated by the optimization layer ($E_{4,opt}$), and a penalization term for avoiding large changes between each sample time and the next.

$$\min_{\boldsymbol{u}_{opt}} J = \min_{\boldsymbol{u}_{opt}} \left[\Phi\left(\boldsymbol{x}(t_{opt})\right) + \int_{t_{0,opt}}^{t_{opt}} L\left(\boldsymbol{x}(t), \boldsymbol{u}(t), t\right) dt \right]$$

Subject to:

$$0 = \boldsymbol{f}_{opt}(\dot{\boldsymbol{x}}_{opt}(t), \boldsymbol{x}_{opt}, \boldsymbol{u}_{opt}(t), \hat{\boldsymbol{d}})$$

$$\boldsymbol{x}(t_{0,opt}) = \hat{\boldsymbol{x}}_{0,opt}$$

$$\boldsymbol{g}(\boldsymbol{x}_{opt}(t), \boldsymbol{u}_{opt}(t), \hat{\boldsymbol{d}}) = 0$$

$$\boldsymbol{h}(\boldsymbol{x}_{opt}(t), \boldsymbol{u}_{opt}(t), \hat{\boldsymbol{d}}) \le 0$$

$$x^{l} \le x_{opt}(t) \le x^{U}$$

$$\boldsymbol{u}^{l} \le \boldsymbol{u}_{opt}(t) \le \boldsymbol{u}^{U}$$

$$\min_{u_{mpc}} J_{NMPC} = \min_{u_{mpc}} \left(\int_{t_{0,mpc}}^{t_{mpc}} \left(x - x_{opt}\right)^{T} Q \left(x - x_{opt}\right) + \left(u - u_{opt}\right)^{T} R \left(u - u_{opt}\right) + \Delta u^{T} P \Delta u \, dt \right)$$

Subject to:

$$0 = \boldsymbol{f}_{mpc}(\dot{\boldsymbol{x}}_{mpc}(t), \boldsymbol{x}_{mpc}, \boldsymbol{u}_{mpc}(t), \hat{\boldsymbol{d}})$$

$$\boldsymbol{x}(t_{0,mpc}) = \hat{\boldsymbol{x}}_{0,mpc}$$

$$\boldsymbol{g}(\boldsymbol{x}_{mpc}(t), \boldsymbol{u}_{mpc}(t), \hat{\boldsymbol{d}}) = 0$$

$$\boldsymbol{h}(\boldsymbol{x}(t), \boldsymbol{u}_{mpc}(t), \hat{\boldsymbol{d}}) \le 0$$

$$\boldsymbol{x}^{l} \le \boldsymbol{x}_{mpc}(t) \le \boldsymbol{x}^{U}$$

$$\boldsymbol{u}^{l} \le \boldsymbol{u}_{mpc}(t) \le \boldsymbol{u}^{U}$$

Figure 3. Mathematical statement of the Optimization layer (left) and the Control layer (right).

Figure 3 shows the general formulation of the optimization and control layer problems, where f_{opt} and f_{mpc} represent the nonlinear process models used in the optimization and control layers respectively. The objective function used in the D-RTO problem is composed of the Mayer term (Φ) which is related to the state of the process at the final time and the Lagrange term (L) which represents an economical function related to the dynamic behaviour of the state variables during the transition from the initial optimization time ($t_{0,opt}$) to the final optimization time (t_{opt}); whereas g and h are the equality and inequality constraints of each optimization problem; and the super-indexes l and U indicate the lower and upper bounds for the states and manipulated variables. Basically, both layers (the optimization and the control

one) consist on a constraint nonlinear optimization problem, which differs mainly on the nature of the objective function, being an economic and a performance objective function for the D-RTO and the NMPC blocks respectively. Finally, the terms Q, R and P are weighting matrices of proper dimensions, which can be seen as tuning parameters for the NMPC.

4 Optimization-based Control for the Bio-ethanol process

The problem of controlling the bio-ethanol process for obtaining optimal operation at each sample time is addressed by applying the two frameworks described in Section 3. It is important to remark that the whole process has six available input variables that can be used as manipulated variables (control degrees of freedom). However, only three of them are taken as decision variables in the optimization layer, because the other three manipulated variables are used in an internal control loop. In this section, it will be first explained the mentioned internal control loops and after that, the results obtained by applying the one and two layer approaches (including the internal control loops) are presented and compared.

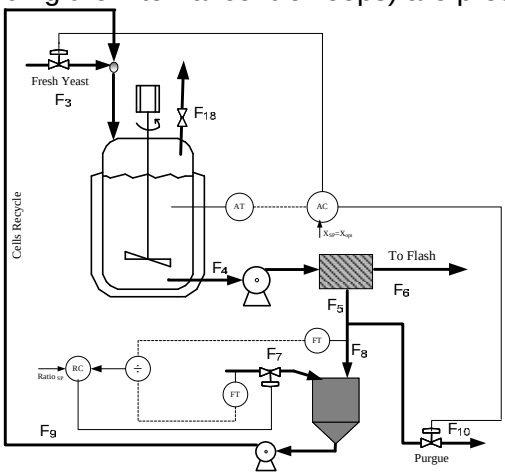

Figure 4. Internal Control loop for the Bio-ethanol Process.

4.1 Internal Control Loops for the Bio-ethanol Process

The internal loops proposed in this work comprise a split-range controller for keeping the biomass concentration in the fermentor at its optimal value and a ratio controller for achieving a suitable viscosity in the biomass recycle slurry. The biomass control loops proposed in this work are treated as independent because i) an optimal biomass concentration should be always guaranteed, in order to avoid a misuse of the substrate (which can be quickly consumed for cells maintenance and growth instead of metabolite production) if a higher concentration than the optimal is available; also, if the biomass concentration is below the optimal, a slower metabolite production rate will occur, affecting the productivity of the process; and ii) the yeast is only involved in the fermentation, filter and cells recycle loop. Figure 4 shows the proposed control loops in which the set point for the biomass in the fermentor (X_{opt}) comes from the optimization layer (tracking control); whereas the set point for the ratio controller (fixed set-point) was calculated following the suggestions given by Maiorella et al (1983), for achieving a suitable viscosity in the biomass recycle slurry.

4.2 Two-layer vs. One-layer Optimizing Control for the Bio-ethanol process

The dynamic optimization problem for both approaches was solved by the direct sequential approach using the Metropolis Monte Carlo-simulated annealing optimization method as presented in Ochoa et al (2007). The process begins at steady state. At time t=5h, a step disturbance on the starch feed concentration occurs (20% reduction). At the same time the optimization layer is called, which calculates the values of the manipulated variables that maximize the following objective function (which only considers the Lagrange term):

$$J_{opt} = w_1 \int_t^{t+\Delta t} E_{17} F_{17} dt - w_2 \int_t^{t+\Delta t} F_0 S_0 dt - w_3 \int_t^{t+\Delta t} F_4 dt + w_4 \int_t^{t+\Delta t} E_4 dt \quad (1)$$

The first term in (1) represents the productivity of the process, the second term penalizes the consumption of raw material, the third term penalizes the energy consumption and the last term incorporates a quality constraint as soft constraint, and Δt is the optimization interval. As previously mentioned, in the one-layer approach, the manipulated variables calculated for the optimization layer are directly applied to the process, and the optimization layer is recalled every 0.5 hours (trigger), in the meanwhile the process kept the manipulated variables at the optimal values given by the last optimization routine. In contrast, in the two-layer framework the optimal values for the manipulated variables are used into the model of the process for calculating the corresponding values for the state variables (i.e. $E_{4,opt}$ which is the "optimal" value for the ethanol concentration in the fermentor); this information is sent to the control layer for minimizing the objective function given by (2). The solution of the optimization problem for the NMPC (optimal values for the manipulated variables F_0, F_1, and F_{13} that minimizes (2) is applied to the process, and the control layer is recalled every 0.2h.

$$J_{NMPC} = \int_{t_{0,mpc}}^{t_{mpc}} Q(E_4 - E_{4,opt})^2 dt + \int_{t_{0,mpc}}^{t_{mpc}} P\,\Delta F_0^{\,2} dt \qquad (2)$$

Figure 5 compares the results of the one and two-layer approaches to the open loop policy. All three frameworks were run considering the biomass internal control loops proposed in Section 4.1 by using a proportional control law (biomass set point was given by the optimization layer in the first two cases, whereas for the open loop case, the set point was the initial steady state). As shown in Figure 5, the one and two-layer approaches have good response to the disturbance, maintaining the ethanol concentration in a higher value when compared to the open loop policy, in which a fast decrease in the ethanol concentration took place. This behaviour can be explained after a careful analysis of biomass dynamics. In the open loop case, in which no optimization was carried out after the disturbance, the biomass was kept in a high value (close to its original steady state), which resulted in a high cells' population using most of the glucose for maintenance and growing tasks (primary cell's tasks) instead of ethanol production. In contrast, the one and two-layer frameworks kept the biomass concentration at a lower value, consuming less substrate in maintenance and growth and reaching a suitable condition leading to higher ethanol concentrations.

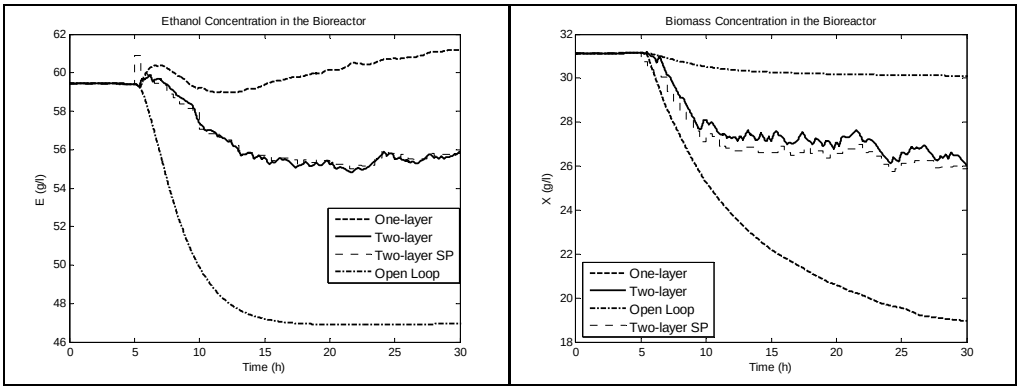

Figure 5. Results one-layer v.s. two-layer: Ethanol (left) and Biomass (right)

On the other hand, the ethanol concentration obtained with the one-layer approach was higher than that obtained with the two-layer during the whole process. To explain this fact, it is necessary to analyze the starch input flow (F_0, main manipulated variable) profiles applied to the process in both cases (Fig. 6). After the disturbance, the first action of the NMPC controller, trying to track the ethanol set point given by the optimization layer, was to reduce F_0 leading to an increase in ethanol concentration in the bioreactor due to a reduced dilution effect. However, by doing this, the process was driven to a condition of less substrate availability and consequently to lower ethanol production compared to the one-layer approach, which increased F_0 after the disturbance. After this short but relevant difference in starch feeding profile, the optimal operation profiles of the state variables in the process (e.g. ethanol and biomass) became completely different for both approaches.

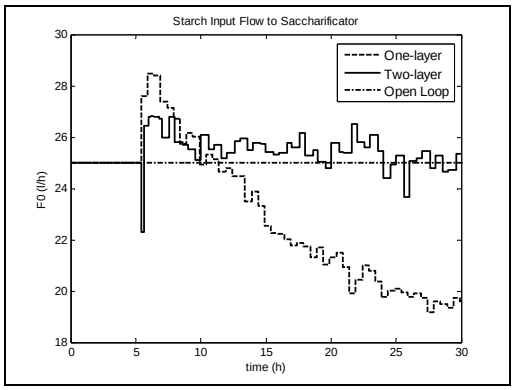

Figure 6. Results one-layer vs. two-layer: Starch Input Flow

At this point some important remarks should be done. First, the success of the one-layer approach depends strongly on the accuracy of the model used on the optimization-layer. Second, the one-layer approach has a certain “dead period” (0.5 h in this case) in which the control system does not have any feedback from the real process measurements. If a disturbance takes place during this “dead period”, it may drive the process to a condition of poor performance, and this will not be corrected until the following optimization task is triggered. In this sense, the two-layer approach seems to be a better choice because the NMPC-layer (which uses a simpler model of the process) acts in a feedback fashion more frequently than the optimization-layer. However, as can be seen in the bio-ethanol example, the objective function of the NMPC-layer is more a performance-type objective than a productivity one, and thus, it is possible that the results obtained are optimal in terms of tracking control but not in terms of productivity. Therefore, much effort should be oriented to the development of a two-layer strategy in which the NMPC takes into account the productivity of the whole process and not only the tracking of a set of variables.

Conclusion

The results presented in this work, demonstrate that the integration of optimization and control in a real-time framework is a very promising approach for achieving optimal operation (higher productivity, good disturbance rejection, increased profit, etc.) in bioprocesses from a plantwide control perspective. The two-layer and one-layer approaches were applied to the bioethanol process combining the use of two internal control loops for tracking the optimal biomass concentration. In a further study, optimization-control integration will be applied to the complete bioethanol process (including distillation and adsorption). Finally, it is important to highlight that there is a need of controlling the process for tracking the optimal operating conditions that lead to maximum productivity, instead of maintaining a predefined operating point calculated by using a steady state model of the process under nominal conditions.

References

Costa, A.C., Atala, D.I.P., Maugeri, F., Maciel, R. (2001). Factorial design and simulation for the optimization and determination of control structures for an extractive alcoholic fermentation. *Process Biochemistry*., 37, 125–137.

Engell, S. (2007). Feedback control for optimal process operation. *Journal of Process Control*, 17, 203-219.

Kadam, J.V., Marquardt, W., Schelegel, M., Backx, T., Bosgra, O.H., Brouwer, P.J., Dünnebier, G., van Hessem, D., Tiagounov, A., de Wolf, S. (2003). Towards integrated dynamic real-time optimization and control. *FOCAPO conference proceedings.*, 593-596.

Maiorella, B.L., Blanch, H.W., Wilke, C.R. (1983). Economic evaluation of alternative ethanol fermentation processes. *Biotechnology and Bioengineering*., 26, 1003-1025.

Manenti, F., Rovaglio, M. (2007). Integrated multilevel optimization in large-scale Poly(ethylene therepthalate) Plants. *Ind. Eng. Chem. Res*, 47, 92-104.

Ochoa, S., Yoo, A., Repke, J-U., Wozny, G., Yang, D.R. (2007). Modeling and parameter identification of the simultaneous saccharification-fermentation process for ethanol production, *Biotechnol. Prog*., 23, 1454-1462.

Proceedings of the 10th International Chemical and
Biological Engineering Conference - CHEMPOR 2008
Braga, Portugal, September 4-6, 2008
E.C. Ferreira and M. Mota (Eds.)

On-Line Adaptive Metabolic Flux Analysis: Application to PHB Production by Mixed Microbial Cultures

João Dias, Filipa Pardelha, Mário Eusébio, Maria A.M. Reis, Rui Oliveira*
[1] CQFB/REQUIMTE, Chemistry Department, FCT/Universidade Nova de Lisboa, 2829-516 Caparica, Portugal

Keywords: Metabolic flux analysis, on-line, adaptive, polyhydroxybutyrate, mixed microbial cultures
Topic: Systematic methods and tools for managing the complexity

Abstract
In this work, an on-line adaptive metabolic flux analysis (MFA) algorithm was developed and applied to the polyhydroxybutyrate (PHB) production by mixed microbial cultures (MMC). In MMC the main source of perturbation is the population dynamics which may cause variability in the energetic and stoichiometric parameters and therefore in the metabolic fluxes. An observer-based estimator (OBE) applied to the central MFA equation was proposed to solve this problem. The role of the OBE was to adjust the values of the unknown parameters such that the concentrations of the intracellular metabolites were forced to converge to zero. The estimator was implemented to the PHB process operated in a sequencing batch reactor (SBR) equipped with the on-line respirometric and titrimetric analysis. The O_2 and CO_2 fluxes were estimated directly through the experimental data. The macroscopic fluxes of acetate, PHB and sludge production was estimated through the on-line measurements and a projection of latent structures (PLS) model constrained by the carbon balance previously validated with off-line data. The proposed algorithm proved to converge exponentially with errors of the metabolites concentration always below 1 mmol/l by adjusting on-line the network parameters associated to biosynthesis. The estimates of the unknown fluxes passed the consistency index test for experimental error as low as 1%.

Introduction
Metabolic Flux Analysis (MFA) is a technique that uses data of some measured fluxes, normally substrate uptake and end-product formation rates, to determine the unknown fluxes of a metabolic network. The calculations required to this analysis are based on the pseudo-steady-state hypothesis to intracellular metabolites (Stephanopoulos et al, 1998). One of the several applications of MFA in metabolic engineering is the on-line estimation of the flux distribution of cells cultivated in bioreactors (Kim et al, 2008; Zhang et al, 2005).

In present work, on-line MFA is applied to polyhydroxybutyrate (PHB) production by mixed microbial cultures (MMC). The metabolic network adopted in this work was previously described (Dias et al, 2005). The main challenge in the MMC process control is the time-varying population composition which indirectly causes dynamics in the metabolic network. Same examples of this dynamic behavior are the undesired production of extracellular polymeric substances (EPS) (Dias et al., 2008a) and the oxidative phosphorylation efficiency (P/O ratio) oscillations that may occur over culture selection process (Dias et al., 2008b).

To deal with the time-variability of the metabolic network parameters, an on-line adaptive algorithm is proposed. The algorithm is based on the application of the observer-based estimator (OBE) (Bastin and Dochain, 1990; Oliveira et al., 2002) to the central MFA equation, whereby the role of the OBE is to force the concentrations of intracellular metabolites to converge to zero by adjusting the values of unknown parameters. The consistency of the on-line adaptive metabolic flux distribution (MFD) calculations was verified through the Chi-squared (X^2) test (Wang and Stephanopoulos, 1983).

* Corresponding author. Tel +351-21-2947804. E-mail: rui.oliveira@dq.fct.unl.pt

Materials and Methods

Experimental set-up and culture conditions

The set of 4 experiments were performed in a Sequencing Batch Reactor (SBR) with a working volume of 1.5 l controlled by a BIOSTAT B unit (Sartorius Biotech). Several probes were connected to the reactor in order to measure on-line temperature, pH, dissolved O_2 and dissolved CO_2. The reactor inlet and outlet gas flow was measured with mass flowmeters and the outlet gas composition in O_2 and CO_2 was detected by a gas analyzer. An analytical balance was used to monitor the weight of the acid solution used to control the reactor pH during the SBR experiments. The SBR cycles and operational conditions are summarized in Table 1.

Table 1- SBR cycles and operational conditions

SBR cycles conditions			
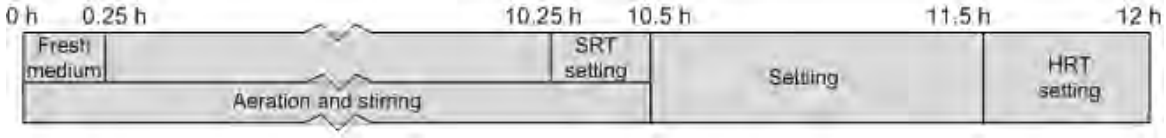			
Operating conditions			
Hydraulic Retention Time (HRT) (h)	24	Aeration rate (ml/min)	400
Sludge Retention Time (SRT) (d)	10	Stirrer speed (RPM)	600
Temperature (ºC)	24		

Metabolic network and metabolic constraints

The metabolic network adopted for the PHB and EPS production can be described by a set of six metabolic reactions (expressed in a carbon-mole basis) which are compiled in Table 2:

Table 2- Metabolic model for PHB and EPS production by mixed microbial cultures

Acetate uptake (R_{Ac})
$CH_2O + ATP \rightarrow CHO_{0.5} + 0.5 \cdot H_2O$
Biomass growth and EPS synthesis (R_{EPS+X})
$Y_{Ac-CoA/(EPS+X)} \cdot CHO_{0.5} + Y_{N/(EPS+X)} \cdot NH_3 + K_{EPS+X} \cdot ATP \rightarrow (EPS + X) + \left(Y_{Ac-CoA/(EPS+X)} - 1 \right) \cdot CO_2$
Catabolism (R_3)
$CHO_{0.5} + 1.5 \cdot H_2O \rightarrow CO_2 + 2 \cdot NADH_2 + 0.5 \cdot ATP$
PHB production (R_{PHB})
$CHO_{0.5} + 0.25 \cdot NADH_2 \rightarrow CH_{1.5}O_{0.5}$
Maintenance (R_5)
$ATP \rightarrow m_{ATP}$
Oxidative phosphorylation (R_6)
$NADH_2 + 0.5 \cdot O_2 \rightarrow H_2O + \delta \cdot ATP$

Additionally to these reactions, R_{CO2} and R_{O2} were defined as fluxes and the steady-state balances of intracellular metabolites (Ac-CoA and ATP), redox, oxygen and total carbon were derived as metabolic constraints. Therefore, to calculate all network fluxes at least three fluxes has to be measure on-line.

In this study five fluxes were available on-line. R_{CO2} and R_{O2} were provided by on-line measurements while the on-line estimation of acetate, PHB, sludge concentration and their respective fluxes were obtained by a projection of latent variables (PLS) model constrained by the carbon balance (Dias et al, 2008a).

On-line adaptive MFA implementation

The central MFA equation was defined as $\mathbf{0} = \mathbf{A} \cdot \mathbf{v}$, where **A** is the stoichiometric coefficients matrix of the metabolic reactions and **v** the vector of fluxes.

The matrix **A** was derived as a function of the time-varying parameters and split into the matrix $\mathbf{A_b}$ and $\mathbf{A_n}$ for the subset of known ($\mathbf{v_b}$) and unknown ($\mathbf{v_n}$) metabolic fluxes. To solve the system, an adaptive MFA system was developed by applying an observer-based estimator (Bastin and Dochain, 1990) to the central MFA equation. The system involves a vector of intracellular concentrations ($\mathbf{c_i}$), the matrices described above, a vector of unknown time-varying parameters ($\boldsymbol{\theta}$) and tuning matrices $\boldsymbol{\Omega}$ and $\boldsymbol{\Gamma}$. The tuning parameters were defined to control the stability and the speed of convergence and were defined according to the rules proposed by Oliveira et al. (2002). The on-line adaptive MFA system is defined as follows:

$$\frac{d\Delta\mathbf{c}_i}{dt} = \mathbf{A_b}(\boldsymbol{\theta}) \cdot \mathbf{v_b} + \mathbf{A_n}(\boldsymbol{\theta}) \cdot \mathbf{v_n} + \boldsymbol{\Omega} \cdot \left(\mathbf{0} - \Delta\mathbf{c_i}\right)$$

$$\frac{d\boldsymbol{\theta}}{dt} = \boldsymbol{\Gamma} \cdot \left(\mathbf{0} - \Delta\mathbf{c_i}\right)$$

$$\mathbf{v_n} = -\mathbf{A_n^{\#}}(\boldsymbol{\theta}) \cdot \mathbf{A_b}(\boldsymbol{\theta}) \cdot \mathbf{v_b}$$

This problem was implemented in a MATLAB™ program. The matrix **A** and **v** were derived according to ATP, Ac-CoA, redox, O_2 and carbon balances.

$$v_b = \left[R_{CO_2}, R_{O_c}, R_{PHB}, R_{EPS+X}, R_{m_{ATP}}\right]^T;\ v_n = \left[R_{Ac}, R_4, R_6\right]^T$$

$$A_n = \begin{bmatrix} 0 & 0 & -Y_{Ac-CoA/(EPS+X)} & -1 & 0 \\ -\sigma_2 & 0 & \sigma_{EPS+X} & \sigma_{PHB} & 0 \\ 0 & 0 & -K_{EPS+X} & 0 & -1 \\ 0 & -1 & -1 & -1 & 0 \\ -2 & 0 & 0 & 0 & 0 \end{bmatrix};\ A_b = \begin{bmatrix} 1 & -1 & 0 \\ -\sigma_{Ac} & 0 & 0 \\ -1 & 0.5 & \delta \\ 1 & 0 & 0 \\ 0 & 0 & 1 \end{bmatrix}$$

The matrix $\boldsymbol{\theta}$ comprises the unknown parameters related to the biomass and EPS biosynthesis:

$$\theta = \begin{bmatrix} Y_{Ac-CoA/(EPS+X)} & \sigma_{EPS+X} & K_{EPS+X} \end{bmatrix}^T$$

The tuning matrices $\boldsymbol{\Omega}$ and $\boldsymbol{\Gamma}$ contain $\boldsymbol{\zeta}$ and $\boldsymbol{\tau}$, which are the natural periods of oscillation and damping coefficients of the desired second order dynamical response, respectively, were defined as following:

$$\Omega = diag\left(2 \cdot \frac{\zeta}{\tau}\right) \text{ with } \dim(\Omega) = 4;\ \Gamma = \frac{1}{\tau^2} \cdot \begin{bmatrix} -\frac{1}{R_{EPS+X}} & 0 & 0 & 0 & 0 \\ 0 & -\frac{1}{R_{EPS+X}} & 0 & 0 & 0 \\ 0 & 0 & -\frac{1}{R_{EPS+X}} & 0 & 0 \end{bmatrix} \cdot e$$

The consistency of the measured fluxes was checked through the consistency index method (Wang and Stephanopoulos, 1983) whenever the MFA system is redundant. The redundancy matrix, $\mathbf{R} = \mathbf{A_b} - \mathbf{A_n} \cdot \mathbf{A_n^{\#}} \cdot \mathbf{A_b}$, was calculated for this propose. When $\mathbf{v_b}$ is fully consistent with the network stoichiometry and devoid of error, the equation $\mathbf{0} = \mathbf{R} \cdot \mathbf{v_b}$ is verified.

In this study, the equation $\mathbf{0} = \mathbf{R} \cdot \mathbf{v_b}$ is equivalent to the steady-state balance $\mathbf{e} = (0 - c_i)$. In general, this relation is not obeyed and the consistency index test, **h**, has to be performed. The index (**h**) is a statistical chi-squared (χ^2) test and was calculated using the following set of equations:

$$\mathbf{e} = -\mathbf{R} \cdot \mathbf{v_b};\ \mathbf{Y} = \mathbf{R} \cdot \mathbf{Y_b} \cdot \mathbf{R}^{\mathbf{T}};\ h = \mathbf{e}^{\mathbf{T}} \cdot \mathbf{Y}^{-1} \cdot \mathbf{e}$$

where **e** is the deviation from zero of $\mathbf{0} = \mathbf{R} \cdot \mathbf{v_b}$ and **Y** the variance-covariance matrix of the metabolic fluxes, **v**, calculated by the propagation of **Y** associated to the measured fluxes, $\mathbf{Y_b}$. The number of degrees of freedom required to choose the χ^2 value is given by the difference between the number of metabolic constraints (5) and the number of unknown fluxes (3). The network consistency fails whenever h > χ^2.

Results and discussion

Direct and indirect measurements used for on-line MFA

The cumulative fluxes of O_2 and CO_2 (R_{O2}, R_{CO2}) were measured directly through respirometry, while PHB and EPS+X fluxes (R_{PHB}, R_{EPS+X}) were estimated indirectly through a PLS model calibrated a priori with the off-line measurements (see Dias et al., 2008a, for details). The maintenance flux for acetate (R_5) was assumed to be known [m_{ATP} = 0.02 mol-ATP/(C-mol.h) (Beun et al., 2002)] and calculated by integrating the theoretical maintenance coefficient obtained by the material and energetic balances of intermediates (Dias et al., 2008b). Figure 1 shows schematically the metabolic network of the PHB production process while in Table 3 are presented the fluxes for R_{O2}, R_{CO2}, R_{PHB}, R_{EPS+X} and R_5 at five different process phases of one SBR experiment.

On-line estimation of the unknown metabolic parameters

The estimation of σ_{EPS+X}, $Y_{Ac-CoA/(EPS+X)}$ and K_{EPS+X} was carried out assuming full knowledge of the remaing metabolic parameters. The oxidative phosphorylation efficiency, δ, was set at 3 mol-ATP/mol-$NADH_2$ (Dias et al., 2008b), while the convergence to unrealistic values of the unknown parameters was prevented by keeping them within biological limits. The estimates of the metabolic parameters presented a high variability within and between the four SBR experiments. The short-term variability was caused by the shift between biomass synthesis and EPS production, while the long-term variability may be explained by the population dynamics. Table 3 compiles the results obtained for these parameters for 5 different process phases.

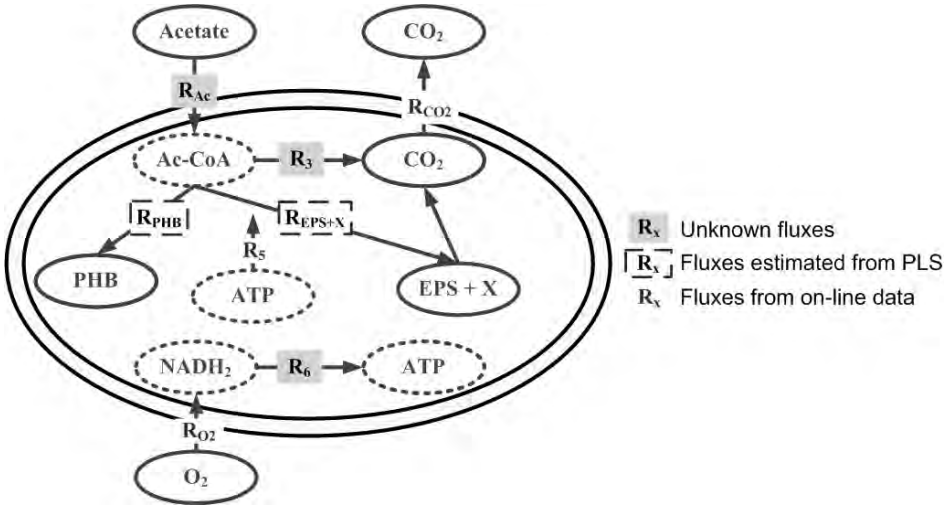

Figure 1 – Metabolic network of PHB and EPS plus biomass production process by MMC.

Table 3 – Values of cumulative fluxes, estimated (Est), expected or experimental (Exp) at five phases of one SBR experiment. Unknown time-varying parameters, consistency index and maximum (0-Δc_i) are also presented at the same SBR phases.

t (h)	R_{Ac}		R_3		R_6		R_{CO2}	R_5	R_{O2}
	Est	Exp	Est	Exp	Est	Exp			
0.00	100.49	100.49	0.00	0.00	0.00	0.00	0.00	0.00	0.00
0.25	69.06	74.05	2.94	3.84	2.59	3.97	1.58	0.39	3.51
0.50	45.01	50.14	8.31	6.61	13.62	13.58	7.11	0.78	12.79
0.75	20.90	26.07	10.87	9.36	24.95	23.91	12.76	1.17	18.07
1.00	0.00	1.90	13.07	13.08	36.00	34.04	18.56	1.59	21.67

t (h)	R_{EPS+X}		R_{PHB}		$Y_{Ac\text{-}CoA/(EPS+X)}$	σ_{EPS+X}	K_{EPS+X}	h	max(0-Δc_i)
	Est	Exp	Est	Exp					
0.00	0.00	0.00	36.45	5.43	1.00	4.50	1.70	0.00	0.00
0.25	27.40	-0.97	37.01	-1.77	1.04	3.91	0.08	0.00	0.08
0.50	32.29	-7.65	46.51	1.92	1.39	3.72	0.78	0.12	0.22
0.75	42.04	-4.26	56.42	-0.90	1.24	3.37	0.48	4.53	0.08
1.00	52.97	-6.94	65.98	0.88	1.06	3.42	0.11	1.55	0.10

Metabolic fluxes

The unknown fluxes R_{Ac}, R_3 and R_6 included in matrix $\mathbf{v_b}$ were estimated and compared with their calculated and experimental values. The expected flux for R_{Ac} and R_6 were obtained directly from acetate and O_2 measurements while the expected R_3 was estimated through the carbon balance and the previous estimate of $Y_{Ac-CoA/(EPS+X)}$. The results obtained for 5 different SBR phases are presented in Table 3. In general, for all SBR experiments a good agreement between the expected and estimated fluxes were observed. Nevertheless, the cumulative $NADH_2$ in R_6 presented some no systematic variations which may be explained by the unknown ATP and redox balances or by time-varying P/O ratio. The introduction of additional metabolic constraints, not accounted by the model, has to be investigated in the future to enhance these last results.

Consistency analysis of the metabolic network

The consistency index test, **h**, was performed for all on-line samples assuming experimental errors below 1 %. The χ^2 coefficient was calculated for 95 % of confidence level and 2 degrees of freedom (number of redundant equations). Under these conditions, in nearly all samples, the estimated fluxes passed the χ^2 distribution test. The higher values for **h**, caused by the deviation from zero of the intracellular concentrations, were mainly due to the transition between the cell growth and EPS metabolism.

Conclusions

The main bottleneck of metabolic flux analysis in bioprocesses is the lack of information in metabolites balances, such as of ATP and $NADH_2$. In the PHB production process by MMC, there is two additional sources of uncertainty, namely the time-varying metabolic network, due to the population dynamics, and the lack of metabolic pathways for the EPS production. In this work, an algorithm that applies an observer-based estimator to central MFA equation was derived and validated for 4 SBR experiments. The algorithm showed an exponential convergence with residual intracellular concentrations always below 1 mmol/l. The consistency index, **h**, was also checked and passed in nearly all samples the χ^2 distribution test for experimental errors as low as 1 %. The ability of the algorithm to identify the shift

between biomass synthesis and EPS production demonstrated that its application for on-line monitoring and control of other biological systems may be very promising.

References

Bastin G., Dochain D. (1990). *On-line Estimation and Adaptive Control of Bioreactors*, Elsevier, Amsterdam.

Beun J.J., Dircks K., van Loosdrecht M.C.M., Heijen J.J. (2002). *Poly-beta-hydroxybutyrate metabolism in dynamically fed mixed microbial cultures*. Water Research, 36(5), 1167-1180.

Dias J.M.L., Pardelha F., Eusébio M., Reis M.A.M., Oliveira R. (2008a). *On-line monitoring of PHB production by mixed microbial cultures using respirometry, titrimetry and chemometric modelling*, Process Biochemistry, Submitted.

Dias J.M.L., Oehmen A., Serafim L.S., Lemos P.C., Reis M.A.M., Oliveira R. (2008b).*Metabolic modelling of polyhydroxyalkanoate copolymers production by mixed microbial cultures*, BMC Systems Biology, Submitted.

Dias J.M.L., Serafim L.S., Lemos P.C., Reis M.A.M., Oliveira R. (2005). *Mathematical modelling of a mixed culture cultivation process for the production of polyhydroxybutyrate*, Biotechnology and Bioengineering, 92(2), 209-222.

Kim H.U., Kim T.Y., Lee S.Y. (2008). *Metabolic flux analysis and metabolic engineering of microorganisms*. Molecular Biosystems, 4(2), 113-120.

Oliveira R., Ferreira E.C., de Azevedo S.F. (2002). *Stability, dynamics of convergence and tuning of observer-based kinetics estimators*, Journal of Process Control, 12(2), 311-323.

Stephanopoulos G.N., Aristidou A.A., Nielsen J. (1998). *Metabolic Engineering: Principles and Methodologies*, Academic Press, San Diego.

Wang N.S., Stephanopoulos G. (1983). *Application of Macroscopic Balances to the Identification of Gross Measurement Errors*, Biotechnology and Bioengineering, 25(9), 2177-2208.

Zhang C.Y., Shi Z.P., Gao P., Duan Z.Y., Mao Z.G. (2005). *On-line prediction of products concentrations in glutamate fermentation using metabolic network model and linear programming.* Biochemical Engineering Journal, 25(2), 99-108.

Proceedings of the 10th International Chemical and
Biological Engineering Conference - CHEMPOR 2008
Braga, Portugal, September 4-6, 2008
E.C. Ferreira and M. Mota (Eds.)

Modelling of Membrane Bioreactors for Wastewater Treatment Incorporating 2D-Fluorescence Monitoring Data

Claudia F. Galinha[1], Carla Portugal[1,2], Gilda Carvalho[1,3], Giuseppe Guglielmi[4], Daniele Chiarani[4], Gianni Andreottola[4], Rui Oliveira[1], Maria A. M. Reis[1], João G. Crespo[1*]

[1] REQUIMTE/CQFB, Chemistry Dept., FCT, Universidade Nova de Lisboa, Campus da Caparica, 2829-516 Caparica, Portugal.

[2] CEBAL, Centro de Biotecnologia do Alentejo, R. Pedro Soares, Apt. 6158, 7801-908 Beja, Portugal.

[3] IBET/ITQB, Apartado 12, 2781-901 Oeiras, Portugal

[4]Department of Civil and Environmental Engineering, University of Trento, Via Mesiano, 77, 38050 Trento, Italy

Keywords: Membrane Bioreactor (MBR), Modelling, PLS, 2D-fluorescence
Topic: Systematic methods and tools for managing the complexity

Abstract

In this work two membrane bioreactor (MBR) systems for wastewater treatment are monitored using 2D-fluorescence spectroscopy as fingerprints of the system status. Fluorescence maps can be correlated with the operational parameters using non-mechanistic methods, such as principal component analysis (PCA) and projection to latent structures (PLS), for performance monitoring and process optimisation. The 2D-fluorescence was used as a tool for monitoring MBR performance. It was found that the combination of the 2D-fluorescence data with selected performance variables capture additional information about the biological system state and substantially enhances MBR modelling and performance prediction.

1 Introduction

Membrane bioreactors are widely applied for wastewater treatment. However, the progressive membrane fouling due to deposition of cells and cell products on the membranes reduces the permeability of the system, resulting in substantial maintenance costs and shortening membrane life span. The major biofouling agents in MBRs are Extracellular Polymeric Substances (EPS), and thus EPS monitoring and control in MBR operation is essential. EPS contain large amounts of proteins and aromatic organic substances that possess natural fluorescence properties, making fluorescence a powerful technique to monitor their production in MBRs.

2D-fluorescence spectroscopy is a highly sensitive, selective and non-invasive technique that can provide rapid information about the composition of complex media such as biological systems. Due to the fact that all organisms contain natural intracellular fluorophores, such as aminoacids (e.g. tyrosine and tryptophan), vitamins, coenzymes and aromatic organic matter in general, fluorescence is a technique suitable to be used in bioprocess monitoring. Furthermore, since this technique is non-invasive, it can be used in situ and on-line without disturbing the biological system. The excitation-emission matrices (EEMs) obtained by scanning the spectra wavelengths can cover a wide diversity of natural fluorophores. The maps obtained from the EEMs can thus correspond to a fingerprint of the physiological status of a biological system.

The richness and complexity of information contained in EEMs should be taken into account when interpreting fluorescence results. Fluorescence fingerprints not only combine

* Corresponding author. Tel + 351-21-294-83-85. E-mail:jgc@dq.fct.unl.pt

physiological patterns of different microorganisms, but also reflect the variation in concentration of some substrate components and microbial by-products which possess fluorescence properties. In addition, some molecules can act as quenchers to fluorescence, by interacting with the excited fluorophores, resulting in alterations of fluorescence signal. Therefore, it is necessary to deconvolute the contextual information contained in the fluorescence maps. Using chemometrics, EEMs can be correlated with key operational and performance parameters of the studied system. When using chemometric modelling techniques, fluorescence spectra are viewed as multivariate descriptors of performance parameters and treated with statistical approaches such as Principal Component Analysis (PCA) and Projection to Latent Structures (PLS). The statistical models are obtained by this approach using on-line fluorescence maps and their corresponding process performance parameters measured for different operating conditions. Through these calibrated models, the EEMs obtained on-line can be used to monitor the status of the process, as well as for prediction, allowing rapid correction of operational parameters for process optimisation.

Fluorescence spectroscopy was previously applied for on-line monitoring of an extractive MBR for degradation of volatile organic compounds in aqueous media (Wolf et al., 2001). The biofilm formed at the membrane surface was monitored in situ using an optical fibre cable for delivering excitation light and capturing emission light. The EEMs obtained were analysed together with operational parameters using artificial neural networks (ANN) for system monitoring and modelling. 2D-scanning fluorometry together with ANN, as a nonlinear and non-mechanistic technique for deconvoluting fluorescence information, proved to be suitable for monitoring this complex biosystem.

In the present study, 2D-fluorescence is applied to monitor two pilot scale MBRs for domestic wastewater treatment, by measuring EEMs of the influent wastewater, the bioreactor mixed liquor and the permeate. The fluorescence maps obtained as fingerprints of the system are correlated with operating and performance parameters using PLS to create models able to predict the selected performance variables.

2 Methodology

In the current work 2D-fluorescence is applied to monitor a pilot scale MBR for domestic wastewater treatment located in a Wastewater Treatment Plant (Lavis, Italy) and a lab MBR in Caparica, Portugal, also with municipal wastewater. Both MBR systems consist in submerged hollow-fibre membranes immersed in a complex matrix containing suspended activated sludge and several products resulting from wastewater feeding and microbial activity, as well as biofilms attached to the membranes.

Fluorescence EEMs are measured in the wastewater feed, in the mixed liquor and in the permeate at the same time that samples are collected for further analysis of wastewater and mixed liquor (chemical oxygen demand (COD), nitrogen and suspended solids). Also transmembrane pressure (TMP), temperature and dissolved oxygen (DO) are measured on-line. All these data collected together with the operating parameters – imposed permeate flux (J), hydraulic retention time (HRT) and solids retention time (SRT) – are used to perform PLS models for each system.

PLS are used to maximize the co-variance between fluorescence maps, selected performance variables (e.g. TMP and COD removal) and operation conditions (e.g. aeration and influent COD).

To perform mathematical models, data needs to be previously processed. Since fluorescence EEMs have one value of intensity of emission for each pair of excitation/emission wavelength that have to be used as independent variables, EEMs have to be linearized and compacted using principal component analysis (PCA). EEMs compacting is needed to decrease the amount of variables described by fluorescence maps, colinearity and noise. Additionally, all data have to be standardized to ensure the same initial weight for all variables, and have to be split in training and validation sets. Standardization

was done by subtracting to each value the average of the corresponding variable and dividing by the standard deviation. Approximately 25% of the data is used to validate the models after the PLS training with the remaining data.

PLS models are developed for these systems in search for a correlation between inputs and outputs that would enable us to predict the systems behaviour. Operating conditions, wastewater characteristics and EEMs are used as inputs of the models. Permeate characteristics, sludge characteristics and membrane performance (measured as TMP) are the parameters predicted by these models (called outputs). PLS models are obtained as one linear correlation of all inputs to predict each output, permitting to infer about the contribution of each input parameter in the outputs behaviour, leading to a possible process optimization.

PLS models are trained using EEMs of either wastewater, sludge or permeate in distinct models, and all together in the same model to access the information contained in each kind of EEMs and their predicting capability. Additionally, changes are introduced in the operating conditions to cover a wider range of conditions used for model training and improve the predictability capacity of the resulting PLS models.

3 Results and Discussion

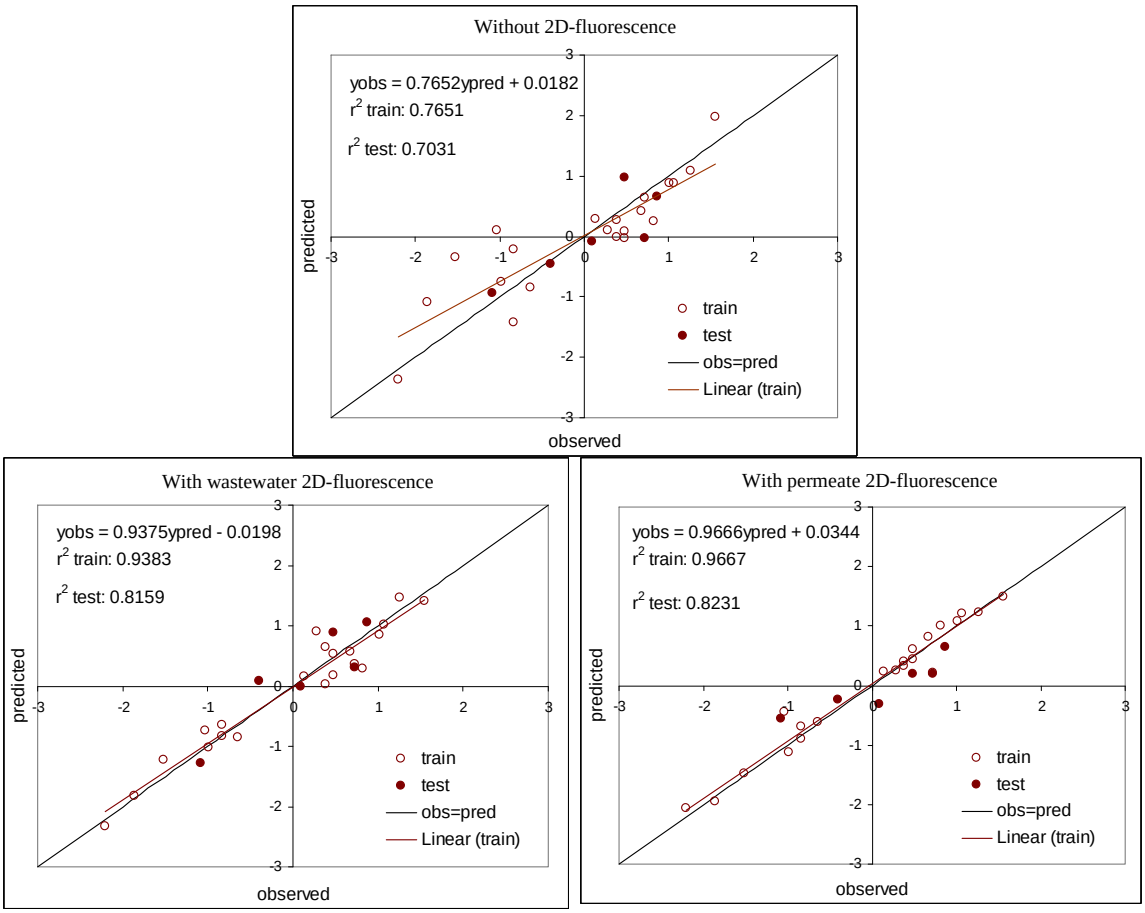

Figure1 – Normalized values of TMP predicted by PLS models against the experimental normalized values of TMP. The first plot shows predicted values by a PLS model without fluorescence information, the other two plots with a PLS model developed with wastewater EEMs and permeate EEMs, respectively.

PLS models obtained with data from the pilot MBR show that the combination of the EEM's additional information about the biological system state with the selected performance variables enhanced MBR modelling and performance prediction. Figure 1 shows that models

using EMMs as input together with analytical and performance data, have a better fitting of the training points for the TMP prediction. Also the validation points fit better in PLS models developed with fluorescence data.

Preliminary results suggest that strong correlated parameters (such as total suspended solids and volatile suspended solids or the information given by each of the three different EEM types) do not improve the information given to the model and can even increase noise, decreasing the predictive capacity of model. Additionally, it was found that fluorescence maps from sludge seem to capture more information about the system than the wastewater or permeate EEMs (data not shown), which is expectable as the information collected by the sludge reflect the biomass status and the microbial activity taking place in the activated sludge tank. Nevertheless different compacting methods of the EEMs are still being studied to ensure that none of the information contained in each type of EEM is lost.

In the future, PLS models and conclusions about the correlation between inputs and outputs obtained from models will be compared for both MBRs since they differ in scale, configuration, membrane manufacturer and wastewater fed.

References

Wolf G., Almeida J. S., Pinheiro C., Correia V., Rodrigues C., Reis M. A. M. and Crespo J. G. (2001). Two-dimensional fluorometry coupled with artificial neural networks: A novel method for on-line monitoring of complex biological processes. *Biotechnology and Bioengineering* 72(3), 297-306.

Acknowledgments

This work was funded by the EUROMBRA research project (Contract No. 018480), under the 6th Framework Programme of the European Commission. FCT (Portugal) is thankfully acknowledged for the grants SFRH / BD / 30253 / 2006 and SFRH / BPD / 30800 / 2006.

Proceedings of the 10th International Chemical and
Biological Engineering Conference - CHEMPOR 2008
Braga, Portugal, September 4-6, 2008
E.C. Ferreira and M. Mota (Eds.)

Performance indicators for reactive distillation design

Rui M. Filipe[1*], Henrique A. Matos[2], Augusto Q. Novais[3]
[1] Departamento de Engenharia Química, Instituto Superior de Engenharia de Lisboa, R. Conselheiro Emídio Navarro, 1, 1959-007 Lisboa, Portugal.
[2] Centro Processos Químicos, Departamento de Engenharia Química e Biológica, Instituto Superior Técnico, Av. Rovisco Pais, 1049-001 Lisboa, Portugal.
[3] Departamento de Modelação e Simulação de Processos, Instituto Nacional de Engenharia, Tecnologia e Inovação, Est. do Paço do Lumiar, 1649-038 Lisboa, Portugal.

Keywords: Reactive distillation, multi-objective optimization, feed quality
Topic: Systematic methods and tools for managing the complexity

Abstract

A cost indicator for the design and multi-objective optimization of reactive distillation columns, designated capacity, was introduced in previous work by the authors. The question of this indicator's effectiveness as a measure of the actual column cost, is herein investigated over a number of designs by comparing it with the value obtained by means of conventional costing procedures. The results show that the level of accuracy obtained when using capacity is satisfactory and certainly acceptable for a preliminary design stage.

1 Introduction

Reactive distillation (RD) combines reaction and separation into the same physical shell. This combination can lead to both economic and environmental gains resulting from process intensification (Malone and Doherty, 2000; Taylor and Krishna, 2000) and therefore to systems with significantly greener engineering attributes (Malone *et al.*, 2003).

However the design of these systems can prove very complex and costly. Design should therefore be preceded by preliminary studies to assess first the potential adequacy of the technology. With this aim some work was developed to create a framework combining feasible regions and optimization techniques to the design and multi-objective optimization of complex reactive distillation columns, for reacting systems with variable degrees of relative volatilities (Filipe *et al.*, 2006; 2007; 2008b).

This led to the consideration of RD columns with distributed feeds, with many of them involving the combination of superheated and subcooled feeds. This combination provides a source or a sink of heat at specified trays of the columns, which favors reaction while reducing the total reactive holdup requirements.

To assess the impact of employing such combined feeds, a cost indicator, designated capacity, was introduced as a novel optimization objective criterion (Filipe *et al.*, 2006). This cost indicator, based on the capacity variables (Jobson *et al.*, 1996), was defined as the weighted sum of liquid and vapor internal flows divided by the total feed to the column.

Together with the total number of stages and reactive holdup this indicator was used to build the Pareto front that contains the efficient set of solutions. Considering the very large number of designs involved in the evaluation, an indicator was preferred to a detailed cost calculation.

Following a strategy of refining the Pareto optimal designs, some aspects related with the practical implementation of a few promising designs were investigated (Filipe *et al.*, 2008a) by means of a number of sensitivity tests on catalyst usage and feed quality. The advantage

* Corresponding author. Tel + 351 218 317 000. E-mail: rfilipe@isel.ipl.pt

of using combined feeds was confirmed, as well as the need for a careful selection of the feed qualities.

The capacity indicator proved valuable as an optimization criterion, not only because it is efficient in comparing thousands of different designs, but also because it effectively limits the range of the feed qualities used. However, some drawbacks have been identified in its formulation, namely it makes no distinction between reactive and non reactive trays and the RD effective capital and operational costs are not explicitly shown.

This work presents a study where the effectiveness of the proposed cost indicator is assessed and, in addition, the optimal solutions identified in previous stages of the design procedure are tested at an advanced level. The size (height and diameter) of the column, energy and catalyst demands are quantified in the Aspen Plus detailed model of some designs and the total cost of the column estimated using common cost correlations. These values can be correlated with the corresponding capacity values, thus allowing the estimation of new weights for the factors present in the initial capacity definition.

As an illustrative example, a system with ideal vapor liquid behavior is employed, i.e., the olefin metathesis system (wherein 2-pentene reacts to form 2-butene and 3-hexene). For this particular reactive system, the reactant boiling point falls between those of the two products, allowing for a wide range of feasible column designs.

2 Methodology

To develop this study, six different solutions belonging to the Pareto front relating reactive and capacity (cost indicator) previously generated (Filipe *et al.*, 2008b) were selected. The main assumptions for the optimization methodology developed in GAMS to achieve the Pareto fronts are: steady state operation, constant pressure, vapor-liquid equilibrium at every stage, kinetically controlled reaction occurring in the liquid phase, and negligible heat effects. For each design, the methodology applied determines the optimal locations for the catalyst, feeds and feed quality.

The selected set of solutions is used to initialize simulations in Aspen Plus, using the RadFrac model and the Ideal property method. All the design specifications, such as the number of stages, reboil ratio, distillate to feed ratio, location and quality of the feeds, as well as the reactive holdup distribution, are taken from the former optimization results. Aspen Plus does not support the direct specification of the feed quality. To overcome this, a design specification is implemented: the feed temperature is adjusted to provide the required energy for a change in the internal liquid flow according to the equation $L_n = L_{n+1} + q \bullet F$, where F is the feed flow, q the feed quality, and L_{n+1} and L_n the liquid entering and leaving the tray, respectively.

The capacity cost indicator previously defined (Filipe *et al.*, 2006) is based on the size of internal flows, feeds and number of stages, providing an expedient method for the evaluation of a large number of solutions. Equation 1 shows how to calculate the capacity for a column with N stages, where i = 1 refers to the condenser and i = N to the reboiler, V_2 is the vapor condensed at the total condenser, B is the bottom liquid flow and w_B and w_C are the weights for the boiling and condensing capacity, respectively. Both weights were set to unity during the optimization step.

$$Capacity = \frac{w_B\left(\sum_{i=2}^{N} V_i\right) + w_C\left(\sum_{i=2}^{N-1} L_i + V_2 + B\right)}{\sum_{i=1}^{N} F_i} \qquad \textbf{Eq. 1}$$

As many reported designs tend to be operationally unrealistic (e.g. very large number of feeds, too large or too small feed temperatures), some modifications of the optimal designs previously obtained were considered. Three different scenarios, A, B and C are defined by

modifying the original optimal design, for each of the selected 6 cases. In scenario A, the number of feeds is limited to two, while maintaining the amount of energy supplied by the feed streams to the column. Scenario B considers a more realistic adaptation, where the number of feeds is reduced to two and the feed quality value is bounded by an upper temperature of 650K and a lower of 298K. In this same scenario, the cooling requirements of the cold stream are reduced to zero. Moreover the elimination of unrealistic temperature conditions by increasing the temperature of the cold feeds, has only a slight effect on product purity as demonstrated previously (Filipe *et al.*, 2008a). Scenario C represents a departing approach from the previous ones, where the advantages of using subcooled and superheated feeds are not considered. Instead, feed conditions - dew and boiling points of the feed stream - usually found in industrially operating columns are assumed. The number of feeds is also reduced to two in this scenario and the behavior of the capacity is tested for a diverse range of feed qualities.

The total annual cost (TAC) is calculated as the sum of the annual capital cost and energy cost, using the correlations reported by Luyben (2000). Annual capital cost is assumed to be the capital investment divided by a payback period of 3 years. The column shell, trays, reboiler, condenser, heat exchangers for feeds and corresponding heating utilities, are considered in the calculations. The cost of the catalyst is not considered, as the capacity is supposed to include only capital and utilities cost, but it is accounted for in the multi-objective optimization methodology, in terms of the reactive holdup variable.

The olefin metathesis system is used, with the physical properties and reaction kinetics being taken from the literature (Okasinski and Doherty, 1998). The reaction is considered only to occur in the liquid phase with a negligible heat of reaction and ideal vapor-liquid equilibrium behavior at atmospheric pressure. The specifications for column operation are taken from Hoffmaster and Hauan (2006), where the goal is to convert a pure 2-pentene feed into product streams of 2-butene and 3-hexene with a purity of at least 98 mole percent using a feed flow of 2 kmol/h and a distillate to feed ratio of 0.5.

3 Results and discussion

The details for the selected cases are shown in Table 1. The number of stages ranges between 29 and 16, the reactive holdup between 3.2 and 8 and the capacity between 90.4 and 41. As discussed earlier (Filipe *et al.*, 2008b) the capacity increases with the number of stages (higher internal flows in larger columns) and, for the same design specification, higher product purities require higher capacities (increased residence time in the reactive trays). Column diameter changes only slightly within each scenario, while between scenarios a significant reduction is observed in C when compared to A and B, which is justified by its lower internal flows due to the feed qualities used.

Although the design specifications used in the optimization methodology required a purity of 98% in the products, the assumptions made at the optimization stage and the more rigorous calculations employed by Aspen Plus lead to different purities. In addition, the changes in the feed qualities also contribute to this effect. Product purity is greatly reduced in scenario C, especially in the columns with larger number of stages, where the reduction in the internal flows is more noticeable. This reduction in the internal flows, also revealed by the reduction in capacity, decreases the residence time in the reactive trays, thus deteriorating the specifications of the products.

Figure 1 depicts the variation of product purity with capacity for scenarios A and B. The dashed line indicates the specification used in the optimization methodology. It is noticeable that the adjustments made in the feed qualities increase the product purities in most of the designs at the expense of a penalty in capacity, which is always increased. This is a somewhat expected result as these scenarios are based in optimal designs where the reactive holdup and capacity had been minimized. In addition, contrary to the observed effect

for a single column, capacity is found not to increase with product purity while comparing different columns, since they correspond to different performance levels.

Table 1 - Case details

		Case	1	2	3	4	5	6
Optimization results		RH	3.2	3.5	4.2	5.2	6.4	8.0
		Cap	90.4	70.7	54.6	46.8	43.4	41.0
		NT	29	25	19	18	17	16
		NF	3	5	3	3	3	3
		FT	9,10,21	9,10,15,16,17	9,11,12	9,10,11	8,9,10	8,9,10
		F (%)	28,26,46	12,45,9,15,19	60,18,22	63,14,23	29,42,29	46,38,16
		q	2,2,-2	2,2,-2,-2,-2	2,-2,-2	2,-2,-2	2,1.3,-2	2,0,-2
Aspen Plus simulations	Scenario	FT	9,21	9,17	9,12	9,11	8,9	8,10
		F (%)	55,45	58,42	60,40	62,38	70,30	46,54
	A	q	2,-2	2,-2	2,-2	2,-2	1.6,-2	2,-0.6
		Cap	96.6	78.2	62.9	49.9	45.5	42.5
		D_{col}	0.18	0.18	0.19	0.18	0.17	0.17
		Purity (%)	97.55	97.92	98.06	97.66	97.70	97.21
		Equipment ($)	58317	53367	50046	46071	42329	41442
		Utilities ($)	5950	5860	6192	5884	5214	5257
		TAC ($)	25389	23649	22874	21241	19323	19071
	B	q	1,-1.7	1,-1.7	0.98,-1.7	0.96,-1.8	0.97,-1.8	0.91,-1.7
		Cap	100.1	83.7	66.5	59.2	51.3	49.8
		D_{col}	0.18	0.17	0.18	0.18	0.17	0.17
		Purity (%)	97.14	97.98	98.20	98.35	98.23	97.83
		Equipment ($)	55022	50718	47241	44806	40994	42335
		Utilities ($)	11110	10983	11751	11175	9965	10375
		TAC ($)	29451	27888	27498	26111	23630	24486
	C	q	1,0	1,0	1,0	1,0	1,0	1,0
		Cap	66.4	58.6	50.3	45.5	41.7	44.1
		D_{col} (m)	0.14	0.14	0.15	0.14	0.14	0.15
		Purity (%)	82.19	88.14	94.97	96.10	96.37	97.06
		Equipment ($)	43596	41166	39646	37755	35556	39268
		Utilities ($)	6832	7009	8001	7665	7244	8719
		TAC ($)	21364	20731	21216	20250	19096	21808

NT number of trays, NF number of feeds, FT feed tray, F amount of feed (%), q feed quality, Cap capacity, D_{col} column diameter, TAC total annualized costs.

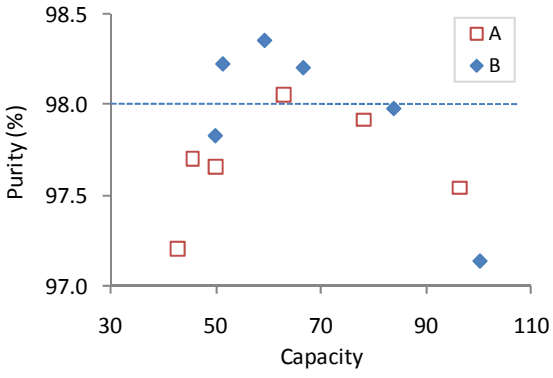

Figure 1 - Purity versus capacity for scenarios A and B

3.1. Comparison of capacity with total annualized costs

In Figure 2, the capacity, and the equipment and utilities costs are depicted for scenario B. All these variables decrease as the height of the column decreases (a high case number indicates a low number of stages). It is noticeable that capacity describes correctly the cost trend, while displaying greater sensitivity at the upper end of the cost curves.

In Figure 3 the variation of the total annual costs and capacity for case B are normalized, by dividing the value of each case by the average value of the six cases. It now becomes clearer that the deviation occurs at both ends of the cost curves. The calculated mean deviation is about 20%, thus capacity may be considered an acceptable cost indicator for an early stage conceptual process design. It is also advantageous when the design is not yet fully specified as only the knowledge of internal flows and feed flows is required. In addition, its calculation is straightforward, making it adequate for the comparison of very large number of designs.

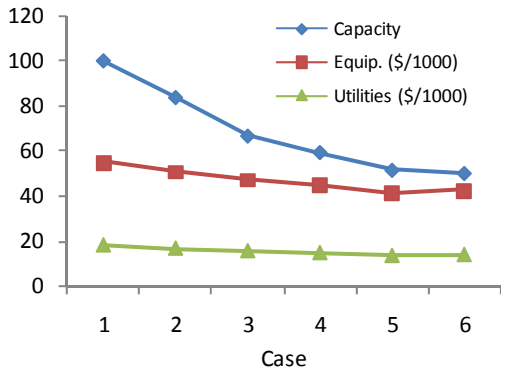

Figure 2 - Capacity, equipment and utilities cost for scenario B

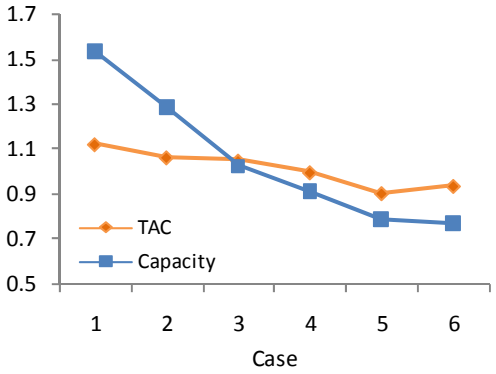

Figure 3 - Normalized capacity and TAC for scenario B

3.2. Capacity weights

The effect of weights w_C and w_B on the capacity cost indicator was assessed and it is concluded that no significant effects were noticed. The values for the individual boiling and condensing capacities (Figure 4) typically differ less than 5%, so the assumed values of $w_B = w_C = 1$, employed for the present study seem justified.

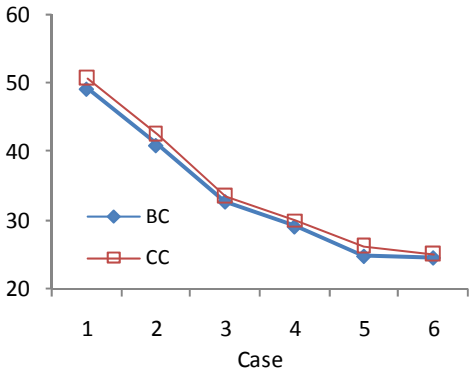

Figure 4 – Boiling capacity (BC) and condensing capacity(CC) for scenario B

4 Conclusions

This paper addresses the use of performance indicators for the design of reactive distillation columns. Specifically, the analysis of a cost indicator previously used in the classification and selection of several thousands of preliminary designs is addressed. The total annualized

costs are calculated and compared to capacity indicator values for several different designs derived from the optimal designs previously obtained from optimization runs performed in GAMS. The results show that capacity and costs have a common trend, within an average error of 20%, pointing to capacity as a suitable indicator for preliminary design analysis.

The influence of the weights used in the definition of capacity was also assessed with a view of improving its accuracy, but no significant improvements could be achieved as the individual capacity values are quite close.

On-going work aims to establish the effect of the weights during the optimization process and to further sophisticate the capacity indicator with a view to make it more selective in terms of the number and characteristics of the optimal preliminary designs.

References

Filipe, R.M., Novais, A.Q., Hauan, S. (2006). Multi-objective optimization of reactive distillation columns using feasible regions. *17th International Congress of Chemical and Process Engineering*, Prague, Czech Republic.

Filipe, R.M., Hauan, S., Matos, H.A., Novais, A.Q. (2007). Multi-Objective Design of Reactive Distillation. *17th European Symposium on Computer Aided Process Engineering*. V. Plesu and P. S. Agachi. 24**:** 407-412.

Filipe, R.M., Hauan, S., Matos, H.A., Novais, A.Q. (2008a). A sensitivity analysis on optimal solutions obtained for a reactive distillation colum. *18th European Symposium on Computer Aided Process Engineering*. B. Braunschweig and X. Joulia. Lyon, France. 25**:** 211-216.

Filipe, R.M., Turnberg, S., Hauan, S., Matos, H.A., Novais, A.Q. (2008b). Multi-objective design of reactive distillation with feasible regions. *Industrial & Engineering Chemistry Research*, (accepted for publication).

Hoffmaster, W.R., Hauan, S. (2006). Using feasible regions to design and optimize reactive distillation columns with ideal VLE. *AIChE Journal*, 52, 1744-1753.

Jobson, M., Hildebrandt, D., Glasser, D. (1996). Variables indicating the cost of vapour-liquid equilibrium separation processes. *Chemical Engineering Science*, 51, 4749-4757.

Luyben, W.L. (2000). Economic and Dynamic Impact of the Use of Excess Reactant in Reactive Distillation Systems. *Industrial & Engineering Chemistry Research*, 39, 2935-2946.

Malone, M.F., Doherty, M.F. (2000). Reactive Distillation. *Industrial & Engineering Chemistry Research*, 39, 3953-3957.

Malone, M.F., Huss, R.S., Doherty, M.F. (2003). Green chemical engineering aspects of reactive distillation. *Environmental Science & Technology*, 37, 5325-5329.

Okasinski, M.J., Doherty, M.F. (1998). Design Method for Kinetically Controlled, Staged Reactive Distillation Columns. *Industrial & Engineering Chemistry Research*, 37, 2821-2834.

Taylor, R., Krishna, R. (2000). Modelling Reactive Distillation. *Chemical Engineering Science*, 55, 5183-5229.

Proceedings of the 10th International Chemical and
Biological Engineering Conference - CHEMPOR 2008
Braga, Portugal, September 4-6, 2008
E.C. Ferreira and M. Mota (Eds.)

The Importance of Models and Practical Integration in Process Development

Cases from the Simulated Moving Bed technology

Pedro Sá Gomes, Mirjana Minceva and Alírio E. Rodrigues*
Laboratory of Separation and Reaction Engineering, Associate Laboratory LSRE/LCM
Department of Chemical Engineering, Faculty of Engineering, University of Porto
Rua Dr. Roberto Frias, 4200-465 Porto, Portugal

Keywords: Simulated Moving Bed, Chromatography, Adsorption, Modeling, Simulation, Optimization, Separation, Process development and Process intensification.
Topic: Systematic methods and tools for managing the complexity

This work is based on the presentation recently awarded with the prize jEPSI at the 6th Workshop Anual de Engenharia de Processos e Sistemas, 12th March 2008 at Coimbra-Portugal, and intends to illustrate why a solid method for process development should be the result of the integration of "theory" (the models) and "practice" (experimental applications). Therefore, are presented some cases from the Simulated Moving Bed technology where developments based on model analysis led to the conception of practical applications, as well as some cases where the restructuration or operation of experimental/industrial units guided improvements in the previously used models, Figure 1.

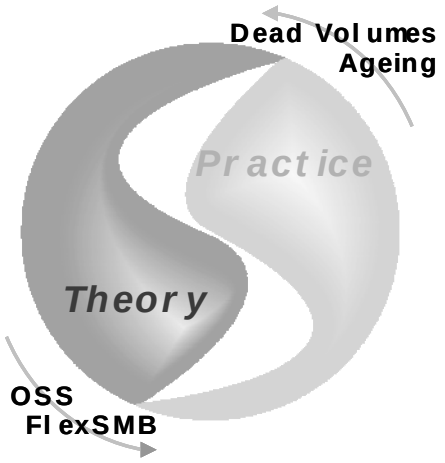

Figure 1 – From models to practice… and from practice to models.

Simulated Moving Bed technology

It is known that industrial-scale continuous adsorption processes are preferable to batch ones. The use of continuous chromatographic counter current operation in particular (here by called TMB, True Moving Bed), maximizes the mass transfer driving force, providing a better utilization of the adsorbent, which may have a rather low selectivity. In addition, with TMB it is possible to reduce the solvent consumption, increase of productivity and purity and therefore less diluted product streams. Contrary to the TMB units, where the solid phase moves counter currently to the fluid phase, in the SMB (Simulated Moving Bed) [1] units the solid motion is simulated by a

* Corresponding author. Tel + 351-225-081671. E-mail:arodrig@fe.up.pt

synchronous shift of all inlet and outlet ports, while the solid phase is held immobile, Figure 2.

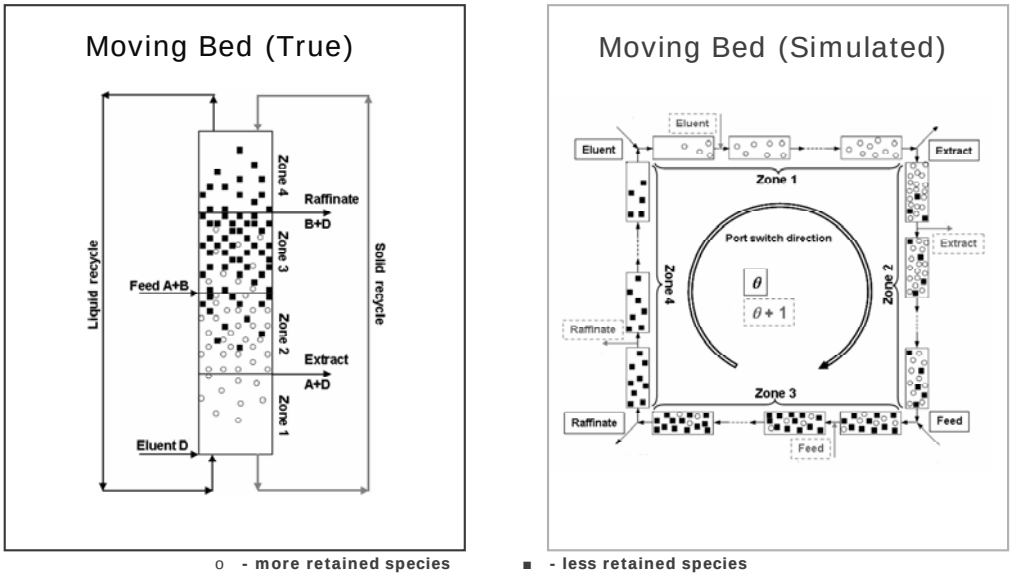

Figure 2 – The True Moving bed (TMB) and Simulated Moving Bed (SMB) analogy.

By this way, several problems usually associated with solid motion, namely, particle and equipment attrition, high pressure drops, particle and flow redistribution are avoid.

The SMB technology has been mainly applied to the so-called “difficult separations”, in fields such as the petrochemical area with the separation of p-xylene from C_8 isomers mixtures. The expansion to new SMB applications in fields such as the biotechnological, fine chemistry and pharmaceutical industries is remarkable in the last decade [2].

From models to practice…

By means of mechanistic models, or more simplistic approaches, it is possible to describe an SMB unit accounting to all its particularities, even the ports discontinuities Table 1 and 2.

Table 1 – SMB nodes balances

j = 1: $C_{bi(4,x=1)} = \frac{u_1^*}{u_4^*} C_{bi(1,x=0)}$	**(1a)**	$u_1^* = u_4^* + u_{Eluent}$	**(2a)**
j = 2,4: $C_{bi(j-1,x=1)} = C_{bi(j,x=0)}$	**(1b)**	$u_2^* = u_1^* - u_{Extract}$	**(2b)**
		$u_3^* = u_2^* + u_{Feed}$	**(2c)**
j = 3: $C_{bi(2,x=1)} = \frac{u_3^*}{u_2^*} C_{bi(3,x=0)} - \frac{u_{Feed}}{u_2^*} C_i^F$	**(1c)**	$u_4^* = u_3^* - u_{Raffinate}$	**(2d)**

Table 2 – SMB model equations with LDF approach.

i. In a volume element of the bulk fluid phase,

$$\frac{\partial C_{bic}}{\partial \theta} = \gamma_j^* \left\{ \frac{1}{Pe_c} \frac{\partial^2 C_{bic}}{\partial x^{*2}} - \frac{\partial C_{bic}}{\partial x^*} \right\} - \frac{(1-\varepsilon_b)}{\varepsilon_b} k_{p\,ic}^{\,*} \left(q_{ic}^* - \langle q_{ic} \rangle \right) \quad \textbf{(3)}$$

ii. in the “adsorbent-phase”,

$$\frac{\partial \langle q_{ij} \rangle}{\partial \theta} = k_{p\,ic}^{\,*} \left(q_{ic}^* - \langle q_{ic} \rangle \right) \quad \textbf{(4)}$$

with the respective initial and boundary conditions,

- $\begin{cases} C_{bic}(x^*,0) = 0; \\ \langle q_{ic}(x^*,0) \rangle = 0; \end{cases}$ **(5)**

- x^*= 0: $C_{bi(c,x^*=0)} = C_{bi}(0,\theta) - \frac{1}{Pe_c} \frac{\partial C_{bic}}{\partial x^*}\Big|_{x^*=0}$ **(6a)**

- x^*= 1: $\frac{\partial C_{bic}}{\partial x^*}\Big|_{x^*=1} = 0$ **(6b)**

plus the multicomponent adsorption isotherms

$q_{ic} = f_i\left(\langle C_{pic} \rangle, \langle C_{pic} \rangle\right)$ with $k \neq i$ and for all species *i* and in column *c* **(7)**

The deep study of these models provided the development of the "non conventional modes of operation", where, and by means of the introduction of asynchronous ports movements, variation of concentration and/or flow rates, it was possible to extend the versatility of this kind of units and by consequence its performance. The development of the OSS (Outlet Streams Swing) [3] mode of operation is one of these cases.

In the OSS mode of operation the more and less retained species are collected in the extract and raffinate ports non-continuously, i. e., during a part of the time switch the more retained species is collected in the extract while the raffinate flow rate is decreased leading to the violation of the equilibrium theory constraints on zone 4; in the rest of the period the opposite procedure is performed, Figure 3.

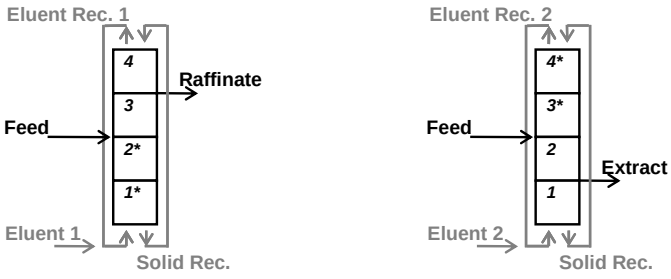

Step 1 Raffinate collection **Step 2** Extract collection

Figure 3 - OSS strategy for the test case, (a) the first half of the switch time, (b) the second half of the switch time, equivalent TMB scheme.

This operation mode leads to expansion and contraction of the collection and contaminating fronts increasing the distance between them, Figure 4.

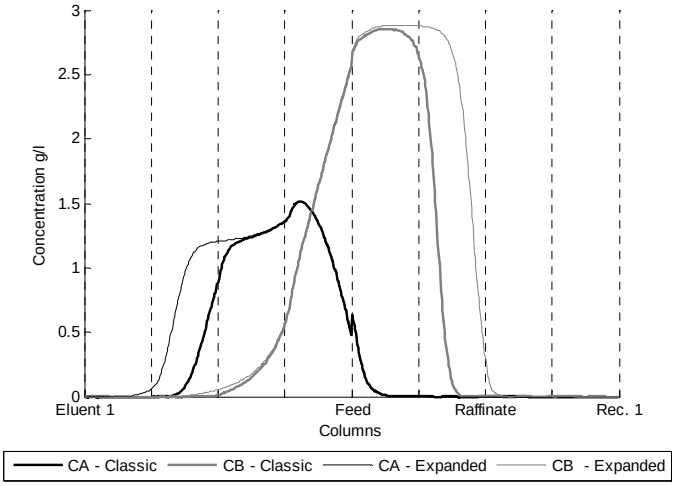

Figure 4 – Classic and expanded fronts from de OSS modus operandi.

However, the practical application of these “non conventional modes of operation” is per itself a challenge. Generally an SMB unit, industrial, pilot of laboratory-scale, is limited to one or two modes of operation and to implement a new operating mode is necessary to contact the supplier, do adjustments, even to reformulate the entire unit if not to acquire a new one. Therefore, flexibility (at least at laboratory-scale) is seen as one of the more relevant qualities for this kind of equipment.

This aspect was the main reason that led to the design and construction of a 6 columns unit, the FlexSMB-LSRE, Figure 5.

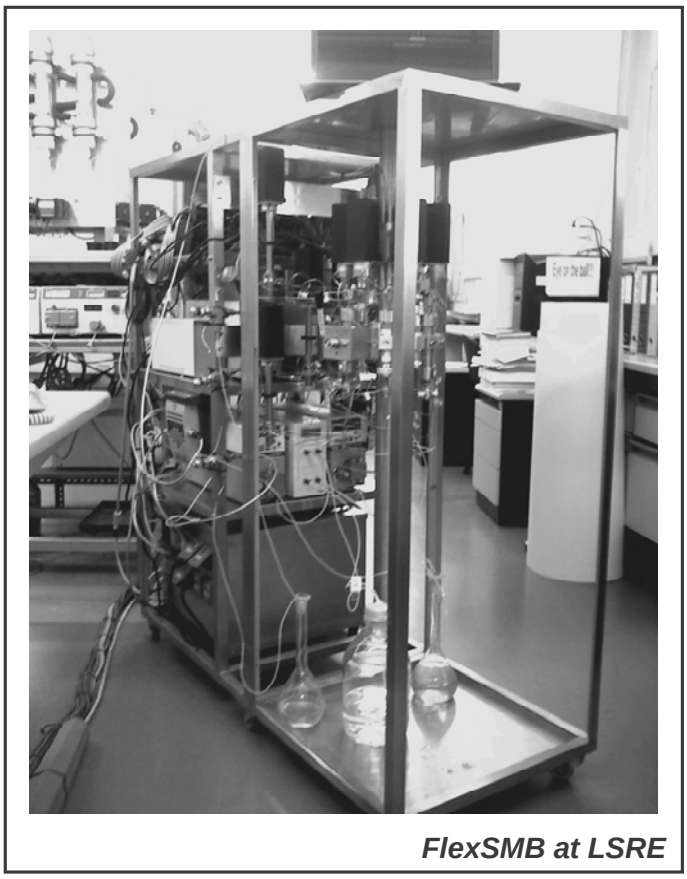

FlexSMB at LSRE

Figure 5 – Flexible SMB unit, the FlexSMB-LSRE.

…from practice to models.

In the published or patented innovative work related with SMB industrial separations, just a few references refer to the adsorbent ageing problems. The “time life” of the adsorbent, a predominant economical factor in the SMB units design as adsorbent cost, has considerable influence on the complete unit design, if not in the main project viability [4].

Nevertheless, the information considering this issue remains restricted to the plant operators and technology owners. Usually an industrial SMB unit operates at the limit (the optimum conditions), a small deviation on its operating parameters will pollute the outlet streams, Figure 6.

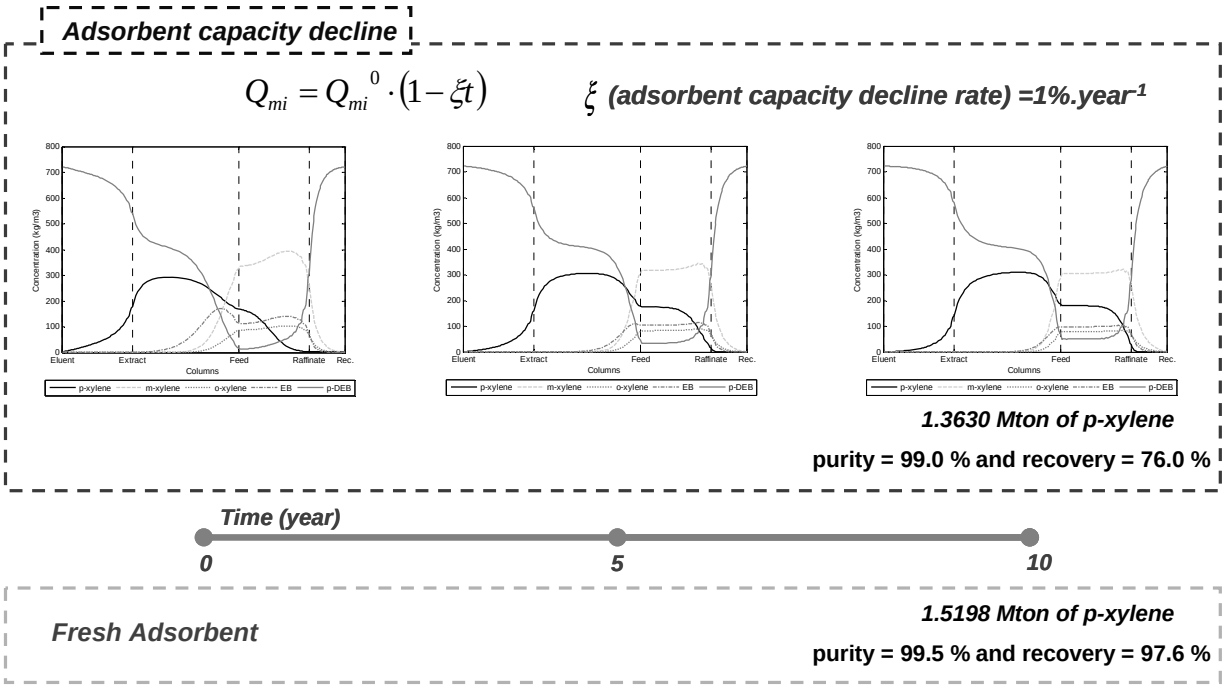

Figure 6 – Concentration profiles of a p-xylene separation unit suffering an adsorbent capacity decline over 10 years. Performance parameters for the ageing and fresh adsorbent cases [5].

In Figure 6, one can observe that p-xylene is being driven to the raffinate port over the time of adsorbent ageing, affecting the p-xylene recovery.

Initially, the unit is designed accounting to the industrial/economical requirements and to equipment/adsorbent restrictions. If the adsorption equilibrium data changes over the time, ageing phenomena, and the unit is kept on the initial operating parameters, the unit will pollute its outlet products, as can be perceived form the separation regions on Figure 7.

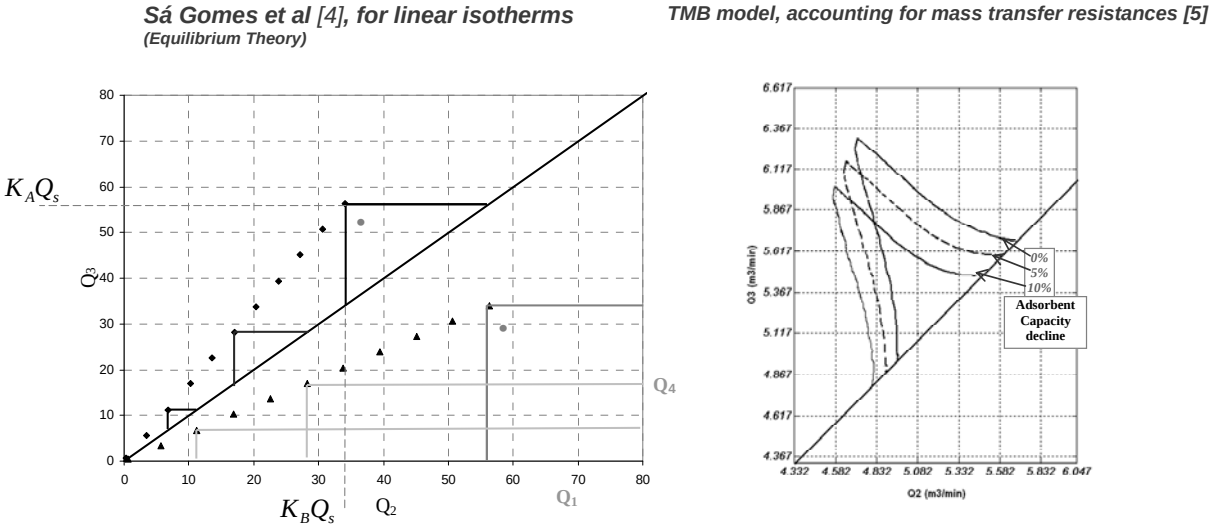

Figure 7 – Adsorbent ageing effect in linear (from [4]) and non linear (from [5]) isotherms case.

The observation of these aspects during an industrial unit operation led to the extension of the common models to account with ageing problems. The analysis of this "extended models" provided some diagnostic methods for the ageing mechanism as well as short cut methods for the compensation (such as the switching time compensation measure or variable zone length, [4,5]) of this kind of problems, Figure 8.

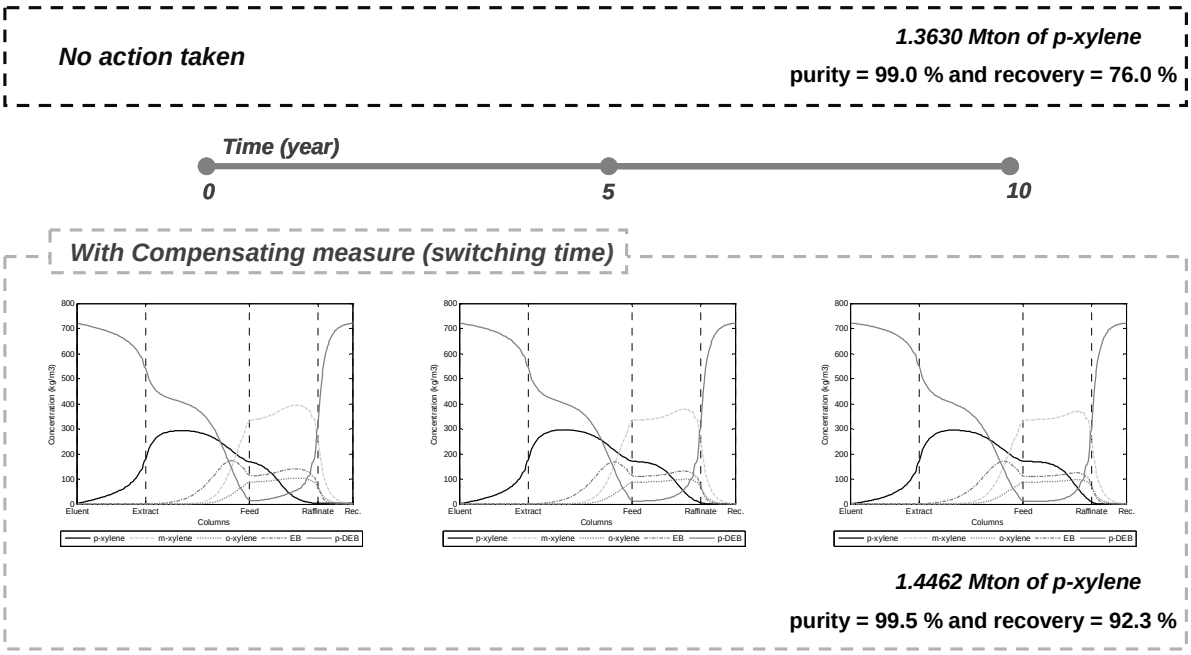

Figure 8 - Concentration profiles of a p-xylene separation unit suffering an adsorbent capacity decline over 10 years, but after implementing a switching time compensation measure. Performance parameters for the adsorbent aged with compensation and with no action cases [5].

By these means it was possible to extend the sieve life maintaining the purity requirments as in the operation of a fresh adsorbent unit.

Conclusion

One can now remind *M. S. Tswett*: “An essential condition for all fruitful research is to have at one’s disposal a satisfactory technique. “*Tout progrès scientifique est un progrès de méthode*” as somebody once remarked. Unfortunately the methodology is frequently the weakest aspect of scientific investigations.”

And in our opinion, a solid method for process development should be the result of the integration of “theory” (the models) and “practice” (experimental applications). Hereby demonstrated with: New operating techniques (the OSS and the FlexSMB-LSRE unit) and More accurate models (dead volumes (SMB units) and Ageing phenomena analysis).

References

[1]. Broughton, D.B., C.G. Gerhold, (1961) Continuous Sorption Process Employing Fixed Bed of Sorbent and Moving Inlets and Outlets. US patent no 2 985 589

[2]. Sá Gomes, P.; Minceva, M.; Rodrigues A. E.; (2006) Simulated Moving Bed: Old and New, Adsorption, 12:375-392.

[3]. Sá Gomes, P.; Rodrigues, A. E.; (2007) Outlet Stream Swing (OSS) and MultiFeed (MF) Operation of Simulate Moving Beds, Separation Science and Technology, 42: 223-252.

[4]. Sá Gomes, P.; Minceva M.; Rodrigues A. E.; (2007) Operation of Simulated Moving Bed in Presence of Adsorbent Ageing, Separation Science and Technology, 42: 3555 – 3591.

[5]. Sá Gomes, P.; Minceva, M.; Rodrigues A. E.; (2008) Operation of an Industrial SMB Unit for p-xylene Separation Accounting for Adsorbent Ageing Problems, Separation Science and Technology, 43(8): 1974 – 2002.

Proceedings of the 10th International Chemical and
Biological Engineering Conference - CHEMPOR 2008
Braga, Portugal, September 4-6, 2008
E.C. Ferreira and M. Mota (Eds.)

A chemometric tool to monitor high-rate anaerobic granular sludge reactors during load and toxic disturbances

José Carlos Costa, M. Madalena Alves, Eugénio C. Ferreira*
IBB – Institute for Biotechnology and Bioengineering, Centre of Biological Engineering, University of Minho, Campus de Gualtar, 4710–057 Braga, Portugal.

Keywords: Control, Organic Loading Disturbance, Principal Components Analysis, Quantitative Image Analysis, Toxic Shock Load
Topic: Systematic methods and tools for managing the complexity.

Abstract

The wide fluctuations in flow rate and the presence of toxic compounds can damage the high efficiency of high-rate anaerobic granular sludge reactors. As earlier these disturbances are detected, more accurate would be the corrective actions, and less damage will be caused to the microorganisms involved in the process. The use of Principal Component Analysis (PCA) determined a latent variable, combining a weighted sum of operational, physiological, and morphological data, which showed high sensitivity to recognize the operational problems occurred when four organic loading disturbances and three toxic shock loads were applied to Expanded Granular Sludge Bed reactors. The high loadings/weights linked with the morphological parameters, specially the aggregates size distribution (>0.1, >1) and filaments length dynamics (TL/VSS), obtained using quantitative image analysis techniques, illustrate the usefulness of monitor the structural changes of the anaerobic granular sludge. The application of PCA chemometric tool to dataset gathering information from all disturbances allowed the differentiation between organic loading and toxic shock disturbances, as well as the main effects caused by each class of disturbance.

1 Introduction

High-rate anaerobic digestion reactors gained significance during the last decades in the field of wastewater treatment processes. However, these systems are designed with reference to a nominal operating condition, in which the organic loading rate is assumed to be constant in time. Also, some compounds can have inhibitory or toxic effects to the microbial populations, such as detergent and solvents. These facts, coupled with the long start-up periods imply the need to monitor the anaerobic granular sludge stability in order to achieve an appropriate control and sustainability of the process.

The recognition of parameters that could be used for monitoring the process is important to efficient control of those processes. It is equally feasible to obtain values of parameters measured in solid, liquid or gaseous phases. However, parameters involved in reactors control had been limited to indicators of the liquid and the gaseous phases (van Lier et al., 2001), due to difficulties in obtain and inaccuracy associated with morphological parameters.

With the rapid development of instrumental methods the amount of diverse data generated in an environmental process monitoring and/or control is increasingly drastically (Bourgeois et al., 2001; Schügerl, 2001; Spanjers and van Lier, 2006). This advance guide analysts and researchers to gathering further more multivariate data. Concurrently, with computer science and technology developments apply computers

* Corresponding author. Tel + 351-253-604407. E-mail:ecferreira@deb.uminho.pt

and advanced statistical and mathematical methods to analyse this data became easier.

In this framework, image analysis techniques appear as a promising tool to provide quantitative parameters of the solid phase evolution. And, chemometrics based techniques, such as Principal Components Analysis (PCA), can be useful to detect groups, trends, correlations, and outliers in datasets gathering vast amounts of information. This method allows identifying patterns in data, and expressing them in order to highlight their similarities and differences. PCA is a projection method for analyze data and reduce it from an n-dimensional space to few latent/hidden variables, while keeping information on its variability.

A multivariate statistical analysis has been used together with image analysis techniques to pattern recognition, such as discriminant analysis, neural networks, and decision trees (Ginoris et al., 2007). The relationships between morphological parameters and biomass properties in aerobic wastewater treatment processes were also assessed by partial least squares regression (Amaral et al., 2005) and principal components analysis (Jenné et al., 2006).

The objective of this work was to apply the chemometric technique Principal Components Analysis in order to recognize fluctuations, and respective effects, in high-rate anaerobic granular sludge reactors performance caused by organic loading and toxic disturbances.

2 Material and Methods

2.1 Datasets

Four organic loading disturbances (OLD) (Table 1) were applied to an Expanded Granular Sludge Bed (EGSB) reactor fed with $1.5g_{COD\text{-}ethanol}/L$ and hydraulic retention time (HRT) of 8 hours, in steady-state conditions. Also, three toxic shock loads (TSL) were applied in EGSB reactors operating in similar conditions (Table 1).

Table 1. Organic Loading Disturbances and Toxic Shock Loads conditions.

Disturbance	OLD1	OLD2	OLD3	OLD4	TSL1	TSL2	TSL3
Ethanol (g_{COD}/L)	5	1.5	15	15	1.5	1.5	1.5
HRT (h)	8	2.5	8	8	8	8	8
[Toxic] (mg/L)	-	-	-	-	1.6	3.1	40
Exposure phase (h)	72	72	72	384	56	222	222
Recovery phase (d)	7	7	7	7	14	12	7

Three programmes previously developed (Amaral, 2003) were used as the final step of a procedure (Costa et al., 2007) to obtain quantitative morphological information from anaerobic granular sludge.

Three datasets were created gathering morphological, physiological, and reactors performance information. Datasets 1 and 2 included observations of OLD and TSL, respectively. The objective consisted in examine the sensitivity of the latent variables to recognize the disturbances. Dataset 3 encompassed all observations and was created to study the differentiation of the OLD from the TSL, and respective effects. The variables used are described in Table 2.

2.2 Principal Component analysis

Principal components analysis aims at finding and interpreting hidden complex, and possibly causally determined, relationships between features in a dataset. Correlating features are converted to the so-called factors which are themselves noncorrelated (Einax et al., 1997).

SIMCA-P (Umetrics AB) software package was used to perform the Principal Components Analysis. The first step of the analysis consists in the pre-treatment of data by standardization of the variables, i.e., guarantee that each individual variable has about the same range, avoiding that some variables would be more important than others because of scale effects. During this work each variable was autoscaled so that each variable has mean zero and unit standard deviation.

Subsequently, the software iteratively computes one principal component at a time, comprising a score vector t_a and a loading vector p_a. The score vectors contain information on how the samples relate to each other. Otherwise, the loading vectors define the reduced dimension space and contain information on how the variables relate to each other. Usually, few principal components (2 or 3) can express most of the variability in the dataset when there is a high degree of correlation among data.

The criterion used to determine the model dimensionality (number of significant components) was cross validation (CV). Part of data is kept out of the model development, and then are predicted by the model and compared with the actual values. The prediction error sum of squares (PRESS) is the squared differences between observed and predicted values for the data kept out of the model fitting. This procedure is repeated several times until data element has been kept out once and only once. Therefore, the final PRESS has contributions from all data. For every dimension, SIMCA computes the overall PRESS/SS, where SS is the residual sum of squares of the previous dimension. A component is considered significant if PRESS/SS is statistically smaller than 1.0.

3. Results and Discussion

3.1 Recognition of organic load and toxic disturbances

The PCA expressed the importance of the proposed morphological parameters to recognize, possible problematic, disturbances to high-rate anaerobic granular sludge reactors. The latent variables t[1] and t[2] showed high percentages of variation in the first hours of exposure in every disturbances applied (Figs. 1 and 2).

As showed in table 1, LD3 and 4 were the most severe organic loading disturbances. Watching at t[1] (Fig. 1) is visible its high variation in this two OLD, essentially caused by the granules fragmentation, biomass washout, and decrease in specific acetoclastic activity (SAA) and COD removal efficiency. These variables had the higher loadings in Principal Component (PC) 1 (Table 2). In LD1, although the COD removal efficiency was unaffected, granule fragmentation was observed. In LD2 (hydraulic shock load) there was no changes in granules distribution sizes, but a severe release of filaments. For that reason the TL/VSS and LfA parameters had high loadings in PC2 (Table 2), and t[2] show the higher variation in the LD2 (data not shown).

Relatively to toxic shock loads was observed that the detergent SL1 had no significant effects on reactor performance and biomass characteristics. These was detected by the PCA, since the variable t[1] do not show large variation during this TSL (Fig. 2). The detergent SL2 caused the biggest decrease in reactor performance, and, solvent SL3 caused granules fragmentation and continuous deterioration of biomass and reactor performance. Observing the evolution of t[1] in figure 2, is clearly visible an immediate deviation between the inoculum observation in SL2 and the first observation during shock load (after 8h), recognizing the operational problems caused by the detergent. In the same figure, is visible a constant decrease of t[1] during SL3. During toxic shock loads, constant filaments release was visible. This morphological change was responsible by the variability detected in PC2 (data not shown) as showed by the high loadings of TL/VSS associated with the latent variable t[2] (Table 2).

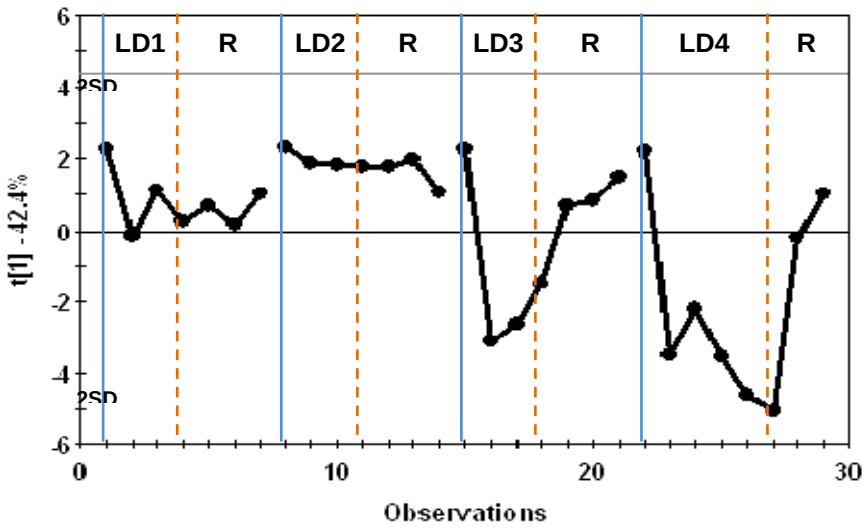

Figure 1. First latent variable (t[1]) evolution during organic loading disturbances. LD – Load Disturbance Phase; R – Recovery Phase.

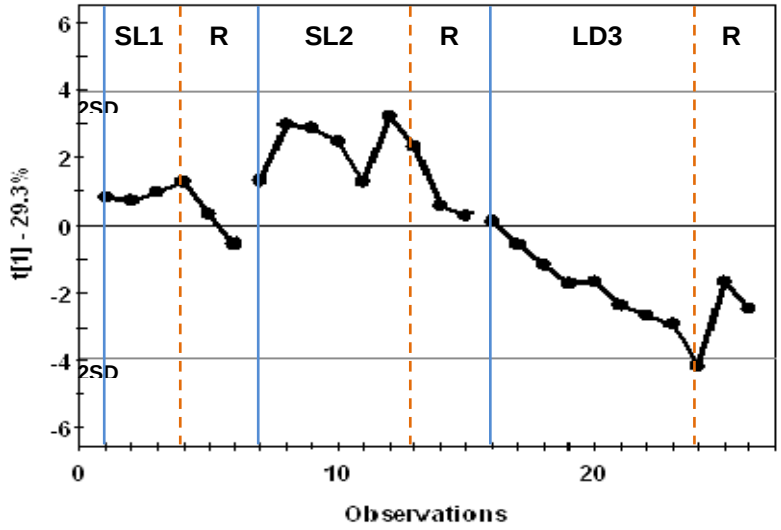

Figure 2. First latent variable (t[1]) evolution during toxic shock loads. SL – Toxic Shock Load Phase; R – Recovery Phase.

Table 2. Loadings/weights associated with the first (t[1]) and second (t[2]) latent variable in organic loading disturbances (LD) and toxic shock loads (SL).

Variable	LD		SL		Name
	t[1]	t[2]	t[1]	t[2]	
OLR	**-0.40**	0.06	0.12	-0.20	Organic Loading Rate
Csd	-	-	**-0.34**	-0.07	Toxic (detergent or solvent) concentration
Eff	**0.40**	0.02	-0.20	**0.30**	Chemical Oxygen Demand (COD) Removal Efficiency
pH	**0.32**	-0.12	0.00	**0.38**	pH
VSS	**-0.40**	-0.12	-0.05	-0.28	Effluent Volatile Suspended Solids
<0.1	-0.12	-0.29	-0.20	**0.30**	% of Aggregates Projected Area with Deq < 0.1 mm
>0.1	**-0.35**	0.19	**-0.43**	-0.09	% of Aggregates Projected Area with 0.1 ≤ Deq (mm) < 1
>1	**0.36**	-0.16	**0.44**	0.07	% of Aggregates Projected Area with Deq ≥ 1 mm
SAA	**0.33**	0.13	-0.26	**0.30**	Specific Acetoclastic Activity
SHMA	0.04	**-0.41**	0.18	-0.04	Specific Hydrogenotrophic Methanogenic Activity
LfA	0.13	**0.55**	0.24	**0.38**	Total Filaments Length / Total Aggregates Projected Area
VSS/TA	0.16	-0.18	0.17	**-0.33**	VSS / Total Aggregates Projected Area
TL/VSS	0.05	**0.55**	0.13	**0.44**	Total Filaments Length / Volatile Suspended Solids
vsed	-	-	**0.46**	0.01	Settling Velocity

Summarising, besides the imposed variables, organic loading rate (OLR) and toxic concentration (Csd), the morphological variables, >1 and >0.1 in t[1], and LfA and TL/VSS in [t2], had the higher loadings/weights, enhancing the need to monitor the biomass morphology to control the reactors. It may be suggested that, from the liquid and gaseous phase, the pH can be an important parameter to monitor/control the process, as reported by others (Liu et al., 2004). The results show the adequacy of use the chemometric technique Principal Component Analysis to recognize disturbances in high-rate anaerobic reactors and detect the respective effects.

3.2 Distinguish organic load disturbances from toxic shock loads

The two firsts Principal Components gathered 51.2% of the total variability in dataset 3 (encompassing observations from organic loading and toxic disturbances). However, analysing the score and loading plots of PC1-PC2 plane (Fig. 3) is possible to visualize the variables with higher influence to distinguish load disturbances from shock load observations and respective effects, i.e. the variables more affected by the disturbances. The organic loading disturbances displaced the observations in direction of negative scores in PC1 and PC2 (line 1 in Fig. 3a). Concerning to the toxic shock load, it was observed that observations were dislocated in the direction of positive scores in PC1 and negative scores in PC2 (line 2 in Fig. 3a).

Watching at the direction lines of the exposure phase observations (Fig. 3a) and the loading plot (Fig. 3b), is visible that the TSL affects mostly the morphological variables LfA and TL/VSS. As stated before a severe release of filaments was observed in these disturbances, being these variables responsible for the detection of operational problems even before the COD removal efficiency decrease. The OLD caused increases in the VSS, and, decreases in the pH and COD removal efficiency. A severe fragmentation phenomenon was also observed, as showed by the increase in the percentage of aggregates projected area with equivalent diameter (D_{eq}) between 0.1–1 mm (>0.1), and consequent decrease in the % of aggregates area with D_{eq} > 1 mm (>1).

The recovery phases observations tend to return to close the inocula observations (Fig. 3a). Effectively, the reactors regain its pre-disturbances performance few hours after their stop, indicating that only temporary inhibitions occurred.

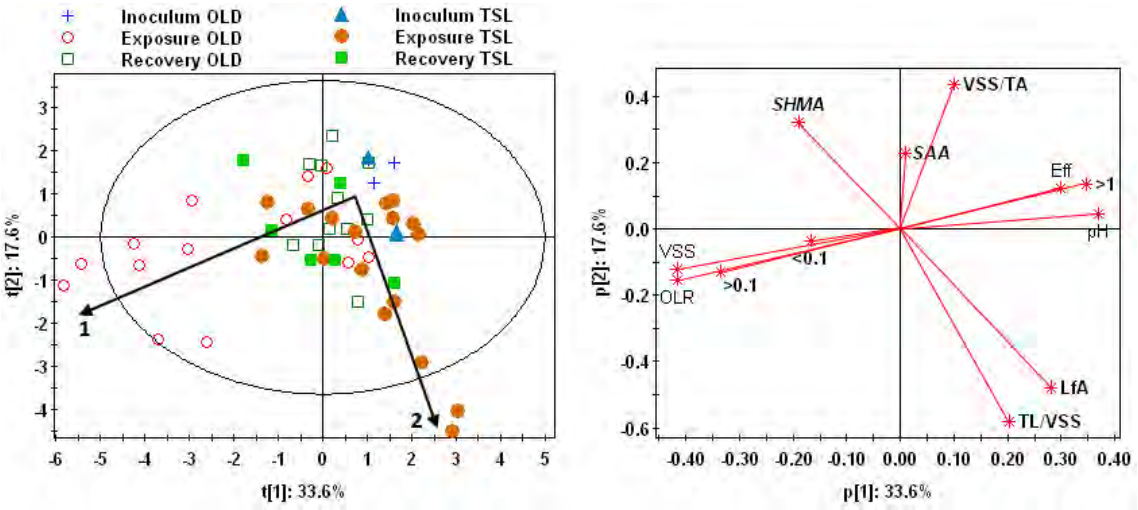

Figure 4. PCA of the first principal component versus the second principal component: (**a**) score plot t[1] *vs.* t[2], and, (**b**) loading plot p[1] *vs.* p[2].

4. Conclusions

The morphological parameters >0.1 and >1, indicator of granules fragmentation, experience high variation in the first hours of disturbances, either when was an organic or a toxic shock load. Their high weights were relevant for the immediate recognition of the deviations to the normal operation of the EGSB reactors detected by the latent variable determined by the PCA. The results enhance the important role that biomass morphology monitoring can have in the recognition of organic loading and toxic disturbances in anaerobic granular sludge reactors. Indeed, the proposed morphological parameters were sensitive enough to detect the disturbances before COD removal efficiency decreased. The PCA allow to distinguish organic loading from the toxic disturbances, and the main effects caused by each other. Increase the OLR caused granules fragmentation and washout (increase in effluent VSS) and decrease in COD removal efficiency. The exposure to detergent and solvent caused the filaments release and consequent increase in LfA parameter, and decrease in the SHMA.

Acknowledgements

We grateful acknowledge the financial support to J.C. Costa through the grant SFRH/BD/13317/2003 and the project POCTI/AMB/60141/2001 from the Fundação para a Ciência e a Tecnologia (Portugal).

References

Amaral, A.L. (2003). *Image Analysis in Biotechnological Processes: Application to Wastewater Treatment.* PhD thesis, University of Minho, Portugal (http://hdl.handle.net/1822/4506).

Amaral, A.L., and Ferreira, E.C. (2005). Activated sludge monitoring of a wastewater treatment plant using image analysis and partial least squares regression. *Analytica Chimica Acta*, 544, 246-253.

Bourgeois, W., Burgess, J.E., and Stuetz, R.M. (2001). On-line monitoring of wastewater quality: a review. *Journal of Chemical Technology and Biotechnology*, 76, 337-348.

Costa, J.C., Abreu, A.A., Ferreira, E.C., Alves M.M. (2007). Quantitative image analysis as a diagnostic tool for monitoring structural changes of anaerobic granular sludge during detergent shock loads. *Biotechnology and Bioengineering,* 98(1), 60-68.

Einax, J.W., Zwanziger, H.W, and Geiss, S. (1997). *Chemometrics in Environmental Analysis*. Weinheim: VCH.).

Ginoris, Y.P., Amaral, A.L., Nicolau, A., Coelho, M.A.Z., and Ferreira, E.C. (2007). Recognition of protozoa and metazoa using image analysis tools, discriminant analysis, neural networks and decision trees. *Analytica Chimica Acta*, 595, 160-169.

Liu, J., Olsson, G., and Mattiasson, B. (2004). Monitoring and control of an anaerobic upflow fixed-bed reactor for high-loading-rate operation and rejection of disturbances. *Biotechnology and Bioengineering*, 87(1), 43-53.

Jenné, R., Banadda, E.N., Gins, G., Deurinck, J., Smets, I.Y., Geeraerd, A.H., and Van Impe, J.F. (2006). Use of image analysis for sludge characterisation: studying the relation between floc shape and sludge settleability. *Water Science and Technology*, 54 (1), 167-174.

Schügerl, K. (2001). Progress in monitoring, modeling and control of bioprocesses during the last 20 years. *Journal of Biotechnology*, 85, 149-173.

Spanjers, H., and van Lier, J.B. (2006). Instrumentation in anaerobic treatment – research and practice. *Water Science & Technology*, 53 (4-5), 63-76.

Van lier, J.B., Tilche, A., Ahring, B.K., Macarie, H., Moletta, R., Dohanyos, M., Hulshoff-Pol, L.W., Lens, P., and Verstraete, W. (2001). New perspectives in anaerobic digestion. *Water Science and Technology*, 43 (1), 1-18.

Proceedings of the 10th International Chemical and
Biological Engineering Conference - CHEMPOR 2008
Braga, Portugal, September 4-6, 2008
E.C. Ferreira and M. Mota (Eds.)

Control of bromelain recovery process through conventional and fuzzy controllers

Manuela S. Leite, Ana M. F. Fileti, Flávio V. Silva*
School of Chemical Engineering, Departament of Chemical Systems Engineering, State University of Campinas (UNICAMP),CP 6066, CEP13083-970, Campinas, São Paulo, Brazil.

Keywords: Fuzzy controller, PID controller, Bromelain, Fieldbus
Topic: Systematic methods and tools for managing the complexity

Abstract

Fuzzy logic has an important role in process control due to its capability to incorporate the empirical knowledge about the process. Systems with unknown behavior can be easily controlled using logical rules. Thus, fuzzy controllers are an important alternative method to the conventional PID control mainly in ill-defined or nonlinear systems. This paper presents an experimental implementation of conventional and fuzzy controllers applied to a bromelain precipitation process.

1 Introduction

Bromelain is a proteolitic enzyme presents in pineapple fruit with high commercial value (Freiman and Sabaa Srur, 1999). As consequence, pharmaceutical and chemical applications have been increasing (Kelly, 1996). Bromelain is recovered from industrial and kitchen waste (pineapple stem and rind).

The enzyme precipitation is a simple operation but the temperature maintenance is crucial. The temperature control avoid the irreversible protein denaturation, improve the process yield and the enzymatic activity (Lucarini et al 2005).

The fuzzy control systems have come into prominence due to their applicable approach, attractive for complex process, their characteristic action based on knowledge of the system and on qualitative dynamic behavior, and when measurements are uncertain, incorporating the non-linearity into the methodology of the project (Eker and Torun, 2006; Traoré et al, 2005; Souza Jr. and Almeida 2001; Babuska et al, 2002; Horiuchi and Kishimoto, 2002; Hiroyuki and Kobayashi, 2000; Martìnez, 1999)

In this work, the design and tuning of conventional PID and fuzzy controllers was experimentally developed for a pilot batch plant to a bromelain recovery process from pineapple juice through the precipitation process with alcohol at low temperature (5℃) in a fed-batch stirred tank, using fieldbus network architecture. The performance between these controllers was evaluated in terms of: ITAE criterion, electrical energy consumption, and mainly in terms of enzymatic activity recovery.

2 Fuzzy Logic

The fuzzy inference simulates a human ability to make decisions using fuzzy logic and approximate reasoning. Mamdani inference is widely applied in fuzzy logic controllers. The output of the inference process is a fuzzy set, specifying a possibility distribution of control

* Corresponding author. Tel + 55-19-3521-3946. E-mail: sl.manuela@gmail.com, flavio@feq.unicamp.br

action. The control action (U or ΔU) is determined by a process called defuzzification. The defuzzifier converts the output of the associate rules (inference) into a single numerical value. The basis of fuzzy control is a set of rules that represent the knowledge of a process operator. Each rule represents a cause and effect relationship and is formatted in an "IF . . . THEN . . ." manner. For a given operating condition (cause), there is a corresponding action (effect) that should be taken to control the process.

For example, the MISO (multiple-input-single-output) rule:

$$\text{IF } x_1 \text{ is } A_1 \text{ and ... and } x_n \text{ is } A_n \text{ THEN } y_i \text{ is } C_i$$

The fuzzy control structure can be classified according to its application. One of the most popular fuzzy structures is based on error (ε) and change-of-error ($\Delta\varepsilon$), constituting the basis of the fuzzy-PD and fuzzy-PI controllers, with U and ΔU output control signals (manipulated variable), respectively.

3 Material and Methods

3.1 Bromelain precipitation plant description

The experimental plant, represented in Figure 1, consisted of a stainless steel stirred tank (1000 mL); a storage tank of the precipitant agent (ethanol 99.5 GL); a variable speed pump for the coolant (1000 L/h maximum capacity) used as manipulated variable; four Pt-100 temperature sensors for monitoring temperatures (ethanol storage, precipitation tank, inlet and outlet cooling fluid); two temperature transmitters (digital output signal) and a level transmitter; a frequency converter to modulate the pump speed of cooling fluid; a micropump that continuously feeds the ethanol into the precipitation tank. This micropump was employed to continuously feed the ethanol into the tank at room temperature (approximately 23 ºC) until the liquid volume reached 750mL, which corresponds to 1:4 v/v ratio between juice and ethanol (best protein precipitation condition, according to Cesar, 1999).

The initial conditions to system variables were determined in order to establish the biases for the control strategy implementation. The analyzed variables, through experimental design, were: the ethanol micropump flow rate; the coolant pump flow rate (manipulated variable); and the coolant inlet temperature. The best values found were, respectively: 2.16 L/h; 374 L/h; and 0 ℃. A 50% (v/v) water propylene glycol s olution was used as cooling fluid and a thermostatic bath kept its temperature constant.

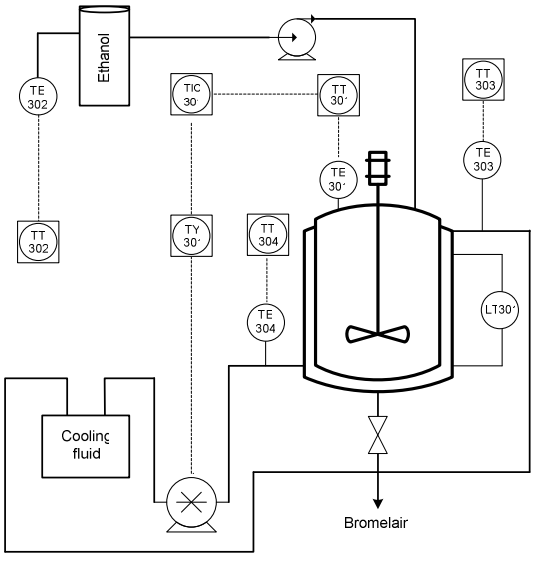

Figure 1. Fed-batch precipitation system flow chart.

3.2 Sample preparation and determination of the enzymatic activity

The stem and rind of pineapple fruit (species “Pérola”) were triturated and mixed to get a uniform solution. Distilled water was used at a dilution rate of 1:1. Solids were filtered out from the mixture by means of paper filters. The filtrate, called pineapple juice, contains the bromelain enzyme. Samples containing 150 mL of pineapple juice were frozen at -18ºC (César et al, 1999) until they were individually used in the experiments (fed into the tank).

The determination of the enzyme activity was used as parameter for evaluation of the performance of both types of controllers. The analysis of the enzymatic activity is based on the biuret colorimetric method. Under alkaline conditions substances containing two or more peptide bonds form a purple complex with copper salts in the reagent. According to this method, a unit (U) of enzymatic activity corresponds to the amount of enzyme able to change in a unit the absorbance reading at 540 nm, during 10 min at 37℃.

3.3 Fieldbus network architecture

The management of the digital control system was performed through a Foundation Fieldbus communication system, according to Figure 2.

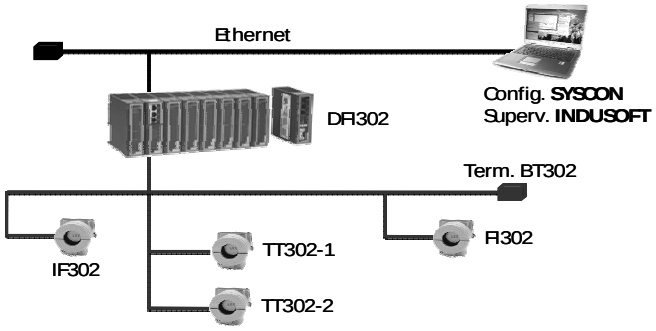

Figure 2. Fieldbus network for bromelain precipitation process.

The field devices used to monitor and control the precipitation tank, are as follows: distributed Fieldbus interface (DFI302), converters device (IF302 and FI302) and temperature transmitters (TT302). Software SYSCON 7.0 was used to implement the conventional control loop and to configure Fieldbus network devices. The software INDUSOFT Web Studio 6.1 was used for the management and data acquisition of the system.

3.4 Controllers design

- Conventional Controller

The first method of Ziegler-Nichols was used for PID tuning purposes in open-loop runs and were obtained values of the parameters K_c, τ_i and τ_d for the PID controller. This controller has the form of Equation 1 (Stephanopoulos, 1984).

$$U(t) = u_{ss} + K_c\left[\varepsilon(t) + \frac{1}{\tau_i}\int_0^T \varepsilon(t)dt + \tau_d \frac{d\varepsilon(t)}{dt}\right] \quad \text{(eq.1)}$$

- Fuzzy Controller

Initially, some experiments were carried out to have expert knowledge about precipitation process. Positive and negative disturbances were applied in the manipulated variable at different moments of the batch run, with different volumes, and the controlled variable behavior was observed. Thus, the process dynamic was identified and precipitation process nonlinearities could be observed. This knowledge was essential to tune fuzzy controller. After that, different universe of discourse, base of rules and support sets of membership functions were experimentally tested.

The implementation of the fuzzy-PI controller was carried out using the Fuzzy Toolbox of software MATLAB 7.0.1. The MISO strategy was used in this controller and three linguistic variables were used: temperature error and change-of-error (input linguistic variable) and change in coolant flow rate (output linguistic variable), represented by Equations 2, 3 and 4, respectively.

$$\varepsilon(t) = Y(t) - Y_{SP}(t) \text{ (Eq.2)} ; \Delta\varepsilon(t) = \varepsilon(t) - \varepsilon(t - \Delta t) \text{ (Eq.3)};$$
$$\Delta U(t) = U(t) - U(t - \Delta t) \text{ (Eq.4)}$$

In this study were used triangular membership functions. The linguistic expressions for the magnitude of the linguistic variables contain the following adjectives: negative large (NL), negative medium (NM), negative small (NS), zero (ZR), positive small (PS), positive medium (PM), positive large (PL). The rule base was implemented using the above adjectives and Mamdani inference system. The center of area was used for the output variable calculation (defuzzification), (Eq. 5).

$$u^* = \frac{\sum_{i=1}^{N} u_i \mu_{OUT}(u_i)}{\sum_{i=1}^{N} \mu_{OUT}(u_i)} \qquad (5);$$

The triangular membership functions, and their corresponding labels of error (ε), incremental error (Δε). and increment output value (ΔU), were determined by observing the system nonlinearities and they are presented in Figure 3 and Figure 4.

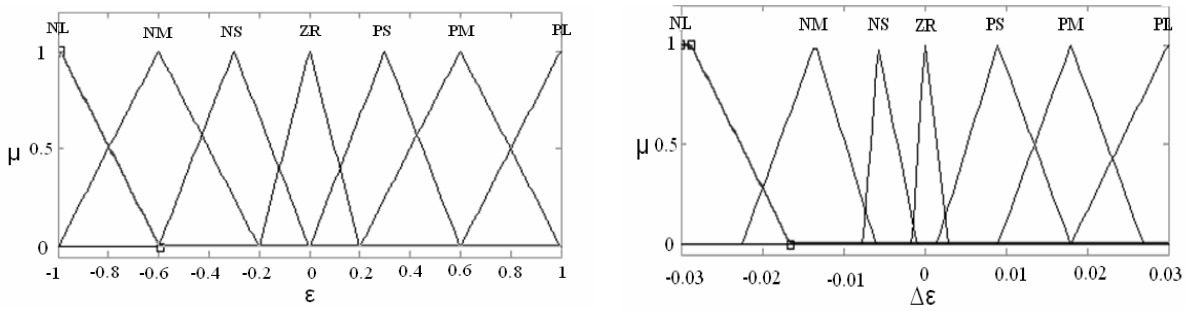

Figure 3. Membership functions of ε and Δε.

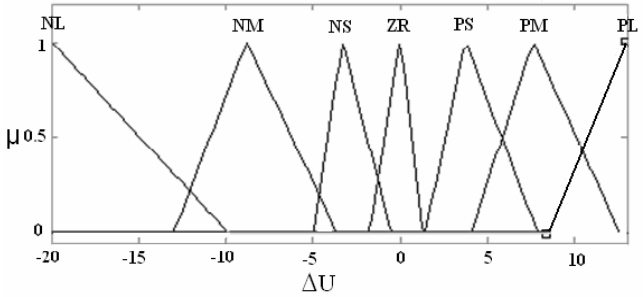

Figure 4. Membership function of ΔU.

Modifications in the configuration of the fuzzy controller (universe of discourse, rule base and support sets of membership function) were made as well, based on the accomplishment of experimental tests. The performance of the controller was evaluated and new strategies in its configuration were implemented when necessary. Table 1 shows 49 rules used for this fuzzy controller

Table 1. Rule base of the fuzzy-PI controller.

ERROR (ε)	CHANGE-OF-ERROR (Δε)						
	NL	**NM**	**NS**	**ZR**	**PS**	**PM**	**PL**
PL	NS	NS	NS	PL	PL	PL	PL
PM	NS	ZR	PS	PM	PL	PL	PL
PS	NM	NS	ZR	PS	PM	PL	PM
ZR	NL	NM	NS	ZR	PS	PM	PL
NS	NL	NL	MN	NS	ZR	PS	PS
NM	NL	NL	NL	MN	NS	ZR	ZR
NL	NL	NL	NL	NL	MN	NS	ZR

4 Results and Discussion

For conventional controller, the best adjusted parameters were: K_c = 35.0 %/℃, τ_i = 28.0 s, and τ_d = 7.0 s. Figures 5a and 5b show the temperature behavior under a well-tuned conventional PID and fuzzy-PI controller, respectively.

From these results, could see that addition of ethanol is critical. In order to keep overshoot at minimum level, intense controller response is required, causing pump saturation, which was noted under both control strategies. In fact the saturation effect was far less noticeable when the fuzzy controller was applied (from 130 to 35 s), favoring conservation of the equipment and smaller electric energy consumption (from 9.11 to 3.65 kWh).

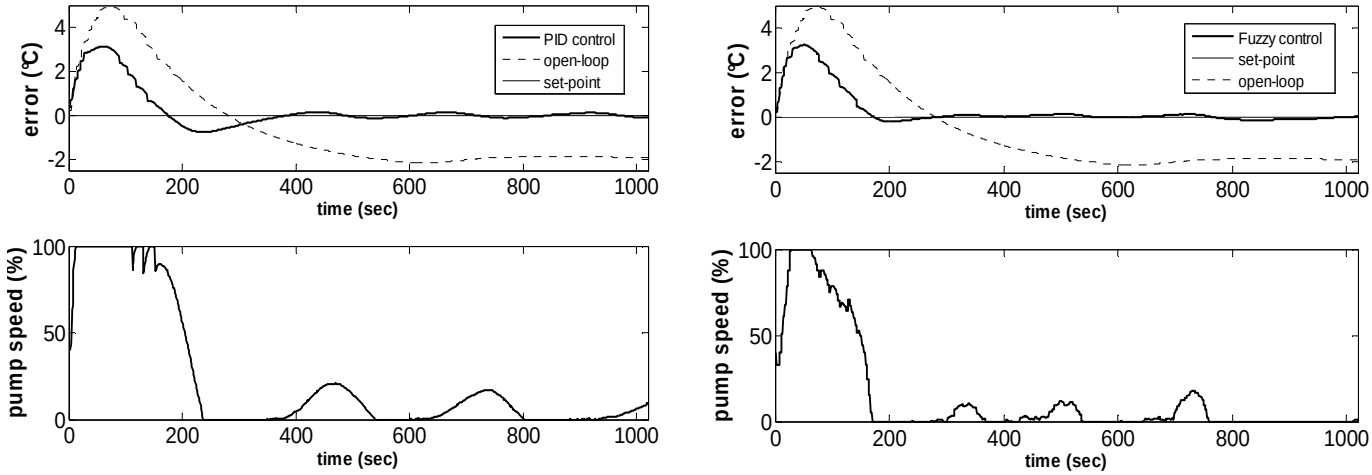

a b

Figure 5. Behavior of the controlled and manipulated variables under: a) PID control and b) fuzzy-PI control.

5 Conclusion

From the results, it could be concluded that both controllers are suitable for the precipitation tank temperature control (same overshoot and rise time value). However, the fuzzy controller showed better global performance criteria: small ITAE, small response time and pump saturation time, and a larger enzymatic activity of the product (79.73 % higher than using PID).

The fuzzy controller presented electric energy consumption that was 59.93% less when compared to the energy required by the conventional controller, providing a significant reduction of operational costs. The greater efficiency of the fuzzy controller can be attributed to its capability of adaptation to the nonlinearities, presenting favorable technical comparison with the conventional feedback controller.

In this application, the fuzzy controller was simple in structure, easy to implement, better in performance, and more versatile than the conventional controller.

Acknowledgs

The authors are grateful to FAPESP and CAPES for financially supporting this study.

References

Babuska R., Oosterhoff, J., Oudshoorn, A., Bruijn, P.M. (2002). Fuzzy self-tuning PI control of pH in fermentation*. Engineering Applications of Artificial Intelligence*, 15,3–15.

Cesar, A.C.W., Silva, R., and Lucarini, A.C. (1999). Pineapple stem and rind proteolytic enzymes recovery (In Portuguese). *Revista de Iniciação Científica – São Carlos/SP*,1, 47-53.

Eker, I., Torun, Y. (2006). Fuzzy logic control to be conventional method. *Energy Conversion and Management*, 47, 377-394.

Hiroyuki, H., Kobayashi, T. (2000). Fuzzy Control of Bioprocess. *Journal of Bioscience and Bioengineering*, 89, 401-408.

Horiuchi, J., Kishimoto, M. (2002). Application of Fuzzy Control to Industrial Bioprocess in Japan, *Fuzzy sets and Systems*, 128, 117-124.

Kelly, G.S. (1996). Bromelain: A literature review and discussion of its therapeutic applications. *Alternative Medicine Review*, 1(4), 243-257.

Martìnez G., Lòpez, A., Esnoz, A., Vírseda, P., Ibarrola, J. (1999). A new fuzzy control system for white wine fermentation. Food Control, 10, 175-180.

Souza Jr., and Almeida, P.I.F. (2001). Design of a fuzzy system for the control of a biochemical reactor in fed-batch culture. *Process Biochemistry*, 37 461- 469.

Stephanopoulos, G., Chemical process control: an introduction to theory and practice. Englewood Cliffs: Prentice-Hall Inc., 1984. 696p.

Traore, A., Grieu,S., Puig,S., Corominas, L., Thiery, F., Polit, , M., Colprim, J. (2005). Fuzzy control of dissolved oxygen in a sequencing batch reactor pilot plant. *Chemical Engineering Journal,* 111, 13–19.

Proceedings of the 10th International Chemical and
Biological Engineering Conference - CHEMPOR 2008
Braga, Portugal, September 4-6, 2008
E.C. Ferreira and M. Mota (Eds.)

Optimal cleaning schedule for heat exchangers in a heat exchanger network based on continuous time approach

Kanyaluk Ao-ekkasit, Slita Nusong, Soorathep Kheawhom*
Department of Chemical Engineering, Faculty of Engineering, Chulalongkorn University
Patumwan, Bangkok 10330, Thailand.

Keywords: Cleaning schedule, Heat exchanger network, MINLP, Optimization, Continuous-time.
Topic: Systematic methods and tools for managing the complexity.

Abstract

In this work, the simulations of fouling in heat exchanger networks are performed based on linear and asymptotic fouling models. The effects of various model parameters on a variation with time of outlet temperature of hot and cold streams, heat transfer coefficient and heat transfer rate are investigated. In addition, the problem of optimal cleaning schedule of heat exchangers is formulated using a new technique based on continuous of time horizon approach. The formulated optimization problem minimizes the summation of operating cost with subject to various operating constraints. Where, the number of cleaning operation is fixed priorly, and the time period for each cleaning operation is then determined. We illustrate the proposed technique and compare our technique with traditional discretization of time approach in case studies: (i) a single heat exchanger for 24 months horizon, (ii) the optimal cleaning schedule of heat exchanger network consisting 10 exchangers for 18 months horizon. Our developed technique can overcome the difficulty in using logical variables encountered in the cleaning schedule optimization problem. Our approach can efficiently solve the cleaning schedule problem while obtain a better solution compared with previous work.

1 Introduction

Energy consumed plays an important role in the operating costs of all chemical industries. Therefore, heat exchanger networks are implemented in almost all chemical plants. However, fouling of heat exchangers is one of major industrial problems. It leads to the reduction of heat transfer efficiency and heat transfer rate. Consequently, it reduces production rate, and increases cleaning and maintenance costs. Thus, the effective methods for fouling mitigation are required. In order to restore thermal performance of the heat exchanger, fouling can be removed by regular cleaning. Normally, cleaning improves the heat exchanger performance resulting in the reduction of energy cost. However, during cleaning period the heat exchanger must be stopped, resulting in the requirement of external utilities. Thus, cleaning too often may not be economically favorable after all.

The approach to address cleaning schedule problem can be classified into two main categories: discrete-time and continuous-time models (Floudas and Lin, 2005). However, all most of the work have been done based on the discrete-time approaches. The major drawbacks of the discrete-time approaches lie on the fact that the discretization time plays an important role in the reliability of the solution obtained. Smaili et al. (1999) studied the optimization of cleaning schedule of heat exchanger network used in sugar industry. This work described the use of a mixed integer nonlinear programming to the problem. They reported that in order to obtain a reliable optimal cleaning schedule, an accuracy mathematical model of the fouling behavior of the network is required.

*Corresponding author. Tel. +66-2-218-6893. E-mail: soorathep.k@chula.ac.th.

Georgiadis and Papageorgiou (2001) proposed a mathematical model of the fouling in batch plant operation, where a short-term scheduling problem was considered. The objective was to determine the optimal utilization of available plant resources over a given time horizon. An iterative procedure for solving the resulting non-convex mixed integer nonlinear programming was proposed. This approach involves solving a series of mixed integer linear programming sub-problems. Further, a mixed integer nonlinear programming formulation of the cleaning schedule problem for continuously operating heat exchanger networks was studied by Smaili et al. (2002). It was reported that even a global optimal solution obtained from mixed integer nonlinear programming formulation may not be the best schedule, if the discretization time is too coarse.

Additionally, Lavaja and Bagajewicz (2004) illustrated a mixed integer linear programming for cleaning schedule optimization. This work was applied in a typical preheat train configuration. They did not approximate the nonlinear equations related to heat transfer or the fouling models. They used a special rearrangement in order to obtain linear expressions. The model was capable of rendering global optimality for small case.

In this work, we develop an algorithm for optimal heat exchanger network cleaning schedule based on continuous time approach. The model considered here does not approximate the nonlinear equations related to heat transfer or the fouling models. The optimal cleaning schedule of heat exchanger network is obtained by solving the optimization problem formulated.

2 Heat exchanger model description

The formulation presented here is based on constant flow inputs and physical parameters. Only changes due to cleaning actions are considered. Film heat transfer coefficients are also assumed to remain constant despite changes in Prandtl and Reynold numbers caused by fouling. In addition, the heat exchanger is bypassed for isolation during cleaning action. And, the fouling in bypass heat exchanger is neglected. Further, each heat exchanger is modeled using a lumped parameter where the change in overall heat transfer coefficient is related to the fouling formation presented in Eq. 1.

$$r_f(t) = \frac{1}{U(t)} - \frac{1}{U_c}. \tag{1}$$

Where, $U(t)$ is overall heat transfer coefficient (BTU/ft^{2}h$^\circ$F), U_c is overall heat transfer coefficient when the unit is clean, and $r_f(t)$ is fouling resistance (BTU/ft^{2}h$^\circ$F).

In this work, linear and asymptotic fouling formulation models were considered for estimating the changes in $r_f(t)$ as shown in Eqs. 2 and 3, respectively.

$$\dot{r}_f(t) = {r_f}^{\infty}(1 - e^{-t/\tau}) \tag{2}$$

$$\dot{r}_f(t) = {r_f}^{\infty} \tag{3}$$

Heat transfer rate of cold stream (Q_c) and hot stream (Q_h) are shown in Eqs. 4 and 5, respectively.

$$Q_c = F_c C_{p,c}(T_{c,out} - T_{c,in}) \tag{4}$$

$$Q_h = F_h C_{p,h}(T_{h,in} - T_{h,out}) \tag{5}$$

The heat transfer rate in a heat exchanger is expressed as in Eq. 6.

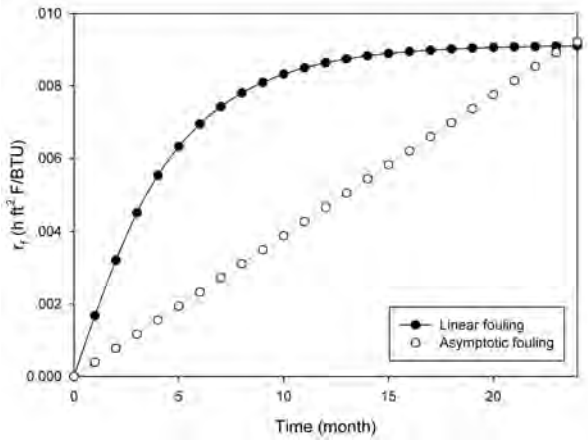

Figure 1: Fouling formation of asymptotic and linear fouling models.

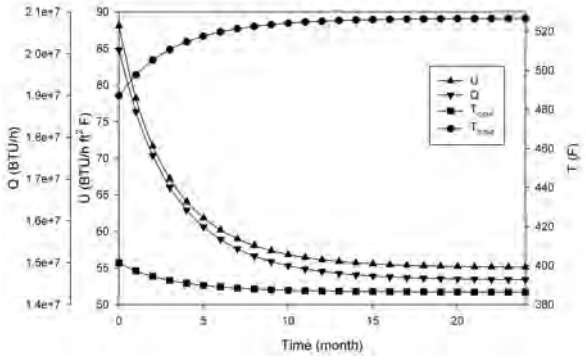

Figure 2: The variation of U, Q, $T_{c,out}$ and $T_{h,out}$ in single heat exchanger with asymptotic fouling.

$$Q = UA\frac{(T_{h,in} - T_{c,out}) - (T_{h,out} - T_{c,in})}{ln(T_{h,in} - T_{c,out})/(T_{h,out} - T_{c,in})} \tag{6}$$

The performance of heat exchanger is calculated using the NTU-effectiveness method. Heat exchangers are modeled as a simple counter current. Where, we can computed $T_{h,out}$ and $T_{c,out}$ by using Eqs. 7 and 8, respectively.

$$T_{h,out} = \frac{1 - \frac{F_hC_{p,h}}{F_cC_{p,c}}}{e^{\frac{UA}{F_cC_{p,c}}(1-\frac{F_hC_{p,h}}{F_cC_{p,c}})} - \frac{F_hC_{p,h}}{F_cC_{p,c}}}T_{h,in} + \frac{1 - e^{\frac{UA}{F_cC_{p,c}}(1-\frac{F_hC_{p,h}}{F_cC_{p,c}})}}{e^{\frac{UA}{F_cC_{p,c}}(1-\frac{F_hC_{p,h}}{F_cC_{p,c}})} - \frac{F_hC_{p,h}}{F_cC_{p,c}}}T_{c,in} \tag{7}$$

$$T_{c,out} = \frac{F_hC_{p,h}}{F_cC_{p,c}}(T_{h,in} - T_{h,out}) + T_{c,in} \tag{8}$$

Figure 1 presents the fouling formation of linear and asymptotic models in 24 months period without cleaning. The variation in asymptotic fouling model of overall heat transfer coefficient, heat transfer rate, outlet temperature of hot stream and outlet temperature of cold stream in 24 months without cleaning are presented in Figure 2. The variation of asymptotic fouling changes rapidly at the early stage of operation and then stabilizes to the final value at asymptote. The increasing of fouling results in the reduction of overall heat transfer coefficient. The outlet temperature of hot stream increases with time, while the outlet temperature of cold stream decreases with time. This is due to the fact that fouling reduces the heat transfer efficiency. Figure 3 shows the variation with time of heat transfer rate with various different parameters in asymptotic fouling model. In comparison, the increasing of time decay fouling formation

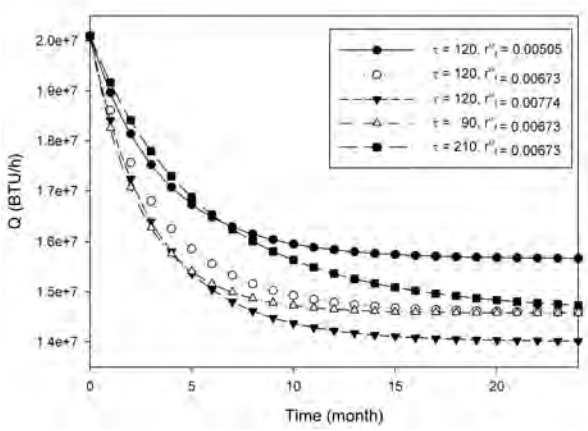

Figure 3: The variation of a single heat exchanger with different parameters in asymptotic fouling model.

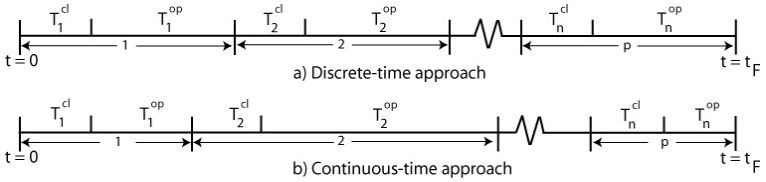

Figure 4: Discrete and continuous time approach.

(τ) results in slow formation of fouling. The effectiveness of heat exchanger increases by increasing the time decay of fouling formation (τ).

3 Optimization of cleaning schedule

We considered the cleaning schedule for a heat exchanger network comprising N heat exchangers during time period t_F of continuous plant operation. The goal is to minimize the total operating cost including cleaning cost and cost on energy losses in each process stream as shown in Eq. 9.

$$F = \sum_{n=1}^{N} C_E \left(\int_0^{t_F} (Q_{n,clean} - Q_n(t)) dt \right) + \sum_{n=1}^{N} C_{cl} k_n \tag{9}$$

where, N is the number of heat exchangers in the network. C_E is the cost of furnace extra fuel. $Q_{n,clean}$ is the heat transfer rate between hot and cold streams of heat exchanger n^{th} in clean condition. Q_n is the heat transfer rate between hot and cold fluids of heat exchanger n^{th}. C_{cl} is the cleaning cost. k_n is the number of cleaning actions of heat exchanger n^{th}.

$Q_n(t)$ is not continuous at a point where cleaning action occurs. There are two approaches, discrete and continuous time approaches, in order to evaluate the objective function based on Eq. 9. The basic idea in the discrete time formulation is to divide the length of time horizon (t_F) considered into a number of specified small periods (P) as shown in part (a) of Fig. 4. The decisions to be made are associated with these time periods. The length of each period can be adjusted as necessary. However, the size of the search space increases with the decreasing of the length of each period. In this work, we applied the continuous-time approach as shown in part (b) of Fig. 4, where the number of cleaning operation is fixed priorly, and the time period for each cleaning operation is then determined. Each time period consists of two subperiods. The first period is a cleaning subperiod (t^{cl}), where heat exchangers are being cleaned. And the second one is an operating subperiod (t^{op}). In the operating subperiod, the heat exchangers are operated, and the formation of fouling occurs.

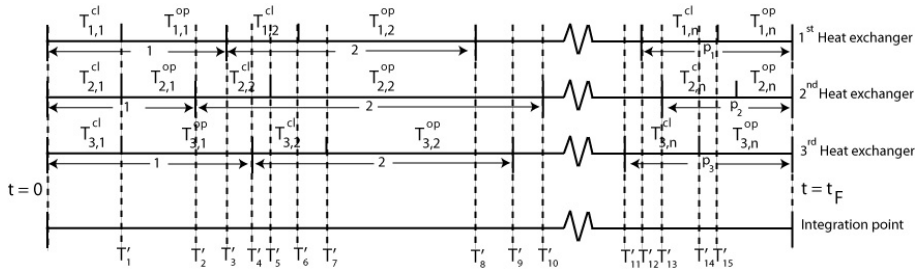

Figure 5: Integration points used in our algorithm.

Various constraints were applied in order to determine the optimal cleaning schedule. The outlet cold temperature of each heat exchanger must be greater than the inlet cold temperature associated, and the outlet hot temperature of each heat exchanger must be lower than the inlet hot temperature associated. Moreover,there is also restriction in minimum value that the temperature of each cold stream is allowed to be reached.

In our algorithm, the integral term appeared in the objective function as shown in Eq. 9 is calculated from the summation of all point to point integration, where the discontinuity occurs at each point. Figure 5 shows integration points in the network with three exchangers.

We proposed using modified differential evolutionary algorithm (DE) to solve the formulated optimization problem. DE is a very simple population based optimizer which is at the same time very powerful and robust (Storn and Price, 1997).

4 Case studies

The optimization of cleaning schedule using our formulation described in previous section are presented and illustrated in two case studies. The first case focuses on the optimal cleaning schedule of a single heat exchanger. The second case is an optimal cleaning schedule of heat exchanger network previously addressed in the work by Smaili et al. (2002). In the discrete time approach, the time horizon is divided into 30 days period. In each period, the cleaning subperiod is 6 days, and the operating subperiod is 24 days. The cleaning cost is 4,000 £/unit. The cost of furnace utility is 0.01 £/kWh. The parameters used in both cases were also taken from Smaili et al. (2002).

4.1 Case study 1

In the first case, the time horizon considered is 24 months. The heat exchanger is counter current shell and tube. The maximum decrease on outlet temperature of cold stream is 2%. We focused on the influence of initial fouling rate and time decay of fouling formation on the number of cleaning actions and objective function obtained using our algorithm and traditional discrete-time approach. Table 1 shows the number of cleaning actions and and objective functions obtained in the case study 1.

Table 1: The comparison of the solutions obtained in the case study 1.

		Discrete time		Continuous time	
Parameters		Cleaning	Objective func.	Cleaning	Objective func.
$r_f{}^{\infty}$	0.003365	10	172,434 £	9	166,085 £
	0.006730	11	176,912 £	10	169,393 £
	0.013461	12	194,756 £	11	177,931 £
τ	90	12	226,524 £	11	221,751 £
	120	11	176,912 £	10	169,393 £
	210	10	170,541 £	9	141,404 £

The rapid change in heat transfer rate occurs in the case of large value of initial fouling rate. Consequently, the rapid reduction of outlet temperature of cold stream requires more cleaning actions. Thus, the operating cost increases when the initial fouling rate increases. The increasing in the decay of fouling formation results in the slow deposition of fouling. In the case of small value of time decay of fouling formation, the outlet temperature of cold stream rapidly decreases. Thus, the operating cost decreases when the time decay of fouling formation increases. The number of cleaning actions decreases with the increasing of the time decay of fouling formation. Because, the large value of time decays of fouling formation provides small value of fouling formation.

4.2 Case Study 2

We considered the optimal cleaning schedule of heat exchanger network under fouling condition. The operating time horizon considered is 18 months. The maximum decrease on outlet temperature of cold stream is also 2%. We focused on the influence of cleaning cost on the number of cleaning actions and objective function obtained using our algorithm and traditional discrete-time approach. Table 2 shows the number of cleaning actions and and objective functions obtained in the case study 2.

Table 2: The comparison of the solutions obtained in the case study 2.

Cleaning cost	Smaili et al. (2002)	Discrete time	Continuous time
$4,000£$	$392,294£$	$351,555£$	$292,050£$
$8,000£$	No reported	$486,035£$	$405,010£$

The performance obtained using continuous time formulation are better than that obtained using discrete time formulation. This is due to the fact that in continuous time approach, the time period between each cleaning operation which is continuous in nature is not required to be defined priorly.

5 Conclusions

In this work, the effects of various model parameters on a variation of outlet temperature of hot and cold streams, heat transfer coefficient and heat transfer rate were investigated. In addition, the problem of optimal cleaning schedule of heat exchangers was formulated using a new technique based on continuous of time horizon approach. The problems formulated were solved by using differential evolutionary algorithm. Our proposed formulation technique was illustrated in case studies. The linear fouling model and asymptotic fouling model were considered. The performance of our technique compares favorably with traditional discretization of time approach approach. The performance obtained using continuous time formulation were better than that obtained using discrete time formulation.

References

Floudas, C., Lin, X., 2005. Mixed integer linear programming in process scheduling: Modeling, algorithms, and applications. *Annals of Operations Research*, 139, 131–162.

Georgiadis, M. C., Papageorgiou, L. G., 2001. Optimal scheduling of heat-integrated multipurpose plants under fouling conditions, *Appl. Therm. Eng.*, 21, 1675–1697.

Lavaja, J. H., Bagajewicz, M. J., 2004. On a new milp model for the planning of heat exchanger network cleaning, *Ind. Eng. Chem. Res.*, 43, 3924–3938.

Smaili, F., Angadi, D. K., Hatch, C. M., 1999. Optimization of scheduling of cleaning in heat exchanger networks subject to fouling: Suger industry case study, *Trans. IChemE.*, 77, 159–164.

Smaili, F., Vassiliadis, V. S., Wilson, D. I., 2002b. Optimization of cleaning schedules in heat exchanger networks subject to fouling. Chem. Eng. Commun. 189:1517–1549

Storn, R., Price, K., 1997. Differential evolution - a simple and efficient heuristic for global optimization over continuous spaces, *J. Global Optim.*, 11, 341–359.

Proceedings of the 10th International Chemical and
Biological Engineering Conference - CHEMPOR 2008
Braga, Portugal, September 4-6, 2008
E.C. Ferreira and M. Mota (Eds.)

Optimal Design of Water-Using Networks

João Teles[1,2], Pedro M. Castro[1*], Henrique A. Matos[2]
[1] Departamento Modelação e Simulação de Processos, Instituto Nacional de Engenharia Tecnologia e Inovação, 1649-038 Lisboa, Portugal.
[2] Departamento de Engenharia Química e Biológica, Instituto Superior Técnico, 1049-001 Lisboa, Portugal

Keywords: Water minimization, water reuse, mathematical programming, optimization
Topic: Systematic methods and tools for managing the complexity.

This paper introduces a novel strategy for designing optimal water using networks (WUN) involving fixed contaminant load and fixed flowrate operations and featuring multiple contaminants and water sources. A mixed integer linear programming (MILP) based procedure is used to generate a few structurally different starting points for the non-convex nonlinear program (NLP). The problem is decomposed into calculation stages by assuming that the water streams go through the units in series. The binary variables then select which unit belongs to a certain stage. The algorithm is compared to a closely related LP-based method taken from the literature and to the one employed by the global optimization solver BARON. The results from a large set of example problems confirm its effectiveness in avoiding local solutions. In contrast to the previous method they are easily scalable and, for some of the larger problems, could find better solutions than BARON with significantly fewer computational resources.

1 Introduction

Water is seen as probably the most broadly used resource in industry. These usages lead to contaminated wastewater, which may pose an environmental pollution problem. Increasing water costs, restrictions on water use and increased environmental awareness have driven designers towards conceiving more efficient water systems looking for both freshwater minimization and wastewater generation. Several contributions have appeared in the literature that look into this problem. In all of them, the identification of water reuse and/or recycling opportunities has been regarded as an innovative step within the two most commonly used scientific solution approaches: the insight-based pinch technology, largely supported by graphical methods, and the more systematic mathematical programming approaches. Targeting/design methods for water systems can also be classified based on the problem being handled. Ideally, a fully integrated water-using and treatment network should be sought but due to the inherent complexity of the problem, many researchers have focused on either the water-using or the distributed wastewater treatment (WTN) design.
When compared to pinch based approaches, mathematical programming methods have the advantage of effectively dealing with multicontaminant systems. All water reuse possibilities can be embedded into a superstructure and the problem formulated as a NLP. However, unless computationally expensive global optimization solvers are employed (e.g. BARON), suboptimal solutions may result. One alternative is to use heuristic procedures to generate multiple, structurally different, starting points to the NLP, thus increasing the probability of finding the global optimal solution. Recent examples of such methods can be found in Teles et al. (2008) for WUNs and in Castro et al. (2007) for WTNs. The former is very effective but may lead to a prohibitively high number of mathematical problems to solve as the number of operations increases. With the aim of reducing the overall computational burden of the search procedure, while keeping the same success rate, this paper proposes a novel MILP-based algorithm. The novelty is to employ binary variables to select the best operation for a particular calculation stage of the initialization procedure.

* Corresponding author. Tel + 351-210924643. E-mail:pedro.castro@ineti.pt

2 Problem Statement

The design of a water-using system involves a set *W* of fresh water sources containing a number of pollutants (set C), with known concentrations ($c_{w,c}^{wat}$), that are available to satisfy the demands of every water-using operation (set O), which fall in two broad categories (Prakash and Shenoy, 2005): fixed contaminant load operations (set O^{fl}) which are quality controlled and may be modeled as mass transfer units, and fixed flowrate operations (set O^{ff}) that are quantity controlled and do not involve any mass transfer. Data for the former is often expressed by a limiting flowrate (f_o^{lim}), together with maximum inlet ($c_{o,c}^{in\,max}$) and outlet ($c_{o,c}^{out\,max}$) concentrations, which can be related to the mass exchange ($\Delta m_{o,c}$) through $\Delta m_{o,c} = f_o^{lim} \cdot \left(c_{o,c}^{out\,max} - c_{o,c}^{in\,max}\right), \ \forall o \in O^{fl}, c \in C$. For the latter, the inlet (f_o^{in}) and outlet (f_o^{out}) flowrates are given. The outlet concentrations are independent on the inlet concentrations (must be lower than $c_{o,c}^{in\,max}$) and so are fixed to $c_{o,c}^{out\,max}$. The objective is to minimize the total freshwater flowrate into the system, Eq 1.

3 Mathematical NLP Formulation

The model variables of the general NLP that includes all reuse and recycling possibilities are the following: $F_{w,o}^{wat}$, represents the flowrate of fresh water source *w* needed to satisfy the demand for operation unit *o*; $C_{o,c}^{in}$ and $C_{o,c}^{out}$ are, respectively, the inlet and outlet concentrations for the fixed contaminant load operations; F_o^{tot} is the total flowrate into fixed load operation *o*; $F_{j,o}^{oper}$ gives the total flow rate from operation *j* to operation *o*; and F_o^{tsys} represents the outlet flowrate from operation *o* heading for the treatment system.

The model constraints are now described. Eq 2 is the total flow balance over the unit's inlet mixers, where the inlet flow to operation *o* (known for fixed flowrate units) may come from freshwater streams and/or from the units' outlet streams. Eq 3 is the total flow balance over the unit's outlet splitters, where the exiting flow may be heading to the same, to other water-using units, or to the treatment system. For fixed contaminant load operations, Eqs 4-7 apply, while for fixed flowrate operations, Eq 8 suffices, which ensures that the inlet concentrations do not exceed their specified maximum values. Eqs 4-5 are the mass balances over the mixers of and over the fixed load units. Eq 6 and 7 are the upper bounds on the concentration variables.

$$\text{Min} \sum_{w \in W} \sum_{o \in O} F_{w,o}^{wat} \tag{1}$$

$$F_o^{tot}\Big|_{o \in O^{fl}} + f_o^{in}\Big|_{o \in O^{ff}} = \sum_{w \in W} F_{w,o}^{wat} + \sum_{j \in O} F_{j,o}^{oper} \quad \forall o \in O \tag{2}$$

$$F_o^{tot}\Big|_{o \in O^{fl}} + f_o^{out}\Big|_{o \in O^{ff}} = F_o^{tsys} + \sum_{j \in O} F_{o,j}^{oper} \quad \forall o \in O \tag{3}$$

$$F_o^{tot} \cdot C_{o,c}^{in} = \sum_{w \in W} F_{w,o}^{wat} \cdot c_{w,c}^{wat} + \sum_{j \in O} F_{j,o}^{oper} \cdot (C_{j,c}^{out}\Big|_{j \in O^{fl}} + c_{j,c}^{out\,max}\Big|_{j \in O^{ff}}) \quad \forall o \in O^{fl}, c \in C \tag{4}$$

$$\Delta m_{o,c} = F_o^{tot} \cdot \left(C_{o,c}^{out} - C_{o,c}^{in}\right) \forall o \in O^{fl}, c \in C \tag{5}$$

$$C_{o,c}^{in} \le c_{o,c}^{in\,max} \quad \forall o \in O^{fl}, c \in C \tag{6}$$

$$C_{o,c}^{out} \le c_{o,c}^{out\,max} \quad \forall o \in O^{fl}, c \in C \tag{7}$$

$$f_o^{in} \cdot c_{o,c}^{in\,max} \ge \sum_{w \in W} F_{w,o}^{wat} \cdot c_{w,c}^{wat} + \sum_{j \in O} F_{j,o}^{oper} \cdot (C_{j,c}^{out}\Big|_{j \in O^{fl}} + c_{j,c}^{out\,max}\Big|_{j \in O^{ff}}) \ \forall o \in O^{ff}, c \in C \tag{8}$$

4 Mathematical Programming Approaches

The presence of non-convex bilinear terms in the constraints imposes significant difficulties for commercial local NLP solvers, which may fail to find feasible solutions or end up with suboptimal networks. One alternative is to use global optimization solvers like BARON, but these tend to be extremely demanding computationally, as will be seen later on. Hence, valid approaches that are able to significantly reduce the computational effort and still obtain the global optimal solution are particularly relevant. This section presents a new efficient method to generate feasible networks for the initialization of the general NLP, after giving an overview of that by Teles et al. (2008).

4.1 Review of LP-based method of Teles et al. 2008 (TCN)

Doyle and Smith (1997) proposed a systematic initialization procedure, where an approximated version of the NLP, which is linear, is generated by replacing the outlet concentrations in all operations by their predefined maximum values and by relaxing the mass balance over the units. The idea behind TCN is similar in the sense that the concentration variables are also replaced by appropriate parameters. However, instead of relying on problem data to preset the fixed load operations' outlet concentrations and solving the full problem, TCN tackles each operation one at a time, so that the concentrations of all water streams that can be used to meet the demand of the unit under consideration are known beforehand. This procedure removes all bilinearities and leads to a succession of partial freshwater minimization, LP problems.

In TCN, the general superstructure is approximated by the complete set of substructures that assume that the water streams go through the operations in sequence, from the point they enter the water-using system up to the point they are sent to the downstream treatment system. For each sequence, every fixed load operation is pre-allocated to a single position, ranging from 1 to $|O^{fl}|$. Fixed flowrate operations are easier to handle since they consist of a linear subsystem that can be considered simultaneously with any fixed load operation. Overall, the proposed strategy involves the solution of a potentially large number of mathematical problems $(|O^{fl}|!\cdot(1|_{|O^{ff}|=0} + |O^{fl}|\Big|_{|O^{ff}|>0}) \cdot (|O^{fl}| \text{LPs} + 1 \text{NLP})$, which is little dependent on the number of fixed flowrate operations. Thus, and although the generation of multiple starting points can improve the chances of escaping local optima, as the number of operations increases, the total computational effort can reach prohibitive values.

4.2 New MILP-based algorithm (M1)

The new algorithm M1 employs a similar decomposition approach, but avoids the generation of redundant sequences, most of them unable to converge to global optimality by local solvers. Like in TCN, all fixed flowrate operations are considered within a single calculation stage. The total number of starting points generated equals the number of fixed load units $|O^{fl}|$. The total number of MILPs solved is equal to $|O^{fl}|^2$.

Figure 1 illustrates the superstructure used in the initialization procedure for the case where the fixed flowrate units are allocated to the second calculation stage. With this strategy, it is possible to reuse the outlet stream from a particular fixed flowrate unit into itself (internal recycling), into the other fixed flowrate units, or still into the fixed load unit that is allocated to the stage in question. Furthermore, the outlet from the chosen fixed load unit can also feed the fixed flowrate units (to avoid bilinear terms, one assumes that the outlet concentrations are at their maximum values, Doyle & Smith, 1997).

The algorithm is now illustrated with the example given in Table 1, for the case where the fixed flowrate system is allocated to stage two, like in Figure 2. Starting with the first stage, the MILP selects unit O_4, leading to $Y_{O_4} = 1$. Afterwards, the dynamic sets that facilitate the writing of the constraints are updated. For the second calculation stage, the unit just selected goes into the set of previous operations, PvO={O_4}, see Figure 2. The active operations, which include the fixed flowrate units, are AcO={O_1, O_2, O_3, O_5, O_6}. The optimizer selects fixed load unit O_2 and so the next assignments are: $Y_{O_2} = 1$,

AcO={O_1, O_3} and PvO={O_2, O_4, O_5, O_6}. In the third stage, unit O_3 is selected leaving O_1 to be the last element in the sequence. After the algorithm has gone through all calculation stages, we get a feasible water-using network and an upper bound on total freshwater consumption. Such network is then used as a starting point for the solution of the general NLP. Table 1 lists the results for this (S2) and the other starting points.

The MILP mathematical formulation is very similar to the general NLP given in section 3. In Eq 10 and 12, unit j can feed unit o if it has been assigned to previous stages or if $j \in O^{ff} \wedge j=o$. More than a single unit will normally be involved, so units j, either fixed load or fixed flowrate, can feed fixed flowrate units o. The maximum inlet concentration constraint over the mixers is given by Eq 12, where all the outlet concentrations from previous selected units are known. Eq 13 replaces the mass balance over the fixed load units (Eq 5). Since the outlet concentrations need not to be determined, it is enough to ensure that the maximum outlet concentration is not exceeded. Note that the mass exchange term is only added for the chosen unit, while for the others, Eq 12 ensures that Eq 13 is always met since $c_{o,c}^{in\,max} \le c_{o,c}^{out\,max}$. Eq 14 assures that the outlet flowrate from previously selected unit j to the chosen unit o, does not exceed the amount still available. Eq 15 ensures a zero inlet flowrate for non-selected fixed mass load units, where the limiting flowrate f_o^{lim} acts as the upper bound. Finally, note that only fixed load units can be selected so the binary variables are restricted to the O^{fl} subset, as it can be seen in Eq. 16, which guarantees that a single unit is selected.

$$\text{Min} \sum_{w \in W} \sum_{o \in AcO} F_{w,o}^{wat} \tag{9}$$

$$F_o^{tot}\Big|_{o \in O^{fl}} + f_o^{in}\Big|_{o \in O^{ff}} = \sum_{w \in W} F_{w,o}^{wat} + \sum_{j \in PvO \vee (j \in AcO \wedge (j \in O^{ff} \vee (j \in O^{fl} \wedge o \in O^{ff})))} F_{j,o}^{oper} \quad , \ \forall o \in AcO \tag{10}$$

$$F_o^{tot}\Big|_{o \in O^{fl}} + f_o^{out}\Big|_{o \in O^{ff}} = F_o^{tsys} + \sum_{j \in O^{ff} \vee (j \in O^{fl} \wedge o \in O^{ff})} F_{o,j}^{oper} \ , \ \forall o \in AcO \tag{11}$$

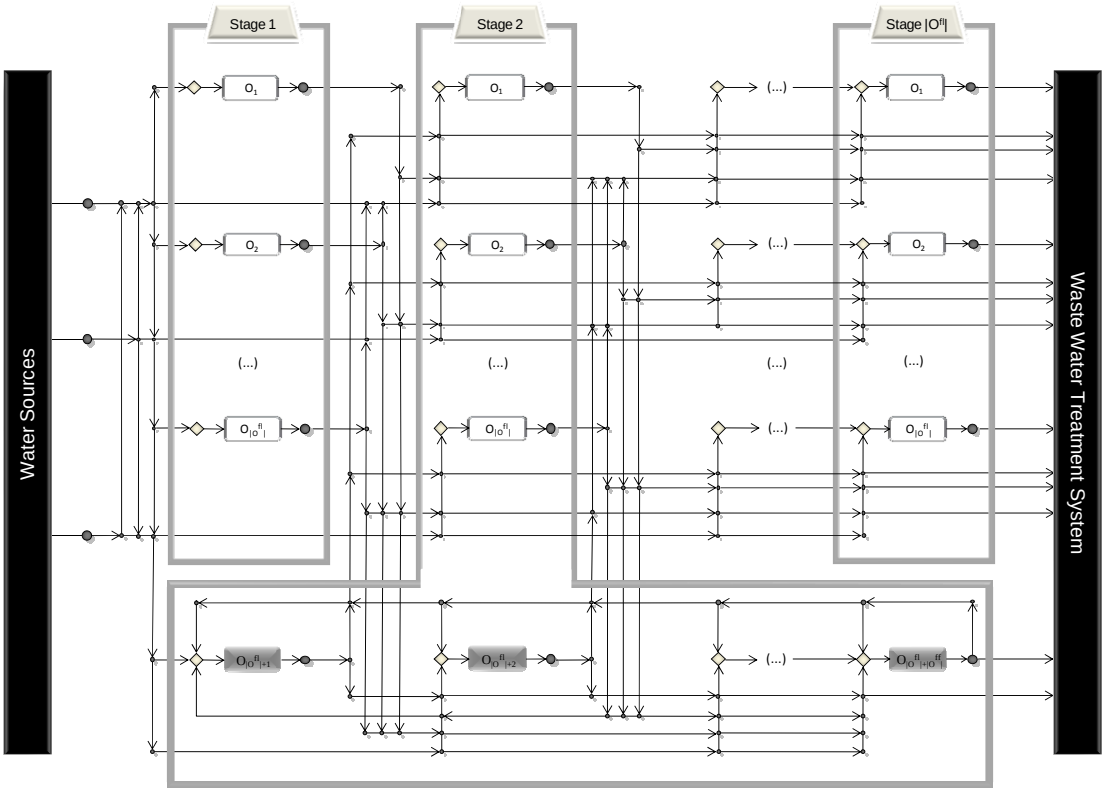

Figure 1 - General superstructure for the initialization process of model M1.

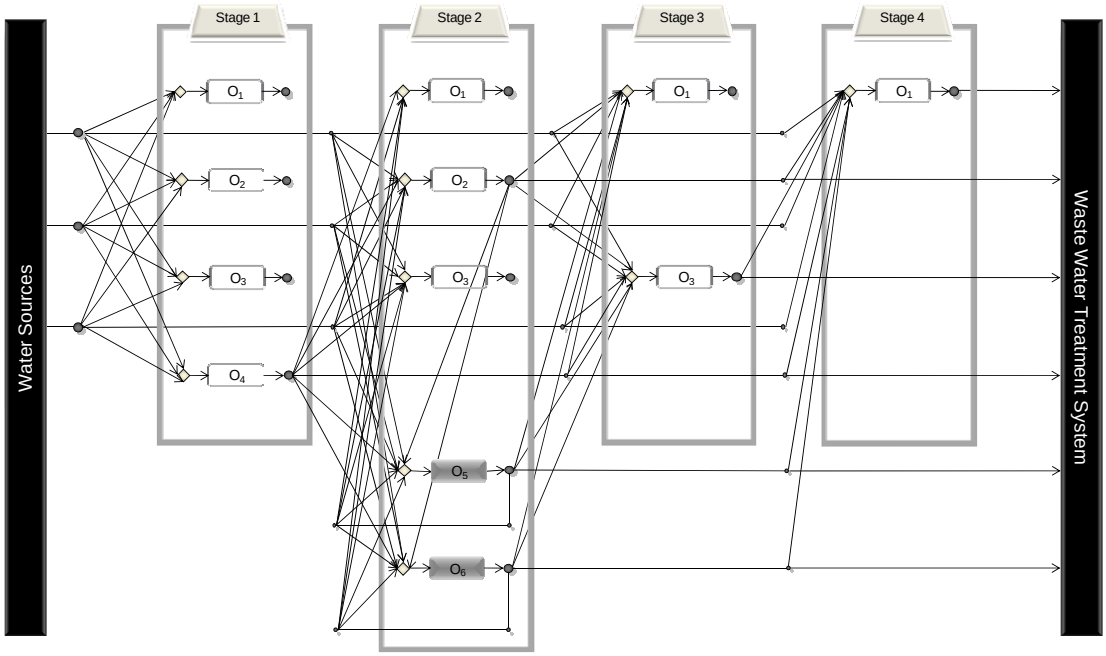

Figure 2 – Illustration of the initialization phase of model M1.

$$\sum_{w\in W} F_{w,o}^{wat}\cdot c_{w,c}^{wat} + \sum_{j\in PvO}\left[\left\langle F_{j,o}^{oper}\cdot c_{j,o}^{out}\right\rangle\Big|_{j\in O^{fl}} + \left\langle F_{j,o}^{oper}\cdot c_{j,c}^{out\,max}\right\rangle\Big|_{j\in O^{ff}}\right] + \sum_{j\in A\,c\,O\wedge(j\in O^{ff}\vee(j\in O^{fl}\wedge o\in O^{ff}))}(F_{j,o}^{oper}\cdot c_{j,c}^{out\,max}) \le \left(F_o^{tot}\Big|_{o\in O^{fl}} + f_o^{in}\Big|_{o\in O^{ff}}\right)\cdot c_{o,c}^{in\,max}, \forall\, o\in A\,c\,O, c\in C \tag{12}$$

$$\sum_{w\in W} F_{w,o}^{wat}\cdot c_{w,c}^{wat} + \sum_{j\in PvO}\left[\left\langle F_{j,o}^{oper}\cdot c_{j,o}^{out}\right\rangle\Big|_{j\in O^{fl}} + \left\langle F_{j,o}^{oper}\cdot c_{j,c}^{out\,max}\right\rangle\Big|_{j\in O^{ff}}\right] + \sum_{j\in Ac\,O\wedge j\in O^{ff}}(F_{j,o}^{oper}\cdot c_{j,c}^{out\,max}) + \Delta m_{o,c}\cdot Y_o \le F_o^{tot}\cdot c_{o,c}^{out\,max}, \forall\, o\in O^{fl}\cap A\,c\,O, c\in C \tag{13}$$

$$\sum_{j\in A\,c\,O} F_{o,j}^{oper} \le f_o^{tsys},\quad \forall\, o\in PvO \tag{14}$$

$$F_o^{tot}\Big|_{o\in O^{fl}} \le f_o^{lim}\cdot Y_o,\quad \forall\, o\in A\,c\,O, o\in O^{fl} \tag{15}$$

$$\sum_{\substack{o\in A\,c\,O\\ o\in O^{fl}}} Y_o = 1 \tag{16}$$

5 Computational Results

Table 2 shows the characteristics of the 36 test problems considered, while Table 3 lists the computational results for TCN, M1 and BARON. The study was performed in an Intel Core 2 Duo 2.4 GHz processor, with 2 GB of RAM memory, running Windows XP Professional. All mathematical formulations and algorithms were executed in GAMS 22.5. The resulting MILPs were solved with CPLEX, while the NLPs were solved by the local solver CONOPT. The results have shown that the new method is slightly less effective than its predecessor in escaping local optima, since it could find the optimal solutions in 21 out of the 25 problems that TCN could tackle. The advantage is that it requires significantly fewer computational resources and so it can go well beyond the previously observed practical limit of seven fixed load units, as illustrated with those examples featuring twenty units, which took less than four minutes to solve. The new method is even more successful than the global optimization solver BARON in Exs 31-

33, with the added advantage of being orders of magnitude faster.

6 Conclusions

This paper has presented a new MILP-based strategy for the optimal design of water-using networks featuring multi-contaminants and both fixed contaminant load and fixed flowrate operations. A new approach has been proposed to generate a small set of very good starting points for the solution of the non-convex NLP. It has been compared to a closely related LP-based method taken from the literature and to the one employed by the global optimization solver BARON. The results from a large set of example problems confirm its effectiveness in avoiding local solutions despite the small number of starting points. In contrast to the previous method they are easily scalable and, for some of the larger problems, could find better solutions than BARON with significantly fewer computational resources.

References

Castro, P.M., Matos, H.A., Novais, A.Q. (2007). Resources, Conservation and Recycling, 50, 158-185.

Doyle, S.J., Smith, R. (1997). Trans IChemE, 75(B), 181.

Prakash, R., Shenoy, U. (2005). Chemical Engineering Science, 60, 255.

Teles, J., Castro, P., Novais, A.Q. (2008). Chemical Engineering Science, 63, 376-394.

Table 1 – Problem data for a particular example and respective generated solution sequences

Problem Data											
	C_1		C_2		C_3		C_4				
Conc. (ppm)	$c^{in\,max}$	$c^{out\,max}$	$c^{in\,max}$	$c^{out\,max}$	$c^{in\,max}$	$c^{out\,max}$	$c^{in\,max}$	$c^{out\,max}$	f^{lim}	f^{in}	f^{out}
O_1	112	212	54	100	12	67	134	234	80		
O_2	32	60	12	50	47	200	56	156	60		
O_3	10	90	80	180	54	100	39	90	60		
O_4	45	89	93	120	70	120	177	200	10		
O_5	200	400	40	70	30	60	80	100		35	20
O_6	300	450	55	155	80	100	120	220		45	40

	W	W	W_3
c^{wat}	0	0	3
c^{wat}	0	3	0
c^{wat}	3	0	0
c^{wat}	1	1	1

Problem Solution			
	Initial Sol.	NLP Sol. (t/h)	Achieved Sequence
S1	204.624	178.263	{ O_4, O_5, O_6 }-O_2-O_3-O_1
S2	196.854	178.263	O_4-{ O_2, O_5, O_6 }-O_3-O_1
S3	196.281	178.263	O_4-O_2-{ O_3, O_5, O_6 }-O_1
S4	190.202	178.263	O_4-O_2-O_3-{ O_1, O_5, O_6 }

Table 2 – Characteristics of the test problems considered

Model					TCN M1	TCN M1	TCN M1	Model					TCN M1	TCN M1	TCN M1	Model					TCN M1	TCN M1	TCN M1
	$\|O^{fl}\|$	$\|O^{ff}\|$	$\|W\|$	$\|C\|$	# NLP	≠ Local Optima	Success Rate (%)		$\|O^{fl}\|$	$\|O^{ff}\|$	$\|W\|$	$\|C\|$	# NLP	≠ Local Optima	Success Rate (%)		$\|O^{fl}\|$	$\|O^{ff}\|$	$\|W\|$	$\|C\|$	# NLP	≠ Local Optima	Success Rate (%)
Ex1	3	1	1	2	18 3	1 1	100 100	***Ex13***	4	2	3	4	96 4	3 1	39 100	***Ex25***	5	2	4	3	600 5	11 2	37 40
Ex2	4	0	3	4	24 4	3 3	88 50	***Ex14***	4	3	2	6	96 4	3 2	59 75	***Ex26***	10	2	4	6	- 10	- 3	- 0
Ex3	4	0	2	4	24 4	1 1	100 100	***Ex15***	5	2	2	6	600 5	2 1	59 100	***Ex27***	8	8	5	4	- 8	- 2	- 13
Ex4	4	2	1	2	96 4	1 1	100 100	***Ex16***	4	1	3	4	96 4	3 1	36 0	***Ex28***	20	0	4	6	- 20	- 7	- 0
Ex5	4	3	2	2	96 4	1 1	100 100	***Ex17***	4	1	3	3	96 4	1 1	100 100	***Ex29***	14	6	3	6	- 14	- 4	- 7
Ex6	5	0	4	5	120 5	3 3	0 60	***Ex18***	3	1	3	4	18 3	1 1	100 100	***Ex30***	15	5	5	6	- 15	- 11	- 20
Ex7	5	0	3	6	120 5	2 2	100 60	***Ex19***	4	0	3	4	24 4	4 3	71 50	***Ex31***	20	0	5	6	- 20	- 20	- 5
Ex8	5	0	3	4	120 5	2 2	35 80	***Ex20***	4	5	4	5	96 4	3 2	78 75	***Ex32***	20	0	3	4	- 20	- 16	- 5
Ex9	6	0	2	6	720 6	2 2	37 17	***Ex21***	4	2	4	6	96 4	3 2	49 50	***Ex33***	11	5	3	4	- 11	- 5	- 18
Ex10	3	1	2	3	18 3	1 3	100 100	***Ex22***	4	3	5	6	96 4	5 3	31 0	***Ex34***	13	3	6	4	- 13	- 8	- 0
Ex11	3	1	4	4	18 3	2 1	67 0	***Ex23***	5	2	5	6	600 5	2 2	42 20	***Ex35***	13	3	4	5	- 13	- 8	- 31
Ex12	4	0	3	2	24 4	1 1	100 100	***Ex24***	4	3	4	6	96 4	2 1	51 0	***Ex36***	9	4	3	5	- 9	- 2	- 11

Table 3 - Computational results

Solver	CPLEX		CONOPT		CPU(s)		BARON			Solver	CPLEX		CONOPT		CPU(s)		BARON		
Model	**TCN**	**M1**	**TCN**	**M1**	**TCN**	**M1**	**LB[a](t/h)**	**OF(t/h)**	**CPU(s)**	**Model**	**TCN**	**M1**	**TCN**	**M1**	**TCN**	**M1**	**LB[a](t/h)**	**OF(t/h)**	**CPU(s)**
Ex1	**86.833**		**86.833**		10.84	5.31	85.97	**86.833**	3600[b]	***Ex19***	**74.605**	75.92	**74.47**		18.65	4.2	74.297	**74.47**	72000[b]
Ex2	**74.605**	75.92	**74.47**		18.25	5.38	74.03	**74.470**	7800[b]	***Ex20***	**407.264**	417.515	**403.196**		100.6	15.83	392.227	**403.196**	111625[b]
Ex3	**143.419**		**143.413**		18.33	5.36	142.52	**143.413**	3600[b]	***Ex21***	**217.105**	217.259	**216.37**		90.67	4.76	216.345	**216.37**	72000[b]
Ex4	**123.929**	129.773	**123.929**		79.74	14.53	123.66	**123.929**	200000[b]	***Ex22***	**327.374**	339.329	**323.505**	327.237	89.03	8.67	323.396	**323.505**	144000[b]
Ex5	**198.111**	201.111	**197.69**		85.52	20.56	-	**197.690**	36	***Ex23***	**381.868**	388.867	**366.473**		740.3	6.79	366.412	**366.473**	72000[b]
Ex6	**144.114**	145.212	**142.082**		120.6	8.71	141.10	**142.082**	3600[b]	***Ex24***	**512.116**	530.281	**511.964**	514.647	88.98	4.49	511.895	**511.964**	93600[b]
Ex7	**280.771**	280.877	**280.771**		126.6	8.82	280.76	**280.771**	63000[b]	***Ex25***	**413.091**	423.389	**410.635**		673.5	6.68	382.221	**410.635**	12100[b]
Ex8	**166.198**	175.282	**164.49**		117.7	8.34	-	**164.490**	2834	***Ex26***	-	846.876	-	800.891	-	29.2	775.645	**797.977**	241200[b]
Ex9	**313.513**	313.72	**312.922**		1079	15.12	311.48	**312.922**	5000[b]	***Ex27***	-	678.52	-	**556.675**	-	21.13	516.678	**556.675**	72000[b]
Ex10	**169.117**	188.839	**169.117**		10.6	6.25	169.102	**169.117**	72000[b]	***Ex28***	-	1876.2	-	1814.238	-	170.5	1668.568	**1812.17**	100800[b]
Ex11	**105.337**	128.585	**104.886**	106.277	12.43	6.18	104.886	**104.886**	51000	***Ex29***	-	1323.09	-	**1285.006**	-	73.51	1237.357	**1285.006**	230400[b]
Ex12	**167.204**	180.073	**165.195**		18.33	6.59	163.902	**165.195**	72000[b]	***Ex30***	-	948.29	-	**744.538**	-	91.46	363.578	758.67	230400[b]
Ex13	**178.954**	190.202	**178.263**		83.12	15.68	177.536	**178.263**	72000[b]	***Ex31***	-	876.512	-	**681.583**	-	166.9	204.761	719.038	230400[b]
Ex14	**330.046**	338.609	**329.57**		83.82	22.12	325.234	**329.570**	72000[b]	***Ex32***	-	788.027	-	**638.717**	-	155.6	305.918	653.735	360000[b]
Ex15	**362.249**	383.652	**361.518**		637.2	22.06	358.718	**361.518**	72000[b]	***Ex33***	-	692.397	-	**565.343**	-	38.52	443.507	572.951	360000[b]
Ex16	**288.306**	320.388	**285.934**	291.175	83.5	10.04	-	**285.934**	37980	***Ex34***	-	713.223	-	**590.299**	-	50.88	452.281	635.395	162000[b]
Ex17	**157.378**	161.621	**157.094**		83.69	10.03	151.764	**157.094**	72000[b]	***Ex35***	-	815.626	-	**783.951**	-	51.3	760.96	**783.951**	17200[b]
Ex18	**239.563**	267.735	**238.733**		11.47	8.24	236.875	**238.733**	72000[b]	***Ex36***	-	679.776	-	**662.807**	-	20.17	594.418	**662.807**	100800[b]

a = lower bound at the time of termination, when unable to prove global optimality; b = maximum resource limit

Proceedings of the 10th International Chemical and
Biological Engineering Conference - CHEMPOR 2008
Braga, Portugal, September 4-6, 2008
E.C. Ferreira and M. Mota (Eds.)

A Shortcut Design Method for Hybrid Separation Processes

M. Sorin, E. Ayotte-Sauvé, F. Rheault and F. Sadeghi

CANMET Energy Technology Centre -Varennes, 1615 Lionel-BouletP.O. Box 4800,
Varennes, Quebec, J3X 1S6, Canada,
Tel: (450) 652-3513, Fax: (450) 652-0999, e-mails:msorin@nrcan.gc.ca

Keywords: Hybrid separation, Power separation, Exergy
Topic: Systematic methods and tools for managing the complexity

Abstract
In recent years, hybrid processes composed of a distillation column coupled with another separation process (membrane, pressure-swing adsorption unit, etc.) have received increased attention by both the industry and the scientific community. Combining such processes often leads to a large number of possible design arrangements. Therefore, efficient design methods are required, even at the conceptual design level. In this paper, general thermodynamic insights relative to the integration of a distillation column with an auxiliary separation process are developed – the aim being to minimize the number of distillation trays within the hybrid system. Two developments are discussed: the first concerns an extension of the definition of the concept of power of separation, previously introduced by Sorin and co-workers, to non-isothermal processes; the second establishes the basis of a shortcut method for finding the redistribution of a given separation duty between the sub-processes of a hybrid system (involving distillation) which minimizes the number of distillation trays.

Introduction

As many authors have reported in the literature (Moganti et al., (1994) and Stephan et al., (1995)), combining a distillation column with a membrane allows for a reduction of the number of distillation trays. Given the significant number of possible hybrid configurations between a distillation column and a membrane network, Kookos (2003) as well as Szitkai et al., (2002) proposed a mathematical programming methodology based on a superstructure representing all possible parallel hybrid arrangements. They considered the problem of finding a distillation column design and a membrane network design forming a hybrid for which the annualized cost was minimal. However, as was mentioned by Bausa and Marquardt (2000), although important and useful, the results of such an optimization will provide “no understanding of whether the solution obtained can be further improved or whether there are inherent constraints which cannot be overcome”.

In this paper, the definition of power of separation, a thermodynamic function introduced by Sorin and Rheault (2007) for isothermal processes will be extended for non-isothermal processes such as distillation. The property of additivity of this function will then be used to decompose a distillation/membrane hybrid process. Through a numerical study, it will be shown that the minimum number of column trays corresponds to the maximum power of separation of the membrane. This observation will offer the advantage of reducing the problem’s complexity by considering, as a first step of the conceptual design, the design of the membrane alone. The separation of the water-ethanol mixture in a process composed of a distillation column and a pervaporation membrane will be used as an example illustrating this shortcut design approach.

Power of Separation of a Non-Isothermal Process

By using the exergy balance around an isothermal separation process, Sorin and Rheault (2007) focused on the part of the exergy rise within the process which is associated with the variation of activities of the species in the products and the feedstock. They called this term the power of separation (P_{sep}) of the process. More precisely, P_{sep} can be expressed through the Gibbs free energy variation rate (ΔG), the process temperature (T) and the environment temperature (T_0) as:

$$P_{sep} = \frac{T_0}{T} \Delta G \,. \qquad (1)$$

The aim of the present section is to extend this definition to a non-isothermal separation process. The following development may be generalized to any non-isothermal separation process with any number of components and streams. However given that the interest of the present paper is mainly focused on distillation processes and given that the conclusions obtained here for binary mixtures may be easily extended to any number of components in the mixture, the following development is restricted to binary distillation.

The increase of the exergy rate of products over the feedstock (ΔE) for a binary distillation process can be expressed using the multi-step separation process presented on a temperature (T) – molar fraction (X_a) of volatile component diagram (figure 1). The shape of saturated liquid and vapor lines presented in figure 1 is chosen only to illustrate the procedure, it can be done for other shapes of T-X diagrams, for example for azeotropic mixtures.

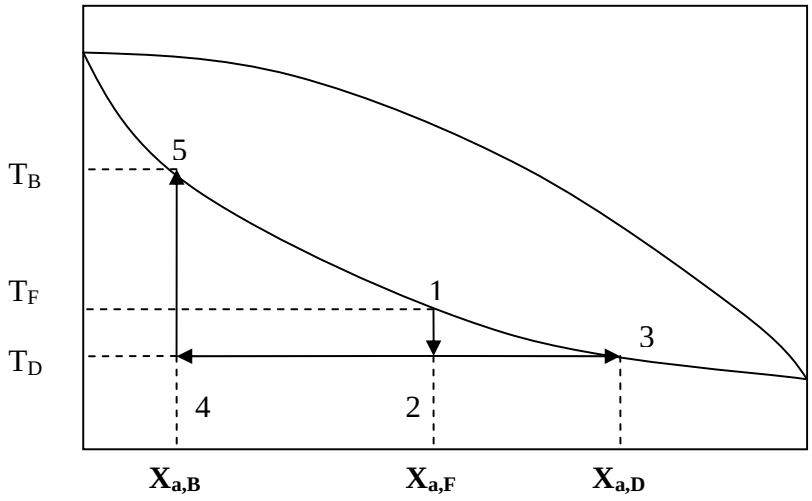

Figure 1. T-X diagram for a binary distillation.

The points 1, 3 and 5 correspond to feedstock, distillate and bottom products. The process of separation can be presented as an assembly of elementary processes, for example, the

feedstock cooling (1-2), the isothermal separation of the feedstock (2-3,4) and the heating of the bottom liquid (4-5). Given that ΔE is a thermodynamic function of state it can be presented as:

$$\Delta E_{1-3,5} = \Delta E_{2-1} + \Delta E_{2-3,4} + \Delta E_{5-4} \qquad (2)$$

Each term on the left and right sides of equation (2) may be expressed through the corresponding difference in enthalpy ΔH and entropy ΔS rates:

$$\Delta E_{out-in} = \Delta H_{out-in} - T_0 \Delta S_{out-in} \qquad (3)$$

where the indexes in and out correspond to the inlet and outlet of each elementary process respectively. For the heat transfer processes 1-2 and 5-4 equation (3) may be written as:

$$\Delta E_{out-in} = \Delta H_{out-in} (1 - \frac{T_0}{\overline{T_{out-in}}}) \qquad (4)$$

where $\overline{T_{out-in}}$ is the average thermodynamic temperature of the corresponding processes of cooling and heating. According to Sorin and Rheault (2007), for the isothermal separation process 2-3,4, equation (3) takes the form:

$$\Delta E_{out-in} = \Delta H_{out-in} (1 - \frac{T_0}{T}) + P_{sep} \qquad (5)$$

and the last term of the right side of equation (5) can be expressed through the variation of the activities $a_{i,j}$ of a component i at a point j (2, 3 and 4).

In turn, according to Prausnitz et al., (1986) the activity variation of the components along the elementary processes 2-1 and 5-4.follows the relation:

$$(\frac{\partial \ln a_i}{\partial T})_{P,X} = (h_i^0 - \overline{h_i}) / RT^2 \qquad (6)$$

where h_i^0 and $\overline{h_i}$ are the molar and the partial molar enthalpy of the component i. Assuming that the term $(h_i^0 - \overline{h_i})$ is constant with temperature, integrating (6) and multiplying by T_0 leads to:

$$RT_0 \frac{\ln a_{i,out}}{\ln a_{i,in}} = (h_i^0 - \overline{h_i})(\frac{T_0}{T_{in}} - \frac{T_0}{T_{out}}) \qquad (7)$$

Multiplying equation (7) by the corresponding molar rates $n_{i,j}$ adding it to equation (2) and substituting the corresponding terms from equations (4) and (5), yields:

$$RT_0 \sum_i n_i \frac{\ln a_{i,out}}{\ln a_{i,in}} = \Delta E_{1-3,5} - \Delta H_{2-3,4}(1-\frac{T_0}{T_2}) - \Delta H_{2-1}(1-\frac{T_0}{\overline{\overline{T_{2-1}}}}) -$$
$$\Delta H_{5-4}(1-\frac{T_0}{\overline{\overline{T_{5-4}}}}) + \sum_i n_i (h_i^0 - \overline{h_i})(\frac{T_0}{T_1} - \frac{T_0}{T_2}) + \sum_i n_i (h_i^0 - \overline{h_i})(\frac{T_0}{T_4} - \frac{T_0}{T_5}) \quad (8)$$

The left hand side of equation (8) is the power of separation for a non-isothermal process. It is the part of exergy rise due exclusively to the activities variation of the product components over the ones of feedstock free from heating, cooling and heat of mixing effects. Equation (8) shows that the power of separation is an additive thermodynamic function. In particular, the power of separation of a hybrid process is the sum of the power of separation of the distillation column and that of the auxiliary separator.

Distillation Column/Membrane Hybrid: Power of Separation Short-Cut Method

Consider a hybrid process with a fixed separation task and composed of a distillation column with a given reflux ratio and an additional separation unit. The present section aims at validating the following hypothesis: the number of trays within the distillation column may be reduced by increasing the power of separation of the additional separator. This hypothesis is verified by using the example of the separation of water-ethanol mixture in a hybrid process composed of a distillation column and a pervaporation membrane (fig. 2).

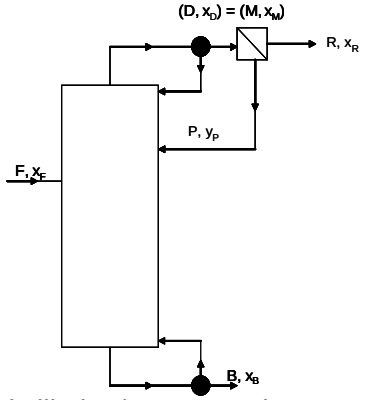

Fig. 2. Distillation/pervaporation membrane hybrid.

Assume that the distillation column verifies the constant molar overflow (CMO) hypothesis and that the hybrid is such that the (saturated vapor) permeate is returned to the column with no mixing, i.e. the position at which the permeate enters the column is determined as the position where the vapor exiting the corresponding tray has the same composition as the permeate. The following hybrid design problem is considered. For given flow rates and compositions of the hybrid's input and output streams (B, x_B, F, x_F, R, x_R), a given reflux ratio for the distillation column, a fixed (and constant) internal pressure for the column and fixed pressures at both sides of the membrane, determine the conditions for the minimum number of trays in the column as well as for the minimum membrane surface area. The membrane area has been evaluated according the shortcut method proposed by Bausa and Marquardt (2000) the number of distillation trays was calculated iteratively using the McCabe-Thiele diagram. The membrane area and the number of distillation trays for the hybrid structure in fig. 2 were evaluated for different molar fractions of ethanol in the distillate. As can be observed in fig. 3 (the membrane surface area and number of distillation trays correspond to square and triangular points respectively), when the membrane's power of separation is increased, its surface area

increases; in that case, the column's power of separation decreases (because the hybrid has constant power of separation and because power of separation is additive), which results in a decrease of the number of distillation trays. As can be seen by these results, the power of separation of the membrane or distillation column is intrinsically linked to the process' size.

This observation, based on thermodynamics, offers the advantage of simplifying the conceptual design task by optimizing only one of the hybrid sub-processes. To be more precise, in the present case study (see Fig. 3), the size of both processes can be studied by considering only one parameter: the power of separation of the membrane. Maximizing the power of separation of the membrane alone would result in a hybrid with minimal number of distillation trays (and minimal power of separation of the column, since the hybrid's power of separation is fixed); on the other hand, minimizing the membrane's power of separation would result in a hybrid design with minimal membrane surface area. These results show that the power of separation of a process seems to be intimately linked to its size.

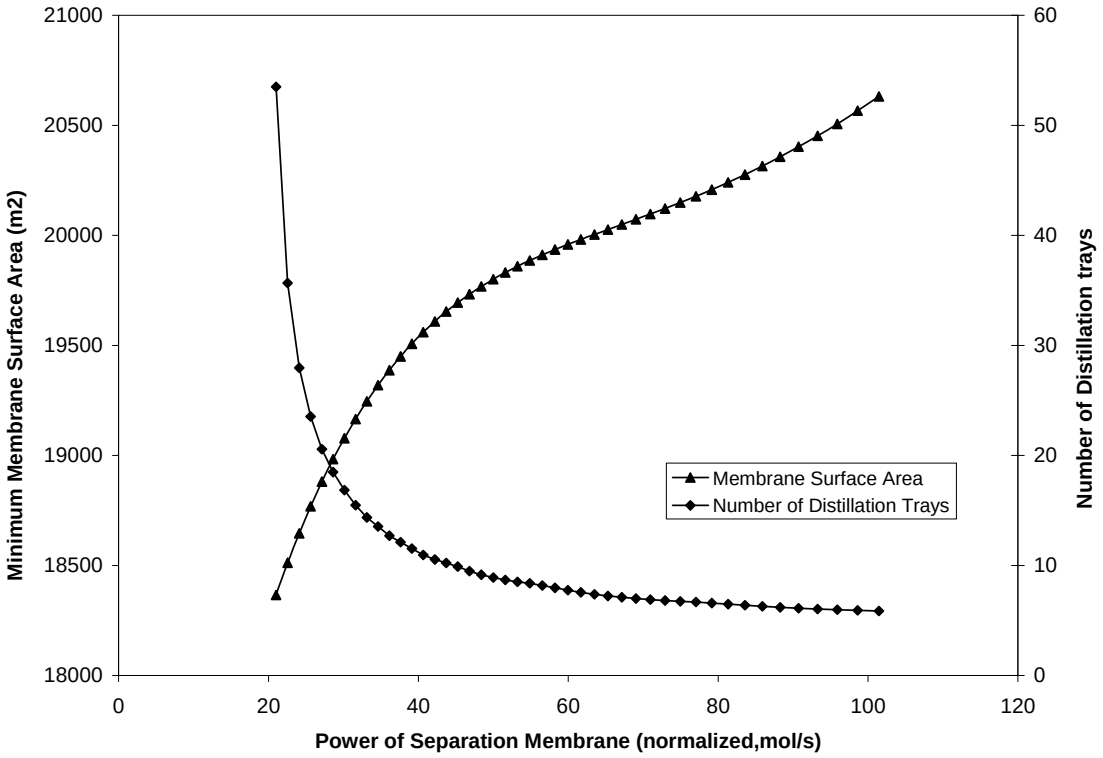

Fig. 3. Numerical results for the water-ethanol separation.

Conclusion

A short-cut method to minimize the number of distillation trays for hybrid processes is proposed. It is based on the property of additivity of power of separation of the units forming the hybrid process, i.e. the power of separation of the process is the sum of the power of separation of each sub-process. The result of this is that by maximizing the power of separation of one of the sub-processes, the optimal design of the column or/and the membrane module can be worked out independently from each other. This allows to reduce the complexity of the conceptual design of hybrid processes.

References

Bausa, J, Marquardt, W. (2000). Shortcut design methods for hybrid membrane/distillation processes for the separation of non-ideal multicomponent mixtures, Industrial & Engineering Chemistry Research, 39, 1658-1672.

Kookos I. (2003). Optimal design of membrane/distillation column hybrid processes. *Industrial & Engineering Chemistry Research*, 42,1731-1738

Moganti S., Noble RD., Koval CA.(1994). Analysis of a membrane/distillation column hybrid process. *Journal of Membrane Science,* ;93, 31-44.

Prausnitz, J.M., Lichtenthaler, R.N., de Azevedo,E.G. (1986). Thermodynamics of Fluid-Phase Equilibria, PTR Prentice-Hall Inc.

Sorin, M. Rheault, F. (2007). Thermodynamically Guided Intensification of Separation *Processes, Applied Thermal Engineering*, 27, 1191-1197

Stephan, W., Noble, RD., Koval CA. (1995). Design methodology for a membrane/distillation column hybrid process. *Journal of Membrane Science,* 99, 259-272.

Szitkai, Z., Lelkes, Z., Rev, E. Fonyo, Z. (2002) Optimization of hybrid ethanol dehydration systems, *Chemical. Engineering. and Processing*, 41, 631-646.

Proceedings of the 10th International Chemical and
Biological Engineering Conference - CHEMPOR 2008
Braga, Portugal, September 4-6, 2008
E.C. Ferreira and M. Mota (Eds.)

Methods and tools for global sensitivity analysis of dynamic models of biological systems

Maria Rodriguez-Fernandez, Julio R. Banga*
IIM - CSIC - Process Engineering Group, Instituto de Investigaciones Marinas (CSIC).
C/ Eduardo Cabello, 6. 36208 Vigo, Spain.

Keywords: Global sensitivity, identifiability, parameter estimation, systems biology.
Topic: Integration of life sciences & engineering.

Abstract

Parameter identification is a critical aspect for mathematical modelling of biological systems. When the number of parameters increases, this task can become very challenging and understanding how sensitive is the model output to variations in parameter values can be very helpful. If a small change in a parameter results in relatively large changes in the state variables, the model answer is said to be sensitive to this parameter. This means that this type of parameters have to be determined very precisely to achieve an accurate model. On the contrary, parameters to which the process dynamics exhibit a small sensitivity do not need to be measured rigourously.

Local sensitivity analysis determines the model sensitivity to changes in the parameters values within a small local region about a given set of nominal values. Global sensitivity methods account for interactions between parameters and explore the entire range of each parameter. Thus, parametric global sensitivity analysis is presented here as a robust alternative for this type of analysis, detecting non influential parameters and their interactions. The performance of this methodology is illustrated with a benchmark dynamic model describing a biochemical pathway.

1 Introduction

Developing suitable dynamic models of biochemical pathways is a key step towards the development of predictive models for cells or whole organisms. Such models can ultimately provide explanations of the biological phenomena becoming a fundamental aspect in Systems Biology. Since the amount and quality of experimental data increases and the underlying mechanisms of biological systems are better understood, the complexity of the models necessarily increases. That usually involves an increase in the number of parameter often leading to over-parametrised models where the parameter identification problem turns very challenging. In that case, the sensitivity analysis (the study of the impact that changes in the value of the parameters have on the output of the model) can be used to decide which parameters should be the focus of the model calibration efforts, or even as an analysis tool to test model identifiability. Moreover, sensitivity methods should serve as diagnostic tools that help to improve mathematical models guiding model reformulations efforts when unidentifiable parameters are found.

Saltelli et al (2005) have reviewed and categorized the available sensitivity analysis methods. Roughly, they can be classified into local and global approaches. Local methods measure the variation of the output due to the change of model parameters around a given nominal value. They have the advantage of being straightforward to implement and computationally cheap. However, although these methods are valid for linear cases or when the value of the parameters is known, they can be misleading for the general nonlinear case. In contrast, global sensitivity analysis methods consider the effects of changing parameters simultaneously while spanning the entire admissible region of the parameter space.

*Corresponding author. Tel. +34 986 214 473. E-mail: julio@iim.csic.es.

In this work, global sensitivities are presented as a robust alternative for this type of analysis, detecting non influential parameters and their interactions in non linear dynamical models. The derivative based global sensitivity measures, presented in Kucherenko et al (2008) for explicit functions, are here extended for models described by deterministic ordinary differential equations (ODEs). These values and the computational time required for their computation are contrasted with the well known Sobol' indices Sobol' (2001). A parameter ranking based on these measures is established and compared with the one based on local sensitivities. These rankings allow the prioritisation of parameters that can be subsequently estimated using robust global optimization methods Egea et al (2007). The performance of this methodology is illustrated with a benchmark problem regarding a model of a biochemical pathway with three enzymatic steps Rodriguez-Fernandez et al (2006).

2 Methods

2.1 Mathematical model

A challenging benchmark problem, involving a biochemical pathway with three enzymatic steps, was considered. The mathematical formulation of the nonlinear dynamic model can be found in Rodriguez-Fernandez et al (2006). The identification problem consists of the estimation of 36 kinetic parameters of the nonlinear biochemical dynamic model (8 nonlinear ODEs) which describes the variation of the metabolite concentration with time.

For this study, model outputs corresponding to 8 metabolite concentrations at 21 time-points taken from 0 to 120 s were considered. In order to get a better understanding of the model structure, the local and global sensitivity measures of each metabolite concentration towards the entire set of 36 parameters were investigated. Hence, each of these methods produced a $8 \times 21 \times 36$ matrix.

2.2 Sensitivity analysis methods

Local sensitivities provide the slope of the calculated model output in the parameter space at a given set of nominal values considered for the parameters so the behavior of the response function is described only locally in the input space. Moreover, preliminary experiments and model calibration tests should be carried out in order to obtain a first guess for the parameter values and an iterative scheme involving both steps is required in order to study the model sensitivity. In addition, these methods are linear thus they are not sufficient for dealing with complex models, especially those in which there are nonlinear interactions between parameters.

In contrast, global sensitivity analysis (GSA) methods evaluate the effect of a parameter while all other parameters are varied simultaneously, thus accounting for interactions between parameters without depending on the stipulation of a nominal point (they explore the entire range of each parameter).

The most widely used methods in GSA are, FAST and extended FAST, the Morris method and its adaptations and the Sobol' method considered as one of the more powerful despite its high computational cost.

2.2.1 Numerical methods for the calculation of local sensitivity indices

They are several numerical methods for calculating the local sensitivity indices although the computed values should be the same among the precision of the considered method.

The decoupled direct method (DDM) has proven to be the best general method for the numerical calculation of local sensitivities (Saltelli et al. (2000)). One of the best known implementations of this method is ODESSA, a package of FORTRAN routines for simultaneous solution of ordinary differential

equations and the associated fist-order parametric sensitivity equations, developed by Leis and Kramer (1988). ODESSA is a modification of the initial-value solver LSODE, and is the one used in this work.

2.2.2 Sobol' global sensitivity indices

The method of global sensitivity indices developed by Sobol' is the most established among the variance-based methods. The method is based on the ANOVA decomposition of the variance of the model output. A detailed description of the method can be found in Sobol' (2001) were Sobol' defines two type of indices: S_{p_a} that accounts only for the effect of the parameters of the subset a and $S^T_{p_a}$ that also accounts for the interactions of the parameters of the subset a with the rest of the parameters.

Calculation of Sobol' indices is based on the evaluation of a series of integrals over the parameter space. For that, the Quasi Monte Carlo algorithm (QMC) using the Sobol' low-discrepancy sequences (LDS) was selected in this work among the existing possibilities. In such a way, the sensitivity indices can be calculated in a straightforward manner according to the formulas:

$$S_{p_a} = \frac{\frac{1}{N}\sum f(p_a, p_b) f(p_a, p'_b) - (\frac{1}{N}\sum f(p))^2}{\frac{1}{N}\sum f^2(p) - (\frac{1}{N}\sum f(p))^2} \tag{1}$$

$$S^T_{p_a} = \frac{1}{2}\frac{\sum \left[f(p_a, p_b) f(p'_a, p_b)\right]^2}{\frac{1}{N}\sum f^2(p) - (\frac{1}{N}\sum f(p))^2} \tag{2}$$

Thus, each Quasi Monte Carlo sample point requires three computations of the model $f(p_a, p_b)$, $f(p'_a, p_b)$ and $f(p_a, p'_b)$. For the computation of the Sobol' indices of an entire set of n parameters, using N sample points, the number of function evaluations is $N_F = N(n+2)$.

2.2.3 Derivative based Global Sensitivity Measures

Kucherenko and co-workers Kucherenko et al (2008) presented the derivative based global sensitivity measures (DGSM) based on averaging local derivatives using Quasi Monte Carlo sampling methods. They applied this technique to a set of explicit functions showing that it is much more accurate than the Morris method. Moreover, they demonstrated that there is a link between these measures and the Sobol' sensitivity indices.

In this work, these measures are extended in order to be able to handle ordinary differential equations (ODEs). The details of this methodology are described below.

Consider a differentiable function $f(p)$, where $p = \{p_i\}$ is a vector of parameters defined in the unit hypercube H^n $(0 \leq p_i \leq 1, i = 1, ..., n)$. Local sensitivity measures are based on partial derivatives

$$E_i\left(p^*\right) = \frac{\partial f}{\partial p_i} \tag{3}$$

Sensitivity measure $E_i\left(p^*\right)$ depends on a nominal point and it changes with a change of p^*. This deficiency can be overcome by averaging $E_i\left(p^*\right)$ over the parameter space H^n. Such a measure can be defined as:

$$\bar{M}_i = \int_{H^n} E_i dp \tag{4}$$

Another measure, which is the variance of $\bar{M}_i$, is also considered

$$\bar{\Sigma}_i = \left[\int_{H^n} \left(E_i - \bar{M}_i\right)^2 dp\right]^{1/2} \tag{5}$$

$\bar{\Sigma}_i$ can also be presented as

$$\bar{\Sigma}_i^2 = \int_{H^n} E_i^2 dp - \bar{M}_i^2 \tag{6}$$

Combining $\bar{M}_i$ and $\bar{\Sigma}_i$ a new measure $\bar{G}_i$ can be introduced

$$\bar{G}_i = \bar{\Sigma}_i^2 + \bar{M}_i^2 = \int_{H^n} E_i^2 dp \tag{7}$$

Being s a number of parameters in a subset we can define the so called "alternative global sensitivity estimator", $\bar{G}_s$, as

$$\bar{G}_s = \frac{\sum_{i=1}^{s} G_i}{\sum_{i=1}^{n} G_i} \tag{8}$$

Non-monotonic functions have regions of positive and negative values of partial derivatives $E_i\,(p^*)$, hence due to the effect of averaging values $\bar{M}_i$ can be very small or even zero: i.e. for a symmetrical at a middle point ($p = 0.5$) function $\bar{M}_i = 0$. To avoid such situations measures based on the absolute value of $|E_i(p^*)|$ can be used:

$$\bar{M}_i^* = \int_{H^n} |E_i|\, dp \tag{9}$$

$$\bar{\Sigma}_i^* = \left[\int_{H^n} \left(|E_i| - \bar{M}_i^* \right)^2 dp \right]^{1/2} \tag{10}$$

Similar measures were introduced in Campolongo et al (2006) within the framework of the Morris method. Using an analogy with variance based global sensitivity measures, the set of measures $\bar{M}_i$, $\bar{\Sigma}_i$ and $\bar{G}_i$ are called derivative based global sensitivity measures (DGSM).

Analogously with the calculation of Sobol' indices, the integrals (Eq. 9-10) were evaluated here by means of the Quasi Monte Carlo algorithm (QMC) using the Sobol' LDS. Local sensitivities (Eq. 3) were computed with ODESSA simultaneously with the original system so the number of function evaluations is reduced to $N_F = N$.

2.3 Extension to ODEs systems

Since dealing with a systems of ODEs, the sensitivity indices of every observed state variable at each measurement time point with respect to each of the parameters, are available. In order to summarize all this information, global sensitivity indices as the average of all the S_i for each parameter are defined:

$$S_i = \frac{1}{N_y} \frac{1}{N_t} \sum_{j=1}^{N_y} \sum_{k=1}^{N_t} S_{ij}(t_k) \tag{11}$$

The same expression is applicable to S_i^T, $\bar{M}_i$, $\bar{\Sigma}_i$ and $\bar{G}_i$.

3 Results and discussion

3.1 Local sensitivity analysis

The local sensitivity indices were computed at a nominal point p^* and at $5p^*$ and their values are shown in Figures 1-2.

With these results a ranking of importance for the parameters was established. For the nominal point, p^*, the ten less influential parameters are p_2, p_3, p_8, p_9, p_{14}, p_{15}, p_{30}, p_{32} p_{33} and p_{36}. They account for the 5 % of information while the ten more influential ones represent the 50 % of the model sensitivity. That

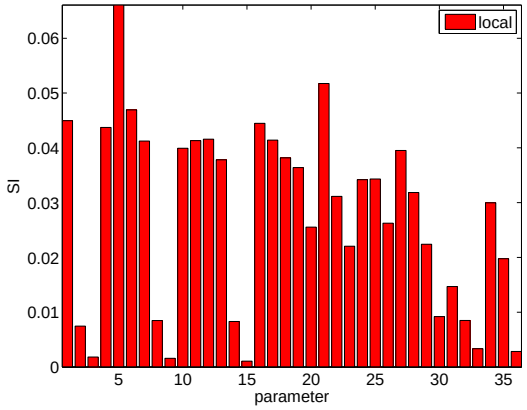

Figure 1: Local sensitivities at p^*

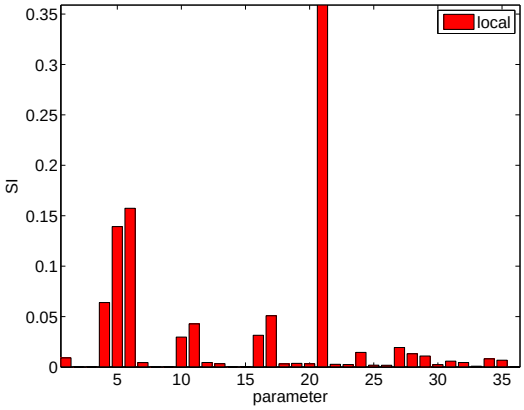

Figure 2: Local sensitivities at $5p^*$

indicates that our efforts must be focused on the proper estimation of the most influential parameters whereas the less important can be fixed to their nominal values.

However, when computing the same ranking for a different point, as $5p^*$, the results are completely different. Since the sensitivity analysis is usually performed before the parameter estimation, more robust methods are needed in order to ensure that small changes in the parameters values will not significantly change the results of the study.

3.2 Global sensitivity analysis

The values of the total Sobol' indices and the $\bar{G}_i$ measure were computed using the same number of sample points ($N = 2^{10}$). The integrations were computed over a logarithmic parameter space assumed to be uniformly distributed within one order of magnitude larger and one order smaller than the nominal values. The results are shown in Figures 3-4.

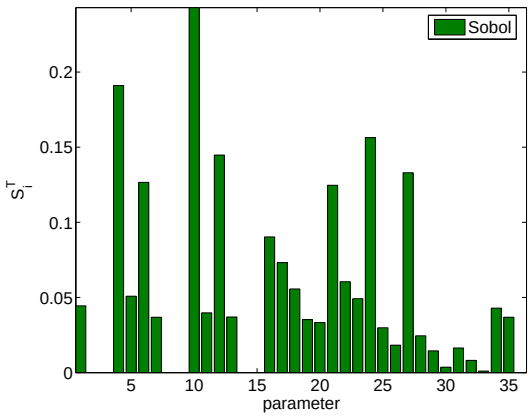

Figure 3: Sobol', Set of bounds I

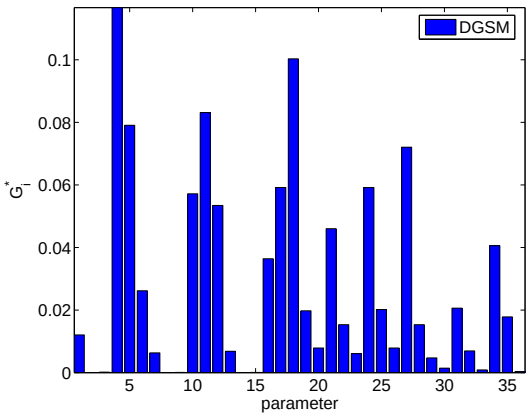

Figure 4: DGSM, Set of bounds I

From the ten less influential parameters, nine are coincident (p_2, p_3, p_8, p_9, p_{14}, p_{15}, p_{25}, p_{33} and p_{36}) showing that $\bar{G}_i$ is a good proxy to S_i^T. Moreover, it can be seen that one third of the parameters accounts for the 50 % of the model sensitivity.

Besides, eight are in agreement with the results of the local sensitivities at the nominal point but no connection can be established with the results for the vector $5p^*$ although this point is included in the considered set of bounds.

4 Conclusion

Accurate parameter estimation of complex dynamical systems can become very challenging as models can contain hundreds or even thousands of parameters. The results of a sensitivity analysis can be used to establish a ranking of importance for the parameters, allowing to fix unessential parameters and to prioritize the most influential ones and facilitating the identification task.

In this contribution, a novel methodology for global sensitivity analysis reducing $(n + 2)$ times the number of function evaluations with respect to the well known Sobol' indices was presented. The results obtained by both methods are equivalent and more robust than those provided by the local sensitivities that are strongly dependent on the selection of the nominal point.

Especial attention should be payed to the number of sample points considered for the integration since low convergence may also be the source of inaccurate results.

References

Sobol, I.M. (2001). Global sensitivity indices for nonlinear mathematical models and their Monte Carlo estimates, *Mathematics and Computers in Simulation*, 55, 271–280.

Saltelli, A., Ratto, M., Tarantola, S., Campolongo, F. (2005). Sensitivity Analysis for Chemical Models, *Chemical Reviews*, 105, 2811–2827.

Egea, J. A., Rodriguez-Fernandez, M., Banga, J. R., Marti, R. (2007). Scatter search for chemical and bio-process optimization. *Journal of Global Optimisation*, 37, 481–503.

Rodriguez-Fernandez, M., Mendes, P., Banga, J.R. (2006). A hybrid approach for efficient and robust parameter estimation in biochemical pathways. *BioSystems*, 83, 248–265.

Kucherenko, S., Rodriguez-Fernandez, M., Pantelides, C., Shah, N. (2008). Monte Carlo evaluation of Derivative based Global Sensitivity Measures, *Reliability Engineering and System Safety*, In press.

Campolongo, F., Cariboni, J., Schoutens, W. (2006). The importance of jumps in pricing European options, *Reliability Engineering and System Safety*, 91(10–11), 1148–1154.

Saltelli, A., Chan, K., Scott, E.M. (2000). Sensitivity Analysis, *Wiley*.

Leis, J.R., Kramer, M.A. (1988). ODESSA - An ordinary differential-equation solver with explicit simultaneous sensitivity analysis, *ACM Transactions on Mathematical Software*, 14(1), 61–67.

Proceedings of the 10th International Chemical and
Biological Engineering Conference - CHEMPOR 2008
Braga, Portugal, September 4-6, 2008
E.C. Ferreira and M. Mota (Eds.)

Stochastic Modelling of the Baculovirus/Insect Cells System: Prediction of Recombinant Protein Expression

António Roldão[1], Manuel J.T. Carrondo[1,2], Paula M. Alves[1] and R. Oliveira[3]
[1] ITQB-UNL/IBET, Apartado 12, 2781-901 Oeiras, Portugal
[2] FCT/UNL, Laboratório de Engenharia Bioquímica, P-2829-516 Caparica, Portugal
[3] REQUIMTE FCT/UNL, P-2829-516 Caparica, Portugal

Keywords: Stochastic Modelling, Insect Cells, Baculovirus, Recombinant Protein Expression, Rotavirus-like Particles
Topic: Systematic methods and tools for managing the complexity

Abstract

Triple-layered Rotavirus-like particles (RLPs), a vaccine candidate against rotavirus disease, are produced using the baculovirus/insect cells system. This extremely complex process has assembly efficiencies of the three constitutive viral proteins of RLPs (VP2, VP6 and VP7) normally around 11-15%. In order to optimize batch performance, it is essential to evaluate *a priori* the effect of critical process parameters as the multiplicity of infection (MOI – #virus.cell^{-1}) on process kinetics. A stochastic mathematical model was developed (Roldão *et al.*, 2008a) and used to find optimal asynchronous infection regimes. Results indicate that maximum productivity for VP2 (used as a model for the remaining viral proteins) is achieved at MOI=0.01 virus.cell^{-1} while the minimum is obtained at MOI=10 virus.cell^{-1}. Moreover, model simulations show that high MOIs have no advantage over low ones in protein expression due to maximum translation capacity. One can conclude that optimal protein production is a compromise between high intracellular protein templates, obtained at high MOIs, and high infected cell densities, obtained at low MOIs. The acquired knowledge demonstrates the potential of mathematical models in process design and will show its usefulness in process optimization. In a second study, several baculovirus titration methods were evaluated to find the one estimating viral titers with best accuracy as it strongly affects MOI variability and consequently batch consistency. The techniques that better combined titer accuracy, cost *per* titration, titration time and labor intensity were the $TCID_{50}$, MTT and flow cytometric assays. Nevertheless, it is compulsory to confirm titers accuracy by at least two different titrations methods.

1. Introduction

Genetically engineered baculovirus are powerful vectors for expression of heterologous proteins in insect cells. This system is being applied to the production of RLPs as a vaccine against rotavirus disease which currently has a higher mortality than AIDS/HIV in under-five children. RLPs based vaccines are non-infectious, highly immunogenic and safer to produce than existing live attenuated ones. Nevertheless, the optimisation of RLPs production is extremely complex as it involves the assembly of VP_2, VP_6 and VP_7. Thus, strategies to maximize individual protein production and to suppress product-derived contaminants negatively impacting the overall process are essential to increase assembly efficiencies for higher values than the normal 11-15%.

The design of such strategies starts from an initial screening of which critical process parameters most affects process kinetics. In this respect, MOI is considered one of the most relevant ones and therefore was investigated. The stochastic mathematical model developed by Roldão *et al.* (2008a) shows here its usefulness in finding optimal asynchronous infection

regimes. This model combines the stochastic nature of infection (randomness of virus binding to the host cells) with intracellular dynamics, namely vDNA replication, mRNA synthesis and protein expression (see Eqs. 1 to 15). These three main intracellular events occurring after infection were simulated for different MOIs (0.01, 0.1, 1, 10 and 40 virus.cell^{-1}) to extract process specificities and verify model robustness. Additionally, final protein yields were compared for a wide range of MOIs (10^{-3} to 10^{2} virus.cell^{-1}) to assess the MOIs maximizing viral protein expression.

The successfulness of an optimized process depends on the robustness and efficiency of the production workflow. One must guarantee that critical parameters are tightly controlled. As an example, irreproducible MOIs caused by inaccurate viral titer estimation have a profound impact on process performance and batch consistency. The selection of an appropriate titration method to the recombinant baculovirus in use, capable of distinguishing between infectious and non-infectious virus is essential to reduce titer errors and MOI variability. Therefore, several methods for baculovirus titration were evaluated in this study and suggestions regarding the ones showing better compromise between time/cost/accuracy were extracted.

2. Model Development

2.1. Assumptions

A set of simplifying hypothesis were assumed based either on the literature or on experimental observations:

i. Stochastic infection: low MOIs are important for process optimisation.
ii. Structured protein expression: intracellular dynamics of vDNA, mRNA and viral protein are considered.
iii. Gene size: intrinsic protein expression kinetics is ruled by the size of the underlying gene.
iv. Maximum translation capacity: maximum translation capacity of mRNA blocks coming from the polyhedrin promoter.

2.2. Mathematical equations

The dynamics of cell density is given by:

$$\frac{dn}{dt} = \mu n - k_d n \qquad \text{Eq. 1}$$

with μ (h^{-1}) the specific growth rate and k_d (h^{-1}) the cells death rate defined as:

$$k_d = \begin{cases} k_{d,\text{int}} + \Delta k_d \log_{10}\left(\sum_k dna_k\right), & \text{t} > \text{TOI} + \delta^* \\ k_{d,\text{int}}, & \text{otherwise} \end{cases} \qquad \text{Eq. 2}$$

where $k_{d,int}$ (h^{-1}) is the intrinsic cell death rate of *Sf*-9 cells, *TOI* (h) the time of infection, δ^* (hpi) the time required for the infection to accelerate host cell death, Δk_d (h^{-1}) the increase in cell death rate due to infection correspondent to 10 intracellular vDNA copies and dna_k (dna$_k$.cell^{-1}) the intracellular vDNA concentration delivered by virus *k* (*k* denotes the foreign gene in the virus). The rate of virus *k* entry, $r_{inf,k}$ (dna$_k$.cell^{-1}h^{-1}) is defined as:

$$r_{\text{inf},k}\,dt = \begin{cases} X_k, & t \le TOI + \delta_{reinf} \\ 0, & t > TOI + \delta_{reinf} \end{cases} \qquad \text{Eq. 3}$$

with X_k a random variable denoting the number of viruses *k* per unit cell (dna$_k$.cell^{-1}) which penetrate the cells in the time interval *[t, t+dt]* and δ_{reinf} (hpi) the time period over which cells continue to be re-infected. It is here assumed that the random variable X_k follows the Poisson probabilistic model:

$$P_{X_k=nk} = \frac{\exp(-\lambda(t))\lambda(t)^{nk}}{nk!} \quad \text{Eq. 4}$$

The shape parameter $\lambda(t)$ of the Poisson distribution is defined here as follows:

$$\lambda(t) = k_a v_k(t) dt \quad \text{Eq. 5}$$

with k_a (ml.cell^{-1}.h^{-1}) the first order attachment constant and v_k (dna$_k$.ml^{-1}) the concentration of extracellular virus k at time t. It can be interpreted as the average number of virus binding to a single cell in the time interval *[t, t+dt]*. The dynamics of extracellular virus v_k is given by:

$$\frac{dv_k}{dt} = \left(-r_{\inf,k} + r_{bud,k}\right) n \quad \text{Eq. 6}$$

Extracellular virus concentration has two contributions: the depletion of virus due to infection and also virus budding, which are the newly synthesized virus in the host cells secreted to the extracellular medium. The intracellular dynamics of vDNA delivered by virus k, dna_k (dna$_k$.cell^{-1}), is defined by:

$$\frac{d\ dna_k}{dt} = \eta_t r_{inf,k} + r_{dnarep,k} - r_{bud,k}, \quad dna_k(0) = 0 \quad \text{Eq. 7}$$

The first term is the rate of infection multiplied by the trafficking efficiency, η_t. The second term is the vDNA replication rate, $r_{dnarep,k}$ (dna$_k$.cell^{-1}.h^{-1}), in the host cells nucleus, defined as:

$$r_{dnarep,k} = \begin{cases} k_{RDNA} dna_k \left(1 - \dfrac{\delta^* - (t - TOI)}{\delta^* - \delta_{DNA,low}}\right), & \delta_{DNA,low} \le t \le \delta^* \\ 0, & otherwise \end{cases} \quad \text{Eq. 8}$$

where k_{RDNA} (h^{-1}) is the first-order vDNA replication constant, $\delta_{DNA,low}$ (hpi) the time for onset of vDNA replication and δ^* is defined as :

$$\delta^* = \frac{\delta_{10}}{\log_{10}\left(\sum_k dna_k\right)} \quad \text{Eq. 9}$$

with δ_{10} (hpi) the critical time instant correspondent to 10 intracellular vDNA copies. The third term in Eq. 7 is the virus budding rate, $r_{bud,k}$ (dna$_k$.cell^{-1}.h^{-1}):

$$r_{bud,k} = \begin{cases} k_{bud} dna_k, & \delta_{bud,low} \le t - TOI \le \delta_{bud,high} \\ 0, & otherwise \end{cases} \quad \text{Eq. 10}$$

with $\delta_{bud,low}$ (hpi) and $\delta_{bud,high}$ (hpi) the time of onset and halt of virus budding, respectively, and k_{bud} (h^{-1}) the first-order virus budding constant. The transcription of foreign gene k into the corresponding mRNA under the control of polyhedrin promoter, is defined as:

$$\frac{d\ rna_k}{dt} = r_{transc,k} - k_{DRNA,k} rna_k, \quad rna_k(0) = 0 \quad \text{Eq. 11}$$

with rna_k the intracellular concentration of mRNA coding for protein k (rna$_k$.cell^{-1}), $r_{transc,k}$ (rna$_k$.cell^{-1}.h^{-1}) the transcription rate of gene k and $k_{DRNA,k}$ (h^{-1}) the first order degradation rate. The transcription rate is as follows:

$$r_{transc,k} = \begin{cases} k_{rna,elong} \dfrac{dna_k}{S_k} \left(1 - \dfrac{\delta^* - (t - TOI)}{\delta^* - \delta_{polh,low}}\right), & \delta_{polh,low} \le t - TOI \le \delta^* \\ 0, & otherwise \end{cases} \quad \text{Eq. 12}$$

with $k_{rna,elong}$ (bp.h^{-1}) the RNA polymerase elongation rate, S_k (bp) the size of gene k and $\delta_{polh,low}$ (hpi) the characteristic time post infection for the onset of polyhedrin promoter transcription. The translation of mRNA into viral proteins is defined by:

$$\frac{dvp_k}{dt} = r_{transl,k}, \quad vp_k(0) = 0 \qquad \text{Eq. 13}$$

with vp_k (μg.cell^{-1}) the concentration of intracellular viral protein k and the $r_{transl,k}$ (μg.cell^{-1}.h^{-1}) the corresponding synthesis rate:

$$r_{transl,k} = \begin{cases} \dfrac{k_{rib,elong} rna_k}{S_k mp_k}\left(1 - \dfrac{\delta^* - (t - TOI)}{\delta^* - \delta_{polh,low}}\right) i_{transl}, & \delta_{polh,low} \le t - TOI \le \delta^* \\ 0, & otherwise \end{cases} \qquad \text{Eq. 14}$$

with $k_{rib,elong}$ (bp.rna$_k^{-1}$.h^{-1}) the ribosomal elongation rate, mp_k (μg) the molecular weight of vp_k and i_{transl} an adimensional parameter to account for the hypothesis of a maximum translation capacity. The term i_{transl} is defined here as:

$$i_{transl} = \begin{cases} 1, & \sum_k S_k rna_k \le L_{transl,\max} \\ \dfrac{L_{transl,\max}}{\sum_k S_k rna_k}, & \sum_k S_k rna_k > L_{transl,\max} \end{cases} \qquad \text{Eq. 15}$$

where $L_{transl,max}$ (rna$_k$.bp.cell^{-1}) is the maximum translation capacity.

2.3. Model calibration

The stochastic/structured model was implemented in MATLAB™. Two integration methods were evaluated: the direct Euler method and the 4th/5th order Runge-Kutta solver (MATLABs' *ode45* function). The Euler method for an integration step of t = 0.1 h was taken as a reasonable compromise between accuracy and computation time. Model calibration was performed using intra and extracellular data of vDNA, mRNA and VP collected over time in experiments with MOI= 5 virus.cell^{-1} and a starting cell density $n(0)$=10^6 cells.ml^{-1}. Process parameters can be viewed in Roldão *et al.* (2008a).

3. Results

All intracellular events were simulated for MOIs of 0.01, 0.1, 1, 10 and 40 virus.cell^{-1}. The population dynamics of healthy and infected cells (Figure 1) show that for high MOIs, 100% infection occurs within the first 3 hpi whereas at low MOIs a high percentage of cells remain healthy and growing in the first 36 hpi, being only infected in a second round of infection due to virus budding (16-36 hpi).

In terms of vDNA replication, maximum intracellular vDNA content is a trade-off between two different factors: high MOI represents more 'seeds' for vDNA replication but reduces the time window for vDNA replication; for low MOIs, virus budding is extended over a long period of time, which will continuously infect and re-infect the existing host cells. Intracellular mRNA and VP follow closely the vDNA replication pattern. Interestingly, model simulations show similar maximum protein yields for the tested MOIs. This apparent insensitiveness to variations in MOI can be explained by the maximum translation capacity of mRNA blocks coming from the polyhedrin promoter. Final volumetric protein productivities, on the other hand, vary significantly for the tested MOIs. Such differences can be explained at the light of the effect of MOI on cellular growth (Figure 2). Since cellular growth is significantly more inhibited at high MOIs than

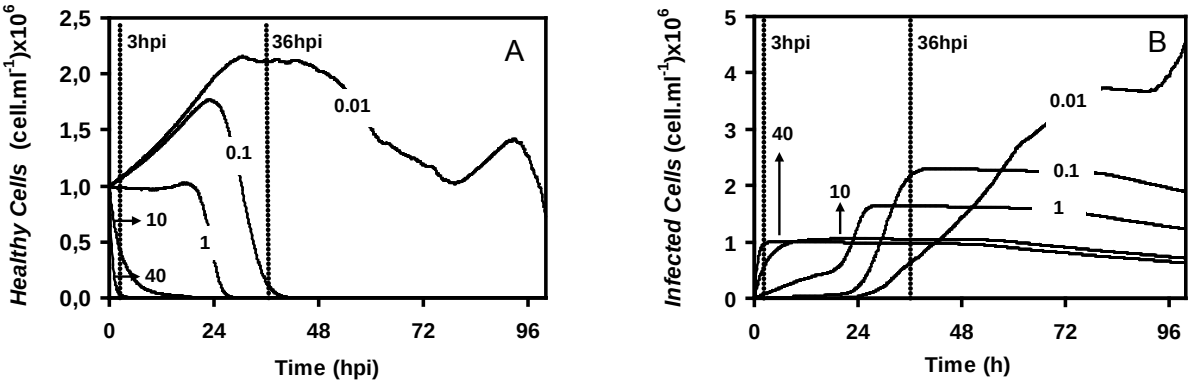

Figure 1. Kinetic profile of healthy (A) and infected (B) cells population. The numbers next to the lines indicate the MOI.

at low MOIs, for similar specific protein yields, the volumetric productivities will be much lower at high MOIs. This phenomenon is visible when comparing the yields of VP2 for MOIs of 0.01 and 10 virus.cell^{-1}. While similar specific productivities are achieved at both MOIs (11 and 12 mg.cell$^{-1}\times10^{-9}$ for 0.01 and 10 virus.cell^{-1} respectively), volumetric productivity at MOI of 0.01 is almost 4-fold higher than at MOI of 10 virus.cell^{-1} (Figure 3).

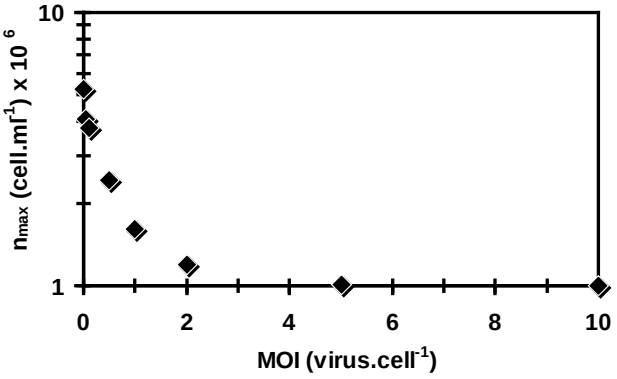

Figure 2. Effect of MOI on maximum cell concentration (n_{max})

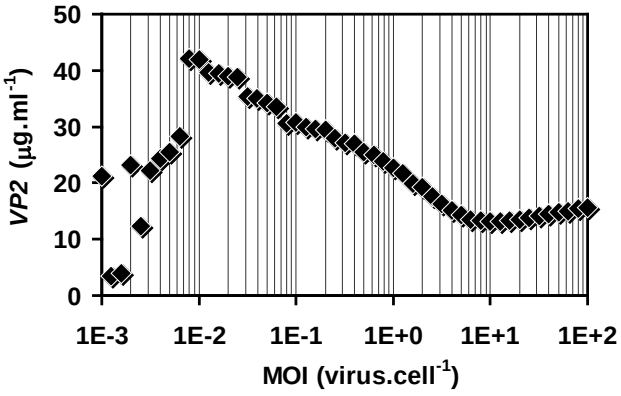

Figure 3. Effect of MOI on VP2 volumetric productivity

Results in Figure 3 indicate the existence of a maximum at MOI=0.01 and a local minimum at MOI=10 which can be attributed to the no-saturation of the translation machinery although 100% infection was obtained in the first infection cycle. For very high MOIs, there is saturation in protein expression due to maximum translation capacity. Therefore, one can conclude that optimal protein production is a compromise between high intracellular protein templates, obtained at high MOIs, and high infected cell densities, obtained at low MOIs. The application of this modelling and optimisation methodology to the remaining VPs, will allow the establishment of optimal operational conditions for optimization of RLPs titre.

Since this model explores the hypothesis of gene size being the main factor affecting the rate of protein expression, the effect of both gene size and MOI on final protein productivities was addressed (Figure 4). Optimal MOIs seem to be independent of the gene size. This result is rational because the recombinant gene size does not affect either the infection kinetics or the vDNA replication rate or the budding of progeny virus. It only affects the transcription and translation mechanisms, meaning that it only impacts on the intracellular accumulation of protein. Moreover, the increase in gene size results in the decrease of protein productivities as

mentioned in Palomares *et al.* (2002).

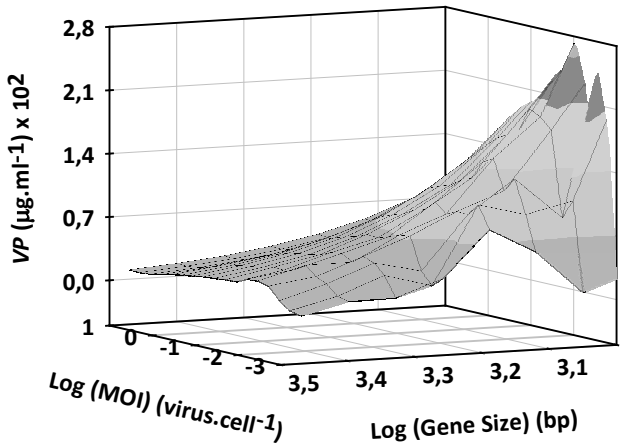

Figure 4. Gene size and MOI effect on final volumetric protein productivity

In the second study, several methods for baculovirus titration were evaluated: $TCID_{50}$ for baculovirus with and without a reporter protein (Green Fluorescent Protein – GFP), microculture tetrazolium assay (MTT), AlamarBlue assay, cell size based assay, growth cessation assay, real time Q-PCR, plaque assay and flow cytometry assay (Roldão *et al.*, 2008b). The techniques that better combined all important variables (accuracy, cost *per* titration, titration time and labor intensity) and therefore proved reliable for titer estimation were the $TCID_{50}$, MTT and flow cytometric assays with titer errors and approximated costs *per* titration of 19% and 14€, respectively. Nevertheless, it is compulsory to confirm titers accuracy by at least two different titrations methods.

4. Conclusion

Mathematical/analytical tools are here demonstrated to play a determinant role in recombinant protein expression. The predictive capacity of the stochastic model will be particularly useful in designing co-infection experiments for optimization of RLPs production as infection statistics becomes a crucial factor and one must guarantee that the infected cells carry all genes required for RLP assembly.

References

Palomares, L.A., Lopez, S., Ramirez, O.T. (2002). Strategies for manipulating the relative concentration of recombinant rotavirus structural proteins during simultaneous production by insect cells. *Biotechnology and Bioengineering*, 78 (6):635.

Roldão, A., Carrondo, M.J.T., Alves, P.M., Oliveira, R. (2008a). Stochastic Simulation of Protein Expression in the Baculovirus/Insect Cells System. *Computers and Chemical Engineering*, 32(1-2): 68-77.

Roldão, A., Oliveira, R., Carrondo, M.J.T., Alves, P.M. (2008b). Error assessment in recombinant baculovirus titration: evaluation of different methods. *Journal of Virological Methods,* submitted.

Proceedings of the 10th International Chemical and
Biological Engineering Conference - CHEMPOR 2008
Braga, Portugal, September 4-6, 2008
E.C. Ferreira and M. Mota (Eds.)

Scaling-up control of yeast fed-batch cultures

L. Dewasme[1], X. Hulhoven[2], A. Vande Wouwer[1]
[1] Service d'Automatique, Faculté Polytechnique de Mons, Boulevard Dolez, 31, B_7000 Mons, Belgium (e-mails : Laurent.Dewasme, Alain.VandeWouwer@fpms.ac.be).
[2] Service de Chimie générale et Biosystèmes, Université Libre de Bruxelles, Av. F.-D. Roosevelt, 50 CP 165/61, 1050 Bruxelles, Belgium (e-mail : Xavier.Hulhoven@ulb.ac.be)

Keywords: fermentation process, robust linear control, internal model principle, observer polynomial, biotechnology.
Topic: Biochemical Engineering.

Abstract

In this paper, experimental investigations of a robust RST control scheme for the regulation of the ethanol in fed-batch cultures of *S. cerevisiae* is presented. Our main objective is to prove its efficiency and robustness in experimental applications ranging from laboratory to industrial scales. The controller only requires one on-line measurement signal, making it easily implementable in an industrial environment. Disturbance rejection is ensured thanks to an on-line parameter adaptation procedure, which delivers as a side product an estimate of the growth rate that can be used for process monitoring purposes. The robustification of the controller is achieved in a simple way, using the observer polynomial.

1 Introduction

S. cerevisae is one of the most popular host microorganism for vaccine production. The possibility to easily express a variety of different recombinant proteins explains its important role in the pharmaceutical industry. In order to maximize productivity, a common strategy is to regulate the ethanol concentration at a low value, thus ensuring an operating point close to the edge between the respirative and respiro-fermentative regimes where the yeast respirative capacity is exactly filled (bottleneck assumption of Sonnleitner and Käppeli's model (1986)). Several applications of this principle can be found, for instance in Chen et al. (1995) and Valentinotti et al. (2003). However, these control schemes all require the on-line measurement of the ethanol concentration, implying the availability of an (unfortunately quite expensive) ethanol probe. This explains that alternative strategies based on more basic measurement signals, such as the dissolved oxygen concentration, have been proposed, e.g. in Akesson (1999), or that software sensors reconstructing ethanol from the measurements of basic signals have been designed (Hulhoven et al., 2006).

In a recent study of Renard et al. (2006), a RST controller with Youla parametrization is developed for the regulation of the ethanol concentration and tested successfully in real-life experiments. One of the main advantage of this approach is that it is based on a simple linear model linking the feed flow rate to the ethanol concentration, and a simple linear model of the disturbance, which represents the substrate demand for cell growth. The prior knowledge of only one stoichiometric coefficient is required, whereas the apparent growth rate can be easily estimated on-line (in order to ensure a good disturbance rejection).

The objective of the present study is to present an alternative and simpler formulation of the RST control scheme based on the observer polynomial (Dewasme et al. (2007)), and to demonstrate its large applicability range and robustness in the scaling-up of the ethanol regulation from laboratory bioreactors to industrial ones.

This paper is organized as follows. The next section introduces the nonlinear model of Sonnleitner and Käppeli (1986). The linearization of the system, the controller design and the on-line parameter adaptation are presented in Section 3. Section 4 illustrates the performance of the ethanol regulation in a series of different real-life experiments from laboratory-scale to industrial-scale bioreactors. The last section is devoted to general conclusions and comments.

2 Modeling yeast fed-batch cultures

The yeast strain *S. cerevisiae* presents a catabolism that can be macroscopically described by the following three main reactions:

Substrate oxidation: $$S + k_5 O \xrightarrow{r_1} k_1 X + k_7 P \quad (1a)$$

Substrate fermentation: $$S \xrightarrow{r_{21}} k_2 X + k_4 E + k_8 P \quad (1b)$$

Ethanol oxidation: $$E + k_6 O \xrightarrow{r_3} k_3 X + k_9 P \quad (1c)$$

where X, S, E, O and P are, respectively, the concentration in the culture medium of biomass, substrate (typically glucose), ethanol, dissolved oxygen and carbon dioxide. k_i are the yield coefficients and r_1, r_2 and r_3 are the reaction rates which are strong non linear functions of the main components, taking the classical form of Monod laws.

This kinetic model, which is often encountered in the literature, is based on Sonnleitner's bottleneck assumption (Sonnleitner and Käppeli, 1986, see Figure 1).

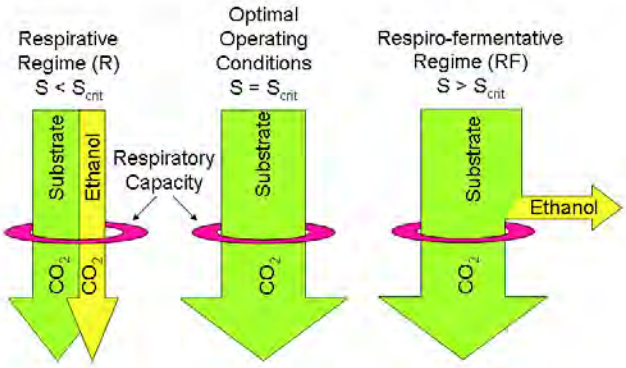

Figure 1: Representation of Sonnleitner's bottleneck assumption (1986).

During a culture, the yeast cells are likely to change their metabolism because of their limited respiratory capacity. When the substrate is in excess (concentration $S > S_{crit}$), the yeast cells produce ethanol through fermentation, and the culture is said in respiro-fermentative (RF) regime. Ethanol has a detrimental effect on the cells growth because it directly inhibits the cells respiratory capacity (Pham, 1999). On the other hand, when the substrate becomes limiting (concentration $S < S_{crit}$), the available substrate (typically glucose), and possibly ethanol (as a substitute carbon source), if present in the culture medium, are oxidized. The culture is then said in respirative (R) regime.

Component-wise mass balances give the following differential equations :

$$\frac{dX}{dt} = (k_1 r_1 + k_2 r_2 + k_3 r_3) X - DX \quad (2a)$$

$$\frac{dS}{dt} = -(r_1 + r_2)X - D(S - S_{in}) \quad (2b)$$

$$\frac{dE}{dt} = (k_4 r_2 - r_3)X - DE \quad (2c)$$

$$\frac{dO}{dt} = -(k_5 r_1 + k_6 r_3)X - DO + OTR \quad (2d)$$

$$\frac{dP}{dt} = (k_7 r_1 + k_8 r_2 + k_9 r_3)X - DP - CTR \quad (2e)$$

$$\frac{dV}{dt} = F_{in} \quad (2f)$$

where S_{in} is the substrate concentration in the feed, F_{in} is the inlet feed rate, V is the culture medium volume and D is the dilution rate ($D = \frac{F_{in}}{V}$). *OTR* and *CTR* represent respectively the oxygen transfer rate from the gas phase to the liquid phase and the carbon transfer rate from the liquid phase to the gas phase. Classical models of *OTR* and *CTR* are given by:

$$OTR = k_L a(O_{sat} - O) \quad (3a)$$

$$CTR = k_L a(P - P_{sat}) \quad (3b)$$

where $k_L a$ is the volumetric transfer coefficient and, O_{sat} and P_{sat} are respectively the dissolved oxygen and carbon dioxide concentrations at saturation.

3 Simple design of an adaptive robust controller

The basic principle of the controller is to regulate the ethanol at a constant low setpoint, leading to a self-optimizing control in the sense of Skogestad (2004) and ensuring that the yeast culture operates in the respiro-fermentative regime, close to the biological optimum, i.e., the edge with the respirative regime.

The control structure is provided following the next decisions:

- The most evident choice of a manipulated variable in a fed-batch system is the feed flow rate F_{in}. Considering that we are looking for the simplest way of modeling the bioreactor, we assume then that F_{in} appears as the main and only input of the system.
- As explained in Valentinotti et al. (2003), the maximum of productivity is obtained at the edge between the respirative and respiro-fermentative regimes, where the quantity of ethanol is constant and equal to zero (*VE=0*). Unfortunately, evaluating accurately the volume is a difficult task as it depends on the inlet and outlet flows including F_{in} but also the added base quantity for pH control and several gas flow rates. So, for those practical limitations, a sub-optimal strategy is elaborated through the control of the ethanol concentration around a low value depending on the sensitivity of commercially available ethanol probes.
- A linear control framework is chosen as it makes the design of robust controllers easier than in a nonlinear framework.
- A RST (2-degree-of-freedom) controller is selected as it offers a great decoupling of the servo/regulation tasks (desired performance specifications and rejection of disturbances).

Substrate consumption represents one of the fastest dynamics of the system. As the theoretical value of S_{crit} is very small (below *0.1g/l*) and assuming a quasi-stationnarity of *S* (i.e. considering that there is no accumulation of glucose in the bioreactor while working not

far from the optimal operating conditions), the very small quantity of substrate is almost instantaneously consumed by the cells ($\frac{d(VS)}{dt} \approx 0$).

Inserting this assumption in the differential system (2), a discrete transfer function linking the ethanol concentration to the feed rate can be obtained for both the respirative and respiro-fermentative regimes:

$$E(k) = \frac{bq^{-1}}{1-q^{-1}}\left[F_{in}(k) - d_i(k)\right] \quad (4a)$$

$$d_i(k) = \frac{c}{1-\gamma q^{-1}}\delta(k) \quad (4b)$$

where the parameters *b* and *c* are functions of the operating regime and d_i is seen as the perturbation representing the cells growth (γ is an image of the cells growth rate). For the sake of clarity, we call bq^{-1} the polynomial *B*, $1-q^{-1}$ the polynomial *A*, *c* the polynomial *C* and $1-\gamma q^{-1}$ the polynomial *D*.

The two-degree-of-freedom RST controller, applied to the linearized model of the bioreactor (see Figure 2), is designed to control the ethanol concentration at E_{ref}. The control law can be written as:

$$R(q^{-1})F_{in}(k) = -S(q^{-1})E(k) + T(q^{-1})E_{ref} \quad (5)$$

and, omitting the backward-shift operator for the sake of clarity, the closed-loop equation takes the form

$$E(k) = \frac{BT}{AR+BS}E_{ref} + \frac{BR}{AR+BS}d_i(k) \quad (6)$$

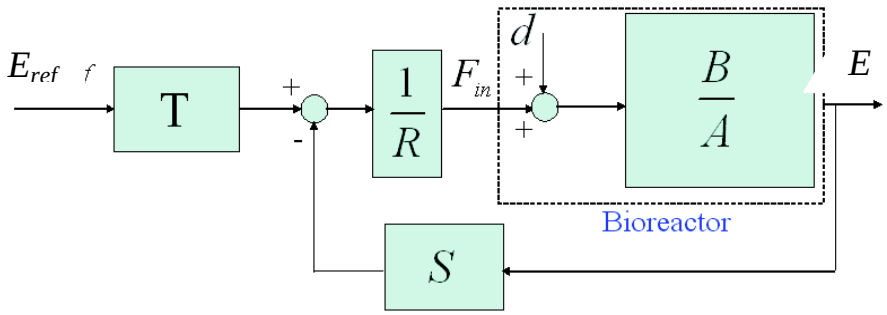

Figure 2: closed-loop control of the bioreactor model where B, A, R, S and T are polynomials in backward-shift operator q^{-1}.

The *RST* controller polynomials are then computed using a pole-placement procedure (Astrom et al, 1997). They are found by solving a diophantine equation of the form:

$$AR + BS = A_0 A_m \quad (7)$$

where A_m is chosen to tune the tracking performances and A_0 is the observer polynomial, which can be selected independently of A_m so as to confer some robustness to the controller.

Following the internal model principle (Francis et al, 1976), the unstable pole γ of the disturbance d_i should be included into the *R* polynomial (i.e, *D* is a factor of *R*). This disturbance will be canceled out if a correct estimation of the parameter γ is available, for

instance through a *Recursive Least Squares* algorithm (Astrom et al, 1997). Indeed, after the initial time, (4b) can be written as:

$$d_i(k) - \gamma\ d_i(k-1) = 0 \qquad (8)$$

4 Experimental results

Experimental applications of the control scheme to fed-batch cultures of *S. cerevisiae* have been performed with laboratory-scale and industrial-scale bioreactors. Experimental results are presented in Figures 3 and 4.

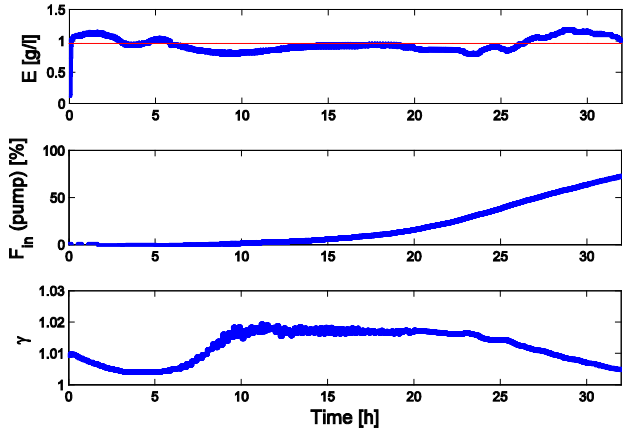

Figure 3: Experimental results of the ethanol regulation applied to laboratory-scale fed-batch cultures of S. Cerevisiae. Evolution of the ethanol concentration E around E_{ref}=1g/l, the feed flow rate F_{in} expressed in % of the maximal pump speed and the parameter γ, image of the cells growth rate.

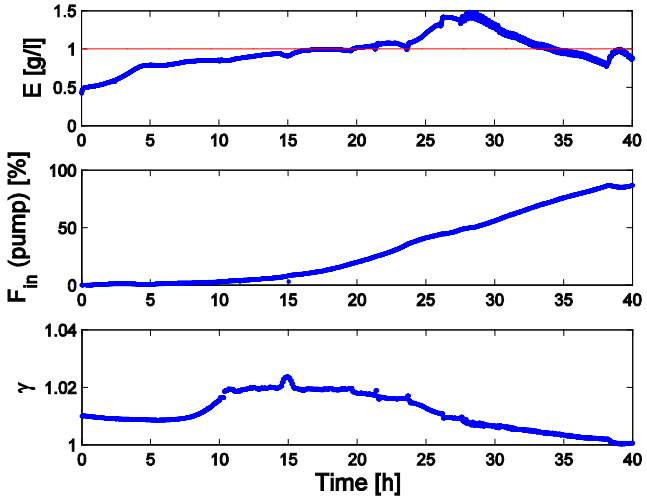

Figure 4: Experimental results of the ethanol regulation applied to industrial-scale fed-batch cultures of S. cerevisiae. Evolution of the ethanol concentration E around E_{ref}=1g/l, the feed flow rate F_{in} expressed in % of the maximal pump speed and the parameter γ, image of the cells growth rate.

The results are comparable independently of the bioreactor scale. Indeed, in the two situations, the ethanol concentration stays around the setpoint E_{ref}=1g/l during the first *10h* and then follows it almost exactly for the next *10h*. Actually, the first hours correspond to the adaptation of the *γ* parameter. When the estimate converges, the regulation of the ethanol concentration becomes more accurate (as the disturbance, which represents the substrate demand for cell growth, can be compensated almost exactly).

After *20h*, the ethanol concentration deviates slightly from the setpoint. This can be explained by an apparent decrease of the cell growth as reflected by the estimated value of *γ*. This limitation phenomenon can be due to a lack of some nutriments in the culture medium. Indeed, cell growth is so efficient that the culture medium is exhausted after a certain batch time. After this time, the feed flow rate evolution becomes linear as *γ* decreases. Despite this deviation, the controller maintains *E* around *1g/l* and prevents it from moving too far from the setpoint. This demonstrates the efficiency of the tracking control even in the presence of unexpected and unmodelled phenomena like the observed limitation.

5 Conclusion

An adaptive RST controller is designed to regulate the ethanol concentration at an imposed setpoint. This design is based on pole placement (for setpoint tracking) and the selection of an observer polynomial (for loop robustification), which can be achieved independently.

In all the experimental validations, the controller performed well independently of the bioreactor scale, demonstrating its reliability under various conditions. As compared to conventional open-loop operation, the application of the control scheme can lead to very significant productivity gain.

Acknowledgements
This work presents research results of the Belgian Network DYSCO (Dynamical Systems, Control, and Optimization), funded by the Interuniversity Attraction Poles Programme, initiated by the Belgian State, Science Policy Office.

References

M. Akesson (1999). *Probing control of glucose feeding in Escherichia coli cultivations*. PhD thesis, Lund Institute of Technology.

K.J. Astrom and B. Wittenmark (1997). *Computer Controlled Systems Theory and Design. Information and System Sciences.* Prentice Hall.

L. Chen, G. Bastin, and V. van Breusegem (1995). *A case study of adaptive nonlinear regulation of fed-batch biological reactors. Automatica*, 31(1):55-65.

X. Hulhoven, F. Renard, Ph. Dehottay, Ph. Bogaerts, and A. Vande Wouwer (2006). *Monitoring and control of a bioprocess for malaria vaccine production*. Toulouse, France. *ROCOND* 2006.

F. Renard, A. Vande Wouwer, S. Valentinotti, D. Dumur (2006). *Control of Yeast Fed-Batch Cultures using Minimal a priori Process Knowledge and Measurement Information*. *Journal of Process Control* 16 (2006), 855-864.

L. Dewasme, F. Renard, and A. Vande Wouwer (2007). *Experimental investigations of a robust control strategy applied to cultures of S. cerevisiae*. Kos, Greece. ECC 2007.

S. Skogestad (2004). *Control structure design for complete chemical plants. Computers and Chemical Engineering*, 28 (1-2):219-234.

B. Sonnleitner and O. Käppeli (1986). *Growth of S. cerevisiae is controlled by its limited respiratory capacity: Formulation and verification of a hypothesis. Biotechnology & Bioengineering*, 28:927-937.

S. Valentinotti, B. Srinivasan, U. Holmberg, D. Bonvin, C. Cannizzaro, M. Rhiel, and U. von Stockar (2003). *Optimal operation of fed-batch fermentations via adaptive control of overflow metabolite. Control engineering practice*, 11:665-674.

B. A. Francis and W. M. Wonham (1976). *The internal model principle of control theory. Automatica*, vol. 12, pp. 457-465.

Proceedings of the 10th International Chemical and
Biological Engineering Conference - CHEMPOR 2008
Braga, Portugal, September 4-6, 2008
E.C. Ferreira and M. Mota (Eds.)

Adaptive extremum-seeking control of yeast fed-batch cultures

L. Dewasme[1], A. Vande Wouwer[1], M. Perrier[2]
[1] Service d'Automatique, Faculté Polytechnique de Mons, Boulevard Dolez, 31, B_7000 Mons, Belgium (e-mails : Laurent.Dewasme, Alain.VandeWouwer@fpms.ac.be).
[2] Département de Génie Chimique, Ecole Polytechnique de Montréal, C.P.6079, Montréal, Que., Canada.

Keywords: Extremum-seeking, fermentation process, nonlinear control, biotechnology.
Topic: Biochemical Engineering.

Abstract

In this study, we consider the problem of optimizing the productivity of fed-batch cultures of *S. Cerevisiae*. This bioprocess is described by nonlinear kinetic models based on the bottleneck assumption of Sonnleitner and Käppeli (1986) and ethanol inhibition resulting from the fermentation of a possible excess of substrate feeding. In contrast with most published studies where the critical substrate level is assumed constant, we investigate the situation where this critical substrate level depends on the yeast respiratory capacity, and in turn on the oxygen and ethanol concentration in the culture medium. The challenge is thus to maintain the process at a high level of productivity by avoiding the accumulation of ethanol. To this end, two adaptive extremum-seeking schemes coupled to a feedback control loop regulating either the substrate or ethanol concentration are developed.

1 Introduction

Yeasts are one of the most important host microorganisms in manufacturing of biopharmaceuticals. Industrial vaccine production is usually achieved using fed-batch cultures of genetically modified yeast strains, which can express different kinds of recombinant proteins.

From an operational point of view, it is necessary to determine an optimal feeding strategy (i.e. the time evolution of the input flow rate to the fed-batch culture) in order to maximize productivity. The main problem that can be encountered at this stage is the presence of an overflow metabolism. The fermentation of an excess of substrate (glucose) can lead to the accumulation of ethanol in the culture medium, and in turn to the inhibition of the cell respiratory capacity.

To avoid this undesirable effect, a closed-loop optimizing strategy is required, which could take various forms (Chen et al. (1995), Renard et al. (2007)). In particular, the use of extremum seeking strategies for bioprocess optimization has received an increasing attention in recent years (Ariyur et al. (2003), Titica et al. (2003)).

In this study, we develop two adaptive extremum-seeking strategies based on Lyapunov stability arguments: (i) in order to determine on-line the critical substrate concentration and to avoid the production of ethanol. (ii) in order to keep the ethanol concentration constant.

2 Modeling yeast fed-batch cultures

The yeast strain *S. cerevisiae* presents a catabolism that can be macroscopically described by the following three main reactions:

Substrate oxidation: $$S + k_5 O \xrightarrow{r_1} k_1 X + k_7 P \quad (1a)$$

Substrate fermentation: $$S \xrightarrow{r_{21}} k_2 X + k_4 E + k_8 P \quad (1b)$$

Ethanol oxidation: $E + k_6 O \xrightarrow{r_3} k_3 X + k_9 P$ (1c)

where X, S, E, O and P are, respectively, the concentration in the culture medium of biomass, substrate (typically glucose), ethanol, dissolved oxygen and carbon dioxide. k_i are the yield coefficients and r_1, r_2 and r_3 are the nonlinear reaction rates given by:

$$r_1 = \min(r_S, \frac{r_o}{k_5}) \quad (2a)$$

$$r_2 = \max(0, r_S - \frac{r_o}{k_5}) \quad (2b)$$

$$r_3 = \max(0, \min(r_E, \frac{r_o - k_5 r_S}{k_6})) \quad (2c)$$

where the kinetic terms associated with the substrate consumption r_S, the oxidative or respiratory capacity r_o and the ethanol oxidative rate r_E are given by $r_S = \mu_S \frac{S}{S + K_S}$, $r_o = \mu_o \frac{O}{O + K_O}$ and $r_E = \mu_E \frac{E}{E + K_E}$, respectively. These expressions take the classical form of Monod laws where μ_S, μ_o and μ_E are the maximal values of specific growth rates and K_S, K_O and K_E are the saturation constants of the corresponding element.

This kinetic model, which is often encountered in the literature, is based on Sonnleitner's bottleneck assumption (Sonnleitner et al, 1986, see Figure 1). During a culture, the yeast cells are likely to change their metabolism because of their limited respiratory capacity. When the substrate is in excess (concentration $S > S_{crit}$), the yeast cells produce ethanol through fermentation, and the culture is said in respiro-fermentative (RF) regime. On the other hand, when the substrate becomes limiting (concentration $S < S_{crit}$), the available substrate (typically glucose), and possibly ethanol (as a substitute carbon source), if present in the culture medium, are oxidized. The culture is then said in respirative (R) regime.

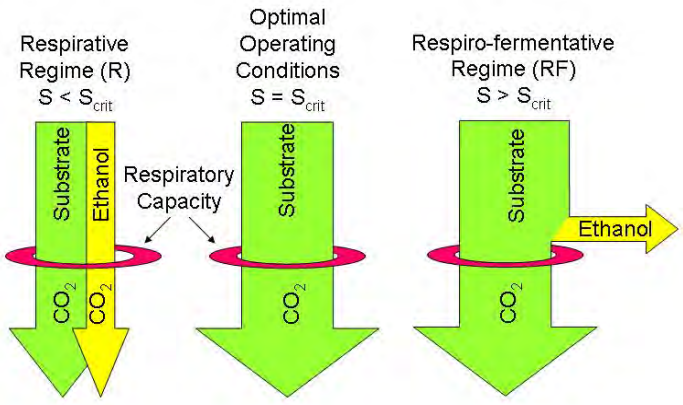

Figure 1: Illustration of Sonnleitner's bottleneck assumption for yeast limited respiratory capacity (1986).

Component-wise mass balances give the following differential equations :

$$\frac{dX}{dt} = (k_1 r_1 + k_2 r_2 + k_3 r_3) X - DX \quad (3a)$$

$$\frac{dS}{dt} = -(r_1 + r_2)X - D(S - S_{in}) \quad (3b)$$

$$\frac{dE}{dt} = (k_4 r_2 - r_3)X - DE \quad (3c)$$

$$\frac{dO}{dt} = -(k_5 r_1 + k_6 r_3)X - DO + OTR \quad (3d)$$

$$\frac{dP}{dt} = (k_7 r_1 + k_8 r_2 + k_9 r_3)X - DP - CTR \quad (3e)$$

$$\frac{dV}{dt} = F_{in} \quad (3f)$$

where S_{in} is the substrate concentration in the feed, D is the dilution rate ($D=F_{in}/V$), F_{in} is the inlet feed rate and V is the culture medium volume. *OTR* and *CTR* represent respectively the oxygen transfer rate from the gas phase to the liquid phase and the carbon transfer rate from the liquid phase to the gas phase. Classical models of *OTR* and *CTR* are given by:

$$OTR = k_L a(O_{sat} - O) \quad (4a)$$

$$CTR = k_L a(P - P_{sat}) \quad (4b)$$

where $k_L a$ is the volumetric transfer coefficient and, O_{sat} and P_{sat} are respectively the dissolved oxygen and carbon dioxide concentrations at saturation.

Ethanol has a detrimental effect on the cells growth because it directly inhibits the cells respiratory capacity (Pham, 1999). The production of ethanol depends on a critical substrate level (S_{crit}) which is not constant. After a trivial mathematical manipulation, a relation between the critical substrate concentration level and the cell respiratory capacity can be obtained as:

$$S_{crit} = \frac{K_S r_o}{k_5 \mu_S - r_o} \quad (5)$$

In order to maintain the system at the edge between the respirative and respiro-fermentative regimes, it is necessary to determine on-line the critical substrate concentration (S_{in}) and to control the substrate concentration in the culture medium around this value.

3 Adaptive extremum-seeking strategies

The adaptive extremum-seeking strategy that is chosen in this study is related to the techniques developed in Titica et al. (2004), Guay and Zhang (2003) and Marcos et al. (2004), which take their roots in the classical work of Ariyur and Krstic (2003). It consists in a permanent estimation of the system dynamics through the analysis of a “control error signal” (which in the present case is a function of the difference between S and the set point S_{crit}) following the injection of a periodical excitation signal d into the adaptive system. This allows the convergence of the parameter estimates to their true values and the stabilization of the error signal around zero (but not exactly zero as the excitation is permanent).

Two original adaptive strategies based on substrate or ethanol control are presented. We first define the main parameters to estimate. Then, we derive adaptation laws and a control law from the consideration of a candidate Lyapunov function ensuring system stability.

The parameters to estimate on line are the kinetic terms in equations (3b) or (3c), depending on the controlled variable, and these terms are denoted $\theta_S = r_1 + r_2$ and $\theta_E = k_4 r_2 - r_3$, respectively . In the case of substrate control, a second parameter is introduced, which represents the angular coefficient of a linear approximation of equation (5), i.e., $S_{crit} \approx \alpha r_0$.

Defining $Z_S = k_p(S - S_{crit}) + k_i \int (S - S_{crit})dt - d$ and $Z_E = k_p(E - E_{sp}) + k_i \int (E - E_{sp})d - td$, the error control variables where *d* is the excitation or *"dither signal"* and E_{sp} the ethanol set point chosen by the user, we consider the following Lyapunov candidate functions:

$$V_S = \frac{1}{2} Z_S^2 + \frac{1}{2\gamma_S} \tilde{\theta}_S^2 + \frac{1}{2\gamma_\alpha} \tilde{\alpha}^2 \quad (6a)$$

$$V_E = \frac{1}{2} Z_E^2 + \frac{1}{2\gamma_E} \tilde{\theta}_E^2 \quad (6b)$$

where γ_i (*i*=*S*,*E*) and γ_α are strictly positive tuning parameters.

A stabilizing controller is obtained if one can prove the strict negativity of the Lyapunov function derivative.

Differentiating V_i (*i*=*S*,*E*) and forcing $\dot{V}_i$ to be negative as in $\dot{V}_i = -k_z Z_i^2$, we obtain:

$$\dot{\hat{\theta}}_i = -\gamma \; k_p Z_i X \quad (7)$$

and, only in the case of substrate regulation:

$$\dot{\hat{\alpha}} = -\gamma \; Z_S (k_p \dot{r}_o + k_i r_o) \quad (8a)$$

$$\hat{S}_{crit} = \hat{\alpha} \; r_o \quad (8b)$$

Finally, the control law is given by:

$$D = \frac{\left[\frac{k_Z Z_S - a + k_d d}{k_p} - \hat{\theta} X \right]}{S - S_{in}} \quad (9)$$

with the dither signal d chosen as:

$$\dot{d} = a + k_i (S - \hat{\alpha} \; r_o) - k_p \hat{\alpha} \; \dot{r}_o - k_d d \quad (10)$$

where *a* is a closed-loop excitation signal and k_d is a new striclty positive design parameter. In a similar way, the ethanol control law can be derived as:

$$D = \frac{\left[\frac{k_Z Z_e - a + k_d d}{k_p} - \hat{\theta} X \right]}{k_4 S_{in} - E} \quad (11)$$

where *d* is chosen as:

$$\dot{d} = a + k_i (E - E_{sp}) - k_d d \quad (12)$$

4 Simulation results

We apply the controller designed in the previous section to a simulated case-study corresponding to classical small-scale (*20 liter* bioreactor) culture conditions.

Figures 2 and 3 present the simulation results. The productivity is quite satisfactory as more than *150 g/l* of biomass are obtained within *less than 40 hours*. Note that in this simulation, a fast convergence to the optimal operating conditions is achieved thanks to a judicious choice of the tuning parameters (typically γ and γ_S).

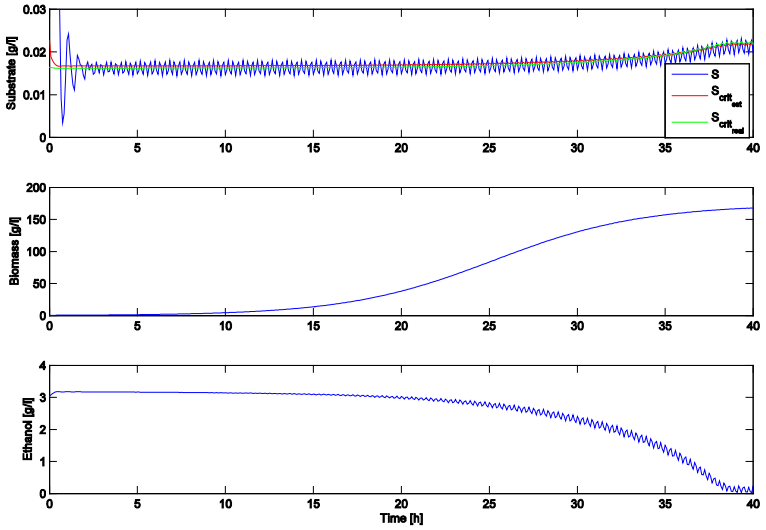

Figure 2: Substrate control. Substrate ($S, \hat{S}_{crit}$ and S_{crit}), biomass (X) and ethanol (E) concentration values.

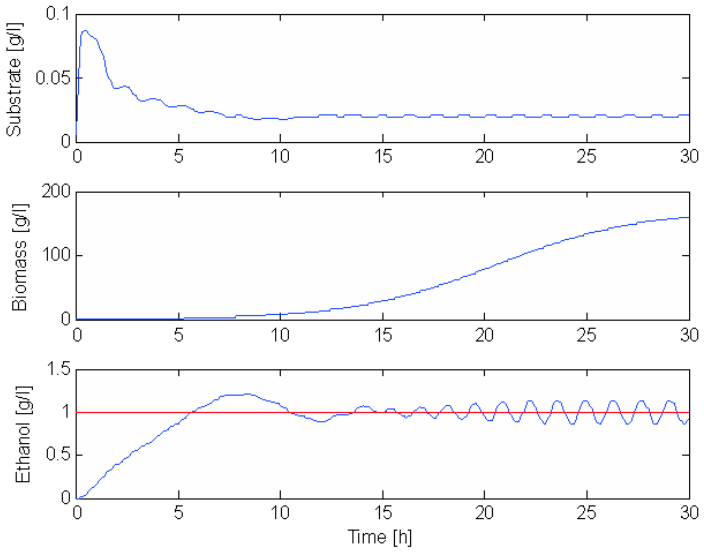

Figure 3: Ethanol control. Substrate ($S, \hat{S}_{crit}$ and S_{crit}), biomass (X) and ethanol (E) concentration values.

In the second case (Figure 3), ethanol control depends only on one parameter adaptation (θ_E) resulting in an easier choice of the tuning parameter values. Results are comparable even if the choice of a measurable reference concentration ($E_{ref} > 0.5$, according to the probe sensitivity) does not correspond to the theoretical extremum ($E=0$).
Finally, note that ethanol measurement is a more practical solution than glucose measurement, as it is difficult to measure the critical glucose concentration with currently available commercial probes. Indeed, the probe sensitivity is generally not sufficient to correctly measure concentrations below *0.1 g/l*. As the ethanol concentration set point can be imposed by the user, it is easier in this case to avoid sensitivity problems. However, the larger the setpoint, the less optimal the solution (fortunately productivity remains quite good for small changes in this value).

5 Conclusion

Two original adaptive extremum seeking strategies based either on substrate or ethanol regulation are derived and applied to yeast fed-batch cultures. The productivity is quite satisfactory as more than *150 g/l* of biomass are obtained within less than *40 hours* for both control strategies. Substrate control leads to the optimal operating conditions in the sense of Sonnleitner and Käppeli's model (1986) while the ethanol control is a very good but sub-optimal solution. However, substrate control has some practical drawbacks related to glucose probe sensitivity.

Acknowledgements
This work presents research results of the Belgian Network DYSCO (Dynamical Systems, Control, and Optimization), funded by the Interuniversity Attraction Poles Programme, initiated by the Belgian State, Science Policy Office.
The authors also gratefully acknowledge the support of the Wallonie-Bruxelles-Québec commission in the framework of the research projet between A. Vande Wouwer and M. Perrier.

References

K. B. Ariyur and M. Krstic (2003). *Real-Time Optimization by Extremum-Seeking Control.* John Wiley & Sons, INC., publication, *wiley-interscience edition*.

L. Chen, G. Bastin and V. van Breusegem (1995). *A case study of adaptive nonlinear regulation of fed-batch biological reactors. Automatica*, 31(1):55-65.

T. B. H. Pham (1999). *Modelling and control of microbii fed-batch and pH-auxostat processes*. PhD thesis, Royal Institute of Technology. Department of Biotechnology, Sweden.

F. Renard and A. Vande Wouwer (2007). *Robust adaptive control of yeast fed-batch cultures. Computers and Chemical Engineering*, May 2007.

B. Sonnleitner and O. Käppeli (1986). *Growth of saccharomyces cerevisiae is controlled by its limited respiratory capacity: Formulation and verification of a hypothesis. Biotechnology & Bioengineering*, 28:927-937.

M. Titica, D. Dochain and M. Guay (2003). *Adaptive extremum-seeking control of fed-batch bioreactors. European Journal of Control*, 9(6):618-31.

M. Titica, D. Dochain and M. Guay (2004). *Adaptive extremum-seeking control of enzyme production in filamentous fungal fermentation. CAB9*, Nancy-France, pages CD-ROM paper 062.

M. Guay and T. Zhang (2003). *Adaptive extremum-seeking control of nonlinear dynamic systems with parametric uncertainties. Automatica*, 39:1283-1293.

N. I. Marcos, M. Guay and D. Dochain (2003). *Adaptive extremum-seeking output feedback control for continous stirred reactors. Proc. Adchem* 2003, Hong Kong, China, pages 333-338.

Proceedings of the 10th International Chemical and
Biological Engineering Conference - CHEMPOR 2008
Braga, Portugal, September 4-6, 2008
E.C. Ferreira and M. Mota (Eds.)

Improvement of baculovirus vectors production based on the metabolic characterization and modelling of Sf-9 cultures

Nuno Carinhas[1]; Vicente Bernal[1]; Adriana Y. Yokomizo[1]; Tiago Vicente[1]; Manuel J. T. Carrondo[1,2]; Rui Oliveira[1,3]; Paula M. Alves[1]

[1]ITQB-Universidade Nova de Lisboa/Instituto de Biologia Experimental e Tecnológica, Av. República, Apt. 12, 2781-901 Oeiras, Portugal. [2]Faculdade de Ciências e Tecnologia, Universidade Nova de Lisboa, 2829-516 Caparica, Portugal. [3]REQUIMTE/CQFB, Departamento de Química, Faculdade de Ciências e Tecnologia, Universidade Nova de Lisboa, 2829-516 Caparica, Portugal.

Keywords: Sf-9 cells; baculovirus vectors; metabolic flux analysis; MOI; high cell density infection; nutrient supplementation
Topic: Systematic methods and tools for managing the complexity.

Abstract

Currently, there is still a gap between studies addressing the physiology of insect cells and reports focusing on increasing the productivity in the insect cell/baculovirus system. A detailed description and modelling of the cellular metabolic state with and without infection would allow to understand how the culture and infection conditions influence growth and productivity. In this work, Metabolic Flux Analysis was applied to assess the metabolic shifts in the *Spodoptera frugiperda* Sf-9 insect cell line as a consequence of growth and baculovirus infection. For that purpose, a simple model of the central metabolism has been constructed and used for the analysis of metabolic adaptations due to cell density and baculovirus infection. The knowledge of how the infection process impacts on the intracellular metabolic fluxes was then used for the rational design of strategies to achieve higher recombinant baculovirus yields in high cell density cultures. Either medium exchange or different suplementation schemes of selected nutrients were emloyed, leading to higher volumetric titers and specific yields.

1 Introduction

Baculovirus (BV)-infected insect cells have been used extensively as an expression system for the production of recombinant proteins (Summers, 2006). More recently, an increasing number of investigators have tackled the use of BVs to direct gene expression in mammalian cells (Kost and Condreay, 2002), for which efficient vector production at high cell density bioreaction is needed. The robustness of suspension cultures of *Spodoptera frugiperda* (Sf-9) cells and the high cell densities and productivities generally attained are advantageous for bioprocess development (Ikonomou et al., 2003). However, early on researchers have come to the conclusion that recombinant protein yields decrease in batch cultures infected during the later stages of growth (Caron et al., 1990). The literature related to the production of BV vectors is very scarce, with some early works demonstrating similar effects of cell density on the yields of wild type viruses. Another significant factor influencing system productivity is the MOI, i.e. the number of infectious particles (IP) per cell added to a culture. More specifically, the interplay between MOI and cell concentration at infection (CCI) is of utmost importance for efficient experimental planning and to better comprehend the BV-insect cell system.

Wth this complex scenario, very few works have attempted to analyze the metabolism of insect cells, trying to understand the effects exerted by BV infection at different MOIs. A detailed description and modelling of the cellular metabolic state with and without infection would help to understand how the culture conditions influence growth and productivity in this system. More specifically, the knowledge of how the infection process impacts on the intracellular metabolic fluxes would enable us to design strategies to achieve higher

productivities in high cell density cultures (Reuveny et al. 1993).
During the last decade, Metabolic Flux Analysis (MFA) has been emerged to quantitatively characterize the metabolism of cells, initially to study the capabilities of engineered microorganism for biotechnological applications. This approach uses mass balancing techniques and the assumption of steady-state to translate the information of a metabolic network supposed to govern the system in a set of linear constraints (Stephanopoulos et al., 1998). These constraints are then combined with measurements of extracellular excretion and uptake rates to calculate the rates of intracellular reactions. The application of mass balance techniques to animal cell cultures has become increasingly popular, although very few studies have been made with insect cell cultures.
In the present work, MFA is used to estimate the intracellular flux distributions of Sf-9 cell cultures subjected to different infection and culture conditions in terms of CCI, MOI and medium composition. For this purpose, the profiles of compounds related to cellular metabolism were analyzed in the culture medium, and several indicators of system productivity were evaluated for the different experiments.

2 Methods

2.1) Experimental cultures

Sf-9 cells were infected with a recombinant BV for evaluation of virus production and culture behavior. Cultures were performed either in 125 mL spinner flasks (Wheaton, USA) or 1-5L biorreactors (B. Braun, Sartorius, Germany) at 27^{o}C. The experiments were performed varying the CCI (1x10^{6} cells.mL^{-1} (CCI 1), 2x10^{6} cells.mL^{-1} (CCI 2) and 3-4x10^{6} cells.mL^{-1} (CCI 3)), using both low (< 5 IP/cell) and high MOIs (> 5 IP/mLI). Additional infections were performed, in which different medium composition coditions were tested, namely by exchanging the medium at the time of infection or adding selected nutrients along with virus inoculation. Every 24 h, culture samples were taken and centrifuged at 1 700 g, during 10 minutes, at room temperature to separate cells from supernatant. Aliquots of the supernatant were then stored at 4^{o}C for virus titration, or at - 20^{o}C to measure the concentrations of glucose and other sugars, lactate, key trycarboxylc acid cycle (TCA) intermediates, ammonia and free amino acids. Additionally, the pools of intracellular co-factors were followed (NAD(H), NADP(H) and ATP). Recombinant BV titration was performed by end point dilution based on the green fluorescent protein (GFP) signal.

2.2) MFA

A model for the central metabolism of Sf-9 cells was built containing the information available from previous models developed for other animal cell lines and the published information available for Sf-9 cells metabolism (Ferrance et al., 1993; Drews et al., 1995 and 2000). The model assumes that the Sf9 cell line uses glucose as the main carbon source. Moreover, it considers the main reactions of central metabolism of cultured animal cells, namely glycolysis, pentose-phosphate pathway, anaerobic fermentation pathway, tricarboxylic acids cycle, respiratory pathways, glutaminolysis, amino acids metabolism and biomass formation (Fig. 1).
On the basis of this metabolic network, a system of mathematical equations was formulated, according to the general MFA theory (Stephanopoulos et al., 1998):

$$\mathbf{r}(t) = \mathbf{A}\mathbf{v}(t) \quad \text{(Eq. 1)}$$

With **r**(t) the vector for the accumulation rates of each compound considered in the network, **A** the stoichiometric matrix of the metabolic network and **v**(t) the vector of the fluxes through the various biochemical reactions. It is generally accepted as reasonable to assume the pseudo-steady-state hypothesis for intracellular metabolites, considering that the accumulation term is negligible. In order to solve this system of equations, some fluxes were experimentally determined. The most common case is to determine trans-membrane rates of

metabolites consumed and/or secreted by the cells. These modelling constraints are crucial when applying the MFA approach because in a typical biochemical network the number of reaction rates is usually higher than the number of metabolites, resulting in an underdetermined system where not all the rates can be uniquely determined. After measuring these rates, the redundant system at hand was solved by the weighted least squares method using the Penrose pseudo-inverse matrix. The balanceable rates, which arise from system redundancy, have been used to calculate the consistency index, *h*, according to the description in Wang and Stephanopoulos (1983). The comparison of *h* with the χ^2-test function was done in order to evaluate the consistency of the experimental values along with the assumed biochemistry and the pseudo-steady-state assumption. To check for the presence of gross measurement errors, the consistency index was calculated for each rate when that rate is not involved, allowing the identification of those rates for which the values of *h* decline the most (i.e., fluxes having higher errors associated). The above-mentioned calculations were performed using the CellNetAnalyzer software (Klamt et al., 2007).

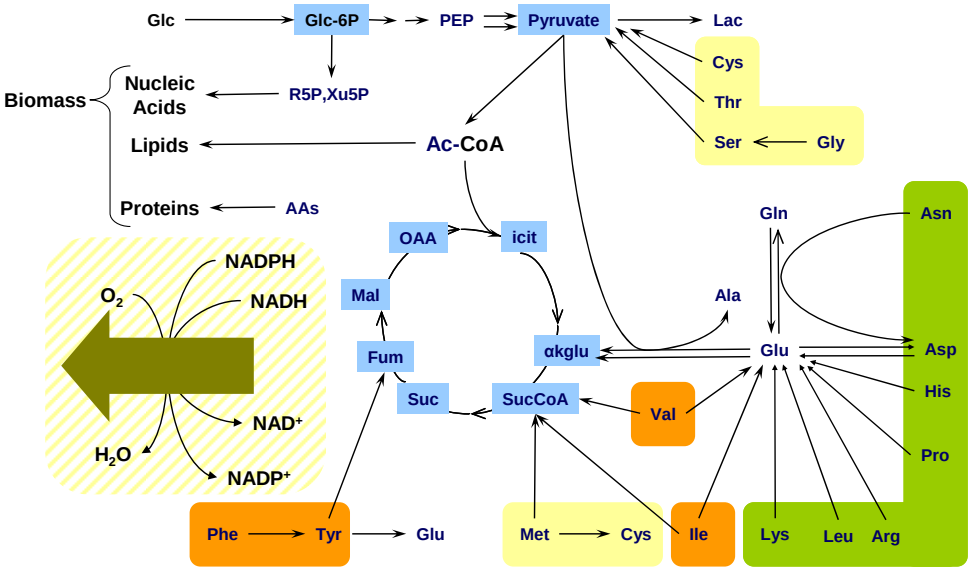

Figure 1 - Model of central metabolism of the *Spodoptera frugiperda* Sf-9 cell line.

3 Results and Discussion

In terms of process productivity, our results confirm that a cell density effect on recombinant baculovirus production occurs which is dependent on the MOI used, with a high MOI "delaying" the drop in production to higher cell densities (Fig. 2). There is a scarcity of data in the literature regarding the factors that affect BV production by insect cells. From a metabolic perspective, the decrease in protein yields when infecting the cells at later stages of growth has been attributed to nutrient depletion rather than the accumulation of inhibitory by-products (Bédard et al., 1994). This is consistent with the fact that the common compounds excreted by mammalian cell lines, ammonia and lactate, do not usually accumulate to toxic levels in Sf-9 cells (Drews et al., 1995). However, most of these studies lacked a detailed description of cellular metabolism, failing to identify the specific components responsible for decreased system productivity. Our results demonstrate that the major alterations of cellular metabolism occurring following infection are related to decreased fluxes through the TCA cycle and growth inhibition, these effects being dependent on the MOI used (Fig. 3). At the same time, the specific consumption rates of glucose are

considerably inhibited after virus infection, which is consistent with the halt in cell replication (data not shown).

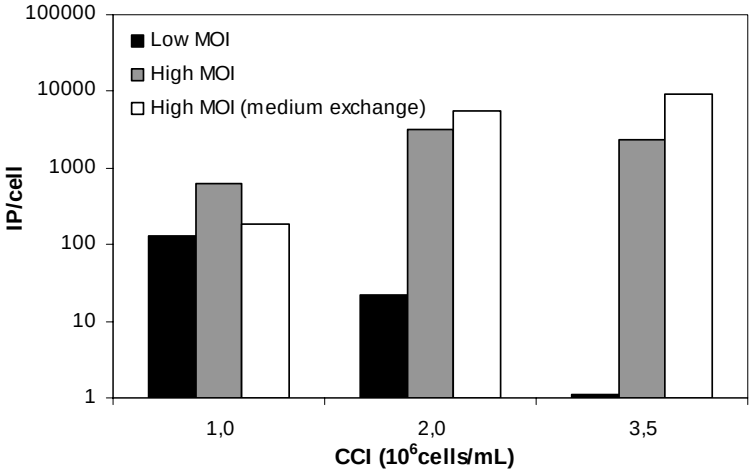

Figure 2 – Effect of different combinations of MOI, CCI and medium exchange at infection on specific productivity.

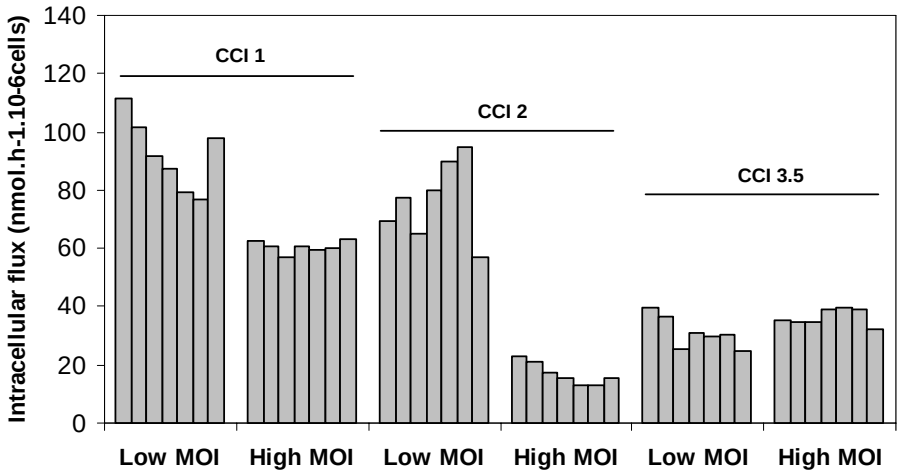

Figure 3 – Effect of different combinations of MOI and CCI on the TCA cycle fluxes.

On the other hand, these findings were corroborated by the marked alterations observed in the intracellular levels of energy and redox co-factors. In fact, it was observed an increase in the levels of intracellular ATP, along with a decrease in the NAD^+/NADH and $NADP^+$/NADPH ratios (data not shown), clearly indicating that the events following BV incorporation have a profound impact on the energetic state of the cells.

We then rationalized that by deliberately altering the cells envirome at the time of infection we could impact the central energy production pathways in order to maintain consistent high energetic levels throughout infection. For this purpose, we performed additional cultures with complete medium exchange, attaining not only higher volumetric titers, but also higher specific yields when compared to the previous cultures (Fig. 2). However, total medium replacement, though feasible for small scale cultures, is not suitable for higher production scales, increasing the cost of the bioprocess due to the need for separation devices and extra medium costs. On the other hand, the addition of complex nutrient mixtures such as different kinds of serum substitutes and hydrolysates could be beneficial for increasing

recombinant BV yields, but hinder the identification of the individual components that may be limiting production. Considering this, selected nutrient supplementation schemes at the time of infection were tested, namely different combinations of key TCA cycle intermediates and glutamine, in order to assess the role of these components on the metabolic state of Sf-9 cells and system productivity. The final results showed an increase in specific yields when compared to non-supplemented cultures. Moreover, after investigating the intracellular flux distributions of infected supplemented cultures, it was observed a relative increase in the TCA cycle rates.

Altogether, the results obtained provide the basis for interconnecting cellular metabolism with infection process allowing culture optimization for BV vectors production. The growing application of recombinant BVs for gene therapy represents an opportunity to deepen the knowledge on this system.

References

Bédard, C., Kamen, A., Tom, R., Massie, B. (1994). *Maximization of recombinant protein yield in the insect cell/baculovirus system by one-time addition of nutrients to high-density batch cultures*,Cytotechnology 15**,** 129-138.

Caron, A. W., Archambault, J., Massie, B. (1990). *High-level recombinant protein production in bioreactors using the baculovirus-insect cell expression system*, Biotechnology and Bioengineering 36**,** 1133-1140.

Drews, M., Doverskog, M., Ohman, L., Chapman, B. E., Jacobsson, U., Kuchel, P. W. and Häggström, L. (2000). *Pathways of glutamine metabolism in Spodoptera frugiperda (Sf9) insect cells: evidence for the presence of the nitrogen assimilation system, and a metabolic switch by $^{1}H/^{15}N$ NMR*, Journal of Biotechnology 78, 23-37.

Drews, M., Paalme, T., Vilu, R. (1995). *The growth and nutrient utilization of the insect cell line Spodoptera frugiperda Sf9 in batch and continuous culture*, Journal of Biotechnology 40, 187-198.

Ferrance, J. P., Goel, A., Ataai, M. M. (1993). Utilization of glucose and amino-acids in insect-cell cutures – quantifying the metabolic flows within the primary pathways and medium development, Biotechnology and Bioengineering 42, 697-707

Ikonomou, L., Schneider, Y. J., Agathos, S. N. (2003). *Insect cell culture for industrial production of recombinant proteins*, Applied Microbiology and Biotechnology 62, 1-20.

Klamt, S., Saez-Rodriguez, J., Gilles, E. D. (2007). *Structural and functional analysis of cellular networks with CellNetAnalyzer*, BMC Systems Biology 1, 2.

Kost, T. A., Condreay, J. P. (2002). *Recombinant baculoviruses as mammalian cell gene-delivery vectors*, Trends in Biotechnology 20, 173-180.

Reuveny, S., Kim, Y. J., Kemp, C. W., Shiloach, J. (1993). *Production of recombinant proteins in high-density insect cell cultures*, Biotechnology and Bioengineering 42, 235-239.

Stephanopoulos, G. N., Aristidou, A. A., Nielsen, J. (1998). *Metabolic Engineering. Principles and Methodologies*, New York: Academic Press, NY.

Summers, M. D. (2006). *Milestones leading to the genetic engineering of baculoviruses as expression vector systems and viral pesticides*, Advances in Virus Research 68, 3-73.

Wang, N., Stephanopoulos, G. (1983). *Application of macroscopic balances to the identification of gross measurement errors*, Biotechnology and Bioengineering 25, 2177–2208.

Proceedings of the 10th International Chemical and
Biological Engineering Conference - CHEMPOR 2008
Braga, Portugal, September 4-6, 2008
E.C. Ferreira and M. Mota (Eds.)

Lactose fermentation by recombinant *Saccharomyces cerevisiae* strains

Pedro M. R. Guimarães, José A. Teixeira, Lucília Domingues*
IBB – Institute for Biotechnology and Bioengineering, Centre of Biological Engineering,
University of Minho, Campus de Gualtar, 4710–057 Braga, Portugal.

Keywords: Lactose fermentation, cheese whey, bio-ethanol, recombinant *S. cerevisiae*
Topic: Integration of life sciences and engineering.

Abstract

The development of *Saccharomyces cerevisiae* strains with the ability to ferment lactose has a high biotechnological interest, particularly for cheese whey bioremediation processes with simultaneous bio-ethanol production. We have developed a flocculent *S. cerevisiae* strain that efficiently ferments lactose to ethanol, using a combination of genetic engineering and evolutionary engineering approaches. This strain fermented efficiently and nearly completely (residual lactose < 3 $g \cdot L^{-1}$) lactose concentrations up to 150 $g \cdot L^{-1}$, including 3-fold concentrated cheese whey, producing ethanol titres up to 8% (v/v). The ethanol productivity obtained with this strain (> 1.5 $g \cdot L^{-1} \cdot h^{-1}$) was higher than that reported for batch or fed-batch fermentations with other lactose-consuming recombinant *S. cerevisiae* strains. The strain is highly flocculent, a property that makes it interesting for the development of high cell density fermentation processes, which may attain much higher productivity.

Introduction

Cheese whey is a by-product of dairy industries, particularly the watery portion that is formed during the coagulation of milk casein in cheese making or in casein manufacture. Whey is produced in large amounts (about 9 litres of whey are generated per each Kg of cheese produced) and has a high polluting load, therefore creating a significant environmental problem (Siso, 1996). The world whey production is estimated to be around 82 million tons per year (Pesta et al., 2007). In Portugal, the production of liquid whey is estimated to be 500 – 560 thousand tons per year (Frazão, 2001), and the largest part of it is processed by concentration and drying. Whey has a BOD (biochemical oxygen demand) of 30 – 50 $g \cdot L^{-1}$ and a COD (chemical oxygen demand) of 60 – 80 $g \cdot L^{-1}$. Lactose is largely responsible for these high BOD and COD; protein recovery reduces the COD only by about 10 $g \cdot L^{-1}$ (Siso, 1996; Domingues et al., 1999a) On the opposite hand, however, whey represents about 85 – 95% of the milk volume and retains 55% of milk nutrients. Among the most abundant of these nutrients are lactose (4.5 – 5% w/v), soluble proteins (0.6 – 0.8% w/v), lipids (0.4 – 0.5% w/v) and mineral salts (8 – 10% of dried extract) (Siso, 1996). Therefore, whey has a vast potential as a source of added value compounds, challenging the dairy industry to face whey surplus as a resource and not solely as a waste problem.

The first step in most procedures for cheese whey valorisation consists in the recovery of the protein fraction. Whey proteins have high nutritional value as well as reported health benefits. Separation of whey proteins is typically done by ultrafiltration, producing whey protein concentrates (WPC), as well as high volumes of a lactose-rich stream, the permeate, that remains a major pollutant since it retains the lactose. The lactose in the permeate (ca. 5% w/v) may be used as a substrate for the production of valuable compounds by fermentation. The classical examples are ethanol and single cell protein (SCP) production in yeast-based

* Corresponding author. Tel + 351-253-604402. E-mail: luciliad@deb.uminho.pt

bioprocesses, although biotechnologists have proposed a multitude of alternative bio-products (see e.g. Siso, 1996; Pesta et al., 2007).

Thus, a bioprocess for the production of ethanol from the lactose in cheese whey can perform two roles: on the one hand it can reduce the whey polluting load, contributing to cheese whey bioremediation, and, on the other hand, an useful product (ethanol) is obtained that can be used as fuel or in food-related applications (e.g. in vinegar manufacturing or in the beverage industry). Being a waste product, whey has advantage over food-related fermentation feedstocks, such as corn, for bio-ethanol production.

Direct fermentation of whey or whey permeate to ethanol is hardly economically competitive with the currently established processes (using cane sugar and cornstarch as substrates) or with emerging second generation technologies (using lignocellulosic biomass as raw material), mainly because the low lactose content (ca. 5% w/v) results in low ethanol titre (2 – 3% v/v), making the distillation process too expensive. Concentration of whey lactose, e.g. by ultrafiltration, is an option to obtain higher ethanol titres. The use of cheese whey powder as an alternative source of concentrated lactose to the production of ethanol has also been recently proposed (Kargi and Ozmihci, 2006; Ozmihci and Kargi, 2007). High ethanol concentrations (10 – 12% v/v) may be obtained by fermentation of concentrated lactose media (up to 200 g L^{-1} lactose) thus significantly reducing the distillation costs. Microbial strains are needed that can efficiently convert such high concentrations of lactose into ethanol, allowing the development of fermentation processes that reach high ethanol titres as well as high ethanol productivities. Such processes must be designed to minimise residual lactose at the end of fermentation, since one of the major motivations for whey utilization is to reduce/eliminate its polluting load.

There are a few established industrial systems to produce ethanol from whey, which has been done in some countries, such as Ireland, Denmark, United States and New Zealand (Siso, 1996; Pesta et al., 2007). Recently, a German dairy company (Müllermilch) announced the construction of a plant near Dresden to produce 10 million liters of bio-ethanol per year from dairy by-products.

Kluyveromyces fragilis has been the microorganism of choice for most industrial plants producing ethanol from whey (Siso, 1996; Pesta et al., 2007), because *Saccharomyces cerevisiae*, the yeast usually chosen for industrial processes involving alcoholic fermentation, is unable to metabolise lactose. Nevertheless, the ability to metabolise lactose can be transferred to *S. cerevisiae* strains by genetic engineering, a problem that has been addressed over the past 20 years by several strategies (for a review see e.g. Rubio-Texeira, 2006). One of those strategies involves cloning of the *LAC4* (β-galactosidase) and *LAC12* (lactose permease) genes of the lactose-consuming yeast *Kluyveromyces lactis* in *S. cerevisiae* strains (Sreekrishna and Dickson, 1985; Rubio-Texeira et al., 1998). However, most strains obtained displayed undesirable characteristics (such as slow growth, genetic instability or problems derived from the use of glucose-galactose mixtures) or were ineffective for ethanol production.

This paper provides an outline of our recent work on engineering a flocculent *S. cerevisiae* strain for efficient lactose to ethanol fermentation. Detailed accounts of the work described here have already been published elsewhere (Guimarães et al., 2008a; Guimarães et al., 2008b).

Construction of a flocculent lactose-consuming *S. cerevisiae* strain

A recombinant *S. cerevisiae* strain with the ability to express both the *LAC4* and *LAC12* genes of *K. lactis* was initially constructed (for details see Domingues et al., 1999b). The plasmid KR1B-LAC4-1 (Sreekrishna and Dickson, 1985), which harbors the *LAC4* and *LAC12* genes, was co-transformed with a linear fragment from the plasmid YAC4 containing the *URA3* gene. The host strain (NCYC869-A3) was a uracil-deficient mutant of the flocculent haploid *S. cerevisiae* strain NCYC869 (*MATα FLO1*).

Using this strategy, a recombinant strain able to metabolize lactose was obtained. However, that original recombinant (strain T1) showed a rather poor lactose fermentation phenotype, growing slowly in lactose and presenting a low ethanol conversion yield (Table 1). The flocculation ability of the strain T1 was also poor when compared with the host strain (Guimarães et al., 2008a).

Evolutionary engineering of the recombinant strain for efficient lactose to ethanol fermentation

In order to improve the lactose fermentation phenotype of the recombinant strain (T1) we used an evolutionary engineering approach. Evolutionary engineering refers to the exploitation of the evolutionary principles to enhance microbial properties in a biotechnological context, provided the desired phenotype is amenable to direct or indirect selection (Sauer, 2001). Evolutionary engineering approaches have been used successfully in the improvement of genetically engineered *S. cerevisiae* strains for xylose and arabinose fermentation (see e.g. Sonderegger and Sauer, 2003; Wisselink et al., 2007).

The strategy that we used to improve the lactose fermentation performance of the recombinant strain T1 consisted in serial transfer/dilution in gently shaken (40 rpm) flasks (for details see Guimarães et al., 2008a). This strategy was designed to keep the recombinant growing in lactose for many generations (>120), as well as to select for the most flocculent cells. The cells recovered at the end of the experiment presented significantly improved lactose fermentation performance compared to T1. These evolved cells were considered to be an independent strain, which was named T1-E (evolved T1). The evolved recombinant strain, T1-E, consumed lactose 2-fold faster and produced 30% more ethanol than T1 (Table 1). Moreover, T1-E flocculated in an earlier phase of the fermentations and formed much bigger flocs than T1, as could be easily observed by visual inspection of the cultivation flasks.

Table 1 – Comparison of fermentation parameters of strains T1 and T1-E in shake-flask cultivations with 25 $g \cdot L^{-1}$ of lactose. Data from a similar fermentation with a *K. lactis* strain (CBS2359) are also show for comparison.[1]

Yeast strain	T1	T1-E	*K. lactis*
Specific growth rate (h^{-1})	0.14 ± 0.01	0.21 ± 0.01	0.28
Final biomass concentration ($g \cdot L^{-1}$)	3.48 ± 0.09	2.81 ± 0.09	2.56
Maximum ethanol concentration ($g \cdot L^{-1}$)	7.08 ± 0.79	10.52 ± 0.04	8.86
Ethanol conversion yield (% of theoretical)	53 ± 5	69 ± 1	65

[1]Shake-flask fermentations were done at 30 ºC with 150 rpm agitation in yeast defined mineral medium (for details see Guimarães et al., 2008a). Data are means ± ranges of duplicate independent cultivations for T1, and means ± standard deviations of triplicate cultivations with single colony isolates for T1-E. Data for *K. lactis* are from a single cultivation.

A series of physiological and genetic studies were done to compare the original recombinant and the evolved strain. Two molecular events that targeted the *LAC* construct in the evolved strain were identified: (1) a 1593 bp deletion in the intergenic region (promoter) between *LAC4* and *LAC12*, and (2) a decrease of the plasmid copy number by about 10-fold compared to the original recombinant. The construction of T1 involved the transfer of a 13 kb *K. lactis* genomic sequence that included the genes *LAC4* and *LAC12* as well as their intergenic region (LACIR) (Domingues et al., 1999b). LACIR is an unusually large intergenic region that works as a promoter for the divergent transcription of both the *LAC* genes. This region contains four functional upstream activating sites (UASs) that synergistically contribute to the activation of both genes by providing binding sites for the transcriptional activator Lac9p, homologous to Gal4p of *S. cerevisiae* (Gödecke et al., 1991). Our results suggest that the intact promoter (endogenous *K. lactis* promoter) was unable to mediate induction by

lactose of the transcription of *LAC4* and *LAC12* in the original recombinant T1, whereas the deletion identified established transcriptional induction of both genes in the evolved recombinant T1-E. We proposed that tuning of the expression of the heterologous *LAC* genes in the evolved recombinant was accomplished by interplay between the decreased copy number of both genes and different levels of transcriptional induction for *LAC4* and *LAC12*, resulting from the changed promoter structure (Guimarães et al., 2008a).

Fermentation of high concentrations of lactose by the evolved recombinant strain

The performance of the evolved recombinant strain (T1-E) was studied in batch fermentations with high concentrations of lactose (up to 200 $g \cdot L^{-1}$). Since aeration has been reported to improve the performance of yeast in fermentations producing very high concentrations of ethanol (see e.g. Alfenore et al., 2004) we have tested T1-E in micro-aerated (shake-flasks) and in well-aerated (bubble column bioreactor) fermentations.

The fermentations were performed in defined mineral medium. Shake-flask fermentations were done in Erlenmeyer flasks filled with medium to 40% of the total volume and incubated at 30 ºC and 150 rpm. The initial pH was adjusted to 5.5 and 100 mM potassium hydrogen phthalate was added to the medium to avoid major drops in pH during cultivation. The bioreactor fermentations were done in a 600 mL bubble column (made in-house) filled with 440 mL of medium. The temperature was maintained at 30 ºC and the pH at 4.0. An air flow rate of 1 vvm was applied using a sintered porous plate located at the bottom of the column and a magnetic stirrer was used to aid in keeping the entire volume well-mixed (for details about the fermentations see Guimarães et al., 2008b).

The evolved recombinant strain consumed rapidly and completely 150 $g \cdot L^{-1}$ lactose in either well-aerated or micro-aerated batch fermentations, producing 5.5% (v/v) and 8.0% (v/v) of ethanol, respectively (Table 2). However, the yeast was unable to consume completely 200 $g \cdot L^{-1}$ lactose in the micro-aerated shake-flask fermentations, but, conversely, consumed totally the same concentration of lactose in well-aerated bioreactor fermentations, although taking a considerable time (about 60 h) to complete fermentation. This may be related with the yeast's inability to synthesize proper amounts of sterols and unsaturated fatty acids under the oxygen limiting conditions found in the shake-flask fermentations. It is well established that yeast needs oxygen in order to synthesise unsaturated fatty acids and sterols (see e.g. Guimarães et al., 2006), and lower amounts of these lipids in the plasma membrane have been correlated with lower ethanol tolerance (see Aguilera et al., 2006 and references therein).

Table 2 – Fermentation of high concentrations of lactose by T1-E in micro-aerated (shake-flasks) and in aerated (bubble column bioreactor) cultivations

Micro-aerated				Aerated			
Initial lactose ($g \cdot L^{-1}$)	Ethanol produced (% v/v)	Ethanol productivity ($g \cdot L^{-1} \cdot h^{-1}$)	Residual lactose ($g \cdot L^{-1}$)	Initial lactose ($g \cdot L^{-1}$)	Ethanol produced (% v/v)	Ethanol productivity ($g \cdot L^{-1} \cdot h^{-1}$)	Residual lactose ($g \cdot L^{-1}$)
114	6.1	2.0	< 1.5	100	4.1	1.2	< 1.5
150	8.0	1.5	< 1.5	150	5.5	1.6	< 1.5
200	8.4	1.4	50	200	7.2	0.95	< 1.5

The ethanol yields were much higher in the shake-flask fermentations (about 80% of the theoretical) than in the bioreactor fermentations (< 60%). This probably resulted from lower oxygen availability for yeast in the shake-flasks (conditions of micro-aeration), leading to

higher sugar flux towards fermentative metabolism. Therefore, under our conditions high aeration was not beneficial to the ethanol production performance of the yeast.

In the design of processes for ethanol production from cheese whey or whey permeate a compromise must be made between maximisation of ethanol titre and productivity and minimisation of the residual lactose concentration at the end of fermentation, since one of the major motivations for whey utilization is to reduce its polluting load. The results suggest that an initial lactose concentration of 150 $g \cdot L^{-1}$ represents the best compromise to obtain high ethanol titre (8% v/v) and productivity (1.5 $g \cdot L^{-1} \cdot h^{-1}$) at the end of fermentation (i.e. with a lactose residual < 1.5 $g \cdot L^{-1}$).

The ethanol productivity obtained in this work was higher than that reported for batch or fed-batch fermentations with other lactose-consuming recombinant *S. cerevisiae* strains: 0.3 $g \cdot L^{-1} \cdot h^{-1}$ (Rubio-Texeira et al., 1998); 0.14 to 0.6 $g \cdot L^{-1} \cdot h^{-1}$ (Ramakrishnan and Hartley, 1993); 1 $g \cdot L^{-1} \cdot h^{-1}$ (Compagno et al., 1995); 1.3 $g \cdot L^{-1} \cdot h^{-1}$ (Farahnak et al., 1986). The utilization of high initial lactose concentrations enabled also to attain higher ethanol titres than previously obtained with recombinant *S. cerevisiae*, with the exception of the work of (Farahnak et al., 1986) that reported an ethanol titre of 13% (v/v). The strain used here was also able to ferment concentrated cheese whey powder solution containing about 150 $g \cdot L^{-1}$ lactose in a batch fermentation with low (0.1 vvm) aeration, consuming nearly all lactose (residual lactose < 3 $g \cdot L^{-1}$) in about 120 h and producing 7% (v/v) ethanol, which corresponds to an ethanol productivity of 0.46 $g \cdot L^{-1} \cdot h^{-1}$ (Guimarães et al., 2008a). The performance of the yeast may be improved by supplementation of the cheese whey with cheap nutrient sources (e.g. corn steep liquor). To our knowledge, the recombinant strain used in this work is the most efficient lactose-fermenting *S. cerevisiae* strain reported in the literature. An additional important advantage of this strain is its highly flocculent phenotype, which makes it particularly suitable for the development of high cell density fermentation processes that, when operated in continuous with flocculated biomass retention, may allow to attain very high ethanol productivities (Domingues et al., 2000).

References

Aguilera, F., Peinado, R.A., Millán, C., Ortega, J.M., Mauricio, J.C. (2006). Relationship between ethanol tolerance, H^+-ATPase activity and the lipid composition of the plasma membrane in different wine yeast strains. *Int J Food Microbiol*, 110, 34-42.

Alfenore, S., Cameleyre, X., Benbadis, L., Bideaux, C., Uribelarrea, J.-L., Goma, G., Molina-Jouve, C., Guillouet, S.E. (2004). Aeration strategy: a need for very high ethanol performance in *Saccharomyces cerevisiae* fed-batch process. *Appl Microbiol Biotechnol*, 63, 537-542.

Compagno, C., Porro, D., Smeraldi, C., Ranzi, B.M. (1995). Fermentation of whey and starch by transformed *Saccharomyces cerevisiae* cells. *Appl Microbiol Biotechnol*, 43, 822-5.

Domingues, L., Dantas, M.M., Lima, N., Teixeira, J.A. (1999a). Continuous ethanol fermentation of lactose by a recombinant flocculating Saccharomyces cerevisiae strain. *Biotechnol Bioeng*, 64, 692-697.

Domingues, L., Teixeira, J.A., Lima, N. (1999b). Construction of a flocculent *Saccharomyces cerevisiae* fermenting lactose. *Appl Microbiol Biotechnol*, 51, 621-6.

Domingues, L., Vicente, A.A., Lima, N., Teixeira, J.A. (2000). Applications of yeast flocculation in biotechnological processes. *Biotechnol Bioprocess Eng*, 5, 288-305.

Farahnak, F., Seki, T., Ryu, D.D., Ogrydziak, D. (1986). Construction of lactose-assimilating and high ethanol producing yeasts by protoplast fusion. *Appl Environ Microbiol*, 51, 362-367.

Frazão, N. (2001). *Estudo de mercado do soro lácteo em Portugal*, Tecninveste - ANIL, Porto.

Gödecke, A., Zachariae, W., Arvanitidis, A., Breunig, K.D. (1991). Coregulation of the *Kluyveromyces lactis* lactose permease and b-galactosidase genes is achieved by interaction of multiple *LAC9* binding sites in a 2.6 kbp divergent promoter. *Nucleic Acids Res*, 19, 5351-5358.

Guimarães, P.M.R., Virtanen, H., Londesborough, J. (2006). Direct evidence that maltose transport activity is affected by the lipid composition of brewer's yeast. *J Inst Brew*, 112, 203-209.

Guimarães, P.M.R., François, J., Parrou, J.L., Teixeira, J.A., Domingues, L. (2008a). Adaptive evolution of a lactose-consuming *Saccharomyces cerevisiae* recombinant. *Appl Environ Microbiol*, 74, 1748-1756.

Guimarães, P.M.R., Teixeira, J.A., Domingues, L. (2008b). Fermentation of high concentrations of lactose to ethanol by engineered flocculent *Saccharomyces cerevisiae*. *Biotechnol Lett*, in press (DOI 10.1007/s10529-008-9779-1).

Kargi, F., Ozmihci, S. (2006). Utilization of cheese whey powder (CWP) for ethanol fermentations: effects of operating parameters. *Enzyme Microb Technol*, 38, 711-718.

Ozmihci, S., Kargi, F. (2007). Kinetics of batch ethanol fermentation of cheese-whey powder (CWP) solution as function of substrate and yeast concentrations. *Biores Technol*, 98, 2978-2984.

Pesta, G., Meyer-Pittroff, R., Russ, W. (2007). Utilization of whey. In: Oreopoulou, V., Russ, W. (editors). *Utilization of by-products and treatment of waste in the food industry*, Springer, New York.

Ramakrishnan, S., Hartley, B.S. (1993). Fermentation of lactose by yeast cells secreting recombinant fungal lactase. *Appl Environ Microbiol*, 59, 4230-5.

Rubio-Texeira, M., Castrillo, J.I., Adam, A.C., Ugalde, U.O., Polaina, J. (1998). Highly efficient assimilation of lactose by a metabolically engineered strain of *Saccharomyces cerevisiae*. *Yeast*, 14, 827-37.

Rubio-Texeira, M. (2006). Endless versatility in the biotechnological applications of *Kluyveromyces LAC* genes. *Biotechnol Adv*, 24, 212-25.

Sauer, U. (2001). Evolutionary engineering of industrially important microbial phenotypes. *Adv Biochem Eng Biotechnol*, 73, 129-169.

Siso, M.I.G. (1996). The biotechnological utilization of cheese whey: a review. *Biores Technol*, 57, 1-11.

Sonderegger, M., Sauer, U. (2003). Evolutionary engineering of *Saccharomyces cerevisiae* for anaerobic growth on xylose. *Appl Environ Microbiol*, 69, 1990-1998.

Sreekrishna, K., Dickson, R.C. (1985). Construction of strains of *Saccharomyces cerevisiae* that grow on lactose. *Proc Natl Acad Sci USA*, 82, 7909-13.

Wisselink, H.W., Toirkens, M.J., Berriel, M.R.F., Winkler, A.A., van Dijken, J.P., Pronk, J.T., van Maris, A.J. (2007). Engineering of *Saccharomyces cerevisiae* for efficient anaerobic alcoholic fermentation of L-arabinose. *Appl Environ Microbiol*, 73, 4881-4891.

Proceedings of the 10th International Chemical and
Biological Engineering Conference - CHEMPOR 2008
Braga, Portugal, September 4-6, 2008
E.C. Ferreira and M. Mota (Eds.)

Studies of fed-batch operation mode on synthesis of short chain ethyl esters catalyzed by cutinase

Dragana P. C. de Barros, Susana M. S. A. Bernardino, Pedro Fernandes, Joaquim M. S. Cabral, Luís P. Fonseca,

IBB – Institute for Biotechnology and Bioengineering, Centre for Biological and Chemical Engineering, Instituto Superior Técnico, Av. Rovisco Pais, 1049-001 Lisboa, Portugal.

Abstract:

The goals of these studies are to determine and optimize the conditions of the synthesis of chain ethyl esters, a group of important fruit flavor compounds, by cutinase in organic media, in particular, isooctane an organic solvent recognized as safety ingredient in food and beverage industrial processes.

The possibility and success to operate in fed-batch operation mode and to determine how much substrate and concentration would be possible to add in consecutive pulse of substrate supply and how these variables affect the enzyme activity and stability were evaluated.

In order to avoid substrate inhibition and to improve the esterification yield a discontinuous feed pulse of substrates strategy (pulse fed-batch mode of substrates supply) was tested which allows achieve concentration of ethyl caproate, important flavor compound of apple and pineapple aromas, of 1.5M in isooctane media. By monitoring the concentration of the substrates this type of cutinase, biosynthesized with a *S. cerevisiae* strain, shows excellent properties on synthesis of short alkyl esters and special achieving very high ester concentration.

Keywords: Cutinase, ethyl caproate, enzymatic processes, fed-batch operation mode, short chain alkyl esters

Topic: Integration of life sciences & engineering.

1. Introduction

Short chain ethyl esters belong to a huge group of flavor compounds that are very important components of natural aromas for the most part used in various food, beverage, cosmetic and pharmaceutical industries. Flavor esters are usually produced by chemical synthesis of an alcohol with an organic acid in the presence of an acid catalyst or by extraction from natural sources. The chemical synthesis of these flavor esters has low-priced but, they are characterized by low purity and not classified like as natural products. Natural aromas obtained by the extraction are very expensive owing to low concentration in the natural product and low extraction yield (Hari-Krishna S. et al., 2002, Berger R.G, 1995).

Biotechnology processes based on enzyme synthesis, as alternative catalysts to chemical route, produce also those esters and other similar flavors. These enzymatic processes have technological and economical interesting characteristics as use mild reaction condition, synthesize flavors with high quality and purity due to the regio- and stereo-specificity of enzymes. The high purity of these flavors allows to be classified as *natural* by food regulatory agencies and better public acceptance as ingredients for food industry in relation to those synthesized by chemical processes (Welsh et al., 1990).

Cutinase are a group of enzymes that can be considered as a link between esterase and lipase. In recent years, the esterolytic activity of cutinase has been largely exploited and several applications in different industrial field have been presented. In the reaction of esterification cutinase showed selectivity for short-chain carboxylic acid esters (Carvalho et al., 1999).

2. Materials and methods

2.1. Materials and chemicals

The acetic, valeric, caproic and octanoic acids (Sigma-Aldrich, Germany), and ethanol 96% (AGA, Portugal) previously dried with were used for ester synthesis while *iso*-octane (Sigma-Aldrich, Germany) used as as organic solvent and n-decane as internal standard of Gas Chromatography (GC) (Merck, Germany). Anhydrous sodium sulfate, powder (Sigma-Aldrich, Germany) used to dry sample media after reaction of esterification and before GC analysis. All other chemicals used were analytical grade.

2.2. Production of cutinase

The *F. solani pisi* cutinase wild-type was biosynthesized by recombinant *S. cerevisiae* SU50 strain as described by Calado *et al*., 2003.. The cutinase producing *S. cerevisiae* SU50 strain (Mata, leu2-3, ura3, gall:URA3, ML-S, MAL3, SUC3) contains the expression vector pUR7320 constructed and provided by the Unilever Research Laboratory, Vlaardingen, the Netherlands. The strain was stored at -80°C in frozen tubes containing selective medium and 50% (v/v) glycerol (Merck, Dannstadt, Germany).

2.3 Purification of cutinase and production of lyophilized enzyme preparation

The isolation and purification of cutinase excreted by recombinant *S. cerevisiae* SU50 strain was carried out by expanded bed adsorption (EBA). Frontal adsorption experiments were carried out in a EBA column Streamline 25 with a settled bed adsorbent height of 15 cm and the column top adjusted to 45 cm. The cation adsorbent Streamline SP XL from Amersham Pharmacia Biotech, Sweden was used to isolate the cutinase directly from the fermentation broth. The cutinase activity and protein concentration of the collected effluent fractions from the column were determined after each run Calado *et al*., 2002. The pool of elution fractions exhibiting highest cutinase activity were previously dialyzed against 20mM phosphate buffer pH 7.0 and then frozen at -80°C and lyophilized (B. Braun Biotech. International CHRIST Alpha 2-4) overnight. Lyophilized pure cutinase was stored at freeze at -20°C before used in esterification reactions.

2.4 Characterization of the cutinase preparations

The cutinase esterolytic activity and protein content were assayed and lyophilized cutinase preparations characterized. The protein concentration was determined by the method of PEARCE (BCA assay). Protein concentrations were determined with reference to a protein standard, the Bovine Serum Albumin (BSA) (Merck).

The cutinase estereolytic activity was assayed using a spectrophotometric method, based on monitoring the hydrolysis of p-nitrophenylbutyrate (p-NPB) to nitrophenol (p-NP), a yellow compound easily identify and quantify by the absorbance at 400 nm Calado *et al*., 2002.

One unit of cutinase estereolytic activity was defined as the amount of enzyme required to convert 1μmol of p-NPB to p-NP per 1 min, under specific condition. The extinction coefficient of p-NP was considered to be 1.84×10^4 (M^{-1} cm^{-1}), as indicated by the supplier (Sigma).Specific activity of lyophilized cutinase preparations was of 170 U/mg protein and

these enzyme samples when loaded in an electrophoresis gel which shows basically only one band of 22kDa, i.e., pure cutinase Sambrook et al.,1989.

2.5 Methods for monitoring substrate and ester concentrations

The concentration of ethanol, carboxilic acids (acetic acid, valeric acid, caproic acid) and ethyl esters (ethyl acetate, ethyl valerate, ethyl caproate) was determined by a Hewllet-Packard model 5890 gas chromatography (GC) equipped with a flame ionization detector (FID). The WCOT Fused Silica coating CP Chirasil- Dex CB column, 25m x 0.25mm, DF=0.25 (Varian Inc.) was used. N-decane was used as the internal standard and to calculate ethyl esters and respective substrates concentrations in the reaction media based on the results of GC analysis according the following specific conditions applied for each particular ethyl ester and respective substrates:

Ethyl acetate: oven temperature was held at 50ºC for 4 min before being elevated to 140ºC for 3 min at 30ºC/min; injector temperature was set at 200 ºC; detector temperature was set at 250 ºC; carrier gas was nitrogen**.**

Ethyl valerate: oven temperature was held at 50ºC for 4 min before being elevated to 170ºC for 2 min at 30ºC/min; injector temperature was set at 200 ºC and detector temperature is set at 250 ºC; carrier gas was nitrogen**.**

Ethyl caproate: oven temperature was held at 50ºC for 4 min before being elevated to 160ºC for 1.67 min at 15ºC/min; injector temperature was set at 200 ºC; detector temperature was set at 250 ºC; carrier gas was nitrogen**.**

2.6 Esterification catalyzed by lyophilized cutinase

Esterification reaction of acid and alcohol by cutinase was carried out in isooctane as organic solvent. Unless otherwise stated a typical esterification reaction for ethyl esters synthesis was carried out in 7 ml of working volume inside of 10 ml capped flasks with rubber (EPDM stoppers, black, Sigma-Aldrich, Germany), used as appropriate reactors that minimizes evaporation or loss of volatile compounds. Alcohol, acid and n-decane were mixed thoroughly in isooctane which consists the reaction medium before the addition of enzyme (lyophilized form) with the objective to minimize enzyme inhibition by the substrates [Claon, P. A. et al., 1993]. First sample (zero point of the reaction) was withdrawn before enzyme addition. The enzymatic ester synthesis occurred in an incubator at 30ºC with multi magnetic stirrer(S.B.S. Instruments A-23). This device enables operation of multiple parallel experiments by simultaneous use of 6 to 12 reactors, as well as, using at least a blank (without enzyme) running in parallel for each ester synthesis reaction. During the reaction a magnetic stirring set at 300 rpm was performed. Samples were withdrawn periodically using a needle without to destroy the rubber cap and then dried before ester and substrates analyzed by GC. The esterfication conversion or reaction yield was calculated according the molar ratio between ethyl ester and respective limiting substrate, alcohol or acid.

The esterification reaction was performed in two different reaction operation modes: batch and discontinuous feed pulse of substrates (fed-batch). In the fed-batch operation mode, the composition of the substrates in the reaction media was assessed first and only then the feed of new substrates was performed in accordance with their observed consumptions

3. Results and discussion

Due to enzyme inhibition for high concentrations of fatty acids and ethyl alcohol and in order to attain high ethyl ester concentration in reaction media was tested a strategy of fed-batch operation mode of stepwise substrates addition because high ester concentrations has significant impact on production cost of any ester. The possibility and success to operate in fed-batch operation mode and to determine how much substrate and concentration would be

possible to add in consecutive pulse of substrate supply and how these variables affect the enzyme activity and stability were evaluated.

Studies of fed-batch operation mode on synthesis of ethyl caproate was initially performed using lower initial concentration of caproic acid (0.05 M) and keeping always the alcohol/acid molar ratio of 2 (Fig. 1). First addition on second day was done with ethyl caproate concentration of 0.054 M. Within the next 9 days of reaction, stepwise substrates additions with R = 2 were carried out for more 5 times. After 11 days, the conversion achieved was of 94 % in relation to caproic acid (limiting substrate) with the final ester concentration of 0.15M (Fig. 1). These results suggest that consecutive substrates supply during the production of caproate ethyl ester by cutinase could be possible to perform without significant effect on enzyme activity after 11 days.

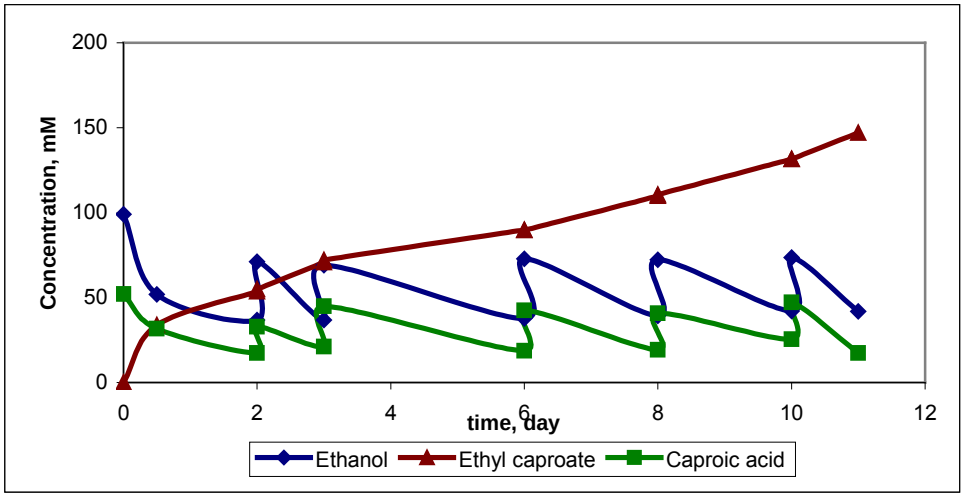

Fig. 1: The effect of the fed-batch operation mode by 5 stepwise additions on synthesis of ethyl caproate by cutinase. (Reaction conditions: Initial concentrations [ethanol] = 0.1M; [caproic acid] = 0.05M; t=30°C; 300 rpm; 2.1 mg/ml enzyme; cutinase specific activity 170 U/mg).

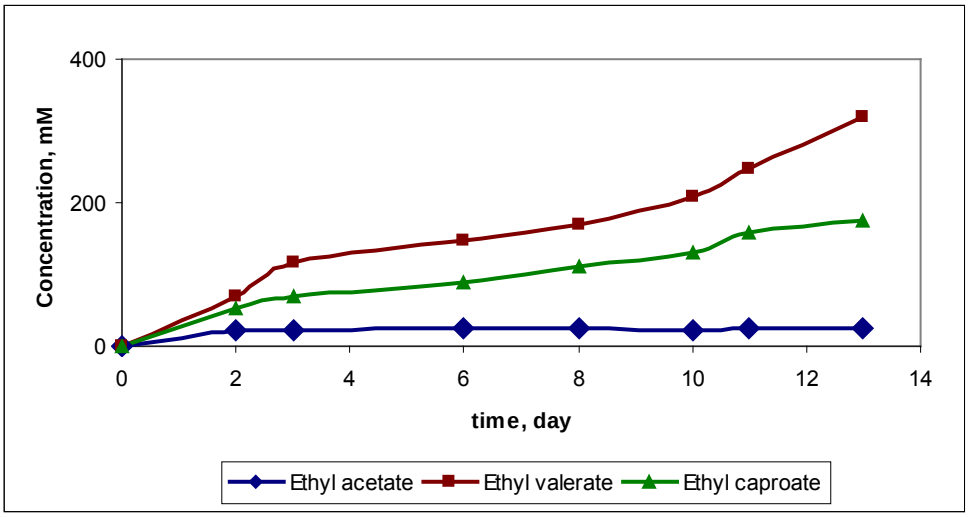

Fig. 2: Effect of acid chain length on synthesis of ethyl esters by cutinase using the fed-batch operation mode (7 stepwise substrates additions). (Reaction condition: [ethanol]=0.1M; 300 rpm, t=30^{0}C, 2.1mg/ml of enzyme, cutinase specific activity 170U/mg).

The same strategy was implemented and evaluated during 13 days for synthesis of acetate, valerate and caproate ethyl esters. Similar profiles of accumulation of ethyl valerate in relation to ethyl caproate was obtained but this strategy was not enough efficient for ethyl acetate. After the initial conversation and seven consecutive stepwise substrates additions

into the reaction medium have not produced more ethyl acetate as apparently the cutinase was deactivated especially due to low pH in the microenvironment surrounding enzyme preparation (Fig. 2)

3.1. Cutinase operational stability evaluated by long esterification reaction

The cutinase catalyzed synthesis of ethyl caproate was observed to evaluate the potential of fed batch reaction operation mode and stability of the lyophilized cutinase in the reaction media under agitation and in equilibrium with respective substrates and different concentrations of product.

a) b)

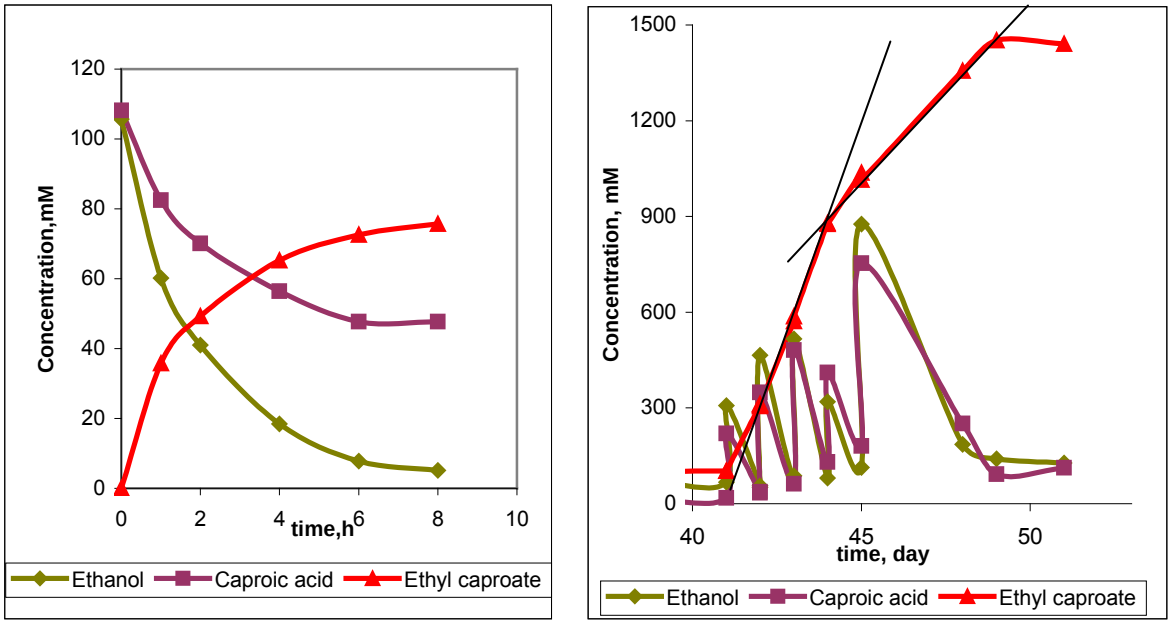

Fig. 3.a),b). Evolution of ester concentration in isooctane media obtained by discontinuous pulse of substrates (fed-batch mode). (Reaction conditions; equimolar alcohol/acid concentrations R=1; t=30°C; 300 rpm; 2.1 mg/ml enzyme; cutinase specific activity 170 U/mg).

The reaction start with equimolar concentration of substrates (0.1M) in batch mode, and after achieving an equilibrium 75.6M concentration of ester (7h) (Fig. 3a), the reaction was left to run 40 days. Between day 41 and 45 days, 5 new stepwise substrates were added (discontinuous feed pulse of substrates).

Monitoring the addition of the substrates was observed. At first 4 addition concentration of substrates was controlled between 0.2M-0.3M and at day 45 was added almost double concentration of substrates. It was noticed that the velocity of production of ester decrease 2.3 times (Fig. 3b), due to the inhibitory effect of substrates. However the yield of ester increase until total consumption of the substrates reaching equilibrium.

These results suggest a enzyme inhibition or deactivation occure with concentration of substrates higher than 0.3M, while the conversion to ethyl caproate was continuously increasing in the reaction medium with lower substrate concentrations.

With fed-batch reaction operation mode at day 45 was observed almost total consumption of substrates and ester concentration increased until about 1.5 M inside of the reaction medium if the substrates concentration was always controlled (Fig. 3b). A similar strategy was also used by Deng at al., 2003 and a good ester yield was also obtained 80.5% with *Candida sp.* 99-125 non-immobilized. By monitoring the concentration of the substrates, an optimal amount can be added in each supply that will not lead to the inhibition or deactivation of the enzyme but at end allows to achieve one of the highest concentration of ethyl caproate. As it was not observed significant accumulation of substrates in the reaction media and for this

reason is possible to think that higher ethyl caproate concentration could be achieved continuing the fed-batch process.

4. Conclusion

Feasibility of using consecutive feeding pulse of the substrates during the production of ethyl esters could be a very productive way to achieve great amount of the product and, at the same time, avoid the substrate inhibition. The feeding should be performed into reaction media to attain substrate concentrations lower than 0.3M and with this strategy minimizes inhibition of enzyme by the substrates.
Furthermore, the lyophilized cutinase showed to be active for long time (more than 50 days) in the reaction media without significant effect of isooctane on its stability. The fed-batch operation mode can be a very rational way to enhance the amount of the ester synthesized and, at the same time, avoid the substrate inhibition and enzyme desactivation since the substrate was added in accordance with its depletion from the reaction mixture.

References

Hari-Krishna, S., Karanth, N.G. (2002). Lipases and lipase-catalyzed esterification in non-aqueous media. Catalysis reviews, 44, 499-591.

Berger, R.G. (1995). Aroma Biotechnology, 1st edn. Springer,Heidelberg.

Wels,h F. W., William, R. E., Dawson, K. H. (1990). Lipase mediated synthesis of low molecular weight flavor ester. J. Food Sci., 55, 1678-1682.

Carvalho, C. M. L., Aires-Barros, M. R., Cabral, J. M. S. (1999). Cutinase: From molecular level to bioprocess development. Biotechnol. Bioeng., 66, 17-34.

Calado, C. R. C.,Almeida C., Cabral, J. M. S., Fonseca, L. P.(2003), Development of a Fed-Batch Cultivation strategy for the Enhanced Production and secretion of Cutinase by a Recombinant *Saccharomyces cerevisiae* SU50 Strain , Journal of Bioscience and Bioengineering 96, No 2,141-148.

Calado, C. R. C., Taipa, M. A., Cabral, J. M. S., Fonseca, L. P. (2002), Optimization of culture conditions and characterization of cutinase produced by recombinant *Saccharomyces cerevisiae*, Enzyme Microb. Technol., 31, 161-170.

Claon,P.A., Akoh C.C.(1993). Enzymatic synthesis of geraniol and citronellol esters by direct esterification in n-heksane , Biotechnol. Lett., 15,1211-1216.

Li Deng, Tianwei Tan, Fang Wang, Xuebing Xu .(2003), Enzimatic production of fatty acid alkyl esters with a lipase preparation from *Candida sp.* 99-125 ,Eur. J. Lipid Sci. Technol. 105, 727 -324.

Sambrook, J., Fritsch, E. F., Maniatis T.(1989),Molecular cloning, a laboratory manual,2nd edition,Cold Sp. Har Lab.Pres, Vol3,1847-1866..

Proceedings of the 10th International Chemical and
Biological Engineering Conference - CHEMPOR 2008
Braga, Portugal, September 4-6, 2008
E.C. Ferreira and M. Mota (Eds.)

New enzymatical process for anaerobic utilization of glycerol

Andrea Balassy [1], Aron Nemeth [1], Bela Sevella [1]
[1] BME-ABET - Department of Applied Biotechnology and Food Science, Budapest University of Technology and Economics, 1111 Budapest, Hungary

Keywords: Glycerol; 1,3-propanediol; enzyme activities; immobilization
Topic: Integration of life sciences & engineering

Abstract

As glycerol is a nontoxic, edible, biodegradable compound, it will provide important environmental benefits to the new platform products. Glycerol can be utilized in various ways of biological transformation to industrially valuable products (Werpy and Petersen, 2004). There are some important derivatives among these such as 3-hydroxypropionaldehyde ((3-HPA) commercial name: reuterin), dihydroxyacetone (DHA), and 1,3-propanediol (PD). 1,3-PD has the largest potential (100.000 t/yr capacity). Several bacteria are able to ferment glycerol to 1,3-PD under anaerobic conditions. A new recombinant technology was worked out with the leadership of DuPont and Genecor in the last decade, in which a recombinant *Escherichia coli* converts glucose directly to 1,3-PD (DuPont Tate & Lyle Bio Products, 2007). Microbiological production of a molecule has always lower yield than an enzymatic method and usually produces a lot of byproducts, which also can be avoided using enzymatic bioconversion. For years we have been working on a new enzymatic process in order to produce 1,3-PD and DHA simultaneously from glycerol. For this enzymatic way three key enzymes are needed (Papanikolaou et. al, 2000). These enzymes must be produced by microbial fermentation. We would like to present the results of developing the fermentation media.

1 Introduction

Although glycerol has been a well-known renewable chemical for centuries, its commercial relevance has increased considerably in the last few years because of its rising formation as an inevitable by-product of biodiesel production. Glycerol can be utilized in various ways of biological transformation to industrially valuable products such as 3-hydroxypropionaldehyde ((3-HPA) commercial name: reuterin), dihydroxyacetone (DHA), and 1,3-propanediol (PD).
1,3-propanediol is mainly used as a starting material polymers, an important diol in the production of polyesters, polycarbonates and polyurethanes. Two examples of large scale applications of 1,3-propanediol are SORONA made by DuPont via biological way and CORTERRA, trade mark of Shell produced via chemical synthesis. Although the fermentative PD production of DuPont is much more environmental friendly then the chemical way, an enzymatic process would be more advantageous. It would not have an upper limit of product yield (decreased also with biomass formation), and would not produce any unwanted metabolites.
For enzyme source several bacteria can be used, which are able to ferment glycerol to PD under anaerobic conditions (Biebl et al. 1999).
We have been working for several years on a process, where glycerol can be converted into 1,3-PD and DHA simultaneously by the fermented enzymes of *Klebsiella pneumoniae* and *Clostridium butyricum*. The process for this method was patented (*P 05 00961*, 2005).
For the enzymatic production of 1,3-PD from glycerol, two key enzymes are responsible: Glycerol-dehydratase (GDHt, E.C.4.2.1.30) and a $NADH_2$-dependent 1,3-propanediol-oxydoreductase (PDOR, E.C.1.1.1.202). In our process the NAD^+ produced by PDOR can be

regenerated by a series of oxydoreductases (alcohol-dehydrogenase, formate dehydrogenase etc.), but we usually use glycerol-dehydrogenase (GDH, E.C. 1.1.1.6) which produces DHA.
It is known that enzyme inactivation can be reduced and its economic value is increased by immobilization. To carry out enzymatic bioconversions, we already used successfully a membrane reactor system retaining the enzymes. With the crude key enzymes of *K. pneumoniae*, we made several successful glycerol transformation to PD and set up a complex mathematical model to describe the whole process (Németh, Á., Sevella, B. 2008). Unfortunatelly acetic acid was always produced as an unfavored byproduct. This byproduct formation cannot be eliminated any way because it serves also the ATP, which is essential for the regeneration of the suicide inactivated key enzyme (B_{12}-dependent GDHt). To overcome this problem we choosed an other enzyme source namely *Clostridium butyricum* VPI 1718 because its GDHt is B_{12}-independent, thus it does not go under suicide inactivation (Raynaud et al., 2004). Crude enzyme solution of *C. butyricum* was obtained by ultrasonic desintegration of cells and were already tested in glycerol to PD bioconversion (Németh, Á. 2008).
Clostridium butyricum is to our knowledge the best natural 1,3-producer from glycerol (Saint-Amans et al., 1994) and the only microorganism identified so far to use a coenzyme B_{12}-independent glycerol dehydratase. Our pleriminary results indicated that the 2xYT medium described by Reynauld et al 2003 is perfect for our Clostridium strain. However in economic aspect the concentrations of yeast extract and bactotryptone are too high to scale-up this fermentation procedure. The first purpose of this study was to optimize the fermentation media.
The other aim of our research was to compare further immobilization technics with the membrane reactor experiments. We tried a covalent method applying chitosan matrix activated with glutaraldehyde. Chitosan – a natural polyaminosaccharide obtained from chitin – was chosen as support material to bind the three key enzymes from the crude enzyme solution.

2 Materials and Methods

Organism and medium

Clostridium butyricum NCIMB 8082 (the same as VPI 1718) was used as enzyme source. The strain were stored at 4°C on Petri dish on modified Reinfored Clostridial Medium (Difco, agar: 12,5 g). Batch cultures of *C. butyricum* were grown anaerobically at 37°C in 2xYT medium (yeast extract, 10 $g \cdot l^{-1}$; bactotryptone, 16 $g \cdot l^{-1}$; NaCl, 5 $g \cdot l^{-1}$), supplemented with 20 $g \cdot l^{-1}$ glycerol or glucose as carbon source (Reynaud et al., 2003). However, as described under "Results", the concentrations of yeast extract, bactotryptone, glycerol and glucose were varied.

Analytical methods

The cell concentations were estimated as cell dry weight using a predetermined correlation factor (K: 1,496 $g \cdot l^{-1}$) between optical density at 600 nm (Pharmacia LKB-Ultrospec Plus spectrophotometer, Pharmacia Co., USA) and cell dry weight.
Substrates and products concentrations were determined by Waters Breeze HPLC System (Waters 1515 Isocratic HPLC Pump, Waters 717 Plus Autosampler, Bio-Rad Aminex HPX 87H chromatography column, Waters 2414 Refractive Index Detector) using the following method: flow rate, 0,5 ml $\cdot$ min^{-1}; mobil phase, 0.01 N H_2SO_4 ; column temperature, 65°C; detector temperature 40°C; sample analyzing time, 30min.

Fermentation experiments

Batch cultivations are shown in Table 1.

Table 1

Number	Type	Anaerobic condition	Medium	Volume	pH regulation	Comment
1	TT	ANAEROSTAT	2xYT substrate: 30g/l Glu or Gly	10 ml	K-phosphates or CaCO3	inoculation: 50 ml cell suspension
2	SF	ANAEROSTAT	2xYT substrate: 30g/l Glu or Gly	50 ml	K-phosphates or CaCO4	inoculation: 1 fringe / flask
3	BQ (1-l)	N_2 gas (periodic)	1. stage: 2xYT; substrate: 20g/l Glu 2.stage: 20 g/l Gly, 10 g/l YE (final concentration) *	0,8 l	20% NH4OH and 25% H2SO4 (by automatic addition)	inoculation (10%): medium: 2xYT contained 20 g/l Glu
4	BQ (1-l)	N_2 gas (periodic)	2xYT substrate: 20g/l Gly	0,8 l	20% NH4OH and 25% H2SO4 (by automatic addition)	inoculation (10%): medium: 2xYT contained 20 g/l Gly
5	BM (2-l)	N_2 gas (periodic)	1. stage: YE: 6 g/l, BT: 4 g/l, NaCl: 5 g/l; substrate: 20g/l Glu 2.stage: 20 g/l GLY, 6 g/l YE (final concentration) *	1,5 l	20% NH4OH and 25% H2SO4 (by automatic addition)	inoculation (10%): medium: 2xYT contained 20 g/l Glu

*After glucose was tottally consumpted in the 1.stage, 20% of the broth was changed with fresh media
TT: test tube (shaked); SF: shaking flask; BQ (1-l): 1-l Bioreactor (B. Braun Biostat® Q DCU); BM (2-l): 2-l Bioreactor (B. Braun Biostat® M); Glu: glucose; Gly: glycerol; YE: yeast extract; BT: bactotryptone

Sampling (in the cases of test tubes) were realized from different parallel test tubes at the corresponding timepoint, because the need of anaerobic cultivation performed in a closed ANAEROSTAT system (Merck).
The growth temperature was 37°C, the agitation speed was 200 rpm.

Preparation of cell-free extracts
Fermentation broth's (number 3-5) were centrifuged at 6000 rpm for 40 min. For resuspending the harvested cells, HEPES buffer pH=7.4 containing 50 mM N-(2-Hydroxyethyl)-piperazine-N′-(2-ethanesulfonic acid) and 0.1 mM MnCl2, and 2 mM dithiothreitol was used. This centrifugation/resuspendation cycle was repeated twice.
Cells were disrupted by ultrasonic desintegration (Labsonic-P, 300W; Sartorius) using the following method: volume, 10 ml; time, 15 min at 0,5 s intervals; efficiency, 60%. Cell debris was separated by centrifugation (10 min at 13000 rpm). The enzyme activity of supernatant was determined.

Enzyme assays

1,3-propanediol-oxydoreductase (PDOR), glycerol-dehydratase (GDH) and glycerol-dehydratase (GDHt) activity was determined photometrically using the method described previously (Németh, Á., Sevella, B. 2008; Németh, Á., Kupcsulik, B., Sevella, B. 2003).

3 Results

Fermentation process development

To reach an economically feasible technology we tried to reduce the costly media components significantly (1. and 2. experiments results shown in Table 3).

Beside the maximum level of bactotryptone (BT;16 $g \cdot l^{-1}$) and two types of substrates we analyzed the effect of yeast extract (YE) concentraion (Figure 1.a). Biomass production decreased significantly below 6 $g \cdot l^{-1}$ YE. While BT concentration was reduced to 4 $g \cdot l^{-1}$ at constant YE (10 $g \cdot l^{-1}$), the biomass was not fallen remarkably (Figure 1.b).

Table 2

Test number	Test Type	Yeast extract ($g \cdot l^{-1}$)	Bactotryptone ($g \cdot l^{-1}$)	Glucose ($g \cdot l^{-1}$)	Glycerol ($g \cdot l^{-1}$)	pH regulation	pH	X ($g \cdot l^{-1}$)	Y_{PD} (mol/mol)	Y_{BP} (g/g)
1	TT	10	16	30	-	A	-	9.228	-	0.43
2	TT	6	16	30	-	A	-	7.682	-	0.13
3	TT	2	16	30	-	A	-	2.132	-	0.09
4	TT	10	12	30	-	A	-	8.679	-	0.83
5	TT	10	8	30	-	A	-	7.871	-	0.10
6	TT	10	4	30	-	A	-	7.625	-	0.21
7	TT	10	16	-	30	A	-	4.680	0.32	0.94
8	TT	6	16	-	30	A	-	3.932	0.30	0.10
9	TT	2	16	-	30	A	-	2.217	0.25	0.56
10	TT	10	12	-	30	A	-	4.356	0.22	0.89
11	TT	10	8	-	30	A	-	4.408	0.23	0.73
12	TT	10	4	-	30	A	-	4.578	0.16	0.44
13	TT	10	16	-	30	A	-	5.054	0.21	0.07
14	TT	6	16	-	30	A	-	4.249	0.24	0.12
15	TT	6	12	-	30	A	-	6.202	0.42	0.18
16	TT	6	8	-	30	A	-	5.049	0.34	0.15
17	TT	6	4	-	30	A	-	3.944	0.24	0.11
18	TT	10	2	-	30	A	-	3.453	0.24	0.11
19	TT	10	16	-	30	B	-	7.497	0.70	0.32
20	TT	6	16	-	30	B	-	7.545	0.67	0.30
21	TT	6	12	-	30	B	-	7.655	0.67	0.27
22	TT	6	8	-	30	B	-	7.493	0.71	0.27
23	TT	6	4	-	30	B	-	8.055	0.67	0.26
24	TT	10	2	-	30	B	-	7.921	0.66	0.26
25	SF	10	16	-	30	A	6.55	6.450	0.19	0.00
26	SF	10	16	-	30	B	6.57	9.203	0.63	0.05
27	SF	6	2	-	30	A	6.63	3.472	0.07	0.00
28	SF	6	2	-	30	B*	6.99	7.940	0.62	0.04
29	SF	10	16	-	30	A*	6.36	6.207	0.20	0.00

A: K_2HPO_4, 5 $g \cdot l^{-1}$; KH_2PO_4, 3 $g \cdot l^{-1}$; B: $CaCO_3$, 30.978 $g \cdot l^{-1}$; B*: $CaCO_3$, 15.489 $g \cdot l^{-1}$; A*: K_2HPO_4, 5 $g \cdot l^{-1}$; KH_2PO_4, 5 $g \cdot l^{-1}$

TT: test tube; SF: shaking flask; PD: 1,3-propanediol; BP: by products

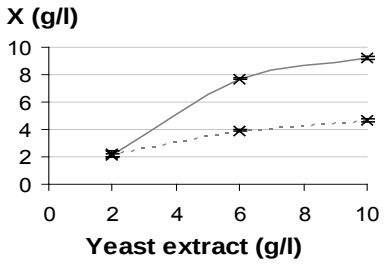

Figure 1.a: −x− substrate: 20 g/l Glucose
··x·· substrate: 20 g/l Glycerol

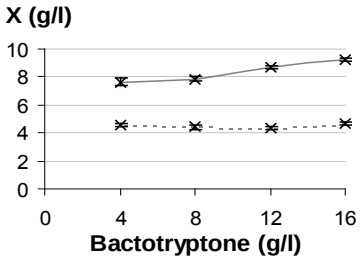

Figure 1. b: −x− substrate: 20 g/l Glucose
··x·· substrate: 20 g/l Glycerol

The 0,72 mol/mol theoretical yield for PD limits the development of an economical fermentation process (Zeng et al., 1996). In the biological production of PD, a series of by-products (acetic acid, butyric acid, lactic acid etc.) decrease the yield of 1,3-PD.

Biebl et al. described the yield (mol/mol glycerol) of PD beside single byproducts such as acetic acid, butyric acid and lactic acid (0.72; 0.59; 0.66 mol/mol respectively). In our experiments the yield of PD did not decrease while BT concentration reduced to 2 $g \cdot l^{-1}$ at constant 10 $g \cdot l^{-}1$ YE (pH regulation with K-phosphates) but fall down beside constant 6 $g \cdot l^{-1}$ YE. However, BT concentration had no effect on PD yield beside pH regulation with $CaCO_3$ (at 6 $g \cdot l^{-}1$ level of YE) and the obtained PD yield approached the theoretical maximum described above.

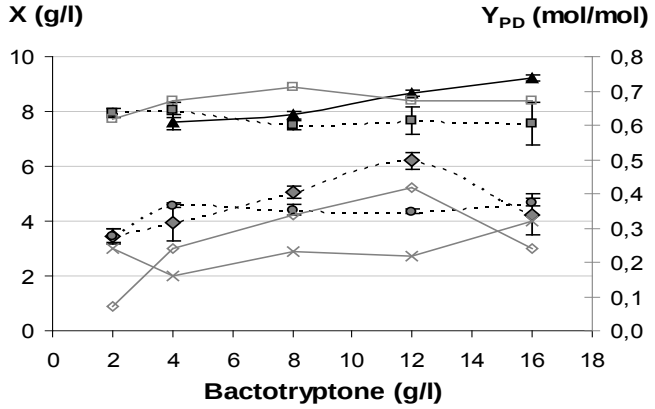

Figure 2.: −▲− (**X g/l**) YE: 10 g/l; pH: A; substrate: Glu; −♦− (**X g/l**) YE: 10 g/l; pH: A; substrate: Gly
−●− (**X g/l**) YE: 6 g/l; pH: A; substrate: Gly; ··■·· (**X g/l**) YE: 6 g/l; pH: B; substrate: Gly
−x− (**Y_{PD}**) YE: 10 g/l; pH: A; substrate: Gly
−◊− (**Y_{PD}**) YE: 6 g/l; pH: A; substrate: Gly; −□− (**Y_{PD}**) YE: 6 g/l; pH: B; substrate: Gly
YE: yeast extract; Glu: glucose; Gly: glycerol; PD: propanediol
A: K_2HPO_4, 5 $g \cdot l^{-1}$; KH_2PO_4, 3 $g \cdot l^{-1}$; B: $CaCO_3$, 30.978 $g \cdot l^{-1}$

Table 3

Number*[1]	Medium Type	YPD		YBP	X	PDOR/GDH
		mol/mol	g/g	g/g	g/l	
3	Substrate: Glu/Gly; YE; BT 10; 16 g/l	0.62	0.60	0.49	11.6	1
4	Substrate: Gly; YE; BT 10; 16 g/l	0.65	0.53	0.29	6.55	10
5	Substrate: Glu/Gly; YE; BT 6; 4 g/l	0.54	0.45	0.42	9.16	1*[2]

*[1] see Materials and methods
*[2] near to the determination lower limit

For enzyme (PDOR, GDH) production we drove several fermentations in lab scale bioreactor (experiments 3-5). If glucose and glycerol were used consecutively as carbon sources (beside of maximum level of YE and BT) the obtained PDOR/GDH ratio was around 1, while in the case of glycerol as sole carbon source the PDOR/GDH ratio was 10 (Table 3). Applying the media with decreased YE and BT content (6 and 4 $g \cdot l^{-1}$ respectively) together with glucose and glycerol as consecutive carbon sources the enzyme activities were hardly measurable and their ratio was around 1 again. These results can be very interesting if we are going to apply the most appropriate enzyme ratio in the enzymatic bioconversion.

References

Werpy, T., Petersen, G. et. al (PNNL, NREL) (2004). Top Value Added Chemicals from Biomass. *U.S. DOE: Biomass* 1, 52-56

DuPont Tate & Lyle Bio Products begins bio-propanediol production (2007). *Focus on Surfactants*, 2, 4-5 DOI: 10.1016/S1351-4210(07)70046-X

Papanikolaou, S., Ruiz-Sanchez, P., Pariset, B., Blanchard, F., Fick, M. (2000). High production of 1,3-propanediol from industrial glycerol by a newly isolated *Clostridium butyricum* strain. *Journal of Biotechnology* 77, 191-208

Biebl, H., Menzel, K., Zeng, A.P., Deckwer, W.D. (1999). Microbial production of 1,3-propanediol. *Applied Microbiology and Biotechnology* 52, 289-297
Németh, Á., Sevella, B. (2008). Development of a New Bioprocess for 1,3-propandiol Production I.: Modeling of Glycerol bioconversion to 1,3-propanediol with *Klebsiella pneumoniae* Enzymes. *Applied Biochemistry and Biotechnology* 144(1) 47-58.
Raynaud, C., Croux, C., Girbal, L., Soucaille, P., Lanzilotta, W.-N. (2004). Insight into the mechanism of the B12-independent glycerol dehydratase from *Clostridium butyricum*: preliminary biochemical and structural characterization. *Biochemistry* 43, 4635-4645
Németh, Á. (2008). Research on biotechnological/bioconversion methods for production of glycerol derivatives. Budapest University of Technology and Economics
Saint-Amans, S., Perlot, P., Goma, G., Soucaille, P., (1994). High production of 1,3-propanediol from glycerol by *Clostridium butyricum* VPI 3266 in a simply controlled fed-batch system. *Biotechnology Letters* 16, 831–836.
Reynaud, C., Sarc., P., Meynial-Salles, I., Croux, C., Soucaille, P. (2003). Molecular characterization of the 1,3-propanediol (1,3-PD) operon of *Clostridium butyricum*. *Applied Biological Sciences* 100(9), 5010-5015
Németh, Á., Sevella, B. (2008). Difficulties and solutions for the assays of the key enzymes of a new enzymatic glycerol bioconversion. *Periodica Polytechnica Chemical Engineering* 52, (1), 1-6.
Németh, Á., Kupcsulik, B., Sevella, B. (2003). 1,3-Propanediol oxidoreductase production with *Klebsiella pneumoniae* DSM2026. *World Journal of Microbiology and Biotechnology* 19. pp. 659-663.
Zeng, A.P., Deckwer, W.D. (1996). Bioreaction techniques under microaerobic conditions: from molecular level to pilot plant reactors. *Chemical Engineering Science* 51 (10) 2305–2314
Zeng, A.P. (1996). Pathway and kinetic analysis of 1,3-propanediol production from glycerol fermentation by *Clostridium butyricum*. *Bioprocess Engineering* 14, 169-175

Proceedings of the 10th International Chemical and
Biological Engineering Conference - CHEMPOR 2008
Braga, Portugal, September 4-6, 2008
E.C. Ferreira and M. Mota (Eds.)

Biosorption of hexavalent chromium by *Arthrobacter viscosus*

Bruna Silva[1*], Hugo Figueiredo[1], Cristina Quintelas[1], Isabel C. Neves[2], Teresa Tavares[1]

[1] IBB – Institute for Biotechnology and Bioengineering, Centre of Biological Engineering, University of Minho, Campus de Gualtar, 4710–057 Braga, Portugal.
[2] Chemistry Department, Centre of Chemistry, University of Minho, Campus de Gualtar, 4710–057 Braga, Portugal.

Keywords: Chromium, Biosorption, *A. viscosus*, Detoxification.
Topic: Integration of Life Sciences and Engineering.

Abstract

Arthrobacter viscosus biomass was used for Cr(VI) biosorption. The effect of biomass concentration on Cr(VI) reduction and removal from aqueous solution was studied in the range of 1.2 to 5.3 g/L. The removal of Cr(VI) and total chromium increased linearly with the increase of biomass concentration. The best removal efficiencies of Cr(VI) and total chromium were reached for the highest biomass concentration, 72.2 % and 44.0 %, respectively. The increase in biomass concentration did not produce significant changes in the uptake values. The maximum uptake value, 8.2 $mg_{Cr}/g_{biomass}$, was obtained for a biomass concentration of 2.3 g/L.

1 Introduction

Heavy metals derived from the release of industrial wastewater present an ongoing and serious hazard to human health and to the environment, because these elements are toxic, not biodegradable and can accumulate in food chain and living tissues (Gavrilescu, 2004; Deng et al., 2006).

Chromium is a common and very toxic pollutant introduced into natural waters from a variety of industrial wastewaters. The major sources of contamination are electroplating, metal finishing industries and tanneries (Agarwal et al., 2006). Among the several oxidation states of chromium, the main forms present in the environment are trivalent and hexavalent, Cr(III) and Cr(VI), respectively. These two oxidation states have widely contrasting toxicity and transport characteristics. Hexavalent chromium poses a greater risk due to its carcinogenic properties to living organisms, while Cr(III) is generally only toxic to plants at very high concentrations and is less toxic or non-toxic to animals (Dakiky et al., 2002; Anderson, 1997). Depending on the solution pH values, Cr(VI) species may be in the form of dichromate ($Cr_2O_7^{2-}$), hydrochromate ($HCrO_4^-$), or chromate (CrO_4^{2-}) and Cr(III) species may take the form of hydrated trivalent chromium, $Cr(H_2O)_6^{3+}$, and chromium hydroxide complexes, $Cr(OH)(H_2O)_5^{2+}$ or $Cr(OH)_2(H_2O)_4^+$. Due to the repulsive electrostatic interactions, Cr(VI) anion species are generally poorly adsorbed by the negatively charged soil particles and can move freely in the aqueous environments. In contrast, Cr(III) species normally carry positive electric charges and therefore can be easily adsorbed on the negatively charged soil particles (Silva et al., 2008 a; Deng et al., 2004).

* Corresponding author. Tel + 351-253-604400. E-mail:bsilva@deb.uminho.pt

The conventional methods used for heavy metals removal are generally expensive and potentially hazardous due to the generation of harmful by-products. Common methods include chemical precipitation, chemical oxidation or reduction, ion exchange, membrane filtration and carbon adsorption (Bailey et al., 1999). These technologies have significant disadvantages, such as incomplete metal removal and generation of huge volumes of toxic sludge, and are often inefficient and/or expensive mainly when applied to diluted solutions up to 100 mg/L (Sağ et al., 1995; Cossich et al., 2004).

As an alternative to traditional physicochemical treatments, a number of biological assays using microbial biomass have been studied and developed to treat chromium-contaminated waste streams and natural waters. Certain types of microbial biomass can retain relatively high quantities of metals by means of passive processes known as biosorption, which is dependent on the affinity between the metallic species and the binding sites on the cell wall (Raras, 1995). Biosorption is a metabolism-independent process and thus can be performed by both living and dead microorganisms. This adsorption is based on mechanisms such as complexation, ion exchange, coordination, adsorption, chelation and microprecipitation (Hu et al., 1996). The accumulation of metals by biological materials is a promising process that can reduce capital costs by 20%, operational costs by 36% and total treatment costs by 28%, compared with conventional systems (Loukidou et al., 2004).

The use of bacteria for biosorption is a fast growing field in metal remediation because of their ubiquity, ability to grow under controlled conditions and small size (Mohan et al., 2006). Many studies have demonstrated that various types of biomaterials such as bacteria are capable of transforming hexavalent chromium, Cr(VI), into the much less toxic and less mobile trivalent form, Cr(III). When Cr(VI) comes in contact with biomaterials, especially in an acidic solution, the Cr(VI) can easily or spontaneously be reduced to the Cr(III), because Cr(VI) has high *redox* potential value (above +1.3 V at standard conditions) (Park et al., 2004, 2005, 2007, 2008). *Arthrobacter* species are of particular interest because of its high potential for bioremediation (Asatiani et al., 2004). The bacteria used in this work, *Arthrobacter viscosus*, is a good exopolysaccharide producer, an aspect which would permit prediction of good metal ion entrapment (Figueiredo et al., 2008; Silva et al., 2008 b).

The purpose of the present work was to assess the potential of *A. viscosus* for the biosorption of hexavalent chromium and to study the effect of biomass concentration on its removal performance.

2 Experimental

2.1 Materials and reagents

Arthrobacter viscosus was obtained from the Spanish Type Culture Collection of the University of Valencia. Aqueous potassium dichromate solution was prepared by diluting $K_2Cr_2O_7$ (Panreac) in deionised water.

All glassware used for experimental purposes was washed in 10% nitric acid to remove any possible interference by other metals.

2.2 Preparation of the biomass

A medium with 10 g/L of glucose, 5 g/L of peptone, 3 g/L of malt extract and 3 g/L of yeast extract was used for the microorganism growth. The medium was sterilized at 121 ºC for 20 min, cooled to room temperature, inoculated with bacteria and kept at 28 ºC for 24 h with moderate stirring in an incubator. The cells were then harvested by centrifugation at 7000 rpm for 15 min and re-suspended in residual culture medium to obtain suspensions with different biomass concentrations to be used in the biosorption assays.

2.3 Biosorption assays

Batch experiments were conducted in 250 mL Erlenmeyer flasks using 15 mL of each suspension of *A. viscosus* and 150 mL of a potassium dichromate solution (100 mg_{Cr}/L). Biomass concentrations of 1.2, 2.3, 4.3 and 5.3 g/L were used and determined by dry weight measurement. The initial pH value of the dichromate solution was adjusted to 3, using a 4 M H_2SO_4 solution. The Erlenmeyer flasks were kept at 28 ºC, with moderate stirring. Samples of 1 mL were taken, centrifuged and analyzed for chromium determination.

2.4 Chromium analysis

Hexavalent chromium was analyzed by measuring absorbance at 540 nm of the purple complex of Cr(VI) with 1,5-diphenylcarbazide, in acidic solution (Eaton et al., 1995). For total Cr determination, the Cr(III) was first oxidized to Cr(VI) at high temperature by the addition of an excess of potassium permanganate previous to the reaction with 1,5-diphenylcarbazide. The Cr(III) concentration was calculated by the difference between the total Cr and Cr(VI) concentration.

3 Results

Cr(VI) removal and its reduction to Cr(III) was observed in the presence of *A. viscosus* cells. In Fig. 1 is shown the time-dependent concentration of Cr(VI) and the initial removal rates, for various biomass concentrations.

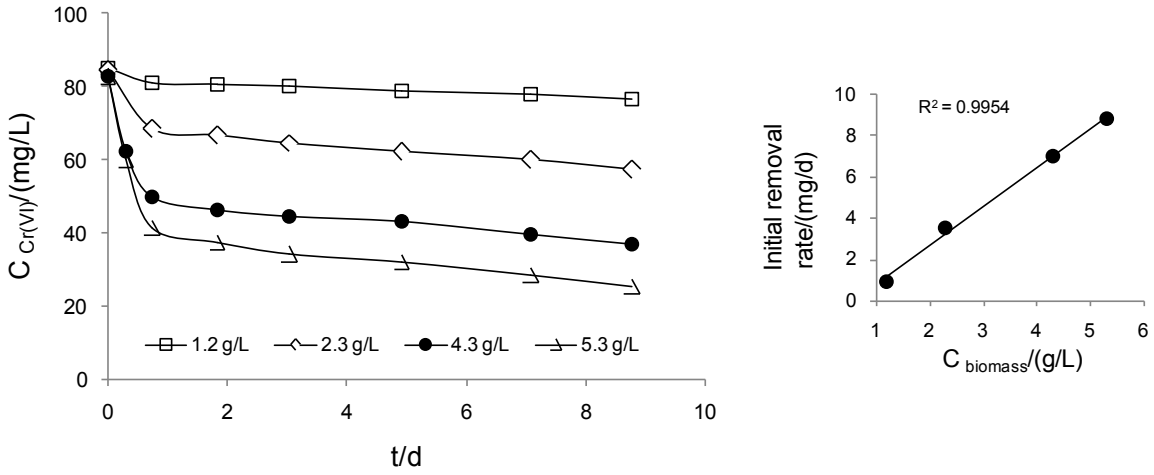

Fig. 1 Concentration of Cr(VI) as a function of contact time and initial removal rates, for biomass concentrations of 1.2, 2.3, 4.3 and 5.3 g/L.

It can be observed that the removal of Cr(VI) is enhanced with an increase in biomass concentration, as it was expected. The initial removal rates were plotted against biomass concentration, as presented in Fig. 1. The plot showed a good linearity, indicating that the reaction was pseudo-first-order with respect to biomass concentration. Total removal of Cr(VI) was not achieved, for the biomass concentrations in study. As the solution pH was not maintained at highly acidic values, the reduction of Cr(VI) to Cr(III) was restricted due to the high pH values of the solutions after 9 days of contact time, which varied from 4.6 to 5.1. Therefore, there was a deficit of protons in solution to allow the complete reduction of Cr(VI).

The concentration values of Cr(VI), Cr(III) and total chromium at the end of the contact time, are presented in Figure 2. It can be seen that the final chromium concentrations in solution showed a linear pattern with respect to biomass concentration, in the range of 1.2 to 5.3 g/L. Cr(VI) concentration decreased lienarly with the increase of biomass concentration, while Cr(III) concentration in solution increased proportionally with the increment of biomass. The lowest total chromium concentration was obtained for the highest biomass concentration, remaining in solution 25.4 mg/L of Cr(VI) and 24.6 mg/L of Cr(III).

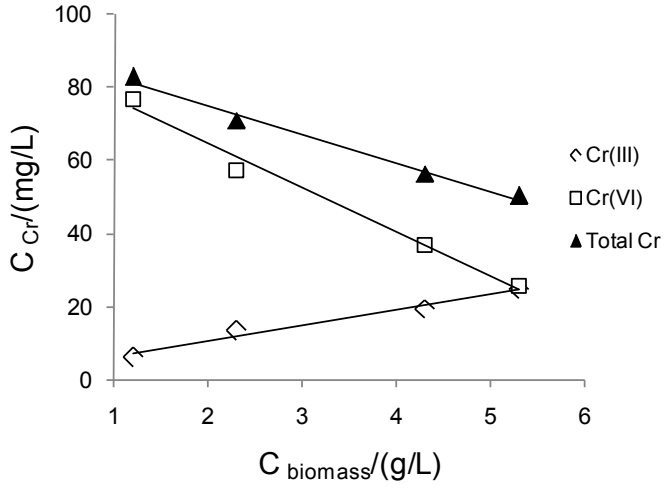

Fig. 2 Chromium concentrations in solution after 9 days of contact time, for different biomass concentrations.

In Fig. 3 are shown the removal efficiencies and the uptake of total Cr attained for the different biomass concentrations. As the biomass concentration increased, the removal efficiency of Cr(VI) and total Cr increased linearly, as discussed above. The best removal efficiencies of Cr(VI) and total chromium were achieved for a biomass concentration of 5.3 g/L, 72.2 % and 44.0 %, respectively. It can be observed in Fig. 3b) that the uptake values did not change significantly with the increase of biomass concentration. The highest uptake value, 8.2 $mg_{Cr}/g_{biomass}$, was obtained for a biomass concentration of 2.3 g/L.

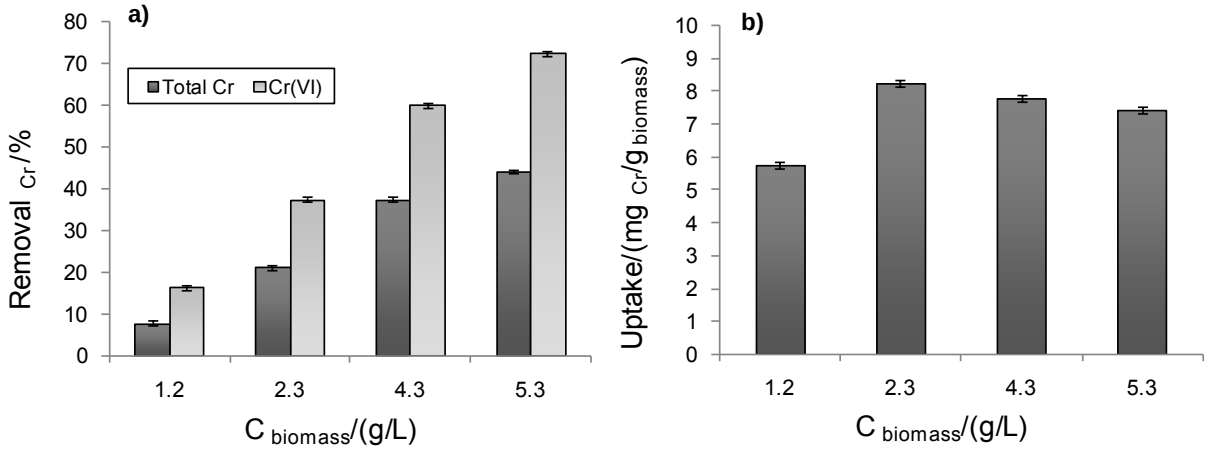

Fig. 3 Removal efficiencies of total Cr and Cr(VI) **(a)** and uptake of total chromium in terms of initial bacteria mass **(b)** after 9 days of contact time, for the different biomass concentrations tested.

4 Conclusions

This work demonstrate the ability of *Arthrobacter viscosus* biomass for the detoxification of Cr(VI) from contaminated wastewaters and highlights the efficacy of using biological agents as an alternative to conventional treatments.

The complete reduction of Cr(VI) was not attained for the biomass concentrations in study, due to the lack of protons in solution. For promoting the Cr(VI) reduction, it is necessary to work with highly acidic pH values. The removal efficiencies of Cr(VI) and total chromium increased linearly with the increase of biomass concentration, in the range 1.2 to 5.3 g/L.

Acknowledgements

H. Figueiredo and B. Silva thank Fundação para a Ciência e Tecnologia (FCT-Portugal) for a Ph.D. grant and C. Quintelas is thankful for the concession of a Pos-Doc grant.

References

Agarwal, G.S., Bhuptawat, H.K., Chaudhari, S. (2006). Biosorption of aqueous chromium(VI) by *Tamarindus indica* seeds. *Bioresource Technology*, 97, 949-956.

Anderson, R.A. (1997). Chromium as an essential nutrient for humans. *Regulatory Toxicology and Pharmacology*, 26, S35–S41.

Asatiani, N.V., Abuladze, M.K., Kartvelishvili, T.M., Bakradze, N.G., Sapojnikova, N.A., Tsibakhashvili, N.Y., Tabatadze, L.V., Lejava, L.V., Asanishvili, L.L., Holman, H-Y. (2004). Effect of chromium(VI) action on *Arthrobacter oxydans. Current Microbiology*, 49, 321–326.

Bailey, S.E., Olin, T.J., Bricka, R.M., Adrian, D.D. (1999). A review of potentially low-cost sorbents for heavy metals. *Water Research*, 33, 2469-2479.

Cossich, E.S., Silva, E.D., Tavares, C.R.G., Filho, L.C., Ravagnani, T.M.K. (2004). Biosorption of chromium (III) by biomass of seaweed *Sargassum* sp. in a fixed bed column. *Adsorption*, 10, 129–138.

Dakiky, M., Khami, A., Manassra, A., Mer´eb, M. (2002). Selective adsorption of chromium(VI) in industrial wastewater using low-cost abundantly available adsorbents. *Advances in Environmental Research*, 6, 533-540.

Deng, L., Su, Y., Su, H., Wang, X., Zhu, X. (2006). Biosorption of copper (II) and lead (II) from aqueous solutions by nonliving green *algae Cladophora fasciculares*: equilibrium, kinetics and environmental effects. *Adsorption*, 12, 267–277.

Deng, S., Bai, R. (2004) Removal of trivalent and hexavalent chromium with aminated polyacrylonitrile fibers: performance and mechanisms. *Water Research*, 38, 2424-2432.

Eaton, D., Clesceri, L.S., Greenberg, A.E. (1995). *Standard methods for the examination of water and wastewater*, American Public Health Association (APHA), Washington.

Figueiredo, H., Silva, B., Raposo, M.M.M., Fonseca, A.M., Neves, I.C., Quintelas, C., Tavares, T. (2008). Immobilization of Fe(III) complexes of pyridazine derivatives prepared from biosorbents supported on zeolites. *Microporous and Mesoporous Materials*, 109, 163-171.

Gavrilescu, M. (2004). Removal of heavy metals from the environment by biosorption – a review, *Engineering Life Science*, 4, 219-232.

Hu, M.Z.-C., Norman, J.M., Faison, B.D., Reeves, M.E. (1996). Biosorption of uranium by *Pseudomonas aeruginosa* strain CSU: characterization and comparison studies. *Biotechnology and Bioengineering*., 51, 237–247.

Loukidou, M. X., Zouboulis, A. I., Karapantsios, T. D., Matis, K. A. (2004). Equilibrium and kinetic modeling of chromium(VI) biosorption by *Aeromonas caviae*. *Colloids and Surfaces A*, 242, 93-104.

Mohan, D., Pittman Jr., C.U. (2006). Activated Carbons and Low-Cost Adsorbents for Remediation of Tri- and Hexavalent Chromium from Water: A Review. *Journal of Hazardous Materials B*, 137, 762-811.

Park, D., Yun, Y.-S., Ahn, C.K., Park, J.M. (2007). Kinetics of the reduction of hexavalent chromium with the brown seaweed *Ecklonia* biomass. *Chemosphere*, 66, 939-946.

Park, D., Yun, Y.-S., Jo, J.H., Park, J.M. (2005). Mechanism of hexavalent chromium removal by dead fungal biomass of *Aspergillus niger. Water Research*, 39, 533-540.

Park, D., Yun, Y.-S., Kim, J.Y., Park, J.M. (2008). How to study Cr(VI) biosorption: Use of fermentation waste for detoxifying Cr(VI) in aqueous solution. *Chemical Engineering Journal*, 136, 173-179.

Park, D., Yun, Y.-S., Park, J.M. (2004). Reduction of Hexavalent Chromium with the Brown Seaweed *Ecklonia* Biomass. *Environmental and Science Technology*, 38, 4860-4864.

Raras, A.G. (1995). Biological and biotechnological waste management in material processing. *Journal of the Mineral Metals & Materials Society*, 47, 56–63.

Sağ, Y, Kutsal, T. (1995). Biosorption of heavy metals by *Zooglodea ramigera*: use of adsorption isotherms and a comparison of biosorption characteristic. *The Chemical Engineering Journal*, 60, 181–188.

Silva, B., Figueiredo, H., Quintelas, C., Neves, I.C., Tavares, T. (2008 a). Zeolites as supports for the biorecovery of hexavalent and trivalent chromium. *Microporous and Mesoporous Materials*, doi: 10.1016/j.micromeso.2008.05.015.

Silva, B., Figueiredo, H., Quintelas, C., Neves, I.C., Tavares, T. (2008 b). Iron and Chromium Removal from Binary Solutions of Fe(III)/Cr(III) and Fe(III)/Cr(VI) by Biosorbents Supported on Zeolites. *Materials Science Forum*, 587-588, 463-467.

Proceedings of the 10th International Chemical and
Biological Engineering Conference - CHEMPOR 2008
Braga, Portugal, September 4-6, 2008
E.C. Ferreira and M. Mota (Eds.)

Treatment of wood hydrolysates for bioethanol production by fermentation

Cátia V.T. Mendes, Jorge M.S. Rocha, Cristina M.S.G. Baptista, M. Graça V.S. Carvalho*
CIEPQPF, Dep. Chemical Engineering, University of Coimbra, R. Sílvio Lima, Pólo II, 3030-790 Coimbra, Portugal

Keywords: bioethanol, wood hydrolysates, xylose, biorefinary, *Eucalyptus globulus*
Topic: Integration of life sciences & engineering

Abstract

The main objective of this work is the valorisation of *Eucalyptus globulus* wood hydrolysates, rich in xylose, by using them as raw material for bioethanol production within the biorefinery concept. The hydrolysates were obtained from two distinct pre-treatments of eucalyptus wood chips: an auto-hydrolysis and an acid-hydrolysis. The liquid extracts resulted from the auto-hydrolysis needed a secondary acid-hydrolysis, which doubled the xylose content. Two treatment methods were tested to reduce the potential inhibitors concentration and to adjust the pH value in the liquid hydrolysates, either using NaOH or $Ca(OH)_2$. The treated liquid hydrolysates were fermented by the yeast *Pichia stipitis*, which was previously adapted to the treated wood extracts. The use of $Ca(OH)_2$ enabled a greater detoxification effect, leading to a better overall yeast performance. An ethanol concentration of 12 g L^{-1}, with a productivity of 0.22 g L^{-1} h^{-1} and a yield based on xylose equivalents of 0.48 g_{eth} $g_{xyl\ eqs}^{-1}$, was achieved so far when using the acid-hydrolysates.

1 Introduction

Several well known factors are leading to an increase in the demand of bioethanol as an alternative fuel. Its advantage as an ecological fuel, obtained from renewable resources, must be supported by non-food competitive materials. Lignocellulosic biomass is abundant, cheap and with a great potential to produce bioethanol, being composed of cellulose (40-50%), hemicelluloses (25-35%) and lignin (15-20%) (Knauf and Moniruzzaman, 2004).The hemicellulosic fraction of *Eucalyptus globulus* wood, the major wood species used in Portugal to produce pulp and paper, is mainly xylan which is partly dissolved during the cooking process and burned in the recovery boiler. For the production of value-added products, such as bioethanol, this fraction could be partly extracted before the cooking start up and undergo an ethanolic fermentation after hydrolysis into simple sugars. The hydrolysis of those polymeric chains releases xylose monomers which can then be fermented by few microorganisms, like *Pichia stipitis* (Pan *et al.*, 2004). Nevertheless, the fermentation efficiency of hemicellulosic sugars is strongly dependent on the hydrolysates inhibitors content coming from the raw material or produced during the hydrolysis reaction (Villareal *et al.*, 2005). Such compounds can stress fermentative microorganisms reducing their performance (sugar use and product formation efficiencies). The type and concentration of inhibitors in the hydrolysates obtained from wood chips depend on both hydrolysis operating conditions and raw materials used and may include sugar-derived by-products (furfural and hydroxymethylfurfural), aliphatic acids (like acetic acid), lignin and its degradation products as well as metals (Villareal *et al*., 2005). The inhibitory effects can be overcome by the hydrolysate detoxification prior to fermentation and several methods have been developed to reduce the inhibitors concentration, or even to convert them into inactive substances. Microbial adaptation, evaporation, solvent extraction, activated charcoal adsorption,

* Corresponding author: Tel +351-239-798746, Email: mgc@eq.uc.pt

enzymatic treatment, the use of ion exchange resins and pH adjustment are some of the most common procedures that can be employed separately or in different combinations, to achieve an efficient detoxification of the hydrolysate (Villareal *et al.*, 2005). pH adjustment is a low-cost treatment (Canilha *et al.*, 2003) and it was used in this work to detoxify the hydrolysates from *Eucalyptus globulus* wood. For that, two procedures with different alkali (NaOH and $Ca(OH)_2$) were tested. *Pichia stipitis* was selected to ferment the treated hydrolysates, due to its ability to ferment xylose and to produce ethanol with a high yield (in the range 0.24 – 0.47 g g^{-1}) over different sources of hydrolysates, including eucalyptus wood (Karimi *et al.*, 2006; Ferrari *et al.*, 1992).

2 Materials and methods

2.1 Wood hydrolysis and treatment methods

The hydrolysates were obtained by two different hydrolysis processes applied to eucalyptus wood chips, both with a solid to liquid ratio of 1:4 kg L^{-1}: 1) an auto-hydrolysis at 150 ºC for 180 min and 2) an acid-catalysed-hydrolysis with sulphuric acid (0.4% w/w) at 140 ºC, for 180 min. The hydrolysate obtained from the auto-hydrolysis process was further submitted to a secondary hydrolysis, also catalysed by sulphuric acid (4% w/w) at 100 ºC for 180 min, to increase monosaccharides content (Carvalho *et al*., 2007). The secondary hydrolysis was worthless for the acid-hydrolysates. The acid-, auto- and secondary-hydrolysates had, respectively, *c.a.* 40, 10 and 16 g L^{-1} of reducing sugars, being xylose the major one. As the optimum pH for *Pichia stipitis* activity is 6.5 (Ferrari *et al.*, 1992), two strategies for hydrolysates treatment by pH adjustment were carried out: the first one was a one-step method consisting in the addition of NaOH or $Ca(OH)_2$ until pH 6.5, being the precipitates removed by centrifugation and vacuum filtration; the second one was a two-steps method which comprised the increase in pH until 10 by adding NaOH or $Ca(OH)_2$, and, after the precipitates removal, the pH correction to 6.5 with concentrated sulphuric acid, followed by vacuum filtration.

2.2 Microorganism and fermentation conditions

Pichia stipitis DSM 3651 (DSMZ, Germany) was primarily grown in both liquid and solid synthetic media and kept in agar slants at 4ºC. The synthetic medium contained analytical grade xylose (10 g L^{-1}, Merck) and microbiological grade peptone (5 g L^{-1}, Fluka), yeast extract (3 g L^{-1}, Sigma) and malt extract (3 g L^{-1}, Fluka). The yeast was then progressively adapted to treated eucalyptus hydrolysates, hereafter referred to as natural media: it was gradually transferred from solid to liquid natural media (and *vice versa*) with increasing volumetric percentages of acid hydrolysate and consequently with higher concentrations of potential inhibitors - 15, 30, 50 and 75% (v/v) diluted in water and non diluted (100% (v/v)). The strain adapted to full strength natural media (100% (v/v) of acid hydrolysate) was kept in agar slants at 4ºC. This adapted strain was grown in liquid natural media, composed of acid-, auto- or secondary-hydrolysates, supplemented with peptone, yeast extract and malt extract in the concentrations referred above. Batch fermentations were carried out in 250 mL erlenmeyer flasks (with cotton stoppers covered by aluminium sheet) using 150 mL of liquid natural media, at 130 rpm and 30 ºC. 10 mL of fresh inoculum, previously prepared under the same conditions of the culture, and at exponential phase were used.

2.3 Analytical methods

Cultures were followed by cell density, reducing sugars consumption and ethanol production. Total reducing sugars, evaluated as xylose equivalents, were determined by a colorimetric method using the dinitrosalicylic acid reagent (DNS) and a UV-VIS spectrophotometer at 540 nm. Optical density of cells suspension was measured at 540 nm in order to follow the yeast growth. Ethanol and xylose concentrations in the cultures were both determined by HPLC, with a PL Hi-Plex Ca 8 μm column, at 85 ºC, using ultra-pure water as eluent at a flow rate of 0.6 mL min^{-1}. The same chromatographic column was used to characterize the hydrolysates.

3 Results and discussion

Besides carbohydrates, the wood hydrolysates also contain other compounds which could inhibit the yeast metabolism. From previous results (Rocha *et al*., 2007; Mendes *et al*., 2008), the yeast growth rate was not limited by furfural (0.1 to 0.8 g L^{-1}) but had a 20-30% reduction in the presence of lignin (1.3 to 7.0 g L^{-1}) and was strongly inhibited by acetic acid (4 to 8 g L^{-1}) since the pH media was lowered to 4. The range of concentrations tested was selected according to the wood hydrolysates composition. In the latter case, the pH correction of the media with NaOH or NH_3 restored the yeast activity, confirming the major influence of pH in a fermentation process. Therefore, two different strategies to adjust the pH value of hydrolysates and to reduce their toxicity level were studied. In addition, microbial cells adaptation to natural media is essential to avoid long lag phases. The adaptation to full strength natural media must be progressive by reducing the dilution rate with water. The level of adaptation was observed to be very dependent on the strategy adopted to adjust the pH of the hydrolysates. All the results regarding the hydrolysates treatment are listed in table 1.

Table 1 – Influence of both treatment method and alkali on the fermentation of eucalyptus wood hydrolysates by *Pichia stipitis* (P – productivity; Y – yield).

Met-hod	Alkali	Medium	Inoculum charact.(1)	Initial sugars g/L	%Sugars consumed	Ethanol g/L	P g/(L h)	Y g/g
	NaOH(2)	Synthetic	Synthetic, Original strain	20.0	100	4.8	0.102	0.23
Acid-Hydrolysates								
1 step(2)	NaOH	50% natural	Synthetic, Original strain	23.4	84.2	3.9	0.081	0.20
	$Ca(OH)_2$	50% natural	Synthetic, Original strain	21.2	81.6	6.5	0.087	0.38
	$Ca(OH)_2$	50% natural	50%natural, 50%adapted	25.9	90.0	6.0	0.063	0.26
	$Ca(OH)_2$	75% natural	50%natural, 50%adapted	33.7	85.5	10.3	0.071	0.36
	$Ca(OH)_2$	100% natural	50%natural, 50%adapted	42.4	0	0	0	0
2 steps	NaOH	100% natural	100%natural, 100%adapted	37.0	0	0	0	0
	$Ca(OH)_2$	100% natural	100%natural, 100%adapted	36.4	85.2	12.3	0.221	0.48
Auto-Hydrolysates								
1 step	NaOH	100% natural	Synthetic, 50%adapted	10	43.6	1.6	0.032	0.27
2 steps	NaOH	100% natural	Synthetic, 50%adapted	10.7	44.9	1.0	0.019	0.26
	$Ca(OH)_2$	100% natural	100%natural, 100%adapted	7.0	50	1.1	0.036	0.41
Secondary-Hydrolysates								
1 step	NaOH	100% natural	100%natural 50%adapted	15.5	87.1	4.0	0.056	0.30
2 steps	NaOH	100% natural	100%natural, 100%adapted	14.7	87.1	3.3	0.046	0.30
	$Ca(OH)_2$	100% natural	100%natural, 100%adapted	9.4	73.4	2.1	0.072	0.43

(1) – type of inoculum growth media and strain adaptation (50% means strain adapted to 50%(v/v) natural media); (2) – Rocha *et al*., 2007.

3.1 pH adjustment by one-step method

Regarding the one-step method, *i.e.* the addition of an alkali (NaOH or $Ca(OH)_2$) to reach the required pH in acid-hydrolysates, our previous work has shown that the use of $Ca(OH)_2$ led to a faster yeast growth and to higher ethanol yield and productivity (Rocha *et al*., 2007). However, using this procedure, the strain adaptation was only achieved for solid media containing up to 50% (v/v) of acid-hydrolysate. Both original and adapted strains were used to inoculate half-strength natural media. The corresponding fermentation evolution for cell density and ethanol and xylose concentrations is shown in figures 1a) and 1b). The main differences between the two assays are the ethanol and xylose equivalents profiles at the beginning of the fermentation. A lag phase of 50 h in ethanol production was observed with the original strain, while an ethanol concentration of 3 g L^{-1} was achieved and 88% of initial xylose equivalents were consumed with the adapted yeast, at the same time (50 h). Using this adapted strain, fermentation of natural media was only feasible till 75% (v/v) as shown in table 1.

The lag phase was also observed at the beginning of auto- and secondary-hydrolysates fermentation both treated with either $Ca(OH)_2$ or NaOH. The ethanol production rate achieved in the fermentation of auto-hydrolysates was very low and was associated to the low initial sugar concentration (table 1). In addition, only half of the reducing sugars were consumed by the yeast, being the xylose monomers totally used. The secondary hydrolysis applied to the auto hydrolyzed extracts did increase the initial reducing sugars (table 1), and particularly xylose content, even though the ethanol concentration obtained was still very low (2 g L^{-1}), corresponding to a rate production of 0.017 g (L h)$^{-1}$ and a yield of 0.19 g_{eth} $g_{xyl\ eqs}^{-1}$ based on the reducing sugars consumed (Rocha *et al*., 2007).

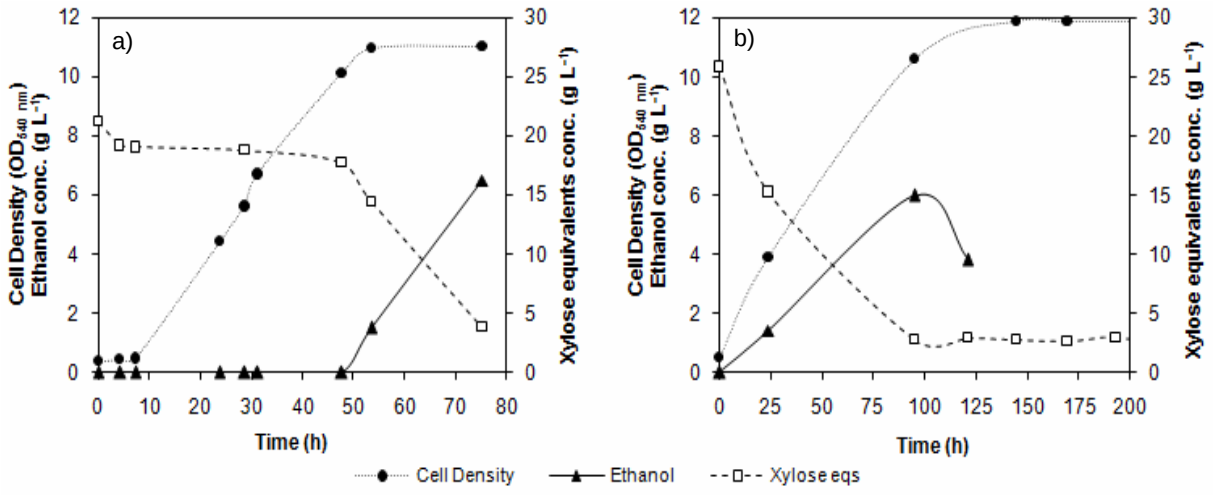

Figure 1 – Cell density, ethanol and xylose equivalents evolution in the fermentation of liquid natural media consisting of 50% (v/v) acid hydrolysate diluted in water, using a) the original strain and b) the strain adapted to half strength natural media.

3.2 pH adjustment by two-steps method

The other pH adjustment method, which consisted in the addition of an alkali to pH 10 followed by its decrease to 6.5 with concentrated acid (sulphuric acid), was then carried out in an attempt to reach a better purification of hydrolysates. According to the results presented above, $Ca(OH)_2$ was the first choice. Using this two-steps method, the strain adaptation and the fermentation of full strength acid-hydrolysate (100% (v/v)) was successfully achieved (table 1). The fermentation of acid-hydrolysates, as depicted in figure 2a), led to a maximum ethanol concentration of 12 g L^{-1}, a productivity of 0.22 g L^{-1} h^{-1} and a yield based on xylose equivalents of 0.48 g_{eth} $g_{xyl\ eqs}^{-1}$. These results are similar to some of the data in the literature

(Ferrari *et al.*, 1992) allowing some expectations on the energetic valorisation of *Eucalyptus globulus* wood hemicelluloses extracted prior to pulping.

The experiments carried out show that a better yeast performance is achieved when acid-hydrolysates are treated with $Ca(OH)_2$ by the two-steps method, due to a greater detoxification effect. However, a decrease up to 9% on the initial sugars concentration was observed. A stronger influence of $Ca(OH)_2$ addition upon sugar content reduction was even registered in the treatment of the auto-hydrolysates (table 1). A decrease up to 35% was verified which, consequently, led to lower ethanol concentrations (1.1 g L^{-1}). Even though, higher productivity (0.036 g L^{-1} h^{-1}) and yield on reducing sugars (0.41 g_{eth} $g_{xyl\ eqs}^{-1}$) were obtained when compared to the one-step method.

Similarly, the secondary-hydrolysates treated with $Ca(OH)_2$ suffered a reduction of the initial xylose equivalents up to 44%. As a consequence, a low ethanol concentration was also obtained (2.1 g L^{-1}), as shown in figure 2b), with a productivity and yield of 0.072 g L^{-1} h^{-1} and 0.43 g_{eth} $g_{xyl\ eqs}^{-1}$, respectively. The fermentation profiles in figures 2 a) and 2 b) show that ethanol production is proportional to xylose equivalents consumption. Therefore, to avoid the sugar content decrease, the treatment procedures must be optimized, particularly for the auto- and secondary-hydrolysates.

The decrease in ethanol concentration latter in all the fermentations assays can be due to its metabolisation when the other nutrients are exhausted, or to its loss by vaporization during the long fermentation period. The remaining reducing sugars at the end of fermentations probably cannot be fermented by the yeast although xylose was totally consumed as confirmed by HPLC analysis.

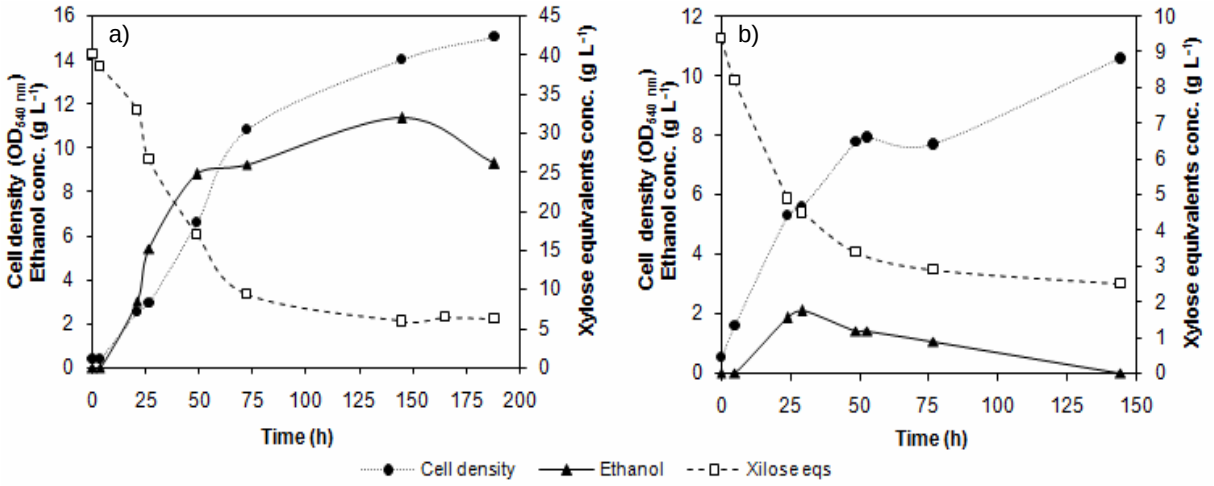

Figure 2 - Ethanol production, xylose equivalents concentration and yeast growth profiles obtained in the fermentation of 100% (v/v) a) acid-hydrolysate and b) secondary-hydrolysate, both treated with $Ca(OH)_2$ by the two-steps method and using the strain adapted to full strength natural media.

A few experiments using NaOH in the two-steps method were carried out with acid- and secondary-hydrolysates as illustrated in table 1. Since this alkali did not promote a significant loss on the initial reducing sugars concentration, a higher amount of sugars was available and the fermentation of the secondary-hydrolysate led to a higher ethanol concentration (3.3 g L^{-1}) than the one achieved when using $Ca(OH)_2$. However, the productivity and the yield were smaller (0.046 g L^{-1} h^{-1} and 0.30 g_{eth} $g_{xyl\ eqs}^{-1}$, respectively). On the other hand, no yeast activity was detected when using the acid-hydrolysate treated with NaOH (table 1) like in the pH adjustment by the one-step method. A greater toxicity level of the acid-hydrolysates when compared to the auto- and the secondary-hydrolysates, not sufficiently reduced by the addition of NaOH, may explain this result.

4 Conclusions

Hydrolysates obtained from eucalyptus wood auto-hydrolysis or acid-hydrolysis have a low pH value and contain a broad range of compounds, including reducing sugars (xylose is the major one) and potential inhibitors, like acetic acid, furfural and lignin. These hydrolysates must be submitted to a detoxification treatment and pH adjustment before fermentation by *Pichia stipitis*, whose metabolic activity is strongly dependent on pH. As different hydrolysis conditions were used to produce the hydrolysates, these did not present equal toxic levels nor composition and therefore different responses were obtained when they were treated by different methods (one-step or two-steps) using two alkalis (NaOH or $Ca(OH)_2$).

The treatment of acid-hydrolysates by the addition of $Ca(OH)_2$ up to pH 10, followed by pH adjustment to 6.5 with concentrated sulphuric acid (two-steps method) promoted a higher detoxification effect. The strain adaptation was achieved with success in 100% acid-hydrolysates, thus enabling the reduction or even the absence of the initial lag phase during their fermentation. The best set of results achieved in the fermentation of the treated acid-hydrolysates comprised a maximum ethanol concentration of 12 $g_{eth}\ L^{-1}$, corresponding to a productivity of 0.22 $g_{eth}\ (L\ h)^{-1}$ and a yield of 0.48 $g_{eth}\ g_{xyl\ eqs}^{-1}$ on reducing sugars.

On the other hand, a significant reduction of the initial sugars concentration was observed in both auto- and secondary-hydrolysates treated by this method and, consequently, the ethanol concentration accomplished was very low (1.1 and 2.1 $g_{eth}\ L^{-1}$, respectively), even though higher yields on the reducing sugars consumed were obtained. Therefore, better procedures must be studied within this treatment strategy, using for example other types of alkali, in order to decrease the percentage of reducing sugars lost when processing auto- and secondary-hydrolysates.

Acknowledgements

The support of RAIZ – Forest and Paper Research Institute (Eixo, Aveiro, Portugal) providing the *Eucalyptus globulus* wood hydrolysates, is gratefully acknowledged.

References

Canilha, L., Silva, J.B.A., Solenzal, A.I.N. (2004). Eucalyptus hydrolysate detoxification with activated charcoal adsorption or ion-exchange resins for xylitol production. *Process Biochemistry*, 39, 1909-1912.

Carvalho M.G.V.S., Baptista C.F.A., Mendes C.V.T., Rocha J.M.S. (2007). *Hemicelluloses: from wood to the fermenter*. BioMicroWorld 2007, Seville, Spain (oral presentation).

Ferrari, M.D., Neirotti, E., Albornoz, C., Saucedo, E. (1992). Ethanol production from Eucalyptus wood hemicellulose hydrolysate by Pichia stipitis. Biotechnology and Bioengineering, 40, 753-759.

Karimi, K., Emtiazi, G., Taherzadeh, M.J. (2006). Production of ethanol and mycelia biomass from rice straw hemicellulose hydrolysate by *Mucor indicus*. *Process Biochemistry*, 41, 653-658.

Knauf, M., Moniruzzaman, M. (2004). Lignocellulosic biomass processing: A perspective. *International Sugar Journal*, 106, 147-150.

Mendes, C.V.T., Baptista, C.M.S.G., Rocha, J.M.S., Carvalho, M.G.V.S. (2008). *Fermentation of wood hydrolysates prior to pulping for valorisation of Eucalyptus globulus hemicelluloses*. 10th European Workshop on Lignocellulosic and Paper, Sweden, 25-28 Aug. (accepted for oral presentation).

Pan, X., Arato, C., Gilkes, N., Gregg, D., Mabee, W., Pye, K., Xiao, Z., Zhang, X., Saddler, J. (2004). Biorefining of softwoods using ethanol organosolv pulping: preliminary evaluation of process streams for manufacture of fuel-grade ethanol and co-products. *Biotechnology and Bioengineering*, 90, 473-481.

Rocha, J.M.S., Gomes, L.F.F., Mendes, C.V.T, Baptista, C.M.S.G., Carvalho, M.G.V.S. (2007). *Xylose from Eucalyotus globulus wood as a raw material for bioethanol production*, Proc. Biomicroworld 2007, II Int. Conf. on Environ., Ind. and Applied Microbiology, Seville, p. 452.

Vilarreal, M.L.M., Prata, A.M.R., Felipe, M.G.A., Silva, J.B.A. (2005). Detoxification procedures of eucalyptus hemicellulose hydrolysate for xylitol production by *Candida guilliermondii*. *Enzyme and Microbial Technology*, 40, 17-24.

Proceedings of the 10th International Chemical and
Biological Engineering Conference - CHEMPOR 2008
Braga, Portugal, September 4-6, 2008
E.C. Ferreira and M. Mota (Eds.)

Biopolymers Production by Microbial Fermentation on Glycerol-Rich Product

Filomena Freitas, Vitor D. Alves, Joana Pais, Nuno Costa, Mónica Carvalheira, Rui Oliveira, M. A. M. Reis*
CQFB-Requimte, Chemistry Department, FCT/Universidade Nova de Lisboa, 2829-516 Caparica, Portugal.

Keywords: Biopolymer, Fermentation, Exopolysaccharide (EPS), Polyhydroxyalkanoates (PHA), Glycerol-Rich Product (GRP)
Topic: Sustainable process-product development through green chemistry.

Abstract

The objective of this work was the conversion of glycerol-rich byproduct (GRP), obtained in biodiesel production facilities, into biopolymers using ***Pseudomonas oleovorans***. Two distinct biopolymers were simultaneously produced: an extracellular polysaccharide (EPS) and intracellular polyhydroxybutyrate (PHB). Under optimized EPS production conditions in fed-batch mode, the cellular PHB content was 21 % of the cell dry weight (CDW) and the EPS concentration was 11.6 g L^{-1}. The use of glycerol as carbon source greatly reduces production costs of the process, since it allows for the valorization of GRP by its conversion into high-value products.

1 Introduction

Microorganisms are generally better suited for biopolymers production than plant or algae, because they usually exhibit higher growth rates and are more amenable to manipulation of conditions for enhancing growth and/or production (Moreno et al., 1998). However, the high cost of the carbon sources used, mainly sugars such as glucose, sucrose and fructose (Kumar et al., 2007) limits the market potential of these biopolymers. As a consequence, less expensive carbon sources must been searched in order to decrease production costs.

Glycerol, a byproduct of biodiesel production, is generated in quantities far beyond current consumption in traditional applications. The development of new routes to convert crude glycerol, which is now considered as a waste with associated disposal costs, into higher value products is an urgent need (Çelik et al., 2008). The use of glycerol rich byproduct (GRP), a low cost substrate, for microbial production of biopolymers presents an advantageous strategy since it allows for the reduction of production costs (Ashby et al., 2005).

Polysaccharides are used in a variety of industrial applications, including food, painting, cosmetic, paper and pharmaceutical, as emulsifiers, stabilizers or thickening agents. Currently, polysaccharides obtained from plants (ex: Guar gum, Arabic gum), algae (ex: alginate, carrageenan, agar) and crustacean (ex: chitin) still dominate the market, with microbial polysaccharides (ex. xanthan, gellan gum, dextran, pullullan) representing only a small fraction of the biopolymers commercialized (Moreno et al., 1998).

Polyhydroxyalkanoates (PHA) are natural polyesters synthesized by bacteria and stored inside the cell. These biopolymers exhibit properties that range from semicrystalline to elastomeric, making them biocompatible substitutes for petrochemical-based polymers (Ashby et al., 2005).

* Corresponding author. Tel + 351-212-948357. E-mail:amr@dq.fct.unl.pt

The objective of this work was the conversion of the GRP obtained in biodiesel production facilities into high-value microbial biopolymers. When grown on GRP as the sole carbon source, ***Pseudomonas oleovorans*** produced two distinct biopolymers: a new extracellular polysaccharide (EPS) and intracellular polyhydroxybutyrate (PHB).

2 Materials and Methods

Pseudomonas oleovorans NRRL B-14682 was grown on a slightly modified Medium E* (pH 7.0), with the following composition (per liter): $(NH_4)_2HPO_4$, 3.3g; K_2HPO_4, 5.8g; KH_2PO_4, 3.7g; 10mL of a 100mM $MgSO_4$ solution and 1mL of a micronutrient solution. The micronutrient solution had the following composition (per liter of 1N HCl): $FeSO_4 \cdot 7H_2O$, 2.78 g; $MnCl_2 \cdot 4H_2O$, 1.98g; $CoSO_4 \cdot 7H_2O$, 2.81g; $CaCl_2 \cdot 2H_2O$, 1.67g; $CuCl_2 \cdot 2H_2O$, 0.17g; $ZnSO_4 \cdot 7H_2O$, 0.29g) (Brandl et al., 1988). Glycerol-rich product (GRP) was added to give a concentration between 30 g L^{-1}.

Inoculums for the bioreactor experiments were prepared by incubating the culture in Medium E* supplemented with GRP (50 g L^{-1}), in shake flasks, for 72 h at 30ºC in an incubator shaker (200 rpm). Fed-batch experiments were performed in a 2L bioreactor (BioStat B, Sartorius), operated with controlled pH (6.75 – 6.85) and temperature (30ºC), constant air flow rate (0.25 slpm, standard liters per minute) and automatic variation of the stirrer speed (400-800 rpm) for controlling the dissolved oxygen (DO) concentration in the culture broth. The inoculum culture (200 mL) was inoculated into the medium described above supplemented with 50 g L^{-1}. Starting around 24 hours of cultivation, a feeding solution was fed to the bioreactor at a constant rate of 5mL h^{-1}. The feeding solution composition was identical to the culture medium described above, with a higher glycerol concentration (200g L^{-1}).

Glycerol concentration in the cell-free supernatant was determined by liquid chromatography (HPLC) with an Aminex HPX-87H column (BioRad), coupled to a refractometer. The analysis was preformed at 50ºC, with H_2SO_4 0.01 N as eluent, at a flow rate of 0.6 ml/min. Ammonium concentration was determined using a potentiometric sensor (Thermo Electron Corporation, Orion 9512).

For EPS quantification, the cell-free supernatant was subjected to protein removal (addition of trichloroacetic acid at a final concentration of 10%), prior to ethanol precipitation. The precipitated EPS was dissolved in deionised water, frieze dried and weighted. For the identification and quantification of the constituent monosaccharides, the EPS samples were dissolved in deionised water and hydrolyzed with trifluoroacetic acid 99%, at 120ºC, for 2 hours. The hydrolysate was analyzed by HPLC with a CarboPac PA10 column (Dionex), equipped with an amperometric detector. The analysis was preformed at 30ºC, with sodium hydroxide (NaOH 4 mM) as eluent, at a flow rate of 0.9 ml/min.

3 Results and Discussion

When cultivated on mineral medium containing GRP as the sole carbon source, ***Pseudomonas oleovorans*** grew, produced extracellular EPS and accumulated intracellular PHB (Figure 1). Bacterial cell growth stopped due to nitrogen limitation, as the ammonium concentration in the culture broth dropped below 0.1 g NH_4^+/l.

Following 1 day of cultivation, the bioreactor was continuously fed with a mineral medium containing glycerol and ammonium, thus keeping a high carbon/nitrogen (C/N) ratio. As a result, the glycerol concentration in the bioreactor was maintained above 25 g L^{-1} throughout the cultivation (Figure 1).

Under these conditions, the culture produced extracellular EPS, reaching a concentration of 11.6 g/l after 6 days of fermentation. Concomitant with EPS production, there was a sharp raise of the culture broth viscosity, which induced mixing limitations decreasing mass and heat transfer. Thus, the experiment shown in Figure 1 was terminated at 6 days of fermentation, because it was no longer possible to maintain appropriate mixing, aeration or

control of bioreactor parameters. Simultaneously with EPS production, the culture accumulated intracellular reserves of PHB, reaching a cellular content of 21% (Figure 1).

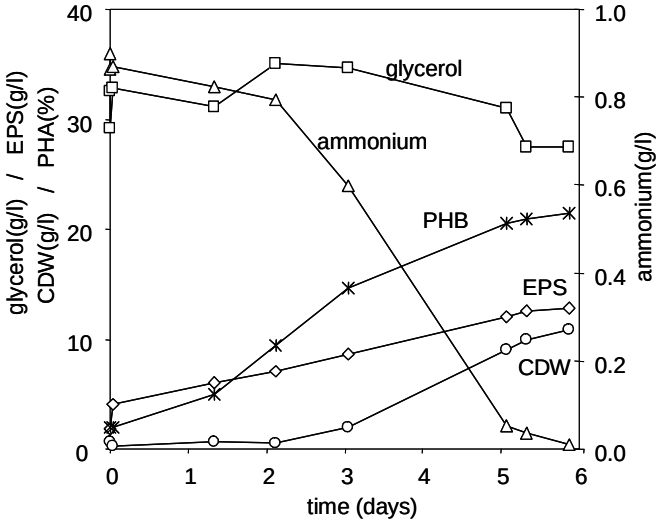

FIGURE 1. Bacterial growth on glycerol and production of PHB and EPS.

The EPS was extracted and its physical-chemical characteristics where studied. The chemical analysis of the EPS revealed that it is composed by galactose (50-90%), glucose (1-25%), rhamnose (1-25%) and mannose (0.5-20%), with an average molecular weight of $2x10^6$. The presence of galactose residues in microbial polysaccharides is rather common, even though it may be present in variable amounts ranging from 21-63 mol%, in galactose-rich heteropolysaccharides produced, for example, by several bacteria of the Genera ***Erwinia*** (Eastgate et al., 2000) and ***Pseudomonas*** (Osman et al., 1989; Hung et al., 2005). Microbial galactose-rich EPS frequently contain other monosaccharides such as glucose, mannose, rhamnose, arabinose and fucose. The unusual high galactose content of the EPS produced by ***Pseudomonas oleovorans*** grown on GRP, distinguishes it from other microbial EPS. Also, many of the known microbial EPS contain, besides neutral sugars, acidic sugars (ex. glucuronic acid, galacturonic acid) or amino sugars (ex. glucosamine, galactosamine) that are absent from the EPS obtained in this study.

Results have also shown that the EPS contains non-saccharide components, namely, acyl groups, which accounts for 3-15 wt% of the polymer's mass. Three different organic acids were identified in the acid hydrolysate: pyruvate (3.35 wt%), succinate (1.04 wt%) and acetate (0.38 wt%). These components are frequently found in microbial EPS and they greatly influence polymer's properties, namely, solubility and rheology (Rinaudo, 2004). As shown by its pyrolysis at 550ºC, the purified polymer had an inorganic content of about 11.6 wt%, which was attributed to the presence of ions, such as potassium (4.7 wt%), magnesium (0.2 wt%) and sodium (0.9 wt%), as detected by ICP analysis. These inorganics were probably remnants of the contents of the culture broth, being present in the polymer after its purification as counter ions for the anionic groups of the polymer (pyruvil and succinyl groups).

The EPS forms highly viscous aqueous solutions with pseudoplastic fluid behavior (Figure 2). The viscosity of an EPS 0.1% (w/v) solution is higher than that of pectin and alginate for the same range of shear rate, and higher than that of carrageenan for shear rates below 30 s^{-1}. It is insoluble in organic solvents and has both flocculating and emulsifying activities, as well as film-forming capacity.

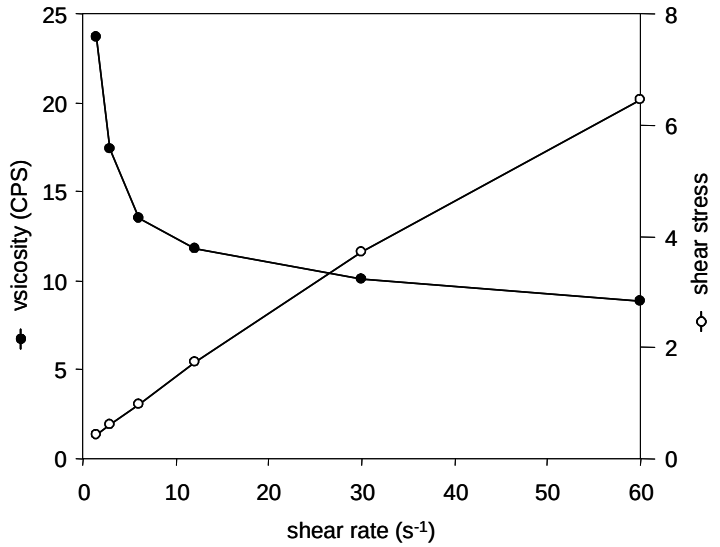

FIGURE 2. Rheological properties of a 0.1% w/v aqueous solution of the EPS.

These chemical and physical properties suggest a broad range of applications in the food, textile and paper industries, in the formulation of pharmaceutical and cosmetic products, for metal recovery in the mining industry, wastewater treatment and many others. The EPS may be used alone or blended/mixed with other polymers as a suspending, thickening, flocculating, emulsifying or film-forming agent.

4 Conclusions

The process described in this work allows for the valorization of GRP, which is currently a waste generated by several industrial processes, especially the biodiesel industry, converting it in high-value products. Thus, glycerol is used as a low cost substrate for the microbial fermentation of ***Pseudomonas oleovorans*** that efficiently converts GRP, a low cost substrate, into two distinct biopolymers, namely extracellular EPS and intracellular PHB. The process may be controlled to favor the production of either or both biopolymers, which makes it very versatile. This new process constitutes a promising technology for the valorization of GRP, since it allows for the production of two biopolymers with relatively low production costs. In addition, the EPS is a novel product with characteristic chemical composition and physical properties which are very competitive when compared to commercially available algal and plant polysaccharides.

5 Acknowledgements

This project was financially supported by 73100, under the project “Production of biopolymers from glycerol”, 2005-2008. Vitor D. Alves acknowledges Fundação para a Ciência e a Tecnologia, scholarship SFRH/BDP/26178/2005.

References

Ashby, R.D., Solaiman, D.K.Y., Foglia, T.A. (2005). Synthesis of short-/medium-chain-length poly(hydroxyalkanoate) blends by mixed culture fermentation of glycerol. ***Biomacromolecules***, 6, pp. 2106-2112.

Brandl, H., Gross, R.A., Fuller, R.C. (1988). ***Pseudomonas oleovorans*** as a Source of Poly(□-Hydroxyalkanoates) for Potential Applications as Biodegradable Polyesters. ***Appl. Env. Microbiol.***, 54(8), pp. 1977-1982.

Çelik, E., Ozbay, N., Oktar, N., Çalık, P., 2008. Use of Biodiesel Byproduct Crude Glycerol as the Carbon Source for Fermentation Processes by Recombinant ***Pichia pastoris***. Ind. Eng. Chem. Res. 47, 2985-2990.

Eastgate, J. A., 2000. ***Erwinia amylovora***: the molecular basis of fireblight disease. Mol Plant Pathol, 1(6), 325-329.

Hung C.C., Santischi P.H., Gillow J.B., 2005. Isolation and characterization of extracellular polysaccharides produced by ***Pseudomonas fluorescens*** Biovar II. Carbohydr Pol, 61, 141-147.

Kumar, A.S., Mody, K., Jha, B., 2007. Bacterial exopolysaccharides – a perception. J. Basic Microbiol., 47, 103-117.

Moreno, J., Vargas, M.A., Olivares, H., Rivas, J., Guerrero, M.G. (1998). Exopolysaccharide production by the cyanobacterium ***Anabaena*** sp. ATCC 33047 in batch and continuous culture. ***J. Biotechnol.***, 60, pp. 172-182.

Osman S.F., Fett W.F.,1989. Structure of an acidic exopolysaccharide of ***Pseudomonas marginalis*** HT041B. J Bacteriol, 171(3), 1760-1762.

Rinaudo, M., 2004. Role of substituents on the properties of some polysaccharides. Biomacromol. 5, 1155-1165.

Proceedings of the 10th International Chemical and
Biological Engineering Conference - CHEMPOR 2008
Braga, Portugal, September 4-6, 2008
E.C. Ferreira and M. Mota (Eds.)

Bacterial Diversity in a Biotrickling Filter Treating High Loads of H_2S

Juan P Maestre[1], Roger Rovira[1], Xavier Gamisans[2], Kerry A Kinney[3], Mary J Kirisits[3], Javier Lafuente[1], David Gabriel[1]*

[1]Department of Chemical Engineering. Universitat Autònoma de Barcelona. Edifici Q. Campus de Bellaterra. 08193 Bellaterra, Barcelona, Spain
[2]Department of Mining Engineering and Natural Resources, Universitat Politècnica de Catalunya, Bases de Manresa 61-73, 08242 Manresa, Spain
[3]Department of Civil, Architectural, and Environmental Engineering, The University of Texas at Austin, 1 University Station C1786, Austin, Texas 78712

Keywords: Biotrickling filter, Hydrogen sulfide, Bacterial community diversity, Clone library, T-RFLP
Topic: Integration of life sciences & engineering

Abstract

The diversity and spatial distribution of bacteria in a lab-scale biotrickling filter treating high loads of hydrogen sulfide (H_2S) were investigated. Community patterns were obtained by means of terminal restriction fragment length polymorphism (T-RFLP) at two locations in the reactor. A 16S rRNA gene clone library was established. Clones were clustered into 24 operational taxonomic units (OTUs). Only 48% of the 16S rRNA gene sequences in the clone library exhibited similarities of more than 96% to classified bacterial species, indicating that a considerable fraction of the clone sequences were derived from unknown taxa. Approximately 45% of the sequences retrieved were affiliated to bacteria of the sulphur cycle including *Thiothrix spp., Thiobacillus spp*. and *Sulfurimonas denitrificans*. Sequences related to *Thiothrix lakustris* accounted for 38% of the collection. Differences in the microbial community were observed among the zones investigated. Although aerobic species were predominant in the reactor, facultative anaerobes had a major relative abundance at the inlet of the reactor, where the sulfide to oxygen ratio is higher.

1 Introduction

With increasingly strict regulations for air pollution control, the necessity for treating gas pollutants is critical. Biogas, produced in multiple industrial processes like the anaerobic treatment of wastewater treatment plant sludge, contains variable amounts (1000-20000ppm$_v$) of hydrogen sulfide (H_2S), which is a corrosive, toxic and odorous gas. Biological processes have proven to be suitable, environmental-friendly, and cost-effective alternatives for low H_2S concentration treatment, but only a few references address biological treatment of high concentrations of H_2S in biotrickling filters (Fortuny et al., 2008). In biofiltration, the gas to be treated is forced through a filter bed where microorganisms are attached. Gaseous pollutants are transferred to a moisturized biofilm, where the transformation of the compounds takes place, involving several physical, chemical and biological interactions.

A thorough study of the microbial community in bioreactors has been shown to be critical to the improved understanding of the underlying biochemical processes. It has been estimated that as many as 99% of all microorganisms are not cultivable by standard methods, biasing cultivated community diversity studies. However, this problem can be overcome by using the novel molecular biology tools targeting the small subunit rRNA-encoding genes. Terminal restriction fragment length polymorphism (T-RFLP) is a molecular technique for characterizing environmental microbial communities and for studying changes in their

* Corresponding author. Tel + 34935811587. E-mail: david.gabriel@uab.es

structure and diversity (Liu et al., 1997). Clone libraries have been extensively used for microbial communities analysis since it provides a collection of the species present in the sample.

In the present work, the microbial diversity in a biotrickling filter treating H_2S was studied using a combination of T-RFLP and clone libraries of the 16S rRNA gene. This combination allowed more accurate identification of individual T-RFLP peaks. Although a few studies have characterized the microbial community of such gas-phase bioreactors, mainly biofilters, using molecular techniques (Friedrich et al., 2002), this work is the first to characterize the populations in a biotrickling filter treating H_2S by constructing an extensive clone library and by using T-RFLP as the fingerprinting technique for studying H_2S-degrading communities.

2 Materials and Methods

Experimental setup. In this work, an experimental reactor based on a conventional biotrickling filter was used. The reactor was initially inoculated with activated sludge from a municipal wastewater treatment plant and then continuously operated for six months in upflow mode at an empty bed residence time of 180 s, an average liquid retention time of 54 ± 7 h, an inlet H_2S concentration of 2,000 ppm_v (load of 55.6 g H_2S m^{-3} h^{-1}) and a liquid recirculation velocity of 3.6 m h^{-1}. Under these conditions, elimination capacities of 53±1 g H_2S m^{-3} h^{-1} were achieved for the whole experimental period, except for few days after the start up. Metered amounts of H_2S, N_2 and air (0.2, 77.3 and 22.4 %, respectively) were used to simulate a controlled biogas inflow. Details of the reactor, mineral medium, other operational conditions and analytical methods can be found elsewhere (Fortuny et al., 2008).

DNA isolation and 16S rRNA gene amplification. Biomass samples were withdrawn from two sampling ports situated at different heights in the reactor, 17 cm and 34 cm out of 50 cm. The first one will be referred as inlet part and the second one as outlet part. For library construction biomass samples from the inlet and the outlet part of the reactor were mixed in a 1:1 ratio (w/w).The DNA was extracted and tested and preserved at -20ºC. The small subunit (SSU) rRNA gene was polymerase chain reaction (PCR) amplified from genomic DNA extracted from the environmental samples and two isolates using universal primers for the Bacterial domain (8F/1492R). These two isolates were obtained from the same reactor and then tested as sulfur oxidizers (data not shown). For isolate identification and clone library generation, the PCR reactions were performed as described elsewhere (Chi-hua and Banks, 2006) but contained 100 ng of template DNA. For isolate identification, PCR products were sent for direct sequencing. For clone libraries, the 16S rRNA gene fragments were cloned with the TOPO TA Cloning® Kit for Sequencing (Invitrogen, CA, USA) according to the manufacturer's instructions.

T-RFLP analysis. For T-RFLP analysis, the labeled forward primer Fam-8F and the unlabeled reverse primer 926R (Molbiol, Germany) were used. T-RFLP was performed as described in Ho and Banks, (2006) with some modification as described by Egert and Friedrich (2005) to reduce partially single-stranded amplicon. The T-RFLP digests (digested with HhaI) were analyzed on an ABI automated sequencer (Model 3100). Duplicates from the initial step of DNA extraction were performed through the whole process to evaluate the reproducibility of the methodology. The distribution of the peaks from the collected profiles was performed using ABI Genemarker 1.51.71 (Softgenetics, PA, USA). A level of 80 fluorescence units was used as a minimum threshold value for all peaks in the selected size range. To assess community similarity, terminal restriction patterns were standardized based on T-RF peak area (Kaplan et al., 2001). Once the samples were normalized, peaks below the threshold were deleted, and new peak area percentages were calculated. Duplicate sample results were grouped, and consensus terminal-restriction fragments (T-RFs) and average peak areas were obtained by using the web tool T-align (http://inismor.ucd.ie/~talign/).

Sequencing and phylogenetic reconstruction. One hundred clone inserts were sequenced in full with pUC/T3-T7 primers by Macrogen (Korea). All sequences were

checked for chimeric artifacts by using the CHIMERA_CHECK program of the Ribosomal Database Project and for similar sequences with the ClustalW program. Near full-length sequences (approximately 1500bp) were compared with similar sequences of the reference organisms by a BLAST search (Altschul et al., 1997). Sequences with the same first accession number were grouped into clusters. Thus, the clustering process was based on the BLAST results obtained for every clone. Similarity among clones within the same cluster was studied by sequence comparison using ClustalW.

Phylogenetic trees - ARB and rarefaction analysis. Sequences were subjected to a BLAST search (Altschul et al., 1997) to get a first suggestion of the phylogenetic affiliation. Sequences were aligned using the automatic alignment tool in the ARB program package (http://www.mikro.biologie.tu-muenchen.de). Then, nearly-complete sequences were inserted into the optimized tree derived from the complete sequence data by the ARB neighbour-joining method. The rarefaction analysis, which indicates if the community diversity is well represented by the number of clones that have been sequenced, was calculated using the defined OTUs. The software Analytic Rarefaction (version 1.3, S.M. Holland, http://www.uga.edu/~strata/software/) was used to perform rarefaction analysis. The 16S rRNA gene sequences of the clones have been submitted to the Genbank /EMBL/DDBJ to obtain the corresponding accession numbers.

3 Results and Discussion

Bacterial diversity. In the present work, a lab-scale biotrickling filter degrading high loads of H_2S was investigated. On the one hand, the high loads of hydrogen sulfide may constrain the bacterial diversity of the biofilter. Besides, comparing to organic packing materials, the inert plastic grid used could decrease the microenvironments available for bacterial communities. On the other hand, the presence of a biofilm enhances bacterial diversity due to the different microenvironments that exist in the biofilm.

A 16S rRNA gene clone library was constructed with near full-length 16S rRNA gene sequences for all the clones. After eliminating putative chimeric sequences, the remaining 75 clones were clustered into 24 groups. Rarefaction analysis demonstrated that the clone library constructed was suitable to describe the vast majority of the bacterial diversity of the reactor since the rarefaction curve almost achieved a plateau (data not shown). Seventy four percent of the sequences were related to the phylum Proteobacteria and 26.0% to Bacteroidetes. Among clones analyzed and clustered, 10 clusters, including 45 clones, were closely related to known sulfur-oxidizing bacteria (SOB) species: *Thiothrix lakustris* (γ-Proteobacteria), *Thiothrix sp. CT3* (γ-Proteobacteria), *Sulfurimonas denitrificans* (ε-Proteobacteria), *Thiobacillus denitrificans* (β-Proteobacteria), *Thiobacillus sajanensis* (β-Proteobacteria) and *Thiobacillus plumbophylus* (β-Proteobacteria) (Fig.1). Thiotrichales was the most predominant order among γ-Proteobacteria (almost 90%). The remaining orders of this class represented in the clone library were related to Xanthomonadales (clones were affiliated with *Dokdonella koreensis* and *Xanthomonas axonopodis*). All clones belonging to ε-Proteobacteria were exclusively related to Campilobacterales (clones were affiliated with *Sulfurimonas denitrificans*). Regarding class β-Proteobacteria, the order most frequently represented was Hydrogenophilales (clones were related to *Thiobacillus spp*.). Concerning the phylum Bacteroidetes, it comprised 26% of the clone library, and the clones were affiliated with *Haliscomenobacter hydrossis*.

Molecular phylogenetic analyses can suggest, but not definitively demonstrate, what metabolic roles are being played by the organisms present in the reactor. *Thiothrix* is a filamentous genus in the γ-Proteobacteria. It can grow under heterotrophic, chemolithoautotropic, and mixotrophic conditions. This could explain the predominance of *Thiothrix* in the bioreactor since it had been operated for 6 months after inoculating with activated sludge from a wastewater treatment plant, and there was a considerable quantity of biomass accumulated in the packing material. *Thiothrix spp*. have been described as a component of biofilms in sulfide-containing flowing water in natural systems and wastewater treatment plants. These filamentous bacteria are believed to be one of the major causes of

activated sludge bulking and foaming.

The genera *Thiobacillus* and *Sulfurimonas*, both found in the library, have been described previously as sulfur-oxidizers (Kelly et al., 1997). The genus *Thiobacillus* is represented in the clone library by the chemolithoautotrophic species *T. denitrificans*, *T. sajanensis* and *T. plumbophilus*. *T. denitrificans* is a facultative anaerobe, and *T. sajanensis* and *T. plumpophilus* are aerobes. Also, the genus *Sulfurimonas* is represented in the collection by the chemolithoautotroph facultative anaerobe *Sulfurimonas denitrificans*. Although both genera represent less than 20% of the clones in the collection, they are presumably playing an active role in the sulfur oxidation process, mostly in microenvironments where oxygen levels are extremely low. These microenvironments are present in thick biofilms like those in this bioreactor.

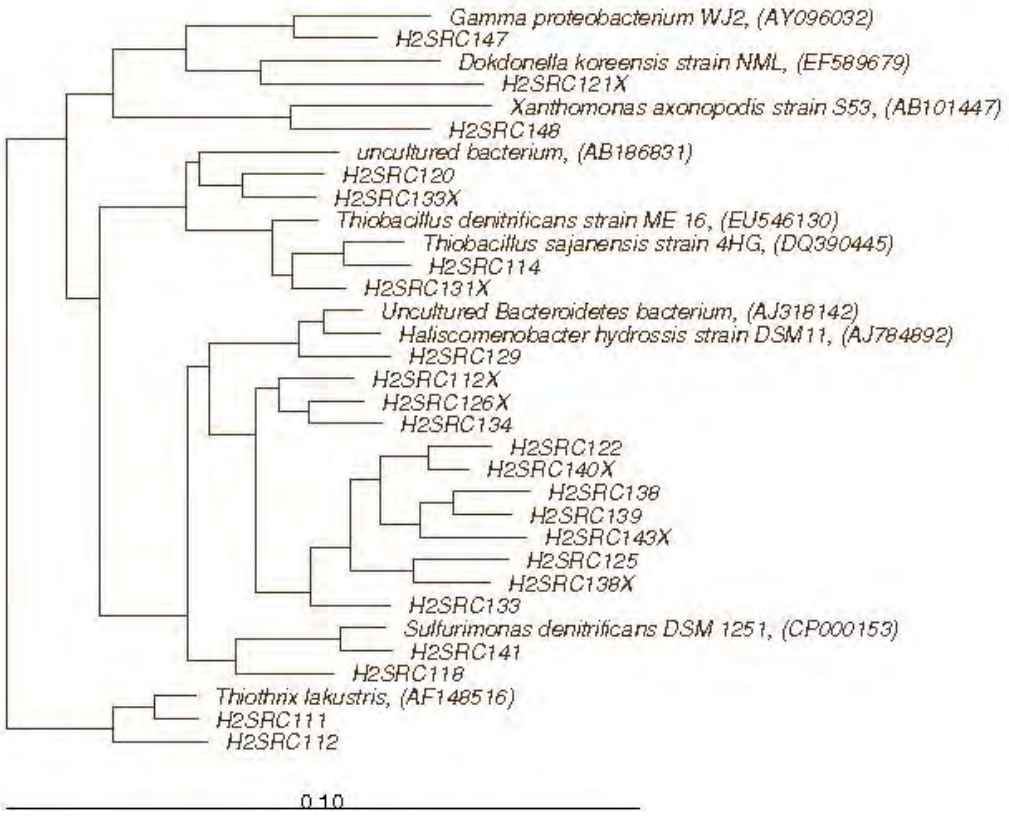

Figure 1. Bacterial phylogenetic tree based on near complete 16S rRNA gene sequences showing the affiliation of the representative clones for each OTU and its closest phylogenetic relatives. Clone names are shown with the code H2SRC1#. The symbol # indicates the number assigned to every clone and in some cases it has an X (clones are organised into two subcollections 1-50 and 1-50X).

Microbial spatial distribution through T-RFLP. T-RFLP is not considered a quantitative methodology, but a comparison between samples can be performed based on the areas of the peaks representing different OTUs. T-RFLP was used for the samples of biomass withdrawn at two different heights of the reactor. Since the most significant clones of the clone library, either in abundance terms or in relation to sulfur cycle, were subjected to T-RFLP analysis, it was possible to identify the populations represented by some of the OTUs found in the T-RFLP patterns (Fig. 2). Clones affiliated with *Thiothrix lakustris* were digested with HhaI and yielded a terminal restriction fragment of 173 bp. Two species isolated from the reactor during the second month of operation also were studied by T-RFLP. Genomic DNA from *Thiobacillus denitrificans* strain DSMZ 807 was used through the whole T-RFLP process as a positive control. This organism has been also described as an SOB previously (Beller et al., 2006). When it was subjected to T-RFLP analysis, it showed a T-RF of 563 bp,

which corresponds to the same OTU as *Thiobacillus plumbophilus* (OTU 9).

Species abundance in the PCR amplicon is related to peak area percentage. It is possible to observe that OTU 6, which was confirmed to include the clone affiliated with *Thiothrix lakustris*, is the most abundant OTU found in the T-RFLP patterns, in accordance with the results obtained in the clone library. It was found that the clones and isolates used for OTU identification by T-RFLP only comprised 30% of the total peak area of the patterns, meaning that there is at least 70% of the peak area represents other OTUs. The distribution this 30% peak area studied is represented in Fig. 3.However, the clones used for OTU identification represented 65% of the clone library diversity.

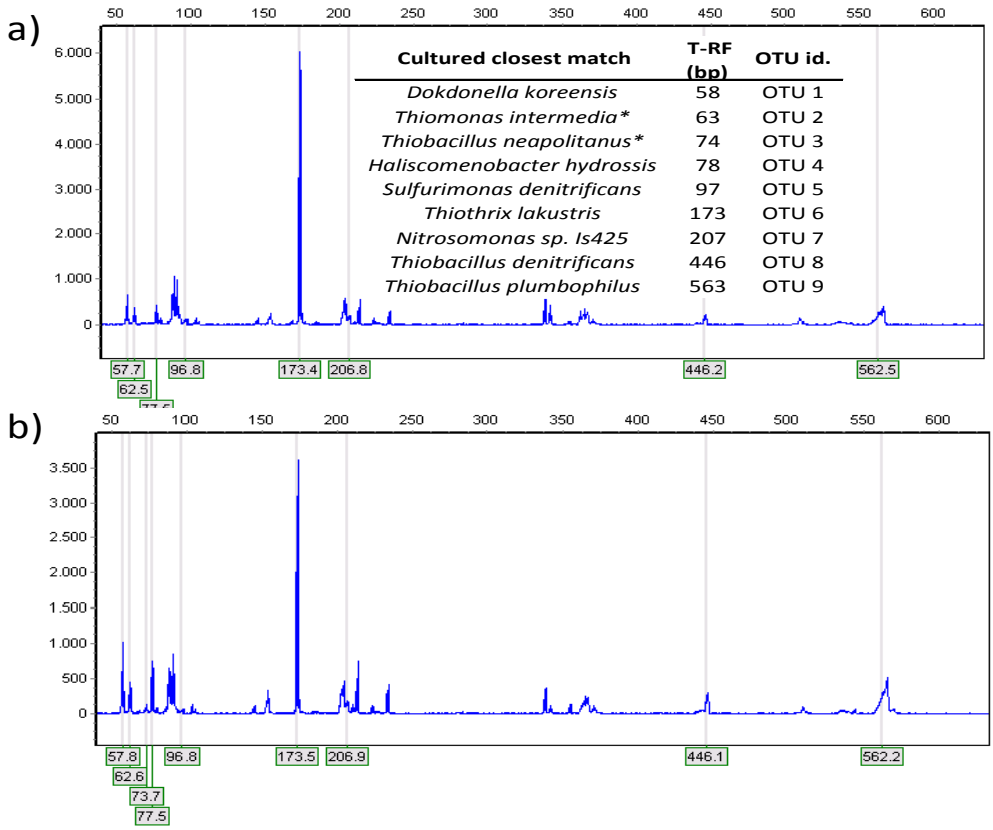

*Two species isolated from the reactor

Figure 2. Electropherograms showing T-RFLP patterns in a) outlet part, and b) inlet part of the reactor. Main OTUs studied are labeled with their respective restriction fragment lengths.

Figure 3. Distribution of studied OTUs in microbial communities of A) outlet part of the reactor and B) inlet part of the reactor. Distribution is based on % peak area from T-RFLP.

OTU 6, related to *Thiothix lakustris*, is predominant among the species studied in both parts of the reactor. It could be hypothesized that this species would be the most adapted to the operational conditions throughout the reactor, most probably because of its mixotrophy. In

the inlet part of the bioreactor, the otherOTUs increased in relative abundance at the expense of OTU 6. This means that the physiological advantage of *Thiothrix lakustris* over the rest of species is reduced near the inlet of the reactor where there is higher sulfide to oxygen ratio. Here, it can be highlighted that OTUs that increment their significance near the inlet of the reactor are related to mainly facultative anaerobic species (*Thiobacillus denitrificans*, *Sulfurimonas denitrificans* and *Haliscomenobacter hydrossis*) so they could use another electron acceptor if oxygen was lacking. It is remarkable that OTUs 2 and 3, linked to the two isolates *Thiomonas intermedia* and *Thiobacillus neapolitanus*, represent a low proportion of peak area. These results agree with those obtained through the clone library where clones affiliated to these species were not even found. This could indicate that either the clone library should be extended to cover a higher portion of the bacterial diversity and/or that in the OTUs where they are represented, there could be other species that we have not analysed individually by T-RFLP.

4 Conclusions

In this study, a molecular approach has been used to characterize the microbial diversity in a biotrickling filter. A clone library potentially representing the most abundant species present was created, and T-RFLP was used to study the differential microbial distribution at two different heights in the reactor. The use of both molecular tools improves the knowledge about the microbiology of gas-phase bioreactors. To our knowledge, this is the first research to retrieve an extensive number of near full-length 16S rRNA gene sequences from a biotrickling filter treating H_2S and to construct a collection representative of the existing diversity. Approximately 45% of the sequences retrieved were affiliated with bacteria of the sulphur cycle including *Thiothrix spp.*, *Thiobacillus spp*. and *Sulfurimonas denitrificans*. Although clones related to aerobic species were predominant in the reactor, facultative anaerobes had a major relative abundance at the inlet of the reactor, where the sulfide to oxygen ratio is higher. Even though these results may help to break new ground in the biofiltration field, further research about the microbial composition and distribution in biotrickling filters is needed in order to fully understand the underlying processes that take place in these systems. Quantification of populations would help to hypothesize about the causes of changes in the microbial community composition and to understand the relation between phylogeny and reactor efficiency.

References

Altschul, S.F., Madden, T.L., Schaffer, A.A., Zhang, J., Zhang, Z., Miller, W., and Lipman, D.J. (1997). Gapped BLAST and PSI-BLAST: a new generation of protein database search programs. *Nucleic Acids Res.* 25, 3389-3402.

Beller, H.R., Chain, P.S.G., Letain, T.E., Chakicherla, A., Larimer, F.W., Richardson, P.M., Coleman, M.A., Wood, A.P., and Kelly, D.P. (2006). The Genome Sequence of the Obligately Chemolithoautotrophic, Facultatively Anaerobic Bacterium Thiobacillus denitrificans. *The Journal of Bacteriology* 188, 1473-1488.

Chi-hua, H. and Banks, M.K. (2006). Degradation of Polycyclic Aromatic Hydrocarbons in the Rhizosphere of Festuca arundinacea and Associated Microbial Community Changes. *Bioremediation Journal* 10, 93-104.

Egert, M. and Friedrich, M.W. (2005). Post-amplification Klenow fragment treatment alleviates PCR bias caused by partially single-stranded amplicons. *Journal of Microbiological Methods* 61, 69-75.

Fortuny, M., Baeza, J.A., Gamisans, X., Casas, C., Lafuente, J., Deshusses, M.A., and Gabriel, D. (2008). Biological sweetening of energy gases mimics in biotrickling filters. *Chemosphere* 71, 10-17.

Friedrich, U., Prior, K., Altendorf, K., and Lipski, A. (2002). High bacterial diversity of a waste gas-degrading community in an industrial biofilter as shown by a 16S rDNA clone library. *Environ.Microbiol.* 4, 721-734.

Kaplan, C.W., Astaire, J.C., Sanders, M.E., Reddy, B.S., and Kitts, C.L. (2001). 16S ribosomal DNA terminal restriction fragment pattern analysis of bacterial communities in feces of rats fed Lactobacillus acidophilus NCFM. *Applied and Environmental Microbiology* 67, 1935-1939.

Kelly, D.P., Shergill, J.K., Lu, W.P., and Wood, A.P. (1997). Oxidative metabolism of inorganic sulfur compounds by bacteria. *Antonie Van Leeuwenhoek* 71, 95-107.

Liu, W.T., Marsh, T.L., Cheng, H., and Forney, L.J. (1997). Characterization of microbial diversity by determining terminal restriction fragment length polymorphisms of genes encoding 16S rRNA. *Appl.Environ.Microbiol.* 63, 4516-4522.

Proceedings of the 10th International Chemical and
Biological Engineering Conference - CHEMPOR 2008
Braga, Portugal, September 4-6, 2008
E.C. Ferreira and M. Mota (Eds.)

Biofilm technology: from support design to reactor operation

Maria F. Matos, Cláudia F. Alves, António G. Brito, Regina B. Nogueira*
IBB – Institute for Biotechnology and Bioengineering, Centre of Biological Engineering,
University of Minho, Campus de Gualtar, 4710–057 Braga, Portugal.

Keywords: sequencing batch biofilm reactor (SBBR), support, nitrogen removal, poly-β-hydroxybutyrate (PHB)
Topic: Integration of life sciences & engineering (Improvement of environmental remediation processes).

Abstract

The aim of this work was to assess the feasibility of a Sequential Batch Biofilm Reactor (SBBR) to perform carbon and nitrogen removal: from support design to reactor operation. The experimental part was conducted in two phases. In the first phase, different supports were tested to select the most suitable one for SBBR operation. In the second phase, the most appropriate support was used in a SBBR to perform carbon and nitrogen removal. The results demonstrate that the support with the highest internal surface area presented a higher biomass accumulation. Time profiles of nitrogen ions and acetate concentration showed the typical behaviour of a SBBR performing carbon and nitrogen removal. Poly-β-hydroxybutyrate (PHB) was formed immediately after acetate depletion and was subsequently consumed for biomass growth, owing to the high oxygen concentration in the reactor.

1. Introduction

The Sequential Batch Reactor (SBR) has been used to remove organic carbon and nutrients from wastewater in one single unit under properly controlled conditions (Brito et al., 1997; Rodrigues et al., 2001). The SBR can be combined with biofilm growth on the surface of a support material, originating the Sequencing Batch Biofilm Reactor (SBBR). In SBBR systems high concentrations of biomass can be maintained independently of the sedimentation characteristics of the biological aggregates and the hydraulic retention time of the reactor. SBBRs are particularly suitable when the required microbial population grow very slowly or when the biomass yield is low (Vieira et al., 2008).

Microorganisms in SBRs are exposed to continuous periodic environmental changes, namely varying liquid volumes and substrate concentrations (donors and receivers of electrons). When confronted with such interchanging periods of high ("feast period") and low ("famine period") substrate concentrations, bacterial populations adopt specific survival strategies. In particular, they often accumulate and set aside organic carbon as internal polymers such as poly-β-hydroxybutyrate (PHB). While such storage phenomena are well studied for suspended biomass systems, as for example SBRs, they are still poorly documented in literature for systems using biofilms, such as the SBBRs (Alves et al., 2004). Nevertheless, they do play an important role in the optimization of operating strategies, which holds particularly true for multiple and interlinked degradation pathways, such as the nitrogen and carbon removal by biological nitrification and denitrification. Therefore, the aim of this work was to assess the feasibility of a SBBR to perform carbon and nitrogen removal: from support design to reactor operation.

* Corresponding author. Tel + 351-253-604414. E-mail: regina@deb.uminho.pt

2. Materials and methods

2.1. Experimental set-up

In the first phase of the experimental work, biomass adhesion and biofilm formation was evaluated in a new developed thermoplastic support (*DupUM*) and in two supports currently available on the market (*Biolox10* and *Bioflow30*) (Table 1). Three SBBRs with working volumes of 2.5 L filled with different supports were operated in parallel. The bed formed by the supports occupied 47 % of the reactors volume. The reactors were operated with a constant cycle time of 6.2 h, a volume exchange ratio of 0.8 L/L and a resulting hydraulic retention time (HRT) of 7.75 h. The duration of the individual operating phases was: 102 min mixed fill, 150 min aerated, 114 min settle and 10 min draw. During the aerated phase airflow was applied through membrane diffusers, causing the reactor contents including the carrier bed to circulate. In the first operation period (days 0 – 127), a synthetic wastewater with acetate as the only carbon source and ammonium as nitrogen source was used. The carbon and nitrogen ratio (C/N) used was 6.25. At day 127, the carbon and nitrogen concentration in the system was increased from 500 mg/L and 80 mg/L to 750 mg/L and 120 mg/L, respectively. The SBBRs were inoculated with biomass from a nitrification/denitrification unit treating effluent from a brewery industry.

Table 1. Characteristics of supports.

Support	Material	Dimensions (mm)	Nº pieces/m^3	Specific surface area (m^2/m^3)
 *DupUM*	PE [a]	height: 10.0 Diameter: 17.0	324 900	407
 *Bioflow30*	PP [b] Recycled	height: 30.0 Diameter: 32.0	21 910	320
 *Biolox10*	PE Recycled	height: 10.0 diameter: 9.5	538 922	640

a) Polyethylene; b) Polypropylene

In the second phase, a SBBR with a working volume of 28 L was operated with a constant cycle time of 5 h, a volume exchange ratio of 0.36 $L \cdot L^{-1}$ and a HRT of 14 h. The duration of the individual operating phases was: 115 min mixed fill, 165 min aerated and 20 min draw. The biofilm was formed on the support selected in the previous phase of the experimental work. The SBBR was operated with synthetic water. The composition of the synthetic substrate solution was: 643 $mg \cdot L^{-1}$ $NaCH_3COO \cdot 3H_2O$, 130 $mg \cdot L^{-1}$ NH_4Cl, 210 $mg \cdot L^{-1}$ $NaHCO_3$, 44 $mg \cdot L^{-1}$ KH_2PO_4, and 1 $mL \cdot L^{-1}$ of a trace element solution in accordance with Vishniac and Santer (1957). The reactor was inoculated with the selected supports coming from the previous phase.

2.2. Analytical methods

The thermodynamic characterization of the interaction support material-biomass was evaluated using contact angle measurements. Contact angles were measured using sessile drop method at 20ºC with distilled water, formamide and 1-bromonaphthalene.The measurements were carried out in a standard contact angle apparatus (Kruss-GmH, Hamburg).

Grab samples were taken and analyzed for ammonium, nitrite, nitrate and chemical oxygen demand (COD) according to *Standard Methods*. The biofilm accumulation on supports was

estimated as dry weight measurements. PHB content of suspended biomass and biofilm (external and internal) was measured by gas chromatography (GC) using the method developed by Smolders et al. (*1994*).

2.3. Calculations

The Extended Derjaguin-Landau-Verwey-Overbeek theory (XDLVO) was used to assess the affinity of the individual support materials to biomass adhesion (van Oss, 1989).

Mass balance calculations were based on an assumed elemental composition of $CH_{1.8}O_{0.5}N_{0.2}$ for 1 Cmol biomass (Beun et al., 2002). The carbon consumption of hereotrophic growth was calculated based on the observed ammonium consumption and a biomass formation rate per mole of acetic acid of 0.40 Cmol·Cmol^{-1} (Beun et al., 2002). Stoichiometric considerations for energy production lead to the following rates of acetate consumption with respect to nitrate, nitrite, and oxygen: 1.25 Cmol acetate·mol^{-1} NO_3^-, 0.5 Cmol acetate· mol^{-1} NO_2^- and 1 Cmol acetate·mol^{-1} O_2, respectively. It was assumed that nitrification is performed by ammonium and nitrite oxidizing bacteria with a biomass formation yield of 0.057 Cmol mol^{-1} NH_4^+ and 0.034 Cmol mol^{-1} NO_2^-, respectively (Henze et al., 1995).

3. Results and Discussion

3.1. Supports surface properties

The free energy of adhesion between the biomass and the support surface immersed in water was calculated to foresee the biofilm adhesion on the supports. According to the results obtained, the surface properties of *Biolox10* and *DupUM* (with values of ΔG of -34.60 mJ.m^{-2} and -30.16 mJ.m^{-2}, respectively) are more favourable to biomass adhesion than the one of *Bioflow30* (-4.04 mJ.m^{-2}) due to their lower free energy of adhesion (Salerno et al., 2004).

3.2. Biofilm formation in supports

The biofilm accumulation profile expressed as dry weight per specific surface area is presented in figure 1.

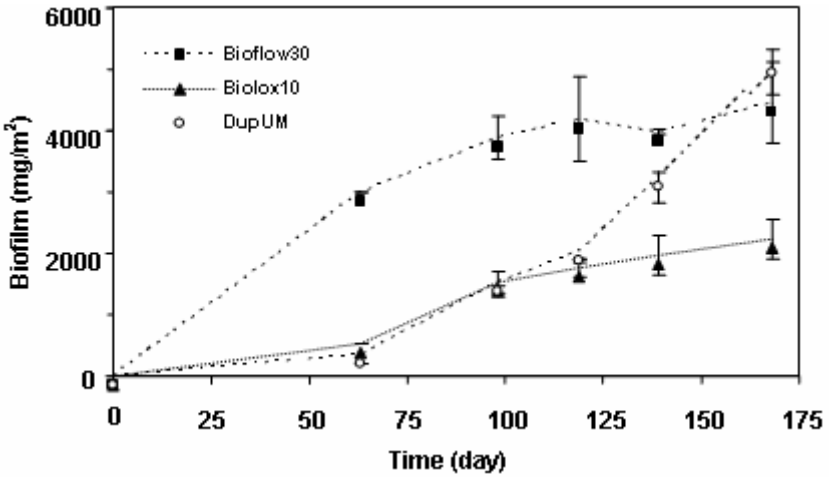

Figure 1. Biofilm accumulation on supports surfaces expressed as dry weight per specific surface area.

Biolow10 and *DupUM* displayed a very slow biofilm growth, whereas *Bioflow30* presented an initial biofilm growth about six times higher. This may be related to the different detachment forces in the reactors as a result of the support geometry. For the same fraction of support

(47 %) and as a result of the different dimension of the supports, the number of support pieces was considerably different in each reactor. This difference is higher for *Biolox30*, where there were only 26 support pieces in the reactor, which is much less than the number of pieces in the reactors with *Biolox10* and *DupUM* (around 633 pieces and 381 pieces, respectively). Hence, the occurrence of collisions and their intensity are expected to be different in the reactors. Probably, the abrasion forces which result from the collisions caused by the high number of pieces of *Biolox10* and *DupUM* in the respective reactors have conditioned initially the biofilm formation on the respective supports.

From day 127, the concentration of carbon and nitrogen in the reactors was increased. Biofilm accumulation on *Bioflow30* and *Biolox10* did not change significantly compared to the increase of biofilm mass observed on *DupUM*. These results have shown that biofilm accumulation on *DupUM* was limited by the amount of available substrate. After 168 days, *DupUM* presented a higher biomass accumulation per unit of surface area (5096 $mg.m^{-2}$) than *Biolox10* and *Bioflow30* (2231 $mg.m^{-2}$ and 4454 $mg.m^{-2}$, respectively). Based on these experimental results *DupUM* was selected for the next phase of the experimental work.

The thermodynamic approach did not allow us to foresee the biofilm formation on the supports. The results obtained through the thermodynamic characterization indicated that *Bioflox10* and *DupUM* had more favourable surface properties to the initial adhesion of biomass than *Bioflow30.* However, after 120 days of reactors operation, *Bioflow30* showed higher biofilm accumulation than the other supports. According to Gjaltema et al. (1997), in airlift reactors the biofilm adhesion and formation is dominated by the reactor hydrodynamic conditions and by collisions among particles. The results from biomass adhesion and biofilm formation studies obtained in the present work suggest that the hydrodynamic conditions established in the reactors and the geometry of the supports played a crucial role in biofilm formation. Biofilm growth was favoured in the supports that presented a higher internal surface area that protected biofilms from erosion and abrasion detachment mechanisms.

3.3. Reactor performance

Figure 2 depicts profiles of nitrogen ions, acetate as COD and dissolved oxygen (DO), during a typical SBBR cycle.

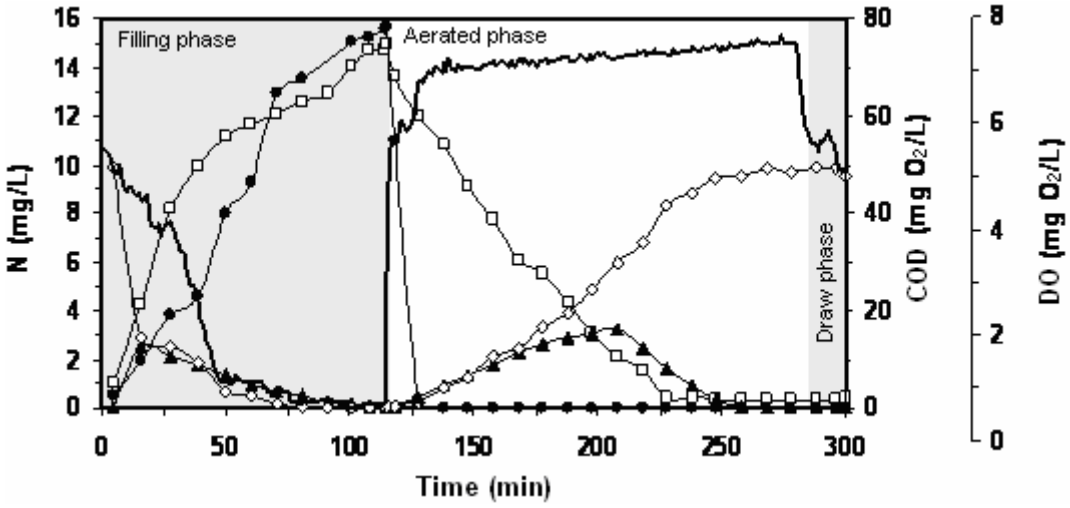

Figure 2. COD (●), DO (-), ammonium (□), nitrite (▲) and nitrate (◊) profiles during a SBBR cycle.

During the mix fill phase, the nitrate left over from the previous cycle was completely denitrified with acetate, so that no nitrite accumulation was observed. Time profiles of ammonium, nitrite and nitrate concentration in the aerated phase showed the typical behaviour of nitrification reactions, via nitrite formation and subsequent oxidation to nitrate. A

nitrogen balance of this phase showed that 66 % of ammonium supplied was oxidized to nitrate with the remainder being used for biomass growth.

According to these results, 46 % of carbon supplied was consumed during the mixed fill phase with the remainder being consumed in the aerated phase. Based on mass balances in the fill phase, it was possible to estimate that 15 % of carbon was used to the growth of biomass, 25 % was used as a source of energy and the remaining 60 % were removed by unknown mechanisms. The quantification of PHB in the biomass has allowed complementing the balance of carbon during the operation cycle illustrated in figure 2. Figure 3 presents schematically the main carbon fluxes in the SBBR.

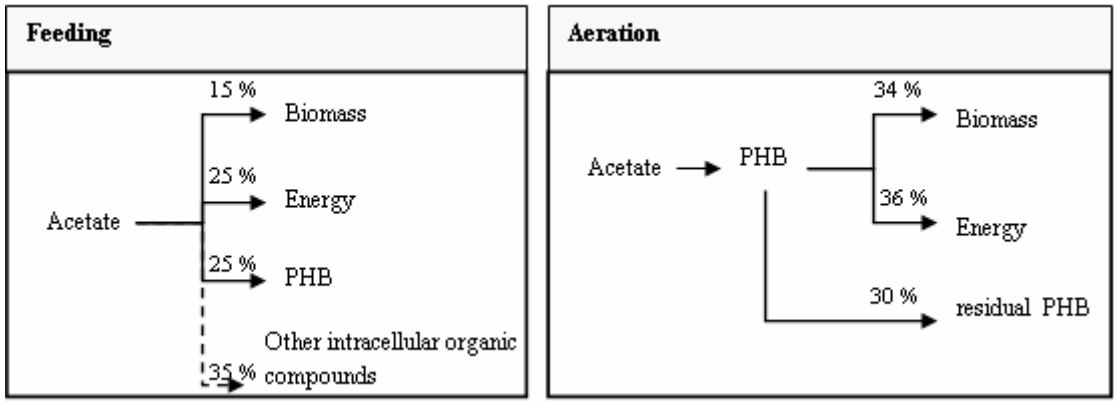

Figure 3. Fate of carbon added as acetate in the feeding and the aeration phase of the SBBR.

As illustrated, the carbon portion missing at the end of the feeding phase was stored as PHB (25 %), while the remaining 35 % were removed by another mechanism such as conversion to intracellular intermediary composts of a low molecular weight or storage as another PHA, besides PHB (Dionisi et al., 2001).

The acetate present at the beginning of the aeration phase is quickly converted and stored in the biomass as PHB. After acetate depletion, a part of the PHB (70 %) is consumed as a source of carbon and energy, while the rest is stored in the biomass (30 %). According to the reactions' stoichiometry, the organic carbon transformed into PHB during the aeration phase would be sufficient to denitrify the entire nitrate previously produced. This did not occur, however, probably due to the high concentration of oxygen dissolved in the liquid. Instead the PHB was consumed in the production of biomass and in energy needs.

Suspended biomass was revealed to play a significant role in the carbon removal mechanism: about 79 % of the total PHB formed was stored in the suspended biomass, although this biomass represented only 20 % of the total biomass present in the reactor. This important result might be attributed to the higher accessibility of suspend biomass to acetate, due to existence of lower mass transfer limitation.

4. Conclusions

Biomass adhesion and biofilm formation studies suggest that the hydrodynamic conditions established in the reactors and the geometry of the supports played a crucial role in biofilm formation. Biofilm growth was favoured in the supports that presented a higher internal surface area that protected biofilms from erosion and abrasion detachment mechanisms.

According to the operation phase of the SBBR, there are two relevant mechanisms in the removal of acetate in the SBBR: (1) use of the acetate simultaneously with the growth of biomass and in the metabolism of PHB storage (feeding phase); and (2) direct storage of the acetate as PHB which is later on used in the growth of biomass (aeration phase). The consumption of acetate and its storage as PHB is mostly carried out by the biomass in suspension. Although the biomass in suspension represented only 20 % of the total biomass

present in the reactor, 79 % of the total PHB formed was stored in the biomass in suspension. This result is due to the lower mass limitations of the biomass in suspension in comparison with the biofilm.

References

Alves C., Nogueira R., Brito A.G. (2004). Poly-β-hydroxybutyrate metabolism in a biofilm reactor. *Biofilms 2004: Structure and Activity of Biofilms*. Las Vegas, USA, 24-26 October.

Beun J. J., Dircks K., van Loosdrecht M. C. M., Heijnen J. J. (2002). Poly-β-hydroxybutyrate metabolism in dynamically fed mixed microbial cultures. *Water Research,* 36, 5, 1167-1180.

Brito A. G., Rodrigues A. C., Melo L. F. (1997). Feasibility of a pulsed sequencing batch reactor with anaerobic aggregated biomass for the degradation of low strength wastewaters. *Water Science and Technology*, 35, 1, 193-198.

Dionisi D., Majone M., Ramadori R., Beccari M. (2001). The storage of acetate under anoxic conditions. *Water Research,* 35, 11, 2661-2668.

Gjaltema A., van der Marel N., van Loosdrecht M.C.M., Heijnen J. J. (1997). Adhesion and biofilm development on suspended carriers in airlift reactors: hydrodynamic conditions versus surface characteristics. *Biotechnology and Bioengineering*, 55, 6, 880-889.

Henze M., Harremoës P., Jansen J. l. C., Arvin E. (1995). Wastewater treatment - biological and chemical processes. *Springer-Verlag Berlin Heidelberg*, New York.

Rodrigues A. C., Brito A. G., Melo L. F. (2001). Post-treatment of a brewery wastewater using a sequencing batch reactor. *Water Environment Research*, 73, 1, 45-51.

Salerno M., Logan B., Velegol D. (2004). Importance of molecular details in predicting bacterial adhesion to hydrophobic surfaces. *Langmuir* 20,10625-10629.

Smolders G. J. F., van der Meij. J., van Loosdrecht M. C. M., Heijnen J. J. (1994). Stoichiometric model of the aerobic metabolism of the biological phosphorus removal process. *Biotechnology and Bioengineering,* 44, 7, 837-848.

van Oss C. J. (1989). Hydrofobicity and hydrophilicity of biosurfaces. *Current Opinion in Colloid Interface Science*, 2, 503, 510.

Vieira M., Brito A. G., Nogueira R. (2008). Nitrogen removal in a sequencing batch biofilm reactor: effect of carbon availability and intermittent aeration. *Int. Journal of Environment and Waste Management* (in press).

Vishniac W., Santer M. (1957). The *Thiobacilli*. *Bacteriological Reviews* 21, 195-213.

Proceedings of the 10th International Chemical and
Biological Engineering Conference - CHEMPOR 2008
Braga, Portugal, September 4-6, 2008
E.C. Ferreira and M. Mota (Eds.)

Lignocellulosic Materials as a Feedstock for Polymer Synthesis

Matjaž Kunaver[1*], Edita Jasiukaityte[1], Vesna Tišler[2], Sergej Medved[2]
[1] National Institute of Chemistry, Hajdrihova 19, SI-1000 Ljubljana, Slovenia.
[2]University of Ljubljana, Biotechnical Faculty, Wood Science Department, Rožna dolina Cesta VIII/34, SI-1000 Ljubljana, Slovenia

Keywords: Liquefied wood, polyester synthesis, adhesives,
Topic: Sustainable process-product development through green chemistry.

Abstract

Wood is one of the most abundant natural polymer, and despite its complex composition it can be used as a potential renewable feedstock for polymer production. The first step is the liquefaction of wood with multifunctional alcohols. The products are low molecular mass liquid oligomers. Liquefied wood can be prepared using all kind of wood biomass, like wood meal and wood residues from wood furniture industry, wood waste from building industry, broken furniture, waste paper and other materials based on cellulose. Glycerine, the industrial byproduct from the production of biodiesel can be utilized in some experiments as the main reactant. Such a reaction mixture is made of 97% of waste material.

In our research native hardwoods and softwoods were liquefied with different glycols and acidic catalyst. The liquefaction took place at 150 – 180 °C for 0.5 - 3 h with more than 95% yields. We have been the first worldwide to utilize the liquefied wood as the feedstock for the synthesis of different polyesters where the liquefied wood is been incorporated into a large polymeric molecule. Such polymers have a potential use in composites, adhesives and polyurethanes. Unsaturated polyesters were prepared by reacting liquid wood with maleic and phthalic acids. Polyester polyols were prepared by using adipic acid. These polymers were reacted with isocyanates to give a series of polyurethane foams that were comparable with commercial foams and could be used for isolation purposes.
Such utilization of lignocellulosic materials can reduce the crude oil consumption and might increase the use of the renewable resources in large extent.

Introduction

Biomass conversion to ethanol, diesel fuel and bio based chemicals are recently the most intensive research goals. However, much remains to be done in synthesis, analysis and characterisation if these materials are to replace the materials, otherwise produced from crude oil. Several attempts to elucidate the mechanisms associated with the liquefaction of lignin, of cellobiose and of cellulose have been published. The liquefaction of lignin with phenol has been studied on the basis of the behaviour of model substances, such as guaiacylglycerol-β-guiacyl ether (Lin et al., 2001), (Lin, Nakagame et al., 2001) . According to Lin et al. the reaction starts with hydrogen ion from acid catalysis attack of β-hydroxyl groups of lignin and it is followed by substitution reaction in C-β of obtained intermediates after scision of unstable β-O-4 linkage. The cellulose behaviour in acidic ethylene glycol was studied by Yamada and Ono (2001). In their paper, the authors proved the formation of ethylene glycol – glucosides in the early stage of liquefaction. These later decomposed into the 2-hydroxyethyl levulinate.
The preparation of low-cost polyols from biomass materials has been investigated by several research groups using different reagents. Kržan and Kunaver (2006) applied microwaves

* Corresponding author. Tel + 386 1 476 0363. E-mail: matjaz.kunaver@ki.si

radiation as the heating source. Cellulose and cellulose derivatives can be considered to be polyhydric alcohols. In the liquefaction process, the presence of hydroxyl group-containing species in the wood components can be used as the polyols for several different purposes. The polyhydric units that are present in the resulting liquefied/derivatised wood can be used in the creation of polyurethane foams, polyurethane resin precursors (Wei et al., 2004) and in the recently developed wood-polyalcohol based urethane adhesives (Tohmura et al., 2005). Lee et al. (2005) have studied the thermal stability, biodegradability and genotoxicity of a range of polyurethane foams that were produced from polyols made from waste paper. They found that the foams possessed the same thermal stability as those made from liquefied starch or wood. The hydroxyl value of the liquefied wood has been determined by several authors and is generally determined to be between the equivalent of 200 and 500 mg of KOH/g. The actual value depends on the liquefaction time. This high number of hydroxyl group sites means that the products have application in those areas in which the hydroxyl component can be used in complex polyester synthesis. Some benefits could be expected from such systems. These include the incorporation of the biomass components into the polymeric compositions and consequently, the provision of a certain degree of biodegradability. The work presented here offers a new approach to the utilisation of the liquefied/derivatised wood in the creation of novel polymeric composite materials.

Materials and methods

Materials

Wood saw dust of poplar (Populus *spp*.), oak (Quercus *spp*.), spruce (Picea *spp*.) and beech (Fagus Sylvatica) were sieved through 1.25 mm^2 screens and dried at room temperature to a constant water content. Waste corrugated board was cut into 10 mm to 10 mm pieces and used without further modification.

Glycerol, diethylene glycol, p-toluene sulfonic acid (pTSA), sulphuric acid, adipic acid, phthalic acid anhydride, dimethylacetamide, styrene and dibutyl tin oxide of reagent grade were used without further purification.

Liquefaction/derivatisation of wood saw dust and waste corrugated board

The respective polyhydroxy alcohol (300g), p-toluene sulphonic acid (9g) and wood saw dust or pieces of corrugated board (100g) were placed into the 1000 cm^3 three necked glass reactor, equipped with the mechanical stirring. Liquefaction was conducted with constant stirring at 150^{o}C to 160^{o}C for 90 minutes. The extent of liquefaction was evaluated by determining the residue after the washing out the reaction mixture with N,N-dimethylacetamide and acetone. The residue was dried in an oven at 110^{o}C to constant weight. The residual ratio was calculated as the weight percentage based on the starting wood material.

Synthesis of polyester polyols and unsaturated polyesters from the liquid/derivatised wood

The liquefied/derivatised wood or corrugated board mixture (400g) was introduced into the four-necked 1000 cm^3 glass reactor, equipped with a water condenser and mechanical stirrer. The reactor was placed in an electric jacket heater. 300g of adipic acid or of phthalic acid anhydride (depending on the required product) were added and 0.6g of dibutyl tin oxide as the transesterification catalyst. The mixture was heated gradually up to 220^{o}C under stirring and was held at this temperature. Water was continuously distilled from the reaction system. A sample was withdrawn periodically from the reaction system and its acid value was determined. After completion of the reaction, when the acid value was reduced to less than 30mg KOH/g, the reaction mixture was cooled to an ambient temperature.

Similar procedure was used for the synthesis of unsaturated polyesters. The formulations are shown in Table 1.

Table 1. Typical formulations for the synthesis of unsaturated polyesters and polyester polyols

Polyester Polyol	Unsaturated polyester
400g Liquid wood	400g Liquid wood
300g Adipic acid	224g Maleic anhydride
0.6g Dibutyl tin oxide	320g Diethylene glycol
	160g Phthalic anhydride
	1.1g Dibutyl tin oxide

Unsaturated polyester was inhibited with 100ppm of hydroquinone and diluted to 60% solids with styrene.

Polyester characterization

Measurement of hydroxyl number and acid number of liquid wood and liquid/derivatised wood species

The hydroxyl numbers of liquid wood and its derivatives were determined according to the method described elsewhere (ASTM).

FTIR Spectroscopic analysis

All of the spectra were obtained using a Perkin-Elmer Spectrum-1 FTIR spectrophotometer. The liquid/derivatised wood samples were applied on NaCl crystal as a thin film. Transmittance spectra were measured in the wavelength range from 4000 cm^{-1} to 500 cm^{-1}.

GPC measurements

Gel permeation chromatographic representations were obtained on an HP – AGILENT system, consisting of isocratic pump HP 1100, a refractive index detector AGILENT 1100 and a Perkin Elmer LC235 diode array detector. Two PLgel columns, connected in series (Plgel 100Å, 5um, Plgel 50Å, 5µm), were used. Poly(styrene) standards were used for the calibration curve. The mobile phase was prepared from N,N-dimethylacetamide containing 0,05M LiBr. The latter was added in order to prevent interaction between the sample molecules and stationary phase. The mobile phase flow rate was 1cm^3/min.

RESULTS AND DISCUSSION

The liquefaction process gave yields of the liquefied wood that were in excess of 98%. The typical reaction yields are shown in Figure 1 for two different wood meals. It is clear that at least 90 minutes of reaction time, under the specified heating regime, is needed if unwanted residues are to be minimised. Apparent further condensation occurs with longer reaction time, increasing the amount of the residue formed in lignocellulosic materials where lignin is also present. The liquefaction of waste corrugated board was completed in 90 minutes with 100% yield.

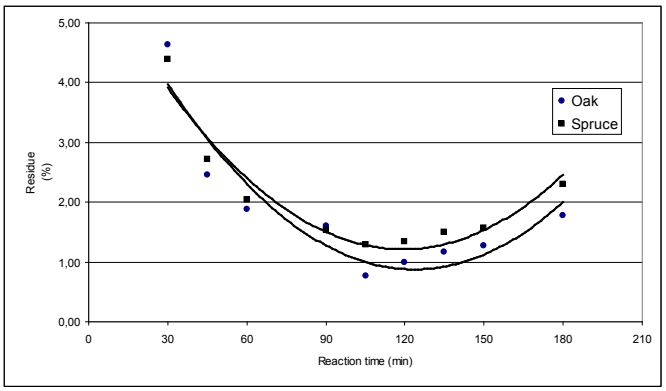

Figure 1: Reaction yields: Liquefaction of Oak and Spruce wood meals. Wood meal to glycerine ratio 1:4; 3% pTSA acid catalyst.

Each of the liquefied wood species was characterised using FTIR spectroscopic evaluations and by gel permeation chromatography/size exclusion chromatography (GPC/SEC). The results of this characterisation and analysis showed that each of the liquefied/derivatised wood products gave very similar FTIR spectroscopic profiles and GPC/SEC characteristics. For the reaction product arising from the liquefaction/derivatisation of the poplar wood meal, at different reaction times, the spectral information shown in Figure 2 was obtained.

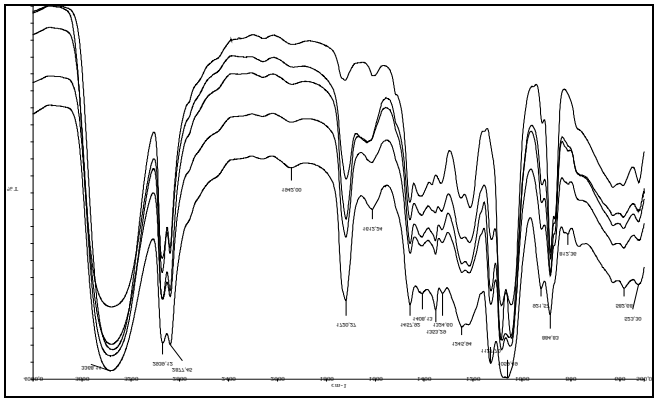

Figure 2: FTIR spectrum of products derived from the liquefied poplar wood samples that were isolated every 15 minutes of reaction: top spectrum - after 30 minutes, lower spectrum – after 120 minutes

With respect to the influence of the time of reaction, the intensity of the 1721 cm^{-1} (C=O stretching) band increased during such reaction because of the formation of the levulinic acid ester of diethylene glycol, (DEG) which is produced by solvolysis of cellulose through cleavage of the β-1,4-glycosidic linkage. The presence of this compound was also verified by identification using GC/MS analysis. The concentration increased during the process of liquefaction.

Liquid wood readily reacted with appropriate dibasic acids to yield a higher molecular mass resin of acceptable viscosity and with appropriate OH numbers. Acid addition was adjusted to either theoretical or experimentally determined OH numbers. The solid remains after liquefaction could be kept in the mix as a filler.

Theoretically all of the hydroxyl groups could be esterified during the polyester synthesis. A liquefied wood with a hydroxyl value 500 mg of KOH/g for complete esterification would need 8.9 mM/g of organic acid. However, such a complete reaction is never achieved due to differences in reactivity of the hydroxyl groups. A certain proportion of the hydroxyl groups are left unreacted since in the case of the polyurethane synthesis they are needed for the polycondensation reaction with the polydiiocynate.

In our studies we have reduced the hydroxyl value from between 500 and 600 mg of KOH/g to values between 10-25 for unsaturated and 150-200 for saturated polyester. As a result of the utilization of liquefied wood in polyester-polyol synthesis, 45% to 25% of polyhydric alcohols were replaced with liquefied wood. The reactivity and the hydroxyl value remained in the range of commercial products.

The liquefied/derivatised wood meals (based on oak meal, beech meal, spruce meal and poplar meal) and the corresponding polyester based materials that were derived from reaction between the liquefied/derivatised wood meal and phthalic acid were subjected to GPC/SEC analysis. The resulting chromatograms were all very similar. Figure 3 gives the chromatogram of the unsaturated polyester derived from the liquefied poplar wood meal and Figure 4 the chromatogram of the liquefied poplar wood and its corresponding phthalate ester.

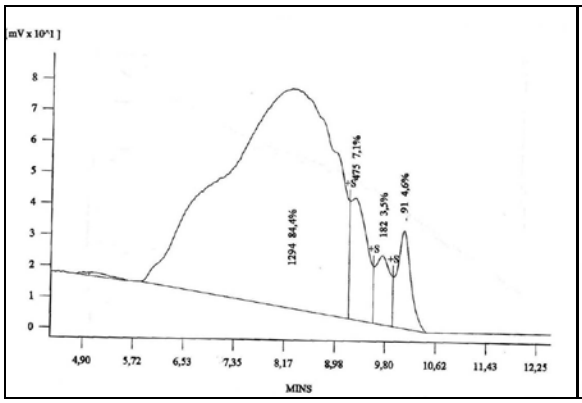

Figure 3. SEC curve of unsaturated polyester resin

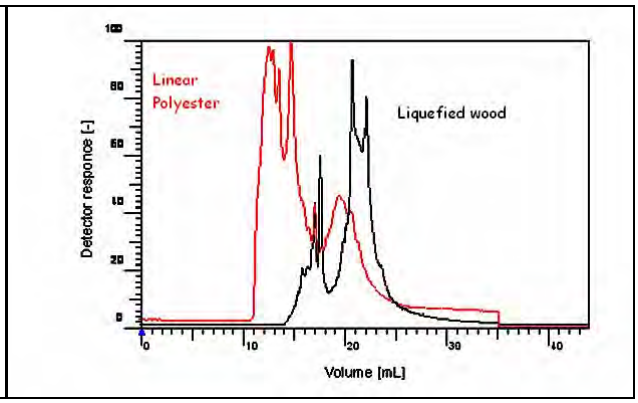

Figure 4. SEC curve of liquefied poplar wood and polyester polyol

Resin use

Unsaturated polyesters were dissolved in styrene and resins were crosslinked with a peroxide initiator and showed normal reactivity. The liquefied wood concentration in 100% unsaturated polyester resin was from 22% to 29%. Saturated polyesters were reacted with MDI isocyanate in the presence of standard foam forming additives. Compressive strength at 10% strain was 46kPa – 74kPa and density from 0.03 g/cm^3 to 0.05g/cm^3. Polyurethane foams appeared less hydrophilic than foams derived directly from liquefied wood.

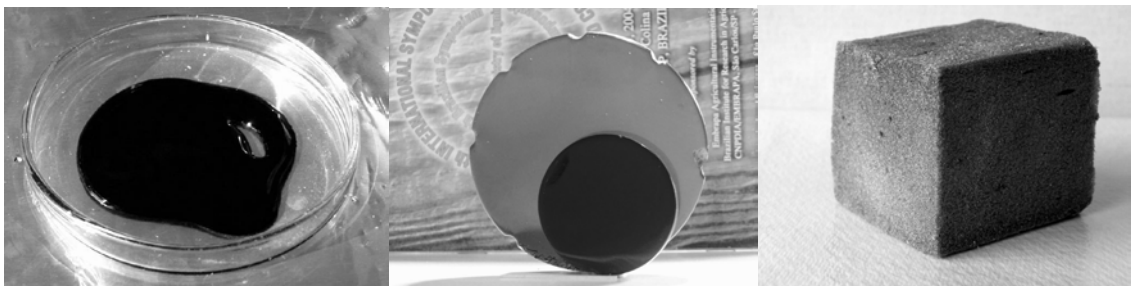

Figure 5: Liquefied wood (left), unsaturated polyester (middle), polyurethane foam (right)

Conclusions

Liquefied/derivatised wood can be used as one of the components in polyester synthesis due to the large number of hydroxyl groups available in the liquefied/derivatised wood. By using adipic acid and phthalic acid anhydride as reagents in the polyester synthesis, polyesters

have been synthesised that have a molar mass distribution that is similar to that of the commercial linear polyesters that are used for polyurethane foam production. 45% of the raw materials that would otherwise be in the linear polyester creation were, thus, replaced with wood. This amount varies according to product requirements.

Linear polyesters that are based on liquid wood species show similar application properties to those of commercial wood composites. They can be used in combination with melamine resin precursors, as wood adhesives in fibre-wood boards production and in plywood boards production as well as in polyurethane foam preparation. The properties of wood based linear polyester and unsaturated polyester products and their potential use are the subject of current further research.

References

Lin L., Yao Y. and Shiraishi N. (2001) Liquefaction Mechanism of β-O-4 Lignin Model Compound in the presence of Phenol under Acid Catalysis, Part 1. Identification of the Reaction Products. Holzforschung 55: 617-624

Lin L.; Nakagame S.; Yao Y.; Yoshioka M. and Shiraishi N. (2001) Liquefaction Mechanism of β-O-4 Lignin Model Compound in the presence of Phenol under Acid Catalysis, Part 2. Reaction Behavior and Pathways. Holzforschung 55: 625-630

Yamada T. and Ono H. (2001) Characterization of the products resulting from ethylene glycol liquefaction of cellulose. Journal of Wood Science 47: 458-464

Kržan A. and Kunaver M. (2006) Microwave heating in wood liquefaction. Journal of Applied Polymer Science 101 (2): 1051-1056

Wei Y., Cheng F., Li H. and Yu J. (2004) Synhesis and properties of polyurethane resins based on liquefied wood. Journal of Applied Polymer Science 92: 351-356

Tohmura S., Li G. and Qin E. (2005) Preparation and characterization of wood polyalcohol-based isocyanate adhesives Journal of Applied Polymer Science 98: 791-795

Lee S.H., Ohkita T. and Teramoto Y. (2005) Polyol recovery from biomass-based polyurethane foams. Journal of Applied Polymer Science 95: 975-980

ASTM Standard D4274-05: Standard Test Method for Testing Polyurethane Raw Materials: Determination of Hydroxyl Numbers of Polyols: ASTM International, Pennsylvania, United States of America

Proceedings of the 10th International Chemical and
Biological Engineering Conference - CHEMPOR 2008
Braga, Portugal, September 4-6, 2008
E.C. Ferreira and M. Mota (Eds.)

Bioethanol production from sugars by yeast having sugar uptake ability by expression of sugar transporter

Takanori Tanino, Chiaki Ogino, Norihisa Kumagai, Naoto Ohmura *
Department of Chemical Science and Engineering, Graduate School of Engineering, Kobe University, 1-1 Rokkodaicho, Nada-ku, Kobe 657-8501, Japan

Keywords: *Saccharomyces cerevisiae*, bioethanol, transporter, xylose, xylose isomerase
Topic: Integration of life science & engineering

Abstract

We constructed *Saccharomyces cerevisae* strain with the xylose isomerase (XI) as the xylose metabolic pathway by multicopy integration of the XI overexpression cassette into the yeast genome. Resulting yeast MT8-1/XKSδXI successfully produced ethanol from xylose as the sole carbon source. Furthermore, MT8-1/XKSδXI strain could also produce ethanol from the mixture of glucose and xylose. These results indicated that MT8-1/XKSδXI strain could be applied to ethanol production from lignocellulose hydrolysate.

1 Introduction

Bioethanol production from lignocellulosic biomass, such as wood, is one way to avoid the problem of competition with food. Glucose and xylose are major components of the lignocellulosic biomass, and the efficient utilization of not only glucose but also xylose is advantageous for large-scale ethanol production. Since the wild type strain of *Saccharomyces cerevisiae* could not metabolite xylose, the engineering of recombinant strains having xylose metabolic pathway has been well investigated previously by various research groups. To be more precise, many research groups introduce xylose reductase (XR)-xylose-xylose dehydrogenase (XDH) as the xylose metabolic pathway. However, the difference of cofactor preference between XR and XDH frequently causes xylitol accumulation and limits the xylose metabolic flux (*Rizzi et al.*, 1989a, b, Toivari *et al.*, 2001). In this study, we selected xylose isomerase (XI) pathway and integrated XI overexpression cassette in yeast genome. The recombinant yeast strain having XI pathway was applied to the fermentation of ethanol from xylose and the mixture of xylose and glucose.

2 Materials and methods

Strains and media

Escherichia coli NovaBlue (Novagen Inc., Madison, WI.) was used as the host strain for recombinant DNA manipulation. *S. cerevisiae* MT8-1 (*MAT**a** ade his3 leu2 trp1 ura3*) (Tajima *et al.*, 1985) was used for introduction of xylose metabolic pathway and fermentation. *E. coli* was cultivated in Luria-Bertani (LB) medium (1% (w/v) tryptone, 0.5% yeast extract and 0.5% sodium chloride) containing 100 μg/ml ampicillin. Yeast was cultivated in YPD medium (1% (w/v) yeast extract, 2% peptone and 2% glucose) or SD medium (0.67% (w/v) yeast nitrogen base supplemented with appropriate amino acids and nucleotides and 2% glucose). For solid media, 2% (w/v) agar was added to the media described.

Construction of plasmids

The pLXKS for overexpression of *S. cerevisiae* xylulokinase (XK) *XKS1* was constructed as follows. A DNA fragment composed of the glyceraldehyde-3-phosphate

* Corresponding author. Tel + 81-78-803-6199. E-mail:ohmura@kobe-u.ac.jp

dehydrogenase (GAPDH) promoter, XK and GAPDH terminator from *S. cerevisiae* was prepared by polymerase chain reaction (PCR) with the following primers: SacII-pGAP (5'-ATTACCGCGGACCAGTTCTCACACGGAACACC-3') and tGAP-XhoI (5'-GCCCGCCTCGAGTCAATCAATGAATCGAAAATGTC-3'), with plasmid pWX1X2XK (Katahira et al., 2004) as template. The amplified fragment was digested *Sac*II and *Xho*I; it was inserted into *Sac*II and *Xho*I site of pRS405 (ATCC87516).

The pδWOXYLA1 for δ integration of XI from *Orpinomyces* sp. *OXYLA1* (under preparation) overexpression cassette into the yeast genome was constructed as follows. Three DNA fragments containing 167 bp of 5' region of□ sequence, 167 bp of 3' region of δ sequence and *TRP1* deficient marker (*TRP1*d) were amplified from the genome of *S. cerevisiae* BY4741 by PCR with the following primers: DS1-(F)-SacI (5'-ATGCGAGCTCTGTTGGAATAGAAATCAACT-3') and DS-167+AscI(R)-SacI (5'-GCATGAGCTCGGCGCGCCATGTTTATATTCATTGATCCTA-3'), DS168+AscI(F)-KpnI (5'-ATGCGGTACCGGCGCGCCATAAAATGATGATAATAATATT-3') and DS-334(R)-KpmI (5'-GCATGGTACCTGAGAAATGGGTGAATGTTG-3'), and TRP1d(F)-XhoI (5'-ATGCCTCGAGTGGAGTATGTCTGTTATTAA-3') and TRP1 (R)-XhoI (5'-GCATCTCGAGTGCAGGCAAGTGCACAAACA), respectively. The amplified fragments were digested *Sac*I, *Kpn*I and *Xho*I, respectively; they were sequentially inserted into *Sac*I, *Kpn*I and *Xho*I sites of pBluescript II KS+ (Agilent Technologies, Inc., Santa Clare, CA.). The resulting plasmid vector was named p□W. A DNA fragment composed of the GAPDH promoter, *OXYLA1* and GAPDH terminator was prepared by PCR with following primers: pGAP-SacI-F (5'-cggccgcggACCAGTTCTCACACGGAACACCACTAATGGA-3') and tGAP-NotI-R (5'-ATTTTAATGACATTTTCGATTCATTGATTGAgcggccgccgg-3') with plasmid pWOXYLA1 (under preparation) as template. The amplified fragment was digested *Sac*I and *Not*I site; it was inserted into *Sac*I and *Not*I site of pδW. The resulting plasmid vector was named pδWXI.

Yeast transformation

The expression plasmid pLXKS was digested with *Hpa*I at *LEU2* maker loci and transformed into *S. cerevisiae* MT8-1 cells using YEAST MAKER™ (Clontech Laboratories Inc.) according to the protocol specified by the supplier. The resulting transformant was named MT8-1/XKS. Subsequently, the expression plasmid pδWXI was also digested with *Asc*I and transformed into MT8-1/XKS using YEAST MAKER™. The resulting transformant was named MT8-1/XKSδXI.

Fermentation

The xylose-utilizing yeast MT8-1/XKSδXI was aerobically culticated in SDC medium (0.67% (w/v) yeast nitrogen base supplemented with appropriate amino acids and nucleotides, 0.5% glucose and 2% Casamino acids) for 48 h at 30°C. The cells were collected by centrifugation for 5 min at 3,000 x g and washed with distilled water twice. Two g wet cell weight of collected cells was inoculated into 50 ml of fermentation medium, containing 1% (w/v) yeast extract, 2% peptone and various concentrations of glucose and xylose. Ethanol fermentation was carried out in 100-ml closed bottles equipped with a bubbling CO_2 outlet. All fermentations were performed at 30°C with mild agitation. Ethanol and sugars were measured by HPLC analysis described in the next section.

HPLC analysis

HPLC analysis of fermentation medium was performed by using a refractive index detector (model RID-10A; Shimadzu, Kyoto, Japan). The column used for separation was a Shim-pack SPR-Pb column (Shimadzu). The HPLC apparatus was operated at 80°C with water at a flow rate of 0.6ml/min as the mobile phase.

3 Results

Fermentation from xylose

For introduction of the xylose metabolic pathway to the *S. cerevisiae* MT8-1 strain, one copy of XK overexpression cassette and multicopy of XI overexpression cassettes were introduced into the MT8-1 strain genome. To confirm the xylose fermentation ability, MT8-1/XKSδXI was applied to the fermentation from xylose as the sole carbon source without adaptation. Figure 1 shows the time course of the fermentation. MT8-1/XKSδXI consumed xylose and produced ethanol and byproduct, xylitol and glycerol. This result shows that MT8-1/XKSδXI have xylose fermentation ability. Ethanol productivity of up to 104 h of fermentation was 0.13 g per liter per h, and the ethanol yield was 0.30 g per g of xylose-consumed consumption.

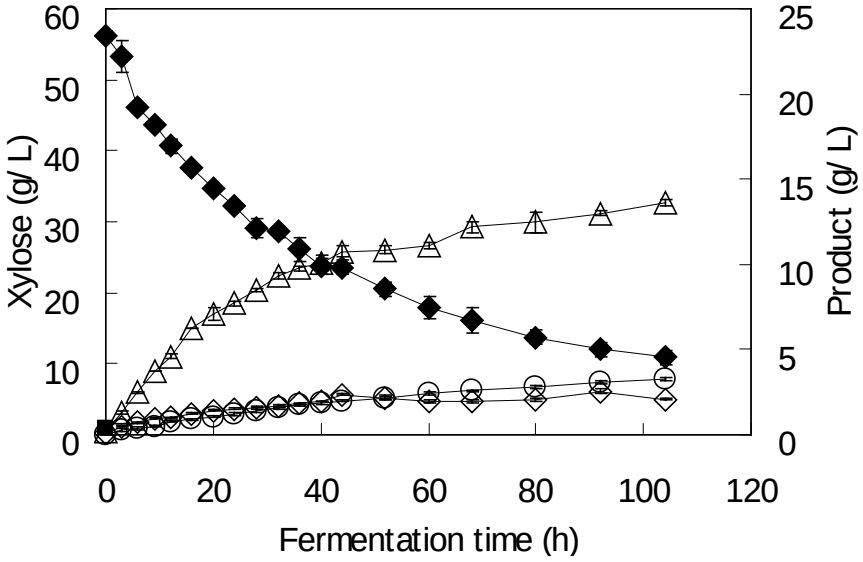

Figure 1. Time course of fermentation from xylose as the sole carbon source by MT8-1/XKSδXI. Xylose (closed diamonds), ethanol (open triangles), glycerol (open diamonds) and xylitol (open circles) contents were measured by HPLC.

Ethanol production in a mixed culture medium consisting of mixture of glucose and xylose

Figure 2 shows the time course of the ethanol production using MT8-1/XKSδXI strain in a mixed culture medium consisting of mixture of the same amount of glucose and xylose. Ethanol and byproduct productions from the mixed culture medium were observed. Ethanol production associated with the glucose consumption was rapidly finished (12 h). In contrast, ethanol production associated with the xylose consumption was slow, but comparably slow rate of ethanol production was observed.

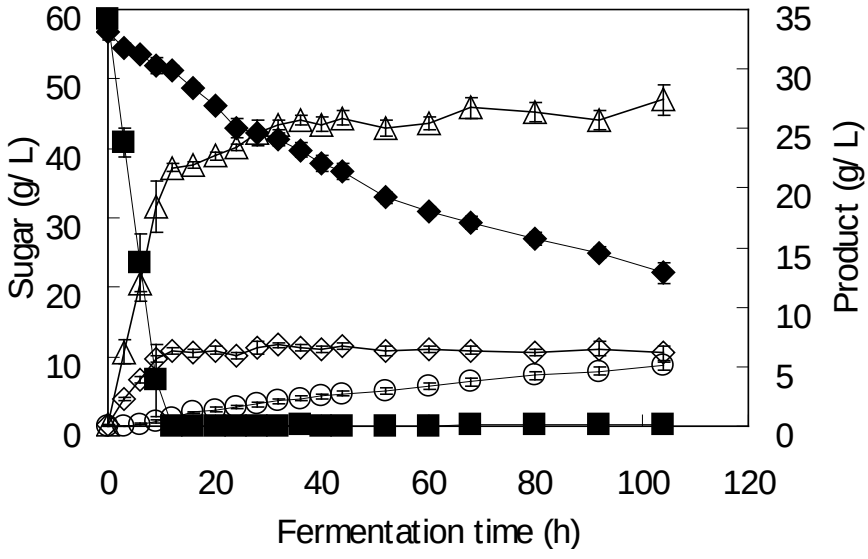

Figure 2. Time course of fermentation from mixture of glucose and xylose by MT8-1/XKSδXI. Glucose (closed squares), Xylose (closed diamonds), ethanol (open triangles), glycerol (open diamonds) and xylitol (open circles) contents were measured by HPLC.

4 Discussion

In the present study, we constructed xylose metabolic yeast with XI pathway by the multicopy integration of XI overexpression cassettes into the genome of *S. cerevisiae* MT8-1 strain. The resulting strain MT8-1/XKSδXI successfully produced ethanol from xylose as the sole carbon source without adaptation (Fig. 1). To the best of our knowledge, this is the first report of xylose metabolic *S. cerevisiae* with the XI pathway by the integration of XI expression cassette into the genome. However, the ethanol yield is very low and a relatively large amount of xylitol (0.07 g per g consumed xylose) was produced. The xylitol production results from the unspecific aldose reductase *GRE3*, and the deletion of *GRE3* is important for the decrease of xylitol production (Träff *et al.*). Kahumaa introduced *Piromyces* sp. XI into the TMB 3044 strain by multicopy plasmid and achieved the ethanol yield 0.43 g per g consumed xylose with 0.04 g per g consumed xylose (Kahumaa *et al*. 2007). The TMB 3044 strain contains deletion of *GRE3* and additional over expressed non-oxidative pentpse phosphate pathway (PPP) (Kahumaa et al. 2005). To achieve a higher ethanol yield in our XI integration system, these genetic modifications would be important.

MT8-1/XKSδXI strain could produce ethanol from the mixture of the glucose and xylose (Fig. 2). This result indicates that MT8-1/XKSδXI strain could be applied to ethanol production from lignocellulose hydrolysate.

Further research including study of the genetic modification of metabolic pathway and xylose uptake are under investigation.

References

Katahira, S., Fujita, Y., Mizuike, A., Fukuda, H., Kondo, A., (2004) Construction of a xylan-fermenting yeast strain through codisplay of xylanolytic enzymes on the xylose-utilizing *Saccharomyces cerevisiae* cells. *Applied and Environmental Microbiology*, 70, 5407-5414

Rizzi, M., Harwark, K., Erlemann, P., Buithanh N.A., Dellweg, H. (1998a) Purification and properties of the NAD+-xylitol dehydrogenase from the yeast *Pichia stipitis*. *Journal of Fermentation and Bioengineering*, 67, 20-24

Rizzi, M., Harqart, K., Buithanh N.A., Dellweg, H. (1989b) A kinetic-study of the NAD+-xylitol dehydrogenase from the yeast *Pichia pastoris*. *Journal of Fermentation and Bioengineering*, 67, 25-30

Tajima, M., Nogi, Y., Fukusawa, T. (1985) Primary structure of the *Saccharomyces cerevisiae GAL7* gene. *Yeast*, 9, 399-409

Träff, K.L., Otero Coedero, R.R., van Zyl, W.H., Hahn-Hägerdal, B. (2001) Deletion of the *GRE3* aldose reductase gene and its influence on xylose metabolism in recombinant strains of *Saccharomyces cerevisiae* expressing the *xylA* and *XKS1* gene. *Applied and Enviromental Microbiolgy*, 67, 5668-5674

Karhumaa, K., Garcia Sanchez, R., Hahn-Hägerdal, B., Gorwa-Grausland, M.F. (2007) Comparison of the xylose reductase-xylitol dehydrogenase and the xylose isomerase pathway for xylose fermentation by recombinant *Saccharomyces cerevisiae*. *Microbial Cell Factories*. 6, 5.

Karhumaa, K., Hahn-Hägerdal, B., Gorwa-Grauslund, M.F. (2005) Investigation of limiting metabolic steps in the utilization of xylose by recombinant *Saccharomyces cerevisiae* using metabolic engineering. *Yeast*. 22, 359-368

Proceedings of the 10th International Chemical and
Biological Engineering Conference - CHEMPOR 2008
Braga, Portugal, September 4-6, 2008
E.C. Ferreira and M. Mota (Eds.)

Nano and micro-biocatalysts manufacture and their impact on the synthesis of β-lactamic antibiotics

Susana M.S.A. Bernardino[1], Juan F.M. Gallegos[2], Filipa Maduro[2], Pedro Fernandes[2*], Joaquim M. S. Cabral[2], Luís P. Fonseca[2]

[1]ESTM – Escola Superior de Tecnologia do Mar, Instituto Politécnico de Leiria, 2524-909 Peniche, Portugal

[2] IBB – Institute for Biotechnology and Bioengineering, Centre for Biological and Chemical Engineering, Instituto Superior Técnico, 1049-001 Lisboa, Portugal

Keywords: Penicillin acylases, β-lactamic antibiotics, immobilization, sol-gel
Topic: Sustainable process-product development through green chemistry

Abstract

Biocatalysis presents a sound alternative to chemical synthesis in the field of drug production, given the highly selective nature of biological catalysts. The use of immobilized biocatalysts in antibiotic production is one of the most relevant. Penicillin G Acylase (PGA) from *E. coli* is currently used to hydrolyze penicillin G (PG) and catalyze the synthesis of β-lactam antibiotics. The enzymatic synthesis of these semi-synthetic antibiotics on a commercial basis is only feasible if immobilized biocatalysts are used, given the cost of enzyme production. In this work, particular emphasis is given to advances in penicillin G acylase immobilization by entrapment in a silica matrix with magnetic properties. A mechanically stable carrier based on porous xerogels silica matrixes, starting from tetramethoxysilane (TMOS), was produced. Diffusion limitations were minimized given the diameter (25 nm- 30 μm) of the nano- and micro-carriers obtained. Immobilization of PGA in these carriers allowed a protein immobilization yield of 95-100%, whereas the recovered activities were 50-65% at 37 ºC, as determined by PG hydrolysis (pH STAT method). These values of activity were kept constant during at least six months. Cephalexin (CEX) synthesis was performed at 14 ºC and pH 8.0, using the immobilized PGA in sol-gel in aqueous medium. Phenylglycine methyl ester (PGME) was used as acyl donor and 7-aminodeacetoxycephalosporanic acid (7-ADCA) was the limiting substrate at 30 mM. Cephalexin stoichiometric yield after 1 hour incubation was close to 65% (19 mM CEX/h), with respect to the limiting nucleophile. Immobilized PGA (682 U/g_{dry} at 37 ºC) retained high specific activity throughout 10 consecutive runs for penicillin G hydrolysis, suggesting adequate biocatalyst stability.

1. Introduction

Penicillins are the most widely used β-lactam antibiotics, but the excessive and too often inadequate use of these antibacterials has led to the development of resistant pathogens. Currently, the only method of overcoming the resistance problem is the use of newer semi-synthetic antibiotics. These penicillins (e.g. amoxicillin, ampicillin, ticarcillin) and cephalosporins (e.g. cephalexin, cefaclor, cefadroxil) correspond to 65% of the ever rising worldwide production

of antibiotics, exceeding 45000 tons in 2000 (Giordano et al., 2006).

The conventional processes of manufacturing these drugs demand harsh conditions. The industrial production of β-lactam antibiotics and their intermediates is, however, undergoing a remarkable transformation where the traditional chemical conversions based on stoichiometry are being replaced by enzyme-catalyzed processes – the so-called "green chemistry" approach. In contrast to the complex solvent-based chemical approach, the one-step enzymatic conversion is regio-and stereo-specific and can be performed under mild conditions (Kim and Lee, 1996).

Penicillin acylases (PACs) (penicillin amidohydrolase, EC 3.5.1.11) are a group of enzymes which are mainly involved in the industrial synthesis of semi-synthetic β-lactam antibiotics and production of 6-aminopenicillanic acid (6-APA), 7-aminodesacetoxycephalosporanic acid (7-ADCA) or 7-aminocephalosporanic acid (7-ACA). The application of PAC in the production of β-lactam antibiotics has been extensively studied by many research groups (Alkema et al., 2002, 2003; Alvaro et al., 1990; Guisan et al., 1998; Grooten et al., 1998; Fernandez-Lafuente et al., 1998; Hernandez-Justiz et al., 1998; Kasche et al., 1986; Kim and Lee, 1996a,b; Svedas et al., 1996; van Langen et al., 1999; Youshko et al., 2000, 2004). PAC is a heterodimeric protein synthesized as an inactive preprotein that contains a leader peptide and a spacer peptide separating the α- and β- subunits. The PAC enzyme belongs to the family of N-terminal nucleophile (Ntn) hydrolases, a class of enzymes that have a catalytic nucleophile at the N-terminal position and a fold around the active site consisting of a four layered catalytically active αββα-core. This core is comprised of two anti-parallel β-sheets packed against one another and covered by a layer of anti-parallel α-helices. In PAC the catalytic nucleophile is an N-terminal serine of the large β-subunit. PAC from *Escherichia coli* is the most studied and used enzyme for commercial purposes (Serenovic et al., 2005). Although PACs have proved effective in their role, better biocatalysts and higher yields than those actually obtained are required (Illanes et al., 2004).

In semi-synthetic antibiotic production, synthesis can be performed under thermodynamic or kinetic control. In both cases the reduction of water activity in the reaction medium will improve it, by displacing the equilibrium towards synthesis (Illanes et al., 2007).

The first strategy considers the direct condensation of the nucleophile and the acyl donor. Non-ionic forms of the substrates are required for the condensation reaction, so that pH will be an important variable in this strategy by altering the ionic equilibrium of the nucleophile and the acyl donor by the substrates. In this strategy, the yield is determined by the thermodynamic equilibrium of the reaction (which is largely independent of the biocatalyst used) and drastic conditions are usually required to displace it in favor of synthesis, so that very robust biocatalysts are required to perform adequately (Schröen et al., 2001).

Synthesis under kinetic control requires an activated acyl donor, in the form of an ester or an amide. It is usually a better strategy when product yield is the main goal, since product concentration is not limited by the equilibrium of the reaction. In kinetically controlled synthesis of β-lactam antibiotics, the reaction of synthesis (synthetase activity) will occur simultaneously with the hydrolysis of both the activated acyl donor (esterase activity) and the antibiotic product (amidase activity). Yields will be favored by reducing water activity, since the rates of the hydrolytic reactions will be reduced (Illanes et al., 2004,2007).

The advantages of using immobilized PGA over the soluble form, e.g., easier handling of the

biocatalyst, facilitated separation of the biocatalyst from the product, lesser product contamination, possible continuous use or re-use of the biocatalyst and enhanced stability and productivity, allow for significant cost saving in the production. However, immobilization brings along some drawbacks, such as loss of activity upon immobilization and diffusion limitations, which reduce the productivity of the immobilized enzyme system (Schroën et al., 2001).

A relatively recent approach for enzyme immobilization is based in the sol-gel process, which allows the room temperature synthesis of silica glasses, although suitably modified to exclude the typical harsh conditions that would cause enzyme denaturation. The concomitant material offers the same beneficial properties as traditional silica based matrices and allows a high biocatalyst load, since the enzyme is entrapped within the polymeric matrix as it forms (O'Neil et al., 2002).

A well-established sol-gel processing technique consists of hydrolyzing the adequate precursors in aqueous solutions to produce soluble hydroxylated monomers, followed by polymerization and phase separation to produce a hydrated metal or semi-metal oxide hydrogel. Removal of water from the wet gel, which is usually accompanied by changes in the structure of the pores and of the gel network, results in a porous xerogel. The most widely used precursors are alkyl-alkoxysilanes (Reetz et al., 1998).

Such materials offer the same beneficial properties as traditional silica based matrices. However, the amount of enzyme that can be immobilized is not limited by the available surface area on the matrix, because the enzyme is also entrapped within the polymeric matrix as it forms and becomes homogeneously throughout the material (O´Neil et al., 2002). This method has been employed for entrapment of a wide range of enzymes, antibodies, and whole cells.

The aim of this study was the development of a suitable methodology for the immobilization of PGA in a sol-gel silica matrix with magnetic properties and the concomitant application of this new biocatalyst on cephalexin synthesis.

2. Material and Methods

PGA solution (26.6 mg mL^{-1}, 35 U mg^{-1}) from *Escherichia coli*, tetramethoxysilane (TMOS), sodium dioctyl sulfosuccinate (AOT), magnetite nanopowder, were all purchased from Sigma-Aldrich. Isooctane was supplied from Riedel de Haën. Penicillin G was obtained from Fersinca Gb. All other reagents used were either laboratory or analytical grade.

Enzyme assay and Operational stability- pH STAT method

One unit of PGA activity (U) for the soluble and immobilized enzymes is defined as the amount of enzyme required to produce 1 μmol of 6-APA (6-Amino Penicillanic Acid) per minute. Enzyme activity was determined in a small batch stirred reactor with automatic pH correction by the pH STAT method (Cardoso and Costa, 1986), using a 4% (w/v) penicillin solution in 0.02 mol dm^{-3} pH 8.0 phosphate buffer at 37ºC. To evaluate the operational stability of the biocatalyst, Penicillin G hydrolysis was performed during 10 minutes at 37 ºC and pH 8.0 (pH STAT method), using the immobilized PGA in sol-gel in aqueous medium.

Assay for protein concentration

The concentration of protein in the enzyme solution before immobilization and in the supernatant and washings, after immobilization, was determined through mass quantification

based on a calibration curve of PGA absorbance at 280 nm. The amount of protein linked to the support was calculated by mass balance.

Activity retention

The percentage of activity retention was calculated as the ratio between the specific activities of the enzyme immobilized on the support and of the free enzyme solution.

Sol-gel

A solution containing 100 μL TMOS (2.32 mol dm^3) and 40 μL HCl (1.37 mmol dm^3) was sonicated in a Transsonic T 460 sonicating water bath for 10 min until the hydrolysis reaction was complete. In a typical immobilization procedure, 75 μL of PGA was suspended in 85 μL of magnetic suspension -10% (w/v) in 100 mmol dm^{-3} phosphate buffer, pH 7.5 - and the whole was mixed with the sol solution. To obtain micro-particles and minimize diffusion limitations, 300 μL of the sol-gel solution with enzyme was immediately added to 6 mL of 150 mmol dm^{-3} AOT/isooctane solution, before gelation. The resulting mixture was placed under vortex for 2 min, washed twice with 100 mmol dm^{-3} phosphate buffer, pH 7.5 and aged at 2-8 ºC during one week. The micro-particles obtained were suspended in 1 mL of the same phosphate buffer. The particles are either used or stored at 2 – 8 °C.

SEM

Dry particles of biocatalyst were put on a double carbon tape and analyzed in a Field Emission Scanning Electron Microscope (Jeol JSM-7001F).

Analysis

Substrates (7-ADCA and PGME) and products (CEX and PG) of synthesis were identified and analyzed by HPLC using a Merck Hitachi delivery system L-6000 with a Perkin Elmer LC 90 UV UV-vis detector and a Merck Hitachi D-2500 (Chromato-Integrator) integrator. The column used was a ChromSpher 5 C18 S250x4.6 from Varian. Samples were eluted isocratically with a mixture of 40% (v/v) acetonitrile, 60% (v/v) 5 mM phosphate buffer and 0,2% (m/v) SDS, pH 3.1, at a flow rate of 1 $mL.min^{-1}$, and analyzed in the UV detector at 214 nm. Elution times were 3.21, 3.91, 8.61 and 10.85, for PG, 7-ADCA, CEX and PGME, respectively. Concentration of substrates and products were calculated from calibration curves using stock solutions with internal standard (acetaminophen).

Synthesis of CEX with immobilized PGA

Synthesis of CEX was performed in temperature controlled, magnetically stirred reactors with 10 mL of reaction medium. Substrate concentrations were 30 mM 7-ADCA, and 90 mM PGME. 20 mg of biocatalyst per mL of reaction, corresponding to 97 U/mmol 7-ADCA, were used). The reaction was performed at 14 ºC and pH 8.0. During synthesis, pH and temperature were monitored and samples were taken to analyze product and substrates to determine yield and volumetric productivity. Yield was defined as the maximum molar conversion of 7-ADCA into CEX (%) and productivity as the amount of cephalexin produced per unit time and unit reaction volume at maximum yield ($mM.h^{-1}$). Specific productivity was determined per gram of dry biocatalyst ($mM.h^{-1}g^{-1}$). Experiments have variations below 5% among them.

3. Results and Discussion

In this work, particular emphasis was given to advances in penicillin G acylase immobilization by entrapment in a silica matrix with magnetic properties. Mechanically stable xerogel carriers

containing magnetite were produced from tetramethoxysilane (TMOS), to yield an immobilized biocatalyst in the form of nano- and micro-carriers, with sizes roughly ranging from 25 nm to 30 μm, as determined by SEM. A typical SEM micrograph of micro-carriers is given in figures 1 and 2. The presence of magnetite considerably eased the recovery of the biocatalyst, from the reaction media, through the use of a magnetic concentrer (figure 3).

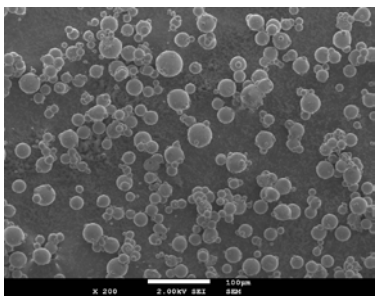

Figure 1: SEM micrograph of the sol-gel matrices (micro-particles) with encapsulated magnetite and PGA (bar match 100 μm).

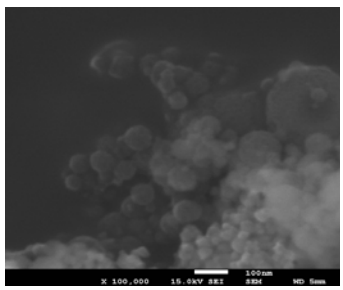

Figure 2: SEM micrograph of the sol-gel matrices (nano-particles) with encapsulated magnetite and PGA (bar match 100 nm).

Figure 3: Magnetic particles recovery on a magnetic concentrer.

Immobilization of PGA in these carriers allowed for an immobilization yield of 95-100%, whereas the recovered activity was 45-70% at 37 ºC, as determined by the pH STAT method, depending on aging. This clearly exceeds results reported in a previous work on PGA immobilization in sol-gel where only 10 % of activity was recovered (Kallenberg et al., 2005). Temperature and pH dependency are similar to soluble and immobilized PGA. The energy of activation also remained roughly unchanged following immobilization, for 10.5 and 10.8 kcal mol^{-1}, for soluble and immobilized enzyme, respectively, were determined from Arrhenius plots. The enzyme can carry out hydrolytic and synthesis reactions efficiently, in aqueous media (Figures 4 and 5).

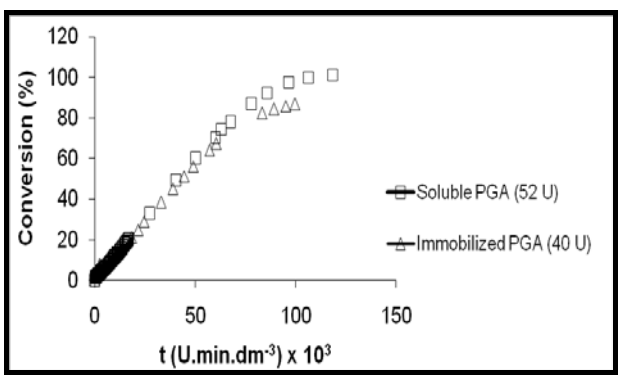

Figure 4: Penicillin G hydrolysis (pH STAT method). T = 37 °C; pH = 8.0; Penicillin G = 4% (m/v); 20 mM phosphate buffer (microparticles).

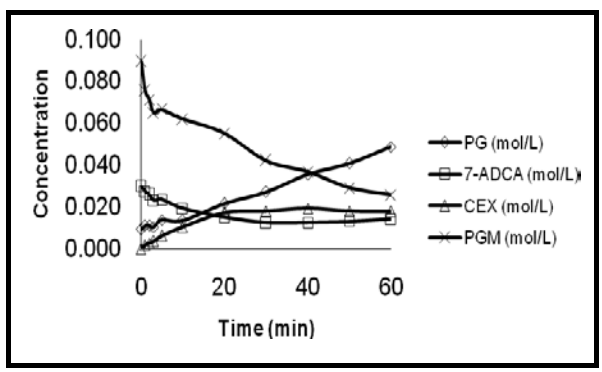

Figure 5: Cephalexin synthesis. T = 14 ºC; pH = 8.0; 29 U; reaction medium = 10 mL Y = 65%; P = 19 $mM.h^{-1}$; P_{sp} = 95 $mM.h^{-1}.g^{-1}$ (microparticles).

Immobilized PGA retained 65% specific activity throughout 10 consecutive runs for penicillin G hydrolysis (data not shown) suggesting adequate biocatalyst stability.

At low substrate concentrations (30 mM 7-ADCA, 90 mM PGME) and low enzyme load (97 $U.mmol^{-1}$ 7-ADCA) a maximum conversion yield of 65% was obtained with a productivity of 19 $mM.h^{-1}$ and a specific productivity of 95 $mM.h^{-1}.g^{-1}$. Illanes et al. (2005) obtained a similar result

for specific productivity (93 $mM.h^{-1}.g^{-1}$) but in organic medium at high substrate concentrations (150 mM 7-ADCA; 450 mM PGME) and low enzyme load (80 $U.mmol^{-1}$ 7-ADCA). The results obtained are thus encouraging and are likely to allow for substantial process improvement in terms of costs and environment.

4. Conclusions

Enzyme immobilization was carried out using penicillin G acylase from *Escherichia coli* in a silica xerogel matrix with magnetic properties. The enzyme is catalytically active and can carry out hydrolytic and synthesis reactions efficiently, but it is necessary to optimize the synthesis reaction conditions in order to depress hydrolytic activity. To prevent some biocatalyst degradation caused by dissolution and abrasion of magnetic agitation, novel developments such design and project an enzymatic reactor compatible with the developed magnetic biocatalysts are being tested, aiming to develop a system in which the biocatalyst can be recycled many-fold, a mandatory feature to render enzymatic catalysis economically feasible.

5. References

Giordano, R.C., Ribeiro, M.P.A, Giordano, R.L.C. (2006). Kinetics of b-lactam antibiotics synthesis by penicillin G acylase (PGA) from the viewpoint of the industrial enzymatic reactor optimization. *Biotecchnol Adv* 24:27-41.

Illanes, A., Anjarí, M.S., Altamirano, C., Aguirre, C. (2004). Optimization of cephalexin synthesis with immobilized penicillin acylase in ethylene glycol mediun at low temperatures. *Journal of Molecular Catalysis B: Enzymatic* 30: 95-103.

Illanes, A., Wilson, L., Altamirano, C., Cabrera, Z., Alvarez, L., Aguirre, C. (2007). Production of cephalexin in organic medium at high substrate concentrations with CLEA of penicillin acylase and PGA-450. *Enzyme and Microbial Technology* 40:195-203.

Kallenberg, AI, van Rantwijk, .F; Sheldon, R.A. (2005). Immobilization of Penicillin G Acylase: The key to optimum performance. *Adv. Synth. Catal.* 347:905-926.

Kim, M.G., Lee, S.B. (1996). Penicillin acylase-catalyzed synthesis of pivampicillin: effect of reaction variables and organic cosolvents. *Journal of Molecular Catalysis B: Enzymatic* 1: 71-80.

O´Neil, H., Angley, C.V., Hemery, I., Evans, B.R., Dai, S., Woodward, J. (2002). Properties of carbohydrate-metabolizing enzymes immobilized in sol-gel beads: stabilization of invertase and β-glucosidase by blue dextran. *Biotechnology Letters* 24:783-790.

Reetz, M.T., Zonta, A., Vijayakrishnan, V., Schimossek, K. (1998). Entrapment of lipases in hydrophobic magnetite-containing sol-gel materials: magnetic separation of heterogeneous biocatalysts. *Journal of Molecular Catalysis A: Chemical* 134: 251-258.

Schroën, C.G.P.H., Eldin, M.S.M., Janssen, A.E.M., Mita, G.D., Tramper, J. (2001). Cephalexin synthesis by immobilised penicillin G acylase under non-isothermal conditions: reduction of diffusion limitation. *Journal of Molecular Catalysis B: Enzymatic* 15:163-172.

Serenovic, L., Stankovic, N., Spizzo, P., Basso, A., Gardossi, L., Vasiljevic, B., Ljubijankic, G., Tisminetzky, S., Degrassi, G. (2005). High-level production and covalent immobilization of *Providencia rettgeri* Penicillin G Acylase (PAC) from recombinant *Pichia pastoris* for the development of a novel and stable biocatalyst of industrial applicability. *Wiley InterScience* 344-354.

Proceedings of the 10th International Chemical and
Biological Engineering Conference - CHEMPOR 2008
Braga, Portugal, September 4-6, 2008
E.C. Ferreira and M. Mota (Eds.)

Integration of bioprocesses in polyesters microbial synthesis

Anabela S. Antunes, Jorge M.S. Rocha*
CIEPQPF, Chemical Engineering Department, Faculty of Science and Technology,
University of Coimbra, Rua Sílvio Lima, 3030-790 Coimbra, Portugal

Keywords: polyhydroxyalkanoates, PHB, *Ralstonia eutropha*, biopolymers
Topic: Integration of life sciences & engineering.

Abstract

Several fermentation conditions were studied to optimize the biological production of polyester by *Ralstonia eutropha* and its posterior extraction. The highest biopolymer concentration obtained was 11 g L^{-1} in fermentor and 7.5 g L^{-1} in Erlenmeyer flasks. Both culture systems showed similar yields but higher productivity in fermentor, in fed-batch operation with a glucose concentration not higher than 10 g L^{-1} (seven supplies of glucose). Oxygenation rate must be low and pH close to neutral is advantageous. Cane molasses were shown to be a good substrate because of the price and its natural buffer ability. The adaptation lag phase of *R. eutropha* can be reduced if molasses are pre-treated by a biocatalytic hydrolysis driven by yeast cells at 45ºC, in bioprocess integration. Polymer extraction by ethanol precipitation favours the selective separation of large polymeric chains.

1. Introduction

The production of environmentally friend ecological plastics, since its manufacture from renewable raw materials till its degradation by biological processes, taking in mind that Nature always knows how to recycle what it is able to synthesize, it is a main contribution to mankind sustainability. The biocompatibility of natural materials enlarges their application to medicine, agriculture, food industry and other quotidian uses. The challenge is to explore Nature gifts without degrading its quality level, creating conditions to biological production in large scale, and economically competitive with traditional chemical synthesis. The polyesters from polyhydroxyalkanoates family (PHAs) are biopolymers that can be processed and used as a change of common petrochemical based plastics (Choi and Lee, 1997). They play the role of reserve compounds in many bacterial strains, such as *Ralstonia eutropha*, and their biosynthesis can be stimulated in fed-batch fermentation, under appropriate incentives and driven stress conditions, like the limitation of an essential growth nutrient and the excess of a carbon and energy source (Braunegg et al., 1998). These biopolymers are produced as discrete inclusions localised in the cell cytoplasm of the fermentative microorganism, being *R. eutropha* the most widely chosen bacterium due to its ability to accumulate large amount of poly-3-hydroxybutyrate (PHB), a particularly PHA, from simple carbon sources, such as glucose or fructose (Khanna and Srivastava, 2005). The large scale production of biopolymers still has several bottlenecks to be overtaken (Luengo et al., 2003) being so far their commercialization strongly limited by high production costs compared with the oil-derived plastics. Their net price is indeed extremely affected by the costs of substrates and by downstream procedures. Therefore, efforts have been made to reduce the production costs through the development of genetic modified bacterial strains, more efficient fermentation strategies using inexpensive and renewable substrates (*e.g.* molasses, sucrose, lactose or glycerol) and more effective downstream processing methods, allowing high levels of productivity and yield (Khanna and Srivastava, 2005). Although a great demand of new and more ecological extraction processes, PHA's are mostly separated from

* Corresponding author. Tel + 351-239-798731. E-mail:jrocha@eq.uc.pt

the producing cells by using solvents or mixtures of them that are toxic to the environment. The non-polymer cell material is degraded by acetone or alcohols, and the polymer, once liberated, is dissolved in chloroform or other chlorinated hydrocarbons, which can be separated from the solvent by evaporation or precipitation, using a polymer non solvent, usually an alcohol (Braunegg et al., 1998).

The large number of references found in literature, but the shortage of new experimental results, led to a set of experiments to test or confirm the effect of several factors in the production of PHB. The aim of this work was to study the fermentation of residual carbon sources and to improve the polymer extraction methods, optimizing the operational conditions in order to achieve high values of productivity and yield.

2. Material and methods

2.1 Microorganism and media

Ralstonia eutropha (DSM 545) was grown on agar slants and kept at 4ºC. The growth medium consisted of **a)** 4.5 g L^{-1} Na_2HPO_4, 1.5 g L^{-1} KH_2PO_4, **b)** 2.5 g L^{-1} $(NH_4)_2SO_4$, 0.2 g L^{-1} $MgSO_4.7H_2O$, **c)** 0.05 g L^{-1} Citrato-NH_4-Fe(III), 0.02 g L^{-1} $CaCl_2.2H_2O$, 0.1 mL trace metal solution and **d)** 10 g L^{-1} glucose. The trace metal solution was prepared with 3 g L^{-1} H_3BO_3, 2 g L^{-1} $CoCl_2.6H_2O$, 1 g L^{-1} $ZnSO_4.7H_2O$, 0.3 g L^{-1} $MnCl_2.4H_2O$, 0.3 g L^{-1} $Na_2MoO_4.2H_2O$, 0.2 g L^{-1} $NiCl_2.6H_2O$ and 0.1 g L^{-1} $CuCl_2.2H_2O$. Solutions a), b), c) and d) were sterilized separately in autoclave to avoid the medium composition degradation.

Liquid media for polymer production were prepared with the same mineral salt composition, varying the carbon source supplied. Cane molasses, sucrose and glucose with initial concentrations in the range 10-40 g L^{-1} were used as carbon source.

2.2 Fermentation conditions

2.2.1 Erlenmeyer flasks

Fed batch fermentations were carried out in 500 mL Erlenmeyer flasks (working volume 200-400 mL), at an orbital incubator (30 ºC;100-125 rpm). 10 mL of fresh inoculum, previously prepared under the same conditions, was used. Additional carbon source was supplied when necessary, to guarantee an excess to stimulate PHB production (trying to regain the initial composition).

In Erlenmeyer flasks the oxygen supply is just by air diffusion through the cotton stopper. In order to evaluate the effect of air accessibility, a set of fermentations with different medium volumes (200, 300, 400 mL) were carried out. The larger the medium volume (consequently smaller the superficial area in the conic flasks), the lower was the oxygenation of the microbial cells.

Mineral salts and the carbon source were dissolved in water (with and without some rough pH adjustment with NaOH 1M), and in buffers like Tris-HCl (0.1, 0.3 and 0.6 M) and HEPES, to provide a buffer environment to the bacterial metabolism.

In a set of assays, cane molasses were previously submitted to a biocatalytic hydrolysis by the action of *Saccharomyces* yeasts (making use of their intracellular enzyme invertase). The biocatalytic hydrolysis of cane molasses was realized by yeasts from a two days culture of 150 mL of a standard yeast growth medium (yeast extract 3 g L^{-1}, malt extract 3 g L^{-1}, peptone 5 g L^{-1} and glucose 10 g L^{-1}) at 30ºC and 125 rpm, that were centrifuged and added to 200 mL of cane molasses solution (100 g L^{-1}, that is equivalent to 50 g L^{-1} of sucrose) and kept in an orbital incubator at 45ºC for 2 h. After the molasses sucrose hydrolysis the suspension was centrifuged to remove the yeast cells (that can be reused) and the hydrolysate liquid was used as carbon source for *R. eutropha* growth. One volume of this sterilized hydrolysate was added to four volumes of the above described growth medium

(without carbon source) and also previously sterilized. This means a dilution 1:5 of molasses solution that was compared with non hydrolysed equivalent molasses solution of 20 g L^{-1}.

2.2.2 Fermentor

Fed-batch fermentation was also carried out in a Biostat® Bplus 5 LCC fermentor, with 5 L of working volume (B. Braun Biotech International, Germany). pH was set at 7.0 and automatically controlled by addition of NaOH 1M and H_2SO_4 1M. Air flow rate was adjusted manually by the air flow valve and the rotameter. Liquid volume was 3 L and culture was done at 30 ºC and 150 rpm (mechanical stirring).

2.3 Extraction methods

Culture broth was centrifuged (3500 rpm, 20 min) to separate the cells that were afterwards mixed with pure acetone, in order to degrade the non-polymer cell material. This suspension was stirred for 24 h at room temperature, filtrated under vacuum and the cellular residues were kept. Chloroform was added to the cellular residues, and the suspension was kept at room temperature in a well closed recipient under constant and magnetic stirring for 24 h, to promote the polymer dissolution in the organic solvent. The cellular residues were removed by filtration and the organic phase with the dissolved polymer was kept. Three procedures were tested to separate PHB from the organic solvent: i) chloroform evaporation, where the solution was submitted to a natural evaporation process; ii) chloroform distillation, where the solution was distilled permitting the chloroform recovery; and iii) ethanol precipitation, where ethanol was slowly added to the solution, acting as a counter solvent and thus promoting the polymer precipitation (the mixture was then filtrated and the polymer recovered).

2.4 Analytical methods

Cell growth was monitored by measuring the optical density of cells suspension at 540 nm on a Beckman D.U. 650 spectrophotometer, after suitable dilution with distilled water. Cell mass concentration was determined by standard plot between optical density and dry cell mass. Cells suspension was centrifuged, washed with water and dried till constant weight. Glucose, sucrose and cane molasses were evaluated by a colorimetric method for total sugars, using phenol and sulphuric acid (485 nm). Glucose and reducing sugars present in cane molasses were also determined by the dinitrosalicylic acid (DNS) method, measuring the optical density at 540 nm. After its removal the biopolymer mass was evaluated and the product was analysed by an infra-red spectroscopy method (FTIR). Its molecular weight was determined by a viscosimetric method, using an Ubbelohde nº1 viscometer.

3. Results and discussion

The use of cheap substrates as carbon source, the increase of their yield conversion into polymers, the use of simple fermentation systems and the development of more efficient and ecological extraction methods, will be the main items to make bioplymers production economically competitive. Simple reaction systems were carried out with *Ralstonia eutropha*, always with the purpose of reducing overall costs of the production process. The temperature control and the culture medium homogenization were relatively easy to achieve, either in small and simple scale, like Erlenmeyer flasks in an orbital incubator, or in larger scale in (more or less sophisticated) fermentor.

PHB production was obtained in all assays, although the productivities and yields varied, as a consequence of changing the operational variables, such as the type of carbon source and its initial concentration, the pH value of the culture, the oxygen supply, and the pretreatment of residual substrates, which affected the metabolic activity of the bacteria. Productivities were reported to the period of polymer accumulation; yields have the mean of real yields, that is, reported to consumed (and not supplied) carbon source.

3.1 The effect of oxygenation

The effect of oxygen in PHB production was initially studied in Erlenmeyer flasks (500 mL capacity). The oxygen supply is simply provided by superficial diffusion of air through the cotton stopper. The availability of oxygen to the cells was changed by varying the working volume in the Erlenmeyer flasks. The higher the culture volume (consequently lower

superficial area), the less was the oxygen supplied to the cells. Table 1 shows the PHB concentration achieved in the fermentation of different initial culture volumes, as well as the corresponding productivity and yield. In the assay D, the culture broth was transferred to an Erlenmeyer flask with a lower capacity (250 mL) after the exponential growth phase and at the beginning of PHB accumulation phase, reducing the superficial area and thereby the air supply.

Table 1. The effect of oxygen supply rate by air superficial diffusion (initial concentration of glucose 10 g L^{-1}, 100 rpm, no pH adjustment, additional supply of glucose)

	A	B	C	D
Volume (mL)	200	300	400	200
PHB conc. (g L^{-1})	0.67	1.42	2.31	1.15
Productivity (g_{PHB} $L^{-1}h^{-1}$)	0.0143	0.0189	0.0257	0.0247
Yield ($g_{PHB}/g_{glucose}$)	0.0733	0.136	0.374	0.1187

The highest PHB concentration, productivity and yield were obtained in assay C, showing the advantage of lower oxygenation rates. In fed-batch D, where the reduction of oxygenation was introduced in PHB production stage, the PHB concentration obtained was higher and productivity and yield almost doubled, when compared to the values registered in assay A where no change of oxygenation was induced. These evidences may have practical advantages in simple reaction systems (it is well known the difficulty to supply enough oxygen to aerobic cultures). Comparing assays C and D it is also evident that oxygen restriction must occur since the fermentation beginning.

3.2 The effect of pH

Cell growth and polymer accumulation are favored by pH close to neutral. The best results were obtained when pH 7 was kept constant during the fermentation either roughly by adding manually NaOH 1M in assay J or automatically in the fermentor (Table 2). The use of buffers was not very efficient in pH control, except with Tris-HCl 0.6 M. However, the presence of a foreign compound in the culture did not favor the polymer productivity. Better results were achieved with cane molasses as carbon source due to their natural buffer effect.

Table 2. The effect of culture pH (initial concentration of glucose 10 g L^{-1})

	E	F	G	H	I	J	Fermentor
Buffer Solution	Water	Tris-HCl 0.1 M	Tris-HCl 0.3 M	Tris-HCl 0.6 M	HEPES 0.1 M	NaOH	NaOH/H_2SO_4
PHB conc. (g L^{-1})	0.55	0.76	0.74	1.57	0.63	7.54	10.9
Productivity (g_{PHB} $L^{-1}h^{-1}$)	0.022	0.056	0.0077	0.0043	0.0209	0.0279	0.1344
Yield ($g_{PHB}/g_{glucose}$)	0.056	0.056	0.045	0.031	0.053	0.2292	0.2601

3.3 The effect of carbon source type and concentration

The kinetic of cell growth and biopolymer production is dependent from the type and concentration of carbon source used. Glucose is the easiest sugar for cells to metabolize but both very low and very high glucose concentration can inhibit the cell metabolism. According to Table 3 initial glucose concentrations in the range 20-40 g L^{-1} (also being the limit in glucose additions) lead to good results on PHB production. The highest molecular weight of polymer obtained (1.8×10^6 Da) was coming from this range of glucose supply. Sucrose, as a disaccharide, either purified or as the main component of cane molasses (residual carbohydrates from sugar industry) can be directly used by *R. eutropha*, with similar polymer production from the same amount of sugar supplied. However, a longer adaptation phase

was observed. In fact, the use of cane molasses is advantageous since they are less expensive and, on the other hand, the culture pH is much more stable, compared to glucose as carbon source, where the pH decrease deeply from 7 to 3-4, and this is not good for polymer production, as reported above.

Table 3. The effect of carbon source concentration (volume 400 mL, 125 rpm, no pH adjustment; additional supply of glucose in assays K and L when its concentration was reduced to zero)

	K	L	M
$[Glucose]_{initial}$ ($g\ L^{-1}$)	10	20	40
PHB conc. ($g\ L^{-1}$)	4.73	7.75	6.2
Productivity ($g_{PHB}\ L^{-1}h^{-1}$)	0.02363	0.0484	0.0620
Yield ($g_{PHB}/g_{glucose}$)	0.1382	0.2194	0.1721

3.4 Biocatalytic hydrolysis integration

A better profit of cane molasses can be made by a previous biocatalytic treatment, using *Saccharomyces sp*. yeasts, with the aim of hydrolysing the sucrose content into reduced sugar, easier to ferment by the bacteria. In fact, at 45ºC the yeasts are not able to reproduce, but their intracellular invertase is active for hydrolysis. The time evolution of this pre-treatment was followed by the DNS method. The reduced sugar content increased till a plateau was reached at 120 min. Table 4 and Figure 1 show the advantages of reducing the lag phase of the bacterial culture and to increase the biopolymer productivity, without a significant reduction of the molasses natural buffer ability. Cane molasses do not need to be sterilized before hydrolytic treatment with yeast cells (a very high concentration of yeasts and a high temperature are enough to avoid contamination).

Table 4. The effect of pretreatment with yeasts over molasses (previously sterilized or not) on polymer production; conditions described in Material and Methods.

	N	O	P
Carbon Source	**Cane Molasses (non hydrolysed)**	**Cane Molasses (sterilized and hydrolysed)**	**Cane Molasses (non sterilized but hydrolysed)**
PHB conc. ($g\ L^{-1}$)	0.13	2.01	2.19
Productivity ($g_{PHB}\ L^{-1}h^{-1}$)	-----	0.0111	0.0177
Yield ($g_{PHB}/g_{glucose}$)	-----	0.1088	0.1663

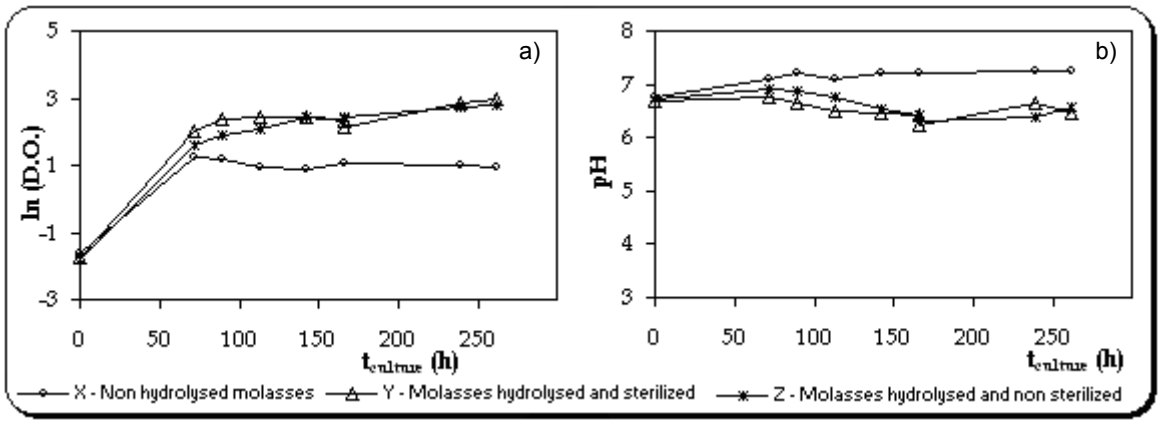

Figure 1. Profiles of a) *R. eutropha* growth and b) pH during fermentation, of non-hydrolysed molasses and hydrolysed molasses (previously sterilized or not).

3.5 Biopolymer extraction

PHB recovery was more efficient when using chloroform, followed by the organic solvent evaporation, or by ethanol precipitation. The mass of polymer obtained by the two methods was similar, but the latter is more advantageous because it is possible to recover both chloroform and ethanol by distillation. Polymer characterization was made by viscosimetric evaluation of molecular weight, making use of Mark-Houwink equation (Figure 2a)) and by FTIR, where the ester bond peak at *c.a.* 1750 cm^{-1} is well evident (Figure 2b)). Molecular weights were greater for polymers recovered by ethanol precipitation, when compared to the fraction recovered by chloroform evaporation. This fact must be ascribed to the loss of small polymeric chains that do not precipitate with ethanol, while in chloroform evaporation all molecular weight range of chains is recovered. So, ethanol precipitation induces a selective extraction of the largest polymeric chains.

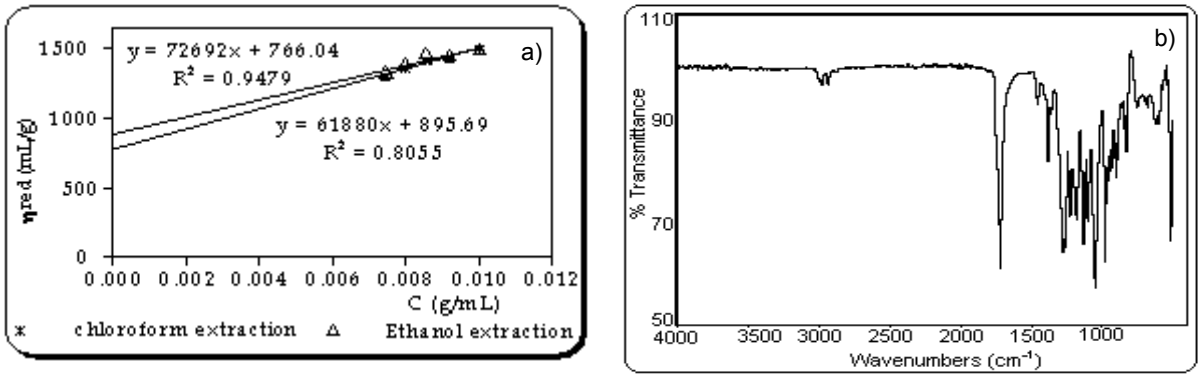

Figure 2 - Characterization of PHB polymer after its recovery by a) viscosimetric determination of molecular weights and b) FTIR.

4. Conclusions

Although cell densities achieved in this work had been quite low, probably due to a nitrogen limitation, with the consequence of low polymer productivities, some insight with practical application was obtained. The need of a low oxygenation rate, the adverse effect of pH reduction during the fermentation, that can be diminished by using cane molasses (a cheap substrate with a natural buffer ability), preferably if submitted to a biocatalytic hydrolysis, can contribute to the simplification of the bioprocess.

The highest PHB concentration registered was *c.a.* 11 g L^{-1} in the fermentor and 7.5 g L^{-1} in Erlenmeyer flasks, but these values are expected that can be increased significantly, to make the bioprocess more competitive. The lower productivity of simple reaction systems can eventually be compensated by the reduction of operation costs. It was achieved a biopolymer content of *c.a.* 80% of cell dry weight.

References

Braunegg, G., Lefebvre, G., Genser, K.F. (1998). Polyhydroxyalkanoates, biopolyesters from renewable resources: physiological and engineering aspects. *Journal of Biotechnology*, 65, 127-161.

Choi, J., Lee, S.Y. (1997). Process analysis and economic evaluation for poly(3-hydroxybutirate) production by fermentation. *Bioprocess Engineering*, 17, 335-342.

Khanna, S., Srivastava, A.K. (2005). Statistical media optimization studies for growth and PHB production by *Ralstonia eutropha*. *Process Biochemistry*, 40, 2173-2182.

Luengo, J.M., Garcia, B., Sandoval, A., Naharro, G., Olivera, E. (2003). Bioplastics from microorganisms. *Ecology and industrial microbiology*, 6, 251-260.

Proceedings of the 10th International Chemical and
Biological Engineering Conference - CHEMPOR 2008
Braga, Portugal, September 4-6, 2008
E.C. Ferreira and M. Mota (Eds.)

Macroscopic control of intracellular regulation: application to mammalian cell cultures

Ana P Teixeira[1,2], João ML Dias[2], Paula Alves[1], MJT Carrondo[1] and Rui Oliveira[2]
1- ITQB-UNL/IBET, Instituto de Tecnologia Química e Biológica, Instituto de Biologia Experimental e Tecnológica, Apartado 12, 2781-901 Oeiras, Portugal;
2- REQUIMTE/CQFB, Departamento de Química, FCT, Universidade Nova de Lisboa, 2829-516 Caparica, Portugal;

Keywords: elementary modes analysis, projection of latent structures, macroscopic control, mammalian cell cultures
Topic: Systematic methods and tools for managing the complexity

Abstract
Elementary modes (EMs) are the simplest pathways within a metabolic network connecting substrates to end-products, which are able to operate coherently in steady-state. In this work, it was developed an algorithm to identify the set of active EMs which best describe the dynamics of the envirome. The algorithm combines the projection to latent structures (PLS) method with the elementary modes (EMs) analysis and aims at the maximisation of the covariance between the EM fluxes and the environmental factors.
The PLSEM algorithm was applied to identify, from a total of 251 EMs, the active subset during different fed-batch cultures of recombinant Baby Hamster Kidney (BHK) cells. A high degree of correlation was obtained between the observed transmembranar fluxes and the ones calculated through the fluxes of the selected EMs, confirming the potential for a macroscopic control of the intracellular fluxes. Therefore, the PLSEM algorithm can be used to design macroscopic control strategies, with its regression coefficients providing specific information of how the envirome impacts EM fluxes.

1. Introduction
The concept of elementary modes (EMs) has been widely applied for metabolic pathway analysis (Schuster et al. 1999; Klamt and Stelling 2003; Palsson et al. 2003). From a biological point of view, these pathways correspond to enzyme subsets that define a solution space circumscribing the functional capabilities of the biochemical network. Particular solutions found within this solution space are achieved by non-negative linear combinations of the EMs. In general, the number of EMs within metabolic networks is very high denoting their innate adaptability and robustness properties. The envirome can reduce the allowable steady-state flux distribution through the network. The knowledge of which of these pathways are carrying higher fluxes under particular envirome conditions is advantageous to understand how cells meet their metabolic “objectives”.
In this work, an algorithm was developed based on the projection to latent structures (PLS) including metabolic constraints to identify the active subset of elementary modes given a set of measured macroscopic fluxes. We demonstrate the potential of the algorithm to map the operation of the metabolic network of BHK cells during different fed-batch cultures.

2. Proposed Methodology
The PLSEM algorithm developed in this study combines two well-known methods: projection to latent structures (PLS) and Elementary modes (EMs) analysis. The objective of this algorithm is to identify a subset of EMs whose fluxes are highly correlated with environmental factors and, at the same time, to eliminate redundancy by excluding all non active EMs. In other words, the design principle is to maximise covariance between EMs fluxes and

environmental factors. Bellow we describe briefly the principles behind EMs analysis followed by the integration of PLS and EMs into the PLSEM algorithm.

2.1. Elementary Modes Analysis

Considering a metabolic network with *m* metabolites and *q* reactions such as the network represented in Figure 2, the following steady state material balance equations can be formulated assuming balanced growth and negligible dilution:

$$\begin{cases} \mathbf{N}\mathbf{r} = \mathbf{0} \\ r_k > 0 \end{cases} \quad (1)$$

with $\mathbf{N} = \{n_{ij}\}$ a $m \times q$ stoichiometric matrix, $\mathbf{r} = \{r_j\}$ the vector of q metabolic fluxes, r_j denoting the net specific rate of reaction j and k denoting the irreversible reactions in the metabolic network. The universe of solutions of system (1) forms a convex polyhedral cone in the solution space (Rockafellar 1970). It is a property of this system that the infinite set of solutions may be expressed as nonnegative linear combinations of a finite set of n fundamental vectors $\mathbf{e}_i$ called elementary modes (EMs):

$$\mathbf{r} = \sum_{i=1}^{nem} \lambda_i \mathbf{e}_i \qquad \forall \mathbf{r} \in \Re^q \quad (2)$$

The non-null elements in each EM, $\mathbf{e}_i$, define a subset of active reactions of the overall metabolic network **N**, which are essentially pathways for the conversion of substrates into end-products. The complete set of EMs can be organized in the columns of a matrix $\mathbf{K}_{EM}$ to obtain an expression relating the measured macroscopic fluxes ($\mathbf{R}_{obs}$) with the fluxes of the EMs ($\mathbf{R}_{EM}$):

$$\mathbf{R}_{obs} = \mathbf{K}_{EM} \,.\, \mathbf{R}_{EM} \quad (3)$$

2.2. The PLSEM Algorithm

The goal of the PLSEM algorithm is to maximise the covariance between measured environmental factors (**X**) and measured extracellular fluxes ($\mathbf{R}_{obs}$) (see Figure 1).

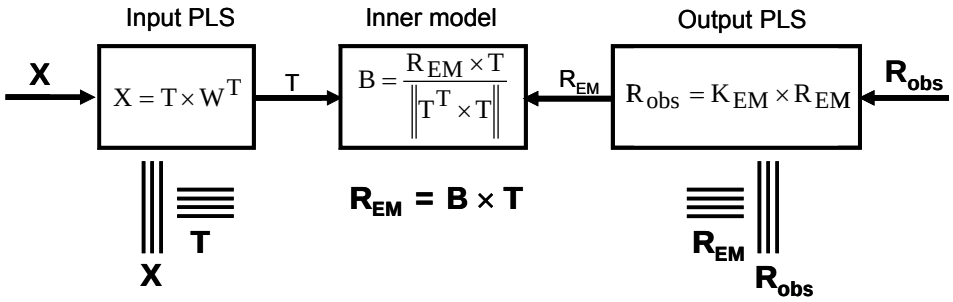

Figure 1 – The PLSEM algorithm.

The core of the PLSEM is identical to the classical PLS. PLS finds latent variables (LVs) of both the predictor and target matrices. The interesting feature of PLS is that these latent structures obey to the principle of orthogonality in relation to the original data. This operation eliminates redundant information of the inputs and outputs. The calculation of the predictor LVs in the PLSEM algorithm is done exactly in the same way as in PLS. The main difference lies in the calculation of the target output LVs. In the PLSEM, the EMs analysis is applied with the loadings matrix replaced by the EMs stoichiometry ($\mathbf{K}_{EM}$). Every flux vector in the solution space can be represented by linear combinations of the unique set of elementary modes. Therefore, the complete set of EMs contains all the orthogonal vectors that constitute the convex basis of the solution space, corresponding to the latent variables of the target output.

3. Materials and Methods

3.1. Culture conditions

A BHK21A cell line expressing the fusion glycoprotein IgG1-IL2 (antibody type one linked to Interleukin two) is the biological system under study. The culture medium used, SFM4CHO (Hyclone), is a serum-free and protein-free medium. The bioreactions were carried out in 2 L vessels. The starting volume was 950 ml, dissolved oxygen was kept at 30% of air saturation through sparging with an aeration rate of 0.02 vvm; the agitation rate was kept at 70 rpm. pH was allowed to vary between 7 and 7.25; the addition of NaOH (0.2 mM) or CO_2 occur only when pH lied outside this range. A set of six experiments were performed, one batch and five fed-batch cultures, using different initial concentrations of glucose, glutamine, glutamate, serine and aspartate and different feeding strategies. The quantification of viable cells, glucose, lactate, ammonia, recombinant protein, amino acids and osmolality is described elsewhere (Teixeira et al.,).

3.3. Metabolic Network

The biochemical network considered in this work is depicted in Figure 2. These reactions represent the major fluxes of carbon and nitrogen through the metabolism of BHK cells. The main metabolic pathways considered include glycolysis, glutaminolysis, TCA cycle, pentose phosphate pathway, recombinant product synthesis and biosynthesis of cellular components (nucleotides, carbohydrates, lipids, and proteins). The network contemplates also the catabolism of all amino acids except tryptophan.

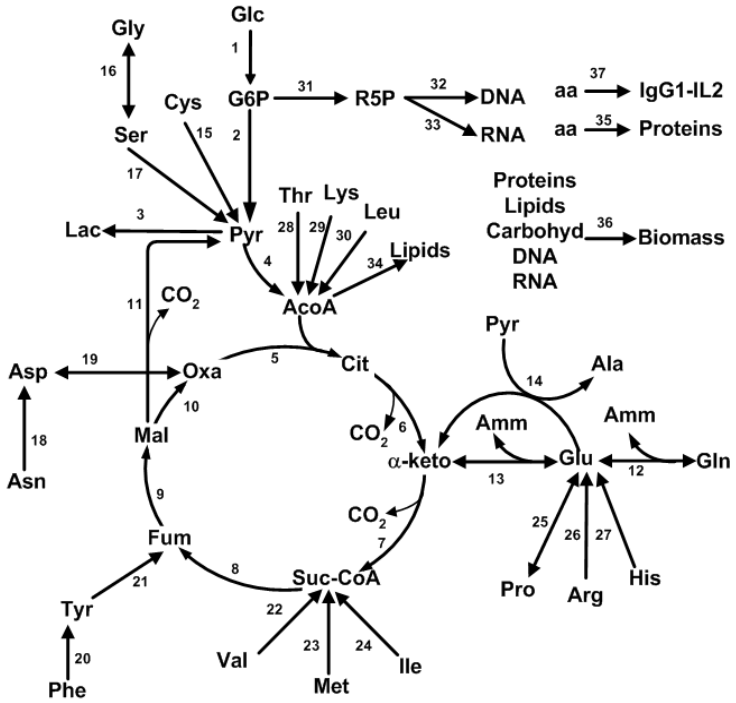

Figure 2 – Metabolic Network of the BHK cells.

4. Results and Discussion

4.1. Elementary Modes of the BHK metabolic network

The Elementary modes of the metabolic network represented in Figure 2 were determined using FluxAnalyzer software (Klamt et al. 2003), giving a total of 251 pathways connecting substrates with end-products. Within the set of EMs, there are 139 for biomass synthesis,

meaning that cells have many alternative routes to produce the biomass building blocks. This denotes the high degree of redundancy of the cellular metabolic network.

4.2. Typical active Elementary Modes during BHK cultures

The PLSEM algorithm was applied to data from the growth phase of six different experiments, in order to disclose the main trends in the operation of the metabolic network of BHK cells. The environmental factors comprising the input predictor of the algorithm are the pH and osmolality of the culture bulk, viable cells density, together with the concentrations of 23 measured compounds, namely glucose, lactate, ammonia, glycoprotein and 19 amino acids. The output matrix consists of 24 measured extracellular rates. Figure 3 shows the correlations obtained between the measured rates and the rates calculated through the fluxes of the active elementary modes; there is a high degree of correlation for the majority of extracellular rates. It should be emphasized that the EMs fluxes describing the observed rates were selected in the sense of maximising the correlation with the envirome factors; thus, these results evidenced the potential for macroscopic control of the intracellular fluxes. Fig. 3b presents the selected EMs together with the variance of the measured rates explained by each one. It can be observed that 20 EMs captured over 92% of the data variance.

(a)

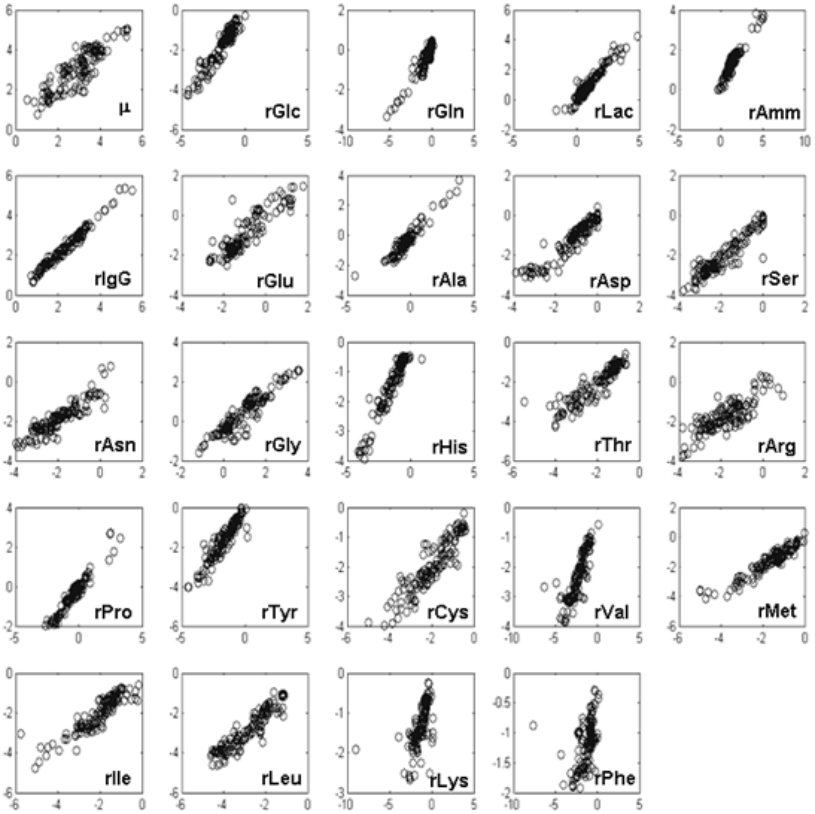

(b)

EM	Added variance (%)
20	61.76
1	69.08
11	74.97
6	79.14
4	81.21
9	83.24
28	84.66
5	85.56
7	86.44
102	87.22
12	88.12
74	89.07
82	89.75
2	90.35
14	90.93
114	91.39
3	91.81
43	92.17
25	92.47
80	92.74

Figure 3 – (a) Correlations between the measured rates and the rates calculated through the fluxes of the active EMs. (b) Rank of EMs obtained with data from the growth phase of six BHK cultures.

The first selected EM is one of the 139 EMs for biomass synthesis, describing more than 60% of the variance of the data. This result was expected since almost all specific extracellular rates can be partially described by an EM for biomass synthesis, as the majority of compounds is consumed or produced in such metabolic pathways. For the same reason, the unique EM for product formation (EM1) is in the rank, since it contributes to describe not

only the specific product formation but also part of the specific rate consumption of every amino acid.
The EM corresponding to the anaerobic conversion of glucose into lactate was selected in third place (EM11: Glc → 2 Lac). This EM is known to be very active in mammalian cell cultures when extracellular glucose concentration is higher than a defined concentration, normally a very low value. Glucose is taken up at high rates and the excess inside the cells enters in overflow metabolism being transformed into the waste and toxic by-product lactate.
Serine transamination into two molecules of glycine was the fourth selected EM (EM6: Ser + Amm → 2 Gly). One molecule of ammonia, the main toxic by-product for mammalian cells, is consumed during this pathway. Thus, this reaction may represent a strategy that cells found for ammonia detoxification.
Finally, it is worth to mention that the complete oxidation of glucose through the TCA cycle (EM43: Glc → 6 CO_2), the main source of energy for mammalian cells, is also present in the rank. After this overview, it can be stated that the PLSEM algorithm allowed the identification of typical pathways which are known to be active in mammalian cells. Thus, a very important structural insight into the operation of metabolic networks can be provided with this algorithm.

4.3. Assessment of the effect of the envirome on fluxome

The most relevant feature of the PLSEM algorithm is the possibility of using its regression coefficients to identify the environmental factors which correlate with the active EMs fluxes. This information can be potentially used to direct the fluxome to a desired state through manipulation of the envirome. There are many envirome factors which positively correlate with the flux of the EM20 corresponding to biomass synthesis, namely the concentration of glucose and lactate and also the concentration of nine amino acids, including glutamine. On the other hand, the pH of the culture bulk and the concentrations of product and histidine correlate negatively with the flux of this EM. Although BHK cells are capable of glutamine synthesis from glutamate (Neermann and Wagner 1996), higher growth rates were achieved in culture media with high levels of glutamine. The remaining amino acids correlate positively with this EM because normally they are more concentrated in the initial stage of the exponential growth phase when the biomass formation is higher. Then, their concentration decreases as they are consumed and cellular growth decreases as well. Therefore, this information may not necessarily mean that high levels of those amino acids promote higher biomass growth.
In terms of product synthesis, the envirome factors that correlate negatively with the flux of EM1 are the pH and the glucose concentration, while the osmolality and the concentrations of valine, isoleucine, leucine and lysine correlate positively with this EM. The high negative correlation with glucose concentration is expectable because in all experiments glucose concentration decreases from the beginning to the end of the batch, whereas the opposite trend is observed for product formation. However, this correlation is explained by reactor operation factors rather than a possible glucose inhibition mechanism on product synthesis. The effect of the pH deserves further attention, since it correlates negatively with both EMs of biomass formation and product synthesis. There are some reports agreeing that maximum growth rates (Yoon et al. 2005) and maximum productivities of recombinant proteins are obtained at pH = 7 (Osman et al. 2001). Regarding the osmolality effect, it has been reported in literature that the specific productivity of mammalian cells increases when the osmolality of the culture medium increases (Ozturk and Palsson 1990; Lin et al. 1999). Our PLSEM results support this observation. Altogether, these results demonstrate that the algorithm provides a basis for the macroscopic control of the intracellular fluxes. Nevertheless, the identification of the envirome factors which correlate with the flux of EMs would profit from a richer data set, obtained from a higher number of perturbations of the system. Although we have data from six experiments, some environmental factors (namely the concentration of essential amino acids) have similar profiles which may not be sufficient to disclose all the relevant information.

Conclusions

The PLSEM algorithm was developed merging two compatible concepts: the projection to latent structures and the elementary modes (EMs) methodologies. As in metabolic flux analysis, the PLSEM algorithm allows to calculate a set of unknown fluxes from a set of measured fluxes under the constraint of the metabolic network stoichiometry. The main difference lies in that the PLSEM uses the additional information contained in the envirome for structural analysis of the metabolic network in the sense of minimising pathway redundancy, by selecting the active EMs.

The method was evaluated by using data obtained from BHK cultures performed under different batch and fed-batch conditions.The algorithm provides two important pieces of information: the set of active EMs (the ones that correlate with the envirome) and the regression coefficients between EM fluxes and envirome factors. From a bioprocess engineering viewpoint, the PLSEM constitutes a powerful tool for process optimisation and control since it links the envirome, which can be manipulated macroscopically, with the fluxome under the constraint of the known network stoichiometry and thermodynamics.

References

Klamt S, Stelling J, Ginkel M, Gilles ED. (2003). FluxAnalyzer: exploring structure, pathways, and flux distributions in metabolic networks on interactive flux maps. *Bioinformatics* 19(2):261-9.

Neermann J, Wagner R. (1996). Comparative analysis of glucose and glutamine metabolism in transformed mammalian cell lines, insect and primary liver cells. *J Cell Physiol* 166(1):152-69.

Osman JJ, Birch J, Varley J. (2001). The response of GS-NS0 myeloma cells to pH shifts and pH perturbations. *Biotechnol Bioeng* 75(1):63-73.

Ozturk SS, Palsson BO. (1990). Effect of medium osmolality on hybridoma growth, metabolism and antibody production. *Biotech and Bioeng* 37:959-993.

Palsson BO, Price ND, Papin JA. (2003). Development of network-based pathway definitions: the need to analyze real metabolic networks. *Trends Biotechnol* 21(5):195-8.

Rockafellar R. (1970). *Convex analysis*. Princeton, Princeton University Press.

Schuster S, Dandekar T, Fell DA. (1999). Detection of elementary flux modes in biochemical networks: a promising tool for pathway analysis and metabolic engineering. *Trends Biotechnol* 17(2):53-60.

Teixeira AP, Portugal CAM, Carinhas N, Dias JML, Crespo JP, Alves PM, Carrondo MJT, Oliveira R. *In situ* 2D fluorometry and chemometric monitoring of mammalian cell cultures. *Biotechnol and Bioeng* (*submmited*).

Yoon SK, Choi SL, Song JY, Lee GM. (2005). Effect of culture pH on erythropoietin production by Chinese hamster ovary cells grown in suspension at 32.5 and 37.0 degrees C. *Biotechnol Bioeng* 89(3):345-56.

Proceedings of the 10th International Chemical and
Biological Engineering Conference - CHEMPOR 2008
Braga, Portugal, September 4-6, 2008
E.C. Ferreira and M. Mota (Eds.)

Towards PAT bioprocess monitoring and control: near infrared and software sensor

Zita I.T.A. Soons[1,2*], Mathieu Streefland[2], Anton J.B. van Boxtel[1]
[1] Wageningen University, Systems and Control Group, P.O. box 17,
6700 AA Wageningen, The Netherlands
[2] Netherlands Vaccine Institute, Unit Research and Development, P.O. box 457,
3720 AL Bilthoven, The Netherlands

Keywords: PAT, software sensor, near infrared spectroscopy, feedback control
Topic: Systematic methods and tools for managing the complexity

Abstract

Two advanced techniques have been compared to enhance bioprocess monitoring and control by online reconstruction of biomass and specific growth rate for feedback control: a software sensor based on standard measurements of the oxygen uptake rate and inline near infrared spectroscopy. An automatic search method for wavelength selection was proposed to enhance the prection ability of the near infrared method. Both techniques perform well, however when it comes to feedback control, the software sensor is preferred, because it is more robust against variations in the operating conditions and noise. The results are shown on real cultivations of *Bordetella pertussis.*

Introduction

Bioprocesses are characterised by natural variability in the raw materials, initial conditions, human intervention, and varying properties of the micro-organism. By setting fixed protocols the current GMP regulations do not encompass reduction of these deviations. This leads to products that have a variable quality, and are even out of specs. The FDA's guidance (2004) on Process Analytical Technology (PAT) finds more and more applications in the biopharmaceutical industry. It involves a shift from testing quality in finished drug products to building quality into products by introducing timely measurement and control of quality variables during the production process.

Wold et al. (2006) defined five levels of chemometrics analysis for PAT and states that the fifth level "PAT process control" in the sense of feedback control based on online monitored variables is still a challenge of the future. The use of spectroscopic instrumentation, although, is often seen as promising for PAT, however in the frame of feedback control it is less well developed. This work describes a step towards real-time feedback control for PAT by comparing two technologies for online monitoring of biomass growth (Soons, 2008). The ensuing controller design is based on the preferred technique. The dual substrate cultivation of *Bordetella pertussis* for the production of whole cell whooping cough vaccine was chosen as a test case.

Materials and methods

Bioprocess monitoring

Data of the near infrared sensor and data from other sensors (dissolved oxygen, pH, etc.) together with offline measurements of biomass concentration were taken from eight batch cultivations with *Bordetella pertussis*. The nutrient and biomass profiles were similar for all experiments. In four batches periods of deviations from the intended

* Corresponding author. Tel + 31-317-484955. E-mail:zita.soons@gmail.com or ton.vanboxtel@wur.nl

profiles, like oxygen limitation or poor pH control, were introduced to enhance the model robustness in counteracting the natural deviations of bioprocesses and to test PLS prediction performance. Every minute a spectrum was recorded consisting of 2074 wavelengths between 833 and 2500 nm. The noise was filtered by Savtisky-Golay smoothing with a 45-point window and a second order polynomial. Out of eight batches, six were assigned for the training dataset, two for the validation set. We refer to Soons (2008) for the more details on the measurement methods, the bioreactor conditions, and the spectral data pre-treatment.

Bioprocess control

The batch cultivations were extended with a fed-batch phase to obtain a higher biomass concentration in a controlled way. The fed-batch phase and the specific growth rate controller automatically started when the limiting substrates were almost depleted and the specific growth rate dropped to the set-point. We refer to Soons et al. (2006) for the more details on measurement methods and bioreactor conditions.

Bioprocess monitoring

The specific growth rate and biomass formation are important variables that we would like to control during the cultivation of bacteria for vaccine production. This is particularly important when the produced bacteria form the basis of a whole cell vaccine like whooping cough. Biomass growth, however, can not be measured online, because there are no suitable sensors.

Software sensor for biomass growth

A software sensor based on an Extended Kalman Filter (EKF) was developed to reconstruct biomass (C_X) and specific growth rate (μ) from standard measurements of the oxygen uptake rate (*OUR*) (Soons et al., 2008). The application of the EKF in biotechnological applications is amongst others discussed by Stephanopoulos and San (1984). The EKF calculates new estimates every minute using the model, the *OUR* measurement, the previous estimation, and the variance. The software sensor is based on a generic model with only two parameters (m_O and Y_O) that are required to be known accurately:

$$\begin{aligned} \frac{dC_X}{dt} &= \left(\mu - \frac{F}{V}\right) C_X \\ \frac{d\mu}{dt} &= 0 \\ OUR &= \left(\frac{\mu}{Y_O} + m_O\right) C_X \end{aligned} \qquad 1$$

Biomass estimation using near infrared sensor

It has also been investigated how nIR spectra can be used to yield an alternative measurement of biomass. Scarff et al. (2006) provide an overview on calibration of near infrared models for cultivation of micro-organisms. The evolvement of the spectra in time contains information on the course of the cultivation process. The interpretation of the spectra is challenging due to the large number of wavelengths and due to the overlapping absorbance bands of specific components. Partial least squares (PLS) is commonly used to regress a response variable (component concentrations) on a set of predictor spectra (near infrared measurements) (Van Sprang et al, 2007). Not all wavelengths in the spectrum, however, contain information relevant to the component of interest. To counteract these effects, wavelength selection is a common tool to

gather wavelengths that do contain relevant information. The complexity of the near infrared spectrum, however, precludes to some extend the use of the classical wavelength selection approach. Most works select spectral regions on the basis of prior knowledge on the absorbance of specific chemical components (amongst others Van Sprang et al., 2007 and Vaidyanathan et al., 1999). As an alternative, automated search methods were suggested by amongst others Triadaphillou et al. (2007). The currently available wavelength search methods are not effective in finding global minima. To overcome this problem, in this paper, the controlled random search procedure presented by Price (1977) is applied to obtain the most informative wavelengths by selecting the center and width of a spectral window and the number of latent variables for the PLS calibration. The window of wavelengths may vary in size, ranging from a single wavelength to 241 wavelengths.

The controlled random search first generates a set of *NT* trial points from the search domain *V*, specified by *n* parameters (center and width of the spectral window and the number of latent variables). The goal function (root mean squared error *RMSE*) is evaluated for all trial points and stored in a matrix *A*. Then the search starts by generating each iteration a new trial point and calculating the goal function for this point (*RMSE*). The new trial point *TP* is generated by choosing *n+1* random distinct points from the set *A* and calculating the next trial point form the centroid of the *n* random points minus the last point. When *RMSE* is smaller than the stored trial point with the greatest *RSS* (*M*), *TP* replaces *M* in *A*. This process continuous until the set in *A* has converged.

Bioprocess control

Control of bioprocesses is a difficult task due to the time-varying characteristics of cultivation processes. The control purpose is to regulate the specific growth rate (μ) to a desired value by adding a feed with limiting substrates. By combining a dual substrate model for biomass growth with a reference model, a controller was derived that adapts its settings in response to time-varying conditions (Soons et al., 2006):

$$F_{G+L} = \frac{ac + bd}{aC_G^{in} + bC_L^{in}} \hat{C}_X V + K_P \cdot (\mu_{set} - \hat{\mu}) + \int_0^t K_I \cdot (\mu_{set} - \hat{\mu})\, dt \qquad 2$$

where the controller gains K_P and K_I are adjusted online to the changing volume:

$$K_P = \frac{V}{\gamma_1 (aC_G^{in} + bC_L^{in})}, K_I = \frac{V}{\gamma_2 (aC_G^{in} + bC_L^{in})} \qquad 3$$

γ_1 and γ_2 are the tuning parameters for the controller and *a*, *b*, *c*, and *d* are constants depending on the micro-organism (in the work *B. pertussis*) and the set-point for specific growth rate.

Results and discussion

Wavelength selection

The controlled random search procedure was applied several to the training dataset and converged to the same spectral window and number of latent variables during each run. Figure 1 indicates that a window of 850-910 nm gives the best prediction of the biomass concentration. The selection of a wide window consisting of 199 wavelengths makes that the model is not too specific for the training dataset and is able to predict biomass concentrations on other batches.

Figure 2 shows the measured (C_X^m) versus the predicted biomass concentrations (C_X^{nIR}). The results show good correspondence for the low and medium values of biomass in the training set. In the high biomass range the biomass concentrations were

slightly overestimated. Out of six batches in the training dataset three contained “natural” deviations in pH and/or dissolved oxygen (PAB0003, PAB0004, and PAB0007). Despite of these hick-ups the near infrared model is capable to estimate biomass properly.

The performance of the PLS model obtained from the controlled random search procedure was compared with the PLS model built on the full spectrum (2074 wavelenths) by comparing *RMSE* of the full spectrum (*FS*) with *RMSE* of the selected wavelengths (*WS*) using Eq. 4. An improvement in PLS modelling accuracy of 62% was obtained.

$$I = \frac{RMSE_{FS} - RMSE_{WS}}{RMSE_{FS}} \cdot 100\% \qquad 4$$

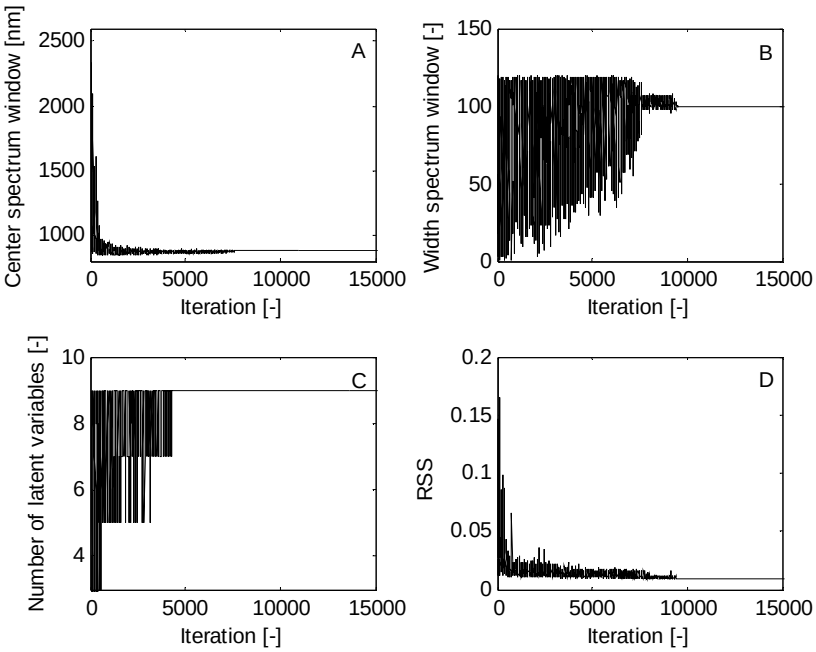

Fig. 1. Example of automatic wavelength selection by applying a controlled random search on the training dataset 2. The lines represent the trial points that were added to dataset A. **A.** Center spectrum window **B.** Width spectrum window **C.** Number of latent variables **D.** Weighted residual sum of squares.

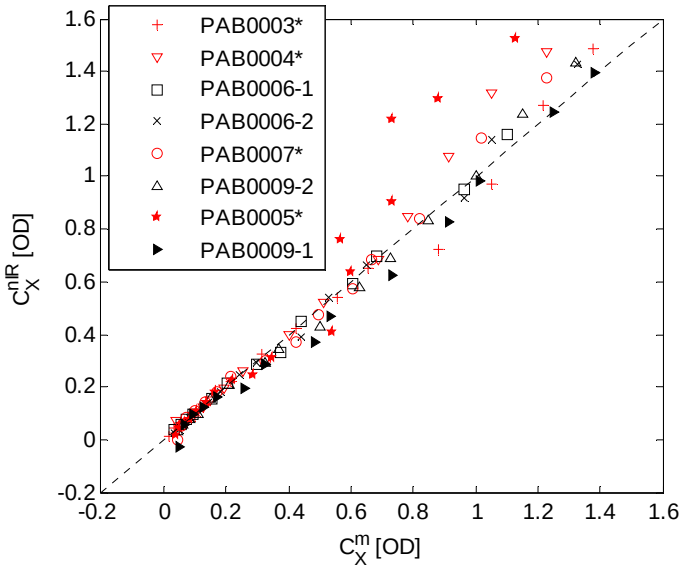

Fig. 2. Measured biomass concentrations versus concentrations predicted using the near infrared sensor. The training set is shown in open symbols, the validation set in filled symbols (PAB0005 and PAB0009-1); the batches in red and indicated with an asterix (*) contain temporary deviations in pH and dissolved oxygen; the batches in black do not contain deviations.

Bioprocess monitoring

The performance of monitoring based on the software and on the near infrared sensor is compared during eight batch cultivations and illustrated on one batch. The biomass estimations for the near infrared sensor were also used for online estimation of the specific growth rate, which is useful in situations where the specific growth rate is

controlled. In fig. 3A it can be seen that the software sensor accurately observes the exponential increasing biomass concentrations. The software sensor was hardly affected by the presence of hick-ups, and performed well over the entire range from start to end. Also the normally distributed noise in *OUR* (shown in Fig. 4A) was effectively filtered out by the software sensor.

In the same figure it can also be seen that the near infrared estimations also predict well the exponential increasing pattern of the biomass concentration. The estimations, however, were relatively noisy over the whole range of the cultivation (Fig. 3C). The software sensor was less sensitive for such disturbances.

The erratic and noisy biomass estimations from the near infrared sensor have important consequences for specific growth rate estimation and control. The variations were not normally distributed and therefore more difficult to filter out, resulting in a delayed reconstruction of the specific growth rate (Fig. 3B). These erratic properties of the spectroscopic biomass growth monitoring may deteriorate performance in feedback control.

Overall, in the cultivations that were consistent with the cultivations of the training dataset the PLS model predicted the biomass growth fairly well. If however variations occurred, which were unseen in the training set, the prediction power deteriorated. For future calibration of PLS models, it is important to assure that the training dataset comprises all sources of natural variation that might be expected during production runs; for instance by performing “design of experiment” batches.

Whilst the accuracy of the PLS model has improved by application of wavelength selection, the online prediction of biomass is not that robust against noise and unseen disturbances. So, if near infrared estimations are intended for feedback control, special care must be taken. It is suggested to check whether the behaviour of the current batch is consistent with the training dataset to detect deviating behaviour, e.g. by performing a principal component analysis on the online process data. In the current state of development the software sensor is the preferred choice when it comes to feed-back control.

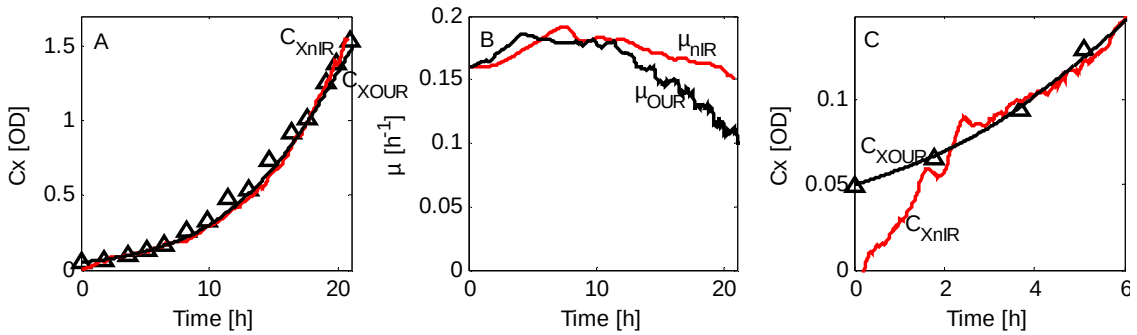

Fig. 3. Bioprocess estimations based on the near infrared and on the software sensor during batch cultivation. **A.** Biomass **B.** Specific growth rate. **C.** Detail of Fig. 1A: biomass estimations in the initial phase of the batch.

Bioprocess control

The next step was to extend the standard batch cultivation with a fed-batch phase by adding a feed with limiting substrates to control the specific growth rate, estimated by the software sensor. This way three times higher biomass concentrations were obtained in laboratory cultivations (Fig. 4) in a controlled way. The controller, therefore, contributes to enhanced batch-to-batch consistency and quality.

Wold et al. (2006) state that “PAT process control” is still a challenge of the future. This work is intended to be a step towards real-time feedback control for PAT by implementing two technologies for online monitoring and control of biomass growth during the cultivation step in vaccine production for *B. pertussis*.

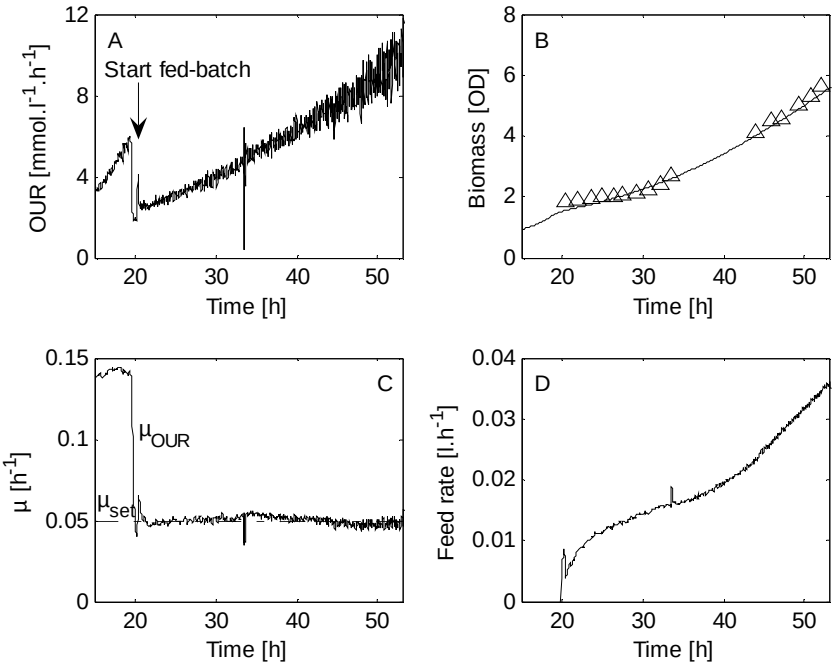

Fig. 4. Bioprocess control based on the software sensor during fed-batch cultivation. **A.** Oxygen uptake rate **B.** Biomass **C.** Specific growth rate. **D.** Feed rate.

Acknowledgements

The Dutch Ministry of Economical Affairs (TSGE3067) funds the project. We would like to thank Remko van Brakel for the helpful discussion about PLS modelling and Bas Speetjens for providing the matlab code of the controlled random search procedure. The experiments were performed at the Netherlands Vaccine Institute.

References

FDA (2004). Guidance for Industry: PAT – A framework for Innovative Pharmaceutical Development, Manufacturing and Quality Assurance.

Price W.L. (1977). A controlled random search procedure for global optimisation, *Computer J* 20, 367-370.

Scarff M., Arnold S.A., Harvey L.M., McNeil B. (2006). Near infrared spectroscopy for bioprocess monitoring and control: current status and future trends, *CRC Crit Rev Biotechnol 26*, 17-39.

Soons Z.I.T.A., Voogt J.A., Van Straten G., Van Boxtel A.J.B. (2006). Constant specific growth rate in fed-batch cultivation of *Bordetella pertussis* using adaptive control. *J Biotechnol* 125, 252-268.

Soons Z.I.T.A., Shi J., Stigter J.D., Van Der Pol L.A., Van Straten G., Van Boxtel A.J.B. (2008) Observer design and tuning for biomass growth and k_La estimation using online and offline measurements. *J Process Contr* 18, 621-631

Soons Z.I.T.A. (2008). Advanced monitoring and control in biopharmaceutical production. Thesis, Wageningen University, The Netherlands.

Stephanopoulos G. and San K.Y. (1984), Studies on On-Line Bioreactor Identification. I. Theory. *Biotechnol Bioeng* 26, 1176-1188.

Triadaphillou S., Martin E.B., Montague G.A., Nordon A., Jeffkins P., Stimpson S. (2007). Fermentation process tracking through enhanced spectral calibration modeling. *Biotechnol Bioeng* 97, 554-567.

Vaidyanathan S., Macaloney G., McNeil B. (1999). Fundamental investigations on the near-infrared spectra of microbial biomass as applicable to bioprocess monitoring. *Analyst* 124, 157-162.

Van Sprang E.N.M., Streefland M., van der Pol L.A., Beuvery E.C., Ramaker H-.J., Smilde A.K. (2007). Manufacturing vaccines: an illustration of using PAT tools for controlling the cultivation of *Bordetella pertussis. Quality Eng* 19, 373-384.

Wold S., Cheney J., Kettaneh N., McCready C. (2006). The chemometric analysis of point and dynamic data in pharmaceutical and biotech production (PAT) – some objectives and approaches. *Chemometrics Intelligent Lab Syst* 84, 159-163.

Proceedings of the 10th International Chemical and
Biological Engineering Conference - CHEMPOR 2008
Braga, Portugal, September 4-6, 2008
E.C. Ferreira and M. Mota (Eds.)

Near-Infrared Reflectance Spectroscopy as a Process Analytical Technology tool in Pharmaceutical Industry

Sílvia S. Rosa[1,2]*; Pedro A. Barata[1]; José M. Martins[1], José C. Menezes[2]

[1] Laboratórios Atral SA; Rua da Estação, 42, Vala do Carregado, P-2600-726 Castanheira do Ribatejo, Portugal

[2] IBB – Institute for Biotechnology and Bioengineering ,Centre for Biological and Chemical Engineering, IST, Technical University of Lisbon; Av. Rovisco Pais, P-1049-001, Lisbon, Portugal

Keywords: Process analytical technology (PAT), Near-infrared spectroscopy, pharmaceutical industry, identification, qualification, quantification.
Topic: Systematic methods and tools for managing the complexity.

Abstract

The FDA's Process Analytical Technology regulatory framework was born to support innovation and efficiency in pharmaceutical development, manufacturing, and quality assurance. PAT is a "system for designing, analyzing, and controlling manufacturing through timely measurements (i.e., during processing) of critical quality and performance attributes of raw and in-process materials and processes, with the goal of ensuring final product quality".

Several PAT tools are described in the FDA guideline for monitoring, process supervision, diagnostics, and control. Among monitoring techniques near-infrared (NIR) spectroscopy, is one of the most powerful and well know since it is intrinsically a PAT tool due to its multi-parametric capabilities (measures different in nature quality attributes) and also fingerprinting capabilities of whole process samples. NIR therefore has the potential to enhance process understanding and control of many pharmaceutical manufacturing processes, at also to replace advantageously quality control by in-process measurements validated and in accordance to regulatory requirements.

Here we describe the use of near-infrared diffuse reflectance spectroscopy as a Process Analytical Tool (PAT) used in a Pharmaceutical industry. NIR has been used for identification and qualification of raw-materials and intermediate manufacturing products, and for quantification purposes, likewise the determination of moisture and active pharmaceutical ingredients (API's), in intermediates and final products.

1 Introduction

The pharmaceutical industry is a highly regulated industry and in many cases innovation is first initiated when there are external requirements. Today's quality systems in pharmaceutical industries are gigantic organizations that are operated under the requirements of Good Manufacturing Practice (GMP), which can be a 'straight jacket' for innovation. To facilitate innovation and encourage the adoption of the PAT approach, FDA has supported the idea that technology innovation does not necessary require a heavy regulatory and bureaucratic process. The FDA PAT initiative is the key driver when it comes to innovation and introduction of PAT in the pharmaceutical industry.

The American FDA published a final PAT Guidance in September 2004. This guidance is a regulatory framework to encourage the voluntary development and implementation of

* bsel@ist.utl.pt

innovative pharmaceutical development, manufacturing, and quality assurance. This guidance does not intend to force the pharmaceutical industries to adopt the PAT concept; it just describes the current opinion of the FDA about this issue. By reading the guidance, we can anticipate that in the future, inspections of companies will be based on risk assessment. This means that if a company uses PAT and proves a high level of process understanding, their products are considered of less risk to the public safety compared to pharmaceutical products manufactured in the traditional way.

Companies that do not prove to have enough process understanding will then be of more concern to the FDA.

According to FDA, PAT is "*a system for designing, analysing, and controlling manufacturing through timely measurements (i.e., during processing) of critical quality and performance attributes of raw and in-process materials and processes, with the goal of ensuring final product quality*" (FDA, 2004).

The goal of PAT framework is to enhance understanding and control of the manufacturing processes, in order to be consistent with the sentence that reflects the ideal drug quality system: "*quality cannot be tested into products; it should be built-in or should be by design*".

PAT aims for the combination of the most recent scientific and technologically advanced resources in an integrated systems approach, in order to reach the desired state of pharmaceutical manufacturing and regulation (FDA, 2004).

Besides the regulatory aspect of PAT other benefits include improved process understanding, improved quality control, less batch rejections and higher throughput which all adds in favour of more competitive processes. Though PAT is not mandatory, the situation could certainly change when a large number of successful applications have been approved by the authorities. PAT is the road to higher quality more affordable drugs, which is both a benefit for pharma companies, patients and public healthcare systems.

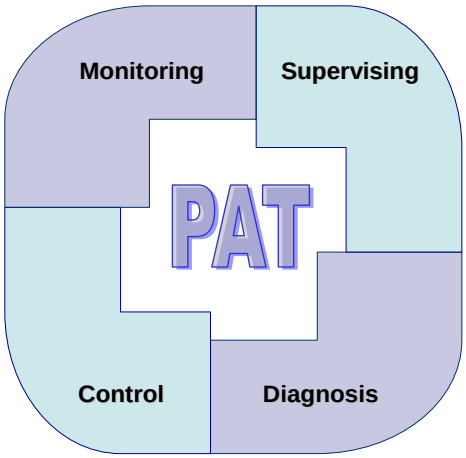

Figure 1 – PAT building blocks

In the last years, a favourable environment has been created around the PAT concept. Beyond any doubt, it is possible to said that the FDA's guidance gave the best contribution to the divulgation and discussion of PAT concept in the scientific world and consequently to its acceptance increase.

Several PAT tools are described in the FDA guideline, but near-infrared (NIR) spectroscopy is those who developed a strait relation with the PAT concept, since it is nowadays, a very well known and advantageous analytical technique, to which doesn't remain much to prove.

NIR has been used as a PAT tool in a pharmaceutical industry, for identification and qualification of raw-materials and intermediate manufacturing products, and for quantification purposes, likewise the determination of moisture and active pharmaceutical ingredients (API's), in intermediates and final pharmaceutical products.

2 Experimental

2.1 Equipment and software

NIR reflectance spectra were collected at-line, with a MPA™ (Multiple Purpose Analyzer) FT-NIR Bruker Optics spectrometer equipped with a reflectance fiber-optic probe. All methods were developed with OPUS software, version 4.2, with QUANT and IDENT packages, from Bruker Optics.

2.2 Identification and qualification of raw material

All the raw-materials used in the manufacturing of pharmaceutical products must be reliable identified. NIR has been used for this purpose for several years, and here we describe the overall strategy used for the development of a NIR identification method for daily use in a pharmaceutical industry.

For the identification process of incoming raw material, two independent spectral libraries were constructed: one for Active Pharmaceutical Ingredients (API's) and another one for excipients, in order to by-pass eventual overlaid problems in the spectra within these groups. During the methods development several chemometric techniques and multivariate data analysis were used for the development of an appropriate model that allow identification of new batches that reach the quality control, which was done for both libraries.

Several qualification methods were also developed, in order to complement the identification process and give a result as reliable as possible not only about the incoming raw material identity but also about its application. The qualification can be required after the identification step, because the same product can have different physical (e.g. particle size, density, compactation), or chemical properties (e.g. polymorphism, hidratation degree) related with different applications.

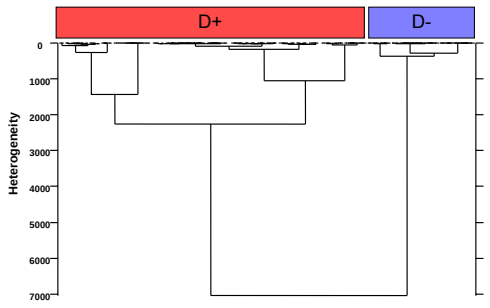

Figure 2 - Dendogram from a qualification cluster method

The global process passes through the identification of new incoming batches, which is positive if the result matches the previously defined threshold for the respective class group in the method. Qualification can be required if we are in presence of a raw-material that shows different properties as said before. Figure 2 is an example of qualification, which represents a dendogram from a cluster model which can qualify correctly several batches of the same API with different dispersability properties in water according to these properties.

The proven advantages of this identification technique include: reduced use of technician time; elimination of the consumption and exposure of noxious solvents used in some sample preparation procedures; faster raw-material approval in the receiving area and more information about it (e.g. chemical and physical properties).

This kind of NIR application could be considered as a PAT initiative, since it is an efficient and innovative approach for the control of critical quality attributes of a raw material to a pharmaceutical manufacturing process. Although this application is used in the first step of the process (raw material analysis), it will enable process control, thus reducing the vulnerability of the process and manufacturing time cycles, to use in the incoming raw material with a positive impact in productivity and final product quality assurance.

2.2 Quantification methods

NIR is being used for quantitative purposes. Several quantitative methods (multivariate calibrations) were developed. Most of all were developed to determine moisture content in process intermediates (i.e. In-Process analysis), and some of them for the content determination of active ingredients (API) in intermediates and end-products simultaneously.

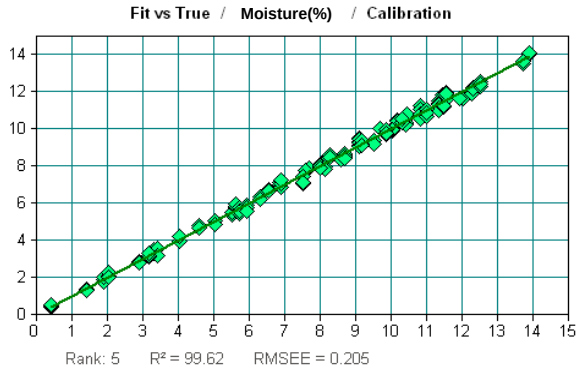

Figure 3 – Calibration for moisture determination

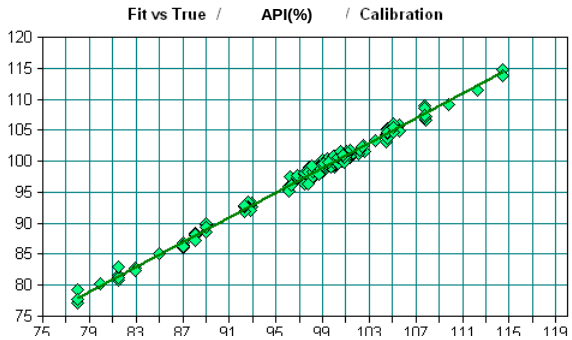

Figure 4 – Calibration for API determination

Figure 3 represents a calibration for moisture determination in an intermediate granulate analysed during manufacturing process (in-process), and figure 4 represents a calibration for an API determination in a final solid dosage form.

Moisture or API content is monitored and controlled during the manufacturing process, which allows to check if the product meets the specification criteria and also to assure its final quality. This could be considered a PAT application, as multiple quality attributes of different nature are included in the NIR evaluation and can be seen as the first step to establish a multi-parametric release system, since it allows the real-time measurement, monitoring, and control of critical quality parameters as it is the moisture or API content in pharmaceutical products.

All calibrations were validated for specificity, linearity, range, accuracy, and precision (repeatability and intermediate precision) parameters, and proved to be suitable for its intended use.

3 Conclusions

The use of NIR spectroscopy for qualitative and quantitative purposes in a pharmaceutical industry has proved its usefulness over conventional analytical techniques. NIR applications could be considered PAT applications, since they represent an efficient and innovative approach for the control of critical to quality attributes of pharmaceutical products over all the manufacturing process (viz. raw materials, intermediates, and final products).

The NIR applications described here enable process control, thus reducing the vulnerability of the process and manufacturing time cycles, with a positive impact in productivity and final product quality assurance

NIR implementations have the potential to enhance process understanding and control of existing and running manufacturing processes, at the same time they provide very valuable quality control analytical results in-process in accordance to regulatory requirements.

References

Food and Drug Administration (FDA) (2004). PAT - A Framework for Innovative Pharmaceutical Manufacturing and Quality Assurance (Guideline), (http://www.fda.gov/CDER/guidance/6419fnl.pdf).

Proceedings of the 10th International Chemical and
Biological Engineering Conference - CHEMPOR 2008
Braga, Portugal, September 4-6, 2008
E.C. Ferreira and M. Mota (Eds.)

Enhancing engineering education in the area of chemical processes through a virtual platform (LABVIRTUAL)

M. G. Rasteiro[1], L. M. Gando-Ferreira[1], J. C.Teixeira[2], F. P. Bernardo[1], M. G. Carvalho[1], A. G. Ferreira[1], R. M. Quinta-Ferreira[1], F. P. Garcia[1], C. M. S. G. Baptista[1], N. C. Oliveira[1], M. J. Quina[1], L. O. Santos[1], P. A. Saraiva[1], A. M. Mendes[3], F. M.Magalhães[3], J. Granjo[1], R. Bastos[1], M. Ascenso[1], R. Borges[1], A. S. Almeida[3], A. Macedo[4]

[1]Departamento de Engenharia Química, Universidade de Coimbra
[2] Departamento de Matemática/Instituto de Telecomunicações, Universidade de Coimbra
[3]Departamento de Engenharia Química, Faculdade de Engenharia da Universidade do Porto
[4]MediaPrimer – Tecnologias e Sistemas Multimédia, Lda., Coimbra

Keywords: Chemical Processes, E-learning, Virtual Laboratories, Web Platform

Abstract

This work describes the development of a Virtual Platform with a wide scope, directed to the learning of Chemical Processes. The platform is organized in five different sections: Separations and Unit Operations, Reaction Engineering, Process Systems Engineering, Biological Processes and Virtual Experiments. The first four sections deal with the chemical/biochemical processes and include simulators, applications and case studies aimed at leading the students to understand those processes. The fifth section, Virtual Experiments, deals both with the laboratory visualization of the basic phenomena related to the processes in the other four sections, and with the remote monitoring of laboratory experiments. Moreover, this platform, which has been constructed as a dynamic Web Portal, will allow discussion forums and is aimed at sharing experiences with other schools. This paper describes the different applications included in the web platform, as well as the simulation strategies and web methodologies used for its construction, presenting also one example of application in the classroom.

1 Introduction

Recent advances on information and communication technologies (ICT) have facilitated the development of educational and laboratorial systems based on distributed multimedia technologies, namely virtual reality, under relatively low costs. The traditional methodology of education conducted only in the classroom does have a number of inherent limitations that include passive learning attitudes, difficulties in applying the concepts introduced to real life problems, and little responsibility on the side of students regarding self-learning. New educational tools, based on virtual learning environments, can contribute to stimulate each student, in order to develop competencies of autonomous and critical thinking, in accordance namely with the Bologna process.

The Chemical Engineering Departments of both the Universities of Coimbra and Porto have been experimenting, on their own, for quite sometime, new teaching methodologies (Rafael et al., 2007, Mendes, 2002) taking into consideration the concerns referred above, and also taking advantage of the information technology skills available in the new students' populations. Recently, these departments got engaged in a broader project, directed towards the development of a virtual platform with a wider scope, aimed at the teaching/learning of Chemical Processes, at the graduation level in Chemical Engineering, for Portuguese-speaking students including those from African countries. A large group of academics (13 Chemical Engineering Faculty members and 5 research students), with complementary competencies and expertise were involved in this project.

This paper describes the different sections included in the web platform built, as well as the simulation strategies and web methodologies used for its construction. The web platform structure adopted is illustrated in Figure 1. The functional areas of the platform are as follows: Separations and Unit Operations, Reaction Engineering, Process Systems

Engineering, Biological Processes and Virtual Experiments. Moreover, our teaching platform also includes an area directed towards secondary school students interested in chemical engineering, where, besides general information on “What Chemical Engineering is all about”, fundamentals of physics and chemistry, in relationship with engineering applications, are covered.

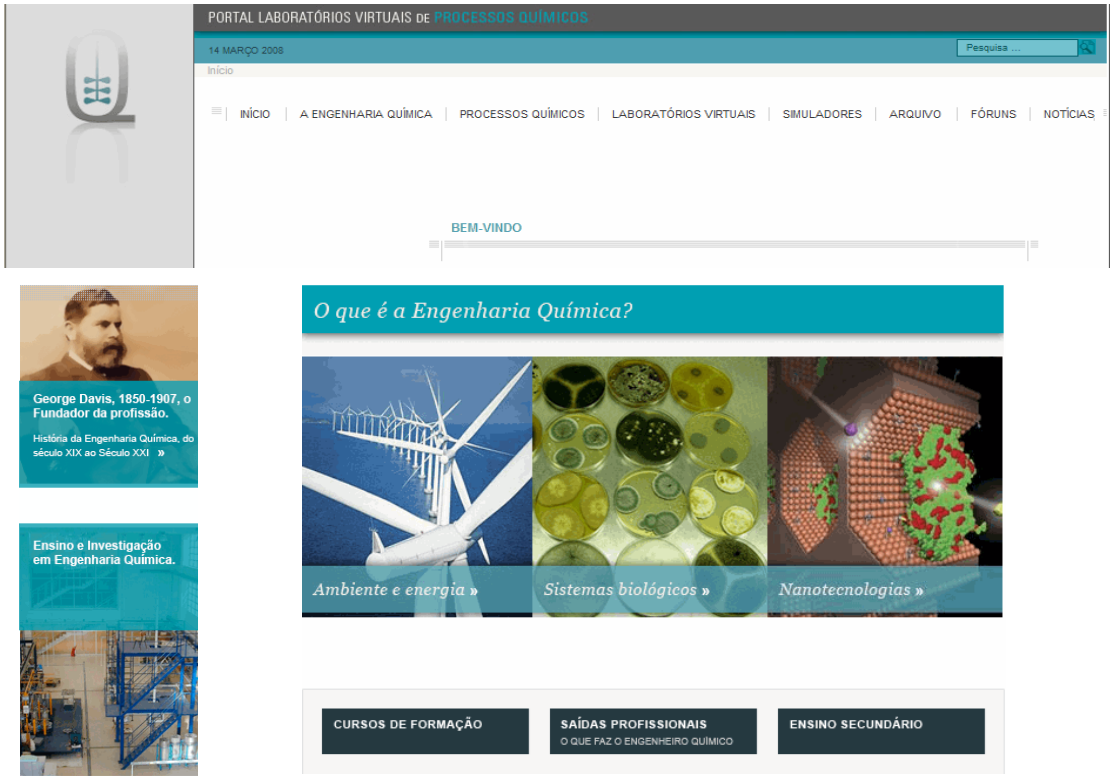

Figure 1 – Structure of our Teaching Web Platform.

2 Development of the virtual platform

The Web infrastructure of the Virtual Laboratories of Chemical Processes Platform is an information platform based on standard open-source and freely available software - *CMS Joomla*!, free software under the GPL license. This approach allows similar functionalities provided by other commercial software, with the flexibility to better adapt code to the specific needs of this Portal. In addition to these functionalities, the use of *Joomla!* allows the installation of additional components and modules, to support other functionalities of the portal such as discussion forums, search boxes, online surveys, lists of documents available for downloading, etc.

One of the key components of the web platform is process simulation. The study of the different chemical processes is supported by twenty interactive simulation modules, covering both fundamental topics as well as more practical and complex applications. Figure 2 depicts the basic architecture of the simulation system, comprehending two main blocks: the *web interface*, which helps the user in entering the data required for simulation and supports the visualization of the corresponding results, and the *computational platform*, where the mathematical model of the chemical process is solved. The exchange of information between these two levels is mediated by a simulation gateway, designed in agreement with the CGI (Common Gateway Interface) protocol. The input data set, collected in an input form, supports numerical values as well as discrete options (chemicals to be processed, type of model to be used or different modes of simulation). The simulation output may include graphics and in some cases several sets of results for different input conditions and also dynamic profiles drawn in real time. Matlab was chosen as the preferential computational

platform, although other tools are also used, such as Octave and FORTRAN, for greater flexibility and faster execution, or to use previously developed codes.

Regarding the mathematical process models embedded in the simulators, they may be sets of algebraic and/or differential equations, depending if the process operation is continuous or batch and if the model has or has not variables distributed on space. These sets of equations are solved using standard numerical methods and in some more complex problems a decomposition strategy and/or iterative procedure may also be needed.

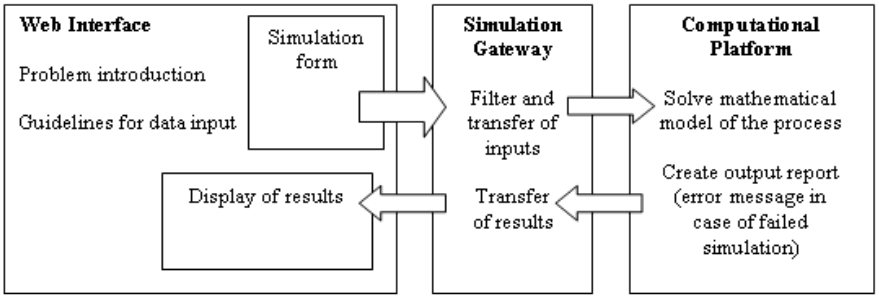

Figure 2 - Flowchart with the simulation Components.

3 The Chemical Processes area

Next, the main features of the different blocks in the Chemical Processes area are presented. Each block includes a library of fundaments, models and applications, simulators and case studies to lead the students through the study of the process concerned. Moreover, some processes in the four main areas previously mentioned are also illustrated through web visualizations of laboratory experiments, in the “Virtual Experiments” section, which interacts with all the other modules.

3.1 Unit Operations and Separation Processes

This section is directed to the study of Unit Operations, especially equilibrium and rate based processes applied to Chemical Processes. Five different separation processes have been considered so far: Distillation, Liquid/liquid extraction, Absorption, Adsorption and ion-exchange and Crystallization. Thermodynamics and Heat and Mass Transfer Fundaments were considered as autonomous modules and have been developed as well in this section, preceding the Separation Processes modules. For the design of distillation equipment both short-cut and the rigorous Wang-Henke method have been implemented. As for the design of liquid/liquid extraction equipment a McCabe-Thiele type method has been implemented, which is only valid when both solvents can be considered immiscible. The design of tray absorption towers, for both Absorption and Stripping, is also being based on the McCabe-Thiele method for the determination of the theoretical number of trays, for concentrated solutions, and on the Kremser equation when the user introduces a linear equilibrium equation (valid, in general, for diluted solutions). The rate-based processes considered in the platform are Gas/Liquid Absorption in packed towers and Adsorption and Ion-exchange in solid/liquid systems. With the simulator “Absorption in packed columns” the user can choose calculating one or all the design parameters: packing height, column diameter, pressure-drop and flooding mass flux. The simulator “Adsorption” consists of two major parts. In the first part, the user gets information on the equilibrium parameters by testing four different isotherms. In the second part, the user can choose models for studying the kinetic behaviour of batch, continuous stirred tank and fixed-bed adsorbers.

3.2 Chemical Reaction Processes

At the Chemical Reaction Engineering level our main goal is focused on the development of e-learning tools in the field of kinetic studies, design and operation of reactors to be used in homogeneous and heterogeneous processes. In what regards reaction kinetics, experimental data can be used to determine kinetic parameters, reaction orders and activation energies in order to obtain reaction rates equations that reflect the influence of

temperature and reactants concentration. The simulator allows using both integral and differential methods. In the context of reactor analysis the platform addresses ideal chemical reactors, stirred tanks under continuous, batch and semi-batch operation as well as plug flow reactors. Catalytic reactors are also addressed with particular emphasis on fixed-bed reactors largely used in the industry. In this domain, pseudo-homogeneous and heterogeneous mathematical models were developed in steady state regime, requiring different numerical techniques for computer simulation of the resulting ordinary differential equations, ODEs, or algebraic and ordinary differential equations, DAEs. Moreover, in the Residence Time Distribution (RTD) section, the students can calculate and plot the response to pulse or step inputs of tracer, which are the experimental techniques used to evaluate the RTD in open systems. The experimental procedure is also illustrated in one of the virtual experiments.

3.3 Process Systems Engineering

The main objective of the PSE section is to introduce the student to a variety of problems and methodologies that can be typically associated to the development and manufacture of chemical related products (pharmaceuticals, novel material, commodities and specialties) and process operating modes (batch or continuous). One basic module of the virtual platform includes a set of examples covering key concepts in the domain of instrumentation, by linking to a multimedia library, and process control. Moreover, a data acquisition system was implemented to monitor outdoor air quality (SO_2, NO_2 and CO emissions) using electrochemical sensors, temperature and relative humidity, in real time.

Students are also introduced to additional concepts related to dynamic systems. The physical examples considered are built starting from simple examples (like hydraulic systems), where most of the basic concepts of instrumentation and single-loop control laws can be illustrated, to more advanced processes, through the gradual introduction of additional chemical and physical phenomena, once the concepts described in other sections of the portal are mastered. Using this approach, both important practical aspects such as the effects of the choice of the sampling rate for discrete control, or the effects of errors introduced by linearizing models at various operating points, to the use of more advanced concepts such as alternative control strategies (adaptive and predictive), and the setup of parameter estimation and system identification schemes can be covered. One additional module in this section addresses the use of process integration and optimization methodologies in the context of rationalization of energy and utility usage in the process industries. Finally, this section includes also a subsection focused on Product Engineering, which links to a more detailed web page developed by the University of Cambridge (Moggridge , 2008).

3.4 Biological Processes

Modelling biological processes using theory, empirical correlations and mathematical tools contributes to the understanding of biological phenomena, to determine process parameters, to predict the performance of the equipment under different working conditions, etc., always considering the properties of the biological entities. This section includes the quantitative analysis of biological kinetic data to evaluate simple or more complex fermentations as affected by process conditions such as cell density and growth rate, substrate concentration, air flow rate, dissolved oxygen concentration, stirrer speed, etc. The recovery of bioactive products is more constrained in comparison with the unit operations that are more traditional in chemical engineering, in order to avoid loss of activity and contamination by other products. At this stage only the basic principles of membrane and chromatographic processes are covered. The simulation of the ultrafiltration process, in batch or continuous mode, can be tested as an example for illustrating the potentialities of the membrane technology in separating macromolecules. Regarding the chromatography, the partition of two components between a mobile and a stationary phase (adsorbent) has been simulated by using the technique of the elution chromatography, in which the sample is injected into the column as a pulse. The students, in both cases, have the opportunity of testing key concepts

involved in these operations and evaluating different operating approaches to achieve the best separation efficiency.

3.5 Virtual Experiments

Experimentation is as fundamental for students' learning process as the theoretical knowledge. The inclusion of a section named "Virtual Experiments" aims to cope with this objective. *Virtual Experiments* is meant to be an independent section, with links to other relevant areas of the site, as reaction, separation, biological systems and processes control. In this way different approaches for facilitating the learning and teaching processes in Chemical Engineering laboratories, will be coupled. Four experiments are included here: Determination of the Kinetic Constant and Activation Energy for the Liquid Phase Homogeneous Reaction between Ethyl Acetate and Sodium Hydroxide; Flow Pattern Characterisation in a Tubular Reactor Packed with Glass Beads; Study of the Sucrose Inversion and Study of a Cation-Exchange Resin. In addition to the description of the experimental setups and procedures and the theoretical background for each lab work, multimedia support is provided in the form of a video, illustrating each setup's components and the major steps in the operation procedures and experimental occurrences. In the section of process control, the students may carry out remotely one feedback control experiment, whose setup is located at the Chemical Engineering Department of the Faculty of Engineering - University of Porto.

4 Using the virtual platform in the teaching of chemical processes

According to the philosophy behind the construction of the platform, the site can be used in the classroom to illustrate the design and operation of process equipment, as for instance to show the influence of operating conditions, feed characteristics, etc. on the design outcome, or still to evaluate the validity of different models to do the design.

In this section of the paper we will next describe one example of the use of the platform to determine kinetic parameters of a reaction (reaction orders and activation energy). The estimation of the kinetic parameters is often addressed in the curricula of chemical engineering based on the liquid phase homogeneous reaction between ethyl acetate (EAc) and sodium hydroxide (NaOH). The reaction rate, r, is given by: $r = k\left(C_{NaOH}\right)^{n}\left(C_{EAc}\right)^{m}$, where k is the kinetic constant, n and m are the partial orders for sodium hydroxide and ethyl acetate, respectively; C_{NaOH} is the sodium hydroxide concentration and C_{EAc} is the ethyl acetate concentration. This reaction was carried out in a batch stirred reactor at 15, 20 and 25 ºC, and the students may determine, using the simulator in the Chemical Reaction Processes section, the partial orders (n, m) based on the integral or differential method. In order to fit the known concentration profile of NaOH, the conversion of this reagent, x_{NaOH}, was used to relate the concentrations of the two reagents and to allow integration and linearization. The students are expected to understand the consequences of admitting different values for n and m. For example, considering $n = m = 1$, the following equation is fitted by the simulator ($r = \mathrm{d}C_{NaOH}/\mathrm{d}t$)

$$\ln\left(\frac{M - x_{NaOH}}{M\left(1 - M - x_{NaOH}\right)}\right) = kC_{NaOH,0}\left(M - 1\right)t \qquad (1)$$

where M corresponds to $C_{EAc,0}/C_{NaOH,0}$, $C_{NaOH,0}$ is the initial concentration of NaOH, t is the time. By plotting the experimental data as indicated in Figure 3 (a) when the temperature of the system is set at 15 ºC, the linear fitting is the one indicated through the solid line, with a coefficient of correlation, $R^2 = 0.999$. The students shall conclude that the orders n=m=1 are adequate trials, and that the kinetic constant is 5.28×10^{-5} $m^3 \cdot mol^{-1}.s^{-1}$. For each case, the user may also validate the model by comparing the predicted values with the experimental ones. Since none experiment was performed at the conditions of excess of one reagent, the differential method is limited to the case of $n = m$; otherwise the linearization is not possible.

For this particular case ($n = m$), students may compare the fitting obtained with this method with the one obtained through the integral method.
Another important analysis that may be performed in the platform concerns the calculation of the activation energy, E , and the pre-exponential factor, k_0 , by using the Arrhenius equation. After knowing the kinetic constant calculated at 15, 20 and 25 ºC, the students may obtain a similar fitting to the one represented in Figure 3 (b). In this case, one may conclude that the system is characterized by $E = 4.79 \times 10^4$ J·mol^{-1} and $k_0 = 2.58 \times 10^4$ m^3·mol^{-1}·s^{-1}.

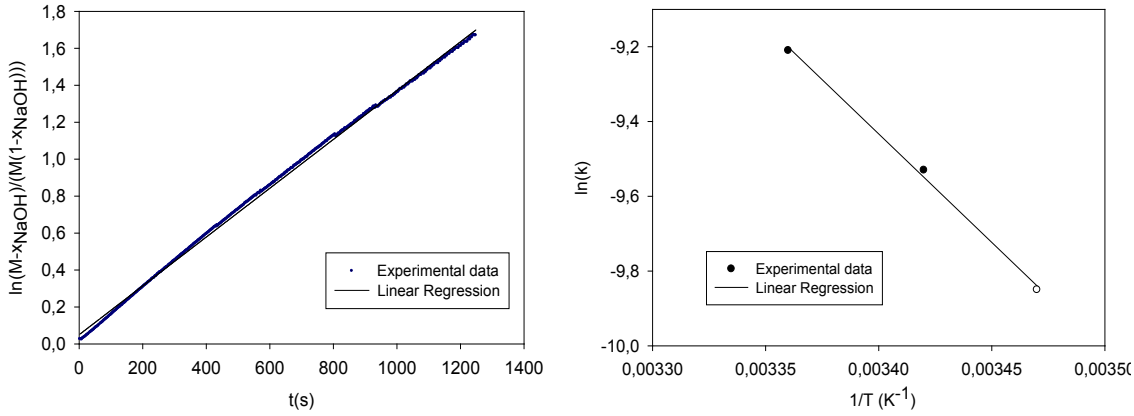

Fig. 3 - (a) - Fitting of the experimental values for the hydrolysis of ethyl acetate using the integral method, when $n = m = 1$; (b) - Fitting of the Arrhenius equation.

5 Conclusions

The Portal LABVIRTUAL (http://labvirtual.eq.uc.pt) showed to be a valuable tool for the teaching of Chemical Processes because of the several features which are usually not combined in a single platform: i) Broad collection of chemical processes being addressed in the same platform, in the different areas of Chemical Engineering; ii) Simulators (twenty in total) which enable designing and dimensioning the different processes addressed, iii) Applications and case studies to help the students in the use of the simulators and give them a practical perspective of the basic concepts; iv) Virtual experiments which enable the students to visualize some basic phenomena on which the design of chemical processes is based, and also help the students to get better prepared to carry out experiments in the real laboratory. These features give to the student an integrated approach to Chemical Processes, and lead to an easier integration of knowledge which is addressed in different courses Moreover, the portal has also been built to disseminate information about Chemical Engineering to the general public, and mainly to students in the basic and secondary education levels. Finally, and because the language of the portal is Portuguese, it is expected that it can be used to strengthen the relations between universities in Portugal and their counterparts in the Portuguese speaking countries, involved in the teaching of Chemical Engineering.

Acknowledgment

The receipt of sponsorship from POSC (Programa Operacional da Sociedade de Conhecimento, Portugal), contract 743/4.2/C/REG, enabling the development of this platform is acknowledged.

References

Mendes, A.M.M. (2002). Laboratórios de Engenharia Química. FEUP Edições, Porto.

Moggridge, G. D., Saraiva P. M., Costa R.. (Acessed Jan. 2008). Chemical Product Design Teaching. http://www.engsc.ac.uk/an/mini_projects/cpd/index.html

Rafael, A.C., Bernardo, F., Ferreira, L.M., Rasteiro, M.G. and Teixeira, J.C. (2007). Virtual Applications Using a Web PLatform to Teach Chemical Engineering: the Distillation Case. *Trans. IChemE, Part D, Ed. For Chem. Engrs.,* 2(D0), 1-9.

Proceedings of the 10th International Chemical and
Biological Engineering Conference - CHEMPOR 2008
Braga, Portugal, September 4-6, 2008
E.C. Ferreira and M. Mota (Eds.)

Add-ins for Shortcut Design and Sizing of Distillation Columns

Fernando G. Martins[1*], Marta I. M. S. Cruz [1], Domingos Barbosa[2]

[1] LEPAE – Chemical Engineering Department, Faculty of Engineering, University of Porto, Rua Dr Roberto Frias s/n, 4200-465 Porto, Portugal.

[2] CBQF – Pólo FEUP – Chemical Engineering Department, Faculty of Engineering,University of Porto, Rua Dr Roberto Frias s/n, 4200-465 Porto, Portugal.

Keywords: Distillation, Shortcut Methods, Design, Column Sizing, Add-ins, Spreadsheet

Topic: Educating chemical and biological engineers for coming challenges

Abstract

A computer program, in Visual Basic for Applications, was developed for design and sizing of binary and multicomponent distillation columns using shortcut methods. The program is in the form of two add-ins for Microsoft Excel, one for binary and the other for multicomponent distillation.

These two add-ins are easy to use and to incorporate in Microsoft Excel, a widespread working tool for engineers, and can be helpful as a teaching aid, or as a tool for operator training or preliminary design and sizing of distillation columns.

1. Introduction

Distillation continues to be one of the most used separation techniques in the chemical industry, in sipte of its energy intensive character. This unit operation uses heat as the separating agent, and the difference in relative volatilities as the separation principle. The design of distillation columns is greatly influenced by the type of mixture to be separated, in particular, its ideal or non-ideal behaviour. In spite of its widespread used, distillation cannot be applied to the separation of all kinds of liquid mixture, more specifically, distillation should not be a first choice for the separation of azeotropic, closed boiling or thermodegradable mixtures.

Due to its generalized use, which is not restricted to the chemical industry, the design of distillation columns is well understood, and many reliable mathematical models for performing distillation calculations are available in the literature. These models can be divided in two main classes: i) shortcut models and ii) rigourous models. The shortcut models are easier to use and can be considered rigorous enough for preliminary design and process evaluation, or for qualitative studies.

This work presents two software tools, in the form of Microsoft Excel add-ins, for the application of shortcut models to the design and sizing of binary and multicomponent distillation columns.

2. The software tools

The add-in for binary distillation uses the McCabe-Thiele method for column design, allowing the user to interact with the program by means of self-explanatory user-forms. The software is able to design and size binary or pseudo-binary distillation columns, with multiple feeds and sidestreams, having different feed entalpic conditions, for ideal vapour and non-ideal

* Corresponding author. Tel + 351-22-5081974. E-mail:fgm@fe.up.pt

liquid mixtures. The design of steam distillation columns is also considered. The vapour-liquid equilibrium can be described by assuming constant relative volatility, ideal mixtures, or by using the Margules, van Laar, Wilson, NRTL, UNIQUAC and UNIFAC models to describe the non-ideality of the liquid phase (Smith et al., 2001). Figure 1 shows the screenshots of the add-in for binary distillation. The calculations are illustrated by means of a graphical interface, and the results summarized in a spreadsheet. The program allows the calculation of the minimum reflux ratio, minimum number of stages, operating reflux ratio, number of ideal trays, and can also be used to perform estimates of the number of real trays, the height, and diameter of the column. The sizing of the column is based on the shortcut method purposed by Douglas (1988). The value of the actual reflux rate may be given as input or estimated by specifying the value of the ratio R/Rmin. This computer program does not only offer to the process engineer a good first estimate for the design and size of binary distillation columns, but is also an important teaching aid for students and operator training, showing graphically the influence of the different design variables in the final project.

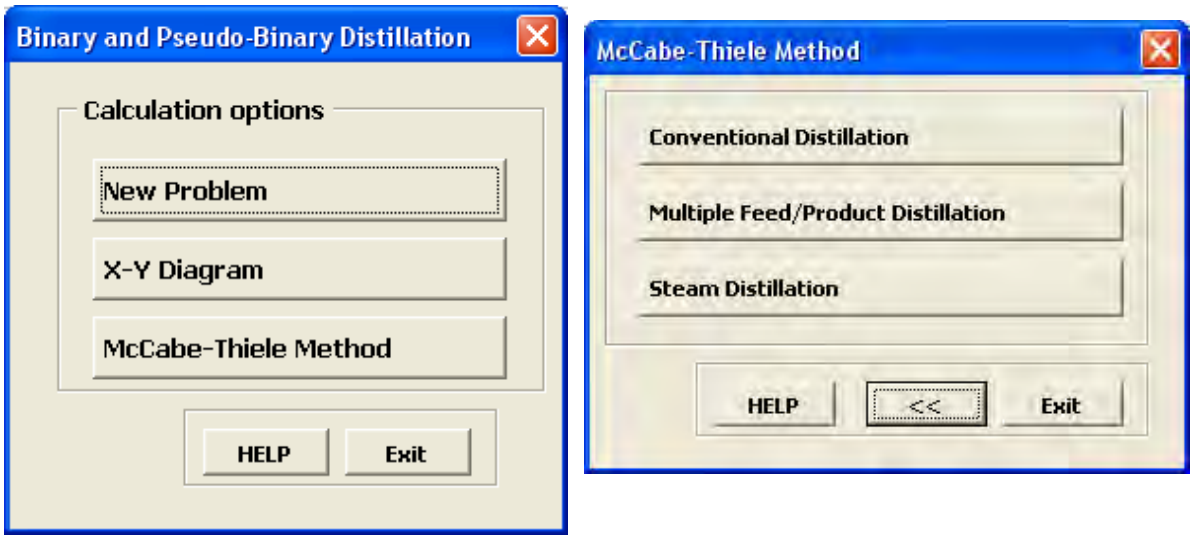

Figure 1 – Screenshots for binary distillation.

The add-in for multicomponent distillation uses the Fenske-Underwood-Gilliland-Kirkbride shortcut method. This method assumes constant internal flows in each section of the column, and constant relative volatility. For systems of variable relative volatility, the equilibrium constants or the parameters for the Antoine equation must be given, in order for the program to calculate an average value for the relative volatility. Two alternative equations are used to fit the Gilliland correlation, the Martins (1999) and Molokanov et al. (1972) equations. For application of the Gilliland correlation either the value of R/Rmin or N/Nmin must be specified. As output, the program gives the following information: minimum number of stages, minimum reflux ratio, composition and flows of both products at total and at minimum reflux ratio, number of ideal stages, operating reflux ratio and feed tray. The software is able of autonomously analyze the possibility of the distribution of non-key components.

3. Examples

This section gives an overview of the potentialities of the developed software, by showing how the two add-ins can be used to design distillation columns for a closely ideal mixture (i.e., benzene/toluene), a highly non-ideal mixtures (i.e., ethanol/water) and a multicomponent mixture.

Example 1: Binary distillation – Separation of the mixture benzene/toluene.

The first example corresponds to the separation of an equimolar saturated liquid mixture of benzene/toluene at 100 kPa. The behaviour of this mixture is closed to ideal, and therefore the phase equilibrium can be described by assuming the relative volatility constant, and equal to 2.456. The recovery of benzene was set equal to 90%, its purity equal to 90 %, and the reflux ratio equal to 2.61. Figure 2 shows the input form with the data used to design this conventional distillation column.

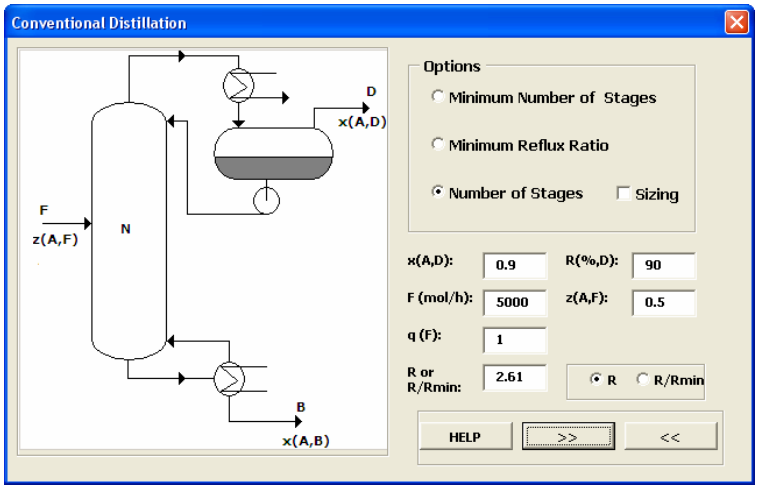

Figure 2 – Input form for the design of a binary conventional distillation column.

Running the add-in, the McCabe-Thiele diagram is created, and the minimum reflux ratio, the operating reflux ratio, and the ideal number of plates shown in the diagram (Figure 3). If the operator chooses the sizing option, the number of real stages and the column diameter and height will also appear in the generated McCabe-Thiele diagram.To further exemplify the capabilities of the software, the same example is now run using a column with 2 feeds and 1 sidestream, and assuming non-ideal liquid phase. The input form for this example is given in Figure 4, and the corresponding McCabe-Thiele diagram shown in Figure 5.

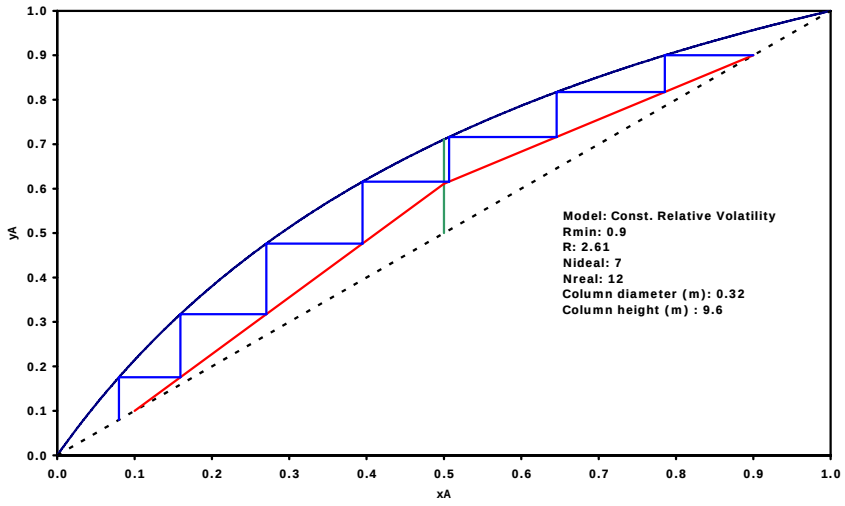

Figure 3 – McCabe-Thiele diagram for the system benzene(A)/toluene(B).

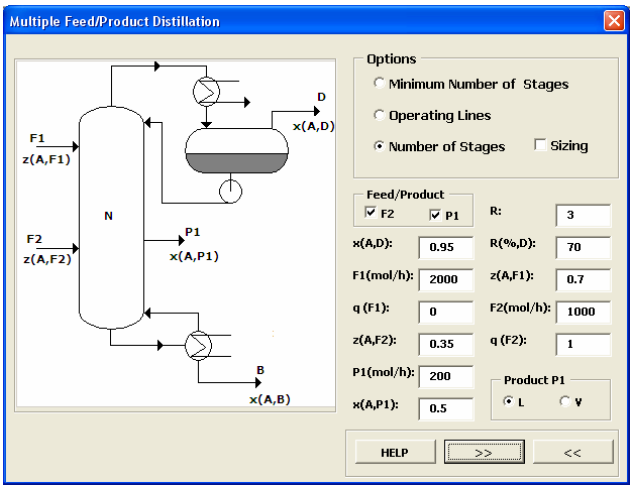

Figure 4 – Input form for a binary distillation column with 2 feeds and 1 sidestream.

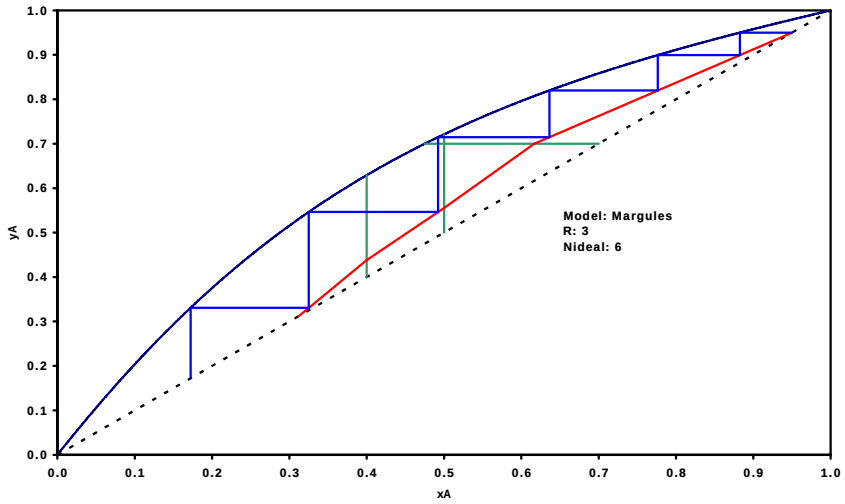

Figure 5 – McCabe-Thiele diagram for the system benzene(A)/toluene(B) in a column with 2 feeds and 1 sidestream

Example 2: Binary distillation – Separation of the mixture ethanol/water.

Figure 6 shows the McCabe-Thiele diagram for the mixture ethanol/water, assuming an ethanol recovery of 90%, and a distillate purity of 89% in ethanol. The feed was considered saturated liquid with 35% ethanol (molar percentage), and the R/Rmin ratio was set equal to 1.3. The vapour/liquid equilibrium was predicted by using the UNIQUAC model.

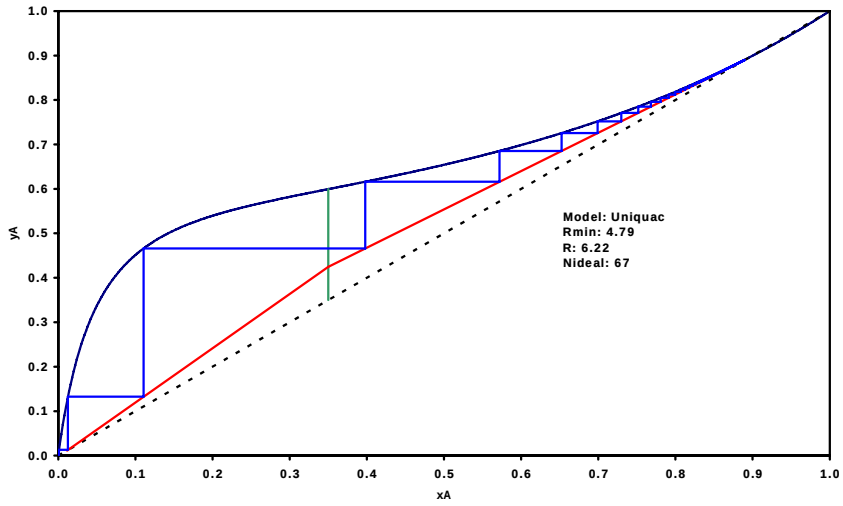

Figure 6 – McCabe-Thiele diagram for the system ethanol(A)/water(B).

As can be seen, for this highly non-ideal system, a large number of stages is necessary to attain the required separation, being most of the stages located in the rectifying section.

This add-in also allows the design of steam distillation columns, a capability that is not easily found in most of the available software applications.

Figure 7 shows the McCabe-Thiele diagram for the separation of the mixture ethanol(A)/water(B) by steam distillation.

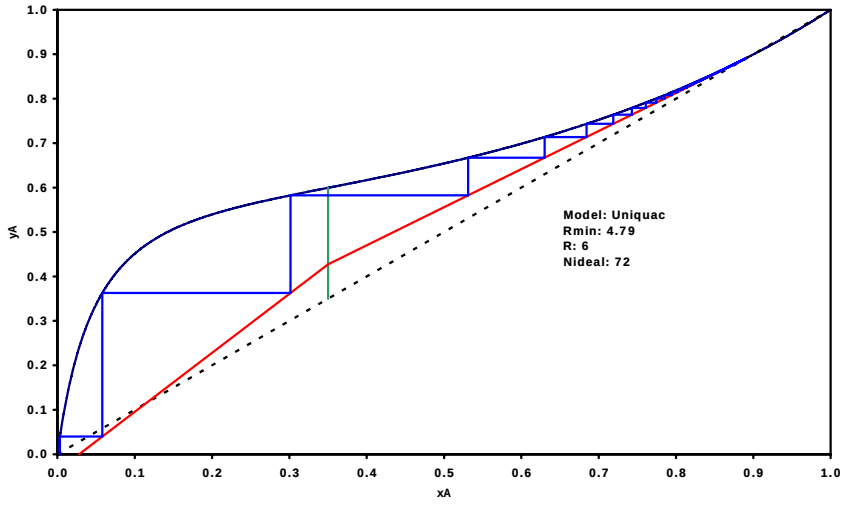

Figure 7 - McCabe-Thiele diagram for the separation of ethanol(A)/water(B) by steam distillation.

Example 3: Multicomponent distillation

The first case to be analyzed for multicomponent distillation deals with the separation of n-butane/n-pentane from a mixture with the following composition (molar percentage): 5% propane, 40% n-butane, 10% i-pentane and 45% n-pentane. The recovery of n-butane in the distillate and n-pentane in the bottom product were both set equal to 95%.

The key components are n-butane (light-key) and n-pentane (heavy-key), the operation pressure is 1000 kPa, and the ratio R/Rmin is 1.3. Table 1 shows the results generated by the add-in.

Table 1 – Results for the Fenske-Underwood-Gilliland-Kirkbride shortcut method.

	Fenske			Underwood			Gilliland (Martins, 1999)	
Components	**xd**	**xb**	**Nmin**	**xd**	**xb**	**Rmin**	**N**	**R**
Propane	0.109	0.000	7	0.108	0.000	1.201	15	1.561
n-Butane	0.830	0.037	**D/F**	0.819	0.037	**D/F**	**Kirkbride**	
i-Pentane	0.032	0.158	0.458	0.044	0.149	0.464	**Nr**	**Ns**
n-Pentane	0.029	0.805		0.029	0.814		8	7

This add-in can be used in alternative to the McCabe-Thiele method for binary systems of constant volatility. Table 2 shows the results of the application of the Fenske-Underwood-Gilliland-Kirkbride shortcut method to the separation of the binary mixture of benzene/toluene studied in example 1. As can be seen, identical results are achieved.

Table 2 – Results of the Fenske-Underwood-Gilliland-Kirkbride shortcut method for the system benzene/toluene.

	Fenske			Underwood			Gilliland (Fernando, 1999)	
Components	**xd**	**xb**	**Nmin**	**xd**	**xb**	**Rmin**	**N**	**R**
Benzene	0.900	0.100	5	0.900	0.100	0.870	7	2.609
Toluene	0.100	0.900	**D/F**	0.100	0.900	**D/F**	**Kirkbride**	
			0.500			0.500	**Nr**	**Ns**
							3	4

4. Conclusions

The potencialities of two Microsoft Excel add-ins developed for the design and sizing of binary and multicomponent distillation columns were discussed. These add-ins use shortcut methods, the McCabe-Thiele and Fenke-Underwood-Gilliland-Kirkbride methods, for design of binary and multicomponent distillation columns, and the method of Douglas for column sizing. The developed add-ins also allow the design of steam distillation columns, columns with multiple feeds and sidestreams, and columns used for the separation of non-ideal mixtures.

This software can be sucessfully used as an aid for teaching, or a tool for operator training and preliminary design and sizing of distillation columns.

References

Douglas, J.M. (1988) *Conceptual Design of Chemical Processes*, McGraw-Hill International Editions, Singapore.

Martins, F.G. (1999). Gilliland plot revisited. *Hydrocarbon Processing*, Volume 78 (12), 41.

Molokanov, Y.K., Korablina, T.P., Mazurina, N.I.; Nikiforov, G.A. (1972). An Approximation Method for Calculating the Basic Parameters of Multicomponent Fractionation. *Int. Chem. Eng.*, 12(2), 209-212.

Smith, J.M., Van Ness, H.C., Abbott, M.M. (2001). *Introduction to Chemical Engineering Thermodynamics*, 6th edition, McGraw-Hill International Editions, New York.

Proceedings of the 10th International Chemical and
Biological Engineering Conference - CHEMPOR 2008
Braga, Portugal, September 4-6, 2008
E.C. Ferreira and M. Mota (Eds.)

Continuous and Batch Distillation in an Oldershaw Tray Column

Carlos M. Silva*, Raquel V. Vaz, Tiago M. F. Canhoto, Patrícia F. Lito, Ana S. Santiago

CICECO, Department of Chemistry, University of Aveiro, 3810-193 Aveiro, Portugal

Keywords: distillation, rectification, McCabe-Thiele, efficiency, Rayleigh

Topic: Educating chemical engineers for coming challenges

Abstract

The importance of distillation in the separation field prompts the inclusion of distillation experiments on chemical engineering curricula. This work describes the performance of an Oldershaw column with 5 sieve trays in the rectification of a cyclohexane/n-heptane mixture. Different modes of column operation are studied, namely continuous rectification, with total and partial reflux, and batch rectification with constant reflux. The effect of internal flows upon the separation and column efficiency is also assessed. With this experimental work students train relevant concepts, including vapour-liquid equilibrium, continuous *versus* batch operation, McCabe-Thiele graphical method, column efficiency, and the generalized Rayleigh equation.

1. Introduction

The distillation is by far the most frequently used separation process. Although not energy-efficient, it has a simple flowsheet and is a low-risk process. It is indeed the benchmark with which all newer processes must be compared. Following Null (1987), distillation should be selected unless $\alpha_{12} < 1.05$, whereas Nath and Motard (1981) and Douglas (1988) indicate $\alpha_{12} < 1.10$, a more conservative critical value. Generally, design heuristics point out that processes using energy separation agents should be favoured.

Previous features justified the inclusion of distillation experiments on the chemical engineering curricula of the Department of Chemistry at University of Aveiro (DCUA). Students start receiving lectures on distillation as part of their course of Separation Processes I, which is essentially devoted to equilibrium-staged unit operations. Afterwards, experiments are carry out in Laboratory EQ, a weekly, six-hour lab course intended to study separation, reaction, and control.

In this paper the lab exercise on continuous and batch rectification developed at DCUA is presented. Experiments are performed in an Oldershaw column with 5 sieve trays to separate cyclohexane/n-heptane under different modes of operation: total reflux, continuous rectification with partial reflux, and batch rectification with constant reflux. The effect of the power supply to the reboiler flask upon the separation and column efficiency is evaluated.

An Oldershaw tray column is a laboratory scale column equipped with perforated trays. Of special importance is the fact it produces separations close to those in large industrial columns (Fair et al., 1983). In fact, experimental results show that commercial towers will

* Corresponding author. Tel + 351 234 401 549. E-mail:carlos.manuel@ua.pt

require a similar number of stages to reach the same separation level obtained in the Oldershaw unit (Humphrey and Keller, 1997).

With this work students train relevant concepts introduced earlier on their curriculum, namely vapour-liquid equilibrium, continuous *versus* batch operation, McCabe-Thiele graphical method, efficiency, and the generalized Rayleigh equation. Examining experimental results students gain insight in this unit operation.

2. Experimental Section

2.1 Experimental set-up

Experiments are performed in an Oldershaw tray column equipped with a dest-star advance controller supplied by Normschliff Gerätebau. The unit is shown in Figure 1 and comprehends five perforated plates, a reboiler, a total top condenser using tap water as cooling fluid, a lateral condenser to remove distillate as liquid, a solenoid valve to divide the vapor stream into reflux and distillate under partial reflux mode. Additional features are: temperature sensors placed between trays; samples of liquid may be withdrawn from each tray to determine its composition by refractive index (RI); temperature sensors immersed in reboiler and located at the top allowing the determination of the bottom and head compositions, respectively.

Figure 1: Oldershaw tray column.

2.2 Experiments at total reflux, $R = \infty$

Continuous rectifications at total reflux were performed at two distinct reboiler powers ($P = 700$ W and 900 W) to evaluate their effect upon separation and column efficiency. The temperature profile of the column was used to detect the stationary state. Top and bottom temperatures (T_D and T_B) were utilized to calculate the corresponding cyclohexane molar compositions, x_D and x_B, by Liquid-Vapor equilibrium relationships.

2.3 Continuous rectification at partial reflux

This equipment is extremely versatile, being possible to devise a continuous rectification under partial reflux. With an adaptation the distillate is directly fed to the reboiler (see Figure 1), allowing us to reach the corresponding stationary state. Such experiment was carried out at $R = 6$ under last power programmed, i.e. $P = 900$ W. Once more, T_D and T_B were utilized to determine x_D and x_B.

2.4 Batch rectification at constant partial reflux

Finally, a semi-continuous or batch distillation was performed with $R = 6$ and $P = 900$ W. Presently, the distillate is not fed to the reboiler, but collected to an independent flask shown in Figure 1. Under this mode of operation, compositions vary along time. T_D and T_B were registered during 1 h approximately, being used yet again to determine the corresponding x_D and x_B. At the end of the batch rectification, the refractive index of distillate was measured.

3. Calculations

3.1 Vapor-Liquid Equilibrium

At low pressures, the vapor-liquid equilibrium may be represented by:

$$y_i P_t = x_i \gamma_i P_i^{\sigma} \quad (1)$$

where y_i and x_i are the molar fractions of component i in the vapor and liquid phases, respectively, P_i^{σ} is its vapor pressure, γ_i is its activity coefficient, and P_t is the total pressure. P_i^{σ} is determined by the Antoine equation, while γ_i is calculated using the Margules equations. The corresponding parameters are listed in Table 1.

Table 1: Antoine (Boublik et al., 1973) and Margules parameters.

	Antoine[a)]			Margules	
	A	**B**	**C**	**A12**	**A21**
Cyclohexane	6.84941	1206.001	223.148	0.0563	-0.0938
n-heptane	6.90253	1267.828	216.823		

a) $\log P^{\sigma} = A - B/(T(^{o}C) + C)$

3.2 Number of equilibrium stages

The number of equilibrium stages is obtained by the well-known McCabe-Thiele method (Seader and Henley, 1998). In this work the column has a rectifying section only. Its operating line is:

$$y = \left(\frac{R}{R+1}\right)x + \left(\frac{1}{R+1}\right)x_D \quad (2)$$

When the column operates at total reflux ($R = \infty$) the rectifying operating line coincides with the diagonal line. The number of equilibrium stages is given by the number of outlined steps between x_D and x_B. One equilibrium stage, corresponding to the reboiler, must be discounted to the total number of stages.

3.3 Overall efficiencies

The experimental overall efficiency is given by:

$$E_{ov}\,(\%) = \frac{N_{ideal}}{N_{act}} \times 100 \quad (3)$$

where N_{ideal} is the ideal number of equilibrium stages and N_{act} is the actual number of trays (in this case $N_{act} = 5$).

The overall efficiency can be predicted by empirical correlations, namely, those by Drickamer and Bradford (1943), and O'Connell (1946). Drickamer and Bradford correlated the overall efficiency in terms of the molar average liquid viscosity, μ, of the column feed at the average tower temperature:

$$E_{ov}\,(\%) = 13.3 - 66.8 \log \mu\,(\mathrm{cP}) \quad (4)$$

O'Connell used viscosity and relative volatility, α, dependence:

$$E_{ov}\,(\%) = 50.3\left[\,\alpha \times \mu\,(\mathrm{cP})\,\right]^{-0.226} \qquad (5)$$

The relative volatility is the geometric average of bottom and top values.

3.4 Generalized Rayleigh equation

The liquid number of moles in the reboiler is related with distillate and residue compositions by the Generalized Rayleigh equation:

$$\ln\frac{B}{F} = \int_{x_{B,0}}^{x_{B,\,ftinal}} \frac{dx_B}{x_D - x_B} \qquad (6)$$

where F and B are the initial and final liquid number of moles in the reboiler, respectively. By knowing experimental (x_D, x_B) pairs, the B/F fraction may be obtained by numerical integration.

4. Results and Discussion

Table 2 presents the results obtained by total reflux experiments at 700 W and 900 W. For illustration, the McCabe-Thiele diagrams at total reflux and 900 W is plotted in Figure 2a. The minimum number of equilibrium stages were 4.76 and 4.61 for $P = 700$ W and 900 W, respectively, giving rise to overall efficiencies of 95.1% and 92.1%. These results indicate the column is more efficient when operated at 700 W, which is usually unexpected for the students. Actually, higher reboiler powers generate higher internal flows. Although such effect leads to a foreseen increase of the mass transfer coefficients, it also decreases the mean residence times of both phases in each tray which has a larger impact in the whole.

Table 2: Experimental conditions and results for total reflux experiments.

$P\,(W)$	T_D(ºC)	T_B(ºC)	x_D	x_B	E_{ov}(%)		
					Exp.	Eq. 4	Eq. 5
700	83.9	92.6	0.878	0.281	95.1	53.1	64.8
900	84.2	92.7	0.864	0.273	92.1	53.2	64.9

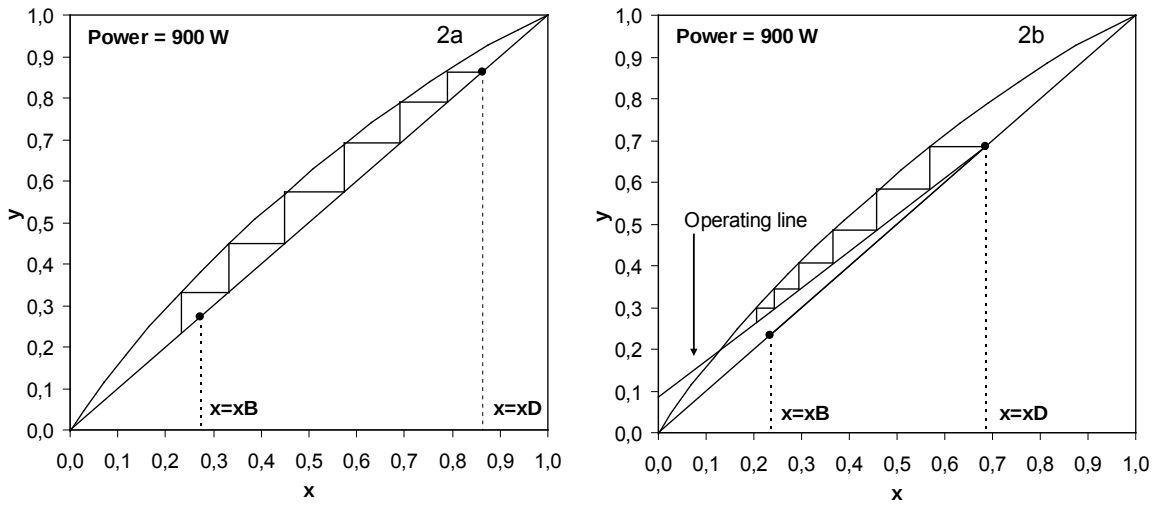

Figure 2: McCabe-Thiele diagram for a) total and b) partial reflux rectifications.

The experimental and predicted overall efficiencies for $P = 700$ W and 900 W are included in Table 2. Obtained results show that the predicted E_{ov} are significantly inferior to the experimental ones. Overall column efficiency is known to be a complex function of the system properties, operating conditions and column geometry; however, empirical correlations used only takes some system properties into account. Moreover, other results from literature (Seader and Henley, 1998) indicate that similar systems exhibit efficiencies 10% to 20% higher than the obtained by O'Connell correlation.

The results obtained for the partial reflux rectification ($P = 900\,W$ and $R = 6$) are given in Table 3. The corresponding McCabe-Thiele diagram is plotted in Figure 2b. As may be observed, the overall efficiency achieved was about the same of that obtained at total reflux for the same reboiler power.

Table 3: Results for partial reflux experiment.

T_D(ºC)	T_B(ºC)	x_D	x_B	E_o(%)
88.2	93.5	0.660	0.234	92.0

Figure 3 shows the evolution of distillate and residue compositions during the batch rectification ($P = 900\,W$ and $R = 6$). As expected, the column was exhausted in cyclohexane along time, because it is the light component.

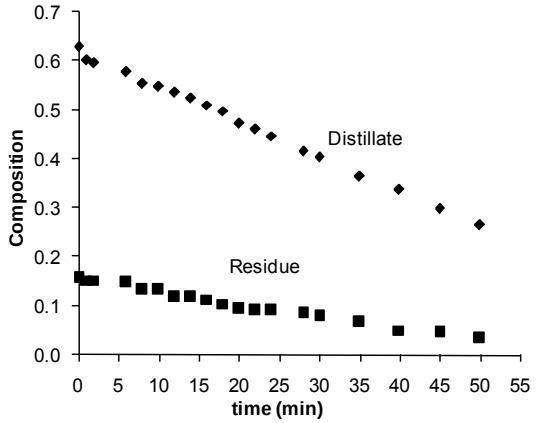

Figure 3: Distillate and residue compositions during the batch rectification.

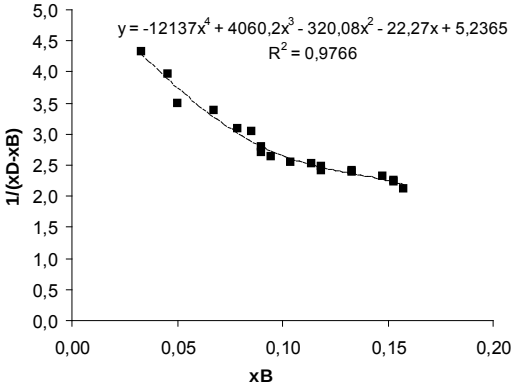

Figure 4: Graphical integration of Rayleigh equation.

The undistillated liquid fraction, B/F, was determined by numerical integration of the Rayleigh equation, using the polynomial fitted to experimental data (see Figure 4). Furthermore, B/F was also calculated by a mass balance using the initial ($x_{B,0}$) and final ($x_{B,final}$) residue compositions, and the composition of final distillate obtained by refractive index. As may be observed, B/F fractions obtained by both methods are very similar (see Table 3).

Table 3: B/F fraction obtained by Rayleigh equation and mass balance.

x_D **(RI)**	B/F **(Rayleigh Eq.)**	B/F **(mass balance)**
0.410	0.696	0.667

5. Conclusions

This work describes an experimental procedure where students have the opportunity to study distillation, using an Oldershaw tray column, under three different modes of operation: total reflux, partial reflux, and batch. The reboiler power (and so the internal flows) effect on column performance was investigated at total reflux. Results show the efficiency decreases slightly with increasing power. Column efficiency measured at partial reflux is analogous to that obtained at total reflux. In batch distillation the evolution of distillate and residue compositions was followed along time. Undistillated liquid fraction was calculated by numerical integration of the generalized Rayleigh equation and global material balance, giving rise to similar results.

With this work students train relevant concepts, including vapour-liquid equilibrium, continuous *versus* batch operation, McCabe-Thiele graphical method, column efficiency, and data analysis with the generalized Rayleigh equation.

Acknowledgments

Patrícia F. Lito wishes to express her gratitude to Fundação para a Ciência e Tecnologia (Portugal) for the PhD grant provided (SFRH/BD/25580/2005).

References

Boublik, T., Fried, V., Hala, E., (1973). *The Vapour Pressures of Pure Substances*, Elsevier, Amsterdam.

Douglas, J.M. (1988), *Conceptual Design of Chemical Processes*, McGraw-Hill, New York.

Drickamer, H.G., Bradford, J.R., (1943). Overall Plate Efficiency of Commercial Hydrocarbon Fractionating Columns as a Function of Viscosity, *Transactions AIChE*, 39, 319-360.

Fair, J.R., Seibert, A.F., (1996). Understand Distillation-Column Debottlenecking Options, *Chemical Engineering Progress*, 92(6), 42-48.

Nath, R., Motard, R.L. (1981), Evolutionary synthesis of separation processes, *American Institute of Chemical Engineering Journal*, 27, 578-587.

Null, H.R. (1987), Selection of a separation process, in R.W. Rousseau (Ed.) *Handbook of Separation Process Technology*, Wiley-Interscience, New York, Chapter 22.

O'Connell, H.E., (1946). Plate Efficiency of Fractionating Columns and Absorbers. *Transactions AIChE*, 42, 741-755.

Seader, J.D., Henley, E.J., (1998). *Separation Process Principles*, John Wiley & Sons, New-York.

Proceedings of the 10th International Chemical and
Biological Engineering Conference - CHEMPOR 2008
Braga, Portugal, September 4-6, 2008
E.C. Ferreira and M. Mota (Eds.)

Regeneration of sulfur poisoned nickel based catalysts for steam-methane reforming

S. Meysam Hashemnejad[1], Matin Parvari[1]*
[1] Chemical Engineering Department, Iran University of Science and Technology, Farjam Str., Tehran, Iran.

Keywords: Methane Steam Reforming; Nickel Catalysts; Sulfur Poisoning; Regeneration.
Topic: Regeneration of Spent Nickel Catalyst.

Abstract

This paper reports the result of regeneration of Razi petrochemical catalyst used for steam methane reforming. Nickel catalyst was poisoned by sulfur component from abnormally available in natural gas. A remarkable loss of sulfur was observed and the catalyst gains its activity. No changes of crystal structure were detected by XRD analyses. The first part leads to the identification of the catalyst by X-ray diffraction (XRD), Scanning Electron Microscope (SEM), carbon and sulfur analyzer. It clearly shows that sulfur and carbon deposition was the main problem in deactivation of catalyst. The catalyst activity of the catalyst contaminated with sulfur before and after regeneration was measured on methane steam reforming at a CH4:H2O ratio of 1:3 at 850Ċ. The result shows that approximately, main quantity of sulfur is removed and the regenerated catalyst gained 80% of its catalyst activity.

1 Introduction

Hydrogen gas or mixtures of hydrogen, carbon monoxide and carbon dioxide (synthesis gas) are used extensively in a wide range of industrial processes [1]. Hydrogen is predicted to become a major source of energy in the future. It is an important raw material in the chemical and petroleum industries; large quantities are used in the manufacture of ammonia and methanol and in a variety of petroleum hydro treatment processes [2, 3]. Methane can be converted into synthesis gas by steam reforming, CO_2 (dry) reforming or by conversion with O_2 through secondary reforming and partial oxidation [4]. Three main methane steam reforming reactions are always carried out as presented in the following equations:

$$CH_4+H_2O \leftrightarrow 3H_2+CO \quad (1)$$

$$CO+H_2O \leftrightarrow CO_2+H_2 \quad (2)$$

$$CH_4+2H_2O \leftrightarrow CO_2+4H_2 \quad (3)$$

Both water–gas shift reaction (Eq. (2)) and reverse methanation (Eq. (3)) are associated with the steam reforming over a catalyst at elevated temperatures [5]. Steam reforming reactions are usually carried out on supported nickel catalysts. Nickel is cheap, sufficiently active, and allows suitable catalysts to be economically produced.

One of the major problems in the application of these catalysts is sulfur poisoning. Even after a thorough desulfurization of the feedstock, sulfur-containing compounds in the feed may reach

* Corresponding author. Tel +98(21)73912755, Email: Parvari@iust.ac.ir

the nickel catalyst at a ppb level. Sulfur is a strong poison for nickel catalysts and blocks the active nickel sites. The sulfur adsorption capacity of steam-reforming catalysts is therefore an important catalyst parameter [6].

2 Sulfur poisoning

The most common cause of poisoning involves strong chemisorptions of gas phase species on the active sites. If the chemisorptions are weak, desorption and reactivation may occur, if it is strong deactivation results. The effectiveness of a poison depends on the equilibrium constant for the poisoning reaction and on the catalysts activity of the product formed. Sulfur is the good case in point.

Sulfur is a severe and common poison for nickel steam reforming catalysts as a sulfur-poisoned nickel catalyst has essentially no activity below 700Ċ. All sulfur -containing compounds in the feed are converted into hydrogen sulfide at reforming conditions [6]. The sulfur atom in hydrogen sulfide adsorbs strongly at the nickel surface by following reaction:

$$H_2S + Ni_{Surface} \leftrightarrow Ni_{Surface}\text{-}S + H_2 \qquad (4)$$

Process (4) is a fast, reversible process in a large range of concentration. Feedstock with S contents lower than 10 ppb are recommended to avoid appreciable deactivation of the Ni catalytic surface [7]. Process (4) is carry out with the adsorption of water in active site

$$H_2O + Ni_{Surface} \leftrightarrow Ni_{Surface}\text{-}O + H_2 \qquad (5)$$

This is to compete with sulfur binding for high water steam contents in the feed.

Concept that contributes to the sulfur poisoning is sulphating of support, which may change the crystalline structure and nature of support [8-10], so we can find out that the type of support may affect on reversible of sulfur poisoning.

3 Experimental Section

3.1. Catalyst preparation and reaction tests

The commercial catalyst was supplied by Razi petrochemical complex (Iran). Ni (14wt %) supported on $CaAl_4O_7$ is an industrial steam methane reforming catalyst. The catalyst was crushed and sieved to the appropriate size (30–50 mesh).

The experimental setup used for these experiments was operated at atmospheric pressure with ratio of methane to steam (CH_4/H_2O = 1/3). High purity methane (not less than 99.99%) was used as the reactant. Runs were carried out in a fixed bed quartz micro reactor (6.6 mm ID). Experiments were performed with 200 mg of the catalyst. After catalyst loading, because XRD study shown that a part of the Ni in the fresh catalysts is found as NiO so catalyst was reduced in situ for 2 h in a 50 mol% H_2/N_2 mixture (60 ml/min), while the temperature was raised from ambient to 600Ċ at a rate of 10Ċ/min. The catalyst was heated to 850 Ċ under the nitrogen flow with the rate of temperature increase of 10 Ċ /min. water and methane were then introduced to the reactor respectively. The composition of the gas stream leaving the reactor was determined by gas chromatography that is able to simultaneously analyze the remaining CH_4 and produced CO, CO_2 and H_2. The remaining water vapor exiting the reactor was removed from the product stream by use of a condenser.

3.2. Catalyst characterization

X-ray diffraction studies were performed in a PW-1800 Philips diffractometer with Cu Kα radiation (λ = 1.5406 Å) at 40 kV, 30 mA for determining crystalline phases.

Chemical analysis of all samples was carried out using a scanning electron microscope (SEM) coupled with an energy dispersive spectroscopy (EDS) analysis for the determination of chemical composition of samples. SEM images were taken on a Philips XL30 microscope.

The amount of deposited carbon and sulfur on species after reaction was quantified by Carbon Analysis (CA) which was performed on a thermal analysis Leco CS-444 from ambient to burned sample temperature. The samples burned on excited oven and amount of gas outlet was determined by a quadruple mass spectrometer.

3.3. Regeneration treatments

The regeneration process was performed in an attempt to remove both sulfur and carbon from the Ni catalyst, using the steam treatment in 700Ċ, higher temperature may increase the risk of sintering of nickel particles. The treatments were carried out in 2 hour. In all cases we added hydrogen to steam to prevent fully oxidation atmosphere, one of the reason of that is help us not to do repetitious reduction of catalyst before reforming reaction. After each satisfactory treatment the catalyst was cooled under nitrogen to room temperature and analyzed the sulfur and carbon content.

4 Results and Discussion

4.1. Catalyst characterization

In this case we have nickel catalyst used for production of synthesis gas with H_2/CO=3/1 ratio. There are three deactivated catalyst from top, middle and bottom of tower, which are compared with each others. As we know, one of the unexpected problems is excess existence of sulfur and sulfur derivations as poison of nickel catalyst in feed. The reaction conditions employed here are rather severe in terms of sulfur and also carbon deposition. Sulfur content in three deactivated catalysts is summarized in table 1. It clearly shows the huge amount of sulfur and carbon in catalyst at top that we do not have this severe condition for catalysts in middle and bottom so we can conclude the operations are take place out of control.

Table 1 sulfur and carbon weight percentage of nickel catalyst at top, middle and bottom of tower in Razi petrochemical complex.

Wt%	Top	Middle	Bottom
Carbon	0.17	0.04	0.03
Sulfur	0.2	0.03	0.03

The powder X-ray diffraction patterns of the deactivated samples in top, middle and bottom of the tower are shown in Fig. 1. NiO give peak at 37.249°, and no indication of $NiAl_2O_4$ is observed for this catalyst. Figure 1 clearly point out that calcium aluminate was used as support. The results demonstrate that there are no considerable changes of nickel crystallite sizes in three deactivated catalysts with each other and also compare with fresh one has been occurred. Sharpen up for support phase at top of the tower, indicating that particles of calcium aluminate became larger; this is consistent with the SEM micrographs of these samples as shown in fig. 2.

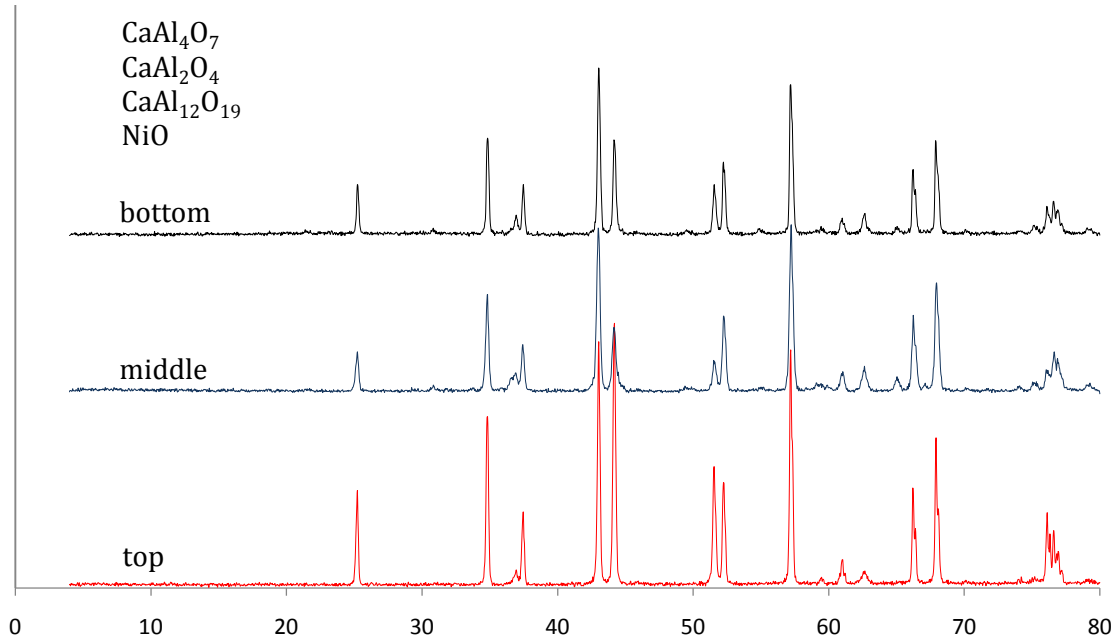

Fig. 1. XRD pattern of active and support phases for top, middle and bottom of tower catalyst sample in Razi petrochemical complex.

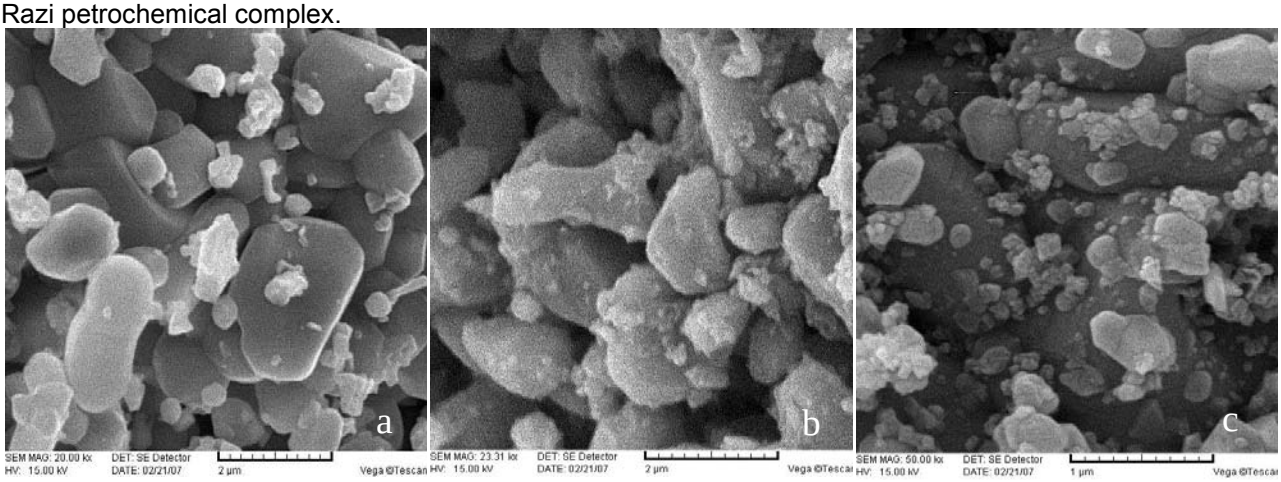

Fig. 2. SEM micrograph of bottom (a), middle (b) and top (c) used catalyst sample, in Razi petrochemical complex.

4.2. Catalyst regeneration

Regeneration of nickel catalyst was shown to be effective upon injection of steam stream at 700Ċ:

$Ni_{Surface}$-S + H_2O ↔ NiO + H_2S (6)

H_2S + 2H_2O ↔ SO_2 + 3H_2 (7)

One of the other reasons for adding hydrogen to the steam stream is to lead forward reaction (7) to prohibit hydrogen sulphide remaining in system and change it to SO_2.

The data in figure 1 show the impressive results in sulfur removal from Ni base catalyst. The degree of regeneration is declared with the ratio S/S_0, S and S_0 are the sulfur contents after

regeneration treatment and in initial deactivated catalyst, we have the same situation for carbon content. We can see the profound changes in sulfur content in regenerated catalyst.

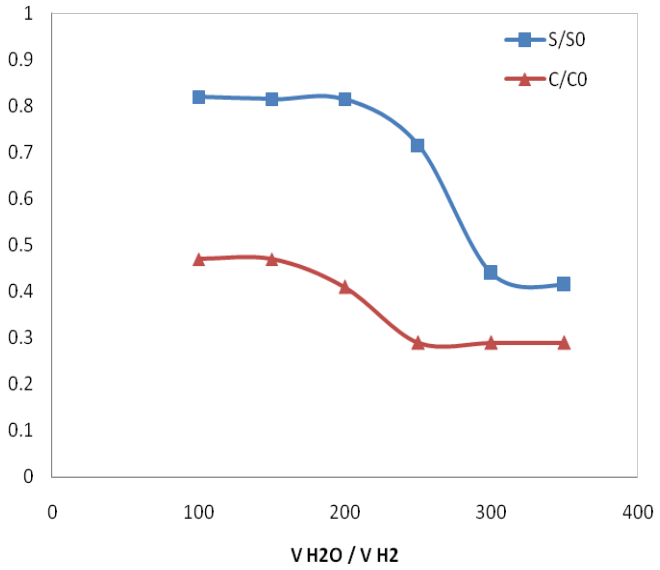

Figure3. Results in regeneration treatment with V_{H_2O}/ V_{H_2} for taking out sulfur and carbon in contaminated Ni based catalyst.

When the ratio VH_2O/ VH_2 was increased no improvement was observed as expected from the chemisorptions experiment. However, at VH_2O/ VH_2 above 200 a significant decrease of sulfur content in regenerated catalyst was observed (fig.1); surprisingly there is the same condition for removal of carbon deposition as shown figure 1. One of the characteristics of this treatment is that the catalyst structure does not change during the regeneration, as we shown in fig. 2.

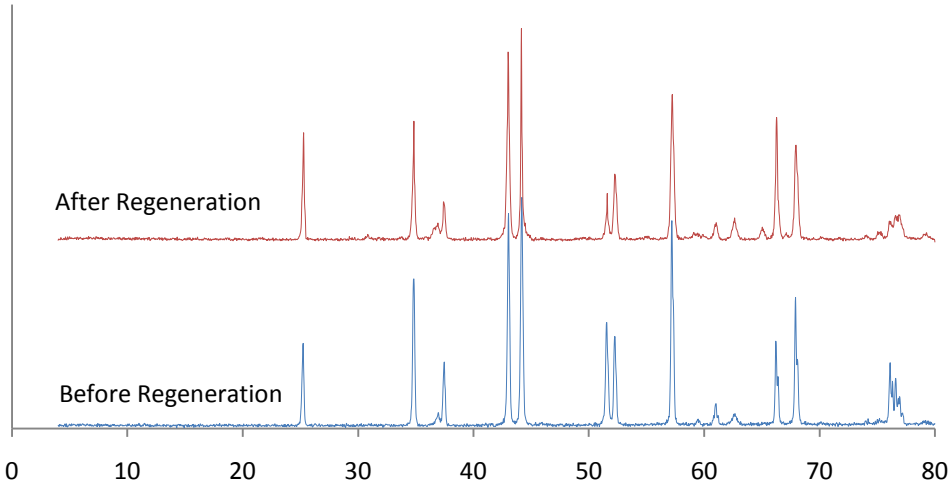

Figure4. XRD pattern of Ni catalysts where denote catalysts structure before and after treatment with steam.

The observed methane conversions for the catalyst before and after regeneration are summarized in figure 3. The catalyst regained more than 80% of its activity at VH_2O/ VH_2 = 350.

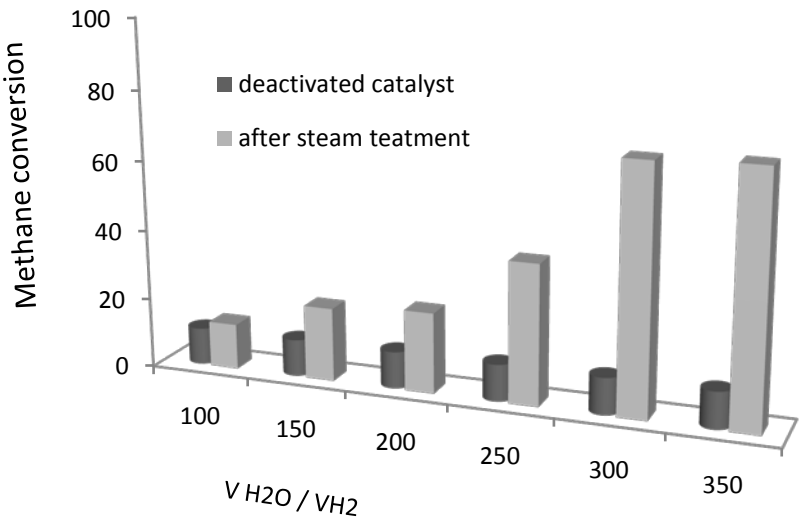

Figure5.methane reforming conversion in deactivated nickel catalyst before and after treatment with steam.

5 Conclusions

Sulfur poisoning is critical subject for steam reforming catalysts. Regeneration experiments have been performed on conventional Ni catalyst ($NiO\text{-}CaAl_4O_7$). The regeneration process is based on an oxidative removal of sulfur and carbon from the deactivated catalyst with steam treatment in 700Ċ. The steam reforming of methane at a CH_4:H_2O ratio of 1:3 was employed to test the catalytic activity of the catalyst. Since most of the sulfur and carbon is thereby removed, catalyst regained its activity more than 80%. One of important thing is no changes of the crystal structure were detected by XRD diagram.

Acknowledgment
The authors would like to thank Razi petrochemical complex for providing Ni catalyst.

References

[1] Frank B. Rasmussen1, Jens Sehested, Herman T. Teunissen, Alfons M. Molenbroek, Bjerne S. Clause, “Sintering of Ni/Al2O3 catalysts studied by anomalous small angle X-ray scattering” Applied Catalysis A: General 267 (2004) 165–173.
[2] J.N. Armor, Appl. Catal. A 176 (1999) 159.
[3] J.I. Villacampa, C. Royo, E. Romeo, J.A. Montoy, P. Del Angel, A. Monzóna, “Catalytic decomposition of methane over Ni-Al2O3 coprecipitated catalysts Reaction and regeneration studies” Applied Catalysis A: General 252 (2003) 363–383.
[4] J.R. Rostrup-Nielsen, Catal. Today 18 (1993) 305.
[5] N. Laosiripojana, S. Assabumrungrat, “Methane steam reforming over Ni/Ce–ZrO2 catalyst: Influences of Ce–ZrO2 support on reactivity, resistance toward carbon formation, and intrinsic reaction kinetics”, Applied Catalysis A: General 290 (2005) 200–211.
[6] Jens Sehested,“Four challenges for nickel steam-reforming catalysts”, Catalysis Today 111 (2006) 103–110.
[7] Christophe Lombard, Stephane Le Doze, Eric Marencak, Paul-Marie Marquaire, David Le Noc, Grégory Bertrand, François Lapicque, “In situ regeneration of the Ni-based catalytic reformer of a 5kW PEMFCsystem”, International Journal of Hydrogen Energy 31 (2006) 437 – 440.
[8] C.P. Hubbard, K. Otto, H.S. Gandhi, K.Y.S. Ng, J. Cata. 144 (1993) 484.
[9] C.P. Hubbard, K. Otto, H.S. Gandhi, K.Y.S. Ng, Cata. Lett. 30 (1995) 41.
[10] M. Waqif, P. Baxin, O. Saur, J.C Lavalley, G. Blanchrd, O. Touret, Appl. Catal. B 11 (1997) 193.

Proceedings of the 10th International Chemical and
Biological Engineering Conference - CHEMPOR 2008
Braga, Portugal, September 4-6, 2008
E.C. Ferreira and M. Mota (Eds.)

Total oxidation of ethyl acetate over TiO_2 supported noble metals catalysts

V. P. Santos, M. F. R. Pereira, J. J. M. Órfão, J. L. Figueiredo*
Laboratório de Catálise e Materiais (LCM), Laboratório Associado LSRE/LCM, Departamento de Engenharia Química, Faculdade de Engenharia, Universidade do Porto, Rua Dr. Roberto Frias, 4200-465 Porto, Portugal

Keywords: catalytic oxidation, VOC, ethyl acetate, platinum, palladium, titania
Topic: Advancing the chemical and biological engineering fundamentals.

Abstract

The catalytic oxidation of ethyl acetate in low concentration (2,000 ppmv) was investigated over noble metal catalysts (palladium or platinum) supported on titania. The influence of several parameters was investigated, such as the crystalline phase of the support, the type and amount of noble metal, the metal dispersion and the activation conditions. Platinum was found to be more active and selective into CO_2 than the corresponding palladium catalyst. The activation conditions influence the activity of the Pt/TiO_2 catalyst. The highest activities were obtained when the catalyst was activated under hydrogen atmosphere. The presence of water vapour in the feed enhances the global conversion and decreases the CO_2 selectivity.

1 Introduction

Volatile organic compounds (VOC) are considered an important class of air pollutants, not only due to their toxic nature but also because they are precursors of ground level ozone and smog. VOC are emitted from a variety of sources such as industrial processes (stationary sources ≈ 40 %) and vehicle exhaust (mobile sources ≈ 60 %). Among the different techniques that can be applied to efficiently control the emissions of VOC, catalytic oxidation seems to be the most efficient and cost-effective technology for emissions containing low concentrations (Everaert and Baeyens, 2004). In this process, high elimination efficiency can be achieved at relatively low temperatures, although the performance of the process critically depends on the type of the catalyst used, operating temperature, VOC type and concentration, space velocity and O_2 concentration.

The optimization of the catalyst formulation is not usually an easy task, due to the large variety of VOC molecules and the complex nature of VOC mixtures. Extensive studies have been done in recent years in order to develop more active catalysts and to understand the factors that determine VOC reactivity over oxidation catalysts (Papaefthimiou et al., 1998a; O'Malley and Hodnett, 1999; Tsou et al., 2004). In general, platinum and palladium supported catalysts are considered more active than metal oxides in the oxidation of several VOC (mainly in the oxidation of non-oxygenated VOC) (Papaefthimiou et al., 1998b; Tsoncheva et al., 2006). As a result, the majority of commercial catalysts consists of either platinum or palladium or both supported on alumina carriers, in pellet or monolith forms.

The main goal of the present work is to study the oxidation of ethyl acetate catalysed by noble metals supported on titania. Several parameters were investigated, such as the structure of the support and type of noble metal (platinum and palladium). The best catalytic system was chosen for further studies, namely the load of noble metal, pre-treatment

* Corresponding author. Tel + 351-22 508 1663 E-mail: jlfig@fe.up.pt

conditions, stability and the influence of the presence of other species in the performance of the catalyst.

Among VOC, ethyl acetate is a common solvent, widely used in the printing industry and is one of the most difficult gaseous pollutants to oxidise completely. Several studies have been reported choosing ethyl acetate as a model for volatile organic compounds (Papaefthimiou et al., 1998a; Papaefthimiou et al., 1998b; Sawyer and Abraham, 1994; Papaefthimiou et al., 1997; Yang et al., 2007).

2 Experimental

2.1 Preparation and characterization of the catalysts

TiO_2 with different amounts of anatase and rutile phases were used in this work. The first sample consists of 100% anatase and was synthesized by a sol-gel process, via hydrolysis of titanium alkoxides, in acidic medium. The second sample is a commercial product (Degussa P-25) containing 80% anatase. The third sample was obtained by submitting P-25 to a thermal treatment at 700 ºC under air, in order to reduce the content of anatase to 47% (Grzechulska-Damszel et al., 2006)

Platinum and palladium supported catalysts were prepared by incipient wetness impregnation on Degussa P-25 using as metal precursors, H_2PtCl_6 and $PdCl_2$, respectively (metal load: 1% or 2%). The resulting materials were dried at 110 ºC overnight and calcined at 500 ºC for 2 hours.

The crystalline structure was identified by X-ray diffraction (XRD) measurement. The metal dispersion was obtained by hydrogen chemisorption at room temperature. The characterization results are shown in Table 1.

Table 1- Properties of the catalysts (crystalline phase and metal dispersion).

Catalyst	Phases	Metal dispersion, D_M (%)
TiO_2 (sol-gel)	100% anatase	-
TiO_2 (P25)	80% anatase	-
TiO_2 (P25, air, 700 ºC)	47 % anatase	-
1% Pt/TiO_2	80% anatase	15
2% Pt/TiO_2	80% anatase	18
1% Pd/TiO_2	80% anatase	14
1% Pt/TiO_2 (air/steam, 500 ºC)	80% anatase	1

2.2. Kinetic study

The reaction was carried out in a BTRS Jr Autoclave Enginners fixed bed reactor at atmospheric pressure and in the temperature range of 150-400 ºC. The reactor was maintained at each temperature for 30 minutes in order to obtain experimental values at steady state. The ethyl acetate conversion (X) and the conversion into CO_2 (X_{CO_2}) were respectively calculated as $X = 1 - \frac{F_{VOC}}{F_{VOC,in}}$ and $X_{CO_2} = \frac{F_{CO_2}}{\nu F_{VOC,in}}$, where F_{VOC} is the outlet molar flow rate of VOC at steady state, $F_{VOC,in}$ is the inlet molar flow rate of VOC, F_{CO_2} is the outlet molar flow rate of CO_2 at steady state and ν is the number of carbon atoms in the VOC molecule (for ethyl acetate, ν = 4). A concentration of ethyl acetate in the feed stream of 2,000 ppmv and a space velocity of 16,000 h^{-1} were used as standard conditions. The catalyst sample (0.05 g) was diluted with glass spheres of the same size as the catalyst particles ($0.2<\phi<0.5$ mm), in order to minimize the thermal effects (catalyst bed length: 2 cm). The temperature was evaluated by a K-type thermocouple placed in the middle of the catalyst bed. Prior the reaction, the best catalytic system was pre-treated in situ according to three different protocols: a) air at 400 ºC for 1 hour; b) hydrogen at 350 ºC for 2 hours; c) mixture of steam and air at 500 ºC for 2 hours.

The analytical system consisted of a gas chromatograph equipped with a flame ionization detector (FID) for the analysis of the organic compounds, and two non-dispersive infrared (NDIR) analyzers for detection and quantification of CO (Analytical Development Company) and CO_2 (NOVA Analytical Systems Inc.).

3. Results and discussion

3.1 Catalyst screening

The oxidation of ethyl acetate was studied over the TiO_2 samples and the noble metal/TiO_2 catalysts. This study was made in order to obtain the best catalyst for this reaction with respect to: a) crystalline phase of the support, comparing three samples with different amounts of anatase; b) type of noble metal (palladium or platinum). The results are presented in Figure 1.

The influence of the TiO_2 crystalline phase was studied in the temperature range of 150-400 ºC. As can be seen, this parameter does not have a major effect on the catalytic activity of TiO_2, although the anatase structure is a little more active than the rutile phase. In the presence of the support, ethyl acetate is completely oxidized at about 340 ºC, but the CO_2 yields are very low at this temperature (XCO_2 values between 47% and 67%, respectively for the 47% and 100% anatase samples). High amounts of by-products were formed, such as acetic acid, acetaldehyde and acetone, due to the large number of acidic sites on titania. This is in agreement with the information reported by other authors (Papaefthimiou et al., 1998a).

Supporting palladium or platinum on TiO_2 considerably reduces the amount of by-products formed and enhances the activity, decreasing the temperature at which ethyl acetate is completely converted into CO_2 to 330 and 280 ºC, respectively. This effect is less pronounced for palladium catalysts, where at high temperatures large amounts of ethylene were formed. Thus, Pt/TiO_2 catalyst was selected for further studies.

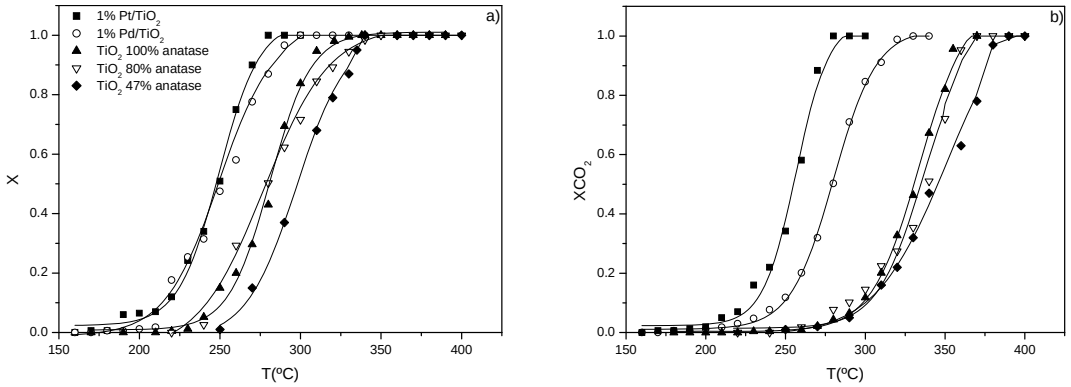

Figure 1- Catalytic activity of 1% Pt/TiO_2, 1% Pd/TiO_2 and TiO_2 (100%, 80% and 47% of anatase), for the oxidation of ethyl acetate: a) Ethyl acetate conversion (X) b) Conversion into CO_2 (XCO_2).

3.2. Influence of the pre-treatment conditions

The effect of the electronic state of platinum was studied in this reaction by comparing the activities of the Pt/TiO_2 catalyst pre-reduced under hydrogen at 350 ºC and pre-calcined under air at 400 ºC. The behaviour of both catalysts is shown in Figure 2. As can be seen, the pre-reduced catalyst is more active in the oxidation than the calcined one. For instance, at 250 ºC the conversion into CO_2 is about 57% with the pre-reduced catalyst, while with the pre-calcined catalysts can only achieve this conversion at 260 ºC. This behaviour is in agreement with reports by other authors, where metallic platinum was also found to be the

most active catalyst, namely in the oxidation of o-xylene and MIBK over Pt/HFAU (Tsou et al., 2005) or n-heptane over Pt/Al_2O_3 (Völter et al., 1987).

Figure 2 also shows the activity of Pt/TiO_2 after a pre-treament in situ with air/steam at 500 ºC. It is well known that a treatment with a mixture of air and steam at high temperatures promotes the sinterization of the platinum particles (Löwendahl and Otterstedt, 1990). In fact, the metal dispersion was found to decrease from 15 to 1% (see Table 1). The results show that the complete oxidation of ethyl acetate into CO_2 over the steamed catalyst occurs at higher temperatures (290 ºC). However, the intrinsic activity of the catalyst was found to increase with increasing particle size of Pt, which makes this reaction structure-sensitive.

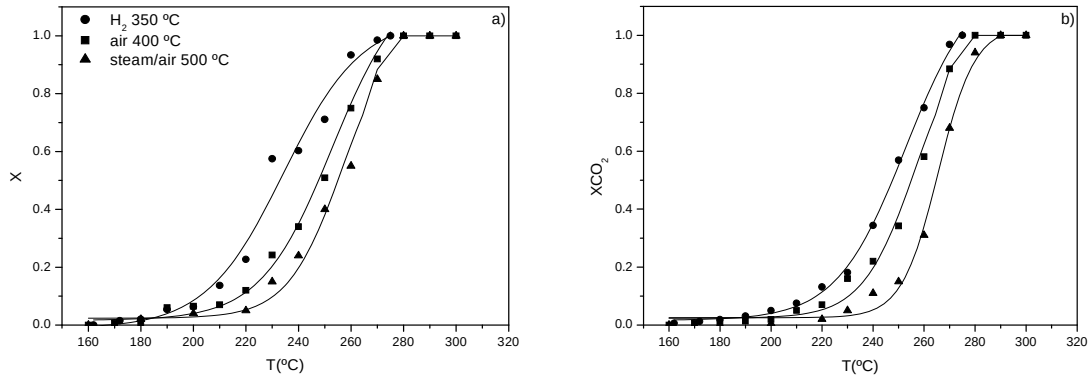

Figure 2- Effect of the activation conditions on the catalytic activity of Pt/TiO_2 catalyst: a) Ethyl acetate conversion (X); b) Conversion into CO_2 (XCO_2).

3.3. Influence of platinum content

The influence of platinum load on the catalytic activity was investigated varying the platinum level from 1 to 2%. The results are presented in Figure 3. For a similar metallic dispersion (see Table 1), the higher the platinum content, the higher the global conversion and the CO_2 yield. For instance, complete oxidation of ethyl acetate into CO_2 is obtained at 290 ºC for a Pt content of 1% and at 280 ºC for 2%.

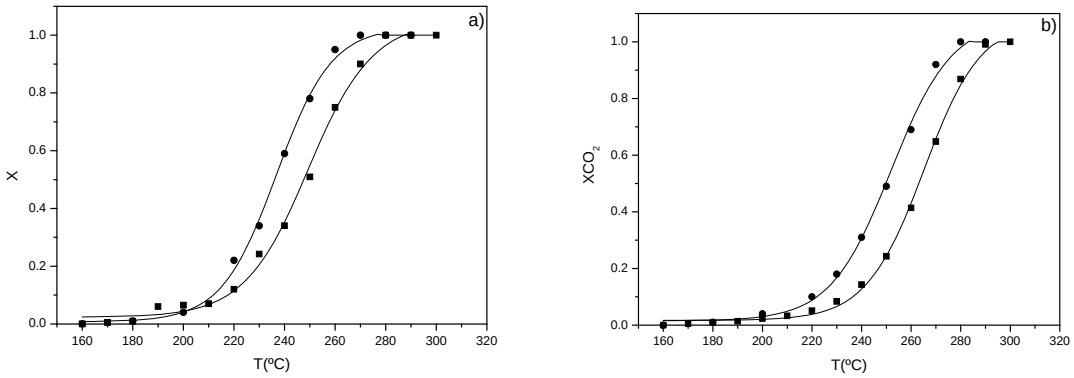

Figure 3- Ethyl acetate conversion (X) and conversion into CO_2 (XCO_2) as a function of temperature over Pt/TiO_2 with different platinum loads: 2%(●) and 1% (■).

3.4 Stability of the catalyst

In order to analyze the stability of the materials, light-off experiments were made with a fresh catalyst and with a sample previously used in a long duration experiment at 450 ºC for 24 hours. It was concluded (data not shown) that the platinum supported catalyst is very stable and does not present any kind of deactivation.

3.5 Effect of the presence of water vapour, CO_2 and ethanol in the feed

In practical situations, the conditions for the oxidation of VOC will not be the same as the standard conditions used in this work. Moisture, CO_2 and other VOC will be present in the feed to be treated. In order to study the effect of these parameters on the performance of the catalyst, kinetic studies were carried out introducing CO_2, water or ethanol in the feed.

It was observed (results not shown) that CO_2 does not have a major effect in the performance of the catalyst, suggesting that CO_2 has a little affinity towards the support.

The presence of water vapour enhances the conversion of ethyl acetate, but decreases the CO_2 selectivity (results not shown). Larger amounts of by-products are formed such as acetaldehyde, ethylene, acetone, acetic acid and ethanol. Water promotes the decomposition of ethyl acetate into ethanol and acetic acid, which are further converted into acetaldehyde and acetone, or oxidized completely into CO_2 and H_2O (Sawyer and Abraham, 1994).

In addition to the results obtained above, the behaviour of Pt/TiO_2 in the oxidation of ethyl acetate and ethanol mixtures was investigated. Kinetic experiments were carried out at different temperatures in the standard conditions described previously (2,000 ppmv of each VOC).

The conversion of ethyl acetate alone and in the presence of 2,000 ppmv of ethanol over Pt/TiO_2 is shown in Figure 4 as a function of the reaction temperature. It was found that the oxidation of ethyl acetate is not affected by the presence of ethanol.

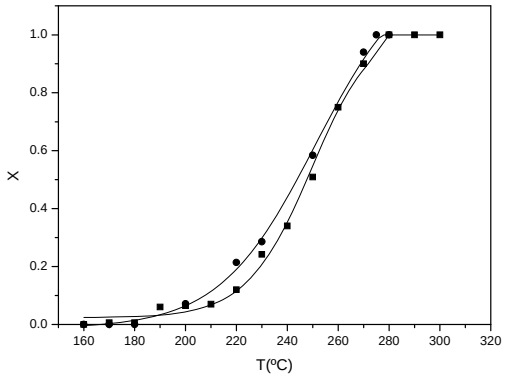

Figure 4- Conversion of ethyl acetate as a function of temperature on 1%Pt/TiO_2: ethyl acetate alone (2,000 ppmv) (■) and with ethanol (2,000 ppmv + 2,000 ppmv) (●).

4 Conclusions

The following conclusions can be drawn from this study:

- The TiO_2 phase does not play a major role on the catalytic activity, in spite of the anatase structure being a little more active than the rutile phase.
- The presence of a noble metal is essential to increase both activity and selectivity into CO_2.
- The platinum catalyst is more active and selective than the corresponding palladium catalyst.
- The pre-reduced catalyst is more active than the pre-calcined one.
- The performance of the Pt/TiO_2 catalyst in the oxidation of ethyl acetate is not very sensitive to the metal dispersion.
- The higher the platinum content, the lower the temperature necessary to convert all ethyl acetate into CO_2.

- Long duration experiments show that the platinum supported catalyst is very stable during the catalytic oxidation.
- The presence of water vapour in the feed stream increases the global conversion but decreases the CO_2 selectivity. On the contrary, CO_2 has no influence on the catalytic activity.
- The presence of ethanol in the feed has no effect on the catalyst performance for the oxidation of ethyl acetate.

Acknowledgments

This work was supported by Fundação para a Ciência e a Tecnologia (FCT) and FEDER under Programme POCI/1181 and PTDC/AMB/69065/2006. V.P.S. acknowledges the grant received from FCT (SFRH/BD/23731/2005).

References

Everaert, K., Baeyens, J. (2004). Catalytic combustion of volatile organic compounds. *Journal of Hazardous Materials,* 109, 113-139.

Grzechulska-Damszel, J., Morawski, A.W., Grzmil, B. (2006) Thermally modified titania photocatalysts for phenol removal from water. International Journal of Photoenergy, 2006, Article ID 96398, 7 pages, doi:10.1155/IJP/2006/96398.

Löwendahl, L., Otterstedt, J.E. (1990). Effect of hydrothermal treatment on alumina as support for noble metal catalysts. *Applied Catalysis,* 59, 89-102.

O'Malley, A., Hodnett, B.K. (1999). The influence of volatile organic compound structure on conditions required for total oxidation. *Catalysis Today,* 54, 31-38.

Papaefthimiou, P., Ioannides, T., Verykios, X.E. (1997). Combustion of non-halogenated volatile organic compounds over group VIII metal catalysts. *Applied Catalysis B-Environmental,* 13, 175-184.

Papaefthimiou, P., Ioannides, T., Verykios, X.E. (1998a). Performance of doped Pt/TiO2 (W6+) catalysts for combustion of volatile organic compounds (VOCs). *Applied Catalysis B: Environmental,* 15, 75-92.

Papaefthimiou, P., Ioannides, T., Verykios, X.E. (1998b). Catalytic incineration of volatile organic compounds present in industrial waste streams. *Applied Thermal Engineering,* 18, 1005-1012.

Sawyer, J.E., Abraham, M.A. (1994). Reaction pathways during the oxidation of ethyl-acetate on a platinum/alumina catalyst. *Industrial & Engineering Chemistry Research,* 33, 2084-2089.

Tsoncheva, T., Linden, M., Areva, S., Minchev, C. (2006). Copper oxide modified large pore ordered mesoporous silicas for ethyl acetate combustion. *Catalysis Communications,* 7, 357-361.

Tsou, J., Magnoux, P., Guisnet, M., Órfão, J.J.M., Figueiredo, J.L. (2004). Catalytic oxidation of methyl-isobutyl-ketone over basic zeolites. *Applied Catalysis B-Environmental,* 51, 129-133.

Tsou, J., Magnoux, P., Guisnet, M., Órfão, J.J.M., Figueiredo, J.L. (2005). Catalytic oxidation of volatile organic compounds – Oxidation of methyl-isobutyl-ketone over Pt/zeolite catalysts. *Applied Catalysis B-Environmental,* 57, 117-123.

Völter, J., Lietz, G., Spindler, H., Lieske, H. (1987). Role of metallic and oxidic platinum in the catalytic combustion of n-heptane. *Journal of Catalysis,* 104, 375-380.

Yang, Y., Xu, X., Sun, K. (2007). Catalytic combustion of ethyl acetate on supported copper oxide catalysts. *Journal of Hazardous Materials,* 139, 140-145.

Proceedings of the 10th International Chemical and
Biological Engineering Conference - CHEMPOR 2008
Braga, Portugal, September 4-6, 2008
E.C. Ferreira and M. Mota (Eds.)

Incidence of the preparation method of the support on the behavior in n-butane dehydorgenation of $Pt/MgAl_2O_4$, $PtSn/MgAl_2O_4$ y $PtPb/MgAl_2O_4$ catalysts

Sonia Bocanegra*, Alberto Castro, Osvaldo Scelza, Sergio de Miguel
Instituto de Investigaciones en Catálisis y Petroquímica (INCAPE)/Facultad de Ingeniería Química-Univ. Nac. del Litoral- CONICET, Santiago del Estero 2654, Santa Fe, 3000, Argentina..

Keywords: Synthesis of $MgAl_2O_4$, Dehydrogenation, Bimetallic catalysts
Topic: Advancing the chemical engineering fundamentals

Abstract

Two preparation methods of $MgAl_2O_4$ have been used: ceramic and co-precipitation. The supports were characterized by measurements of the textural properties (BET isotherms), XRD and 2-propanol dehydration. The XRD characterization shows the formation of $MgAl_2O_4$ spinel for both materials.The textural properties indicated that the specific surface of $MgAl_2O_4$ obtained by co-precipitacion was much higher than that obtained by the ceramic method. The results of 2-propanol dehydration reaction show a scarce activity for both $MgAl_2O_4$, mainly for $MgAl_2O_4^{co\text{-}precipitation}$. This means that these materials have very low acidity.
The monometallic catalysts were prepared by impregnation of both supports with solution of H_2PtCl_6 such as to obtain a Pt loading of 0.3 wt%. The bimetallic catalysts (PtSn and PtPb) were obtained by impregnation of the corresponding monometallic ones with an aqueous solution of $SnCl_2$ or $Pb(NO_3)_2$. The Sn contents were 0.3 and 0.5 wt%. The Pb contents were 0.52 and 0.87 wt%. These catalysts were characterized by H_2 chemisorption, TEM, TPR, XPS, test reactions of the metallic phase (cyclohexane dehydrogenation and cyclopentane hydrogenolysis) and evaluated in the n-butane dehydrogenation reaction at 530 ºC. The H_2 chemisorption and TEM results show that $Pt/MgAl_2O_4^{co\text{-}precipitation}$ displays a lower metallic dispersion than the Pt supported on $MgAl_2O_4^{ceramic}$. The characterizations carried out by TPR, XPS and test reactions show good interaction for bimetallic catalysts, except for $PtPb/MgAl_2O_4^{co\text{-}precipitation}$. The evaluation of catalysts in n-butane dehydrogenation displays a lower activity of $Pt(0,3)/MgAl_2O_4^{co\text{-}precipitation}$ than $Pt(0,3)/MgAl_2O_4^{ceramic}$ and a similar selectivity to all butenes. The bimetallic catalysts that contain Sn showed better activities and selectivities with regard to the monometallic ones, but the PtPb catalysts did not show the above mentioned behavior. Likewise, the $PtSn(0.3)/MgAl_2O_4^{ceramic}$ shows the best catalytic performance.

1 Introduction

$MgAl_2O_4$ is a material with interesting properties to be used as a support of metallic catalysts for dehydrogenation. This material has a high thermal stability, low acidic character and good interaction with the metallic phase (Armendariz et al, 2001). The traditional method to obtain this material is the ceramic one (reaction in solid phase at high temperature). This preparation method has certain disadvantages such as the low specific surface area and chemical heterogeneity. In order to avoid these problems others preparation methods have been used: mechanochemical, sol gel and co-precipitation (Li et al., 2001) . With respect to the nature of the metallic phase, it must be indicated that Pt has been intensively used as the active metal. Pt has a high activity of alcanes dehydrogenation and low hydrogenolytic capacity. In spite of these properties, the performance of the metallic phase can be enhanced by addition of metals of the 14 group as Sn, Pb and Ge (Pakhomov et al., 1980).

* Corresponding author. Tel + 54-0342-4555279. E-mail:sbocane@fiqus.unl.edu.ar

2 Materials and methods

Synthesis of $MgAl_2O_4$

i) Ceramic method (***$MgAl_2O_4^{cer}$***)

$MgAl_2O_4$ was prepared by a solid phase reaction between MgO (Alfa Aesar, purity 99.99%) and γ-Al_2O_3 (CK 300 from Cyanamid Ketjen, purity 99.9%). The stoichometric ratio was 1 mol of MgO/1mol γ-Al_2O_3. The mixed solids were grounded and then calcinated in an electric furnace at 900 ºC for 24 h.

ii) Co-precipitation method (***$MgAl_2O_4^{cop}$***)

$Mg(NO_3)_2$.6 H_2O (Merck, 99.0% purity), $Al(NO_3)_3$.9 H_2O (Merck, 98.5% purity) and ammonia solution (Merck, 28%, analytical grade) were used as reagents. A solution of the nitrates was prepared, with a Al/Mg molar ratio = 2. The precursor was prepared by adding the ammonia solution into the mixed salt solution under stirring, until reaching pH 11 at 40ºC. The resulting gel was aged and then washed. The dried gel was calcinated in flow air at 800ºC for 4 h.

Catalysts Preparation

The Pt(0.3 wt%)/$MgAl_2O_4$ catalysts were prepared by incipient impregnation of both supports with an aqueous solution of H_2PtCl_6 for 6 h. Then the samples were dried at 100º C.

The bimetallic catalysts (PtSn and PtPb) were obtained by impregnation of the corresponding monometallic ones with an aqueous solution of $SnCl_2$ in HCl medium or $Pb(NO_3)_2$ for 6 h. The Sn contents were 0.3 and 0.5 wt%. The contents of Pb went equimolares to those of Sn (equivalent to 0.52 and 0.87 wt% Pb). After impregnation the catalysts were dried at 100 ºC. After the preparation all catalysts were calcined at 500ºC.

Characterization of $MgAl_2O_4$ supports and catalysts

The different stages of preparation of the supports were characterized by XRD which were performed in a Shimadzu model XD3A instrument using CuK_α radiation (λ =1542 Å).

The specific surface area and pore volume of both supports were determined through the BET isotherm in a Quantachrome Corporation NOVA-1000 equipment.

In order to characterize the acid properties of supports, isopropanol dehydration experiments at atmospheric pressure were carried out in a flow reactor. H_2/isopropanol molar ratio=19. The space velocity of feed was 0.52 mol alcohol h^{-1} g cat^{-1} and the temperature was 200ºC.

The characteristics of the metallic catalysts were determined by different techniques:

H_2 chemisorption measurements were made in volumetric equipment at room temperature and performed in the range of 25-100 torr. The isotherms were lineal in the range of used pressures. From the data of chemisorbed H_2 the metallic dispersion was calculated.

TEM measurements were carried out on a JEOL 100CX microscope with a nominal resolution of 6 Å, operated with an acceleration voltage of 100KV.

TPR experiments were performed in a quartz flow reactor. The samples were heated at 6ºC min^{-1}. The reductive mixture (5 v/v % H_2-N_2) was fed to the reactor with a flow rate of 10 ml min^{-1}. Catalysts were previously calcined “in situ” at 500ºC in air flow for 3 h.

XPS measurements were carried out in a VG-Microtech Multilab spectrometer, which operates with an energy power of 50 eV (radiation $MgK\alpha$, $h\nu$ = 1253.6 eV). Samples were previously reduced “in situ”. Binding energies were referred to the C1s peak at 284.9 eV.

Cyclohexane dehydrogenation (CHD) and cyclopentane hydrogenolysis (CPH) were carried out in a differential flow reactor. Prior to these reactions, samples were reduced “in situ”. In both reactions the H_2/hydrocarbon molar ratio was 26. The reaction temperatures in CHD were 300ºC, whereas in CPH the temperature was 500ºC.

n-butane dehydrogenation reaction

The n-butane dehydrogenation test was carried out in a continuous flow reactor at 530 ºC. The reactor was fed with 18 ml min^{-1} of the reactive mixture (n-butane + hydrogen, H_2/n-C_4H_{10} molar ratio= 1.25). Prior to the reaction, catalysts were reduced "in situ" at 530ºC. The reactor effluent was analyzed in a GC-FID equipment. With this analytical device, the amounts of methane, ethane, ethylene, propane, propylene, n-butane, 1-butene, cis-2-butene, trans-2-butene and 1,3 butadiene were measured.

3 Discussion of results

Figure 1 shows XRD results corresponding to the synthesis of $MgAl_2O_4^{cer}$. Figure 1a displays the diffractograms corresponding to the mixture of the reactives (MgO and γ-Al_2O_3). In Figure 1 b it can be observed that the main product of the solid phase reaction was the $MgAl_2O_4$ spinel thus remaining traces of MgO and γ-Al_2O_3. After purifying the solid with a aqueous solution of $(NH_4)_2CO_3$ (1M), the XRD shows the complete elimination of the MgO (Figure 1c).

Figures 2 shows XRD results that correspond to the synthesis of $MgAl_2O_4$ by the coprecipitation method. Figure 2a displays the diffractogram corresponding to the coprecipitated precursor, thus showing that the main phase is a $MgAl_2(OH)_8$, together with meixnerite and bayerite (Armendariz et al., 2001). After the calcination at 800ºC, the characteristic peaks of the $MgAl_2O_4$ spinel are clearly observed in the X-ray diffractogram (Figure 2c).

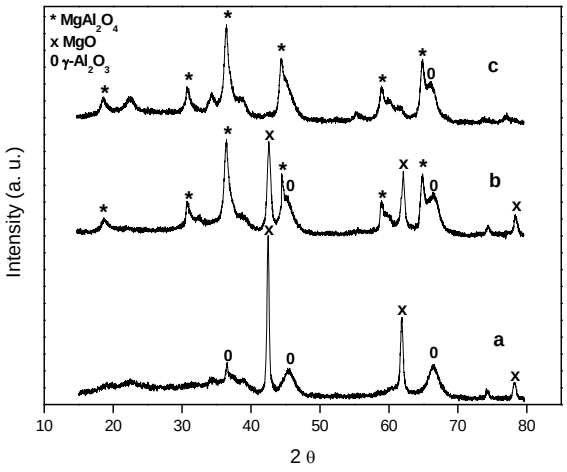

Figure 1: XRD of $MgAl_2O_4^{ceramic}$, impurified (b) y purified (c), and mixture MgO whit γ-Al_2O_3 before reaction (a).

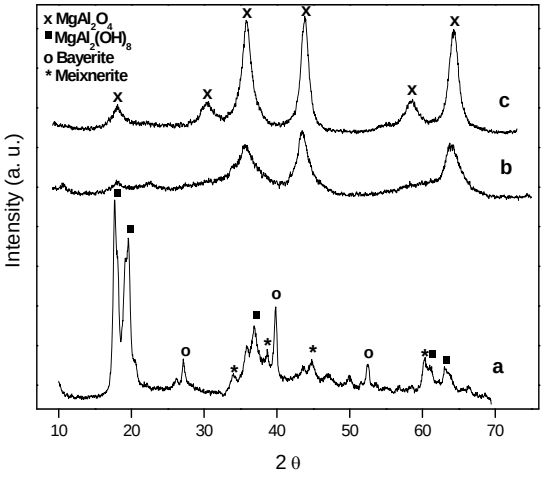

Figure 2: XRD of $MgAl_2O_4^{co\text{-}preicpitation}$, precursor (a), precursor calcinated at 500ºC (b) and calcinated at 800ºC (c).

The results of specific surface area and pore volume, reported in Table 1, indicate that the support obtained by co-precipitation have higher specific surface area and pore volume that the $MgAl_2O_4^{cer}$, which are more suitable characteristics for the deposition of the metallic precursor. However, the metal dispersion also depends on other factors such as the interaction strength between the metallic precursor and the support.

In order to determine the acid properties of the supports, the 2-propanol dehydration reaction was carried out. Results are shown in Table 1. It can be observed that γ-Al_2O_3 (reference material), which has Lewis acid centers, shows an important activity in this reaction. On the other hand, both $MgAl_2O_4$ display a very low dehydration activity, mainly for $MgAl_2O_4^{cop}$.

Table 2 displays the H_2 chemisorption results for the different catalysts. It can be observed that the Pt/$MgAl_2O_4^{cop}$ catalyst displays a lower metallic dispersion than Pt/$MgAl_2O_4^{cer}$. In the case of bimetallic catalysts it is observed that the H_2 chemisortion capacities are clearly lower than the corresponding of the monometallic ones. This effect can be attributed to a blocking and/or dilution of the Pt by Sn or Pb, besides, a probable formation of alloys.

The distribution of Pt particle sizes (by TEM) shows a mean particle diameter of 1.83 nm for $Pt/MgAl_2O_4^{cop}$ catalyst and a mean particle diameter of 1.32 nm for the $Pt/MgAl_2O_4^{cer}$ catalyst. These results are in agreement with the H_2 chemisorption results, and with acid properties of supports. Hence during the metallic impregnation, the $MgAl_2O_4^{cer}$ would be able to adsorb $PtCl_6^{2-}$ with a higher interaction, thus leading probably to a higher metallic dispersion.

Table 1: Textural properties of supports and conversion in 2-propanol dehydration

Support	Specific surface ($m^2\ g^{-1}$)	Pore Volume ($cm^3\ g^{-1}$)	$X_{initial}$ (%) (2-propanol)	X_{final} (%) (2-propanol)
$MgAl_2O_4^{cer}$	37	0.11	1.8	1.3
$MgAl_2O_4^{cop}$	108.2	0.33	0.2	0.2

Table 2 shows the results obtained in the reaction tests of the metallic phase for different catalysts supported on both $MgAl_2O_4$. In the cyclohexane dehydrogenation (CHD) reaction can be observed that $Pt/MgAl_2O_4^{cop}$ and $Pt/MgAl_2O_4^{cer}$ catalysts show similar values of the initial CHD rate. The addition of Sn or Pb to Pt decreases the initial reaction rate in CHD, though the addition of Pb appears to have a more marked effect on the reaction rate. This fact would be in agreement with results obtained in the literature [15,21], which indicate that both lead and tin produce blockage of the superficial platinum atoms, but the first one produces a larger effect than the second one. Respect to the activation energy in this reaction, it is mesured an increase of the values only when Sn is added to $Pt/MgAl_2O_{4\ cer}$, which would indicate a certain electronic effect in these bimetallic catalysts.

Table 2 also shows the results of cyclopentane hydrogenolysis (CPH). It can be observed that when Pb and Sn are added to Pt supported in the $MgAl_2O_4^{cop}$, there is a small decrease of the CPH rate values, being this effect more pronounced for PtPb catalysts. This means that Sn or Pb are intercalated between Pt atoms, but in a low extension. On the other hand when Sn or Pb are added to $Pt/MgAl_2O_4^{cer}$, the initial reaction rates of CPH are lower than those found for bimetallic catalysts supported on $MgAl_2O_4^{cop}$. These results would indicate higher dilution and blocking effects than in the other catalyst series.

Table 2: hydrogen chemisorption, initial rate of CH dehydrogenation reaction (R^o_{CH}) and initial rate of CP hydrogenolisis (R^o_{CP}) of Pt, PtSn and PtPb catalysts.

Catalyst	H_2 ($\mu mol\ g_{cat}^{-1}$)	Dispersion (%)	R^o_{CH} ($mol\ h^{-1} g_{Pt}^{-1}$)	R^o_{CP} ($mol\ h^{-1} g_{Pt}^{-1}$)
$Pt/MgAl_2O_4^{cer}$	3.75	49	52,1	7.6
$Pt/MgAl_2O_4^{cop}$	2.35	31	68.1	6.0
$PtSn(0.3)/MgAl_2O_4^{cer}$	1.52	-	20.8	2.0
$PtSn(0.5)/MgAl_2O_4^{cer}$	1.52	-	0.2	2.0
$PtSn(0.3)/MgAl_2O_4^{cop}$	1.63	-	52.7	4.4
$PtSn(0.5)/MgAl_2O_4^{cop}$	1.00	-	40.0	3.6
$PtPb(0.52)/MgAl_2O_4^{cer}$	0.62	-	10.9	1.0
$PtPb(0.87)/MgAl_2O_4^{cer}$	0.28	-	7.0	0.8
$PtPb(0.52)/MgAl_2O_4^{cop}$	1.75	-	40.4	3.5
$PtPb(0.87)/MgAl_2O_4^{cop}$	1.96	-	34.0	2.8

Figures 3 and 4 show the results obtained by TPR on mono and bimetallic catalysts supported on both $MgAl_2O_4$. It can be observed in Figure 3 for catalysts supported on $MgAl_2O_4^{cer}$ that the $Pt/MgAl_2O_4^{cer}$ has a main reduction peak located at about 270 ºC and a secondary peak at about 425 ºC. This fact was explained by the existence of two different oxychlorinated Pt species (Lietz et al., 1983). When Sn or Pb are added to Pt, the main reduction peaks are broader and are shifted to higher temperatures, which can indicate a Pt-Sn (or Pt-Pb) co-reduction and a good interaction of Pt with the second metal. For the Pt catalysts supported on $MgAl_2O_4^{cop}$ (Figure 4), two reduction peaks can be observed, the main one, placed at 254 ºC, and the secondary one located at about 450 ºC. The appearance of two reduction peaks was previously explained. The main peak is shifted to higher

temperatures when increasing Sn amounts are added to the monometallic catalyst. This behaviour indicates a good interaction between both metals. In the case of PtPb catalysts supported on $MgAl_2O_4^{cop}$, the main reduction peak is shifted to slightly lower temperatures and it is not observed a broadening of this peak. Besides, for these catalysts, two reduction zones are found at about 250-350 ºC and 350-500 ºC. These broad reduction zones are associated to the reduction of free Pb species. These facts would indicate both a Pt-Pb segregation and a low interaction between Pt and Pb.

XPS results of PtSn catalysts supported on both $MgAl_2O_4$ indicate that a small fraction of Sn (10-15%) is in the zerovalent state and probably alloyed with Pt, while the remainder are attributed to oxidized species of Sn. The presence of Sn(0) in bimetallic catalysts and the absence of this species in the Sn monometallic one, would indicate a higher Sn reducibility in PtSn catalysts, these results agreeing with TPR ones. Considering the TPR and cyclohexane dehydrogenation results for $PtPb/MgAl_2O_4^{cop}$, although an important fraction of the lead is like Pb(0), it would not be forming alloy with Pt, but isolated.

The n-butane dehydrogenation results are displayed in Figures 5 and 6. The n-butane conversion (Figure 5) shows that the initial activity of $Pt/MgAl_2O_4^{cer}$ is higher than that of $Pt/MgAl_2O_4^{cop}$, thus agreeing with TEM and dispersion measurements. Besides, the addition of Sn to both monometallic catalysts increases the conversion. However, the Pb addition to Pt supported in both $MgAl_2O_4$ decreases the n-butane conversion with respect to the corresponding monometallic ones. With respect to the selectivity to all butenes (Figure 6), $Pt/MgAl_2O_4^{cop}$ catalyst show a slightly higher selectivity than that of $Pt/MgAl_2O_4^{cer}$. The Sn addition to Pt clearly increases the selectivity to butenes reaching values near 98%. On the other hand, the Pb addition to Pt does not produce an increase of the selectivity to all butenes, except for PtPb(0.52 wt%)/ $MgAl_2O_4^{cop}$. It must be noted that the best catalytic performance is obtained by the PtSn(0.3 wt%)/$MgAl_2O_4^{cer}$. In general it can be seen in Figures 5 and 6 that the ceramic method for the support preparation and the lower Sn content added to Pt lead to better dehydrogenation catalysts.

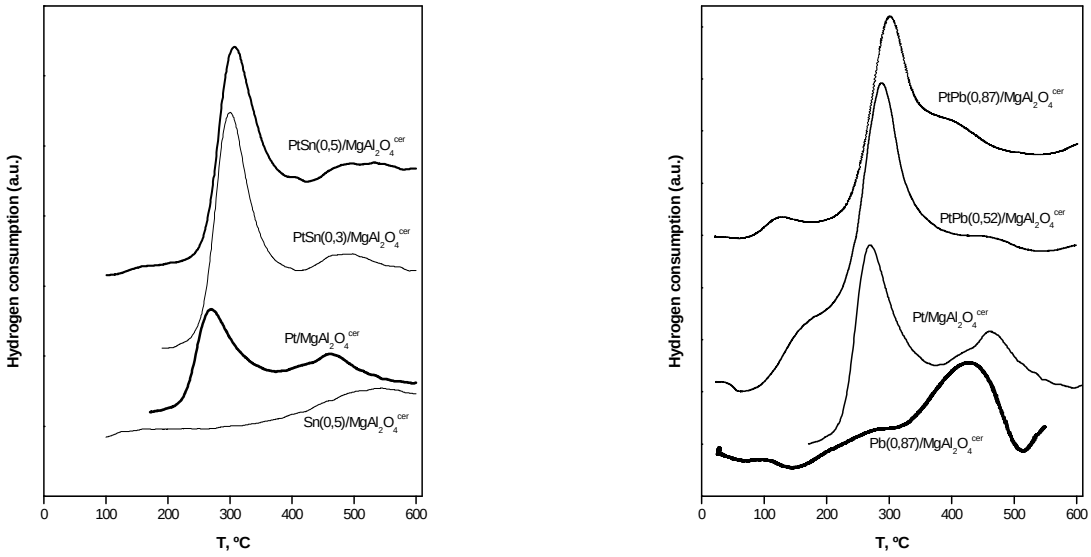

Figura 3: TPR experiencies of Pt, Sn, Pb, PtSn y PtPb catalysts supported on $MgAl_2O_4^{cer}$.

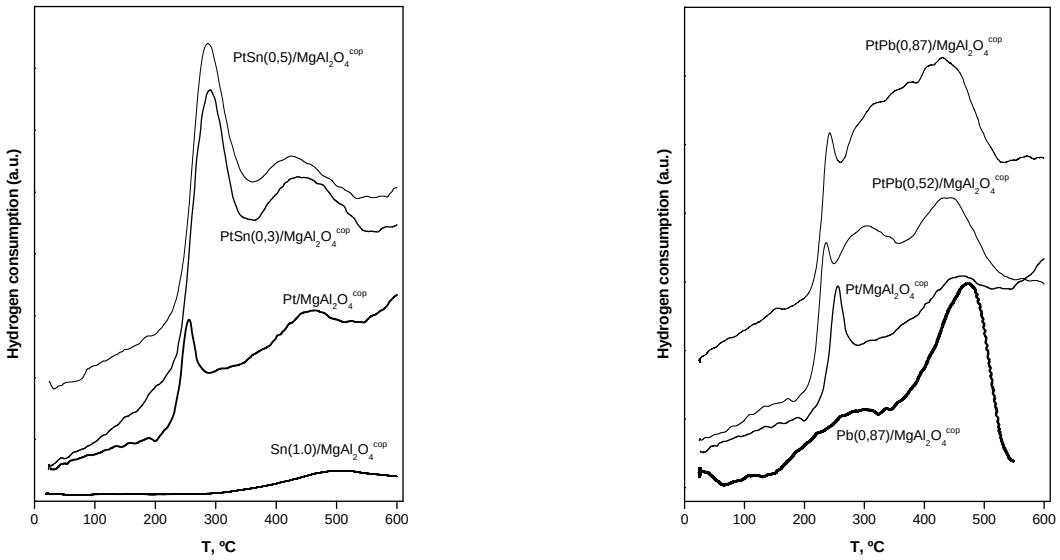

Figura 4: TPR experiencies of Pt, Sn, Pb, PtSn y PtPb catalysts supported on $MgAl_2O_4^{cop}$.

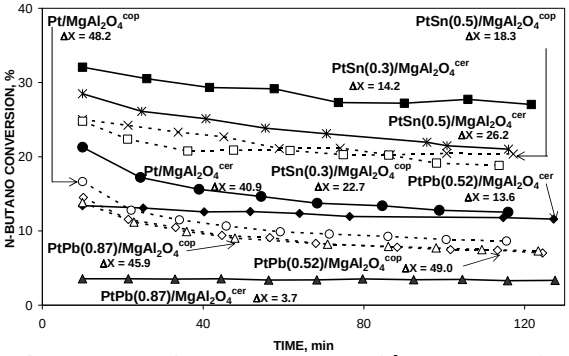

Figure 5: n-butane conversión vs reaction time for Pt, PtSn and PtPb catalysts.

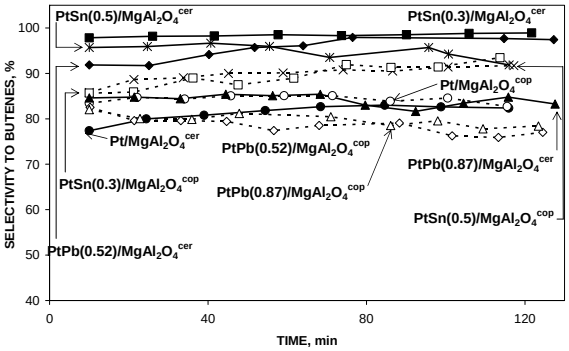

Figure 6: Selectivity to butenes vs reaction time for Pt, PtSn and PtPb catalysts.

4 Conclusions

The $MgAl_2O_4$ spinels show very low acidity and good interaction with the metallic phase. However, the $MgAl_2O_4^{cop}$ displays lower acidity than the $MgAl_2O_4^{cer}$, which seems to influence in the metal-support interaction, since that $Pt/MgAl_2O_4^{cer}$ catalyst shows higher metallic dispersion and better catalytic behavior than the $Pt/MgAl_2O_4^{cop}$ one. The Sn addition to Pt catalysts improves its performance in the dehydrogenation. This behavior is according to catalysts characterization results, where good Pt-Sn interaction is observed, mainly for bimetallic catalysts supported in $MgAl_2O_4^{cer}$. Oppositely, the Pb addition to Pt catalysts does not enhance its catalytic behavior in dehydrogenation. This conduct is in agreement with the characterization results of metallic phase that indicate low interaction Pt-Pb, especially for $PtPb/MgAl_2O_4^{cop}$ catalysts. In conclusion, the synthesis of ceramic method and the Sn addition to Pt lead to better dehydrogenation catalysts, being the $PtSn(0.3)/MgAl_2O_4^{cer}$ catalyst that showed the better performance.

References

Armendáriz, H., Guzmán, A.,Toledo, J., Llanos, M., Vazquez, A., Aguilar-Ríos, G. (2001). *Appl. Catal. A*, 211, 69-80.

Li, J., Ikegami, T., Lee, J., Mori, T., Yajima, Y. (2001).*J. European Ceram. Soc*. 21, 139-148.

Bocanegra, S., Guerrero-Ruíz, A., de Miguel, S., Scelza, O. (2004). *Appl. Catal. A: General* 277, 11-22.

Lietz, G., Lieske, H., Spindler, H., Hanke, W., Völter, J. (1983). *Journal of Catal.* 81, 17-23.

Proceedings of the 10th International Chemical and
Biological Engineering Conference - CHEMPOR 2008
Braga, Portugal, September 4-6, 2008
E.C. Ferreira and M. Mota (Eds.)

Hydrogen production from methane reforming: thermodynamic assessment

Tatiana V. Franco, Cícero N. Ávila-Neto, Lucienne L. Romanielo, Carla E. Hori, Adilson J. Assis[1]

[1] School of Chemical Engineering – Federal University of Uberlândia – Av.João Naves de Ávila, 2121 – Santa Mônica – CEP: 38408-100 – Uberlândia – MG – Brazil

Keywords: Methane reforming, hydrogen, chemical equilibrium, scilab software.
Topic: Advancing the chemical engineering fundamentals.

Abstract

The main contributions of this study are to conduct a comparative thermodynamic analysis of methane reforming reactions and to asses the influence of key operational variables on chemical equilibrium using an in-house code, developed in the open-source software Scilab (www.scilab.org). Equilibrium compositions are calculated by two distinct methods: (1) evaluation of equilibrium constants; (2) Lagrange multipliers. Both methods result in systems of non-linear algebraic equations, solved numerically using the Scilab function "fsolve". Comparison between experimental and simulated equilibrium data, published in the literature, was used to validate the simulated results. Effects of temperature, pressure, initial H_2O/CH_4 ratio (steam reforming), initial CH_4:CO_2:N_2 ratio (dry reforming) and initial O_2/CH_4 (partial oxidation) ratio on the reaction products were evaluated.

1 Introduction

Hydrogen can be produced using several routes. At the present moment, the main route is the catalytic reforming of methane, which includes steam-methane reforming (SMR), partial oxidation (POX), autothermal reforming (ATR) and dry-methane reforming (DMR).

Steam-Methane Reforming produces a H_2/CO ratio equals to three, which is high, when compared to other reforming processes (Seo et al., 2002). Xu and Froment (1989) demonstrated that besides steam reforming of methane (Equation 1), there is another important reaction which takes place in these systems: the water-gas shift reaction (Equation 2). The sum of both reactions results in the Equation 3.

$$CH_4 + H_2O \rightarrow CO + 3H_2 \qquad \Delta H^{\circ}_{298} = 206.0 kJ/mol \tag{1}$$

$$CO + H_2O \rightarrow CO_2 + H_2 \qquad \Delta H^{\circ}_{298} = -41.0 kJ/mol \tag{2}$$

$$CH_4 + 2H_2O \rightarrow CO_2 + 4H_2 \qquad \Delta H^{\circ}_{298} = 165.0 kJ/mol \tag{3}$$

Nevertheless, steam reforming has the disadvantage of intensive energy requirements due to the overall endothermic nature. In order to reduce energy costs, partial or stoichiometric oxidation (Equation 4) of methane has been investigated as an alternative (Corbo and Migliardini, 2006).

$$CH_4 + 1/2\,O_2 \rightarrow CO + 2H_2 \qquad \Delta H^{\circ}_{298} = -35.7 kJ/mol \tag{4}$$

The autothermal reforming process combines the endothermic reforming with the exothermic oxidation. In the reaction process, it is assumed that the heat required for the endothermic reforming can be supplied by the heat released from the oxidation reaction. (Li et al. *In press;* Tomishige et al., 2007).

Finally, dry-methane reforming (Equation 5) produces a synthesis-gas with a H_2/CO ratio near one, which can be used for adjusting H_2/CO ratio in steam reforming, suitable for

[1]Corresponding author. Tel + 55 34 3239-4292, Ramal: 233 – E-mail: ajassis@ufu.br

Fischer–Tropsch reactions and methanol production (Schuurman et al., 2006).

$$CH_4 + CO_2 \leftrightarrow 2CO + 2H_2 \quad \Delta H^{\circ}_{298} = 247.4kJ/mol \tag{5}$$

Although the thermodynamics equilibrium is widely discussed in the literature, it has a scarce systematization and the available programs are usually proprietary, except the CANTERA's software. Therefore, the main objectives of this study are to conduct a comparative thermodynamic analysis for methane reforming reactions and to asses the influence of key operational variables on chemical equilibrium using an in-house code, developed in the open-source software Scilab (www.scilab.org).

2 Simulation methods

Equilibrium compositions are calculated by two distinct methods: (1) evaluation of equilibrium constants; (2) Lagrange multipliers. Both methods result in systems of non-linear algebraic equations, solved numerically.

2.1 Evaluation of Equilibrium Constants method (EEC)

An independent multi-reaction system was organized and each reaction is associated with a reaction coordinate (ξ) and with a distinct equilibrium constant (K_j). The equilibrium constant for each reaction is described by Smith et al. (2000). In this work, the fugacity coefficient for each species in the mixture, $\hat{\phi}_i$, is calculated using the virial's equation considering that there are interactions between the gases (Equations 6). The cross virial's coefficient, used in the Equation 7, follow the correlation proposed by Tsonopoulos and Reidman (1990).

$$\ln \hat{\phi}_i = \frac{P}{RT}\left[B_{ii} + \frac{1}{2} M_{ijk} \right] \tag{6}$$

$$M_{ijk} = \sum_k \sum_j y_k y_j \left(2\delta_{ki} - \delta_{kj} \right) \tag{7}$$

This method is interesting to evaluate when a determined operational condition (T, P, composition) favours a certain reaction, through the analysis of the value of the equilibrium constant of this reaction compared to another one present in the system (Smith et al., 2000).

2.2 Lagrange Multipliers method (LM)

In agreement with Smith et al. 2000, the system composition in the equilibrium can be found solving *N* equilibrium equations, *w* mass balance equations and a restriction equation, represented by Equations 8-10, respectively:

$$\Delta G_{fi} + RT \ln\left(y_i \hat{\phi}_i \frac{P}{P_0} \right) + \sum_k \lambda_k a_{ik} = 0 \tag{8}$$

$$\left(i = 1, 2, ..., N\right)$$

$$\sum_i n_i a_{ik} = A_k \quad \left(k = 1, 2, ..., w\right) \tag{9}$$

$$\sum_i y_i = 1 \quad \left(i = 1, 2, ..., N\right) \tag{10}$$

Where ΔG_{fi} is the standard Gibbs function of the formation of species *i*, *R* is the universal

gas constant, y_i is the molar fraction of species *i* in the mixture, $\hat{\phi}_i$ is the fugacity coefficient of species *i* in the mixture, λ_k is the Lagrange's multipliers oh each element *k*, a_{ik} is the number of atoms of each *k* element of molecule *i* and A_k is the total number of atomic mass of the *k* element. The advantage of this method is to be independent of the reaction system because the choice of a group of molecules is equivalent to choice a system of independent reactions between the species (Smith et al., 2000).

2.3 Simulation method

In both cases, the variation of standard enthalpy and Gibbs free energy of the reaction system ($\Delta H°_j$ e $\Delta G°_j$, respectively) are functions of the temperature and must be corrected with the heat capacities of the gas, *Cp*. The input parameters of the simulator are: molar fraction of the reactants, temperature and pressure in the reactor input and operational temperature and pressure. The resolution of the equations is made through implemented computational codes in the free platform of calculation Scilab © INRIA-ENPC. The numeric calculation uses a function "fsolve", which one utilizes a modification of the hybrid Powell method with a tolerance of 10^{-10}.

3 Results and discussion

3.1 Steam-Methane Reforming

Accordingly to Seo et al. (2002), in the equilibrium, the species of the steam-methane reforming are CH_4, H_2O, CO, CO_2 and H_2, C(solid) and the radicals H, O, OH, HO_2, HCO, CH e CH_2. However, the simulations indicate that the radicals concentrations are neglected when compared to the concentrations of the other products. Therefore, they will be disrespected in this work.

Applying the Denbigh method with the products considered by Seo et al. (2002), one concludes that only Equations 1 and 2 are necessary for the calculation of the thermodynamic balance through the analysis of the balance constants.

The H_2 yield and the H_2/CO selectivity are defined by Fogler (1999) as:

$$Y_{H_2} = \frac{N_{H_2}^{Out}}{N_{CH_4}^{In} - N_{CH_4}^{Out}} \tag{11}$$

$$S_{H_2/CO} = \frac{N_{H_2}^{Out}}{N_{CO}^{Out}} \tag{12}$$

As the reactor temperature is raised from 600 to 800 ℃, CH_4 conversion increases from 44 to 90 %. In agreement with the Figure 1 (a), for temperatures around 800 ℃, the raise of initial H_2O/CH_4 ratio from one to two increases H_2 yield in 4.67%. For temperatures around 430 ℃, this yield is practically the same for all conditions.

Table 1 shows the comparison between the simulated results and literature data for the steam-methane reforming. Lutz et al. (2003) used the software CHEMKIN with the program for chemical equilibrium calculations Stanjan, with a ratio H_2O/CH_4 = 2 and *P* = 10 atm. The average relative error between the results of this work (EEC method) and those one of Lutz et al. (2003) is 7.21% and the average relative error for the LM method is 7.68%. The same analysis is done for the results reported by Seo et al. (2002), but they use the software Aspen Plus™ for the equilibrium compositions with a ratio H_2O/CH_4 = 1 and *P* = 1 bar. This time, the average relative error between the simulated results of this work (EEC method) and

those of Seo et al. (2002) is 24.85%, while for the LM method the average relative error is 24.89%. The discrepancy of the errors between the two author's data can be a function of the consideration of carbon solid in the reforming products by Seo et al. (2002). It's important to note that both softwares used by the authors, use the LM method for the calculation of the equilibrium composition.

The software ScanIt was used to obtain the data of Table 1-3 because all the authors showed the results by graphics.

3.2 Dry-Methane Reforming

Dry-methane reforming analysis is carried out considering the same species as in the case of steam-methane reforming, with the addition of N_2 as an inert. As the reactor temperature is raised from 600 to 800 ℃, CH_4 conversion increases from 43 to 91%. Figure 1 (b) shows the H_2 yield simulation for the DMR with CH_4:CO_2:N_2 sensitivity. Table 2 shows the validation of the simulated results by comparison with CH_4 equilibrium conversion data of Akpan et al. (2007). The average relative error between the results of this work (EEC method) and those one of Akpan et al. (2007) is 6.32% and the average relative error for the LM method is 6.40%.

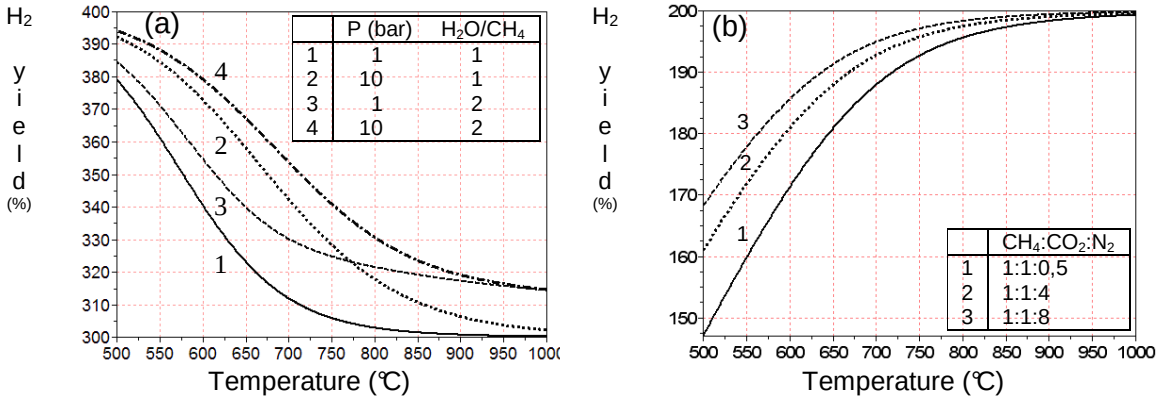

Figure 1. (a) H_2 yield for SMR, pressure and H_2O/CH_4 sensitivity; (b) H_2 yield for DMR, CH_4:CO_2:N_2 sensitivity.

3.3 Partial Oxidation of Methane

For partial oxidation, the following species are considered: CH_4, H_2O, CO, CO_2, H_2 and O_2. Despite of Zhu et al. (2001) consider the formation of others hydrocarbons such as C_2H_6, C_2H_4, C_2H_2, CH_3OH, HCHO and HCOOH, they have a very small yield ($<10^{-7}$%) and, for this reason, they are not consider in this work.

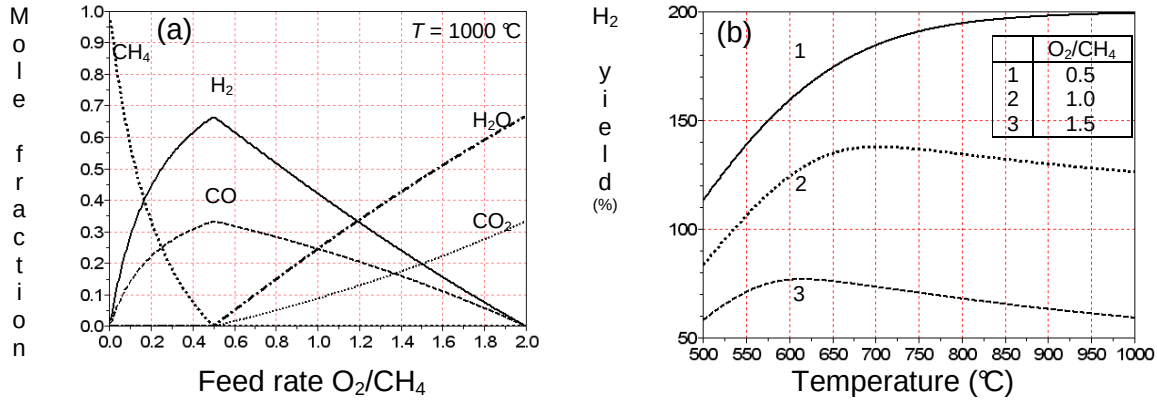

Figure 2. (a) Equilibrium composition of the POX products (P = 1 atm); (b) H_2 yield for POX, O_2/CH_4 sensitivity.

Table 1. Comparison between simulates and data results for SMR equilibrium composition.

Operational conditions	Compounds	500 °C			600 °C			700 °C			800 °C			900 °C			1000 °C		
		Simulation		Liter.	Simulation		Liter.	Simulation		Liter.	Simulation		Liter.	Simulation		Liter.	Simulation		Liter.
		LM	EEC		LM	EEC		LM	EEC		LM	EEC		LM	EEC		LM	EEC	
Lutz *et al.* (2003) $H_2O/CH_4 = 2$ P = 10 atm	CH_4	0.267	0.260	0.260	0.210	0.202	0.203	0.133	0.126	0.126	0.058	0.054	0.050	0.015	0.013	0.015	0.003	0.003	0.004
	H_2O	0.537	0.524	0.524	0.434	0.420	0.421	0.322	0.309	0.314	0.230	0.222	0.222	0.185	0.181	0.184	0.175	0.173	0.176
	CO	0.002	0.002	0.004	0.015	0.016	0.015	0.055	0.056	0.061	0.114	0.115	0.115	0.154	0.154	0.153	0.169	0.168	0.168
	CO_2	0.037	0.041	0.038	0.059	0.063	0.061	0.065	0.068	0.065	0.051	0.053	0.050	0.036	0.038	0.038	0.029	0.030	0.027
	H_2	0.157	0.173	0.174	0.282	0.299	0.300	0.425	0.441	0.434	0.547	0.556	0.563	0.610	0.614	0.61	0.624	0.626	0.625
Seo *et al.* (2002) $H_2O/CH_4 = 1$ P = 1 bar	CH_4	0.320	0.317	—	0.194	0.192	0.137	0.079	0.078	0.055	0.027	0.026	0.018	0.009	0.009	0.004	0.004	0.004	0.000
	H_2O	0.249	0.245	—	0.132	0.128	0.151	0.054	0.053	0.064	0.019	0.019	0.018	0.007	0.007	0.004	0.003	0.003	0.000
	CO	0.019	0.019	—	0.090	0.091	0.059	0.185	0.185	0.155	0.229	0.229	0.224	0.243	0.243	0.242	0.247	0.247	0.246
	CO_2	0.071	0.072	—	0.062	0.063	0.046	0.025	0.025	0.023	0.007	0.007	0.004	0.002	0.002	0.000	0.001	0.001	0.000
	H_2	0.341	0.347	—	0.522	0.526	0.525	0.657	0.659	0.652	0.718	0.719	0.716	0.729	0.739	0.739	0.745	0.745	0.748

Table 2. Comparison between simulates and data results for DMR equilibrium conversion.

Operational conditions	Conv. (%)	400 °C			500 °C			600 °C			700 °C			800 °C		
		Simulation		Liter.	Simulation		Liter.	Simulation		Liter.	Simulation		Liter.	Simulation		Liter.
		LM	EEC		LM	EEC		LM	EEC		LM	EEC		LM	EEC	
Akpan *et al.* (2007) $CH_4:CO_2:N_2 = 2:2:1$ P = 1 atm	CH_4	3.96	3.95	3.38	16.02	16.02	15.8	43.01	43.10	45.1	74.43	74.59	77.8	91.24	91.35	93.2

Table 3. Comparison between simulates and data results for POX equilibrium conversion.

Operational conditions	Compounds	$O_2/CH_4 = 0.5$		$O_2/CH_4 = 1.0$		$O_2/CH_4 = 1.5$	
		Simulation	Liter.	Simulation	Liter.	Simulation	Liter.
		LM		LM		LM	
Zhu *et al.* (2001) T = 600 °C P = 1 atm	CH_4	0.214	0.156	0.060	0.023	0.005	0.000
	H_2O	0.107	0.078	0.237	0.198	0.409	0.401
	CO	0.155	0.200	0.118	0.148	0.062	0.063
	CO_2	0.107	0.078	0.195	0.175	0.270	0.268
	H_2	0.417	0.488	0.390	0.456	0.254	0.268

Figure 2 (a) shows the simulated results of the POX equilibrium composition, and it's also possible to note that, at 1000℃, CH_4 is completely consumed when O_2/CH_4= 0.5.

The H_2 yield is strongly influenced by the temperature and by the O_2/CH_4 ratio in the feed. As it is shown in Figure 2 (b), the highest values are achieved for bigger values of temperature and smaller initial O_2/CH_4 ratios. Table 3 shows the validation of the results by comparison with equilibrium composition data of Zhu et al. (2001). The average relative error between the results of this work (LM method) and those of Zhu et al. (2001) is 28.7%.

4 Conclusions

Thermodynamics analysis was carried out for the steam-methane reforming, dry-methane reforming and partial oxidation of the methane. Literature's data were compared with the results of Lagrange's multipliers method and the Equilibrium constants evaluation method. The analyses enabled to validate the simulated results of this work and to verify the best operational conditions for each methane reforming reaction. The developed computer codes in Scilab are available upon request.

Acknowledgements

This work has been supported by Brazilian funding agencies, CAPES and CNPq (Grant n. 475934/2006-7).

References

Akpan, E., Sun, Y., Kumar, P., Ibrahim, H., Aboudheir, A., Idem, R. (2007). Kinetics, experimental and reactor modelling studies of the carbon dioxide reforming of methane (CDRM) over a new Ni/CeO_2–ZrO_2 catalyst in a packed bed tubular reactor. *Chemical Engineering Science*, 62, 4012-4024.

Bottino, A., Comite, A., Capannelli, G., Di Felice, R., Pinacci, P. (2006). Steam reforming of methane in equilibrium membrane reactors for integration in power cycles. *Catalysis Today,* 118, 214-222.

Corbo, P., Migliardini, F. (2006). Hydrogen production by catalytic partial oxidation of methane and propane on Ni and Pt catalysts. *International Journal of Hydrogen Energy*, *In press*.

Denbigh, K. G. (1981). The principles of chemical equilibrium, *Cambridge University Press,* 4. ed.

Dias, J. A. C., Assaf, J. M. (2004). Autothermal reforming of methane over Ni/γ-Al_2O_3 catalysts: the enhancement effect of small quantities of noble metals. *Journal of power sources*, 130, 106-110.

Li, B, Maruyama, K., Nurunnabi, M., Kunimori, K., Tomishige, K. (2004). Temperature profiles of alumina-supported noble metal catalysts in autothermal reforming of methane. *Applied Catalysis A*, 275, 157-172.

Lutz, A. E., Bradshaw, R. W., Keller, J. O., Witmer, D. E. (2003). Thermodynamic analysis of hydrogen production by steam reforming. *International Journal of Hydrogen Energy*, 28, 159-167.

O'Connor, A. M., Schuurman, Y., Ross J. R. H., Mirodatos, C. (2006). Transient studies of carbon dioxide reforming of methane over Pt/ZrO_2 and Pt/Al_2O_3. *Catalysis Today*, 115, 191-198.

Seo, Y.-S., Shirley, S. T., Kolaczkowski, S. T. (2002). Evaluation of thermodynamically favourable operating conditions for production of hydrogen in three different reforming technologies. *Journal of Power Sources*, 108, 213-225.

Smith, J. M., Van Ness, H. C., Abbott, M. M. (2000). Introdução à termodinâmica da engenharia química. *LTC Rio de Janeiro*, 5 ed.

Tsonopoulos, C., Heidman, J. L. (1990). From the virial to the cubic equation of state. *Fluid Phase Equilibria*, 57, 261-276.

Zhu, J., Zhang, D., King, K. D. (2001). Reforming of CH_4 by partial oxidation: thermodynamic and kinetic analyses. *Fuel*, 80, 899-905.

Proceedings of the 10th International Chemical and
Biological Engineering Conference - CHEMPOR 2008
Braga, Portugal, September 4-6, 2008
E.C. Ferreira and M. Mota (Eds.)

Hydrogen production from methane autothermal reforming: mathematical modeling and parametric optimization

Sandra C. Dantas[1], Fabiano de A. Silva[1], Carla E. Hori[1], Adilson J. de Assis[1*]

[1]Federal University of Uberlândia – School of Chemical Engineering – Av. João Naves de Ávila, 2121, Campus Sta. Mônica. CEP: 38408-100, Uberlândia-MG, Brazil.

Keywords: Modeling and simulation; process optimization; hydrogen production.
Topic: Advancing the chemical and biological engineering fundamentals.

Abstract

The goals of this study were to present and to validate a small scale reactor model for the autothermal reforming of methane reaction. In addition, the model should be able to describe the influence of temperature on methane conversion profiles, aiming to maximize hydrogen production. The developed mathematical model considered the mass balance equation for each component, and the set of ordinary differential equations was integrated using the software Scilab^{TM}. The validation was accomplished using experimental data available in the literature. The experimental results and the model presented good agreement with the methane conversion in all studied temperature range. Through simulated data of methane conversions, hydrogen yields and H_2/CO selectivity, it was observed that the best reaction conditions to maximize hydrogen production are around 723 K.

1 Introduction

In recent years, hydrogen has been attracting great interest as a clean fuel for combustion engines and fuel cells (Ayabe *et al*., 2003). Among all the potential sources of hydrogen, the natural gas, which has methane as the main component, has been considered a good option because this gas is very abundant, clean and can easily be converted to hydrogen (Dias and Assaf, 2004).

Nowadays steam reforming of methane is the main route to produce hydrogen in industrial scale. However, this process is highly endothermic, and therefore it requires high temperatures to obtain high equilibrium conversions. This results in a high operational cost. On the other hand, partial oxidation of methane is a slightly exothermic reaction that produces a H_2/CO ratio of approximately 2. This ratio is adequate for Fischer-Tropsoe synthesis. The coupling of steam reforming and partial oxidation of methane main advantage is to use the heat generated from the exothermic reaction as an energy source for the endothermic reaction. This process is called autothermal reforming of methane (ATR). Since this system presents higher energy efficiency and more satisfactory H_2/CO ratio for H_2 production, this reaction can be considered as an important alternative route in the hydrogen production (Dias and Assaf, 2004).

Although the autothermal reforming of methane has a potential interest for industrial application, there is still a limited number of works in literature referring to the reactor design and studies of operational conditions optimization. Therefore, the main objective of this work is to present and to validate a reactor model in small scale for this reaction. In addition, the effect of reactor temperature influence in methane conversions and in the yield and selectivity for H_2 formation were investigated, aiming to maximize the production of H_2.

2 Mathematical model

2.1 Chemical reaction

In this study, ATR is defined as a combination of partial oxidation and steam reforming of methane. In the reactor, several chemical reactions occur, and their rates are strongly dependent of reactions conditions. In order to reduce the number of reactions and to keep the model as simple as possible, only the reactions with significant reaction rates will be considered. According to the literature (Hoang *et al.*, 2006), the reactions that prevail in the autothermal reforming of methane process are represented by Equations 1-4.

R_1: $CH_4 + H_2O \leftrightarrow CO + 3H_2, \qquad \Delta H_1(298K) = 206.2kJ/mol$ (1)

R_2: $CH_4 + 2H_2O \leftrightarrow CO_2 + 4H_2, \qquad \Delta H_2(298K) = 164.9kJ/mol$ (2)

R_3: $CO + H_2O \leftrightarrow CO_2 + H_2, \qquad \Delta H_3(298K) = -41.1kJ/mol$ (3)

R_4: $CH_4 + 2O_2 \leftrightarrow CO_2 + 2H_2O, \qquad \Delta H_1(298K) = -802.7kJ/mol$ (4)

Thus, the model takes into account four reactions and six gas species: methane, oxygen, carbon dioxide, water, carbon monoxide and hydrogen. Nitrogen is present in the inlet air and it is considered as an inert, which affects only the gas properties and the equilibrium conversions.

2.2 Reaction kinetic model

There are a large number of kinetic models for steam reforming and water-gas shift reactions in literature. The model proposed by Xu and Froment (1989) for nickel catalysts is considered to be more general and it has been the most used in literature. For methane total combustion, the rate equation proposed by Trimm and Lam (Trimm e Lam, 1980 apud Smet *et al.*, 2001) will be adopted in this work. This kinetic model was developed for supported platinum catalysts and the corresponding adsorption parameters were adjusted for nickel. Ni catalyst was assumed to be in the reduced state, which implies that total combustion and reforming occur in parallel (Smet *et al.*, 2001).

The rate equations corresponding to the considered reactions are presented in Table 1 (Equations 5-9).

Table 1 – ATR kinetic reaction model

Reaction rate equation	
$R_1 = \frac{k_1}{p_{H_2}^{2,5}}\left(p_{CH_4} p_{H_2O} - \frac{p_{H_2}^3 p_{CO}}{K_I} \right) \times \frac{1}{\Omega^2}$	(5)
$R_2 = \frac{k_2}{p_{H_2}^{3,5}}\left(p_{CH_4} p_{H_2O}^2 - \frac{p_{H_2}^4 p_{CO_2}}{K_{II}} \right) \times \frac{1}{\Omega^2}$	(6)
$R_3 = \frac{k_3}{p_{H_2}}\left(p_{CO} p_{H_2O} - \frac{p_{H_2} p_{CO_2}}{K_{III}} \right) \times \frac{1}{\Omega^2}$	(7)
$R_4 = \frac{k_{4a} p_{CH_4} p_{O_2}}{\left(1 + K_{CH_4}^C p_{CH_4} + K_{O_2}^C p_{O_2}\right)^2} + \frac{k_{4b} p_{CH_4} p_{O_2}}{\left(1 + K_{CH_4}^C p_{CH_4} + K_{O_2}^C p_{O_2}\right)}$	(8)
$\Omega = 1 + K_{CO} p_{CO} + K_{H_2} p_{H_2} + K_{CH_4} p_{CH_4} + K_{H_2O} \frac{p_{H_2O}}{p_{H_2}}$	(9)

The equilibrium constants and the parameters of Arrhenius equation ($k_j = k_{0j} * \exp\left(-E_j / RT\right)$) are presented in Table 2 and the adsorption constants ($K_i = K_{0i} \times \exp\left(-\Delta H_i / RT\right)$) in Table 3.

Table 2 – Equilibrium constants and Arrhenius kinetic parameters

Reaction, j	*Equilibrium constant, K_j*	*k_{0j} (mol/kg$_{cat}$xs)*	*E_j (m^3×bar/mol)*
1	$K_I = \exp\left(\frac{-26830}{T} + 30.114\right)$ (bar^2)	1.17×10^{15} (bar$^{0.5}$)	2.401
2	$K_{II} = K_I . K_{III}$ (bar^2)	2.83×10^{14} (bar$^{0.5}$)	2.439
3	$K_{III} = \exp\left(\frac{4400}{T} - 4.036\right)$	5.43×10^5 (bar^{-1})	0.6713
4		8.11×10^5 (bar^{-2})	0.8600
		6.82×10^5 (bar^{-2})	0.8600

Table 3 – Van't Hoff parameters for adsorption of different species

	K_{0i} (bar^{-1})	*ΔH_i (m^3×bar/mol)*	*K^C_{0i} (bar^{-1})*	*ΔH^c_i (m^3×bar/mol)*
CH_4	6.65×10^{-4}	-0.38280		
CO	8.23×10^{-5}	-0.70650		
H_2	6.12×10^{-9}	-0.82900		
H_2O	1.77×10^5 (bar)	0.88680		
CH_4 (combustion)			1.26×10^{-1}	-0.27300
O_2 (combustion)			7.78×10^{-7}	-0.92800

The rate of consumption or formation of each gas species is determined by summing up the reaction rates of each species in all the reactions, as shown below in Equations 10-15.

$$r_{CH_4} = R_1 - R_2 - R_4 \quad (10)$$

$$r_{O_2} = -2R_4 \quad (11)$$

$$r_{CO_2} = R_2 + R_3 + R_4 \quad (12)$$

$$r_{H_2O} = -R_1 - 2R_2 - R_3 + 2R_4 \quad (13)$$

$$r_{H_2} = 3R_1 + 4R_2 + R_3 \quad (14)$$

$$r_{CO} = R_1 - R_3 \quad (15)$$

2.3 Reactor Model

A one dimensional model was constructed to represent a fixed bed reactor, with nickel-based catalyst, in small scale, in steady state. The reactor considered with 4 mm length is operated with 120 mL/min of inlet flow and 1 cm^3 of catalyst volume. In this condition, is reasonable to adopt the following simplifying assumptions:

i. interfacial mass transfer resistance and intraparticle diffusion limitations were not incorporated;

ii. pressure drop is negligible;

iii. the reactor can be considered as isothermal.

With the assumptions adopted previously, the molar flow along the axial direction, for each component, Fi (mol/s), can be described by the following mass balance equation (Barrio *et al.,* 2007):

$$\frac{dF_i}{dz} = \rho_b * S * \sum_j r_{ij} \quad (16)$$

where i denotes the gas species; j represents reaction index; z is the reactor length (0 to L); density of catalyst bed is ρ_b; with a value of 1.87×10^6 g/m^3; *S* (m^2) is the reactor transversal area and r_{ij} are the reaction rates.

The model is constituted by a set of ordinary differential equations (ODE's), non-linear, of initial value in length. The initial condition is given by $F_i=F_{i0}$, and the inlet composition in molar ratio is 16.7% CH_4: 1.7% O_2: 41.6% H_2O: 40% N_2. The EDO's system was integrated numerically using the function "ode" of free software Scilab™ (www.scilab.org).

2.4 Equilibrium Composition

The chemical equilibrium compositions were calculated using two distinct and classic methods: (1) evaluation of equilibrium constants; (2) Lagrange multipliers. Both methods result in non-linear algebraic equation, solved numerically in Scilab™, through the function "fsolve".

The program developed for the equilibrium composition calculation was validated with data published in the literature and the results are in publication process. The authors are part of same research group, and the results will be published separately.

3 Results and discussions

3.1 Model experimental validation

The model experimental validation was accomplished by comparing the simulated data with experimental data reported by Ayabe *et al.* (2003), in the same operational conditions. Ayabe *et al.* (2003) analyzed the activity of 10%Ni/Al_2O_3 catalyst in ATR reaction, as a function of temperature (light-off curve). The authors observed that there is a large difference in methane conversions when the reaction begins at low temperatures and the temperature is increased gradually, when compared to the inverse procedure, starting the reaction at high temperatures and gradually reducing it. The results show a strong hysteresis of conversion behavior in relation to temperature.

Figure 1 presents a comparison among methane conversions in reactor exit (or in *z* = L), simulated, experimental (Ayabe *et al.,* 2003) and at thermodynamic equilibrium. The agreement between simulated and experimental data is better at higher temperatures, which could be due to poor adjustment of the kinetic parameters or differences between the kinetic model considered and the real one at low temperatures.

3.2 Reaction conditions optimization

It is also possible to observe in Figure 1 that high methane conversions are favored at high temperatures. The experimental results present a strong drop in activity of Ni catalyst at 573 K. In fact the activity experimental value at this temperature is approximately zero, fact that is contemplated in the model.

Figure 2 presents the composition simulated profiles (in molar fraction in dry base) as a function of reaction temperature (light-off curve). The results show at lower temperatures, that methane total oxidation reaction is favored, generating CO_2, while at higher temperatures, methane reforming with CO_2 and steam reforming occur, favoring the formation of synthesis gas (H_2 and CO).

Usually the mechanism for ATR is considered as a coupling of steam reforming of methane with partial oxidation reactions. CO_2 formation at low temperatures, followed by synthesis gas formation at higher temperatures, are indications that the reaction occurs in two stages as described by Mattos *et al.* (2002), for partial oxidation of methane reaction.

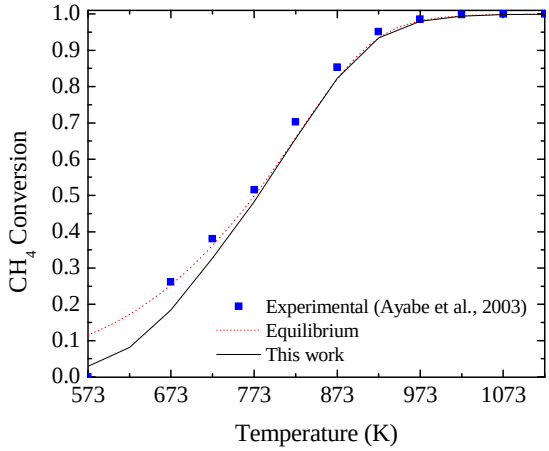

Figure 1 – CH_4 conversion: simulated, equilibrium and experimental (Ayabe *et al.*, 2003), temperature function, in reactor final ($z = L$).

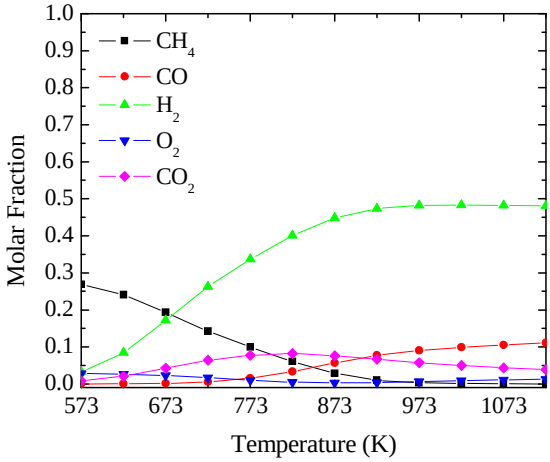

Figure 2 – Molar fraction in dry base of productions of autothermal reforming of methane at different temperatures.

Figure 3 presents the yield for hydrogen production as a function of reaction temperature, as defined by Fogler (1999). The yield was higher than 100%, which shows just that the hydrogen formation does not occur only in steam reforming reaction, but also in water-gas shift reaction. The yield profile decreased with the temperature increase, showing that at low temperatures there is larger hydrogen production in relation to the reacted methane. Starting from 723 K, approximately, the fall in yield value becomes less marked, indicating that the variation of the amount of formed H_2 by reacted CH_4 is small.

Figure 4 presents the profile of selectivity of hydrogen formation to carbon monoxide. There is an exponential decrease in selectivity values with the temperature increase. This result is related to small CO formation at low temperatures, as observed in Figure 2. For temperatures above 773 K, the H_2/CO selectivity is low. These results show that, for larger hydrogen selectivity, the use of lower temperatures is more appropriate.

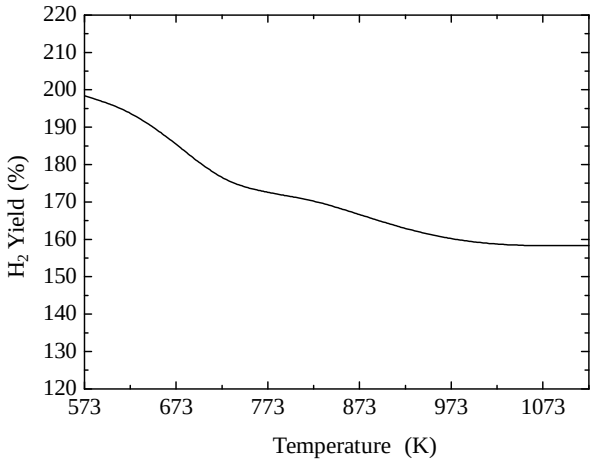

Figure 3 – Yield for H_2 production in autothermal reforming of methane at different temperatures.

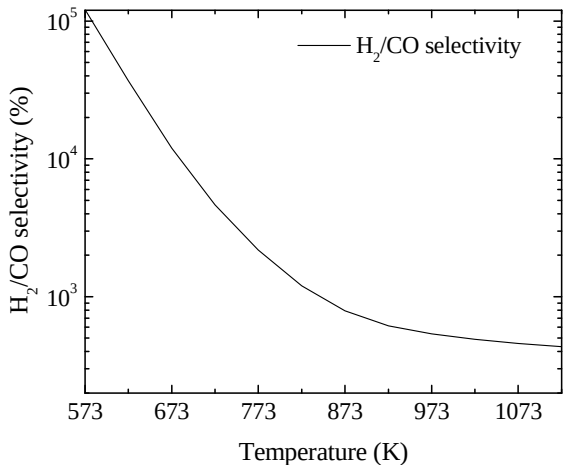

Figure 4 - H_2/CO selectivity in different temperatures for autothermal reforming of methane.

Through the results of methane conversion, yield of hydrogen and H_2/CO selectivity it is

possible to verify coherence among these results. For a maximum in hydrogen production, associated with smaller operational costs, the best reaction conditions are between 723 and 773 K. At these temperatures, there is a high H_2 yield, an elevated selectivity and a methane conversion around 50%. Besides, in these conditions, the catalyst properties are maintained and with smaller chances of sintering. In addition, these conditions have the advantage of smaller energy costs, because the reaction temperature is lower.

4 Conclusions

The proposed mathematical model has a good adjustment to the experimental data of Ayabe *et al*. (2003), presenting a good agreement of methane conversions and H_2 yields in all studied grade. The simulated data showed that the best reaction condition to maximize hydrogen production is around 723 K.

Acknowledgements

This work has been supported by Brazilian funding agencies, FAPEMIG, CAPES and CNPq (Grant n. 475934/2006-7), as well as, “Rede Brasileira de Combustíveis e Hidrogênio” (CTPETRO/FINEP/PETROBRAS).The authors would like to thank Chemical Engineers Tatiana V. Franco and Cícero N. de Ávila-Neto for the help in the calculation of equilibrium compositions.

References

Ayabe, S., Omoto, H., Utaka, T., Kikuchi, R., Sasaki, K., Teraoka, Y., Eguchi, K. (2003) Catalytic autothermal reforming of methane and propane over supported metal catalysts. *Applied Cat. A: General*, v.241, p. 261-269.

Barrio, V.L., Schaub, G., Rohde, M., RABE, S., Vogel, F., Cambra, J.F., Arias, P.L., Guemez, M.B. (2007) Reactor modeling to simulate catalytic partial oxidation and steam reforming of methane. Comparison of temperature profiles and strategies for spot minimization. *International Journal of Hydrogen Energy*, v. 32, p.1421-1428.

Dias, J.A.C, Assaf, J.M. (2004) Autothermal reforming of methane over Ni/γ-Al_2O_3 catalysts: the enhancement effect of small quantities of noble metals. *J. of Power Sources*, v.130, p.106-110.

Fogler, H.S. (1999) *Elements of Chemical Reaction Engineering*, Third Edition.

Halabi, M.H., Croon, M.H.J.M., Van Der Schaaf, J., Cobden, P.D., Schouten, J.C. (2008) Modeling and analysis of autothermal reforming of methane to hydrogen in a fixed bed reformer. *Chem. Eng. Journal*, v.137, p.568-578.

Hoang, D.L., Chan, S.H., Ding, O.L. (2006) Hydrogen production for fuel cells by autothermal reforming of methane over sulfide nickel catalyst on gamma alumina support. *J. of Power Sources*, v.159, p.1248-1257.

Mattos, L.V, Oliveira, E.R., Resende, P.D., Noronha, F.B., Passos, F.B. (2002) Partial oxidation of methane on Pt/Ce-ZrO_2 catalysts. *Catalysis Today*, v.77, p.245-256.

Smet, C.R.H., Croon, M.H.J.M., Berger, R.J., Marin, G.B., Schouten, J.C. (2001) Design of adiabatic fixed-bed reactors for the partial oxidation of methane to synthesis gas. Application to production of methanol and hydrogen-for-fuel-cells. *Chem. Eng. Science*, v.56, p.4849-4861.

Xu, J., Froment, G.F. (1989) Methane Steam Reforming, Methanation and Water-Gas Shift: I. Intrinsic Kinetics. *AIChE Journal*, v.35, p.88-96.

Proceedings of the 10th International Chemical and
Biological Engineering Conference - CHEMPOR 2008
Braga, Portugal, September 4-6, 2008
E.C. Ferreira and M. Mota (Eds.)

Fluid Dynamics of Fluidized and Vibrofluidized Beds Operating with Flat Particles

Renata de Aquino B. Lima[1] and Maria C. Ferreira[1*]
[1]Drying Center of Pastes, Suspensions and Seeds, Chemical Engineering Department, Federal University of São Carlos, P.O. Box 676, Zip Code:13565-905 – São Carlos – SP, Brazil.

Keywords: Fluidization, Biomass particles, Minimum fluidization velocity, Vibrofluidized beds.
Topic: Advancing the chemical and biological engineering fundamentals – Multiphase flow.

Abstract

Fluid dynamic behaviors of fluidized and vibrofluidized beds operating with flat particles were investigated. Particles made of blank paper sheets cut into different shapes were used to simulate the geometry of actual leaves. Leaf-shaped and square-shaped 'particles', with $\varphi<0.1$ were tested. Curves of pressure drops versus air velocity were obtained in a rectangular column of cross section of 0.20x0.11 m^2, 0.30 m high, at dimensionless vibration parameters of 0; 0.5; 1.0 and 1.5. The flat particles produced poor fluidization patterns and highly non-homogeneous beds. The introduction of vertical vibration contributed to reduce channeling and to decrease the transition velocities from fixed to expanded beds. An additional effect of the vibration was the alignment of the particles into the bed, resulting in a configuration of maximum contact area between particles and fluid.

1. Introduction

Due to the good mixing and high heat and mass transfer rates, fluidized beds are widely applied in industrial operations and many papers have been published on equipment design and testing for a broad range of particulate materials (Hajidavalloo, 1998; Colters and Rivas, 2004). The appealing characteristics of fluidized beds for drying of particulate materials encouraged some authors to investigate their application on the drying of leaves (whole or in pieces) of tea and medicinal plants (Shah and Goyel, 1980; Zanoelo, 2007). Post-harvesting storage of dehydrated plants is an alternative to ensure good-quality products for processing along the whole year, minimizing supplying oscillations due to the seasonal crops. Leaves are particles of irregular and flat shapes, with sphericities (φ) under 0.5, out of the range of the usually fluidized particulate materials. The shape of a particle is one of the parameters that affect their fluid dynamic behavior in fluidized and vibrofluidized beds (Gupta and Mujumdar, 1980). In a recent review, Cui and Grace (2007) pointed out that non-standard particles – such as those large in size and extreme in shape – have flow characteristics not readily predictable; noting that characterization of the multiphase flow aspects of such flat particles is weak. They state about the necessity of additional research to provide a general understanding of how the shape and size of low-sphericity particles affect their fluid dynamic behavior in multiphase flows. It is worth noting that even the definition of which shape factor should be used to characterize irregular and flat particles is not clear and differ from one author to another. According to Taylor (2002), a generalized quantitative definition of shape does not exist and different definitions may be used depending on the application. Few works have been found in the consulted literature reporting the operation of fluidized beds with particles of low φ. Lucas et al. (1986) obtained experimental data and fitted a correlation to predict minimum fluidization velocity (U_{mf}) for particles of $0.1 \leq \varphi \leq 0.5$. Reina et al. (2000) investigated fluidization and segregation patterns of a polydisperse system formed by scrap-wood particles of low mean sphericity ($\varphi=0.35$), and

* M.C. Ferreira, Phone: 55-16-33518442; E-mail: mariaf@ufscar.br

observed that the low particle density and extreme irregular shape presented strong influence on the fluid dynamic behavior during fluidization.

Aiming future applications in the drying of medicinal plants, in this work the fluid dynamic behavior of flat particles in fluidized beds is investigated. Tests will be conducted using particles made of blank paper sheets cut into two different shapes. The use of particles made of paper sheets allows avoiding interfering effects on the bed dynamics caused by surface roughness and segregation due to size distribution. Such effects would necessarily be present if natural particles were used and might difficult the analysis of results on this initial stage of investigation. Vibrofluidized beds will be evaluated as an alternative to fluidization, as the literature suggests that the introduction of a vertical mechanical vibration contributes to reduce U_{mf} and bed pressure drop, and to minimize channeling and dead regions as well, resulting in more homogeneous fluidization patterns and increased heat and mass transfer rates.

2. Materials and Methods

2.1. Particulate Materials

The particles used in the experiments were made of paper sheets (density of 833 $kg.m^{-3}$) cut into the shapes of leaves and squares with previously specified dimensions. The paper used had a gramature of 75 $g.m^{-2}$ and was 90 μm thick. For each shape, ten particles were randomly selected and their main dimensions were measured using a particle analyzer (Galai Macro Viewer) and software Image Pro Plus 3.0. Feret diameters, areas and perimeters of the particles are in Table 1, as well as their sphericity, defined as the relationship between the surface area of a sphere having the same volume of the particle and the surface area of a particle.

Table 1: Properties of particulate materials

Particle	Feret diameters (cm)	Area (cm^2)	Perimeter (cm)	φ
leaf-shaped	maximum – 3.28	4.45	4.98	0.063
	minimum – 1.90			
square-shaped	maximum – 1.49	1.51	8.41	0.090
	minimum – 1.41			

2.2. Equipment and Experimental Procedure

The experimental apparatus is composed of a rectangular column, with a height of 0.30 m, and cross section of 0.20 x 0.11 m^2, made of galvanized iron (a detailed diagram and a full description may be found in Daleffe et al., 2005). The air is provided by a blower and the airflow rate is measured using a previously calibrated orifice plate. Pressures at the orifice plate and at the bottom of the bed were measured by pressure transducers linked to a data acquisition system (acquisition board A/D PCI-6024E from National Instruments). For operation in vibrofluidized mode, an eccentric mechanism was used to adjust the amplitude of vibration and a mechanical controller located at the axle of the electric motor allows for the adjustment of frequency of vibration. Frequency of vibration was measured with an optical tachometer Minipa MDT-2244. Different amplitudes (A) and frequencies (f) of vibration were tested, with vibration parameters Γ of 0.5; 1.0 and 1.5. The vibration parameter is defined as $\Gamma=A(2\pi f)^2/g$. To allow visual inspection of particle's dynamic into the bed, some tests were carried out using an acrylic chamber, with the same dimensions of the original galvanized iron chamber. For the conditions investigated, it was observed neither the presence of electrostatic effects nor significant changes on the behavior of fluidization in comparison to the observed with the galvanized iron chamber.

Experiments were conducted by increasing the gas flow rate step-by-step from zero to the maximum value prior to elutriation of particles. The air flow rate was then gradually decreased, and data of pressure drops versus air flow rates were obtained. Each point was obtained from the mean value of

512 samples, collected during 3 seconds. The air mean temperature was kept at 25 ^{o}C. All the experiments were carried out in triplicates. The voidage at minimum fluidization condition (ε_{mf}) was obtained by filling the fluidization chamber with a known mass of particles (about 128 g) and measuring simultaneously the pressure drops and bed heights as the air flow rate was gradually increased, in tests conducted in the acrylic chamber. The bed height at minimum fluidization condition was then obtained and ε_{mf} was estimated by the classical equation established for fluidization (Reina et al., 2000).

3. Results and Discussion

To check equipment and measurement systems, preliminary tests were carried out using "ballotini" glass spheres (d_p= 925 μm). Data of pressure drop (ΔP) versus the air velocity (U) were obtained and U_{mf} was obtained from the characteristic curve by the classical procedure. The experimental value, U_{mf}=0.47 m.s^{-1}, is in excellent agreement with the estimated from Wen and Yu (1966) correlation, equals to 0.46 m.s^{-1}. This result corroborates the quality of equipment and measuring instruments. In Figure 1(a) are the curves of pressure drops versus air velocity obtained in tests with the square-shaped paper particles.

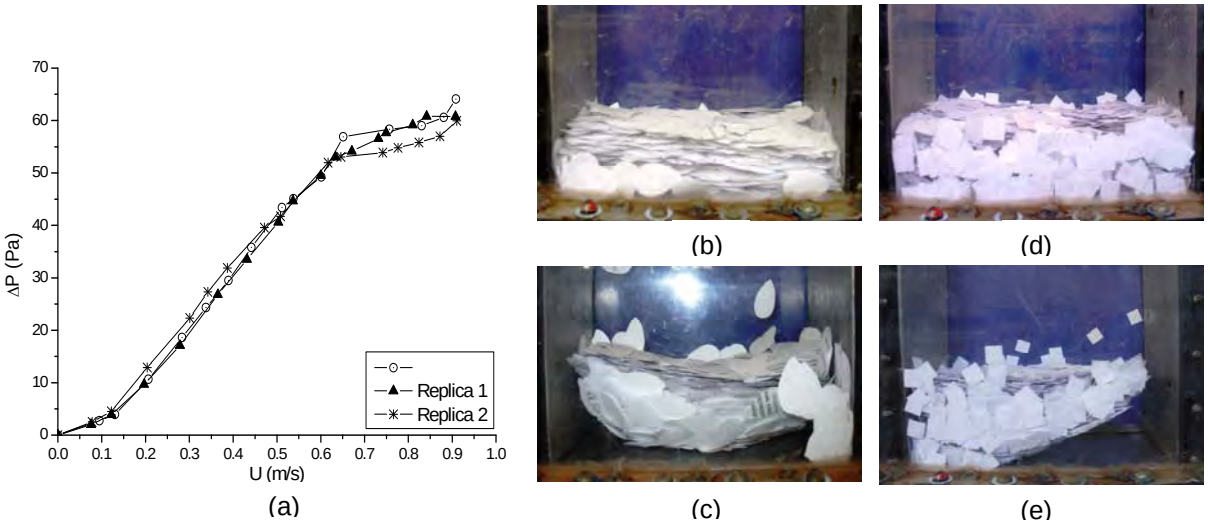

Figure 1: Fluidized bed (Γ=0.0); (a) ΔP vs. U for square-shaped particles; Photos: (b) Leaf-shaped particles; initial static bed (c) U=1.0m.s^{-1}; (d) Square-shaped particles; initial static bed (e) U=1.0m.s^{-1}l.

It is possible to note a region where ΔP increases linearly with the increase of U, a typical behavior for flow through fixed beds. As the air velocity continues to be increased, a change in the slope of the curve is noted, from U≈0.59 m.s^{-1}. In a conventional fluidized bed, this change characterizes the transition to the fluidized regime, in which ΔP is expected to remain constant as U is increased. For the particles tested here though, ΔP does not remain constant as U is raised, but continues to increase at a lower rate, a behavior that may be attributed to the poor quality of fluidization. Visual observation of flow patterns corroborates this evidence, as can be observed in Figures 1(b) and 1(c) for the leaf-shaped particles and in Figures 1(d) and 1(e) for the square-shaped ones, where typical patterns observed during the experiments are depicted. In the 'fluidized' condition, it is possible to note the presence of channeling, with very large voids located preferentially near the chamber walls (see Figures 1c and 1e). The arrangement of particles in the bed, with their surfaces facing the air flow, introduces a great resistance to the flow, preventing a homogeneous percolation of the fluid through the bed. Instead of a bed of particles uniformly percolated by the air, the particles are lifted by the flow as an aggregated bed, almost in a whole block. As channeling has not been observed in the previous tests with glass spheres, it is attributed to the particular characteristics of the particles, which are extremely flat, with φ<0.1. The transition velocity between the fixed bed and expanded regimes was obtained by fitting linear curves to

the points located in the fixed and expanded regions and finding the intercepting point between the lines (in a similar procedure to the one used to finding U_{mf} in classical fluidized beds). In spite of the poor homogeneity of the beds formed, the transition between fixed and expanded regimes is consistently reproducible (Figure 1a). The good reproducibility was also observed for the leaf-shaped particles, (the curves are not presented here for concision). A value of 0.63±0.03 $m.s^{-1}$ for the transition velocity was obtained for the square-shaped particles and of 0.58±0.04 $m.s^{-1}$ for the leaf-shaped ones. The mean voidages of these beds were estimated as 0.84 and 0.86 for the leaves and squares, respectively. These values are not considered representative of real voidages though, due to the large voids caused by channeling. Zanoelo (2007) reported a mean voidage of around 0.92 in a fluidized bed formed by mate leaves, square-shaped and with dimensions very similar to the square-shaped particles used in the present work.

Figure 2(a) shows curves of ΔP versus U for the square-shaped particles in vibrofluidization, with $A=4.0x10^{-3}m$ and $\Gamma=1.0$. These curves were obtained by initially fluidizing the bed and then introducing vibration. After, the bed was defluidized.

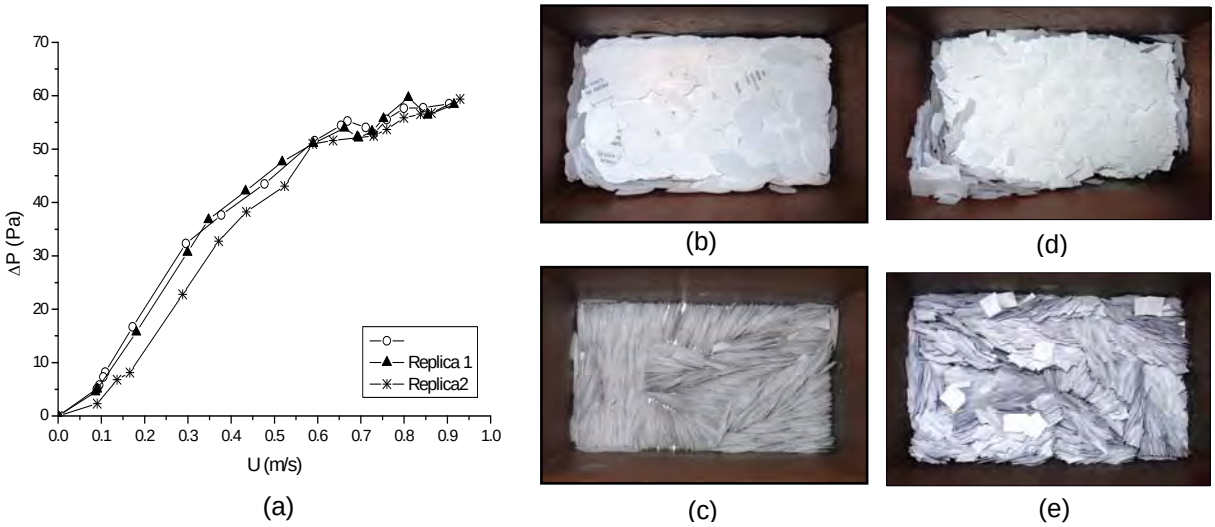

Figure 2 Vibrofluidized bed ($A=4.0x10^{-3}m$; $\Gamma=1.0$). (a) ΔP vs. U (square-shaped particles).Photos (top views): (b) leaf-shaped particles, initial static bed; (c) vibrofluidized bed after a time of 30 min; $U=1.05U_{mf}$ (d) square-shaped particles, initial static bed; (e) vibrofluidized bed after a time of 20 min; $U=1.05U_{mf}$.

By comparing the curves with the ones obtained in fluidization, it is possible to note that the use of vibration extends the range of transition between the fixed and fluidized regimes, a typical behavior of vibrofluidized beds (Daleffe et al., 2005), making the identification of transition velocity more difficult. Reduction of channeling was detected with the use of vibration, because the particles were rearranged and their relative position concerning the direction of air flow rate changed along the essays – the particles gradually become aligned, with their major axis positioned horizontally and their surface area parallel to the direction of air flow (see Figures 2b to 2e). The photos show top views of the beds at the initial static condition and after a period of operation at $A=4.0.10^{-3}m$ and $\Gamma=1.0$ (they illustrate typical patterns observed for practically all the conditions tested). The time for the complete alignment of the particles was a function of the amplitude and frequency of vibration and also of the air velocity. The reproducibility of the characteristic curves in Figure 2a has not been as good as in fluidized beds, which is attributed to the fact that the bed packing structure changed significantly along the process.

The effects of vibration parameters on the fluid dynamic behavior of vibrofluidized beds of square-shaped particles at vibration amplitudes of $4.0x10^{-3}$ and $5.0x10^{-3}m$ may be observed in Figure 3. The extended transition region the fixed to the expanded regimes prevents an accurate identification of the transition velocities. Literature does not present a consensual definition for the transition velocity in vibrofluidized

beds (Daleffe et al, 2005). Here, they were obtained using the same methodology applied for fluidization, and the values are indicated in Figure 3. Although the notation U_{mf} is maintained, it is convenient to note that the transition velocities here are not equivalent to the classical definition applied for conventional fluidized beds, since even for Γ=0 the regime observed may not be considered as really fluidized. According to Gupta and Mujundar (1980), in homogeneous beds the vibration should reduce both U_{mf} and ΔP_{mf}. The results show that the transition velocities in vibrofluidized beds are lower than in the fluidized ones, but the effect of increasing Γ on U_{mf} is not clear. The values of U_{mf} for the leaf-shaped particles (curves not showed here for concision), varied in the range of experimental uncertainty. Concerning the effects of vibration parameters on the fluid dynamics, curves in Figure 3 show that at Γ>0, ΔP in the fixed bed region is always greater than at Γ=0, while in the expanded regime it is not possible to identify significant effects of the vibration on the pressure drops.

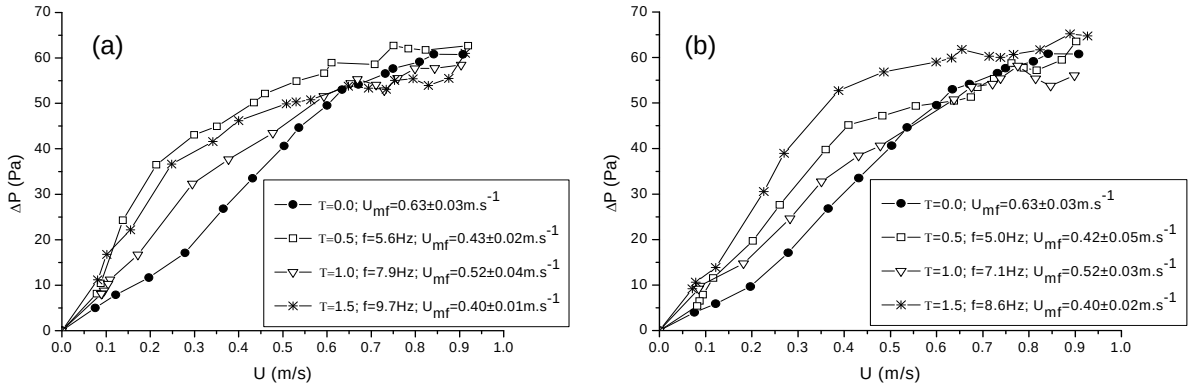

Figure 3: ΔP vs. U; square-shaped particles; (a) A=4.0x10^{-3} m; (b) A=5.0x10^{-3} m.

The shapes tested in the present work have sphericity lower than 0.1, and the superficial area of square-shaped particle is about 30% minor than the leaf-shaped oneparticles. The fluid dynamic behavior for the different shapes are depicted in Figures 4(a) for Γ=0 and 4(b). In fluidization, the increase in the particle dimensions resulted in greater pressure drops at fixed bed region, while opposite behavior is observed for vibrofluidized beds. At values of U>U_{mf}, the pressure drops are similar for the different shapes, because the mass of particles used in the experiments was the same and the particles have the same density, so the pressure drop does not change.

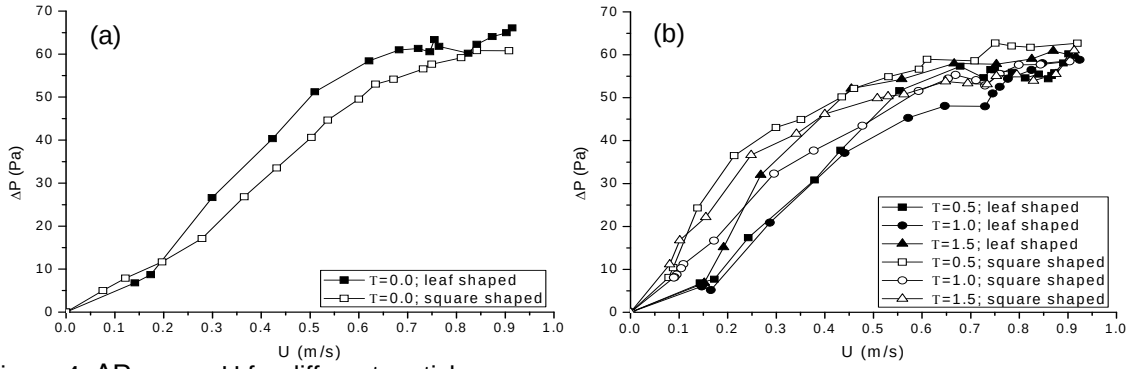

Figure 4: ΔP versus U for different particles.

A correlation developed by Lucas et al. (1986), recommended for particles of 0.1≤ φ ≤0.5 was tested to estimate U_{mf} for our conditions, as well as one suggested by Reina et al. (2000). The deviations were quite large though, exceeding an order of magnitude. The classical correlation from Wen and Yu (1966) was the one which best predicted the experimental results, yielding values of 0.97 and 0.77 m.s^{-1} for the leaf-shaped and square-shaped particles, respectively. Experimental values of ΔP_{mf} in fluidization were compared to the ones predicted by the theoretical relationship. The predicted values

(57 Pa for both particle shapes) agree well with the experimental ones (56±3 e 54±2 Pa for the leaf-shaped and square-shaped particles, respectively).

4. Conclusions

The use of particles made of paper and cut into specified sizes and shapes permitted the measurement of fluid dynamic data in fluidization of particles with very low φ, eliminating variations in size and shape inherent to natural particles. Tests with leaf- and square-shaped particles with $\varphi<0.1$ showed that they produce poor fluidization patterns, very different from the obtained in conventional fluidization of particles with $\varphi>0.5$. The particle beds are expanded by the air flow, but they are strongly non-homogeneous and intense channeling is observed. The results yield to the conclusion that methodologies developed for particles of $\varphi>0.5$ should be applied with caution for flat particles. The use of vertical vibration minimized channeling and reduced U_{mf}. An important effect of vibration was the alignment of the particles, which rest with their major axis positioned horizontally and their surface areas parallel to the air flow. The particle shapes tested presented similar fluid dynamic behaviors in both fluidized and vibrofluidized configurations, with values of U_{mf} and ΔP_{mf} not significantly different for each shape. The correlation developed by Wen and Yu (1966) predicted U_{mf} for the leaf-shaped particles with deviations of 67% (square-shaped particles) and 22% (leaf-shaped particles). Additional experimental data, for other shapes and different ranges of φ, are necessary to the establishment of reliable methodologies for estimating fluidization parameters of low-sphericitiy particles. The results obtained here suggest that the use of fluidized beds for drying of leaves may lead to a non-uniform drying, since the contact between the particles and the percolating fluid along the bed is irregular. Vibration may be used as a preliminary operation before fixed bed drying, since the alignment of the particles may favor heat and mass transfer by maximizing the area of particles in contact with the fluid.

Acknowledgments

The authors thank CNPq for financial support and Prof. J.T. Freire for the valuable suggestions.

References

Colters, R., Rivas, A.L. (2004). Minimum fluidization velocity correlations in particulate systems. *Powder Technol.*, 147, 34-48.

Cui, H., Grace, J.R. (2007). Fluidization of biomass particles: A review of experimental multiphase flow aspects. *Chem. Eng. Sci.*, 62, 45-55.

Daleffe, R.V., Ferreira, M.C., Freire, J.T. (2005). Drying of pastes in vibro-fluidized beds: effects of the amplitude and frequency of vibration. *Drying Technol.*, 23, 1765-1781.

Gupta, R., Mujumdar, A.S. (1980). Aerodynamics of a vibrate fluid bed. Ca*n. J. Chem. Eng.*, 58, 332-338.

Hajidavalloo, E. (1998). Hydrodynamic and thermal analysis of a fluidized bed drying system. PhD Thesis, Faculty of Engineering, Dalhouse University-Daltech, Halifax, Nova Scotia, 173 p.

Lucas, A., Arnaldos, J., Casal, J., Puigjaner, L. (1986). Improved equation for the calculation of minimum fluidization velocity. *Ind. & Eng. Chem. Proc. Des. Devel.*, 25, 426-429.

Reina, J., Velo, E., Puigjaner, L. (2000). Predicting the minimum fluidization velocity of polydisperse mixtures of scrap-wood particles. *Powder Technol.*, 111, 245-251.

Shah, R.M., Goyel, S. K. (1980). Drying characteristics of tea fluidized on a vibrating bed (Part I). In: *Drying'80*, Volume 2, Hemisphere Publishing Corporation, New York, 176-181.

Taylor, M.A. (2002). Quantitative measures for shape and size of particles. *Powder Technol.*, 124, 94-100.

Zanoelo, E. F. (2007). A theorical and experimental study of simultaneous heat and mass transport resistances in a shallow fluidized bed dryer of mate leaves. *Chem. Eng. Proc.*, 46, 1365-1375.

Proceedings of the 10th International Chemical and
Biological Engineering Conference - CHEMPOR 2008
Braga, Portugal, September 4-6, 2008
E.C. Ferreira and M. Mota (Eds.)

Heterogeneous model for mass transfer of dissolved lignin during kraft pulping of *Eucalyptus globulus*

João P. F. Simão, Cristina M. S. G. Baptista, M. Graça Carvalho*
CIEPQPF, Department of Chemical Engineering, University of Coimbra,
P-3030 790 Coimbra, Portugal

Keywords: Kraft pulping, mass transfer, lignin, kinetic model, *Eucalyptus globulus*
Topic: Advancing the chemical and biological engineering fundamentals.

Abstract

The mass transfer of lignin from the inside of wood chips to the bulk liquor during the kraft pulping of *Eucalyptus globulus* was studied and a kinetic model to describe this process is proposed. The kraft pulping experiments were carried out with target temperatures ranging from 80 to 165 ºC, effective alkali charges from 10 to 45 g Na_2O/L and sulphidities from 15 to 75%. The model is based on extensive experimental data on the dissolved lignin concentration profiles along pulping time, both inside and outside the chips. The lignin concentration in the entrapped liquor was much higher than in the free liquor, and reached a maximum value during the cook. The model follows a lumped parameter estimation approach, where the spatial concentration profile of lignin inside the chip is represented by its spatial average, enabling to estimate the effective diffusion coefficient while taking into account the contribution of the film surrounding the wood chips to the overall mass transfer resistance. The model enabled a good prediction of the dissolved lignin concentration in the free liquor. The effective diffusion coefficient was expressed by an Arrhenius-type equation with an estimated activation energy for diffusion of 29 kJ/mol, being also dependent on the cooking yield raised to 5,07. This exponent high value is explained by the increasing resistance to lignin diffusion along pulping time. The mass transfer resistance in the external film was found to have a significant contribution to the overall resistance (20 to 30% at the beginning of the cook) and should not be neglected.

1 Introduction

The kraft pulping process is strongly dependent on the mass transfer of the reagents and reaction products that occurs between the free (bulk) liquor and the liquor entrapped in the chips. The highly heterogeneous nature of the process comes from the fact that the pulping reactions occur between the reagents in the entrapped liquor and the wood components in the solid matrix of the chips and the chemicals' concentrations in the entrapped liquor are substantially different from those in the free liquor (Egas et al., 2002). The main objective of the pulping process is to remove the lignin from the wood, preserving, as much as possible, the carbohydrates. However, besides promoting the reaction of lignin with the alkaline reagents in the cooking liquor, it is required to withdraw the dissolved lignin from inside the chip to the free liquor, since it can re-precipitate onto the wood after the cook. The mass transfer of the dissolved lignin from the entrapped liquor to the free liquor occurs both during the cook and in the following washing stages.

The majority of the kinetic studies on the kraft pulping of wood are focused on the chemical reactions involving the wood components or the mass transfer of the cooking reagents, and therefore there are very few studies in the literature on the mass transfer of the dissolved organic compounds to the free liquor (Li and MacLeod, 1993; Li and Mui, 1999). Besides, these studies are mostly focused on the mass transfer in the washing stages rather than

* Corresponding author. E-mail:mgc@eq.uc.pt

during the cook. As an example, the model based on experimental studies developed by Li et al. (1997) is one of the few kinetic approaches to describe the diffusion of dissolved lignin within the pulp fibres, during the washing stage. The kinetic model follows Fick's law with cylindrical coordinates in the radial dimension of the fibre walls, being the diffusion coefficient independent of the radial position. According to this model, the diffusion coefficient was found to vary with the pH, leading to a faster diffusion rate at higher pH values.

The dissolved lignin mass transfer kinetics is relevant not only for the washing process that follows the cook, where a deeper knowledge of the mass transfer of organic compounds is needed, but also during the cook. By knowing the dissolved lignin concentration in the free liquor and the mass transfer rate between the free and the entrapped liquors, the lignin concentration in the entrapped liquor can be determined, and consequently the amount of lignin removed from wood at every instant of the cook.

2 Experimental

The proposed model is based on experimental data from laboratory cooking experiments. The experimental procedure is described elsewhere in more detail (Egas et al., 2002; Simão et al., 2008). Pulping of handmade *Eucalyptus globulus* chips (30x30x6 mm) was performed in a six-vessel computer controlled batch-digester system described by Romanenko and Castro (2000). Each cooking experiment consisted of six simultaneous cooks in the same conditions of temperature, pressure and reagents concentration, but with different pulping times. The chips were fully impregnated with water prior to the cooks, which allows disregarding the penetration mechanism. The effective alkali charge, the sulphidity and the target temperature varied among experiments in the ranges 10 to 45 g Na_2O/L, 15 to 75% and 80 to 165 ºC, respectively. The liquid-to-wood ratio remained at 8 L/kg in all experiments (Simão et al., 2008).

After each cook, samples of free and entrapped liquors were withdrawn, being the latter obtained by pressing the cooked chips. The liquor samples were analyzed for dissolved lignin concentration according to the method developed by Trinh (1988): the samples were diluted with NaOH solution at 0.01 N and their absorbance was measured at 280 nm.

3 Model Development

The proposed model is based on a lumped parameter estimation approach, where the spatial lignin concentration profile along the chip thickness is replaced by its spatial average, which corresponds to the lignin concentration in the whole of the entrapped liquor that was measured in the cooking experiments. A similar model for the diffusion of effective alkali was already presented (Simão et al., 2008). This approach is illustrated in figure 1. Therefore, the overall mass transfer coefficient (K_{OL}) relates the lignin concentration in the average of the entrapped liquor with the one in the free liquor. This coefficient can be related to the effective diffusion coefficient (D_{eff}) and the mass transfer coefficient in the external film (k_L).

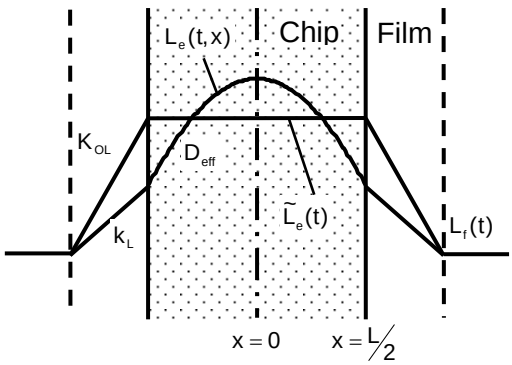

Figure 1. Dissolved lignin profile across the chip and its space average equivalent.

In order to build the lignin mass transfer model, the following assumptions were made:

- The free liquor phase is homogeneous and well agitated;
- The resistances to heat transfer are considered negligible;
- The chip is treated as a infinite slab and its critical dimension is the thickness;
- The convective flux inside the chip is negligible;
- The lignin activity coefficient is the same in the free and entrapped liquors;
- The effective diffusion coefficient is constant along the chip thickness;
- The re-precipitation of lignin on the wood fibres is considered not to occur.

A microscopic mass balance to the dissolved lignin in the entrapped liquor leads to Eq. 1:

$$\frac{\partial(\varepsilon L_e)}{\partial t} = D_{eff}\left(\frac{\partial^2 L_e}{dx^2}\right) + r \tag{1}$$

with the following boundary and initial conditions:

$$x = 0 \quad \Rightarrow \quad \left(\frac{\partial L_e}{\partial x}\right)\Bigg|_{x=0} = 0 \tag{2}$$

$$x = \frac{L}{2} \quad \Rightarrow \quad D_{eff}\left(\frac{\partial L_e}{\partial x}\right)\Bigg|_{x=\frac{L}{2}} = -k_L\left[L_e\left(t,\frac{L}{2}\right) - L_f(t)\right] \tag{3}$$

$$t = 0 \quad \Rightarrow \quad \begin{cases} L_e(0,x) = 0 \\ L_f(0) = L_f^0 \end{cases} \tag{4}$$

where $L_e(t,x)$ and $L_f(t)$ are the dissolved lignin concentrations in the entrapped and free liquors, ε is the chip porosity, r is the chemical reaction rate, L is the chip thickness, D_{eff} is the effective diffusion coefficient and k_L is the mass transfer coefficient in the external film. By using the spatial average of the lignin concentration profile, $\tilde{L}_e(t)$, and average reaction rate, $\tilde{r}$, in the entrapped liquor, and assuming that this profile is represented by an inverted second-order polynomial, symmetric at $x = 0$, the following lumped parameter model is obtained where the microscopic balance is expressed as a function of $\tilde{L}_e(t)$:

$$\frac{\partial(\varepsilon \tilde{L}_e)}{\partial t} = \frac{12 D_{eff} k_L}{L(6D_{eff} + Lk_L)}\left[L_f(t) - \tilde{L}_e(t)\right] - \tilde{r} \tag{5}$$

On the other hand, the macroscopic balances to the lignin concentration in the free and entrapped liquors are expressed by Eq. 6 and 7:

$$\frac{d(V_f L_f)}{dt} = -K_{OL} A_T\left[L_f(t) - \tilde{L}_e(t)\right] \tag{6}$$

$$\frac{d(V_e^T \tilde{L}_e)}{dt} = K_{OL} A_T\left[L_f(t) - \tilde{L}_e(t)\right] - V_{chip}^T \tilde{r} \tag{7}$$

where V_e^T and V_f are the total volumes of entrapped and free liquor in the system, V_{chip}^T is the total volume of chips and A_T is the total mass transfer area. By multiplying Eq. 5 by V_{chip}^T, the microscopic balance can be related to the macroscopic balance in Eq. 7, and therefore the following relationship is inferred:

$$\frac{1}{K_{OL}} = \frac{1}{k_L} + \frac{L}{6D_{eff}} \tag{8}$$

The mass transfer coefficient in the film k_L was determined using correlations for liquid-solid systems published by Dwidevi and Upadhyay (1977) and the experimental data for the properties of free liquor.

The effective diffusion coefficient was considered to follow an Arrhenius-type equation for diffusion, multiplied by the cooking yield (η) raised to an exponent:

$$D_{eff} = \varepsilon k_D \sqrt{T}\, e^{-\frac{E_a}{RT}} \eta^n \quad (13)$$

where k_D is the preexponential constant, E_a is the activation energy for diffusion and R is the gas constant. The yield factor was added to account for a high decrease in the lignin transfer rate along cooking time which was found to occur. This strategy is similar to the one used by Gustafson et al. (1983) in their kinetic model, where the cooking yield was related to the lignin content in the solid phase.

4 Results and Discussion

Some of the experimental results are illustrated in figures 2 and 3. Unlike the liquor reagents, the lignin is dissolved within the chips and diffuses from the entrapped liquor to the free liquor. Therefore, the lignin concentration in the entrapped liquor is much higher than that in the free liquor. A decrease in the lignin concentration in the entrapped liquor is also observed later in the cook, for the cooks with a high temperature. The maximum lignin concentration value corresponds to the equilibrium between the rates of chemical reactions that produce the dissolved lignin and the rate of mass transfer towards the outside of the chip. Once this equilibrium is reached, the mass transfer rate becomes higher than the chemical reaction rate, and the lignin concentration in the entrapped liquor begins to decrease.

The lignin concentration increased, both in the free and in the entrapped liquors, for higher temperatures and alkali charges, as also shown in figures 2 and 3. The same effect was observed when the sulphidity was increased (results not shown). This behaviour was expected, since it is known that an increase in temperature, alkali charge or sulphidity leads to a higher reaction rate of wood lignin, and consequently to a higher dissolved lignin concentration.

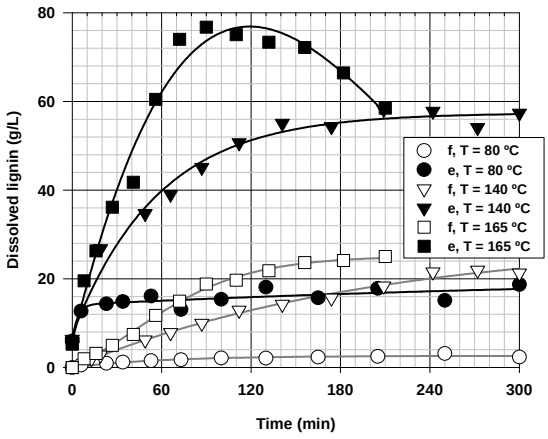

Figure 2. Effect of temperature (T) on the dissolved lignin concentration in the free (f) and entrapped (e) liquors (effective alkali charge = 15 g Na_2O / 100 g odw, sulphidity = 30%)

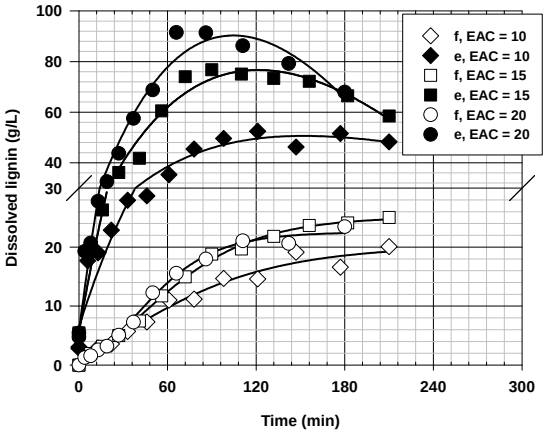

Figure 3. Effect of effective alkali charge (EAC) on the dissolved lignin concentration in the free (f) and entrapped (e) liquors (temperature = 165 ºC, sulphidity = 30%)

The proposed model contains a total of three parameters to estimate: the preexponential constant and the activation energy for the effective diffusion coefficient and the exponent of the cooking yield (Eq. 14). From the 35 cooking experiments available for model development, 22 were chosen to solve the parameter estimation problem, while the remaining 13 were left for model validation. Re-parametrization was performed in k_D and E_a, being the estimated parameters $\beta_1 = \ln(k_D) - E_a / 300R$ and $\beta_2 = E_a / 300R$.

Figures 4 and 5 show the experimental and predicted values for the dissolved lignin in the free liquor in cooks used for model development (Fig. 4) and for model validation (Fig. 5). Taking into account that the lignin concentration in both free and entrapped liquors is subject to experimental error, a good fit of the model predictions to the experimental values was obtained, with R^2 values of 0.968 for the data used for parameter estimation and 0.909 for the validation data.

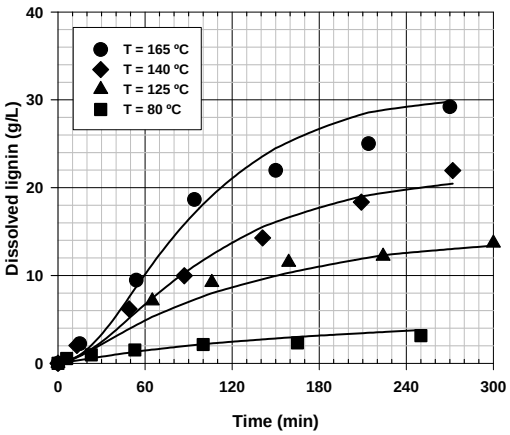

Figure 4. Experimental values and model predictions for the dissolved lignin in the free liquor in cooks used for parameter estimation (effective alkali charge = 15 g Na_2O / 100 g odw, sulphidity = 30%).

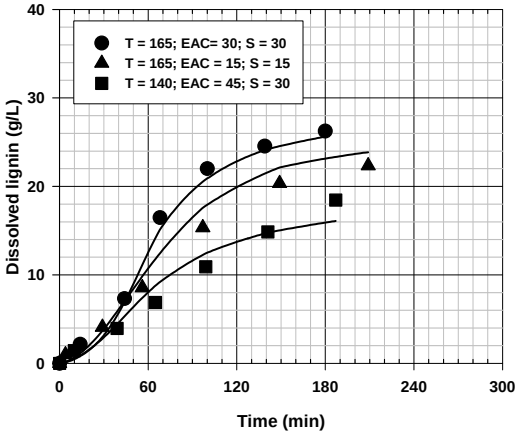

Figure 5. Experimental values and model predictions for the dissolved lignin in the free liquor in cooks used for model validation (temperature, T, in ºC, effective alkali charge, EAC, in g Na_2O / 100 g odw, sulphidity, S, in %)

The estimated values of the parameters and their standard deviations are presented in Table 1. The estimated values show a high confidence level, with deviations reaching a maximum of 7.6% of these values. The activation energy (29 kJ/mol) is in the range of literature values for diffusion (Gustafson et al., 1983), while being higher than the one found for the diffusion of alkali (21 kJ/mol) in a previous model developed by the authors (Simão et al., 2008). This is to be expected since the diffusion of lignin is supposedly slower than alkali diffusion.

However, the diffusion of lignin is also significantly affected by the cooking yield, as suggested by the high value of the yield exponent. The high influence of the yield factor is reflected on a continuous increase of the resistance to lignin diffusion within the chip throughout the cook, as illustrated in Figure 6 where the overall, internal and external resistances to mass transfer are shown. The increase in the internal resistance is only compensated at the beginning of the cook, where the temperature increase would normally lead to a lower resistance to mass transfer. This occurrence can be tentatively explained by the molecular weight distribution of the dissolved lignin: the lignin with lower molecular weight diffuses faster to the free liquor, leaving behind the lignin of higher molecular weight whose diffusion is slower. The increase in the viscosity of the entrapped liquor also contributes to hinder the diffusion of lignin out to the free liquor. On the other hand, the resistance to mass transfer in the external film decreases along the cook, influenced by the temperature and the surface velocity of the free liquor. At the beginning of the cook, as shown in Figure 6, it has a relatively high value, reaching almost 30% of the overall mass transfer resistance in some cooks. This indicates that, at least during the heating stage of the cook, the mass transfer in the film should not be neglected. However, after this period the internal resistance to mass transfer starts to increase, and the importance of the external film resistance fades away as the cook progresses.

Estimated parameter	β_1	β_2	n
Parameter value	– 48,8	11,8	5,07
Standard deviation	1,3	0,9	0,25
Model parameter	k_D	E_a (J/mol)	
Parameter value	$8{,}58 \times 10^{-17}$	29×10^3	

Table 1. Optimal parameter estimates for the mass transfer model.

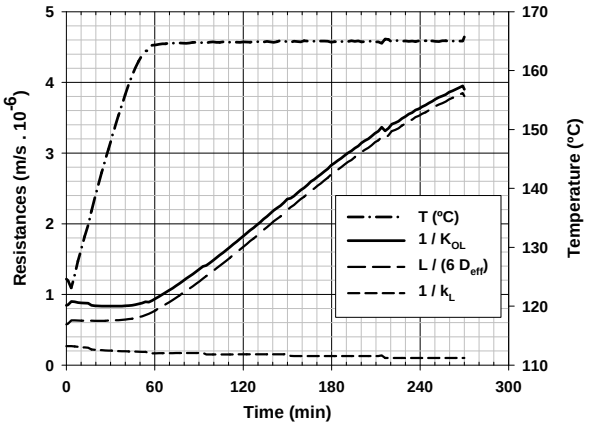

Figure 6. Evolution of the overall ($1/K_{OL}$), internal ($L/6D_{eff}$) and external ($1/k_L$) resistances to mass transfer along pulping time for a particular cook. (T = 165 ºC; CAE = 15 g Na_2O/100 g odw; S = 30%).

5 Conclusions

The proposed model for the mass transfer of dissolved lignin is fully based on experimental data on the dissolved lignin concentration in both free and entrapped liquors, and therefore is independent of the chemical reactions that produce the dissolved lignin. The model provides a good prediction of the lignin transferred to the free liquor at each instant of the cook in a wide range of operating conditions.

According to the model, the diffusion of lignin is dependent on the cooking yield, resulting on a significant increase of the corresponding resistance to mass transfer along the cook. This increase may be explained by an increase in the liquor viscosity and in the average molecular weight of the dissolved lignin that are believed to occur during the cook. The resistance to mass transfer of lignin in the film surrounding the chips was found to be significant at the beginning of the cook, up to 30% of the overall mass transfer resistance.

References

Dwidevi, P. N., Upadhyay, S. N. (1977). Particle-fluid mass transfer in fixed and fluidized beds. *Ind. Eng. Chem. Proc. Des. Dev.*, 16(2), 157–165.

Egas, A. P. V., Simão, J. P. F., Costa, I. M. M., Francisco, S. C. P., Castro, J. A. A. M. (2002). Experimental methodology for heterogeneous studies in pulping of wood. *Ind. Eng. Chem. Res.*, 41(10), 2529-2534.

Gustafson, R. R., Sleicher, C. A., McKean, W. T., Finlayson, B. A. (1983). Theoretical model of the kraft pulping process. *Ind. Eng. Chem. Proc. Des. Dev.*, 22(1), 87-96.

Li, J., MacLeod, J. M. (1993). The effects of alkaline leaching on pulp bleachability and physical-properties. *Tappi J.*, 76(12), 159-166.

Li, J., Mui, C. (1999). Effect of lignin diffusion on kraft delignification kinetics as determined by liquor analysis. Part I: An experimental study. *J. Pulp Paper Sci.*, 25(11), 373-377.

Li, J., Phoenix, A., MacLeod, J. M. (1997). Diffusion of lignin macromolecules within the fibre walls of kraft pulp. Part I: Determination of the diffusion coefficient under alkaline conditions. *Can. J. Chem. Eng.*, 75, 16-22.

Romanenko, A., Castro, J. A. A. M. (2000). An RT-Linux based control system of a pilot plant for reaction kinetics and process control studies. *Comp. Chem. Eng.*, 24, 1063-1066.

Simão, J. P. F., Egas, A. P. V., Carvalho, M. G.,Baptista, C. M. S. G., Castro, J. A. A. M. (2008). Heterogeneous studies in pulping of wood: modelling mass transfer of alkali. *Chem. Eng. J.*, 139, 615-621.

Trinh, D. T. (1988). The measurement of lignin in kraft pulping liquors using an automatic colorimetric method. *J. Pulp Paper Sci.*, 14(1), J19-J22.

Proceedings of the 10th International Chemical and
Biological Engineering Conference - CHEMPOR 2008
Braga, Portugal, September 4-6, 2008
E.C. Ferreira and M. Mota (Eds.)

Axial mixing in extractor column liquid-liquid, without mechanical agitation

Brandão, M., M.; De Góis, L.M.N.

Masters Degree Chemical Engineering – Federal University of Bahia, Politécnica School, Aristides Novis Street nº 2, 2º floor, Federação – CEP: 40210-630 – Salvador – Ba –Brasil
Phone: (55XX71) 3283-9809 – Fax: (55XX71)3283-9810
E-mail: mmb@ufba.br and lmario@ufba.br

Abstract

In this paper was presented the assessment of an liquid-liquid extration column, without mechanical agitation, by experimental and theoretical determination of axial dispersion data from related equipment and also posterior analyses of these results.
Experimentally, the method used for determination of axial dispersion number,it was about the test of tracer (type pulse), using water as solvent and the orange of metila as soluto, however for attainment of the axial dispersion values, it was used the Levenspiel model (1962), always to the ambient temperature (25ºC).
In the theoretical part was proposal an equation based on pi of Buckingham theorem of dimensional analysis, so that also the behavior of the axial dispersion in function of selected variable , using a program elaborated in FORTRAN language.
In this study was analyzed influence of outflow continuous phase, the number of compartments utilized and the free area of draining perforateed plates in the extractor column liquid-liquid, it based on the comparison final values of axial dispersion, these gotten in experimental way against the theoretical values, formulated for empirical correlations.

Key Word: Separation, Extraction, Axial Dispersion.

1. Introduction

The liquid-liquid extraction studied hear has as object an extractor column of perforated plates, without mechanical agitation and laboratorial scale. It´s operating with water (continuous phase) and orange of metila (tracer) in countercurrent and normal conditions of bench. Some references about axial dispersion and their areas had been produced throughout these years. Moustiri (2001) considered the study of the axial dispersion in a column with bubbles considering the two-phase flow. It also admitted an unified empirical correlation, to predict the coefficient axial dispersion of the liquid, the holdup of gas and the size of the bubble at column in operation. On another study for Thanos (2001) studied the axial dispersion and holdup of mix at high pressures and temperatures, also it´s using empirical correlations to predict the coefficient of axial dispersion. In other source, Zítný (2004) considered the determination of the values of axial dispersion through the theorem of the finite values for making a perfect analogy with the transfer of heat and mass. Another premise of its model none case that will have bigger velocity for disturbance influence at temperature in the flow.
Already Góis (1995), exactly not being one of the studies most recent related to the axial dispersion, however including a relation to the hydraulical study of extractor columns, this contribution spoken about the performance of an extractor column evaluated through tree distinct groups, as demonstrated in Figure 1 below.
Of this study, it was possible for the Laboratory of Separation in the Chemical Engineer Masters Degree (MAEQ) on politécnica School at UFBA, to be bred 3 sources of study, it related to the hydarulical of columns extractor, as mentioned in Figure 1.

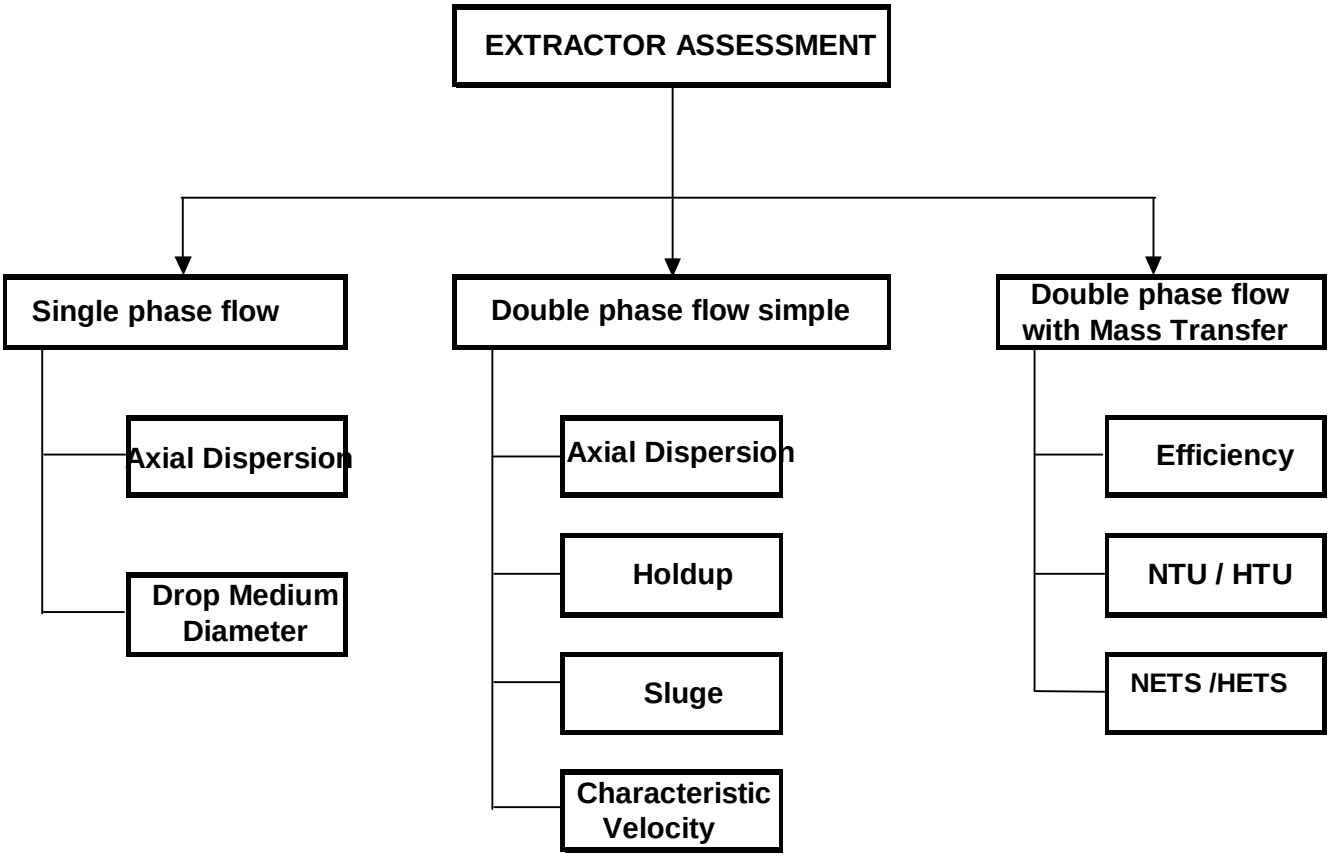

Figure 1- Diagram of assessment for+ extractor columns (Góis, 1995)

Amongnst the cited, the study of the single-phase flow through the assessment of coefficient axial dispersion is the focus of the present work, until presented here.

2. Experimnt

For accomplishment the present work was used na extracting column with perforated Prates, as demonstrated in figure 2.

2.1. Apparatus Describe

The configuration operational geometric of the extracting column was 3 and 4 compartments, with height of 72 ou 92 cm and an internal diameter of 9,50 cm.
This extracting column also is composed of aluminumm perforated plates. So, each plate have diameter of 11,72 cm, an area of 108,82 cm^2 and a fixed area of puncture for plate. The area of each puncture is 0,55 or 0,35 cm, it providing, respectively, a free area of flow approximately of 6% or 29%.

2.2. Experiment Procedure

For experimental determination of the axial dispersion number was used the test of tracer type pulse, which consists in injection one pulse of plotting (orange of metila) with know concentration, in the base of the extracting column under flowed phase (water), It followed of collections of samples (plotting + solucion) in the top of the same.

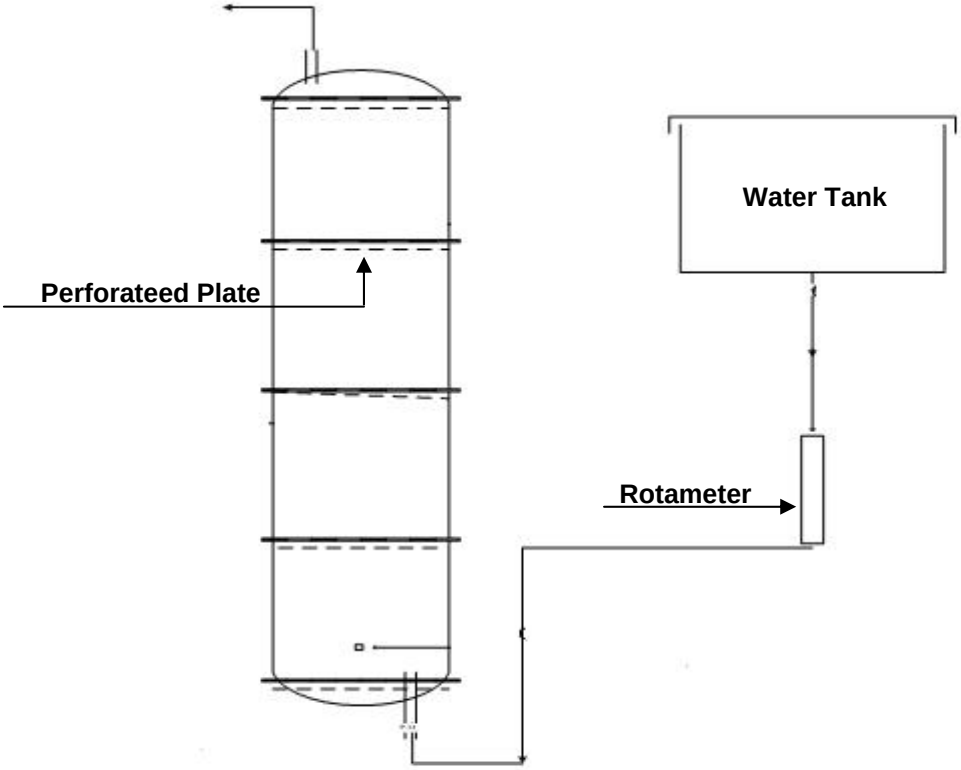

Figure 2- Diagram of laboratorial apparatus of extractor column with perforated plates.

The extracting columnn perforateed plates endowed terminals for feeding/sampling is fed by a hose, which the flowed phase (water) from the feeding, it compound for action of gravity the extractor column in vertical and ascending direction at maximum level operation.
Therefore, 5 ml of orange of metila (plotting), was injected, with know concentration in the base. So, itself collecting samples in the top of the column of 30 in 30 seconds, logically at different values of the same one.
Each experimental attempt was repeated 3 times, for reduce experimental error quantity and attributed an average value of same one sample, independent of evaluated parameter.

2.3. Axial Dispersion Determination

With the experimentally values obtained of, it was determined axial dispersion number by differential model propost at Levenspiel (1962).
The model Levenspiel (1962), affirms that since that mixture process involves a redistribuition of material for agitation, but this reflect a considerable time in the flow, such redistribuition can be considered as statistical nature and analogous to molecular diffusion. So, the author describes the axial dispersion similar form then molecular diffusion (Fick Law).
In such way, for each experiment, with their respective times and measured concentrations, it possible to be gotten experimental numbers of axial dispersion at na axial dispersion of small intensity.

3. Results

The evaluated operational variable are continuous phase flow and axial dispersion efficiency at the operational geometry of perforateed plate column with 3 or 4 compartment, free area or 6% or 29%, according the table 1 on the sequence this topic.

Table 1. Resume of parameters and operational variables used.

Parameters	Operational Range
Outflow continuous phase (cm^3/s)	14 – 63
Compartments number	3 ou 4
Plates number	4 ou 5
Lenght of column (cm)	72 ou 92
Free Area (%)	6 ou 29

The axial dispersion values in this present work are presented for graphs D/vL (axial dispersion number) double Qc (flow continuous phase flow), for differents free areas of operation and geometric arrangements, in accordance with Figures 3 and 4.

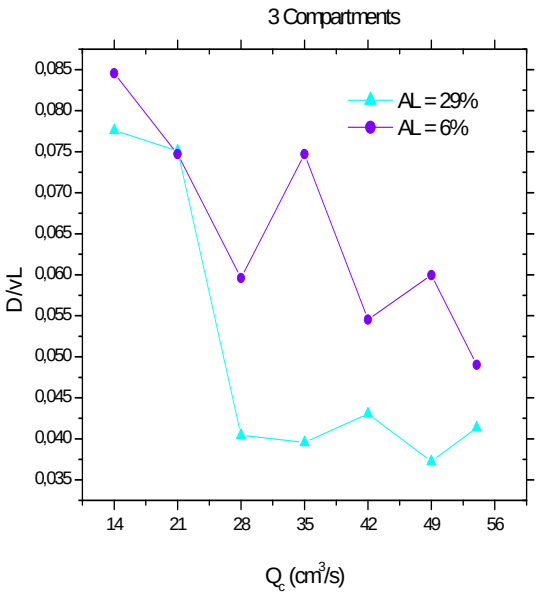

Figure 3 – Variability of axial dispersion number with outflow continuous phase at an extracting column with 3 compartments

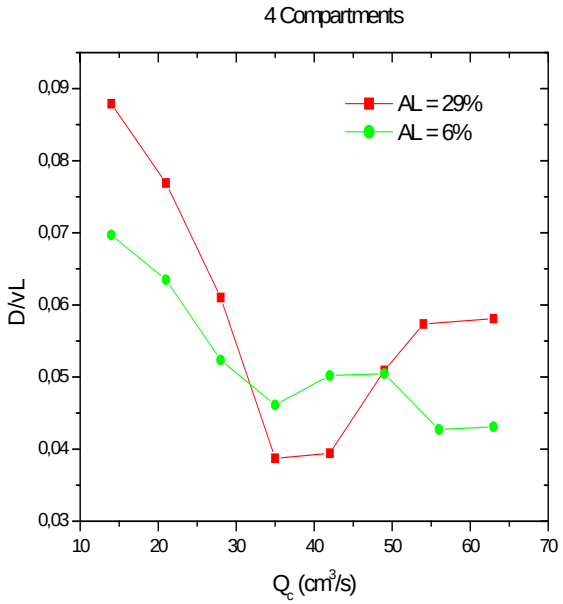

Figure 4 – Variability of axial dispersion number with outflow continuous phase at an extracting column with 4 compartments

3.1. Efficiency Analysis of Axial Dispersion

Analyzing the graph of Figure 3, it was observed that for operation of the extrcating column with 3 compartments and a free area of 6% for each plate (puncture), It had been gotten higher values of axial dispersion, since, for this arrangement in the tested operational band (range), it happens a bigger recirculation of the fluid in interior of each compartment. In such a way, it has an increase of the contact time enters the phases per compartment. Therefore, it also increasing the time of residence on same ones of samples in each compartment.

Already analyzing the graph of Figure 4, it was observed that for operation of the extracting column with 4 compartments and a free area of 6% or 29% for plate, it had been gotten for operational range, different efficiencies. Firts, for low outflows (14 - 34 cm^3/s) with a free area of 29%, it had been gotten the biggest performances, because in this arrangement it has a bigger contact between the dispersed phases and continuous (bigger free area) and also decreases outflows (bigger time of residence for solution in extractor column). But, for intermediate outflows (28 - 44 cm^3/s), it was obtained an optimum performance with free area of 6%. In this study case had to

propitiate the arrangement an increase of contact time enters phases in each compartment, so it also raising the time of residence of same in extracting column in each compartment and then getting bigger values of axial dispersion, for this arrangement in question.
Finally, for high outflows (above of 49 cm^3/s), with free area of 29%, it had been gotten the best performances of this experiment, because in this scene is necessary a bigger area of contact between phases. Being thus, with a free area of 29%, it has a higher contact between phases, proportional the operational outflows.
After analysis of efficiency at two arrangements, it was consisted that the extractor column with 3 compartmentes and a free area of 6%, it presents raised average values of axial dispersion in all experiment.
However, on the graphs of Figures 3 and 4, it was observed that for outflows continuous phase (Qc) between 35 and 49 cm^3/s in both geometric arrangements, it had occurred an inversion of values on axial dispersion. These facts had been possible, for the occurrence of Backmixing. This phenomenom, that means inversion of sense in axial direction (longitudinally).

3.2. Efficiency Analysis of Outflow Continuous Phase

The analysis of influence on outflow continuous phase in the axial dispersion was also based on graphs D/vL double Qc, presented in Figures 4 and 5.
In all the graphs are observed that the reduction of the values of the axial dispersion is characteristic of the experiment, with the gradual increase of the outflow continuous phase (water). This fact occurs, because with the increase on outflow of water, the phase that contains the tracer, it will consequently have little time of contact with the flowed phase and it will be less dispersed longitudinally in direct current (water), thus originating an axial dispersion of low intensity.

4. Empirical Equations

In this currently study has too the attainment of empirical correlations, that will predict theoretical values of experiment, so that is possible to compare theoretical double experimental, these obtained accord with section 3.
When is respect with a situation, which doesn't exist a distinguishing equation that governs clearly the phenomenon study in this work, the theorem Pi de Buckingham was applied. It based on the technique of dimensional analysis.
So, the admitted admensional groups were created matrixes and this premised to use method of Square Minimum.
After that, with an implementation one program in FORTRAN language, it has possible to obtain 2 empirical equations, in the sequence this topic. They empirical equations conduct each operational arrangement, in time which it isn't possible to attribute only one empirical equation to present good results, for both arrangements.
After analysis of the graphs in figures 5, it was observed that pairs of values for axial dispersion number experimental and theoretical are inside the limits of permissible error (+/- 30%). This range is applicable for works at this search area, over all that their objective the comparison the results experimental with theoretician.

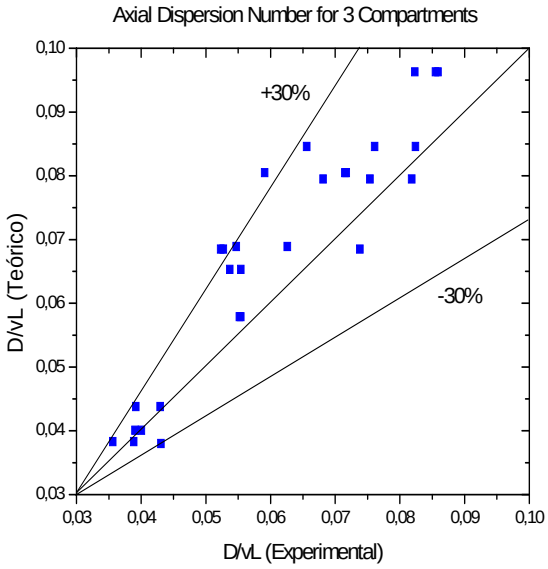

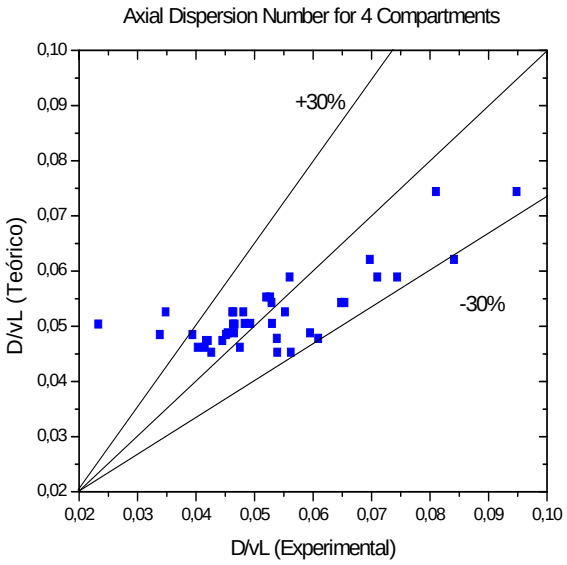

$$D/vL = 0{,}186\,(D/L)^{-0{,}202}\,(1/Fr)^{0{,}308}\,(Re)^{0{,}0243} \quad (1)$$

$$D/vL = -\,0{,}198\,(1/AL)^{-0{,}368}\,(1/Fr)^{0{,}226}\,(Re)^{0{,}0189} \quad (2)$$

Figure 5 - Axial Dispersion Number Experimental double Axial Dispersion Number theoretical for a extractor column, respectly with 3 and 4 compartments.

5. Appreciation

The CAPES, at Master's Degree in Chemical Engineering at Federal University of Bahia - (MAEQ-UFBA).

6. Bibliography References

- FOX , R. W., Mcdonald, A. T.; e Pritchard, P. J.; Introdução à Mecânica dos Fluidos, 2001, 504 p., editora LTC
- GAMBARRA, M. M. P.; Estudo da eficiência em uma coluna de extração de pratos perfurados. Salvador / Bahia: Universidade Federal da BAHIA, 2006. 87 p. Tese (Mestrado).
- GÓIS, L. M. N. DE; Estudo e Desenvolvimento de um Extrator de Pratos Perfurados Pulsantes. Campinas / São Paulo: Faculdade de Engenharia Química, Universidade Estadual de Campinas, 1995. 183 p. Tese (Doutorado).
- LEVENSPIEL, O.; Engenharia das reações Químicas, Vols.1 e 2, 6º reimpressão 1995, 211p. e 4º reimpressão 1994, 481p.
- MOUSTIRI, S.; HEBRARD, G.; THARKRE S. S.; ROUSTAN, M.; A undified correlation for predicting liquid axial dispersion coefficient in bubble columms. Chemical Engineering Science, p.1041-1047, 2001.
- SÁ, R. M. DE; Estudo da Retenção da Fase Dispersa em Colunas de Extração Líquido-Líquido. Salvador / Bahia: Universidade Federal da BAHIA, 2005. 96 p. Tese (Mestrado).

- THANOS, A. M.; GALTIER, P. A; PAPAIANAKOS, N.G.; Liquid Dispersion and holdup in a small scale upflow hydroteater at high temperatures and pressure, Chemical Engineering, 693-698, 2001.
- ZITNÝ, R.; Thýn, J.; Axial dispersion model in finite element analysis of heat and mass transfer in pipes, CTU in Prague, Faculty of mechanical engineering, Process Engineering department, Technická 4, 166 07 Prague 6, (2004).

Proceedings of the 10th International Chemical and
Biological Engineering Conference - CHEMPOR 2008
Braga, Portugal, September 4-6, 2008
E.C. Ferreira and M. Mota (Eds.)

THREE-DIMENSIONAL SIMULATION OF BUBBLY FLOW: INFLUENCE OF BREAKUP AND COALESCENCE MODELS

Marcela K. Silva[1], Renato Dionísio[1], Marcos A. d'Ávila[1], Milton Mori[1*]
[1] School of Chemical Engineering, University of Campinas, UNICAMP
P.O. Box 6066, 13083-970, Campinas-SP, Brazil

Keywords: Bubble Columns, Breakup, Coalescence, CFD
Topic: Advancing the chemical and biological engineering fundamentals

Abstract

Three-dimensional gas-liquid simulations in a cylindrical bubble reactor with an external loop were performed. The effects of average bubble size, bubble size distribution and gas inlet plate geometry were evaluated. The population balance models of Luo and Svendsen (1996) and Prince and Blanch (1990) were used in order to simulate the breakup and coalescence effects, respectively. The drag force was modeled using the Ishii-Zuber model, which takes into account bubble deformation effects. The k-epsilon turbulence model was applied only for the continuous phase and the dispersed one was considered laminar. Lift, Magnus and added mass forces were neglected. Simulations at different superficial gas velocities were performed using two different inlets: a uniform and a perforated plate entrance. Breakup and coalescence effects were studied only for the uniform gas inlet geometry and the particle size distribution was obtained using a probability density function. Results show that the approach used in this work provided physically consistent results with transient effects in the column. Good agreement of the time-averaged gas holdup with experimental data on gas holdup available in the literature was obtained. It was found that the simulation approach used in this work was able to capture the complex transient fluid dynamics in bubbly flows.

1 Introduction

Reactors based on bubbly flows, such as bubble column and airlift reactors, have been widely used in biochemical, petrochemical and metallurgical industries due to their simple construction and operation, high mass and heat transfer rates. In spite of the cited advantages, the multiphase flow behavior exhibited in such reactors is not fully understood due to its complexity. However, the use of adequate numerical models can be very important in understanding flow behavior and in developing scale-up strategies. Due to the emergence of high speed computers and the advancement of numerical techniques, numerical studies of bubbly flows have increased. These numerical techniques are now capable of performing three-dimensional simulations of multiphase flows in complex geometries (Santos, et al., 2007).

Gas-liquid fluidization systems operate by the injection of the gas phase at the bottom of a column filled with liquid. This operation depends on several factors, such as fluid physical properties, column dimensions and inlet gas velocity. There are basically two types of flow regime: the homogeneous and the heterogeneous. The homogeneous flow regime is characterized by low superficial gas velocity, bubbles that are nearly uniform in size and shape and bubble breakup and coalescence phenomena that are considered to be insignificant. On the other hand, in the heterogeneous flow regime, where the superficial gas velocity is high, higher turbulence is observed and bubble breakup and coalescence effects become significant. In this case, models able to capture these phenomena are necessary. Thus, for a good reactor design and operation, it is very important to know the parameters

* Corresponding author. Phone + 55 19 3521-9363. E-mail:mori@feq.unicamp.br

over which the respective regime prevails (Mena, et al., 2005).

In the past decade, computational fluid dynamics (CFD) emerged as an important tool for modeling multiphase flows. Currently, in order to evaluate bubbly flow behavior using CFD it is necessary to combine it with population balance models. These models were implemented as the so-called multiple size group method (MUSIG) in the commercial CFD package ANSYS-CFX (Wang, et al., 2007). The present work shows three-dimensional gas-liquid simulations in a cylindrical bubble reactor with an external loop using the Eulerian-Eulerian approach with the commercial CFD package CFX 11 from ANSYS. The aim of this study was to present the effects of important parameters in CFD simulations, such as bubble size and geometrical modeling of the gas sparger.

2 Mathematical Modeling

The equations used to describe bubbly flows in the present work are the mass and momentum conservation equations, which consider the interaction between the phases using an Eulerian-Eulerian approach, given respectively by

$$\frac{\partial}{\partial t}\left(\varphi_\alpha \rho_\alpha\right) + \nabla \bullet \left(\varphi_\alpha \rho_\alpha \vec{U}_\alpha\right) = 0 \qquad (1)$$

$$\frac{\partial}{\partial t}\left(\varphi_\alpha \rho_\alpha \vec{U}_\alpha\right) + \nabla \bullet \left(\varphi_\alpha (\rho_\alpha \vec{U}_\alpha \vec{U}_\alpha)\right) = \varphi_\alpha \nabla P_\alpha + \nabla \bullet \left(\varphi_\alpha \mu_\alpha \left(\nabla \overrightarrow{U_\alpha} + \left(\nabla \overrightarrow{U_\alpha}\right)^T\right)\right) + M_\alpha + \rho_\alpha \vec{g} \qquad (2)$$

Here, ρ is the density, φ is the volume fraction, $\vec{U}$ is the velocity vector, μ is the viscosity and M_α are the interphase forces, which are the sums of all forces:

$$M_\alpha = \sum_{\beta \neq \alpha} M_{\alpha\beta} = M_{\alpha\beta}^D + M_{\alpha\beta}^L + M_{\alpha\beta}^{LUB} + M_{\alpha\beta}^{VM} + M_{\alpha\beta}^{TD} + \ldots, \qquad (3)$$

where α and β indicate continuous and dispersed phases, $M_{\alpha\beta}^D$ is the drag force, $M_{\alpha\beta}^L$ is the lift force, $M_{\alpha\beta}^{LUB}$ is the wall lubrification force, $M_{\alpha\beta}^{VM}$ is the virtual mass force and $M_{\alpha\beta}^{TD}$ is the turbulence dispersion force. In this study only the drag force, which is the main interphase force affecting the bubble column flow was considered. The mathematical term is given by

$$M_{\alpha\beta}^D = \frac{C_D}{8} A_{gl} \rho_l \left(\overrightarrow{U_l} - \overrightarrow{U_g}\right)\left|\overrightarrow{U_g} - \overrightarrow{U_l}\right| \qquad (4)$$

where C_D is the drag coefficient and $A_{gl} = 6r_g/d_g$ is the interfacial area per unit of volume of an ensemble of particles of diameter d_g and volume fraction r_g. The expression for the drag coefficient varies according to the multiphase system; in this work the drag force model used was the Ishii-Zuber model, which considers the bubble deformation:

$$\begin{aligned} C_D^{(dist)} &= \min\left(C_D(\text{ellipse}), C_D(\text{cap})\right) \\ C_D &= \max\left(C_D(\text{sphere}), C_D(\text{dist})\right) \end{aligned} \qquad (5)$$

$$C_D^{ellipse} = \frac{2}{3} E_O^{1/2} E(r_d) \qquad (6)$$

$$E(r_d) = \frac{\left(1 + 17.67 f(r_d)^{6/7}\right)}{18.67 f(r_d)}, \quad f(r_d) = \frac{\mu_l}{\mu_m}\left(1 - r_d\right)^{1/2}, \quad E_O = \frac{g \Delta\rho d_p^2}{\sigma} \qquad (7)$$

where, E_O is the Eotvos number, $\mu_m = \mu_l(1\text{-}r_g/r_{dm})^{-2.5 r g \mu^*}$ is the bulk viscosity and $\Delta\rho = \rho_l - \rho_g$.

$$C_D^{sphere} = \frac{24}{Re}\left(1 + 0.15 Re_m^{0.687}\right), \quad Re_m = \frac{\rho_l \left|\overrightarrow{U_g} - \overrightarrow{U_l}\right|}{\mu_m} \qquad (8)$$

$$C_D^{cap} = \frac{8}{3}(1-r_d)^2 \qquad (9)$$

The turbulence model used was the standard k-epsilon, which was used only for the continuous phase. This model was chosen because of its satisfactory results in bubble columns simulations (Krishna and Van Baten, 2004). The parameters values of $C_\mu = 0.09$, $C_{\varepsilon 1} = 1.44$, $C_{\varepsilon 2} = 1.92$, $\sigma_k = 1$ and $\sigma_\varepsilon = 1.3$ were used.

The MUSIG model was used for modeling the bubble size distribution. The population balance discretized equation in this model is written as

$$\frac{\partial}{\partial t}(\rho_d r_d f_i) + \frac{\partial}{\partial x^i}(\rho_d r_d U_d^i f_i) = S_i \qquad (10)$$

Defining the size fraction as $f_i = r_i / r_d$, r_i is the volume fraction of the i-group; r_d is the bubbles total volume fraction; x^i is the position component; and S_i is the source term, which contains the rates of bubble birth and death due to the breakup and coalescence:

$$S_i = B_{Bi} - D_{Bi} + B_{Ci} - D_{Ci} \qquad (11)$$

The contributions to birth and death due to the breakup and coalescence processes are given respectively by

$$B_{Bi} = \rho_d r_d \left(\sum_{j>i} g(v_j; v_i) f_j \right); \quad D_{Bi} = \rho_d r_d \left(f_i \sum_{j<i} g(v_i; v_j) \right) \qquad (12)$$

$$B_{Ci} = (\rho_d r_d)^2 \left(\frac{1}{2} \sum_{j \le i} \sum_{k \le 1} Q(v_j; v_k) X_{jki} f_j f_k \frac{m_j + m_k}{m_j m_k} \right); \quad D_{Ci} = (\rho_d r_d)^2 \left(\sum_j Q(v_j; v_k) f_i f_j \frac{1}{m_j} \right) \qquad (13)$$

where $g(v_j; v_i)$ is the specific breakup rate, $Q(v_j; v_k)$ is the specific coalescence rate and X_{jki} is the fraction of mass due to coalescence between the jth and the kth groups which goes to group i.

$$X_{jki} = \begin{cases} \dfrac{(m_j + m_k) - m_{i-1}}{m_i - m_{i-1}} & \text{if} \quad m_{i-1} < m_j + m_k < m_i \\ \dfrac{m_{i+1} - (m_j + m_k)}{m_{i+1} - m_i} & \text{if} \quad m_i < m_j + m_k < m_{i+1} \end{cases} \qquad (14)$$

In this work the Luo and Svendsen breakup model was used to describe the bubble breakup. The breakup rate is written as

$$g(v_i; f_B v_i) = 0.923 F_B (1-r_d) \left(\frac{\varepsilon_C}{d_i^2} \right)^{1/3} \int_{\xi_{min}}^{1} \frac{(1+\xi)^2}{\xi^{11/3}} e^{-\chi} d\xi \qquad (15)$$

$$\text{where } \chi = \frac{12\left[f_{BV}^{2/3} + (1-f_{BV})^{2/3} - 1\right]\sigma}{\beta \rho_c \varepsilon_c^{2/3} d_i^{5/3} \xi^{11/3}} \qquad (16)$$

Here, F_B is a calibration coefficient, β=2 and ξ is the dimensionless size of eddies in the inertial subrange of isotropic turbulence:

$$\xi_{min} = 11.4 \frac{\eta}{d_i}; \qquad \eta = \left(\frac{1}{\varepsilon_c} \nu_c^3 \right)^{1/4} \qquad (17)$$

ε_C is the continuous phase eddy dissipation rate, ν_c is the continuous phase kinematic viscosity and σ is the surfance tension coefficient.

For the coalescence process, the model used was that of Prince and Blanch, which models the coalescence by a collision rate of two bubbles and a collision efficiency relating to the time required for coalescence:

$$Q(v_i;v_j) = (\theta_{ij}^T + \theta_{ij}^B + \theta_{ij}^S)\eta_{ij}; \quad \eta_{ij} = e^{-t_{ij}/\tau_{ij}} \tag{18}$$

$$t_{ij} = \left(\frac{\rho_c r_{ij}^3}{16\sigma}\right)\ln\left(\frac{h_0}{h_f}\right); \qquad \tau_{ij} = \frac{r_{ij}^{2/3}}{\varepsilon_c^{1/3}}; \qquad r_{ij} = \left[\frac{1}{2}\left(\frac{1}{r_i}+\frac{1}{r_j}\right)\right]^{-1} \tag{19}$$

where η_{ij} is the collision efficiency; t_{ij} is the time required for coalescence; τ_{ij} is the actual contact time during the collision; h_0 is the initial film thickness and h_f is the critical film thickness when the bubble rupture occurs, which are chosen as 1.10^{-4} and 1.10^{-8}m respectively; and r_{ij} is the equivalent radius.

The expressions for the collision contributions due to θ_{ij}^T turbulence and θ_{ij}^B buoyancy are shown below; the share contribution θ_{ij}^S is neglected:

$$\theta_{ij}^T = F_{CT}S_{ij}(u_{ti}^2 + u_{tj}^2)^{1/2}; \quad \theta_{ij}^B = F_{CB}S_{ij}\left|U_{rj} - U_{ri}\right| \tag{20}$$

where: $S_{ij} = \frac{\pi}{4}(d_i + d_j)^2$ is the interfacial area, $u_{ti} = \sqrt{2}\varepsilon_c^{1/3}d_i^{1/3}$ is the tubulence velocity, F_{CT} and F_{CB} are calibration factors and $U_{ri} = [(2.14\sigma/\rho_c d_i) + 0.505 g d_i]^{1/2}$.

3 Simulation Parameters

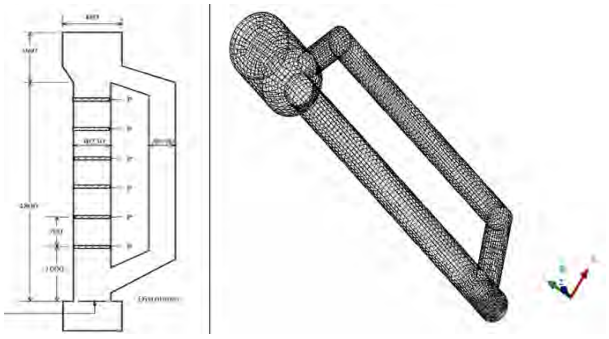

The geometry used in this work consisted in a cylindrical bubble reactor with an external loop, as shown in Figure 1. The mesh used contained approximately 55 thousand control volumes, which were chosen after performing mesh independence tests. The results were compared with the experimental data of Wang, et al., (2004), who present data for a column heigth of 4.6m.

Figure 1: Bubble column reactor and mesh.

Simulations were performed considering air and water at 25ºC as dispersed and continuous phases, respectively. The column was assumed to be initially filled up to a height of 5 m. Non-slip conditions were adopted for both phases and the time step used was 0.01s. Two kinds of inlets were tested: one uniform and the other with a gas distributor with 133 holes, each 1mm in diameter; the former referred to a sintered plate entrance and the latter to a perforated plate entrance in the experimental system. Gas superficial velocities of 0.08, 0.016 and 0.032 m/s were simulated for both geometries. The tests referring to the breakup and coalescence phenomena were achieved only with the uniform inlet and the air superficial velocity of 0.032 m/s. For the test with the population balance models, air was assumed to be the polydispersed phase, with six bubble size groups varying according to a probability density function (Wang, et al., 2004). The bubble diameter is shownin Table 1.

Table 1: Bubble groups used in population balance simulations.

Group	1	2	3	4	5	6
Diameter (mm)	0.5	1.5	2.4	3.3	4.2	7.0

For the initial condition, bubble group 2 was considered as 1 because of the correlation proposed by Chen, et al., (2005), in which the bubble diameter at the inlet is a function of the orifice diameter given by $d_b = 2.9(\sigma.d_o/\rho_l g)^{1/3}$, d_b is the bubble diameter, σ is the surface tension coefficient, ρ_l is the liquid density and d_o is the orifice diameter, considered to be 30μm, which is the average pore size of the sintered plate used in the work of Wang, et al., (2004). All simulations were performed in a commercial CFD package, CFX 11 from ANSYS; in all tests real-time simulation was approximately 200 seconds.

4 Results and Discussion

The gas holdup results from the two different inlets are presented in Figure 2.

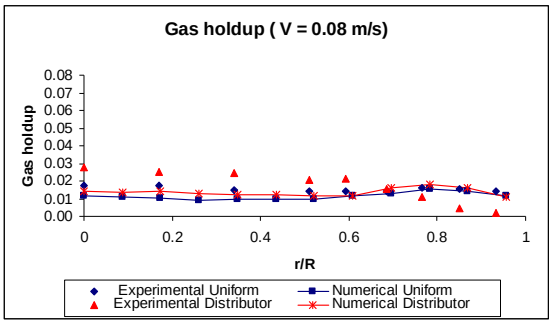

Figure 2a: Gas holdup at 0.08 m/s

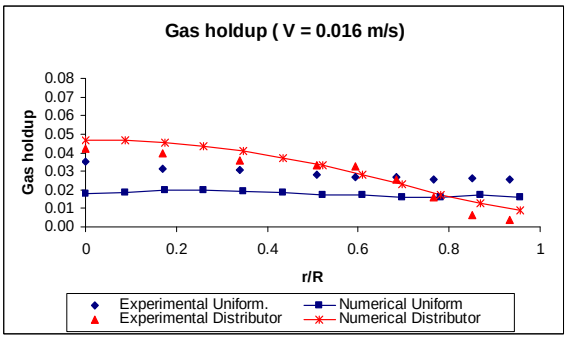

Figure 2b: Gas holdup at 0.016 m/s.

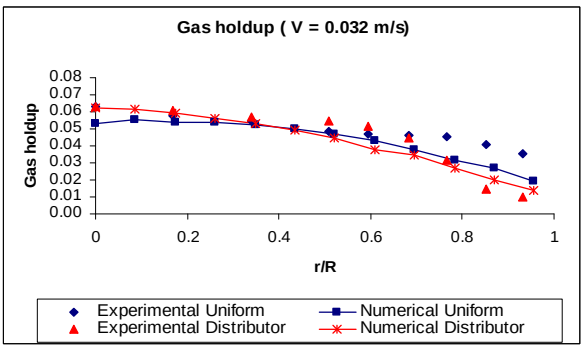

Figure 2c: Gas holdup at 0.032 m/s

For the gas superficial velocity of 0.08 m/s (Figure 2a), it is observed that the simulation results for the uniform gas entrance were in good agreement with experimental data; however, for the perforated plate case, simulations show an increase in the gas holdup near the wall, which is not corroborated by the experimental data. For the gas superficial velocity of 0.016 m/s (Figure 2b), different behaviors are observed for the two inlets; for the uniform inlet a uniform radial profile is noted, whereas for the perforated plate lower values of gas holdup near the wall are observed. For both gas entrances, simulations were in qualitative agreement with experimental data. For the case in which the gas superficial velocity was 0.032 m/s (Figure 2c) is observed a decrease in gas holdup near the wall for both geometries. In this case, good agreement was obtained for the perforated plate distributor.

The simulation data referring to the influence of the breakup and coalescence models are shown in Figure 3 (a and b) for the gas superficial velocity of 0.032 m/s.

It is noted that the breakup and coalescence models underpredict the average gas holdup in the region close to center of the column, whereas the gas holdup prediction is similar to that without the population balance models in the region close to the column wall. Although that homogeneous flow regime would be expected for an air/water system at the gas superficial velocity of 0.032 m/s, effects on the flow field due to the population balance modeling can be observed. In Figure 3b the gas holdup profile for both kinds of regime is shown. A bigger concentration of air at the external loop is observed when the population balance was used. Further studies are currently being performed in the heterogeneous regime.

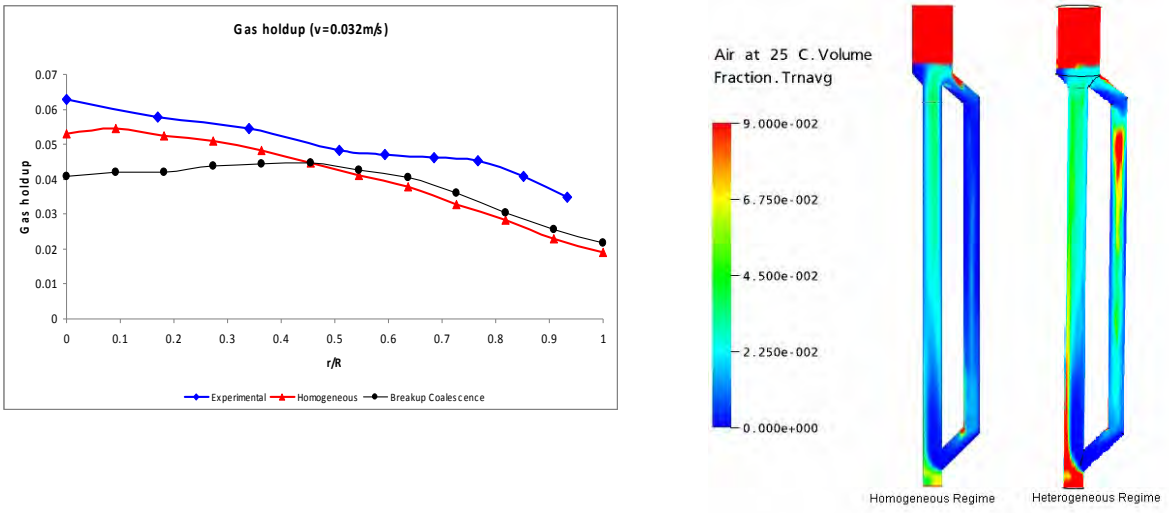

Figure 3: Comparison of heterogeneous and homogeneous regimes: (a) Gas holdup at the 4.6m height**;** (b) Gas holdup profile

5 Conclusions

This article presented gas-liquid flow CFD simulations in a cylindrical bubble reactor with an external loop, where the effects of differents kinds of inlets and the influence of the implementation breakup and coalescence models were evaluated. The results corresponding to the different kinds of inlet show good agreement with the experimental data. The inlet geometrical modeling showed that this consideration is important in simulations considering the perforated plate geometry presented. In evaluating the breakup and coalescence models the results showed a decrease in the gas holdup at the center of the column, suggesting the influence of the population balance implementation.

References

Chen, P., Sanyal J., Dudukovic´, M.P. (2005). Numerical Simulation of Bubble Columns Flows: Effect of Different Breakup and Coalescence Closures. *Chemical Engineering Science*, Volume 60, 1085-1101.

Krishna, R., Van Baten, J.M., Urseanu, M.I. (2004). Three-phase Eulerian Simulations of Bubble Columns Reactors Operating in the Churn-turbulent Regime: A Scale up Strategy. *Chemical Engineering Science*, Volume 55, 4483-4493.

Luo, H., Svendsen, H.F. (1996). Theoretical Model for Drop and Bubble Breakup in Turbulent Dispersions*, AIChE Journal*, Volume 42, No. 5, 1225-1233.

Mena, P.C., Ruzicka, M.C., Rocha, F.A., Teixeira, J.A., Drahos, J. (2005). Effect of Solids on Homogeneous-Heterogeneous Flow Regime Transition in Bubble Columns. *Chemical Engineering Science*, Volume 60, 6013-6026.

Prince, M.J., Blanch, H.W. (1990). Bubble Coalescence and Break-up in Air-Sparged Bubble Columns. *AIChE Journal*, Volume 36, No. 10, 1485-1499.

Santos, C.M., Dionisio, R., Cerqueira , H.S., Sousa-Aguiar, E.F., Mori, M., d´Avila, M.A. (2007). Three-Dimensional Gas-Liquid CFD Simulations in Cylindrical Bubble Columns, *The International Journal of Chemical Reactor Engineering*, Volume 5, A90,

Wang, T., Lin, J., Han, M., Zhang, T., Wang, J., Jin, W. (2004) Influence of the Gas Distributor on the Local Hydrodynamic Behavior of an External Loop Airlift Reactor, *Chemical Engineering Journal*, Volume 102, 51-59.

Wang, T., Wang, J., Jin, Y. (2007). Slurry Reactors for Gas-to-Liquid Processes: A Review. *Industrial and Chemical Engineering Research*, Volume 46, 5824-5847.

Proceedings of the 10th International Chemical and
Biological Engineering Conference - CHEMPOR 2008
Braga, Portugal, September 4-6, 2008
E.C. Ferreira and M. Mota (Eds.)

Mass transfer coefficient in three airlift reactors with internal loop using Newtonian fluid

Lucas M. Policarpo[1], Marcel O. Cerri[1] Antonio J. G. Cruz[1], Carlos O. Hokka[1], Alberto C. Badino[1]

[1]DEQ-UFSCar - Department of Chemical Engineering, Federal University of São Carlos, P.O. Box 676, Post Code 13565-905, São Carlos, SP, Brazil

Keywords: airlift reactor, scale-up, Newtonian fluid, volumetric oxygen transfer coefficient.
Topic: Advancing the chemical engineering fundamentals

Abstract

Oxygen transfer was evaluated in three internal-loop airlift reactors (ALR) of different working volumes (2, 5 and 10 dm^3) with similar geometric configuration utilizing eight Newtonian fluids. The effects of superficial gas velocity (U_{GR}) and liquid viscosity (ν_L) had contrary effects on k_La, however they presented the same orders of magnitude, showing that the viscosity effect on oxygen mass transfer cannot be neglected. A correlation for k_La based on dimensional analysis, taking into account the effects of geometric parameters, physical properties of the fluid and operational conditions proposed and a very good fitting between calculated and experimental data were obtained. The influence of the internal diameter of the reactor on k_La was analyzed as positive, showing that in larger-scale reactors an appropriate oxygen transfer can be reached under smaller aeration conditions.

1 Introduction

Internal-loop airlift reactors are a special class of pneumatic reactors. Using this type of reactor is attractive for chemical and biological reactions due to their inexpensive and simple construction without moving mechanisms and low energy costs, when compared with stirred tank reactors (Blažej *et al.,* 2004a).

One of the most significant parameters in the design of such airlift reactors is the volumetric mass transfer coefficient (k_La) commonly used to evaluate the capacity of oxygen transfer in bioreactors. This quantity depends on the system geometry and fluid properties which are related to several other parameters (Ruen-ngam *et al.*, 2008).

The application of airlift reactors in industry is still limited due to several reasons. The most important one is the lack of methods able to measure primary hydrodynamic parameters (e.g. gas hold-up, gas-liquid mass transfer, linear circulation velocity) and the absence of appropriate hydrodynamic models that take into account the reactor scale (Blažej *et al.*, 2004b).

Although scale-up studies related to airlift reactors are important for industrial applications, few studies have been found in literature focusing on this matter, in comparison with scale-up of conventional stirred and aerated tank bioreactors. For an appropriate study on the performance and scale-up of bioreactors, obtaining correlations to foresee hydrodynamic and heat and mass transfer parameters are important. Correlations based on dimensional analysis offer advantages given that the correlations obtained for a known system can be used to estimate more precisely the parameters in other similar systems with different dimensions. Meanwhile, it is more secure for scale-up use, to obtain dimensionless correlations for a wide range of fluids, experimental conditions and bench and pilot scales of bioreactors. The literature presents several works related to obtaining dimensional correlations for bubble column bioreactors. One of the first works that employed dimensional analysis to investigate the behavior of pneumatic bioreactors was by Hughmark (1967), which used Yoshida and Akita's (1965) experimental data to obtain a dimensional correlation that describes the oxygen transfer in a bubble column bioreactor. Some years later, Akita

and Yoshida (1973) proposed a classical work to investigate the effects of the reactor diameter, liquid height, superficial gas velocity (U_G) and liquid density (ρ_L), liquid kinematic viscosity (ν_L) and liquid surface tension (σ_L) on global gas hold-up (ε_G) and on volumetric oxygen transfer coefficient (k_La) in different scales of bubble column bioreactor, ranging from 18 to 63 dm^3. The empiric correlations were proposed based on dimensional analysis for Newtonian fluids**.** With respect to airlift bioreactors, few works related with obtaining correlations for k_La based on dimensional analysis are found in the literature. Thus, the aim of the present work was to investigate the oxygen transfer coefficient three bench-scale internal-loop airlift bioreactors (2, 5 and 10 dm^3) utilizing different Newtonian fluids.

2. Materials and Methods

Fluids: Distilled water and glycerol solutions were used as Newtonian fluids. Liquid dynamic viscosity (μ_L) of the distilled water and glycerol solutions were determined from rheograms using a digital concentric-cylinder rheometer (Brookfield Engineering Laboratories) model LV-DVIII+, at 28ºC. Table 1 shows the physical properties of the fluids used in this study.

Table 1. Physical properties of the Newtonian fluids

Fluid	Concentration (% $v.v^{-1}$)	$\mu \cdot 10^3$ (Pa.s)	ρ_L ($kg.m^{-3}$)	$D_L \cdot 10^9$ ($m^2.s^{-1}$)	σ_L ($kg.s^{-2}$)
GS12	58.0	12.54	1164.7	0.39	0.068
GS10	55.0	10.77	1158.1	0.42	0.069
GS8	50.0	8.90	1149.5	0.48	0.069
GS6	46.1	6.84	1136.9	0.57	0.069
GS5	40.3	5.33	1124.0	0.63	0.070
GS3	32.3	3.76	1104.5	0.81	0.070
GS2	26.1	2.75	1085.3	1.10	0.071
water	-	0.84	996.0	2.84	0.072

Equipments: concentric-tube airlift reactors (ALR) with 2, 5 and 10 dm^3 total working volume were used in this study. The external tube was made of glass, but the bottom and top plates, the draft tube, the gas sparger, and the condenser were made of stainless steel. The temperature of the reactor was controlled by the circulation of water through the hollow draft tube. A scheme of the concentric-tube airlift bioreactor is shown in Figure 1. Geometrical characteristics and relationships between distances are shown in Table 2 for the three different scales of the airlift bioreactor. The type of sparger was designed to obtain a system with efficient heat and mass transfer. The holes of the cross-piece type sparger are 0.5 mm diameter and are spaced 5 mm along the length of the sparger rods (Badino *et al.*, 2006).

Volumetric oxygen transfer coefficient (k_La): the volumetric oxygen transfer coefficient (k_La) was determined by the dynamic pressure-step method (Blažej et al. 2004c). In this experimental method, the pressure in the vessel is changed abruptly by approximately 15 kPa, and an increase in the dissolved oxygen concentration (C_e) in the bubble dispersion occurs regardless of the gas flow pattern. Equation 1 was fitted to the experimental data (C_e as a function of time) and k_La values were estimated through the procedure that uses the least squares non-linear regression.

$$C_e = C_{e0} \cdot e^{-k_e \cdot (t-t_0)} + C_{es} \cdot (1 - e^{-k_e \cdot (t-t_0)}) + \frac{k_e \cdot (C_{es} - C_{e0})}{k_e - k_L a} \cdot (e^{-k_e \cdot (t-t_0)} - e^{-k_L a \cdot (t-t_0)}) \quad (1)$$

In Equation 1, C_{e0} is the signal of the electrode in the initial condition when $t = t_0$; C_{es} is the signal of the electrode or the dissolved oxygen concentration in the liquid phase in the saturation with air, and k_e is the time constant of the oxygen probe calculated from the inverse of the response time (τ_e). The response to a unit step function, in triplicate, allowed the calculation of k_e = 0.125 s^{-1} assuming the "first order response". The dissolved oxygen concentration was measured with a sterilizable amperometric electrode (Mettler-Toledo,

model InPro 6800) bearing a Teflon membrane (Mettler-Toledo, model InPro T96). Values of k_La were obtained in duplicate for Newtonian and non-Newtonian systems with the superficial gas velocity (U_{GR}) for the three scales of the airlift bioreactor.

Global gas hold-up (ε_G): The gas holdup was determined by measuring the increase in height of the dispersion upon aeration as follows (Chisti, 1989):

$$\varepsilon = \frac{h_D - h_L}{h_D} \tag{2}$$

where h_D is the height of the gas-liquid dispersion and h_L is the height of gas free liquid.

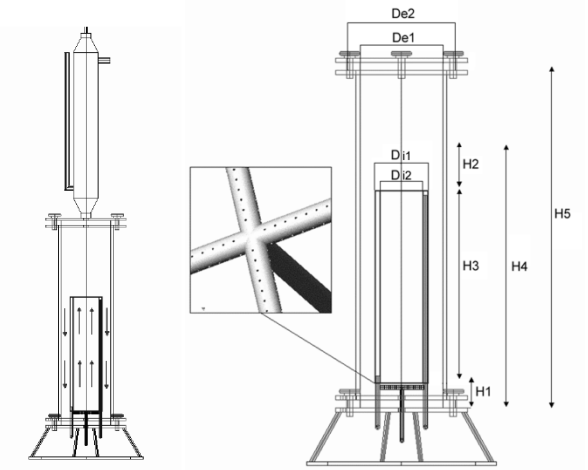

Figure 1. Scheme of concentric-tube internal-loop airlift reactors (ALR)

Table 2. Geometric characteristics of the three scales of concentric-tube internal-loop ALR

Liquid volume (dm^3)	2.0	5.0	10.0
H1 (m)	0.032	0.045	0.055
H2 (m)	0.033	0.055	0.045
H3 (m)	0.262	0.350	0.450
H4 (m)	0.327	0.450	0.550
H5 (m)	0.450	0.600	0.700
De2 (m)	0.100	0.135	0.170
H4/De1	3.63	3.60	3.44
A_D/A_R	1.68	1.78	1.84
D_{i2}/De1	0.61	0.60	0.59

3. Results and Discussion

When only one fluid is used in the oxygen mass transfer study, simpler correlations are found in the literature. Shah *et al.* (1982) proposed the following correlation, in which k_La is related to only the superficial gas velocity (U_G) for water aerated in a bubble column reactor.

$$k_La = 0.47 \cdot U_G^{0.82} \tag{3}$$

The experimental dependency of k_La on U_{GR} is plotted in Figure 2 for the three scales of airlift bioreactors utilized in the present work. A positive influence of the gas flow rate on k_La is evident from the almost linear dependency of k_La on U_{GR}. Values of k_La were practically equal for the three scales up to U_{GR} of 0.04 $m.s^{-1}$. For higher values of U_{GR}, the values of k_La for the scale of 2 dm^3 were greater than for the k_La values of 10 dm^3, which were greater than the 5 dm^3. The correlations of k_La as function of U_{GR} are presented as follows:

2 dm^3 - $k_La = 0.760 \cdot U_{GR}^{0.954}$ R^2=0.991 (4)

5 dm^3 - $k_La = 0.440 \cdot U_{GR}^{0.864}$ R^2=0.994 (5)

10 dm^3 - $k_L a = 0.550 \cdot U_{GR}^{0.898}$ R^2=0.995 (6)

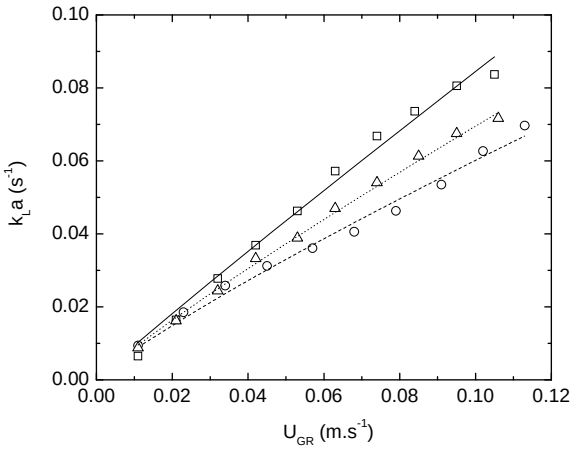

Figure 2. Volumetric oxygen transfer coefficient ($k_L a$) as a function of the superficial air velocity in the riser (U_{GR}) for water in the 3 scales of airlift bioreactors: (□) 2 dm^3, (○) 5 dm^3, (Δ) 10 dm^3, (—) correlation 2 dm^3, (-----) correlation 5 dm^3, (·····) correlation 10 dm^3.

In spite of the difference between the reactors, the values estimated by the correlations of the present work are close to the values estimated by the correlation proposed by Shah et al. (1982). The close values of $k_L a$ obtained in the reactors of 2, 5 and 10 dm^3 under equal aeration conditions are due to the geometric similarity of the scales used in the present work. This is a good indicative for the scale-up of this bioreactor model, when the volumetric oxygen transfer coefficient ($k_L a$) is the criterion of the chosen scale-up.

According to Moo-Young and Kawase (1987), the $k_L a$ depends on the superficial gas velocity (U_{GR}), the geometry of the reactor and the physical properties of the fluid. Liquid viscosity has a significant effect on the gas-liquid oxygen transfer. Figure 3 illustrates the effect of the dynamic viscosity on the $k_L a$ in the scale of 2 dm^3. At constant U_{GR} of 0.053 m.s^{-1}, the $k_L a$ decreased from 0.046 s^{-1} (water: μ=0.84 mPa.s) to 0.015 s^{-1} (GS2: μ=2.75 mPa.s).

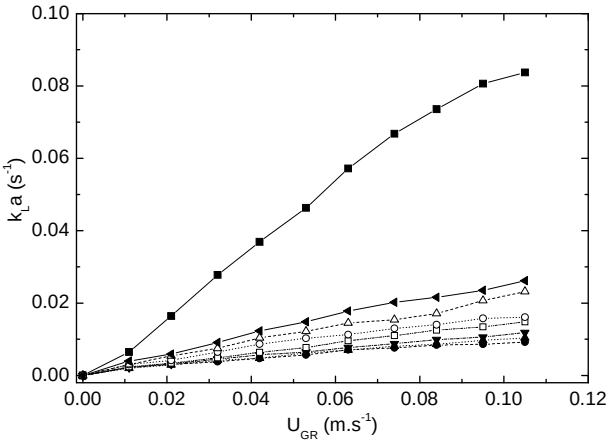

Figure 3. Volumetric oxygen transfer coefficient ($k_L a$) as a function of the superficial air velocity in the riser (U_{GR}) in a scale of 2 dm^3 for Newtonian fluids: (■) water, (●) GS12, (▲) GS10, (▼) GS8, (□) GS6, (○) GS5, (Δ) GS3, (◄) GS2.

Shariati *et al.* (2007) investigated the oxygen transfer in an ALR with internal loop using Newtonian petroleum fluids (diesel and microemulsions of water and diesel). The authors observed the strong influence of the viscosity on k_La and proposed the following correlation to show the effects of U_{GR} and kinematic viscosity ($\nu_L=\mu_L/\rho$) on k_La:

$$k_La = 1.552 \cdot 10^{-4} \cdot U_{GR}^{0.935} \cdot \nu_L^{-0.683} \quad (7)$$

In the present work equation 8 was fitted to the experimental data of the three scales of airlift bioreactors. It can be observed that the exponents of U_{GR} and ν_L were very close.

$$k_La = 10^{-5} \cdot U_{GR}^{0.847} \cdot \nu_L^{-0.746} \qquad R^2=0.98 \quad (8)$$

According to equation 8, k_La increases with the increase of the U_{GR} and decreases with the increase of the viscosity (ν_L). Although U_{GR} and ν_L have contrary effects on k_La, its effects presented the same orders of magnitude. The results show that the effect of the viscosity on oxygen mass transfer cannot be neglected.

The effects of the internal tube diameter (D_{12}), superficial gas velocity (U_{GR}), liquid density (ρ_L), liquid viscosity (μ_L), liquid surface tension (σ_L) and oxygen diffusivity in the water (D_L) on the volumetric oxygen transfer coefficient (k_La) were evaluated in the three scales of the airlift reactors (2, 5 and 10 dm^3) utilizing eight Newtonian fluids. A correlation based on those originally proposed by Akita and Yoshida (1973) for different scales of bubble column bioreactor ranging from 18 to 63 dm^3 was fitted to the experimental data. It is based on dimensional analysis related to modified Sherwood number (Sh) to Schmidt (Sc), Galileo (Ga) and Bond (Bo) numbers, to global gas hold-up (ε_G) and additionally to Froude number (Fr):

$$Sh = 0.00041 \cdot Fr^{0,31} \cdot Sc^{0,81} \cdot Ga^{0,68} \cdot Bo^{0,197} \cdot \varepsilon^{0,554} \qquad R^2=0.98 \quad (9)$$

$$\left(\frac{k_La \cdot D_{l2}^2}{D_L}\right) = 0.00041 \cdot \left(\frac{U_{GS}}{\sqrt{g \cdot D_{l2}}}\right)^{0.310} \cdot \left(\frac{\mu_L}{\rho_L \cdot D_L}\right)^{0.810} \cdot \left(\frac{g \cdot D_{l2}^2 \cdot \rho_L^2}{\mu_L^2}\right)^{0.680} \cdot \left(\frac{g.D_{l2}^2.\rho_L}{\sigma}\right)^{0.197} \cdot \varepsilon_G^{0.554} \quad (10)$$

230 experimental data were utilized in the fitting. The ranges of dimensionless numbers were the following: 4921<Sh<256768; 0.011<Fr<0.143, 297.0<Sc<27544.5, 410.1<Bo<1509.7, $1.4 \cdot 10^7$<Ga<$1.8 \cdot 10^{10}$ and 0.009<ε_G<0.17.

A very good fitting represented by the high value of R^2 can be noted. Figure 4 illustrates the quality of the fitting, where the differences between calculated and experimental data were lower than 15%.

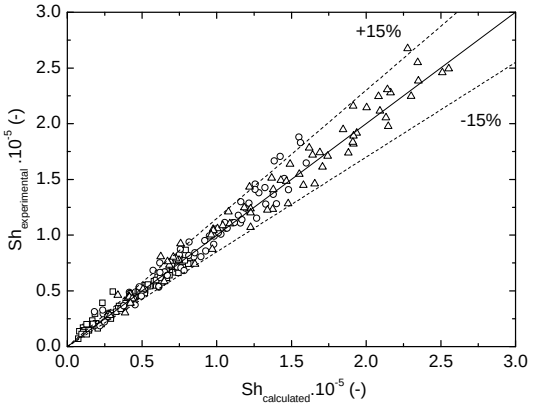

Figure 4. Comparison between calculated and experimental data of the Sherwood number for Newtonian fluids in three scales of internal loop ALR (□) 2 dm^3, (○) 5 dm^3, (Δ) 10 dm^3.

With the rearrangement of equation 10, the dependence of the k_La in relation to internal diameter of the reactor (D_{l2}) is given by:

$$k_La \propto D_{l2}^{0.17} \quad (11)$$

Akita and Yoshida (1973) also observed similar behavior in bubble column reactors. The exponent value of D_{I2} equal to 0.17 found in the present work was the same found by Akita and Yoshida (1973) for reactors with D_I in the 0.15 to 0.60 m range. According to equation 11, the influence of the internal diameter of the reactor on k_La is important for the scale-up of this bioreactor model, because the larger the reactor, the larger the k_La. Therefore, in larger-scale reactors an appropriate oxygen transfer can be reached under smaller aeration conditions.

4. Conclusions

The effects of geometric parameters (D_{12}), physical properties of the fluid (ρ_L, μ_L, σ_L and D_L) and operational conditions (U_{GR}) on the volumetric oxygen transfer coefficient (k_La) were evaluated in the three scales of airlift reactors (2, 5 and 10 dm^3) utilizing eight Newtonian fluids. The effects of U_{GR} and μ_L had contrary effects on k_La, however they presented the same orders of magnitude, showing that the effect of the viscosity on oxygen mass transfer cannot be neglected. A correlation for k_La based on dimensional analysis was proposed and a very good fit between calculated and experimental data was obtained. The influence of the internal diameter of the reactor on k_La was analyzed as positive. This observation is important for scale-up strategies, because in larger-scale reactors an appropriate oxygen transfer can be reached under smaller aeration conditions.

Acknowledgements

The authors thank the financial support provided by the Brazilian foundations FAPESP (Grant Procs. 03/11722-5 and 05/55079-4) and CAPES.

5. References

Akita, K. & Yoshida, F. (1973), Gas Holdup and Volumetric Mass-Transfer Coefficient in Bubble Columns - Effects of Liquid Properties, *Industrial & Engineering Chemistry Process Design and Development* 12(1), 76-80.

Badino, A. C.; Hokka, O. & Cerri, M. O. (2006), Pneumatic reactor with an inner and a transparent outer cylinder gas injection for circulation and temperature control of the enclosed reaction mixture, *Brazilian Patent* BR200404703-A.

Blažej, M.; Annus, J. & Markos, J. (2004a), Comparison of gassing-out and pressure-step dynamic methods for k_La measurement in an airlift reactor with internal loop, *Chemical Engineering Research & Design* 82(A10), 1375-1382.

Blažej, A.; Kisa, A. & Markos, J. (2004b), Scale influence on the hydrodynamics of an internal loop airlift reactor, *Chemical Engineering and Processing* 43(12), 1519-1527.

Blažej, M., Juraščík M., J. A. J. M. (2004c), Measurement of mass transfer coefficient in an airlift reactor with internal loop using coalescent and non-coalescent liquid media, *Journal of Chemical Technology and Biotechnology* 79, 1405 - 1411.

Chisti, M.Y. (1989). Air-Lift Bioreactors, Elsevier, New York.

Ruen-ngam D., Wongsuchoto P, A. L. T. C. & Pavasant, P. (2008), Influence of salinity on bubble size distribution and gas–liquid mass transfer in airlift contactors, *Chemical Engineering Journal*, doi:10.1016/j.cej.2007.12.024.

Hughmark, G. A. (1967), Holdup and Mass Transfer in Bubble Columns, *Industrial & Engineering Chemistry Process Design and Development* 6(2), 218-220.

Moo-Young, M. & Kawase, Y. (1987), Gas Hold-up and Mass-Transfer in a Bubble Column with Viscoelastic Fluids', *Canadian Journal of Chemical Engineering* 65(1), 113-118.

Shah, Y. T.; Kelkar, B. G.; Godbole, S. P.; Deckwer, W. D., (1982). Design parameters estimations for bubble column reactors, AIChE, 28, 353-379.

Shariati, F. P., Bonakdarpour, B., Mehrnia, M. R., (2007) Hydrodynamics and oxygen transfer behavior of water in diesel microemulsions in a draft tube airlift bioreactor, Chemical Engineering and Processing, 46, 334-342.

Yoshida, F. & Akita, K. (1965), 'Performance of Gas Bubble Columns - Volumetric Liquid-Phase Mass Transfer Coefficient and Gas Holdup', AIChE Journal 11(1), 9-13.

Proceedings of the 10th International Chemical and
Biological Engineering Conference - CHEMPOR 2008
Braga, Portugal, September 4-6, 2008
E.C. Ferreira and M. Mota (Eds.)

Evaluation of parameters and process conditions of the ethylbenzene dehydrogenation in a fixed bed reactor wrapped with permselective membrane

Paulo Jardel P. Araújo[1,*] e Teresa M. K. Ravagnani[1,]**
[1]School of Chemical Engineering - University of Campinas
CP6066, CEP 13083-910, Campinas, SP, Brazil
Email: *jardelengenharia@gmail.com; **kakuta@feq.unicamp.br

Keywords: Permselective membrane, Mathematical modeling, Ethylbenzene dehydrogenation.
Topic: Advancing the chemical and biological engineering fundamentals.

Abstract

One of the most important raw materials of the industry of thermoplastic is the styrene. Its demand grows considerably due its recyclable nature. The main chemical route for styrene production is the ethylbenzene dehydrogenization. The kinetic model presenting six reactions with only one reversible proposed by Shell and Crowe (1969) was adopted here. The presence of produced hydrogen affects the styrene productivity provoking the reversibility of the main reaction and undesirable secondary reactions. Therefore, the use of permselective composed membranes for removal of hydrogen is suggested, increasing the process productivity.

In this context, a mathematical model was developed taking in account the different mechanisms of transport that take advantage in the fixed bed and in the various layers of the membrane proposal. The system presented in this paper involves a catalytic tubular reactor of fixed bed wrapped with permselective composed membrane. The membrane is composed by three layers: A macroporous layer used as a support; a microporous intermediate layer to increasing the separation factor; and a metal dense layer which promote the selectivity at hydrogen.

The system simulation was carried out with application transmembrane pressure differential to promote the removal of permeated hydrogen. The computational program was implemented to determine the productivity of the styrene. The effect of various parameters on this system performance was analyzed.

The process simulation with all conditions determined for its better industrial development presented an increase of 40.98% in the styrene productivity compared with the process developed with conventional fixed bed reactor.

1 Introduction

In reactors of catalytic fixed bed, commonly used in industrial processes, the application of connected membranes provides to these multi-functional characteristics.

The membranes allow the separation of the key component, what reduces the tax of the reversible and secondary reactions (Armor, 1989). Its more important characteristics are the selectivity and permeability, which depend on the configuration of the membrane layers, of the pores structure, the process temperature, the molecular weight of the components and the different mechanisms of transport through membrane.

According to Hermann et al. (1997), there is in the literature, three different types of membranes proposals: dense metal membranes (e.g. Pd or Pd-Alloys), porous membranes

* Paulo Jardel Araujo. + 55-3521-3978. E-mail: jardelengenharia@gmail.com

(e.g. alumina, zirconia), and composites membranes (e.g. metal/stainless steel, metal/alumina).

The composite membranes are most applied, because they combine the advantages of other types of membrane: the high permselectivity of the dense membranes and the high permeability of the porous support. The stainless steel support is commonly used in these membranes, because its structural properties are clearly superior to other types of porous supports and the great domain of its manufacture technology for setting of the palladium (Mardilovich et al., 1998).

An important application for such reactor configuration is the catalytic dehydrogenization of the ethylbenzene. This chemical route represents 90% of the total styrene production. This reaction is reversible and endothermic, and the maximum conversion of the ethylbenzene in real process conditions, is limited about 45% due to the thermodynamic equilibrium (Wu and Liu, 1992).

1. C_6H_5-C_2H_5 (EB) ⇆ C_6H_5-C_2H_3 (ST) + H_2
2. C_6H_5-C_2H_5 (EB) → C_6H_6 (BEN) + C_2H_4
3. C_6H_5-C_2H_5 (EB) + H_2 → C_6H_5-CH_3 (TOL) + CH_4 (MET)
4. ½C_2H_4 (ET) + H_2O → CO + $2H_2$
5. CH_4 (MET) + H_2O → CO + $3H_2$
6. CO + H_2O → CO_2 + H_2

The industrial process is lead to a temperature of 550-650ºC, normally atmospheric pressure or subatmospheric, and in the presence of Fe_2O_3-catalysts doped with other metallic oxides. To supply the necessary energy, the reaction is carried out in great excess of steam.

The presented equations, show the reversibility of the reaction of styrene production, and the secondary reactions that occur in the hydrogen presence. Therefore, this paper propose the removal of hydrogen providing increase of productivity of styrene. It will be also analyzed some parameters that control the performance of the reactor fixed bed wrapped in membrane.

2 Mathematical Modeling

A computational program in Fortran 95 was developed for the simulation. A pseudo-homogeneous model with plug flow was assumed to describe the catalyst bed. The membrane configuration proposal is composed of a macroporous stainless steel support, a fine microporous layer, and a Pd-film.

The heat transfer resistance through the membrane is neglected. The balances of mass, energy and momentum are described to follow:

Mass balance.

$$\frac{d\dot{n}_i}{dz} = A\rho_b \sum_{j=1}^{n} v_{ij} r_j - 2\pi R J_i \Big|_R \quad (1)$$

Energy balance.

$$\frac{dT}{dz} = \left[\sum_j -\left(\Delta H_{R,j}\right) r_j \right] \frac{A_R \rho_b}{n_{tot}\left(c_p\right)_m} \quad (2)$$

Momentum balance.

The pressure drop in fixed bed is described by Ergun equation:

$$\frac{dp}{dz} = -150 \frac{\eta u}{d_{cat}^2} \frac{(1-\varepsilon_B)^2}{\varepsilon_B^3} - 1.75 \frac{\rho u^2}{d_{cat}} \frac{(1-\varepsilon_B)}{\varepsilon_B^3} \quad (3)$$

Stagnant gas film

To describe the multicomponent diffusion in a stagnant gas film, it was applied the Stefan-Maxwell equation (Deckman et al. 1995):

* Paulo Jardel Araujo. + 55-3521-3978. E-mail: jardelengenharia@gmail.com

$$\frac{dy_i}{dr} = \frac{RT}{P} \sum_{j=1}^{n} \frac{J_j y_i - y_j J_i}{D_{ij}} \qquad (4)$$

Temperature and pressure are supposed to be constants in this stagnant gas film.

Macroporous support

In this layer, the mechanism of diffusion include effective multicomponent diffusion, effective Knudsen diffusion and viscous flow. Therefore, it was used the *Dusty Gas* model (Sloot et al., 1992):

$$\frac{dy_i}{dr} = \frac{RT}{P}\left(\sum_{j=1}^{n} \frac{J_j y_i - y_j J_i}{(\varepsilon/\tau) D_{ij}} - \frac{J_i}{D_{iK}^{e}} \right) \qquad (5)$$

Microporous layer

The flux through this layer is controlled by Knudsen diffusion. Hence, the flux is given by:

$$J_i = -D_{iK}^{e} \frac{dc_i}{dr} \quad (6)$$

Pd-Film

According to the Sievert's law (Abdalla and Elnashaie, 1994):

$$J_{H_2} = \frac{D_{H_2} C_0}{P_0^{1/2} \ln \frac{r_{m2}}{r_{m1}}} \frac{1}{r} \left[(P)_{m1}^{1/2} - (P)_{m2}^{1/2} \right] \qquad (7)$$

with:

$$D_{H_2} = 2.3x10^{-7} e^{\left(-\frac{21700}{RT}\right)} \qquad (8) \qquad C_0 = 3.03x10^{2} T^{-1.0859} \qquad (9)$$

As the Pd-Film is permeable only for hydrogen, the minimum condition is assumed for the other species in the membrane wall.

The equations (1) at (3) are resolved by Runge-Kutta 4th order method.

Considering the membrane is inert and the process occurs in steady state, the ODE system (Equations 4-7) is resolved with a generalized Newton-Raphson method.

3 Simulations and Results

The styrene productividy is the main parameter of analysis of the reactor performance, therefore reflects the amount of styrene produced from initial ethylbenzene. This parameter was determined by equation 10 at follow:

$$PDT_{ST}(\%) = \frac{ST_f}{EB_i}.100 \qquad (10)$$

i – Inlet amount in the reactor.
f – Outlet amount in the reactor.

The driven force for removal of hydrogen from catalyst bed was established by application of a pressure differential between retentate and permeate.

The simulations are carried out with the range of parameter described in Table 1.

TABLE 1 – Range of operational parameters, configuration of reactor and membrane.

Operational conditions		*Reactor configuration*	
Inlet temperature	873.15 – 953.15K	Lenght	0.39 – 1.2m

* Paulo Jardel Araujo. + 55-3521-3978. E-mail: jardelengenharia@gmail.com

Inlet pressure	100.0 – 250.0kPa	D_{in} (fixed bed)	¾" – 2"
WHSV	1 – 1.6h^{-1}	*Membrane configuration*	
S/O ratio	6 – 12	Thickness (Macro)	1 – 3mm
Catalyst proprieties		Thickness (Micro)	10 – 30µm
Void fraction	0.5	Thickness (Pd)	1 – 20µm
Density	2150kg/m^3	*Membrane proprieties*	
Diameter	3mm	Void Fraction (Macro e Micro)	0.5
		Tortuosity (Macro e Micro)	3
		Pore diameter (Macro)	0.2µm

The range permitted in this analysis it was fixed as given of industrial operation (Kumar et al., 2006) and taking care of the process restrictions.

To conduct a comparative analysis, the system was simulated with the proposed model for a conventional fixed bed reactor, without membrane, in standard conditions of industrial process (Hermann et al, 1997), resulting in a styrene productivity of 52.76%.

- Inlet temperature and steam to oil ratio (S/O).

The inlet temperature was analyzed in a range that took care of energy necessity of the process, as well as to avoid the degradation of the equipment.

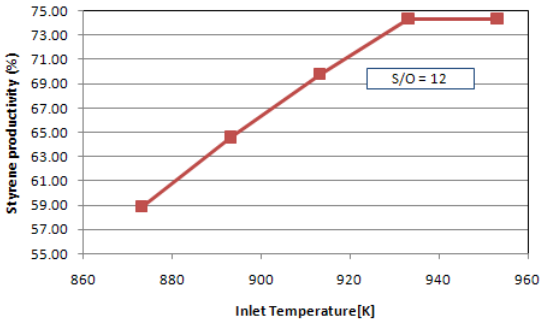

FIGURE 1 – Influence of inlet temperature in the styrene productivity.

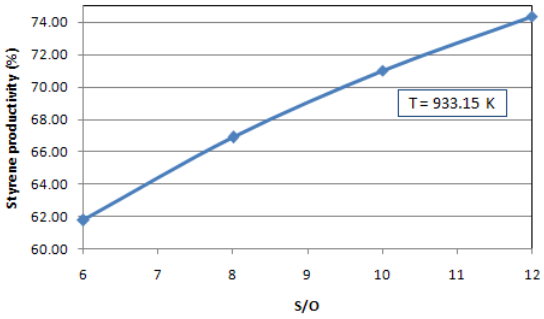

FIGURE 2 – Influence of S/O ratio in the styrene productivity.

It was observed for Figure 1 that, as waited, the styrene productivity increases with the increase of inlet temperature, however, from 933.15K was not observed any alteration in the productivity.

The common range used in literature of 6-12 was admitted for S/O ratio analysis. The S/O ratio must be enough high to supply, together with inlet temperature, the energetic necessity of the endothermic reaction. According to for Figure 2, the S/O equal to 12 reached satisfactory value of styrene productivity, hence this value is recommended for development of the process.

- Fixed bed sizing.

Industrially, the cost related to the sizing of the equipment is decisive for promoting the project. Therefore, the lesser size possible for the reactor is primordially searched.

It was analyzed the sizing of the fixed bed to a constant inlet feeding of the reactants, that is, without depending of a already established WHSV.
The analysis was conducted with stainless steel tubing of constant internal diameter of 0.0254m (1in). The variation of volume was obtained through the change in the reactor length. Considering a fixed mass flow of 9.08x10^{-5}kg/s, determined according data in Table 1, it was realized the simulation with reactor length in a range of 0.39 at 1.2m, corresponding at volumes between 197.62 and 608.05cm^3. The Figure 3 presents the results.

* Paulo Jardel Araujo. + 55-3521-3978. E-mail: jardelengenharia@gmail.com

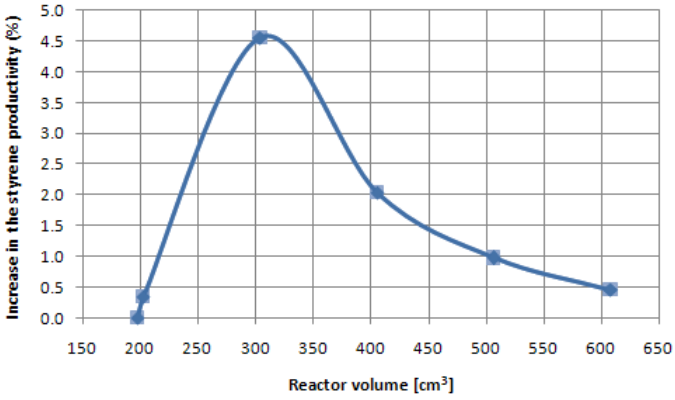

FIGURE 3 – Influence of reactor length in the styrene productivity.

According with Figure 3, can be determined that the recommended reactor volume that take care of the process restrictions and reduces cost of implantation of the system and is of 304.02 cm^3, which represents in a internal diameter of 1in, a reactor length of 0.6m.

- Membrane sizing.

The configuration of the membrane proposal is treated by accounting for up to three membrane layers: a macroporous support, a microporous providing molecular sieving and a Pd-film ensuring selectivity at the membrane.

In the simulation it was obtained a better value of styrene productivity (74.38%) in lesser thickness of macroporous and microporous layer, as well as in Pd-film. Presenting thickness of $1x10^{-3}$m for macroporous layer, 10µm for microporous layer and 1µm for Pd-film. Such result reflects that a lesser way to permeates, provides a bigger hydrogen flux through of membrane. This behavior is ideal for applications of composite palladium membranes in industrial processes, because to the high cost of acquisition of this material. And ahead the manufacture techniques available currently, such configuration is perfectly possible to achieve (Ma et al., 2004).

4 Conclusions

Analysing the styrene productivity, the carried simulations allowed the determination of the operational condition of the process, of the sizing of reactor and of membrane that was provided better system performance.

With the process simulation using the recommended values for each analyzed parameter, the styrene productivity was gotten 40.98% superior to the styrene productivity in the process with conventional fixed bed. This increase proves how is important the determination of favorable conditions for better development of the process.

References

ARMOR, J. N., Catalysis with permselective inorganic membrane, Journal of Applied Catalysis, Vol. 49, (1989) 1-25.

ABDALLA, B. K. and ELNASHAIE, S. S. E. H., Catalytic dehydrogenation of ethylbenzene in membrane reactors, AIChE J., 40 (1994), 2055.

ASSABUMRUNGRAT, S., SUKSOMBOON, K., PRASERTHDAM, P., TAGAWA, T. and GOTO, S., Simulation of a palladium membrane reactor for dehydrogenation of ethylbenzene, Journal of Chemical Engineering of Japan, 35 (2002), 263-273.

DECKMAN, H. W., CORCORAN, E. W., MCHENRY, J. A., MELDON, J. H. and

* Paulo Jardel Araujo. + 55-3521-3978. E-mail: jardelengenharia@gmail.com

PAPAVASSILIOU, V. A., Pressure drop membrane reactor equilibrium analysis, Catal. Today, 25 (1995), 357.

HERMANN, CH., QUICKER, E. and DITTMEYER, R., Mathematical simulation of catalytic dehydrogenation of ethylbenzene to styrene in a composite palladium membrane reactor, Journal of Membrane Science, 136 (1997) 161-172.

KUMAR, SHASHI, SHANKAR S., SHAH P. R. and KUMAR, SURENDRA, A comprehensive model for catalytic membrane reactor, International Journal of Chemical Reactor Engineering, 4 (2006), No pp. given.

MA, Y. H., AKIS, B. C., AYTURK, M. E., GUAZZONE, F., ENGWALL, E. E., and MARDILOVICH, I. P., Characterization of Intermetallic Diffusion Barrier and Alloy Formation for Pd/Cu and Pd/Ag Porous Stainless Steel Composite Membranes, Ind. Eng. Chem. Res., 43 (2004), 2936-2945.

MARDILOVICH, P. P., SHE, Y., REI, M. H. and MA, Y. H., Defect-free palladium membranes on porous stainless-steel support, AIChE J. 44 (1998), p. 310-322.

SHELL, J. G. P. and CROWE, C.M., Simulation and optimization of an existing ethylbenzene dehydrogenation reactor, Can. J. Chem. Eng., 47 (1969) 183 apud ABDALLA, B. K., ELNASHAIE, S. S. E. H., ALKHOWAITER, S. and ELSHISHINI, S. S., Intrinsic kinetics and industrial reactors modeling for the dehydrogenation of ethylbenzene to styrene on promoted iron oxide catalysts, Appl. Catal. A: General, 113 (1994), 89-102.

SLOOT, H. J., SMOLDERS, C. A., VAN SWAAIJ, W. P. M. and VERSTEEG, G. E., High-temperature membrane reactor for catalytic gas-solid reactions, AIChE J., 38 (1992), 887.

WU, J. C. S. and LIU, P. K. T., Mathematical analysis on catalytic dehydrogenation of ethylbenzene using ceramic membranes, Ind. Eng. Chem. Res., 31 (1992) 322.

* Paulo Jardel Araujo. + 55-3521-3978. E-mail: jardelengenharia@gmail.com

Proceedings of the 10th International Chemical and
Biological Engineering Conference - CHEMPOR 2008
Braga, Portugal, September 4-6, 2008
E.C. Ferreira and M. Mota (Eds.)

Effect of kinds of gas on gas holdup in bubble columns

Fukuji Yamashita* and Megumi Nakajima
Dept. of Applied Chemistry, Kanagawa Institute of Technology, Atsugi, 243-0292, Japan;

Keywords: Gas holdup, Bubble column, Gas, Gas density, Bubble coalescence
Topic: Advancing the chemical engineering fundamentals-Multiphase flow

Abstract

The effect of kinds of gas on gas holdup in bubble columns was experimentally studied. Average gas holdup E_G for H_2, He, Ar, O_2 and CO_2 gas – tap water system was visually measured in bubble columns. E_G increased with increasing gas density and was correlated. The gas holdup data of Ozturk et al. (1987) for H_2, He, N_2, Air, CO_2 gas -xylene system were correlated by nearly the same equations as those in this work. The frequencies and volumes of bubbles which generated from horizontal single nozzles (7 and 10 mm I.D.) into tap water did not depend on kinds of gas. The reason why E_G increases with increasing gas density may be because the rate of coalescence of bubbles into larger ones is much larger for the gas of lower gas density.

1 Introduction

Bubble columns are widely used as bioreactors and gas-liquid reactors. Gas holdup E_G is a very important parameter for design and scale-up of bubble columns. Therefore, there have been many studies about gas holdup in bubble columns. It has been reported that gas holdup depends on many factors such as gas and liquid velocity, physical property of gas and liquid, type and arrangement of gas spargers, gas inlet height and inclination angle of bubble columns. However, the effect of kinds of gas on E_G is not yet clear. In this work, the effect of kinds of gas on E_G was experimentally studied.

1.1 Previous studies

Akita and Yoshida (1973) have reported that E_G does not depend on kinds of gas in a 15cm square bubble column with 4.5 mm orifice, although the gas holdup with He appears slightly lower at higher gas velocities. They used Air, O_2, He, CO_2 / water system. Hikita et al. (1980) studied the effect of gas and liquid properties on gas holdup in the bubble column of 10 cm inner diameter and 1.5 m height. They have reported that E_G depends on $\rho_G^{0.062}\rho_L^{0.069}\mu_G^{0.107}\mu_L^{-0.053}$ and presented the following correlation:

$$E_G = 0.672\,(U_G\mu_L/\gamma)^{0.578}[\mu_L^4 g/(\rho_L\gamma^3)]^{-0.131}\,(\rho_G/\rho_L)^{0.062}(\mu_G/\mu_L)^{0.107} \quad (1)$$

Koetsier and Van Swaaij (1976) studied the effect of kinds on E_G in a bubble column with porous gas sparger. In pure water system, E_G for N_2 gas is much larger than that for He gas.

*Corresponding author. Tel +81- 046-291-3083. E-mail:yamasita@chem.kanagawa - it.ac.jp

However, in 0.6 mol/dm^3 Nacl aqueous solution, E_G for N_2 gas is nearly equal to that for He gas. They concluded that bubbles for He gas coalesced into larger ones much easier than those for N_2 gas and rise faster in the pure water system and that E_G for He gas is much lower than that for N_2 gas.

Ozturk et al. (1987) have also studied the effect of kinds of gas on E_G in the 9.5 cm I.D. and 85 cm tall bubble column with organic liquids and reported that E_G depends on kinds of gas. They have concluded that the gas-specific effects are probably related to the bubble formation at the sparger rather than the hydrodynamics in the bulk of the dispersion. Therefore, E_G depends on kinds of gas in bubble columns with small height (H_T < 1 m), however, E_G does not depend on kinds of gas in tall bubble columns (H_T > 2 m). H_T means a bubbling height.

2. Experimental

Two bubble columns were used. They were made of transparent acrylic resin. They are a rectangular and a circular bubble columns. The rectangular bubble column whose cross section is 5cm x 10cm is 60 cm high with a perforated plate as a gas sparger. The diameter, number and pitch of holes were 1 mm, 18 and 10 mm, in order. The circular bubble column has 8 cm inner diameter and 165 cm height with a 6mm I.D. single nozzle as a gas sparger. H_2, He, Ar, O_2 and CO_2 gas from cylinders were used as gases. The flow rate of gases was controlled by the mass flow controller made by Alicat. Tap water was used as a liquid. Liquid was used in a batch. All runs were conducted at room temperature. Average gas holdup E_G was measured visually.

When the effect of kinds of gas on frequencies and volumes of bubbles which generated from a nozzle was studied, single horizontal 7 and 10 mm I.D. glass tubes were used as a nozzle. The nozzles were set on a bottom of a rectangular water bath at room temperature. The water bath was 16 cm wide, 29 cm deep and 21 cm high. Water depth was 15 cm. Frequencies of bubbles were measured by the electric resistance probe.

3. Experimental results and discussion

3.1 Effect of kinds of gas on E_G

Fig.1 shows the effect of kinds of gas on E_G in the rectangular bubble column with 35 cm clear water height. E_G depended slightly on kinds of gas at small superficial gas velocity U_G. However, E_G depended remarkably on kinds of gas at large U_G and increased with density of gas.

Fig.2 shows the effect of kinds of gas on E_G in the circular bubble column with 165cm bubbling height. E_G also depended slightly on kinds of gas at small U_G. However, E_G depended remarkably on kinds of gas at large U_G and increased with density of gas.

Fig.3 shows photos of bubbles in rectangular bubble column. Bubbles for O_2-tap water system are much denser than those for He-tap water. Therefore, E_G for O_2 becomes much larger than that for He.

Ozturk et al (1987) have concluded that the gas-specific effects are probably related to the bubble formation at the sparger rather than the hydrodynamics in the bulk of the dispersion. Therefore, E_G depends on kinds of gas in bubble columns with small height (H_T < 1 m), however, E_G does not depend on kinds of gas in tall bubble columns (H_T > 2 m). But, E_G depended on kinds of gas in the bubble column with H_T = 165 cm in this work. This finding shows that E_G may depend on kinds of gas in tall bubble columns (H_T > 2 m).

3.3 Correlation of average gas holdup E_G

3.3.1 E_G for the circular bubble column

Fig.4 shows the effect of U_G on E_G in the circular bubble column. E_G increased with U_G and was expressed by the following equation:

$$E_G = AU_G^{\ B} \tag{2}$$

Where A and B are constants. Table 1 shows the effect of kinds of gas on values of A and B. Figs.5 and 6 show the effect of gas density ρ_G on A and B, respectively. A and B were expressed by the following equations, respectively.

$$A = 3.23\rho_G^{-0.0121} \tag{3}$$

$$B = 1.05\rho_G^{0.122} \tag{4}$$

Eqs.(3) and (4) are applicable in the range of ρ_G = 0.083-1.83 kg/m^3.

Fig.7 shows the comparison between $E_{G,exp}$ and $E_{G,cal}$. $E_{G,exp}$ means experimental values of E_G. $E_{G,cal}$ means values of E_G calculated by Eqs.(2)-(4). It is clear from Fig.7 that $E_{G,cal}$ shows a good agreement with $E_{G,exp}$.

3.3.2 E_G for the rectangular bubble column

Fig.8 shows the the effects of U_G on E_G in the rectangular bubble column. E_G increased with U_G and was expressed by the following equation:

$$E_G = CU_G^{\ D} \tag{5}$$

Where C and D are constants. Table 2 shows values of C and D. Figs.9 and 10 show the effect of gas density ρ_G on C and D, respectively. C and D were expressed by the following equations, respectively.

$$C = 5.7\rho_G^{0.042} \tag{6}$$

$$D = 0.96\rho_G^{0.114} \tag{7}$$

Eqs.(6) and (7) are applicable in the range of ρ_G = 0.083-1.83.

Fig.11 shows the comparison between $E_{G,exp}$ and $E_{G,cal}$. $E_{G,cal}$ means E_G calculated by Eqs.(5)-(7). It is clear from Fig.11 that $E_{G,cal}$ shows a good agreement with $E_{G,exp}$.

3.3.3 E_G for H_2, He, N_2, Air, CO_2 gas -xylene system by Ozturk et al. (1987)

E_G data for H_2, He, N_2, Air, CO_2 gas -xylene system by Ozturk et al. (1987) in a 9.5cm I.D. and 85 cm tall bubble column were correlated by the following equations:

$$E_G = EU_G^{\ F} \tag{8}$$

$$E = 3.22\rho_G^{-0.0122} \tag{9}$$

$$F = 0.91\rho_G^{0.122} \tag{10}$$

Fig.12 shows the comparison between Eqs.(8)-(10) and the experimental data of Ozturk et al.

(1987). $E_{G,cal}$ obtained from Eqs.(8)-(10) shows a good agreement with $E_{G,exp}$.

3.4 Frequencies *N* and volumes of bubbles *V* generated from a horizontal single nozzle

In order to study the effect of kinds of gas on size of bubbles which generate from a gas sparger, frequencies of bubbles which generated from a horizontal single nozzle were measured. Figs.13 -15 show the effect of kinds of gas on *N* and V for 7 and 10 mm nozzle, respectively. It is clear from these figures that *N* and *V* don't depend on kinds of gas.

Conclusion

1) E_G increased with increasing gas density and was correlated. The reason why EG increases with gas density may be because bubbles of smaller gas density coalesce into larger bubbles more easily at the same superficial gas velocity.

2) The gas holdup data of Ozturk et al. (1987) for H_2, He, N_2, Air, CO_2 gas -xylene system were correlated by nearly the same equations as those in this work.

3) Frequencies of bubbles which generated from the 7 mm and 10 mm I. D. horizontal nozzles did not depend on kinds of gas at the same gas flow rate.

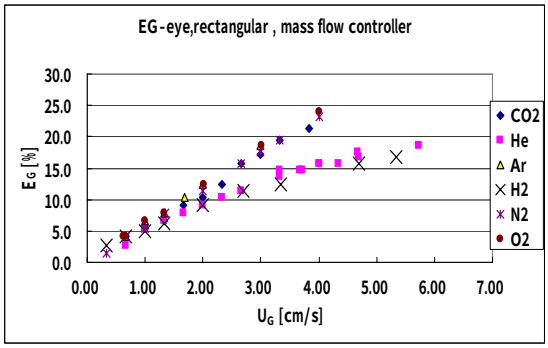

Fig.1 E_G for the rectangular column.

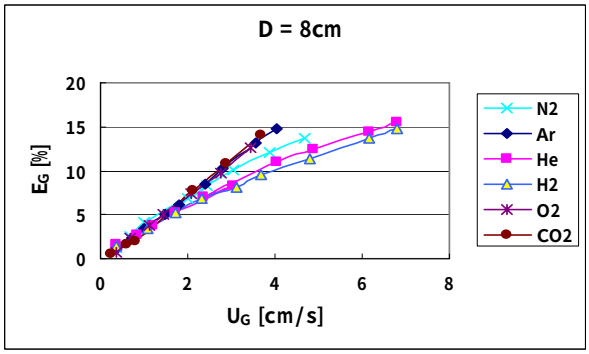

Fig.2 E_G for the 8cm I.D. column

Fig.3 Photos of bubbles in the rectangular bubble column in the range of h=10-20cm..
Left: oxygen – tap water at UG =4.47 cm/s. Right: He-tap water at UG = 4.80 cm/s

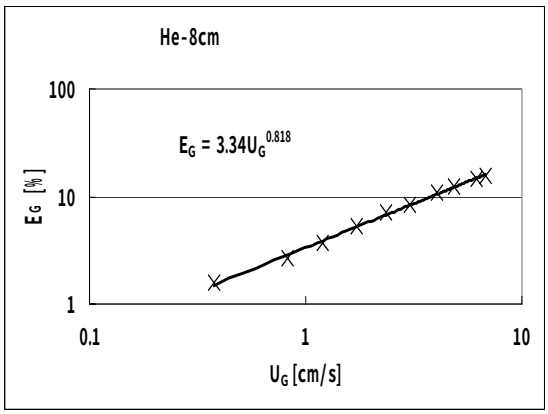

Fig.4 E_G vs. U_G for He- tap water system in the circular bubble column

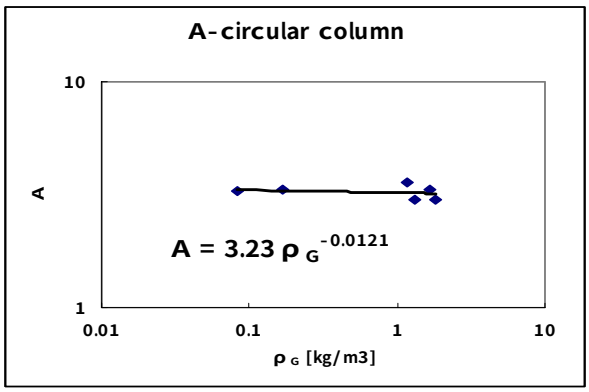

Fig.5 A vs. ρ_G for the circular column.

Table1 Details of A and B

Gas	ρ_G[kg/m^3]	A	B	C	D
H_2	0.083	3.26	0.805	5.45	0.678
He	0.166	3.34	0.818	4.88	0.935
N_2	1.16	3.57	0.922	5.39	1.089
O_2	1.33	3.02	1.230	6.32	0.963
Ar	1.66	3.32	1.084	6.24	0.986
CO_2	1.83	2.99	1.20	5.42	0.973

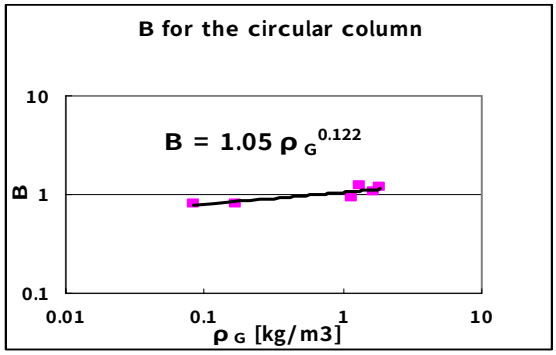

Fig.6 B vs. ρ_G for the circular column.

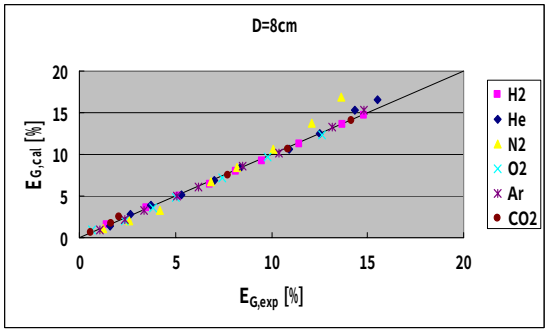

Fig.7 $E_{G,exp}$ vs. $E_{G,cal}$ for the circular column

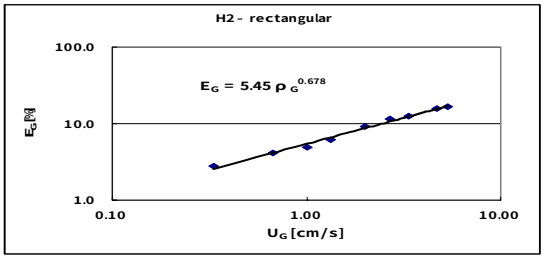

Fig.8 E_G vs. U_G for H_2 in the rectangular column

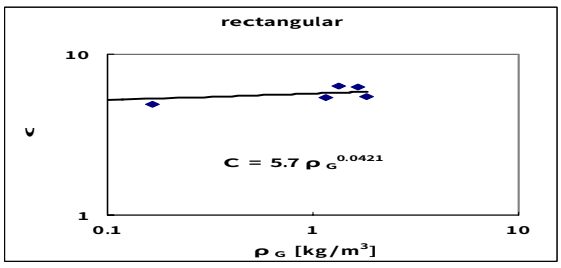

Fig.9 C vs. ρ_G for the rectangular column.

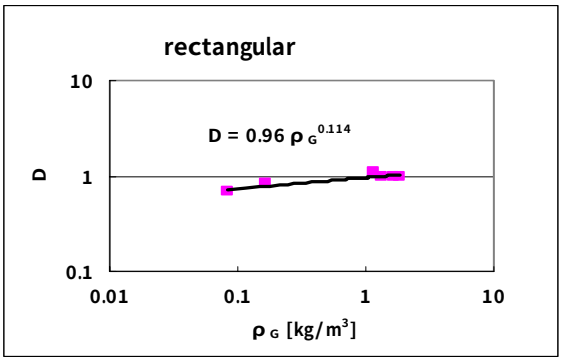

Fig.10 D vs. ρ_G for the rectangular column.

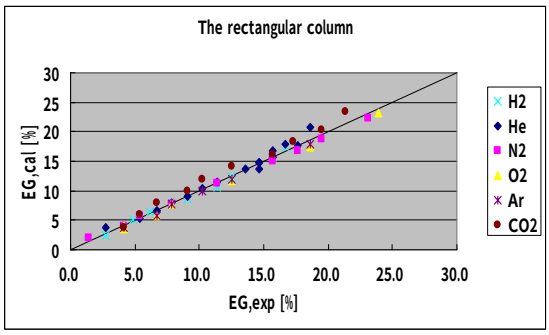

Fig.11 $E_{G,cal}$ vs. $E_{G,exp}$ for the rectangular column

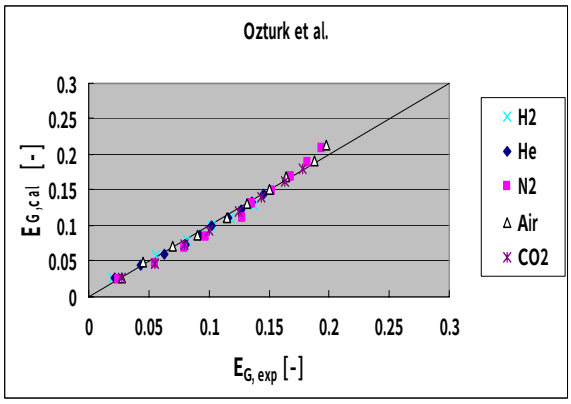

Fig12 $E_{G,cal}$ vs. $E_{G,exp}$ for the rectangular column

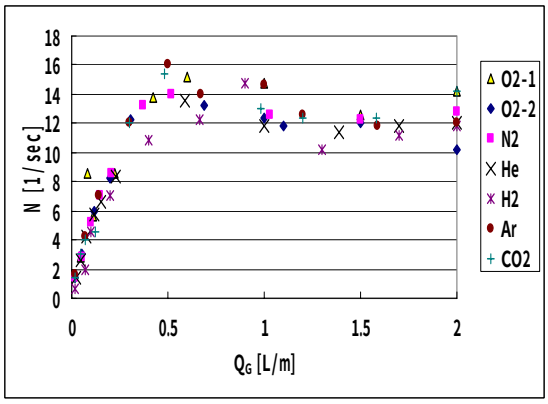

Fig.13 N vs. Q_G for 7mm nozzle

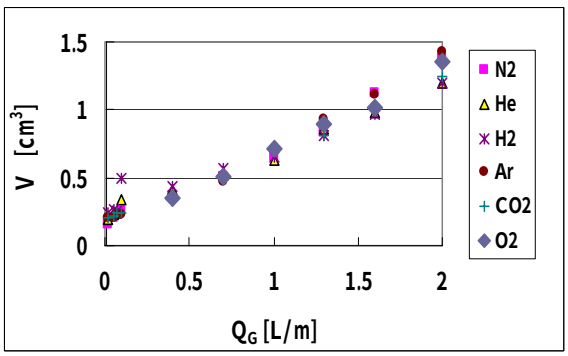

Fig.14 V vs. Q_G for the 7mm I.D. nozzle.

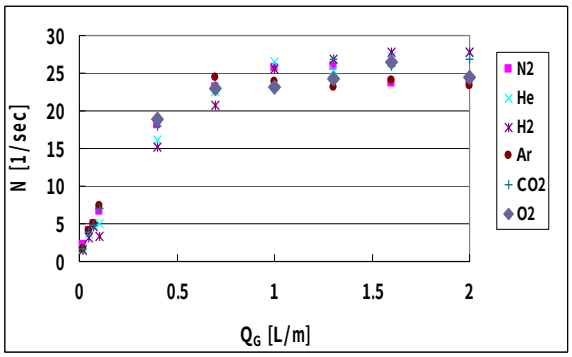

Fig.15 N vs. Q_G for the 10 mm I.D. nozzle.

References

Akita, K., Yoshida F. (1973). Gas holdup and volumetric mass transfer coefficient in bubble columns. *Industrial Engineering Chemistry Process Design Development*, 12, 76-80.

Hikita, H., Asai, S., Tanigawa, K., Segawa, K., Kitano, M. (1980). Gas holdup in bubble columns. *The Chemical Engineering Journal*, 20, 59-67

Ozturk, S. S., Schumpe, A., Deckwer, W. -D. (1987). Organic liquids in a bubble column: hold-ups and mass transfer coefficients. *AIChE Journal*, 33, 1473-1480.

Koetsier, W. T., Van Swaaij, W. P. M. (1976). Maximum gas holdup in bubble columns. *Journal of Chemical Engineering of Japan*, 9, 332-333.

Bhaga, D., Pruden, B. B., Weber, M. E. (1971). Gas holdup in a bubble column containing organic liquid mixture. *The Canadian Journal of Chemical Engineering*, 49, 417-420.

Proceedings of the 10th International Chemical and
Biological Engineering Conference - CHEMPOR 2008
Braga, Portugal, September 4-6, 2008
E.C. Ferreira and M. Mota (Eds.)

Simulation of dynamic performance of ozonation treatment of surfactants in a semi－batch bubble column reactor by CFX

Fukuji Yamashita[1]*, Tomoyuki Suzuki[1], Haruki, Kobayashi[2]

[1] Dept. of Applied Chemistry, Kanagawa Institute of Technology, Atsugi, 243-0292, Japan

[2] Ansys K.K, 6-10-1 Nishishinjuku, Shinjuku-ku, Tokyo, 160-0023, Japan

Keywords: Simulation, Ozonation**,** Surfactant, Bubble column, CFD

Topic: Advancing the Chemical Engineering fundamentals-Catalysis & reaction engineering

Abstract

Simulation of dynamic performance of ozone dissolution into pure water and ozonation treatment of surfactants in a semi-batch bubble column reactor by CFX 11.0 software was done using a two-fluid Eulerian model. Turbulence was modeled by the SST model. The results of simulations showed a good agreement with experimental results of this work and Uchiyama et al.(2007).

1 Introduction

Recently, much attention has been paid to environment. In order to keep clean environment, waste gas and liquid must be completely treated. Ozone is a strong oxidizer and has been widely used for treating water and wastewater. Surfactants are predominant pollutants of wastewater and must be decomposed. There have been many researches about decomposition of pollutants by ozone. Uchiyama et al. (2007) studied the dynamic performance of ozonation treatment for nonionic surfactants SS-90 (Polyoxyethylene Alkyl Ether) in a bubble column and simulated the experimental results by using the tank-in series model. Recently, CFD has developed remarkably because of development of cheap efficient PC and good software. Simulation by CFD is very useful for research, design and scale up of bubble columns. In this work, rate of ozone dissolution into pure water was experimentally measured, and simulation of dynamic performance of ozone dissolution into pure water and ozonation treatment of surfactants in a semi-batch bubble column reactor by CFX software was done. The simulation results were compared with experimental results of this work and Uchiyama et al. (2007).

2. Experiment and Simulation

2.1 Experimental apparatus and method

The bubble column used was made of transparent acrylic resin. Its inner diameter and

*Corresponding author.Tel.+81-046-291-3083. E-mail: yamasita @ chem. kanagawa - it.ac.jp.

height were 0.16 m and 1.0 m, respectively. The gas distributor was a perforated plate. The diameter, number and pitch of holes of the perforated plate were 0.5 mm, 193 and 5 mm in order. Oxygen gas from an oxygen cylinder was used as a gas and ultra pure water was used as a liquid. Liquid was used in a batch. Ozone was generated from oxygen gas by an ozone generator (PO-10 by Fuji Electric). Concentrations of ozone in gas and liquid were measured by ozone meters OZ-1 and OZ-2 by TOA DKK. A liquid pump was used to improve liquid mixing in the bubble column. All runs were done at room temperature.

2.2 Simulation

Commercially available CFD code-CFX 11 (Ansys Inc.) was used to solve the differential equations involved in two-fluid Eulerian approach. Two bubble columns were used as the simulation models. A 16 cm I.D. and 90 cm tall bubble column with 10 mm mesh was used for the simulation of dynamic performance of ozone dissolution into pure water. A 10 cm I.D. and 100 cm bubble column with 10 mm mesh was used for the simulation of dynamic performance of ozonation treatment of surfactants. The gas inlet was 10 mm and set in the center of bottom of the bubble column. The condition of the gas outlet (= top of the bubble column) was degassing condition. Turbulence was modeled by the SST model. The liquid was fed in a batch. The bubble diameter was 5 mm.

In case of pure water, the interfacial transfer of ozone between the gas and the liquid is modeled as follows:

$$dC/dt = k_L a(C^* - C) - k_d C \quad (1)$$

where k_d is the rate constant of ozone self decomposition in the liquid phase.

In case of water with the surfactant, the rate of change in dissolved ozone is given by

$$dC/dt = K_L a(C^* - C) - k_d C - b\, d(TOC)/dt \quad (2)$$

$$d(TOC)/dt = -k_1(TOC) \quad (3)$$

$$k_1 = 3.75 \times 10^6 Y^{0.29} Q_g^{0.67} \exp(-47800/RT)(TOC)_0^{-0.835} \quad (4)$$

where b represents the consumed ozone per *TOC* degradation rate and b = 3 was used. The third term on the right-hand side of Eq.(2) represents loss of ozone in the liquid phase due to oxidation of the substrates.

The volumetric mass transfer coefficient $K_L a$ was estimated on the basis of the empirical correlation proposed by Shah et al. (1982) for oxygen transfer from air to water.

$$K_L a = (D_{O3}/D_{O2})^{0.5}\, 0.467 U_G^{0.82} \quad (5)$$

where U_G is the superficial gas velocity.

Henry's law constant *H* was given by Miyahara et al. (1994)

$$H \text{ (in kg/ m}^3\text{Pa)} = 1/\{1.4 \times 10^9 \exp(-2.62 \times 10^3/T)\} \quad (6)$$

3 Results and discussion

3.1 Dynamic behavior of ozone dissolution into pure water

Fig.1 shows contours of ozone dissolution into pure water at superficial gas velocity U_g = 0.166 cm/s. The concentration of ozone increased with time. Fig.2 shows comparison

between the simulation and experimental results of dynamic change of ozone concentration with time. At small time experimental concentrations increased much slowly than simulation ones because the experimental bubble column had a 4 dm^3 gas chamber under the perforated plate. However, simulation concentrations became nearly equal to experimental ones at large time.

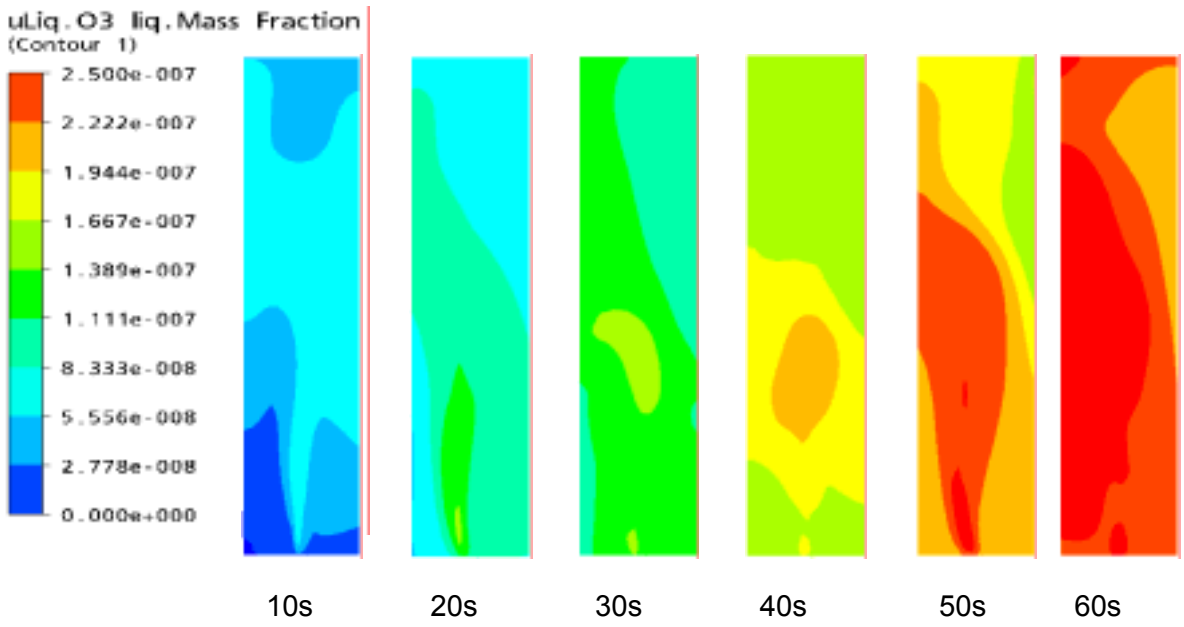

Fig.1 Contours of dissolved ozone concentration in the bubble column at U_g = 0.166cm/s in case of water with no surfactants.

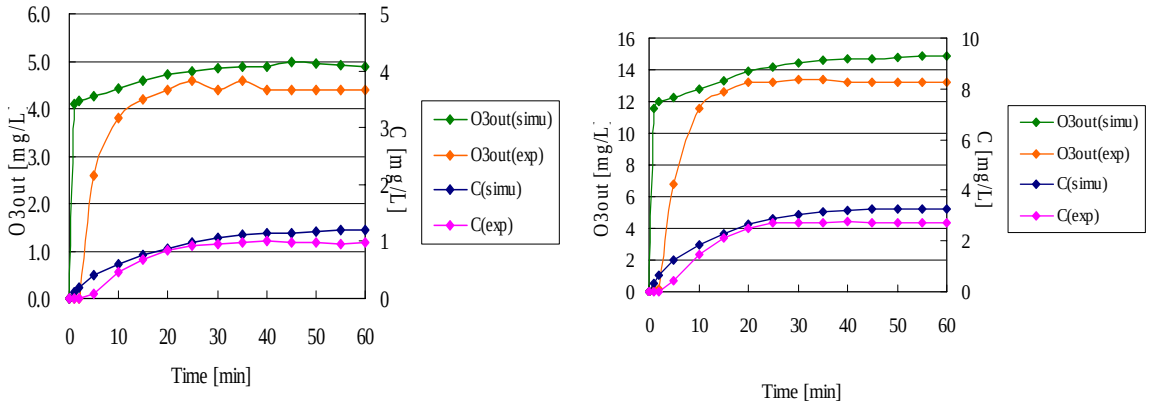

(a) Y_{in} = 5 mg / L (b) Y_{in} = 15 mg/L

Fig.2 Comparison between simulation concentration and experimental ones at U_g = 0.166 cm/s. Y_{in} means ozone concentration in the gas at gas inlet.

3.2 Dynamic behavior of ozone dissolution into water with SS-60

Figs.3 and 4 show 5 snapshots of contours of dissolved ozone and *TOC* in the water at U_g =

0.166 cm/s, respectively. Concentrations of ozone in the water increased with time. However, *TOC* decreased with time because surfactants reacted with ozone.

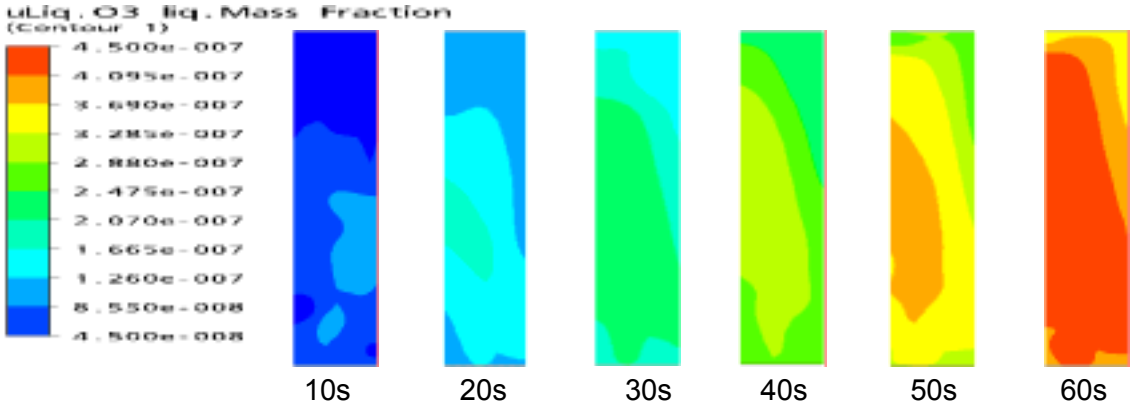

Fig.3 Contours of dissolved ozone in the bubble column with time at U_g = 0.106 cm/s, Y_{in} = 25 mg/L and *TOC* = 7.16 mg/L.

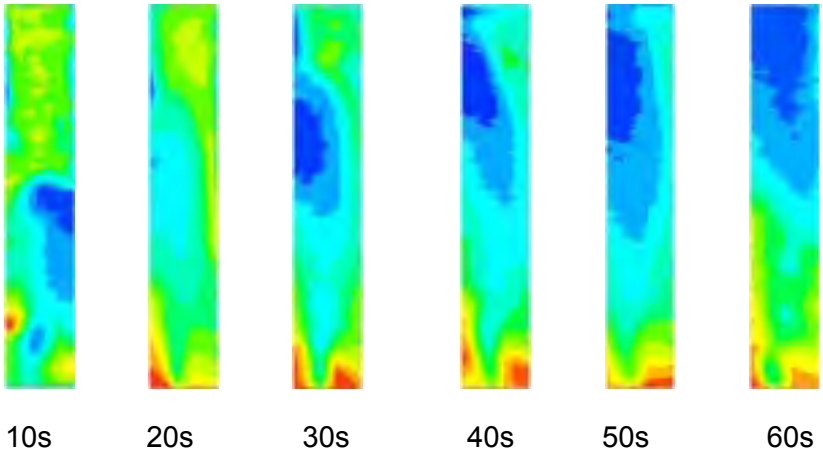

Fig.4 Contours of *TOC* in the bubble column with time at U_g = 0.106 cm/s, Y_{in} = 25 mg/L and *TOC* = 7.16 mg/L.

Fig.5 shows the dynamic behavior of *C*, *TOC* and Y_{in} at U_g = 0.106 cm/s, Y_{in} = 15 g/m^3 and *TOC* = 7.16 mg/L. (a) shows the simulation results in this work and (b) shows the experimental results by Uchiyama et al. (2007). It is clear from Fig.5 that the simulation results show a good agreement with experimental ones of Uchiyama et al. (2007).

Fig.6 shows the effect of Y_{in} on $TOC/(TOC)_0$ at U_g = 0.106 cm/s and *TOC* = 7.16 mg/ L in the range of Y_{in} = 10 – 25 mg/L. $TOC/(TOC)_0$ decreased with increasing Y_{in}. Though the experimental results of Uchiyama et al. (2007) decreased linearly with time *t*, those of simulation results in this work did not decrease linearly with time. This reason is not yet clear.

Fig.7 shows the effect of ozone gas flow rate Q_g on $TOC / (TOC)_0$ *at* $(TOC)_0$ = 7.16 mg/L and Y_{in} =10 mg/L in the range of Q_g = 0.25 – 1.0 L/min. $TOC/(TOC)_0$ decreased with increasing Q_g.

Fig.8 shows the effect of $(TOC)_0$ on the ratio *TOC* at Y_{in} = 25 mg/L and Q_g = 0.5 L/min (U_g = 0.106 cm/s). *TOC* became larger with increasing $(TOC)_0$. The simulation results showed a

good agreement with the experimental results of Uchiyama et al. (2007).

4. Conclusion

Simulation of the dynamic performance of ozone dissolution into pure water and ozonation treatment of surfactants in a semi-batch bubble column reactor by CFX 11.0 software was done using a two-fluid Euler-Euler model. The simulation results showed a good agreement with experimental results of this work and Uchiyama et al. (2007).

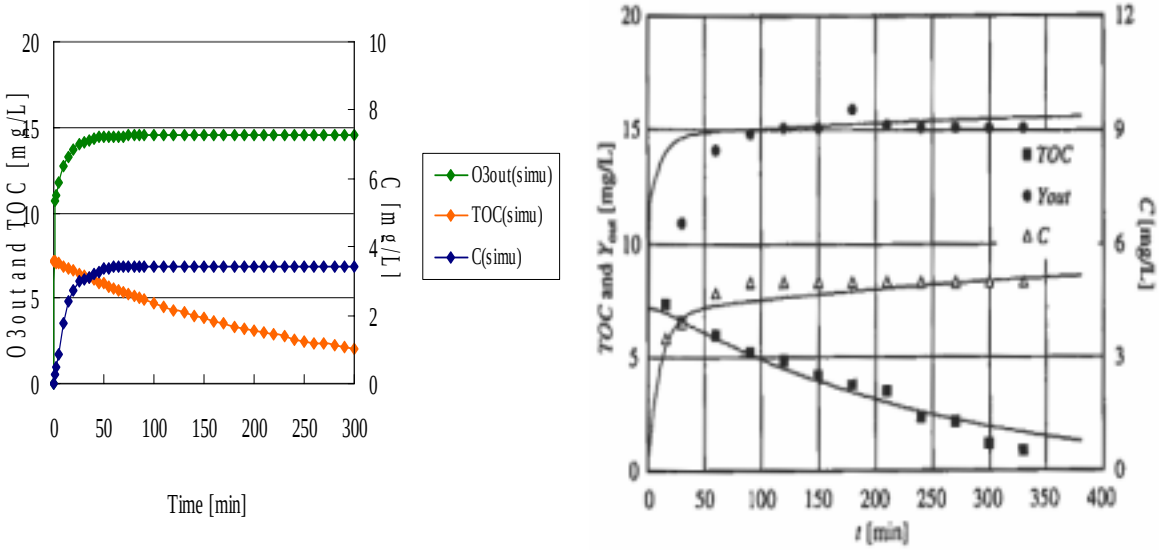

(a) simulation results (b) experimental results by Uchiyama et al.

Fig.5 Dynamic simulation for ozonation of surfactants lat U_g = 0.106 cm/s, Y_{in} = 15 g/m^3 and *TOC* = 7.16 mg/ L.

Solid lines in (b) means simulation results by Uchiyama et al. (2007)

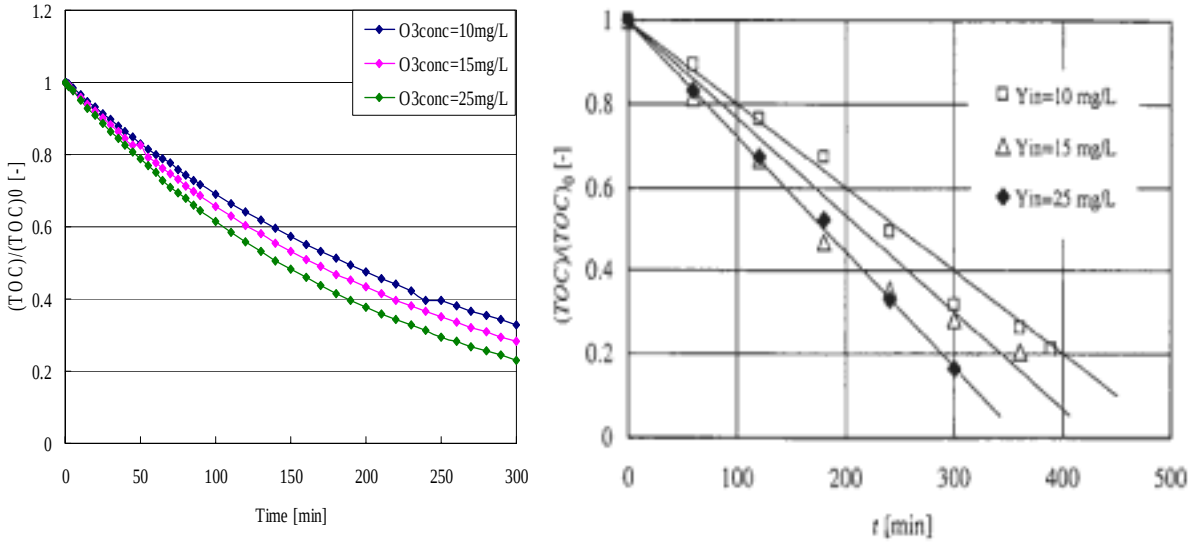

Fig.6 *TOC*/ $(TOC)_0$ vs. t. at U_g = 0.106 cm/s and *TOC* = 7.16 g/ m^3 in the range of Y_{in} = 10 – 25 mg/L.

$(TOC)_0$ means *TOC* at *t* = 0. Solid lines in (b) means simulation results by Uchiyama et al. (2007).

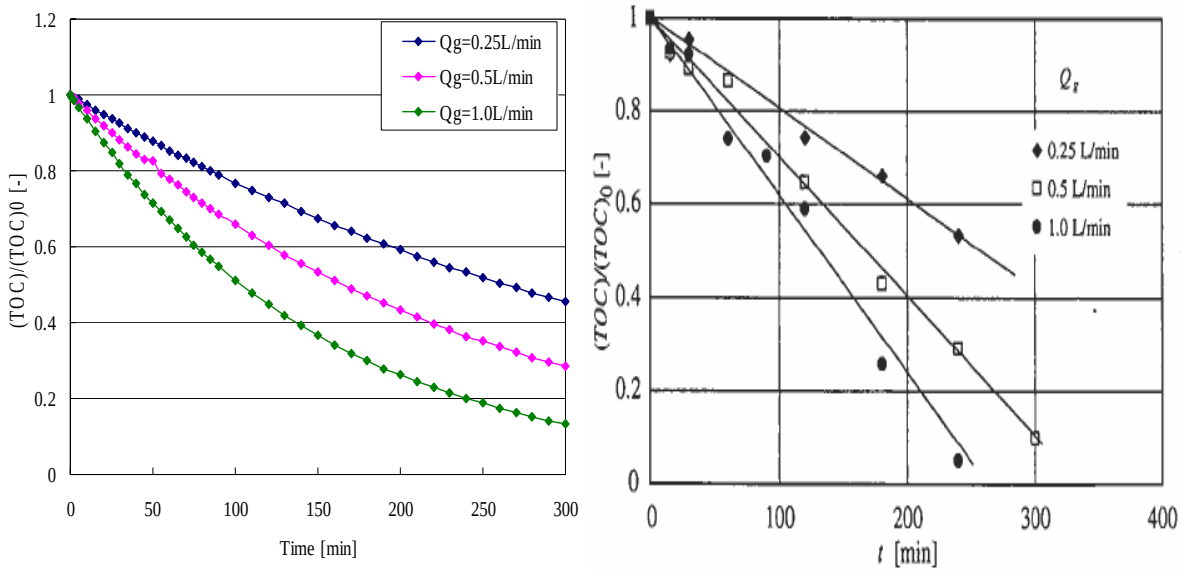

Fig.7 Effect of ozone gas flow rate Q_g on $TOC / (TOC)_0$ *at* $(TOC)_0$ = 7.16 mg/L and Y_{in} = 10 mg/L

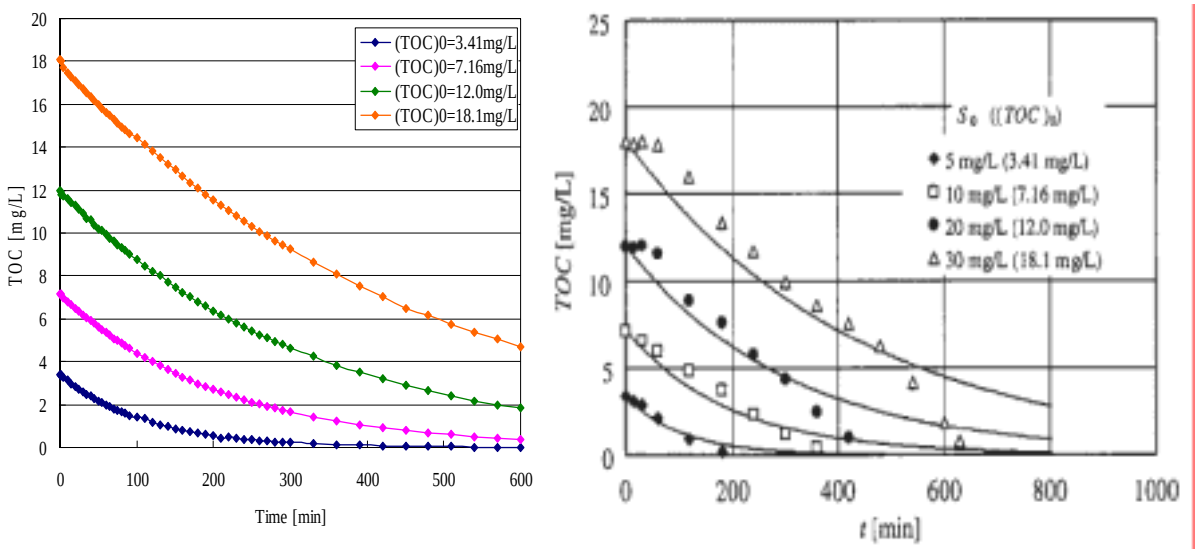

Fig.8 Effect of initial *TOC* on ozonation rate at U_g = 0.106 cm/s and Y_{in} =25 mg/L.

References

Miyahara, T., Hirokawa, M., Ueda, M. Yoshida, K. (1994). Solubility of Ozone into Water in a Bubble Column, *Kagaku Kogaku Ronbunshu*, 20, 497-503

Shah, Y. T., Kellkar, B.G., Godbole, G. P., Deckwer, W. –D., (1982), Design Parameters Estimations for Bubble Column Reactors, *AIChE J.*, 28, 353-379

Uchiyama, T., Kobayashi, H., Znad, H. T., Tokumura, M., Kawase, Y. (2007). Dynamic Performance of Ozonation Treatment for Nonionic Surfactants (Polyoxyethylene Alkyl Ether) in a Bubble Column Reactor. *Ozone: Science and Engineering*, 29, 65-72

Proceedings of the 10th International Chemical and
Biological Engineering Conference - CHEMPOR 2008
Braga, Portugal, September 4-6, 2008
E.C. Ferreira and M. Mota (Eds.)

Particle Interaction with Coherent Structures in a Confined Two-Phase Jet

J.C.S.C. Bastos[1], R.K. Decker[1], U. Fritsching[*1], M. Mori[*2]

1. University of Campinas, Campinas, São Paulo, Brazil
2. University of Bremen, Institut für Werkstofftechnik, Bremen, Germany

Keywords: Gas-Solid Flows, Coherent Structures, Particle Interaction
Topic: Advancing the chemical and biological engineering fundamentals

Abstract: The purpose of this research was the study of flow structures and the contact between phases in a two-phase confined jet. Flow structures are related to quasideterministic strutuctures (large-scale), randomly distributed in space and time. Analysis of the contact between the phases in such structures allows the identification of different mixture behaviors mainly due to gas-particle and particle-particle interactions. A pentagonal plexiglass chamber was used as a confined system to investigate these phenomena. Three different nozzles were used to feed air at the top of the chamber, but just the central nozzle was loaded with particles between 10μm and 200μm. The other two were used to increase the interaction between the phases at the chamber. An optical technique known as Phase Doppler Anemometry (PDA) was used to measure the instantaneous velocity of the particulate phase and particle diameter in five different axial positions of the jet nozzle. Radial profiles were also obtained for each axial position. The data analyzed were presented in terms of mean velocity, fluctuation velocity known as rms velocity, turbulence intensity and interparticle arrival time (in terms of Chi^2 distribution and deviation number). The experiments were carried out under different conditions, such as initial velocity (all nozzles), particle distribution (central nozzle) and gas/particle load ratio (central nozzle). These investigations rovid important information on local flow structures and their effect on the macrocospic and turbulent transport of particles between the jet center and the jet contour regions.

1. Introduction

The study of large-scale coherent structures (LSCS) and the contact between phases in gas-solid two-phase flow can be attributed to their technological importance to many industrial processes. Particles in finite gravity tend to accumulate in two types of regions downward flows sandwiched between counter-rotating quasi-streamwise vortex tubes and regions beneath the vortex layers with negative spanwise vorticity. This accumulation of particles may be a problem in the jet mixing processes, causing efficiency to be lower when a good mixture of particles is required. However, if coherent structures are suppressed and incoherent structures dominate the flow, a higher efficiency of mixture may be obtained, mainly due to the chaotic behavior of the incoherent particulate phase, avoiding cluster formation. Based on an application of the interparticle arrival time methodology proposed by Edwards and Marx (1995A, 1995B), this work aims to analyze the flow structure of the dispersed phase in a two-phase jet under different flow and

[1] Corresponding author. E-mail: mori@feq.unicamp.br
[2] Corresponding author. E-mail: ufri@iwt.uni-bremen.de

operational conditions. Due to effects of interference of the tracer particles on the dispersed phase measurement, addressed by Gillandt *et al*. (2000) and Hussainov *et al*. (2000), it is the objective of this investigation to study the particle cluster formation just in relation to the particulate phase, thereby avoiding unnecessary measurements. Moreover, also aims this work to identify physical regions and operational conditions were LSCS occur and within cluster structures. A summary of the interparticle arrival time analysis developed by Edwards and Marx (1995A, 1995B) and improved by Heinlein and Fritsching (2004) is presented in Heinlein and Fritsching (2006).

2. Theory

A summary of the interparticle arrival time analysis developed by Edwards and Marx (1995A, 1995B) and modificated by Heinlein and Fritsching (2004) of the interparticle histogram and its acquisition are presented in Heinlein and Fritsching (2006). The theoretical interparticle function is compared with the experimental interparticle distribution function and particulate flow steadiness or unsteadiness is assessed, where

$$h_{th}(\tau_j) = \frac{\lambda^2 (T-\tau)\exp(-\lambda\tau)}{\lambda T - 1 + \exp(-\lambda T)} \text{ and } h_{\exp}(\tau_j) = \frac{H(\tau_j)}{N\Delta\tau_j}.$$

The statistical analysis of the Chi^2 test is used to obtain the significance, or confidence level, at which the experimental results can be argued to be the same as the theoretical values. In a Chi^2 analysis, the random variable χ^2, the deviation of the observed values from the corresponding expected values, can be measured and can determine the validity of the hypothetical model (Luong and Sojka (1999)). Once Chi^2 has been determined, the hypothetical model can be accepted or rejected depending on the desired significance level.

3. Experimental Setup and Measurement Device

An air compressor supplies a stream of filtered and dried air to the measurement system, which four different lines, as shown in Figure 1. The first line or the main line was connected to the mixture chamber where particles were loaded from a particle deposit, forming a mixture of gas/particles to be fed in through the central nozzle. The second line provided a small amount of air for particle deposit, which was kept at a positive pressure of 0.4bar. When a positive pressure was not achieved, particles were not able to flow through the 1.5mm orifice due to the opposite pressure of the main line. This orifice regulated a constant particle feed into the mixture chamber and consequently the mass load ratio. The third and the fourth lines were used to feed air into the measurement section (confined jet) through two different nozzles, one on the left and the other on the right side of the central nozzle. These three nozzles were located side by side at the top of a closed chamber and were the only entrance, characterizing a confined flow. The main characteristics of the chamber three inlets at the top each with a diameter of 12mm (left, central and right), one outlet at the base (entire base) and a height of 1 meter. Both lateral nozzles were used to supply air at different velocities in order to investigate the flow instabilities due to the presence of different local velocities in the chamber, and consequently local flow structures. Inside this chamber, different radial profiles were obtained at five different axial distances from the jet nozzles, providing data on the mean velocity, rms velocity, turbulence intensity and interparticle arrival time. The data were acquired at each point by a PDA system, which is a nonintrusive and highly accurate measurement device.

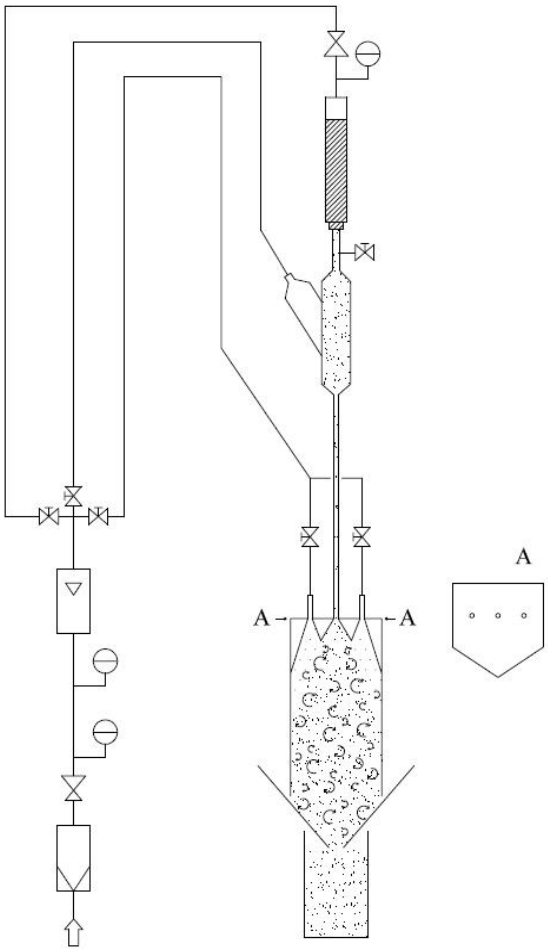

Figure 1 – Experimental setup of the confined two-phase jet.

The PDA measurements were conducted in refractive mode at an off-axis angle of 30º. The particles used during the experiment were spherical glass beads. The instantaneous velocities acquired by the PDA system were interpreted in post-processing mode. Therefore, a complete signal line was sampled for a preselected time of 5s, providing approximately 15000 samples in regions of higher intensity. The minimum particle number considered for sample acquisition is 1000 samples.

4. Boundary conditions

For analysis of the gas-solid flow in a two-phase particle-laden jet, a mixture of different particle diameters between 10µm and 200µm was used. The physical properties of the gas and particulate phase used in the experiments were particle density of 2500Kg/m^3, a gas density of 1.014Kg/m^3 and a gas viscosity of 1.81x10^{-5}Kg/m.s. The mean particle diameter of the particles measured was obtained for all experiments by the granular distribution analysis expressed in terms of Sauter mean particle diameter.

An overview of the initial velocities analized and their respective positions are shown in Table 1.

Table 1 – Initial velocities in different jet nozzles.

Case	U_0 (m/s) - Jet 1	U_0 (m/s) - Jet 2	U_0 (m/s) - Jet 3
1	0	11.5	0
2	8	8.5	8
3	10	9.5	10

5. Results and Discussion

The results obtained for three different cases are presented in terms of mean velocity, rms velocity, turbulence intensity and LSCS in terms of Chi^2 and number of deviations. These results can provide an overview of the behavior of the gas-solid flow in a confined jet at different flows, as shown in Table 1. Measurements were taken at two

different axial distances from the jet nozzle, 210mm and 240mm, in a region where the flow is developed and interaction with the flow from the adjacent nozzles already exists.

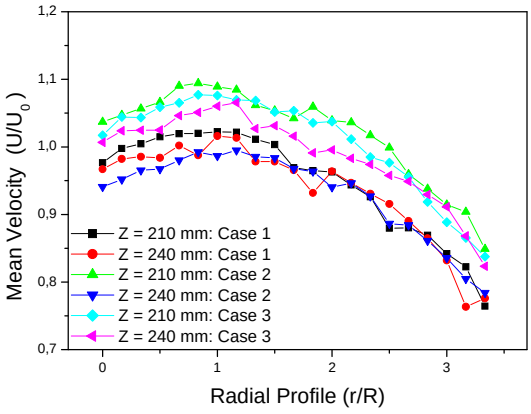

Figure 2 – Mean velocity profiles.

In Figure 2 the radial mean velocity profiles for the above mentioned axial positions are presented for the three cases under analysis. It is interesting to observe that with the increment in the adjacent velocities in jets 1 and 3, the radial profiles with particles loaded in jet 2 tend to be more uniform. For instance, the differences between maximal and minimal velocity in the same profile for cases 1 and 3 are respectively 3m/s and 2.2m/s. These differences are not huge, but show the tendency toward a flat profile. This flat profile is not seen in other studies, such as for the study developed by Decker et al. (2007) where a free jet flow with the same operational and geometrical characteristics was studied.

In that situation the authors found a difference between velocities around 8m/s in the same profile with flow characteristics similar to those found in this study. This shows that the walls and the adjacent flows have a strong effect on jet behavior and consequently on the homogeneity of the flow.

In Figure 3 it is possible to observe the rms velocity for the same conditions at those analyzed in Figure 2. It is interesting to observe a radial region for both profiles in case 1, where there are more interactions between particle. This region between 0.007m and 0.012m indicates the presence of strong flow structures (coherent or incoherent ones) and indicates the shared region of the jet, where the main flow interacts with a region of small velocities. This happens because in case 1 there is no adjacent velocity in nozzles 1 and 3 and the flow interactions are strongly affected by the chamber wall. This increment in rms velocity in the shared region is also observed for free jet flows.

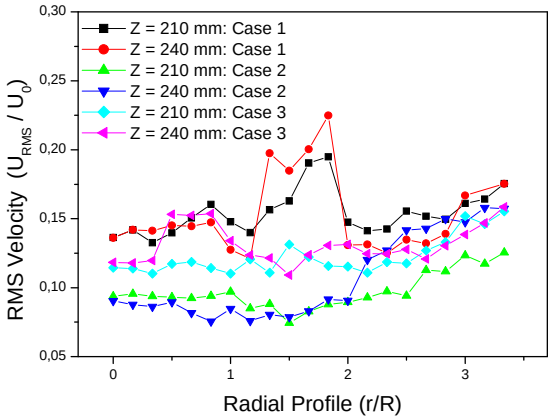

Figure 3 – Rms velocity profiles.

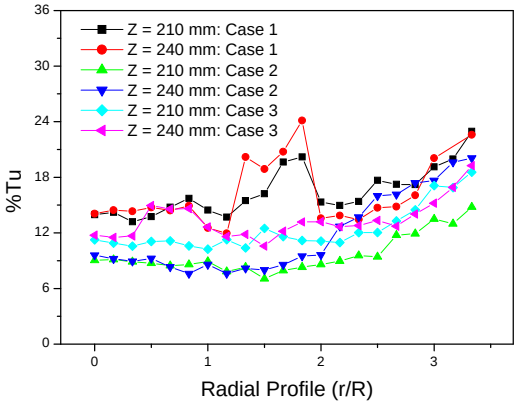

Figure 4 – Turbulence intensity profiles.

The presence of adjacent velocities provided by jets 1 and 3 produces the uniform behavior in the rms velocity profile, which is in agreement with the observations obtained for the mean velocity. In other words, the presence of adjacent flows affects the flow into the chamber in such away that the flow structures tend to become uniform in all radial positions. However such structures are still strong due to the high level of turbulence in the flow.

In Figure 4 the turbulence intensity profile is shown. It is important to observe that the turbulence intensity values are obtained from mean velocity and rms velocity values. As the mean velocity has almost the same profile for all the radial positions, the turbulence intensity profiles become similar to the rms velocity profiles. Furthermore, these results show a uniform behavior in the jet when there are adjacent flows, as previously mentioned.

The large-scale structures may be understood by the statistical study of multiple points, as reported by Heinlein and Fritsching (2006). This technique is based on time distribution between successive arrival particles, known in the literature as interparticle arrival time (IAT). This analysis can be expressed in terms of Chi^2 and number of deviations, which provide data about the flow structures and instabilities in two-phase flows. By definition, steady flows are those whose IAT distribution obeys inhomogeneous Poisson statistics and unsteady flows are those that the IAT distribuition does not obey. Are LSCS in two-phase flows examples of unsteadiness.

It is important to mention that alone the Chi^2 analysis does not guarantee confidence regarding the existence and location of LSCS. This is because the Chi^2 values may be obtained due to random fluctuation and no conclusion can be obtained. Based on this necessity, a parallel analysis of number of deviations must also be developed so the steadiness and unsteadiness of the flow can be assessed.

In Figures 5 and 6 the Chi^2 and the number of deviations analysis, respectively, are presented for the cases and axial positions in Figure 2. It is interesting to observe in Figure 5 that large values for Chi^2 are obtained at position Z = 210mm for case 2. Furthermore, in Figure 6, a larger number of deviations can also be observed for the same case, but at Z = 240mm. However, neither of the cases is able to identify LSCS, because they are not in agreement with the Chi^2 and number of deviations criteria. In other words, no LSCS exist under these conditions. In these cases, the values of Chi^2 observed in Figure 5 are due to random fluctuation since the majority of the values in Figure 6 are under the zero line.

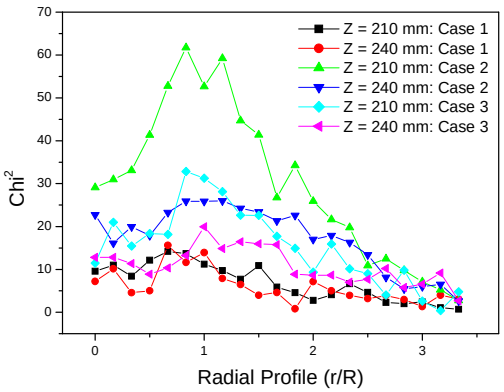

Figure 5 – Chi^2 profiles.

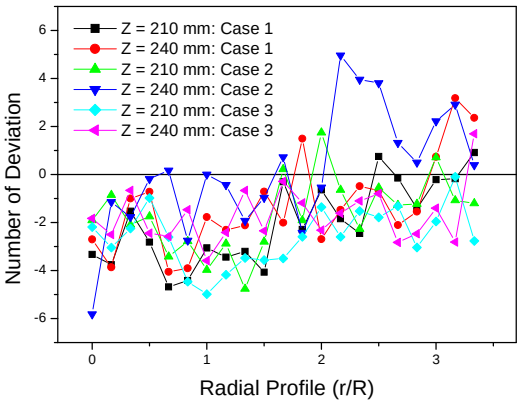

Figure 6 – Number of deviations profiles.

6. Conclusions

In this study flow structure and particle interaction are analyzed for a confined two-phase jet flow with three different nozzles: one main nozzle where particles are loaded together with the gas phase and two adjacent ones without particles. Three different cases are analyzed for two different axial positions of the jet nozzle: 210 and 240mm. The results are presented in terms of mean velocity, rms velocity, turbulence intensity, Chi^2 and number of deviations radial profiles. In all these analyse the confined jet had similar characteristics, such as flat radial profiles with the increment in adjacent velocities in the adjacent nozzles. Another behavior observed is in relation to LSCS. In all cases presented in this study, no such flow structures are observed and incoherent structures dominate the flow field. This happens due to two different characteristics of this study: high velocities in the jets and the presence of the wall. Under these conditions, a high level of flow structures exists, mainly due to the direction and redirection of the main flow and the presence of secondary flows, which produce the dissipation and suppression of these coherent structures.

References

Schöne, F., Bauckhage, K., Wriedt, T. (1994). Size of the Detection Area of a Phase-Doppler Anemometer for Reflecting and Refracting Particles. *Particle & Particle Systems Characterization*, 11, 327-338.

Edwards, C.F., Marx, K.D. (1995). Multipoint Statistical Structure of the Ideal Spray, Part 1: Fundamental Concepts and the Realization Density. *Atomization and Sprays*, 5, 435-455.

Edwards, C.F., Marx, K.D. (1995). Multipoint Statistical Structure of the Ideal Spray, Part 2: Evaluating Steadiness Using the Interparticle Time Distribution. *Atomization and Sprays*, 5, 457-505.

Gillandt, I. (2000). Analyse der Turbulenzmodulation im dispersen zweiphasigen Freistrahl; Shaker, Aachen.

Lie, J., Kuipers, J.A.M. (2007). Effect of Competition between Particle-Particle and Gas-Particle Interactions on Flow Patterns in Dense Gas-Fluidized Beds. *Chemical Engineering Science*, 62, 3429-3442.

Luong, J.T.K., Sojka, P.E. (1999). Unsteadiness in Effervescent Sprays, *Atomization & Sprays* 9, 217-257.

Decker, R. K., Fritsching, U., Meier, H. F., Mori, M. (2007). Particle Interaction with Coherent Structures in a Two-Phase Jet. *In: 6th International Conference on Multiphase Flow, Leipzig.*

Bastos, J. C. S. C., Rosa, L. M., Mori, M., Marini, F., Martignoni, W. P. (2008). Modelling and Simulation of a Gas-Solids Dispersion Flow in a High-flux Circulating Fluidized Bed (HFCFB) Riser. *Catalysis Today*, 130, 462-470.

Heinlein, J., Fritsching, U. (2004). Detection and evaluation of droplet concentration variations in sprays; Shaker Verlag, Aachen, 2004.

Heinlein, J., Fritsching, U. (2006). Droplet Clustering in Sprays, *Experiment in Fluids* 40, 464 – 472.

Hussainov, M., Kartushinsky, A., Rudi, Ü., Shcheglov, I., Kohnen, G., Sommerfeld, M. (2000). Experimental investigation of turbulence modulation by solid particles in a grid-generated vertical flow. *International Journal of Heat and Fluid Flow*, 21,365-373.

Proceedings of the 10th International Chemical and
Biological Engineering Conference - CHEMPOR 2008
Braga, Portugal, September 4-6, 2008
E.C. Ferreira and M. Mota (Eds.)

Heat transfer in the freeboard of a bubbling fluidized bed

P. Neto[1], A.M. Ribeiro[1*], C. Pinho[2]

[(1)] Instituto Superior de Engenharia do Porto, Rua Dr. António Bernardino de Almeida, 431, 4200-072 Porto – Portugal.
[(2)]CEFT-DEMEGI, Faculdade de Engenharia da Universidade do Porto, Rua Dr. Roberto Frias, s/n, 4200-465 Porto – Portugal

Keywords: bubbling fluidized bed, heat transfer coefficients, propane combustion
Topic: Advancing the chemical engineering fundamentals

Abstract

The main objective of this investigation was to experimentally study, in the free board of a bubbling fluidized bed of sand, the heat transfer towards a water cooled confining membrane wall. New results were obtained on the heat transfer mechanisms occurring in the membrane walls placed above a bubbling fluidized bed heated by an electrical resistance of 2 kW. Two kinds of experiments were performed: in the first part, the bed was fluidized with air and the temperature in the bed reached values in the range of 400 – 700 ºC, and in the second set of experiments, propane was injected and mixed with the fluidizing air and combustion took place in and above the bubbling bed. For the latter situation, the temperature in the bed reached values above 700ºC. An empirical correlation was developed to determine overall heat transfer coefficients.

1. Introduction

The temperature of fluidized bed boilers and furnaces is controlled by the heat transfer rate towards non-refractory walls, either membrane walls or heat transfer bundles placed in the gas flow path. The understanding and explanation of heat transfer mechanisms among the bed or particles and confining walls, like membrane walls, is of great importance. Published data concerning the heat transfer in this region are scarce, and are essentially concerned with the heat transfer towards tube bundles placed in the free board region, while data on heat transfer towards membrane walls are almost non-existent. Wen–Ching (2003) refers to numerous works using laboratory scale fluidized bed reactors and confirms that the information available on the transport region of bubbling beds is quite limited.

Several heat transfer studies were carried out in fluidized beds for operating conditions different than those considered in the present work. Al-Busoul (2002) used bed immersed surfaces while several other studies consider the membrane wall, but only in the bubbling bed region. Pagliuso and Lombardi (2000) presented results for an experimental set-up quite similar to that considered in this investigation and so their work was used for a preliminary analysis. However, these authors refer to a circulating fluidized bed operating at around 150 ºC, while the present study covers a higher range of temperatures.

The literature search carried out also reveals no information about studies of heat transfer in fluidized beds with the combustion of propane. Some authors (Gayan et al, 2004; Dounit et al,

* Corresponding author. Tel + 351-228340500. E-mail:asr@isep.ipp.pt

2001 and Ribeiro and Pinho 2004) experimentally studied combustion reactions in fluidized beds, but only to characterize reaction kinetics and not the heat transfer phenomena involved.

The current investigation presents new results on the heat transfer mechanisms occurring in the membrane walls placed above a bubbling fluidized bed. Based on the experimental data obtained, a new empirical correlation was developed to determine overall heat transfer coefficients.

2. Experimental

2.1 Experimental apparatus

The fluidized bed reactor used in the present study was able to work in either bubbling or circulating bed conditions. A full description of the apparatus is found in Neto (2008). The system was built in stainless steel and was thermally insulated with Kaowool ceramic fibre. The riser portion of the reactor was formed by two vertical sections with water jacket membrane walls. The first part of the reactor, from the distributor to the flange separating it from the first membrane wall section, was 420 mm long, whereas each membrane wall section was 1000 mm long. The internal diameter of the reactor, made in stainless steel AISI 316, was 54.5 mm.

The fluidized bed reactor was heated by means of a 2 kW electrical resistance wrapped around the bubbling bed region of the reactor. Alternatively, propane could be injected and mixed with the fluidizing air, with combustion taking place in and above the bubbling bed, according to the bed particle size.

Heat from the gas solid suspension was transferred to these regions and the corresponding rate of transfer was determined through the energy balance of the cooling water flow. Temperatures were measured with K-type thermocouples, with a precision of 0.4% of the measured value, and were linked to a data acquisition system operating with Labview software. The thermocouple measuring the bed temperature was also connected to a PID temperature controller, which acted upon the bed heating electrical resistance.

To evaluate the pressure drop in the bubbling bed and in the riser section of the reactor, Omega PX 142 pressure transducers were used. These were also connected to the same data acquisition system as the thermocouples.

The fluidizing air flow was measured using a calibrated orifice plate equipped with a differential pressure transducer connected to a data acquisition system. The uncertainties associated with the air flow rates were in the range from 6 to 10 %. The water flow sent to the water jackets was measured by a calibrated rotameter and the uncertainties associated with these flow rates varied between 5 and 10 %.

Throughout the experiments, the bed was formed by silica sand with the following average diameters: 107.5 μm, 142.5 μm, 180 μm, 282.5 μm and 357.5 μm (all belonging to type *B* of the Geldart classification). For all the experiments, the sand was introduced into the bed until a fluidizing pressure drop of 10-15 cm H_2O was obtained.

2.2 Experiments without combustion

During normal operating conditions, in the 400 to 700 ºC bed temperature range and at 1 atm, the air mass flow rate was varied from 0.82 to 1.5 kg/h. Three cooling water flows through the membrane walls were used (35, 73 and 140 kg/h), always in laminar regime. Their values had no influence on the heat transfer rate because the overall resistance to the energy transfer was in the bed side wall.

The experimental work took place above the minimum fluidization velocity and below the terminal settling velocity of the bed particles, with the exception of the smaller bed particles where the fluidizing air superficial velocity was above this value. However no bed pressure drop reduction was found, which meant that no carry over of bed sand particles took place during these runs. All tested situations were therefore for bubbling bed fluidization, and the objective was to find out the importance of the projection of bed particles high above the bed surface on the heat transfer rate towards the water cooled membrane wall of the riser portion of the reactor.

2.3 Experiments with combustion

For these experiments, the electrical resistance was used to reach a bed temperature of 700 - 720ºC, this being the minimum temperature necessary to ignite the propane. The air was fed to the reactor below the distributor plate at flow rates between 0.85 -1.2 kg/h, enabling a bubbling fluidized bed to be obtained. Following this, the propane gas was fed to a point below the reactor at flow rates in the range of $0.095 < \dot{m}_{pro}$ (kg/h) < 0.12, in order to obtain an air to fuel ratio in the range of 8 to 10, so that the mixture equivalence ratio, *r*, was always above one.

The operating conditions which were adopted lead to a bubbling fluidized bed for all air and propane mass flow rates that were used. One of the objectives of this work was to compare the influence of particle size, so the operating conditions were similar in all the experiments made with combustion.

3. Results and Discussion

3.1 Experiments without combustion

In the experiments carried out in the bubbling bed fluidized with air, the following parameters were studied for each particle size: cooling water mass flow rate, bed temperature and fluidized bed air flow rate. Although two sections of water cooled membrane walls were used, there was only significant heat transfer in the region close to the bubbling bed.

From the results obtained it may be concluded that the water mass flow had no influence on the heat transfer rate towards the confining membrane walls. The experiments showed that an increase in the air flow rate increases the temperature difference of the cooling water as heat transfer rate increases, not only by convection of the gas solid flow, but also through radiation effects and, more importantly, due to the augmentation of particle projection towards the membrane walls. This increase in the cooling water outlet temperature is stronger for the smaller bed particle size when the projection of particles from the bed surface is strongest. Higher bed temperatures also means that bed hydrodynamic conditions enhance particle projection and thus the increase in the heat transfer rate.

3.2 Experiments with combustion

These experiments allowed the study of the heat transfer mechanisms in the presence of combustion reactions taking place simultaneously in the bed and immediately above it. They allowed the correlation of bed particle size with combustion, and evaluation of the importance of this interaction on the global heat transfer rate.

The experiments carried out showed that the beds exhibited two different behaviours, depending on the bed particle size. For the three smaller particles (107.5 μm, 142.5 μm, 180 μm) the combustion reaction took place both inside and at the surface of the bed. In addition, as the experiment was occurring, a decrease in the mass of the particles in the bed was observed. The

cause of this decrease was the carryover of particles due to the explosions occurring during the combustion reaction.

For the larger particle sizes (282.5 μm and 357.5 μm), the combustion reaction started inside the bed but rapidly moved towards the transport zone. For these experiments, and in the determination of the global heat transfer coefficient, only the data corresponding to combustion inside the bed was considered. This procedure was assumed in order to ensure that the combustion conditions were similar for all of the particle sizes under study.

The experiments with combustion showed, for all bed particle sizes tested, an increase in the enthalpy of the water when compared with the results obtained without combustion. This increase in the enthalpy of the water was more pronounced for the particle sizes of 107.5 μm, 142.5 μm, 180 μm, and decreased as the particle size was increased.

3.3 Correlation to calculate global heat transfer coefficients with and without combustion

The results obtained indicated that the heating of the cooling water was due to three mechanisms of heat transfer: convection due to the gas flow; radiation between the fluidized bed and the wall, and radiation due to the flame (in the experiments carried out with combustion); convection heat transfer due to particle splashing and projection away from the bed surface. The importance of these mechanisms is enhanced by the combustion reaction.

To calculate the importance of the heat transfer rate towards the confining membrane walls, the enthalpy increase of the cooling water flow was determined and compared with the air convection, the bed, and with the flame radiation components. The difference was attributed to the heat transferred through the particles' movement as they were expelled from the bed by the bursting bubbles reaching the free surface of the bed. The heat transfer area is the membrane wall area and the temperature difference adopted was given by:

$$\Delta T_{ln_{b-w}} = \frac{T_b - T_{go}}{ln\left(\frac{T_b - T_w}{T_{go} - T_w}\right)} \quad (1)$$

where T_b is the bed temperature, T_{go} is the temperature of the gas flow at the end of the first membrane wall heat exchanger, and T_w is the membrane wall temperature determined through the heat transfer balance of the membrane wall heat exchanger.

On the other hand, the cooling water enthalpy increase, $\dot{Q}_w$, was calculated through:

$$\dot{Q}_w = \dot{m}_w c_w \left(T_{wto} - T_{wti}\right) \quad (2)$$

where T_{wi} and T_{wo} are, respectively, the inlet and outlet water temperature, $\dot{m}_w$ is the water mass flow rate, and c_w is the specific heat of the water. From this the overall heat transfer coefficient, h_{glo}, based upon the internal area of the bed riser, or membrane heat exchanger pipe, A_p, and on $\Delta T_{ln_{b-w}}$, was determined according to:

$$Q_w = h_{glo}\, A_p\, \Delta T_{ln_{b-w}} \quad (3)$$

The area of the heat transfer surface was calculated by: $A_p = \pi\, d_i\, L_p$, where L_p is the height of each membrane wall section and d_i is the bed internal diameter.

A simple correlation was determined by means of a dimensional analysis, taking into account the main physical parameters characterizing the experimental conditions, both with and without combustion. The adjustment of this correlation to the experimental data through adequate fitting parameters leads to:

$$Nu = 17{,}3\, Re^{-0.24} Pr \left(\frac{U_0}{U_{mf}}\right)^{-0.024} \left(\frac{d_p}{d_i}\right)^{-0.30} \left(\ln\left(\frac{T_b - T_w}{T_b - T_{go}}\right)\right)^{0.17} r^{0.78} \qquad (4)$$

where U_o and U_{mf} are, respectively, the superficial gas velocity and the minimum fluidization velocity. Re is the Reynolds number $\left(Re = \rho_g U_o d_i / \mu_g\right)$, Pr is the Prandtl number, and r is the mixture equivalence ratio. The fluidizing air properties were determined at the film temperature.

Equation (4) is valid for a bed of sand with an ID of 54.5 mm, either fluidized with air or with combustion of propane, at atmospheric pressure in the region above the bed free surface and according to the following operating limits:

- 107.5 < d_p (µm) < 357.5
- 0.85 < $\dot{m}_a$ (kg/h) < 1.2
- 0.09 < $\dot{m}_{pro}$ (kg/h) < 0.12
- 1.4 < r < 1.9 (r = 1 for the experiments without combustion)
- 400 < T_b (ºC) < 820
- 200 < Re < 400
- 2 < U_o / U_{mf} < 40

An average deviation of 17 % was determined between the calculated and the experimental Nusselt numbers $\left(Nu = h_{glo} d_i / k_g\right)$. Figure 1 validates the Nu calculated from equation (4) against the experimental data.

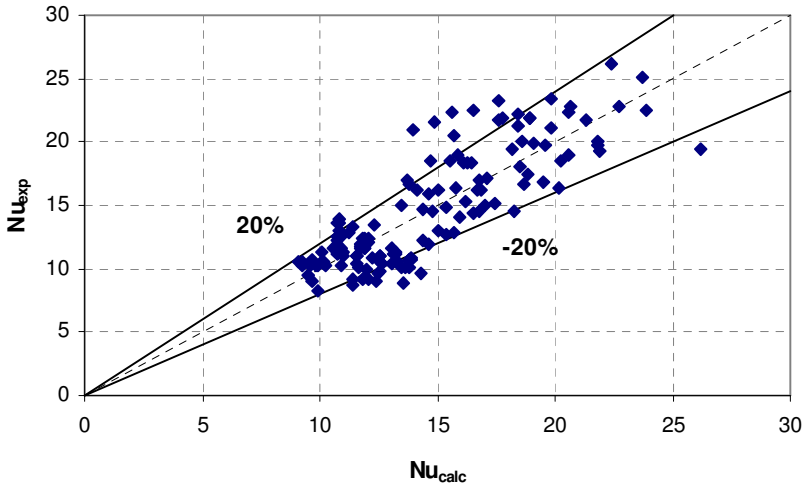

Figure 1 – Validation of equation (4).

4. Conclusions

In these experiments heat transfer was quantified in terms of a global heat transfer coefficient, taking into account the following mechanisms: convection due to the gas solid flow, radiation from the bed surface, and convection heat transfer due to particle projection away from the bed. The importance of these mechanisms is enhanced by the combustion reaction, especially the latter, due to the action of bursting bubbles that appear during the combustion. A correlation for the global heat transfer coefficient was proposed with an average deviation of 17%.

Acknowledgment

The authors wish to thank the Portuguese *Fundação para a Ciência e Tecnologia* for the financial support of this work under the Research Project POCTI/EME/44300/2002.

References

Al-Busoul, A. (2002). Bed-to-surface heat transfer in a circulating fluidized bed. *Heat and Mass Transfer*, 38, 295-299.

Dounit, S., Hemati, M. Steinmetz, D. (2001). Natural gas combustion in fluidized bed reactors between 600 and 850 ºC: experimental study and modelling of the freeboard. *Powder Technology*, 120, 49-54.

Gayan, P, Adanez, J., Diego, L.F., García-Labiano, F., Cabanillas, A., Bahillo, A., Aho, M., Veijonen, K. (2004). Circulating fluidized bed co-combustion of coal and biomass. *Fuel*, 83, 277-286.

Neto, P. (2008). *Transferência de calor acima da superfície livre de um leito fluidizado borbulhante*. PhD Thesis, Faculty of Engineering, University of Porto.

Pagliuso, J.D., Lombardi G. (2000). Experiments on the local heat transfer characteristics of a circulating fluidized bed. *Experimental Thermal and Fluid Science*, 20, 170-179.

Ribeiro, L., Pinho, C. (2004). Generic behaviour of propane combustion in fluidized beds. *Chemical Engineering Research and Design*, 82, 1597-1603.

Wen-Ching, Y. (2003) *Handbook of Fluidization and Fluid-Particle Systems*, Marcel Dekker, Inc, New York. Basel.

Proceedings of the 10th International Chemical and
Biological Engineering Conference - CHEMPOR 2008
Braga, Portugal, September 4-6, 2008
E.C. Ferreira and M. Mota (Eds.)

Dispersion in packed beds determined by NMR

Ulrich M. Scheven[1]*, **Rob Harris**[2], **Mike L. Johns**[2]
[1]REQUIMTE/CQFB, Departamento de Química, Faculdade de Ciências e Tecnologia,
Universidade Nova de Lisboa, 2829-516 Caparica, Portugal
[2] Magnetic Resonance Research Centre, Department of Chemical Engineering,
University of Cambridge, Cambridge CB2 3RA, United Kingdom.

Keywords: Nuclear magnetic resonance, pulsed field gradients, dispersion, porous media, laminar flow.
Topic: Advancing the chemical snd biological engineering fundamentals.

Abstract

Displacement encoding Pulsed Field Gradient Nuclear Magnetic Resonance (PFG-NMR) complements traditional elution measurements of axial dispersivities in packed beds by measuring the variance of the displacement distribution of inert tracers as they move down the packed column. It is clear, however, that NMR derived dispersivities in packed beds of monodisperse solid spheres, the fundamental random porous system for which there exist canonical (1; 2; 3) but incompatible theoretical predictions with few or no adjustable parameters, can be affected by the same experimental complications which have substantially contributed to the puzzling scatter in published dispersion results based on elution experiments. Notable among these are macroscopic flow heterogeneities near walls (4), and inhomogeneous flow injection. Analyzing PFG-NMR results we delineate a transition from a pre-asymptotic to a quasi-asymptotic dispersion regime and extract the true dispersivity of the ideal (unbounded) random pack of solid monodisperse spheres with perfectly homogeneous flow injection.

1 Introduction

In an idealized traditional tracer elution experiment with creeping and constant uni-axial flow of velocity v_o through a random pack of identical spheres a narrow pulse of inert tracers is injected uniformly in a plane perpendicular to the mean flow, at time $t = 0$. Moving through the sample the tracer cloud spreads by a combination of random processes, diffusion and mechanical mixing, and asymptotically a tracer band with Gaussian concentration profile is expected to develop, centered around the mean displacement $\langle\zeta\rangle = v_0 t$. The variance σ^2 of the tracer concentration is proportional to time or to the distance traveled. This proportionality defines the Péclet number dependent dispersion coefficient $D = \sigma^2/2t$ or equivalently the dispersivity $l_d = D/v_0 = \sigma^2/2v_0 t$. The shape of the tracer distribution and its variance σ^2 can then be determined from time series measurements of tracer concentration in the eluent, and from the known flow velocity. With repeat experiments at different flow velocities one determines the Péclet number dependence of the dispersion coefficient, at a fixed degree of mechanical mixing set by the porespace geometry and the length of the sample. In real samples of packed particles complications arise due the presence of macroscopic stagnation zones, which are not the subject of this paper, or due to non-uniformity of flow on the scale of the sample. The latter may be caused for example by uneven flow injection into the sample, by faster flow near containing walls (4), by filtration effects in the sample, or due to sample preparation. One then observes non-Gaussian tracer distributions whose variance grows super-linearly with time or mean displacement as the tracers traverse the sample. The measured dispersion coefficient (or dispersivity) is "effective", meaning sample dependent, and hence the consistency of nominally comparable dispersion data is not what one might hope for (5), as can been seen for example in Fig.1a reproduced from reference (6). It plots measured dispersion coefficients normalized by the molecular diffusion coefficient of the fluid. Many similar canonical plots exist in the literature and

*Corresponding author. Tel. +351-212-949621. E-mail: ums@dq.fct.unl.pt.

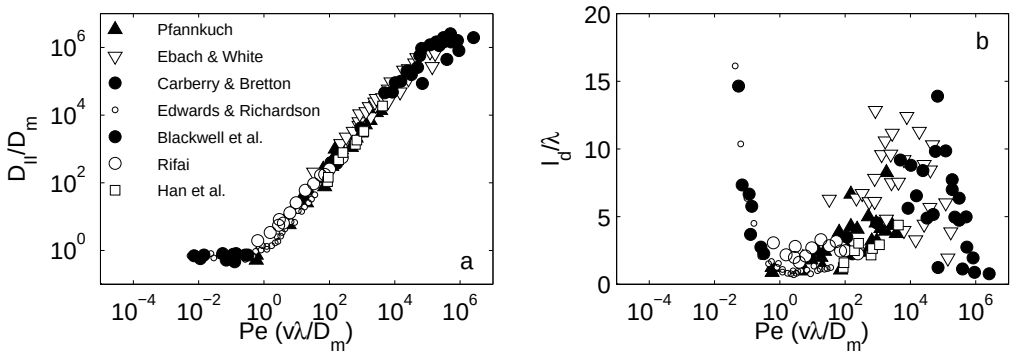

Figure 1: (a) A reproduction of fig. 11 in ref. (6), plotting longitudinal dispersion coefficients for a number of experiments, normalized by the molecular diffusion coefficients, against Péclet number, D/D_m vs. Pe. (b) The same data now replotted as dispersivity normalized by the length scale used to define the Peclet number, $l_d/\lambda = 1/Pe \times D/D_m$, with $\lambda = d\epsilon/(1-\epsilon)$. The porosity of the pack is ϵ, and the diameter of constituent solid spheres is d.

in text books. The two logarithmic axes of Fig.1a are useful in plots of dispersion coefficients spanning several decades, and not coincidentally the Pe-dependence of the dispersion coefficient is frequently discussed in terms of an effective power law coefficient $\delta \ll 1$, $D \propto Pe^{1+\delta}$. It is worth noting, however, that a value of $\delta = 0$ corresponds trivially to pure mechanical mixing, while the interesting physics of the mixing process is buried in the small parameter δ. After dividing the normalized dispersion coefficients by the associated Péclet numbers and replotting the resulting normalized dispersivity on a semi-logarithmic plot in Fig.1b, one appreciates the amount of scatter and uncertainty associated with typical measurements of longitudinal dispersion. The expedient power law description of the data in Fig.1a is considerably less compelling when the data are viewed, closely, on the semi-logarithmic axes in Fig.1b. We also note that Fig.1b contains valuable information which is not readily apparent in the double logarithmic plot of Fig.1a. First, there appears to be a lower bound on the dispersivity approximately where $l_d/\lambda = 0.4$. Second, the data for the largest Pe appear to recover the low dispersivities seen near $Pe = 1$, suggesting that turbulent mixing at high Pe has the same effect on the mixing process as diffusive mixing does near $Pe = 1$.

2 NMR experiments

Many displacement encoding PFG-NMR measurements (7) have been conducted on Stokes flows through randomly packed beds of identical spheres, in order to elucidate a wide range of dispersion phenomena accessible to PFG-NMR investigation (8; 9; 10; 11; 12; 13; 14; 15; 16; 17; 18; 19; 20; 21; 22). The particular case of longitudinal dispersion in packed beds of identical solid spheres is widely studied both because of its theoretical (1; 2; 3) and practical importance, generally using PFG-sequences compensating for internal gradients (23). In our displacement encoding PFG-NMR measurement with flowing water all protons act as tracers. The NMR-signal is is a complex number $S(q) = \langle e^{iq\zeta_j} \rangle = \int P(\zeta) e^{iq\zeta} d\zeta$ where q is the magnitude of the magnetization wave vector $\vec{q}$ set up by the pulsed field gradients, ζ_j is the displacement of the spin o tracer molecule j during an evolution period Δ, typically ranging up to a few seconds, and $P(\zeta)$ is the probability distribution of molecular displacements along the direction of the pulsed field gradients. The PFG-NMR analogue of a traditional tracer elution experiment is one where the degree of mechanical mixing is kept constant by adjusting the evolution time Δ to keep the mean displacement ζ_0 constant, $\Delta = \zeta_0/v_0$. Then the fixed mean displacement ζ_0 takes the role of the sample length in the elution experiment. In contrast to the elution experiment, where mechanical mixing is fixed and the tracer distribution is observed at the end of the sample alone, the NMR experiment can track the displacement of all tracers as they sweep through different mean displacements ζ_0; the degree of mechanical mixing is thus variable continuously. We make use of this property to analyze measurements conducted at fixed velocities v_0 for variable evolution times Δ and correponding mean displace-

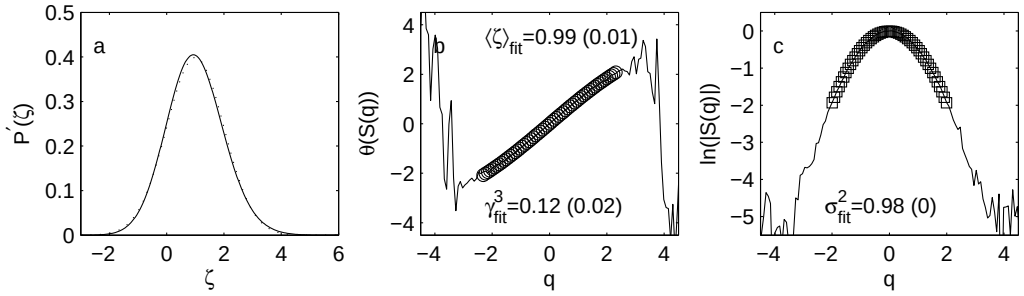

Figure 2: (a) Synthetic skewed displacement distribution P' (solid) with $\langle\zeta\rangle = \sigma^2 = 1$ and skewness factor $\gamma^3/\sigma^3 = 0.15$. Gaussian distribution (dots) with $\langle\zeta\rangle = \sigma^2 = 1$ and $\gamma^3/\sigma^3 = 0$ for comparison. Odd (b) and even (c) cumulant fits (symbols) to synthetic noisy NMR data (solid) calculated from P'. Fit ranges set by self consistent cumulant analysis (20).

ments $\zeta_0 = \Delta v_0$. We find and discuss a transition from a pre-asymptotic (16) to a "quasi-asymptotic" regime (22) in which the intrinsic dispersivity of the random pack of spheres can be determined.

We established creeping water flow through three different packs made of monodisperse borosilicate glass beads of diameter $100\mu m$. They were filled into a plexiglass tube with inner diameter $37.5mm$, to a pack length of $70mm$. Flow distributors placed at the inlet and outlet of the packs assured reasonably homogeneous but presumably imperfect flow injection. The tube was placed into an $85MHz$ imaging system fitted with an imaging gradient set whose maximal gradient strength was a modest $10g/cm$. Axial water flow was established using pulse free ISCO piston pumps. We employed (22) the 13-interval APGSTE sequence (23). All results reported here refer to displacements along the direction of mean flow. The first three terms of a cumulant (16; 24) analysis of the NMR signal $S(q)$, $\ln(S(q)) = \ln(|S(q)|) + i\theta(S(q)) = \sum_{j=1}^{\infty} \frac{(iq)^j}{j!} X_j$ sampled at low q yield the mean $\langle\zeta\rangle = X_1$, the variance $\sigma^2 = X_2$ and the skewness $\gamma^3 = X_3$. These are the first moment and the second and third central moments of $P(\zeta)$, respectively. Evidently odd cumulants appear in the phase θ of the signal, while even cumulants appear in the logarithm of its magnitude. One obtains the effective dispersivity $l_{eff} = \sigma^2/2\langle\zeta\rangle$ and skewness factor γ^3/σ^3 which is a useful non-dimensional measure of the symmetry of a nearly Gaussian distribution. We employed a self consistent cumulant analysis (SCA) (20) to verify that our data was not fitted over excessive fitting ranges in q-space, and to extract the first three cumulants and error bars. The analysis is illustrated in Fig. 2, using synthetic near gaussian displacement distribution constructed to have a realistic skewness factor of $\gamma^3/\sigma^3 = 0.15$, with fit results indicated in the figures. Below we discuss and analyze comparable experimental cumulant results.

3 Results and Discussion

Figure 3 shows SCA-derived flow velocities (a), effective dispersivities (b) and the skewness factors (c) versus mean displacement, obtained in three nominally identical packs labelled P1, P2, P3, using the same volumetric flowrate $\dot{V} = 44ml/min$ and sampling times Δ. The inset shows three full probability distributions obtained in packs P1, P2 and P3 respectively, of displacements at a mean displacement of approximately 37 bead diameters; to the eye they do resemble the skewed distribution of figure 2a. The velocities v_0 of figure 3a are obtained by dividing the phase-derived mean displacement by the corresponding evolution time Δ. First we observe that for displacements larger than some 10 bead diameters d the measured velocity in all samples is constant to within 0.4%. Second, the mean velocity differs from one sample to the next, spanning a range of 5%, despite the fact that the samples were made with the same particles, contained in the same tube, and were prepared, nominally, in the same manner. This is indicative of different packing densities known to occur for random packs. Each sample's porosity can be calculated by $\epsilon = \dot{V}/Av$, where A is the cross section of the tube containing the pack. Third, the measured velocities for displacements of less than about 10 particles are enhanced above the asymptotic value, by up to 2%. This is attributed to surface relaxation which preferentially removes slow spins, near

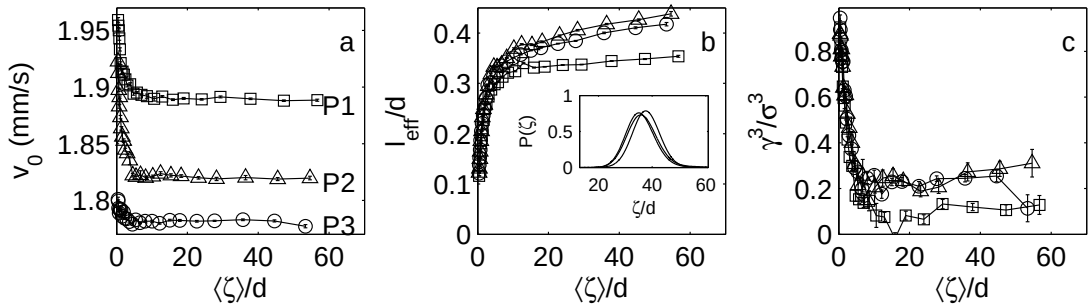

Figure 3: Cumulant derived velocities $v_0 = \langle\zeta\rangle/\Delta$, effective non-dimensional dispersivities $l_{eff} = \sigma^2/2\langle\zeta\rangle d$ and skewness factors γ^3/σ^3, in three nominally identical samples, at the volumetric flow rate 44ml/min. (a) Non-vanishing displacement-relaxation correlations result in enhanced NMR derived velocity readings in the pre-asymptotic regime $\langle\zeta\rangle/d \lesssim 10$. Final velocity readings reflect different packing densities. (b) Effective dispersivities grow approximately linearly with mean displacements, in the quasi-asymptotic regime $\langle\zeta\rangle/d \gtrsim 10$. (c) Decreasing skewness factor in the pre-asymptotic regime, but constant skewness factor in the quasi-asymptotic regime.

the walls, from the measurement. This relaxation-induced bias, also seen in earlier NMR measurements with flow through microporous beads (19), is transient because mechanical mixing ensures that all surviving spins have seen all relaxation environments equally, for mean displacements above about 10 bead diameters. One might therefore suppose that for $\langle\zeta\rangle/d \gtrsim 10$, where the relaxation becomes asymptotic, the dispersion would be asymptotic as well. This, however, is not the case. Figure 3b reveals that the effective dispersivity continues to grow approximately linearly with increasing mean displacement rather than tending towards an asymptotic value. Furthermore figure 3c reveals that after a steep initial drop in the skewness factor occurring roughly where $\langle\zeta\rangle/d < 10$ the displacement distributions remain skewed with approximately constant skewness factor. The linear growth of the effective dispersivity and the roughly constant skewness can be understood quantitatively using a simple model allowing for spatial variations in the drift velocity within the sample. When variations of drift velocities occur on scales larger than the mean displacements attained in the experiments, then variations of the mean velocity are not averaged out by the experiment. We call this regime "quasi-asymptotic" because it is locally asymptotic after about a mean displacement of 10 to 15 sphere diameters, as indicated by the asymptotic relaxation behavior, but globally pre-asymptotic, because all tracers have not yet seen all mean velocities which are present in the sample. In a recent paper(22) we have therefore written the "quasi-asymptotic" displacement distribution as a convolution of a dispersive Gaussian displacement distribution - governed by a single dispersivity l_d which depends on the geometry of the pore space and the Péclet number - with a distribution of mean displacements governed by a reasonably narrow distribution of mean velocities defined over an experimental coarse graining volume given by the longitudinal ($\approx \langle\zeta\rangle$) and transverse ($\approx \sqrt{\langle\zeta\rangle d}$) tracer displacements. One obtains

$$l_{eff} = \sigma^2/2\langle\zeta\rangle = l_d + \frac{1}{2}\langle\beta^2\rangle\langle\zeta\rangle \tag{1}$$

for the measured effective dispersivity l_{eff}. It is equal to the intrinsic dispersivity l_d plus a term proportional to mean displacement and the variance of the distribution of mean velocities divided by the squared mean velocity, $\langle\beta^2\rangle \equiv \langle(v - v_0)^2/v_0^2\rangle$. $\langle\beta^2\rangle$ is approximately constant when the dominant variations of the mean velocity occur on scales larger than the ones set by the experimental coarse graining volume. The observed growth of effective dispersivity is thus linear in $\langle\zeta\rangle$ in figure 3b. The skewness factor is

$$\gamma^3/\sigma^3 = \frac{6l_d\zeta_0^2\langle\beta^2\rangle + \langle\beta^3\rangle\zeta_0^3}{(2l_d\zeta_0 + \langle\beta^2\rangle\zeta_0^2)^{3/2}} \Rightarrow \frac{\langle\beta^3\rangle}{\langle\beta^2\rangle^{3/2}} \tag{2}$$

and it asymptotically approaches the constant and finite skewness factor of the velocity distribution $\langle\beta^3\rangle \equiv \langle(v - v_0)^3\rangle/\langle(v - v_0)^2\rangle^{1.5}$. Using expression (1) we could determine intrinsic dispersivities l_d for different values of the Péclet number $Pe = v\lambda/D_m$ in all three samples, where D_m is the molecular

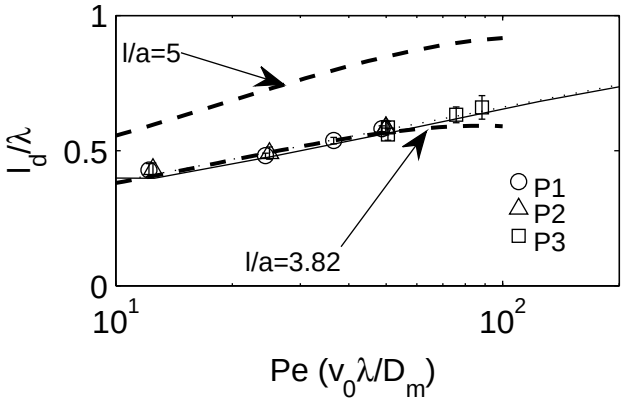

Figure 4: Adapted from ref. (22): Dispersivity vs. Péclet number, scaled by the hydrodynamic length $\lambda = 6r_h$. The dotted line is a linear fit to our data, the solid line from simulations (25), and dashed lines are Saffman's prediction for random networks of identical capillaries having length l and radius a.

diffusion coefficient. When scaled by the hydrodynamic length $\lambda = d \times \epsilon/(1-\epsilon)$ of the pore space all values of l_d/λ collapse onto a straight line in Fig. 4, to within the errors which we carried through the entire analysis. The numerical results by Maier(25) et al. are shown in a thin solid line and agree with our findings, as do Saffman's (1; 2) theoretical results for the dispersivity in a random network of identical capillaries with length l and radius a, shown with a dashed line for the best fit $l/a = 3.82$. The agreement of experiments, simulations and theory are remarkable. For reference we also show Saffman's original estimate $l/a = 5$ which to date has often served for comparisons between theory and experimental results.

4 Conclusion

Large random packs of identical solid spheres are a special case among porous samples where displacement encoding NMR measurements can distinguish dispersion regimes associated with two widely separated length scales: a pre-asymptotic regime, where the relevant dispersive length scale is on the order of a few particle diameters, and a quasi-asymptotic regime, where the relevant macroscopic dispersion length scale is larger than the experimental coarse graining length. The measurements are sensitive to displacement-relaxation correlations which give rise to enhanced measured velocities where the local mixing process is incomplete. The disappearance of enhanced velocity readings signals the end of the pre-asymptotic dispersion regime and the beginning of the quasi asymptotic regime, where measurement and analysis of effective dispersion coefficients yield Péclet-number dependent intrinsic dispersivities of the random pack of spheres, and the variance $\langle \beta^2 \rangle$ particular to the sample. This variance is a measure of macroscopic hydrodynamic sample heterogeneity and is perhaps not irrelevant for a linkage of dispersion and permeability data in other more heterogeneous samples.

References

[1] Saffman, P.G., (1959). A theory of dispersion in a porous medium, *Journal of Fluid Mechanics*, 6, 321-349

[2] Saffman, P.G., (1960). Dispersion due to molecular diffusion and macroscopic mixing in flow through a network of capillaries, *Journal of Fluid Mechanics*, 7, 194-208

[3] Koch, D., Brady, J.F., (1985). Dispersion in fixed beds, *Journal of Fluid Mechanics*, 154, 399-427

[4] Vortmeyer, D., Schuster, J., (1983). Evaluation of steady flow profiles in rectangular and circular packed-beds by a variational method, *Chemical Engineering Science*, 38, 1691-1699
[5] Delgado, J.M.P.Q., (2006). A critical review of dispersion in packed beds, *International Journal of Heat and Mass Transfer*, 42, 279-310
[6] Han, N.W., Bhakta, J., Carbonell, R.G., (1985). Longitudinal and lateral dispersion in packed beds: Effects of column length and particle size distribution. *AIChE Journal*, 31, 277-288
[7] E. O. Stejskal and J.E. Tanner, (1965). Spin diffusion measurements: Spin echoes in the presence of a time-dependent field gradient, *Journal of Chemical Physics*, 42, 288-292
[8] Ding, A., Candela, D., (1996). Probing nonlocal tracer dispersion in flows through random porous media, *Physical Review E*, 54, 656-660
[9] Lebon, L., Oger, L., Leblond, J., Hulin, J.P., Martys, N.S., Schwartz, L.M., (1996). Pulsed gradient NMR measurements and numerical simulation of flow velocity distribution in sphere packings, *Physics of Fluids*, 8, 293-301
[10] Seymour, J.D., Callaghan, P.T., (1996). Flow-Diffraction Structural characterization and measurement of hydrodynamic dispersion in porous media by PGSE NMR, *Journal of Magnetic Resonance A*, 122, 90-93
[11] Tallarek, U., Albert, K., Bayer E., Guiochon, G., (1996). Measurement of transverse and axial apparent dispersion coefficients in packed beds, *AIChE Journal*, 42, 3041-3054
[12] Seymour, J.D., Callaghan, P.T., (1997). Generalized approach to NMR analysis of flow and dispersion in porous media, *AIChE Journal*, 43, 2096-2111
[13] Tallarek, U., Dusschooten, D.v., As, H.v., Bayer, E., Guichon, G., (1998). Study of transport phenomena in chromatographic columns by pulsed field gradient NMR, *Journal of Physical Chemistry B* 102, 3486-3497
[14] Manz, B., Alexander, P., Gladden, L.F., (1999). Correlations between dispersion and structure in porous media probed by nuclear magnetic resonance, *Physics of Fluids*, 11, 259-267
[15] Kandhai, D., Hlushkou, D., Hoekstra, A.G., Sloot, P.M.A., Van As, H., Tallarek, U., (2002). Influence of Stagnant Zones on Transient and Asymptotic Dispersion in Macroscopically Homogeneous Porous Media, *Physical Review Letters*, 88, 234501
[16] Scheven, U.M., Sen, P.N., (2002). Spatial and temporal coarse graining for dispersion in randomly packed spheres, *Physical Review Letters*, 89, 254501
[17] Stapf, S., (2002). NMR investigations of correlations between longitudinal and transverse displacements in flow through random structured media, *Chemical Physics*, 284, 369-388
[18] Khrapitchev, A.A., Callaghan, P.T., (2003). Reversible and irreversible dispersion in a porous medium. *Physics of Fluids*, 15, 2649-2660
[19] Scheven, U.M., Seland J.G., Cory, D.G., (2004). NMR propagator measurements on flow through a random pack of porous glass beads and how they are affected by dispersion, relaxation, and internal field inhomogeneities, *Physical Review E*, 69, 021201
[20] Scheven, U.M., Verganelakis, D., Harris, , Johns, M.L., Gladden, L.F., (2005). Quantitative nuclear magnetic resonance measurements of preasymptotic dispersion in flow through porous media, *Physics of Fluids*, 17, 117107
[21] Holland, D.J., Scheven, U.M., Middelberg, A.P.J., Gladden, L.F., (2006). Quantifying transport within a porous medium over a hierarchy of length scales, *Physics of Fluids*, 18, 033102
[22] Scheven, U.M., Harris, R., Johns, M.L., (2007). Intrinsic dispersivity of randomly packed monodisperse spheres, *Physical Review Letters*, 99, 054502
[23] Cotts, R.M., Hoch, M.J.R., Sun, T; Markert, J.T., (1989). Pulsed field gradient stimulated echo methods for improved NMR diffusion measurements in heterogeneous systems, *Journal of Magnetic Resonance*, 83, 252-266
[24] Kubo, R., Toda, M., Hashitsume, N., (1991) *Statistical Physics II: Nonequilibrium Statistical Mechanics*, 2nd edition, Springer Verlag, New York
[25] Maier, R.S., Kroll, D.M., Bernard, R.S., Howington, S.E., Peters, J.F, Davis, H.T., (2000). *Physics of Fluids*, 12, 2065-2079

Proceedings of the 10th International Chemical and
Biological Engineering Conference - CHEMPOR 2008
Braga, Portugal, September 4-6, 2008
E.C. Ferreira and M. Mota (Eds.)

Operating the segregated flows of particulate materials as a principle of technological process organization

Dolginun V.N.*, Ivanov O.O., Klimov A.M. and Ukolov Al-dr. A.
Department of Technological Equipment and Food Technology,
Tambov State Technical University,
106 Sovetskaya str., 392000, Tambov, Russia

Keywords: particulate solids, mixing, separation, segregated flows, operation, modeling.
Topic: Advancing the chemical engineering fundamentals (Particulate systems)

Introduction

The treatment of the nonuniform particulate solids mixtures with high inclination to segregation is a widespread technological problem. First of all, this problem is the consequence of the necessity to provide the distribution homogeneity of particles differing in size or density in the apparatus working volume. The ignorance of this condition leads to the different residence time of nonuniform particles in the apparatus working volume and reduces the product quality.

On the other hand, the high segregating components make difficult their mixture production and place exacting technological standards upon the mixing equipment. In consequence of high nonuniformity of the mixture particles their segregated flows arise. These flows are situated in dominate areas of the working volume and differ from each other by structural and kinematical characteristics. Traditionally these flows are destructed by means of several special methods.

In the present paper the principle of operating segregated flows is suggested in order to solve the technological problems during the treatment of nonuniform particulate solids. The basic advantage of this principle consists in its realization possibility for many technological applications. These applications may be as follows:

a) differentiation of technological conditions for different particles by means of operation of their residence time in the apparatus working volume;
b) increasing the mixture quality of particulate solids inclined to segregation due to the intensification of longitudinal and transversal mixing segregated flows;
c) separation process organization of traditionally hard separated mixtures by means of intensification of segregated flows of mixtures.

In the present paper a version of practical realization of the above mentioned principle is discussed.

A version of segregated flow operation in apparatus with rotating drum.

The segregated flows especially occur in the course of granular materials treatment when there are steady or cyclic repeated shear flows in apparatus working volumes. That is why the segregated flows are revealed brightly during particulate solids treatment in apparatus having rotating drums. It is well known [1] that the segregated flows formation in a rotating bed of granular materials is very active. The rotating bed process takes place in a rotating drum which has not any nozzles in its working volume.

However our investigation has shown that there are significant segregated flows not only in a nozzleless drum but also in drums provided with peripheral lifting blades (Fig.1.) It is explained by necessity to provide the conditions of blade filling for all the drum length.

* Corresponding author. E-mail: ioo_c4@rambler.ru

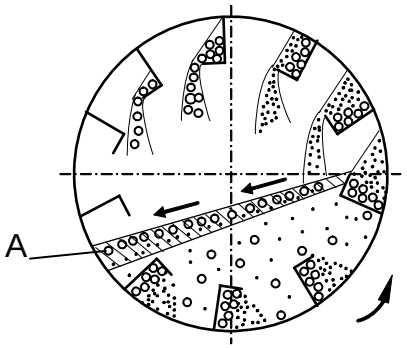

Fig.1. Schematic of segregated flow formation in a cross section of a rotating drum apparatus with peripheral blades: A – is the area of segregated flows formation

In order to carry out this condition it is necessary that the material heap in the lower drum part must be sufficiently big. Then it is evidently that the heap height must be grater than the blade height. In this case a shear gravity flow of particles arises near the free surface of the heap. Because of that the segregated flows of granular materials take place in the upper part of the heap. These flows are characterized by the movement of big or light particles over small or dense ones.

Since the blades are filled at the contact with the above mentioned segregated flow (Fig.1) then initially the blade takes big or light particles from the free surface of the heap. The further filling the blade is fulfilled by small or dense particles from segregated flow depth.

On the other hand as it is shown on Fig.1 when the blade rises from the heap initially small and dense particles are falling from the blade. When the blade goes down towards the heap big and light particles are falling from the blade.

Thus the effect of segregated flows arising in the drum heap is extended to the bed of falling particles in the cross drum section. Taking into consideration that the apparatus with rotating drums widespread are used for heat and mass transfer as well as for hydromechanical process organization we developed a realization version of the principle of operating the segregated flows of granular materials on the basis of the above discussed physical effect.

This version uses the traditional construction of apparatus which consists of horizontal rotating drum with peripheral lifting blades. Basing on the investigation results in terms of segregated flows in the apparatus of the traditional construction we suggested a device allowing the operation by named flows.

The device operating the segregated flows realize the principle of the multistage counter current flows of nonuniform particles [2] and additionally provides the possibility to change their value and direction along and across of the drum axis. The addition of the traditional apparatus by the suggested device allows to set the different treatment time for particles differing in size and density. If the main technological aim is the qualitative mixture production then the residence time of nonuniform components is equalized and longitudinal and transversal mixing segregated flows is organized in the working volume.

Moreover this equipment may be used for separation of particles differing in size and density. In this case the longitudinal countercurrent flows of segregated particles are intensified in the apparatus.

Experimental and analytical research on the efficiency and dynamic characteristics of a multifunctional apparatus

The paper presents the results of experimental and analytical investigations of technological efficiency and dynamic characteristics for multifunctional apparatus at various versions of its technological application.

The basic application versions are the periodic and continuously working mixers also the separator for hard separated materials. Thereby it is noteworthy, that the apparatus construction is rather suitable simultaneously to organize heat-mass transfer processes, because of existence of the falling particles bed in the apparatus working volume.

The experiments on the mixing and separation carried out with the use of hard mixed and hard separated materials respectively. In order to prepare these materials we have used glass beads and polyethylene granules differing in size and density (see Table 1). The particle sizes were choused to complicate the mixing and separation processes.

Table 1 Characteristics of modeling particulate mixtures

Process	Mixture materials	Fraction size $d \cdot 10^{-3}$, m; and its concentration, kg kg^{-1}	Density ρ, kg·m^{-3}
Separation	glass beads	+3,0–3,5; 0,7	2500
	polyethylene granules	+2,5–4,0; 0,3	920
Mixing (periodic)	glass beads	+3,0–3,5; 0,7	2500
	polyethylene granules	+4,0–5,0; 0,3	920
Mixing (continuous)	glass beads	+2,5–3,5; 0,6	2500
	polyethylene granules	+4,0–5,0; 0,4	920

In order to forecast the effect of the segregated flow operation an analytical approach is developed in the paper. This approach is based on an adaptation of the general mass transfer equation for conditions of segregating particulate media.

The dynamics of test component distribution along the drum length *z* is described in the following way

$$S(z)\cdot\frac{\partial(\rho_b\cdot c(z,\tau))}{\partial\tau}=-\frac{\partial(c(z,\tau)\cdot G(z))}{\partial z}+ \\ +D_{dif}\cdot\frac{\partial}{\partial z}\left(S(z)\cdot\rho_b\cdot\frac{\partial c(z,\tau)}{\partial z}\right)+I_l\cdot c_0+S(z)\cdot\rho_b\cdot\left(I_v^+ + I_v^-\right) \quad (1)$$

where *G(z)* is the mixture flux in the drum heap along the drum length, *kg·s*$^{-1}$; $I_v^-(z)=\omega\cdot n\cdot F\cdot c(\tau,z)/(2\pi S(z))$ is the function, describing the exhausting action of the lifting blades; $I_v^+(z)$ is the function modeling the effect of operation of the segregated flows in the falling bed of particles in the drum.

Equation (1) was integrated numerically at the boundary conditions

$$\left.\frac{\partial c}{\partial z}\right|_{z=0,L}=0$$

and initial conditions:

$c(z,0)=c_0$ for separation process,

$c(z,0)=\begin{cases}1, & 0<z<0.42L\\ 0, & 0.42L<z<L\end{cases}$ for periodic mixing process.

The mixture non homogeneity was estimated by means of the variation coefficient determination. This coefficient is calculated as the ration of the standard concentration deviation of the test component to its mean concentration in the mixture expressed as the percentage.

The investigation results for different technological application versions of apparatus are presented on Figs. 2-5. Thereat Figs. 2 and 4 show the mixing and separation dynamics respectively, as the comparison of experimental and calculated data. The authors explain particularly the observed deviation of these data from each other by technical difficulties arising during mixture concentration measuring along the drum length for high segregating materials.

The investigation results reveal that the suggested apparatus is rather effective especially when it is important to process the high segregating materials without sieves and separating gas-liquid flows.

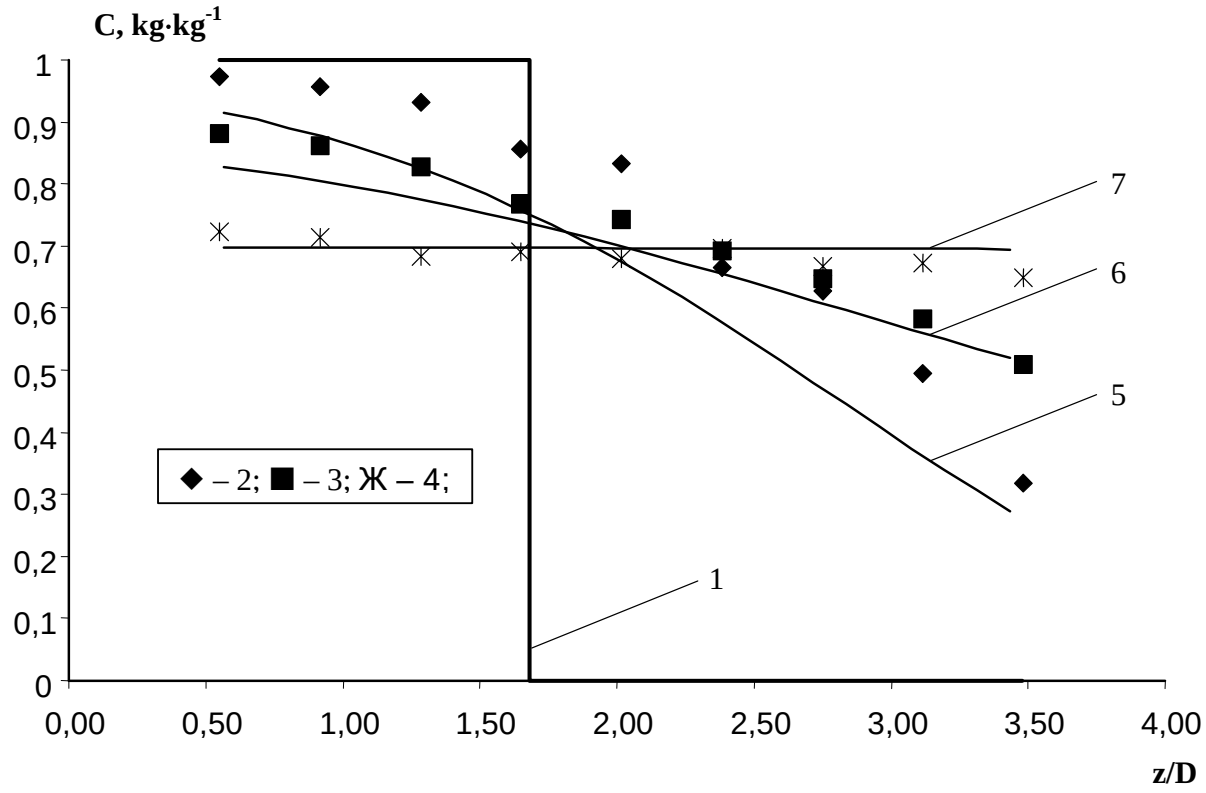

Fig. 2. Experimental dynamics of the test component distribution along the apparatus length z/D in the course of the periodic mixture preparing: 1 – 0 s., 2, 5 – 24 s., 3, 6 – 72 s., 4, 7 – 360 s. (1, 2, 3, 4–experimental, 1, 5, 6, 7– calculated)

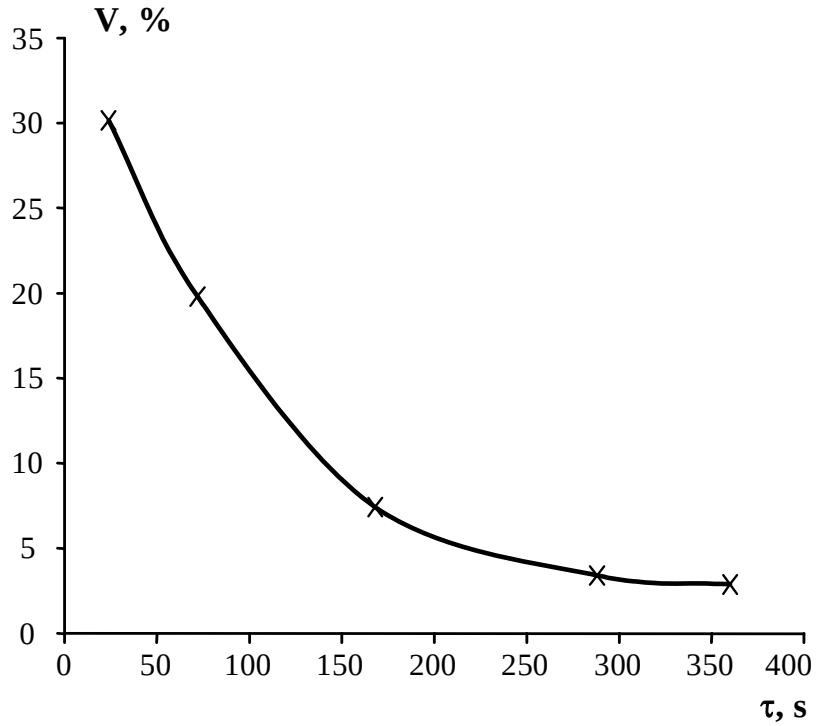

Fig. 3. Variation coefficient evaluation (experimental) in the course of the periodic mixture preparing high segregating particles.

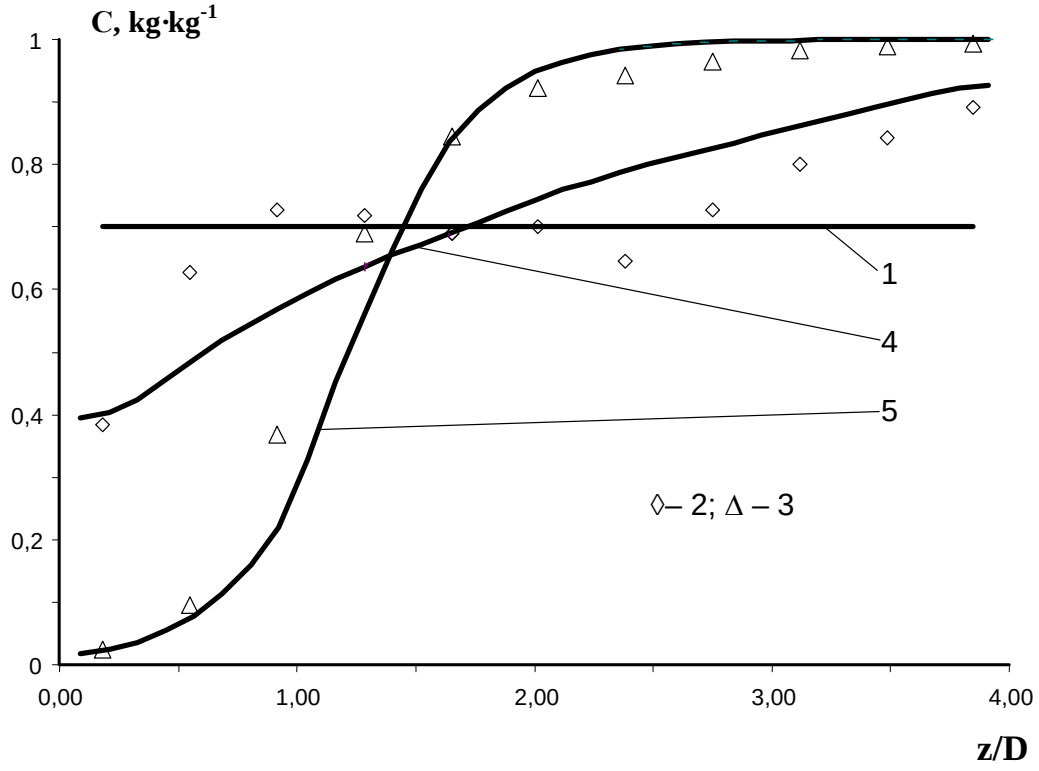

Fig. 4. Dynamics of concentration distribution along the drum length z/D during continuous granular mixture separation (Table 1) at the initial condition: 1– 0 s, 2, 4–24 s, 3, 5– 360 s. (2, 3 –experimental; 1, 4, 5–calculated)

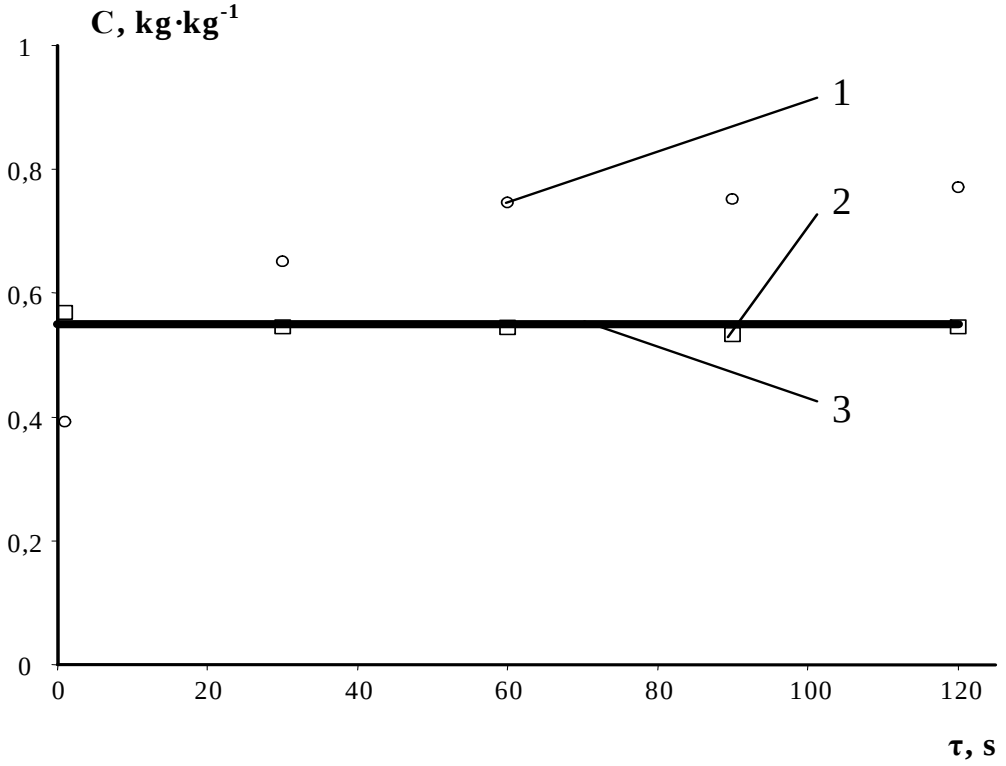

Fig. 5. Dynamic of the product concentration evaluation (experimental) in the course of the continuous mixture preparing: 1 – without operating segregated flows; 2 – with operating segregated flows; 3 – is the mixture concentration (nominal).

Conclusions

The principle of operation of segregated flows is suggested in order to solve the technological problems during the treatment of nonuniform particulate solids. The basic advantage of this principle consists in its realization possibility for many technological applications. These application versions are determined as follows:

a) differentiation of technological conditions for different particles by means of operation of their residence time in the apparatus working volume;
b) increasing the mixture quality of particulate solids inclined to segregation due to the intensification of longitudinal and transversal mixing segregated flows;
c) separation process organization of traditionally hard separated mixtures by means of intensification of segregated flows of mixtures.

Variant of practical realization of the above mentioned principle on the bases of a rotary apparatus, having rotating drum with peripheral lifting blades is suggested.

The results of experimental and analytical investigations of technological efficiency and dynamic characteristics for multifunctional apparatus at its basic application versions are presented. These basic versions are the periodic and continuously working mixers also the separator for hard separated.

In order to forecast the effect of the segregated flows operation an analytical approach is developed.

The investigation results reveal that the suggested apparatus is rather effective especially when it is important to process the high segregating materials without sieves and separating gas-liquid flows.

List of symbols

c – test component concentration, $kg \cdot kg^{-1}$

c_0 – nominal mixture concentration, $kg \cdot kg^{-1}$

D – drum diameter, m

D_{dif} – quasi-diffusion coefficient, $m^2 s^{-1}$

F – cross section area of a heap on a blade, m^2

$I_l(z)$ – function of the test component distribution in the charging part of apparatus, $kg \cdot s^{-1} m^{-1}$

L – drum length, m

n – lifting blade number

$S(z)$ – cross section area of a heap in the drum, m^2

z – longitudinal coordinate, m

Greek letters

ρ_b – bulk density, $kg \cdot m^{-3}$

τ – time, s

ω – angular velocity, s^{-1}

References

1. Bates, L. (1997). User Guide to Segregation. British Materials Handling Board, Elsinore house, United Kingdom.
2. Dolgunin, V.N., Kudy, A.N., Ivanov, O.O., Klimov, A.M. (2007). Gravity separation technology of grain materials differ in complex of physical and mechanical properties of particles. *European Congress of Chemical Engineering – 6*, Book of abstracts, Volume 2, 233–234, Copenhagen, Denmark.

Proceedings of the 10th International Chemical and
Biological Engineering Conference - CHEMPOR 2008
Braga, Portugal, September 4-6, 2008
E.C. Ferreira and M. Mota (Eds.)

Hindered Motion in Highly Porous Media: Steric and Fractal Approaches

Manuel Mota*, Alexander Yelshin
IBB – Institute for Biotechnology and Bioengineering, Centre of Biological Engineering, University of Minho, Campus de Gualtar, 4710–057 Braga, Portugal.

Keywords: Hindered diffusion, Porous media, Fractal, Simulation
Topic: Advancing the chemical and biological engineering fundamentals.

Abstract

Two-dimensional simulation of porous media using a pore fractal dimension D was performed. Obtained results can be outlined as follows: 1). Starting from large pores with aspect ratio of micro-particle size to pore size λ > 0.001, molecules (or test object) recognise the pore volume as a partially restricted space with reduced fractal dimension. 2). The restriction effect on a molecule depends on pore topology (in the present case on the type of packing). 3). Dramatic reduction of D is observed when λ overcomes 0.01 and approaches λ ~ 0.1 in a 2-D approach, meaning that the test object recognises the pore as one dimensional rather than a 2-D space; in turn, a 3-D system will be recognised by the the test object as a 2-D system. 4). Concerning the hydrodynamic chromatography (HDC) the simulation explains why micro-objects become significantly retarded even at λ ~ 0.01, that is, even when the ratio between the Stokes-Einstein diameter of the diffusing micro-object to the equivalent pore diameter is very small. The developed approach confirms that even for micro-object with a very simple geometry (a square test box) a molecule might be much more sensitive to pore topology than what could be expected by a steric effect. It is possible to expect a more pronounced effect for asymmetric micro-objects in tortuous channels. These results show that the problem of molecular sensitivity towards pore topology may be understood using fractal analysis. Further work will apply this fractal approach to diffusivity behaviour in gel-like and fibre-like or foam structures.

1. Introduction

The quest for higher resolution in macromolecules bio-separation, nano-particles, viruses and micro-organisms, together with the requirement to keep their full bioactivity by preserving their shape and conformation is calling for new approaches in the bio-separation field. A hydrodynamic theory developed for the diffusion and convection of micro-objects in porous media for the case of hindered motion was presented in a previous work of Mota et al. (2006) and can be briefly summarised as follows.

The pore topology plays an important role in the separation of micro-particles of different shapes when the aspect ratio (micro-particle size)/(pore size) approaches λ = 0.1. The complexity of the observed retardation phenomenon needs further investigation to clarify the interaction particle-pore topology mechanism. The obtained results may open interesting applications for bio-separation, for deep bed filtration, and to understand the motion of micro-objects (for instance viruses and nano-particles) in porous media.

2. Hindered diffusion

The effective diffusion coefficient D_e of a solute in a channel is composed of two correction functions, $F_1(\lambda)$ and $F_2(\lambda)$: $D_e = D_0 F_1(\lambda) F_2(\lambda)$, where D_0 is the bulk diffusion coefficient and λ is the ratio of Stokes-Einstein diameter of the diffusing

* Corresponding author. Tel + 351-25360-1191. E-mail: mmota@reitoria.uminho.pt

micro-object d_m to the equivalent pore diameter d_{por}, $\lambda = d_m / d_{por}$. The parameter $F_1(\lambda)$ is the steric partition coefficient, which is defined as the cross-sectional area of the pore available to the solute molecule divided by the total cross-sectional area of the pore

$$F_1(\lambda) = (1-\lambda)^2 \tag{1}$$

The correction factor $F_2(\lambda)$ accounts for the effect of the pore wall on the solvent properties (an increase in the local solvent viscosity near the pore wall) and is often represented by a polynomial series, as displayed in equation (2), or by an exponential function, as displayed in (3). Other model functions are particular cases of (2) or (3)

$$D_e / D_0 = (1-\lambda)^2\left[1 - 2.1044\lambda + 2.089\lambda^3 - 0.948\lambda^5\right],\ \lambda \le 0.5 \tag{2}$$

$$D_e / D_0 = (1 - 1.83\lambda + 4.18\lambda^2)\exp(-6.52\lambda) \tag{3}$$

Numerous experimental results show that hindered diffusion and convection depend not only on equivalent micro-object and pore sizes, but on the pore topology as well, (Mota et al., 2006). Havsteen (1993) analysed non-classical flow through narrow-pored membranes and concluded that when the passages through the membrane become small enough in comparison with the size of the percolating molecules, fractal properties of the pore must be accounted for. Giona et al. (1996) admit that the topology complexity of a fractal pore network modifies the scaling properties of diffusion.

Using a 2-D model, when pore size is significantly larger than a molecule, fractal dimension tends to the topological value of 2. When the pore scale gets close to the size of a molecule, the fractal values become close to the topological dimension of unity. For better understanding transport phenomena in porous materials it is interesting to know how a molecule will behave in the porous space geometry between the aforementioned boundaries.

To consolidate the experimental observations, a two-dimension porous media simulation was made with a disc packing.

3. Simulation conditions

Pore area fractal analysis was performed by a test-box counting method

$$\log\left[N(r)\right] = \log(k) - D_{pa}\log(r) \tag{4}$$

where D_{pa} is the porous area fractal dimension; $N(r)$ is the number of boxes of side length r needed to cover a porous medium image. The test-box simulates a compact micro-object inside the pore space formed by discs packing.

The fractal dimension was measured by means of the commercial software *Fractal Vision* 2.5, Oliver (1992). This software was successfully applied to quantify the surface roughness of flocs and granules and gave a quite reasonable estimation of the fractal dimension, as reported by Bellouti et al. (1997). The *Fractal Vision* algorithm allows determining the fractal dimension of an image tested by three types of box size r = 2, 4 and 6 pixels, Oliver (1992). The molecule size in simulation was assumed to be equal to the test box size r.

Image in pixel's representation has rough bounds with a minimal size resolution of 1 pixel. This roughness simulation imitates the rough channel surface. The ratio of roughness scale to the discs size, that builds the porous medium skeleton, will be variable. The ratio increases when disc size decreases. Such behaviour means that, for a fixed molecule size, decreasing the porous medium scale results in a more active role of roughness. This fact does not contradict known reports. For instance, Douglas, (1989) during simulation of fractal surface adsorption observed a great probability of polymer-surface interaction with increasing roughness.

All images of porous media are considered as cross-sections that are perpendicular to the direction of the molecule diffusion and the measured parameter was the fractal dimension of pore area D_{pa}. The following two-dimensional models of porous media have been used: 1) binary and ternary mixtures of different size and fraction of discs; 2) regular uniform disc square and hexagonal packings.

4. Results and discussion

4.1. Binary and ternary packings

Binary and ternary mixtures of different size and fraction content of discs were built by the algorithm described by Mota et al. (1999). The mixture model was used in the cited research for investigation of porous media geometry: porosity, tortuosity, etc. Procedure of the binary porous medium building was based on randomly packing and compacting of discs in order to obtain high-density packing. The ternary mixture model is built by filling the void space of a binary mixture with smaller discs. In simulation the following model of porous media were used: binary packing of discs with disc size ratio (1) : (1.9), (1) : (3.8), and (1) : (15.7); ternary packing, obtained from binary (1) : (1.9) and (1) : (3.8) packings, disc size ratio (1) : (4.5) : (8.6) and (1) : (3.36) : (12.8).

Fractal dimension of pores cross-section area D_{pa} is shown in Fig. 1 for two types of ternary (data sets 1 and 2) and three types of binary (data sets 3 – 5) systems as a function of fraction of large disc (x_D) in the packing. Discs size ratio is shown in Fig. 1 in brackets. Test disc boundary roughness was 1 pixel.

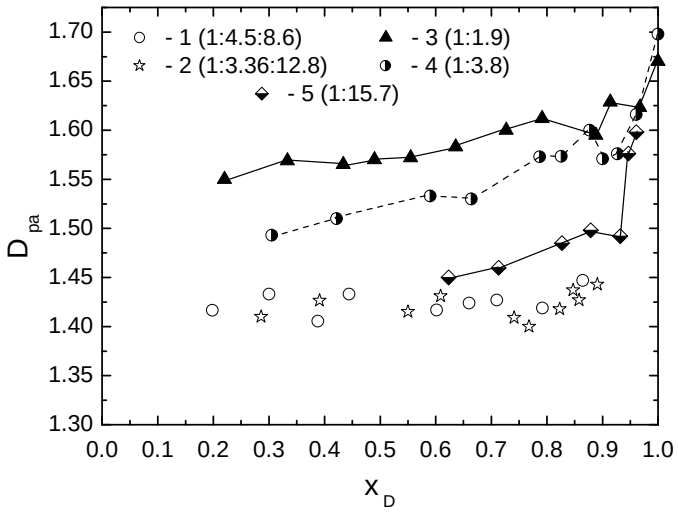

Figure 1. Fractal dimension of the porous area, D_{pa}, vs. fraction of largest discs in the mixture, x_D.

In binary packing, at the same fractional content x_D, increasing discs size ratio significantly reduced the fractal dimension that also depends on the large particle fraction in the mixture, x_D. The most dramatic D_{pa} decrease in mixtures with minimum porosity, occurs for x_D ~ 0.85 – 0.9 (Mota et al., 1999). Ternary mixtures built by filling the appropriate binary mixture free area by smallest discs have lower D_{pa} but are less sensitive to x_D.

For all binary mixtures the fraction of smallest discs which was possible to insert in free space, to get the ternary packing, was less than 10%. This observation leads to the conclusion that even a small amount of fine particles present in the binary packing can significantly affect on macromolecule diffusion because of the change in pores network topology.

Decreasing D_{pa} in binary packings for x_D below 0.8 is related with pore size

distribution when smallest pores have greater impact of the fractal dimension (Mota et al., 2004).

Concerning application to hydrodynamic (HDC) and slalom chromatography, we may assume that the process resolution may be improved by transition from monosize to the binary packing, at the same time saving the number of small size particles, usually more expensive. Binary packing is a well controlled system and the molecule's sensitivity can be controlled by particle fraction content and size ratio.

4.2. Fractality and diffusivity (fractal and steric approach)

To evaluate fractal and diffusive behaviour of porous media regular uniform square and hexagonal disc packings were investigated. The measured parameter was D_{pa} at different disc size versus the aspect ratio r/d_{por}: the ratio between the test-box size (r) and the equivalent pore size was determined based on disc size.

To compare the measured 2-D fractal dimension and 3-D diffusivity D_e/D_0 models (1-3), a re-normalisation procedure was performed based on the assumption that the equivalent pore diameter is $d_{por} = (2/3)[\varepsilon/(1-\varepsilon)]d$, where d is the sphere diameter; ε is the sphere packing porosity, ε = 0.476 for cube packing and 0.26 for hexagonal packing. Hence, the equivalent pore diameter is for cube packing $d_{por} \approx 0.6d$ and for hexagonal packing $d_{por} \approx 0.234d$, consequently, for other packing structures $d_{por} \approx a \cdot d$, a < 1, where d is the diameter of sphere equal to the diameter of disc. Finally, normalised pore size becomes $\lambda = d_m/d_{por} \sim r/d_{por} = r/(a \cdot d)$. Obtained results are shown in Figure 2.

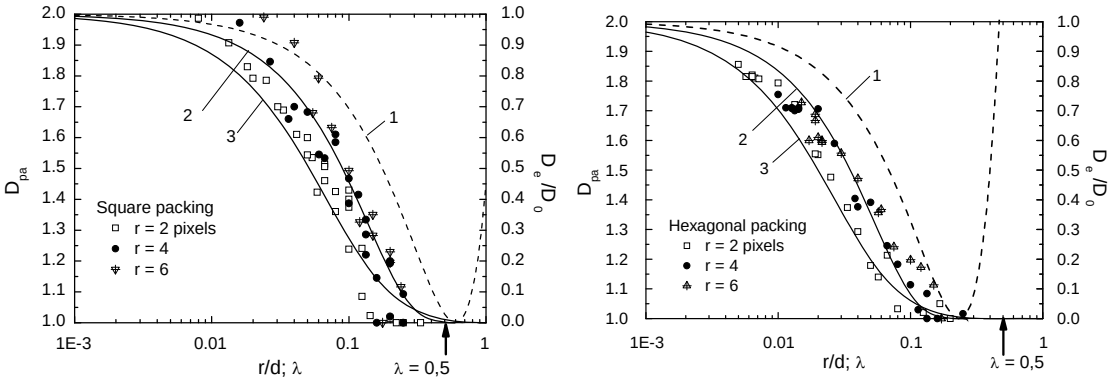

Figure 2. Dependence of D_{pa} on r/d and diffusivity D_e/D_0 on λ for square packing (a) and hexagonal packing (b) of uniform discs. 1 – Equation (1); 2 – Equation (2); and 3 – Equation (3).

The most important simulation result is the following: the range of molecule's "sensitivity" to the pore network cross-section area coincides to the hindered diffusion range. The main measured values of D_{pa} occupy an area between curve 1, equation (1) for steric partition coefficient, (cylindrical pore and spherical molecule) and curve 3, equation (3) for hindered diffusion of a macromolecule, whereas Renkin equation (2) is close to the scattering zone of the determined fractal dimension.

Concerning three dimension porous media, obtained results can be treated as follows: 1). Starting from large pores with λ > 0.001, molecules recognise the pore volume as a partially restricted space with reduced fractal dimension. 2). The restriction effect on a molecule depends on the pore topology (in present case on the type of packing). 3). Dramatic reduction of D_{pa} is observed when λ overcomes values around 0.01 and

approaches λ ~ 0.1 in 2-D approach meaning that the test object recognises the pore as one dimensional rather than a 2-D space; in a 3-D system the test object will recognise the pore with a behaviour closer to a 2-D system. 4). Concerning the hydrodynamic chromatography (Mota et al., 2006) the simulation explains why micro-objects become significantly retarded even at λ ~ 0.01, that is, even when the ratio between the Stokes-Einstein diameter of the diffusing micro-object d_s to the equivalent pore diameter is very low.

The developed approach confirms the fact that even for simple micro-object geometry (= test box) a molecule might be much more sensitive to pore topology than the predicted by the steric effect. It is possible to expect an even more pronounced effect for asymmetric micro-objects in tortuous channels, for example, branched and long macromolecules.

These results show that the problem of molecular sensitivity to pore topology may be satisfactorily solved using fractal analysis. Further work will apply this kind of approach to molecular diffusion inside gel-like, fibre-like or foam structures.

4.3. Molecule – pore size scale estimation

Based on fractal analysis let us estimate the pore diameter and disc (particle) size of uniform hexagonal packing model and the Tyn and Gusek (1990) list of protein sizes, assuming also that the test molecular size is equal to the protein size.

Calculations will be made 1) for hexagonal uniform sphere packing at two cases, namely, when test object recognises pore cross-section area with two fractal dimensions D_{pa} = 1.5 and 1.77.

Noting that $\lambda = r/(a \cdot d)$, for a hexagonal uniform sphere packing when D_{pa} ~ 1.5, the ratio $r/(0.234d)$ is around 0.03, and for D_{pa} ~ 1.3, $r/(0.234d)$ ~ 0.059, therefore, $d = r/(0.234\lambda)$. Assuming that twice the molecular gyration radius r_g is equal to the test box size ($r = 2r_g$), for the above defined D_{pa} we have the particle diameter $d = 2r_g/0.03/0.234$ or $d = 2r_g/0.059/0.234$. Obtained results are given in Table 1.

Table 1

Estimated packing particle size d for hexagonal uniform sphere packing recognised by test-box molecule as fractal medium with fractal dimension D_{pa} = 1.3 and 1.5.

Protein	Molecular weight	r_g, nm	D_{pa} = 1.5		D_{pa} = 1.3	
			d, μm	d_{por}, μm	d, μm	d_{por}, μm
Myoglobin	17,500	1.63	0.46	0.11	0.24	0.055
Ovalbumin	44,000	2.03	0.56	0.14	0.29	0.069
Catalase	225,000	3.98	1.13	0.27	0.58	0.13
Fibrinogen	340,000	14.2	4.05	0.95	2.06	0.48
Collagen	345,000	87.0	24.8	5.8	12.6	2.95
Myosin	493,000	46.8	13.3	3.12	6.78	1.59
DNA	4,000,000	117.0	33.3	7.8	16.9	3.97

Obtained data in Table 1 show that for a spherical particle we may expect a system's molecule-porous medium fractal behaviour in the submicron and micron range close to chromatographic column and micro-column packings for macromolecules such as fibrinogen. Moreover, the obtained particle size falls in the range of HDC and slalom chromatography modes (Hirabayashi and Kasai, 1996). Nevertheless, for proteins such as myoglobin, or ovalbumin, the determined particle/pore size is smaller and locates in nano-scale where data on chromatography are still scarce.

The carried out analysis considers the molecule as a square (2-D), but real

macromolecules are shaped, therefore, such type of macromolecules would be sensitive to pore topology even for r/d_{por} << 0.01 if the pore channel is rough and tortuous.

The drawback to porous media model analysis by the rectangular test box (molecule) is that such approach cannot be considered as a pure fractal analysis because of spatial scales dependence. Nevertheless, it seems interesting to get some “pseudo-fractal” dimension measurements for investigation of linear macromolecule interaction with porous media channel topology.

5. Conclusion

Images of 2-D porous media cross-section area generated on the simplest level of rough disc were analysed by test count method. The range of molecule’s sensitivity to the pore network cross-section area includes the range where hindered diffusion is observed. Renkin equation for hindered diffusivity is close to centreline of fractal dimension measured values.

The results confirm the idea that hindered diffusion effect may be described in fractality terms when pore wall is rough. It is possible to expect a more pronounced effect for asymmetric macromolecules in tortuous channel which can be subject of further investigation.

It was shown that hindered diffusion might be partially described in fractal dimension terms for porous media. Estimation based on bio-molecules size shows that the calculated by D_{pa} particle size is in the submicron and micron ranges close to chromatographic column packings.

It can be concluded that the problem of molecule sensitivity to the pore topology may be satisfactorily solved using fractal features but future work must validate obtained results. Other important point is to study the molecule sensitivity to roughness and tortuosity of pore channels. The present results can contribute theoretically and practically to the development of the hydrodynamic separation methodology and to determine the effective range of HDC method.

References

Mota, M., Teixeira, J., Yelshin, A., Cortez, S. (2006). Utilisation of controlled pore topology for the separation of bioparticles in a mixed-glass beads column. *Journal of Chromatography B*. 843, 63–72.

Havsteen, B. H. (1993). Anomalous filtration, *Advances in colloid and interface science*. 45, Elsevier: Amsterdam, 79-213.

Giona, M., Schwalm, W. A., Schwalm, M. K., Adrover, A. (1996). Exact solution of linear transport equation in fractal media - Part. I. Renormalization analysis and general theory. *Chem. Eng. Sci.* 51, 4717-4729.

Oliver, D. (1992) *Fractal Vision: Put Fractals to Work for You*, SAMS Publishing: USA.

Bellouti, M., Alves, M.M., Novais, J.M., Mota, M. (1997). Flocs vs granules: differentiation by fractal dimension. *Wat. Res.* 31, 1227-1231.

Douglas, J.F. (1989). How does surface roughness affect polymer-surface interaction? *Macromolecules*. 22, 3707-3716.

Mota, M., Teixeira, J.A., Yelshin, A. (1999). Image analysis of packed beds of spherical particles of different sizes. *Sep. Purific. Technol*. 15, 59-68.

Mota, M., Teixeira, J.A., Dias, R., Yelshin, A. (2004). Effect of real particles packing with large size ratio on porosity and tortuosity of filter bed. *Proceedings of 9th World Filtration Congress, April 18 - 22, 2004, New Orleans, Louisiana, USA*, AFS: New Orleans, Louisiana, USA, 1-30.

Tyn, M.T., Gusek, T.W. (1990). Prediction of diffusion coefficients of proteins. *Biotech. Bioeng.* 35, 327-337.

Hirabayashi, J.,Kasai, K. (1996). Applied slalom chromatography improved DNA separation by the use of columns developed for reversed-phase chromatography. *Journal of Chromatography A*. 722, 135-142.

Proceedings of the 10th International Chemical and
Biological Engineering Conference - CHEMPOR 2008
Braga, Portugal, September 4-6, 2008
E.C. Ferreira and M. Mota (Eds.)

Maxwell-Stefan based model for ion exchange in microporous materials

Patrícia F. Lito, Carlos M. Silva[1]
University of Aveiro, Department of Chemistry, CICECO, 3810-193 Aveiro, Portugal

Keywords: Ion Exchange, Titanosilicates, Maxwell-Stefan Equations, Nernst-Planck Equations
Topic: Advancing the chemical and biological engineering fundamentals.

Abstract

The aim of this work is to describe a batch ion exchange process with microporous zeolites using a model based on the generalized Maxwell-Stefan equations and to establish a comparison with the results obtained using the Nernst-Plank equations. Model capability to represent and predict experimental data is analyzed using data available in literature concerning batch experiments on mercury (II) removal from aqueous solution using ETS-4 microporous titanosilicate. Results reveal both models provide good and similar representations as well as fine predictive capability. Therefore, under the particular conditions investigated here, both models can be successfully applied to describe intraparticle ionic transport.

1. Introduction

The use of microporous zeolites as decontaminating agents has gaining considerably attention, mainly due to their interesting adsorption properties and ion exchange capability (Rocha and Anderson, 2000).

Beyond experimental measurements, modelling and simulation are unquestionably valuable tools to study and design a chemical plant. It is fundamental to be able to predict the dynamic behavior of any unit, optimize their operating conditions, and scale up from laboratory to large scale. The objective of this work is to present a theoretical model comprising external and intraparticle mass transport resistances to describe and predict the concentration profiles of a batch ion exchange process in a microporous solid.

Mass transport in dilute ionic systems can be described by the Nernst-Planck (NP) equations (Helfferich, 1995; Rodrigues et al. 1998). In an electrolyte solution, the electrical field induced by the different mobility of counter ions produces an additional force responsible for transference of ions; NP Equations accounts for both concentration and electric potential gradients. However, in this approach the interdiffusion coefficients of counter ions are composition-dependent and the ionic interactions are lumped into effective diffusivities, Furthermore, NP Equations do not take non-ideality effects into account. An alternative approach concerns the application of the Maxwell-Stefan (MS) equations. In the MS based model presented here, the exchanger solid pellets are considered to be pseudo component in the ionic mixture, in a way similar to the Dusty Gas Model approach (Jackson, 1977), and both ion-ion and ion-solid interactions are considered and distinguished (Graham and Dranoff, 1982a,b; Wesselingh et al., 1995). In this treatment one diffusivity coefficient is defined for each pair of components, being dependent on their properties only. In addition, surface diffusion of adsorbed species is taken as the transport mechanism occurring in zeolite micropores, since ions never escape from the force field of the matrix co-ions, due to their small diameters.

[1] Corresponding author. Tel +351 234 401549. E-mail: carlos.manuel@ua.pt

In this work a batch ion exchange process in a microporous material is described using a model based on the generalized MS equations. Model capability to represent and predict experimental data is analyzed using data available in literature concerning batch experiments on mercury (II) removal from aqueous solution using ETS-4 microporous titanosilicate. Model results are compared with results obtained using the NP equations.

2. Modelling

The models presented here to describe batch ion exchange were derived assuming the following hypothesis: i) there exist film and intraparticle mass transfer resistances; ii) spherical solid particles; iii) perfectly stirred tank; iv) isothermal and isobaric operation; v) liquid and solid volume changes are neglected; (vi) co-ions are excluded from the zeolite particles (Donnan exclusion); (vii) effect of competitive ions (e.g. H^+) is neglected and (viii) ideal solution.

Maxwell-Stefan Equations. Intraparticle resistance to ion exchange in microporous materials can be described by the generalised MS equations (Krishna and Wesselingh, 1997):

$$-\nabla\mu_i - Fz_i\nabla\phi = \sum_{j=1}^{N}\frac{y_j\Re T(u_i-u_j)}{Đ_{ij}} \tag{1}$$

where $\nabla\mu_i$ is the surface chemical potential gradient of i, F is the Faraday constant, z_i is the charge of component i, $\nabla\phi$ is the electrostatic potential gradient, $Đ_{ij}$ is the MS surface diffusivity of pair i - j, u_i and u_j are the velocities of i and j, $\Re$ is the gas constant, and T is the absolute temperature. The derivation of our MS based model has been presented elsewhere (Silva and Lito, 2007), and considers the following assumptions: i) Surface diffusion is the unique transport mechanism, since due to the very small pore diameters ions never escape from the force field of the matrix co-ions; ii) The solid matrix is considered to be a uniform distribution of fixed charges corresponding to the $(N+1)^{th}$ component. Therefore, $u_{N+1}=0$, as in the well known Dusty Gas Model (Jackson, 1977). Besides, conditions of electroneutrality and nonexistent electric current are assumed:

$$\sum_i q_i z_i = 0 \qquad \text{and} \qquad \sum_i z_i N_i = 0, \qquad i = 1,...,N+1 \tag{2}$$

where q_i is molar concentration of i and N_i is its molar flux. The resulting multicomponent Maxwell-Stefan equations are, in matrix notation:

$$(N) = -q_t[B]^{-1}(\nabla y) - q_t[B]^{-1}(z.y)\varphi \tag{3}$$

where

$$y_i = \frac{q_i}{q_t},\ q_t = \sum_{1=1}^{N+1} q_i,\ B_{ii} = \frac{y_s}{Đ_{is}} + \sum_{\substack{j=1\\ j\neq i}}^{N}\frac{y_j}{Đ_{ij}},\ B_{ij} = -\frac{y_i}{Đ_{ij}},\ \varphi = \frac{-\sum_{i=1}^{N} z_i\left(\sum_{j=1}^{N} L_{ij}\nabla y_j\right)}{\sum_{i=1}^{n} y_i z_i\left(\sum_{i=1}^{n} z_j L_{ji}\right)},\ [L] = [B]^{-1} \tag{4}$$

Nernst-Plank Equations. In dilute ionic solutions, intraparticle flux of each counter ion can be described by the Nernst-Planck equations (Helfferich, 1995):

$$J_i = -D_i\nabla q_i - D_i z_i q_i\frac{F}{RT}\nabla\phi \tag{5}$$

where D_i is the self-diffusion coefficient of species i, q_i is the molar concentration of counter ion i in the particle, z_i is the electrochemical valence of i, F is Faraday constant, $\Re$ is gas constant, T is absolute temperature, ϕ is the electrostatic potential and r is the radial position. NP equations presented here are recast as a special form of Fick's first law, in nondimensional form, with concentrations expressed in equivalents:

$$N_i^* = -D_{ij}^*\left(\frac{\partial y_i}{\partial \xi}\right), \text{ with } \quad D_{ij}^* = \frac{\delta\left(z_i y_i + z_j y_j\right)}{z_i y_i + \delta z_j y_j}, \tag{6}$$

Nondimensional variables are defined as follows:

$$\delta = \frac{D_j}{D_i}\ y_i = \frac{z_i q_i}{Q},\ \xi = \frac{r}{R},\ N_i^* = \frac{z_i R}{Q D_i} N_i \tag{7}$$

where Q is the ion exchanger capacity and R is the particle radius. The above equations were developed assuming conditions of electroneutrality and nonexistent electric current.

Material balances, initial and boundary conditions, and equilibrium isotherm. Concerning diffusing components, we deal with counter ions A and B: A is the pollutant we want to remove from solution $\left(\mathrm{Hg}^{2+}\right)$, using an ion exchanger initially in B– form $\left(\mathrm{Na}^{+}\right)$. Therefore, the material balances in the particle and in the reservoir are, respectively:

$$\left(\frac{\partial q_A}{\partial t}\right) = -\frac{1}{r^2}\frac{\partial}{\partial r}\left(r^2 N_A\right) \tag{8}$$

$$\frac{\partial C_A}{\partial t} = -\frac{V_s}{V_L}\frac{\partial \bar{q}_A}{\partial t} \tag{9}$$

where C_A is the concentration of A in bulk solution, and V_s and V_L are the solid and fluid phase volumes, respectively. The average loading per unit particle is given by:

$$\bar{q}_A = \frac{3}{R_p^3}\int_0^R r^2 q_A dr \tag{10}$$

The above differential equations are subjected to the following initial and boundary conditions:

$$t = 0, \qquad \begin{cases} q_A = \bar{q}_A = 0 \\ C_A = C_{A,0} \end{cases} \tag{11}$$

$$r = R, \qquad q_A = q_{A,R} \tag{12}$$

$$r = 0, \qquad \left(\frac{\partial q_A}{\partial r}\right) = 0 \tag{13}$$

The concentration at the interface is determined by the equality of internal and external fluxes, i.e.,

$$N_A A\big|_{r=R} = A k_c\left(C_A - C_{A,R}\right) \tag{14}$$

where k_c is the convective mass transfer coefficient and A is the particle surface area.

In this work, the equilibrium between bulk solution and ion exchanger is represented by the Freundlich equation, given the good equilibrium representation obtained in the experimental conditions studied. Thus

$$q_A = K_F C_A^{1/n} \tag{15}$$

where K_F and n are the Freundlich parameters.

Solution Approach. The simultaneous solution of that set of differential and algebraic equations gives the concentration of counter ions in the fluid, and their concentration profiles in the solid phase as function of position and time. The models have been solved numerically using the Method of Lines (Schiesser, 1991) and integrated by the Finite-Difference approach. For that purpose, two programs in Matlab has been written to solve the resulting Ordinary Differential Equations (ODEs) with finite-difference approach. Ode15s has been used to integrate these set of ODEs of the initial-value type. Maxwell-Stefan diffusivities, self-diffusion coefficients and film mass transfer coefficient were obtained by optimization.

Data Source. The case studied is this work is mercury (II) removal from aqueous solution using ETS-4 microporous titanosilicate. Experimental data and physical properties of ETS-4 may be found elsewhere (Lopes et al., 2007). Experimental conditions are listed in Table 1.

Table 1 – Experimental conditions of data used in calculations (Lopes et al., 2007).

Exp. Conditions	Exp. 1	Exp. 2	Exp. 3
Temperature, K	295 ± 1		
Solution volume, 10^{-3} m^3	2		
Initial Hg^{2+} conc., $10^{-6}\ kg/m^3$	50		
Mass of ETS-4, $10^{-6}\ kg$	1.63	5.06	12.2

3. Results and Discussion

Figure 2 shows experimental data and results obtained with both MS and NP based models, plotted in $C_A(t)/C_{A0}$ *versus* time form. Calculated results, namely MS diffusivities and NP self-diffusion coefficients, the mass transfer coefficients for each model, and average absolute deviations (AAD) found are listed in Table 2. Figure 1 points out the good representations achieved for the experimental data, corresponding to $AAD_{\mathrm{MS}} = 5.37\%$ and $AAD_{\mathrm{NP}} = 5.27\%$; an accurate correlation is accomplished even in the transition from steep descent to the horizontal branch, where kinetic curves are most difficult to fit. Furthermore, the comparison of results shows their similar fitting capability to represent such data.

The diffusion coefficients optimized with both models (Table 2) have the same order of magnitude, i.e., $10^{-20} - 10^{-18}$ m^{2}s^{-1}. These values are consistent with the small pore diameters of ETS-4 (0.3-0.4 nm) and follows others found in literature (Barrer and Rees, 1959; Coker and Rees, 2005). It should be noted, however, that MS and NP diffusivities do not have to be identical because of their distinct intrinsic physical meaning; MS diffusivities characterize the interaction between each pair of species in the mixture, including the solid fixed ionic charges, whereas NP self diffusion coefficients represent the mobility with which counter ions diffuse in the ion exchanger. Moreover, the calculated convective mass transfer coefficients are almost the same (4.748×10^{-3} m.s^{-1} and 4.740×10^{-3} m.s^{-1}, respectively).

The predictive capability of both models may be assessed from Figure 3, where simulations of Exp. 1 and 2 obtained with parameters optimized from Exp.3 alone are graphed. It may be observed that both models perform similarly, as NP and MS predictive curves practically overlap. The $AADs$ of the correlations and predictions are compiled in Table 3, and prove that both models offer good predictions with modest global deviations increments over those corresponding to correlation. With respect to the individual $AADs$, they are equally ordered, i.e. $AAA_3 < AAA_2 < AAA_1$. Furthermore, passing from correlation to prediction both $AADs$ for Exp.2 diminish and both $AADs$ for Exp.1 increase. Nonetheless, Nernst-Planck based model results are still slightly better. Therefore, under the conditions investigated, both approaches can be applied successfully to describe intraparticle ionic transport.

Table 2 – Calculated results with the MS and NP based models of this work.

Maxwell-Stefan				
$Đ_{As}\,[m^2 s^{-1}]$	$Đ_{Bs}\,[m^2 s^{-1}]$	$Đ_{AB}\,[m^2 s^{-1}]$	$k_c\,[m\,s^{-1}]$	AAD [%]
5.027×10^{-18}	1.982×10^{-19}	6.029×10^{-20}	4.748×10^{-3}	5.37
Nernst-Planck				
$D_A\,[m^2 s^{-1}]$	$D_B\,[m^2 s^{-1}]$	$k_c\,[m\,s^{-1}]$	AAD [%]	
1.147×10^{-19}	1.155×10^{-18}	4.740×10^{-3}	5.27	

Table 3 – Analysis of predictive capability of the MS and NP based models of this work.

	Maxwell-Stefan		**Nernst-Planck**	
	Optimization	Prediction	Optimization	Prediction
AAD Exp.1	7.36	7.43	7.04	7.05
AAD Exp.2	5.42	5.40	5.46	5.45
AAD Exp.3	3.46	-	3.44	-
Global AAD	5.37 / 6.42*	6.45	5.27 / 6.28*	6.28

* Global AAD for experiences 1 and 2.

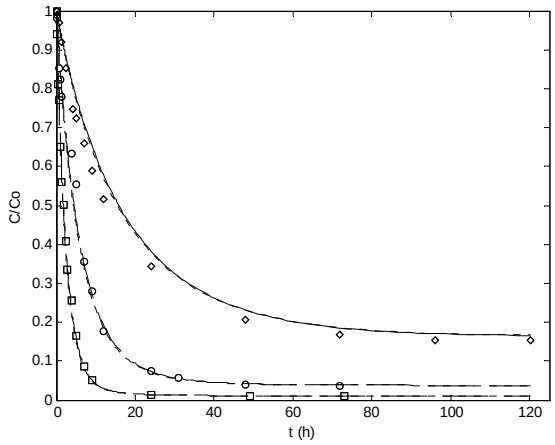

Figure 2 – Normalized concentration of bulk solution *versus* time: modelling and experimental data. Full and dashed lines are representations achieved optimising all data with NP and MS based models, respectively; Symbols: ◊ Exp.1; ○Exp.2 and □ Exp.3 (see Table1).

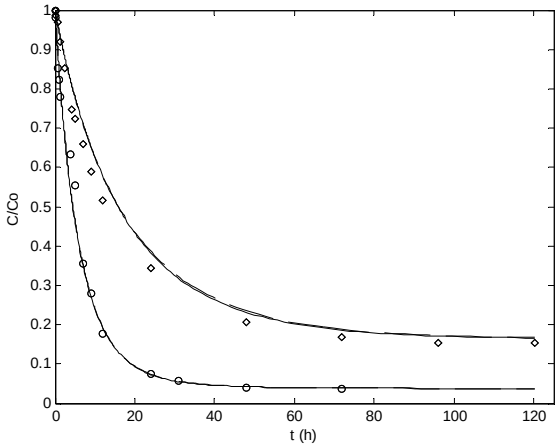

Figure 3 – Prediction ability of MS and NP based models. Full and dashed lines are predictions obtained with parameters independently fitted to the third set of data (not represented here, for simplicity), with NP and MS based models, respectively. Symbols: same as Figure 2.

4. Conclusions

A comparison between MS and NP based models to describe ion exchange in microporous materials has been accomplished, using experimental data from literature. Results reveal both models provide good data representation, as well as exhibit fine predictive capability. The advantageous of the MS description, which arise particularly from taking into account ion-ion and ion-solid interactions, are not highlighted here. Such result can be ascribed to the experimental conditions used, namely dilute ionic solutions and binary exchange. However, it is expected theoretically that these models will behave differently in concentrated solutions and in multicomponent systems; NP equations lump ionic interactions into effective diffusivities and are not able to take non-ideality effects into account. In the whole, under the conditions studied here both models can be successfully applied to describe ion exchange process in microporous crystalline solids.

Acknowledgments

Patrícia F. Lito wishes to express her gratitude to Fundação para a Ciência e Tecnologia (Portugal) for the PhD grant provided (SFRH/BD/25580/2005).

References

Barrer, R.M., Rees, L.V.C., (1959). Self-diffusion of alkali metal ions in analcite. *Transactions of the Faraday Society*, 55, 709-721.

Coker, E.N., Rees, L.V.C., (2005). Kinetics of ion-exchange in quasi-crystalline aluminosilicate zeolite precursors. *Microporous and Mesoporous Materials*, 84, 171-178.

Graham, E.E., Dranoff, J.S., (1982a). Application of the Stefan-Maxwell equations to diffusion in ion exchangers. 1. Theory. *Industrial and Engineering Chemistry Fundamentals*, 21, 360-365.

Graham, E.E., Dranoff, J.S., (1982b). Application of the Stefan-Maxwell equations to diffusion in ion exchangers. 2. Experimental results. *Industrial and Engineering Chemistry Fundamentals*, 21, 365-369.

Helfferich, F. (1995) Ion Exchange. Dover, NY, USA.

Jackson, R., (1977). Transport in Porous Catalysts. Elsevier, Amsterdam, The Netherlands.

Krishna, R., Wesselingh, J.A., (1997). The Maxwell-Stefan approach to mass transfer. *Chemical Engineering Science*,

Lopes, C. B., Otero, M., Lin, Z., Silva, C. M., Pereira, M.E., Rocha, J., Duarte, A., (2008). Mercury removal from aqueous solution using ETS-4 – kinetic and equilibrium study. (submitted)

Rodrígez, J.F., Valverde, J.L., Rodrigues, A.E., (1998). Measurement of effective self-diffusion coefficients in a gel-type cation exchanger by the zero-length-column method. *Industrial and Engineering Chemistry Research*, 37, 2020-2028.

Schiesser, W. E., (1991). The Numerical Method of Lines. Academic Press, USA.

Silva, Carlos M., Lito, Patrícia .F., (2007). Application of the Maxwell-Stefan Approach to Ion Exchange in Microporous Materials. Batch Process Modeling. *Chemical Engineering Science*, 62, 6939-6946.

Wesselingh, J.A., Vonk, P., Kraaijveld, G., (1995). Exploring the Maxwell-Stefan description of ion exchange. *The Chemical Engineering Journal*, 57, 75-89.

Proceedings of the 10th International Chemical and
Biological Engineering Conference - CHEMPOR 2008
Braga, Portugal, September 4-6, 2008
E.C. Ferreira and M. Mota (Eds.)

A sequencing method applied to the solution of a linear model of an adsorption column

R. L. Wu, M. F. Cuel, C. O. Hokka, M. Barboza, W. H. Kwong*
Department of Chemical Engineering
Federal University of São Carlos
P.O Box 676, ZIP Code 13565-905 São Carlos SP, Brazil

Keywords: fixed bed adsorption column, numerical solution, sequencing method, finite difference method, breakthrough curve
Topic: Advancing the chemical and biological engineering fundamentals

Abstract

This paper discusses the application of a new transient simulation method, called the sequencing method, to solve a model representing a fixed bed adsorption column. In each time step, convection and mass transfer are applied successively on the column's mesh. Numerical simulations are given for linear adsorption isotherms. These results are compared with the traditional finite difference method. The results show that the sequencing method yields excellent fluid and solid concentration profiles along the column's length and a more accurate prediction of breakthrough time than the finite difference method.

1. Introduction

Most separation and purification processes based on sorption technology use continuous flow columns. Starting at the inlet, the saturated solid sorbent zone gradually extends throughout the column, the sorbate eventually breaking through the column. The breakthrough time represents the duration of ongoing sorption until a predefined exit threshold sorbate concentration is reached. Any optimized column system is based on the accurate prediction of breakthrough time under given specific operating conditions.

Several common numerical methods have been used to approximate partial differential equations (PDEs) to ordinary differential equations (ODEs) for numerical simulation: finite difference methods (FDM), finite element methods (FEM) and orthogonal collocation methods (OCM) (Santacesaria, *et al.* 1982; Srivastava and Joseph, 1984; Gu *et al*., 1990; Gu *et al*., 1992; Gu *et al*., 1993; Altenhöner *et al*., 1997; Strube *et al*., 1997; Kaczmarski *et al*., 1997). When treating a method without diffusion, most methods introduce some form of diffusion called numerical diffusion (Finlayson, 1992). A numerical method called the Sequencing Method (SM) for solving convection-dispersion-reaction equations of homogeneous tubular reactor was recently proposed by Renou et al. (2003). The SM is based on the separation of the various phenomena. At each time step, convection, dispersion and reaction are applied successively on the reactor mesh. This method exhibits excellent shock capturing features for weakly dispersive reactors, and accurate simulations are also obtained for highly dispersive reactors. In the latter case, the only minor drawback is the fact that the SM has some problems to capture the inlet gradient correctly

The aim of this work was to investigate the sequencing method for solving the mathematical model depicting a fixed bed adsorption column, including the column's hydrodynamics and mass transfer on the fluid and solid phases. In the solution of the mathematical model, an extension of the sequencing method is proposed for solving heterogeneous column systems consisting of convection and transport equations. These are compared with the traditional numerical method of finite differences.

* Corresponding author. Tel + 55-16-33518711. E-mail:wu@ufscar.br

2. Mathematical modeling

The effect of axial dispersion is neglected because in real chromatographic systems, which are dominated by convection rather than by diffusion, this simplification can be applied without loss of accuracy (Zhong &Guiochon 1996, Dünnebier *et al*., 1998; Dünnebier & Klatt, 2000). The differential equations governing linear adsorption are given by two equations, the first a mass balance in the fluid phase and the second a mass balance in the stationary phase (Finlayson, 2006).

$$\phi\frac{\partial c}{\partial t'}+\phi V\frac{\partial c}{\partial x'}+(1-\phi)\frac{\partial n}{\partial t'}=0 \tag{1}$$

$$\frac{\partial n}{\partial t'}=k(\gamma c-n) \tag{2}$$

where c is the fluid concentration (moles per fluid volume), n is the concentration on the solid adsorbent (moles per solid volume), ϕ is the void fraction in the bed, V is the fluid velocity, t' is time, x' is distance down the bed, k is a mass transfer coefficient, and γ is the slope of the equilibrium line, n vs. c. The initial conditions give the concentration in the fluid phase and adsorbed phase at time zero, which, in this example, is no concentration at all.

$$c(x,0)=0 \tag{3}$$

$$n(x,0)=0 \tag{4}$$

The only boundary condition is the inlet concentration, here taken as 1.0.

$$c(0,t)=1 \tag{5}$$

The equations are written nondimensionally using the following variables:

$$x=\frac{x'k}{V}\qquad t=kt' \tag{6}$$

Equation (1) is

$$\frac{\partial c}{\partial t}+\frac{\partial c}{\partial x}+\frac{1-\phi}{\phi}(\gamma c-n)=0 \tag{7}$$

$$\frac{\partial n}{\partial t}=\gamma c-n \tag{8}$$

3. Simulation results

The model proposed here consists of a system of partial differential equations (Equations 7 and 8), whose solution is required for the transient simulations. Two approximation methods were used: the sequencing method and the finite difference method.

3.1. Sequencing method

At each time step, convection and mass transfer between the fluid and solid phases are applied successively on the column's phase mesh. The solution for each subsystem becomes the initial condition of the next subsystem. This can be described mathematically by the following algorithm. For a given column, let the initial condition be the profile of the fluid phase and the profile of solid phase. The initial profile of the fluid phase is used as an initial condition for the following convective subsystem, which is solved for one time step Δt

$$\frac{\partial c^*(x,t)}{\partial t}=-\frac{\partial c^*(x,t)}{\partial x} \tag{9}$$

$$c^*(x,0)=c_0(x) \tag{10}$$

$$c^*(0,t) = c_{in}(t) \tag{11}$$

where $c^*(z,t)$ represents the variable state associated with the convection part of the simulated problem. Next, the result of the solution for the fluid phase convection profile is passed through the following transfer subsystem, where it serves as the initial condition such that $c^*_{\Delta t}(x) = c^*(x,\Delta t)$ for a time step Δt

$$\frac{\partial c(x,t)}{\partial t} = -\gamma \frac{1-\phi}{\phi} c(x,t) + \frac{1-\phi}{\phi} n(x,t) \tag{16}$$

$$c(x,0) = c^*_{\Delta t}(x) \tag{17}$$

and the solid phase

$$\frac{\partial n(x,t)}{\partial t} = \gamma c(x,t) - n(x,t) \tag{18}$$

with an initial condition of $n(x,0)$.

For a time step Δt, N elements of dimension Δx are used to define the reactor mesh. The following values are used:

$$\Delta x = \frac{L}{N} \tag{19}$$

$$\Delta t = \frac{\Delta x}{V} \tag{20}$$

Therefore, the choice of the mesh's dimensions determines the time and space discretization. The resolution of the convection subsystem can be treated as a delay system from an input-output standpoint. Thus, at each time step, the data are moved one step forward in the mesh, the column's output concentration is removed and the concentration at the column inlet is placed at position one in the mesh. The mass transfer subsystem (Equations 16 and 18) is a linear system:

$$\begin{bmatrix} \dot{c}_1 \\ \vdots \\ \dot{c}_N \\ \\ \dot{n}_1 \\ \vdots \\ \dot{n}_N \end{bmatrix} = \begin{bmatrix} -\gamma\frac{1-\phi}{\phi} & \cdots & 0 & \frac{1-\phi}{\phi} & \cdots & 0 \\ & \vdots & & & \vdots & \\ 0 & \cdots & -\gamma\frac{1-\phi}{\phi} & 0 & \cdots & \frac{1-\phi}{\phi} \\ & \cdots & & & \cdots & \\ \gamma & \cdots & 0 & -1 & \cdots & 0 \\ & \vdots & & & \vdots & \\ 0 & \cdots & \gamma & 0 & \cdots & -1 \end{bmatrix} \begin{bmatrix} c_1 \\ \vdots \\ c_N \\ \\ n_1 \\ \vdots \\ n_N \end{bmatrix} \tag{21}$$

Since this system is linear, it can be solved for a given Δt using a transition matrix formulation:

$$\frac{d\mathbf{y}}{dt} = \mathbf{A}\mathbf{y} + \mathbf{b} \qquad \mathbf{y}(0) = \mathbf{y}_0 \tag{22}$$

The solution of this equation is the solution to the general Equations (7) and (8) for a time step Δt and is given by:

$$\mathbf{y} = \exp(\mathbf{A}\Delta t)\mathrm{y}_0 \tag{23}$$

Two different values are considered for the slope of the equilibrium line: 2 and 0.1. A value of 2 represents a high adsorption capacity while 0.1 indicates low adsorption capacity. The numerical values adopted for the process parameters are taken from Finlayson (2006). Figures 1-3 show the results for $\gamma = 2$ and were obtained using only 101 nodes. The solution is plotted at $t = 0.2$, $t = 0.4$, $t = 0.6$, $t = 0.8$, and at $t = 1.0$. Figure 1 shows the solution for c, using the sequencing method, while Figure 2 shows the corresponding solution for n. Figure 3 shows the breakthrough curve found with the sequencing method. The c profiles are steep while the n profiles are not.

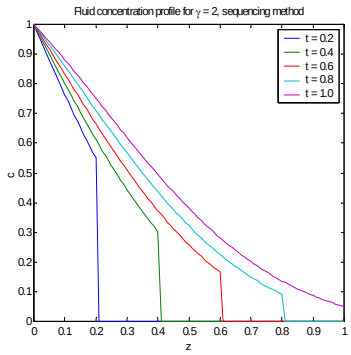

Figure 1. Fluid concentration for $\gamma = 2$ by the sequencing method

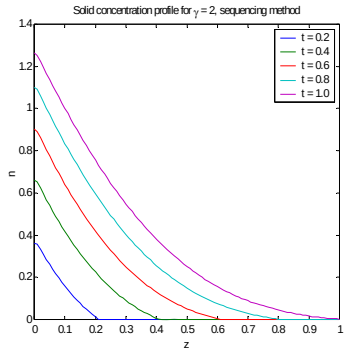

Figure 2. Solid concentration for $\gamma = 2$ by the sequencing method

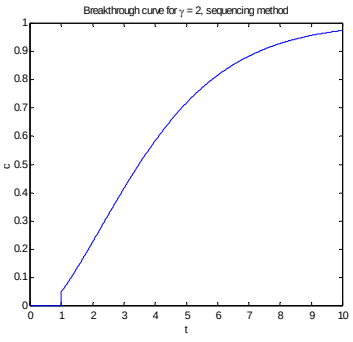

Figure 3. Breakthrough curve for $\gamma = 2$ by the sequencing method

At equilibrium, the value of n is $\gamma c = 2$. This indicates that the adsorption capacity of the bed is very large, resulting in a rapid reduction of c with distance; all the material is adsorbed.

3.2. Finite difference method

Simulation by the FDM is done using the explicit, upstream finite difference method, i.e., upstream difference for the first order partial derivative, and the explicit method is applied to the time derivative to obtain the working equations (Finlayson, 2006).

$$\frac{c_i^{k+1} - c_i^k}{\Delta t} = -\frac{c_i^k - c_{i-1}^k}{\Delta x} - \frac{1-\phi}{\phi}\left(\gamma c_i^k - n_i^k\right) \tag{24}$$

$$\frac{n_i^{k+1} - n_i^k}{\Delta t} = \gamma c_i^k - n_i^k \tag{25}$$

The solution obtained with this method when the inlet condition undergoes a step change is shown in Figures 4-6. This solution was obtained using only 101 nodes; the sharp front is steady over quite a large region. Keep in mind that the exact solution is a vertical line at the position $x = t$.

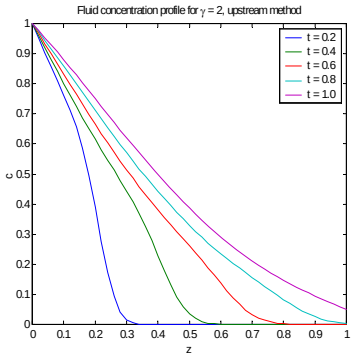

Figure 4. Fluid concentration for $\gamma = 2$ by the upstream method

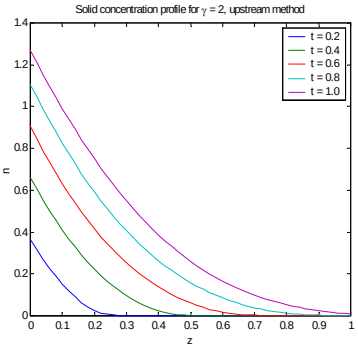

Figure 5. Solid concentration for $\gamma = 2$ by the upstream method

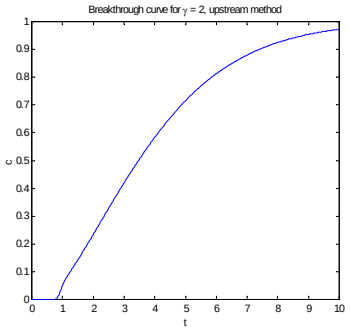

Figure 6. Breakthrough curve for $\gamma = 2$ by the upstream method

Next, the value of γ is changed to 0.1. The bed's adsorptive capacity is lower, so the problem resembles the advection equation. The liquid and solid concentration profiles and the breakthrough curve are shown in Figures 7-12, which also indicate that the results are evened out by the upstream explicit method.

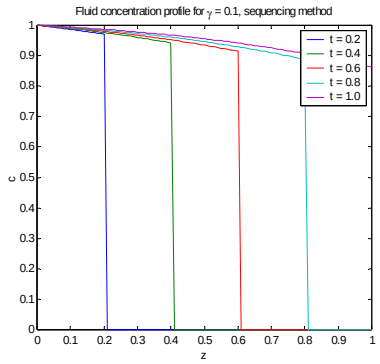

Figure 7. Fluid concentration for $\gamma = 0.1$ by the sequencing method

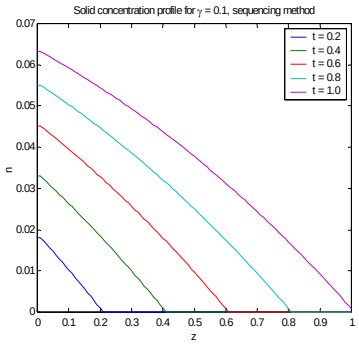

Figure 8. Solid concentration for $\gamma = 0.1$ by the sequencing method

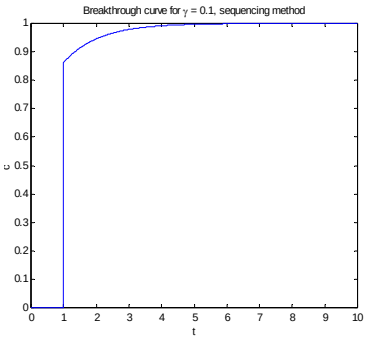

Figure 9. Breakthrough curve for $\gamma = 0.1$ by the sequencing method

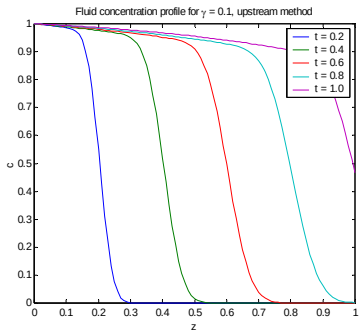

Figure 10. Fluid concentration for $\gamma = 0.1$ by the upstream method

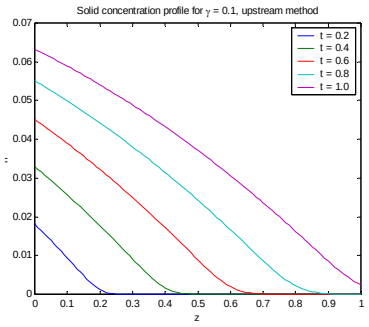

Figure 11. Solid concentration for $\gamma = 0.1$ by the upstream method

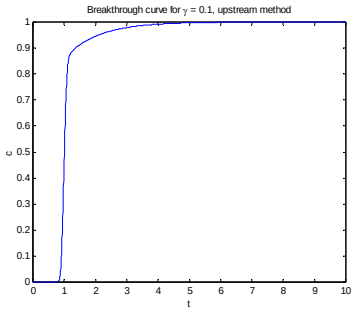

Figure 12. Breakthrough curve for $\gamma = 0.1$ by the upstream method

An analysis of the results confirms that, overall, both the numerical approaches capture the behavior of the column. Although the FDM method yields good results, the profile for c is not as steep as that obtained with the sequencing method. In Table 1 indicates the computation times (on a 800 MHz PC with 256 Mb RAM) for the transient profiles displayed in Figures 1-12. As can be seen, the sequencing method is generally faster.

Table 1. Computation time for transient profiles.

	$\gamma = 2$	$\gamma = 0.1$
SM	2.47 s	2.31 s
FDM	12.47 s	12.52 s

Conclusions

A new algorithm was proposed for simulating adsorption columns, based on a time solution approach of the PDE model, and was validated by phenomenological arguments. This approach implies the successive solution of a specific sub-problem describing each phenomenon. The column simulations showed that the SM method yields adequate transient responses to step inputs. The FDM method also provided good results, but the concentration profile was steady and considerably less steep than the sequencing method solution. Because the SM method can account for sharp inputs, it can more accurately predict breakthrough time. Finally, a comparison was made of the computational efficiency of two numerical methods for solving the transient

problem, i.e., the sequencing method and the finite difference method used in this work.

References

Abel, S., Erdem, G., Mazzotti, M., Morari, M., Morbidelli, M. (2004) Optimizing control of simulated moving beds - linear isotherm. *Journal of Chromatography A* 1033, 229-239.

Altenhöner, U., Meurer, M., Strube, J., Schmidt-Traub, H. (1997) Parameter estimation for the simulation of liquid chromatography. *Journal of Chromatography A* 769, 59-69.

Dünnebier, G., Klatt, K. U. (2000) Modelling and simulation of nonlinear chromatographic separation processes: a comparison of different modelling approaches. *Chemical Engineering Science* 55, 373-380.

Dünnebier, G., Weirich, I., Klatt, K. U. (1998). Computationally efficient dynamic modelling and simulation of simulated moving bed chromatographic processes with linear isotherms. *Chemical Engineering Science* 53, 2537-2546.

Finlayson, B. A. (1992). *Numerical methods for problems with moving fronts*. Seattle: Ravenna Park Publishing.

Finlayson, B. A. (2006). *Introduction to Chemical Engineering Computing*. New Jersey: John Wiley & Sons.

Gu, T., Truei, Y. H., Tsai, G. J., Tsao, G. T. (1992) Modeling of gradient elution in multicomponent nonlinear chromatography. *Chemical Engineering Science* 47, 253-262.

Gu, T., Tsai, G. J., Tsao, G. T. (1990) New approach to a general nonlinear multicomponent chromatography model. *AIChE Journal* 36, 784-788.

Gu, T., Truei, Y. H., Tsai, G. J., Tsao, G. T. (1993) Modeling nonlinear multicomponent chromatography. *Advances in Biochemical Engineering.* 49, 45-71.

Kaczmarski, K., Antos, D. (1996) Fast finite difference method for solving multicomponent adsorption- chromatography models. *Computers Chemical Engineering* 20, 1271-1276.

Kaczmarski, K., Mazzotti, M., Storti, G., Morbidelli, M. (1997) Modeling fixed-bed adsorption columns through orthogonal collocations on moving finite elements. *Computers Chemical Engineering* 21, 641-660.

Renou, S., Perrier, M., Dochain, D., & Gendron, S. (2003). Solution of the convection-dispersion-reaction equation by a sequencing method. *Computers Chemical Engineering* 27, 615-629.

Santacesaria, E. Morbidelli, M. Servida, A., Giusepe, S. Carrà S. (1982) Separation of xylenes on Y zeolites. 2. Breaktrhough curves and their interpretation. *Industrial Chemical Process Desenvolvment Devlopment* 21, 446-451.

Strube, J., Altenhöner, U., Meurer, M., Schmidt-Traub, H., Schulte, M. (1997) Parameter estimation for the simulation of liquid chromatography. *Journal of Chromatography A* 769, 81-92.

Srivastava, R.K., Joseph, B. (1984) Simulation of packed-bed separation processes using orthogonal collocation. *Computers & Chemical Engineering.* 8, 43-50.

Zhong, F & Guiochon, G. (1996) Analytical solution for the linear ideal model of simulated moving bed chromatography. . *Computers & Chemical Engineering.* 51, 4307-4319.

Proceedings of the 10th International Chemical and
Biological Engineering Conference - CHEMPOR 2008
Braga, Portugal, September 4-6, 2008
E.C. Ferreira and M. Mota (Eds.)

Study of the adsorption process of methanol and water over a SAPO-18 catalyst by means of pulse techniques

Irene Sierra, Andrés T. Aguayo, Javier Ereña, Ana G. Gayubo, Javier Bilbao
Departamento de Ingeniería Química, Universidad del País Vasco, Apartado 644, 48080, Bilbao, Spain

Keywords: adsorption, methanol, water, SAPO-18
Topic: Advancing the chemical and biological engineering fundamentals

Abstract

This work deals with the adsorption process of both water and methanol over SAPO-18, studied by means of pulse techniques. The values of the kinetic and equilibrium constants have been calculated by fitting the experimental response of the injections. Runs have been performed in an Autochem II equipment coupled to a mass spectrometer. It is concluded that the capacity of water vapour to be adsorbed on acid sites effectively hinders the transformation of methanol into dimethyl ether, since the equilibrium values are similar for both systems, while the adsorption rate of water is one order of magnitude higher.

1. Introduction

Dimethyl ether (DME) has aroused great interest, as it can be used directly as a diesel fuel for automobiles with a high cetane number, lower NO_x emission, near-zero exhaust production and reduced engine noise compared to conventional diesel fuel (Bo et al., 2006). The use of this new fuel is a way of promoting the utilization of diesel engine cars, since these engines are more efficient in reducing CO_2 emissions than those of gasoline (Fei et al., 2006a,b). Moreover, DME is a substitute for LPG in geographic areas with no oil supplies, and it is suitable for the generation of the H_2 required for fuell cells, especially in automotion.

The synthesis of DME from methanol leads to a high amount of water in the reaction medium, which has a considerable unfavourable effect, as it causes a decrease in the equilibrium values of DME yield and selectivity. Moreover, it may attenuate the activity of the acid function, due to the adsorption on active sites. In a previous work, Aguayo et al. (2005) reported the poor hydrothermal stability of γ-Al_2O_3, an acidic function commonly used in the synthesis of DME.

The possibility of using an alternative acidic function has been investigated. The selected catalyst for this paper is a SAPO-18 silicoaluminophosphate. Several authors have suggested that water in the reaction medium may attenuate the deactivation of the catalyst, as it might shift the coke formed over its active sites (Morán, 2002).

2. Experimental

The catalyst has been prepared in the laboratory following the method proposed by Chen et al. (1994). Runs have been performed by using pulse techniques, in a mass spectrometer (Omnistar from Pfeiffer) coupled to a catalyst characterization equipment (Autochem II 2920), provided with a TCD detector.

The experimental procedure is as follows. The first step is a sweeping stage with an inert gas (helium) at 400 ºC, in order to remove the physically adsorbed impurities. Subsequently, the temperature required for the adsorption process is established. Runs have been performed using different temperatures, in the range 200-400 ºC for water vapour-SAPO system, and 150-250 ºC for methanol-SAPO system. The adsorption of methanol has been carried out at

lower temperature in order to limit the methanol dehydration reaction, which takes place at temperatures above 250 ºC. In each run five pulses of helium saturated with water or methanol have been injected, in order to saturate the catalyst sample.

The modelling of the experimental response (signal of water or methanol collected in the mass spectrometer) allows for calculating the mass transfer coefficients, diffusivities and kinetic constants of the adsorption process. In order to simplify the model, the following assumptions have been made: (i) there is no radial temperature or concentration gradient, (ii) there is no axial heat or mass dispersion in the gas phase, (iii) the physical properties of both gas and solid phase are constant, (iv) pressure drop is negligible, (v) mass transfer rate is expressed by means of an equation including a linear gradient, (vi) the mass transfer resistances in both gas and solid phase are included in an overall mass transfer coefficient, k.

The mass balance for the catalyst is:

$$\frac{\partial x}{\partial t} = \frac{k}{(1-\varepsilon)\rho_{solid}}\left[(K_{eq}\, y) - x\right] \quad (1)$$

where x is the adsorbate (water or methanol) concentration in the solid phase, y is the concentration of the adsorbate in the gas phase, ε the porosity, k the kinetic constant and K_{eq} the equilibrium constant of the adsorption process. On the other hand, the mass balance for the gas phase is:

$$\frac{\partial y}{\partial t} = -\frac{Q}{S\varepsilon}\frac{\partial y}{\partial l} - \frac{RT}{\varepsilon}k\left[(K_{eq}\, y) - x\right] \quad (2)$$

where Q is the gas flow and S the cross section of the catalyst bed.

The Langmuir model has been used to describe the adsorption equilibrium:

$$\frac{1}{k_{eq}} = \frac{1}{k_L x_m} + \frac{y}{x_m} \quad (3)$$

where k_L is the Langmuir equilibrium constant (ratio between the adsorption and desorption rates) and x_m the maximum amount of adsorbate in the solid phase.

The system of partial differential equations has been solved by means of a programme written in MATLAB. The differential equations have been approximated using the line method, which is a numerical method based on finite differences. The parameters to optimize are the kinetic and equilibrium constants of adsorption. The objective function used for kinetic parameter optimization is the sum of square residuals:

$$\Phi = \sum \left(y_{cal} - y_{exp}\right)^2 \quad (4)$$

where Φ is the objective function, and y_{cal} and y_{exp}, respectively, the calculated and experimental values of the response (partial pressure of the adsorbate, obtained from the data collected in the mass spectrometer).

Figure 1 displays, as an example, the fitting between the experimental values and those calculated of partial pressure of methanol for a pulse injected at 200 ºC. It is concluded that the chosen methodology is suitable to describe the adsorption process over SAPO-18 catalyst.

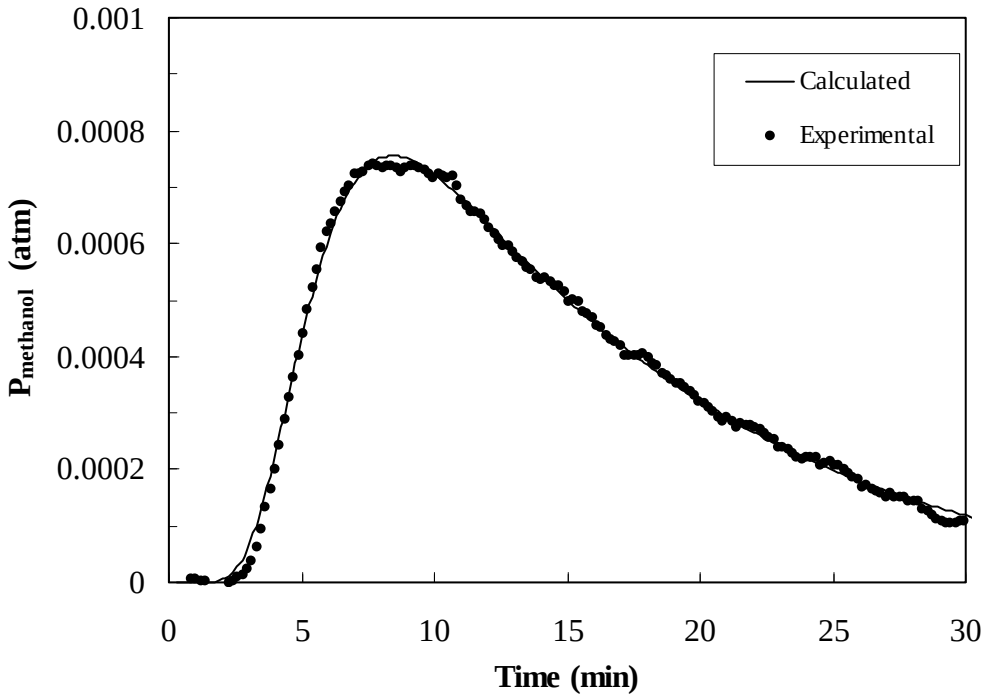

Figure 1. Fitting of the experimental response of an injection of methanol over SAPO-18 at 200 ºC.

3. Results and discussion

Adsorption of water over SAPO-18

First of all, the adsorption process of water vapour over SAPO-18 has been studied, using four different temperatures: 200, 250, 275 and 300 ºC. Figures 2 and 3 display the TCD signal obtained for two experiments performed at 200 ºC and 300 ºC, respectively. It is observed that in the experiment performed at 200 ºC, the signal corresponding to the first peak is lower than the signal of subsequent peaks. This means that part of the volume injected in the first pulse is retained in the surface of SAPO-18 catalyst (irreversibly adsorbed or chemisorbed). The fraction of the injected volume which is not chemisorbed, generates a signal of lower area than that of the last peaks of the experiment, corresponding to a process of physical adsorption, in which all the injected volume is desorbed.

When the adsorption process takes place at temperatures higher than 250 ºC (Figure 3 shows, as an example, the signal obtained at 300 ºC), on the contrary, the adsorption of water is a reversible process (there is only physical adsorption). It is observed that the peaks of the experimental response have a similar area, which means that there is no chemical adsorption at this temperature. The sharp peaks detected in the TCD correspond to a very fast kinetics, with high values of the kinetic constant.

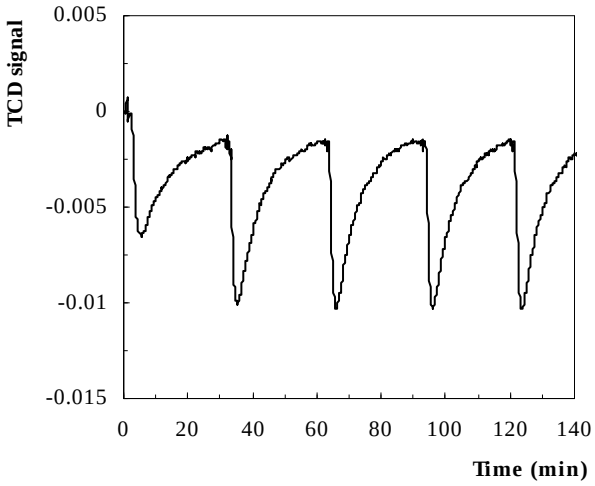

Figure 2. TCD signal of the adsorption process of water vapour over SAPO-18 at 200 ºC.

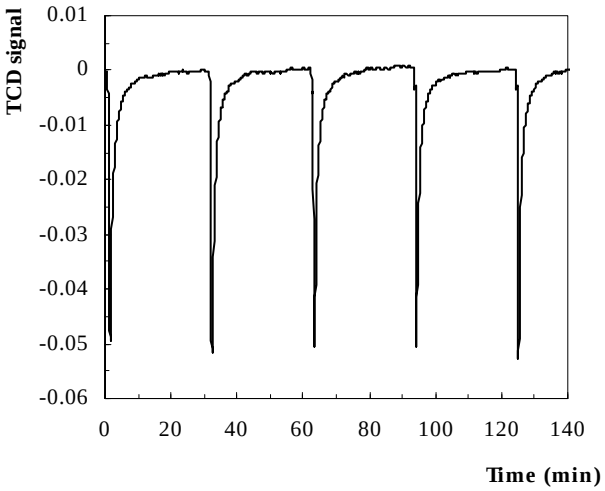

Figure 3. TCD signal of the adsorption process of water vapour over SAPO-18 at 300 ºC.

Figure 4 displays the effect of the partial pressure of water on the equilibrium constant. It is clear that an increase in the partial pressure of adsorbate leads to a decrease in the equilibrium constant of adsorption. Consequently, the equilibrium of water-SAPO system cannot be described using Henry's Law. The experimental data have been fitted to the Langmuir isotherm. The following values of the parameters have been obtained: x_m= 1.66 mol (kg of catalyst)$^{-1}$, k_L= 17 atm^{-1}.

Finally, the infuence of temperature on the adsorption process of water over SAPO-18 has been studied. Figure 5 shows that the equilibrium is severely affected by temperature. The explanation is that the level of chemical adsorption is higher at low temperatures, which results in a higher equilibrium constant.

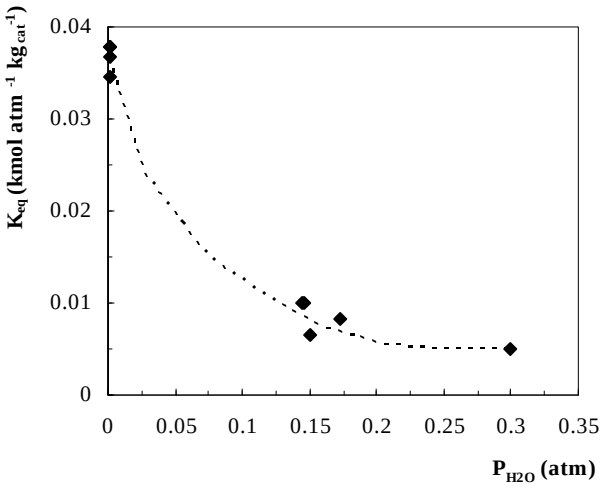

Figure 4. Influence of the partial pressure of the adsorbate on the equilibrium for water-SAPO system.

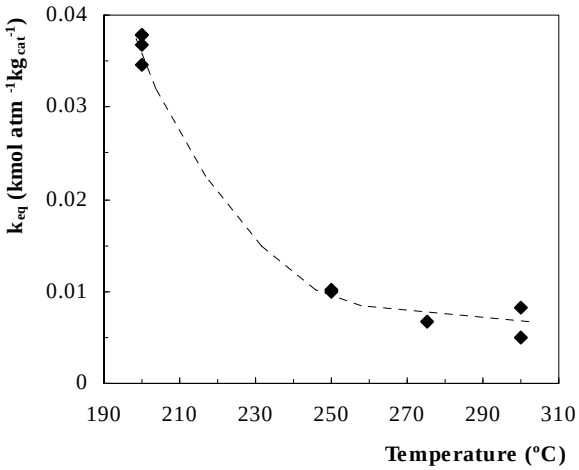

Figure 5. Influence of the adsorption temperature on the equilibrium for water-SAPO system.

Adsorption of methanol over SAPO-18

The adsorption process of methanol over SAPO-18 has been carried out at three different temperatures: 150, 200 and 250 ºC. The data of the TCD signal show that the adsorption is fundamentally physical at temperatures above 250 ºC, while for lower temperatures there is also chemical adsorption. The equilibrium constant decreases as the partial pressure of methanol increases (Figure 6). The equilibrium of the methanol-SAPO system can be described using the Langmuir isotherm. The following parameters have been calculated: x_m=0.12 mol (kg of catalyst)$^{-1}$; k_L=400 atm^{-1}.

Finally, the effect of temperature on the equilibrium for methanol-SAPO system has been studied (Figure 7). The results show that the adsorption equilibrium is severely affected by temperature. It is observed that the equilibrium constant is higher for the first pulses, as a consequence of the chemical adsorption. This process is more evident at low temperatures, due to the higher level of chemisorption. At temperatures above 250 ºC, the equilibrium value is constant for the different pulses, as the adsorption process is basically physical.

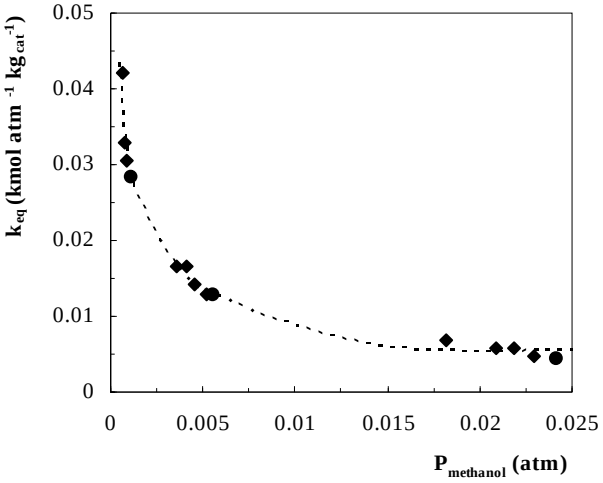

Figure 6. Influence of the partial pressure of the adsorbate on the equilibrium for methanol-SAPO system.

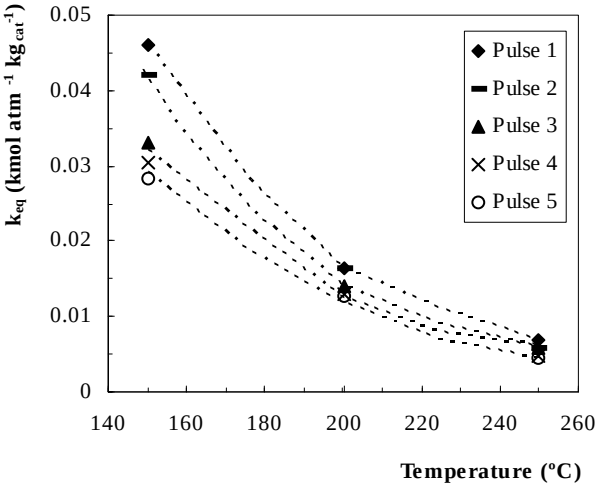

Figure 7. Influence of the adsorption temperature on the equilibrium for methanol-SAPO system.

Comparison of the adsorption process for both adsorbates

Table 1 shows the values of the kinetic and equilibrium constants of adsorption for both systems. These values have been calculated from the modelling of the experimental response collected in the mass spectrometer.

It is observed that the equilibrium constant is similar in both cases (water-SAPO and methanol-SAPO systems). Nevertheless, the adsorption process of water vapour is much faster than that of methanol, since the kinetic constant is one order of magnitude higher. Thus, water in the reaction medium competes with methanol for the acid sites of the catalyst, leading to a decrease in the activity of the catalyst to carry out the dehydration of methanol.

Consequently, the low hydrothermal stability of SAPO-18 catalyst must be considered in reactions in which water concentration is high, such as the MTO process (methanol to olefins) and the dehydration of methanol to DME.

Table 1. Values of the kinetic and equilibrium constants for the adsorption of water and methanol over SAPO-18.

System	Kinetic constant (min^{-1} m^{-3} kg_{cat}^{-1})	Equilibrium constant (mol atm^{-1} kg_{cat}^{-1})
water-SAPO	$>$ 500	5-40
methanol-SAPO	50-75	5-45

4. Conclusions

The adsorption process of methanol and water over SAPO-18 has been studied. The aim of this work is to investigate the suitability of this catalyst in the dehydration of methanol to DME, without being affected by the high amount of water produced.

It is concluded that the chosen methodology (modelling of the experimental response of several injections of helium saturated with the adsorbate) is suitable to describe the adsorption process, and calculate the parameters (kinetic and equilibrium constants).

The results reveal that water in the reaction medium effectively hinders the methanol dehydration reaction, as it competes with methanol for the acid sites of SAPO-18 catalyst. The equilibrium values are similar for both adsorbates, while the kinetics of the adsorption process is one order of magnitude faster for water-SAPO system. Therefore, the acidic sites of the SAPO-18 catalyst are partially deactivated when the concentration of water in the reaction medium is high (for example, during the dehydration of methanol to DME).

References

Aguayo, A.T., Ereña, J., Sierra, I., Olazar, M., Bilbao, J. (2005). Deactivation and regeneration of hybrid catalysts in the single-step synthesis of dimethyl ether from syngas and CO_2. Catal. Today, 105, 265-270.

Bo, Z., Weibiao, F., Jingsong, J. (2006). Study of fuel consumption when introducing DME or ethanol into diesel engine. Fuel, 85, 778-782.

Chen, J., Thomas, J.M., Wright, P.A., Townsend, R.P. (1994). Silicoaluminophosphate number eighteen (SAPO-18): a new microporous solid acid catalyst. Catal. Letters, 28, 241-248.

Fei, J., Tang, X., Huo, Z., Lou, H., Zheng, X. (2006a). Effect of copper content on Cu-Mn-Zn/zeolite-Y catalysts for the synthesis of dimethyl ether from syngas. Catal. Commun., 7, 827-831.

Fei, J., Hou, Z., Zhu, B., Lou, H., Zheng, X. (2006b). Synthesis of dimethyl ether (DME) on modified HY zeolite and modified HY zeolite-supported Cu-Mn-Zn catalysts. Appl. Catal. A: General, 304, 49-54.

Morán, A.L. (2002). Progresos en el modelado cinético de los procesos MTG y MTO y de la desactivación del catalizador, Universidad del País Vasco, Bilbao, Spain.

Acknowledgements

This work has been financed by the University of the Basque Country (Project GIU06/21) and by the Spanish Ministry of Science and Technology (Project CTQ2004-04903).

Proceedings of the 10th International Chemical and
Biological Engineering Conference - CHEMPOR 2008
Braga, Portugal, September 4-6, 2008
E.C. Ferreira and M. Mota (Eds.)

Optimization of Mobile Phase Composition for Preparative Separation of Profens Enantiomers by Chiral Liquid Chromatography

António E. Ribeiro[1], Nuno S. Graça[1], Luís S. Pais[1*], Alírio E. Rodrigues[2]
Laboratory of Separation and Reaction Engineering
[1] School of Technology and Management, Bragança Polytechnic Institute,
Campus de Santa Apolónia, Apartado 1134, 5301-857 Bragança, Portugal
[2] Faculty of Engineering, University of Porto, Rua Dr. Roberto Frias,
4200-465 Porto, Portugal

Keywords: Mobile phase composition, Preparative liquid chromatography, Chiral separation, Non-Steroidal Anti-Inflammatory Drugs, Profens.
Topic: Advancing the chemical engineering fundamentals.

Abstract

In this paper it will be presented and discussed the experimental and simulation results obtained for the preparative separation of ketoprofen and flurbiprofen enantiomers by chiral liquid chromatography. Experimental results include solubility studies, elution and frontal chromatographic experiments and the measurement of competitive adsorption isotherms, using different mobile phase compositions. Modeling and simulation tools are used to predict the behavior and the performance of fixed bed and simulated moving bed processes. These prediction tools are used to select the proper mobile phase composition for the enantiomers separation in a preparative and production-scale point of view.

1 Introduction

Ketoprofen (R,S)-2-(3-benzoylphenylpropionic acid) and Flurbiprofen (R,S)-2-(2-fluoro-4-biphenylpropionic acid) are both examples of profens, the actual most relevant subclass of the Non-Steroidal Anti-Inflammatory Drugs (NSAIDs). These drugs are frequently prescribed worldwide in relieve of pain and in the treatment of several forms of inflammation and in the treatment of main articular diseases such as rheumatoid arthritis, osteoarthritis, ankylosing spondylitis (Burian and Geisslinger, 2005). The recent literature presents several studies concluding for different pharmacological proprieties for R and S profen enantiomers. Following these findings, chiral resolution of profen enantiomers can contribute to the development of new drugs with distinct therapeutic applications and/or safer pharmacological actions (Panico ***et al.***, 2006).

The optimization of preparative chiral liquid chromatography and Simulated Moving Bed (SMB) processes is a complex task that requires a careful selection of mobile phase composition. In this selection, high resolution (or high selectivity) is not the only aspect, since other parameters, such as high solubility and low retention times, are crucial aspects that must also be considered (Ribeiro ***et al.***, 2008).

In this work, experimental results obtained for the ketoprofen and flurbiprofen enantiomers will be shown, including solubility and adsorption measurements, and pulse and breakthrough experiments. Additionally, simulation results, based on the experimental adsorption isotherms measured, will be presented to compare the performance of fixed-bed and SMB processes.

* Corresponding author. Tel + 351-273-303087. E-mail: pais@ipb.pt

2 Experimental tools, modeling and simulation

The experimental tools, modeling and simulation procedures for the optimization of mobile phase composition are described in a recent published work (Ribeiro ***et al.***, 2008). This includes experimental methods for solubility and adsorption isotherms measurements, and simulation tools to predict the operation of fixed-bed and simulated moving bed processes.

3 Results and Discussion

3.1 Solubility of profen racemic mixtures

Firstly, the solubility of ketoprofen and flurbiprofen enantiomers was measured in three pure solvents, all with a composition of 0.01%TFA: 100%n-hexane, 100%ethanol and 100%methanol. These solubility measurements were performed in duplicate and at a temperature of 23ºC (room temperature). Obtained results (not shown) indicate that profens solubility increases when the solvent is changed from 100%n-hexane to 100% ethanol and from this to 100% methanol. On a second stage, the dependency of solubility with the alcoholic composition in an ethanol/n-hexane mixture was investigated. Results were consistent with the previous ones. Ketoprofen and flurbiprofen enantiomers have high solubility values in solvents with a high polar composition. On the other hand, a mobile phase with an increased polar content is referred as an advantage in preparative chromatography due, not only because it allows higher racemate solubility, but also because presents lower retention times (Lynam and Stringham, 2006).

3.2 Elution chromatography

Several experiments of elution chromatography (pulses) were performed on different solvent mixtures of ethanol/n-hexane and methanol/n-hexane, in order to characterize the system selectivity at preparative conditions. A preparative column (Chiralpak AD, Daicel, Japan), with a particle size of 20 μm, was used on these experiments. Six level concentrations were prepared in the range between 0.05 and 4.0 g/L, and injected using two different loops: 100 μL and 1 mL. Obtained results are presented in Figure 1, for ketoprofen, and in Figure 2, for flurbiprofen.

For ketoprofen enantiomers, results show that the 20%ethanol/80%n-hexane mobile phase presents considerable higher retention times than the pure mobile phases (ethanol and methanol). The hydrocarbon mobile phase also leads to important chromatographic tails, which is an indication of strong non-linear behavior and not welcome for preparative separations. Comparing the results obtained for the two pure alcohol mobile phases it can be clearly concluded that, despite higher ketoprofen solubility, pure methanol does not allows acceptable selectivity values and, consequently, ketoprofen enantioseparation.

For the flurbiprofen enantiomers, high selectivity values can be obtained for mobile phase compositions lower than 10%ethanol/90%h-hexane (results not shown). However, this mobile phase composition exhibits retention times substantially higher and very low solubility values, which means a clear disadvantage for high productivities. For an ethanol/n-hexane-based mobile phase, a 10/90 composition represents a reasonable compromise between selectivity, retention time and solubility. For methanol/n-hexane-based mobile phase, due to the immiscibility range between 6% and 60% methanol, its use is not possible. Taking into account the very low solubility values, experiments with less than 6% of methanol in n-hexane were also not carried out, since they are not attractive under preparative point of view. On the other side, and despite high solubility, the use of a mobile phase with higher methanol content (more than 60%) does not allow selectivity values as the ones obtained with ethanol/n-hexane mixtures.

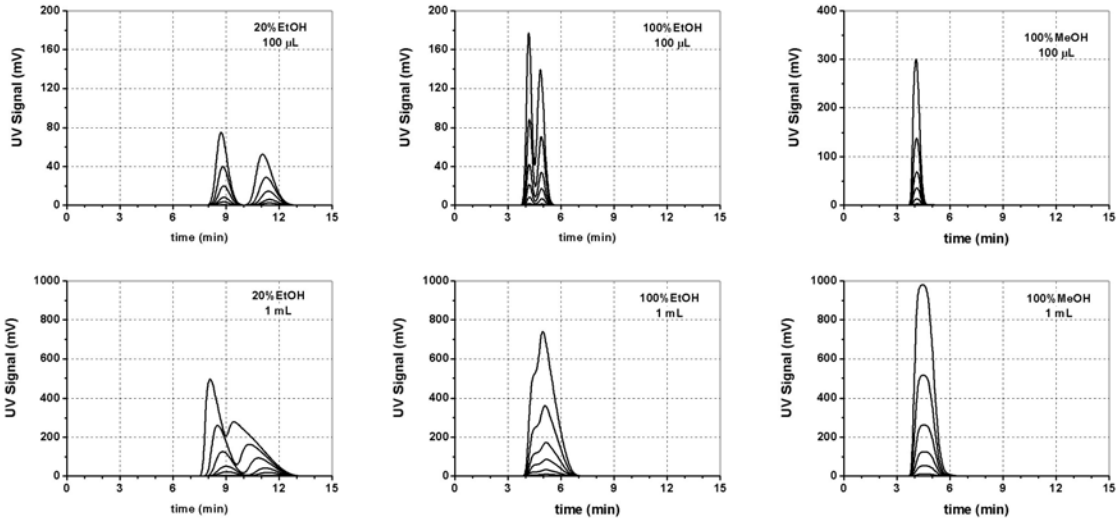

Figure 1. Experimental elution profiles of ketoprofen enantiomers in different mobile phase compositions: 20%ethanol/80%n-hexane, 100%ethanol and 100%methanol. Racemic ketoprofen concentrations in six different levels: 0.05, 0.2, 0.5, 1.0, 2.0 and 4.0 g/L; preparative column (particle diameter of 20 µm); UV detection at 260 nm; flow rate of 1 mL/min; temperature of 23ºC; injection volumes of 100 µL and 1 mL.

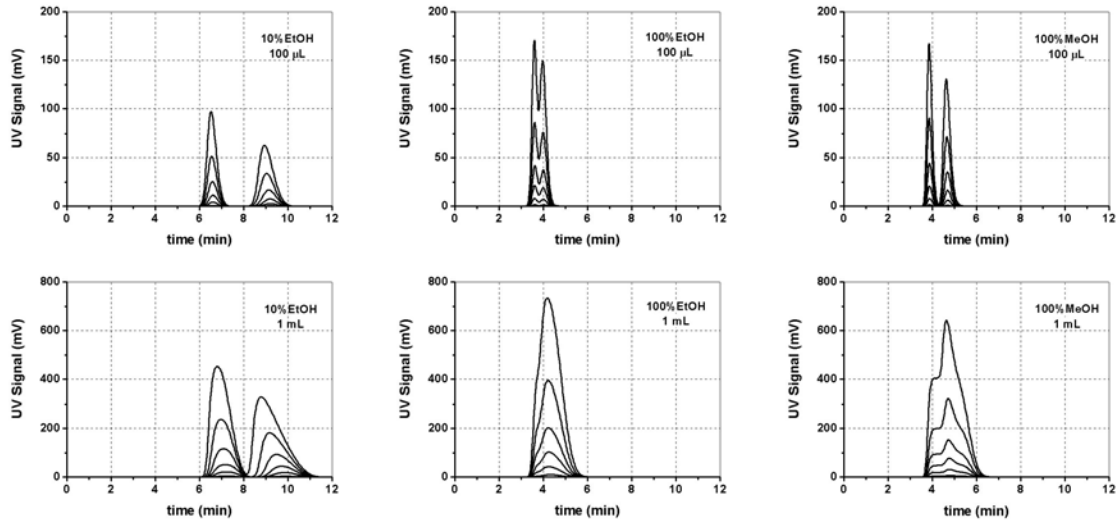

Figure 2. Experimental elution profiles of flurbiprofen enantiomers in different mobile phase compositions: 10%ethanol/90%n-hexane, 100%ethanol and 100%methanol. Racemic flurbiprofen concentrations in six different levels: 0.05, 0.2, 0.5, 1.0, 2.0 and 4.0 g/L; preparative column (particle diameter of 20 µm); UV detection at 260 nm; flow rate of 1 mL/min; temperature of 23ºC; injection volumes of 100 µL and 1 mL.

3.3 Multicomponent adsorption isotherm experiments and modeling

Figure 3 (for ketoprofen) and Figure 4 (for flurbiprofen enantiomers) present the experimental results obtained for the adsorption isotherms measurements in different mobile phase compositions, showing a good agreement with model predictions. In these figures, the prediction of the selectivity factor and its concentration dependency is also represented.

Ketoprofen results clearly show three different situations: for 100%methanol, selectivity is low and constant, which means that the separation of ketoprofen enantiomers hardly can be achieved using pure methanol as mobile phase. Despite its high selectivity for low concentrations, the common 20%ethanol/80%n-hexane mobile phase presents a strong decrease in selectivity with the increase of enantiomers concentrations. The better situation

is obtained for 100%ethanol, where selectivity maintains high values even for high enantiomer concentrations.

Results obtained for flurbiprofen enantiomers confirm a decrease in selectivity with the increase of the alcoholic content. High selectivity values can be observed for high hydrocarbon content. However, this mobile phase composition exhibits retention times substantially higher and very low solubility values. As stated before, for the separation of the flurbiprofen enantiomers, a 10%ethanol/90%n-hexane mobile phase composition is a reasonable compromise between selectivity, retention time and solubility.

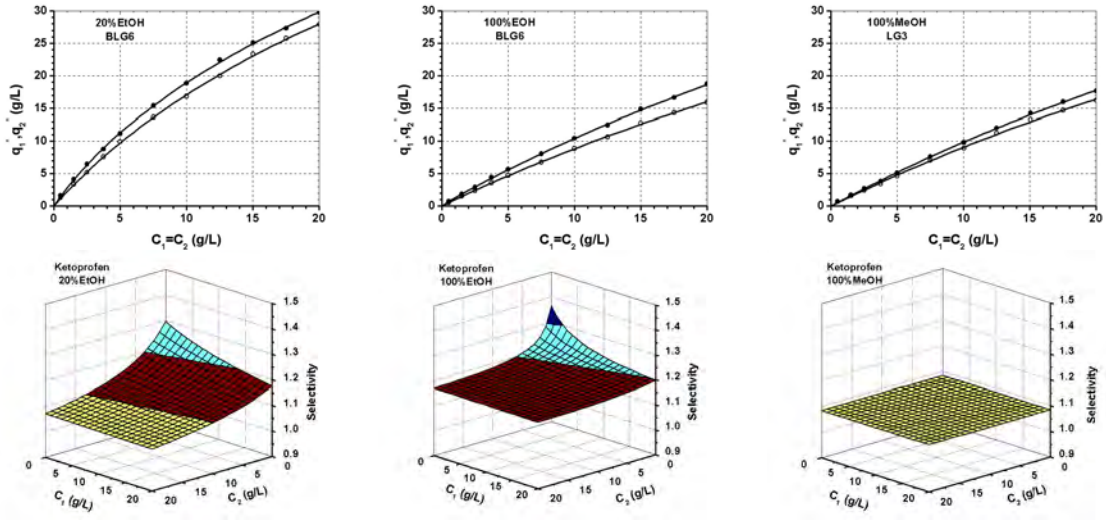

Figure 3. Comparison between model and experimental results for the equilibrium adsorption isotherms of ketoprofen enantiomers using the bi-Langmuir model (BLG6) in 20%ethanol/80%n-hexane and 100%ethanol and using the Langmuir model (LG3) in 100%methanol. Open and closed circles for the experimental concentration of the less and the more retained enantiomer, respectively; solid lines for the adsorption isotherm model. Temperature: 23ºC. The second line presents the prediction of the selectivity factor as a function of both enantiomers concentration.

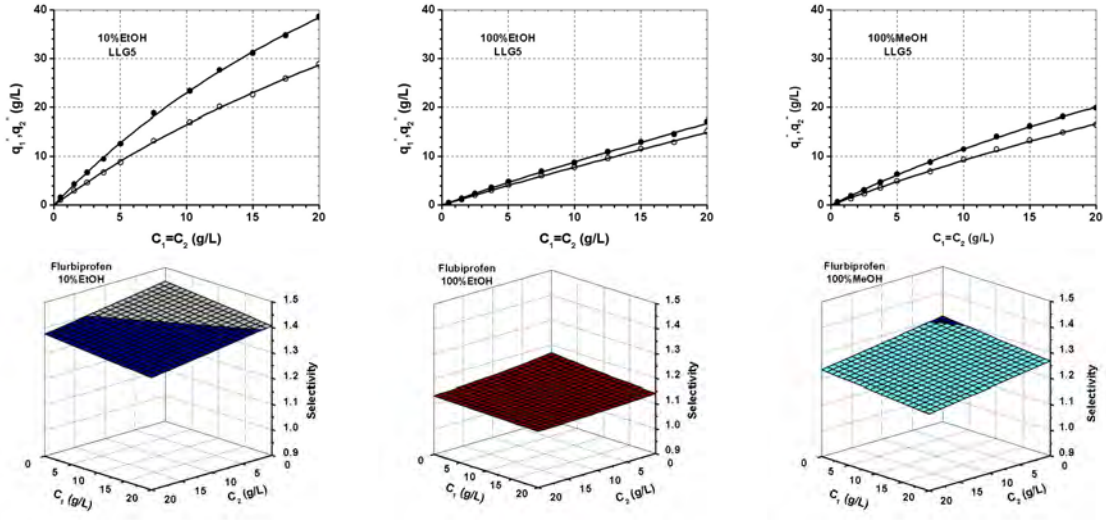

Figure 4. Comparison between model and experimental results for the equilibrium adsorption isotherms of flurbiprofen enantiomers using the modified linear+Langmuir model (LLG5) in 10%ethanol/90%n-hexane, 100%ethanol and 100%methanol. Open and closed circles for the experimental concentration of the less and the more retained enantiomer, respectively; solid lines for the adsorption isotherm model. Temperature: 23ºC. The second line presents the prediction of the selectivity factor as a function of both enantiomers concentration.

3.4 Frontal chromatography experiments and simulation

Breakthroughs experiments were carried out with the purpose of testing the selected adsorption isotherm models. In the present work it is shown experiments using a racemic feed solution of 40 g/L and the selected mobile phase composition: 100%ethanol for the ketoprofen and 10%ethanol/90%n-hexane for flurbiprofen enantiomers. It can be clearly observed from Figure 5 that both the selected models describe very well the experimental data behaviour in the whole concentration range.

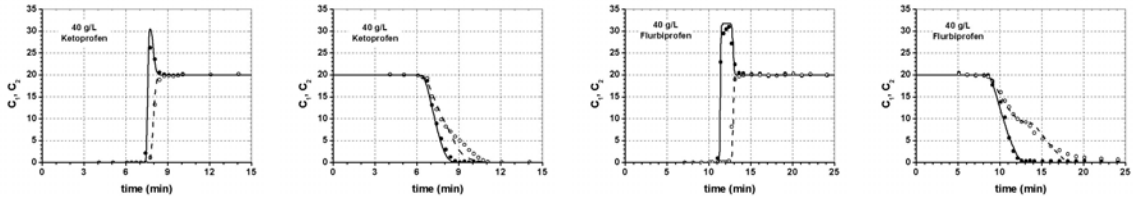

Figure 5. Saturation (adsorption) and regeneration (desorption) curves for a racemic feed concentration of 40 g/L. Comparison between experimental (points) and simulation (lines) results. Closed and open circles for the less and the more retained enantiomer, respectively. Temperature: 23ºC. Flow rate: 0.5 mL/min. Ketoprofen: 100%ethanol and bi-Langmuir model (BLG6); Flurbiprofen: 10%ethanol/90%n-hexane and modified linear+Langmuir model (LLG5). Model parameters: ε=0.4, ***Pe***=3500, ***St***=$k\tau$=1000 (see Ribeiro ***et al.***, 2008)***.***

3.5 Performance of SMB operation

The performance of the ketoprofen enantiomers separation by SMB technology is compared in Figure 6 for different mobile phase compositions using the Equilibrium Theory model. The separation region (see plot $\gamma_3 x \gamma_2$) for 20%ethanol/80%n-hexane has operating conditions considerable different from the ones obtained for the pure alcohol mobile phases (pure ethanol and pure methanol) due to the higher retention times. Comparing the separation regions for the three mobile phases, it can be concluded that, for the 20/80 composition, the separation region becomes quickly smaller with the increase of feed concentration. This is a sign of stronger non-linear behavior of the adsorption process and a reason for lower productivities.

The comparison of the SMB performance for the two pure alcohol mobile phases is clear: both have similar operating conditions due to similar retention times, but pure ethanol presents considerable better performances due to higher selectivity. Figure 6 also presents the productivity and the solvent consumption obtained for the different mobile phase compositions, as a function of feed concentration. These simulation results also clearly show that pure ethanol is the better choice for the separation of ketoprofen enantiomers through SMB operation: at high feed concentrations, the productivity using pure ethanol is three times the ones obtained with the other two solvents, and solvent consumption is only 75% and 25% of the one needed with pure methanol and 20%ethanol/80%n-hexane, respectively.

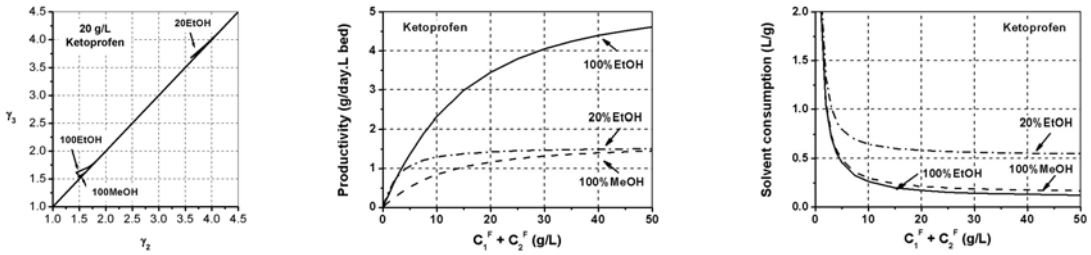

Figure 6. SMB separation regions and prediction of the performance of SMB operation for ketoprofen enantiomers: productivity and solvent consumption as a function of feed concentration for the different mobile phase compositions.

For flurbiprofen enantiomers (see Figure 7) it can be observed high retention time values in mobile phases with high hydrocarbon contents (the separation regions are progressively located at higher values of γ_2 and γ_3 with an increase of the n-hexane content). On the other side, these results are very different from the ones obtained for the separation of the ketoprofen enantiomers. The dimension of the separation regions progressively decrease with the decrease of the n-hexane content (increase of the ethanol content). Therefore, the best performance (bigger separation region) is obtained with a 10%ethanol/90%n-hexane composition through all feed concentration range. The performance parameters predictions also support the previous conclusions. Under preparative conditions, maximum productivity is achieved with the 10/90 composition, while solvent consumption does not significantly differ for all mobile phase compositions.

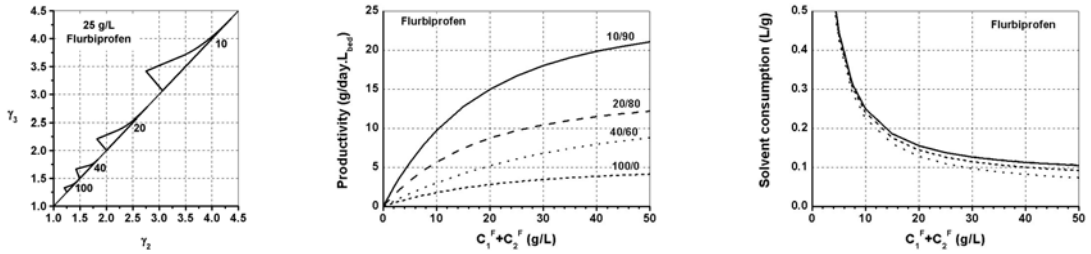

Figure 7. SMB separation regions and prediction of the performance of SMB operation for flurbiprofen enantiomers: productivity and solvent consumption as a function of feed concentration for the different mobile phase compositions.

4 Conclusions

For the separation of ketoprofen enantiomers, best situation is achieved using pure ethanol as mobile phase. For flurbiprofen enantiomers, the experimental results obtained lead to different conclusions: a 10%ethanol/90%n-hexane composition is the better choice since it represents a good compromise between selectivity, retention time and solubility. The present work shows that the choice of the proper mobile phase composition is a topic of utmost importance for the optimization of preparative liquid chromatographic separations. This choice will affect the throughput of the separation process since solubility, retention time, and selectivity are all parameters very sensitive to changes in mobile phase composition.

Acknowledgements

Financial support by the Portuguese R&D foundation FCT (Fundação para a Ciência e a Tecnologia) and the European Community through FEDER (project POCI/EQU/59738/2004) is gratefully acknowledged. The authors wish to thank Simão P. Pinho (Bragança Polytechnic Institute) for the support on the solubility measurements.

References

Burian, M., Geisslinger, G. (2005). ***COX-dependent mechanisms involved in the antinociceptive action of NSAIDs at central and peripherical sites***. Pharmacol. Ther. 107, 139-154.

Lynam, K., Stringham, R. (2006) ***Chiral Separations on Polysaccharide Stationary Phases Using Polar Organic Mobile Phases***. Chirality 18, 1-9.

Panico, A., Cardile, V., Gentile, B., Garuti, F., Avondo, S., Rosisvalle, S. (2006). ***"In vitro" differences among (R) and (S) enantiomers of Profens in their activities related to articular pathophysiology.*** Inflammation 29, 119-128.

Ribeiro, A., Graça, N., Pais, L., Rodrigues, A. (2008). ***Preparative separation of ketoprofen enantiomers: Choice of mobile phase composition and measurement of competitive adsorption isotherms***. Sep. Pur. Technol. 61, 375-383.

Proceedings of the 10th International Chemical and
Biological Engineering Conference - CHEMPOR 2008
Braga, Portugal, September 4-6, 2008
E.C. Ferreira and M. Mota (Eds.)

Gas Filtration at High Pressure

Ana B.N. Brito[1], Sandra G.R. Azevedo [1], Eduardo H. Tanabe[1], Edison Ricco Jr[1,2], José R. Coury[1], Mônica L. Aguiar[1*]

[1] UFSCar – Federal University of Sao Carlos, Chemical Engineering Department,
P.O. box 676, Washington Luis Km 235, 13565-905 Sao Carlos-SP, Brasil.
[2] Apexfil Industry and Commerce Ltda – Curuçá, 111- Vila Maria
02120-000 São Paulo-SP, Brasil.

Keywords: Filtration, High pressure, permeability, gas cleaning, filter media
Topic: Advancing the chemical and biological engineering fundamentals.

Abstract

The growing consumption of natural gas and the stringency of environmental legislation have created a greater demand for knowledge of the behavior of diverse means of filtration that can be used under high pressure. To remedy this need, we sought to develop a research project to present a preliminary investigation of cellulose filters which are commonly employed, but also of acrylic, treated and untreated polyester that can be reutilized and avoid the accumulation of residue on disposable filters. A battery of trials at pressures varying from 98 to 900 kPa and air leaks of 0.00028 to 0.0019 m^3/s, were used to determine the permability coefficient and the porosity of the filters media. At the end of the trials, Darcian and non-Darcian permeability coefficient (k_1 and k_2) increased with the increase in system pressure. Small alterations in porosity and no variation in the shape of the filter media fibers over time occurred when submitted to high pressure.

1 Introduction

The utilization of natural gas has risen in recent years due to its diverse applications and has substituted conventional forms of energy (petroleum derivatives, electricity and coal). While these energy sources have specific areas of utilization, natural gas has no captive market and easily adapts to the energy needs of many sectors. Aside from this, as a combustible that is less polluting due to its simple chemical structure, its use has grown more rapidly than petroleum derivatives. This advantage has made natural gas a more appropriate product for use in urban centers with pollution problems.

Natural gas has a substantial participation in industry, as it is utilized by the principal equipment in this segment: vapor generators (steam generator), hot air ovens (drying ovens), Fluid heaters, melting ovens, refrigeration systems, etc. It is also a viable alternative for improving environmental problems associated with automotive vehicles, because it burns more completely than gasoline, alcohol or diesel. For this reason, natural gas powered vehicles emit less of pollutants such as nitrate oxides, carbon dioxide (CO_2) and principally carbon monoxide (CO) – gases responsible for global warming (Alonso, 1999). Another advantage of natural gas is that it does not require stockage which eliminates the need for logistic control, delivery vehicles at the factory, and other costs and risks associated with the storage and handling of combustible liquids. In addition, use of natural gas also lowers operational costs in industry by eliminating the expenses with maintenance, cleaning and purchasing antipollution equipment.

* Corresponding author. Tel + 55-16-33518443. E-mail: mlaguiar@ufscar.br

One inconvenient factor, however, is the residue that accumulates on the inside of pipelines that transport natural gas, called black powder. This particulate material may originate from contamination during the construction or maintenance of the gas pipeline from lamination, soil or electrodes. Black powder may also originate from silica and inorganic salts from petroleum wells, or jointly as the erosion residue from solid residues traveling at high velocity and the corrosion residue from carbon steel pipes with no interior covering.

These residues can damage equipment and shorten its usable lifetime and are generally eliminated by filtration at high pressure.

Filtration is an important operation utilized for the separation of solid gas by fluid flowing through a permeable porous filter (Dickenson, 1994). This filtration initially captures solid particles or liquid on the inside of the filter media, known as internal filtering, where the filter media becomes impregnated and then forms a layer of particulate material called cake.

Given the notable of natural gas use, innumerous advances are being proposed for the study of the filtration process of this gas to improve operational conditions. Very few researchers have studied the filtration process in the field of natural gas, a combustible that is considered to be extremely important today in the concretization of sustainable development, due to the inherent difficulties in working with high pressure systems.

For good filter media performance, it is desirable that this presents high permeability and porosity generating a low pressure drop and keeping maximum efficiency.

Porosity is a structural parameter of filter media which corresponds to the amount of empty space (pores) present in the sample that can be determined by picnometry.

Permeability is the property that indicates the greater or lesser facility a liquid has passing through a porous media. Fluid flow generates a loss of energy reflected in pressure drop along the filter surface. Permiability can be determined by Equation 1, known as the Forchheimer equation for compressible fluids, where the pressure drop through the porous media describes the non-linear dependence on fluid velocity (Innocentini, 2008):

$$\frac{P_e^2 - P_s^2}{2P_eL} = \frac{\mu}{k_1} v_s + \frac{\rho}{k_2} v_s^2 \quad (1)$$

where P_e and P_s, are the absolute pressures before and after filtering, μ and e ρ, are the viscosity and density of the fluid, L, the thickness of the filter media and v_s, the superficial velocity of the gas, given by the relation of the volumetric leak and the area of the transversal section area, perpendicular to fluid flow. The k_1 and k_2 parameters are the Darcian and non-Darcian permeability, respectively. The first term of the Equation (1) represents the contribution of the viscous forces on pressure drop, caused by friction between the fluid molecules and the filter media. The following term represents the inertial forces, caused by the turbulence of the fluid flow and or the cake of the filter media.

For this reason, the objective of this study was to determine the parameters for permiability and porosity, as well as identify the behavior of the filter media fibers when submitted to gas filtration at high pressure.

2 Materials and methods

This section presents the equipment used in gas filtration, as well as the characteristics of the filters media of cellulose, acrylic, treated and untreated polyester.

The experimental unit, illustrated in Figure 1, is basically constituted of powder aspersor (to simulate residues in the gas), a high pressure compressor connected to three air filters, an air dryer, absolute filter, rotating valves and manometers.

Previously dried and filtered air was used instead of natural gas for the experimental trials because it was safer and cheaper. The filters media were cut in 0.07 m circular sections for a

total filtering area of 0.0038 m^2.

For the permeability trials, the acrylic filter media was placed in the experimental unit (item 7 in Figure 1). System pressure was adjusted to 98 kPa (item 2 in Figure 1), varying the gas leak from 0.00028 to 0.0019 m^3/s and noting the pressure drop values obtained by the differential manometer (item 8 in Figure 1) for the filter media without the addition of powder. This procedure was repeated at pressures of 196, 294, 392, 490 and 588 kPa. The filter media was substituted by cellulose, treated and untreated polyester and the pressure drop was measured as previously described.

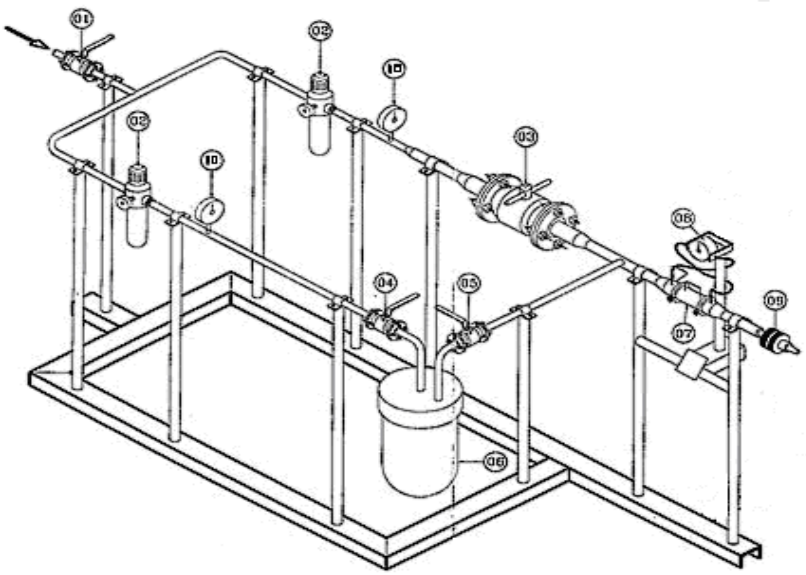

1 – Ball valve class 150
2 – High Pressure Regulator
3 – Ball valve class 150WCB
4 – Ball valve class 150
5 – Ball valve class 150
6 – Powder aspersor
7 – Filter media
8 – Differential manometer
9 – Absolut Filter
10– Safety manometer

Figure 1 – Experimental Unit

From the data for pressure drop, air viscosity varied by system pressure and the characteristics defined in Table 1, the filter media permeability was obtained utilizing Equation 1.

Table 1 – Filter media characteristics

Filter Media	Thickness (m)	Grams (g/m^2)
Acrylic	0.0028	550
Treated Polyester	0.0025	550
Untreated Polyester	0.0032	550
Cellulose	0.0035	120

To determine porosity, the filters media (cellulose, acrylic, treated and untreated polyester) were submitted to maximum system pressure (900 kPa) and maximum leak (0.0019 m^3/s) for periods of 3,600 and 43,200 seconds. Following this, the solid volume was measured by Gás Micromeritics AccuPyc 1330 picnometer to calculate porosity.

For image analysis, these same filters media underwent the treatment technique developed by Coury and Aguiar (1995). This analysis was performed by an Image Pro-Plus analyzer, to visually verify the condition of the fibers and any possible wear.

3 Results and discussions

This section presents the graphics obtained from the experimental data for pressure drop in function of superficial gas velocity and permeability in function of system pressure, as well as the porosity calculated for the filters media.

The fluid flow permeability trials were performed by varying the superficial velocity of the gas from 98 to 588 kPa band of system pressure. For each applied pressure, a graphic of pressure drop in function of the superficial gas velocity, utilizing the experimental system presented in Figure 1. The results are presented in Figures 2 and 3.

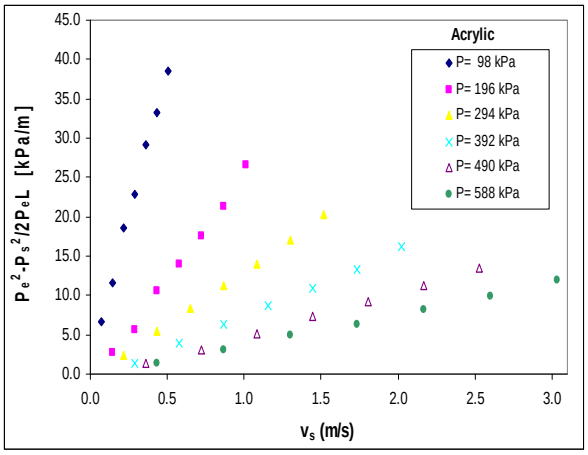

(a)

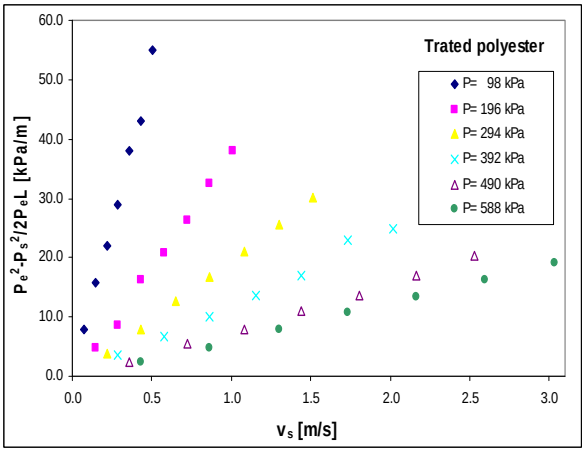

(b)

Figure 2 – Pressure drop in function of superficial velocity at different system pressures for: (a) acrylic filter media and (b) treated polyester filter media.

In Figure 2a, for acrylic filter media, the pressure drop values present a quadratic tendency with the superficial velocity of gas increase. This shows that the contribution of viscous and inertial terms were significant, as observed in the adjustments ($R^2 \approx 0.99$) of the curves seen in the graphs. It was also verified that an increase in system pressure lowered the filter pressure drop. This may have occurred due to the variation in system pressure that may have modified the position of the fibers by forcing air through the filter media and increasing the permeability. Similar behavior can be seen in the treated polyester (Fig. 2b), untreated polyester (Fig. 3a) and cellulose (Fig. 3b).

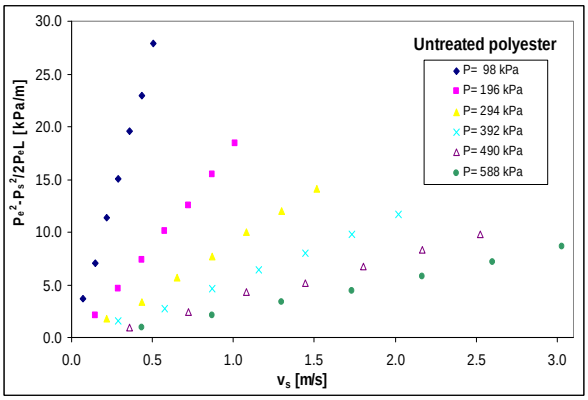

(a)

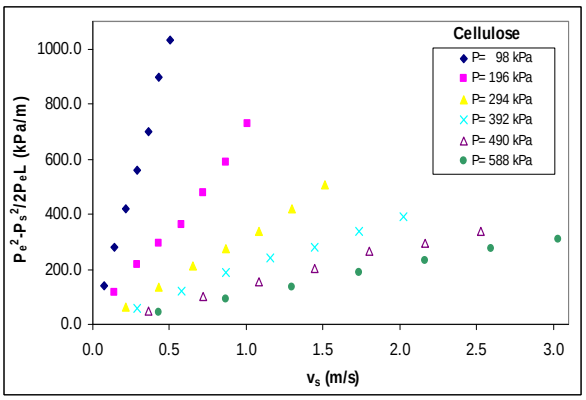

(b)

Figure 3 – Pressure drop in function of superficial velocity at different system pressures for: (a) untreated polyester filter media and (b) cellulose filter media.

Comparing Figures 2 and 3 of the filters media studied, greater pressure drops occurred for cellulose, followed by acrylic, untreated and treated polyester. This can be explained by the lower porosity of cellulose, as presented in Table 2 that increases resistance to fluid flow.

Figure 4 presents the behavior of Darcian and non-Darcian permeability (k_1 and k_2) for the different filters media in function of the pressure system. The constant was determined by the adjustment of Equation 1, which showed the significance for viscous and inertial effects as verified by the behavior of the Figures presented previously.

The analysis of Figure 4 shows the Darcian and non-Darcian permeability (k_1 and k_2) increased with the pressure system variations. This indicates that the permeability trials at elevated pressures contributed to alterations in the properties of the fluids, as well as the structure of the filter elements. Such changes may have occurred in the position of the fibers when gas was forced through at increased pressure.

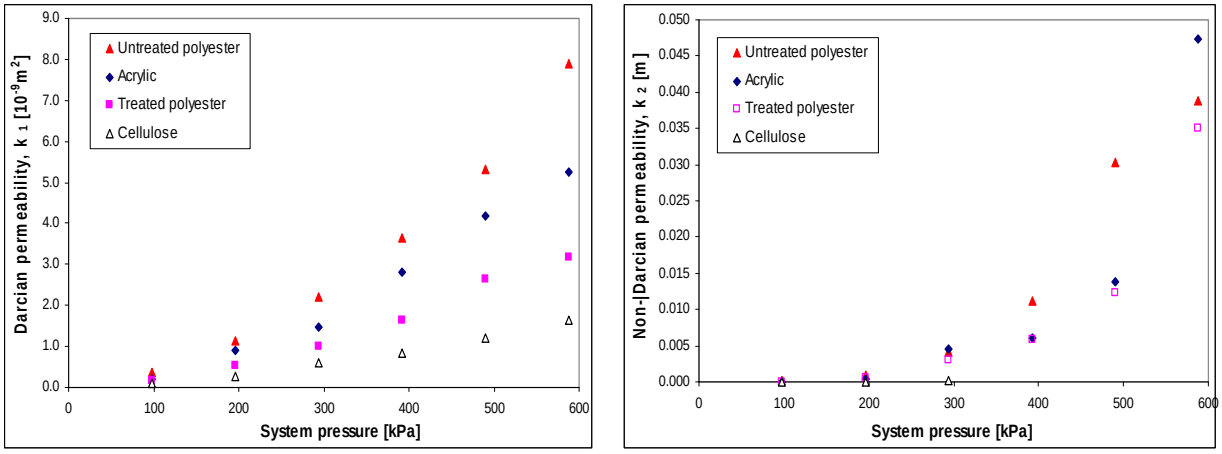

(a) (b)

Figure 4 – Air permeability Darcian (a) and non-Darcian (b) in relation to system pressure for acrylic, cellulose, treated and untreated polyester filters media.

Untreated polyester presented the greatest permeability which showed that treatment confers greater stability to filter media fibers. This greater permeability would not be appropriate for performing filtration trials because the great accumulation of particles on the interior of the filter media would interfere with the filter cleaning and increase the residual system pressure drop as observed in the study by Tanabe (2008) in an ambient pressure system. The filters utilized in the removal of particulate matter should present high collection efficiency and a low residual pressure drop in order to minimize operation costs.

To investigate the possible changes in the structure of the filter media, results for porosity in function of exposure time were analyzed for filter media made from cellulose, acrylic, treated and untreated polyester submitted tor 900 kPa pressure for exposure periods of 3,600 and 43,200 seconds and are presented in Table 2. The porosity of the original filter media (not submitted to pressure) was also determined.

Table 2 – Porosity calculated by equation 1

Filter Media / Time (s)	Acrylic	Treated Polyester	Untreated Polyester	Cellulose
0	0.82	0.77	0.88	0.78
3600	0.74	0.72	0.84	0.77
43200	0.78	0.75	0.85	0.76

Note that in Table 2, after the application of system pressure, a small variation in porosity occurred with the increase in exposure time. The alteration in porosity values over time may occur due to the rearrangement of the fiber structure by increased pressure, which may cause the structure to become more or less permeable and further investigation of these results is warranted.

Transversal section images of filter media sample were used to verify any possible alteration in fiber morphology and microstructure and are presented in Figures 5 and 6.

The images presented show that the fibers did not result in any great changes in shape from pressure or periods of the exposure applied. A possible change may have occurred only in their position.

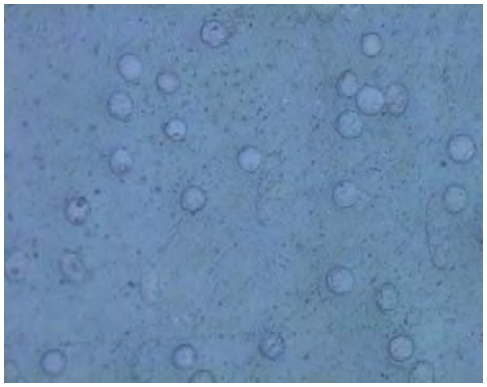

Figure 5 – Original transversal image of the untreated polyester filter media (200 X).

Figure 6 – Transversal imagem of untreated polyester filter media submitted to pressure for 43,200 seconds (200 X).

4 Conclusions

This section presents the principal conclusions obtained from the filtration trials performed for cellulose, acrylic, treated and untreated polyester.

The Darcian permeability coefficients (k_1) increased with the system pressure increase, due to the variations in the fluid properties and possibly, in the disposition of the fiber structure that facilitated the gas flow through the filter media.

The pressure versus velocity curves presented a linear behavior, greatly influenced by the system pressure.

The research performed showed that the filters media, when submitted to high pressure do not present any flattening of the fibers and only small alterations in porosity.

Acknowledgements

Authors would like to thank the Brazilian research funding institution CNPq for financial support.

References

Alonso, P. S. R. (1999) O Gás Natural na Matriz Energética Brasileira: avaliação global de seus impactos, estratégias para disseminar sua utilização e criação de um suporte de tecnologias para o Brasil. Rio de Janeiro: UFRJ/COPPE.

Coury, J. R., Aguiar, M. L. (1995) Rupture of dry agglomerates. Powder Technology, v.85, p.97-43.

Dickenson, C. (1994) Filters and Filtration Handbook. 3 ed. Oxford: Elsevier Advanced Technology.

Innocentini, M. D. M., Rodrigues, V. P., Romano, R. C. O., Pileggi, R. G., Silva, G. M. C., Coury, J. R. (2008) Permeability optimization and performance evaluation of hot aerosol filters made using foam incorporated alumina suspension, Journal of Hazardous Materials, in press.

Tanabe, E. H. (2008) Estudo do comportamento da deposição das partículas em diferentes meios filtrantes, Master Science Dissertation, Federal University of Sao Carlos, Brazil (in Portuguese).

Proceedings of the 10th International Chemical and
Biological Engineering Conference - CHEMPOR 2008
Braga, Portugal, September 4-6, 2008
E.C. Ferreira and M. Mota (Eds.)

Kinetics of carbon dioxide absorption with chemical reaction in piperidine aqueous solutions

Alicia G. Abuín[1], Diego Gómez-Díaz[1] José M. Navaza[1*], Isabel Vidal[1]

[1] Department of Chemical Engineering – ETSE. Lope Gómez de Marzoa s/n. University of Santiago de Compostela. E-15782, Santiago de Compostela. Spain.

Keywords: absorption, piperidine, kinetic

Topic: Advancing the chemical and biological engineering fundamentals

Abstract

Chemical reaction kinetics of carbon dioxide with aqueous solutions of piperidine has been studied using a stirred tank reactor with a planar interfacial area. The operational variables considered in this work have been the amine concentration and the reaction temperature. Specific absorption rates have been obtained and different correlations have been employed to estimate physicochemical properties of carbon dioxide in piperidine aqueous solutions. Results indicate that the absorption process occurs in a fast reaction regime with a first-order kinetic for amine and carbon dioxide. The reaction rate constant was calculated and correlated as a function of temperature.

1. Introduction

Carbon dioxide is a very important greenhouse gas that is emitted by several industrial processes. Carbon dioxide accompanying natural gas necessitates carrying out different cleaning operations for its later use. Recent methods for carbon dioxide capture, separation and sequestration, involve different options such as physical and chemical absorption (and adsorption), membranes separations, mineralization, etc.

The use of aqueous solutions of amines in gas-liquid reactors (stirred tanks, bubble and packed columns, air-lift, etc) for the capture of acid gases (mainly carbon dioxide) is a common procedure that is adopted in numerous industrial processes and has been the aim of a great number of research studies during the last decades [1].

Currently, aqueous alkanolamines solutions based on monoethanolamine, diethanolamine, 2-dipropanolamine and methyldiethanolamine are most commonly used in industry. These amines have shown fast regimes of absorption accompanied by a chemical reaction, which has a high importance as regards the aim of capturing higher quantities of carbon dioxide, as well as the scale-up of operation units. The most recent research studies are also related to the development and testing of new reagents and/or amines to capture carbon dioxide, as well as the use of blends of different amines [2] with the aim of achieving a certain enhancement in pollutant gas capture, due to their combined action. For these reasons, it is important to determine kinetic data for these kinds of reactions with the aim of understanding the behaviour of different amines or blends when reacting with the carbon dioxide present in a gas stream, so that we can calculate the capture efficiency or the geometrical characteristics [3] to design gas-liquid contactors.

* Corresponding author. E-mail:eqnavaza@usc.es

2. Experimental section

Commercial grade CO_2 gas of 99.998% purity, supplied by Carburos Metálicos, (Spain) was used in this work. Piperidine of 99% purity was obtained from Fluka (USA). Aqueous solutions of piperidine were prepared with double distilled water.

The experiments were conducted in a stirred cell (1) having a planar interfacial area working in batches as regards both phases (see figure 1). Four baffles have been placed in its internal wall to improve the mixing and prevent vortex formation during stirring. The gas to be absorbed, carbon dioxide, was passed through two humidifiers (2) to prepare the gas phase. This procedure removed other resistance to mass transport and allowed only the evaluation of the liquid phase resistance to the gas transfer. Water was placed into the “humidifiers”. A soap flow-meter (3) was used to determine the absorption rate of carbon dioxide by the absorption accompanying the chemical reaction produced by the glucosamine present in the liquid phase. The absorption rate was measured by analysing the movement (produced by the consumption of carbon dioxide) of the soap film along the calibrated glass tube. The absorption processes have been carried out at different temperatures (7 to 55 ºC) by connection of humidifiers, stirred cell and flow-meter to a thermostat-cryostat (4).

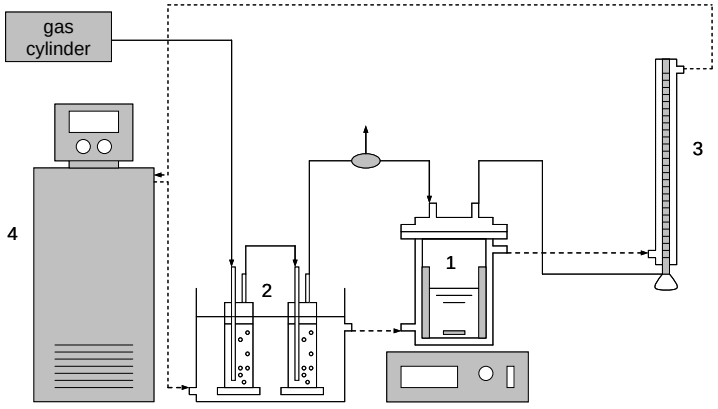

Figure 1. Experimental set-up for kinetic studies of gas-liquid systems.

3. Results and Discussion

The kinetics of reaction between carbon dioxide absorbed in water and piperidine were studied by employing gas phase absorption data. The flow densities were calculated assuming that the gas phase follows an ideal behaviour, taking previous studies into account [4].

Carbon dioxide flow density was calculated by means of experimental data corresponding to the absorbed quantity of carbon dioxide along the operation time. Figure 2 shows the experimental results which were obtained in relation to the flux density determined for the liquid phases employed in this work. Experimental data shows a linear trend in all cases in the studied operation time range, and this kind of behaviour allows the use of experimental data for kinetic studies. The slope of the linear plot shown in figure 2 allows the calculation of the absorption volumetric flux at different operation conditions. Similarly, results from figure 2 indicate that there is certain influence of initial piperidine concentration in the liquid phase upon the carbon dioxide absorption rate or upon the slope of linear fits. This observation confirms the existence of chemical reaction in the liquid phase of carbon dioxide with the amine.

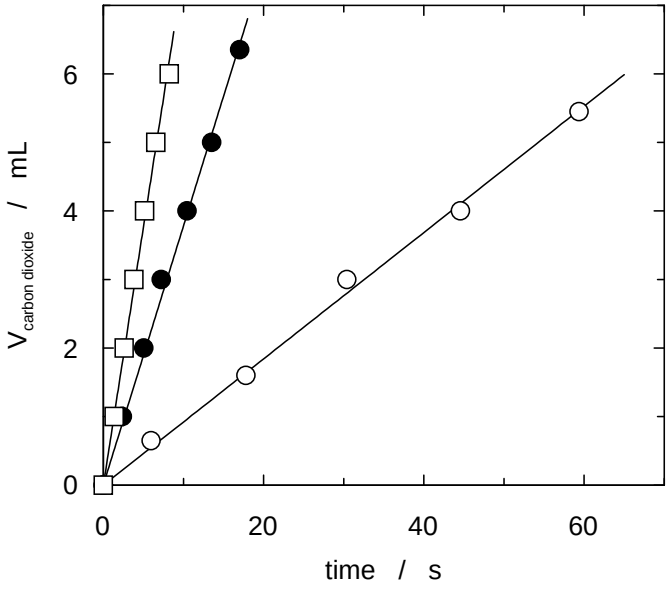

Figure 2. Influence of amine concentration on carbon dioxide absorption rate in gas-liquid kinetic studies. (○) [piperidine] = 0 M; (●) [piperidine] = 0.05 M; (□) [piperidine] = 0.1 M. T=25 ºC.

The reaction between carbon dioxide and amine involves different parallel chemical reactions, such as the reaction between this gas and hydroxyl ions (bicarbonate formation) and water (carbonic acid formation). However, the influence of these reactions under the conditions employed in the present work could be considered negligible. As regards the carbonic acid formation and reaction, it is very slow and it must be considered of no influence on the system studied. The other parallel reaction abovementioned between carbon dioxide and hydroxyl ions could be negligible due to the low hydroxyl ions concentration in the system, such as different studies have proved. Based on conclusions reached by different studies which indicate that carbamic reaction is the mechanism of reaction between carbon dioxide and amines when the carbonation relationship (moles of carbon dioxide/moles of amine) is lesser than 0.5, we could develop the analysis of our experimental results using this hypothesis, that is in agreement with results based on pH measurements (<11), previously commented.

A value of carbonation ratio lesser than 0.5 indicates that the reaction takes place by means of a second-order mechanism with three possible regimes: physical absorption, fast-reaction and instantaneous regime. Since the glucosamine concentration is high in the liquid phase and implies values of $C_{Bo}/C_{Ao} >> 1$, the physical absorption regime must be ruled out, so it is necessary to analyse the instantaneous and fast-reaction regimes.

An instantaneous regime relates carbon dioxide flow density (N_A) with initial glucosamine concentration with a linear trend. Figure 3 shows this relation, which indicates that this regime doesn't govern the reaction mechanism.

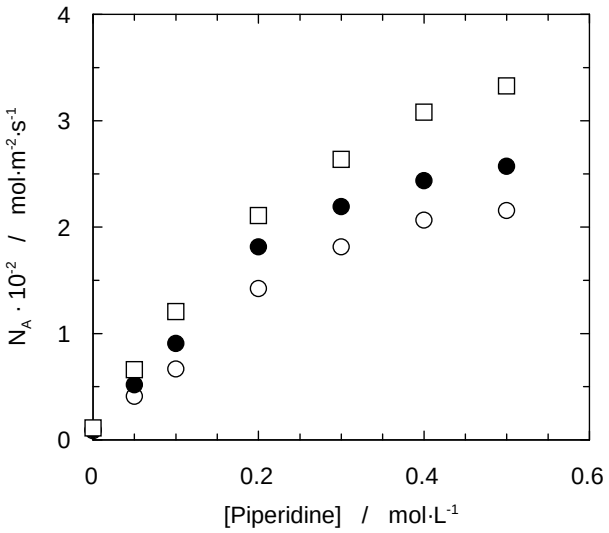

Figure 3. Influence of amine concentration and temperature on gas absorption rate with chemical reaction. (○) T = 15 ºC; (●) T = 35 ºC; (□) T = 55 ºC

The fast reaction regime allows the calculation of the carbon dioxide flow density by means of equation 1, taking into account that the reaction order, as regards the carbon dioxide when reacting with aqueous solutions of primary amines, is one.

$$N_A = C_{Ao}\sqrt{D_A \cdot k_{1,n} \cdot C_{Bo}^n} \qquad (1)$$

where C_{Ao} and C_{Bo} are the initial concentrations of carbon dioxide and piperidine in the liquid phase, D_A is the gas diffusivity in glucosamine aqueous solutions and $k_{1,n}$ is the overall reaction rate constant.

The diffusion coefficient corresponding to carbon dioxide in aqueous solutions of piperidine was calculated employing the expression shown in equation 2 [5].

$$D_A = D_{A,w} \cdot \left(\frac{\eta_w}{\eta}\right)^{0.8} \qquad (2)$$

where $D_{A,w}$ is the diffusivity of carbon dioxide in pure water, η_w and η are the viscosity of pure water and aqueous solutions of amine, respectively. The value of carbon dioxide diffusivity in pure water was determined employing the expressions proposed by different studies[12, 16]. On the other hand, the water viscosity and piperidine aqueous solutions have been obtained from literature [6].

The initial carbon dioxide concentration in the liquid phase must coincide with the concentration in equilibrium in gas phase. This parameter could be replaced in equation 1 employing Henry's law. These considerations allow us to obtain the linearized expression shown in equation 3 to fit experimental data as well as to calculate the reaction order corresponding to glucosamine:

$$\log\left(\frac{N_A^2 \cdot He^2}{P_A^2 \cdot D_A}\right) = \log\left(k_{1,n}\right) + n \cdot \log\left(C_{Bo}\right) \qquad (3)$$

where He is Henry's constant and P_A is the carbon dioxide partial pressure.

Figure 4 shows the results obtained after using equation 3 to fit the experimental results obtained in the present work. These results indicate a good agreement between the

experimental data and the linear fits of equation 3 under de operation conditions employed in this work.

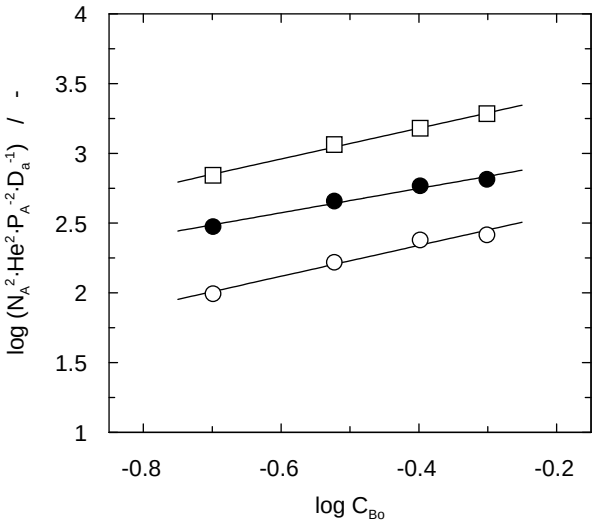

Figure 4. Linear fits according to equation 3 to obtain the reaction order and kinetic constant of the gas-liquid reaction. (○) T = 15 ºC; (●) T = 35 ºC; (□) T = 55 ºC.

Linear fits of the experimental data (i.e. in figure 4) have been used to calculate the reaction order regarding the piperidine, as well as the value of the kinetic constant employing the intercept with the origin. The slope of linear fits obtained at different temperatures contributes values close to 1. This is the reaction order corresponding to glucosamine, being in agreement with previous studies of chemical absorption of carbon dioxide with other primary amines [7].

Literature

[1] Idem R, Wilson M, Tontiwachwuthikul P, Chakma A, Veawab, A, Aroonwilas A, Gelowitz D. Pilot plant studies of the CO_2 capture performance of aqueous MEA and mixed MEA/MDEA solvents at the University of Regina CO2 capture technology development plant and the boundary dam CO_2 capture demonstration plant. Industrial & Engineering Chemistry Research. 2006; 45: 2414-2420.

[2] Liao C-H, Li, M-H. Kinetics of absorption of carbon dioxide into aqueous solutions of monoethanolamine + N-methyldiethanolamine. Chemical Engineering Science. 2002; 57: 4569 – 4582.

[3] Xiao J, Li C-W, Li M-H. Kinetics of absorption of carbon dioxide into aqueous solutions of 2-amino-2-methyl-1-propanol+monoethanolamine. Chemical Engineering Science. 2000; 55: 161-175.

[4] Camacho F, Sánchez S, Pacheco R. Absorption of carbon dioxide at high partial pressures in 1-amino-2-propanol aqueous solution. Considerations of thermal effects. Industrial & Engineering Chemistry Research. 1997; 36: 4358-4364.

[5] Ratcliff G. A., Holdcroft J. G. Diffusivities of gases in aqueous electrolyte solutions. Transactions of the Institution of Chemical Engineers. 1963; 41: 315-319.

[6] Gómez-Díaz, D., Navaza, J. M., Sanjurjo, B. Densities, viscosities, surface tensions and speed of sound of aqueous solutions of piperidine + pyrrolidine + water. J. Chemical. 2007, 52: 1996-1999.

[7] Chakraborty A. K., Astarita G, Bischoff K. B. CO_2 absorption in aqueous solutions of hindered amine. Chemical Engineering Science. 1986; 41: 997-1003.

Proceedings of the 10th International Chemical and
Biological Engineering Conference - CHEMPOR 2008
Braga, Portugal, September 4-6, 2008
E.C. Ferreira and M. Mota (Eds.)

Absorption of carbon dioxide by MDEA aqueous solutions in a bubble column reactor

Estrella Álvarez[1], Diego Gómez-Díaz[2], M. Dolores La Rubia[3], José M. Navaza[2], Lourdes C. Quintáns-Riveiro[2*]

[1] Department of Chemical Engineering – ETSEI. Maxwell s/n. University of Vigo. E-36310, Vigo. Spain.

[2] Department of Chemical Engineering – ETSE. Lope Gómez de Marzoa s/n. University of Santiago de Compostela. E-15782, Santiago de Compostela. Spain.

[3] Department of Chemical, Environmental and Materials Engineering – EPS. Las Lagunillas s/n. University of Jaén. E-23071, Jaén. Spain.

Keywords: absorption, MDEA, bubble column, interfacial area.

Topic: Advancing the chemical and biological engineering fundamentals.

Abstract

Present work analyzes the mass transfer process using N-methyldiethanolamine (MDEA) in the removal process of carbon dioxide using a bubble column reactor (BCR) as gas-liquid contactor. The use of this type of equipment requires the interfacial area determination for the following mass transfer coefficient calculation based on absorption kinetics. The effect of contactor, operation conditions, liquid phase nature and chemical reaction upon the mass transfer coefficient and interfacial areas have been analyzed.

1. Introduction

In general, the reaction between CO_2 and primary and secondary alkanolamines in aqueous solutions is described by the zwitterion mechanism reintroduced by Danckwerts [1]. According to this mechanism, the primary and secondary alkanolamines react directly and reversibly with CO_2 to form a zwitterion intermediate, which is deprotonated by the bases existing in solution including alkanolamines, OH^- ions, and water to produce a stable carbamate and a protonated base, except for the CO_2- MEA reaction, which is independent of the concentration of OH^- ions [2].

Certain authors revealed that the addition of tertiary amines with primary or secondary amines presents certain advantages to increase CO_2 absorption capacity [3]. In contrast to primary and secondary amines, the tertiary amines do not react directly with CO_2 to form stable carbamates. Specifically, MDEA (N-methyldiethanolamine) seems a very good amine to get the previously commented characteristics.

For the reaction of CO_2 with tertiary alkanolamines, Donaldson and Nguyen [4] proposed the following reaction mechanism. This reaction mechanism is essentially a base-catalyzed hydration of CO_2, and the mechanism implies that tertiary amines cannot react directly with CO_2. In most of the literature on CO_2 kinetics with tertiary amines in aqueous solutions, it is assumed that reaction of CO_2 with MDEA is a pseudo-first order reaction.

* Corresponding author. E-mail:eqnava2@usc.es

2. Experimental section

Aqueous solutions employed as liquid absorbent phases have been produced using different quantities of N-methyldiethanolamine (MDEA) supplied by Aldrich (CAS number 105-59-9). The solutions were prepared by mass using a balance with a precision of $\pm 10^{-7}$ kg. To prepare the absorbent phases (in the range 0-1 $mol \cdot L^{-1}$), bi-distilled water has been employed.

All experiments were performed at room temperature, operating in batches with respect to the liquid phase. The bubble column is made of methacrylate, 1.03 m height, and has a square cross-section (side length 6 cm). For the injection and uniform distribution of the gas phase, a gas sparger (three glass capillary sparger) is installed at the centre of the bottom plate. The simplicity of the gas sparger produces a small dead zone near to the gas inlet.

The absorption process has been carried out at 25 ºC using a similar experimental set-up employed by our research team in previous studies [5]. The gas to be absorbed, carbon dioxide, was passed through two bubbling flasks at 25 ºC to prepare the gas phase. This procedure removed other resistance to mass transport and allowed only the evaluation of the liquid phase resistance to the gas transfer. Pure water was placed into the bubbling flasks. The gas flow-rate fed to contactor was controlled with a mass flow controller (5850 Brooks Instruments) and measured with a soap flow-meter. The mass flow controller employed in the present study was calibrated by the supplier for the used gas flow-rates and pressures ranges. The gas flow-rates employed have been included into 15-30 $L \cdot h^{-1}$. The outlet gas flow-rate has been measured using a soap gas flow-meter and gas absorption rate was calculated as the difference between inflow and outflow rates.

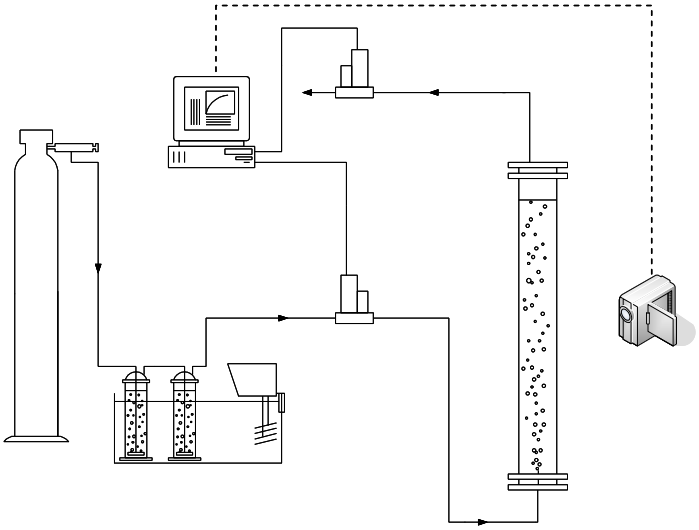

Figure 1. Experimental set-up employed in carbon dioxide absorption studies.

The use of a BCR to analyse carefully the experimental results implies the knowledge of the interface area employed in the gas/liquid mass transfer. For this reason the present paper includes the determination of the interfacial area to the operation conditions under which the mass transfer experiments have been carried out. The methodology employed implies the use of a rectangular bubble column.

The bubble diameter was measured using a photographic method based on taking images of the bubbles along the height of the column, from bottom to top. A Sony (DCR-PC330E) video camera was used to obtain the images. A minimum number of 80 well-defined bubbles along the bubble column were used to evaluate the size distribution of bubbles in the different liquid phases employed (different concentration of MDEA), and for each gas flow-rate which has

been used. We used the Image Tool v2.0 software to carry out the necessary measurements of the geometric characteristics of the bubbles. Photographs of different bubble column zones were analyzed, taking into account the possible influence of mass transfer accompanying of chemical reaction upon the bubble size along the liquid phase height.

3. Fundamentals

The interfacial area in gas-liquid contactors is commonly determined using physical or chemical methods. In relation to physical methods, the photographic one is the most employed methodology. In relation to the chemical method, it is based on absorption measurements of a chemical absorption process with a well known reaction kinetic. Due that the kinetic of the chemical absorption of carbon dioxide in aqueous solutions of MDEA has been determined in a previous paper, and in the basis of the equations previously commented, the interfacial area could be calculated. The knowledge of the interfacial area is necessary for the posterior mass transfer coefficient determination.

The images we obtained of the bubbles in the liquids employed show an ellipsoid shape. For this reason, major (*E*) and minor (*e*) axes of the projected ellipsoid (in two dimensions) were determined. The diameter of the equivalent sphere (equation 1) was taken as the representative bubble dimension.

$$d = \sqrt[3]{E^2 \cdot e} \tag{1}$$

Different authors recommend to use the Sauter mean diameter (d_{32}), which is possible to determine using the data calculated for the equivalent diameter.

$$d_{32} = \frac{\sum_i \left(n_i \cdot d_i^3\right)}{\sum_i \left(n_i \cdot d_i^2\right)} \tag{2}$$

where n_i is the number of bubbles which have an equivalent diameter (d_i).

The Sauter mean diameter and the gas hold-up values allow the calculation of the specific interfacial area using equation 3.

$$a = \frac{6 \cdot \varepsilon_G}{d_{32} \cdot \left(1 - \varepsilon_G\right)} \tag{3}$$

The overall gas hold-up, ε_G, was measured using the volume expansion method:

$$\varepsilon_G = \frac{\Delta V}{\Delta V + V_L} \tag{4}$$

where V_L is the ungassed liquid volume and ΔV is the volume expansion after gas dispersion, calculated from the liquid level change and the cross sectional area. The change in the volume in the bubble column was calculated based on the change observed in the liquid level and the increase in this value after gassing.

Due that the mass transfer process is the slowest step of the global process, is necessary to study the carbon dioxide transport to the liquid phase. The enhancement factor depends on the value of the mass transfer coefficient in absence of chemical reaction, the amine concentration, diffusivity of the reactants in the liquid phase and the values for the kinetic constants for the reactions evolved in the global process. Under certain conditions, the amine concentration at gas / liquid interface could be the same that in the liquid bulk and the reaction could be carried out completely at interface.

$$N = C_A^* \cdot a \cdot \sqrt{D_A \cdot k_2 \cdot C_B^{bulk}} \tag{5}$$

where *N*, is the absorption rate of carbon dioxide, C_A^* and D_A, the solubility and diffusivity of carbon dioxide in the aqueous phase, *a*, is the interface area, k_2, the rate constant for the reaction between carbon dioxide and hydroxyl ions and C_B^{bulk}, the MDEA concentration in the bulk of the aqueous phase.

The use of this expression (equation 5) needs that the concentration of amine remains constant practically along the time. If this condition is not satisfied implies that a part of the chemical reaction between carbon dioxide and hydroxyl ions is carried out at interface and the other part in the bulk of the liquid. The surface renewal theory developed by Dankwerts contributed the expression shown in equation 6.

$$N = C_{CO_2}^* \cdot a \cdot \sqrt{D_A \cdot k_2 \cdot C_B^{bulk} + k_L^2} \qquad (6)$$

4. Results and Discussion

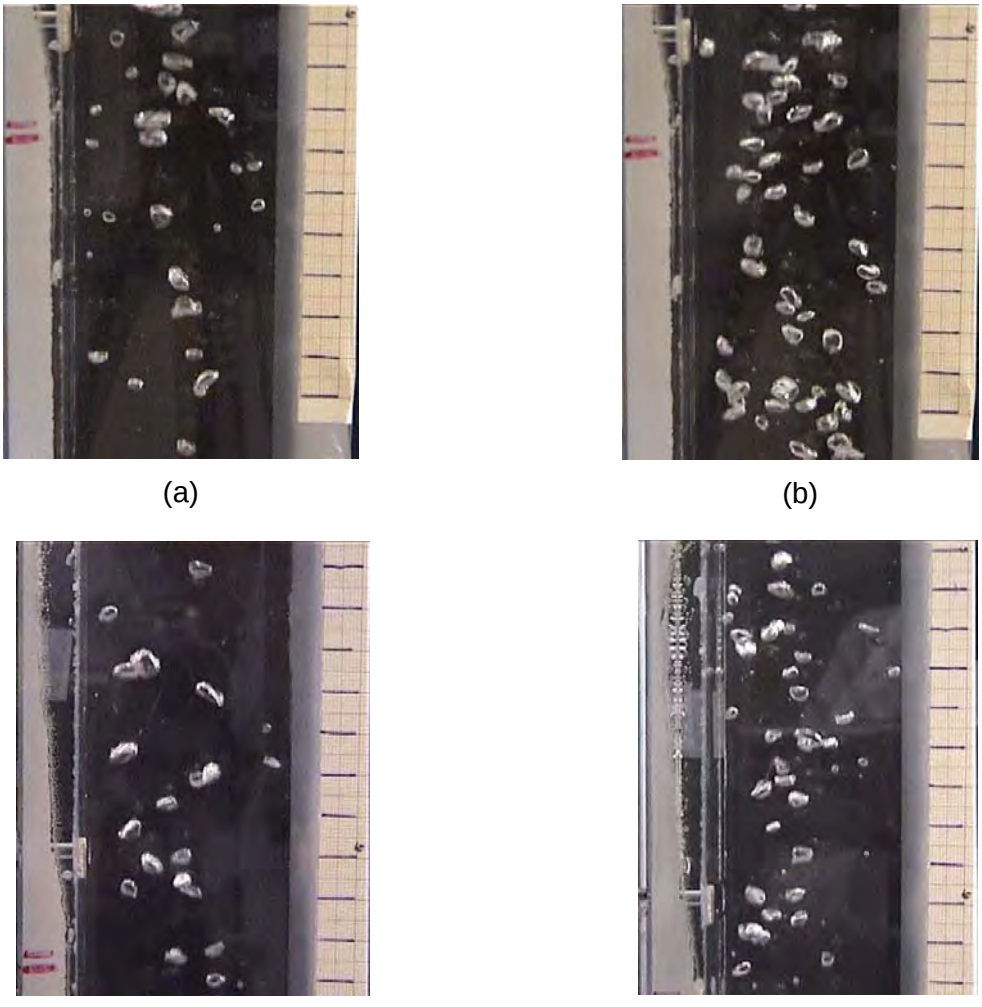

(a) (b)

(c) (d)

Figure 2. Photographs from bubble column under different operation conditions (gas flow-rate and MDEA concentration). (a) [MDEA] = 0.5 M; Q_g = 14 L·h^{-1}; bottom section. (b) [MDEA] = 0.5 M; Q_g = 30 L·h^{-1}; bottom section. (c) [MDEA] = 0.1 M; Q_g = 20 L·h^{-1}; top section. (d) [MDEA] = 1 M; Q_g = 20 L·h^{-1}; top section.

An example of photographs obtained from the bubble column reactor under different conditions is shown in figure 2. The effect of gas flow-rate could be analysed in photographs (a) and (b) observing a higher number of bubbles in (b) photograph. This behaviour causes a direct effect on gas hold-up. Also, figures (c) and (d) allow analyse the effect of MDEA concentration. These photographs show that an increase in MDEA concentration in the liquid phase produces an increase in the number of bubbles and in their size. This kind of photographs have been employed to determine the bubbles size and it distribution and to obtain the reasons for these behaviours.

An example of the experimental results obtained in this analysis is shown in figure 3. In the experimental section, the method indicates that the bubble column must be analysed along the equipment height because bubble size distribution could vary significantly along the bubble column due to the absorption process that carry out into the contactor.

Figure 3 shows that this hypothesis must be taken into account because a clear difference in the bubble size distribution exists at the bottom and the top of the bubble column reactor. Smaller bubbles were detected at the top of the contactor respect the bubbles present at bottom zone. This size bubbles decrease is due principally to the transfer of gas carbon dioxide to the liquid phase.

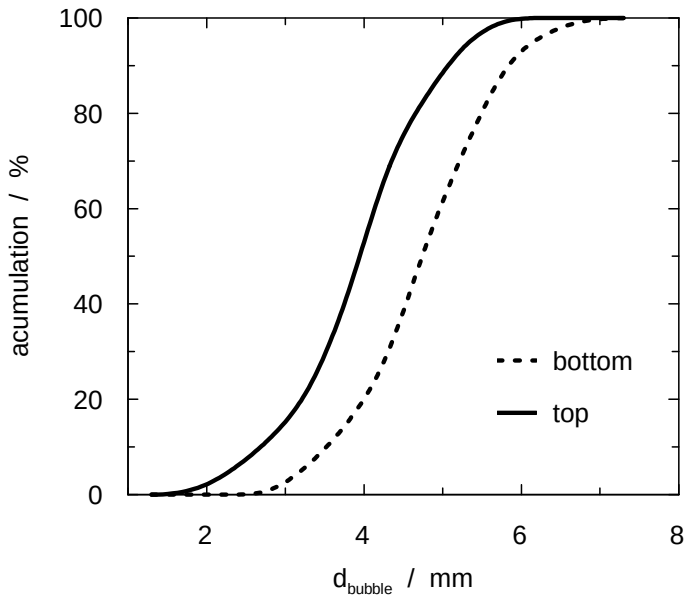

Figure 3. Bubbles size distribution obtained at different column zones. C_{Bo} = 0.5 mol·L^{-1}. Q_g = 30 L·h^{-1}.

Using equation 1-4 and experimental data of bubbles diameter is possible to determine the area between both phases (gas and liquid) and analyse the influence of amine initial concentration and gas flow-rate on the generated interfacial area in the bubble column reactor. Figure 4 shows the influence of both operational variables upon the value of interfacial area. An increase in the gas flow-rate produces a clear increase in the value of interfacial area. This behaviour is due to the increment in the gas hold-up because a higher volume of gas phase is introduced in the contactor. On the other hand, bubble diameter increases too but it has negative effect on the interfacial area value.

An increase in the initial amine concentration in the liquid phase produces also an increase in the value of the interfacial area. This behaviour is assigned to the influence of surface tension of liquid phase upon the diameter of bubbles generated in this liquid phase. Different authors have studied the influence of this physical property on the hydrodynamic of bubble

contactors [6, 7] and they have concluded that a decrease in the surface tension produces a reduction in the bubbles size and it inhibits the coalescence phenomenon.

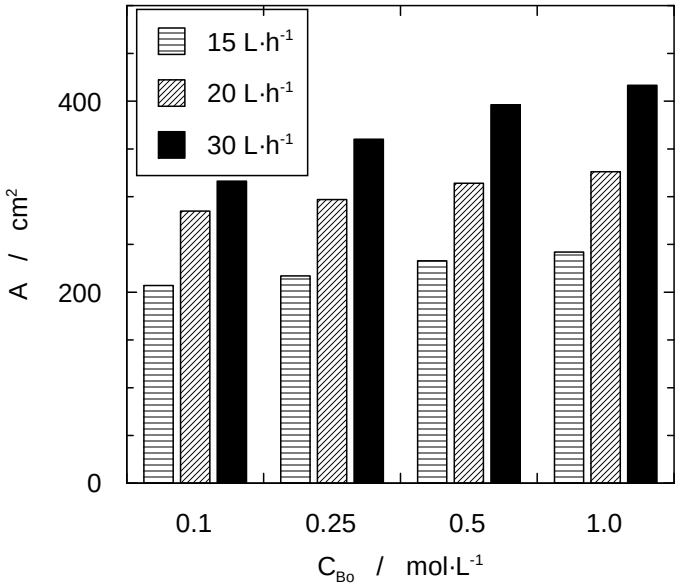

Figure 4. Effect of amine concentration and gas flow-rate upon the interfacial area.

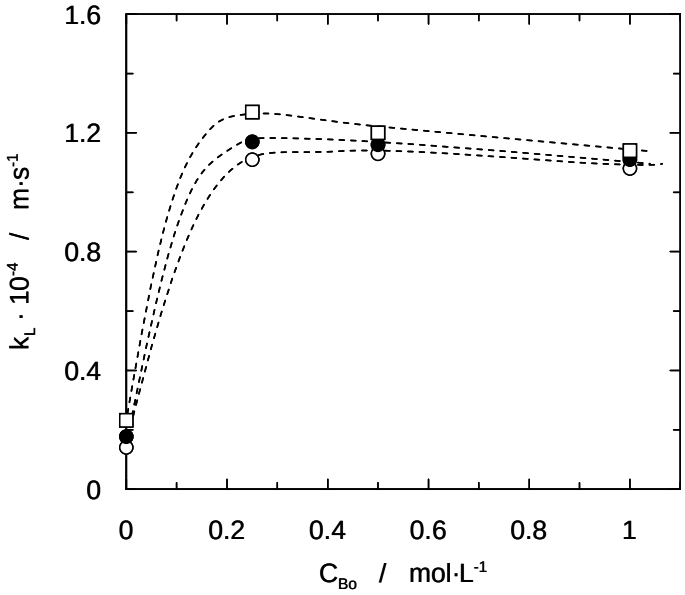

Figure 5. Influence of initial MDEA concentration and gas flow-rate on mass transfer coefficient. (○) Q_g = 15 L·h^{-1}; (●) Q_g = 20 L·h^{-1}; (□) Q_g = 30 L·h^{-1}.

The experimental data corresponding to interfacial area under the experimental conditions employed in present work is employed in the mass transfer coefficient using equation 6 by fitting absorption intensity and amine concentration data.

The calculated results obtained for the mass transfer coefficient and the influence of initial MDEA concentration and gas flow-rate, are shown in figure 5. This figure shows that a higher

initial concentration of amine produces an increase in the mass transfer coefficient until a maximum because higher values of amine concentration produce a slight decrease in this coefficient. The decrease in the value of mass transfer coefficient is due to the viscosity of the liquid phase that increases with the amine concentration. The influence of this physical property upon the mass transfer coefficient has been commented widely by [6, 7].

Literature

[1] P. V. Danckwerts, The reaction of carbon dioxide with ethanolamines, Chem. Eng. Sci. 34 (1979) 443-446.

[2] P. M. M. Blauwhoff, G. F. Versteeg, W. P. M. van Swaaij, A study on the reaction between CO_2 and alkanolamines in aqueous solutions, Chem. Eng. Sci. 39 (1984) 207-225.

[3]. G. F. Versteeg, A. J. van Dijck, W. P. M. van Swaaij, On the kinetics between CO_2 and alkanolamines both in aqueous and non-aqueous solutions. An overview, Chem. Eng. Commun. 144 (1996) 113-158.

[4] T. L. Donaldson, Y. N. Nguyen, Carbon dioxide reaction kinetics and transport in aqueous amine membranes, Ind. Eng. Chem. Fundam. 19 (1980) 260-266.

[5] D. Gómez-Díaz, J. M. Navaza, B. Sanjurjo, L. Vázquez_Orgeira. Carbon dioxide absorption in glucosamine aqueous solutions. Chem. Eng. J. 122 (2006) 81–86.

[6] E. Álvarez, B. Sanjurjo, A. Cancela, J. M. Navaza, Mass transfer and influence of physical properties of solutions in a bubble column, Chem. Eng. Res. Des. 78 (2000) 889-893.

[7] M. Nakanoh, Y. Fumitake, Gas absorption by Newtonian and non-Newtonian liquids in a bubble column, Ind. Eng. Chem. Res. 19 (1980) 190-195.

Proceedings of the 10th International Chemical and
Biological Engineering Conference - CHEMPOR 2008
Braga, Portugal, September 4-6, 2008
E.C. Ferreira and M. Mota (Eds.)

Simulation of membrane separations using a modified Maxwell-Stefan model

Paulo Brito[1,2*], Licínio M. Gando-Ferreira[2], António Portugal[2]
[1] Chemical and Biological Technology Department, School of Technology and Management, Bragança Polytechnic Institute, Campus de Santa Apolónia, 5301–857 Bragança, Portugal
[2] CIEPQPF, Department of Chemical Engineering, University of Coimbra, Pólo II, 3030–790 Coimbra, Portugal

Keywords: Modeling, Ultra-filtration, Transport phenomena, Apparent rejection, Adaptive methods
Topic: Advancing the chemical and biological engineering fundamentals – Membranes and membrane science

Abstract

A modified Maxwell-Stefan model, which considers both the concentration polarization and the transport through the membrane, is tested for the simulation of Dextran-98000 aqueous solutions filtration.

The model is able to successfully simulate experimental data in the high rejection/low flux region, but does replicate the observed rejection drop/pressure build-up which occurs for increased fluxes, which may be due to limitations of the model itself.

1 Introduction

The modeling of mass transfer phenomena in solute separations through inert membranes is essential for the efficient design and optimization of these operations, namely ultra-filtration processes, widely applied in an important range of industries, that include food and biotechnological industrial processes. In this work, a model is applied to simulate the ultra-filtration of aqueous solutions, based on a particular aproach to the Maxwell-Stefan general equations (Kerkhof, 1996). The ultra-filtration process simulation provides an analysis of the solute rejection phenomenon, which, in general, depends on the solution components properties (namely, their molecular sizes), the membrane characteristics and the process operational conditions. Therefore, through the intramolecular transport modelation, we can quantify the influence of each former conditions in the refered rejection phenomenon. This strategy provided promising results in the simulation of PEG-3400 aqueous solutions ultra-filtration (Brito et al., 2004, Ferreira et al., 2003). Now, the purpose is to test the ultra-filtration simulation performance for more massive solutes, specifically dextran-98000.

2 Model

The model considers both the concentration polarization and the transport through the membrane and incorporates a binary friction model based on the Maxwell-Stefan-Lightfoot equation (Kerkhof, 1996). Hence, for the polarization layer, we have:

$$\frac{\partial c}{\partial t} = -\frac{\partial N}{\partial z} \tag{1}$$

with the flux, *N*, defined as,

* Corresponding author. Tel + 351-273-303110. E-mail:paulo@ipb.pt

$$N = -(D + D_t)\frac{\partial c}{\partial z} + u_v c \tag{2}$$

where, $D = D_{12}\Gamma_c$, being D, the Fickian diffusion coefficient; D_t, the turbulent diffusivity; D_{12}, the Maxwell-Stefan diffusion coefficient; and Γ_c, the thermodynamic factor. The turbulent diffusivity is defined assuming an unitary turbulent Schmidt number ($\mathrm{Sc_t} = \nu_t / D_t$), and taking account the turbulent cinematic viscosity computed by the Vieth correlation (Brito et al., 2004):

$$\frac{\nu_t}{\nu} = \left(\frac{2}{9}\pi\sqrt{3}\right)^3 \left(\frac{f}{2}\right)^{3/2} \left(y^+\right)^3 \tag{3}$$

with the normalized distance from the membrane wall, y^+, calculated by,

$$y^+ = \frac{y\langle u_t \rangle \sqrt{f/2}}{\nu} \tag{4}$$

being f, the Fanning friction factor, defined by the Blasius equation, $f = (0.3164/4)\mathrm{Re}^{-0.25}$, and u_t, the circulating fluid velocity.

For the membrane, on the other hand, the molar concentration temporal gradient is given by:

$$\varepsilon \frac{\partial c'}{\partial t} = -\frac{1}{\tau}\frac{\partial N_m}{\partial z} \tag{3}$$

in which, τ is the tortuosity factor, and ε is the porosity. The intramembrane flux, N_m, is calculated by:

$$N_m = -\frac{\Gamma_c}{G}\frac{\partial c'}{\partial z} + u_v \frac{F}{G} c' \tag{4}$$

where, F and G are the convective and friction factors respectively, defined as in Kerkhof (1996) for a monosolute system, with the solute and the solvent represented by subscripts 1 and 2, respectively:

$$F = \left(\frac{1}{D_{12}} + \frac{{c_t}^2 \overline{V}_1 \overline{V}_2}{B_o}\kappa_2\right)\frac{\tau}{\varepsilon} \tag{5}$$

$$G = \left(\frac{1}{D_{12}} + \frac{c_t}{B_o}\left(\phi_2 \kappa_1 \overline{V}_1 + \phi_1 \kappa_2 \overline{V}_2\right)\right)\frac{\tau}{\varepsilon} \tag{6}$$

where, c_t is the total molar concentration, $B_o = r_p^2/4$, is the permeability parameter, r_p, the porous radius, and $\overline{V}_i$, ϕ_i and κ_i are the molar volume, the volume fraction and the viscosity fractional coefficient of component i, respectively. The thermodynamic factor Γ_c is given by (Kerkhof, 1996):

$$\Gamma_c = 1 + c\frac{\partial \ln \gamma}{\partial c} - \frac{c}{c_t}\left(1 - \overline{V}_1 / \overline{V}_t\right)$$

However, ideality is assumed.

The model is completed by the definition of: boundary conditions, fixed bulk concentration at the polarization layer extreme, and equilibrium and flux equalization conditions at the membrane/polarization and membrane/permeate interfaces;

$$z = -\delta \quad \Rightarrow \quad c = c_b$$
$$z = 0 \quad \Rightarrow \quad c' = K_{eq} c \; ; N = N_m \tag{7}$$
$$z = L_m \quad \Rightarrow \quad c' = K_{eq} c_p \; ; N = u_v c_p$$

and initial conditions, zero concentration profile start-up,

$$t = 0 \quad \Rightarrow \quad c = c_b \quad (z = -\delta) \quad \wedge \quad c = c' = 0 \quad (z > -\delta) \tag{8}$$

The problem is discretized in the spatial direction and solved in the temporal dimension until a steady-state profile is reached, which implies a constant profile for the flux over all the spatial domain. Therefore, a simulated stationary permeate concentration, c_p, becames available, that can be used to calculate the apparent solute rejection, R_{app}:

$$R_{app} = 1 - {c_p}/{c_b} \tag{9}$$

The fluxes profiles allow the computation of the pressure drop due to the flow and the simulated total pressure drop,

$$\Delta P_{flow} = \frac{\tau}{\varepsilon} \frac{RT}{B_o} \int_0^{L_m} c_t \sum_{i=1}^{2} \kappa_i N_i \overline{V}_i dz \tag{10}$$

$$\Delta P_{total} = \Delta P_{flow} + \sigma \, \Delta\Pi \tag{11}$$

where $\Delta\Pi$ is the osmotic pressure drop through the membrane and σ, the osmotic reflection coefficient. The membrane resistence may be computed relating the flow pressure drop and the flux using pure water filtration experiments.

$$R_m = \frac{\Delta P_{flow}}{\eta_w u_v} \tag{12}$$

On the other hand,

$$R_m = \frac{L_m}{B_o} \frac{\tau}{\varepsilon} = \frac{8 L_m}{r_p^{\,2}} \frac{\tau}{\varepsilon} \tag{13}$$

which allows the estimation of relations between the structural properties of the membrane, namely of τ/ε, a critical model parameter.

For the particular monosolute system under study (dextran-1 and water-2), the following relations are used in the computation of the specified properties (Blox, 2003):

$$D = 5.96 \times 10^{-11} + 2.12 \times 10^{-11} \tanh(0.0284\rho - 1.491) \tag{14}$$

$$\Pi = 37.0\rho + 0.752\rho^2 + 76.4 \times 10^{-4} \rho^3 \tag{15}$$

and

$$\kappa_1 = \kappa_2 \left(1 + \frac{\eta_{sp}}{\phi_1} \right) \tag{16}$$

$$\kappa_2 = {\eta_w}/{c_t RT} \tag{17}$$

with,

$$\eta_{sp} = a\rho \exp(b\rho) \tag{18}$$

where, ρ represents the solution mass concentration.

3 Numerical Solution

The numerical solution of a normalized version of the partial differential-algebraic equation system, defined over a space-time coordinate system of variables, is accomplished with an adaptive resolution algorithm, based on the Adaptive Method of Lines, and presented by Brito and Portugal (1998). This method is used to solve simultaneously the two modules of the model (polarization layer and membrane) over a one-dimensional discretized space direction, in the time direction until a steady state solute concentration profile is reached. The spatial derivatives are approximated by central finite differences and the time integration is accomplished with DASSL numerical integrator. The normalized concentrations (y and y') are defined in relation to the bulk concentration, c_b, and the spatial coordinate ($-\delta \le z \le L_m$) is normalized to the total spatial domain extent:

$$z^* = \frac{z + \delta}{L_m + \delta} \tag{19}$$

being δ, the polarization layer size and L_m, the membrane thickness. The operational conditions, the solution components and membrane properties, and the simulation parameters used in the obtainance of all results presented in the next section, are resumed in Table 1.

Table 1. Operational conditions, properties, and simulation parameters.

Properties	Operational conditions and parameters
$\overline{V}_1 = 45.6$ m^3/kmol	$\rho_b = 10$ kg/m^3
$\overline{V}_2 = 0.018$ m^3/kmol	$u_t = 0.76$ m/s; 1.57 m/s
$L_m = 5\times10^{-7}$ m	$T = 298$ K
$r_p = 4.5\times10^{-9}$ m	$\delta = 86\times10^{-6}$ m
$\varepsilon = 0.5$	

4 Results

A typical run provides evolutionary profiles like the ones presented in Figures 1 and 2, for normalized concentration (y and y') and space (z^*) variables. The formation of significant solute accumulation at the membrane/polarization interface (in the presented case, the solute concentration is roughly four times higher than bulk concentration - c_b) is verified, together with diminished permeate concentrations, leading to high levels of apparent rejection of solute.

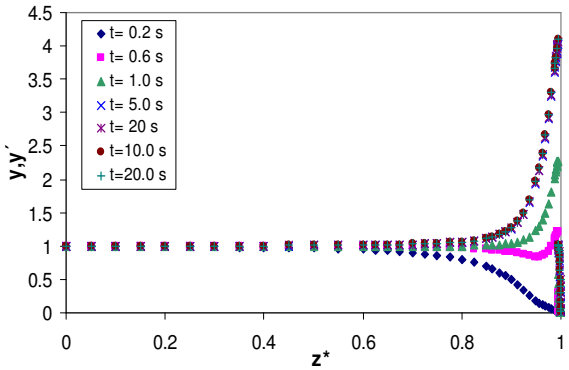

Figure 1. Normalized concentration profiles (polarization and membrane): u_t= 1.57 m/s, u_v= 1.0×10^{-5} m/s and K_{eq}= 0.25.

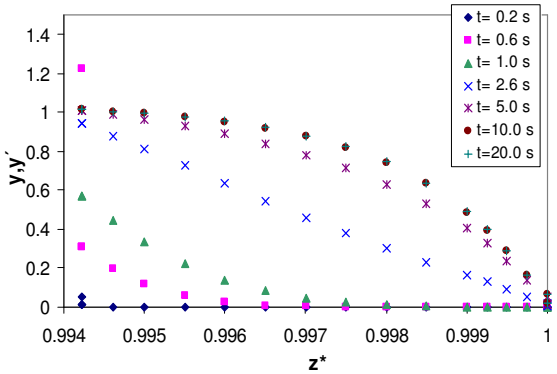

Figure 2. Normalized concentration profiles (membrane): u_t= 1.57 m/s, u_v= 1.0×10^{-5} m/s and K_{eq}= 0.25.

The large levels of rejection are maintained over a reasonable range of flux values (vd. Figure 3). It is verified that fixing K_{eq} at 0.25 allows a good agreement between experimental and simulated results in the practically constant rejection area. However, a sudden important decrease in rejection beyond a flux threshold is observed, which the model seems unable to

replicate, in spite of a slight decreasing tendency that does not fit at all to the experimental data.

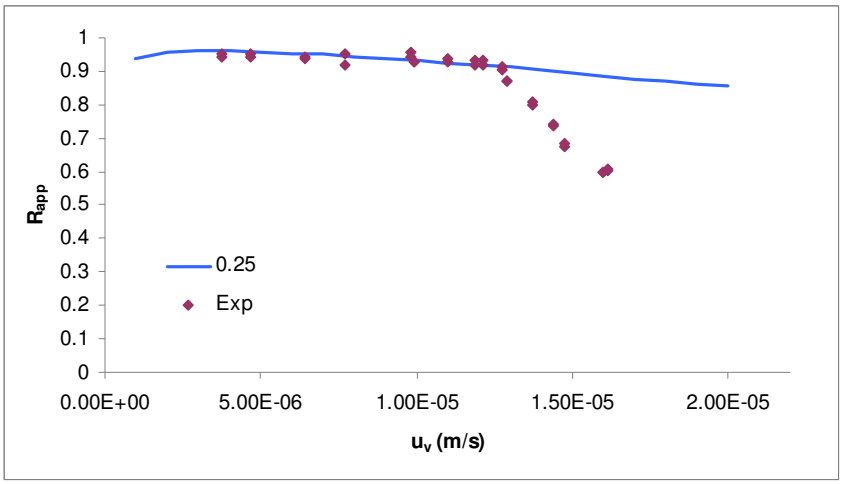

Figure 3. Apparent solute rejection profiles: u_t = 1.57 m/s, K_{eq} = 0.25.

The problem stated above becomes more notorious for results concerning u_t=0.76 m/s. In this case the decrease in rejection occurs earlier and in much stronger manner (vd. Figure 4). Again, the model can successfully replicate experimental results in the high plateau region with the same K_{eq} value, but fails to fit the sudden decrease.

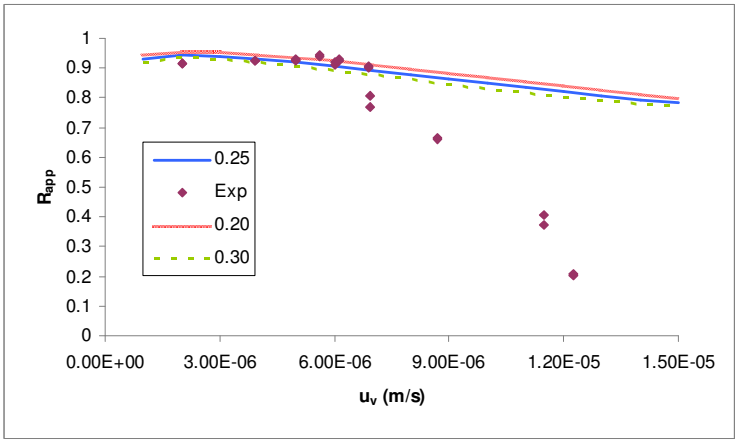

Figure 4. Apparent solute rejection profiles: u_t = 0.76 m/s, for various K_{eq}.

These discrepancies may be due to two major reasons: phenomenon driven, main phenomena enter a different regime in which the model considerations become no longer valid; or parameter driven, the assumptions concerning parameter non-variance in the problem conditions are invalidated. Considering the later case, two important parameters able to affect considerably the results are: membrane resistance, R_m and equilibrium constant, K_{eq}. R_m is estimated using Pure Water Filtration (PWF) experiments in the same conditions (vd. Figure 5; in this case, $R_m = 5.1394 \times 10^{12}$ m^{-1}), a questionable procedure since it is noticeable a typical lack of reproducibility of this kind of PWF data (Blox, 2003). For PEG-3400 filtration experiments this procedure seems to be acceptable, because the experimental pressure drop profiles are very similar to the PWF profiles (Brito et al, 2004). However this is clearly not the case in Dextran experiments. On the other hand, K_{eq} is assumed constant and it is the sole parameter tuned to fit the experimental data available, as stated above. Therefore, it is chosen to test the sensitivity of the model toward these two parameters in order to explain the sudden rejection drop.

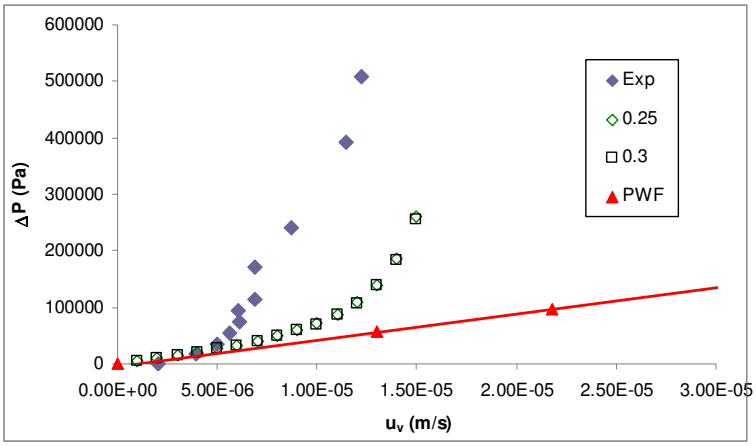

Figure 5. Total pressure drop profiles: u_t = 0.76 m/s, K_{eq} = 0.25; 0.30. (PWF- Pure Water Filtration)

It could be argued that this dramatic rejection drop would be due to sudden changes in the membrane geometry or structure. However, this behavior suggests an important drop in membrane resistance R_m, which is inconsistent with the also dramatic increase in the pressure drop that occurs simultaneously with the rejection fall (vd. Figure 5). In general, this pressure drop rising should be connected with a resistance increase. The same conclusions could be driven by the analysis of the model behavior to changes in K_{eq}. Changing these parameters values in the right direction to account the rejection evolution, will decrease its fitness of pressure data. Alternatively, the pressure drop rising conjugated with rejection drop could be explained with massive solute build-up at the membrane interface leading to extremely high solute concentration values (much higher than the computed by the model in these conditions – up to 25 times the bulk concentration). So, the pressure drop dramatic increase would be due essentially to the osmotic contribution. The model provides a rise in pressure drop and the osmotic pressure drop contribution increases significantly for higher fluxes but overall this rise is insufficient to follow the experimental data. Similar conclusions could be drawn by the analysis of the u_t =1.57 m/s experimental data, which are not presented here. Therefore, it is concluded that the behavior observed is explained by phenomenogical features that are not successfully represented by the model used in the rejection drop zone, and that are particularly visible for lower values of u_t.

5 Conclusions

It is concluded that the model successfully simulates experimental data in the high rejection/low flux region, but it is unable to replicate the observed rejection drop/pressure build-up which occurs for increased fluxes, which may be due to phenomenogical reasons or limitations of the model itself.

References

Blox, M. (2003). Ultrafiltration of multicomponent systems, *Interim Report*, Separation Processes and Transport Phenomena Group, Eindhoven University of Technology.

Brito, P.M.P., Portugal, A.A.T.G. (1998). Application of adaptive methods based on finite difference discretizations in the simulation of a tubular reactor system. *Proceedings of ACOMEN'98 – Advanced Computational Methods in Engineering,* Ghent, Belgium, 697-704.

Brito, P., Ferreira, L.M., Portugal, A., Blox, M., Kerkhof, P. (2004). Modelização de separações por membrana através de métodos de refinamento de malha. *Proceedings of Congresso de Métodos Computacionais em Engenharia*, Lisboa, Portugal, 473 & CD-ROM

Ferreira, L.M., Brito, P., Portugal, A., Blox, M., Kerkhof, P. (2003). A simulation study on the transport phenomena in ultrafiltration. *Workshop on Modelling and Simulation in Chemical Engineering*, Coimbra, Portugal, 8 p.

Kerkhof, P.J.A.M. (1996). A modified Maxwell-Stefan model for transport through inert membranes: the binary friction model. *Chemical Engineering Journal*, 64, 319-343.

Proceedings of the 10th International Chemical and
Biological Engineering Conference - CHEMPOR 2008
Braga, Portugal, September 4-6, 2008
E.C. Ferreira and M. Mota (Eds.)

Influence of pyrolysis parameters on the performance of CMSM

Marta C. Campo, Fernão D. Magalhães, Adélio M. Mendes*
LEPAE – Laboratory of Process, Environment and Energy Engineering, Chemical Engineering Department, Faculty of Engineering, University of Porto, 4200-465 Porto, Portugal.

Keywords: CMSM, Pyrolysis, Gas Separation, Carbon Membranes
Topic: Advancing the chemical and biological engineering fundamentals.

Abstract

Carbon hollow fiber membranes have been prepared by pyrolysis of a co-polyimide P84/S-PEEK blend. The precursor was submitted to proximate analysis by thermogravimetry (TGA) revealing a yield of fixed carbon around 40%. This study aimed at understanding the influence of pyrolysis parameters: end temperature, quenching effect and soaking time on the membrane properties. Permeation experiments were performed towards N_2, He and CO_2. The specie N_2 was again tested after CO_2 to assess if any loss of performance of the membranes had occurred. Scanning electron microscopy (SEM) has been done for all carbon hollow fibers. The highest permeances and ideal selectivities were obtained for the membranes submitted to an end temperature of 750 ºC, previous to quenching.

1 Introduction

Carbon molecular sieve membranes (CMSM), pioneered by Koresh and Soffer in the 80's, are a very recent research topic in the area of gas separation. These inorganic membranes present great advantages over polymeric membranes, since they have comparatively high permeabilities and selectivities, together with high thermal and chemical stability (Saufi and Ismail, 2004; Ismail and David, 2001). The main applications for this type of membranes are, among others, air separation, landfill gas recovery, olefin/paraffin separation, hydrogen recovery and natural gas processing.

Carbon membranes are produced by pyrolysis of a polymeric precursor under an inert atmosphere (Saufi and Ismail, 2004). The preparation of CMSM should always be directed towards the tailoring of the final carbonaceous micropore network. The influence of the pyrolysis parameters and complementary treatments used for producing the final carbon membranes should be studied in order to better suit a certain application. Some previous studies indicate general requests to be fulfilled. The precursors should have high yield of carbon and should be thermosetting. The temperature programs followed in the pyrolysis, the cooling steps and the gas atmosphere employed, are all important aspects that have to be studied and optimized according to the precursor selected, having in mind the final application. Nevertheless, CMSM have two major disadvantages that still have to be overtaken: brittleness and aging effects (Ismail and David, 2001; Menendez and Fuertes, 2001). Nowadays, it is known that oxygen chemisorption on the surface of CMSM reduces the performance of these membranes (Menendez and Fuertes, 2001). This phenomenon may reduce the size of the pores affecting the separation of the gases. In cases that the feed mixture is humidified, the oxygen content on the carbon matrix may lead to the adsorption of water vapor which may block the passage of other species (Lagorsse et al., 2005).

* Corresponding author. Tel + 351-22 508 1695. E-mail:mendes@fe.up.pt

2 Experimental

2.1 Precursor TGA

The precursor used in this study was a co-polyimide P84/S-PEEK blend. It was submitted to a proximate analysis performed in a Netzsch TG 209 F1 Iris, thermogravimetric balance, revealing a yield of fixed carbon approaching 40 %. The temperature protocol followed is described elsewhere (Ottaway, 1982).

2.2 Fabrication of carbon hollow fiber membranes

The pyrolysis occurred inside a quartz tube heated by a Carbolite® TZF 12/100 High Temperature Tubular Furnace, under a 50 $ml_N \cdot min^{-1}$ nitrogen atmosphere, together with a Eurotherm 2408 CP temperature controller. The temperature program employed is based on a temperature program described by Barsema (2004). The main differences from this protocol relate to the end temperature, quenching and soaking time.

The quenching consisted on a quickly cooling down inside a box with a nitrogen flow; *"No"* quenching means that the sole driving force for cooling was the difference between the temperature inside the furnace and the room temperature. The process of removing the carbon hollow fibers from the oven and introducing them into the quenching box was done as fast as possible, in order to minimize air exposure.

The influence of a final step – soaking time – in which the end temperature was kept constant for 2 h before quenching was also analysed.

These two steps, soaking and quenching, may probably lead to microstructural rearrangements, affect the pore size distribution and consequently the selectivity of the membrane.

Table 1 shows the identification of each kind of carbon membrane prepared, concerning its type and pyrolysis' parameters.

Table 1. Identification of the samples and pyrolysis' parameters.

Sample	T_{END} (ºC)	Soaking time (h)	Quenching
HF-700-A	700	0	Yes
HF-700-B	700	0	No
HF-750-A	750	0	Yes
HF-750-B	750	0	No
HF-800-A	800	0	Yes
HF-800-B	800	0	No
HF-700-ST2h	700	2	Yes

2.3 Scanning electron microscopy

All samples identified on table 1 were characterized by means of SEM. Through the pictures taken it was possible to measure the thickness, ℓ, of the selective layer, the inner and outer diameter of each fiber, and consequently the wall thickness. With this information the area, A_m of the membrane was calculated.

2.4 Permeation

After pyrolysis, the resulting carbon membranes were assembled on 3/8'' stainless steel cylinders filling it with a polyurethane resin isolating feed from permeate stream. Figure 1 illustrates the membrane module, where it is evidenced that the feed circulates on the shell side, whereas the permeate is evacuated from the bore side (right side). This edge of the membrane was left open for permeate removal. In order to protect the fibers from breaking, a PVC support rod was used. The other edge was introduced within a plastic tube full with glue. This was the closed edge (left side). These individual modules were then connected to a stainless steel housing which was introduced in a temperature controlled cabinet.

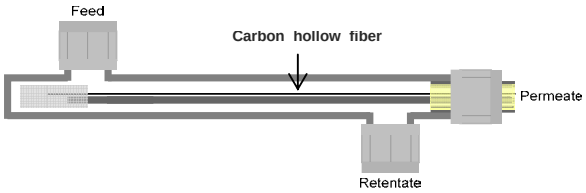

Figure 1. Scheme of the membrane module.

The permeation experiments were conducted at 30 ºC, using a pressure increment method. The several carbon membranes were tested towards N_2, He and CO_2. All the modules were submitted to 2 bar feed pressure on the shell side whereas vacuum was applied on the bore side. Here, ideal gas behavior was assumed and, hence, the monocomponent permeance, $\mathbf{P}$ was calculated according to equation (1),

$$\frac{\mathbf{P}}{\ell} = \frac{V_P \, \upsilon_M \, \left(P_l^t - P_l^0\right)}{\Re \, T \, t \, A_m \left(P_h - P_l\right)} \tag{1}$$

where V_P is the volume of the tank where the permeate is collected, P_l and P_h are respectively, the permeate pressure and the feed pressure, A_m is the effective area of the fiber, T is the absolute temperature, υ_M is the molar volume of the gas, $\Re$ is the gas constant, and t is the time. The ideal selectivity $\alpha_{i/j}$ for a certain pair of gases i and j is obtained by equation (2),

$$\alpha_{i/j} = \frac{\mathrm{P}_i}{\mathrm{P}_i} \tag{2}$$

where $\mathbf{P}_i$ and $\mathbf{P}_j$ are the permeances of species i and j, respectively.

3 Results and Discussion

3.1 Scanning electron microscopy

SEM pictures were taken to compare the structures of the different samples. Although fiber dimensions decrease in opposition to the end temperature, no further observations can be reliably taken. Figure 2 provides an example of micrographs taken for sample HF 700B.

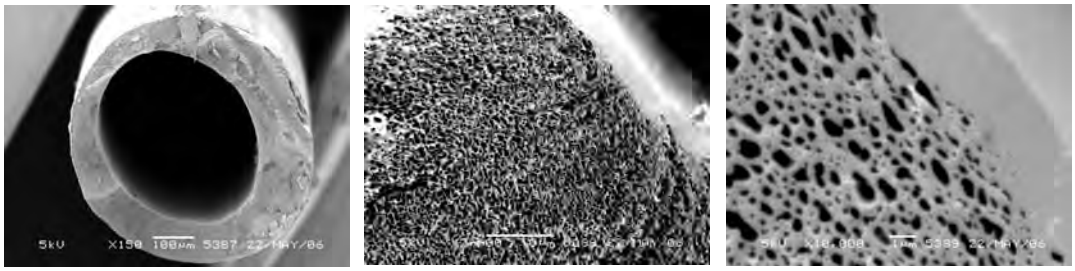

Figure 2. SEM pictures from HF 700 B carbon hollow fiber membrane.

3.2 End temperature effect

The effect of the end temperature on the performance of carbon hollow fiber membranes can be studied by determining monocomponent permeances. On table 2 are listed permeances and ideal selectivities for samples pyrolysed up to 700, 750 and 800 ºC towards N_2, He and CO_2. Figure 2 gives a better overlook on these results.

Table 2. Effect of end temperature on the permeance of carbon hollow fibers.

	Permeance / GPU*			Ideal Selectivity		
Sample	**N_2**	**He**	**CO_2**	**CO_2/N_2**	**CO_2/He**	**He/N_2**
HF-700-A	8	95	136	18	1.5	12
HF-750-A	24	151	356	15	2.4	6.4
HF-800-A	11	79	117	10	1.5	7.0

* $GPU = 10^{-6} cm^3 cm^{-2} s^{-1} cmHg^{-1}$

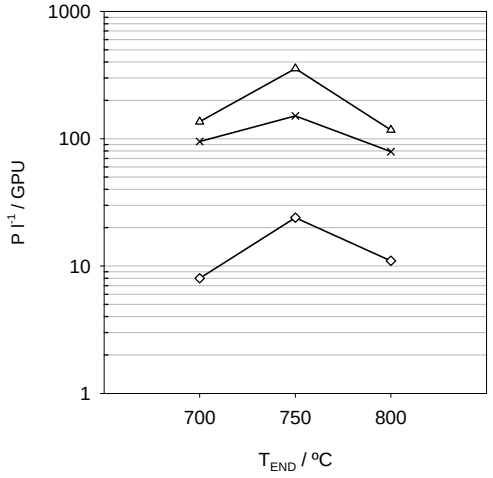

Figure 3. Permeation data through carbon membranes prepared up to 700, 750 and 800 ºC:
◇ - N_2, × - He and △ - CO_2.

From table 2 and figure 3 it is clear that for 750 ºC end temperature there is a maximum in permeance for all the species studied. For each end temperature, the species with lower

permeance is N_2 (L-J kinetic diameter 0.364 nm). However, despite CO_2 (0.33 nm) having a higher kinetic diameter than He (0.26 nm), the shape of the two species is different: the first one is linear and the second one is spherical. This difference in shape may be favorable to CO_2 that might get into smaller pores if it passes in it smallest dimension. Besides, it is known that normally CO_2 has a high affinity towards carbon matrixes, in opposition to He, which mostly does not adsorb. It is being assumed that adsorption plays a significant role in the mass transport mechanism through these membranes: molecular sieving combined with surface diffusion. A general look at the values of selectivities reflects that the highest are achieved for 700 ºC. From 700 to 750 ºC the increase in permeances for all species might indicate that the total pore volume has increases. On the other hand, the decrease in selectivity for the pairs CO_2/N_2 and He/N_2 is suggesting that the mean pore width is eventually enlarging.

3.3 Quenching effect

On this study, as previous mentioned, it was intended to analyze the permeance dependency on the way membranes are cooled from the pyrolysis end temperature to room temperature. Table 3 summarizes permeation data and ideal selectivities of the membranes obtained up to 750 ºC.

Table 3. Quenching effect on the permeance of carbon hollow fibers.

	Permeance / GPU			Ideal Selectivity		
Sample	**N_2**	**He**	**CO_2**	**CO_2/N_2**	**CO_2/He**	**He/N_2**
HF-750-A	24	151	356	15	2.4	6.4
HF-750-B	14	100	203	14	2.0	7.1

It is observed that the highest permeances are generically obtained when the membranes are quenched just after achieving 750 ºC. As for selectivities, table 3 shows that these values are reasonably constant. Qualitatively, it is possible to infer that the mean pore width was kept constant but the total volume of pore has decreased.

3.4 Soaking time effect

The soaking time consisted on keeping the membranes at the end temperature for a certain time interval, just before quenching. The effect of such a soaking time on the performance of carbon membranes is presented on table 4.

Table 4. Effect of soaking time on the permeance of carbon hollow fibers.

	Permeance / GPU			Ideal Selectivity		
Sample	**N_2**	**He**	**CO_2**	**CO_2/N_2**	**CO_2/He**	**He/N_2**
HF-700-A	8	95	136	18	1.5	12
HF-700-ST2h	14	118	159	11	1.3	8.2

In this case, from table 4, all the permeances are enhanced by the existence of a final isothermal step at 700 ºC end temperature but all the selectivities are lower. Higher permeances allied to lower selectivities might be an indication that the total pore volume has increased as well as the mean pore width.

3.5 CO_2 exposure

After exposure to CO_2 a reference experiment with N_2 was performed to assess any possible decrease in the permeance of the membrane. CO_2 is electron-deficient and thus, acts as a Lewis-acid (Raveendran et al., 2005). Although the membranes are essentially carbon, there may be some oxygenated groups on the surface (Brennan et al., 2001), acting as a Lewis-base, enhancing interactions with CO_2. Nevertheless, experiments showed no loss in permeance due to CO_2 exposure.

4 Conclusions

The pyrolysis parameters studied influence the characteristics of the resulting carbon membranes. The highest permeances and ideal selectivities were obtained for the membranes submitted to an end temperature of 750 ºC, previous to quenching. It was also concluded that the existence of a final soaking time after reaching the end temperature, just before quenching, improved the permeance of the carbon membranes, but causes a decrease in selectivity. Furthermore, it was observed that the membranes revealed higher permeances when quenched at the end of the process than the ones naturally cooled down to room temperature. No decrease in the performance of the membrane due to CO_2 exposure was observed.

Acknowledgments

The work of Marta Campo was supported by FCT, grant SFRH/BD/23833/2005. The authors would like to acknowledge the funding provided by FCT in the context of the research project POCI/EQU/60246/2004. The authors would also like to thank Doctor Tymen Visser, Doctor Kitty Nymeijer and Professor Matthias Wessling for their support during the stay of Marta Campo at MTG, Twente.

References

Saufi, S.M., Ismail, A.F. (2004). Fabrication of carbon membranes for gas separation - a review. *Carbon*, 42(2),241-259.

Ismail, A.F., David, L.I.B. (2001). A review on the latest development of carbon membranes for gas separation. *Journal of Membrane Science*, 193(1),1-18.

Menendez, I., Fuertes, A.B. (2001). Aging of carbon membranes under different environments. *Carbon*, 39(5),733-740.

Lagorsse, S., Campo, M.C.,Magalhães, F.D., Mendes, A.M. (2005). Water adsorption on carbon molecular sieve membranes: Experimental data and isotherm model. *Carbon*, 43(13), 2769-2779.

Barsema, J. (2004). *Carbon Membranes - Precursor, preparation and functionalization*. *PhD Thesis*, Enschede.

Ottaway, M. (1982). Use of Thermogravimetry for Proximate Analysis of Coals and Cokes. *Fuel* 61(8), 713-716.

Raveendran, P., Ikushima, Y. Wallen, S. L. (2005). Polar attributes of supercritical carbon dioxide. *Accounts of Chemical Research*, 38(6), 478-485.

Brennan, J. K., Bandosz, T. J., Thomson, K. T., Gubbins, J. K., (2001). Water in porous carbons. *Colloids and Surfaces a-Physicochemical and Engineering Aspects*, 187, 539-568.

Proceedings of the 10th International Chemical and
Biological Engineering Conference - CHEMPOR 2008
Braga, Portugal, September 4-6, 2008
E.C. Ferreira and M. Mota (Eds.)

Influence of Pressure on the Yield of Supercritical CO_2 Extraction of Linseed (*Linum usitatissimum* L.) Oil and Investigation of its Antioxidant Potential

Elisângela. L. Galvão[1], Joanna A. C. Barros[2], Ana V. B. Moreira[2], Humberto N. M. Oliveira[1], Elisa M. B. D. Sousa[1]*

[1] Universidade Federal do Rio Grande do Norte, Departamento de Engenharia Química, Campus Universitário s/n, CT/ DEQ/PPGEQ , Lagoa Nova, 59072-970- Natal, RN, Brasil; TEL: 55-84-32153769-224, FAX: 55-84-32153770.

E-mail: elgalvao@eq.ufrn.br, elisa@eq.ufrn.br

[2] Universidade Federal do Rio Grande do Norte, Departamento de Nutrição, Av. Gen. Cordeiro de Farias, s/n. Petrópolis – 59010-180-Natal, RN- Brasil; TEL: 84-32154322.

E-mail: ana.vladia@terra.com.br

Keywords: linseed oil, supercritical CO_2 extraction, lipid composition.

Topic: Advancing the chemical and biological engineering fundamentals – extraction.

Abstract

The present study proposes to investigate the effect of pressure on the yield of supercritical CO_2 extraction of linseed oil and its influence on the lipid profile of the oil obtained. Moreover, the antioxidant potential of the linseed oil through thin-layer chromatography (TLC) and the evaluation of the co-oxidation of substrates of the system β-carotene/ linoleic acid were determined. The supercritical extractions were performed isothermally (at 50°C) for two extraction pressures (P = 150 and 250 bar) in a fixed bed extractor operating at a constant solvent flow of 1.5 gCO_2/min. Experimental extraction time was set at 5h. The yield values for each pressure condition tested in the supercritical CO_2 extraction assays varied from 3.8% (at 150 bar) to 8.3% (250 bar). The oil samples were esterified and submitted the chromatographic analysis. The main fatty acids (FA) found in the brown linseed oil were palmitic (6.51-6.52%), stearic (5.19-5.31%), oleic (21.96-22.09%), linoleic (13.85-13.86%) and α-linolenic (51.23-51.49%). The presence of antioxidant phenolics compounds was evidenced in all the samples, however, the best protection factor against the oxidation (21.33%) was obtained for the extracted oil samples at 250bar (volume of 200 μg/100g). The results showed that the linseed oil besides being an important source of essential fatty acids, also presents natural antioxidants, ratifying its role as an important food for the human nutrition.

1. Introduction

The extraction technique using supercritical fluids to obtain natural products has promoted a great deal of scientific and technological development in recent years, mainly in sectors linked to the food, pharmaceutical and chemical industries. In the food sector, in particular, there has been an explosion of interest on the part of consumers in the role of specific foods or physiologically active food components, the supposedly functional foods that improve health (Roberfroid, 1999). In this context, linseed (*Linum usitatissimum L.*), recognized for its rich composition of family acids of the ω3 family has received considerable attention.

Although it is an oleaginous seed widely used in industrial oil production, there are few published studies on linseed oil recovery using supercritical extraction. Accordingly, this study proposes to investigate the effect of operating extraction pressure on the yield of supercritical CO_2 extraction of linseed oil and its influence on the lipid profile of the linseed oil obtained.

2. Materials and Methods

Raw Material Preparation.

The brown linseeds (from a single lot collected in March 2007 in the city of Guarani das Missões, Brazil) were homogenized, sifted and stored in glass flasks at -20ºC until use. Sample moisture was determined according to the AOCS 2-54 method. To prepare the particle bed, the seeds were ground in a domestic multiprocessor for 10 seconds and separated in a sieve agitator containing Tyler sieves. Sample granulometry was composed of a mixture of particles with 30% of 24, 30% of 28, 20% of 32 and 20% of 48 mesh. A fixed mass of 140 ± 2 g of linseed was introduced into the extraction cell, forming the fixed particle bed for each experiment.

SC-CO_2 Extraction. The tests were performed isothermically (at 50ºC) for two extraction pressures (P = 150 and 250 bar) in a fixed bed operating at a constant solvent flow of 1.5 gCO_2/min (measured under ambient conditions). Experimental extraction time was fixed at 5 h. Linseed oil extraction at each pressure condition was carried out in duplicate and the mean of the results was used. The oil samples were collected at predetermined time intervals, weighed on an analytical scale, sealed and stored at -20°C for subsequent analyses.

Analyses. The oil samples obtained in supercritical extraction were sterified according to the Hartman and Lago method (1973) and submitted to chromatographic analyses. The analyses were performed in an Agilent 6850 series GC system capillary gas chromatography (CGC). The column used was the DB-23 Agilent (50% cyanopropyl) – methylpolysiloxane, 60m x 0.25mm x 0.25µm). The chromatographic conditions were as follows: 1) Temperature gradient: the initial temperature was 150°C/2 min, increasing 5°C/min up to 215°C, remaining at this temperature for 12 minutes; 2) Injector temperature: 250°C; 3) Detector temperature: 280°C; 4) Entrainment gas: nitrogen at a flow of 1mL/min and injector split ratio of 1/50. The identification of fatty acids in the samples was compared to the spectra of fatty acid patterns determined under the same conditions.

Antioxidant activity. Thin-layer chromatography (TLC) was used for the qualitative identification of the presence of antioxidant composites in the linseed oil samples. For the TLC, the plates were coated with Merck's silica gel G 60 (0.25mm) and activated at 110°C for 1 hour. We then applied 100µL (10µg/mL) of each sample, obtained at different operating pressures. Chromatographic development was performed using n-butanol: acetic acid: water (4:1:5) with a 15 cm path as solvent system. The developing reagents used were β-carotene/linoleic acid and ferric chloride/potassium/ferricyanide, according to procedures described by Nascimento (2002). The plates were exposed to natural light and were observed after 12h and 24h. The β-carotene developer is specific for identifying the presence of substances with likely antioxidant activity and can be observed by the orange coloration on the plates. Ferric chloride and potassium ferricyanide show the presence of likely phenolic composites, visualized by the blue coloration on the plates (Duve and White, 1991). According to Degani, Cass and Vieira (1998), the retention factor (Rf) is the most important parameter to be considered in TLC and is calculated from the ratio between the distance traveled by the substance under study and the distance traveled by the mobile phase. The antioxidant activity of the linseed oil was determined from the assessment of the co-oxidation of the substrates in the β-carotene/linoleic acid system, according to methodology developed

by Marco (1968) and modified by Miller (1971). This is an *in vitro* method that uses β-carotene and linoleic acid as oxidant agents and tween as emulsifying agent. The method is based on spectrophometric measures of decoloration (oxidation) of the β-carotene induced by the products of the oxidative degradation of linoleic acid. The concentrations of the samples used in the assays (100 and 200 µL/100g) were proposed by Moreira and Mancini Filho (2003a) and the spectrophotometric measures of the solutions were performed every 15 min for two hours. All the determinations were carried out in duplicate and were followed by a control without antioxidants. The results are expressed as a percentage of oxidation inhibition (%I), which is calculated considering the decline in optical density of the control (Dc) as 100% oxidation (Equation 1).

$$\%I = \left(\frac{Dc - Dam}{Dc} \right) 100 \qquad (1)$$

The decrease in the optical density reading of the samples (*Dam*) is given by $Dam = Abs_{initial} - Abs_{final}$ and for control $Dc = Abs_{initial} - Abs_{final}$.

3. Results and Discussion

The linseed sample had a moisture content of 7.6% and particle diameter of 0.42mm.

Process yield. The mean yield values for each pressure condition used in the supercritical extraction assays are shown in Figure 1. A yield of 3.8% was obtained for the minimum pressure used (150 bar), with an average collection of 5.2g of oil. For the maximum pressure used (250 bar), the mean yield was 8.3%, with an average collection of 12.01g of oil. The yield of each extraction was calculated from the ratio between the oil mass obtained in each assay and the linseed mass introduced into the extractor column.

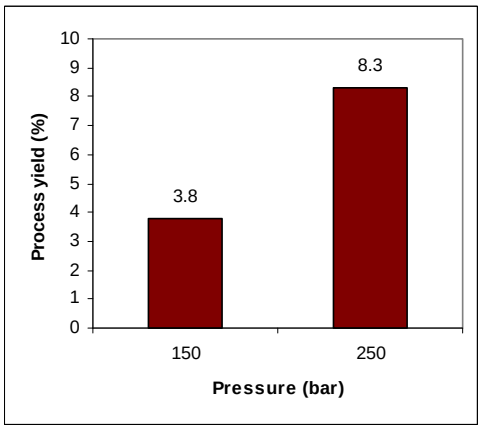

Figure 1. Process yield of the supercritical extraction of linseed oil as a function of extraction pressure**.**

Higher yield values were obtained with higher pressures. This result was expected, since increased operating temperatures cause a rise in CO_2 density, which induces better oil solubilization in supercritical CO_2, resulting in greater oil recovery.

Thin-layer chromatography (TLC). The chromatographic profiles of the linseed oil samples for the different extraction pressures studied are shown in Figure 2.

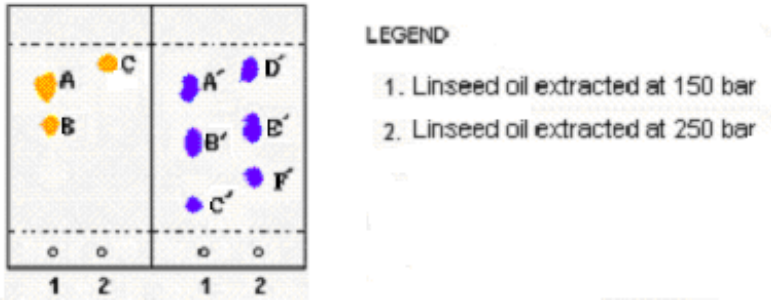

Figure 2. Chromatographic behavior of linseed oil samples obtained by supercritical CO_2 extraction at different operating pressures. (P = 150 and 250 bar)

All the linseed oil samples developed with β-carotene displayed bands with antioxidant activity. These bands were identified by the permanence of the orange coloration on the chromatographic plates, indicating the antioxidants present in the oil impeded the photooxidation of β-carotene. Retention factors varied between 0.64 and 0.96 for samples 1 (with linseed oil obtained at 150 bar) and 2 (with linseed oil obtained at 250 bar). Rf can vary according to a number of factors such as: adsorbent layer thickness, temperature and saturation of the vat containing the solvent system. The development of the plates with the ferricyanide/ferric chloride system showed the presence of phenolic composites, a fact indicated by the appearance of blue stains on the chromatographic plates, with a variation in Rf between 0.14 and 0.94. According to Moreira and Mancini Filho (2003b), phenolic composites are considered natural antioxidants. Thus, this result corroborates those obtained in the development with β-carotene, in which the linseed oil samples contained composites with antioxidant activity. A similar situation was observed by Nascimento (2002) for extracts of *Turnera ulmifolia* Linn., where he detected phenolic composites that inhibited β-carotene oxidation and therefore, had antioxidant activity.

Table 1**.** Rf of the linseed oil samples in TLC.

BANDS		**Rf**	
β-carotene	Ferricyanide/ Ferric Chloride	β-carotene	Ferricyanide/ Ferric Chloride
A	A'	**0.77**	**0.80**
B	B'	**0.64**	**0.63**
C	C'	**0.96**	0.14
	D'	-	**0.94**
	E'	-	0.58
	F'	-	0.17

bold – bands relationship between phenolics compounds and antioxidant activity.

Antioxidant Activity. The presence of antioxidant activity in the linseed oil samples was determined in the β-carotene/linoleic acid system and the results are presented in Figure 3.

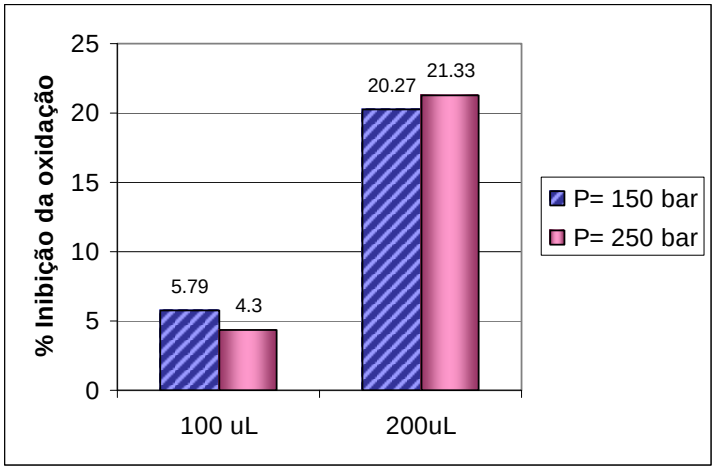

Figure 3 – Percentage of oxidation inhibition in the β-carotene/linoleic acid system for the linseed oil samples obtained at different extraction pressures.

The results show distinct levels of protection against the oxidative process; however, the best protection factor against oxidation (21.33%) was obtained for the oil samples extracted at 250 bar (sample volume of 200 μg/100g).

FA Composition. The main fatty acids (FA) found in the brown linseed oil were palmitic (6.51%), stearic (5.19-5.31%), oleic (21.96-22.09%), linoleic (13.85-13.86%) and α-linolenic (51.23-51.49%).

The percentage of each fatty acid found in linseed oil did not vary significantly with extraction pressure used. Brown linseed oil had a mean value of 65.22% of polyunsaturated fatty acids (C18:2n-6 and C18:3n-3), 22.03% of unsaturated fatty acids (C18:1) and 11.77% of saturated fatty acids (C16:0 and C18:0).

Table 2. Composition of brown linseed oil fatty acids (% m/m) obtained at different extraction pressures.

Fatty acid	150 bar	250 bar
Palmitic (C16:0)	6.51	6.51
Stearic (C18:0)	5.31	5.19
Oleic (C18:1)	22.09	21.96
Linoleic (C18:2n-6)	13.85	13.86
Linolenic (C18:3n-3)	51.23	51.49
Unidentified	1.01	0.99

4. Conclusions

The pressure range used in the supercritical extraction of linseed oil resulted in yield percentages of 3.8% and 8.3% (at 150 and 250 bar, respectively) for a total extraction time of 5h at a temperature of 50°C and mean solvent flow rate of 1.5 gCO_2/min. The results suggest a proportional relationship between the increase in linseed oil recovery and the rise in operating pressure. With respect to oil composition, no significant differences were observed between FA concentration values as a function of the extraction pressure used in the

experiments. In regard to the potential antioxidant of the linseed oil, the presence of antioxidant phenolic compounds was observed in all the samples; however, the best protection factor against oxidation (21.33%) was obtained for the extracted oil samples at 250bar (volume of 200 μg/100g). The results showed that linseed oil, in addition to being an important source of essential fatty acids, contains natural antioxidants, confirming its role as an important food for human nutrition.

5. References

DUVE, K.J.; WHITE, P.J. Extraction and identification of antioxidants in oats. Journal of the American Oil Chemists' Society, Champaign, v.61, n.6, p.365-370, 1991.

DEGANI, A. L. G., CASS, Q. B., VIEIRA, P. C. Cromatografia: um breve ensaio. Química Nova na Escola, São Paulo, v. 7, p. 21-25, Maio 1998.

HARTMAN, L., LAGO, R.C.A. (1973). Rapid preparation of fatty acids methyl esters. Lab. Pract., London, 22, 475-476.

MARCO, G. J. A rapid method for evaluation of antioxidants. Journal of the American Oil Chemists' Society. Champaign, v.45, p.594-598, 1968.

MILLER, H. E. A simplified method for the evaluation of antioxidants. Journal of the American Oil Chemists' Society, Champaign, v.48, p.91, 1971.

MOREIRA, A. V. B; MANCINI-FILHO, J. Atividade antioxidante das especiarias mostarda, canela e erva-doce em sistemas aquosos e lipídicos. Nutrire: rev. Soc. Bras. Alim. Nutr., v. 25, p. 31-46, jun., 2003a.

MOREIRA, A. V. B.; MANCINI FILHO, J. Efeito dos compostos fenólicos de especiarias sobre lípides poliinsaturados. Rev. Brasileira de Ciências Farmacêuticas, vol. 39, supl. 3, p.130-133, 2003b.

NASCIMENTO, Maria Aparecida. Avaliação da atividade antioxidante in vitro dos extratos etéreo, etanólico, hidroetanólico e aquoso de *Turnera ulmifolia Linn*. (*Turneraceae*). Natal: UFRN, 2002. 61p. Dissertação (Mestrado), Programa de Pós-Graduação em Ciências Farmacêuticas, Universidade Federal do Rio Grande do Norte, Natal, 2002.

Official Methods and Recommended Practices of the American Oil Chemists' Society, 4th edn., AOCS Press, Champaign, vol.1, 1993.

ROBERFROID, M.B. (1999). What is beneficial for Health? The Concept of Functional Food. Food and Chemical Toxicology, 37, p.1039.

Proceedings of the 10th International Chemical and
Biological Engineering Conference - CHEMPOR 2008
Braga, Portugal, September 4-6, 2008
E.C. Ferreira and M. Mota (Eds.)

Supercritical Fluid Extraction of Grape Seed Oil using an Enzymatic Pre-treatment

C P. Passos[1], R.M. Silva[1], F.A. da Silva[1], M.A. Coimbra[2], C.M. Silva[1,1]
[1]CICECO, Department of Chemistry, University of Aveiro, 3810-193 Aveiro, Portugal
[2] Department of Chemistry, University of Aveiro, 3810-193 Aveiro, Portugal

Keywords: Supercritical Fluid Extraction, Enzymatic treatment, grape seed
Topic: Advancing the chemical engineering fundamentals.

Abstract

In this work, the supercritical fluid extraction of grape seed oil has been investigated. Grape (*Vitis vinifera*) seeds have been previously treated with an enzymatic cocktail of protease, xylanase, pectinase, and cellulose to increase the oil extractability upon partial hydrolysis of the vegetable cell walls. At 160 bar and 40ºC, the extraction yield of pre-treated biomass reached 16.5%, which is 43% superior to that of untreated samples. The first extraction curve clearly overcomes the one obtained for non-treated seed. Modelling has been accomplished providing good representations.

1. Introduction

Grape seed (Vitis vinifera L.) is a well known oilseed crop and a major by-product resultant from the wine industry, containing typically between 7-15% (w/w) of oil (Gomez, et al. 1996, Sovova 2005). It is also an appealing product due t its large availability, as a major by-product resultant from the wine industry. This research group is investigating ways of increasing the worth of such sub-products.

The extraction of vegetable oils using supercritical (SC) carbon dioxide is being studied as a potential alternative to conventional extraction methods. The most important reasons in this application come from the use of a harmless solvent, mild operating conditions, and the possibility to tailor inherent important properties such as solubility, selectivity, etc. Supercritical carbon dioxide is the usual solvent of choice, sometimes combined with polar co-solvents.

In recent years, supercritical fluid extraction (SFE) of grape seed oil has demonstrated that the amount of extracted oil is equivalent to that obtained by conventional soxhlet *n*-hexane extraction (Gomez, et al. 1996). Sovová et al. (2001) investigated the solubility of grape seed oil in SC CO_2 obtaining similar results to the one's presented in earlier studies from experimental extraction curves, where it was stated it becomes appreciable at 40°C for pressures around 200 bar, for vegetable oils whose main components are triglycerides (Bamberger, et al. 1988).

In the SFE process, the pressurised solvent flows continuously through the bed of particles and dissolves the solute. Behind the extractor, the pressure of the solution is reduced; solvent power of the fluid expanded to gaseous state dramatically decreases and the solute precipitates in a separator where its amount can be measured. The process is most easily characterised by extraction curve, i.e. the plot of the

[1] Corresponding author. Tel + 351-234-401549. E-mail:carlos.manuel@ua. pt

accumulated extract *versus* the time or the amount of solvent passed through the extractor.

To account for the sudden reduction of the extraction rate observed after a first extraction period, (that is particularly observed when vegetable oil is extracted from seed), the concept of broken and intact cells has been introduced (Sovova 1994). Close to the surface there is a region of broken cells whose walls have been damaged by pre-treatment processes, and particle core contains intact cells. Mass transfer resistance due to cell walls is high and therefore there is a large difference in diffusion rates from both regions; the initial fast extraction from broken cells is followed by a much slower extraction period from intact cells (Sovova 2005).

In this work, grape seed oil extraction is carried out using SC CO_2. To enhance the yield of the process, the extraction is combined with an enzymatic pre-treatment (cocktail of enzymes with pectinase, xylanase, protease and cellulase actions).

2. Experimental Procedure

2.1. Processing of the solid plant material

Seeds were collected from grapes (*Vitis vinifera* L.) of the red variety *Touriga Nacional* harvested at technological maturity in *Caves Messias* (Anadia, Portugal) during September 2007. Seeds were collected during transfer of the musts in wine fermentation, and separated from pulp and skins by decantation and sieving. A first wash removed immature grains floating at water surface. Subsequently, the seeds were submitted to several washes with water (200 g/L) under gentle stirring with a magnetic bar at 4 ºC during a minimum of three days, with two water exchanges per day, until a minimum constant turbidity was observed. The purified seeds were finally washed with ethanol, air dried at room temperature, and stored at 4 ºC until use. Finally, milling was carried out on a domestic coffee mill, and the particles classified in a standard sifter with several mesh sizes. For further analyses only paticles with a size diameter between 1.0-1.4 mm were selected.

2.2. Enzymatic pre-treatment

Prior to the SFE, an enzymatic pre-treatment was performed based on previous optimized results by Passos et al. (2008). Following to that essay, the experimental conditions selected are: reaction time of 24h, 40ºC, pH=4, and a concentration range of enzymes of 29, 142, 1191, and 21 U/g of seed sample of cellulase, pectinase, protease and xylanase, respectively.

2.3. Supercritical Fluid Extraction

Extraction measurements were run in a semi-batch flow extraction apparatus built/assembled at the University of Aveiro. It has been operated with nearly 95 g of crushed grape seeds, a CO_2 flow rate of 0.6 kg h^{-1}, at 160 bar and 40ºC. Two sets of experiments were carried out: one with enzymaticaly pre-treated seed, and another one with untreated seed for comparison. The extraction yield was defined (% w/w) as the quantity of oil extracted divided by the quantity of dried vegetable matrix loaded in the extractor multiplied by 100.

3. Mathematical Modelling

Among the various models presented in literature to describe SFE from solid biomass, the model developed by Sovová (2005) has been chosen in this essay. It represents experimental data fairly well. The model assumes that the oil is distributed between an easily accessible part of the seed and another fraction corresponding to the intact core cells where oil is entrapped. Therefore, three material balances were writhen (one to the extractor and one for each particle region):

a.1 (Fluid Phase)

$$\left[\varepsilon\rho_f \frac{\partial y}{\partial t}\right] + \left[\varepsilon\rho_f u \frac{\partial y}{\partial z}\right] = j_f = j_{f1} + j_{f2} \qquad [2]$$

a.2 (Solid phase with broken cells)

$$\left[(1-\varepsilon) r \rho_s \frac{\partial x_1}{\partial t}\right] = -j_{f1} \qquad [3]$$

a.3 (Solid phase with intact core cells)

$$\left[(1-\varepsilon)\cdot(1-r)\rho_s \frac{\partial x_2}{\partial t}\right] = -j_{f2} \qquad [4]$$

During the extraction, solute diffuses from intact core cells to the broken ones at surface, and then from these to the bulk by convection.

4. Results and discussion

In Figure 1 some eppendorfs with collected oil for both treated and non-treated samples are shown. It may be observed at naked eye the colour gradient between extracts, the darker ones being obtained at the beginning and at the end of experiments.

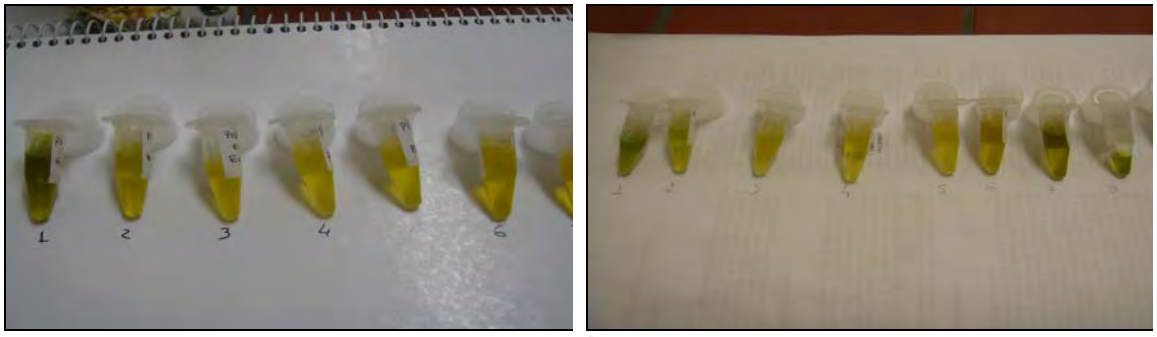

a **b**

Figure 1 – Eppendorfs containing grape seed oil collected along time under supercritical conditions with (a) and without (b) enzymatic pre-treatment.

Figure 2 shows the results for the grape seed oil extraction with SC CO_2 at 160 bar and 40ºC, where yield is graphed against the ratio between solvent consumption and seed charge (m_{CO_2}/m_{seed}). Here, yield is expressed as the percentage ratio between extracted oil and seed charge. Two cumulative curves are plotted for samples which have and have not suffered the enzymatic pre-treatment. Both curves present similar trends, comprehending a first period approximately linear, and a second asymptotic period which represents only 3-8% of the total extracted oil, which justifies the hypothesis of the theory proposed by Sovová (Sovova 2005, 1994) and also adopted in this work.

The maximum oil yield obtained for the untreated seeds was 11.5%. This result agrees with a 4 h conventional *n*-hexane soxhlet extraction. When the enzymatic pre-treatment was introduced, the broken to intact cells ratio was enlarged, which explains why the corresponding extraction curve clearly overcomes the former for non-treated sample. In addition, maximum yield becomes 16.5%, representing an increase of about 43% over the first result. It is important to detach that 11.5% of oil is nearly attained for $m_{CO_2}/m_{seed} \cong 8$, whereas untreated biomass reaches the same recovery for $m_{CO_2}/m_{seed} \cong 4$. Such fact implies that only half of the CO_2 has to be spent to get the same oil quantity. Equivalently, the extraction time is reduced to one half also, for the same mass flow rate of SC solvent. In the whole, the contribution of the first extraction period, where equilibrium and diffusion in the film dominate, is increased, expanding the extractability of the grape seed oil,

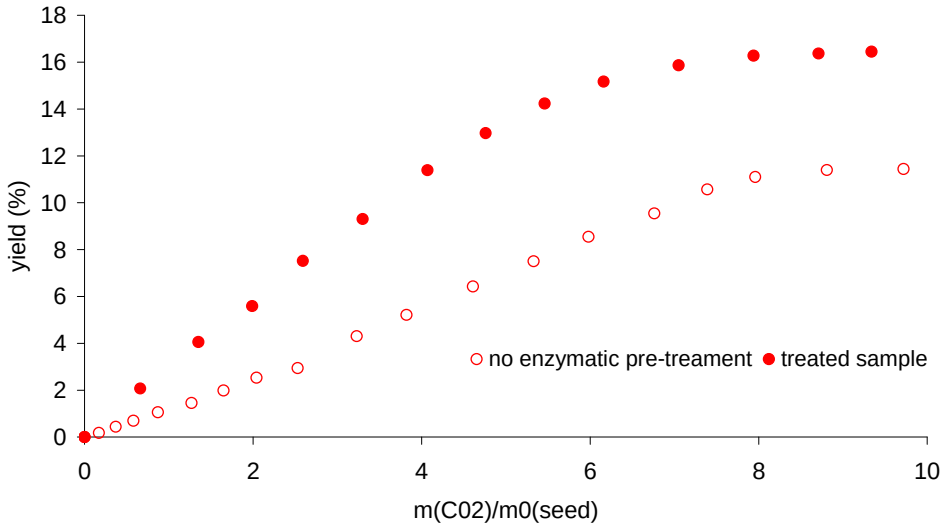

Figure 2 – SFE curves of grape seed oil at *T* = 40ºC and *P* = 160 bar. Comparison between treated and non-treated samples.

Modelling has also been carried out in order to represent and simulate the process. According to Figure 3, it may be concluded the SC CO_2 washes the easily accessible fraction of the crushed seed exhausting its oil content. The inner part, containing most non-easily accessible oil, exhibits somewhat smother profiles. Results corroborate experimental data plotted in Figure 2, as the contribution of the second extraction period to the global yield is almost negligible.

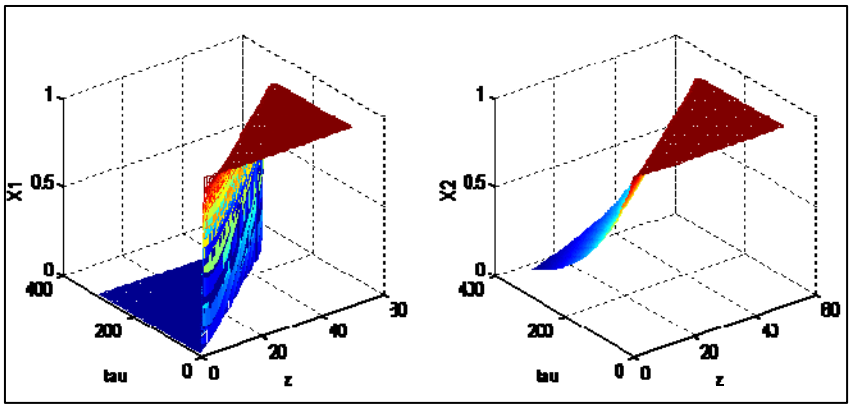

Figure 3 – Distribution of the oil normalised concentrations in easily and non-accessible fractions of grape seed (X_1 and X_2) as function of both the axial coordinate of the bed (z) and dimensionless time (tau). Experimental conditions: T =40ºC and P = 160 bar

4. Concluding remarks

In this essay, the SFE of grape seed oil using CO_2 achieved yields similar to those obtained by conventional soxhlet with n-hexane. Taking into account the well reported advantages of SFE and carbon dioxide, such results confirm that this is an efficient separation alternative.

By introducing an enzymatic pre-treatment, the broken/intact cells ratio was enlarged, thus increasing extraction yield by 43% for experiments at 40ºC and 160 bar. The corresponding extraction curve clearly overcomes the one for non-treated sample.

Results were modelled considering the fundamental assumption due to Sovová, i.e. the oil is distributed between broken and intact fractions of the grape seed. Good representations were accomplished, thus confirming such hypothesis.

5. Notation

$j_f = j_{f1} + j_{f2}$	$kg.m^{-3}s^{-1}$	mass transfer rate to the fluid phase;
j_{f1}	$kg.m^{-3}s^{-1}$	mass transfer rate between the free oil within the broken cells and the fluid phase;
j_{f2}	$kg.m^{-3}s^{-1}$	mass transfer rate between the oil entrapped in the intact core cells and the fluid phase;
r		fraction of broken cells, grinding efficiency;
t	s	extraction time;
u	$m.s^{-1}$	fluid velocity;
x_1	kg(solute)/ kg(insoluble solid)	concentration in broken cells;
x_2	kg(solute)/ kg(insoluble solid)	concentration in intact cells;
y	kg(solute)/ kg(solvent)	fluid-phase concentration;
ε	-	bed void fraction;
ρ_f	$kg.m^{-3}$	fluid density;

ρ_s	kg(insoluble solid) /m(solid phase)^3	solid density;

References

Gómez, A. M., López, C. P., De la Ossa, E. M. (1996). Recovery of grape seed oil by liquid and supercritical carbon dioxide extraction: A comparison with conventional solvent extraction. *The Chemical Engineering Journal and the Biochemical Engineering Journal*, 61, 227-231.

Sovová, H. (2005). Mathematical model for supercritical fluid extraction of natural products and extraction curve evaluation. *Journal of Supercritical Fluids*, 33, 35-52.

Bamberger, T., Erickson, J.C., Cooney, C.L., Kumar, S.K. (1988). Measurement and model prediction of solubilities of pure fatty acids, pure triglycerides, and mixtures of triglycerides in supercritical carbon dioxide. *J. Chem. Eng. Data*, 33, 327-333.

Sovová, H. (1994). Rate of the Vegetable Oil Extraction with Supercritical Co2 .1. Modeling of Extraction Curves. *Chemical Engineering Science*, 49, 409-414.

Proceedings of the 10th International Chemical and
Biological Engineering Conference - CHEMPOR 2008
Braga, Portugal, September 4-6, 2008
E.C. Ferreira and M. Mota (Eds.)

SUPERCRITICAL ANTISOLVENT PROCESS APPLIED TO THE PHARMACEUTICAL INDUSTRY

A. Tenorio, M. D. Gordillo, C. M. Pereyra* and E. J. Martínez de la Ossa
Department of Chemical Engineering, Food Technology and Environmental Technologies,
Faculty of Sciences, University of Cádiz,
11510 Puerto Real (Cádiz), Spain

Key words: supercritical antisolvent, nanoparticles, precipitation, carbon dioxide, antibiotics

Abstract
Pharmaceutical preparations are the final product of a technological process that gives the drugs the characteristics appropriate for easy administration, proper dosage and enhancement of the therapeutic efficacy. The design of pharmaceutical preparations in nanoparticulate form has emerged as a new strategy for drug delivery [1]. Particle size (PS) and particle size distribution (PSD) are critical parameters that determine the rate of dissolution of the drug in the biological fluids and, hence, have a significant effect on the bioavailability of those drugs that have poor solubility in water, for which the dissolution is the rate-limiting step in the absorption process [2,3]. Supercritical AntiSolvent (SAS) processes have been widely used to precipitate Active Pharmaceutical Ingredients (APIs) [4, 5] with a high level of purity, suitable dimensional characteristics, narrow PSD and spherical morphologies.
SAS process is based on the particular properties of the supercritical fluids (SCFs). These fluids have diffusivities of two orders of magnitude larger than those of liquid resulting in a faster mass transfer rate SCFs properties (solvent power and selectivity) can be also adjusted continuously by altering the experimental conditions (temperature and pressure). As consequence, the SCFs can be removed of the process by a simple change from the supercritical to room conditions which avoid difficult post – treatments of waste liquid streams. Carbon dioxide (CO_2) at supercritical conditions, among all possible SCFs, is largely used because of its relatively low critical temperature (31.1 ºC) and pressure (73.8 bar), low toxicity and low cost.
In this paper, we show some results about processed antibiotics (ampicillin and amoxicillin), two of the worlds most widely prescribed antibiotics, when they are dissolved in 1-methyl-2-pyrrolidone (NMP) and carbon dioxide is used as antisolvent.

1.- Introduction

The utilization of supercritical fluids in the processing of pharmaceutical compounds has become important in recent years [6].
Advantages such as high purity products, environmental protection, and greater experimental versatility are significant and all combine to create a viable alternative to certain conventional processing currently used in the pharmaceutical industry [7].
The supercritical antisolvent process (SAS) uses both the high power of supercritical fluids to dissolve the organic solvents and the low solubility of the pharmaceutical compounds in supercritical fluids [8] to cause the precipitation of such compounds once they are dissolved in the organic phase.
The dissolution of the supercritical fluid into the organic solvent is accompanied by a large volume expansion and, consequently, a reduction of the liquid density, and therefore, of its solvent power, causing a sharp rise in the supersaturation within the liquid mixture. Because of the high and uniform degree of supersaturation, small particles with a narrow particle size distribution are expected [9].
Furthermore, antibiotics can be entrapped in nanoparticles of various formulations using supercritical antisolvent process. In particular, polymeric micro- and nano-particles have

been found successful in the preparation of sustained drug delivery systems, hence they display enhanced therapeutic performance compared to traditional formulations [10-12].
Ampicillin and amoxicillin are some of the most widely prescribed antibiotics. Using controlled-sized microparticles of ampicillin or amoxicillin it is possible to increase its bioavailability and decrease its therapeutic dosage (thus improving efficiency). It is also possible to change its drug delivery system (transdermal, tracheobronchial and pulmonary delivery systems) by eliminating undesired secondary effect as a result of oral consumption of this pharmaceutical compound [1].
In this work, ampicillin and amoxicillin have been processed at 90 bar, 308.15 K, 100 mg/mL, 5 mL/min solution flow rate, washing time 180 min, noozle 100 µm and 32 g/min CO_2 flow rate using 1-Methyl-2-pyrrolidone (NMP) as solvent.

2.- Material and Methods

2.1. Experimental equipment and procedures

A schematic diagram of the pilot plant, developed by Thar Technologies® (model SAS 200), is shown in Fig. 1. The SAS 200 system is made up of the follow components: two high pressure pumps, one for the CO_2 (P1) and the other for the solution (P2), which incorporate a low dead volume head and check valves to provide efficient pumping of CO_2 and many types of solvent; a stainless steel precipitator vessel (V1) with 2 L volume, consisting of two parts, the main body and the frit; it also has an electric heating jacket (V1–HJ1); an automated back pressure regulator (ABPR1) of high precision attached to a motor controller with a position indicator; a jacketed (CS1–HJ1) stainless steel cyclone separator (CS1) with 0.5 L volume to separate the solvent and CO_2, once the pressure is released by the manual back pressure regulator (MBPR1). Auxiliary elements are necessary too, such as: a low pressure heat exchanger (HE1); cooling lines and cooling bath (CWB1) to keep the CO_2 inlet pump cold and to chill the pump heads. An electric high pressure heat exchanger (HE2) is used to preheat the CO_2 to bring the temperature in the precipitator vessel to the required level rapidly; safety devices (rupture discs and safety valve MV2) are included; pressure gauges measure the pump outlet pressure (P1, PG1), the precipitator vessel pressure (V1, PG1) and cyclone separator pressure (CS1, PG1) and continuous temperature measurements are made by means of thermocouples placed inside (V1–TS2) and outside (V1–TS1) the precipitator vessel, inside the cyclone separator (CS1–TS1) and on the electric high pressure heat exchanger; a FlexCORTM coriolis mass flowmeter (FM1) is used to measure CO_2 mass flow rate and other parameters such as total mass, density, temperature, volumetric flowrate, and total volume. All parameters that influence in the precipitation process (temperature, flow rate, pressure) can be controlled either manually or automatically (using ICM software). All the experiments were performed following the same procedure described in a previous work [13].

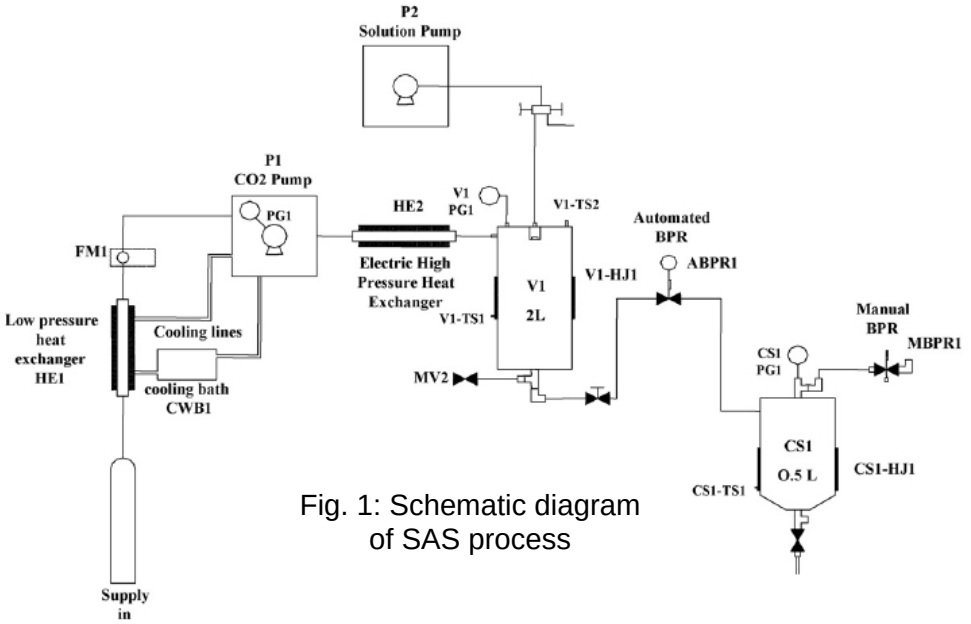

Fig. 1: Schematic diagram of SAS process

2.2. Materials and analytical methods

1-Methyl-2-pyrrolidone (NMP) (purity 99.5%) was purchased from Sigma–Aldrich Chemical (Spain). CO_2 with a minimum purity of 99.8% was supplied by Carburos Metálicos S.A. (Spain). Ampicillin sodium salt (minimum purity 91.0%) and amoxicillin (AMC) (purity ≥97%) were purchased from Sigma–Aldrich Chemical (Spain) and were used in the precipitation experiments. SEM pictures of amoxicillin and ampicillin as received are shown in Fig. 2. Samples of the powder precipitated both on the vessel wall and in the frit were observed using a Sirion scanning electron microscopy (SEM). Previously, the samples were put onto carbon tape and then were covered with a gold coating using a sputter coater.

(a)

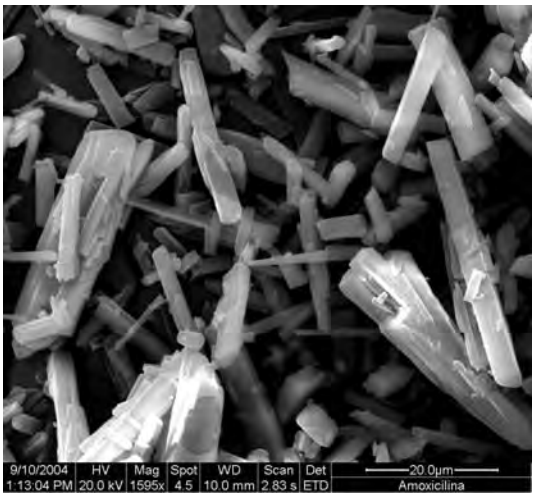

(b)

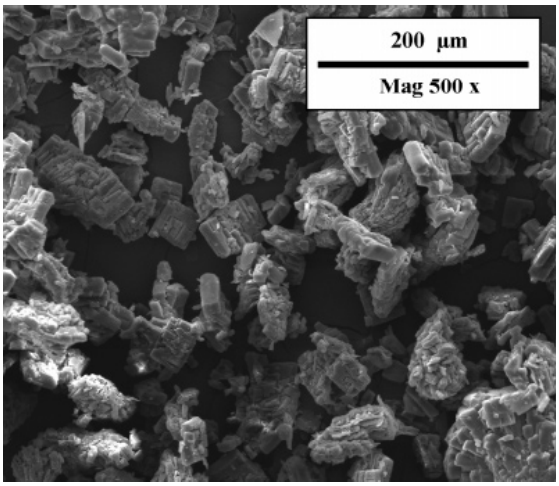

Fig 2. SEM images of unprocessed amoxicillin (a) and ampicillin (b)

3.- Results

SEM pictures of processed amoxicillin and ampicillin are shown in Figure 3 [13, 14].

(a)

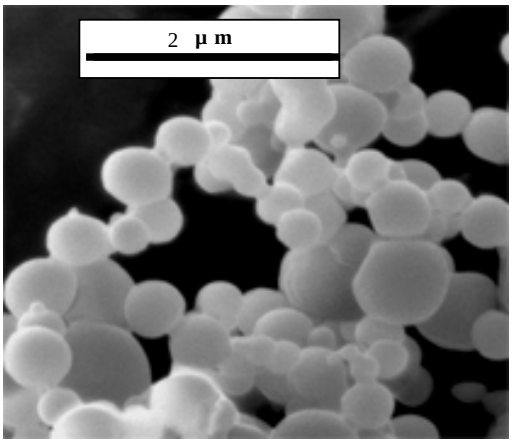

(b)

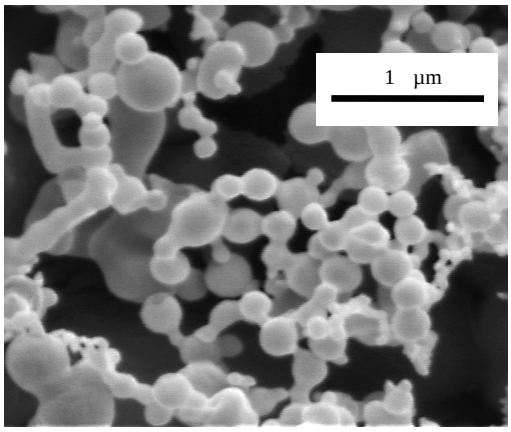

Fig. 3. SEM image of amoxicillin (a) and ampicillin (b) nanoparticles precipitated from 100 mg/mL, 308.15 K, 90 bar, 5 mL/min solution, 32 g/min CO_2, washing time 180 min, noozle 100 µm

The SEM images were processed using Scion image analysis software (Scion Corporation) to obtain the particle sizes. After that, the mean particle size (PS) and particle size distribution (PSD) were calculated using Statgraphics plus 5.1 software. More than 200 particles were counted to carry out the analysis in each experiment.
The SEM images of amoxicillin and ampicillin samples micronized show the formation of spherical nanoparticles with a mean particle size of 450 nm and 291 nm respectively, uniformly distributed with a coefficient of variation equal to 0.4.

References

[1] Pasquali, I., Bettini, R., Giordano, F. (2006). *Solid-state chemistry and particle engineering with supercritical fluids in pharmaceutics.* European Journal of Pharmaceutical Sciences, 27, 299.

[2] Perrut, M., Jung, J., Leboeuf, F. (2005). Enhancement of dissolution rate of poorly-soluble active ingredients by supercritical fluid processes: Part I: Micronization of neat particles. International Journal of Pharmaceutics, 288, 3.
[3] Van Nijlen, T., Van Den Mooter, G., Kinget, R., Augustijns, P., Blaton, N., Brennan, K. (2003). Improvement of the dissolution rate of artemisinin by means of supercritical fluid technology and solid dispersions. International Journal of Pharmaceutics, 254, 173.
[4] Chattopadhyay, P., Gupta, R. B. (2001). Production of antibiotic nanoparticles using supercritical CO_2 as antisolvent with enhanced mass transfer. Industrial and Engineering Chemistry Research, 40, 3530.
[5] Rehman, M., Shekunov, B. Y., York, P., Colthorpe, P. (2001). Solubility and precipitation of nicotinic acid in supercritical carbon dioxide. Journal of Pharmaceutical Sciences, 90, 1570.
[6] Reverchon, E. (1999). Supercritical antisolvent precipitation of micro- and nanoparticles, J. Supercrit. Fluids 15, 1
[7] Dehghani, F. and Foster, N. R. (2003). Dense gas anti-solvent processes for pharmaceutical formulation, Curr. Opin. Solid State Mater. Sci. 7, 363.
[8] Shekunov, B. Y., York, P. (2000). Crystallization processes in pharmaceutical technology and drug delivery design, J. Cryst. Growth 211,122.
[9] Dukhin, S. S., Shen, Y., Dave, R., Pfeffer, R. (2005) Droplet mass transfer, intradroplet nucleation and submicron particle production in two-phase flow of solvent-supercritical antisolvent emulsion, Colloid Surf. A: Physicochem. Eng. Aspect. 261, 163.
[10] Liu, H.; Finn, N., Yates, M. Z. (2005) Encapsulation and sustained release of a model drug, indomethacin, using CO_2-based microencapsulation, Langmuir 21, 379.
[11] Tai, H., Wang, W., Howdle, S. M. (2005) Dispersion polymerization of vinylidene fluoride in supercritical carbon dioxide using a fluorinated graft maleic anhydride copolymer stabilizer, Macromolecules 38, 1542.
[12] Y. Wang, R. Pfeffer, R. Dave, R. Enick, Polymer encapsulation of fine particles by a supercritical antisolvent process, AIChE J. 51 (2005) 440
[13] Tenorio, A., Gordillo, M. D., Pereyra, C. M., Martínez de la Ossa, E. J. (2007). Controlled submicro particle formation of ampicillin by supercritical antisolvent precipitation Journal of Supercritical Fluids, 40(2), 308.
[14] Tenorio, A., Gordillo, M. D., Pereyra, C. M., Martínez de la Ossa, E. J. (2008). Screening design of experiment applied to supercritical antisolvent precipitation of amoxicillin. Journal of Supercritical Fluids, 44(2), 230.

Proceedings of the 10th International Chemical and
Biological Engineering Conference - CHEMPOR 2008
Braga, Portugal, September 4-6, 2008
E.C. Ferreira and M. Mota (Eds.)

Solvent effects on ionic association of 2,6-lutidinium chloride salt at 60.00 ºC: A QSPR study

M. Reis[1], L. Moreira[1], R. E. Leitão[2], F. Martins[1*]
[1] Departamento de Química e Bioquímica - FCUL, CQB, Campo Grande, 1749-016 Lisboa, Portugal
[2] Departamento de Engenharia Química - ISEL, CQB, R. Conselheiro Emídio Navarro, 1950-007, Lisboa, Portugal

Keywords: Conductance, organic salts, association constant, QSPR, solvent effects.
Topic: Advancing the chemical and biological engineering fundamentals

Abstract

Conductivity values (σ_{sln}) for 2,6-lutidinium chloride were obtained in twelve protic and aprotic solvents at 60.00 ± 0.01 ºC, for ten concentrations ranging from 0.001 to 0.01 mol dm^{-3}. The obtained $c = f(\sigma_{sln})$ curves do not follow the Fuoss-Hsia equation, modified by Fernández Prini, but rather adjust well to the Ostwald´s law.

Molar conductivities at infinite dilution (Λ^0_m), association constants (K_A) and respective errors were determined from the application of an iterative curve fitting procedure which was also applied with success to another set of $c = f(\sigma_{sln})$ curves previously reported for other ten solvents at the same working temperature (60 ºC).

The application of a suitable equation within the QSPR (quantitative structure-property relationships) context, the enlarged TAKA equation, allowed a proper understanding of solvent effects on ionic association of this salt in solution and the discrimination and quantification of the involved physicochemical properties. It is shown that that the chosen equation is able to adequately model K_A in terms of specific and non-specific ion-solvent-solvent interactions which all contribute to enhance the dissociation process. Our results indicate that a considerable amount of positive charge density is located on the hydrogen directly attached to the nitrogen of the heterocyclic ring.

1 Introduction

Conductivity measurements of salts in a diversified set of solvents are of great importance due to their contribution for an in-depth understanding of solvent effects on ion association and mobility phenomena (Prini et al., 2000).

A considerable amount of work has been devoted to establish mathematical models to accurately reproduce molar conductivity (Λ_m) *vs*. concentration (c) curves. Expressions such as the Fuoss-Hsia equation (Hsia and Fuoss, 1968), later modified by Fernández-Prini (Prini, 1969) or newer models which use a full radial distribution function as given by the Mean Spherical Approximation (Blum and Turq, 1992) are some possible examples.

The ionic association of salts, defined as an equilibrium between dissociated ions and associated salt molecules [ion$^-$] + [ion$^+$] $\leftrightharpoons$ [ion pair], is among the first recognized influences on the referred plots. An association constant (K_A) can thus be defined from the equilibrium equation which represents the concentration dependence of the process of accounting for strong Coulombic forces at short interionic distances (Cotê et al., 1998).This description of the association constant implies that log K_A can be considered an energetic related term dependent on both salt and solvent features.

* Corresponding author. Tel +351-21-7500870. E-mail: filomena.martins@fc.ul.pt

Quite recently, the use of a suitable equation (eq. 1) allowed us to determine K_A values and respective errors at 60.00 ºC for 2,6-lutidinium chloride salt in ten different non-aqueous solvents (Moreira et al, 2006). In eq. 1 Λ^0_m represents the molar conductivity at infinite dilution, S is a dielectric constant and viscosity dependent parameter, α is the ionization degree and $f_\pm$ the mean ionic activity coefficient.

$$\Lambda_m = \Lambda^0_m - S(c\alpha)^{1/2} - K_A \Lambda_m f_\pm^2 c\alpha \qquad \text{eq. 1}$$

The obtained results revealed strong deviations from the predictions of classical dielectric theories. It was therefore reasoned that specific ion-solvent-solvent interactions could play an important role in explaining the observed results. The aim of this work is therefore the application of a suitable methodology to determine and quantify the relevant solvent properties which influence the ionic association of the above mentioned 2,6-lutidinium salt at 60.00 ºC.

Quantitative structure-property relationships (QSPR) are among the most powerful methodologies used to study solvent effects on physicochemical processes and, in particular, the TAKA equation (Abraham et al., 1987) has been one of the most used equations built upon these concepts. We have enlarged its scope by including an extra solvent property related to the solvent's stiffness, thus deriving the denominated enlarged TAKA equation, eq. 2 (Moreira *et al.*, 2005).

$$\text{Energetic term} = a_0 + a_1 \pi^* + a_2 \alpha + a_3 \beta + a_4 C + a_5 \log \eta \qquad \text{eq. 2}$$

According to the above equation, solvents are characterized by their dipolarity/polarizability (π^*), taken as a measure of non-specific solvent–solute interactions related to the capacity of the solvent to generate a spread of charges in the cybotatic region of the solute; their hydrogen bond donor (HBD) acidity (α) and hydrogen bond acceptor (HBA) basicity (β) abilities, regarded as measures of specific solvent–solute interactions of the Lewis type (see fig. 1); their structuredness, given by the cohesive energy density parameter, C, which accounts for solvent–solvent interactions determining the disruption and reorganization of the solvent structure; and the solvent's stiffness, given by the logarithm of viscosity ($\log \eta$). The a_i coefficients are the complementary solute-dependent coefficients of the solvent parameters.

The determination of K_A values in a diversified set of solvents allows a correct application of eq. 2, the accomplishment of statistically meaningful results and the quantification of solvent effects on ion association phenomena.

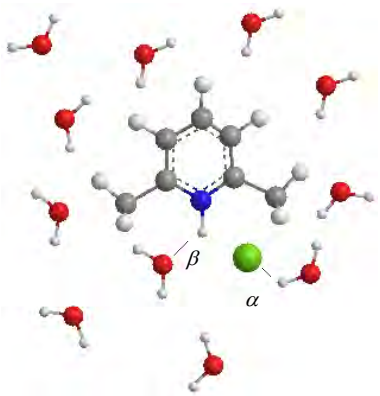

Fig. 1 - Scheme describing α (HBD) and β (HBA) solvation modes on a 2,6-lutidinium chloride – water cluster representation.

2 Results and discussion

The results here presented refer to conductivity measurements (σ_{meas}) of 2,6-lutidinium chloride in twelve protic and aprotic solvents for ten different concentrations ranging from 0.001 mol dm^{-3} to 0.01 mol dm^{-3}, at 60 ± 0.01 ºC. Together with these determinations, residual conductivity, emerging from the solvent itself, was considered and subtracted from σ_{meas} to determine the solution's conductivity (σ_{sln}).

Equation 1 was tentatively applied to the obtained data following a formerly optimised procedure (Moreira et al, 2006). However, for this particular set of solvents the methodology was not suitable to determine the necessary K_A (and Λ^0_m) values, since there was no convergence to a minimum in the fitting process.

A different approach, based on the Ostwald´s law for weak electrolytes (Robbins, 1972) was therefore devised to obtain the required values. Traditionally, the linearized form of this law (eq. 3) has been used with the argument that it allows a more reliable determination of Λ^0_m. However, this linearized form overweighs the lower concentration (and conductivity) data, for which the experimental uncertainty is higher. Also, considering that errors in c are always higher than those in σ_{sln}, it is more appropriate to derive a $c = f(\sigma_{sln})$ expression to compute K_A and Λ^0_m values. Equation 3 was therefore reorganized to equation 4, were K_A and c maintain the mol dm^{-3} units, as Λ^0_m remains in S cm^2 mol^{-1} and σ_{sln} in S cm^{-1}.

$$\frac{1}{\Lambda_m} = \frac{1}{\Lambda_m^0} + \frac{K_A \Lambda_m c}{\left(\Lambda_m^0\right)^2} \qquad \text{eq. 3}$$

$$c = \frac{1000\sigma_{sln}}{\Lambda_m^0} + \frac{1000^2 K_A \sigma_{sln}^2}{\left(\Lambda_m^0\right)^2} \qquad \text{eq. 4}$$

A formerly designed Microsoft Excel spreadsheet (Moreira et al, 2006) was modified to allow the determination of both K_A, Λ^0_m values and respective errors from an iterative curve fitting procedure. The obtained results for the eleven (σ_{sln}, c) curves are reported in table 1, together with those obtained by the application of the same procedure for the ten solvents previously reported at the same temperature (Moreira et al, 2006).

One of the most important aspects regarding QSPR studies is the importance of attaining results with statistical robustness and significance. Commonly, some general rules are considered: an adequate sample size must contain at least three points for each descriptor; the descriptor's space should be fully covered and homogeneous and have no leverage points; the set of descriptors should not be intercorrelated (the determination coefficient, R^2, among pairs of descriptors should be no greater than 0.50 and as low as possible for one descriptor against all others; the regression coefficients should have a significance level of at least 95%.

As referred before, the enlarged TAKA equation (eq. 2) was used to quantify solvent effects on K_A values derived from (σ_{sln}, c) curves. The five descriptors' values for each of the 22 solvents used in this work are also reported in table 1.

Table 1 - Solvent descriptors[a] and K_A, Λ^0_m values and respective associated errors determined at 60 ºC.

N	Solvents[b]	Descriptors					Λ^0_m	Std. error	K_A	Std. error
		π^*	α	β	C	log η	S cm^2 mol^{-1}	%	mol^{-1} dm^3	%
1	**MeOH**	0.60	1.09	0.73	0.858	-0.259	**151.47**	**1.59**	**22.90**	**13.27**
2	1-PrOH	0.53	0.79	0.85	0.597	0.288	34.28	1.99	291.89	5.82
3	**TFE**	1.13	1.51	0.00	0.573	0.244	**59.71**	**1.45**	**28.41**	**10.51**
4	**1,2-Pr(OH)$_2$**	0.76	0.83	0.78	0.840	1.625	**11.80**	**0.55**	**22.85**	**4.55**
5	**1,2-Bu(OH)$_2$**	0.71	0.80	0.71	0.739	1.699	**9.04**	**1.13**	**42.19**	**6.56**
6	**DiEtglycol**	0.92	0.72	0.67	0.838	1.477	**12.28**	**0.58**	**17.49**	**5.83**
7	**TriEtglycol**	0.88	0.66	0.69	0.737	1.690	**10.25**	**0.57**	**24.43**	**4.57**
8	DMSO	1.00	0.00	0.76	0.707	0.299	60.31	0.50	59.61	2.46
9	**DMF**	0.88	0.00	0.69	0.582	-0.096	**82.57**	**6.25**	**1030.70**	**15.36**
10	Nitromethane	0.85	0.22	0.25	0.663	-0.212	29.76	6.42	1012.71	15.62
11	Prop. Carb.	0.83	0.00	0.40	0.737	0.403	35.36	8.18	1120.31	19.71
12	Acetonitrile	0.75	0.19	0.37	0.576	-0.467	90.19	9.54	3041.33	21.32
13	**Aniline**	1.18	0.26	0.50	0.583	0.576	**0.32**	**4.02**	**86.38**	**16.70**
14	EtOH	0.55	0.88	0.80	0.679	0.034	64.48	3.60	73.66	15.98
15	1-BuOH	0.54	0.74	0.84	0.542	0.410	17.30	4.72	553.09	12.37
16	2-Me-1-PrOH	0.50	0.71	0.92	0.520	0.523	13.25	7.15	743.40	18.01
17	**2-Me-1-BuOH**	0.51	0.64	0.93	0.480	0.681	**3.77**	**7.20**	**681.42**	**18.35**
18	EthoxyEtOH	0.66	0.71	0.64	0.469	0.267	18.63	3.56	245.29	10.83
19	**2,3-Bu(OH)$_2$**	0.75	0.68	0.88	0.621	1.818	**5.75**	**0.74**	**36.54**	**4.60**
20	DMA	0.85	0.00	0.76	0.502	-0.033	61.77	8.31	2020.15	19.05
21	**Formamide**	0.97	0.71	0.60	1.567	0.519	**59.09**	**5.19**	**93.33**	**20.77**
22	**H_2O**	1.09	1.17	0.47	2.297	-0.050	**196.69**	**0.59**	**8.14**	**10.74**

[a] Descriptors reported at 25ºC and assumed not to vary considerably with temperature.
[b] Solvents studied in this work are represented in bold.

Equation 2 was first applied to the full set of solvents. The regression presented poor statistical parameters (sd_{fit}=0.38, R^2_{adj}=0.76 and F=15), an apparent outlier and both C and log η with SL < 95%. However, the exclusion of either and both of these descriptors lead to worse regressions from a statistical point of view. Therefore, the descriptors space was analyzed to check the existence of possible leverage points. This procedure revealed that water and formamide were indeed leverage points in C. The removal of these solvents lead to a significant improvement in the statistical figures of merit (sd_{fit}=0.21, R^2_{adj}=0.92 and F=47), to the disappearance of any outliers and to a loss of statistical significance of log η (SL=49%). This descriptor was therefore withdrawn from the regression equation and a new fitting lead to equation 5:

$$\log K_A = 8.01_{\pm 0.45} - 2.74_{\pm 0.33}\pi^* - 1.34_{\pm 0.12}\alpha - 1.72_{\pm 0.26}\beta - 2.75_{\pm 0.40}C \qquad \text{eq. 5}$$

(N = 20, R^2_{adj} = 0.927, sd_{fit} = 0.203, F = 61, SL > 99%)

Results must also be externally validated. For that purpose, remaining data were divided in two sets: a training set, designed according to the above mentioned rules, which was used to determine regression coefficients; and a test set, with a similar descriptors' variablity, used to assess the ability of the established regression equation to predict log K_A values for solvents not used in the training set. Solvents 1 to 13 were chosen as the training set and solvents 14 to 20 were selected as the test set. Equation 6 shows the attained results. The magnitude and sign of regression coefficients are almost identical to the ones from eq. 5, confirming the

robustness of the fit. Figure 2 shows the quality of the fit and also that external validation was fully accomplished for the test set.

$$\log K_A = 8.04_{\pm 0.46} - 2.79_{\pm 0.29}\pi^* - 1.23_{\pm 0.11}\alpha - 1.71_{\pm 0.24}\beta - 2.80_{\pm 0.51}C \qquad \text{eq. 6}$$

(N = 13, R^2_{adj} = 0.960, sd_{fit} = 0.160, F = 74, SL > 99%)

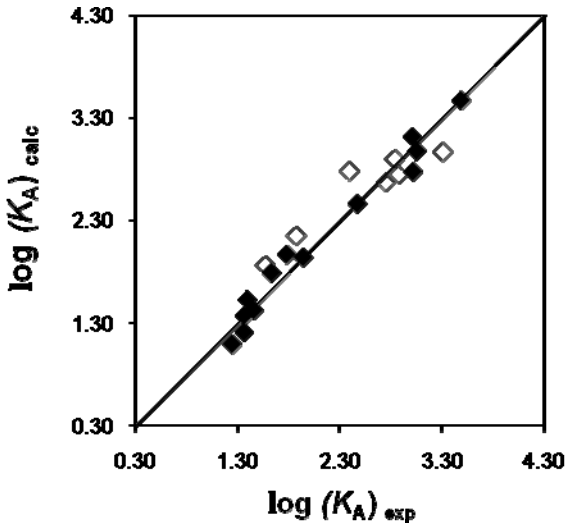

Fig. 2 – Calculated *vs*. experimental log K_A values:

◆ – training set (solvents 1 to 13)
◇ – test set (solvents 14 to 20)

The obtained model equation for the full data set, eq. 5, explains 93% of the overall log K_A variability with a standard deviation of 0.2 log units. Results also indicate that specific and non-specific solute-solvent interactions, together with the structuring degree of the solvent decrease K_A. All solvent effects contribute to increase the ionic character of the salt in solution. The relevance of π^* and α was foreseen, given the nature of the studied process. On the other hand, the significance and magnitude of the β parameter are rather unexpected and are only consistent with accepting a considerable amount of positive charge density located on the hydrogen directly attached to the nitrogen of the heterocyclic ring and not on the nitrogen itself, as usually assumed (see fig. 1).

This study's main outcome, *i.e.*, the abiltiy to model K_A through the TAKA equation, confirms our earlier conjecture (Moreira *et al.*, 2006) for the need to consider extensive ion-solvent and solvent-solvent interactions to correctly assess solvent effects on ion association phenomena.

3 Conclusions

Twelve new $c = f(\sigma_{sln})$ curves obtained at 60 ºC, together with previously reported curves for ten other solvents obtained at the same temperature, were successfully analysed using an equation derived from the Ostwald´s law for weak electrolytes. An iterative curve fitting approach allowed the computation of statistically meaningful and discernible Λ^0_m and K_A values and respective errors.

The gathered data allowed the analysis of log K_A values using a QSPR methodology. Dipolarity/polarizability (π^*), hydrogen bond donor (HBD) acidity (α) and hydrogen bond acceptor (HBA) basicity (β) abilities and solvent structuredness, were found to be the significant factors to explain the energetics of ion association phenomena showing therefore

its dependence on extensive ion-solvent and solvent-solvent interactions. Moreover, our results clarify specific charge localization features.

4 Experimental

Measurements were obtained using a digital Wayne Kerr B905 conductance bridge at a working frequency of 1 kHz. Temperature resistant commercial Sentek KI10 cells were used and their cell constants were determined using a 0.01 mol dm^{-3} solution of KCl. A thermostatic bath Haake V filled with silicon oil was used to maintain temperature within $\pm$ 0.01 ºC. For each solvent a 0.01 mol dm^{-3} stock solution was prepared, weighing the necessary amount of solvent in a Precisa 205A SCS balance (precision $\pm 10^{-4}$ g). All other solutions were subsequently prepared by dilution. Solutions were left in the oil bath for fifteen minutes to reach thermal equilibrium, after which conductance was measured. The reading was confirmed five minutes later. Anomalous measurements were always repeated.

The solvents, provided by Merck, BDH or Aldrich, were used without further purification. The salt was in-house produced from hydrochloric acid addition to 2,6-lutidine in acetone, followed by standard purification and drying procedures. ^{1}H NMR spectrum of the salt showed no contaminants, accessing therefore its purity.

References

Bianchi, H.L., Dujovne, I., Prini, R.F. (2000). Comparison of Electrolytic Conductivity Theories: Performance of Classic and New Theories. *Journal of Solution Chemistry*, Vol. 29, No 3, 237-253.

Hsia, K.L., Fuoss, R.M. (1968). Condutance of alkali halides. XI. Cesium bromide and iodide in water at 25 degrees. *Journal of the American Chemical Society*, Vol. 90, 3055-3060.

Prini, R.F. (1969). Conductance of electrolyte solutions. A modified expression for its concentration dependence. *Trans. Faraday Soc,* Vol. 65, 3311-3313.

Bernard, O., Kunz, W., Turq, P., Blum, L. (1992). Condutance in Electrolyte-Solutions using the mean spherical approximation. *Journal of Physical Chemistry,* Vol. 96, 3833-3840.

Côté, J.F., Perron, G., Desnoyers, J.E., Benson, G.C., Lu, B.C.Y. (1998) Application of the Bjerrum association model to electrolyte solutions. II. Enthalpies of dilution in water and non-aqueous solvents. *Journal of Solution Chemistry*, Vol. 27, 685-705.

Moreira, L., Leitão, R.E., Martins, F. (2006). Solvent and temperature effects on ion association and mobility of 2,6-lutidinium chloride in non-aqueous solvents. *Molecular Physics*, Vol. 104, No 12, 1905-1913.

Abraham, M.H., Doherty, R.M., Kamlet, M.J., Harris, J.M., Taft, R.W. (1987). Linear solvation energy relationships. 37. An analysis of contributions of dipolarity polarizability, nucleophilic assistance, electrophilic assistance, and cavity terms to solvent effects on tert-butyl halide solvolysis rates. *J. Chem. Soc., Perkin Trans 2*, Vol. 7, 913-920.

Martins, F., Moreira, L., Elvas Leitão, R., (2005). Recent Advances in Correlation Analyses of Tertiary Alkyl Halides Heterolysis Reactions. Communication to ESORX, Rome, Italy.

Robbins, J. (1972). *Ions in Solution 2*, Oxford University Press, Oxford.

Proceedings of the 10th International Chemical and
Biological Engineering Conference - CHEMPOR 2008
Braga, Portugal, September 4-6, 2008
E.C. Ferreira and M. Mota (Eds.)

Modelling of the solvent extraction equilibrium of cadmium(II) in neutral chloride medium using Cyanex 923

A.A. Leopold[1*], A. Fortuny[1], M.T. Coll[1], N.S. Rathore[1] and A.M. Sastre[2]
[1]Department of Chemical Engineering, Universitat Politecnica de Catalunya, EPSEVG, Av. Victor Balaguer s/n, 08800 Vilanova i la Geltru, Spain
[2] Department of Chemical Engineering, Universitat Politecnica de Catalunya, ETSEIB, Av. Diagonal 647, 08028 Barcelona, Spain

Keywords: Cadmium(II), Cyanex 923, Solvent Extraction, Stability Constants, Extraction Equilibrium.
Topic: Advancing the chemical and biological engineering fundamentals.

Abstract

Speciation of aqueous cadmium(II) chloride complexes and determination of the equilibrium extraction constant for cadmium(II) in neutral chloride medium by applying solvent extraction with organophosphorous solvating extractant Cyanex 923 have been investigated. The cumulative stability constants of Cd–Cl complexes in aqueous neutral chloride solutions have been evaluated. The modelling of the extraction equilibrium constant for cadmium(II) in Cyanex 923/Exxol D-100 system has been described.

1 Introduction

Cadmium is considered as one of the most dangerous elements. Because cadmium is widely used in a number of industries, cadmium-contaminated wastewaters can originate from a multitude of sources associated with human activities. Therefore, it is of paramount importance to find an effective method to remove it from liquid effluents. The removal of cadmium(II) from aqueous chloride solutions by solvent extraction (SX) using the phosphine oxides mixture Cyanex 923 as extractant has been reported to be promising, mainly due to high extraction efficiency [1, 2, 3]. As a result, the present study proposes the application of this extractant to the modelling of cadmium(II) solvent extraction in neutral chloride medium. Determination of the cumulative stability formation constants of Cd-Cl complexes and the equilibrium extraction constant of cadmium(II) from neutral chloride medium is described.

2. Experimental procedure

Chemicals

Cyanex 923 is a neutral solvating extracting agent; it is a mixture of four phosphine oxides with the general formulae R_3PO (8,5 %), $R_2R'PO$ (37,4 %), RR'_2PO (30,4 %), R'_3PO (16,1 %), where $R=CH_3(CH_2)_7$ and $R'=CH_3(CH_2)_5$ [4]. It was used as received (Cytec Ind. Canada). Aliphatic diluent Exxol D-100 was also used as supplied by the manufacturer (Exxonmobil Chemical Europe Inc. Belgium). Both of them were used without further purification. All other chemicals were of AR grade. Aqueous solutions of cadmium(II) chloride were prepared by dissolving the required amount of $CdCl_2 \cdot 2{,}5H_20$ (Probus, S.A. Badalona, Barcelona) in double-distilled water. The selected concentrations of chloride ions were obtained by adding NaCl. As the stripping agent was used double distilled water.

Apparatus and procedure

The liquid-liquid extraction experiments were carried out in separatory funnels in which the equal volumes (10 mL) of the aqueous and organic phases, containing the required concentrations of reagents, were shaken on a mechanical shaker (SBS Instruments SA) at room temperature (20±2) for 20 minutes to guarantee complete equilibration. The phases

* Corresponding author. Tel + 34 93 896 77 54. E-mail: agnieszka.leopold@upc.edu

were then allowed to separate. The cadmium(II) concentrations of the suitable aliquots of the aqueous phases were determined by atomic absorption spectrometry using VARIAN AA 240FS. The metal content of the organic phases was determined by mass balance between the total concentration of cadmium(II) in the feed solutions and the metal content measured by spectrometer in the aqueous aliquots.

3. Modelling of cadmium(II) solvent extraction from neutral chloride medium using Cyanex 923 as extractant

In aqueous neutral chloride solutions, cadmium(II) forms strong chloride complexes, presented by $CdCl^+$, $CdCl_2$, $CdCl_3^-$ and $CdCl_4^-$. Formation of the Cd-Cl complexes is described by the stability formation constants which represent the theoretical distribution of cadmium(II) presented in aqueous solution into different species at given conditions. Each complex of cadmium(II) chloride formed in the aqueous phase owns its stepwise formation constant expressed as K_1, K_2, K_3, K_4.

$$Cd^{2+} + Cl^- \xleftrightarrow{K_1} CdCl^+ \quad (1)$$

$$CdCl^+ + Cl^- \xleftrightarrow{K_2} CdCl_2 \quad (2)$$

$$CdCl_2 + Cl^- \xleftrightarrow{K_3} CdCl_3^- \quad (3)$$

$$CdCl_3^- + Cl^- \xleftrightarrow{K_4} CdCl_4^{2-} \quad (4)$$

The stepwise stability constants can be expressed as follows:

$$K_1 = \frac{\left[CdCl^+\right]}{\left[Cd^{2+}\right]\cdot\left[Cl^-\right]} \quad (5)$$

$$K_2 = \frac{\left[CdCl_2\right]}{\left[CdCl^+\right]\cdot\left[Cl^-\right]} \quad (6)$$

$$K_3 = \frac{\left[CdCl_3^-\right]}{\left[CdCl_2\right]\cdot\left[Cl^-\right]} \quad (7)$$

$$K_4 = \frac{\left[CdCl_4^{2-}\right]}{\left[CdCl_3^-\right]\cdot\left[Cl^-\right]} \quad (8)$$

where the ion concentrations are given in mol/L.
The nominators of Eq. (5) – (8) present the concentrations of neutral cadmium(II) chloride species formed in the aqueous phase in equilibrium.
Moreover it is possible to use the cumulative stability formation constants of cadmium(II) complexes which can be expressed as β_1, β_2, β_3, β_4. A cumulative constant can always be considered as the product of stepwise constants. Thus the relation between stepwise and cumulative stability formation constants can be expressed as:

$$\beta_1 = \mathrm{K}_1 \quad (9)$$

$$\beta_2 = \mathrm{K}_1 \cdot \mathrm{K}_2 \quad (10)$$

$$\beta_3 = \mathrm{K}_1 \cdot \mathrm{K}_2 \cdot \mathrm{K}_3 \quad (11)$$

$$\beta_4 = \mathrm{K}_1 \cdot \mathrm{K}_2 \cdot \mathrm{K}_3 \cdot \mathrm{K}_4 \quad (12)$$

The overall equation presenting the values of the cumulative stability formation constants of each Cd – Cl complex is as follows:

$$\beta_n = \frac{[CdCl_n^{2-n}]}{[Cd^{2+}]\cdot[Cl^-]^n} \quad (13)$$

where *n=1, 2, 3, 4* is the number of chloride ions complexed with the metal ion.
The concentration of cadmium(II) in the feed phase is the sum of all the species presented in aqueous solution:

$$[Cd]_{aq} = [Cd^{2+}] + [CdCl^{+}] + [CdCl_2] + [CdCl_3^{-}] + [CdCl_4^{2-}] \quad (14)$$

Deriving Eq. (5) – (8) for the concentrations of the neutral cadmium(II) chloride species which are formed in equilibrium in feed phase it is obtained:

$$[CdCl^{+}] = K_1 \cdot [Cd^{2+}] \cdot [Cl^{-}] = \beta_1 \cdot [Cd^{2+}] \cdot [Cl^{-}] \quad (15)$$

$$[CdCl_2] = K_2 \cdot [CdCl^{+}] \cdot [Cl^{-}] = K_1 \cdot K_2 \cdot [Cd^{2+}] \cdot [Cl^{-}]^2 = \beta_2 \cdot [Cd^{2+}] \cdot [Cl^{-}]^2 \quad (16)$$

$$[CdCl_3^{-}] = K_3 \cdot [CdCl_2] \cdot [Cl^{-}] = K_1 \cdot K_2 \cdot K_3 \cdot [Cd^{2+}] \cdot [Cl^{-}]^3 = \beta_3 \cdot [Cd^{2+}] \cdot [Cl^{-}]^3 \quad (17)$$

$$[CdCl_4^{2-}] = K_4 \cdot [CdCl_3^{-}] \cdot [Cl^{-}] = K_1 \cdot K_2 \cdot K_3 \cdot K_4 \cdot [Cd^{2+}] \cdot [Cl^{-}]^4 = \beta_4 \cdot [Cd^{2+}] \cdot [Cl^{-}]^4 \quad (18)$$

Having presented relations (15) – (18), it is possible to substitute the concentration of each of the Cd – Cl complex formed expressed in the Eq. (14), therefore it is got:

$$[Cd]_{aq} = [Cd^{2+}] + \beta_1 \cdot [Cd^{2+}] \cdot [Cl^{-}] + \beta_2 \cdot [Cd^{2+}] \cdot [Cl^{-}]^2 + \beta_3 \cdot [Cd^{2+}] \cdot [Cl^{-}]^3 + \beta_4 \cdot [Cd^{2+}] \cdot [Cl^{-}]^4 \quad (19)$$

By rearranging Eq. (19), the concentrations of all Cd-Cl species formed in neutral chloride medium in equilibrium can be known from the relations:

$$[Cd^{2+}] = \frac{[Cd]_{aq}}{M} \quad (20)$$

$$[CdCl^{+}] = \frac{[Cd]_{aq} \cdot \beta_1 \cdot [Cl^{-}]}{M} \quad (21)$$

$$[CdCl_2] = \frac{[Cd]_{aq} \cdot \beta_2 \cdot [Cl^{-}]^2}{M} \quad (22)$$

$$[CdCl_3^{-}] = \frac{[Cd]_{aq} \cdot \beta_3 \cdot [Cl^{-}]^3}{M} \quad (23)$$

$$[CdCl_4^{2-}] = \frac{[Cd]_{aq} \cdot \beta_4 \cdot [Cl^{-}]^4}{M} \quad (24)$$

where:

$M = 1 + \beta_1 \cdot [Cl^{-}] + \beta_2 \cdot [Cl^{-}]^2 + \beta_3 \cdot [Cl^{-}]^3 + \beta_4 \cdot [Cl^{-}]^4$.

Moreover, it is necessary to establish the concentration of free chloride ions in the system $[Cl^{-}]$. The concentration of chloride ions presented in the aqueous feed solution $[Cl^{-}]_{aq}$ can be divided between free chloride ions and chlorides forming the Cd – Cl complexes and which concentrations we already know from relations (20) – (24). It can be presented as follows:

$$[Cl^{-}] = [Cl^{-}]_{aq} - [CdCl^{+}] - 2 \cdot [CdCl_2] - 3 \cdot [CdCl_3^{-}] - 4 \cdot [CdCl_4^{2-}] \quad (25)$$

The extraction mechanism of cadmium(II) from chloride medium using neutral extractant Cyanex 923 is related to the solvation of the neutral $CdCl_2$ species and formation of the $CdCl_2 \bullet L_2$ complexes in the organic phase, where L is the extractant [2]. The extraction of the neutral $CdCl_2$ species and the equilibrium extraction constant can be decribed by the equations:

$$CdCl_2 + 2\ L_{org} \xleftrightarrow{K_{e1}} (CdCl_2 \bullet L_2)_{org} \quad (26)$$

$$K_{e1} = \frac{[CdCl_2 \bullet L_2]_{org}}{[CdCl_2] \cdot [L]^2_{org}} \quad (27)$$

where $[L]_{org}$ is the concentration of the free extractant in the system.

Working in neutral medium it is obvious that all of the cadmium(II) extracted into the organic phase is in the form of the $CdCl_2$ species complexed with the extracting agent. So that, the total concentration of metal presented in the feed solution is considered as cadmium(II)

divided between the both phases, the organic and the aqueous one:

$$[Cd]_{total} = [Cd]_{org} + [Cd]_{aq} \quad (28)$$

$$[CdCl_2 \bullet L_2]_{org} = [Cd]_{org} = [Cd]_{total} - [Cd]_{aq} \quad (29)$$

where: $[Cd]_{org}$ is the concentration of cadmium(II) in the form of complexes with extracting agent $[CdCl_2 \bullet L_2]$, it is calculated by the mass balance between the total concentration of cadmium(II) presented in the feed phase and cadmium(II) that has not been extracted into the organic phase, measured by spectrometry, and denominated as $[Cd]_{aq}$.
Applying the same way of thinking it is possible to determine the concentration of the free extracting agent in our system. Thus, the total concentration of the Cyanex 923, $[L]_{total}$, is distributed between the concentration of the free extractant, $[L]_{org}$, and the concentration of the extracting agent bound with extracted species $CdCl_2$, $[L]_{complex}$.

$$[L]_{total} = [L]_{org} + [L]_{complex} \quad (30)$$

As it was stated before, all of the cadmium(II) extracted into the organic phase is in the form of the $CdCl_2$ species forming complexes with the extracting agent, thus the extractant complexed with neutral species is the concentration of cadmium(II) in the organic phase; taking into account the stoichiometry of the extraction the latter one has to be multiplied by two, as it is supposed that each $CdCl_2$ extracted is bounded with two molecules of the extractant [2].

$$[L]_{org} = [L]_{total} - 2 \cdot [Cd]_{org} \quad (31)$$

Eq. (28) – (31) allow simplifying the Eq. (27). Thus, we obtain:

$$K_{e1} = \frac{[Cd]_{total} - [Cd]_{aq}}{[CdCl_2] \cdot ([L]_{total} - 2 \cdot ([Cd]_{total} - [Cd]_{aq}))^2} \quad (32)$$

The presence of the extracting agent also changes the concentration of free chlorides in the system. Apart from the aqueous cadmium(II) chloride species, which have to be subtracted from the total concentration of chlorides presented in the feed solution phase, there must be taken into account also the chlorides bounded with the extractant as the $CdCl_2 \bullet L_2$ complexes. So we obtain:

$$[Cl^-] = [Cl^-]_{total} - [CdCl^+] - 2 \cdot [CdCl_2] - 3 \cdot [CdCl_3^-] - 4 \cdot [CdCl_4^{2-}] - 2 \cdot [Cd]_{org} \quad (33)$$

4. Model resolution

Series of solvent extraction experiments in neutral chloride medium have been carried out. The influence of the concentration of extractant in the organic phase, the concentration of chloride ions in the feed phase, and the extraction isotherm have been investigated. The experimental results have been applied to an Excel programme where using a numerical solution method the theoretical models based on all of the previously presented equations have been calculated. The curve-fitting simulation technique along with consequent comparison of the experimental data with the modelling resolution have been used to determine the unknown variables which include cumulative stability constants of aqueous Cd-Cl complexes and equilibrium extraction constant of cadmium(II) in neutral chloride medium.
There are a few reviews reporting the determination of the speciation of aqueous cadmium(II) chloride species [5, 6, 7, 8]. It has been tried to adjust all of these sets of stability constants of Cd-Cl complexes to the presented in this work model of cadmium(II) solvent extraction and, as a result, only the ones obtained through the chemical equilibrium software MEDUSA worked out. In the cited programme there is no data for the $CdCl_4^-$ species, thus this one has been obtained on the modelling way. Adding the latter one to the speciation system has forced us to change the value for the $CdCl_3^-$ complex.
As a continuation, the results for the experiments, where determined model of the extraction

system is fitted to the experimetal data, are presented. At the end the values of the unknown variables are proposed.

Influence of the Cyanex 923 concentration in the organic phase

Carrier plays a decisive role in making the extraction process efficient and economically viable. Influence of the extracting agent on the extraction process has been studied with concentration of Cyanex 923 ranging from 0 to 20% (v/v) and in two different constant initial concentrations of chloride ions in the feed phase, namely 0,5M and 1M. The initial metal content has been maintained as 1 g/L. It can be seen in Fig. 2 and 3 that in smaller concentrations of extractant the theoretical model of extraction fits better to the investigation's data. Cadmium extraction increases practically lineally by raising the carrier concentration in the organic phase. In both of the experiments, at concentrations of extractant higher than 15% (v/v) the experimental data and the results obtained by modelling of the extraction system don't fit to each other. That is why, the further experiments of extraction properties of Cd(II) were done with 5 or 10% the Cyanex 923 in Exxol D-100 (v/v).

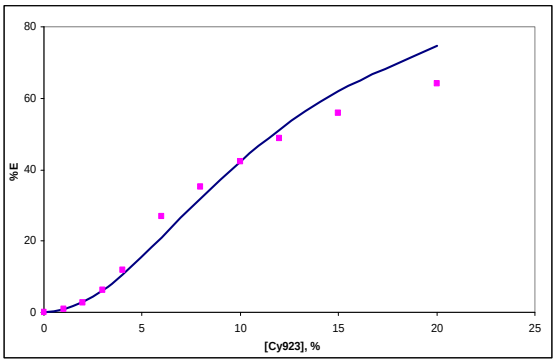

Fig. 2. Effect of the concentration of Cyanex 923 in the organic phase: $[Cd]_{total}$=1 g/L, $[Cl^-]_{total}$=1M, $[Cy923]_{total}$=0-20% (v/v); ■ experimental data, – model results.

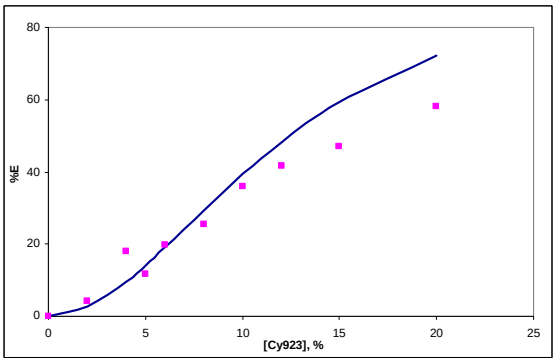

Fig. 3. Effect of the concentration of Cyanex 923 in the organic phase: $[Cd]_{total}$=1 g/L, $[Cl^-]_{total}$=0,5M, $[Cy923]_{total}$=0-20% (v/v); ■ experimental data, – model results.

Influence of the concentration of chloride ions Cl^- in the aqueous feed phase

The studies of the effect of $[Cl^-]$ ions in neutral medium have been performed in two different constant initial concentrations of extractant: 5% and 10% (v/v). In both of the cases initial metal content has been kept as 1 g/L. Total chloride concentrations have varied from 0,1M to 3M. The results in Fig. 4 and 5 show that the concentration of Cl^- ions in the aqueous phase has effect on the extraction of Cd(II) and the metal extraction increases with the $[Cl^-]$ up to 1M and reaches to maximum of 43% and 17% for studies with Cyanex 923 of 10% and 5%, respectively. Then the percentage of extraction slightly decreases. The first increase in the extraction is due to the Cl^- ion effect, which enhances the formation of extractable $CdCl_2$ species in the aqueous phase [42]. For the experiments made by with 10% (v/v) Cyanex 923, the experimental data fit better to the theoretical model of extraction.

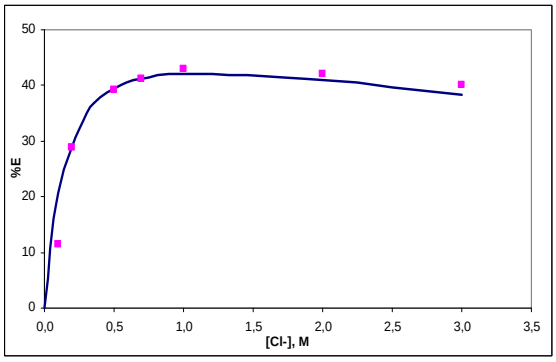

Fig. 4. Effect of the concentration of chloride ions in the aqueous phase: $[Cd]_{total}$=1 g/L, $[Cl^-]_{total}$=0,1-3M, $[Cy923]_{total}$=10% (v/v);■ experimental data, – model results.

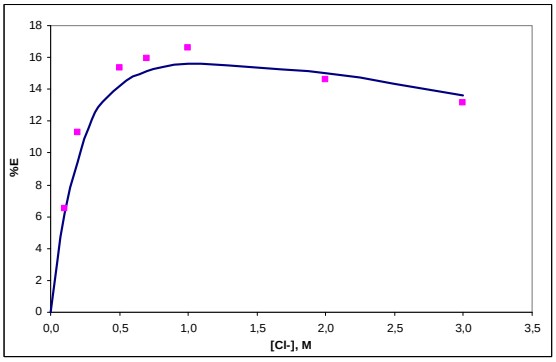

Fig. 5. Effect of the concentration of chloride ions in the aqueous phase: $[Cd]_{total}$=1 g/L, $[Cl^-]_{total}$=0,1-3M, $[Cy923]_{total}$=5% (v/v); ■ experimental data, – model results.

Extraction isotherm

The study of the extraction isotherm has been carried out in the range of initial cadmium and chloride concentrations in aqueous phases of 0,3 – 10 g/L and 0,5M, respectively. The Cyanex 923 of 5% has been chosen as a concentration of extractant. The experimental data and the modelling results fit well to each other. The extraction percentage of Cd(II) is slightly superior in the case of smaller concentrations of metal ions in the aqueous feed phase, what can be seen in Fig. 6.

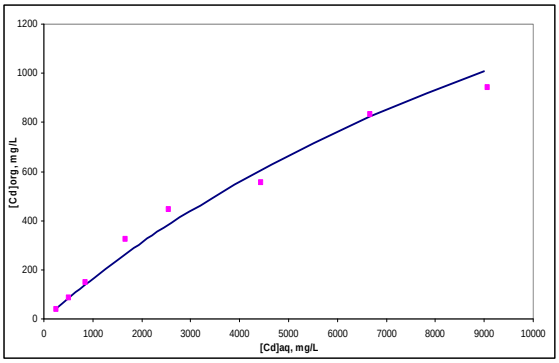

Fig. 6. Extraction isotherm of cadmium(II): $[Cd]_{total}$=0,3 – 10 g/L, $[Cl^-]_{total}$=0,5M, $[Cy923]_{total}$=5% (v/v); ■ experimental data, ─ model results.

Application of the numerical resolution method presented above to the experimental data has resulted in determination of the cumulative stability constants of aqueous Cd-Cl complexes and equilibrium extraction constant of cadmium(II) in neutral chloride medium which are proposed to be as follows: $\beta_{CdCl^+} = 95{,}5(L/mol)$, $\beta_{CdCl_2} = 398(L^2/mol^2)$, $\beta_{CdCl_3^-} = 60(L^3/mol^3)$, $\beta_{CdCl_4^{2-}} = 6(L^4/mol^4)$ and $K_{e1} = 19{,}8$ (L^2/mol^2), respectively.

5. Conclusions

Experimental and teorethical data fit to each other.As a future objective it is planned to apply the determine unknown variables to the modelling of cadmium(II) solvent extraction from acidic chloride medium using Cyanex 923 as extractant.

References

1. Bina Gupta, Akash Deep, Poonma Malik, Extraction and recovery of cadmium using Cyanex 923, *Hydrometallurgy* 61 (**2001**) 65–71
2. M. Alonso, A. Lopez-Delgado, A. M. Sastre, F. J. Alguacil, Kinetic modelling of the facilitated transport of cadmium (II) using Cyanex 923 as ionophore, *Chemical Engineering Journa*l 118 (**2006**) 213 – 219.
3. F.J. Alguacil, H. Tayibi, Carrier-facilitated transport of Cd(II) from a high-salinity chloride medium across a supported liquid membrane containing Cyanex 923 in Solvesso 100, *Desalination* 180 (**2005**) 181 – 187.
4. M. Wisniewski, M. Pierzchalska, “Recovery of carboxylic acids C1-C3 with organo-phosphine oxide solvating extractants”, *Journal of Chemical Technology and Biotechnology*, 80 (**2005**) 1425 – 1430.
5. K. Rasa, T. Peltovuori, H. Hartikainen, Effects of de-icing chemicals sodium chloride and potassium formate on cadmium solubility in a coarse mineral soil, *Science of the Total Environment* 366 (**2006**) 819 – 825.
6. T. Sato, T. Nakamura, The stability constants of the aqueous chloro complexes of divalent zinc, cadmium and mercury determined by solvent extraction with tri-n-octylphosphine oxide, *Hydrometallurgy* 6 (**1980**) 3 – 12.
7. T. Makino, K. Sugahara, Y. Sakurai, H. Takano, T. Kamiya, K. Sasaki, T. Itou, N. Sekiya, Remediation of cadmium contamination in paddy soils by washing with chemicals: Selection of washing chemicals, *Environmental Pollution* 144 (**2006**) 2 – 10.
8. Ignasi Puigdomenech, Inorganic Chemistry Royal Institute of Technology, Stockholm, Sweden.

Proceedings of the 10th International Chemical and
Biological Engineering Conference - CHEMPOR 2008
Braga, Portugal, September 4-6, 2008
E.C. Ferreira and M. Mota (Eds.)

Models to correlate the surface tension of solvent mixtures

Alicia G. Abuín[1*], Diego Gómez-Díaz[1], José M. Navaza[1], Isabel Vidal[1]
[1] Department of Chemical Engineering – ETSE. Lope Gómez de Marzoa s/n. University of Santiago de Compostela. E-15782, Santiago de Compostela. Spain.

Keywords: surface tension, chemical model, empiric model
Topic: Advancing the chemical and biological engineering fundamentals

Abstract

Surface tension has high industrial importance in chemical reactions as the reactions in the surface region are quite different from the bulk region. The surface tension also is an essential property in mass-transfer calculations, in various chemical engineering processes such as, distillation, extraction and absorption, because surface tension has a determining effect. In electrochemical reactions, biological membranes operation, environmental engineering and several other processes namely; corrosion, adherence, detergency, floating and lubricating the surface tension plays a significant role.

The aim of this study is to analyse the different models to correlate surface tension of mixed solvents and pure liquids, for the purpose of the simplest applications, as the property which determines the degree of dispersion, the dynamics of motion of liquids or the wettability, models are looked for.

1. Scope

Several approaches to describe surface tension of pure liquids and mixtures have been proposed. Some of them are empirical; others have more complexity. The most complicated models include an activity coefficient.

It is a review adapted to an actual interest: to design mixtures for fine chemistry. These mixtures are pirrolydone-based, aqueous two phases systems-based and ionic liquids. For the purpose of the simplest applications of the surface tension, as the property which determines the degree of dispersion, the dynamics of motion of liquids or the wettability, models are looked for.

The aim is to collect models with a minimum of parameters to describe the systems with sufficient accuracy for a practical purpose, not for an in-depth academic knowledge. The interest is not prediction *ab initio*. The scope is on a systematic approach in order to design new systems in knowing some basic ones. It is interesting to correlate surface tension after collecting a reasonable number of experimental data and then prediction with interpolation techniques.

There are several kinds of issues that can be approached in different ways - the true speciation in reactive systems, the activity coefficients in strong non-ideal aqueous systems or multicomponent– but there is insufficient data in the fine chemistry literature to test possible applications, moreover, with the scope of designing new mixtures and evaluate their potential as separation or reaction media, the use of complicated thermodynamic models –and surface tension is not a thermodynamic property- or models with a lot of parameters seems to be too much effort and it is not meaningful for people in fine chemistry industry. The correlation of extra-thermodynamics properties is not as rigorous as that of thermodynamic ones.

* Corresponding author. E-mail: alicia.garcia@rai.usc.es

For these reasons the search will be directed towards models that describe surface tension with the concentration of apparent components or other physical properties.

2. Models

2.1 Classification

The models selected according to the scope are presented in Table 1

2.2 Description

Any of the method presented here must not be seen as a substitute of other method: They must be seen as complementary schemes because it is frequently useful to have different methods available for estimating physical properties,

For organic compounds, Mcleod *(via* Reid, Prausnitz and Poling,1987) proposed a relation between surface tension and vapour and liquid densities based on the *parachor*, a temperature independent parameter which is estimated from the structure of the molecule, but it must be emphasized that surface tension depends on $([P])^4$ and therefore is very sensitive to the values of *parachor* . Below boiling point, at low pressure, $\rho_v << \rho_L$ and then the vapour density term is neglected.

Goldhammer and Gambill (*via* Reid, Prausnitz and Poling,1987) suggest correlating the density by relating it to temperature. The exponent *n* is 0.25 for alcohols, 0.29 for hydrocarbons and ethers and 0.31 for other organic compounds.

Brock and Bird (1955) suggested a method based on the corresponding states. Mcleod's method requires knowledge of the liquid densities, whereas this method requires critical properties and normal boiling point. The corresponding states method is a more general method capable of being applied to a variety of properties, whereas Mcleod's method is more specific and the main problem lies in the structural determinations needed.

About the simple methods proposed by Pelofsky (1966) and Schonhorn (1967) no more comments are needed.

The surface tension of a liquid mixture is not a simple function of the surface tension of pure components because the composition of the surface is not the same as that of the bulk and usually surface composition is not known.

For mixtures, parameter [P] can be obtained from structural data as for pure liquids or from regression of experimental data. The modified Macleod-Sugden's method has the advantage the, at the extremes of composition, it yields the correct values ($\sigma_m \rightarrow \sigma_i$ as $x_i \rightarrow 1$).

The equation of state based methods result in complex calculations, as well as the method proposed by Escobedo and Mansoori (1997), but they provide general expressions and accurate results if neededd.

The method proposed by Rice and Teja (1982) is based on the corresponding states principle. The main disadvantage of this method is that two reference fluids are needed as well as acentric factor and an interaction parameter for polar liquids.

Both classical and statistical thermodynamics have been employed to derive expressions for σ_m and the most arrive at a similar equation. The main difficulty of this class of methods is that a model for activity coefficients is needed and then a more complicate calculations. Santos et. Al. (2002) present an extensive review of thermodynamic methods and no more comments will be presented here.

Connors and Wright (1989) proposed a simpler model based on involving binding to the surface, an approach from adsorption theory. An example of the behaviour of this method is shown in figure 1. In the way of simple models, Jouyban et. Al. (2004) provide a model based on Nearly Binary Solvent/ Redlich-Kister equation. Both of them show good agreement.

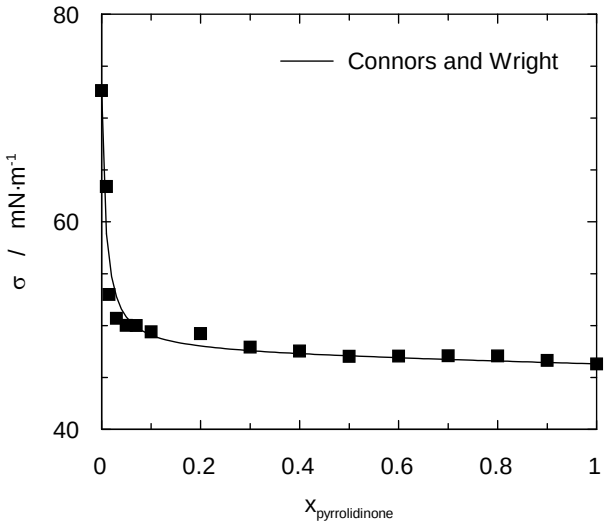

Figure 1. Fit behaviour of Connors and Wright model for water+2-pyrrolidinone mixture.

References

Reid, R. C., Prausnitz, J. M., Poling, B. E. (1987). The properties of gases and liquids. 4th Ed. Mc Graw Hill, New York.

Fishtine, S. H. (1963). Estimates of saturated f fluid densities and critical constants. *I & EC Fundamentals, 2, 2, 149-155.*

Brock, J. R., Bird, R. B. (1955). Surface tension and the principle of corresponding states *AIChE Journal*, 1, 2 174-177.

Miller, D. G.(1963). On the reduced Frost-Kalwarf vapour pressure equation. *I & EC Fundamentals*. 2, 1, 78-79.

Hakim, D. I., Steimberg, D., Stiel L. I. (1971). Generalized Relationship for the Surface Tension of Polar Fluids. *I & EC Fundamentals*, 10, 1: 174-175.

Pelofsky, A. H. (1966). Surface Tension-Viscosity Relation for Liquids. *Journal of Chemical and Engineering Data*,11, 394-397

Schonhorn, H. (1967). Surface Tension-Viscosity Relation for Liquids *Journal of Chemical and Engineering Data*,12, 4 524-525.

Carey, B. S., Scriven E. , Davis, H. T. (1978). Semiempirical Theory of Surface Tensions of Pure Normal Alcanes and Alcohols. *AIChE Journal*, 24,6, 1076-1080

Escobedo, J., Mansoori, A. G. (1998). Surface-Tension Prediction for Liquid Mixtures. *AIChE Journal*, 44,10, 2324-2332

Rice, P., Teja, S. (1982). A Generalized Corresponding-States Method for the Prediction of Surface Tension of Pure Liquids and Liquid Mixtures. *Journal of Colloid and Interface Science*, 86, 1 158-163

Santos, B. M. S., Ferreira, A. G. M., Fonseca, I. M. A. (2002). Surface and interfacial tensions of the systems water + *n*-butyl acetate + methanol and water + *n*-pentyl acetate + methanol at 303.15 K. *Fluid Phase Equilibria,* 208, 1-21

Connors, K. A., Wright, J. L. (1989). *Analitical Chemistry*, 61, 3, 194-198

Jouyban, A., Azarbayjany, A. F., Jalali-Barzegar, M., Acree, W. E. (2004).Correlation of surface tension of mixed solvents with solvent composition. *Pharmazie*,59, 937-941

Asprion, N., Ind. Eng. Chem. Res., 44: 7270 (2005)

Table1. Single models to correlate surface tension data

Model	suggestions	Empiric Thermodinamic Physico-Chemical	Equation	Notes (Extended away from the table)
1	Macleod-Sugden (*via* Reid, Prausnitz and Poling,1987)	Empiric	$\sigma^{1/4} = [P](\rho_L - \rho_V)$	**Pure liquids (non aqueous)** σ in dynes per centimetre ρ in moles per cubic centimetre
	Goldhammer Gambill		$\rho_L - \rho_v = \rho_{Lb}\left(\frac{1-T_r}{1-T_{br}}\right)^n$ $\sigma = ([P]\rho_{Lb})^4\left(\frac{1-T_r}{1-T_{br}}\right)^{4n}$	ρ_{Lb} in moles per cubic centimetre (at the normal boiling point)
2	Brock and Bird (1955) Miller (1963)	Empiric Corresponding states	$\sigma = P_c^{2/3}T_c^{1/3}Q(1-T_r)^{11/9}$ $Q = 0.1196\left[1+\frac{T_{br}\ln(P_c/1.01325)}{1-T_{br}}\right]-0.279$	**Pure liquids (non aqueous)** For non polar liquids Not applicable to compounds exhibiting strong hydrogen bonding
	Hakim et al. (1971)			Broaden approach to include polar liquids A lot of parameters Doubtful reliability
3	Pelofsky (1966) Schonhorn (1967)	Correlated with viscosity	$Ln\sigma = \frac{B}{\eta} + LnA$ $\sigma = A'C\frac{Mk}{R\eta}$	**Pure liquids** σ in dynes per centimetre Viscosity in centipoises An extended equation Doubtful reliability
4	Carey et al. (1978)	Semiempiric, based on Equation of State		**Pure liquids** Complicated functions Applicability limited
5	Macleod-Sugden (*via* Reid, Prausnitz and Poling,1987)	Empiric	$\sigma_m^{1/4} = \sum_{i=1}^{n}[P_i](\rho_{Lm}x_i - \rho_{vm}y_i)$	**Non-aqueous mixtures** Recommended for polar liquids σ in dynes per centimetre ρ in moles per cubic centimetre

Table1. Cont.

6	Macleod-Sugden Modified (*via* Reid, Prausnitz and Poling,1987)	Empiric	$\sigma_m^{1/4} = \rho_{Lm} \sum_{i=1}^{n} \frac{x_i \sigma_i^{1/4}}{\rho_{Li}}$	**Non-aqueous mixtures** σ in dynes per centimetre ρ in moles per cubic centimetre
7	Rice et al. (1982)	Empiric Corresponding states		**Pure fluids and non-aqueous mixtures**
8	Several authors	Classical and statistical thermodynamic	General form $\sum_{i=1}^{n} \left(\frac{x_i^B \gamma_i^B}{\gamma_i^\sigma} \right) \exp \frac{A_i(\sigma_m - \sigma_i)}{RT} = 1$ $A_i = (V_i)^{2/3} (N_0)^{1/3}$	Ai in square centimetres per mol A liquid model must be assumed for activity coefficients A more exhaustive discussion by Santos et al.
9	Meissner and Michaels (*via* Reid, Prausnitz and Poling,1987)	Empiric	$\frac{\sigma_m}{\sigma_W} = 1 - 0.411 log\left(1 + \frac{x}{a}\right)$	**aqueous mixtures** valid for x ≤ 0.01 a, model parameter x, mol fraction
10	Connors and Wright (1989)	Physic-chemistry of surface	$\sigma = \sigma_1 - \left[1 + \frac{bx_1}{1 - ax_1}\right] x_2(\sigma_1 - \sigma_2)$	**aqueous mixtures of organic cosolvents** a, b, model parameters x, mol fraction
11	Jouyban-Acree (2004)	Empiric	$Ln\sigma_m = x_1 Ln\sigma_1 + x_2 Ln\sigma_2 + x_1 x_2 \sum_{i=0}^{2} K_i (x_1 - x_2)^i$	**aqueous mixtures** K_i, model parameter
12	Asprion (2005)	Empiric	$\sigma_m = \sigma_1 + \sum_{i \geq 2} \frac{S_i x_i}{1 + \sum_{i \geq 2} (S_j - 1) x_j} (\sigma_i - \sigma_1)$	**aqueous mixtures** S_i, model parameter

Extended notes to Table 1.

(1)

σ surface tension. The same notation for the entire document

ρL liquid density

ρv vapor density

ρLb molal liquid density at the normal boiling point

[P] parachor, correlated with structure, Quayle (1953), (via Reid, Prausnitz and Poling,1987)

n from Fishtine (1963)

Tb normal boiling point

T_r reduced temperature, T/T_c, T_b/T_c, T_c is the critical temperature. For critical and reduced properties: The same notation for the entire document.

(3)

η Viscosity

k Thermal conductivity in cal/s·cm·K

R Gas constant, 1986 cal/mol·K

A, B, C Constants

(5)

σ_m surface tension of mixture. The same notation for the entire document

ρ_{Lm} liquid mixture density

ρ_{vm} vapor mixture density

x_i, y_i mole fraction of i in liquid and vapor phases. The same notation for the entire document

$[P_i]$ parachor of component i

(8)

x_i^B mol fraction of i in bulk liquid

γ_i^B activity coefficient of i in bulk liquid normalizad so that $\gamma_i^B \to 1$ as $x_i \to 1$

γ_i^σ activity coefficient of i in surface phase normalizad so that $\gamma_i^\sigma \to 1$ as surface phase composition becomes identical pure i

σ_m, σ_i surface tension of mixture and component i

Ai partial molar surface area of i

Vi pure liquid i molal volume

N_0 Avogadro's number

Proceedings of the 10th International Chemical and
Biological Engineering Conference - CHEMPOR 2008
Braga, Portugal, September 4-6, 2008
E.C. Ferreira and M. Mota (Eds.)

Thermodynamic analysis of surface tension in water / pyrrolidone system

Alicia G. Abuín[1], Antonio Blanco[1], Diego Gómez-Díaz[1], José M. Navaza[1*], Isabel Vidal[1]

[1] Department of Chemical Engineering – ETSE. Lope Gómez de Marzoa s/n. University of Santiago de Compostela. E-15782, Santiago de Compostela. Spain.

Keywords: 2-pyrrolidone, N-alkyl-2-pyrrolidone

Topic: Advancing the chemical and biological engineering fundamentals.

Abstract

In the present study, the surface tensions of aqueous solutions of several pyrrolidones have been determined using a Krüss K-11 tensiometer using the Wilhelmy plate method to different concentrations and different temperatures from 20 to 50 ºC and its behaviour has been analysed.

The addition of small quantities of pyrrolidone to water produces a drastically decrease in surface tension value. The bigger decrease in the surface tension was produced in low concentration of pyrrolidone. However, in high concentrations of pyrrolidone, the influence of the mixture composition can be considered negligible. This behaviour seems to indicate that an aggregation phenomenon exists between the two components pyrrolidone and water.

1. Introduction

2-Pyrrolidone is an organic compound consisting of a five-membered lactam. When the proton on the lactam is replaced for an alkyl group, this results in a great solvency (C_1P is the most active member) and as N-alkyl chain increases the surface activity increases. This reaches a maximum at a chain with 12-14 atoms of carbon (1).

The polarity of the N-alkyl-pyrrolidones makes possible strong hydrogen bonding with organic molecules and solvents.

Nowadays, pyrrolidones have increased their industrial interest as solvent for a wide variety of applications such as hard-surface cleaners because of its wetting properties and synergy with anionic surfactant, extractor agents of antibiotics which contain a phenolic- or carboxylic-group, formulation agents for shampoos, personal care products such as dyeing, bleaching or permanent waving and agricultural products like herbicides or plant virus growth inhibitors, etc. This is possible because pyrrolidones besides being surface-active compounds, they have low vapour pressure and low toxicity.

During the last few years the N-alkyl-pyrrolidones have also been porposed as skin-penetration enhacers. The use of these enhacers allow the administration of therapeutic agents to the bloodstream without pain and in a controlled manner.

2. Experimental section

2-Pyrrolidinone (CAS number 616-45-5) and 1-ethyl-2-pyrrolidinone (CAS number 2687-91-4), were supplied by Fluka with a purity of > 99 % and > 98 %. Respectively. Bidestilled water was used to prepare the mixtures of water and amine. All the mixtures were prepared by

* Corresponding author. E-mail: alicia.garcia@rai.usc.es

mass using an analytical balance (Kern 770) with a precision of 10^{-4} g. The uncertainty of the samples preparation in mole fraction was ± 0.0002.

The surface tension was determined employed a Krüss K-11 tensiometer used the Wilhelmy plate method. The plate employed was a commercial platinum plate supplied by Krüss. The platinum plate was cleaned and flame-dried before each measurement. The surface tension of pure water was determined and compared with literature to confirm that this method contribute suitable results [1]. The uncertainty of the measurement was ±0.05 $mN \cdot m^{-1}$. The detailed experimental procedure has been described elsewhere. In general, each surface tension value reported was an average of ten measurements. The samples were thermostated in a closed vessel under stir, before surface tension measurements to prevent evaporation. Surface tension measurements were carried out at different temperatures between 20 and 50 ºC.

3. Results and Discussion

Effect of Composition

In the present work we have determined and analysed the surface tension of aqueous solutions of 2-pyrrolidinone and 1-ethyl-2-pyrrolidinone over the entire range of mixture composition. The experimental values of this physical property for the mixtures used in this study have been collected for different values of temperature and composition. The trends observed abour the influence of mixture composition upon the experimental data obtained for these mixtures are shown in Figure 1 for both systems at a constant temperature.

The behaviour shown in this figure proved that the addition of small quantities of solutes to water produces a drastically decrease in surface tension value for all systems. The higher decreases in the surface tension was produced in low concentration of pyrrolidinones. The behaviour shown for these two systems is similar that the observed by other authors for mixtures i.e. employed amines [2].

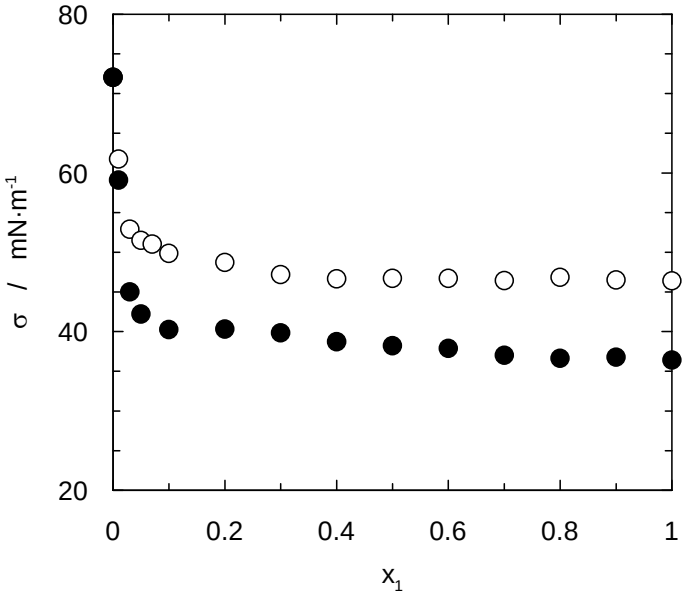

Figure 1. Influence of composition on surface tension of (○) water + 2-pyrrolidinone and (●) water + 1-ethyl-2-pyrrolidinone at 25 ºC.

Effect of temperature

The effect of the temperature upon the value of surface tension has been analysed and the behaviour observed is shown in Figure 2. A decrease in this property is produced when the operation temperature increases, and this behaviour was observed for both analysed systems.

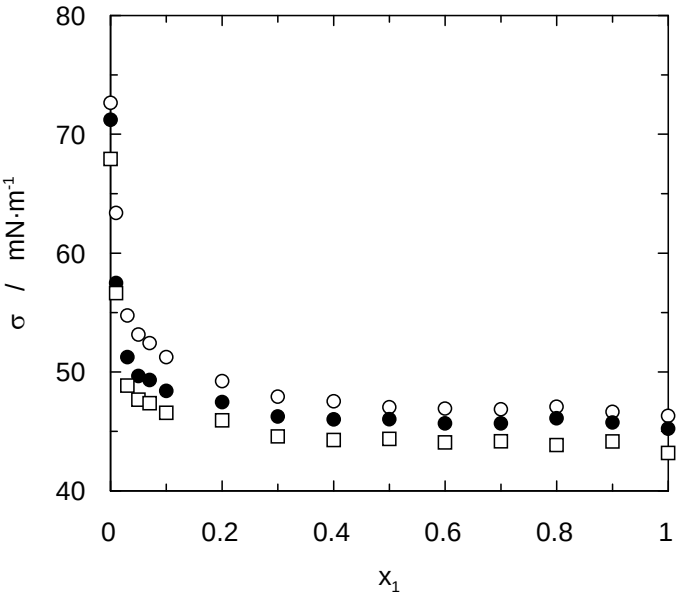

Figure 2. Influence of composition and temperature on surface tension of water + pyrrolidinone system. (○) T = 20 ºC; (●) T = 40 ºC; (□) T = 50 ºC.

Also, a linear trend was observed when the plot of surface tension versus temperature was carried out. Our research group has observed this behaviour for other binary systems. In previous work of our group and other authors [3] the surface tension *vs* temperature data has been fitted with a linear regression employing eq. 1.

$$\sigma = K_1 - K_2 \cdot t \qquad (1)$$

where σ is the surface tension, t is the temperature, K_1 and K_2 are fitting coefficients corresponding to equation 1.

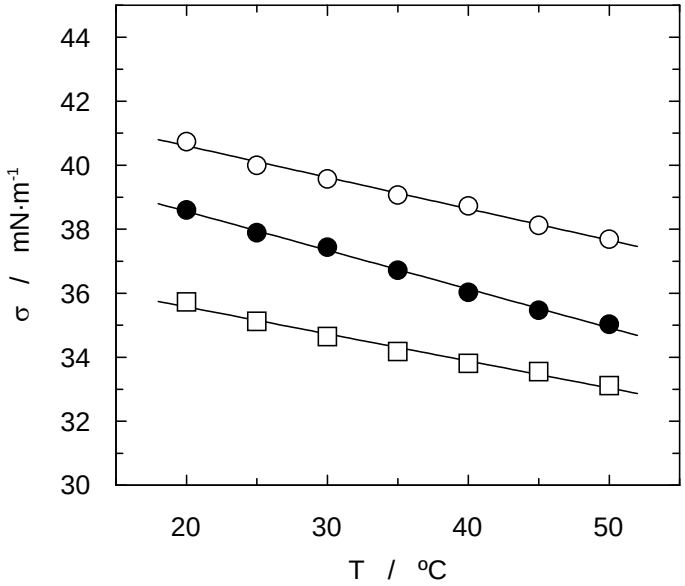

Figure 3. Influence of temperature on surface tension of water + 1-ethyl-2-pyrrolidinone system. (○) x = 0.3; (●) x = 0.6; (□) x = 1.

Surface thermodynamics

The last point has been related with the thermodynamic properties of the surface for this kind of mixtures. The surface enthalpy and entropy have been calculated using equations employed by Glinski et al [4] (eqs. 2 and 3).

$$S = -\left(\frac{\delta\sigma}{\delta T}\right)_{C,P} \qquad (2)$$

$$H = \sigma - T\left(\frac{\delta\sigma}{\delta T}\right)_{C,P} \qquad (3)$$

In relation with the trend observed for the entropy, this parameter has a constant value along the compositions upper the 0.5 molar fraction and near to pure water a notable increase in its value is produced. Other authors have found maximas for other systems [1] related with the molecular organization of different substances in the water surface.

The value of surface enthalpy corresponding to the water + 1-ethyl-2-pyrrolidinone system is shown in figure 4. The behaviour is similar than the effect of mixture composition on the surface tension because an important decrease was observed at very low 1-ethyl-2-pyrrolidinone concentration.

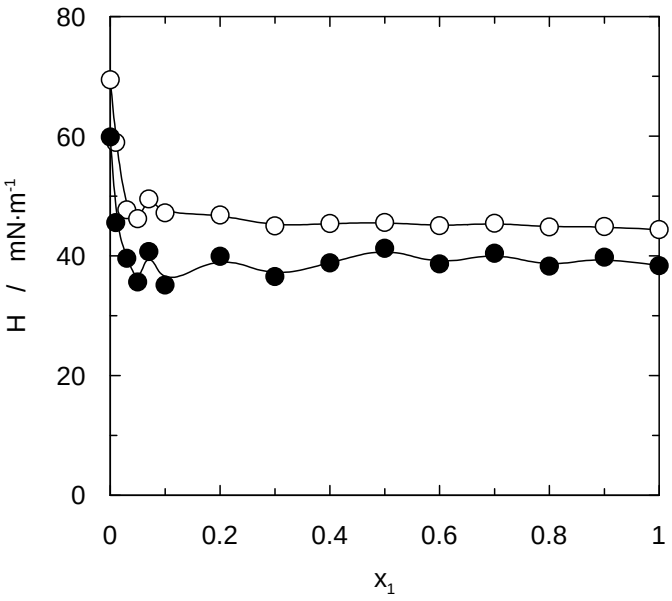

Figure 4. Surface enthalpy for water + 1-ethyl-2-pyrrolidinone system. (○) T = 20 ºC; (●) T = 50 ºC.

Literature

[1] Maham, Y.; Mather, A. E. Surface thermodynamics of aqueous solutions of alkylethanolamines. Fluid Phase Equilib. 2001, 182, 325-336.

[2] Vázquez, G.; Álvarez, E.; Navaza, J. M.; Rendo, R.; Romero, E.. Surface tension of binary mixtures of water + monoethanolamine and water + 2-amino-2-methyl-1-propanol and tertiary mixtures of these amines with water from 25 °C to 50 °C. J. Chem. Eng. Data. 1997, 42, 57-59.

[3] Álvarez, E.; Vázquez, G.; Sánchez-Vilas, M.; Sanjurjo, B.; Navaza, J. M. Surface tension of organic acids + water binary mixtures from 20 °C to 50 °C. J. Chem. Eng. Data. 1997, 42, 957-960.

[4] Glinski, J.; Chavepeyer, G.; Platten, J. K. Surface properties of diluted aqueous solutions of 1,2-pentanediol. J. Chem. Phys. 1999, 111, 3233-3236.

Proceedings of the 10th International Chemical and
Biological Engineering Conference - CHEMPOR 2008
Braga, Portugal, September 4-6, 2008
E.C. Ferreira and M. Mota (Eds.)

Volumetric properties for the ternary mixture Methanol-Formamide-Acetonitrile

Nelson Nunes[1*], Filomena Martins[2], Lídia Pinheiro[3], Ruben E. Leitão[1]

[1] Department of Chemical Engineering, Engineering Institute (ISEL), Polytechnical Institute of Lisbon, CQB, R. Conselheiro Emídio Navarro 1, 1950-062 Lisboa, Portugal.

[2] Department of Chemistry and Biochemistry, Faculty of Sciences, University of Lisbon, CQB, Ed. C8, Campo Grande 1749-016 Lisboa, Portugal

[3] CBT/iMed.UL, Faculty of Pharmacy, University of Lisbon, Av. Prof. Gama Pinto, 1649-003 Lisboa, Portugal

Keywords: solvents, ternary mixture, molar volume, partial molar volume
Topic: Advancing the chemical and biological engineering fundamentals

Abstract

Densities have been measured for the ternary mixture methanol-formamide-acetonitrile as a function of mole fraction at 298.15 K. The correspondent molar volume was determined along with two relevant connected properties: the excess molar volume and the partial molar volume of the mixtures. Excess molar volumes of the binary mixtures have been fitted with a Redlich-Kister type relationship and ternary fractions with the Cibulka polynomial relationship. Results have been used to interpret the nature of solvent-solvent interactions among mixtures' components.

1 Introduction

An increasing number of chemical industrial processes use mixtures of organic solvents, and a significant number of these show non-ideal behavior. Optimization and adequate design of equipment are conditioned by the correct assessment of mixing properties of these mixtures. Mixing properties and their corresponding derived values are also of primary interest for theoretical purposes namely for model development, estimation of parameters, etc.

Following previous studies on characterization of solvent mixtures (Leitão *et al.*, 2002) we now present the volumetric results for the ternary mixture methanol-formamide-acetonitrile. The experimental results have been used to calculate excess molar volumes (V^E), and partial molar volumes of the mixtures' components ($\overline{V_i}$) and interpret the behavior of the liquid mixtures under study.

2 Experimental

All the solvents used in the study were reagent grade, methanol (Riedel de Häen, HPLC, >99.5% purity), formamide (Aldrich, HPLC, >99.5% purity) and acetonitrile (Aldrich, HPLC, >99.5% purity) and were used without further purification. In all cases the water content was less than 0.1%.

Mixtures were prepared by weight, using a Mettler H35 balance with a precision of ± 0.1 mg. Densities were measured using an Anton-Paar vibrating-tube digital densimeter (cell unit DMA 512, processing unit DMA 60 and temperature unit DT 100-30).

* Corresponding author. Tel + 351-218 317 266. E-mail:nnunes@deq.isel.ipl.pt

A total of 61 molar fractions including ternary, binary and pure solvents were obtained at 298.15 ± 0.01K, with each value resulting from at least three individual density measurements.

3 Results and Discussion

Molar volumes have been calculated from density results according to the relationship

$$V = \sum_{i}^{n} \frac{x_i M_i}{\rho} \tag{1}$$

where x_i and M_i are the mole fraction and molecular weight of component i and ρ the solution density.

Figure 1 summarizes the obtained volumetric results for the ternary mixture, along with the corresponding 3D surface.

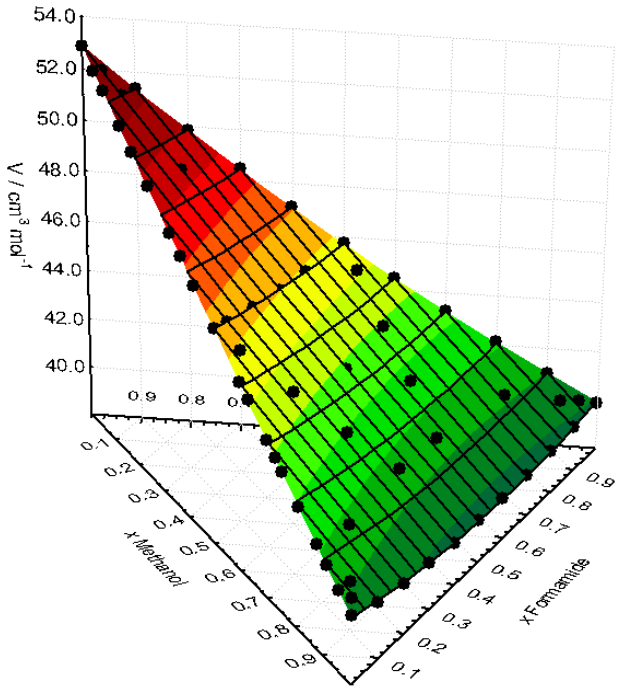

Figure 1 – Molar volume surface for the ternary mixture methanol-formamide-acetonitrile at 25 ºC.

The analysis of the molar volume of the mixtures shows a monotonous variation with no apparent singularities. In order to investigate the interactions between the mixtures' components, it is therefore necessary to determine excess molar volumes, V^E, which were calculated for each binary mixture from the volume data according to,

$$V^E = V - \sum_{i=0}^{N} x_i V_i \tag{2}$$

where V is the experimentally obtained molar volume and V_i the molar volume of each component.
For these mixtures, excess molar volumes were fitted using the Redlich-Kister equation (Redlich-Kister, 1948),

$$V^E_{i,j} \,/\, \mathrm{cm^3 mol^{-1}} = x_i x_j \sum_{P=0}^{n} a_P (x_i - x_j)^P \qquad (3)$$

Estimates of coefficients a_P were obtained by the least squares method and are summarized in table 1, along with the relevant statistical figures of merit. The standard deviation of the fit was calculated according to,

$$\sigma(V^E) = \sqrt{\frac{\sum (V^E - V^E_{calc})^2}{N - P}} \qquad (4)$$

where N is the number of observations and P the number of parameters.

Table 1 – Redlich-Kister equation and statistical parameters for each binary mixture

Parameters \ Mixtures	methanol / acetonitrile	formamide / acetonitrile	methanol / formamide
$a_0 \pm \sigma\ (a_0)$	–0.547 ± 0.007	–2.48 ± 0.03	–2.56 ± 0.05
SL(%)	(100%)	(100%)	(100%)
$a_1 \pm \sigma\ (a_1)$	–0.25 ± 0.03	---	–0.9 ± 0.1
SL(%)	(100%)		(100%)
$a_2 \pm \sigma\ (a_2)$	–0.25 ± 0.03	---	–0.6 ± 0.2
SL(%)	(100%)		(95.5%)
$a_3 \pm \sigma\ (a_3)$	–0.30 ± 0.06	---	---
SL(%)	(100%)		
R	0.998	0.997	0.996
sd_{fit}	0.004	0.02	0.02
F	817	1580	376
p (%)	100	100	100

Excess molar volumes of the ternary fractions were adjusted through the Cibulka relationship, eq. 5, which combines the Redlich-Kister relations of the three binary mixtures with other empirical fitting parameters (A, B_1, B_2) (Cibulka, 1982).

$$V^E_{1,2,3} = V^E_{1,2}(x_1, x_2) + V^E_{1,3}(x_1, x_3) + V^E_{2,3}(x_2, x_3) + x_1 x_2 x_3 \times \left(A + B_1(x_1 - x_2) + B_2(x_2 - x_3)\right) \qquad (5)$$

Fitted parameters and relevant statistical figures of merit are summarized in table 2.

Table 2 –Cibulka equation fitting and statistical parameters methanol/formamide/acetonitrile.

Parameters \ Mixture	methanol / formamide / acetonitrile
$A \pm \sigma\ (A)$	–1.7 ± 0.2
SL(%)	(100%)
$B_1 \pm \sigma\ (B_1)$	---
SL(%)	
$B_2 \pm \sigma\ (B_2)$	---
SL(%)	
R	0.9977
sd_{fit}	0.02
F	13010
p (%)	100

Figure 2 represents the determined excess molar volumes along with the surface defined by volumes calculated by the Cibulka equation.

Analysis of figure 2 shows the existence of a negative deviation from ideal behavior for all binary mixtures. Volume contraction is smaller in methanol/acetonitrile, but it suggests, nevertheless, the presence of hydrogen bond of the type OH---N≡C and also of specific interactions between OH groups and the π system electrons which cause the observed volume contraction. In methanol/formamide and formamide/acetonitrile mixtures, large volume contractions are observed which are probably linked to formamide molecules since this is a highly polar component and also highly associated by hydrogen bonding, due to a strong H-bond acceptor group (C=O) and a proton donating group ($-NH_2$). The negative excess molar volume clearly points out the presence of specific interactions between formamide and the other components, and with the breakdown of some of the original hydrogen bonds, new heteromolecular ones can occur, such as OH---N-H e CN---H-N. Other negative contributions seem attributable to acetonitrile (in methanol/acetonitrile mixture) and to methanol (in methanol/formamide mixture) which are accommodated in pre-existing free spaces. Figure 2 also shows that there is a ternary interaction: in fact, the largest negative deviation is observed for the ternary fraction 0.350/0.500/0.150, which indicates that the strongest interaction among all three components occurs for this mole fraction, along with the most effective mutual component accommodation.

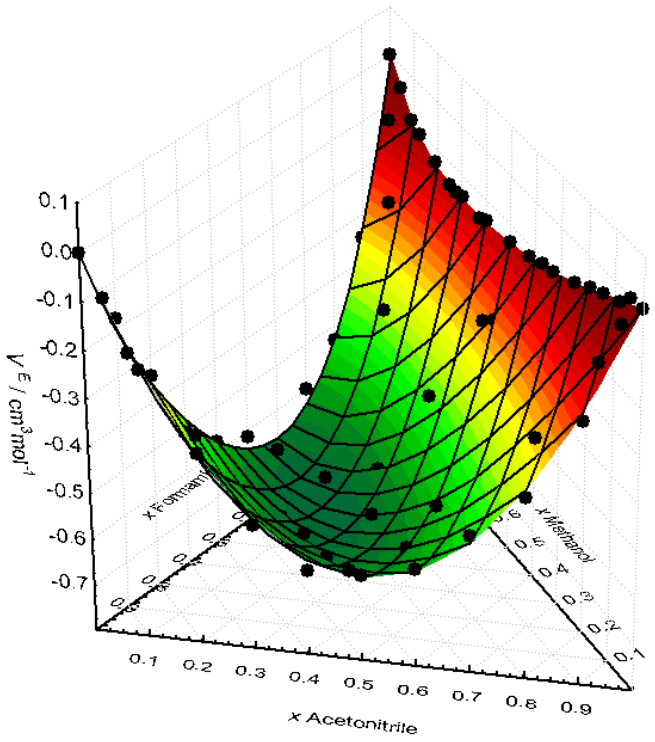

Figure 2 – Excess molar volume surface for metanol/formamide/acetonitrile at 25 ºC.

Partial molar volumes, $\overline{V_i}$, were also calculated in order to better identify the various molecular interactions present. The chosen relationship for the determination of $\overline{V_i}$ (Lepori, 1998) is based in the excess partial molar volume, $\overline{V_i}^E$

$$\bar{V}_i^E = V^E - x_j \left(\frac{\partial V^E}{\partial x_j} \right)_{T,p,x_k} - x_k \left(\frac{\partial V^E}{\partial x_k} \right)_{T,p,x_j} \quad (6)$$

which is then added to the components' molar volume, V_i^0

$$\bar{V}_i = V_i^0 + \bar{V}_i^E \quad (7)$$

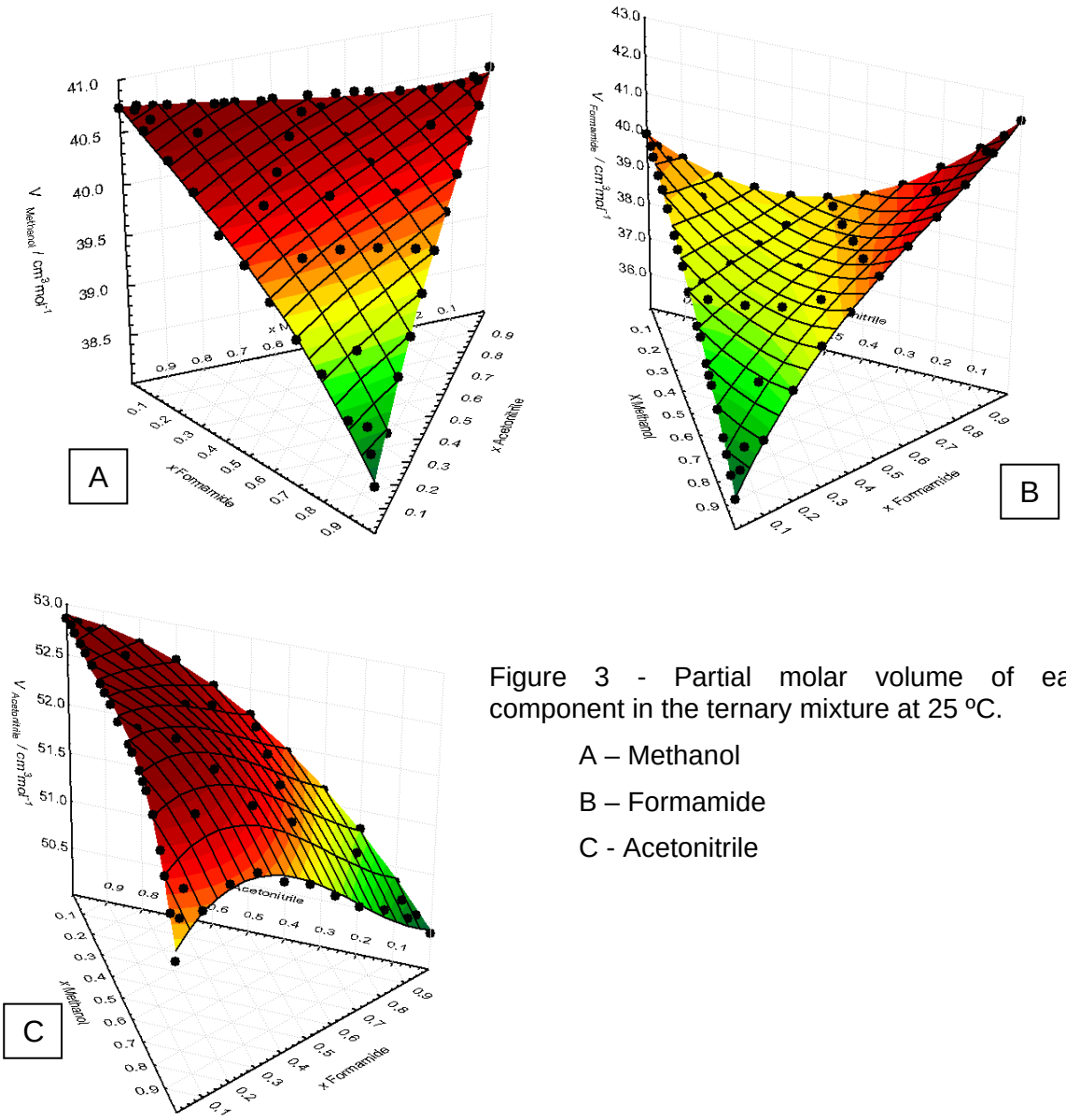

Figure 3 - Partial molar volume of each component in the ternary mixture at 25 ºC.

A – Methanol

B – Formamide

C - Acetonitrile

Figure 3 confirms some of the assumptions previously discussed within the context of excess molar volumes. In acetonitrile containing mixtures, the partial molar volume of methanol shows a slight decrease to a minimum (close to rich acetonitrile fractions). This is possibly

due to the accommodation of acetonitrile molecules within the methanol structure, and to interactions established between acetonitrile and methanol.
In the methanol/formamide mixture there is strong contraction of methanol's volume with the increase of formamide's fraction, characteristic of the formation of new bonds, particularly hydrogen bonds.

The partial molar volume of acetonitrile molecules increases with the increase of their mole fraction. For formamide a gradual and constant rise is observed whereas for methanol one observes a rise followed by a plateau. This type of behavior reveals the accommodation of acetonitrile molecules in the original structural network, and the increase of specific interactions, especially in acetonitrile poor regions.

The partial molar volume of formamide shows a decrease as its mole fraction decreases. In acetonitrile mixtures the minimum value occurs at an acetonitrile mole fraction of 0.65. This situation suggests that until this fraction of acetonitrile is reached, formamide is progressively forming new H-bonds, and from this fraction on, acetonitrile molecules break down some of the formamide bonds. In mixtures with methanol, the partial molar volume of formamide always decreases, suggesting that the eventual breaking of bonds is well compensated by the formation of new ones.

References

Cibulka, I., (1982) Estimation of Excess Volume and Density of Ternary Liquid-Mixtures of Non-Electrolytes from Binary Data. *Collection of Czechoslovak Chemical Communications*, 47, 1414-1419.

Leitão, R. L., Martins, F., Ventura, M. C., Nunes, N. (2002). Structural characterization of the ternary solvent mixture methanol-acetonitrile-1-propanol. *Journal of Physical Organic Chemistry*, 15, 623-630.

Lepori, L., Matteoli, E. (1998) Excess volumes of the ternary system ethanol plus tetrahydrofuran plus cyclohexane at 298.15 K. *Fluid Phase Equilibria* 145, 69-87.

Redlich, O., Kister, A.T., (1948) Algebraic Representation of Thermodynamic Properties and the Classification of Solutions. *Industrial and Engineering Chemistry*, 40, 345-348.

Proceedings of the 10th International Chemical and
Biological Engineering Conference - CHEMPOR 2008
Braga, Portugal, September 4-6, 2008
E.C. Ferreira and M. Mota (Eds.)

An effective method for calculation of homogeneous azeotropes in reactive and nonreactive mixtures

Adrián Bonilla-Petriciolet [1*], Gustavo A. Iglesias-Silva [2], and José Enrique Jaime-Leal [1]

[1] Chemical Engineering Department, Instituto Tecnológico de Aguascalientes, 20256 Aguascalientes, México.

[2] Chemical Engineering Department, Instituto Tecnológico de Celaya, Guanajuato, México

Keywords: azeotropy, global optimization, chemical equilibrium, phase equilibrium
Topic: Advancing the chemical and biological engineering fundamentals.

Abstract

In this work we introduce an alternative approach to find homogeneous azeotropes in reactive and nonreactive mixtures. Specifically, the Simulated Annealing optimization method is used to solve a system of nonlinear equations that results from the equalities of the orthogonal derivatives of the Gibbs energy, and the Gibbs energy of mixing in the vapor and liquid phases. For nonreactive systems, this system is solved using conventional composition variables while for reactive cases we use the transformed variables proposed by Ung and Doherty. Numerical performance of this approach is illustrated using several examples and results show that this method is effective for the calculation of homogeneous azeotropes in mixtures with or without chemical equilibrium.

1. Introduction

Azeotropy is a phase equilibrium phenomenon that occurs in many industrial applications and its presence restricts the separation grade of a multi-component mixture that can be achieved by distillation. In particular, the description of homogeneous azeotropy is essential for the selection of strategies in the synthesis, design, and operation of separation units. This description consists on establishing the temperature, pressure, and composition as well as the component number of the azeotrope.

An azeotrope can occur in reactive and nonreactive mixtures. For nonreactive systems, several methods for finding homogeneous azeotropes have been proposed. For example, Fidkowski *et al.* (1993) developed a robust method to locate all the homogeneous azeotropes using a homotopy technique together with a robust phase stability analysis. Harding *et al.* (1997) used a deterministic global optimization procedure with convex underestimating functions for the thermodynamic equations to perform a global minimization. The success or failure of this technique depends upon proper construction of the convex functions. Maier *et al.* (1998) used an interval-Newton/generalized-bisection algorithm to locate all the solutions of the thermodynamic conditions for homogeneous azeotropy using solution models and ideal gas behavior. Recently, Aslam and Sunol (2006) used a homotopy continuation method to study the sensitivity of azeotropic states to activity coefficient model parameters and operating conditions.

For systems with chemical equilibrium, few robust methods have been developed to address the problem of locating all reactive homogeneous azeotropes. Okasinski and Doherty (1997) reported a homotopy continuation method to locate multi-component reactive azeotropes. Later, Harding and Floudas (2000) applied their deterministic optimization method in the calculation of all reactive azeotropes of multi-component systems. This method offers a theoretical guarantee for finding all azeotropes, but depending on the thermodynamic model, it is necessary to reformulate the problem. Maier *et al*. (2000) have also extended their

* Corresponding author. Tel + 52-449-9105002 ext. 127. E-mail: petriciolet@hotmail.com

interval-Newton/generalized-bisection algorithm to locate all reactive azeotropes using solution models and ideal gas behavior. Finally, Qi and Sundmacher (2005) proposed a geometrical approach to locate all kind of azeotropes (reactive, nonreactive and kinetic). Although these methods have demonstrated to be very promising, some of them are model dependent, may require problem reformulations or a significant computational time for multi-component systems.

In this context, stochastic optimization methods offer some advantages for the calculation of homogeneous azeotropes and may overcome the difficulties described above. These methods are robust numerical tools that present a reasonable computational effort in the optimization of multivariable functions; they are applicable to ill-structure or unknown structure problems; they are efficient and require only calculations of the objective function. Many thermodynamic problems that are very difficult to solve by conventional techniques can be solved using stochastic methods. In Thermodynamics, Simulated Annealing and other stochastic methods have been successfully applied in phase equilibrium and stability problems, critical point calculations, parameter estimation in non-linear models, among other applications. To the best of our knowledge, these methods have been not applied in the calculation of homogeneous azeotropes in both reactive and nonreactive mixtures.

In this work we introduce an alternative technique to find homogeneous azeotropes in reactive and non-reactive mixtures which is based on the application of Simulated Annealing optimization technique. Specifically, this optimization method is used to solve a system of nonlinear equations that results from the equalities of the orthogonal derivatives of the Gibbs energy, and the Gibbs energy of mixing in the vapor and liquid phases.

2. Formulation of Thermodynamic Problem

Recently, Iglesias-Silva *et al*. (2003) have shown that two-phase equilibrium in a nonreactive mixture of c components results from solving

$$\left(\frac{\partial g}{\partial x_i}\right)^{\alpha}_{T,P,x_{j\neq i}} - \left(\frac{\partial g}{\partial x_i}\right)^{\beta}_{T,P,x_{j\neq i}} = 0 \quad i = 1,2,\cdots,c-1 \tag{1}$$

$$\left(g^{\beta} - g^{\alpha}\right) - \sum_{j=1}^{c-1}\left(x_j^{\beta} - x_j^{\alpha}\right)\left(\frac{\partial g}{\partial x_j}\right)^{\alpha}_{T,P,x_{l\neq j}} = 0 \tag{2}$$

$$z_i = x_i^{\alpha}\varphi^{\alpha} + x_i^{\beta}\varphi^{\beta} \qquad i = 1,2,\cdots,c-1 \tag{3}$$

where g is the Gibbs free energy of mixing, z_i is the mole fraction of component i in the feed, x_i^k is the mole fraction of component i in the phase k, φ^k is the fraction of moles in phase k, α and β denote the vapor and liquid phases, respectively. If this mixture shows homogeneous azeotropy ($z_i = x_i^{\alpha} = x_i^{\beta}$), the above equations simplify to

$$F_1 = g^{\alpha} - g^{\beta} = 0 \tag{4}$$

$$F_{i+1} = \left(\frac{\partial g}{\partial x_i}\right)^{\alpha}_{T,P,x_{k\neq i}} - \left(\frac{\partial g}{\partial x_i}\right)^{\beta}_{T,P,x_{k\neq i}} = 0 \quad i = 1,2,\cdots,c-1 \tag{5}$$

where Eqs. (4) and (5) are a system of c nonlinear equations with $c-1$ unknown compositions (mole fractions, x) plus the unknown temperature or pressure of the azeotrope. For reactive systems, Eqs. (1)–(3) can be extended if we consider the transformed composition variables proposed by Ung and Doherty (1995). These variables depend only on the initial composition of each independent chemical species and restrict the solution space to the compositions that satisfy stoichiometry requirements. As a consequence, they reduce

the dimension of the composition space by the number of independent reactions. Thus, the transformed mole fractions X of a mixture with R independent chemical reactions are given by

$$X_i = \frac{x_i - \nu_i N^{-1} \vec{x}_{ref}}{1 - \nu_{TOT} N^{-1} \vec{x}_{ref}} \quad i = 1,..., c - R \tag{6}$$

where $\vec{x}_{ref}$ is the column vector of R reference component mole fractions, ν_i is the row vector of stoichiometric coefficients of component i for each reaction, ν_{TOT} is a row vector where each element corresponds to the sum of the stoichiometric coefficients for all components that participate in reaction r, and N is a square matrix formed from the stoichiometric coefficients of the reference components in the R reactions. Using these transformed variables as an alternative for the conventional composition quantities (mole numbers or fractions), the Gibbs free energy in a reactive system behaves as in a non-reactive system. Therefore, all thermodynamic properties of the reactive mixture are functions of the transformed composition variables.

Hence, the two-phase equilibrium in a reactive system can be calculated using

$$\left(\frac{\partial \hat{g}}{\partial X_i}\right)^{\alpha}_{T,P,X^{\alpha}_{j\neq i,\, j\in\{1,...,c-R-1\}}} - \left(\frac{\partial \hat{g}}{\partial X_i}\right)^{\beta}_{T,P,X^{\beta}_{j\neq i,\, j\in\{1,...,c-R-1\}}} = 0 \quad i = 1,..., c - R - 1 \tag{7}$$

$$\hat{g}^{\beta} - \hat{g}^{\alpha} - \sum_{i=1}^{c-R-1} (X_i^{\beta} - X_i^{\alpha}) \left(\frac{\partial \hat{g}}{\partial X_i}\right)^{\alpha}_{T,P,X^{\alpha}_{j\neq i,\, j\in\{1,...,c-R-1\}}} = 0 \tag{8}$$

$$Z_i = X_i^{\alpha}\Phi^{\alpha} + X_i^{\beta}\Phi^{\beta} \qquad i = 1,..., c - R - 1 \tag{9}$$

subject to

$$K_{eq}^{r} = \prod_{i=1}^{c} a_i^{\nu_i^r} \qquad r = 1,..., R \tag{10}$$

where $\hat{g}$ is the transformed Gibbs free energy of mixing, Z_i is the transformed feed composition of component i, K_{eq}^{r} is the reaction equilibrium constant, a_i is the activity of component i, Φ^{α} and Φ^{β} are the transformed fractions of moles at the vapor and liquid phases, respectively.

Ung and Doherty (1995) showed that $Z_i = X_i^{\alpha} = X_i^{\beta}$ is a necessary and sufficient condition for the presence of a homogeneous reactive azeotrope. If we replace this condition into Eqs. (7)-(9), then

$$F_1 = \hat{g}^{\beta} - \hat{g}^{\alpha} = 0 \tag{11}$$

$$F_{i+1} = \left(\frac{\partial \hat{g}}{\partial X_i}\right)^{\alpha}_{T,P,X^{\alpha}_{j\neq i,\, j\in\{1,...,c-R-1\}}} - \left(\frac{\partial \hat{g}}{\partial X_i}\right)^{\beta}_{T,P,X^{\beta}_{j\neq i,\, j\in\{1,...,c-R-1\}}} = 0 \quad i = 1,..., c - R - 1 \tag{12}$$

These equations can be used to find $c - R - 1$ transformed composition variables and the temperature or pressure of reactive azeotrope. The material balance is meaningless for both reactive and nonreactive azeotropes. If the Gibbs energy, or transformed Gibbs energy, is plotted for both liquid and vapor phases *versus* the corresponding composition variable at the homogeneous azeotrope pressure and temperature, the Gibbs curves of each phase will intersect at one point satisfying the equality criterion of the tangent plane and the equality of chemical potentials. Note that Eqs. (4)-(5) and (11)-(12) are an alternative set of

thermodynamic conditions to locate all homogeneous nonreactive and reactive azeotropes in multi-component systems, which can be applied with any thermodynamic model. They are nonlinear and may have one, more than one or no solutions (one azeotrope, several azeotropes or the nonexistence of a homogeneous azeotrope). Conventional root-finders are not suitable for solving these equations. Hence, a reliable and efficient numerical strategy must be used for the calculation of homogeneous reactive and nonreactive azeotropes. In the next section, we describe our approach to solve this thermodynamic problem.

3. Description of solution approach

We use an optimization approach to locate all solutions of Eqs. (4)-(5) and (11)-(12). These equations are formulated as a single objective function that should minimize by a suitable optimization technique. This objective function is given by

$$F_{obj} = F_1^{\,2} + \sum_{i=2}^{nec} F_i^{\,2} \tag{13}$$

where nec = $c-1$ for nonreactive mixtures and $nec = c - R - 1$ for reactive mixtures, respectively. At azeotropy condition, the global minimum of this function must be zero, but we assume that an azeotrope is found when we find the composition variables (x_i or X_i) and temperature or pressure that make the value of the function less than or equal to 1×10^{-9}; otherwise, we consider that an azeotrope does not exist in the mixture at the given conditions. For systems with polyazeotropy, this function have several optimums where F_{obj} $\leq 1\times10^{-9}$. The following procedure is used to locate all homogeneous azeotropes. First, we define the initial search intervals for the composition variables and the temperature or pressure. In these intervals, the objective function is minimized using a suitable optimization method and, once a minimum is found, we create new search intervals using the found solution for the temperature or pressure. In these new intervals, we again minimize the objective function. This procedure is repeated until the convergence criterion cannot be satisfied. For polyazeotropy, the objective function is penalized in the limits of the intervals obtained from segmentation to avoid convergence to the last solution. Usually, the value of the objective function is greater than 1×10^{-4} if testing conditions do not contain an azeotrope.

The Simulated Annealing method (SA) is used to find the global optimum of Eq. (13). In general, SA method overcomes most of the numerical difficulties that local optimization methods show. Because of the stochastic nature of SA, a local minimum can be avoided much more easily than in conventional methods. SA simulates the process of slow cooling of metals to achieve the minimum function value in a minimization problem. The cooling phenomenon is modeled by controlling a temperature like parameter introduced with the concept of Boltzmann probability distribution. Using a proper decrease of temperature, the convergence of the algorithm can be manipulated. In the present study, the SA algorithm developed by Corana *et al.* (1987) was used. This algorithm has been successfully applied in several thermodynamic problems (e.g., Bonilla-Petriciolet *et al*., 2006). Note that the numerical performance (reliability and efficiency) of SA method is affected by the cooling schedule. SA is a robust optimization method if an appropriate cooling schedule is used. So, the parameters of cooling schedule were tuned for the current application.

4. Case of study

We have calculated the homogeneous azeotropes of several binary, ternary and quaternary reactive and nonreactive mixtures that appear in the literature for testing the numerical performance of proposed strategy. In these calculations, solution models and equations of state were used. In all performed calculations, our method finds all azeotropes without any numerical problem independently of the initial values for optimization variables. In fact, our

method is very reliable for finding homogeneous azeotropes in both reactive and nonreactive mixtures.

With illustrative purposes, Figure 1 shows the performance of our method in the calculation of the homogeneous azeotrope for the reactive mixture: isobutene (1) + methanol (2) ⇔ methyl ter-butyl ether (3) with n-butane (4) as inert at 20 atm. Wilson model and ideal gas behavior are used to calculate the thermodynamic properties of this mixture, where three transformed mole fractions (X_1, X_2, X_4) and temperature are used as decision variables.

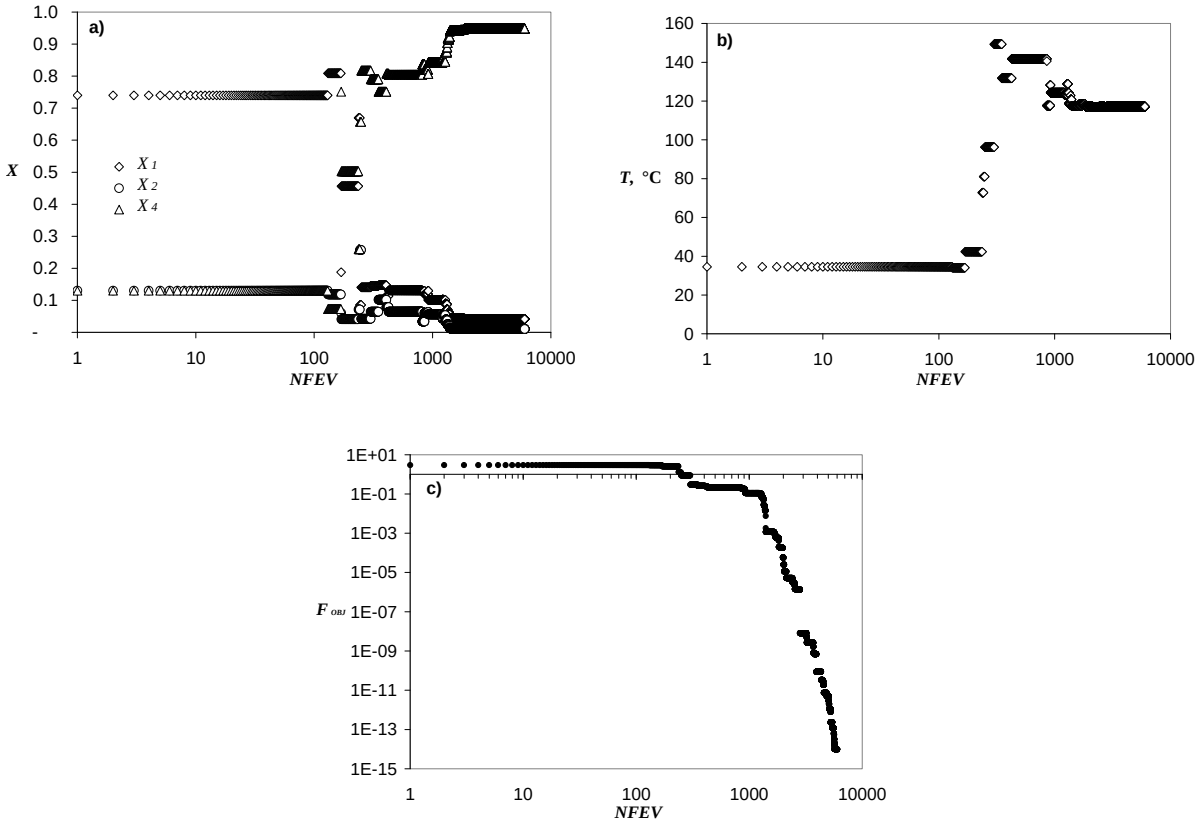

Figure 1. Performance of decision variables in the calculation of a reactive azeotrope using the Simulated Annealing method. a) Transformed mole fractions vs. NFEV, b) Temperature vs. NFEV, c) F_{obj} vs. NFEV.

From Fig. 1, we can observe that SA method requires a significant number of function evaluations (NFEV) for improving the accuracy of azeotrope conditions after F_{obj} has reached a value lower than 1x10^{-04}. Based on these results, we tried a hybrid approach starting with SA method as a robust algorithm for ensuring certain progress from poor initializations, and ending with a more efficient local method to accelerate convergence. Specifically, we used the Newton method as local strategy to solve Eqs. (4)-(5) or (11)-(12) using the solution obtained by SA method. The switch to the Newton method takes place once F_{obj} is lower or equal than 1x10^{-04}. All examples were solved using this approach with random initial values and, for all performed calculations, the azeotropes were found without any numerical problem. Note that a proper initialization for Newton method is available after application of SA method, and convergence is easily achieved. However, computational time is significantly reduced for both reactive and nonreactive systems. Generally, there is a 3:1 rate between the computational times of SA method and SA-Newton hybrid method.

Our experience with local solvers for finding homogeneous azeotropes indicates that these methods may show a success rate from 70 to 99 % using random initial values. When the unknown number increases, the performance of local solvers is poor. Clearly, local methods are more efficient than SA method; however they are less reliable and more dependent on the initial guesses.

5. Conclusions

We present an alternative set of thermodynamic conditions to locate all homogeneous azeotropes in multi-component reactive and nonreactive mixtures. Specifically, we showed that a homogeneous azeotrope (reactive or nonreactive) must satisfy an equality of the Gibbs free energy of mixing between vapor and liquid phases and an equality of the orthogonal derivatives of Gibbs energy with respect to composition variables in each phase. The resolution of these thermodynamic conditions can be done with confidence using the Simulated Annealing method. This optimization method is robust for finding all homogeneous azeotropes in reactive and nonreactive mixtures, and is almost independent of the initial values and its algorithm parameters. Finally, our method can be used with any thermodynamic model without the problem reformulation and it is suitable for multi-component calculations.

References

Aslam, N., Sunol, A.K., (2006). Sensitivity of azeotropic states to activity coefficient model parameters and system variables. *Fluid Phase Equilibria* 240, 1-14.

Bonilla-Petriciolet, A., Vázquez-Román, R., Iglesias-Silva, G.A., Hall, K.R., (2006). Performance of stochastic optimization methods in the calculation of phase stability analyses for nonreactive and reactive mixtures. *Industrial Engineering Chemistry Research* 45, 4764-4772.

Corana, A., Marchesi, M., Martini, C., Ridella, S., (1987). Minimizing multimodal functions of continuos variables with the simulated annealing algorithm. *ACM Transactions on Mathematical Software* 13, 262-280.

Fidkowski, Z.T., Malone, M.F., Doherty, M.F., (1993). Computing azeotropes in multicomponent mixtures. *Computers Chemical Engineering* 17, 1141-1155.

Harding, S.T., Floudas, C.A., (2000). Locating all heterogeneous and reactive azeotropes in multicomponent mixtures. *Industrial Engineering Chemistry Research* 39, 1576-1595.

Harding, S.T., Maranas, C.D., McDonald, C.M., Floudas, C.A., (1997). Locating all homogeneous azeotropes in multicomponent mixtures. *Industrial Engineering Chemistry Research* 36, 160-178.

Iglesias-Silva, G.A., Bonilla-Petriciolet, A., Eubank, P.T., Holste, J.C., Hall, K.R., (2003). An algebraic method that includes Gibbs minimization for performing phase equilibrium calculations for any number of components or phases. *Fluid Phase Equilibria* 210, 229-245.

Maier, R.W., Brennecke, J.F., Stadtherr, M.A., (1998). Reliable computation of homogeneous azeotropes. *AIChE Journal* 44, 1745-1755.

Maier, R.W., Brennecke, J.F., Stadtherr, M.A., (2000). Reliable computation of reactive azeotropes. *Computers Chemical Engineering* 24, 1851-1858.

Okasinski, M.J., Doherty, M.F., (1997). Thermodynamic behavior of reactive azeotropes. *AIChE Journal* 43, 2227-2238.

Qi, Z., Sundmacher, K., (2005). Geometrically locating azeotropes in ternary systems. *Industrial Engineering Chemistry Research* 44, 3709-3719.

Ung, S., Doherty, M.F., (1995). Necessary and sufficient conditions for reactive azeotropes in multireaction mixtures. *AIChE Journal* 41, 2383-2392.

Proceedings of the 10th International Chemical and
Biological Engineering Conference - CHEMPOR 2008
Braga, Portugal, September 4-6, 2008
E.C. Ferreira and M. Mota (Eds.)

A Portable Library for Equilibrium and Thermodynamics Properties Calculations based on Object Oriented Paradigms

Joana C. Vieira[1], Miguel A. Mesquita[2], Francisco A. Da Silva[3*]
[1] IINEGI – Institute of Mechanical Engineering and Industrial Management, UMEC (Composite Materials and Structures Unit), Rua Doutor Roberto Frias, 378, 4200-465 Porto, Portugal.
[2] Portugal Telecom Inovação, SA, Rua Eng. José Ferreira Pinto Basto, 3810-106 Aveiro, Portugal
[3] University of Aveiro, Department of Chemistry, CICECO, 3810-193 Aveiro, Portugal

Keywords: Vapor-liquid equilibrium, thermodynamic library, object oriented, Thermolib.
Topic: Systematic methods and tools for managing the complexity.

Abstract

A new thermodynamic library programmed in Java named Thermolib is presented. It is designed to be portable, command friendly and versatile. It is proposed as a pedagogical and research tool for performing vapour-liquid equilibrium and thermodynamic properties calculations directly from command driven computing environments.

1 Introduction

This work presents the development of a portable and embeddable numerical library aimed at the calculation of equilibrium and thermodynamics properties. This library, identified as ThermoLib, is being developed using object-oriented concepts. It was created with part of the core code from an arcane application called Ekilib (Báez, et al., 1990; Vieira, 2007). That application was compressed by a group of six thermodynamic modules assembled with a user friendly interface, using classical procedural programming in Turbo-Pascal, being free distributed in the academic community. At that time, the availability of easy to use thermodynamic number cruncher applications was rare and commercial software only ran in huge mainframes. The portability of the code was constrained by tough limitations in hardware. Fortran 77 language was the “king of hill” in the scientific computing area and C language was directed to operating system development.

Nowadays, computer power and its availability are fairly common and software development has been revamp with object-oriented paradigms, allowing the management of complexity with well established patterns. The object-oriented paradigm is well supported in languages like C++ and Java, which in last years have been shifting Fortran from scientific programming crown. In this work, we have chosen Java as developing language platform, because it adopts a shorter but a flexible sub-set of C++ powerful characteristics, due to its omnipresence, even increasing performance and acceptation by scientific computing community (Pang, 2006).

The scenario in thermodynamic libraries for process modeling continues to be limited. It has raised recently a free object-oriented library developed in C++ (Landschützer, 2007), which seems will become in a large open source process simulator application, shareware packages callable from inside worksheets or thermodynamic packages with too narrow application. However, a portable, embeddable, easy to use, command driven, wide thermodynamic numerical library continues to be scarce or expensive, most of them restricted to commercial applications environments or not easily portable.

* Corresponding author. Tel +351-234 401 549. E-mail:fsilva@ua.pt

General propose computing environments as Matlab or Octave are used in academy and research, normally solving problems with thermodynamic requirements. It is always hard to include in dynamic models, rigorous thermodynamic treatment for determining properties and/or solving equilibrium equations. This library will try to fulfill this gap, both pedagogically and as a research working toolbox. The new library uses a database with critical data for pure components, easily accessible with single commands. The possibility to have a live object in memory for direct inspection with the “pure” component data and behavior, ready to use “mixture” objects allocating all data and methods for computing mixture properties and “mixture-stream” objects with vapor-liquid capacities are the main add-ons of the library we are developing.

2 Library Structure

Figure 1 shows the main class diagram of Thermolib library where at the middle is placed the package thermo, where all thermodynamic calculations implemented are located. Figure 2 shows a detailed class diagram for the package thermo, where it is prominent the Pure ← Mixture ← MixtureStream ← skeleton, inherited from Ekilib simulator (Báez *et. al.,* 1990). Pure class defines the behaviour of a single component and the access to pure component database. Mixture is an extension of single component where all mixture properties are assembled, while MixtureStream allocates all vapour-liquid equilibrium calculations: Flash, Bubble and Dew points. At the left side of Figure 2 it is shown the Eos and ExcessProperties interfaces, where new models extensions will be anchored, not originally avalilable in Ekilib.

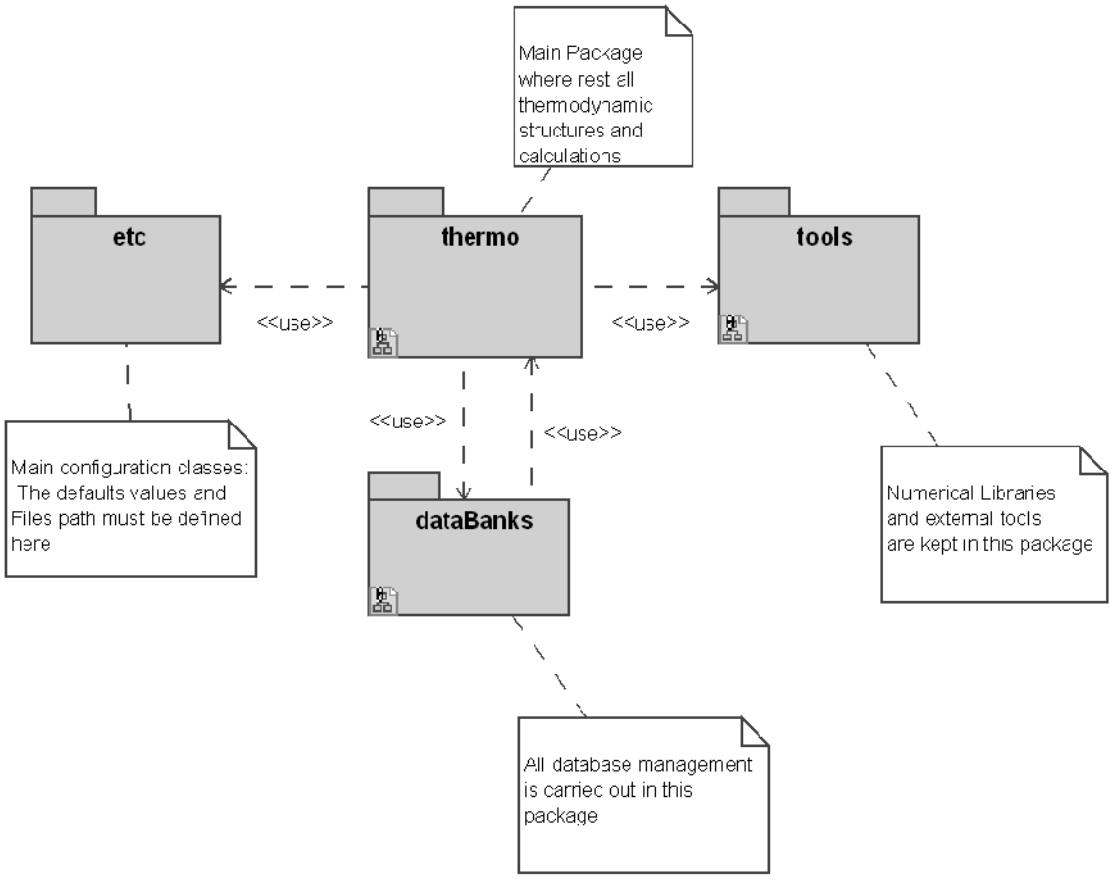

Figure1: Global class diagram of Thermolib toolbox written in Java language.

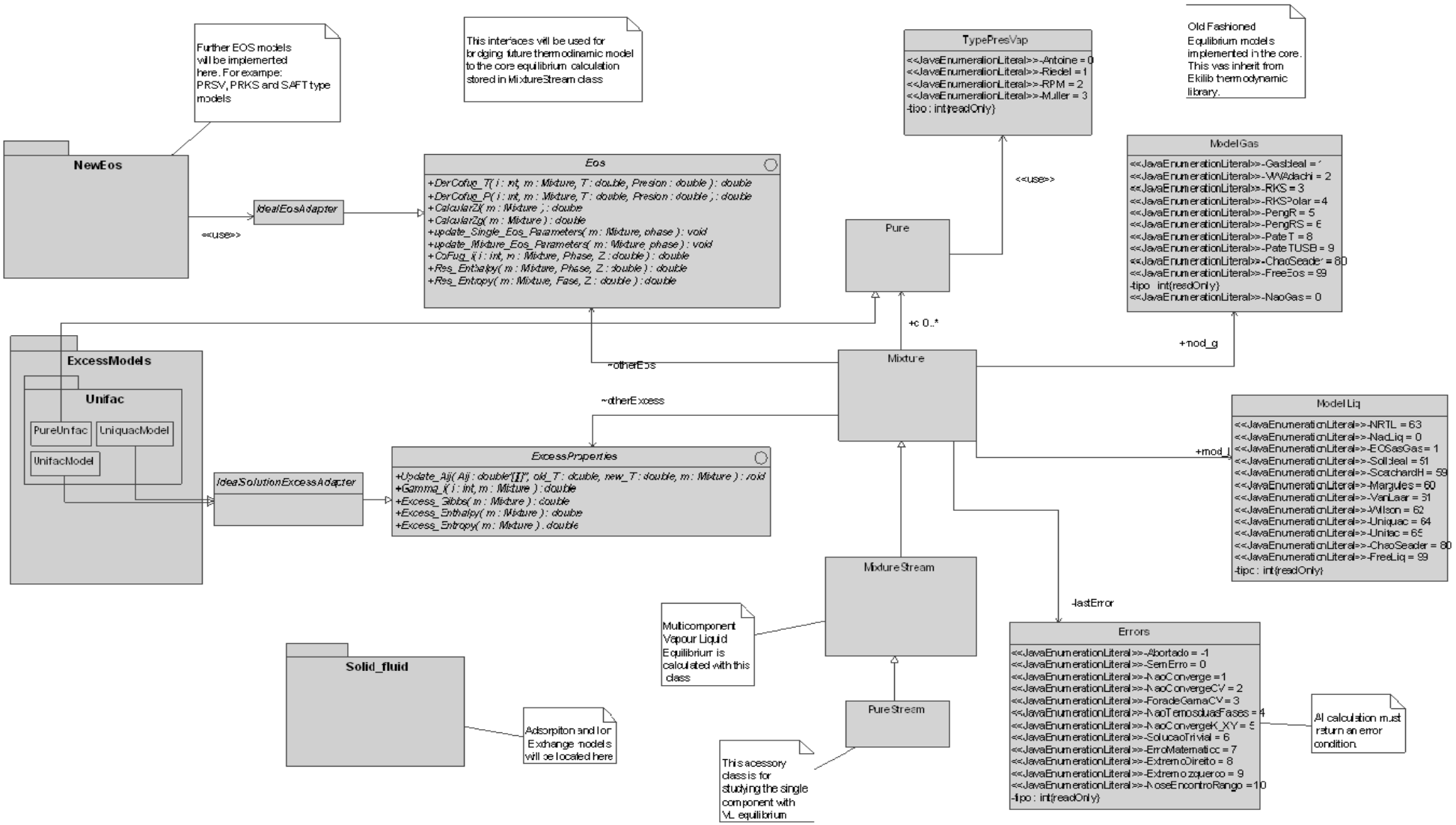

Figure 2: Detailed class diagram of “Thermo” package showed in Figure 1.

3 Simple examples

Figure 1 shows a textbook problem (Smith, *et al.*, 2005) solved with our library, using Matlab. The plots are obtained from standard commands, while the thermodynamic calculations where carried out with Thermolib embedded or imported directly in the computer environment. Figure 2 shows how to create an instance of a pure component directly from Matlab console window, after three commands, and a simple vapor pressure calculation. The scroll-window over the white pane shows the internals of the pure component available in memory at a finger distance. Further pedagogical examples and research application of Thermolib library can be found elsewhere (Viera, 2007; Silva, 2008).

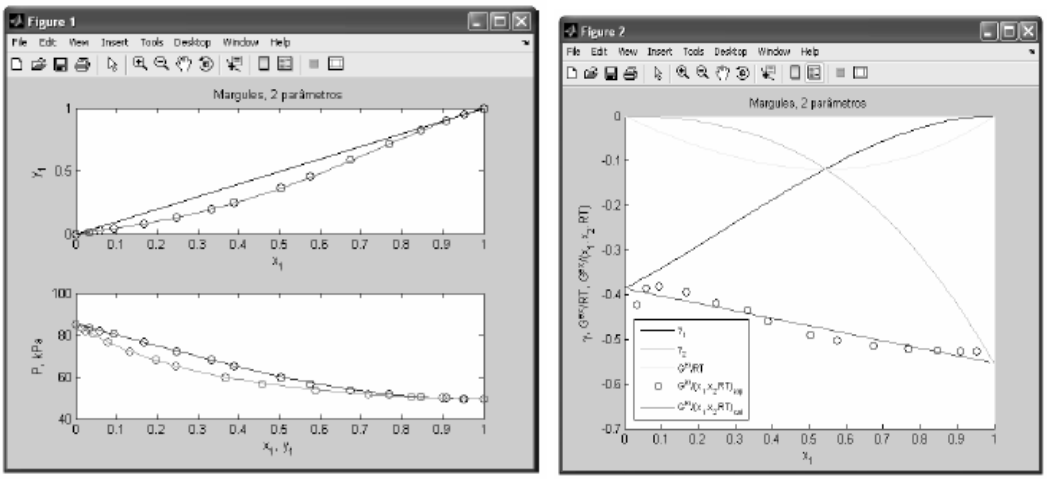

Figure 1: VLE data for tert-butyl ether(1)/dichloromethane(2) at 308.15K and equilibrium calculations using two-parameters Margules equation (A12 = -0.3861, A21=-0.5534). Problem adapted from Smith *et al.*, 2005.

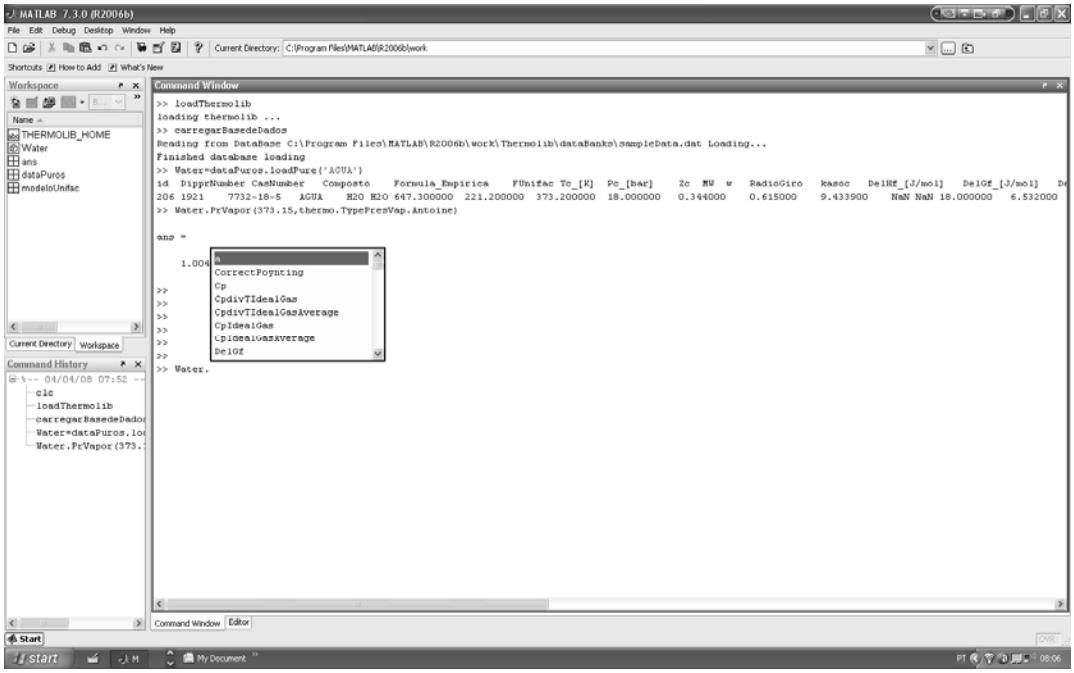

Figure 2: Using ThermoLib in a direct command driven session, showing how to get a “water molecule”, its internal class data and methods.

4 Conclusions

A promising thermodynamic library is being developed called Thermolib. It is aimed to be portable, command driven and direct accessible from the main console of well known numerical/computing systems. In the midterm, we expect to have a robust thermodynamic library easy to use with pedagogical and research interest.

Acknowledgments

The authors gratefully acknowledge the financial support from Programa Operacional "Ciência, Tecnologia, Inovação" QCA III and FEDER, project POCTI/EQU/46055/2002.

References

Báez, L. A., Da Silva, F. A and Müller, E.A. (1990), "A User-Friendly Program for Vapor-Liquid Equilibrium", Chem. Eng. Edu., winter, 24-27, 32-33.

Joana C. Vieira, (2007), "Desenvolvimento de uma Biblioteca para Cálculo de Propriedades Termodinâmicas", MSc. Thesis in Chem. Eng., Univ. of Aveiro.

Herwig Landschützer (2007), "Thermopack: A Free Object-Oriented Thermodynamic and Process Engineering Library", http://members.liwest.at/thermopack.

Pang, T., (2006) "An Introduction to Computational Physics", Second Edition, Cambridge University Press.

Silva, C.M., Alves, S. A., Da Silva, F.A. (2008) "Modelling Solubility of Amino Acids in Aqueous Solutions", Chempor 2008, 10th International Chemical and Biological Engineering Conference, 4-6 Sep, Braga, Portugal

Smith, J. M., H.C. Van Ness, and M. M. Abbott (2005); "Introduction to Chemical Engineering Thermodynamics", 7th ed., New York, McGraw-Hill.

Proceedings of the 10th International Chemical and
Biological Engineering Conference - CHEMPOR 2008
Braga, Portugal, September 4-6, 2008
E.C. Ferreira and M. Mota (Eds.)

Thermophysical properties of aqueous solutions of CNTs in the temperature range (298.15-318.15) K

Filipa A.M.M. Gonçalves[1], Abel G.M. Ferreira[1], Isabel M.A. Fonseca[1*]
J. Ponmozhi[2], Mónica S.A.O. Correia[2], Subramani Kanagaraj [2]
[1]Departamento de Engenharia Química, Universidade de Coimbra, Pólo II, Rua Sílvio Lima, 3030-790 Coimbra, Portugal
[2]Departamento de Engenharia Mecânica, Universidade de Aveiro, Campo Universitário de Santiago, 3810-193 Aveiro

Keywords: Nanofluids, CNT, Viscosity, Shear thinning, Shear thickening
Topic: Thermophysical Properties

Abstract

This article reports an experimental study on the flow characteristics of the aqueous suspensions of carbon nanotubes (CNTs) and also a suspension of CNT-EG (ethylene glycol). The viscosity of nanofluids was measured using a rheometer over a wide range of temperatures (298.15 to 318.15K), shear rate and carbon nanotubes concentration. Nanofluids with particle volume fraction ranging from 0.25 to 4 vol% were examined. Non-Newtonian behaviour was observed for the particle volume fraction of CNT-Water; the results show that CNT-Water and CNT-EG suspensions exhibit shear thinning behaviour at low shear rates. However the CNT-EG suspension exhibits at higher shear rate a Newtonian behaviour. The viscosity of nanofluids decreases with an increase of temperature independently of the CNTs concentration. It´s observed that viscosity of the nanofluids increases by increasing the concentration of CNTs even at high temperature and high shear rate.

1 Introduction

Nanofluids are diluted liquid suspensions of nanoparticles with at least one of their critical dimensions smaller than about 100 nm [1]. Such a type of composite materials has been shown to exhibit certain enhanced behaviour such as heat transfer and mass transfer [2]. Nanofluids can be regarded as functionalized colloids with special requirements of low particle loading, high thermal performance, great physical and chemical stability over a wide range of temperature and solution chemistry, and favorable flow/rheological behaviour. Because of the unusually high thermal conductivity of CNTs, it can be expected that the suspensions containing CNTs would enhance thermal conductivity and their improved thermal performance would be applied to energy systems [3]. Multiwalled carbon nanotubes (MWNTs) have an interesting set of properties with a wide variety of potential applications in liquid suspensions, polymer solutions, polymer melts, and polymer composites. Their unusual properties include excellent thermal and electrical conductivities, and magnetic properties [4]. Thought nanofluids can be used as a replacement for conventional oil, their rheological properties are needed to be known because they influence the required pumping power in a heating system [5].

* Corresponding author. Tel +351-239798728 ; Fax: +351-239798703 E-Mail: fonseca@eq.uc.pt

The measurement of viscosity of the nanofluids is essential to establish adequate pumping power as well as the convective heat transfer coefficient, since the Prandtl and Reynolds numbers will be influenced [6]. Presently there are two major areas in which CNTs are being used, which include electronics [7] and nano electromechanical systems [8] – mechanical memory elements, nanoscale electric motors. In electronic applications, CNTs are used to dissipate unwanted static charge build-up and are used as a conducting agent to aid in electrostatic painting [7].

2 Experimental

2.1 Materials

The multiwalled carbon nanotubes were purchased from M/s Shenzhen Nanotech Port Co., Ltd, China. The specifications of MWCNTs are as follows: range of diameter 60-100nm, length of the tubes 5-15 micron, density 2.16g/cc and purity $\geq$ 95%

2.2 Chemical treatment on CNTs

The effective utilization of nanotubes in nanofluids depends on the ability to disperse CNTs homogeneously in the fluid without destroying their integrity. It is also required to perform a chemical treatment on CNTs to have a homogeneous dispersion of CNTs in water [9]. The required quantity of CNTs was suspended in the mixture of concentrated nitric acid (65%) and sulphuric acid (95-97%) by the volume ratio of 1:3 and refluxed at 140ºC for 30 minutes. After washing the nanotubes with deionised water until the supernatant attained a pH around 7, the samples were dried at 100ºC. The chemically treated CNTs were studied in FTIR where it was observed different functional groups like carboxyl, carbonyl and others. The advantages of processing CNTs with chemicals are to modify their surface with functional groups, purify the tubes and to increase the surface area and pore volume of CNTs.

2.3 Preparation of nanofluids

In this study, a stable and homogeneous dispersion of chemically treated CNTs were prepared in deionised water by reducing the hydrophobic linkage of CNTs. The chemically treated CNTs were added with deionised water and sonicated for 1 hour to have a homogeneous and uniform dispersion of CNTs in water. In this study, nanofluids are prepared with difference concentration of CNTs.

2.4 Rheological study of nanofluids

The viscosity was measured using a controlled stress rheometer, Haake, Model RS1. The rheological tests were carried out with a sensor system Z34 DIN that comprises one rotor and one beaker, with a connected thermocontroller. The spindle used was 20.00 mm (radius) at a clearance to bottom 7.2 mm. The measurements were performed in the shear rate range from 0 to 1200 sec^{-1} for temperatures from 298.15 to 308.15K; at 318.15K the shear rate was from 0 to 600 sec^{-1}. For all the nanofluids at least three measurements were made, to test the precision of the results, including 250 or 125 data points, depending on the range of shear rate. The maximum precision was ±0.01 and ±0.17 the minimum, for the range of shear rate from 50 to 150 sec^{-1}. The accuracy of data was performed using a Brookfield viscosity standard (4.30 mPas) from Engineering Laboratories, Inc., Stoughton, U.S.A.

3. Results and discussion

3.1 Viscosity of CNT nanofluids

Figure 1 represents the viscosities of CNT-EG nanofluids (0.1 vol%) at two temperatures, 298.15 and 308.15K. There is a slight shear thinning behaviour for both temperatures at lower shear rate. It can be seen in Fig. 1 (a) that the viscosity is almost independent of the shear rate, indicating a close Newtonian behaviour of EG based

nanofluid. In Fig.1 (b) shear stress developed in the nanofluids is directly proportional to the shear rate being applied at any temperatures. At particular shear rate, the stress developed in the nanofluid decreases with an increase of temperature.

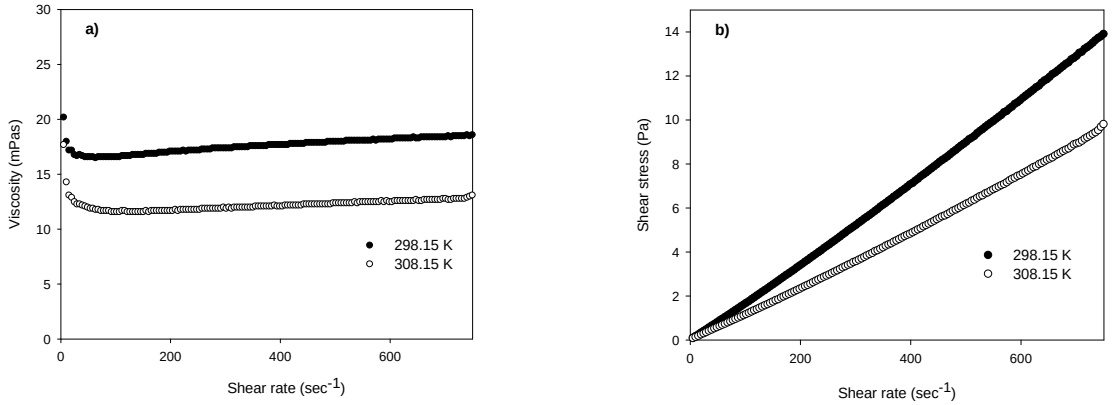

Fig.1. (**a**) Viscosity of EG-water nanofluids as a function of shear rate at 298.15 and 308.15 K; (**b**) Shear rate as a function of shear stress at same temperatures

In Table 1 the viscosities for the CNT based water nanofluid are presented as a function of temperature and composition. This data are plotted in Figure 2.

Table 1: Viscosity (mPas) for CNT nanofluids at three different shear rates at 298.15 and 308.15 K

T (K)	γ (sec^{-1})	Viscosity of CNT Nanofluids (mPas)								
		0.25%	***0.50%***	***0.75%***	***1.00%***	***1.50%***	***2.00%***	***2.50%***	***3.00%***	***4.00%***
298.15	10	3.22	3.46	3.52	3.58	3.60	3.82	3.69	4.22	4.66
	50	1.53	1.53	1.58	1.64	1.71	1.69	1.88	2.09	2.34
	100	1.64	1.72	1.75	1.76	1.77	1.78	1.73	1.88	2.10
308.15	10	3.31	3.30	3.29	3.45	3.73	3.71	3.90	4.02	5.84
	50	1.55	1.56	1.46	1.58	1.60	1.72	1.74	2.24	2.51
	100	1.58	1.595	1.66	1.65	1.69	1.71	1.76	1.96	2.04

With the increasing of CNT concentration, the viscosity increases for all fixed values at shear rate considered. At 4 vol% the nanofluid exhibits higher values of viscosity, at 10 sec^{-1}, as expected. However, for the remaining shear rates similar viscosities were found.

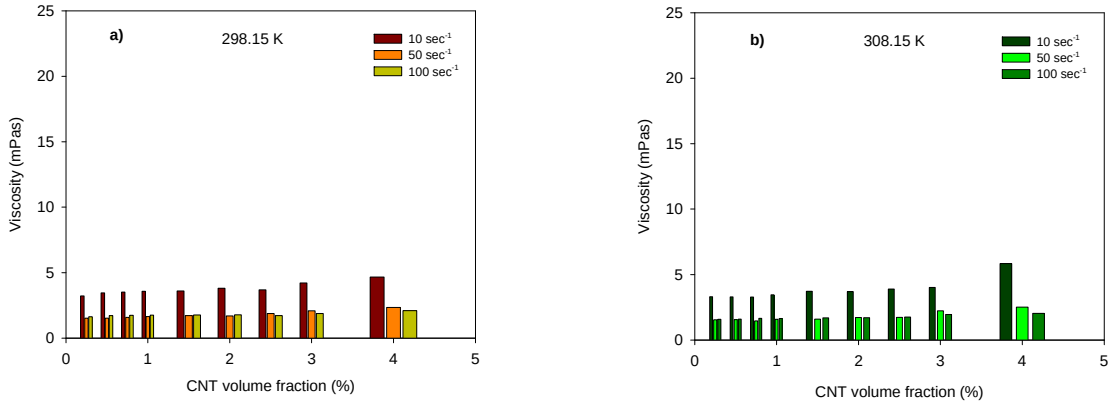

Fig. 2. Viscosity as a function of particle volume fraction, at shear rates of 10, 50 and 100 sec^{-1}, at (**a**) 298.15 K and (**b**) 308.15 K

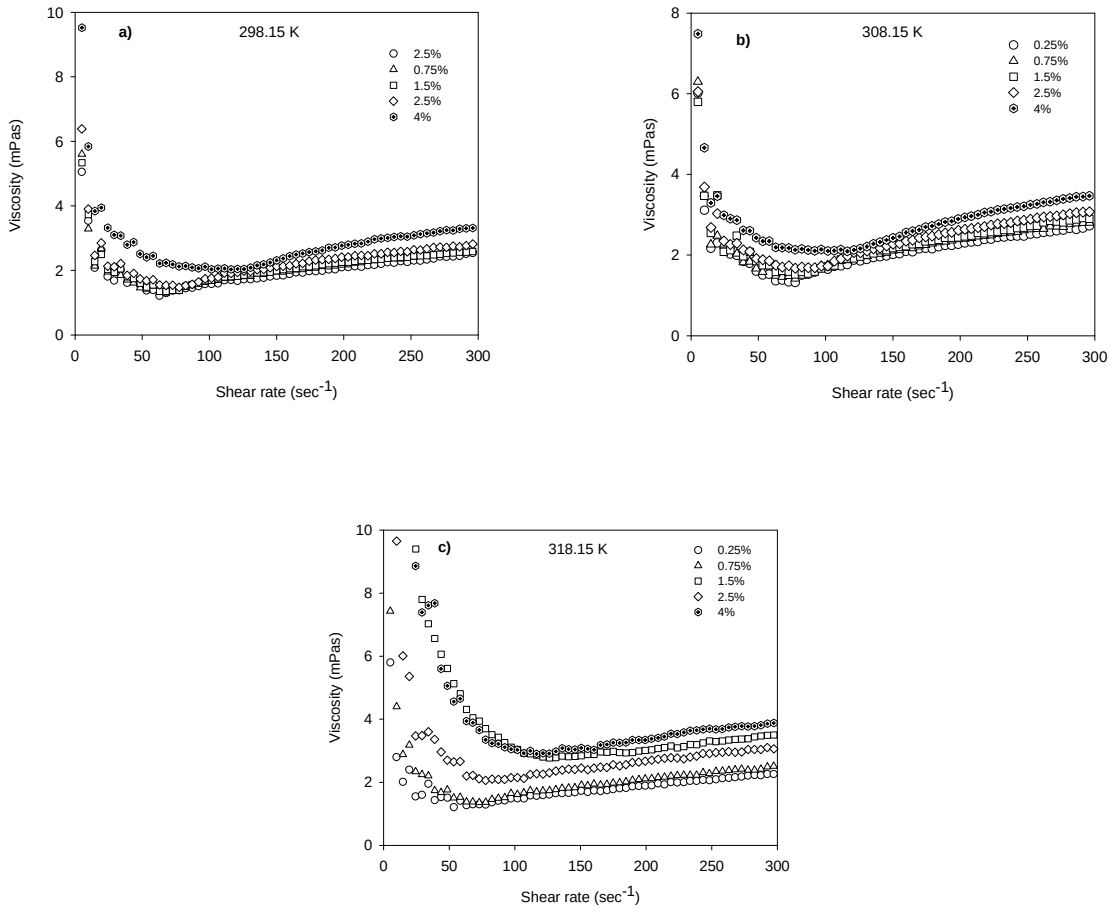

Fig.3. Viscosity as a function of shear rate for nanofluids 0.25 vol%, 0.75 vol%, 1.5 vol%, 2.5 vol% and 4 vol% at (**a**) 298.15 K, (**b**) 308.15 K and (**c**) 318.15 K

Figure 3 illustrates the viscosity as a function of shear rate at temperatures of 298.15, 308.15 and 318.15 K, for three different volume concentrations from 0.25 to 4.0 vol%. It can be seen that the viscosity increases with increasing CNT volume fraction and at lower shear rate the dispersions exhibits shear thinning behaviour. This non-Newtonian behaviour, probably the most common, is often observed for the polymers solutions, like paints, emulsions and dispersions of many types. It is well-known in rheology studies that in polymer solutions, the thread-like structured polymers, which are initially entangled, are rearranged along the flow direction under the shear stress, and consequently the viscosity of the solution decreases with shear rate. However, shear thinning behaviour is not the only non-Newtonian behaviour present on these CNT nanofluids. An increasing of viscosity with an increase in shear rate characterizes the dilatant fluid or shear thickening flow behaviour. Although less common than pseudoplasticity, dilatancy is frequently observed in fluids containing high levels of deflocculated solids, such as slurries, candy compounds and sand/water mixtures.
Figure 4 shows the variation of viscosity with the temperature and volume fraction for CNT nanofluids 0.25, 0.75 and 3.0 vol%. The viscosity of nanofluids decreases with an increase of temperature and increases with an increase in the CNT concentration. All the nanofluids samples exhibit the same trend. However, only at higher concentrations we observed a reasonable rise on the viscosity of CNT nanofluids; for example, doesn´t exist a large difference in viscosity between nanofluid 0.25 and 0.50 vol%, or even between 1.0 and 1.5 vol% nanofluids.

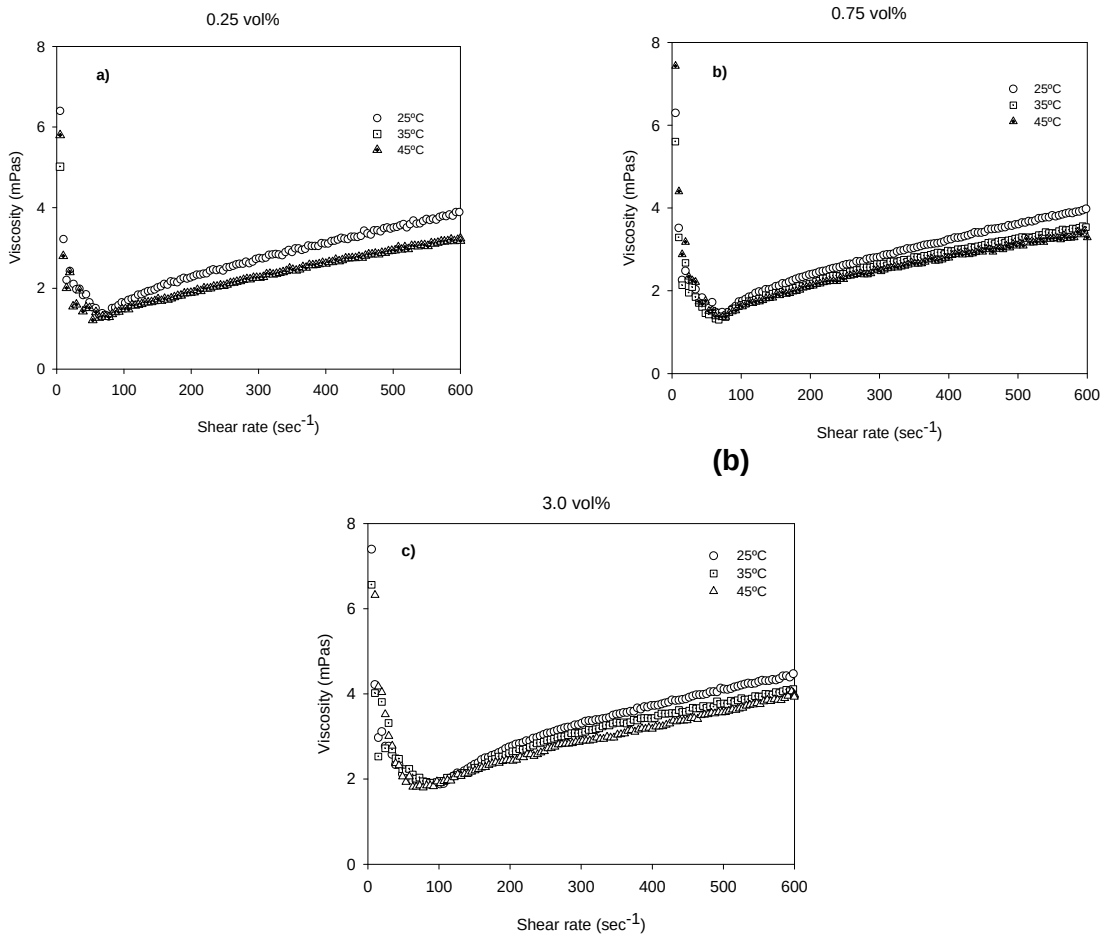

Fig.4. Viscosity as a function of shear rate for nanofluids **(a)** 0.25 vol%, **(b)** 0.75 vol% and **(c)** 3.0 vol% at 298.15 K, 308.15 K and 318.15 K

4. Conclusions

In this study we have measured the viscosity of the CNT nanofluids and the effects of the CNTs concentration and temperature were investigated. CNT nanofluids show the features of shear thinning behaviour, at low shear rate, for which viscosity increases with decreasing shear rate. At higher shear rates, the nanofluids behave like a dilatant fluid or shear-thickening. The viscosity of nanofluids increases with the increase on volume concentration of nanoparticles but more importantly the viscosity difference becomes much larger at high volume fraction. We found that the EG-water nanofluid is close to the Newtonian behaviour, with the viscosity depending strongly on temperature, though it also exhibits shear thinning behaviour but only at shear rates below 25 sec^{-1}. As the temperature increases, viscosity of CNT-water and CNT-EG nanofluids decreases. The shear thinning behaviour is much high for the CNT-Water nanofluids than for the CNT-EG nanofluid.

Acknowledgment

This work was supported by Fundação para a Ciência e Tecnologia (FCT) Project PTDC/EME-MFE/66482/2006. Filipa Martins Gonçalves acknowledge the financial support from FCT through the scholarship.

References

[**1**] H.Chen, Y. Ding and C.Tan (2007), Rheological behaviour of nanofluids, *New Journal of Physics*, 9, 367.

[**2**] H. Chen, Y. Ding, Y. He and C.Tan (2007), Rheological behaviour of ethylene glycol based titania nanofluids, *Chemical Physics Letters* 444, 333-337.

[**3**]G. H. Ko, K. Heo, K. Lee, D.S. Kim, C. Kim, Y. Sohn and M. Choi (2007), An experimental study on the pressure drop of nanofluids containing carbon nanotubes in a horizontal tube, *Heat an Mass Transfer* 50, 4749-4753.

[**4**] J. Hilding, E. A. Grulke, Z. G. Zhang and F. Lockwood (2003), Dispersion of Carbon Nanotubes in Liquids, Journal of Dispersion Science and Technology 24, Issue 1, 1–41.

[**5**] S. Kanagaraj, F.R. Varanda, A. Fonseca, A.O. Simões, J. Ponmozhi, J.A.L. Silva, M.S.A. Oliveira, Rheological Study of Nanofluids at Different Concentration of Carbon Nanotubes, Heat and Mass Transfer Conference, JNTU Hyderabad, India, 3-5 January, 2008.

[**6**] P.K. Namburu, D.P. Kulkarni, D. Misra and D.K. Das (2007), Viscosity of copper oxide nanoparticles dispersed in ethylene glycol and water mixture, *Experimental Thermal and Fluid Science* 32, 397-402.

[**7**] M. Seo, S. Park (2004), Electrical resistivity and rheological behaviors of carbon nanotubes-filled polypropylene composites, *Chemical Physical Letters* 395, 44-48.

[**8**] S.M.S. Murshed, K.C. Leong, C. Yang (2008), Thermophysical and Electrokinetic properties of nanofluids – A critical review, *Applied Thermal Engineering*, *xxx*

[**9**] K. Esumi, M. Ishigami, A. Nakajima, K. Sawada and H. Honda (1996), Chemical treatment of carbon nanotubes, *Carbon* 34, 279-281.

Proceedings of the 10th International Chemical and
Biological Engineering Conference - CHEMPOR 2008
Braga, Portugal, September 4-6, 2008
E.C. Ferreira and M. Mota (Eds.)

Liquid-liquid equilibria, and interfacial tensions of the system water+butyl acetate+1-propanol at 323.15 K

H. F. Costa[1], Y. Johnson[2], F. M. Gonçalves[1], A.G.M.Ferreira[1*], I.M.A.Fonseca[1]
[1]Departamento de Engenharia Química, Universidade de Coimbra, Pólo II, Rua Sílvio Lima, 3030-790 Coimbra, Portugal
[2] Department of Physics, St. Joseph´s College, Trichy-620 002, India

Keywords: LLE; Interfacial tension; Water ; N-Butyl Acetate; 1- Propanol
Topic: Thermodynamics and Thermophysical Properties

Abstract

This work belongs to a systematic study of this property for binary and ternary systems of the type water + ester + alcohol which has being developed by our research group. Liquid-liquid equilibrium (LLE) data are determined for the system water+N- butyl acetate+1-propanol at 323.15 K and atmospheric pressure. The experimental tie-line data was correlated by UNIQUAC equations and were predicted by UNIFAC. The empirical method of Othmer and Tobias is used for tie-line correlation, and the method of Pick et al was applied for binodal data correlation. The liquid interfacial tension has been measured for the corresponding tie-lines at the same temperature and pressure and this property was correlated using the relation proposed by Li and Fu.

1 Introduction

The importance of liquid-liquid extraction in separation technology has increased over the last 30 years. It is now usually used in pharmaceutical and food industries for recovering valuable organic materials for example the alcohols from aqueous solutions. The published studies on liquid-liquid equilibrium and on the thermophysical properties data of ternary systems of practical interest are scarce when compared with the wide variety of binary systems which have been investigated. The surface and interfacial tensions of solutions have a great effect on the efficiency of the extraction. In the last years we have made measurements of this properties and we have correlated the data for systems of the type water+alcohol+ester.[1-3] The aqueous solutions of alkanols can be efficiently extracted with esters and precise liquid-liquid equilibrium (LLE) data are needed for extraction processes. Some LLE measurements on ternary systems of the type water+alkanol+aliphatic ester can be found in the literature.[4-7]. The purpose of this study is to determine the liquid-liquid equilibria for the water+N-butyl acetate+1-propanol at 323.25 K and to study the interfacial tension at this temperature. The experimental tie-line data were regressed to the UNIQUAC model to obtain the interaction parameters of the model and addicionaly the data were compared with those predicted by means of UNIFAC group contribution method [8] using the LLE interaction parameters reported by Magnussen et al [9]. The tie line data have been correlated by the simple method of Othmer and Tobias [10], and the binodal curve was represented following a method proposed by Pick et al [11]. For the ternary system studied, the interfacial tension was determined in the immiscible range at the same temperature and the experimental data was correlated with the Li and Fu model [12].

2 Experimental

2.1 Materials. Tridistilled water was used. 1-Propanol (Riedel de Häen) was supplied with a weight fraction purity better than 0.995. N-butyl acetate was supplied by Sigma-Aldrich with a stated purity better than 0.995. The purity of the chemicals was checked by measuring their density, viscosity and surface tension.

* Corresponding author. Tel +351-239798729 ; Fax: +351-239798703 E-Mail: abel@eq.uc.pt

The liquid mixtures were prepared by mass using a Mettler AT 200 balance with a precision of $\pm 1\times10^{-5}$ g. The uncertainty of the mole fraction is estimated to be of the order $\pm 1\times10^{-4}$.

2.2 Methods

Binodal curve. The binodal curve was determined by the cloud-point method. Water+1-propanol or N-butyl acetate+1-propanol binaries of known compositions were shaken in an equilibrium cell equipped with a magnetic stirrer and a jacket for circulating water from a HAAKE circulator. The temperature was controlled up to ±0.01 K. The third component (the ester or the water) was added until the transition point was reached. Next some alcohol was added until the disappearance of the cloud point occurs. The return to the transition point was next made by adding the third component used for a particular binary initial mixture. The contents of the components were determined by mass.

Chromatographic calibration curve. The analysis of the conjugate phases was carried out by gas chromatography in a TRE METRICS 9001 gas cromatograph equipped with a capillary column (J & W Scientific DB1: 25m×0.2 mm; film thickness, 0.3 µm). The internal standard method was used for the calibration of the detector (FID) response in order to achieve high reproducibility on the concentration of each compound in the conjugate phases on the binodal curves. N-butanol was the internal standard in the studied systems and was chosen because it has chromatographic properties close to those of the compounds in the considered multicomponent systems. Each point on the calibration curve for each compound was obtained from multicomponent systems of different known concentration prepared in the completely miscible region. All the mixtures of known concentration used for the calibration curves of the ternary system studied in this work were prepared by mass.

The FID's response (i.e. chromatographic areas) as a function of mass of each compound, so called response factor, was fitted to a straight line, Eq 1, by the least square method:

$$w_i = \left(\frac{A_i}{A_s} - b\right)\left(\frac{w_s}{m}\right) \qquad (1)$$

where w_i is the mass of the i component of the system, A_i the chromatographic area of the component *i*, A_s the chromatographic area of the internal standard (buthanol), w_s the constant mass of the internal standard, m and b the slope and the ordinate of the fitted straight line, respectively.

Liquid-liquid Phase Behavior. The experimental investigation on the liquid-liquid equilibrium of the ternary system water+n-butyl acetate+1-propanol was made in an equilibrium cell built of Pyrex glass with a total volume of 25 cm^3, which was enough to take samples from the two equilibrium liquid phases to perform the quantification of their concentration, and interfacial tension. This cell represented schematically in Figure 1 is similar to that used by Garcia-Flores et al [13]. The temperature control in the equilibrium cell was achieved by means of a constant temperature bath-circulator, Haake D8-G with a temperature precision of ±0.02 K, which uses water as thermal fluid in the thermal jacket of the cell. The temperature was measured in the cell thermowell with a Alpha Technics digital thermometer, model 4400, with a platinum resistance probe, certified by NIST, whose readings have an accuracy of 0.015 K and resolution of 0.01 K.

Five different tie-lines of known global concentration were prepared by weighing. The heterogeneous liquid mixtures were transferred into the equilibrium cells and stirring was carried out with magnetic bars during a period of at least 4 h, then allowed to settle for a 10 h period to obtain two liquid phases in equilibrium in each cell, at 323.15 K. The samples of both phases were obtained simultaneously with syringes with a capacity of 5 cm^3 through the sampling glass capillaries in the equilibrium cells (Figure 1), to ensure the right amount of sample for measuring the LLE, the density of the saturated liquid phases, and the interfacial tension between the liquid phases.

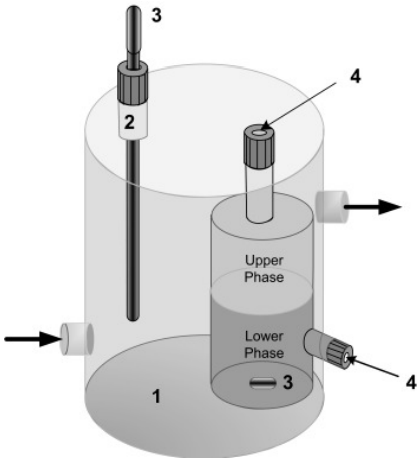

Figure 1. Equilibrium cell used for study the LLE: 1.Thermal jacket; 2.Thermowell; 3. Digital thermometer probe; 4. Sampling port.

Interfacial tension . Equilibrium liquid-liquid interfacial tensions were measured using a PC controlled KSV Sigma 70 tension balance which employs the Du Noüy ring-detachment method. The temperature inside the surface tension measurement vessel was maintained and controlled at 323.15±0.10 K using a UltraTerm bath.

For the liquid interfacial tension measurements, the liquid mixtures with a known global composition were prepared and kept at 323.15 K in a thermostated cell and shaken several times during a period of at least 24 h to reach the equilibrium.

3. Results and Discussion

In Table 1 the experimental equilibrium concentration results of the conjugate phases are given. Each result is the average of at least four injections of the same equilibrium sample into the chromatograph.

Table 1. Experimental values of the mole fraction, x, for the liquid-liquid equilibrium and liquid Interfacial Tension, γ, for the ternary system water(1)+n-butyl acetate(2)+1-propanol(3) at 323.15 K.

Overall Composition		Water layer		Organic layer			γ (mN·m^{-1})
z_1	z_3	x_1	x_3	x_1	x_3	γ(mN·m^{-1})	
0.8599	0	0.9998	0	0.1305	0	21.74	14.2
0.8487	0.0407	0.9842	0.0154	0.2009	0.1664	22.40	7.3
0.8400	0.0686	0.9757	0.0238	0.2769	0.2593	22.21	5.4
0.8175	0.1109	0.9643	0.0349	0.4117	0.3279	22.43	2.8
0.8159	0.1284	0.9580	0.0410	0.4889	0.3363	22.56	0.0

The experimental LLE data were correlated using UNIQUAC model. The parameters of this model were determined by fitting using an iterative computer program which uses simplex method [14] by minimizing the objective function

$$F = \sum_{k}^{n} \sum_{i}^{3} \sum_{j}^{2} (x_{i,exp} - x_{i,calc})_j^2 \qquad (2)$$

where n is the number of tie lines, (n=5), x_{exp} indicates the experimental mole fraction, x_{calc} is the calculated one, the subscript i indexes components, j phases and k=1,2,…, n are the tie-lines.

The LLE of the ternary mixtures were predicted using UNIFAC. The group-interaction parameters used for estimating the activity coefficients in the liquid phases were those given by Megnussen et al. [9] obtained from experimental LLE. Figure 2 shows the experimental LLE diagram, the correlation by UNIQUAC model, and the predictions from UNIFAC. As it can be seen the correlation results from UNIQUAC (point lines) are in poor agreement with the experimental data (solid lines) with exception of the aqueous phase and the organic

phase far from the critical point. The UNIFAC predicts a two-phase region in good agreement with that observed experimentally. The slopes of the predicted tie-lines are similar to those measured. The uncertainty of correlation and estimation has defined by the root mean square deviation (RMSD):

$$RMSD = \left\{ \sum_{k}^{n} \left[\sum_{i}^{3} \sum_{j}^{2} (x_{i,exp} - x_{i,calc})_j^2 / 6n \right] \right\}^{1/2} \quad (3)$$

The values of RMSD for UNIQUAC and UNIFAC are espectively 4.3×10^{-2} and 2.94×10^{-4} .

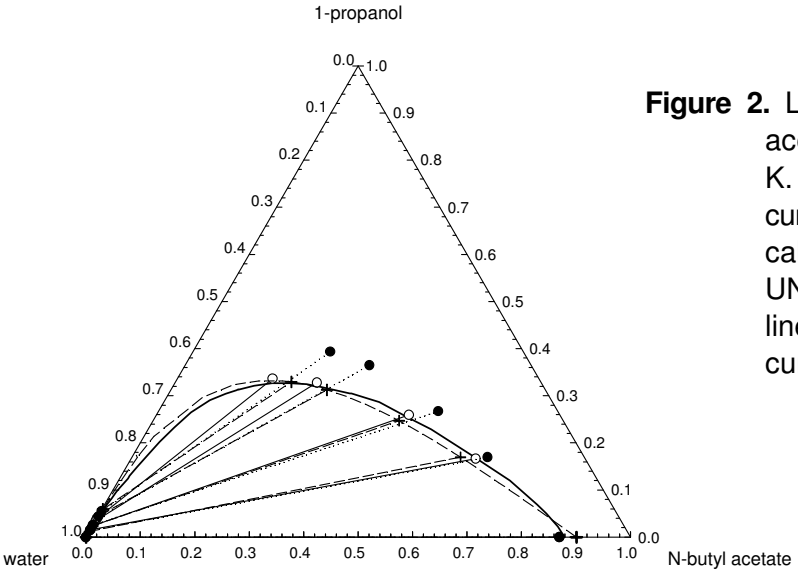

Figure 2. LLE data for water+N-butyl acetate+1-propanol at 323.25 K. Experimental: (–), binodal curve; (–○–) tie-lines; (●···●) calculated UNIQUAC tie-line; UNIFAC predictions: (+) tie-line data, and (----) binodal curve.

The reliability of experimentally measured tie-lines was determined by the application of Othmer-Tobias [10] one of the most used correlation for this purpose. This method employs the linear relationship

$$\ln[(1 - w_{1,aq}) / w_{1,aq}] = m + k \ln[(1 - w_{2,org}) / w_{2,org}] \quad (4)$$

where $w_{1,aq}$ and $w_{2,org}$ are respectively, the mass fraction of water (component 1) in the aqueous phase and ester (component 2) in the organic phase. The linearity of the plot in Figure 3 indicates the degree of consistency of the measured data. The values of parameters are m= -2.0413 and k=0.4911 and the standard deviation is σ =0.050.

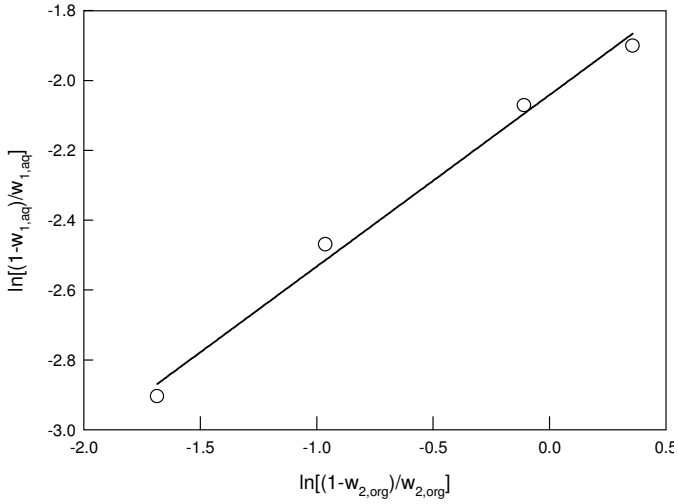

Figure 3. Othmer-Tobias correlation for water(1)+N butyl acetate(2)+1-propanol(3) at the temperature of 323.15 K, where w_i denotes the mass fraction of component i. The symbols refers to the experimental tie-line data and the line to the correlation.

The binodal curve has been correlated using the method of Novák et al. [11] obtaining

$$\ln[(x_1 / x_2)]/(x_1 - x_2) = 2.8536 + 0.9218(x_1 - x_2) + 1.0762(x_1 - x_2)^2 + 3.004(x_1 - x_2)^{10} \quad (5)$$

where x_1 and x_2 are molar fractions on the binodal curve. The standard deviation of the fit is σ= 0.097. In Figure 4 the experimental data and the results of correlation from equation (5) are compared. We conclude that the equation (5) describes very well the binodal curve data.

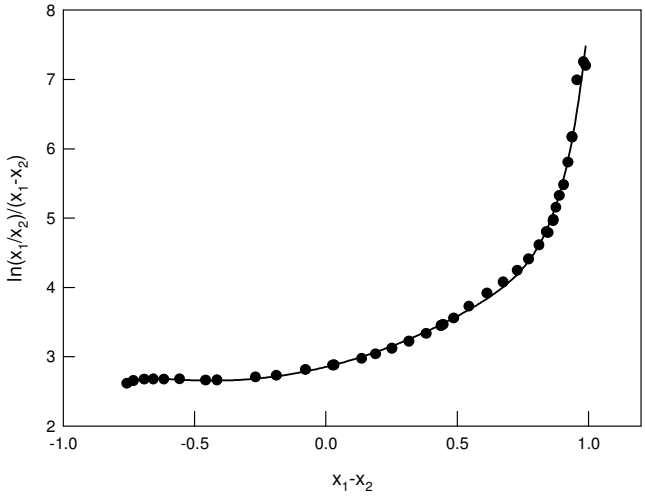

Figure 4. Dependence of

$[\ln(x_1/x_2)]/(x_1-x_2)$ on (x_1-x_2)

for the binodal curve. The symbols refers to the experimental data and the line to the correlation with equation (5).

To correlate the liquid interfacial tension, the Li and Fu model [12] was used. The equation of the model is

$$\gamma' = \gamma_0' \left(\frac{X}{X_0} \right)^k \quad , \quad X = -\ln\left[x_1^{\alpha} + x_2^{\beta} + x_{3p} \right] \tag{6}$$

γ' is the interfacial tension between the two immiscible liquid phases α and β in the ternary system and γ_0' is the interfacial tension of the partially miscible binary pair which corresponds x_3 = 0 and $X = X_0$ in Eq. (6). x_1^{α} is the mole fraction of component 1 in the liquid phase α richer in component 2, x_2^{β} is the mole fraction of component 2 in the phase richer in component 1 and x_3^{p} is the mole fraction of component 3 in the phase poor in it. The parameter k is adjustable in Eq. (6) and a general form, $k = \sum_{i=0} k_i X^i$ can be used. The results for the fitting of the Li and Fu model trough Eq. (6) to the liquid interfacial tension, γ', are shown in Figure 5. The use of one parameter in the fitting (k= 2.0775) results in an inadequate representation. A satisfactory representation of γ' is obtained taking into account the dependence of k on the composition (k=-6.1638-8.1540X+3.7210X^2). The same conclusion was already taken from past studies on the same type of systems [1].

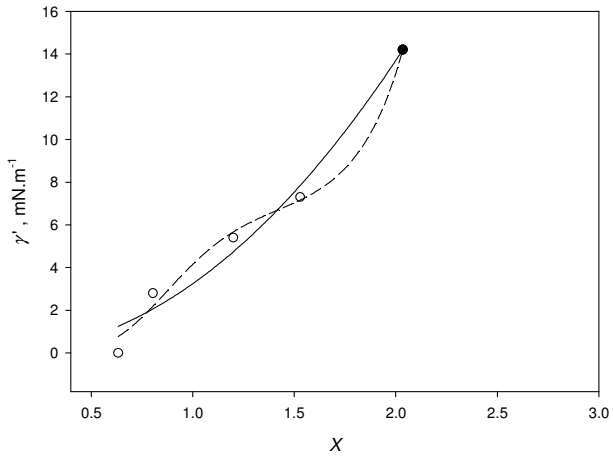

Figure 5. Liquid interfacial tension,γ' , as a function of X for the ternary system water+ N-butyl acetate +1-propanol at 323.15 K. The symbols (•, ○) represent the experimental data of the binary and ternary systems respectively, and the lines the curves fitted with the Li and Fu model, eq 4: (—) k = constant and (- - - -) $k = k_1 + k_2 X + k_2 X^2$.

4. References

[1] Santos, B. M. S., Ferreira A. G. M., Isabel M. A. Fonseca, (2003). Surface and interfacial tensions of the systems water + n-butyl acetate + methanol at 303.15 K. *Fluid Phase Equilibria* 208,1-21.

[2] Mirjana Lj. Kijevcanin, Inês S. A. Ribeiro, Abel G. M. Ferreira, Isabel M. A. Fonseca,(2003). Densities, Viscosities and surface and interfacial tensions of the ternary mixture water + ethyl butyrate + methanol at 303.15 K. *J. Chem. Eng. Data*. 48 ,1266-1270.

[3] Mirjana Lj. Kijevcanin, Inês S. A. Ribeiro, Abel. G. M. Ferreira, Isabel M. A. Fonseca. (2004). Water+esters+methanol: experimental data, correlation and prediction of surface and interfacial tensions at 303.15 K and atmospheric pressure. *Fluid Phase Equilibria* 218, 141-148.

[4] Rao R. J.; Rao, C. V. (1957). Ternary liquid equilibria: methanol-water-esters. *J. Appl. Chem*. 7, 435-439.

[5] Rao R. J.; Rao, C. V. (1959). Ternary liquid equilibria systems: n-propanol-water-esters. *J. Appl. Chem.* 9, 69-73.

[6] Arce, A.; Alonso, L.; Vidal, I. (1999) Liquid_Liquid Equilibria of the Systems Ethyl Acetate+Ethanol+Water, Butyl Acetate+Etanol+Water, and Ethyl Acetate+Butyl Acetate+ Water. *J. Chem. Eng. Japan* 32, 440-444.

[7] Arce, A.; Blanco, A.; Martínez-Alonso,J.; Vidal, I. (1995) LLE data for the systems water+(methanol or etanol) + n-amyl acetate. *Fluid Phase Equil*. 109, 291-297.

[8] Fredenslund, Aa.; Gmehling, J.; Rasmussen, P. (1977) Vapor-Liquid Equilibria Using UNIFAC, Elsevier, Amsterdam.

[9] Magnussen T.; Rasmussen, P.; Fredenslund, Aa. (1981) UNIFAC Parameter Table for Prediction of Liquid-Liquid Equilibria. *Ind. Eng. Chem. Processs Des. Dev*. 20, 331-339.

[10] Othmer, D. F.; Tobias, P. E. (1942) Tie-Line Correlation. Ind. Eng. Chem. 34, 690-693.

[11] Novák, J. P., Matous, J.; Pick, J. (1987) Liquid-Liquid equilibria in studies in modern thermodynamics, Elsevier, New York.

[12] B. Li and J. Fu, Interfacial Tensions of Two-Liquid-Phase Ternary Systems. *J. Chem. Eng. Data* 37 (1992) 172-174.

[13] Garcia-Flores, B. E.; Trejo, A.; Águila-Hernández, J. (2007) Liquid-Liquid phase behaviour, liquid-liquid density, and interfacial tension of multicomponent systems at 298 K, *Fluid Phase Equil.* 255, 147-159.

[14] Nelder, J. A.; Mead, R. (1965) A simplex method for function minimization. *J. Computer* 7, 308-313.

Proceedings of the 10th International Chemical and
Biological Engineering Conference - CHEMPOR 2008
Braga, Portugal, September 4-6, 2008
E.C. Ferreira and M. Mota (Eds.)

Thermodynamic analysis of leather tanned with different tanning agents

Mónica Rosas[1], Valentina Domingues[2*], Teresa Oliva-Teles[2], Paulo Silva[1], António Crispim[1]

[1]CIETI/*Instituto Superior de Engenharia do Porto,* R. Dr. António Bernardino de Almeida, 431, 4200-072 Porto Portugal.

[2] REQUIMTE/*Instituto Superior de Engenharia do Porto,* R. Dr. António Bernardino de Almeida, 431, 4200-072 Porto Portugal.

Keywords: leather, tanning agents, DSC
Topic: Suitable Integration of life sciences & engineering

Abstract

Traditionally, quality, cost and yield are the three main concerns of leather manufacturers. However, the issue of environmental impact is now a worldwide concern. This environmental concern, combined with consumer preference, particularly in the European market, for chromium-free leather now makes the development of new tanning methods.

It is well known that collagen cross-linked with various cross-linking agents such as metal ions and aldehydes is made resistant against the degradation by collagenase and also that the thermal stability of collagen is increase owing to the cross-links formation. This cross-linking is the main objective of tanning, a process that converts raw hide/skin into leather. Understanding the effect of them on the dimensional stability of collagen will also aid in understanding the process of tanning.

The thermal stability of collagen has been investigated by measuring the hydrothermal shrinkage of collagen fibres, the characteristic temperature at which collagen fibre shrinks to one-third its original length and by differential scanning calorimetric (DSC) measurements. DSC allows the study of enthalpy changes, which are associated with the denaturation of collagen.

In this work the effect of different tanning agents in the stabilization of collagen was evaluated by DSC. The alternative agents selected were: mimosa extract, acrylic resin, glutaraldehyde, genipin. Chromium at 7% as been also tested as tanning agent, in the same scale, to be used as a reference.

The leather tanned with 7% of cromium was undoubtely the best results about themodynamic stability but several tanning agents can be choosed for and a good themodynamic stability was achieved. The DSC data of leather thermodynamic stability were correlated with test of leather shrinking temperature described in ISO 3380.

1 Introduction

The collagen molecule consist of a triple helix held together mainly by hydrogen bonds. Denaturation is simply a term which implies the physical change of the hydrated collagen complex. It is commonly defined as the transition from the triple helix to a randomly coiled form that has been caused by any one of the many deterioration agents that could affect leather. Collagen molecules are assembled into fibers stabilized by various cross-links between the molecules. When saturated with water and heated, the hydrogen bonds are broken, and the linear structure of the collagen molecules is transformed into a disorder structure. The temperature, at which the structure transforms, depends on the number and nature of the cross-links between the collagen molecules. The methods of tannage, as well as the degree of deterioration influence the stability of the collagen molecules, and this stability may vary

* Corresponding author. Tel + 351-228340500. E-mail:vfd@isep.ipp.pt

considerably from molecule to molecule. The change in structure is easily recognized, and the changes observed range from a small bending to a complete coiling of a fiber – the fiber shrink (Larsen et al., 1993). Our present understanding is that denaturation is the result of the loss of collagen's higher structural features due to disruption of the hydrogen bonding and other secondary forces that hold the molecule together. The temperature at which fully hydrated collagen or leather shrinks under defined conditions is called the shrinkage temperature (Ts).

Part of the benefit of tanning and lubricating leather is the ability to resist fiber sticking upon drying. Of the changes in appearance and properties that are a consequence of tanning, one of the more important is increase in hydrothermal stability (Kite and Thomson, 2005).

The Ts of undeteriorated mature collagen is around 65ºC but it can be as low as 30ºC in deteriorated collagen. The Ts for new vegetable-tanned leather is from 70 to 90ºC depending. In chrome-tanned leather the weak hydrogen bonds keeping the collagen polypeptides together are replaced by strong covalent chromium chemical bonds, thus the shrinkage temperature is around 100ºC (Young, 1998), (Chahine, 2000).

There's a chrome-free movement in several industry to answers to environmental and health concerning. Market demand has always been a main impetus for technological development and innovation, and now legislation demands careful environmental considerations as well.

Some vegetable extracts has been tried as tanning agent the mimosa extract and genipin. The application of Mimosa extract (from *Acacia negra* and *Acacia molíssima*) is very common worldwide and it can be modified by mixing with other types of tanning materials to adopt its characteristics to the specific leather type in re-tanning. Particularly suitable for the re-tanning of chrome leather where fullness, buff ability and good printing and plating properties are required. The combination with other anionic tanning agents such as resins and polymers is common practice to enhance the finishing of the leather. In general, Mimosa extract is now the favorite natural tanning agent in the use of fast modern tanning systems in pits or drums.

Genipin is a hydrolytic product of geniposide, which is found in the fruit of *Gardenia jasminoides Ellis*. The structure of genipin was discovered in the 1960's (Djerassi et al., 1961), Fig. 1. Because it is a naturally occurring, biodegradable molecule with low cytotoxicity, genipin has recently been investigated as a crosslinking material. The most common crosslinking agent has been glutaraldehyde, but because of concerns about its toxicity new methods are being tested like genipin. The tanning effect of genipin was found to be similar to that of glutaraldehyde, an organic tanning agent currently being used to produce chrome-free leather (Vaandering, 2006).

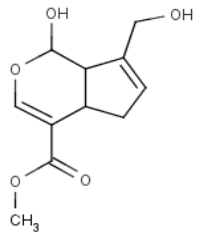

Figure 1. Structure of Genipin

One of the more important consequences of tanning is increasing the hydrothermal stability. The evaluation of the thermal behavior in the different leather samples obtained with the different tanning agents can be measured by different methods: by direct observation or under a microscope of the hydrothermal shrinkage temperature, by using the isometric tension test, or by differential scanning calorimetry (DSC). The latter allows the study of enthalpy changes which are associated with the denaturation of collagen, of which shrinkage is the macroscopic manifestation (Chahine, 2000).

In the present investigation, an attempt has been made to achieve different tanning agents and get high thermostability leather.

2 Experimental

2.1 Materials and reagents

Pickled bovine pelt was kindly supplied by NEIC and Curtumes Aveneda. Genipin was purchased from Wako Chemicals GmbH. Glutaraldehyde (Drasil GL) from Cognis, chromium sulphate with 25% Cr_2O_3 and 33% basicity (Cromosalt B) from Bayer, Plenatol HBE from Cromogénia Units SA, mimosa extract from Seta and the acrylic resin was developed by Indinor. The brine solution (6ºBe) was prepared using

commercial sodium chloride. The pH adjust was performed with sulfuric acid, formic acid or sodium carbonate and magnesium oxide from Riedel-de Haën.

2.2 Apparatus

Reactions with hide powder were carried out in a thermostated shaking bath, SBS30, with temperature controlled and assure uniform mixing. The skin powder was obtained using a laboratory cutting mill, Pulverisette 15 from Fritsch. The pH was controlled using a pHmeter GLP22 from Crison. Laboratory drums, Mathis CH-8155, were used to prepare the leather samples with the different tanning agents to perform the tests of leather shrinking temperature described in ISO 3380.

The measurements were performed using a Netzsch DSC 204 differential scanning calorimeter equipped with a controlled TASC 414/3A. It was calibrated for temperature and heat flow using Bismuth (Bi), Indium(In), Potassium nitrate (KNO_3), Tin (Sn) and Zinc (Zn) as standards (obtained from Netzsch).

2.3 Sample preparation

The tanning procedures were the same for the tests carried out in a thermostated shaking bath, with hide powder, and in the laboratory drums, with skin pieces. The hide were weighted and immersed in NaCl solution (6ºBe), then the first pH adjust was done. The tanning agents are added and the reaction occurs with temperature controlled and a uniform mixing. In the end of the reaction a second pH adjusts is made. All the samples are washed with distilled water; the tanned leather obtained in the laboratory drums is tested for shrinkage temperature. And the tanned hide powder obtained in the thermostated shaking bath is soaked in distilled water overnight, filtered in vacuum and dried in a desiccator and, finally analyzed in DSC for thermal stability.

However for each tanning agent the amount of the agent, pH conditions, time of reaction and temperature were different. In Table 1 are described the steps for the tanning procedures for chromium, mimosa extract, glutaraldehyde, genipin and acrylic resin.

Table 1. Tanning agents, percentage, time, temperature and pH conditions for hide tanning.

Process/Chemicals	Percentage (%)(*)	Duration	Temperature (ºC)	Remarks
Chromium tanning				
Brine (6ºBe)	500			
Sulfuric acid (1:10)				Cross section pH 2.8
Chromium salt	7	120	30	
Plenatol HBE	0.7	240	35	
		240	40	Final pH~4
Glutaraldehyde tanning				
Brine (6ºBe)	500			
Sodium carbonate				to pH 5
Gluteraldehyde	6	480	40	
Mimosa Extract tanning				
Brine (6ºBe)	500			
Sodium carbonate				to pH 5
Mimosa extract	10	120	35	
Mimosa extract	15	720	35	
Formic acid				to pH 4
		240	40	
Acrilic resin tanning				
Brine (6ºBe)	500			
Sulfuric acid				to pH 2.5
Acrilic Resin	8	24h	35	
Sodium carbonate				to pH 4
		240	35	
Genipin tanning				
Brine (6ºBe)	500			
Magnesium oxide				to pH 7.5
Genipin	5	24h	35	
Magnesium oxide				to pH 7.5
		240	35	

(*) % of the pickled pelt amount used

The tanned hide powder samples were filtered and maintained in a desiccator with silica gel at least 5 days.
The thermal stability of collagen has been investigated by measuring the hydrothermal shrinkage of the collagen fibers, the characteristic temperature at which collagen fiber shrinks to one-third its original length and by differential scanning calorimetric (DSC) measurements.

2.4 Differential scanning calorimetric analysis

The heating rate was maintained constant at 10ºC/min in the temperature range of 25 to 175ºC under continuous flow of dry nitrogen gas (20 mL/min). The samples were weighed (around 3 mg) and placed in aluminum crucibles with a pierced lid. An empty aluminum pan was used as reference.

2.5 Thermal properties

The hydrothermal shrinkage temperatures of the leathers were tested with total immersion in a water bath.

A piece of leather samples (around 8 cm^2) was held in water with controlled temperature in a period up to 3 minutes. The tested temperatures were between 30ºC to 95ºC with a variation of 5ºC each. Experiments using a Standards method, ISO 3380, were executed.

3 Results and discussion

To establish a basis for evaluating the tanning effects on temperature shrinking two tests were done: ISO 3380 in a Certified laboratory and an immersion in a water bath. The hydrothermal shrinkage temperatures of native and leather treat with several tanning agents are given in Table 2.

This high increase in hydrothermal stability on treatment with chromium when compared to others is due to the fact that chromium forms co-ordinate covalent linkages with the carboxyl group of the collagen and increases the long range ordering of collagen by forming a larger number of cross-links (Fathima et al., 2004).

Preliminary tests in DSC with pieces of leather showed a high standard deviation (28%). However studies with hide powder revealed a lowers standard deviation (6%).

Improvements in thermal stability of a hide, hide powder, or even collagen are often cited as evidence of the tanning potential of the process that resulted in increased thermal stability of collagen (Ding et al., 2006). The transition of protein from a native to a denatured conformation is accompanied by the rupture of inter- and intra-molecular bonds, and the process has to occur in a cooperative manner to be discerned by DSC (Ma et al., 1991). Analysis of a DSC thermogram enables the determination of an important parameter; the enthalpy of denaturation (ΔH).

Table 2. Shrinkage temperature analyses by two methods and enthalpy of denaturation obtained for hide powder tanned with different agents.

Tanning agent	Ts (℃) ISO 3380	Ts (℃) Water bath	ΔH(J/g)
Native	40	40-45	
Chromium 7%	95	90-95	336
Mimosa extract 25%	77	75-80	316
Glutaradehyde 6%	72	70-75	229
Genipin 5%	59	70-75	231
Acrilic Resin 8%	58	60-65	264

The thermal stability of collagen is considered as the marker of the reaction. Thermally induced structural transitions in the fibrous collagenous network leads to shrinkage. The enthalpy of denaturation of native and various samples of hide powder treated with different tanning agents are given in Table 2. It could be seen that the denaturation temperature measured using DSC follows the same trend as the hydrothermal shrinkage temperature as described by other authors (Fathima et al., 2004).

Both methods are based on the principle that when heated in water, the collagen will deform to randomly disordered chains over a distinct temperature interval (Larsen et al., 1993).

The Fig. 2 shows the thermograms obtained with the same tanning agents in hide powder.

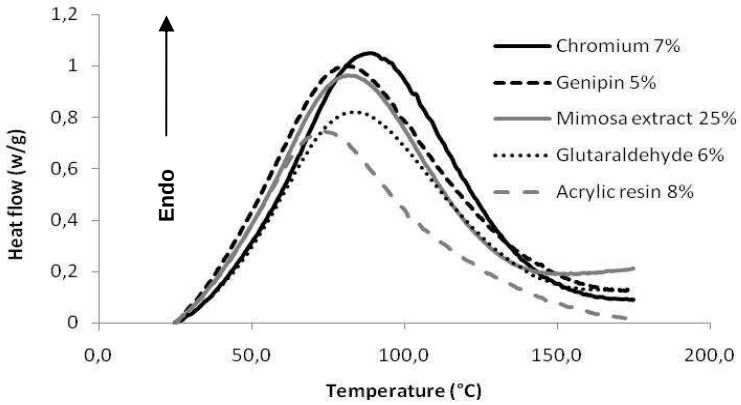

Figure 2 - Thermal absorption recording of denaturation of tanned leather with: chromium 7%, mimosa extract 25%, glutaraldehyde 6%, genipin 5% and acrylic resin 8%

It is an endothermic process in which a phase transition takes place involving changes in the lattice and long-range order. An increase in thermal stability could be related to the increase in the number of cross-links because they decrease the entropy of transition (Privalov and Tiktopul.Ei, 1970). However, the thermal stability measured using DSC is not the some phenomena measured by the water bath and ISO 3380. The collagen fibers were kept in the presence of water during the hydrothermal shrinkage measurements and in the absence of water during DSC measurements. And it is known that the thermal helix-coil transition depends on the degree of hydration (Pineri et al., 1978). It could also be seen from Fig 2 that the enthalpy of the endothermic peaks has increased for the chromium-treated collagen. ΔH is the amount of heat energy required to bring about the transition. An increase in ΔH indicates that cross-linking has occurred, which then requires more energy to undergo the helix-coil transition.

The chromium tanning shows a higher endothermic process than the others as expected. The studies of thermal stability of hide powder of chromium, mimosa extract and glutaraldehyde are identical as the results obtained for the hydrothermal shrinkage temperature by water bath and ISO 3380 (Table 2). However leather genipine tanning shows differences between the values of the thermal stability obtained by DSC analysis and the shrinkage temperature tests (with water bath and by ISO 3380).

Although the genipin data from DSC with hide powder are comparable with the results from chromium tanned, the Ts tests (with water bath and by ISO 3380) achieved lower Ts (70-75ºC and 59ºC). Those differences between these data shows different information which can be explained by the leather samples size used in tanning process. While DSC samples were tanned as hide powder the samples for Ts testes were tanned as hide pieces. The penetration and reaction of genipin is easier on hide powder, more difficult with hide pieces and even more complicated in bigger amount of leather obtained in the laboratory drums for the ISO 3380 determination.

4 Conclusions

Improvements in thermal stability (generally reported as shrinkage temperature) of a hide, hide powder, or even collagen are often cited as evidence of the tanning potential of the process that resulted in increased thermal stability of collagen.

The results of this study show that other tanning agents can be effective at increasing the thermal stability of hide powder.

Optimization of procedures for applying the agents studied to hides as a tanning agent or a component of a combination tannage is under development.

The results so far obtained support the assumption that genipin can act as a new type of crosslinking reagent of natural origin, with many potential applications.

References

Chahine, C. (2000). Changes in hydrothermal stability of leather and parchment with deterioration: a DSC study. *Thermochimica Acta*. 365:101-110.

Ding, K., M.M. Taylor, and E.M. Brown. (2006). Effect of genipin on the thermal stability of hide powder. *Journal of the American Leather Chemists Association*. 101:362-367.

Djerassi, C., T. Nakano, E.J. Eisenbraun, A.N. James, L.H. Zalkow, and J.N. Shoolery. (1961). Terpenoids .47. Structure of Genipin. *Journal of Organic Chemistry*. 26:1192-&.

Fathima, N.N., B. Madhan, J.R. Rao, B.U. Nair, and T. Ramasami. (2004). Interaction of aldehydes with collagen: effect on thermal, enzymatic and conformational stability. *International Journal of Biological Macromolecules*. 34:241-247.

Kite, M., and R. Thomson. (2005). *Conservation of Leather and Related Materials*. Butterworth-Heinemann. 340 pp.

Larsen, R., M. Vest, and K. Nielsen. (1993). Determination of Hydrothermal Stability (Shrinkage Temperature) of Historical Leather by the Micro Hot Table Technique. *Journal of the Society of Leather Technologists and Chemists*. 77:151-156.

Ma, C.Y., V.R. Harwalkar, and E.K. John. 1991. Thermal Analysis of Food Proteins. *In* Advances in Food and Nutrition Research. Vol. Volume 35. Academic Press. 317-366.

Pineri, M.H., M. Escoubes, and G. Roche. (1978). Water-Collagen Interactions - Calorimetric and Mechanical Experiments. *Biopolymers*. 17:2799-2815.

Privalov, P.L., and Tiktopul.Ei. (1970). Thermal Conformational Transformation of Tropocollagen .1. Calorimetric Study. *Biopolymers*. 9:127-&.

Vaandering. 2006. Genipin. Vol. 2008.

Young, G.S. (1998). Thermodynamic characterization of skin, hide and similar materials composed of fibrous collagen (Fine arts conservation). *Studies in Conservation*. 43:65-79.

Proceedings of the 10th International Chemical and
Biological Engineering Conference - CHEMPOR 2008
Braga, Portugal, September 4-6, 2008
E.C. Ferreira and M. Mota (Eds.)

Effect of Isooctane on Vapor-Liquid Equilibria of Water and TEG Solution

A. Khosravanipour Mostafazadeh, M. R. Rahimpour*, A. Shariati
Chemical and Petroleum Engineering Department, School of Engineering, Shiraz University, Shiraz 71345, Iran

Keywords: Experimental data; Activity Coefficient; NRTL; UNIQUAC

Abstract
In this study, vapor-liquid equilibria for systems water-triethylene glycol (TEG) and water-TEG-isooctane were measured experimentally. The VLE data were determined in a modified Othmer still which is the continuous-distillation still that recirculates the vapor phase and the samples were analyzed using gas chromatography and titration method. NRTL and UNIQUAC models were correlated for liquid phase behavior. It was observed that the correlations can provide good agreement with experimental data. The results of multi-component VLE demonstrate the enhancement of volatility of water in water-TEG solutions and increasing the purity of the dehydrated TEG by the addition of isooctane (2,2,4 trimethyl pentane).

1. Introduction

The natural gas dehydration is an important operation in the gas processing and conditioning industry. The standard method for natural gas dehydration is by absorption of water using TEG. TEG is used in about 95% of the glycol dehydration units for natural gas streams. Glycol dehydration units conventionally consist of a contactor, and a regenerator. An alternate approach for the enhancement of reconcentrator performance is the use of stripping agent. In this approach a volatile hydrocarbon liquid is added into the glycol regeneration system. The hydrocarbon increases the volatility of water in the solution of water-TEG. Smith and Skiff (1990) reported that this type of process can achieves concentrations of over 99.99% with triethylene glycol, resulting in potential dry gas with the water dew points range in -100 to -140°F. Isooctane (2,2,4 trimethyl pentane) are used as entrainers in the stripping column of natural gas dehydration unit (Francis S. Manning, Richard E. 1992, A. Ryba, 2005). Knowledge of vapor-liquid equilibrium (VLE) data is necessary for accurate design and simulation of stripping columns. Therefore, vapor-liquid equilibria for water-TEG and water-TEG with addition of isooctane (as stripping agents) have been studied in this work. Morrison et al. (1990) investigated the salt effect in vapor-liquid equilibrium of water-ethanol system and they showed the relative volatility of ethanol is increased by the addition of salt. Herskowitz and Gottlieb (1984) determined the activity coefficient of water in a water-triethylene glycol solution using an isopiestic method. Gupta et al. (1989) determined isobaric vapor-liquid equilibria for the systems TEG-benzene, toluene-TEG and benzene-N-Methylpyrrolidone. Scauzillo (1961) presented equilibrium ratios and activity coefficients of water in the systems water-TEG-natural gas. Chorng et al. (2005) developed an advanced EoS for prediction of triethylene glycol and water system. In this work, experimental procedure was done in order to determine vapor-liquid equiliria data for binary water-TEG and ternary water-TEG-isooctane systems. Modified Othmer still was used for taking samples and they were analyzed by gas chromatography (GC) and titration method. The results were used to optimization the interaction parameters of the NRTL and UNIQUAC equations.

* Corresponding author, Phone: +987112303071, Fax: +987116287294;
E-mail: rahimpor@shirazu.ac.ir (Prof. M. R. Rahimpour)

2. Experiments

2.1. Materials

The materials were used from commercial sources. They were obtained from Merck with nominal purities that are tabulated in Table 1.

Table 1 Materials used in this study

chemical	purity	water content	density gr/cm^3	supplier
triethylene glycol	> 99 %	< 0.3 %	1.123	Merck
isooctane	> 99.5 %	< 0.01 %	0.691	Merck
distillated water	-	-	1.00	Shiraz University

2.2. Apparatus and experiments

The VLE data were determined at atmospheric pressure in a modified Othmer still which is the continuous-distillation still that recirculates the vapor phase. The modified Othmer still provides accurate vapor-liquid equilibrium data in a relatively short experimental time. The still comprises a distillation flask, a reflux condenser and condensate return. The detail description has been reported in that paper. In this research, the all seal glass recirculating still with two magnetic homogenizers was used. The still was slightly modified by providing a magnetic stirrer in condensate and liquid sections. Also, the vacuum was performed by a vacuum pump before any experiments and then the atmospheric pressure was applied. Thermocouple model was Pt 100 and the digital temperature detector within ±0.1 K accuracy was used. The schematic procedure of experiments is shown in Fig. 1.

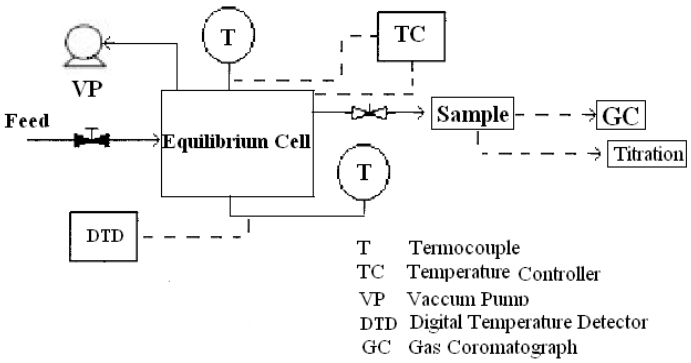

Fig. 1. Schematic procedure of vapor-liquid equilibrium measurement

2.3. Sample analysis

At steady state condition the samples were taken. Only the vapor (condensate) sample need be analyzed. Incidentally this method also possesses the advantages of producing experimental data rapidly and of giving liquid composition on a single phase directly. Analysis of samples was carried out by gas chromatography (GC) on a Varian coupled with a personal computer by use of relative program. The GC apparatus equipped with 2m×1/4in column packed with Propack Q. Helium was used as a carrier gas. Two different detectors were used to analyze the amounts of components in this work. Flame ionization detector (FID) was applied to obtain the concentration of isooctane and thermal conductivity detector (TCD) was chosen to detect the water content. The temperatures of the injector and detector were maintained at 300 ^{o}C, the column temperature was controlled by programming the temperature. The concentration of TEG was determined using titration method. This method contains the acetylation of hydroxyl group by acetic anhydride with perchloric acid (Fritz and Schenk, 1959). Liquid compositions throughout the experiment are calculated by overall material balance based on that of initial mixture.

3. Correlation

The liquid-phase activity coefficients of the components in the mixtures were calculated from UNIQUAC (Abrams and Prausnitz, 1975) and NRTL (Renon and Prausnitz, 1968) equations. The general equation of the activity coefficient for component *i* in a mixture with *n* components is given by Abrams and Prausnitz (1975):

$$\ln \gamma_i = \ln \frac{\varphi_i}{x_i} + \frac{z}{2} q_i \ln \frac{\theta_i}{\phi_i} + l_i - \frac{\varphi_i}{x_i} \sum_j x_j l_j - q_i \ln \left[\sum_j \theta_j \tau_{ji} \right] \quad (1)$$

$$+ q_i - q_i \sum_j \frac{\theta_j \tau_{ij}}{\sum_k \theta_k \tau_{kj}}$$

$$\tau_{ij} = \exp(A_{ij} / T) \quad (2)$$

NRTL equation was also applied on liquid phase for calculation of activity coefficients. The activity coefficients are calculated from the NRTL model as follows:

$$\ln \gamma_i = \frac{\sum_j x_j \tau_{ji} G_{ji}}{\sum_k x_k G_{ki}} + \sum_j \frac{x_j G_{ij}}{\sum_k x_k G_{kj}} \left(\tau_{ij} - \frac{\sum_k x_k \tau_{kj} G_{kj}}{\sum_k x_k G_{kj}} \right) \quad (3)$$

$$G_{ij} = \exp(-\alpha_{ij} \tau_{ij}) \quad (4)$$

$$\tau_{ij} = \frac{A_{ij}}{T}$$

4. Results

Experimental data for system water and TEG is presented in Table 2. Since there is a high difference between the boiling points of TEG and water, the amount of water in the vapor phase was very small. Fig. 2 depicts *y-x* diagram of water in water-TEG solution. Also, the experimental vapor-liquid data for ternary system containing water, TEG, and isooctane is given by Table 3. From this table, the volatility of water increases in the presence of isooctane. Also the equilibrium temperature declines while isooctane is added to the mixture.

Table 2 Vapor-liquid data for system water (1) +TEG (2), P=638 mm Hg

T (^{0}C)	x_1	x_2	y_1	y_2
148.1	0.117	0.882	0.98287	0.017127
141.6	0.176	0.823	0.99076	0.009234
139.4	0.250	0.749	0.99444	0.005551
127.7	0.372	0.627	0.99771	0.002284
117.3	0.543	0.457	0.99920	0.000800
107	0.704	0.296	0.99974	0.00026
103.5	0.781	0.219	0.99985	0.000149
101.8	0.826	0.174	0.99990	0.000100
100.8	0.856	0.144	0.99992	0.000076
99.8	0.877	0.123	0.99993	0.000061
99.2	0.893	0.107	0.99994	0.000051
98.4	0.914	0.085	0.99996	0.000038
97.7	0.928	0.072	0.99996	0.000031
97.3	0.942	0.058	0.99997	0.000024
96.9	0.956	0.044	0.99998	0.000018

Table 3 Vapor-liquid data for system TEG +water+isooctane, P=638 mm Hg

T C	x_{Water}	x_{TEG}	$x_{Isooctane}$	y_{water}	y_{TEG}	$y_{isooctane}$
127.7	0.3725	0.6275	0.0	0.997779	0.002221	0.0
118.2	0.369	0.62	0.011	0.482	0.00096	0.51704
111.2	0.3651	0.61503	0.01987	0.3326	0.00059	0.66681
106.9	0.3608	0.6078	0.0314	0.2409	0.000407	0.758693
102.9	0.3566	0.6007	0.0427	0.1909	0.000302	0.808798
149.4	0.250	0.750	0.0	0.994449	0.005551	0.0
129.8	0.2455	0.73662	0.01788	0.351	0.0018	0.6472
115.5	0.2434	0.72561	0.03099	0.2205	0.00084	0.77866
101.0	0.239	0.7109	0.0501	0.139	0.00038	0.86062
94.3	0.23446	0.70067	0.06487	0.1032	0.00025	0.89655
93.4	0.2304	0.6914	0.0782	0.096	0.00022	0.90378

The relative volatility of water rather than TEG is shown in Fig. 3(a). In this figure, it is observed that the relative volatility increases by addition of isooctane and also Fig. 3(b) shows the temperature declines by addition of isooctane and water volatility increases with decreasing temperature.

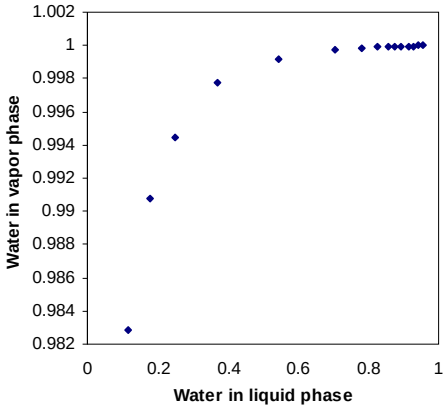

Fig 2 *x-y* diagram for water in water-TEG solution at P=638 mmHg

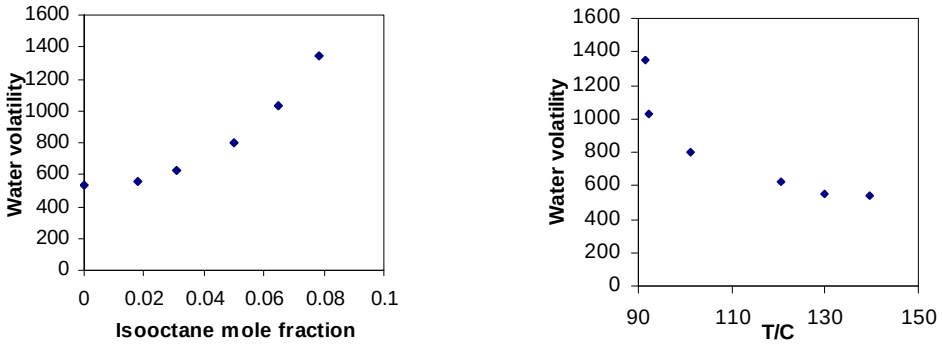

(a) (b)

Fig. 3 Relative volatility of water in water-TEG solution with addition of isooctane, (a) as a function of Isooctane mole fraction, (b) as a function of temperature

The experimental data of the water-TEG and water-TEG- -isooctane systems were correlated using UNIQUAC and NRTL equations. Estimation of the binary interactions of these models was based on minimization of the objective function O*F* in terms of calculated and experimental activity coefficient values. The function O*F* used in this work can be expressed as:

$$OF = Min\sum_{i=1}^{n}\sum_{j=1}^{m}\left(\gamma_{\exp} - \gamma_{cal}\right)^2 \tag{5}$$

where γ_{exp} and γ_{cal} are the experimental and calculated activity coefficients, respectively. The subscripts *i, j* denote the component and data, respectively. The binary interaction parameters in UNIQUAC and NRTL equations between TEG-water and TEG-water-isooctane are listed in Table 4. Good agreements are observed between model results and experimental data.

Table 4 Binary interaction parameters between water (1)-isooctane (2)-TEG (3)

	Interaction Parameters (UNIQUAC)		Interaction Parameters (NRTL)		
Water+TEG					
Water-TEG	A_{13}=-428.627	A_{31}=331.663	A_{13}=248.949	A_{31}=-172.965	α_{13}=2.366
Water+TEG+Isooctane					
Water- Isooctane	A_{12}=-647.140	A_{21}=-464.858	A_{12}=-72.078	A_{21}=314.051	α_{12}=-2.060
Water-TEG	A_{13}=-99.311	A_{31}=151.290	A_{13}=-155.068	A_{31}=-67.819	α_{13}=-4.103
Isooctane-TEG	A_{23}=-608.41	A_{32}=52.198	A_{23}=1081.279	A_{32}=1181.917	α_{23}=0.501

Root mean square deviation (RMSD) in activity coefficients are shown in Table 5. The errors are acceptable for applying theses correlations.

Table 5 Root mean square deviation[1] (RMSD)

Comp in the mix	NRTL	UNIQUAC
Water	0.037	0.027
TEG	0.013	0.001
Isooctane	0.101	0.033

1- $RMSD = \left\{\sum_i^n \left\{\gamma_i^{\exp} - \gamma_i^{calc}\right\}^2 / n\right\}^{0.5}$

5. Conclusions

Isobaric vapor-liquid equilibria of water-triethylene glycol (TEG) and the effect of isooctane on this solution have been investigated experimentally. The experimental data of the binary (water+TEG) and ternary systems (water+TEG+isooctane) were tuned using UNIQUAC and NRTL activity coefficients models. Good agreements were obtained. The results demonstrate the volatility of water increases in water-triethylene glycol solution by the addition of isooctane and decreasing equilibrium temperature. By use of this approach, the separation of TEG and water is done with higher performance in a stripping column of natural gas dehydration unit.

Symbols Used

A_{ij}	binary interaction parameter
p_i^{sat}	vapor pressure of component *i*
P_c	critical pressure (kPa)
q	surface area parameter
r	volume parameter
R	universal gas constant (J/mol K)

T temperature (K)
T_c critical temperature (K)
V volume (m^3/mole)
V_c critical volume (m^3/kmole)
x_i mole fraction of component *i* in liquid phase
y_i mole fraction of component *i* in vapor phase

Greek Letters

γ_i activity coefficient of component *i*
φ volume fraction in UNIQUAC equation
Θ area fraction in UNIQUAC equation
τ binary interaction parameter
α_{ij} third non-random parameter in NRTL equation

Subscript and Superscript

calc calculated
exp experimental

References

Abrams, D.S., Prausnitz, J.M. (1975). Statistical thermodynamics of liquid mixtures: a new expression for the excess Gibbs energy of partly or completely miscible systems. A.I.Ch.E. Journal, 21, 116.

Fritz, J. S., Schenk, G. H. (1959). Acid-catalyzed acetylation of organic hydroxyl groups, Anal. Chem. 31, 1808.

Gupta, S. K., Rawat, B. S., Goswami, A N., Nanoti S. M., and Krishna, R. (1989). Isobaric vapour-liquid equilibria of the systems: benzene-triethylene glycol, toluene-triethylene glycol and benzene-n-methylpyrrolidone, Fluid Phase Equilibria*,* 46, 95.

Herskowitz, M., and Gottlieb, M. (1984). Vapor- liquid equilibria in aqueous solutions of various glycols and Poly(ethylene glycol). 1. triethylene glycol, J. Chem. Eng. Data*,* 29, 173.

Manning, F. S., Thompson, R. E. (1992). Oilfield processing of petroleum*, Volume one: Natural gas,* Pennwell, p. 149.

Morrison, J.F., Baker, J.C., Meredith III, H.C., Newman, K.E., Walter, T.D., Massle, J.D., Perry, R.L., and Cummings, P.T., (1990). Experimental measurement of vapor-liquid equilibrium in alcohol/water/salt systems, J. Chem. Eng. Data, 35, 395.

Renon, H., and Prausnitz, J. M. (1968). AICHE J., 14, 135.

Ryba, A. (2005). Reduction in Emissions and Energy use at Mackowice Natural gas dehydration Facility, Diploma Thesis Faculty of Drilling, Oil and Gas AGH University of Science and Technology in Cracow Trondheim.

Scauzillo, F. R. (1961). Equilibrium ratios of water in the water-triethylene glycol-natural gas system, Journal of Petroleum Technology, 697.

Smith, T. E., and Bonner, R. F. (1949). Vapor-liquid equilibrium still for partially miscible liquids, Ind and Eng Chem, 2867.

Smith, R. S., Skiff, T. B., (1990). Drizo Gas Dehydration, Solution for Low Dew Points of Aromatics Emissions, *Proc.* Laurance Reid Gas Conditioning Conf*,* University of Oklahoma, Norman, OK. 61.

Smith, J. M., Van Ness, H. C., Abbott, M. M. (2001). Introduction to Chemical Engineering Thermodynamics, Sixth edition, Mc Graw-Hill International Edition.

Twua, C. H., Tassoneb, V., Simb, W. D., Watanasiric, S. (2005). Advanced equation of state method for modeling TEG–water for glycol gas dehydration, Fluid Phase Equilibria*,* 228–229. 213.

Proceedings of the 10th International Chemical and
Biological Engineering Conference - CHEMPOR 2008
Braga, Portugal, September 4-6, 2008
E.C. Ferreira and M. Mota (Eds.)

Optimized force fields for predicting vapour-liquid equilibrium of binary mixtures involving alkanes and xenon at low temperatures

Carlos E.C. Laginhas, A.J. Palace Carvalho, J.P. Prates Ramalho and Luís F.G. Martins
CQE – Centro de Química de Évora, University of Évora, Rua Romão Ramalho, 59, 7000–671 Évora, Portugal.

Keywords: Monte Carlo, Alkanes, Xenon, Vapour-liquid equilibria, Force field
Topic: Advancing the chemical and biological engineering fundamentals (thermodynamics)

Abstract

Although TraPPE-UA is able to predict vapour-liquid coexistence curves and vaporization enthalpies for many linear alkanes at wide temperature ranges, this is not so for vapour pressures of the shortest alkanes at low temperatures. In view of this fact, we did an optimization of non-bonded parameters of typical units of TraPPE force field so that experimental and calculated liquid density and vapour pressure match for ethane and propane. Using the new optimized parameters, vapour pressures and orthobaric liquid densities of butane at low to moderately high temperatures were calculated by Monte Carlo (Gibbs ensemble) simulation as well as vapour-liquid diagrams for systems xenon+ethane, xenon+propane and xenon+butane at cryogenic temperatures. The calculation results presented excellent agreement with experimental ones and the optimized parameter sets proved to be transferable.

1. Introduction

Our research team has dedicated a lot of work on thermodynamic properties of liquid mixtures involving noble gases (in particular, xenon) and the lightest alkanes (except methane). As stated elsewhere, xenon, being a structureless spherical particle, is an ideal component to use as reference when the liquid structure and intermolecular interactions of the other component of a binary mixture has to be assessed. Linear alkanes constitute a chemical family whose thermodynamic properties usually presents pronounced regularities, varying gradually with the number of carbon atoms in the molecule. This fact implies that it is possible to predict, with reasonable accuracy, one given thermodynamic property for a specific alkane based on values for the same property (at corresponding conditions) previously obtained for other alkanes by simple extrapolation. This behaviour extends also to mixtures of alkanes by applying theoretical or phenomenological approaches such as segment theories (Blas, 2000) or congruence principle (Weiguo *et al.*, 1990). Despite the effort that has been made to integrate the thermodynamic behaviour of all the akanes under the same united scheme, the lightest alkanes hardly follow some of the regularities encountered among the longer ones, probably due to the absence of a fully developed angle-type molecular structure.

Among the force fields that have been proposed recently, TraPPE-UA was one of the most successfully in describing the vapour-liquid equilibria of hydrocarbons, while keeping a simple form which allow the calculations to be made with low computational cost. TraPPE-UA was able to predict the vapour-liquid coexistence curves from methane do dodecane, but failed to reproduce the vapour pressure curves for the lightest alkanes, in particular at low temperatures (Martin and Siepmann, 1998).

We have recently reported Monte Carlo computer simulations of excess enthalpies and excess volumes for the binary systems of xenon with ethane, propane and butane at low

temperatures (Carvalho *et al.*, 2007). Simulation results presented an excellent agreement with experimental ones for xenon+ethane, whereas for the remaining systems, some deviations were observed, which became progressively more significant as the alkane chain length increased. For these systems it is also important to obtain VLE simulation results. In the paper aforesaid, the TraPPE-UA force field was chosen to model all the alkanes studied because, among other tested force fields, was the one that was found to give the best agreement between calculated and experimental liquid density of pure components. However, TraPPE-UA was unable to predict vapour pressures of the lightest alkanes at cryogenic temperatures, which prevents the prediction of VLE of mixtures involving such components. On the other hand, the Lennard-Jones potential from Bohn *et al*. (1985) didn't give the best prediction of the vapour pressure curve of xenon. For this reason, we did a reparameterization of both force fields in order to match the results of Gibbs ensemble simulations of vapour-liquid equilibrium to experimental data specifically for the lightest alkanes and xenon at temperatures between 150 K and 350 K. In the case of alkanes, we found that there is no a unique set of non-bonded (Lennard-Jones) parameters that can predict the entire vapour pressure curve as a function of temperature. Two sets of parameters for each alkane were obtained, one for low temperatures and the other for not too low or higher temperatures. With these sets of parameters, a better prediction of vapour-liquid equilibrium for systems involving xenon and the alkanes ethane, propane and butane has been accomplished.

2. Simulation Details

The computer simulations both for pure liquids and liquid mixtures were done by Monte Carlo method, using MCCCS Towhee Monte Carlo molecular simulation package, version 5.2.12. We start the calculation by the optimization of the non-bonded Lennard-Jones parameters of both used force fields. For xenon, the optimization of ε and σ, was done simultaneously, by trial and error, in order to obtain the best fit of orthobaric liquid densities and vapour pressure as a function of temperature in the range 160-200 K, using the Bohn *et al.* potential as a starting point. In the case of short alkanes studied, a stepwise procedure was attempted. Starting from TraPPE-UA force field and keeping its structure and all of its intramolecular parameters, a trial and error optimization of the CH_3 Lennard-Jones parameters was done by trying to fit orthobaric liquid density and vapour pressure curves for ethane. Since, as stated above, no unique set of non-bonded parameters was obtained, the ethane liquid range was divided in two portions: 150-200 K and 205-305 K. For each one, the optimization was possible and a set of parameters was found that fit orthobaric liquid density and vapour pressure curves for ethane. Then, following TraPPE philosophy, the transferability of CH_3 was assumed and the Lennard-Jones parameters for CH_2 were also optimized by the same trial and error procedure, matching simulation and experimental results for orthobaric liquid densities and vapour pressures of propane. As for ethane, two sets of non-bonded parameters were obtained, one for each temperature range considered, 160-210 K and 215-350 K. The optimized parameters were then used to predict the vapour pressure and orthobaric liquid density curves for pure butane and vapour pressures of xenon+ethane, xenon+propane and xenon+butane mixtures for a series of predefined total compositions at temperatures for which experimental results exist.

The computer simulations were carried out in the *NVT* Gibbs ensemble. For pure components, each simulation consisted of a total of 500 molecules, distributed to each cubic simulation box so that the "liquid" box have side lengths of about 30-40 Å. The simulations were done in large temperature ranges at intervals of 5 or 10 K. Mixtures were "prepared" by varying the proportions of molecules of each component, being the total number of molecules between 500 and 1000 molecules, observing the same criteria as above to fill the simulation boxes. The simulations were carried out at temperatures for which experimental results exist to allow comparison between simulation and experience.

In each simulation, a preliminary equilibration run of between 20 000 and 50 000 steps (in which each step is in fact a MC cycle, consisting of an amount of moves equal to the number of molecules in the system) was done, followed by a production run for the calculation of averages, consisting of another 100000 to 200000 steps, which were divided into 20 blocks in order to estimate errors. The Monte Carlo moves consisted simulation box volume exchanges, coupled-decoupled configurational-bias regrowths, translations and of the centre of mass, rotations about the centre of mass, configurational-bias molecule reinsertions in the same simulation box and aggregation volume-bias and configurational-bias molecules exchanges between boxes.

3. Results and Discussion

In table 1 the non-bonded parameters for CH_3 and CH_2 obtained from trial and error optimization are presented. For comparison, the original TraPPE-UA parameters are also shown. The fitting results for ethane and propane at low and high temperatures are shown in figures 1 and 2. Those are the best fittings that it was possible for each temperature range with just one set of parameters per range per compound. For xenon, ε/k_B = 226.3 K and σ = 3.948 Å were found.

Table 1. Optimized TraPPE-UA non-bonded parameters for two sets considered and comparison with the corresponding original parameters

	"Low temperature"		"High temperature"		Original TraPPE-UA	
unit	ε/k_B [K]	σ [Å]	ε/k_B [K]	σ [Å]	ε/k_B [K]	σ [Å]
CH_3	102.2	3.773	100.75	3.787	98	3.75
CH_2	48.55	4.01	47.2	4.03	46	3.95

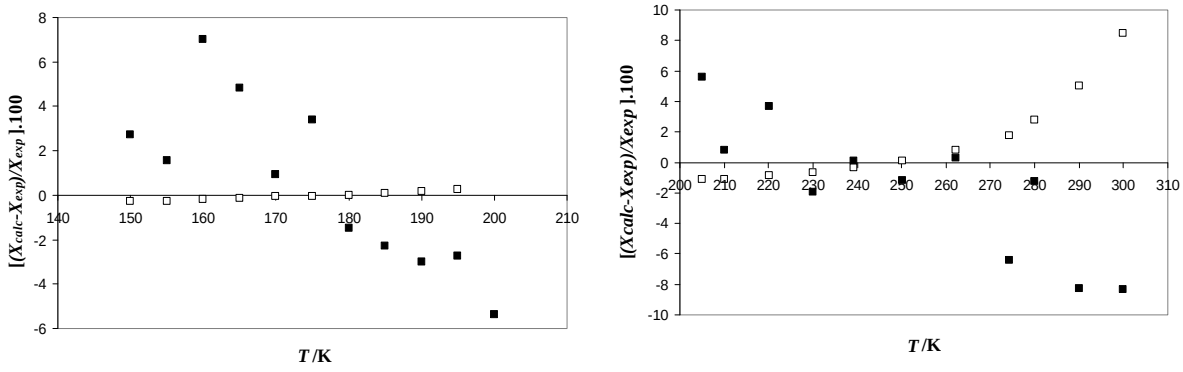

a) b)

Figure 1. Relative deviations between calculated and experimental values of saturated liquid densities (empty squares) and vapour pressures (filled squares) for ethane with low [a)] and high [b)] temperature sets.

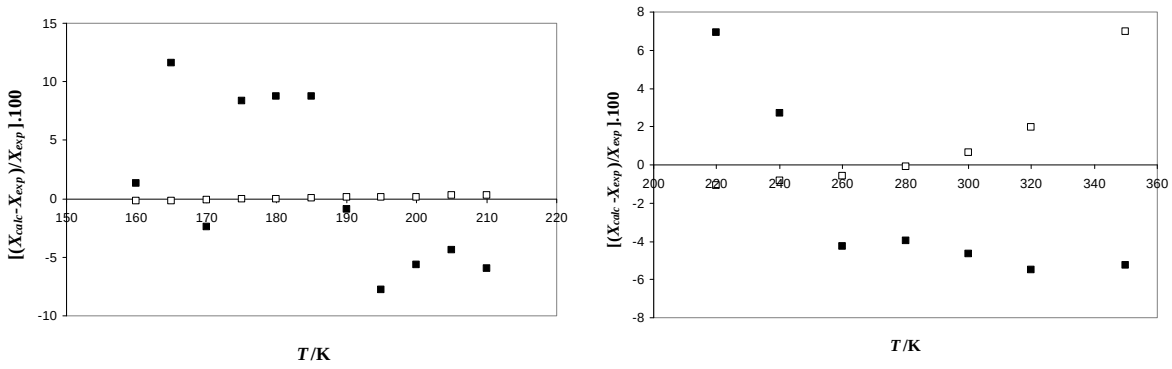

a) b)

Figure 2. Relative deviations between calculated and experimental values of saturated liquid densities (empty squares) and vapour pressures (filled squares) for propane with low [a)] and high [b)] temperature sets.

Using both sets of parameters for each unit, vapour pressure and orthobaric liquid density of pure butane were obtained by simulation and presented in figures 3 and 4. The agreement is very good, except in the high temperature region of "low temperature" set, where the calculations probably were extended outside the temperature range of the fitting procedure. The results show that the parameters so obtained are reasonably transferable.

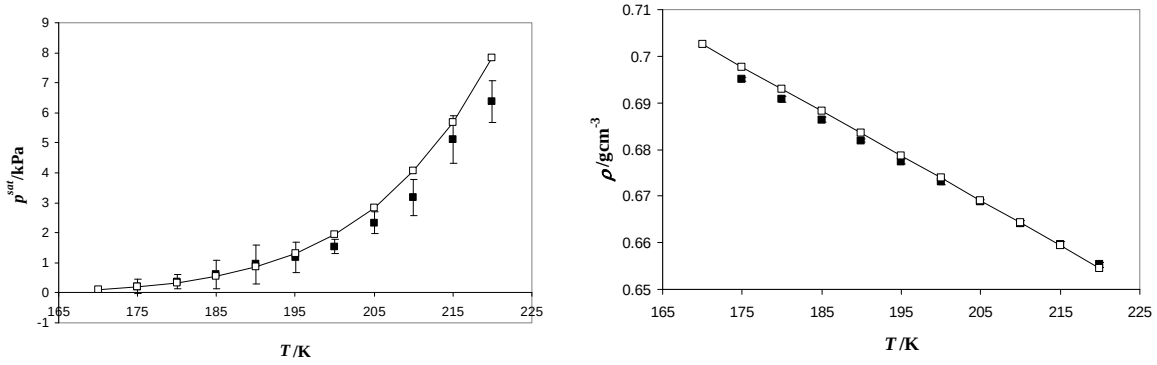

a) b)

Figure 3. Vapour pressures [a)] saturated liquid densities [b)] as a function of temperature for butane in the low temperature parameter set. Filled squares: simulation results; empty squares: experimental results (NIST).

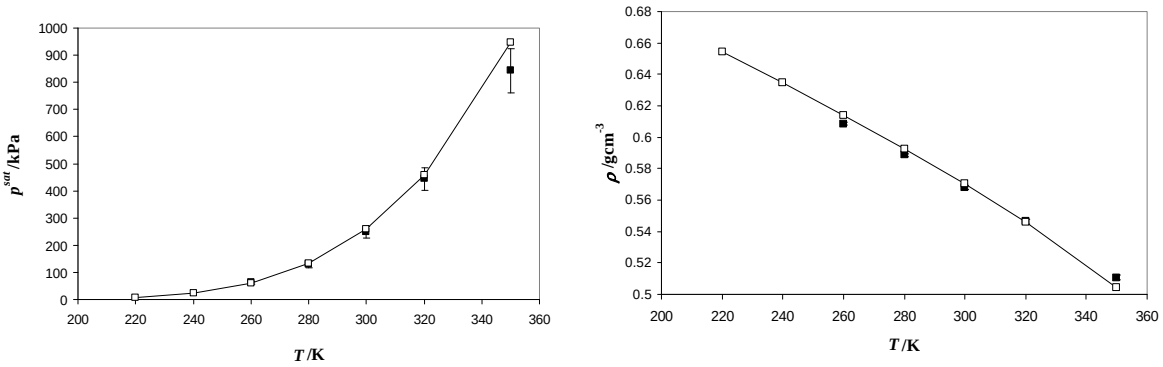

a) b)

Figure 4. Vapour pressures [a)] saturated liquid densities [b)] as a function of temperature for butane in the high temperature parameter set. Filled squares: simulation results; empty squares: experimental results (NIST).

Finally, as the main goal of this work, vapour-liquid phase diagrams of binary systems of xenon with ethane, propane and butane were calculated at two (fixed) temperatures, for which experimental results have already been reported. In figure 5 phase diagrams of

xenon+ethane system at temperatures between 161.40 K and 230.05 K are shown. The vapour-liquid equilibria of xenon+propane and xenon+butane are presented, respectively, in figures 7 and 8. For all the cases, the agreement between simulation and experiment is excellent, the experimental results lying within the error bars of the simulation results. The new TraPPE-UA parameters can predict phase diagrams of mixtures involving xenon and light alkanes by computer simulation without any fit to mixture properties.

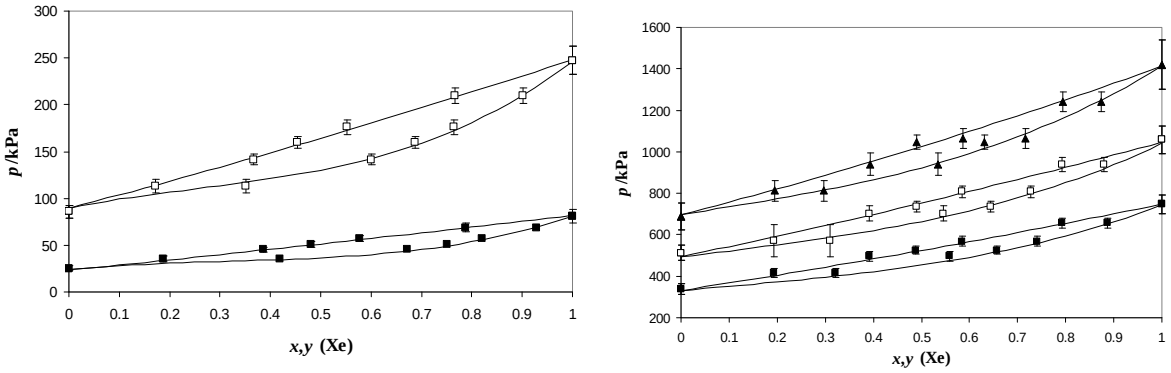

a) b)

Figure 5. Vapour-liquid equilibrium for the binary system xenon+ethane. a): filled squares,161.40 K; empty squares, 182.34 K. b): filled squares, 210.03 K; empty squares, 220.14 K; filled triangles, 230.05 K . Lines: experimental results from Filipe *et al.* (2000a) [a)] and Nunes da Ponte *et al.* (1985) [b)]

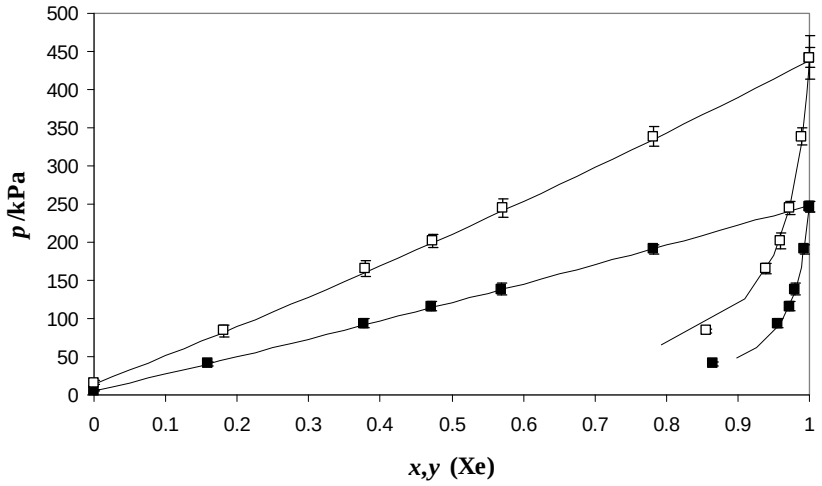

Figure 6. Vapour-liquid equilibrium for the binary system xenon+propane at 182.34 K (filled squares) and 195.49 K (empty squares). Lines: experimental results from Filipe *et al.* (2000a).

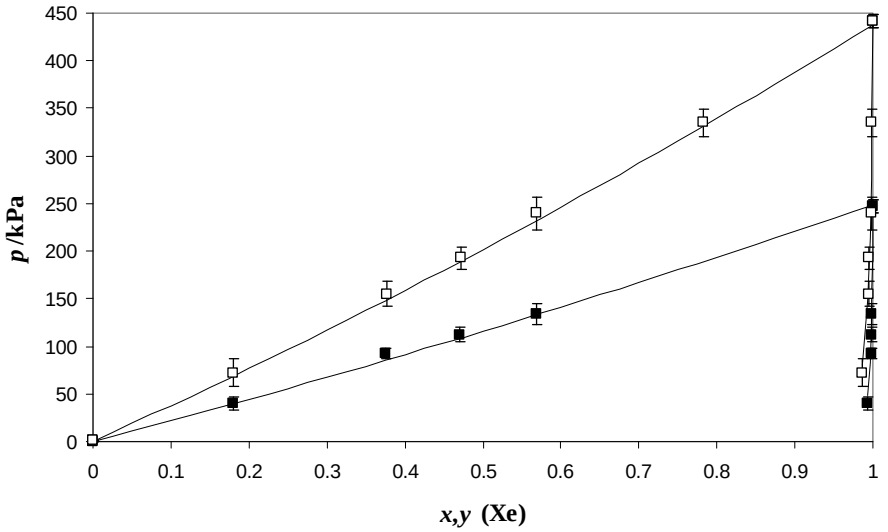

Figure 7. Vapour-liquid equilibrium for the binary system xenon+butane at 182.34 K (filled squares) and 195.49 K (empty squares). Lines: experimental results from Filipe *et al.* (2000b).

3. Conclusions

We have optimized the non-bonded parameters from TraPPE-UA force field for alkanes by matching Monte Carlo simulations and experimental orthobaric liquid densities and vapour pressures for ethane and propane (for CH_3 and CH_2 parameters). We also optimize the Bohn *et al.* potential for xenon at low temperatures. The parameters proved to be transferable to butane and, with them, we were able to predict vapour-liquid phase diagrams of binary systems involving the alkanes from ethane to butane and xenon.

References

Blas, F.J. (2000). Excess Thermodynamic Properties of Chainlike Mixture: 1 Prediction from the soft-SAFT Equation of State and Molecular Simulation. *J. Phys. Chem. B*, 104, 9239-9248

Bohn, M., Lago, S., Fischer, J., Kohler, F. (1985). *Fluid Phase Equilibria,* 23, 137-151

Filipe, E.J.M., Gomes de Azevedo, E.J.S., Martins, L.F.G., Soares, V.A.M., Calado, J.C.G. (2000a). Thermodynamics of Liquid Mixtures of Xenon with Alkanes: (Xenon+Ethane) and (Xenon+Propane). *J. Phys. Chem. B*, 104, 1315-1321

Filipe, E.J.M., Martins, L.F.G., Calado, J.C.G. (2000b). Thermodynamics of Liquid Mixtures of Xénon with Alkanes: (Xenon+*n*-Butane) and (Xenon+Isobutane). *J. Phys. Chem. B*, 104, 1322-1325

Martin, M.G., Siepmann, J.I. (1997). Predicting Multicomponent Phase Equilibria and Free Energies of Transfer for Alkanes by Molecular Simulation. *J. Am. Chem. Soc.,* 119, 8921-8924

Martin, M.G., Siepmann, J.I. (1998). Transferable Potentials for Phase Equilibria: 1 United-Atom Description of n-Alkanes. *J. Phys. Chem. B*, 102, 2569-2577

Nunes da Ponte, M., Chokappa, D., Calado, J.C.G., Clancy, P., Streett, W.B. (1985). Vapor-Liquid Equilibrium in Xénon+Ethane System. *J. Chem. Phys.*, 89, 2746-2751

Palace Carvalho, A.J., Prates Ramalho, J.P., Martins, Luís F.G. (2007). Excess Thermodynamics of Mixtures Involving Xenon and Light Alkanes by Computer Simulation. *J. Phys. Chem. B*, 102, 2569-2577

Weiguo, S., Qin, A.X., McElroy, P.J., Williamson, A.G. (1999). (Vapour+liquid) equilibria of (*n*-hexane + *n*-hexadecane), (*n*-hexane + *n*-octane) and (*n*-octane + *n*-hexadecane). *J. Chem. Thermodyn.,* 22, 905-914

Proceedings of the 10th International Chemical and
Biological Engineering Conference - CHEMPOR 2008
Braga, Portugal, September 4-6, 2008
E.C. Ferreira and M. Mota (Eds.)

Kinematic viscosity of ternary solutions of ethanol, glycerol and water from 293.1 to 318.1 K

R. Moreira[1*], F. Chenlo[1], D. Le Gall[2]
[1] Departamento de Enxeñaría Química. ETSE, Universidade de Santiago de Compostela, 15782 Santiago de Compostela. Spain.
[2] ENGSTI, Université de Pau et des Pays de l'Adour, Rue Jules Ferry, 64075 Pau, France.

Keywords: Capillary viscosimetry, Concentration, Temperature, Modeling.
Topic: Rheology.

Abstract

Kinematic viscosity of ternary aqueous solutions of ethanol and glycerol were determined at several temperatures (from 20 up to 45 ºC) and different molar fractions of component (up to 0.75 of ethanol and 0.60 of glycerol) covering a wide range of experimental conditions. A capillary viscosimeter was employed as equipment.

Experimental data of kinematic viscosity showed non-ideal behaviour and were modelled employing previous proposed correlations for aqueous ethanol solutions modified with an additional exponential term where is taken into account the influence the presence of glycerol. The final model reproduces the experimental data of kinematic viscosity of ternary solutions of glycerol, ethanol and water with deviations less than 6% in the range of concentrations and temperatures tested.

1. Introduction

Viscosity is an important transport property for equipments design and for evaluation of operational costs. Glycerol is very employed in the pharmaceutical and food industries because is nontoxic and can be considered as good solvent for organic and inorganic compounds. Aqueous solutions of glycerol with presence of alcohols are also frequently found in several industrial processes. Nowadays, these systems have also specially importance in the production of biofuels from vegetal oils and ethanol where glycerol is a by-product (Ito et al., 2005).

Several approaches with theoretical or semi-theoretical bases have been proposed in the literature for estimating viscosity of pure (electrolytic and non-electrolytic) liquids, but well understood theories have not been developed (Poling et al., 2001; Viswanath et al., 2007). The estimation of viscosity of mixture fluids can usually carried out by extension of pure component methods by semi-theoretical methods or by application of mixing rules to experimental data or values calculated by means of a model for pure component. There are a lot of proposed equations for systems with specific chemical properties (Viswanath et al., 2007).

One of the aims of this work is to determine experimentally the kinematic viscosity of glycerol/ethanol/water ternary solutions. Viscosity of the corresponding ethanol/water and glycerol/water binary solutions are already studied in wide range of temperatures and concentrations. High non-ideal behaviour of kinematic viscosity of binary ethanol-water solutions was reported (Pemberton et al., 1978) with maximum values of kinematic viscosity varying with concentration and temperature. In this way, the maximum was determined at 0.25 ethanol molar fraction at 293.1 K and at 0.35 at 318.1 K (Moreira et al., 2007). These last authors modelled the kinematic viscosity employing Redlich-Kister equation (Redlich and

* Corresponding author. Tel + 34-981-563100. E-mail:eqmoncho@usc.es

Kister, 1948) for the concentration effect and, for the dependence on temperature, empirical Vogel-Fulcher-Tamman (Cocchi et al., 1999) relation was selected. The model is given by:

$$\upsilon_{eth/water} = x\upsilon_{eth} + (1-x)\upsilon_{water} + x(1-x)\left[\exp\left(\frac{3255}{T} - 9.41\right) + \exp\left(\frac{-3917}{T} + 11.44\right)(1-2x) + \exp\left(\frac{5113}{T} - 16.06\right)(1-2x)^2\right] \quad (1)$$

where $\nu_{eth/water}$ (m^2/s) is the kinematic viscosity of ethanol/water binary solutions, x is the molar fraction of ethanol, T (K) the absolute temperature, ν_{eth} and ν_{water} (m^2/s) are the kinematic viscosity of pure ethanol and water, respectively.

Aqueous glycerol solutions were also studied in different ranges of temperatures and concentrations (Chenlo et al., 2004; Cheng, 2008). These solutions show a strong dependency of kinematic viscosity on glycerol concentration at high glycerol concentrations. In general, viscosity modelling is carried out by means of exponential relationships with temperature and concentration as variables.

2. Materials and Methods

The solutions were prepared by weight, with a Mettler AJ150 balance with a precision of ± 0.0001 g using degassed distilled water, commercial ethanol (Panreac, 96% v/v) and glycerol (Merck > 99%).

Kinematic viscosities were determined by using a Schott-Gerate AVS 350 automatic Ubbelohde viscosimeter with the procedure previously described (Vázquez et al., 1994). All measurements were made at least in five replicates. Temperature control was assured by inserting the capillary viscosimeter into a water thermostatic bath with a Selecta Digiterm heating system (precision of ± 0.1ºC). The temperature was varied from 20 ºC up to 45 ºC by steps of 5 ºC. Upper temperature was limited by the presence of ethanol. The uncertainty in the measurements was within $\pm 10^{-9}$ m^2/s and capillaries were periodically calibrated by determination of tri-distilled water at several temperatures.

In terms of concentration, the ternary system was generated from ethanol/water binary solutions with concentrations ranged from 0.05 up to 0.75 molar fraction adding different amounts of glycerol in order to obtain 0.05, 0.1, 0.2, 0.3, 0.45, and 0.60 molar fraction of this component. In this way, ternary mixtures were created maintaining the ethanol/water ratio constant. Table 1 shows the initial binary solutions of ethanol and water and the corresponding ethanol/water averaged ratios and standard deviation of ternary solutions with glycerol.

Table 1. Initial ethanol/water solutions and experimental ethanol/water ratios of ternary solutions.

Molar fraction of ethanol of aqueous solutions	Water/ethanol ratio in ethanol/glycerol/water solutions
0.05	19.245 ± 0.290
0.15	5.746 ± 0.096
0.25	3.048 ± 0.058
0.35	1.891± 0.041
0.45	1.249 ± 0.032
0.60	0.687 ± 0.024
0.75	0.349 ± 0.019

Statistical analysis of experimental data, non-linear fittings and parametric optimization, were carried out using the program TableCurve 3D®.

3. Results and discussion

Figure 1 shows the changes of kinematic viscosity of glycerol/ethanol/water mixtures at a fixed molar fraction of glycerol. At low molar fraction of glycerol, at all assayed temperatures, a maximum value of kinematic viscosity can be observed around 0.23 molar fraction of ethanol (Fig. 1a). This maximum value of viscosity is also presented at higher concentrations of glycerol, but at lower concentrations of ethanol and the curves are more smoothed. In fact, at the highest glycerol concentration tested in this work (0.6 molar fraction, Fig. 1b), the maximum value is around 0.06 molar fraction of ethanol and viscosity values of solutions from this concentration up to 0.14 molar fraction of ethanol are closed. On the other hand, as it was expected, the kinematic viscosity of ternary solutions decreases with temperature and increases with glycerol concentration in all mixtures.

These results indicate that the presence of glycerol at high concentrations moves the typical maximum of aqueous solutions of ethanol towards lower ethanol concentrations because in the limit case of aqueous solutions of glycerol (ethanol concentration equal to zero) there is not a maximum value at intermedeate concentrations (Weast, 1983). Different molecular interactions associations between the components can explain these results that reveal strong deviations from the ideal behaviour.

Taking into account the previous comments and the non-ideal behaviour of the systems, the modelling of kinematic viscosity of the ternary systems can not be simple as mixing rule models, and interactions must be included.

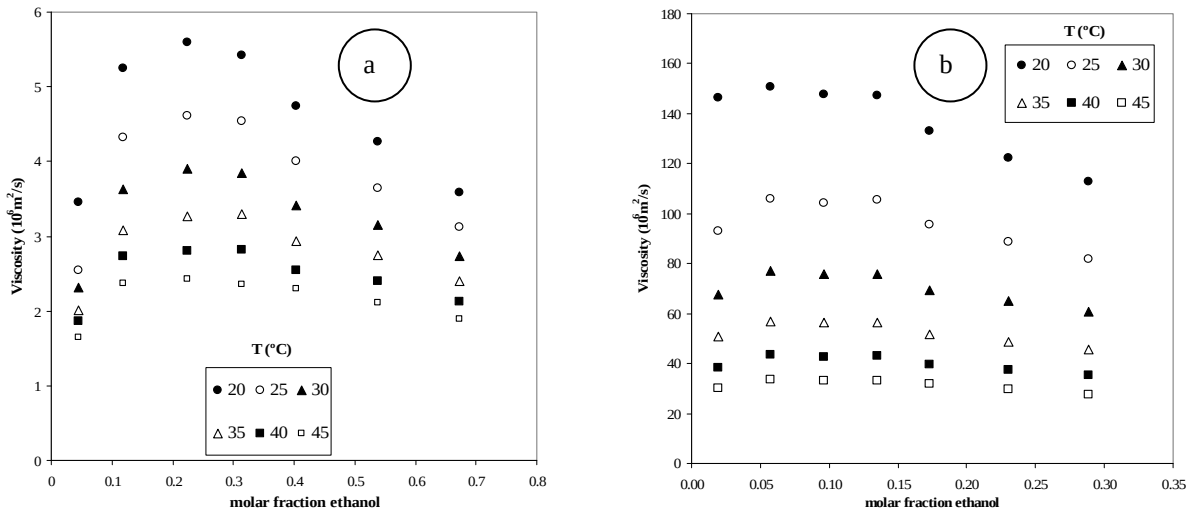

Fig. 1. Kinematic viscosity of glycerol/ethanol/water mixtures at a fixed molar fraction of glycerol: a) 0.1 and b) 0.6.

The modelling of kinematic viscosities, ν (m^2/s), corresponding to the ternary solutions was carried out applied the following equation which is a modification from the originally proposed by Torok et al., (1993):

$$\nu = \nu_{eth/water} + a\left[\exp(bx_{gly}) - 1\right] \quad (2)$$

where $\nu_{eth/water}$ (m^2/s) is given by the Eq. (1), x_{gly} is the molar fraction of glycerol in ternary solution, a (m^2/s) and b are parameters of fitting.

Parameter *a* was correlated by means of non-linear fittings simultaneously to *T* and *x* (ethanol concentration corresponding to binary system after removal glycerol), obtaining the following expression:

$$a = 1.39 + 5.64\left[\exp(-T/62.03)\right] + \left[3.56 - \frac{89.18}{T^{1.5}}\right] x - 8.80\,x^2 + 5.91\,x^3 \qquad (3)$$

Parameter *b* showed only dependence on temperature according to:

$$b = 4.11 + 5.54\left[\exp(-T/25.03)\right] \qquad (4)$$

Figure 2 shows experimental data of kinematic viscosity of ternary solutions at two different water/glycerol ratios, as examples. One more time, it can be observed as viscosity increases with glycerol concentration at a fixed water/ethanol ratio and the strong influence of temperature on viscosity. Comparing Figs 2a and 2b it can be also observed kinematic viscosity values decrease when ethanol concentration increases (lower values of water/ethanol ratio). In Figs. 2a and 2b are also plotted the proposed model, involving the Eqs 1 to 4, and a good agreement between experimental data and predicted values can be observed.

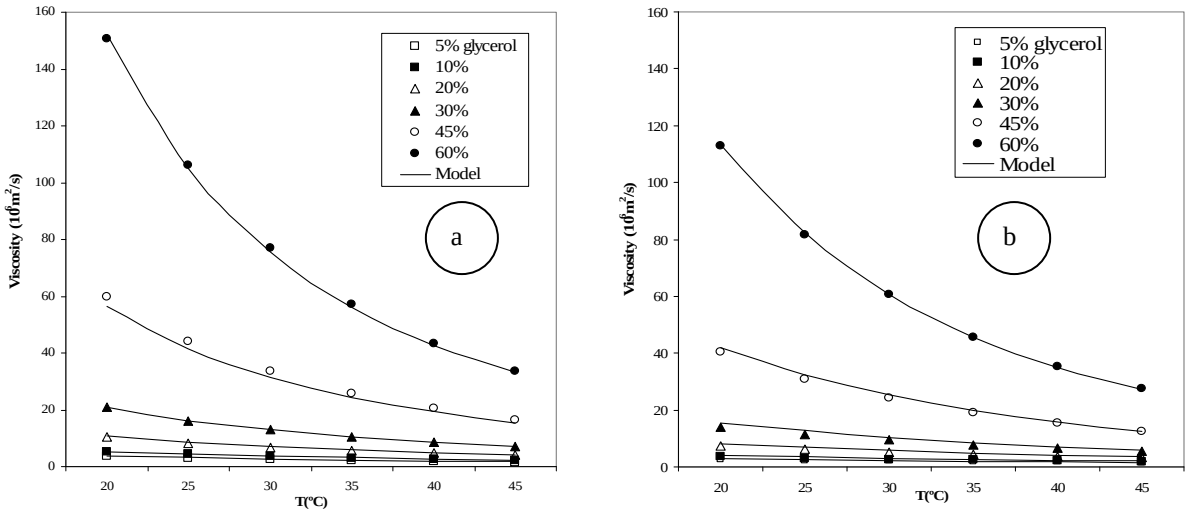

Fig. 2. Experimental data (dots) and modelled values (lines) by means of Eqs (1 to 4) of glycerol/ethanol/water mixtures at fixed ethanol/water ratios: a) 5.746 and b) 0.349.

Using the model is possible to reproduce successfully the kinematic viscosity of ternary solutions of glycerol, ethanol and water in the range of concentrations and temperatures tested with deviations less than 6%. Fig. 3 shows the good agreement between the experimental data and calculated values for all tested conditions of concentration and temperature.

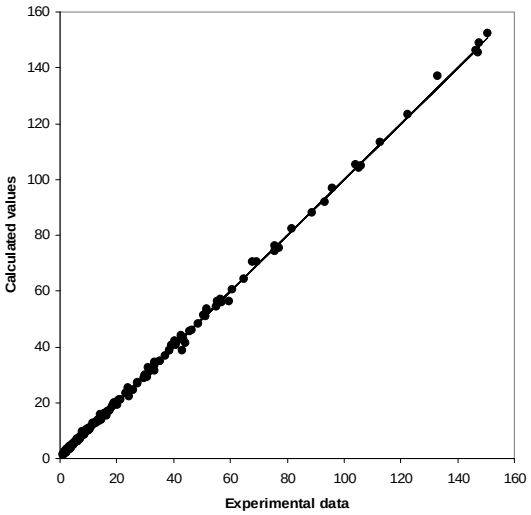

Fig. 3. Calculated kinematic viscosities (10^6 m^2/s) in comparison with experimental data.

4. Conclusions

Kinematic viscosity for Newtonian ternary systems, consisting in a mixture of ethanol, glycerol, and water was determined using a capillary viscosimeter showing a strongly non-ideal behaviour due to typical water/ethanol interactions. In this way, maximum values of kinematic viscosity was detected at determined ethanol concentration and being modified by the presence of glycerol in the ternary system. Higher glycerol concentrations increases kinematic viscosity values. In all cases, as it was expected, temperature decreases the kinematic viscosity.

In spite of the commented behaviour, a model to correlate the kinematic viscosity with temperature and component concentration is proposed and satisfactorily tested by statistical analysis.

5. Acknowledgements

Authors acknowledge the financial support to Ministerio de Educación y Ciencia of Spain and FEDER (CTQ 2007-62009/PPQ).

References

Cheng, N.S. (2008). Formula for the viscosity of a glycerol-water mixture. *Industrial & Engineering Chemical Research*, 47, 3285-3288.

Chenlo, F., Moreira, R., Pereira, G., Bello, B. (2004). Kinematic viscosity and water activity of aqueous solutions of glycerol and sodium chloride. *European Food Research and Technology*, 219, 403-408.

Cocchi, M., Marchetti, A., Sanna, G., Tassi, L., Ulrichi, A., Vaccari, G. (1999). Kinematic viscosities of ternary mixtures containing ethane-1,2-diol, 2-methoxyethanol and water from -10ºC to 80ºC. *Fluid Phase Equilibria*, 157, 317-342.

Ito, T., Nakashimada, Y., Senba, K., Matsui, T., Nishio, N. (2005). Hydrogen and ethanol production from glycerol-containing wastes discharged after biodiesel manufacturing process. *Journal of Bioscience and Bioengineering*, 100, 260-265.

Moreira, R., Chenlo, F., Correia, G.R. (2007). Viscosity of water based solutions of ethanol and sucrose. *International Journal of Food Properties*, 10, 435-444.

Pemberton, R.C., Mash, C.J. (1978). Thermodynamics properties of aqueous non-electolyte mixtures. 2. Vapor-pressures and excess Gibbs energies for water+ethanol at 303.15 to 363.15 K determined by an accurate static method. *Journal of Chemical*

Thermodynamics, 10, 867-888.
Poling, B.E., Praustnitz, J.M., O'Conell, J.P. (2001). *The properties of gases and liquids*, McGraw-Hill, New York, USA.
Redlich, O., Kister, A.T. (1948). Thermodynamics of nonelectrolyte solutions –X-Y-T relations in a binary system. *Industrial Engineering Chemistry*, 40 (2), 341-345.
Torok, T.I., Rard, J.A., Miller, D.G. (1993). Viscosities, electrolytic conductivities, and volumetric properties of HCl-MCl_x-H_20 as a function of temperature up to high molal ionic strengths. *Fluid Phase Equilibria*, 88, 263-275.
Vázquez, G., Chenlo, F., Álvarez, E., Moreira, R., Pardo, P. (1994). Viscosities of solutions of interest for studies of absorption processes*. Journal of Chemical Engineering Data*, 39, 87-89.
Weast, R.C. (1983). *CRC Handbook of Chemistry and Physics,* (67^{th} Ed), Chemical Rubbing Publishing, Boca Raton.
Viswanath, D.S., Ghosh, T.K., Prasad, D.L., Ndutt, N.V.K., Rani, K.Y. (2007). *Viscosity of liquids: theory, estimation, experiment and data*, Springer Verlag, Dordrecht, The Netherlands.

Proceedings of the 10th International Chemical and
Biological Engineering Conference - CHEMPOR 2008
Braga, Portugal, September 4-6, 2008
E.C. Ferreira and M. Mota (Eds.)

Aqueous Biphasic Systems with Ionic Liquids

Catarina M. S. S. Neves[1], Sónia M. P. Ventura[1], Mara G. Freire[2], Maria Alice Z. Coelho[3], Isabel M. Marrucho[1] and João A. P. Coutinho[1*]

[1] CICECO, Departamento de Química, Universidade de Aveiro, 3810-193 Aveiro, Portugal

[2] Instituto de Tecnologia Química e Biológica, ITQB2, Universidade Nova de Lisboa, 2780-901 Oeiras, Portugal

[3]Departamento de Engenharia Bioquímica, Escola de Química/UFRJ, Centro de Tecnologia, Lab.113, Rio de Janeiro, RJ 21949-900, Brasil

Keywords: Ionic liquids, aqueous biphasic systems, inorganic salt, chaotropic, kosmotropic
Topic: Advancing the chemical and biological engineering fundamentals.

Abstract

The main goal of this study is to determine Aqueous Biphasic Systems (ABS) phase diagrams at 298.15 K to evaluate the salting-in *versus* salting-out strength of ionic liquids (ILs) ions. The separation of both aqueous phases was achieved between the inorganic salt K_3PO_4 and hydrophilic ILs addition. The selected ILs combination allowed the study of the cation alkyl chain length and the type of functional groups at the cation impact in their water-structuring ability. The coexistence curves were determined using an empirical mathematical description from relationships from volume and density data collected for each aqueous phase (Merchuk et al.,1998).

1. Introduction

The efficiency of any fermentation process depends largely on downstream processing which ensures the purity and quality of the biochemicals and represents about 60-90 % of the cost of the biological processes (Kula et al., 1982). Nevertheless, many biomolecules have narrow tolerance limits of pH, temperature, osmotic pressure and surface charges, and the extraction and isolation techniques should be specific and compatible to the product (Banik et al. 2003). The conventional techniques used for product recovery, are not only expensive but also result in lower yields. Keeping this problem in mind, the industrial community has carrying a large effort in the use of cost-effective ecofriendly simple separation techniques: the aqueous biphasic systems (ABS). These systems consist in two mutually incompatible solutes such as polymers/polymer, polymer/salt or salt/salt dissolved in water. Above critical concentrations of these components the spontaneous phase separation takes place.
Environmental concerns about volatile organic compounds have increased in the last few years and there is a growing interest nowadays in finding ‘‘greener’’ replacement solvents for extractions and liquid-liquid separations. In this context, ionic liquids (ILs) have aroused as a new class of organic solvents with high potential as “green” solvents. It is essentially their specific characteristic of negligible vapor pressure (Freemantle, 1998; Anderson et al., 2002) that make of them suitable “green” candidates for a large range of applications.
The first publication of ABS with ILs was reported by Rogers and his co-workers (Gutowski et al., 2003). In this paper, the authors have demonstrated that the addition of K_3PO_4 to an aqueous solution of an hydrophilic IL produces a salting-out effect and promotes the separation of phases. On the other hand, the extraction of different organic compounds by ILs was reported by a larger number of authors. Li and his co- workers (He et al., 2005; Li et al., 2005) have studied the extraction of biochemical compounds and drugs such as, testosterone, epitestosterone and opium alkaloids. The extraction of metals ions (Dietz, et al., 2003), and organic molecules, such as penicillin (Liu, et al., 2006), antibiotics (Cull et al.,

* Corresponding author.Tel +351-234-370200. E-mail: jcoutinho@ua.pt

2000), alcohols (Fadeev et al., 2001) and acids (Matsumoto et al., 2004) were also described in literature. Nevertheless, there are still many gaps in what concerns the IL impact in promoting ABS.
The main goal of this study is to determine the impact of different characteristics of the IL cation, such as the presence of a long or short alkyl chain length, the presence of a double bond or an hydroxyl group in generating ABS. The results show that the cation structural differences have an important influence in the binodal curves behavior and in the formation of ABS. The cation alkyl chain length increase decrease the IL affinity for water and this facilitates the phases separation. In general, ILs with a smaller solubility in water have a higher ability to promote a salting-out effect, resulting in a binodal curve closest to the origin and indicating that less inorganic salt is needed to form the ABS.
The present work shows different phase diagrams (binodal curves and tie-lines) for selected systems of hydrophilic ILs + K_3PO_4 + water. The binodal curves were fitted to a three-parameter equation and the tie-lines are determined for a mathematical method well described by Merchuck et al. (Merchuk et al.,1998).

2. Materials and Methods

The K_3PO_4 (purity level > 98 %) was from Sigma-Aldrich. The ILs 1,3-dimethylimidazolium chloride, [C_1mim]Cl, with a purity level > 98 %, 1-ethyl-3-methyl-imidaziolium chloride, [C_2mim]Cl, with a purity level > 98 %, 1-butyl-3-methyl-imidaziolium chloride, [C_4mim]Cl, with a purity level > 99 %, 1-hexyl-3-methyl-imidaziolium chloride, [C_6mim]Cl, with a purity level > 98 %, 1-allyl-3-methyl-imidaziolium chloride, [amim]Cl, with a purity level > 98 %, 1-hydroxyethyl-3-methyl-imidaziolium chloride and [hydemim]Cl, with a purity level > 99 %, were acquired at Iolitec. Prior to the experimental measurements all the ILs samples were dried under vacuum and at moderate temperature (353 K) for at least 48 h.
The liquid-liquid phase separation inducing measurements between the aqueous solutions of K_3PO_4 and ILs were carried out at atmospheric pressure and 298 K. The binodal curves were determined through the visual cloud point titration method. For each system studied (water + IL + K_3PO_4) at least one tie-line (TL) was determined by a simple gravimetric method. The TLs were determined by application of the lever arm rule to the relationship between the mass phase composition and the overall system composition (Merchuk et al.,1998).

3. Results and Discussion

The experimental binodal data obtained are shown in Figure 1.

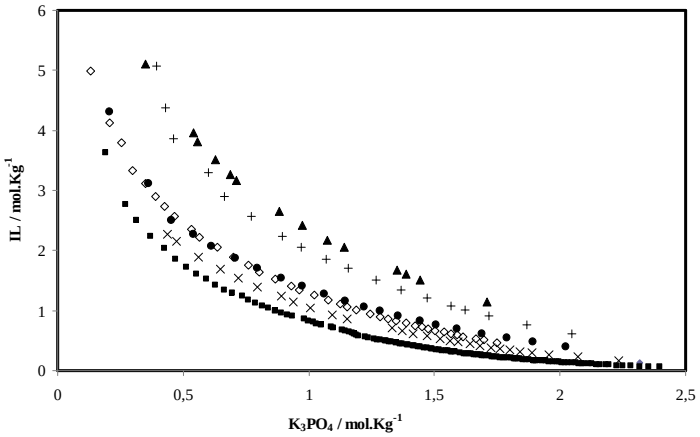

Figure 1. Experimental binodal curves for the IL and K_3PO_4 aqueous systems studied for the following ILs: ■, [C_6mim]Cl; ×, [C_4mim]Cl; ●, [C_2mim]Cl; +, [C_1mim]Cl; ◊, [amim]Cl; ▲, [hydemim]Cl.

Figure 1 presents the binodal curve for the different ILs studied. Perusal of Figure 1 indicates that the increase in the alkyl chain length of the IL cation promotes phase separation. The higher the IL alkyl chain length less inorganic salt is needed to promote ABS. On the other hand, the presence of a double bond at the alkyl chain length of the imidazolium cation or the presence of an hydroxyl group decreases the IL salting-out inducing capacity. This arises from the IL affinity for water increase (or IL hydrophilic nature increase) by the presence of double bonds or hydroxyl groups.

In general, ILs with a higher ability to promote a salting-out effect, indicate that less salt is needed to promote the phase separation, which results in a binodal curve closer to the origin and in a higher biphasic region. It can be seen from Figure 1 that the phase-forming ability of the ILs follows the order: [C_6mim]Cl > [C_4mim]Cl > [C_2mim]Cl > [amim]Cl > [C_1mim]Cl > [hydemim]Cl.

Tie-lines for these cloud point curves were fitted by a least-squares method. Figures 2 and 3 present two examples of a complete phase diagram for [C_2mim]Cl and [C_6mim]Cl + K_3PO_4 + H_2O systems, respectively.

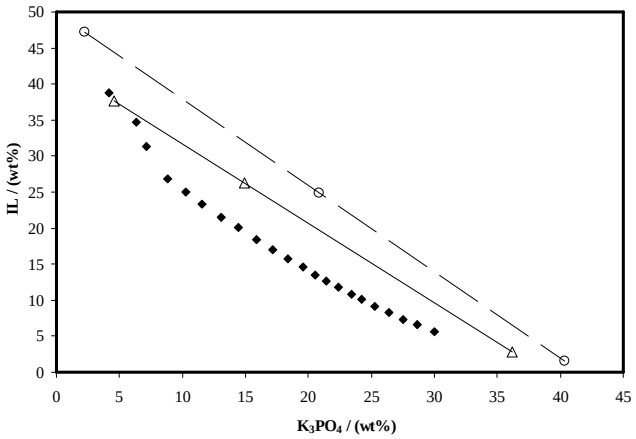

Figure 2. Experimental coexistence binodal curve (♦) for the aqueous systems [C_2mim]Cl + K_3PO_4 and respective tie-lines.

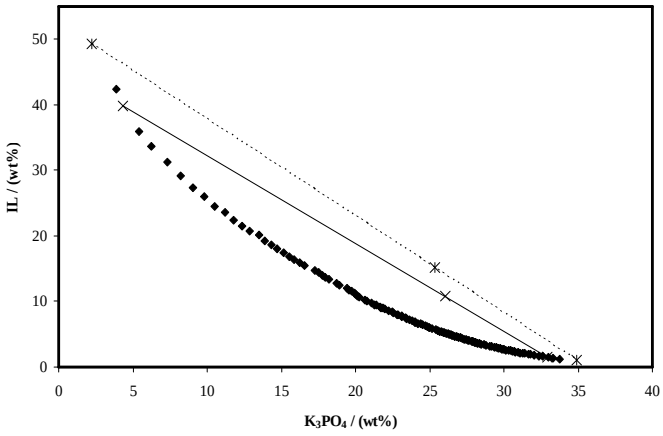

Figure 3. Experimental coexistence binodal curve (♦) for the aqueous systems [C_6mim]Cl + K_3PO_4 and respective tie-lines.

A phase diagram provides information about the concentration of phase-forming components required to form two aqueous phases, the concentration of the phase components at the top and bottom phases (given by the tie-lines) and finally, information about the ratio of the phase volumes**.**

Conclusion

The ability to form salt-salt ABS allows for hydrophilic ILs to be used in aqueous separation systems. Phase equilibrium experimental data were determined for systems involving hydrophilic ILs + K_3PO_4 + water, at atmospheric pressure and 298 K. Binodal data were fitted according to the empirical relationship of Merchuk (Merchuk et al.,1998) and the parameters for this equation were determined by a least-squares regression of the cloud point data.
The results show that aqueous biphasic systems can be obtained over a large range of concentrations both for ILs and the inorganic salt. The IL cation alkyl side chain length increase facilitates the phase separation formation. On the other hand, the inclusion of double bond or hydroxyl groups decreases the ability of phases separation. In this context, the ILs capacity for phase separation follows the order: $[C_6mim]Cl > [C_4mim]Cl > [C_2mim]Cl >$ [amim]Cl > $[C_1mim]Cl >$ [hydemim]Cl.

References

Anderson, J.L., et al. (2002), Characterizing Ionic Liquids On the Basis of Multiple Solvation Interactions. *Journal of the American Chemical Society*, 124, 14247-14254.

Banik, R.M., Santhiagu, A., Kanari, B., Sabarinath C. and Upadhyay, S.N. (2003). Technological aspects of extractive fermentation using aqueous two-phase systems. *World Journal of Microbiology & Biotechnology*, 19, 337–348.

Cull, S.G., Holbrey, J.D., Vargas-Mora, V., Seddon, K.R. and Lye, G.J. (2000) Room-Temperature Ionic Liquids as Replacements for Organic Solvents in Multiphase Bioprocess Operations. *Biotechnology and Bioengineering*, 69, 227-233.

Dietz, M.L., Dzielawa, J.A., Laszak, I., Young, B.A. and Jensen, M.P. (2003) Influence of solvent structural variations on the mechanism of facilitated ion transfer into room-temperature ionic liquids. *Green Chemistry*, 5, 682-685.

Fadeev, A.G. and Meagher, M.M. (2001) Opportunities for Ionic Liquids in Recovery of Biofuels. *Chemical Communications*, 3, 295-296.

Freemantle, M. (1998) Designer solvents - Ionic liquids may boost clean technology development. *Chemical & Engineering News*, 76, 32-37.

Gutowski, K.E., Broker, G.A., Willauer, H.D., Huddleston, J.G., Swatloski, R.P., Holbrey, J.D. and Rogers, R.D. (2003) Controlling the Aqueous Miscibility of Ionic Liquids: Aqueous Biphasic Systems of Water- Miscible Ionic Liquids and Water-Structuring Salts for Recycle, Metathesis, and Separations. *Journal of the American Chemical Society*, 125, 6632- 6633.

He, C.Y., Li, S.H., Liu, H.W., Li, K. and Liu, F. (2005) Extraction of testosterone and epitestosterone in human urine using aqueous twophase systems of ionic liquid and salt. *Journal of Chromatography A*, 1082, 143-149.

Kula, M.-R., Kroner,K.H. and Hustedt, H. (1982) Advances in Biochemical Engineering/Biotechnology. *Purification of enzymes by liquid-liquid extraction*, 24, 73-118.

Li, S.H., He, C.Y., Liu, H.W., Li, K. and Liu, F. (2005) Ionic liquid-based aqueous two-phase system, a sample pretreatment procedure prior to high-performance liquid chromatography of opium alkaloids. *Journal of Chromatography B*, 826 58-62.

Liu, Q., Yu, J., Li, W.L., Hu, X.S., Xia, H.S., Liu, H.Z. and Yang, P. (2006) Partitioning Behavior of Penicillin G in Aqueous Two Phase System Formed by Ionic Liquids and Phosphate. *Separation Science and Technology*, 41, 2849-2858.

Matsumoto, M., Mochiduki, K., Fukunishi, K. and Kondo, K. (2004) Extraction of organic acids using imidazolium-based ionic liquids and their toxicity to Lactobacillus rhamnosus. *Separation and Purification Technology*, 40, 97-101.

Merchuk, J.C., Andrews, B.A. and Asenjo, J.A. (1998). Aqueous two-phase systems for protein separation Studies on phase inversion. *Journal of Chromatography B*, 711, 285-293.

Proceedings of the 10th International Chemical and
Biological Engineering Conference - CHEMPOR 2008
Braga, Portugal, September 4-6, 2008
E.C. Ferreira and M. Mota (Eds.)

Hydrophobic Ionic Liquids and Water Mutual Solubilities

Catarina M. S. S. Neves[1], Mara G. Freire[2], Luís M. N. B. F. Santos[3], Isabel M. Marrucho[1], João Oliveira[4] and João A. P. Coutinho[1*]

[1] CICECO, Departamento de Química, Universidade de Aveiro, 3810-193 Aveiro, Portugal

[2] Instituto de Tecnologia Química e Biológica, ITQB2, Universidade Nova de Lisboa, 2780-901 Oeiras, Portugal

[3] CIQ, Departamento de Química, Faculdade de Ciências da Universidade do Porto, R. Campo Alegre 687, 4169-007, Porto, Portugal

[4] CESAM, Departamento de Química, Universidade de Aveiro, 3810-193 Aveiro, Portugal

Keywords: solubility measurements, ionic liquids, water.
Topic: Sustainable process-product development through green chemistry.

Abstract

In this work a systematic study of the mutual solubilites between hydrophobic ionic liquids (ILs) and water from (288.15 to 318.15) K and at atmospheric pressure was conducted for imidazolium, pyridinium and pyrrolidinium-based cations and bis(trifluoromethylsulfonyl)imide and hexafluorophosphate-based anions ILs. The main goal of this work is to determine the impact of several IL structural modifications in their liquid-liquid phase behaviour with water keeping the possibility to design a solvent for a specific application, in this case to fine-tune a particular IL with known mutual solubilities with water. Moreover, from the experimental results the ILs hydrophobic tendency, and thus their toxicity impact, was predicted. The predictive capability of COSMO-RS, a model based on unimolecular quantum chemistry calculations, was evaluated for the description of the binary systems investigated providing an acceptable agreement between the model predictions and experimental data both with the temperature dependence and the ILs structural variations.

1. Introduction

In recent years ionic liquids (ILs) have gathered special attention from the scientific community and an exponential increase of studies involving different features, properties and applications of ILs have been presented in literature. Their particular physicochemical characteristics such as high solvation ability and coordination properties, non flammability, wide liquidus range, wide electrochemical window, high thermal stability and negligible vapor pressures make of them suitable candidates for a large range of applications (Earle et al., 2006). Moreover, the possibility of controlling their polar/apolar characteristics by correctly choosing the cation and/or the anion allows them to present selective solubilities for particular components in fluid mixtures. This characteristic, coupled with their negligible vapor pressures, has transformed ILs into excellent alternatives as potential green solvents with an obviously high industrial interest.

Besides the many possible applications already reported in literature such as solvents for electrochemical applications (Seddon, 1997), recyclable alternatives to aprotic solvents or catalysts for organic or organometallic synthesis and as media for analytical chemistry (Armstrong et al., 1999), ILs are very promising solvents for separation processes where they could serve as media for clean liquid-liquid extraction or absorption processes (Bosmann et al., 2001). Nevertheless, for the extraction of organic products from chemical reactions that proceed in aqueous media and for liquid-liquid extractions from aqueous phases, ionic liquids with lower solubility in water are preferred.

* Corresponding author.Tel +351-234-370200. E-mail: jcoutinho@ua.pt

While ILs cannot contribute to air pollution due to their negligible vapour pressures, they may have in fact a significant solubility in water (even the ones known as “hydrophobics”) and, as a result, this is the most likely medium through which ILs will enter and pollute the environment (Freire et al., 2007a and Freire et al., 2008a). In addition, their release to aquatic environments could cause water contamination because of their potential toxicity and limited biodegrability. The ILs toxicity is directly related and mainly controlled by their lipophilicity (Ranke et al., 2006). This kind of studies have demonstrated that the ILs toxicity is primordially determined by the cation nature and it is essentially driven by the cation alkyl side chain length (Ranke et al., 2006). Therefore, the ILs bioaccumulation is directly proportional to their hydrophobicity and thus, the knowledge of their water solubility can be a way of predicting the toxicity and bioaccumulation impact of an ionic liquid in the ecosystem.

Some contributions dealing with experimental solubilities between ILs and water have already been reported (Freire et al., 2007c). However, careful and methodical studies of the cation and anion influence in a common series and in a wide range of temperature, which thus allow the calculation of derived properties, are still scarce.

Traditional approaches to predict fluid properties or phase equilibria require an extense data bank of vapor-liquid (VLE) and liquid-liquid equilibrium (LLE) experimental measurements. COSMO-RS (Klamt and Eckert, 2000) is a predictive method based on unimolecular quantum chemical calculations of the individual molecules, which has already proved to be a promising approach to model phase equilibria for ionic liquids (Freire et al., 2007d and Freire et al., 2008b). The performance of this predictive method is here analyzed in the prediction of the water-IL binary systems which have also been experimentally measured.

2. Materials and Methods

The ILs 1-alkyl-3-methylimidazolium bis(trifluoromethylsulfonyl)imide (with the alkyl group ranging from methyl to octyl), $[C_n mim][Tf_2N]$, 1-butyl-3-methylimidazolium hexafluorophosphate, $[C_4 mim][PF_6]$, 3-methyl-1-propylpyridinium bis(trifluoromethylsulfonyl)imide, $[C_3 mpy][Tf_2N]$ and 1-methyl-1-propylpyrrolidinium bis(trifluoromethylsulfonyl)imide, $[C_3 mpyr][Tf_2N]$, were acquired at IoLiTec with purity levels > 99 % for all samples. In order to improve the ILs purity level and reduce the water content and volatile compounds to negligible values, the ILs individual samples were dried under constant agitation at vacuum and moderate temperature for a minimum of 48 h. The water used for equilibration was ultra-pure water, double distilled, passed by a reverse osmosis system and further treated with a Milli-Q plus 185 water purification apparatus.

The mutual solubilities measurements were performed at temperatures from (288.15 to 318.15) K and at atmospheric pressure. The two phases were vigorously agitated and allowed to reach equilibrium for a minimum of 48 h. The vials were thermostated on an aluminum block, immersed in an isolated air bath, and capable of maintaining the temperature within ± 0.01 K by means of a PID temperature controller driven by a calibrated Pt100 (class 1/10) temperature sensor inserted into the aluminum block. In order to achieve temperatures below the room temperature, a Julabo circulator, model F25-HD, is coupled to the overall oven system allowing the passage of a thermostatized fluid flux around the aluminum block.

The solubility of water in the IL-rich phase was determined with a Metrohm 831 Karl-Fischer (KF) coulometer. IL-rich phase samples of ≈ (0.1 to 0.2) g were taken from the equilibrium vials using a glass syringe maintained in dry and warm conditions. The solubility of ILs in the water-rich phase was determined by UV-spectroscopy using a SHIMADZU UV-1700, Pharma-Spec Spectrometer. Samples of ≈ (0.3 to 1.0) g were taken from the water-rich phase by means of a glass syringe and diluted by a factor ranging from (1:50 to 1:1000) (v:v) in pure water, depending on the IL solubility under study, and in order to read values of

absorbance in an adequate range. The solubility results at each temperature were determined as the average of at least five independent measurements.

3. Results and Discussion

Figure 1 presents both the experimental and COSMO-RS predictions of the liquid-liquid phase diagram between the [C_2-C_8mim][Tf2N] ILs series and water.

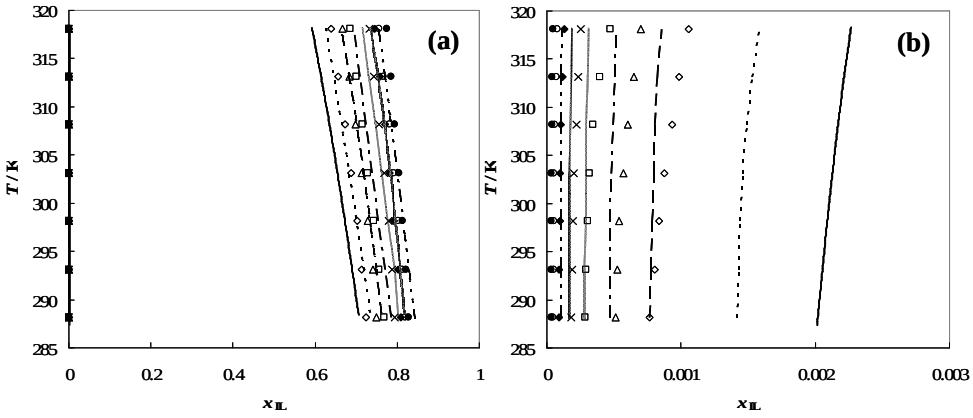

Figure 1. Complete liquid-liquid phase diagram for water and ILs (a) and water-rich phase side (b): (◊) (————) [C_2mim][Tf_2N]; (□) (- - - - - - -) [C_3mim][Tf_2N]; (□) (—— ——) [C_4mim][Tf_2N]; (×) (— - —) [C_5mim][Tf_2N]; (♦) (▪▪▪▪▪▪▪▪▪▪▪▪) [C_6mim][Tf_2N]; (○) (▪▪▪▪▪▪▪▪▪▪▪▪) [C_7mim][Tf_2N]; (●) (— - - —) [C_8mim][Tf_2N]. The single symbols and the lines represent respectively the experimental data and the COSMO-RS predictions.

It should be noted, for instance, the asymmetrical behavior of these binary systems (involving ILs and usual molecular solvents) when adopting the mole fraction basis. Experimentally, there is an increase in the IL hydrophobic nature with the alkyl chain length increase (decreasing therefore the mutual solubilities values). The results obtained from COSMO-RS calculations show an acceptable agreement with the experimental data and follow the same hydrophobic tendency, depicting the good qualitative prediction capability of this model when dealing with the alkyl chain length impact in these mutual solubilities. Nevertheless, higher relative deviations were observed at the water-rich phase, probably due to the low solubility of the studied ILs in water.

Figure 2 depicts the experimental results obtained and the COSMO-RS prediction values for the cation family impact in the mutual solubilities with water maintaining the [Tf_2N] anion in common for imidazolium, pyridinium and pyrrolidinium-based ILs.

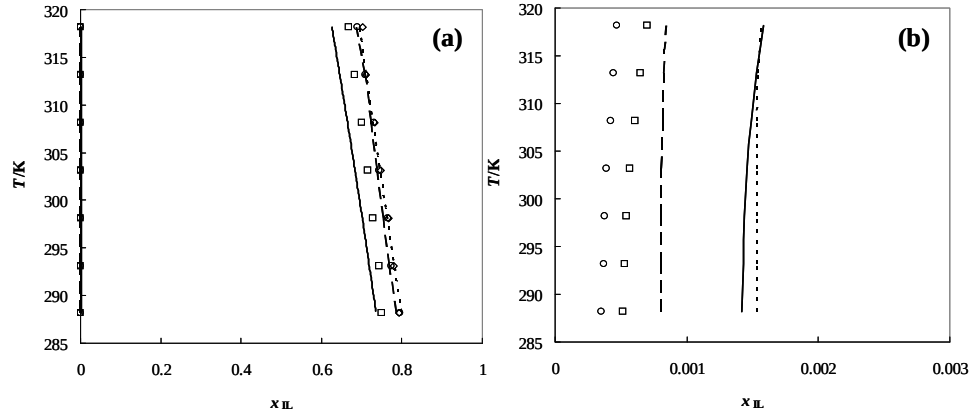

Figure 2. Complete liquid-liquid phase diagram for water and ILs (a) and water-rich phase side (b): (□) (————) [C_3mim][Tf_2N]; (○) (—— ——) [C_3py][Tf_2N]; (◊) (- - - - - - -) [C_3pyr][Tf_2N]. The single symbols and the lines represent respectively the experimental data and the COSMO-RS predictions.

The hydrophobic tendency increase derived from the cation class family follows the order: [C_3mim] < [C_3mpy] < [C_3mpyr]. The overall trend is shown to be well predicted by COSMO-RS. Besides the qualitative description, the predictions also provide a good quantitative description of the experimental data. For the water-rich phase the predictive hydrophobic tendency is also well described.

Figure 3 shows the comparison between the experimental data and COSMO-RS predictions for the liquid-liquid phase behaviour of the [C_4mim] cation in combination with the anions [PF_6] and [Tf_2N].

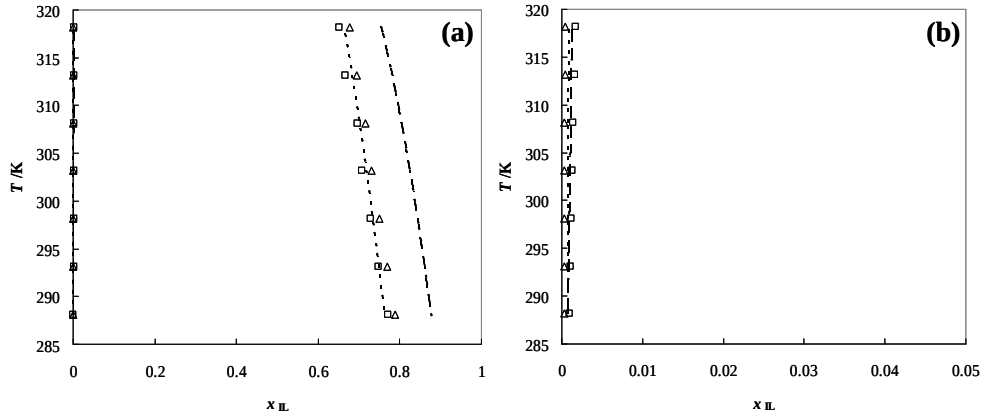

Figure 3. Complete liquid-liquid phase diagram for water and ILs (a) and water-rich phase side (b): (□) (—— ——) [C_4mim][PF_6]; (Δ) (- - - - - - -) [C_4mim][Tf_2N]. The single symbols and the lines represent respectively the experimental data and the COSMO-RS predictions.

The solubility of ILs and water decreases from the [PF_6] to the [Tf_2N] anion. At the water-rich phase, COSMO-RS proved to predict the increase in the IL hydrophobicity nature due to the anion identity following the experimental mutual solubilities results. However, in the IL-rich phase the hydrophobic tendency between [PF_6] and [Tf_2N] is not well described when compared to the experimental data. COSMO-RS predicts a higher solubility of water in [C_4mim][Tf_2N] than in [C_4mim][PF_6]. Clearly the phase behavior is the result of several competing interactions in the solution and all types of interactions should be considered.

4. Conclusions

Experimental data for mutual solubilities between water and hydrophobic imidazolium, pyridinium and pyrrolidinium-based cations in combination with bis(trifluoromethylsulfonyl)imide and hexafluorophosphate anions in the temperature range between (288.15 and 318.15) K and at atmospheric pressure were presented. The hydrophobic tendency of the cation family increases from imidazolium to pyridinium to pyrrolidinium-based ILs and with the alkyl chain length increase within the same cation family. On the other hand, the anion hydrophobic tendency increases from hexafluorophosphate to bis(trifluoromethylsulfonyl)imide-based anions ILs. In addition, the results depicting the ILs amphiphilic character can be used to fine tune the ILs mutual solubilities with water and to manage their ecotoxicity impact. COSMO-RS showed to be an *a priori* method of selection for the IL-water binary systems phase behavior qualitative prediction, which may be of considerable value for the design of suitable ILs for practical applications and with expected mutual solubilities.

References

Armstrong, D.W.; He, L. and Liu, Y.S. (1999). Examination of Ionic Liquids and Their Interactions with Molecules, When Used as Stationary Phases in Gas Chromatography. *Anal. Chem.*, 71, 3873-3876.

Bosmann, A.; Datsevich, L.; Jess, A.; Lauter, A.; Schmitz, C. and Wasserchеid, P. (2001). Deep Desulfurization of Diesel Fuel by Extraction with Ionic Liquids. *Chem. Commun.,* 2494-2494.

Earle, M.J.; Esperança, J.M.S.S.; Gilea, M.A.; Lopes, J.N.C.; Rebelo, L.P.N.; Magee, J.W.; Seddon, K.R. and Widegren, J.A.P. (2006).The Distillation and Volatility of Ionic Liquids. *Nature*, 439, 831-834.

Freire, M.G., Neves, C., Carvalho, P.J., Gardas, R.L., Fernandes, A.M., Marrucho, I.M., Santos, L. and Coutinho, J.A.P. (2007a). Mutual Solubilities of water and hydrophobic ionic liquids. *J. Phys. Chem. B*, 111, 13082-13089.

Freire, M.G.; Carvalho, P.J.; Fernandes, A.M.; Marrucho, I.M.; Queimada, A.J. and Coutinho, J.A.P. (2007b). Surface Tensions of Imidazolium Based Ionic Liquids: Anion, Cation, Temperature and Water Effect. *J. Colloid Interface Sci.*, 314, 621-630.

Freire, M.G., Santos, L.M:N.B.F.; Fernandes, A.M.; Coutinho, J.A.P. and Marrucho, I.M. (2007c) An Overview of the Mutual Solubilities of Water-Imidazolium-Based Ionic Liquids Systems. *Fluid Phase Equilib.*, 261, 449-454.

Freire, M.G., Santos, L.M:N.B.F.; Marrucho, I.M. and Coutinho, J.A.P. (2007d). Evaluation of COSMO-RS for the Prediction of LLE and VLE of Alcohols + Ionic Liquids. *Fluid Phase Equilib.*, 255, 167-178.

Freire, M.G., Carvalho, P.J., Gardas, R.L., Marrucho, I.M., Santos, L.M.N.B.F. and Coutinho, J.A.P. (2008a). Mutual Solubilities of Water and the $[C_n mim][Tf_2N]$ Hydrophobic Ionic Liquids. *J. Phys. Chem. B*, 112, 1604-1610.

Freire, M.G., Ventura, S.P.M., Santos, L.M:N.B.F.; Marrucho, I.M. and Coutinho, J.A.P. (2008b). Evaluation of COSMO-RS for the prediction of LLE and VLE of water and ionic liquids binary systems. *Fluid Phase Equilib.*, 268, 74-84.

Klamt, A.and Eckert, F. (2000). COSMO-RS: a Novel and Efficient Method for the a priori Prediction of Thermophysical Data of Liquids. *Fluid Phase Equilib.*, 172, 43-72.

Ranke, J., Müller, A., Bottin-Weber, U., Stock, F., Stolte, S., Arning, J., Störmann, R. and Jastorff, B. (2007). Lipophilicity Parameters for Ionic Liquid Cations and their Correlation to in Vitro Cytotoxicity. *Ecotoxicol. Environ. Saf.*, 67, 430-438.

Seddon, K.R. (1997). Ionic Liquids for Clean Technology. *J. Chem. Technol. Biotechnol.,* 68, 351-356.

Proceedings of the 10th International Chemical and
Biological Engineering Conference - CHEMPOR 2008
Braga, Portugal, September 4-6, 2008
E.C. Ferreira and M. Mota (Eds.)

Carbon Dioxide Solubilities in $[C_nmim][Tf_2N]$ Ionic Liquids at High-pressure

Pedro J. Carvalho[1], José J. B. Machado[1], Jérôme Pauly[2], Jean-Luc Daridon[2], Isabel M. Marrucho[1], João A. P. Coutinho[1]

[1]CICECO, Dep. de Química, Universidade de Aveiro, 3810-193 Aveiro, Portugal
[2]Laboratoire des Fluides Complexes, UMR 5150, BP 1155, 64013 Pau Cedex, France

Keywords: Solubilities, High pressure, Ionic liquids, Carbon dioxide

Introduction

Recently, a class of *neoteric* solvents composed of large organic cations and organic or inorganic anions, that cannot form an ordered crystal and thus remain liquid at or near room temperature, have become one of the fastest growing "green" media for chemists and engineers. Ionic liquids (ILs) outstanding tunable properties through the combination of cations and anions, place them on a green and sustainable level where more efficient and renewable processes and products can be developed by minimizing wastes and avoiding the use of toxic and/or hazard solvents and reagents. Among the several applications foreseeable for ionic liquids such as solvents in organic synthesis [1, 2], homogeneous and biphasic transfer catalysts [3-5], separation processes [6-9] their use in processes with supercritical gases is one of the most exciting.

Several authors [9-12] described potential applications for ILs systems + supercritical fluids, demonstrating the possibility of solute extraction from an IL without any contamination of the extracted solute and solving one of the shortcoming of the use of ILs in solvent extraction processes: the recovery of the compounds from the IL media, by phase separation induction.

Muldoon et al. [13] and Lopez-Castillo [14] reported that the solubility of gases, that typically present low solubilities, could be enhanced by the presence of CO_2, even at low partial pressures. Solinas et al. [15] reported that inducing CO_2 pressure improves the activation, tuning, and immobilization of chiral iridium catalysts in IL/CO_2 for the enantioselective hydrogenation reaction of imines. High-pressure NMR showed that the CO_2 presence increases the amount of H_2 dissolved in the IL, lowering the system viscosity, and thus allows the catalyst, known to be sensitive to the H_2 availability, to operate more effectively [15].

Task-specific ILs are also becoming usual, Bates et al. [6] reported amine functionalized ILs while Yuan et al. [16] and Sun et al. [17] presented hydroxyl-functionalized ILs as novel efficient catalyst for chemical fixation of CO_2. Yu et al [18] and Huang et al. [19] presented guanidinium based ILs, where the electron-donating groups attaching to -NH_2 coupled with the intramolecular hydrogen bonds and associated with H atom on -NH_2 raises the strength of the donor-acceptor interactions energy on -NH_2 and consequently enhance the interactions between -NH_2 and CO_2.

However, the successful development of separation methods based on supercritical fluids depends on the adequate knowledge of the phase behavior of the systems. Several authors, such as Brennecke [11, 20, 21], Peters [22-24] Noble [25], Lim [26], Baltus [27], Outcalt [28], Yokozeki [29] and Majer [30] have been reporting supercritical carbon dioxide solubility in common ILs, but few have focused their studies on the Tf_2N anion based ionic liquids [22, 24-28].

In this work, a new apparatus was developed to investigate the high pressure phase

behavior of gas + ionic liquid systems. Two ionic liquids based on the Tf_2N anion were selected for this study to try to contribute for a better understanding of the solubility of supercritical CO_2 on these fluids. The system of CO_2 + 1-ethyl-3-methyl-imidazolium bis(trifluoromethylsulfonyl)imide ([C_2mim][Tf_2N]) was chosen because it allows the evaluation of the quality of the measurements by comparison with literature data [24] and the CO_2 + 1-methyl-3-pentyl-imidazolium bis(trifluoromethylsulfonyl)imide ([C_5mim][Tf_2N]) system was studied to investigate the effect of the alkyl chain length on the CO_2 solubility in ionic liquids. Both systems were measured in temperatures up to 363 K and pressures of 50 MPa.

Experimental Section

Materials: Two imidazolium based ILs, 1-ethyl-3-methyl-imidazolium bis(trifluoromethylsulfonyl)imide, [C_2mim][Tf_2N] and 3-methyl-1-pentyl-imidazolium bis(trifluoromethylsulfonyl)imide, [C_5mim][Tf_2N], were used on this study. All compounds were acquired at IoLiTec with mass fraction purities > 99 % and bromide impurity mass fraction < 10^{-4}. The purities stated by the supplier, of each ionic liquid, were checked by ^{1}H NMR, ^{13}C NMR and ^{19}F NMR.

It is well established that IL physical properties are influenced by their water content [31-34]. To reduce to negligible values both water and volatile compounds, vacuum (0.1 Pa), stirring and moderate temperature (353 K), for a period of at least 48 hours, were applied prior to the measurements. The final IL water content was determined with a Metrohm 831 Karl Fischer coulometer, indicating a water mass fraction of (42 and 20)•10^{-6} for [C_2mim][Tf_2N] and [C_5mim][Tf_2N] respectively.

The CO_2 used was from Air Liquide with a purity of ≥ 99.998 % and H_2O, O_2, C_nH_m, N_2 and H_2 impurities volume fractions lower than (3, 2, 2, 8 and 0.5)•10^{-6}, respectively.

Experimental measurements: The high pressure equilibrium cell developed on this work is based on the synthetic method and is sketched in Figure 1. The cell, based on the design of Daridon et al. [35-39], consists of a horizontal hollow stainless-steel cylinder, closed at one end by a movable piston and at the other end by a sapphire window. This window, along with a second window on the cell wall through which an optical fiber lights the cell chamber, allow the operator to follow the behavior of the sample with pressure and temperature. The orthogonal positioning of the sapphire windows minimizes the parasitic reflections and improves the observation in comparison to axial lighting.

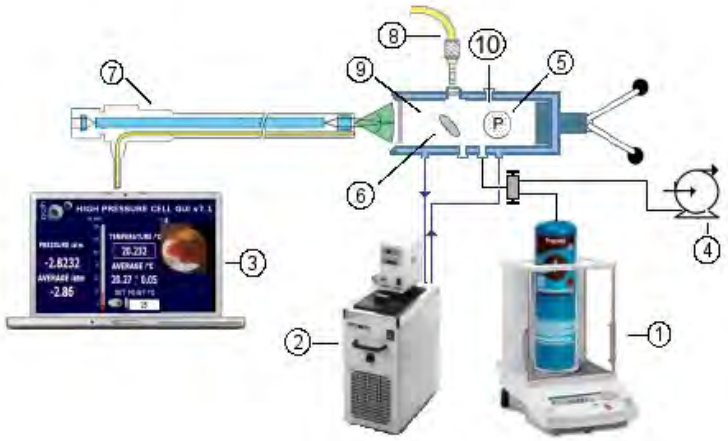

Figure. 1. Schematic apparatus: 1 – Analytical balance; 2 – Thermostatized bath circulator; 3 – Computer to data and video acquisition; 4 – Vacuum pump; 5 – Piezoresistive pressure transducer; 6 – Magnetic bar; 7 – Endoscope plus a video camera; 8 – Light source with optical fiber cable; 9 – High-pressure variable-volume cell; 10 – Temperature probe.

A small magnetic bar placed inside the cell allows the homogenization of the mixture by means of an external magnetic stirrer. The presence of the magnetic stirrer as well and the sapphire window on the cell wall limit the minimum internal volume of the cell to 8 cm^3, while the maximum value is set to 30 cm^3. The cell reduced volume helps to minimize the inertia and temperature gradients within the sample.

The cell is thermostatized by circulating a heat-carrier fluid through three flow lines directly managed into the cell. The heat-carrier fluid is thermo-regulated with a temperature stability of ±0.01 K by means of a thermostat bath circulator (Julabo MC). The temperature is measured with a high precision thermometer, Model PN 5207 with an accuracy of 0.01 K connected to a calibrated platinum resistance inserted inside the cell close to the sample. The pressure is measured by a piezoresistive silicon pressure transducer (Kulite) fixed directly inside the cell to reduce dead volumes, that was previously calibrated and certified by an independent laboratory with IPAC accreditation, following the EN 837-1 standard and with accuracy better than 0.2%. The accuracy of the transducer in the experimental range studied is 0.2 MPa.

Due to the high viscosities of the ionic liquids, a fixed amount of ILs was introduced directly inside the cell. The exact mass of the samples was determined by weighting, using a high weight/high precision balance with an accuracy of 1 mg (Sartorius). In order to avoid any interference of atmospheric gases during the manipulation, after placing the IL inside the cell this was kept under vacuum overnight, while stirring and heating at 353 K.

The CO_2 was introduced under pressure from an aluminum reservoir tank. Its quantity was measured on the precision balance and introduced into the measuring cell by means of a flexible high pressure capillary.

After preparation of a mixture of known composition, this was allowed to reach the desired temperature at low pressure; the pressure was then slowly increased at constant temperature until the system becomes monophasic. The pressure at which the last bubble disappears represents the equilibrium pressure for the fixed temperature.

The purity of the IL is checked again by NMR at the end of the study to confirm that no degradation of the IL takes place during the measurements.

Results and Discussion

Although measurements were previously carried by us and other in similar apparatuses [35-39], to validate the methodology and experimental procedure adopted in this work, [C_2mim][Tf_2N] was selected and compared against data from Schilderman et al. [24]. High pressure binary vapor-liquid mixtures data, of CO_2 in ILs, are scarce and significant discrepancies among data from different authors [24, 26, 28] are common in literature, since previous authors where not aware to the influence of water as well as other impurities or even degradation products on ILs physical properties and phase equilibria. The identification of the data with the highest quality available in the literature was carried using a thermodynamic consistency test. Valderrama and Àlvarez [40], proposed a thermodynamic consistency test for systems with incomplete *PTxy* data and based on the Gibbs-Duhem equation that was recently extended by Àlvarez and Aznar [41] to systems of supercritical fluid + IL systems. Their work allows the identification of the more reliable phase equilibrium data for supercritical fluids in ionic liquids. The most reliable data identified y Àlvarez and Aznar [41] was the Schilderman et al. [24] data for the system CO_2 + [C_2mim][Tf_2N], where the isotherms at 313 K, 323 K e 363 K were found thermodynamically consistent. For this reason this system was here chosen to validate the measurements on the new high pressure cell developed on this work. A comparison of the data here measured with the data by Schilderman et al. [24] is presented in Figure 2 showing very good agreement.

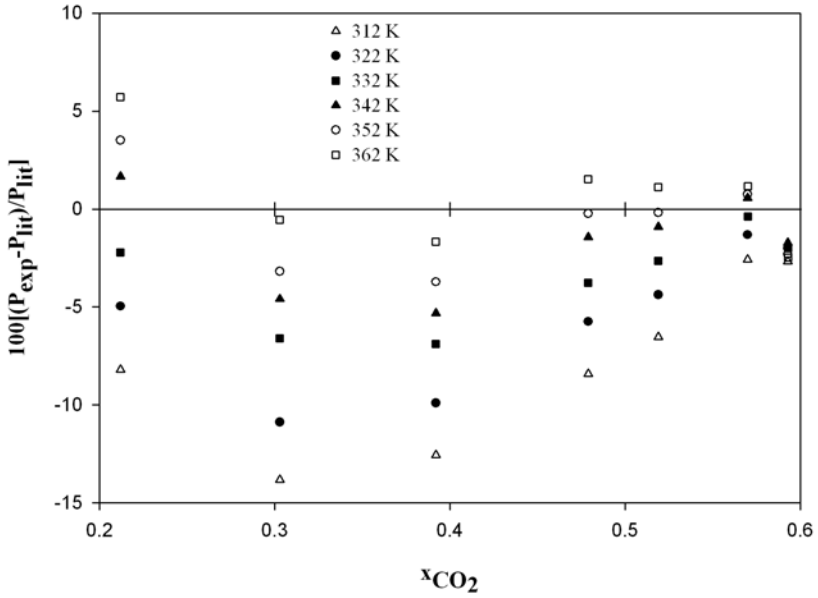

Figure 2. Percent average deviations between the experimental data of this work and those reported by Schilderman et al. [24] for the system CO_2/[C_2mim][Tf_2N].

The solubility of carbon dioxide in the ILs studied was measured for mole fractions from (0.2 to 0.8), in the temperature range (293 to 363) K and pressures from (0.6 to 50) MPa, are depicted in Figures 3 a and 3b.

The temperature increase leads to an increase on the equilibrium pressure and by increasing CO_2 concentration, the equilibrium pressures increase gradually, at first, and rapidly for higher CO_2 contents.

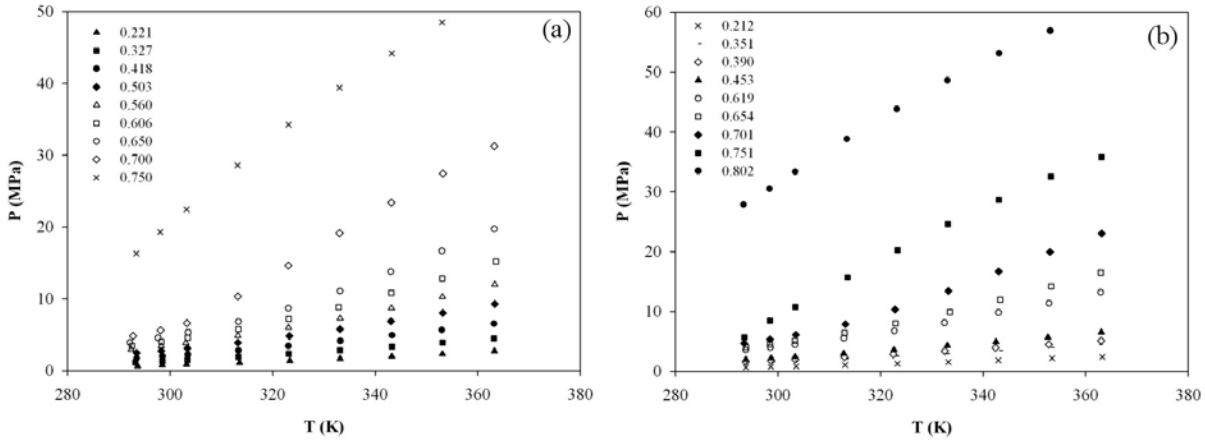

Figure 3. Pressure – temperature diagram of the binary systems (a) CO_2 + [C_5mim][Tf_2N] and (b) CO_2 + [C_2mim][Tf_2N].

It is well established that Tf_2N anion based ILs, due to the presence of fluoroalkyl groups which are known to be "*CO_2-philic*", present higher CO_2 solubilities than other common ILs. In fact, results show that Tf_2N anion based ILs exhibit considerable low equilibrium pressures for higher mole fractions, as can be seen in Figure 3. This behavior, yet poorly understood, is related to the interaction between the negative fluorine atoms and the positive charge on the carbon of the CO_2 molecule [20, 21].

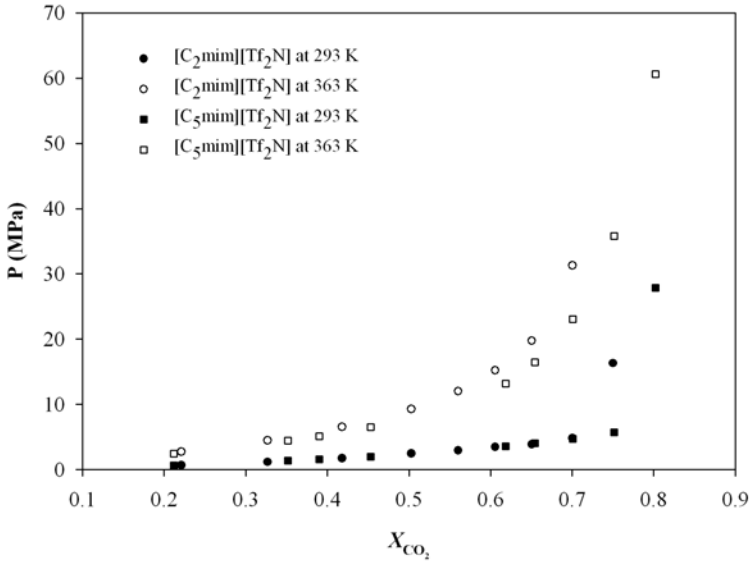

Figure 4. Pressure – composition diagram of CO_2 in [C$_n$mim][Tf_2N].

It is well established that the substituents on the imidazolium ring can affect the ILs properties [22, 23, 31, 34, 42-45]. For CO_2 solubility an slight increase can be seen with the alkyl chain length increase, for all pressures [11, 20, 22, 24]. Nonetheless, Tf_2N anion based ILs present lower alkyl chain length influence on the solubility than other ILs, even for higher CO_2 concentrations, as can be seen in Figure 4 [20, 24]. Kazarian et al. [46], using ATR–IR spectroscopy, reported that the solubility is not related to any specific interactions between the CO_2 and the cation, furthermore, the high solubility of CO_2 in ILs is not either related to the interaction with the most acidic hydrogen on the C_2 position of the imidazolium ring or with the nitrogens in the imidazolium or pyridinium rings [46, 47]. Shariati et al. [22] and Aki et al. [20] explained this entropic rather enthalpic behavior due to the decrease of the compounds densities, with the increase of the alkyl chain length, and by its turn, to a greater free volume in the ILs.

Conclusions

A new high pressure cell to measure supercritical fluid + liquid phase behaviour was developed and tested. The 1-ethyl-3-methyl-imidazolium bis(trifluoromethylsulfonyl)imide was choosed to validate both the apparatus because high quality data for this systems by Schilderman et al. [24] Was available. It is shown that the data measured is in good agreement with the data by these authors.

New experimental data are reported for CO_2 solubility in 3-methyl-1-pentyl-imidazolium bis(trifluoromethylsulfonyl)imide in a wide range of temperature, pressure and carbon dioxide mole fractions.

As commonly observed, the increase of the temperature leads to a decrease on the solubility, while the opposite behavior can be observed by increasing the pressure. As the CO_2 mole fraction increases, the equilibrium pressure starts to increase gradually, for low concentrations, and ends increasing rapidly for higher CO_2 contents. While CO_2 solubility increases marginally when increasing the alkyl chain length, on the imidazolium ring, the Tf_2N anion based ILs present a lower influence than other common ILs, even for higher CO_2 concentrations. This behavior can be explained by the fact that the pentyl group impose a bulkier behavior, in the [C_5mim][Tf_2N], than the ethyl group in the [C_2mim][Tf_2N]. Nonetheless, since the density decreases with the alkyl chain length increase, leading to a greater free volume in the ILs, an increase of the solubility with the alkyl chain length increase is expected and can be understood as a entropic behavior.

Aknowledgments

The authors are thankful for financial support from Fundação para a Ciência e a Tecnologia (Project POCI/EQU/58152/2004) and Ph.D. grant (SFRH/BD/41562/2007) of Pedro J. Carvalho

Literature Cited

[1] J.A. Boon, J.A. Levisky, J.L. Pflug, J.S. Wilkes, Friedel-Crafts reactions in ambient-temperature molten salts, The Journal of Organic Chemistry 51 (1986) 480-483.
[2] S.E. Fry, N.J. Pienta, Effects of molten salts on reactions. Nucleophilic aromatic substitution by halide ions in molten dodecyltributylphosphonium salts, Journal of the American Chemical Society 107 (1985) 6399-6400.
[3] H. Zhao, Innovative Applications of Ionic Liquids as Green Engineering Liquids, Chem. Eng. Comm. 193 (2006) 1660-1677.
[4] R. Sheldon, Catalytic reactions in ionic liquids, Chem. Commun. (2001) 2399-2407.
[5] H. Wong, S. Han, A.G. Livingston, The effect of ionic liquids on product yield and catalyst stability, Chemical Engineering Science 61 (2006) 1338-1341.
[6] E. Bates, R. Mayton, I. Ntai, J. Davis, CO2 Capture by a Task-Specific Ionic Liquid, JACS 124 (2002) 926-927.
[7] J.L. Anthony, E.J. Maginn, J.F. Brennecke, Solution thermodynamics of imidazolium-based ionic liquids and water, J. Phys. Chem. B 105 (2001) 10942-10949.
[8] J.G. Huddleston, H.D. Willauer, R.P. Swatloski, A.E. Visser, R.D. Rogers, Room temperature ionic liquids as novel media for clean liquid-liquid extraction, Chem. Commun. 16 (1998) 1765-1766.
[9] L. Blanchard, J. Brennecke, Recovery of Organic Products from Ionic Liquids Using Supercritical Carbon Dioxide, Ind. Eng. Chem. Res. 40 (2001) 287-292.
[10] L.A. Blanchard, D. Hancu, E.J. Beckman, J.F. Brennecke, Green processing using ionic liquids and CO2, Nature 399 (1999) 28-29.
[11] L. Blanchard, Z. Gu, J. Brennecke, High-Pressure Phase Behavior of Ionic Liquid/CO2 Systems, J. Phys. Chem. B 105 (2001) 2437-2444.
[12] A. Scurto, S. Aki, J. Brennecke, CO2 as a Separation Switch for Ionic Liquid/Organic Mixtures, Journal of the American Chemical Society 124 (2002) 10276-10277.
[13] M. Muldoon, S. Aki, J. Anderson, J. Dixon, J. Brennecke, Improving Carbon Dioxide Solubility in Ionic Liquids, Journal of Physical Chemistry B 111 (2007) 9001-9009.
[14] Z. Lopez-Castillo, S. Aki, M. Stadtherr, J. Brennecke, Enhanced Solubility of Hydrogen in CO2-Expanded Liquids, Ind. Eng. Chem. Res. 47 (2008) 570-576.
[15] M. Solinas, A. Pfaltz, P. Cozzi, W. Leitner, Enantioselective Hydrogenation of Imines in Ionic Liquid/Carbon Dioxide Media, Journal of the American Chemical Society 126 (2004) 16142-16147.
[16] X. Yuan, S. Zhang, J. Liu, X. Lu, Solubilities of CO2 in hydroxyl ammonium ionic liquids at elevated pressures, Fluid Phase Equilib. 257 (2007) 195-200.
[17] J. Sun, S. Zhang, W. Cheng, J. Ren, Hydroxyl-functionalized ionic liquid: a novel efficient catalyst for chemical fixation of CO2 to cyclic carbonate, Tetrahedron Letters 49 (2008) 3588-3591.
[18] G. Yu, S. Zhang, X. Yao, J. Zhang, K. Dong, W. Dai, R. Mori, Design of Task-Specific Ionic Liquids for Capturing CO2: A Molecular Orbital Study, Industrial & Engineering Chemistry Research 45 (2006) 2875-2880.
[19] J. Huang, A. Riisager, R.W. Berg, R. Fehrmann, Tuning ionic liquids for high gas solubility and reversible gas sorption, Journal of Molecular Catalysis A: Chemical 279 (2008) 170-176.
[20] S.N.V.K. Aki, B.R. Mellein, E.M. Saurer, J.F. Brennecke, High-Pressure Phase Behavior of Carbon Dioxide with Imidazolium-Based Ionic Liquids, J. Phys. Chem. B 108 (2004) 20355-20365.
[21] J.L. Anderson, J.K. Dixon, J.F. Brennecke, Solubility of CO2, CH4, C2H6, C2H4, O2,

and N2 in 1-Hexyl-3-methylpyridinium Bis(trifluoromethylsulfonyl)imide: Comparison to Other Ionic Liquids, Acc. Chem. Res. 40(11) (2007) 1208-1216.
[22] A. Shariati, C.J. Peters, High-pressure phase behavior of systems with ionic liquids: II. The binary system carbon dioxide+1-ethyl-3-methylimidazolium hexafluorophosphate, J. Supercrit. Fluids 29 (2004) 43-48.
[23] A. Shariati, C.J. Peters, High-pressure phase behavior of systems with ionic liquids: Part III. The binary system carbon dioxide + 1-hexyl-3-methylimidazolium hexafluorophosphate, J. Supercrit. Fluids 30 (2004) 139-144.
[24] A.M. Schilderman, S. Raeissi, C.J. Peters, Solubility of Carbon Dioxide in the Ionic Liquid 1-Ethyl-3-Methylimidazolium Bis(trifluoromethylsulfonyl)imide, Fluid Phase Equilib. 260 (2007) 19-22.
[25] A. Finotello, J. Bara, D. Camper, R. Noble, Room-Temperature Ionic Liquids: Temperature Dependence of Gas Solubility Selectivity, Ind. Eng. Chem. Res. 47 (2008) 3453-3459.
[26] E. Shin, B. Lee, J.S. Lim, High-pressure solubilities of carbon dioxide in ionic liquids: 1-alkyl-3-methylimidazolium bis(trifluoromethylsulfonyl)imide, J. Supercrit. Fluids 45 (2008) 282-292.
[27] Y. Hou, R. Baltus, Experimental Measurement of the Solubility and Diffusivity of CO2 in Room-Temperature Ionic Liquids Using a Transient Thin-Liquid-Film Method, Ind. Eng. Chem. Res. 46 (2007) 8166-8175.
[28] B. Lee, S. Outcalt, Solubilities of Gases in the Ionic Liquid 1-n-Butyl-3-methylimidazolium Bis(trifluoromethylsulfonyl)imide, J. Chem. Eng. Data 51 (2006) 892-897.
[29] M. Shiflett, A. Yokozeki, Solubility of CO2 in Room Temperature Ionic Liquid [hmim][Tf2N], J. Phys. Chem. B 111 (2007) 2070-2074.
[30] J. Jacquemin, M.F. Costa Gomes, P. Husson, V. Majer, Solubility of carbon dioxide, ethane, methane, oxygen, nitrogen, hydrogen, argon, and carbon monoxide in 1-butyl-3-methylimidazolium tetrafluoroborate between temperatures 283 K and 343 K and at pressures close to atmospheric, J. Chem. Thermodyn. 38 (2006) 490-502.
[31] M.G. Freire, P.J. Carvalho, A.M. Fernandes, I.M. Marrucho, A.J. Queimada, J.A. Coutinho, Surface Tensions of Imidazolium Based Ionic Liquids: Anion, Cation, Temperature and Water Effect, J. Colloid Interface Sci. 314(2) (2007) 621-630.
[32] K.R. Seddon, A. Stark, M. Torres, Influence of Chloride, Water, and Organic Solvents on the Physical Properties of Ionic Liquids, Pure Appl. Chem. 72 (12) (2000) 2275-2287.
[33] J.G. Huddleston, A.E. Visser, W.M. Reichert, H.D. Willauer, G.A. Broker, R.D. Rogers, Characterization and Comparison of Hydrophilic and Hydrophobic Room Temperature Ionic Liquids Incorporating the Imidazolium Cation, Green Chem. 3 (2001) 156-164.
[34] R.L. Gardas, M.G. Freire, P.J. Carvalho, I.M. Marrucho, I.M.A. Fonseca, A.G.M. Ferreira, J.A.P. Coutinho, High Pressure Densities and Derived Thermodynamic Properties of Imidazolium Based Ionic Liquids, J. Chem. Eng. Data 52(1) (2007) 80-88.
[35] S. Vitu, J.N. Jaubert, J. Pauly, J.L. Daridon, D. Barth, Phase Equilibria Measurements of CO2 + Methyl Cyclopentane and CO2 + Isopropyl Cyclohexane Binary Mixtures at Elevated Pressures, J. Supercrit. Fluids 44 (2008) 155-163.
[36] J. Pauly, J. Coutinho, J.L. Daridon, High Pressure Phase Equilibria in Methane + Waxy Systems: 1. Methane + Heptadecane, Fluid Phase Equilib. 255 (2007) 193-199.
[37] S.P.M. Ventura, J. Pauly, J.L. Daridon, J.A.L. da Silva, I.M. Marrucho, A.M.A. Dias, J.A.P. Coutinho, High Pressure Solubility Data of Carbon Dioxide in Tri-iso-butyl(methyl)phosphonium Tosylate - Water Systems, J. Chem. Thermodyn. In Press, Accepted Manuscript (2008) -.
[38] A.M.A. Dias, H. Carrier, J.L. Daridon, J.C. Pamies, L.F. Vega, J.A.P. Coutinho, I.M. Marrucho, Vapor-Liquid Equilibrium of Carbon Dioxide-Perfluoroalkane Mixtures: Experimental Data and SAFT Modeling, Ind. Eng. Chem. Res. 45 (2006) 2341-2350.
[39] S.P.M. Ventura, J. Pauly, J.L. Daridon, I.M. Marrucho, A.M.A. Dias, J.A.P. Coutinho, High-Pressure Solubility Data of Methane in Aniline and Aqueous Aniline Systems, J. Chem. Eng. Data 52 (2007) 1100-1102.
[40] Valderrama, José O;Àlvarez, Víctor H, A Versatile Thermodynamic Consistency Test for

Incomplete Phase Equilibrium Data of High-pressure Gas-liquid Mixtures, Fluid Phase Equilib. 226 (2004) 149-159.
[41] V.H. Alvarez, M. Aznar, Thermodynamic Modeling of Vapor-liquid Equilibrium of Binary Systems Ionic Liquid + Supercritical {CO2 or CHF3} and Ionic Liquid + Hydrocarbons using Peng-Robinson Equation of State, J. Chin. Inst. Chem. Eng. In Press, Corrected Proof (2008) -.
[42] M.G. Freire, C.M.S.S. Neves, P.J. Carvalho, R.M. Gardas, A.M. Fernandes, I.M. Marrucho, L.M.N.B.F. Santos, J.A.P. Coutinho, Mutual Solubilities of Water and Hydrophobic Ionic Liquids, J. Phys. Chem. B 111(45) (2007) 13082-13089.
[43] M.G. Freire, P.J. Carvalho, R.L. Gardas, I.M. Marrucho, L.M.N.B.F. Santos, J.A.P. Coutinho, Mutual Solubilities of Water and the [Cnmim][Tf2N] Hydrophobic Ionic Liquids, J. Phys. Chem. B 112 (2008) 1604-1610.
[44] R.L. Gardas, M.G. Freire, P.J. Carvalho, I.M. Marrucho, I.M.A. Fonseca, A.G.M. Ferreira, J.A.P. Coutinho, P, r, T Measurements of Imidazolium Based Ionic Liquids, J. Chem. Eng. Data 52 (2007) 1881-1888.
[45] P.J. Carvalho, M.G. Freire, I.M. Marrucho, A.J. Queimada, J.A.P. Coutinho, Surface Tensions for the 1-Alkyl-3-methylimidazolium Bis(trifluoromethylsulfonyl)imide Ionic Liquids, J. Chem. Eng. Data 53 (2008) 1346-1350.
[46] S.G. Kazarian, B.J. Briscoe, T. Welton, Combining ionic liquids and supercritical fluids: in situ ATR-IR study of CO2 dissolved in two ionic liquids at high pressures, Chem. Commun. (2000) 2047-2048.
[47] J. Deschamps, M.F. Costa Gomes, A.A.H. Padua, Molecular Simulation Study of Interactions of Carbon Dioxide and Water with Ionic Liquids, ChemPhysChem 5 (2004) 1049-1052.

Proceedings of the 10th International Chemical and
Biological Engineering Conference - CHEMPOR 2008
Braga, Portugal, September 4-6, 2008
E.C. Ferreira and M. Mota (Eds.)

Physicochemical characterization of surface sized paper surfaces

Isabel M. T. Moutinho*, M. Margarida L. Figueiredo, Paulo J. T. Ferreira
Chemical engineering Department , Coimbra University, Polo II da Universidade de Coimbra, Rua Sílvio Lima, 3030-290 Coimbra, Portugal

Keywords: Contact Angle, PCA, PLS, Printing quality, Profilometry, Surface sizing
Topic: Interfacial & colloidal phenomena and/or Product design & innovation

Abstract

At present, there is an increasing demand concerning the quality of printing and writing paper grades. Printing quality strongly depends on the properties of the fibrous matrix and on the characteristics of the paper surface, which are influenced by the quality of the pulp fibers and by all the operations of the papermaking process, which include the surface treatments, such as calendering and/or coating and surface sizing. Regarding surface sizing, typically only starch is used as sizing agent, but there is an increasing tendency for combining this compound with synthetic polymers.

The present study aims at correlating the surface properties and the printing quality of printing and writing papers, prepared with different surface sizing formulations. The samples were characterized by using profilometry and contact angle measurements. A mask was printed onto the paper samples, by inkjet printing, and optical densities, Gamut areas and line quality were computed. The results were analyzed using Principal Component Analysis (PCA) and Partial Least Squares (PLS).

1 Introduction

The increasing demand from costumers and the competition from other information media challenge the papermaking industry to increase its know-how and improve the quality of all paper grades. The printing and writing papers performance depends on the properties of the fibrous matrix and on the characteristics of the paper surface, which are influenced by the quality of the pulp fibers, the refining process, the chemicals added in the preparation of the furnish, the operations at the paper machine and the modifications of the paper surface (Koskela, 2003; Carceller, 2004). Surface modifications include calendering and/or chemical treatments such as coating and surface sizing (Koskela, 2003). Today, chemical modifications of paper surface for improving printing quality is a common practice in papermaking and, as a consequence, there is a large increase in the production of new chemicals that meet specific end-use paper requirements.

For surface sizing, cationic starch alone or mixed with a synthetic polymer are used to control the hydrophilic character of paper surface, preventing excessive absorption of liquids and inks. A thin film is formed at paper surface, reducing the number and size of pores as well as paper roughness, and modifying paper surface energy, so that not only liquid penetration but also liquid spreading is attenuated (Koskela, 2003).

For selecting the most appropriate surface sizing agent for a specific paper grade it is essential to evaluate surface energy, porosity and roughness, which largely influence ink spreading, penetration and drying. Furthermore, it is also crucial to study the effect of surface sizing on printing quality. Optical density, raggedness, sharpness, mottling, bleeding, line and dot quality and Gamut area are some of the relevant properties that should be taken into account when printing processes are involved (Koskela, 2003).

* Corresponding author. Tel + 351-239 798 700. E-mail:isamim@gmail.com

This study aims at correlating the surface properties and the printing quality of UWF (Uncoated Wood Free) printing and writing papers, prepared with different surface sizing formulations. For that, and considering the large quantity of samples and the resulting large amount of data, PCA (Principal Components Analysis) and PLS (Partial Least Squares) were used.

2 Materials and Methods

A calendered uncoated base paper produced with an Eucalyptus globulus Kraft pulp was surface sized using a series of distinct surface sizing formulations. These formulations were produced by the combination of cationic starch with different synthetic polymers. A sample surface sized with cationic starch alone was produced has reference (Table 1).

The polymers were selected considering the current trends in the papermaking industry. So, mostly commercial products were selected. As for the cationic starch, it was collected immediately before the size press of a paper machine, in order to be as close as possible to the industrial practice. All the additives introduced before the size press are presented in the starch suspension.

Table 1 - Polymers used in the production of the surface sizing formulations.

Compound	Ref.	Compound	Ref.
Cationic starch collected at the paper	St	Methylated Melamine	S6
Co-styrene-acrylate	S1	Co-styrene-dimethylaminopropylamine	S7
Co-styrene-maleic anhydride	S2	Co-styrene-butyl acrylate	S8
Co-acrylonitrile-acrylate	S3	Co-styrene-acrylate	S9
Co-styrene-maleic anhydride	S4	Co-styrene-acrylate	S10
Quaternary ditallow methyl epoxypropyl	S5		

The surface sizing formulations were prepared with a synthetic sizing agent content of 5, 10 or 20% (w/w) and, accordingly, a starch content of 95, 90 and 80% (w/w) (Table 2). Then they were applied on the surface of the base paper using a Mathis laboratory device, SVA-IR-B. A 0.15 mm roll was used and its velocity adjusted to 6m/min. The drying process was performed with an IR drier followed by air drying. The total surface sizing pick-up was 3.5 ± 0.3 g/m^2. The surface sized samples were no further calendered.

The physical characterization of the samples surface was performed by optical profilometry using the AltiMet perfilometer Altisurf 500 and the PaperMap software. For each sample, pieces of 4x4 mm^2 were scanned with a scanning resolution of 2 μm. From the 2000 profiles obtained for each piece, several relevant surface texture parameters were computed (Cohen, n.d.; Stout, 1994): average roughness (Sa, μm); root mean square roughness (Sq, μm); maximum peak height (Sp, μm); maximum valley depth (Sv, μm); total height of the surface (St, μm); skewness of the 3D surface texture (Ssk); root-mean-square slope of the surface (Sdq); texture aspect ratio of the surface (Str); arithmetic mean summit curvature of the surface (Ssc) and developed interfacial ratio (Sdr, %).

For the evaluation of the surface energetics of the paper samples, contact angle measurements were performed with the DataPhysics equipment OCA20, using the sessile drop method (Brigs, 1989). The initial contact angle using water was measured to evaluate the ability of the paper surface to interact with the water based inks. The total, as well as the dispersive and polar components of the solid surface energy were determined by measuring on the same sample the initial contact angle with other different liquids whose surface tension components are known (Diodomethane, Ethileneglycol, Formamide, and Propileneglycol). For that, the WORK method was applied. The theory behind this method and the surface tension values of the liquid probes used are presented elsewhere (Brigs, 1989). For each paper sample, pieces from at least three different sheets were used and for each liquid probe a minimum of 10 drops were measured.

Inkjet printing quality was evaluated by measuring the optical density (OD), Gamut area and some line quality parameters in a specified mask printed on the paper samples. The OD and the Gamut area, defined elsewhere (Moutinho, 2007) were chosen since they correlate well with the end users perception. The former was determined in a gretag 19C spectrophotometer. The CIE lab color coordinates necessary to compute the Gamut area were obtained by using the AvaMouse spectrophotometer (Avantes). The line quality parameters, image area, borderlenght and roughness, which are commonly used in many paper mills, were determined using the image analysis system PIA BASF – 8042319.

Table 2 - Sample description.

Sample	Surface Sizing Formulation (% w/w)	Sample	Surface Sizing Formulation (% w/w)	Sample	Surface Sizing Formulation (% w/w)
St	100% Cationic Starch	St**S4**-*05*	95% Cationic Starch 5% S4	St**S7**-*10*	90% Cationic Starch 10% S7
St**S1**-*05*	95% Cationic Starch 5% S1	St**S4**-*10*	90% Cationic Starch 10% S4	St**S7**-*20*	80% Cationic Starch 20% S7
St**S1**-*10*	90% Cationic Starch 10% S1	St**S4**-*20*	80% Cationic Starch 20% S4	St**S8**-*05*	95% Cationic Starch 5% S8
St**S1**-*20*	80% Cationic Starch 20% S1	St**S5**-*05*	95% Cationic Starch 5% S5	St**S8**-*10*	90% Cationic Starch 10% S8
St**S2**-*05*	95% Cationic Starch 5% S2	St**S5**-*10*	90% Cationic Starch 10% S5	St**S8**-*20*	80% Cationic Starch 20% S8
St**S2**-*10*	90% Cationic Starch 10% S2	St**S5**-*20*	80% Cationic Starch 20% S5	St**S9**-*10*	90% Cationic Starch 10% S9
St**S2**-*20*	80% Cationic Starch 20% S2	St**S6**-*05*	95% Cationic Starch 5% S6	St**S9**-*20*	80% Cationic Starch 20% S9
St**S3**-*05*	95% Cationic Starch 5% S3	St**S6**-*10*	90% Cationic Starch 10% S6	St**S10**-*05*	95% Cationic Starch 5% S10
St**S3**-*10*	90% Cationic Starch 10% S3	St**S6**-*20*	80% Cationic Starch 20% S6	St**S10**-*10*	90% Cationic Starch 10% S10
St**S3**-*20*	80% Cationic Starch 20% S3	St**S7**-*05*	95% Cationic Starch 5% S7	St**S10**-*20*	80% Cationic Starch 20% S10

3 Results and Discussion

PCA was used to choose the best set of topographic parameters that describe all the paper samples. The ten variables that were measured, plotted in Figure 1a, describe 73% of the results variability (51% 1st component; 22% 2nd component). According to the correlation loadings, the variables Ssc, Sdq and Sdr can be eliminated from the set. The resulting PCA analysis, which includes the seven variables Sa, Sq, Sp, Sv, St, Ssk and Str, is presented in Figure 1b. A higher degree of explanation (90%: 61% 1st component; 29% 2nd component) is now achieved. Therefore, these seven parameters are enough to adequately describe and analyze the effect of surface sizing in the topography of all the paper samples.

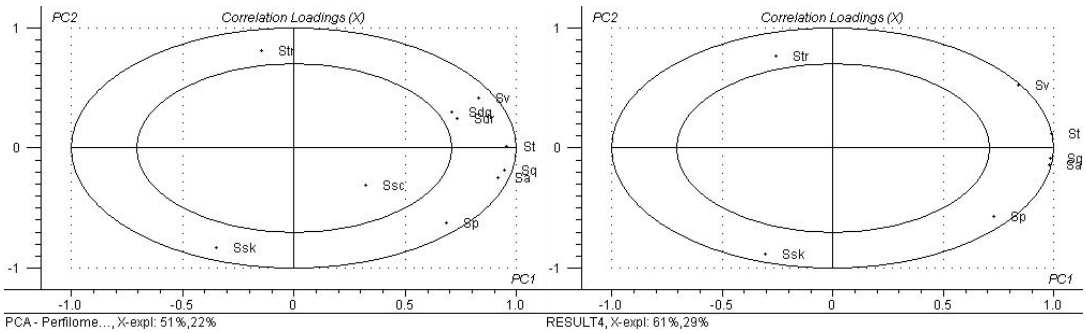

(a) (b)

Figure 1 - PCA analysis (a) using the descriptive variables obtained by profilometry; (b) using 7 descriptive variables.

The ANOVA results corresponding to the seven topographic parameters selected after the PCA analysis are listed in Table 3. Has can be seen, the results are statistically significant ($p << 0.05$ and $F > F_{critical}$) and reveal that the major contribution to the variability of the results is due to the differences among the samples. However, the variability due to the measurements within each sample is not negligible.

Table 3 – ANOVA analysis results for the most important profilometry variables, resolute by PCA analysis.

Variable	Contribution to total variation (%)		Reproducibility Factor	p	F	Fcritical
	Among Samples	Within Samples				
Sa	56.72	43.28	0.40	1.7E-14	6.25	1.54
Sq	63.57	36.43	0.45	1.3E-15	7.16	1.55
Sp	53.49	46.51	1.39	9.2E-09	4.29	1.56
Sv	60.53	39.47	1.87	5.7E-17	7.31	1.54
St	57.53	42.47	2.65	5.4E-15	6.46	1.54
Ssk	62.64	37.36	0.23	2.5E-14	6.65	1.56
Str	57.32	42.68	0.22	3.7E-08	4.25	1.58

The values of the contact angle with the five distinct liquids, as well as the total surface energy, its dispersive and polar components and the polar character, were analyzed by PCA (Figure 2a). The two components with the nine variables describe 73% of the variability of the data (51% 1st component; 22% 2nd component). After discarding the polar component of the surface energy, which is redundant relatively to the polar character, and the contact angle with ethileneglycol, which has the smaller correlation loading, and new PCA with seven variables was performed (Figure 2b). A higher degree of explanation was now obtained (95%: 59% 1st component, 36% 2nd component).

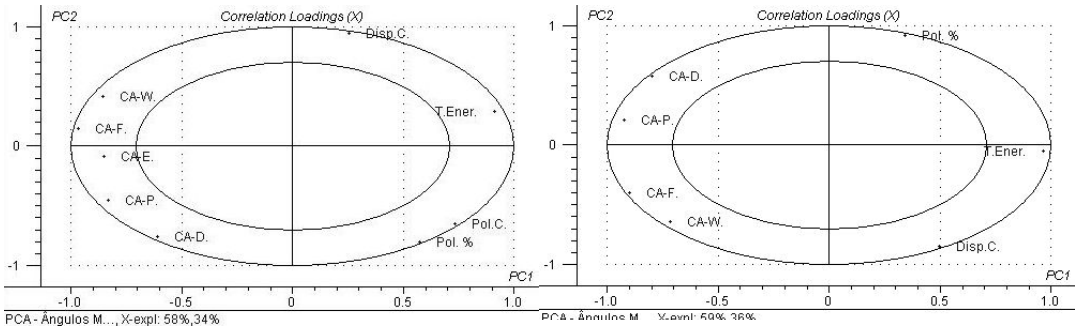

(a) (b)

Figure 2 – PCA analysis (a) for all variables computed from the contact angle variables; (b) using 7 variables achieved through contact angle measurements.

ANOVA was also applied to the results of the contact angle measurements performed with each one of the five aforementioned different liquid probes. The results, listed in Table 4 are once again statistically significant and show that the variability is mostly due to the differences between the 31 paper samples. This indicates that the contact angle results, and those of the properties derived from them (the total surface energy and its dispersive and polar components) clearly distinguish samples, contrary to the Profilometry results. Thus, it is legitimate to conclude that the use of different surface sizing agents has a predominant effect on the surface energetics and a reduced impact on the surface texture.

Table 4 - ANOVA Analysis of the contact angle values.

Variables (Contact Angles)*	Contribution to total variation (%)		Reproducibility Factor	p	F	Fcritical
	Among Samples	Within Samples				
Diodomethane	96.81	3.19	3.57	3.5E-263	382.95	1.49
Propileneglycol	97.82	2.18	4.06	7.2E-223	434.52	1.50
Ethileneglycol	98.59	1.41	3.75	1.7E-276	743.27	1.49
Formamide	98.93	1.07	3.69	0.0E+00	1029.46	1.49
Water	98.88	1.12	4.01	0.0E+00	1099.36	1.49

* ANOVA Analysis performed using the measured values for the contact angle with the different liquids tested, since all the calculations are based in these values.

PCA was also used with the following printing quality parameters: optical densities for black, cyan, magenta and yellow, gamut area, image area and contour perimeter and roughness (Figure 3a). From this set of eight variables, the cyan and magenta optical densities were removed for further analysis since, in the graph these are close to the yellow OD. For the same reason, the image area was also discarded. The remaining five variables (black and yellow Optical densities, Gamut area and contour perimeter and roughness) were used in a new PCA analysis (Figure 3b) and, as can be seen, it was possible to increase th explanation from 74% (42% 1st component; 32% 2nd component) up to 85% explanation (49% 1st component, 36% 2nd component).

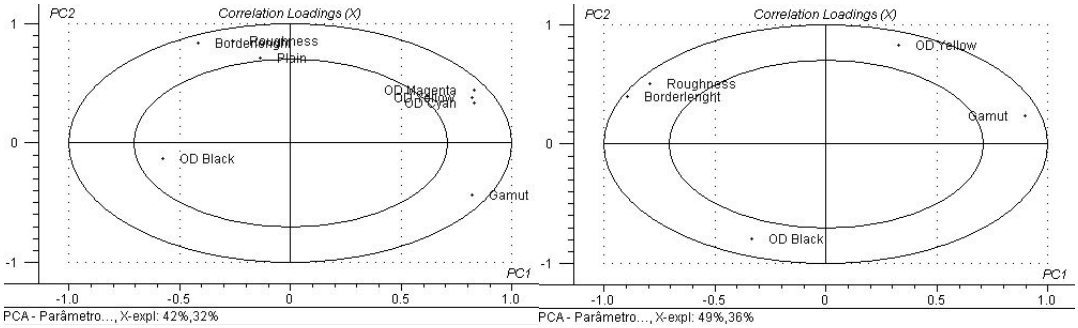

(a) (b)

Figure 3 – PCA analysis (a) for all the printing quality parameters; (b) using 5 printing quality parameters.

The corresponding ANOVA results for these 5 variables are presented in Table 5. The quality of the ANOVA analysis is once again ensured by the good values of the parameters P, F and Fcritical.

Table 5 – ANOVA analysis results for the most important printing quality variables.

Variable	Contribution to total variation (%)		Reproducibility Factor	p	F	Fcritical
	Among Samples	Within Samples				
OD Black	67.58	32.42	0.21	4.0E-25	10.84	1.53
OD Yellow	64.90	35.10	0.07	1.7E-22	9.55	1.53
Gamut Area	73.00	27.00	952.59	1.4E-03	2.97	1.81
Borderlenght	57.53	42.47	0.90	8.7E-17	7.00	1.53
Roughness	49.12	50.88	0.02	1.2E-11	4.99	1.53

From this table, it is possible to conclude that OD and Gamut area are significantly different from sample to sample, whereas for the line quality parameters the variations between samples or within the same sample have similar relevance. These findings indicate that caution must be taken in the interpretation of the line quality parameters, and they must always be analyzed in combination with other printing quality parameters in order to avoid misleading conclusions.

Next, in this study, PLS models were computed in order to determine whether the physical and/or the chemical surface parameters previously described can explain the printing performance of the distinct sized papers, as evaluated by the printing quality in terms of optical densities, Gamut area and line quality parameters.

Three different sets were created: one with the seven independent topographic variables (Figure 1b), assigned as “Physical”; another with the seven independent chemical variables evaluated by the contact angle measurements (Figure 2b), assigned as “Chemical”; and another with these 14 variables all together, assigned as “Total”. The above five printing quality variables (Figure 3b) were used as the “dependent” variables, either isolated or grouped as follows: all dependent; OD (OD black + OD yellow); line quality (borderlenght + roughness). Thus, 24 models were considered. Table 6 presents the results of the resultant models with a degree of explanation superior to 10%.

Table 6 – Results achieved by PLS models.

Independent Variables Set (xx)	Dependent Variables Set (yy)	Explanation %*	Correlation Coeficcient
Total	All Printing Variables	17% (11; 6)	0.43
Total	Optical Densities	20% (13; 7)	0.47
Chemical	Optical Densities	15% (5; 10)	0.29
Total	Line Quality	23% (21; 2)	0.42
Physical	Line Quality	14% (13; 1)	0.28
Total	Gamut Area	22% (13; 9)	0.36
Chemical	Gamut Area	26% (8; 18)	0.28
Total	OD - Black	25% (20; 5)	0.45
Physical	OD - Black	15% (12; 3)	0.35
Chemical	OD - Black	10% (12; 3)	0.28
Total	OD - Yellow	32% (15; 17)	0.70
Chemical	OD - Yellow	41% (8 ; 2)	0.67
Total	Borderlenght	20% (16; 4)	0.40
Total	Roughness	29% (27; 2)	0.54
Physical	Roughness	20% (18; 2)	0.45

* Total% (1st component; 2nd Component)

The explanation percentages as well as the coefficients of correlation are in general small. This means that other paper surface properties than those measured is this study and used in the PLS analysis are also necessary to explain the printing quality parameters that were assessed in the distinct samples. Nonetheless, some interesting features are clear in Table 6: the optical densities and gamut area are more affected by the chemical properties, while the line quality variables are more related to the physical structure of the paper surface. In other words, the paper topography mostly affects the printed image contours while the chemical properties of the surface have a more pronounced influence on the color related properties.

4 Conclusions

The mathematical tools applied in this work proved to be most useful in the treatment of the large amount of information achieved. Using PCA it was possible to identify the most relevant parameters regarding paper surface characterization (physical and chemical) and printing quality evaluation. The ANOVA analysis demonstrated that surface sizing operation influences more significantly the chemical rather than the physical properties of the paper surface, while from the PLS analysis it was possible to conclude that the topography is more important in the explanation of the printing properties related to the definition of the contours while the chemical properties achieved from contact angle measurements are more useful in the explanation of the printing quality variables related to the colour.

References

Briggs, D., Rance, D.G., Briscoe, B.J. (1989). *Comprehensive Polymer Science*, C., Price, C. (book eds.), Allen, G, Bevington, J.C. (series eds.), Pergamon Press, Oxford; 707-732.

Carceller, R., Juppo, A. (2004). New surface size composition changes paper surface properties for improving ink jet printability of copy paper. *Paperi ja Puu,* 86(3), 161-163.

Cohen D. K. (n.d.).*Glossary of Surface Texture Parameters*, Michigan Metrology.

Koskela, J P.; Hormi, O. E. O. (2003). Improving the printability of paper with long-chain quaternaries. *Appita Journal*, 56(4), 296-300.

Moutinho, I. M. T., Ferreira, P. J. T., Figueiredo, M. M. L. (2007); Impact of surface sizing on inkjet printing quality; *Ind. Eng. Chem. Res.*; 46 (19); 6183-6188.

Stout K.J., Sullivan P.J., Dong W.P., Mainsah E., Luo N., Mathia T., Zahouani H. (1994). *The development of methods for the characterization of roughness on three dimension*, Publication no. EUR 15178 EN of the Commission of the European Communities, Luxembourg.

Proceedings of the 10th International Chemical and
Biological Engineering Conference - CHEMPOR 2008
Braga, Portugal, September 4-6, 2008
E.C. Ferreira and M. Mota (Eds.)

SUB-MICRON SIZE ARAGONITE SYNTHESIS BY DOUBLE-JET PRECIPITATION

Carmencita Mateescu[1], Mihaela Mihai[2], Raluca Isopescu[2*], Irinela Chilibon[3], Florina Branzoi[4]

[1]National Institute for Materials Physics , Magurele, Romania,
[2]University Politehnica Bucharest, 1-7 Polizu Street, Bucharest,
[3]National Institute for Optoelectronics, INOE, Magurele, Romania,
[4]Institute of Physical Chemistry, 303 Splaiul Independetei Bucharest, Romania

Keywords: Aragonit, Precipitation, Ultrasonic field, Size distribution
Topic: Advancing the chemical and biological engineering fundamentals.

Abstract

Aragonite with sub-micron size particles was synthesized in a liquid-liquid reaction by the controlled double jet precipitation method. The reaction medium was an ethanol-water solution. The precipitation process depends on supersaturation, pH, temperature, reaction time, agitation specific energy, feeding order of the reacting solutions, the nature, and the presence/absence of the additives. This parameters influence the final solid phase morphology and also the particle sizes. All samples were characterized by FT-IR spectroscopy, XRD, optical and electron microscopy, particle size distribution by laser granulometer and microscopic measurements methods. The results proved that a very small amount of the precipitated particles were agglomerated.

The population balance equation describing the precipitation process was integrated using the method of classes (Marshal P. et al, 1988). The kinetic parameters were estimated using a random search optimization method. The results obtained were in good agreement with experimental data and proved that in the present working conditions nucleation and growth are the main mechanisms while agglomeration is inhibited.

1 Introduction

Nano calcium carbonate finds applications in advanced materials like composites and biomaterials. The controlled double-jet precipitation method allows the production of colloidal particles with a good control of their monodispersity .The precipitation of calcium carbonate (PCC) by liquid-liquid reaction usually provides a mixture of polymorphs since calcium carbonate has at least three stable polymorphs: calcite, aragonite and vaterite. In order to induce the crystallization of aragonite, the high pressure polymorph, the precipitation conditions, such as supersaturation, temperature, pH, feeding order, stirring, additives, must be carefully controlled.

This paper reports the synthesis of aragonite by the double jet precipitation method. The reaction medium was either bi-distilled water or a solution of bi-distilled water and ethanol. The influence of ultrasonic agitation on the particle size distribution was investigated in comparison with magnetic stirrer.

The final PSD, measured in a mass base system, on a laser beam particle size analyzer (PSA) was used for the kinetic parameter estimation considering that the final shape of the PSD is the result of overlapping primary and secondary crystallization mechanisms such as nucleation, growth and agglomeration.

* Corresponding author. Tel + 4072265848. E-mail:ralucaisopescu@yahoo.com

The parameters were estimated by fitting the experimental PSD to the computed values obtained by solving the population balance equation as defined in a large number of publications.

2 Experimental

Aragonite was synthesized by liquid-liquid reaction using 0.1 M solutions in bi-distilled water of analytical grade, calcium nitrate tetrahydrate (Riedel-de Haen) and potassium carbonate (Sigma-Aldrich). The reagents were introduced into a glass reactor by means of peristaltic pumps at the same flow rate of 10 ml/min. The reaction medium was either 50 cm^3 of bi-distilled water or a mixture of water and ethanol 1:1 in volumes. The reaction temperature was kept constant at 50°C by means of a thermostate.
In a first set of experiments a magnetic stirrer performed the agitation into the reaction medium. In a second set of experiments the glass reactor was placed into an ultrasonic bath and agitation was resumed to the influence of ultrasonic field. The experiments were set up in absence and in presence of polyelectrolyte type additive: *polyoxyethilene sorbitan monolaureate* (Tween 20) at two different concentrations. The precipitate was aged for 1hour, then filtered and washed several times with bi-distilled water and dried at 100°C.

Phase composition was established by FT-IR spectroscopy using a Perkin-Elmer spectrophotometer. PCC samples were dispersed in spectral grade KBr and pressed. Using powder X-ray diffraction (diffractometer Bruker D8 Advantage) quantitative phase composition was established and particles mean size was calculated with Debye-Scherrer formula. Particle size distribution was also investigated using a laser beam particle size analyzer (Analysette 22 Micro Tech). TEM was performed using a JEOL 200CX electron microscope. Samples were deposited on carbon coated 3 mm diameter copper electron microscope grids.

3 Results and discussion

FT-IR spectroscopy of PCC proved to be mainly aragonite. The other two anhydrous polymorphs (calcite and vaterite) are present in various ratios (table 1). XRD measurements confirmed the conclusions drawn on the basis of FT-IR spectra.

Table 1. Experimental results

Sample no	Agitation mode	Reaction medium	Composition	Mean diameter PSA [µm]	XRD Mean diameter [nm]
1	magnetic	50 cm^3 bi-distilled water	65.05% aragonite; 2.78% calcite; 32.17% vaterite	15.314	102.0 190.0 60.7
2	magnetic	50 cm^3 ethanol – water ratio 1:1	98.76 % aragonite; 1.24 % calcite;	1.457	25.4 33.3
3	US 50 kHz;	50 cm^3 bi-distilled water	71.48% aragonite; 20.99% calcite; 7.53% vaterite	13.282	57.5 570.0 47.9
4	US 50 kHz;	50 cm^3 ethanol – water ratio 1:1	98.18 % aragonite; 1.82 % calcite	1.075	18.2 21.2
5	magnetic	50 cm^3 bi-distilled water with TWEEN 20 1.2 10^{-4} mmol/l	65.05% aragonite; 2.78% calcite; 32.17% vaterite	12.54	-
6	US 50 kHz	50 cm^3 bi-distilled water with TWEEN 20 1.2 10^{-4} mmol/l	71.48% aragonite; 20.99% calcite; 7.53% vaterite	1.12	-

The reaction medium proved to have a significant influence on the composition of the precipitate and on the particle size distribution. When the reagents are dropped and react in bi-distilled water, the proportion of the other stable polymorphs of $CaCO_3$ is significant, PCC is a mixture of the three polymorphs, aragonite being still the dominant phase with a percentage of 65-70 %. When the reaction medium is a solution of 1:1 ethanol and bi-distilled water, the phase composition determined both by FT-IR spectrometry and XRD measurements, shows that aragonite is only slightly impurified with calcite (1.24-1.28 %). The temperature of 50 °C is reported to be specific for aragonite development but from our experiments the reaction medium is in fact more important. The presence of alcohol – water clusters, at 50°C proved to be favorable to aragonite development

The PSD diagram registered by means of a particle size analyzer shows that when the reaction medium was a mixture of ethanol and bi-distilled water 1:1 in volumes, a diminishing of the particles size by one order of magnitude appears. The PSA (laser beam analyzer) measures in fact not the individual crystallites size but the size of agglomerates and it registers a mass base distribution, emphasizing the contribution of agglomerates. The diminishing of the dimensions when additives are used proves that additives prevent the aggregates formations (figure 3).

From XRD spectra, using the Debye-Scherrer formula, the crystallites size was estimated using the most intensive maxima for each phase. These measurements proved that using the double jet precipitation method nanoparticles of PCC develop. In the presence of ethanol solution aragonite dimensions dropped to 25 nm.

TEM images reveal the presence of nanometric particles gathered in agglomerates of micrometric dimensions (figure 1a) in the case when ethanol is present in the reaction medium. When bi-distilled water is used as reaction medium longer aragonite needels of several microns form and gather in bunches (figure 1b).

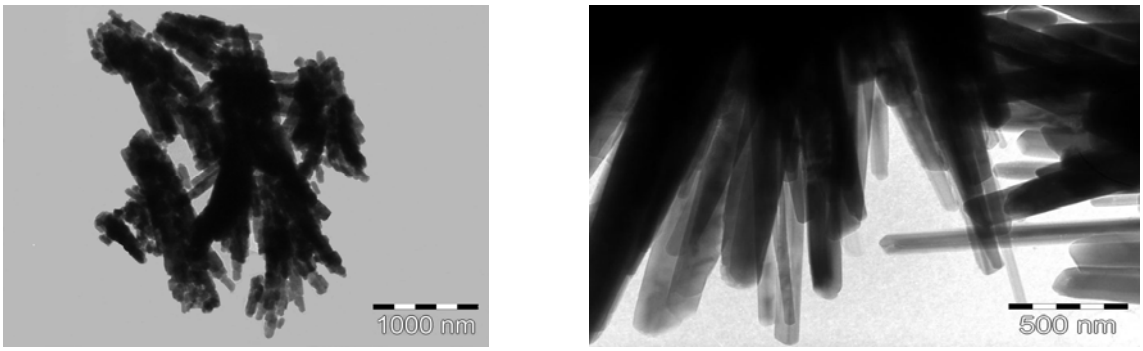

(a) (b)

Figure 1. TEM images of PCC. (a) sample 4; (b) sample 3.

Figure 2 presents SEM images of the PCC obtained in the two experimental runs. The images show a significant contribution of spherical vaterite and calcite in sample 1 (figure 2b) while in sample 2 (figure 2a) mainly rod and needle like aragonite are present.

4 Kinetic parameters estimation

The kinetic parameters estimation relays on mathematical modelling of the precipitation process considering the mechanisms assumed according to the analyses of experimental PSD data. These mechanisms are: nucleation, non-ideal crystal growth and agglomeration.

The PBE for a batch crystalliser is generally represented by an integro-partial differential equation. Considering nucleation, growth and agglomeration as main mechanisms and adopting a discretisation of the particle size range as defined by Marshal et all (1998), the PBE can be transformed in a system of differential equation. Considering Ni the number of particles in unit volume of slurry in class i (according to the method of classes first defined in

(Marshal et all 1998) the PBE for class i becomes:

$$\frac{dN_i}{dt} + \frac{1}{V}\frac{dV}{dt}N_i + [G(d_i) * n(d_i) - G(d_{i-1}) * n(d_{i-1})] = B_i + r_{A,i} \quad (1)$$

where V is the volume of suspension, B_i is the nucleation contribution in class i, $r_{A,i}$ the agglomeration term. G(d) stands for the size dependent crystal growth rate and n(d) is the population density function.

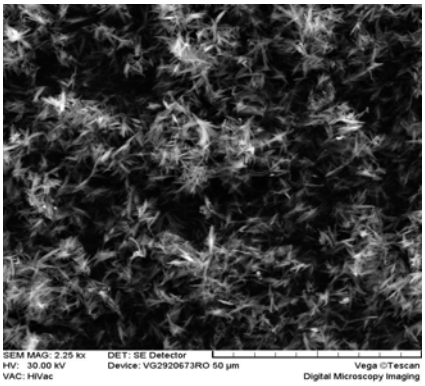

(a)

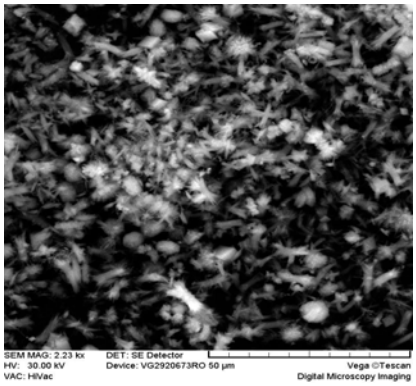

(b)

Figure 2. SEM images for PCC. (a) Run 2, (b) Run 1, (c)

Reaction without TWEEN	Reaction with TWEEN 20
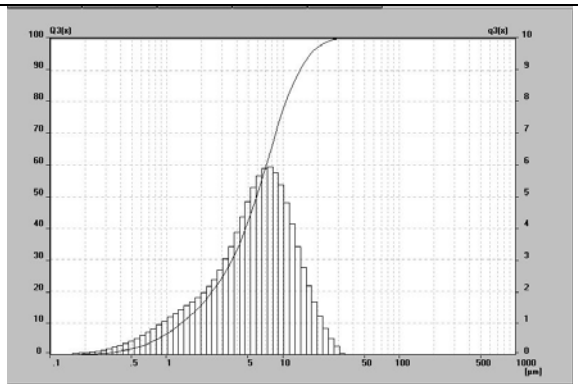	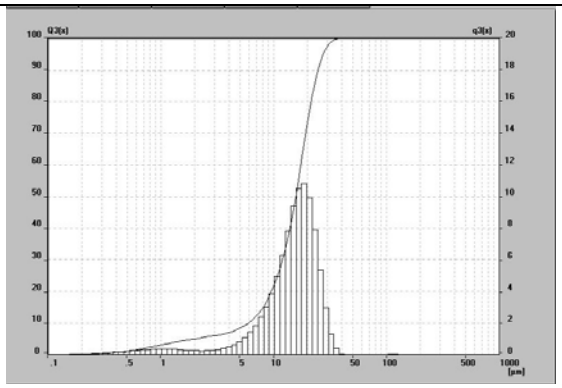
PSD at the end of reaction	
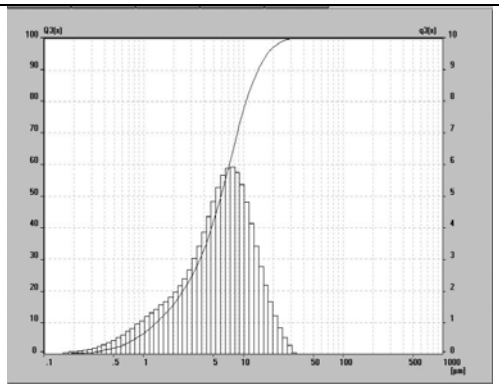	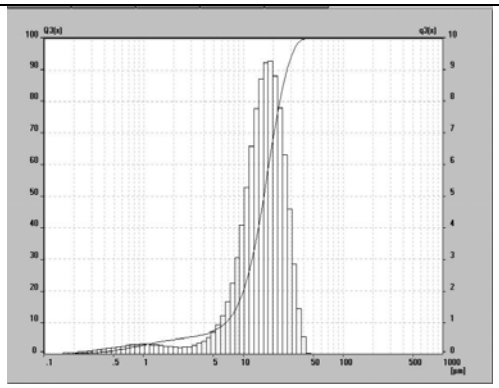
PSD for 40 minutes aging period.	

Figure.3. The PSD dynamic for calcium carbonate precipitation.

Further, we consider that nucleation occurs only in the first class at the nuclei size, so B_i is termed B^0 for this class and is null for all other classes. The agglomeration term is calculated considering the equation derived by Hounslow et all (1988):

$$r_{A,i} = N_{i-1}\sum_{j=1}^{i-2} 2^{j-i+1}\beta_{i-1,j}N_j + \frac{1}{2}\beta_{i-1,i-1}N^2_{i-1} - N_i\sum_{j=1}^{i-1} 2^{j-i}\beta_{i,j}N_j - N_i\sum_{j=i}^{Nc}\beta_{ij}N_j \quad (2)$$

The kinetics G, B^0 and $\beta_{i,j}$ depend on the nature of the system and operating condition. As revealed by experimental data analysis, a non-ideal crystal growth can be assumed. For the definition of G(d) the ASL model was selected. As concerning the agglomeration rate, a size independent kernel was assumed: $\beta_{i,j}=\beta$. Deriving equation (1) for all classes, a system of differential equations is formed and solved by a standard numerical method. The kinetic parameters (B^0, G_0, a, b, β) were estimated by minimising a least squares criterion.

$$F = \sum_{i=1}^{Nc}[\ln(N_{i,\exp}) - \ln(N_{i,comp})]^2 \quad (3)$$

where N_c is the number of classes in accordance with experimental data.

The use of logarithm in equation (3) assures the same contribution of all classes in the definition of the minimisation criterion. The minimisation was performed using a random adaptive search method recommended for multimodal objective functions, which is generally the case in kinetic parameters estimation.

The solution found by solving the PBE and fitting the results to experimental data are presented in table 2, together with the best value of the least squares criterion. The kinetic parameters were identified for the first 15 minutes of the precipitation process.

Table 2. Estimated kinetic parameters

Run	B^0, no·m^{-3}s^{-1}	G_0, m·s^{-1}	a, m	b	β, m^3·s^{-1}	F_{min}
1	$1.8625\cdot10^{14}$	$1.3297\cdot10^{-11}$	$3.91\cdot10^{7}$	0.278	$4.4159\cdot10^{-15}$	12.20
2	$4.0002\cdot10^{14}$	$1.1597\cdot10^{-10}$	$2.45\cdot10^{5}$	0.098	$1.0578\cdot10^{-17}$	3.67
3	$6.2148\cdot10^{14}$	2.167810^{-10}	$2.74\cdot10^{7}$	0.470	$2.1678\cdot10^{-15}$	16.40
4	$4.0789\cdot10^{14}$	$2.3600\cdot10^{-10}$	$4.89\cdot10^{7}$	0.017	$3.2700\cdot10^{-18}$	2.35
5	$1.9600\cdot10^{8}$	$1.9700\cdot10^{-13}$	$4.84\cdot10^{7}$	0.790	$3.2700\cdot10^{-18}$	4.57
6	$3.1000\cdot10^{9}$	$2.8000\cdot10^{-10}$	$3.37\cdot10^{7}$	0.680	$3.2700\cdot10^{-18}$	1.39

It may be noticed from the data in table 2 that the mathematical model gives more reliable results in the case of ethanol-water precipitation medium where few agglomerates are formed. In this case the constant mean shape factor considered from the transformation of mass based PSD into number based distribution introduces lower errors. On the other hand when large agglomerates are formed, the constant kernel agglomeration model might not be enough accurate to capture the complexity of the process. Figure 4 presents calculated and experimental PSD data for 1 and 2 runs.

The data in table 2 confirm that nucleation is the dominant mechanism in all experimental runs. The ultrasonic filed slightly increases the nucleation rate, more evident for bi-distilled water medium than for ethanol-water mixture and decreases the agglomeration. The linear crystal growth rate, G_0 is affected by the US waves as expected, increasing the crystal growth rate probably by an enhanced mass transfer close to the crystal surface. In the case of bi-distilled water, where larger agglomerates are formed, a size dependent crystal growth was revealed, as the values of parameters “a” and “b” show (table 2). The effect of the precipitation medium is even more important on the mechanisms involved than the presence of ultrasonic field. The agglomeration rate is drastically reduced in ethanol water mixture. The

newborn particles seem to grow mainly by linear growth mechanism while efficient particle collisions leading to agglomerates are very rare.

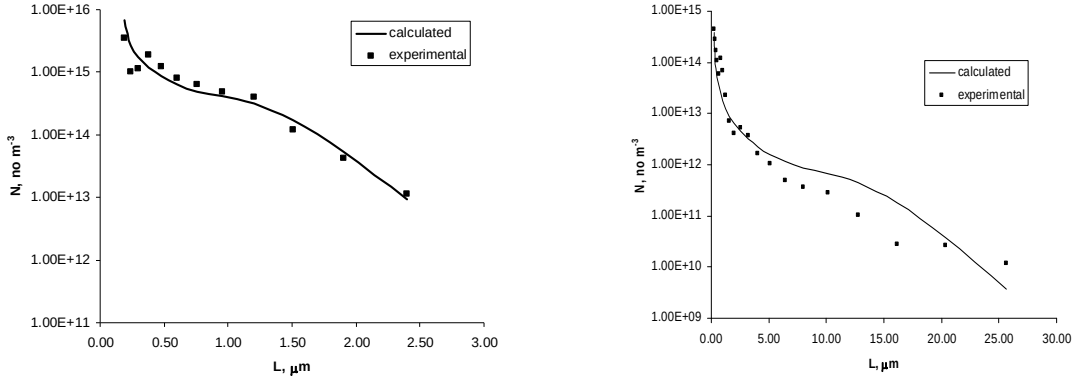

(a) (b)

Figure 4 Experimental and computed PSD, N_i for sample 4 (a) and sample 3 (b).

The presence of several polymorphs may also increase the agglomeration rate by creating a larger free surface of the solid phase capable to attach other solid particles. The polymorphic transformation that probably occurred when the precipitation took place in bi-distilled water may also be responsible for the shape of PSD and a reason for a poorer data fitting with the model based on nucleation, growth and agglomeration.

5 Conclusions

PCC was synthesized by the double jet precipitation method using two mixing systems, either ultrasonic waves or magnetic mixer, in a reaction medium of bi-distilled water or ethanol-water solution.

The presence of ethanol in the reaction medium and aditives had an important influence on the final solid phase properties both from morphological point of view and particle size distribution.

The mathematical model derived and the values of estimated kinetic parameters confirm that nucleation is the dominant mechanism in all experimental runs. The agglomeration process is significantly decreased when precipitation takes place in ethanol-water medium.

The double-jet calcium carbonate precipitation in ethanol-water mixtures may be a challenging solution to obtain pure polymorphic phase and submicron size particles.

References

Marshal P., David R., Klein J. P., Villarmaux J., (1988) Crystallization and precipitation engineering I: An efficient method of solving population balance in crystallization with agglomeration, *Chemical Enginerting Science*, 43, 59-67.

Hounslow, M., Ryall, R.L., Marshall V. R., (1988) A discretized population balance for nucleation, growth and aggregation, *AIChEJ*, 34 1821-1832.

Acknowledgement

This research was supported by The Romanian Ministry of Education and Research through “Research of Excellency” Program, Project no. 18/2005

Proceedings of the 10th International Chemical and
Biological Engineering Conference - CHEMPOR 2008
Braga, Portugal, September 4-6, 2008
E.C. Ferreira and M. Mota (Eds.)

Change on rheological properties of mushroom cream due to freezing process

E. Álvarez*, M. A. Cancela, N. Delgado-Bastidas, R. Maceiras
Chemical Engineering Department, University of Vigo, E.T.S.E.I. Rúa Maxwell, s/n, 36310 Vigo, Spain

Keywords: Rheological properties, activation energy, mushroom cream, freeze-thaw treatment.
Topic: Advancing the chemical and biological engineering fundamentals

Abstract

The effect of the freeze-thaw treatment on rheological behaviour and activation energy in mushroom cream has been investigated. Freeze-thaw treatment was made at different times of frozen storage; it was within a range of 0 to 6 weeks. For each freezing cycle, the sample was submitted to rheological measurements within a range of temperature between 20 and 40°C. Mushroom cream exhibited pseudo plasticity following the Ostwald Waele model in all cases. This model described very well the flow behaviour of analyzed samples, for each temperature and time of frozen storage (R^2 > 0.999). Furthermore, it was observed that sample viscosity increased with freeze-thaw treatment respect to the not treated sample. Finally, an equation type Arrhenius was used to determine and quantify the temperature effect on the consistency index during the heating and shearing program; moreover, activation energy values were obtained.

1. Introduction

The increasing social and economic importance of food production, together with the complexity of production technology, processing, handling and acceptance of these highly perishable and fragile food materials requires a more extensive knowledge of their physical properties; because of this, the viscoelastic properties play an important role in the handling and quality attributes of both minimally processed foods, such as fruits and vegetables, and fabricated foods such as sauces and creams (Rao and Steffe, 1992). In the alimentary industry the foods undergo a lot of transformations during their processing therefore there is a significant relationship between industrial practice and research studies on properties of foods.

Most foods are subjected to variations in their temperature during production, transport, storage, preparation and consumption, e.g., pasteurization, sterilization, evaporation, cooking, freezing, chilling etc. Temperature changes cause alterations in the physical and chemical properties of food components which influence the overall properties of the final product, e.g., taste, appearance, texture and stability. Chemical reactions, such as hydrolysis, oxidation or reduction, may be promoted or physical changes, such as evaporation, melting, crystallization, aggregation or gelation, may occur. A better understanding of the influence of temperature on the properties of foods enables food manufacturers to optimize processing conditions and improve product quality (Osborne and Voogt, 1986).

An important factor in the studies on the flow properties is the effect on rheological behaviour of thawing conditions. Works have been carried out to determine the effect of freeze-thawed cycles on the apparent viscosity of commercial and natural purees (Alvarez and Canet, 2001a, b;

* Corresponding author. Tel + 34-986-812213. E-mail: ealvarez@uvigo.es

Downey, 2003). They observed that time of frozen storage plays an important role on the apparent viscosity and others rheological parameters, whose negative effect is more significant for commercial creams. This effect is related to ice crystal growth caused by fluctuations when time increases. It maybe causes a break in the cell structure of the fluid, and it originates a greater fluid loss (Alvarez *et al.*, 2004). These factors indicated that freezing treatment causes a greater structural damage in commercial purees, due to retrogradation of gelatinized starch and operation conditions during the manufacturing process.

The objective of this work was to evaluate the effect of the freeze-thaw treatment on rheological behaviour and on activation energy in a commercial mushroom cream.

2. Materials and Methods

Sample Preparation

Mushroom puree was prepared according the maker instructions, weighing 18.375 g with a balance Mettler AJ150 with a precision of ±0.1 mg, and they were dissolved in 250 ml of warm water. The ingredients of mushroom cream was: vegetal fat, starch, milky solids, wheat flour, salt, flavour enhancer (E-621), animal fat, mushroom (3.4 mass %), sucrose, aroma, spices and antioxidants (E-304/E-307).

Frozen Storage and Conditions of Freeze-Thaw Treatment

Freeze-thaw treatments were performed by storing in a refrigerator for 16 h at 4ºC, followed by freezing at -24ºC in a freezer. Samples of each system were subjected to 0, 1, 2, 3, 4, 5 and 6 weeks of frozen storage. Afterwards, all samples were thawed at room temperature of 20ºC for 14 h to ensure them same conditions of thaw before realizing the experiments. Each testing date was repeated twice.

Rheological Measurement

A rotation viscometer, Viscotester VT550 (Haake, Germany), equipped with SV1 rotor (bob length = 61.4 mm, bob diameter = 20.2 mm, gap width = 1.45 mm) in a concentric cylindrical cup assembly interfaced to a computer for control and data acquisitions was used for rheological measurements. The viscometer was operated in controlled shear rate mode, where the shear rate (γ) was set and the resultant shear stress was measured (τ). The sample compartment was maintained at a constant temperature using a water/bath circulator and it was varied from 20 to 40 ºC.

For each test, the filled sample cup and spindle were temperature equilibrated for about 10 min and the samples were subjected to shear changes from 17.8 and 445 s^{-1}. The rheograms were evaluated using the Ostwald Waele model (Eq. 1) and the apparent viscosity was computed as the ratio of shear stress to shear rate ($\eta = \tau/\gamma$).

$$\tau = K\gamma^{n} \quad (1)$$

where τ is the shear stress (Pa), γ is the shear rate (s^{-1}), *K* is the consistency index ($Pa \cdot s^{n}$) and *n* is the flow behaviour index (dimensionless).

Model fitting was carried out using Origin 7.0. The model parameters were varied simultaneously to achieve the minimum residual square error between the predicted and the actual flow curves data.

3. Results and Discussion

Rheological Properties

All test samples of mushroom cream exhibited shear-thinning behaviour at different temperatures and different frozen storage times. The viscosity decreased with temperature for the same frozen storage time (Figure 1). This behaviour was observed in starchy foods and reported by Alvarez and Canet (2004).

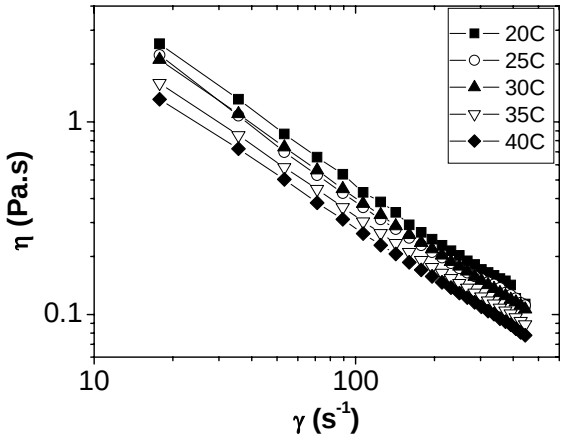

Figure 1. Viscosity vs. shear rate for 6th week, at all temperatures.

Figure 2 shows rheograms at different frozen storage time of mushroom cream samples. In these rheograms, it can be observed that viscosity increases with time frozen storage in all cases. Our results show a clear tendency to increase viscosity with respect to time of frozen storage, despite of possible structural damage caused by freeze-thaw treatment. Analyzed frozen cream was more affected by the starch behaviour as a swelling agent that by breakdown of the cell structures caused by freeze-thaw treatment. The cell structures were destroyed progressively under the effect of shear rate; this can be seen in Figure 2.

The crystallization on cooling and frozen storage is the cause of that frozen storage stability decreases. In this study, one of the reasons, that viscosity did not diminished with the frozen storage time, was the use of cryoprotectants and other hydrocolloids, such as thickness, starches and sugars. The water binding ability (high but relatively weak) of hydrocolloids can provide body and texture to foodstuffs, this is main reason for using starches as an additive in commercials creams, moreover they are claimed to offer temperature resistance, shear and storage stability and smooth texture.

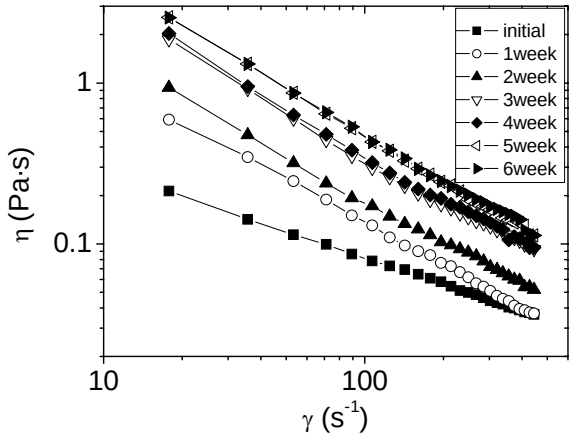

Figure 2. Viscosity vs. shear rate at all time of frozen storage and 30 ºC.

The causes of the viscosity increase with frozen storage time are possibly related to the transformation of the starch into a sponge-like material after freezing (Eliasson and Kim, 1992). During frozen process, cell walls are broken due to crystallization of water and association of amylose molecules, as well as a redistribution of amylopectin in swollen starch granules (Vermeylen et al., 2004; Van Hung et al., 2006). In addition, a growth of ice crystals happens during frozen treatment. The dissolution of ice crystals happens and it promotes differences in local concentration of amylose and amylopectin. The increase of the local concentration of amylose and amylopectin could be cause by the formation of aggregated; it leads to shrinkage and disruption of swollen starch granules (Alvarez and Canet, 1999). It is important to mention that the growths of intercellular ice crystals, as well as their dissolution, are related to the time of frozen storage. Because of this, it is possible to find relationship between experimental evidences defined by others authors with the experimental results obtained in this work.

Once obtained viscosity values, these data were fitted to Ostwald Waele model, since this model described very well the flow behaviour of analyzed samples, for each temperature and time of frozen storage. For all cases, R^2 values were greater that 0.999.

Figure 3 was plotted to describe the influence of temperature and time of frozen storage on the consistency and flow index in all analyzed cases. It can be observed that *n* has a value less than unity in all cases. It indicates a pseudoplastic behaviour of analyzed samples. In relation with the dependence of flow index with temperature, it was observed a strong detrimental effect on flow index values when samples were submitted to freeze-thaw treatment. On the other hand, consistency index values experimented a diminution with respect to temperature, although these values shown an ascending trend with respect to time of frozen storage. These values presented a linear trend with temperature and with the time of frozen storage.

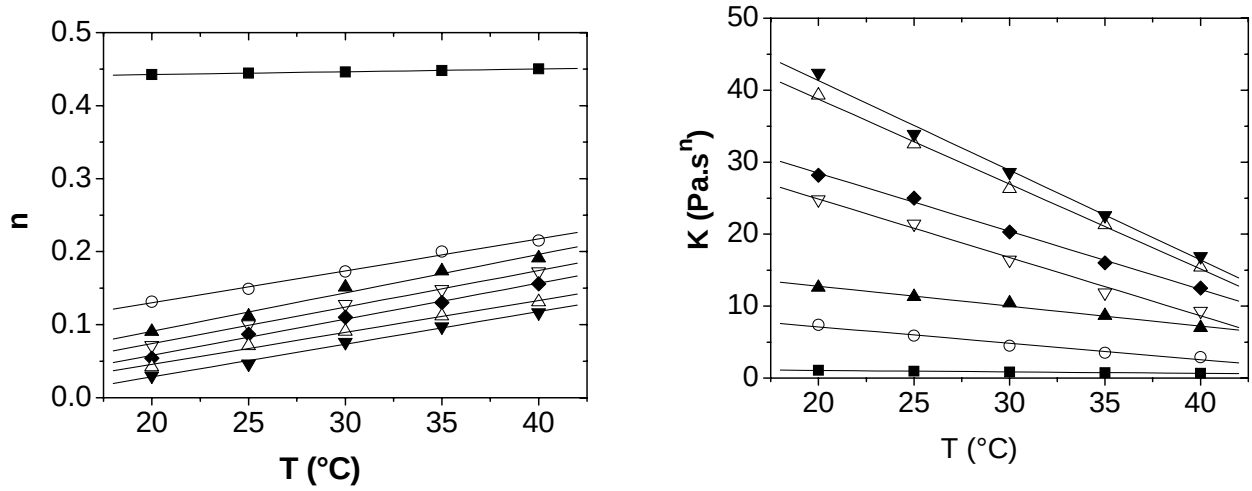

Figure 3. Flow and consistency index at different time of frozen storage: (■) 0 Week, (○) 1st Week, (▲) 2nd Week, (▽) 3rd Week, (◆) 4th Week, (△) 5th Week, (▼) 6th Week

Activation Energy

In the literature, the Arrhenius model has been most widely used to describe the effects of temperature. Therefore, an equation type Arrhenius (Eq. 2) was used to determine and quantify the temperature effect on the consistency index during the heating and shearing program.

$$K = K_T \, e^{\left(\frac{E_A}{RT}\right)} \tag{2}$$

where K is the consistency coefficient (Pa.s^n), K_T is Arrhenius constant (Pa.s^n), E_A is the activation energy (KJ/mol), R is the gas constant and T is the temperature (K). Constants of the Arrhenius model are displayed in Table 1.

Table 1. Parameters of Arrhenius Model.

Time of frozen storage (weeks)	E_A (KJ/mol)	R_T (Pa.s^n)
0	19	$5.4 \cdot 10^{-4}$
1	37	$2.2 \cdot 10^{-6}$
2	22	$1.6 \cdot 10^{-3}$
3	39	$3.1 \cdot 10^{-6}$
4	27	$5.2 \cdot 10^{-4}$
5	33	$4.5 \cdot 10^{-5}$
6	34	$4.5 \cdot 10^{-5}$

From the results, it can be concluded that the effect of temperature is lightly significant in all studied cases.

4. Conclusions

The Ostwald Waele model was effective to describe the rheological behaviour of mushroom cream behaved as a pseudoplastic fluid. The samples exhibited a reduction viscosity when these were suffered a shearing and heating program, when the used temperature was always smaller to the gelatinization temperature of starches. Furthermore, viscosity increased in all cases when they were exposed to freeze-thaw treatment with respect to not treated samples.

The consistency index presented a downward linear trend with respect to temperature and increased linearly with the time of frozen storage. On the other hand, the flow index increased linearly with temperature and presented a clear downwards trend with the time of frozen storage. Finally, Arrhenius model was used to describe the effects of temperature on the consistency index, observing a high dependence with respect to the temperature.

References

Alvarez, M. D., Canet, W. (1999). Rheological properties of mashed potatoes made from dehydrated flakes, effect of ingredients and freezing. *European Food Research and Technology,* 209, 335-342.

Alvarez, M. D., Canet, W. (2001a). Influence of cooking and freeze-thawing cycles on viscoelastic properties of vegetable purees*. Lebensmittel-Wissenschaft and Technology,* 34, 549-555.

Alvarez, M. D., Canet, W. (2001b). Rheological properties of frozen vegetable purees. Effect of freeze-thaw cycles and thawing conditions*. European Food Research and Technology,* 213, 30-37.

Alvarez, M. D., Canet, W. (2004). Rheological behaviour of fresh and frozen potato puree in steady and dynamic shear at different temperatures. *European Food Research and Technology,* 218, 544-553.

Downey, G. (2003). Effects of cryoprotectant mixture on physical properties of frozen and thawed purèed cooked potatoes, some introductory studies. *International Journal of Food Science and Technology,* 38, 857-868.

Eliasson, A. C., Kim, H. R. (1992). Changes in rheological properties of hydroxypropyl potato starch pastes during freeze-thaw treatments I. A rheological approach for evaluation of freeze-thaw stability. *Journal of Texture Studies,* 23, 279-295.

Rao, M.A., Steffe, J.F. (1992). *Viscoelastic Properties of Foods*, Elsevier Applied Science, London.

Osborne, D.R., Voogt, P. (1986). *Análisis de los nutrientes de los alimentos*, Ed. Acribia, Zaragoza

Van Hung, P., Maeda, T., Morita, N. (2006). Waxy and high-amylose wheat starches and flours -characteristics, functionality and application. *Trends in Food Science & Technology*, 17, 448-456.

Vermeylen, R., Goderis, B., Reynaers, H., Delcour, J. A. (2004). Amylopectin molecular structure reflected in macromolecular organization of granular starch. *Biomacromolecules,* 5, 1775-1786.

Proceedings of the 10th International Chemical and
Biological Engineering Conference - CHEMPOR 2008
Braga, Portugal, September 4-6, 2008
E.C. Ferreira and M. Mota (Eds.)

The Effect of operating conditions on styrene bulk polymerization in a spinning disk reactor

S.Mohammadi, M.Alavi [1], M.R.Moghbeli
Chemical engineering Department, Iran university of Science and Technology(IUST), Farjam Str., Tehran, Iran

Abstract: in this paper the influence of operating parameters on performance of spinning disk reactor (SDR) in styrene bulk (without solution) polymerization by 2, 2-azobisisobutyronitrile (AIBN) as an initiator has been studied. The parameters that used for this study are temperature initiator, disk speed and pre-polymer conversion. The results are compared to those observed in a stirred batch reactor. It is believed that centrifugal and shear conditions on rotating disk are the reasons of enhancements in the rate of free radical polymerization.

Key words: bulk polymerization, polystyrene, spinning disk reactor, stirred batch reactor

Introduction

Free radical polymerization technique is widely used by industry for polymerization of styrene. Industrial polymerization process has been traditionally carried out in large stirred tanks. In the market world quality is one of the most important parameters of competition. SDR reactor technology uses centrifugal accelerations to create thin highly sheared films on rotating surfaces so it provides good mixing as well as high mass and heat transfer [1,2]. These characteristics can solve problems of bulk process significantly in high polymer concentration and viscosity during polymerization and we can have uniformity in the mixture. Excellent mixing as well as plug flow characteristics should aid in producing polymer products characterized by narrow molecular weight distribution [3,4]. In the application of the spinning disk technology time scale is the other benefits in polymerization process.

2. Experimental

2.1. Material

Styrene monomer and 2, 2-azobisisobutyronitrile (AIBN) as initiator from Merck Co are being used for experiments.

2.2.Apparatus

Stirred tank reactor

The apparatus used for this study, consisted of a batch reactor and a spinning disk reactor (SDR). The batch consisted of 250 ml capacity volume Pyrex flat glass .the reactor stood in water bath in the center of a magnetic plate which together with a magnetic stirrer in the reaction mixture was used to provide uniform temperature and polymer melt. a thermometer was inserted in the water bath.

SDR

[1] Corresponding author. Tel +982173912716. E-mail:alavi.m@iust.ac.ir

It consists of a chamber enclosed in water cooled housing; the chamber is located on a double pipe rotating shaft driven by an electric motor. The rotating disk system is made of stainless steel 316 and was 20 mm in diameter. The surface of disk is smooth. The disk is rotated by an electromotor positioned on the central shaft, which supported double disk arrangement. The speed of disk is variable by inverter system that is connected to the rotating shaft. The system can used to vary the disk speed in the range 0-3000 rpm. Several copper coils are around the out side of reactor for preventing further polymerization and cooling the product. The temperature of disk is controlled by continues flow of water through a narrow channel underneath it. The water is pumped from a temperature – controlled water bath up the central shaft pipe and is returned to the bath through the outlet shaft pipe. Performance of heating cooling system is shown in figure1

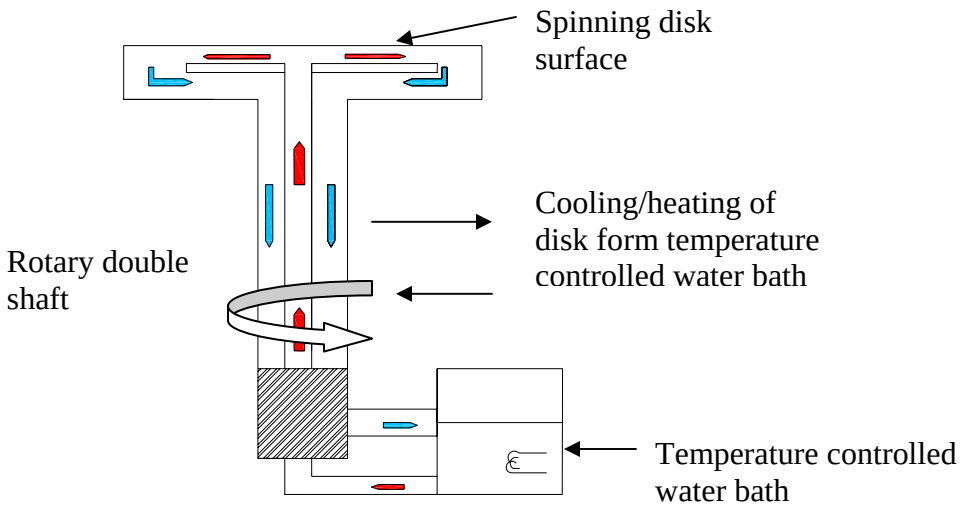

Figure1. internal heat transfer system of SDR

Various parameters for flow on the spinning disk surface have been derived on the basis of centrifugal model.[5] The SDR parameters of interest in this study are the disc residence time t_{res} and the average shear rate $\dot{\gamma}_{ave}$ as expressed in eqs (1),(2)respectively.[5,6]

$$t_{res} = \left(\frac{81\pi^2\nu}{16\omega^2 Q^2}\right)^{1/3}\left(r_o^{4/3} - r_i^{4/3}\right) \quad (1)$$

$$\dot{\gamma}_{ave} = 1.5\left(\frac{Q\omega^4 r}{18\pi\upsilon^2}\right)^{1/3} \quad (2)$$

The mean residence time represents the contact time between the various
Reacting species on the rotating disc while the average shear rate characterizes the degree of mixing achieved in the reacting film.

3.3. Polymerization procedure

3.3.1. Polymerization in batch reactor

Tests were carried out to investigate the effectiveness of the spinning disk on bulk polymerization of styrene. 200 ml styrene polymerized with (0.5-1.5 %) w/w AIBN as initiator at (70-90) °C. Samples were taken every 20 minutes for determining the conversion.

3.3.2 Polymerization in SDR.

Polymerization in SDR consists of 2 stages 1-pre-polymerization in batch as described above and SDR polymerization. The pre-polymer mixture containing monomer polymer and initiator was fed to the center of disk by feeder. Centrifugal forces created by disk rotation force the liquid to flow over the disk surface in the form of a very thin film, after reaching the edge of disk, the product gets thrown off the surface, hits the cold walls and collect for analysis.
The disk temperature (70, 80, 90°C), pre-polymer conversion (32-61%) initiator (0.5, 1, 1.5%w/w) and the disk speed (400-1500rpm) were varied.

4. Results and discussion

4.2 Spinning disk reactor

4.2.1. Effect of pre-polymer feed conversion

The conversion results of runs in SDR can be seen in fig 2. In this experiment different feed conversions are led to disk and as it has shown by increasing feed conversion, there is an increase in product conversion. As we know by proceeding polymerization the viscosity of mixture will be increased so at fixed rotating speed the residence time will be increased so the liquid has higher time exposure on disk and polymerization proceed to higher conversions.[5] The batch time means the time that need to reach to the same conversion in the batch.

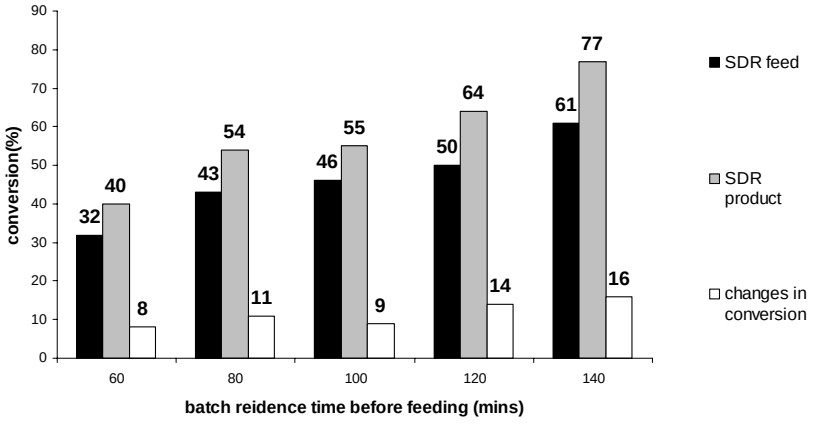

Figure2. Effect of pre-polymer conversion at fixed speed of 1500rpm in SDR

4.2.2. Effect of disk speed

The changes in conversion of the polymer collected from spinning disk surface at disk rotational speeds in the range 400-1500 rpm and fixed SDR feed conversion of 61% can be seen in figure 3. The maximum increase in conversion of 19.6% can be obtained at disk speed of 1500 rpm. By increasing the speed the residence time will be decreased but shear will increase and the shear has more influential role for increasing the conversion.

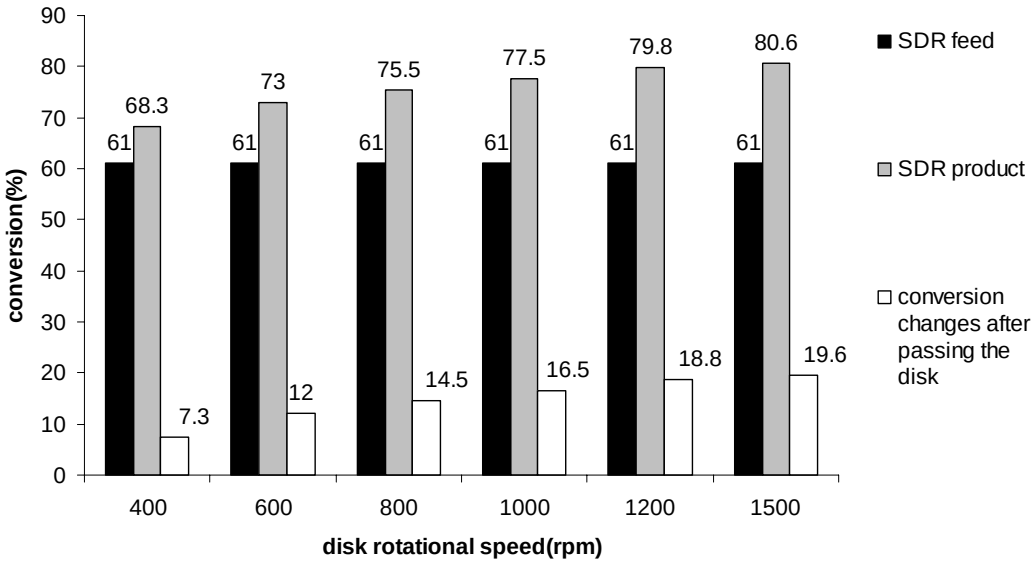

Figure3. Effect of disk speed at fixed pre-polymer conversion of 61%in SDR

For finding disk optimum speed in fixed pre-polymer conversion of 50% led to disk at different disk speed from 400-2000 rpm and the result is shown in figure4.

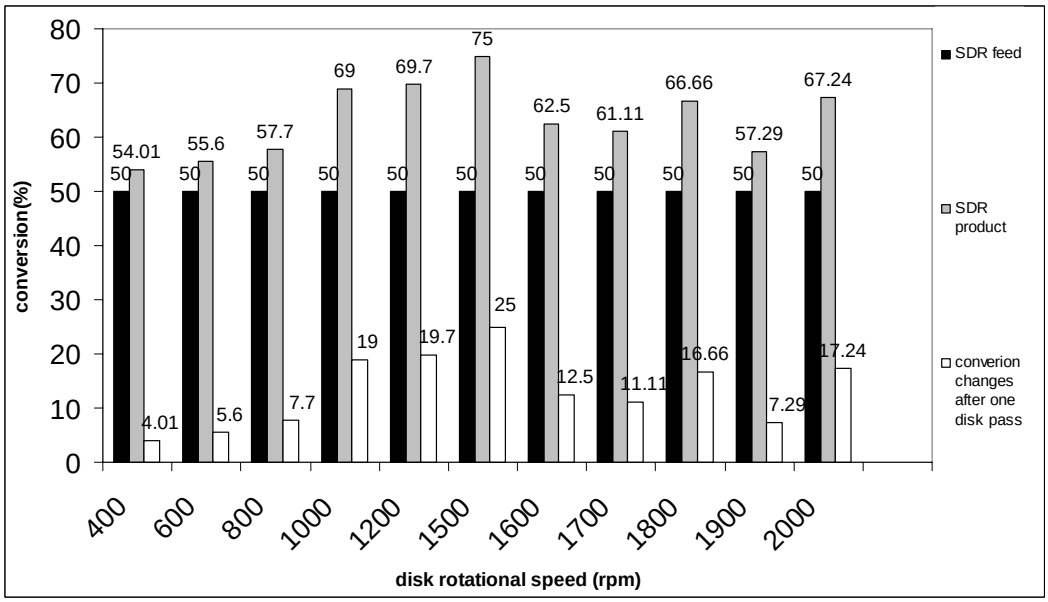

Figure4. Effect of speed on conversion in SDR at fixed pre-polymer conversion of 50%

As we can see after speed of 1500 rpm the conversion will be decreased and residence time is more influential than shear.

For finding an optimum pre-polymer conversion, We have done several tests with different pre-polymer conversion at different disk speed at fixed initiator concentration of 1% and fixed disk temperature 0f 70°C. The results are shown in figure5. As we can see the conversion of 50% has the most changes in one disk pass.

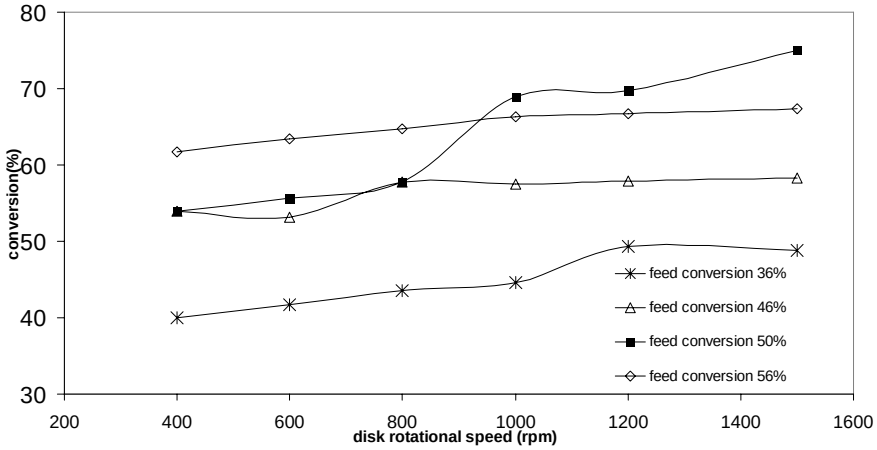

Figure5.effect of pre-polymer at different disk speed in SDR

4.2.3. Effect of temperature

For study the effect of temperature several tests have been carried out that the results are shown in figure 6. as we expected by increasing disk temperature at fixed pre-polymer conversion of 46% and fixed initiator concentration of 1%(w/w) the polymerization rate will be increased, so the conversion will increase.

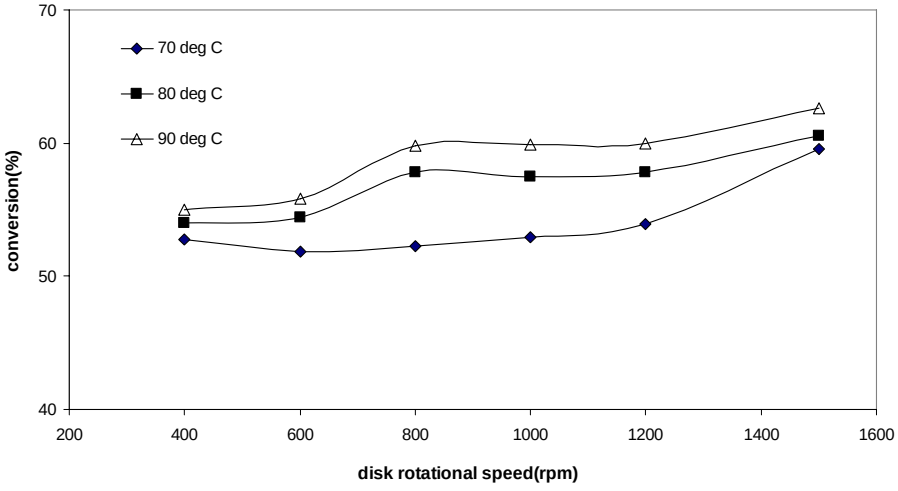

Figure6.Effect of disk temperature on conversion changes at fixed pre-polymer 46% in SDR

5. Conclusion

This work was carried out in an attempt to gain the optimum operating condition in SDR to have the highest changes in conversion of product of SDR at one disk pass. it is hoped that the finding of the effect of parameters, the work will forward our understanding the mechanism of SDR in bulk polymerization.

References:

[1].K.V.K. BoodhooI R.J. JachuckG" Process. intensification. spinning: disk reactor for styren.polymerisation, Applied Thermal. Engineering: 2. (2000). 1127-1146.

[2]P. Leveson, W. A. E. Dunk, R. J. Jachuck "Numerical Investigation of Kinetics of Free-Radical Polymerization on Spinning Disk Reactor" Journal of Applied Polymer Science Volume 90, Issue 3, Date: 17 October 2003, Pages: 693-699

[3]Leveson, W. A. E. Dunk, R. J. Jachuck "Investigation of Shear Effects on Styrene Free Radical Polymerization Using a Narrow Channel Reactor "Applied Polymer Science Volume 94, Issue 4, Date: 15 November 2004, Pages: 1365-1369.

[4]Vicevic,K.Novakovic,K.V.K.Boodhoo,A.JMorris "kinetics of styrene free radical polymerization in the spinning disk reactor,chem..Eng.J(2007)

[5]Kamelia V. K. Boodhoo,1 William A. E. Dunk,1 Marija Vicevic, Roshan J. Jachuck, Valerie Sage,2 Duncan J. Macquarrie, James H. Clark "Classical Cationic Polymerization of Styrene in a Spinning Disc Reactor Using Silica-Supported BF3 Catalyst "Applied Polymer ScienceVolume 101, Issue 1, Pages: 8-19

[6]M.Vicevic,R.J.J.Jachuck, K.Scott,J.H.cllark and K.Wilson "rearengment of α-pinene oxide using a surface catalysed spinning disk reactor" Green Chem ,2004,6,533-537

Proceedings of the 10th International Chemical and
Biological Engineering Conference - CHEMPOR 2008
Braga, Portugal, September 4-6, 2008
E.C. Ferreira and M. Mota (Eds.)

Synthesis of Crosslinked Poly(vinyl chloride): Study of Polymer Properties

Tomás[1],A., Gil[2], M.H., Bordado[3], J.C., Gonçalves[1], P., Rodrigues[1], P.
[1] Companhia Industrial de Resinas Sintéticas, CIRES, S.A., Estarreja, Portugal
[2] Chemical Engineering Department, Coimbra University, Coimbra, Portugal
[3] Chemical and Biological Eng. Department, IBB, Instituto Superior Técnico, Lisboa, Portugal

Keywords: Poly(vinyl chloride), copolymerization, crosslink, polymer properties.
Topic: Advancing the Chemical and Biological Engineering Fundamentals

Abstract

Vinyl chloride (VC)/difunctional derivative copolymerization was carried out in the suspension process for preparing chemically crosslinked poly(vinyl chloride) (PVC). Effects of concentration of the divinyl monomer on the structure of crosslinked PVC (such as the gel fraction, polymerization degree of sol and crosslinking density of gel) were investigated. We could observe that the yield of crosslinking was dependent on the type of crosslink agent. The crosslinking efficiency of diallyl maleate (DAM) was higher than ethylene glycol dimethyl acrylate (EGDMA) Moreover, for DAM, it was possible to achieve a slight increase in the glass transition temperature of the obtained copolymers.

Introduction

The world consumption of poly(vinyl chloride) (PVC) in 2007 was around 33.5 million of metric tons, being the second polymer, considering the different types of poly(ethylene) (Bryen, 2007). Although the vast majority of applications are linked directly with its excellent mechanical properties, compatibility with additives, recyclability and good cost to performance ratio, the major disadvantages comes from its lower heat stability and, consequently, a limited range of final applications (Beltran *et al*, 1998; Yong-Zhong *et al*, 1999). To overcome these deficiencies, the application of the copolymerization technique intends to incorporate a new monomer on the poly(vinyl chloride) growing chain, in order to provide new properties or improve the original ones (Burgess, 1982)

A particular type of copolymerization, consists in the application of a small percentage of a difunctional (divinyl or diallyl) monomer to prepare a chemically crosslinked PVC (Burgess, 1982). Besides other properties, this technique has been continuously studied and developed for the production of special polymers for matte surfaces in top coated finished products (Amano *et al*, 1992; Yong-Zhong *et al*, 1999; Koga *et al*, 1997).

The crosslinked polymer normally follows significant changes on the structure and final behaviour of the material. If previous soluble in the presence of a solvent, the crosslinked polymer swells as the solvent penetrates the network, producing a solvent-swollen crosslinked polymer so called a gel (Stevens, 1990).

The denominated crosslinking agents, such as divinylbenzene, glycol dimethyl acrylate, diallyl maleate or phthalate, have been reported on the literature as efficient gel promoters (Burgess, 1982).

The aim of this paper was to study the effect of new difunctional monomers, like diallyl maleate (DAM), ethylene glycol dimethyl acrylate (EGDMA), polyethylene glycol dimethyl acrylate (PEG Mn: 550) and the correspondent high molecular weight (PEG Mn: 750). Also, besides the study of the effect of co-monomer dosage on the obtained gel fraction, the study of the correspondent glass transition temperature (Tg), could give us a valuable information over the produced copolymer and potential market applications.

* Corresponding author. Tel + 351-234-811212. E-mail: arnaldo.tomas@cires.pt

Experimental

Chemicals

Vinyl chloride monomer (VCM) from Shin Etsu B.V. (purity 99.99% (w/w) from chromatographic method). Deionized industrial water (conductivity < 10µS.m^{-1})
Dially Maleate, tech. (purity min. 93%) (DAM), Ethylene glycol dimethyl acrylate (purity min. 98%) (EGDMA), Polyethylene glycol dimethyl acrylate (PEG Mn: 550), Polyethylene glycol dimethyl acrylate (PEG Mn: 750) from Sigma Aldrich.
Suspending agents: Partially hydrolyzed poly(vinyl alcohol) with 72.5% (PVA 72.5) and 88% (PVA 88) hydrolysis degree (purity min. 95%) – commercial grades from Synthomer Ltd.
Initiator: Tert-butyl peroxydeodecanoate (purity min. 95%) – commercial grade from Akzo Nobel Polymer Chemicals BV.
Tetrahydrofuran (THF) (purity min. 99.9%) and Cyclohexanone (purity min. 99.5%) – chemically pure grades from Riedel-den Haën

Polymerization

The polymer samples studied in this work were prepared in a 150dm^3 pilot reactor equipped with a blade agitator and an external jacket. All standard procedures are described in the literature (Burgess, 1982; Butters, 1982).
The partially hydrolyzed poly(vinyl alcohol) grades were used as colloidal protectors and were dispersed in the deionized water during the reactor charge sequence.
The free radical generator was an organic peroxide (Tert-butyl peroxydeodecanoate), half life 3.9h at 53ºC, and it was charged after the vacuum operation into the reactor mixture.
The polymerization reactions were carried at constant temperature (53ºC), and the unreacted monomer was recovered when the reactor pressure reached 6.60 bar G.
The concentration on monomer (VCM) mass and absolute quantities of water and chemicals are shown in Table 1.

Table 1: Standard Recipe for the VCM polymerization with divinyl monomers.

Chemical	% (on VCM)	Mass, g
Vinyl chloride monomer	--	37000
Deionized water	190.0	70300
PVA 72.5	0.055	20.4
PVA 88	0.012	4.44
Initiator	Variable	
Divinyl monomer	Variable	

The amount of divinyl monomer was variable considering the initial mass concentration based on VCM.

Separation and structure characterization of the sol and gel

A dry sample of polymer was immersed in THF to swell at ambient temperature (20ºC) for 24h. After that, the swollen gel was centrifuged and weighed before the drying operation at 50ºC to obtain the sol. The gel fraction (w_g) of polymer is the ratio of the weight of the dry residue to that of the original resin. The molecular weight (M_c) between crosslinks was determined according to the Flory–Rehner equation (Flory, 1950), according to Eq. (1):

$$M_c = \frac{-\rho_{PVC} \cdot V_{THF} \cdot V_2^{1/3}}{\ln(1 - V_2) + V_2 + \chi \cdot V_2^2} \quad (1)$$

Where, ρ_{PVC} is the density of PVC (1310 kg.m^{-3}), V_{THF} is the molar volume of THF (0.0811 dm^3.mol^{-1}), χ is the polymer-solvent interaction parameter (0.14). The volume fraction of polymer in the swollen gel, V_2, was calculated according to Eq. (2):

$$V_2 = \frac{1}{1 + \frac{\rho_{PVC}}{\rho_{THF}} \cdot \frac{w_s - w_0}{w_0}} \quad (2)$$

Where, ρ_{THF} is the density of THF (0.889 kg.dm^{-3}), w_s is the weight of the swollen gel, and w_0 is the weight of PVC.

The crosslink density (ν) was determined from M_c (Eq. 1) as reported in Eq. (3):

$$\nu = \frac{\rho_{PVC}}{M_c} \quad (3)$$

The gel fraction (w_g) is calculated according to Eq. (4):

$$w_g = \frac{w_s}{w_0} \quad (4)$$

Following the industrial standards, the molecular weight distribution of PVC is estimated from the dilute solution viscosity measurements. According to a reduced viscosity method (ISO 1628-2), using cyclohexanone as the solvent based component for the polymer solution, the Fikentscher "K- value" was determined.

Results and Discussion

Crosslinking Efficiency of Different Divinyls

The polymerizations with a mixture of VCM and the selected divinyl monomers were carried out according to the stated recipe and procedure. After the reaction, the polymer samples were dried in a fluidized bed until a moisture content target lower than 1% (w/w) was reached. The effects of the initial concentration of each divinyl monomer F_x (mass concentration on VCM) on the obtained gel fraction of copolymer are shown in Fig. 1.

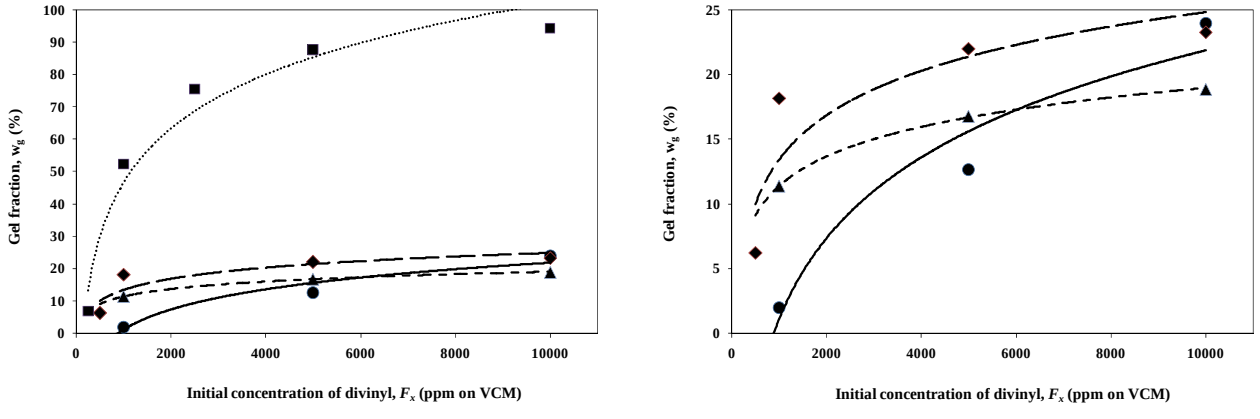

a) b)

Figure 1: Effect of the initial concentration (F_x) of each divinyl monomer on the obtained gel fraction (w_g): (●) VC/PEG Mn550; (♦) VC/PEG Mn750; (▲) VC/EGDMA; (■) VC/DAM.

From Fig. 1 it is possible to conclude that the gel fraction (w_g) increases with the dosage of divinyl co-monomer. Nevertheless, the curve behaviour is different for each divinyl, namely

the gel fraction of VC/DAM copolymer increases rapidly with F_x and a high gel fraction is achieved at a relatively low dosage. The gel fraction of VC/EGDMA copolymer increases slowly as F_x increases, but and it difficult to obtain a crosslinked polymer with a gel fraction higher than 19% (w/w). Also, it seems that the different types of EGDMA have a different behaviour at lower dosage. In fact, for F_x equal to 1000ppm, the PEG Mn550 produced the lower gel fraction (2%), followed by a steady increase in EGDMA (11%) and PEG Mn750 (18%). Although these relative differences are kept lower for higher F_x values, PEG Mn550 and Mn750 had a similar final performance (≈24%).

The different behaviour of the VC/Divinyls in the copolymerization and the different crosslinking efficiencies, are strictly correlated with the reactivity ratios of each pair of VC/Divinyl monomers. In the previous work of Yong-Zhong *et al* (2000), some of the reactivity ratios of VC/ Divinyl monomers were published following the Mayo-Lewis equation for a standard free radical copolymerization system (table 2).

Table 2: Reactivity ratios of VC/crosslinking monomers at 45ºC (Yong-Zhong *et al*, 2000).

(second monomer-2)	DAM	EGDMA
r_1	0.425	0.844
r_2	0.480	23.1
r_1/r_2	0.885	0.0365

From the data in Table 2, It is possible to see that r_1, r_2 of VC/DAM are smaller than 1, showing is copolymerization tendencies. Also, r_1 of VC/EGDMA is smaller than 1, but r_2 much greater than 1, showing the strong tendency of EGDMA towards homopolymerization. Thus, the gel fraction of VC/EGDMA copolymer and the crosslinking efficiency of EGDMA are lower. Moreover, although the reactivity ratios are not published for VC\PEG Mn550 and VC\PEG Mn750, from the obtained results, it is possible to conclude that those reactivity ratios should be similar to the ones of VC\EGDMA system.

Crosslinking Density of Different Divinyls

From the stated calculation procedure (eq. 3), fig. 2 shows that the crosslinking density (ν) of the gel. Again, the major differences in the results of DAM are observed in Fig. 2a).

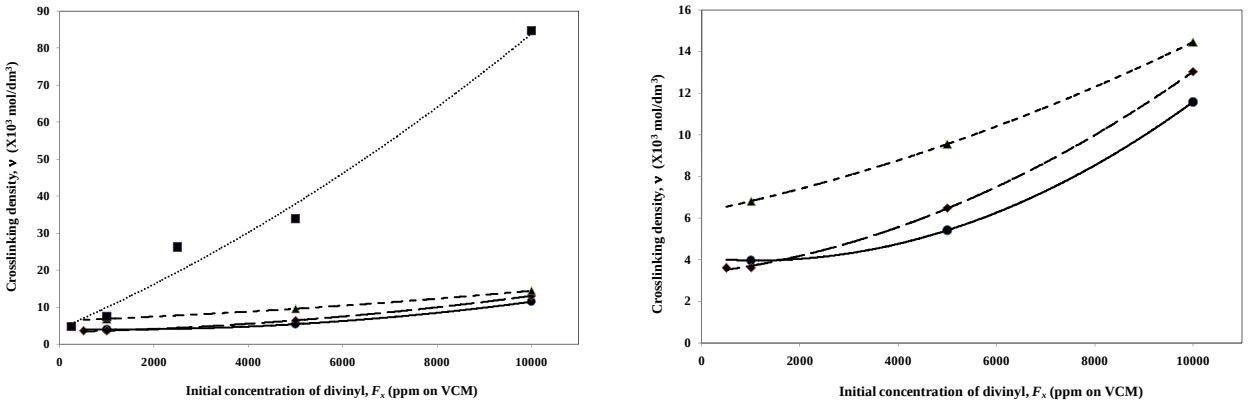

a) b)

Figure 2: Effect of the initial concentration of each divinyl monomer on the crosslinking density of the gel (ν). (●) VC/PEG Mn550; (♦) VC/PEG Mn750; (▲) VC/EGDMA; (■) VC/DAM.

The crosslinking density increases gradually with the increase of the gel fraction, nevertheless for EGDMA, PEG Mn550 and PEG Mn750, there is only a steady increase to 12~14 x10^3 mol.dm^{-3} (fig. 2b). For DAM, the gel fraction becomes noticeable higher for higher divinyl dosages. These results are in direct tune with the higher crosslinking efficiency of DAM.

K Value of Sol for Different Divinyls

The effect of the concentration of each divinyl monomer on the K value of sol is shown in Fig. 3.

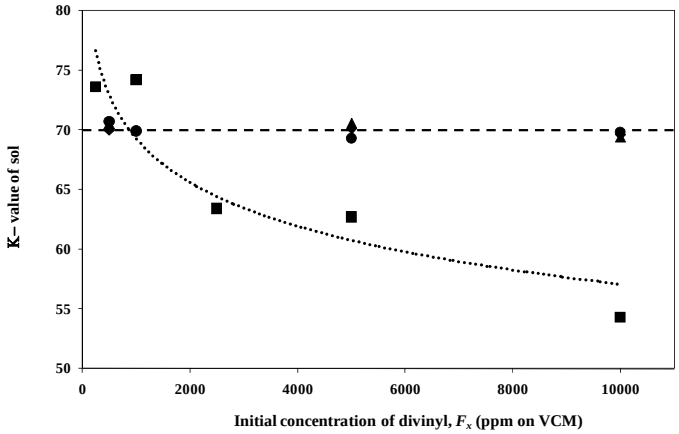

Figure 3: Effect of the initial concentration of each divinyl monomer on the K value of sol: (--) K value homopolymer; (●) VC/ PEG Mn550; (♦) VC/ PEG Mn750; (▲) VC/EGDMA; (■) VC/DAM.

Besides the known dependence of the reaction temperature, there is a sudden decrease in K value only for a concentration of DAM higher than 1000 ppm. That is, it seems that only for a very high gel fraction (>50%), there is a lowering effect of the K value of the sol. Thus, comparing with the homopolymer data, for an efficient gel promoter like DAM, the longer primary chains will have a higher probability of participating in the crosslinking reaction.

Glass transition (Tg) for Different Divinyls

The glass transition temperature was determined by Differential Scanning Calorimetry (DSC) according to a standard procedure for poly(vinyl chloride). In fig. 4 it is shown the Tg for each polymer sample.

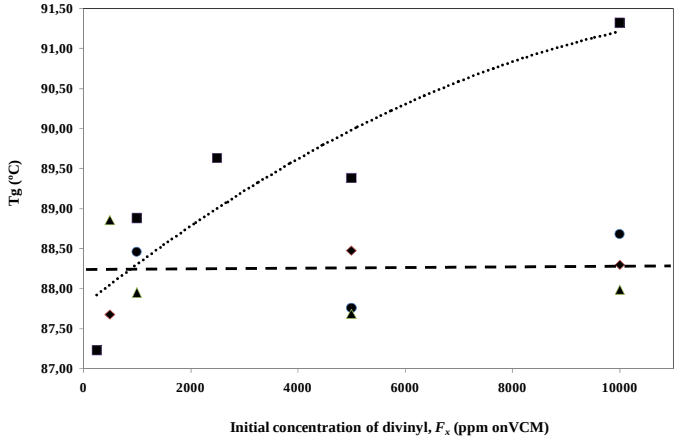

Figure 4: Effect of the initial concentration of each divinyl monomer on the Tg of the copolymer: (--) Tg homopolymer; (●) VC/PEG Mn550; (♦) VC/PEG Mn750; (▲) VC/EGDMA; (■) VC/DAM.

Although the data variation around the homopolymer target (88.48º), mainly related with the fluctuations from the polymer production process, it is possible to observe in Fig 4. an increase trend of Tg with the DAM dosage. This result it's in tune with the fundamentals of the Tg definition, mainly the modifications in the polymer chemical structure by a lower molecular free volume or rotational freedom, related with the crosslinking effects in the carbon chains.

Conclusions

Chemically crosslinked PVC can be obtained by VC/difunctional monomer suspension copolymerization. Its structure is influenced by the concentration of the difunctional monomer and the correspondent reactivity with VCM. The crosslinking efficiency of the divinyls changes in the following order of relative magnitude: DAM>>PEG Mn750>PEG Mn550>EGDMA. The crosslinking efficiency of EGDMA is very low due to its higher probability of homopolymerization. Also, the similar behaviour of PEG Mn750 and PEG Mn550, induces the fact that the correspondent reactivity ratios should be within the same range of the system VC\EGDMA. The crosslinking density of the gel increases as the concentration of the divinyls increases, but markedly for DAM rather than all the others. Also, for DAM, the K value of the sol of the copolymer decreases with the increase of the gel fraction. The opposite effect is observed for the glass transition temperature (Tg), with an abrupt increase of more than 2.5ºC, from the standard homopolymer, when the gel fraction reached over 90% (w/w).

Acknowledgments

The financial support of FCT, SFRH/BDE/15534/2005, is gratefully acknowledged.

References

Bryen, S. (2007). Vinyls Industry update. *World Vinyl Forum 2007*, Boston, USA.

Yong-Zhong, B., Zhi-Xue, W., et al. (2000), Synthesis of chemically crosslinked poly(vinyl chloride) by vinyl choride/divinyls suspension polymerization. *Europ. Polym. Journal*, 36, 981-986.

Beltran, M.I., García, J.C., et al. (1999), Thermal decomposition behaviour of crosslinked plasticized PVC. *Polymer Degradation and Stability*, 65, 65-73.

Amano,T., Hoshida, S. (1992). US patent, 5,130,387.

Koga, T., *et al.* (1997), US patent, 5,614,593.

Burgess, R.H. (1982), Manufacture and Processing of PVC, Applied Science Publishers LTD, London, UK.

Butters G. (1982). Particulate nature of PVC: Formation, structure, and processing, London: Applied Science Publishers

Stevens, M.P. (1990). Polymer Chemistry 2nd Edition. Oxford University Press, New York, USA.

Flory, PJ., Krigbaum, W.R. (1950). Thermodynamics of high polymer solutions, *Journal Chemical Physics*,18,108.

Proceedings of the 10th International Chemical and
Biological Engineering Conference - CHEMPOR 2008
Braga, Portugal, September 4-6, 2008
E.C. Ferreira and M. Mota (Eds.)

Experimental Study of the TEMPO Mediated Copolymerization of Styrene with Divinylbenzene

Miguel A.D. Gonçalves[1], **Rolando C.S. Dias**[1] *, **Mário Rui P.F.N. Costa**[2]
[1]LSRE-Instituto Politécnico de Bragança
Quinta de Santa Apolónia, 5300 Bragança, Portugal.
[2] LSRE-Faculdade de Engenharia da Universidade do Porto
Rua Roberto Frias s/n, 4200-465 Porto, Portugal.

Keywords: Crosslinking, Nitroxide-Mediated, Kinetic, Modeling, Radius of Gyration.
Topic: Advancing the chemical engineering fundamentals.

Introduction

Since the discovery of controlled radical polymerization (CRP) in the early nineties (Georges et al., 1993), an ever increasing activity has been focused on the production of polymers with narrow molecular weight distributions and well-defined architectures (such as block copolymers, stars or brushes). This work describes an experimental research on the nitroxide-mediated radical polymerization (NMRP) of styrene (S) and divinylbenzenes (DVB) in xylene (X) solution at 130 °C, using the stable radical TEMPO (2,2,6,6-tetramethylpiperidinyl-1-oxy) as mediator and AIBN (azobisisobutyronitrile) as initiator. Measurements of absolute molecular weights and *z*-average radius of gyration of the produced copolymers have been performed for different polymerization times using a SEC system with coupled refractive index (RI) and multi-angle laser light scattering (MALLS) detectors.

The main difference between conventional free radical polymerization (FRP) and NMRP is due to the dynamic equilibrium described by Eq. (1), where $-\mathrm{P}^{\bullet}$ represents an active polymer radical, X a stable radical (e. g. TEMPO) and $-\mathrm{P}-\mathrm{X}$ a dormant alkoxyamine:

$$-\mathrm{P}^{\bullet} + \mathrm{X} \underset{k_{act}}{\overset{k_{deact}}{\rightleftharpoons}} -\mathrm{P}-\mathrm{X} \tag{1}$$

This intermittent equilibrium reduces substantially the concentration of active radicals and concomitantly the probability of termination. Consequently, the expected life time (t_l) of a polymer molecule in NMRP attains several hours, in contrast with the few seconds characteristic of FRP, as described by Eq. (2):

$$t_l = \frac{R}{r_t} \simeq \frac{1}{2k_t R} \tag{2}$$

with R representing the concentration of active radicals, r_t the rate of termination and k_t the correspondent rate coefficient. Is therefore possible to reduce the frequency of termination of polymer chains to levels below 5% , the result being a huge increase in the homogeneity of the products. Nowadays, besides NMRP other CRP techniques like Atom Transfer Radical Polymerization (ATRP) or Reversible Addition-Fragmentation Chain Transfer Polymerization (RAFT) are used with the aim of synthesizing

* Corresponding author. Tel. +351-273-303088. E-mail: rdias@ipb.pt.

more homogeneous linear polymers. More recently these concepts have been extended to non-linear polymerizations by trying to obtain also more homogeneous polymer networks with potential applications as advanced materials (Ide and Fukuda, 1997, 1999; Achilleos et al., 2007; Gao et al., 2008). Considering the NMRP of S/DVB, here we also show that a recently developed general kinetic approach can be used to assist in the design of such branched polymers.

Experimental Part

Experiments were carried out at 1 dm^3 scale using a 2.5 dm^3 maximum capacity stainless steel semi-batch reactor which has been described in detail elsewhere (Gonçalves et al., 2007). In this work the reactor was operated only in batch mode. Xylene at 98.5% purity, AIBN at 98% purity, TEMPO at 98% purity, styrene stabilized with 0.005% w/w 4-tert-butylcatechol at 99% purity and commercial grade divinylbenzene stabilized with 0.1% w/w 4-tert-butylcatechol at 80% purity have been purchased from Sigma Aldrich and used as received. That commercial DVB is a mixture of isomers, comprising 56.2% m-divinylbenzene and 24.2% p-divinylbenzene, plus 19.6% of ethylvinylbenzene. Xylene solvent is also a mixture of xylenes plus ethylbenzene ($\leq$ 25% in the latter component). Typically, NMRP and conventional S/DVB copolymerizations were carried out as follows: the empty reactor was purged with an argon stream (40 cm^3/min) and the heating process in order to reach 130 °C was started. After 15 min, the predetermined amounts of styrene, xylene, divinylbenzene and TEMPO (in NMRP experiments) were charged to the reactor. Until completion of the heating process the polymerization system was bubbled with argon at a flow rate of 40 cm^3/min. Owing to energy losses and insufficient heating power, around 100 and 120 min were needed to reach the set-point temperature of 130 °C in the conventional and NMRP experiments, respectively. This difference is caused by the heat generated by the auto-initiation of styrene in the conventional runs during the heating period. When the set-point was reached, samples of polymer were withdrawn from the reactor to be analyzed by SEC/RI/MALLS and immediately afterwards AIBN was added to the system, defining the initial time of the polymerization $t = 0$. The analysis of these samples has confirmed the existence of some thermal initiation of styrene during the heating process in conventional runs (monomer conversion of about 4 % was experimentally measured) and conversely, the absence of this phenomenon in the NMRP experiments has been found. After $t = 0$ samples of polymer were withdrawn from the reactor at prescribed polymerization times and analyzed by SEC/RI/MALLS. During the polymerization process the flow rate of the argon stream spargeing the system was reduced to 20 mL/min in order to prevent appreciable mass losses from the reactor, since it is operated at atmospheric pressure and the polymerization temperature is close to the xylene boiling point (around 140 °C).

Kinetic Modeling

Based upon a work started in the early nineties (Costa and Dias, 1994), it has been recently shown that molecular size distributions (MSD), sequence size distributions (SSD) and *z*-average radius of gyration distributions (RGD) can be predicted for complex irreversible non-linear polymerization systems (Costa and Dias, 2005, 2007; Dias and Costa, 2006, 2007). Besides the detailed molecular architecture which becomes feasible to describe, this general kinetic approach is valid for different kinds of reactors (batch, plug flow, semi-batch or CSTR) and is free of several mathematical simplifications with non-universal applicability. Moreover, this approach allows the development of a computational tool that can be used to simulate different polymerization systems in an automated fashion. Eqs. (3), (4) and (5) are the general master equations allowing the prediction of the MSD, SSD and RGD after specification of the chemical

Table 1: Chemical groups and kinetic scheme considered in the modeling studies of NMRP of S/DVB.

Chemical Groups	Chemical Reactions
Five Monomers: S, *m*-DVB, *p*-DVB and pendant double bonds (*m*-PDB, *p*-PDB). Five kinds of polymer growing Radicals. Five kinds of polymer dormant Radicals. Initiator, primary radicals from initiator, from monomeric styrene and from the dimer. Two kinds of dormant primary radicals and saturated nitroxyl radical. Nitroxyl radical (TEMPO), Dimer of Styrene, solvent and correspondent primary radical.	Mayo Dimerization of Styrene. Thermal Initiation of Styrene. Initiator Decomposition. Living/dormant exchange of radicals. Initiations of monomers and pendant double bonds. Chain transfers to monomers, solvent, dimer and initiator.

groups and kinetic scheme of the polymerization system.

$$\frac{\partial G}{\partial t} = G_{\mathcal{R}_P} + \frac{G_F(t) - G}{\tau} - \mathcal{R}_v G; \qquad G_{|t=0} = G_0\left[\mathbf{s_0}(t, \mathbf{s})\right] \tag{3}$$

$$\frac{\partial U}{\partial t} = G_{\mathcal{R}_S} + \frac{U_F(t) - U}{\tau} - \mathcal{R}_v U; \qquad U_{|t=0} = U_0\left[\mathbf{s}_0(t, \mathbf{s})\right] \tag{4}$$

$$\frac{\partial G_n^H}{\partial t} = G_{\mathcal{R}_{H_n}} + \frac{G_{n\ F}^H(t) - G_n^H}{\tau} - \mathcal{R}_v G_n^H; \qquad G_{n\ |t=0}^H = G_{n\ 0}^H\left[\mathbf{s_0}^-(t, \mathbf{s}^-), \mathbf{s_0}^+(t, \mathbf{s}^+)\right] \tag{5}$$

In the present polymerization system, modeling studies were performed considering a kinetic scheme comprising a total of 36 chemical groups and 125 different chemical reactions, as briefly summarized in Table 1. Note that due to the existence of two isomers in commercial DVB, this polymerization system becomes more complex than a crosslinking process involving for instance pure diacrylates or dimethacrylates. Indeed, *m*-DVB, *p*-DVB and the correspondent pendant double bonds (*m*-PDB and *p*-PDB, respectively) have different reactivities (Gonçalves et al. (2007) and references therein) and therefore must be distinguished in the kinetic modeling. Moreover, due to the relatively high polymerization temperature (130 °C) which is required, other complex details arising from the thermal initiation of styrene must be taken into account in the present studies.

Results and Discussion

In Figure 1(a) is presented a typical kinetic plot showing the living character of a NMRP run. The modified monomer conversion $ln(M_0/M) = -ln(1-p)$ should roughly (after an initiation period) follow a linear growth with reaction time and this is confirmed with the experimental measurements presented in Figure 1(a). The predicted values were obtained using kinetic parameters available in the literature for linear NMRP polymerization systems (Zhang and Ray (2002), Fu et al. (2007) and references therein). Note that monomer conversion is almost not affected by the reactivities of *m*-PDB and *p*-PDB, since the concentrations of these species in the polymerization system is very low.

Figure 1(b) shows in detail the improved control of the molecular architecture achievable in NMRP synthesized polystyrene (PS) samples as compared to the FRP products. From the chromatograms of PS samples with different polymerization times shown in Figure 1(c) it is possible to observe the growth of molecular weights without concomitant broadening of the distribution. In fact, linear products with an

approximately constant polydispersity index (around 1.1) can be produced at increasing polymerization times (monomer conversions) using the NMRP technique.

Measured and predicted time evolution of $\overline{M}_n$ and $\overline{M}_w$ in a NMRP copolymerization of S/DVB with $y_{DVB} = 0.5\%$ and initial molar ratio TEMPO/AIBN=1.1 are presented in Figure 1(d). A good agreement between experimental observations and predictions is here observed using the reactivity of pendant double bonds as fitting parameters. It was estimated that the apparent reactivity ratio of PDB comparatively to styrene is $r = k_p^*/k_{p11} = 0.35$ (similar to the one found in Gonçalves et al. (2007) with FRP of S/DVB). It is plausible that the value of this reactivity ratio becomes affected by the effect of intramolecular cyclization reactions which were neglected in the present calculations. Indeed, these effects should be more important at 50% dilution as compared with bulk conditions used to estimate the equal reactivity of pendant vinyls in related works (Ide and Fukuda, 1997). An apparent decrease of the reactivity ratios of pendant vinyls with respect to the monomers has been found by these authors (Trigo et al., 2008) and other research groups (Gao et al., 2008) for other polymerization systems at diluted conditions, namely dimethacrylates and diacrylates, respectively.

Figure 1(e) compares the observed and predicted evolution of $\overline{M}_w$ for linear and non-linear polymer formation. The well-known linear growth of $\overline{M}_w$ for linear polystyrene does not occur with S/DVB copolymerization owing to the build-up of branched products. These results show that non-linear copolymerizations can be used to modify the properties of linear polymers with the goal of producing advanced materials (such as hyperbranched polymers). Figure 1(f) shows in detail the impact on the polymer molecular sizes of the presence of a small amount of DVB (about 0.5% mole fraction) in the NMRP polymerization system. A fraction of polymer molecules of molecular architecture close to linear polystyrene is present (showing an ill-separated peak at higher elution times) but most of polymer is branched.

Figure 2 compares experimental measurements (by SEC/MALLS) and theoretical predictions of the *z*-average radius of gyration of these non-linear polymers. This confirms the usefulness of the proposed kinetic approach namely to design with improved detail the molecular architecture of such materials. Note that results presented in Figure 2(b) show a more compact structure of NMRP S/DVB copolymers as compared with the FRP analogues. This means that the properties of these polymers can be manipulated in a known way through the use of CRP techniques.

Conclusions

Molecular architecture of NMRP S/DVB copolymers measured by SEC/MALLS shows important differences not only when compared with the linear case but also with respect to the FRP of the same monomers. It has now been shown that a recently developed general kinetic approach can deal with the complexities of this polymerization system, namely those caused by the huge number of different chemical species and involved reactions. The final goal of this research is to design hyperbranched polymers and networks with a well defined structure (which should be predicted by appropriate theoretical means) to be used for biomedical purposes or exploited as advanced materials. Earlier works on similar chemical systems (Ide and Fukuda, 1997) have now been extended with predictions and measurements of average molecular weights and radius of gyration of sol fraction. Likely influence of intramolecular reactions has been detected at 50 % dilution, showing that at best only in bulk conditions more or less ideal networks can be produced. Ongoing researches are expected to provide more assertive results.

Acknowledgments

Financial support by Fundação para a Ciência e a Tecnologia (FCT), Ministry of Science and Technology of Portugal and European Community through FEDER (projects POCI/EQU/44784/2002 and POCI/EQU/60483/2004 - PPCDT/EQU/60483/2004) is gratefully acknowledged.

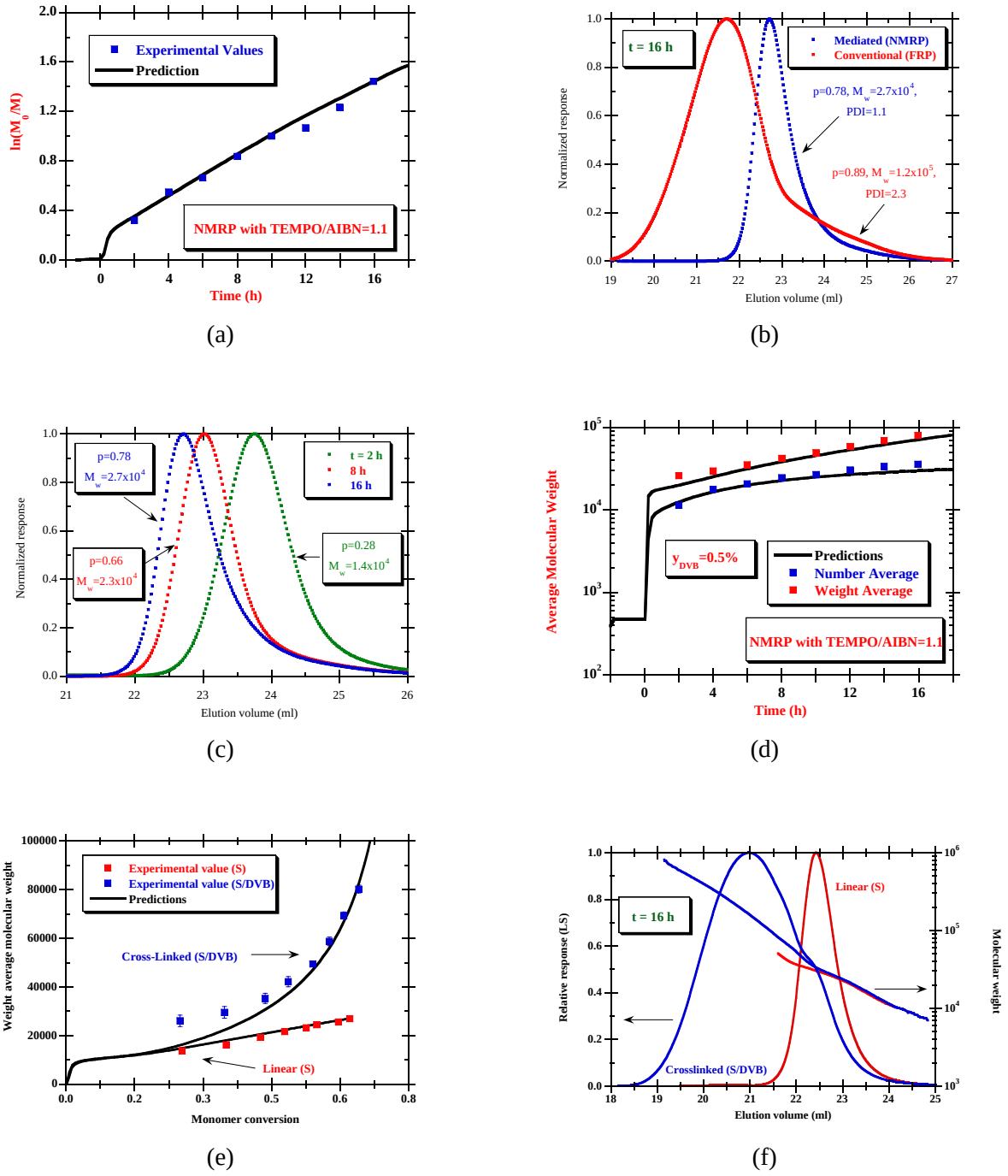

Figure 1: (a) Kinetic plot showing the living character of a NMRP run with TEMPO/AIBN=1.1. (b) Observed chromatograms (RI) of polystyrene (PS) samples synthesized at 130 °C using conventional free radical polymerization (FRP) and NMRP. In both cases the polymerization time is $t = 16$ h. Polymerizations in S/X solution (50 % v/v) using the same initial ratio S/AIBN in both runs: S_0 = 4.4, $AIBN_0$ = 0.0086 and $TEMPO_0$ = 0.0096 $\mathrm{mol\ dm^{-3}}$ (NMRP experiment). (c) Observed chromatograms of NMRP synthesized PS samples (same conditions as (b)) with different polymerization times showing the growth of MW without concomitant broadening of the distribution (PDI around 1.1). (d) Measured and predicted time evolution of $\overline{M}_n$ and $\overline{M}_w$ in a NMRP copolymerization of S/DVB with $y_{DVB} = 0.5\%$ and initial molar ratio TEMPO/AIBN=1.1. (e) Predicted and measured $\overline{M}_w$ in linear (S) and non-linear (S/DVB) NMRP polymerizations. (f) Observed chromatograms (MALLS) of PS and S/DVB samples synthesized using NMRP. Copolymerization S/DVB was performed with DVB_0 = 0.022 $\mathrm{mol\ dm^{-3}}$.

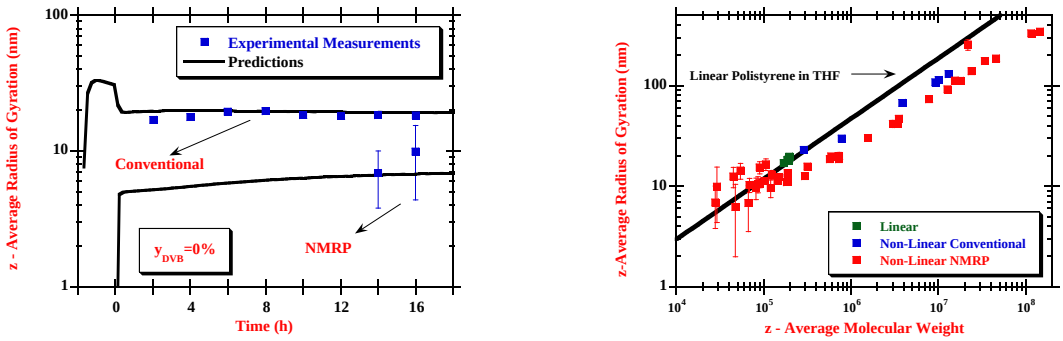

(a) (b)

Figure 2: (a) Predictions and experimental observations for $\overline{R}_g$ in conventional and NMRP linear runs. (b) Experimentally observed relation $\overline{R}_g$ vs. $\overline{M}_z$ in different conventional and NMRP runs in the S/DVB copolymerization.

References

Achilleos, M., Krasia-Christoforou, T., Patrickios, C. (2007). Amphiphilic Model Conetworks Based on Combinations of Methacrylate, Acrylate, and Styrenic Units: Synthesis by RAFT Radical Polymerization and Characterization of the Swelling Behavior, *Macromolecules*, 40, 5575–5581.

Costa, M.R.P.F.N., Dias, R.C.S. (1994). A general kinetic analysis of non-linear irreversible copolymerizations, *Chem. Eng. Sci.*, 49, 491–516.

Costa, M.R.P.F.N., Dias, R.C.S. (2005). An Improved General Kinetic Analysis of Non-Linear Irreversible Polymerizations, *Chem. Eng. Sci.*, 60, 423–446.

Costa, M.R.P.F.N., Dias, R.C.S. (2007). Prediction of Mean-Square Radius of Gyration of Tree-Like Polymers by a General Kinetic Approach, *Polymer*, 48, 1785–1801.

Dias, R.C.S., Costa, M.R.P.F.N. (2006). A general kinetic method to predict sequence length distributions for non-linear irreversible multicomponent polymerizations, *Polymer*, 47, 6895–6913.

Dias, R.C.S., Costa, M.R.P.F.N. (2007). Branching and Cross-Linking in Coordination Terpolymerizations, *Macromol. React. Eng.*, 1, 440–467.

Fu, Y., Cunningham, M.F., Hutchinson, R.A. (2007). Modeling of Nitroxide-Mediated Semibatch Radical Polymerization, *Macromol. React. Eng.*, 1, 243–252.

Gao, H., Li, W., Matyjaszewski, K. (2008). Synthesis of Polyacrylate Networks by ATRP: Parameters Influencing Experimental Gel Points, *Macromolecules*, 41, 2335–2340.

Georges, M.K., Veregin, R.P.N., Kazmaier, P.M., Hamer, G.K. (1993). Narrow Molecular Weight Resins by a Free-Radical Polymerization Process, *Macromolecules*, 26, 2987–2988.

Gonçalves, M.A.D., Dias, R.C.S., Costa, M.R.P.F.N. (2007). Time programmed feed of semibatch reactors with non-linear radical copolymerizations: an experimental study of the system styrene+divinylbenzene using SEC/MALLS, *Macromol. Symp.*, 259, 124–134.

Ide, N., Fukuda, T. (1997). Nitroxide-Controlled Free-radical Copolymerization of Vinyl and Divinyl Monomers. Evaluation of Pendant-Vinyl Reactivity, *Macromolecules*, 30, 4268–4271.

Ide, N., Fukuda, T. (1999). Nitroxide-Controlled Free-Radical Copolymerization of Vinyl and Divinyl Monomers. 2. Gelation, *Macromolecules*, 32, 95–99.

Trigo, I.M.R., Gonçalves, M.A.D., Dias, R.C.S., Costa, M.R.P.F.N. (2008). Molecular Architecture of Non-Linear Polymers: Kinetic Modeling and Experimental Characterization of the System Methyl Methacrylate + Ethylene Glycol Dimethacrylate, *Macromol. Symp.*, Accepted.

Zhang, M., Ray, W.H. (2002). Modeling of "Living" Free-Radical Polymerization Processes. I. Batch, Semibatch, and Continuous Tank Reactors, *J. Appl. Polym. Sci.*, 86, 1630–1662.

Proceedings of the 10th International Chemical and
Biological Engineering Conference - CHEMPOR 2008
Braga, Portugal, September 4-6, 2008
E.C. Ferreira and M. Mota (Eds.)

Styrene polymerization under high shear

S. Mohammadi, M.R. Moghbeli, M. Alavi [1]
Chemical engineering Department, Iran University of Science and Technology(IUST), Farjam Str., Tehran, Iran

Abstract: free radical bulk polymerization of styrene with 2,2-azobisisobutironitrile (AIBN) as an initiator has been studied in a spinning disc reactor (SDR).multi pass technology has been used in this study. It is believed that multi passed product has better quality than one passed. The excellent heat and mass transfer that can be achieved in the highly sheared thin films that produced on the surface of disc due to centrifugal acceleration are the most important reasons of improving the product quality.

Keywords: polymerization, polystyrene, shear, AIBN

1-Introduction

Spinning disc technology has been demonstrated to achieve significant enhancements in free radical polymerization rate. [1, 2] it is believed that these enhancements are related to the centrifugal and shear conditions that exist on the disc. [2].

Bulk polymerization of styrene is a mass and heat transfer limited process. we have designed a thin film spinning disc reactor. This reactor provides good heat and mass transfer as well as micro mixing characteristics.
In bulk processes where the viscosity of the mixture increases by about seven orders of magnitude during the course of polymerization SDR can solve the problem. The occurrence of hot spots and temperature peaking results in broadening of the molecular weight distribution , he effects of which are translated into a poor polymer product quality.[3]
Benefits that can be obtained by using SDR are high quality of product, time saving, temperature controlling and high rate polymerization. In this study has been used multi pass disc and the data has been compared to those has been passed single time from the disc and also the data has been obtained from batch reactor.

2. Experimental

2.1.Materials

Styrene monomer and AIBN as initiator from Merck Co are being used for experiments.

2.2.Apparatus

The apparatus used for this study, consisted of a batch reactor and a spinning disc reactor (SDR). The batch reactor system shown schematically in figure 1 consisted of 250 ml capacity volume Pyrex flat glass .the reactor stood in water bath in the center of a magnetic plate which together with a magnetic stirrer in the reaction mixture was used to

[1] Corresponding author. Tel +982173912716. E-mail:alavi.m@iust.ac.ir

provide uniform temperature and polymer melt. A thermometer was inserted in the water bath.

A schematic of SDR reactor is shown in figure 1. It consists of a chamber enclosed in water cooled housing; the chamber is located on a double pipe rotating shaft driven by an electric motor. The rotating disc system is made of stainless steel 316 and was 20 mm in diameter. The surface of disc is smooth. The disc is rotated by an electromotor positioned

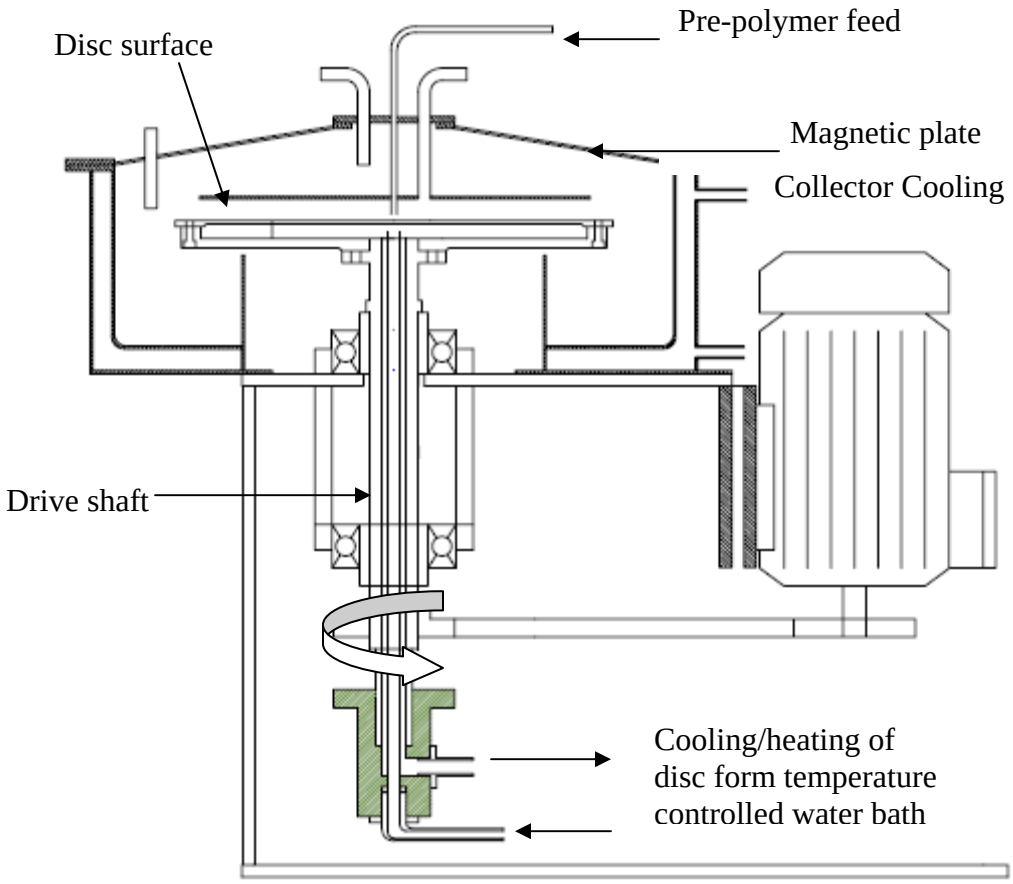

Figure 1. Schematic of spinning disc reactor

on the central shaft, which supported double disc arrangement The speed of disc is variable by inverter system that is connected to the rotating shaft. The system can used to vary the disc speed in the range 0-3000 rpm. Several copper coils are around the out side of reactor for preventing further polymerization and cooling the product. The temperature of disc is controlled by continues flow of water through a narrow channel underneath it. The water is pumped from a temperature – controlled water bath up the central shaft pipe and is returned to the bath through the outlet shaft pipe. The reactor set-up is shown in figure 2.

Figure2.Spinning disc reactor

3.3. Procedure

3.3.1.Polymerization in batch reactor

Tests were Carried out to investigate the effectiveness of the spinning disc on bulk polYmerization of styrene. 200 ml styrene polymerized with 1 % w/w AIBN as initiator at 70 °C. samples were taken everx 20 minutes for detarmining the conversikn. for experiments runs were perfmrmed each having different prepolymer stage eNding to conversion of 30% and 50% t(at has been chosen for this study.

3.3.2.Polymerization in SDR reactor

The SDR reactor(temperature of heating disc system) is set to 70°C and hot Pre-polymer from batch stage is fed into the center of disc through a feeder. centrifugal forces of rotating disc force the liquid to flow over the disc from the center to edge of surface in form of very thin film , the sheared film gets thrown off the surface, hits the cold walls and polymerization is being stopped. The product collected and conversion were determined. Polymer that collected from collector is being preheated and then fed in to the disc again and the product collected and conversion were determined and for 3 times the polymer is passed on the surface of disc.

4.Samples analysis

The quality of the polymer and conversion in the samples collected from the batch and spinning disc surface were assessed using gel permeation chromatography (GPC).

5.Results and discussion

5.1. batch reactor

The data that obtained from batch reactor is shown in figure 3.these test carried out for comparison of performance of SDR and obtained profile has been used as a standard.

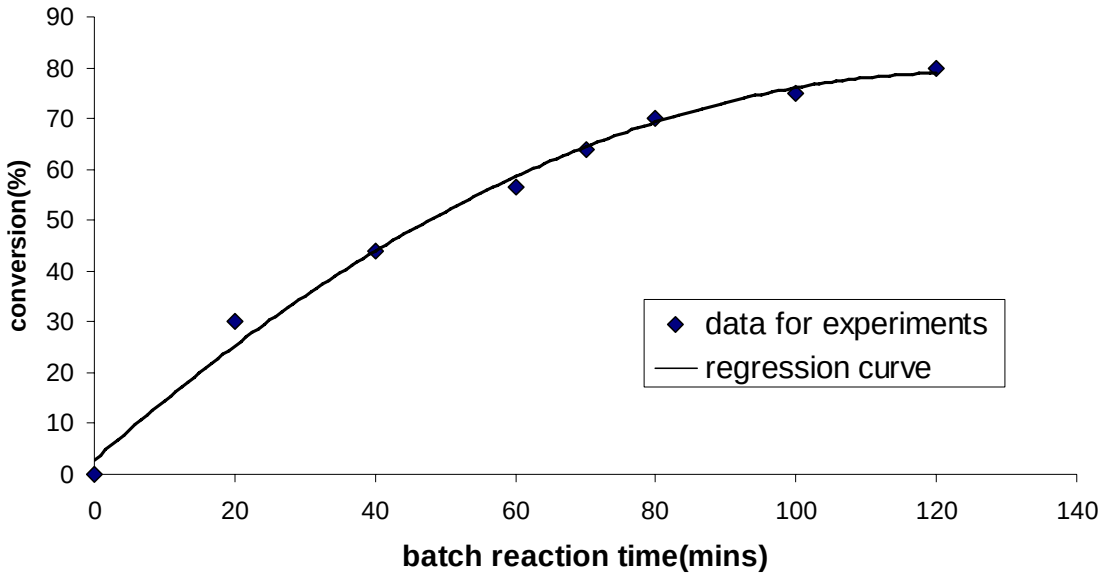

Figure3 .batch styrene polymerization profile

5.2 SDR reaCtor

Several test has been carried out tg study performance of SDR with fixed disc speed of 1500 rpm and different feed conversion. The general procedure of performing SDR runs include 4 steps: 1. preparation of feed (pre-polymer) in batah reactor that explained above 2. Transferring fee$ to disc.3 and 4 are transferring SDR product as feed to disc again. It means thap each beed step is the product of previous step.

5.2&1.Effect of pre-polymer conversion

The conversion result of runs are given in fig 4-5.
From fig 5,6 it can be seen that a rise in the conversion of feed in to the SDR is accompanied by steady increase in product conversion in one pass on the disc rotating at 1500 rpm. It is known that a direct proportionality relationship exists between the residence time on the disc and liquid viscosity, it is expected that the corresponding rise in exposure time on the spinning disc allows polymerization proceed to higher conversion.[4] In fig 5 the changes of conversion after each pass on the disc for prepolymer of 30% and in fig6 for pre-polymer of 50% can be seen.

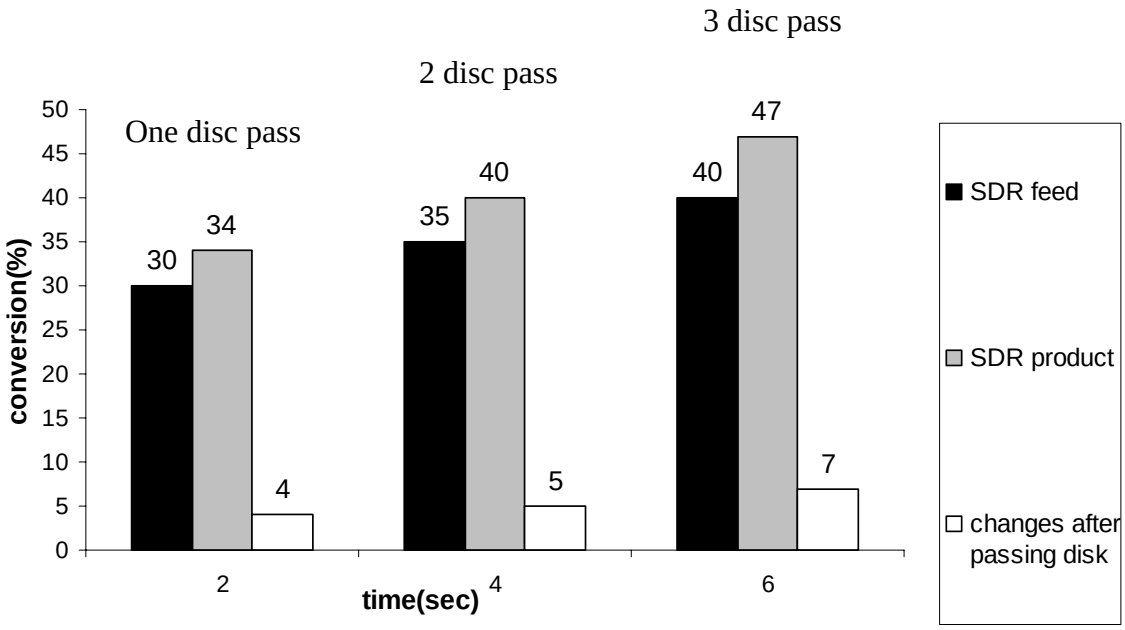

Fig4.Styrene polymerization changes after 3 disc pass for pre-polymer 30%

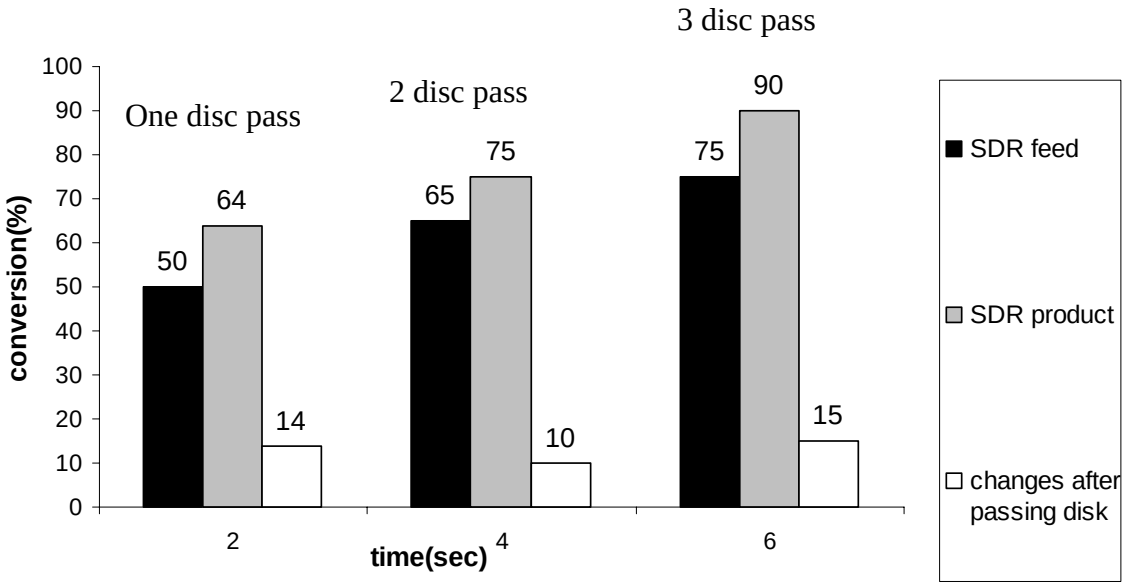

Fig5.Styrene polymerization changes after 3 disc pass for pre-polymer 30%

As it has shown in fig 5 and fig 6 total times for each step is 2 seconds and by comparing the results in fig 4 , 5 and fig 3 we can see the time saving by using SDR reactor.

Table1.Molecular weight properties of final polymer product from batch and SDR reactor

Reactor type	Conversion(%)	M_n(gr/mol*10^4)	M_w(gr/mol*10^4)	PDI
batch	30	2.3929	4.1132	1.71
SDR	34	2.3720	4.0479	1.70
SDR	45	2.4302	4.4441	1.82
Batch	50	3.0175	4.5394	1.5
SDR	75	2.3272	4.6965	2.018
SDR	90	2.7164	4.5299	1.667

results of GPC test has shown in table 1. a slight decrease in the number average and weight average molecular weight of the SDR product was observed compared with the pre-polymerized SDR feed as well as significant decrease in monomer concentration(increase in conversion) combined with a slight increase in polydispersity. As we can see multi passing has good effect on polydispersity of product.

References:

[1].Kamelia V. K. Boodhoo,1 William A. E. Dunk,1 Marija Vicevic, Roshan J. Jachuck, Valerie Sage,2 Duncan J. Macquarrie, James H. Clark “Classical Cationic Polymerization of Styrene in a Spinning Disc Reactor Using Silica-Supported BF3 Catalyst “Applied Polymer ScienceVolume 101, Issue 1, Pages: 8-19

[2].P. Leveson, W. A. E. Dunk, R. J. Jachuck “Numerical Investigation of Kinetics of Free-Radical Polymerization on Spinning Disk Reactor” Journal of Applied Polymer Science Volume 90, Issue 3, Date: 17 October 2003, Pages: 693-699

[3].K.V.K. BoodhooI R.J. JachuckG” Process. intensification. spinning: disk reactor for styren.polymerisation, Applied Thermal. Engineering: 2. (2000). 1127-1146.

Proceedings of the 10th International Chemical and
Biological Engineering Conference - CHEMPOR 2008
Braga, Portugal, September 4-6, 2008
E.C. Ferreira and M. Mota (Eds.)

Novel Stimulus Responsive Coating for Polystyrene Particles

Bruno Reis[1*], Simon Biggs[1]

[1] IPSE-SPEME – Institute of Particle Science and Engineering, School of Process, Environmental and Materials Engineering, University of Leeds, Leeds LS29JT, UK

Keywords: Stymulus-Responsive Polymers, Poly(N,N-Dimethylaminoethylmethacrylamide), Poly(N-Methylmethacrylate), Rheology Behaviour
Topic: Advancing the chemical and biological engineering fundamentals

Abstract

Smart or intelligent (co)polymers are materials which exhibit reversible changes in properties, in response to small physical or chemical changes in their environment. Our main purpose is to characterize novel stimulus responsive coatings on polystyrene latex particles which, in this case, are based upon in the coating with poly(N, N-dimethylaminoethylmethacrylate) (pDMAEMA)-poly(N-methylmethacrylate) (pMMA). For this stimulus responsive polymeric system, it was observed three pH regions of interest as function of temperature: (i) for pH below 5, the particles diameters underwent a monotonic rise with increasing pH and then reached a peak value of $\approx$380 nm, and the fluid presented Shear Thinning behaviour; (ii) from pH = 5 to 6, the hydrodynamic diameter remained constant and the fluid had Newtonian behaviour; (iii) from pH = 6 to 8.40, the diameter began to decrease and dropped to $\approx$230 nm and the fluid presented once again Shear Thinning behaviour. It was showed that the same transition occurs with different properties, by DLS and Rheology.

1 Introduction

Stimulus responsive polymers, also referred to as “intelligent”, “smart”, or “environmentally sensitive” polymers, are systems that exhibit large and sharp, physical or chemical reversible changes in response to small external changes in environmental conditions (Aguilar *et al*, 2007). The stimulus can be the exposure to the light (UV irradiation), a mechanic constraint, an application of an electric or magnetic field, changes in environmental conditions (like pH, ionic strength, temperature) or the polymer molecular weight and its polydispersity and tacticity. The applications of these kind of materials have wide ranging uses in areas such as: environmental (depollution of water), biomedical (Aguilar *et al*, 2007), biological molecules recognition (Gil and Hudson, 2004), pharmaceutics (drug-delivery systems), personal care products (shampoos, cosmetics) and agrochemical formulations (B. Jeong and A. Gutowska, 2002).

Particle surfaces can be modified to enhance properties by changing the chemical composition or the physical particle structure using polymeric materials. One approach is to synthesize intelligent latex particles by coating them with a stimulus-responsive polymer sheath (Yang *et al*, 2007). The polymer coating will expand or collapse depending of the applied stimulus. In the collapsed state, the particles are attracted to each other and can form an aggregate network where the solids are easily separated from the liquid phase. Switching the trigger (under appropriate conditions) will allow the particle system to re-disperse and form a stable dispersion (Binks (2004)). In this way, we may accurately control the dispersion properties.

* Corresponding author. Tel + 44 (0) 113 343 2380. E-mail: reisbruno24@gmail.com

1.1 Temperature Responsive Polymers

Some polymer solutions become cloudy upon either cooling or heating, due to the fluctuations in the refraction index caused by the partitioning into a polymer rich phase and a solvent rich phase. When a polymer solution exhibits a cloud point upon cooling, it is said to have an upper temperature critical solution (UCST), and upon heating a lower critical solution temperature (LCST) (Gil and Hudson, 2007). The phase separation and precipitation are reversible with no inherent limit in lifetime. Polymers such as poly (N,N'-diethyl acrylamide) (PDEAAm) exhibit a sharp phase transition in water (LCST) in the range of 25-35ºC (Gil and Hudson, 2004), poly(dimethylaminoethyl methacrylate) (PDMAEAMA) close to 50ºC (Aguilar *et al*, 2007) and poly (N-(L)-(1-hydroxymethyl) propylmethacrylsmide) close to 30ºC (Aguilar *et al*, 2007).

Although less popular and studied than pNIPAM, in terms of transition mechanism and also in specific applications, the scientific and practical interests for pDMAEMA are continuously increasing (Pagonis and Bokias, 2004). These poly (N-substituted acrylamides) are soluble in water and in polar organic solvents, with pDMAEMA being more hydrophilic than pNIPAM. Some applications of pDMAEMA based products have been proposed, ranging from two-phase catalysts to hydrogels for drug-delivery purposes or polymer supports for protein synthesis.

At very low temperatures, under its lower critical solution temperature, the solution is stabilized by the presence of hydrogen bonds between the amine groups, water and by ice-like structures which water molecules form around the hydrophobic groups. As the temperature increases, the hydrogen bonding weakens and the attraction between hydrophobic groups increases leading to an eventual demixing of the pDMAEMA chains, above the LCST (J. Koetz, 2001). The loss of entropy, by demixing, is more than compensated by the gain of entropy from the water molecules that lose their ice-like structure in the presence of dimethyl.

1.2 pH Responsible Polymers

pH-sensitive polymers are polyelectolytes that have, in their structure, weakly ionisable pendant groups, which can accept or release protons in response to changes in environmental pH, The pH-responsive polyelectrolytes can be divided in two main classes: weak poly(acid)s, that are dissociated at high pH, and weak poly(base)s that are protonated at low pH (Amalvy *et al*, 2003). When these polymers are near the critical pH, they gradually suffer a reversible transition in their conformation, from an expanded to collapsed state and most of them become water insoluble. The rapid change in hydrodynamic volume is caused by the variation in the charges that surround the ionic groups.

pDMAEMA is a pH responsive polybase where the amine groups, in its side chains, gain protons under acidic condition and release them under basic condition (Pagonis and Bokias, 2004). This polymer also has hydrophobic groups on the amine group. The nitrogen from pDMAEMA, under acidic conditions, is protonated giving rise to internal charge repulsion between neighbouring dymethyl groups. This leads to the expansion of the polymer overall dimensions. As the pH of the solution increases, the nitrogen becomes less ionised and the charge repulsion is gradually reduced giving rise to an increase of polymer-polymer interaction. When certain critical charge density is attained, conformational transition occurs (Amalvy *et al*, 2003).

The aim of this research is to characterize the stimuli responsiveness, colloidal stability and also the rheological properties of a novel stimulus responsive particle coating, polystyrene based upon poly (N, N-dimethylaminoethylmethacrylate) (pDMAEMA) - poly (N-methylmethacrylate) (pMMA). The styrene block is an excellent anchor point for linkers, however it has the disadvantage of being quite hydrophobic. Coupling pDMAEMA-pMMA to the styrene polymer should provide a greater range solvent compatibility over pure grafted DMAEMA or MMA.

2 Experimental

2.1 Material

Poly (N-methylmethacrylate) (pMMA)-Poly(N,N-(dimethylamino)ethyl methacrylate) stabilized polystyrene latex particles suspension, also known as pS/(pDMAEMA-pMMA), with a solid content of 11.9%, an average hydrodinamic diameter of 350 nm, a surface tension of supernatant of 70nm and a polydispersity index about 0.021 (DLS) were kindly provided by Dr. Syuji Fujii of Sheffield University.

2.2 Procedure

The hydrodynamic diameter and the size distribution of the pS/(pDMAEMA-pMMA) suspension, as a function of temperature, pH and salt concentration were measured using a BI-200SM Laser Light Scattering Goniometer (Brookhaven Insturments, Ltd.). A Zetasizer Nano ZS (Malvern Insturments, Ltd.) was used to measure the zeta potential as a function of the pH and KNO_3 concentration. A Bohlin C-VOR Rheometer was used to study the rheology at different pH values and solids concentrations.

3 Results and Discussion

3.1 Zeta Potential

Polystyrene and pMMA are hydrophobic and have a negative surface charge (zeta potential negative) at all pHs. pDMAEMA is more hydrophilic due to the protonation of the amine groups in water and has a positive zeta potential at low pH. Positive zeta potentials were detected at low pH values due to the cationic nature of the pDMAEMA brushes. Three experiments were undertaken to investigate how the zeta potential varies with pH and salt concentration in the system. The first measurement was carried out without any electrolyte and the other two with different KNO_3 concentrations, i.e 0.01 M and 0.1 M. The isoelectric point (IEP) of the particle suspension, without salt, was found to be close to pH 8. Below this pH the outer polymeric shell of the particles swells and pDMAEMA is found to dominate the zeta potential and the overall behaviour of the particles. For a pH above 8, the pDMAEMA shrinks and eventually collapses on the particle surface and the underlying polystyrene dominates the recorded zeta potential.

Addition of KNO_3, was seen to shift the IEP from pH 8.05 to 7.81, with 0.01M of KNO_3, and to 7.50 when with 0.1M of KNO_3. In this case, the variation of the IEP is significant and as the salt concentration increases the IEP of the pS/(pDMAEMA-pMMA) decreases. The concentration of salts is known to influence the phase transition of responsive polymers (Ballauff and Borisov, 2006, and Read *et al*, 2005). In relation to the behaviour of zeta potential with pH, we observe that it is broadly the same for the 3 salt conditions. When the pH increases from an acidic to a basic environment, the zeta potential switches from a cationic to anionic state as the pDMAEMA discharges.

3.2 Dynamic Light Scattering

Dynamic light scattering (DLS) was used to characterize the solution properties of the pS/(pDMAEMA-pMMA) copolymer under alkaline and acidic conditions. The size of a particle is calculated from the translational diffusion coefficient which is directly related to the hydrodynamic diameter for DLS measurements. The measurements were performed at 25, 30 and 35 ºC, below the LCST of pDMAEMA, for two different salt concentrations (0.1M and 0.01M KNO_3) and different pHs (Figure 1). For each experimental condition, the reported values are averages of 2 measurements. It was observed that the diameter of pS/(pDMAEMA-pMMA) particles (i) for a low pH shows a monotonic rise with increasing

pH, and then reaches a peak value of ≈380 nm, (ii) from pH = 5 to 6, the hydrodynamic diameter stays approximately constant and (iii) from pH = 6 to 8.40 it decreases gradually to ≈230 nm. For pH values above 8.40, the hydrodynamic diameter increases due to flocculation. Flocculation leads to a broader size distribution.

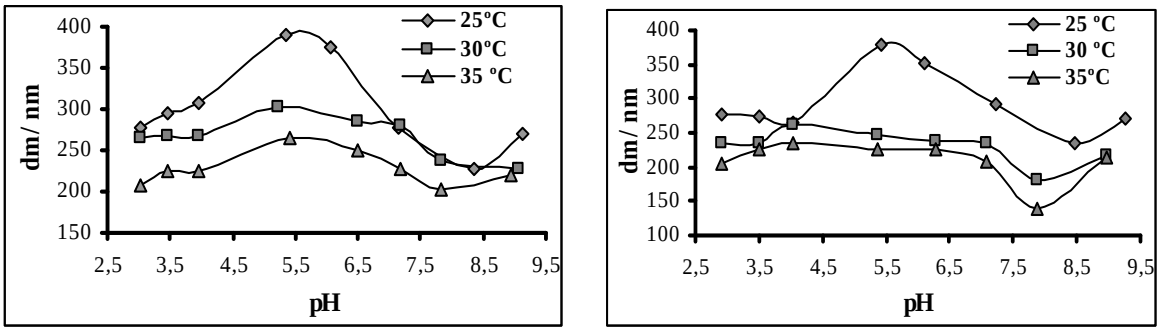

Figure 1. Hydrodynamic diameter average *versus* pH for pS/(pDMAEMA and pMMA) particle concentration of 0.01% (*w/w*) in 0.01M KNO_3 (right) and in 0.1M KNO_3 (left).

Under pH 6, the PDMAEMA are protonated and the repulsion between NH^+ tends to swell the polymeric chains grafted to the polystyrene surface. A decrease in pH (pH< 5) leads to a higher protonation degree of PDMAEMA chains and thereby a stronger repulsion, increasing the hydrodynamic diameter. However, the decrease of the pH also results in adverse effects of swelling. Indeed, for a lower pH range, the concentration of NO_3 ions increase (from HNO_3 solution) and this tends to disrupt the hydrophobic hydration, therefore the chains collapses due to the polymer-polymer interactions. In collapse state polystyrene rule the suspension and the zeta potential decrease. A higher concentration of HNO_3 induces a higher ionic strength; hence a higher concentration of counterions induces a smaller repulsion between the polymeric chains on the particles surface as the protonated nitrogen ions are screened from each other. The $[NO_3^-]$ is enough to penetrate into the brushes of the polymers chains, to push over the water molecules and to relocate, between NH^+ and the adjacent polymer chains. In this case, we suggest that this mechanism is the same as the one acting in the presence of high salt concentrations. As salt concentration rises, the isoelectric point (IEP) and hydrodynamic diameter average of PS/(PDMAEMA-PMMA) suspension decreases.

Another process that can also occur is the cationic flocculation. We realize that the H^+ from the acid solution may establish bonds between nitrogens. When the samples are dipped in an acidic concentrate solution for equilibrium, the band N-H becomes more intense than when dipped to equilibrium in pure water or alkali solutions. Hence, the hydrogen bonding can be a non-negligible force in this system and can act to facilitate aggregation of the PDMAEMA chains. At pH = 8.40 the flocculation occurred, as we mentioned, in DLS measurements. A KOH solution was used to increase the pH, which resulted in the deprotonation of nitrogen atoms. The attraction force between hydrophobic groups increases and the PDMAEMA chains start to collapse and the aggregation between the chains of different particles occurs (pH> 8.50).

3.3. Rheology

To concentrate the pS/ (pDMAEMA and pMMA) particles at 23% (*w/w*), it was used a centrifuge (20 000 rpm/ 5 minutes) and, above it, filtration technique (0.2 μm filter). We observed, for all concentrations studied, that for 5< pH< 7, the pS/(PDAEMA-pMMA) fluid has a Newtonian behaviour and for pH values under 5 and above 7, the pS/(pDMAEMA and pMMA) presents a Shear Thinning fluid (Model Cross). The aggregation phenomenon occurs in this pH range. For pH's 7.31 and 7.84, the viscosity is larger than for basic pH, because it is near to the IEP. The Van der Walls forces are higher than the repulsion forces between the

electrical double layers under these conditions and flocculation occurs. Shear promotes the rupture of the weak flocs and the viscosity decreases as shear rate increases. At around pH 7 the flocs are more resistant, but less dense than basic pH values. If we observe the DLS measurements it will be possible to establish a relation between the swelling and shrinking polymer chains with the flocculation phenomenon and thus with the rheology. For pH's above 7 (Figures 2) the pDMAEMA collapses and as flocculation occurs it will form hard flocs - Charge Patch Flocculation. For 5< pH< 7, the polymer swells and therefore the chains aggregate - Bridging Flocculation. In this last flocculation mode, the flocs have no resistence and are destroyed when exposed to the bob movement. It was to be expected for pH 4.28 the same rheological behaviour (Newtonian behaviour) that it was observed at pH 6.04. As previoulsy mentioned, it was suggested that H^+ and NO_3^- played bonds between the amine group nitrogens and that is why the polymeric chains shrunk. As the particles become once again hydrophobic, they repel the water molecules and tend to aggregate.

At hight concentrations and low shear rate, the Newtonian plateau seems to disappear and to develop into a yield stress (Figures 2). At shear rates exceeding 10^3 s^{-1}, the high concentration samples display a shear thickenning behaviour. For higher shear rate values, the network does not have time to re-arrange and the particles do not acquire flow properties. In this case, the elastic force is greater than the viscous force.

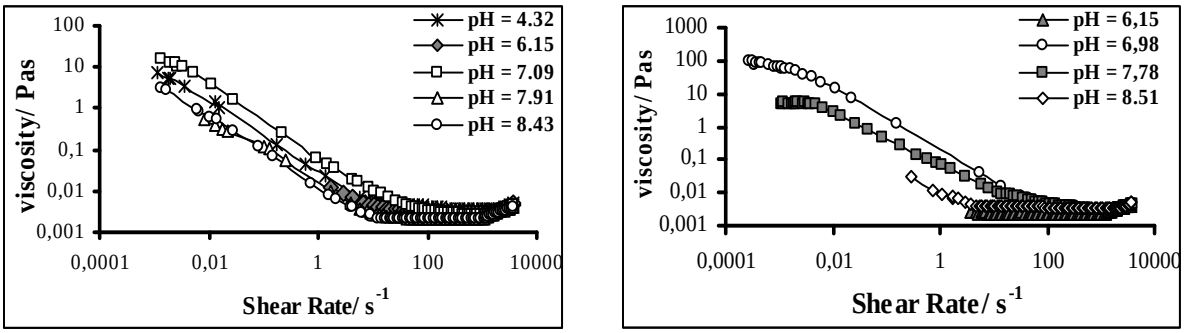

Figure 2. Viscosity *versus* shear rate for different pH's. Filtration Technique, 29% (*w/w*) (right). Filtration Technique, 38% (*w/w*) (left).

Figure 2 (graphic on left) shows for pH 8.51 Newtonian behaviour. In this situation, with the increase of particle concentration, the flocs sedimentation occurred, as it was observed in the end of the measurement.

If we plot a high shear viscosity (or low shear rate) and hydrodynamic diameter average versus pH, we observed that the range, where the diameter and viscosity decrease, are the same (Figure 3). Once again it was showed the relation between DLS and Rheology. The same transition occurs with different properties.

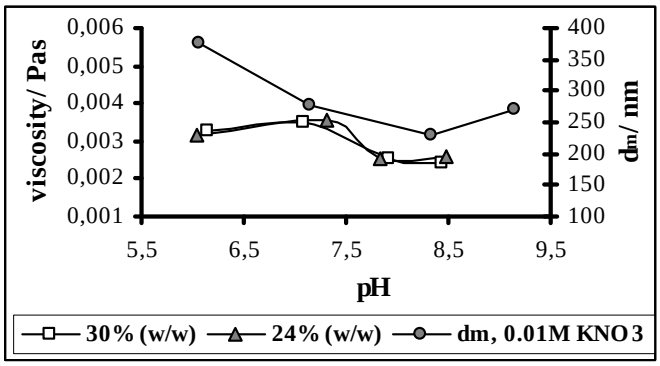

Figure 3. High shear viscosity, η_∞ , hydrodynamic diameter average of the core-shell latex versus pH.

4 Conclusions

Smart polymers have attracted our attention as versatile system stimuli responsive. In the course of our work, it was observed three pH regions of interest: (i) for pH below 5 the particles diameters underwent a monotonic rise with increasing pH and then reached a peak value of $\approx$380 nm; (ii) from pH = 5 to 6 the hydrodynamic diameter remained constant; (iii) from pH = 6 to 8.40 the diameter began to decrease and dropped to $\approx$230 nm. For pH values below 6, the hydrodynamic diameter decreased, because the NO_3 anions coming from the acid solution within the pS/(pDMAEMA-pMMA) suspension were placed between the protonated nitrogens, decreasing the repulsion between them. The results also show that with the increased of KNO_3 concentration, the particles become more compact, since the NO_3 anions are enough to penetrate the brushes of the polymers chains, to force out the water molecules and to be placed between the amine's nitrogens. At pH 8.40 the flocculation occurred due to the deprotonation of nitrogen atoms. Rheological measurements show us the same transitions that we observed by DLS technique. The pS/(pDMAEMA and pMMA) suspension presents as Shear Thinning fluid (Model Cross) for pH values below 5 and above 7. The aggregation phenomenon occurs in these pH values. The fluid has a Newtonian behaviour for pH around 6. It was also observed that with the increasing of pH, the flocs are more compact and dense and rapidly settled on the Money Cell's cup. It was demonstrated that the same transition occurs with different properties, by DLS and Rheology.

5 References

Aguilar, M.R., Elvira, C., Gallardo, A., Vásquez, B., Román, J.S. (2007). Smart Polymers and Their Applications as Biomaterials*. Topics in Tissue Engineering*, 3.

Gil, E. S., Hudson, S. M. (2004). *Stimuli*-Responsive Polymers and Their Bioconjugates. *Prog. Polymer Science*, 29, 1173-1222.

B., Jeong, A., Gutowska (2002). Lessons from Nature: Stimuli-Responsive Polymers and Their Biomedical Applications.*Trends in Biotechnology*, 20, 305-311.

Yang, Y., Zhang, J., Liu, L., Li, C., Zhao, H. (2007). Synthesis of PS and PDMAEMA Mixed Polymer Brushes on the Surface of Layered Silicate and Their Application in Pickering Suspension Polymerization. *Journal of Polymer Science: Part A: Polymer Chemistry*, 45, 5759–5769.

Gil, E. S., Hudson, S. M. (2007). Effect of Silk Fibroin Interpenetrating Networks on Swelling/ Deswelling Kinetics and Rheological Properties of Poly(N-isopropylacrylamine group) Hydrogels. *Biomacromolecules*, 8, 258-264.

Binks, Bernard P. (2004). Synthesis of Sterically-Stabilized Polystyrene Latex Particles using Cationic block Copolymers and Macromonomers and Their Application as Stimulus-Responsive Particulate Emulsifiers for Oil-in-Water Emulsions. *Langmuir*, 20, 4345-4354.

Pagonis, K., Bokias, G. (2004). *Upper* Critical Solution Temperature-Type Cononsolvency of Poly (N,N-dimethylacrylamide) in Water - Organic Solvent Mixtures. *Polymer*, 7(4), 2149-2153.

J., Koetz, S., Kosmella, Beitz, T. (2001). Self-assembled Polyelectrolyte Systems. *Progress in Polymer Science*, 26(8), 1199-1232.

Amalvy, J. I., Armes, S. P., Binks, B. P., Rodrigues, J. A. Rodrigues (2003). Use of Sterically-Stabilised Polystyrene Latex Particles as a pH-Responsive Particulate Emulsifier to prepare Surfactant-Free Oil-in-Water Emulsions. *Chem. Commun.*, 1826-1827.

Read, E.S., Fujii, S., Amalvy, J.I., Randall, D.P., Armes, S. P. (2005). Effect of Varying the Oil Phase on the Behavior of pH-Responsive Latex-based Emulsifiers: Demulsification versus Transitional Phase Inversion. *Langmuir*, 20(18), 1662-1662.

Ballauff, M., Borisov, O. (2006). Polyelectrolyte Brushes. *Colloid & Interface Science*, 11(6), 316-323.

Proceedings of the 10th International Chemical and
Biological Engineering Conference - CHEMPOR 2008
Braga, Portugal, September 4-6, 2008
E.C. Ferreira and M. Mota (Eds.)

Cadmium (II) removal from aqueous solution using microporous titanosilicate ETS-4 and ETS-10

Lidiana Barreira, Elizabeth Camarinha, Patrícia F. Lito, João Rocha, Zhi Lin, Armando C. Duarte, Eduarda Pereira, Carlos M. Silva[1]
University of Aveiro, Department of Chemistry, CICECO, 3810-193 Aveiro, Portugal

Keywords: ETS-4, ETS-10, Ion Exchange, Batch experiments
Topic: Advancing the chemical and biological engineering fundamentals.

Abstract

Cadmium is one of the most toxic non-essential heavy metals present in the environment, even at low concentrations. In this work the ability of microporous titanosilicates ETS-4 and ETS-10 for the uptake of Cd^{2+} ion from aqueous solutions has been investigated, assessing the potential of these materials in water remediation. With this purpose, batch stirred tank experiments have been carried out by contacting a fixed volume of solution with known masses of titanosilicate. The evolution of the cadmium concentration with time has been monitored by Inductively Coupled Plasma Mass Spectrometry. pH is an important variable in ion-exchange processes, hence its effect has been studied. Results have shown expected trends, and revealed that Cd^{2+} uptake is clearly more effective at pH values around 6.

1. Introduction

The removal of toxic heavy metal ions from sewage, industrial and miningwaste effluents has been widely studied, especially in recent years. Their presence in streams and lakes has been responsible for several types of health problems in animals, plants and human beings (Hui et al., 2005). Cadmium is a non-essential element and one of the most hazardous trace elements, being considered a “priority metal” from the standpoint of potential hazard to human health. Aquatic ecosystem pollution by Cd^{2+} usually arises from several industrial processes, such as electroplating, battery and accumulator manufacturing, production of ceramics and pigments, plastic manufacturing, metallurgical alloying, smelting and acid mine drainage. Different technologies are described in literature for removal of heavy metals, such as chemical precipitation, electro-flotation, reverse osmosis, adsorption and ion exchange. Although ion exchange may be considered attractive because of the relative simplicity of application, the cost and the regeneration of adsorbents are limiting factors (Petrus and Warchol, 2003), hence it is of interest to research new materials to replace expensive activated carbons and resins. Natural and synthetic zeolites are gaining considerable interest because of their high selective and ion exchange capacity (Trgo et al. 2006; Lopes et al., 2007).

Titanosilicates are three-dimensional crystalline solids with remarkable physical and chemical properties, such as selective sorption, ion exchange and catalytic activity (Rocha and Anderson, 2000; Lv et al., 2005). The structure of these materials is built from SiO_4 tetrahedral and TiO_6 octahedral units linked to each other by shared oxygen atoms, forming regular cavities and channels of molecular dimensions. Each TiO_6 octahedron in the titanosilicate global structure carries a -2 charge, which can be neutralized by extra-framework cations (usually Na^+ and K^+). These compensation species, as well as water molecules or other adsorbed molecules, are located in the channels of the structure and may be exchanged by others (e.g., Cd^{2+}).

[1] Corresponding author. Tel +351 234 401549. E-mail:carlos.manuel@ua.pt

Titanosilicate ETS-4 is a small pore member of the Engelhard Titano Silicate (ETS) family. It has a distinct interconnected octahedral–tetrahedral framework structure, which can be systematically fined through dehydration at elevated temperatures. ETS-10 is a wide pore titanosilicate with a remarkable high thermal stability. The most interesting point of its structure is that ETS-10 contains infinite – Ti – O – Ti – O chains, which are surrounded by silicate ring structures. This material shows a disordered structure and has excellent diffusion characteristics. Both ETS-4 and ETS-10 have been suggested as good ion exchangers (Rocha and Anderson, 2000).

2. Experimental

2.1 Materials and solutions

All chemicals used were of analytical reagent grade and obtained from commercial suppliers without further purification. The certified standard stock solution of cadmium (1001 ± 2 mg/L) was purchased from Merck. ETS-4 and ETS-10 used consisted of an off-white microcrystalline powder, whose features may be found in Table **1.** Their synthesis is described elsewhere (Ferreira, et al., 2007; Lv et al.,2007). All glass ware used in the experiments were acid-washed prior to use (nitric acid 25%, 12 hours followed by hydrochloric acid 25% another 12 hours).

Table 1– Features of the ETS-4 and ETS-10 particles used.

Material	ETS-4	ETS-10
Formula	$[Na_9Ti_5Si_{12}O_{38}(OH).12H_20]$	$[(Na,K)_2TiSi_5O_{13}.4H_2O]$
Density, kg/m^3	2200	1800
Ion exchanger capacity, eq/kg	6.39	4.52
Particle diameter, 10^{-6} m	0.5-0.9	5
Pore diameter, 10^{-10} m	3-4	4,9×0,76

2.2 Batch Experiments

Experiments with both ETS-4 and ETS-10 have been carried out following the same procedure. Therefore, they are both indistinctly referred has titanosilicate.

All experiments were carried out in batch conditions, at 295 K ± 1 in a 2 L volumetric flask. Cadmium solutions were prepared daily by diluting the stock solution to the desired concentrations in high purity water (18 MΩcm). Known masses of titanosilicate were added to the cadmium solutions and this time was considered the starting point of the experiment. Table 2 depicts the experimental conditions including the initial solution concentrations and titanosilicate masses. The pH initially registered is 4, and remained approximately constant during the experiment 1. NaOH was added to cadmium solution in order to fix the initial pH of experiments 2 to 4 (see Table 2).

Titanosilicate powder and aqueous solutions were maintained in contact under constant stirring. The time required for solution-solid equilibration was evaluated by carrying out each experiment until the Cd^{2+} concentration remained constant. During this period, several aliquots (10 mL) were taken at different times and each aliquot was filtered through a 0.45 µm Acetate Plus Osmonics filter. The filtrate was adjusted to pH<2 with HCl, stored at 277.15 K, and then analysed. Besides, new experiments were carried out in order to obtain some

additional equilibrium points. With this purpose, solutions with known Cd^{2+} concentrations were contacted with the titanosilicate until the equilibrium was attained. A blank experiment (without titanosilicate) was always run as control, to check that the removal of cadmium occurred by ion-exchange onto the solid and not by, e.g., adsorption on the vessel walls. Cadmium analysis was performed by Inductively Coupled Plasma Mass Spectrometry.

Table 2 – Experimental conditions for isothermal batch operation.

Experimental Conditions	**Exp. 1**	**Exp. 2**	**Exp. 3**	**Exp. 4**
pH (~constant during experiment)	4	6.5	6	6
Temperature, K	295 ± 1			
Solution volume, 10^{-3} m^3	2			
Initial Cd^{2+}concentration, 10^{-3} kg/m^3	0.85			
Mass of titanosilicate, 10^{-6} kg	ETS-4		ETS-10	
	25	25	5	20.1

3. Results and Discussion

Figures 1 and 2 show the normalized Cd^{2+} concentration in the fluid as a function of time, measured for the same initial solution concentrations (C_{A0}), for different ETS-4 and ETS-10 masses, respectively.

Results follow expected trends: cadmium removal increases with increasing pH (see Figure 1), and with increasing titanosilicate mass (Figure 2) since the extensive ion-exchange capacity is proportional to solid mass.

Fast metal uptake occurs in the first few hours of the process, followed by the characteristic slower removal towards the equilibrium (Figures 1 and 2). Such fact dues to the large mass transport driving forces observed at the beginning, since ETS-4 and ETS-10 particles are initially free of cadmium.

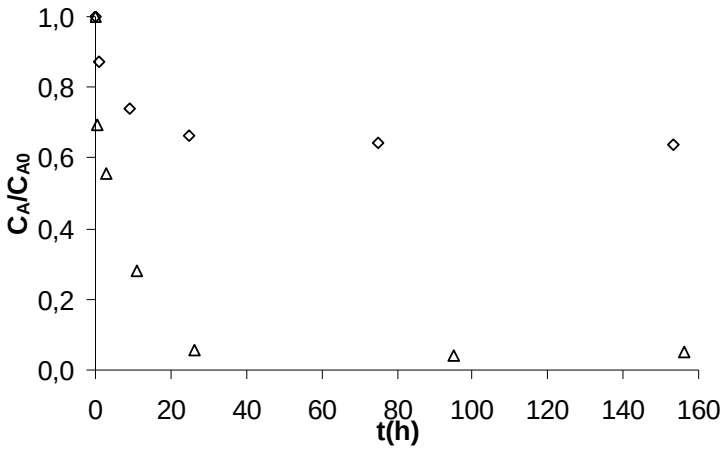

Figure 1: Normalised concentration of bulk solution *versus* time for experiments with ETS-4. Experimental conditions (see Table 2): ◊ Exp.1 and Δ Exp.2.

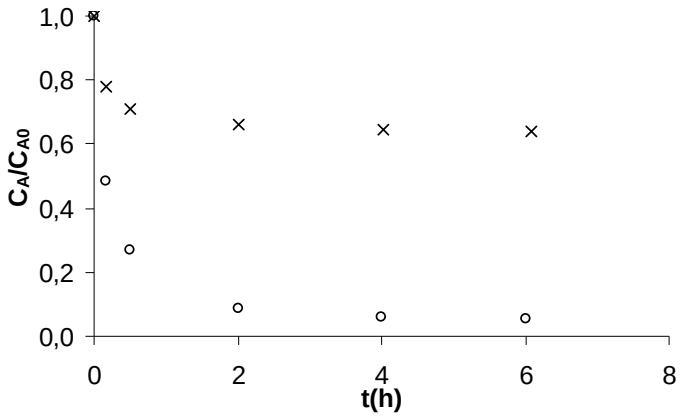

Figure 2: Normalised concentration of bulk solution *versus* time for experiments with ETS-10. Experimental conditions (see Table 2): × Exp.3 and ○ Exp.4.

Figure 3 shows equilibrium data for ETS-4 at pH=4 and pH=6.5. As has been mentioned above, the amount of adsorbed metal by ETS-4 increases with higher pHs. This is a very important result since the pH of industrial effluents and other waste water are around 6.

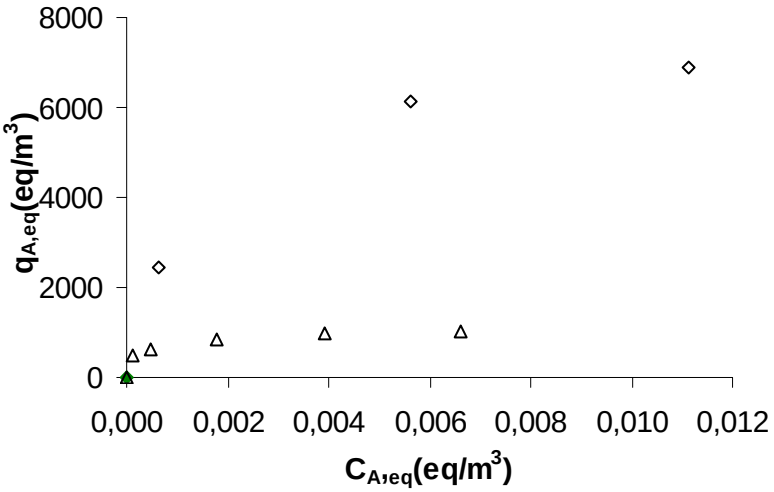

Figure 3: Comparison between equilibrium data measured for ETS-4 (◊, pH=6,5 and Δ, pH=4).

4. Conclusions

In this work the removal of Cd^{2+} from aqueous solution using titanosilicates ETS-4 and ETS-10 has been investigated with batch stirred tank experiments. The effect of pH and titanosilicate mass has been studied. The obtained results follow expected trends and evidence that metal uptake is more effective for pH values around 6.

Acknowledgments

Patrícia F. Lito wishes to express her gratitude to Fundação para a Ciência e Tecnologia (Portugal) for the PhD grant provided (SFRH/BD/25580/2005).

References

Álvarez-Ayuso, E., García-Sánchez, A., (2007). Removal of Cadmium from aqueous solutions by palygorskite. *Journal of Hazardous Materials* 147, 594-600.

Biškup, Biserka, Subotic, Boris, (2004). Kinetic analysis of the exchange processes between sodium ions from zeolite A and cadmium, copper and nickel ions from solutions. *Separation and Purification Technology* 37, 17–31.

Ferrreira, T.R., Lopes, C.B., Lito, P.F., Otero, M., Lin, Z., Rocha, J., Pereira, E., Silva, C.M., Duarte, A., (2007), Cadmium(II) Removal from Aqueous Solution using Microporous Titanosilicate ETS-4, *Chemical Engineering Journal*, (accepted).

Hui, K.S., Chao, C.Y.H., Kot, S.C., (2005). Removal of mixed heavy metal ions in wastewater by zeolite 4A and residual products from recycled coal fly ash. *Journal of Hazardous Materials* B127, 89-101.

Lopes, C. B., Otero, M., Lin, Z., Silva, C.M., Pereira, E., Rocha, J., Duarte, A., (2007). Mercury removal from aqueous solution using ETS-4 – kinetic and equilibrium study. (submitted).

Lv, Lu, Hor, Mei Peng, Su, Fabing, Zhao, X.S., (2005). Competitive adsorption of Pb2+, Cu^{2+}, and Cd^{2+} ions on microporous titanosilicate ETS-10. *Journal of Colloid and Interface Science*, 287, 178–184.

Lv, Lu, Wang, Kean, Zhao, X.S., (2007). Effect of operating conditions on the removal of Pb2+ by microporous titanosilicate ETS-10 in a fixed-bed column. *Journal of Colloid and Interface Science* 305, 218–225.

Petrus, R., Warchol, J., (2003). Ion exchange equilibria between clinoptilolite and aqueous solutions of Na^{+}/Cu^{2+}, Na^{+}/Cd^{2+} and Na^{+}/Pb^{2+}. *Microporous and Mesoporous Materials,* 61,137-146.

Rocha, J., Anderson, M.W., (2000). Microporous titanosilicates and other novel mixed octahedral-tetrahedral framework oxides. *European Journal of Inorganic Chemistry*, 801-818.

Trgo, M., Peric, J., Medvidovic, N.V., (2006). A comparative study of ion exchange kinetics in zinc/lead – modified zeolite-clinoptilolite systems. *Journal of Hazardous Materials* B136, 938-945.

Yilmaz, B., Miraglia, P.Q., Warzywoda, J., Sacco, A., (2004). Synthesis of titanosilicate ETS-4 with controlled morphology and investigation of its crystallization kinetics. *Microporous and Mesoporous Materials,* 71, 167-175.

Proceedings of the 10th International Chemical and
Biological Engineering Conference - CHEMPOR 2008
Braga, Portugal, September 4-6, 2008
E.C. Ferreira and M. Mota (Eds.)

Poly(vinyl alcohol) with sulfonic acid groups as catalyst for the alpha-pinene alkoxylation

José E. Castanheiro[1*], Isabel M. Fonseca[2], Ana M. Ramos[2], Joaquim Vital[2]
[1] Centre of Chemistry of Évora, University of Évora, 7000–671 Évora, Portugal.
[2] REQUIMTE/CQFB, FCT, New University of Lisbon, Campus de Caparica, 2829-516 Caparica, Portugal

Keywords: α-pinene, alkoxylation, PVA, sulfonic acid groups
Topic: Advancing the chemical and biological engineering fundamentals

Abstract

The alkoxylation of α-pinene was carried out over poly(vinyl alcohol) containing sulfonic acid groups, as catalyst. The main product of α-pinene alkoxylation was α-terpinyl methyl ether being also formed bornyl methyl ether, fenchyl methyl ether, limonene and terpinolene as by-products.

The absorption band at 1037 cm^{-1} in the FTIR spectrum of PVA_SSA40 (PVA membrane containing 40% of –OH groups esterified with SSA) which does not appear in the spectrum of PVA, indicates the presence of the sulfonic acid groups.

The catalytic activity of PVA with sulfonic acid groups increases when the amount of sulfosuccinic acid used in the polymer crosslinking is increased from 5% to 40%. However, when the crosslinking degree increases from 20% to 40%, the conversion of α-pinene increases only slightly.

Good values of selectivity to α-terpinyl methyl ether were obtained over poly(vinyl alcohol) with sulfonic acid groups.

A simple kinetic model, which fits experimental concentration data quite well, was developed.

1 Introduction

Alpha-Pinene is a renewable raw material usually obtained from pine gum or as a waste from the Kraft process. Its acid catalysed methoxylation yields a complex mixture of monoterpenic ethers, being alpha-terpinyl methyl ether the main product. The alpha-terpinyl methyl ether smells grapefruit-like and might be used as flavour and fragrance for perfume and cosmetic products, as additive for pharmaceuticals as well as in food industry. Strong homogeneous acid catalysts, e.g sulphuric acid, have been used, but the effluent disposal leads to environmental problems and economical inconveniences. These problems can be overcome by the use of solid acid catalysts. Beta zeolite (Hensen et al., 1997) and acidic cation exchange resins have been used for the α-pinene alkoxylation.

Homogenous and heterogeneous catalysts could be immobilized in polymeric membranes in order to improve their selectivity or activity, thanks to environment created by the polymeric matrix around the catalyst (Ozdemir et al., 2006, Vankelecom, 2002). In a previous work, it was observed that PVA membranes with $–SO_3H$ groups have catalytic activity in esterification of acetic acid by isoamylic alcohol (Castanheiro et al., 2006).

In the present work, we report the α-pinene alkoxylation over poly(vinyl alcohol) containing sulfonic acid groups. These groups were introduced by the direct reaction between -OH of PVA and sulfosuccinic acid.

* Corresponding author. Tel + .: +351-266-745311. E-mail:jefc@uevora.pt

2 Experimental

PVA catalysts were prepared by dissolving PVA (MERCK, average molecular weight: 72000) in water at 90ºC, during 6 h. Aqueous 10 wt.% PVA solutions were mixed with the appropriate amounts of sulfosuccinic acid (SSA) and then the mixtures were vigorously stirred at room temperature for 24 h. After that, the homogeneous solutions were poured and cast on a Teflon plate. The cast membranes were allowed to dry at 60ºC during 24 h. The dried membranes were heated at 120ºC, during 2 h (Rhim et al. 2004). The code PVA_SSAx means a membrane containing 2x% of its –OH groups esterified.

The amount of sulfonic acid groups in PVA_SSA was measured by a classic titration. The samples were equilibrated with 10 ml of 0.1 mol/L NaOH solution for 24 h. Then, the amount of H^+ was calculated from the reduction in alkalinity determined by titration.

The FTIR spectra were recorded in a Bio-Rad FTS 155 instrument.

Catalytic experiments were carried out in a batch reactor equipped with a stirrer, at 60ºC. In a typical experiment, the reactor was loaded with 1 mL of α-pinene, 50 mL of methanol and 0.5 g of catalyst. Samples were taken periodically and analysed by GC, using a Konic HRGC-3000C instrument.

3 Results and Discussion

Table 1 shows the results of membrane characterisation. The swelling measurements for each pure component decreased, when the SSA contents increased. This is due to the decrease of the free volume, even though the membrane contains more hydrophilic functional groups (Rhim et al., 2004). The amount of sulfonic groups in PVA_SSA membranes expressed in milli-equivalent (meq) by weight of dry membrane (g), increase with SSA contents.

Table 1. Membrane characteristics[a]. $Q_{methanol}$, $Q_{\alpha\text{-pinene}}$ – swelling degree for methanol and α-pinene, respectively.

Membrane	Thickness (mm)	meq./g_{memb}	$Q_{methanol}$	$Q_{\alpha\text{-pinene}}$
PVA_SSA5	0.112	0.50	0.329	0.054
PVA_SSA20	0.104	2.02	0.223	0.044
PVA_SSA40	0.108	4.00	0.114	0.029

[a]The code PVA_SSAx means a membrane containing 2*x%* of its –OH groups esterified.

Fig. 1 shows the FTIR spectra of PVA and the PVA crosslinked with sulfosuccinic acid, PVA_SSA40. The absorption band at 1730-1735 cm^{-1}, in the spectrum of PVA_SSA40, usually assigned to the ester group (-CO-O-), suggests that the crosslinking with SSA was succeeded. The absorption band at 1037 cm^{-1} in the spectrum of PVA_SSA40, which does not appear in the spectrum of PVA, indicates the presence of the sulfonic acid groups by the introduction of SSA (Rhim et al., 2004).

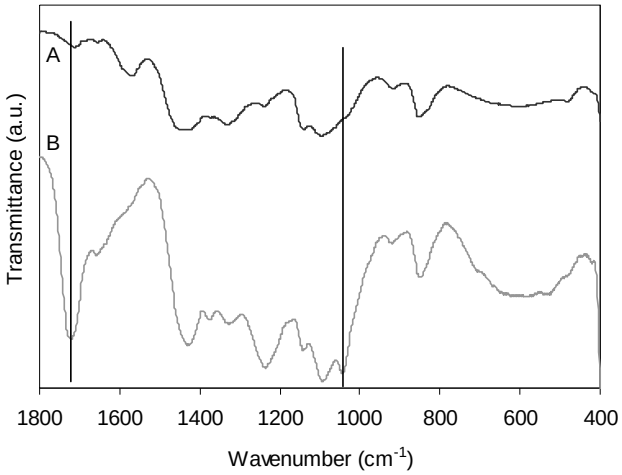

Fig. 1. FTIR spectra of PVA matrixes. (A) pure PVA; (B) PVA_SSA40.

The main product of α-pinene methoxylation was α-terpinyl methyl ether being also formed bornyl methyl ether, fenchyl methyl ether, limonene and terpinolene as by-products (scheme 1).

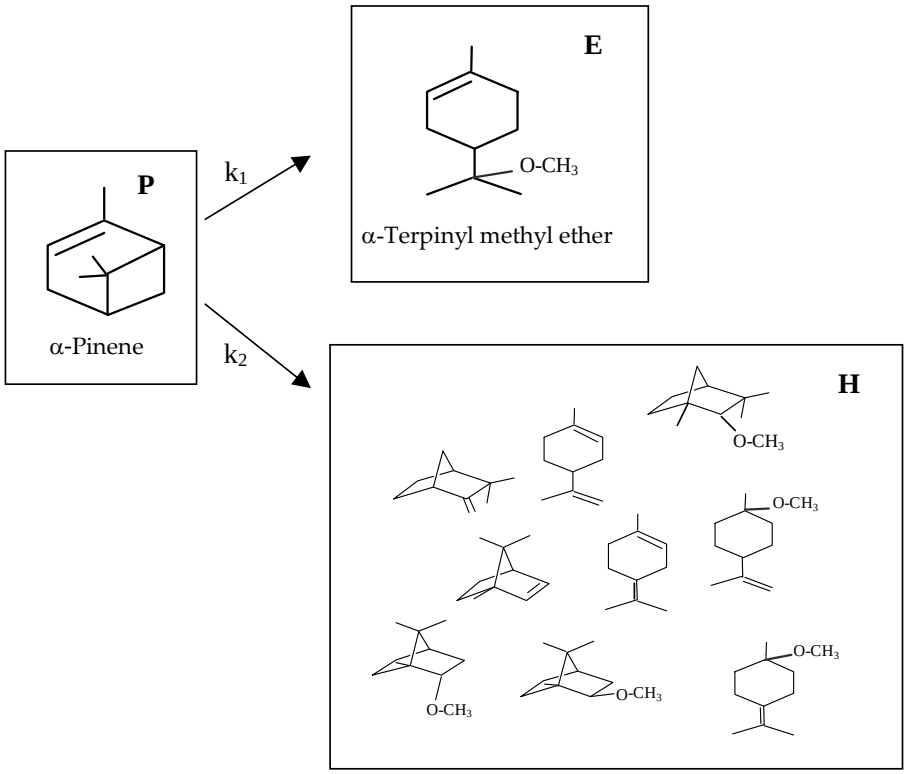

Scheme 1

Fig. 2 shows the concentration profiles obtained for the catalyst PVA_SSA20. In the Fig. 2, “others” lumps all the minor products.

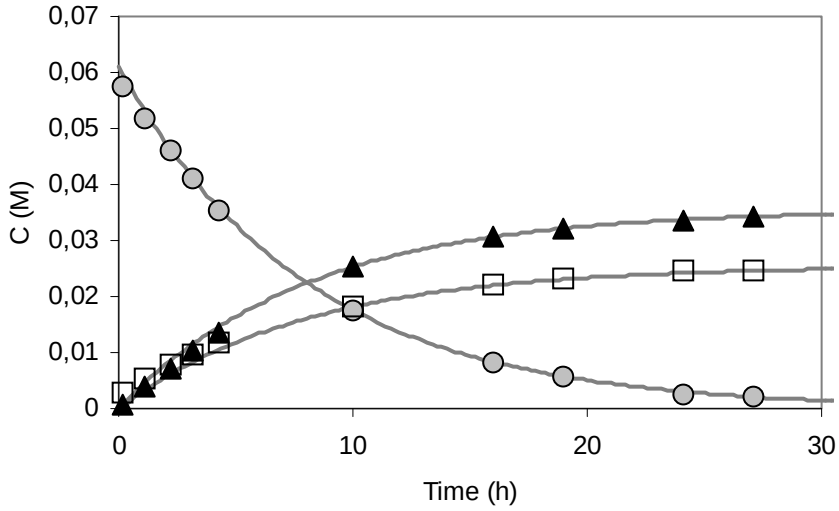

Fig. 2. Alkoxylation of α-pinene over PVA_SSA40. Concentration vs. time. (⊙) α-pinene; (▲) α-Terpinyl methyl ether; (□) H-lumps all the minor components. The solid lines represent the model fitted to the data points.

The α-pinene concentration profile over PVA_SSA5, PVA_SSA20 and PVA_SSA40 catalysts were shown in Fig. 3. It was observed that the conversion increases when the amount of sulfosuccinic acid used in the polymer cross-linking is increased from 5% to 20%. This behaviour can be explained by the increase of the amount of sulfonic acid groups in the PVA matrix. However, when crosslinking degree increases from 20% to 40%, the conversion of α-pinene increases only slightly. This is, probably, due to the increase of restrictions on the mobility of molecules, in the polymer matrix.

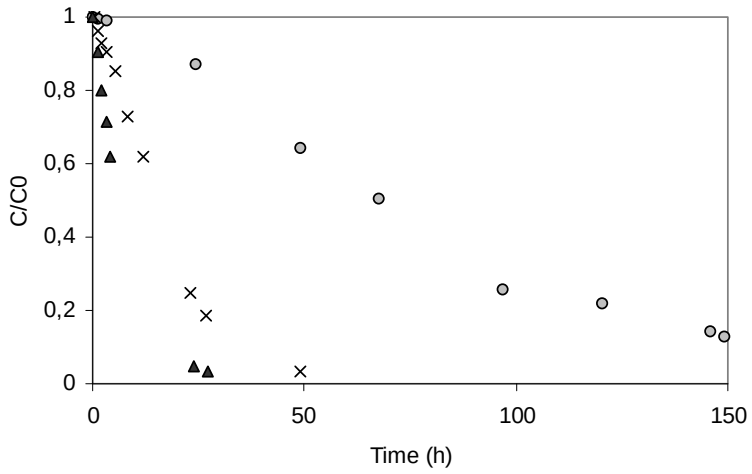

Fig. 3. Alkoxylation of α-pinene over poly(vinyl alcohol) with sulfonic acid groups. Effect of crosslinking degree on the concentration profiles of α-pinene. (⊙) PVA_SSA5; (x) PVA_SSA20; (▲) PVA_SSA40.

Fig. 4 shows the selectivity to the α-terpinyl methyl ether at 95% of α-pinene conversion, for PVA_SSA5, PVA_SSA20 and PVA_SSA40. It was observed that all of the catalysts tested on α-pinene alkoxylation exhibited good selectivity to α-terpinyl methyl ether (about 60% near complete conversion).

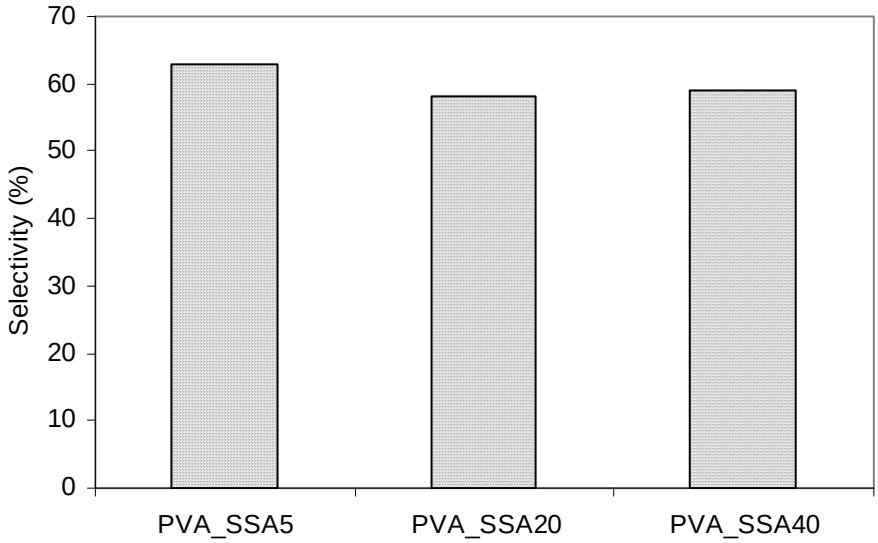

Fig. 4. Alkoxylation of α-pinene over poly(vinyl alcohol) with sulfonic acid groups. Selectivity to α-terpinyl methyl ether at 95% of α-pinene conversion.

A simple kinetic model is proposed. It is assumed first order kinetics. The reaction rate of these two pseudo elementary reaction are expressed as:

$$r_1=k_1C_p \quad (1)$$

$$r_2=k_2C_p \quad (2)$$

For batch reactor the mole balance equations may be written as:

$$\frac{dCp}{dt}=-\frac{W}{V}\left(r_1+r_2\right) \quad (3)$$

$$\frac{dC_E}{dt}=\frac{W}{V}r_1 \quad (4)$$

$$\frac{dC_H}{dt}=\frac{W}{V}r_2 \quad (5)$$

The fitting of the model to data points is shown in Fig. 2.

4. Conclusions

Poly(vinyl alcohol) crosslinked with succinic acid containing sulfonic acid groups, was used as catalysts in the alkoxylation of α-pinene.

The main product of α-pinene alkoxylation was α-terpinyl methyl ether being also formed bornyl methyl ether, fenchyl methyl ether, limonene and terpinolene as by-products.

The conversion increases when the amount of sulfosuccinic acid used in the polymer crosslinking is increased from 5% to 20%. However, when crosslinking degree increases from 20% to 40%, the conversion of α-pinene increases only slightly.

All of the catalysts tested on α-pinene alkoxylation exhibited good selectivity to α-terpinyl methyl ether.

A simple kinetic model, which fits experimental concentration data quite well, was developed.

Reference

Castanheiro, J.E., Ramos, A.M., Fonseca, I.M., Vital, J., (2006). Esterification of acetic acid by isoamylic alcohol over catalytic membranes of poly(vinyl alcohol) containing sulfonic acid groups, *Applied Catalysis A: General*, 311, 17-23.

Hensen, K., Mahaim, C., Hölderich, W.F., (1997). Alkoxylation of limonene and alpha-pinene over beta zeolite as heterogeneous catalyst, *Applied Catalysis A: General*, 149, 311-329.

Ozdemir, S.S., Buonomenna, M.G., Drioli, E., (2006). Catalytic polymeric membranes: Preparation and application, *Applied Catalysis A: General*, 307, 167-183.

Rhim, J.W., Park, H.B., Lee, C.S., Jun, J.H., Kim, D.S., Lee, Y.M., (2004). Crosslinked poly(vinyl alcohol) membranes containing sulfonic acid group: proton and methanol transport through membranes, *Journal of Membrane Science*, 238, 143-151.

Vankelecom, I.F.J., (2002). Polymeric Membranes in Catalytic Reactors, *Chemical Reviews*, 102, 3779-3810.

Proceedings of the 10th International Chemical and
Biological Engineering Conference - CHEMPOR 2008
Braga, Portugal, September 4-6, 2008
E.C. Ferreira and M. Mota (Eds.)

Carbon aerogel supported platinum catalysts for selective hydrogenation of cinnamaldehyde

B.F. Machado[1], S. Morales-Torres[2], H.T. Gomes[1,3], A.F. Pérez-Cadenas[2], F.J. Maldonado-Hódar[2], F. Carrasco-Marín[2], J.L. Figueiredo[1], J.L. Faria[1*]

[1] Laboratório de Catálise e Materiais (LCM), Laboratório Associado LSRE/LCM, Departamento de Engenharia Química, Faculdade de Engenharia, Universidade do Porto, Rua Dr. Roberto Frias s/n, 4200-465 Porto, Portugal

[2] Grupo de Investigación en Materiales de Carbón, Facultad de Ciencias, Universidad de Granada, Avda. Fuentenueva s/n, 18071 Granada, España

[3] Departamento de Tecnologia Química e Biológica, Escola Superior de Tecnologia e de Gestão, Instituto Politécnico de Bragança, Campus de Santa Apolónia, 5300-857 Bragança, Portugal

Keywords: carbon aerogels, platinum, surface groups, cinnamaldehyde hydrogenation
Topic: Advancing the chemical and biological engineering fundamentals: (Bio) Catalysis & reaction engineering

Abstract

This paper describes the preparation and characterization of 1% wt. Pt catalysts supported in carbon aerogels for the application in the liquid-phase selective hydrogenation of cinnamaldehyde. Carbon aerogel supports with different textures were activated with hydrogen peroxide and ammonium peroxydisulfate leading to large amounts of surface groups but keeping unchanged their textural properties. After introducing Pt, the surface chemistry and morphology of the catalysts was characterized by analytical techniques like SEM, TPD, N_2 adsorption isotherms, mercury porosimetry and H_2 chemisorption. Catalysts prepared with activated aerogels exhibited good selectivity towards the desired product, cinnamyl alcohol. A high temperature post-treatment of the catalysts failed to enhance their selectivity, mainly leading to hydrocinnamaldehyde production.

1. Introduction

The synthesis of carbon aerogels was first reported by Pekala (1990). Depending on the solvent removal step, these materials are referred to as: (i) aerogels if supercritical CO_2 is used; (ii) xerogels when the removal takes place under ambient temperature and pressure conditions; and (iii) cryogels: if a freeze-drying method is used. Carbon aerogels are one of the most promising new carbon forms for many applications such as adsorbents, catalysts or capacitors (Moreno-Castilla, 2005; Maldonado-Hodar, 2007). Their potential is based on their unique properties: purity, homogeneity and above all, controllable porosity. Between the different precursors and methods developed during the last years, the sol-gel polymerization of resorcinol (R) and formaldehyde (F) is the most common. The porous texture of carbon aerogels, and consequently their applications, strongly depends on several experimental conditions. The most important is the polymerization step, since it defines the structure and consequently the porous texture of the organic aerogels.

Polymer-based (Moreno-Castilla, 2005; Samant, 2004) and other carbon materials like nanofibers, nanotubes or fullerenes (Serp, 2003) are an important class of materials to produce noble metal supported catalysts. This type of catalysts is extremely useful in the liquid phase heterogeneous selective hydrogenation of unsaturated aldehydes to the corresponding unsaturated alcohols. This is a key process for the production of important intermediates in the preparation of fine chemicals for fragrance, pharmaceutical and

*Corresponding author. Tel + 351-225 081 645. E-mail: jlfaria@fe.up.pt

agrochemical industries. Unfortunately, there are some constrictions, both thermodynamic and kinetic, that limit the selectivity towards the unsaturated alcohol formation. In spite of these drawbacks, the selectivity to unsaturated aldehydes using heterogeneous catalysts can be improved by careful design of the catalysts, controlling the type and surface chemistry of the support, the nature of the active metal, and the addition of a promoter, among others.

In this work, we prepared several carbon aerogel supported Pt catalysts, using materials with different textures and surface chemistries, seeking to establish appropriate structure/activity relationships, which are useful for smart catalyst design.

2. Experimental

2.1 Catalyst preparation

Organic aerogels were synthesized by polymerization of resorcinol with formaldehyde in aqueous solution, according to the methodology developed originally by Pekala *et al.* (1990) using alkali carbonates (M_2CO_3; M = Li or Cs) as polymerization catalysts. This process yields organic RF-aerogels which were carbonized in N_2 flow at 900ºC. Carbon aerogels will be here referred as Li900 and Cs900 indicating the metal alkali and the carbonization temperature used in their synthesis.

Samples of Li900 carbon aerogel were further oxidized (1 g carbon/10 mL of solution) with concentrated hydrogen peroxide (HP, H_2O_2, 9.8 M) and with a saturated solution of ammonium peroxydisulfate (AP, $(NH)_4S_2O_8$) in sulfuric acid (H_2SO_4, 1M) during 48 h at ambient temperature (Moreno-Castilla, 1995). After oxidation, the samples were washed with distilled water and dried at 120ºC in an oven during 24 h. The samples oxidized with H_2O_2 and with $(NH)_4S_2O_8$ will be here referred as Li900H and Li900S, respectively.

Supported Pt (1 wt. %, $Pt(NH_3)_4(NO_3)_2$) catalysts were prepared by incipient wetness impregnation on the above described materials. Prior to reaction, the resulting catalysts (Li900Pt, Li900HPt, Li900SPt and Cs900Pt) were treated in N_2 for 4 hr and reduced in H_2 for 2 hr. A post-reduction treatment (2 hr, N_2) was performed at 700ºC to remove part of the surface groups (Li900Pt700, Li900HPt700, Li900SPt700 and Cs900Pt700).

2.2 Catalyst characterization

The surface morphology of the aerogels was studied by SEM (LEO, model Gemini-1530, equipped with EDX microanalysis). Textural characterization was carried out using mercury porosimetry (Quantachrome Autoscan 60) and N_2 adsorption at -196ºC (Quantachrome autosorb-1). Mercury porosimetry allowed the determination of pore volume (V_{MES}: 3.5 nm < dpore < 50 nm and V_{MAC}: dpore > 50 nm) and the external surface area (S_{EXT}: dpore > 3.7 nm). The BET equation (Brunauer, 1938) and Dubinin-Raduskevich and Stoeckli *et al.* (2002) relations were used for analysis of N_2 adsorption isotherms.

The surface chemistry of the carbon aerogels was characterized by temperature-programmed desorption (TPD). TPD experiments were carried out by heating the samples to 1000ºC in He flow (60 cm^3 min^{-1}) at a heating rate of 50ºC min^{-1}. The amount of evolved gases was recorded as a function of temperature using a quadrupole mass spectrometer (Balzers, model Thermocube), as described elsewhere (Alvarez-Merino, 2000). The oxygen content was calculated from the amounts of CO and CO_2 released during the TPD experiments.

Pt dispersion (D_{Pt}) and average particle size (d_{Pt}) were obtained by H_2 chemisorption measurements performed at 40 ºC. Assuming the formation of spherical particles and a H:Pt = 1:1 stoichiometry it was possible to determine the Pt particle size (d_{Pt} = 1.08/D_{Pt} (nm)). H_2 chemisorption isotherms were measured in conventional volumetric equipment made of Pyrex glass, free of mercury and grease, which reached a dynamic vacuum better than 10^{-6}

mbar at the sample location. Equilibrium pressure was measured with a Baratron transducer from MKS.

2.3 Catalytic hydrogenation

Hydrogenation of cinnamaldehyde was carried out in a 100 mL well-stirred stainless steel high pressure reactor at 90ºC and 10 bar (total pressure). The reaction mixture contained heptane (solvent), cinnamaldehyde, decane (internal standard for gas chromatography) and the catalyst. As the reaction proceeded samples were withdrawn to monitor product distribution. The analysis was performed in a DANI GC-1000 Gas Chromatograph, equipped with a WCOT Fused Silica column (length 30 m, 0.32 mm i.d., film thickness 1 µm). The results of the reaction runs were analyzed in terms of cinnamaldehyde conversion, turn-over frequency and product selectivity.

3. Results and discussion

3.1 Support characterization

The selection of the polymerization catalyst had a great influence over the porous texture of the aerogel: smaller cations like Li were found to produce materials with significant mesoporous volume, whereas larger Cs cations led to macroporous materials (Figure 1). The higher BET surface area (increase of about 150 $m^2\ g^{-1}$) of the Li900 materials relatively to the macroporous material (Table 1) is explained in terms of smaller particle size.

The aerogel surface oxidation treatments resulted in the formation of different oxygen-containing groups like carboxylic acids, lactones and phenols. The introduction of these groups was achieved without any significant changes of the initial textural properties of the aerogels (a decrease of only *ca.* 4% was observed in the S_{BET} values). On the other hand, the surface acidity of the material was seriously affected by the oxidation procedure. The acidic character of the samples, determined by pH_{PZC} measurements, was found to increase in the following order: Li900S (3) > Li900H (5) > Li900 ≈ Cs900 (10). In addition, the amount of O_2 present at the surface was found to increase with decreasing pH_{PZC}, i.e.: Li900S (10 wt.%) > Li900H (3% wt.%) > Li900 ≈ Cs900 (1 wt.%).

Table 1. Textural properties of the carbon aerogels.

Support	S_{BET} ($m^2\ g^{-1}$)	V_{MIC} † ($cm^3 \cdot g^{-1}$)	L_0 † (nm)	S_{ext}* ($m^2 \cdot g^{-1}$)	V_{MES}* ($cm^3 \cdot g^{-1}$)	V_{MAC}* ($cm^3 \cdot g^{-1}$)
Li900	902	0.37	1.0	191	1.06	0.00
Li900H	863	0.35	1.1	-	-	-
Li900S	861	0.35	1.1	-	-	-
Cs900	758	0.30	0.7	59	0.07	1.20

†Dubinin-Radushkevich and Stoecki equations applied to N_2 adsorption data.
*Determined by mercury porosimetry.

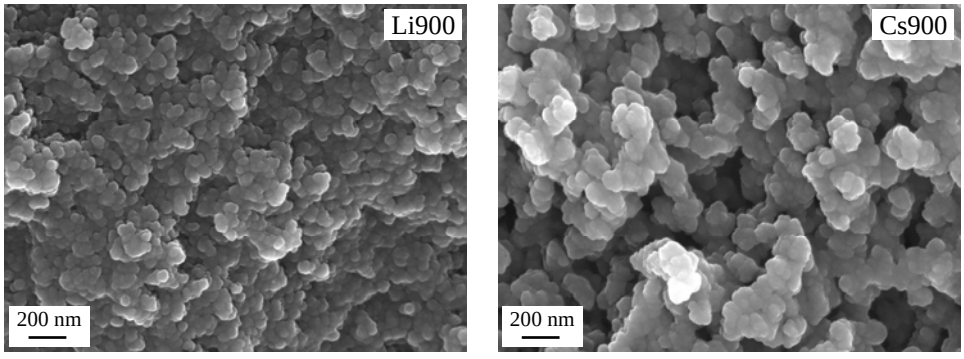

Figure 1. SEM images of Li900 and Cs900 aerogels.

3.2 Metal-phase characterization

Platinum dispersions and particle sizes of the carbon aerogel supported catalysts are given in Table 2. Excellent Pt dispersions over the untreated aerogels (Li900Pt and Cs900Pt) were observed, but somewhat lower values were detected when using the oxidized supports (Li900HPt and Li900SPt). There are two main factors that can affect the metal dispersion over a support: (i) the available surface area and (ii) the interaction between the surface and the precursor solution. The textural properties of the supports were not significantly changed by the oxidation treatments, as already showed, but the presence of oxygenated surface groups increased the hydrophilic character of the surface. Taking into consideration that the surface is negatively charged (pH_{PZC} < pH precursor solution) and the cationic nature of the precursor ($[Pt(NH_3)_4]^{+2}$) an improved metal dispersion was expected when using the oxidized supports, in comparison to the catalysts prepared using the untreated ones. However this is not the case, because the oxygen surface groups act as anchoring sites, which can retain the Pt-precursor molecules at the entrance of the pores preventing the Pt diffusion through the porous structure. On the other hand, during the reduction treatment, the less stable oxygen surface complexes will be removed, which can promote the mobility of the platinum particles favoring their agglomeration (Román-Martínez, 1994).

When a post-reduction treatment is carried out in N_2 at 700 ºC, the experimental conditions are severe enough to induce some sintering of the Pt particles. This seems to be related to the surface chemistry of the materials as the Pt particle size supported in untreated aerogels increases *ca.* 2.3 times while for the activated supports an increase of only 1.5-1.6 times is observed. Besides a sintering effect, the treatment at 700ºC is also able to purge the surface of many of the oxygenated surface groups.

Table 2. Pt dispersion and particle size for the aerogel supported catalysts.

Catalyst	**D_{Pt} (%)**	**d_{Pt} (nm)**
Li900Pt	74.1	1.5
Li900Pt700	31.3	3.4
Li900HPt	46.1	2.3
Li900HPt700	30.5	3.5
Li900SPt	44.4	2.4
Li900SPt700	28.7	3.8
Cs900Pt	87.3	1.2
Cs900Pt700	40.3	2.7

3.3 Hydrogenation of cinnamaldehyde

Some of the possible pathways for the selective hydrogenation of cinnamaldehyde (CAL) in a non alcohol solvent are shown in Figure 2. The thermodynamically preferred path goes through the hydrogenation of the C=C bond yielding the saturated aldehyde (hydrocinnamaldehyde, HCAL). Selective hydrogenation of the C=O bond gives the unsaturated alcohol (cinnamyl alcohol, COL). Both COL and HCAL can be further hydrogenated to produce the fully saturated alcohol (hydrocinnamyl alcohol, HCOL). In some experiments, a number of side-products involving the loss of the hydroxyl group (*β*-methylstyrene (MS) and 1-propylbenzene (PB)) were also detected in different amounts, indicating a strong adsorption over the metal sites and a possible poisoning effect.

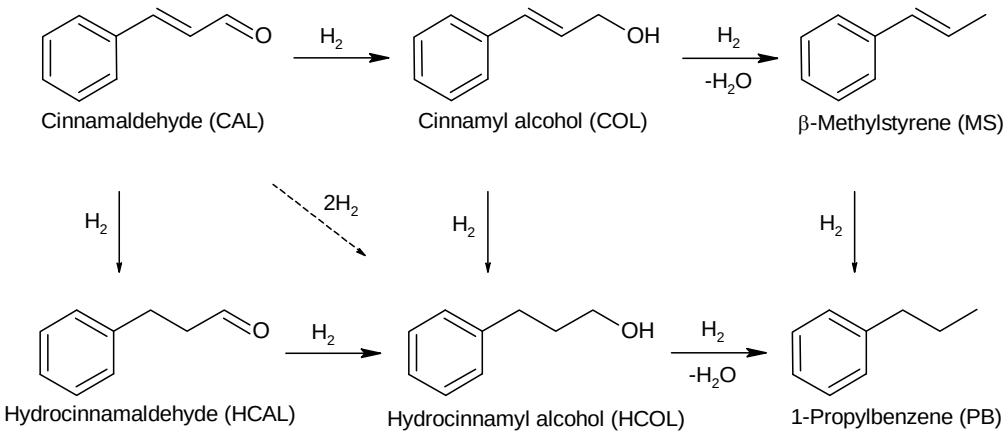

Figure 2. Reaction scheme for the selective hydrogenation of cinnamaldehyde.

The reaction results obtained at 90ºC and 10 bar (total pressure) are gathered in Table 3. Taking into account the average pore size diameter in both aerogels (12 and 48 nm) and the cinnamaldehyde molecule size (< 1 nm) we could expect the absence of internal mass transfer limitations during the reaction. This assumption was confirmed by the higher activity (TOF) exhibited by Li900Pt regarding the macroporous Cs900Pt catalyst.

Table 3. Initial turn over frequency and selectivities towards COL, HCAL and HCOL, measured at 50% conversion of CAL.

Catalyst	TOF (s^{-1})	S_{COL} (%)	S_{HCAL} (%)	S_{HCOL} (%)
Li900Pt	1.6	11	54	20
Li900Pt700	3.4	12	54	25
Li900HPt	1.6	53	18	20
Li900HPt700	3.5	21	41	28
Li900SPt	2.3	36	23	25
Li900SPt700	4.4	21	44	27
Cs900Pt	0.9	24	34	35
Cs900Pt700	2.8	12	54	19

Oxidation of the carbon materials had a marked effect over the selectivity towards cinnamyl alcohol. Selectivity increased by a factor of 4.8 for Li900HPt (53% at 50% conversion of cinnamaldehyde) and 3.3 for Li900SPt (36%) compared with the catalyst prepared using the non-treated support (11%).

In previous studies we used a high temperature treatment to enhance selectivity of the catalysts (Solhy, 2008). In the present study a thermal treatment at 700ºC in N_2 increased the TOF up to a factor of 3 and shifted selectivity to the C=C bond. The selectivity towards the carbonyl group appears to be related to the surface chemistry of the material, as a more acidic surface favors the interaction with the carbonyl group and a more basic surface favors the reduction of the olefinic bond.

4. Conclusions

Macro or mesoporous carbon aerogels were obtained depending on the type of polymerization catalyst used. Oxidation treatment with H_2O_2 and $(NH_4)_2S_2O_8$ allowed the porous structure to remain relatively unchanged while introducing significant amounts of oxygenated groups. The acidic character of most groups led to a strong decrease of the pH_{PZC} of the support surface. The Pt dispersion over the aerogels was strongly influenced by these chemical modifications, decreasing in all cases after oxidation treatments. The

increased acidity of the Li900HPt and Li900SPt supports leads to a higher selectivity towards cinnamyl alcohol when compared with that obtained with Li900Pt. A thermal treatment at 700ºC removed most of the support surface groups and shifted the selectivity back to the hydrogenation of the C=C bond.

Acknowledgements

SMT and AFPC acknowledge the Spanish Ministry of Education and Science for a F.P.U. research fellowship and a Ramón y Cajal research contract. These investigations were supported by the MEC-FEDER (CTQ2007-61324), Junta de Andalucia (RNM 547), FCT and POCI/FEDER (POCI/EQU/58252/2004 and PhD grant SFRH/BD/16565/2004 for BFM).

References

Pekala, R.W., Alviso C.T., LeMay, J.D. (1990). Organic aerogels: microstructural dependence of mechanical properties in compression. *Journal of Non-Crystalline Solids*, 125, 67-75.

Moreno-Castilla, C., Maldonado-Hodar, F.J. (2005). Carbon aerogels for catalysis applications: An overview. *Carbon*, 43, 455-465.

Maldonado-Hodar, F.J., Moreno-Castilla, C., Carrasco-Marin, F., Perez-Cadenas, A.F. (2007). Reversible toluene adsorption on monolithic carbon aerogels. *Journal of Hazardous Materials*, 148, 548-552.

Samant, P.V., Gonçalves, F., Freitas, M.M.A., Pereira, M.F.R., Figueiredo, J.L. (2004). Surface activation of a polymer based carbon. *Carbon*, 42, 1321-1325.

Al-Muhtaseb, S.A., Ritter, J.A. (2003). Preparation and properties of resorcinol-formaldehyde organic and carbon gels. *Advanced Materials*, 15, 101-114.

Serp, P., Corrias, M., Kalck, P. (2003). Carbon nanotubes and nanofibers in catalysis. *Applied Catalysis A: General*, 253, 337-358.

Moreno-Castilla, C., Ferro-Garcia, M.A., Joly, J.P., Bautista-Toledo, I., Carrasco-Marin F., Rivera-Utrilla, J. (1995). Activated carbon surface modifications by nitric acid, hydrogen peroxide, and ammonium peroxydisulfate treatments. *Langmuir*, 11, 4386-4392.

Brunauer, S., Emmet, P.H., Teller, E. (1938). Adsorption of gases in multimolecular layers. *Journal of the American Chemical Society*, 60, 309-319.

Stoeckli, F., Guillot, A., Slasli, A.M., Hugi-Cleary, D. (2002). The comparison of experimental and calculated pore size distributions of activated carbons. *Carbon*, 40, 383-388.

Alvarez-Merino, M.A., Carrasco-Marín, F., Fierro, J.L.G., Moreno-Castilla, C. (2000). Tungsten catalysts supported on activated carbon: I. Preparation and characterization after their heat treatments in inert atmosphere. *Journal of Catalysis*, 192, 363-373.

Román-Martínez, M.C., Cazorla-Amorós, D, Linares-Solano, A, Salinas-Martínez de Lecea, A. (1994). Metal support interaction in Pt/C catalysts. Influence of the support surface chemistry and the metal precursor. *Carbon*, 33, 3-13.

Solhy, A., Machado, B.F., Beausoleil, J., Kihn, Y., Gonçalves, F., Pereira, M.F.R., Órfão, J.J.M., Figueiredo, J.L., Faria, J.L., Serp, P. (2008). MWCNT activation and its influence on the catalytic performance of Pt/MWCNT catalysts for selective hydrogenation. *Carbon*, 46, 1194-1207.

Proceedings of the 10th International Chemical and
Biological Engineering Conference - CHEMPOR 2008
Braga, Portugal, September 4-6, 2008
E.C. Ferreira and M. Mota (Eds.)

Extraction of nickel from spent nickel catalyst with inorganic acid

S. Meysam Hashemnejad[1], Matin Parvari[1]*
[1] Chemical Engineering Department, Iran University of Science and Technology, Farjam Str., Tehran, Iran.

Keywords: Nickel recovery, Leaching, Hydrometallurgical, Spend catalyst
Topic: Recovery of Nickel Catalyst.

Abstract

This study examined the recovery of nickel from spent nickel catalyst ($NiO/CaAl_4O_7$) by hydrometallurgical technique with sulfuric acid. The influences of temperature, acid concentration, solid: liquid ratio and contact time has been studied. Under optimum conditions (temperature: 120℃, acid concentration: 70% (v/v), solid: liquid 1/20, time of reaction: 220min) 99% Ni were extracted as sulfate phase. In addition to the economical advantages the proposed procedure will be helpful in saving the wastage of metal and protecting the environment from metal pollution.

1 Introduction

A considerable attention is given to the problem of utilization and processing of solid wastes containing nonferrous metals. Wastes of this kind are toxic substances hazardous to the environment, on the one hand, and a valuable chemical raw material, on the other [1]. For many years, nickel has been considered as the most suitable metal in steam reforming of hydrocarbons. Nickel is cheap, sufficiently active, and allows suitable catalysts to be economically produced [2]. In the course of operation, the catalysts lose activity as a result of changes in their composition and structure. At high temperatures, the catalyst undergoes sintering and its active surface area decreases. In the course of time, a considerable fraction of nickel cations diffuses from the catalyst surface deep inside alumina, active nickel oxide is converted on alumina into inactive nickel aluminate, and spinel-like compounds, inactive in catalysis, are formed [1].The increasing demand for metals in the world has required intensive studies for the extraction of metals from low-grade ores and/or secondary resources. Extraction of nickel can be performed from secondary resources like spent catalysts [3]. Regeneration of spent catalysts after many cycles of use is not possible by ordinary techniques and it poses a significant waste disposal problem for most of the hydrogenation and fertilizer plants [4].

Commonly, two methods are suggested for recovery of nickel from ores and raw materials of technological origin: pyrometallurgical technique, whose main product is ferronickel obtained at high temperatures, and hydrometallurgical, based on leaching-out of nickel from raw materials with various acids and solutions of ammonia and ammonium salts. The hydrometallurgical method for nickel recovery, compared with the pyrometallurgical technique, is the most promising because it conforms to the principle of combination of environmental and economical interests (markedly diminishes the number of technological procedures, does not require fuel expenditure for high-temperature processes, minimizes the amount of solid wastes and toxic discharges into the atmosphere). One more advantage of the given technique is that it can recover from leaching solutions, at an appropriate choice of methods used, both metallic nickel (electrolytically) and its salts [1].

* Corresponding author. Tel +98(21)73912755, Email: Parvari@iust.ac.ir

Increasing environmental concerns and legislation regarding the disposal of hazardous residues are forcing companies and countries to process their own waste products and residues, Spent hydroprocessing catalysts have been classified as hazardous wastes by the Environmental Protection Agency in the USA (Rapport, 2000) [5]. So the treatment of this waste is compulsory due to its toxicity and polluting character. This situation has resulted in increasing emphasis on the production of nickel from secondary sources like spent catalysts.

2 Experimental section

2.1. Apparatus and Materials

A Perkin-Elmer ® Model 2380 atomic absorption spectrometry (AAS) with air-acetylene flame and hallow cathode lamps were used for the analysis of nickel. All instrumental settings were those recommended in the manufacturer's manual book and the instrumental conditions were shown in Table 1.

Structural characterization of the nickel catalyst was performed by powder X-ray diffraction (XRD) data were collected at room temperature using a PW-1800 Philips diffractometer with Cu Kα1 radiation (λ = 1.5406 Å) at 40 kV, 30 mA for determining crystalline phases.

The chemical composition of catalysts was analyzed semiquantitatively by standardless X-ray fluorescence (XRF) spectroscopy (EAGLE II μ-Probe, EDAX) with RhKα radiation using the fundamental parameter model. The X-ray beam was focused to a spot size of 300 μm on the sample surface.

Spent nickel oxide catalyst used in this study was kindly provided (supplied) by Arak petrochemical complex (Iran). We can find out, structure of nickel catalysts by X-ray diffraction (XRD). Figure1 shows presence of NiO and CaAl4O7 as the major phases and CaAl2O4 as the minor phase. The content of nickel in the catalyst sample was 14.06% as indicated by X-ray fluorescence analysis.

2.2. Procedure

The spent catalyst was ground and sieved to achieve appropriate particle size. Leaching experiments were carried out in a 250mL thermostatically controlled stirrer tank. In each experiment we used particle size<100μm and also stirring velocity adjusted at the maximum rate (1000 rpm) to eliminate these factor in leaching [4, 2]. At first, 5 g of spent catalyst was added to certain amount of sulfuric acid having a specified concentration (30, 50, 70 and 90%) and different temperature (80,100,120 andĊ140 or higher) to determine best temperature and acid concentration and then other factors, solid: liquid ratios (S/L) and time of reaction were analyzed. Nickel was leached-out from the catalyst in accordance with following reaction [3].

$NiO + H_2SO_4 \rightarrow NiSO_4 + H_2$

The reaction of support phase with acid is very week that we can obviously say it is totally inactive toward H_2SO_4 .After separation of nickel sulfate solution and washing the solid which settles at the bottom of a liquid, the specimens were chemically examined for determination of nickel content using atomic absorption spectroscopy (AAS), and then the percentage extraction of nickel was calculated by following equation.

Ni recovery (%) = (mass of nickel out by acid / total mass of nickel determined by XRF analyses) *100

Table 1: FAAS instrumental condition employed to determination of metal ions.

Flame type	Air acetylene
Air flow rate	11.0L/min
Acetylene flow rate	0.5L/min
Slit width	0.7 nm
Lamp width	5 mA
Burner height	13 mm
Integration time	5 second

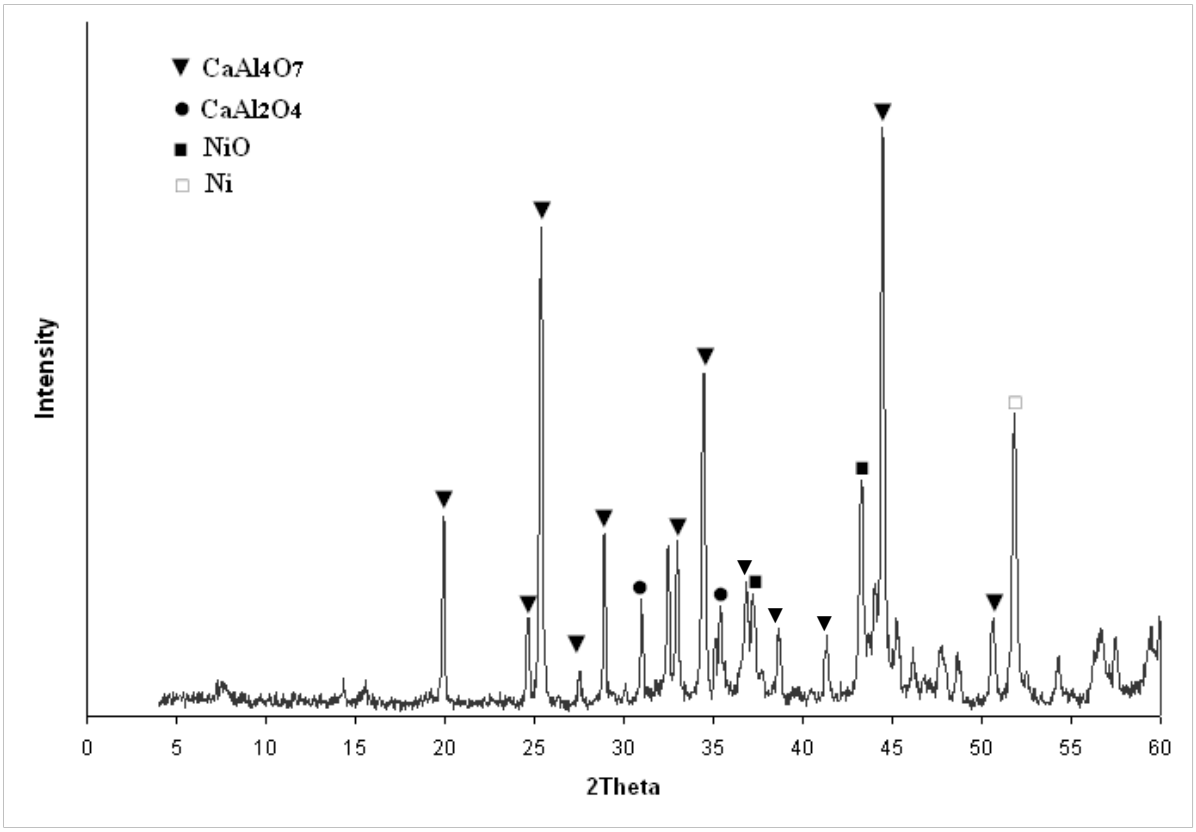

Fig. 1. The X-ray diffraction result of spent nickel catalyst

3 Results and discussion

3.1. Effect of temperature and acid concentration

Leaching of spent nickel catalyst was carried out at different temperatures and acid concentration ranging from 80 to 140 Ċ and 30 to 90% respectively. Solid: liquid ratio was maintained in S/L: 1/10 (gr/ml) in each experiment and the treatment of solid with acid was kept in one hour. Fig. 2 demonstrates the effect of varying acid concentration by volume and temperature. The obtained result shows that the maximum nickel recovery was found 82% at 120Ċ and 70% acid concentration.

O

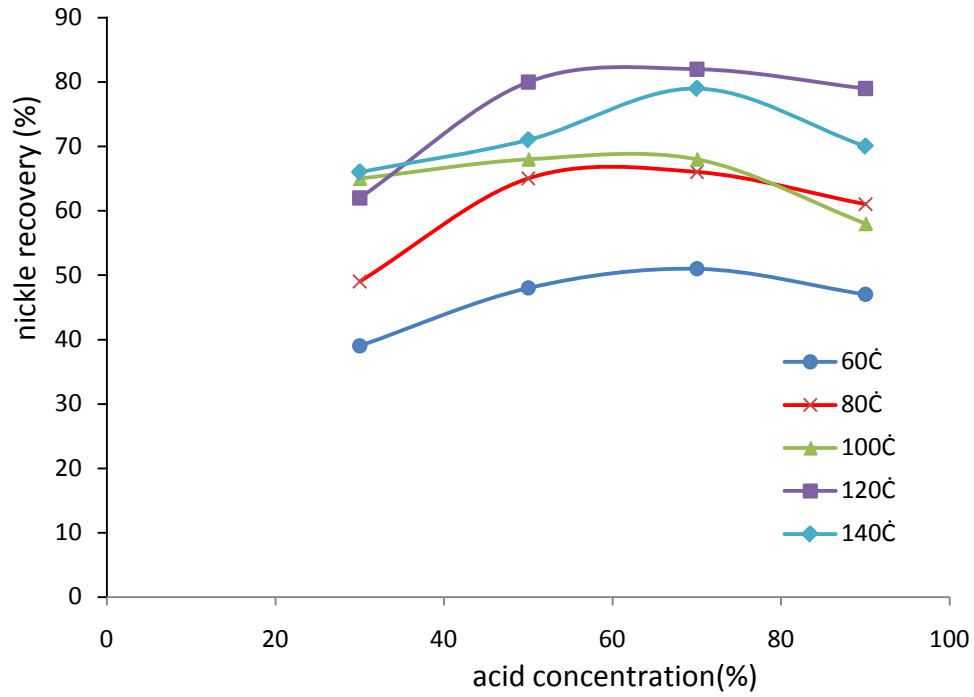

Fig. 2. Effect of temperature and acid concentration on recovery of nickel from spent nickel catalyst. S/L: 1/10, time of reaction: 1 hr.

3.2. Effect of solid/liquid ratio

The other important factor that affects on extraction yield is the ratio of solid to acid solution. It was found that the minimum ratio of S/L is approximately 1/20 (gr/ml) to reach the highest value of nickel recovery (figure3).

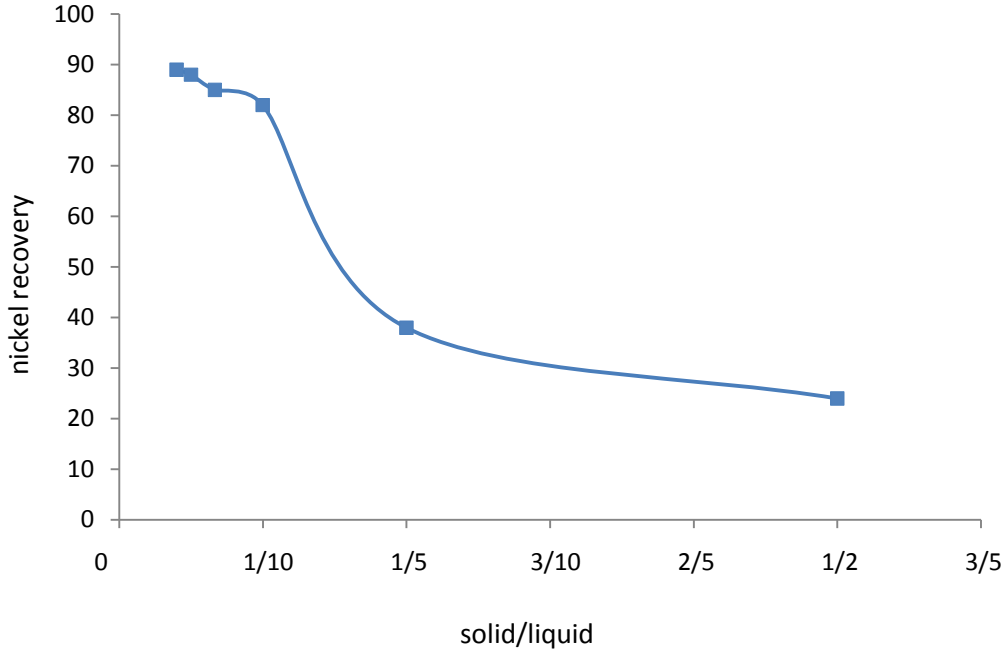

Fig. 3. Effect of solid/liquid ratio on recovery of nickel catalyst. H_2SO_4 concentration 70%(v/v) and temperature:120Ċ.

3.2. Effect of reaction time

Extraction of nickel from spent Ni catalyst was carried out at different time of reaction from 20 to 220 minute. In all these experiment other factors were adjusted at their best condition (temperature: 120Ċ, acid concentration: 70% (v/v) and S/L: 1/20). We can obviously find out from figure 4 that time of contact is the other mains factors. Metal removal can be continued till 220 minute. At this time all nickel can be removal as sulfate.

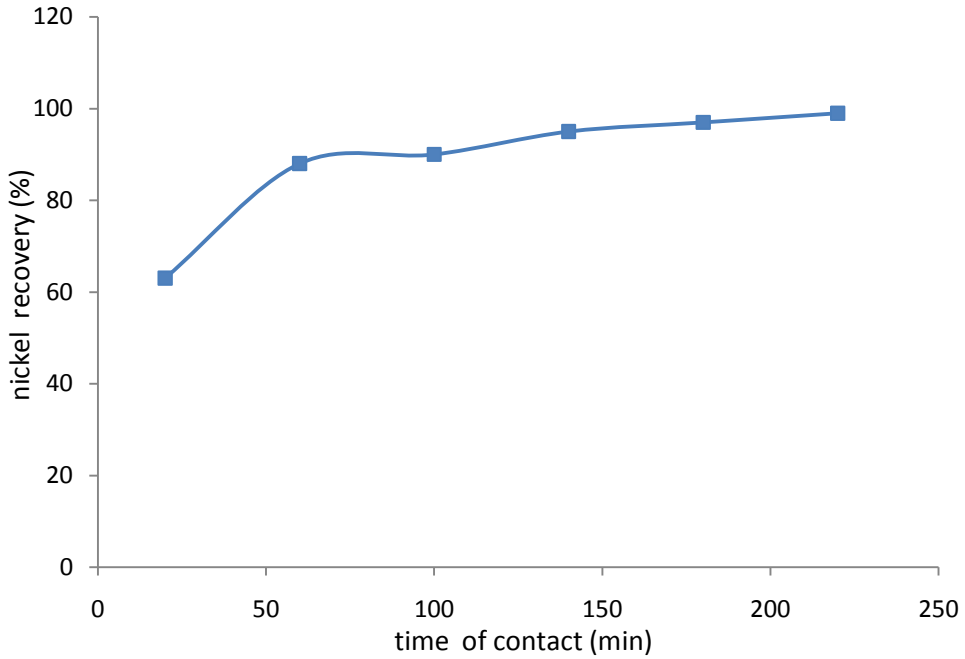

Fig. 4. Effect of contact time on nickel recovery. H_2SO_4 concentration 70 %(v/v) and temperature: 120Ċ, S/L: 1/20.

4 Conclusions

Extraction of nickel was carried out from spent nickel catalysts using in steam methane reforming by sulfuric acid as inorganic component, also there is chance to regenerate these catalysts and reuse in the processes. The recovery of nickel was more than 99 percentages during the leaching process. The optimum experimental parameters achieved under the following conditions: temperature 120Ċ, acid concentration 70% (v/v), solid: liquid 1: 20 and contact time 220 minute. Although in all these experiments eliminate the stirring rate and particle size diameter factors.

Acknowledgment

The authors would like to thank Arak petrochemical complex for providing Ni catalyst.

References

[1] V. S. Kolosnitsyn, S. P. Kosternova, O. A. Yapryntseva, A. A. Ivashchenko, and S. V. Alekseev, “Recovery of Nickel with Sulfuric Acid Solutions from Spent Catalysts for Steam Conversion of Methane,” published in Zhurnal Prikladnoi Khimii, (2006).

[2] N.M. Al-Mansi, N.M. Abdel Monem, “Recovery of nickel oxide from spent catalyst” Waste Management 22 85–90, (2002).

[3] E.A. Abdel-Aal, M.M. Rashad, “Kinetic study on the leaching of spent nickel oxide catalyst with sulfuric acid” Hydrometallurgy 74 189–194, (2004).

[4] Kamala K. Sahu Archana Agarwal Banshi D. Pandey, “Nickel recovery from spent nickel catalyst,” Waste Management & Research: 23: 148–154, (2005).

[5] Yun Chen, Qiming Feng, Yanhai Shao, Guofan Zhang, Leming Ou, Yiping Lu, “Research on the recycling of valuable metals in spent Al2O3-based catalyst,” Minerals Engineering 19 94–97, (2006).

Proceedings of the 10th International Chemical and
Biological Engineering Conference - CHEMPOR 2008
Braga, Portugal, September 4-6, 2008
E.C. Ferreira and M. Mota (Eds.)

Oxidation of Fe(II) in sulphuric medium

Sílvia M.C. Santos, Ana E. Ferreira, Rita C. Figueiredo, Maria J.N. Correia, Maria T.A. Reis, Maria R.C. Ismael, Remígio M. Machado, Jorge M.R. Carvalho *

CPQUTL – Centre for Chemical Processes of UTL, DEQB – Department of Chemical and Biological Engineering, Instituto Superior Técnico, Av. Rovisco Pais, 1049-001 Lisboa, Portugal,

Keywords: Iron oxidation, Leaching, Zinc concentrate
Topic: Advancing the chemical and biological engineering fundamentals.

Abstract

Ferric ion is one of the most important oxidants used in leaching processes. In this study a comparison between the oxidation of iron at atmospheric pressure and under an oxygen pressure of 2 and 6 bar was carried out. The results showed that H_2O_2 was the most effective oxidant agent. However, it is a very expensive reagent to be used in a leaching process at industrial scale. As an alternative, ferrous ion oxidation may be carried out in an autoclave, where it is possible to have more than 20% of the total iron in its ferric form at 95 ºC and $P(O_2)$=6 bar in 1 h, with the expected beneficial effects on the leaching rates of sulphide minerals.

1 Introduction

Ferric ion is commonly used as oxidant agent in the leaching of sulphide minerals. Thus, for example, the leaching reaction of zinc sulphide follows the reaction below (Aydogan et al., 2005; Dutrizac et al., 2003):

$$ZnS + Fe_2(SO_4)_3 \rightarrow ZnSO_4 + 2FeSO_4 + S^0 \quad (1)$$

When the leaching is carried out in acid media under oxygen pressure, the ferric ions spent in reactions 1 or 2 are regenerated through reaction 3 (Filippou, 2004):

$$2ZnS + 2Fe_2(SO_4)_3 \rightarrow 2ZnSO_4 + 4FeSO_4 + 2S^0 \quad (2)$$

$$4FeSO_4 + 2H_2SO_4 + O_2 \rightarrow 2Fe_2(SO_4)_3 + 2H_2O \quad (3)$$

Therefore, according to reaction 3, oxygen is transferred from the gaseous phase to the liquid phase and reacts with ferrous ions, in the presence of sulphuric acid, to produce ferric ions. The ferric ions will then dissolve zinc sulphide (equation 2).

The consumption of ferric ions in the leaching reaction (Eq. 1 and 2) leads to the decrease of the redox potential and to the observed reduction of the leaching rate. Therefore, it is advantageous to carry out the oxidation of Fe(II) to Fe(III) during the leaching by the addition of external oxidants. In fact, this procedure would allow maintaining the concentration of the oxidant and the redox potential but minimizing the consumption of fresh reagent. Oxidizing agents such as air, oxygen (O_2) and hydrogen peroxide (H_2O_2) may be used to promote the oxidation of ferrous ions in aqueous solution. In acidic solutions, the oxidation of ferrous ion with O_2 follows reaction 4 (Rönnholm, 1999):

$$Fe^{2+} + \frac{1}{4}O_2 + H_3O^+ \rightarrow Fe^{3+} + \frac{3}{2}H_2O \quad (4)$$

* Corresponding author. Tel + 351-21-8417311. E-mail: jcarv@ist.utl.pt

The kinetics of the oxidation of Fe(II) ions by gaseous oxygen (reaction 4) is a second order reaction with respect to Fe(II) concentration (Chmielewski, 1984, Vracar, 1997). Thus, the equation of the process rate is:

$$\frac{d[Fe(III)]}{dt} = -\frac{d[Fe(II)]}{dt} = k[Fe(II)]^2 \quad (5)$$

or:

$$\frac{1}{[Fe(II)]_t} = kt + \frac{1}{[Fe(II)]_0} \quad (6)$$

Where $[Fe(II)]_t$ is the concentration of the ferrous ions within a determined period of time (mol/L), $[Fe(II)]_0$ is the concentration of ferrous ions at time=0 (mol/L); k is the rate constant (L/(mol.min) and t is the time (min). Therefore the kinetic constants may be calculated from the slope of the lines that represent $[Fe(II)]^{-1}$ vs time, for t=0.

Hydrogen peroxide is also used as an oxidizing agent for iron. In fact, the reduction potential of the pair H_2O_2/H_2O (E_0 (H_2O_2/H_2O) = 1.77 V) is very high and will oxidize the ferrous ions in accordance with the following reaction (Aydogan, 2006):

$$H_2O_2 + 2Fe^{2+} + 2H^+ \leftrightarrow 2H_2O + 2Fe^{3+} \quad (7)$$

The use of H_2O_2 in hydrometallurgical processes, despite its relatively high price, has a great potential, as mentioned in several recent studies concerning the sphalerite leaching (Aydogan, 2006, Pecina et al., 2008).

In this study, oxidation tests using synthetic solutions containing only ferrous sulphate and sulphuric acid were performed at atmospheric pressure and at pressures of 2 and 6 bar using a Parr autoclave.

2 Materials and methods

All the chemicals were Analytical Grade and all solutions were prepared with deionised water. Measurements of the pH and of the redox potential were carried out with a pH/E meter from Metrohm. The solutions were analysed for iron concentration by atomic absorption spectroscopy (Perkin Elmer, AAnalyst 200) and ferrous ion was determined by volumetric analysis with potassium dichromate (Vogel, 1972).

3 Experimental procedure

Oxidation tests at atmospheric pressure were performed in a five-necked round bottom reactor (1 L, 13 cm diameter) heated by a thermostatic oil bath. For stirring, a single round paddle (6.5 cm diameter) was used. The 800 mL of leaching solution ($FeSO_4$ + H_2SO_4) was added to the reactor and when the temperature was reached, air was added and the stirring started. The addition of small volumes of H_2O_2 130 V (2 mL after each sample), were also tested.

The autoclave tests were carried out using a Hastelloy C-276 autoclave (Parr, model 4843). In this case, 1000 mL of solution ($FeSO_4$ + H_2SO_4) was added to the reactor under stirring and the selected O_2 pressure. The first sample was collected when the selected temperature was reached.

The redox potential of the solution was monitored throughout the experiments with a silver/silver chloride reference electrode. The pH of the solution was also monitored during the tests. At pre-set time intervals, samples of 2 to 5 mL were withdrawn from the reactor and analysed for total and for ferrous iron.

4 Results and discussion

At atmospheric pressure, the oxidation of ferrous ions was performed by the addition of air and H_2O_2 130 V. The comparison between these two oxidizing agents is presented in Figure 1.

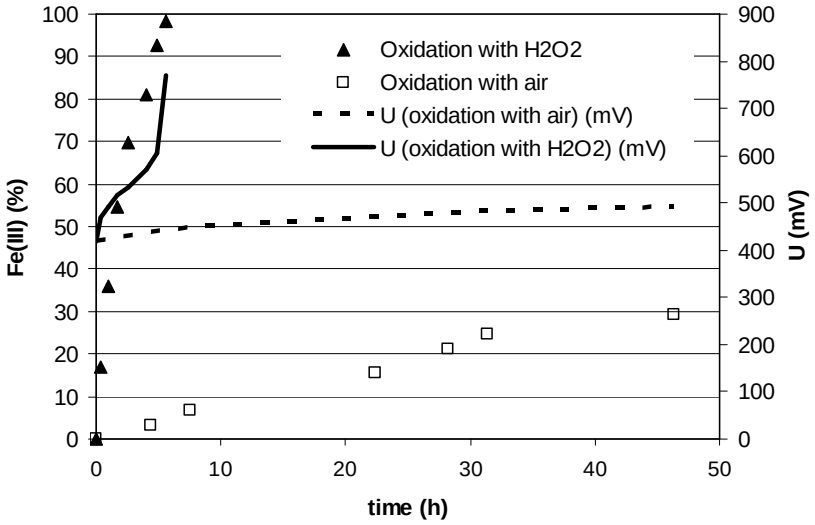

Figure 1: Effect of the addition of air and H_2O_2 on Fe(II) oxidation. Experimental conditions: solution with $[Fe(II)]_{initial}$=15 g/L, $[H_2SO_4]$=0.5 M, T=80 ± 3 ºC, stirring speed=500 rpm, air=64 L/h, V_{H2O2} =14 mL ($V_{solution}$=800 mL). Reference electrode: silver/silver chloride.

The results show that at atmospheric pressure, hydrogen peroxide was more effective than air. In fact, the addition of 14 mL of H_2O_2 130 V (addition of 2 mL after each sample) to 800 mL of solution allowed the complete oxidation of Fe(II), whereas after 46 h of air injection, only 30% of the ferrous ion was oxidized.

The autoclave tests were performed at two different O_2 pressures: 2 and 6 bar. Figure 2 presents the influence of the temperature in the oxidation rate of ferrous ion.

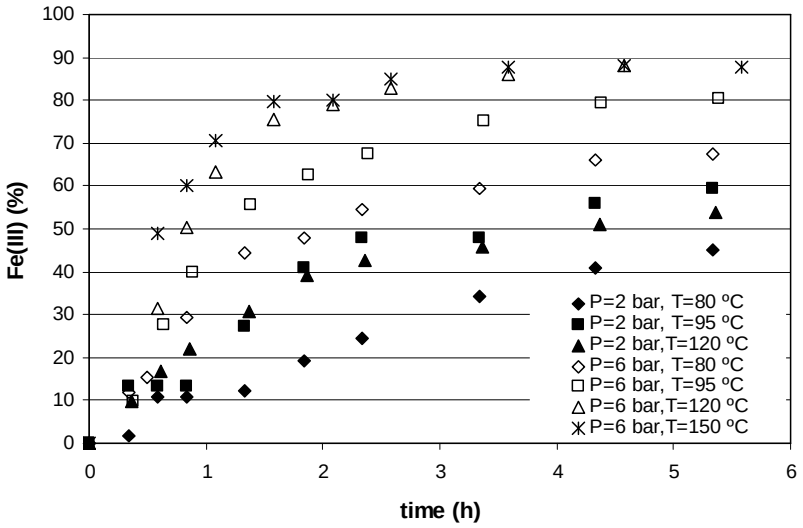

Figure 2: Autoclave oxidation of Fe(II). Experimental conditions: solution with $[Fe(II)]_{initial}$=15 g/L, $[H_2SO_4]$=0.5 M, stirring speed=500 rpm.

It is possible to conclude from Figure 2 that at 80 ºC and 2 bar of oxygen 44% of the ferrous ion was oxidized in 5 h. The results obtained were improved when the temperature was increased to 95 ºC. In fact, 60% of the ferrous ion was in its trivalent form after 5 h of reaction but there was no improvement of these results when the temperature was increased up to 120 ºC.

As expected, the kinetics of the oxidation reaction increased directly with the oxygen pressure and temperature, being the temperature effect more pronounced at 6 bar. Thus, for example, at 95 ºC and PO_2=2 bar, 40% of the ferrous ion was oxidized in 2 h, whereas this value increased to 63% at 6 bar. On the other hand, the temperature increase from 80 to 120 ºC allowed an augment of the amount of ferric ions in solution of about 30%.

The effect of the stirring speed on the oxidation rate of ferrous ion is presented in Figure 3. The results showed that, at 6 bar oxygen pressure, the oxidation rate was not significantly affected by the increase of the stirring speed. This result indicates that the rate controlling step of the ferrous ion oxidation is not the diffusion in the liquid phase. On the other hand, the effect of the temperature on the kinetics of ferrous iron oxidation presented in Figure 2 suggests a reaction rate control of the global process.

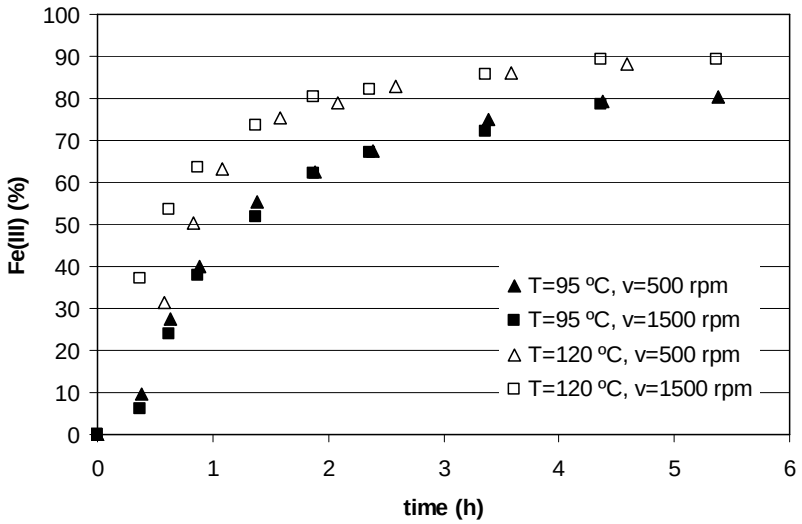

Figure 3: Autoclave oxidation of Fe(II). Experimental conditions: solution with $[Fe(II)]_{initial}$=15 g/L, $[H_2SO_4]$=0.5 M, $P(O_2)$=6 bar.

The activation energy value helps to identify the rate controlling step. Therefore, the kinetic constants for the experiments carried out at PO_2= 6 bar were calculated from the slope of the lines $[Fe(II)]^{-1}$ vs time and Figure 4 shows the correspondent Arrhenius plot. The value of the activation energy calculated for the reaction was E_a= 40 kJ/mol, which clearly suggests a reaction controlled process.

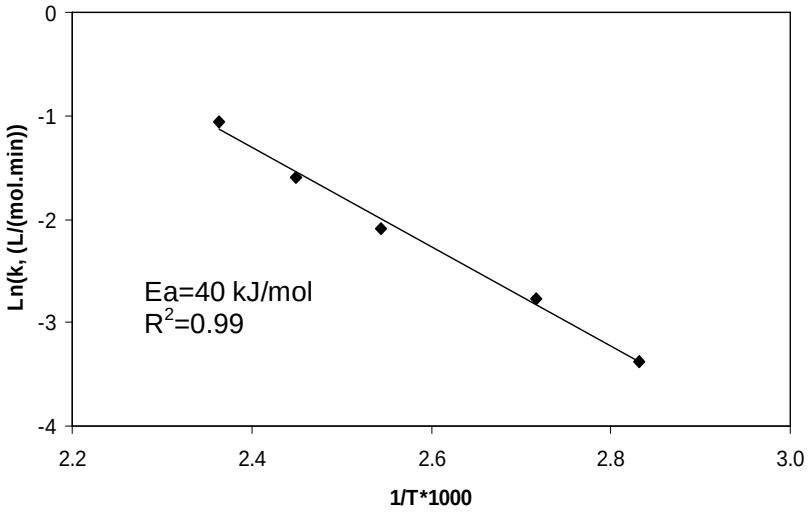

Figure 4: Arrhenius plot.

The above presented results are important in the optimization of the leaching conditions to be used in, for example, the leaching of the metals contained in a zinc sulphide concentrate. As shown in Figure 1, at atmospheric pressure, H_2O_2 was the most effective oxidant agent. However, its price may affect the economics of the hydrometallurgical process at industrial scale and, therefore, the autoclave leaching under an oxygen pressure should be used instead. In fact, Figure 5 clearly shows the benefits of carrying out the autoclave leaching described by the zinc leaching curves from a zinc sulphide concentrate with 45% of zinc. The change of the percentage of ferric ions in solution with time is also shown in this Figure.

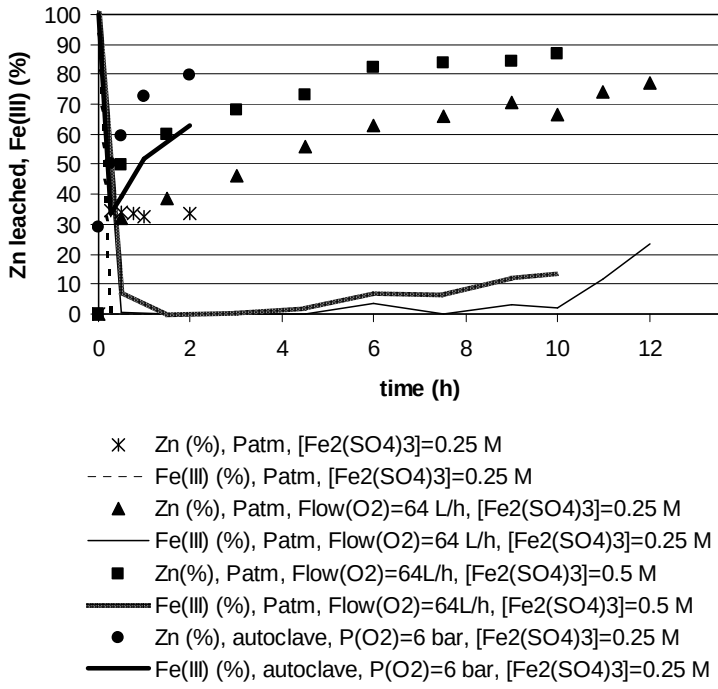

Figure 5: The effect of Fe(II) oxidation on Zn leaching. Experimental conditions: s/l=10% (w/v), T=80 ºC, solution with $[H_2SO_4]$=0.5 M, stirring speed=500 rpm.

As illustrated above, at atmospheric pressure and without iron oxidation, the maximum extraction of zinc (35%) was attained in 30 min and increasing the leaching time did not lead

to the increase of zinc extraction. Furthermore, after 15 min all the iron was in its ferrous form. At atmospheric pressure, the introduction of oxygen in the reactor allowed a slight improvment of the leaching results and the maintenance of a residual amount of ferric ions in solution for reaction times higher than 4 h. However, this effect was very slow. On the contrary, the resuls were improved significantly when the leaching was carried out in autoclave under an oxygen pressure of 6 bar. In this case, the ferrous iron was rapidly oxidated to Fe(III), allowing to maintain its percentage value higher than 35% during all the experiments and to leach in 2 h more than 80% of the zinc contained in the concentrate.

5 Conclusions

It was demonstrated that H_2O_2 at atmospheric pressure, as well as air/oxygen, may be used to perform the oxidation of ferrous ion. Whereas the reaction is very slow with air/oxygen, the price of hydrogen peroxide may not allow its application at industrial scale. As an alternative, ferrous ion oxidation may be carried out in an autoclave. In fact, the regeneration of the ferric ions in situ would allow a significant decrease of the consumption of fresh ferric oxidant, without decreasing the leaching efficiency. The results obtained in this work show that zinc leaching was considerably enhanced when the oxidation of the ferrous iron to the ferric state was performed during the leaching reaction and it was possible to leach in 2 h around 80% of the zinc contained in a zinc sulphide concentrate with 45% of zinc.

Acknowledgements

The authors would like to acknowledge to Somincor for the support and for supplying the samples of the zinc sulphide concentrate. Financial support for this study by “Fundação para a Ciência e a Tecnologia” (FCT, Portugal) and the European Community, through the project FCT PDCT/EQU/61733/04 and “Agência de Inovação” (Adi, PRIME-IDEIA, Portugal) through the project PROJECTO ZINCO 70/00191, is gratefully acknowledged. S.M.C. Santos is also thankful to FCT, Portugal, for her PhD financial support (fellowship ref: SFRH/BD/25598/2005).

References

Aydogan, S., Aras, A., Canbazoglu, M. (2005). Dissolution kinetics of sphalerite in acidic ferric chloride leaching. Chemical Engineering Journal, 114, 67-72.

Aydogan, S.(2006). Dissolution kinetics of sphalerite with hydrogen peroxide in sulphuric acid medium. Chemical Engineering Journal, 123, 65-70.

Chimielewsky, T., Charewicz, A. (1984). The oxidation of Fe(II) in aqueous sulphuric acid under oxygen pressure. Hydrometallurgy, 12, 21-30.

Dutrizac, J.E., Pratt, A.R. and Chen, T.T. (2003). The mechanism of sphalerite dissolution in ferric sulphate – sulphuric acid media. Yazawa International Symposium, Metallurgical and Materials Processing: Principles and Technologies, Volume III: Aqueous and Electrochemical Processing, 139-161.

Filippou, D. (2004). Innovate hydrometallurgical processes for the primary processing of zinc. Mineral Processing & Extractive Metall. Rev., 25, 205-252.

Pecina, T., Franco, T., Castillo, P., Orrantia, E. (2008). Leaching of a zinc concentrate in H_2SO_4 solutions containing H_2O_2 and complexing agents. Minerals Engineering,21,23-30.

Rönnholm, M.R., Wärna, J., Salmi, T., Turunen, I., Luoma, M. (1999). Kinetics of oxidation of ferrous sulphate with molecular oxigen. Chemical Engineering Science, 54, 4223-4232.

Vogel, A.I. (1972). A Text Book of Quantitative Inorganic Analysis Including Elementary Instrumental Analysis, 3th ed., Longman Group Limited, London.

Vracar, R.Z., Cerovic, K.P. (1997). Kinetics of oxidation of Fe(II) ions by gaseous oxygen at high temperatures in an autoclave. Hydrometallurgy, 44, 113-124.

Proceedings of the 10th International Chemical and
Biological Engineering Conference - CHEMPOR 2008
Braga, Portugal, September 4-6, 2008
E.C. Ferreira and M. Mota (Eds.)

Influence of temperature and internal devices on the drying of fine particles in a conical spouted bed

H. Altzibar*, G. Lopez, J. Bilbao, M. Olazar
Department of Chemical Engineering, University of the Basque Country, P.O. Box 644, 48080 Bilbao, Spain.

Keywords: Conical spouted bed, Non-porous draft-tube, Open-sided draft-tube, Moisture content, Drying time
Topic: Advancing the chemical engineering fundamentals

Abstract

A study has been conducted on the performance of a draft-tube conical spouted bed for drying fine particles. Batch operation has been performed at several temperatures using different draft-tubes (non-porous and open-sided) in order to ascertain the influence of temperature and draft-tube configuration on the drying of fine particles. The open-sided draft-tube is the one with best performance and a maximum air temperature of 200 ºC is recommended for energy optimization. An open-sided tube that protrudes above the bed by at least 2/3 the stagnant bed height produces much lower and denser fountains.

1 Introduction

The applicability of the spouted bed technique lies in its ability to treat (drying, coating, encapsulation and so on) granular products that are too coarse for fluidized beds, or solids that are heat sensitive (Brennan, 1989; Ando and Maki, 2002; Rosiane et al., 2000). This is the case in the food and pharmaceutical industries. Thus, the spouted bed regime is an alternative contact method that is especially interesting when the conventional regimes have limitations imposed by the physical characteristics of the solid and by gas residence time (Rosiane et al., 2000; Olazar et al., 1992).

Spouted beds with fully conical geometry combine the features of the cylindrical spouted beds (such as the capacity for handling coarse particles, small pressure drop, cyclic movement of the particles and so on) with those inherent to their geometry, such as stable operation in a wide range of gas flowrates (Olazar et al., 1992). This versatility in the gas flowrate allows for handling particles of irregular texture, fine particles and those with a wide size distribution and sticky solids, whose treatment is difficult using other gas-solid contact regimes (Aguado et al. 1999). Moreover, operation in the dilute spouted bed can be carried out with short gas residence times (as low as milliseconds) (Olazar et al., 1997).

Conical spouted beds have low segregation (Olazar et al., 1994), which allows for handling particles with a wide size distribution without stability problems. This property is interesting for both physical operations, such as drying, and chemical operations, such as waste material pyrolysis, for improving the distribution of products and consequently increasing their commercial interest (Olazar et al., 2001).

A crucial parameter that limits the scaling-up of spouted beds is the ratio between inlet diameter and particle diameter. In fact, the inlet diameter should be no more than 20-30 times the average particle diameter in order to achieve spouting status. The use of a draft-tube is the usual solution to this problem. Nevertheless, solid circulation, particle cycle time, gas distribution and so on, are governed by the space between the bottom of the bed and the draft-tube, Moreover, minimum spouting velocity and operating pressure drop are also

* Corresponding author. Tel + 34-946012527. E-mail:haritz.altzibar@ehu.es

functions of the type of draft-tube used.

A conventional spouted bed with draft-tube has proven to be an efficient dryer of simple construction (Passos and Mujumdar, 1989). Thus, it provides a high interface area for gas and solid contact, high heat and mass transfer coefficients and high production rates.

In previous papers (Altzibar et al., 2008), a conical spouted bed provided with draft-tube has been studied to verify their potential application in the drying of fine particles. Batch runs have been carried out using non-porous, porous and open-sided draft-tubes at ambient conditions and their performance has been compared. In this paper, batch runs have been carried out in a conical spouted bed using non-porous and open-sided draft-tubes at different temperatures.

2 Experimental

The experimental unit used for drying, Figure 1, consists of the following components: feeding system, device for feeding nitrogen and/or air, preheater, the conical spouted bed reactor, cyclone and the filter.

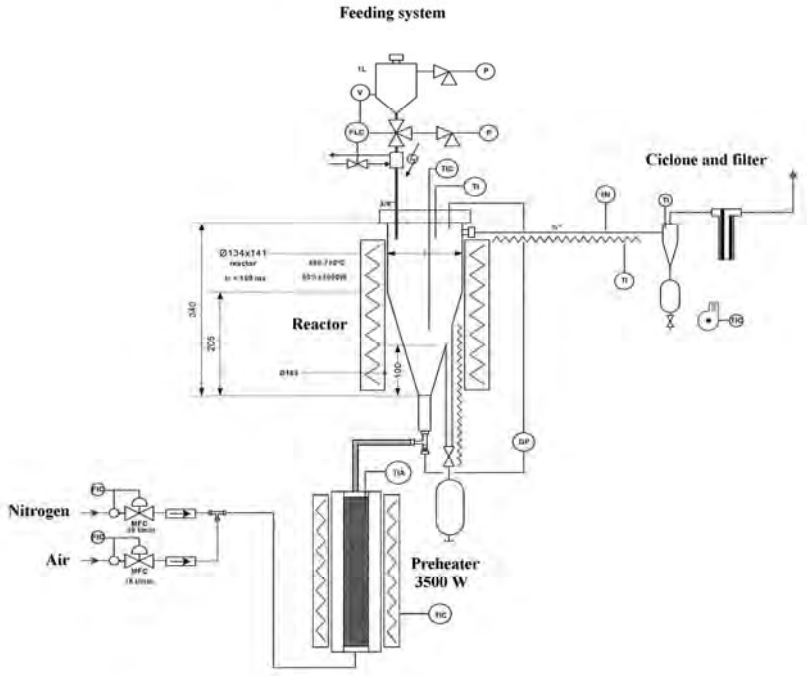

Figure 1. *Diagram of the experimental unit.*

This experimental unit has been used previously in other operations, as a pyrolysis of waste plastics (Elordi et al., 2007), pyrolysis of biomass (Aguado et al., 2000) and pyrolysis of scrap tyres (Arabiourrutia et al., 2007).

The reactor is the main component of the unit and is of conical geometry provided with an upper cylindrical section. The reactor is made of 316-L stainless steel. Figure 2a shows the different zones in the bed with a standard non-porous draft-tube and particle movement. The geometric factors of the reactor, Figure 2b, are the following: height of the conical section, H_C = 0.205 m; angle of the conical section, γ = 28º; diameter of the cylindrical section, D_C = 0.123 m; base diameter, D_i = 0.02 m; inlet diameter, D_0 = 0.01 m. These dimensions have been established from previous hydrodynamic studies carried out in the spouted bed regime in conical contactors (Olazar et al., 1992) and bearing in mind the versatility of the equipment.

The reactor allows the insertion of draft-tubes. Two draft-tubes with different configurations have been used, Figure2c, which are open-sided and non-porous ones. The dimensions of

the open-sided draft-tube are the following: length of the tube, L_T = 0.16 m; width of the faces, W_H = 0.006 m; diameter of the tube, D_T = 0.01 m. In case of the non-porous draft-tube, the dimensions are: length of the tube, L_T = 0.115 m; height of entrainment zone (distance between the gas inlet nozzle and bottom of draft tube), L_H = 0.033 m; diameter of the tube, D_T = 0.01 m.

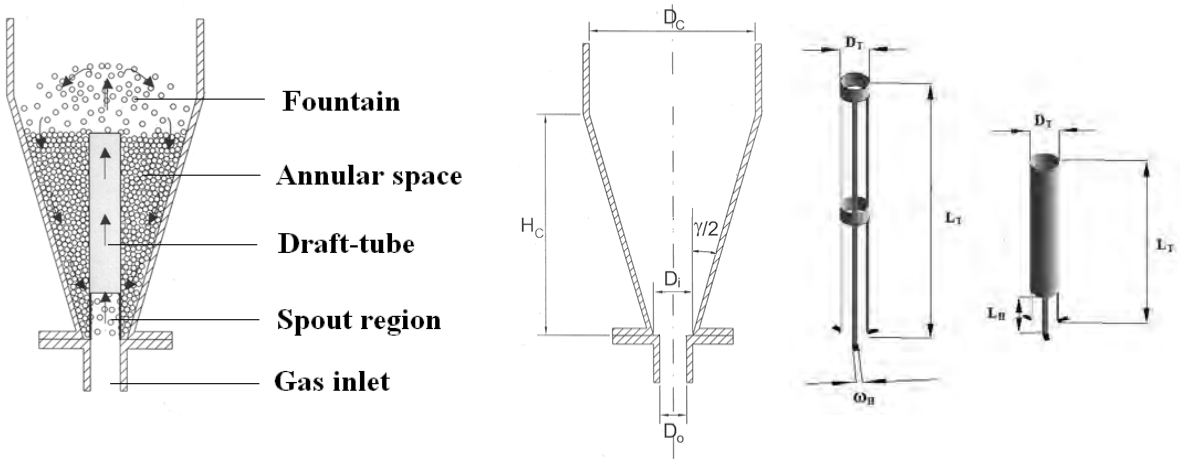

(a) (b) (c)

Figure 2. (a) *Zones in the conical spouted bed with draft-tube, (b) Geometric factors of the contactors, (c) Open-sided and non-porous draft-tubes.*

The unit is provided with two devices for heating the bed. A ceramic resistance for heating the gas that enters the reactor and another one that is coiled outside the reactor and covered with insulator. These resistances are controlled by means of measurements taken by several thermocouples, which are located at the bed inlet and at several positions in the bed.

Furthermore, there are thermal conductivity detectors (Alhborn MT8636-HR6) for measuring air moisture content at the bed inlet and outlet. Temperature and moisture contents are also stored in the Alhborn Almeno 2290-8 data logger, which allows for monitoring their evolution over time. The gas stream leaves the dryer and passes through a cyclone and a filter where fine solid particles are retained.

The gas flowrate is regulated by means of a mass flow controller that allows for a feed of up to 50 l min^{-1}, which is dosed by high sensitivity control valves that may be operated either from the computer or from the control panel. The gas used for operation is air.

The material used for drying is building sand. Table 1 shows the particle size distribution of this material.

Table 1. Particle size distribution of the sand.

Particle size (mm)	0.05	0.1	0.23	0.47	0.81	1.5	3	4	TOTAL
Weight (%)	0.172	3.974	20.210	31.476	26.793	16.852	0.489	0.034	100

Based on the values in Table 1, the average particle size (reciprocal mean diameter) has been calculated by means of the expression:

$$\overline{d_p} = 1/\left[\sum\left(x_i/d_{p_i}\right)\right] \quad (1)$$

The average size of the sand obtained using eq (1) is 0.5 mm and its density is 2358 kg m^{-3}.

3 Results

Batch runs have been carried out in a conical spouted bed with and without draft-tubes at four different temperatures: 25, 100, 200 and 300 ºC. The evolution of the air moisture

content with time has been monitored at the bed outlet. In the experimental study, an air flowrate 75% higher than the minimum one has been used in order to achieve a stable performance of the spouted bed.

In all runs, a bed with 200 grams of sand has been used. The initial moisture content of the sand is about 1%, and the specification is that it should be dried to approximately 0.005 kg of water/kg of dried solid for subsequent use. This solid is usually dried in rotary driers where mass transfer and efficiency are low.

Figure 3, 4 and 5 show the evolution of air moisture content with drying time at several temperatures with and without draft-tubes.

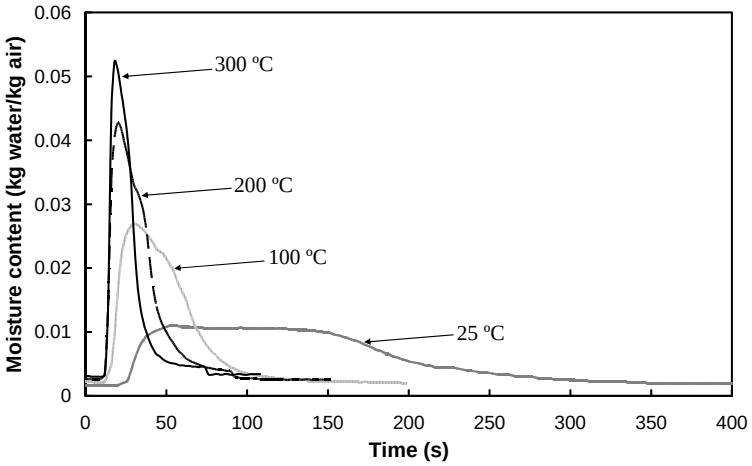

Figure 3. *Evolution of air moisture content with drying time at several temperatures without draft-tube.*

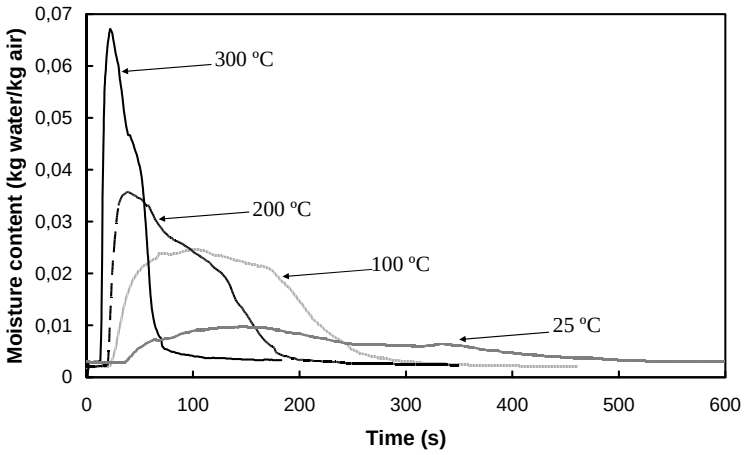

Figure 4. *Evolution of air moisture content with drying time at several temperatures using the non-porous draft-tubes.*

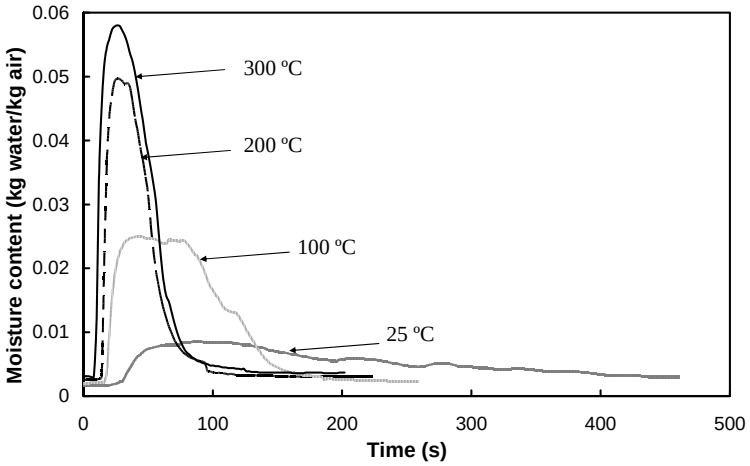

Figure 5. *Evolution of air moisture content with drying time at several temperatures using the open-sided draft-tubes.*

Figure 3, 4 and 5 show that the time required for drying the solid to the specification given decreases when the drying temperature is increased. As observed, the drying time required at ambient conditions (25 ºC) is significantly higher than that at high temperatures.

Furthermore, conical spouted beds are more stable at high temperatures than at ambient conditions, because under the latter conditions wet sand behaviour is much worse and the bed is more unstable.

In addition, it is also observed that without using any draft-tube and using open-sided draft-tube, the time required for drying above 200 ºC, Figures 3 and 5, is almost the same, which is evidence that the process is controlled by the internal diffusion in the particle.

Nevertheless, this is not the case when the non-porous draft-tube is used.Thus, the drying time required at 300 ºC is much higher than at 200 ºC. This is explained by the lower fraction of air rising through the annular space with the non-porous draft-tube and the resulting poorer gas-solid contact. Thus, when the non-porous draft-tube is used, until 300 ºC the process is not controlled by the internal diffusion in the particle.

On the other hand, Figures 3-5 show that the drying time required without using any draft-tube is shorter than using draft-tubes. The reason lies in the fact that the air required to achieve a stable spouted bed is much higher (2 or 3 times) and consequently the gas-solid contact is more vigorous. Consequently, energy efficiency for this operating procedure is low due to the excessive air flowrate required.

When draft-tubes are used, the drying time required with the open-sided draft-tube is shorter than with the non-porous draft-tube. The reason for that lies in the much higher solid circulation rate, which helps air percolation to the annulus and provides a better gas-solid contact. The only drawback of the open-sided draft-tube is that air flowrate required is slightly higher than with the non-porous draft-tube. Altzibar et al. (2008) proved that open-sided draft-tubes always require higher minimum spouting velocity and operation pressure drop than non-porous ones. This higher values are due to the solid-cross flow from the annulus into the spout along the whole length of the spout.

Despite these inconveniences, as proven by Altzibar et al. (2008), the solid circulation rate and the drying efficiency of the open-sided draft tube are superior to any other spouted bed configuration. Moreover, it allows for reducing the height of the fountain.

4 Conclusions

Conical spouted beds fitted with a draft-tube perform well in the drying of fine solids, given that they allow for stable operation in a wide range of operating conditions.

Conical spouted beds without any draft-tube require the shorter drying time, but the excessive air flowrate required does not advise this way of operation.

The non-porous draft-tube requires lower air flowrates but needs a longer drying time.

The open-sided draft-tube has the best performance on the drying of fine solids. Although the air flowrate required is slightly higher than the non-porous draft-tube, the time required for drying is much shorter. Besides the open-sided tube has the higher solid circulation rate. In addition, the open-sided tubes that protrude above the bed by at least 2/3 the stagnant bed height produce much lower and denser fountains. Consequently, the height required for the dryer is much shorter and particle entrainment will also be avoided.

Thus, conical spouted beds provided with open-sided draft-tubes have their best performance for drying sand at a temperature of 200 ºC. Higher temperartures do not have influence on the drying time and imply higher energy consumption.

References

Aguado, R.; Olazar, M.; Gaisan, B.; Bilbao, J. (1999). Kinetics of polystyrene pyrolysis in a conical spouted bed reactor. *Chemical Engineering Journal*, 92, 91-99.

Aguado, R., Olazar M., San José, M.J., Aguirre, A., Bilbao, J., (2000). Pyrolysis of sawdust in a conical spouted bed reactor. Yields and product composition, *Industrial & Engineering Chemistry Research*, 39, 1925-1933.

Altzibar, H., Lopez, G., Alvarez, S., San José, M.J., Olazar, M. (2007). A draft-tube conical spouted bed for drying fine particles, *Drying Technology*, 26, 308-314.

Ando S., Maki T. (2002). Analysis of the drying process of seed particles in a spouted bed with a draft tube, *Advanced powder technology* 13(1), 73-91.

Arabiourrutia, M., López, G., Elordi, G., Olazar, M., Aguado, R., Bilbao, J., (2007). Product distribution obtained in the pyrolysis of tyres carried out in a conical spouted bed. *Chemical Engineering Science* 62, 5271 – 5275.

Brennan, J.G. (1989). Dehydration of Foodstuffs in Water and Food Quality, Ed. T.H. Hardman, *Elsevier Applied Science*, New York, pp.33-70.

Elordi, G., López, G., Arabiourrutia, M., Olazar, M., Aguado, R., Bilbao, J. (2007). Catalytic pyrolysis of high density polyethylene in a conical spouted bed reactor. *Journal of Analalytical and Applyed Pyrolysis* 79, 450–455.

Olazar M., San José M.J., Aguayo, A.T., Arandes, J.M., Bilbao. J. (1992). Stable Operation Conditions for Gas-Solid Contact Regimes in Conical Spouted Beds. *Industrial & Engineering Chemistry Research*, 31, 1784-1791.

Olazar, M.; San José, M.J.; Peñas, F. J.; Bilbao, J. (1994). Segregation in conical spouted beds with binary and tertiary mixtures of equidensity spherical particles. *Industrial & Engineering Chemistry Research*, 33, 1838-1844.

Olazar, M.; Arandes, J.M.; Zabala, G.; Aguayo, A.T.; Bilbao, J. (1997). Design and operation of a catalytic polymerization reactor in a dilute spouted bed regime. *Industrial & Engineering Chemistry Research*, 36, 1637-1643.

Olazar, M.; Aguado, R.; San José, Bilbao, J. (2001). Kinetic study of fast pyrolysis of sawdust in a conical spouted bed reactor in the 400-500 °C range. *Journal of Chemical Technology & Biotechnology*, 76, 469-476.

Passos, M.L.; Mujumdar, A.S. (1989) Spouted and spout-fluidized beds for grain drying. *Drying Technology*, 7, 663-697.

Rosiane L. Cunha, Karen G. Maialle and Florencia C. Menegalli (2000). Evaluation of the drying process in spouted bed and spout fluidized bed of xanthan gum: focus on product quality, *Powder Technology* 107(3), 234-242.

Proceedings of the 10th International Chemical and
Biological Engineering Conference - CHEMPOR 2008
Braga, Portugal, September 4-6, 2008
E.C. Ferreira and M. Mota (Eds.)

Decolourization of Reactive Red 180 by laccase: optimization by Response Surface Methodology

Raquel O. Cristóvão, Ana P.M. Tavares, José M. Loureiro, Rui R. Boaventura, Eugénia A. Macedo*

LSRE/LCM - Laboratory of Separation and Reaction Engineering, Faculdade de Engenharia da Universidade do Porto, Rua Dr. Roberto Frias, 4200-465 Porto, Portugal

Keywords: Optimization, Laccase, Reactive dye, Enzymatic catalysis, Decolourization
Topic: Advancing the chemical and biological engineering fundamentals

Abstract

Three-level Box–Behnken factorial design with three factors and response surface methodology were used to optimize the colour removal of C.I. reactive red 180 by commercial laccase. A mathematical model was developed to study the effect of temperature, pH, enzyme concentration and their interactions on the decolourization. Enzyme concentration and pH as well as their interaction were the main factors that affected the decolourization. The dye degradation was independent of temperature. The model estimated that the highest decolourization (> 92 %) was obtained for pH 7.5 and 85 U l^{-1}. This predicted value was experimentally validated, obtaining dye colour removal (540 nm) of 93 ± 1.5 %.

1 Introduction

Reactive dyes are the principal class of dyes employed in textile industries to colour cellulosic fibres [1]. However, around 30 % of the applied reactive dyes are discarded causing serious environmental problems and the conventional treatments of wastewater are not efficient to completely remove the residual colour [2]. Classical treatments including adsorption, chemical precipitation, ozonation and flocculation have been reported for decolourization of effluents. However, in many cases they are inefficient and have a high cost. Conversely, biological processes such as biodegradation are an efficient alternative. Nevertheless, few studies involving enzymatic degradation of reactive dyes with commercial laccase are available [3].

Laccase is a copper-containing oxidoreductase (EC 1.10.3.2, *p*-diphenol:dioxygen oxidoreductase), which catalyzes the oxidation of phenolic compounds with reduction of oxygen to water [4]. However, the substrate range can be extended to non-phenolic compounds by the addition of a mediator [5]. Catalytic degradation of dyes with the laccase-mediator system (LMS) is an environmentally friendly technology which constitutes a promising alternative to conventional decolourization.

Experimental design and Response Surface Methodology (RSM) are useful statistical techniques that can be used in decolourization processes to identify and optimize the relevant factors that influence the colour removal. RSM can also be used to evaluate the relative significance of several factors and their possible interactions. It is an experimental strategy to obtain the optimum conditions for a multivariable system. Few reports are available to optimize reactive dyes degradation [6, 7].

In this study the RSM using the full Box-Behnken design of experiments was applied to optimize the decolourization conditions of C.I. reactive red 180 (RR180) by commercial laccase. A synthetic effluent containing the reactive dye was used to obtain a constant

* Corresponding author. Tel + 351-22-5081653. E-mail:eamacedo@fe.up.pt

composition in order to understand more easily the effects of the treatment.

2 Materials and Methods

Chemicals and enzyme

Textile dye: C.I. Reactive red 180 (Remazol Brilliant Red F3B), a monoazo dye, was kindly provided by DyStar (Porto, Portugal) and was used for degradation experiments without any further purification.

Enzyme: Commercial laccase formulation (DeniLite II S; 120 U g^{-1}) from genetically modified *Aspergillus* was kindly provided by Novozymes (Denmark). This formulation is used for indigo dye decolourization in denim finishing operations and includes a buffer and an enzyme mediator.

Box–Behnken Design of Experiments

A 3^3 Box–Behnken full factorial design was used to identify the factors having significant effects on RR180 decolourization by laccase. Three factors, i.e., temperature, enzyme concentration and pH were chosen. The experimental Box–Behnken design, analysis of variance (ANOVA) and 3D response surface were carried out using the software Statistica v.5.1 (Statsoft Inc.). Equation (1) describes the regression model of the present system, which includes the interaction terms:

$$Y = \beta_0 + \beta_1 X_1 + \beta_2 X_2 + \beta_3 X_3 + \beta_{12} X_1 X_2 + \beta_{13} X_1 X_3 + \beta_{23} X_2 X_3 + \beta_{11} X^2_1 + \beta_{22} X^2_2 + \beta_{33} X^2_3 \quad (1)$$

where Y is the predicted response, *i.e.* the colour removal; X_1, X_2 and X_3 are the coded levels of the independent factors temperature, pH and enzyme concentration. The regression coefficients are: β_0 the intercept term; β_1, β_2 and β_3 the linear coefficients; β_{12}, β_{13}, β_{23} the interaction coefficients and β_{11}, β_{22}, β_{33} the quadratic coefficients. The model evaluates the effect of each independent factor on the response.

Dye Decolourization Experiments

To study the decolourization of the reactive textile dye, 50 mg l^{-1} of C.I. RR180 were incubated in a 25 ml Erlenmeyer flask under stirring for one day. The dye degradation conditions are: laccase concentrations (24, 48 and 96 U l^{-1}), temperature (25, 35 and 45 ºC) and pH (6, 7 and 8). The pH values of dye solutions were adjusted with 50 mM phosphate buffer.

Determination of Dye Degradation

Dye decolourization was determined by monitoring the decrease in the absorbance peak at the maximum absorbance wavelength of RR180 (540 nm) (peak) or by calculating the total area under all the entire visible spectrum (area). UV-visible spectrophotometer (Thermo, model UV1) was used in all experiments. Decolourization is reported as: % decolourization = $(A_i - A_f)/A_i \times 100$, where A_i is the initial absorbance or total area under the initial spectrum and A_f is the final absorbance or total area under the final spectrum.

3 Results and Discussion

The most important factors, which affect the efficiency of enzymatic dye degradation,

are temperature and pH of the solution and enzyme concentration. In order to study the combined effect of these factors, experiments were performed for different combinations using factorial design methodology. The results show that the quadratic model, including linear interactions, fits adequately to the experimental data giving a coefficient of determination R^2 of 0.9306. Equation (2), which indicates the effect of factors on RR180 decolourization, is shown below, in terms of coded factors:

$$Y = 68.7 + 0.65X_1 + 10.5X_2 + 16.1X_3 + 0.5X_1^2 + 9.6X_2^2 + 6.7X_3^2 - 3.3\,X_1X_2 - 0.78X_1X_3 + 9.0X_2X_3 \quad (2)$$

Comparing the results of the dye decolourization by absorbance reduction at the maximum wavelength and results of the total decolourization based on the overall spectrum, the RR180 total decolourization (area) was always lower than decolourization at maximum wavelength (peak). The decolourization of RR180 causes a reduction of absorbance at the peak but not fully decolourization considering the entire visible spectrum.

The model was found to be adequate for prediction within the range of factors chosen. The optimum operating conditions for RR180 decolourization can be predicted from the second order polynomial function. The Pareto chart displays the statistically relevant effect of each factor on the response and it is a practical way to view the results. These are sorted from the largest to the smallest, and the effects to the right of the divisor line are significant. From Figure 1, the enzyme concentration (X_3) and pH (X_2) and their interaction $X_3 \times X_2$ showed to have effect on RR180 decolourization whilst the temperature did not affect the decolourization.

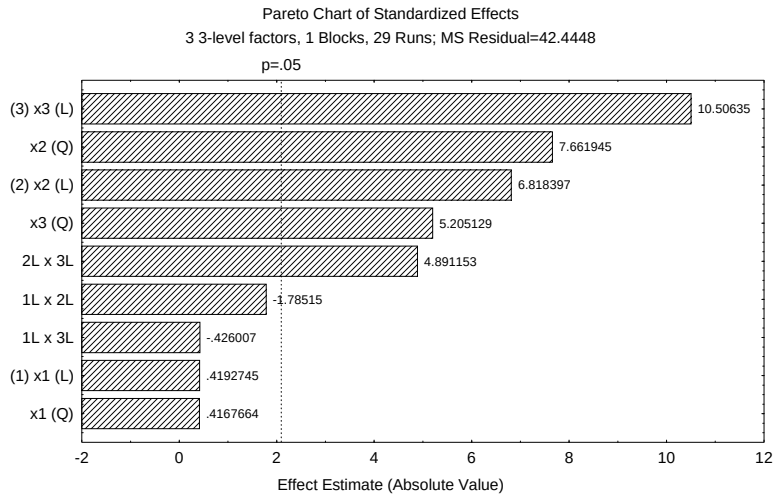

Figure 1 – Pareto chart of standardized effects for 3^3 Box-Behnken factorial design. (1) Temperature; (2) pH; (3) enzyme concentration.

The significance of the estimated effects was tested by analysis of variance (ANOVA). The ANOVA (Table 1) test indicates that the model adequately describes the decolourization of RR180 by commercial laccase. The significance of each coefficient was determined through a *p* value test considering 95 % of confidence in which low *p* values ($p < 0.05$) indicate high significance of the corresponding coefficient. The effect of pH and enzyme concentration and their interaction on RR180 decolourization is significant whilst the temperature did not influence the decolourization.

Table 1 – Analysis of variance (ANOVA) for the fitted quadratic polynomial model for optimization of C.I. reactive red 180 decolourization by commercial laccase.

Source	Sum of squares (SS)	df[a]	Mean square (MS)	*F*-value	*p*-value
(1) X_1 (L[b])	7.5	1	7.5	0.18	0.6797
X_1 (Q[c])	7.4	1	7.4	0.17	0.6815
(2) X_2 (L)	1973	1	1973	46	0.0000
X_2 (Q)	2491	1	2491	58	0.0000
(3) X_3 (L)	4685	1	4685	110	0.0000
X_3 (Q)	1149	1	1149	27	0.0001
1L by 2L	135	1	135	3.2	0.0902
1L by 3L	7.7	1	7.7	0.2	0.6749
2L by 3L	1015	1	1015	24	0.0001
Error	806	19	42.4		
Total SS	11618	28			

The response surface plots, generated from Box–Behnken design, are showed in Figure 2 a-c. The plots represent the decolourization of RR180 over changes in two independent factors (temperature, pH or enzyme concentration) while a third one was kept constant. Figure 2a shows the response surface of interactions between pH and temperature at 55 U l^{-1}. Decolourization increases with pH up to 7.5, and then decreases. The decolourization was practically independent of temperature changes as observed in Figures 2a and 2c. Figure 2b represents the effect of changes in enzyme concentration and pH at 35 ºC. It clearly shows that the optimum conditions for obtaining the maximum decolourization are within the experimental ranges tested. The decolourization increased with increasing pH and enzyme concentration up to approximately 7.5 and 85 U l^{-1}, respectively. Then the decolourization decreased slowly. Maximum decolourization was observed at those conditions and dye degradation above 92 % was predicted by the response surface metodology.

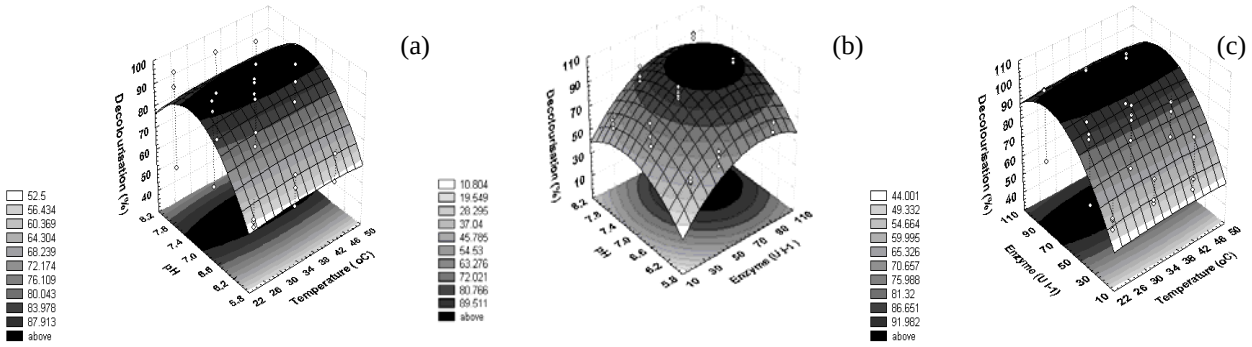

Figure 2 – Response surface plots of the reactive red 180 decolourization by commercial laccase: (a) effect of temperature (X_1) vs pH (X_2) at 55.4 U/l; (b) effect of enzyme concentration (X_3) vs pH (X_2) at 35 ºC; (c) effect of temperature (X_1) vs enzyme concentration (X_3) at pH 7.0.

The adequacy of the regression model for RR180 decolourization by laccase was checked by using the calculated optimum conditions: 85.4 U l^{-1} and pH 7.5 in triplicate experiments. Under these conditions, 93 ± 1.5 % of RR180 decolourization was obtained which is in good agreement with the predicted value (above 92 %).

DeniLite II is a commercial laccase with great potential to decolourise textile dyes. However a few studies regarding the use of this commercial laccase on the treatment of effluents containing dyes and especially with reactive dyes (RR 180) are available. It is a formulation containing laccase, mediator and a non-ionic surfactant used in the finishing process for indigo stained clothes [8]. In this study DeniLite II was used for decolourization of RR180 and the obtained results prove that pH and enzyme concentration play an important role on decolourization. Recent reports showed that a mediator is necessary for the decolourization of dyes by laccase [9, 10]. To confirm these findings, some experiments were carried out with pure commercial laccase (DeniLite Base) and no degradation of RR180 was detected (data not shown). Apparently, mediator is necessary for its degradation by laccase in order to complete the mechanism of electron transfer from the substrate to the enzyme. It seems that the mediator acts as an electron carrier, an intermediate substrate for the laccase [11]. The overall catalytic cycle is the reduction of the oxygen molecule to water molecule with the concomitant oxidation of the substrate.

4 Conclusions

Commercial laccase (DeniLite II S) was tested for decolourization of RR180. 3^3 Box–Behnken full factorial design was found to be an efficient tool for optimisation of RR180 decolourization. Enzyme concentration and pH were the factors that influenced the decolourization whilst the temperature changes did not affect the dye degradation. Validation experiments were carried out in order to check the suitability of the model. The results showed that the predicted decolourization was in agreement with the experimental value. Dye degradation by commercial laccase proved to be an efficient alternative treatment for decolourization of RR180 (> 92 %).

5 Acknowledgments

Financial support for this work was in part provided by LSRE financing by FEDER/POCI/2010, for which the authors are thankful. The authors wish to thank Novozymes (Denmark) for commercial laccase and DyStar (Porto, Portugal) for C.I. reactive red 180. R. Cristóvão acknowledges her Ph.D. scholarship from Fundação para a Ciência e a Tecnologia (FCT) (SFRH/BD/28529/2006) and A.P.M. Tavares acknowledges her Post-Doc scholarship from FCT (SFRH/BPD/22697/2005).

References

1. Allègre, C., Moulin, P., Maisseu, M., Charbit, F. (2006). Treatment and reuse of reactive dyeing effluents. *J. Membrane Sci.,* 269, 15–34.

2. Vandevivere, P.C., Bianchi, R., Verstraete, W. (1998). Treatment and reuse of wastewater from the textile wet-processing industry: Review of emerging technologies. *J. Chem. Technol. Biotechnol.,* 72, 289-302.

3. Soares, G.M.B., Amorim, M.T.P., Hrdina, R., Costa-Ferreira, M. (2002). Studies on the biotransformation of novel disazo dyes by laccase. *Process Biochem*., 37, 581-587.

4. Thurston, C.F. (1994). The structure and function of fungal laccases. *Microbiology*, 140, 19-26.

5. Bourbonnais, R., Paice, M.G. (1990). Oxidation of non-phenolic substrates. An expanded role for laccase in lignin biodegradation. *FEBS Lett*., 267, 99-102.

6. Myers, R.H., Montgomery, D.C. (2002). *Response surface methodology*, 2nd ed. John

Wiley & Sons Inc., U.S.A.

7. Hanrahan, G., Lu, K. (2006). Application of factorial and response surface methodology in modern experimental design and optimization. *Crit. Rev. Anal. Chem.,* 36, 141-151.

8. Soares, G.M.B., Amorim, M.T.P., Oliveira-Campos, A.M., Hrdina, R., Costa-Ferreira, M. (2002). Specificity of phenolic disazo dyes in relation to transformation by laccase. *Enzyme Microb. Tech.,* 30, 607-612.

9. Murugesan, K., Dhamija, A., Nam, I.H., Kim, Y.M., Chan, Y.S. (2007). Decolourization of reactive black 5 by laccase: Optimization by response surface methodology. *Dyes Pigments*, 75, 176-184.

10. Camarero, S., Ibarra, D., Martínez, M.J., Martínez, A.T. (2005). Lignin-derived compounds as efficient laccase mediators for decolorization of different types of recalcitrant dyes. *Appl. Environ. Microb*., 71, 1775-1784.

11. Riva S. (2006). Laccases: blue enzymes for green chemistry. *Trends Biotechnol.*, 24, 219-226.

Proceedings of the 10th International Chemical and
Biological Engineering Conference - CHEMPOR 2008
Braga, Portugal, September 4-6, 2008
E.C. Ferreira and M. Mota (Eds.)

Modeling Orange II Azo Dye Degradation by Fenton's Reagent

J. Herney Ramirez, Filipa M. Duarte, F. G. Martins, Carlos A. Costa and Luis M. Madeira*

LEPAE – Departamento de Engenharia Química, Faculdade de Engenharia da Universidade do Porto. Rua Dr. Roberto Frias, 4200-465 Porto, Portugal.

Keywords: Orange II, Kinetics, Fenton's Reagent, Hydrogen Peroxide, Oxidation.
Topic: Advancing the chemical and biological engineering fundamentals.

Abstract

A semi-empirical kinetic model was used to study the degradation of the azo dye orange II (OII) using Fenton's reagent, in the Fenton-like stage. The effect of temperature and initial concentrations of OII, hydrogen peroxide and ferrous ion catalyst on the degradation rate has been investigated in a batch reactor. The apparent kinetic constants (k_{ap}) were determined in a wide range of experimental conditions, using a pseudo-first-order reaction rate with respect to OII concentration. Besides, k_{ap} depends on the initial conditions following a power-law dependency. This equation, without further fitting parameters, was then successfully used to validate experiments performed in a continuous stirred tank reactor.

1 Introduction

Some azo dyes and their precursors have shown to be, or are suspected to be, human carcinogens as they form toxic aromatic amines (Brown et al., 1993). In particular, orange II (OII), also called acid orange 7, is a molecule with N=N bonds that is widely used in the dyeing of textiles and cosmetics, and thus found in the wastewaters of the related industries (Méndez-Paz et al., 2005). The processes used to decontaminate such wastewaters are physical, biological and chemical. Recent progress in this field has led to the development of advanced oxidation processes (AOPs). Among them, the oxidation using Fenton's reagent has proved to be a promising and attractive treatment method for the effective decolourization and degradation of dyes, as well as for the destruction of a large number of hazardous and organic pollutants (Lin et al., 1997; Malik et al., 2003). Moreover, the process is simple, taking place at low temperatures and atmospheric pressure (Bigda et al., 1995).

Oxidation with Fenton's reagent is based on ferrous ion and hydrogen peroxide and exploits the very high reactivity of the hydroxyl radical produced in acidic solution by the catalytic decomposition of H_2O_2. The $HO^{\bullet}$ species produced through these reaction will then attack the organic matter present in the reaction medium, because the hydroxyl radical is a powerful inorganic oxidant that reacts non-selectively with numerous compounds.

A main goal of the present work is to find a simple semi-empirical equation that describes the degradation of Orange II in a batch reactor by the Fenton's reagent. Several operational parameters, such as OII concentration, H_2O_2 dosage, Fe^{2+} concentration and temperature, which affect the degradation efficiency, were investigated. Finally, the kinetic law obtained was used to validate experiments carried out in a continuous reactor. To the best of the author's knowledge, there are available only a few studies about Fenton's reagent application in continuous reactors (e.g., Rivas et al., 2004), and none was found for the OII dye. Studies dealing with the modelling of such continuous process are also scarce.

2 Materials and methods

Chemical oxidation of azo dye Orange II aqueous solutions was conducted in two stirred jacketed glass reactors: a batch and a continuous stirred tank reactor (CSTR), with 0.30 L

and 0.92 L capacity, respectively. In both cases, temperature was controlled through a Huber thermostatic bath (Polystat CC1 unit). The absorbance and the pH were continuously monitored using a Philips PU8625 UV/VIS spectrophotometer and a pH-meter from EDT instruments (RE 357 TX), respectively. More details about the apparatus can be found in Ramirez et al. (2005).

In all batch experiments initial pH was adjusted to 3.0 through addition of 1 M NaOH or 0.1 M H_2SO_4 solutions, this optimal pH value being chosen based on our previous work (Ramirez et al., 2005). After pH adjustment, solid iron sulphate ($FeSO_4.7H_2O$, from Panreac) was added to the reactor, followed by the hydrogen peroxide solution (30% w/w, from Merck), which corresponds to the initial instant of the runs.

Orange II concentration was obtained from a calibration curve at the characteristic dye wavelength (486 nm), because this corresponds to the maximum of absorption and in this range interference by oxidation products does not occur (Ramirez et al., 2007a).

For operation of the CSTR, a Watson-Marlow 5055 peristaltic pump was used to feed two streams: one acidic containing the dye solution with the dissolved iron catalyst and another with the H_2O_2 solution. Both flow rates were carefully measured so that the concentration of each species, at the reactor inlet, was known. The exit stream flowed through the spectrophotometer flow-through cell until a steady dye concentration was measured. All experiments were carried out at pH ~3.0. In experiments carried out in duplicate, conversion varied by less than 10% (Ramirez et al., 2008).

3 Results and Discussion

3.1 Batch Reactor - Kinetic study

In the Fenton's process the formation of hydroxyl radicals has been demonstrated by several researchers and suggested to be the main oxidant species. In spite of the oxidation kinetics complexity, it is often assumed that, under certain conditions, the mechanism of the process can be significantly simplified, being of particular relevance the reaction between the organic matter and such radicals (Sun et al., 2007). The corresponding kinetic equation, assumed to be elementary, can thus be expressed as follows:

$$\left(-r_{OII}\right) = kC_{HO^{\bullet}}.C_{OII} = k_{ap}C_{OII} \qquad (1)$$

where k_{ap} is an apparent pseudo first-order kinetic constant that involves the radical HO concentration (assumed to remain constant along one experiment, due to the hypothesis of a pseudo steady-state concentration of hydroxyl radicals). The value of this rate constant depends therefore on the initial reactants concentrations (H_2O_2 and Fe^{2+}), on the temperature and also on the concentration of scavenger species present in the reaction mixture (such as intermediates, $HO_2^{\bullet}$, etc.) (Sun et al., 2007). On the other hand, these scavenger species concentrations depend on the initial orange II concentration, and for this reason k_{ap} is a function of all these variables: $k_{ap} = f(C_{OII_o}, C_{H2O2_o}, C_{Fe^{2+}{}_o}, T)$.

The dependence of k_{ap} from the operating conditions can be found by performing independent experiments, changing each factor at a time, after appropriate linearization of the data. On the other hand, the k_{ap} values in each run can be obtained from the mass balance in the batch reactor ($dC_{OII}/dt = -k_{ap}.C_{OII}$), thus yielding:

$$\frac{C_{OII}}{C_{OII_o}} = exp\left(-k_{ap}t\right) \qquad (2)$$

However, the reaction exhibits a change on its kinetics, which is a consequence of the complexity of the mechanism. This has been widely reported in the literature associated with the Fenton's process, and for that reason the k_{ap} values were calculated from experimental data covering only the Fenton-like phase of the process, this means where most of the Fe^{2+} has been converted into Fe^{3+} ($Fe^{2+} + H_2O_2 \rightarrow Fe^{3+} + HO^- + HO^{\bullet}$). Actually, it is known that the Fenton's process is divided in two stage-reactions. In the first stage the organic compounds

are decomposed rapidly and somewhat less rapidly in the second one (Malik et al., 2003). Because the above-mentioned reaction in which Fe^{2+} is converted into Fe^{3+} is very fast, the first stage is short and afterwards the process enters into a so-called pseudo steady-state, wherein Fe is mainly in the 3+ oxidation state (although it regenerates to Fe^{2+}).

3.2 Batch Reactor – Effect of the main operating conditions

3.2.1 Effect of the initial orange II concentration

The effect of the initial dye concentration was tested at constant initial H_2O_2 and Fe^{2+} concentrations and temperature. Results are shown in Fig. 1A, with the corresponding fitting lines (in the second Fenton's stage), and the obtained apparent kinetic constants are shown in Fig. 1B. Results show that the degradation rate decreases for increasing initial dye concentrations. The apparent rate order for Orange II was then determined to be -0.67 from the slope of a ln k_{ap} vs. ln C_{OIIo} plot (Fig. 1B). The negative effect of the parent organic compound on the apparent kinetic constant was also reported by other authors (e.g., Sun et al., 2007). Because the amount of hydrogen peroxide molecules available is the same, this indicates that the higher the dye concentration in the reactor, the smaller is the hydroxyl radicals concentration at the pseudo steady-state.

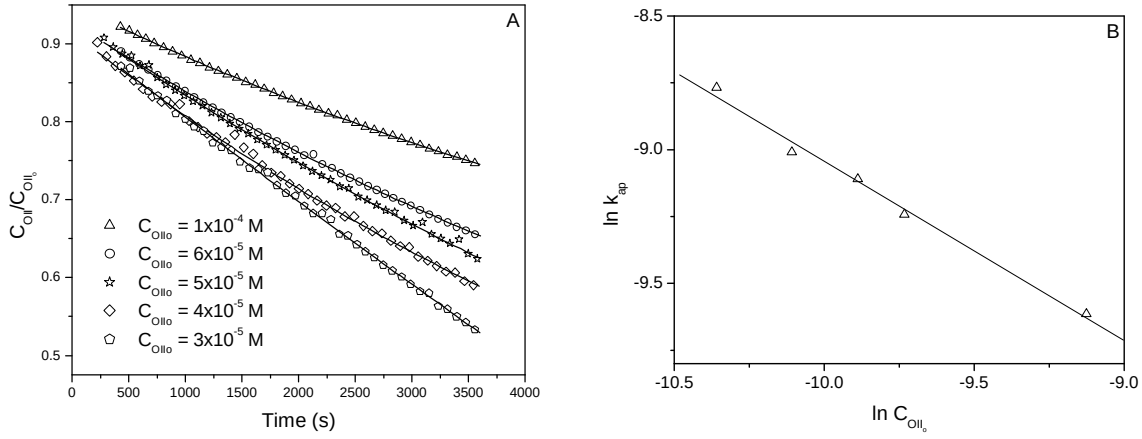

Fig. 1 – (A) Plot of the normalized dye concentration over time in the second Fenton stage at different initial OII concentrations and respective model fitting. (B) Effect of the initial OII concentration on the apparent rate constant of OII degradation. T = 30°C, $C_{H_2O_2}$ = 2.0×10^{-4} M, $C_{Fe^{2+}}$ = 5.0×10^{-6} M.

3.2.2 Effect of the initial hydrogen peroxide concentration

The effect of the initial hydrogen peroxide concentration on k_{ap} evidenced that the degradation rate increases for increasing hydrogen peroxide loads, in the range studied (data not shown). This trend was expectable. The apparent rate order for initial H_2O_2 concentration was determined to be 0.77 from the slope of a ln k_{ap} vs. ln $C_{H_2O_{2_o}}$ plot.

3.2.3 Effect of the initial ferrous ion concentration

The procedure described above was also applied to analyze the effect of $C_{Fe^{2+}_o}$. Data obtained put into evidence that the degradation rate is very sensitive to the iron concentration, because it acts as catalyst in the Fenton or Fenton-like process. The rate order for initial Fe^{2+} dose was determined to be 1.43.

3.2.4 Effect of the temperature

It was observed that the temperature has a strong positive effect on the OII degradation rate, due to an increment in the pseudo-first-order rate constant. The data exhibit Arrhenius-type behaviour, with an apparent activation energy of 58.1 kJ mol^{-1}, calculated from the usual ln k_{ap} vs. 1/T plot. The value obtained is very similar to that previously reported by the authors for a Fe-impregnated activated carbon (56.1 kJ mol^{-1}) (Ramirez et al., 2007b).

3.2.5 Rate equation for the degradation of OII in a batch reactor

The rate equation can be expressed in a simple way, as shown in Eq. (1), wherein k_{ap} depends on the initial conditions as follows:

$$k_{ap} = 4.06\times10^{13} C_{OIIo}^{-0.67} C_{H_2O_2o}^{0.77} C_{Fe^{2+}o}^{1.43} \exp(-58092/RT) \qquad (3)$$

It is noteworthy that the pre-exponential coefficient indicated was calculated by regression, minimising the sum of the square residues between the k_{ap} data obtained from Eqs. (2) and (3), for each experiment.

Up to now a first-order rate law for OII degradation was established, which can be useful for predicting the pseudo steady-state (i.e., when Fe is essentially at the 3+ oxidation state) in a chemical reactor. Obviously, in a batch system this can fail, depending on the initial conditions and extension of the initial (Fenton) phase, which in most experiments performed is short. However, it can be valuable to predict the behaviour of open reactors, operating at steady-state conditions, if the residence time is enough so that Fe^{2+} is almost completely converted into Fe^{3+}.

3.3 Continuous stirred tank reactor (CSTR) experiments

In an ideal CSTR, the contents are well-stirred and uniform throughout; therefore the exit stream has the same composition as the fluid within the vessel. Tracer experiments have confirmed that the reactor used in this work closely matches these ideal mixing conditions (Ramirez et al., 2008).

In Figs. 2 to 6, is shown the effect of the reagents concentrations (at the reactor inlet), temperature and residence time on the outlet concentration of OII. In all of them, closed symbols refer to conditions within the batch range, whereas open symbols to values out of it. It can be concluded that the effect of each parameter on the OII outlet concentration is similar to that observed in the batch reactor. First, C_{OIIout} increases when the dye concentration in the reactor feed increases (Fig. 2). It is evident that when the H_2O_2 concentration is increased in the feed, a decrement in the OII outlet concentration is noticed (Fig. 3), because more hydroxyl radicals are available for oxidation, in the range studied. The same behaviour is observed when the ferrous iron is changed, as showed in the previous figures and also in Fig. 4. In the latter, an increase in the Fe^{2+} load fed to the reactor from 5×10^{-6} to 6×10^{-5} M lead to a significant increase in the steady-state OII conversion, however runs carried out at higher Fe^{2+} doses ($1\text{-}2\times10^{-4}$ M) resulted in no appreciable differences in terms of OII removal. Temperature effect was investigated in the range 283 to 336 K, showing to be an important parameter in the Fenton process (Fig. 5), particularly when low catalyst doses are employed. Finally, when the residence time was incremented, better results were obtained in terms of OII removal, as expected (Fig. 6).

3.4 Validation of the model in the continuous reactor

Since the reaction is of a pseudo first-order type, the outlet concentration of OII can be predicted by the CSTR mass balance, which yields (Fogler 1999):

$$C_{OII_{out}} = \frac{C_{OII_{in}}}{1 + k_{ap}\,\tau} \qquad (4)$$

where τ = V/Q is the space-time, V is the reactor volume (0.92 L) and Q is the total flow rate. k_{ap} is obtained by Eq. (3), based on the concentration of each species at the reactor inlet, because these are the conditions that determine the steady-state radicals concentration. This issue can also be rationalized from the well known total segregation model (Fogler 1999, Rodrigues 1981). Actually, the computation of conversion/exit concentration in a continuous reactor by the total segregation model makes use of an expression for a “micro” batch reactor that is based on the reactor feed conditions. Figures 2 to 6 show the model predictions (Eq. (4)) for all the experiments performed.

In what concerns the effect of the inlet OII concentration (Fig. 2), it is remarkable the adherence of the model to experimental data in which iron concentrations within the range used in the batch runs have been employed (closed symbols). However, even when catalyst doses one order of magnitude higher are employed, the model is able to predict the negative

effect of increasing dye concentrations, related with a decrease in the number of oxidant molecules (or radicals) available per dye molecule (lower H_2O_2/OII ratios). The model fits also reasonably the data obtained in experiments where increasing oxidant dosages were employed (Fig. 3), particularly for low iron loads. The model adherence is however worst when the catalyst concentration approaches the upper limit employed in the kinetic study.

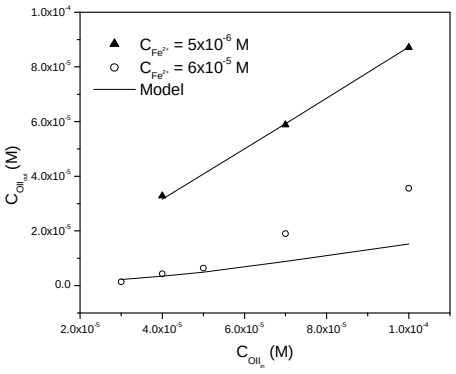

Fig. 2 – Effect of the inlet dye concentration on the OII outlet concentration in the CSTR $\left(C_{H_2O_2} = 4.0\times10^{-4}\ M, T = 30\ ^oC\right)$.

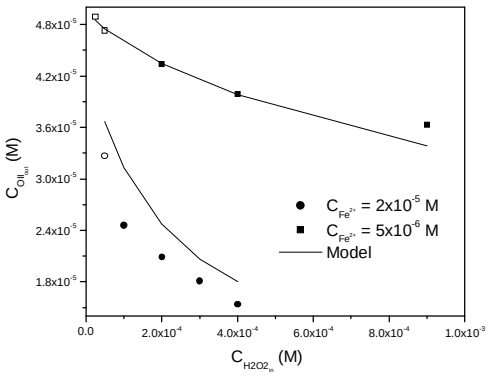

Fig. 3 – Effect of the inlet H_2O_2 concentration on the OII outlet concentration in the CSTR $\left(C_{OII} = 5.0\times10^{-5}\ M, T = 30\ ^oC\right)$.

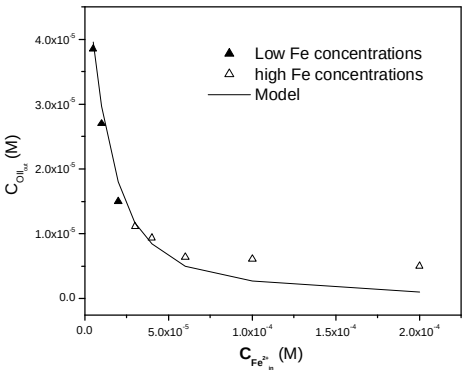

Fig. 4 – Effect of the inlet Fe^{2+} concentration on the OII outlet concentration in the CSTR $\left(C_{H_2O_2} = 4.0\times10^{-4}\ M, C_{OII} = 5.0\times10^{-5}\ M,\ T = 30\ ^oC\right)$

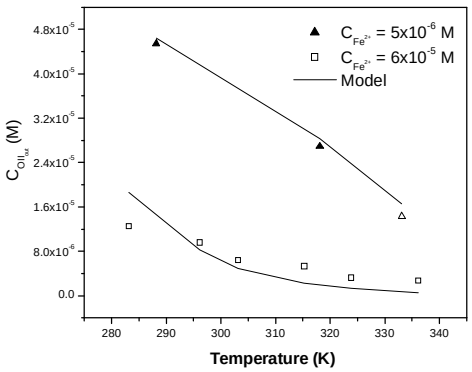

Fig. 5 – Effect of the temperature on the OII outlet concentration in the CSTR $\left(C_{H_2O_2} = 4.0\times10^{-4}\ M, C_{OII} = 5.0\times10^{-5}\ M\right)$.

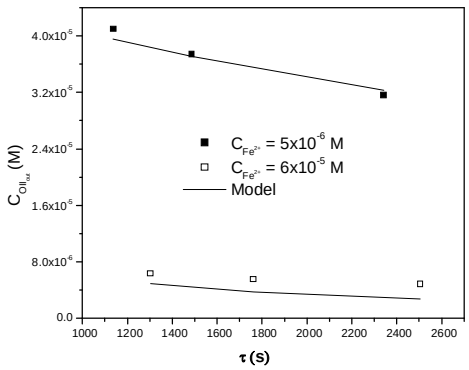

Fig. 6 – Effect of the space time on the OII outlet concentration in the CSTR $\left(C_{H_2O_2} = 4.0\times10^{-4}\ M, C_{OII} = 5.0\times10^{-5}\ M, T = 30\ ^oC\right)$.

Fig. 4 reinforces what was said in the previous paragraph, i.e., the good adherence of the

model to experimental data when using conditions (now iron concentrations) within those employed when establishing the rate equation. However it has some difficulties to predict the scavenging effect, i.e., the parallel and undesirable reaction that occurs between the catalyst and the hydroxyl radicals at high Fe loads. The results obtained when the temperature and residence time were changed (Figs. 5 and 6, respectively) show that the model also predicts well the positive effect of both parameters.

Conclusions

In this study, and particularly in the batch reactor experiments, low initial concentrations of hydrogen peroxide and ferrous ion were applied to eliminate the useless use of excessive reagent doses, commonly found at high Fe^{2+} and/or H_2O_2 doses. Experiments carried out in the batch reactor evidenced the positive effect of increasing the reaction temperature, H_2O_2 or Fe^{2+} concentrations, and the negative effect of increasing dye concentrations, trends that were corroborated with experiments in the CSTR.

The dye history concentration showed a change in the kinetics, typical of this process, being initially very rapid (Fenton stage) and afterwards the slower Fenton-like stage proceeds, where iron is mostly in the 3+ oxidation state. For the longer and last stage, a pseudo steady-state approach was employed to deduce the reaction rate, which was found to be of the first-order type with respect to OII concentration. The dependence of the apparent kinetic constant on the initial operating conditions was then deduced, leading to a power-law rate equation with Arrhenius dependency.

This rate equation revealed to be useful to predict the steady-state OII outlet concentration in the CSTR, in a wide range of operating conditions. In all cases, it was observed a reasonably good agreement between experimental and model results, even for experiments performed out of the range used in the batch kinetic study.

References

Bigda, R.J. (1995). Consider Fenton chemistry for wastewater treatment. *Chemical Engineering Progress,* 91, 62-66.

Brown, M.A., De Vito, S.C. (1993). Predicting azo dye toxicity. *Critical Reviews in Environmental Science and Technology,* 23, 249-324.

Fogler, H.S. (1999). *Elements of Chemical Reaction Engineering,* Prentice-Hall, 3rd ed., New Jersey.

Lin, S.H., Lo, C.C. (1997). Fenton process for treatment of desizing wastewater. *Water Research,* 31, 2050-2056.

Malik, P.K., Saha, S.K. (2003). Oxidation of direct dyes with hydrogen peroxide using ferrous ion as catalyst. *Separation and Purification Technology,* 31, 241-250.

Méndez-Paz, D., Omil, F., Lema, J.M. (2005). Anaerobic treatment of azo dye Acid Orange 7 under fed-batch and continuous conditions. *Water Research,* 39, 771-778.

Ramirez, J.H., Costa, C.A., Madeira, L.M. (2005). Experimental design to optimize the degradation of the synthetic dye Orange II using Fenton's reagent. *Catalysis Today,* 107-108, 68-76.

Ramirez, J.H., Duarte, F., Martins, F., Costa, C.A., Madeira, L.M. (2008). Modelling of the synthetic dye orange II degradation using Fenton's reagent: from batch to continuous reactor operation. Submitted.

Ramirez, J.H., Costa, C.A., Madeira, L.M., Mata, G., Vicente, M.A., Rojas-Cervantes, M.L., Lopez-Peinado, A., Martin-Aranda, R.M. (2007a). Fenton-like oxidation of Orange II solutions using heterogeneous catalysts based on saponite clay. *Applied Catalysis B: Environmental,* 71, 44-56 (a).

Ramirez, J.H., Maldonado-Hodar, F.J., Perez-Cadenas, A.F., Moreno-Castilla, C., Costa, C.A., Madeira, L.M. (2007b). Azo-dye Orange II degradation by heterogeneous Fenton-like reaction using carbon-Fe catalysts. *Applied Catalysis B: Environmental,* 75, 317-328 (b).

Rivas, F.J., Navarrete, V., Beltran, F.J., Garcia-Araya, J.F. (2004). Simazine Fenton's oxidation in a continuous reactor. *Applied Catalysis B: Environmental,* 48, 249-258.

Rodrigues, A.E. (1981). *Theory of residence time distributions, in Multiphase Chemical Reactors,* A.E. Rodrigues, J.M. Calo and N.H. Sweed (Eds.), NATO ASI Series, Sijthoff Noordhoff.

Sun, J.H., Sun, S.P. Fan, M.H., Guo, H.Q. Qiao, L.P.,Sun, R.X. (2007). A kinetic study on the degradation of p-nitroaniline by Fenton oxidation process. *Journal of Hazardous Materials,* 148, 172-177.

Proceedings of the 10th International Chemical and
Biological Engineering Conference - CHEMPOR 2008
Braga, Portugal, September 4-6, 2008
E.C. Ferreira and M. Mota (Eds.)

Viscosity of Heavy Oil and Distillation Residues with Diluents

Andreia Amaro de Lima[1], Krishnaswamy Rajagopal[2]*, Marco Antonio Farah[3]
[1,2] Universidade Federal do Rio de Janeiro, Escola de Química, Laboratório de Propriedades do Petróleo, LATCA, Av. Horácio Macedo, 2030, Ed. do Centro de Tecnologia, Bloco E - sala 209 ,CP 68542 Cidade Universitária, Rio de Janeiro, RJ - CEP: 21941-909, Brazil,
[3] Petroleo Brasileiro S.A., Rua General Canabarro, 500, Maracana , Rio de Janeiro, RJ CEP 2057-900, Brazil.

Keywords: Heavy Oil, Distillation Residues, Viscosity Correlations, Viscosity Reduction, Solvent Dilution
Topic: Advancing the chemical and biological engineering fundamentals

1. Introduction

The oil and its derivatives are complex mixtures that must be characterized by special methods to determine their chemical composition and other properties. As these experimental methods are expensive, and at times, insufficient, several empirical methods of calculation are applied, which easily allow estimating the composition basic properties of the substance. Among these characterization properties, the one that differentiates the description of the oil and its fractions is the viscosity, due to its easy and fast determination, and its possibility of use for heavy fractions.

The field of applications of viscosity characterization for oils and fractions is vast, especially for the heavy ones. The production and processing of heavy crude oil is constantly increasing as more heavy and viscous oil resources are being exploited to satisfy the rising world demand for petroleum. The viscosity correlations are important, in evaluating the performance in all operations and processes to which the oil and its derivatives are subjected, so that the method with the best performance of its production, refining, transport and storage can be selected.

There are several correlations and methods in literature that predict the viscosity of pure hydrocarbons and their mixtures, as well as estimate the viscosity of oil and its derivatives, which takes in to consideration the composition of the mixture. Almost all of them are of empirical nature, since there isn't a basic theory that predicts fluid transport properties.

The mixture can be modeled as a homogeneous solution or as a non-homogeneous mixture with a dispersed phase made of heavier components. This study aims at selecting a simple model that can quantify the dilution and the reduction of viscosity, as well as getting a good correlation between the viscosity of the mixture with temperature and the concentration of the diluent. We measured the kinematic viscosity of solutions of two atmospheric and one vacuum residues of distillation in toluene for different concentrations of diluent at several temperatures. The kinematic viscosity of a naphthenic crude oil was also measured for a wide temperature variation.

2. The Viscosity Prediction Models

2.1. Viscosity Prediction of the crude oil with temperature variation

The correlation usually used in petroleum industry proposed initially by Walther (1931), and later modified by ASTM (1982), where the parameters are a function of the kinematic

* Corresponding author. raja@eq.ufrj.br <mailto:raja@eq.ufrj.br>

viscosity (ν) and can be seen in the reference:

$$\log(\log(z)) = A - B \times \log(T)$$

$$z = \upsilon + 0{,}7 + C - D + E - F + G - H$$

The Eyring model (1936) shows that the dynamic viscosity decreases exponentially with the increase of temperature, depending on each substance, for example the presence mainly of aromatic hydrocarbons and little for the presence of paraffins. The viscosity, which is related with the energy necessary to initiate the draining of a substance, varies depending on the type and the form of molecules, besides being dependent on intra and intermolecular forces. Therefore, the parameters to predict the dynamic viscosity (μ) depend on the size of the molecule, its molar density and its activation energy.

$$\ln \mu = A + \frac{B}{T}$$

2.2. Viscosity Prediction of Residues in Toluene Mixtures

The viscosity prediction of these mixtures of residue in the solvent, toluene, can be obtained considering two kinds of models: those, in which the sample concentration is low, defined as less than 10%; and those in which the residue concentration is higher, defined as less than 50%. The first type of mixture was defined as dilute solution and the second type, as emulsions.

2.2.1. Dilute solutions

Dilute suspensions can be treated as if a particle were alone in an infinite liquid. Most of the existing models estimate the relative viscosity of the solution (η_r), defined as the ratio between the viscosities of the solution (η) to that of the continuous phase (η_C).

Taylor (1932) has considered the influence of the viscosities of both the dispersed and continuous phase and proposed an expression valid for emulsions with low concentration of dispersed spherical drops. His model is a function of volumetric fraction of the dispersed phase *(ϕ),* and the parameter *k*, which is the ratio of the viscosity of the dispersed phase (η_D) to that of the continuous phase (η_C).

Mooney (1951) has developed an equation based on Einstein's model, but for a suspension at a finite concentration, which is a function of an agglomeration factor defined by the value of null fluidity and the volumetric fraction of the dispersed phase *(ϕ).*

Roscoe (1952) has proposed a correlation for micro emulsions, modifying the Einstein's equation, using just the volumetric fraction of the dispersed phase *(ϕ).*

Choi and Schowalter (1975) and Yaron and Gal-Or (1972) have proposed correction factors to take into account the deformation of droplets. Both factors $f(\phi^{1/3})$ depend on the volume fraction (ϕ) and the ratio (k), given in the references.

Phan-Thien and Pham (1997) have developed a correlation based on the Taylor model, for a band of particles size above of which the Brownian movement is not so important anymore. Their model is a function of the parameter *k* and the volumetric fraction of the dispersed phase *(ϕ).*

2.2.2. Emulsions

An emulsion is a dispersed system in which the phases are immiscible or partially miscible liquids. Theoretical studies in the oil emulsions area have been limited to the case of suspensions of rigid spheres, especially for semi-dilute suspensions, in which the interactions between the pairs are dominant. For concentrated suspensions there are some semi-empirical models that can be used in the calculation of viscosity.

Guth and Simha (1936) have extended the results of Einstein to another concentration band, involving the interaction between particles, just applying the volumetric fraction of the dispersed phase *(ϕ).*

Brinkman (1952) has proposed a correlation especially recommended for high concentration samples, just as a function of the volumetric fraction of the dispersed phase *(ϕ).*

Richardson (1953) has observed an exponential increase of the relative viscosity also as a function of the volumetric fraction of the dispersed phase.

Krieger and Dougherty (1959), based in the model of Taylor, have considered a model where the concentration of the dispersed phase depends on the size of the drops. The correlation, restricted to Newtonian fluids, is a function of maximum volumetric fraction of the dispersed phase (ϕ_m), that is the limit of fluidity above of which the system is not in a liquid state to behave as an elastic solid. The correlation is also a function of intrinsic viscosity ([η]), which takes in consideration the ratio between the viscosity of the dispersed phase and the one from the continuous phase.

All these models only describe the variation of viscosity as a function of dispersed phase volume fraction or the ratio between the viscosity of dispersed phase and that of the continuous phase. The significant effect of temperature on the viscosity is not considered in any of these models.

3. Materials and Methods

For this study a stable medium heavy naphthenic crude oil (**OIL**), a very light atmospheric residue similar to several heavy oils (**AR I**), a typical atmospheric residue (**AR II**) and a typical vacuum residue from same oil (**VR II**) were selected . The samples were characterized by chemical analysis (elemental and SARA) and several relevant physical properties were measured. Table 1 lists molecular weight obtained by cryoscopy, density by Anton-Paar densimeter and molal average boiling point obtained by simulated distillation. Toluene was chosen as diluent as it dissolves all the asphaltenes present in chosen residues. Toluene high purity "HPLC / Spectra grade " was purchased from TEDIA Inc of United States and was used with out further purification.

Table 1 – Samples characteristics

	Oil	**AR I**	**AR II**	**VR II**
Molecular Wt.	340	565	604	1037
Density (ºAPI)	20,2	26,7	12,6	7,9
Molal Avg. Boiling Point	373,3	490	383	518

The kinematic viscosity is determined experimentally by the method ASTM D 445 (Brazilian standard MB-293), where a given volume of liquid sample is introduced into a standard viscometer and viscosity is determined by the time of flow by gravity through a capillary, under precise and reproducible control of temperature. We used calibrated Cannon-Fenske reverse flow viscometers for opaque fluids. The calibration factor was obtained by the standard procedure ASTM 446. This analysis takes about 60 minutes, with a reproducibility of approximately 0,35% of the average value, and a repeatability of 0,7% of average.

4. Results and Discussion

4.1. Viscosity prediction of Crude Oil

To obtain kinematic viscosity of the crude oil, 37 experiments were performed, each one with 2 repetitions. A temperature range of 20 to 200° C, with steps of 5° C was studied. The empirical result for the viscosity experiment for the oil showed an exponential decrease of the property by the increase of the temperature, as was expected.

Next it can be seen in the results for the kinematic viscosity prediction of the crude oil where the ASTM method and the Eyring's correlation is applied, both of which are extensively used in oil industry, a graph with the comparison of both methods, where the calculated results of the prediction are plotted against the experimental kinematic viscosity of the heavy crude oil. Values of the R-square coefficient from the observed figure, standard deviations and average absolute deviations of the experiments are presented in Table 2 and Figure 1.

Table2 – Crude oil viscosity prediction

Model	R2	SD	AAD
ASTM	0.9967		3.21614
Eyring	0.9582		20.05004

When the kinematic viscosities obtained experimentally are compared against the generated values from Eyring's correlation, an average absolute deviation (AAD) of 20 cSt, with a correlation coefficient (R^2) of 0.9582, is observed which makes it clear that this correlation is not well applied to the heavy crude oil. On the other hand, the same analysis for the ASTM method using the parameters obtained for this oil shows an average absolute deviation of 3 cSt and a correlation coefficient of 0.9967.

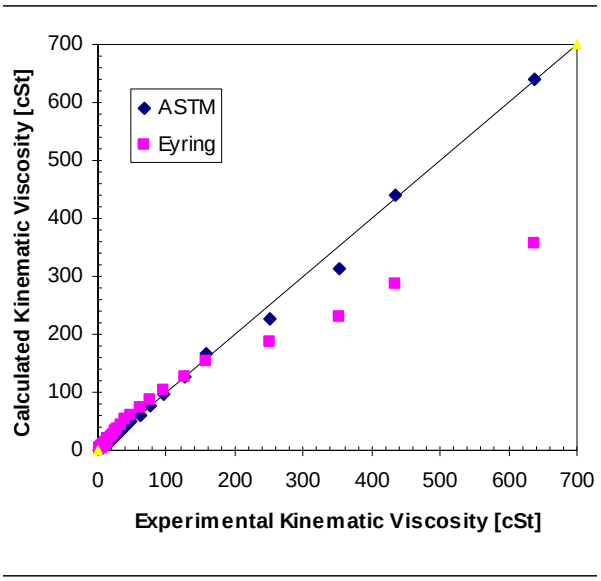

Figure 1 – Crude oil viscosity prediction

As a result, it can be concluded that when the Eyring's correlation is applied to heavy crude oils, it is noticed that this is only well adjusted at low temperatures, whereas when the ASTM method is applied, the results are perfectly adjusted for all temperatures, including high temperatures. These satisfactory results were already expected, since ASTM method is vastly applied to oils, while the Eyring's correlation is better adjusted to dilute solutions.

4.2. Viscosity prediction of Dilute Mixtures

The variation with concentration of residues correlates accurately with literature correlations for colloids and emulsions. Results of the average absolute deviation of the predictions of relative viscosity of residues at low concentrations mixed in toluene using literature correlations at a standard temperature of 20º C are presented in Table 3 and Figure 2. Dilute mixtures were prepared using volumetric fraction from 1% to 10% of the dispersed phase.

Table 3 – Average Absolute Deviations (AAD) of dilute mixtures

Correlation	AR I	AR II	VR II
Taylor	0.0737	0.0991	0.0985
Mooney	0.0833	0.1146	0.1186
Roscoe	0.0952	0.0982	0.0529
Yaron - Gal-or	0.0841	0.0965	0.0843
Choi - Schwlater	0.0645	0.0691	0.0762
Phan-Thien - Pham	**0.0465**	**0.0588**	**0.0586**

Figure 2 – Dilute mixtures relative viscosity prediction

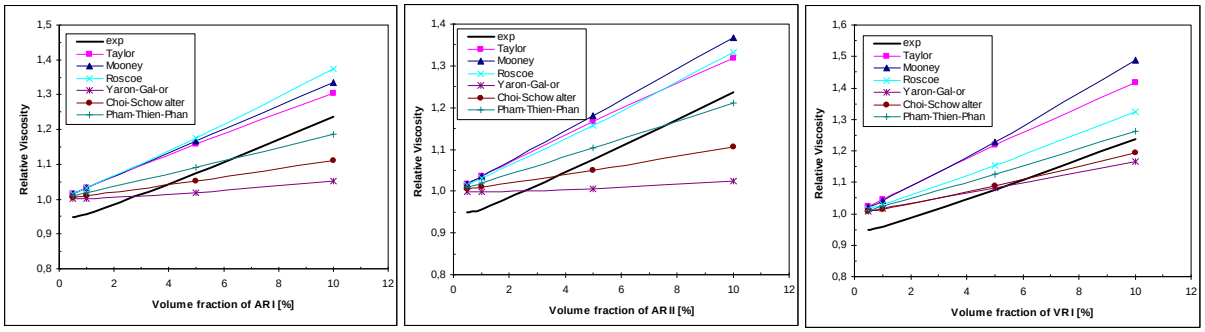

Deviation results for all residues studied were satisfactory when all correlations were applied. As it can be observed, the lighter the residue is, the better the deviation results are. At low concentrations, the relation of Phan-Thien and Pham best correlates the viscosity data effectively. By the information given above, it can be affirmed that dilute mixtures of residues of oil can be treated as pure ones.

4.3. Viscosity prediction of Emulsions

Results of the average absolute deviation of the predictions of relative viscosity of one residue at high concentrations mixed in toluene using literature correlations with temperature variation are presented in Table 4 and Figure 3. Concentrated solutions can be treated as emulsions. Those were prepared using volumetric fraction from 1% to 50% of the dispersed phase, a light atmospheric residue called AR I. Relative viscosity was obtained varying temperature from 30º to 60º C, with a 10º C step.

Table 4 – Average Absolute Deviations (AAD) of emulsions

Correlation	***30º C***	***40º C***	***50º C***	***60º C***	***Temp Avg***
Guth - Simha	0.1462	0.1372	0.3191	0.3683	*0.2427*
Brinkman	0.2316	0.2894	0.1583	0.2064	*0.2214*
Richardson	0.1131	0.0886	0.0444	0.0462	*0.0731*
Krieger	0.0417	0.1054	0.0344	0.0593	*0.0602*

Figure 3 – Emulsions relative viscosity prediction

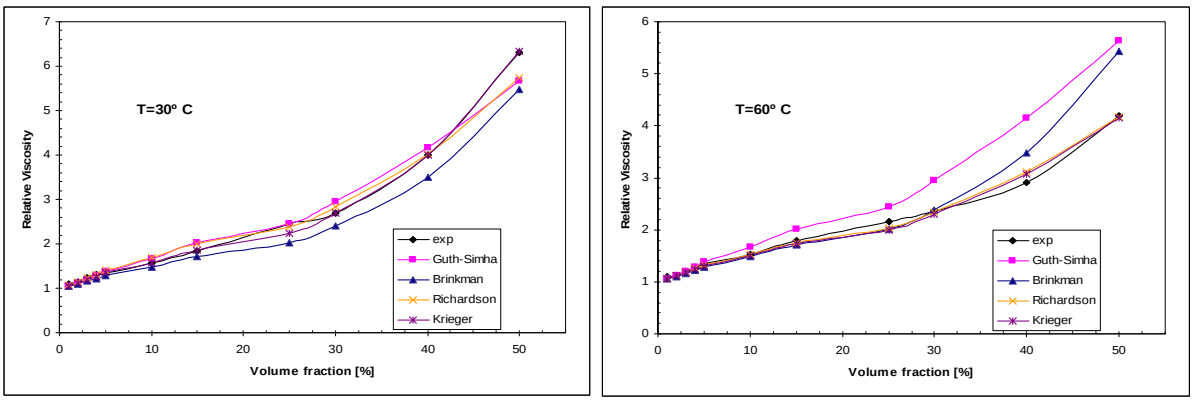

Results of average absolute deviations above show that the higher the temperature the higher the deviation results, which can be better observed on the figures. Krieger correlation best correlates all concentrations of the residue at all temperatures. The parameter used in this correlation depends linearly on temperature, which explains this best fit to even higher temperatures. Therefore, these correlations were well adjusted to residue in toluene, even in high concentrations, what confirms the hypothesis that this synthetic mixture behaviors as an emulsion.

5. Conclusions

From the measured kinematic viscosities of heavy naphthenic crude oils over a wide temperature range, it was concluded that the Eyring's correlation is accurate only at low temperatures, whereas ASTM results are perfectly adjusted in all temperatures. This was expected since ASTM method is widely applied to oils, while Eyring's correlation is better adjusted to dilute solutions.

The relative viscosity of residues mixed in toluene at low concentrations were correlated using several literature correlations. It was observed, that the lighter the residue, the better the deviation results. At low concentrations, the relation of Phan-Thien and Pham correlated the viscosity data most effectively.

Finally, predictions of relative viscosity of one residue at high concentrations mixed in toluene were obtained using literature correlations for viscosities of emulsions at several temperatures . The results showed that the deviation increases with the temperature. Krieger correlation best correlated the viscosity at all concentrations of the residue and at all temperatures. Therefore, these correlations, in general, were well adjusted to residue in toluene, even in high concentrations, which confirms the hypothesis that synthetic mixtures behave as emulsions.

Acknowledgments
The authors thank A.A. Robaina, G.F.Moraes, V.S.L.A. Correia, I. Hovell and L.A.M. Rutledge for help in experimental work and acknowledge the financial support of CENPES/PETROBRS and of MCT/FINEP/CTPETRO/PETROBRAS under the project number: FBR 2528-06 entitled, "Distribuição do Gás Sulfídrico entre Óleos Pesados, Gás Liberado e a Água de Formação nas Condições de Reservatório". The authors also thank CNPq for the scholarship " bolsa de produtividade to Krishnaswamy Rajagopal. and FAPERJ for scholarship to Andreia Amaro de Lima.

References
Farah M.A, Oliveira R.C Caldas J.N. Rajagopal ,K.. (2005) Viscosity of water-in-oil emulsions: Variation with temperature and water volume fraction.. Journal of Petroleum Science and Engineering 48 (3-4): 169-184
Farah, M.A. Caracterização de Frações de Petróleo pela Viscosidade.(2006). D.Sc. Thesis, Escola de Química, , Universidade Federal do Rio de Janeiro, Rio de Janeiro.
Lima, A.A. A viscosidade de óleo cru e de soluções de frações pesadas de petróleo. (2006). M.Sc. Thesis, Escola de Química, , Universidade Federal do Rio de Janeiro, Rio de Janeiro.

****

Proceedings of the 10th International Chemical and
Biological Engineering Conference - CHEMPOR 2008
Braga, Portugal, September 4-6, 2008
E.C. Ferreira and M. Mota (Eds.)

Solving population balance models in precipitation using orthogonal collocation and stochastic optimization

Raluca Isopescu, Vasile Lavric*
University Politehnica of Bucharest, Department of Chemical Engineering,
RO-011061, 1-7 Polizu Street, Bucharest, Romania

Keywords: population balance, precipitation, orthogonal collocation, genetic algorithms
Topic: Advancing the chemical and biological engineering fundamentals.

Abstract

The present work focuses first on modeling the semi-continuous precipitation using the population balance (PB) technique, considering homogenous nucleation, size dependent growth and agglomeration, then on estimating the parameters that describe the crystallization kinetics. The mathematical model includes the reaction kinetic characterization together with the mass and particle number conservation laws. Additional novel relations characterizing the crystallization processes like nucleation, growth and agglomeration are defined. The method of choice to solve the integral-differential PB equation is the orthogonal collocation. The parameter estimation was performed using genetic algorithms (GA) throughout minimization of the sum of squares of the residuals experimental - calculated density function in the collocation points. The methodology was applied using data obtained for the precipitation of $CaCO_3$ by pouring into a given volume of $CaCl_2$ solution, initially placed in a well-stirred vessel, an equivalent volume of K_2CO_3 solution during a specified time.

1 Introduction

The precipitation of sparingly soluble salts as a result of a homogeneous reaction in semi-batch crystallizers is a common procedure in industrial fabrications of chemicals. This procedure is experimentally very convenient but entails a lot of problems especially when the final product has to be carefully controlled from morphological and particle size distribution (PSD) points of view. The homogeneous nucleation induced by the fast chemical reaction generates new particles all over the reaction time. Besides nucleation, particle growth and side processes such as agglomeration act concomitantly to establish the final PSD; this overlap of mechanisms worsens the control of PSD (Jones *et al.* 2005). The PB technique is widely used to model crystallization and precipitation processes as it captures the changes in PSD seen as the result of four basic processes acting upon the particles within a control volume: birth, growth, break-up and agglomeration (Qamar *et al.*, 2006). Considering the characteristic particle size as the internal co-ordinate of the solid phase that is formed, denoted by *L*, the dynamic population balance equation (DPBE) can be written as:

$$\frac{\partial n(L,t)}{\partial t} + \frac{\partial \left[G(L,t) \cdot n(L,t) \right]}{\partial L} = r\left(L,t,n\right) \tag{1}$$

where *n(L,t)* is the population density function, *G(L,t)* is the growth rate function and *r(n,L,t)* is a complex functional, with integral terms, agglutinating generation and/or death functions that model nucleation, agglomeration and/or breakage processes. Several numerical methods are proposed in literature to solve the DPBE, among them the methods of classes' moments, line characteristics and pivot being the most used, while the collocation methods are seldom taken into consideration. In the present work the DPBE for the precipitation of calcium carbonate in semi-batch crystallizer was built and solved by orthogonal collocation with Legendre polynomials.

* Corresponding author. E-mail:v_lavric@chim.upb.ro

Applying orthogonal collocation to equation (1) transforms it into a system of ordinary differential equations (ODEs) with respect to time written for the collocation points which are the roots of the considered orthogonal polynomials. The overlapping of homogenous nucleation and agglomeration could render the ODEs stiff for some periods of the integration time, implying to switch the integration methods from non-stiff to stiff and back accordingly.

2 Experimental

The precipitation was carried on in a 0.5 L crystallizer at 30°C. A volume of 0.250 L of 0.1 M $CaCl_2$ solution was initially placed in the vessel. An equivalent volume of 0.1 M K_2CO_3 solution was added at a flowrate of 1 L/h. Suspension samples were taken at different feeding moments and PSD was measured on a laser beam particle analyzer, in terms of mass distribution. Concomitantly, Ca^{2+} ion concentration was measured in solution using a volumetric method. The precipitated solid phase was identified as pure calcite according to *IR* spectra analysis.

The population density function *n(L)* was computed from the final experimental PSD using the common transformation of first order approximation:

$$n(L) = \frac{\left[M(L_i) - M(L_{i-1})\right] \cdot m_T}{\bar{L}_i^3 \cdot \rho_S \cdot k_v \cdot (L_i - L_{i-1})} \tag{2}$$

where *M(L)* is the cumulative mass distribution, m_T is the solid mass in the unit volume of suspension, evaluated from Ca^{2+} concentration measurements, ρ_s is the density of calcite and k_v the volumetric shape factor which, for calcite, takes the value of 1.

3 Mathematical model

The supersaturation is generated by the chemical reaction:

$$CaCl_2 + K_2CO_3 \rightarrow CaCO_3 + 2KCl \tag{3}$$

The resulted calcium carbonate has a very low solubility and precipitation occurs almost instantaneously. The relative supersaturation is calculated according to the general mass action law for the ionic reactions and assuming perfect mixing of the reaction system:

$$S = \sqrt{\frac{\left[Ca^{2+}\right] \cdot \left[CO_3^{2-}\right]}{K_{sp}}} \tag{4}$$

where the solubility constant, K_{sp}, has the value of $3.4 \cdot 10^{-9}$ $(mol/L)^2$ for calcite. The concentration of Ca^{2+} and CO_3^{2-} ions are calculated from mass balances at the given flowrate. The variation of the calculated supersaturation is presented in Figure 1.

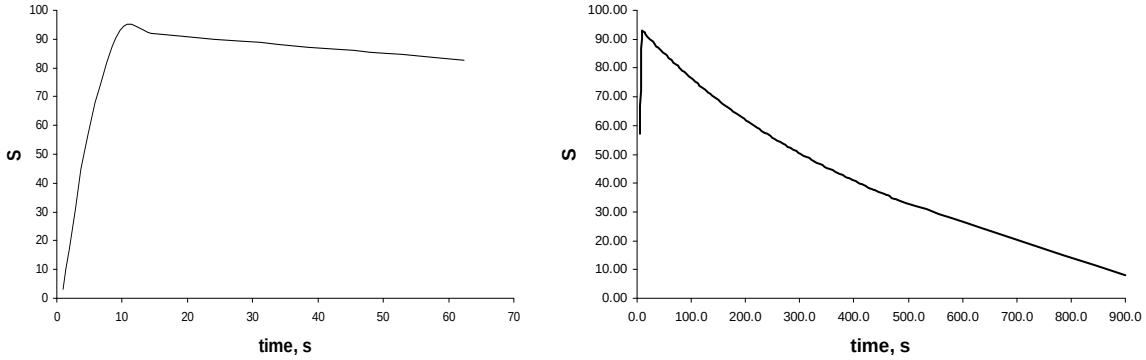

a) variation of relative supersaturation in the first minute

b) variation of relative supersaturation during the reagent addition

Figure 1. Time profile of the calculated relative supersaturation: (a) details, (b) whole time

As Figure 1 shows, the computed supersaturation increases very rapidly to rather high values; this is common in precipitation where supersaturation is created by a fast chemical reaction and the solubility product is very small. After less than 10 s from the beginning of the second reactant's addition, the supersaturation reaches a maximum value. During this period the nuclei are formed faster than the precipitation rate of the solid phase. After this short period the supersaturation starts decreasing till the end of the reaction time as Ca^{2+} ions are consumed.

Nucleation and growth (primary mechanisms) are mainly influenced by supersaturation. The relations assumed in this work to define nucleation and growth rates are of power low type:

$$B^0(t) = k_B\left[S(t)\right]^{n_B} \tag{5}$$

$$G(L,t) = G_0(t)\cdot(1+a\cdot L)^b \tag{6}$$

$$G_0(t) = k_G\cdot\left[S(t)\right]^{n_G} \tag{7}$$

where $B^0(t)$ is the nucleation rate depending only on supersaturation and $G(L,t)$ is the crystal growth rate depending on the crystal characteristic length, L. $G_0(t)$ is the growth rate at zero nucleus-size while a and b are the parameters of the size dependent growth model. The zero nucleus-size growth rate depends on supersaturation, and hence on time, according to equation (7).

The general DPBE for precipitation describes the time variation of the number based density function $n(L, t)$ when several possible antagonist mechanisms are present:

$$\frac{1}{V(t)}\frac{\partial\left[n(L,t)\cdot V(t)\right]}{\partial t}+\frac{\partial\left[G(L,t)\cdot n(L,t)\right]}{\partial L}=B^0\delta(L-L_0)+B(L,t)-D(L,t) \tag{8}$$

where $V(t)$ is the reaction volume while $B(L,t)$ and $D(L,t)$ represent the *birth* (two combining crystals) and *death* (growth beyond the current crystal characteristic length) functions characterizing the agglomeration process.

$$B(L,t)=\frac{1}{2}\int_0^L\beta(L,y,t)\cdot n(L-y,t)\cdot n(y,t)\cdot dy \tag{9}$$

$$D(L,t)=\int_0^\infty\beta(L,y,t)\cdot n(L,t)\cdot n(y,t)\cdot dy \tag{10}$$

where β is the agglomeration kernel representing the rate constant for the agglomeration process. Like for chemical processes, this constant can be also expressed as:

$$\beta(L,y,t)=\beta_0(t)\cdot\beta'(L,y) \tag{11}$$

In this study, since the experiments were performed at intense agitation and for moderate concentrations, the time dependency of the agglomeration kernel was defined throughout supersaturation:

$$\beta_0(t)=k_\beta\left[S(t)\right]^{n_\beta} \tag{12}$$

Agglomeration accompanies the primary mechanisms all over the precipitation process. As one of the reagents is continuously fed new nuclei are generated which can either grow or attach to the already formed crystals. At high supersaturation, bridges can form between particles that collide and larger particle could be generated. In the assumed crystal growth mechanism we included a size dependency that, formally, could be responsible for a faster growth of larger particles due to the addition of newly formed nuclei. Thus, we model the agglomeration process introducing a correction factor that reduces the contribution of the agglomerates formed throughout the collisions between very large and very small particles; the

agglomeration kernel therefore includes a particle size dependency. The value of this correction factor has to be established from experimental data fitting.

4 Numerical integration of the population balance equation

The DPBE was rendered dimensionless using the notations $\xi = \frac{L}{L^{\max}}$ and $\nu(\xi,t) = \frac{n(\xi,t)}{n^{\max}}$:

$$\frac{\partial \nu(\xi,\tau)}{\partial \tau} + \frac{\partial\left[G(\xi,\tau)\cdot\nu(\xi,\tau)\right]}{\partial \xi} + \frac{\nu(\xi,\tau)}{(1+\tau)} = \\ = B^{*}\cdot\delta(\xi-\xi_0) + \frac{1}{2}\int_0^{\xi}\beta^{*}(\xi,\zeta,\tau)\cdot\nu(\xi-\zeta,\tau)\cdot\nu(\zeta,\tau)\cdot d\zeta - \nu(\xi,\tau)\int_0^{1}\beta^{*}(\zeta,\xi,t)\cdot\nu(\zeta,t)\cdot d\zeta \tag{13}$$

The equation (13) is transformed throughout orthogonal collocation into a set of ODEs defined on the N interior collocation points (*j=1,N*; *j=0* and *j=N+1* represent de boundary conditions):

$$\frac{d\nu(\xi_i,\tau)}{d\tau} + \sum_{j=0}^{N+1} A_{ij}\left[G^{*}(\xi_j,\tau)\cdot\nu(\xi_j,\tau)\right] + \frac{\nu(\xi_i,\tau)}{(1+\tau)} = \\ = B^{*}\cdot\delta(\xi_i-\xi_0) + \frac{1}{2}\beta^{*}\int_0^{\xi_i}\nu(\xi_i-\zeta,\tau)\cdot\nu(\zeta,\tau)\cdot d\zeta - \nu(\xi_i,\tau)\cdot\beta^{*}\int_0^{1}\nu(\zeta,t)\cdot d\zeta, \quad i = 0,N+1 \tag{14}$$

In equation (14) the elements in matrix A depend on the collocation point (Finlayson, 1972). The significance of *B**, *G** and β^{*} is the following:

$$B^{*} = \frac{B^{0}\cdot\delta(\xi-\xi_0)\cdot\bar{t}}{n^{\max}} \tag{15}$$

$$G^{*} = \frac{G(L,t)\cdot\bar{t}}{L^{\max}} \tag{16}$$

$$\beta^{*} = \frac{\beta_0(\tau)\cdot\bar{t}\cdot n^{\max}\cdot L^{\max}}{2} \tag{17}$$

The function chosen for the correction factor to reflect the particle size dependency of the agglomeration kernel, as mentioned above, is:

$$\beta^{*}(\zeta,\xi,\tau) = \beta^{*}\cdot\sqrt{\zeta}\cdot(1-\zeta^{2})\cdot\sqrt{\xi}\cdot(1-\xi^{2}) \tag{18}$$

The system of ODEs was integrated for the initial and boundary conditions:

$$\tau = 0, \quad \nu(\xi,0) = 0 \tag{19}$$

$$\zeta = 0, \quad \nu(0,\tau) = \frac{B^{0}(\tau)}{G^{0}(\tau)} \tag{20}$$

The model parameters are k_B, n_B, k_G, n_G, *a*, *b*, k_β, n_β. These parameters were estimated by fitting the computed values for population density function with experimental data. The objective function used in the search for the optimal vales of the parameters was:

$$Fob = \min\sum_i\left[\frac{\ln\nu(\xi_i)_{comp}}{\ln\nu(\xi_i)_{\exp}} - 1\right]^2 \tag{21}$$

The minimization was carried out using GA which is expected to give good results due to its capability to explore a wide range of parameter variation and find the global optimum even for multimodal objective functions which is the case when 8 kinetic parameters are to be simultaneously identified. Inspired from the natural selection of biological organisms (survival

of the fittest), GA have several specific features: (a) the representation of parameters on chromosome-like structure, either binary encoded or directly stored for a faster retrieval and processing – the later is the method we used in the present study; the restrictions are dealt with simply eliminating the individuals violating them; (b) the optimal value is searched for within a group of candidate solutions, assimilated to a population; (c) the objective function is used to compute a fitness value, for each individual, measuring its adequacy; there is no need to employ derivatives or other additional information regarding the problem. Several probabilistic rules, known as genetic operators (selection, crossover, mutation and cloning), are used to create new offspring from best fitted individuals. Two important improvements are implemented into the standard GA, making it converging more rapidly: 1) when a large part of the population has too bad fitted individuals, preventing them to participate at multiplication, apply cloning by selecting randomly from the better fitted individuals and 2) if elitism is sought, the individuals from the new population not born through crossover are generated randomly around the best fitted individual, using a shrinking standard deviation (Răducan *et al.*, 2004).

5 Results and discussions

The mathematical model was solved for a period of 480 s from the beginning of reagent addition and fitted to the experimental distribution data using equation (21) as objective function. In this time interval about half of the reagent quantity was added. We tried several ortogonal collocation interior points from 7 to 19 – the lower the value the approximation error increases, while for high numbers the solution starts oscillating. In our case, 15 interior points was a good compromise. The values of kinetic parameters obtained regressing the mathematical model over the experimental data set are presented in Table 1.

Table 1. The values of the parameters implied in the mathematical model

k_B, no·m^{-3}	n_B	k_G, ms^{-1}	n_G	a, m^{-1}	b	β_0, m^3·s^{-1}	n_β	*Fmin*
$4.844 \cdot 10^{14}$	1.115	$1.009 \cdot 10^{-9}$	0.167	$1.67 \cdot 10^{6}$	0.862	$3.782 \cdot 10^{-17}$	0.959	0.022

The quality of the fit is also represented in Figure 2. As it can be seen analyzing Figure 2, the computed and experimental values are in a rather good agreement, although at very small particle sizes the distance model – experiment is fairly high. Experimental data show a more important small particle sizes population that could not be reproduced by the model, although a very high nucleation rate was identified (see Table 1 for details). An explanation can be the fact that in this range of particle sizes the experimental data are not very reliable as they were obtained on a laser beam particle size analyzer which do not include information for particles below 0.5 μm. Another source of errors could come from equation (2) which uses backward finite differences to compute the first derivative of the cumulative mass distribution with respect to the characteristic length of the crystal. In the very small particle domains, this means zero extrapolation, with the unavoidable attached errors. At the same time, the lack of dense experimental point on the last five μm makes the model fluctuate, although being close to the experiments in the range 18 – 27 μm.

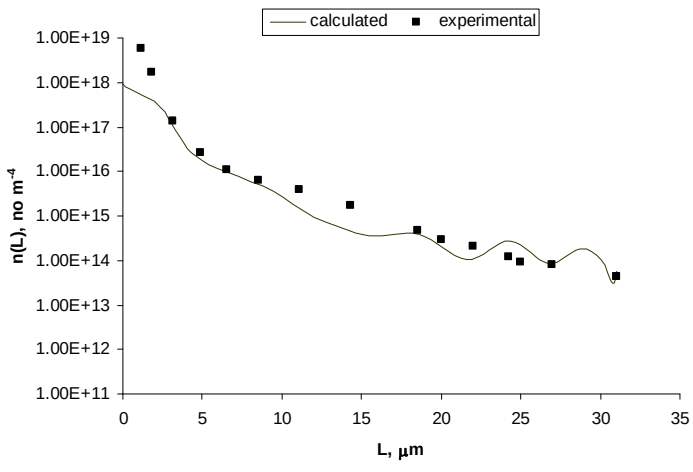

Figure 2. Computed and experimental distribution of the population density function

Under the experimental conditions investigated, nucleation is very important all along the reaction

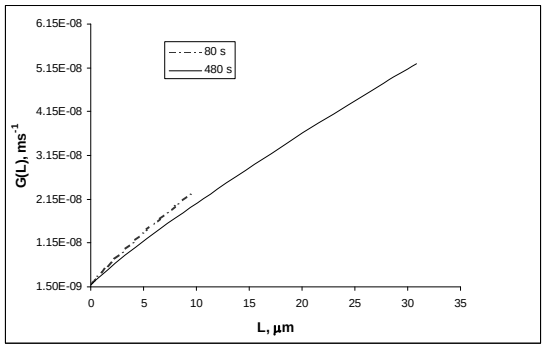

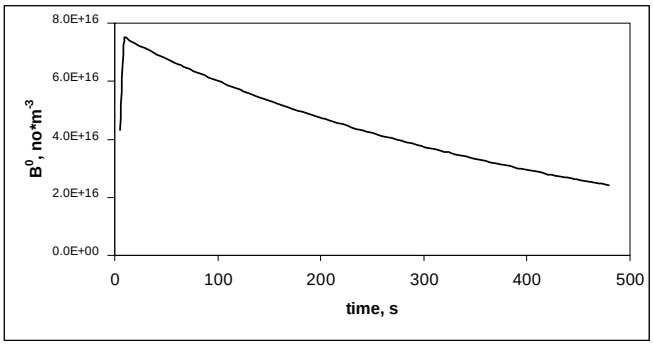

a) b)

Figure 3. Variation of the crystal growth rate with the characteristic length of the crystal (a) and time profile of the nucleation rate (b) during the precipitation process

time (Figure 3b). Following supersaturation, it almost doubles during the first 10 s then asymptotically decays due to the decrease of Ca^{2+} ion concentration. The crystal growth rate significantly increases with the particle size (Figure 3a), with a higher slope at the beginning of the process, when only small crystals are present (dashed line), and a lower one towards the end (solid line), when the nuclei growth rate, $G_0(\tau)$ decreases due to the supersaturation decrease – see equations (7).

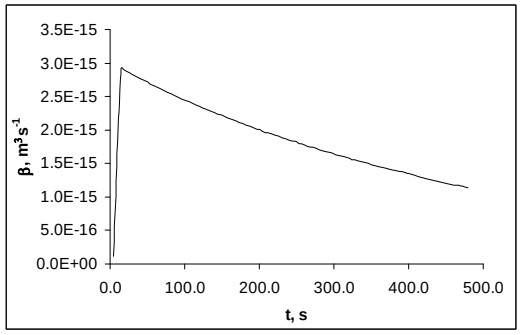

Figure 4. Time profile of agglomeration kernel

The agglomeration kernel (Figure 4) has quite significant values, meaning that agglomeration mechanism is important all along the precipitation process. The value of n_β parameter obtained in the regression analysis step proves that supersaturation strongly influences the solid bridge formation between particles that collide. Due to its dependency upon supersaturation – see equation (12) – its shape closely follows the supersaturation time profile. The agglomeration kernel should change profile after the second reactant adding will cease (the ageing period) when the supersaturation is very low but an important mass of solid phase is formed.

6 Conclusions

A mathematical model describing precipitation was built based upon PBE and using as basic mechanisms solely homogenous nucleation, crystal growth and agglomeration. Some additional novel relationships characterizing these crystallization processes have been proposed, relating them to relative supersaturation and crystal size. Satisfactory agreement between the mathematical model and the experiment was observed. Improvements could be sought changing the way the experimental distribution of the population density is computed, replacing in equation (2) the backward finite difference with a more appropriate formula.

References

Finlayson, B.A. (1972). *The Method of Weighted Residuals and Variational Principles*, Academic Press, New York.

Jones, A., Rigopoulos, S., Zauner R., (2005). Crystallization and precipitation engineering, *Comp. Chem. Eng.*, 29, 1159-1166.

Qamar, S., Elsner, M. P., Angelov, I.A.,Warneke, G., Seidel-Morgenstern, A., (2006). A comparative study of high resolution schemes for solving population balance in crystallization, *Comp. Chem. Eng*., 30, 1119-1131.

Răducan, O., Lavric, V., Woinaroschy, A. (2004). Time Optimal Control of Batch Reactors through Genetic Algorithms, *Rev. Chim.*, 55(8), 638-642.

Proceedings of the 10th International Chemical and
Biological Engineering Conference - CHEMPOR 2008
Braga, Portugal, September 4-6, 2008
E.C. Ferreira and M. Mota (Eds.)

Analyzing regimes in chemical reactors with allowing for the multistage kinetics and non-perfection of a system

Brener A.M.*, Tauasarov B.R.
State University of South Kazakhstan, Tauke Khan av. 5, Shimkent, Kazakhstan

Keywords: s, Reactor, Multistage Kinetics, Non-perfect Systems, Stability, Wave Front
Topic: (Bio) Catalysis & reaction engineering.

Abstract

The paper deals with problems of dynamical systems describing reaction-diffusion systems distinguishing by multistage and non-perfect kinetics. We consider main types of dynamical behaviour of such systems using two characteristis examples.

As a result of investigations we conclude that multistage and non-perfect kinetics can essentially affect reactor regimes and change their important characteristics. Moreover we submit the set of parameters controlling the regime stability and describing the regime bifurcations. The main types of possible dissipate structures induced by these factors as well as conditions of their formation have been determined. The results of investigations are likely to be useful for calculating intensity of mass transfer processes in chemical reactors.

1 Theoretical details and discussion

Multistage kinetics and non-perfection of reaction-diffusion systems have an essential influence on the process regime in chemical reactors. At the same time engineers often don't give due attention to these aspects of chemical processes and apparatuses design. In our work this problem has been theoretically investigated and illustrated by means of two model auto-catalytic reactions as examples.

Firstly we consider the following model scheme with main reagents X, Y and intermediate products A, C, despite the first stage is supposed to be an auto-catalytic reaction (Saul and Showalter, 1985):

$$X + Y \xrightarrow{k_1} X\,,\; X \xrightarrow{k_2} A,\; Y \xrightarrow{k_3} C\,, \tag{1}$$

where k_1, k_2, k_3 are the reactions rate constants.

Let's assume that the component Y enters the reactor continously with constant supply rate q, and the reagent X is the initial priming-tube.

Thus the system of kinetic equations for main reagents reads

$$\begin{aligned} \frac{dX}{dt} &= k_1 XY - k_2 X\,, \\ \frac{dY}{dt} &= q - k_1 XY - k_3 Y. \end{aligned} \tag{2}$$

[1]Here $X \geq 0$ and $Y \geq 0$ denote concentrations of reagents X and Y.

Provided the rate q satisfying the inequation

$$q < \frac{k_2 k_3}{k_1} \tag{3}$$

there is the only stable rest point of the system (2)

$$X_{01} = 0;\ Y_{01} = \frac{q}{k_3}. \tag{4}$$

But when this rate exceeds the critical value

$$q > q^* = \frac{k_2 k_3}{k_1} \tag{5}$$

the system acquires yet another rest point:

$$X_{02} = \frac{q k_1 - k_2 k_3}{k_1 k_2}\ ;\ Y_{02} = \frac{k_2}{k_1}. \tag{6}$$

Jacobians of the linearized system of kinetic equations at the rest points have the following

$$J_{01} = \begin{pmatrix} -k_2 + \dfrac{k_1 q}{k_3} & 0 \\ -\dfrac{k_1 q}{k_3} & -k_3 \end{pmatrix}, \tag{7}$$

$$J_{02} = \begin{pmatrix} 0 & \dfrac{q k_1 - k_2 k_3}{k_2} \\ -k_2 & -\dfrac{q k_1}{k_2} \end{pmatrix}. \tag{8}$$

Provided $q > q^*$ the rest point (4) becames unstable. And the springing up rest point (6) becomes stable on the contrary and it has a type of stable node or stable spiral.

The regimes analysis gives the folowing results:

1) for $(k_3/k_2) \geq 1$ at any q the rest point (6) is a stable node, and oscillations don't exist;

2) for $(k_3/k_2) < 1$ at q exceeding the critical value q^* rest point (6) can be a spiral.

At $(k_3/k_2) < 1$ we have

* Corresponding author. Tel 007-725-2210933. E-mail:amb_52@mail.ru

$$q^* < \frac{2k_2^2}{k_1}\left[1-\sqrt{1-\frac{k_3}{k_2}}\right]. \tag{9}$$

From this it follows that provided $(k_3/k_2)<1$ and $q > q^*$ the rest point (6) is a stable spiral, and appropriate transition regime goes on in the form of oscillations at the rate range

$$q_1 < q < q_2\,, \tag{10}$$

where

$$q_1 = \frac{2k_2^2}{k_1}\left[1-\sqrt{1-\frac{k_3}{k_2}}\right], \tag{11}$$

$$q_2 = \frac{2k_2^2}{k_1}\left[1+\sqrt{1-\frac{k_3}{k_2}}\right]. \tag{12}$$

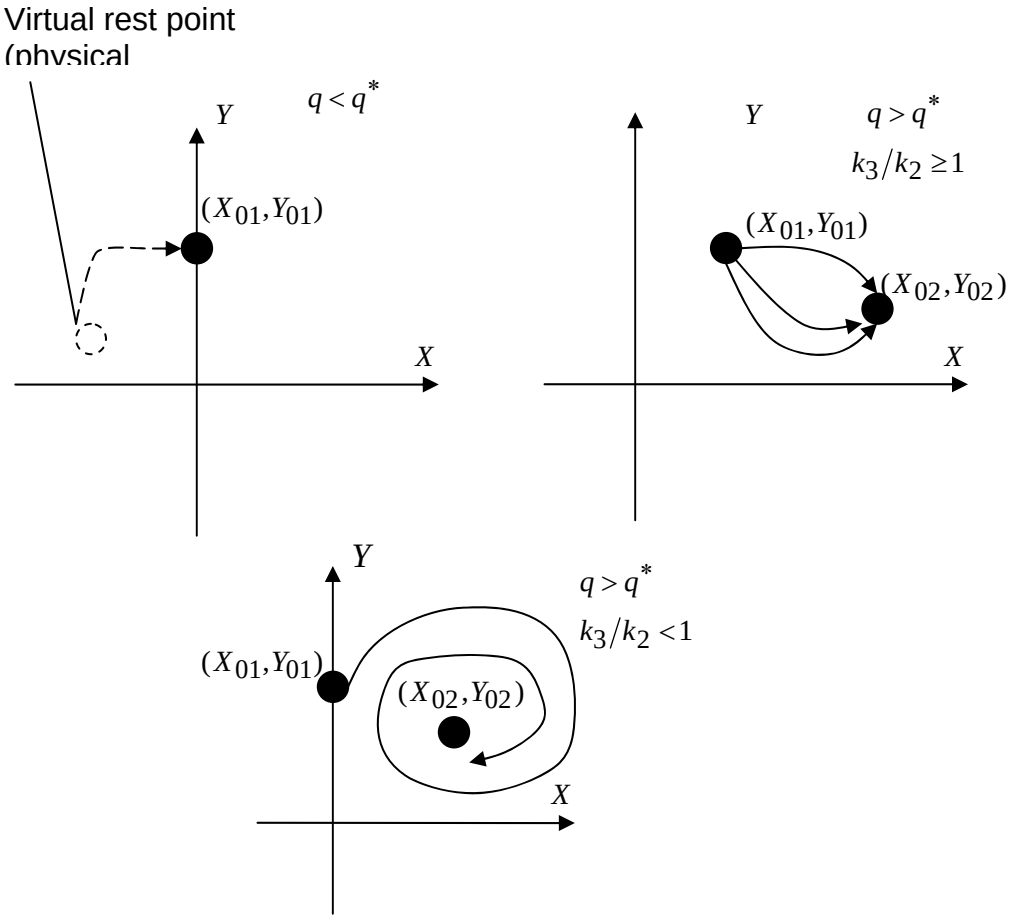

Figure 1- Phase curves near rest points of the system (2)

Thus the system has the control parameter

$$\alpha = \frac{k_3}{k_2}. \tag{13}$$

The value $\alpha = \alpha^* = 1$ is the bifurcation point, and for the transition regime we can obtain the frequency of oscillations ω and the logarithmic fading decrement ν :

$$\omega = \sqrt{\frac{2q}{k_3} - \frac{2k_2k_4}{k_1k_3} - \frac{k_3k_4^2}{4}}, \tag{14}$$

$$\nu = -\frac{k_4}{2} \tag{15}$$

The second example is the auto-catalytic reaction of the following type (Saul and Showalter, 1985; Kudryavtsev, 1987):

$$A + X \underset{k_2}{\overset{k_1}{\rightleftarrows}} 2X + C. \tag{16}$$

In the perfect thermodynamic system the following relation is true

$$\mu = \mu^* + RT \ln X, \tag{17}$$

where μ is a chemical potential and μ^* - its standard value, R is gas constant, T is a temperature.

Let's consider the case of non-perfect reaction-diffusion system, where the chemical potentials of reagents read (Karapetianz, 1975; Jou et all, 2001).

$$\mu = \mu^* + RT \ln X + \omega_{AX} (1 - X)^2. \tag{17}$$

Here

$$\omega_{AX} = \kappa[2\varepsilon_{AX} - (\varepsilon_{AA} + \varepsilon_{XX})], \tag{18}$$

and ε_{AX}, ε_{AA}, ε_{XX} are energies of an interaction between molecules of reagents, κ is a parameter depending on the model of liquid state.

Supposing $X << 1$ we obtain the following approximate relation

$$\mu = \mu^* + RT \ln X + \omega_{AX} (1 - 2X). \tag{19}$$

According to thermodynamics of diluted solutions the diffusion coefficients determine by the derivatives of chemical potentials over the concentrations.

Thus we obtain:

$$\frac{\partial \mu}{\partial X} = \frac{RT}{X} - 2\omega_{AX} = \frac{RT}{X}(1 - 2\omega_{AX} X), \tag{20}$$

From this it follows

$$D = D_i\left(1-2\omega_{AX}X\right), \tag{21}$$

where D_i is the diffusion coefficient in perfect system, D is the one in a real system.

And so, the mass transfer equation for the reaction (15) proceeding in a tubular through-reactor can be written as follows

$$\frac{\partial X}{\partial t}+q\frac{\partial X}{\partial z}=\frac{\partial}{\partial z}\left(D_i\left(1-2\omega_{AX}X\right)\frac{\partial X}{\partial z}\right)+f\left(X\right), \tag{22}$$

where

$$f\left(X\right)=k_1AX-k_2X^2. \tag{23}$$

Using method of an auto-model variable the equation (22) can be reduced to the following ordinary differential equation

$$\frac{d^2X}{ds^2}-\frac{q-c}{D_i\left(1-2\omega_{AX}X\right)}\frac{dX}{ds}-\frac{2\omega_{AX}}{1-2\omega_{AX}X}\left(\frac{dX}{ds}\right)^2+\frac{f\left(X\right)}{D_i\left(1-2\omega_{AX}\right)}=0, \tag{24}$$

where $s=x-ct$, c is a phase velocity or a velocity of wave front.

Equations of the appropriate dynamical system read

$$\begin{cases} \dfrac{dX}{dt}=Y, \\ \dfrac{dY}{dt}=\dfrac{q-c}{D_i\left(1-2\omega_{AX}X\right)}Y+\dfrac{2\omega_{AX}}{1-2\omega_{AX}X}Y^2-\dfrac{f\left(X\right)}{D_i\left(1-2\omega_{AX}X\right)}=0 \end{cases} \tag{25}$$

There are two rest points of the system

$$X_{01}=0,\quad X_{02}=A\frac{k_1}{k_2}. \tag{26}$$

Jacobians of the linearized system (25) at the rest points (26) read

$$J_{01}=\begin{pmatrix} 0 & 1 \\ -\dfrac{k_1A}{D_i} & \dfrac{q-c}{D_i} \end{pmatrix}, \tag{27}$$

$$J_{02} = \begin{pmatrix} 0 & 1 \\ \dfrac{k_1 A}{D_i(1-\gamma)} & \dfrac{q-c}{D_i(1-\gamma)} \end{pmatrix}. \quad (28)$$

where

$$\gamma = 2\omega_{AX} A \frac{k_1}{k_2}. \quad (29)$$

As for diluted solutions $\omega_{AX} << 1$ the following inequation is correct

$$\gamma < 1. \quad (30)$$

From detail analysis which is analogous with the analysis of system (2) we conclude that non-perfect kinetics in the case of high diluted solutions doesn't change types of rest points and reactor regimes. At the same time concrete values of regimes characteristics have undergone changes.

Particularly, the velocity of wave front which generates from transient oscillatory regimes differs from the velocity of wave front in a perfect system. The appropriate relation reads

$$c_{0r} = c_0 + \gamma\sqrt{k_1 D_i A}\ . \quad (31)$$

Here c_0 is the wave front velocity calculated for the perfect system:

$$c_0 = \left| q - 2\sqrt{k_1 DA} \right|, \quad (32)$$

and $\gamma < 1$ is the special amendment coefficient for which we obtain the following relation

$$\gamma = 2\omega_{AX} \frac{k_1}{k_2} A. \quad (33)$$

2 Conclusion

It can be concluded that rate of reagents supply not only controls an output of the reactor but also can essentially change a set of stationary and transition process regimes. Usually engineers connect such transformations with heat phenomena. At the same time the mentioned above factors can also cause regime transitions.

As regards the non-perfection of systems its influence for high diluted solutions manifests only in increasing the wave front velocity under transition regimes.Incidentally, transition regims theirself are determined by a system non-linearity. However in the case of strong solutions the situation may be different. This problem needs an additional study.

References

Saul, A., Showalter, K. (1985). Propagation of wave fronts in reaction-diffusion systems. *Oscillations and Traveling Waves in Chemical Systems, Ed. R.J. Field and M. Burger*, Wiley, New York, 451-471.

Kudryavtsev, I.K. (1987). *Chemical Instabilities*, Moscow Univ. Publ., Moscow. (in Russian).

Karapetyanz, M.K. (1975). *Chemical Therodynamics*, Himia, Moscow. (in Russian)

Jou, D., Casas-Vazquez, J., Criado-Sancho, M. (2001) *Thermodynamics of Fluids Under Flow*, Springer, Berlin.

Proceedings of the 10th International Chemical and
Biological Engineering Conference - CHEMPOR 2008
Braga, Portugal, September 4-6, 2008
E.C. Ferreira and M. Mota (Eds.)

Optimisation of a package production process for the implementation of a "Total Productive Maintenance"

Ana Rita Seita, Rui Alves[2], M.Mercedes Esquível[1*]
[1]Centre for Biological and Chemical Engineering, IBB, DEQB, Instituto Superior Técnico, Av. Rovisco Pais, 1049-001 Lisboa, Portugal
[2]Seda Ibérica Embalagens SA, Oeiras, Portugal

Keywords: Lamination, TPM, packages, factorial design, optimisation
Topic: Multi-scale and/or multidisciplinary approach to process-product innovation

Abstract

This research consists of the detailed study on the powder detergent packages production process, focusing especially on optimal control variable levels' selection and stipulation, with the purpose of minimising the number of defective board boxes. Although the production process has four stages, this study focuses mainly on the second stage, where the laminated board boxes are produced.

Among the several defects these boxes may have, one in particular was studied, as it is responsible for the major problems that have happened since the company started producing these boxes. This defect is the curling of the laminated board boxes, which, when reaching the third stage, cause the machine to stop, as well as a high level of waste. By using a factorial design, the conclusion is that the variables which influence the boxes curling the most are: paper's tension (tp); the position of the fibre breakers 2 (QF2); and the interactions among board box grammage and wax's temperature (Gc.Tw) and (tp.QF2).

1 Introduction

One of today's companies' primary concerns is the increase of global productivity, including the production tasks, as well as the technical activities and all the other company's functions. This high production's increase can only be obtained by increasing work efficiency, constituting the company's economical and social progress thrust.

In this context, the Seda Ibérica S.A. Company, where this study took place, is in the middle of a TPM's implementation process around the factory, which will represent a change in its organisation's culture. One of TPM's goal is to "achieve zero stops, zero malfunctions, zero accidents and zero defects" and in order to succeed all the processes must be known in detail. This means a deep knowledge of each process, the flaws must be identified and formally recognised, their causes discovered and attempts have to be made to eliminate them. In this context, it is essential to keep the process controlled so that it can be adjusted, later on, obtaining the expected results. This way, to implement TPM, a multi-departmental team in each process of the factory is constituted so that all the workers are involved in improving production.

* Corresponding author. Tel + 351-218417312. E-mail: mercedes.esquivel@ist.utl.pt

After a detailed knowledge of the process, optimal values are to be found for each parameter and, so that the maximum efficiency of the manufacturing process is obtained, increasing production, increasing the quality and the costumers' satisfaction and reducing waste.

Therefore, this process control was achieved through the following steps: i) a corrective control – to study the best environmental conditions in which the board boxes must be subjected after leaving the machine, and which is the best way palletization can be made so that deformation doesn't increase during the waiting period, before beginning the following stage; ii) a preventive control – in order to discover the machine's working parameters optimal values for each format, so that the board boxes deformation can be reduced.

TPM

Japan introduced TPM around 1971. At that time, industries were trying to improve the preventive maintenance techniques, system production maintenance and trustworthy engineering, to achieve zero failure and zero equipment malfunctions, as well as zero defective products and zero losses in the process. TPM is a program of continuous improvement, which requires the cooperation of all workers: from the equipment handler, to the maintenance workers, to the intermediate managership, to the higher levels of management. In this sense, the five TPM main goals are: (a) to guarantee the global installation efficiency, (b) to implement a maintenance program that optimises the equipment life-cycle, (c) to call for every department involved in the increasing of the installed capacity plan, (d) to request data and information about all the workers of the company and (e) to encourage the team-work principle, in order to consolidate actions of continuous improvement.

2 Description of the conditioning powder detergents packages manufacturing process

This process consists of four stages. During the first stage, the paper is printed through rotogravure printing, by entering and leaving through the paper rolls. That being said, we can consider this to be a continuous production. The printing is done with gravure cylinders, immersed in paint so that when the paper is pressed against them, the printing stays in the paper. The paper goes through several gravure cylinders printing each colour at a time.

During the second stage, the printed paper and the board are united. This union is achieved through microcrystalline wax that is applied in one of the board sides and by pressing it with a system of rolls. This operation is called lamination and is accomplished with a special machine in a continuous production. The board and the printed paper enter the machine through paper rolls and are glued together, using a hot melt lamination, followed by the tear strip application. After the lamination process, the glued material is diecutted, according to the specific format, so that in the end of stage two, the boxes are ready to go to the third stage of the process.

During the third stage, the laminated detergent boards are folded, glue is applied to the sides of the box and a corrugated cardboard support is pasted inside the box, providing the endurance needed to support the powder detergent. In this stage, the laminated detergent boards are shaped and glued overall, although its bases and tops are left unglued. They then proceed to the final stage, to a machine where the handles are placed, to ease transportation.

At the end of the process, the laminated detergent boards are conditioned inside board boxes, stacked and stored up, and this is a process that can produce boxes with diverse formats and has the ability to produce 3000 boxes per hour.

3 Problem description

In the process of making laminated detergent boards, some problems such as decentralized printing, incorrect folding or curling can occur. From all these, only the one which causes stops at the third stage of the process was studied. This problem is the boxes' curling and is responsible for 25% of the total registered defects.

Performance's Characteristic is defined as the deformation height, in centimetres, from the upper and lower left corners (y_1 and y_2), exhibited by the laminated board boxes. The maximum deformation height to considerer the product conform is $2X10^{-2}$ m

Only 7 parameters out of the usual registered 20 were considered critical. Chosen as critical factors are: *velocity* (v) because it represents the process' yield; *paper's tension* (tp) because it is applied near the laminating area and it influences the boxes' curling; the *fibre breakers' position 1*(QF1) and *2* (QF2), because they make sure the board box is stretched; the *wax's temperature* (Tw); The board box *grammage* (Gc) as it affects its resistance; and the *board box's humidity* (Hc) because it influences most of the board box mechanic characteristics, such as resistance and elasticity.
The factorial design was applied on two levels and in two stages to optimize the working conditions. The optimization strategy used, in which factors vary simultaneously, reduces the number of trials in comparison to the classical approach in which only one factor varies. In table 1 the values considered for the selected factors are presented.

Table 1- Variables' levels

Variables	**High level (+1)**	**Low level (-1)**
v(pc/min)	100	60
tp (kg.f)	40	35
Hc (%)	7	5
QF1 (%)	61	18
QF2 (%)	95	0
Tw (ºC)	200	100
Gc (g/m^2)	430	378

4 Results and Discussion

On the first stage a factorial 2^{7-3} was applied corresponding to a total of 16 trials with the objective to quickly identify the set of factors with significative effect on the deformation of the boxes. The obtained data confirmed that the *fibre breaker's position* (QF1) and the *board box humidity* (Hc) did not have any influence in the cardboard box deformation.
On a second stage of the work a factorial 2^{5-1} was applied to the remaining 5 factors according to the matrix presented on table 2.

Table 2: 2^{5-1} matrix and its resulting data

Trial Nº	Factors					Results ($\times 10^2$ m)	
	A(v)	B(tp)	C(QF2)	D(Gc)	ABCD (Tw)	y1 (Upper Left)	y2 (Lower Left)
1	-1	-1	-1	-1	1	1	1,5
2	1	-1	-1	-1	-1	0,5	1
3	-1	1	-1	-1	-1	0,5	3
4	1	1	-1	-1	1	0	0,5
5	-1	-1	1	-1	-1	1,5	4
6	1	-1	1	-1	1	2	1,5
7	-1	1	1	-1	1	0	0
8	1	1	1	-1	-1	0	0
9	-1	-1	-1	1	-1	0	0
10	1	-1	-1	1	1	0	0
11	-1	1	-1	1	1	0	0,5
12	1	1	-1	1	-1	0	0
13	-1	-1	1	1	1	2,5	5
14	1	-1	1	1	-1	1	1
15	-1	1	1	1	-1	0	0
16	1	1	1	1	1	1,5	3

The factor effects were calculated by measuring the difference between the average of the trials, were the factor is in the + level, and the average of the trials, were the factor is in the level – (eq.1).

$$Effect_{Factor} = \bar{y}_{Factor^+} - \bar{y}_{Factor^-} \qquad \text{eq. 1}$$

In figure 1 a graph of the probability of the effects is shown. All the effects that fall on the line are negligible while the significant effects are represented further form the line. The important effects from this analysis are paper's tension (tp) the position of the fibre breakers (QF2) and the interactions tp.Qf2 and GC.Tw.

The two principal factors tp and QF2 and the interactions tp.QF2 and Gc.Tw are those which may produce the most deformation on the boxes.

In figure 2 a geometrical representation of factorial design 2^{5-1} is shown, in which vertices of the cubes the values of the answer variables y_1 and y_2 are written between brackets. The shaded areas represent the combination of the variables for which the box deformation is minimized.

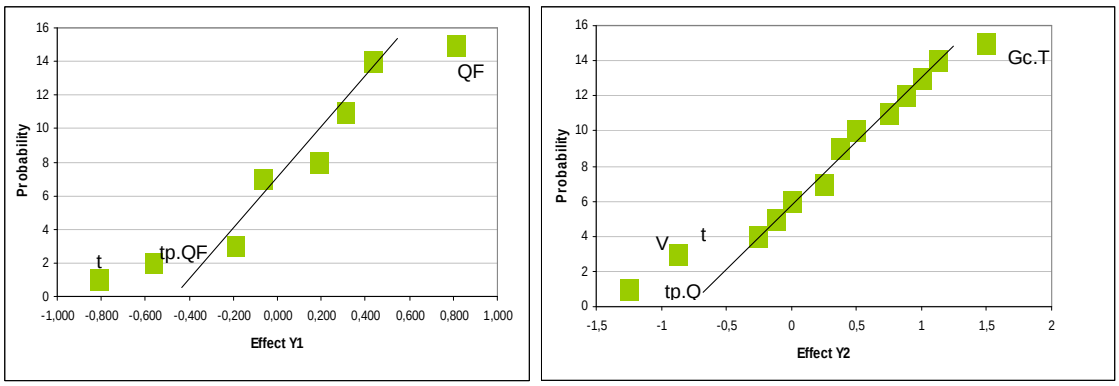

Figure 1 - Graph of the normal probability of the effects for factorial 2^{5-1}

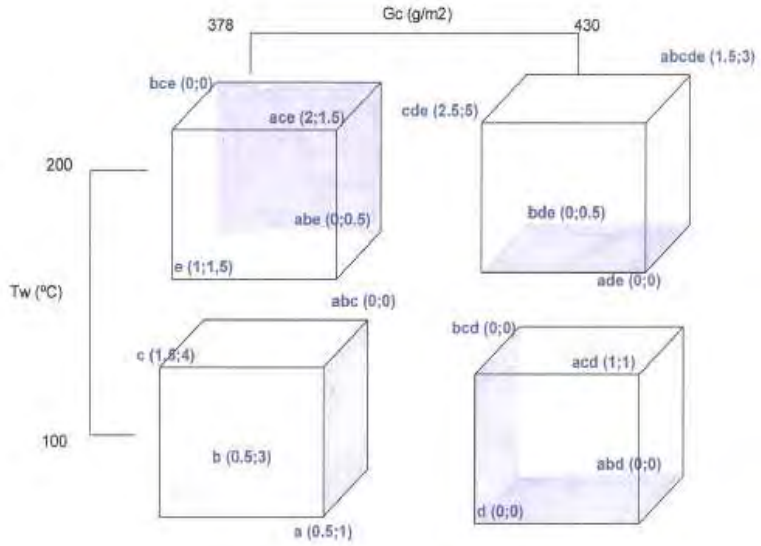

Figure 2: Geometrical representation of factorial design 2^{5-1} and its respective results y_1 and y_2 (between brackets)

First order model building

For the four variables mentioned before, a first order model was made, as exemplified in the equation 2 and 3. Figure 3 shows the normal probability for y1 and y2 residuals. The points in the graph are reasonably located over a straight line confirming the hypothesis that the factors tp, QF2, tp.QF2 and Gc.Tw are the only ones with significative effect in the process being studied.

$$\hat{y}_1 = 0.656 - \frac{0.813}{2}x_2 + \frac{0.813}{2}x_3 - \frac{0.563}{2}x_2x_3 + \frac{0.313}{2}x_4x_5 \qquad \text{eq. 2}$$

$$\hat{y}_1 = 1.313 - \frac{0.875}{2}x_2 + \frac{1.000}{2}x_3 - \frac{1.250}{2}x_2x_3 + \frac{1.500}{2}x_4x_5 \qquad \text{eq. 3}$$

$$x_i = \frac{Factor - (Factor_{low} + Factor_{high})/2}{(Factor_{high} + Factor_{low})/2} \qquad \text{eq. 4}$$

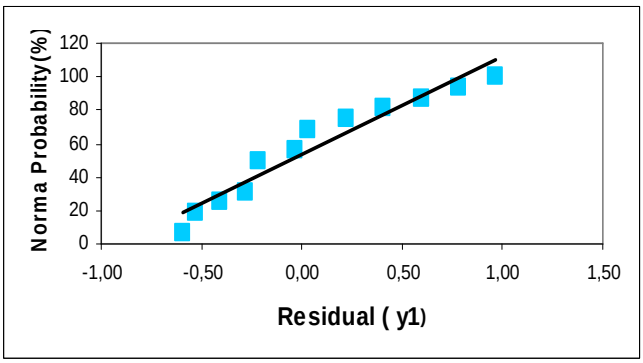

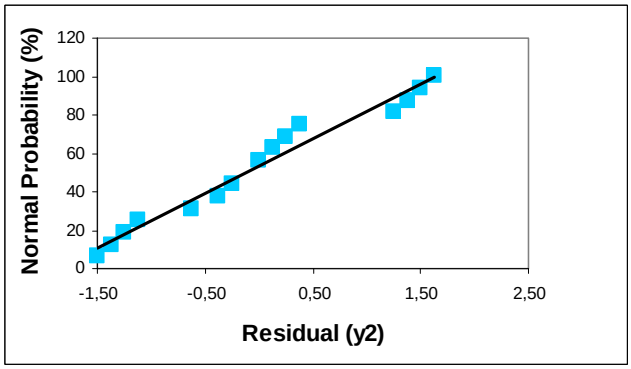

Figure 3- Normal probability graph of the residues

5 Conclusions

The purpose of this research was to select the control variables and to calculate its effects on the “RPL” machine during the laminated board boxes production process.

From the seven critical variables pointed out, it was determined that only the paper’s tension (tp), the fibre breaker’s position (QF2), the interactions (tp.QF2) and (Gc.Tw) cause the board boxes to curl.

From the data shown on figure 2 a decision diagram was constructed which allows, depending on cardboard grammage (Gc) and wax temperature (Tw), to select the remaining conditions of the process towards minimal cardboard deformity.

References

Box, G.; Hunter, W.; Hunter, J.; *Statistics for Experimenters: An Introduction to Design*, Data *Analysis, and Model Building*, Jonh Wiley & Sons, 1978.

Hockman, K.; Dupont, D.; *Design of experiments*, Chemical Engineering, November 1995, pg 142-147.

Isaacson, W.; *Statistical Analyses for Multivariable Systems,* Chemical Engineering, June 29, 1970, pg 69-75

Proceedings of the 10th International Chemical and
Biological Engineering Conference - CHEMPOR 2008
Braga, Portugal, September 4-6, 2008
E.C. Ferreira and M. Mota (Eds.)

Rheological and thermodynamic study on a biodiesel production process

Álvaro F. C. Vaz[1], Andreia C.S. Fial[1], Ana P. R. Gomes[2], Rogério M. S. Simões[1]

[1] DCTP – Department of Paper Science and Technology, [2] Optics Center
University of Beira Interior, Rua Marquês d'Ávila e Bolama, 6200–001 Covilhã, Portugal.

Keywords: Biodiesel, Rheology, Surface Energy, Thermogravimetry, Differential Scanning Calorimetry.
Topic: Multi-scale and/or multi-disciplinary approach to process-product innovation.

Most of the world energy consumption is based on oil, coal and natural gas. The rise in energy demand related with new global players resulted in a surge of the conventional energy sources prices. The global concern on environmental issues such as greenhouse effect and threats related with future supply shortage have opened the way for new sustainable alternatives based on renewable sources, and the conversion of natural oils into biodiesel. Biodiesel is a fatty acid mono-alquil esther derived from vegetable oils and animal fats obtained by a transestherification process with an alcohol (methanol or ethanol), as represented by the equation (Knothe et al.):

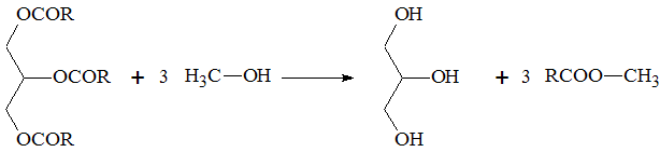

(Equation 1)

The oil in the industrial process passes trough a pre-treatment (such as filtering, degumming, free fatty acids removal and catalyst mixing), a transestherification reaction, a phase separation from glycerol, a washing step, a purification step and a drying step. This work characterizes different vegetable oils such as rape seed, sunflower seed and soybean, and biodiesel produced industrially by methanolic via. All samples were furnished by PRIO, from an industrial site. The scope of this study embraces rheological and surface tension characterization and a thermodynamic study on thermogravimetry and differential scanning calorimetry (DSC). The reason behind these options is the importance of these itens on the biodiesel flow, atomization and proper combustion through the injector (Ejim et al.). The evolution throughout a PRIO industrial process was the goal of this study, represented by steps A trough H.

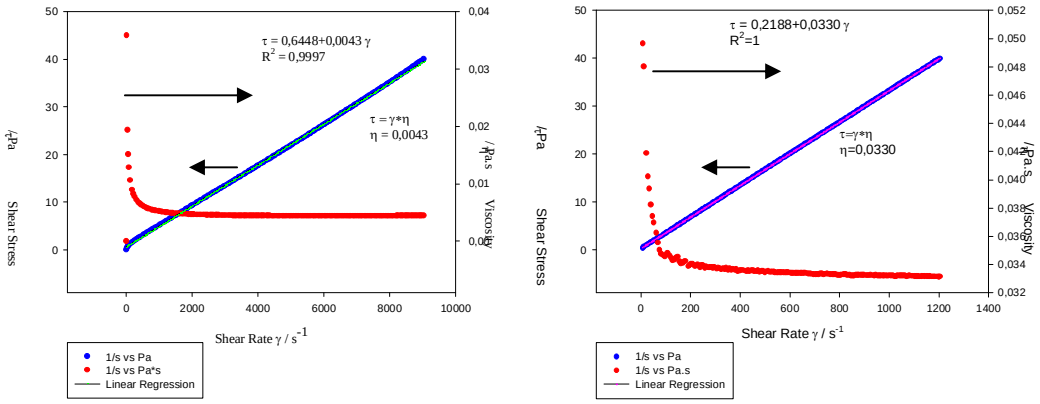

Graphic 1: Oil and Biodiesel pseudoplastic responses.

The oil and biodiesel viscosity evaluation was made on a HAAKE RS150 rheometer with baths at 40ºC and 5ºC. The surface tension was made using a DATAPHYSICS Contact Angle System OCA. Both oils and biodiesel have shown pseudoplastic responses, as exemplified in Graphic 1. It shows the values of shear stress (kPa) in the left vertical axis, and apparent viscosity (Pa.s) in the right vertical axis, as a function of shear rate in s^{-1}. The value of the apparent viscosity can be considered constant for high shear rates.

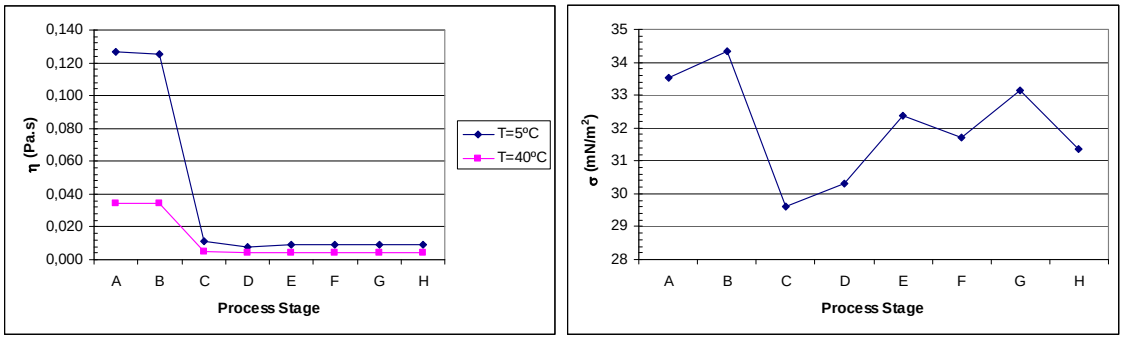

Graphic 2: Process viscosity (Pa.s) at 5ºC and 40ºC and surface tension (mN/m^2) evolutions.

Graphic 2 shows the evolution during the process of the apparent viscosity (at 5ºC and 40ºC) and surface tension. It can be seen that there is a steep viscosity reduction after the transestherification step. This can be justified by the molecular length reduction and a more linear structure in the biodiesel. The surface tension similarly reduces after the transestherification step, but it increases regularly in the subsequent steps.

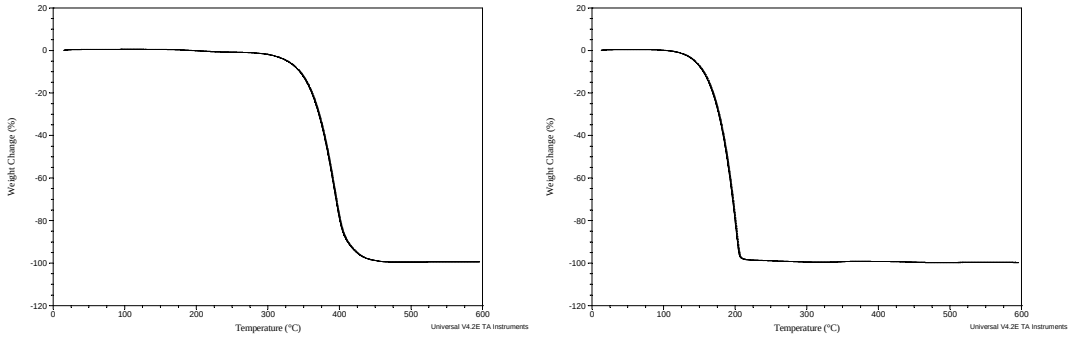

Graphic 3: Oil and biodiesel thermogravimetric evolution.

Thermogravimetry is a technique which obtains a sample mass variation as the temperature increases regularly. Graphic 3 represents thermogravimetric results for a sample of oil and sample of biodiesel, where the maximum evaporation rate took place at close to 375ºC for the oil and close to 175ºC for the biodiesel.

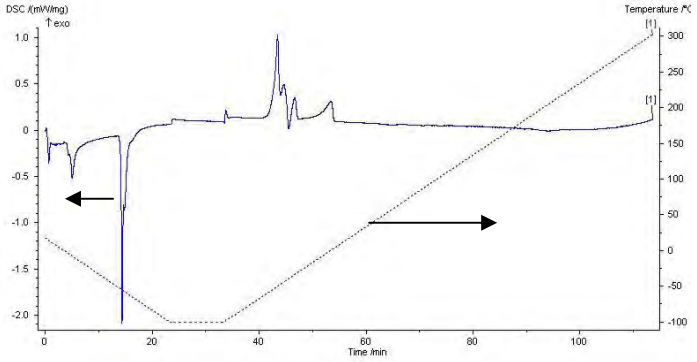

Graphic 4: Differential scanning calorimetry for a biodiesel sample.

Differential Scanning Calorimetry compares the heat flow to a sample and a standard material, with a programmed temperature evolution. It permits to study phase transitions and reactions. A study has been made between -100ºC and 300ºC in a nitrogen inert atmosphere. As seen in Graphic 4, two significant phase transitions where obtained in the -100ºC–20ºC interval. The first one, close to 0ºC, corresponds to wax crystallization, being the crystallization onset temperature (or Cloud Point). The latter results from a crystallization/solidification step (Pour Point) (Knothe et al.). Further studies with non-inert air atmosphere were already made and are being prepared for publication.

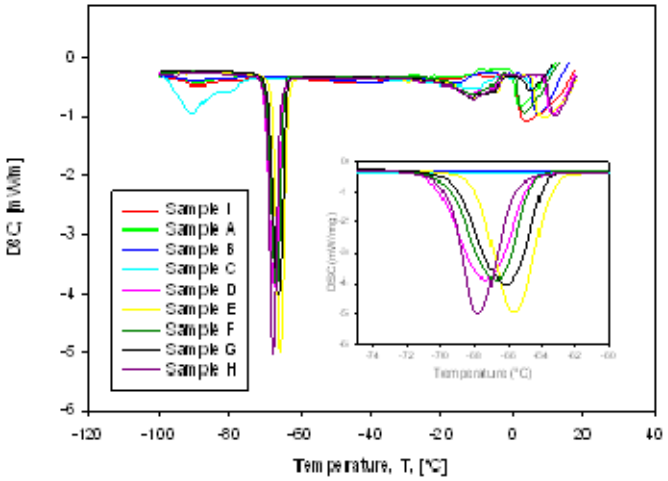

Graphic 5: DSC for all samples from 20ºC to -100ºC.

Graphic 4 5 show the DSC diagram for the different samples throughout the process from 20ºC to -120ºC. It can be seen two exothermic peaks, the first one in the -80ºC—60ºC range and the second one in the 0ºC-20ºC. The first one is the Pour Point, being the lowest temperature at which the biodiesel can be poured. The second one, as explained above, is the temperature at which the waxes begin to crystallize (Cloud Point). It can be seen in the graphic that a reduction in the Cloud Point occurs in steps F trough H, being then in the range -20ºC–0ºC.

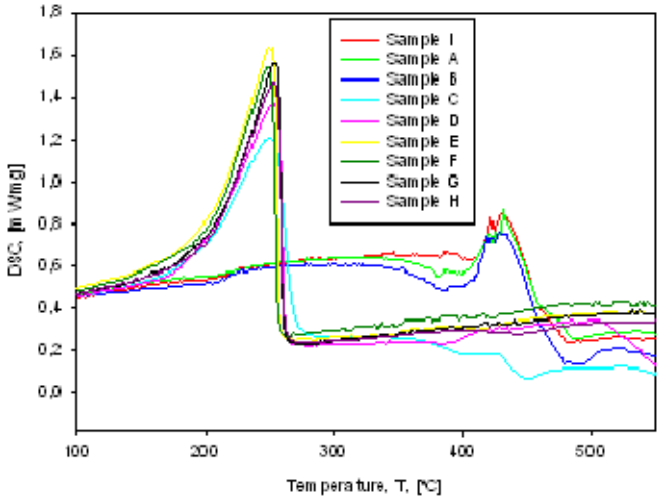

Graphic 6: DSC for all samples from 100ºC to 550ºC.

Graphic 6 shows the DSC diagram for the different samples in the 100ºC–550ºC range.

An endothermic step is observed, as in the thermogravimetric results. Anyway, vaporization temperatures are comparatively slightly higher, being around 430ºC for the oil steps (I, A and B) and around 230ºC for the biodiesel steps (C trough H). This corresponds to the final evaporation temperatures in the thermogravimetric plots.

Subsequent studies will focus on establishing the relationship between the process operation and biodiesel composition, and how it determines the evolution of physical, rheological and thermodynamic properties.

References

Knothe, G.; Gerpen, J.V.; Krahl, J. (2005). *The Biodiesel Handbook*, AOCS Press.

Ejim, C.E.; Fleck, B.A.; Amirfazli, A. (2006) Analytical study for atomization of biodiesels and their blends in a typical injector: surface tension and viscosity effects. *Fuel*, 86, 1534-1544.

Proceedings of the 10th International Chemical and
Biological Engineering Conference - CHEMPOR 2008
Braga, Portugal, September 4-6, 2008
E.C. Ferreira and M. Mota (Eds.)

Comparison of ozonolysis and steam explosion of wheat straw as pretreatments to obtain bioethanol

M. Teresa García[1*], Silvia Bolado[1], Gerardo González[1], Isabel Catalina[1], Andrés Miranda[1]

[1] Univ. Valladolid, Dep. Chemical Engineering and Environmental Technology, Pº Prado de la Magdalena s/n, 47011 Valladolid, Spain.

Keywords: bioethanol, lignocellulosic biomass, steam explosion, ozonolysis, straw
Topic: Multi-scale and/or multi-disciplinary approach to process-product innovation. Energy and environment

Abstract

In this work ozonization and steam explosion of wheat straw have been compared as adequate pretreatments in the bioethanol production process from lignocellulosic materials. The pretreatment stage is necessary before enzymatic hydrolysys in order to leave cellulose accesible to enzymes when lignocellulosic raw material is employed. For both selected pretreatments, the influence of the main process variables was analysed and operation conditions were optimized. Hydrolysis tests for each pretreated sample were performed in order to determine the improvement produced in the enzymatic saccharification under the different pretreatment conditions used. From the statistical treatment of the obtained experimental results, it can be concluded that the maximum yields (87.1 % on glucose) on enzymatic hydrolysis were obtained when wheat straw is ozonized, operating with 40 % of solid moisture, 3-5 mm of particle size and 90 L/h of ozone, whereas a 80,9 % of glucose after enzymatic hydrolysis was obtained when the raw material was steam exploded at 210 ºC, 20 mm of particle size and 10 min of residence time.

1 Introduction

Locomotion is a key factor in the present economy progress representing around 20-25% of total world energy consumption. Therefore, its integration in a sustainable development is decisive. Among the whole renewable fuels one of the best to reduce the present dependence on crude oil is bioethanol. The reason for worldwide interest in bioethanol lies in its numerous advantages. It's a renewable combustible, non toxic, highly soluble and quickly biodegradable. Ethanol can be used as fuel for automobiles either alone or blended with gasoline to reduce the consumption of petroleum fuels. The National Renewable Energy Laboratory in the USA establish that the use of bioethanol blended gasoline results in fall of around 1.85-2.65 Kg CO_2 emissions /L of gasoline. It can also be used as an additive for standard gasoline as ETBE (ethyl tertiary butyl ether), being a replacement for MTBE (methyl t-butyl ether), the most common additive, which use is being limited in the United States owing to its probed groundwater contaminant effect.

Nevertheless, despite the efforts made to decrease the production cost of ethanol, this is still too high compared with petroleum derived fuels. Moreover, the production of bioethanol from the traditional raw materials (starch and carbohydrates) must compete with the food market, so the development of process employing new raw materials is an important challenge in this area. To reduce this cost, lots of researchers have focused on the exploitation of lignocellulosic materials which abundance and low prices would guarantee process self-sufficiency (Sánchez y Cardona, 2007).

However, the main obstacle for the better use of lignocellulosic materials to produce ethanol is their low digestibility because of the tight association between their components: cellulose,

* Corresponding author. Tel + 34 983 423237. E-mail:maite@iq.uva.es

hemicellulose and lignin. It is well known that lignin content have a large impact in enzymatic hydrolysis of lignocellulosic biomass (Palonen, 2004; Mosier, 2005). Vidal and Molinier (1988) shown that the accessibility to the enzyme was inversely proportional to the lignin content. Therefore delignification appears to be necessary to enhance enzymatic saccharification. Cardona and Sánchez (2007) reviews and compare the use of different mature and developing technologies leading to an improvement on the global process.

The different alternatives tested for lignocelluloses pretreatment involve the use of physical, chemical, physicochemical and/or biological methods, e.g. steam explosion, ammonia fiber explosion (AFEX), ozonolysis and wet oxidation (Sun and Cheng, 2002; Silverstein et al., 2007). This research compares ozonization and steam explosion as adequate techniques to the removal and/or degradation of lignin structure, leaving cellulose accessible to enzymes and avoiding toxic wastes which can inhibit the subsequent enzymatic hydrolysis and fermentation processes.

2 Material and Methods

Raw material. Wheat straws were kindly donated by Institute of Technological Agriculture of Castilla y León. The straw was ground in a blender, sieved to obtain the size desired and kept in an oven at 45ºC. The composition range (% w/w) of wheat straw is shown in Table 1.

Table 1. Composition of wheat straw

Composition (% w/w)	
Moisture	9.0 – 6.0
Cellulose (as glucose)	34.2 – 26.7
Hemicellulose (as xilose)	20.1 – 17.5
Acid Insoluble Lignin	17.1 – 23.8
Acid Soluble Lignin	5.2 – 3.8

Ozonolysis Pretreatment. Experimental work was designed to examine the influence of the initially proposed main operation factors [Moisture (M), particle size (S), air/O_3 flow rate (C), ozone concentration (O) and type of biomass (L)] on the percentage of lignin removal during ozone pre-treatment. The ozonolysis was performed in a fixed bed reactor under room conditions. Ground material was firstly hydrated to the required moisture value and exposed to an ozone/air gas stream in the fixed bed reactor (glass column 50 cm in heigh and 2.7 cm in diameter). The ozone production was controlled by varying either the oxygen flow rate or the electrical power supply and its concentration was measured according to the iodometric method (Standard Methods, 1995). Reactor's outlet went past through a 2% KI solution in order to remove the unreacted ozone from the gas stream. The resulting ozone-treated substrate was dried in an oven at 45ºC, stored in a freezer and used for enzymatic hydrolysis and analysis. The experiments were programmed through a 2^{5-1} factorial design in which the variables were evaluated at two levels (Table 2). The study of the influence of main operating factors and their interactions were calculated and exposed in a normal probability plot to draw the most significant process variables. The estimation of the effect is defined as the change in the response that is produced by a change in the level of the parameter.

Table 2. Experimental levels of the parameters studied in ozonation experiments

Factor	Level value	
	Lower (-1)	Upper (1)
Moisture (M) (%w/w)	20	40
Particle size (S) (mm)	<1	3-5
Air/ozone flow rate (C) (L/h)	60	90
Ozone concentration (O) (%w/w)	2.7	3.0

Steam explosion Pretreatment. The steam explosion was carried out in a 5L stainless steel batch reactor in which the straw was loaded at the top and heated to the desired temperature with saturated steam. When the pre-set residence time was concluded, the steam-treated biomass was released from the reactor by rapid depressurization of the vessel. After the pre-treatment, the product was washed with warm water and the residual solid was separated by filtration. Both, solid and liquid portions were dried in an oven at 45ºC, stored in a freezer and used for enzymatic hydrolysis and analysis. The experiments arranged as a 2^{4-1} factorial design. The main process variables selected for this pretreatment being temperature (T), residence time (R), particle size (S) and the use or not of 4,5% w/w SO_2 as acid catalyst (A) as it is shown in Table 3. Results were statistically studied as indicated in ozonolysis experiments.

Table 3. Experimental levels of the parameters studied in steam explosion experiments

Factor	Level value	
	Lower (-1)	Upper (1)
Temperature(T)(ºC)	180	210
Residence time (R) (min)	4	10
Particle size (S) (mm)	3	20
Catalyst (4.5%w/w SO_2) (A)	no	yes

Enzymatic Hydrolysis. The enzymatic hydrolysis was carried out using a mixture of cellulose complex (NS50013) and β-glucosidase (NS50010), both enzymes kindly donated by Novozymes (Denmark). The tests were performed with 0.3 g of freeze stored biomass suspended in 5 mL acetate buffer 0.1 M (pH 4.8), containing 10 FPU g-1 and 10 CBU g-1 of substrate (dry basis) at 50 ºC for 96 h. The flasks were shaken in a rotary incubator at 150 rpm. After the hydrolysis, liquid portion is analyzed for carbohydrates.

Analytical methods. Acid insoluble lignin, acid soluble lignin and carbohydrates were estimated according to NREL laboratory analytical procedures Lap 003, 004 and 002 respectively (NREL, 1995), except that a Bio-Rad HPX-87H ion-exclusion column was used to measure sugar concentration. The mobile phase was 5 mM H_2SO_4 at a flow rate of 0.6 mL min-1 at 60 ºC. The detector was based on the refraction index measurement. Carbohydrates after enzymatic hydrolysis were analyzed by HPLC with the same method indicated before.

3 Results

Ozonolysis Pretreatment. The statistical treatment of the results is collected in Table 4. Capital letters refer to upper level and lower case letters refer to lower level of the analysed variables, the moisture variable presents the most significant effects from the studied parameters working always with identical operation time (2.5 h). According to the factorial design, as the percentage of water content increased, it was observed an increase in the removal of acid insoluble lignin for wheat straw. The rest of the studied parameters didn't have major importance from the point of view of delignification yield and digestibility. However, these parameters have to be taken into account to make this pretreatment feasible from an economical point of view.

Figure 1 represents the normal probability plot, in which the moisture effect gets off from the line that goes through the rest of the points. The content of acid soluble lignin increased after the ozonolysis pre-treatment and some times the total acid lignin content decreased, showing that exist a lignin fraction refractory to the ozonation pre-treatment, as suggested by Neely (1984).

Table 4. Results obtained in the 2^{5-1} experimental design for ozonolysis.

Variables	% AIL (% w/w)	% ASL (% w/w)	Effect estimation		% glucose hydrolyzed (% w/w)
			Parameter	% AIL removed	
msco	11.8	7.3	M	13.9	81,0
MSco	13.5	8.8	MS	-8.3	63,2
MsCo	12.2	10.4	MC	2.1	75,9
msCo	13.5	8.6	C	-0.6	69,3
MscO	11.8	8.6	MO	-4.3	74,8
mScO	14.4	7.1	SO	-8.9	81,3
msCO	13.9	9.7	CO	-16.1	56,4
MSCO	11.2	8.4	MSCO	-0.6	87,1

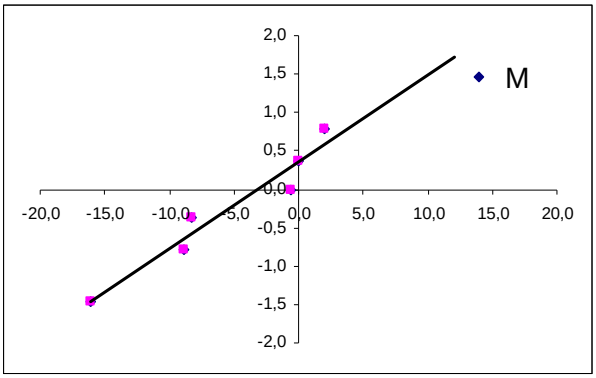

Figure 1. Normal probability plot of the effects of parameters in the ozonation experimental design for AIL variation

The yield obtained after enzymatic hydrolysis of the pretreated samples defined as the percentage of glucose hydrolyzed is shown in Table 4. There is a correlation between the % of glucose hydrolyzed and the acid insoluble lignin concentration. In all cases, when the ozonated materials were hydrolyzed, the yield obtained increased compared with the untreated straw. The enzymatic hydrolysis yield improved from 29% corresponding to untreated raw material to 56.4 – 87.1 % for pretreated wheat straw as the acid insoluble lignin content decreased from 17.1% to 13.9% and 11.7% respectively.

The operating conditions leading the maximum yield on enzymatic hydrolysis were: 40 % of moisture, 3-5 mm of particle size, 90 L/h of ozone and a ozone concentration corresponding the 76% of ozonizator power. These values agree with the higher lignin removal observed.

Steam Explosion Pretreatment. The statistical treatment of the results is shown in Table 5. Capital letters refer to upper level and lower case letters refer to lower level of the analysed variables. At this moment, there are not available results of experiments using the acid catalyst. The residence time variable has the higher influence on acid insoluble lignin removal but however it is not statistically important. The other analysed parameters didn't show major influence from the point of view of delignification yield and digestibility. The acid insoluble lignin values obtained in the different experimental conditions are very similar, no relevant differences are found. The same behaviour has been observed by Cullis et al (2004).

The variation in the content of acid insoluble lignin after steam explosion, in the operating conditions tested, was not significantly different. There is not a clear relationship between %AIL in the steam exploded straw and the yield of the further enzymatic hydrolysis stage.

Table 5. Results obtained in the 2^{4-1} experimental design for steam explosion

Variables	% AIL (% w/w)	% ASL (% w/w)	% glucose hydrolyzed (% w/w)	Effect estimation		
				Parameter	% AIL variation	% glucose hydrolyzed
Trsa	18.6	2.4	48.5	T	5.9	58.1
tRsa	19.4	2.7	23.4	R	-3.8	0.4
trSa	19.7	25.3	23.5	S	1.7	23.5
TRsa	19.5	2.5	34.8	TR	-2.1	10.8
TrSa	17.9	3.7	56.0	TS	5.9	30.1
tRSa	19.4	2.7	23.4	RS	2.9	22.6
TRSa	18.4	1.3	80.9	TRS	-1.3	16.0
trsa	18.7	2.5	31.9	-	-	-

Figure 2 represents the normal probability plot for acid insoluble lignin removal and enzymatic hydrolysis. The effect on %AIL removed did not indicate a clear influence of none of the parameters considered in the experimental design, as it is inferred on the results of %AIL. The effect on the yield of enzymatic hydrolysis is greater and always positive and the temperature seems to be the more influent parameter.

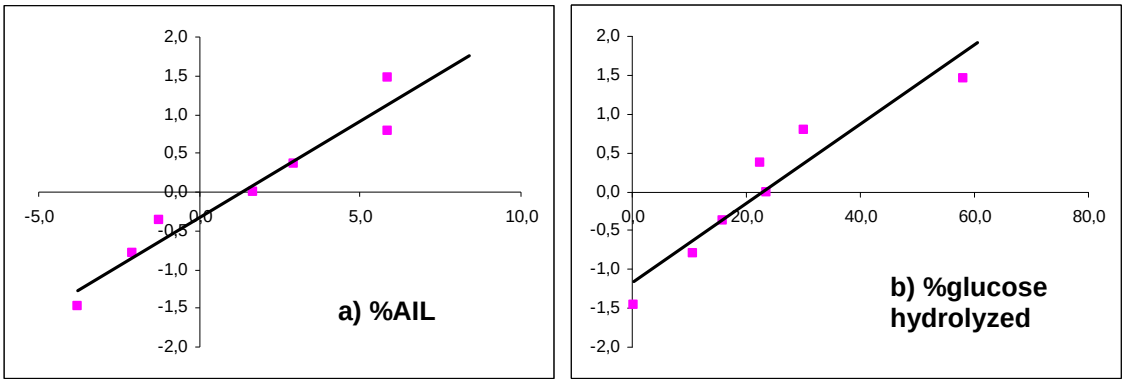

Figure 2. Normal probability plot of the effects of parameters in the steam explosion experimental design for a) AIL variation and b) % glucose hydrolyzed

On the other hand, higher temperature and size particle leads in a higher extent on enzymatic hydrolysis, in accordance with results obtained by Ballesteros et al (2002). The influence of residence time is also positive (higher the time, higher the yield of enzymatic hydrolysis). The enzymatic hydrolysis yield for this pre-treatment ranged in a largest interval from 23.4 – 80.9 % whereas the acid insoluble lignin content varies only from 19.4% to 18.4%.

The operating conditions leading the maximum yield on enzymatic hydrolysis were: temperature of 210 ºC, reaction time of 10 min and particle size of 20 mm.

4 Conclusions

It can be concluded that the maximum yields (87.1 % on glucose) on enzymatic hydrolysis were obtained when wheat straw is ozonized, operating with 40 % of solid moisture, 3-5 mm of particle size and 90 L/h of ozone, whereas a 80.9 % of glucose after enzymatic hydrolysis

was obtained when the raw material was steam exploded at 210 ºC, 20 mm of particle size and 10 min of residence time.

Results derived from the experimental designs reveal different mechanisms to improve cellulose accessibility to enzymes. The ozone degrades and solubilizes the acid lignin content in the biomass, whereas steam explosion seems to open the lignocellulosic structure without significant changes in the lignin composition.

Moreover, ozonolysis has demonstrated to be a very suitable pre-treatment for wheat straw to be used for bioethanol production. More research must be done in this way, in order to have a costly effective pretreatment.

Acknowledgements
The authors acknowledge the financial support of this research to the Instituto Tecnológico de Castilla y León, ITACyL, and to the Ministerio of Ciencia y Tecnología (MCyT, PPQ2006-15217/PPQ).

References

Ballesteros I., Oliva J.M., Negro M.J., Manzanares P. and Ballesteros M. (2002). *Enzymic hydrolysis of steam exploded herbaceous agricultural waste (Brassica carinata) at different particule sizes*, Process Biochem 38, 187–192

Cardona, C.A., Sánchez, O.J. (2007). Fuel ethanol production: Process design trends and integration opportunities. *Bioresource Technology*, 98, 2415-2457.

Cullis, F., Saddler, J. ,Mansfield, S.D. (2004). *Effect of Initial Moisture Content and Chip Size on the Bioconversion Efficiency of Softwood Lignocellulosics*, Biotechnology and Bioengineering,85,20,413-421.

Emmel, A., Mathias, A.L., Wypych, F., Ramos, L.P. (2003). *Bioresource Technology*, 86, 105-115.

Indacoechea I., Bolado S., García-Cubero M.T., Diez R. (2006). *17th International Congress of Chemical and Process Engineering*, Chisa, Prague.

Mosier, N., Wyman, C., Dale, B., Elander, R., Lee, Y. Y., Holtzapple, M., Ladish, M. (2005). *Bioresource Technology*, 96, 673-686.

National Renewable Energy Laboratory (NREL) (1995). *Chemical Analysis and Testing Laboratory Analytical Procedures:* LAP-002, LAP-003, LAP-004. NREL, Golden, CO, USA.http://www.eere.energy.gov/biomass/analytical_procedures.html.

Palonen, H. (2004). Role of Lignin in the Enzymatic Hydrolysis of Lignocellulose. Espoo 2004. VTT Publications 520. 80p. +app. 62p.

Sánchez, O.J., Cardona, C.A. (2007). Trends in biotechnical production of fuel ethanol from different feedstocks. *Bioresource Technology*, doi:10.1016/j.biortech.2007.11.013

Silverstein, R.A., Chen, Y., Sharma-Shivappa, R.R., Boyette, M.D., Osborne, J. (2007). A comparison of chemical pre-treatment methods for improving saccharification of cotton stalks. *Bioresource Technology*, 98, 3000-3011.

Standard Methods for the Examination of Water and Wastewater, 1995. 19th ed. Washington DC., USA., APHA-AWWA-WEF.

Sun, Y., Cheng, J. (2002). Hydrolysis of lignocellulosic materials for ethanol production: a review. *Bioresource Technology*, 83, 1-11.

Vidal, P.F., Molinier, J. (1988). Ozonolysis of lignin-improvement of in vitro digestibility of poplar sawdust. *Biomass*, 16, 1-17.

Proceedings of the 10th International Chemical and
Biological Engineering Conference - CHEMPOR 2008
Braga, Portugal, September 4-6, 2008
E.C. Ferreira and M. Mota (Eds.)

The vegetative cycle of *Lavandula luisieri* – influence on essential oils and antioxidants

Ana Rita B. Mancelos Beirão, M. Gabriela Bernardo-Gil, Humberto E. Ferreira

Centre for Biological and Chemical Engineering, IBB, DEQB, IST,
Av. Rovisco Pais, 1049 – 001 Lisboa, Portugal

Keywords**:** *Lavandula luisieri*, essential oil, antioxidant, Rancimat, peroxide value
Topic: Multi-scale and/or multi-disciplinary approach to process-product innovation

Abstract

The *Lavandula luisieri* was studied in terms of yield and composition of essential oil and antioxidant activity during the vegetative cycle of life. The essential oil was obtained by hydrodistillation (Clevenger apparatus), and the liquid and the solid residues were solvent extracted to obtain extracts, which were studied in terms of antioxidant activity. The composition of essential oils was determined by gas chromatography and confirmed by GC-MS. The main components found included α-pinene, 1,8-cineole and α-terpineol. The antioxidant activity was determined in terms of induction time by the Rancimat method and the peroxide value. The highest value of essential oil yield was 0.59 %, obtained from the plant harvested in September. The extracts with the highest antioxidant activity were obtained from the plant harvested in May.

1. Introduction

A number of reasons point to the need of an in-depth study of the mechanisms of oxidation (rancidity), not only on fats, but more generally in food. Among them, nutritional problems caused by changes in modern life, accompanied by changes in our diet, the evidence of the existence of degenerative diseases in the developed countries caused by a longer but more stressed live, a complex food production market accompanied by a higher quality demand, are some of the reasons that explain the public consumers demands upon scientists ("When do they finally dominate the issue and give some concrete answers?"). But the issues raised are not easy to answer, and seem to become more and more complicated. Antioxidants of synthetic origin introduced in the industry over the last 50 years have become notorious not only to the public, but to some of the scientists. There is growing concern about the safety of synthetic antioxidants, despite their superior efficacy and high stability (Kiokias, Sotirios *et al.*, 2008). Discussion is centered around the advantages and disadvantages of natural and synthetic antioxidants (Pokormý, Jan, 2007), the need to use them, and the ability to resolve the actual anxiety of the public *vis-a-vis* a longer shelf life, but above all a longer human life. In the meantime, antioxidants of plant origin, known since the earlier days of man's culture, regained the right to be restudied and understood, in their composition and plant production technics, with the help of higher resolution scientific instruments of our days, such as liquid and gas chromatography and others related technics. Extraction methods have also been improved, and new methods invented (Esquivel, 1999), so that a new scientific horizon has been created. It joins nutritionists, chemists, pharmacologists, toxicologists, medicinal doctors and agronomic scientists, as well as technical and instrumental engineers, in providing new insights into one of the most ancient puzzles of the world: food science and human health.

The term antioxidant is not restrained by any international accepted definition. However, an antioxidant can be defined as "any substance that in small quantities, normally in concentrations much lower than the oxidizable materials to be protected, is able to prevent or greatly delay its oxidation".

Antioxidants are applied to foods for two different purposes:

- To suppress lipid oxidation and the formation of free radicals under conditions of prolonged storage, heating, frying or deodorization;
- To reduce the concentration of free radicals *in vivo* after food ingestion.

Antioxidants can be of synthetic or natural origin. The use of synthetic antioxidants is restricted in several countries, because of their undesirable long-term toxicological effects, including carcinogenicity (Branen, 1975; Barlow, 1990, Gazzini et al., 1998). As a result, there is a great interest in finding antioxidants from natural sources for food and medicinal applications.

As previously mentioned, the extraction of natural substances with antioxidant activity, to replace synthetic food preservatives has gained great importance (Economou et al, 1991, Esquivel et al., 1999, Ribeiro et al., 2001, Reddy et al., 2005). Extensive research has been dedicated to the identification of antioxidant compounds obtained from natural sources, and the antioxidant activity of many plants has been investigated. However, only rosemary and sage are commercially available as flavourless, odourless, and colourless antioxidant extracts. Previous work shows that the majority of active antioxidant substances occurs in extracts, but some essential oils were also studied to analyze their antioxidant activity, namely essential oil containing thymol and carvacrol, and other phenolic compounds, which exhibit high antioxidative activity. However, these compounds are highly volatile and, when high temperatures are involved, they provide scarce antioxidative protection.

There are several methods for the evaluation of antioxidative action on fats and oils (Frankel and Meyer, 2000; Becker et al, 2004). Some methods are used for the assessment of early oxidative changes (loss of reactants – active oxygen, unsaturated fatty acids; formation of free radicals – ESR detection of spin adducts; and formation of primary oxidation products – peroxide value (POV), hydroperoxides) and late oxidative changes (formation of secondary oxidation products – hydrocarbons, aldehydes, ketones, acids, p-anisidine value, trolox value, TBARS; protein damage – carbonyls, cross-linking). In the Rancimat method the conductivity caused by short-chained acids is measured, after a process of acceleration of oxidation. Rancimat method has some advantages such as being fast and able to study stability at high temperatures, which are important for the use of the antioxidants in food processing (frying). However, the oxidation analysis under these conditions is also pointed out as the principal disadvantage, as significant losses of volatile antioxidants may occur. Furthermore, at high temperatures, marked differences in energies of activation may result in overestimated oxidation levels.

Lavandula luisieri is an aromatic *Labiatae* endemic of the Iberian Peninsula, common in the South of Portugal and in the Southwest of Spain. Sanz et al. (2004) found 1,8-cineole, lavandulol, linalool and their acetates and necrodane derivatives in essential oils of this *Lavandula*, harvested in Spain.

2. Materials and Methods

2.1. Materials

Wild *Lavandula luisieri* was collected from August 2003 until July 2004 in Alentejo (South of Portugal) and was air-dried. Before extraction, leaves and/or flowers were coarsely cut. The particle diameter after size reduction was estimated by using a sieving machine Retsch KS 1000 (Retsch, Haan, Germany), being the medium particle diameter calculated as 0.3 mm. All the chemicals were obtained from several suppliers, but they were of the highest purity available.

2.2 Methods

2.2.1 Extraction of essential oil

The essential oils of *Lavandula luisieri* were obtained by using a modified Clevenger apparatus. About 100 g of dried plant powder (leaves and/or flowers) were used and the distillation was conducted for 4h. The amount of recovered oil was measured gravimetrically.

2.2.2. Solvent extraction

Both the solid residue and the liquid residue of Clevenger distillation were used for preparation of extracts with eventual antioxidant activity by using the method described by

Ribeiro et al. (2001). The ground solid residues were boiled with distilled water for about 2 h, and then filtered through a coffee filter paper. The collected filtrate was acidulated with a solution of HCl 25% to a pH 2.5 and filtered. The aqueous phase was shaken with diisopropilether (10:3) and allowed to separate. The upper aqueous layer was extracted twice more with diisopropilether. The organic phases were combined, dried with anhydrous $MgSO_4$, filtered, and evaporated using a rotary evaporator (Heidolph VV2000).

2.2.3. Analysis of essential oils

The essential oils were analysed by gas chromatography (GC) on a Hewlett-Packard 5890 Series II chromatograph equipped with a FID detector and a DB5 column (5% phenyl, 95% dimethylpolysiloxane), 0.32 mm id x 50m, film thickness 0.17 μm. The column oven temperature was programmed to hold at 60 ºC for 10 minutes, then heated to 180 ºC at a slope of 2 ºC/min, with a final isothermal hold at 180 ºC for 30 minutes. Injector and detector temperatures were 200 and 250ºC, respectively. Nitrogen carrier gas was adjusted to a linear velocity of 2 ml/min. Aliquotes of 0.2 μl were injected using the split mode (split ratio 1:20).

The sample components were identified by comparing the retention times with those of chromatographic standard of the compounds (Sigma-Aldrich, Madrid, Spain). Peak areas were determined using a Hewlett-Packard 3396 Series II integrator. For quantitative analyses, the peak areas were converted to absolute values using response factors estimated from the calibration curves of the standard compounds. Results were compared to those obtained by GC-MS.

2.2.4. Rancimat method

Rancimat method (Metrohm Rancimat 679) was used for detection and estimation of the antioxidant activity. Sample extracts dissolved in sunflower oil (7.0 g), with concentrations varying from 0 to 4000 ppm, were heated at 110 ºC. A continuous air stream (20 L/h) was passed through the heated samples, and the volatile compounds were absorbed in a conductivity cell. Conductivities were continuously monitored until a sudden rise appears. The oxidative stability was determined as the time corresponding to the inflection point of the curve, named the induction time (IT). Protection factor (PF) was determined by the ratio between the induction period found for the sunflower oil with a certain quantity of extract and the induction time obtained for sunflower oil with no addition of extract.

2.2.5. Peroxide value

The peroxide value (PV) was expressed as mEq of oxygen / kg of fat, and was determined by the iodine titration method. Extracted oil samples (2 g) were weighed into test tubes. The oxidation of the potassium iodide, in acetic medium, by the active oxygen of the fat is followed by titration of the free iodine with sodium thiosulphate, using starch as an indicator. The evolution of the peroxide value with storage time was studied.

2.3 Results and Discussion

2.3.1 Essencial oils

Table 1 summarizes the major components of the *Lavandula luisieri* essential oil obtained from plants harvested in May 2004. The yields obtained, in terms of grams of essential oil per 100 g of plant were 0.12 % from flowers and 0.3 % from leaves + flowers. The main antioxidative component present is α-Terpineol, either when the essential oil was obtained from flowers only or from flowers + leaves. The content in 1,8-Cineole and α-Pinene is higher in leaves than in flowers. On other hand, the content of viridiflorol is higher in flowers than in leaves. Figures 1 and 2 show seasonal variations of the major antioxidative components in essencial oil.

Components	Mass percentage	
	Flowers	Flowers + Leaves
α-Pinene	2.85	8.47
α-Terpinene	1.22	2.51
Limonene	0.33	0.43
1,8-Cineole	4.00	16.6
Linalool oxide	0.96	1.76
Fenchone	1.91	3.67
Terpinolene	0.79	1.16
Camphor	8.92	1.91
Borneol	2.24	2.16
Menthol	2.15	2.01
Dihydrocarveol Acetate	1.63	1.60
Lavandulil Acetate	1.71	1.31
Eucarvone	5.00	4.41
Menthatriene	2.15	1.84
α-Terpineol	13.85	17.15
Carvacril Acetate	1.21	1.07
Eugenol	2.01	0.74
β-Caryophyllene	1.48	0.84
Viridiflorol	6.77	2.97

Table 1. Some components of essential oils obtained from flowers and flowers + leaves of *Lavandula luisieri* harvested in May.

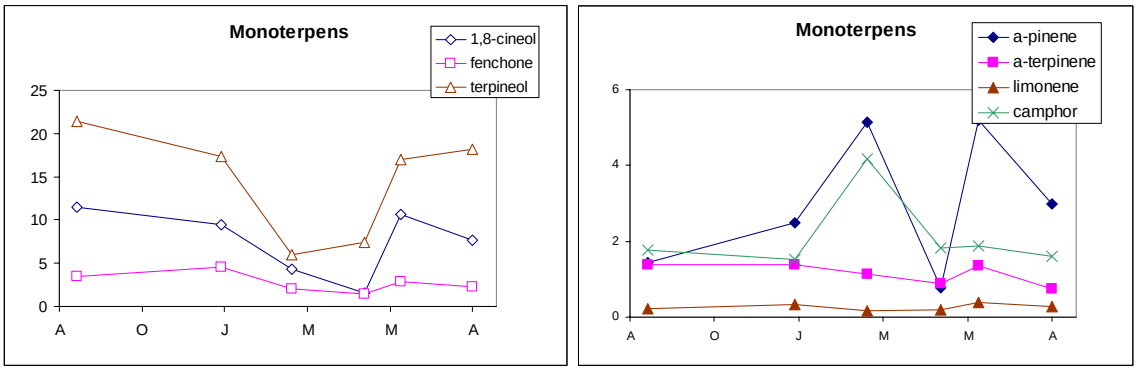

Figure 1 and 2 – Variation of monoterpene composition along the vegetative cycle. From left to right, the months represented are August, October, January, March, May and August again. Amounts are expressed as mass percentage of the extract.

2.3.2 Diisopropylether Extracts

After the solvent extraction of essential oils by 'Clevenger distillation' the liquid and solid residues left were extracted with diisopropilether. Yields, in terms of grams of antioxidative extract per 100 g of plant were 2.10 % and 0.39 %, respectively for the extraction from liquid and solid residues. The yields obtained from the plants harvested in June 2004 were 2.7 % for the extraction from the Clevenger distillation' liquid residue, and 0.24 % for the solid residue.

Figures 3 and 4 show the protection factor results of extracts, obtained from solid and liquid residues of Clevenger distillation, of plant harvested in May and June, respectively. In general, liquid residues presented higher antioxidant activity than solid residues, although the differences in results are not statiscally significant.

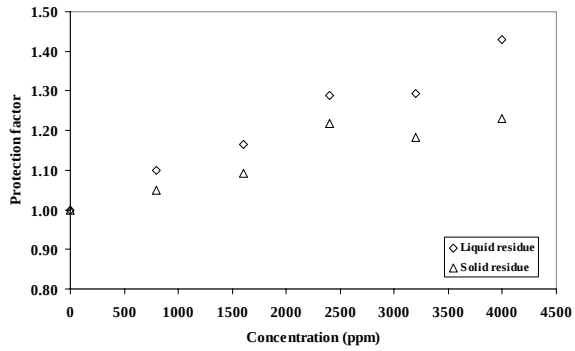

Figure 3. Protection factors of extracts obtained from liquid and solid residues of Clevenger distillation of *Lavandula luisieri* harvested in May.

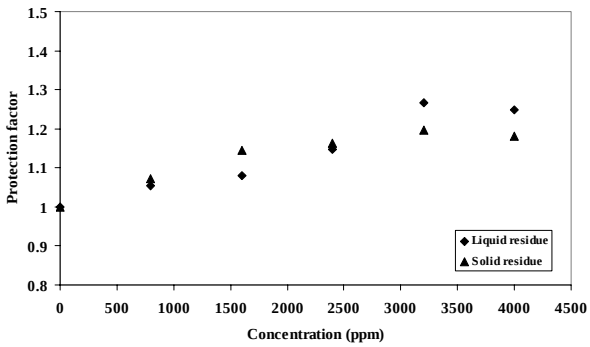

Figure 4. Protection factors of extracts obtained from liquid and solid residues of Clevenger distillation of *Lavandula luisieri* harvested in June

The evolution of the oxidation process (peroxide value) of the sunflower oil was followed in 4 different storage conditions: under direct sunlight exposure at room temperature, simulating shelf exposure; in the dark at 4ºC (refrigerator); under indirect natural light at room temperature (20-22ºC); and under artificial light at room temperature (15-18ºC). For each one of these 4 storage conditions, 3 essays were conducted in parallel: one with sunflower oil only (reference, blank essay); another with sunflower oil spiked with 4000 ppm of the antioxidative plant extracts (*Lavandula luisieri)*; and a third with sunflower oil spiked with butylated hydroxytoluene (BHT, 4000 ppm). Several aliquotes of these 3 essays were taken over time, and titrated as described previously under section 2.2.5 to obtain the peroxide value. Similar essays were conducted with extracts obtained from plants harvested during March, May, June. The results of the June extracts are presented in Figures 5 to 8.

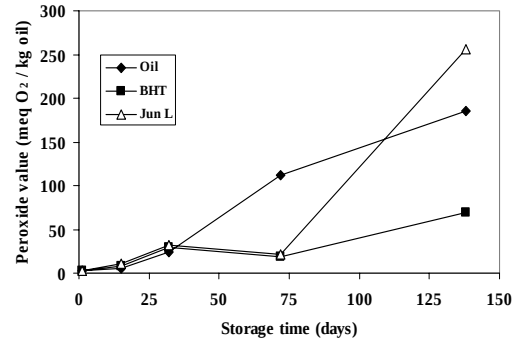

Figure 5. Peroxide values of sunflower oil (Oil), of sunflower oil with BHT, and sunflower oil with *Lavandula luisieri* extract, obtained from plant harvested in June, during storage at sun exposure.

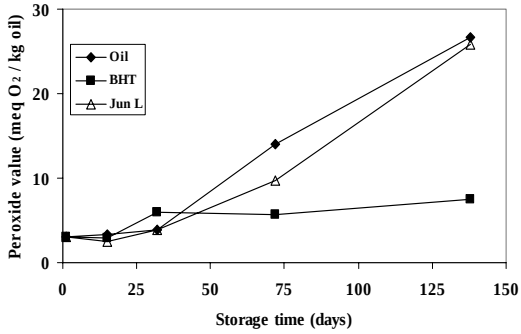

Figure 6. Peroxide values of sunflower oil (Oil), of sunflower oil with BHT, and sunflower oil with *Lavandula luisieri* extract, obtained from plant harvested in June, during storage in refrigerator.

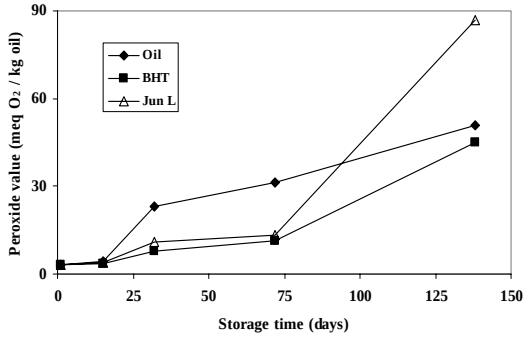

Figure 7. Peroxide values of sunflower oil (Oil), of sunflower oil with BHT, and sunflower oil with *Lavandula luisieri* extract, obtained from plant harvested in June, during storage at natural light.

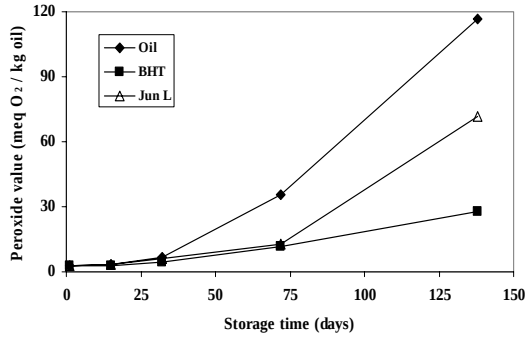

Figure 8. Peroxide values of sunflower oil (Oil), of sunflower oil with BHT, and sunflower oil with *Lavandula luisieri* extract, obtained from plant harvested in June, during storage at artificial light.

As it was expected, the oil samples stored under direct sunlight exposure at room temperature, presented higher peroxide values than all the other storage conditions, since the oxidative process occurs through radical formation, a process known to be enhanced by UV light. Furthermore, direct sun exposure seems to alter the plant antioxidative molecules that are supposed to reduce oxidation, as can be seen in Figure 6 above 75 days. The peroxide value of the oil plus *Lavandula luisieri* extract increased its oxidation drastically, from the 75th day onward, supplanting the peroxide value of the oil alone, in the conditions of storage at sun exposure.

Storage under artificial light at room temperature (15-18ºC) showed that the *Lavandula luisieri* extract prevented the oil oxidation as well as BHT, until, at least, 75 days of storage (Figure 8).

2.3.3 Plant extracts obtained under new alternative experimental conditions

Components of the plants of May, June and July were extracted with alcohols under a sonication protocol and analysed by HPLC (Wang *et al*, 2004) to identify fenolic acids. Using comparisons with standards, it was possible to identify the presence and quantitate rosmarinic and caffeic acids(Figure 9). A correlation has been found between Protection Factor of the samples and the quantity of rosmarinic acid present in extracts (Figure 10).

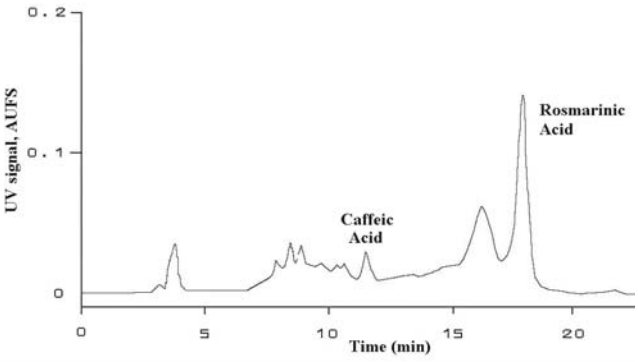

Figure 9 –HPLC chromatogram of the June extract

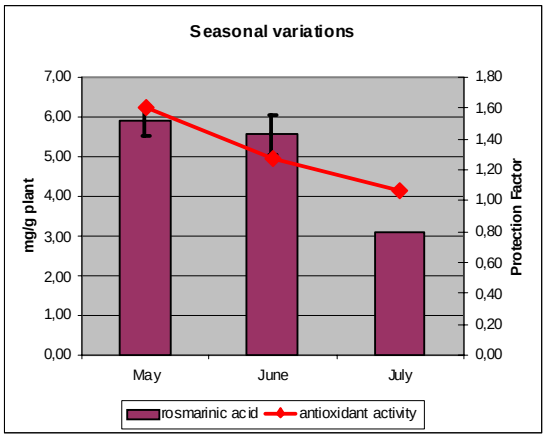

Figure 10 – Correlation between quantity of rosmarinic acid and Protection Factor

This result highlights the possibility that rosmarinic acid may be one of the substances responsible for the antioxidant activity of *Lavandula luisieri*. Further efforts are required to confirm the results, and to improve the analytical method, both in terms of increasing the antioxidant extraction yield and to better resolve and identify de various unknown components of the extract by HPLC-MS-Electrospray.

References

Atoui, A.K.; Mansuri, A.;Boskon, G.;Kefalas,P. (2005) Tea and herbal infusions: Their antioxidant activity and phenolic profile *Food Chemistry*,89(1),27-36

Becker, E. M., Nissen, L. R., Skibsted, L. H. (2004). Antioxidant evaluation protocols: food quality or health effects, *Eur. Food Res. Technol.*, 219, 561-571.

Economou, K. D., Oreopoulu, V., Thomopoulos, C. D. (1991). Anti-oxidant activity of some plant extracts of the family *Labiatae*, *JAOCS* 68, 109-113.

Esquível, M. M., Ribeiro, M. A., & Bernardo-Gil, M. G. (1999). Supercritical extraction of savory oil: study of antioxidant activity and extract characterization. *Journal. Supercritical Fluids, 14*, 129-138.

Frankel, E. N., & Meyer, A. S. (2000). The problems of using one-dimensional methods to evaluate multifunctional food and biological antioxidants. *Journal Science Food Agriculture, 80*, 1925-1941.

Kiokias, Sotirios et al.(2008). In Vitro Activity of Vitamins, Flavonoids, and Natural Phenolic Antioxidants Against the oxidative Deterioration of Oil-based Systems. .*Critical Reviews in Food Science and Nutricion,* 48:78-93

Pokorný, Jan (2007). Are naturel antioxidants better – and safer – than synthetic antioxidants? *Eur.J.Lipid Sci. Technologie* 109 (2007) 629-642

Reddy, V., Urooj, A., Kumar, A. (2005). Evaluation of antioxidant activity of some plant extracts and their application in biscuits. *Food Chemistry, 90*, 317-321.

Ribeiro, M. A., Bernardo-Gil, M. G., & Esquível, M. M. (2001). *Melissa Officinalis* L.: Study of antioxidant activity in supercritical residues. *Journal Supercritical Fluids, 21*, 51-60.

Wang, H., Provan, G.J.;Helliwell, K..(2004) Determination of rosmarinic acid and caffeic acid in aromatic herbs by HPLC*, Food Chemistry, 87, 307-311*

Proceedings of the 10th International Chemical and
Biological Engineering Conference - CHEMPOR 2008
Braga, Portugal, September 4-6, 2008
E.C. Ferreira and M. Mota (Eds.)

Pectin extraction from guavas using response surface methodology

Cláudia L. Munhoz[1*], Eliana J.Sanjinez-Argandoña[2], Manoel S. Soares Júnior [3]
[1] IAGRO – State Agency Defense Animal and Plant, 79710-000, Vicentina, MS, Brasil.
[2] UFGD – University Federal of Great Dourados, 79804-970, Dourados, MS, Brasil.
[3] UFG – University Federal of Goias, 748001-970, Goiania, GO, Brasil

Keywords: Pectin, Extraction acid, Guava
Topic: Multi-scale and/or multi-disciplinary approach to process-product innovation. Integration of life sciences & engineering.

Abstract

Extraction of natural hydrocolloid carbohydrate polymers, such as pectin, from de surplus of the crop of fruits becomes interesting commercially. Thus, the extraction of pectin from guavas pulp and pulp with peel was carried out in an aqueous acid medium under different concentrations using a experimental design for two extraction parameters (acid concentration and time). Considering the efficiency, the economization of energy and the feasibility of experiment, the optimum conditions of pectin extraction were extraction time 60 min and citric acid solution 5%, getting up yield of extracted pectin from guavas pulp and pulp with peel the range of 12–13.65% and pectin of low degree of esterification.

1 Introduction

Pectin is a polysaccharide composed of molecules of acid galacturônico united by glycosidic alpha-(1.4) and neutral sugars that contribute to the structure of the fruit. Pectins obtained have different characteristics, which vary according to their origin, allowing for wider use in industry (Willats; Knox; Mikkelsen, 2006).

The raw material commonly used is the citrus peel or apple pomace (May, 1990). Studies of new sources have been the target of several searches, particularly of fruits and agro-industrial waste. The guava (*Psidium guajava* L.), considered a source of pectin, is a fruit with high rates of post-harvest loss (Linhares et al., 2007), allowing its use for that purpose.

The process of extraction of pectin covers the steps of extraction, separation and drying. The extraction can be performed with acids, bases or enzymes, and the most common procedure acid. The factors that influence the efficiency of extraction are the type and concentration of acid, temperature and time of extraction (May, 1990). However the use of inorganic acids, as HCl and HNO_3, generate waste pollutants. A viable alternative could be the use of organic acids such as citric acid.

The research aimed to extract pectin from the pulp and the pulp with peel of flour of red guavas *cv* Pedro Sato, and characterized by degree of esterification.

2 Materials and methods

2.1 Materials

Red guavas (*Psidium guajava* L.) *cv* Pedro Sato were acquired in the district of Santa Terezinha, Itaporã city, MS state, Brazil.

The fruits were washed and sanitized with dichloro s. dicloro s. triazinatriona sodium dihydrate (Sumaveg), the concentration of 0.66% per 10 min. Then the fruits were separated into two lots and broke up pulp and pulp with peel for further drying in stove. The fractions

* Corresponding author. Tel + 55-67-34681169. E-mail:clmunhoz@yahoo.com.br

were dried in stove with forced movement of air at 55 ºC for 72 hours until moisture of 12.55 and 13.24% for pulp and pulp with peel, respectively. The fractions were ground into mill knives (Marconi), to obtain the flour and stored in glass containers tightly closed. All reagents used in the analyses were analytical grade.

2.2 Experimental design

The composed central rotational design 2^2 with four axial points and three replicates in the central point was applied to obtain the yield on the extraction of pectin (Table1). The independent variables were the concentration of citric acid (g $L)^{-1}$ and the time of extraction (min). Tests were conducted with two repetitions and random.

Table 1. Matrix of experimental design.

Test	Variables coded		Variables original	
	Acid (%)	Time (min)	Acid (%)	Time (min)
1	-1	-1	3.5	35
2	1	-1	6.5	35
3	-1	1	3.5	85
4	1	1	6.5	85
5	-1.414	0	3	60
6	1.414	0	7	60
7	0	-1.414	5	25
8	0	1.414	5	95
9	0	0	5	60
10	0	0	5	60
11	0	0	5	60

2.3 Extraction of the pectin from the pulp and pulp with peel of flour of guava

The extraction of pectin was performed in acidic medium with the citric acid. Samples were taken of each flour (4 g) and dissolved in 200 ml of distilled water. The extractions were performed to 97 ºC under different experimental conditions of concentration of citric acid (3.5-7.0%) and time (25-95 min). After extraction, the samples were cooled to 4 ºC for two hours, once filtered. The residue of filtered, containing pectin, was precipitated with ethanol (95%) in the proportion of 1:2 (one part of the residue and two parts of ethanol). After one hour of rest, the pectin precipitated was separated by filtering and dry in stove at 55 °C until weight constant. The yield of pectin was calculated from the initial quantity of raw material (Equation 1):

$$Yield = \frac{pectin_{extracted} \times 100}{mass_{flour\,(dryed)}} \qquad \text{Equation (1)}$$

Where $\text{pectin}_{\text{extracted}}$ is the mass of pectin obtained after extraction and drying in grams and $\text{mass}_{\text{flour (dryed)}}$ is the mass of sample on dry basis in grams.

2.4 Titration characterization of pectin

Samples of pectin obtained in experimental conditions 5 g (100 g $)^{-1}$ and time of 60 min were quantified by titration the content of acid galacturonic and the degree of esterification (Wang; Pagan; Shi, 2002 Apud Fertonani, 2006).

2.5 Analyses of results

The data were statistically assessed by average, standard deviation and coefficient of variation, analysis of variance and Tukey test in the level of 5% probability.

3 Results and discussion

3.1 Pectin extraction

Table 2 shows the average yields of pectin extracted from the pulp and pulp with peel of flour of guava.

Table 2. Yields of extraction of pectin obtained from the flours of pulp and pulp with peel guava by experimental planning.

Experiment	Pulp [g (100 g)$^{-1}$]	Pulp with peel [g (100 g)$^{-1}$]	Independent variables	
			Acid [g (100 g)$^{-1}$]	Time (min)
1	7.83^{c}	7.31^{e}	3.5	35
2	13.64^{a}	10.57^{b}	6.5	35
3	9.38^{b}	8.87^{c,d,e}	3.5	85
4	12.90^{a}	10.64^{b,c,d}	6.5	85
5	9.56^{b}	8.49^{d,e}	3	60
6	13.66^{a}	13.24^{a}	7	60
7	7.91^{c}	5.91^{f}	5	25
8	12.77^{a}	12.85^{a,b}	5	95
9	12.52^{a}	11.41^{a,b}	5	60
10	12.75^{a}	11.81^{a,b}	5	60
11	12.44^{a}	11.36^{a,b,c}	5	60

*Letters equal columns do not differ statistically between them (P>0,05).

The average yields of pectin extracted from pulp of flour of guava *cv* Pedro Sato ranged from 7.83-13.66 g (100 g)$^{-1}$. The yields obtained in the concentrations of citric acid from 5 to 7 g (100 g)$^{-1}$ (experiments 2, 4, 6, 8, 9, 10 and 11) did not differ ($P > 0.05$) between them, but differed ($P \leq 0.05$) than of 3 and 3.5 g (100 g)$^{-1}$. In these experiments were the biggest yields of pectin. The lowest yields were found in experiments 1 and 7. It appears that the increased concentration of the acid gradually affected the yield of extraction.

The analysis of variance of the results of yields from pectin extraction from pulp of flour of guava (Table 3) shows the effects linear, quadratic and the interaction of variables: concentration of acid and time of extraction. The linear and quadratic effects of variable time and the linear effect of variable acid, in the yield of extraction of pectin, were significant, which leads to the conclusion that both the acid as the time of extraction influence the yield of extraction of pectin. However, relatively long time of extraction may degrade the pectin, reducing the amount of waste being precipitated by alcohol due to the formation of a gel weak, during final precipitation (Pagan et al., 2001), and higher concentrations of acid may degrade the pectin. According Fertonani (2006) pectin extracted with high concentrations of citric acid can drag other compounds or may also occur to link of citric at pectic structure precipitate in ethanol. Canteri-Schemin et al. (2005) on the extraction of pectin from apple pomace using tartaric, malic, citric, phosphoric, sulfuric, nitric and hydrochloric acid, had greater yields from the citric acid to 97 ºC in a time ranging from 10 to 210 min and concentration of 0.05 to 9.95 g (100 mL)$^{-1}$.

Tablea 3. Analysis of variance of yield of pectin extraction from pulp and pulp with peel of flour of guava *cv* Pedro Sato depending on the concentration of citric acid cítrico [g (100 g)$^{-1}$] and the time of extraction (min)

Factor analysis	Sum squares	Degrees of freedom	Square average	F	P
(1) Acid (L)	**57.98**	**1**	**57.98**	**71.60**	**0.0001**
Acid (Q)	2.64	1	2.64	3.26	0.0896
(2) Time (L)	**14.63**	**1**	**14.63**	**18.07**	**0.0006**
Time (Q)	**14.15**	**1**	**14.15**	**17.98**	**0.0006**
1L by 2L	2.62	1	2.62	3.24	0.0907
Residue	10.78	16	0.674		
Total	102.80	21			

Coefficients in bold are significant.

In tests, from the planning, it was found that there was better training of the gel (visually observed by its firmness) to the concentration of 5 g (100 g)$^{-}$ de citric acid and time of extraction of 60 min. So, as this condition, there was no significant difference in average yield obtained from the use of higher concentrations of acid and longer time, it was concluded that this condition is the combination better suited for obtaining pectin with good yield.

The yields of pectin extraction obtained from the pulp with peel of flour of guava are also shown in Table 2. The amounts found ranged from 5.91-12.85 g (100 g)$^{-1}$. The experiments 6, 8, 9, 10 and 11 provided the highest yield, whose values are in the range of 11.36 to 13.24 g (100 g)$^{-1}$, with no significant difference ($P > 0.05$) among themselves.

Table 4 presents the analysis of variance of yield of pectin extraction from pulp with peel of flour of guava.

Table 4. Analysis of variance for adjusted model of yield of pectin extraction from pulp with peel of flour of guava *cv* Pedro Sato depending on the concentration of citric acid [g (100 g)$^{-1}$] and time of extraction (min)

Factor analysis	Sum of squares	Degree of freedom	Square average	F	P
(1) Acid (L)	**34.15**	**1**	**34.15**	**25.68**	**0.0002**
Acid (Q)	3.46	1	3.46	2.60	0.1500
(2) Time (L)	**32.44**	**1**	**32.44**	**24.39**	**0.0003**
Time (Q)	**18.36**	**1**	**18.36**	**13.80**	**0.0030**
1L by 2L	1.11	1	1.11	0.83	0.4040
Residue	21.28	16	1.33		
Total	110.80	21			

Coefficients in bold are significant.

The results obtained by analysis of variance show that the linear effects of concentration of citric acid and time of extraction, and the quadratic effect of variable time were significant ($P \leq 0.05$). The other effects were not significant ($P > 0.05$).

The yield on the extraction of pectin from the pulp with peel of flour of guava was higher concentrations of 5 and 7% of citric acid, except for the experiment 7 (Table 2). In experiments with 6.5% of acid the yield was lower, probably the time of 35 min was not enough for extraction of pectin, as also observed in the extraction of acid with 5% and 25 min of extraction. For concentrations greater than 6.5% of the time extraction seems positively influence, as noted for the extraction of pectin the pulp of flour of guava, but depending on the temperature of extracting more time could lead to degradation of pectin (Pagan et al., 2001). From the above, the concentration of 5 g (100 g)$^{-1}$ citric acid and extraction of time of 60 min was also considered the best condition for extraction of pectin.

The use of peel of plants in the extraction of pectin is little studied. Kliemann (2006)), in samples of peel of yellow passion fruit with and without flavedo, won best performance of pectin in conditions for extraction of 90 °C, pH of 1.2 with citric acid for 10 min. Kalapathy and Proctor (2001) studied the acquisition of pectin from the peels of soybeans, the authors assessed the efficiency of extraction using hydrochloric acid in concentrations of 0.06 to 0.18 g. 100 g^{-1} (0.05 e 0.3 N) and found that the higher incomes (17 and 19%) were obtained at concentrations 0.06 e 0.12 g. 100 g^{-1} with no significant difference between both concentrations.

3.2 Characterization of pectin

The characteristics of quality of pectins are presented in Table 5. For galacturonic acids, despite the values make a significant difference ($P \leq 0.05$), they are close to the minimum percentage of galacturonic acid (65%) to commercial pectin established by the FAO (Food and Agriculture Organization of the United Nations).

Table 5. Titration quality of pectin extracted from pulp and pulp with peel of flour of guava with citric acid 5 g (100 g)$^{-1}$, time of extraction of 60 min at 97 ºC and of commercial pectin

Pectin	**Galacturonic acid (%)**	**Degree of esterification (%)**
Pulp	64.88 ^{C} ± *0,11*	38.94 ^{B} ± *1,50*
Pulp with peel	68.84 ^{B} ± *0,77*	40.99 ^{B} ± *1,30*
Commercial	75.38 ^{A} ± *0,54*	72.01 ^{A} ± *1,27*

Averages followed by the superscripted letters in the same column do not differ at the level of 5% probability by Tukey test

Pectins obtained in this study were considered low-esterification (38.94% and 40.99%) and are characterized how pectins of low levels of esterification and can form gels stable in the absence of sugar, but require the presence of bivalent ions. Compared with pectins of high power of esterification, are less sensitive to changes in pH, can form gels in the range of pH 2.6-6.0. It can be stated as a thickener and stabilizer in food emulsions (Sharma; Liptay; Le Marguer, 1998; Yapo et al. 2007). Calliari (2004) obtained similar value (37.50%) for pectin extracted with citric acid from orange pomace, under the conditions of 4% of pomace, 3.5% of citric acid at 75 °C. Kliemann (2006) also extracted pectin low-esterification (45.94%) using citric acid in pH 1.2 to 90 ºC for 10 min in the extraction of peel of passion fruit. Marcon et al. (2005) extracted pectin of low esterification (14.3% to 29.4%) from apple pomace, with citric acid to 5%, times of extraction between 30-80 min and temperatures between 50-100 °C. (2005).

4 Conclusion

The best condition for the pectin extraction from pulp and pulp with peel of flour of guava was: concentration acid 5 g (100 g)$^{-1}$ and time of extraction of 60 min, in that condition the yield around 11 %.

Pectins extracted obtained under the best conditions for extraction, from pulp and pulp with peel of flour of guava showed up low-esterification with degree of esterification of 38.94% and 40.99% respectively. However, the concentration of galacturonic acid was close to the standard commercial.

References

Calliari, C.M. (2004). *Extração térmica, química e enzimática de pectina de bagaço de*

laranja. Tesis, Universidade Estadual de Londrina, Londrina.
Canteri-Schemin, M.H., Fertonani, H.C.R., Waszczynskyj, N., Wosiaki, G. (2005). Extraction of pectin from apple pomace. *Brazilian Archives of Bbiology and Technology,* 48 (2), 259-266.
Fertonani, H.C.R. (2006). *Estabelecimento de um modelo de extração ácida de pectina de bagaço de maçã.* Tesis, Universidade Estadual de Ponta Grossa, Ponta Grossa.
Food and Agriculture organization of the United Nations. *Health (emulsifiers, stabilisers, thickeners and gelling agents in food) regulations 1994.* (FAO). Disponível em:<http://www.fao.org.com>. Acesso em: 15.12.2007.
Kalapathy, U., Proctor, A., (2001). Effect of acid extraction and alcohol precipitation conditions on the yeld and purity of soy hull pectin. *Food Chemistry,* 73 (4), 393-393.
Kliemann, E. (2006). *Extração e caracterização da pectina da casca do maracujá amarelo (Passiflora edulis flavicarpa).* Tesis, Universidade Federal de Santa Catarina, Florianóplois.
Linhares, L.A., Santos, C.D., Abreu, C.M.P., Corrêa, A.D. (2007). Transformações químicas, físicas e enzimáticas de goiabas Pedro Sato tratadas na pós-colheita com cloreto de cálcio e 1-metilciclopropeno e armazenadas sob refrigeração. *Ciência e Agrotecnologiay,* 31 (3), 829-841.
Marcon, M.V., Vriesmann, L.C., Wosiaki, G., Beleski-Carneiro, E. (2005). Pectins from apple pomace. *Polímeros: Ciência e tecnologia,* 15 (2), 127-129.

May, C.D. (1990). Industrial pectins: sources, production and applications. *Carbohydrate polymers,* 12 (15), 79-99.
Pagán, J.; Ibarz, A.; Llorca, M.; Pagán, A.; Barbosa-Cánoas, G. V. (2001). Extraction and chacarterization of pectin from stored peach pomace. *Food Research International,* 34 (7), 605-612.
Sharma, S. K.; Liptay, A.; Le Marguer, M. (1998). Molecular characterization, physico-chemical and functional properties tomato fruit pectin *Food Research International,* 30 (7), 543-547.
Willats, W. G. T.; Knox, J. P.; Mikkelsen, J. D. (2006). Pectin: new insights into and old polymers are starting to gel. *Trends in Food Science & Technology,* 17 (3), 97-104.
Yapo, B. M.; Robert, C.; Etienne, I.; Wathelet, B.; Paquot, M. (2007). Effect of extraction conditions on the yield, purity and surface properties of sugar beet pulp pectin extracts. *Food Chemistry,* 100 (4), 1356-1364.

Proceedings of the 10th International Chemical and
Biological Engineering Conference - CHEMPOR 2008
Braga, Portugal, September 4-6, 2008
E.C. Ferreira and M. Mota (Eds.)

Study on persimmons (*Diospyrus kaki* L.) fruit osmotic dehydration treatments

Paulo M. Castro[1], Eliana J. Sanjinez-Argandoña[2], Iriani R. Maldonade[2]
[1]Departamento de Engenharia de Alimentos, Universidade Estadual do Centro Oeste (UNICENTRO), CEP 85010-990, Guarapuava-PR, Brasil.
[2]Faculdade de Ciência Exatas e Tecnologia (FACET), Universidade Federal da Grande Dourados (UFGD), CP 533, CEP 79804-970, Dourados-MS, Brasil.

Key words: Osmotic dehydration, *Diospyrus kaki* L., mass transfer, Reynolds Number, response surface methodology
Topic: Multi-scale and/or multi-disciplinary approach to process-product innovation. Integration of life sciences & engineering.

Abstract

The dehydration of persimmon fruit (*Diospyrus kaki* L.*)* using osmotic process in sugar solutions was studied. Weight reduction, water loss and solid gain were obtained as a function of the temperature (40, 50 e 60ºC) and immersion time (60, 180 e 300 min) in order to choice the best conditions of the osmotic process. Response surface methodology was used to estimate the effects of osmotic dehydration treatments and to optimize those conditions. The best osmotic treatment was at 40ºC during 4 hours of immersion.

1 Introduction

In Brasil, great part of fruits and vegetables produced is lost in the production centers for not using efficient techniques, which assure a longer time of shelf life. The non-processed fruits are sufficiently perishable, their losses postharvest, in the developed countries, not exceed 20% of total production. On persimmon fruit production, specifically, the high perishability of these fruits and the local market, make the demand lower than the offer, causing collapse of prices and diverse losses for the farmer, in the short period of harvest (Brackmann et al., 2006). Thus, the search of alternative methods to minimize these losses is constant. The effect of osmotic dehydration, as pre-treatment, on fruits conservation methodology, is mainly related to the improvement of its nutritional, sensorial and functional properties. The type and degree of alteration in the composition of the osmotic dehydrated fruit depend, specially, on: the intrinsic characteristics of the fruit, the posterior process of conservation and the desired qualitative characteristics (Torreggiani and Bertolo, 2001). The knowledge of mass transfer rates on persimmon osmotic system between the fruit and the dehydrated solution can improve nutritional and sensorial properties to the fruit. The goal of this work was to: construct a system of osmotic dehydration with recirculation of the drying solution; dehydrate slices of persimmon osmotically in the system with recirculation; determine the mass transfer parameters and determine the best condition of osmotic treatment.

2 Material and methods

Persimmon fruits (*Diospyrus Kaki* L.) of variety Fuyu, from the same orchard, were supplied in the local market by the same provider. They were chosen in accordance to size, appearance (healthy fruits), shape and degree of maturation (mature, however firm), in order to get more homogeneous samples. Sugar (sucrose) was commercial provided by Açúcar União (Brasil). Persimmon samples had the rind and seeds

removed, cut into slices of 1 cm of thickness, and then washed with water and dried with absorbent paper, before being submitted to the osmotic process. The samples were weighed, placed on polypropylene trays and put into the osmotic solution (60ºBrix), previously warmed at 40ºC. The flow of the solution was established by a peristaltic bomb with outflow of 0,003 L/h, to guarantee the contact of the sample with the solution. The weight reduction (WR), water loss (WL) and solid gain (SG) at different time of dehydration had been calculated according to equations 1, 2 and 3:

$$PM(\%) = 100 \times \left(\frac{m_i - m_t}{m_i} \right) \quad (1)$$

$$PA(\%) = 100 \times \left(\frac{m_i \cdot X_{bu_i} - m_t \cdot X_{bu_t}}{m_i \cdot X_{bu_i}} \right) \quad (2)$$

$$GS(\%) = 100 \times \left(\frac{ART_t - ART_i}{ART_i} \right) \quad (3)$$

Where: $\mathbf{m_i}$ e $\mathbf{m_t}$ the total mass of sample at the initial time and at time (t), respectively; $\mathbf{X_{bu}}$ e $\mathbf{X_{bu\ t}}$ the humidity at initial humid base and at time (t) of the sample; $\mathbf{ART_i}$ e $\mathbf{ART_t}$ **,** the total reducing sugars at initial time and at time (t).

Analytical methods were determined according to AOAC (1996). Soluble solids content were determined by refractometric index, using refratometer (Zeiss West Germany). The Reynolds number was determined according to Mavroudis, Gekas, and Sjoholm (1998). The experimental data obtained were analyzed through regression and graphical analysis by the software STATISTICA version 5.0 (Statsoft, USA). A full 2^2 factorial design with three replicate at the center point was used to study the effect of the two variables of process: temperature (40, 50 e 60 ºC) and period of immersion time (60, 180 e 300 min) on water loss (WL), weight reduction (WR), solid gain (SG) ratio. The flow type in the system was determined by the Reynolds Number (Re). Where: ρ_{sol}: fluid density, μ_{sol}: fluid viscosity,V_s: fluid velocity, D_L: diameter

$$\mathrm{Re} = \frac{\rho_{sol} \cdot V_s \cdot D_L}{\mu_{sol}}$$

3 Results and conclusion

The selected fruits were analyzed to determine humidity, total sugars, titratable acidity, soluble solids and pH (Table 1). The results obtained were in accordance to the literature for the same variety of fruit (Sato & Assumpção, 2002; Daniele et al., 2002; Vasconcelos, 2000). The differences observed can be attributed to the degree of maturation of the fruit, as well as the climate and soil conditions.

Table 1: Chemical and physical characteristics of persimmon fruits, cultivar *Fuyu.*

Characteristics	Theorical*	Experimental
pH	4.20 a 6.60	5.94 a 6.33
Titratable acidity (g acid malic/100g sample)	0.07 a 0.11	0.06 a 0.13
Soluble solids (^{o}Brix)	9 a 21	16.5
Humidity (%)	82	80.5 a 83.5
Total sugars (%)	17 a 26	16.97 a 19.09

* SATO & ASSUMPÇÃO (2002)

The results determined for the mass transfer coefficients, water loss (WL), weight reduction (WR), solid gain (SG) are shown in Table 2.

Table 2: Experimental results obtained from experimental design: water loss (WL), weight reduction (WR), solid gain (SG).

Independent variables				Dependent variables		
Codified		Decodified		Response		
Temperature (X1)	Time (X2)	T (°C)	t (min)	WL (%)	WR (%)	SG (%)
-1	-1	40	60	31.50	13.08	5.03
-1	1	40	300	55.79	24.74	9.98
1	-1	60	60	39.07	24.17	14.90
1	1	60	300	68.84	46.96	21.88
-1.41	0	36	180	43.32	25.25	18.07
1.41	0	64	180	64.87	48.18	20.69
0	-1.41	50	11	25.60	9.10	16.50
0	1.41	50	350	68.32	48.46	19.86
0	0	50	180	51.64	33.14	18.50
0	0	50	180	55.67	37.41	18.26
R^2	---	---	---	0,99	0,93	0,53

The data of the estimative effect indicate how much each factor influenced in the studied region. Regression coefficients describing the effect of osmotic dehydration variables on the water loss (WL) of persimmon fruit slices are given in Table 3. The determination coefficient (R^2) for water loss and weight reduction was 0.99 and 0.93, respectively, indicating a good adjustment of the experimental data (Table 2). It is observed that the linear effect of temperature (L) and linear term of time (L) had positive effect on the water loss, or either, an increase in any one of these factors caused an increase the water loss, while that the effect of the factors temperature (Q) and time (Q) have negative influence, in the same way, an increase in these factors causes reduction of the loss of water. The interaction between time and temperature presented positive effect, showing that the interaction of both factors contributed to increase water loss. However, among the factors studied, only the immersion time (L) was statistically significant values for the water loss.

Table 3: Effect estimated, pure error, p-value and regression coefficient on water loss

Variables	Effect estimated	Pure error	P-values<0.05	Regression coefficient
Temperature (L)	12.83	2.03	0.099	0.654
Temperature (Q)	-0.44	2.71	0.898	-0.002
Time (L)	28.67*	2.02*	0.045*	0.158*
Time (Q)	-7.62	2.66	0.214	-0.000
Time x Temperature (L)	2.74	2.85	0.512	0.001

*Significant at 95% of level; (L) = linear term; (Q) = quadratic term

In Figures 1 and 2 show the typical response surface diagram of the osmotic treatments,

representing the water loss (WL) and weight reduction (WR) as function of immersion time (min) and temperature (ºC). During the three first hours of immersion treatment, the loss of water was 53-60%, and after 5 hours of immersion, the water loss increased to 60-67%. The high rate of water loss in the beginning of the process can be explained by the driving forces, between the internal solute fruit concentration and the hypertonic solution concentration. Rapid removal of water in early stages of osmotic dehydration has been reported in carrots (Uddin et al. 2004) and in guavas (Sanjinez-Argandoña, 2005). The influence of the temperature on the water loss is barely observed at the beginning of the process, and it can only be verified after 180 min, at 40°C, when losses of water (above of 50%) increases with enhancing time of immersion. However, high temperatures damage the cellular structure (Sanjinez-Argandoña et al., 2004), which increase the solids content in intracellular, besides it makes the fruit soft.

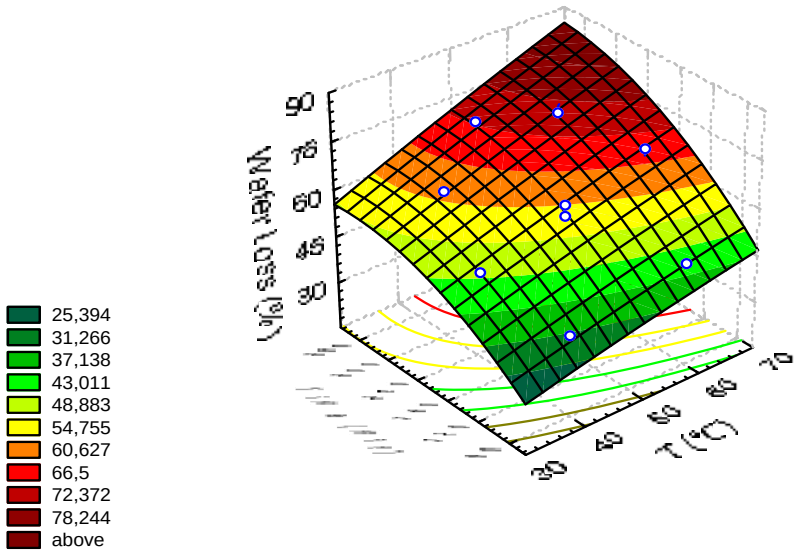

Figure 1: Water loss during osmotic dehydration of persimmon fruit slices as function of immersion time (min) and temperature (°C).

The fluidynamic of the osmotic system was conducted by the laminar flow, and the Reynolds Number determined was 3.33. The water loss was influenced mainly by the period of time of immersion and had less influence by temperature. Sanjinez-Argandoña et al. (2004) had observed, on batch and semi-continuous osmotic treatments of guavas, that the mass transfer is positively affected by the speed of the flow. Consequently, raising outflows (from laminar to turbulent flow) would be more effective to water loss. Although, the solution flow was laminar, the results obtained were similar to the data determined by Azeredo e Jardine (2000) that dehydrated pineapples using osmotic dehydration from 2 to 5 hours, at temperatures of 30 to 50ºC with osmotic solution concentration between 60 and 70ºBrix, they observed that pineapples had 32.3 to 52% of water loss; 17.5 to 32.9% of weight reduction and an increase of solids of 11.4 to 22.3%. Figure 2 shows the weight reduction as function of immersion time and temperature. It can be observed that at three hours of process (180 minutes), at 50 and 60°C, the weight reduction was 43 and 49%, respectively. It is interesting to observe that at temperature of 50°C, the weight reduction for 180 min and 350 min of process was the same (Table 2). These results proved that the reduction of weight was influenced by

temperature and immersion time of osmotic treatment.

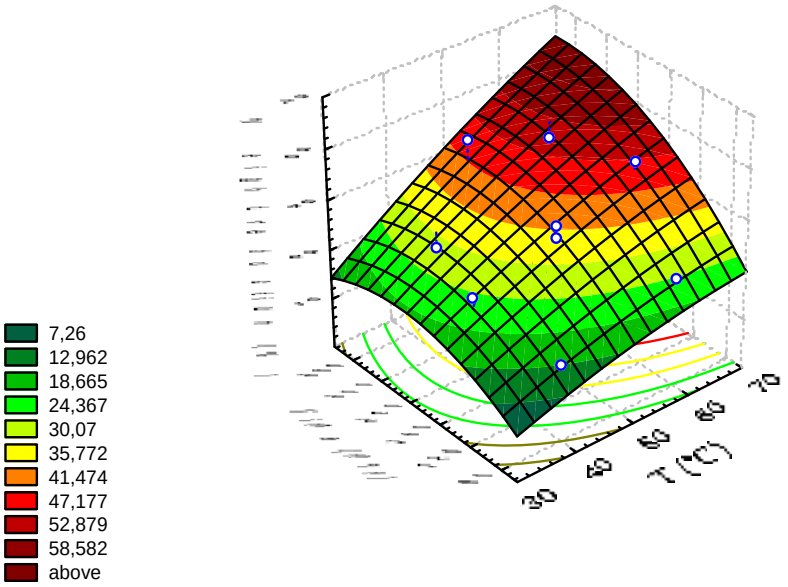

Figure 2: Weight reduction (WR) during osmotic dehydration of persimmon fruit slices as function of immersion time (min) and temperature (°C).

The Pareto chart (Figure 3) shows the influence of immersion time and temperature on the gain of solids. The solid gain is more influenced by temperature than the immersion time. Probably, this fact is due to the temperature that affects directly on the selectivity of the cellular membranes of fruit. The model adjusted for solid gain was statistically significant at the level of 95% for the variables: time, linear (L) and quadratic (Q) term; and temperature, linear (L) term. However, the determination coefficient of predicted values was lower (53%) than the results, determined for water loss and weight reduction (99 and 93%, respectively). This lack of fit can be attributed to the insufficient number of terms, which means that the omission factors had influenced on the response as, for example, different concentrations of osmotic solution.

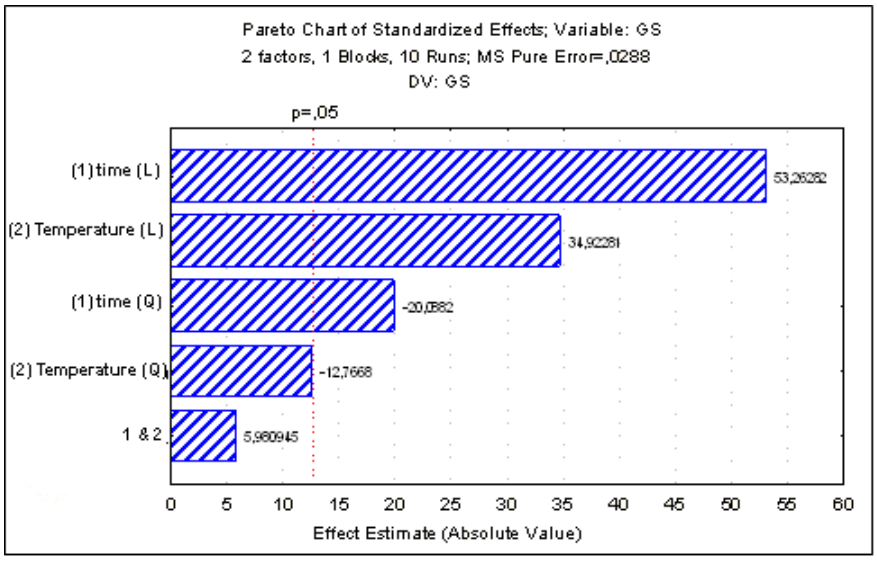

Figure 3: Pareto's chart for solid gain on osmotic treatment of persimmon fruits.

4. Conclusion

The osmotic fluidynamic system was conducted by the laminar flow, and the Reynolds Number determined was 3.33. The water loss was influenced mainly by the time of immersion and had less influence by temperature. The solid gain was significantly influenced by the temperature and time of immersion; however, the analysis of variance demonstrated that the polynomial model did not have good adjustment for the experimental data. The osmotic dehydration of persimmon fruit slices at 40°C, in sucrose solution (60 ºBrix) for 4 hours was chosen as the best condition for water loss (53.5%), weight reduction (38.5%) and solid gain (15%).

References

AOAC (1996). *Official methods of Analysis*. Arlington, VA, USA: Association of Official Analytical Chemists.

Azeredo, H Mc; Jardine JG (2000). Desidratação osmótica de abacaxi aplicada à tecnologia de métodos combinados. Ciênc. Tecnol. Aliment, 20 (1), 74-82.

Brickman, A.; Pinto, J.A.V; Gómez, A.C.S.; Steffens, C.A.; Sestari, I. (2006). Condições de armazenamento de caqui 'Fuyu'. Revista Brasileira Agrociência, 12(2) 183-186.

Danieli, Roque et al. (2002). Efeito da aplicação de ácido giberélico e cloreto de cálcio no retardamento da colheita e na conservabilidade de caqui, Fuyu. **Rev. Bras. Frutic.** , Jaboticabal, v. 24, n. 1, p. 69-75.

Mavroudis, N.E., Gekas, V., Sjoholm, I. (1998). Osmotic dehydration of apples. Effects of agitation and raw material characteristics. *Journal of Food Engineering,* 35, 191-209.

Sanjinez-Argandoña, E.J., Menegalli, F.C.; Cunha, R.L. Hubinger, M.D. (2004). Comparação da cinética de desidratação osmótica de goiabas em sistema batelada e semicontínuo. Revista Ciências Exatas e Naturais, Vol. 6, no 1, p.57-66.

Sanjinez-Argandoña et al. (2005)

Sato, G.S.; Assumpção, R. (2002), Mapeamento E Análise Da Produção Do Caqui no Estado De São Paulo. Informações Econômicas IEA, São Paulo. 32 (6).

Torreggiani, D. E Bertolo, G. (2001). Osmotic pre-treatments in fruit processing: chemical, physical and structure effects. *Journal of Food Engineering*, v.49, p.247-253.

Uddin, M.B.; Ainsworth P.; Ibanoglu, S. (2004). Evaluation of mass exchange during osmotic dehydration of carrots using response surface methodology. *Journal of Food Engineering* 65, 473–477.

Vasconcelos, 2000

Proceedings of the 10th International Chemical and
Biological Engineering Conference - CHEMPOR 2008
Braga, Portugal, September 4-6, 2008
E.C. Ferreira and M. Mota (Eds.)

High Pressure Treatment of Grape Seed to Enhance the Yield of Oil Extraction

Ana L. Magalhães[1], C P. Passos[1], Jorge A. Saraiva[2,*], Manuel A. Coimbra[2], Carlos.M. Silva[1]

[1]CICECO, Department of Chemistry, University of Aveiro, 3810-193 Aveiro, Portugal
[2] Department of Chemistry, University of Aveiro, 3810-193 Aveiro, Portugal

Keywords: High pressure treatment, grape seed, extraction yield, supercritical fluid extraction.
Topic: Multi-scale and/or multi-disciplinary approach to process-product innovation.

Abstract

The combination of pre-treatments with natural matrices processing may induce higher extraction yields and/or reduce the treatment times involved. In this essay, the application of a high pressure treatment prior to the supercritical fluid extraction of grape seed (*Vitis vinifera*) oil has been investigated.

Experiments show that, under the operating conditions adopted, the final extraction yield slightly decreases with increasing processing pressure. Up till 3000 bar such effect is negligible, though a variation of 15.5% was measured at 5000 bar.

With respect to the supercritical fluid extraction results, the comparison between cumulative curves achieved with treated and untreated grape seed evidenced faster kinetics in the former case, despite final yields were approximately the same. Therefore, combining a high pressure treatment with supercritical fluid extraction may certainly reduce CO_2 consumption to reach the same extractability under optimized operating conditions.

1. Introduction

Increasing consumer demand for high quality, freshlike, safe foods that are minimally processed, incited the industry to continuously improve the existing technologies and gave birth to many research efforts on novel technologies (Ludikhuyze et al., 2003), such as high-pressure processing. In addition to food preservation, high-pressure treatment (HPT) may result in food products acquiring novel structure and texture, and hence can be used to develop new offers or increase the functionality of certain ingredients (Saraiva et al., 2002; Castro et al., 2006). The application of high pressure leads to rearrangement in the tissue architecture, which may result in increased extractability, even at ambient temperature. The combination of high pressures and lower temperatures could become a viable alternative to some current industrial practice (Rastogi et al., 2007). The inclusion of HPT as a preceding step of other unit operations, such as solid-liquid extraction, is being considered as one of the emerging possibilities in the path leading to novel products and new process development opportunities (Garcia et al., 2001). When applied as a pre-treatment, it may promote higher solute extractability and increase extraction kinetics, which ultimately reduces processing times.

* Corresponding author: Tel. +351 234 370 716; E-mail: jorgesaraiva@ua.pt.

Grape seed (*Vitis vinifera*) is a well known oilseed crop and a major by-product resultant from the wine industry, containing typically between 7-15% (w/w) of oil (Gomez, et al. 1996). It is also an appealing product due to its large availability, as a major by-product resultant from the wine industry. The aim of this study is to investigate and improve the yield of grape seed oil extraction by applying an HPT prior to supercritical fluid extraction (SFE) with CO_2.

2. Experimental Procedure

2.1. Processing of solid plant material

Seeds were collected from grapes (*Vitis vinifera*) of the red variety *Touriga Nacional* harvested at technological maturity, provided by a local wine industry (*Caves* Messias, Anadia, Portugal) during September 2007. Seeds were collected during transfer of the musts in wine fermentation, and separated from pulp and skins by decantation and sieving. A first wash removed immature grains floating at water surface. Subsequently, the seeds were submitted to several washes with water (200 g/L) under gentle stirring with a magnetic bar at 4 ºC during a minimum of three days, with two water exchanges per day, until a minimum constant turbidity was observed. The purified seeds were finally washed with ethanol, air dried at room temperature, and stored at 4 ºC until use. Finally, milling was carried out on a domestic coffee mill, and the particles classified in a standard sifter with several mesh sizes.

In this work, to ensure the biomass used in different runs had the same size distribution, the extractor load was prepared by combining fixed masses of crushed seed from each mesh interval. Specifically, a mean particle diameter $\overline{d}_p = 1.3$ mm was adopted, being calculated by Sauter's equation (Povh et al., 2001) to a set of fractions within [0.71;1.4]:

$$\overline{d}_p = \frac{1}{\sum_{i=1}^{k} \frac{\Delta m_i}{d_{p_i}}} \qquad [1]$$

where d_{p_i} is the size of sieve i, which retains a mass of solid Δm_i.

2.2. High pressure treatment

Prior to both conventional Soxhlet and supercritical fluid extractions of grape seed oil, the HPT was applied. It has been accomplished in a Hydrostatic press (Unipress Equipment, Model U33, Poland). Experiments were conducted at several pressures during 15 min at 22ºC. The milled seed was previously subjected to an overnight water floating (2 mL_{water}/g_{seed}) and only then subjected to the HPT. After the samples were freeze dried.

2.3. Soxhlet extraction

The yield of grape seed oil extraction was assessed by conventional Soxhlet carried out with 150 mL of *n*-hexane in a Soxhlet apparatus (50 mL capacity; 23×100 mm cartridge) during 4 h. The mass oil was determined gravimetrically after solvent evaporation. Furthermore, to ensure that the resultant oil carries no water, the

extracted samples were passed over sodium sulfate anhydrous under vacuum in a G1 sintered glass filter, and evaporated in a rotary evaporator at 30 ºC. The oil was then transferred to speed-vacuum tubes and dried by centrifugal evaporation. The yield of the process is expressed as the mass of oil extracted from 100 g of dried grape seed. The results thus obtained were assumed as reference values, being used for comparison with those achieved by SFE. The yield of the process $(\eta,\%)$ was expressed as the mass of oil extracted from 100 g of dried grape seed.

2.4. Supercritical fluid extraction

The experiments of SFE of grape seed oil were carried out in a semi-batch extraction apparatus built/assembled at the University of Aveiro. It has been operated with nearly 65 g of crushed grape seed, a CO_2 flow rate of 0.6 kg h^{-1}, at 180 bar and 40ºC. Two sets of experiments were carried out, using treated and untreated samples for comparison.

3. Results and discussion

The results obtained by conventional Soxhlet confirmed that the average particle diameter has a strong effect on the yield of the grape seed oil extraction. Figure 1 shows an increase in the oil recovery of 128% when d_p is reduced from range 1-1.4 mm $(\eta = 6.7\%)$ to $d_p < 0.5$ mm $(\eta = 15.3\%)$. These determinations evidenced it is fundamental to ensure that the same size distribution is being processed to allow comparisons between them. Therefore, the procedure based on Eq.1 and described in section 2.1 was always carried out in this essay, and the average value $\overline{d}_p = 1.3$ mm has been adopted and fixed since then.

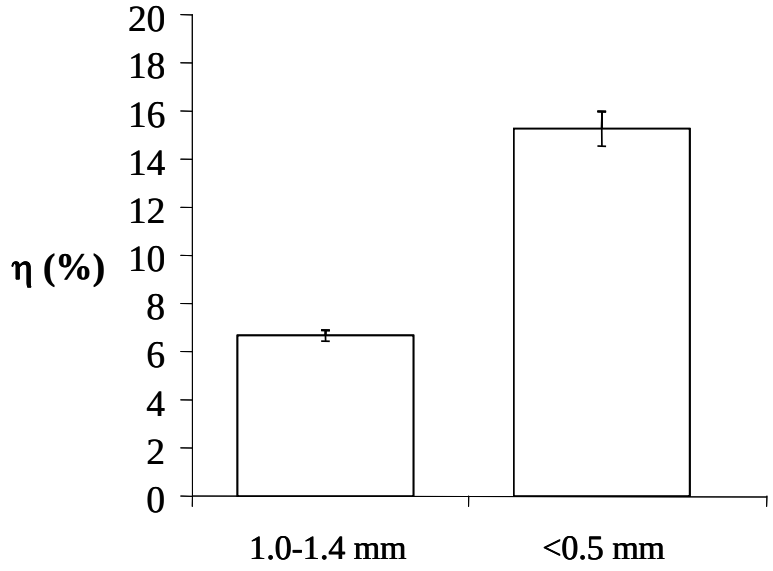

Figure 1. Extraction yield (%) against granulometry of crushed seed particles.

Introducing HPTs prior to conventional Soxhlet extractions, slightly lower recoveries were obtained by increasing the operating pressure, P, (Figure 2). The lowest pressures applied (1000 and 3000 bar) produced nearly the same yields, $\eta = 6.5\%$ and 6.4%, respectively, while $P = 5000$ bar decreases oil removal to 5.8%. These observations correspond to a global variation of 15.5%, and suggesting that pressure treatment change the oil availability, givin rise to lower yields.

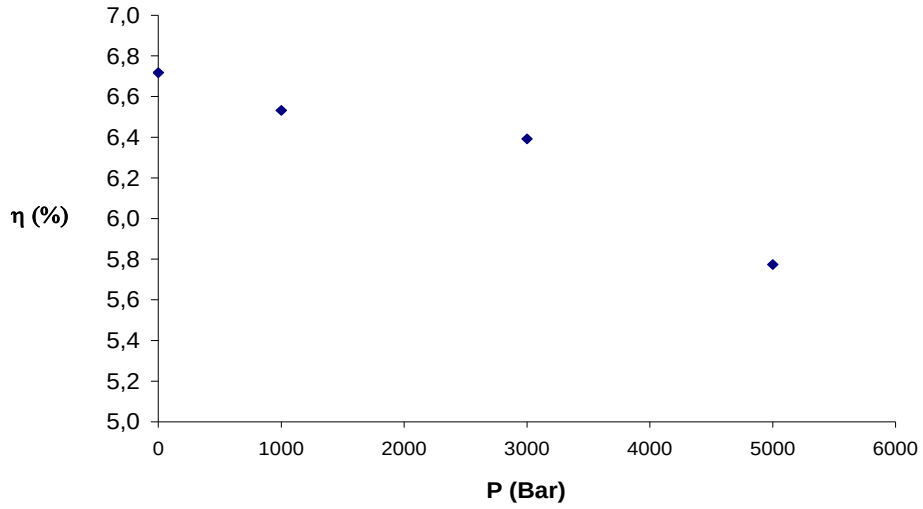

Figure 2. Extraction yield (%) as function of the operating pressure of several high pressure treatments, for $\overline{d}_p = 1.3$ mm and $t = 15$ min.

In Figure 3 cumulative curves for grape seed oil extraction with supercritical CO_2 are plotted, for the operating conditions of 180 bar and 40ºC, and $\overline{d}_p = 1.3$ mm. In abscissas the ratio of solvent consumption to seed charge $\left(m_{CO_2} / m_{seed}\right)$ is presented. The two cumulative curves correspond to measurements achieved with untreated samples and with high pressure pre-treated biomass at $P = 1000$ bar during 15 min. These results exhibit the characteristic behaviour associated to seed oils (e.g., Sovova et al., 1994): a first equilibrium and film controlled period approximately linear, followed by a second diffusional controlled period with more asymptotic behaviour.

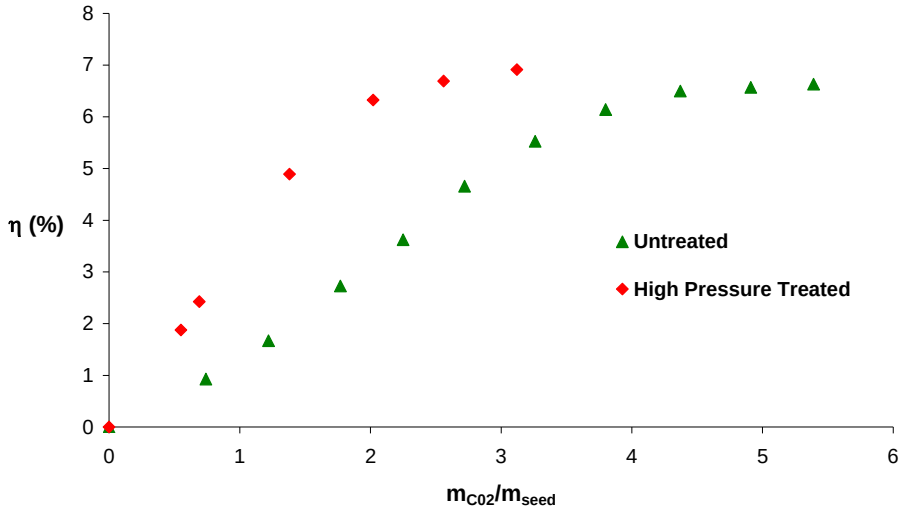

Figure 3 – Effect of HPT ($P = 1000$ bar; $t = 15$ min) upon the cumulative extraction curves obtained by SFE of grape seed oil at 40ºC and 180 bar, for $\overline{d}_p = 1.3$ mm.

Figure 3 corroborates previous finding by Soxhlet experiments, *i.e.* HPT does not increase the final yield, as both curves tend nearly for the same plateau. Nonetheless, a distinct behaviour was observed during extraction, since the curves are different for the intermediate conditions. Such fact shows that the extraction kinetic is faster for the treated samples. It is worth noting that the CO_2 consumption necessary to achieve complete oil removal almost doubles from pre-treated $\left(m_{CO_2}/m_{seed} \cong 3\right)$ to untreated $\left(m_{CO_2}/m_{seed} \cong 5.5\right)$ samples. In terms of processing time, it additionally implies that only half extraction time is need to accomplish total oil removal.

4. Concluding remarks

In this work, the effect of a high pressure pre-treatment upon the yield and efficiency of grape seed oil extraction has been evaluated.

Experiments show a slight impact of HPT on the final yield up till 3000 bar performed during 15 min. Nonetheless a weak yet consistent decrease has been observed with increasing operating pressure, which may suggest possible changes on the oil availability from the biomass.

The comparison between cumulative curves of the SFE of treated and untreated grape seed evidenced faster kinetics in the former case, despite final yields are approximately the same. Therefore, combining HPT and SFE we may reduce CO_2 consumption to reach the same extractability under optimized operating conditions.

Acknowledgements

The authors gratefully acknowledge Dr. Joeli Muños for technical support.

References

Ludikhuyze, L., Van Loey, A., Indrawati, Smout, C., Hendrickx, M. (2003). Effects of combined pressure and temperature on enzymes related to quality of fruits and vegetables: From kinetic information to process engineering aspects. *Critical Reviews in Food Science and Nutrition,* 43, 527-586.

Saraiva, J., Vitorino, R., Nunes, C., Coimbra, M.A. (2002). Effect of high pressure treatments on protease and beta-galactosidase activities of table olives. *High Pressure Research*, 22, 669-672.

Castro, S.M., Van Loey, A., Saraiva, J.A., Smout, C., Hendrickx, H. (2006). Inactivation of pepper (Capsicum annuum) pectin methylesterase by combined high-pressure and temperature treatments. *Journal of Food Engineering*, 75, 50-58.

Rastogi, N.K., Raghavarao, K., Balasubramaniam, V.M., Niranjan, K., Knorr., D. (2007). Opportunities and challenges in high pressure processing of foods. *Critical Reviews in Food Science and Nutrition,* 47, 69-112.

Garcia, A.F., Butz, P., Tauscher, B. (2001). Effects of high-pressure processing on carotenoid extractability, antioxidant activity, glucose diffusion, and water binding of tomato puree (Lycopersicon esculentum Mill.). *J. Food Science,* 66, 1033-1038.

Gomez, A.M., Lopez, C.P., De la Ossa, E.M. (1996). Recovery of grape seed oil by liquid and supercritical carbon dioxide extraction: A comparison with conventional solvent extraction. *The Chemical Engineering Journal and the Biochemical Engineering Journal,* 61, 227-231.

Povh, N.P., Marques, M.O.M., Meireles, M.A.A. (2001). Supercritical CO2 extraction of essential oil and oleoresin from chamomile (*Chamomilla recutita* [L.] Rauschert).*The Journal of Supercritical Fluids,* 21, 245-256.

Sovova, H., Kucera, J., Jez, J. (1994). Rate of the Vegetable Oil Extraction with Supercritical Co2. II. Extraction of Grape Oil.*Chemical Engineering Science,* 49, 415-420.

Proceedings of the 10th International Chemical and
Biological Engineering Conference - CHEMPOR 2008
Braga, Portugal, September 4-6, 2008
E.C. Ferreira and M. Mota (Eds.)

Relations between oxidative stability and antioxidant content in vegetable oils using an accelerated oxidation test –Rancimat

M. Mercedes Esquível*, M. Albertina Ribeiro, M. G. Bernardo-Gil
Centre for Biological and Chemical Engineering, IBB, DEQB, Instituto Superior Técnico,
Av. Rovisco Pais, 1049-001 Lisboa, Portugal

Keywords: Antioxidant activity, Rancimat Method, vegetable oil, antioxidant extract
Topic: Multi-scale and/or multidisciplinary approach to process-product innovation

Abstract

In vegetable oils, particularly virgin olive oil and sunflower oil and in lard, the effects of temperature and antioxidant extracts concentration on the induction time were investigated using a sequence of simple factorial designs.

The antioxidant extracts were obtained from aromatic plants by hydrodistillation followed by liquid-liquid extraction using diisopropyl ether as a solvent. Vegetable oils and lard were spiked with those extracts in a range of concentrations from 250 to 2500 ppm and then subjected to oxidation in a 679 Rancimat apparatus.

In the sequence of factorial designs, two blocks of 2^3 design were run. In the first block only peppermint extract was used in two different matrices (virgin olive oil and sunflower oil). In the second block the antioxidant extract was introduced as a new variable but keeping the same matrix (sunflower oil). A simple equation was derived trying to relate the induction time (T_I) with the extract concentration (C_{Ext}): $T_I / T_{I_0} = 1 + k^{\alpha} C_{Ext}$. The model was validated with data obtained from rosemary (Rosmarinus officinalis), peppermint (Mentha piperita), lemon balm (Melissa officinalis) and marjoram (Origanum majorana) in virgin olive oil and sunflower oil at temperatures of 100, 110, 120, 130, 140 and 150 ºC. To confirm the results, supplementary experiments were done with peppermint in lard at 120 and 130 ºC.

1 Introduction

One of the great challenges in food and cosmetic industries is to find new ways to control the degradation in food and in biological systems. Since the lipids are one of the major bulk constituents in food, the antioxidants susceptible of delaying the oxidation process have attracted a lot of attention as food additives. Lipid oxidation causes the development of off-flavor compounds, reduces the shelf life and nutritive value of food products and can be related with some health problems like arteriosclerosis, cancer, coronary diseases and the aging process (1).

The compounds widely used to delay the lipid oxidation in foods are synthetic (phenolic type) like butylated hydroxyanisole, butylated hydroxytoluene, tert – butylhydroquinone and propyl gallate commonly named BHA, BHT, TBHQ and PG, respectively. The effectiveness of those compounds depends on several factors which include the concentration used, the chemical nature of the food and the storage or processing conditions. However, the information about the possible carcinogenic effect of the synthetic antioxidants restricts their use (2) and instigates the research in the development and utilisation of antioxidants from natural sources, such as plants.

* Corresponding author. Tel + 351-218417312. E-mail: mercedes.esquivel@ist.utl.pt

Antioxidant activity, of herbs and spices extracts, have created widespread interest. Several authors have reported data about the utilisation of natural substances to stabilise edible oils against oxidation. These natural substances include rosemary (3), oregano, thyme, marjoram, dittany (4,5) and clove (6).

Methods for the determination of the oxidative stability of oils and fats have been reviewed by Rajalakshmi and Narasimhan (7). Rancimat method used in the present work allows the stability evaluation at high temperatures (up to 220 ºC with 679 Metrohm Rancimat) which is important in the use of the antioxidants in food products as French fries, potato chips, margarine uses, etc. However, there have been no reports about general predictive correlations for the antioxidant activity of natural products in oils.

This study reports the antioxidant effect of natural extracts in vegetable oils during accelerated oxidation in order to establish an empirical equation between protection factor and extract concentration.

2 Materials and Methods

Raw material

Two commercial oils, extra virgin olive oil – Azeite de Moura (ATOM, nº190369) and refined sunflower oil – 3a's Girassol – SOVENA (lote nº 093AG2) were purchased from local market. Lard without additives was supplied by local shop.

Rosmarinus officinalis was collected in the central region of Portugal, Lisbon, Mentha piperita and Origanum majorana were collected in the north of Portugal– Mirandela, and Melissa officinalis was obtained from Dietoforma (Lisboa). The air-dried materials were grounded using an Armfield mill to give the particle size of $3X10^{-3}$ m.

Organic solvents and all the other chemicals used of the highest available purity were purchased from Merck.

Apparatus

Antioxidant activity evaluation was conducted in a model 679 Rancimat apparatus Metrohm, Switzerland (8). For the preparation of the samples (vegetable oil or lard with the extract dissolved), the calculated quantities of each extract were first solubilized in a few drops of methanol, then added to the vegetable oil. The mixture was homogenised in an ultrasound bath for 5 minutes and finally the methanol traces were evaporated using nitrogen gas. The air flow was set to 20 L/h. Induction time was determined automatically by the inflection point of the conductivity vs. time curve.

The temperature calibration was done monthly. The reproducibility of the results was calculated from three to five repetitions using the same kind of sample at the same temperature.

Extraction

Ground vegetable material (100 g) was extracted with boiling distilled water (2 L), at normal pressure for 90 minutes with stirring. The aqueous extract was filtered (filter paper Whatman 4) and the pH was rendered to a value of 2.0 (pH Meter E603, Metrohm, Switzerland) by the addition of 25% hydrochloric acid.

The precipitated by-products were separated by filtration (filter paper Whatman 1) and the resulting solution was extracted four times with diisopropyl ether (Vibromatic, Selecta, Spain), using 30 mL of ether for 100 mL of solution each time.

The combined organic phases were dried over anhydrous magnesium sulfate, filtered (filter paper Whatman 1) and evaporated to dryness using a vacuum rotary evaporator VV2000. The extracts were kept under inert atmosphere in the dark until subsequent analyses. The

yield of dried water extracts from the rosemary, peppermint, marjoram and lemon balm were 0.5%, 0.4%, 0.6% and 0.8% respectively.

3 Results and Discussion

In the first part of the work a factorial design was applied on two levels to determine the main effects and the interaction of the following items:

A: Type of vegetable oil.

B: Oxidation temperature.

C: Extract concentration in vegetable oil.

D: Vegetable material used wyle obtaining the extract.

Because it was impossible to do the complete randomization of all the trials of a factorial design of 2^4 we chose to do two blocks of 2^3 each. This impossibility is due both to dry plants validity limits (if results are to be reproducible, plants should be harvested at the same time of the year and in the same place) and also due to the antioxidant extracts which only keeps its properties during approximately one week.

In the first block only peppermint extract was used in two different matrices (sunflower and virgin olive oil). In the second block the antioxidant extract was introduced as a new variable but keeping the same matrix (sunflower oil). Two variable answers were considered: the induction time *TI* (h) and the protection factor *PF* calculated by the ratio of the induction time of the sample (mixture of oil and antioxidant extract) to the induction time of oil without additives (TI_0). The variables and levels are summarized in table 1.

Table 1: Variables and levels of factorial designs

Variables	Level	
Block 1: Peppermint extract	-	+
A: Vegetable Oil	Sunflower	Virgin Olive Oil
B: Temperature, ºC	110	130
C: Extract Concentration, ppm	250	2500
Block 2: sunflower oil		
A: Extract	peppermint	rosemary
B: Temperature, ºC	110	130
C: Extract Concentration, ppm	250	2500

The results obtained in the trials are shown in Figures 1a) and 1b).

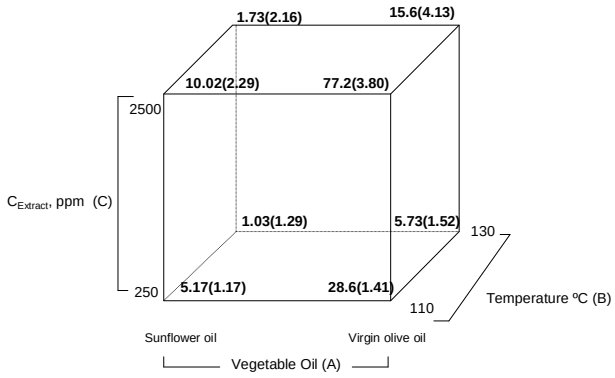

Figure 1a) first block of 2^3 factorial design. Protection factors in parenthesis.

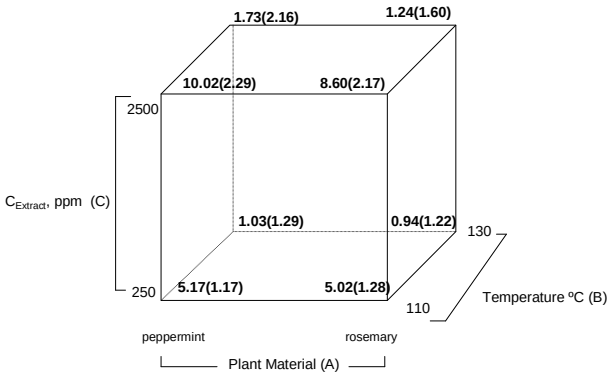

Figure 1b) second block of 2^3 factorial design. Protection factors in parenthesis.

The factor effects were calculated by measuring the difference between the average of the trials, were the factor is in the + level, and the average of the trials, were the factor is in the level – (eq.1).

$$Effect_{Factor} = \bar{y}_{Factor^+} - \bar{y}_{Factor^-} \qquad \text{eq. 1}$$

The error of each effect was estimated by the equation:

$$Error_{Efeito} = \sqrt{\frac{4}{8} s_n^2} \qquad \text{eq. 2}$$

being s_n^2 the variance obtained from four trials done in intermediate conditions (central points). In table 2 the factor effect and its respective confidence intervals are shown. The most significant effect shown is the matrix type used followed by the concentration effect. It seams that the plant used in the extracts doesn't have a noticeable relevance.

Table 2: Factor effects

		TI	*PF*
Block 1: Peppermint extract	Effect A (Vegetable Oil)	27.30±0.07	0.99±0.08
	Effect B: (Temperature, ºC)	-24.23±0.07	0.10±0.08
	Effect C: ($C_{Extract,\ ppm}$)	16.00±0.07	1.75±0.08
Block 2: sunflower oil	Effect A: (Extract)	0.54±0.07	-0.16±0.08
	Effect B: (Temperature, ºC)	-5.96±0.07	-0.16±0.08
	Effect C: ($C_{Extract,\ ppm}$)	2.35±0.07	0.82±0.08

A simple equation was derived trying to relate the induction time with extract concentration:

$$T_I / T_{I_0} = 1 + kC_{Ext}{}^{\alpha} \qquad \text{eq. 3}$$

being the linear form:

$$\ln(T_I / T_{I_0} - 1) = \ln k + \alpha \ln C_{Ext} \qquad \text{eq. 4}$$

where T_I and T_{I_0} are the induction time of the mixture and of the control sample respectively (h), C_{Ext} is the concentration of the extract in the mixture (ppm), and k and α are constants that should depend on the matrix type. The figures 2 and 3 show a graphic representation of the results.

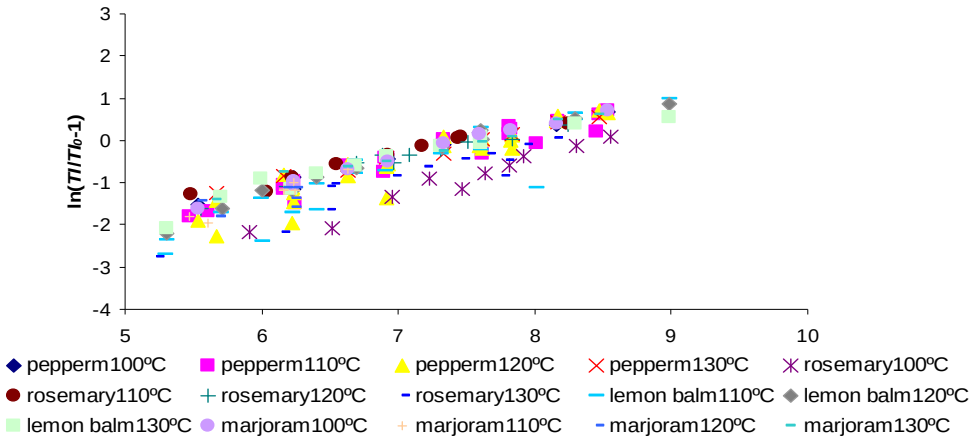

Figure 2: Experimental results from different extracts in sunflower

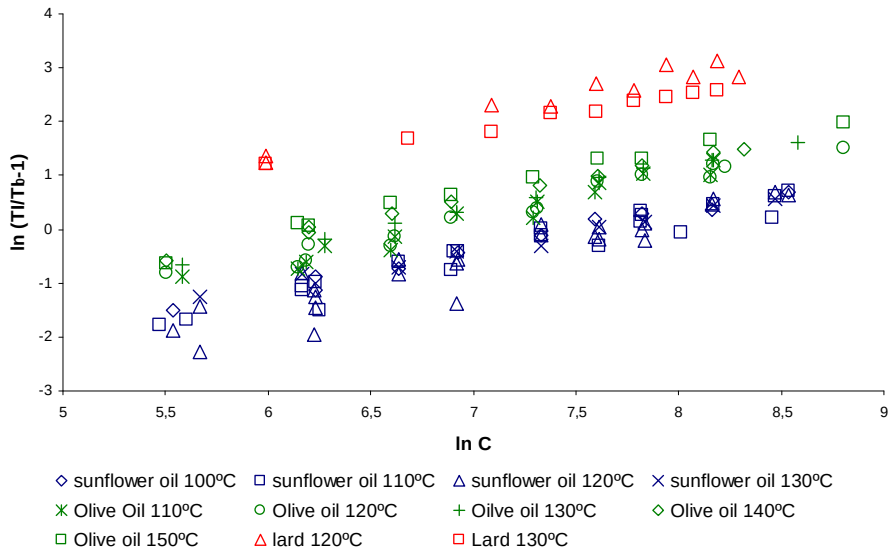

Figure 3: Experimental results from peppermint extracts on sunflower oil, olive oil and on lard

The equations obtained were:

Table 3: Model parameters

System	Equation 4b	Observations	F
Vegetal extract on sunflower oil	$\ln(T_I / T_{I_0} - 1) = (-6.3 \pm 0.3) + (0.82 \pm 0.05) \ln C_{Ext}$	208	1165.6
Peppermint on sunflower oil	$\ln(T_I / T_{I_0} - 1) = (-6.2 \pm 0.6) + (0.80 \pm 0.04) \ln C_{Ext}$	55	417.9
Peppermint on olive oil	$\ln(T_I / T_{I_0} - 1) = (-5.2 \pm 0.5) + (0.79 \pm 0.07) \ln C_{Ext}$	58	490.0
Peppermint on lard	$\ln(T_I / T_{I_0} - 1) = (-3.01 \pm 0.05) + (0.7 \pm 0.1) \ln C_{Ext}$	19	126.7

Conclusions

The proposed equation adjusts itself to the experimental points obtained in the different conditions. As previewed by the factorial design, the ratio TI/T0 (protection factor) only depends on the type of oil and the extract concentration used and not of the temperature.

By the analysis of the parameters used, it can be said that the parameter α is constant and equal to 0.8 while the parameter K depends on the type of matrix used. The equation does not depend of the type of plant extracts, which could be explained because the extraction process is selective towards a type of antioxidants – phenols, being the extract components expected to be similar.

The range of temperatures selected in this work is limited and took into consideration that, for lower then 100 ºC temperatures the induction times are extremely high and for values greater then 140 ºC the degradation of the chemical components takes place.

References

1. Frankel, Edwin N; German, J Bruce (2006), Antioxidants in foods and health: problems and fallacies in the field, *Journal of the Science of Food and Agriculture*, 86 (13),1999-2001.
2. Madhavi, D.L., S.S. Deshpande, and D.K. Salunkhe (1996), Summary, Conclusions, and Future Research Needs, in *Food Antioxidants,* edited by D.L. Madhavi, S.S. Deshpande, and D.K. Salunkhe, Marcel Dekker Inc, New York, 471-477.
3. Chang, S.S, C.-T Ho, and C.M. Houlihan (1987), Isolation of a Novel Antioxidant Rosmaridiphenol from *Rosmarius Officinalis L.,* U.S. Patent 4,638,095.
4. Banias, C., V. Oreopoulou, and C.D. Thomopoulos (1992), The effect of Primary Antioxidants and Synergists on the Activity of Plant Extracts in Lard, *J. Am. Oil Chem. Soc*. *73*:520-524.
5. Economou, K.D., V. Oreopoulou, and C.D. Thomopoulos (1991), Antioxidant Activity of Some Plant Extracts of the Family Labiatae. *Ibid*. *68*:109-113.
6. Kim, S.Y., J.H. Kim, S.K. Kim, M.J. Oh, and M.Y. Jung (1994), Antioxidant Activities of Selected Oriental Herb Extracts. *Ibid. 71*:633-640.
7. Rajalakshmi, D., and S. Narasimhan (1996), Food Antioxidants: Sources and Methods of Evaluation, in *Food Antioxidants,* edited by D.L. Madhavi, S.S. Deshpande, and D.K. Salunkhe, Marcel Dekker Inc, New York, 65-157
8. Frank, J., J.V. Geil, and R. Freaso(1982), Automatic Determination of Oxidation Stability of Oil and Fatty Products, *Food Techonology*, June:71-76.

Proceedings of the 10th International Chemical and
Biological Engineering Conference - CHEMPOR 2008
Braga, Portugal, September 4-6, 2008
E.C. Ferreira and M. Mota (Eds.)

Experimental sorption isotherms of loquat and quince fruits in the range from 20 to 65 ºC.

R. Moreira[1*], F. Chenlo[1], M.D. Torres[1], N. Vallejo[1]
[1] Departamento de Enxeñaría Química, Universidade de Santiago de Compostela, Rúa Lope Gómez de Marzoa s/n, E-15782 Santiago de Compostela, Spain.

Keywords: Water activity, Gravimetric method, Equilibrium moisture content, Isosteric heat.
Topic: Food Engineering.

Abstract

Sorption isotherms of loquat (pulp and seeds) and quince fruits were determined by a static gravimetric method at different temperatures (20 to 65ºC). Curves obtained can be considered as type II at 20ºC and type III at higher temperatures according to the Brunauer–Emmett–Teller (BET) classification. Equilibrium moisture content data were correlated by different mathematical models applied to foodstuffs (GAB, Oswin, Henderson, Peleg and Halsey). Most of these models showed high coefficients of determination (R^2>0.943), acceptable standard error (E<18 %) and low root mean square error (E_{RMS}<0.147). These results indicate that all models can be considered as acceptable for predicting the equilibrium moisture content of these fruits. Peleg and GAB models (four and three parameters, respectively) were found to have the highest coefficient of determination.

1 Introduction

Loquat is an edible fruit (*Eriobotrya japonica Lindl.*) belonging to the Rosaceae family, originated in China and is widely cultivated in the subtropical regions of Southern China, Japan, Mediterranean area, United States, Brazil and Australia (Badenes *et. al*, 2000). Loquats have a thin but tough skin. Each fruit contains 3 to 5 dark-brown seeds (1-2 cm long). The harvest is short (around two months) and is susceptible to decay, with moisture and nutritional losses during postharvest life. Loquat composition reported (wet basis) refers water 78.0%, carbohydrates 10.6%, fibre 10.2%, fat 0.5%, protein 0.40% and other components (Mataix *et al.*, 1998). It is high in vitamin A and potassium, but low in vitamin C and sodium. Loquat has been used as a pharmaceutical plant, particularly; is used in a traditional herbal medicine for skin diseases, inflammation and expectoration (Koba *et al.*, 2007). Loquat fruit can be eaten fresh or lightly cooked for use in gelatine desserts and jams and is also employed by its high pectin content to make jelly.

The world production of loquat in 2006 is estimated at 550,000 t, being the main commercial producer China (453,600 t). Spain (43,300 t) is the leader in loquat production in the Mediterranean area. Other producers are Turkey (12,000 t) and Japan (10,200 t) (Lin, 2007).

The quince (*Cydonia Oblonga Mill*) belongs to the pome fruit family. Quince is one of the earliest known fruits. For over 4,000 years, quince trees have grown in Asia and the Mediterranean countries. Today, quince is also found in South America and United States. In the raw form, the rind is rough and woolly, and the flesh is hard and unpalatable and acidulous taste. It is rarely used in its raw form, the hard and dry flesh of the quince becomes softer and sweeter and its colour turns from light pink to purple when it is cooked. The main constituents of quince are water 84% and carbohydrates 15% (wet basis). Other small constituents include proteins 0.4% and fats 0.6%. It is also considered a good source of fibre, potassium and vitamin C. High dietary fibre content 12% (dry basis), makes dried quinces an excellent ingredient for cereals, cakes and desserts.

* Corresponding author. Tel + 34-981-563100 ext. (16759). E-mail:eqmoncho@usc.es

The world production of quince in 2006 is estimated at 490,000 t, being the main commercial producers, Turkey (106,000 t), China (85,000 t), Uzbekistan (49,000 t), Iran (39,300 t), Marocco (28,000 t), Argentina (25,700 t) and Spain (20,000 t) (FAO, 2007).

The expense of hand harvesting, together with the fact that the fruit does not travel or keep well, limit its commercial expansion, so the study of these edible fruits has become of recent interest. Data on moisture content and water activity is important to predict the physical, chemical and biological changes occurring during storage and processing of food materials. The water sorption isotherm represents the equilibrium relationship between moisture content of food sample and water activity at constant temperature and pressure. Food systems typically exhibit Type II and III according to the BET classification (Brunauer *et al.*, 1940). As theoretical prediction is not possible, experimental studies are necessary. Knowledge of the sorption isotherm of food materials is very important for prediction of quality and optimisation of the drying, storage and other processes. Moisture sorption isotherm models, therefore, constitute an essential component of the overall drying theory. In the literature there is a long list of available isotherms models, which can be classified into several categories: kinetic models based on an absorbed mono-layer of water, e.g. BET model, kinetic models based on a multi-layer and condensed film, e.g. Guggenheim-Anderson-de Boer (GAB) model (Van den Berg and Bruin, 1981), semi-empirical models, e.g. Halsey and Peleg models (Halsey, 1948; Peleg, 1993), and purely empirical models, e.g. Oswin and Henderson models (Oswin, 1946; Henderson, 1952). GAB equation is recognised as the most widely utilised and versatile. This work was developed due to absence of experimental data on sorption isotherms of loquat and quince fruits.

2 Materials and methods

2.1. Preparation of samples

Loquat and quince were purchased from a local market; pieces were selected according to its size and ripeness. The fruits were peeled and cut into thin slabs of about 3 mm. Loquat seeds were separated and their peel was also removed, seeds were cut into thin slabs.

2.2. Determination of sorption isotherms

The equilibrium moisture contents of loquat and quince were determined by static gravimetric technique, which is based on the use of saturated salt solutions to maintain constant water activity at determined values of the samples when equilibrium is reached between atmosphere and sample food. The salt solutions used to obtain constant relative humidity of surrounding air were KOH, LiCl, $MgCl_2$, K_2CO_3, $Mg(NO_3)_2$, NH_4NO_3, NaCl, KCl and $BaCl_2$ which were prepared according to recommendations (Greenspan *et al.*, 1977); this group of salts allows to obtain a wide range of relative hymidity of air (7 to 91 %RH) in equilibrium. The determination of sorption isotherms for loquat pulp and seeds and quince pulp was carried out in the same range of temperatures from 20 to 65ºC. The temperatures studied for loquat samples were 20, 35, 50 and 65ºC while for the quince fruits were 20, 45, and 65ºC.

In order to inhibit microbial growth a small quantity of thymol was also placed in the flasks in which water activity was greater than 0.5. Triplicate samples of 2 g were placed on Petri dishes inside the jars. Samples were weighted at regular intervals until constant weight (±0.0005 g) in an analytical balance (Mettler AJ150). The equilibrium period was about 8 weeks. The moisture content was determined using a vacuum oven (Heraeus Vacutherm VT 6025) at 70ºC and 13 kPa, achieving constant weight after three days (A.O.A.C., 1995).

2.3. Data analysis

Sorption isotherm represents the equilibrium moisture content (X) variation with water activity (a_w), which is defined as the ratio between vapor pressure of water in the food surface and vapor pressure of pure water at the same temperature. Sorption isotherm models used to fit experimental data are showed in Table 1 (Eq. (1- 5)).

Table 1. Sorption isotherm models applied to the fitting of experimental data

Model	Mathematical equation	
GAB	$X = \frac{X_M C K a_w}{(1 - K a_w)(1 - K a_w + C K a_w)}$	(1)
Oswin	$X = A\left[\frac{a_w}{(1 - a_w)}\right]^B$	(2)
Henderson	$X = \left[\frac{-\ln(1 - a_w)}{A}\right]^{\frac{1}{B}}$	(3)
Halsey	$X = \left[\frac{-a}{\ln a_w}\right]^{\frac{1}{r}}$	(4)
Peleg	$X = m_1 a_w^{n_1} + m_2 a_w^{n_2}$	(5)

The parameters of the models were estimated by non-linear regression procedure employing Table Curve software (Jandel Scientific), in order to select the best correlation and to improve the analysis of the experimental data. The goodness of the fitting of each sorption model was evaluated based on statistical parameters like coefficient of determination (R^2), mean relative percentage deviation modulus (E) and root mean square error (E_{RMS}).

$$E = \frac{100}{N} \sum_{i=1}^{N} \frac{|X_{exp} - X_{cal}|}{X_{exp}} \quad (6)$$

$$E_{RMS} = \left[\frac{1}{N} \sum_{i=1}^{N} (X_{exp} - X_{cal})^2\right]^{1/2} \quad (7)$$

where N is the number of samples, X_{exp} and X_{cal} are experimental and model calculated moisture content, respectively.

In the GAB model there are three parameters (C, K, and X_M), which are functions of temperature. These parameters can be associated to some physical meanings, X_M is the monolayer moisture content, C is a constant related to heat of sorption of the first layer and K is related to the heat of sorption of the multilayer. The influence of temperature on GAB parameters can be calculated by Arrhenius equations:

$$X_M = X_{MO} \exp(\Delta H / RT) \quad (8)$$

$$C = C_O \exp[(H_M - H_N)/RT] \quad (9)$$

$$K = K_O \exp[(H_L - H_N)/RT] \quad (10)$$

where R is the ideal gas constant, T is the absolute temperature (K), H_M, the monolayer enthalphy, H_N is the multilayer enthalpy and H_L is the average heat of condensation of water vapor (43.14 kJ/mol in the investigated range of temperature from 20 to 65ºC). The heats ΔH, H_M, and H_N and were determined by fitting of the equations (8), (9) and (10) after fit of the experimental data values to the GAB model to obtain the three-parameters (C, K, and X_M).

3 Results and discussion

Figure 1 show the experimental data of equilibrium sorption isotherm for quince, loquat pulp and loquat seed at different temperatures.

According to BET classification (Brunauer et al., 1940) curves obtained are type II at 20ºC and type III at higher temperatures.

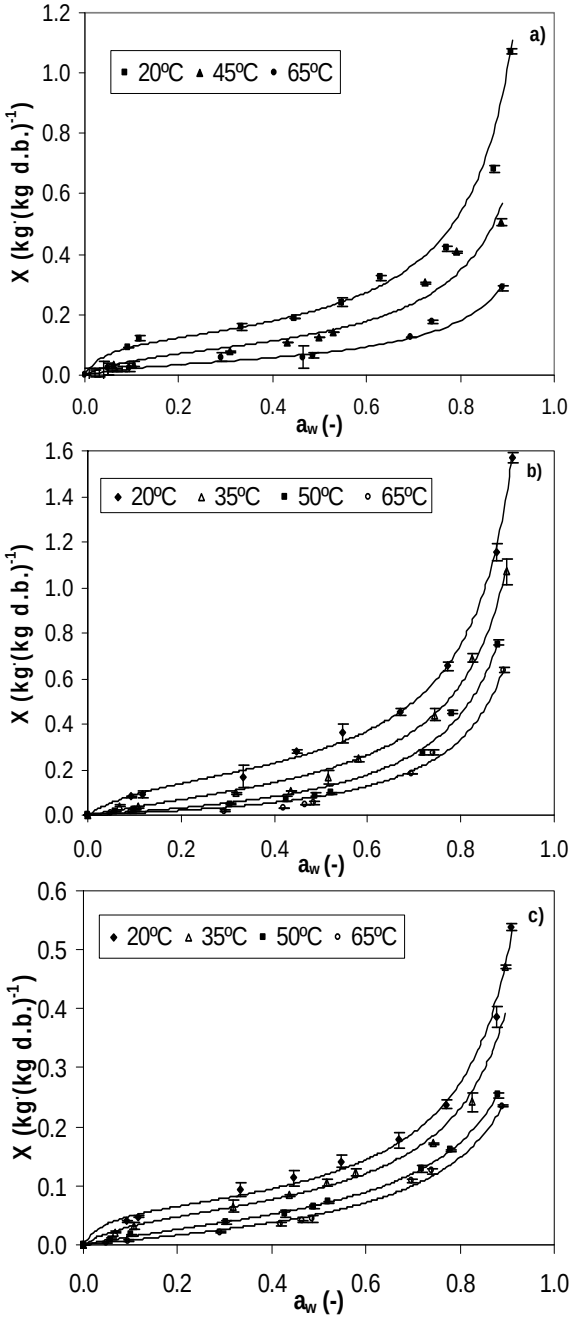

Fig.1. Experimental data of equilibrium moisture content of (a) quince, (b) loquat pulp and (c) loquat seed. Lines correspond to GAB model (Eq. 1).

As expected, the equilibrium moisture content increased with water activity at constant temperature. These changes in are due to the tendency of the food material to lower vapour pressure when decreasing the relative humidity of air. A more detailed analysis lead to identify two regions in the sorption isotherm, at low water activities, the so-called multilayer sorption region, moisture content increases linearly with water activity, whereas at high water activity, the so-called capillary condensation region, water content rapidly increases with water activity. Falade and Aworh (2004) explain this behaviour based on sugar state.

There is also an increase in moisture content with decreasing temperatures, at constant water activity. This can be explained because at higher temperatures, the activation of the water molecules changes to higher energy levels and the links become less stable and break away from the water-binding sites of food material, consequently the equilibrium moisture content decreases (Palipane and Driscoll, 1992). The increase of temperature has also an important effect on chemical and microbiological reactions relative to the spoilage. The temperature influences the physicochemical properties of fruits, which in turn reduces the number of active sites for water binding.

An interesting phenomenon was observed when Figs.1a and 1b are analysed. Sorption isotherms of quince are lower than those of loquat fruit in the range of temperatures. This means that quince presents lower strength in holding water in comparison with loquat. This behaviour is observed when comparing experimental data of pulp fruits with seeds too, Figs.1b and 1c. In this case, the sorption isotherm of seeds is the lowest by its composition, as expected.

Most of these models showed high coefficients of determination (R^2 0.943), acceptable standard error (E<18 %) and low root mean square error (E_{RMS}<0.147). These results indicate that all models can be considered as acceptable for predicting the equilibrium moisture content of these fruits. However, Peleg (Eq. 5) and GAB (Eq. 1) models (four and three parameters, respectively) were found to have the lowest standard error and the highest coefficient of determination (R^2). It is expected that models with more parameters give best results; comparing only two-parameter models, Oswin model (Eq. 2) gives the best adjustment; Henderson (Eq. 3) was the model that worst fitting of the experimental results. Coefficients of the five sorption models tested at different temperatures are shown in Table 2.

Table 2. Sorption isotherm models to fit of experimental data of loquat and quince.

Model	Parameter	Loquat								Quince		
		Fruit				Seed				Fruit		
		20ºC	35ºC	50ºC	65ºC	20ºC	35ºC	50ºC	65ºC	20ºC	45ºC	65ºC
GAB	X_M	0.163	0.136	0.121	0.0989	0.0620	0.0550	0.0484	0.0450	0.115	0.0802	0.0435
	K	0.986	0.981	0.979	0.976	0.971	0.962	0.933	0.929	0.985	0.968	0.960
	C	8.58	2.70	1.07	0.795	22.5	9.59	3.39	1.88	24.9	10.0	7.39
	R^2	0.998	0.993	0.989	0.988	0.997	0.995	0.999	0.998	0.984	0.961	0.977
	E (%)	3.95	4.39	8.37	8.67	7.84	7.39	4.82	7.01	6.11	11.7	7.35
	E_{RMS}	0.0207	0.0264	0.0145	0.00738	0.0147	0.00731	0.00267	0.00334	0.00379	0.04483	0.0120
Oswin	A	0.302	0.192	0.119	0.0871	0.133	0.0998	0.0685	0.0507	0.219	0.143	0.0747
	B	0.620	0.797	0.931	0.950	0.579	0.618	0.665	0.874	0.685	0.653	0.652
	R^2	0.994	0.996	0.992	0.990	0.990	0.994	0.999	0.999	0.987	0.985	0.969
	E (%)	7.07	4.97	9.35	9.51	8.58	8.17	4.94	7.55	13.78	10.82	8.58
	E_{RMS}	0.109	0.0282	0.0167	0.0111	0.0209	0.00860	0.00282	0.00420	0.0489	0.0297	0.0109
Henderson	A	2.08	2.19	2.46	2.79	6.26	6.70	6.97	7.35	2.48	3.74	6.81
	B	0.981	0.627	0.545	0.520	1.140	0.989	0.855	0.813	0.766	0.887	0.895
	R^2	0.983	0.996	0.996	0.995	0.995	0.993	0.994	0.997	0.943	0.983	0.976
	E (%)	17.9	17.6	13.8	13.9	17.4	15.3	15.2	12.4	17.9	18.4	12.9
	E_{RMS}	0.147	0.0338	0.124	0.0618	0.0416	0.0129	0.00658	0.00685	0.0677	0.0232	0.0108
Halsey	a	0.1599	0.1199	0.1049	0.0836	0.0402	0.0359	0.0244	0.0722	0.0968	0.0565	0.0222
	r	1.17	1.04	0.833	0.769	1.33	1.26	1.23	0.701	1.25	1.32	1.35
	R^2	0.998	0.981	0.992	0.985	0.995	0.990	0.992	0.989	0.985	0.969	0.978
	E (%)	7.34	11.4	9.43	11.1	8.91	11.7	8.8	12.3	6.9	16.9	7.94
	E_{RMS}	0.126	0.0325	0.0294	0.0238	0.0251	0.00924	0.00639	0.00625	0.0338	0.0353	0.0114
Peleg	m_1	0.660	0.289	0.114	0.0544	0.257	0.194	0.115	0.0546	0.427	0.0533	0.0732
	n_1	0.951	0.941	0.734	0.710	0.925	0.919	0.889	0.876	0.778	0.103	0.411
	m_2	3.31	1.60	1.46	1.10	1.39	1.22	0.339	0.236	4.01	0.690	0.368
	n_2	13.3	6.64	6.33	5.42	16.0	13.1	6.29	3.47	18.8	2.99	4.46
	R^2	0.997	0.999	0.998	0.995	0.993	0.998	0.999	0.999	0.992	0.996	0.991
	E (%)	6.89	4.79	5.30	8.09	7.65	6.85	4.76	5.01	11.24	10.0	4.99
	E_{RMS}	0.0304	0.0246	0.0133	0.00678	0.0112	0.00548	0.00280	0.00317	0.0277	0.0150	0.00760

The sorption equilibrium isotherms of quince and loquat (pulp and seeds) using the GAB model, are plotted in Fig.1. It can be observed a good quality of fitting. A correlation of the GAB model parameters with temperature was established. The monolayer moisture content (X_M) is the minimum moisture content covering hydrophilic sites on the material surface at a given temperature, the safest water activity level is that corresponding to X_M or lower. Estimated values for X_M are within the reported values for fruits, which vary between 4% and 15% (dry basis) (Moraga et. al., 2006). Rizvi (1986) noted that X_M decreases with temperature increases, which has been ascribed to a reduction in the number of active sites induced by temperature. The values of C and K parameters are also within the reported limits for fruits. A more detailed analysis of the GAB parameters can provide further valuable information. Value of (H_M-H_N) represents the difference in enthalpy between monolayer and multilayer sorption and (H_L-H_N) represents the difference between the heat of condensation of water and heat of sorption of the multilayer (Van den Berg and Bruin, 1981). Values of C_O, K_O, X_{MO}, (H_M-H_N), (H_L-H_N) and ΔH evaluated with Eqs. (8), (9) and (10) are showed in Table 3. They agree with literature data for other fruits (Goula et al. 2008).

Table 3. Values of the parameters of the Eqs. (8), (9) and (10).

	C_0	K_0	X_{M0}	ΔH	(H_M-H_N)	(H_L-H_N)
			kg water/kg d.b.	kJ/mol	kJ/mol	kJ/mol
Ouince	$2.14.10^{-3}$	0.815	$1.00.10^{-4}$	17.31	110	0.461
Loquat pulp	$8.15.10^{-8}$	0.912	$4.34.10^{-2}$	8.84	44.6	0.189
Loquat seed	$1.08.10^{-7}$	0.675	$5.28.10^{-3}$	5.99	46.7	0.892

The values of (H_M-H_N) and (H_L-H_N) indicate how strong water molecules are bound in the respective layers. The estimated (H_M-H_N) values have positive values as expected, due to the strong exothermic interaction of water vapour with primary sorption sites of the material. The (H_L-H_N) values are in agreement with the literature (Samaniego-Esguerra et. al, 1991).

4 Conclusions

The results obtained for both fruits are analogous, but different. This was expected since each food is a complex combination of various constituents, which not only can sorb water independently but can also interact among themselves. Sorption isotherms of quince and loquat can be described as belonging to type II at 20ºC and type III at higher temperatures according to BET classification. An increase in temperature caused a decrease in the amount of adsorbed water for a water activity. After testing five equations describing moisture sorption isotherm in the temperature range investigated (20-65ºC), the kinetic three-parameters GAB model and the empirical four-parameters Peleg equation were found the best correlations for the quince and loquat data in the range of water activity studied (0-0.9).

5. Acknowledgements

Authors acknowledge the financial support to Ministerio de Educación y Ciencia of Spain and FEDER (CTQ 2007-62009/PPQ).

References

A.O.A.C. (1995). *Official methods of analysis*. Association of Official Analytical Chemists.

Badenes, M., Martínez- Clavo, J., Yacer, G. (2000). *Analysis of a germplasm collection of loquat (Eriobotrya japonica Lindl.)*. Kluwer Academic Publishers, Netherlands, 187-194.

Brunauer, S., Deming, L., Deming, W., Teller, E. (1940). On a theory of the Van der Waals adsorption of gases. *Journal of the American Chemical Society,* 62, 1723–1732.

Falade, K., Aworh, O. (2004). Adsorption isotherms of osmo oven dried African star apple (Chrysophyllum albidum) and African mango (Irvingia gabonensis) slices. *European Food Research and Technology,* 218, 278–283.

FAO. (2007). <http://faostat.fao.org/site/567/DesktopDefault.aspx?PageID=567>.

Goula, A.M., Karapantsios, T.D., Achilias, D.S., Adamopoulus, K.G. (2008). Water sorption isotherms and glass transition temperature of spray dried tomato pulp. *Journal of Food Engineering*, 85, 73-83.

Greenspan, L. (1977). Humidity fixed points of binary saturated aqueous solutions. *Journal of Research of the National Bureau of Standards Section A,* 81, 89-102.

Halsey, G. (1948). Physical adsorption on non-uniform surfaces. *Journal of Chemistry Physics,* 16, 931–937.

Henderson, S. (1952). A basic concept of equilibrium moisture. *Agricultural Engineering,* 33, 29–32.

Koba, K., Matsuoka, A., Osada, K., Huang, Y. (2007). Effect of loquat (Eriobotrya japonica) extracts on LDL oxidation. *Food Chemistry,* 104, 308-316.

Lin, S. (2007). World Loquat Production and Research with Special Reference to China. *Acta Hortoculturae*, 750, 37-43.

Mataix, J., Mañas, M., Llopis, J. (1998). *Tabla de Composición de Alimentos españoles*, Universidad de Granada, Granada, Spain.

Moraga, G., Martínez-Navarrete, N., Chiralt, A. (2006). Water sorption isotherms and phase transitions in kiwifruit. *Journal of Food Engineering,* 72, 147-156.

Oswin, C. (1946). The kinetics of package life III. *Journal of Chemical Industry*, 65, 419–421.

Palipane, K., Driscoll, R. (1992). Moisture sorption characteristics of inshell macadamia nuts. *Journal of Food Engineering*, 18, 63–76.

Peleg, M. (1993). Assessment of a semi.empirical four parameter general model for sigmoid moisture sorption isotherms. *Journal of Food Process Engineering*, 16, 21-37.

Rizvi, S.S.H. (1986). *Thermodynamics of foods in dehydration*. In: Engineering Properties of Food, 133–214. Marcel Dekker, New York.

Samaniego-Esguerra, C., Boag, I., Robertson, G. (1991). Comparison of regression methods for fitting the GAB model to the moisture isotherms of some dried fruits and vegetables. *Journal of Food Engineering*, 13, 115–133.

Van den Berg, C., Bruin, S. (1981). *Water activity and its estimation in food systems; Theoretical aspects*, Academic Press Inc., New York.

Proceedings of the 10th International Chemical and
Biological Engineering Conference - CHEMPOR 2008
Braga, Portugal, September 4-6, 2008
E.C. Ferreira and M. Mota (Eds.)

The Influence of Sucrose Osmotic Pretreatment on the Kinetics of Rehydrated Dried Chestnuts

R. Moreira*, F. Chenlo, L. Chaguri
Departamento de Enxeñaría Química, Escola Técnica Superior de Enxeñaría (ETSE), Universidade de Santiago de Compostela, Rúa Lope Gómez de Marzoa, s/n 15782 Santiago de Compostela, Spain.

Keywords: Dehydration, Water sorption, Rehydration indexes, Peleg's model
Topic: Food engineering.

Abstract

Rectangular prisms of chestnuts (10 x 10 x 15 mm) previously dried at 65 ºC without and with sucrose treatment (60 % (p/p) at 25 ºC during 8 hours) until different moisture content (0.33 and 0.15 kg water/kg d.b.) were rehydrated by inmersion in water at 25 ºC during different periods of time (10, 30, 60, 120 and 180 min). Rehydration kinetics were obtained by measuring their weigths at several intervals of time. At the same time, the swelling was experimentally determined.

Peleg's model was succesfully applied to describe the water uptake in all experiments. The parameters K_1 and K_2 were obtanined and it was observed that both Peleg's constants decrease when osmotic treatment was carried out. Rehydration indexes, such as dry basis holding capacity (DHC), water absorption capacity (WAC) and rehydration ability (RA) were determinated. The results indicated that rehydration capacity of sample with sucrose treatment was greater than chestnuts dried at same moisture content without osmotic treatment. The chestnuts volume recovery can be considered as ideal swelling.

1. Introduction

Chestnut (*Castanea sativa* Mill.) is a traditional seasonal fruit (autumn) from Mediterranean countries. It presents high water content (50 % wet basis, approximately) and also is an important carbohydrate source (46 % dry basis; mainly starch and several sugars like sucrose and, glucose and fructose in less proportion) and (Scharz, 1990; De la Montaña et al., 2004). The main chestnut countries producers (10^3 t/year) in the European Community are Italy (50), Portugal (31), Greece (19), France (12) and Spain (10), (FAOSTAT, 2007). Owing to chestnut high moisture content and it seasonal characteristics, drying can be considered as a useful method to improve product availability. Air drying is the method frequently used in the drying of food materials. Some process variables during drying as temperature, velocity of air, relative humidity could have a highly negative effect on the quality of the product. Furthermore, most of dehydrated products need to be rehydrated before consumption or further processing. So many reconstitution properties can be obtained through control of the dehydration and rehydration processes conditions (Marabi et al., 2006) to achieve a product with characteristics similar to the fresh.

The study of the rehydration kinetics is very important to improve the global food processing. In this way, it is necessary the knowledge on the food product composition, pre-drying treatment, drying techniques and conditions, composition and temperature of rehydration media (Funebo and Ohlsson, 1998; Lewicki, 1998a). The determination of rehydration indexes is useful to quantify the degree of cellular and structural disruption caused during processes previous to rehydration so as to establish the market acceptability (Lewicki, 1998b). The water absorption capacity (WAC) index

* Corresponding author. Tel + 34-981-563-100. E-mail:eqmoncho@usc.es

provides information on the ability of the material to absorb water and increases with water absorption. WAC value can be calculated according to equation:

$$WAC = \frac{M_r X_r - M_d X_d}{M_0 X_0 - M_d X_d} \quad (1)$$

where M is the dry mass (kg d.b.), X is the moisture content (kg water/kg d.b.), and subscripts d, o and r refer to after drying (or before rehydration), before drying and after rehydration, respectively.

The dry matter holding capacity (DHC) index is a measure of the ability of the material to hold soluble compounds and represents the extent of tissue damage and its permeability to soluble compounds. The DHC was calculated according to equation:

$$DHC = \frac{M_r s_r}{M_d s_d} \quad (2)$$

where s is the solid content and subscript r and d are refer to after and before rehydration.

Finally, rehydration ability (RA) index is a measure of ability of the product to rehydrate and shows the damage of the tissue by drying and rehydration processes. The RA was calculated according to equation:

$$RA = (WAC)\,(DHC) \quad (3)$$

The rehydration kinetics of dehydrated chestnut was obtained and the resulting data were fitted to the Peleg's model (Peleg, 1988) defined by:

$$X = X_0 + \frac{t}{K_1 + K_2 t} \quad (4)$$

where K_1 (s·kg d.b./kg water) is a kinetic parameter and K_2 (kg d.b./kg water) is other parameter related to equilibrium moisture content, X_e. When $t \rightarrow \infty$, equilibrium moisture content can be calculed by:

$$X_e = X_0 + \frac{1}{K_2} \quad (5)$$

Equation (4) can be linearized:

$$\frac{t}{X - X_0} = K_1 + K_2 t \quad (6)$$

allowing for the determination of K_1 and K_2 values by linear regression of experimental data.

The effect of the previous dehydration steps (osmotic treatment and convective air drying) on rehydration kinetics of chestnuts was evaluated.

2. Materials and Methods

Raw Material. Chestnut samples (*Castanea sativa* Mill), variety Famosa, with similar initial moisture content (0.55 ± 0.02 kg water/kg wet product) were carefully prepared with rectangular prismatic geometry (10x10x15 mm) from the parenchymatic tissue with a cuter mechanized in longitudinal direction to the basis of the chestnut. The moisture content was determined using a vaccum oven (< 15 kPa) and 70 ºC (Heraeus

Vacutherm VT650) up to constant weight of samples, following standard procedure (AOAC, 1995).

Dehydration Experiments and Conditions. Prisms were previously dehydrated by osmosis in aqueous sucrose solutions (60 % w/w) at 25 ºC during 8 h (optimal conditions (Chenlo *et al*., 2007)). The relation of weights solution sample was around 10 in order to maintain constant sucrose concentration of solution during the osmotic process. After, convective air-drying was carried out in a chamber at pilot-plant scale, with a hot air closed circuit and assisted by a heat pump (Vázquez *et al*., 1997), at 65 ºC, 30 % of relative humidity and speed of air at 2.4 m/s, (Moreira *et al*., 2005). Different drying times (0.5, 1.5, 3 and 6 hours) were assayed (obtaining samples with different moisture content).

Rehydration Experiments and Conditions. After drying, samples of chestnuts were immersed into distilled water at 25 ºC during different periods of time (10, 30, 60, 120, and 180 min). Rehydrated samples were carefully blotted with absorbent paper in order to remove external water and after they weighted and introduced into the vaccum oven to obtain the dry solid.

Determination of swelling. Four samples, for each experimental condition tested, were used at the specified rehydration times to evaluate swelling of samples during rehydration and after determination of dry solids contents. Swelling was determined by displacement technique and samples were weighed at 20 ºC in air and in n-heptane liquid (ρ_{hep} = 710 kg/m^3), consecutively. On the basis of Archimedes' principle, volume of sample, V, was calculed by:

$$V = \frac{m - m_{hep}}{\rho_{hep}} \quad (7)$$

where m (kg) is the weight of chestnut in air and m_{hep} (kg) is the weight of the same sample immersed in n-heptane.

3. Results

Figure 1a,b shows, as examples, rehydration kinetics of chestnuts, with or without osmotic pre-treatment with sucrose, partially air-dried at 65 ºC up to 0.33 and 0.15 kg of water/kg d.b. Rehydration kinetics showed initially high water absorption rates that decrease as samples achieve to equilibrium. Initial moisture content is also a significant variable in rehydration kinetics. Samples previously dried for longer periods (lower initial moisture contents) showed less rehydration capacity, indicating the presence of modified structures (Moreira et al., 2008). In this manner, the amount of water imbibed during rehydration depends on the extension of the drying step. After long drying periods (chestnut dried until 0.15 kg water/kg d.b.) samples showed a diminution of rehydration rate regard as samples dried for shorter periods (chestnut dried until 0.33 kg water kg d.b.). Similar behaviour in rehydration of chestnuts (without pre-treatment) at several temperatures and initial moisture contents (after dried) has been found by Moreira et al., 2008. It could be explained due the occurrence of shrunken and closed structures that avoid the passage of water. The osmotic pre-treatment increased the rate and the amount of water gained during rehydration process regarding to chestnuts without pre-treatment. Basically, the explanation of these results is based on the fact of the dry solid of samples increases during osmotic treatment due to the osmotic solute acquisition that contributes to retain greater water amount.

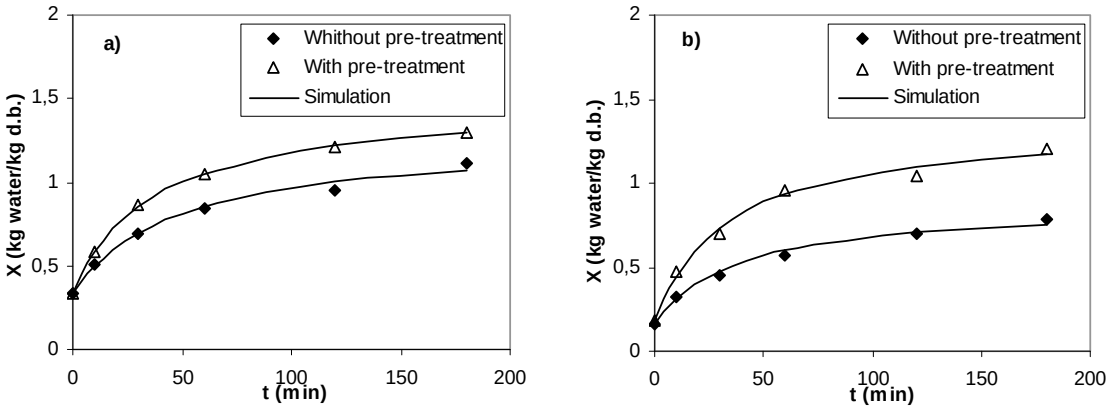

Figure 1. Rehydration kinetics at 25 ºC of chestnuts, with and without sucrose pre-treatment, and dried at 65 ºC up to a) 0.33 and b) 0.15 kg water/kg d.b.

Table 1 shows values of K_1 and K_2 parameters and equilibrium moisture content obtained from equations (5) and (6) at 25 ºC and to the initial moisture content tested at 0.33 and 0.15 kg water/kg d.b., respectively. All values of coefficients of determination (R^2) were equal or higher than 0.98 indicating that Peleg's model was satisfactorily applied (lines in Figure 1a,b) to describe rehydration kinetics of chestnuts at the experimental conditions tested. Values of K_1 and K_2 decrease with osmotic treatment at each initial moisture content. This behaviour indicates that water transfer and water absorption capacity (related to the inverse of K_1 and with K_2, respectively) are promoted by osmotic treatment. The water capacity absorption depends on the type of material, structure of tissue, and chemical composition and can be modified by application of treatments. This behaviour is in accordance with other authors who considered that parameter K_2 can change if structure or other properties are modified during rehidration (García-Pascual et al., 2005; Lopez et al., 1995). Otherwise, values of equilibrium moisture increase when the osmotic treatment was carried out.

Table 1 Parameters and coefficients of determination of equation (6) and values equilibrium moisture content, equation (5), for rehydration at 25 ºC of chestnuts dried with and without sucrose treatment until 0.33 and 0.15 kg water/kg d.b.

Treatment	K_1 s.(kg water/kg d.b.)$^{-1}$	K_2 (kg water/kg d.b.)$^{-1}$	R^2	X_e (kg water/kg d.b.)
X_0 (kg water/kg d.b.) = 0.33 ± 0.05				
Without	2990.9	1.07	0.98	1.26
With	1861.0	0.86	0.99	1.49
X_0 (kg water/kg d.b.) = 0.15 ± 0.03				
Without	3264.3	1.39	0.99	0.88
With	1747.4	0.85	0.99	1.36

Table 2 shows values of DHC, WAC and RA rehydration indexes, as function of the applied osmotic treatment, rehydration times and initial moisture content (chestnuts pre-dried until 0.33 and 0.15 kg water/kg d.b.). These results confirm that the rehydration ability is reduced due to the drying modifies the structure of the chestnut. This behaviour is more emphasize in samples pre-dried at low moisture contents. According to expectations, DHC index decreases and WAC and RA indexes increase with rehydration time for samples with and without pretreatment. Chestnuts previously dried with osmotic treatment show WAC and RA indexes higher than chestnut dried without pre-treatment. This result indicates a largest rehydration capacity without additional loss of soluble compounds acquired during osmotic treatment.

Table 2 Values of DHC, WAC and RA indexes at different times of rehydration (and moisture content) for chestnuts dried at 65 ºC without and with sucrose (60%, 25 ºC, 8 h) treatment at 0.33 and 0.15 kg water/kg d.b.

t (min)	X (d.b.)	DHC	WAC	RA	X (d.b.)	DHC	WAC	RA
X_0 (kg water/kg d.b.) = 0.33 ± 0.05								
	Without pretreatment				With pretreatment			
10	0.510	1.056	0.437	0.462	0.584	1.043	0.145	0.151
30	0.689	0.928	0.828	0.768	0.865	1.007	0.616	0.620
60	0.847	0.908	1.087	0.987	1.048	0.994	0.940	0.935
120	0.953	0.890	1.230	1.095	1.207	0.975	1.455	1.419
180	1.113	0.901	1.537	1.385	1.302	0.846	1.487	1.259
X_0 (kg water/kg d.b.) = 0.15 ± 0.03								
	Without pretreatment				With pretreatment			
10	0.319	1.000	0.255	0.255	0.478	0.981	0.227	0.223
30	0.454	0.982	0.474	0.465	0.702	0.970	0.364	0.353
60	0.569	0.952	0.599	0.570	0.955	0.963	0.624	0.601
120	0.703	0.929	0.775	0.720	1.039	0.911	0.636	0.579
180	0.784	0.926	0.864	0.800	1.203	0.880	1.076	0.947

Figure 2 shows the variations of the volume of samples with and without osmotic pretreatment at different initial moisture content obtained experimentally with n-heptane by displacement techinique (calculed by Equation (7)) versus the volume of samples imbibed water, which is calculed from the mass of water obtained from rehydration kinetics. Experimental data are appromixately on the diagonal (random differences). In this way, the volume recovery can be considered ideal swelling. These results are different regarding to volumetric shrinkage of chestnut during drying. In that case, it was observed the presence of collapsed structure due to volumetric shrinkage was higher than equivalent volume occupied by water that was removed (Moreira et al., 2005). Ideal volumetric swelling can mean that water firstly fills the open void spaces of chestnut and after tissue structure. So, the chestnut is partially rehydrated in the more external areas.

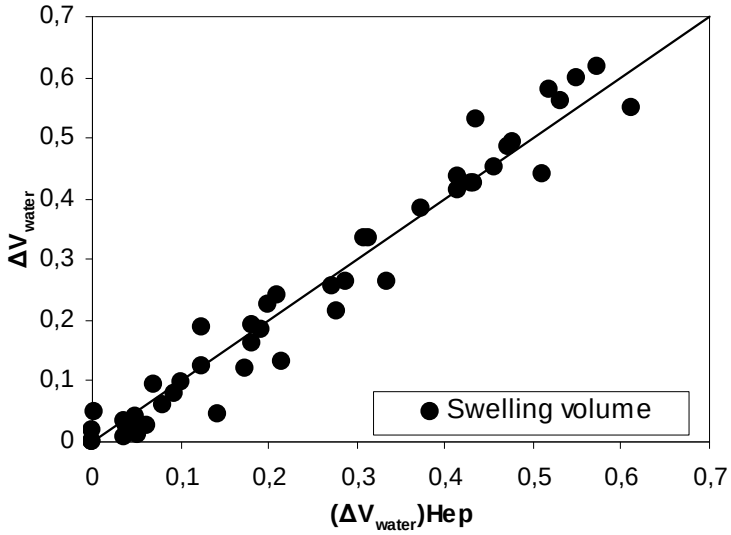

Figure 2 Volumetric swelling during rehydration of chestnuts samples

4. Conclusions

Rehydration kinetics show high initial water absorption rates that decreases during rehydration time. Samples previously dried during longer period showed a minor rehydration, indicating the existence of modified structure. Osmotic treatment increases water absortion rates and the amounts of absorbed water. Peleg's model was successfully applied to the experimental data of rehydration of chestnuts. Equilibrium moisture content increases and K_1 and K_2 decrease when osmotic treatment was carried out. With regard to rehydration indexes, DHC index decreases and WAC and RA indexes increase with time. The osmotic treatment increases the values of WAC and RA indexes regard as samples was rehydrated without pre-treatment. Analisys of indexex rehydration confirms that drying modifies the structure of chestnuts, reducing the rehydration ability. By other hand, the pre-treatment increase the rehydration capacity without additional loss of soluble compounds that was acquired during osmotic treatment. No effect of pre-treatment and initial moisture content was observed on the swelling and the volume recovery can be considered as ideal swelling.

References

AOAC. (1995). Official methods of analysis, 16th ed. Association of Official Analytical Chemists, Washington DC.

Chenlo, F., Moreira, R., Fernández-Herrero, C., Váquez, G. (2007). Osmotic dehydration of chestnut with sucrose: mass transfer processes and global kinetics modelling. *Journal of Food Engineering*, 78, 765-774.

De la Montaña Míguelez, J., Míguez Bernárdez, M., García Queijeiro, J.M. (2004). Composition of varieties of chestnuts from Galicia (Spain). *Food Chemistry*, 84, 401-404.

FAOSTAT. (2007). Statistical database. In: *http://faostat.fao.org*.

Funebo, T., Ohlsson, T. (1998). Microwave-assisted air dehydration of apple and mushroom. *Journal of Food Engineering*, 38, 353-367.

García-Pascual, P., Sanjuán, N., Bon, J., Carreres, J.E., Mulet, A. (2005). Rehydration process of Boletus edulis mushroom: characteristics and modelling. *Journal of the Science of Food and Agriculture*, 85, 1397-1404.

Lewicki, P.P. (1998a). Some remarks on rehydration of dried foods. *Journal of Food Engineering*, 36, 81-87.

Lewicki, P.P. (1998b). Effect of pre-drying treatment, drying and rehydration on plant tissue properties:a review. *International Journal of Food Properties*, 1, 1-22.

Lopez, A., Pique, M., Clop, M., Tasias, J., Romero, A., Boatella, J., Garcia, J. (1995). The hygroscopic behaviour of the hazelnut. *Journal of Food Engineering*, 25, 197-208.

Marabi, A., Thieme, U., Jacobson, M., Saguy, I.S. (2006). Influence of drying method and rehydration time on sensory evaluation of rehydrated carrot particulates. *Journal of Food Engineering*, 72, 211-217.

Moreira, R., Chenlo, F., Chaguri, L., Fernandes, C. (2008). Water sorption, texture, and color kinetics of air-dried chesnuts during rehydration. *Journal of Food Engineering*, 86, 584-594.

Moreira, R., Chenlo, F., Chaguri, L., Vázquez, G. (2005). Mathematical modelling of the drying kinetics of chestnut (*Castanea sativa* M.): influence of the natural shells. *Food and Bioproducts Processing*, 83, 306-314.

Scharz, H. (1990). Food composition and nutrition tables. Wissenchaftli-che Vivlagsgesselchaft, mbtf., Stuttgart, Germany.

Peleg, M. (1988). A empirical model for the description of moisture sorption curves. *Journal of Food Science*, 53, 1216-1219.

Vázquez, G., Chenlo, F., Moreira, R., Cruz, E. (1997). Grape drying in a pilot plant with a heat pump. *Drying Technology*, 15, 899-920.

Proceedings of the 10th International Chemical and
Biological Engineering Conference - CHEMPOR 2008
Braga, Portugal, September 4-6, 2008
E.C. Ferreira and M. Mota (Eds.)

Production of polygalacturonase from *Coriolus versicolor* grown on tomato pomace and its chromatographic behaviour on immobilized metal chelates

Maria do Rosário Freixo[1,2], Amin Karmali[2*], José Maria Arteiro[1]
[1] Department of Chemistry, Universidade de Évora,
Rua Ramalho Ortigão Nº59, Évora, Portugal
[2] Chemical Engineering and Biotechnology Research Center of Instituto Superior de Engenharia de Lisboa, Rua Conselheiro Emídio Navarro 1950-062 Lisboa, Portugal.
[*] corresponding author

Keywords: Tomato pomace; polygalacturonase production; IMAC purification; *Coriolus versicolor* ; lignocellulosic enzymes.
Topic: Multi-scale and/or multi-disciplinary approach to process-product innovation

Abstract

Tomato pomace and pectin were used as the sole carbon sources for production of polygalacturonase from a strain of *Coriolus versicolor* in submerged culture. The culture of *C. versicolor* grown on tomato pomace exhibited a peak of polygalacturonase activity (1427 U/L) on the 3rd day of culture with a specific activity of 14.5U/mg protein. The production of polygalacturonase by *C. versicolor* grown on pectin as sole carbon source, increased with the time of cultivation, reaching a maximum activity of 3207 U/L of fermentation broth with a specific activity of 248 U/mg protein. Differential chromatographic behaviour of lignocellulosic enzymes produced by *C. versicolor* (i.e polygalacturonase, xylanase and laccase) was studied on immobilized metal chelates. The effect of ligand concentration, pH, the length of spacer arm and the nature of metal ion were studied for enzyme adsorption on immobilized metal affinity chromatography (IMAC). The adsorption of polygalacturonase as well as other enzymes to immobilized metal chelates was due to coordination of histidine residues which are available at the protein surface since the presence of imidazole in the equilibration buffer abolished the adsorption of the enzyme to immobilized metal chelates. A one-step purification of polygalacturonase from C*. versicolor* was devised by using a column of Sepharose 6B-EPI 30-IDA-Cu(II) and purified enzyme exhibited a specific activity of about 150 U/mg protein, final recovery of enzyme activity of 100% and a purification factor of about 10. The use of short spacer arm and the presence of imidazole in equilibration buffer exhibited a higher selectivity for purification of polygalacturonase on this column with a high purification factor. The purified enzyme preparation was analysed by SDS-PAGE as well as by “in situ” detection of enzyme activity.

1 Introduction

A major issue faced by the food processing industries involves the accumulation, handling and disposal of wastes which arise both economical and environmental problems. Tomato (*Lycopersicon esculentum* Mill.) is a widely cultivated vegetable crop in Mediterranean countries. During tomato processing, a huge amount of a by-product is produced known as tomato pomace which consists of tomato peel, seeds as well as some pulp. The chemical composition of tomato pomace consists of proteins, lipids, carbohydrates including pectins, amino acids, carotenoids and minerals (Alvarado, Pacheco-Delahaye, Hevia, 2001; Knoblich, Anderson, Latshaw, 2005; Valle, Cámara, Torija, 2006). Several pectin-rich substrates such as wheat, deseeded sunflower head, apple pomace and citrus peel have been used for the production of microbial pectinases in both submerged and solid-state fermentation. However, to our knowledge tomato pomace has not been used for production of pectinases.

Pectins are a family of polysaccharides with a backbone of 1,4-linked α-D-galacturonic acid residues, partially present as their methyl esters. Pectinases are widely used in biotechnological applications [19], namely in food industry (i.e fruit juice extraction, coffee and tea fermentation, oil extraction, improvement of chromaticity and stability of red wines), textile, paper and pulp industries and in waste water treatment. However, industrial production of pectinases makes use almost exclusively of *Aspergillus niger* strains [31].
Polygalacturonases (EC 3.2.1.15 and EC 3.2.1.67) catalyse the hydrolysis of α-1,4-linkages between α-D- galacturonic acid units in pectin, by endo and exo action. There is only one report in the literature about the production of endo and exo-polygalacturonases from a white rot fungi, *Coriolus trogii* (Levin, Forchiassin, 1998). Polygalacturonases are of industrial interest since they are used in specific applications, such as in baby and functional foods (Jayani, Saxena, Gupta, 2005; Gummadi, Panda, 2003).
Since this enzyme is secreted extracelularly by white-rot fungi as well as other lignocellulosic enzymes, it is of great interest to devise a simple and cheap separation method for these enzymes so as to be used in different industrial applications.
Immobilized metal affinity chromatography (IMAC) has been used for purification of wild-type and recombinant proteins. The interactions between accessible coordination sites of metal ions and electron-donating groups present on the protein surface are responsible for retention of proteins in IMAC. Several factors affect the adsorption process, such as the nature of metal ion involved in coordination, the matrix, the length of spacer arm, the ligand concentration, the pH and buffer used (Porath, 1992; Gutiérrez, Valle, Galán, 2007).
To our knowledge, IMAC has not been reported in the literature for fractionation and purification of polygalacturonase as well as xylanase and laccase from microbial sources.
The present work is concerned with the production of polygalacturonase from *Coriolus versicolor* by using either tomato pomace or pectin as sole carbon source in culture media. Subsequently, the chromatographic behavior of this enzyme as well as other lignocellulosic enzymes (i.e xylanase and laccase) on immobilized metal chelates will be investigated as a function of ligand concentration, pH, length of spacer arm and nature of metal ion. The selective adsorption of polygalacturonase on immobilized metal chelates will be carried out for purification of this enzyme with high yield and activity.

2 Methods

2.1 Fungal growth conditions
Fungal growth conditions were previously described (Freixo, Karmali, Arteiro, 2008).

2.2 Enzyme assays
Enzymatic assays were performed as described in the literature (Freixo, Karmali, Arteiro, 2008).

2.3 Preparation of chromatographic matrices
Chromatographic matrices were prepared as described in the literature (Freixo, Karmali, Arteiro, 2008).

2.4 Adsorption tests of polygalacturonase, xylanase and laccase on metal chelates
As previously described (Martins, Andrade, Karmali, Serralheiro, 2006), a rapid batch method carried out in ELISA microtiter plates was used to study the adsorption of polygalacturonase, xylanase and laccase on the following Cu(II), Ni(II), Zn(II) and Co(II) metal chelate supports: Sepharose 6B- BDGE-30-IDA- M(II), Sepharose 6B- EPI-30-IDA- M(II) and Sepharose 6B- EPI-10-IDA- M(II).

2.5 Purification of polygalacturonase from *Coriolus versicolor*

Based on the results of the batch mode on ELISA microtiter plates, a set of experimental conditions were selected to purify polygalacturonase from this fungal strain, as described in the literature (Freixo, Karmali, Arteiro, 2008).

3. Results and Discussion

3.1 Production of polygalacturonase and protein content in culture supernatants

The cultivation of *Coriolus versicolor* on tomato pomace and pectin media was followed for 14 days (Fig.1) and the content of soluble reducing sugars, protein and polygalacturonase activity were measured throughout the cultivation process. Polygalacturonase activity in culture medium containing tomato pomace displayed a "two peaks" time-course curve for this strain of basidiomycete, as shown in Fig. 1A. Such feature was observed by other authors which suggested that it was due to catabolic repression of polygalacturonases in the presence of glucose and other sugars which were released to the medium during fermentation of other polysaccharides. The culture of *Coriolus versicolor* exhibited a peak of polygalacturonase activity (1427 U/L of fermentation broth) on the 3rd day of culture with a specific activity of 14.5 U/mg protein (Fig. 1A). The data presented in the literature revealed that C*oriolus trogii* secreted polygalacturonase with a lower activity (1000 U/L of fermentation broth) on the 15th day of culture [22]. On the other hand, several strains of *Aspergillus sp.* have been used for production of polygalacturonase in submerged culture which exhibited the highest levels in the range of 1000 – 6500 U/L of fermentation broth containing either citrus pectin, dried orange peel or sugar beet as carbon sources.

A

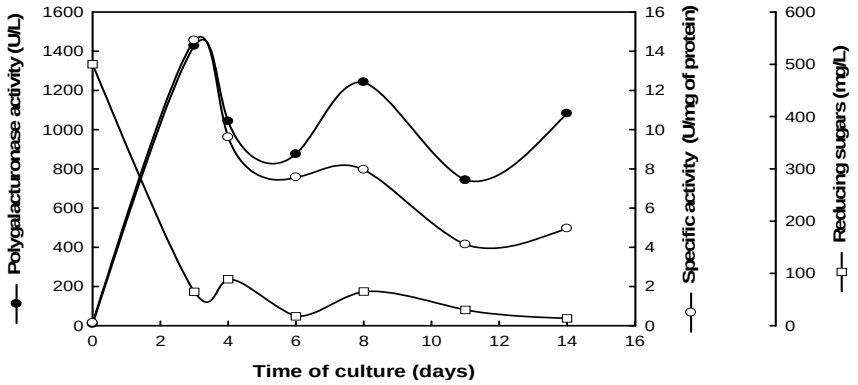

B

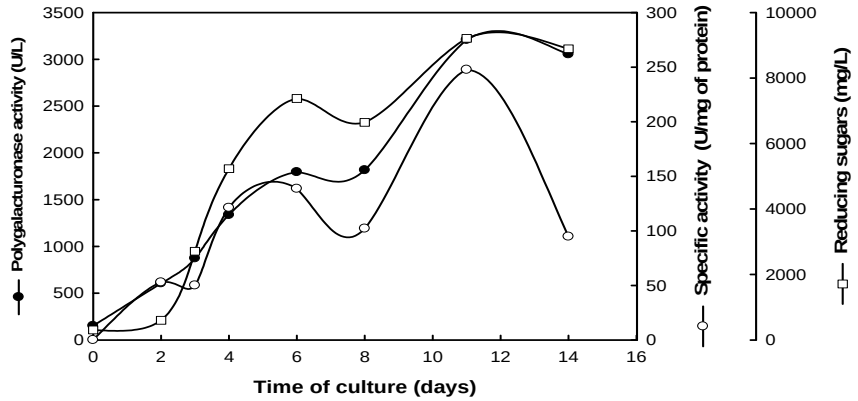

Figure 1 – Total protein content and polygalacturonase activity assayed in culture supernatant of fermentation broth of *Coriolus versicolor* by using either tomato pomace or pectin as carbon sources. A- Tomato pomace as carbon source and B- Pectin as carbon source (Polygalacturonase activity - ●; Specific activity - ○ and Soluble reducing sugars - □).

3.2 Chromatographic behaviour of polygalacturonase, xylanase and laccase on immobilized metal chelates

The chromatographic behaviour of these lignocellulosic enzymes is summarized in Table 1, for different stationary phases (Sepharose 6B-BDGE 30 – IDA, Sepharose 6B EPI 30–IDA, Sepharose 6B–EPI 10–IDA) as well as for different immobilized metal ions. The results from adsorption assays did not vary with either different ligand concentration or length of spacer arm, suggesting that protein adsorption takes place through the immobilized metal ion at different pH (Table 1). Xylanase exhibited partial adsorption to immobilized Cu(II)-IDA chelates at pH 7.0 and 8.0 whereas it did not adsorb at pH 6.0. Polygalacturonase and laccase revealed full adsorption to immobilized Cu(II)-IDA chelates at pH 6.0, 7.0 and 8.0 (Table 1).

Table 1 – Differential chromatographic behaviour of lignocellulosic enzymes from *Coriolus versicolor* on immobilized metal chelates

	pH	Stationary phase	Cu(II)	Ni(II)	Zn(II)	Co(II)
Xylanase	6	BDGE-30, EPI-30, EPI-10	–	–	–	–
	7	BDGE-30, EPI-30, EPI-10	±	–	–	–
	8	BDGE-30, EPI-30, EPI-10	±	–	–	–
Polygalacturonase	6	BDGE-30, EPI-30, EPI-10	+	–	–	–
	7	BDGE-30, EPI-30, EPI-10	+	–	–	–
	8	BDGE-30, EPI-30, EPI-10	+	–	–	–
Laccase	6	BDGE-30, EPI-30, EPI-10	+	–	–	–
	7	BDGE-30, EPI-30, EPI-10	+	–	–	–
	8	BDGE-30, EPI-30, EPI-10	+	-	-	-

3.3 Purification of polygalacturonase by using imidazole in equilibration buffer

The combination of tailor-made stationary phases for IMAC and a correct choice of the adsorption conditions permitted to design a one-step purification procedure for polygalacturonase from *Coriolus versicolor*. The chromatographic behaviour of polygalacturonase on Sepharose 6B – EPI 30 – IDA- Cu(II) column at pH 6.0 (Fig.2B) resulted in partially purified enzyme according to the electrophoretic analysis (data not shown). However, the presence of 2mM imidazole in the equilibration buffer abolished the adsorption of several protein contaminants to Sepharose 6B – EPI 30 – IDA- Cu(II) column including laccase and xylanase (data not shown). Hence, polygalacturonase was desorbed from the column with a linear gradient of imidazole (Fig. 2C) with a specific activity of about 150 U/mg protein, a final recovery of enzyme activity of about 100% and a purification factor of about 10 (Table 2). The degree of purification of this polygalacturonase activity peak was high and exhibited no contamination (data not shown) with either laccase or xylanase activities (Table 3). However, the final recovery of enzyme activity was only about 50% with a specific activity of about 180 U/mg protein in the presence of 4mM imidazole in the equilibration buffer (Table 3).

The purity of chromatographic fractions from Sepharose 6B – EPI 30 – IDA- Cu(II) was analysed by SDS-PAGE which revealed that the purified fractions exhibited three protein bands and three activity bands of polygalacturonase with Mr of 63.3, 43 and 30 kDa. The presence of two additional activity bands of polygalacturonase may be due to other forms of this enzyme in white-rot fungi. However, the Mr value of 41.7 kDa was also reported in the literature for purified preparations of endopolygalacturonases from *Phanerochaete chrysosporium*. On the other hand, an extracellular polygalacturonase from *Trichoderma harzianum* exhibited a Mr of 31 kDa on SDS-PAGE.

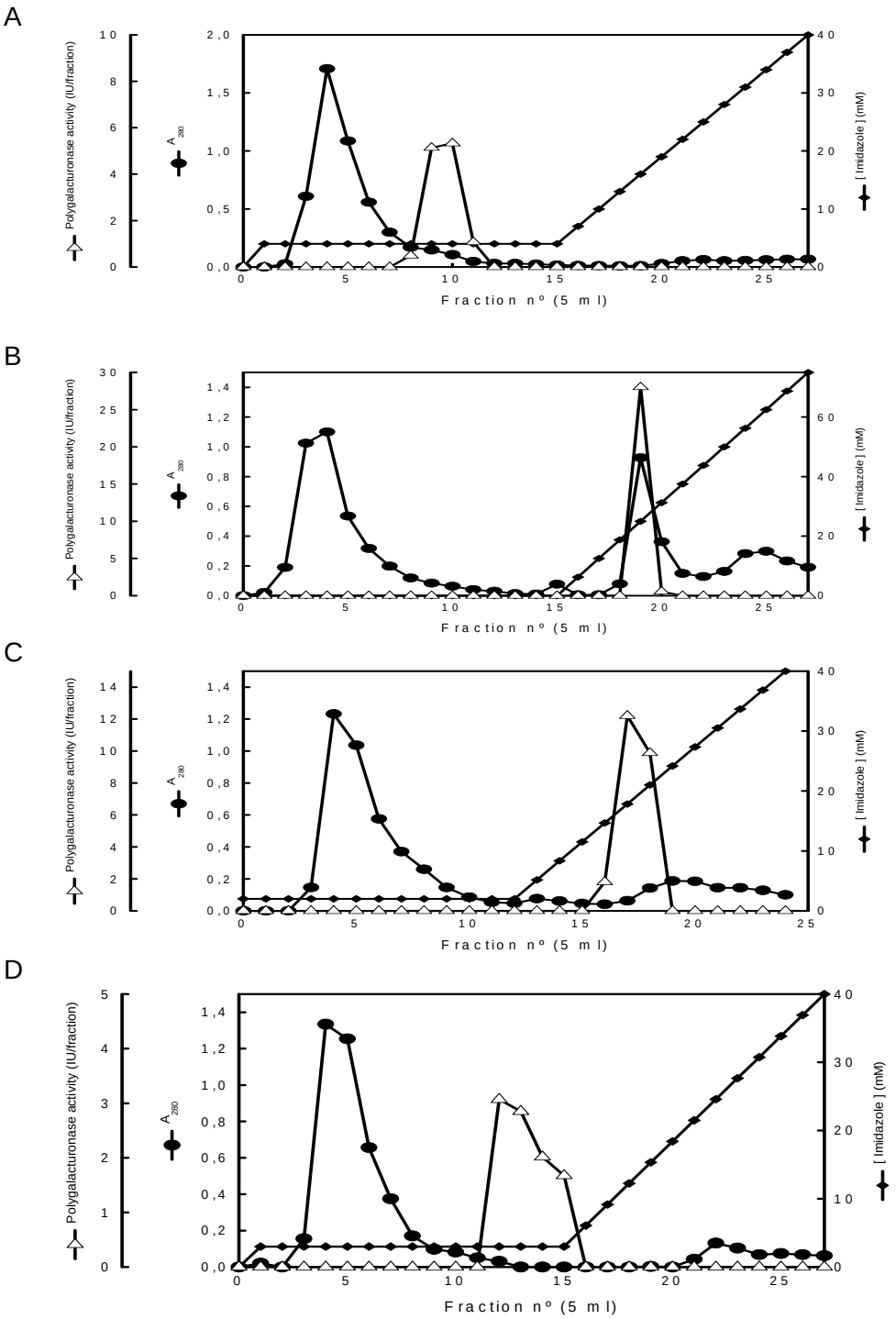

Figure 4 - Chromatographic behaviour of polygalacturonase from *Coriolus versicolor* on a Sepharose 6B–EPI-30–IDA-Cu(II) column at pH 6.0. Elution was carried out with a linear gradient of imidazole, as described in Materials and Methods. A- 4mM imidazole in the equilibration buffer (increments of 3 mM imidazole per fraction); B- No imidazole in the equilibration buffer (increments of 3.33 mM imidazole per fraction); C- 2mM imidazole in the equilibration buffer (increments of 3.17 mM imidazole per fraction); D- 3 mM imidazole in the equilibration buffer (increments of 3.08 mM imidazole per fraction).

Table 2 - Purification of polygalacturonase from *Coriolus versicolor* by Immobilized Metal Affinity Chromatography on Sepharose 6B – EPI 30 – IDA - Cu(II) at pH 6.0 in the mobile phase containing 2mM imidazole.

	Purification Steps	Total protein (mg)	Total activity (U)	Specific activity (U/mg protein)	Recovery (%)	Purification factor
1.	Culture supernatant	1.4	20.62	14.73	100	1
2.	Cu (II) column eluate	0.140	20.58	147.0	99.8	9.97

Table 3 - Purification of polygalacturonase from *Coriolus versicolor* (CV) by Immobilized Metal Affinity Chromatography on Sepharose 6B – EPI 30 – IDA - Cu(II) at pH 6.0 in the mobile phase containing 4 mM imidazole.

	Purification Steps	Total protein (mg)	Total activity (U)	Specific activity (U/mg protein)	Recovery (%)	Purification factor
1.	Culture supernatant	1.4	20.22	14.44	100	1
2.	Cu (II) column eluate	0.0587	10.46	178.19	51.7	12.34

Acknowledgements

MRF is grateful to Évora University for finantial support and the authors thank Fundação para a Ciência e Tecnologia for partial financial support (Research Unit 702, POCTI/EQU/48812/2002) as well as Instituto Politécnico de Lisboa (Research Grant No. 25/2003).

References

Alvarado, A., Pacheco-Delahaye, E., Hevia, P. (2001). Value of a tomato byproduct as a source of dietary fiber in rats. Plant Foods for Hum Nutr, 56, 335-348.

Knoblich, M., Anderson, B., Latshaw, D. (2005). Analyses of tomato peel and seed byproducts and their use as a source of carotenoids. J Sci Food Agric, 75, 1166-1170.

Valle, M.D., Cámara, M., Torija, M.E. (2006). Chemical characterization of tomato pomace. J Sci Food Agric, 86, 1232-1236.

Jayani, R.S., Saxena, S., Gupta, R. (2005). Microbial pectinolytic enzymes: A review. Process Biochem, 40, 2931-2944.

Gummadi, S.N., Panda, T. (2003). Purification and biochemical properties of microbial pectinases – a review. Process Biochem, 38, 987-996.

Levin, L., Forchiassin, F. (1998). Culture conditions for the production of pectinolytic enzymes by the white-rot fungus *Coriolus troggi* on a laboratory scale. Acta Biotechnological, 18, 157-166.

Porath, J. (1992). Immobilized metal ion affinity chromatography. Protein Expr Purif;, 3, 1-7.

Gutiérrez, R., Valle, E.M.M., Galán, M.A. (2007). Immobilized Metal-Ion Affinity Chromatography: Status and Trends. Separation & Purification Reviews, 36, 71-111.

Martins, S., Andrade, J., Karmali, A., Serralheiro, M.L. (2006). Screening of suitable immobilized metal chelates for adsorption of monoclonal antibodies against mutant amidase from *Pseudomonas aeruginosa*. J Mol Recognit, 19, 340-347.

Freixo, M.R., Karmali, A., Arteiro, J. M. (2008). Production of polygalacturonase from *Coriolus versicolor* grown on tomato pomace and its chromatographic behaviour on immobilized metal chelates. J Ind Microbiol Biotechnol, 35, 475-484.

Proceedings of the 10th International Chemical and
Biological Engineering Conference - CHEMPOR 2008
Braga, Portugal, September 4-6, 2008
E.C. Ferreira and M. Mota (Eds.)

Biological deacidification of wine - must

Susana Ribeiro[1], Ana Xavier[1], Filipe Centeno[2,3], Pierre Strehaiano[3], Inês Portugal[1*]
[1] Departamento de Química/CICECO – Universidade de Aveiro, 3810 – 193 AVEIRO
[2] Proenol, Indústria Biotecnológica Lda., Travessa das Lages 267, 4405 – 194 Canelas, V. N. GAIA
[3] Laboratoire de Génie Chimie UMR CNRS 5503, INP-ENSIACET 118 Route de Narbonne, 31062 TOULOUSE, France

Keywords: Maloalcoholic fermentation, *Schizosaccharomyces pombe*, immobilized yeast, wine deacidification
Topic: Integration of life sciences & engineering

Abstract
Maloalcoholic fermentation of wine-must by *Schizosaccharomyces pombe* immobilized in alginate double-layer beads was studied in batch mode in Erlenmeyers and in a total recycle fixed-bed reactor. The influence of some parameters on must deacidification was discussed: the concentration of sulphur dioxide didn't affect the reaction rate significantly; the reaction is 1st order in relation to L-malic acid concentration with k=0,00174 h^{-1} at 15ºC and Ea= 16 ± 2 kcal/mol; the presence of ethanol slows the reaction by a factor of 2-3. Under similar conditions conversion of L-malic acid is faster in the recycle reactor than in the closed flaks. The recycle reactor handles larger volumes of must and this enables its implementation in wineries. The reaction can be stopped by adding *Saccaromyces cerevisiae* to inhibit the activity of *Schiz. pombe.*

1 Introduction

Total acidity is a key parameter for the organoleptic equilibrium and the stability of wines during ageing. It depends essentially on the relative amounts of tartaric and malic acids. It can be reduced by biological, chemical or mechanical methods but biological deacidification is usually preferred (Garcia *et al,* 2006). Traditional biological deacidification involves the growth of lactic acid bacteria, either spontaneously or induced by inoculation methods depending on the wine's microflora.

Malolactic fermentation (MLF) is a naturally occurring biological process where lactic acid bacteria transform malic acid (a dicarboxylic acid) into lactic acid (a monocarboxylic acid) and CO_2. This transformation reduces the wine's total acidity but it also changes wine's aromatic characteristics. Furthermore, MLF is often difficult to occur because during wine fermentation the pH, the temperature and the concentration of SO_2, ethanol and micronutrients can reduce the activity of lactic acid bacteria (Silva *et al*, 2003).

Maloalcoholic fermentation (MAF) is an alternative to MLF that uses yeast species such as *Schizosaccharomyces pombe* to transform malic acid into pyruvic acid which is further metabolised to ethanol and CO_2 (Fig. 1). The transformation of a dicarboxylic acid (malic acid) into an alcohol has the double effect of reducing acidity and increasing ethanol yield. Another advantage of MAF is the fact that *Schiz. pombe* yeasts are more tolerant to the above mentioned factors that inhibit lactic acid bacteria (Silva *et al,* 2003; Delpech, 2002).

* Corresponding author. Tel + 351-234 370 708… . E-mail:inesport@ua.pt

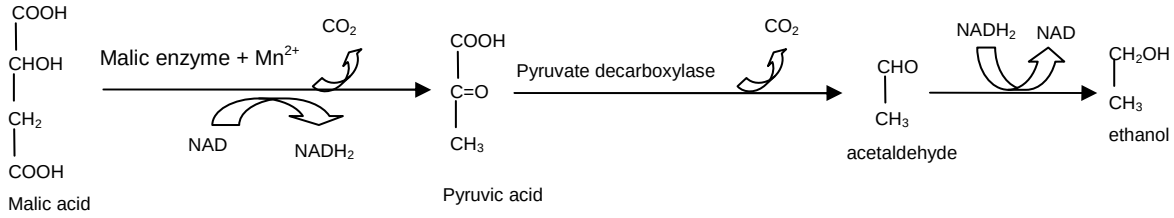

Figure 1 – Schematical representation of maloalcoholic fermentation (Garcia *et al,* 2006).

The consumption of L-malic acid by *Schiz. pombe* occurs without consumption of sugars and with similar activity when used either as free cells or immobilized cells (Silva *et al,* 2003). After total breakdown of L-malic acid *Schiz. pombe* yeast must be removed from the fermentative medium because prolonged contact with the deacidified must causes an unpleasant taste associated with the sugars' metabolism and thus the wine's organoleptic qualities are reduced (García *et a*l, 2006; Lepe, 1997). Yeast removal is easier to accomplish when using immobilized cells.

The purpose of this work was to study the activity of *Schiz. pombe* yeast encapsulated in double-layer alginate beads (diameter ~2 mm) for the biological deacidification of wine-must in a batch recycle fixed-bed reactor.

2 Materials and Methods

The yeast used for MAF was *Schizosaccharomyces pombe* immobilized in alginate double layer, commercially known by ProMalic®. Fermentative media (must) contained aprox. 200 g/L of sugar, the concentration of L-malic acid was adjusted to 2, 4 or 8 g/L , the initial pH was aprox. 3 and ProMalic® load was aprox. 1 g/L.

Total and free sulphur dioxide, total acidity and pH were evaluated at the beginning and at the end; sugars and L-malic acid concentrations were evaluated along time using enzymatic methods (ABX Pentra 400). The occurrence of MAF was confirmed by HPLC (Eurokat® 10 µm, refractive index detector, 0,4 mL/min H_2SO_4 0,01N, 25ºC).

Batch experiments in Erlenmeyers

Sterile must (430 mL, sterilized by ultrafiltration) was placed in 500 mL sterile Erlenmeyers closed with a cotton stopper. The concentration of L-malic acid was adjusted to the desired initial value (2, 5 or 8 g/L) and the pH was adjusted with 85% orthophosphoric acid to aprox. 3. This medium was inoculated with 1 g/L re-hydrated ProMalic® (re-hydration in a 40 g/L sugar solution during 4 to 5 hours) and reaction proceed at controlled temperature (± 1ºC). In some experiments must was replaced by wine to evaluate the influence of ethanol.

Experiments in a total recycle fixed bed reactor

The reactor scheme and photo are shown in Fig. 2. The glass reactor (h=20 cm, ϕ= 4cm) contained glass beads (Dp=3 mm) and re-hydrated ProMalic® beads (Dp=2 mm). Sterile must was placed in the feed-deposit (5 L) and pumped with an Ismatec MCP-Z peristaltic pump. Before each experiment all parts of the experimental set-up were sterilized by chemical methods using a 2-5 oxonium solution or by autoclaving during 15 minutes at 121ºC. The experimental assembly was placed in a controlled temperature chamber (±1ºC).

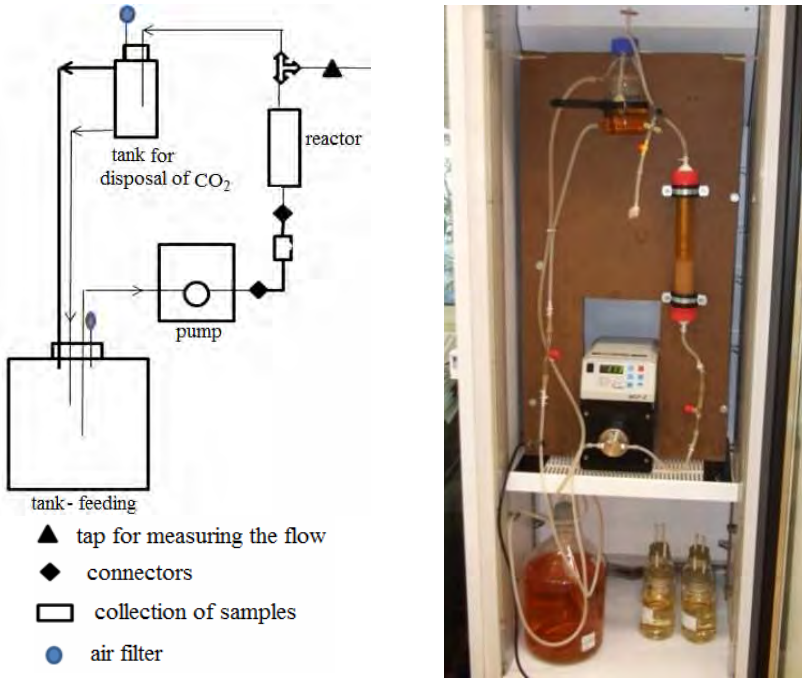

Figure 2 - Scheme and photo of the experimental assembly.

3. Experimental Results and Discussion:

The influence of L-malic acid initial concentration, ethanol and temperature on MAF rate was evaluated performing batch experiments in Erlenmeyers.

Experimental results for MAF at 15ºC using different initial concentrations of L-malic acid are presented in Fig. 3 and Table 1. L-malic concentration curves present a 1st order characteristic behaviour represented by equations (1) and (2)

$$\frac{d[L-malic]}{dt} = -k[L-malic] \quad (1)$$

$$[L-malic] = [L-malic]_0 . e^{-kt} \quad (2)$$

with k=0,00174 h^{-1} at 15ºC.

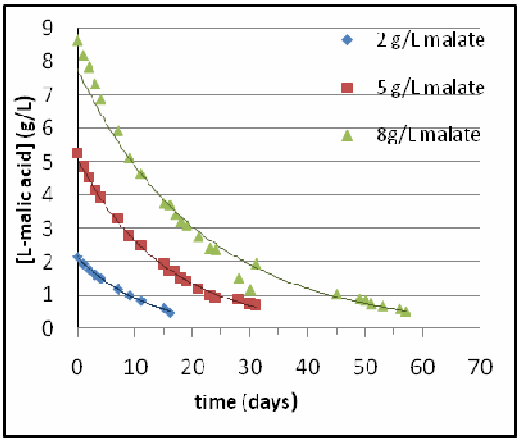

Table 1- Initial reaction rates (r_0) for different initial substrate concentrations (1 g/L ProMalic ® , 15ºC).

$[L\text{-malic acid}]_0$ (g/L)	r_0 (g/L day)
2	0,14
5	0,27
8	0,39

Figure 3 – MAF of L-malic acid in must using immobilized *Schiz. pombe* (1g/L ProMalic ®, 15ºC): experimental data and 1st order model curves.

Experimental results for MAF at different temperatures in the range 10 – 22 ºC are presented in Fig. 4 and Table 2. The results obtained with free yeast are also presented in Fig. 4 to discuss the effect of immobilization on deacidification rate.

Temperature increases the rate of MAF with an apparent energy of activation (Arrhenius type equation) of 16±2 kcal/mol and 31±8 kcal/mol for immobilized and free *Schiz. pombe* yeast, respectively. This difference is attributed to the existence of mass transfer limitations in the case of immobilized yeast due to the alginate's double layer. (Gòdia and López-Santín, Eds – 2005).

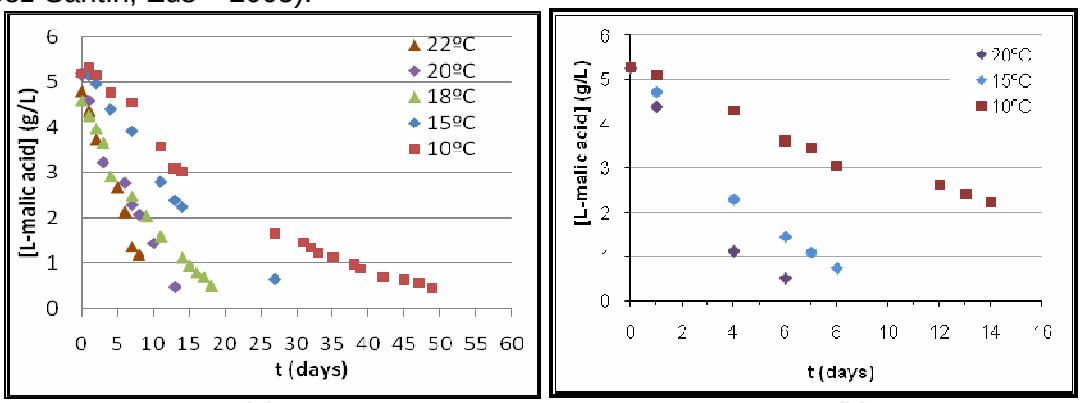

Figure 4 –Evolution of L-malic acid concentration with time during MAF of must by immobilized (a) and free (b) *Schiz. pombe* (1 g/L ProMalic ®) at different temperatures.

Table 2 – Initial rate of MAF at different temperatures by immobilized and free *Schiz. Pombe.*

	immobilized	free
T (ºC)	r_0 (g/L day)	r_0 (g/L day)
22	0,42	----
20	0,39	1,05
18	0,32	----
15	0,20	0,67
10	0,17	0,28

The inhibition of yeast's activity by ethanol is well known. To ascertain the effect of ethanol on the activity of immobilized *Schiz. pombe* the results for MAF of must were compared with the results for MAF of wine (11,3 º) (Fig. 5 and Table 3). Ethanol lowers the initial reaction rate by a factor of 1,5 to 3,5 and inhibition is stronger for higher concentrations of L-malic acid.

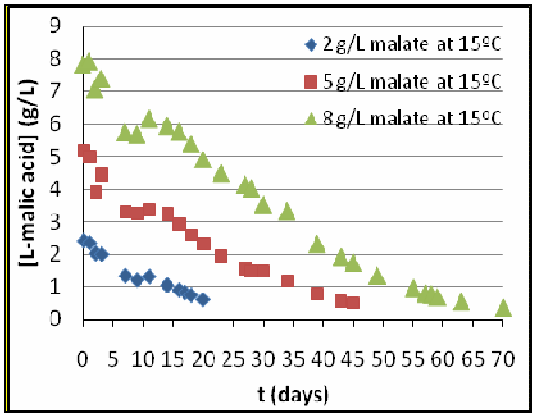

Table 3- Initial reaction rates (r_0) for MAF of wine and must with different initial substrate concentrations (1 g/L ProMalic ®, 15ºC).

$[L\text{-malic acid}]_0$ (g/L)	r_0 (g/L day)	
	must	wine
2	0,14	0,085
5	0,27	0,097
8	0,39	0,11

Figure 5 –Evolution of L-malic acid concentration in wine during MAF (1 g/L ProMalic ®, 15ºC).

Further experiments were performed in a recycle fixed-bed reactor operating in batch mode (i.e. closed circuit). Fermentation media flows at constant flow rate (~100 mL/min) through a fixed-bed of ProMalic® (~1 g/L) connected to a 5-L deposit. Samples were collected at the reactor's inlet and outlet and analyzed for sugar and L-malic content. These results are identical and thus the reactor may be considered a differential type of reactor. Since the fermentative media is not withdrawn during the experiment the reactor operates in batch mode and the substrate concentration changes with time.

The evolution of L-malic acid concentration with time during MAF of must with *Schiz. pombe*, in the recycle reactor and in Erlenmeyers, is presented in Fig. 6. The rate of deacidification is higher in the recycle reactor. This may be related to the fact that in the Erlenmeyers the reactions were performed without agitation and this causes mass transfer limitations of substrate diffusion into the yeast beads. In the recycle reactor mass transfer limitations are lower because the flow rate used causes some "agitation" around the yeast beads.

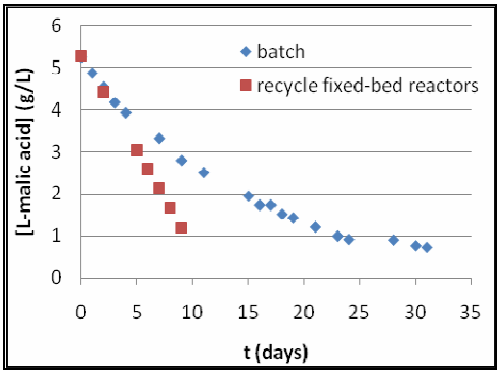

Figure 6 –Evolution of L-malic acid concentration in wine during MAF in Erlenmeyers (batch) and in the recycle reactor (1 g/L ProMalic ®, 15ºC).

The influence of mass transfer limitations was further discussed by performing experiments in similar conditions with higher yeast loads (Fig. 7 and Table 4). Higher loads of ProMalic® increased MAF rates, as expected, for this corresponds to longer contact times. With this type of reactor it is possible to obtain a residual value of L-malic acid (0.5 g/L) in 3 days. This represents a great process improvement. Presently, in wineries that are using ProMalic® the reduction of must acidity by MAF requires 2 to 3 weeks to reach 0,5 g/L of L-malic acid.

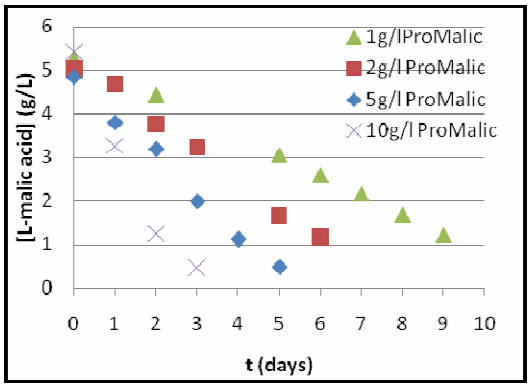

Table 4- Initial reaction rates (r_0) for MAF of must in the recycle reactor with different ProMalic® loads at 15ºC.

ProMalic® (g/L)	r_0 (g/L day)
1	0,47
2	0,71
5	0,89
10	1,70

Figure 7 –Influence of the recycle reactor's yeast load (ProMalic ®) on the evolution of L-malic acid concentration during MAF of must at 15 ºC.

The process of wine making from must requires inoculation with other yeasts such as *Saccharomyces cerevisiae* for example. Since *S. cerevisiae* is known to inhibit the activity of *Schiz. pombe* (Strehaiano and Taillandier, 2001) it is important to know exactly when to

inoculate. A reaction was performed in the recycle reactor as describe before and after two days *S. cerevisiae* was inoculated (Fig 8). During a period of aprox. 2 days MAF proceeded as usual: sugar concentration remained constant and the concentration of L-malic acid was reduced. After this period a drop of sugar concentration was observed and the concentration of L-malic acid remained aprox. constant, i.e. MAF was halted. Inhibition of *Schiz. pombe's* activity was not immediate after inoculation probably due to a lag-phase of *S. cerevisiae*.

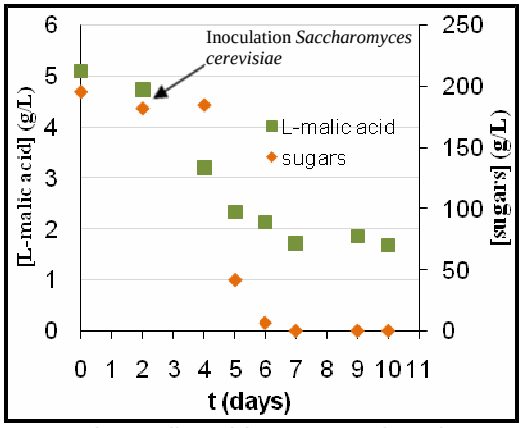

Figure 8 – Evolution of sugars and L-malic acid concentrations in must during MAF in the recycle reactor (1 g/L ProMalic ®, 15ºC): influence of inoculation with *S. cerevisiae*.

4. Conclusions:

Grapes and musts may present different values of L-malic acid concentration. This parameter was found to influence the MAF rate of must deacidification by immobilized *Schizosaccharomyces pombe*. The reaction is 1st order in relation to L-malic acid with k=0,00174 h^{-1} at 15ºC and Ea = 16±2 kcal/mol. Although immobilization reduces the rate of deacidification the advantages associated with yeast removal after reaction and the use of a total recycle fixed-bed reactor are favourable. In this type of reactor a residual value of L-malic acid (0.5 g/L) is obtained in 3 days while in a conventional batch process it takes 2 to 3 weeks to reach the same value.

References:

Delpech, C. (2002). Une nouvelle voie de désacidification dês moûts. Viti Technique 273, 46-48.

Lepe, J.A.S. (1997).Levaduras vínicas: Funcionalidad Y Uso en Bodega; Ediciones Mundi-Prensa.

Garcia, A.P., Suarez-Martínez C., Heras-Manso, J.M. (2006). Manejo de la acidez del vino base cava desde el punto de vista organoléptico, ACE revista de Enologia, Nº 66.

Silva S., Ramón-Portugal, F., Andrade, P., Abreu, S., Texeira, M.F., Strehaiano, P. (2003). Malic Acid Consumption by Dry Immobilized Cells of *Schizosaccharomyces pombe*. Am. J. Enol. Vitic., 54: 50 - 55.

Strehaiano, P., Taillandier, P. (2001). Nouvelles utilisations des levures *Schizosaccharomyces* encapsulées pour la désacidification des mouts de raisin. Journée Technique Régionale, Institut Technique du Vin, Toulouse.

Gòdia F., López-Santín J., Editors (2005). Ingeniería Bioquímica – Editorial Sintesis

Proceedings of the 10th International Chemical and
Biological Engineering Conference - CHEMPOR 2008
Braga, Portugal, September 4-6, 2008
E.C. Ferreira and M. Mota (Eds.)

Using GC-MS and Multivariate Statistics to Safeguard the Identity of Madeira Wine: a Preliminary Study

Ana C. Pereira[1,2], Marco S. Reis[1], Pedro M. Saraiva[1], José C. Marques[2]

[1]Department of Chemical Engineering, University of Coimbra Pólo II - Pinhal de Marrocos, 3030-290 COIMBRA

[2]Madeira Research Chemistry Center, Department of Chemistry, University of Madeira, Complexo da Penteada, 9000-390 Funchal

Topic: Multi-scale and/or multi-disciplinary approach to process-product innovation: Food Engineering

Keywords: Madeira wine, GC-MS, principal component analysis, maximum likelihood principal component analysis

Abstract:

The results presented here outline the preliminary developments of a study which aims to find out and characterize the ageing phenomenon of Madeira wine, understanding the evolution of its aroma profile over ageing time, in such a way that it will be possible to develop a tool for assessing Madeira wine authenticity. For this purpose, a preliminary screening of volatile compounds by gas chromatography, coupled with mass spectrometry detection (GC–MS) was carried out, in order to perform the necessary wine flavour fingerprinting.

The amount of information obtained was simplified in order to support an easier analysis. In this work, two different methods for dimensional reduction of the original data set were applied: principal component analysis (PCA) and maximum likelihood principal component analysis (MLPCA). Two models were obtained, and the performance of each one was evaluated regarding the possibility of finding patterns of ageing in different samples of Madeira wine. PCA was also applied to differentiate varieties used in wine production, given that ageing time is known.

I. Introduction

Our image as a country which produces distinctive wines implies the responsibility and the need for conducting research aimed at supporting wine production, and the optimization of the procedures involved, such as ageing. Madeira wine, despite being one of the world's most famous dessert and aperitif wines, does not have yet many studies carried out in order to keep up with the increasing demand for higher quality in the current global markets. Moreover, its peculiar characteristics, namely regarding its exceptional longevity, makes of it a product with high economic value, attractive for possible fraudulent copies. For these reasons, a reproducible method, able to provide a credible evaluation of the authenticity and identity of Madeira Wines, is opportune and of the utmost relevance.

Understanding the chemical nature of wine aroma demands quantitative determination

of a quite large number of different odour-active compounds. The use of mass spectrometry as an on-line GC-detector for the identification of flavour compounds is perhaps the most widely used analytical technique for wine flavour chemical analysis due to the good results that have been reported on the literature (Ferreira, Jarauta et al. 2006; Ortega-Heras, González-Sanjosé et al. 2007).

Such an analytical measurement procedure generates large amounts of experimental data, with strong correlations among them. Therefore, such data are well suited to be analysed through multivariate statistical techniques, in order to efficiently extract useful information from the data sets available. The usefulness of multivariate techniques is reported in different areas: in process analysis, monitoring and control (Kourti and MacGregor 1995; Hu and Yuan 2008), in pharmaceutical applications (Gabrielsson, Lindberg et al. 2002), in the field of metabolomics (Jansen, Hoefsloot et al. 2004) and in the food industry, to characterize and authenticate products either for quality control or marketing purposes (Preys, Vigneau et al. 2007). The latter applications usually fall under the heading of “Chemometrics” a discipline described by Wold, in 1998, as able to solve the following problems in chemistry: to get chemical relevant information out of measured chemical data, to represent and display this information and to get such information into data.

The focus of this study is to conduct an exploratory data analysis related to the changes in the aroma profiles that take place during maturation of Madeira wine in oak casks.

Most multivariate statistical methods require more samples (wines) than variables (volatiles/flavour compounds), in order to perform the data analysis. This is frequently a problem, since instrumental techniques are sensitive enough to identify and quantify a large number of compounds. Therefore, statistical pre-processing is usually required to reduce the number of variables. In flavour chemistry the work involved in analyzing 5 or 10 wines is enormous. Therefore, most studies do not use many samples to model the relationships between chemical data and flavour compounds.

In this context, principal components analysis (PCA) has been used to look for patterns in a data set with a large number of variables, including the cases where there are more variables than samples. PCA is a very useful methodology for looking at patterns or trends and simplify large data sets, by finding linear combinations (principal components, PC) of variables (the compounds identified) that still describe the major trends present in the original data set. The relationships between the original variables can be seen by looking at the loading coefficients, which represent the most important linear correlations present in the original data. The first principal component (PC) explains the largest amount of variation among the samples. The second PC and subsequent PCs are then derived in such a way that they maximize the amount of unexplained variation under the constraint of being orthogonal to the previous components (Johnson and Wichern 2007).

In this work, another method for the dimensional reduction of the original data set was also applied: maximum likelihood principal component analysis (MLPCA). This is also a PCA method that estimates subspaces explaining the maximum variability present in the original data sets, differing from the first one mentioned due to the information that it uses, while solving its related objective functions. While in conventional PCA only the (scaled) data are used, in MLPCA (Wentzell, Andrews et al. 1997; Jansen, Hoefsloot et al. 2004) one further considers their associated uncertainties, which are used to weight the relative impact of each data point in the estimation of the PCA subspace (compounds containing smaller experimental errors are more influential in the MLPCA

estimation process). In our study the weights used are the uncertainties of each measurement, given by the standard deviation of the GC-MS replicates.

The application of these techniques results in two different models. An analysis of each one is performed separately, to identify how well each one best describes trends in our data set. It is useful to have a quantitative measure of similarity between them in order to have an idea of how different the subspace estimates obtained from both methodologies are. Some geometric concepts are pointed out as useful criteria to evaluate similarity between PCA models (Krzanowski 1979; Raich and Çinar 1995).

II. Materials and Methods

Samples

Two groups of samples were considered in this study: one group collected after 5 years of ageing in casks (five year old wines), and another group collected after 10 years of ageing in casks (10 year old wines). All samples, within each group, were submitted to the same ageing conditions, and submitted to the same vinification process. In each group, samples were collected for the four most important and recommended white wine varieties used in Madeira Wine production, namely: “Malvasia”, “Boal”, “Verdelho” and “Sercial”.

Experimental procedures and data analysis

Volatiles compounds were extracted from samples according to the following procedure: 3 mL of distilled water were added to 5 mL of sample and mixed with 1 mL of ethyl acetate and 10 µL of 3-octanol (internal standard). After mechanical agitation, during 30 min at 2500 rpm, the organic phase was dried with anhydrous sodium sulphate. The extract was analysed in an Agilent 6890N gas chromatograph coupled to an Agilent 5975 quadrupole inert mass selective detector. The identification of compounds was carried out by comparison of the mass spectra obtained for the analysis and those included in the NIST MS Library Database. Afterwards, the results obtained were analyzed using multivariate statistical techniques.

Data for the mean values of the two injections, corresponding to the relative response area for each wine volatile compound to an internal standard, were organized in a matrix with 24 rows (samples analysed) by 37 columns (compounds identified). In this format, it is very difficult to identify any significant trend in the behaviour of samples. Therefore, we proceeded by reducing the number of relevant dimensions present in this data set, in order to highlight the underlying analytical information that is really relevant for characterizing the wine flavours. All data analysis tasks were performed with the computational platform Matlab (version 7.6, The Mathworks Inc.).

Results

Using both approaches, two PCA models were estimated. The scores and loading coefficients obtained confirm that there are indeed differences between the MLPCA and PCA models. Analysing the scores plot shown in Figure 1, for the first and second principal components (explaining 61% of the overall data variability), one can see that samples from each wine variety, with different ageing times in casks, appear quite well separated under the conventional Principal Components Analysis representation (Figure 1a). Results regarding the “Malvasia, (M5)” variety seem rather distinct in this analysis from the remaining varieties with same ageing time, but its trend in the projection space is similar, namely regarding the second principal component (PC2). All samples (of the same variety) have one underlying similarity, concerning their evolution in the ageing process: the value of the second principal component (PC2) decreases with wine ageing. In Figure 1a) arrows highlight the direction of varieties ageing over time. Another result worth mentioning is the similarity of trends found in wine samples that are similar from the organoleptic point of view: “Malvasia” and “Boal”, the sweetest wines, follow one direction, and the remaining two, “Sercial” and “Verdelho”, wines with lower values of residual sugar, follow another one. The coupled analysis of the score and loading values does allow one to identify which set of volatile compounds are responsible for this trend, namely the furanic lactones and the ethyl and diethyl ester amounts.

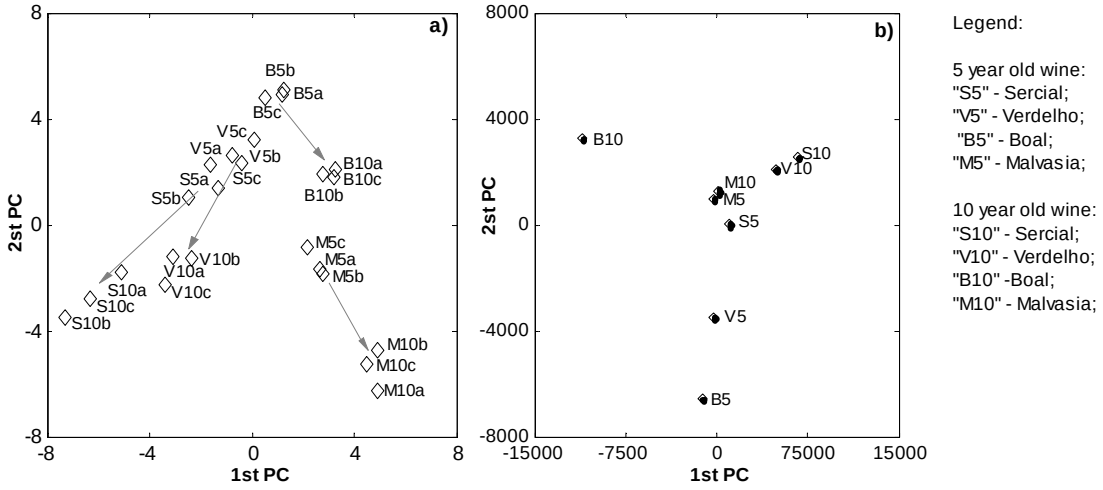

Figure 1 – Scores plots for the 1st and 2nd principal components, with ageing signature for samples from different wine varieties: a) Principal Components of Analysis; b) Maximum Likelihood Principal Components of Analysis.

As can been seen from Figure 1b), using MLPCA the separation obtained is not so clear. This may be due to the fact that the uncertainty estimates, based on three replicates only, may not be reliable enough, and thus contributes to deteriorate the analysis, rather than improving it. In future work, more samples should be considered, in order to verify if this approach can indeed improve performance over conventional PCA in capturing the natural underlying data variation.

In this study, the evaluation of the similarity between the two estimate subspaces was done by considering the angle between their coordinate axes. Using PCA decomposition, the angle β, between PCA coordinate direction sets P_{PCA} (loading values of conventional PCA) and P_{MLPCA} (loadings values of MLPCA), corresponds to eigenvalues $\left(s_k^{1/2}\right)$ of the following matrix:

$$P_{PCA}^{T} P_{MLPCA} P_{MLPCA}^{T} P_{PCA} = L^{'} S L \quad (1)$$

$$\beta = \cos^{-1}\left(s_k^{1/2}\right) \quad (2)$$

where L gives a set of coordinates and s_k corresponds to the k^{th} largest values in S (Raich and Çinar 1995), corresponding to the smallest angle β between *2*-dimensional subspaces. In our case, the angle from the two subspaces was equal to 52,11º, a value that expresses a highly significant difference between them.

Each group of aged samples was also analysed separately (i.e., the 5 year old group and the 10 year old group), as shown in Figure 2. In this case, the first two components do show good separation capabilities for all of the four varieties, each one of them explaining approximately 80% of the overall original data variance (Johnson and Wichern 2007). Therefore, using PCA, one is indeed able to identify: 1) the period that wines were in casks – ageing time (using the PCA model estimated considering all the groups); and 2) the wine variety (using the PCA models for each group).

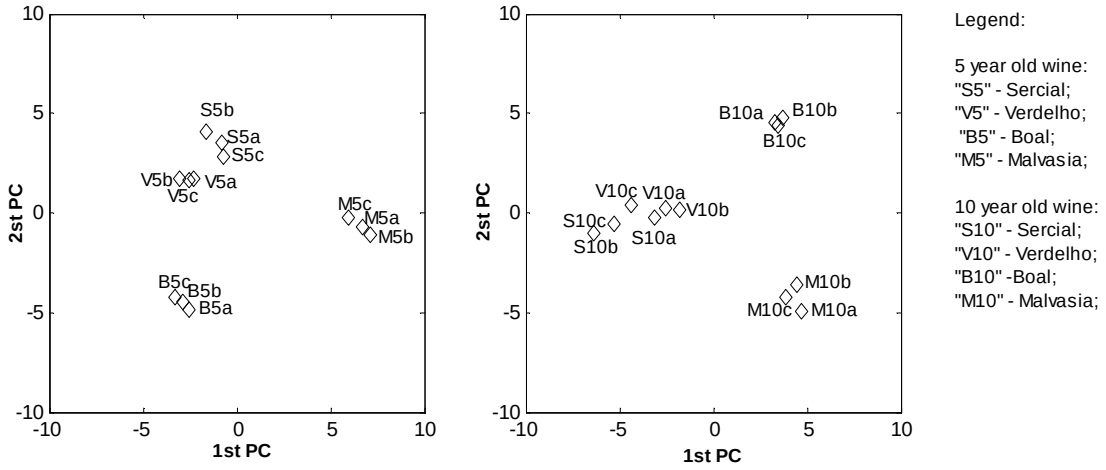

Figure 2 – Scores plots for the 1st and 2nd principal components for different varieties of wine with the same ageing period: a) 5 year old wines; b) 10 year old wines.

Conclusions

A global strategy to analyse the characteristic bouquet of Madeira Wine was presented.

The data set, with many variables obtained by GC/MS analysis, was simplified, through the use of multivariate projection methods. The application of such multivariate statistical methods revealed patterns of the original measurement variables, increasing the diagnostic value of laboratory assays.

These preliminary results reveal that the different varieties employed in Madeira Wine production have one similarity, concerning their evolution in the ageing process. Nevertheless, each one follows a particular trend in the proposed model, whereas new studies have been conducted considering one variety individually but in more detail across ageing time. We are also planning in the future to consider a more representative set of samples, in order to validate the ability of our methodology. In the end, we hope to come up with a credible evaluation procedure, able to safeguard Madeira Wine identity and assure its quality of ageing over time.

Acknowledgments

A. C. Pereira would like to thank *Fundação para a Ciência e Tecnologia* for the PhD grant SFRH / BD / 28660 / 2006. The authors acknowledge Madeira Wine Company, which kindly supplied wine samples.

References

Ferreira, V., I. Jarauta, et al. (2006). Physicochemical Model To Interpret the Kinetics of Aroma Extraction during Wine Aging in Wood. Model Limitations Suggest the Necessary Existence of Biochemical Processes. J. Agric. Food Chem., 54, 3047-3054.

Gabrielsson, J., N.-O. Lindberg, et al. (2002). Multivariate methods in pharmaceutical applications. J. Chemometrics, 16, 141-160.

Hu, K. and J. Yuan (2008). Multivariate statistical process control based on multiway locality preserving projections. Journal of Process Control, 18, 797–807.

Jansen, J. J., H. C. J. Hoefsloot, et al. (2004). Analysis of longitudinal metabolomics data. Bioinformatics, 20, 2438-2446.

Johnson, R. A. and D. W. Wichern (2007). Applied Multivariate Statistical Analysis, Pearson Education.

Kourti, T. and J. F. MacGregor (1995). Process analysis, monitoring and diagnosis, using multivariate projection methods. Chemometrics and Intelligent Laboratory Systems, 28, 3-21.

Krzanowski, W. J. (1979). Between-Groups Comparison of Principal Components. J. Am. Stat. Assoc. 74:367, 703– 707.

Ortega-Heras, M., M. L. González-Sanjosé, et al. (2007). Consideration of the influence of aging process, type of wine and oenological classic parameters on the levels of wood volatile compounds present in red wines. Food Chemistry, 103, 1434–1448.

Preys, S., E. Vigneau, et al. (2007). Multivariate prototype approach for authentication of food products. Chemometrics and Intelligent Laboratory Systems, 87, 200-207.

Raich, A. C. and A. Çinar (1995). Multivariate statistical methods for monitoring continuous process. Chemometrics and Intelligent Laboratory Systems, 30, 37-48.

Wentzell, P. D., D. T. Andrews, et al. (1997). Maximum Likelihood principal components of analysis. J. Chemometrics, 11, 339-366.

Wold, S., Sjöström, M. (1998), Chemometrics, present and future success. Chemometrics and Intelligent Laboratory Systems, 44, 3-14.

Proceedings of the 10th International Chemical and
Biological Engineering Conference - CHEMPOR 2008
Braga, Portugal, September 4-6, 2008
E.C. Ferreira and M. Mota (Eds.)

A new strategy for using banana as an ingredient in the brewing process

Giovani B.M. Carvalho[1], Daniel P. Silva[2], António A. Vicente[2], Maria das Graças A. Felipe[1], José A. Teixeira[2], João B. Almeida e Silva[1*]

[1] Biotechnology Department, Engineering School of Lorena, University of São Paulo, Campus I, P.O.Box116, 12602-810, Lorena-SP, Brazil.
[2] IBB - Institute for Biotechnology and Bioengineering, Centre of Biological Engineering, University of Minho, Campus de Gualtar, 4710-057 Braga, Portugal.

Keywords: Beer, Adjunct, Banana, Brewing, Fermentation
Topic: Multi-scale and/or multi-disciplinary approach to process-product innovation

Abstract

Beer is a traditionally fermented beverage made from malted grains of barley, hops, yeast, and water, while banana is an important food crop cultivated widely in tropical and subtropical areas and is one of the major fruits in Brazil. Besides, the banana is also very favorable to food industry (*e.g.* fermented beverages) due to its rich content on soluble solids, presence of minerals, and providing low acidity. In this context, the objective of this work was to evaluate a new strategy for using banana as adjunct to increase the fermentable sugars and to supply a specific aroma in pilot-plant brewing experiments. For this, static fermentations were conducted in a 180 L cylindrical-conical reactor using 140 L as working volume. Addition of banana was evaluated when changing the concentration of the wort from 10 to 12 ºP and from 10 to 13.5 ºP (ºP is the weight of the extract or the sugar equivalent in 100 g solution, at 20 ºC) and fermented under a constant temperature of 10 and 12.5 ºC, respectively. The results showed that the increment in the initial sugar concentration (12 to 13.5 ºP, due to the use of banana juice as adjunct), and in the temperature (10 to 12.5 ºC), increased approximately 17% the ethanol productivity. Thus, it was concluded that by using of simple preparation techniques of banana juice, banana can be used as adjunct in brewing processes, helping in the development of new products as well as in the elaboration of more concentrated worts when compared the traditional brewing worts.

1 Introduction

Produced in large quantities in tropical and subtropical areas, due to the special climatic conditions needed to its growth, banana is one of the most extensively consumed fruits and one of the most significant foodstuffs in the world, while being a good source of mineral salts and vitamins. Sensorial attributes of this fruit, as flavor, taste, texture and color are significantly influenced by its chemical composition, especially by acids, sugars and phenolic compounds. Studies have revealed physicochemical, nutritional and sensorial differences according to the region of origin of the bananas (Cano *et al.*, 1997; Hardisson *et al.*, 2001).

According to Food and Agriculture Organization of the United Nations (FAO, 2008), among the major producers of the banana worldwide in 2006, India was the first with 11.7×10^6 tonnes, which corresponded to 16.5% of the worldwide production, and Brazil was the second with 7.1×10^6 tonnes (approximately 10% of the worldwide production). Thus, banana can be regarded as a important staple food that is critical to the nutritional and economic well being of millions of people throughout the developing world and are grown in about 120 countries (Olorunda, 2000).

* Corresponding author. Tel +55-12-3159-5044. E-mail: joaobatista@debiq.eel.usp.br

On the other hand, biotechnology includes a wide range of diverse technologies that may be applied in each of the different food and agriculture sectors. In this context, several studies to obtain foods or beverages from fruits, such as orange, grape or apple, have been carried out. In brewing process, the conventional beer fermentation technology is initially based in the wort preparation and on its batch fermentation. With no mechanical stirring and with a temperature profile along appropriate fermentation time, fermentable sugars present in the wort are transformed to ethanol and in several taste and aroma compounds in order to obtain the desired characteristics on the final product (Linko, 1998; Almeida e Silva, 2005).

Nowadays, the brewing industry has applied a whole spectrum of technical, biochemical, microbiological and genetic innovations. Furthermore, in today's competitive beer-market it is very important to develop different types of beers, *e.g.* obtained by the use of new ingredients or new adjuncts. Thus, in previous works we have evaluated the feasibility of new technologies, *e.g*. for selectively producing beers from more concentrated wort (using high maltose syrup), aiming at obtaining good quality beer in a shorter time and in the least expensive way, or using different processing ways (Almeida *et al*., 2001; Almeida e Silva *et al*., 2004; Dragone *et al*., 2004; Brányik *et al*., 2006; Silva *et al*., 2008). By increasing wort concentration, after preparation, the beer is adjusted to the desired ethanol concentration with oxygen-free water, which makes of this process of considerable interest as higher levels of ethanol per given plant capacity and labor costs are obtained.

In this work, the objective was to describe and evaluate the performance of the use of banana juice as adjunct to increase the fermentable sugars and to supply a specific aroma, in pilot-plant brewing experiments. Special attention was paid to fermentation performance in terms of fermentation parameters as volumetric productivity, ethanol yield, and sugars consumption. For this, the addition of banana was evaluated when changing the concentration of the wort from 10 to 12 ºP and from 10 to 13.5 ºP (ºP is the weight of sugar extract equivalent to the weight of sucrose in a 100 g solution/20 ºC), fermented under a constant temperature of 10 and 12.5 ºC, respectively.

2 Materials and methods

The yeast strain used in this work was a commercial lager brewing strain (*Saccharomyces cerevisiae*). The yeast biomass for initial inoculation in the fermentation reactor was cultivated using all malt wort (12.5 ºP) firstly on a rotary shaker (200 mL / 30 ºC / 200 rpm, 18 h), followed by a 4 L Erlenmeyer flask under static and aerobic conditions (2 L / 15 ºC / 0.1 vvm of aeration, 30 h), then in a 40 L stainless steel vessel under static and aerobic conditions (20 L / 15 ºC / 0.01 vvm of aeration, 54-60 h) until the cell concentration was sufficient to provide a cell concentration of 10-20×10^6 cellsmL^{-1} in the beginning of the fermentation in the pilot tank (140 L).

All-malt worts and worts with banana as adjunct were produced according to conventional brewing techniques in the pilot installation used for the experiments, as shown in Figure 1. Banana juice, prepared with fruits of the variety *Prata* (*Musa spp*) and provided by EMATER (Empresa de Assistência Técnica e Extensão Rural do Estado de Minas Gerais, Cristina-MG/Brazil), was used to change the concentration of the all malt wort from 10 to 12 ºP and and from 10 to 13.5 ºP. This banana variety was chosen considering the great production and availability in Brazil which results in accessible price at markets. They were sanitized with running potable water, manually peeled, cut in the form of discs (thickness: 0.5 cm) and triturated in a blender before use. The typical carbohydrate profile of the banana used in this work, classified by the peel color as ripening stage 8 - yellow with more brown specks, according to Loeseck (1950), was: sugars as glucose and fructose (12.4 %ww^{-1}), sugars as sucrose (3.2 %ww^{-1}) and starch (0.5 %ww^{-1}). The banana juice was produced in a concentration of 0.29 gL^{-1} by enzymatic treatment (43.2 ºC during 1.3 h, with agitation at 32 rpm, pH 5 and 8.4x10^{-7} L of Ultra Pectinex SP-L enzymatic pectinolytic solution by gram of medium) followed by a thermal treatment (84 ºC during 0.67 h).

After wort preparation, the initial pH value was adjusted at 5 (by the addition of lactic acid) and the initial dissolved oxygen concentration was set at approximately 8 mgL^{-1}; static fermentations were performed in a 180 L cylindrical-conical tank (brewing fermenter) with 140 L working volume at constant temperature of 10 ºC to wort of 12 ºP and 12.5 ºC to wort of 13.5 ºP. The fermentation runs were carried out until the apparent attenuation was about 70-75% (1.0 ºP above the final value of fermentable sugars).

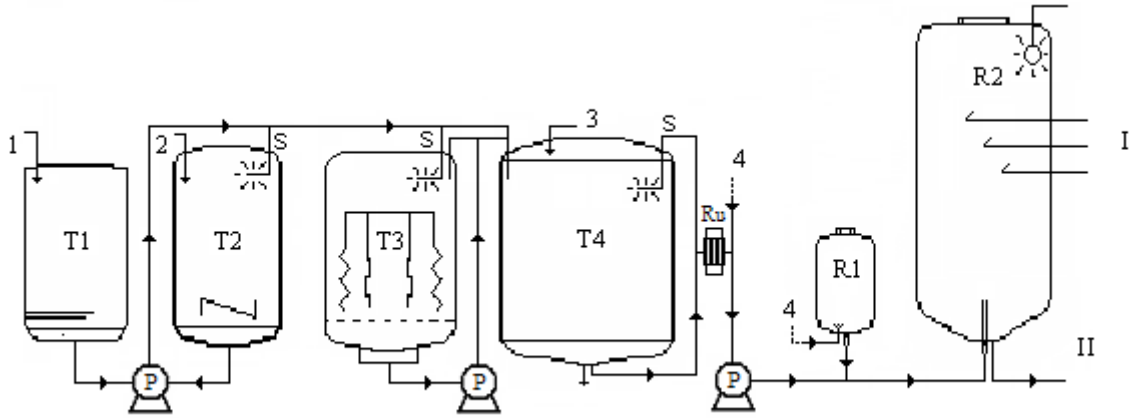

Figure 1. Pilot brewery for wort preparation and beer fermentation (Biotechnology Department at the Engineering School of Lorena, University of São Paulo EEL-USP/Brazil): T1 hot water tank, T2 wort treatment tank, T3 filtration tank, T4 boiling tank, P pumps, S spray-balls (in-line cleaning system), Ru refrigeration unit, R1 inoculation/propagation tank, R2 fermentation/maturation reactor, I and II sampling points or final product, 1 water supply, 2 malt supply, 3 hops supply, 4 air/O_2 supply.

During fermentations, samples were taken in triplicate at specified intervals and the yeast was removed by centrifugation at 4000 g for 20 min. The apparent extract and ethanol concentrations in the supernatant were measured at 20 ºC using an automatic beer analyzer (Beer Analyzer 2, Anton Paar, Graz, Austria). Part of the supernatant was also filtered through a syringe filter (Sep-Pak C18 cartridge, Waters, Milford, MA), and 20 µL were injected into an HPLC system which consisted of an Aminex HPX-87H column (300 × 7.8 mm^2, Bio-Rad Laboratories Ltd, Hercules, CA) at 45 °C using a Shimadzu chromatograph LC-10AD (Shimadzu Co., Tokyo, Japan) with refractive-index detector. The mobile phase was 0.005 $molL^{-1}$ H_2SO_4 at 0.6 $mLmin^{-1}$ flow rate. Sugar concentrations, reported as glucose, fructose, maltose and maltotriose, were determined from calibration curves obtained with pure compounds. The yeast cell number was determined using a Neubauer counting chamber and the viability was determined by methylene blue staining. All analyses were based on the techniques described in ASBC (1996). The ethanol productivity (ratio between ethanol produced and total fermentation time, $gL^{-1}h^{-1}$) and the ethanol yield coefficient (ratio between produced ethanol and consumed extract, gg^{-1}) were determined after conversion of the apparent extract (ºP) to grams of extract per liter of wort (gL^{-1}).

3 Results and discussion

According with the Figures 2 and 3, in both experiments, the final fermentation time was achieved at 120 h. These Figures show the performance of *S. cerevisiae* (yeast in suspension, lager strain), extract consumption and ethanol production as a function of the time of fermentation. As can be observed, during the first 24 and 36 h of fermentation, using banana as adjunct on 12.0 ºP/10.0 ºC and 13.5 ºP/12.5 ºC, respectively, the substrate consumption (measured in terms of apparent extract) was closely related to the increase of yeast biomass in suspension.

However, and after this time, the concentration of yeast in suspension decreased until the final time due to flocculation effect. This profile is in agreement with conventional profiles for brewing processes (Silva *et al*., 2008; Dragone *et al*., 2004). Besides, several factors are known to affect the cell viability in fermentative process, however, in both experiments obtained in this work the cell viability showed few variations (100-95%).

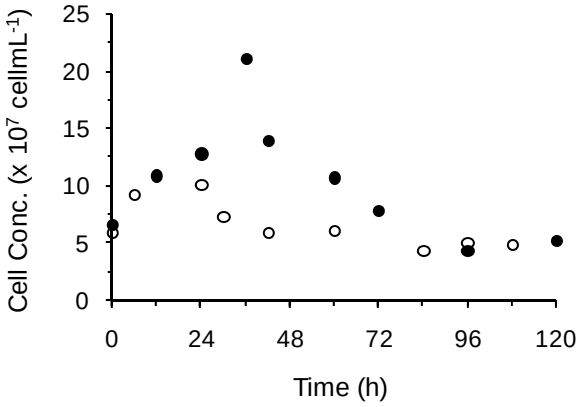

Figure 2. Performance of *S. cerevisiae* (yeast in suspension, lager strain) during fermentation of wort with banana as adjunct under the following conditions of concentration and temperature: (●) 13.5 ºP/12.5 ºC and (○) 12.0 ºP/10.0 ºC.

For the fermentation conditions of this work, the increment in the initial sugar concentration (12 to 13.5 ºP), due to the use of the banana as adjunct, and in the temperature (10 to 12.5 ºC), increased approximately 17% the ethanol productivity. The final productivity of the 12 ºP/10 ºC process was 0.29 $gL^{-1}h^{-1}$, while in the 13.5 ºP/12.5 ºC process was 0.34 $gL^{-1}h^{-1}$. Ethanol yield values were close at the end of each experiment (approximately 0.45 gg^{-1}).

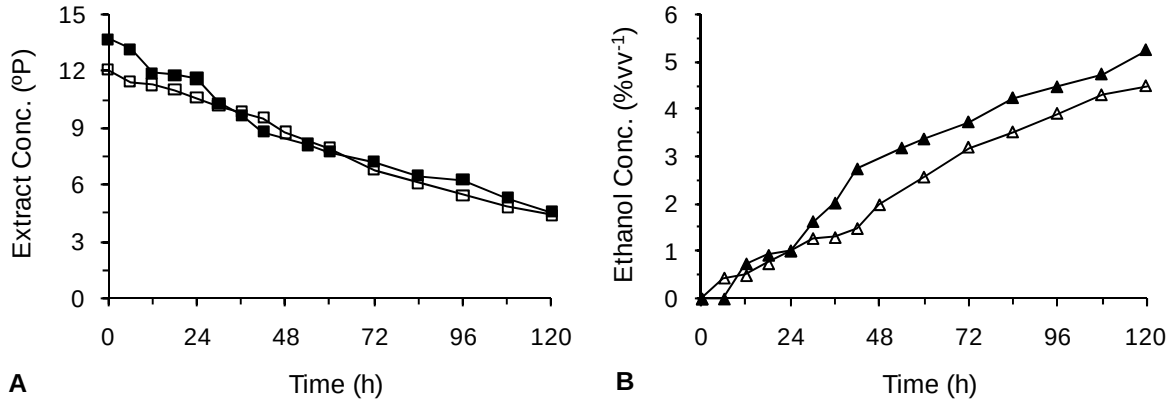

Figure 3. Extract consumption (A) and ethanol production (B) during fermentation of wort with banana as adjunct under the following conditions of concentration and temperature: (■, ▲) 13.5 ºP/12.5 ºC and (□, Δ) 12.0 ºP/10.0 ºC.

Figure 4 shows the profile of the glucose, fructose, maltose and maltotriose concentrations as a function of the time of fermentation. According to Navarro *et al.* (2007), the sugars in wort are not all fermented equally well. Since the yeast has to hydrolyze sugar polymers before it can use them, it always attacks hexoses first. In our work, as shown in Figure 4, comparing the consumption rate for each fermentable sugar found in concentrated wort with banana juice as adjunct, in general the following order of assimilation was observed: part of the glucose was consumed firstly, followed by fructose, maltose and finally maltotriose.

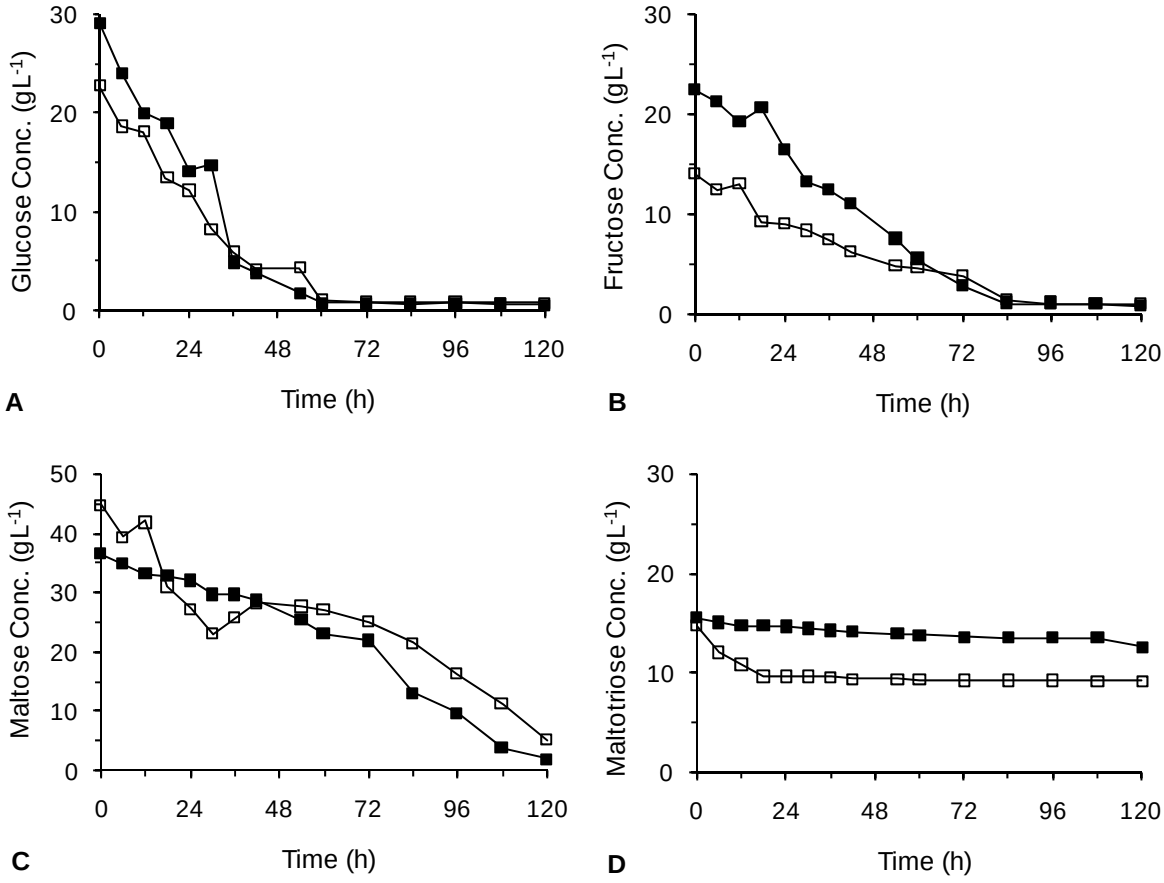

Figure 4. Fermentation performance of glucose (A), fructose (B), maltose (C) and maltotriose (D) at wort with banana as adjunct under the following conditions of concentration and temperature: (■) 13.5 ºP/12.5 ºC and (□) 12.0 ºP/10.0 ºC.

4 Conclusion

From this work it can be concluded that, by using simple preparation techniques of banana juice, banana can be used as adjunct in brewing processes, helping in the development of new products as well as in the elaboration of more concentrated worts when compared the traditional brewing worts (11-12 ºP). As a complement, the authors suggest the use of statistical designs to evaluate the optimization conditions of the variables simultaneously considered in this work (temperature and concentration). Besides, an increased productivity in brewing processes cannot be achieved at the expense of an unbalanced flavor profile of the final product and therefore future works are needed, especially to provide an understanding of the organoleptic profile obtained during the process of beer production using banana juice as adjunct.

Acknowledgements

FAPESP, Malteria do Vale, Corn Products Brasil, Wallerstein Industrial e Comercial, and DiverseyLever (Brazil); FCT (Portugal); and CAPES/GRICES (Brazil/Portugal).

References

Almeida, R.B., Almeida e Silva, J.B., Lima, U.A., Silva, D.P., Assis, A.N. (2001). Evaluation of fermentation parameters during high-gravity beer production. *Brazilian Journal of Chemical Engineering*, 18, 459-465.

Almeida e Silva, J. B. (2005). Cerveja. In: Venturini Filho, W. G. *Tecnologia de Bebidas*. Edgar Blucher, São Paulo, p.347-380.

Almeida e Silva, J. B., Lima, U. A., Silva, D. P., Almeida, R. B., Assis, A. N. (2004). Evaluation of factors involved in the concentration of vicinal diketones in beer produced by high gravit. *Cerevisia*, 29, 147-154.

ASBC, American Society of Brewing Chemists (1996). *Methods of Analysis of American Society of Brewing Chemists*. ASBC. 8ª. ed. Saint Paul Minnesota. USA.

Brányik T., Silva, D.P., Vicente, A.A., Lehnert, R., Almeida e Silva, J.B., Dostálek, P., Teixeira, J.A. (2006). Continuous Immobilized Yeast Reactor System for Complete Beer Fermentation using Spent Grains and Corncobs as Carrier Materials. *Journal of Industrial Microbiology and Biotechnology*, 33, 1010-1018.

Cano, M.P., Ancos, B., Matallana, M.C., Camara, M., Reglero, G., Tabera, J. (1997). Differences among Spanish and Latin-American banana cultivars: morphological, chemical and sensory characteristics. *Food Chemestry*, 59, 411-419.

Dragone, G., Silva, D.P., Almeida e Silva, J.B. (2004). Factors Influencing Ethanol Production Rates at High Gravity Brewing. *Food Science and Technology / Lebensmittel-Wissenschaft + Technologie*, 37, 797-802.

FAO, Food and Agriculture Organization of the United Nations (2008) FAOSTAT statistics database http://faostat.fao.org/site/567/DesktopDefault.aspx?PageID=567 (last updated 11 May 2008).

Hardisson, A., Rubio, C., Baez, A., Martin, M., Alvarez, R., Diaz, E. (2001). Mineral composition of the banana (*Musa acuminata*) from the island of Tenerife. *Food Chemistry*, 73, 153-161.

Linko, M., Haikara, A., Ritala, A., Penttilä, M. (1998). Recent advances in the malting and brewing industry. *Journal of Biotechnology*, 65, 85-98.

Loeseck, H. W. (1950). *Chemical changes during ripening. Bananas – chemistry, physiology and technology*, Volume 4, Interscience, New York.

Navarro, S., Pérez, G., Navarro, G., Mena, L., Vela, N. (2007). Variability in the fermentation rate and colour of young lager beer as influenced by insecticide and herbicide residues. *Food Chemistry*, 105, 1495-1503.

Olorunda, A.O. (2000). Recent advances in post harvest technologies of banana and plantains in Africa. *Acta Horticulture* 534, 517-527.

Silva, D. P., Brányik, T., Dragone, G., Vicente, A. A., Teixeira, J. A., Almeida e Silva, J. B. (2008). High gravity batch and continuous processes for beer production: evaluation of fermentation performance and beer quality. *Chemical Papers*, 62, 34-41.

Proceedings of the 10th International Chemical and
Biological Engineering Conference - CHEMPOR 2008
Braga, Portugal, September 4-6, 2008
E.C. Ferreira and M. Mota (Eds.)

β-Galactosidase from *Aspergillus oryzae* immobilized onto different magnetic supports: A comparative experimental and modelling study of the galactooligosaccharides production

David F.M. Neri[1,2*], Victor M. Balcão[1], Rafael S. Costa[1], Eugénio M.F.C. Ferreira[1], Duarte P.M. Torres[1], Lígia R. Rodrigues[1], Luiz B. Carvalho Jr[2], José A. Teixeira[1]

[1]IBB – Institute for Biotechnology and Bioengineering, Centre of Biological Engineering, University of Minho, Campus de Gualtar, 4710-057 Braga, Portugal.

[2]Departamento de Bioquímica and Laboratório de Imunopatologia Keizo Asami, Universidade Federal de Pernambuco, Brazil.

Keywords: β-galactosidase,immobilization,magnetic supports,GOS,mathematical modeling**.**
Topic: Multi-scale and/or multi-disciplinary approach to process-product innovation.

Abstract

β-Galactosidase from *Aspergillus oryzae* is an enzyme with a wide industrial application, mostly in the hydrolysis of lactose and, more recently, in the synthesis of oligosaccharides. Several advantages are associated with the application of immobilized enzymes on magnetic supports. In this work, β-galactosidase was covalently immobilised onto a Polysiloxane-Polyvinyl Alcohol Magnetic Composite (mPOS-PVA), Magnetic Polysiloxane with Polyaniline (mPOS-PANI), Magnetized Dacron (DACRON) and Magnetite with Polyaniline (MAG-PANI) using glutaraldehyde as activating agent being the synthesis of GOS evaluated and compared at different temperatures (30, 40, 50 and 60 ^{o}C) and various initial lactose concentration (50, 100, 200, 300, 400 and 500 g/L). The kinetic parameters obtained by fitting the experimental data were compared in order to determine the effect of the immobilization process with different supports on the synthesis of oligosaccharides. These results clearly demonstrate that all supports may be used for β-galactosidase immobilization as, besides improving the enzyme hydrolytic and GOS synthesis properties, its separation from the obtained reaction products is easy to accomplish.

1 Introduction

During the lactose hydrolysis catalyzed by β-galactosidase GOS are produced by transgalactosylation activity and the production increases by increasing the initial concentrations of lactose in the reaction mixture (Albayrak and Yang, 2002). GOS are nondigestible oligosaccharides, which are prebiotics acting as growth-promoting substrates for bifidobacteria in the human intestine. Enzymes have been utilized in a large number of practical applications, particularly in biomedical and biotechnological fields, through immobilization on a variety of supports (Bayramoglu *et al*., 2008). The applications of immobilized enzymes may be challenged by difficulties that arise in enzyme recovery and recycling, which are the most important processes that can decrease the overall cost of the enzyme immobilization process (Lee *et al*., 2007). The use of magnetic micro-beads as supports for enzyme immobilization is mainly based on the magnetic feature of the solid-phase that enables to achieve a rapid separation in a magnetic field, as well as decrease of operation cost. In addition, the nano-scaled immobilized enzyme can greatly alleviate the transfer barrier, and thus improve the catalytic efficiency (Hong *et al*., 2008). Immobilization of enzyme or biomolecules to the magnetic microbeads is usually accomplished through reactive groups existing on their surface. Nowadays, these functional composites cold be produced in many ways, i.e. emulsion polymerization (Csetneki *et al*., 2004), in situ formation (Li *et al*., 2006) and sol-gel (Luo *et al*., 2006), but usually involve the coating of magnetically susceptible particles with synthetic polymers or biomacromolecules (Hong *et al*., 2008). Actually, the use of magnetic particles in enzyme technology is constantly increasing.

Permanent magnetization could cause the particles to aggregate even if the supports are removed from the magnetic field (Neri *et al*., 2008 and Bayramoglu *et al*., 2008). In this study, β-galactosidase from *Aspergillus oryzae* was covalently immobilized onto different magnetic supports (mPOS-PANI, DACRON, mPOS-PVA and MAG-PANI) for GOS production. The effects of the temperature, initial lactose concentration and reutilization were investigated. In addition, the kinetic parameters were determined and compared between the four supports using experimental data (10-50% initial lactose concentration).

2 Materials and methods

Supports synthesis: mPOS-PVA – beads were synthesized according to the procedure described by Barros *et al.* (2002) and the magnetized particles were obtained by Carneiro-Leão *et al*. (1991); MAG-PANI – magnetite (MAG) was obtained by co-precipitation (Carneiro-Leão *et al*., 1991) and after coated with polyaniline (PANI) as was done by Oliveira *et al*. (2008); mPOS-PANI – POS was prepared polymerizing the tetraethylorthosilicate and after was coated with polyaniline as described in Oliveira *et al*. (2008); DACRON – was converted to magnetic DACRON according to Pinheiro *et al*. (1999). The immobilization of β-galactosidase was done using glutaraldehyde as activating agent. The supports activated (100 mg) were incubated with 10 mL β-galactosidase solution (4 mg solid/mL) in 20 mM citrate-phosphate buffer, pH 4.5, for 18 h at 4 °C and 20 rpm. Production of GOSs from lactose was studied with immobilized enzyme on various supports in different conditions. The reaction kinetics was studied at six different initial lactose concentrations (5, 10, 20, 30, 40, and 50 %, w/v and four different temperatures (30, 40, 50, and 60ºC). GOSs, lactose, glucose and galactose concentration were determined using HPLC. As the concentration (w/v) of these sugars is proportional to their peak areas, normalized sugar concentrations as weight percentages of total sugars or initial lactose were determined from peak areas and are reported in this work.

Trisaccharides synthesis and lactose hydrolysis mechanisms including glucose and galactose competitive inhibition was mathematically modelled following four ordinary differential equations:

The lactose hydrolysis (*L*) is given by,

$$\frac{dL}{dt}=\frac{n_{1L}[L][H_2O]+n_{2L}[Tri][H_2O]+n_{3L}[L]^2}{d_1} \quad \text{where,} \quad n_{1L}=\frac{-k_1k_2}{k_4};n_{2L}=k_2;n_{3L}=\frac{-2k_1k_3}{k_4} \qquad \text{Equation 1}$$

the glucose (*G*) formation by,

$$\frac{dG}{dt}=\frac{n_{1G}[L]^2+n_{2G}[L][H_2O]}{d_1} \quad \text{where,} \quad n_{1G}=\frac{k_1k_3}{k_4};n_{2G}=\frac{k_1k_2}{k_4} \qquad \text{Equation 2}$$

and the galactose (*Gal*) by,

$$\frac{dGal}{dt}=\frac{n_{1Gal}[H_2O][L]+n_{2Gal}[Tri][H_2O]}{d_1} \quad \text{where,} \quad n_{1Gal}=\frac{k_1k_2}{k_4};n_{2Gal}=k_2 \qquad \text{Equation 3}$$

Finally, the trisaccharides production (*Tri*) is described by the equation 4

$$\frac{dTri}{dt}=\frac{n_{1Tri}[Tri][H_2O]+n_{2Tri}[L]^2}{d_1} \quad \text{with,} \quad n_{1Tri}=-k_2;n_{2Tri}=\frac{k_1k_3}{k_4} \qquad \text{Equation 4}$$

and $$d_1=\frac{k_2}{k_4}[H_2O]+\left(\frac{k_3}{k_4}+\frac{k_1}{k_4}\right)[L]+[Tri]+\frac{k_2k_5}{k_4k_6}[G][H_2O]+\frac{k_3k_7}{k_4k_8}[Gal][L]+\frac{k_2k_7}{k_4k_8}[Gal][H_2O]+\frac{k_3k_5}{k_4k_6}[G][L]$$

The kinetic model was adapted from the work of Boon *et al.* (1999) and the rate expressions were derived with the King-Altman method (King and Altman, 1956; BioKin, Lda). The model used only lactose as substrate and temperature effect was not included. The parameters were grouped into five parameters (k_1,is the overall reaction rate constant; k_4, describes the reaction of water with the galactosyl-enzyme complex; k_3/k_4, ratio between rate constants oligosaccharides synthesis and hydrolysis of the formed oligosaccharides; k_5/k_6 and k_7/k_8 ,account for glucose and galactose inhibition, respectively) that were estimated and one fixed

parameter (k_2, describes the reaction of water with the galactosyl-enzyme complex), which was assumed constant. The estimation of the model parameters was performed by the simulated annealing algorithm of the Systems Biology toolbox for *Matlab* (Mathworks) software (Schmidt and Jirstrand, 2006) using the results of the independent batch experiments, with the sets of experimental data from different initial lactose concentration (10%-50%; w/v) as substrate. All experimental data points were fitted simultaneously for each concentration and support.

3 Results and Discursion

Effects of lactose concentration on GOS production by free and immobilized enzyme on different magnetic supports

The percent of total GOS plotted against the percent of lactose conversion at 5% and 50% of initial lactose concentration, 40 ºC and pH 4.5 by different supports and free enzym, is shown in Figure 1A. Similar experiments were performed for different initial lactose concentrations (10 to 40%, w/v) and the tri- and the tetra-saccharides were quantified (data not show). GOS (tri- and tetra-saccharides) production increased with increasing lactose concentration. However, for each lactose concentration the GOS production decreased after a certain degree of lactose conversion. This can be attributed to a preferential hydrolysis (formation of glucose and galactose) rather than GOS synthesis. Furthermore, there was no marked difference between the free and immbilized enzyme performances. As the initial lactose concentration increased from 5% to 50%, the maximum GOS content in the product increased from 11.2% (at 35% conversion) to 26.1% (at 56% conversion) for the free enzyme, from 10.3% (at 38% conversion) to 25.7% (at 49% conversion) for the immobilized enzyme on mPOS-PANI, from 10.1% (at 34% conversion) to 26.2% (at 54% conversion) for the immobilized enzyme on DACRON, from 10.4% (at 30% conversion) to 26.0% (at 55% conversion) for the immobilized enzyme on mPOS-PVA, and from 10.8% (at 33% conversion) to 26.0% (at 52% conversion) for the immobilized enzyme on MAG-PANI. The maximum amount of tri-, tetra-saccharides and total GOS obtained for the free enzyme were 104.5 g L^{-1}, 33.2 g L^{-1} and 130.3 g L^{-1} for a lactose conversion of about 48%, 61% and 56%, respectively, in 500 g L^{-1} of lactose. For the immobilized enzyme, the corresponding values of 103.7 g L^{-1} on DACRON, 31.9 g L^{-1} on MAG-PANI and 131.0 g L^{-1} on DACRON were obtained for about 46%, 59%, and 54% lactose conversion, respectively in 500 g L^{-1} of lactose. These results suggest that enzyme immobilization on different supports does not impose any limitation or changes on GOS formation from lactose. Similar results were obtained with β-galactosidase from *A. oryzae* immobilized on cotton cloth (Albayrak and Yang, 2002). Thus, the GOS formation ability of the enzyme was not affected by the immobilization of the enzyme onto different supports, what is a clear demontration of the absence of mass transfer limitations using mPOS-PANI, DACRON, mPOS-PVA and MAG-PANI as supports.

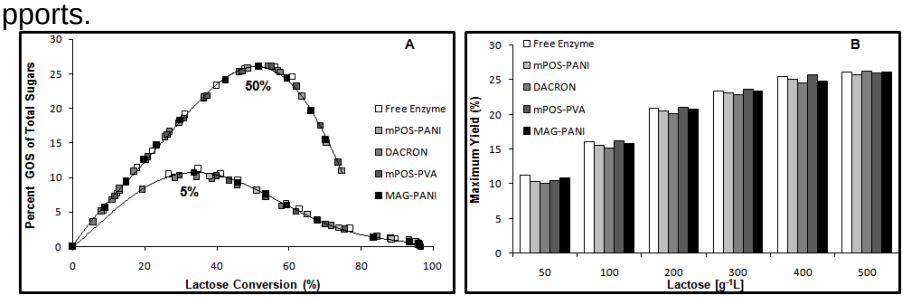

Figure 1. Total GOS (A) formation by free and immobilized (closed symbols) *A. oryzae* β-galactosidase on different supports at pH 4.5 and 40° C catalysing the hydrolysis of initial lactose concentrations (5 and 50%, w/v). GOS Yield (B) *versus* lactose concentration by free and immobilized *Aspergillus oryzae* β-galactosidase on different suports.

GOS yields during lactose hydrolysis catalyzed by the free and the immobilized β-galactosidase on different supports are shown in Figure 1B. The maximum GOS yield

increased with the initial lactose concentration for both enzyme preparations. It was observed that the hydrolysis and transgalactosylation reactions occurred simultaneously and that the product profile of the reaction is largely dependent on lactose concentration. The hydrolysis reaction dominates at low lactose concentration while GOS formation dominates at high lactose concentrations. β-Galactosyl groups should have a higher probability of attaching to lactose than water at increasing lactose concentrations (Iwasaki et al., 1996).An increase was observed up to 300 g L^{-1} of initial lactose concentarion, while for higher lactose concentrations the GOS yield was almost constant at 22.8–26.2% for free and immobilized enzyme on different suports. Park et al (2007) observed the same behavior for high lactose concentration with a thermostable β-galactosidase from *Sulfolobus solfataricus*. It is possible that some disaccharides such as allolactose and galactobiose are formed by the enzymatic transfer of galactose to glucose and galactose, respectively. The absence of this side reactions, was confirmed by checking the molar balances on glucose and galactose over the course of the reaction, assuming that all GOS only contained one unit of glucose with galactose as the remaining sugar. It is also possible that different trisaccharides were also formed, but were not detected by HPLC.

Higher operational and thermal stability, making possible its reuse, has been demonstrated to be one of the advantages of this system for enzyme immobilization (Neri *et al*, 2008). An immobilized β-galactosidase on different supports preparation acting on 20% (w/v) lactose was successively reutilized for 10 cycles at 25 ºC and at the end the enzymatic derivative retained approximately 87% for mPOS-PANI, 90% for DACRON, 84% for mPOS-PVA, and 85% for MAG-PANI of its initial activity (see Figure 2), confirming the advantages of the magnetic supports β-galactosidase derivative.

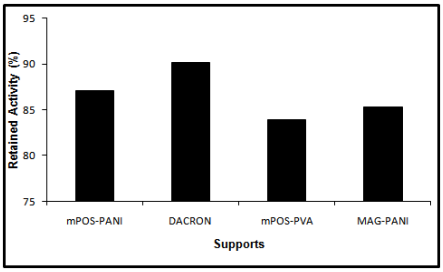

Figure 2. Effect on the activity of β-galactosidase immobilized on different supports after 10 reutilization.

Effects of temperature

Temperature normally has a pronounced effect on the enzyme reaction rates but showed to have a minimal effect, if any, on GOS production (Iwasaki et al., 1996; Monsan and Paul, 1995; Albayrak and Yang, 2002). As shown in Figure 3A and B, GOS production was almost unchanged despite temperatures varying from 30° C to 60° C (Figure 3B) for the conversion of 40% (w/v) lactose, for both the free and immobilized enzyme preparations. Albayrak and Yang (2002) reported similar results for β-galactosidase from *Aspergillus oryzae* immobilized on cotton cloth. It is well known that enzymes do not affect equilibrium constant of the reactions.

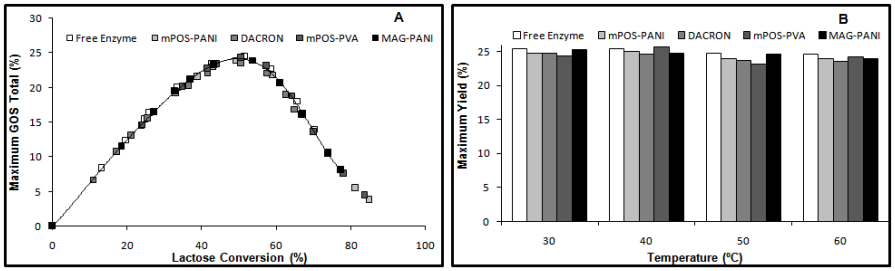

Figure 3. Effects of temperature on the GOS production from the hydrolysis of 40% (w/v) lactose catalyzed by the free and immobilized *A .oryzae* β-galactosidase on different supports at 60 ºC (A). GOS Yield (B) on different supports at various temperature.

Kinetic analysis β-galactosidase free and immobilized on different supports

To verify the precondition that the model parameters are independent of the initial lactose concentrations and in this way to use the parameters by taking the average values, the 95% confidence interval of the slope of the linear dependence of the kinetic parameters on initial lactose concentration was estimated (data not shown). For all the simulations runs the average parameters from each initial lactose concentration were used (Table 1).
To determine the effect of the different supports on the kinetic parameters, experiments were carried out at various initial lactose concentrations ranging from 10-50% (w/v). Figure 4 shows a comparison of the experimental and calculated concentrations profiles with the averaged parameters obtained for the supports at 20% initial lactose concentration. As can be seen, the good quality of the model is remarkable. The model describes well the time course of lactose conversion, glucose and galactose formation and overpredicts slightly the trisaccharides concentration for all the runs.

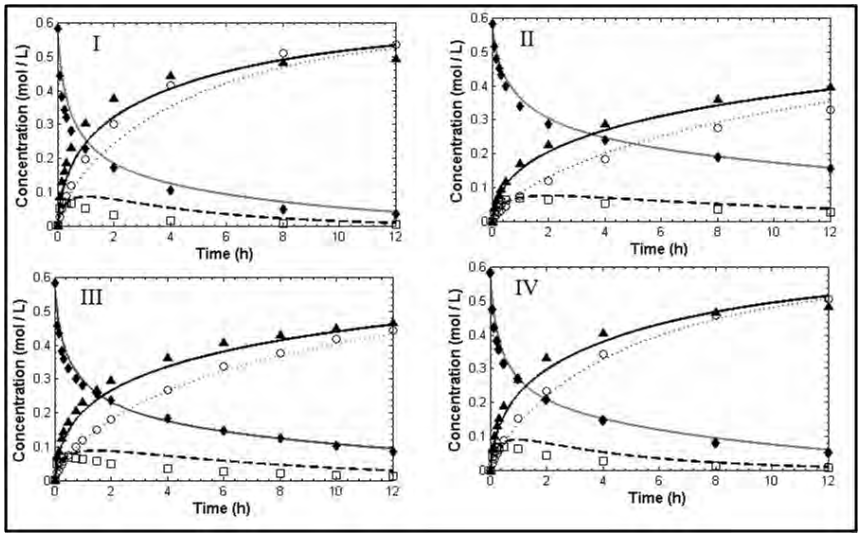

Figure 4. Comparison between experimental (symbols) and simulated data (descending gray solid line: lactose; ascending black solid line: glucose; depicted line; galactose and dashed line: trisaccharide) of (♦) lactose, (▲) glucose, (○) galactose and (□) trisaccharides concentration by immobilized β-galactosidase on Support I (mPOS-PANI), II (DACRON), III (mPOS-PVA) and IV (MAG-PANI) at pH 4.5, 40ºC for 20% initial lactose concentration. Lines represent the simulation using the fitted parameters.

The parameter k_3, that regulates the oligosaccharides synthesis and k_4, which regulates the hydrolysis of the formed oligosaccharides are assumed to be key parameters in the overall process. Not surpringly, as can be observed in Table I, the ratio between k_3 and k_4 is of the same order of magnitude for free and immobilized enzyme on different supports, indicating that the relative extent of the synthesis and hydrolysis reactions is not affected by the immobilization procedure. This is in accordance with the obtained experimental data (see Figure 1).

Table I. Estimated average values and 95% confidence intervals of parameters for the immobilized at different supports and free β-galactosidase obtained by fitting the experimental data for *A. oryzae* at different initial lactose concentration, pH 4.5 and 40ºC.

Parameter (units)	mPOS-PANI	DACRON	mPOS-PVA	MAG-PANI	Free
k_1 (h^{-1})	1.93 ± 0.93	1.09 ± 0.78	1.87 ± 0.70	1.59 ± 0.76	3.06 ± 2.90
Log(k_3/k_4) (-)	1.50 ± 0.043	1.52 ± 0.029	1.49 ± 0.013	1.50 ± 0.017	1.55 ± 0.22
k_4 (h^{-1})	3.69 ± 2.82	4.83 ± 1.613	4.59 ± 1.37	6.15 ± 2.50	3.45 ± 5.06
Log(k_5/k_6) (-)	1.023 ± 0.22	1.12 ± 0.24	1.015 ± 0.17	1.012 ± 0.46	1.50 ± 0.33
Log(k_7/k_8) (-)	0.75 ± 0.35	1.480 ± 0.13	1.45 ± 0.026	0.85 ± 0.41	1.51 ± 0.21

4 Conclusions

All supports proved to be an adequate support for *Aspergillus oryzae* **β**-galactosidase immobilization and its use on GOS production using lactose as substrate. The galacto-oligosaccharides formation ability of the enzyme was not affected by its immobilization onto the magnetic supports that can be easily recovered by applying a magnetic field. The galacto-oligosaccharides production was almost unchanged despite temperatures varying from 30° C to 60° C for the free and immobilized enzyme preparations on different supports. The model describes the experimental data well in the range of the initial lactose concentration used. Such kinetic model may be used bio-process engineering studies to increase knowledge of catalytic studies and the most appropriate support for immobilization process can be selected.

5 Acknowledgments

David F. M. Neri gratefully acknowledges support by the Programme Alβan, the European Union Programme of High Level Scholarships for Latin America (Scholarship no. *E05D057787BR*). Luiz B. Carvalho Jr. is recipient of a scholarship of the Brazilian National Research Council (CNPq).

6 References

Albayrak N, Yang ST. (2002) *Biotechnol Bioeng.* 77: 8-19.
Bakken AP, Hill CG, Amundson CH. 1992*. Biotechnology and Bioengineering* 39:408-417.
Barros AL, Almeida AMP, Carvalho Jr LB, Azevedo WM. (2002). *Brazilian J Med Biolog Research*, 35:449.
Bayramoglu G, Yilmaz M, Senel AU, Arica MY. (2008) *Biochem Eng Journal,* 40:262-274.
BioKin,Ltd. http://www.biokin.com/king-altman/index.html. (2008) Ref Type: Electronic Citation
Boon MA, Janssen AEM, van der Padt A. (1999) *Biotechnol Bioeng,* 64:558-567.
Carneiro-Leão AMA, Oliveira EA, Carvalho Jr LB. (1991) *Appl Biochem Biotechn*, 31: 53-56.
Csetneki I, Kabai M, Szilágyi A, Kovács A, Németh Z, Zrinyi M. (2004) *J. Polym. Sci. Chem.* 42: 4802.
Hong J, Xu D, Gong P, Yu J, Ma H, Yao S. (2008) *Microporuos and Mesoporous Materials*, 109: 470-477.
Huber RE, Kurz G, Wallenfels K. (1976) *Biochem* 15:1994-2001.
Iwasaki K, Nakajima M, Nakao S. 1996. *Process Biochem* 31:69-76.
King EL, Altman C. (1956) *Journal Physical Chemical*, 60:1375-1381.
Lee SH, Doan TTN, Ha SH, Koo Y-M. (2007) *Journal of Molecular Catalysis B: Enzymatic,* 45: 57-61.
Li B, Jia D, Zhou Y, Hu Q and Cai W. (2006) *J Magnetism Magn Mater,* 306: 223-227.
Luo M, Tang W, Zhao J, Pu C. (2006) *J. Mater. Process Technol.* 172: 431.
Monsan P, Paul F. (1995) *FEMS Microbiol* 16:187-192.
Neri DFM, Balcão VM, Carneiro-da-Cunha MG, Carvalho Jr LB, Teixeira JA. (2008) *Catalysis Commun.* doi: http://dx.doi.org/10.1016/j.catcom.2008.05.022
Oliveira G, Lima-Filho J, Chaves M, Azevedo W, Carvalho Jr L. (2008) *Reactive Funct Polymers*, *68: 27-32*
Park HY, Kim HJ, Lee JK Kim D, Oh DK. 2007. *World J Microbiol Biotechnol* doi: 10.1007/s11274-007-9642-x
Pinheiro SMB, Carvalho Jr. LB, Chaves MEC. (1999) *Biotechnology Techniques*, 13: 919-922.
Schmidt H, Jirstrand M. (2006) Bioinformatics, 22: 514-515.
Wadiak DT, Carbonell RG. (1975) *Biotechnol and Bioeng*, 17:1157-1181.

Proceedings of the 10th International Chemical and
Biological Engineering Conference - CHEMPOR 2008
Braga, Portugal, September 4-6, 2008
E.C. Ferreira and M. Mota (Eds.)

Multivariate Analysis of DNA Microarrays

Marco S. Reis *
Department of Chemical Engineering, University of Coimbra
Rua Sílvio Lima, 3030-790, Coimbra, Portugal

Keywords: DNA Microarrays, Gene expression, Multivariate data analysis, PLS-DA, Fisher discriminant analysis
Topic: Systems Biology

Abstract

cDNA microarrays and oligonucleotide chips have the capability of performing genome-wide gene expression analysis, that potentially bring insights and relevant information on how cell and microorganisms are organized or behave at the transcriptome level. Even though this is only a part of the big picture that Systems Biology tries to describe and elucidate, it is certainly an important piece in the puzzle of life, to be properly integrated with the subsequent analysis levels (proteome, metabolome, microbiome, etc.). However, the specific nature of data generated in these experiments does raise relevant difficulties in their analysis which may hinder the full exploitation of their information content. In this paper, an integrated multivariate approach is proposed for analysing gene expression data for classification purposes, incorporating intermediates steps of gene screening, data projection, transformation and classification, in a coherent way. A VIP measure for the combined mapping PLS-DA/FDA is proposed in order to rank genes according to their relevance for achieving a given level of class separation, as well as a "non-classification" option is included in the method, with the purpose of informing the user about the uncertainty in class predictions.

1 Introduction

The analysis of processes going on at the cell scale plays a central role in bioengineering activities. In this field, fundamental knowledge about the complex behaviour of such systems is continuously increasing through the application of the scientific method to well defined biologic problems, through iteration between data analysis stages and hypothesis testing stages, until a mechanistic explanation is found that is consistent with all known results. Between the wide range of currently available data gathering methodologies from biologic systems operation, cDNA microarrays and oligonucleotide chips have become standard techniques, since all cellular processes originate at the transcription stage of cell operation (Stephanopoulos et al., 2002), enabling the simultaneous monitoring of the gene expression levels at a genome-wide scale. Therefore, this class of techniques is able to provide fundamental data-driven information over which explanations about system operation can be elaborated, or through which one is capable to characterize a variety of physiologic states (classification) or discover new ones (discovery).

DNA microarrays result from the hybridization of target samples of labelled mRNA representative of different cells states, with genomic DNA sequences immobilized in a solid matrix (probes). The magnitude of signal intensity at each probe location is then interpreted as a measure of the expression level of that particular gene, at the state corresponding to the label being analyzed.

Data from cDNA microarrays and oligonucleotide chips have been analyzed through univariate techniques, where genes that most differentiate between the states under analysis are identified through F and t statistics, or through other techniques, such as the signal to

* Corresponding author. Tel + 351-239-798700. E-mail:marco@eq.uc.pt

noise ratio (Golub et al., 1999) and the SAM method (Tusher et al., 2001). The simplicity of these methodologies enables the adequate control of classification error rates, such has the False Positive Rate (FPR), Family-Wise Error Rate (FWER) and the False Discovery Rate (FDR). However, they do disregard the cooperative behaviour of gene expression, a widely recognized feature of biologic systems.

Multivariate approaches, on the other hand, are more suitable for taking into account gene co-expression, but still present some methodological limitations. For instance, Fisher Discriminant Analysis (FDA) requires the number of variables (genes, in microarray data) to be less than the number of observations, a condition not met in practice in microarrays studies, where the number of genes whose expression levels are assessed is much larger than the number of analyzed samples. Therefore, such multivariate techniques do require a preliminary stage of variable selection, usually based on the simpler univariate approaches, a clear manifestation that some coherency and integration is lacking in the way the problem is being addressed.

In this work, an intrinsic multivariate approach is presented where such preliminary univariate variable reduction stage is not needed, but where genes screening can still be conducted after a first run of the proposed methodology, on the basis of multivariate information thus generated (genes VIP's). The proposed classification approach, to be described in the second section of this paper, combines PLS-DA (Barker and Rayens, 2003) and FDA (Johnson and Wichern, 2002), and has incorporated a "non-classification" option, that results from the analysis of the uncertainty associated with each class prediction, according to two distance measures of the expression profile in new samples, when compared to those in the training dataset.

2 Methods

In this section, the main steps of the proposed classification methodology are briefly described. In the first stage (training stage), a model is preliminarily estimated using all genes in the training data set, after selecting the number of PLS-DA dimensions (an adjustable parameter of the method). The X-scores thus obtained, are then transformed again, now using Fisher's Discriminant Analysis, in order to maximize the separation of class clusters in the resulting transformed space. If such separation is acceptable, it is then possible to estimate the importance of each gene in this process, after such a PLS-DA / FDA combination, using the following Variable Importance in Projection (VIP) metric:

$$VIP_{PLS-DA/FDA}(i) = n_{genes} \sum_{j=1}^{LV_{FDA}} \sum_{l=1}^{LV_{PLS}} \left\{ W(i,l)^2 \cdot L_N(l,j)^2 \cdot d(j) \right\} \tag{1.1}$$

where, $VIP_{PLS-DA/FDA}(i)$ is the VIP metric for observation i, n_{genes} stand for the original number of genes present in the data set, W is weighting matrix of PLS-DA, L_N the normalized eigenvector matrix of FDA (Johnson and Wichern, 2002; Stephanopoulos et al., 2002) and d is the vector with the inter/intra distances for each FDA component ($LV_{FDA} \leq LV_{PLS}$), a separability metric of classes, given by the ratio of the interclass to the intraclass variability. In Figure 1, it can be seen that the order suggested by the proposed VIP scores does correlate well with the ordering obtained with the Wilks's lambda statistic (a univariate measure of the classification ability of an isolated gene), but, being multivariate in nature, it necessarily leads to differences between the two methodologies.

Selecting the genes with the highest VIP values, it is possible to estimate a more parsimonious classification model, without the deleterious influence of genes not correlated with the cell states, which are the objects of classification. Such number of selected genes

can be put forward by estimating the classification performance using cross-validation, while the number of genes is successively reduced by removing the ones with the lower VIP scores. The maximum of the curve *cross-validated classification performance* versus *number of genes retained*, provides the desired number of retained genes. Using only such set of genes with highest VIP scores, result in a reduced training data set, for which a new combined PLS-DA/FDA model is estimated. Finally, for the scores in the FDA space, a suitable classifier is estimated, according to the topology of the data clusters for each class in this domain.

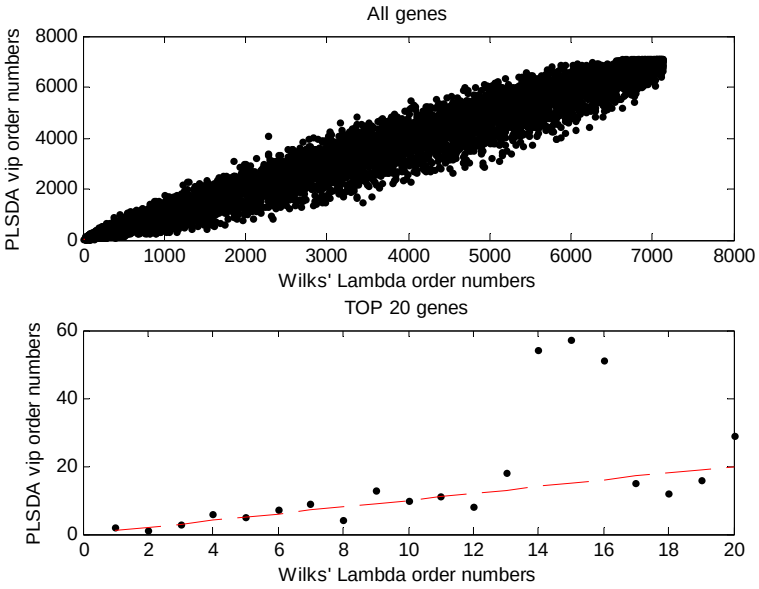

Figure 1. Correlation study of the order numbers proposed by the VIP metric and by the Wilks' Lambda statistic, for all genes in the data set.

Using some results of the estimated models, namely the classification probabilities for the attributed classes, computed using the Bayesian formalism for all samples in the training data set, and their distances to the PLS-DA's X-scores subspace, it is possible to put forward two metrics that characterize: (i) the "normal" distance of each sample (gene expression profile) to the subspace fitted with the training data, and the (ii) "normal" probabilities with which classes were assigned in the training samples. After analysing the variability of these metrics in the training data set, thresholds can be set for each one of them. Then, for a gene expression profile relative to a new sample, metric (i) will allow the user to verify whether it falls in the region where the model was estimated, and therefore it can be applied for assigning a class label to it, or not, in which case the model is no longer valid; metric (ii), on the other hand, addresses the problem of how confident are we in a given proposed classification (assuming that the sample is close enough to the PLS-DA subspace, which can be verified by analysing metric (i)), relatively to what was done in the training stage: classes that are predicted with probabilities significant lower than those for the training stage, should be taken with caution, or even rejected, if such probability is really low. In the next section we provide an illustrative example of this methodology.

3 Results and Discussion

In order to illustrate the proposed methodology, a well known data set was used (Golub et al., 1999), where different expression phenotypes were measured in samples from patients with different types of leukaemia: acute lymphoblastic leukaemia (ALL), subdivided according

to their lineage (ALL-B and ALL-T) and acute myeloid leukaemia (AML). The combined multivariate approach was applied to the training set containing 38 samples (19 ALL-B, 8 ALL-T and 11 AML) with 7129 genes, using LV_{PLS}=5 and LV_{FDA}=2. We would like to point out that, in this work, these parameters were not optimized for achieving the best classification performance, but are set to these values only for the sake of illustrating the approach. Analysing the curve of *cross-validated classification performance* versus *number of genes retained*, it was decided to select only the TOP-30 genes in the VIP ranking. Figure 2 provides de VIP scores in a decreasing order of magnitude, where we can see that the few TOP genes do indeed present magnitudes significantly higher than most of the others.

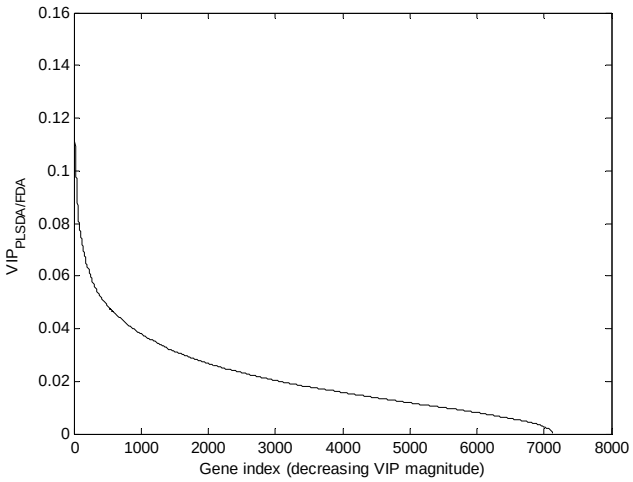

Figure 2. Profile of gene VIPs, by decreasing order of magnitude, in the leukaemia case study (Golub et al., 1999).

Even though the results obtained by using only PLS-DA over the entire training data set (Figure 3-a), do provide already an interesting class separation, it can be significantly improved by selecting the most important genes, according to the proposed VIP criteria, as a large number of them do not carry relevant information for classification purposes (Figure 3-b).

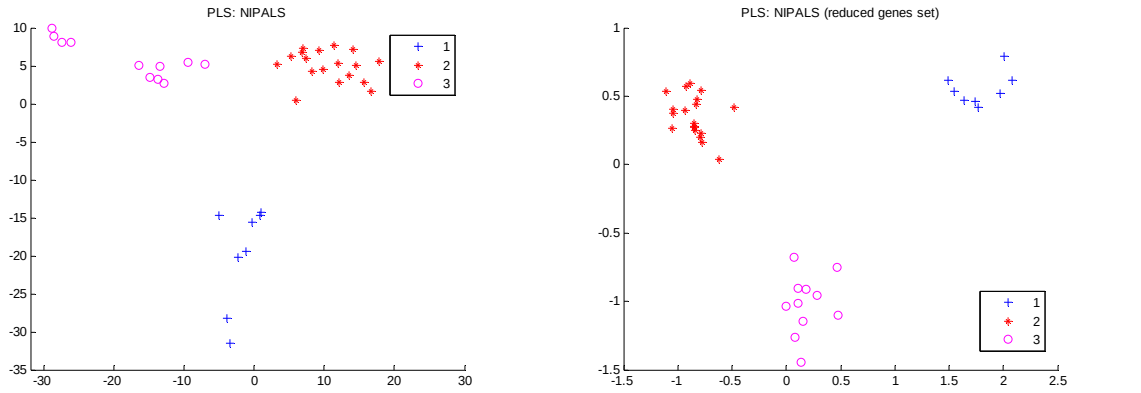

Figure 3. Scatter plots for the several leukaemia classes in the reduced dimensional space after a first run analysis (a) and after gene selection using the VIP criteria (b). (1:ALL-T; 2:ALL-B; 3:AML)

Applying the estimated classification model to the test data set containing 34 samples (19 ALL-B, 1 ALL-T and 14 AML), an average classification rate (per class) of ~9% was achieved (which can be significantly improved through a better choice of the adjustable parameters,

LV_{PLS} and LV_{FDA}). What is interesting to analyse here, being something that is generally overlooked in the literature, is the strong dissimilarity of the test set, when compared to the training samples. This can be confirmed by looking at the combined plot for the squared distance to the PLS-DA subspace versus the log-probability of classification, for each sample in the training data set (Figure 4), where most of the samples are in the “safety classification region”, located in the lower-right corner, whereas for the test set, most of them are outside such region. Therefore, even though in this example the classification rate achieved for the test set was reasonably good, it should be looked quite carefully, since the new samples are now arranged differently in the classification subspace, most of the falling outside the “safety classification region”.

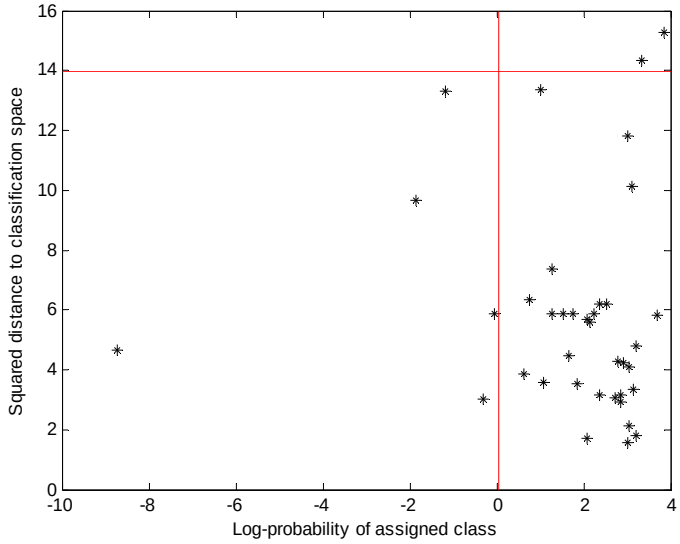

Figure 4. Combined plot for the squared distance to the PLS-DA subspace versus the log-probability of classification, for each sample in the training data set.

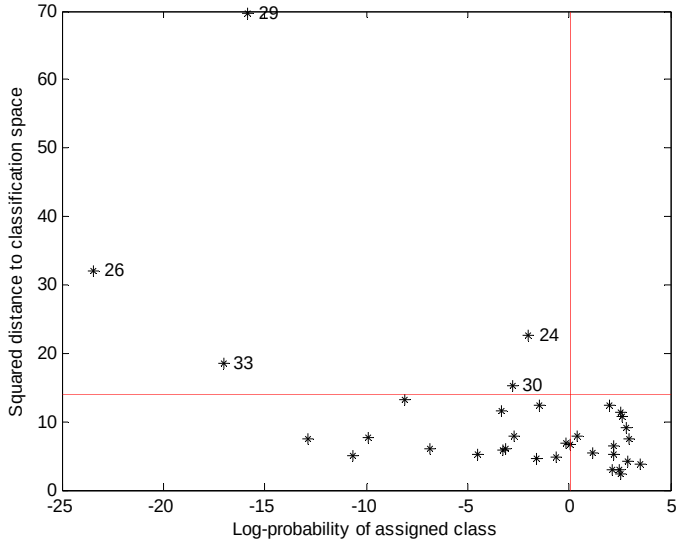

Figure 5. Combined plot for the squared distance to the PLS-DA subspace versus the log-probability of classification, for each sample in the test data set.

4 Conclusions

In this paper an integrated multivariate approach was presented for addressing classification tasks using gene expression data. The proposed approach has the capability of performing genes screening on the basis of multivariate information thus generated (genes VIP's), and it combines PLS-DA and FDA. Furthermore, it has incorporated a "non-classification" option that results from the analysis of the uncertainty associated with each class prediction, according to two distance measures of the expression profile: the squared distance to the PLS-DA subspace and the probability of classification. The proposed approach was illustrated with a classic gene expression data set (Golub et al., 1999), where its potentialities were explored, leading to the conclusion that, in spite of the reasonable accuracy of the classifier, the test samples were significantly different from those in training data set, which may prevent, in real world situations, the possibility of making class predictions.

References

Barker, M., Rayens, W. (2003). Partial Least Squares for Descrimination. *Journal of Chemometrics*, 17, 166-173.

Golub, T.R., Slonim, D.K., Tamayo, P., Huard, C., Gaasenbeeck, M., Mesirov, J.P., Coller, H., Loh, M.L., Downing, J.R., Caligiuri, M.A., Bloomfield, C.D., Lander, E.S. (1999). Molecular classification of cancer: Class discovery and class prediction by gene expression monitoring. *Science*, 286, 531-537.

Johnson, R.A., Wichern, D.W. (2002). Applied Multivariate Statistical Analysis. Prentice Hall, Upper Sadle River, NJ.

Stephanopoulos, G., Hwang, D., Schmitt, W.A., Misra, J., Stephanopoulos, G. (2002). Mapping Physiological States from Microarray Expression Measurements. *Bioinformatics*, 18(8), 1054-1063.

Tusher, V.G., Tibshirani, R., Chu, G. (2001). Significance analysis of microarrays applied to the ionizing radiation response. *Proc. Natl. Acad. Sci. USA*, (98), 5116-5151.

Proceedings of the 10th International Chemical and
Biological Engineering Conference - CHEMPOR 2008
Braga, Portugal, September 4-6, 2008
E.C. Ferreira and M. Mota (Eds.)

Evaluation of olive oil-lemon juice emulsion stability through digital image analysis

Kelly A. Silva[1], Maria H. Rocha-Leão[2], Maria A.Z.Coelho[2*]

[1]Instituto de Química, Centro de Ciências Matemáticas e da Natureza, Universidade Federal do Rio de Janeiro, Campus Ilha do Fundão, 21949-900 – Rio de Janeiro, Brazil.

[2]Escola de Química, Centro de Tecnologia, Universidade Federal do Rio de Janeiro, Campus Ilha do Fundão, 21949-900 – Rio de Janeiro, Brazil

Keywords: Emulsion, image analysis, xanthan gum, starch modified, maltodextrin
Topic: Integration of life sciences & engineering

Abstract

The aging mechanisms of olive oil-lemon juice emulsion were investigated using image analysis. The emulsions were prepared with different ratios of modified starch (or maltodextrin) and xanthan gum. After preparation, emulsions stability was followed through analysis of the evolution of mean droplet size. The results indicate that stability of this salad dressing may take place for two aging mechanisms, coalescence or molecular diffusion. Analysis of the evaluation of the mean droplet size during 63 days indicated that coalescence is more common amongst the samples, the mean diameter droplets were greater in the samples with maltodextrin and with only xanthan gum and although this, during the storage time studied, any samples presented separation of phases.

1 Introduction

Emulsions are thermodynamically unstable systems because of the positive free energy needed to increase the surface area between oil and water phases and because oil and water have different densities. To form emulsions kinetically stable for a reasonable period of time, chemical substances known as emulsifiers must be added prior to homogenization (McClementes and Decker, 2000).

The Mediterranean diet has been associated with greater longevity and quality of life in epidemiological studies (Majem-Serra, Roman and Estruch, 2006). “Greek salad dressing” is, by definition, mixtures of virgin olive oil and lemon juice instantly prepared before use. Due to their compositions, they are a good source of biophenols as well as lipid-soluble and water-soluble vitamins. Besides, it has highly appreciated nutritional characteristics (Paraskevopoulou, Boskou and Paraskevopoulou, 2007).

Several kinds of physicochemical mechanisms contribute to the instability of an emulsion, including gravitation separation (creaming), coalescence, and flocculation. Polysaccharides are usually added to the aqueous phase of oil-in-water food emulsions to improve creaming stability of emulsions (Quintana et al, 2002).They are generally odorless, colorless and tasteless, have low energy and digestibility. The majority of such polysaccharides show little surface activity and their incorporation into oil-in-water emulsions is aimed inhibiting droplet creaming by increasing the viscosity of the aqueous phase thus preserving the desired textural properties of the emulsion (Paraskevopoulou, Boskou and Kiosseoglou, 2005). Starch, similar to other major polysaccharides, has low surface activity and is often used as a thickening agent or stabilizer in food emulsions. However, it has been found recently that starch causes a decrease in the creaming stability of beverage emulsions via depletion flocculation, similar to other major polysaccharides (Ye, Hemar and Singh, 2004).

* Corresponding author. Tel + 55 21 2562-7572. E-mail: alice@eq.ufrj.br

Emulsions containing maltodextrin as stabilizers therefore require an additional emulsifying agent for the production of a stable emulsion. In an emulsion system containing surfactant and polysaccharide, the nature and strength of emulsion stability will depend on surfactant–polysaccharide interactions at the surface of the emulsion droplets as well as in the aqueous medium between the droplets (Klinkesorn, 2004). Xanthan gum is a heteropolysaccharide aquosoluble produced industrially by fermentation of sucrose by *Xanthomonas campestris*. Excellent gum rheological properties contribute to its use in a wide range of applications in the food industry (Druzian, 2007). Hydrophobically modified starch, such as octenyl succinate anhydride starch, is an amphiphilic macromolecule. It offers properties that have many applications within the formation and stabilization of dispersed food systems such as emulsions.

Emulsion stability can be studied through the evolution of the droplet size and size distribution. The increase in droplet diameter is an indicator of the loss of stability of the emulsion and the growth rate of the droplets reveals the mechanism responsible for their aging. Two main mechanisms have been proposed for the loss of stability of these emulsions: coalescence and molecular diffusion (Sjoblom, 1996).

The objective of the present work was to develop oil-in-water emulsions containing two basic ingredients, olive oil and lemon juice, added by different combinations of xanthan gum with modified starch or maltodextrin that would exhibit reasonable stability over prolonged storage. Digital image processing was used to evaluate the stabilization of the emulsion by distribution of the droplet sizes along storage time at room temperature (± 27 ^{o}C).

2. Aging Mechanisms

The physical degradation of emulsions is due to the spontaneous trend toward a reduction in the Gibbs free energy *(∆G)*, achieved by reducing the size of the oil/water interface, *A*, and/or of the interfacial tension between the continuous and the dispersed phases, *γ* :

$$\Delta G = \gamma \Delta A - T \Delta S \quad (1)$$

The reduction of the interfacial area is achieved mainly by two mechanisms: coagulation, followed by coalescence, and molecular diffusion. Coalescence is the formation of a larger droplet from the merging of smaller ones. This requires that the small droplets come into contact, with thinning and disruption of the film that covers them. Emulsion degradation by coalescence is characterized by a broadening in particle size distribution, with an exponential increase in the mean droplet size with time, according to the Van den Tempel Theory,

$$a^{-3} = a_0^{-3} \exp(Kt) \quad (2)$$

where $\bar{a}_o$ is the initial average particle radius, $\bar{a}$ is the average particle radius at time t , and K is the coalescence constant. The coarsening of emulsions through molecular diffusion, also known as Ostwald ripening, is due to the gradual growth of the larger droplets of the emulsion at the expenses of smaller ones. This is a direct consequence of the Kelvin effect, which states that the solubility of a particle is inversely proportional to its radius, meaning that individual molecules tend to leave smaller particles and to diffuse through the continuous phase to join larger ones. There is essentially one theoretical treatment known as the Lifshitz–Slyozov–Wagner (LSW) theory and its modifications, where the molecular diffusion mechanism is characterized by linear growth of the droplet volume with time,

$$d(\bar{a})^3/dt = 8CD\gamma V m^2/9RT \quad (3)$$

where C and D are respectively the solubility and the diffusion coefficient of the dispersed phase in the continuous medium, V_m is the molar volume of the dispersed substance, R is the usual gas constant, and T is the absolute temperature. (Freire et al, 2005; Trindade et al, 2008). According to Eq. (3), an increase in the particle's volume is proportional to the solubility, the diffusion coefficient, and the interfacial tension of the dispersed phase (olive oil) in the continuous phase (lemon juice). Therefore, emulsions that undergo Ostwald ripening can be stabilized by decreasing at least one of these three factors.

3. Materials and methods

Oil-in-water emulsions (50% v/v) were prepared as follows: a lemon juice polysaccharide solution was first prepared by slowly dispersing 1% w/v arabic gum and 0.5% w/v xanthan gum (control), and different concentrations of modified starch (or maltodextrine) and xanthan gum with composition summarized in Table 1. After, the olive oil was added stirring it with a vortex (2200 rpm) for 2 min. The resulting crude emulsion was then homogenized for 1 min at 9500 rpm using Ultra-Turrax T25 homogenizer (IKA Instruments, Germany) equipped with a dispersing tool. Benzoic acid was added at a concentration for 1% w/v in the continuous phase to lemon juice.

Table 1. Emulsions composition olive oil-lemon juice (50% v/v) studied and optimal fitted for mechanisms of stability loss for the studied ($\bar{a}^3$ = droplet diameter (μm^3) and t = time(days)).

Emulsion	Starch modified (%)	Xanthan gum (%)	Maltodextrin (%)	Fitted equation
I	1,0	0,5	-	$\bar{a}^3 = 1{,}43\ t + 107{,}19$
II	1,0	0,6	-	$\bar{a}^3 = 75{,}91\ e^{0{,}0081t}$
III	2,0	0,5	-	$\bar{a}^3 = 69{,}70\ e^{0{,}0295t}$
IV	2,0	0,6	-	$\bar{a}^3 = 62{,}35\ e^{0{,}0236t}$
V	-	0,4	1,0	$\bar{a}^3 = 110{,}87\ e^{0{,}017t}$
VI	-	0,5	1,0	$\bar{a}^3 = 23{,}49\ t - 758{,}62$
VII	-	0,6	1,0	$\bar{a}^3 = 33{,}36\ t - 1150{,}4$
VIII	-	0,5	-	$\bar{a}^3 = 173{,}76\ e^{0{,}0267t}$

3.1. Image analysis

The measurement of emulsions droplet size distribution was carried out during a storage period 63 days. Images acquisition was conducted using an optical microscope (Eclipse E200, Nikon) with 400× magnification coupled with digital camera (Media Cybernetics, QImaging) linked to a personal computer. The images were focused in such a way as to enhance droplet contours. Afterwards, a step to suppress objects connected to the image border, and a hole-fill procedure were performed. Application of operations, such as erosion (to remove small debris) and reconstruction, produced the final binary image. These image processing were developed using the Matlab® v.7.0.4 (The Mathworks, Natick, Mass.) package and were fully automated. A micrometer and appropriate software, Image-Pro® Plus 5.0, were used for calibration of the droplet size. For each 7 days an average of 25 different pictures from different samples were analyzed. The quantification step from image analysis supplies a statistical analysis of the data providing the total number of analyzed objects, the average droplet diameter and its standard deviation as well as the particle size distribution (Freire et al, 2005; Trindade et al, 2008). It also provides the particle roundness and its distribution, useful detecting if other objects than droplets are being analyzed.

4. Results and discussion

The emulsions are formed from two immiscible liquids, olive oil-juice lemon that added of emulsifiers in ratios appropriate to remain themselves steady a long time. Analysis realized through digital image processing permitted the accomplishment of the stability of emulsions studied. The emulsions droplets size was carried out during 63 days. For each 7 days an average 25 different pictures from each sample was analyzed varying of 250 the 1800 droplets. The quantification step from image analysis supplies a statistical analysis of the data providing the total number of analyzed objects, the average droplet diameter and its standard deviation as well as the particle size distribution. It also detects if other objects than droplets are being analyzed.

The oil droplets are stabilized against flocculation and coalescence due to strong steric barrier effect arising from polysaccharide blocks protruding towards the emulsion continuous phase from neighboring droplet surfaces, where they are anchored though the more hydrophobic protein moiety of the gum (Dickinson, 2003).

A statistical analysis of the experimental data aiming to assure that no systematic errors (or bias) were made during the particle diameter measurements was also performed for all the samples. Among other issues, it is important to ensure that the program is detecting the smallest droplets and that the samples are randomly analyzed with no preferential droplet size detection (Trindade et al, 2008). When no systematic errors are present, the population of all the studied emulsions follows a Gaussian distribution. During the 63 days of storage, all the samples were visually steady and homogeneous, that is, they had not presented formation of creaming or separation of phases. Although this the results through the image processing shown that some samples already had initiated the process of stability loss.

Table 2. Distribution of the droplet size populations for emulsions.

	Width			Peak		
Emulsions	0 day	63 day	Ratio	0 day	63 day	Ratio
Control	0,083 ± 0,004	0,069 ± 0,003	0,8313 *	2,003 ± 0,094	1,922 ± 0,084	0,9599 *
I	0,107 ± 0,005	0,085 ±0,004	0,7943 *	2,198 ± 0,105	2,185 ± 0,090	0,9939 *
II	0,117 ± 0,004	0,089 ± 0,003	0,7594 *	2,394 ± 0,085	2,253 ±0,070	0,9411 *
III	0,078 ± 0,004	0,096 ± 0,005	1,2266 **	2,027 ± 0,101	2,255 ± 0,115	1,1124 **
IV	0,121 ± 0,005	0,065 ± 0,002	0,5357 *	2,352 ± 0,101	2,137 ± 0,067	0,9087 *
V	0,054 ± 0,003	0,068 ± 0,004	1,2584 **	1,640 ± 0,090	1,952 ± 0,103	1,1904 **
VI	0,091 ± 0,007	0,051 ± 0,005	0,5634 *	1,886 ± 0,138	1,139 ±0,097	0,6042 *
VII	0,095 ± 0,007	0,079 ± 0,007	0,8360 *	2,124 ± 0,141	1,557 ± 0,126	0,7330 *
VIII	0,075 ± 0,004	0,057 ± 0,003	0,7533 *	1,857 ± 0,104	1,690 ± 0,088	0,9096 *

***** Widht = Homogeneous; * Peak = dislocated for lesser values
****** Widht = Heterogeneous; ** Peak = dislocated for bigger values

The molecules of xanthan gum adopt a helical conformation that they can be described as rigid connecting rods without trend to associate resulting in a thickener behavior. The most important property is ordered state of the macromolecule; therefore the xanthan gum can always be used in the electrolyte presence. These characteristics become xanthan gum appropriate as acid thickener and stabilizer agent in acid pH, as dressing salad in general (Multon, 2000; Fonseca, 2008). The sample control was characterized as steady during 63 days of storage, because of mechanism loss of stability wasn't detect, therefore as it can be seen in fig. 1a the evaluation of droplet size remains around a specific value. This can be explained since the sample was characterized as homogeneous in table 2 and this sample was chosen for comparative in this study due to the good results gotten in the works carried out by Paraskevopoulou and collaborators in 2005 and 2007.

The emulsions content mixture of xanthan gum with maltodextrin (emulsions V, VI and VII) and the emulsion VIII with only xanthan gum had the biggest cube diameter when compared with the results of the emulsions that contained xanthan gum and modified starch. In agreement with Dickinson (2003), emulsifiers are surface-active ingredients that adsorb to the surface of emulsion droplets and prevent them from aggregating. Maltodextrins are not particularly surface-active, and so their main stabilizing action in oil-in-water emulsions is believed to be through viscosity modification or gelatinization of the aqueous continuous phase surrounding the oil droplets. The starch-modified enzimatically contain hydrophobic as well as hydrophilic groups, the starch molecules are attracted to the interface between the water and the oil droplets in an emulsion. As a result, a tougher, more cohesive, more continuous, and less easily disrupted film is formed about the oil droplet. This makes it more difficult for the dispersed phase to coalesce and separate (Wurzburg, 1986).

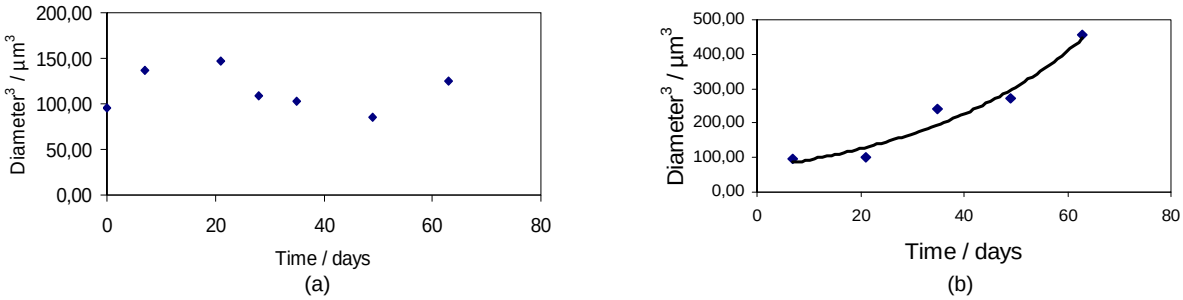

Fig.1. Droplet size evolution as a function of time for emulsion control (a) and emulsion III (b).

It was observed that in accordance with the data presented in table 1 and table 2 samples II and IV had exponential growth of droplets characterizing mechanisms of stability loss by coalescence. The modified starch, such octenyl succinate anhydride starch, is amphiphilic macromolecule. It offers properties that have many applications within the formation and stabilization of dispensed food systems such emulsions (Modig et al, 2006). The result from distribution of the droplet size populations (table 2) showed the emulsions III and V had been characterized as heterogeneous and presented droplets growth since the values of size to 63 days increased in contrast with the initial time. In figs. 1b these sample show an exponential growth what characterizes an increase of droplet size and probable loss stability by coalescence mechanism.

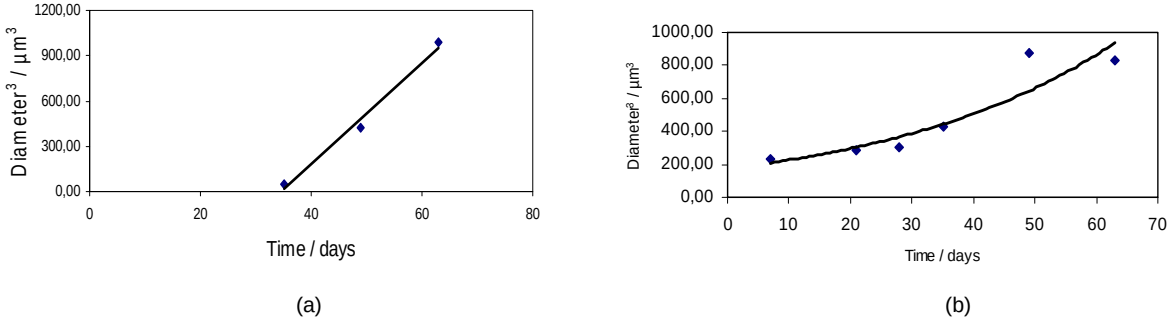

Fig. 2. Droplet size evolution as a function of time for emulsion VII (a) and emulsion VIII (b)

Sample I that contain lesser ratio of modified starch and xanthan gum, as well samples VI and VII (fig. 2a), that contain different ratios of xanthan gum and maltodextrin, had a linear growth of the droplet size characterizing the beginning of stability loss by molecular diffusion, as can be visualized in table 1, through the fitted equation. In accordance with Klinkesorn (2004), the molecular characteristics of maltodextrin, such as concentration and chain length, affect the stability of oil-in-water emulsions. Already sample VIII (fig. 2b) that contain only 0.5% xanthan gum show exponential growth of droplet size however during the 63 analyzed days all samples were homogeneous.

5. Conclusions

The image processing procedure showed to be a good method to the evaluation of oil in water emulsions stability. Analysis of the evaluation of the mean droplet size during 63 days indicated that coalescence is more common amongst the samples, the mean diameter droplets were greater in the samples with maltodextrin and with only xanthan gum and although this, during the storage time studied, no samples presented separation of phases. It can be conclude that the polysaccharides xanthan gum, maltodextrin and starch modified, have the ability for the stabilize oil-in water emulsions. The emulsifiers influence allowed the characterization the system along time besides to contribute to the development of more consistent formulation.

Acknowledgments

The authors are grateful for the financial support give by CAPES.

References

Fonseca, V.C. (2008). *Elaboração de molho para salada com soro de queijo minas frescal estabilizado por combinações ternárias de alginato de propileno glicol, goma xantana e carboximetilcelulose*. Dissertação (mestrado em tecnologia de alimentos) - Universidade Federal do Paraná, Curitiba, Brasil. 133p.

Freire, M.G., Dias, A.M.A., Coutinho, J.A.P., Coelho, M.A.Z., Marrucho, I.M. (2005). Aging Mechanisms of Perfluorocarbon Emulsions using Image Analysis. *Journal of Colloid and Interface Science*, 286, 224-232.

Dickinson, E. (2003). Hydrocolloids at interfaces and the influence on the properties of dispersed systems. *Food Hydrocolloids*, 17:1, 25–39.

Druzian, J.I., Pagliarini, A.P. (2007). Xanthan gum production by fermentation from residue of apple juice. *Ciência e Tecnologia de Alimentos*., Campinas, 27, 1.

Majem-Serra, M., Roman, B., Estruch, R. (2006). Scientific evidence of interventions using the Mediterranean diet: A systematic review. *Nutrition Reviews*. 64, S27-S47.

Klinkesorn, U; Sophanodora P; Chinachoti, P; McClements, D.J. (2004). Stability and rheology of corn oil-in-water emulsions containing maltodextrin. *Food Research International*. 37, 851–859.

McClements, D.J., Decker, E.A. (2000). Lipid oxidation in oil-in-water emulsions: impact of molecular environment on chemical reactions in heterogeneous food systems. *Journal of food science*, 65: 8, 1270-1282.

Modig, G., Nilsson, L., Bergenstahl, B., Wahlund, K.G. (2006) Homogenization-induced degradation of hydrophobically modified starch determined by asymmetrical flow field-flow fractionation and multi-angle light scattering. *Food Hydrocolloids,* 20, 1087-1095.

Multon, J. L. (2000). Aditivos y auxiliares de fabricación en las industrias agroalimentarias. 2. ed. Zaragoza: acribia, 277p.

Paraskevopoulou, A., Boskou, D., Kiosseoglou, V. (2005). Stabilization of olive oil - lemon juice emulsion with polysaccharides. *Food Chemistry*, 90, 627 – 634.

Paraskevopoulou, D. Boskou, D. Paraskevopoulou, A. (2007). Oxidative stability of olive oil-lemon juice salad dressings stabilized with polysaccharides. *Food Chemistry*,. 101, 1197-1204.

Quintana.J.M., Califano, A.N., Zaritzky, N.E., Partal, P., Franco, J.M. (2002). Linear and nonlinear viscoelastic behavior of oil-in-water emulsions stabilized with polysaccharides. *Food & nutrition press*, 33, 215-236.

Sjoblom, J. (1996). Emulsion and Emulsion Stability, *Surfactant Science Series*,61, Dekker, New York.

Trindade, J.R., Freire, M.G., Amaral, P.F.F., Coelho, M.A.Z., Coutinho, J.A.P., Marrucho, I.M. (2008). Aging mechanisms of oil-in-water emulsions based on a bioemulsifier produced by Yarrowia lipolytica. Colloids and Surfaces A: *Physicochem* Eng. Aspects 324, 149-154.

Yea A., Hemar Y., Singh H. (2004). Flocculation and coalescence of droplets in oil-in-water emulsions formed with highly hydrolysed whey proteins as influenced by starch. *Colloids and Surfaces B: Biointerfaces*. 10, 1-9.

Wurzburg, O.B. (1986). Modified starches: properties and uses. 1. ed. CRC Press, *Boca Raton*, Florida, 277p.

Proceedings of the 10th International Chemical and
Biological Engineering Conference - CHEMPOR 2008
Braga, Portugal, September 4-6, 2008
E.C. Ferreira and M. Mota (Eds.)

Looking Toward New Biomolecules: IR and ^{1}H NMR Spectroscopies and DFT Calculations on N_α-Benzoyl-L-Arginine Ethyl Ester Hydrochloride

Ana C. Fonseca[1*], Susana Jarmelo[1,2], Rui A.Carvalho[3], Rui Fausto[2], Maria H. Gil[1], Pedro Simões[1]

[1]Chemical Engineering Department, University of Coimbra, Polo II, Pinhal de Marrocos, 3030-790 Coimbra, Portugal.
[2] Department of Chemistry, University of Coimbra, 3004-535 Coimbra, Portugal.
[3] Department of Biochemistry, University of Coimbra, 3001-401 Coimbra, Portugal.

Keywords: Biomolecules, N_α-benzoyl-L-arginine ethyl ester hydrochloride (BAEE·HCl), IR, NMR, DFT calculations.
Topic: Advancing the chemical engineering fundamentals.

Abstract

High level molecular modeling and experimental studies by IR and ^{1}H NMR spectroscopies on an L-arginine derivative, N_α-benzoyl-L-arginine ethyl ester hydrochloride (BAEE·HCl) were carried out.

A systematic conformational search on the less expensive semi-empirical PM3 Potential Energy Surface (PES) of the two tautomers of BAEE·HCl was done. The lowest-energy conformations obtained with the PM3 method were afterwards optimized using the density functional theory (DFT) method and the B3LYP/6-31++G(d,p) level of approximation.

The IR spectrum of BAEE·HCl was recorded in the range 4000–600 cm^{-1}, at room temperature. The ^{1}H NMR spectra of BAEE·HCl was recorded in DMF-D_7, at 25ºC.

The information provided by the theoretical methods for the most stable conformers, in combination with the experimental data, allowed a detailed characterization of the molecular structure of BAEE·HCl.

1 Introduction

In recent years, there has been a growing interest in developing new materials for biomedical applications that can mimic some of the functions of biomolecules (Zhang *et al.*, 2007). Polydepsipeptides, copolymers of α-hydroxy acids and α-amino acids, are promising materials for that end. These copolymers present an amide (–CONH–) and an ester linkage (–COO–) in the main chain. From the point of view of pharmaceutical and biomedical applications, these materials represent particularly promising systems, since they have the ability to establish strong biospecific intermolecular hydrogen bond interactions (through their amide groups) with cell components. Hydrogen bonds involving the amide groups may also enhance mechanical and thermal properties of polydepsipeptides compared to the related polyesters, while degradability is ensured by the presence of ester groups (He *et al.*, 2003, Deng *et al.*, 2007). Thus, it is of great importance the investigation of their properties, not only at the macroscopic, but also at the microscopic level. In this context, vibrational and NMR spectroscopies, combined with molecular modeling methods, have been shown to be a valuable approach in the development and characterization of new materials (Strittmatter and Williams, 2000, Zhang *et al.*, 2007).

* Corresponding author. Tel + 351-239-798760. E-mail:anafs3@eq.uc.pt

Despite the promising capabilities of polydepsipeptides, these materials have been studied very scarcely. In fact, they have essentially been investigated as models to predict some of the properties of polypeptides and proteins, due to their structural similarity. For example, the study of polydepsipetides has allowed the investigation of the role of hydrogen bonds in the helical structure of peptides (Ingwall *et al.*, 1976, Zhang *et al.*, 2007).

In this work, molecular modeling calculations and experimental studies by IR and ^{1}H NMR spectroscopies on an L-arginine derivative, BAEE·HCl, were carried out. This compound is an appropriate model to better understand some of the polydepsipeptides properties, since its structure comprises an amide and an ester bond. The study of small model systems can stimulate and provide crucial data for the development of better, more efficient and reliable computational methods to be applied for more complex systems. To the best of our knowledge, no studies have been reported on this compound hitherto.

2 Materials and Methods

Computational Details

A systematic conformational search on the semi-empirical PM3 Potential Energy Surface (PES) of two tautomers of BAEE·HCl was performed to generate a sequence of conformations sorted by their relative energies. The most stable structures were afterwards submitted to geometry optimization and to magnetic shielding tensors and harmonic vibrational calculations through quantum chemical methods. These calculations have been performed within the DFT framework at the B3LYP/6-31++G(d,p) level of theory in vacuum, using the Gaussian03 package (Frisch *et al.*, 2004).

Experimental Details

BAEE·HCl (purity ≥ 99%) was purchased from Fluka and used without any further purification.

The IR spectrum of solid BAEE·HCl (4000–600 cm^{-1}, at room temperature) was obtained, with 4 cm^{-1} spectral resolution, using a Bomem (MB104) Fourier Transformer spectrometer equipped with a Zn/Se optics. The solid BAEE·HCl was pressed in a KBr pellet (Sample:KBr ratio – 1:400).

^{1}H NMR spectra of BAEE·HCl in DMF-D_7 was obtained on a Unity 500 MHz Spectrometer using a 5 mm broadband NMR probe. Each spectrum consisted of 32 averaged scans and acquisition parameters included 36k points covering a spectral width of 6 kHz, a 30º radiofrequency pulse and a total repetition time of 10 s. Digital zero filling to 64k and a 0.5 Hz exponential were applied before Fourier transformation. Samples were prepared by dissolving 10 mg of BAEE·HCl in 600 μL of the deuterated solvent.

3 Results and Discussion

Theoretical Calculations on the Structure of BAEE·HCl

A thorough conformational search on two BAEE·HCl tautomers (see Figure 1) has been performed.

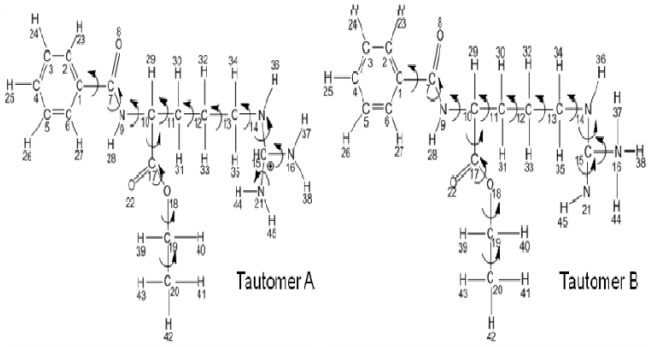

Figure 1 – Schematic representation of the tautomers of BAEE·HCl considered for conformational search. The single bonds indicated by the arrows were chosen for rotation.

For each tautomer shown in Figure 1, fourteen different internal rotation axes that can give rise to conformational isomers were considered in the conformational search procedure, yielding a quite large number of conformers for these compounds. Thus, our first approach was to perform a systematic conformational search on the PES of each tautomer by semi-empirical PM3 method. This strategy allowed the selection of the most stable set of conformations to be submitted to further refinement by more sophisticated theoretical approaches.

The optimized PM3 structures, with relative energies up to *ca.* 3 kJ mol^{-1}, which accounts for fourteen structures for tautomer A and four structures for tautomer B, were used as starting point for DFT calculations carried out at the B3LYP/6-31++G(d,p) level of theory. According to this method, nine conformers, with relative energies up to *ca.* 9 kJ mol^{-1}, were found for tautomer A, whereas for tautomer B only three different conformers were obtained, with relative energies up to *ca.* 2 kJ mol^{-1} (see Table 1).

Table 1 – Relative energies and molecular dipole moments for the most stable BAEE·HCl conformers obtained at the B3LYP/6-31++G(d,p) level of theory.

Tautomer	Conformer	ΔE(kJ mol^{-1})[a]	$\|\mu\|$(D)
A	I.A	0.00	10.34
	II.A	1.37	10.40
	III.A	1.60	10.48
	IV.A	1.63	10.39
	V.A	3.23	10.35
	VI.A	9.32	8.60
	VII.A	65.11	20.76
B	I.B	0.00	6.40
	II.B	1.52	6.24
	III.B	1.82	6.40

[a] The calculated energies for the most stable conformers are -2704385.26 kJ mol^{-1} and -2704220.65 kJ mol^{-1} for BAEE·HCl tautomer A and tautomer B, respectively.

From Table 1 one can observe that the conformers of tautomer A present a higher value of dipole moment than the conformers of tautomer B. This is indicative that tautomer A is more stabilized by polar solvents and this will be the form that will occur predominantly in polar media. It also should be mentioned that the most stable structure of tautomer B (I.B) is less stable than the most stable structure of tautomer A (I.A) by almost 165 kJ mol^{-1}. These facts suggest that the occurrence of tautomer B should be much less probable when compared with tautomer A.

The structures of the most stable conformers, for both tautomers, are depicted in Figure 2.

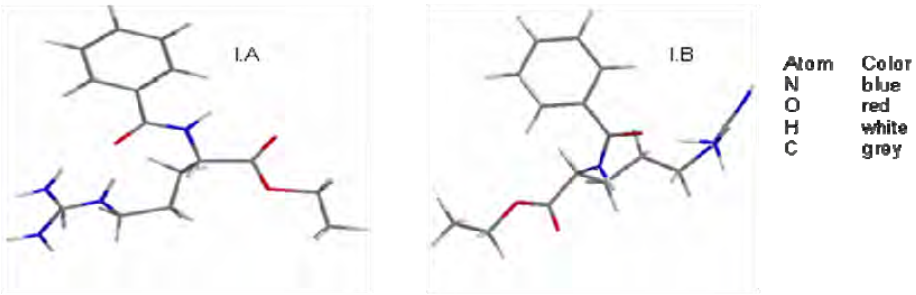

Figure 2- Structures of the most stable conformers of tautomers A and B of BAEE, as predicted by the B3LYP/6-31++G(d,p) calculations.

The most stable DFT conformers for both tautomers have a tendency to form a folded structure (Figure 2). These structures are stabilized by intramolecular H-bonds formed between the guanidine group [$NH_2C(=NH)NH–R$] and the carbonyl oxygen atom of the amide linkage. The remaining obtained low energy conformers follow the same trends.

Based on X-Ray diffraction data (unpublished preliminary results) it is known that in the crystalline phase these BAEE molecules adopt an unfolded structure (see Figure 3). For the isolated molecule, this structure is more energetic than the folded ones by almost 40 kJ mol^{-1} (see Table 1). Thus, the stabilization of this structure in the crystal phase should be explained by a network of intermolecular H-bonds and packing effects.

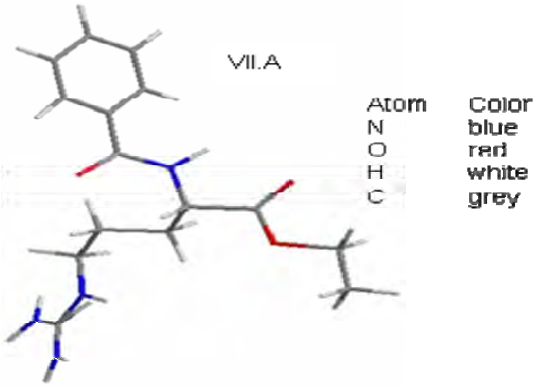

Figure 3- Structure of BAEE present in the solid.

Infrared Spectrum of BAEE·HCl

Figure 4 shows the experimental FT-infrared spectrum of solid BAEE pressed in a KBr pellet in the wavenumber range 3750–600 cm^{-1}, recorded at room temperature. The simulated [B3LYP/6-31++G(d,p)] infrared spectrum of BAEE is also presented (see Figure 3 for the structure chosen in these simulations).

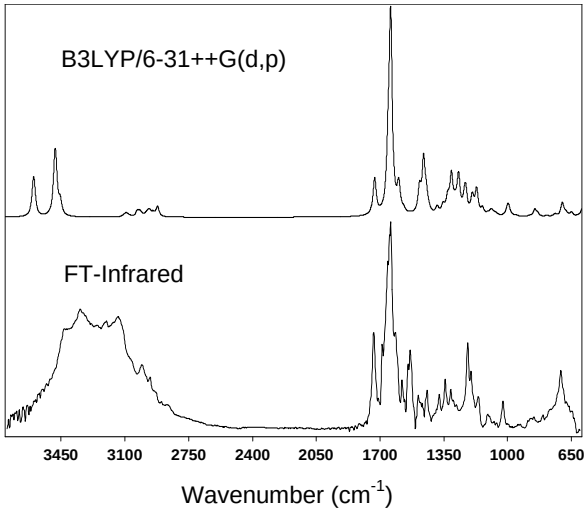

Figure 4- Bottom: experimental FT-infrared spectrum of BAEE·HCl; Top: simulated infrared spectrum of BAEE (see Figure 3) in vacuum calculated at the B3LYP/6-31++G(d,p) in the harmonic approximation. The calculated wavenumbers were scaled down by a factor of 0.965. For the simulation, Lorentzian functions centered at the scaled calculated wavenumbers and with bandwidths at half-height equal to 20 cm^{-1} were used.

Table 2 summarizes some representative experimental and calculated vibrational modes and respective assignments.

Table 2 - Observed (polycrystalline sample pressed in a KBr pellet) and B3LYP/6-31++G(d,p) calculated representative IR data for BAEE.

Experimental	Calculated B3LYP/6-31++G(d,p)		Approximate description
Wavenumbers (cm^{-1})	Wavenumbers (cm^{-1})[a]	IR Intensities (km mol^{-1})	
			GUANIDINE GROUP
3348[b]	3603	136.8	νNH_2 as.
	3599	86.4	νNH_2 as.
	3494	7.4	νNH_2 s.
	3485	214.6	νNH
	3480	166.3	νNH_2 s.
			AMIDE GROUPS
	3455	71.5	νNH_{amide}
			CARBONYL GROUPS
1734; 1711	1729	194.9	$\nu C{=}O_{Ester}$
1688	1654	235.7	$\nu C{=}O_{Amide}$
			GUANIDINE GROUP
1657; 1649;1642	1643	523.1	δNH_2
	1640	523.7	δNH_2
1617	1598	131.2	δNH_2

[a]The B3LYP/6-31++G(d,p) calculated wavenumbers were scaled by a single factor of 0.965.
[b] Broad band whose maximum is at 3348 cm^{-1}.

Since the experiment was done in the solid phase, the simulated spectrum of BAEE was obtained by considering an optimized structure similar to that present in the crystalline phase (see Figure 3). Considering that the calculation is referred to the isolated molecule in vacuum, thus not accounting for crystalline effects (force field, intermolecular H-bonding), the agreement between the experimental and calculated spectra is quite acceptable in a fairly large spectral range.

^{1}H NMR Spectrum of BAEE·HCl

Table 3 summarizes the calculated GIAO [B3LYP/6-31++G(d,p)] and experimental ^{1}H NMR chemical shifts, with respect to TMS, for BAEE.

Table 3- Comparison between calculated B3LYP/6-31++G(d,p) and experimental chemical shifts ^{1}H NMR (ppm) for BAEE, in DMF-D_7.

Protons	Calculated B3LYP/6-31++G(d,p)		Experimental
	I.A	VII.A	
$N\text{-}H_{amide}$	7.81	7.23	8.64
N-H	10.80	4.66	8.22
NH_2/NH_2	4.60/4.51; 7.35/4.38	4.71/4.69;4.59/4.55	7.58
$C\text{-}H_{orto}$	7.63	8.22	7.85
$C\text{-}H_{para}$	8.05	7.99	7.31
$C\text{-}H_{meta}$	7.90	7.76	7.24
$C\text{-}H_{methine}$	4.01	4.83	4.30
$CH_{2\ ester}$	4.70	4.36	3.92
$CH_{2\ (1)}$	3.16	3.20	3.11
$CH_{2\ (3)}$	2.41	1.76	1.79
$CH_{2\ (2)}$	2.22	2.37	1.54
$CH_{3\ ester}$	1.41	1.40	0.98

These results are indicative that the quality of the calculated chemical shifts values is dependent on the presence of H-bonds. In fact, it is for the protons that can actually be involved in intermolecular H-bonds (not accounted in the theoretical calculations) that the agreement between theoretical and experimental results is worse.

4 Conclusions

In this work DFT calculations performed at the B3LYP/6-31++G(d,p) level of theory and IR and ^{1}H NMR spectroscopies were used to investigate the molecular structure of an L-arginine derivative, BAEE·HCl.

The obtained results show that, in the vacuum, the conformers of this compound adopt a folded structure, stabilized by intramolecular H-bonds.

The overall results also clearly suggest that the tautomer A is the predominant species both in the solid and in solution.

5 References

Deng, C., Chen, X., Sun, J., Lu, T., Wang, W., Jing, X. (2007). RGD Peptide biodegradable amphipilic triblock copolymer poly(glutamic acid)-b-poly(L-lactide)-b-poly(glutamic acid): synthesis and self-assembly. *Journal of Polymer Science A*, 45, 3218-3230, 2007.

Frisch, M.J., *et al.* .(2004).*Gaussian 03 (Revision D.01)*. Gaussian Inc., Wallingford CT. (And references therin.)

He, B., Bei, J., Wang, S. (2003). Synthesis and characterization of a functionalized biodegradable copolymer: poly(L-lactide-co-RS-malic acid). *Polymer*, 44, 989-994.

Ingwall, R.T., Gilon, C., Goodman, M. (1976). Polydepsipeptides.5. Experimental Conformational Analysis of Poly(L-alanyl-L-lactic acid)and related model compounds. *Macromolecules*, 5, 802-808.

Strittmatter, E. F., Williams, E. R. (2000). Structures of Protonated Arginine Dimer and Bradykinin Investigated by Density Functional Theory: Further Support for Stable Gas-Phase Salt Bridges, *Journal of Physical Chemistry A*, 25, 6069–6076.

Zhang, J., King, M., Suggs, L., Ren, P. (2007). Molecular modeling of conformational properties of Oligodepsipeptides. *Biomacromolecules*, 8, 3015-3024.

Proceedings of the 10th International Chemical and
Biological Engineering Conference - CHEMPOR 2008
Braga, Portugal, September 4-6, 2008
E.C. Ferreira and M. Mota (Eds.)

CFD Analysis of Blood Rheology

Filipa Carneiro[1*], Vasco Gama Ribeiro[2], José C.F. Teixeira[1], Senhorinha F.C.F Teixeira[3]

[1] Mechanical Engineering Department, University of Minho, Campus de Azurém, 4800–058 Guimarães, Portugal.

[2] Centro Hospitalar de Vila Nova de Gaia, Rua Conceição Fernandes, Vilar de Andorinho, 4430-502 Vila Nova de Gaia, Portugal.

[3] Production and Systems Department, University of Minho, Campus de Azurém, 4800–058 Guimarães, Portugal.

Keywords: Blood rheology, Numerical modelling, non-Newtonian
Topic: Advancing the chemical and biological engineering fundamentals

Abstract

A three-dimensional model of the aorta bifurcation of the iliac arteries was used to study numerically the blood rheology influence on the hemodynamics, by using the Carreau-Yasuda model to account for the shear-thinning behaviour of blood. The simulations were carried out with the finite volume method, using the FLUENT computational software. A non-Newtonian model for the fluid viscosity has been implemented for assessing the recirculation zone, and also the velocity and wall shear stress distributions. The vicinity of the iliac bifurcation was characterized by complex flow patterns, such as separation of flow and recirculation, which are believed to play an important role in the atherosclerosis lesions.

1 Introduction

Cardiovascular diseases, such as atherosclerosis, are the major cause of death in the developed countries, and are normally associated with complex blood flow patterns. This disease is characterized by the adhesion of lipidic plaque on degraded endothelium or regions of low wall shear stress (WSS) resulting in the stiffening and thickening of the artery, or stenosis. This occurs mostly in the arteries bifurcations and curvatures, like aorta, iliac, coronary, carotid and femoral arteries. The recirculation, stagnation and separation of the blood flow and the low wall shear stress, which contribute to the plaque deposition, are affected by different factors, such as the artery geometry (Carneiro et al., 2008a) and blood rheology (Carneiro et al., 2008b).

The Computational Fluid Dynamics (CFD) analysis of hemodynamics in complex artery geometries has become an important tool in research. In most of CFD simulations, blood is modelled as a Newtonian fluid, particularly in large arteries, where the influence of shear thinning properties is not so significant. However, the rheological model for blood viscosity is a key factor in the simulation of hemodynamic flows. Rheology models of varying complexity have been proposed to capture the shear-thinning behaviour of blood (Abraham, 2005, Chen and Lu, 2006, Owens, 2006). Gijsen et al. (1999) proved experimentally that the blood flow should be simulated by the Carreau-Yasuda model in the carotid arteries, at both low and high shear stress. It was suggested that the non-Newtonian properties of blood are an important feature in the hemodynamics, which affect the interaction between the fluid and the vessel. This interaction plays an important role in vascular biology and pathophysiology.

The work reported in this paper aims to simulate numerically the influence of the blood rheology, by using the Carreau-Yasuda model, of the hemodynamics on the abdominal aorta bifurcation into the iliac arteries.

* Corresponding author. Tel + 351-253-510220. E-mail:afcarneiro@dem.uminho.pt

2 CFD model

2.1 Space discretization

The flow patterns are described by differential equations that are solved by the finite volume method. This method requires the domain discretization into control volumes. The geometry and the computational mesh were created using the GAMBIT software. A schematic representation of the three-dimensional geometry, considered in this investigation, and the relevant details are given in Figure 1. To reduce the computational time, symmetry is assumed in the medium planes y and z, reducing the computational domain by 75%.

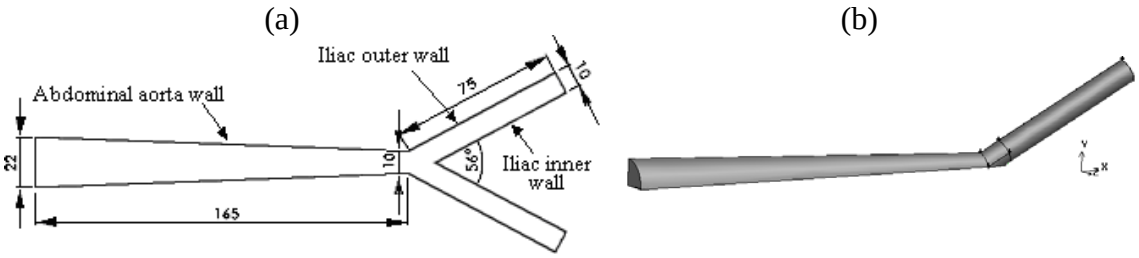

Figure 1. Geometry of the abdominal aorta in the iliac arteries: (a) medium z plane, (b) three-dimensional view.

The abdominal aorta bifurcation of the iliac arteries is modelled as a rigid wall with a circular cross section. This approach enables the subsequent model validation with experimental data.

The number of control volumes is a balance between the desired low computational time and a high precision. The domain was decomposed into four connected subdomains. Specifically, two of these are at the bifurcation region, to refine the local mesh, where higher velocity gradients are expected. Boundary layers were considered at the cross section throughout the entire domain, to refine the mesh near the walls, at the inlet and in the vicinity of the bifurcation. The resulting computational domain for this model was built with 13376 hexahedral elements, such as depicted in Figure 2.

Figure 2. Computational mesh of the model (inlet and z=0 planes).

2.2 Mathematical model

The FLUENT is a computational fluid dynamics software that solves the three-dimensional equations for mass (equation 1) and momentum (equation 2), assuming conservation for each variable:

$$\nabla \vec{v} = 0 \tag{1}$$

$$\frac{\partial}{\partial t}(\rho \vec{v}) + \nabla \cdot (\rho \vec{v}\vec{v}) = -\nabla p + \nabla \cdot (\bar{\bar{\tau}}) \tag{2}$$

where $\vec{v}$ is the fluid velocity vector, ρ is the density, p is the static pressure and $\bar{\bar{\tau}}$ is the stress tensor. The turbulence k-ε model is described by the equations 3 and 4:

$$\frac{\partial}{\partial t}(\rho k) + \nabla(\rho \vec{v} k) = \nabla\left[\left(\mu + \frac{\mu_t}{\sigma_k}\right)\frac{\partial k}{\partial x_j}\right] + G_k - \rho\varepsilon + S_k \tag{3}$$

$$\frac{\partial}{\partial t}(\rho \varepsilon) + \nabla(\rho \vec{v} \varepsilon) = \nabla\left[\left(\mu + \frac{\mu_t}{\sigma_\varepsilon}\right)\frac{\partial \varepsilon}{\partial x_j}\right] + C_{1\varepsilon}\frac{\varepsilon}{k}G_k - C_{2\varepsilon}\rho\frac{\varepsilon^2}{k} + S_\varepsilon \tag{4}$$

where k is the kinetic energy, ε the dissipation rate, μ the viscosity and μ_t the turbulent (or eddy) viscosity. G_k represents the generation of turbulence kinetic energy due to the mean velocity gradients. $C_{1\varepsilon}$ and $C_{2\varepsilon}$ are constants. σ_k and σ_ε are the turbulent Prandtl numbers for k and ε, respectively. S_k and S_ε are user-defined source terms.

2.3 Boundary conditions

The fluid was considered incompressible, non-Newtonian, with the density of 1057 kg/m^3. The inflow is laminar and the generated turbulence was simulated with the k-ε model with enhanced wall treatment. An uniform inlet velocity of 0.234 m/s was assumed. The outflow is equally distributed by the two iliac arteries. The abdominal aorta bifurcation of the iliac arteries is modelled as a stationary wall with no-slip shear condition.

2.4 Numerical discretization and solution

In the finite volume method the partial differential equations are approximated by a set of algebraic equations over the computational domain that is subsequently solved. It was used the standard scheme to solve pressure equation and the second order upwind scheme to solve momentum, turbulence kinetic energy and turbulence dissipation rate equations.

Solutions are obtained iteratively, solving the equations sequentially, using the segregated solver with the SIMPLE algorithm. The convergence is accepted when the residuals are below 1e-05.

3 Blood rheology

The blood, a liquid tissue, circulates in the vascular blood system, maintaining the organism living. It is a complex medium composed by plasma, a Newtonian fluid, and a suspension of various cells, such as erythrocytes, leucocytes and platelets, which are related to its microscopic structures, as aggregation, deformation and alignment of the erythrocytes (Chen and Lu, 2006).The blood cells are about 45% of blood by volume, forming a non-Newtonian fluid, with a shear-thinning viscoelastic behaviour. The rheological model for blood viscosity is a key factor in the simulation of hemodynamic flow. To study the flow patterns that promote the atherosclerosis development the flow was modelled as a non-Newtonian fluid described by the Carreau-Yasuda model.

The shear viscosity (η) is a function of the shear rate $(\dot{\gamma})$ this being written as:

$$\dot{\gamma} = \sqrt{\frac{1}{2}\overline{\overline{D}}:\overline{\overline{D}}} \tag{5}$$

with

$$\overline{\overline{\tau}} = \eta\left(\overline{\overline{D}}\right)\overline{\overline{D}} \tag{6}$$

and

$$\overline{\overline{D}} = \left(\frac{\partial u_j}{\partial x_i} + \frac{\partial u_i}{\partial x_j}\right) \tag{7}$$

where $\overline{\overline{D}}$ is the deformation rate.
The non-Newtonian Carreau-Yasuda shear thinning model used is:

$$\eta = \eta_\infty + \left(\eta_0 - \eta_\infty\right)\left[1 + \left(\dot{\gamma}\lambda\right)^a\right]^{(n-1)/a} \tag{8}$$

where η_0 and η_∞ are, respectively, the upper and lower limiting values of the fluid viscosity, n is the power-law index, λ is the time constant. In this work, the Carreau-Yasuda model parameters, obtained from Gijsen et al. (1999), are: $\eta_0 = 22 \times 10^{-3}$ kg.m^{-1}s^{-1}, $\eta_\infty = 2.2 \times 10^{-3}$ kg.m^{-1}s^{-1}, $a = 0.644$, $n = 0.392$ and $\lambda = 0.110$ s.

4 Results and discussion

The equations and the numerical procedure described above were applied throughout the abdominal aorta bifurcation into the iliac arteries. The velocity distribution, in the vicinity of the bifurcation, is shown in Figure 3.

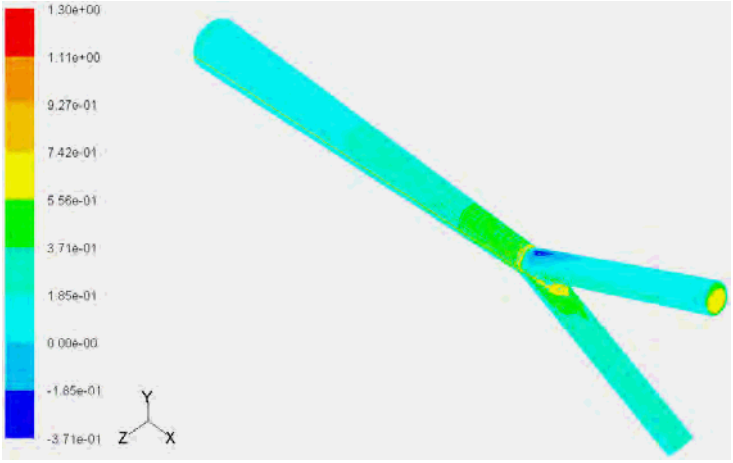

Figure 3. Velocity distribution.

The velocity increases along the abdominal aorta reaching the maximum velocity of 1.2m/s, just downstream the bifurcation. A recirculation zone is developed downstream the bifurcation with flow separation. The recirculation zone disappears and the maximum peak velocity shifts from the inner wall to the iliac artery center, due to the flow development. The wall y^+ is a non-dimensional parameter that measures the refinement mesh at the wall. The wall y^+ distribution, is showed in Figure 4, throughout the geometry.

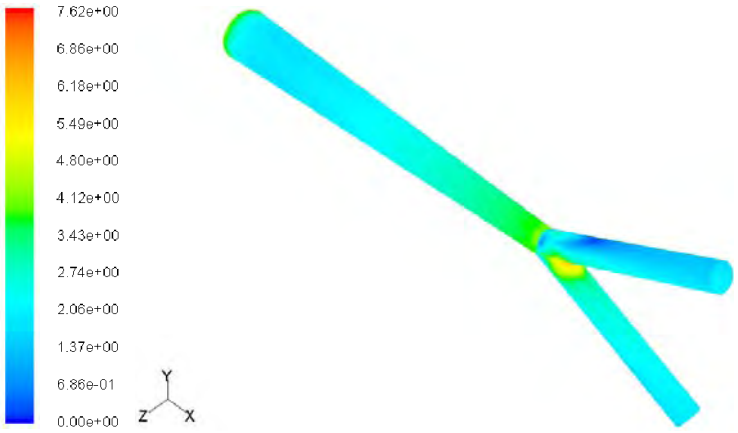

Figure 4. Wall y^+ distribution.

As it is almost less than 5, it indicates that almost of the elements are enough refined. Thus, the present calculations are catching the high gradients expected near the wall. Just for the beginning of the inner wall (177.6-179.3 mm), the wall y plus exceed the limit of 5 (only 1.2% of the elements are from 5 to 6.3). Figure 5 illustrates the detailed velocity vectors, at medium plane z.

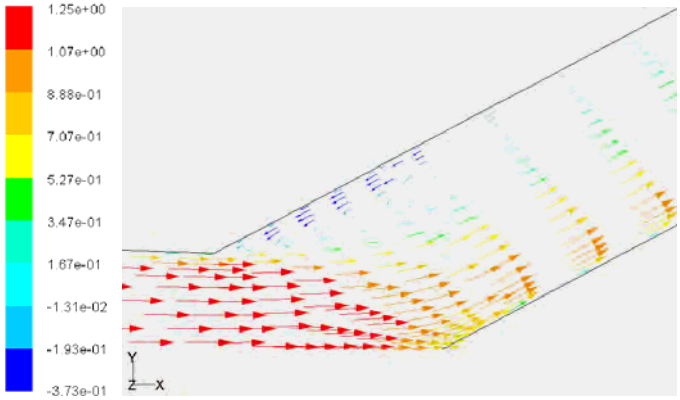

Figure 5. Velocity vectors in the vicinity of the iliac bifurcation.

The flow split into the recirculation zone and the main flow field, that shifts from the center of the aorta to the inner wall of the iliac artery. The recirculation zone is located near the outer wall, from 168.0 to 192.5 in the axial direction, with a length of 24.5 mm. Velocity profiles were obtained at different line locations (at x= 150, 165, 175 and 185 mm, x_1, x_2, x_3, x_4 respectively) in the medium z plane (Figure 6) and can be observed in the Figure 7.

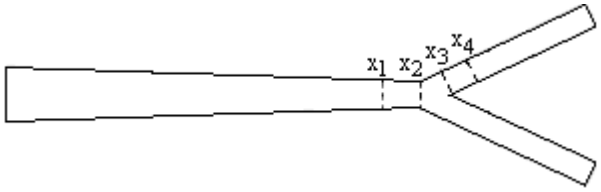

Figure 6. Location of the cross sections for velocity profile analysis.

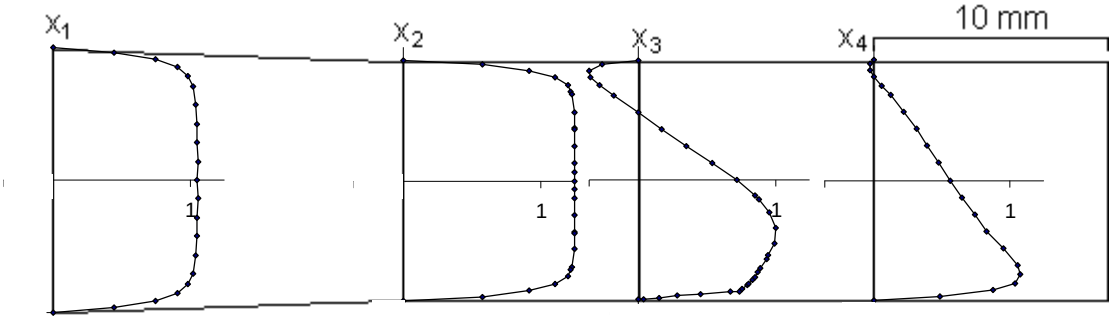

Figure 7. Velocity profiles (m/s) at x_1, x_2, x_3 and x_4.

At x=150 mm the axial velocity has no influence of the bifurcation, but at 165mm there are two slight peaks corresponding to each branch. It indicates the flow separation. Downstream the bifurcation, at the axial position of 175 mm, there is a recirculation zone near the outer wall, due to the flow separation. At the axial position of 185 mm, the recirculation zone is much smaller. Figure 8 shows the WSS distribution along the abdominal aorta and into the iliac arteries.

The WSS increases along the abdominal aorta up to the iliac bifurcation, and decreases along the iliac arteries. However, the maximum peak is obtained at the entrance of the inner iliac artery. At the outer wall, there is a sharp decrease approaching zero in the vicinity of the iliac bifurcation, due to the recirculation zone. The appearance of this low WSS coincides with early intimal thickening in the abdominal aorta.

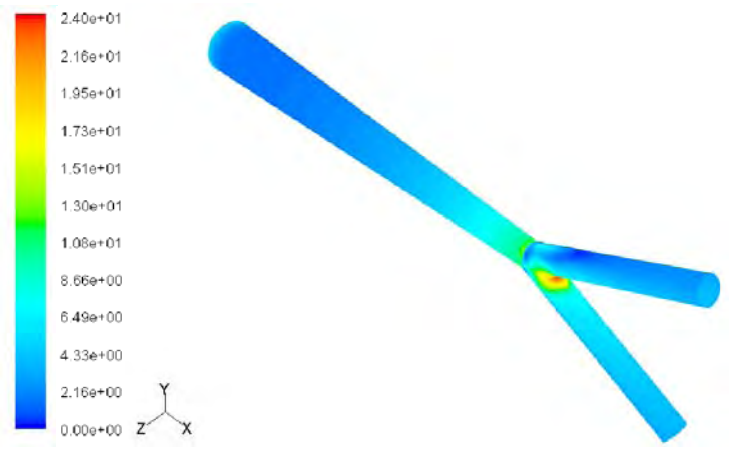

Figure 8. Wall Shear Stress distribution.

5 Conclusions

A numerical CFD model to simulate the blood flow dynamics has been implemented. The flow was modelled as a shear thinning non-Newtonian fluid, described by the Carreau-Yasuda model. There is flow separation and a recirculation zone in the vicinity of iliac bifurcation. The wall shear stress values decreases at the iliac outer wall, in the recirculation zone. These observations are consistent with the observed clinically. The non-Newtonian model assumption is valid for hemodynamic simulations in the abdominal aorta. Further studies should consider the flow unsteadiness to analyse the wall shear stress oscillation through the cardiac cycle.

Acknowledgements

The author Filipa Carneiro gratefully acknowledges the Portuguese Foundation for Science and Technology (FCT) by the support of this work, through the grant SFRH/BD/31793/2006.

References

Carneiro, F., Ribeiro, V.G., Teixeira, J.C., Teixeira, S.F.C.F. (2008a) A influência da geometria da bifurcação ilíaca no desenvolvimento da aterosclerose. *II Conferência de Métodos Numéricos em Mecânica de Fluidos e Termodinâmica*, 8-9 May University of Aveiro, Portugal (in portuguese).

Carneiro, F., Ribeiro, V.G., Teixeira, S.F.C.F., Teixeira, J.C.F. (2008b) Numerical study of blood fluid rheology in the abdominal aorta bifurcation. *Design & Nature*, 24-26 June, Algarve, Portugal.

Abraham, F. (2005) Shape optimization in steady blood flow: A numerical study of non-Newtonian effects. *Computer Methods in Biomechanics and Biomedical Engineering*, 8(2), 127-137.

Chen, J., Lu, X-Y (2006) Numerical investigation of the non-Newtonian pulsatile blood flow in a bifurcation model with a non-planar branch. *Journal of Biomechanics*, 39(5), 818-832.

Owens, R. G. (2006) A new microstructure-based constitutive model for human blood, *Journal of Non-Newtonian Fluid Mechanics*, 140(1-3), 57-70.

Gijsen, F. J. H., van de Vosse, F. N., Janssen, J. D. (1999) The influence of the non-Newtonian properties of blood on the flow in large arteries: steady flow in a carotid bifurcation model. *Journal of Biomechanics*, 32(6), 601-608.

Proceedings of the 10th International Chemical and
Biological Engineering Conference - CHEMPOR 2008
Braga, Portugal, September 4-6, 2008
E.C. Ferreira and M. Mota (Eds.)

Study of Cerebrospinal Fluid Dynamics in a Computational Model of Stenosed Aqueduct

N.Masoumi[1], D. Bastani[2], S.Najarian[3]
[1] MSc Student, Sharif University of Technology, Chemical and Petroleum Department
[2] Teacher assistant, Sharif University of Technology, Chemical and Petroleum Department
[3] Professor, Amirkabir University of Technology, Biomedical Engineering Department

Key words: Computational Fluid Dynamic (CFD), Cerebrospinal Fluid (CSF), Stenosed aqueduct,
Topic: Study of Cerebrospinal Fluid Dynamics in a Computational Model of Stenosed Aqueduct

Abstract

In this study we evaluate the cerebrospinal fluid (CSF) dynamic using computational fluid dynamic (CFD) analysis in an anatomical 2D model of a ventricular system. The anatomical basis of our simulation was generated from Magnetic Resonance Imaging (MRI). Stenosed aqueduct, leading to an obstructive hydrocephalus was modeled and the results of CSF velocity in the aqueduct and CSF pressure in the lateral ventricle were compared with those in the normal condition. Modeling the ventricles as flexible components based on solid-fluid interaction analysis for hydrodynamic study is a new approach in our work, enabling a more accurate simulation of CSF flow. The CSF production rate is considered pulsatile and relates to arterial pulsation in the choroid plexus. Since the CSF is a Newtonian fluid, the CFD software was applied to solve the equation of the continuity and momentum for CSF flow. Also the brain tissue was modeled as an elastic compartment. The mesh boundary of the CSF was immersed in a marker and-cell staggered grid to take into account fluid-solid interaction in ADINA software packege. Increase of velocity and an up to two-fold pressure drop were observed due to aqueduct stenosis.

1 Introduction

The cerebrospinal fluid (CSF) has several functions, such as physical support, excretion, intracerebral transport and control of the chemical environment of the central nervous system (CNS). CSF is mostly located in the ventricular system and the subarachnoid space (SAS) and in part is produced by the choroid plexus [1,2]. Pathologic conditions of the cerebrospinal fluid space are usually of a critical nature. Hydrocephalus - an abnormal accumulation of CSF in the brain - is the most prominent of a number of such conditions. Mostly, hydrocephalus is treated by surgical placement of a shunt. There is a need for intelligent shunts that can adjust themselves dynamically to different operating conditions and thereby reduce the number of shunt revisions a patient has to undergo [3]. The aqueduct of Sylvius is a narrow channel connecting the third and fourth ventricle (Fig 1). It is a narrow pathway for CSF flow and hence maybe an important site for development of hydrocephalus.

Therefore, a better understanding of the local hydrodynamics (pressures, velocities, strains, etc.) and the interaction between the CSF and the surrounding brain matter could be valuable for neurosurgeons to predict the efficiency of a highly invasive operation. Also, the computer model could be used to help the medical practitioner decide whether a patient should be shunted and what kind of shunt should be used. With advances in computing, work has been undertaken using CFD to model CSF flow and understand its nature [4-6]. These novel representations yield the distribution of CSF pressure and velocity. Advances in MRI have made it possible to capture significant parts of the geometry of the CSF system, such as the ventricles and their connecting

pathways. Thus, the possibility exists to set up a CFD model of the ventricular space based on accurate geometric information. However, CFD calculations based on accurate ventricular geometry are not straightforward due to the complex shape of the domain. These challenges are compounded by meshing and loading problems in the presently available software packages. These factors strengthen the need for 2D or simple 3D models of human ventricular system (HVS) [3,6,7]. Fin and Grebe [8] have published a three-dimensional CFD model of the aqueduct of Sylvius based on MRI anatomy scans; they found that the deformability of the walls has a strong influence on the pressure drop. In recent work, Kurtcuoglu *et al* [3] evaluate the CSF hydrodynamic in a stenosed aqueduct. In their new approach [9] the cerebrospinal fluid flow was studied in a model of the third ventricle of the brain and the aqueduct of Sylvius, derived from magnetic resonance imaging (MRI) scans, using CFD detailed quantitative information of the flow field in his spaces. This increase in ICP was observed by authors [10-11].

All these models include some simple approximations for their geometries, boundary conditions or input and output values such as CSF constant production rate and rigid condition for the HVS. None of the present models consider the real pulsatile flow pattern underlying choroid plexus expansion, synchronized with the heart beat, the importance of which has been previously described [10-12]. Moreover, for the purpose of simplicity all current models neglect consideration of the solid interaction effect, further limiting their accuracy.

Therefore, the fundamental limitations of recent simulations increase the necessity for the development of sophisticated and comprehensive models. In the present study, an idealized 2D geometry of the HVS from the MRI data, based on our previous study [13] with perfect boundary conditions around the model was constructed. Evaluating the CSF pulsatile hydrodynamic in a stenosed aqueduct in a 2D model based on Fluid–solid interaction analysis in the obstructive hydrocephalus is a new approach in our study. As this is one of the very first reported attempts to model the CSF space and behavior for hydrocephalus case, driven in a practical manner by pulsatile inflow and FSI boundary conditions for HVS, we believe that the qualitative and quantitative data on the pressure and flow patterns in the ventricular system are reliable.

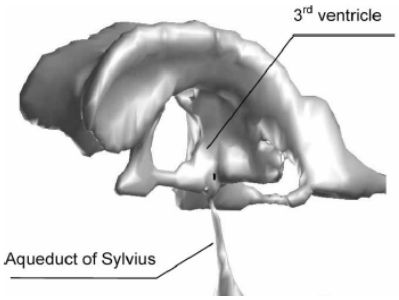

Figure 1: Three dimension representing of

2 Material &Method

Our aim is to use the physical principles of the fluid flow and solid material to quantify intracranial CSF hydrodynamics in the hydrocephalus condition. The procedure is performed in three stages. In step one, MRI techniques are used to accurately define the ventricle geometry. In step two, the MR image is converted into an accurate two-dimensional surface with two models of normal and stenosed aqueduct that are imported into CFD analyzer software. Mesh generation is then used to partition these spaces into a large number of small finite elements. In step three, CFD software solves the equations of fluid motion and solid tissue numerically over the brain geometry.

Table I: Parameters used for CSF fluid and brain tissue

Parameters	value	references
E-Young modulus	14-30 kPa	[13]
ν-Poassion's ratio	0.49	[11]
μ-CSF viscosity	0.001003 (Pa.s)	[11]
ρ-CSF density	1000-1007 kg/m^3	[4,11]
ρ_w-brain tissue density	Specific gravity: 1.02	Web

Figure 2 shows the 2D model of the HVS with and without stenosis. The JPEG pictures were imported to the CATIA 5.16 software. The models in IGES format were meshed in ADINA software (ADINA^{TM}, version 8.2, Automatic Dynamic Incremental Nonlinear Analysis, Watertown, MA). Solid components have been constructed in ADINA and the fluid segment in ADINA-F domain. The values of physical constants used in our model are depicted in Table I. For the solid, a rule-based mesh of 10065 point and 3665 rectangular solid elements of the plane strain type and for the fluid sub domain, a rule-based mesh of 1734 points and 300 rectangular elements were used in normal model.

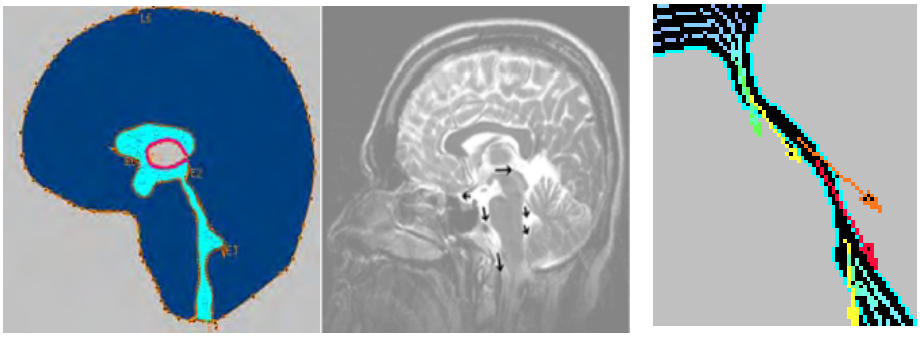

(a) (b) (c)

Figure 2: (a) 2D model of normal case (b) the MRI scan and (c) a model of 50% Stenosed aqueduct

The elements are arranged so that the aspect ratios are reduced in elements which are under compression to achieve higher compression strength. This avoids potential issues with overlapping of solid and fluid elements in the ALE mesh when deformation in the compression direction is imposed to fluid elements. ALE formulation and leader and follower points are used to keep the mesh quality in fluid elements during the solution time. A mesh with rectangular elements will lead to a good convergence.

CSF motion is described by the equations of mass and momentum conservation for an incompressible Newtonian fluid. These conservation balances lead to a system of partial differential equations known as the continuity and the Navier-Stokes equations. The governing equations for CSF flow are given in vector form by equations (1) and (2) as shown below. The surrounding tissue was modeled as an elastic compartment and for mathematical modeling the Arbitrary Lagrangian-Eulerian (ALE) formulation is used as the governing rule. This yields in formula (3). For solving the problem with Fluid-Solid interaction (FSI), the compatible kinematic and dynamic conditions in solid–fluid boundary should be defined.

Conservation of mass:

$$\nabla.\mathrm{u} = 0 \qquad (1)$$

Conservation of momentum:

$$\left(\left(\mathrm{u} - \mathrm{u}_{\mathrm{g}}\right).\nabla\right)\mathrm{u} = -\frac{1}{\rho}\Delta\mathrm{p} + \upsilon\nabla^{2}\mathrm{u} \qquad (2)$$

Lagrangian-Eulerian (ALE) formulation:

$$\frac{\partial \tau_{ij}^{s}}{\partial x_{j}} = \rho^{s}\frac{\partial^{2} d_{i}^{s}}{\partial t^{2}} \qquad (3)$$

Many studies confirm the pulsatile CSF production pattern relate to the heart beat and its effect on CSF hydrodynamic [8,10]. The bulk CSF production is implemented as input flux at the choroid plexus. This amount is considered 600 ml/day. The frequency of the pulsatile motion is set to 1 Hz approximating the normal cardiac cycle [10].

Therefore the CSF generation in choroid plexus is as follows:

$$q(t)=q_{bulk}+q_{ulse}(t) \qquad (4)$$

$$q_{bulk}=constant \qquad (5)$$

$$q_{ulse}(t)=\alpha[\sin(\omega t-\pi/2)-1/2.\cos(2\omega t-\pi/2)] \qquad (6)$$

The expansion of the vascular bed also causes the displacement of CSF from the cranium into the spinal SAS. For simplification we considered a partial pressure (zero value) at the end of Magendie foramina [4]. The results of the CSF analysis are the flow rate, velocities, and intracranial pressure (ICP) gradients of CSF in the ventricular system. Obtaining the volume changes of lateral ventricle (LV) from FSI condition is the new approach which was accessible with a deformable system modeling.

3 Results

Fig 3 shows the pressure contour for both cases. The ICP is highest in the LV and lowest in the Magendie foramina during systole. The pressure gradients within HVS never exceed 3 Pa. The highest CSF velocity occurs within the cerebral aqueduct reported as -2.5/+8 mm/s and the pressure drop along the region reaches 1.5 Pa in systolic time for normal case. However, there are a number of regions within the HVS that have CSF flow velocity about zero. In the hydrocephalus case, the results of pressure drop and velocity magnitude of the aqueduct region are almost two times larger than the normal condition. Volume changes of the LV of about 5% were observed in the case of hydrocephalus. Moreover the stenosis also affects the CSF flow pattern. While clinical evidences also validate the reverse flow of CSF in the aqueduct in diastolic time [11], the observation showed that there is no backflow in diastolic time in the case of hydrocephalus.

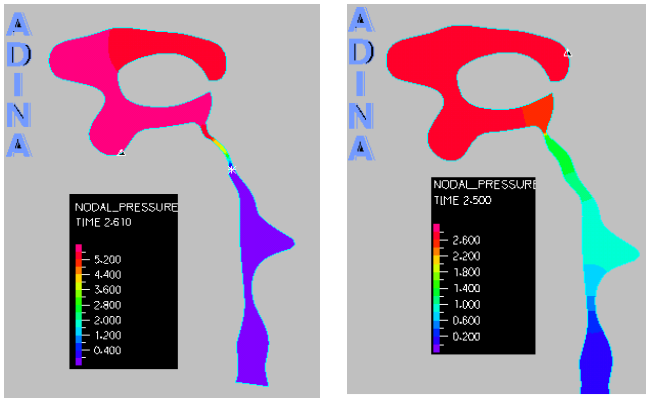

Figure 3:Pressure distribution in normal (left) and stenosed model (right)

The results of CSF pressure and velocity are depicted in Table II of both conditions for comparison.

Table II: CSF pressure and velocity in HVS for normal and Stenosed case

parameter	Normal	Stenosed	Published difference
Aqueduct velocity	-2.5 - 8.5 mm/s	0-6 mm/s	20%-50% [11,3]
Magandy velocity	3 mm/s	4.5 mm/s	
Monro velocity	2 mm/s	2 mm/s	
AS pressure drop (Pa)	4	1.1	2-10 times
Total Pressure drop (Pa)	5.8	2.6	10%-50% [11,3]
Expansion Vertical	5%	1%	2 times

4 Discussion

Linninger *et al* [11] are currently, to the best of our knowledge, the only group to have published a 2D, CFD model of the intracranial system with the base of CSF pulsatile production in order to obtain the CSF hydrodynamic pattern. However, in their model the approximation of boundary conditions remaines; a 2D model of the HVS considering surrounding brain tissue as intracellular fluid is an example. Therefore, in this study we declare a model with fewer limitations and more accuracy for simulation of CSF flow that is able to calculate ventricular wall displacement and evaluate hydrocephalus condition for the first time.

The main difference between the model with and without stenosis lies in the amplitude of the lateral ventricle (LV) displacement, which decreased while the LV volume increased. In the present configuration with the aqueduct cross-sectional area reduced 50% a maximum relative pressure increase of 46% is observed (Fig 4).

The stenosis also led the velocity to increase in the aqueduct. At the smallest cross section, the maximum velocity increased by 50%. Hence, aqueduct stenosis might not only indirectly damage the ventricular walls through the development of hydrocephalus, but also directly increase the amplitude of the CSF pressure oscillation and velocity magnitude. This shows that single ventricles or pathways should, in general, not be modeled detached from the remainder of the system. The results are in good agreement with Kurtcuoglu's stenosed model [3].

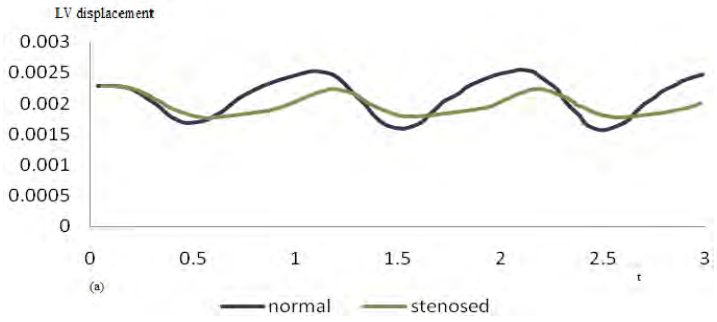

(a)

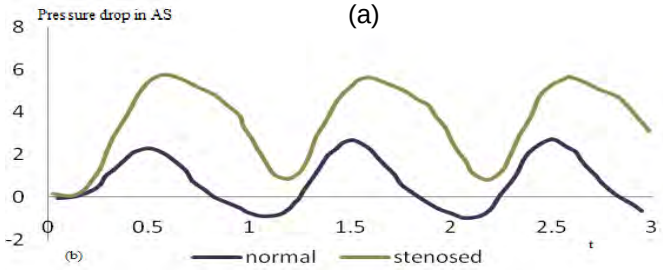

(b)

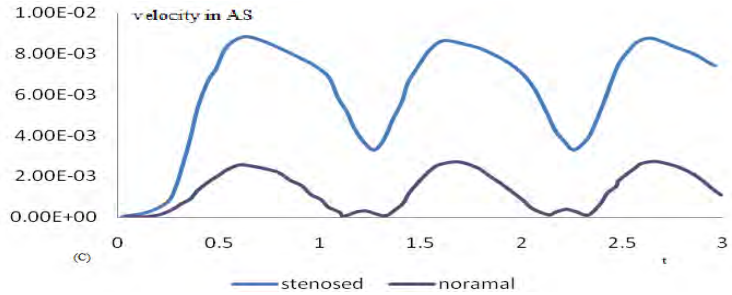

(c)

Figure (4): (a):LV displacement, (b) pressure drop in AS, (c) velocity magnitude in AS

References

[1] Tipold, A. (2003). Cerebrospinal fluid. In: Clinical Neurology in Small Animals Localization, Diagnosis and Treatment.

[2] Fishman, R.A. (1992). Cerebrospinal Fluid in Diseases of the Nervous System. WB Saunders Co, Philadelphia, 1–42.

[3] Kurtcuoglu, V., Poulikakos, D., Yiannis, V. (2005). Computational Modeling of the Mechanical Behavior of the Cerebrospinal Fluid System. J.Biomechanical Engineering, 127, 264-269.

[4] Ammourah, S., Aroussi, A. (2003). Cerebrospinal Fluid dynamics in a Simplified Model of the Human Ventricular System. 11th Annual Conference on CFD . Vancouver BC, Canada, 28-30.

[5] Jacobson, E., Fletcher, D.F. (1999). Computer modelling of the cerebrospinal fluid flow dynamics of aqueduct stenosis." Medical & Biological Engineering & Computing, 37,59-63.

[6] Loth, F., Yardimci, M.A., Alperin, N. (2001). Hydrodynamic modeling of cerebrospinal fluid motion within the spinal cavity" J.Biomechanical Engineering—Transactions of the ASME, 123, 71–79

[7] Linninger, A.A, Tsakiris, C., Zhu,D.,C. (2005) Pulsatile Cerebrospinal Fluid Dynamics in the Human Brain." IEEE Transaction on Biomedical Engineering, 52, 557-565.

[8] Fin, L., Grebe, R. (2003). Three dimensional modeling of the cerebrospinal fluid dynamics and brain interactions in the aqueduct of Sylvius. Computer Methods in Biomechanics and Biomedical Engineering, 6, 163–170.

[9] kurtcuoglu, V., Soellinger, M. (2007). Computational investigation of subject-specific cerebrospinal fluid. J. Biomechanics, 40,1235–1245.

[10] Greitz, D.(1993). Cerebrospinal Fluid Circulation and Associated Intracranial Dynamics: A Radiologic Investigation using MR Imaging and Radionuclide Cisternography. Acta Radiol., Sul. 386, 1–23

[11] Linninger, A.A, Xenos, M., Zhu,D.,C. (2007). Cerebrospinal Fluid Flow in the Normal and Hydrocephalic Human Brain. IEEE Transaction on Biomedical Engineering, 54,.291-302.

[12] Bhadelia, R.A., Bogdan, A.R., Kaplan, R.F., Wolpert, S.M.(1997). Cerebrospinal fluid pulsation amplitude and its quantitative relationship to cerebral blood flow pulsations: a phase-contrast MR flow imaging study", Neuroradiology, 39, 258–264.

[13] Masoumi,N., Seddighi.A.M., Bastani, D., Najarian, S., Framanzad**,** F. (2008). 2D Computational Fluid Dynamic Modeling of the Human Ventricle System Base on Fluid-Solid Interaction and Pulsatile flow. Unpublished.

Proceedings of the 10th International Chemical and
Biological Engineering Conference - CHEMPOR 2008
Braga, Portugal, September 4-6, 2008
E.C. Ferreira and M. Mota (Eds.)

Multiphase flow inside the Volumatic® spacer: a CFD approach

Sofia Abreu[1*], Luís F. Silva[1], Henedina Antunes[2], Senhorinha F. C. F. Teixeira[3]

[1] Department of Mechanical Engineering, School of Engineering, University of Minho, Campus Azurém, 4800–058 Guimarães, Portugal.

[2] Pediatrics Service, S. Marcos Hospital, Largo Carlos Amarante, 4701-965 Braga, Portugal.

[3] Department of Production and Systems Engineering, School of Engineering, University of Minho, Campus Azurém, 4800–058 Guimarães, Portugal.

Keywords: Asthma, Respiratory flow, Volumatic® spacer, Computational Fluid Dynamics.
Topic: Advancing the chemical and biological engineering fundamentals.

Abstract

Over the last years, allergic diseases, particularly asthma, have been acquiring an increasing importance in the developed countries, due to the rising of its prevalence and morbidity and the economic burden associated. In the preventive and urgent treatment of asthma, the oral pharmacological therapeutics assumes a major role. Therefore, this paper will report another step further to the research been undertaken at the University of Minho, to understand the behaviour of drug flow inside a spacer device, combined with pressurized metered-dose inhalers (or pMDIs), based on the use of Computational Fluid Dynamics (CFD) tools to study multiphase flows inside a Volumatic® spacer device.

1 Introduction

For children with less than seven years, the main mechanism of drug distribution has been the use of pMDIs coupled with spacers, since it minimizes the problems of a poor technique of inhalation associated with the use of pMDIs. Indeed, they are often reported to achieve a better drug delivery to the lungs than pMDI alone (O'Callaghan and Barry, 2003).

Spacer devices have a port at one end to which the pMDI is attached and a mask or mouthpiece fitted at the other end. These devices constitute a volume into which the patient actuates the pMDI and from which the patient inhales, without necessarily having to coordinate both actions. By acting as an aerosol reservoir, these devices slow the aerosol velocity and increase transit time and distance between the pMDI actuator and the patient's mouth, allowing particle size to decrease (Newman, 2005).

Thus, it is essential to identify all the spacer characteristics that may optimize the drug distribution to the low respiratory tract combined with a reduced drug loss inside the spacer, in order to achieve more efficient treatments in young children.

The purpose of the present study is to use CFD tools in order to develop a tridimensional computational model of the Volumatic® spacer able to predict the flow patterns during the respiratory cycle, in order to compare with the experimental results.

An Eulerian-Lagrangian approach has been taken in simulating the dispersed phase. The drug droplets are treated as inert particles.

* Corresponding author. Tel + 351-253-510344. E-mail:sofiachavesabreu@gmail.com.

2 The Analysed Spacer

The selected spacer for the CFD analysis, reported in this paper, was the Volumatic® (750 ml, Glaxo Wellcome Inc.), as highlighted in Figure 1. The Volumatic® is a high volume spacer made only of polycarbonate that is susceptible to the electrostatic charge. On the other hand, it is one of the most commonly used spacers in all countries as well as in the Portuguese public hospitals.

Figure 1 – The Volumatic® spacer.

3 Model and Numerical Formulation

The geometric model used in the simulations was created in Gambit™. A computational mesh of finite volumes was created for the spacer, and the boundary conditions were defined: inlet, outlet and wall. The meshes were imported to the FLUENT™, where the continuity and momentum equations were solved, as well as, the turbulence equations. The software also allowed the solution processing.

3.1 CFD Model

Figure 2 highlights different views of the Volumatic® spacer. Due to the symmetrical shape of the spacer and in order to reduce the processing time, the computational domain was reduced to one quarter.

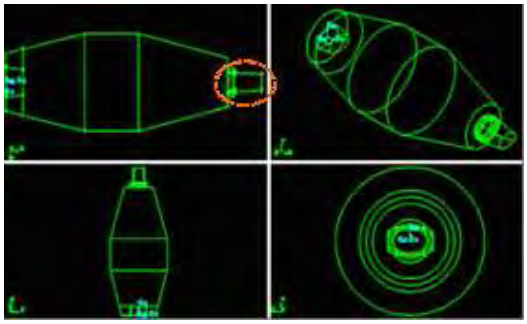

Figure 2 - Representation of the Volumatic® spacer, with the mouthpiece region located in the first view.

3.2 Mesh

The numerical mesh was created with a number of elements that did not compromise the precision of the results and, simultaneously, allowed reasonable computational times. Figure 3 shows the final mesh generated for the Volumatic® spacer, using the Hexahedral/Wedge Cooper scheme with different intervals, resulting in a 3D computational grid with 65326 hexahedral elements.

(a) 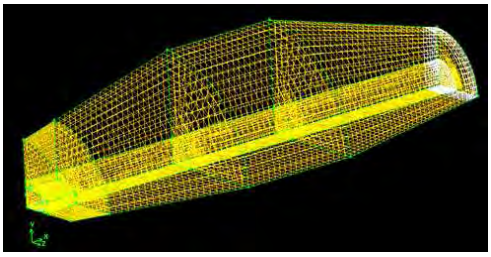 (b) 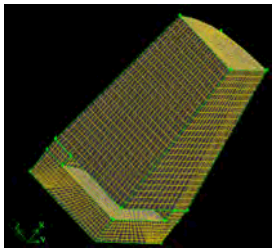

Figure 3 - Computational grid for the Volumatic®, with (a) the body and (b) the mouthpiece.

3.3 Mathematical Model

The air flow is considered incompressible, Newtonian, in transient state and turbulent.The mass conservation equation, often called the equation of continuity is expressed as follows (FLUENT INC., 2005):

$$\frac{\partial u_i}{\partial x_j} = 0 \qquad (1)$$

in which u_i is the mean velocity in the direction i, with $i = x, y \text{ and } z$.

The velocity field is described by the Navier-Stokes equations (equation 2). They describe the principle of momentum conservation for a Newtonian fluid in turbulent regime (FLUENT INC., 2005):

$$\rho \frac{\partial u_i}{\partial t} + \rho u_j \frac{\partial u_i}{\partial x_j} = -\frac{\partial p}{\partial x_i} + \frac{\partial}{\partial x_j}\left[\mu\left(\frac{\partial u_i}{\partial x_j} + \frac{\partial u_j}{\partial x_i} - \frac{2}{3}\delta_{ij}\frac{\partial u_l}{\partial x_l}\right)\right] + \frac{\partial}{\partial x_j}\left(-\rho\overline{u_i' u_j'}\right) + S_D \qquad (2)$$

where ρ is the air density, p the static pressure, μ the air viscosity, the term $-\rho\overline{u_i' u_j'}$ is called the Reynolds stresses and the last term represents the source terms due to the presence of particles/droplets.

Turbulent flow was simulated through the renormalization-group (RNG) *k-ε* model with enhanced wall treatment.

In Fluent, the trajectories of a discrete phase particle (droplet) are predicted by integrating the force balance on the particle which is written in a Lagrangian reference frame, for the x-direction in Cartesian coordinates, as:

$$\frac{du_D}{dt} = F_D(u - u_D) \qquad (3)$$

where u_D is the particle (droplet) velocity. The first term in the right side of equation (3) accounts for the drag force and F_D is the drag force, given by:

$$F_D = \frac{18\mu}{\rho_D d_D^2}\frac{C_D \,\mathrm{Re}}{24} \qquad (4)$$

where μ is the molecular viscosity of the fluid, d_D is the droplet diameter and ρ_D is the droplet density.

3.4 Boundary Conditions

The air inlet velocity in the spacer was calculated based on the respiratory cycle performed by the patient during the inhalation. Figure 4 shows, in detail, the inhaler adaptor face (in grey) where the air inlet occurs during the inspiration.

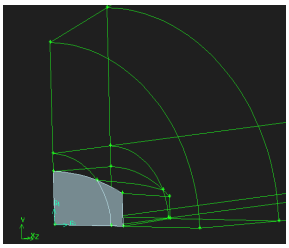

Figure 4 - Representation, in grey, of the zone defined with the boundary condition of velocity inlet in the Volumatic®.

This zone corresponds to the inlet boundary condition where the function of the respiratory velocity of a child (as expressed by Boron, 2003), has already been shown elsewhere for two tested spacers (Abreu et al., 2008a, b). Figure 5 shows this sinusoidal function and also the time instants reported the study of the periodic air inlet, namely 0.4 s (ascending phase), 1 s (maximum velocity inlet), 1.6 s (descending phase), 2 s (beginning of expiration), and 4 s (beginning of inspiration).

The fluid was taken as air at atmospheric conditions. The dispersed phase was defined in the mathematical model as a continuous injection of inert particles with an inlet velocity of 40 m/s.

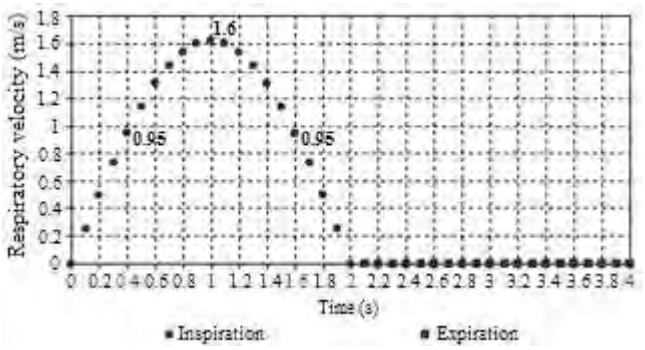

Figure 5 - Periodic velocity in a respiratory cycle, defined in the inlet face of Volumatic®.

3.5 Solution Procedure

In this study, the differential equations for pressure and velocities were solved in a sequential manner, using the SIMPLE (Semi-Implicit Method for Pressure-Linked Equations) algorithm (FLUENT INC., 2005). The air flow was assumed as transient and the first order implicit method was used in the discretization of the temporal derivative. The second order implicit method was applied in the momentum and turbulence equations discretization. FLUENT™ solves the continuity and momentum equations in every control volume of the domain (FLUENT INC., 2005). The mass and momentum conservation is tested at the end of each iteration, and the solution is accepted when the defined convergence criterion (in this case 10^{-3}) is achieved.

4 Results and Discussion

Figure 6 represents the axial velocity along the centerline of the Volumatic® spacer, considering only the continuous phase (black profile) and the biphasic flow (red profile), respectively, for the instant of 0.4 s after the beginning of the respiratory cycle.

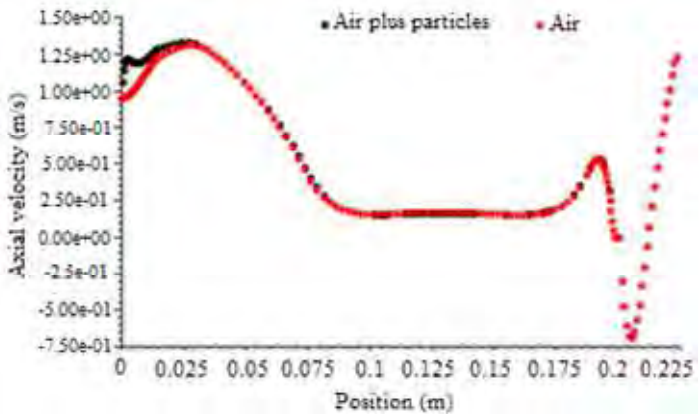

Figure 6 - Comparison between the profiles of axial velocity along the centerline, considering only the continuous phase (black profile) and the biphasic flow (red profile), respectively, for the instant of 0.4s.

It is possible to observe that the profiles of axial velocity along the centerline associated with the monophasic and biphasic flow are practically overlapped with only a small difference on the initial part of the spacer, where particles are injected. On the other hand, it is also noted the existence of recirculation region in the two profiles, between, approximately, 0.2 m and 0.218 m (corresponding to the zone of the mouthpiece).

The profiles of axial velocity inside the Volumatic® spacer for the evaluated five instants of the respiratory cycle are depicted in Figure 7.

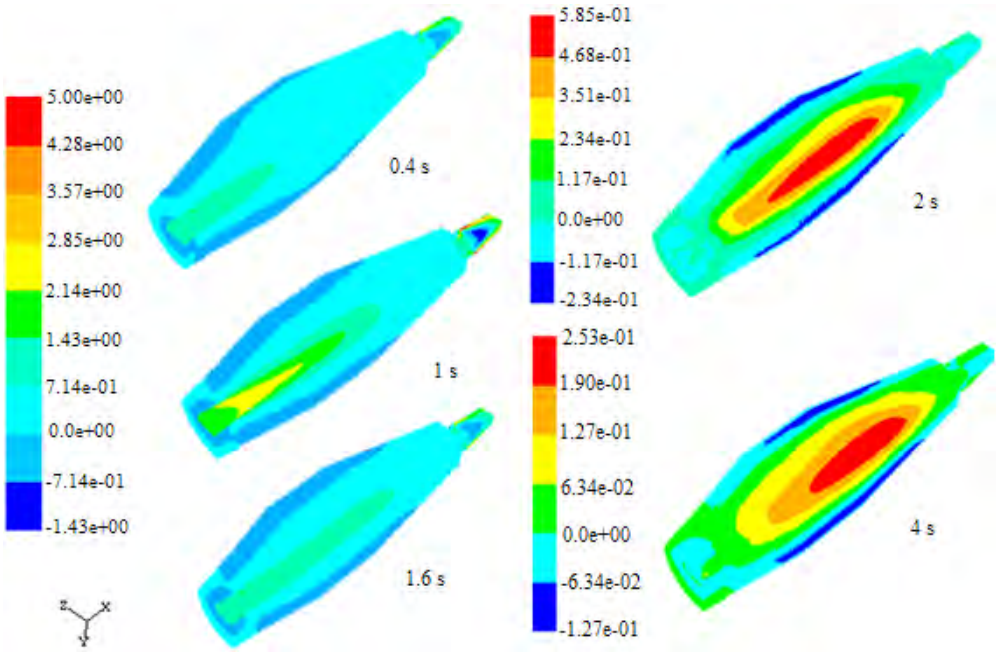

Figure 7 - Isokinetic profiles of axial velocity (m/s) in the Volumatic®.

It is observed that for the three instants of the inspiratory cycle, as the flow moves towards the final part of the spacer its velocity decreases, and increases again close to the cylinder that connects the spacer's body and mouthpiece, reaching the maximum velocity near the wall of the mouthpiece. As expected, the velocity reaches a maximum value, of approximately 5 m/s, when the inlet velocity is also the highest, which

happens after 1 s. On the other hand, the maximum velocity reached in the mouthpiece, after 0.4 s and 1.6 s, is approximately the same and assumes a value of 3 m/s. Also according to Figure 7 there are no significant differences detected for the recirculation zones in the three studied instants of inspiration. These zones are essentially localized next to the top of the wall of the spacer body.

For the instant of 2 s after the beginning of the respiratory cycle, as observed in Figure 5, the expiratory period performed by the patient starts and lasts till the instant of 4 s. In this instant, an anti-return valve located on the mouthpiece prevents the air entry through the adapter.

In opposition to the instants previously analysed, the highest velocity at 2 s (approximately 0.6 m/s) is located in the central part of Volumatic® (see Figure 7). This observation reveals that the closing of the valve, which occurs during the expiration, is being correctly simulated, since the fluid is forced to remain inside the spacer during this period and the velocity in the zone of the mouthpiece is near zero.

At the end of the respiratory cycle (see again Figure 7), it is observed that the fluid inside the spacer is practically stagnated, with a maximum velocity of about 0.25 m/s, located in the constant section of the Volumatic®'s body.

These numerical results are being compared with the experimental results obtained in vitro concerning the deposition of salbutamol sulphate in the spacer, through a simulator of the respiratory tract (Abreu et al., 2008c).

5 Conclusions

From the results obtained so far using Fluent™ simulations, it is possible to conclude that the spacer shape influences the air flow. Several recirculation zones were observed in the spacer for different instants of the respiratory cycle. These zones are essentially localized next to the wall of the spacer body, in other words, in these zones it happens a higher deposition of drug particles.

References

Abreu, S., Silva, L.F., Teixeira, S.F.C.F., Antunes, H. (2008a). The spacer shape effect on the flow field within the Volumatic® and Nebuchamber®. The 17th IASTED International Conference on Applied Simulation and Modelling – ASM'2008, June 23-25, Corfu, Greece.

Abreu, S., Silva, L.F., Teixeira, S.F.C.F., Antunes, H., Marques, H., Ramalhete, N. (2008b). Experimental study and CFD analysis of the Volumatic® spacer. 3rd Frontiers in Biomedical Devices Conference and Exhibition - ASME BioMed'08, June 18-20, Irvine, California, USA.

Abreu, S., Silva, L.F., Teixeira, S.F.C.F., Marques, H., Ramalhete, N., Antunes, H. (2008c). Avaliação do desempenho de três câmaras de expansão. *Act Med Port.* (To be submited).

Boron, W.F. (2003). Medical Physiology: A Cellular and Molecular Approach - 1st edition. Philadelphia, Elsevier Science.

O'Callaghan, C. and Barry P. (2003). The influence of inhaler selection on efficacy of asthma therapies. *Advanced Drug Delivery Reviews, 55*, 879-923.

FLUENT INC. (2005). User's Guide, Lebanon, New Hampshire.

Newman, S. (2005). Principles of Metered Dose Inhaler Design. *Respiratory Care, 50,* 1177-1190.

Proceedings of the 10th International Chemical and
Biological Engineering Conference - CHEMPOR 2008
Braga, Portugal, September 4-6, 2008
E.C. Ferreira and M. Mota (Eds.)

Computational Fluid Dynamics (CFD) behavior of Water Flow in a Packed Column Filled with Spherical Particles

Bardia Hasanzadeh[1],Morteza Baghalha[1*], Hamed Shahsavan[1], Seyed A. Monemian[2]

[1] Sharif University of Technology, Department of chemical and Petroleum Engineering
[2] University of Tehran, School of Chemical Engineering

Keywords: Simulation, Computational Fluid Dynamics, Packed Column, Porosity.
Topic: Multi-scale and/or multi-disciplinary approach to process-product innovation

Abstract

Water flow behavior in a packed column was modeled based on computational fluid dynamics. The parameters of Ergun's equation were modified by applying the CFD results into the empirical Ergun's equation. The range of Reynolds number considered in the present CFD work was far wider than that already obtained experimentally that are reported in literature.

Introduction

Nowadays expensive process operations can be simulated by Computational Fluid Dynamics (CFD) with considerable reduced expenses. The modeling of flow patterns in porous media has attracted many attentions due to the complication of simulation (Puncochar et al., 2002, Nemec et al., 2005). Ergun's equation (1952) explains the pressure drop in a random structured bed. He showed that the equation satisfies the experimental data for cylindrical, spherical and crushed packing in a wide range of Reynolds numbers. In the present work, the pressure drop of fluid water was investigated in a packed column of spherical particles as well as the effect of roughness of the wall. Also, validity of experimental parameters of Ergun's equation was verified using CFD. Finally, the analytical data were compared to experimental data.

Modeling and Simulation

The geometry of porous media was generated in Solid Works software as the preprocessor. Figure 1 (a) depicts the geometry of porous media. It is composed of a column packed with spherical particles with free spaces at the beginning and the end of the column.

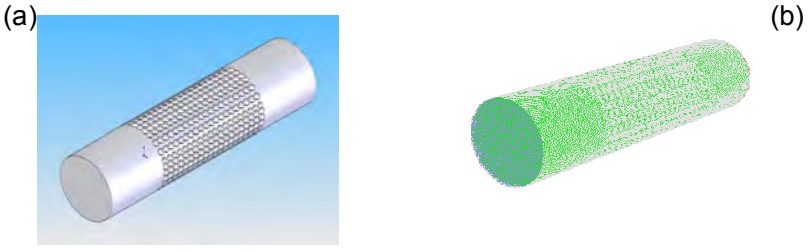

Figure 1. The geometry (a) and meshing (b) of column packed with spherical particles

The free space at the beginning makes the inlet stream to be uniform and such a space at the end of column prevents the formation of vortices. The mechanical characteristics

* Corresponding author. Tel (+98-21) 6616-4577 E-mail: baghalha@sharif.edu

of the model is as follows: total length: 0.6 m, porous length: 0.298 m, Inlet (outlet) empty space: 0.151 m, bed to particle diameter (D/dp): 9.625 and porous volume of the bed: 46.9 %. The arrangement of the packing is a state between random arrangement and ordered one. The contact area between the spherical particles is defined to be a circle i.e., the packing is not complete spheres in agreement with experimental conditions.

After meshing of such a complicated volumetric model (see Figure 1 (b)), the meshed geometry was examined to ensure the agreeable quality of the meshing. Then, it was exported to Fluent software as the processor. The solver was three-dimensional double precision (3ddp) and due to incompressibility of the water, the solving method was selected as implicit segregated. The flow calculation was done using $K-e$, laminar and Realizable $K-e$ models. After determining the physical properties of the fluid and the boundary conditions, the problem should be initialized. The solving procedure was iterated until the convergence criteria were obtained.

Results and Discussion

The present simulation results in 28 descritized points that half of them are related to the smooth wall condition and the others are related to the glass lined wall with roughness height of 0.3 mm. The solver took 5 h to converge for any of these points. Experimental parameters of Ergun's equation were modified by the CFD. Also, the analytical data were compared to experimental data based on a previous work done by Rumpf et al. (1971). As observed in Figure 2, the analytical data fits well the experimental data. It is noticeable that Ergun's equation overestimates the pressure drop.

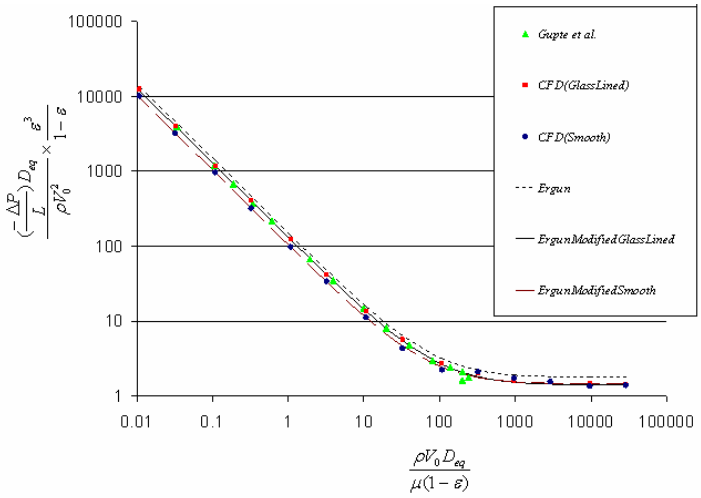

Figure 2. Comparison between experimental (Rumpf et al., 1971) and analytical data

Conclusion

Water flow behavior in a packed column was modeled based on computational fluid dynamics. The parameters of Ergun's equation were modified by applying the CFD results into the empirical Ergun's equation. The range of Reynolds number considered in the present CFD work was far wider than that previously existed in literature. The obtained CFD results were in good agreement with the available experimental data in literature.

References

Ergun, S. (1952). Fluid flow through packed columns, *Chemical Engineering Progress,* 48, 89-94.

Nemec D., Levec J. (2005). Flow through packed bed reactors: 1. Single-phase flow. *Chemical Engineering Science,* 60, 6947-6957.

Puncochar, M., Drahoš, J. (2000). Limits to model for pressure drop correlation. *Chemical Engineering Science,* 55, 3951–3954.
Rumpf, H., Gupte, A. R. (1971). Einflüsse der Porosität und Korngrößenverteilung im Widerstandsgesetz der Porenströmung. *Chemie Ingenieur Technik,* 43, 367-375.

Proceedings of the 10th International Chemical and
Biological Engineering Conference - CHEMPOR 2008
Braga, Portugal, September 4-6, 2008
E.C. Ferreira and M. Mota (Eds.)

Application of CFD in the Study of Supercritical Fluid Extraction with Structured Packing – pressure drop calculations

João B. Fernandes[1], Pedro C. Simões[1*], José P. B. Mota[1], Esteban Saatdjian[2]
[1] REQUIMTE, Departamento de Química, Faculdade de Ciências e Tecnologia,
Universidade Nova de Lisboa, 2829-516 Caparica, Portugal
[2] LEMTA-CNRS, 2 ave. de la forêt de Haye, 54500 Vandoeuvre, France

Keywords: Pressure drop, CFD modeling, structured packing, supercritical fluids
Topic: Multi-scale and/or multidisciplinary approach to process-product innovation.

Abstract

Liquid phase SFE has been carried out mainly in packed extraction columns, with structured packings particularly of the gauze type. Structured packing performs very well during extractions under these conditions, mainly due to their relatively large surface area and free volume. Nevertheless, there are also important disadvantages such as high cost, low capacities at high flow rates, premature flooding, and entrainment of the liquid phase due to low density differences [1]. The assessment of the real efficiencies of these packings poses extreme difficulties related to the moderately high pressures involved in these processes. Computational Fluid Dynamics (CFD) can be used to characterize the complex multiphase flow inside the packed bed and evaluate the influence of the shape and geometry of the packing on the hydrodynamics and mass and heat transfer rates in the SFE packed column [2]. The final objective of our work is to model the complex transport phenomena present in SFE columns with structured packing in order to predict rates and to optimize the process. The first stage, presented here, consists in an accurate modelling of the hydrodynamics inside the relatively complex geometry of the structured packing. The current paper presents a CFD model to predict the pressure drop in these columns; the results are compared to a wide variety of experimental data available in the literature.

This model was applied to the study of Sulzer EX structured gauze packing. For that purpose two different geometrical models were developed. A simpler one which consists of two contacting corrugated packing sheets (two packing sheets model), includded in a box. This geometry tries to mimic the volume existent between two packing sheets.The other one, more complex, which consists of thirteen packing sheets forming a packing element (packing element model).

To validate the geometric model comparisons were drawn between simulation results and the data of Stockfleth and Brunner [12,13], Meyer [14] (carbon dioxide at 313K,10.1<P<13.1) and Olaño *et al* [15] for data obtained with air at ambient pressure.

1 Introduction

Liquid phase SFE has been carried out mainly in packed extraction columns, with structured packings particularly of the gauze type. The assessment of the real efficiencies of these packings poses extreme difficulties related to the moderately high pressures involved in these processes. Computational fluid dynamics (CFD) can be very helpful to characterize the multiphase flow inside the packed bed and evaluate the influence of the shape and geometry of the packing on the hydrodynamics and mass and heat transfer kinetics of the SFE packed column. One main and very important advantage of using CFD simulation is its potential to reduce the extent and number of experiments required to describe such a type of flow.

Among the numerical investigations on the flow behaviour in structured packing, Hodson *et al.* [3] used CFD to simulate the flow pattern of the vapor phase on the micro-scale. Van Gulijk [4] presented a simplified “Toblerone” model of a packing sheet to investigate the transversal dispersion behaviour in structured packing. Von Scala et al. [5] centered their

study on the hydrodynamics and energy transfer inside structured packing; for that purpose they produced a model incorporating three different types of flow: inside the valleys of the corrugations, flow crossing the valleys, and ideal mixture. The proposed geometry was rather simple and the calculations were made for four staggered packing elements. Based on van Gulijk´s work, Higler *et al.* [6] and van Baten et al. [7,8] studied the liquid phase mixing and mass transfer within a catalytic packed bed reactor which contained Katapak-S structure. Petre et al. [9,10] considered the structured packing layers as the combination of four representative elementary units (REU), simulated the hydrodynamics in each REU using three-dimensional CFD and reconstructed the overall pressure drop in single gas-phase flow. Haghshenas *et al.* [2] modelled a whole packing module and determined its pressure drop, these authors also studied the mass transfer inside structured packing by using a two sheet model in counter-current gas-liquid flow.

The final objective of our work is to model the complex transport phenomena present in SFE columns with structured packing in order to predict rates and to optimize the process. In this first stage, a very accurate modelling of the single phase hydrodynamics inside the relatively complex geometry of the structured packing is presented. The porosity of the gauze packing is explicitely taken into account using a porous media formulation and considering the specific thickness of the packing sheets.This very detailed model can run under both laminar and turbulent flow conditions and for supercritical fluids. To our knowledge this is the first time that a packed supercritical extraction column is modeled with such detail. Another important issue is the compromise between a three-dimensional model of the entire packing, and which will be much more CPU time consuming and a model of just one or two layers of packing which will yield results much faster. Here we present these two CFD models to predict the dry pressure drop in SFE columns; the results are compared to a very wide range of experimental data available in the literature.

2 Problem formulation and numerical simulation

As indicated above, two CFD models are used to predict the dry pressure drop of a structured packed column running at supercritical conditions. The structured packing inside the column is SULZER EX, with the characteristics listed in Table 1.

Column internal diameter: 24mm	
Packing	SULZER EX
Material	Gauze
Fractional void volume, ε	0.86
Specific surface area, a_s [m^2/m^3]	1710
Particle diameter, d_p [mm]	0.4912
Hydraulic diameter, d_h [mm]	1.886
Inclination angle, α [deg]	45

Table 1- Geometric data of SULZER EX structured gauze packing

The characteristic diameter of the channels, d_p, and the hydraulic diameter, d_h, are defined as follows:

$$d_p = \frac{6(1-\varepsilon)}{a_s} \quad (1)$$

$$d_h = \frac{4\varepsilon}{a_s} \quad (2)$$

where ε is the fractional void volume of the packing and a_s is the specific surface area.

The two proposed geometrical models for the simulation consist (i) of two contacting corrugated packing sheets (two packing sheets model), included in a box, and (ii) of thirteen

packing sheets forming a packing element (packing element model). The first geometry tries to mimic the volume existent between two packing sheets, and the second tries to mimic a whole packing element.

The commercial CFD software package, Fluent v.6.3, was used to predict the velocity profiles and pressure drop inside the packing. Under turbulent flow conditions, a modification of the standard k-ε model [11] was employed with standard wall functions. This modified turbulence model differs from the standard one in that it contains a new formulation for the turbulent viscosity and a new equation for the dissipation rate. In all of our simulations the fluid was considered to be Newtonian, incompressible and isothermal, the properties of the fluid were assumed constant and its thermophysical properties were taken from NIST Database.

The geometry of the first model corresponds to two packing sheets included in a box. A bottom-up strategy was used to generate the computational grid. First the vertices of the grid were defined, then the vertices were linked by lines, the lines generated surfaces and finally the surfaces originated volumes. This computational domain is composed of about 1 million tetrahedral cells (applying a mesh with hexahedral cells turned out to be very difficult due to the extreme complexity of the geometry). The smallest element of the grid has a dimension of 0.31mm. Figure 1 shows a top view of the Sulzer EX packing. The region within the white rectangle is modelled by the grid shown on the second part of the figure.

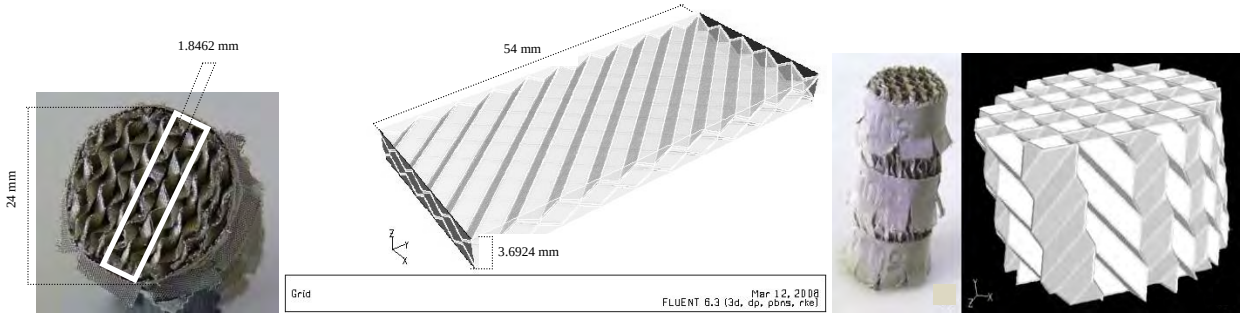

Fig. 1- Sulzer EX packing and computational grids

The walls of the box in the *x*-direction are modelled as solid walls with no-slip boundary condition while the walls in the *z*-direction are modelled as translational periodic to account for the effect of neighbouring packing sheets. At the bottom, the gas inlet is defined as velocity inlet with an imposed uniform velocity profile. At the upper side, the gas exit was defined as pressure outlet boundary condition. The packing sheets have a thickness of 0.31mm and were modelled using the porous media formulation of FLUENT [11]. This porous media formulation incorporates an empirically determined flow resistance in the region of the model defined as porous. In essence this is nothing more than an added momentum sink in the governing momentum equations. It was also assumed that there is continuity of the velocity vectors across the porous media interface.

The second model or packing element module, consists of thirteen porous sheets stacked together forming a packing element contained in a cylinder to mimic the column wall. Due to computational power constraints only one third of the actual packing element was modelled (see third part of Fig.1).

The porosity of the porous sheets was modelled by the addition of a momentum source term to the standard fluid equations for the computational cells corresponding to the sheets. The permeability, α, which contributes to the viscous loss term, and the inertial resistance factor, f_R, were determined experimentally as discussed below. The boundary condition at the wall of the column was defined as a no-slip boundary condition.

To derive the input data for the porous region, we measured experimentally the pressure drops produced by water flowing inside a straight empty tube and flowing in the straight tube with a single sheet of the packing. Measurements of the pressure drop were made for

several liquid velocities and the data was represented in a plot of pressure drop versus flow Reynolds number. The mass flow rates of water were measured by simply measuring the volume of liquid falling into a collecting vessel during a determined time interval.

The actual pressure drop, Δp, produced by the packing sheet was obtained by subtracting the empty tube pressure drop from the one obtained for the tube plus the packing sheet. The coefficients for the viscous and inertial resistance factors of the porous sheet were obtained by fitting the experimental data to:

$$\Delta p = -\left(\frac{\mu}{\alpha}u + \frac{1}{2} f_R \rho u^2\right)\Delta s \qquad (13)$$

where Δs is the thickness of the sheet. From the fitting the following values were obtained $1/\alpha = 1.26\times10^{10}$ and $f_R = 6214.58$.

3 Results and Discussion

In order to validate both computational models we proceeded to simulate the pressure drops measured by different authors, Stockfleth and Brunner [12,13], Meyer and Brunner [14], and Olaño et al [15].

3.1 Data of Stockfleth and Brunner and Meyer and Brunner, Two Packing Sheets and Packing Element Models with CO2 at supercritical conditions

Similar to the pressure drop in tubes, the pressure drop over the packing is a function of the resistance factor and the dynamic head. In the next plot one can see a comparison of the experimental results obtained by these authors and the ones generated in the simulations:

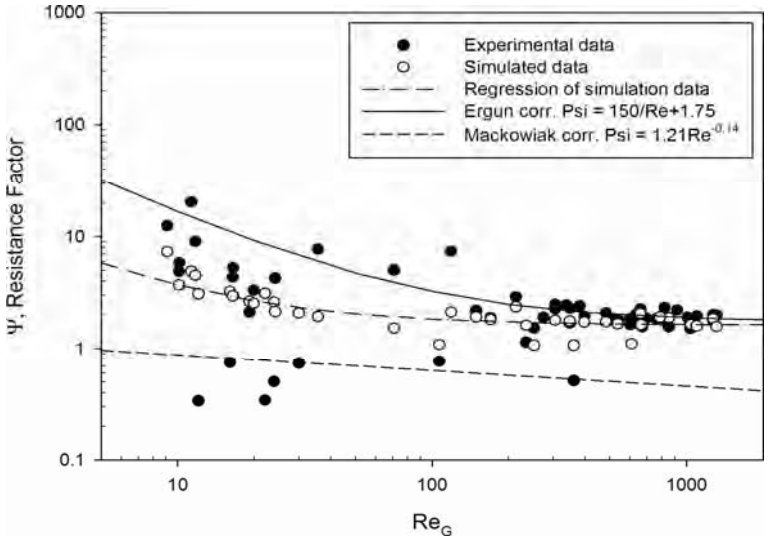

Fig. 2 - Comparison between experimental and simulated resistance factors. Data of Stockfleth and Brunner, Meyer and Brunner.

In the above plot you can see that the resistance factors calculated are well within the experimental data, moreover, they show much less scattering. In the same plot there are represented the regressions of Ergun, Mackowiak and another one developed based on the simulated data. This last correlation is simply an Ergun type correlation, fitted to our simulated data and whose parameters have taken the following values:

$$\Psi = \frac{20.992}{\mathrm{Re}} + 1.632$$

3.2 Data of Olaño, Two Packing Sheets Model – air at ambient pressure

This data concerns the dry pressure drop of Sulzer Ex packing for air at ambient pressure. In this case, the packing had slightly different dimensions, the column where the study was conducted possessed a smaller diameter than the ones considered previously, and the crimp height of the corrugation was unknown, so we decided to rescale the computational grid in order to simulate the packing with smaller diameter. The results for the predicted and experimental pressure drops are shown in Figure 9. In this case, the experimental points were simulated both using the laminar model and the realizable k-ε turbulence model. Both assumptions in the simulation model generated data able to follow the trend of the experimental data, but, as expected, the laminar model showed a better performance in the low Reynolds number data while the realizable k-ε model performed better at the highest Reynolds number data. In the same figure is also plotted a trend line for the experimental data. This line shows at which Reynolds number occurs the transition from laminar to turbulent flow (a line fitted to the last data would have a higher slope indicating a stronger dependency of the pressure drop on the flow conditions). Looking at the figure it is possible to see that the transition occurs when Re is about 500; after this value the adapted turbulence model chosen performs very well.

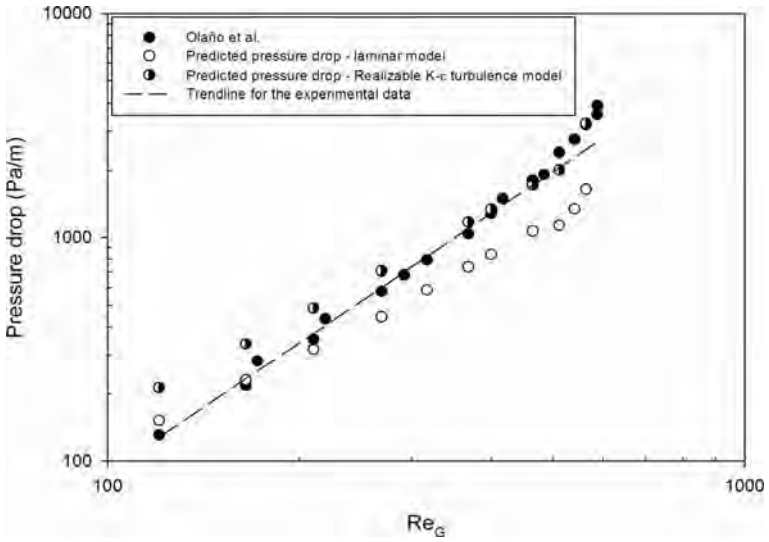

Fig. 3- Comparison between predicted and experimental pressure drops for the data of Olaño et al

4 Conclusions

Two very detailed computational models were presented for the estimation of the pressure drop caused by Sulzer EX packing. The first one being a simple representation of two packing sheets and assuming periodicity perpendicularly to the main flow direction and the second one a partial packing module, this one with periodicity in the flow direction. In both models, which can simulate either laminar and turbulent flow, the packing thickness and its permeabilty are taken into account.

Simulations were carried out to determine the pressure drops of Sulzer EX at various gas mass flowrates and various conditions of pressure (0.1 to 30 MPa) and temperature (298 to 393K) and good agreement was found between predicted and experimental pressure drops. The flow field inside the structured packing is also analyzed.

Even though the dry pressure drop is a very important factor in the design of supercritical fluid extraction columns and is used in many correlations for the determination of wet pressure drop, alone it is not enough to determine their hydrodynamics. Our next step will be to modify and test these models against real extraction conditions where liquid is flowing

countercurrently to the supercritical solvent. This implies a study of the simultaneous heat and mass transfer in the column.

References

[1] Gamse, T. (2005). *Industrial applications and current trends in supercritical fluid technologies*, Volume 59(9/10) 207-212, Hemijska Industrija.

[2] Haghshenas, F., Zivdar, M., Rahimi, R., Esfahany, M. N., Afacan, A., Nandakumar, K., Chuang, K. T. (2007). CFD simulation of mass transfer efficiency and pressure drop in a structured packed distillation column, *Chem. Eng. Technol.*, 30(7), 854-861.

[3] Hodson, J. S., Fletcher, J. R., Porter, K. E. (1997). Fluid mechanical studies of structured distillation packings, in: *Institution of Chemical Engineers Symposium Series, AIChE,* New York, 142, 999-1007.

[4] Van Gulijk, C. (1998). Using computational fluid dynamics to calculate transversal dispersion in a structured packing bed, *Comput. Chem. Eng.*, 22, 767-770.

[5] Von Scala, C., Wehrli, M., Gaiser, G. (1999). Heat transfer measurements and simulation of Katapak M® catalyst supports, in: International Symposium on multifunctional reactors, *Chem, Eng. Sci. 54(10),*1375-1381.

[6] Higler, A. P., Krishna, R., Ellenberger, J., Taylor, R. (1999). Counter-current operation of a structured catalytically packed-bed reactor: Liquid phase mixing and mass transfer, *Chem. Eng. Sci*., 54, 5145-5152.

[7] Van Baten, J. M., Ellenberger, J., Krishna, R. (2001). Radial and axial dispersion of the liquid phase within a Katapak-S structure: Experiments vs. CFD simulations, *Chem. Eng. Sci.*, 56 , 813-821.

[8] Van Baten, J. M., Krishna, R. (2002). Gas and liquid phase mass transfer within Katapak-S structures studied using CFD simulations, *Chem. Eng. Sci*., 57, 1531-1536.

[9] Petre, C. F., Larachi, F., Iliuta, I., Grandjean, B. P. A. (2003). Pressure drop through structured packings: Breakdown into the contributing mechanisms by CFD modeling, *Chem. Eng. Sci.,* 58, 163-177.

[10] Petre, C. F., Larachi, F., Iliuta, I., Grandjean, B. P. A. (2003). Tailoring the pressure drop of structured packings through CFD simulations, *Chem. Eng. Process.,* 42, 535-541.

[11] Yang, Z., Zhu, J. (1995). A new k-ε eddy viscosity model for high Reynolds number turbulent flows, *Computers Fluids*, 24(3), 227-238.

[12] Stockfleth, R., Brunner, G. (1999). Hydrodynamics of a packed countercurrent column for the gas extraction, *Ind. Eng. Chem.*, 38, 4000-4006.

[13] Stockfleth, R., Brunner, G. (2001). *Holdup, pressure drop, and flooding in packed countercurrent columns for the gas extraction, Ind. Eng. Chem., 40, 347-356.*

[14] Meyer, Jens-Torge (1998). Druckverlust und Flutpunkte im Hochdruckgegenstrom-kolonnen mit überkritischen Kohlendioxid, PhD. Dissertation, *Technische Universität Hamburg-Harburg*, Germany

[15] Olaño, S., Nagura, S., Kosuge, H., Asano, K. (1995). Mass transfer in binary and ternary distillation by a packed column with structured packing, *J. Chem. Eng. Japan*, 28(6).

Proceedings of the 10th International Chemical and
Biological Engineering Conference - CHEMPOR 2008
Braga, Portugal, September 4-6, 2008
E.C. Ferreira and M. Mota (Eds.)

Application of CFD techniques in a high-flux riser-reactor flow prediction

Rosa, L.M.[1], Bastos, J.C.S.C.[1] , Mori, M.[1], Martignoni, W.P.[2]
[1] University of Campinas, Department of Chemical Processes, School of Chemical Engineering, P.O. Box 6066, 13083-907 Campinas, SP, Brazil.
[2] PETROBRAS/CENPES – Centro de Pesquisas e Desenvolvimento Leopoldo Américo Miguez de Mello, 21941-915 Rio de Janeiro, RJ, Brazil.

Keywords: CFD, simulation, FCC riser, gas-solid, catalytic cracking
Topic: CFD & Chemical Engineering.

Abstract

The application of computational fluid dynamics (CFD) in industrial operations has been increasing not only in the design of new equipment, but also in the optimization of that already existing. The present work shows a set of three-dimensional two-phase and adiabatic conditions using the two-fluids model for the calculation of gas-solid flow in high-flux risers with two different geometries, one with a height of 10m and an internal diameter of 76mm, and the second with a height of 18m and an internal diameter of 50mm. The k-epsilon model was applied to consider the influence of turbulence on the gas phase. The four-lump and ten-lump kinetic model schemes were used to predict the catalytic cracking reactions in the two different reactors. The riser with a height of 10m and an internal diameter of 76mm had two entrances, one for particle inlet and one for the organic materials. The size of the mesh for this case was 584,000 control volumes. The second riser studied with geometry a height of 18m and an internal diameter of 50mm had one entrance for vapor, one for organic materials, and a third for particle inlet. The mesh generated for this geometry had 650,000 control volumes. The numerical results of gas-solid dispersion flow in a high-flux riser were compared with the experimental data from the work of Pärssinen and Zhu (2001), the four-lump scheme for the mass concentration of chemical species was compared with the work of Ali et al. (1997), and the ten-lump scheme was compared with the work of Nayak et al. (2005). The catalytic cracking reaction models have an important role in the prediction of all phenomena present in the reactor. The simulated results show that the kinetics models are important not only for the variation in the gas phase and the temperature profiles inside the reactor, but also because these parameters interfere directly in the dynamic behavior of the gas-solid flows.

1 Introduction

A fluidized catalytic cracking unit (FCCU) consists in a riser reactor, where the catalytic reactions occur, and a regenerator, where the catalyst is reactivated. The main purpose of the riser is to put into contact hydrocarbons and catalyst particles, causing the catalytic cracking reactions. The cracking process converts the hydrocarbons fed into products with a higher commercial value. Although this equipment is widely used, phenomena in risers have not been entirely explained. They are operated with a high concentration of particles in a fluidized bed regime (fast transport regime). The adoption of fluidized beds is related to the catalytic cracking of gasoil in gasoline. Cracking had previously been done in fixed bed reactors.

Multiphase flows are more difficult to predict and analyze because their phases can assume complicated configurations (Hanratty et al., 2003). The phases do not mix uniformly and interactions (on a small scale) between the phases can have a strong effect on the macroscopic properties of the flow. The formation of heterogeneous structures in gas-particle systems (e.g., clusters) strongly affects the gas-solid contact and transport processes in dense fluidized beds. These structures depend on the overall forces acting on the particles. The drag force plays a fundamental role in the coupling of gas and particles. Zhang and Reese (2003) propose a new equation for the mean drag force that considers not only the solids volumetric fraction, but also the

Corresponding author. Phone + 55 19 3521-3963. E-mail:mori@feq.unicamp.br

random fluctuations in the particle movement.

In the modeling of chemical reactions, the use of groups of chemical species (or *lumps*) is common. A lump is the representation of a group of chemical species that have similar chemical properties. Thus, the catalytic cracking reactions that occur concurrently between numerous chemical species can be modeled as reactions between a fewer number of lumps (Farkas, 1999). The advantage of this procedure is the small number of chemical species and of reaction rates that have to be calculated separately, requiring a data bank for their calculation, and proportional computational resources. In the literature simulations that apply lumps to model the catalytic cracking of hydrocarbons, in gas-solid reaction systems (Ali and Rohani, 1997; Ali et al., 1997), or three-phase systems (Nayak et al., 2005) are mainly one-dimensional. However, one-dimensional simulations cannot provide realistic solutions for radial distributions and are not able to properly handle some phenomena, such as particle reflux and swirls in a turbulent flow, and one-dimensional balances cannot be applied at the entrance region due to the high nonhomogeneity and turbulence in this region.

This article shows the influence of cracking models on the fluid flow through simulations with and without calculating reactions and with different cracking models. The finite volume method was utilized.

2 Mathematical Modeling

For simulation of the flow inside the reactor, the flow of two phases was considered: the particulate phase, formed of catalyst particles, and the gaseous phase, which is a mixture of water vapor and organic compounds. The formation of new products and consumption of the existing ones alter the physicochemical properties of the gaseous phase. Both phases are fed at different temperatures; thus, at the bottom of the reactor, high temperature gradients exist.

Gas-solid systems can be modeled by several techniques. One consists in modeling each phase separately with the established equations for one-phase flows with a moving surface between them. However, when the phases are well mixed, as in many industrial operations, these cases require an average procedure to make solution of the equations possible.

Ishii (1975) divides the models for solution of fluid flow problems into two categories: diffusion models and two-fluid models. A diffusion model is formulated considering the mixture to have one transport equation for the continuity, momentum and energy, and a diffusion equation. A two-fluid model consists in two equations for the continuity, momentum and energy, one for each phase. In this work, the Eulerian-Eulerian approach was also applied. The *k-epsilon* model was applied to take account of the turbulent behavior of the flow. The equations of the model are given in the Appendix section.

3 Chemical Kinetic Models

Several models are being proposed for the calculation of catalytic cracking reactions. The advances in both the analytical techniques and mathematical routines for determining the parameters lead to the progression from simple models with three and four lumps, to more complex models with ten, twelve, and more lumps.

The four-lump kinetic model classifies the hydrocarbon fractions into four groups, as illustrated in Figure 1a. Oil cracking follows a second-order kinetics, while gasoline cracking follows a first-order kinetics. Parameters for the determination of reaction rates and heat were found in Ali et at. (1997).

Analogously, the ten-lump model describes the relationship of ten groups of hydrocarbons – four light hydrocarbon groups, four heavy hydrocarbon groups, coque and gasoline (Figure 1b). Parameters for the determination of reaction rates and heat were found in Nayak et at. (2005).

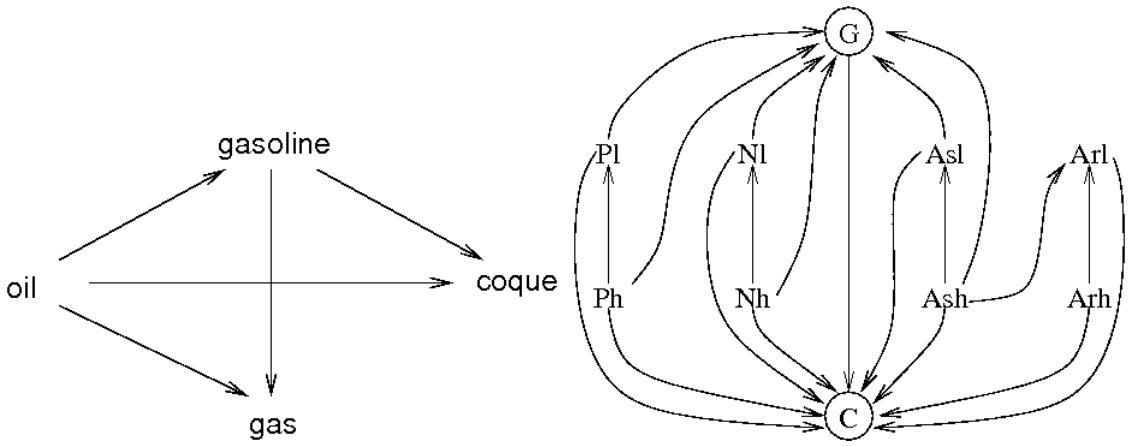

Figure 1. Kinetic models: (a) four lumps and (b) ten lumps

3 Meshes

Several three-dimensional meshes were elaborated with two different geometries. All had a first volume (at the walls) thickness of about 1mm, which provided the value of y+ needed for the turbulence model. The first geometry, shown in Figure 2a, had a height of 10m and an internal diameter of 76mm, and was based on the equipment presented by Pärssinen and Zhu (2001). It is a combination of a cylindrical duct with a lateral junction that has the purpose of injecting the catalyst, and ends in a curve. A construction known as “O-Grid” was applied for the generation of a higher quality mesh. Meshes of different sizes were tested, and the mesh chosen for the simulations had 584,000 control volumes. The second geometry, shown in Figure 2b, had a height of 18m and an internal diameter of 50mm. It is also a combination of a cylindrical duct with a lateral junction, and terminates with another junction that forms a 90 degrees angle with the main duct. It has two more entrances inside the reactor for vapor and feed inlet. These details made the elaboration of the meshes more difficult, which was solved with an “L-Grid” construction for the curved inlet. The final mesh had 650,000 control volumes.

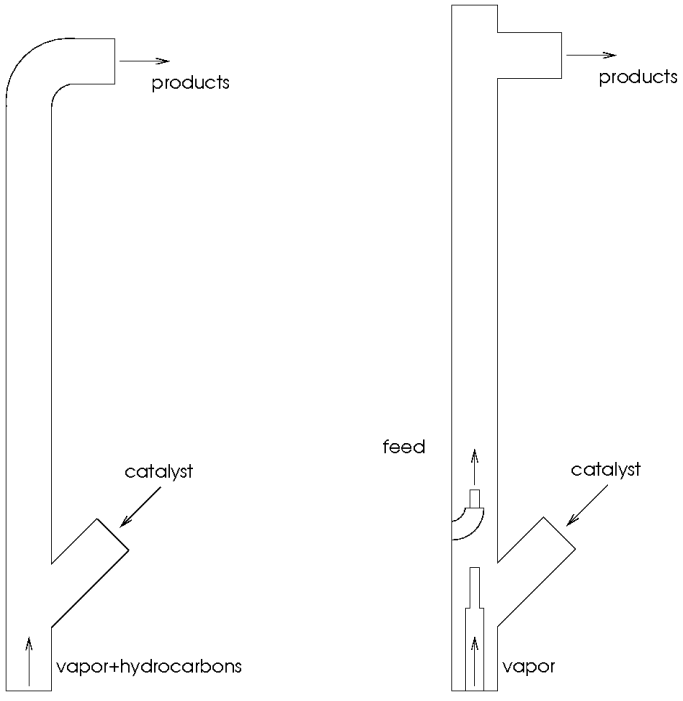

Figure 2. Geometries utilized

4 Results

Figure 3 shows the concentration profile of hydrocarbons calculated with the four-lump model for geometry A. The values obtained follow the same trends as the experimental ones (given by Ali et al., 1997), but the conversion was a little lower than expected (i.e., the final values of the products do not reach the experimental values). One possible explanation for this behavior could be the heat transfer model: chemical reactions are greatly influenced by temperature.

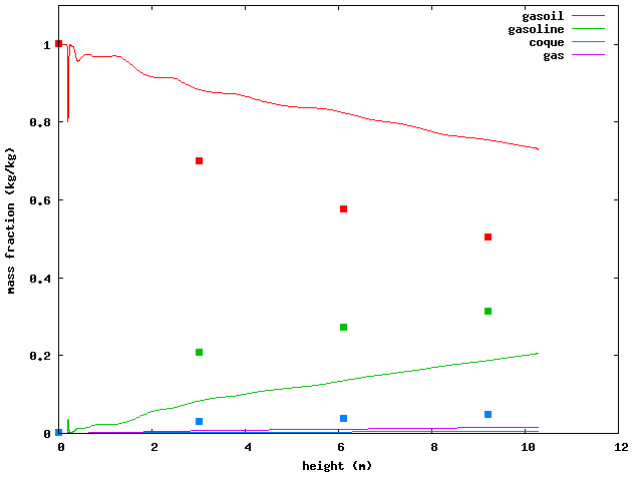

Figure 3. Hydrocarbons conversion

In Figure 4 the gas-phase temperature maps calculated for the two geometries considered are shown. In both cases it could be seen that these values are influenced by the temperature of the particle phase. In Figure 4a, more heat is transferred to the gas phase, whereas the temperature after contact with hot catalysts is higher than the temperature in Figure 4b.

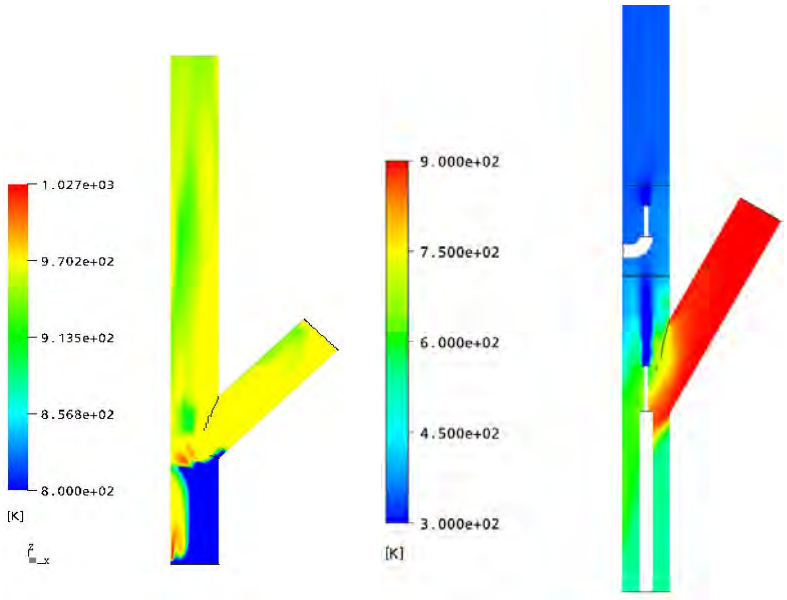

(a) (b)

Figure 4. Temperature maps

The behavior of the flow with reaction (labeled as case 04) compared with the flow without reaction (case 02) are shown in Figure 5. When the composition of the gas phase varies, its properties are not the same because it depends on the properties of each chemical species. Figure 5a shows the flow in the lower section of the reactor at a height of 1.53m. There are few differences between the profiles, but these are greater at higher heights (Figure 5b) because there are more products formed in this region.

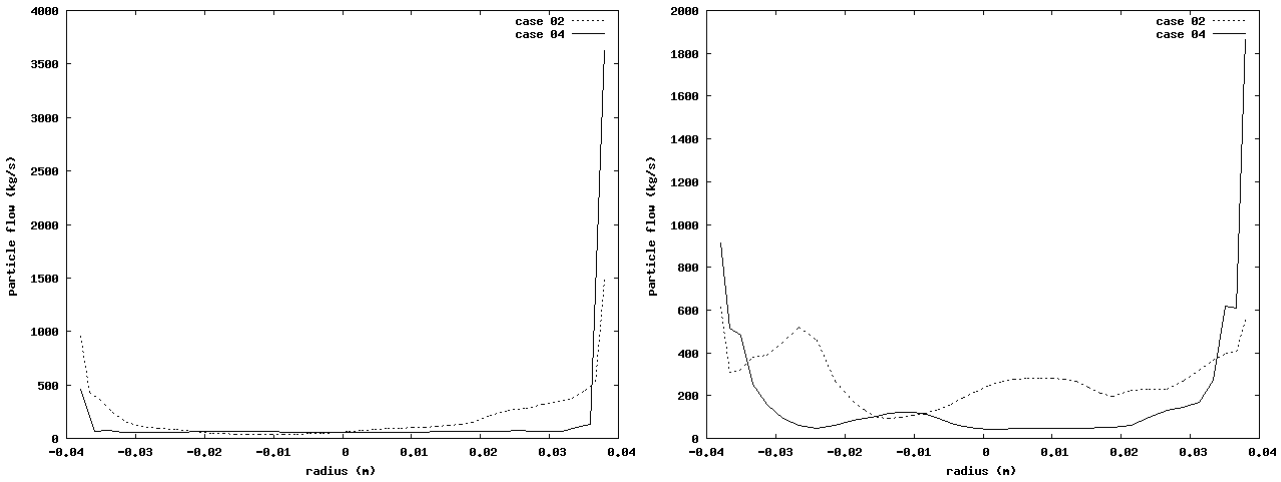

(a) (b)

Figure 5. Comparison of flows at heights of 1.53m and 9.42m

5 Conclusions

The simulation of a reacting gas-solid fluid flow, coupling the four-lumps and ten-lumps kinetic models with the two-fluids model, was calculated for two different riser configurations in the CFX package. Simulation of the reacting flows resulted in conversions a little lower than what was expected, but with the same trends, thereby showing them to be different from simulations without chemical reactions. More studies can be done on the heat transfer model coefficient, and on the dynamics of the flow at high temperatures.

References

Ali, H., Rohani, S. Dynamic modeling and simulation of a riser-type fluid catalytic cracking unit. *Chem. Eng. Technol.*, n. 20, p. 118-130, 1997.

Ali, H., Rohani, S., Corriou, J.P. Modelling and Control of a riser type fluid catalytic cracking (FCC) unit, *Trans. IchemE.*, 75A, 401-412, 1997.

Farkas, G. Kinetic lumping schemes. *Chemical Engineering Science*, 54, p. 3909-3915, 1999.

Hanratty, T.J., Theofanous, T., Delhaye, J.M., Eaton, J., McLaughlin, Prosperetti, A., Sundaresan, S., Tryggvason, G. Workshop findings. *International Journal of Multiphase Flow*, n. 29, p. 1047-1059, 2003.

Ishii, M. *Thermo-Fluid Dynamic Theory of Two-Phase Flow*. Eyrolles, 1975.

Nayak, S.V., Joshi, S.L., Ranade, V.V. Modeling of vaporisation and cracking of liquid oil injected in a gas-solid riser. *Chemical Engineering Science*, n. 69, p. 6049-6066, 2005.

Pärssinen, J.H. and Zhu, J.X. Particle velocity and flow development in a long and high-flux circulating fluidized bed riser. *Chemical Engineering Science*, 56, 5295-5303, 2001.

Zhang, Y., Reese, J.M. The drag force in two-fluid models of gas-solid flows. *Chemical Engineering Science*, v. 58, p. 1641-1644, 2003.

Appendix

continuity

$$\frac{\partial}{\partial t}\left(\varepsilon_g \rho_g\right)+\nabla\cdot\left(\varepsilon_g \rho_g u_g\right)=0 \quad (1)$$

$$\frac{\partial}{\partial t}\left(\varepsilon_p \rho_p\right)+\nabla\cdot\left(\varepsilon_p \rho_p u_p\right)=0 \quad (2)$$

momentum transport

$$\frac{\partial}{\partial t}\left(\varepsilon_g \rho_g u_g\right)+\nabla\cdot\left(\varepsilon_g \rho_g u_g u_g\right)=-\varepsilon_g \nabla p_g+\nabla\left(\varepsilon_g \mu_g\left(\nabla u_g+\left(\nabla u_g\right)^T\right)\right)+\varepsilon_g \rho_g g+\beta_{gp}^m\left(u_p-u_g\right) \quad (3)$$

$$\frac{\partial}{\partial t}\left(\varepsilon_p \rho_p u_p\right)+\nabla\cdot\left(\varepsilon_p \rho_p u_p u_p\right)=-G\nabla\varepsilon_p+\nabla\left(\varepsilon_p \mu_p\left(\nabla u_p+\left(\nabla u_p\right)^T\right)\right)+\varepsilon_p \rho_p g+\beta_{pg}^m\left(u_g-u_p\right) \quad (4)$$

chemical species transport

$$\frac{\partial}{\partial t}\left(\varepsilon_g \rho_g c_i\right)+\nabla\cdot\left(\varepsilon_g \rho_g u_g c_i\right)=\nabla\left(\varepsilon_g \Gamma_i \nabla c_i\right)+S_g^i \quad (5)$$

energy transport

$$\frac{\partial}{\partial t}\left(\varepsilon_g \rho_g H_g\right)+\nabla\cdot\left(\varepsilon_g \rho_g u_g H_g\right)=\nabla\left(\varepsilon_g \lambda_g \nabla T_g\right)+\beta_{gp}^h\left(T_p-T_g\right)+\sum_r \Delta H\frac{\partial c_r}{\partial t} \quad (6)$$

$$\frac{\partial}{\partial t}\left(\varepsilon_p \rho_p H_p\right)+\nabla\cdot\left(\varepsilon_p \rho_p u_p H_p\right)=\nabla\left(\varepsilon_p \lambda_p \nabla T_p\right)+\beta_{pg}^h\left(T_g-T_p\right) \quad (7)$$

closure equations

solids pressure: $G=\exp\left(600\left(\varepsilon-0.62\right)\right)$ (8)

drag force for dilute flows: $\beta_{gp}^m=\frac{3}{4}\mathrm{Cd}\frac{|\,u_p-u_g\,|\,\varepsilon_p\rho_p}{d_p}f\left(\varepsilon\right)$ (9)

(Re<=1000) $\mathrm{Cd}=\frac{24}{\mathrm{Re}}\left(1+0.15\,\mathrm{Re}^{0.687}\right)$ (10)

(Re>1000) $\mathrm{Cd}=0.44$ (11)

drag force for dense flows: $\beta_{gp}^m=150\frac{\varepsilon_p^2\mu_g}{\varepsilon_g d_p^2}+1.75\frac{|\,u_p-u_g\,|\,\varepsilon_p\rho_p}{d_p}$ (12)

heat transfer coefficient: $\beta_{gp}^h=\pi d_p Nu\lambda_g$ (13)

Ranz-Marshall model: $\mathrm{Nu}=2+0.6\,\mathrm{Re}_p^{1/2}\,\mathrm{Pr}^{1/3}$ (14)

2nd order kinetic model: $\frac{\partial c_r}{\partial t}=-k_r\varepsilon_s c_i^2$ (15)

1st order kinetic model: $\frac{\partial c_r}{\partial t}=-k_r\varepsilon_s c_i$ (16)

Arrhenius equation $k_r=k_0\exp\left(\frac{-E_r}{RT}\right)$ (17)

Nomenclature

c	species concentration	[kgmol/m³]
Cd	drag coefficient	[kg.m³/s]
d_p	particle diameter	[m]
E	activation energy	[J/mol]
g	gravity	[m/s²]
H	enthalpy	[J/kg]
k	reaction rate coefficient	[s-¹]
Nu	Nusselt number	[–]
R	gas universal constant	
Re	Reynolds number	[–]
Pr	Prandtl number	[–]
T	temperature	[k]
u	velocity	[m/s]
β	interphase transfer coefficient	
ε	volumetric fraction	
λ	thermal conductivity	[W/(m.K)]
μ	viscosity	[kg/(m.s)]
ρ	density	[kg/m³]

Proceedings of the 10th International Chemical and
Biological Engineering Conference - CHEMPOR 2008
Braga, Portugal, September 4-6, 2008
E.C. Ferreira and M. Mota (Eds.)

Gas holdup in laboratory scale bubble column: CFD [1]simulations vs. measurements

M. Simcik[1]*, L. Kulaviak[1], J. Havlica[1], M. C. Ruzicka[1], J. Drahoš[1], J. Teixeira[2]
[1]Institute of Chemical Process Fundamentals, Czech Academy of Science, Rozvojová 135, Prague 6, 165 02, Czech Republic
[2]Centro de Engenharia Biológica-IBQF, Universidade do Minho, Campus de Gualtar, 4710-057 Braga

Keywords: CFD, Euler-Euler, rectangular bubble column
Topic: CFD & Chemical Engineering.

This contribution deals with CFD Euler-Euler simulation of laboratory scale rectangular bubble column. Horizontal profiles of gas holdup obtained from simulations are compared with experimentally measured profiles using optical fibre probe.

Goal

The goal of the presented contribution was two-fold. Goal 1 was to examine effect of interphase forces and turbulent models on simulation results and effect of front-rear flow field symmetry assumption. Goal 2 was to compare simulated horizontal profiles of gas holdup with profiles measured with optical fiber probe.

Experiments

Experimental column width was 20 cm, measurements were done for column thickness (D) 4 and 10 cm. Ungassed liquid height (H) was 25 and 50 cm. Water and air were used as liquid and gas phase. Gas distributor consisted of one line of 33 orifices (0.5 mm orifice diameter, 5 mm distance between two neighbouring orifices). Experiments were done for air flow rates 800, 1200 and 1800 l/h. Gas holdup profiles were measured at height 11, 21, 31 and 41 cm above the gas distributor. There were 19 measuring points in horizontal profile with distance 1 cm. Local gas holdup at each point was measured for 2 minutes - the obtained values are 2 minute time averages.

Simulations

Euler-Euler model was used for the simulation of gas-liquid flow in the bubble column. Model equations were solved using commercial code Fluent 6.2. In Euler-Euler model all involved phases (gas, liquid) are treated as interpenetrating continua (see e.g. [1], [2], [3]). There is continuity and momentum equation for each particular phase. These equation sets for each phase are coupled together through pressure, phase volume fractions (which sum to unity) and interphase force terms like drag, lift, added mass force. Closure relations for the interphase forces are needed to solve the equations. Also turbulence has to be modelled. The equations for phase q have the following form [1], [2]:

$$\partial(\alpha_q \rho_q)/\partial t + \nabla . (\alpha_q \rho_q \mathbf{u}_q) = 0 \qquad (1)$$

$$\partial(\alpha_q \rho_q \mathbf{u}_q)/\partial t + \nabla . (\alpha_q \rho_q \mathbf{u}_q \mathbf{u}_q) = -\alpha_q \nabla p - \nabla .(\alpha_q \tau_q) + \alpha_q \rho_q \mathbf{g} + \mathbf{F}_{qp} \qquad (2)$$

*Corresponding author. Email: simcik@icpf.cas.cz

where α_q is volume fraction of the phase q. Here $\tau_q = \tau_{l,q} + \tau_{t,k}$ is effective stress tensor which contains not only the contributions from viscous effects ($\tau_{l,q} = \mu_q (\nabla \mathbf{u}_q + \nabla \mathbf{u}_q^{\mathrm{T}})$, but also the contributions from velocity fluctuations arising from averaging - $\tau_{t,k}$ – turbulent stresses. This (turbulent) term can be modeled as ($\tau_{t,q} = \mu_{t,q} (\nabla \mathbf{u}_q + \nabla \mathbf{u}_q^{\mathrm{T}})$, where $\mu_{t,q}$ is turbulent viscosity. Turbulent viscosity was calculated with k-ε turbulence model, which solves transport equations for turbulent kinetic energy and dissipation rate, see [1] for details. Last term in (2) $\mathbf{F}_{qp}$ is the total force (N/m^3) exerted on phase q by phase p (if there are more than two phases then the force is contribution from all other phases) – interphase force. Interphase coupling terms satisfy the following relation:

$\mathbf{F}_{qp} = -\mathbf{F}_{pq}$

We did 3-dimensional transient simulations of the flow field in the bubble column. One set of simulations was done assuming front-rear symmetry of the flow field, another set was done without this assumption (full 3D). Gas inlet was modelled using velocity inlet boundary condition with gas velocity set to 41cm/s and gas void fraction adjusted to obtain required flow rate. Constant static pressure was prescribed at the outlet boundary. The outlet boundary was 25-50cm above the level of ungassed liquid. Three version of k-ε turbulence model were tested (standard, RNG and realizable). Also simulations with different combinations of enabled interphase forces (drag, drag + lift, drag + added mass, drag + lift + added mass force) were run to see how they influence the output. Drag coefficient was modelled according to [4]. Added mass coefficient (when used) was set to 0.5. Influence of the lift coefficient value (from -0.3 to 0.5) on results was examined. If not said otherwise, the lift coefficient was 0.5.

Simulations results presented here were done on 5x5x2.5mm, timestep was 0.005s. Time averaged horizontal profiles of gas holdup were compared with experimental data. Profiles obtained from simulations were averaged over 60s time interval. Time averaging was started after 30s to let the flow field reach a pseudosteady state.

Results

Results are shown in the following figures. See Fig.1 for comparison between full 3D and front-rear symmetric simulation, Fig.2 for comparison of different versions of k-ε turbulence model, Fig. 3 and 4 for the effect of various combinations of interphase forces considered in simulations, Fig.5 for effect of lift coefficient value, and Fig. 6, 7, 8 and 9 for comparison between simulations and experimentally measured gas holdup profiles. See Conclusions for brief discussion of the results.

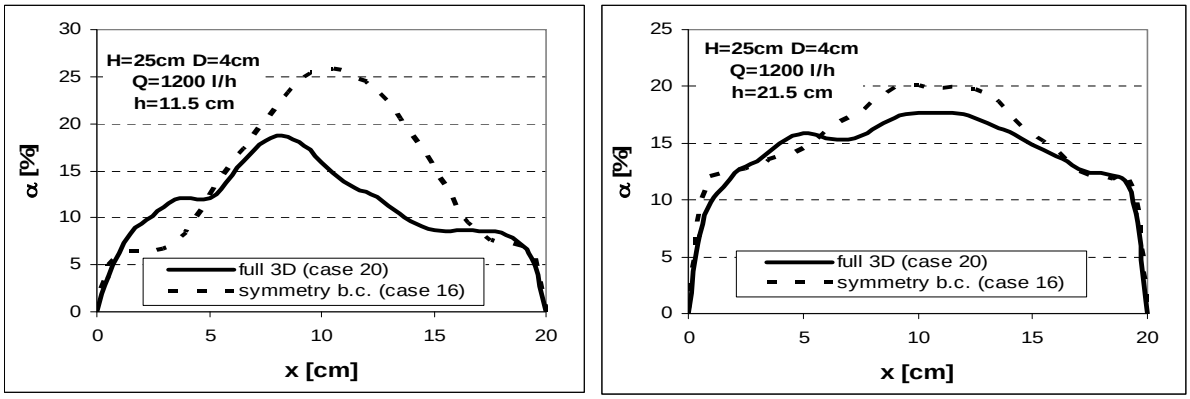

Fig. 1: Gas holdup profile (at h=11.5 and 21.5cm), full 3D vs. symmetry b.c. simulation, air flow rate 1200 l/h

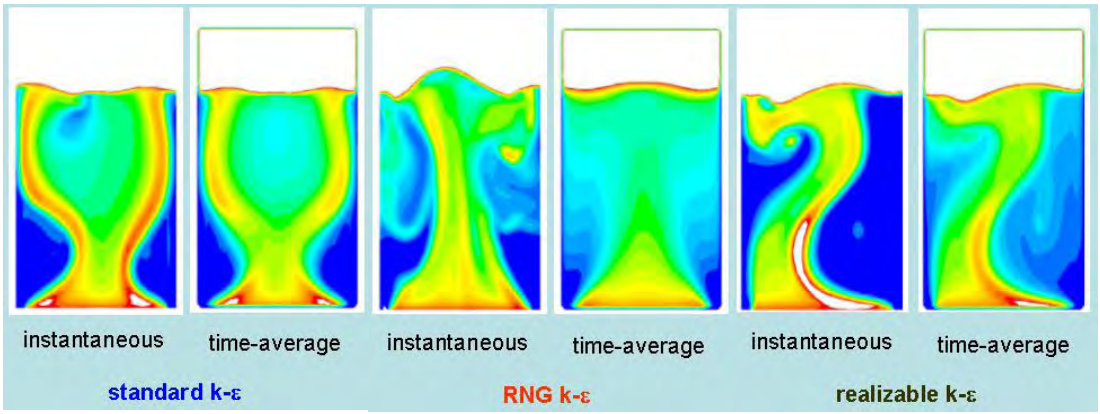

Fig. 2: Instantaneous and time-averaged gas holdup fields (blue...clear water, red...50% holdup) calculated with different turbulent models under otherwise same conditions, H=25cm, D=4cm, Q=1200l/h, symmetry b.c.

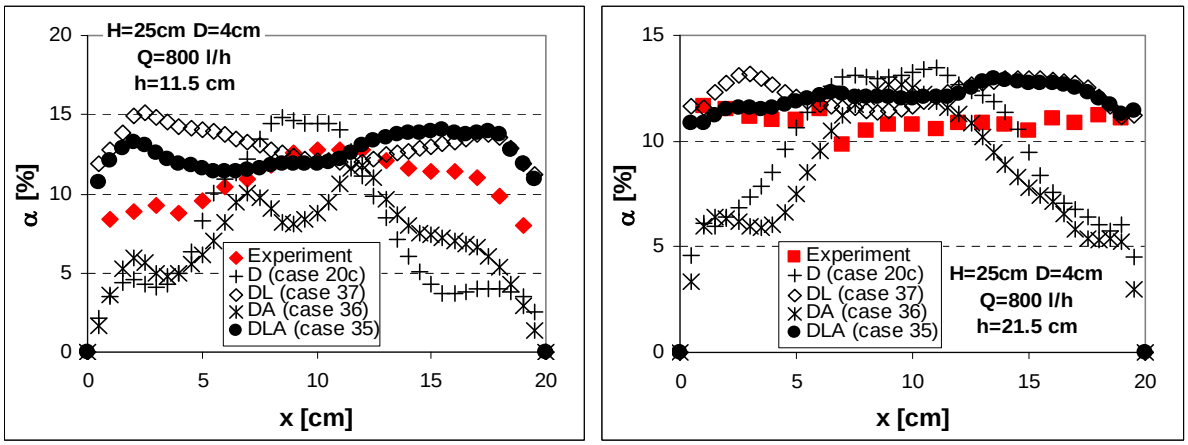

Fig. 3: Time-averaged gas holdup profiles (at h=11.5 and 21.5cm) obtained with different combinations of interphase forces (D-drag, L-lift, A-added mass), H=25cm, D=4cm, Q=800 l/h

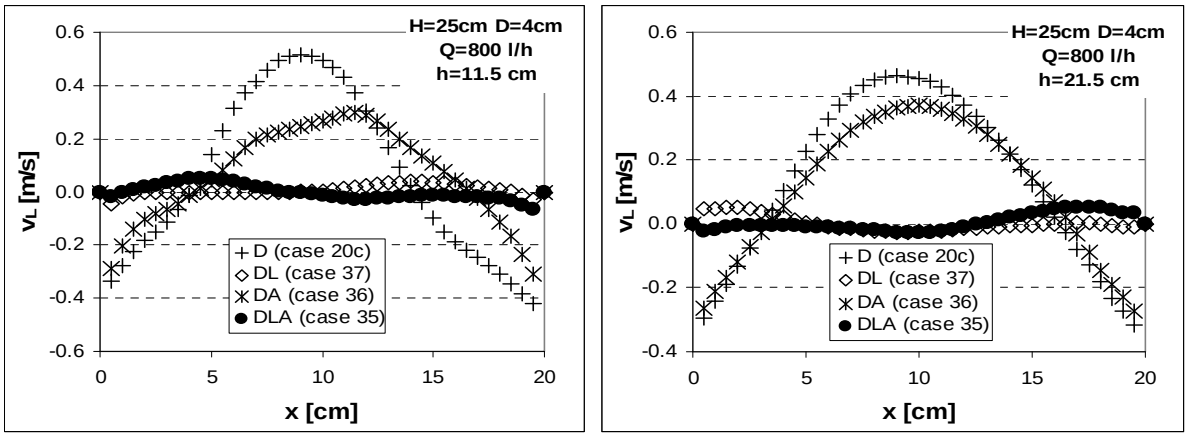

Fig. 4: Time-averaged profiles of vertical liquid velocity (at h=11.5 and 21.5cm) obtained with different combinations of interphase forces (D-drag, L-lift, A-added mass), H=25cm, D=4cm, Q=800 l/h

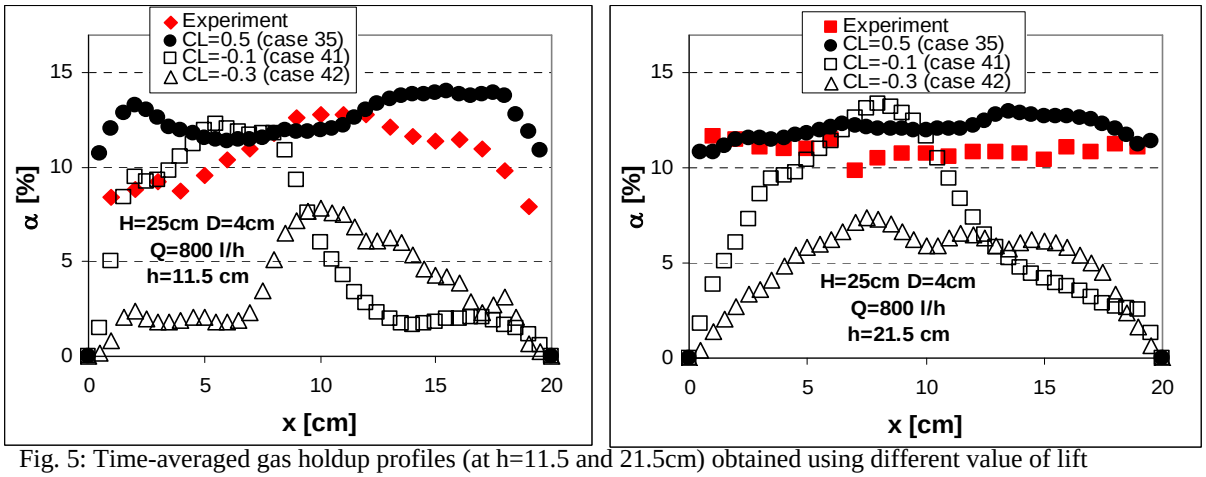

Fig. 5: Time-averaged gas holdup profiles (at h=11.5 and 21.5cm) obtained using different value of lift coefficient

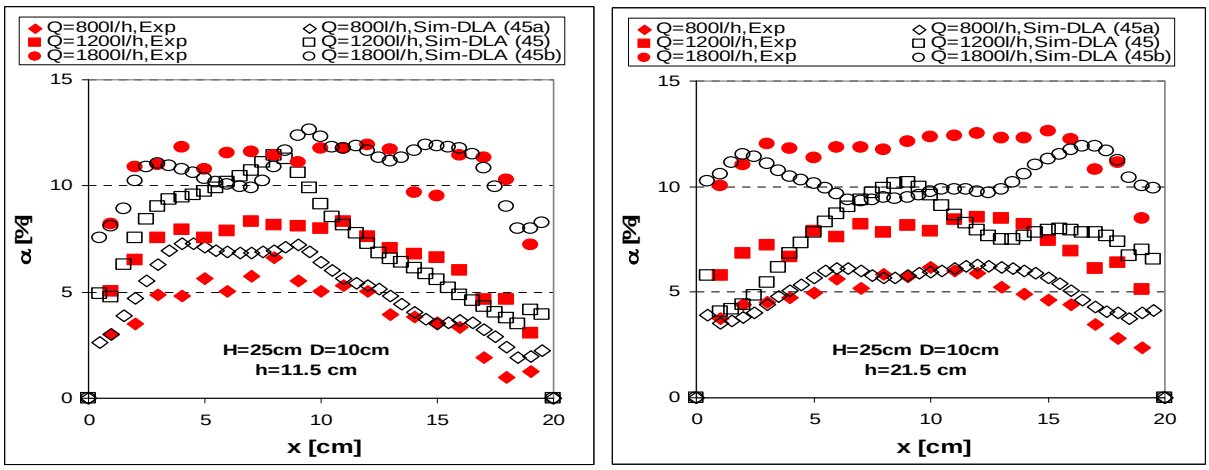

Fig. 6: Time averaged gas holdup profiles (at h=11.5 and 21.5cm): simulation vs. experiment (for different gas flow rates Q, drag, lift and added mass force included in simulations

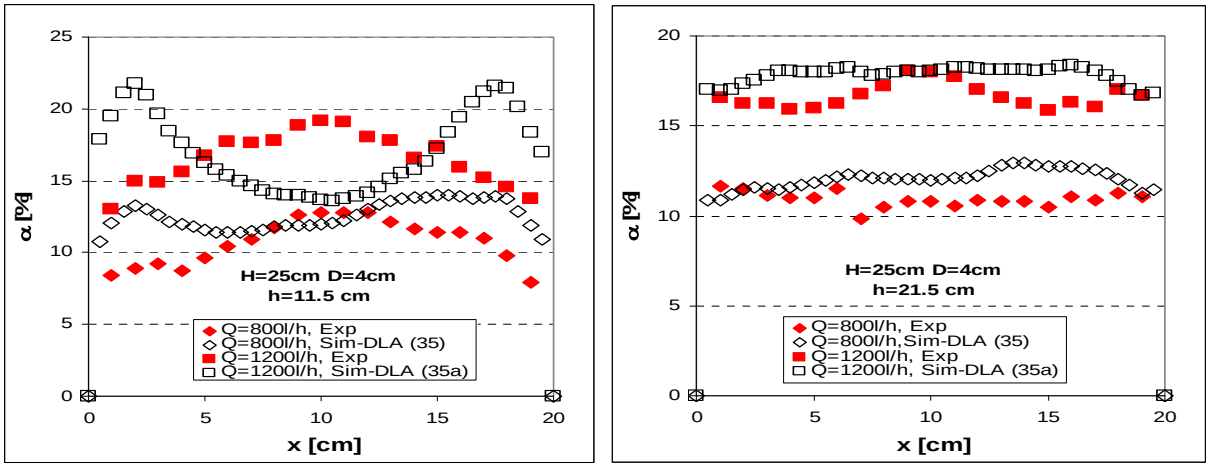

Fig. 7: Time averaged gas holdup profiles (at h=11.5 and 21.5cm): simulation vs. experiment (for different gas flow rates Q, drag, lift and added mass force included in simulations

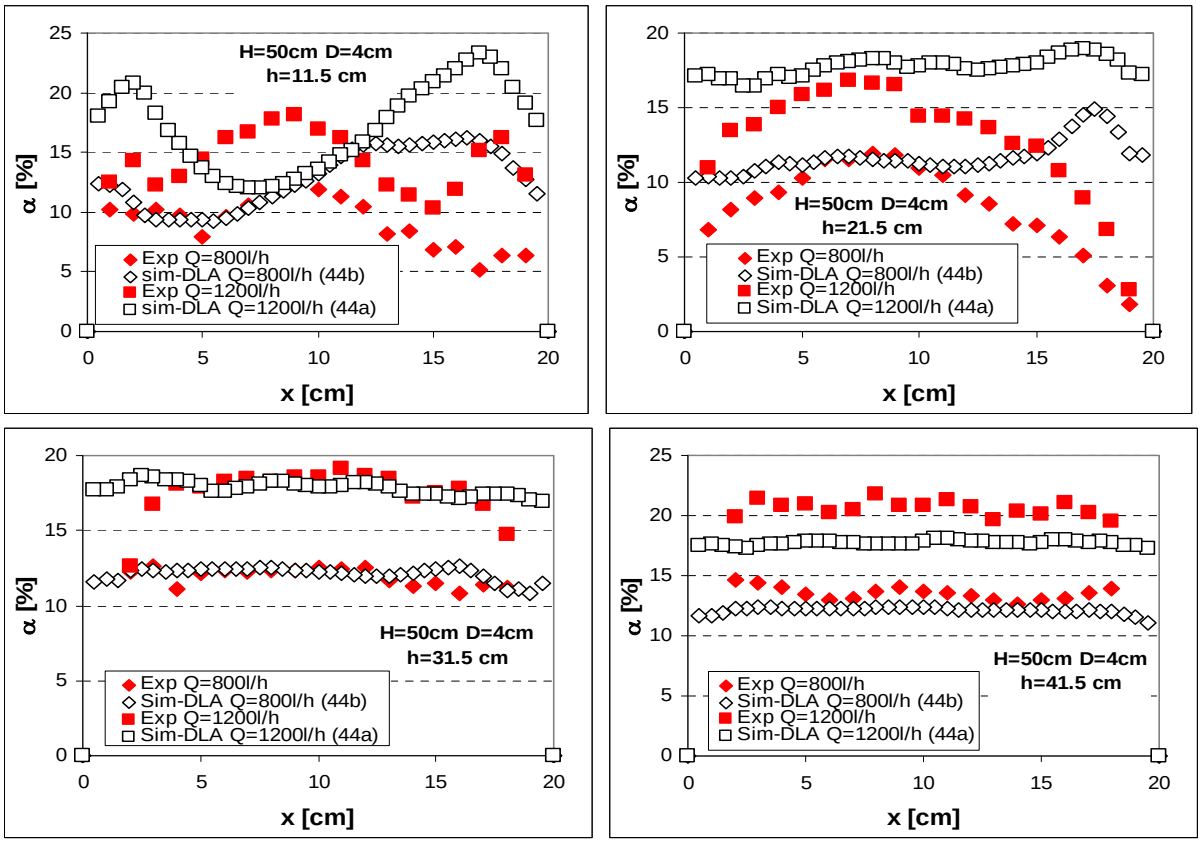

Fig. 8: Time averaged gas holdup profiles (at h=11.5-41.5cm): simulation vs. experiment (for different gas flow rates Q), “fine grid”, drag, lift and added mass forces included in simulations

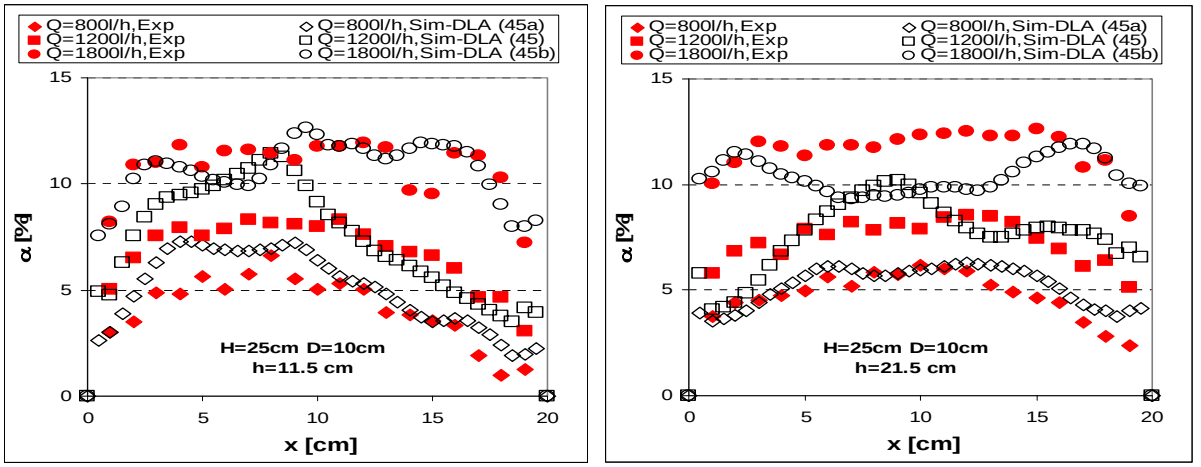

Fig. 9: Simulated (white marks) and experimental (red marks) holdup profiles at two heights h above gas distributor for air flow rates 800, 1200 and 1800l/h. Ungassed liquid level 25 cm, column thickness 10 cm.

Conclusions

Goal 1. The difference in gas holdup profiles calculated with and without the front-rear symmetry assumption was often larger than 20 %, thus the symmetry assumption is not recommended for column simulation even when the column thickness is only 4cm. Each of the simulations using different version of k-ε turbulence model predicted qualitatively different results – two different steady flow fields in the case of standard and realizable model, unsteady flow field in the case of RNG model. RNG k-ε model gave best agreement with experiments. Lift force (lift coefficient values) significantly influenced simulation output, influence of the added mass force was smaller.

Goal 2. Qualitative agreement between simulations and experiments was reached, when drag, lift and added mass force were accounted for.

Acknowledgements

Financial support of the research by GACR through contract No. GA104/07/1110 is gratefully acknowledged.

References

[1] Fluent 6.2 User's Guide, Fluent Inc.
[2] Ranade (2002). Computational Flow Modeling for Chemical Reactor Engineering. Academy Press.
[3] Jakobsen et al. (2005). Modeling of bubble column reactors: Progress and limitations. *Ind. Eng. Chem. Res.,* 44: 5107-5151
[4] Tomiyama et al., 1998, Bubble Tracking Method for the Prediction of Spatial Evolution of Bubble Flow in a Vertical Pipe. 3rd ICMF98, Lyon, France, Jun 8-12.

Proceedings of the 10th International Chemical and
Biological Engineering Conference - CHEMPOR 2008
Braga, Portugal, September 4-6, 2008
E.C. Ferreira and M. Mota (Eds.)

Healthcare Decision Support System

Conceição Granja[1, 2], Paulo Cruz[2], Adélio Mendes[1, *]
[1] LEPAE, Chemical Engineering Department, Faculty of Engineering, University of Porto
Rua Roberto Frias, 4200-465 Porto, Portugal
[2] Siemens S.A., Estrada Nacional 107, no 3570 Freixieiro
Apartado 5145, 4460-901 Perafita, Portugal

Keywords: Healthcare Management, Decision Support System, Job-Shop Scheduling
Topic: Systematic methods and tools for managing the complexity.

Abstract

In this paper a decision support system, based on a scheduling model, is presented. A case study is described based on an imaging clinic of a private hospital. The case study is discretized in a set of jobs J and resources R, based on Job-Shop Scheduling Problem (JSSP) methodology (Brucker, 2004). Jobs are composed of a sequence of tasks that follow precedence relations, according to the job requirements, which restrain some tasks to start until others are completed. It is considered that tasks cannot be interrupted (non-preemptive scheduling) and resources can perform more than one task simultaneously (cumulative scheduling). Furthermore, it is considered in this research that each task establishes restrictions in the resource allocation and may have to be processed in more than one resource, denoted as multiprocessor tasks. These restrictions impose limits in resources selection according to their capabilities (each resource may have more than one capability, denominated as multipurpose machines) and their use in the job (the selection of the resource may be limited to one that was used in a previous task). Additionally, the set of resources have elements that exhibit the same capabilities - machine repetition. Resources may also have different processing requirements for different tasks - multimode machine (Brucker and Knust, 2006). The selection of a resource may restrict the choice of another resource in the subsequent tasks. The objective of the developed model is to describe accurately a clinical workflow.

1 Introduction

In the last decades, the healthcare sector has experience substantial transformations. An unequivocal example is the increasing demand for healthcare services as a result of demographic growing. Other reasons for these transformations are the development of the technology applied to healthcare, patients' mobility and the increasing volume of clinical information. Combined, these factors impel the healthcare providers to diminish their costs and improve the quality, and the efficiency, of their services (Martins et al., 2007).

Mammography is a reference technique in breast cancer trace, analysis and definition of nodules and other breast lesions, as well as in the evaluation and foil of micro-calcifications (benign and malign). Comparatively to breast ultra sound, which does not allow the detection of breast micro-calcifications (although it may be complementary to mammography), mammography allows the detection of malign breast lesions with high sensitivity in a premature stage and a better definition of breast nodules also called infraclinic breast lesions (Kasper et al., 2005; Schwab, 2001). For these reasons, mammography departments evidence high workloads which allied to the clinic workflows stochastic nature, make these departments an evident case study.

An overview over clinical workflows leads to the choice of Job-Shop to deal with the scheduling in the healthcare environment. If patients are considered as jobs each patient has to follow a given path, and has to be treated at varied stations, to reach discharged, the job end. The case study is discretized in a set of jobs *J* and resources *R*, based on Job-Shop Scheduling Problem (JSSP) methodology

[*]Corresponding author. Tel. +351-22-508-1695. E-mail: mendes@fe.up.pt

(Brucker, 2004).

The JSSP generalizes the Flow-Shop Scheduling Problem. There are n jobs $J_j(j=1,\ldots,n)$ and m machines $\{M_1,...,M_m\}$. The job j is composed of n_j tasks $A_{j,i}(i=1,\ldots,n_j)$, linked by precedence constrains. Each task $A_{j,i}$ has a machine $\mu_{i,j} \in \{M_1,...,M_m\}$ and a processing time $p_{i,j}$ associated. The problem is to find a feasible schedule that fulfills some objective function. Only a few JSSP can be solved based on polynomials, or pseudo-polynomials time dependency, meaning that most of the JSSP are $\mathcal{NP}$-hard.

In this paper, a case study of a mammography department from a private imaging clinic is considered. The clinic is located in the north of Portugal but its name will not be mentioned due to ethical reasons.

2 Methodology

In this section, it is presented the methodology applied to the mammography department. All the information was gathered aiming the characterization of the mammography processes to simulate its operation with the developed algorithms. In this sense, all the activities associated to the exams were object of characterization according to:

- **Involved tasks identification** – name, time distribution need for accomplishment, operating mode and human, physical and technical resources required;
- **Resources characterization** (human, technical and physical) – competences/technical specifications, work load, availability, team working/technical interdependences;

To better understand the resources utilization at this department, it was investigated and characterized 1760 medical exams, which took place from January 2nd to April 27th of 2008.

The collected data evidences a characteristic pattern concerning the exams frequency by weekday, as seen in Figure 1.

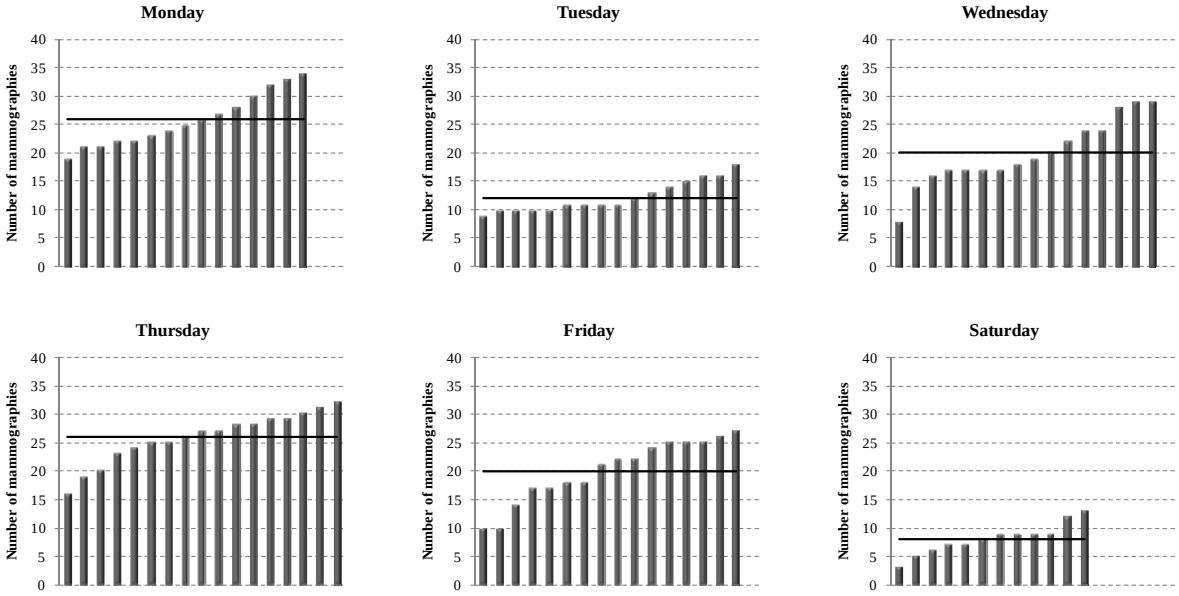

Figure 1: Workload histogram by weekday.

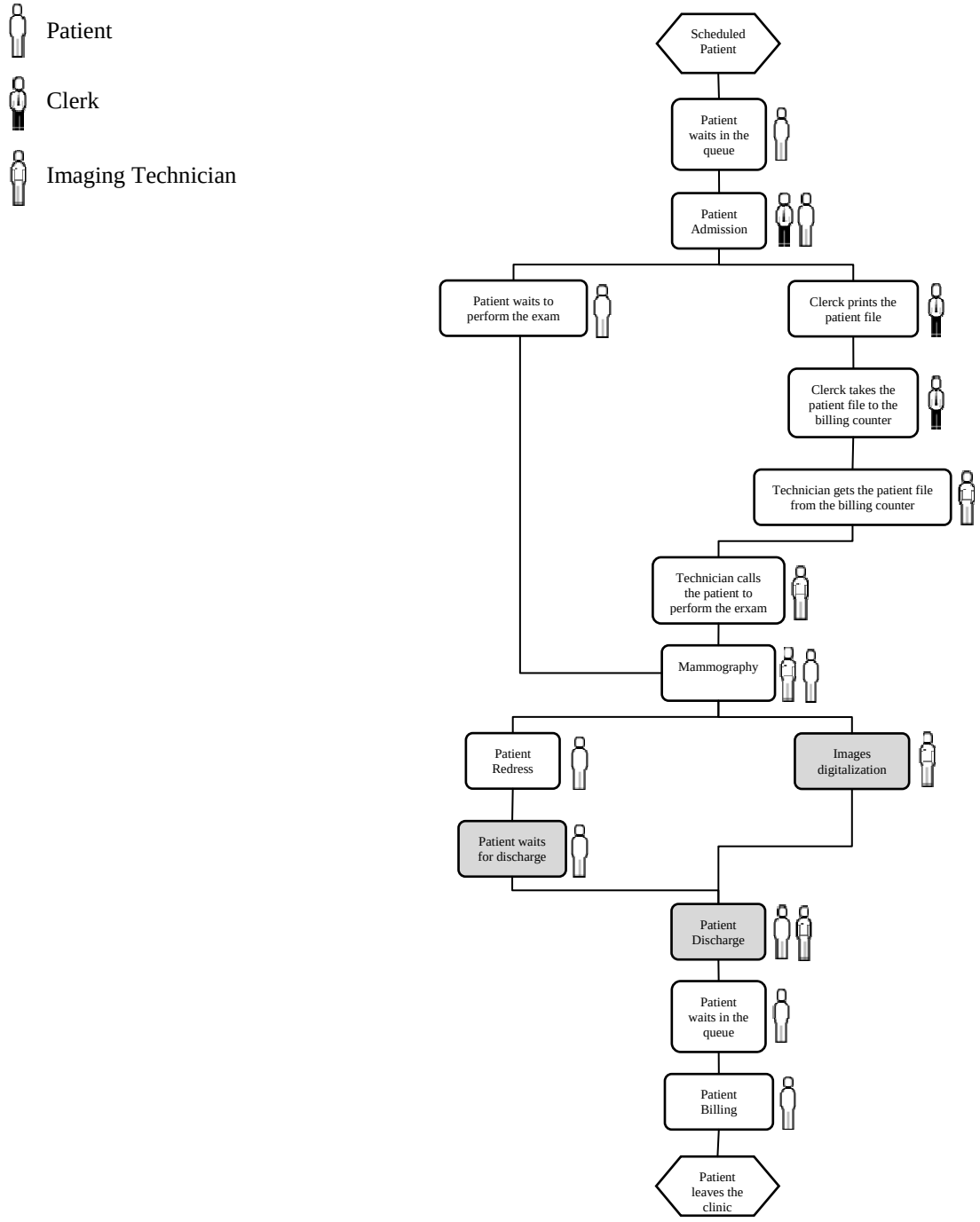

Figure 2: Mammography workflow in the case study Clinic.

Considering each activity as stand-alone processes, i.e. performed by the same resources (human, technical and physical) in the same time space, it was possible to model the department workflow, schematized in Figure 2. The data collected to define the activities time distribution was fitted to a Normal Distribution $X \sim N(\mu, \sigma^2)$, as presented in Figure 3.

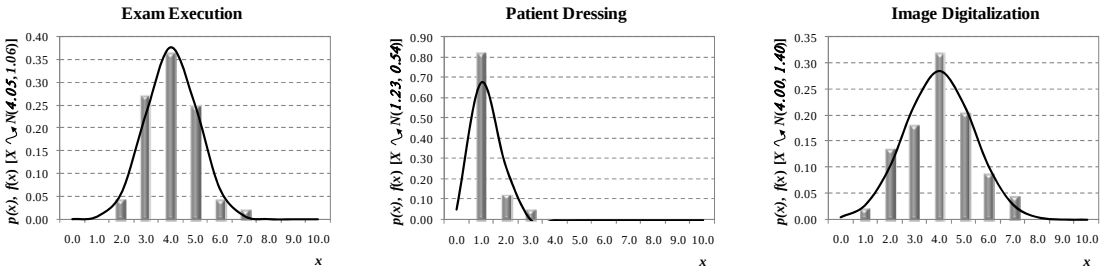

Figure 3: Sample approximation to a Normal Distribution $X \sim N(\mu, \sigma^2)$.

3 Results and Discussion

The developed algorithms were applied to the mammography department current workflow and to the workflow reengineered to embody a digital mammography system instead of an analog. Theoretically, when an analog system is replaced by a digital the activities represented with grey background in Figure 2, meaning that the completion time required to perform the exams should diminish and, because a patient waiting activity is removed from the workflow, their waiting time ought to be reduced as well.

Table 1 Simulation parameters and results, for the current workflow.

Week Day	Work Load	Total Completion Time, hh:mm:ss	Total Waiting Time, hh:mm:ss
Monday	26	04:25:42	01:50:09
Tuesday	12	02:06:33	00:52:35
Wednesday	20	03:18:27	01:41:19
Thursday	26	04:26:09	01:28:17
Friday	20	03:29:07	01:33:04
Saturday	8	01:28:14	00:28:15

The simulation parameters are based in the data collect in the department. The workload simulated was defined from the real workload average, with the intention that the simulation runs represent a typical workweek of the department. According to Figure 1, the simulation parameters were defined as presented in Table 1.

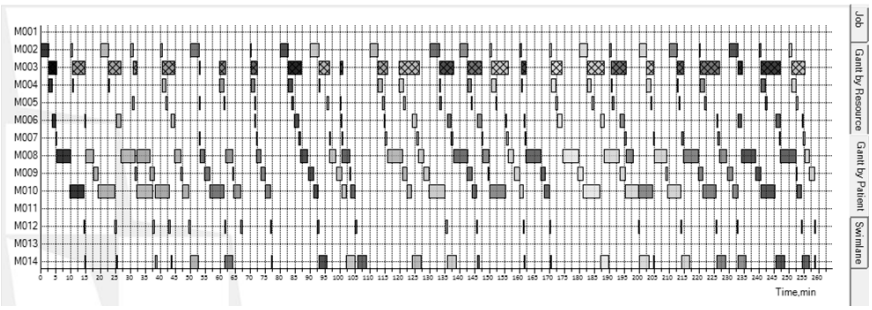

Figure 4: Graphical output of simulation results: Gantt chart by process.

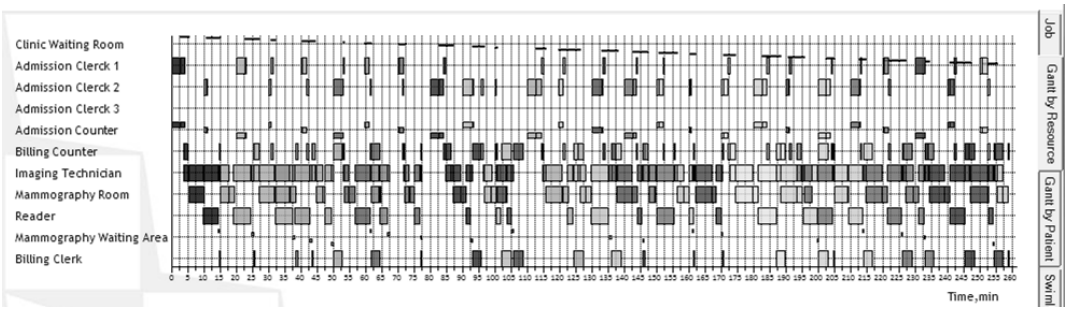

Figure 5: Graphical output of simulation results: Gantt chart by resource.

As expected, the total completion time presented values in the three to the four hours range, which is in agreement with the experimental data, as the technician eight hours of work are shared by the mammography and the densitometry departments. The waiting times were expected to show high values because the patient has to wait while the images are digitalized, activity that lasts approximately the same time as the mammography exam. This fact was confirmed by the simulation results shown in Table 1. In Figure 5 and Figure 5 are presented the Gantt charts originated by the developed simulation system. These charts exhibit the activities' time distribution and the resources utilization, respectively.

The simulation runs performed with the reengineered workflow, are given in Table 2. According with these results, the implementation of a digital mammography system allows average gains, in the total completion time, of 35 % (week based), being the maximum achieve on Saturdays with 41 % and the minimum on Wednesdays with 30 %.The major gains in the total waiting time of the patients are achieved on Wednesday, with 56 %. Saturday is the day of the week when the gains concerning the waiting time are less significant, 25 %. This is due to a higher availability of the resources as a result of the low workload evidenced by the department. In average, the gains in the total waiting time are of 43 %.

Table 2 Simulation parameters and results, for the reengineered workflow.

Week Day	Work Load	Total Completion Time, hh:mm:ss	Total Waiting Time, hh:mm:ss
Monday	26	02:58:35	00:59:14
Tuesday	12	01:20:47	00:24:50
Wednesday	20	02:17:42	00:43:51
Thursday	26	02:57:56	00:52:47
Friday	20	02:16:24	00:55:48
Saturday	8	00:51:53	00:21:17

4 Conclusions

The developed algorithm associated with the modeling strategy evidenced a high accuracy simulating clinical workflows. The model allowed the evaluation that modifications in the workflow and existing resources have in the process productivity and quality, taking the total completion time and total waiting time as metric, respectively. Therefore, it reveled to be a powerful decision support tool for healthcare management.

References

Brucker, P. (2004). *Scheduling Algorithms*, Springer-Verlag Berlin Heidelberg, New York.

Brucker, P., Knust, S. (2006). *Complex Scheduling*, Springer-Verlag Berlin Heidelberg, New York.

Kasper, D.L., Braunwald, E., Fauci, A.S., Hauser, S., Longo, D.L., Jameson, J.L. (2005). *Harrison's Principles Of Internal Medicine*, McGraw-Hill, New York.

Martins, J., Granja, C., Mendes, A., Cruz, P. (2007). Gestão do fluxo de trabalho em diagnóstico por imagem: Escalonamento baseado em simulação. *Informática de saúde – boas práticas e novas perspectivas*, 85-96.

Schwab, M. (2001). *Encyclopedic Reference of Cancer*, Springer-Verlag Berlin Heidelberg, Italy.

Proceedings of the 10th International Chemical and
Biological Engineering Conference - CHEMPOR 2008
Braga, Portugal, September 4-6, 2008
E.C. Ferreira and M. Mota (Eds.)

Optimization of hydroxyapatite synthesis

João F. P. Gomes[1,2*], Cristina C. Granadeiro[1], Miguel A. Silva[1], Milton Hoyos[1], Rodrigo D. Silva[1], Filipe Antunes[1], José E. Amaral[1*], Teresa Vieira[3]

[1] ISEL – Instituto Superior de Engenharia de Lisboa, Chemical Engineering Department. R. Conselheiro Emídio Navarro 1, 1959 – 007 Lisboa, Portugal

[2] IST – Instituto Superior Técnico, CEBQ/IBB, Av. Rovisco Pais, 1049-001 Lisboa, Portugal

[3] IPN – Instituto Pedro Nunes, R. Pedro Nunes, 3030-199 Coimbra, Portugal

Keywords: Optimization, Hydroxyapatite, Chemical Reaction
Topic: Sustainable process-product development through green chemistry

Abstract

Hydroxyapatite (HAP) is one of the inorganic components of the hard tissues of living bodies such as bones and teeth. HAP is a calcium phosphate based bio-ceramic, which has been used for several years in medicine and dentistry because of its excellent biocompatibility with human tissues. The success of its application in these fields depends upon factors such as the composition, crystallinity, size and morphology of HAP particles. This paper describes work performed regarding the synthesis of this compound by a wet method comprising the direct precipitation of orthophosphoric acid solution and a calcium hydroxide solution. The synthesis was performed in a laboratory reactor, 700 mL in capacity, instrumented and controlled using a computer interface, so that the influence on process variables could be assessed. The influence of these parameters was, therefore, evaluated in terms of the required composition and morphology of HAP formed particles, analysing them by FTIR, XRD, SEM and EPMA for determination of the Ca/P ratio. From the obtained results, it can be concluded that HAP particles having suitable properties for use in medicine, could effectively be prepared by this technique, provided that a good control of the involved process variables is maintained.

1 Introduction

Hydroxyapatite (HAP) is described as $Ca_{10}(PO_4)_6(OH)_2$ and was identified as the mineral component of bone and teeth. Being a bioactive mineral it has a crystalline structure similar to the existing minerals in bones which makes its synthesis process particularly interesting [1]. Synthetic HAP precursors can be obtained by several processing routes, such as precipitation, sol-gel or hydrothermal. Some of these techniques do not allow a rigorous process control which can result in obtaining different HAP structures other than those occurring in human body [7]. The aqueous precipitation synthesis of HAP is based on the reaction of calcium hydroxide and ortophosphoric acid [5] - [9], as follows:

$$10Ca(OH)_2 + 6H_3PO_4 \rightarrow Ca_{10}(PO_4)_6(OH)_2 + 18H_2O$$

It is important to maintain the correct molar proportion between calcium and phosphorus, the theoretical value being Ca/P=1.67 [7]. Any changes occurring in the reaction environment, as well as in the rate of drying of the obtained final precipitate will result in changes both in shape and in the size distribution of particulate. Aqueous precipitation is the most common technique for obtaining powder HAP. However, this technique requires a rigorous control of the Ca/P ratio [10]. This was the production reaction selected in this study because of its versatility, ease of implementation and acceptable production costs [11-13]. Apart from that, this method can be possibly scaled-up to the industrial production of HAP, as it can provide the desired stoichiometric composition, as the reaction does not involves other reactants apart from

the ones entering the main reaction and the only by-product is water [7].

2. Experimental

The studied precipitation process uses powdered calcium hydroxide for preparing a aqueous suspension of calcium hydroxide 0.5M. The suspension was then stirred, deaerated with nitrogen and pre-heated in a glass reactor 700 mL in capacity at several test temperatures (20ºC, 40ºC, 60ºC and 80ºC) during 1h, before the acid addition. The orthophosphoric acid solution, 0.3M, was also deaerated with nitrogen and feed into the reactor by means of a peristaltic pump, at a constant rate. The pH control was performed by adding small portions of a NH_4OH solution during the precipitation process. The obtained gel precipitate is then left to rest overnight and is decanted and washed afterwards using distilled water and small portions of a 1mmol solution of orthophosphoric acid, in order to remove the unreacted Ca^{2+} ions, without interfering in the HAP structure. The obtained precipitates are then dried overnight in a oven at 80ºC. In order to evaluate the thermal stability of the obtained HAP powder, they are sinterized afterwards during 1h in a oven at temperatures ranging from 500 to 800ºC. This study also comprised the evaluation of the effects of inert atmosphere, reaction pH media, stirring rate and addition flow rate of acid on the quality of obtained HAP. Regarding product characterisation, the size distribution of synthesised HAP particulate was determined by SEM, JEOL-JSM 5310, using an acceleration voltage of 30kV. The HAP samples were dissolved in water and ethanol and observed at 75x and 1500x magnifications. The HAP samples were also analysed by FTIR, using a Nicolet Impact 400D and by X-ray diffraction, PHILIPS, X'PERT, using Bragg-Brentano geometry, a cobalt anti-cathode at 0.17886nm. The latter analysis were performed in the range 2θ=10-100º, with a rate of 0.025º and an acquisition time of 0.5s/°. The observed phases were indexed by comparison with the distances indicated in the ICDD (International Centre for Diffraction Data) guidelines. This technique allowed for the determination of the crystallite sizes, by calculating the width at half height of the HAP peak of higher intensity, using Scherrer formula after adjustment by a Voigt curve.

3. Results and discussion

The analysis of the IR spectra of the synthesized HAP precipitates showed that all obtained samples are indeed HAP as all exhibits the characteristic peaks in accordance with the theoretical spectra described in the literature [15, 16]. The characteristic detected peaks are: 565-603cm^{-1} and 1035-1093cm^{-1} for the PO_4^{3-}group; 1420-1457cm^{-1} for the CO_3^{2-} group and 3571cm^{-1} for the OH^- group. As a whole, the obtained spectra are quite similar, but some differences exist that can be attributed to changes in operational reaction conditions such as the degree of inert atmosphere and sintering temperature of the HAP precipitates. In fact, a decrease of the intensity of the characteristic peaks for the carbonate group can be observed when the reaction atmosphere is inertized with nitrogen (as well as the deaeration of the used solution is also made) as can be noticed in figures 1a) and 1b) where the peaks at 1419, 1470 and 1637 cm^{-1} are somewhat smaller. Figures 1b), 1c) and 3d) show that, increasing the HAP sintering temperature results in the intensity decrease, and even in the disappearance of the peak characteristic for water (2001cm^{-1}), as the water is suppressed during the sintering process. The same figures show that a decrease in the intensity of the peak characteristic for the carbonate group is also observed with the increase of the HAP sintering temperature, as this temperature increase results in the degradation of any carbonates. This is also related with the decrease of water in the structure as carbonate groups present in the samples are mainly present in aqueous solution. Micrographs obtained by SEM analysis of the HAP precipitates are shown in Figure 2. Regarding HAP morphology, this compound can exist in the acicular or spheroid form [7, 9]. In this particular study it was not possible to determine the exact shape as the particles were strongly agglomerated. Therefore, it was only possible to ascertain the shape of the agglomerates. The HAP crystallites have the tendency to

form agglomerates [17], the global dimensions are in the range of 200 to 400nm, and then the average size of the crystallites is estimated to be in the range of 15-50nm [18]. The obtained X-ray difractograms of the HAP samples are shown in Figure 3. When heated at 500ºC (samples 23 E-H) and at 800ºC (samples 23 I-L), a crystallinity increase occurs when compared with the samples heated at 80ºC (samples 23 A-D). As reported by De-Aza et al. [19], the increase in crystallinity is also shown by the increase of peak intensity and varies directly with temperature increases. Also, as temperature increases, overlapping between peaks occurs, and this is due to the fact that these samples are formed by smaller crystallites. Measured X-ray diffraction data allowed for the determination of crystallite sizes in the range of 18 to 26 nm. SEM analysis of those samples, as shown in Figures 2a and 2b, leads to the conclusion that the first one has a bigger size as bigger crystallites form smaller agglomerates. Thus, the compound present in all samples analysed by X-ray diffraction is HAP ($Ca_5(PO_4)_3(OH)$, and the obtained difractograms do not show significant differences between them. However, samples which were submitted to sintering at a temperature of 800ºC, show a secondary phase of whitlockite ($Ca_3(PO_4)_2$). Apart from this, HAP peaks are much more defined, which is probably due to an increase of size. As previously mentioned, the Ca/P ratio for HAP samples is a basic parameter in what concerns its properties and thermal stability. The obtained results show clearly that the obtained Ca/P ratio is in accordance with the theoretical stoichiometric value of 1.67, as only the HAP phase was formed. Along with the temperature increase, Ca^{2+} is released from HAP structure which leads to the formation of CaO. In this case, the HAP structure is deficient in terms of Ca^{2+} and the Ca/P ratio changes to the characteristic value for whitlockite [15]. It was also noticed that, sample washing does not originate significant differences in the X-ray difractograms, as shown in Figure 3 and in Table 1. The weight loss occurring during temperature increase was also studied by performing thermogravimetric analysis of the HAP samples at sintering temperatures of 80, 500 and 800ºC. In a first stage, until T=80ºC, a weight loss of about 43% takes place, which is due to the evaporation of water trapped within the HAP structure. In a second stage, taking place between 80 and 500ºC, the weight loss is of about 64%, which is now due to dehydroxilation (loss of OH groups) accompanied by calcium carbonate formation. In the temperature range of 500 to 800ºC, the observed weight loss if only of 5%, and can now be attributed to $CaCO_3$ decomposition and release of CO_2 [5]. All samples showed similar variations to the ones described. This behaviour is in accordance with the IR analysis where a decrease of the intensity of the peak characteristic for water and carbonates could be noticed.

Table 1 – Treatment temperature and washing

Sample	T (ºC)	Washing
23A	80	No washing
23B	80	2x H_3PO_4
23C	80	H_2O
23D	80	1x H_3PO_4
23E	500	No washing
23F	500	2x H_3PO_4
23G	500	H_2O
23H	500	1x H_3PO_4
23I	800	No washing
23J	800	2x H_3PO_4
23K	800	H_2O
23L	800	1x H_3PO_4

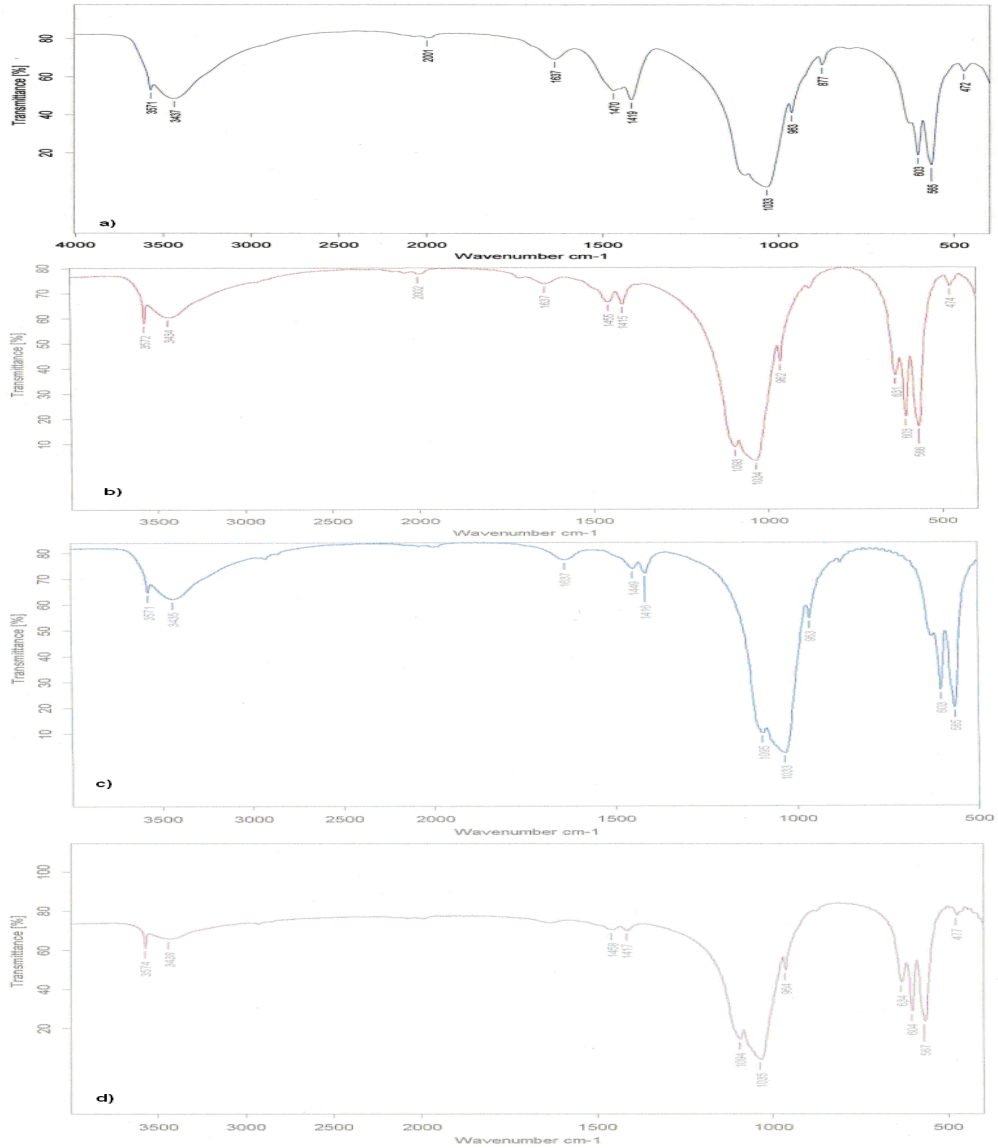

Figure 1 – IR spectra: a) Air and sintering at 500ºC; b) Nitrogen and sintering at 80ºC; c) Nitrogen and sintering at 500ºC; d) Nitrogen and sintering at 800ºC.

a)

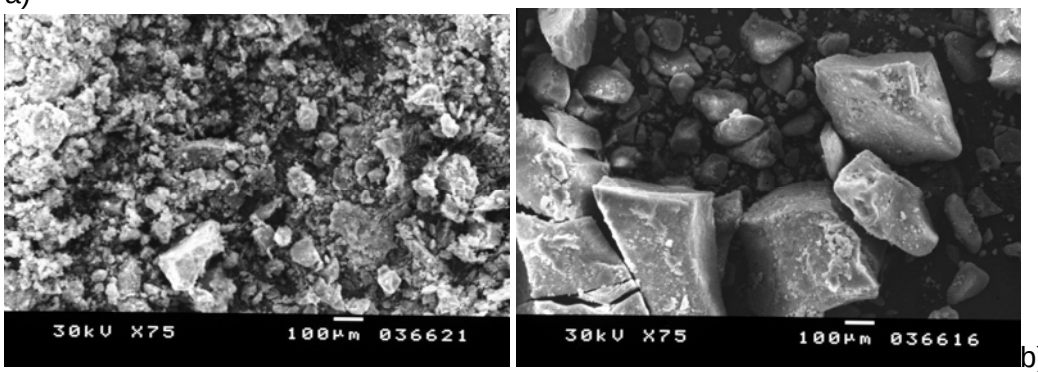

b)

c) 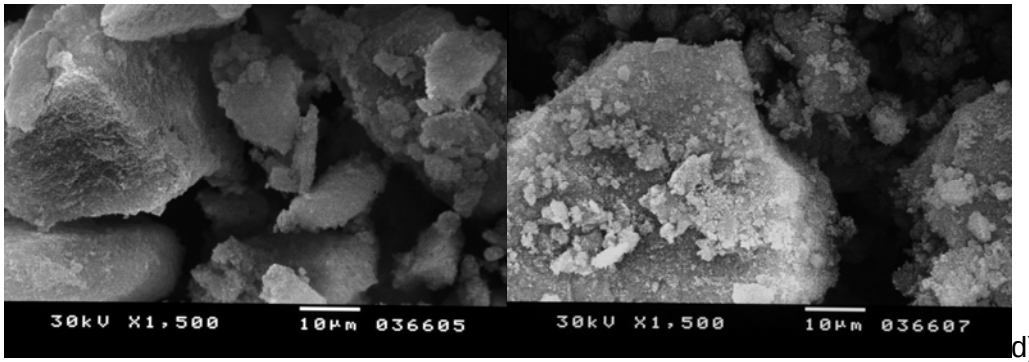

d)

Figure 2 – HAP agglomerate micrographs obtained by SEM, magnifications 75x and 1500x a and c) T=80ºC; b) T=800ºC; d) T= 500ºC.

4 Conclusion

It was found that the main variable influencing the Ca/P ratio is the pH value, as described by Ranito e al. [11]. During this study, the reaction pH initiated at 12, for all tests, decaying slowly with the acid addition until the equivalence point is reached near the completion of the acid addition.

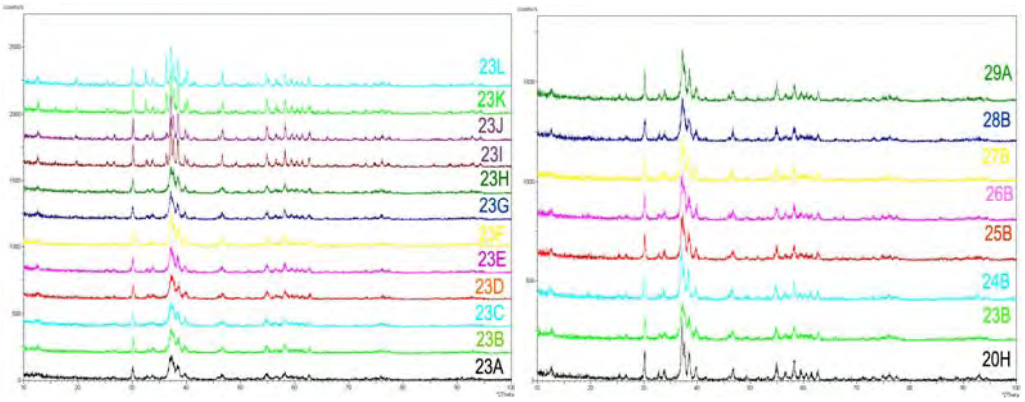

Figure 3 – X-ray difractograms.

Table 2 – T and pH values

Sample	Test T (ºC)	Treatment T (ºC)	pH
20H	80	500	5
23B	40	80	5
24B	40	80	7
25B	40	80	9
26B	40	80	11
27B	40	80	5
28B	40	80	5
29[a]	60	80	5

As it is important that the reactional mixture has the correct stoichiometric quantities, pH has to be controlled effectively, otherwise, at pH levels lower than 7, the formation of calcium monophosphate and dehydrated calcium, which are quite soluble in water medium, can take place [20,21]. Considering the obtained X ray diffraction spectra (Figure 3: samples 23B, 24B and 25B) it can be concluded that the optimum range for pH is from 7 to 9. Also, the analysis of difractograms (Figure 3: samples 28B and 29A) revealed a higher degree of crystallinity for the sample obtained at 60ºC, as indicated in Table 2. Also, the use of deionised water, instead of distilled water for preparation of reagents may lead to the need to use a higher temperature so that to promote the dissolved CO_2 removal. On the other hand, a very high temperature will lead to dehydroxilation and will also increase the energy consumption. The optimal temperature was, then, determined to be 60ºC. Stirring should be mechanical and vigorous in order to promote an homogenous HAP precipitate. An insufficient stirring may allow the formation of monetite and brushite [20,22]. Apart from that, an adequate stirring will contribute to a better pH control of the reactional mixture and promotes a better interaction of the reagents. In the performed tests, the optimal stirring velocity was of 150 r.p.m. At this velocity it is possible to visualise the phase separation involved in precipitate formation. Regarding the acid addition flow rate, the obtained difractograms do not allow to derive further conclusions, but it is expected that lower addition flowrates will lead to bigger crystallites as referred by Saeri et al. [9]. HAP exhibits susceptibility to the substitution of CO_2 in its crystalline structure, as CO_3^{2-} ions could substitute the hydroxyl or phosphate groups, originating then the formation of carbonated HAP [7]. The presence of carbonate ions in the HAP structure diminishes its thermal stability. Thus, in order to avoid this problem, an effective inertization (for instance, using nitrogen) of the reactional medium and reagent used is needed. This effect can be observed in the obtained IV spectra, shown in Figure 1, where a diminishing of peak intensity corresponding to CO_3^{2-}can be noticed. X ray diffraction showed that an increased sintering temperature results in a slight increase of particle size and, therefore, to the formation of crystallites. This could be due to the decrease of CO_3^{2-} ions in the HAP structure and, therefore, to an increased stability. At 800ºC, carbonated HAP experience a significant decomposition [23], and when calcination temperatures are higher than 800º C, the release of Ca^{2+} takes place, thus resulting in CaO oxidation [11], which in turn forms whitlockite, as a secondary phase calcium deficient in the HAP structure. Comparing X-ray analysis with IV spectra it was concluded that the optimal sintering temperature is 500ºC, showed by diminishing the intensity of the peak characteristic for the carbonate group and thus the presence of the HAP monophase. X-ray diffraction allowed to determine the crystallite size in the range of 18 to 26 nm, as well as the occurrence of HAP monophase until a temperature of 500ºC, and additionally a secondary whitlockite phase at 800ºC. The IV spectra of the obtained precipitates showed that all of them are, indeed, HAP; while SEM analysis allowed to identify two types of agglomerates of different sizes. The global conclusion is that the synthesized HAP nanoparticles are structurally identical to biological apatites, which makes the development of this process at an industrial scale very attractive within the scope of bone tissue engineering.

References

Doraiswami, L.K., Sharma, M.M. (1984). *Heterogeneous Reactions: Analysis, Examples and Reactor Design*, Volume 2, Wiley, New York.

Wang, J., Han, S., Wei, F., Yu, Z., Jin, Y. (1997). An axial dispersion model for gas-liquid reactors based on penetration theory. *Chemical Engineering and Processing,* 36, 291-299.

[1] C.M.S Ranito, F.A. Costa Oliveira, J.P. Borges, *Materials Science Fórum.* **514-516** (2006) 1083-1086

[2] M.I. Kay, R.A. Young, A.S. Posner: *Nature*, **204** (1964) 1050

[3] J.C. Elliot, P.E. Mackie, R.A. Young: *Science*, **180** (1973) 1055

[4] T.S.B. Narasaraju, D.E. Phebe: *J. Mat. Sc.* **31** (1996) 1

[5] G.G. Vásquez, C.P. Barba, N. Munguía,: Revista Mexicana de Física, **51(3)** 284-293

[6] Silva, Marcelo H. Prado da; *Apostila de Biomateriais*, CERAMED 2007
[7] A. Afshar, M.R. Saeri, M. Ghorbani, N. Ehsani, C.C. Sorrell,: *Materials & Design*, (2003) 197-202
[8] R.R. Ramachandra, H.N. Roopa, T.S. Kannan, *J. Mater Sci. Mater. Med.* **8** (1997) 511
[9] M. R. Saeri, A. Afshar, M. Ghorbani, N. Ehsani, C. C. Sorrell,: *Materials Letters*, **57** (2003) 4064-4069
[10] N.Y. Mostafa,: *Materials Chemistry and Physics* **94** (2005) 333-341
[11] C.M.S Ranito, C.A. Nogueira, J. Domingues, F. Pedrosa, F.A. Costa Oliveira, J.P. Borges,: *Materials Science Forum*, **514-516** (2006) 1025-1028
[12] S. Raynaud, E. Champion, D. Bernache-Assollant, P. Thomas: *Biomaterials*, **23** (2002), 1065
[13] S. Kwon, Y. Jun, S. Hong, H. Kim: *J. Europ. Ceram. Soc*. **23** (2003), 1039
[14] M.S. Tung, "Calcium phosphate type standard reference material: development, preparation, and characterization", in: E. Horowtiz, J.E. Parr (Eds.), Characterization and Performance of Calcium Phosphate Coatings for Implants, ASTM STP1196, American Society for Testing Materials, Philadelphia; 1994, 99
[15] Ratner, Buddy D.; Hoffman, Allan S.; Schoen, Frederick J. Lemons, Jack E.; *Biomaterials Science- An Introduction to Materials in Medicine*, Elsevier 2nd Ed, London, 2004
[16] C.M.S. Ranito, F.A. Costa Oliveira, J. P. Borges,: *Key Engineering Materials*, **284-286** (2005), 341-344
[17] G. Bazzi, G. Celotti, E. Landi, T.M.G. La Torreta, I. Sopyan, A. Tampieri,: *Materials Chemistry and Physics*, **78** (2003) 816-824
[18] V.M. Rusu, C.H. Ng, M.W. Wilke, B. Tiersch, P. Fratzl, M.G. Peter,: *Biomaterials*, **26** (2005) 5414-5426
[19] A.D. Randolph, M.A. Larson, "Theory of Particulate Processes", 2nd Ed., Academic Press, NY, 1986
[20] P.N. de-Aza, C. Santos, A. Pazo, S. de Aza, R. Cusco, L. Artus: *Chem. Mater*. **9** (1997) 915
[21] C.C. Berndt, G.N. Haddad, A.J.D. Farmer, K.A. Gross: *Mater Forum*, **14(3)** (1990) 161–173
[21] A.J. Ruys, K.A. Ziegler, O.C. Standard, A. Branwood, B.K. Milthope, C.C. Sorrell, "Hydroxyapatite-ceramicmetal Composites; Quantification of Additive-induced Dehydration": Bannister MJ, editor, Proceeding of the International Ceramic Conference, Vol. **1**, Melbourne: CSIRO 1992, 591–97
[22] Conn J.F., Jessen L.A., "Process for predicting Hydroxyapatite", US Patent 4324772, 1980.
[23] A. Slósarczyk, Z. Paszkiewicz, C. Paluszkiewicsz, , *Journal of Molecular Structure*, **744(7)** (2005) 657-661

Proceedings of the 10th International Chemical and
Biological Engineering Conference - CHEMPOR 2008
Braga, Portugal, September 4-6, 2008
E.C. Ferreira and M. Mota (Eds.)

Metallocene Immobilized within Silica by a Sol-Gel Method: Investigation of the Support Structure

Adriano G. Fisch[1], Nilo S.M. Cardozo[1], Argimiro R. Secchi[1], Nadya P. da Silveira[2], João H.Z. dos Santos[2*]

[1] Chemical Engineering Department, Universidade Federal do Rio Grande do Sul, 92010-010 Porto Alegre, Brazil.

[2] Chemistry Institute, Universidade Federal do Rio Grande do Sul, 92010-010 Porto Alegre, Brazil.

Keywords: metallocene; sol-gel method; SAXS; polymerization; polyethylene
Topic: Multi-scale and/or multi-disciplinary approach to process-product innovation.

Abstract

A series of homogeneous metallocenes (Cp_2ZrCl_2, (^{n}BuCp)$_2ZrCl_2$, (^{i}BuCp)$_2ZrCl_2$, (^{t}BuCp)$_2ZrCl_2$, Cp_2TiCl_2, Cp_2HfCl_2, $EtInd_2ZrCl_2$ and $Et(IndH_4)_2ZrCl_2$) was immobilized within silica matrix concomitantly with its preparation using a non-hydrolytic sol-gel method. Resulting catalysts were characterized by Small Angle X-ray Scattering (SAXS) and nitrogen adsorption. The results show that the silica particle was formed by the aggregation of primary structures having a diameter of about 160 Å. This result suggests that the metallocene is surrounded by primary particles deep inside the silica matrix. The low polymer productivity exhibited by the less active metallocene could be related to the problems of particle fragmentation due to monomer mass transfer limitations along the partially fragmented particle, which would subsequently affect catalytic activity. In order to overcome this problem the metallocene content in the silica should be increased.

1 Introduction

The performance of a supported metallocene might change due to the electronic and steric effects from the carrier. Most of the supported metallocenes exhibit lower catalytic activities and lead to different polymer properties in comparison with the equivalent unsupported complexes (Severn et al., 2005). Despite the fact that the carrier might result in some negative effect on the performance of the metallocene (e.g. lower catalytic activity), it is worth noting that some of the outcomes are desirable including the reduction in the quantity of methylaluminoxane (MAO) used for the catalyst activation. Because of these considerations, the choice of the support and the immobilization method play important role in the performance of the metallocene during the polymerization reaction.

In order to overcome some of the aforementioned problems arising from the metallocene immobilization, several methods have been proposed addressing the support methodology, new supports, or chemical treatments of the support (Severn et al., 2005). In a previous work, we have proposed the immobilization of zirconocenes into a silica matrix concomitantly with the oxide synthesis by a non-hydrolytic sol-gel method (Fisch et al., 2006). The resulting catalysts showed to be active for ethylene polymerization with similar activities to those found in Cp_2ZrCl_2 grafted on commercial SiO_2. As an extension of this previous study, the present work addresses the immobilization of different metallocenes within silica by the proposed method (Fisch et al., 2006) and the characterization of the resulting silica by Small Angle X-ray Scattering (SAXS) and N_2 adsorption (BET isotherm). In addition, the catalysts were evaluated in ethylene polymerization in an attempt to obtain some correlation with the silica structural parameters.

* Corresponding author. Tel + 55 51 3308-7238. E-mail: jhzds@iq.ufrgs.br

2 Materials and Methods

Catalysts synthesis

All chemicals were analytical reagent grade and the experiments were performed under inert atmosphere using the Schlenk technique. Heterogenization of the metallocenes was concomitantly performed on the silica synthesis and was carried out according to a non-hydrolytic sol-gel route based on the studies of Hay and Haval (1998) and Bourget et al. (1998). However, modifications were performed to avoid metallocene deactivation.

Scheme 1 shows the synthetic route used in this study. Zirconocene (ca. 0.10 g) was dissolved in toluene (1 cm^3), followed by the addition of $FeCl_3$ (0.02 g), $SiCl_4$ (2.5 cm^3), and 5 cm^3 of tetraethylorthosilicate (TEOS). The reaction was performed at 70 °C until gelation. Following, the resulting oxide was washed (20×2 cm^3) with a triethylaluminum (TEA) n-hexane solution (ca. 0.5 wt.%) at room temperature in order to eliminate residual ethoxide groups (dos Santos et al., 2001). The solid was further dried under vacuum for 12 h at room temperature and milled under inert atmosphere (argon) until reaching a diameter of 20-53 μm. A more detailed description of the synthesis methodology and the catalyst characterization can be found elsewhere (Fisch et al., 2006).

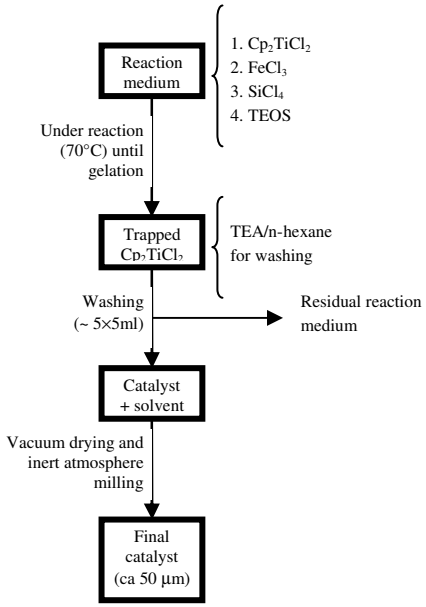

Scheme 1: Route for the catalyst synthesis

Catalyst characterization

Rutherford Backscattering Spectrometry (RBS) was used for evaluation of the Zr loadings (wt.-% Zr/SiO_2) in catalysts.

The Small Angle X-ray Scattering (SAXS) experiments were carried out using synchrotron radiation at LNLS (Campinas, Brazil) at wavelength λ= 1.488 nm. The beam was monochromatized by a silicon monochromator and collimated by a set of slits that define a pinhole geometry. A solid-stated CCD detector (MAR 160) was used to collect two-dimensional (2D) images with 2048×2048 pixels located at 6752.5 mm on the sample. The angular range of the scattering curves was 0.02 $Å^{-1} \leq q \leq 0.49$ $Å^{-1}$, where q is the scattering vector ($q = \frac{4\pi}{\lambda}\sin\left(\frac{\theta}{2}\right)$). The data were corrected for sample transmission and background scattering using an empty cell as reference. Samples were placed in stainless steel sample holders closed by two mica windows.

Morphological characterization of silica particles was performed by Nitrogen adsorption-desorption isotherms. Samples were previously degassed (10^{-2} mbar) at 85 °C for 10 h. Adsorption-desorption nitrogen isotherms were measured at -196 °C in a Gemini 2375 (Micromeritics). The specific surface area (SBET) was determined by the Brunauer-Emmett-

Teller equation (P/P0 = 0.05-0.35). The mesopore size and distribution were calculated by the Barrett-Joyner-Halenda (BJH method) using the Halsey standards. A desorption branch was used. Micropore volumes were calculated by the t-plot method, using the Harkins and Jura standard isotherm.

Scanning Electron Microscopy (SEM) was performed in a JSM 5800 (JEOL) microscope, operating between 10 and 20 kV. The samples were coated with a thin layer of sputtered conductive carbon.

Polymerization

Ethylene polymerization reactions were performed in 150 cm^3 of dried toluene in a 300 cm^3 Pyrex glass reactor connected to a constant temperature circulator and equipped with magnetic stirrer and inlets for Argon and the monomer. Methylaluminoxane (MAO) was used as the co-catalyst. For each experiment, a mass of catalyst system corresponding to 10^{-5} M of the metal was suspended in 5 cm^3 of dry toluene and transferred into the reactor under argon. The polymerizations were performed at 1.6 bar of absolute pressure of ethylene for 30 min at 60 °C. Acidified (HCl) ethanol was used to quench the process, and reaction products were separated by filtration, washed with distilled water, and finally dried under reduced pressure at 60°C overnight.

3 Results and Discussion

A typical SAXS profile found for the supported metallocenes is shown in Figure 1, in which two distinct regions are identified as follows: D_1 for $q<q_b$ and D_2 for $q>q_b$. A characteristic length (ξ) corresponding to the spatial scale of the primary particles was estimated as $\xi = 2\pi/q_b$.

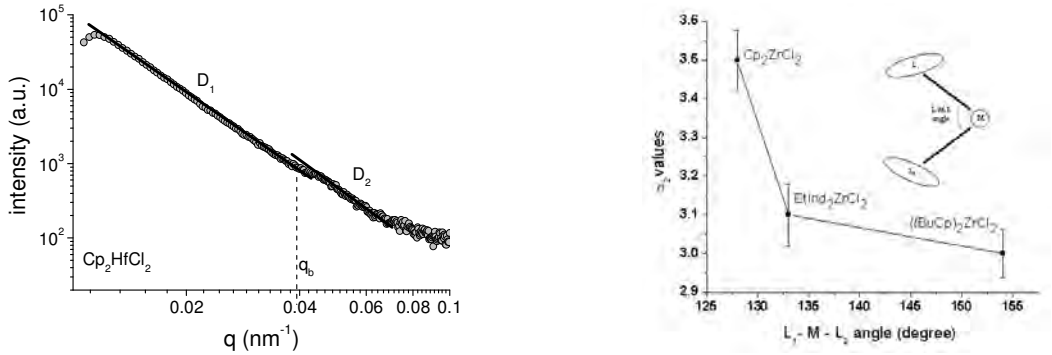

(a) (b)

Figure 1: Typical SAXS profile found for the synthesized catalysts (a) and relationship between fractal dimension and the metallocene bit angle (b).

The scattering intensity profile for $q<q_b$ shows characteristics of the particle with dimensions higher than ξ (D_1 region). Conversely, the characteristics of the particle with dimensions lower than ξ are found in the region of the scattering profile where $q>q_b$, which corresponds to the D_2 region. Therefore, information about the influence of the metallocene in the silica structure could be found in this region considering that the organometallic complex is trapped within the interstices formed by the primary particle agglomeration.

In these regions, the scattering intensity (I) is given by $I = A.q^{-\alpha}$ where the exponent α is usually related to a fractal dimension and the parameter A is a proportionality constant. As shown in Table 1, all α_1 values were found to be between 3.1 and 3.4, which represents the interval attributed to surface fractal structures (Hiemenz, 1997). Furthermore, no clear trend can be established between α_1 values and the metallocene structures. Conversely, α_2 values lie between 3.0 and 3.5, with the exception of $Et(IndH_4)_2ZrCl_2$. In addition, a correlation between α_2 values and the ligand-metal-ligand angle of the metallocenes, which describes a steric hindrance measurement of its structure (Cruz et al., 2004), was found as shown in

Figure 1b. Moreover, α_1 values did not show a clear correlation with the steric hindrance of the metallocene.

Table 1: Fractal dimension for catalysts prepared through concomitant metallocene immobilization with the silica synthesis and its performance in ethylene polymerization.

Entry	Catalyst	α_1	α_2	ξ (Å)	R_g (Å)	Metallocene content (wt.% M)	Activity (kg_{pol}/mol_M)[1]
1	Cp_2ZrCl_2/SiO_2	3.2	3.5	157	95	0.50 ± 0.048	2300
2	Cp_2TiCl_2/SiO_2	3.3	3.5	157	98	0.30 ± 0.0039	Traces
3	Cp_2HfCl_2/SiO_2	3.4	3.3	157	92	0.44 ± 0.0033	100
4	$EtInd_2ZrCl_2/SiO_2$	3.4	3.1	157	93	0.27 ± 0.0064	Traces
5	$Et(IndH_4)_2ZrCl_2/SiO_2$	3.1	2.1	153	96	0.27 ± 0.032	Traces
6	$(n\text{BuCp})_2ZrCl_2/SiO_2$	3.1	-	-	106	0.35 ± 0.017	3600
7	$(i\text{BuCp})_2ZrCl_2/SiO_2$	3.4	3.2	161	100	0.30 ± 0.011	Traces
8	$(t\text{BuCp})_2ZrCl_2/SiO_2$	3.1	3.0	157	98	0.19 ± 0.027	Traces
9	Cp_2ZrCl_2/SiO_2[2]	-	-	-	-	0.71 ± 0.058	200
10	Cp_2TiCl_2/SiO_2	-	-	-	-	1.36 ± 0.037	700
11	Cp_2HfCl_2/SiO_2	-	-	-	-	1.45 ± 0.042	1000
12	$EtInd_2ZrCl_2/SiO_2$	-	-	-	-	1.43 ± 0.065	800

1- Polymerization conditions: 1.6 bar of ethylene, Al(MAO)/M= 1000, 60°C, toluene, 30 min.
2- Catalyst particles with diameter 53-100 μm.
Activities of the homogeneous metallocenes under same polymerization conditions: Cp_2TiCl_2: 1150 kg_{pol}/mol_{Ti}; Cp_2HfCl_2: 1750 kg_{pol}/mol_{Hf} and $EtInd_2ZrCl_2$: 3000 kg_{pol}/mol_{Zr}.

The spatial scale of the primary particles, which was estimated by $\xi = 2\pi/q_b$, was found to be about 160 Å for all samples. Therefore, the influence of the metallocene behavior on the primary particle dimension (ξ) was not clearly observed.

It is possible to evaluate the radius of gyration (R_g) of the particles from the SAXS profile (Figure 1a) considering the Guinier regime and obeying the condition $qR_g << 1$, i.e., $q \rightarrow 0$. Table 1 shows that the R_g values are around 100 Å, which are comparable to the value found for the spatial scale of the primary particles ($\xi \approx 2R_g$= 200 Å).

The texture of the catalysts was also analyzed by N_2 adsorption as shown in Table 2. The resulting specific area seems to be dependent on the steric effect of the metallocene itself. On the other hand, the average pore diameter remained roughly constant.

Table 2: Specific area and average pore diameter of the supported catalysts.

Entry	Catalyst	Specific area ($m^2.g^{-1}$)	Pore diameter (Å)
1	Cp_2ZrCl_2/SiO_2	17 ± 0.040	30
2	Cp_2TiCl_2/SiO_2	29 ± 0.038	31
3	Cp_2HfCl_2/SiO_2	48 ± 0.046	26
4	$EtInd_2ZrCl_2/SiO_2$	170 ± 0.041	26

The catalysts characterization results show that the silica particle produced by a sol-gel method with the concomitant metallocene immobilization could be interpreted using the model of aggregation of the primary structures for the formation of the final silica particle structure (Kuramada et al., 1998; Boukari et al., 1997). Taking into account the presented results, the metallocene seems to be entrapped within the primary structures that form the oxide network, or in other words, the metallocene is surrounded by primary structures. In fact, the deeper location of the metallocene complex could cause quite a different performance for the catalysts.

The catalytic activity in the ethylene polymerization as well as the metallocene content (wt. % M, M= Zr, Ti or Hf) measured by RBS are shown in Table 1. Cp_2ZrCl_2, Cp_2HfCl_2 and $(^n\text{BuCp})_2ZrCl_2$ showed to be actives but, in general way, all catalysts showed poor catalytic activity. $(^n\text{BuCp})_2ZrCl_2$ exhibited a higher activity than Cp_2ZrCl_2, which follows the same trend observed in homogeneous polymerization. The electronic donation by the alkyl chain to the Cp ring, which in turn acts on the Zr center, renders the catalyst site less acidic and

increases the catalytic activity. In addition, no clear correlation between activity and fractal dimension was found.

To complement these results, Figure 2 shows SEM micrographs of the polymer obtained in the ethylene polymerization using catalysts with diameters between 53-100 μm (entry 9 in Table 1). The presence of spherical polymer particles can be observed on the residual non-fragmented catalyst. In this sense, it is possible to observe the importance of catalyst breakup with respect to its activity.

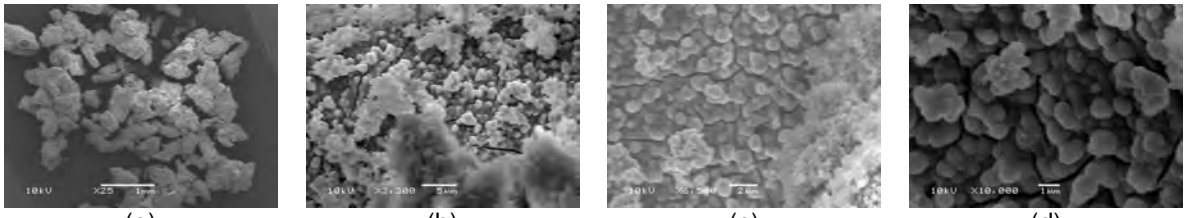

(a) (b) (c) (d)

Figure 2: Micrographs of polymer particle obtained in the ethylene polymerization with Cp_2ZrCl_2/SiO_2. Particle diameter around 53-100 μm (entry 9 in Table 1). Magnification: (a) 25×, (b) 3300×, (c) 6500×, and (d) 10000×.

The reduction in the catalytic activity observed for the resulting catalysts could be attributed to restrictions of monomer access to the active sites due to an inadequate particle fragmentation during the early moments of the polymerization. The pores of the remaining larger pieces of support are full of polymer hindering the access of the monomer to the active sites and leading to a decrease in the catalytic activity. Experimental results addressing this issue have been reported in the literature for supported metallocene catalysts (Hammawa and Wanke, 2007; Zheng et al., 2005), silica-supported Ziegler-Natta catalysts (Ruddick and Badyal, 1997), and Philipps catalysts (Weist et al., 1989). Such studies have shown that the fragmentation is closely related to the physical resistance of the support to break up into many pieces of 0.1 to 20 μm in diameter.

In fact, the activity of the majority of the metallocenes used in the present study is lower than that found in homogeneous Cp_2ZrCl_2 and $(^nBuCp)_2ZrCl_2$ and it might be insufficient to promote an effective rupture of the oxide matrix. Additionally, a huge shell of oxide matrix around the metallocene hinders the breakup of the particle due to the deep location of the metallocene complex into the silica matrix. Under these conditions, monomer mass transfer along the particle radius could hinder the polymerization, which subsequently reduces catalytic activity (Zheng et al., 2005; Ruddick and Badyal, 1997). Taking the aforementioned results, the influence of the particle diameter on the catalyst activity was evaluated by comparing the performance of Cp_2ZrCl_2/SiO_2 with particle diameters of 20-53 μm and 53-100 μm (entries 1 and 9 in Table 1, respectively) in the ethylene polymerization. The resulting activities suggest that the fragmentation hinders the performance of the catalyst when metallocenes of lower activity are immobilized following the proposed methodology.

In an attempt to solve the described diffusion problems, the supported catalysts Cp_2TiCl_2, Cp_2HfCl_2 and $EtInd_2ZrCl_2$ were synthesized with higher metallocene content (ca. 1.5 wt-% Zr) which is possible since the immobilization does not depend on reactions with hydroxyl groups located on the pore surface, such as in the case of the traditional methods (dos Santos et al., 1999). Ethylene polymerization was used to evaluate the performance of these systems as shown in Table 1 (entries10-12). The obtained activities were lower than those resulting from polymerizations with the same homogeneous metallocene (see footnote in Table 1), as expected for most immobilized metallocenes by different methodologies, but much higher than those of the respective catalysts with lower metallocene content (entries 3-4, Table 1). So, it is noticeable that an increase in the amount of metallocene allows the catalysts to break up more adequately during the early moments of the polymerization, and therefore helps to overcome the monomer accessibility hindrance to the active sites in comparison with other studies.

According to the obtained results, it could be pointed out for these catalytic systems that the activity is not related to the particle morphology on the scale of molecular structure of the metallocene complex and its closer surroundings. Conversely, the activity depends on the catalyst fragmentation once the catalytic species have a deep location within the support matrix.

4 Summary

The immobilization of metallocenes within a silica matrix using a non-hydrolytic sol gel route shows that the silica particle was formed by the aggregation of the primary structures with a diameter of about 160 Å. The aggregation process seems to be affected by the metallocene structure which suggests that the organometallic complex is surrounded by primary particles having a deeper location in the oxide matrix. Some metallocenes, which in homogeneous systems are less active, showed a negligible activity when entrapped within the oxide matrix by the proposed method. This result seems to be related to problems of catalyst fragmentation leading to monomer mass transfer limitations along the partially fragmented particle. In order to solve this problem, the amount of metallocene in the catalyst should be increased.

References

Bourget, L., Corriu, R.J.P., Leclereq, D., Mutin, P.H., Vioux, A. (1998). Non-hydrolytic Sol-gel Routes to Silica. *J. Non-Cryst. Solids*, 242, 81-91.

Boukari, H., Lin, J.S., Harris, M.T. (1997). Small-Angle X-Ray Scattering Study of the Formation of Colloidal Silica Particles from Alkoxides: Primary Particles or Not? *J. Colloids Interf. Sci.*, 194, 311-318.

Cruz, V., Ramos, J., Muñoz-Escalona, A., Lafuente, P., Peña, B., Martinez-Salazar, J. (2004). 3D-QSAR Analysis of Metallocene-based Catalysts Used in Ethylene Polymerisation. *Polymer*, 45, 2061-2072.

dos Santos, J.H.Z., Krug, C., da Rosa, M.B., Stedile, F.C., Dupont, J., Forte, M.C. (1999). The effect of silica dehydroxylation temperature on the activity of SiO_2-supported zirconocene catalysts. *J. Mol. Catal. A: Chem.*, 139, 199-207.

dos Santos, J.H.Z., Ban, H.T., Teranishi, T., Uozumi, T., Sano, T., Soga, T. (2001). Indenyl-silica xerogels: new materials for supporting metallocene catalysts. *Appl. Catal. A: Gen.*, 220, 287-302.

Fisch, A., Pozebon, D., Stedile, F.C., Cardozo, N.S.M., Secchi, A.R., dos Santos, J.H.Z. (2006). Immobilization of Zirconocene into Silica Prepared by Non-Hydrolytic Sol-Gel Method. *Macromol. Symp.*, 245-246, 77-86.

Hay, J.N., Haval, H.M. (1998). Preparation of Inorganic Oxides via a Non-hydrolytic Sol-gel Route. *J. Sol-Gel Sci. Technol.*, 13, 109-112.

Hammawa, H., Wanke, S.E. (2007). Influence of support friability and concentration of alpha-olefins on gas-phase ethylene polymerization over polymer-supported metallocene/methylaluminoxane catalysts. *J. Appl. Polym. Sci.*, 104, 514-527.

Hiemenz, P. (1997). *Principles of Colloid and Surface Chemistry*, 3rd ed., CRC, New York.

Kuramada, K., Nakabayashi, H., Murataki, T., Tanigaki, M. (1998). Structure and Formation Process of Silica Microparticles and Monolithic Gels Prepared by the Sol-Gel Method Colloids. *Surf. A: Physicochemical and Engineering Aspects*, 139, 163.

Ruddick, V.J., Badyal, J.P.S. (1997). AFM Study of the Breakup of Catalyst Particles during Ethylene Polymerization. *J. Phys. Chem. B*, 101, 1791-1793.

Severn, J.R., Chadwick, J.C., Duchateau, R., Friederichs, N. (2005). "Bound but not Gagged" – Immobilizing Single-site-olefin Polymerization Catalyts. *Chem. Rev.*, 105, 4073-4147.

Weist, E.L., Ali, A.H., Naik, B.G., Conner, W.C. (1989). Morphological Study of Supported Chromium Polymerization Catalysts. 2. Initial Stages of Polymerization. *Macromol.*, 22, 3244-3250.

Zheng, X., Smit, M., Chadwick, J.C., Loos, J. (2005). Fragmentation Behavior of Sílica-supported Metallocene/MAO Catalyst in the Early Stages of Olefin olymerization. *Macromol.*, 38, 4673-4678.

Proceedings of the 10th International Chemical and
Biological Engineering Conference - CHEMPOR 2008
Braga, Portugal, September 4-6, 2008
E.C. Ferreira and M. Mota (Eds.)

Studies on developing the red mud capability of binding the tannery residual chromium

Mihaela-Doina (Ghiga) Niculescu[1*], Laurentiu Filipescu[2], Ion Ion[2], Zoltan Ecsedi[3], Marian Crudu[1],

[1] The Research-Devlopment National Institute for Textile and Leather, Division Leather and Footwear Research Institute of Bucharest, 93 Ion Minulescu St, 3, Bucharest, Romania
[2] POLITECHNICA University of Bucharest, Faculty of Applied Chemistry and Materials Science, 1 Polizu St, 6, Bucharest, Romania
[3] POLITECHNICA University of Timisoara, Faculty of Industrial Chemistry and Environmental Engineering, 2 Piata Victoriei St, Timisoara, Romania

Keywords: red mud, chromium, adsorption, levigability
Topic: Sustainable process-product development through green chemistry - Sustainable & clean technologies

Abstract

This study has involved the investigation of how the sulphuric acid and alkaline-earth metals neutralize the red mud and measurement of zero charge points (ZCP) in the neutralized red mud with the aim of assessing their neutralization level.

Red mud neutralized with sulphuric acid down to pH = 8 was used as adsorbent for Cr^{3+} ions found in tannery effluents. Subsequently the leaching of the chromium bound to the red mud was tried by levigation tests at pH = 3.5. Even though there was a good chromium adsorption onto the red mud neutralized with sulphuric acid, this has resulted from an reversible interaction. Under such conditions, other neutralization types were tried by means of alkaline-earth metals. Trials for red mud neutralization from pH=12.5 down to pH=11 and 9 by means of $CaCl_2$, $MgSO_4$, $MgCl_2$ and combinations of these have led to sludges showing ZCP values below the pH values for the neutralized sludge, in the range of negative charges, proper for positively charged ion adsorption.

Neutralization by alkaline-earth metals has resulted in new solid phases of higher chemical stability, able for chromium seizing.

1. Introduction

90 % of hides processed currently in the world are subjected to tannage with basic chromium salts that give rise unavoidably to a great amount of chrome leather wastes containing about 75-85 % organic matter and not less than 2.5 % Cr_2O_3. Leather wastes containing chromium (LWCC) reach about 25 % of the whole weight of salted hides to be processed, that is a burden for the leather sector performances and success related to the environment protection [1].

Waste processing by hydrolysis and protein reclamation for a variety of viable applications (biofertilizers, surfactants, eco-adhesives etc.) [2] cause the chromium compound transfer (with economically non-convincing applications) into the effluents and sludge, and their treatment and disposal has to be considered from the environmental point of view.

This work suggests an adsorbing material prepared particularly by neutralization of the residual red mud, collected in large ponds from the alumina refining plants [3], to be used in binding the tannery residual chromium in the solid phases and stabilizing it with the view of long term storage.

* Corresponding author. Tel + 40-727-941170. E-mail:doina_ghiga@yahoo.com

The environmentally compatible mineral complex resulting from the two noxious wastes is a potential source to obtain embedded compounds or for other applications [4].

2. Experimental

In this study the neutralization by 20 % sulphuric acid at various pH values was chosen.

Method: 20 % sulphuric acid was added to each raw red mud sample of pH = 13.30 while stirring and the pH was recorded after 10 minutes of stirring for every adding until the pH becomes steady, showing such values as 8, 9 and 10, respectively. The resulting dispersions were vacuum filtered, and deposits were dried progressively at 50°C, 70 °C in an oven for 6 hours each and subsequently let stay at 110°C for 3 hours. After cooling samples were mixed in a mortar and sealed in flasks.

For the trials of chromium retention on the neutralized red mud some solutions of basic chromium sulphate of a variety of concentrations within the common range found in the tannery effluents were prepared and the red mud was neutralized to pH =8.

The chromium absorption efficiency was assessed by levigation tests.

Method: Adsorption and levigation tests were carried out at the ambient temperature and at a liquid/solid ratio of 10/1, contact time between phases of 4 hours, under mixing.

Neutralization with calcium and magnesium salts were conducted in different ways because of the slow reactions involved and delayed crystallization in the new solid phases.

Method: 1 mol/L solutions of $MgCl_2$, $MgSO_4$ and $CaCl_2$ were prepared. Small portions (0.5 – 5 ml) of each solution were taken and stirred within the sludge at every 24 hours at pH values of 11.0 – 9.00 under control. Samples both of liquid and solid phase were subjected thereafter to analysis.

Methods of analysis: The pH was measured with Consort C833 ionmeter. Calcium and magnesium were analyzed by complexometric titration. Mineralogical phases were identified by XRD using Dron 2 spectrometer along with their semi-quantitative assessment by Philips PW2400 X-ray fluorescence spectrometer. Chromium in liquid phases was analyzed by Varian AA240FS fast sequential AAS spectrometer.

Zero charge point (ZCP) providing information on neutralization level in the red mud was assessed from the plot of surface charge against the pH values registered in the acidic-alkaline titration, $\sigma = f(pH)$, being the point where the curve crosses the pH axis. With that end in view, the mud neutralized with calcium and magnesium salts were subjected to the potentiometric titration [5] with 0.1 N hydrochloric acid.

Method: Each sample of 0.1 g (weighed on an analytical balance) red mud, raw and neutralizat by calcium and/or magnesium salts, spread by stirring in 100 ml solution of 0.01 M, 0.1 M and 0.5 N NaCl electrolyte and degassed by nitrogen bubbling was subjected to titration with 0.1 N HCl solution of established factor, under the nitrogen atmosphere.

Also, 100 ml electrolyte solution of every concentration degassed previously by nitrogen bubbling was subjected to titration with 0.1 N HCl and 0.1 N NaOH solutions of established factors, under the nitrogen atmosphere.

Data obtained from potentiometric titration were used to compute the surface charge σ, with the following formula (1):

$$\sigma = \frac{\Delta \upsilon \times M \times F \times 100}{S \times A \times V} \qquad (1)$$

where:

$\Delta \upsilon$ = volume of HCl solution used in the red mud sample titration – volume of HCl or NaOH solution used in blank (electrolyte) titration at the same pH value;

M = normality of the titrating solution (0.1 N);

F = 96500 C;

S = specific area of the red mud;

A = amount of red mud weighed on the analytical balance;

V = the electrolyte volume being used (100 ml);

Specific areas of the raw and neutralized red mud samples were measured on an ASAP (Accelerated Surface Area and Porosimetry) 2020 System with nitrogen as analysis adsorbent.

After having the ZCP assessed, the chromium adsorption capabilities of the mud samples neutralized with calcium and magnesium salts were tested by techniques similar to those for mud neutralized with sulphuric acid.

3. Results and discussions

Phase composition was not changed by neutralization with sulphuric acid, the major participation of every red mud constituent being kept unchanged when pH was decreased from the initial one of 12.0-12.5 to 8.0, feature revealed in Table 1.

Table 1

COMPOSITION OF THE MUD NEUTRALIZED WITH SULPHURIC ACID

Composition	**Level in the neutralized red mud, %**		
	at pH = 10	**at pH = 9**	**at pH = 8**
Al_2O_3	Al_2O_3	19.0	18.0
SiO_2	SiO_2	7.4	7.4
P_2O_5	P_2O_5	0.7	0.6
SO_3	SO_3	1.0	1.5
Cl	Cl	1.1	1.2
CaO	CaO	3.3	3.4
TiO_2	TiO_2	8.6	9.2
V_2O_5	V_2O_5	0.2	0.2
Cr_2O_3	Cr_2O_3	0.3	0.3
MnO	MnO	0.1	0.2
Fe_2O_3	Fe_2O_3	50.9	57.8
PbO	PbO	0.1	0.1

Sulphuric acid has neutralized the sodium ions, promoting the $Al(OH)_3$ precipitation as gibsit and was removed as soluble sodium sulphate from the red mud.

No red mud constituent containing calcium dioxide and silicon dioxide (calcium aluminates, calcium silicates, calcium alumino-silicates etc.) has been decomposed and changed molar ratios to other constituents.

Event though the sulphate ion concentration in the solid phase has increased with the neutralization progress, this is only because of including in the alumino-silicate formulae and not the calcium sulphate crystallization. Though, the neutralization process has stabilized the material and increased its ion exchange capability.

Red mud neutralized with sulphuric acid down to pH = 8 was used as adsorbent for Cr^{3+} ions. Trial results are shown in Table 2.

Table 2

CHROMIUM ADSORPTION ONTO THE RED MUD
NEUTRALIZED WITH SULPHURIC ACID

Sample	**Inital Cr concentration, g /l**	**Final Cr concentration, mg/l**	**Cr load in the red mud mg/g**
1	1.7105	3.954	3.954
2	1.3684	1.709	1.709
3	1.0263	1.236	1.236
4	0.6842	0.006	0.006
5	0.3421	0.048	0.048

The random sizes of red mud particles and porosity spreading account for the irregular variation in the output chromium level.

Subsequently the leaching of the chromium bound to the red mud was tried by levigation tests at pH = 3.5.

Data in Table 3 have revealed the strong Cr^{3+} binding on the solid adsorbing phase and reasonable chromium amounts released in the leaching water.

Table 3

DATA ON THE CHROMIUM LEACHING AT pH 3.5

Sample	Cr in the washing I effluent, mg/g	Cr in thr washing II effluent, mg/g	Cr in thr washing III effluent, mg/g
1	33×10^{-5}	37×10^{-5}	0
2	42×10^{-5}	45×10^{-5}	26×10^{-5}
3	13×10^{-5}	40×10^{-5}	80×10^{-5}
4	15×10^{-5}	58×10^{-5}	68×10^{-5}
5	23×10^{-5}	12×10^{-5}	56×10^{-5}

Even though there was a good chromium adsorption onto the red mud neutralized with sulphuric acid, this has resulted from an reversible interaction.

Under such conditions, other neutralization types were tried by means of alkaline-earth metals.

The common calcium and magnesium salts can remove alumina from the diluted alumina solution by binding it as insoluble aluminates and aluminate-silicate compounds with or without captured sodium ions. Such compounds give a high specificity for the heavy metal adsorption.

Trials for red mud neutralization from pH=12,5 down to pH=11 and 9 by means of $CaCl_2$, $MgSO_4$, $MgCl_2$ and combinations of these have led to sludges showing ZCP values below the pH values for the neutralized sludge, in the range of negative charges, proper for positively charged ion adsorption.

Data obtained from the potetiometric titration (acid/base) were use in calculating the surface charges σ required to assess the ZCP, as shown in Figures 1 and 2.

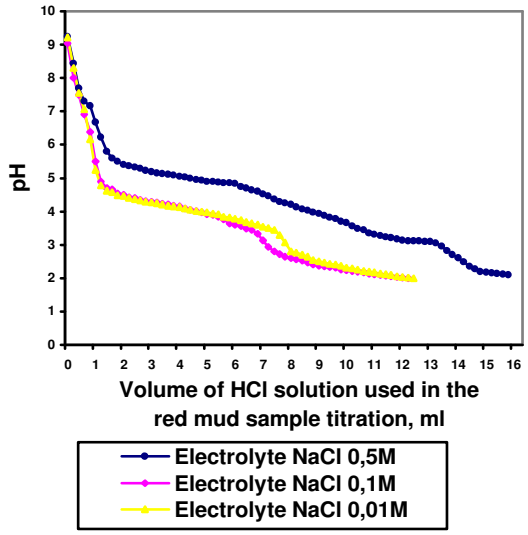

Figure 1. Titration of raw red mud, pH = 12.5, dry

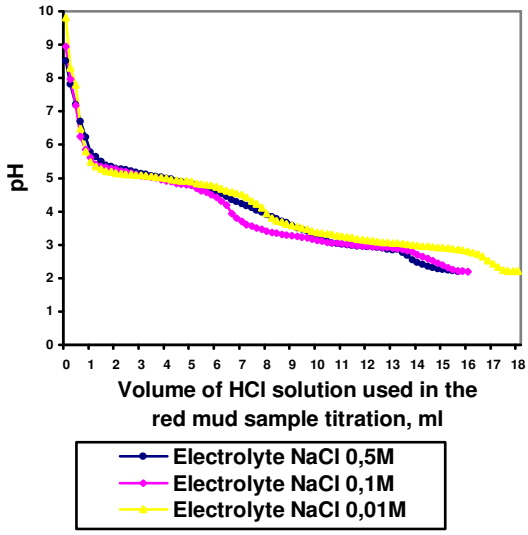

Figure 2. Titration of the red mud, neutralized with $MgCl_2$, pH = 9, dry

ZCPs assessed from the plots σ = f (pH) in Figures 3 and 4 are shown in Table 4.

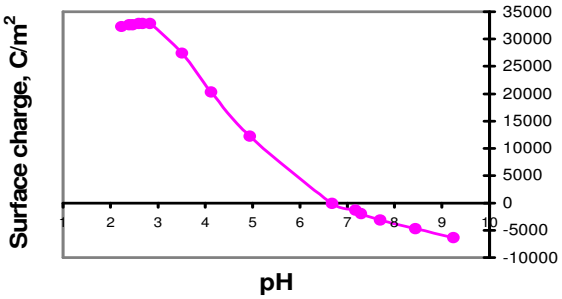

Figure 3. Assessing the ZCP in the 0.5 M NaCl electrolyte solution of the red mud, dry

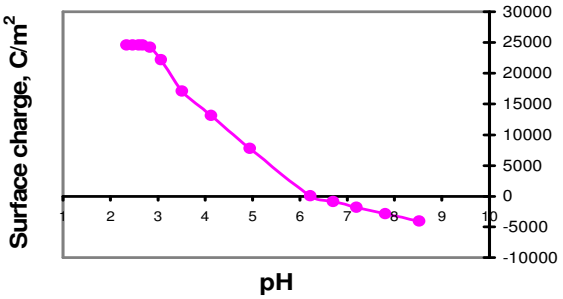

Figure 4. Assessing the ZCP in the 0.5 M NaCl electrolyte solution of the red mud neutralized with $MgCl_2$ at pH = 9

Table 4

ZCP VALUES OBTAINED FROM TRIALS

Ref. No.	Neutralizing agent	Initial pH	Zero charge point for:					
			Wet mud, in NaCl solution			Dry mud, in NaCl solution		
			0.01M	0.1M	0.5M	0.01M	0.1M	0.5M
1	- (raw mud)	12.5	6.25	6.26	6.50	6.05	6.28	6.69
2	$CaCl_2$	11	592	5.89	6.38	6.09	6.44	6.76
3	$CaCl_2$	10.5	5.83	5.93	6.37	5.74	6.39	6.73
4	$MgSO_4$	11	5.58	6.12	6.31	5.88	6.24	6.54
5	$MgSO_4$	9	5.98	6.33	6.38	5.88	6.24	6.52
6	$CaCl_2 + MgSO_4$	11	5.74	6.30	6.37	5.89	6.44	6.56
7	$CaCl_2 + MgSO_4$	9	5.94	5.83	6.34	5.61	6.45	6.53
8	$MgCl_2$	11	6.40	5.89	6.86	6.12	6.42	6.83
9	$MgCl_2$	9	5.62	6.05	6.40	6.28	6.13	6.21
10	$MgCl_2 + CaCl_2$	11	6.76	6.13	7.17	6.50	6.72	6.64
11	$MgCl_2 + CaCl_2$	9	5.71	5.91	6.33	5.84	6.00	6.58

When comparing the ZCP values for the mud samples investigated by potentiometric titration, no significant changes in such parameter based on the concentration the electrolyte wherein the mud samples were spread were found, and these changes fall in the acid range below the initial mud pH, in the negative charge range that is proper for the adsorption of positively charged ions.

Inducing the new solid phase by neutralization with calcium and magnesium salts used in trials has preserved the surface properties of the red mud particles, favourable for chromium adsorption, meaning that the red mud subjected to neutralization with calcium chloride, magnesium sulpahte and magnesium chloride or blends of these can become an adequate adsorbent for chromium.

Even though the red mud can bind the chromium that has been revealed by the values found for ZCP, this was proved not to be enough for a long lasting adsorption under critical conditions such as large pH variation. From the other point of view, use of the red mud waste as such in some applications is unacceptable because of the pH values and very high free alkalinity inducing environmentally adverse action. Considering these, the red mud neutralization is a significant stage, sensitive because of its outcomes for the process of irreversible binding of chromium within the mineral complex making up the red mud.

A comparative review of the ZCPs for the wet and dry red mud samples has revealed a more homogenous variation in the dry mud samples because of the removal of crystallization

water contained in some of the new compounds resulting during neutralization, leading thus to a behaviour lightly different in the acid-alkaline titration.

The mud samples neutralized with magnesium chloride and blend of magnesium chloride and calcium chloride have shown titration curves of very different shapes as compared to the raw mud that suggests some new compounds occurring, as it was predicted.

The tests for chromium adsorption onto the red mud samples neutralized with magnesium chloride and blend of magnesium chloride and calcium chloride have shown adsorption efficiencies above 99 % resulting at a maximum load of cca. 32 mg chromium/1 g mud for the mud sample neutralized with magnesium chloride, and of cca. 30 mg chromium/1 g mud for the mud neutralized with the blend of magnesium chloride and calcium chloride.

Even though the amount of bound chromium above these limits was found in the mud sample, the efficiency has shown a significant decrease, and, therefore, the limits of 32 and 30 mg chromium / 1 g mud, respectively, can be considered the maximum adsorption capabilities for the two neutralized red mud samples.

4. Conclusions

- Red mud neutralization by sulphuric acid is an outstanding solution recommended for its treatment previously to storage in ponds.
- Neutralization by alkaline-earth metals has resulted in new solid phases of higher chemical stability, able for chromium seizing.
- Solid phases induced into the red mud by neutralization have created the premises for a long lasting chromium adsorption so that the resulting mineral complex can be preserved under environmental conditions as an inert waste until some economically viable application would have been developed.
- Simultaneous dumping of two hazardous wastes (residual chromium resulting from the hide processing that is a source of Cr (VI), and highly alkaline red mud resulting from alumina industry) under safe conditions is e solution for rendering the referred two activities environmentally friendly.

References

[1] Integrated Pollution Prevention and Control (IPPC), Council Directive 96/61/EC. (2003). http:/eippcb.jrc.es.

[2] Cot, J. (2004). J. Soc. Leather Technol. Chem. 99 (8), 322-350.

[3] Liu, Y., Lin , C., Wu, Y. (2007). Characterization of red mud derived from a combined Bayer Process and bauxite calcination method, J. of Haz. Materials, 146, 255–261.

[4] Brunori, C., Cremisini, C., Massanisso, P., Pinto, V., Torricelli, L. (2005). Reuse of a treated red mud bauxite waste: studies on environmental compatibility, J. of Haz. Materials, B117, 55-63.

[5] Chvedov, D., Ostap, S., Le, T. (2001). Surface properties of red mud particles from potentiometric titration, Colloids and Surfaces, 182, 131–141.

Proceedings of the 10th International Chemical and
Biological Engineering Conference - CHEMPOR 2008
Braga, Portugal, September 4-6, 2008
E.C. Ferreira and M. Mota (Eds.)

Statistics model and optimization of uranium extraction in ultrasounds field in sulphuric acid medium

Eugenia Panturu[1*], Rozalia Radulescu[1], Antoneta Filcenco-Olteanu[1],
[1]Research & Development National Institute for Metals and Radioactive Resources-ICPMRR
Blvd. Carol I, no.70, 020917 sector 2, Bucharest, Romania

Keywords: ultrasounds, dissolution, uranium, dumps, extraction efficiency
Topic: Advancing the chemical engineering fundamentals;
Sustainable process-product development through green chemistry

Abstract

This paper provide an experimental study based on mathematical statistic that is the factorial experiment designs regarding the effects of ultrasounds power on the extraction efficiency of acid solubization of uranium originated from dumps. The operation parameters varied using a 2^{5-1} factorial experiment were the temperature, the pH of the reaction medium, the operating time and the ultrasound power (Şayan and Bayramoğlu, 2004) . The mathematic model obtained through the experimental results processing was determined using the least squares method and it describes dependency of the extraction efficiency on the technical and economical significant operation parameters. Mathematical model optimization was performed using a maximum slope algorithm and it points out the major factors that influence the uranium extraction efficiency, namely: the temperature, the oxidant amount and the ultrasounds power within the range of studied experimental values. Ultrasound utilization has positive effects on radioactive pollution diminution, obtaining extraction efficiencies above 96% respectively 10% much higher values than those obtained in identically conditions but in the absence of the ultrasonic field.

1 Introduction

According to Sevcenco, V.B., Suderrov, B.N. (1961) the main object of activity of hydrometallurgy as technological discipline is the extraction of metals from ores, concentrates, sterile or other different industrial byproducts using the aqueous solutions of some chemical reagents followed by the separation of extracted metal from solution.

The extraction efficiencies rarelly overlap 95 – 98%, which means that about 2 – 5% of useful element remains undissoluted.

In order to intensify the extraction process of uranium from sterile and to transfer it to solution in the present paper the authors use beside the mechanical stirring the ultrasound field.

Ultrasound effects on the chemical reactions improvement were studied by Thompson and Doraiswamy (1999) and Polyukhin (1978), who have developed ultrasounds application in extractive metallurgy. Researches concerning sonochemistry application in extractive metallurgy beside the classic methods conducted to the achievement of rapid and selective extractions of the metals.

The dumps from Banat-Bihor area, where the uranium mining activity was ceased, cause severes problems due to the radioactive pollution to the environment and to the population living near by the affected areas. Therefore many researches concerning the radioactive pollutants recovery using different technologies for soils remediation were performed.

* Corresponding author. Tel + 40-21-369-04-67. E-mail: eugenia.panturu@icpmrr.ro

This paper aims to develop a model of ultrasounds effects on uranium dissolution in sulphuric acid medium and to optimize them. The results presented in this paper can provide ground information for a much more detailed study concerning the process development.

2 Experimental activity

Factorial calculus is applied on a large scale to the statistic planning of the experiments in order to develop empiric linear models concerning the process response to operation factors. Models of first order are obtained using a 2^n factorial experiment one where each variable works on 2 levels.

Their optimization is done by performing additional experiments that point out the major factors that influence the extraction efficiency.

Similar papers have demonstrated that the application of this type of experimental project for the useful elements dissolution out of different types of raw materials is valid.

Uranium solubilization experiments were performed on samples of 50 g dump waste (0.03% uranium) with particles of 0.100 mm grinding size, the solid/liquid mass ratio was 1:1 and the stirring velocity was maintained invariable at 500 min^{-1}(Panțuru et al. ,2006).

Experimental conditions were reached in respect to the experimental matrix. Uranium solubilization was performed in two stages; after phases separation by filtration, the residue was washed with water (S/L=1:1, mass ratio).

The efficiency of uranium extraction from the solid samples was determined with formula:

$$\eta = \frac{cU_i.g_i - cU_r.g_r}{cU_i.g_i}.100 \qquad (1)$$

In order to determine the ultrasound power, W_{abs}, the calorimeter method (Margulis et al.,2003), which is used frequently for the determination of adsorbed power at lower frequencies, was applied.

The operation period, t_{us}, of the ultrasound source is rather high (10 minutes per stage) for ΔT measuring (minimum 1^oC). The reaction vat temperature was maintained invariable to the experimentation value using a thermostatic bath.

Ultrasound generator consists into a bath ultrasound UR1 Resch (480 W, 35 kHz), the reaction vat being coupled with a reflux condenser.

The experiments were performed using as extraction reagent sulphuric acid 96% and as oxidant reagent potassium chlorate 0.5%-1% depending on the amount of solid sample used in the test, which provides an oxidation potential between 450 and 500 mV necessary to the dissolution of uranium (Okur,H.,Techin,T,2002).

There were also used specific analytic pure reagents for quantitative determinations of the elements from solid samples and for the quantitative chemical analysis of the solutions and residues formed in the solubilization process. The analytical methods used depend on the analyzed elements content namely: atomic adsorption - using a VARIAN spectrAA-88 adsorption with adequate lamps for the determined elements, colorimetry - using a UV-VIS CECIL 1011 spectrometer, volumetry, gravimetry and HPGe γ spectral method – using an ORTEC multichannel analyser with Ge detector for γ radiations (0-3 MeV)

3. Results and discusions

The studied process factors are: the reaction temperature (A), the reaction medium pH (B), the operation duration (C), the oxidant amount (D) and the ultrasounds power ($W_{abs)}$. These factors, except ultrasounds power, were used in another study of our research team and it concerned the uranium acid solubilization but only under mechanic stirring conditions in order to disperse the solid particles and to increase the solubilization velocity .The factors

levels presented in table 1 are similar to the previously used ones, hence, the performances of those two procedures can be easily compared.

Table 1. The factors used in the ultrasounds field factorial model

Factors	UM	Factor code	Range $x_{jmin} \rightarrow x_{jmax}$	The experiment centre X_{jo}	Δx_j	Level	
						inf. -	sup. +
Temperature	^{0}C	A	40→80	60	20	40	80
pH	-	B	1→1,5	1.25	0.25	1	1.5
Duration	hours	C	6→10	8	2	6	10
Oxidant	kg/t	D	6→10	8	2	6	10
US Power	watt	E	75.58→79.002	77.29	1.71	75.58	79.002

A 2^{5-1} fractional factorial calculus was used in order to develop the first order model with the interaction terms.

The experiments were randomly performed in order to avoid a systematic error. Furthermore, it was performed 2 central reproductions (1^0, 2^0) for experimental error calculation. Experimental results represented in Figure 1 point out the efficiency surface, which is obtained by rising of a vertical line at the intersection point between the temperature and ultrasounds power values.

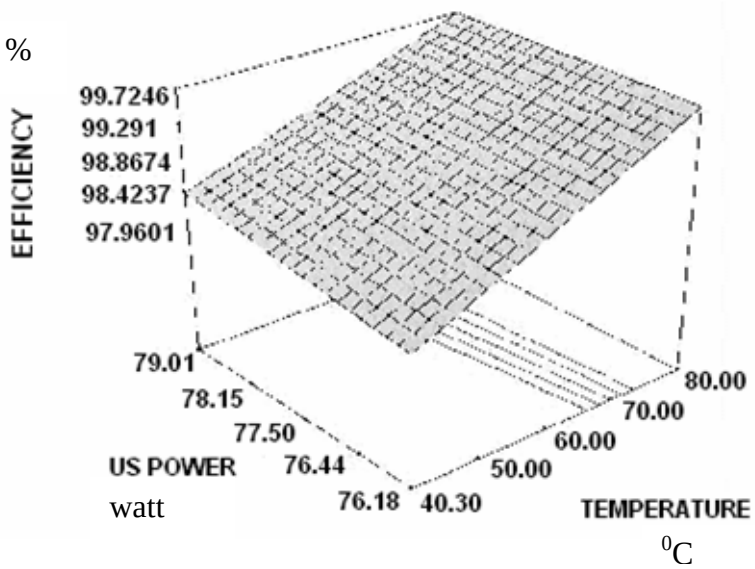

Figure 1. 3D representation of temperature/US power/efficiency interaction

The considered regression models for the selected factors are first order polynomial models that are obtained by variation analysis using Design Expert v.6 program. Hence, after the elimination of the insignificant interactions, the following 2 regression equations were obtained:

The regression equation expressed depending on the codified terms (-1/+1):

$$\eta = 98.739 + 0.981*A + 0.154*B + 0.210*C + 0.260*D + 0.076*E - 0.126*A*B - 0.085*A*C - 0.257*A*D - 0.106*A*E + 0.055*B*D + 0.049*C*D - 0.056*B*E + 0.020*C*E + 0.037*D*E \quad (2)$$

The regression equation express depending on real terms:

$$\eta = 68.910 + 0.388*T + 11.391*pH - 0.316*t - 0.564*Co + 0.260*W_{abs} - 0.025*T*pH - 0.002*T*t - 0.006*T*Co - 0.003*T*W_{abs} + 0.11*pH*Co - 0.131*pH*W_{abs} + 0.012*t*Co + 0.006*t*W_{abs} + 0.011*Co*W_{abs} \quad (3)$$

The coefficients of equation (3) were calculated with the codified values (+1, -1) of the factors and are valid for null values of the factors A, B, C, D, E. These emphasize the medium value

of the efficiency (98.739). The coefficients of equation (3) were calculated using the least squares method. The equation emphasizes the extraction efficiency for certain values of the factors (the studied range).

One can observe that the experimental values of extraction efficiency and the ones determined using the regreassion model have the liniar abnormality of ± 0.02%, and the adjustment accuracy is of 38.73 (to which a value higher then 4 is optimal), obtained in this case and indicates the presence of some data , which aren't affected by experimental errors.

The accuracy of mathematic model is tested through ANOVA variance of analysis and with Fisher's test.

The value of the Fisher's test (F = 217) of the model emphasizes that this is adequate for the experimental data, existing a 4.32% probability that this value to be a simple occurrence.

It is important to point out the fact that in this case the optimization is not necessary because the extraction efficiencies obtained reach maximum values, which determine a high efficiency of ultrasound utilization beside the mechanical stirring one. In order to emphasize the major factors that influence the uranium extraction efficiency namely the temperature, oxidant amount, and ultrasounds power in the studied experimental values range the optimization was achieve.

Design-Expert is a soft that presents an independent module of optimization that permits a numerical or graphical optimization starting with the determined regression models.

The optimization was performed imposing certain values to all the factors within the experimentation domains but on condition that the obtained efficiency is 98-100%.

In table 2 are presented the imposed conditions for the optimization process.

Table 2. Conditions imposed for optimization

Name, MU	Condition	Inferior level	Superior level	Weight
Temperature, ^{O}C	is in domain	40	80	3
pH	is in domain	1	1.5	3
Time, hours	is in domain	6	10	3
Oxidant, kg/t solid	is in domain	6	10	3
US power, watt	is in domain	75.58	79.01	3
Efficiency, %	maximization	98	100	3

In figure 2 is graphically represented (on cube) an optimized solution; it can be noticed that the global optimum – efficiency 100% - (A+D+E-) placed on the cube corner in the front up right, meaning the maximal values of the temperatures ($80^{o}C$), of the oxidant (10 kg/t) and minimal value of the ultrasound power (75.58 W) correspondent to an ultrasound action time of 10 minute per stage.

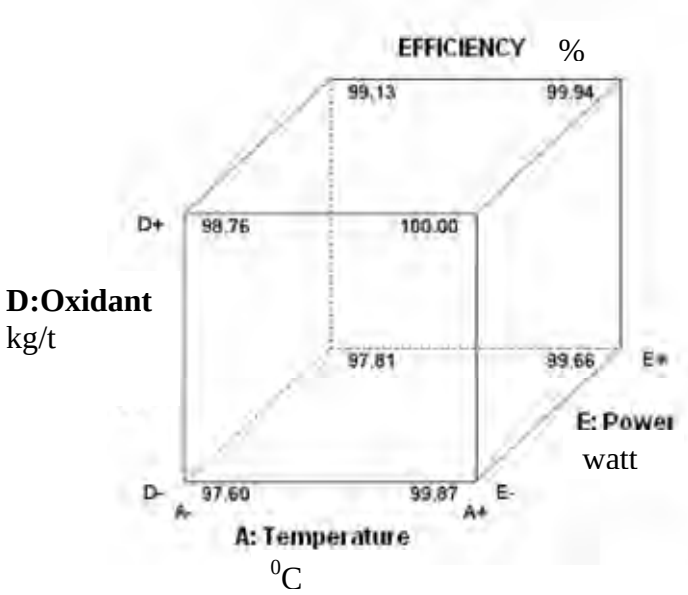

Figure 2. Graphical representation of optimal solution

The minimal value of the efficiency is, in this representation, the value of 97.60 that corresponds to the minimum values of the temperature, the oxidant amount and of the ultrasounds power (A-D-E-) and to the maximum value of the medium pH and of the operation time.

4 Conclusions

The model proposed for the recovery of uranium from waste dumps gets us to the following conclusions, namely:

- the recommended optimal parameters necessary to obtain extraction efficiencies over 96 % are as follows:

- size of beads of 0.100 mm ;

- mass ratio solid/liquid 1 :1 ;

- stirring rotation 500 min^{-1}, in order to hinder the settlement of coarse particles and to provide good conditions for the dispersion of reagents;

- oxidant regent amount, potassium chlorate is 0.75% of the solid amount 8 $kg_{oxidant}/t_{solid}$; this amount is required in order to get in the system a oxidation potential of 450-500 mV ;

- the optimal recommended dissolution temperature is of 50^{o}C ;

- sulphuric acid concentration in uranium bearing solution was correlated to the necessary oxidation potential; the optimal pH is 1, which corresponds to the consumption of a 96% sulphuric acid solution of about 100 kg $_{acid}/t_{solid;}$

- the operation duration was determined to be 2.5 hours in 2 stages ;

- the ultrasounds action duration is of 10 minutes /stage;

- the ultrasounds power is 77 W .

- the extraction efficiencies obtained were with about 10 % higher than the ones in the classic operation case respectively in the absence of the ultrasounds field;

- the ultrasound field action (10 minutes per stage) combined with the mechanical stirring allows the operation time and working temperature diminution with about 33-50%, comparatively to the classic procedure, and the same maximal values of extraction efficiency are obtained therefore the decontamination takes place faster and the electric power consumption is reduced;

- The proposed mathematical model is able to calculate the extraction efficiencies for uranium for any value of considered parameters (temperature, pH of reaction medium, operation duration, oxidant reagent amount, ultrasounds power) only in the range of studied experimental values with a precision of 95%.

This paper emphasizes the major factors that influence the uranium extraction efficiency, namely the temperature, the oxidant amount, the ultrasound power in the studied experimental values range. There are necessary economic analyses in order to establish the costs of ultrasound utilization for waste dumps decontaminations through uranium recovery.

List of symbols:

cU_i –initial concentration of uranium , %
cU_r – uranium concentration in residue, %
g_i – weight of the solid sample, g
g_r – residue weight, g
m – water mass, g
W_{abs} –acoustic power adsorbed by reaction medium, W
ΔT – temperature increasing under ultrasounds source action, ^oC
η - efficiency, %

References

Margulis,M.A.,Margulis,I.M. (2003),*Calorimetric method for measurement of a liquid,* Ultrasonics sonochemistry,volume 10,6, 343-345 ;

Okur,H.,Techin,T. (2002) ,*Effect of ultrasound on the dissolution of colemanite in H_2SO_4, Hydrometallurgy ,* volume 67, 79-86;

Panțuru, E., Jinescu, Ghe., Rădulescu,R., Filip,Gh. (2006), *Reactive extraction of uranium from ores having high content of organic substance* ,Revista de Chimie, volume 57,**,**4, 350-354;

Polyukhin, P.I. (1978) , *The Use of Ultrasonics in Extractiv Metallurgy.* Technicopy, Stonehouse, UK, 32-35;

Sevcenco, V.B., Suderrov, B.N. (1961), *Tehnologia uraniului*, Gosatomizdat, Moscova, 250-252;

Şayan , E., Bayramoğlu , M. (2004), *Statistical modeling and optimization of ultrasound – assisted sulfuric acid leaching of TiO_2 from red mud, Hydrometallurgy*,volume 71,397-401;

Thompson, L.H. , Doraiswamy, L.K. (1999), *Sonochemistry :science and engineering* . Ind.Eng.Chem.Res.,38**,** 1215-1219;

Proceedings of the 10th International Chemical and
Biological Engineering Conference - CHEMPOR 2008
Braga, Portugal, September 4-6, 2008
E.C. Ferreira and M. Mota (Eds.)

Stability of Binary Mixtures in a Novel Combustor Conical Spouted Bed with a Draft Tube of different Length

María J. San José, Sonia Alvarez, Alvaro Ortiz de Salazar, Alberto Morales
Departamento de Ingeniería Química. Universidad del País Vasco. Facultad de Ciencia y Tecnología. Aptdo 644. 48080 Bilbao. Spain. Tel: 34-94-6015362. Fax: 34-94-6013500. e-mail: mariajose.sanjose@ehu.es

Keywords: spouted bed, conical spouted bed, draft tube, length of the draft tube, mixtures
Topic: 1 Sustainable Process-Product Development through green chemistry.
2 Multi-scale and/or multi-disciplinary approach to process-product innovation

Abstract

The stability of binary mixtures of different particle diameter with a non-porous draft tube located at the bottom of the contactor in a novel combustor conical spouted bed has been studied. In order to design the appropriate length of the non-porous draft tube without any instability or operating drawbacks in conical spouted beds, the length of the draft tube located centrally at a height from the bottom of the contactor has been varied up to a maximum values in which the top of the draft tube is at the same level the upper bed surface.

1 Introduction

In spite of the versatility of the conical spouted beds, there are situations in which the gas-solid contact is not fully satisfactory due of the bed instability. In previous papers (Olazar et al., 1992; San José, 1991; San José et al., 1991) the ranges of the geometric factors of the conical contactor and of the contactor-particle system for stable operating condition have been established in order to become the stability.

The insertion of a draft tube in a conventional spouted bed overcomes the limitations of the spouted for improving gas-solid contact. Several advantages of using a draft tube in a conventional spouted bed are the following (Buchanan et al., 1965; Muir et al., 1990; Konduri et al., 1995; Ishikura et al., 2003): greater flexibility in the operation; lower gas flow and pressure drop; solids of any size or nature may be treated; narrower residence time distribution; better control of solid circulation; avoids maximum spoutable bed height. Consequently, solid circulation may be controlled by changing independently column diameter, stagnant bed height or particle diameter. Among the disadvantages the following are worth mentioning: lower mixing degree; complexity of design; risk of tube blockage; lower contact between gas and solids; lower heat and mass transfer; longer recirculation time.

Applications of conventional spouted beds with a draft tube cover a wide range of operations and chemical processes including: drying (Khoe and Van Brakel, 1983; Freitas and Freire, 2002; Szafran and Kmiec, 2004), combustion (Konduri et al., 1995; 1999; San José et al., 2002, 2006), pyrolysis (Stocker et al., 1989), pharmaceuticals (Littman et al., 1997) and mixing (Krambrock, 1976).

In some papers the results of the effect of non-porous draft tube in conventional spouted beds mainly focussed on: hydrodynamics (Matthew et al., 1988; Stocker et al., 1990) and particle circulation (Muir et al., 1990; Yang and Keairns, 1983; Hattori et al., 1998) have been published.

In order to widen the range of the bed stability in conical spouted beds, in this paper the bed stability of binary mixtures of different particle diameter with a non-porous draft tube of different length is analyzed in a conical spouted bed combustor.

2. Experimental

The experimental unit, Figure 1, design on a pilot scale is provided with a blower that supplies a maximum air flow rate of 300 $Nm^3\ h^{-1}$ at a pressure of 15 kPa. The flow rate is measured by means of two mass flow meters in the ranges of 50-300 and 0-100 $m^3\ h^{-1}$, with both being controlled by a computer. The accuracy of this control is 0.5% of the measured flow rate (Olazar et al., 2004; San José et al., 2005):

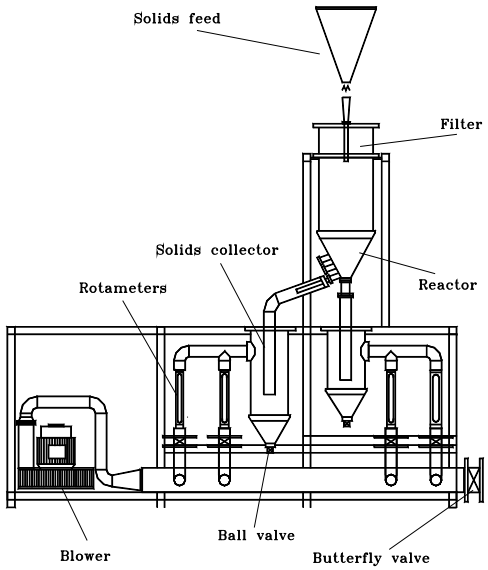

Figure 1. Diagram of the experimental equipment.

The measurement of the bed pressure drop is sent to a differential pressure transducer (Siemens Teleperm), which quantifies these measurements within the 0-100% range (Olazar et al., 2004). This transducer sends the 4-20 mA signal to a data logger (Alhborn Almeno 2290-8), which is connected to a computer where the data are registered and processed by means of the software AMR-Control. The software AMR-Control also registers and processes the air velocity data, which allows for the acquisition of continuous curves of pressure drop against air velocity.

Five conical contactors made of poly(methyl methacrylate) have been used. Figure 2 shows the geometric factors of these contactors, whose dimensions are as follows: column diameter, D_c, 0.36 m; contactor angle, γ, between 28 and 45°; height of the conical section, H_c, from 0.60 to 0.36 m; gas inlet diameter, D_o, in the range of 0.03-0.06 m. The values of the stagnant bed height, H_o, used are in the range between 0.05 and 0.35 m. Operation has been carried out at the minimum spouting velocity and at velocities 20 and 30% above this value.

The influence of the length of the device in each solid particle bed (in the same experimental conditions) has been studied by inserting centrally a draft tube in the contactor and varying the length of the draft tube from a minimum value of 0.02 m to a maximum value in which the top of the draft tube is at the same level that the upper bed surface (Erbil, 2003).

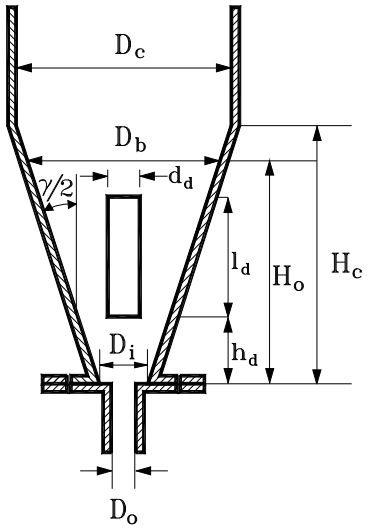

Figure 2. Geometric factors of the contactor and of the draft tube.

The draft tube, Figure 2, is a cylindrical tube made of poly(methyl methacrylate) located centrally at the bottom of the contactor. Figure 2 shows the draft tube geometries. The draft tube diameter, d_d, and height of the entrainment zone, h_d, have been determined experimentally in a previous paper (San José et al., 2007) from a viewpoint of stability of spouting and of the clogging of solid particles. The diameter of the draft tube, d_d, was varied from 0.03 m to 0.05 m. The diameter of the draft tube, d_d, was determined experimentally in a previous paper (San José et al., 2007) for a viewpoint of stability of spouting and was varied from 0.03 m to 0.05 m. The choice of the upper limit of the draft tube diameter, d_d, was made based on to the average spout diameter, (Olazar et al., 2004), which is between the gas inlet diameter, D_o, and the base diameter, D_i, and in conical spouted beds is nearer to the base diameter, D_i (Olazar et al., 2004). The entrainment zone, distance between the base of the contactor and the lower base of the device, h_d, has been determined experimentally in a previous paper (San José et al., 2007) is in the range 0.01-0.09 m. The length of the draft tube, l_d, has been varied from 0.02 m to a value calculated as $l_d = H_o - h_d$. and it is in the range 0.02-0.34 m.

The solids studied are limestone, which corresponds basically to the D group of the Geldart classification (Geldart, 1973, 1986) and their properties are set out in Table 1. Table 1 summarizes the geometric factors of the conical contactors, the dimensions of the central draft tubes and particle properties of solids studied.

Table 1. Geometric factors of the contactors and of the draft tube and particle properties

Contactor poly(methyl methacrylate)		
Column diameter	D_c (m)	0.36
Contactor angle	γ (deg)	28, 33, 36, 39, 45
Height of the conical section	H_c (m)	0.60, 0.50, 0.45, 0.42, 0.36
Gas inlet diameter	D_o (m)	0.03, 0.04, 0.05, 0.06
Stagnant bed height	H_o (m)	between 0.03 and 0.35 m
Draft tube poly(methyl methacrylate)		
Inside diameter	d_d (m)	0.03, 0.04, 0.05, 0.06
Tube length	l_d (m)	from 0.02 to 0.34
Distance of entrainment zone	h_d (m)	from 0.01 to 0.09
Particle (Limestone)		
Diameter	d_p (mm)	between 0.9 and 3.85
Density	ρ_p (kg/m^3)	2650

3. Results

In order to provide the effect of the length of the central draft tubes in conical spouted bed contactors on bed stability, a novel diagram has been proposed in this paper. In this diagram the length of the draft tube, l_d, has been plotted against the gas velocity, u.

In this diagram, Figure 3, the length of the draft tube, l_d, has been plotted against the gas velocity, u, corresponding to a system taken as an example, of contactor angle, γ= 36º, gas inlet diameter, D_o= 0.04 m, with a bed of mixtures of limestones of Sauter average diameter, $\overline{d_S}$ = 3.03 mm and stagnant bed height, H_o= 0.20 m. The draft tube dimensions are: diameter, d_d= 0.04 m, height of the entrainment zone, h_d= 0.05 m and length varied from a minimum length of l_d= 0.02 m to the maximum length of l_d= 0.15 m (corresponding to the level of the stagnant bed, $l_d = H_o - h_d$).

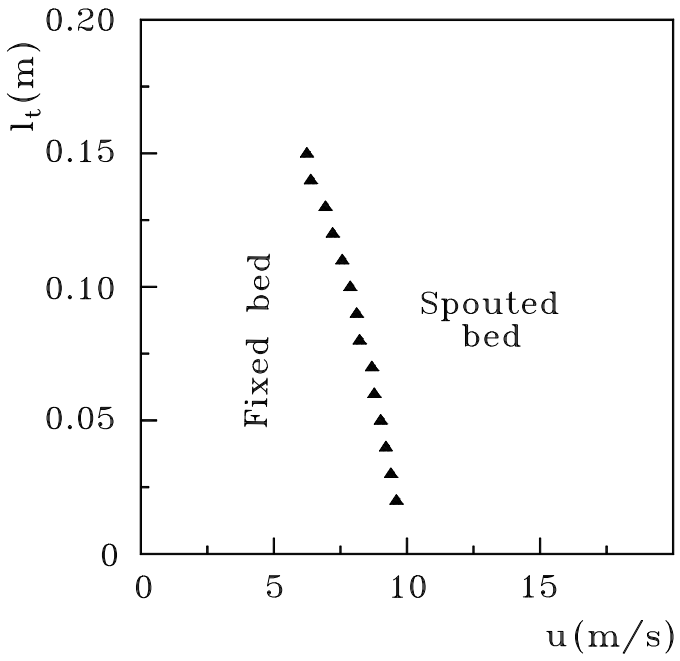

Figure 3. Operating map. System: γ= 36º, D_o= 0.04 m, beds of mixtures of limestone of Sauter average diameter $\overline{d_S}$ = 3.03 mm. Draft tube of d_d= 0.04 m and h_d= 0.05 m.

As is observed, as the gas velocity is increased, the bed passes form the fixed bed to the stable spouted bed regime. As the length of the central draft tube is increased the minimum spouting velocity decreases. Therefore, the increasing in the draft tube length enhances the stable operating conditions. Thus, with the longest draft tube the maximum range of stable operating conditions is reached.

The bed stability for binary mixtures of limestone of Sauter average diameter, $\overline{d_S}$ = 1.45 mm is plotted in Figure 4 for the same experimental conditions than in Figure 3. As it is observed as Sauter average diameter decreases the minimum spouting velocity decreases, therefore the stable operating conditions zone enlarges.

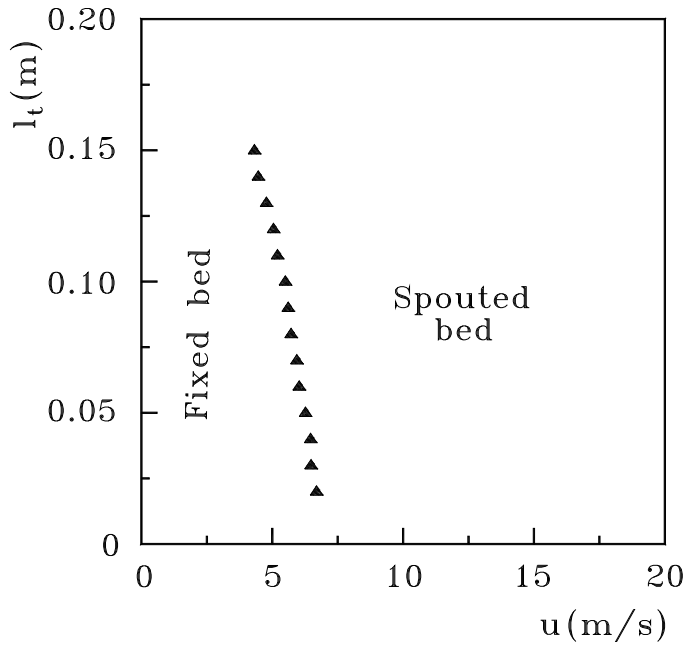

Figure 4. Operating map. System: γ= 36º, D_o= 0.04 m, beds of mixtures of limestone of Sauter average diameter $\overline{d_S}$ = 1.45 mm. Draft tube of d_d= 0.04 m and h_d= 0.05 m.

4. Conclusions

In all the experimental systems studied, the introduction of a central draft tube in the bed enlarges the range of operating conditions in conical spouted beds.

The stability of binary mixtures of different particle diameter in conical spouted beds with draft tube depends on the length of the draft tube. The increasing in the length of the draft tube gives way to a decreasing in the minimum spouting velocity, therefore an increasing in the range of operating conditions in spouting regime. It has been proven that by means of an appropriate design of the draft tube, the range of stable operating conditions of binary mixtures in conical spouted beds with a draft tube is wider than without draft tube without any instability or operation drawbacks.

References

Buchanan, R.H., Wilson B. (1965). Fluid-Lift Solids Recirculator, *Mech. & Chem. Eng. Transactions,* Vol. 1(1), 117-124.

Erbil, A.C. (2003). Annulus Leakage and Distribution of the Fluid Flow in a Liquid Spout-Fluid Bed with a Draft Tube, *Chem. Eng. Sci.* Vol. 58(20), 4739-4745.

Freitas, L.A.P., Freire, J.T. (2002). Sensitivity Analysis on the Fluid Dynamics of a Draft Tube Spouted Bed with Bottom Particles Feed, *Drying Technol*., Vol. 20(6), 1161-1175.

Geldart, D. (1973). Types of Gas Fluidization, *Powder Technol.* Vol. 7(5), 285-292.

Geldart, D. (1986). *Gas Fluidization Technology*, John Wiley, New York.

Hattori, H., Ito, S., Onezawa, T., Yamada, K., Yanai, S. (2004). Fluid and Solids Flow Affecting the Solids Circulation Rate in Spouted Beds with a Draft-Tube, *J. Chem. Eng. of Jpn.,* Vol. 37(9), 1085-1091.

Ishikura, T., Nagashima, H., Ide, M. (2003). Hydrodynamics of a Spouted Bed with a Porous Draft Tube Containing a Small Amount of Finer Particles. *Powder Tehnol*. Vol. 131, 56-65.

Khoe, G.K., Van Brakel, J. (1983). Drying Characteristics of a Draft Tube Spouted Bed, *Can. J. Chem. Eng*., Vol. 61, 411-418.

Konduri, R.K., Altwicker, E.R., Morgan, M.H.III. (1995). Atmospheric Spouted bed Combustion: the Role of Hydrodynamics in Emissions Generation and Control, *Can. J. Chem. Eng*. Vol. 73(5), 744-754.
Konduri, R.K., Altwicker, E.R., Morgan, M.H.III. (1999). Design and Scale-up of a Spouted-Bed Combustor, *Chem. Eng. Sci*., Vol. 54(2), 185-204.
Krambrock, W. (1976). Mixing and Homogenizing of Granular Bulk Material in a Pneumatic Mixer Unit, *Powder Technol.,* Vol. 15, 199-206.
Littman, H., Morgan, M.H.III., Morgan, C.B. (1997). A new Computer Controlled Wurster-type Particle Coating Apparatus, *AIChE Symp. Ser*. Vol. 317, 125-130.
Matthew, M.C., Morgan, M.H.III, Littman, H. (1988). Study of the hydrodynamics within a draft tube spouted bed system", *Can. J. Chem. Eng.,* Vol. 66(6), 908-918.
Muir, J.R., Berruti, F., Behie, L.A. (1990). Solids Circulation in Spouted and Spout-Fluid Beds with Draft Tubes, *Chem. Eng. Commun*. Vol. 88, 153-171.
Olazar, M., San José, M.J., Aguayo, A.T., Arandes, J.M., Bilbao, J. (1992). Stable Operation Conditions for Gas-Solid Contact Regimes in Conical Spouted Beds, *Ind. Eng. Chem. Res.,* Vol. 31(7), 1784-1792.
Olazar, M., San José, M.J. Alvarez, S. Morales, A., Bilbao, J. (2004). Design in Conical Spouted Beds for the Handling of Low-Density Solids, *Ind. Eng. Chem. Res.,* Vol. 43, 655-661.
San José, M.J. (1991). Operation Regimes in conical Spouted Beds. Stability Conditions and Hydrodynamics. Ph.D. Thesis. University of the Basque Country, Bilbao, Spain.
San José, M.J., Olazar, M., Aguayo, A.T., Arandes, J.M., Bilbao, J. (1991). Design and Hydrodynamics of Conical Jet Spouted Beds", *Récent Progrès en Génie des Procédés, La Fluidisation*, Laguerie, C. and Guigon, P. eds; Lavoisier-Technique et documentation: París, Vol 5, 146-153.
San José, M.J., Alvarez, S., Izquierdo, M.A., Aguado, R., Olazar, M. (2002). Conical Spouted Bed Technology with Internal Devices for Combustion of Wood Wastes". *15th International Congress of Chemical and Process Engineering-CHISA,* Praga, 271-272.
San José, M.J., Alvarez, S., Ortiz de Salazar, A., Olazar, M., Bilbao, J. (2005). Spout Geometry in Shallow Spouted Beds with Solids of Different Density and Different Sphericity, *Ind. Eng. Chem. Res.*, Vol. 44, 8393-8400.
San José, M.J., Alvarez, S., Ortiz de Salazar, A., Olazar, M. and Bilbao, J. (2006). Operation Conditions in the Treatment of Biomass Wastes by Combustion in a Conical Spouted Bed. *Science in Thermal and Chemical Biomass Conversion*, Bridgwater, A.V., Boocock, D.G.B., Newbury Berks, UK: CPL press. vol. 1, 228-236.
San José, M.J., Alvarez, S., Ortiz de Salazar, A., Olazar, M., Bilbao, J. (2007). Operating Conditions of Conical Spouted Beds with a Draft Tube. Effect of the Diameter of the Draft Tube and of the Height of Entrainment Zone, *Ind. Eng. Chem. Res.*, Vol. 46, 2877-2884.
Stocker, R.K., Eng, J.H., Svrcek, W.Y., Behie, L.A. (1989). Ultrapyrolysis of Propane in a Spouted-Bed Reactor with a Draft Tube, *AIChE J.* Vol. 35 (10), 1617-1624.
Stocker, R.K., Eng, J.H., Behie, L.A. (1990). Hydrodynamic and Thermal Modeling of a High-Temperature Spouted-Bed Reactor with a Draft Tube, *Can. J. Chem. Eng*., Vol. 68(2), 302-311.
Szafran, R.G., Kmiec, A. (2004). CFD Modeling of Heat and Mass Transfer in a Spouted Bed Dryer, *Ind. Eng. Chem. Res*., Vol. 43(4), 1113-1124.
Yang, W.C., Keairns, D.L. (1983). Studies on the Solid Circulation Rate and Gas Bypassing in Spouted Bed with a Draft Tube, *Can. J. Chem. Eng.,* Vol. 61(3), 349-355.

Acknowledgements

This work was carried out with the financial support of the Ministry of Industry of the Basque Government (Project EPIMATP2 and Project DIPE 07/09).

Proceedings of the 10th International Chemical and
Biological Engineering Conference - CHEMPOR 2008
Braga, Portugal, September 4-6, 2008
E.C. Ferreira and M. Mota (Eds.)

Production of hydrogen by methane steam reforming coupled with CO_2 sorption

Eduardo L. G. Oliveira, Carlos A. Grande, Alirio E. Rodrigues

LSRE – Laboratory of Separation and Reaction Engineering, Faculty of Engineering, University of Porto. Porto, Portugal (arodrig@fe.up.pt)

Keyword: Sorption-enhanced reaction process, steam methane reforming, carbon dioxide, hydrogen production
Topic: Sustainable process-product development through green chemistry

1. Abstract

Hydrogen is becoming the fuel of the future. The most important technology for the production of hydrogen is methane steam reforming (SMR) (Twigg, 1989). However, there are high costs associated, both in energy and materials, as the reaction has to be carried out at high temperatures (973 K) to achieve high methane conversions.

The combination of reaction and sorption in the reactor displaces the equilibrium maintaining a high conversion at lower temperatures (~773 K) which reduces the material and energy costs of the process. The sorption of carbon dioxide is also of interest as we are able to produce hydrogen with very low (or inexistent) carbon dioxide emissions. The sorbed carbon dioxide can be sent to storage facilities.

2. Experimental

Three commercial hydrotalcite extrudates (MG30, MG50, MG70) from Sasol (Germany) were impregnated with K_2CO_3 and Cs_2CO_3 (ACS reagents) from Sigma-Aldrich. The impregnation protocol was based on literature (Nataraj, et al., 2000). Scanning Electron Microscopy (SEM) was performed on a JEOL JSM-6301F (JEOL, Japan) coupled with an Energy dispersive X-ray spectroscope (EDX) Oxford INCA Energy 350 (Oxford Instruments, UK). The surface area of the fresh sorbents was determined by N_2 adsorption at 77 K with a Coulter Omnisorp 100 CX apparatus.

The CO_2 sorption equilibrium was measured by breakthrough experiments. The feed stream comprises helium, carbon dioxide and water while helium and water were employed for sorbent regeneration. The liquid water flowrate was controlled using a HPLC pump (Merck-Hitachi, Japan) and was vaporized before entering into the column. Both CO_2 and He flowrates were controlled by independent mass flow controllers. After the column the water was condensed using an ice trap, and CO_2 concentration was measured each 10 seconds using an infrared detector (Madur, Austria). In Table 1 are reported the operating conditions of all the CO_2 sorption experiments using the MG30-K and Mg30-Cs samples.

Table 1. Experimental conditions used in the equilibrium sorption experiments

Temperature [K]	579, 676, 783
Pressure [bar]	2
P_{CO2} [bar]	0.05, 0.09, 0.19, 0.40

The SERP experiments were performed with just the catalyst and with the catalyst and the adsorbent combined in a proportion of 3:1 adsorbent/catalyst. In the experiments with combined adsorbent and catalyst a layered structure was used combining 2 layers of catalyst with a layer

of adsorbent separating them and a layer of adsorbent in the end. Each layer had half the catalyst/adsorbent and the layers were separated by a metal mesh. The experimental conditions and the mass of catalyst and sorbent used for each of the experiments performed can be seen in Table 2.

Table 2. Experimental conditions used in the SERP experiments

P [bar]	T [K]	Y_{CH4} [%]	Q_{H2O}(l) [ml/min]	Q_{CH4} [SLPM]	m_{cat} [kg]	m_{ads} [kg]
2 ± 0.05	823.15	20.6	0.9	0.147	2.053×10^{-2}	0
2 ± 0.05	773.15	20.6	0.9	0.147	1.8206×10^{-2}	5.6024×10^{-2}

The methane flowrate was started at time 0 and samples of the reactor effluent were taken. All the compositions were analyzed by gas chromatography.

3. Results

In this work, the sorption enhanced reaction process (SERP) concept was tested for SMR using a Ni/Al_2O_3 catalyst and a hydrotalcite sorbent.

3.1. Sorbent selection

The commercial hydrotalcite samples received from SASOL were impregnated with potassium and cesium (Nataraj, et al., 2000). The three pure hydrotalcite samples (MG30, MG50 and MG70) as well as the alkali-modified (with K and Cs) materials were tested to determine the material with higher capacity for CO_2 sorption in the presence of water vapor. The screening was based in a single point of CO_2 sorption equilibrium at 676 K obtained by breakthrough curves employing a stream with carbon dioxide, water vapor and helium (considered as inert gas). In all the experiments, the partial pressure of CO_2 was close to 0.40 bar and the total pressure of the system was 2 bar. The purpose of this screening was to select the two best samples, one modified with cesium and other modified with potassium to measure sorption equilibrium isotherms at three different temperatures. The screening results can be seen in Figure 1.

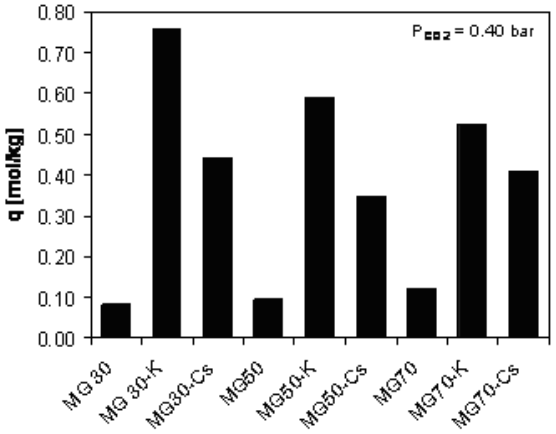

Figure 1. Comparison of the sorption capacity of CO_2 for pure and alkali-modified (Cs and K) hydrotalcites at 676 K, 2 bar total pressure, P_{CO2} of 0.40 bar in the presence of water vapor.

The pure hydrotalcite samples show a CO_2 sorption capacity lower than 0.1 mol/kg and thus cannot be used for SERP. The potassium modified sample that presented the higher sorption capacity was the MG30-K (0.76 mol/kg). In the cesium modified samples the MG70-Cs presented the highest sorption capacity followed by the MG30-Cs. The MG30-K was selected to

measure sorption equilibrium. To study the effect of Cs in the hydrotalcites, the MG30-Cs was also selected to measure sorption equilibrium.

Carbon dioxide breakthrough experiments were performed at various temperatures and CO_2 partial pressures (see Table 1). The equilibrium sorption capacity was determined and the sorption isotherms are presented in Figure 2.

In the isotherms, the capacity at 676 K is higher than at 579 K and the sorption is reversible. This "crossing" in isotherms and the reversibility cannot be explained by sorption alone (physical or chemical). One possible explanation is that together with sorption, an endothermic reaction also occurs and its conversion increases together with temperature. The bi-Langmuir model (equation 1) was selected to describe this behavior as it allows for the combination of 2 distinct sorption mechanisms. A recent work (Lee, et al., 2007) using a similar sorbent proposed a combination of chemisorption and complexation to account for the CO_2 sorption but the maximum in the sorption capacity was not reported. The bi-Langmuir parameters can be seen in Table 3.

$$q_{ads} = q_{max1}\frac{K_1(T)P}{1+K_1(T)P} + q_{max2}\frac{K_2(T)P}{1+K_2(T)P} \qquad (1)$$

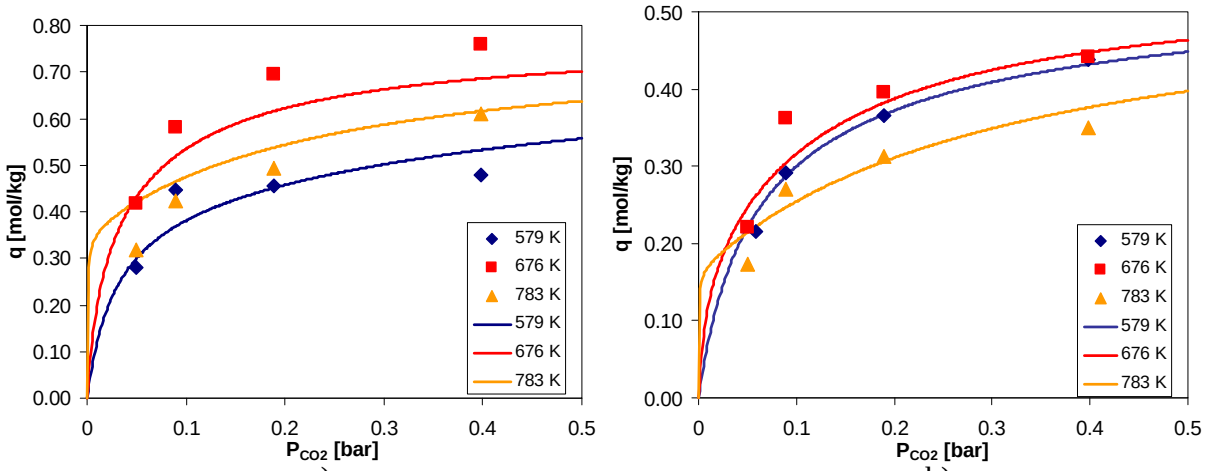

Figure 2. Sorption equilibrium isotherms of CO_2 (in the presence of water vapor) on: a)MG30-K and b) MG30-Cs hydrotalcite samples at 579, 676 and 783 K (points). Bi-Langmuir model fit (lines).

Table 3. Fitting parameters of the bi-Langmuir model for the MG30-K and MG30-Cs hydrotalcite samples (Oliveira, et al., 2008)

Parameters	MG30-K	MG30-Cs
q_{max1} [mol/kg]	0.423	0.383
k_{01} [bar^{-1}]	9.07 x10-3	1.26x10-2
(-ΔH_1) [kJ/mol]	40.0	35.9
q_{max2} [mol/kg]	0.351	0.164
k02 [bar^{-1}]	1.01 x1012	9.13x1011
(-ΔH_2) [kJ/mol]	-130.8	-127.4

3.2. SERP proof of concept

A Ni/Al_2O_3 catalyst from Degussa (Germany) was used in combination with the cesium modified hydrotalcite sample to perform the SERP proof of concept. In Figure 3 the evolution of the methane conversions in the first 500 s of operation of the SERP experiment and the traditional steam reforming are compared. Due to restrictions of the hydrotalcite material, the SERP experiment was performed at a lower temperature than the SMR experiment.

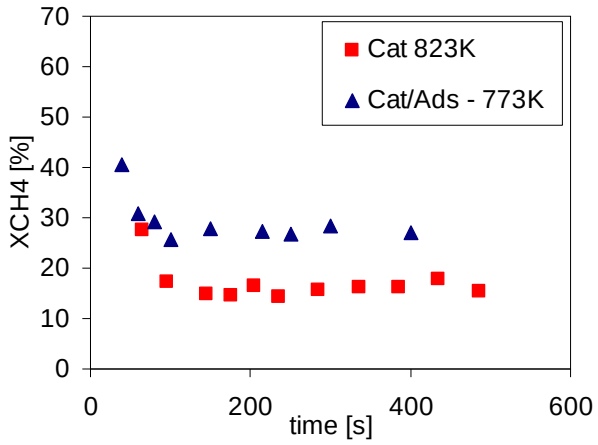

Figure 3. Methane conversion for traditional SMR and SERP (see Table 2).

The methane conversion of the traditional steam reforming was approximately 15% while in SERP we were able to achieve 27% methane conversion. As the same mass of catalyst was used in both experiments we can say that the SERP enhanced the conversion in more than 10 percentage points even though it was operating at a lower temperature. The use of lower temperatures has an impact both in the energy and material costs of hydrogen production.

In Figure 4 we can see the evolution of the compositions of the various components of the dry effluent.

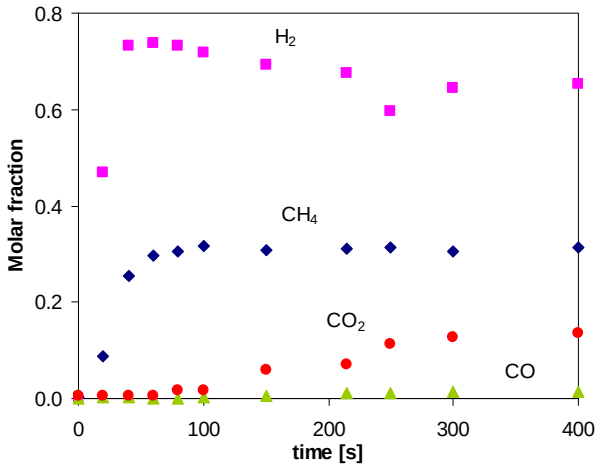

Figure 4. Dry effluent composition vs time for the SERP experiment at 773 K, 2 bar total pressure and 20% CH_4 at inlet.

The effluent stream was composed only of methane and hydrogen during the first 80 s of operation. Comparing with the traditional SMR, the results of Figure 4 indicate that fewer separation processes will be necessary after the SERP reactor. When the sorbent is saturated it is necessary to regenerate by pressure swing adsorption. During the regeneration step it is possible to recover the CO_2 for sequestration.

This proof of concept indicates that there are three main advantages of the use of SERP when compared to tradition SMR:

1. It is possible to produce hydrogen without carbon oxides, reducing the separation train after the reactor – reduction of investment and operation costs;
2. The temperature of operation can be reduced – decreasing operation and investment costs;
3. The carbon dioxide can be recovered for sequestration – reduction of the CO_2 emissions (Kyoto protocol).

4. Conclusions

Nine hydrotalcite materials were prepared and screened for carbon dioxide sorption at high temperatures [579-783] K. The MG30-K and MG30-Cs samples were selected for sorption equilibrium studies.

The sorption equilibrium isotherms showed a maximum in the sorption capacity at 676 K. The bi-Langmuir isotherm was used to describe this behavior.

The sorption enhanced reaction process proof of concept was also performed in this study. Comparing SERP with traditional steam methane reforming, the SERP was able to produce hydrogen with methane as the only impurity during 80 s. The conversion of methane of the SERP at 773 K was 27% while conversion of the traditional SMR was only 15% at 823 K, showing the advantage of the SERP.

5. References

Lee, K. B.; Verdooren, A.; Caram, H. S.; Sircar, S. (2007). Chemisorption of carbon dioxide on potassium-carbonate-promoted hydrotalcite. *Journal of Colloid and Interface Science*, 308, 30-39.

Nataraj, S.; Carvill, B. T.; Hufton, J. R.; Mayorga, S. G.; Gaffney, T. R.; Brzozowski, J. R. (2000). Materials selectively adsorbing CO_2 from CO_2 containing streams. European Patent 1006079 A1.

Oliveira, E. L. G.; Grande, C. A.; Rodrigues, A. E. (2008). CO_2 sorption on hydrotalcite and alkali-modified (K and Cs) hydrotalcites at high temperatures. *Separation and Purification Technology*, 62, 137-147.

Twigg, M. V. (1989). *Catalyst Handbook*, Wolfe Publishing Ltd, England.

Proceedings of the 10th International Chemical and
Biological Engineering Conference - CHEMPOR 2008
Braga, Portugal, September 4-6, 2008
E.C. Ferreira and M. Mota (Eds.)

Modelling of Light Olefin Transformation over ZSM-5 Zeolites with Different Acid Strengths

P. Oliveira[1], P. Borges[1], R. Ramos Pinto[1,2], M.A.N.D.A. Lemos[1], F. Lemos[1*], F. Ramôa Ribeiro[1]

[1] IBB – Institute for Biotechnology and Bioengineering, Centre for Biological and Chemical Engineering, Instituto Superior Técnico, Av. Rovisco Pais, 1049-001 Lisboa, Portugal.

[2] ISCSP, Pólo Universitário do Alto da Ajuda, Rua Almerindo Lessa, 1349-055 Lisboa, Portugal.

Keywords: olefin transformation; acid catalysis; ZSM-5 zeolite; kinetic model

Topic: Catalysis and reaction engineering

Abstract

Data for the acid-catalysed transformation of propylene over four ZSM-5 zeolites with different degrees of sodium exchanged, at various temperatures and partial pressures, was analysed. This transformation is characterized by the fact that, as the temperature increased, the propene consumption rate decreased. In this work the rather complex network mechanism involved in the transformation of these light olefins was approximated by one simple kinetic model. It only details the products by the number of carbon atoms and was developed without the explicit inclusion of the step corresponding to the adsorption of the reactant molecules, altough adsorption effects are, in fact, the reason why apparent negative activation energies are obtained. Polanyi equations were used to derive quantitative relations between the ammonia adsorption energy and the activation energy. It was observed that, for the various ZSM-5 zeolites with different acidities, the model describes well the product distribution.

1 Introduction

The transformation of alkenes over acid catalysts is a very significant reaction with impact in many different applications for the chemical and petrochemical industries (O'Connor & Kojima, 1990) such as the catalytic oligomerization of light olefins, relevant in many fuel-related processes which produce hydrocarbons in the gasoline (C5 to C10) and diesel (C10 to C20) ranges (Tabak & Krambeck, 1986). These reactions are also relevant in the MTG and MTO, which convert methanol to gasoline and to olefins. The use of the ZSM-5 zeolite and other similar zeolites, to perform this reaction, was proposed in the mid 70' and 80's, in the MOGD process (Mobil olefin to gasoline and distillate) (Garwood, 1979 & 1980; Tabak, 1981 & 1985), as possible replacements for the classical phosphoric acid impregnated catalyst. This process, which produces highly branched hydrocarbons with high octane number, acquires a renovated interest with the current petroleum crises and the demand for more efficient catalysts becomes even more critical. To achieve this goal, a deep understanding of the fundamental aspects of these transformations is vital and creates a drive for the development of practical models that enable the rapid analysis of new catalytic materials and even that will allow the prediction of the catalytic behavior of these materials based on very simple characterization tests. This need is particularly

* Corresponding author. E-mail:francisco.lemos@ ist.utl.pt

important in the context of high-throughput catalyst development techniques. Aspects pertaining to the kinetics and thermodynamics of this reaction, covering different operating conditions, have been the subject of various publications (van den Berg et al., 1983; Wilshier, Smart, Western, Mole, & Behrsing, 1987; Yarlagadda, Lund, & Ruckenstein, 1990).

The simplified kinetic mechanism for this kind of reactions (Tabak & Krambeck, 1986) is initiated by a series of oligomerization steps, where linear dimers, trimers, etc, of the original olefin are produced. These newly formed molecules can undergo secondary reactions, (isomerisation, cracking, aromatization, etc.), originating a wide variety of other hydrocarbon molecules.

The objective of this paper is to initiate the mechanistic analysis of the catalytic transformation of propylene, over four ZSM-5 zeolites with different degrees of sodium exchanged, at atmospheric pressure, under different conditions of temperature and inlet concentration of the reactant. It was observed that for propene, the overall activity decreased with increasing temperature, thus presenting an apparent negative activation energy. This effect has been explained by us, as the coupling of adsorption and kinetic effects (Borges et al., 2007).

Despite the fact that the four different catalysts that were used have different acidities we can show that the same reaction network, with the same kinetic rate constants, can be applied to describe the results for all ZSM-5 zeolites, indicating that not only the underlying mechanism is the same for all catalysts, but that the transformation can be described by the same kinetics if the acid strength distribution is taken into account.

2 Experimental

Catalyst preparation

The HZSM-5 catalyst was prepared from a zeolite (ammonia form), with molar silica to alumina ratio of 30, from Zeolyst (CBV 3024G). The other three zeolites, with different acidity strength and total amount of sites, were obtained exchanging the original zeolite (designated as HZSM-5 above) with different aqueous solutions of sodium nitrate, to replace proton by sodium. This prevents the modified sites from showing Brønsted acidity, by decreasing the total amount of hydrogen obtained after the calcinations. All the exchanges were performed at room temperature varying only the concentration of the solution used and the number of exchanges that each sample was subjected to, as shown in Figure 1.

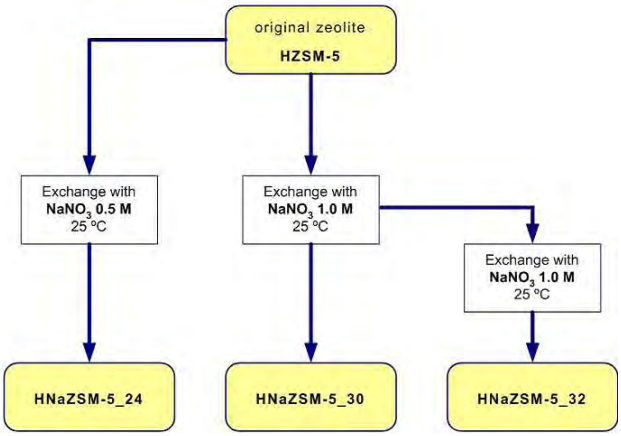

Figure 1 – Schematic of the ionic exchange paths

The new different zeolites prepared, were designated as HNaZSM-5_24, HNaZSM-5_30 and HNaZSM-5_32. The last index in their code name indicates the percentage of sodium that was exchanged, as obtained from the elemental analysis, that is, the percentage of sites exchanged with sodium in comparison to the total amount of sites in the same zeolite sample.

All zeolites were calcined at 500 ºC during 8 hours under a flow of 0.5 litres of dry air per hour and per gram of catalyst. After calcination, the zeolite was kept at room temperature in a constant and high humidity container.

Transformation of small olefins

The transformation of propene was carried out in a fixed-bed continuous flow reactor, at atmospheric pressure and within a temperature range from 300 ºC to 450 ºC. The partial pressure of the reactant was varied from 5 % to 30 %, diluted with nitrogen. Total flow of the reaction mixture was 120 ml/min. The reactant was fed for a few minutes and then the effluent stream was sampled and analysed, while reactant feeding was interrupted. During the analysis time the catalyst was kept under a flow of pure nitrogen at the working temperature. Fresh catalyst was used for each run. No deactivation with time-on-stream was detected during the experiment and no coke was detected (by thermal analysis, under air, up to 700 ºC) on the used catalyst.

External transport limitations were checked by varying the flow rate while keeping the same catalyst mass; no changes in reaction rate were observed. Internal limitations were checked, using the Weisz-Prater criterion (Froment & Bischoff, 1990). This has been reported elsewhere (Borges et al., 2007).

The analysis of the effluent was carried out with a Shimadzu GC-9A gas chromatograph equipped with a Chrompack Plot CP7515 fused silica column and a flame ionization detector. The chromatogram was integrated with a Shimadzu C-R3A integrator.

For the transformation of propene, 75 mg of each HZSM-5 catalyst (wet basis) was used.

3 Results and discussion

Kinetic model

It is assumed that the first step in the transformation of small olefins is oligomerization, leading to heavier species. These heavier species will be able to transform by a variety of processes, including β-scission, establishing a complex reaction network. In the first attempts to build the reaction network, we have only detailed products by their number of carbon atoms (no distinction between olefins and paraffins is made at this stage). Under this approach a model was developed and assumes that the reaction network occurs in pseudo-homogeneous conditions (without adsorption). This way, since only oligomerization/cracking reactions are accounted for, the reaction network can be described by the following equation:

$$C_n + C_m \underset{\leftarrow}{\overset{\rightarrow}{}} C_{n+m} \tag{1}$$

where n and $m \geq 2$ and $n+m \leq 8$. (no protolytic cracking was considered at this stage, and, thus, the formation of methane was excluded). Within this framework, the reaction network is described by just 9 different reactions. Assuming that reactions are of simple order in relation to the different species involved and that requires a total of 18 kinetic rate constants, the forward (k_i corresponding to the oligomerization) and backward (k_{-i} corresponding to the cracking) rate constants.

$$r_i = k_i \cdot p(C_n) \cdot p(C_m) - k_{-i} \cdot p(C_{n+m}) \tag{2}$$

These were assumed as obeying the Arrhenius law and Polanyi equations.

$$k_i = k_{ref,i} \cdot e^{-\frac{E_{a0,i}}{R}\left(\frac{1}{T}-\frac{1}{T_{ref}}\right)} \sum_j q_j \cdot e^{-\frac{\delta_i \cdot E_{a_j}^{NH_3}}{R \cdot T}} \tag{3}$$

where $k_{ref,i} = k_{0,i} \cdot e^{-\frac{E_{a0,i}}{R \cdot T_{ref}}}$, $k_{0,i}$ is the pre-exponential factor for reaction i, $E_{a_{0,i}}$ is the

activation energy for a specific reaction without the acidity effect, δ_i reflects the effect of the acid strength in the activation energy for a given reaction and q_j is proportional to the acid centres number with strength $E_{a_j}^{NH_3}$.

Experimental results

Values for the catalytic activity obtained for propene with the four different zeolites are shown in Figure 2.

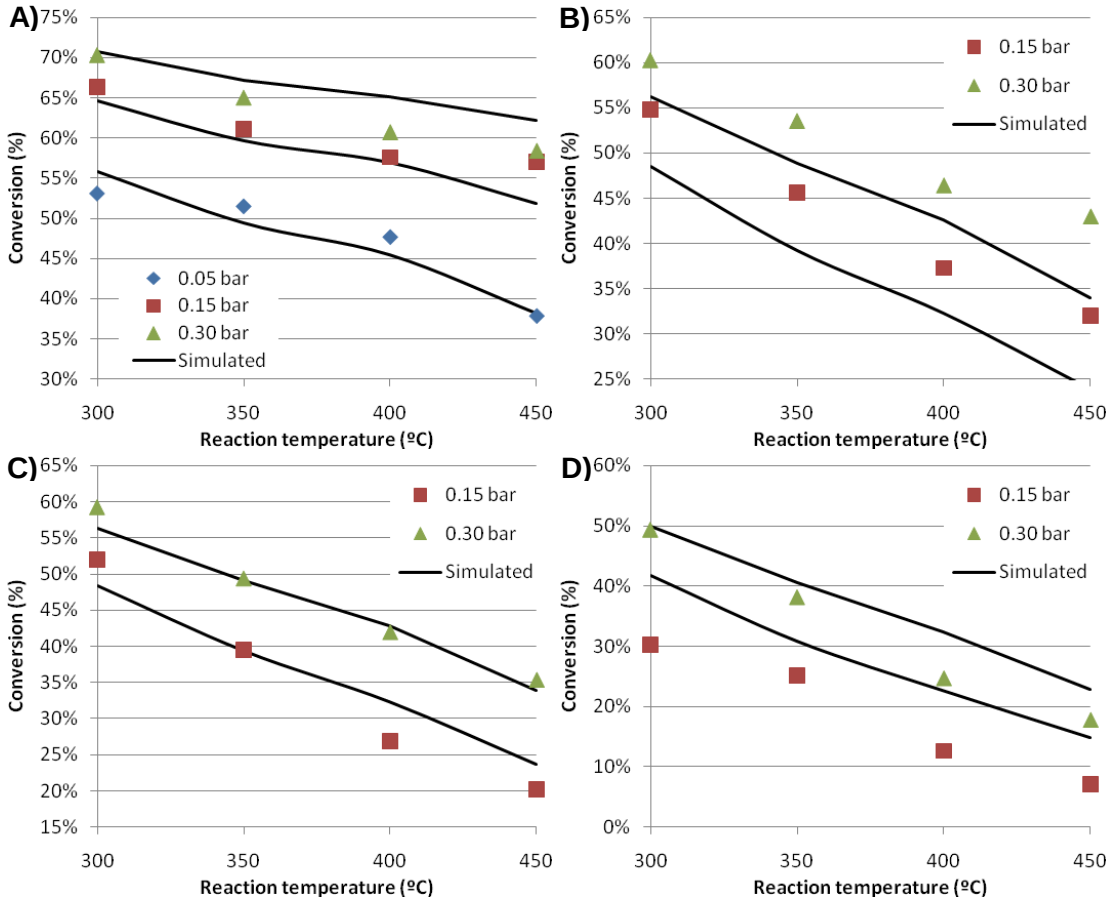

Figure 2 – Conversion of the transformation of propene with the different zeolites and model results. A) HZSM-5; B) HNaZSM-5_24; C) HNaZSM-5_30; D) HNaZSM-5_32

In the above figure is visible that conversion of propene lowers with the increase of temperature. The main products observed are olefins, resulting from oligomerization reactions, and followed by cracking; however, significant quantities of aromatic and paraffinic products are also observed, resulting from aromatization and hydrogen transfer secondary reactions (see Borges et al., 2007 for details). The increase in operating temperature produced a shifting of the products towards lighter hydrocarbons, while an increase in partial pressure had the opposite effect, as it would be expected.

The kinetic model was fitted to the experimental data using a non-linear least-squares regression technique implemented in commercial spreadsheet software (Excel). The set of experimental data used comprises all the results obtained for all the catalyst, i.e., the model will describe all the experiments with a single set of parameters, regardless of catalyst, partial pressure or temperature.

All material balances were numerically integrated using the Euler method, to obtain a computed product distribution. The sum of the squares of the residuals (difference between the experimental values and those obtained from the model) were minimized, using the Solver tool. In order to reduce correlation between the pre-exponential factors

and the activation energies, in the Arrhenius kinetic term a reference temperature was used; this temperature was the experimental temperature closest to the mean of the temperature range covered in the experiments.

The parameters obtained are shown in Table 1 and, in order to allow a simple evaluation of the quality of the fittings, the parity plot obtained and some examples of the product distributions obtained using the model for the different catalysts that were used are depicted in Figure 3.

Table 1. Parameters obtained by fitting the model, to the tests performed with the four HZSM-5 catalysts. k' is reported at 350 ºC.

Reaction network	k_{ref} mol·min^{-1} $g_{zeolite}$		E_{a0} kJ.mol^{-1}		δ	
	forward	backward	forward	backward	forward	backward
$2C_2 \rightleftarrows C_4$	1,31×10^{-1}	1,43×10^{-4}	1,18×10^{4}	1,10×10^{5}	0,00	-0,16
$C_2 + C_3 \rightleftarrows C_5$	3,31×10^{-4}	1,04×10^{-2}	-4,79×10^{4}	1,19×10^{5}	0,01	0,45
$C_2 + C_4 \rightleftarrows C_6$	1,36×10^{-1}	7,64×10^{-4}	5,35×10^{4}	1,05×10^{5}	0,14	-0,08
$C_2 + C_5 \rightleftarrows C_7$	2,15×10^{-2}	1,22×10^{-3}	2,85×10^{2}	1,67×10^{4}	0,01	0,03
$C_2 + C_6 \rightleftarrows C_8$	1,37×10^{-2}	4,77×10^{-3}	2,48×10^{4}	5,06×10^{4}	0,05	0,78
$2C_3 \rightleftarrows C_6$	9,66×10^{-7}	3,34×10^{-2}	-7,95×10^{3}	4,85×10^{4}	0,00	0,41
$C_3 + C_4 \rightleftarrows C_7$	1,09×10^{-3}	4,78×10^{-2}	9,53×10^{4}	5,36×10^{4}	0,01	0,37
$C_3 + C_5 \rightleftarrows C_8$	3,17×10^{-3}	1,04×10^{-2}	5,69×10^{4}	1,47×10^{3}	0,00	0,34
$2C_4 \rightleftarrows C_8$	1,43×10^{-3}	2,04×10^{-2}	8,73×10^{4}	4,32×10^{4}	0,00	0,30

As it can be seen from table 1, some of the apparent activation energies are negative because this model does not explicitly take adsorption into account,as it would be expected from the results presented before (Borges et al., 2007).

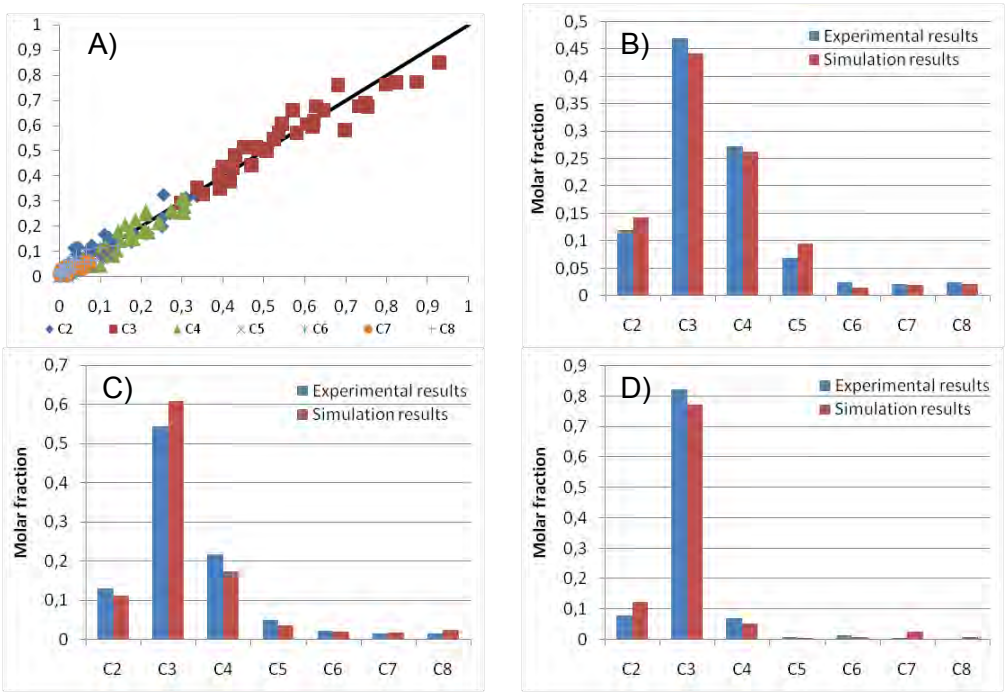

Figure 3 – A) Parity plot. B) Product distribution obtained for the transformation of propylene at 5 kPa and 300ºC for catalyst HZSM-5 and predicted by the Model. C) Product distribution obtained for the transformation of propylene at 15 kPa and 350ºC for the less sodium exchanged HZSM-5 catalyst and predicted by the Model. D) Product distribution obtained for the transformation of propylene at 30 kPa and 450ºC for the most sodium exchanged HZSM-5 catalyst and predicted by the Model

4 Conclusions

Although the model used was relatively simple, it is able to provide a generally acceptable description of the activity and distribution of products for the experiments under analysis.

It is very important to note, that, although the number of parameters is relatively high, only one set of parameters is used to describe all the available experimental data, covering not only all the temperatures and partial pressures used in this study, but also all the catalyst tested. This result opens the way for the development of universal kinetic models that may be applied to any HZSM-5 catalyst, or even to any mixture of HZSM-5 catalysts, for a given reactant.

5 References

van den Berg, J. P., Wolthuizen, J. P., Clague, A. D. H., Hays, G. R., Huis, R., & van Hooff, J. H. C. (1983). Low-temperature oligomerization of small olefins on zeolite H-ZSM-5. An investigation with high-resolution solid-state 13C-NMR. *Journal of Catalysis*, *80*(1), 130-138.

Borges, P., Pinto, R. R., Lemos, M., Lemos, F., Védrine, J., Derouane, E., et al. (2007). Light olefin transformation over ZSM-5 zeolites: A kinetic model for olefin consumption. *Applied Catalysis A: General*, *324*, 20-29.

Froment, G. F., & Bischoff, K. B. (1990). *Chemical Reactor Analysis and Design* (2nd ed., p. 167). Wiley.

O'Connor, C. T., & Kojima, M. (1990). Alkene oligomerization. *Catalysis Today*, *6*(3), 329-349.

Tabak, S. A., & Krambeck, F. J. (1986). Conversion of propylene and butylene over ZSM-5 catalyst. *AIChE Journal*, *32*(9), 1526-1531.

Wilshier, K., Smart, P., Western, R., Mole, T., & Behrsing, T. (1987). Oligomerization of propene over H-ZSM-5 zeolite. *Applied Catalysis*, *31*(2), 339-359.

Yarlagadda, P., Lund, C., & Ruckenstein, E. (1990). Oligomerization of ethene and propene over composite zeolite catalysts. *Applied Catalysis*, *62*(1), 125-139.

Garwood, W.E., Caesar, P.D., Brennan, J.A. (1979), U.S. Patent 4,150,062.

Garwood, W.E., Lee, W. (1980), U.S. Patent 4,227,992.

Tabak, S.A. (1981), U.S. Patent 4,254,295.

Tabak, S.A., Wright, B.S., Owen,H. (1985), U.S. Patent 4,504,693.

Acknowledgments

The authors wish to thank to Fundação para a Ciência e Tecnologia for financial support for the PhD grants SFRH/BD/35820/2007 for Pedro Oliveira, SFRH/BD/3007/2000 for Pedro Borges and SFRH/BD/3006/2000 for Ricardo Ramos Pinto.

Proceedings of the 10th International Chemical and
Biological Engineering Conference - CHEMPOR 2008
Braga, Portugal, September 4-6, 2008
E.C. Ferreira and M. Mota (Eds.)

Abstract template for the CHEMPOR 2008 conference

CARBON DIOXIDE REFORMING OF METHANE OVER NI/γ-Al_2O_3 IN FLUIDIZED-BED REACTOR

José A. Pacífico[1*], Ana, C. Cabral[1], Nelson, M.L. Filho[1], Augusto, Knoechelmann[1], César, A.M. Abreu[1]

[1] UFPE – Chemical Engineering Department, Centre of Technology and Geo-Science Federal University of Pernambuco, Av. Prof. Artur de Sá, S/N, 50670–901 Recife-PE, Brazil.

Keywords: Methane reforming, nickel catalysts, fluidized bed reactor
Topic:Multi-scale and/or multi-disciplinary approach to process-product.

Abstract: To establish operational relations for the catalytic carbon dioxide reforming of methane into syngas, a one-dimensional Kunii-Levenspiel heterogeneous model for the fluidized bed reactor was developed. Effects of reaction parameters as temperature, and pressure on the dry reforming reaction were analyzed in terms of conversion, reagent and product concentrations. The fluidized-bed reactor presented the following dimensions: height of the reactor H_t = 1,180 mm, internal diameter D_{int} = 38 mm, particle diameter d_p = 70-85 μm, minimum fluidization velocity U_{mf} = 0.0011 m/s, superficial velocity U_o = 0.0191 m/s, mass of catalyst m_{cat} = 300 g, and the catalyst 4.98 wt% Ni/γ-Al_2O_3. The reactions were evaluated at 1023K, 1073K, and 1123K respectively, and under atmospheric pressure. Under these conditions and employing a Langmuir-Hinshelwood kinetic model, for 1073 K to 1123 K a methane conversion of 85,62 to 97.89% was obtained.

1. Introduction

Conventional fixed-bed steam methane reformers have some disadvantages, such as low heat transfer rates, diffusional resistance in catalyst pores and large temperature gradients. In addition, steam methane reforming, a highly endothermic process, is affected by the efficiency of the heat input into the reformer. The carbon dioxide reforming of methane may be presented as an alternative process, mainly when employed in a fluidized bed reactor. Improved heat transfer, catalyst uniformity, and the virtual elimination of diffusion limitations are the major advantages of when this reactor is employed (Chen, Honda and Zhang, 2004; Bradford and vannice, 1996; Souza, Aranda and Schmal, 2002). The catalyst particles in a fluidized bed has to be in a proper range, and they have to withstand the mechanical environment. Catalyst particles with a mean diameter in the range of 70 to 85 μm were employed and the thermal uniformity of the fluidized-bed was obtained at a flow rate three times the minimum fluidization velocity.

2. Experimental

The column was built in stainless steel, it has a diameter of 38 mm and a height of 1.180 mm (Figure 1). The bed pressure drops were measured with a differential

pressure transducer . The experimental fluidynamic data were obtained relating the pressure drop in the bed with the superficial velocity.

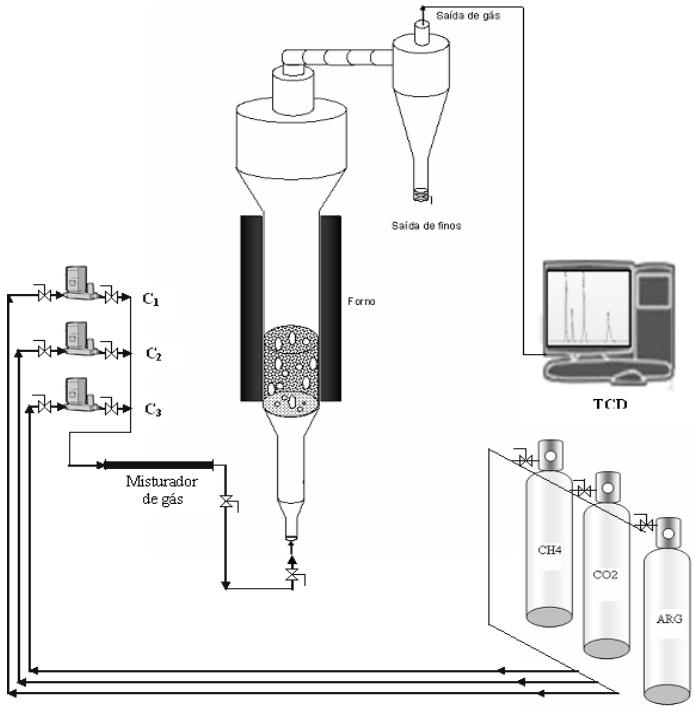

Figure 1. The Schematic representation of fluidized bed reactor

2. Results and Discussion

For evaluation of the process the main reaction considered were:

$$CO_2 + H_2 \leftrightarrow CO + H_2O \quad \Delta H_{298} = 41 kJ/mol \tag{1}$$

$$2CO \leftrightarrow CO_2 + C \ \Delta H_{298} = -172 kJ/mol \tag{2}$$

$$CH_4 \leftrightarrow C + 2H_2 \ \ \Delta H_{298} = 75 kJ/mol \tag{3}$$

Considering the reaction steps the following rate equations were proposed:

$$r_{CH_4} = \frac{k_1 K_{CH_4} C_{CH_4}}{1 + K_{CH_4} C_{CH_4}} \qquad \text{(step I)} \tag{4}$$

$$r_{CO_2} = k_2 \left(C_{H_2} C_{CO_2} - \frac{C_{CO} C_{H_2O}}{K_{eq}} \right) \quad \text{(step II)} \tag{5}$$

$$r_{CO_2} = k_3 C_{CO_2} \quad \text{(step III)} \tag{6}$$

The values of the kinetic parameters of the reaction steps obtained from the optimization procedures and the value of the equilibrium constant of the reverse water gas-shift reaction, are expressed in function of the operating temperature (Pacífico, Abreu, Santos and Lima Filho, 2008).

$$k_1 = 3{,}58 \times 10^9 \times \exp(-248.547 / RT) \tag{7}$$

$$k_2 = 1{,}07 \times 10^{13} \times \exp(-350.080 / RT) \tag{8}$$

$$k_3 = 1{,}16 \times 10^5 \times \exp(-115.860 / RT) \tag{9}$$

$$K_{CH_4} = 1{,}39 \times 10^{-11} \times \exp(167.320 / RT) \tag{10}$$

$$\begin{aligned} lnK_{eWRGS}(T) &:= 5.1377 + 0.2596 x ln(3.3540 x 10^{-3} xT) - \\ & 7.7989 x 10^{-4} xT + 2.2653 x 10^{-7} xT^2 - 2.9724 x 10^{-11} xT^3 - \\ & 4932.0430 xT^{-1} \end{aligned} \tag{11}$$

The solution of the mass balances, from the kinetic laws obtained from the experimental evaluation of steps 4, 5, and 6 of the reaction, and the temperature and the pressure employed, simulations were considered which produced the profiles presented in Figures 2. 3 and 4 in mass base..

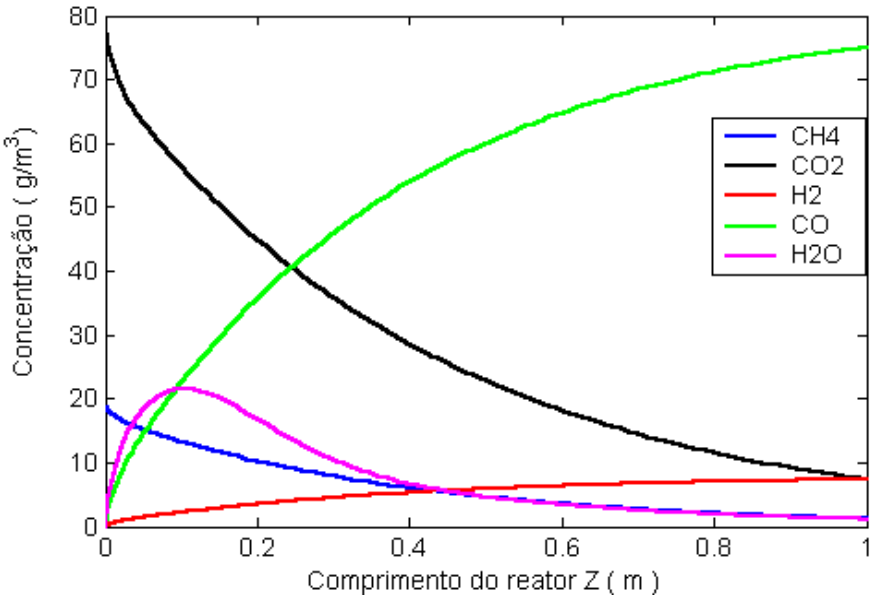

Figure 2. Schematic Profiles of reagents conversion and products.

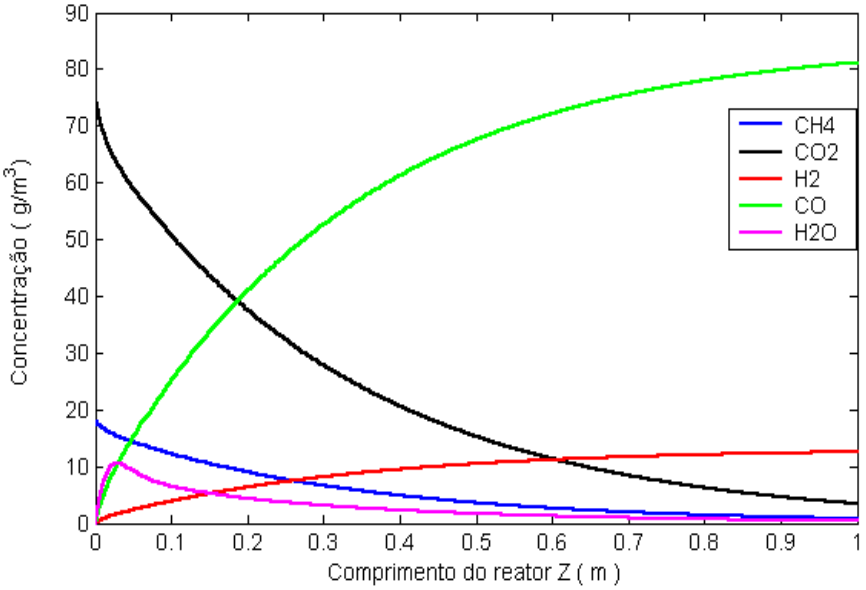

Figure 3. Schematic Profiles of reagents conversion and products.

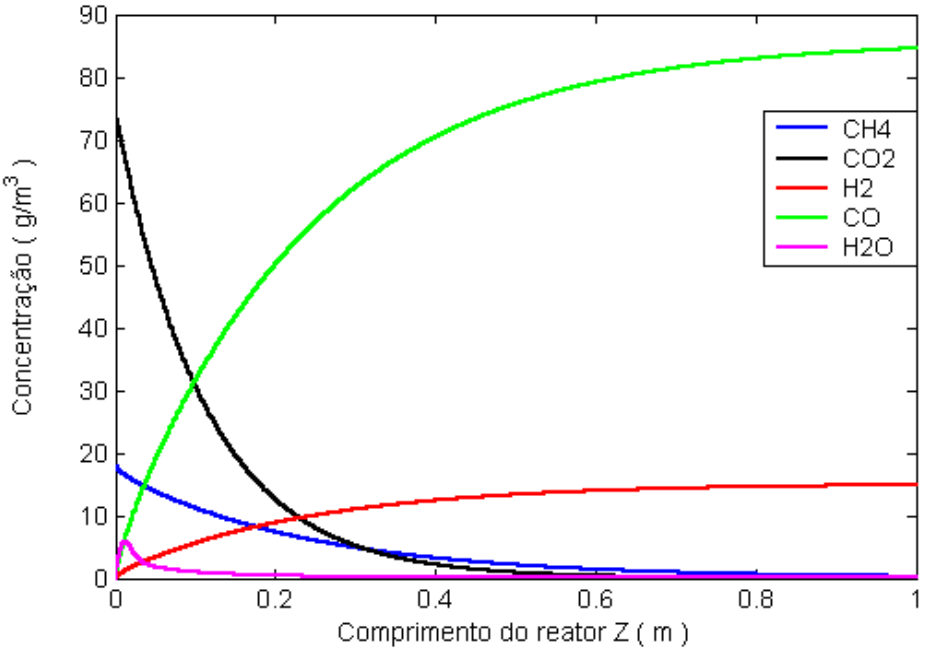

Figure 4. Schematic Profiles of reagents conversion and products.

3. Conclusions

From modeling and the simulation of the reforming process the concentration profiles of CH_4, CO_2, CO, and H_2O along of the fluidized-bed reactor were obtained. The curves in Figures 2, 3, and 4 indicate that, as the temparature of carbon dioxide reform of methane in the the fluidized bed reactor is maintained at a high level, water production via reverse water gas shift diminishes (Edward and Maitra,1995; Yaw and Amin 2005). So, the temperature increase

indicated a higher hydrogen and carbon monoxide production and less coke, as the Boudouard reaction is exothermic and at high temperatures it shifts to the left in the direction of carbon monoxide production.

References

Kunii, D., Levenspiel, O. (1987). Fluidization Engineering, volume 1, Krieger, Florida.

Chen, X., Honda, K., Zhang, Z.G. (2004). CO_2-CH_4 reforming over NiO/γ-Al_2O_3 in fixed-bed/fluidized-bed switching mode. *Catalysis Today*, 93-95, 87-93.

Bradford, M.C.J., Vannice, M.A. (1996). Catalitic Reforming of Methane With Carbon Dioxide Over Nikel Catalysts I – Catalysts Characterization and Activity. Apllied catalisys A: General, 142, 73-96.

Souza, M.M.V.M., Aranda, D.A.G., Schmal, M. (2002). Coke Formation on Pt/ZrO_2/Al_2O_3 Catalysts During CH_4 Reforming with CO_2. Industrial and Engineering Chemical Reserch, 41, 4681-4685.

Pacífico, J.A., Abreu, C.A.M., Santos, D. A., Lima Filho, N. (2008). Kinetic Evaluation of Methane – Carbon Dioxide reforming Process Based on the Reactions Steps. Industrial and Engineering Chemical Reserch, 47, 4617-4622.

Edward, J.H., Maitra, A.M. (1995). The Chemistry of Methane Reforming with Carbon Dioxide and its Current and Potential Applications. Fuel Processing Technology, 42, 269-289.

Yaw, T.C., Amin, N.A.S. (2005). Analysis of Carbon Dioxide Reforming of Methane via Thermodynamic Equilibrium Aproach. Journal Teknology, 43, 31-50.

Proceedings of the 10th International Chemical and
Biological Engineering Conference - CHEMPOR 2008
Braga, Portugal, September 4-6, 2008
E.C. Ferreira and M. Mota (Eds.)

New polystyrene-based polymers as supports for ethylene polymerisation

Joana Tudella[1,2], Maria do Rosário Ribeiro[1], Henri Cramail[2] and Alain Deffieux[2]
[1] Instituto de Ciência e Engenharia de Materiais e Superfícies - ICEMS, Departamento de Engenharia Química e Biológica, Instituto Superior Técnico, Av. Rovisco Pais, 1049-001 Lisboa, Portugal
[2] Université Bordeaux 1; ENSCPB; CNRS; UMR 5629; Laboratoire de Chimie des Polymères Organiques, 16 Avenue Pey-Berland, F-33607 Pessac Cedex, France

Keywords: Ethylene polymerisation, Polymeric supports, Spherical Polyethylene, Hydroxypolystyrene, polystyrene-b-polyisoprene
Topic: Multi-scale and/or multi-disciplinary approach to process-product innovation.

Abstract

The industrial use of metallocene/methylaluminoxane catalytic systems and late transition metal catalysts requires the use of supports to improve the operational conditions, catalyst stability and directly get polyethylene with spherical morphology. However, the presence of residues of the inorganic support at the end of the polymerisation reaction gives rise to some inconvenients and contamination problems. Therefore, important efforts are being nowadays employed in the replacement of inorganic supports ($MgCl_2$, Al_2O_3, SiO_2) by organic supports. The latter are mainly based on polymers like polystyrene. In this work, linear hydroxypolystyrene (PSOH), polystyrene-block-isoprene copolymer (PS-b-PI) and plurihydroxy-functionalised PS-b-PI (PSPI-OH_n) were tested as supports for ethylene polymerisation. The ability of these various polymers when dissolved in a selective solvent to self assemble and form micelles was investigated first by Light Scattering techniques. Then, the capacity of these polymer micelles to act as active supports towards MAO-activated MeDIP(2,6-iPrPh_2FeCl_2) catalyst was analysed through ethylene polymerisation tests and morphology studies of the obtained polyethylene.
The most promising results were obtained for the PS-b-PI copolymer in heptane, which enabled the obtention of Polyethylene with spherical morphology and higher densities than polyethylene obtained in homogeneous conditions.

1 Introduction

Various routes have been investigated to support metallocenes onto organic particles and a special interest has been focused in polystyrene-bound polymerisation precatalysts. This derives from the idea that the catalytic species reside within a mobile hydrocarbon-rich matrix providing a polymerisation microenvironment that more closely resembles to a homogeneous solution polymerisation. Moreover, polystyrene supports are very versatile materials in terms of the incorporation of functional groups, enabling the development of numerous routes to anchor metallocene and/or postmetallocene systems on these organic supports. Therefore, polystyrene-based polymers are largely the most popular organic polymeric supports.

Hong et al. [1] carried out the ethylene copolymerisation using metallocene catalysts encapsulated in gel-type polystyrene-co-divinylbenzene beads. The zirconocene is introduced in the polystyrene-co-divinylbenzene particles by a simple swelling-shrinking process carried out in the presence of the solvent. The polyethylene synthesized particles using this supported catalytic system replicate the polystyrene-co-divinylbenzene particles.

Klapper and co-workers [2] describe the synthesis of polystyrene supports with polyethylene oxide (PEO) and polypropylene oxide (PPO) functionalities. These functional groups containing electronegative oxygen atoms enable to anchor the MAO-metallocene catalytic

complex by electrostatic (non-covalent) interactions with the oxygen atoms.

Bouilhac et al. [3] synthesized star shape polystyrene supports having –O-CH_3 or –OH functionalities at the end of the chain and new polystyrene functionalised microgels containing benzoic acid or benzophenone functionalities [4]. Over this functionalised supports, they added an alkylaluminum to generate the MAO like activating species in situ. At the end, the iron catalyst is anchored on the activator-support complex. The polyethylene synthesized with these new supports presents a spherical morphology and activities may vary from 100 to 1020 KgPE/ (molFe.h.bar). More recently, Bouilhac et al. [5] have developed another strategy based on the self-assembly of end-capped PS and PS-based block copolymers that spontaneously form well defined micelles in a selective solvent [6] which is another important feature for the use of these polymers as organic supports.

On this basis, linear hydroxypolystyrene (PSOH), polystyrene-block-isoprene copolymer (PSPI) and plurihydroxy-functionalised PSPI (PSPI-OH_n) are tested, in this work, as supports for ethylene polymerisation.

2 Materials and Methods

Reagents:
PS, PS-OH and PS-b-PI (PS=37 wt %; PI=63 wt %) were synthesised at LCPO (Université de Bordeaux I). The correponding molecular weights are: Mp=7840, Mn=7240, Mw=7520; Mp=5040, Mn=4860, Mw=5030 and Mp=49000, Mn=37000, Mw=44400. The iron catalyst [MeDIP(2,6-iPrPh_2FeCl_2)] was also synthesised at LCPO (Université de Bordeaux I) according to literature. Trimethylaluminium (2M solution in heptane) and Methylaluminoxane (10% w/v in toluene) were purchased from Aldrich and were used without further treatments. Heptane and toluene were purified according to standard procedures.

Light Scattering Studies of Polymer Solutions in toluene or heptane:
The desired amount of polymer was dried under vacuum during 3-4 hours. The polymer was then solubilized/dispersed in 10 ml of purified toluene or heptane. The light scattering measurements were carried out in a Malvern (Zetasizer 3000 HSA) apparatus.

Polymerisation Tests:
First, the polymeric support was dispersed in the solvent, then MAO or TMA and the catalyst were added. Polymerisations were performed in a modified schlenk (with an adapted cell for light scattering measurements) allowing “in-situ” light scattering studies. The polymerisation reactions were carried out in the following conditions: n (Fe)= $0,8*10^{-6}$ mol; Pethylene=1 bar, T=30 ºC; t= 1 h.

Characterisation of Obtained PE:
The polyethylene images were obtained in Scanning Electronic Microscope JEOL JSM 2500.

3 Results and Discussion

3.1 Light Scattering Studies

3.1.1 Hydroxy-polystyrene (PSOH) polymer

Light scattering measurements were performed to check the formation of micelles/aggregates of PS based polymers when in toluene solution. As expected, when polystyrene is dissolved in toluene, no agregation is observed all over the whole range of concentrations studied indicating that polystyrene is present in the form of single chains in the solvent. The situation changes with PSOH polymer, as shown in Figure 1a). Although at low PSOH concentrations (equal or inferior to 10 g/l), no formation of aggregates/micelles is

observed, aggregates are detected for higher PSOH concentrations (20, 50, 100 g/l). The presence of –OH group induces the self assembling of the polymer chains in toluene. The possible structure of the PSOH micelles (spherical shaped) is illustrated in Figure 1b). The core of the micelles is formed by the –OH groups whereas PS chains will constitute the corona.

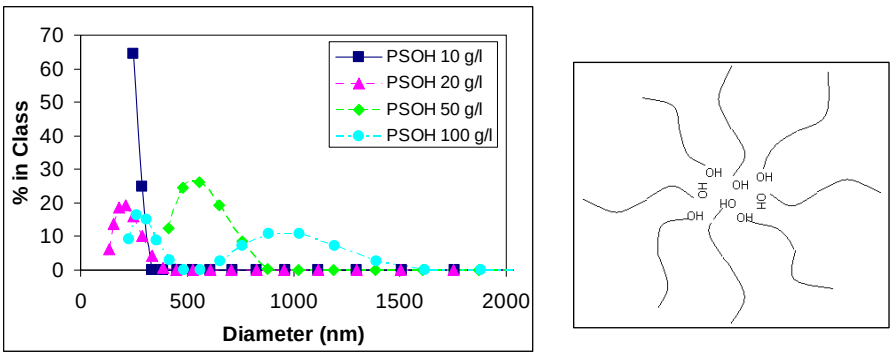

Figure 1a)- Light Scattering of PSOH polymer in toluene and b) Aggregates formed.

The ability of PSOH to form micelles after MAO addition was then investigated. Light scattering results after the addition of MAO over a 10 g/l solution of PSOH are presented in Figure 2. Initially, at this concentration (10 g/l), the PSOH solution in toluene does not form aggregates. However, the addition of MAO to the solution of PSOH leads to the formation of aggregates at lower PSOH concentrations (3 g/l). The diameter of the PSOH/MAO aggregates is around 1000 nm. However, in a solution containing only commercial MAO, the presence of well defined aggregates with cc. 750 nm diameter is also observed. We assume that in PSOH/MAO systems, MAO molecules are in the center of the aggregates, as illustrated in Figure 2b).

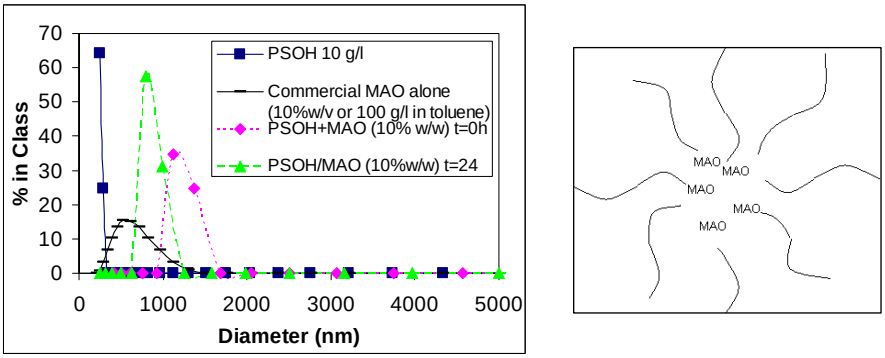

Figure 2a)- Light Scattering of PSOH+MAO polymer in toluene and b) Aggregates formed.

3.1.2 Polyisoprene-b-polystyrene (PS-b-PI) block copolymers

The PS-b-PI in heptane solutions form well defined micelles, with sizes ranging between 200 and 250 nm (in average). Once formed, the micelles are stable and do not change significantly neither with the dilution of the solution nor with time. It is known that the size of the formed aggregates/micelles depends both on the molar mass of the block copolymer and on the relative amount of the isoprene and styrene units [7]. This fact may in part explain why the size of the micelles with this PS-b-PI block copolymer is larger in this case than the one observed by Borsali and co-workers (between 50 and 60 nm).[6] Although both PS-b-PI present quite similar molar masses, the relative lengths of the two blocks are quite different. While the block copolymer used in Ref [6] shows a polystyrene block larger than the polyisoprene block (DP_{PS}=290 and DP_{PI}=110). In our case the situation is reversed; the length of the polyisoprene (PI) block is larger than the polystyrene (PS) block (DP_{PS}=239 and DP_{PI}=280) and a large corona may be expected- Figure 3b).

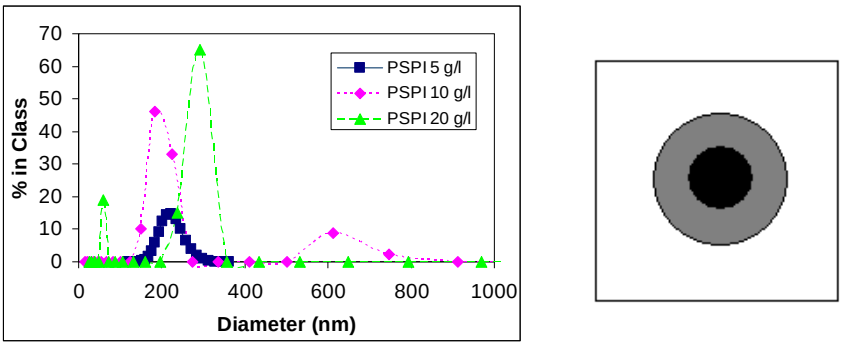

Figure 3a)- Light Scattering of PSPI polymer in heptane and b) Micelles formed (PS Core and PI Shell).

When toluene is used as solvent, both PS and PI blocks are soluble. Therefore, very small objects corresponding to single PS-b-PI chains of lower molecular mass are formed.

In order to anchor the MAO cocatalyst on the PS-b-PI support, functional groups containing oxygen atoms were introduced in the PSPI chains (PI- moieties) via epoxydation and hydrolysis reaction. Two Modified polymers containing OH groups, with two degrees of functionalisation (5 % and 30 %) were obtained and characterised by ^{1}H-NMR and FT-IR. The spectra of these modified polymers confirms the presence of –OH groups.

The behaviour of both modified PS-b-PI copolymers [PSPI-$(OH)_n$] in toluene and heptane was studied. For the PS-b-PI with 5 % of –OH groups, no important changes were observed comparing to the non-modified PS-b-PI. However, for the PS-b-PI with 30 % of –OH groups, some significant changes were observed due to the presence of -OH groups. As both PS and PI-OH blocks are not soluble in heptane, this copolymer becomes insoluble and precipitation of the polymer occurs. Light scattering studies confirm, in fact, the destabilisation of the micelles observed for the non-modified PS-b-PI. By exchanging the solvent from heptane to toluene, the solubility of the two blocks in the PSPI-$(OH)_n$ copolymer is changed. The PS block that is not soluble in heptane is easily solubilized in toluene. However, the PI-OH block (with high extent of functionalisation) will probably remain insoluble in toluene. This way, the formation of soluble PSPI-OH micelles is expected. In fact, Light Scattering studies on modified PSPI (30 % -OH groups) in toluene showed the formation of some micelles with approximately 200 nm diameter and some aggregation tendence. In this case, micelles have a PI-OH core and a PS shell.

The situations observed for the four different systems examined by light scattering are briefly resumed in Table 1.

Table 1- Light Scattering and solubility studies carried out for the PSPI-based polymers.

Polymer	Heptane	Toluene
Non-Modified PSPI	PI block: soluble PS block: not soluble *Formation of micelles* *(PS Core; PI Shell)* 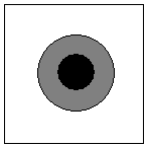	PI block: soluble PS block: soluble *Single PSPI Chains.* *No Micelles* 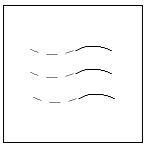
Modified PSPI (PSPI-OH_n)	PI-OH block: not soluble PS block: not soluble *Destabilization of micelles, precipitation of the polymer* 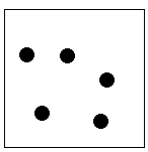	PI-OH block: not soluble PS block: soluble *Aggregation depending on the % of –OH groups inserted* *(PS Shell; PI-OH_n core)* 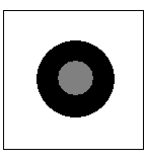

Note: Average diameter of the micelles: 200-250 nm determined by Light Scattering.

Only the two systems which showed the formation of micelles and/or aggregates (PS-b-PI in heptane and PS-b-PI-OH in toluene) were kept to be evaluated in polymerisation tests.

3.2 Polymerisation Tests and Characterisation of the Synthesized PE

3.2.1 Hydroxypolystyrene (PSOH) in toluene

The morphology of the polyethylene synthesized with the PSOH/MAO catalytic systems is shown in Table 2. The obtention of polyethylene in the form of aggregates of spherical particles is clearly observed. In agreement with this morphology, an increase in the PE density as compared to homogeneous conditions is also observed.

Table 2- Morphology of the polyethylene obtained with PSOH/MAO catalytic systems

Co-Catalyst	Polymerisation Activity KgPE/(molFe.h.bar)	PE Photographs obtained by SEM (Scanning Electronic Microscopy)	Density PE (g/l)
Commercial MAO	3960	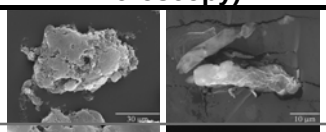	157
PSOH/MAO 20% w/w	2720	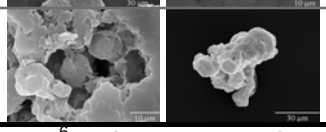	252

Note: Al/Fe=400; V(toluene)= 50 ml; n(Fe)= $0,8*10^{-6}$ mol; T=30ºC; t=1h; Pet=1 bar;

3.2.1 Polyisoprene-polystyrene (PSPI) in heptane

Polymerisation tests were conducted using the PS-b-PI polymer as support in heptane. Besides the obtention of polyethylene with well defined spherical micelles quite good polymerisation activities are attained – See Table 3.

Table 3- Polymerisation activities and morphologies of the polyethylene obtained with PS-b-PI/TMA catalytic systems.

Support/ Co-catalyst System	Al/Fe	Polymerisation Activity KgPE/(molFe.h.bar)	PE Photographs obtained by SEM (Scanning Electronic Microscopy)
TMA	2000	1678	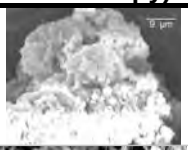
PSPI/TMA m(PSPI)/m(TMA)=0,054	1000	391	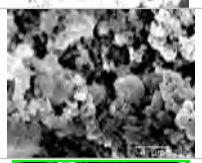
PSPI/TMA m(PSPI)/m(TMA)=0,026	2000	975	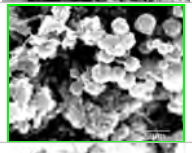
PSPI/TMA m(PSPI)/m(TMA)=0,05	2000	1461	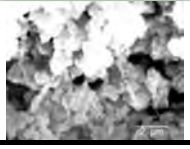

Note: n(Fe)=$0,8*10^{-6}$ mol; V(heptane)=50 ml; T=30ºC, Pet=1 bar.

3.2.2 Plurihydroxy Polyisoprene-polystyrene PSPI(OH)$_n$ in toluene

The (PS-b-PI(OH)n) polymer in toluene was also tested as support in ethylene polymerisation. Although quite acceptable polymerisation activities are achieved, in the range from 600 to 1400 KgPE/(molFe.h.bar), the formation of micelles observed by light scattering was not reflected in the polymer morphology.

4 Conclusions

Concerning the behaviour of hydroxy-polystyrene (PSOH) copolymers in toluene, we may conclude that the –OH groups already yield the formation of polymer aggregates in toluene relatively to non modified polystyrene (PS). However the formation of aggregates was observed only for high PSOH concentrations (above 20 g/l). Nevertheless, the addition of MAO over a PSOH solution in toluene allows the obtention of aggregates with sizes in the order of 1000 nm at lower PSOH concentrations – around 3-5 g/l. The ethylene polymerisation activities do not decrease significantly in the presence of PSOH/MAO cocatalysts in comparison to homogeneous MAO polymerisation values. Moreover, the obtained polyethylene shows spherical particles for high PSOH/MAO ratios which are not visible in PE obtained in homogeneous conditions (MAO alone as cocatalyst).

The polyisoprene-polystyrene (PS-b-PI) block copolymers gave very promising results when used as supports for ethylene polymerisation in heptane. Well defined micellar systems of PS-b-PI with sizes around 200-250 nm are formed in heptane. Moreover, the polymerisation activities in heptane (in the order of 900-1000 KgPE/(molFe.h.bar) are quite acceptable if compared with the corresponding activities in homogeneous conditions (around 1600 KgPE/(molFe.h.bar)). The formation of spherical PE may be tentatively attributed to the catalyst system heterogenisation around the micelles through the electrostactic interaction between the free double bonds of the PI block of the micelle and the cationic active species (formed by the reaction of the cocatalyst with the metal catalyst). A quite different behaviour is observed for the same PSPI block copolymers in toluene. In this case, no stable micelles are formed.

Through the introduction of functional protected groups containing oxygen in the PSPI chain, it was aimed to anchor more efficiently MAO or TMA by electrostatic interactions (that are expected to be stronger than with the single double bonds). However the presence of free –OH groups in the PSPI chain reflected negatively both in polymerisation activities and in polyethylene morphology. In fact, when using heptane, the presence of –OH groups in PSPI(OH)$_n$ chains leads to the insolubility of the two block copolymers and therefore inhibits the self assembling of PSPI(OH)$_n$ chains. When using toluene as solvent, the self assembling of PSPI chains is slightly favoured and aggregates with insoluble PI-OH block in the core and PS soluble block in the corona are expected to be formed. Nevertheless, no improvement of polymer morphology was achieved in this case. The obtained activities are although quite acceptable.

References

[1] Hong, S.; Rief, U., Kristen, M. (2001) *Macromol. Rapid Commun.*, 22**,** 1447-1454
[2] Klapper, M.; Jang, Y-G; Nemnich, T.; Nenov, N.; Mullen, K. (2004) *Macromol. Symp.*, 213, 131-145
[3] Bouilhac, C.; Cloutet, E.; Cramail, H.; Deffieux, A.; Taton, D. (2005) *Macromol. Rapid Comm.*, 22, 1447-1454.
[4] Bouilhac, C.; Cloutet, E.; Cramail, H.; Deffieux, A.; Taton, D. (2007) *Macromol. Chem. Phys.*, 208, 1349-1361
[5] Bouilhac, C.; Cloutet, E.; Cramail, H.; Deffieux, A.; Taton, D. (2007), FR N° 0704328
[6] Minatti, E.; Viville, P.; Borsali, R.; Schappacher, M.; Deffieux, A.; Lazzaroni, R. (2003) *Macromolecules*, 36, 4125-4133.

Proceedings of the 10th International Chemical and
Biological Engineering Conference - CHEMPOR 2008
Braga, Portugal, September 4-6, 2008
E.C. Ferreira and M. Mota (Eds.)

Cure of a fiberglass-vinyl ester I beam composite: a new heating strategy

Lizandro S. Santos[1], Rogério L. Pagano[2], Verônica M.A. Calado[1], Evaristo C. Biscaia JR.[2*]

[1] Escola de Química, Universidade Federal do Rio de Janeiro, Av. Horácio Macedo, 2030, Cidade Universitária, Rio de Janeiro, Brasil
[2] PEQ, Universidade Federal do Rio de Janeiro, Rio de Janeiro, Brasil

Abstract

Pultrusion is a continuous process used for manufacturing constant cross section composite materials. In this process, fibers are continuously pulled and impregnated in a resin bath before entering in a heated die, where occurs an exothermic cure reaction. Normally the die is heated by electrical heaters coupled on its outer surface. The known of cure kinetic is relevant to improve process parameters as heat flux and pulling velocity. It was observed that the most usual heat configuration used in the present literature can be improved by changing the geometry of heaters. In this paper, it was used a CFD package (Ansys CFX 11.0™) to simulate a volume finite mesh of a die with a I beam cavity. The strategy adopted was to minimize the superficial area of heaters in order to reduce the energy consumption. The results were compared with results from the literatute and showed that the proposed heat configuration is a more efficient way to conduce the pultrusion process in terms of energy.

1 Introduction

Polymer composites are materials consisted by a cure reaction of thermosetting or thermoplastic resin associated with reinforcement. These materials can be manufactured by several industrial processes as rtm, filament widing, hand lay-up and pultrusion. Among these technologies, pultrusion stands out because of its ability to combine a high production rate with high quality of produced parts. In pultrusion, fibers are continuously pulled and impregnated in a resin tank before entering into a heated die, where occurs an exothermic cure reaction. The die may be heated by electrical heaters, strip heaters, hot oil or by steam, although electrical heaters are the most common (Coelho and Calado, 2001). Outside the die, the composite part is pulled by a continuous pulling system and then a cut-off saw cuts the part into a desired length. In Fig. 1 is represented a scheme of a pultrusion equipment:

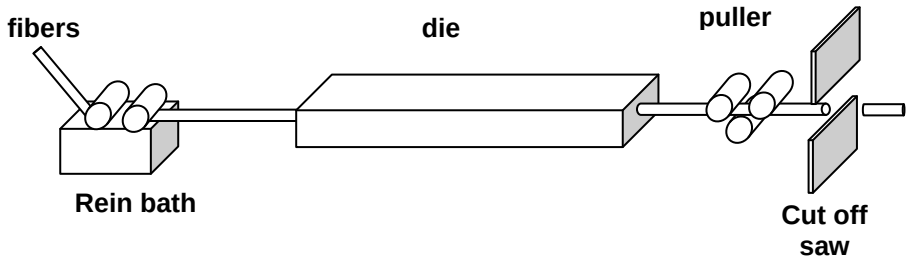

Figure 1. A simplyfied diagram of pultrusion process.

* Corresponding author. Tel +55 21 2562-8345. E-mail:evaristo@peq.coppe.ufrj.br

The heat flux provided by die must be sufficient to promote the polymerization reaction of thermosetting matrix. Besides, the cure process of composite should be uniform and enough to reach good properties of final product. Variables, such as die temperature, pulling speed, pulling force, internal pressure and resin cure kinetics control the composite process during the pultrusion. Among these variables, the die temperature (the temperature imposed on the die wall) is the most relevant one for obtaining a part with uniform and excellent mechanical properties (Pagano *et al.* 1996).

Han *et al.* (1986) studied the pultrusion process to solve the mathematical model by finite difference method. Moschiar *et al.* (1996) also solved the pultrusion model using finite difference and the viscosity, temperature and degree of cure profiles were studied. A good agreement between simulated and experimental results was obtained in low pulling velocities of the process. Liu and Hillier (1999) studied the pultrusion process simulating a composite of geometry like I beam using a vinyl resin/glass fiber system and also achieved a good agreement between results. Other paper using the same geometry was proposed by Liu XL. (2001), however, in order to study the temperature and degree of cure profiles, he proposed a heating configuration to improve the cure of product and consequently to obtain a part with homogeneous cure. The FE packages are appropriate to model irregular shapes in three-dimensions and a variety of boundary conditions and material properties can be defined easily. Jianhua *et al.* considered the simulation of three heaters on the top and three on the bottom of the die wall. Srinivasagupta *et al.* (2003) affirmed that the number of heating zones is variable, but three are found to be sufficient in practice. These authors (Jianhua *et al*, 2001, Srinivasagupta *et al.,*2003) have used this heater arrangement to model the pultrusion process of composites with different dimensions and properties. However, no attention was given to the effects of heater arrangement changes on the necessary thermal energy and composite quality.

In the present investigation, a numerical procedure based on CFD technique for the three-dimensional simulation of pultrusion process of a I beam composite was developed. The heater arrangement on the die wall and its influence on the energy consumption were studied here and compared with results from Liu XL. (2001). The suggestion of a heating configuration to reduce the energy consumption in the pultrusion process is the main objective of this work.

2 Mathematical Model

The mathematical model of the steady state pultrusion process is composed by the energy balance and the kinetic cure reaction. These equations can be written, respectively, as:

$$\rho_c \; C_C\left(u_i \nabla T\right) = k_c \nabla^2 T + c_{in}(1-\phi)\left(-\Delta H\right) R_a \tag{1}$$

$$u_z \frac{d\alpha}{dt} = R_a = \left(A e^{\left(\frac{-Ea}{RT}\right)} \right) (1-\alpha)^n \tag{2}$$

where T is temperature, u velocity vector, C_c specific heat of the composite, k_c thermal conductivity of the composite, ($-\Delta H$) total heat generated, ρ_c the density of the composite, R_a resin reaction rate, Φ fiber volume fraction, c_{in} resin initial concentration, α degree of cure, A frequency factor, E activation energy, and $m + n$ reaction order.

The fiber-resin system was assumed to be epoxy resin and glass fiber. The physical properties of the composite were calculated by the following equations:

$$\rho_c = \phi_r \rho_r + \phi_f \rho_f \tag{3}$$

$$\rho_c Cp_c = \rho_r \phi_r Cp_r + \rho_f \phi_f Cp_f \quad (4)$$

$$\frac{1}{k_c} = \phi_r \frac{1}{k_r} + \phi_f \frac{1}{k_f} \quad (5)$$

where the subscripts r, f and c represent resin, fiber and composite respectively.

In this work, the degree of cure was assumed to be zero *($\alpha = 0$)* before the fiber-resin system entering into the die, and the inlet temperature was considered as 298 K. In order to compare our results with the results presented by Liu X.L (2001), the same physical parameters and kinetic parameters were here considered, shown in Table 1.

Table 1. Physical and Kinetic Parameters

Fiber fraction ***(Φ)***	0.72
Density of the resin ***(ρ_r)***	1100 (kg/m^3)
Density of the fiber ***(ρ_f)***	2560 (kg/m^3)
Thermal conductivity of the resin ***(k_r)***	0.169 (J/m.s)
Thermal conductivity of the fiber ***(k_f)***	1.04 (J/m.s)
Thermal capacity of the resin ***(Cp_r)***	1640 (J/kg.K)
Thermal capacity of the fiber ***(Cp_f)***	640 (J/kg.K)
Initial temperature ***(T_0)***	300 K
Initial concentration of resin ***(c_{in})***	1100 (kg/m^3)
Frequency Factor ***(A)***	1.869x10^6 (s^{-1})
Activation Energy ***(E_{a1})***	71.688x10^3 (J/mol)
Order of reaction ***(n+m)***	2
Universal constant of gases ***(R)***	1.98 (cal/mol. K)
Heat generated ***(ΔH)***	398 (J/g)

For the numerical solution, it was used a CFD-type model. Computational Fluid Dynamics (CFD) is a computer tool for simulating the behavior of systems involving fluid flow, heat transfer, and other related physical processes. Fluid flow equations can be solved over a region of interest with specified conditions on the boundary of that region. The numerical method on which ANSYS CFX 11.0© is based is known as the finite volume technique. In this technique, the region of interest is divided into small sub-regions, called control volumes. The equations are discretized and solved iteratively for each control volume. In this work, a mesh with 34590 nodes and 37690 elements were suficient to integrate with fidelity the system equations.

3 Results and Discussion

According to the reported literature [2-4], the heat flux at the final stage of the cure reaction can be decreased due to the fact that the heat generated by the cure reaction inside the die can provide suficient energy to cure the material at this stage. Hence, the temperature may assume different values along the die length and it may be reduced at the final stage of the cure reaction. The procedure here was based on the simulation of pultrusion process by several times, assuming different values of heat rate at each heater, until finding a minimum value of energy consumption to totally cure the material. Assuming this fact, our methodology was to decrease the superficial area of heaters in order to minimize the spent heat flux along the die length. We believe that the typicial heater configuration suggested by Liu X.L. (2001), Fig. 2, can be configurated in a more efficient way in order to avoid energy loss during the process.

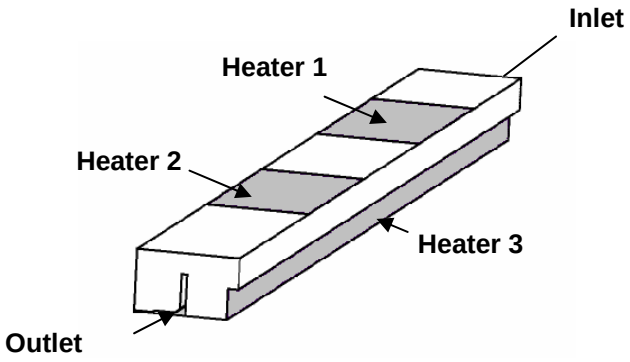

Figure 2 – Typical heating configuration for pultrusion die of composite I beam.

The proposed heat configuration was a tooling pultrusion die consisted of internal heaters inside an insulated die, as shown in Fig. 3. The distance between each heater was set to be 0,2 m. It was assumed the dimensions of 0.002 m×0.002 m×0.06 m.

Considering this heat configuration, simulated temperature and cure profiles along the beam are shown in Figures 4 and 5, and temperature profiles at three points of the beam are presented in Figure 6. It should be pointed out that the proposed configuration was able to cure the material in a more efficient way. This efficiency is characterized by approximately a 20 % reduction of the energy consumption in comparison with the heat strategy used by Liu X.L. (2001). According to the proposed configuration, the necessary power of heaters to cure the material was 7.3 kW.

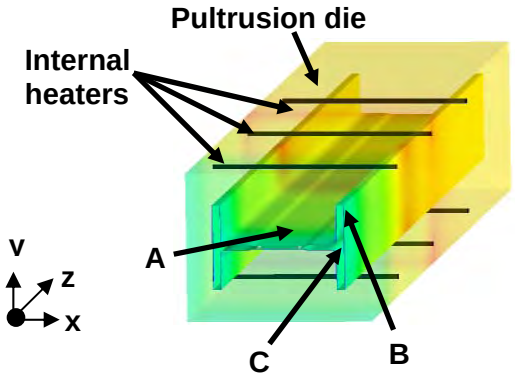

Figure 3 – Internal heating configuration.

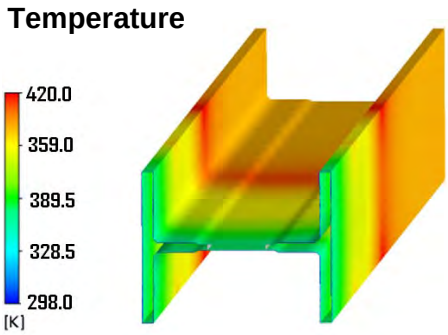

Figure 4 – Composite temperature.

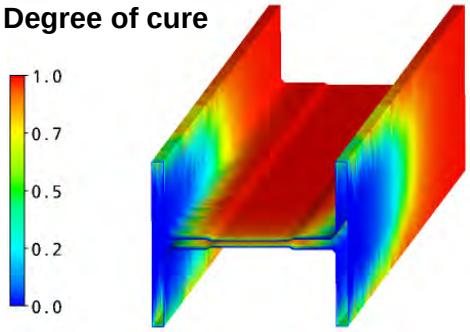

Figure 5 – Degree of cure of the composite.

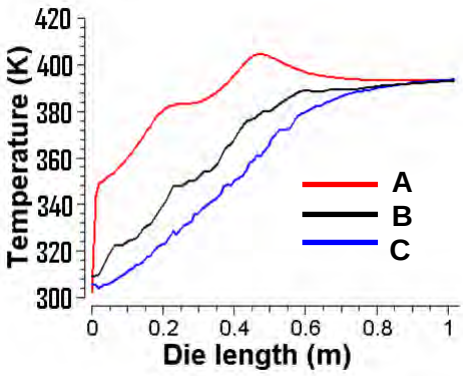

Figure 6 – Temperature profile.

As seen in Fig. 5, the composite part was totally cured at the exit of composite. In Fig. 6 it is possible to see the temperature distribution in funtion of pulling direction at three diferent points. The final temperature of the conjunct was around 400 K reaching a maximum value of 410 K.

4 Conclusions

Through intensive computer simulations, were verified that smaller energy consumption can be obtained with the suggested heat strategy in pultrusion process. This economy was verified by the reduction of the surface area of the heaters causing a significant decrease of the energy consumption. This internal heat configuration appears to be a good alternative to improve global thermal efficiency of the process. The following conclusions can be drawn from the results presented in this paper:

1. The temperature profile depends strongly upon the heat configuration of the die. Heaters with small transversal area must be primarily assumed to simulate the process in order to provide a adequate temperature distribution along the die length. According to the results, heaters with wide transversal area may spend excessive thermal energy to cure the resin.

2. The results suggest new studies about heater arrangements of the pultrusion process. Each particular case must be examined, taking account the variables and the geometry of the desired composite to be obtained.

5 Acknowledgements

Authors would like to thank CAPES, CTPETRO/FINEP (# 0104081500) and CNPq for financial support.

References

Coelho, R.M.L., Calado, V.M.A. (2001). An optimization procedure for the pultrusion process based on a finite element formulation. *Polymer Composites,* 23, 329-341.

Han, C.H., Lee, D.S., Chin, H.B. (1986). Development of a mathematical model for the pultrusion process. *Polymer Engineering and Science*; 26, 393-403.

Jianhua, L., Joshi. C.S., Lam, Y.C. (2001). Curing optimization for pultruded composite sections. *Composite Science and Technology*, 62, 457-467.

Kommu S., Khomami, B., Kardos J.L. (1998). Modeling of injected pultrusion processes. *Polymer Composites,* 19, 335-346.

Liu, X.L. Numerical modeling on pultrusion composite I beam. (2001). *Composites Part A: Applied Science and Manufacturing*, 32, 663-681.

Liu, X.L., Hillier, W. (1999). Heat transfer and cure analysis for the pultrusion of a fiberglass-vinyl ester I beam. *Composite Structures*, 47, 581-588.

Moshiar, S.M., Reboredo, M.M., Larrondo H., Vazquez, A. (1996). Pultrusion of epoxy matrix composites: puling force model and thermal stress analisys. *Polymer Composites,* 17, 850-858.

Pagano, R.L., Santos, L.S., Calado, V.M.A., Biscaia, E.C. (2006). Pultrusion process: modeling of heat transfer and cure kinetic*.* In: *World Polymer Congress - MACRO 2006*, Rio

de Janeiro, Brazil, Vol. 245-246, 1-680.

Srinivasagupta, D., Kardos, J. L., Joseph B. Rigorous dynamic model-based economic design of the injected pultrusion process with controllability considerations. (2003). *Journal of Composite Materials*, 37, 1851-1880.

Proceedings of the 10th International Chemical and
Biological Engineering Conference - CHEMPOR 2008
Braga, Portugal, September 4-6, 2008
E.C. Ferreira and M. Mota (Eds.)

Preparation of Polymeric Hydrogel Microparticles for Textile Applications

Carvalho, A. S.[1,2], Vieira, R.[2] and Gil, M. H.[1*]

[1] Department of Chemical Engineering, University of Coimbra, Portugal, 3030-790 Coimbra
[2] MICROPÓLIS – Production and Development of Polymeric Powders, S.A., Park of Science and Technology of Maia, Rua Frederico Ulrich, 2650 – Moreira da Maia, 4470-605 Maia

Keywords: hydrogel, poly(acrylic acid), microparticles, hydrophobicity/hydrophilicity, inverse-emulsion polymerization, textiles, swelling behaviour.

Topic: Advancing the chemical engineering fundamentals.

Abstract

In this work we wish to report the synthesis of polymeric microparticles based on a hydrogel made of Poly(Acrylic Acid) (PAA). They were prepared by inverse-emulsion polymerization. This material is intended to be used in textile industry in order to improve confortability.

The polymerization conditions and their effects on the morphology (analyzed by Scanning Electron Microscope (SEM)), structure (analysed by Attenuated Total Reflectance - Fourier Transform Infrared (ATR-FTIR)) were determined.

The swelling and water adsorption behavior of the PAA microparticles before and after his incorporation in the textiles (cotton) were evaluated. The morphology of the polymeric microparticles after the incorporation, in the textiles was also assessed.

1 Introduction

Polymeric hydrogels are three-dimensioned networks obtained either by chemical bonds and/or physical forces. They are able to absorb high quantities of water without dissolving. Recently, the interest in the development of hydrogels has increased considerably due to their intrinsic properties. (Hoffman, J., 1999; Can, H., 2003) The polymer particles prepared in this work have been produced by inverse-emulsion polymerization (Lim, D., 2002).

The hydrogel properties are directly dependent on the amount of water that the hydrogel can imbibe into his molecular matrix which is referred as the degree of swelling (Devine, D., 2005).

During human history, the functions of textiles were, for long time, important not only from cultural and technologic development aspects but also from the fashion and comfort aspects. Although their variety was dependent on the available of natural fibres (Schuster, K., 2006). These natural fibres could be either hydrophobic or hydrophilic, being these aspects the main reason for specific selections. However, nowadays the specificity of the textile fibres properties, and the features that are possible to incorporate in those materials, are the main goal for their success.

The hydrogels proposed in this work are referred to be incorporated into the textile fibbers in order to enhance the hydrophilic/hydrophobic character, and, in this way, to improve the comfortability.

Here we report the synthesis of polymeric microparticles based on a hydrogel – PAA, crosslinked with N,N'-Methylene Bisacrylamide.

[*] Corresponding author: Professor Maria Helena Mendes Gil, Tel: + 351-239-798743, Fax: +351-239-798703. E-mail: hgil@eq.uc.pt

2 Experimental Results

Synthesis Procedure

The PAA microparticles were prepared by inverse-emulsion polymerization, and the final structure of the polymer is represented in the Figure 1. The polymerization occurs under inert atmosphere (N_2), at 75ºC for 2h. The mixture components were stirred with mechanical stirring during the reaction time.

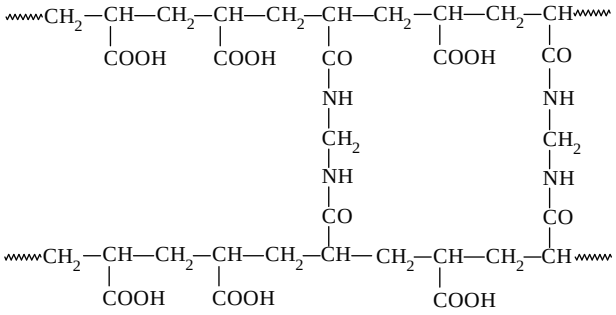

Figure 1 – Structure of the PAA polymer particles produced.

The scale up of the production was carried out for 250mL, 500mL and 1L reactional systems with success and good yields were observed (70-95%).

The size and morphology of the polymeric microparticles have been optimized by the manipulation of critical reaction factors, such as: the organic and aqueous solutions homogeneity phases; the addition time of the monomer and initiator; the cleaning time of the oxygen in the reactional atmosphere with N_2; and the isolation and cleaning of the solid polymer.

ATR-FTIR

The prepared hydrogel was characterized by ATR-FTIR analysis.

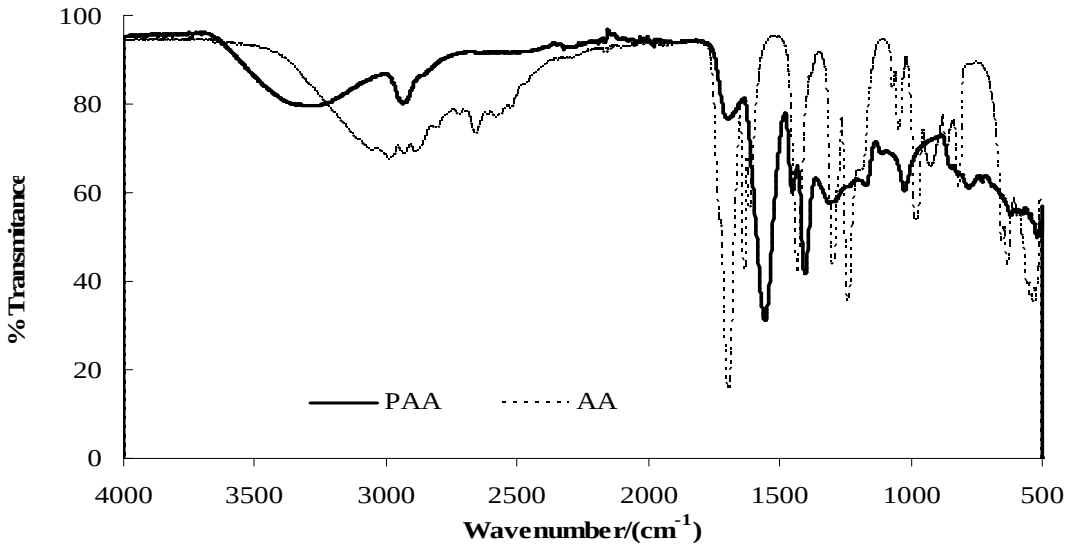

Figure 2 – FTIR spectrum of the prepared polymer (PAA) and of the monomer (AA) used to prepare the polymer.

In the polymer and monomer spectrums (see Figure 2), it is observed the presence of the characteristic COO^- bands (symetrical and assymetrical stretching bands) at 1715cm^{-1}, 1443cm^{-1} and 1408cm^{-1}; Due absence in the polymer spectrum of the characteristic band (1633 -1630cm^{-1}) that belong to the double bands, confirms the polymerization success; The

presence in the polymer spectrum of the amide (N-H linkage) characteristic band at 1699cm^{-1} confirm the crosslinking reaction of the acrylic acid with the N,N'-methylene bisacrylamide.

Swelling Behaviour

The swelling behaviour corresponds to the increase in the volume or changing in the shape of an area or surface. This property was evaluated in the PAA polymer particles and in the textiles fibres after hydrogel incorporation. This test is important to assess the capacity of the polymer to swell, in the presence of water.

The degree of swelling was calculated by evaluating the mass differences, which considers the initial mass as the dry weight of the polymer and end as the mass of polymer after the swelling, using the following equation:

$$\% \text{ swelling} = [(\text{final weight} - \text{initial weight}) / \text{initial weight}] \times 100 \quad (1)$$

Experimentally, for PAA swelling evaluation, two samples of 500mg of dried polymer, were weighted (initial weight), and then dispersed in 50mL of deionized water for 15 minutes, at room temperature (20±1ºC). The excess of water was removed and the samples were weighted (final weight). By the equation (1), it is possible to determine the swelling percentage.

The results obtained for the swelling of the polymeric particles in deionized water are presented in the Table 1. It is possible to verify that the material is an hydrogel with very high and fast swelling capacity. This result is a direct consequence of the very small particles (see SEM results), that possess very high surface areas.

Table 1 – Experimental results for the swelling percentage the PAA in deionized water.

Medium used for promote the polymer swelling	% Swelling
Deionized water (pH~ 5-6)	4512.4 ± 23.5

For the case of the textiles, the swelling capacity was determined after 12 hours of contact with the medium. The dry and wet weight were determined and related by the same equation (1), and the results are referred in the Table 2.

Table 2 – % swelling of the various cotton textiles samples with different treatments.

Sample	% Swelling
Cotton Standard	178.9 ± 4.4
Cotton + PCM + PAA	167.4 ± 3.8
Cotton +PCM + Conditionator	115.0 ± 4.9
Cotton + PCM	127.2 ± 5.3

The cotton fibbers are hydrophilic by nature, but some specific treatments to those fibbers decrease significantly that swelling behaviour. In the case has been incorporated in the textile fibbers PCM's (Phase Change Materials) refered by Su, J., and its colaborators (Su, J., 2006) as materials with capacity to store thermal energy, that could be released over a

defined temperature range, while itself changes phase.

In this case, the textiles swelling decreases from around 179% to around 127%, when they are treated with PCM. The refered decreasing is more significant when the final material is also treated with the conditionator. To counteract the hydrophobic behaviour, PAA hydrogel particles were incorporated in the textile fibbers, at the same time that PCM was incorporated. This incorporation permit to increase the swelling behaviour of the textiles (167%), to values close to the values obtained to the cotton sample without treatment (179%).

Water adsorption behavior

In this study it is important to know what the behaviour of the PAA regarding the ability to adsorb liquids from its surface.

The water adsorption capacity of the polymer particles was availed during 24h at room temperature (T=20±1ºC), putting the samples in contact with a atmosphere with a saturated solution of $CuSO_4.5H_2O$. The dry and wet weight of the samples were determined, along the time and related by the follow relation:

$$\% \text{ Water adsorption} = [(\text{final weight} - \text{initial weight}) / \text{initial weight}] \times 100 \quad (2)$$

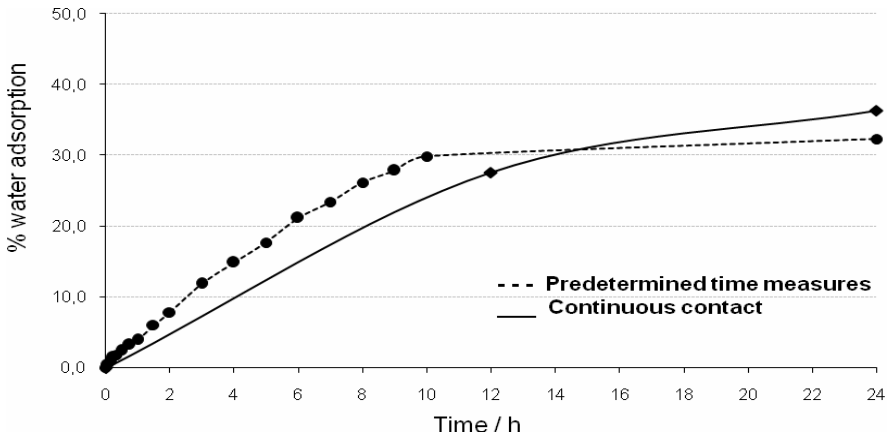

Figure 3 - Water adsorption capacity of the PAA polymer particles.

The results obtained in this test (Figure 3), reveal that the polymer prepared (PAA) is an hydrogel, because it has capacity to adsorb more than 30% of water in his surface for an saturated atmosphere.

SEM

By scanning electron microscope (SEM) analysis it is possible to verify the morphology of the polymeric material.

The Figure 4 – [A] suggest that the prepared material has spherical shape and small sizes (≤10μm). In the Figure 4 – [B] it is possible to verify that the hydrogel microparticles, after the incorporation in the textiles, keep their morphology and they are perfectly attached to the textile fibres.

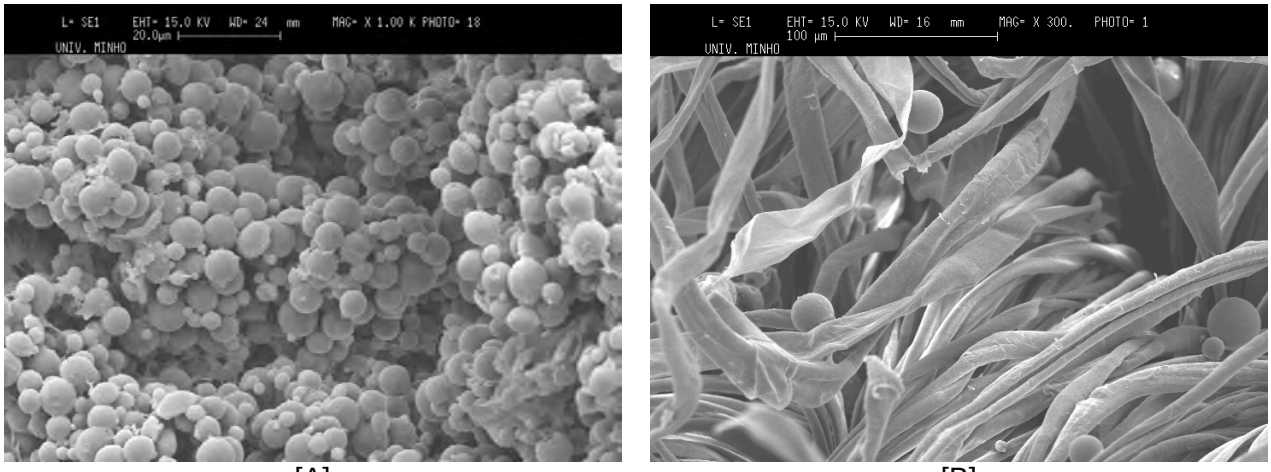

[A] [B]

Figure 4 – SEM images of the PAA microparticles [A] and of the PAA microparticles incorporated in the textiles fibers [B].

3 Conclusions

The PAA hydrogel were efficiently prepared by inverse emulsion polymerization with good yields (about 70-90%). These materials are morphologically spherical and have small sizes (≤10µm). As expect the PAA hydrogel behave as a superabsorbent, because they swell over than 4500%. The hydrogel keep his swelling capacity after the incorporation in the textiles.

This work allows us to conclude that the incorporation of these microparticles in the textiles fibbers increases their swelling properties.

References:

Can, H., Kirci, B., Kavlav, S., Guner, A. (2003). Removal of some textile dyes from aqueous solutions by poly(N-vinyl-2-pyrrolidone) and poly(N-vinyl-2-pyrrolidone)/ $K_2S_2O_8$ hydrogels. *Radiation Physics and Chemistry*, 68, 811-818;

Devine, D., Geever, C., Higginbotham, C. (2005). Drug release from a N-vinylpyrrolidinone/acrylic acid lubricious hydrophilic coating. *Journal of Materials Science*, 40, 3429-3436;

Hoffmann, J., Plotner, M., Kuckling D., Fischer, W. (1999). Photopatterning of thermally sensitive hydrogels useful for microactuators. *Sensors and Actuators*, 77, 139-144;

Lim, D., Song, K., Yoon, K., Ko, S. (2002). Synthesis of acrylic acid-based superabsorbent interpenetrated with sodium PVA sulfate using inverse-emulsion polymerization. *European Polymer Journal*, 38, 579 -586.

Schuster, K., Suchomel, F., Manner, J., Abu-Rous, M., Firgo, H., (2006), Functional and confort properties of textiles from TENCEL® fibres resulting from the fibres water-absorbing nanostructure: A review. *Macromolecular Symposium*, 244, 149-165;

Su, J., Wang, L., Ren, L., (2006), Fabrication and thermal properties of MicroPCMs: Used Melamine-Formaldehyde resin as shell material. *Journal of Applied Polymer Science*, 101, 1522-1528.

Proceedings of the 10th International Chemical and
Biological Engineering Conference - CHEMPOR 2008
Braga, Portugal, September 4-6, 2008
E.C. Ferreira and M. Mota (Eds.)

Photocatalytic oxidation of clofibric acid using nanocrystalline sol-gel TiO_2 under visible irradiation

Cláudia G. Silva, Joaquim L. Faria*
Laboratory of Catalysis and Materials (LCM), Associate Laboratory LSRE/LCM,
Chemical Engineering Department, University of Porto, Rua Dr. Roberto Frias s/n,
4200-465 Porto, Portugal

Keywords: Titanium dioxide, Sol-gel, Photocatalysis, Clofibric acid, Pharmaceuticals
Topic: Environmental engineering & management

Abstract

In this paper different titanium dioxide (TiO_2) powders are used as photocatalysts in the liquid phase heterogeneous photodecomposition of clofibric acid, a current lipid regulator drug. The preparation of the TiO_2 powders was made following an acid-catalyzed sol-gel method starting from titanium isopropoxide. It is described how temperature can be used to control surface and morphological properties of the material. Extensive characterization of the materials by spectroscopic, microscopic and calorimetric techniques is given. The performance of TiO_2 catalysts under visible light activation is quantified in terms of kinetic rate constant and total organic carbon removal. The photo-activity is found to increase with calcination temperature up to 673K and to decline afterwards. This behavior is explained in terms of morphological and structural changes associated with the thermal treatment. The photochemical and photocatalytic oxidation is shown to follow a pseudo-first order kinetic rate law, with 4-chlorophenol, isobutyric acid, hydroquinone, benzoquinone and 4-chlorocatechol being the main detected intermediates.

1 Introduction

Treatment systems for water and air based in semiconductor heterogeneous photocatalysis represent an area of major technical importance in our days (Fujishima et al., 2000). However the implementation of such systems in an efficient way requires very efficient photocatalysts. Titanium dioxide (TiO_2) is the most popular semiconductor material in photocatalytic applications, mainly due to its strong oxidizing power, high chemical stability and relative inexpensiveness. TiO_2 exists in different crystalline forms such as anatase, rutile and brookite. It has been long recognized and recently reviewed that TiO_2 photocatalytic efficiency is related to surface and structural properties of the semiconductor such as crystal structure, surface area, particle size distribution, porosity, band gap and surface hydroxyl density (Carp et al., 2004). In addition, resistance to mechanical stress may be important in industrial applications.
Although TiO_2 is readily available from commercial sources and is quite inexpensive, synthesizing the material can be advantageous when there is a need to control several of the above mentioned surface and structural properties. Liquid phase, sol-gel synthesis is very used to produce thin films, powders and membranes. This technique advantages include ease of processing, control over the composition, purity and homogeneity of the final materials. This method involves formation of a TiO_2 sol or gel, or precipitation by hydrolysis and condensation of titanium alkoxides (a common starting material). The synthesis is followed by a thermal treatment to remove the organic part and to induce the crystallization of TiO_2.

* Corresponding author. Tel + 351-22-5081645. E-mail:jlfaria@fe.up.pt

The physical-chemical properties of the so obtained semiconductor are found to be directly related to preparation parameters such as type of Ti(IV)-alkoxide precursor, solvent, aging time and calcination temperature (Hsiang and Lin, 2006).
In the present work, we produced TiO_2 nanocrystalline powders from Ti(IV) isopropoxide by an acid catalyzed sol-gel method. We used the calcination temperature to induce the appropriate changes on several properties including crystal structure, phase composition, surface area and particle size. We tested the materials in the visible photocatalytic oxidation of clofibric acid (2-(*p*-chlorophenoxy)-2-methylpropionic acid).
Clofibric acid is the active metabolite of several fibrate drugs prescribed to reduce blood cholesterol levels. These drugs act to lower elevated serum lipids by reducing the very low density lipoprotein fraction that is rich in triglycerides. It is also classified as a plant growth regulator (antiauxin) pesticide (Emblidge and DeLorenzo, 2006). Pharmaceuticals are a class of emerging environmental contaminants that are extensively and increasingly being used in human and veterinary medicine. A considerable percentage of these compounds are excreted unchanged through urine and feces, or as metabolites entering the waste water streams. If they are not biodegraded or eliminated in sewage treatment plants they may enter the aquatic environment and eventually reach drinking water. Clofibric acid is resistant to degradation, having an estimated persistence in the environment of 21 years. We describe the photocatalytic degradation kinetics of clofibric acid along with the identification of the reaction intermediates. A correlation between morphological, crystalline and spectroscopic properties of the synthesized TiO_2 materials and its ability for the degradation of this organic pollutant is attempted.

2 Experimental

TiO_2 was prepared by a modified acid-catalyzed sol-gel method as described in the following. An ethanol solution 0.5M in $Ti(OC_3H_7)_4$ was stirred for 30 minutes and acidified with 0.8% v/v nitric acid. The solution was loosely covered and kept stirring until the homogeneous gel formed. The gel was aged in air for one week. The resulting xerogel was ground into a fine powder and dried at room temperature. The powder was divided in several batches and thermally treated (calcination) at different temperatures (from 573 to 973K) in a nitrogen flow for 2 hours. Catalysts were labeled as TX, where X is the calcination temperature. Catalysts were characterized by thermogravimetric (TG) and differential scanning calorimetry (DSC) analysis, N_2 adsorption-desorption, powder X-ray diffraction (XRD), X-ray photoelectron spectroscopy (XPS), atomic force microscopy (AFM), diffuse reflection infrared Fourier transformed (DRIFT) spectroscopy and UV-Vis diffuse reflectance spectroscopy.
The photocatalytic activity of the prepared materials was evaluated following clofibric acid degradation in aqueous solution under visible irradiation. The experiments were carried out in a glass immersion photochemical reactor charged with 250 ml of suspension. The reactor was equipped with a Heraeus TQ 150 medium-pressure mercury vapor lamp (the UV line at 254 nm was filtered by a DURAN 50® glass jacket, excitation being carried out by the more intense lines at λ_{exc} of 366, 436 and 546 nm) which was located axially and held in a quartz immersion tube. In a typical experiment, the initial clofibric acid concentration and the amount of suspended TiO_2 were set at 8.33×10^{-5} M (~18 mg l^{-1}) and 1 g l^{-1}, respectively. An oxygen/argon stream (20% *vol.* of oxygen) was continuously supplied to the reactor. Reactions took place under natural pH conditions (pH~4.2). Before turning on the illumination, the suspensions were saturated with the gas mixture and magnetically stirred for 30 minutes. Then, the suspensions were irradiated at constant stirring speed. Samples were withdrawn regularly from the reactor and centrifuged for separation of any suspended solid, prior to analysis.
The clean transparent solution was then analyzed by HPLC using a Hitachi Elite LaChrom liquid chromatograph equipped with an L-2450 diode array detector. The stationary phase consisted in a YMC-Pack ODS-AQ endcapped column (250 mm × 4.6 mm, 5μm particles) working at room temperature. The mobile phase was a mixture of a 20 mM NaH_2PO_4/H_3PO_4 (pH=2.8) buffer solution and acetonitrile with a gradient concentration at a flow rate of

1 ml min^{-1}. Total organic carbon (TOC) measurements were performed in a Shimadzu TOC-5000 analyzer.

3 Results and Discussion

3.1 Catalysts characterization

Nanocrystalline TiO_2 was obtained by hydrolysis starting from titanium isopropoxide. In acidified ethanol solution the alkoxide is hydrolyzed and then condensation of the polymeric chains takes place. This acid catalyzed hydrolysis prevents premature TiO_2 precipitation. The resulting xerogel was treated thermally under nitrogen flow.

The mass loss and heat release from xerogel samples during calcination was followed by thermal analysis. As shown in Fig. 1a, DTG curve of TiO_2 xerogel presents one intense band at 373K and a broad band centered around 553K. The corresponding peaks could be observed in DSC profiles (Fig. 1b). The former can be attributed to the evaporation of remained ethanol and adsorbed water, which corresponds to an endothermic process. The second band is ascribed to the exothermal crystallization of the amorphous gel to anatase form. The glass transition point can be observed at around 650K, ascribed to the inflection of the DSC curve at this temperature. The strong and well-defined exothermic peak centered at 800K corresponds to the anatase to rutile phase transition.

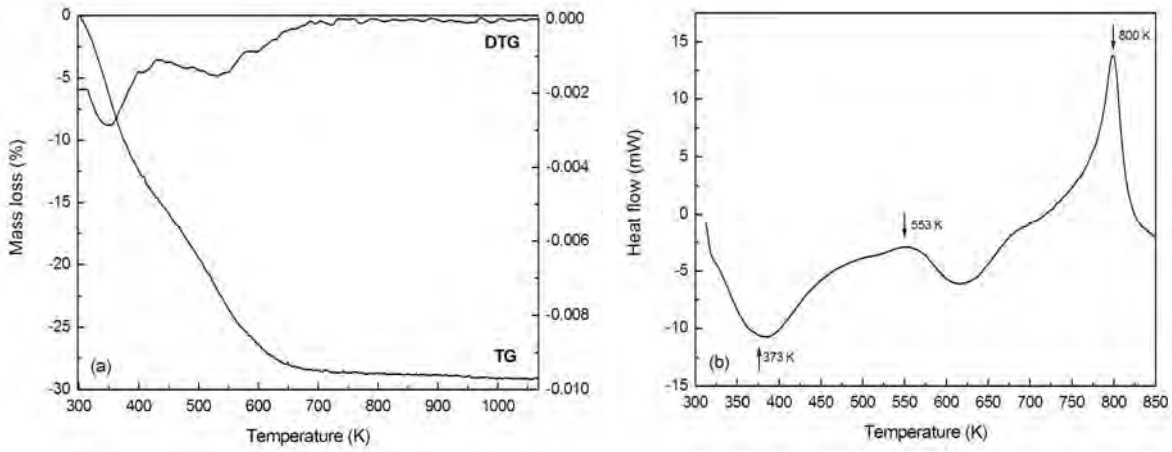

Figure 1. Xerogel evolution during calcination process: (a) TG/DTG and (b) DSC profiles.

The crystal phase of TiO_2 was studied by powder X-ray diffraction. At temperatures below 723K only anatase phase was detected. Anatase to rutile transformation was found to occur between 723 and 773K, thus, at temperatures above 723K, and to a certain point, there is a mixture of anatase and rutile phases. At 973K only the rutile phase was observed. Crystallite size and phase composition obtained by XRD are listed in Table 1.

Table 1. Anatase (d_A) and rutile (d_R) crystallite dimensions, surface area (S), anatase content (x_A), absorption edge (AE) and band gap energy (E_g) of the TiO_2 samples obtained at different calcination temperatures.

Catalyst	d_A (nm)	d_R (nm)	S (m^2 g^{-1})	x_A (%)	AE (nm)	Eg (eV)
T573	5.7	-	134	100	389	3.19
T673	8.5	-	107	100	391	3.17
T723	10	-	84	100	403	3.08
T773	14	20	26	69	410	3.03
T823	23	24	13	38	412	3.01
T873	37	39	3	5	413	3.00
T973	-	39	3	0	413	3.00

The crystallite sizes of both anatase and rutile forms increased with calcination temperature. The TiO_2 surface area was determined by nitrogen adsorption isotherms at 77K. Results show that higher the temperature, lower the surface area. Catalysts obtained at the lowest temperature (T573) exhibited a surface area of 134 m^2 g^{-1}. As the temperature increases, the surface area gradually decreases, reaching 3 m^2 g^{-1} at temperatures higher than 873K. This increase is paralleled by an increase in the crystallite dimensions. The anatase to rutile transformation was confirmed by the change on the DR UV-vis spectra of the solids (Fig. 2). On decreasing the calcination temperature, the absorption edge moved towards shorter wavelengths (blue shift), which corresponded to an increase in the band gap energy.

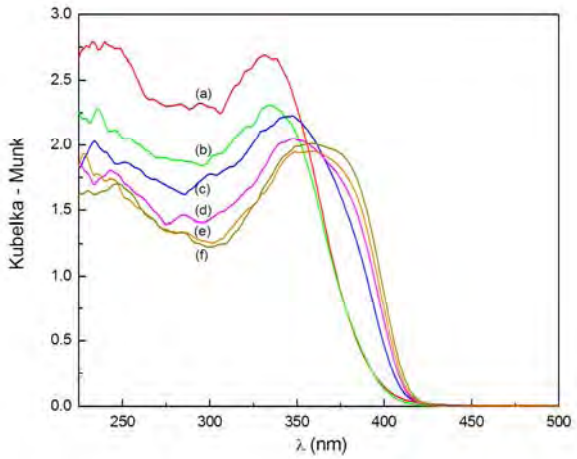

Figure 2. Diffuse reflectance UV-vis spectra of the catalysts: (a) T573, (b) T673, (c) T773, (d) T823, (e) T873, and (f) T973.

The 335 nm characteristic band of anatase disappears progressively as temperature increases. The absorption edges and the calculated band gap energies for each catalyst are given in Table 1. For samples T673 (pure anatase) and T973 (pure rutile) the measured band gap energies were 3.17 and 3.00 eV, respectively, in agreement with 3.20 and 3.02 eV referred in the literature (Carp et. al, 2004).

3.2 Phtotocatalytic degradation of clofibric acid

In order to explore the photo-efficiency of the prepared materials, we tested TiO_2 nanocrystalline catalysts in the photocatalytic oxidation of clofibric acid aqueous solutions under visible irradiation. First, we conducted the neat photochemical reaction, without any catalyst, to have a comparison standard. Both, photochemical and photocatalytic degradation of clofibric acid followed a pseudo-first order kinetic model. Kinetic rate constants (k_{app}) are listed in Table 2.

Table 2. Pseudo-first order apparent kinetic rate constants (k_{app}), clofibric acid conversion after 30 minutes of irradiation ($\chi_{30\ min}$) and total organic carbon removal at the end of 4 hours of irradiation ($\chi_{TOC,4h}$).

Catalyst	k_{app} (min^{-1})	$\chi_{30\ min}$ (%)	$\chi_{TOC,\ 4h}$ (%)
T573	8.03×10^{-2}	91.0	76.1
T673	1.11×10^{-1}	97.4	79.4
T723	7.50×10^{-2}	88.2	72.9
T773	4.76×10^{-2}	74.2	64.5
T823	2.76×10^{-2}	59.3	51.1
T873	2.14×10^{-2}	50.5	40.5
T973	1.02×10^{-2}	27.9	20.0
Blank*	3.62×10^{-3}	14.6	2.6

* no catalyst

The degradation was faster with T673 (k_{app} of 1.11×10^{-1} min^{-1}) even when compared with pure photochemical reaction (3.62×10^{-3} min^{-1}). For this catalyst, close to complete clofibric acid removal was achieved after only 30 minutes of irradiation. Catalysts obtained at higher temperatures resulted on progressively lower kinetic rate constants. Catalyst T973, constituted by pure rutile crystals, showed a k_{app} of 1.02×10^{-2} min^{-1}, close to one order of magnitude lower than the pure anatase catalyst (T673).

The main reaction intermediates detected by HPLC analysis were found to be 4-chlorophenol, isobutyric acid, hydroquinone, benzoquinone and 4-chlorocatechol. Figure 3 shows the concentration profiles of clofibric acid and reaction intermediates for photocatalytic experiments using T673 and T973. The difference in performance between the two catalysts is evident. With T673 there is an abrupt abatement on clofibric acid concentration and it is completely removed very early. The concentration of the main intermediates initially rises and then decreases until complete disappearance after 4 hr of irradiation (Fig.3a). With T973 the rate of removal is much slower. At the end of the irradiation run (4 hr) there was still a considerable amount of the initial compound and reaction intermediates in solution (Fig. 3b). The most important intermediate was 4-chlorophenol, the others being detected at lower concentrations.

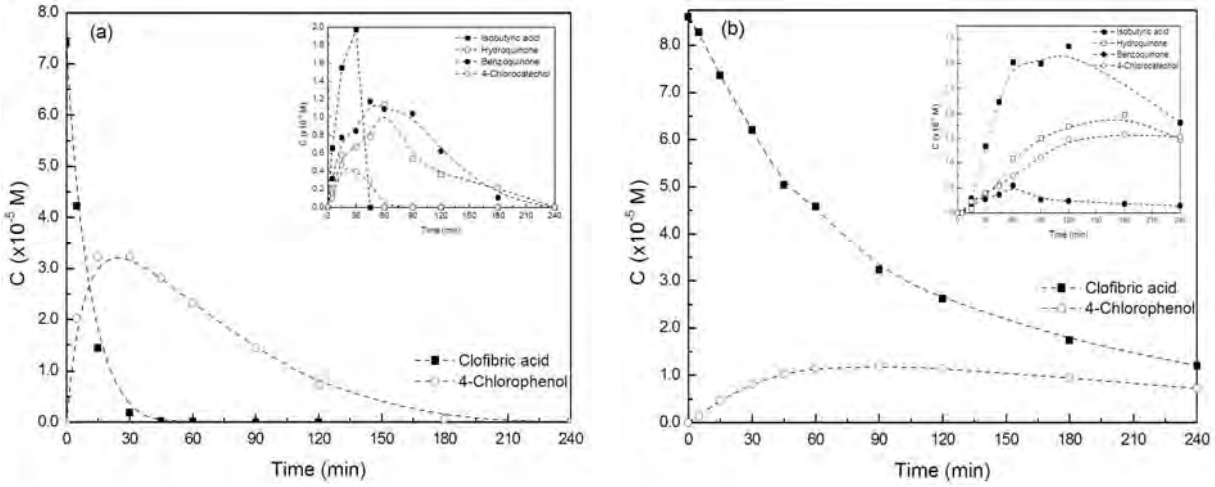

Figure 3. Concentration profiles of clofibric acid and reaction intermediates during the photocatalytic reaction using T673 (a) and T973 (b) catalysts.

Total organic carbon (TOC) analysis provided valuable information about the efficiency of the photo-assisted processes. At the end of the photodegradation runs (4 hr of irradiation) it was observed a merely 2.6% decrease in TOC for reaction without catalyst while for reaction in the presence of T673 the observed TOC removal was 79.4%. The fraction of non-mineralized organics probably corresponds to aliphatic acids, such as lactic, acetic, formic, maleic, oxalic and others resulting from the aromatic ring opening, not detected by HPLC in these experimental conditions. A possible degradation pathway is presented on Fig. 4.

From the presented results it is obvious that the photocatalytic performance depends on the structure and morphology of the TiO_2 powder induced by the final thermal treatment. The 573K treatment leads to the material with the highest surface area, mainly composed of anatase. In XRD measurements (not shown) was possible to observe some peak broadening indicating that the crystallization process was not complete. It is known that amorphous titania has low photocatalytic activity due to a high electron-hole recombination rate and this is in agreement with the observed poor performance of this material.

As the calcination temperature increases up to 673K the performance also increases and T673 is the most active photocatalyst for degradation of clofibric acid. As we increased the calcination temperature a progressive loss in photocatalytic efficiency was observed. The T973 photocatalyst was the less active of all series.

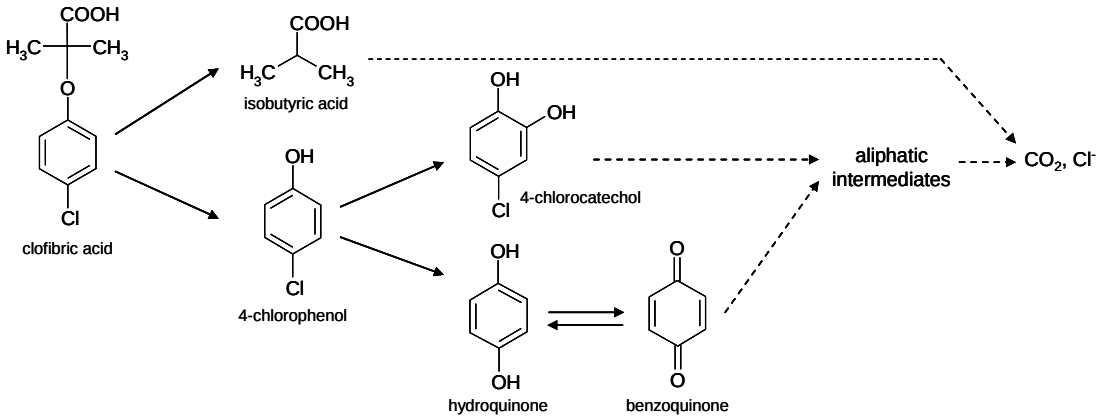

Figure 4. Simplified degradation pathway for the photocatalytic degradation of clofibric acid.

The observed decline in photoefficiency is explained in terms of phase transformation from anatase to rutile. In addition, there is an increase in crystallite size which also contributes to a more efficient electron-hole recombination. Finally, the surface area of the catalyst is also drastically reduced (Table 1) which leads to a lower surface to volume ratio, which is critical in heterogeneous catalysis.

4 Conclusions

The nitric acid catalyzed sol-gel method, using titanium(IV) isopropoxide as precursor leads to the formation of nanocrystalline TiO_2. The control of the calcination temperature in the thermal treatment step, in the range of 573-973K, allowed the production of materials with distinct physical-chemical properties such as crystal phase composition, crystallite dimensions and specific surface area. Pure anatase TiO_2 obtained at 673K produced the best catalyst: complete removal of clofibric acid and its main reaction intermediates (4-chlorophenol, isobutric acid, hydroquinone, benzoquinone and 4-chlorocatechol) after four hours of irradiation. Pure rutile produced at 973K revealed to be a rather inefficient catalyst.
At 573K there is a fraction of titania that is still not crystallized reducing the photo-efficiency of this material. Higher calcination temperature promotes phase transition from anatase to rutile and simultaneously the increase in crystallite and particle dimensions, with the corresponding decrease in surface area, leading to a loss on the activity of the photocatalysts.
From this study, it is clear that the composition of the TiO_2 powders (anatase to rutile ratio) greatly affects the photocatalytic performance. Having the catalytic system well characterized is essential to develop efficient TiO_2-assisted photocatalysis for the mineralization of persistent pharmaceutical compounds in wastewaters.

Acknowledgments
The authors gratefully acknowledge FCT and FEDER for financial assistance (fellowship SFRH/BD/16966/2004 and project POCI/EQU/58252/2004).

References

Fujishima, A., Rao, T.N., Tryk, D.A. (2000). Titanium dioxide photocatalysis. *Journal of Photochemistry and Photobiology C: Photochemistry Reviews*, 1, 1-21.
Carp, O., Huisman, C.L., Reller, A. (2004). Photoinduced reactivity of titanium dioxide. *Progress in Solid State Chemistry*, 32, 33-177.
Hsiang, H.-I., Lin, S.-C. (2006). Effects of aging on the kinetics of nanocrystalline anatase crystallite growth. *Materials Chemistry and Physics*, 95, 275-279.
Emblidge, J.P., DeLorenzo, M.E. (2006). Preliminary risk assessment of the lipid-regulating pharmaceutical clofibric acid, for three estuarine species. *Environmental Research*, 100, 216-226.

Proceedings of the 10th International Chemical and
Biological Engineering Conference - CHEMPOR 2008
Braga, Portugal, September 4-6, 2008
E.C. Ferreira and M. Mota (Eds.)

Catalytic cracking of n-decane as representative of Fisher-Tropsch products

N. Fonseca[1,2], S. Laforge[1], P. Magnoux[1], F. Lemos[2], F. Ramôa Ribeiro[2]

[1]Laboratoire de Catalyse en Chimie Organique, UMR 6503,
40 Avenue du Recteur Pineau, 86022 Poitiers Cedex, France
[2]Centro de Engenharia Biológica e Química, Instituto Superior Técnico,
Av. Rovisco Pais,1049-001 Lisboa, Portugal

Keywords: Catalytic cracking; n-decane; Acid zeolites; Activity; Selectivity; Deactivation
Topic: Advancing the chemical and biological engineering fundamentals

Abstract
In this work, n-decane cracking, taken as a model reaction, was carried out at 350°C over various protonic zeolites (H-Y, H-β, H-ZSM-5 and H-MCM-22) with similar silica-to-alumina ratio (Si/Al~15). The initial catalytic activity depends on both the size of the pore apertures and the pore architecture (channels or cages). On the other hand, the selectivity only depends on the size of the pore apertures: the smaller the pore apertures, the higher the selectivity towards light products (C_3 and C_4). Finally, although all the zeolites undergo deactivation by coke formation, this deactivation is more important for large pore zeolites (H-Y, H-β) than for medium pore size zeolites (H-ZSM-5, H-MCM-22).

1. Introduction
With the declining of petroleum resources, combined with its increased demand and the social and political instability of the petroleum exporter countries, it is imperative to develop economical and energy-efficient processes for the sustainable production of transportation fuels and chemicals [1]. In this way, it can be possible to continue to ensure the global economical development and the improvement of standards of living.

The Fisher-Tropsch (FT) synthesis is an attractive route to produce not only high-quality liquid fuels and lubricants but also valuable materials for petrochemical industry, such as premium naphtha and α-olefins [2]. This industrial process uses alternative sources to petroleum, such as coal, natural gas and biomass via conversion of syngas (mixture of CO and H_2) and produces mostly straight chain paraffins, ranging from C_1 to C_{50} [1, 2]. Another advantage of this process is the almost inexistence of aromatic and sulphur compounds in the final products [2].

The FT products can then be fed in fluid catalytic cracking (FCC) units to produce high-octane gasoline (with high content of isoparaffins) and light olefins, which are valuable materials for petrochemistry. FCC is, in fact, one of the most frequent petroleum-refining processes because it allows to obtain crucial products: mainly gasoline, but also, diesel and light olefins (notably propene) [3].

In this context, n-decane cracking, taken as a model reaction, was carried out at 350°C over various protonic zeolites: H-Y and H-ZSM-5, which form the active phase of FCC catalysts, but also H-β and H-MCM-22, which are used in other commercial processes.

The objective of the present work was to determine the influence of the zeolite pore topology (apertures size and architecture) on the catalysts activity, stability and selectivity, using samples with the same silica-to-alumina bulk ratio (Si/Al~15).

2. Experimental

2.1 Catalysts preparation

The H-Y (CBV 720) and H-ZSM-5 (SM 27) zeolites were purchased from Zeolyst International and AlSi-penta respectively. The H-β zeolite was synthesized in the "*Laboratoire des Matériaux Minéraux*, UMR 7016, Mulhouse, France''. The H-MCM-22 zeolite was prepared in our laboratory, following the procedure reported in reference [4].

2.2 Characterization of zeolite samples

The elementary analysis of silicium and aluminium, which allowed to estimate the bulk Si/Al ratios were done by Inductively Coupled Plasma - Optical Emission Spectrometer (ICP-OES) on a Optima 2000 DV equipment.

The zeolite crystallite sizes were estimated by a high resolution scanning electron microscopy, on a Philips CM 120 microscope.

Nitrogen adsorption measurements were performed at -196°C on a Micromeritics ASAP 2000 apparatus. The microporous volumes were estimated by the t-plot method, using the Harkins and Jura standard isotherm. Before measurement, the samples were out gassed under vacuum for 12 h at 350°C.

The acidity of the samples was measured by adsorption of pyridine and subsequent desorption at increasing temperature (150-450°C), followed by IR spectroscopy, on a ThermoNicolet - Nexus spectrometer. The experimental procedure is reported elsewhere [5]. The amounts of pyridine retained over Brönsted and Lewis acid sites were calculated from the areas of the IR bands at 1545 and 1455 cm^{-1}, respectively, using the extinction coefficients previously determined [6].

The carbon content of the used samples was measured by total burning at 1020°C under helium and oxygen on a Thermoquest NA2100 analyser.

The sample nomenclature and main chemical characteristics are summarized in Table 1.

Table 1: Characterization of zeolite samples

Samples	Bulk Si/Al ratio	Crystallites size (µm)	Pore volume (cm^3/g)		Acidity (µmol/g)			
					Brönsted		Lewis	
			Micro	Meso	Total	Strong	Total	Strong
H-Y	13.3	0.5	0.317	0.190	271	13	101	26
H-β	10.6	1.5	0.212	0.039	398	73	504	345
H-MCM-22	16.8	<< 1	0.218	0.292	651	55	76	63
H-ZSM-5	10.8	1.0	0.158	0.027	1161	459	27	16

2.3 Catalytic experiments

The catalytic tests were performed in a tubular Pyrex fixed-bed continuous-flow reactor, at 350°C and atmospheric pressure. The n-decane (Fluka, 98%), fed to the reactor system using a syringe pump, was diluted with dry nitrogen to achieve a partial pressure of 0.13 atm ($p_{nitrogen}/p_{n\text{-}decane}$= 7). Prior to the catalytic experiments, the zeolite samples were activated, *in situ*, for 12 h at 450°C, in dry air (60 mL/min). The deactivation profile was obtained by accumulating samples of the reactor effluent for different values of time on stream (TOS): 1, 2, 5, 10, 30 and 60 minutes. Different contact time values were obtained by varying the mass of catalyst (10 – 300 mg) and maintaining the n-decane flow constant (2.92 g/h). The reaction effluent was analysed using a VARIAN 3400 chromatograph equipped with a 100 m PONA CP-Sil CB capillary column and a flame ionization detector.

3. Results and discussion

3.1 Initial activity

Figure 1 shows the evolution of the initial n-decane conversion (1 min reaction) as a function of the contact time τ (taken as the reciprocal of the weight hourly space velocity WHSV), for the different zeolite samples.

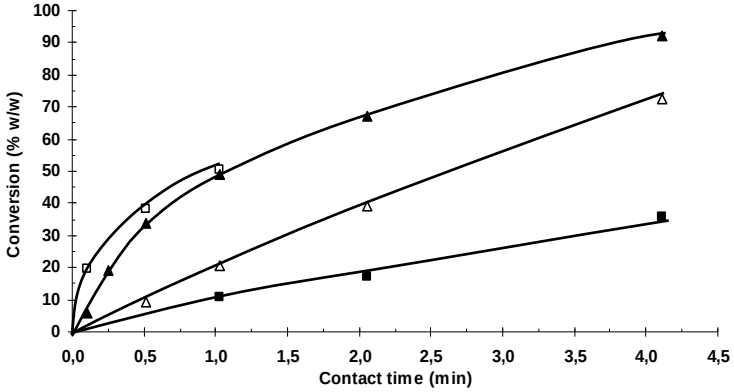

Figure 1: Initial conversion vs. contact time for the different zeolite samples: (■) H-Y, (Δ) H-MCM-22, (▲) H-ZSM-5, (□) H-β

The values of the initial activity of the different catalysts (slope of the tangent of the activity curves in Figure 1 for $\tau = 0$) are reported in Table 2. H-β is the most active catalyst, followed by H-ZSM-5, H-MCM-22 and H-Y. Moreover, Table 1 shows that the concentrations in protonic sites, which are the active sites for catalytic cracking, differ greatly from one zeolite to another: they vary from 1161 µmol g^{-1} in the H-ZSM-5 sample to 271 µmol g^{-1} in the H-Y sample. Therefore turn-over frequency (TOF) values were estimated by dividing the activity values by the total number of protonic acid sites (Table 2), although this calculation implies that all the acid sites have the same activity (hence the same strength). A very high TOF value (2032 h^{-1}) was obtained for H- β, which is 7.7, 12 and 16 times more active than H-ZSM-5, H-Y and H-MCM-22, respectively.

Table 2: Initial activity and TOF for the different zeolite samples

Zeolites	Initial activity (mmol.g^{-1}.h^{-1})	TOF (h^{-1})
H-Y	45	167
H-β	809	2032
H-MCM-22	81	125
H-ZSM-5	307	264

Observing the values reported in the Table 2, one can see that the zeolite structure influences strongly the activity of zeolite samples. These values suggest that the main criterion is not the size of the pore apertures: the large pore H- β zeolite is much more active than H-ZSM-5, which is a medium pore size zeolite, but H-ZSM-5 is more active than H-Y. Therefore, the catalytic activity could depend firstly on the pores architecture (presence of channels or cages): the catalysts exhibiting channel systems, such as H-β and H-ZSM-5 samples, are more active than the zeolites presenting supercages pore structures (H-Y). This could be due to a slower diffusion of n-decane molecules in the channels, which signifies a greater residence time inside of zeolite structure, favouring their adsorption over acid sites, and, subsequently, their cracking in smaller ones. In the case of zeolites presenting supercages, the diffusion of n-decane molecules is much faster and their adsorption less plausible, because residence time is too low.

The channels size also plays an important role because it influences strongly the diffusion velocity inside of the structure. If comparing H-β (large channels) and H-ZSM-5 (medium

channels), one can see that the first one presents a TOF value much higher than the second one (7.7 times).

3.2 Initial selectivity

Whatever the zeolite sample, at least 97% (%wt) of identified products result (directly or indirectly) from the cracking of n-decane and only 3% are aromatic compounds and isomers.

The cracking products distributions (at 10 % of n-decane conversion) obtained after 1 minute of reaction over the different zeolite samples are reported in Figure 2. Similar product distributions are obtained for both large pore zeolite samples (H-Y and H-β): C_4 alkanes and alkenes are the main reaction products, followed by C_5, C_6 and C_3. This suggests that the product distribution depends on the size of the pore apertures, but not on the pore architecture.

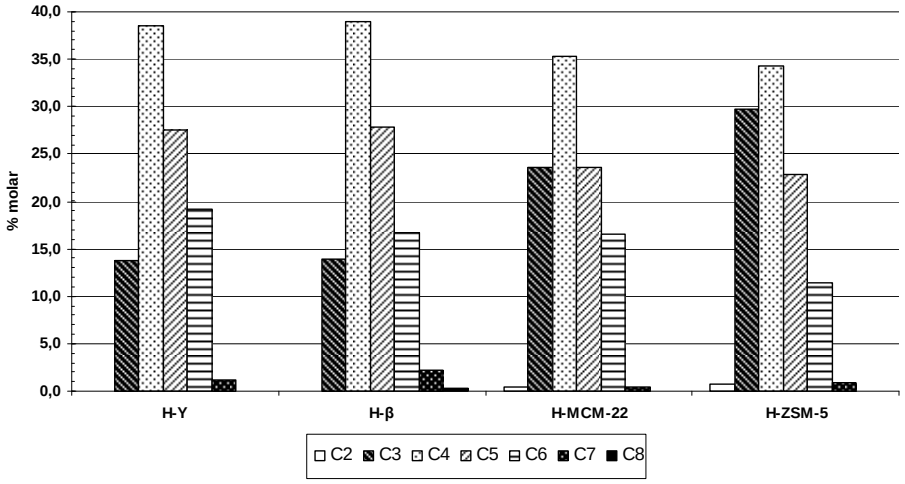

Figure 2: Initial cracking product distribution obtained over the different zeolites for 10% of conversion

On the other hand, the product distributions obtained over H-ZSM-5 and H-MCM-22 suggest that the acid sites concentration (or density) strongly influences the selectivity of the n-decane transformation. The very high C_4/C_6 ratio obtained for H-ZSM-5, associated with the large amount of C_3 products, shows that secondary cracking of the C_6 products (mainly hexenes) happens in a large scale over H-ZSM-5. This could be due to the slow diffusion of these compounds in the narrow channels of this zeolite, which would favour their cracking in smaller products. Nevertheless, the distribution found for the H-MCM-22 sample is not the one expected, it is intermediate between those obtained over large pore zeolites (H-Y and H-β) and over H-ZSM-5. This result cannot be explained by the size of the pore apertures of H-MCM-22 zeolite, which is smaller than that of H-ZSM-5 (hence should lead to an enhanced formation of C_3 products compared to H-ZSM-5). Therefore, the acid sites concentration (and density) could be an explanation: the higher the concentration, the higher the probability of secondary cracking reactions. In this case, the probability for secondary cracking reactions would vary in the following order: H-ZSM-5 >> H-MCM-22 > H-β > H-Y.

3.3 Zeolites deactivation

Figure 3 shows the evolution of n-decane conversion as a function of time-on-stream (TOS), for a contact time value of 1 minute, over the different zeolite samples.

All zeolite samples suffer deactivation, which is more evident during the first 10 minutes of reaction. The extent of the deactivation depends very much on the zeolite structure: it is faster and stronger over the large pore zeolites (H-Y and H-β) and more limited over H-ZSM-5. H-MCM-22 presents, once again, an intermediate behaviour, that could be related to the coexistence of large internal cages and narrow 10-MR pores in its structure [7]. The same order was found for the carbon content (%C, Table 3), indicating that deactivation is due to the formation of bulky polyaromatic compounds (“coke”), which is known to be favoured over large pore zeolites.

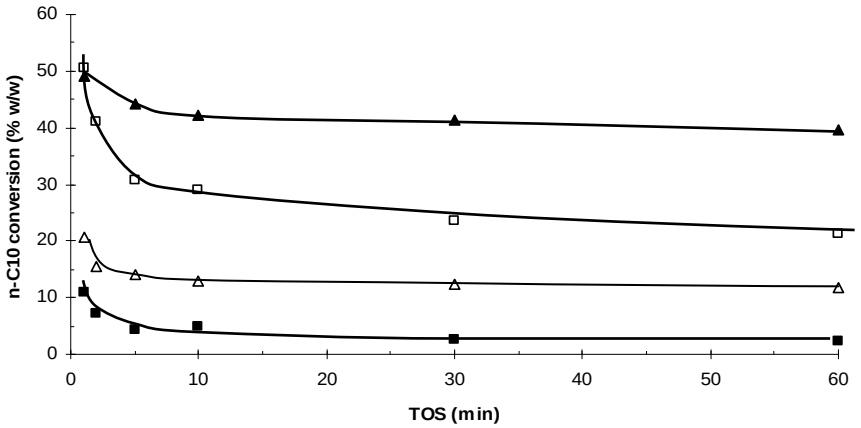

Figure 3: Deactivation profiles for 1.0 min of contact time for the different zeolite samples: (■) H-Y, (Δ) H-MCM-22, (▲) H-ZSM-5, (□) H-β

Table 3 shows that the toxicity of coke depends on the zeolite. For example, H-Y lost nearly 80 % of its initial activity when 2.2 wt% of carbon were deposited, whereas the formation of 3.3 wt% of coke over the H-β zeolite leads to a 57 % reduction of its catalytic activity. This variation in toxicity could be related to the concentration of protonic sites: this concentration is very low over H-Y, which could explain that a low amount of coke could be sufficient to poison (hence deactivate) the most part of its acid sites.

Table 3: Residual activity and carbon content for the different zeolite samples

Zeolites	Residual activity (%) [(1)]	Carbon Content (% wt) [(2)]
H-Y	22	2.2
H-β	43	3.3
H-MCM-22	59	3.5
H-ZSM-5	88	1.0

[(1)] – Ratio of the activities determined after 60 min and 1 min of reaction
[(2)] – For 10% of n-decane conversion and after 60 min of reaction

Catalytic experiments for TOS longer than 60 minutes were also performed with H-MCM-22 and H-ZSM-5 samples, for the same value of the contact time (1 min). After 4 hours, the zeolite samples presented approximately the same activity obtained after 1 hour. This fact can be explained by a slowdown in coke formation after the first 10 minutes of reaction, as suggested by the evolution of the n-decane conversion (Figure 3).

This hypothesis is in agreement with the evolution of the paraffin to olefin (P/O) ratio with TOS (Table 4). If only primary cracking of n-decane molecules happened, one would obtain the same quantity of paraffins and olefins (P/O = 1). However, when the secondary cracking of olefins (mainly hexenes) takes place, two other olefins are produced, reducing the paraffins/olefins ratio. On the other hand, olefins molecules can undergo several reactions (hydrogen transfer, oligomerisation, etc.) leading to the coke formation and to an increase of the P/O value.

Table 4: Parafins/Olefins* ratios at 10% conversion for fresh and coked zeolites samples

TOS (min)	H-Y	H-β	H-MCM-22	H-ZSM-5
1	2.3	2.0	1.6	0.85
60	1.2	1.2	0.95	0.87

* Calculated only for C_4, C_5 and C_6 compounds

The values in Table 4 clearly indicate that these reactions are very important over the fresh H-Y and H-β zeolites and very limited over H-ZSM-5 zeolite, which is consistent with the coke contents (Table 3). Moreover, the decrease of the P/O value, when TOS increases, suggests that coke formation mainly occurs during the first minutes of reaction.

Finally, deactivation has a limited effect on the product distributions obtained over H-Y, H-β and H-ZSM-5 zeolites. This is not the case of H-MCM-22: increase of the C_3 and C_4 products at the expense of C_5 and C_6. This particular behaviour could be related to the presence of two different pore systems in H-MCM-22, which would not be affected in the same way by coke formation. Indeed, it has been previously shown that coking mainly occurs in the large supercages [8]. Therefore, it can be suggested that the evolution with TOS of the product distribution is due to the progressive deactivation of the active sites located in the supercages, which causes an increase of the relative contribution of the active sites located in the sinusoidal channels. The shape of these channels, which are narrow and tortuous, would favour the desorption (hence the formation) of the lighter C_3 and C_4 products.

4. Conclusions

The initial catalytic activity depends on both the size of the pore apertures and the pore architecture. The presence of channels is the main criterion to achieve a very high activity level, but the size their apertures also plays an important role. The following catalytic activity order can be proposed: H-β >> H-ZSM-5 > H-Y > H-MCM22.

On the other hand, the selectivity depends on the size of the pore apertures: the smaller the pore apertures (ZSM-5 and MCM-22), the higher the selectivity towards light products (C_3 and C_4). Nevertheless the acid sites concentration can also influences the selectivity of the n-decane transformation.

Finally, although all the zeolites undergo deactivation by coke formation, this deactivation is more important for large pore zeolites (Y, β) than for medium pore size zeolites (ZSM-5, MCM-22).

5. References

[1] – Huber, G.W. et al (2006). Synthesis of Transportation Fuels from Biomass: Chemistry, Catalysts and Engineering. *Chemical Reviews*, 106, 4044-4098.

[2] – Martínez, A. et al (2007). Detailed study of the activity and deactivation of zeolites in hybrid Co/SiO_2-zeolite Fischer-Tropsch catalysts, *Journal of Catalysis*, 249, 162-173.

[3] – Hollander M.A. et al (2002). Gasoline conversion: reactivity towards cracking with equilibrated FCC and ZSM-5 catalysts. *Applied Catalysis A*, 223, 85-102.

[4] – Corma A. et al (1995). Synthesis and characterization of the MCM-22 zeolite. *Zeolites*, 15, 2-8.

[5] – Morin S. et al (1998). Influence of the framework composition of commercial HFAU zeolites on their activity and selectivity in m-xylene transformation. *Applied Catalysis A*, 166, 281-292.

[6] – Guisnet M. et al (1997). Acid properties of dealuminated mordenites studied by IR spectroscopy. 2. Concentration, acid strength and heterogeneity of OH groups. *Polish Journal of Chemistry*, 71, 1455-1461.

[7] – Leonowicz M.E. et al (1994), MCM-22: a molecular sieve with two independent multidimensional channel systems, *Science* 264, 1910-1913.

[8] – Laforge S. et al (2003). m-Xylene transformation over H-MCM-22 zeolite 1. Mechanisms and location of the reactions. *Journal of Catalysis*, 220, 92-103.

Proceedings of the 10th International Chemical and
Biological Engineering Conference - CHEMPOR 2008
Braga, Portugal, September 4-6, 2008
E.C. Ferreira and M. Mota (Eds.)

Optimization Tools and Economical Issues in the Design of a Residential Cogeneration System

Luís A.S.B. Martins[1*], Francisco Madureira[1], Celina P. Leão[2], Angela M. Silva[2], Manuel L. Nunes[2], Senhorinha F.C.F. Teixeira[2]

[1] DEM – Mechanical Engineering Department, University of Minho, Campus de Azurém, 4800–058 Guimarães, Portugal.

[2] DPS, System and Production Department, University of Minho, Campus de Azurém, 4800–058 Guimarães, Portugal

Keywords: Micro-cogeneration, Thermo-economic optimization, Heat Recuperating system design, multi-disciplinary project.
Topic: Multi-scale and/or multi-disciplinary approach to process-product innovation: Product design & innovation.

Abstract

A numerical optimization method, previously applied to a large cogeneration plant has been adapted for a small-scale unit delivering 100 kWe of electricity and 0.5 kg/s of saturated steam. The unit is based on a micro gas-turbine and includes an internal pre-heater (typical of these types of small-scale units) and the usual HRSG (Heat Recuperator Steam Generator). Despite difficulties in obtaining data for some of the components cost-equations, the preliminary results indicate that the optimal compressor pressure ratio is about half of the usual value in large installations, while the turbine inlet temperature remains virtually unchanged. The method is being adapted to a micro-scale cogeneration unit (<6 kWe), for single household applications, that involves different components including an IC engine and a novel two-step heat recuperator. This methodology is invaluable in the undergoing design and construction of this micro-cogeneration prototype which is part of this project.

1 Introduction

Cogeneration or Combined Heat and Power (CHP), is the simultaneous production of thermal and electric energies. It is a major option to achieve primary energy savings, avoid grid network losses and reduce GHGs emissions. It has been worldwide implemented in large scale installations (>1 MWe) but the use of microcogeneration units (<50 kWe), for domestic or small commercial buildings, is still at an incipient level. This scenario will change rapidly, triggered by rocketing fuel prices, climate change awareness and government support mechanisms (Onovwiona and Ugursal, 2006; DL n.º 363/2007; Directive 2004/8/EC).

The development of a new technology must take into account the socio-economic aspects, thus providing a realistic way to evaluate the production and operation costs of these systems. The economic aspects are important, namely for the final consumer.

Thus far, numerical methods of optimization have been used for the thermo and economic optimizations of large systems. The aim of these procedures is to minimize the total costs including those related with the thermodynamic inefficiencies (Silva et al., 2003). However, applications of these methodologies to small-scale installations cannot be found in the literature.

In the present project, a multidisciplinary team has been adapting a thermoeconomic optimization method, which gave good results with multi-megawatt cogeneration systems (Silva et al., 2003), to small-scale (<1 MWe) and micro-scale cogeneration units (<50 kWe).

* Corresponding author. Tel + 351-253-510344. E-mail: lmartins@dem.uminho.pt

Different technologies are available for cogeneration systems, and the choice depends on, among other factors, the size of the unit and the required power to heat ratio. A small scale cogeneration plant based on a gas turbine has been studied (Martins et al., 2008) and the optimization tool is now being used in the design of a micro-scale cogeneration prototype.

2 Small-scale Gas Turbine Cogeneration Plant

In a still recent past the gas-turbine engines available as prime movers for electricity generation were only large industrial or expensive aeroderivative models typically with powers in the order of tens of megawatts. In recent years, however, this type of engines has undergone major improvements both in efficiency and cost reductions. Nowadays, several inexpensive models are available in the range of 30 to 250 kWe, with electrical efficiencies already exceeding 30%, thanks to the use of a basic air-compressor associated to an internal air pre-heater.

Gas turbine engines offer significant advantages over Diesel or IC engines, particularly when Natural Gas is used as fuel. Working with high levels of excess air, they do not need a cooling system, the emission of pollutants and noise are lower and, in cogeneration mode, total efficiencies of up to 90% are feasible, with the further advantage of flexible heat production through the possible use of post-combustion.

With the current market trends toward Distributed Generation, and the increased substitution of boilers with NG powered cogeneration units for CO_2 emissions reduction, small-scale gas turbine units are the ideal solution for energy systems located in urban areas.

2.1 Plant description

A small-scale cogeneration plant that delivers 100 kW of electricity and 0.05 kg/s of saturated steam has been simulated (Martins et al., 2008). This system is constituted by a compressor, a combustion chamber, a gas turbine, a pre-heater that uses the burnt gases thermal energy to heat the air before entering the combustion chamber, and an exhaust heat recuperator to generate steam.

2.2 Mathematical Model and Numerical Solution

In general, for micro-cogeneration systems, two different optimization criteria can be considered: on the one hand the maximization of the annual cash flow and on the other hand the minimization of the generation cost of the plant (Valdés et al., 2003). The main objective of this study is to minimize the annual cost of the micro-cogeneration system. A mathematical model has been developed to simulate this cost analysis.

In engineering economics, the unit of time intervals for such purpose is usually taken as one year (Zhang et al., 2004). The energy system produces in unit time the desired amounts of products. The total cost per year includes the fuel cost, the initial investment (initial cost) and the operation and maintenance cost. The monetary balance equation for unit time can be applied to the complete system, as well as to its components, in the following general form:

$$C_t = \left(P \rightarrow A, i_e, n\right) C_i + C_{tf} + C_{om} \tag{1}$$

where C_{tf} is the total cost of the fuel (€/year), C_i the initial investment (initial cost), ($P \rightarrow A, i_e, n$) the capital recovery factor, n the system economic life (years) and C_{om} the operation and maintenance cost per year (€/year). The initial investment (C_i) for a micro-cogeneration system consists of purchasing costs of j components, C_j.

The initial investment is distributed over years equally. The capital recovery factor (*CRF*) is used to determine the equal amounts of n cash transactions for an investment and can be expressed as:

$$CRF = \left(P \rightarrow A, i_e, n\right) = \frac{i_e\left[\left(1+i_e\right)\right]^n}{\left[\left(1+i_e\right)\right]^n - 1} \quad (2)$$

where A is called annuity, a series of equal amount cash transactions, P is the present value of the initial cost, i_e is the effective rate of return, and n is years of operation. Effective rate of return is imposed by the owner of funds who makes these funds available for the investment. For thermoeconomic optimization the effective rate of return can be approximated as: nominal rate of return (i.e interest rate) minus inflation rate plus owners' risk factor and correction for the method of compounding (Gogus, 2005).

The fuel cost rate is an important parameter. It can be expressed as the product of the price of unit energy with the input energy rate. The total fuel cost is determined as:

$$C_{tf} = C_f\left(\frac{\bar{W}}{\eta}\right) \times h \quad (3)$$

where C_f is the fuel cost per kWh (€/year), $\bar{W}$ the mean annual output power of the plant (kW), h the system working hours per annual system operation period (h/year), and η the thermal efficiency. The rate of operation and maintenance cost per year was assumed equal to 6% of the equal amount of initial investment per year:

$$C_{om} = 0.06\left(P \rightarrow A, i_e, n\right) C_i \quad (4)$$

Thus, the objective function can be formulated as a minimization of the total annual cost of operation for the micro-cogeneration system, when the components are analyzed separately:

$$\min C_t = 1.06 \sum_j C_{ij}\ CRF + C_{tf} \quad (5)$$

To complete the mathematical model, the equations that describe the purchase cost of the main components of the micro-cogeneration system, must be known. Despite difficulties in obtaining data for these components cost-equations, the authors have adapted some coefficients of the mathematical model used for cogeneration systems (Silva et al., 2003). In addition to these cost equations, a set of nonlinear inequality constraints must be imposed by the operability of the system, taking into account safety considerations, legal regulations, among others.

This system defines a nonlinear optimization problem with constraints, where the pressure ratio of the compressor (P_2/P_1), the isentropic efficiencies of the air compressor and the gas turbine (η_c, η_t, respectively) and the temperatures of the combustion gases at the gas turbine inlet (T_3) and at the outlet of the gas chamber (T_4), are the decision variables.

This optimization problem has been solved by a direct method, the Box method (Rao, 1996). This method, implemented in Fortran, is similar to the simplex method used for linear programming. In previous works, this method shows to be efficient (Silva et al., 2003). Two subroutines must be supplied by the user: one to compute the objective function for any given set of independent variables, and the second one where the upper and lower bounds on the independent variables and the constraints are specified. The method assumes that an initial feasible point, that satisfies all the constraints, is available.

2.3 Some Results

The system delivers a 100kW of electricity, for a combined supply of 0.05 kg/s of saturated steam at 9.8 bar. The fuel is natural gas with LHV (Lower Heating Value) equal to 45100 kJ/kg.

When the optimization method reaches the convergence, the optimal values for the decision variables and costs are obtained. All the temperature and pressure values for the streams in the optimal design of the micro-cogeneration plant are also obtained (see Figure 1).

The preliminary results indicate that the optimal compressor pressure ratio is about half of the usual value in large installations, while the turbine inlet temperature remains virtually unchanged (Martins et al., 2008).

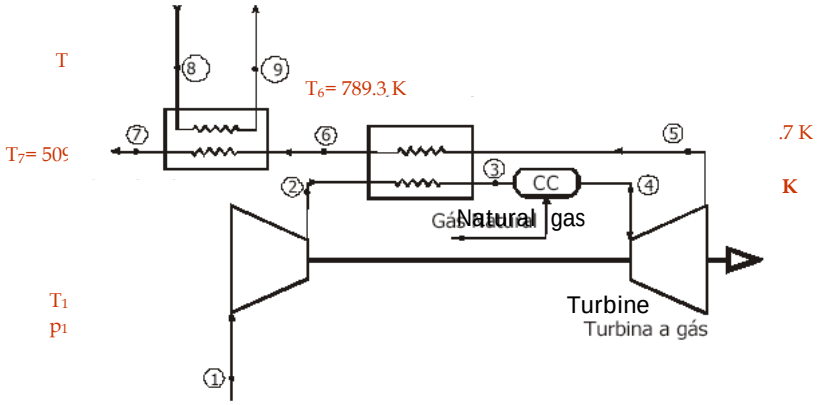

Figure 1. Temperature and pressure values for the streams in the optimal design of the micro-cogeneration plant.

3 Development of a Micro-scale Cogeneration Prototype

The micro-cogeneration prototype that is being designed and constructed (<6 kWe), is aimed at the single household market and is based on a commercial IC engine-generator, complemented with a heat recuperating system. The system layout is shown in Figure 2.

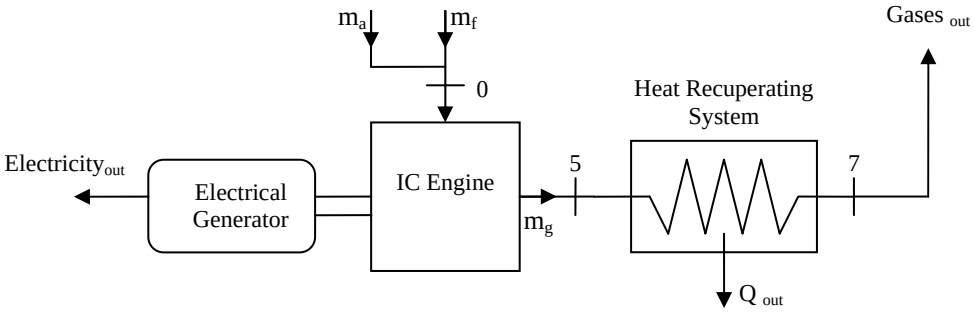

Figure 2. Micro-cogeneration system layout

3.1 Design and Construction

The main component is the Spark Ignition Internal Combustion engine, a single-cylinder with 390 cc capacity, undergoing a four-stroke thermodynamic cycle. It is currently running on gasoline as fuel which is evaporated and fed into the incoming air via a carburettor. The engine powers a 3-Phase synchronous electric generator rated at 6.5 kVA and 50 Hz.

The unit will be converted to Natural Gas and it is expected that, depending on the optimized operating conditions and other engine modifications, the unit will deliver an electric power in the range of 3 to 5 kWe. The conversion to NG will involve the substitution of the carburettor with a proper gas-injector.

The incoming air passes through a filter and is premixed with the NG via the gas injector, immediately upstream of the cylinder inlet valve (point 0). After the 4-stroke cycle the high-

temperature burnt-gases leave the engine through the exhaust valve (point 5). For the sake of simplicity, the intermediate thermodynamic states (1 to 4) are not presented in Figure 2.

With an Internal Combustion Engine there are two possible sources for recovered heat: the high temperature exhaust gases and, as the thermodynamic cycle is non-adiabatic, the engine cooling system. In this work and for the first stage of the prototype development, only the energy associated to the exhaust gases will be taken into account. Thus, the main innovation will be the exhaust gases heat recuperating system, which consists on a series of two counter flow gas-water heat-exchangers (Figure 3). The first one is a direct-heat exchanger where the incoming hot gases are mixed with cold water and as a result the two outgoing streams (water and saturated gases) will leave at approximately the same temperature (T_{W2}=T_6). In the process, a portion of the inlet water evaporates and the exhaust gases become saturated before flowing into the second heat-exchanger for further cooling and partial condensing, with the gases exiting at a low temperature (T_7).

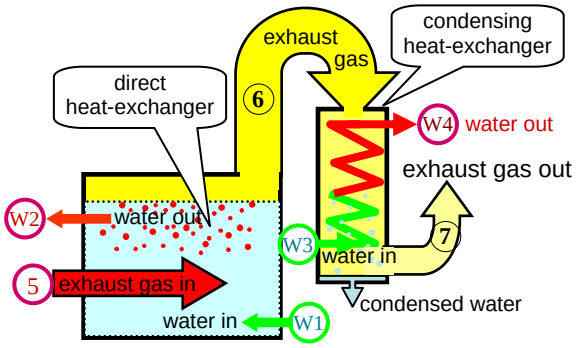

Figure 3. Heat recuperating system.

This novel thermal system and engine cycle analysis has been implemented in Excel in order to study its efficiency. It has been demonstrated that this layout leads to a lower exhaust gas temperature, i.e. to a higher global efficiency by comparison with traditional heat recuperators (Teixeira, 2007).

3.2 Thermoeconomical Optimization Model

At the moment, this optimization tool is being applied to the new microcogeneration system in order to improve design and to study the economical viability of the project.

The expressions and parameters used for obtaining the purchase costs are presented bellow (Table 1). They are based upon available literature for heat exchangers and other components (e.g Haslego and Polley, 2002; Honda, 2007) with the constants tuned for the Spanish and Portuguese market. All the costs are in Euros. As for the equations describing the physical energy system, they are based on the analysis previously done by Teixeira (2007) and are not presented here. The r_v is the engine volumetric ratio with reference value is 8.0, typical of commercial small engines running on gasoline, P_{mec} the engine nominal mechanical power (kW), T_{max} the temperature (K), η_G is the generator efficiency and thr reference equal to 0.825, P_{elect} the nominal electrical power (kW), $\dot{m}_g$ the exhaust gases mass flow rate (kg/s), and A_{HE2} the heat transfer area (m^2) of the cooling heat exchanger.

The decision variables selected for the optimization are the engine volumetric ratio (r_v), the combustion equivalence ratio (ϕ), the temperature of the gases after combustion (T_{max}) and the generator efficiency (η_G). The imposed operational conditions for the unit are 3.5 kW of electricity and 5.5 kW of thermal power.

Table 1 Purchase costs equations for the main components

Component	**Purchase cost equation**
Internal Combustion Engine	$C_{Eng} = 805\left(P_{mec}\right)^{0.5}\left(\frac{r_v}{8}\right)^{0.62}\left(\frac{T_{\max}}{2300}\right)^{7.42}$
Electric Generator	$C_G = 327\left(P_{elect}\right)^{0.7}\left(\frac{0.175}{1-\eta_G}\right)$
Direct Heat-exchanger	$C_{HE1} = 4280\dot{m}_g^{0.37}$
Second Heat-exchanger (condensing)	$C_{HE2} = 800A_{HE2}^{0.46}$

4 Conclusions

After good results with a 5 MW plant and small-scale 100 kW cogeneration unit, both centred on gas-turbine technology, it is expected that the optimization methodology herein presented will be a redoubtable guidance tool in the design of the domestic-scale cogeneration prototype, by allowing the research team to define the optimal values for design variables such as engine volumetric-ratio, excess air, maximum combustion temperature and in the sizing of the heat recuperating system. These objectives will be accomplished, provided that realistic cost-equations and a good thermodynamic model are used as inputs to the computational model.

References

Decreto-Lei n.º 363/2007, Diário da República, 1.ª série – N.º 211 – 2 de Novembro de 2007, 7978-7984.

Directive 2004/8/EC of the European Parliament and of the Council, Official Journal of the European Union, February 2004.

Gogus, Y. A. (2005), Thermoeconomic optimization, International Journal of Energy Research, 29, 559-580.

Haslego, C., Polley, G. (2002) Designing Plate-and-Frame Heat Exchangers, CEP Magazine, September.

Honda (2007). European Engine Catalogue.

Martins, L.A.S., Leão, C.P.,Teixeira, S.F.C.F. (2008) *Optimização termoeconómica de um sistema inovador de micro-cogeração*, in 13º Congresso da APDIO-IO2008, Ambiente e Energia, Vila Real, Portugal (abstract).

Onovwiona, H.I. and Ugursal, V.I. (2006). Residential Cogeneration System: Review of the Current Technology, Renewable and Sustainable Energy Reviews, 10, 389-431.

Rao, S.S. (1996). *Engineering Optimization*, John Wiley and Sons.

Silva, A.M.; Teixeira, J.C.F.; Teixeira, S.F.C.F. (2003). *A numerical thermoeconomic study of a co-generation plant*, In Proceedings of ECOS 2003, Copenhagen: Denmark, 195-202.

Teixeira, L.I.P. (2007). *Micro-Cogeração Doméstica com Recuperador de Calor Bifásico*, MSc Thesis, Universidade do Minho, Portugal.

Valdés, M., Durán, M. D. and Rovira, A., (2003), Thermoeconomic optimization of combined cycle gas turbine power plants using genetic algorithms, 23, 2169-2182.

Zhang, G. Q., Wang, L., Liu, L. And Wang, Z. (2004), *Thermoeconomic optimization of small size central air conditioner*, Applied Thermal Engineering, 24, 471-485.

Proceedings of the 10th International Chemical and
Biological Engineering Conference - CHEMPOR 2008
Braga, Portugal, September 4-6, 2008
E.C. Ferreira and M. Mota (Eds.)

Environmental performance assessment in process design

Florinda Martins[1], Carlos Costa[2]
[1] REQUIMTE, ISEP, Rua Dr. António Bernardino de Almeida, 431, 4200-072 Porto
[2] FEUP, Rua Dr. Roberto Frias, s/n 4200-465 Porto

Keywords: environmental performance; life cycle assessment; environmental impacts
Topic: Sustainable process-product development through green chemistry

Abstract

An important issue in process design is related to which tools (indicators) should be used to include environmental concerns on the analysis and synthesis steps. According to Cano-Ruiz and McRae (1998) environmental indicators have been developed based on several concepts: minimization of the more concerning pollutants in the emissions, minimization of generated total waste mass, minimization of contributions to specific problems and minimization of an aggregated indicator. The environmental assessment based on the total mass of waste generated is not sufficiently enlightening since it does not consider the characteristics of the different substances emitted. The environmental assessment based on specific indicators is very restrictive and does not allow for the consideration of various aspects of the environmental impacts. The consideration of different environmental impacts is the best way to evaluate the environmental performance of a process.

This paper proposes a methodology to develop and determine a global (aggregated) potential environmental impact indicator based on the Guinée model (2002). In this model the impact categories were chosen considering a base list proposed by SETAC (*the Society of Environmental Toxicology and Chemistry*). To determine the global environmental indicator one should consider the baseline category impacts suggested by Guinée (2002) and select those that apply to the case in study. Since for the category human toxicity there aren't internationally accepted impact indicators it is suggested to use the ones that are more suitable for the case in study including the use of other models like the IChemE (2007). Then it follows characterization and normalization steps and finally, the establishment of weights to obtain an aggregated indicator. The normalization can be done using the mean value of the indicators values for all the compounds in each category as suggested by the WAR methodology (Cabezas et al., 1999). The application of this methodology implies the establishment of the scope (time and space). The environmental performance evaluation should be compatible with the information available since it can be interesting to perform a cradle to grave, a cradle to gate, a gate to grave or a gate to gate assessment. The energy environmental impacts should always be taken in consideration. This methodology was applied to the HDA process (Douglas, 1988) in a gate to gate approach considering energy environmental impacts, to select the best topologies by sorting.

1 Introduction

The consideration of the different environmental impacts can be used to evaluate the environmental performance of a process. There are several methodologies to evaluate the potential environmental impacts (Cabezas et al., 1999, IChemE, Janeiro/2007). These methodologies imply the scope definition, space and time, and the choice of a set of impact categories, its characterization, normalization and the selection of weights to obtain a global indicator. To calculate the global potential environment impact it is necessary to use a

weighted sum of the normalized impacts of the several impact categories and for that reason it is necessary to establish weights, that show the importance of each impact category. This is usually done using a panel, or weights developed by others whether by value judgement or with some scientific base.

The environmental performance evaluation should be compatible with the information available since it can be interesting to perform a cradle to grave, a cradle to gate, a gate to grave or a gate to gate assessment. An indicator based in a cradle to grave procedure allows for a very complete analysis, although it may become very difficult to calculate since the information available in the conceptual design step is limited and uncertain. For that reason it seems more logic and interesting to perform a gate to gate approach, considering the process and including its energy requirements impacts. As a time basis one can consider a year of operation.

The methodologies mentioned below were chosen since they calculate or allow the determination of a global indicator, taking into consideration the several environmental impacts and represent an acceptable trade-off between objectivity and simplicity. The determination of a global indicator is very useful to compare different topologies and for optimization purposes, since it easily allows the definition of an environmental objective function.

- WAR methodology (*Waste Reduction*) developed by Cabezas et al. (1999) and Young and Cabezas (1999), initially based on Heijungs et al. (1992), and considering eight impact categories: global warming potential, ozone depletion potential, photochemical oxidation potential , acidification, human toxicity potential by ingestion, human toxicity potential by exposure both dermal and inhalation, aquatic toxicity potential and terrestrial toxicity potential.
- IChemE methodology (IChemE, Janeiro/2007) that considers the following environmental compartments: air (impact categories: acidification, global warming, stratospheric ozone depletion, human health – carcinogenic effects and photochemical ozone (smog) formation), water (impact categories: aquatic acidification, aquatic oxygen demand, ecotoxicity to aquatic life and eutrophication) and soil (impact categories: total hazardous solid waste disposal).

2 Environmental assessment

In order to develop a methodology to calculate a global potential environmental indicator it is necessary to define the impact categories that should be included considering the Guinée model (2002) and the process studied, namely the predicted emissions.

In the Guinée model (2002) the environmental impact categories were chosen taking into consideration the basic list developed by the SETAC group (*the Society of Environmental Toxicology and Chemistry*) concerning the impact assessment. It is a problem-oriented approach, because it is driven by environmental problems (the mid-point of the cause-effect chain), rather than by damage (end-point of the chain). The impact categories chosen belong to the first group, namely the baseline impact categories for which there is a characterization method available in the literature (Guinée, 2002). The impact categories considered are: depletion of abiotic resources, impacts of land use, climate change, stratospheric ozone depletion, human toxicity, ecotoxicity, photo-oxidant formation, acidification and eutrophication. For global warming there are impact factors internationally accepted but for human toxicity there aren't. So for the impact category human toxicity it may be more important to use a characterization more specific for the process considered (ex.: in a process where carcinogenic chemicals are emitted it is more suitable to use the IChemE impact category: human health – carcinogenic effects).

Since it is important to obtain a global indicator for environmental impacts it is necessary to proceed to the normalization, in this case adopting the WAR strategy (Young and Cabezas, 1999) , namely dividing each chemical indicator by the mean value of the indicators values for all the compounds in each category. According to the ISO14042 normalisation is to calculate the magnitude of an indicator towards a reference information. The reference information can be related to a community (country, continent, world), a person or other system, for a given period of time. A goal to be achieved can also be a reference information. Although the normalisation within each category, using the mean value of the indicators values for all the compounds in each category, allows for an analysis more independent of space and time referentials, in the case of the design and optimisation of chemical processes it can have some advantages, specially if that reference information do not exist (more importance of regional and local impact categories).

If there isn't a local defined to the production unit, we may consider that all the impact categories have the same importance, so the weight given to each category will be 1. The sensitivity analysis can be replaced by the application of an end point approach like Eco-indicator 99 or the EPS system (Guinée, 2002).

2.1 Case study

As case study was selected a well documented process, namely the non catalytic hydrodealkylation of toluene to benzene (HDA). To this process several topologies with different options of mass and heat conservation can be established. The raw-material streams are toluene and hydrogen with 3% of methane at 3.964X10^6 Pa and 303.2 K, normally used and referred by Qiu et al. (2000), Luyben et al. (1999) and Douglas (1988). The benzene stream product should be of high purity.
The main reactions are:

$$C_7H_8 + H_2 \rightarrow C_6H_6 + CH_4 \quad (6)$$

$$2C_6H_6 \Leftrightarrow C_{12}H_{10} + H_2 \quad (7)$$

2.2 Topologies for environmental evaluation

There were 21 topologies available for environmental evaluation. For each topology a set of simulations were performed (using PRO/II as simulator) according to a statistical design plan. The next figure shows the flowsheet of one of those topologies.

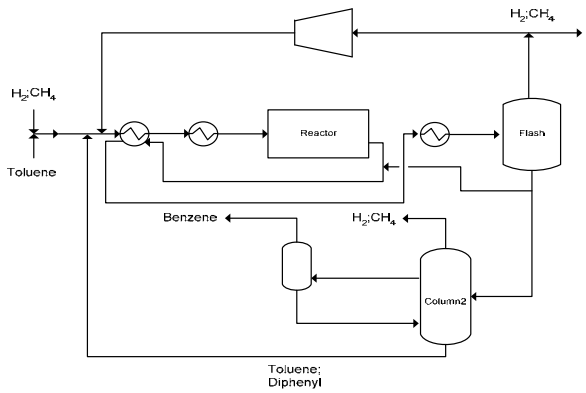

Figure 1 Topology CrTBRe

2.3 Application to the case study

When applying the methodology proposed to calculate the value of the global potential environmental impact indicator we concluded that some impact categories are empty and others were not selected. The impacts of land use weren't considered because the study performed didn't included any detailed project information like the necessary area and the local of implantation of the unit. Ecotoxicity was not considered because it presented very low values to the chemicals of the case study, so its impacts wouldn't be significant. The category stratospheric ozone depletion is an empty category since there aren't chemicals emitted that contribute to this impact category. Also from the Guinée model (2002) the category human toxicity wasn't considered because it was replaced by a more suitable impact category, namely the human health – carcinogenic effects from the IChemE model, since in this process carcinogenic chemicals (benzene) will be emitted. In the IChemE model and for the above mentioned impact category the factors are calculated using occupational exposure limits set by the *UK Health and Safety Executive*.

Table 1 shows the impact categories, the models and the indicators used. The chemicals emitted or necessary by the process that contributed to each impact category are also indicated.

In the reference document on best available techniques, Integrated Pollution Prevention and Control- IPPC, to this type of industry (European_Commission, February 2003) is stated that for this process (HDA) there aren't significant emissions to water or soil, so they weren't considered. It was also considered that there are no direct emissions; the existing emissions are fugitive or emissions related to the use of subproduct streams as fuel and in this last case complete combustion was considered. To estimate the fugitive emissions emission factors were used. The emissions to air are mainly due to fugitive emissions, use of subproduct streams as fuel and use of energy. The environment impacts due to the use of energy (compressor, reboilers and furnace) were calculated by doing the inventory of the related production emissions and considering the selected impact categories.

Table 1 Impact categories, models and indicators

Scale	**Impact categories and models**	**Reference chemical**	**Emitted or necessary chemicals**
Global	Climate change (Guinée model)	CO_2	CO_2 CH_4
Global Regional Local	Depletion of abiotic resources (Guinée model)	antimony	Fuel
Regional Local	Acidification (Guinée model)	SO_2	NO_x SO_2
Local	Eutrophication (Guinée model)	PO_4^{3-}	NO_x
	Photo-oxidant formation (Guinée model)	ethylene	C_6H_6; CH_4 C_7H_8; SO_2
	Human health – carcinogenic effects (IChemE model)	benzene	C_6H_6

3 Results

For each topology and set of simulations the mean value of the global potential environment impact (GPEI) was calculated and the results distribution analysed (the range of responses was divided in 10 intervals and the percentage of results falling in the first interval was calculated for each topology). The average values were used to rank the topologies (Table 2).

Table 2 Topology ranking according to GPEI mean value

Topology	GPEIx10^{-5}	Percentage of results falling in the first interval
Ae	7.1	100%
As	8.5	100%
Es	14.2	100%
Ee	17.3	100%
GrTBe	20.3	100%
GrTBe5	34.3	83%
GrTB	40.3	63%
GrTBe4	43.9	67%
Ce	85.4	0%
ErTB	107.5	33%
ErTBe3	108.4	33%
ErTBe4	112.0	33%
CRe	127.5	75%
ErTBe2	130.7	33%
CrTBR	163.5	33%
GrTBe3	170.6	0%
DrTB	184.3	40%
CsR	201.7	67%
GrTBe2	226.4	0%
ErTBe	240.0	0%
CrTBRe	286.6	0%

Since the normalisation was done within each category the values to the global potential environmental indicator are high.

From table 2 it is possible to conclude that the topology Ae presents the best average value. Topologies As, Ae, Es, Ee and GrTBe are the most promising since they present the best average values and simultaneously have a percentage of results falling in the first interval of the response distribution equal to 100%.

.

4 Conclusions

The methodology proposed to calculate the global potential environmental impact can be used to rank a set of different topologies allowing for the selection of the more promising ones. The way it was developed considers the specific characteristics of the process under studied, taking into account the emissions and chemicals released. For the impact categories that don't have internationally accepted factors this methodology proposes the selection of the more suitable indicators in order to calculate a more process specific value for the global potential environmental indicator.

References

Cabezas, H., Bare, J. C. and Mallick, S. K. (1999). "Pollution prevention with chemical process simulators: the generalized waste reduction (WAR) algorithm-full version." Computers and Chemical Engineering **23**: 623-634.

Cano-Ruiz, J. A. and McRae, G. J. (1998). Environmentally conscious chemical process design, Ann. Rev. Energy Environ. **23**: 499-523.

Douglas, J. M. (1988). Conceptual Design of Chemical Processes. Singapore, McGraw-Hill Chemical Engineering Series.

European_Commission (February 2003). Integrated Pollution Prevention and Control (IPPC). Reference Document on Best Available Techniques in the Large Volume Organic Chemical Industry.

Guinée, J. B. (2002). Handbook on life cycle assessment. Operational guide to the ISO standards. Dordrecht, Kluwer Academic Publishers.

IChemE. (Janeiro/2007). The Sustainability Metrics. **www.icheme.org**.

Luyben, W. L., Tyréus, B. D. and Luyben, M. L. (1999). Plantwide Process Control. New York, McGraw-Hill.

Qiu, Q. F., Krishnaswamy, P. R. and Rangaiah, G. P. (2000). Modeling and simulation of HDA process for plant-wide design and control studies. Chemical and Process Engineering Conference (CPEC), Singapore.

Young, D. M. and Cabezas, H. (1999). "Designing sustainable processes with simulation: the waste reduction (WAR) algorithm." Computers and Chemical Engineering 23: 1477-1491.

Proceedings of the 10th International Chemical and
Biological Engineering Conference - CHEMPOR 2008
Braga, Portugal, September 4-6, 2008
E.C. Ferreira and M. Mota (Eds.)

ENVIRONMENTAL PERFOMANCE OF THE WINE INDUSTRY. OPPORTUNITIES FOR UPTAKE CLEANER PRODUCTION

Rosa A. Rodriguez[1*], Carlos Palacios[1], Stella M. Udaquiola[1]
[(1)]Instituto de Ingeniería Química -Facultad de Ingeniería -Universidad Nacional de San Juan
Libertador 1109 (O) CEP 5400, San Juan, Argentina

Keywords: winery, environment, water, energy, water vapour, wastewater, infrastructure.
Topic: Sustainable process-product development through green chemistry

Abstract

The wine industry is one of the main industries in San Juan, Argentina. The majority of the large firms still consider the environmental issues as a cost driver. As a result of this consideration firms do not use more resources for environmental technologies. On the other hand, the more important impacts associated with wine making are: energy and water consumption, solid wastes generation and gaseous emission.This work presents an environmental diagnosis of winery industry, taking into account the main aspects and the collected data. The evaluation was carried out applying the Schaltegger and Sturm´s definition. This diagnosis originates the necessity to propose the opportunities for uptake of Cleaner Production to wineries in San Juan. In this work, these opportunities are proposed using Cleaner Production Assessment. They are focused in each unit operation, stage process and services and utilities.

1. Introduction

The United Nations Environment Program defined Cleaner Production (CP) as “the continuous application of an integrated, preventative environmental strategy to processes, products and services to increase eco-efficiency and reduce risks to humans and the environment”.

The term Eco-efficiency (EE) is used in different ways and other terms are used overlapping with these meanings, like environmental cost-effectiveness and environmental productivity.

Starting point for the formal definition of EE is the general definition of WBCSD (World Business Council for Sustainable Development, 1992): "To provide goods and services to a competitive price that satisfies the human necessities and the life quality, at time that reduces the environmental impact and the use intensity of resources progressively along the cycle of life, until a compatible level with the dear carrying capacity of the planet." Schaltegger and Sturm (1989), describing EE as a ratio between two elements: environmental impact, to be reduced, and value of production, to be increased.

The connection between CP and EE varies according different bibliographies. Howgrave-Graham and van Berkel (2007) say: “CP is most commonly understood as positive economic benefits arising from efficient use of materials and energy. EE is concerned with positive environmental benefits from economic efficiency”. For Pagan and Prasad (2007), CP and EE are similar concepts. However, for van Berkel (2002), the CP and EE are complimentary. EE focus on the strategic side of business (value creation) and Cleaner Production on the operational side of business (production).

This work presents the results of EE evaluation (applying the Schaltegger and Sturm´s definition) and the opportunities for uptake of CP (using Cleaner Production Assessment) for the wine industry. This industry is one of the main industries in San Juan, Argentina. The wine making process varies greatly between sites, winemakers, quality and style of wine. The vinification process can be divided into unit operations. Every unit operation was drafted as a block and by connecting all the individual unit operations in the form of diagram.

2. Environmental Perfomance of Wine Production

The EE is suited to the industrial world, because its practical approach makes it possible to balance environmental and economic benefits in an integrated way. The concept represents one of the most tangible paths to sustainability for economic players. Its objectives are to reduce the consumption of resources, as well as the impact on nature, while maintaining or enhancing the value of the manufactured product (producing an equivalent amount, or even more). The EE indicators (EEIs) are the tools used for condensing information and assisting with decision making. In order to describe the initial situation of the winery, different intensity indicators defined by Industry and Environment Council, (Murcia, Spain, 2002) were calculated. The data were gathered of eight wineries located in San Juan, Argentina. Table 1 shows each EE indicators definitions. The obtained results are plotted in figures 2 to 7.

Table 1: Quantities used for the EEIs.

Title	Symbol	Units
Specific consumption of Electrical Energy	Es	Kwh/ product ton
Specific consumption of water	Ws	m^3/ product ton
Specific consumption of additives	As	ton/ product ton
Specific quantity of generated wastewater	WWs	m^3/ product ton
Specific quantity of generated solid wastes	Ss	ton/ product ton
Specific consumption of combustible	Cs	ton/ product ton

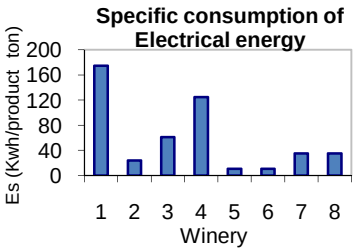

Figure 2*:* Specific consumption of electrical energy for different winery.

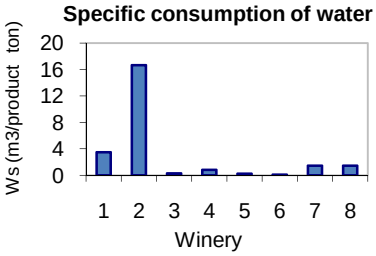

Figure 3: Specific consumption of water for different winery.

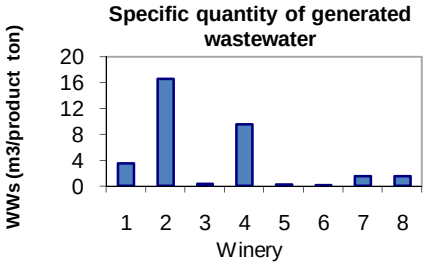

Figure 4: Specific quantity of generated wastewater for different winery.

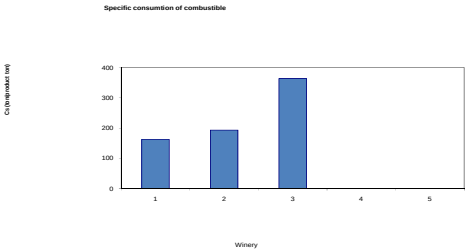

Figure 5: Specific consumption of aditives for different winery.

3. Discussion

The wine industry has the ability to manage some of environmental issues and potentially reduce the extent of their impacts. The more important impacts associated with wine making are: energy and water consumption, solid wastes generation and gaseous emission. These topics are analyzed in this section and the environmental evaluation results are discussed.

Energy consumption: In order to evaluate this consumption, Es was calculated. The wineries 1 and 4 present the highest values. Generally, this consumption in wine production is high. Refrigeration has been estimated to account for 50-70% of used total energy (Broadbridge, 1994). The frigorific energy consumption is produced especially during different process

operations such as pre-fermentative maceration, must cooling for clarifying, fermentation, cold burling, cold stabilization, bottles rinsing and pasteurization. Other power uses include pumping, heating water, cooling cellars, operating machinery, running compressed air systems along with standard business uses such as lighting, air conditioning and running office equipment. In large wineries, pumping can account for around 20% of energy use (Hislop, 1995). Heating, cooling and filtration operations require movement of large volumes of liquid, often utilising several pumps in different stages.

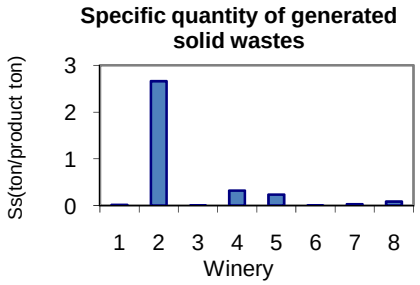

Figure 6: Specific quantity of generated solid wastes for different winery.

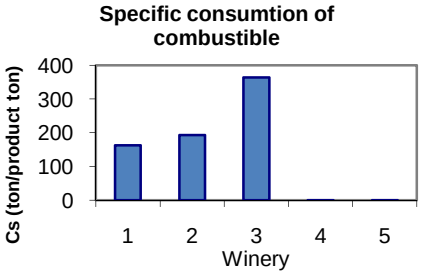

Figure 7: Specific consumption of combustible for different winery.

Water consumption and wastewater generation: Comparing the calculated Ws and WWs values, the highest were observed for winery 2. Water is mainly used in cleaning tasks, disinfection, heat exchange, winery work areas, barrels, process water associated with filtration, ion exchange, sterilizing bottles and cooling system. Solid components in effluent streams arise from tanks, solids settled in tanks and filter media, which may be flushed into treatment systems during cleaning. Spilt and waste juice and wine also add to the wastewater system. Wastewater from wineries is characterized by high biological oxygen demand (BOD), salinity and sodicity from contamination with caustic, mild acids and sometimes biocides (Chapman, et al. 2001). The amount of water used at a winery can easily be associated with design and management of the system rather than tonnes of grapes processed. Calcium tartrate and other residues may also remain once a tank is emptied. Caustic soda (NaOH) is commonly used to remove calcium and potassium residues leading to high sodium ions in wastewater, resulting in sodicity and salinity problems (Chapman, et al. 2001). Following initial tank cleaning using caustic, acidic rinses are used to remove alkaline residues. These chemicals can pose problems in managing wastewater.
Modern production systems generally use more water; 2-5 litres per litre of wine compared to 0.5 litres of water per litre of wine previously. Increased technology and processing methods may be partially responsible; however, given the increasing size of the industry and related increasing demand for water resources, there is a limit on potential water and wastewater resources.
Solid wastes: In order to evaluate the generated solid wastes, Ss was calculated. The winery 2 presents the highest value. Solid wastes generated directly from wine production include marc, filter earth solids from barrels and tanks (lees) and barrels. Grape marc is generated from initial crushing and pressing stages of wine making and is made up of skins, seeds and stalks of grapes. Pressing is performed to remove solids following crushing operations (white wine) or fermentation (red wine). At different stages through the wine making process varied filtration methods are used to remove solid particles. Diatomaceous earth filtering is used to remove tartaric acid crystals and other solid particles from wine. Safety issues are also associated with diatomaceous earth use and disposal due to the risks associated with exposure to fine dust particles if diatomaceous earth dries out. According the higher Ss, winery 2 shows the higher As, also. As was calculated taking into account the quantities of all additives: bentonite, diatomaceous earth, tartaric acid, activated carbon, SO_2, etc.
Gaseous emissions: The main gaseous emission in the wine industry comes from the sulphication and fermentation processes as well as from the boilers. The first process

mentioned emits SO_2. The fermentation process produces CO_2.The boilers are used to provide hot water and steam. If clean fuels are used, the emissions will mainly contain water vapor and CO_2. If other kind of fuels (not the cleaner ones) are burnt, besides the above mentioned pollutants, NO_x, SO_x, among others will be emitted. Although, the emission of gases has not been evaluated, the specific consumption of combustible and the additive are calculated. Considering the first indicator, the winery 3 shows the highest value. Taking into account the specific additive consumption, the winery 2 shows the higher value. During the gaseous substances addition, there are emissions, decreasing the working atmosphere quality. In this case, safety issues are also associated with it. Other aspect to consider is the corrosion by the sulphuric acid; the lost SO_2 react with the air humidity producing this acid.

4. Opportunities for uptake of Cleaner Production

Taking into account the previously exposed diagnosis, the opportunities for uptake of CP were determined. For that, the Cleaner Production Assessment was applied to wineries in San Juan. The cleaner alternatives was proposed, analysing each stage of winery and identifying the environmental impact modifications and possible impediment or restriction for each stage of the wine making process and services-utilities. Tables 2 and 3 detail the current practices and the substitute alternatives identified, to carry out each unit operation of the wine making process and services-utilities respectively.

5. Conclusion

The wine industry is facing serious challenges comprised of internally driven factors, such as rising costs of production due to carry out environmental practice. The majority of the large firms still consider the environmental issues as a cost driver. As a result of this consideration firms do not use more resources for environmental technologies. According to the indications, the firms use more resources for end-of-pipe technologies than the other environmental technologies. However, in this moment, a Program of Cleaner Production is implemented for this industry in San Juan, offering different economic opportunities. In this study, an environmental diagnosis of winery industry was carried out, taking into account the main aspects and the collected data. A great results variation was observed. The winery 2 presented the highest indicators values almost in all analyzed cases. Generally, the high indicators values result of bad management of process or effluents, inadequate technical equipment or planning. The previously exposed diagnosis originated the necessity to propose the opportunities for uptake of CP to wineries in San Juan. These opportunities were focused in each unit operation, stage process and services and utilities.

References

Broadbridge W. (1994). Energy management for quality and value in the Australian grapegrower and winemaker. Ryan Publications : 24-25.

Chapman J., Baker P., Wills S. (2001). Winery wastewater handbook: production, impacts and management. Winetitles, Adelaide.

Consejería de Industria y Medio Ambiente, Región de Murcia España. 2002. Aproximación a la medida de la ecoeficiencia en las empresas agroalimentarias de la Región de Murcia. Programa de calidad ambiental y ecoeficiencia.

Graham A., van Berkel R. (2007). Assessment of cleaner production uptake: method development and trial with small businesses in Western Australia. Journal of Cleaner Production 15: 787-797.

Musee N., Lorenzen L., Aldrich C. 2007. Cellar waste minimization in the wine industry: a systems approach. Journal of Cleaner Production 15: 417-431.

Pagan B., Prasad P. (2007). The Queensland food eco-efficiency project: reducing risk and improving competitiveness. Journal of Cleaner Production 15: 764-771.

Schaltegger and Sturm (1989). Ecology induced management decision support. Starting points for instrument formation. WWZ-Discussion Paper Nº 8914.

van Berkel R. (2002). Cleaner Production Uptake in small to medium size enterprises. Waste and Recycle 2002 Conference Proceedings. Perth September 285-394.

Table 2: Current practices and substitute alternatives to each unit operation and stage process.

Process Stage		Current Practice	Substitute Alternative
Grape transport		Grape transport in bulk in trucks.	Grape transport in plastic bins in trucks.
Reception and sampling		Unprogrammed grape inputs to the winery.	Programmed grape input to the winery.
Destemming - Crushing	Stems transport	Pneumatic extractor and conveyor.	Not found.
	Crushing	Roller crushing, centrifuge crushing.	Not found.
	Transport (The crushed grape is transported using the vintage pump.)	Percussion disk pump, rotating piston pump.	Not found.
	Vintage cooler (Used only for white wines.)	Double tube heat exchanger using water with ethylene glycol as refrigerant.	Not found.
Sulphication	Additives used	Burning of sulfur pellets, potasium methabisulfite dusting, dosage system for SO_2 solution injection, pressure bottles for gaseous SO_2 injection.	The possible substitute alternatives depend on the process stage in which the chemical substance is used.
	Handling	No use of personal safety equipment.	Use appropiate mask and gloves.
	Ventilation	Natural room ventilation.	Extractors, extracting chimney and further treatment, gas sensors.
Maceration	Maceration options	At ambient temperature, warming, or carbonic maceration.	No significant benefits found.
	Remounting options	Use of pumps.	Automatic remounting vessels, agitators, immersed suction tube.
	Agitation options	Use of wooden pistons, or centrifugation pumps.	No significant benefits found.
Fermentation	Fermentation vessels	Stainless steel tanks, metallic tanks stainless steel coated metallic tanks epoxidic resins coated, wooden vessels, masonry vessels coated with epoxidic resins.	No significant benefits found.
	Yeasts addition	Yeast purchasing from other companies.	Yeast growing in the winery's own lab.
	CO_2 generation	Natural ventilation.	Extractors, extracting chimney and later treatment, gas sensors.
	Cooling	Coils introduced in the must, jacketed tanks, refrigeration plates, or refrigerated cellar**.**	Heat transfer engineering revision, automation, heat transfer engineering revision and automation.
	Cooling solution (The cooling solution flows from the cooling plant to the tanks and vessels where the cold is required.)	Aqueous solution of ethylene glycol or aqueous solutions of ethylic alcohol.	No significant benefits found.
Pressing	Press types	Discontinuous hydraulic press, discontinuous screw press, discontinuous pneumatic press, continuous press.	No significant benefits found.
Racking	White wine burling	Cooling, using SO_2 .	Centrifugation.
Clarification		Natural clarification, use of organic clarifiers or use of inorganic clarifiers.	No significant benefits found.
Stabilization	Limpidity	Cooling or addition of ascorbic acid, citric acid, bentonite or arabic gum .	Pasteurization.
	Microbiologic stabilization	Pasteurization, use of SO_2 or use of sorbic acid.	No significant benefits found.

Filtration	Spillage	Leaking spillages not prevention.	Leaking spillages prevention.
	Burling	Use of vacuum filter, or plaque filter.	Use of ecologic earth filter.
	Brightness	Plaque filter, cartridge filter.	No significant benefits found.
Aging		In oak barrels or in masonry vessels.	No significant benefits found.
Bottling		Non-use of personal safety equipment, use of non biodegradable lubricants, use of new bottles.	Use of personal safety equipment, biodegradable lubricants, recycled bottles, waterproof labels and less use of glue in the packaging.

Table 3: Current practices and substitute alternatives to services and utilities.

Service and utility		Current Practice	Substitute Alternative
Refrigeration	Refrigeration system	There is no energetic integration, cool transfer optimization, nor automation.	Energetic integration makes use of the cooling solution coming from activities such as refrigeration of the grape at the process input and vintage cooler. Cold accumulation by using ice.
	Refrigerants used	Ammoniac, Freon 22, HFC-134[a] and HCFC123.	Isobutene.
Water		Cleaning with pressurized water. Water is not recycled or reused. Control meters to control water leaks are not used.	Reuse Meters to control water leaks. Hot water Dry cleaning followed by washing with pressurized water using hoses provided with automatic shut-off nozzles.
Steam and Hot Water		Cleaner fuels are not used. No energy integration	Use of cleaner fuels Energy integration, to make use of the hot water that comes from activities where high temperatures are required, into activities that use water at lower temperatures.
Infrastructure and electric energy		Refrigeration equipment location improperly planned. Location of steam and hot water generation devices improperly planned. Illumination installation without considering the energetic consumption. Absence of meters to improve motors and equipment efficiency. Insufficient or inadequate preventive maintenance.	Re-location of refrigeration equipment to where the cold is demanded. Re-location of steam and hot water generation devices to where these services are demanded. Low consumption illumination. Installation of meters to improve motors and equipment efficiency. Preventive maintenance.

Proceedings of the 10th International Chemical and
Biological Engineering Conference - CHEMPOR 2008
Braga, Portugal, September 4-6, 2008
E.C. Ferreira and M. Mota (Eds.)

REDUCING THE POLLUTION OF LEATHER MANUFACTURING PROCESS

Viorica Deselnicu*, F. Platon, L. Albu, M. Crudu
Leather and Footwear Research Institute, 93 Ion Minulescu Street, 031215, Bucharest
Romania

Keywords: tanning, wet white leather, free chrome leather
Topic: Sustainable process-product development through green chemistry

Abstract

Even the optimization of common chromium tannage, and combined tannage with chromium and other tanning materials have led to outstanding results related to the lowered pollution level in effluents and sludge, the problem has not been solved wholly. The single solution for this problem is finding out an environmentally friendly alternative to chromium tannage. This work also is within the above line, aiming to obtain wet-white leather by an organic tanning process.

1 Introduction

Chromium III salts are used extensively in the tanning process. Approximately 90% of the leather manufactured around the word is tanned using chromium III. It has been used in the leather industry for almost 100 years, primarily because it remains the most efficient and versatile tanning agent available; it is also relatively cheap. Due to toxicity of chromium III, which can convert to chromium VI with higher toxicity, tanners around the word are often place under pressure to reduce the chromium content of their effluent discharges and the resulting sluges. (1)

While much of the chromium used in the tannery may be recycled or reused or removed from waste streams on-site by precipitation as insoluble chromium III hydroxide, a small amount may be discharged to the sewage treatment works. This chromium will be disposed of with the waste sluge from the treatment works and this is one of the main disposal routes by which waste chromium leaves the tanning industry.

By the term „tannage" we understand an additional grind-like interlinking of the skin's collagen network, which results in stabilization against heat and micro-organisms and production of a material which remains supple after drying, retaining the flexibility of the fiber structure. Chrome tannage is quite obviously particularly suited to obtaining these desirable new properties in the hide material. These can be no other explanation for the 70-80% share held by this method in the main tannage of leather produced around the world and the resulting international Cr tanning agent consumption of approx. 400000 tons per annum (2). If we look at alternatives to chrome tannage, quite irrespectively of the question of actual ecological benefits to be drawn from using a different method, it is necessary to consider the extent to which a comparable tanning effect and the achievement of the required characteristics are possible at all on basis of the existing natural circumstances. To permit optimum stabilization of the hide material by the tannage process, it is necessary for the tanning agent to penetrate into the interior of the fibrils to cross-link the polypeptide chains. A stable bond is formed with the hide in the case of tanning with reactive organic substances as a result of reaction with the reactive groups in the collagen. The fact that the shrinkage temperature of leather tanned in this way hardly, in contrast to chrome tannage, exceeds the 800C mark is an indicative of stabilizing effect. The extent to which this type of tanning system can assert itself on a broad basis in the future in the field of pre-tannage or intermediate stabilization due to ecological and economic advantages remains to be seen. One class of syntans that has found application in high stability organic tanning (2) is resins

* Viorica Deselnicu, Tel. +4021-323.52.80, viorica.deselnicu@icpi.ro

(melamine resins, phenol resins, etc.). This resin can react with collagen under typical post tanning conditions, when their expected effect is to fill the fiber structure selectively, but they have little effect on raising the shrinkage temperature, either singly or as part of a combination tannage. A practical option is to use pre-polymer with defined particle size, which are incompletely cross linked and then to complete the polymerization reaction in situ using a cross linking agent. In general, this does not work, yielding only moderate shrinkage temperatures. The critical factor that controls the shrinkage temperature is the particle size of depending on the temperature of the solution. this is because the particles are aggregates of smaller particles; the distribution of particle sizes depends on exactly how the resin was polymerized.

2 The basic procedure

In the framework of this paper the tannage is performed in situ by making use of two pre-polymers, one based on a dialdehyde and the other on a diphenol, in the pickling bath. Having bound in hide the above two materials, the pH is risen up to 4.6 – 4.8 by sodium hydrogen carbonate or magnesium oxide. During this time a tanning resin is made within the leather that increases the hydrothermal resistance of leather, resulting in a shrinkage temperature of 70 – 720C. The obtained leather is white and resistant to the mechanical operations. The wet white leather may be subsequently processed with chromium or only with vegetable and synthetic tanning agents according to the finished leather type to be obtained.

The process is capable of fitting into the current process flow and use existing equipment. The following flow chart, comparing „normal" practice with „wet-white" production indicates that this can be achieved.

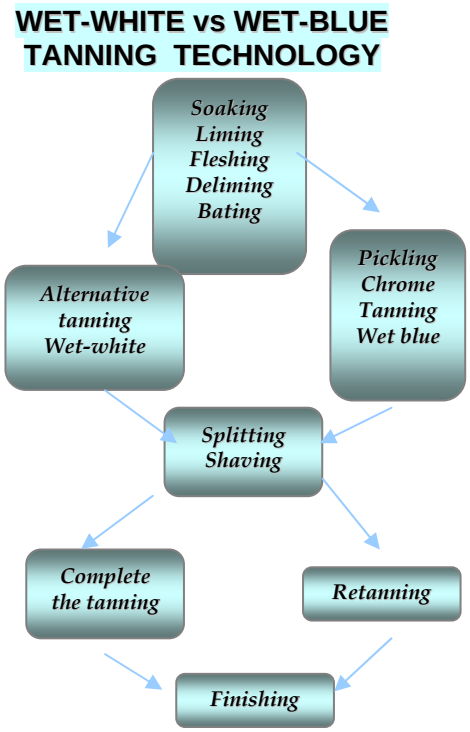

Figure 1. Flow Chart

* Viorica Deselnicu, Tel. +4021-323.52.80, viorica.deselnicu@icpi.ro

The wet-white stock can be tanned with low chrome, vegetable tannins, aldehyde, acrylic/ Zirconium, aldehyde / Aluminum. The variety of leathers produced using „wet-white" stock has adequately demonstrated the versatility of the material.

This procedure was developed for shoe upper leather from bovine hides. This allows good quality, metal-free shoe for garment and upholstery leathers to be produced with no problem.

3. The effect on leather quality

The quality of the crust leathers was directly comparable with those from standard procedures.

Taking the type of tannage into account there are no obvious problems shown in chemical analysis results. If any major differences are to show it is more likely to be highlighted by physical properties. But with appropriate process optimization, these differences would be minimized.

Table 1. Chemical analysis and physical test of leathers

Test	Chrome tanned leather	Wet white tanned leather
Moisture,%	16.14	17.06
Total Ash,%	6.30	3.22
Cr_2O_3,%	5.24	2.35
Extractible fat and grease,%	9.27	5.42
Total Nitrogen,% - Nitrogen from protein,% - Nitrogen from syntan,%	13.98 13.98 -	15.87 13.98 2.31
Hide substance,%	78.58	78.58
Total soluble matters,%	0.79	0.82
Combined tannin,%	10.94	15.51
Degree of tannage ,%	18.30	25.94
Tensile strenght, N/mm^2 - at break	9.8 11.4	15.2 22.7
Elongation,% - 10N/mm - at break	 65 74	 33 61
Tear strenght, N/mm	44.7	51.4

Obs: All results related to 0% moisture

4 The environmental impact

4.1 The environmental impact of shavings

One of the main benefits hoped for as a result of this type of wet-white process lies in the elimination of chrome shavings, which occur at a quantity of approx. 5-10% of the hide weight as a permanent by-product of the chrome main tannage process (in the whole of the Single European Market to approximately 100 000 tons per annum is produced) (2). For the wet-white shavings produced as a result of organic tanning, in contrast, according to studies

* Viorica Deselnicu, Tel. +4021-323.52.80, viorica.deselnicu@icpi.ro

not only the recovery of protein hydrolyzed, but also use for fertilizers and for gelatin, glue and other industrial products.
The comparative chemical composition of shavings from wet blue stock vs. wet white stock is given as Table 2.

Special attention is drawn to the digestibility of the shavings. This figure is often as key value for degradation as well as for utilization.

Table 2. Chemical composition of shavings

Test	Wet blue shavings	Wet white shavings
Moisture,%	59.0	67.06
Ash,%	16.6	0.6
Cr_2O_3,%	5.24	2.35
Extractible fat and grease%	1.2	5.6
Total Nitrogen,%	12.7	15.13
Hide substance,%	78.12	85.01
Cr, mg/Kg	4.2	2.1
pH	3.5	6.0
Digestibility, %	52	65

4.2 The environmental impact of effluents

Legal requirements relating to the chrome content of tannery effluent also cause problems in the chrome tannage process. The high chloride, sulfate and chromium concentrations play a decisive role her. The advantage of the new process is that, besides reducing the salt load of the effluent (about 50% of the total sulfate load arises during tanning), the ash content of a skin is reduced from Also, in the next step, the chrome uptake was improved and the volume of sludge was reduced.

5. Feasibility and financial viability

As wet-white stabilization can be carried out with equipment that is already available, no further machine or drum investment will required. The process costs can be estimated, but no significant increase of costs are anticipated. When fully optimized savings due to improved auxiliary exhaustion and reduced disposal costs can be expected.

The objective of the EU chemical policy is to ensure a high level of protection of human health and the environment for both present and future generations, while ensuring the efficient functioning of the chemical industry. Another important objective is to encourage the substitution of dangerous chemicals by less harmful alternatives.

The actual making of the leather is a multi-step, time consuming process involving the use of a variety of materials.

* Viorica Deselnicu, Tel. +4021-323.52.80, viorica.deselnicu@icpi.ro

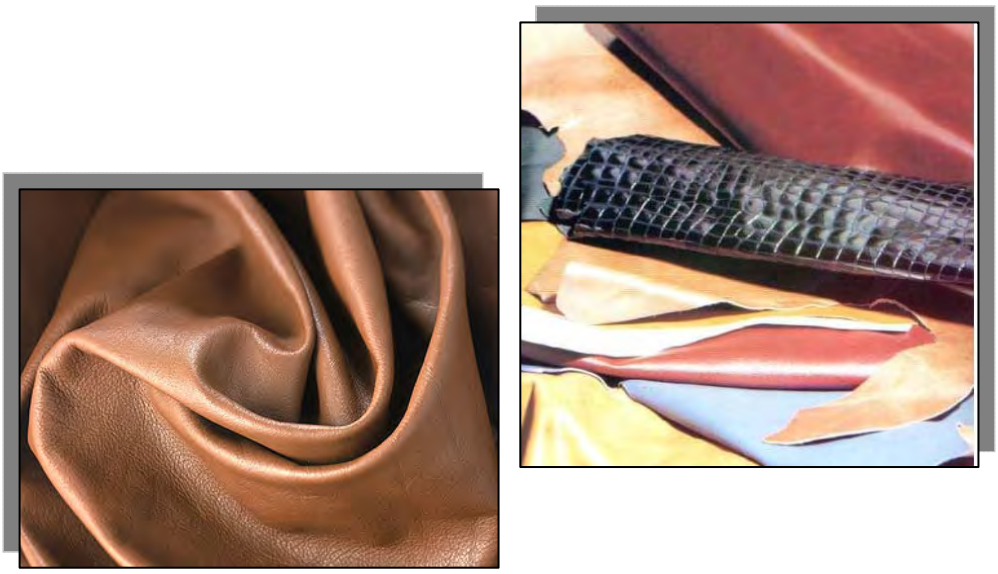

6. Conclusion

The wet-white leathers obtained have a white shade and a shrinkage temperature of 70-720C. It can be mechanically processed in the same way as wet blue leather. By after treating this tannage with chromium, the shrinkage temperature can be increased over 1000C; with synthetic or vegetable replacement tannins, the shrinkage temperature can be increased to 90-950C. This allows well –quality, metal-free shoe, garment and upholstery leathers to be produced with no problem.

The salt content of the effluent considerably reduced, pickling being eliminated. In piling and storing, care must be taken to ensure that the skin do not starts to dry. Owing to their low salt content, the water content and thus the weight of the skin is slightly reduce. Subsequent tanning is better as the actual tan extracts can diffuse into the hide more easily and than form a more stable bond with collagen in the inter fibril spaces.

This new „wet white" procedure does not claim to be a replacement for chrome, vegetable or other tannages, but an alternative. It is a pretannge which can subsequently be tanned with chromium, vegetable or synthetic tanning agents. The advantage of this is that the shavings arising are metal free and, therefore, a valuable by-product. Like untanned solid waste, they can be recycled and used as a starting material for gelatin, fertilizer, glue and other industrial products.

While it is true that from a manufacturing point "wet-white" production will fit into current tannery practice, it is also true that an „overnight" switch cannot be made. Machine handling, sorting and grading characteristics, although acceptable, are different and require that operators gain a familiarity with the material. At the same time the effort required to adjust tanning / retanning processes to produce acceptable leather should not be overlooked.

References

1. Senior K., (2000), „Chromium in the leather industry",
World Leather, nov. pg. 51
2. Germann, H.P, (1995), „Chrome tannage from the viewpoint of ecology", *Journal of the Society of Leather Technologists and Chemists*, Vol. 79, pg. 82
3. Covington A.D and Ma S. (1996), *UK Patent*, 2,287,953

* Viorica Deselnicu, Tel. +4021-323.52.80, viorica.deselnicu@icpi.ro

Proceedings of the 10th International Chemical and
Biological Engineering Conference - CHEMPOR 2008
Braga, Portugal, September 4-6, 2008
E.C. Ferreira and M. Mota (Eds.)

ECO-FRIENDLY TANNING AGENTS TO BE USED IN LEATHER MANUFACTURE

M.Crudu[1], V.Deselnicu[1], L.Albu[1], M.Niculescu[1], I.Rosca[2], D.Sibiescu[2], D.Sutiman[2], A.Cailean[2], N.Boca[3], D.Capac[3], E.Ioanid[4], A.Ioanid[4]

[1]INCDTP Division Leather and Footwear Research Institute – Bucharest, RO
[2]Technical University 'Gh.Asachi – Iassy, RO
[3]SC ZIROM SA – Giurgiu, RO
[3]Macromolecular Chemistry Institute 'Petru Poni' - Iassy , RO

1. SUMMARY

Leather industry has to cope nowadays with major environmental problems because of the polluting processes (a World Bank report has placed the leather industry in the ninth place when considering the environmental impact). Therefore, increasing the environmental efficiency in the leather sector is the major aim of leather, auxiliary materials and equipment manufacturers.

To achieve this, a new concept has arisen that is trying to join new processing rules leading to the harmonization of economic performance of the manufacturing units with the human and environmental protection criteria.

An environmental efficient process has to minimize the raw materials being used, meet the users' requirements, and minimize the emissions (polluting byproducts, wastes, refuses).

The current hide processing can be only thought to be controlled environmentally aggressive, inclining to be limited environmentally aggressive.

The wish of bringing the current hide processing up to the environmentally admitted level has required some decisions to be made on the implementation of new environmentally friendly processes and materials, and this work is in line with this.

The original contribution of this work in solving the above problems has involved the use of solid titanium wastes (cuttings) resulting from the process of obtaining highly pure titanium (ingots) in the preparation of new tanning compounds intended to increase the environmental efficiency of the leather sector.

2. KEY WORDS

Solid titanium wastes, reclaiming, environmentally friendly tanning agents

3. INTRODUCTION

Leather is perhaps the first material being processed chemically by the man (as yearly as 8000 years B.C. – leather was obtained by fat tannage) [1].

Leather belongs to our life; daily we are coming into contact with leather objects making our life more comfortable. Art, traditions, culture, and science have been employing over time leather and parchment [2].

Leather manufacture involves the processing of hides (byproducts of meat industry) into finished leather (a steady material) that can be used in making a large range of products.

Because of the specific tannery processes (use a raw material of organic nature and a large range of chemicals known to be noxious, and not the last, large water consumption and energy expenditure), they are currently facing up to major environmental problems.

Integrating the environment protection into the quality concept is a priority objective of the hide processing field because of the need of reducing water consumption and energy expenditure, and pollution under the general economic context, limited and varying resources at the economic operators' disposal, and a new regulation on chemicals - REACH (Registration, Evaluation and Authorization of Chemicals) to be adopted by the EU [2].

One of main ways of pollution prevention is the implementation of so-called 'clean' or 'environmentally friendly' processes developed onto three directions: [3]

- reduced offer of chemical auxiliaries simultaneously with the application of hide support activation treatment;
- high bath exhaustion;
- replacing the 'classic' chemical auxiliaries of high toxicity and adverse environmental impact with others ones of low or no toxicity.

The development of new tanning agents is required to cope with the increasingly higher environmental pressure on the current tanning materials and processes such as tanning with chromium salts.

4. EXPERIMENTAL

Chromium is the major heavy metal polluting source in the leather sector. Basic Cr^{3+} salts are found currently in the effluents from tanning and wet finishing, and solid wastes from mechanical processing of leather and sludge resulting from the waste water treatment, all these falling within the class of hazardous wastes.

When dealing with the total or part removal of chromium in hide tanning and its replacement with other tanning compounds, even though some new product and processes have been developed, such a problem is kept on opened because of some drawbacks regarding the profitability and productivity while the environmental benefits are obvious.

There have been a variety approaches in obtaining new tanning materials in the last time, such as complicated syntheses, direct processing from ores, charging the chemicals directly into the (pre)tanning baths for in situ synthesis.

This work deals with the preparation of tanning solutions based on titanium by processing solid wastes resulting from the process of obtaining highly pure titanium and that cannot be recycled in the industry yielding them.

The main classification criterion for titanium wastes was their contaminant level [4]. The highest contaminant level in titanium wastes and titanium alloys is in cuttings resulting from the mechanical processing of ingots and cast articles (Figure 1).

Figure 1:
a) Titanium ingot b) Cutting and shaping the ingots c) Unrecyclable cuttings



Therefore, a part of the above wastes cannot be recycled in the remelting process as this is not profitable.

Chemical compositions of the titanium wastes placed at our disposal by SC ZIROM SA – Giurgiu, Romania is shown in Table 1.

Table 1. Titanium waste classification based on their chemical composition

Ref. No.	Alloy type	Ti [%]	Al [%]	V [%]	Nb [%]	Contaminants [%] (Al, V, Nb, Fe, Ni Cr, C, N, O, s.a.)	Remarks
1	Non-alloyed titanium	97	Cont.	Cont.	Cont.	3	Cont.- maximum level
2	Ti 6Al 4V	88	6	4	Cont.	2	Cont.- maximum level
3	Ti 6Al 7Nb	85	6	Cont.	7	2	Cont.- maximum level

Chemical composition of cuttings processed for trials is presented in Table 2.

Element	Ti	Al	V	Fe
%	89.61	6.25	4.07	0.00695

Chemical composition of the cuttings was established by plasma optical emission spectrometry.

The first step in obtaining new tanning solutions based on recovered titanium (from recyclable solid wastes-cuttings) involved the design of a new process for obtaining water soluble salts.

The dissolution of titanium wastes was carried out based on the properties of metals contained in them (considering that there are low levels of Fe, V and Al in such wastes).

Titanium is dissolved by acids at high temperature, the hydrofluoric acid having the best action; nitric acid has no action on the titanium, hydrochloric acid only acts at high temperature, and sulphuric acid at a concentration > 10 % acts at the room temperature.

Vanadium is attacked by nitric acid, concentrated sulphuric acid, perchloric acid, hydrobromic acid etc.

Iron is attacked by sulphuric and hydrochloric acid.

Aluminium is not attacked by the nitric acid while the other oxygenated acids acts on it at high rates even when highly diluted.

Considering the above features, the sulphuric acid was selected to dissolve the unrecyclable titanium cuttings according to the following reaction:

$$Ti + H_2SO_4 + O_2 + H_2O \longrightarrow TiOSO_4 \cdot 2H_2O$$

Following a large number of dissolution trials with solid titanium wastes (cuttings), the process for the preparation of solutions based on titanium/titanyl sulphate (containing V, Al and Fe) was designed and tried.

The framework process for obtaining water soluble salts such as titanium/titanyl sulphates (containing V, Al and Fe) is shown in Figure 2.

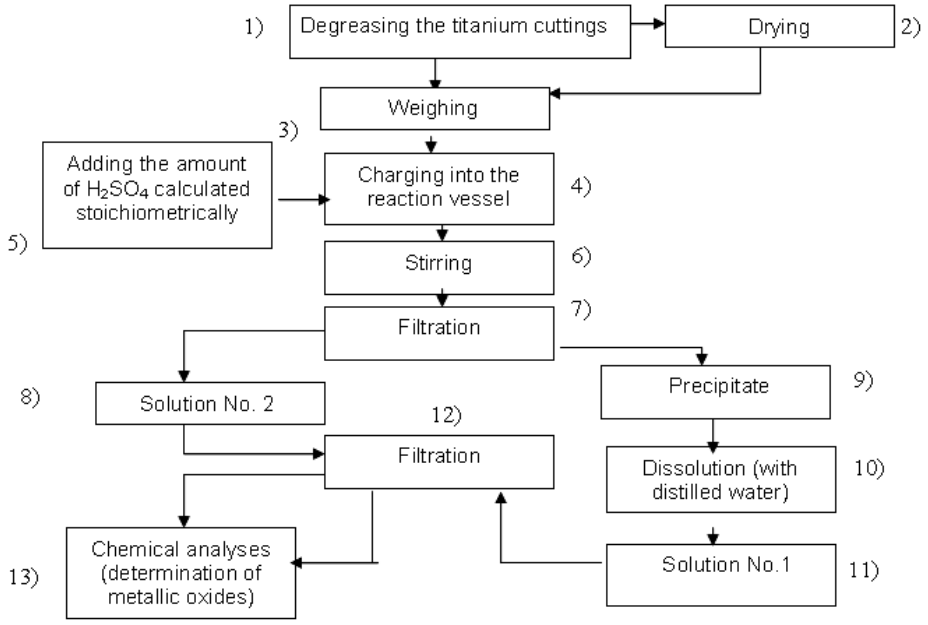

Figure 2. Framework process for obtaining water soluble titanium salts

Considering the difficulty in obtaining tanning compounds from titanium salts (single) because of their instability in solution (hydrolysis at relatively low pH values), the stabilizing possibilities by masking, complexing, basification, and/or combining them with more stable (of chromium and aluminium) or less stable (zirconium) compounds were investigated [6-16].

Analysis (plasma optical emission spectrometry) results for metal level in some of resulting environmentally friendly tanning products are shown in Table 3.

Table 3. Metal level in the new resulting tanning solutions

Sample	Ti	Al	V	Cr	Zr
Ti-Al	2,660	4,995	0,120	-	-
Ti	8,050	0,561	0,365	-	-
Ti-Zr	4,300	0,299	0,195	-	-
Ti-Cr	7,570	0,527	0,343	0,930	-
Ti-Zr-Al	3,680	2,046	0,167	-	-
Ti-Al-Cr	2,830	3,787	0,128	0,480	-

Tanning trials ere performed in laboratory as follows:

- pickled bovine hides of 25/30 type, unsplit (130-250 g);
- rotational speed of the drum(FAVE -Italy): 14 rpm;
- temperature of the tanning bath: 25^{o}C;
- ratio of tanning liquor: 300 %.

Leather resulting from application of the new materials in pre-tanning has shown a common appearance (smooth grain) and colours lighter then in chrome leather (Figure 3) in the most of cases.

Figure 3. Leather pre-tanned with some of the suggested solutions

5. RESULTS AND DISCUSSIONS

The tanning operation is difficult to be defined but it should to be based on o comparison of the raw hide with the tanned one by considering at least three criteria [17]:

- storage and preservation characteristics obtained by tanning;
- changes resulting in the leather structure following the tannage;
- characteristics resulting from tanning treatment.

The protein structures in the dermis have changed their reactivity following the tannage while remaining unsaturated chemically (becoming inactive or stable), imparting leather a long time preservation ability.

Following the treatment known as ‘’tanning’, leather shows such characteristics as follows:

- increased physical-mechanical resistance because of the increased fibrous structure isotropy;
- stability to the enzyme and bioenzyme attack;
- increased hydrothermal resistance as a result of the increased shrinkage temperature of the dermis:
- a porous character and acceptable wettability level in dermis after drying.

Considering the above features, the hydrothermal resistance values for the treated leather and characteristics of leather semi-finished products assessed by electron microscopy can be thought to provide the required information on the tanning characteristic of the environmentally friendly materials suggested in this work.

Shrinkage temperature was performed both by the common method of heating the sample immersed in water (Giuliany device-Italy) and DSC.

Shrinkage temperatures for leather samples tanned with the new tanning solutions are shown in Figure 4.

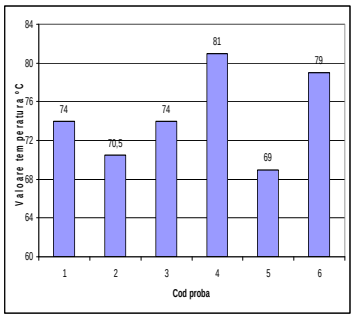

Figure 4. Shrinkage temperatures for leather samples tanned with the new tanning solutions

Figure 5. Leather tanned with the new tanning materials subsequently split

Hydrothermal resistance values for all the leather samples tanned with the new materials are not as higher as those tanned with chromium salts but provide a very good mechanical processing in the operations subsequent the tannage such as splitting and shaving (Fig. 5).

The results of thermal analysis [18] and electron microscopy [19] presented in Figures 6 and 7, and Figures 8 and 9, respectively have revealed the tanning characteristic of the suggested new materials.

Figure 6. DSC curve (obtained in nitrogen flow) for the pickled hides

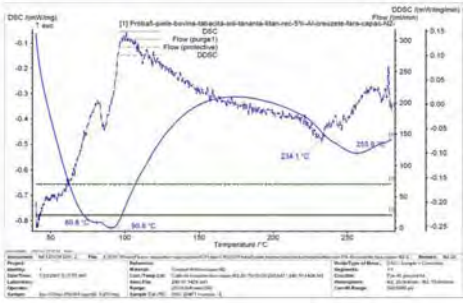

Figure 7. DSC curve (obtained in the nitrogen flow) for the leather tanned with the tanning solutions containing titanium

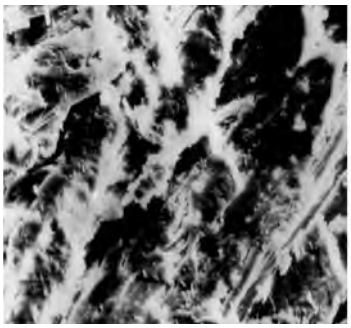

Figure 8. Electron microscopy (SEM) photos for pickled (untanned) bovine leather; the magnification 1500 x

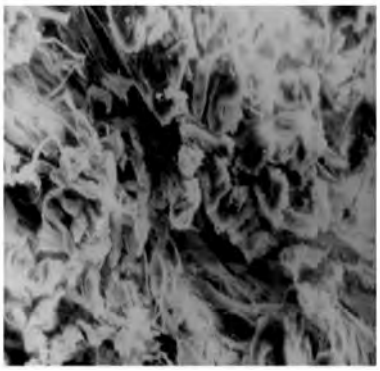

Figure 9. Electron microscopy(SEM) photos for bovine leather tanned with product containing titanium; magnification 1600 x

6. CONCLUSIONS

- Obtaining low cost new auxiliary materials with low environmental impact and easy to be applied, resulting in leather of high quality is nowadays the aim of any investigation in leather manufacture.
- This work suggests to solve some of problems in the leather sector by making original use of some solid titanium wastes (cuttings), resulting from highly pure titanium and its alloy manufacture, to obtain tanning solutions.

- Increased eco-efficiency in the leather manufacture sector by making use of un recyclable wastes (because of the contained contaminants) resulting from nonferrous metal industry as abase for obtaining environmentally friendly products intended to substitute the chromium salts in hide tanning.
- Development of new simple methods for solid titanium waste (cuttings) processing to obtain soluble salts intended to be used in the preparation of new tanning materials, and results (values of hydrothermal resistance, and light coloured or white dense leathers showing smooth grains) obtained in (pre) tanning trials is reason to keep on with the investigations with the aim of improving the methods of waste processing to make them more efficient, and diversifying and rendering more rentable the tanning materials, application processes and wet-white leather semi-finished products.

7. REFERENCES

1. Kochta J.- Alternatives to the Chromium Tannage, das Leder, 1990, 9.
2. Gustavo Gonzales, Quijara –Investigation, Assessment and Authorization of Chemicals (REACH) and Leahter Industry, COTANCE, 2005.
3. Burrows G.H. – Clean Technologies in Hide Processing, IULTCS Congress, Cape Town, March 2001.
4. Buzatu M., Moldovan P.- Reacting and Light Alloys –Part I: Alloys Based on Titanium, PUB Lecture, 1994.
5. ASM Handbook, Formely Tenth Edition, Metals Handbook Volume 2 – Properties and Selection : Nonferrous Alloys and Special – Purpose Materials – Printed in the United States of America, 1995.
6. U.M.Modrei – Study on the Interaction of Tanning Aluminium, Zirconium and Titanium Salts - Tehnologia Legkoij promislenosti, 1984, 2, 53-57.
7. V.F.Sidorin – Interactivity of Ti-Zr Tanning Materials with the Collagen, Tehnologia legjoi promislenosti, 1983, 73-76.
8. D.Anthony, Covington – Pretannings and Tannings Based on Polynuclear Complexes , JALCA, 1981, 1, LXXXII.
9. E.Heidemann – Fundamenmtals of leather manufacture, Eduard Roether KG, Darmstadt, 1993.
10. Pacrisaamy, Manckam; Kama-, Dattaguru – Proces for preparation of tanning agent containning titanumand chronium and use in leather processing, Brevet India : (Cl-Cl4C3 106) 17 July, 2004.
11. A.Covington, RL Sykes – The use aluminium (III) and titan (IV) complexes JSLTC 82' 1987 p 1-13.
12. P.Arbaud – Use of Magnesium-Titanium-Aluminium Complexes in Processing Hides - ICI Colours and Fine chemicals 1995.
13. Vychadilova L, Ludvik J, - Studies on Zirconium Tanning, Kozarstvi, CGK, No.7/1991, p 190-194.
14. Maslava, M.V, Motov, D.L. - Preparation of Complex Titanium-Aluminium Material from Low-Grade Sphene Concentrate, Izvestia Vysshikh Uchbnykh Zavedenii, Kimya i Khimicheskava Tekhnologiya, 2006, 49(2)-Russia.
15. AD. Conington, GS Lampard – Studies on semi-metal tanning, JALCA, 2004, 99(12) 502-509.
16. K.J.Sreeram, R.Aravindhan – Mixed Metal Complexes of Zirconium: a Step Toward Reducing Usage of Chronium in Tanning, JALCA, 2004, 99(3) 110-118.
17. N.Badea, F.Vitan, S.Maier – Chemistry and Technology of Chromium Tanning of Hides, Ed.Cronica, Iassy, 1991.
18. Budrugeac P.;Miu L.;Popescu C.; Wortmann, Term,Anal.Cal, 77 (2004) 975.

Proceedings of the 10th International Chemical and
Biological Engineering Conference - CHEMPOR 2008
Braga, Portugal, September 4-6, 2008
E.C. Ferreira and M. Mota (Eds.)

Biodiesel Production from Leather Industry Wastes

Luís Ramos, Rui Fernandes, António Crispim Ribeiro, Elisa Ramalho*, Nídia S. Caetano, Paula Silva

CIETI-Centro de Inovação em Engenharia e Tecnologia Industrial, Instituto Superior de Engenharia do Porto, R. Dr. António Bernardino de Almeida, 431, 4200 Porto, Portugal

Keywords: Biodiesel, Fleshings, Transesterification, Methyl esters, Beef tallow
Topic: Multi-scale and/or multi-disciplinary approach to process-product innovation

Abstract

Animal fat was extracted from fleshings, a residue from the leather industry, by a two step procedure. First the fleshings are mixed with water (60 ºC) and then the fat rich phase obtained is treated with n-hexane to extract the fat and leave the proteic residue. This fat presents a high acid value and therefore the direct transesterification to biodiesel with an alkaline catalyst was not possible. A pre-treatment step was performed, consisting of an esterification reaction with methanol in the presence of sulfuric acid, and acid values were lowered below 3 mg KOH/g. The transesterification with methanol was carried out with KOH as catalyst at 65ºC in two stages using 80% of the methanol/KOH solution in the first step and the remaining in the second step.

The methyl ester product was characterized and the parameters are, in most cases, within the specifications. The exception is the methyl ester content (94,2%) indicating that further adjustments are needed in the production process in order to improve the quality of the final product.

1 Introduction

Sustainable energy management is a main world concern, considering the fact that fossil fuels supplies are limited and energy demand continues to rise. Search for alternative renewable fuels has therefore gained fundamental importance. Among biofuels, biodiesel has very good utilization and environmental properties, and became a widely used alternative to fossil fuels, with ten years long commercial use in Europe and a rapidly growing world market. Biodiesel cost is mainly determined by feedstock prices. Presently, the cost of the cereals that are used to produce biodiesel is increasing due to the growing market demand. Also, this huge demand introduces a sustainability problem for the next coming years.

Significant research effort is being dedicated to the search for alternative feedstocks. Among these, animal fats from different sources, leather industry, butcher's and slaughterhouses, are potentially interesting. Furthermore, the re-use of these wastes is an environmental friendly disposal option.

Animal fats present usually a high acid value and its fatty acid composition shows a more saturated character than vegetable oils, as can be seen in table 1.

Biodiesel is a mixture of fatty acid esters, obtained by the transesterification of vegetable oils or animal fats with a low molecular weight alcohol, with glycerol as a by-product, as shown in fig. 1.

* Corresponding author. Tel + 351-22-8340500. E-mail:err@isep.ipp.pt

Table 1.Typical fatty acid compositions of vegetable oils and animal fats (Scrimgeour, 2005).

	Fatty acid (wt %)						
	Myristic (14:0)	Palmitic (16:0)	Palmitoleic (16:1)	Stearic (18:0)	Oleic (18:1)	Linoleic (18:2)	Linolenic (18:3)
Soybean oil	0.1	11	0.1	4	23.4	53.2	7.8
Beef tallow	2,7-4,8	20,9-28,9	2,3-9,1	7,0-26,5	30,4-48,0	0,6-1,8	0,3-0,7

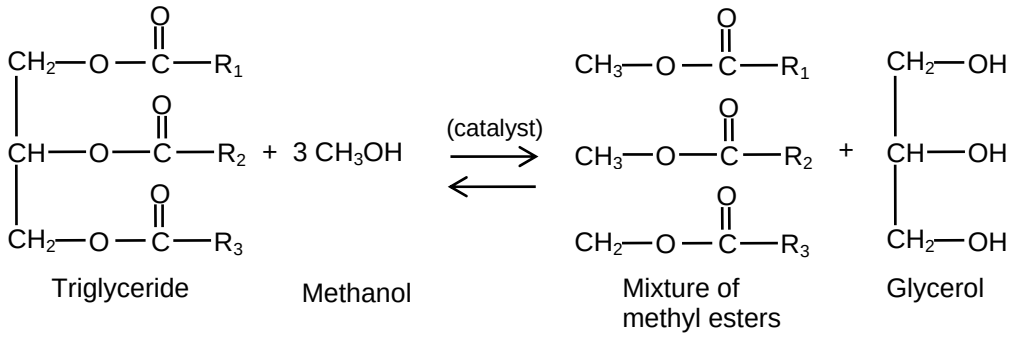

Figure 1. Transesterification reaction of vegetable oils or fats.

Almost all biodiesel production processes are based on the transesterification of triglycerides with methanol using an alkaline homogenous catalyst (NaOH or KOH), in batch or continuous plants. This process requires feed stocks with low free fatty acid (FFA) and water contents. Typical animal fats contain from 5% to 30% FFAs (Gerpen, 2005), and soap formation (fig. 2) occurs in considerable amounts, making product separation very difficult.

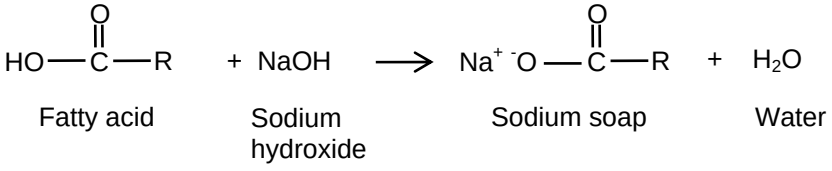

Figure 2. Saponification reaction of free fatty acids.

To avoid this problem, a pretreatment step is required to convert FFAs to methyl esters, thereby reducing the FFA level. This treatment consists of an esterification with methanol and sulfuric acid as catalyst, as shown in fig. 3.
After this reaction, the treated fat can be transesterified with an alkali catalyst to convert the triglycerides to methyl esters.

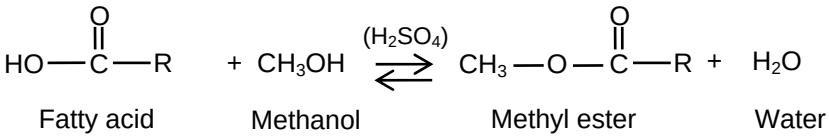

Figure 3. Esterification reaction of free fatty acids.

The purpose of this work is to investigate the possibility of using fleshings (bovine) from the leather industry in biodiesel production. These leather industry wastes contain 40 to 60 wt % of fat (dry basis). Beef tallow is also tested for comparison purposes, because it is a similar residue and previous works showed the feasibility of this feedstock for biodiesel production (Lebedevas, 2006).

2 Methods

Analytical methods

Acid value was determined according to EN 14104 Standard and iodine value was determined according to EN 14111 Standard.
Viscosity was determined according to EN ISO 3104 Standard and density was determined using a picnometer method.
Methyl ester content was determined by a GC method, according to EN 14103 Standard.

Fat extraction

To obtain the fat from beef tallow, the solid is melted at 140 ºC and the product is filtered to remove any solid particles that may be present.

To obtain fat from fleshings two steps are needed: first, the solids are mixed with water and heated in order to break the bonds between the fat and protein material. The optimal conditions for this step are solid:water mass ratio of 1:0.75, for 2h at 70 ºC. Three different phases are obtained, a fat rich phase, a water rich phase and a protein rich phase. In the second step, the fat rich phase is treated with n-hexane to extract the fat and leave the proteic residue. The operating conditions for extraction are: fat rich phase:solvent mass ratio of 1:10, ambient temperature and 1h. The product is filtered to remove the proteins and n-hexane is separated from the fat by distillation.

Biodiesel production

All these animal fats present high acid values depending on the source, and thus a pre-treatment step is needed. This pre-treatment consists of an esterification of the free fatty acids with methanol and sulfuric acid as catalyst at 70ºC. After the phases are separated, the fat phase is transesterified with methanol using potassium hydroxide as catalyst. Initial experiments with a single step transesterification of the fleshings (fat:methanol:KOH mass ratio of 1:0.238:0.01 at 65ºC and 3h) resulted in a product with a low ester content (70%). Therefore a two-stage operation procedure was performed (Baptista, 2008). The first step consisted of a transesterification using 80% of the total volume of the methanol/KOH solution at 65 ºC. The glycerol phase was then removed and the ester rich phase was reacted again with the remaining methanol/KOH solution. After the separation of the glycerol phase, the ester phase was washed with water and dried. The acid value, iodine number, ester content, density and viscosity of the product were determined.

3 Results and discussion

Concerning fat extraction, in the first step the mass of fat rich phase/mass of dryed fleshings ranged from 0,81 to 0,89. For the hexane extraction step, yields of 58-70% were obtained (mass of fat /mass of fat rich phase).
Acid esterification reaction times were studied and the results are shown in figure 4. As can be seen, one hour is sufficient to reduce the acid number to acceptable values for the transesterification step.

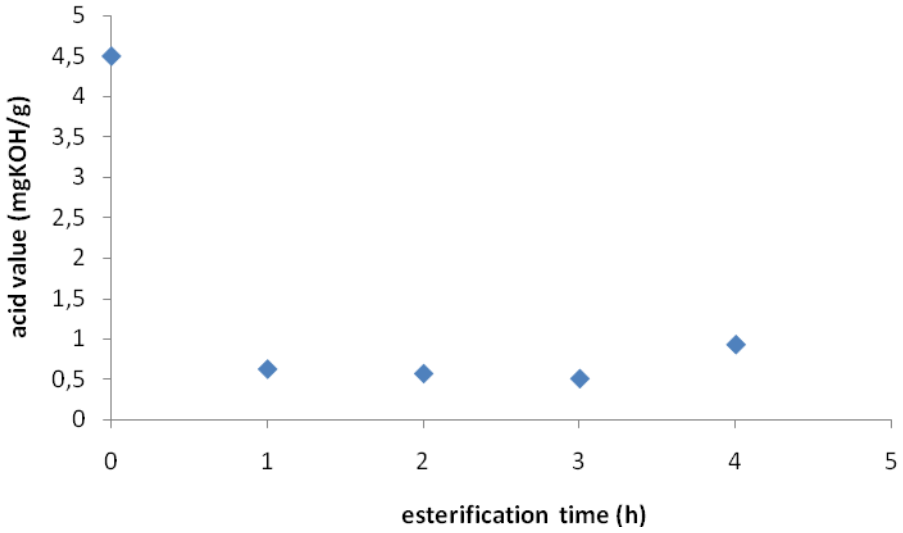

Figure 4. Acid value of the fat as a function of the esterification time.

The results of two step transesterification preliminary studies (3h+2h) presented in table 2, show that the methyl ester products from both raw-materials are similar. This behaviour was expected, as fat from bovine fleshings should have the same composition as beef tallow.

Further studies allowed to reduce reaction times to 1h+1h, and product characterization is presented in table 3.

Table 2. Characterization and yield of methyl ester product (reaction times 3+2h).

Fat source	Acid value (mg $_{KOH}$/g)	Ester content (%)	Density, 15ºC (g/cm^3)	Viscosity, 40ºC (mm^2/s)	Yield (%)
Beef tallow	0.17	94.2	0.87	4.8	65
Fleshings	0.18	94.1	0.87	4.8	57

Table 3. Methyl ester characterization (reaction times 1+1h).

Parameter	Result	EN 14214 reference values
Methyl esters (wt%)	94,2	≥ 96.5
Density, 15ºC (g/dm^3)	872	860-900
Viscosity, 40ºC (mm^2/s)	4,8	3,5-5,0
Acid value (mg $_{KOH}$/g)	0,172	< 0,5
Iodine value (g I_2 /100g)	48,5	< 120

The values obtained are, except for methyl ester content, within the specifications for biodiesel (EN 14214 standard). The product presents methyl ester contents close to the standard value, so further optimization of operating and purifying conditions is needed.

4 Conclusions

This study shows the feasibility of using the fleshings from the leather industry to produce biodiesel, but further adjustments are needed in the production process in order to improve the quality of the final product. Biodiesel produced from this kind of raw material, will present a high CFPP and will need to be blended (with biodiesel produced from vegetable sources or petroleum diesel) prior to final utilization.

Acknowledgements

Authors are thankful to Agência de Inovação (AdI) for financial support (Project VEGOR-ADI/2007/U 4.1/ 0061).

References

Baptista, P., Felizardo, P., Menezes, J.C., Correia, M.J.N., (2008). Multivariate near infrared spectroscopy models for predicting the methyl esters content in biodiesel. *Analytica Chemica Acta*, 607, 153-159

Gerpen, J.V., (2005). Biodiesel processing and production, *Fuel Processing Technology*, 86, 1097-1107

Lebedevas, S., Vaicekauskas, A., Lebedeva, G., Makareviciene, V., Janulis, P., Kazancev, K., (2006). Use of waste fats of animal and vegetable origin for the production of biodiesel fuel: quality, motor properties and emissions of harmful components. *Energy and Fuel*, 20, 2274-2280

Scrimgeour, C., (2005). *Chemistry of fatty acids*, in *Bailey's Industrial Oil and Fat Products*, Volume 6, Wiley, New York.

Proceedings of the 10th International Chemical and
Biological Engineering Conference - CHEMPOR 2008
Braga, Portugal, September 4-6, 2008
E.C. Ferreira and M. Mota (Eds.)

INFLUENCE OF FEEDSTOCKS AND OPERATION CONDITIONS IN BIODIESEL PRODUCTION

Alexandra Nicolau, Pedro Felizardo, Nuno Canha, José Cardoso Menezes[1], M. Joana N. Correia[*]

CPQUTL – Centre for Chemical Processes of UTL, DEQB – Department of Chemical and Biological Engineering, Instituto Superior Técnico, Av. Rovisco Pais, 1049-001 Lisboa, Portugal

[1] IBB - Institute for Biotechnology and Bioengineering, Centre for Biological and Chemical Engineering, Instituto Superior Técnico, Av. Rovisco Pais, 1049-001 Lisboa, Portugal

Keywords: Biodiesel, feedstocks, transesterification, oxidative stability
Topic: Sustainable process-product development through green chemistry

Abstract

Due to the increasing cost and depletion of fossil fuels, there is a growing need for alternative fuels. Biodiesel, being a renewable, non toxic and biodegradable resource with positive influence in the environment, is the main alternative to fossil diesel. The production of biodiesel is usually achieved by an homogeneous transesterification reaction (catalysed by sodium hydroxide or methoxyde) between a lipid (vegetable oils or fats) and a short chain alcohol, such as methanol, to produce an ester and glycerol as a by-product. One of the main goals of this work was to study the effect of different transesterification reaction conditions as well as of the type of oils used on the final biodiesel properties. Another goal was to establish a relationship between the iodine value of the oils and the oxidative stability of biodiesel and the effect of the addition of several commonly used anti-oxidants. The results show that using a methanol/oil molar ratio of 6:1 and a temperature of 65ºC, it was possible to produce soybean biodiesel with a methyl ester content above 97%, using $NaOCH_3$ as catalyst. On the other hand, the samples produced from waste frying oils (WFO) presented low values for the oxidative stability (induction times between 2 and 3h) but this property can be improved by the addition of anti-oxidants.

1 Introduction

One of the main problems for biodiesel commercialization is its high cost. The feedstock, usually semi-refined vegetable oils, represents a wide part of the total cost of the biodiesel production. Therefore, these costs may be considerably reduced if biodiesel is produced from low cost materials such as waste frying oils (WFO) or animal fats. However, the quality of biodiesel must be guaranteed and the European Standard (EN) 14214 specifies the limits for 25 quality parameters. WFO and fats often contain significant amounts of free fatty acids (FFA) and water, which makes them inadequate for direct base catalyzed transesterification reaction. The presence of a small amount of water is a problem because it can lead to a decrease in the quantity of methyl esters produced because water promotes hydrolysis reactions, which convert the methyl esters in FFA. On the other hand, if the amount of FFA is high (> 2 mg KOH/ 100g) it is necessary the use of an extra amount of catalyst during the transesterification reaction to balance the oil acidity and/or a previous esterification reaction with an acid or with glicerol to convert the FFA into esters (Canakci, 2007).

The production of biodiesel is usually achieved by an homogeneous transesterification reaction (catalysed by sodium hydroxide or methoxyde) between a lipid (vegetable oils or fats) and a short chain alcohol, such as methanol, to produce an ester and glycerol as a by-product (Reaction 1) (Felizardo et al., 2006).

[*] Corresponding author: Tel + 351-21-8417344. E-mail: qjnc@ist.utl.pt

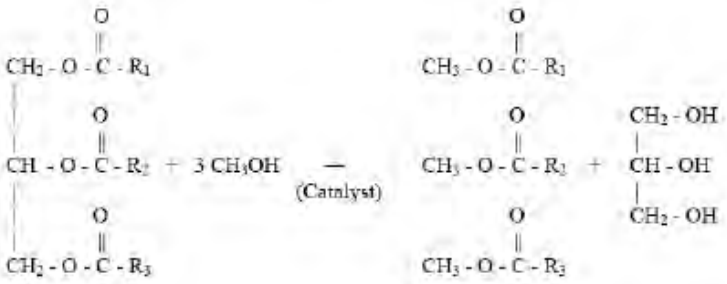

Reaction 1-Transesterification reaction. R1, R2 and R3 represent linear fatty acid chains.

This work presents the effect of different transesterification reaction conditions as well as of the type of oils used on the final biodiesel properties. The relationship between the iodine value of the oils and the oxidative stability of biodiesel and the effect of the addition of several commonly used anti-oxidants is also presented.

2 Materials and methods

All the chemicals were Analytical Grade and the aqueous solutions were prepared with deionised water. The acid value of the oils was obtained by titration with a KOH solution (prEN 14104), whereas the oils iodine value was determined by the Wijs method (prEN 14111). The oxidative stability of methyl esters, with and without antioxidant, was determined by the Rancimat method according to the European Standard EN 14112.
The samples' near-infrared spectra were acquired with an ABB BOMEM MB160 spectrometer equipped with an InGaAs detector and a transflectance probe from SOLVIAS (diffuse transflectance spectra). Spectra were recorded in duplicate for each biodiesel sample at room temperature, with the assistance of the Galactic Grams software package, between 12 000 to 4 000 cm^{-1} and with a spectral resolution of 16 cm^{-1}. The average of the two measurements was used to determine several previously calibrated properties (Felizardo et al., 2007; Baptista et al., 2008).

3 Experimental procedure

Biodiesel samples were prepared by transesterification of soybean, rapeseed, palm and WFO using the following procedure: 300 g of oil was transferred into a stirred tank reactor (1000 cm^3) immersed in a temperature-controlled water bath. For stirring, a single paddle round impeller (diameter = 6.5 cm) at 350 revolutions min^{-1} was used. The oil was heated until the desired temperature was reached (65°C). At this point, a mixture of methanol and sodium methoxide was added to the oil and the transesterification reaction began. The reactor was kept at around 65°C for 90 to 180 min. The majority of the reactions were performed using a molar ratio of methanol/oil of 6:1 and an amount of catalyst corresponding to 0.6% of the mass of oil sample. After the reaction, the two phases obtained, the glycerol-rich phase and the methyl ester (biodiesel) phase, were separated in a decantation funnel. Afterwards, the biodiesel was washed with water, with a 0.1M HCl solution and once again with water. It was centrifuged, filtered and finally dried at 80–90°C under vacuum using a rotary evaporator.

4 Results and discussion

1. Effect of the use of different transesterification reaction conditions on the biodiesel purity

It is known that several factors, including the reaction time and temperature, catalyst type and concentration (cat./oil) and alcohol/oil molar ratio (MeOH/oil), influence the efficiency of

the transesterification reaction and the biodiesel purity (Felizardo et al., 2006).

The results show that increasing the temperature from 55 to 75ºC influences very slightly the reaction kinetics, which is faster at higher temperatures. On the other hand, the methanol/oil molar ratio is one of the most important variables in methyl esters production. The quantity of methanol influences significantly the purity of the final product, which decreases with the decreasing of the molar ratio methanol/oil. Relatively to the amount of catalyst, it was possible to verify a decrease in the esters content in the purified biodiesel when, maintaining the remaining conditions, the quantity of $NaOCH_3$ decreased from 0.60 to 0.30%. However, the reduction of 1 to 0.45% of NaOH did not influence very much the final purity of biodiesel, although more time is required to meet the specification value for the methyl esters content (96.5%), when the amount of catalyst decreases.
The effect of the catalyst type was also studied in this work. The results show that, for the same amount of sodium added, in the form of NaOH or $NaOCH_3$, the methyl esters content of the produced biodiesel is similar, although the kinetic of the reaction is faster when $NaOCH_3$ is used as a catalyst. Hence, for a methanol/oil molar ratio of 6:1 and a temperature of 65ºC, it was possible to produced biodiesel with a methyl ester content above 97%, using NaOH or $NaOCH_3$ as catalyst.

2. Effect of the use of different types of oils on the biodiesel purity

As already mentioned, biodiesel can be produced from different vegetable oils. So, one of the aims of this work was to study the effect of the type of oil used in the transesterification reaction on the final content of methyl esters in biodiesel. The results showed that, independently of the types vegetable oil (soybean, rapeseed, palm oils, WFO or mixtures), the methyl esters content of the final biodiesel increases with the reaction time up to a certain value, which depends on the type of oil, and remains constant after that. The biodiesel samples produced from soybean oil and from the mixtures of soybean, palm and/or rapeseed oils presented the best results in terms of biodiesel purity, in some cases, above 98%. On the other hand, the worst results for the semi-refined oils were obtained with palm oil, which seems to need more time to reach the limit value established by the European Standard EN 14214. The soybean and rapeseed oils only required 30 min of reaction to reach the 96.5% methyl esters content limit.

3. Oils Iodine value
Another goal of the present work was to establish a relationship between the iodine value of the oils and the oxidative stability of the corresponding biodiesel. The iodine value is an important parameter to determine the unsaturation degree of the oil and/or of biodiesel and influences several important properties of biodiesel. In fact, it is known that oils and biodiesel with higher values of the iodine number have higher CFPP (Cold Filter Plugging Point) and a lower oxidative stability (Knöthe et al., 2005).
The iodine value of the oils samples used in this work varied from ≈60 g I_2/100 g for palm oils to values higher than 120 g I_2/100 g for the soybean oils (the EN 14214 imposes and iodine value for biodiesel lower than 120 g I_2/100 g). The results obtained allowed to confirm that the oxidative stability of biodiesel, measured in terms of its induction time, tends to decrease with the increase of the iodine value of the oil used in its production. In fact, the biodiesel samples with higher induction times (above 13h) were the ones produced from palm oil, whereas soybean and rapeseed biodiesel samples have induction times of 5.3 h and 5.8h, respectively. As expected, the samples produced from WFO presented the lowest values of the oxidative stability (induction times between 2 and 3h).

4. Determination of the oxidative stability. Addition of antioxidants
Due to the fact that oxidative degradation affects the biodiesel quality, the European biodiesel standard EN 14214 specifies a minimum induction time (IT) of 6h for the oxidative stability of biodiesel. As mentioned above, the biodiesel samples produced in this work with

higher induction times (above 13h) were the ones produced from palm oil. Soybean and rapeseed biodiesel have induction times of 5.3 h and 5.8h, respectively, whereas biodiesel produced from WFO presented induction times lower than 3h. Therefore, to comply with the EN 14214 specification it is often necessary to prepare blendings with, for example, palm oil biodiesel that presents the highest value of the IT, or to add anti-oxidants to the final biodiesel. Thus, to study the effect of the addition of anti-oxidants, five antioxidants (identified as A to E) were added to biodiesel samples produced from soybean, rapeseed and WF oils and the results are presented in Figure 1.

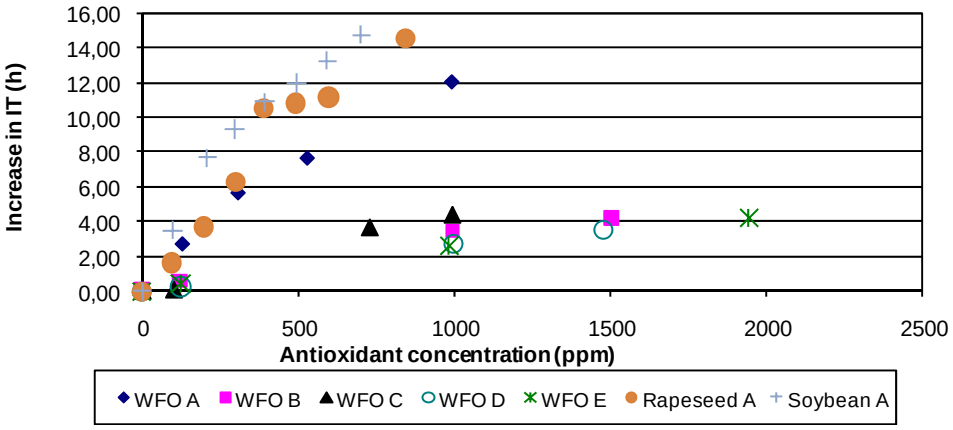

Figure 1 - Effect of the antioxidant concentration on the induction time.

As shown in Figure 1**,** the best results were obtained with the antioxidant A, even though all the antioxidants were able to increase the samples induction time. Furthermore, the curve obtained for the biodiesel sample produced from WFO with the anti-oxidant A was similar to the ones obtained for the soybean and rapeseed biodiesel samples. From Figure 1 it is also possible to conclude that the IT increases directly with the concentration of antioxidant for low concentration of the latter. For higher values the induction time reaches a plateau.

With the aim of testing the durability of the effect of the addition of the antioxidants and confirm the influence of light in the oxidative degradation, some of the samples (with and without antioxidant) were stored in a closed cupboard in dark jars, whereas others were exposed to the sunlight in transparent jars. After an exposure time between 14 and 69 days, the induction time was measured again with a Rancimat apparatus. With this experiment it was possible to confirm that, as expected, the samples exposed to the sun in transparent jars were quickly degraded (IT<1 h after 14 days). On the other hand, the decreases in the IT (degradation) of the samples that had been stored in a dark place were considerably small and never higher than ≈ 3h. Furthermore, for some of the tested antioxidants, it was possible to maintain the IT>6h after 62 days of storage in a dark place.

5 Conclusions

The transesterification reaction conditions and the type of oil used as raw-material affect the ester content of the biodiesel. However, for a methanol/oil molar ratio of 6:1 and a temperature of 65ºC, it is possible to produced biodiesel with a methyl ester content above 97%, using NaOH or $NaOCH_3$ as catalyst. Another goal of this work was to establish a relationship between the iodine value of the oils and the oxidative stability of the corresponding biodiesel. As expected, it was verified that the oxidative stability of biodiesel decreases with the increase of the iodine value. The effect of several anti-oxidants added to the biodiesel was also analysed. The results showed that some of the antioxidants studied

were very effective and allowed obtaining induction times higher than 6h (minimum value imposed by the EN 14214), even for the biodiesel samples produced from WFO after 62 days of storage in a dark place.

Acknowledgements
The authors thank to Prof. Gabriela Bernardo Gil (DEQB,IST) for the use of the Rancimat equipment and to *Iberol, Biovegetal* and *Space* for supplying the oils. Pedro Felizardo would also like to thank *Fundação para a Ciência e Tecnologia* (SFRH/BDE/15566/2005) and Space for is PhD financial support.

References

Canakci, M. (2007). The potential of restaurant waste lipids as biodiesel feedstocks; Bioresource Technology, 98, 183–190.

Baptista P., Felizardo P., Menezes J.C., Correia M. J. N. (2008). Multivariate Near Infrared Spectroscopy Models for Predicting the Methyl Esters Content in Biodiesel, *Analytica Chimica Acta* 607, 153-159.

Felizardo, Pedro, Correia, M. Joana N., Raposo, Idalina, Mendes, João F., Berkemeier R., Bordado, João M. (2006). Production of Biodiesel from Waste Frying Oils, Waste Management, V26, nº 5, 487-494.

Felizardo, P., Baptista, P., Uva, Margarida S., Menezes, J. C., Correia, M.J.N. (2007). Monitoring biodiesel fuel quality by near infrared spectroscopy,, Journal of Near Infrared Spectroscopy, Volume 15, Issue 2, 97–105.

Felizardo, P., Baptista, P., Menezes, J. C., Correia, M.J.N.(2007). *Multivariate near infrared spectroscopy models for predicting methanol and water content in biodiesel*; Analytica Chimica, Acta 595,107 – 113.

Knöthe, G., VanGerpen, J., Krahl, J., (2005). The Biodiesel Handbook, AOCS Press.

Proceedings of the 10th International Chemical and
Biological Engineering Conference - CHEMPOR 2008
Braga, Portugal, September 4-6, 2008
E.C. Ferreira and M. Mota (Eds.)

HIGH FREE FATTY ACIDS OILS FOR BIODIESEL PRODUCTION

Pedro Felizardo, João Machado, Daniel Vergueiro, M. Joana N. Correia*, João Moura Bordado[1]

CPQUTL – Centre for Chemical Processes of UTL, DEQB – Department of Chemical and Biological Engineering, Instituto Superior Técnico, Av. Rovisco Pais, 1049-001 Lisboa, Portugal,

[1] IBB - Institute for Biotechnology and Bioengineering, Centre for Biological and Chemical Engineering, Instituto Superior Técnico, Av. Rovisco Pais, 1049-001 Lisboa, Portugal

Keywords: Biodiesel feedstock, acid oils, soap-stocks, methanolysis, glycerolysis

Topic: Sustainable process-product development through green chemistry.

Abstract

Biodiesel is the main alternative to fossil diesel and it may be produced from different feedstocks such as several semi-refined vegetable oils, waste frying oils (WFO) or animal fats. However, WFO and fats often contain significant amounts of free fatty acids (FFA) that make them inadequate for the direct base catalyzed transesterification reaction (where the FFA content should be lower than 4%). The present work describes two possible methods for the pre-treatment of oils with high content of free fatty acids (20 and 50%) by esterification with methanol and glycerol. In order to reduce the free fatty acids content, the reaction between these FFA and an esterification agent is carried out before the transesterification reaction. The results showed that both methanolysis and glycerolysis are promising pre-treatments to acidic oils or fats (>20 %) because they led to the production of an intermediary material with a low content of FFA (< 4%) that can be used directly in the transesterification reaction for the production of biodiesel.

1 Introduction

Biodiesel (fatty acid methyl esters or FAME) is the main alternative to fossil diesel. The key advantages of its use are the fact that it is a non-toxic renewable resource, which leads to lower emissions of gaseous pollutants. European governments are targeting the incorporation of 20% of biofuels in the general fuels until 2020.

FAME can be produced through a transesterification reaction between a lipid source (vegetable oils and fats) and an alcohol (mainly methanol) to produce an ester and a by product, glycerol (Reaction 1). This reaction occurs stepwise, with mono and diglycerides as intermediate products.

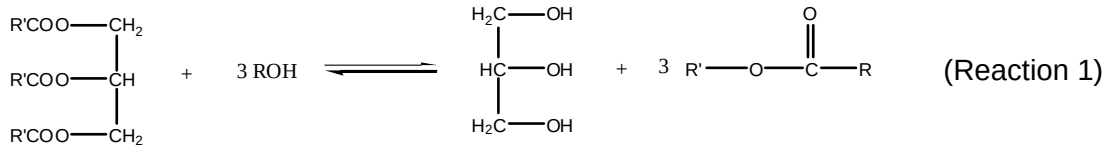

(Reaction 1)

Triglyceride Methanol Glycerol Biodiesel

* Corresponding author: tel-351-21-8417344; email: qjnc@ist.utl.pt

The feedstock represents a wide part of the total cost of biodiesel production. Therefore, these costs may be considerably reduced if biodiesel is produced from low cost materials, such as WFO, animal fats or soap-stocks. However, these raw-materials often contain significant amounts of free fatty acids (FFA), which makes them inadequate for direct base catalyzed transesterification. In fact, for acidic materials (FFA > 2 mg KOH/ 100g) it is necessary the use of an extra amount of catalyst in the transesterification reaction to balance the oil acidity (oils and fats with a FFA content below 4%) or to carry out a previous esterification reaction with methanol (Reaction 2) or with glycerol (Reaction 3) to convert the FFA into esters ((Felizardo et al., 2006; Canakci, 2007).

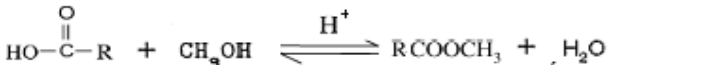

(Reaction 2)

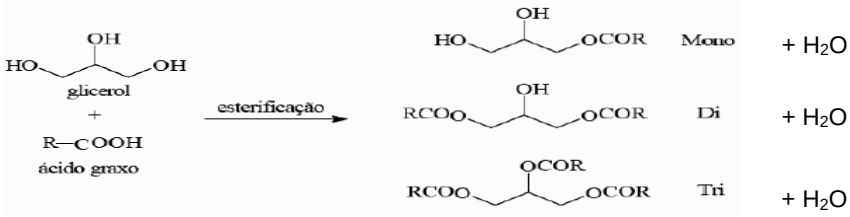

(Reaction 3)

Reactions 2 and 3 show that both pre-treatments involve the reaction of the FFA with an alcohol, such as methanol (methanolysis), or with glycerol (glycerolysis), in order to produce the corresponding esters (methyl esters or glycerides, respectively) (Canakci et al., 2001, 2003; Pereda M. et al., 2003). Methanolysis or glycerolysis are used only when the free fatty acids content is high (5-60% of FFA). After these pre-treatments, the glycerides in the oil/ester phase can be transesterified by basic catalysis.

To study the influence on methanolysis efficiency of the several experimental variables, it was used a factorial design planning of the experiments with three factors (methanol to FFA molar ratio, catalyst to oil mass ratio and the reaction time) and three factor levels. Factorial experiments are especially important in the beginning of an experimental study and they reveal high precision with minimum experimental effort and they enable detection of factor interactions (Otto M., 1999). A full factorial three-level design is described as 3^k design that means *k* factors at 3 levels and 3^k experiments.

The present work describes the application of methanolysis and glycerolysis for the pre-treatment of acidulated soap-stocks with a high content of free fatty acids (20 and 50%). The potential use of these raw materials for biodiesel production is very interesting because they are available at low cost and present a regular quality.

2 Experimental procedures

Acidulated soap-stocks were produced in a lab scale reactor from industrial soap-stocks produced in the soybean oil neutralisation process. This material contains soaps, oil and salts and yields, after treatment, an oil rich phase with FFA and triglycerides, which is usually refered to as acidulated soap-stocks. The procedure used in this work to produce this acidulated soap-stock consisted in adding into the reactor 150 g of soap-stocks plus 150 ml of hydrochloric acid (37%) and 500 ml of water. After three hours of reaction at ≈100ºC, the reaction yields two immiscible phases, one containing the oil and the FFA and an aqueous phase containing the acid and salts (Figure 1). The oil-rich phase was then washed several times with water, and finally dried under vacuum at 90º C, resulting in an acidulated soap-stock with an acid value of 120 to 130 mg KOH/g (60 – 65% of FFA).

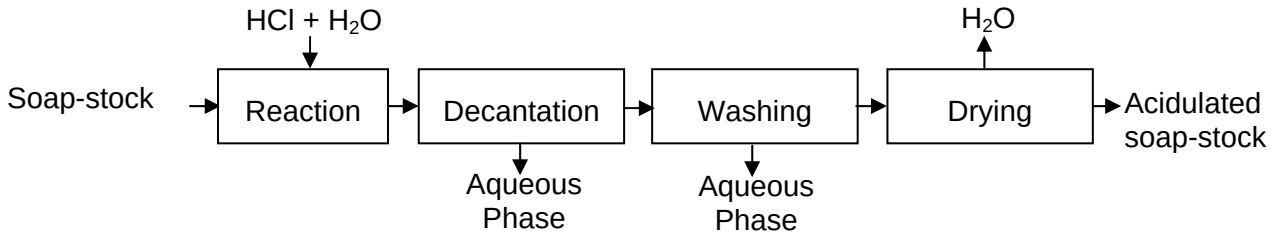

Figure 1 – Process for the production of acidulated soap-stocks

The methanolysis reactions were carried out using the following procedure: 200g of WFO (75% m/m) were mixed with the acidulated soap-stock (25% m/m) and transferred to a glass reactor equipped with a condenser and a mechanical stirrer. The resulting mixture presents an acid value of 40 mg KOH/g (≈ 20% FFA). The reactions were carried out at 350 rpm and 65 ºC.

As mentioned above, to study the influence on methanolysis efficiency of the several experimental variables, it was used a factorial design planning of the experiments with three factors (methanol to FFA mixture molar ratio, catalyst to oil mass ratio and the reaction time) and three factor levels. In this study, the MeOH:FFA molar ratio values were: 4:1, 8:1 and 12:1 and the Catalyst:Oil mass ratio values were: 2%, 3% and 4%. The effect of the reaction time was studied by collecting samples at 5, 90 and 180 minutes of reaction. Therefore, this factorial design led to the execution of nine (3^2) experiments. At the end of the pre-determined reaction time, the excess methanol was removed/recovered from each sample/final product by distillation at 50º C under vacuum in a Rotorvapor- RE-111 from BUCHI. The two phases formed were separated by decantation and the esters/oil phase was washed with water and dried at 90º C under vacuum.

The *Glycerolysis* was carried out using the following procedure: the industrial acidulated soap-stock and glycerol were added to a stirred reactor equipped with a condenser. The reaction was carried out at 200 ºC, 350 rpm for 2 hours. The glycerol was supplied by a biodiesel company (SPACE) and was neutralized with sulphuric acid before use. The samples withdrawn from the reactor were analyzed without further purification steps.

All chemicals used in this study that are not mentioned above were analytical grade and were supplied by Merck. The acid value of the samples was determined after sample purification according to EN 14104, whereas EN ISO 12185 was used to determine the samples' density. Whenever possible, fatty acid methyl esters content of the samples was estimated by Near Infrared Spectroscopy (Baptista et. al, 2008).

3 Results and discussion

3.1 Methanolysis

In order to understand the influence of the variation of the experimental conditions on the obtained results, the data was analysed using the Principal Components Analysis (PCA). This technique is a well establish method that greatly simplifies the analysis of complex interactions. Figure 2 presents the loadings analysis (Otto M., 1999) of the methanolysis experiments. From this Figure it may be concluded that that the acid value decreases with the increase of the MeOH:FFA molar ratio. This is an expectable result because the use of an excess of methanol drift the equilibrium towards the products (Reaction 2). It is also worth noting that the time is collinear with the methyl esters content (%ME). This reveals that increasing the reaction time increases the methyl ester content. Also, increasing the amount of catalyst enhances the formation of fatty-acid methyl esters.

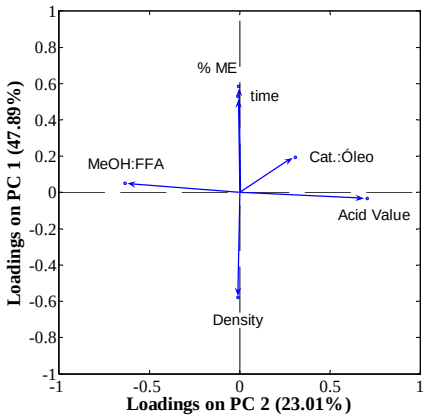

Figure 2 - Principle Component Analysis of Methanolysis

Factorial design analysis also shows that the amount of methanol is of major importance for the reduction of the acid value. Time, on the other hand, has little importance on the esterification reaction, although it was found to have a determinant effect on the reduction of the samples' density. Furthermore, the interaction between the studied factors is, in general, benign to the goals of the experiment.

Figures 3 A and B show the influence of the MeOH:FFA ratio on the samples acid value and methyl esters content, respectively. The results confirm the information obtained with the preliminary PCA. As a consequence, the increase of the MeOH:FFA ratio decreases the acid value and augments the methyl esters content. As anticipated by the analysis of Figure 2, Figure 3 shows that, in these experiments, the FFA content remains almost constant after the first 5 minutes of reaction, whereas the content of methyl esters continues to increase.

The results obtained concerning the ME content (Figure 3B) show that two reactions: the esterification of FFA (Reaction 2) and transesterification of triglycerides (Reaction 1) are occurring in the reaction vessel. In fact, the increase of the ME content to values up to 45%, higher than the initial content of FFA in the WFO-Soap stock mixture (≈20%), indicates the occurrence of both reactions. Furthermore, the decrease of the density is generally related to the transformation of triglycerides into fatty acid methyl esters. Figure 2 also shows that, as concluded from the factorial design analysis, the acid value is almost independent from the reaction time (they are almost orthogonal). This result indicates that after an initial decrease detected in the first samples, there is no significant change in the content of FFA with the increase of the reaction time.

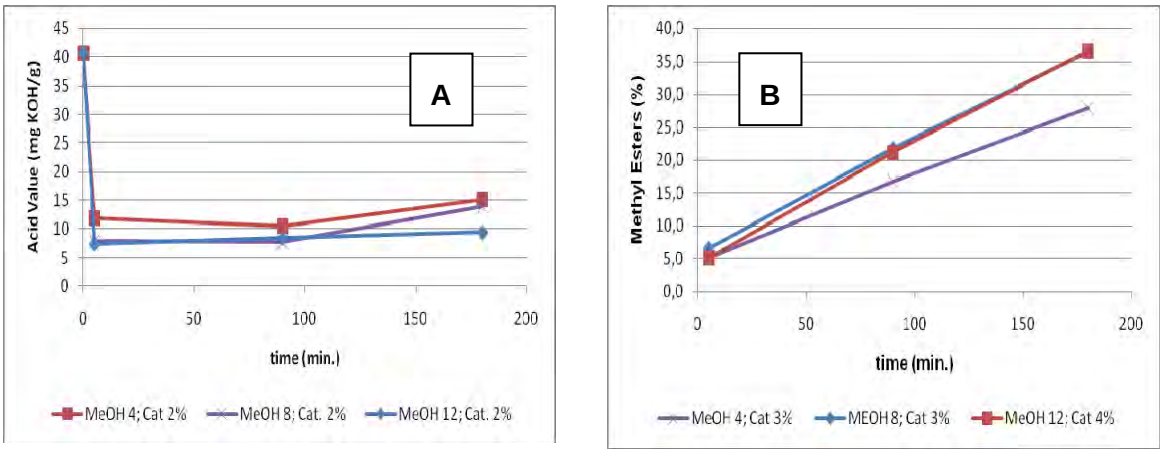

Figure 3A and 3B –Influence of the MeOH:FFA in the Acid value (A) and Fatty Acid Methyl Esters content (B).

The effect of the catalyst:oil mass ratio is shown in Figures 4 A and B. From these figures it is possible to conclude that, although the amount of catalyst has only a slight influence in the FFA content, the methyl esters content increases with the increase of the catalyst:oil ratio. Figure 4 B shows that the methyl esters content surpasses the content of FFA in the initial feed (≈20%), resulting in a mixture that has a higher amount of esters thus leading to a materials that can be easily transesterifyed.

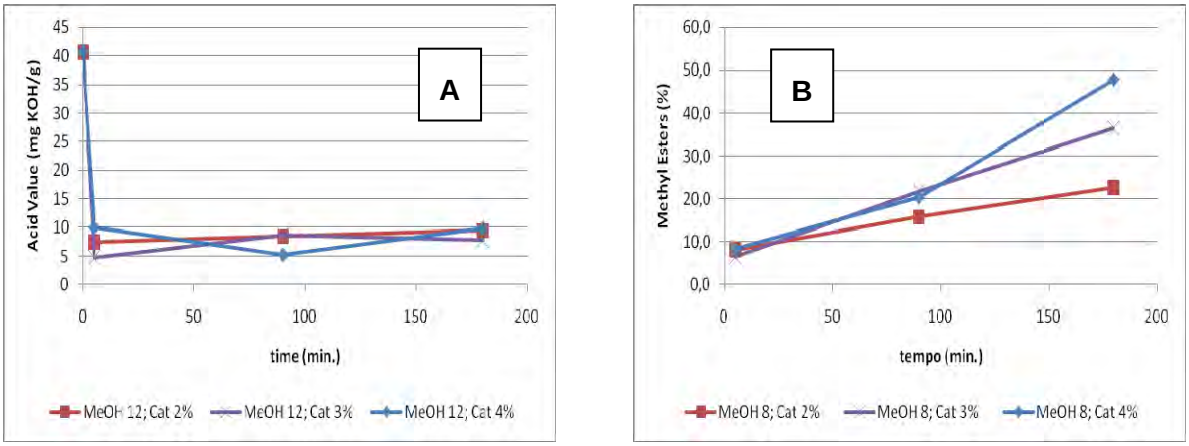

Figure 4 - Catalyst:Oil influence in Acid value (A) and Fatty Acid Methyl Esters content (B).

3.2 Glycerolysis

The preliminary study of glycerolysis was carried out with industrial acidulated soap-stocks produced from the soybean oil neutralisation process. For the glycerolysis experiments, three levels of glycerol:FFA molar ratios were used (1.1, 1.3 and 1.5) and Figure 5 presents the results. From this Figure it is possible to conclude that the addition of glycerol to the reaction mixture improved the kinetics of glycerolysis. However, for a molar ratio higher than 1.3, the final acid value obtained after 120 minutes of reaction is the same. The best results (acid value ≈ 10 mg KOH/g) were obtained using a ratio of glycerol:FFA of 1.3 or 1.5 and a reaction time of 180 minutes (Figure 5). The use of tetrapropyl orthotitanate as catalyst was also tested but no significant improvements were achieved.

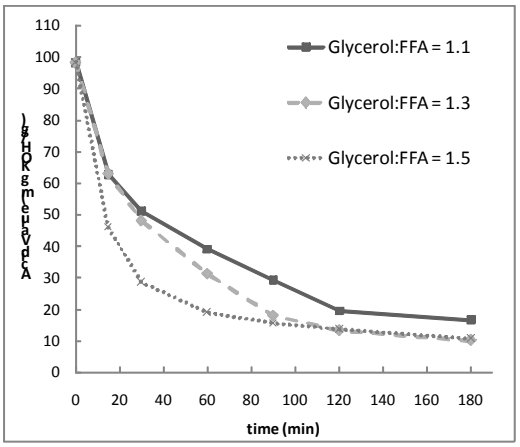

Figure 5 – Glycerolysis reaction kinetics

From Figure 5 it is possible to conclude that the rate of the reaction is lower when compared to the methanolysis. To reach a FFA content lower than 5% (Acid Value ≈ 10 mg KOH/g) it is necessary more than 3 h of reaction. The use of high temperatures is also a disadvantage of

glycerolysis, in spite of allowing the continuous removal of water and therefore the drift of the reaction towards the products. However, glycerolysis has the advantage of using as a reagent a by-product of the biodiesel production process.

4 Conclusions

The results presented in this work show that glycerolysis and methanolysis may be used to reduce the free fatty acids content in acidic and low-cost feedstocks for biodiesel production. In fact, it was possible to reduce the FFA content of a mixture of WFO and soap-stocks from 20% to 4% in 5 minutes by methanolysis. Glycerolysis, which has the advantage of using glycerol from the biodiesel production process, allowed reducing the content of FFA in an industrial soap-stock from 50 to 5 % after 3 hours of reaction at 200ºC. Also, it was effective in the reduction of the FFA content without the addition of any catalyst. However, the use of temperatures around 200º C is clearly a disadvantage, although it allows the continuous removal of the water formed in the reaction (Reaction 3) and the drift of the equilibrium towards the products. On the contrary, methanolysis takes place at 65 ºC and presents therefore lower energy costs. In this temperature range water is not removed from the process and this limits the esterification reaction after the equilibrium is reached. When compared to glycerolysis, methanolysis presents another disadvantage by requiring a large amount of methanol to obtain an effective reduction of the FFA content. It is however worth noting that one of the greatest advantages of methanolysis is the production of fatty-acid methyl esters (biodiesel) instead of mono-, di- and triglycerides, which is very interesting when the main objective is the production of biodiesel after the esterification. Furthermore, as shown above, the transesterification of the glycerides, which is the main goal of the global process, occurs simultaneously with the esterification reaction.

Acknowledgements

The authors thank Iberol and Space for supplying industrial samples of soap-stocks and the waste frying oils for the development of this work. Pedro Felizardo would also like to thank Fundação para a Ciência e Tecnologia (SFRH/BDE/15566/2005) and Space for his PhD financial support.

References

Felizardo, P., Neiva Correia, M.J., Raposo, I., Mendes, J.F., Berkemeier, R. and Bordado, J.M. (2006). *Production of biodiesel from waste frying oils*. Waste Manag. 26 (2006) 487–494.

Canakci, M (2007). *The potential of restaurant waste lipids as biodiesel feedstocks.* Bioresource Technology 98 , 183–190.

Canakci, M., Van Gerpen, J., 2001. *Biodiesel production from oils and fats with high free fatty acids*. Trans. ASAE 44, 1429–1436.

Canakci, M., Van Gerpen, J., 2003. *A pilot plant to produce biodiesel from high free fatty acid feedstocks*. Trans. ASAE 46, 945–954.

Otto, M. (1999). Chemometrics: Statistics and Computer Application in Analytical Chemistry, Wiley-VCH, New York, 1999

Pereda Marín, J., Barriga Mateos, F., Álvarez Mateos, P. (2003). *Aprovechamiento de las oleinas residuales procedentes del processo de refinado de los aceites vegetales comestibles, para la fabricación de biodiesel*. Grasas y Aceites 54, 130–137.

Patricia Baptista, P., Felizardo, P., Menezes, J.C., Neiva Correia, M.J. (2008). *Multivariate near infrared spectroscopy models for predicting the methyl esters content in biodiesel*. Analytica Chimica Acta Volume 607, Issue 2, 153-159.

Proceedings of the 10th International Chemical and
Biological Engineering Conference - CHEMPOR 2008
Braga, Portugal, September 4-6, 2008
E.C. Ferreira and M. Mota (Eds.)

Comparison between biodiesel produced from sunflower oil and waste frying oil

Joana M. Dias[1*], Maria C. M. Alvim-Ferraz[1], and Manuel F. Almeida[2]
[1] Departamento de Engenharia Química, LEPAE, Faculdade de Engenharia, Universidade do Porto, R. Dr. Roberto Frias, 4200-465, Porto, Portugal
[2] Departamento de Engenharia Metalúrgica e de Materiais, LEPAE, Faculdade de Engenharia, Universidade do Porto, R. Dr. Roberto Frias, 4200-465, Porto, Portugal

Keywords: Biofuels, Biodiesel, Sunflower oil, Waste frying oil, Transesterification
Topic: Sustainable process-product development through green chemistry - Environmental engineering & management

Abstract

The objective of the present study was to evaluate the difference of using sunflower oil or waste frying oil for the production of biodiesel through transesterification, using different concentrations of the currently more used catalyst in the industry (CH_3ONa). For that purpose, different experiments were conducted using a 6:1 methanol/oil molar ratio, temperature of 60 ºC, and varying the amount of catalyst used. The biodiesel yield was evaluated and so was the quality of the final product; the characterisation of the produced biodiesel was made according to the European Biodiesel Standard EN 14214.

It was possible to obtain a product in agreement with the EN 14214 using both oils. All samples fulfilled the specifications regarding the following parameters: acid value, density, flash point, copper corrosion and linolenic acid methyl ester content. In terms of iodine value, biodiesel from waste frying oil was within the limit but the one from sunflower oil showed a slightly higher value.

Viscosity and purity were the limiting parameters to select the best catalyst concentration; at 0.6 %, both samples fulfilled the specification in terms of kinematic viscosity; however, higher catalyst concentration (0.8 %) was needed to achieve minimum purity using waste frying oil.

The highest yield (93.4 %) and purity (99.4 %) was obtained using sunflower oil as raw material.

Considering the present study, the optimum catalyst concentrations were: i) 0.6% for the production of biodiesel with a yield of 90 % and presenting a purity of 99.4 % using sunflower oil; and ii) 0.8 % catalyst concentration for the production of biodiesel with a yield of 89 % and presenting a purity of 97.9 % using waste frying oil.

1 Introduction

Increased attention has been given to biodiesel, which is currently being used as an alternative fuel in compression-ignition engines. Biodiesel is an ester that can be produced by transesterification of vegetable oils or animal fats. During this reaction, the triglyceride is converted step by step into a diglyceride, monoglyceride and glycerol; at each step, one mol of ester is produced (Fig. 1). There are many parameters affecting the transesterification reaction. The ones known to greatly influence the reaction are: temperature, methanol/oil molar ratio, mixing rate, catalyst type and amount of catalyst (Meher, L. C., et al., 2006, Ma, F. and Hanna, M. A., 1999).

* Corresponding author. Tel +351-508-1976. E-mail:joana.dias@fe.up.pt

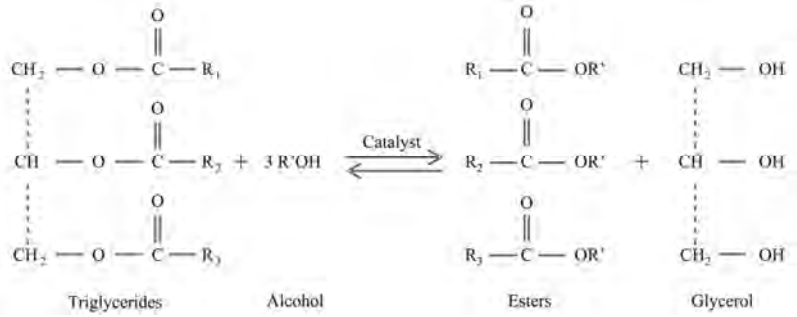

Fig.1 - Transesterification reaction of triglycerides (global reaction).

The increasing costs of refined oils are currently a great concern for biodiesel industry; therefore, alternative raw materials are being studied with more emphasis. The use of waste frying oils and other greasy wastes as raw materials for biodiesel production has two major advantages: i) decreases biodiesel production costs (because it uses readily available raw-materials with low economic value); and ii) reduces waste treatment costs (related with the waste management and wastewater treatment processes) (Wang, Y., et al., 2006, Encinar, J. M., et al., 2005, Tomasevic, A. V. and Siler-Marinkovic, S. S., 2003).

The objective of the present study was to evaluate the difference of using sunflower oil or waste cooking oil for the production of biodiesel through transesterification, using different concentrations of the currently more used catalyst in the industry (CH_3ONa).

2 Materials and Methods

2.1 Materials

The sunflower oil used was from the brand “3Ás equilíbrio” and was donated by Sovena, SA, Portugal. This oil was in agreement with Portuguese specifications for food oil. The waste frying oil was obtained from a voluntary collection system implemented at the Engineering Faculty of Oporto University and consisted of waste frying oil from different domestic sources. The reagents used during synthesis and purification procedures were: methanol 99.5% (analytical grade, Fischer Scientific), sodium methoxide solution 30% in methanol (synthesis grade, Panreac) and anhydrous sodium sulphate 99% (analytical grade, Panreac).

2.1 Methods

2.1.1 Raw materials Pre-treatment

Waste cooking oil was filtered under vacuum, after dehydrated using anhydrous sodium sulphate (left over night) and finally again filtered under vacuum.

2.1.2 Biodiesel Synthesis

Synthesis of biodiesel was made by transesterification. A defined amount of methanol (6:1 molar ratio to oil) was pre-mixed with CH_3ONa. The amount of catalyst varied from 0.4 to 1% of oil mass, in 0.2 intervals. The mixture of methanol and catalyst was then added to the reactor, which already had 200 g of the oil (sunflower 227.4 mmol and waste frying oil 227.9 mmol) preheated at the reaction temperature (60 ºC). At this point, the reaction started; the reactor consisted on a 1L flat-bottom flask immersed in a temperature controlling bath, equipped with a water-cooled condenser and a magnetic stirrer. Reaction occurred for 60 min under vigorous stirring; at the end of the reaction, products were left to settle for 2 hours to ensure the separation of the two phases: biodiesel and glycerol.

2.1.3 Biodiesel Purification

Both phases were separated and excess methanol was recovered from each phase, using a rotary evaporator under reduced pressure. After, biodiesel was washed, first with 50% (v/v) of an acid solution (0.2% HCl) and after repeatedly with 50% (v/v) of distilled water until the pH of the washing water was the same as the distilled water. To remove residual water, biodiesel was after dried over anhydrous sodium sulphate (left over night) and finally filtered under reduced pressure to obtain the final product.

2.1.4 Analytical methods

Different properties of the raw materials were determined: i) composition (using gas chromatography (GC) according to EN 14103 (2003) and NP EN ISO 5508 (1996)); ii) acid value, by volumetric titration according to the standard NP EN ISO 660 (2002); iii) iodine value, by volumetric titration using Wijs reagent, according to the standard ISO 3961 (1996); and iv) water content, using coulometric Karl Fischer titration.

The biodiesel quality was evaluated according to the European biodiesel standard EN 14214 (2003). The following properties were determined: i) acid value, by volumetric titration according to the standard EN 14104 (2003); ii) kinematic viscosity, determined at 40 ºC using glass capillary viscometers according to the standard ISO 3104 (1994); iii) density, determined using a hydrometer method according to the standard EN ISO 3675 (1998); iv) flash point, using a rapid equilibrium closed cup method, according to the standard ISO 3679 (2004); v) copper corrosion, using a copper strip test according to the standard ISO 2160 (1998); vi) water content, by Karl Fischer coulometric titration according to the standard NP EN ISO 12937 (2003); vii) ester and linolenic acid methyl ester contents, by GC according to the standard EN 14103 (2003) and; viii) iodine value, determined from ester content according to annex B of EN 14214 (2003). Regarding to chromatographic analysis, a Dani GC 1000 DPC gas chromatograph (DANI Instruments S.p.A.), with an AT-WAX (Heliflex capillary, Alltech) column (30 m, 0.32 mm internal diameter and 0.25 μm film thickness) was used. The injector temperature was set at 250 ºC, while the detector (FID) temperature was set at 255 ºC. The carrier gas used was N_2 with a flow of 2 mL/min. Injection was made in a split mode, using a split flow rate of 50 mL/min, the volume injected was 1 μL.

3 Results and discussion

3.1 Raw material characterisation

The fatty acid composition and the mean molecular weight (calculated from the composition) of the oil samples are presented in Table 1. Composition of waste frying oil did not vary much from the sunflower oil; main difference was found in C16:0 and C18:3 which might indicate the presence of a small fraction of soybean oil. Regarding C18:1 and C18:2; differences could be expected due to oxidation reactions with temperature; however, this was not the case and similar results have also been found in related studies. Çetinkaya and Karaosmanoğlu (2004) attributed this fact to sunflower oil exposed to high temperature for a short period of time. Because the waste frying oil used in this study was from a domestic source, this might justify these findings. Sunflower oil had an acid value of 0.08 mg KOH/g and an iodine value of 123 g I_2/100 g. Waste frying oil had an acid value of 0.82 mg KOH/g and an iodine value of 117 g I_2/100 g. The water content was 0.05 (% wt) for the waste frying oil and 0.04 (% wt) for soybean oil.

The acid value of the virgin oil was lower than the waste frying oil, however much higher acid values have been reported in waste frying oils; the previously discussed low variation in composition, which indicates smaller degree of oxidation reactions, should be related with such small value found.

Table 1: Fatty acid composition (% wt) and mean molecular weight (g mol^{-1}) of the sunflower oil and waste frying oil

	Sunflower oil	Waste frying oil
Fatty acid		
Palmitic (C16:0)	5.7	8.4
Palmitoleic (C16:1)	n.d	0.2
Stearic (C18:0)	4.0	3.7
Oleic (C18:1)	35.2	34.6
Linoleic (C18:2)	53.5	50.5
Linolenic (C18:3)	0.1	0.6
Arachidic (C20:0)	0.3	0.4
Eicosenoic (C20:1)	0.2	0.4
Eicosadienoic (C20:2)	0.1	n.d
Behenic (C22:0)	0.7	0.8
Docosadienoic (C22:2)	0.1	n.d
Lignoceric (C24:0)	0.2	0.3
Mean molecular weight	879.5	877.5

n.d. not detected

3.2 Biodiesel production yields

Table 2 shows production yields using both raw materials. The lowest yield obtained was for the highest catalyst concentration using both oils; the highest yield using waste frying oil was obtained at the lowest catalyst concentration; however, using sunflower oil, it was obtained using 0.8 % wt catalyst (differences were less than 2% compared to the lowest catalyst concentration). It can be seen that at lower catalyst concentrations (0.4, 0.6 %wt), the difference of using both oils was not very much reflected; however, at higher catalyst concentrations, biodiesel produced using CH_3ONa showed yields approximately 4 % higher for both catalyst concentrations. This fact should be related with the formation of soaps at higher catalyst concentrations, due to the higher fatty acid value of waste frying oil.

Table 2: Biodiesel production yields (wt %) using sunflower oil and waste frying oil as raw materials

Catalyst (% wt)	Sunflower oil	Waste frying oil
0.4	91.6	92.0
0.6	90.0	89.2
0.8	93.4	89.0
1.0	89.6	85.3

3.3 Biodiesel quality

As it can be seen in Table 3, all samples fulfilled the EN 14214 regarding the following properties: acid value, density, flash point, copper corrosion and linolenic acid methyl ester content. From the parameters analysed in biodiesel samples, the ones that were not fulfilled in some cases were the kinematic viscosity and methyl ester content (purity); the ones that were not fulfilled in any case were the water content and the iodine value in the case of using sunflower oil as raw material.

Table 3: Quality parameters of biodiesel from sunflower oil and waste frying oil and the respective standard limits according to EN 14214

Parameter	Results	EN 14214
Acid value (mg KOH g^{-1})	0.09-0.27	<0.50
Water content (mg kg^{-1})	949-1216	<500
Kinematic viscosity at 40 ºC (mm^2 s^{-1})	4.48-5.20	3.50-5.00
Density at 15ºC (kg m^{-3})	881-886	860-900
Flash point (º C)	174-180	>120
Copper corrosion (3h/50 º C)	All samples-Class 1a	Class 1
Methyl ester content (wt %)	88.9-99.4	>96.5
Linolenic methyl ester content (wt %)		
Sunflower oil	0.1	<12.0
Waste frying oil	0.6	
Iodine value*(g I_2/100g)		
Sunflower oil	123	<120
Waste frying oil	119	

*Calculated from the methyl ester composition

It was found that biodiesel viscosity decreases with increasing catalyst concentration and purity increases with increasing catalyst concentration (Fig. 2). For both parameters, almost no restrictions regarding the fulfilment of EN 14214 were found using sunflower oil; however, using waste cooking oil, at least 0.6% catalyst was needed to fulfil viscosity requirements and only at 0.8% catalyst concentration it was possible to obtain enough purity.

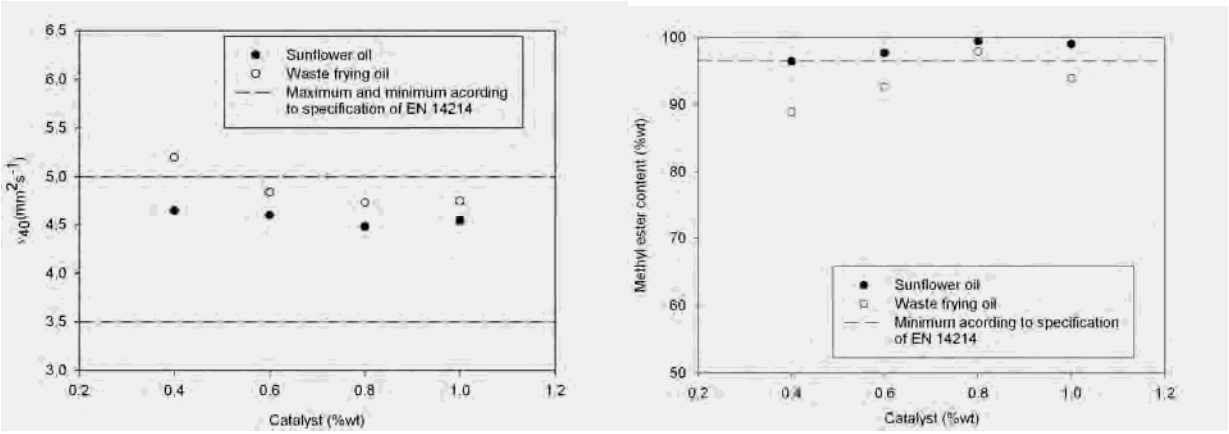

(a) (b)

Fig. 2 - Biodiesel produced using CH_3ONa as catalyst: (a) kinematic viscosity (mm^2s^{-1}) and (b) methyl ester content (% wt).

Regarding the biodiesel water content, the adopted diagram production included a dehidration step using a salt (anhydrous sodium sulphate). However, the use of this salt was shown to be very ineffective. To reduce water content to acceptable values, a different procedure was evaluated using biodiesel from sunflower oil. The sample (water content of 0.10 (% wt)), was subjected to evaporation under reduced pressure using a rotary evaporator at 40 and 60 ºC (163 mbar, 45 min). The water content was then reduced to 0.04 (% wt) at 40 ºC and to 0.02 (% wt) at 60 ºC. These results show that evaporation under reduced pressure might be a suitable procedure to ensure the fulfilment of the European specification for water content.

Regarding the iodine value, as this parameter depends only on the raw material used, samples obtained using the same vegetable oil should present similar iodine value. That was confirmed in

results presented in Table 4, and, for this reason, sunflower oil is not a very attractive raw material aiming to fulfill this parameter.

3 Conclusion

It was possible to obtain biodiesel in agreement with the EN 14214 by transesterification of both virgin and waste frying oil; however, in terms of iodine value, sunflower oil showed a value slightly higher than the limit. Also, biodiesel water content was always above the limit and therefore, a dehydration step using an anhydrous salt was not effective. Evaporation at reduced pressure was evaluated and might be an efficient alternative.

Considering the variations in catalyst concentration, the following parameters were fulfilled in all cases: acid value, density, flash point, copper corrosion and linolenic acid methyl ester content. Viscosity and purity were the limiting parameters to select the best catalyst concentration; at 0.6 %, both samples fulfilled the specification in terms of kinematic viscosity; however, higher catalyst concentration (0.8 %) was needed to achieve minimum purity using waste frying oil.

The highest yield (93.4 %) and purity (99.4 %) was obtained using 0.8 % catalyst concentration and sunflower oil as raw material. However, in order to optimize production costs, a smaller amount of catalyst might be used (0.6 %).

Considering the present study, the optimum catalyst concentrations were: i) 0.6 % for the production of biodiesel with a yield of 90% and presenting a purity of 99.4 % using sunflower oil; and ii) 0.8 % catalyst concentration for the production of biodiesel with a yield of 89 % and presenting a purity of 97.9 % using waste frying oil.

References

Encinar, J.M., González, J.F., Rodríguez-Reinares, A. (2005). Biodiesel from Used Frying Oil. Variables Affecting the Yields and Characteristics of the Biodiesel. ***Industrial and Engineering Chemistry Research***, 44, 5491-5499.

Çetinkaya M, Karaosmanoğlu F. (2004). Optimization of Base-Catalyzed Transesterification Reaction of Used Cooking Oil. ***Energy Fuels***;18,1888-95.

Ma, F., Hanna, M.A. (1999). Biodiesel production: a review. ***Bioresource Technology***, 70, 1-15.

Meher, L.C., Vidya Sagar, D., Naik, S.N. (2006). Technical aspects of biodiesel production by transesterification--a review. ***Renewable and Sustainable Energy Reviews***, 10, 248-268.

Tomasevic, A.V., Siler-Marinkovic, S.S. (2003). Methanolysis of used frying oil. ***Fuel Processing Technology***, 81, 1-6.

Wang, Y., Ou, S., Liu, P., Xue, F., Tang, S. (2006). Comparison of two different processes to synthesize biodiesel by waste cooking oil. ***Journal of Molecular Catalysis A: Chemical***, 252, 107-112.

Proceedings of the 10th International Chemical and
Biological Engineering Conference - CHEMPOR 2008
Braga, Portugal, September 4-6, 2008
E.C. Ferreira and M. Mota (Eds.)

Development of heterogeneous catalysts for transesterification of triglycerides in Biodiesel

J. F. Puna[1*], João F. Gomes[1,2], J. Carlos Bordado[2], M. Joana N. Correia[3]

[1] Chemical Engineering Department, ISEL, Lisboa, Portugal
[2] Catalysis and Reaction Engineering Group, IBB/Centre for Chemical and Biological Engineering, IST/UTL, Lisboa, Portugal
[3] Centre for Chemical Processes, IST/UTL, Lisboa, Portugal

Keywords: Biodiesel, heterogeneous catalysis, efficiency, transesterification, catalyst
Topic: Sustainable process-product development through green chemistry

Abstract:
This paper describes preliminary work done by the authors towards the development of new metallic heterogeneous catalysts that are to be used in the transesterification reaction of triglycerides, which is of considerable interest in the production of biodiesel. Biodiesel, is a mixture of mono-alkyl esters of fatty acids, and is currently manufactured by transesterification of triglycerides with methanol using NaOH or KOH as liquid base catalyst. Catalysts as such are corrosive to the equipment and another drawback is that these catalysts are in liquid phase and must be neutralized after the completion of the reaction, typically using HCl, thus producing salt streams. Moreover, due to the presence of free fatty acids it reacts to form soaps as unwanted by-products, hence requiring more expensive separation processes. Therefore, there is a great need on the development of industrial processes for biodiesel production using solid acid catalysts. The key benefit of using solid acid catalysts is that no polluting by-products are formed and the catalysts do not have to be removed since they do not mix with the biodiesel product.

Introduction:

Biofuels are all the fuel substances produced from Biomass and includes the Biodiesel (single alkyl ester of fatty acids), bioethanol and biogas (a mixture of methane and CO_2). The highway transports activity, in a global level, is 98% oil dependent. In the EU, this activity is responsible by more than 20% of total CO_2 emissions and, more than 50% of these emissions concerns to the individual transport, which increase 22% since 1999. The climate changes, the increase of crude prices and the supply energetic security leads to the growing interest about biofuels potential as substitutes of oil fuels, like gasoline's and diesel (OE, 2007). Actually, the biodiesel production is made essentially, from oleaginous plants by transesterification process (as shown in figure 3), which involves, as reactants, alcohol, essentially, methanol (CH_3OH) and a catalyst, preferably alkaline, liquid phase (NaOH, KOH, sodium methoxide). This process occurs with homogeneous catalysis. The main raw materials, which are the mentioned oils from oleaginous plants, previously refined, are, in majority, of colza, sunflower and soya. It can be done, also, by other plants, such as palm oil. Chemically, biodiesel is described as a mixture of methyl ester's of fatty acids, where, through the transesterification process, are produced those ester's (single, double and triple triglycerides), and produces also, Glycerine as co-product reaction (OE, 2007 and BRP, 2004). The quality of biodiesel must comply with several specifications in order to ensure a final product with good quality, main issue to guarantee his suitably introduction in the market. Naturally, the oil quality has significantly influence in the labour process qualification and in the biodiesel final specifications. It's important, also, refer that, to ensure those specifications, the production process has to be controlled, either at the reaction control level, either, basically, at the purification process level, where occurs the biodiesel/methanol,

* Corresponding author. Tel + 351-218317254. E-mail:jpuna@deq.isel.ipl.pt

biodiesel/catalyst and biodiesel/water separation steps, through the washing of biofuel. One of the most important control parameters of biodiesel is the maximum proportion of total glycerine, which is 0,25% in the European and American technical standards, in order to avoid the formation of particles in the combustion chamber and, also, to avoid the production of higher percentages of acrolein on the automobile combustion gases (BPR, 2004). Other important parameters are the viscosity, the water content, the iodine index, the proportion of single, double and triple triglycerides, the methanol proportion, the sulphur proportion, ashes, carbon residue, total contamination and cetane number. The biodiesel specifications currently available and used are described on the EN 14214 standard. The table 1 presents the goals stipulated by the EU to the incorporation of biofuels in the fuel oils until 2010, which includes the incorporation of biodiesel on the diesel fuel (Pelkmans, 2007). Figure 1 shows the process diagram of biodiesel production and figure 2 shows a generic flow-sheet of the same process.

Table 1: Targets of biofuels incorporation on oil fuels (Pelkmans, 2007)

2005	2006	2007	2008	2009	2010
2%	2,75%	3,5%	4,25%	5%	5,75%

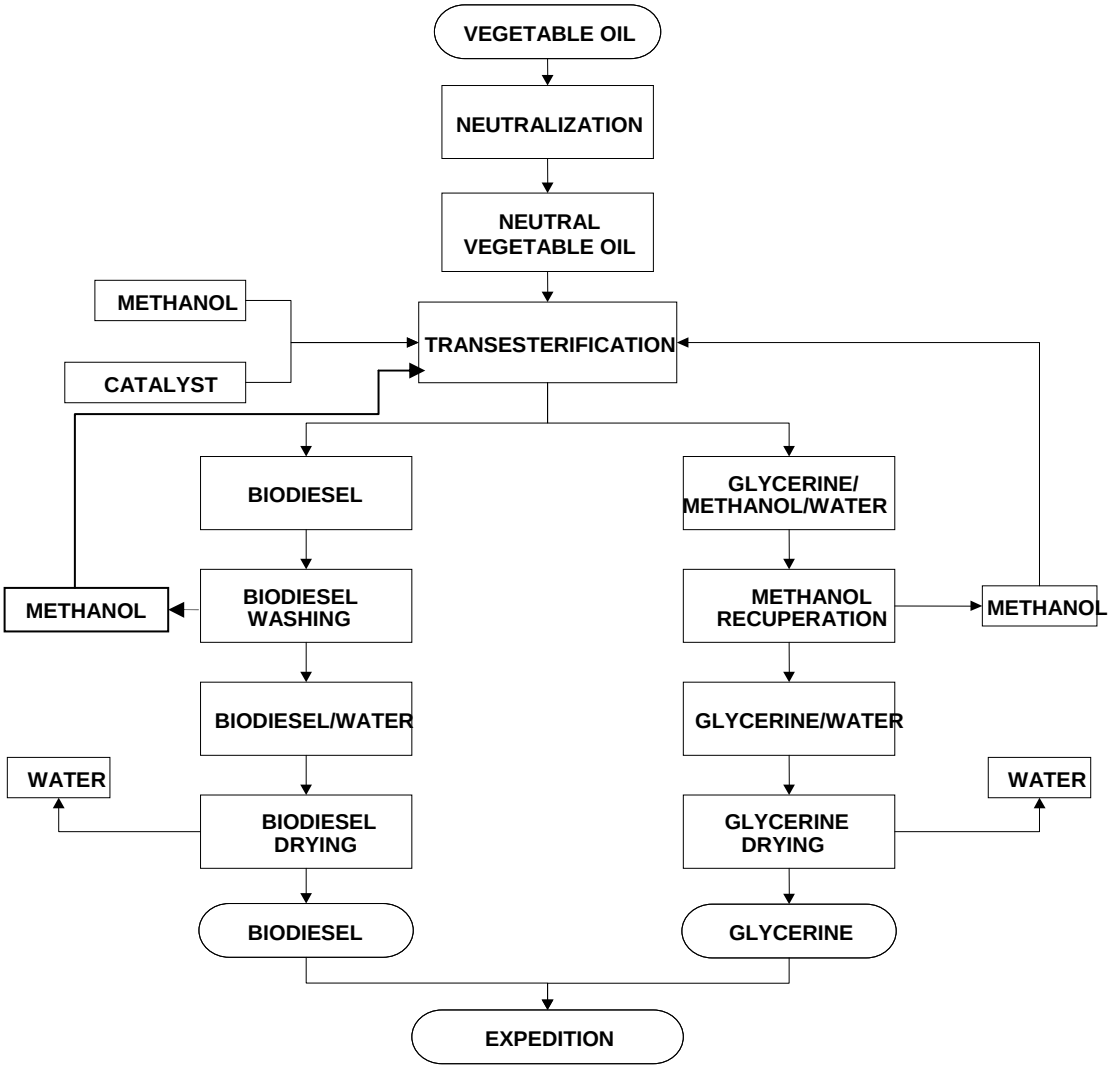

Figure 1: Schematic process diagram of biodiesel production

Development of newest heterogeneous catalysts for biodiesel production:
The transesterification reaction is considered the process with more technical effectiveness and with higher efficiency for biodiesel production using large scale, with minimization of co-products. Nevertheless, it's essential that, the raw materials (vegetable oils) keep a minimum level of quality, which can be achieved in the presence of acids, alkaline or enzymatic catalysts, simples or supported. The use of acid catalysts, like sulphur acid, leads to a reaction kinetic much lower when compared with alkaline catalysts. Other disadvantage in the utilisation of these kinds of catalysts is concerned with biodiesel separation from the process, in order to prevent possible damages to the engines structures, caused by the acid catalyst. On the opposite side, basic catalysts are faster and, in many cases, the steady-state is achieved at 15-30 minutes and leads to higher biodiesel yields, generally higher than 50%. However, they have the inconvenient of being sensible at the presence of water and free fatty acids. These last ones consume the catalyst and conducts to the formation of gels and soaps. These demands difficult the utilisation of used fried oils. On another hand, the enzymatic catalysts offer some advantages when compared with acids and alkaline catalysts, like, for instance, less sensibility to water presence, more catalyst recovery and more efficiency in the biodiesel separation steps. However, their utilisation implies higher costs (BRP, 2004). Other different option is the employment of heterogeneous catalysts in the biodiesel production, in order to replace the conventional homogeneous alkaline or acids catalysts, to eliminate the difficulties founded in the current biodiesel/catalyst separation. These new catalysts are solid. On another hand, these alternative and innovative solutions in the biodiesel production system allowed, more economic profitability and competitiveness to the process and, brings also, more environmental compatibility, when compared with the conventional processes. In this last issue, the use of heterogeneous catalytic systems in the transesterification of triglycerides implies the elimination of several washing/recovery biodiesel/catalyst process steps, in order to ensure a higher efficiency and profitability of the process, lowering the production costs.

There is, also, the strong possibility of being implemented in a continuous way, with the construction of a fixed bed catalytic reactor. The utilisation of heterogeneous catalysts implies higher lifetimes, because there is no need in their recirculation to the initial step (mixture), since the catalyst utilisation time is higher than the homogeneous catalytic processes. This means less catalyst replacements on the fixed bed catalytic reactor, which leads to a higher quality of the final product and, also, to the co-product, the glycerine. However, either the reaction conversion, either the *turnover number*, in order to keep constants, there is the necessity of optimize the operating conditions in the reactor. A literature search on these subjects was already done and the main results and contributions of several authors are synthesized in table 2. The optimization process at industrial scale needs, to perform a previous study, at laboratory scale, which concerns to perform several modifications of concentration ratios, temperature, catalyst structure and composition and time residence, in a fixed bed catalytic reactor. After that, we intend to optimize the biodiesel process production with heterogeneous catalysis, performing the scale-up in a pilot unit and quantify his composition, according to the EN 14214 standard specifications. Figure 4 shows a possible *flow-sheet* for biodiesel production process with heterogeneous catalyst.

The main aspects for Biodiesel production, in order to ensure that there aren't problems and difficulties in the vehicles performances, are, the following ones:

- Complete reaction;
- Glycerin removal;
- Catalyst removal;
- Alcohol and Water removal;
- Absence of Free Fatty-Acids.

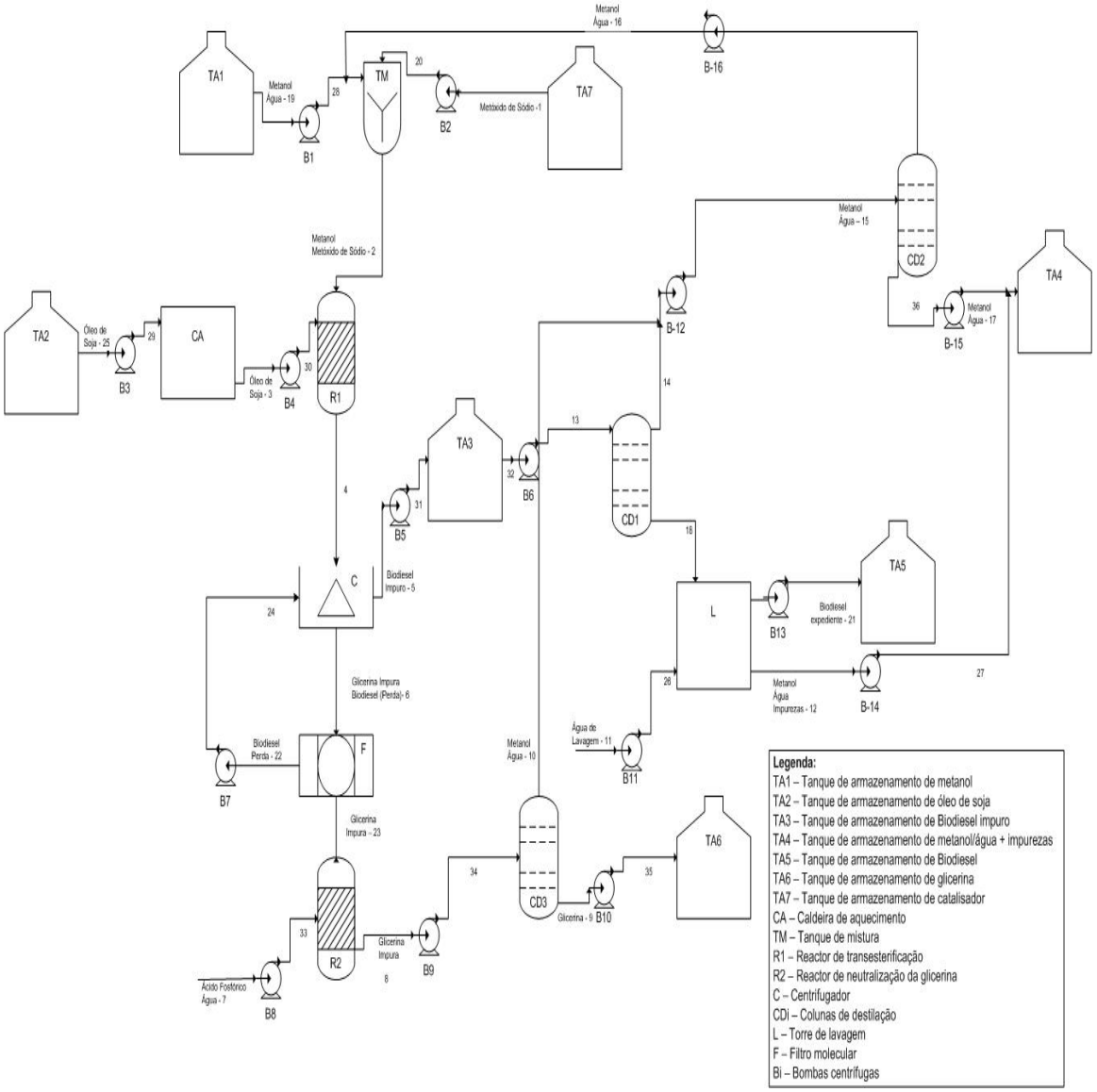

Figure 2: Conventional process flowsheet using homogeneous catalysis for biodiesel production.

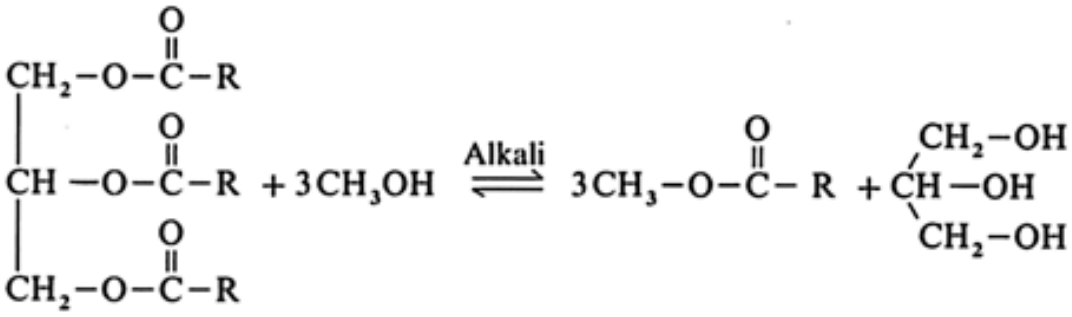

Figure 3: Transesterification reaction for biodiesel production.

Table 2: Used heterogeneous catalysts, experimental conditions and respective results obtained, found in literature research, for biodiesel production

Authors (year)	*Catalysts tested and their properties*	*Experimental conditions and obtained results*
Kiss *et al* (2006)	Zeolites Y, β and ZSM-5, Cationic Resins Amberlite-15 and Nafion-50, metallic oxides such as ZrO_2/SO_4^-, TiO_2/SO_4^{2-} and SnO_2/SO_4^{2-} and $Cs_{2,5}H_{0,5}PW_{12}O_{40}$.	Good results in the reaction conversion and yield for ZrO_2/SO_4^-, in a large gap of temperatures.
Rosa *et al* (2005)	Butilestanoic acid ($(C_4H_9)SnO(OH)$), Dibutyltin oxide ($(C_4H_9)_2SnO$) and Dibutyl dilaurat of tin ($(C_4H_9)_2Sn(C_{12}H_{23}O_2)_2$).	Soya oil transesterification. Molar ratio oil/ methanol/ catalyst: 100/400/1, 10 h of residence reaction time. Higher conversion (35%) for dibutyltin oxide.
Srivastava *et al* (2006)	Supported catalysts Fe-Zn in cyanidric complexes, with and without ter-buthanol (complex agent) and with a co-polymer ($EO_{20}PO_{70}EO_{20}$).	Higher activity and selectivity with complex agent in the catalytic matrix
Perin *et al* (2006)	SiO_2/H_2SO_4, SiO_2/KOH e Al_2O_3/KOH, SiO_2/HCl, $SiO_2/ZnCl_2$, $SiO_2/AlCl_3$ e Al_2O_3/H_2SO_4,	Mamona and Soya oil transesterification, with methanol, temperatures of 25ºC and 65ºC, ratio support/catalyst of 50% (w/w), ratio oil/methanol of 1:6, mass ratio of 5 g oil/0,25 g of catalyst. Best results for supported alumina catalysts for alkaline catalysis, whilst the silica catalysts showed best results for acid catalysis.
Rosa *et al* (2007)	K_2CO_3, Na_2CO_3 e $CaCO_3$	Mamona oil transesterification with methanol, ratio oil/ methanol/ catalyst of 100/600/1, reaction time of 10 h. K_2CO_3 showed best catalytic activity and higher yields in biodiesel production. $CaCO_3$ do not show any catalytic activity.
Brito *et al* (2007)	Zeolite Y	Employment of used fried oils. Good results regarding biodiesel yield.
West *et al* (2007)	ZrO_2/SO_4^{2-},	Good results at catalyst activity and in the biodiesel yield production.
Santos *et al*(2007)	Hydrotalcytes of Mg and Al (ratio Mg/Al of 3), modified with Zn, Sn, Ba, Mn, Ce and Ca, with 5% catalyst (%w/w)	Soya oil transesterification with methanol, 70ºC, reaction time of 3 h, ratio methanol/oil of 9:1. Good results regarding biodiesel yield and product quality.

Conclusions:

On a first approach, it is possible to conclude that, the main advantages of replacing the actual homogeneous catalysts by heterogeneous catalytic matrices (solids structures), concerns with the establishment of surplus-values in a process, economic and environmental points of view, in which this last one depends of minimization of waste solid and liquid production on the labour process. On another hand, it's possible affirm that, through the experimental results searched on the performed bibliographic research that, either the catalytic activity, either the biodiesel yields obtained, either the biofuel quality (fulfilment of the control quality parameters stipulated in the EN 14214 standard) were maximized with supported metallic catalysts matrices, mostly the ZrO_2/SO_4 heterogeneous catalyst matrix, for several temperatures, preferably, the higher ones, in the gap between 65 and 70ºC, with large quantities of methanol, six times higher that the vegetable oil quantity and with percentages rounded 1% of catalyst comparatively with the vegetable oil used in the transesterification process.

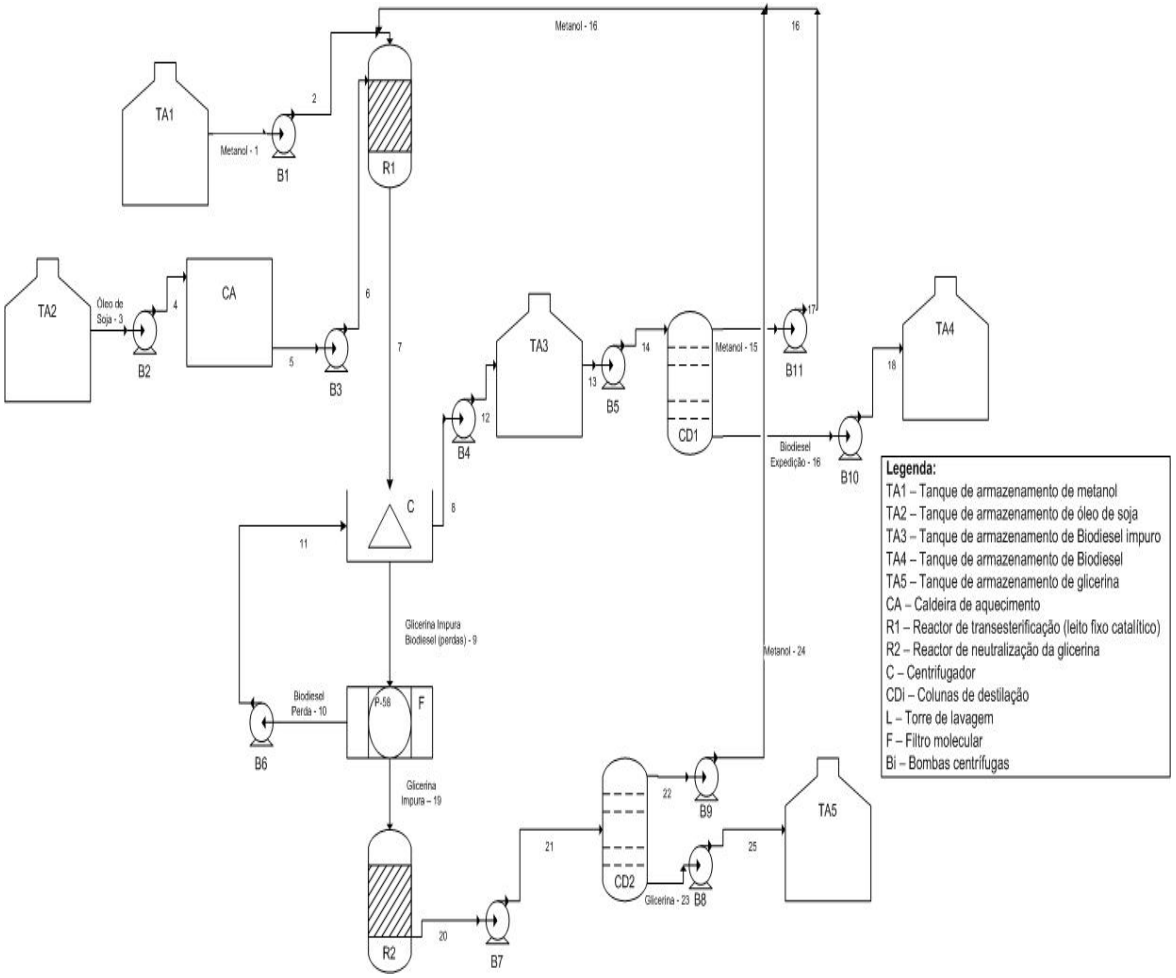

Figure 4: Previewed flowsheet for biodiesel production using heterogeneous catalysis

References:

BPR (2004), *Strategic Issues*, Department of Brazilian Republic Presidency, Biofuels, NAE copy-book – long term strategically process, Vol. 2, 83-94

Brito et al (2007), Reuse of Fried Oil to Obtain Biodiesel: Zeolites Y as a Catalyst, *International Journal of Chemical Reactor Engineering*, Vol. 5, Article A104

Kiss et al (2006), The heterogeneous advantage: Biodiesel by catalytic reactive distillation, *Topics In Catalysis*, Vol. 40, No. 1-4, 141-150

OE (2007), *Biodiesel and Sustainable Development*, Ingenium, 2nd Series, No. 99, pp. 53

Pelkmans, L et al (2007), European Biofuels Strategy, *International Journal of Environmental Studies*, Vol. 64, No. 3, 325-346

Perin et al (2006), Heterogeneous Catalysis in the transesterification of mamona and soy oils *Proceedings of 29th Annual Reunion of Chemical Brazilian Society*, Brazil

Rosa et al (2005), Synthesizing of Biodiesel by Tin (IV) complexes, *Proceedings of 3rd Brazilian Congress of Petroleum and Gas* – IBP, Brazil

Rosa et al (2006), Carbonates utilization as heterogeneous catalysts of transesterification, *Proceedings of 29th Annual Reunion of Chemical Brazilian Society*, Brazil

Santos, A. (2007), *Heterogeneous Catalysts for Biodiesel production – Metanolysis of Soy Oil over Hidrotalcytes of Magnesium and Aluminium changed*, Master Thesis on Environmental Engineering, IST/UTL, Lisbon, 2007

Srivastava et al (2006), Fe-Zn doubles metal cyanide complexes as novel, solid Transesterification catalysts, *Journal of Catalysis*, Vol. 241, Issue 1, 34-44

West et al (2007), Simulation Case Studies and Optimization of a Biodiesel Process with a Solid Acid Catalyst, *International Journal of Chemical Reactor Engineering*, Vol. 5, Article A37, 2007

Proceedings of the 10th International Chemical and
Biological Engineering Conference - CHEMPOR 2008
Braga, Portugal, September 4-6, 2008
E.C. Ferreira and M. Mota (Eds.)

MODELING AND SIMULATION OF PROCESS CONTINUOUS PRODUCTION OF BIODIESEL FROM SOYBEAN OIL USING IMMOBILIZED CANDIDA ANTARCTICA IN FLUIDIZED BED BIOREACTOR

G. F. Silva[1*], F.A. S.Mota[1], J. S. Mendes[2], L. B. R. Gonçalves[2],. A. L. O. Ferreira[2]
(Tecnologias Bioenergéticas – TECBIO)[1]
R. Rômulo Proença, S/N – Campus do Pici, NUTEC, PAR-TEC, Bloco A – Galpão 01, Pici, 60455-760 – Ceará – Brazil
(Universidade Federal do Ceará – UFC)[2]
Campus do Pici, Bloco 709, Pici, 60455-760 – Ceará – Brazil
E-mail:giovanilton@gmail.com[*]

Keywords: Biodiesel, Candida Antarctica, Fluidized Bed

Abstract

The objective this work was investigated a new route for biodiesel production using Immobilized Candida Antarctica in continuous Fluidized Bed Bioreactor. Conventionally, Biodiesel (fatty acid methyl esters) is produced by transesterification in which, oil or fat is reacted with a monohydric alcohol in presence of a catalyst. In recent years, the use of lipases as biocatalysts for biodiesel production has become of great interest due to its environment friendly. But some alcohols such as methanol inactivated the lipases to some extent and the enzymatic stability was poor. In order to enhance the stability of the lipase, three-step methanolysis was adopted, however, glycerol, as one of the products was easy to adsorb on the surface of lipase resulting in serious negative effect on the enzymatic activity. For to solve problems was used the interesterification kinetics of triglycerides and methyl acetate for biodiesel production was modeled. A heterogeneous model describing the interesterification process in an immobilized enzyme fluidized-bed bioreactor was developed. A simplified model based on Ping Pong Bi Bi with substrate competitive inhibition mechanism was proposed to describe the reaction kinetics of the interesterification.The model without any adjustable parameters was used to predict the interesterification process. The key parameters which measured the extent of external and internal mass-transport resistances, as well as the degree of back-mixing were quantified and discussed. The fluidized-bed bioreactor considered in this investigation is composed of two phases: a fluid phase comprised mainly of the triglycerides and methyl acetate and the product (Biodiesel); and a solid phase which is the immobilized enzyme. The effects of some operating and design parameters on the performance of the fluidized-bed bioreactor were also analyzed. The model was also tested for its sensitivity to changes in hydrodynamic parameters.

1 Introduction

Biodiesel is mono-alkyl esters of long chain fatty acids derived from renewable vegetable oils and animal fats. Biodiesel (fatty acid methyl esters) is produced by transesterification in which, oil or fat is reacted with a monohydric alcohol in presence of a catalyst. In the transesterification of vegetable oils, a triglyceride reacts with an alcohol in the presence of a strong acid or base, producing a mixture of fatty acids alkyl esters and glycerol. The overall process is a sequence of three consecutive and reversible reactions, in which monoglycerides are formed as intermediates. The stoichiometric reaction requires 1 mol of a triglyceride and 3 mol of the alcohol. However, an excess of the alcohol is used to increase the yields of the alkyl esters and to allow its phase separation from the glycerol formed. The alcohols employed in the transesterification are generally short chain alcohols such as methanol, ethanol, propanol butanol, and methyl acetate.

Biodiesel has become more attractive recently because of its environmental benefits and the fact that it is made from renewable resources (Schuchardt et al., 1998). The

transesterification of vegetable oils with methanol or ethanol as well as the main uses of the fatty acid methyl esters are studied in this paper. The general aspects of this process and the applicability of different types of catalysts (acids, alkaline metal hydroxides, alkoxides and carbonates, enzymes and non-ionic bases, such as amines, amidines, guanidines and triamino(imino)phosphoranes) (Jordan and Gutsche, 2001; Fangrui and Hanna, 1998; Filippis et al., 1995; Antolín et al., 2002) are described, and ambient or elevated pressures and temperatures.

Conventionally, biodiesel was produced by transesterification of triglycerides and alcohols in the presence of an acid or an alkaline catalyst. In recent years, the use of lipases as biocatalysts for biodiesel production has become of great interest due to its environment friendly. However, some alcohols such as methanol inactivated the lipases to some extent and the enzymatic stability was poor. In order to enhance the stability of the lipase, three-step methanolysis was adopted, however, glycerol, as one of the productswas easy to adsorb on the surface of lipase resulting in serious negative effect on the enzymatic activity Xu et al (2003), Dossat et la (1999) and Du et al (2004).

In order to solve the above-mentioned problems, we previously reported that using methyl acetate as acyl acceptor instead of methanol for biodiesel production could enhance the stability of the lipase significantly and in the process, triacetylglycerol instead of glycerol would be produced and it has been demonstrated that triacetylglycerol had no negative effect on the activity of the lipase. Moreover, triacetylglycerol was an important by-product with a higher value than glycerol and this novel route was thought to be very promising for large scale production of biodiesel.

2. Model Development

2.1 Kinetic Model

The enzymatic model used to describe the interesterification kinetics was based on the model Ping Pong Bi Bi with competitive inhibition for the substratum. The equation of that mechanism is shown:

$$V_i = \frac{V_{\max}[TG][AM]}{K_{M_{TG}}[AM]\left(1+\frac{[MA]}{K_I}\right)+K_{M_{AM}}[TG]+[TG][AM]} \quad (2.1)$$

where V_i was the initial reaction rate; [TG] and [A] the initial molar concentrations of triglycerides and methyl acetate, respectively; K_{mTG} and K_{mA} the apparent Michaelis constants for triglycerides and methyl acetate, respectively; K_i the apparent inhibition constant of methyl acetate and Vmax the initial maximum velocity of the reaction. The kinetic constants are shown in Table 2.1 Xu et al (2005).

Parameters	Value
V_{max} (mol/lmin)	1.9
K_{mTG} (mol/l)	1.0
K_{mA} (mol/l)	16
K_i (mol/l)	0.0455

2.2 Solid Phase Mass Balance

The fluidized-bed bioreactor considered in this investigation is composed of two phases: a fluid phase comprised mainly of the substrate (oil and methyl acetate) and the product (Biodiesel); and a solid phase which is the immobilized enzyme. The following assumptions are employed in the model: (1) the system is isothermal; (2) the movement of reactant within the biocatalyst can be described mathematically by Fick's law of diffusion where the effective diffusion coefficient is constant and independent of concentration; (3) the enzyme activity is uniform throughout the particle; (4) the fluid phase back-mixing can be quantified by an axial dispersion coefficient.

The general mass balance equation governing the concentration distribution in the fluid phase of the biocatalyst is given by:

$$D_L \frac{d^2 C_f}{dZ^2} - U_0 \frac{dC_f}{dZ} - (1-\varepsilon) r_V \tag{2.2}$$

and the Danckwert's boundary conditions are:

$$when\ Z = 0,\ -D_L \frac{dC_f}{dZ} + UC_f = UC_f \tag{2.3}$$

$$when\ Z = L,\ \frac{dC_{x,P,S}}{dZ} = 0 \tag{2.4}$$

This set of boundary conditions, that is equations 7 and 8, is widely used in modeling immobilized enzyme fluidized-bed bioreactors

2.3 Solid Phase Mass Balance

The general mass balance equation governing the concentration distribution in the fluid phase of the biocatalyst is given by equation 2.5.

$$\frac{dC_s}{dZ} = k_m (C_f - C_s) \tag{2.5}$$

with the boundary conditions given by:

$$when\ Z = 0,\ C_s = 0 \tag{2.6}$$

2.4 Evaluation of the relevant parameters

The relevant parameters relating to the dispersion coefficient, external mass-transfer resistance and bed voidage are evaluated using correlations obtained from the literature and are given below.

2.4.1 Dispersion coefficient

The dispersion coefficient, D_L, in the fluidized-bed containing light, non-porous, solid particles was evaluated using the correlation of Tang and Fan (1990) given by Equation (2.7) below.

$$D_L = \frac{U_0 H}{Pe} \tag{2.7}$$

$$\frac{1}{Pe} = 4.35 \left(\frac{\rho_s}{\rho_f} \right)^{2.64} \varepsilon^{1.467} \tag{2.8}$$

The external particle-liquid mass-transfer coefficient was obtained using the correlation of Nore et al. (1992) given by:

$$k_m = 1.1 \left(\frac{U_0}{\varepsilon} \right)^{0.43} D_p^{0.24} \tag{2.9}$$

The bed porosity in the bed is determined by the mechanics of fluidization. Hence, a realistic mathematical expression for the bed fluidization is necessary. For bed of uniform spherical particles, the following relation was proposed. The Richardson and Zaki (1954) relates bed voidage to the upflow superficial liquid velocity given as:

$$\varepsilon = \left(\frac{U_0}{U_t} \right)^{1/n} \tag{2.10}$$

The terminal velocity given by Equation (2.11) was obtained using the correlation of Khan and Richardson (1990).

$$U_t = \frac{\mu}{\rho_f D_p} \left(2.33 Ga^{0.018} - 1.53 Ga^{-0.016} \right)^{13.3} \tag{2.11}$$

where

$$Ga = \frac{\left(\rho_s - \rho_f\right)\rho_f D_p^3 g}{\mu^2} \tag{2.12}$$

The fractional conversion, Y, shown in Fig. 1 against the flow rate is defined by Equation (2.13).

$$Y = \frac{C_0 - C_L}{V_{\max} L/u} = \frac{X}{\theta} \tag{2.13}$$

where θ dimensionless residence time.

3. Results and Discussion

The modeling equations presented here constitute a system of non-linear boundary value problems which were solved by finite difference techniques. The details of solution methodology are omitted here for the sake of brevity.

Figure 1 shows the concentration of each composition triglycerides, methyl acetate and biodiesel against the height of the fluidized bed. From the Figure 2, it can be observed that, the model indicate the high concentration of biodiesel were reached in the end of the reactor. Indicating that the dispersion has influences in the interesterification of triglycerides for biodiesel production with methyl acetate.

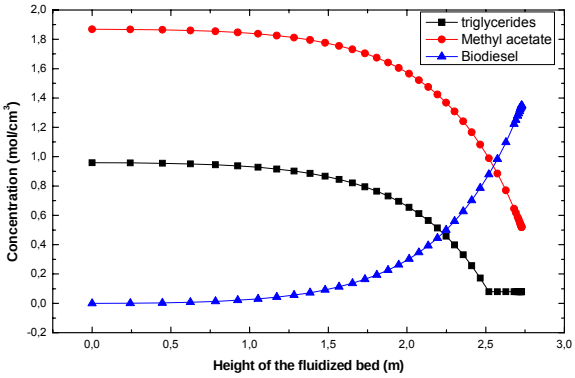

Figure 1: The concentration of triglycerides, methyl acetate and biodiesel.

The Figure 2 show the conversions obtained for the model for fluidized bed in function of the dimensionless residence time. It can be observed that the measure that the dimensionless residence time increases the values of the conversions increased. Therefore, they are high necessary times of residence for the reactor to reach high conversions.

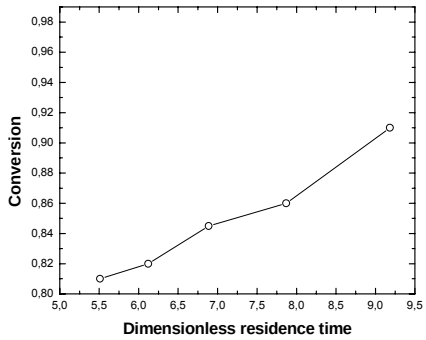

Figure 2: Conversion in fluidized bed bioreactor

Another parameter of common interest in the design of fluidized bed reactors is the Peclet number which is the measure of the degree of back-mixing in the flow vessel. As the Peclet number approaches infinity plug-flow behavior is approached, while complete mixing is approached for a Peclet number approaching zero. It is obvious from the plot of Peclet number against the dimensionless residence time. The according Equations 2.7 and 2.8 when the value the Peclet increases the dispersion coefficient value decrease. This is also indicative of dominance of mixing over segregation. Thus, the conversion increases when the value de Peclet increases.

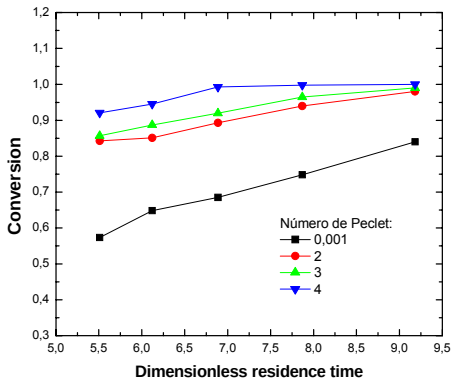

Figure 3: Effect of number of Peclet on the conversion de the fluidized bed.

4. Conclusions

In this work a continuous fluidized bed bioreactor model with Immobilized Candida Antarctica in continuous Fluidized Bed Bioreactor was developed for simulating the steady-state performance of a bioreactor for production biodiesel.

It was examined effect Peclet number and dimensionless residence time at conversion in fluidized bed. It the Peclet number decreases with the increase conversion production of biodiesel. It can be observed that conversion increased when the dimensionless residence time increased.

The model can be used to simulate the biodiesel production by interesterification in fluidized bed bioreactor and the results of the simulation were satisfactory.

References

Antolín, G., Tinaut, F. V., Briceño, Y. et alii (2002). Optimisation of biodiesel production by sunflower oil transesterification. Bioresource Technology, 83, 111-121.

Dossat, V.; Combes, D.; Marty, A. (1999) Lipase-catalysed transesterification of high oleic sunflower oil, Enz. Microb. Technol., 30 (1), 90-94.

Du, W.; Xu, Y. Y.; Liu, D. H.; Zeng, J. (2004) Comparative study on lipase-catalyzed transformation of soybean oil for biodiesel production with different acyl acceptors. Journal Molecular. Catalysis . B: Enzyme., 30 (3-4), 125-129.

Khan, A. R. & Richardson, J. F. (1990). Pressure gradient and friction factor for sedimentation and fluidization of uniform spheres in liquidg Chem. Engng. Sci., 45, 255-265.

Fangrui, M., Hanna, M. A. (1998). Biodiesel production: a review. Bioresource Tecnology, 70, 1-9.

Filippis, C. G. Scarsella, M., Sorrentino, M. (1995). Transesterification process for vegetable oils: A simple control method of methyl ester content. Journal American Oils Chemistry Society, 72, 1399-1407-1415.

Jordan, V., Gutsche, B. (2001). Development of environmentalyy benign processes for the production of fatty acid methyl esters. Chemosphere, 43, 99-108.

Nore, O., Briens, C., Margarilis, A. & Wild, G. (1992). Hydrodynamics, gas-liquid mass transfer and particle liquid heat and mass transfer in a three-phase fluidized bed for biochemical process application. Chem. Engng. Sci., 47, 3573-3580.

Richardson, J. F. & Zaki, W. N. (1954). Sedimentation and fluidization: Part I~ Trans. Inst. Chem. Engrs., 32, 35-53.

Schuchardt, U., Sercheli, R., Matheus, V. R. (1998). Transesterification of vegetable oils: a Review. Journal of the Brazilian Chemical Society, 9, 199.

Tang, W. T. & Fan, L. S. (1990). Axial liquid mixing in liquid-solid and gas-liquid fluidized-beds containing loq density particles. Chem. Engng. Sci., 45, 543-551.

Xu, Y. Y.; Du, W.; Liu, D. H.; Zeng J. (2003), A novel enzymatic route for biodiesel production from renewable oils in a solvent-free medium. Biotechnology letters, 25 (15), 1239-1241.

Xu, Y. Y.; Du, W.; Liu, D. H. (2005), Study on the kinetic of enzymatic interesterification of triglycerides for biodiesel production with methyl acetate as the acceptor. Journal Molecular. Catalysis . B: Enzyme., 32, 241-245.

Proceedings of the 10th International Chemical and
Biological Engineering Conference - CHEMPOR 2008
Braga, Portugal, September 4-6, 2008
E.C. Ferreira and M. Mota (Eds.)

Kinetic models for the homogeneous alkaline and acid catalysis in biodiesel production

José F.O. Granjo[1], Nuno M.C. Oliveira[1*]
[1] GEPSI – PSE Group, Department of Chemical Engineering, University of Coimbra
Rua Sílvio Lima – Pólo II, 3030–790 Coimbra, Portugal.

Keywords: Biofuels, Biodiesel, Reaction engineering, Kinetic models
Topic: Sustainable process-product development through green chemistry.

Abstract

In this work, kinetic models were obtained from experimental data in the open literature, for both the alkaline (NaOH) and acid (H_2SO_4) homogeneous catalysis of the transesterification reaction used to produce biodiesel from vegetable oils. Two approaches, here designated as statistical and empirical, were adopted to obtain these models. For the alkaline catalysis, the results show that kinetic models fitted better a pseudo 2nd-order reaction, presenting an average error of 4% and 4.5%, using the empirical and the statistical approaches, respectively. In the acid catalysis, the kinetic models obtained fitted better a pseudo 1st-order reaction and presented average errors of 7.2% and 5.9%, also using the empirical and the statistical approaches, respectively.

1 Introduction

Currently, the transport activity in the EU accounts for approximately 30% of the total energy consumption, and is responsible for 67% of the oil demand. Consequently, oil prices and energy dependences assume a significant impact on the countries' GDPs, and represent an ever-increasing geostrategic weakness. To mitigate this, and also to comply with the Kyoto's protocol, the European Directive 2003/30/EC, transposed to Portuguese legislation in 2006, established a series of measures to promote a more intense use of biofuels, in order to attain a share of 5.75% in the transport sector, by 2010. The use of biodiesel (a mixture of fatty acid methyl esters) is one possible and attractive alternative to fossil fuels, because of its simple and established technology, and high combustion efficiency.

Biodiesel can be produced from distinctive renewable sources (edible and non-edible), e.g., greases, vegetable oils or animal fats, through a transesterification reaction with methanol, leading to glycerol as a main by-product, also with some interesting industry applications. Many process alternatives are available for biodiesel production, which can be classified by type of catalytic system used in transesterification reactions: homogeneous – alkaline or acid; heterogeneous – alkaline, acid or enzymatic; non-catalytic – supercritical alcohol. Numerous studies regarding the kinetics of transesterification and other aspects of the biodiesel production technology have been made; critical reviews by van Gerpen (2005), Sharma et al. (2008) and Vasudevan and Briggs (2008) are also available. Despite the considerable amount of work done relative to the kinetics of this system, no systematic study, which integrates experimental results from different authors, is available at the moment, in the open literature. This makes it hard to compare the performance of different catalysts at diverse reaction operation conditions, and difficults the comparison of alternative design configurations and set-up conditions for this process, based on systematic process optimization methodologies.

* Corresponding author. Tel + 351-239-798700. E-mail: nuno@eq.uc.pt

The goal of the present work is therefore to provide some preliminary results relative to kinetic models derived from experimental data available in the open literature, for the transesterification reaction of vegetable oils, through homogeneous alkaline and acid systems (the most common technologies used in industry).

Assumptions and considerations

Previous works (Noureddini and Zhu, 1997; Zheng *et al.*, 2006) studied the mass transfer limitations in the reaction's kinetics and concluded that the heterogenous effect is more pronounced for low intensity mixing rates and at the beginning of the reaction, leading to the formation of a lag phase and lower reaction rates. However, they also noted that with an intense mixing intensity (N_{Re}>6000) and with the formation of biodiesel (an emulsion agent), the reaction will be chemically controlled, and therefore the mass transfer resistance between the oil and alcohol phases is no longer important. Therefore, in this situation the reactant mixture can be considered as pseudo-homogeneous.
As described in Ma and Hanna (1999), the alcoholysis reaction consists in a group of parallel and reversible reactions. To prevent low yields of biodiesel and to avoid the formation of intermediary chemical components, an excess of alcohol is normally used, to push the equilibrium towards the products. Normally, a minimum molar ratio methanol/oil of 6:1 is chosen, making the reaction behave as practically irreversible, with a pseudo single step mechanism (Freedman *et al.*, 1984).
Freedman *et al.* (1984), Ma and Hanna (1999), and Canacki and van Gerpen (1999) reported that the free fatty acid (FFA) and water contents can have a significant inhibition effect on the reaction, for both catalysis types. In the alkaline catalysis, it was stressed that the FFA and water contents in oil should be below 0.5 % (w/w) and 0.3 % (w/w), respectively, to avoid soap formation that consumes catalyst and reduces the yield. With the acid catalysis, it was concluded that water and FFA strongly inhibit the reaction for concentrations above 0.5 % (w/w) and 5% (w/w), respectively. Water promotes the hydrolysis of triglycerides, fatty acids or esters, which is undesirable because it reduces the conversion efficiency of biodiesel. Hence, in industry, pretreatments are usually included to eliminate water and FFA in the transesterification reactors, preventing this negative effect (Zhang *et al.*, 2003).
To obtain kinetic expressions for the acid and alkaline catalysis as functions of the operating variables, the following major assumptions were considered: intense mixing rate; excess of methanol; negligible water and free fatty acid contents. Literature data was selected to fulfill the former conditions; consequently, the kinetic models obtained are only applicable to those situations.

Problem Formulation

We now describe the procedure used to obtain the kinetic models for the acid and alkaline homogenous catalysis. Considering the conversion of the limiting reactant (A), the mass balance for a batch system with a *nth* order of reaction is:

$$\frac{dX}{dt} = -kC_{A0}^{n-1}X \qquad (1)$$

At constant temperature, for the 1st and 2nd orders, if the initial time and conversion are both zero, k can be evaluated using values of conversion X_i and time t_i from

$$k_i' = \frac{-\ln(1-X_i)}{t_i} \quad [\text{min}^{-1}] \quad (2); \qquad k_i'' = \frac{X_i}{(1-X_i)C_{A0,i}t_i} \quad [\text{min}^{-1}\times\text{w(oil+methanol)/w oil}] \quad (3)$$

These expressions were used with available experimental data and fixed operating variables, such as temperature (T) in ºC, catalyst concentration in %(w/w oil) (xa) and dimensionless molar ratio methanol/oil (xm). In this case, oil is the limiting reagent, since an excess of methanol is used, and therefore C_{oil0} is used instead of C_{A0}, defined in mass units.

Two approaches, here designated as *statistical* and *empirical*, were used to fit the experimental data to the mathematical models, for each catalysis type. In the *statistical approach*, each experimental data set was used to fit the dependent variables to a set of possible predictors, using linear regression. The dependent variables considered were the kinetic constants for first (***K'***) and second (***K''***) order reactions, and their respective logarithmic transformations. As predictors, the main operating variables (***T***, ***xa***, ***xm***) and various transformations of them were considered, as shown in Table 1.

Table 1. *List of dependent variables and predictors used in the statistical analysis.*

Dependent variables	Predictors		
K'	T	xa	xm
K''	$(T+273.15)^{-1}$	xa^2	xm^2
$Ln(K')$	$Ln(T)$	$Ln(xa)$	$Ln(xm)$
$Ln(K'')$	$\sqrt{T}$	$\sqrt{xa}$	$\sqrt{xm}$
	T^2		

For each dependent variable (***Y)*** a multivariable linear regression was computed (4) with STATISTICA 7, using a forward stepwise regression procedure for variable selection, including the intercept (β_0). This guarantees that only predictors that showed statistically significant regression coefficients with a p-value of 0.05 were included in the final model. Data points that presented a standard residual greater than 2σ were considered outliers, and were consequently eliminated from both strategies.

$$Y = \beta_0 + \sum_{j=1}^{n} \beta_j X_j \tag{4}$$

In the *empirical approach*, models were obtained from a postulated general form of reaction kinetics for all species:

$$r_j = \alpha_j k(T) \prod_{i=1}^{n} (a_i^{\beta_i}) \tag{5}$$

$$a_i = \gamma_i C_i \tag{6}$$

Here β_i and α_i are, respectively, the reaction order and the stoichiometric coefficient of component *i*. If the reaction is taking place in a pseudo-homogeneous medium, from (5) and (6) we obtain:

$$r_j = \alpha_j k(T) \prod_{i=1}^{n} (\gamma_i^{\beta_i}) \prod_{i=1}^{n} (\theta_i + \frac{\alpha_i}{(-\alpha_a)} X)^{\beta_i} C_{AO}^{(\sum_{i=1}^{n} \beta_i)} \tag{7};$$

$$\theta_i = C_{io} / C_{Ao} \tag{8}$$

The activity coefficient γ_i describes the solution non-ideality, which we empirically relate with ***xa*** and ***xm***. Expressing $k(T)$ in Arrhenius law form, and considering the effects of ***xa*** and ***xm*** independent from each other, $K(T, xa, xm)$ can be expressed as:

$$K(T, xa, xm) = A e^{\frac{-Ea}{R \times (T+273.15)}} \prod_{i=1}^{n} (\gamma_i^{\beta_i}) = f(T) \times f(xa) \times f(xm) \tag{9}$$

$$r_j = \alpha_j K(T, xa, xm) \prod_{i=1}^{n} (\theta_i + \frac{\alpha_i}{(-\alpha_a)} X)^{\beta_i} C_{AO}^{(\sum_{i=1}^{n} \beta_i)} \tag{10}$$

Expression (10) can be simplified if all except one reactant (*A*) are in excess. In our case C_{A0} is replaced by C_{oil0} and the order of reaction β_A can be 1 or 2. Therefore:

$$r_j = \alpha_j K(T, xa, xm) C_{oil0} (1 - X)^{\beta_A} \tag{11}$$

A first estimate of $K(T, xa, xm)$ can be obtained through evaluation of the functions $f(T)$, $f(xa)$ and $f(xm)$ from careful chosen subsets of experimental data, changing only one variable at a time. For instance, considering a first order reaction in the acid catalysis, in order to obtain $K(T, xa, xm)$, $f(xm)$ can be determined by choosing data with $f(xa = 3)$ and $f(T = 60)$. Then for each run, $f(xm_i) = k_i'$ was considered. Here the program

CurveExpert® v1.3 was used for a rapid screen of various function families, in order to find the one that coud better fit the data. After $f(xm)$ was determined, $f(T)$ was obtained similarly, where for each run $f(T_i) = k_i' / f(xm_i)$ was considered. This was achieved with a linearization of the Arrhenius equation, leading to the values of the parameters ***A*** and ***Ea***. This sequential methodology allowed therefore a first guess of the function $K(T, xa, xm)$ for both types of catalysis, considering either first or second reaction orders. In these cases, the conversion of the reaction is given by:

$$X = (1 - e^{-K(T,xa,xm)t}) \qquad (12); \qquad X = \frac{K(T,xa,xm)C_{oil0}t}{1 + K(T,xa,xm)C_{oil0}t} \qquad (13)$$

The kinetic constant in (12) is given in *min*$^{-1}$ and in (13) is in *min*$^{-1}$× *(w(oil+methanol))/w oil*. The values obtained during this phase were afterwards used as initial guesses for a rigorous nonlinear regression of (11), considering all data points simultaneous. This was performed in *Mathematica 6*. After the kinetic models were obtained, the predicted and experimental conversions were compared for each run, and the mean relative errors were evaluated for each model, again considering first and second order reaction orders.

Results

In the acid catalysis, all studies used sulfuric acid; experimental values from Freedman *et al.,* (1984), Canacki and van Gerpen (1999), Goff *et al.* (2004), and Zheng *et al.* (2006) were considered. The regression results obtained are summarized below.

Table 2. *Mean relative error and correlation factors for acid catalysis using a statistical and an empirical strategy and considering a pseudo 1st and 2nd order.*

	1st order		2nd Order	
	Empirical	**Statistical**	**Empirical**	**Statistical**
Mean error / %	7.171	5.925	12.87	5.531
R^2 f(T)	0.9830	-	0.9996	-
R^2 f(xa)	0.8829	-	0.2931	-
R^2 f(xm)	0.9922	-	0.9565	-
R^2 K(T,xa,xm)	-	0.9866	-	0.9614

Table 2 shows that data from literature fits better to a 1st order kinetic model, since the mean error considering the average obtained for both strategies is lower and the correlation factors are consistently higher. The 1st order kinetic model expression obtained in the statistical approach is in (14) and expressions (15) to (17) are relative to the empirical approach. Using these expressions with the parameter values of Table 3 and (12) it is possible to calculate the time dependence of the with a given set of operating conditions (*T,xa,xm*).

$$K(T, xa, xm) = e^{(\beta_0 + \beta_1\sqrt{T} + \beta_2 T^2 + \beta_3\sqrt{xa} + \beta_4 \ln(xa) + \beta_5 \ln(xm))} \qquad (14)$$

$$f(T) = \beta_0 e^{\frac{-\beta_1}{(T+273.15)}} \qquad (15); \qquad f(xa) = \beta_0 - \beta_1 e^{-\beta_2 xa} \qquad (16); \qquad f(xm) = \beta_0 - \beta_1 e^{-\beta_2 xm} \qquad (17)$$

The alkaline catalyst studied here was sodium hydroxide and the experimental data was retrieved from Freedman *et al.* (1984), Noureddini and Zhu (1997), Jeong *et al.* (2004) and Leung and Guo (2006). Because in most kinetic studies with alkaline catalysis, *xm*=6 (methanol/oil=6:1), therefore *f(xm)=1* for all experiments which means that the kinetic constant will be only a function of the temperature and catalyst concentration (*K(T,xa)*). Table 4 presents the correlation factors and the mean relative error of the values predicted by each kinetic model, relatively to literature data.

Table 3. *Parameter values for expressions (14) to (17) considering a 1st order reaction, using data from Freedman et al. (1984), Canacki and Gerpen (1999), Goff et al. (2004) and Zheng et al. (2006).*

	Empirical			Statistical
	f(T)	***f(xa)***	***f(xm)***	***K(T,xa,xm)***
β_0	1.195E12	1.38382E0	2.088E-4	-1.586E1
β_1	9.189E3	1.378E0	1.721E-3	9.148E-1
β_2	-	3.357E-1	3.282E-2	1.971E-4
β_3	-	-	-	4.978E-1
β_4	-	-	-	1.131E0
β_5	-	-	-	2.792E-1

Table 4. *Mean relative error and correlation factors for alkaline catalysis using a statistical and an empirical strategy, and considering a pseudo 1st and 2nd order.*

	1st order		2nd Order	
	Empirical	**Statistical**	**Empirical**	**Statistical**
Mean error / %	8.542	8.564	4.029	4.512
R^2 f(T)	0.6216 0.7232	-	0.9003 0.9257	-
R^2 f(xa)	0.8067	-	0.9869	-
R^2 k	-	0.9309	-	0.9716

In Noureddini and Zhu (1997) the temperature effect is studied for a catalyst concentration of *xa*=0.2% (m/m oil), while other authors used *xa*=1%. To account all of these experiments, the *f(T)* function in the empirical approach was obtained for each of these catalyst concentrations, and a mean value of E_a was considered at the end. After the function f(xa) was obtained, the pre-factor *A* was re-estimated using (18), by calculating the mean value of *np* experimental values K_{exp} at a central set of operating conditions (*T*=60ºC, *xa*=1). Note that K_{exp} is evaluated from experimental data using expressions (2) or (3), depending on whether a 1st or 2nd pseudo-order kinetic reaction is considered, respectively. Again, these values were considered as initial estimates in a simultaneous nonlinear regression of all data, in the empirical approach.

Table 4 shows that data from literature fits better to a 2nd order kinetic model, since the mean error for both strategies is lower and the correlation factors are higher. The 2nd order kinetic model expression obtained in the statistical approach is in (19) and expressions (21) to (23) are relative to the empirical approach. Using these expressions with the parameter values of Table 5 and (13) it is possible to calculate the time dependence of the conversion with a given set of operating conditions (*T,xa*).

$$A = \frac{\sum_{i}^{np} K_{\exp,i}(T = 60^{o}C, 1\ \%(\text{m/m oil}))}{np \exp(T = 60) f(xa = 1)} \tag{18}$$

$$K(T, xa) = e^{(\beta_0 + \beta_1 \sqrt{xa} + \beta_2 \ln(T))} \tag{19}$$

$$f(T) = \beta_0 e^{\frac{-\beta_1}{(T + 273.15)}} \quad (20); \qquad f(xa) = \beta_0 + \beta_1 xa + \beta_2 xa^2 + \beta_3 xa^3 \quad (21); \qquad f(xm) = 1 \quad (22)$$

$$K(T, xa, xm) = e^{(\beta_0 + \beta_1 \sqrt{T} + \beta_2 T^2 + \beta_3 \sqrt{xa} + \beta_4 \ln(xa) + \beta_5 \ln(xm))} \tag{23}$$

Table 5. *Parameter values for the expressions (19) to (21) considering a 2nd order reaction, using data from Freedman et al.(1984), Noureddini and Zhu(1997), Leung and Guo(2006), and Jeong et al. (2004).*

	Empirical		Statistical
	F(T)	**F(xa)**	**K(T,xa)**
β_0	1.852E7	-1.090E-1	-1.277E1
β_1	5.575E3	2.333E0	4.303E0
β_2	-	-5.331E0	2.200E0
β_3	-	4.796E0	-

Conclusions

The results obtained show that for the acid catalysis (H_2SO_4) the best models assume a pseudo 1st-order reaction and were obtained, respectively, with a statistical and empirical approaches, with mean errors of 7.2% and 5.9%. In the alkaline catalysis with NaOH, the models fitted better assuming a 2nd pseudo-order reaction, with a mean error of 4% and 4.5%, also with the empirical and statistical approaches, respectively. This study is being extended to other alkaline catalysts, such as KOH, $NaOCH_3$ and $KOCH_3$, with the introduction of a catalytic activity correction factors in the kinetic models.

References

Canakci, M., van Gerpen, J. (1999). Biodiesel Production Via Acid Catalysis. *Transactions of the American Society of Agricultural Engineers*, 42(5), 1203-1210.

Freedman, B., Pryde, E.H., Mounts, T.L. (1984). Variables affecting the yields of fatty esters from transesterified vegetable oils. *Journal of the American Oil Chemists' Society*, 61(10), 1638-1648.

Goff, M.J., Bauer, N.S., Lopes, S., Sutterlin, W.R., Suppes, G.J. (2004). Acid-Catalyzed Alcoholysis of Soybean Oil. *Journal of the American Oil Chemists' Society*, 81(4), 415-420.

Jeong, G.T., Park, D.H., Kang, C.H., Lee, W.T., Sunwoo, C.S., Yoon, C.H., Choi, B.C., Kim, H.S., Kim, S.W., Lee, U.T. (2004). Production of Biodiesel Fuel by Transesterification of Rapseed Oil, *Applied Biochemistry and Biotechnology*, 113-166, 747-758.

Leung, D.Y.C., Guo, Y. (2006). Transesterification of neat and used frying oil: Optimization for biodiesel production. *Fuel Processing Technology*, 87, 883-890.

Ma, F., Hanna, M.A. (1999). Biodiesel production: a review, *Bioresource Technology*, 70, 1-15.

Noureddini, H., Zhu, D. (1997). Kinetics of Transesterification of Soybean Oil, *Journal of the American Oil Chemists' Society*, 74(11), 1457-1463.

Rashid, U., Anwar, F. (2008). Production of biodiesel through optimized alkaline-catalyzed transesterification of rapeseed oil. *Fuel*, 87, 265-273.

Sharma, Y.C., Singh, B., Upadhyay, S.N. (2008). Advancements in development and characterization of biodiesel: A review. *Fuel*, doi:10.1016/j.fuel.2008.01.014.

van Gerpen, J. (2005). Biodiesel Processing and Production, *Fuel Processing Technology*, 86(10), 1097-1107.

Vasudevan, P.T., Briggs, M. (2008). Biodiesel production – current state of the art and challenges. *Journal of Industrial Microbiology & Biotechnology*, doi:10.1007/s10295-008-0312-2.

Zhang, Y., Dubé, M.A., McLean, D.D., Kates, M. (2003). Biodiesel production from waste cooking oil: 1. Process design and technological assessment, *Bioresource Technology*, 89, 1-16.

Zheng, S., Kates, M., Dubé, M.A., McLean, D.D. (2006). Acid-catalyzed Production of Biodiesel from Waste Frying Oil. *Biodiesel and Bioenergy*, 30(3), 267-272.

Proceedings of the 10th International Chemical and
Biological Engineering Conference - CHEMPOR 2008
Braga, Portugal, September 4-6, 2008
E.C. Ferreira and M. Mota (Eds.)

On line monitoring of the transesterification reaction

Flávio Vasconcelos da Silva[1], Ana Maria Frattini Fileti[2], Lílian C. Roder[3], Marcelle Fernanda Carulo [4*]

[1,2,3,4] School of Chemical Engineering, Departament of Chemical Systems Engineering, State University of Campinas (UNICAMP),13083-970, São Paulo, Brazil.

Keywords: On line monitoring, Biodiesel, Viscosity, Fieldbus, rate of conversion
Topic: Sustainable process-product development through green chemistry

Abstract

Biodiesel is defined as the primary alkyl esters of long-chain fatty acids produced from renewable sources, such as vegetable oil or animal fats; it is intended to use in compression-ignition engines. In this work, biodiesel is obtained from soy oil refined by transesterification with ethanol and an acidic catalyst. The process is carried out in a batch stirred tank (1000 mL) with jacked cooling. Samples containing soy oil and ethanol (99.5%) are fed to the tank. The final result in the batch is the conversion of about 94-99% of the mixture into ethyl esters. Conventional analytical methods for the evaluation of the ethyl ester content are becoming common but, the time required for the analysis is long, and the on-line application in a transesterification plant is very difficult. This work aims to develop a quick method to give an indication of the ethyl esters content in a transesterification product to be used as a process control. The literature has revealed that the rate of reaction can be related to its kinematical viscosity. The use of Coriollis effect-based flow meters and the additional differential pressure transmitter makes possible to measure the viscosity of laminar flow of Newtonian fluid.

1 Introduction

One of the main problems in the study or in the industrial application of transesterification process for vegetable oils is how to measure the bio diesel content. Conventional analytical methods for the evaluation of the ethyl esters content are based on gas-liquid chromatography, or thin-layer chromatography/flame-ionization detector, high performance liquid chromatography and gel permeation chromatography systems.

Unfortunately these methods have some drawbacks – their results are often unreliable or directly misleading and high accuracy is required during sample preparation; moreover, chemical modification of the sample is often necessary for analysis, and the time required for the analysis is usually long (Fillipis et al., 1995). In this study, an experimental control method of ethyl esters content was applied using industrial transducers. This methodology involves the design of the viscometer system. This viscosity difference is sufficient to give an indication of the biodiesel content in a transesterification product.

2 The transesterification process

In Brazil, transesterification reaction has been extensively investigated due to addition in petroleum – derived diesel fuel. There are several advantages in using bio diesel; these are: lower concentration of sulphur compounds, carbon dioxide and aromatic polycyclic burned in diesel engines (Knothe *et al.*, 2006).

* Corresponding author. Tel + 55 19 35213969. E-mail:carulo@feq.unicamp.br

The use of vegetable oils in diesel engines is limited due to high viscosity. The transesterification process results in a lower viscosity through separation of glycerol by conversion of fatty acids to ethyl esters (Barnwal & Sharma, 2004). The viscosity is on of most important properties of fuels and it will determine the combustion quality. The highest viscosity of bio diesel when compared to diesel –petroleum is what makes the fuel more lubrificant; however, it results in a lower efficiency during the combustion process in diesel engine (Vicente *et al*., 2006; Knothe & Steidley, 2005).

Tate *et al.* (2006) obtained kinematic viscosity experimental values of biodiesel produced by canola oil, soy oil and fish oil in a range of temperatures of 20ºC until 300ºC. He noticed the viscosity decreased with an increase of temperature following a logarithmic equation.

Is very difficulty to determine the on – line viscosity in a transesterification process, therefore, various methods were studied to correlate the kinematics' viscosity with methyl/ethyl ester produced (Knoth & Steidley, 2005). A different level of viscosity in bio diesel was studied at 40ºC, in several compositions of it. It was concluded that the viscosity of bio diesel decreases significantly with an increase of in saturation of compounds and the presence of glycerides affects the viscosity measurement (Allen *et al.*, 1999). Similar results were obtained by Krisnangkura *et al.* (2006). He predicted the values of bio diesel viscosity at composition $C_{12:0}$ -$C_{18:0}$ in many temperatures. He noticed that this method provided good results when it is compared to experimental values of biodiesel produced from palm oil and cocoa oil.

2.1 Batch Transesterification Tank

The transesterification process is carried out in a batch stirred heater tank (1000mL), at 500W, according to Figure 1. The mixture containing soy oil (400 mL) and ethanol (450 mL) is added to the tank. After this, the addition of catalyst is made during a continuous stirring at 40 rpm to avoid low conversion rate. Inside the jacketed tank, the mixture goes under a range of operating conditions during the period in which the catalyst agent (sulphuric acid) is added.

In order to avoid the low conversion rate, the lower bound for bulk temperature is 45ºC and the cooling flow rate is manipulated through a variable speed pump (pump 2). The set point of bulk temperature is 50ºC. Calibrated PT-100 temperature sensors are located at the precipitation mixture bulk and at the inlet and outlet of cooling fluid (water) stream.

The on line viscosity system is used to monitor the conversion rate of the process.

3 The control method

The whole process of ethyl ester production is managed by the digital control system from Fieldbus communication. Fieldbus network is connected to our laboratory network and provides us with the following variables; Temperature, pressure and mass flow. These analog signals would be converted to the digital signals through analog to digital conversion (A/D).

The management of the digital control system is performed through a Foundation Fieldbus communication system, according to Figure 1. Four field devices compose the field bus network used to monitor and control the precipitation tank:

- Distributed Fieldbus Interface (DFI302): bridge to link different speed networks. It manages the communication between the Local Area Network (High Speed Ethernet) and the Fieldbus network (H1);

- Temperature Transmitter (TT302-3): performs temperature data acquisitions and transmits them to the interface (DFI302);

- Electric Current Converter/Fieldbus (IF302 -2) and (IF302 -3): receives 4-20mA signal from devices (Temperature transmitters, pressure transmitter and mass flow transmitter) and converts to digital signal to DFI302;
- Fieldbus/Electric Current Converter (FI302): receives digital signal from DFI302 and converts to 4-20mA to operate the variable speed pump.

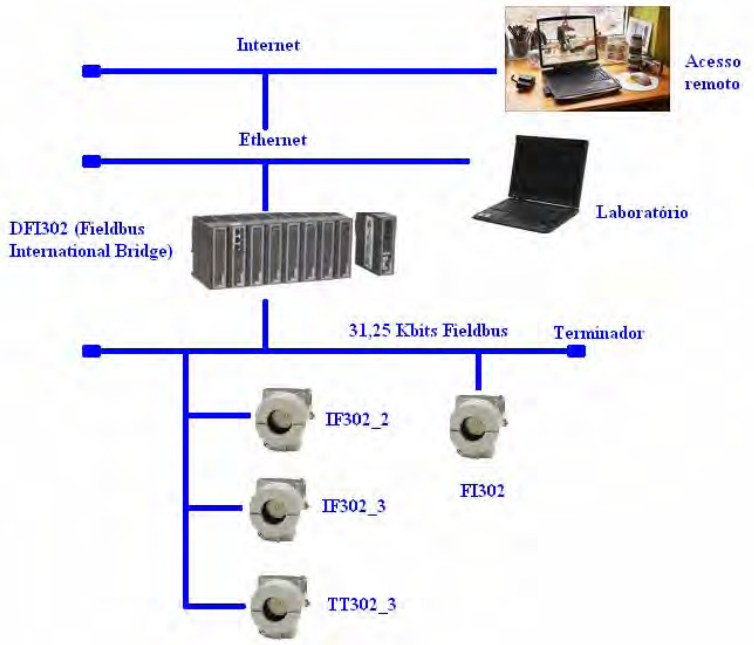

Figure 1. Fieldbus network for transesterification tank monitoring and control.

The digital signal sent to the pump is computed by controllers, which were implemented through the software Syscon (function blocks) and supervisory software Indusoft.

4 Materials and Methods

4.1 Materials

Soy oil refined and ethanol anidro (99,5%) from VETEC. Sulphuric acid (99, 9%) from VETEC.

4.2 Supervisory system development

The supervisory software INDUSOFT was employed in the development of the friendly graphic interface for real time monitoring of the transesterification reaction. The main tasks of this supervisory system are: display of monitoring screens and trends of process variables, the storage of measured data and the implementation of the controller equations.

4.3 A control method of ethyl ester content

The method of viscosity was employed for conversion rate monitoring purposes in biodiesel production. In a transesterification process a change of viscosity can be an indication of the chemical reaction status.

5 Results

5.1 Design procedures

The design of the viscometer system requires uniform flow velocity and Reynolds number for a laminar flow.
The reometer analysis was made to know about reological properties of soy oil and results are shown in Table 1. The reometer used in this work was HAAKE REO-STRESS.

Temperature (°C)	Absolute Viscosity (mPa.s)
20	62,789
25	50,675
30	41,392
40	28,746
50	20,844

Table. 1. Absolute viscosity values for soybean oil.

The fluid is not shear sensitive and Newtonian. In summary, the shear rate itself does not affect the apparent viscosity of the process fluid. In the Table 2 are shown density and kinematic viscosity values of soybean oil.

Temperature (°C)	***Density (g/m***	Kinematic viscosity (cSt)
20	0,902	68,307
25	0,9169	55,320
30	0,9134	45,355
40	0,9066	31,731
50	0,8997	23,181

Table. 2. Density and kinematic viscosity for soybean oil

The number Reynolds obtained must be lower that 2300. The values of biodiesel kinematic viscosity at 40°C is 4,20 mm^2/s and specific gravity at 15,5°C is 0,885 (Tate *et al*., 2006).

Fluid	**Velocity (m/s)**	*Reynolds number (max.)*
Soya oil	3,92	338
Biodiesel	7,99	1905

Table. 3. Velocity and Reynolds number values calculated

All things considered, the soybeans oil did not exhibit time-dependent rheological properties and this approach can be used for viscosity measurement. Fortunately, the laws of physics are not limited to the application of online viscosimeter in this study.

Initially experimental tests were carried out by loading the stirred tank only with oil. The real kinematic viscosity values were obtained through reometer analysis. Table 4 shows results.

Kinematics viscosity biodiesel (cSt)	
Reometer	On-line viscosimete
50,32	55,32
42,3	45,35
28,14	31,73
21,52	23,18
15,79	17,146

Table. 4. Kinematic viscosity of soy oil of 20°C until 60°C

5.2 Transesterification tests

The process is carried out in batch with stirred heated tank (1000mL), with cooling jacket in order to keep the heating temperature in desired value, the heater has a power of 400W and mechanical mixing process is driven by electrical motor rotating at 40 rpm both heat and mechanical movement are the energy input of the system. The set point of bulk temperature is 50ºC. Soybean oil, ethanol and an acidic catalyst are used to accelerate the reaction. In the early moments of catalyst addition, there is a heat generation that immediately cause an decrease on the heating in the closed-loop system. The pump operates at fixed flow rate (220 mL/s) and the batch time is one hour, five samples are withdrawn in time intervals of 15 min.

The transesterification product, a mixture of ethyl esters, unreacted oil, and mono-and diglycerides, was analyzed by gas chromatography (GC). The final result of this process is a batch of ethyl esters with conversion rate of about 95% of the mixture. The results are shown in the Table 5.

Table 5. Comparison between ethyl ester contents measured by GC and calculated from Viscosity of mixture data at 50°C ($\eta_{50°C}$)

Samples	Time (min	ln ($\eta_{50°C}$)	$\eta_{50°C}$ (cSt)	Ethyl ester (wt %)		Error (%)
				by GC	from ($\eta_{50°C}$)[a]	
1[b]	0	-	16,1130	45		
2	15	2,6588	14,2793	86	86	0,0
3	30	2,3921	10,9369	89	89	-0,2
4	45	2,1262	8,3828	92	92	0,8
5	60	2,0130	7,4855	94	94	-0,5

[a]EE=a ln ($\eta_{50°C}$) + b, x= $\eta_{50°C}$ (cSt), a= -12,905 ; b= 120,39; R^2= 0,9789

[b]If the ethyl ester content is higher than 85% the correlation allows the determination by a single viscosity measurement.

6 Conclusions

This paper discussed the use of online viscosimeter. It was accomplished through high precision viscosity measurements for the transesterification process. The viscosity is an important parameter because provide specified characteristics of the biodiesel obtained.

The viscosity difference is sufficient to give an indication of the biodiesel content in a transesterification product. Initially, the samples were analyzed in laboratory to determine the rate of conversion of biodiesel. To gather accurate measurements, the on line viscosimeter was used replacing tedious sampling and procedures.

On line viscosimeter is suitable for the control ethyl ester content in a transesterification process.

7 References

ALLEN, C. A. W.; WATTS, K. C.; ACKMAN, R. G.; PEGG, M. J.; Predicting the viscosity of bio diesel fuels from their fatty acid ester composition, **Fuel**, v.78, 11, 1999, p.1319-1326.

FILIPPIS, P.; GIAVARINI, C. SCARSELLA, M. SORRENTINO, M.; Transesterification Processes for Vegetable Oils: A Simple Control Method of Methyl Ester Content, **JAOCS,** v. 72, 11, 1995, p.1399-1404.

GEABKOPLIS, C. J.,*Transport Processes and Unit Operations*, New Jersey: Prentice Hall PTR, 1993, p.153.

KNOTHE, G., STEIDLEY, K. R. Kinematical viscosity of bio diesel fuel components and related compounds. Influence of compound structure and comparison to petro diesel fuel components. **Fuel 84**. 2005. 1059-1065.

KNOTHE, G., GERPEN, J. V., KRAHL, J., RAMOS, L. P. *The bio diesel handbook.* AOCS Press, 2006, p. 340.

KRISNANGKURA, K., YIMSUWAN, T., PAIRINTRA, R. An empirical approach in predicting bio diesel viscosity at various temperatures. **Fuel 85**. 2006. 107-113.

TATE, R. E., WATTS, K. C., ALLEN, C. A. W., WILKIE, K. I. The viscosities of three bio diesel fuels at temperature up to 300ºC. **Fuel 85**. 2006. 1010-1015.

VICENTE, G., MARTINEZ, M., ARACIL, J. A comparative study of vegetables oils for bio diesel production in Spain. **Energy & Fuels**, 2006, 20, 394-398.

Proceedings of the 10th International Chemical and
Biological Engineering Conference - CHEMPOR 2008
Braga, Portugal, September 4-6, 2008
E.C. Ferreira and M. Mota (Eds.)

Exploitation of Agroindustrial Biomass by Fractionation of Its Components. Characterization of Hemicelluloses, Celluloses and other Fractionation Products

F. López[1], Juan C. García[1]*, A. Pérez[1], G. Garrote[2]

[1] Department of Chemical Engineering. Faculty of Experimental Sciences. *University of Huelva*. *Campus del Carmen. 21007. Huelva*. Spain

[2] Department of Chemical Engineering. Faculty of Sciences. *University of Vigo*. *Campus de Ourense. 32004. Ourense.* Spain

Keywords: lignocellulosic biomass, autohydrolysis, agroforestry residues.

Topic: Sustainable process‐product development through green chemistry. Sustainable & clean technologies

Introduction

The world is experiencing a growing shortage of raw materials which is especially severe in the energy sector and being worsened by the unfavourable environmental impact of a consumerist culture revolving around the exploitation of non-renewable resources. Accomplishing sustainable development and renewability entails finding and using new resources and chemical and consumer products where lignocellulosic biomass constitutes a “necessary” source of raw materials on account of its ubiquity, availability and low polluting power. In fact, lignocellulosic biomass has been widely acknowledged as the largest source of renewable energy available in the world to respond to the decline in fossil fuel sources (Ozcimen and Karaosmanoglu, 2004; Jefferson, 2006; Semelsberger, 2007). Processing the whole material rather than only its sugar and amylaceous fractions to obtain ethanol by fermentation, its fibre fractions to produce cellulose pulp and some residual fractions or all for burning is the only way of exploiting the whole potential of such an abundant resource (Kim and Dale, 2004).

The alternative to integral exploitation of lignocellulosic biomass in a single process (usually of the thermal type) inevitably involves its fractionation; this is hindered by the inability to separate its main components without degrading the chemical structure of some. The complex structure, composition and network of chemical and physical bonds of lignocellulosic biomass precludes the use of separation techniques such as distillation, precipitation, crystallization and extraction for this purpose (Nimz and Casten, 1986). Extensive research in this field has focussed on a variety of highly specific issues and hindered systematic, comprehensive compilation of available fractionation methods. In dealing with such methods, Rijkens (1984) discriminates between those based on delignification (i.e. the solubilization of lignin) and those relying on hydrolysis (i.e. the solubilization of polysaccharides). This was the origin of the “lignocellulosic material biorefinery” concept as the source of a wide range of products by analogy with the oil refinery concept. Although a number of refining schemes have been tested at the laboratory or pilot plant scale, none has to date been implemented on a commercial scale (Kamm and Kamm, 2004).

In this context, the most promising approaches to the integral valorization of lignocellulosic biomass by fractionation revolve around the obtainment of ethanol from hydrolysis products of the raw material by using a “biorefinery” scheme. Bioethanol can be used as an automotive fuel (Hamelinck and Faaij, 2006). Also, it would be desirable to utilize the different polymer fractions

* Corresponding author. Tel + 34-959 219 982. E-mail:juan.garcia@diq.uhu.es

(lignin, hemicelluloses and valorizable compounds) to obtain other valorizable products or by-products in order to help offset the associated storage, pre-treatment and post-treatment costs. Identifying the most suitable pre-treatments or steps for the fractionation of lignocellulosic material is one of the most interesting areas for scientific research and development (Mosier et al., 2005).

The interest in this topic is justified by the renewability and environmental sustainability of the raw material, and also by the increasing awareness of the need for and advantages of its integral exploitation and economic valorization. In fact, lignocellulosic materials can be used to extract fermentable substrates, xilooligosaccharides and chemical products such lignin or furfural

Lignocellulosic raw materials are abundant and renewable. In fact, an estimated 10 - 50 billion ton dry matter of this type is produced each year in the world (Claassen et al., 1999; Galbe and Zacchi, 2002).

The integral fractionation of lignocellulosic biomass can be addressed by using hydrolysis (hemicellulose, cellulose) and delignification reactions.

Delignification has been accomplished by using chemical processes involving organic solvents and high temperatures. The earliest such process was probably the ethanol pre-treatment developed in the 1970s by General Electric to obtain biofuel (Yonghao and Van Heiningen, 1996). The process also provided high-quality unaltered lignin with various potential industrial uses (Lora and Glasser, 2002). Using ethanol as the technological core for refining lignocellulosic materials has led to organosolv processes such as Lignol, which uses temperatures in the region of 200ºC and pressures of 400 psi to maximize extraction of lignin from wood chips and other types of lignocellulosic biomass. Fractionation processes based on a delignification treatment usually focus on the subsequent hydrolysis or saccharification of the cellulose fraction in order to obtain fermentable media for producing ethanol (Mai et al., 2004; Pan et al., 2005; Pan et al., 2006).

Incorporating the hydrolysis of hemicelluloses into a more general process involving the integral fractionation of the raw material can be easier if the use of chemical reagents other than those strictly needed for separation is minimized. This can be specially easy with autohydrolysis. At high temperatures, acetyl groups in the lignocellulosic material give acetic acid, which catalyses the solubilization of hemicelluloses. The resulting liquor essentially contains oligomers, acetic acid, furfural (or hydroxymethylfurfural) and some lignin (Garrote et al., 1999).

In this work, we characterized the raw material and the liquor resulting from the autohydrolysis of five different lignocellulosic materials (*viz. Eucalyptus globulus*, *Arundo donax*, sunflower stalks, *Chamaecytisus proliferus* (tagasaste) and *Pawlonia fortunei*) with a view to assessing their utility for the obtainment of energy and chemical products by integral fractionation based on autohydrolysis.

The final aim was to establish the viability of using effective crops in order to reduce the dependence of Spain on foreign countries as suppliers of energy materials and chemical products, and also to reduce agrifood surpluses by using a fraction of agricultural land to crop alternative plants.

Material and Methods

Characterization of the raw Materials

Chips of materials samples were milled to pass a 8 mm screen, since no diffusional limitations were observed for this particle size in preliminary studies. Samples were air-dried, homogenized in a single lot to avoid differences in composition among aliquots, and stored. Aliquots from the homogenized wood lot were subjected to moisture determination (drying at 105 ºC to constant weight), quantitative acid hydrolysis with 5 mL of 72 % sulfuric acid for an hour and quantitative posthydrolysis with 4 % H_2SO_4 (adding water until 148.67 g) at 121 ºC during 60 min. Before HPLC analysis, the solid residue from posthydrolysis stage was recovered by filtration and considered as Klason lignin, sugar degradation and acid soluble

* Corresponding author. Tel + 34-959 219 982. E-mail:juan.garcia@diq.uhu.es

lignin. The monosaccharides and acetic acid contained in hydrolysates were determined by HPLC in order to estimate the contents of samples in cellulose (as glucan), hemicelluloses (xylan, araban), and acetyl groups.Chromatographic determination was performed using an Agilent 1100 HPLC equipped with an ion-exchange resin Aminex HPX-87H column under the following conditions: mobile phase, 0.05 mol·L-1 of sulphuric acid; flow rate, 0.6 mL·min-1; and column temperature, 40 °C. The volume injected was 20 µL.

Hydrotermal treatment

Raw materials were mixed in the desired proportions, heated in a 2 L stainless steel Parr reactor. Temperatures between 175ºC and 200ºC were ensayed. The solid/liquid ratio was fixed at 1/8 kg oven-dry raw material/kg water for *Arundo donax*, *Paulownia fortunei* and sunflower stalks and 1/6 for eucalyptus and tagasaste.

After treatment, solid residues were recovered by filtration, washed with distilled water, and milled to a particle size less than 0.5 mm to determine α-cellulose (glucan), hemicellulose (xylan, araban and acetyl groups) and lignin, using the same methods as for the raw material.

The liquor was filtered through membranes of 0.45 µm pore size and used for direct HPLC determination of oligosaccharides, monosaccharides (glucose, xylose and arabinose), furfural, 5-hydroxymethylfurfural (HMF), and acetic and formic acids. A second aliquot of the liquid phase (25 mL) were subjected to quantitative posthydrolysis (with sulphuric acid at 4% at 121 °C during 60 min) before HPLC analysis. The increase in the concentrations of monosaccharides and acetic acid caused by this posthydrolysis measured the concentration of oligomers and acetyl groups bound to oligosaccharides.

Results and discussion

Table 1 summarizes the chemical composition of various materials studied here. Because *E. globulus* is the most widely studied material, its values can be used as references for comparison with the others. In fact, the operating conditions used were based on previous work by Garrote (2001) on this material where oligosaccharide extraction was found to be maximal (10.3%) at 196ºC. Note the low glucose contents and high xylose contents in the liquor remaining upon autohydrolysis –which suggest that the polymer retains most of its integrity even at high temperatures–, and also the increased amounts of xylose extracted from all materials.

The holocellulose contents of tagasaste and sunflower stalks exceed those of eucalyptus by 20% and 10.9%, respectively, and are comparable or higher than others materials. On the other hand, the glucan content of eucalyptus is 20.3% and 38.5% higher than that of tagasaste and sunflower stalks, respectively; also, the lignin content is 15.5 and 15.5% higher, respectively, than those of the latter two. Based on these contents, one can expect increased yields in oligosaccharides and xylose in the liquor resulting from the hydrolysis of eucalyptus. Finally, the contents in hemicelluloses (holocellulose-glucan) of tagasaste (41.1%) and sunflower stalks (40.4%) are higher than that of eucalyptus (20.1%).

The xylan contents of tagasaste and *A. donax*, 19.0% and 19.9%, are similar or higher than those of eucalyptus. The highest value for the studied materials is that for sunflower stalks (23.9%). Other authors (Ververis, 2004) have obtained similar glucan and lignin contents, but substantially lower xylan and araban contents, for *A. donax*. *P. fortunei* exhibited the lowest holocellulose content and highest cellulose content among the studied materials. Our xylan, araban and acetyl contents are similar to those found in other materials.

Table 2 shows the concentrations of oligomers, sugars and various other substances in the liquors resulting from the hydrothermal treatments. The table also contains additional data for the less widely studied materials (tagasaste, sunflower stalks and *P. fortunei*) as obtained at hydrolysis temperatures below and above those used with *E. globulus* and *A. donax* (175ºC to 200ºC), however.

* Corresponding author. Tel + 34-959 219 982. E-mail:juan.garcia@diq.uhu.es

Overall, solubilization increased with increasing temperature of the hydrothermal treatment (especially in tagasaste, where the amount of oligomers dissolved rose by a factor of 4 from 175ºC to 195ºC). Xylose and acetic acid were also solubilized maximally at high temperatures (185ºC-195ºC). As noted earlier, the oligomer yield for tagasaste exceeded that for eucalyptus at temperatures from 185ºC to 195ºC. Arabinose was solubilized in very high proportions with respect to its content in the raw material (viz. 95.2% at 195ºCC); however, its concentration was very small in absolute terms owing to its low proportion in the raw material.

Solubilization of oligomers in sunflower stalks increased by 28% from 180ºC to 190ºC and then decreased up to 200ºC by effect of their thorough hydrolysis to simple sugars or other decomposition products. In fact, the content in acetic acid at 200ºC (4.6 g/L, equivalent to 3.7% of the dry mass of raw material) was much higher than that for any other raw material at any temperature. The concentration of formic acid reached levels of up to 1 g/L, but those of furfural and 5-hydroxymethylfurfural never exceeded 0.1 g/L. The oligomer yield of this raw material was higher than were those of eucalyptus and tagasaste (viz. 21.5% with respect to dry mass of raw material and 90.0% of oligomers, which were the highest figures of all).

Oligomer solubilization in *P. fortunei* increase 1.9 times from 180ºC to 200ºC; however, the increase from 190ºC to 200ºC was less marked and accompanied by a decrease in the proportion of xylose extracted.

Only 3.1% of cellulose present in the raw material was solubilized under the most drastic heating conditions used in the autohydrolysis of tagasaste (195ºC); this suggests that the process is quite selective and cellulose is scarcely degraded, so it can be useful for other purposes such as obtaining cellulose pulp. This is an advantage as it allows scarcely degraded cellulose to be obtained as a valorizable product. Similar results were obtained with the other materials and temperatures: cellulose degradation never exceeded 2.8% and 1.6% relative to glucan in the raw material for sunflower stalks and *Pawlonia fortunei*, respectively; these values, however, are still higher that those for *E. globulus* wood, which never exceeded 0.5%.

The amounts of oligomers that can be extracted from tagasaste (13.9%), sunflower stalks (21.5%) and *P. fortunei* (11.7%) at the highest operating temperature (195ºC with the former and 190ºC with the latter two) are greater than those for eucalyptus. The amounts of oligomers obtained from tagasaste at temperatures below 185ºC (3.3%-9.4%) and sunflower stalks below 180ºC (16.8%) are greater than those obtained from eucalyptus wood (8.7%) in some cases. Note the small amounts of degradation products such as furfural present in their liquors and in those resulting from the autohydrolysis of *P. fortunei.*

A. donax exhibited the highest proportions of extracted oligomers and xylose in addition to relatively high proportions of glucose and acetic acid in the hydrolysis liquor. This make it the least suitable material for exploitation by autohydrolysis of all studied here.

Overall, both sunflower stalks and *P. fortunei* can be efficiently hydrolysed at 180ºC and 190ºC while minimizing degradation of the solid phase and maximizing the extraction of xylan. At temperatures in the region of 200ºC, Heitz et al.(50) and Garrote (51) observed substantial depolymerization of cellulose and a decreased amount of cellulose fibers in the autohydrolysis process.

References

Claassen P., Van Lier, J.B., Contreras, A., Van Niel, E., Sijtsma, L., Stams, A., de Vriess, S.S., Weusthuis, R.A. (1999). Utilisation of biomass for the supply of energy carriers. Applied Microbiology and Biotechnology 52 : 741-755.

Galbe, M., Zacchi, G. (2002). A review of the production of ethanol from softwood. Applied Microbiology and Biotechnology, 59: 618-628.

* Corresponding author. Tel + 34-959 219 982. E-mail:juan.garcia@diq.uhu.es

Garrote, G., Domínguez, H., Parajó, J.C. (1999). Mild autohydrolysis: and environmentally friendly technology for xylooligosaccharide production from wood. Journal of Chemical Technology and Biotechnology 74: 1101-1109.

Garrote, G. 2001. Estudio del procesamiento hidrotérmico de materiales lignocelulósicos. PhD Thesis. Departamento de Ingeniería Química. Universidad de Vigo.

Garrote, G.; Dominguez, H.; Parajó, J.C. (2002) Autohydrolysis of corncob: study of non-isothermal operation for xylooligosaccharide production. Journal of Food Engineering 52: 211–218.

Hamelinck, C.H., Faaij, A.P.C. (2006). Outlook for advanced biofuels. Energy Policy 34: 3268-3283

Heitz, M.; Capek-Ménard, E.; Koeberle, P.G.; Gagné,J.; Chornet, E.; Overend, R.P.; Taylor, J.D.; Yu, E. (1991). Fractionation of Populus tremuloides at the pilot plant scale: Optimization of steam pretreatment conditions using the STAKE II technology. Bioresources Technology 35: 23-32.

Jefferson, M. (2006). Sustainable energy development : performance and prospects. Renew Energy, 31: 571-582.

Kamm, B., Kamm, M. (2004). Principles of biorefineries. Applied Microbiology and Biotechnology, 64:137-145.

Kim, S. Dale, B.E. (2004) Global potential bioethanol production from wasted crops and crops residues. Biomass and Bionergy, 26 : 361-375.

Lora, J.H., Glasser, W.G. (2002). Recent industrial applications of lignin: a sustainable alternative to nonrenewable materials. Journal of Polymer Environmental, 10: 39-48

Mai, C., Kües, U., Militz, H. (2004). Biotechnology in the wood industry. Applied Microbiology and Biotechnology 63: 477-494

Mosier, N., Wyman, C., Dale, B., Elander, R., Lee, Y.Y., Holtzapple, M., Ladisch, M. (2005). Features of promising technologies for pretratment of lignocellulosic biomass. Bioresources Technology 92: 673-686

Nimz, H.H. y Casten, R. (1986). Chemical processing of lignocellulosics. Holz Roh-Werkstoff, 44: 207-212

Ozcimen, D., Karaosmanoglu, F. (2004). Production and characterization of bio-oil and biochar from rapeseed cake. Renw Energy, 29 : 779-787.

Pan, X., Arato., C., Gilkes, N., Gregg, D., Mabee, W., Pye, K., Xiao, Z., Zhang, X., Saddler, J. (2005). Biorefining of Softwoods Using Ethanol Organosolv Pulping: Preliminary Evaluation of Process Streams for Manufacture of Fuel-Grade Ethanol and Co-Products. Biotechnology and Bioengineering, 90 (4): 473-481

Pan, X., Gilkes, N., Kadla, J., Pye, K., Saka, S., Gregg, D., Ehara, K., Xie, D., Lam, D., Saddles, J. (2006). Bioconversion of Hybrid Poplar to Ethanol and Co-Products Using an Organosolv Fractionation Process: Optimization of Process Yield. Biotechnology and Bioengineering, 94 (5): 851-861

Rijkens, B.A. (1984). Hydrolyses processes for lignocellulosic material. Presentado en: CECD Workshop Cellulose Programme. Brunscheweig

Semelsberger, T.A., Borup, R.L., Greene, H.L. (2007) Dimethyl ether (DME) as an alternative fuel. Journal of Power Sources, 156: 497-511.

Ververis C., Georghiou K., Christodoulakis N., Santas P. y Santas R. (2004) Fiber dimensions, lignin and cellulose content of various plant materials and their suitability for paper production. Industrial Crops and Products 19 (3): 245-254.

Yonghao, N., Van Heiningen, A.R.P. (1996). Lignin removal from Alcell pulp by washing with ethanol and water. Tappi Journal, 79 (3): 239-243.

* Corresponding author. Tel + 34-959 219 982. E-mail:juan.garcia@diq.uhu.es

Table 1. Chemical composition of *Eucalyptus globulus*, sunflower stalks, tagasaste, *Pawlonia fortunei* and *Arundo donax* .

	Eucaliptus Globulus	Sunflower Stalks	*Chamaecytisus proliferus (tagasaste)*	*Paulownia Fortunei*	*Arundo Donax*
Glucan, %	46,8	33,8	38,9	34,2	34,8
Klason Lignin , %	22,9	19,9	19,8	27,2	23
Holocelluloses	66,9	74,2	80,3	56,9	64,5
Xylan, %	16,6	23,9	19,9	18,3	19,4
Araban, %	0,54	0,37	0,63	1,13	1,5
Acetyl Groups, %	3,49	4,32	4,39	3,31	3,4

* Percentages relative to the raw mass (100 kg dry mass). Average value of four replicated.

Table 2. Oligomer and monomer contents in the liquor relative to dry mass of raw material and (/) the content in each polymer fraction of the raw material, also as dry mass (oligomer contents are given as xylose equivalents).

	Hydrothermal Temperature											
	Eucaliptus Globulus		**Tagasaste**			***Arundo donax***	**Sunflower Stalks**			***Paulownia Fortunei***		
	181ºC	196ºC (39)	175ºC	185ºC	195ºC	185ºC	180ºC	190ºC	200ºC	180ºC	190ºC	200ºC
Olygomers, %	8,70/52,4	10,30/62,0	3,30/16,6	9,40/47,2	13,90/69,8	2,40/12,4	16,79/70,3	21,51/90,0	18,63/77,9	7,80/42,6	11,70/63,9	14,80/80,9
Glucose, %	0,17/0,4	0,25/0,5	1,10/2,8	1,10/2,8	1,20/3,1	0,89/2,6	0,96/2,8	0,80/2,4	0,56/1,7	0,84/2,5	0,74/2,2	0,56/1,6
Xylose, %	1,01/6,1	2,21/13,3	0,70/3,5	0,90/4,5	1,70/8,5	0,73/3,8	1,60/6,7	2,08/8,7	1,68/7,0	0,99/5,4	0,74/4,0	0,56/3,1
Arabinose, %	-	-	0,20/31,7	0,40/63,5	0,60/95,2	0,15/10,0	0,24/64,9	0,48/100,0	0,48/100	0,38/33,6	0,48/42,5	0,47/41,6
Acetic Acid, %	0,21/6,0	0,40/11,5	0,20/4,6	0,40/9,1	0,80/18,2	1,26/37,1	0,88/20,4	1,90/44,0	3,70/85,6	0,40/12,1	0,74/22,4	0,98/29,6

* Corresponding author. Tel + 34-959 219 982. E-mail:juan.garcia@diq.uhu.es

Proceedings of the 10th International Chemical and
Biological Engineering Conference - CHEMPOR 2008
Braga, Portugal, September 4-6, 2008
E.C. Ferreira and M. Mota (Eds.)

Influence of different chemical treatments in lipase immobilization in a lignocellulosic support

Ana I. S. Brígida[1], Luciana R. B. Gonçalves[2], Maria A. Z. Coelho[1]*

[1] Escola de Química, Centro de Tecnologia, Universidade Federal do Rio de Janeiro, Cidade Universitária, 21941–909 Rio de Janeiro, Brasil.

[2] Departamento de Engenharia Química, Universidade Federal do Ceará, Campus do Pici, 60455-760 Fortaleza, Brasil

Keywords: Green coconut fiber, *Candida antarctica* B lipase, Immobilized enzyme, stability, chemical treatments
Topic: Integration of life sciences & engineering

Abstract

Chemical treatment for surface fiber has been reported to remove some impurities, to improve wettability and to modify microstructure and surface chemical groups. In this study we investigated the effect of different chemical treatments on the immobilization of *Candida antarctica* lipase B (CALB) in green coconut fiber. For this purpose, two immobilization strategies were used: adsorption and covalent attachment. The results showed that the chemical treatment with H_2O_2 was more efficient in the removal of the pigments and residues of waxes and fatty acids from fiber surface. During the immobilization process, the chemical treatments not promoted considerable influence on enzyme loading.

1 Introduction

Lipases (triacylglycerol ester hydrolases, E.C. 3.1.1.3) are enzymes that catalyze both the hydrolysis and synthesis of esters from glycerol and long-chain fatty acids. These enzymes, under special conditions, can also catalyze interesterification, aminolysis and thiotransesterification reactions (JAEGER and REETZ, 1998). Thus, the increase on lipases applications in enzymatic synthesis and biotransformations impelled the study of immobilized biocatalysts preparation.

Considering the high cost of some available commercial support matrixes to enzyme immobilization, studies have been intensified in order to obtain cheaper supports. Some papers have reported the use of agroindustrial wastes as immobilization matrix for α-amylase, invertase and lipase. These studies showed that agroindustrial wastes are a suitable raw material source for immobilization matrix. In Brazil, an increase in the green coconut water market had a direct impact on the increase in coconut husk production, an agroindustrial waste (BRÍGIDA *et al*., 2007). However, the presence of impurities on the surface of green coconut fibers requires treatment studies.

Chemical treatment for surface fiber has been reported to improve wettability and to modify microstructure, surface topography, surface chemical groups and tensile strength of fibers (SILVA *et al.*, 2000; ROUT *et al.*, 2001). These characteristics influence enzyme – support interaction and it is an important factor for immobilization process. Moreover, the distribution of surface chemical groups is intrinsically linked to success of functionalization step for immobilization by covalent attachment (FERREIRA *et al*., 2003). Therefore, the aim of this study was to investigate the effect of different chemical treatments on the immobilization of *Candida antarctica* lipase B (CALB) in green coconut fiber. For this purpose, two immobilization strategies were used: adsorption and covalent attachment. In order to evaluate the immobilization process in different chemical treated supports, the lipase loading and stability of the obtained derivates was evaluated.

2 Material and Methods

Materials: Commercial *C. antarctica* lipase type B was kindly donated by Novozyme Latin America Ltd. Substrate p-nitrophenyl laurate were obtained from Fluka and 3-glycidoxypropyltrimethoxysilane (GPTMS) was obtained from Sigma-Aldrich Chemical Co. All chemicals were of analytical grade.

Chemical treatments: Green coconut fiber was obtained from green coconut husks through a process developed by Embrapa Agroindústria Tropical, Ceará State, Brazil. Before being used as support, green coconut fibers were previously cut and sieved to obtain particles between 32 and 35 mesh, washed with distilled water, dried at 60ºC and then they were submitted to three different treatments: (i) 2 g of coconut fibers were submitted to oxidation using 40 mL of a H_2O_2 solution in basic medium (0.05 g NaOH and 18 mL of H_2O_2 30%, v/v, for 100 mL of solution), at 85ºC for 2 h; (ii) 5 g of fibers were soaked in 100 mL of 0.4% NaOCl (v/v, in glacial acetic acid) for about 2 h at 85ºC, and (iii) the last treatment was performed by soaking 5 g of fibers in 100 mL of a solution NaOCl 4-6% (v/v):H_2O (1:1) for 2 h at 30ºC and, after this time, the fibers were washed with water and soaked in 100 mL of 10% NaOH for 1 h at 30ºC.

Support activation: The support activation procedure was a four-step sequential process. The first step was the support protonation with nitric acid (10%, v/v) under low stirring for 30 min at 30 ºC. It was then rinsed with nitric acid (10%, v/v) and acetone-water solutions (20, 50 and 100%, v/v) and dried at 60ºC for 1 h. The support was then silanized using a GPTMS solution at pH 8.5 under low stirring for 5 h at 60ºC. The fiber was rinsed with water, acetone-water solutions, and dried. In the third step, the hydrolysis of epoxy groups was done with 0.1M sulphuric acid at 85ºC under low stirring for 2 h. Again, the fiber was rinsed with water, acetone and dried. For each gram of dry support used in the previous stages, 30 mL of each solution was used. Finally, oxidation process was achieved by reaction with 0.04 M sodium periodate solution (5 mL/g fiber) under low stirring at room temperature for 1 h. After oxidation, the activated fiber was thoroughly rinsed with water and, later, with 5 mM sodium phosphate buffer pH 7.0. Before immobilization, activated fiber was dried under vacuum (BRÍGIDA *et al.*, 2007). In this study, GPTMS solution concentration was evaluated at 1, 2.5 or 5 %, v/v.

Preparation of immobilized enzyme: Lipase was immobilized by adsorption or by covalent attachment by contact at room temperature using treated or treated and functionalized fiber, respectively. The enzyme and support were mixed using a rotative stirring. For each gram of dry support, 10 mL of lipase solution in 25 mM sodium phosphate buffer pH 7.0 were used. After immobilization, the biocatalyst was separated by filtration, rinsed with phosphate buffer (10 mL) and dried at vacuum for 10 min.

Assay of hydrolytic activity: The hydrolysis of p-nitrophenyl laurate was defined as standard method to determine lipase activity from commercial *C. antarctica* lipase type B (CALB) solution and CALB immobilized in coconut fiber. For enzyme solutions, the reaction occurred at 37 ºC by the addition of 0.2 mL of enzyme solution to 1.8 mL of 560 µM p-nitrophenyl laurate (pNP-laurate) dissolved in 50mM potassium-phospate buffer (pH 7.0), containing 1% (v/v) of dimethyl sulfoxide (AMARAL *et al*., 2005). For immobilized enzymes, the reaction occurred at 37ºC by addition of 0.3 g of CALB immobilized to 30 mL of pNP-laurate solution. The reaction development was followed for 100 seconds or 10 minutes, for soluble and immobilized enzyme respectively, in a spectrophotometer (HACH, DR/4000U) at λ= 410 nm. One unit (pNPLU) is defined as the amount of enzyme which releases 1 μmol of p-nitrophenol per minute at pH 7.0 and 37ºC.

Scanning electron microscopy: In order to evaluate changes in the surface provoked by the chemical treatment, natural and treated fibers were analyzed by scanning electron microscopy (SEM) using a Zeiss DSM 940A SEM operating at 15 kV. All samples were glued onto special stubs and gold-coated with a Sputter Emitech K550 to avoid electrostatic charge and to improve image resolution.

Thermal stability: Thermal stability of soluble or immobilized enzyme was determined by incubating the biocatalyst in 100 mM sodium phosphate buffer pH 7 at 60ºC. Periodically, samples were withdrawn and their residual activities were assayed by the hydrolysis of pNP-laurate. Residual activity is given as percentage of initial activity (hydrolytic activity before incubation).

3 Results

Several studies has reported chemical treatment of coconut fiber to remove somes impurities and to improve wettability (SILVA *et al.*, 2000; ROUT *et al.*, 2001). In this study, we evaluated three treated fiber as matrix to immobilization. Figure 1 shows scanning electron micrographs of natural fiber and treated fibers. A visual analysis showed that, for treatment with NaOCl, the presence of residues of waxes and fatty acids in derived fiber samples still occurs in high concentrations (Figure 1b). Already NaOCl treatment followed by treatment with NaOH, showed a liberation of celulose helical spiral, probably caused by the removal of part of hemicellulose and lignin that link the fibrils forming fibres (Figure 1c), while the presence of residues of waxes and fatty acids is still observed. Regarding the treatment with H_2O_2, this was the most efficient in the removal of the pigments in coconut leading to colour change. Thus, the color of natural fiber (brown) switched to a light yellow after treatment. Also, among the three treatments studied, this was the most efficient in removing residues of waxes and fatty acids (Figure 1d).

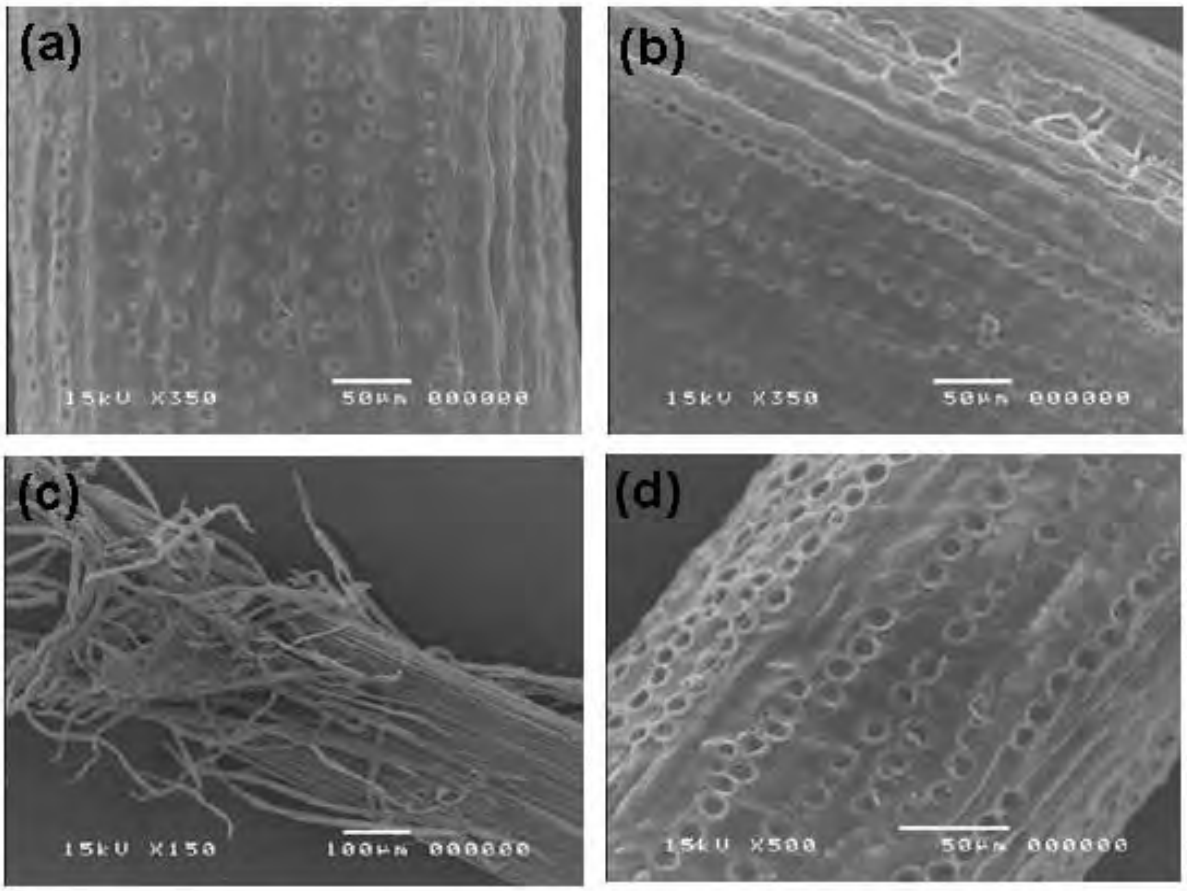

Figure 1 – Scanning electron micrographs of: (A) natural green coconut fiber; (B) NaOCl treated fiber; (C) NaOCl and NaOH treated fiber; (D) H_2O_2 treated fiber.

In addition to structural changes, chemical treatments can possibly modify the distribution of available groups on fiber surface. These changes can have influence on enzyme – support interaction and it is an important factor for immobilization process. Thus, to investigate chemical treatments influence on the immobilization process, immobilization studies of CALB

in natural and treated coconut fiber were realized both by adsorption and covalent attachment.

Immobilization studies showed that lipases immobilized by adsorption had similar activity when immobilized in natural fiber and in treated fiber with NaOCl and NaOCl - NaOH, 263.0 ± 17.5 U/kg, 246.6 ± 26.5 U/kg and 233.1 ± 10.13 U/kg, respectively. On the other hand, a slight increase in activity were achieved by lipase immobilized in H_2O_2 treated fiber, 307.7 ± 1.3 U/kg. All immobilizations carried out with treated fibers showed lower catalytic efficiency (59.0%, 51.2%, 48.3% and 47.0% for natural, H_2O_2, NaOCl and NaOCl – NaOH treated fiber, respectively) and lower thermal stability (Figure 2) when compared to the enzyme immobilized in natural fiber. In addition to physical changes, observed by scanning electron microscopy, variations in the surface charge, indicated by pH change, may have influenced the immobilization process.

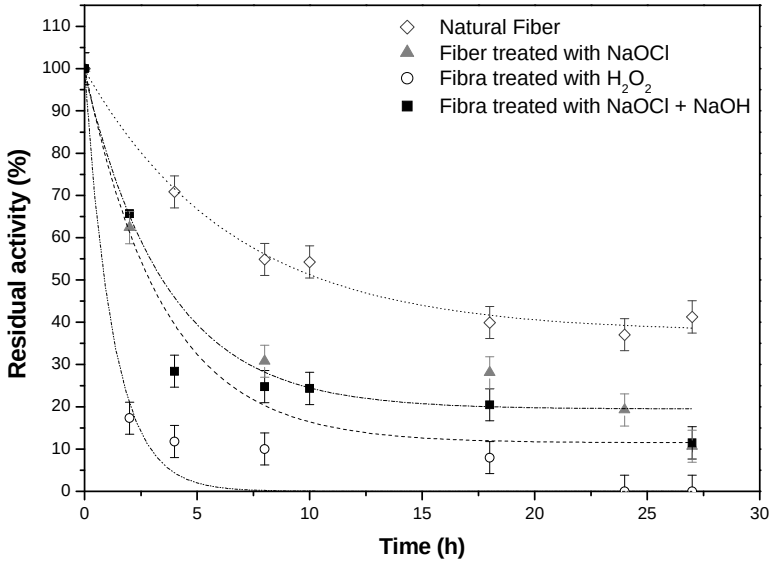

Figure 2 – Influence of chemical treatment in thermal stability of lipase immobilized by adsorption in coconut fiber.

For immobilization by covalent attachment, a GPTMS solution of 1% (v/v) was initially adopted. Immobilization studies showed that lipases immobilized by covalent attachment had similar activity when immobilized in natural and in treated fiber with NaOCl and H_2O_2, 160.9 ± 10.5 U/kg, 156.4 ± 8.0 U/kg and 155.3 ± 10.5 U/kg, respectively. On the other hand, a reduction in activity was achieved by lipase immobilized in NaOCl-NaOH treated fiber, 123.5 ± 9.0 U/kg. These values are lower than those found in adsorption studies. The degree of activation of fibers by silanization with GPTMS at 1% was 104.5, 104.2, 104.8 and 105.1 μmol de CHO/g de fibra, for natural, H_2O_2, NaOCl and NaOCl-NaOH treated fibers, respectively.

To evaluate the silanization efficiency and stability of immobilized enzyme, thermal stabilitiy analyses of CALB immobilized in natural or treated coconut fibers were realized (Figure 3). It was observed that stability of CALB immobilized by covalent attachment in natural coconut fiber is similar to that obtained with H_2O_2 treated fiber. For NaOCl-NaOH and NaOCl treated fibers, deactivation was slightly higher. It was expected that with the removal of some impurities and waxes and fatty acids residues through the chemical treatment of coconut fiber, a greater number of OH groups could be protonated, promoting a more efficient silanization and, consequently, greater stability. However, it was observed that during the last stage of activation (oxidation with sodium periodate), the obtained degree of fiber activation

by silanization with GPTMS to 1% (v / v) was similar in the different types of treatments evaluated. This fact shows that, in covalent attachment immobilization employing 1% GPTMS, there isn't a significant influence on the enzyme stability.

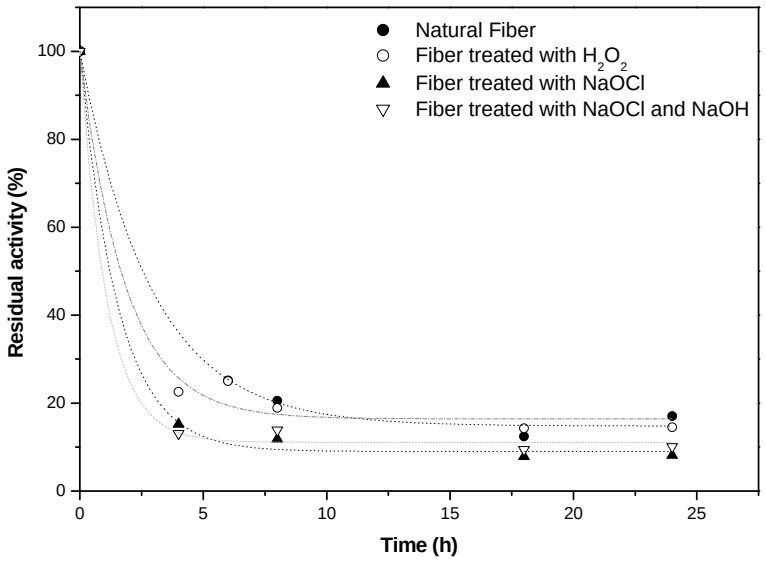

Figure 3 – Influence of chemical treatment in thermal stability of lipase immobilized by covalent attachment in coconut fiber.

In other studies, it was observed that GPTMS concentration during silanization step may influence the derivate stability (FERREIRA *et al.*, 2003). Thus, stability studies with lipases immobilized by covalent attachment in silanizated fibers under different concentrations of GPTMS should be made. Figure 4 shows thermal stability of CALB immobilized by covalent attachment in natural coconut fiber for different GPTMS concentrations. It can be seen that only for GPTMS at 5%, a significant increase in immobilized enzyme stability was detected. Studies of functionalization fibres treated using different concentrations of GPTMS must be made. In addition, other GPTMS concentrations could be studied, considering that the cost of the imobilization procedure can raise, not providing a biocatalyst of low cost.

Conclusions

Among the chemical treatments realized to remove some impurities from natural coconut fiber, treatment with H_2O_2 was more efficient in pigments and residues of waxes and fatty acids removal from fiber surface. From the immobilization studies it is possible to conclude that chemical treatments do not promote considerable difference in the immobilized enzyme charge. However, they may interfere in a negative way on the stability of these enzymes. To effectively assess the influence of such treatments in immobilization by covalent attachment, further studies should be carried using different concentrations of GPTMS during silanization.

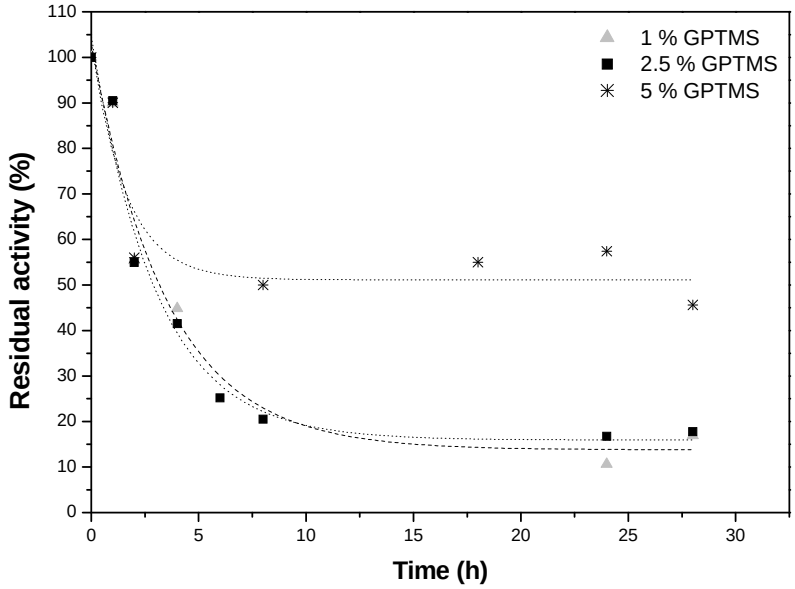

Figure 4 – Influence of GPTMS concentration in thermal stability of lipase immobilized by covalent attachment in coconut fiber.

Acknowledgements

The authors are grateful for the financial support given by CNPq, FAPERJ and CAPES. We are also grateful to L. R. Andrade for the SEM analysis.

References

Amaral, P. F. F., Rocha-Leão, M. H. M., Marrucho, I. M., Coutinho, J. A. P., Coelho, M. A. Z. Improving Lipase Production using a Perfluorocarbon as Oxygen Carrier. *J. Chem. Technol. Biotechnol.* 2005; 81: 1368-1374.

Brígida, A.I.S., Pinheiro, A.D.T., Ferreira, A.L.O., Pinto, G.A.S., Gonçalves, L.R.B. (2007) Immobilization of *Candida antarctica* lipase B by covalent attachment to green coconut fiber. *Applied Biochemistry and Biotechnology*, 137, 67-80.

Brígida, A.I.S., Pinheiro, A.D.T., Ferreira, A.L.O., Gonçalves, L.R.B. (2008) Immobilization of *Candida antarctica* lipase B by adsorption to green coconut fiber. *Applied Biochemistry and Biotechnology*, 146, 173-187.

Ferreira, L., Ramos, M.A., Dordick, J.S., Gil, M.H. (2003) Influence of different sílica derivatives in the immobilization and stabilization of a *Bacillus licheniformis* protease (Subtilisin Carlsberg). *Journal of Molecular Catalysis B: Enzymatic*, 21, 189-199.

Jaeger, K., Reetz, M.T. (1998) Microbial lipases form versatile tools for biotechnology. *Tibtech*, 16, 396-403.

Rout, J., Tripathy, S.S., Nayak, S.K., Misra, M., Mohanty, A.K. (2001) Scanning electron microscopy study of chemical modified coir fibers. *Journal of Applied Polymer Science*, 79, 1169-1177.

Silva, G.C., Souza, D.A., Machado, J.C., Hourston, (2000) Mechanical and thermal characterization of native brazilian coir fiber. *Journal of Applied Polymer Science,* 76, 1197-1206.

Proceedings of the 10th International Chemical and
Biological Engineering Conference - CHEMPOR 2008
Braga, Portugal, September 4-6, 2008
E.C. Ferreira and M. Mota (Eds.)

Information CALS-model of the innovation technology of biologically active additives of a new generation

Arkadiy M. Bessarabov*, Alexey A. Alyakin, Alexey L. Kochetigov
The State Scientific-Research Institute of Chemical Reagents and High Purity Chemical Substances (IREA), Bogorodsky Val, 3, 107076, Moscow, Russia

Keywords: System analysis, CALS-technologies, Biologically active additives, Drying-agglomeration.
Topic: Systematic methods and tools for managing the complexity.

At the present time, as a promising information technology, methods of the Continuous Acquisition and Life Cycle Support (CALS) concept are widely implemented (Bessarabov et al., 2002). The CALS concept is based on a complex of unified information models and the standardization of methods for information access and correct information interpretation according to the international standard ISO 10303 (STEP). A series of CALS projects were developed for a number of technologies for producing special-purity substances (Bessarabov et al., 2006, 2007); however, in all the cases, CALS methods were used only to create project documentation.
In this work, using CALS methods, an information model was elaborated which includes all the steps (marketing, design, production, service and repair, and realization and sale) of the technology of producing biologically active additives of a new generation from an extract of medicinal herbs and gelatin--starch complex (Bessarabov et al., 2003). In recent years, biologically active food additives---therapeutic and prophylactic preparations produced from herbal raw material---have successfully competed with synthetic drugs.
Let us sequentially consider elements of the information model that correspond to various steps of the technology of biologically active additives.

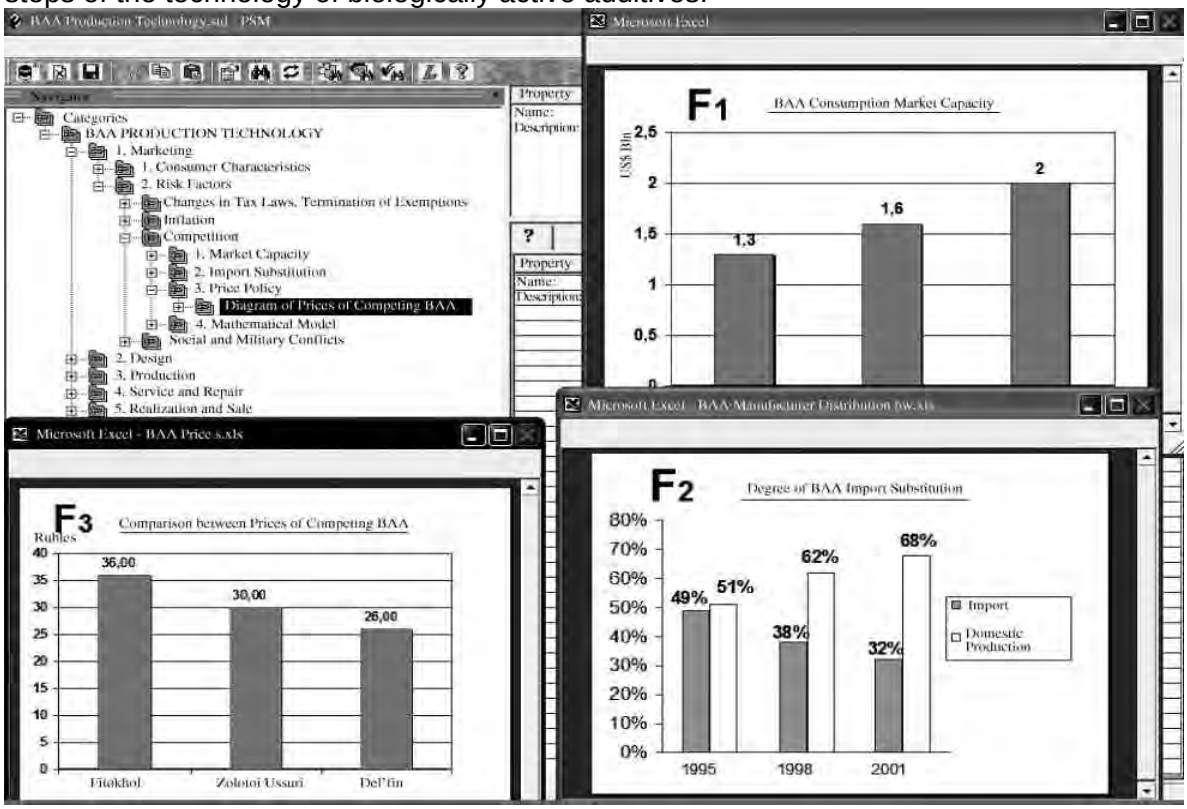

Fig. 1. CALS Project element at the marketing step.

* Corresponding author. Tel + 7(495)963-7527. E-mail:bessarabov@irea.org.ru

On the basis of marketing research results, at the marketing step, two information-analytical blocks are formed: consumer characteristics and risk factors. Each of the blocks includes lower-level parameters, whose analysis gives a complete pattern of the entire analytical block. For convenience of using the system, the parameters are inputted in text and table formats, as well as in graphic form. As basic consumer characteristics, the income, age, and sex distributions of consumers are analyzed. In this block, the reasons for buying biologically active additives and the main factors affecting the purchase decision are also studied. In the block of risk factors (Fig. 1), an analysis is undertaken regarding the possibility of a change in tax laws and concerning inflation and competition, market capacity, degree of import substitution, and prices for similar products. At the marketing step, a conclusion is drawn about the expedience and prospects of developing technology and equipment for producing biologically active additives of new generation.

At the design step (Fig. 2), the initial data for design are analyzed, which contain information on six basic stages: grinding of medicinal raw material, extraction, concentration, mixing, drying--agglomeration, and packing. Particular attention was given to the limiting stage---drying--agglomeration.

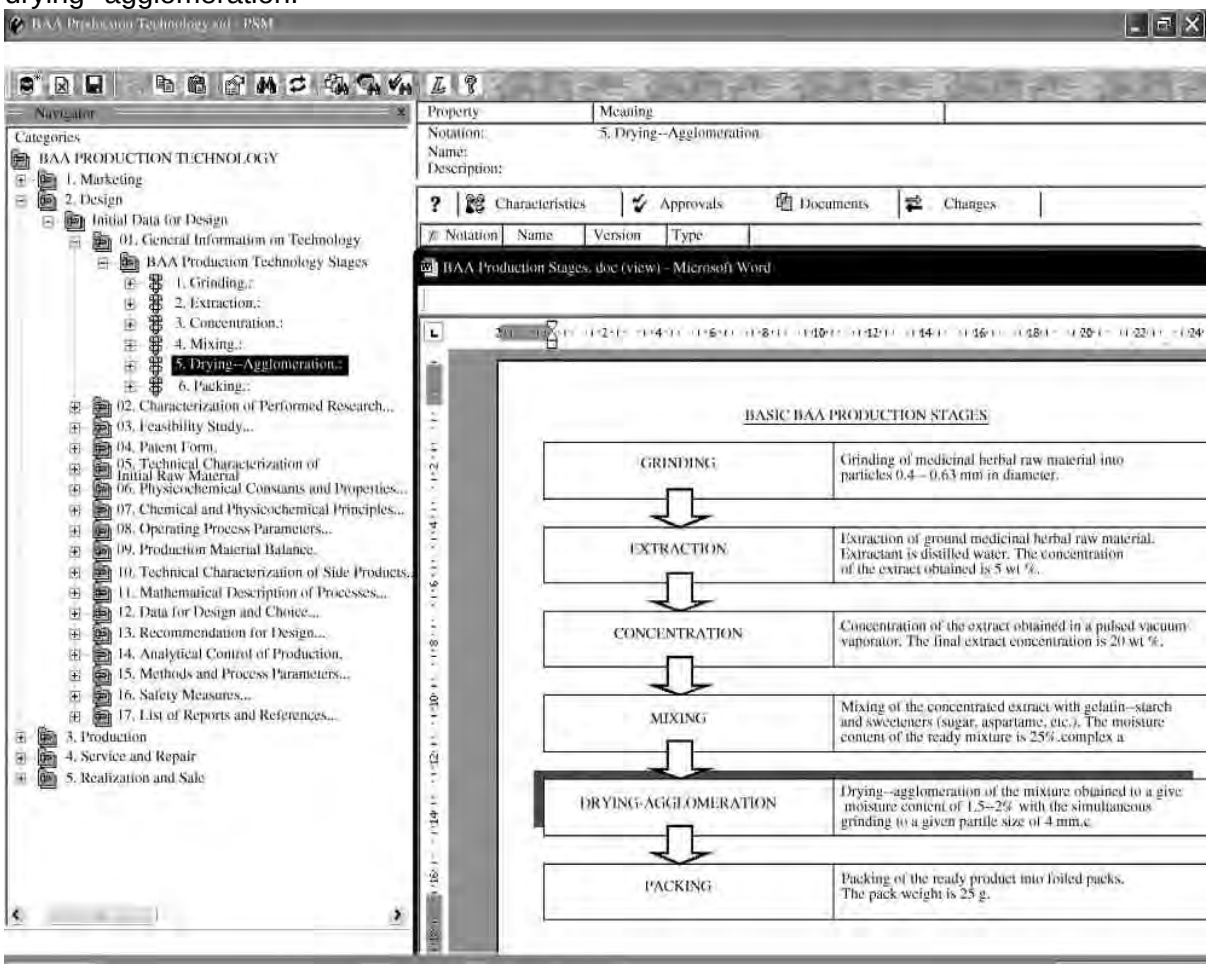

Fig. 2. CALS Project element at the design step (basic stages of the technology of biologically active additives).

The main methods for drying biologically active additives were analyzed; these are spray drying, fluidized-bed drying, infrared drying, and drying in a vacuum dryer equipped with a rake agitator. It was shown that the equipment considered is inefficient if the product contains astringent substances (fructose, lactose, gelatin--starch complex, and others), which, during drying--agglomeration, form clots, stick to moving parts and the housing of the apparatus, and can render the apparatus inoperative. Therefore, a continuous convective agitator dryer was proposed, which gives a product of required quality and given particle size distribution (Fig. 3).

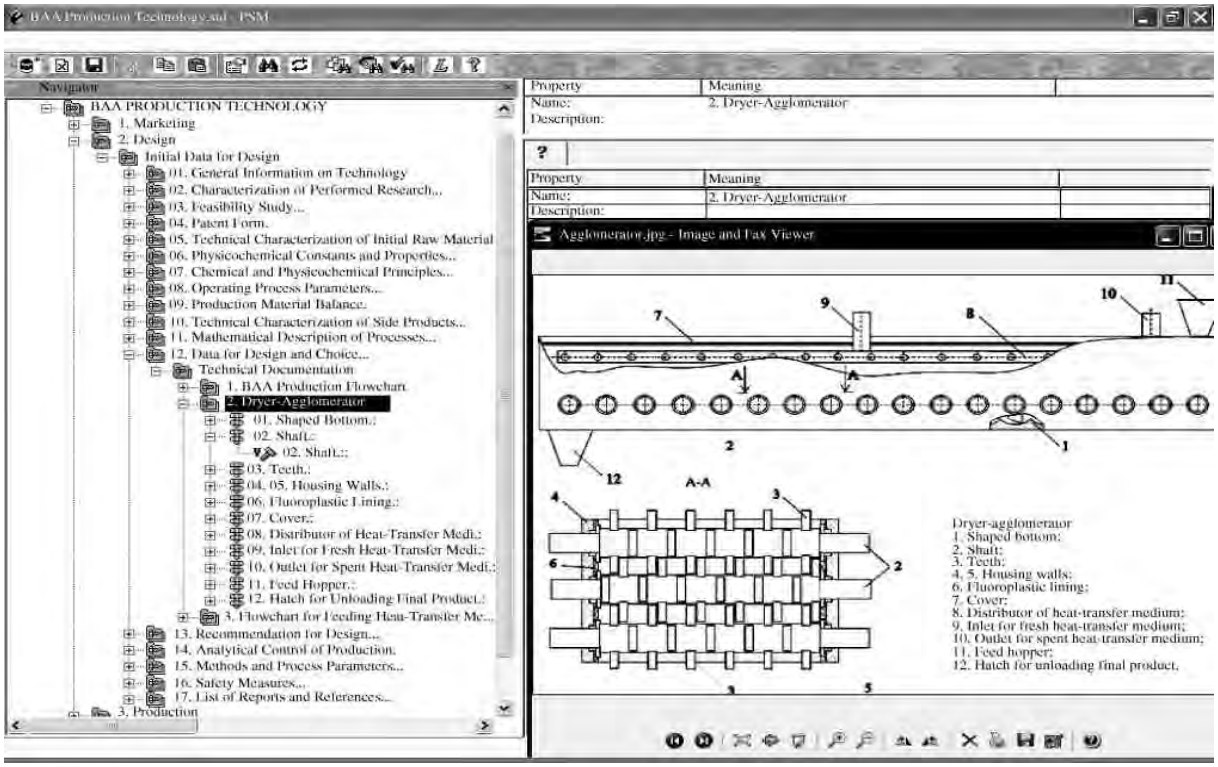

Fig. 3. CALS Project element at the design step (dryer–agglomerator design).

At the design step, four variants of agitator design are considered (Fig. 4). The ultimately chosen variant was the design that ensured required product quality at minimal energy consumption, with the agitator of this design being constructed at minimal material and labor expenditures. Three methods for introducing a heat-transfer medium were analyzed, and the optimal variant ensuring the maximal uniformity and efficiency of heat transfer was chosen. Intermediate and final variants described in text and graphic files were included into the CALS project.

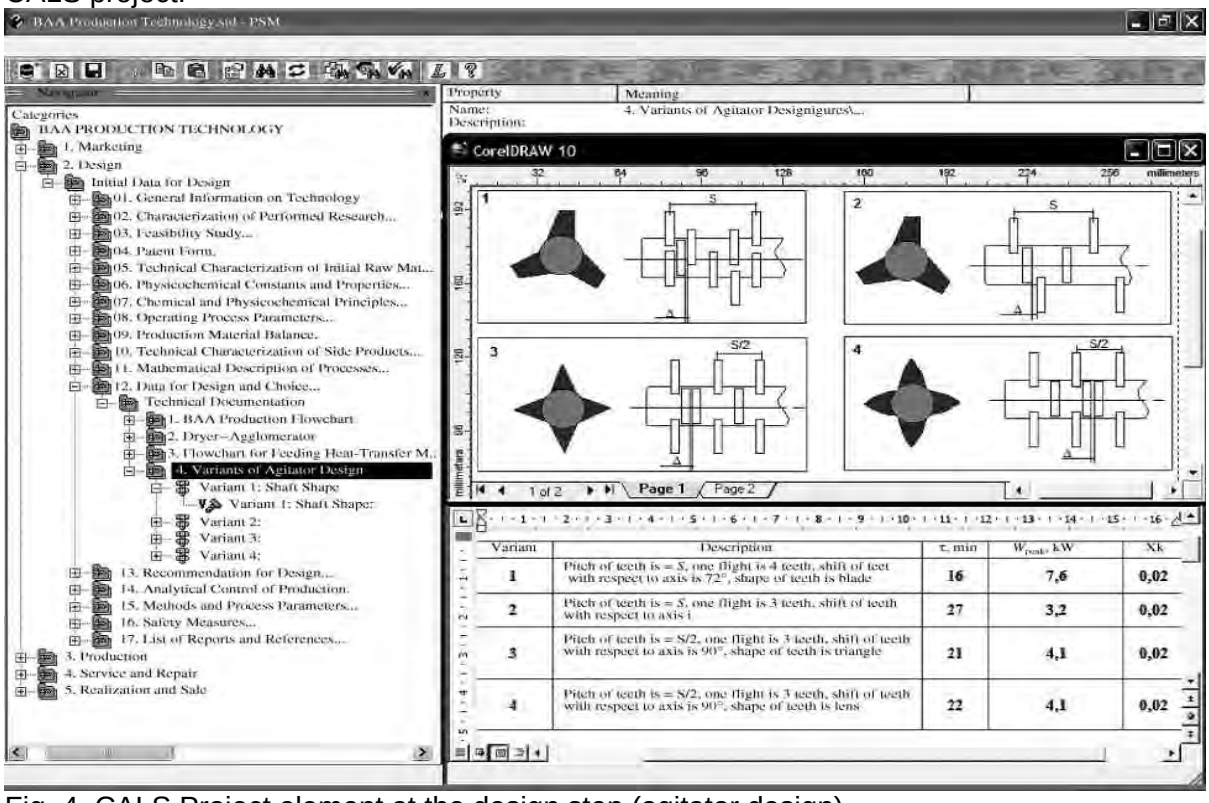

Fig. 4. CALS Project element at the design step (agitator design).

At the production step, technical documentation of extractors, dryers--agglomerators, and other equipment is analyzed by industrial equipment manufacturing plants.
At the service step, technical information on the main stages (switching on, operation, switching off, washing) of service of extractors, dryers--agglomerators (Fig. 5), and other equipment is introduced.

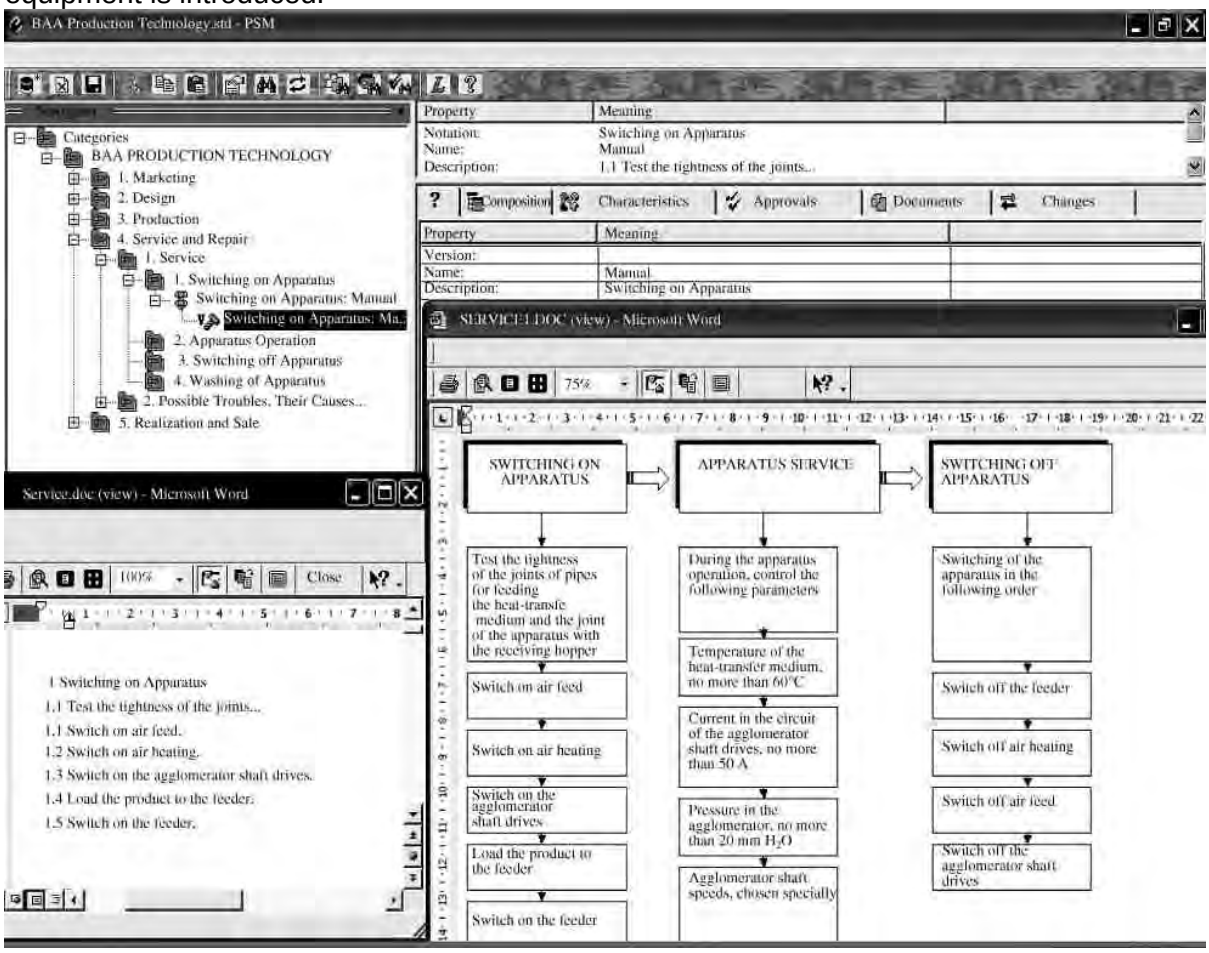

Fig. 5. CALS Project element at the step of service of the dryer–agglomerator.

Information at the repair step (Fig. 6) is structured at three levels: trouble--cause--troubleshooting. The developed module enables one to promptly, in dialog mode, select the optimal variant of troubleshooting.
The step of realization and sale includes product promotion to market (advertising in printed and electronic mass media; participation in exhibitions, contests, tenders, etc.) and also analysis of information on the use of the developed equipment not only in the technology of biologically active additives but also in the chemical and pharmaceutical industries. Under the conditions of the rapid development of the Internet with allowance for its potentialities, one of the elements of this step is the development of the information web site of OOO Ob''edinenie IREA-PENZMASh, the parent organization in the production of the biologically active additives considered in this work and promising equipment for drying highly viscous extracts of medicinal raw material. On the basis of accumulated information, the optimal structure of the web site was developed, necessary information contents were analyzed, and a system for rapidly surfing the site was implemented. The site combines two main Internet systems: FTP and WWW. The WWW system is used to illustratively and conveniently store information, to structure information, and to easily move between sections. The FTP service is used for data (file) storage and exchange.
Basic elements of the CALS project for the technology of biologically active additives are placed on the Internet on the CALS-khimiya (CALS Chemistry) web site in the Pilot Projects section. Also here are links to CALS files containing data in STEP exchange format. The files

themselves are located on an FTP server and are accessed via FTP protocol with an ordinary WWW browser. This scheme (in which information is place in FTP rather than WWW) is chosen for new files to be conveniently uploaded to the CALS-khimiya web site by various developers, rather than solely by the server administrator. The CALS-khimiya web site is one of the promising elements for training scientists and specialists of industrial plants in implementing CALS methods to the chemical industry.

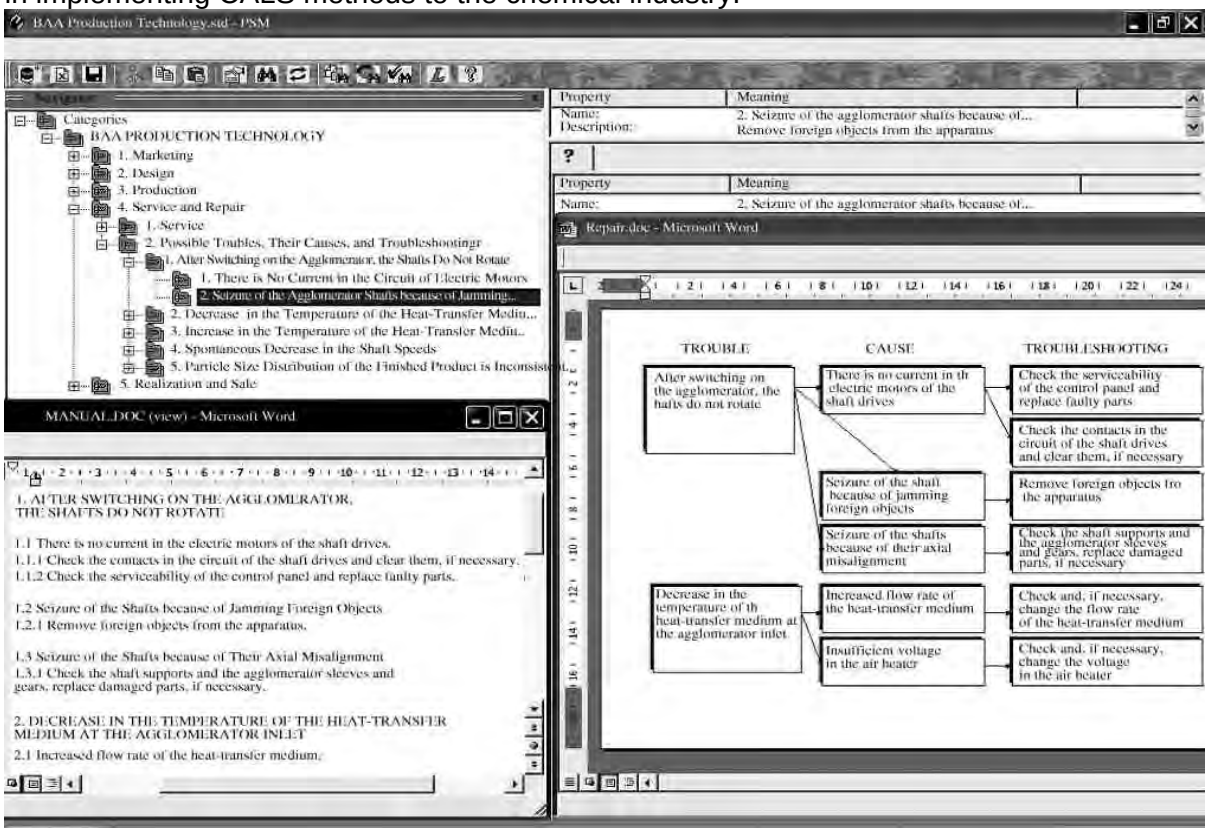

Fig. 6. CALS Project element at the step of repair of the dryer–agglomerator.

The results of this work were implemented at plants of the OOO Ob''edinenie IREA-PENZMASh. The developed CALS documentation significantly reduces the service, maintenance, and repair costs. According to predictions of foreign specialists, after 2005, it will be impossible to sell high-tech products in the international market without electronic documentation created in compliance with international CALS standards (ISO 10303 (STEP)) (Bessarabov et al., 2002). Therefore, one can believe that the electronic description of the technology of biologically active additives in accordance with the international CALS standard ISO 10303 (STEP) enables one to increase sales of new equipment.

References

Bessarabov, A.M., Afanas'ev, A.N. (2002). CALS Technologies in the Design of Promising Chemical Production Plants, 3, 26-30, *Khim. Tekhnol*.

Bessarabov, A.M., Zhdanovich, O.A. (2006). Development of information CALS-technologies in the industry of chemical reagents and high-pure substances. *Synthesis and Properties of Low- and High-Molecular Compounds. Quantitative Level. Published by Nova Science Publishers, Inc*. 75-83, New York.

Bessarabov, A.M., Ponomarenko, A.N., Ivanov, M.Ya. (2007). CALS Information Technologies (ISO-10 303 STEP) in Development of Plasmochemical Processes for Synthesis of Ultrapure Ultradispersed Oxides. *Russian Journal of Applied Chemistry.* Volume 80, 1, 13-18.

Bessarabov, A.M., Malyshev, R.M., Dem'yanyuk, A.Yu., et al. (2003). CALS Modeling of Drying (Sol–Gel Transition) of Highly Viscous Extracts of Medicinal Raw Material, 12, 23-30 ,*Khim. Prom–st. Segodnya.*

Proceedings of the 10th International Chemical and
Biological Engineering Conference - CHEMPOR 2008
Braga, Portugal, September 4-6, 2008
E.C. Ferreira and M. Mota (Eds.)

Stability of hydrolase enzymes in ionic liquids

F.J. Hernández-Fernández[1], A.P. de los Ríos[2], F. Tomás-Alonso[2],D. Gómez[2], M.Rubio[2], G. Víllora[2*]

[1]Department of Chemical and Environmental Engineering, Polytechnic University of Cartagena, Paseo Alfonso XIII, 52, E-30203 Cartagena, Murcia, Spain.
[2]Department of Chemical Engineering, Faculty of Chemistry, University of Murcia, P.O. Box 4021, Campus de Espinardo, E-30100, Murcia, Spain.

Keywords: stability, hydrolase enzyme, lipase, penicillin acylase, ionic liquid.
Topic: Sustainable process-product development through green chemistry

Abstract

In this work we attempted to evaluate the stability of penicillin G acylase (PGA) from *Escherichia coli* in their native form and free *Candida antarctica* lipase B (CaLB) at low water content. The hydrolysis of penicillin G to 6-aminopenicillanic acid (6-APA) and phenyl acetic acid (PAA) catalysed by PGA and the synthesis of butyl butyrate from vinyl butyrate and 1-butanol catalyzed by CaLB were chosen as activity tests. The influence of these new solvents on enzyme stability was studied by incubating the enzyme (PGA or CaLB) in ionic liquids based on dialkylimidazolium cations associated with perfluorinated and dicyanamide anions at 40°C and 30°C, respectively. Stability studies indicate that CaLB and PGA exhibited greater stability in water-immiscible ionic liquids than in water-miscible ionic liquids. Specifically, native penicillin G acylase shows greater stability in IL media than in organic solvents. For example, a half-life time of 23 h was obtained in 1-ethyl-3-methylimidazolium bis{(trifluoromethyl)sulfonyl}imide, $[emim^+][TfN_2^-]$, which was about 2000-fold higher than that in 2-propanol. The higher half-life time of CaLB was observed in $[omim^+][PF_6^-]$ ($t_{1/2}$=84 h).

1. Introduction

In nature, enzymes act as catalysts of living systems and are designed to function in aqueous solutions. However, anhydrous conditions are needed for synthetic transformations using enzymes. The use of organic solvents as non-aqueous environments offers the possibility of carrying out synthetic reactions by hydrolytic enzymes, increasing the solubility of organic substrates (Klibanov, 2001). However, volatile organic solvents have a detrimental impact on the environment, and it is therefore necessary to develop new alternatives for enzyme-catalyzed synthesis in environmentally friendly reaction media. ILs have recently been shown to be an appropriate non-aqueous media for many enzyme-catalyzed reactions, including the synthesis of aminoacids (Eckstein et al., 2002) and aliphatic esters (Berberich *et al*., 2003), the kinetic resolution of rac-aromatic alcohols (Noël et al., 2004) and the carbohydrate ester synthesis (Kim et al., 2003). Ionic liquids are organic salts that are liquid close to room temperature. They normally consist of an organic cation, being the most commonly used dialkylimidazolium and tetraalkylammomiun salts, and a polyatomic inorganic anion having a strongly delocalized negative charge (e.g. hexafluorophosphate, tetrafluoroborate) (Brennecke and Maginn 2001).

From an environmental point of view, the most important properties of ionic liquids are their negligible vapour pressure, which makes them environmentally benign solvents compared with volatile organic solvents and their good chemical and thermal stabilities (Sheldon 2001). Additionally, the physical-chemical properties of ionic liquids, such as their hydrophobicity, density, viscosity, melting point, polarity and solvent properties, may be modified by altering

* Corresponding author. Tel + 034-968-367363. E-mail:gvillora@um.es

the anion or the cation (Dzyuba and Bartsch 2003). Indeed, this feature is a key factor for realizing successful reactions since appropriate combinations of the cationic and anionic parts of the solvent can be made. In this sense, ionic liquids are often referred to as designer solvents (Freemantle 1998). Lipase has shown good behaviour as a catalyst in non-conventional media (Hernández et al. 2006, Paiva et al. 2002). Among the ionic liquids used for lipase-catalyzed reactions, those containing alkylimidazolium cations are showed to be one of the most interesting. In spite of this, it is known that some of these ionic liquids have a strong impact on the activity and stability of lipases (Lau et al. 2004). On the other hand Penicillin G acylase (PGA; EC 3.5.1.11) is the key enzyme used in the industrial production of β-lactam penicillin antibiotics. This enzyme hydrolyzes the side chain of penicillin G and related β-lactam antibiotics, releasing 6-amino penicillanic acid (6-APA), which is the building block in the manufacture of semisynthetic penicillins. PGA can also be used for the production of semisynthetic β-lactam antibiotics, in which the enzyme catalyses the condensation of an acyl group and a 6-APA molecule. The use of non-conventional media such us organic solvents or water-cosolvent mixtures has increased the performance of enzymatic β-lactam synthesis (Illanes *et al*., 2002). Thermodynamic equilibrium could be shifted toward the synthesis using hydrophobic solvents in the reaction medium. It has been demonstrated that PGA is highly active in apolar organic solvents, catalysing the resolution and protection of L-amino acids, D-amino acids and amines (Carboni et al., 2004).

This work studies the stability of free *Candida antarctica* lipase B (CaLB) and penicillin G amidase (PGA-450) in several ionic liquids consisting of dialkylimidazolium cations combined with a range of anions, including hexafluorophosphate, bis(trifluoromethylsulfonyl)imide and dicyanamide (see Figure 1), as well as in a common organic solvents.

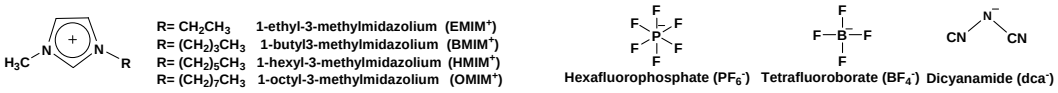

Figure 1. Ions involved in the assayed ionic liquids.

Butyl butyrate synthesis from vinyl butyrate and 1-butanol catalyzed was chosen as reaction model (see Figure 2) for CaLB. The hydrolysis of penicillin G (PG) to 6-aminopenicillanic acid (6-APA) and phenyl acetic acid (PAA) was chosen as activity test for PGA. A comparison of the stability of CaLB and PGA in ionic liquids was also performed.

2. Materials and Methods

2.1. Materials

A commercial lipase (EC 3.1.1.3) preparation was used as catalyst: free *Candida antarctica* lipase B aqueous solution (Lipozyme® CaLB L), which was a gift from Novo España S.A. Prior to use, the enzyme solution was 4-fold diluted in 20 mM phosphate buffer at pH 7. Penicillin G acylase (EC 3.5.1.11) from *Escherichia coli* was purchased from Sigma-Aldrich-Fluka Chemical Co., 29 U/mg. Activity units (U) are reported based on the manufacturer´s determination of activity using the hydrolysis of a 2% (w/v) solution of penicillin G potassium salt (PG) in 0.1 M phosphate buffer pH 7 at 37 ºC.

[bmim$^+$][PF_6^-], [hmim$^+$][PF_6^-], [omim$^+$][PF_6^-], [bmim$^+$][BF_4^-], [hmim$^+$][BF_4^-], were purchased from Solvent Innovation (purity > 99%). The ionic liquids [emim$^+$][TfN_2^-] (purity >99%) and [bmim$^+$][TfN_2^-] (purity >99%) were purchased from Sigma-Aldrich-Fluka Chemical Co. and Strem Chemical Inc., respectively and [hmim$^+$][TfN_2^-] (purity >99%) from Merck KgaA. *1-Butyl-3-methylimidazolium dicyanamide, [bmim$^+$][dca$^-$]* was synthetized as described in a

previous work (de los Ríos et al., 2007). Substrate, solvents and other chemicals were purchased from Sigma-Aldrich-Fluka Chemical Co., and were of the highest purity available.

2.2. CaLB stability in ionic liquids

Mixtures containing 457 μL of ionic liquid and 10 μl of *Candida antarctica* lipase B (8.5 mg mL^{-1} in 20 mM phosphate buffer at pH 7) were incubated at 30 ºC in different screw-capped vials of 1.5 mL total volume. At different incubation times, 19.2 μL (150 μmol) vinyl butyrate and 13.8 μL (150 μmol) 1-butanol were added and the activity of CaLB was measured as described bellow.

2.3. CaLB activity in ionic liquids

19.2 μL (150 μmol) vinyl butyrate and 13.8 μL (150 μmol) 1-butanol were added to 1.5 mL screw-capped vials containing 457 μL of each ionic liquid, or hexane. The reaction was started by adding 10 μL of *Candida antarctica* lipase B (8.5 mg mL^{-1} in 20 mM phosphate buffer at pH 7) and run for 2 h at 30ºC. At different times, 15 μL aliquots were extracted and suspended in 485 μL hexane. The biphasic mixture was strongly shaken for 2 min to extract all the substrates and products into the hexane phase. Then, the hexane solution of ethyl hexanoate (internal standard) (100 μL, 30 mM) was added into the hexane extract (400 μL) and resulting solution (5 μL) was analyzed by GC. The synthetic activity was defined as the amount of enzyme that produces 1 μmol of butyl butyrate per minute.

2.4. PGA stability in ionic liquids

Into a screw-capped vial of 1.5 mL total volume containing 490 μL of ILs or 2-propanol, 10 μL of 35 mg/mL of PGA in 0.1 M phosphate buffer were added and the mixture incubated at 40ºC. At different times, a 30 μL aliquot of the incubation medium was taken and the hydrolytic activity of PGA was measured as described below.

2.5. Enzymatic hydrolisis of penicillin G

The reaction was started by adding a 30 μL aliquot of the incubation medium (PGA incubated in the IL or 2-propanol at 40ºC as described in 2.4) into a screw-capped vial of 1.5 mL total volume containing 470 μL 50 mM PG in in 0.25 M phosphate buffer pH 8 and run at 40 ºC for 24 h. At different times, 50 μL aliquots were extracted and dissolved in 150 μL of 50 mM HCl to stop the reaction and then 50 μL of this solution were added to 575 μL of 0.72 mM resorcinol in 0.25 mM phosphate buffer (internal standard). Finally, 5 μL of the resulting solution was analyzed by high-performance liquid chromatography (HPLC). One unit of hydrolytic activity was defined as the amount of enzyme that produces 1 μmol of PAA per minute at 40ºC pH 8 from 50 mM PG in 0.25 M phosphate buffer.

2.6. Analytical methods

Substrate and product concentrations of penicillin G hydrolysis were determinated by HPLC using a LiChrospher RP-18 column (25 cm length and 4 mm internal diameter, 5 μm particle size and 10 nm pore size). Samples were eluted isocratically with 80% (v/v) 20 mM potassium phosphate buffer pH 6,0 and 20% (v/v) acetronitrile at a flow rate of 0.8 ml/min, and analysed by a UV detector at 220 nm.

GC analysis of the substrates and product of butyl butyrate synthesis was performed with an Agilent 6890 N instrument equipped with FID detector and a Nukol™ capillary column (15m × 0.53mm ×0.5μm, Supelco), using ethyl hexanoate as internal standard. The chromatographic conditions were as follows: carrier gas (N_2) at 1.89 psi (51 mL /min total flow); temperature program: 40 ºC, 4 min; 5 ºC/min, 135ºC; split ratio: 7.9/1; detector: 220 ºC.

3. Results and Discussion

A key criterion for selecting an enzyme-IL system is the stability of the catalyst within the reaction medium. The influence of these new solvents on *Candida antarctica* lipase B stability was studied by incubating the enzyme in different ionic liquids at 30ºC and 2% (v/v) water content. The ionic liquids selected for this study were: [bmim$^+$][PF_6^-], [hmim$^+$][PF_6^-], [omim$^+$][PF_6^-], [hmim$^+$][TfN_2^-], [hmim$^+$][BF_4^-] and [bmim$^+$][dca$^-$]. In all cases, the activity loss followed a second order deactivation kinetics, which permitted the half-life time ($t_{1/2}$) of the enzyme to be determined (see Table 1).

Table 1. Half-life times of *Candida antarctica* lipase B exhibited by incubation in diferent ionic liquids at 30ºC.

Medium	Half-life time (h)
[bmim$^+$][PF_6^-]	48
[hmim$^+$][PF_6^-]	78
[omim$^+$][PF_6^-]	84
[hmim$^+$][NTf_2^-]	72
[hmim$^+$][BF_4^-]	7
[bmim$^+$][dca$^-$]	1.5

As can be seen, the stability of CaLB seems to increase with the increase in the alkyl chain length of the cation, which agrees with the increase in ILs hydrophobicity, although no significant differences in stability has been observed between [hmim$^+$][PF_6^-] and [omim$^+$][PF_6]. These results are in accordance with those obtained by Lozano et al. (2004), who found that the enzyme was very sensitive to deactivation when hydrophobicity decreased, at 2 % water content. The most important effect on CaLB stability was observed by changing the nature of IL anions, as can be observed in Table 1 by comparing the half-life times of CaLB in ionic liquids containing the same cation. For the ionic liquids containing the cation [bmim$^+$], the half-life times increased in the following order: [bmim$^+$][dca$^-$] < [bmim$^+$][PF_6^-], and for those containing the cation [hmim$^+$] in the following order: [hmim$^+$][BF_4^-]<[hmim$^+$][TfN_2^-]< [hmim$^+$][PF_6^-]. Bearing in mind the nucleophilicity sequence for the anions [dca$^-$]> [BF_4^-] >[TfN_2^-]> [PF_6^-] (Irimescu and Kato 2004b, Muldoon et al. 2001), the increase in half-life time was in agreement with the decrease in this parameter. This could be explained by the fact that the most nucleophilic anion may interact more strongly with the enzyme, causing changes in the active enzyme structure. [omim$^+$][PF_6^-], composed of the least nucleophilic anion and the most hydrophobic cation, was seen to be the best IL for protecting the enzyme, with a half-life time of 84 h. In contrast, [bmim$^+$][dca$^-$], which contained the most nucleophilic anion and the least hydrophobic cation, produced a fast fall on CaLB activity, with a half-life time of 1.5 h. The same tendency was observed by Kaar et al. (2003) with Novozym® 435, which was more stable in [bmim$^+$][PF_6^-] than in [bmim$^+$][NO_3^-] and by Persson and Bornscheuer (2003) [33] using an esterase from *B. stearothermophilus*, which showed greater stability in [bmim$^+$][PF_6^-] than in [bmim$^+$][BF_4^-]. The influence of ILs on PGA stability was studied by incubating in several ILs: [bmim$^+$][BF_4^-], [bmim$^+$][PF_6^-], [omim$^+$][PF_6^-], [emim$^+$][NTf_2^-], [bmim$^+$][NTf_2^-] and in organic solvents (2-propanol, toluene, dichloromethane) at 40 ºC.Half-life times of PGA are shown in Table 2.

Table 2. Half-life times of Penicillin G acylase exhibited by incubation in diferent ionic liquids at 40ºC.

Medium	Half-life time (h)
[emim$^+$][Tf_2N^-]	23.21
[bmim$^+$][Tf_2N^-]	9.42
[bmim$^+$][PF_6^-]	1.27
[omim$^+$][PF_6^-]	0.80
[bmim$^+$][BF_4^-]	0.29
2-propanol	0.01

Full enzyme deactivation was practically instantaneous in toluene and dichloromethane, so the only assayed organic solvent in which PGA showed significant stability at the assayed conditions was 2-propanol. As can be seen from Table 1, the half-life time of PGA in ILs was notably improved with respect to 2-propanol. As CaLB, the most important effect on PGA stability was observed by changing the nature of IL anions by comparing the half-life times of PGA in ionic liquids based on the same cation. As can be seen in Table 1, in ionic liquids containing the [bmim$^+$] cation the half-life times increased in the following order: [bmim$^+$][NTf_2^-] > [bmim$^+$][PF_6^-] > [bmim$^+$][BF_4^-]. The low half-life time of PGA in [bmim$^+$][BF_4^-], which is fully miscible with water, could be attributed to the interaction with the absolute amount of water indispensable for acquisition and maintenance of the catalytic conformation of the enzyme. This solvent could strip off the tightly bound water molecules, resulting in either alteration or sometimes distortion of the catalytic conformation and consequently result in deactivation of the enzyme (Nara et al., 2002). The cation also exerts a strong effect on the denaturation of PGA, since, contrary with CaLB, the enzyme is more stable when suspended in the ILs containing cation with shorter 1-alkyl chain length. This effect was even more evident in the most hydrophobic ionic liquids, those based on [NTf_2^-] anions. This behavior has been also described by Basso *et al*. (2005) using the enzyme in an immobilized form, PGA-450.

4. Conclusions

The stability of *Candida antarctica* lipase B and Penicillin G acylase was tested for a wide range of 1,3-dialkylimidazolium based ionic liquids. In both cases, The most important effect on enzyme stability was observed by changing the nature of IL anions. It is worthing to note how the presence of ILs enhance the stability of PGA and, in the case of [emim$^+$][NTf_2^-], an over-stabilization phenomenon is produced, increasing the half-life time by about 2000-fold with respect to 2-propanol, used as reference organic solvent. The lower half-life time of enzymes was observed in [bmim$^+$][BF_4^-] for PGA and in [bmim$^+$][dca^-] for CaLB. This could be explained by the fact that these ILs are fully miscible with water, so they could interact with the absolute amount of water indispensable for acquisition and maintenance of the catalytic conformation of the enzymes.

Accordingly, the potential advantages of these new solvents, together with the unique stabilization effect on enzymes, may open up the possibility of development of new biocatalytic processes based on ionic liquids.

Acknowledgment

This work was partially supported by the CICYT CTQ2005-09238/PPQ and SENECA Foundation 05786/PI/07 grants.

References

Basso, A., Cantone, S., Linda, P., Ebert, C. (2005). Stability and Activity of Immobilised Penicillin G Amidase in Ionic Liquids at Controlled a_w, *Green Chem,* 7, 671-676.

Berberich, J.A., Kaar, J.L., Russell, A.J. (2003). Use of Salt Hydrate Pairs to Control Water Activity for Enzyme Catalysis in Ionic Liquids. *Biotechnol Prog* 19: 1029-1032.

Carboni, C., Quaedflieg, P.J.L.M., Broxterman, Q.B., Linda, P., Gardossi, L. (2004). Quantitative Enzymatic Protection of D-Amino Acid Methyl Esters by Exploiting "Relaxed" Enantioselectivity of Penicillin-G Amidase in Organic Solvent, *Tetrahedron Lett.,* 45, 9649-9652.

de los Ríos, A.P., Hernández-Fernández, F.J., Martínez, F.A., Rubio, M., Víllora, G. (2007). The effect of ionic liquid media on activity, selectivity and stability of Candida antarctica Lipase B in transesterification reactions, Biocatal Biotransform, 25, 151-156.

Dzyuba, S., Bartsch, A. (2003). Recent Advances in Applications of Room-Temperature Ionic Liquid-Supercritical Carbon Dioxide Systems, Angewandte Chemie-International Edition, 42,148-150.

Eckstein, M., Sesing, M., Kragl, U., Adlercreutz, P. (2002). At Low Water Activity α-Chymotrypsin is More Active in an Ionic Liquid than in Non-Ionic Organic Solvents, *Biotechnol Lett,* 24, 867-872.

Freemantle, M. (1998). Designer solvents. Ionic liquids may boost clean technology development, Chemical Engineering News, 76, 32-37.

Hernández, F.J., de los Ríos, A.P-, Gómez, D., Rubio, M., Víllora, G. (2006). A new recirculating enzymatic membrane reactor for ester synthesis in ionic liquid/supercritical carbon dioxide biphasic systems, Applied Catalysis B: Environmental, 67, 121-126.

Illanes, A., Anjari, S., Arrieta, R., Aguirre, C. (2002). Optimization of Yield in Kinetically Controlled Synthesis of Ampicillin with Immobilized Penicillin Acylase in Organic Media, *App Biochem Biotechnol,* 97, 165-180.

Irimescu, R., Kato, K. (2004). Investigation of ionic liquid as reaction media for enzymatic enantioselective acylation of amines, J. Mol. Catal. B: Enzym., 30, 189-194.

Kaar, J.L., Jesionowski, A.M., Berberich, J.A., Moulton, R., Russell, A.J. (2003). Impact of ionic liquid physical properties on lipase activity and stability, Journal of the American Chemical Society, 125, 4125-4131.

Kim, M.-J., Choi, M.Y., Lee, J.K., Ahn, Y. (2003). Enzymatic Selective Acylation of Glycosides in Ionic Liquids: Significantly Enhanced Reactivity and Regioselectivity, *J. Mol. Catal. B Enzym.,* 26, 115-118.

Klibanov, A.M. (2001). Improving enzymes by using them in organic solvents. *Nature* 409, 241-246.

Lau, R.M., Sorgedrager, M.J., Carrea, G., van Rantwijk, F. (2004). Dissolution of Candida antarctica lipase B in ionic liquids: effects on structure and activity, Green Chem., 6, 483-487.

Lozano P, De Diego T, Gmouth S, Vaultier M, Iborra JR. 2004. Criteria to design green enzymatic processes in ionic liquid/supercritical carbon dioxide systems. Biotechnology Progress 20: 661-669.

Muldoon, M.J., Gordon, C.M., Dunkin, I.R. (2001). Investigations of solvent-solute interactions in room temperature ionic liquids using solvatochromic dyes, Journal of Chemical Society Perkin Transactions, 2, 433-435.

Nara, S.J., Harjani, J.R., Salunkhe, M.M. (2002). Lipase-Catalysed Transesterification in Ionic Liquids and Organic Solvents: a Comparative Study, *Tetrahedron Lett.,* 43, 2979-2982

Nara, S.J., Mohile, S.S., Harjani, J.R., Naik, P.U., Salunkhe, M.M. (2004). Influence of Ionic Liquids on the Rates and Regioselectivity of Lipase-Mediated Biotransformations on 3,4,6-Tri-O-Acetyl-D-Glucal, *J. Mol. Catal. B Enzym.,* 28, 39-43.

Noël, M., Lozano, P., Vaultier, M., Iborra, J.L. (2004). Kinetic Resolution Of rac-2-Pentanol Catalyzed by Candida antarctica Lipase B in the Ionic Liquid, 1-Butyl-3-methylimidazolium Bis[(Trifluoromethyl)Sulfonyl]amide, *Biotechno.l Lett.,* 26, 301-306.

Paiva, A.V., Rossum, D.V., Malcata, F.X. (2002). Kinetics of lipase-mediated synthesis of butyl butyrate in n-hexane, Biocatalysis and Biotransformations, 20, 43-51.

Persson, M., Bornscheuer, U.T. (2003). Increased stability of an esterase from Bacillus stearothermophilus in ionic liquids as compared to organic solvents, J. Mol.Catal. B: Enzym., 22,21- 27.

Sheldon, R. (2001). Catalytic reactions in ionic liquids, Chemical Communications, 23, 2399-2407.

Proceedings of the 10th International Chemical and
Biological Engineering Conference - CHEMPOR 2008
Braga, Portugal, September 4-6, 2008
E.C. Ferreira and M. Mota (Eds.)

Fructooligosaccharides production using immobilized cells of *Aspergillus japonicus*

Solange I. Mussatto*, Giuliano Dragone, Lígia R.M. Rodrigues, José A. Teixeira
IBB – Institute for Biotechnology and Bioengineering, Centre of Biological Engineering,
University of Minho, Campus de Gualtar, 4710–057 Braga, Portugal.

Keywords: Sucrose, Fermentation, *Aspergillus japonicus*, Fructooligosaccharides, Immobilization.
Topic: Multi-scale and/or multi-disciplinary approach to process-product innovation.

Abstract

The fructooligosaccharides (FOS) production using immobilized cells of the fungus *Aspergillus japonicus* ATCC 20236 was evaluated. Polyurethane foam, stainless steel sponge, vegetal fiber sponge, pumice stones, zeolites and cork were tested as immobilization carrier during the fermentation under submerged conditions. Experiments were carried out in 500 ml Erlenmeyer flasks containing 1 g of carrier and 100 ml of sucrose medium (165 g/l) enriched with nutrient sources. The flasks were agitated in an orbital shaker at 160 rpm, 28°C, for 48 h. Samples were withdrawn during the fermentation to determine the consumption of sucrose, liberation of glucose and fructose to the medium, production of FOS (1-kestose (GF_2), 1-nystose (GF_3) and 1-β-fructofuranosyl nystose (GF_4)) and enzymatic activity of β-fructofuranosidase. At the fermentation end, the cell mass adhered to the carrier was quantified. The microorganism adhesion to the carrier varied to each tested material. Consequently, the FOS production and enzymatic activity also varied to each medium, due to the differences in the amount of free and immobilized cells present. The highest values of immobilized cells, FOS production and enzymatic activity were achieved by using vegetal fiber sponge as immobilization carrier, while cork gave the worst results.

1 Introduction

Fructooligosaccharides (FOS) are naturally occurring sugars that have beneficial effects as food ingredients, because of its low calorie, noncariogenic nature and ability to promote the growth of beneficial bifidobacteria-rich intestinal flora and immune system modulation. Although FOS is present in several plants, the concentration of them in these sources is low and choice of plants as a source of FOS is limited by seasonal conditions (Wang & Zhou, 2006). Hence, microbial FOS production by the action of fungal fructosyltransferase on sucrose is more feasible at industrial level (Sangeetha et al., 2005).

In the process of FOS production with fructosyltransferase, the main problem is that the activity of the enzyme is severely inhibited by glucose, which is generated as a byproduct. As a result, maximum conversion yield of sucrose to FOS ranges from 55 to 60% (w/w) due to unreacted sucrose and glucose. Since the produced FOS mixture contains considerable amounts of sucrose and glucose, its use has been limited (Yun, 1996). Therefore, the development of processes that permit the FOS production in industrial scale with higher yields, and lower necessity of purification of the final product, is necessary.

The use of immobilized enzymes or cells can be useful for the development of effective and economic methods for large-scale production of FOS. Nevertheless, the selection of the immobilization material is essential to design an effective system for this purpose. The aim of the present work was to evaluate the FOS production using immobilized cells of the fungus *Aspergillus japonicus* ATCC 20236. Polyurethane foam, stainless steel sponge, vegetal fiber

* Corresponding author. Tel + 351- 253 604400 Ext. 605413. E-mail: solange@deb.uminho.pt

sponge, pumice stones, zeolites and cork were tested as microorganism carrier during the production of FOS under submerged fermentation conditions.

2 Material and methods

2.1. Carrier's preparation

Six porous carriers were tested: Polyurethane foam, stainless steel sponge, and vegetal fiber sponge (Scotch Brite, 3M Spain, SA), pumice stones (Elite, purchased at a local department store), zeolites molecular sieves type 4A (BDH Chemicals Ltd., Poole, England), and cork. Polyurethane foam, vegetal fiber sponge and cork were 0.3 cm^3 cubes. Stainless steel sponge was used as cuttings of irregular size. Pumice stones were granules of 8–24 mesh (2.36 mm to 0.71 mm – sieve opening), and zeolites were approximately 0.1 cm in diameter and 0.4 cm length. To be used as immobilization carrier, all the materials were pre-treated by boiling for 10 min, washed three times with distilled water, and then dried overnight at 60 ºC. Prior to use, all the carrier materials were autoclaved at 121 ºC for 20 min.

2.2. Microorganism maintenance

The strain *Aspergillus japonicus* ATCC 20236 was used in the experiments. The strain was maintained on potato dextrose agar (PDA - Difco) plates at 4 ºC, and the spores were maintained mixed with glycerol solution in ultra-freezer at −80 °C. For the production of spores the strain was grown on PDA medium, at 25-30 ºC for 7–8 days.

2.3. Fermentation conditions

The fermentation experiments were carried out in 500 ml Erlenmeyer flasks containing 1 g of carrier and 100 ml of culture medium with the following composition (% w/v): sucrose 16.5, yeast extract 2.75, $NaNO_3$ 0.2, K_2HPO_4 0.5, $MgSO_4 \times 7H_2O$ 0.05, and KCl 0.05. Sterilization of the medium was carried out at 121 ºC for 20 min.

Flasks were inoculated with 1.0 ml of a spore suspension containing around 1.8×10^7 spores/ml, which was prepared by scrap down the spores from the PDA plates with a sterilized solution of 0.1% w/v Tween 80, and counted in a Neubauer chamber. The inoculated flasks were incubated in a rotary shaker at 28 °C and 160 rpm for 48 h. Cells were immobilized in situ in the flasks by natural adsorption.

Samples for analysis were collected at regular intervals and filtered, using 0.2 μm filters to separate the cell pellets from the culture fluid. In the filtered broth, FOS (1-kestose, 1-nystose, and 1-β-fructofuranosyl nystose), residual concentration of other sugars (sucrose, fructose, and glucose), pH and extracellular enzyme activity were measured. The concentrations of free and immobilized cells were determined at the fermentation end.

All the fermentation experiments were conducted in duplicate and the average values are reported. The relative standard deviation was less than 5%.

2.4. Analytical methods

Cell mass concentration. Free cell mass concentration was determined by dry weight per volume (g/l). At the end of the fermentation, the biomass was collected by vacuum filtration of the fermentation broth through pre-weighed 0.45 μm membranes, washed with distilled water and dried at 105 °C to constant weight.

The amount of biomass attached to the carriers was determined after washing the support material with distilled water for three times, and drying at 105 °C to constant weight. The biomass dry weight was determined from the difference between the cells plus carrier and the carrier itself.

Enzymatic activity: Samples of the fermentation media were filtered (through 0.2 μm membranes) to remove the cell mass and the filtrate was utilized as extracellular enzyme

source. The β-fructofuranosidase (FFase) activity was determined by measuring the amount of glucose produced from sucrose (Yoshikawa et al., 2006). The reaction mixture contained 100 ml of the crude FFase extract, 300 mmol of sucrose and 50 mmol of sodium acetate buffer (pH 5.0) in a total volume of 1 ml. After incubation for 20 min at 30 ºC, the reaction was stopped by heating for 5 min at 100 ºC. After cooling, the amount of glucose released into the supernatant was measured by high-performance liquid chromatography (HPLC, see below). One unit (U) of the FFase activity was defined as the amount of enzyme required to release 1 µmol of glucose per min, from sucrose under the above conditions.

Transfructosylating and hydrolyzing activities. The reaction was carried out for 180 min using 0.5 U/ml of FFase in the reaction mixture described above (Yoshikawa et al., 2006). Transfructosylating activity (Ut) and hydrolyzing activity (Uh) were determined by measuring the concentrations of 1-kestose and fructose by HPLC, respectively. One unit of transfructosylating activity was defined as the amount of enzyme required to transfer 1 µmol of fructose per min. One unit of hydrolyzing activity was defined as the amount of enzyme required to release 1 µmol of free fructose per min.

Sugars and FOS concentrations. FOS (1-kestose, 1-nystose, and 1-β-fructofuranosyl nystose) and other residual sugars (sucrose, glucose, and fructose), were directly analyzed by high performance liquid chromatography (HPLC) on an equipment LC-10 A (Jasco, Japan) with a Prevail Carbohydrate ES column (5 um, 250 x 4.6 mm, Alltech) at room temperature, and a refractive index detector. The response of the refractive index detector was recorded and integrated using the Star Chromatography Workstation software (Varian). A mixture of acetonitrile and 0.04% ammonium hydroxide in water (70/30 v/v) was used as mobile phase at a flow rate of 1.0 ml/min. Before injection, the samples were filtered through 0.2 µm filters and diluted with Milli-Q water when needed. The sugars and FOS concentrations were determined from standard curves made with known concentrations of each compound. The total yield of FOS (Y_{FOS}) was calculated as the sum of 1-kestose (Y_{GF2}), 1-nystose (Y_{GF3}), and 1-β-fructofuranosyl nystose (Y_{GF4}), to initial sucrose concentration.

3 Results and discussion

3.1. Immobilized cells concentration

Concentration of cells immobilized in the different carriers is given in Table 1. It can be noted that all the evaluated materials were able to immobilize cells, but with different capacities. Among them, pumice stones, cork and zeolites gave the lower immobilized cells concentration. A major quantity of cells was adhered into polyurethane foam, but the highest cell mass was adhered into stainless steel and vegetal fiber sponges, with the result of vegetal fiber sponge being 10% higher than that of stainless steel sponge.

Table 1. Free and immobilized cells concentration during FOS production by *A japonicus* immobilized in different materials.[a]

Immobilization carrier	Immobilized cells (g/g carrier)	Free cells (g/l)
Pumice stones	0.13	20.83
Zeolites	0.19	19.36
Stainless steel sponge	1.13	2.59
Polyurethane foam	0.48	6.44
Vegetal fiber sponge	1.25	5.09
Cork	0.14	9.97

[a] Values after 48 h of fermentation

All the experiments presented free cells in the medium besides those immobilized. Pumice stones, cork and zeolites, which gave the lowest immobilized cells concentration, presented the major amounts of free cells; while stainless steel sponge and vegetal fiber sponge, which immobilized the major proportion of cells, resulted in the lowest free cells concentration.

3.2. Sucrose consumption and FOS production with immobilized cells

Fermentation with the different carriers had similar behaviors of sucrose consumption and FOS production, with an initial lag phase of approximately 12 h where few substrate was consumed (Figure 1A). As a consequence, practically was not observed FOS production during this period (Figure 1B). Nevertheless, in the subsequent 12 h the process attained the maximum FOS production for practically all the carriers evaluated, as result of the almost depletion of sucrose from the media. 1-Kestose was the main FOS formed in the media at this time, followed by 1-nystose and 1-β-fructofuranosyl nystose that required a larger fermentation time to be formed. On an average, maximum 1-kestose concentration was observed in 24 h of fermentation; 1-nystose concentration was maximum around 36 h of fermentation, while the concentration of 1-β-fructofuranosyl nystose required approximately 48 h to attain the highest value. Similar behavior was observed by Cruz et al. (1998) during the FOS production by *Aspergillus japonicus* immobilized in calcium alginate. According to these authors, the fructooligosaccharide synthesis was always sequential in the sense $GF \rightarrow GF_2 \rightarrow GF_3 \rightarrow GF_4$ as a consequence of the increasing *Km* values for such products presented by the transfructosylase. Thus, high concentrations of the preceding oligosaccharide are always necessary for the synthesis of its homologue with one more fructose unit. This would also explain why the content of 1-kestose is higher at the beginning of the enzymatic reaction.

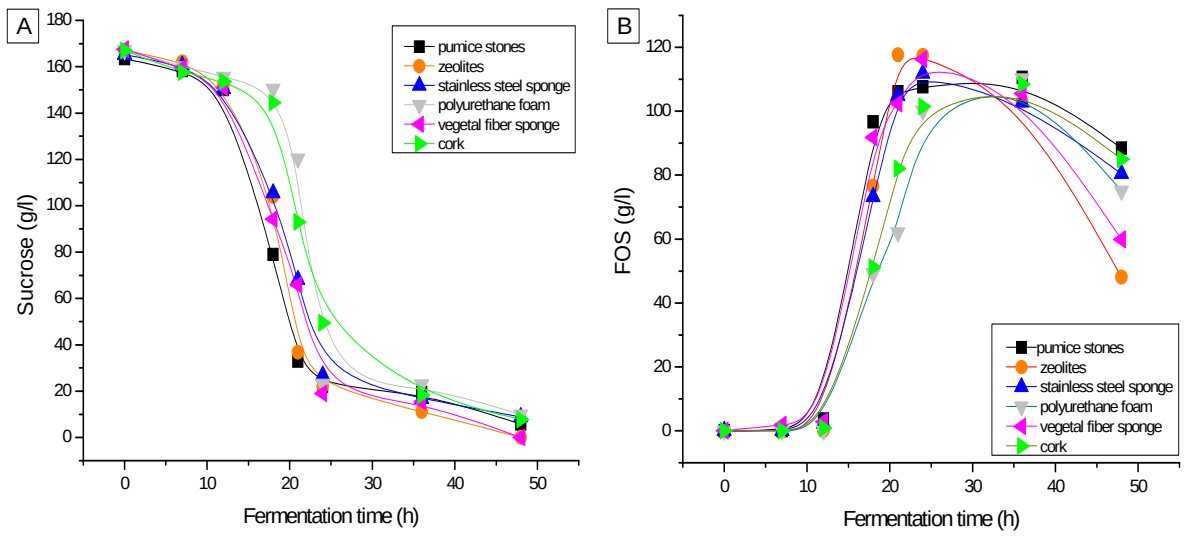

Figure 1. Sucrose consumption (A) and FOS production (B) using *A. japonicus* immobilized in different carriers.

After the initial 24 h fermentation, due to the sucrose exhaustion from the media, the microorganism passed to consume 1-kestose, and therefore, even being observed formation of the other two FOS, the total FOS concentration started to decrease in all media, as can be noted in Figure 1B. Consequently, when the reaction time was extended to over 48 h, changes in the total FOS content occurred, with an increase in GF_3 and GF_4 contents, and a corresponding loss of 1-kestose.

Although the kinetic behaviors of sucrose consumption and FOS production have been similar for all the assays, the fermentative parameters were different to each one of them,

due to the differences in residual sucrose content and total FOS produced, probably as a consequence of the different values of free and immobilized cells. As can be observed in Table 2, the medium containing zeolites gave the best results, but cells in this medium were mostly free (only few amounts were immobilized in the carrier – see Table 1). The media containing vegetal fiber or stainless steel sponges as carriers gave fermentative parameters values for FOS production close similar to those achieved with zeolites, but with an important advantage that in these cases the carrier was able to immobilize the large amounts of cells (Table 1). This means that using vegetal fiber or stainless steel sponges as carrier, it was possible to immobilize large amounts of cells and produce FOS with elevated yields. The medium containing cork as carrier resulted in the lowest values of FOS concentration, $Y_{P/S}$, and Q_P.

Table 2. Fermentative parameters of FOS production by immobilized *A. japonicus*.

Immobilization carrier	Maximum FOS (g/l)	Fermentation time (h)	$Y_{P/S}$ per total substrate (g/g)	$Y_{P/S}$ per consumed substrate (g/g)	Q_P (g/l.h)
Pumice stones	110.55	36	0.68	0.76	3.07
Zeolites	117.45	24	0.70	0.81	4.89
Stainless steel sponge	111.80	24	0.68	0.81	4.66
Polyurethane foam	110.26	36	0.66	0.76	3.06
Vegetal fiber sponge	116.26	24	0.69	0.78	4.84
Cork	108.47	36	0.65	0.73	3.01

3.3. Enzyme activity

Results for the FFase activity by *A. japonicus* immobilized in the different carriers are shown in Figure 2. The best value of enzyme production (42.92 U/ml) was found after 36 h with cells immobilized in vegetal fiber sponge. These values can be favorably compared to those obtained during FOS production by other fungus species. For example, under optimized cultivation conditions, *A. japonicus* JN-19 yielded the highest FFase activity of 55.42 U/ml at 96 h fermentation (Wang and Zhou 2006). In the present study, the maximum FFase activity was achieved after only 36 h fermentation, giving thus a much higher productivity.

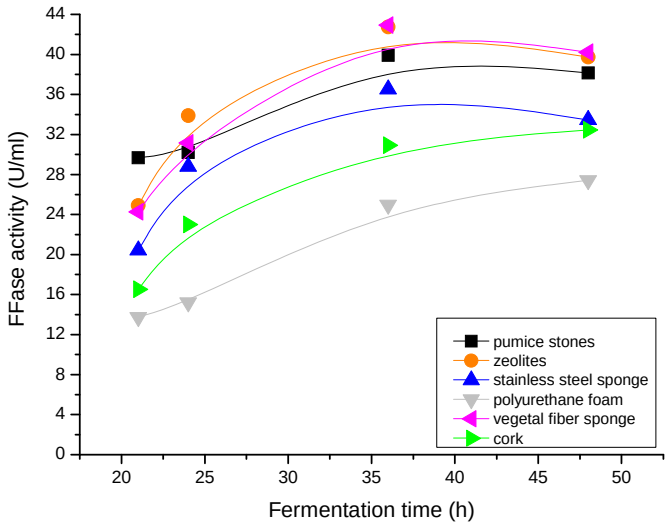

Figure 2. FFase activity by *A. japonicus* cells immobilized in different carriers.

FFases commonly possess both hydrolytic (Uh) and transfructosylating (Ut) activities. Nevertheless, for an efficient FOS production it is preferable to have a high Ut/Uh ratio (Chen & Liu, 1996). Table 4 shows the Ut/Uh, ratio of FFase obtained for *A. japonicus* immobilized in the different carriers. Maximum values were achieved at 48 h fermentation using vegetal fiber sponge as immobilization carrier.

Table 3. Ratio between the transfructosylating and hydrolyzing activities of FFase during FOS production by immobilized *A. japonicus*.

Immobilization carrier	Ut/Uh ratio at 48 h fermentation
Pumice Stones	4.31
Zeolites	3.12
Stainless steel sponge	2.93
Polyurethane foam	4.15
Vegetal fiber sponge	4.82
Cork	2.34

Conclusions

Among the six different materials evaluated for immobilization of the fungus *Aspergillus japonicus* during FOS production, vegetal fiber sponge proportioned the best fermentation results, being able to immobilize the major amount of cells, and giving the highest values of FOS production and FFase activity. Such material was thus selected for use in subsequent experiments aiming to maximize the FOS production by *Aspergillus japonicus* ATCC 20236.

Acknowledgements

The financial support from FCT, the Portuguese Foundation for Science and Technology (research project SFRH/BPD/38212/2007) is gratefully acknowledged.

References

Chen, W.-C., Liu, C.-H. (1996). Production of β-fructofuranosidase by *Aspergillus japonicus*. *Enzyme and Microbial Technology,* 18, 153-160.

Cruz, R., Cruz, V.D., Belini, M.Z., Belote, J.G., Vieira, C.R. (1998). Production of fructooligosaccharides by the mycelia of *Aspergillus japonicus* immobilized in calcium alginate. *Bioresource Technology*, 65, 139-143.

Sangeetha, P.T., Ramesh, M.N., Prapulla, S.G. (2005). Recent trends in the microbial production, analysis and application of fructooligosaccharides. *Trends in Food Science & Technology*, 16, 442-457.

Wang, L.-M. Zhou, H.-M. (2006). Isolation and identification of a novel *Aspergillus japonicus* JN19 producing β-fructofuranosidase and characterization of the enzyme. *Journal of Food Biochemistry*, 30, 641-658.

Yoshikawa, J., Amachi, S., Shinoyama, H., Fujii, T. (2006). Multiple β-fructofuranosidases by *Aureobasidium pullulans* DSM2404 and their roles in fructooligosaccharide production. *FEMS Microbiology Letters*, 265, 159-163.

Yun, J.W. (1996). Fructooligosaccharides – occurrence, preparation, and application. Enzyme and Microbial Technology, 19, 107-117.

Proceedings of the 10th International Chemical and
Biological Engineering Conference - CHEMPOR 2008
Braga, Portugal, September 4-6, 2008
E.C. Ferreira and M. Mota (Eds.)

Development of a biosensor based on ion-selective electrode for urea in milk by using immobilized amidase from *Pseudomonas aeruginosa*

Ana Rita Barbosa and Amin Karmali*
Chemical Engineering and Biotechnology Research Center and Department of Chemical Engineering of Instituto Superior de Engenharia de Lisboa– Rua Conselheiro Emídio Navarro, 1, 1950-062 Lisboa, Portugal
* Corresponding author, e-mail: akarmali@deq.isel.ipl.pt

Keywords: Urea in milk; Amidase from *Pseudomonas aeruginosa*; Biosensor based on ISE; Membranes; Active-site inhibitor
Topic: Sustainable process-product development through green chemistry.

Abstract

The present work involves the development of a biosensor based on ion-selective electrode (ISE) for assay of urea in milk by using a novel enzymatic method. Urea is a powerful time-dependent active-site directed inhibitor for aliphatic amidase (acylamide amidohydrolase EC 3.5.1.4) from *Pseudomonas aeruginosa* which catalyses the hydrolysis of a small number of aliphatic amides producing the corresponding acid and ammonia (Martins *et. al*. 2006; Tata *et al*, 1994) according to the following reaction:

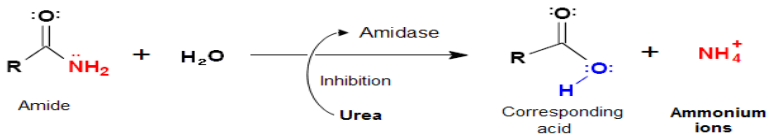

Increasing concentrations of urea were found to inhibit proportionally amidase activity which was detected by the hydrolase reaction. Therefore, urea concentration in samples was inversely proportional to amidase activity which was measured with acetamide as substrate by using ISE for ammonium ions.

Cell-free extracts containing amidase activity were immobilized on nylon and polyethersulfone membranes in the presence of gelatin and glutaraldheyde as the bi-functional reagent. Membranes containing immobilized amidase activity were used to set up a biosensor based on ISE for ammonium ions by using acetamide as the substrate and the enzyme reaction was followed by measurement of ammonium ions due to hydrolysis of the aliphatic amide (Fig.1)

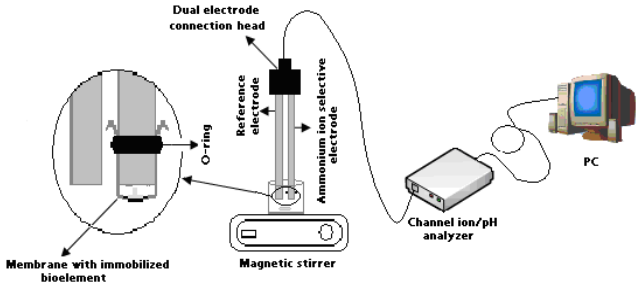

Fig.1 - Experimental set-up for potentiometric biosensor: ammonium ion selective electrode containing polyethersulfone membrane with immobilized cell-free extract and reference electrode, electrochemical cell, magnetic stirrer, ISE analyser and PC.

Subsequently, this biosensor was washed and incubated with milk containing increasing concentrations of urea in the range of 0 – 1.0 mM, for 1 h. After the incubation period, the biosensor containing amidase activity was assayed again by using acetamide as the substrate. There was a linear relationship between a decrease of the biosensor response in mV and urea concentration in milk. This biosensor exhibited a linear response in the range of 2.0 – 10.0 x 10^{-6} M of urea either in a buffer solution or in milk and a response time of 60 s.

The biosensor containing amidase activity could be re-used again by reactivating enzyme activity with hydroxylamine for 2h. This biosensor was stable for at least 1 month since it did not lose enzyme activity and it is cheap because cell-free extracts containing amidase activity can be used for quantification of urea in milk.

Introduction

The food processing industry requires suitable analytical methods for quality control of food which are fast, reliable, specific and cost-effective since current wet chemistry tests are time-consuming and some may require highly skilled labour as well as expensive equipment (Verma *et al.*, 2003). This urgent need is due to increased regulatory action and consumer concern about food composition and safety (Luong *et al.*, 1997).

Milk has been considered as a human's most nearly perfect food as far as nutritional properties are concerned and its consumption depends on strict sanitary control employed by the dairy industry (Potter and Hotchkiss, 1995). Urea is present as an adulterant in milk since it is not a natural constituent of milk which has originated increasing concern from the public as the consumer. The presence of urea in milk may be due to excessive nitrogen uptake whose concentration is in the range of 1.66 – 4.16 mM and high urea concentrations are responsible for reduced fertility rates in dairy cattle (Butler *et al.*, 1996) There are several methods available for quantification of urea in food, industrial effluents and biological fluids. However, all these analytical and biosensor methods present some advantages and drawbacks (Koncki, R. (2007). Therefore, a biosensor development based on enzyme electrode could be useful for quantification of urea in food as well as in industrial effluents. Although purified enzymes exhibit very high specificity either for their substrates or inhibitors, their application in biosensor development may be limited due to time-consuming and costly enzyme purification, requirement of multiple enzymes or the need of cofactor/coenzyme. The use of whole cells containing the desired activity may provide an ideal alternative to overcome these problems. However, the presence of many enzymes and co-factors that are present in whole cells may catalyse undesirable reactions which can compromise the biosensor selectivity (Lei *et. al*., 2006).

The present work involves the development of an enzyme inhibition-based biosensor by using amidase from *Pseudomonas aeruginosa* (Amine et. al, 2006). This biosensor is based on ion-selective electrode (ISE) for assay of urea in milk by using a novel enzymatic method. Urea is a powerful time-dependent active-site directed inhibitor for aliphatic amidase (acylamide amidohydrolase EC 3.5.1.4) from *Pseudomonas aeruginosa* which catalyses the hydrolysis of a small number of aliphatic amides producing the corresponding acid and ammonia. Increasing concentrations of urea were found to inhibit proportionally amidase activity which was detected by the hydrolase reaction. Therefore, urea concentration in samples was inversely proportional to amidase activity which was measured with acetamide as substrate by using ISE for ammonium ions. The bio-component consists of cell-free extract containing amidase activity from *Pseudomonas aeruginosa* which was immobilized on several types of membranes and they could be re-used several times.

Materials and Methods

Materials

Glutaraldehyde was obtained from Sigma Chemical Co. (St. Louis, MO, USA). Modified polyethersulfone (PES) membranes (Ultrabind, US450 0,45 µm) were purchased from Gelman (USA) and Porablot® nylon (NY) plus was supplied by Macherey-Nagel, Germany. Milk (Mimosa brand) was purchased from a local supermarket. A

constitutive mutant strain L10 of *Pseudomonas aeruginosa* was isolated in our laboratory. All other reagents used were of analytical grade.

Methods

Bacterial strain, media and growth conditions for enzyme production

A constitutive mutant strain L10 of *Pseudomonas aeruginosa* was used as the source of amidase. Microbial strain (L10) was grown overnight in minimal salt medium as described previously (Brown and Clarke, 1972).

Enzyme extraction from P. aeruginosa

The cultures were harvested by centrifugation at 7000 x g for 10 min, the pellet was washed twice with saline, centrifuged and the resulting pellets stored at -20 ºC as described previously (Martins *et.al*., 2006).

Protein assay

Protein concentration was determined by the Coomassie blue dye binding method (Bradford 1976).

Immobilization of cell-free extract containing amidase activity

The immobilization of cell-free extract of *P. aeruginosa* was based on covalent bonding of cellular proteins to polyethersulfone membrane. Membrane discs were cut with 20mm of diameter and a mixture was prepared in an eppendorf tube containing 65 μl of cell-free extract in 50 mM Tris-HCl buffer pH 7.2 containing 1 mM β-mercaptoethanol, 1 mM EDTA, 10 % (v/v) glycerol and 1mM benzamidine (TMEGB buffer), 10 l gelatin (25%) and 5 μl of glutaraldehyde (5%, v/v). This mixture was immediately transferred to the center of membrane disc which was incubated at room temperature for 30 min. Subsequently, the membrane discs were washed three times with 3 ml of TMEGB buffer to remove unbound proteins of *Pseudomonas aeruginosa* to the membrane and were kept at 4ºC in a final volume of 3ml of TMEGB buffer.

Transducer

The transducer was a potentiometer with ammonium-ion selective electrode (ELIT) as described previously (Martins et. al, 2006) which was run in a personal computer (Fig. 1). Amidase catalyses the hydrolysis of acetamide forming acetic acid and ammonium ions as described above. The enzyme electrode consisted of immobilized cell-free extract containing amidase activity on several membranes and the side containing the cells was in contact with the surface of an ISE for ammonium ions through an O-ring as shown in Fig. 1. The calibration curve of NH_4Cl as a function of mV reading was carried out in 20 mM Tris buffer pH 7.2 containing 1 mM EDTA and 1mM -mercaptoethanol (TME buffer). The mV readings were plotted against the log of ammonium chloride concentration to provide the calibration data (Martins *et. al.* 2006). All potentiometric measurements were carried out in a final volume of 4 mL containing 0.1M acetamide in an appropriate buffer at room temperature in a magnetic stirrer. The enzyme electrode was placed in the reaction mixture and the biosensor response was determined from the steady state of the voltamogram obtained. All measurements were carried out in triplicates .

Urea assay

The biosensor response was determined by using a reaction mixture containing 0.1M acetamide in 20mM Tris buffer pH 7.2 in the absence of urea. Subsequently, the same membrane disc was washed with the same buffer several times and it was incubated with different concentrations of urea solutions either in Tris buffer or in milk for 30 min. The membrane discs were washed with buffer and used to determine biosensor response by using 0. 1M acetamide in the reaction mixture. There is a linear decrease

in biosensor response with increasing concentrations of urea solutions either in buffer or in milk. All experiments were carried out in triplicates. The biosensor response was measured as the difference between the slopes of the reaction with and without urea incubation (i.e ∆mV/min) of the membrane disc.

Enzyme assay by potentiometry

Amidase activity in free and immobilized cell-free extracts of *P. aeruginosa* was determined by using ISE for ammonium ions. The assays were carried out by using 0.1 M acetamide as a substrate in appropriate buffer, the progress curve of the reaction was followed and recorded for a few minutes and the values of ppm of NH_4^+ were converted in E (mV/min) as the biosensor response. Therefore, the increase in the ammonium ions formation was measured as a function of time in order to monitor the rate of amide hydrolysis in the presence of amidase which was present in cell-free extracts. One enzyme unit was defined as the amount of enzyme required to produce a change of 1 mV per minute in E at 25ºC and in aTris buffer.

Effect of [glutaraldehyde] for immobilization of cell-free extract.

A mixture was prepared containing 65 µL of cell-free extract, 10 µL of gelatin (25%) and final concentrations of glutaraldehyde solution in the range of 0 – 2.5% (v/v) in a final volume of 85 µL of the reaction mixture. The mixture was applied to a PES membrane disc with 20mm diameter with a surface area of 3.14 cm^2 and the biosensor response was obtained by using a reaction mixture containing 0.1 M acetamide in Tris buffer .

Performance of the biosensor for urea.

After optimization of the biosensor response, the analytical characteristics of the biosensor with polyethersulfone membrane were obtained by potentiometry for urea concentrations in the range of 0.02 – 1.0 x 10^{-3} M in Tris buffer. The biosensor response was measured as difference between the slopes of the reaction with and without urea incubation (i.e ∆mV/min) of the membrane disc.

Biosensor regeneration

Membrane discs previously used for assay of urea in milk were regenerated by reactivation with 20 mM hydroxylamine for 30 min and the regenerated membrane discs were used to measure the biosensor response in the reaction mixture described above. The biosensor response was measured in triplicates as a rate of reaction in mV/min in a final volume of reaction mixture of 4 ml.

Biosensor stability

In order to optimize the best storage conditions of the biosensor as well as its stability, different membranes containing immobilized cell-free extract of *P. aeruginosa* were stored in TMEGB buffer at 4ºC.

Determination of [urea] in milk

Urea recovery experiments were carried out by using commercial milk as well as in Tris buffer which were spiked with known amounts of urea. Biosensor response was measured in triplicates as a function of [urea] by using a Porablot NY Plus containing immobilized cell-free extract of *P. aeruginosa* which exhibited amidase activity as described above. The biosensor response was measured as the difference between the slopes of the reaction with and without urea incubation (i.e ∆mV/min) of the membrane disc.

Results and discussion

A typical sensogram is presented in Fig. 2 which reveals the hydrolysis of acetamide in the presence of immobilized cell-free extract of *P. aeruginosa* containing amidase activity since the values of NH_4^+ (ppm) were converted in E (mV) as the biosensor response. This figure also exhibits the progress curve of the reaction after incubation of the biosesnsor with urea solution which inhibited the rate of the reaction. Therefore, it represents a progress curve for the reaction catalysed by amidase which shows that there is an increase in the formation of ammonium ions as a function of time due to the hydrolysis of acrylamide producing acrylic acid and ammonia. From this data, the initial rate (mV/min) was determined from the initial linear part of the progress curve.

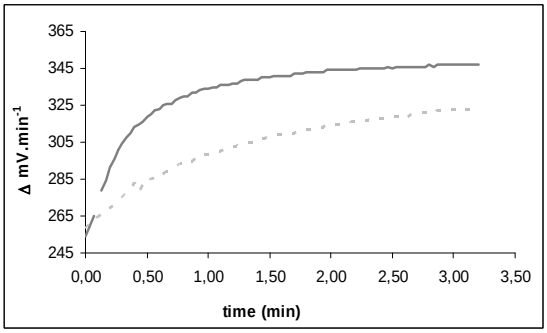

Figure 2 – Biosensor response as a function of time by using immobilized cell-free extract containing amidase activity on PES membrane. Measurements were carried out in a reaction mixture containing 0.1M acetamide in Tris buffer as described in Materials and Methods : - - - - - Incubation in 0.01mM Urea in TME buffer; —— No urea incubation .

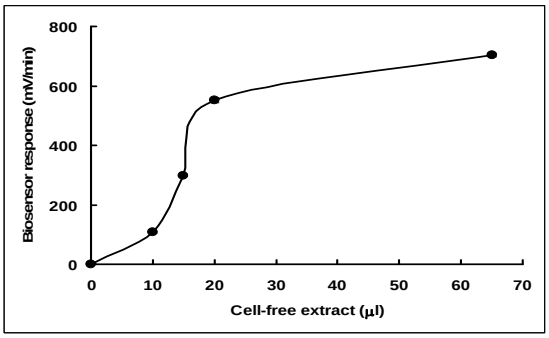

Figure 3 – Effect of immobilization of increasing concentration of cell-free extract on biosensor response with polyethersulfone(PES) membrane

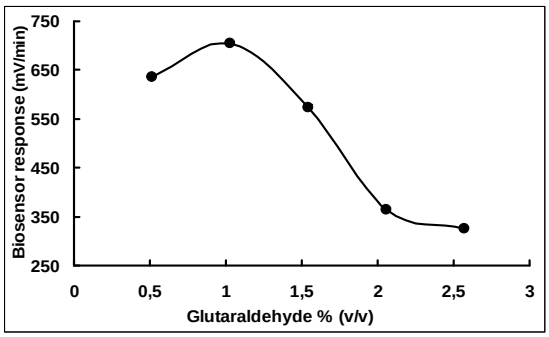

Figure 4 – Effect of glutaraldehyde concentration on biosensor response with polyethersulfone (PES) membrane.

The effect of immobilization of increasing concentration of cell-free extract of *P. aeruginosa* on biosensor response was also investigated which revealed a linear response in mV/min as a function of cell-free extract concentration up to 700 mV/min . The maximum biosensor response was obtained at a glutaraldehyde concentration of 1.0 % (v/v) by using PES membrane as the immobilization support as shown in Fig. 4.

Once the biosensor response was optimized, a calibration curve of the biosensor response in ΔmV/min was carried out as a function of urea concentration in the range of 0.02 – 1.0 x 10^{-3} M in TME buffer (Fig. 5).

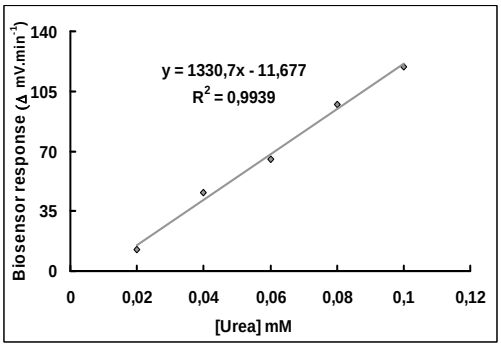

Figure 5- Calibration curve for urea by using the biosensor.

Linear response of the biosensor in ΔmV/min in the range of 0.02 _ 0.1 x 10^{-3} M which was carried out in Tris buffer.

The application of the present method to the detection and determination of urea was investigated by recovery experiments (Andreou and Clonis 2002) by using a sample of milk which was spiked with a known amount of urea (Fig. 6). Control experiments using urea-free milk samples were made in Tris buffer in order to investigate the matrix effects of the recovery in milk and an average substrate recovery of about 93.3% was obtained. As far as the biosensor stability is concerned, Porablot NY Plus membranes containing immobilized cell-free extracts were stored in TMEGB

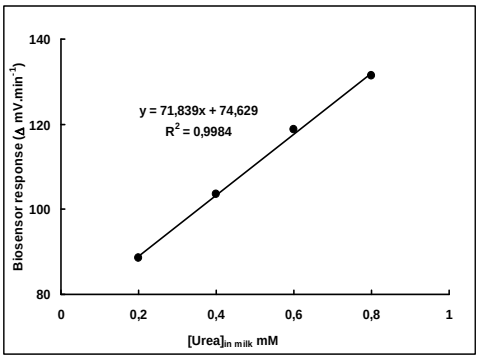

Figure 6 – Determination of urea in milk. Acrylamide recovery experiments were carried out by using milk and Tris buffer which were spiked with known amounts of urea

buffer at 4ºC which revealed that they were stable for over 70 days without any loss of amidase activity (Fig. 7). The membrane discs used for urea assay could be regenerated by incubation with hydroxylamine which resulted in about 80% recovery of biosensor activity as shown in Fig. 8

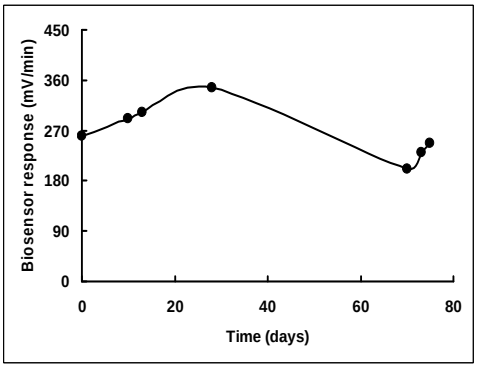

Figure 7 – Stability of biosensor response with PES membrane as a function of time which was stored at 4ºC in TMEGB buffer

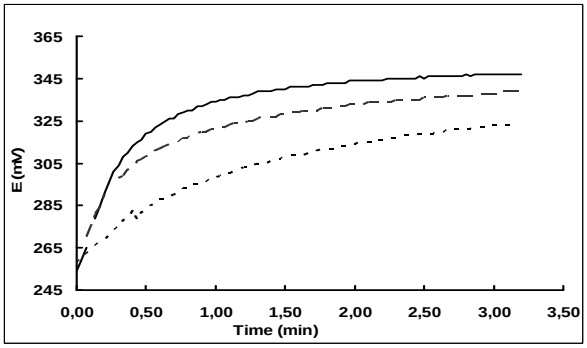

Figure 8 – Regeneration of the biosensor containing PES membrane which was incubated with urea. : ……. Incubation in 0.01mM Urea in TME buffer; - - - - - Reactivation with hydroxylamine and —— No urea incubation

The data presented suggest a potential use of this biosensor for urea assay in milk.

Acknowledgements

We acknowledge financial support from Fundação para a Ciência e a Tecnologia (Unit 702, PTDC/AGR-AAM/73460/2006).

References

Amine, A., Mohammadi, H., Bourais, I.,Palleschi, G. (2006) Review:Enzyme inhibition-based biosensors for food safety and environmental monitoring *Biosensors and Bioelectronics* 21, 1405–1423.

Andreou VG, Clonis YD.(2002). A portable fiber-optic pesticide biosensor based on immobilized cholinesterase and sol-gel entrapped bromocresol purple for in-field use. Biosensors and Bioelectronics 17: 61–69.

Brown P.R. Clarke P.H. (1972). Amino acid substitution in an amidase produced by an acetanilide utilizing mutant of *Pseudomonas aerug*inosa*. J. Gen. Microbiol*. 70, 287-298.

Butler, W.R., Calaman, J.J., Beam, S.W. (1996). Plasma and milk urea nitrogen in relation to pregnancy rate in lactating dairy cattle. *J. Anim. Sci.* 74 (4), 858-865.

Koncki, R. (2007) Review : Recent developments in potentiometric biosensors for biomedical analysis. *Analytica Chimica Acta* 599, 7–15.

Luong, J.H.T., Bouvrette, P., Male, K.B. (1997). Development and and applications of biosensors for food analysis. *Trends Biotechnol* 15, 367-377.

Martins, S., Karmali, A., Serralheiro, M.L. (2006). Kinetic properties of wild-type and altered recombinant amidases by the use of ion-selective electrode assay method. *Analytical Biochemistry* 355, 232-239.

Potter, N.N., Hotchkiss, J.H., (1995). Milk and milk products. In: Food science. *Chapman and Hall*, New York, pp. 279-315.

Tata, R, Marsh, Philip, Brown, Paul R. (1994). Arg-188 and Trp-144 are implicated in the binding of urea and acetamide to the active site of the amidase from *Pseudomonas aeruginosa*. *Biochimica et Biophysica Acta*, 1205, 139-145.

Verma, N., Singh, M. (2003). A disposable microbial based biosensor for quality control in milk, *Biosensors & Bioelectronics,* 18, 1219-1224.

Proceedings of the 10th International Chemical and
Biological Engineering Conference - CHEMPOR 2008
Braga, Portugal, September 4-6, 2008
E.C. Ferreira and M. Mota (Eds.)

Characterization of the fungi tissue of *Agaricus bisporus* for its future use as a component of a biosensor for phenolic compounds determination

Lívia Maria da Costa Silva[1*], Andréa Medeiros Salgado[1], Maria Alice Zarur Coelho[1]

[1]School of Chemistry – Federal University of Rio de Janeiro - Center of Technology, Block E, Laboratory number 103, University City – 21949-900, Rio de Janeiro - RJ, Brazil.

Keywords: tyrosinase, *Agaricus bisporus*, fungi, phenol
Topic: Sustainable process-product development through green chemistry

Abstract

Phenols are pollutant toxics found in several industrial effluents, being its determination of extreme environmental importance. In order to make possible an analytic methodology for a monitoring *in-situ*, this work intends to study the application of tissue of Paris mushroom as a source of the enzyme tyrosinase and its best reaction conditions seeking to develop a biosensor to phenols. Such enzyme is one poliphenol oxidase that transforms the phenolic composites into a lesser soluble product in water. This work aimed to characterize the fungi tissue for its future use as bio-component of a biosensor for the determination of phenolic compounds It was carried out an experimental process of successive extractions of tyrosinase and measurement of its activity. Additionally, the existence of phenol adsorption in the mushroom tissue and presence of phenol in the mushroom tissue had been verified. Obtained results showed that a significant amount of the enzyme remained in the paste of mushrooms even though extracting the first one. Finally, phenol is present in the composition of mushrooms, and the average concentration is 0.307 ppm and the hypothesis of adsorption of the phenol in the pieces of tissue of *Agaricus bisporus* can be eliminated.

1. Introduction

Phenolic compounds are extremely diverse. Although they may have hazardous adverse effects, they are a major pollutant present in the wastewaters from several industrial activities: coalmining, petrol refining, pharmaceutical production, founding and steel and iron manufacture, and the tanning and finishing of leather (Atlow et al., 1984).

Phenolic compounds are produced as secondary metabolites by most plants, in which they probably act as natural antimicrobial agents, as natural deterrents to grazing animals or as inhibitors of pre-harvested seed germination. Furthermore, these compounds are also formed during the natural decomposition of humic substances, tannins, and lignins.

Several procedures have been developed for the determination of phenolic compounds, such as chromatographic techniques, fluorimetric, and spectrophotometric methods. However, these techniques do not easily allow continuous monitoring in actual samples. They are expensive, time-consuming, need skilful operators, and sometimes require preconcentration and extraction steps that increase the risk of sample loss.

Biosensors are generally defined as an analytical device, incorporating a biological or biologically derived sensing element, such enzymes, either intimately associated with or integrated within a physicochemical transducer. They represent promising tools to supplement already existing techniques, due to their intrinsic characteristics such as

* Corresponding author. Tel + 55-21-25627629. E-mail:silva.livia@gmail.com

selectivity, low cost, potential for miniaturization and for the construction of simple flow devices for fast continuous monitoring. Among biosensors for phenols there is the enzyme tyrosinase as a bio-component, which is isolated from mushrooms due to economic reasons.

Tyrosinases (monophenol, o-diphenol:oxygen oxidoreductase, EC 1.14.18.1) belong to a larger group of proteins named type-3 copper proteins. Tyrosinase has been found widely distributed throughout the phylogenetic scale (van Gelder et al., 1997), which catalyses the *o*-hydroxylation of monophenols (cresolase activity or monophenolase) and the subsequent oxidation of the resulting *o*-diphenols into reactive *o*-quinones (catecholase activity or diphenolase), both reactions using molecular oxygen. Subsequently, the *o*-quinones undergo non-enzymatic reactions with various nucleophiles, producing intermediates, which associate spontaneously in dark brown pigments (Topçu et al., 2004; Marin - Zamora et al., 2006).

This work aimed to study the possibility of using tyrosinase naturally present in the tissue of the mushroom *Agaricus bisporus* to quantify phenol contained in standardized samples to finally, in future works, quantify phenol present in samples taken directly from the environment. Some works were met in literature using tyrosinase of this mushroom as biological component of a biosensor (Topçu et al., 2004; Marin-Zamora et al., 2006), however they do not use it in the immobilized form of the natural tissue, that is, immobilization *in-natura* (main objective of this work).

2. Materials and Methods

2.1. Studied Material

Fruit bodies of mushrooms (*Agaricus bisporus*), usually known as champignon Paris mushrooms, used throughout this work, were obtained from a two local dealers. They are Cadeg and Cobal Humaitá (Rio de Janeiro – RJ, Brazil). In both dealers, the lots of mushrooms were always bought on the same retail customer. Validation dates to consume the mushrooms were equally taken into account.

2.2. Source of Tyrosinase

Fruit bodies of mushrooms were triturated in 1750 ml of a pre-cooled acetone for enzymatic extraction. The pulp was then frozen by 24 hours, and then suspended in 300 ml of distilled water, and left overnight in a freezer. The resultant suspension was centrifuged or filtered to produce the first extract (Kameda et al., 2006). The steps of water addition and centrifugation were repeated once or twice to obtain more extracts.

2.3. Tyrosinase Activity

Tyrosinase activity was measured spectrophotometrically according to Campos et al. (1996). A diluted sample (ratio 1:10) of enzyme was added to a L-tyrosine solution (0.2M) in a phosphate buffer (0.2M and pH 6.0). The resulted mixture was homogenized and the changes of the absorbance were monitored at 280 nm in a DR/4000UV spectrophotometer at a regular interval of 30 seconds during 999 seconds.

One unit of enzymatic activity (U) was defined as the amount of enzyme that increased absorbance 0.001 (λ=280 nm) per minute. The enzymatic activity was calculated using the following formula:

$$A = \frac{(Abs_2 - Abs_1) \times 1000 \times D_E}{(t_2 - t_1) \times V_E} \text{ (U/mL)}$$

,

where: Abs_1 and Abs_2 are the absorbances in times t_1 and t_2 at the linear increase; V_E is the volume of the enzymatic solution (1 ml), and D_E is the dilution of the enzymatic solution.

2.4. Verification and quantification of the presence of phenol in mushroom tissue

In this research the enzymatic reactions due to the presence of phenol in the mushroom tissue had been carried out following the conditions: 5 g of mushroom tissue in two different sizes (0.5 and 1.0 cm^3); erlenmeyer with 250 ml of distilled water free of phenol and chlorine; the agitation was rated at 200 rpm in a shaker (agitator orbital Tecnal TE - 420), and the temperature was kept constant in 30 °C.

2.5. Phenol Determination

Phenol analysis was done according to the direct colorimetric method per Standard Methods (Apha, 1996). 250 milliliters of ammonium hydroxide (0.5N) was mixed to 10 ml of samples or blank and pH was adjusted to 7.9 ± 0.1 with potassium phosphate buffer. 100 µl of 4-amino-antipyrine solution (2% w/v) was added additionally. The final step was to mix a 100 µl of potassium ferricyanide solution (8% w/v) to obtain the final mixture. Fifteen minutes later, the absorbance was read at 500 nm. It is Important to clarify that each sample was previously filtered in a C18 PR-COLA cartridge for the interference removal.

3. Results and Discussion

3.1. Extraction and Determination of the Enzymatic Activity of Tyrosinase

The effect of the re-extraction of the enzyme in the enzymatic activity retained on different extracts was studied. With the obtained results (Figure 1) it could be observed that a significant amount of the enzyme remained in the paste of mushrooms even though extracting the first one. That result is corroborated by the literature; see Papa et al. (1994) and Kameda (2003). From the obtained results it could be observed that in function of the different lots, diverse activities were obtained. They varied from 20.2 U/ml to 980.36 U/ml.

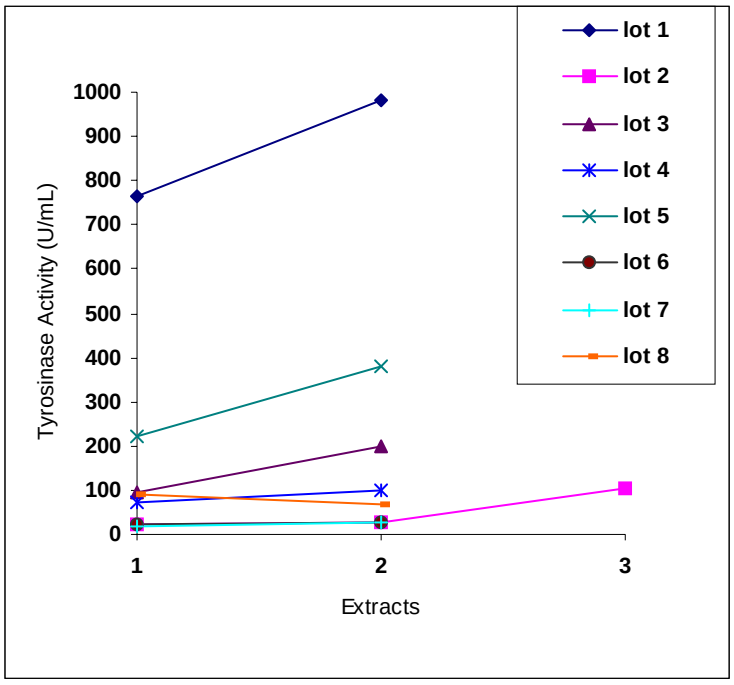

Figure 1: Effect of the re-extraction on the enzymatic activity of tyrosinase.

The tyrosinase present in the tissue mushroom, as in case of *Agaricus bisporus*, most likely comes from the cytoplasm of the cell (van Gelder et al., 1997). Therefore, a larger activity in the second (or third) enzymatic extract in relation to the first one may be due to the largest cellular breaking during the re-extraction process. This one makes the diffusion of the enzyme inside the cells towards the enzymatic extract.

Although the mushrooms were visually quite similar, an enormous difference was observed among the enzymatic activities of the lots under evaluation. And where they were bought is not an issue. Nevertheless, Ingebrigtsen et al. (1989), identified the degree of maturation of the mushrooms as the weight factor to interfere with the activity of the tyrosinase in the extract. In fact, Bevilaqua (2000) equally reported such variation in the extract caused by aged mushrooms. These ones contributed to an increase of 48% in the enzymatic activity in relation to the controlled lot. He concluded, "The aging of the mushroom is responsible for the activation in latent ways of the enzyme ". The presence of isoforms of tyrosinase of *Agaricus bisporus* was already mentioned in the literature by (Whichers et al., 1996; Espín and Whichers, 1999). According to van Leeuwen and Whichers (1999), the mushroom tyrosinase was present as a latent form in ~98-99% of the total tyrosinase activity.

Finally, phenol is present in the composition of mushrooms, and the average concentration is 0.307 ppm and the hypothesis of adsorption of the phenol in the pieces of tissue of *Agaricus bisporus* can be eliminated based on the satisfactory results of experiments that were performed during this work and results of Kameda (2003).

4. Conclusions

The tissue of mushroom *Agaricus bisporus* has showed to be an excellent source of the enzyme tyrosinase for the construction of a biosensor to phenol in the future. Throughout this work the results showed that a significant amount of the enzyme remained in the paste of mushrooms even though extracting the first one. Additionally, phenol is present in the composition of mushrooms, and the average concentration is 0.307 ppm and the hypothesis of adsorption of the phenol in the pieces of tissue of *Agaricus bisporus* can be eliminated.

5. Acknowledgement

The financial support of CNPq is gratefully acknowledged.

References

Apha. (1992): *Standard Methods for the examination of water and wastewater*, 18thed, American Public Health Association, Washington, DC.

Atlow, S.C., Bonadonna-Aparo, L., Klibanov, A.M. (1984): Dephenolization of industrial wastewater catalyzed by polyphenol oxidase. *Biotechnology and Bioengineering,* 26, 599-603.

Bevilaqua, J.V. (2000): Utilização de tirosinase de *Agaricus bispora* no tratamento de efluente contendo fenóis. *Tese de Mestrado em Engenharia Química, COPPE, Federal University of Rio de Janeiro,* Rio de Janeiro, Brazil.

Campos, C.F., Souza, P.E.A., Coelho, J.V. (1996): Chemical composition, enzyme activity and effect of enzyme inactivation on flavor quality of green coconut water. *Journal of Food Processing and Preservation,* 20, 487-500.

Espín, J. C., Wichers, H. J. (1999): Activation of a Latent Mushroom (*Agaricus bisporus*) Tyrosinase Isoform by Sodium Dodecyl Sulfate (SDS). Kinetic Properties of the SDS-Activated Isoform*. Journal of Agricultural and Food Chemistry*, 47, 3518-3525.

Ingebrigtsen, J., Kang, B., Flurkey, W.H. (1989): Tyrosinase Activity and isoenzyme in Developing Mushrooms. *Journal* of *Food Science,* 54, 1, 128-131.

Kameda, E. (2003): Estudo do processo de obtenção de extrato enzimático de *Agaricus bisporus* para remoção de fenol em efluente sintético. *Dissertação de Mestrado em Tecnologia de processos Químicos e Bioquímicos*, *Escola de Química, Federal University of Rio de Janeiro,* Rio de Janeiro, Brazil.

Kameda, E., Langone, M.A.P., Coelho. M.A.Z. (2006): Tyrosinase extract from *Agaricus bisporus* mushroom and its *in natura* tissue for specific phenol removal. *Environmental Technology*, 27, 1209-1215.

Marín-Zamora, M.E, Rojas-Melgarejo, F., García-Cánovas, F., García-Ruiz, P.A. (2006): Direct immobilization of tyrosinase enzyme from natural mushrooms (*Agaricus bisporus*) on D-sorbitol cinnamic ester. *Journal of Biotechnology*, 126, 3, 295-303.

Papa, G., Pessione, E., Leone, V., Giunta, C. (1994): *Agaricus bisporus* tyrosinase 1: Progress made in preparative methods. *International Journal* of *Biochemistry,* 26, 2, 215-221.

Topçu, S., Sezgintürk, M.K., Dinçkava, E. (2004): Evaluation of a new biosensor-based mushroom (*Agaricus bisporus*) tissue homogenate: investigation of certain phenolic compounds and some inhibitor effects. *Biosensors & Bioelectronics*, 20, 3, 592-597.

van Gelder, C.W.G., Flurkey, W.H., Wichers, H.J. (1997): Sequence and structural features of plant and fungal Tyrosinases. *Phytochemistry*, 45, 7, 1309-1323.

van Leeuwen, J., Whichers, H.J. (1999): Tyrosinase activity and isoform composition in separate tissues during development of *Agaricus bisporus* fruit bodies, *Mycol. Res.,* 103, 413-418.

Wichers, H.J., Gerritsen, Y.A.M., Chapelon, C.G.J. (1996): Tyrosinase isoforms from the fruitbodies of *Agaricus bisporus. Phytochemistry,* 43, 2, 333-337.

Proceedings of the 10th International Chemical and
Biological Engineering Conference - CHEMPOR 2008
Braga, Portugal, September 4-6, 2008
E.C. Ferreira and M. Mota (Eds.)

Influence of the concentration of locust bean gum on the gelling ability of whey peptic hydrolysates

Cristina Rocha[1*, 2, 3], Loïc Hilliou[1,4], José A. Teixeira[2], Maria Pilar Gonçalves[1]

[1] REQUIMTE, Departamento de Engenharia Química, Faculdade de Engenharia, Universidade do Porto, Rua Dr. Roberto Frias, 4200-465 Porto, Portugal.
[2] IBB – Institute for Biotechnology and Bioengineering, Centre of Biological Engineering, University of Minho, Campus de Gualtar, 4710–057 Braga, Portugal.
[3] Escola Superior de Tecnologia e Gestão, Instituto Politécnico de Viana do Castelo, Apartado 574, 4900-348 Viana do Castelo, Portugal.
[4] I3N-Institute for Nanostructures, Nanomodelling and Nanofabrication, University of Minho, Campus de Azurem, 4800-058 Guimarães, Portugal.

Keywords: Whey Protein, Locust Bean Gum, Gelation, Hydrolysis, Rheology
Topic: Multi-scale and/or multi-disciplinary approach to process-product innovation.

Abstract

The gelling ability of whey proteins can be changed by limited hydrolysis and by the presence of other components such as polysaccharides; depending on the environmental conditions it can either be improved or impaired.

In this work the effect of LBG on the heat-set gelation of aqueous whey protein hydrolysates (10 % w/w) from pepsin was assessed at pH 7.0 by small deformation rheology. Whey protein concentrate (WPC) and hydrolysates with a degree of hydrolysis (DH) of 1.5, 2.5 and 4.9 % were used. Different LBG concentrations were tested: 0, 0.1, 0.3 and 0.55 % (w/w).

The behaviour of gels from whey proteins or whey protein hydrolysates towards the presence of LBG was very similar. The evolution of the viscous and storage moduli followed the general behaviour reported for many biopolymer heat-set gelation processes including whey proteins gelation. The increase in the LBG concentration generally led to a decrease in the gel strength. However, for whey proteins a small amount of LBG (0.1 %) leads to a big enhancement in the gel strength probably due to an increase in the protein concentration of the protein enriched phase. Further increases in the LBG concentration led to a decrease in the gel strength.

The gelation process is very sensible to environmental conditions and to processing and often leads to rather coarse data. The factorial planning used allowed validating conclusions using fewer experiments than those needed if no planning had been used, while still getting statistical significance out of the results. However, as many factors are involved, the modelling of the process was not straightforward.

1 Introduction

The gelling ability of whey proteins can be changed by limited hydrolysis; depending on the environmental conditions it can either be improved or impaired.

The functionality of whey proteins can also be changed by the presence of other components. For instance, protein-polysaccharide complexes exhibit many functional properties able to provide new food texturization and stabilization methods (Schmitt and others, 1998).

Synergistic effects have been found between whey proteins and several polysaccharides such as galactomannans, xanthan or carrageenan (Croguennoc et al.,

* Corresponding author. Tel + 351-258-819700. E-mail:crocha@deb.uminho.pt

2001; Turgeon and Beaulieu, 2001; and many others). The effect of limited proteolysis in the interaction with polysaccharides is hardly ever mentioned.

Locust bean gum (LBG) is a galactomannan (non gelling neutral polysaccharides found in the endosperm of *Leguminosae*) widely used in the food industry as a thickening agent (Pollard and Fischer, 2006).

Rheological studies are useful to evaluate the gelling ability of biological macromolecules; in particular, they allow accessing the structure of the gel, evaluating its texture, controlling the gelling behavior or complementing the information provided by sensory methods. In fact, as gelation is essentially a phase transition from liquid to solid, monitoring the changes in mechanical properties is important. Small amplitude oscillatory shear techniques can be used to monitor continuously the evolution of the viscoelastic properties, avoiding any modification of the molecular structure caused by shear. This is an advantage over other rheological tests.

In this work the effect of LBG on the gelation of aqueous whey protein hydrolysates (10 % w/w) from pepsin was assessed at pH 7.0.

2 Materials and methods

All chemicals used were of analytical grade and supplied by Sigma, Co (St. Louis MO, USA). Pepsin from hog stomach with an activity of 2540 units/mg $_{protein}$ (one unit will produce a ΔA_{280} of 0.001 per min at pH 2.0 at 37 °C, measured as TCA-soluble products using hemoglobin as substrate in a reaction final volume of 16 mL and 1 cm light path) was obtained from Sigma Chemical Co.

A commercial whey protein concentrate (WPC) powder (Lacprodan 80, batch Q500246) kindly supplied by Arla Food Ingredients (Viby, Denmark) was used for the experiments. According to the suppliers, the WPC dry basis protein content was 82 % (5.5 % moisture), the ash content was 3.5 % max., the lactose content was 7 %, and fat content was 8 %. max. Locust bean gum (> 75 % galoctomanan content) was kindly supplied by Danisco Portugal (Faro, Portugal).

Locust bean gum was purified by precipitation with isopropanol as described by da Silva and Gonçalves (1990).

Whey protein concentrate (WPC) and hydrolysates with a degree of hydrolysis (DH) of 1.5 (P1.5), 2.5 (P2.5) and 4.9 % (P4.9) were used. Different LBG concentrations were tested: 0, 0.1, 0.3 and 0.55 % (w/w).

Dynamic oscillatory tests were performed in a controlled stress rheometer AR2000 (TA Instruments, Delaware, USA) fitted with a parallel plate geometry (40 mm diameter, gap 800 μm). Each sample was equilibrated during 5 min; this step was followed by a frequency sweep ("mechanical spectrum") from 100 to 0.1 Hz at a strain of 5 %. Then a temperature ramp from 20 to 80 ºC was applied, at a rate of 2 º C.min^{-1}, after which the temperature was maintained at 80 ºC for 3 h. At the end of this time sweep the sample was cooled back to 20 ºC, at the same constant rate (2 ºC.min^{-1}). The mechanical properties of the resulting gel were monitored at 20 ºC for 1 h.

A full factorial design was used considering two factors (LBG concentration and degree of hydrolysis) and three levels for each factor and a quadratic model was adjusted with Design Expert 6.0.6 (Stat-Ease, Inc. Minneapolis). Two replicates of the experiments with WPC (DH = 0) were used to estimate errors and determine if the lack of fit of the chosen model was significant. Further refinement of the empirical model was made by excluding the factors that were found to be insignificant, one at a time, as the exclusion of one factor may influence the other.

3 Results and discussion

The evolution of rheological parameters follows the general behaviour reported for

many biopolymer heat-set gelation processes including whey proteins gelation (see for instance Paulsson et al., 1990; Gosal and Ross-Murphy, 2000). Initially *G"* is slightly higher than *G'* because of the liquid nature of the sample and the absence of pre-aggregated protein molecules (Figure 1).

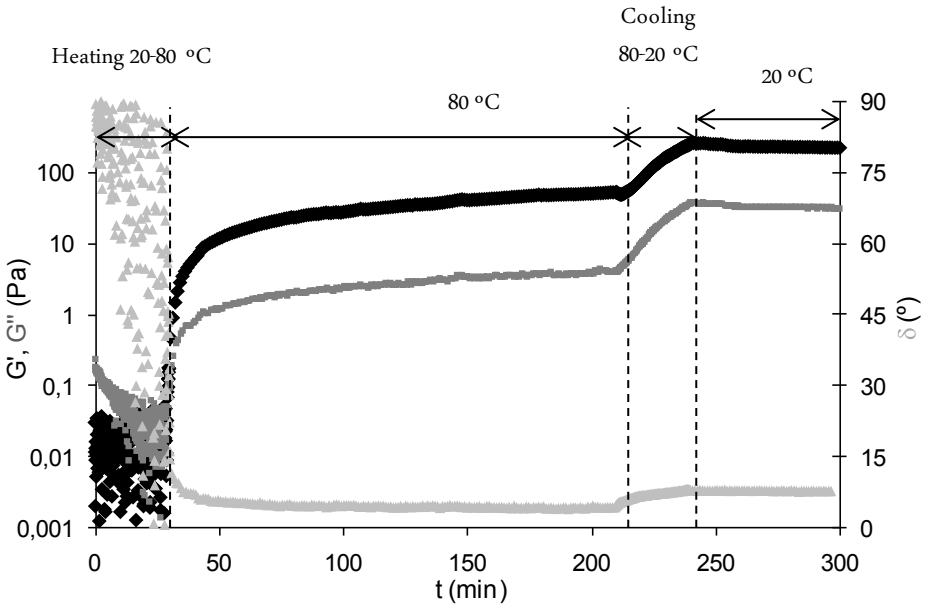

Figure 1 Gelling ability of whey protein concentrate (10 % w/w): black – *G'*; dark grey – *G"*; light grey – δ

As the temperature rises both moduli decrease until the gelation treshold is achieved (either before the end of the temperature ramp or during the time sweep step). As this point approaches, a sudden increase in the values of *G'* and *G"* is observable. However *G'* rises much faster and the crossover *G'-G"* point was considered the gelling point. By the same time the values of the loss angle decrease even more markedly, sign of the increase of the elastic behaviour.

Table 1 Influence of the LBG concentration and hydrolysis degree on the gelling ability of whey protein hydrolysates

Hydrolysate (% w/w)		LBG (% w/w)	*DH* (%)	*G'* (Pa)	*G"* (Pa)	*tan* δ	*Tg* (ºC)	*tg** (s)
WPC	10	0	0	204±33	28.6±3.8	0.14±0.00	79.5±0.0	-
WPC	10	0.1	0	1436±334	207±47	0.14±0.00	75.2±0.1	-
WPC	10	0.3	0	596±420	97.9±69.1	0.17±0.00	76.0±1.4	-
WPC	10	0.55	0	119±7	30.7±1.1	0.26±0.03	78.9±0.6	-
WPC	10	0.80	0	108	39.0	0.36	80	326
P1.5	10	0	1.5	657	92.8	0.14	80.0	36.0
P1.5	10	0.1	1.5	588	105	0.18	77.6	-
P1.5	10	0.3	1.5	118	19.4	0.17	77.9	-
P2.5	10	0	2.5	138	24.8	0.18	73.7	-
P2.5	10	0.1	2.5	107	16.2	0.15	72.6	-
P2.5	10	0.3	2.5	27.8	5.00	0.18	72.4	-
P2.5	10	0.55	2.5	29.5	11.4	0.39	78.7	-
P2.5	10	0.8	2.5	31.5	13.0	0.41	80	745
P4.9	16.5	0	4.9	18.4±18.4	3.35±3.04	0.20±0.04	80.0±0.0	0.0±0.0
P4.9	16.5	0.1	4.9	284	43.2	0.15	74.9	-
P4.9	16.5	0.3	4.9	207	37.3	0.18	72.8	-
P4.9	16.5	0.55	4.9	76.0±17.1	23.8±2.3	0.32±0.04	80.0	35.9±0.1

The increase in the storage modulus and the reduced phase angle indicate the formation of viscoelastic gels. *G'* continues to increase after the gel point as more and more protein reinforces the weak tridimensional network initially formed, enhancing its elasticity.

Although the overall gelation patterns were similar for all tested samples the corresponding gelling parameters (*G'*, *G''*, δ, *Tg*, *tg*) were quite different (Figure 2 and Table 1).

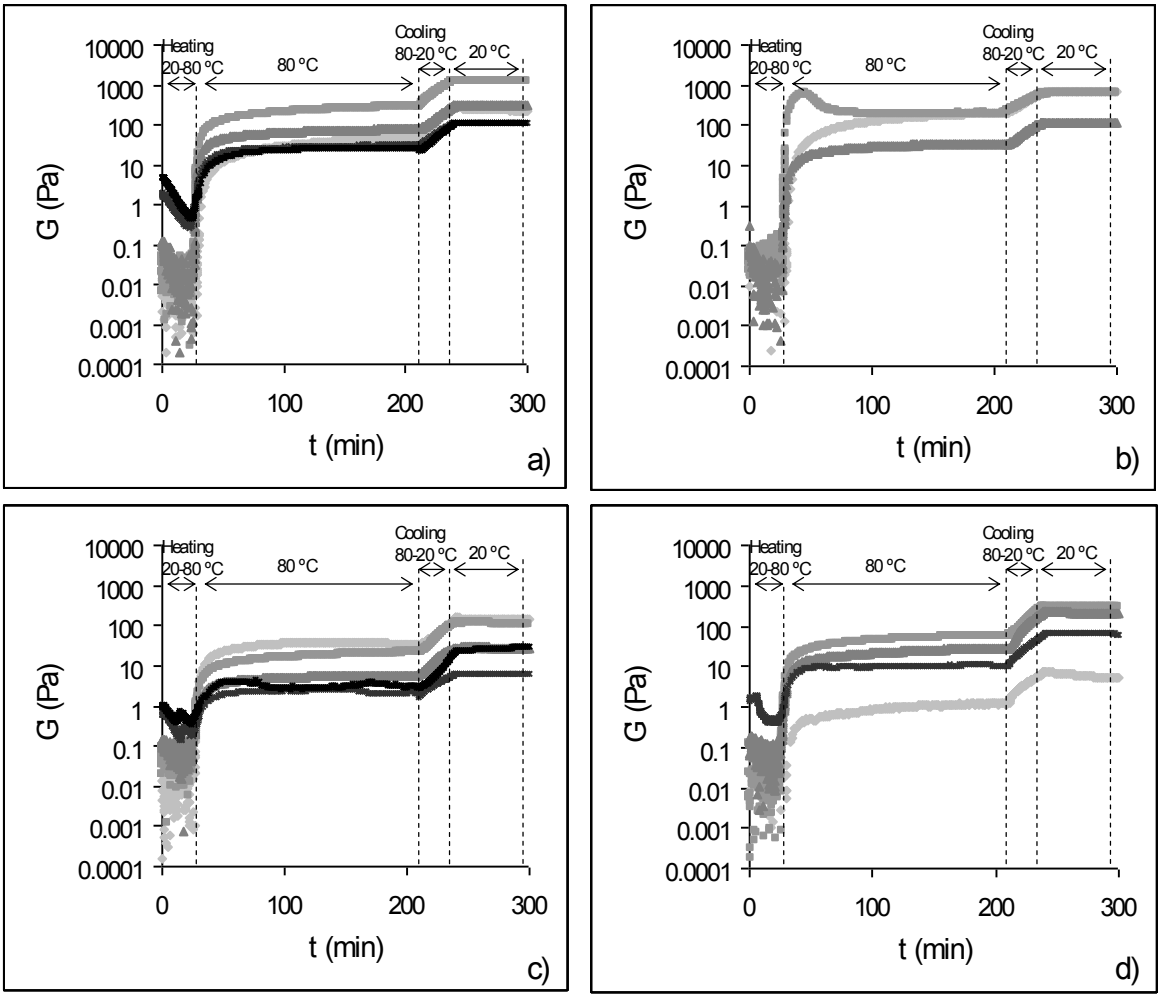

Figure 2 Influence of the LBG concentration on the gelling ability of whey peptic hydrolysates: the darker the colour the higher the LBG amount (0, 0.1, 0.3, 0.55, 0.8): a) WPC 10 % (w/w); b) P1.5 10 % (w/w); c) P2.5 10 % (w/w); d) P4.9 16.5 % (w/w)

In the case of hydrolysates alone, *G'* was higher for P1.5 (657 Pa) followed by P2.5 (138 Pa). These two were stronger than WPC at this concentration (*G'* = 204 Pa) indicating that they were stiffer. They were also more elastic as the loss angle was smaller. Apparently pepsin is effective in improving the gelling ability of whey protein gels for low degree of hydrolysis, possibly because β-Lg (the main gelling protein) is resistant to pepsin. In fact, P1.5 still has all the β-Lg intact and P2.5 still has 96 % of intact β-Lg. This improvement might be due either to the presence of low molecular weight hydrophilic peptides which can reduce electrostatic repulsions between intact β-Lg molecules enhancing protein-protein interaction or to the partial unfolding of α-La and BSA exposing their hydrophobic residues, therefore improving their individual gelling ability and/or allowing for a better interaction with the intact β-Lg.

LBG alters the microstructure of whey protein gels by modifying the equilibrium between aggregation and segregation. The gelation time was also decreased. The behaviour of gels from whey proteins or whey protein hydrolystates towards the presence of LBG was very similar. The increase in the LBG concentration generally led

to a decrease in the gel strength. However, for whey proteins a small amount of LBG (0.1 %) leads to a big enhancement in the gel strength probably due to an increase in the protein concentration of the protein enriched phase. Further increases in the LBG concentration led to a decrease in the gel strength.

When analysing the influence of the concentration of LBG on gelling properties (*G'*, *G''*, tan δ and temperature of gelation), the differences between the hydrolysates and WPC with no polysaccharide and the hydrolysates with 0.1 % of LBG were usually sharp (an example is presented in Figure 3); this difficults modelling with a simple quadratic function.

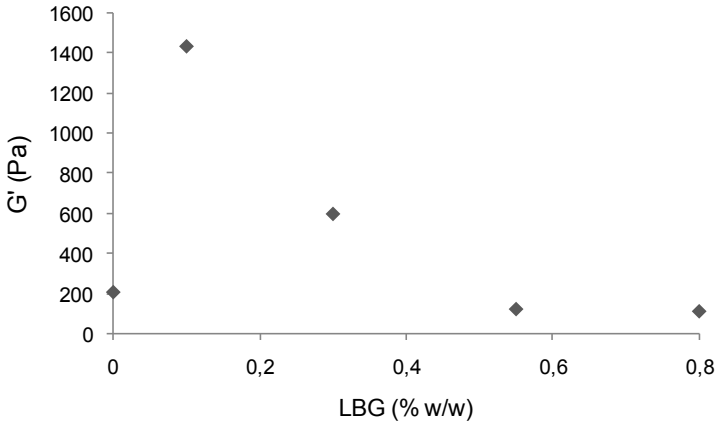

Figure 3 Influence of the LBG concentration on the final storage modulus of whey protein gels (10 % w/w)

Therefore the statistical analyses and empirical modelling were performed only with the data from mixed systems for the LBG range of 0.1 – 0.55 %. A quadratic model as described by Eq. 1 was used.

$$y = b_0 + b_1 x_1 + b_2 x_2 + b_{11} x_1^2 + b_{22} x_2^2 + b_{12} x_1 x_2 + residual \qquad \text{Eq. 1}$$

By means of an analysis of variance it was concluded that all the adjusted models are significant. The effect of LGB concentration and of the degree of hydrolysis on peptic hydrolysates gelation was negative for *G'* and *G''*, though an interaction factor has also to be considered. For tan δ and the temperature of gelation a minimum value exists in the studied range of LBG concentration, while a maximum exists in the studied range of *DH* for the temperature of gelation.

Table 2 Statistical analysis of the influence of the LBG concentration and hydrolysis degree on the gelling ability of 10.0 % (w/w) whey peptic hydrolysates

Variable	Regression coefficients						Regression quality	
	b0	*b1*	*b2*	*b11*	*b22*	*b12*	*PF* (%)	Lack-of-fit
G' (Pa)	1619	**-2886**	-618	-	-	1086	0.20	Not significant
G'' (Pa)	235	**-393**	-87.3	-	-	146	0.31	Not significant
$tan\ \delta$ (º)	0.193	-0.470	-0.012	1.09	-	0.102	0.05	Not-significant
T_g (ºC)	75.8	-10.4	5.40	31.3	-2.50	-	0.51	Not-significant

Items in **bold** correspond to non significant model terms that could not be withdrawn from the model because they were required to support hierarchy.

The gelation process is very sensible to environmental conditions and to processing and often leads to rather coarse data. The factorial planning used allowed validating conclusions using fewer experiments than those needed if no planning had been used, while still getting statistical significance out of the results. However, as many factors are involved, the modelling of the process was not straightforward. A simple quadratic function was generally not enough to accurately describe the system behaviour.

4 Conclusion

WPC mild hydrolysis (up to 2.5%) ameliorates the gelling ability, but affects the WPC synergism with LBG (no max found in the G' dependence on LBG content).

As a general conclusion, it can be stated that it is possible to make all kinds of different gels (fast gelling, slow gelling, hard and stiff, or weak gel) by manipulating the protein concentration, the degree of hydrolysis and the amount of LBG. It is important though to master the mechanism of phase separation in order to be able to design the adequate conditions for the desired texture.

References

Croguennoc, P., Nicolai, T., Durand, D., and Clark, A. (2001). Phase separation and association of globular protein aggregates in the presence of polysaccharides: 2. Heated mixtures of native beta-Lactoglobulin and k-Carrageenan. *Langmuir,* 17(14), 4380-4385.

da Silva, J.A.L. and Gonçalves, M.P. Studies on a purification method for locust bean gum precipitation with isopropanol. *Food Hydrocolloids,* 4, 277-287, 1990.

Gosal, W.S. and Ross-Murphy, S.B. (2000). Globular protein gelation. *Current Opinion in Colloid & Interface Science,* 5(3-4), 188-194.

Paulsson, M., Dejmek, P., and Vanvliet, T. (1990). Rheological Properties of Heat-Induced Beta-Lactoglobulin Gels. *Journal of Dairy Science,* 73(1), 45-53.

Pollard, M.A. and Fischer, P. (2006). Partial aqueous solubility of low-galactose-content galactomannans - What is the quantitative basis? *Current Opinion in Colloid & Interface Science,* 11(2-3), 184-190.

Schmitt, C., Sanchez, C., Desobry-Banon, S., and Hardy, J. (1998). Structure and technofunctional properties of protein-polysaccharide complexes: a review. *Critical Reviews in Food Science and Nutrition,* 38(8), 689-753.

Turgeon, S.L. and Beaulieu, M. (2001). Improvement and modification of whey protein gel texture using polysaccharides. *Food Hydrocolloids,* 15(4-6), 583-591.

Proceedings of the 10th International Chemical and
Biological Engineering Conference - CHEMPOR 2008
Braga, Portugal, September 4-6, 2008
E.C. Ferreira and M. Mota (Eds.)

Enzymatic Agent from Red King Crab Hepatopancreas and Its Applications

V. A. Mukhin, V. Yu. Novikov, K. S. Rysakova
Knipovich Polar Research Institute of Marine Fisheries and Oceanography (PINRO),
Murmansk, Russia.

Keywords: King crab hepatopancreas, enzyme, hydrolysis, enzymatic hydrolysates.
Topic: Integration of life sciences & engineering.

Abstract

In this review, the results of the investigation of proteolytic and chitinolytic activity of enzyme systems of invertebrates, in particular, the enzymatic agent preparing from the Red King crab (*Paralithodes camtschaticus*) hepatopancreas are described.

Enzymatic agent from Red King crab hepatopancreas was shown to be capable of producing protein hydrolysates. Properties and characteristics of enzymatic agents and protein hydrolyzates are investigated in detail.

1 Introduction

Currently, biochemists in different countries are aimed at the development and improvement of enzymatic processes that are used in the production of enzymatic protein hydrolysates and modification of natural polysaccharides.

Special attention to this direction is determined by the high specificity of enzymatic reactions, which makes it possible to obtain unique compounds of a certain structure, and environmental friendliness of biochemical manufacture, in contrast to purely chemical manufacture, which is expressed in renunciation of large volumes of aggressive chemicals and absence of contaminated chemical discharges. Peptides and chitooligosaccharides are interesting as substancts, whose biological activity is higher than that of natural protein and chitin.

Studies performed at the Polar Research Institute of Marine Fisheries and Oceanography demonstrated that invertebrates occurring in the Barents Sea contain proteins whose content of essential amino acids is competitive with common sources of nutrient proteins. The invertebrates of the Barents Sea have the great importance for development of a fishery of Northwest region of Russia. Except for food industry these objects have interest as sources of enzymes with various substrate activities.

The research of enzyme properties is actual for an evaluation of a physiological state of trade objects, for extraction high-activity enzymes, and also to prepare with the its help the enzymatic protein hydrolysates.

The alimentary systems of some marine invertebrates contain diverse and highly active proteases. In particular, Red King crab (*Paralithodes camtschaticus*) hepatopancreas can be used as a source of protease preparations. Their high activity was demonstrated on common protein substrates, including collagen.

The waste of Red King crab processing includes hepatopancreas, which is of interest as a source of various enzymes, including proteolytic ones (Kupina et al., 1999). Total proteolytic and collagenolytic activity of enzyme system of crab is greatly higher that activities in digestive organs of Vertebrates (Chen et al., 1991).

It is expedient to use the internals of sea invertebrates being waste products of a catch, as a source of proteinases. In particular, the hepatopancreas of the Red King crab is most perspective for extraction of highly active complex enzymatic agents of proteolytic action.

2 Experimental Methods

We have studied some ways of enzymatic agent (EA) preparing: fat extraction from hepatopancreas by organic solvents (acetone and n-butanol), fractionation by ultrafiltration and degreasing by the chitosan solution (Mukhin and Novikov, 2001a). EA, obtained on the

first method, (“Acetonic powder”) had smaller specific proteolytic activity, but the yield of product was higher and its cost was much lower. These factors have made its most suitable for wide practical use.

For the most objective reflectance of depth and degree of protein and chitin degradation we simultaneously took into account the data obtained with use of gravimetric, spectral analysises, exclusion chromatography, determination of the contents of the total and amine nitrogen, free amino acids, total reducing sugars and carbohydrates – D-glucosamine and N-acetyl-D-glucosamine.

Anson method with several modifications was used to estimate proteolytic activity of the EA using hydrolysis of 1 % haemoglobin solution (pH 3.6) and 1 % sodium caseinate solution (pH 7.0). Proteolytic activity was expressed in mmol Tyr (280 nm) per 1 g EA after 30 min of incubation 37 °C.

Chitinolytic (exochitinase) activity was determined by the formation of N-acetyl-D-glucosamine as a result of chitin hydrolysis; total glycolytic activity, by the total content of N-acetyl-D-glucosamine, D(+)-glucosamine and other reducing sugars in hydrolysis products. Colloidal chitin and chitosans with different deacetylation degrees were used as substrates. The concentration of N-acetyl-D-glucosamine was determined by the reaction with 4-dimethylaminobenzaldehyde (Reissig et al., 1955). The total concentration of reducing sugars was determined by the reaction with potassium hexacyanoferrate (Imoto and Yagishita, 1971).

Fractionation of protein was carried out by exclusion HPLC on system LC-10AVP (Shimadzu Corp., Japan) with columns TSK-gel Alpha-4000 (30 x 0,78 cm) and TSK-gel guardcolumn Alpha (6 x 0,4 sm) (TOSOH, Japan). Eluent - 0,3 M NaCl, eluent rate - 1 ml/min, UV-detector SPD-10AVP. Determination of D-glucosamine as OPA derivative was carried out also by HPLC on column Supelkosil LC-18 (30 cm x 4 mm). Binary eluent - acetonitrile:CH_3COONa, eluent rate - 1 ml/min, refractometric detector RF-10 AXL.

UV spectrum analysis of solutions (240-320 nm) was carried out with spectrophotometer UV-3101PC (Shimadzu Corp., Japan).

3 Results and Discussion

The proteolytic and chitinolytic activity of enzymatic agents from different taxons of the Barents Sea invertebrates, such as mollusks (*Serripes groenlandicus*, *Biccinum undatum*), crustaceans (*Paralithodes camtschaticus*, *Pandalus borealis*) and echinoderms (*Cucumaria frondosa*, *Asterias rubens*), was studied. The choice of them was conditioned by essential stocks of these animal species in the Barents Sea and insufficient development of rational technologies to process them.

Table 1. Proteolytic (A_{280}) and chitinolytic activity (U_{endo}, U_{exo}) of enzymes from different Invertebrates

Hepatopancreas or entrails	A_{280}	U_{endo}	U_{exo}	U_{exo}/U_{endo}
Serripes groenlandicus	7.6	0.836	0.198	0.237
Buccinum undatum	10.9	0.409	0.352	0.861
Cucumaria frondosa	-	0.346	0.077	0.223
Asterias rubens	30.3	14.544	0.091	0.0063
Paralithodes camtschaticus	100.9	4.324	1.825	0.422
Enzymatic agent from *Paralithodes camtschaticus*	284.0	9.277	3.866	0.417

Proteolytic activity in the hepatopancreas of crab and sea star was found to be an order higher than in other study objects. High protease activity in crab hepatopancreas is an evolutionary mechanism compensating for a poor differentiation of digestive system, low substrate specificity of enzymes, and cold environment.

The greatest chitinolytic activity was observed in the hepatopancreas and enzymatic agents extracted from the Invertebrates. Correlation between proteolytic and chitinolytic

activity exists in most cases. Exception is observed for the hepatopancreas from a starfish in which anomalously high endochitinolytic activity is found.

Properties of Enzymatic agent from Red King crab hepatopancreas

Enzymatic agent from Red King crab hepatopancreas has the greatest proteolytic activity and it can be yielded in great volumes. Therefore it is the most suitable for practical use in various fields of the industry, medicine, an agriculture, etc.

The EA contained over 90 % protein and was active under neutral conditions with respect to sodium caseinate (200-250 mmol Tyr/g for “Acetone powder” and 450-500 mmol Tyr/g for EA, preparing by ultrafiltration).

We studied the temperature, pH, and time dependence of proteolytic activity of enzymatic agent obtained from Red King crab hepatopancreas (Mukhin et al, 2001a).

It is established, that a temperature optimum of activity in relation to casein is 50°C, and in relation to a haemoglobin - 55°C. According to other researchers maximal activity against a collagen is also at 50-55°C (Chen et al., 1991; Sakharov, 1992; Litvin, 1993).

Reaction of proteolytic cleavage of proteins reaches a saturation about 3-4 hours of incubation. The linear part on the kinetic curve was observed within the first hour of incubation (Mukhin and Novikov, 2001a).

The highest digesting ability of EA was shown in relation to tissues of Icelandic scallop and Nothern shrimp which enter into a diet of the Red Ring crab, and also in relation to own tissues (Mukhin et al., 2001b, Mukhin and Novikov, 2001). To a lesser degree EA digests other protein products (meat of the hen, a beef, pork, etc.).

It has been shown, that proteolytic activity of crab hepatopancreas is subject to significant seasonal fluctuations. Apparently, these fluctuations are concerned with stages of sexual cycle of development gonads, larval stage of a chitinous shell, and also with trophic activity. Maximal proteolytic activity is found out in adults in November-March, and in the spring-and-summer season conforming to the season of molting and spawning it drops in two and more times.

It was discovered also a chitin-degrading activity of EA (Novikov and Mukhin, 2003).

Our study confirms the presence of chitinolytic and chitosanolytic activities in the hepatopancreas of the red king crab, related to the specific diet of this species (Novikov and Mukhin, 2003; 2005).

The maximum rate of chitin/chitosan hydrolysis by EA from crab hepatopancreas occurs at 36.5–37.0°C.

The optimal temperature of glycolytic (45°C) and exochitinase (35°C) activities are shifted towards lower temperatures relative to the optimum for the proteolytic activity (55°C) (Rysakova et al., 2008). This finding confirms the conclusion that glycolytic and proteolytic activities are exhibited by different enzymes contained in the enzyme preparation from the red king crab hepatopancreas.

Two pH optimums have been found for the enzymatic reaction under mildly alkaline and acidic conditions for both exo- and endochitinase activities. The optimum pH values for exochitinase and total glycolytic activities coincided and were found to be 4.5. The second maximum of exochitinase activity, which was absent in the case of glycolytic activity, was recorded at pH 8.0. The pH value at which the proteolytic activity of the enzyme preparation was maximum (pH 8.5) did not coincide with the pH corresponding to the maximum glycolytic activity but was close to the pH at which the exochitinase activity was maximum.

The enzyme preparation is most affine to partly deacetylated chitin with an acetylation degree within 40–50 % (Novikov et al., 2007).

By HPLC we have not found the formation of D-glucosamine during enzymatic hydrolysis of chitin and chitosan. It can be concluded that EA exhibits only chitinase activity since it does not cleave single D-glucosamine molecules.

We have confirmed the presence and quantified the exochitinase, endochitinase, and deacetylase activity of the enzymatic agent as well as demonstrated the absence of exochitosanase, and N-acetylglucosamine deacetylase activities. We assumed that the

chitinase and protease activities of the enzyme preparation are apparently exhibited by different enzymes.

It was studied the distribution of specific activities in various fractions of EA from hepatopancreas of the Red King crab.

The data obtained at fractionating of EA by ultrafiltration, a gel-filtration and preparing exclusion HPLC (Table 2) show, that maximal chitinolytic activity is concentrated in fractions with the greater molecular weight (more than 100 kD) in comparison with proteases (50-100 kD).

Table 2. Distribution of exochitinolytic and proteolytic activity of EA on fractions with different molecular weight

Fraction	U_{exo}, μmol AcGlcN/g	A_{prot}, μmol Tyr/g
> 100 kD	**1.53**	33.16
50-100 kD	0.13	**119.90**
10-50 kD	0.70	83.20
< 1 kD	1.96	0.99

Observable increase of exochitinolytic activity in 4-th fraction explains by predominance of amino acids, namely tryptophan which reacts with 4-dimethylaminobenzaldehyde giving a coloured complex.

Obtained results are suggested, that different enzymes are responsible for exochitinolytic and proteolytic activities.

Production and properties of enzymatic protein hydrolysates

Enzymatic agent from Red King crab hepatopancreas was shown to be capable of producing protein hydrolysates. Hydrolysis of protein-containing waste of Northern shrimp, King crab and Iceland scallop occurs most successfully at pH about 8 and 50-55°C for 5-6 h in presence of 3-6 g enzyme per kg substrate (Mukhin and Novikov, 2001; 2001a).

It is demonstrated that the hydrolysates can be used for growing test cultures (Mukhin et al., 2001b; Mukhin and Novikov, 2005), and feed supplement for chickens and fishes (Mukhin and Novikov, 2001a).

The maximum hydrolysis rate was observed at 55°C and pH 7.5. The degree proteolysis also depended on the incubation duration, concentration of the enzymatic agent, and concentration of the substrate. The reaction is described by a set of exponential curves whose steepness depends on the listed factors.

Dry hydrolysate was prepared from protein-containing waste of Icelandic scallop and Northen shrimp processing by means of EA from Red King crab hepatopancreas. The resulting product contains no less than 80 % free amino acids and oligopeptides. Predominant are aspartic acid, leucine, isoleucine, arginine, and lysine, which account for more than 50 % of the free amino acids.

Various types of protein hydrolysates are used in microbiology, medicine, and the food industry. Production of nutrient media requires high-quality inexpensive protein hydrolysates.

1. The potential of using the protein hydrolysate as a nutrient for microorganism cultivation is estimated. It is demonstrated that the hydrolysate can be used for growing test cultures.

Microbiological studies demonstrated that the test cultures satisfactorily grew on a nutrient agar containing enzymatic protein hydrolysates. The colonies demonstrated no morphological deviations.

The biological properties of protein hydrolysates from Icelandic scallop and Northen shrimp were evaluated on the test strains *Shigella flexnerila* 8516, *Shigella sonnei* “S form”, *Pseudomonas aeruginosa* 27/99, *Serratia marcescens* 1, *Corynebacterium xerosis* 1911, *Escherichia coli* 3941/12 (055:K59), *Staphylococcus aureus* Wood-46, *Klebsiella pneumoniae* 3534/51, *Salmonella typhi* II-901, *Salmonella typhimurium* 79, and *Citrobacter freundii* 101/57 grown on the following model media: fish-meal hydrolysate (FMH) No. 1, FMH agar, FMH broth, Endo-FMH agar, and Levin FMH.

Microbiological studies demonstrated that these enzymatic protein hydrolysates can be used as a protein component in nutrient media.

2. We have shown an opportunity of application of hydrolysates as additives in feed of chichens and young fish *Salmo salar* (Mukhin and Novikov, 2002; Mukhin et al., 2003).

For example, the results of experimental feeding of chickens (age 47 day) have shown, that additives of enzymatic protein hydrolysates in feed had led to increase of safety (from 88 to 91 %), average daily weight increment (from 30 to 34 u) and average mass of one specimen (from 1,4 to 1,6 kg).

3. As a result of the researches carried out in our laboratory optimal technologies of preparing of enzymatic agents from digestive organs of sea invertebrates, the enzymatic protein hydrolyzates intended for enteral tube feeding of people have been developed.

For preparing of food hydrolysate the enzymatic agent from hepatopancreas of the Red King crab was used as the proteolytic agent. The sub-standard muscle of the Icelandic scallop was applied as a source of protein.

Protein hydrolyzate for for enteral tube feeding of the postoperative patients, obtained on the developed technology, possesses the increased biological value due to the high contents of low molecular weight protein components. It is capable to run through a probe with a diameter 5 mm without padding pressure that facilitates its uptake in a gastrointestinal path of the patient. The ready form of a drug is characterized by the high contents of high-grade protein products and corresponds to the demands showed to products of a children's food on Hygienic norms of FAO (1991).

Clinical approbation of protein hydrolyzate for medical purpose has shown harmlessness of the given drug. Allergic and toxic reactions at the surveyed patients are not marked. Biochemical analysis of a blood testify to enriching of parameters of a nitrogen metabolism.

4. The developed enzymatic agents allow to make salty delicacy production with good organoleptic properties from fishes and invertebrates: the perch, henfish, sea cock, common whelk and other. The muscle tissue of these organisms is unable to ripen self-contained under influence of own proteolytic enzymes. Processing of muscle tissue of these objects by solution of EA from hepatopancreas of the Red King crab (concentration of 0,025-0,05 %) results in its particulate hydrolysis, a ramollissement and enriching of gustatory advantages of finished goods.

Enzymatic processing of low-grade meat semifinished products at the presence of 0,01-0,1 % of enzymatic agent from hepatopancreas allows to modify a complex of physical and chemical and consumer properties of meat products. Analysis of aminoacid composition has shown, that total composition of amino acids has not changed during enzymatic processing of beef forcemeat. The contents of free amino acids has grown almost in 2 times.

The practical significance of our results is that they demonstrated that crab hepatopancreas can be used as a source of enzymes exhibiting chitinolytic and chitosanolytic activities for industrial modification of chitin and chitosan. This enables maximum utilization of all components of commercial aquatic organisms and increases the efficiency of sea fishery owing to utilization of its processing waste. The study of the glycolytic activity of the enzyme preparation from the red king crab hepatopancreas is of practical interest in terms of designing chitinase preparations for fighting against pests and treating fungal infections.

References

Chen Y. L., Lu P. J., Tsai I. (1991). Collagenolytic activity of crustacean midgut serine proteases: Comparison with the bacterial and mammalian enzymes. Comparative Biochemistry and Physiology. Part B, 100 (4), 763-768.

Imoto T., Yagishita K. (1971). A simple activity measurement of lisozyme. Agricultural and Biological Chemistry. 35 (7), 1154-1156.

Kupina N. M., Gerasimova N. A. (1999). Characterization of poteolytic preparations from crab hepatopancreas. Applied Biochemistry and Microbiology, 35 (3), pp. 270-273.

Litvin F. E. (1993). Collagenolytic proteases from hepatopancreas of Kamchatka crab. Ph.D. thesis. Moscow. 20 pp.

Mukhin V. A., Novikov V. Yu. (2001). Enzymatic hydrolysis of proteins from Crustaceans of the Barents Sea. Applied Biochemistry and Microbiology, 37 (5), 538-542.

Mukhin V. A., Novikov V. Yu. (2001a). Enzymatic protein hydrolysates of marine organism tissues: production, properties, and applications. Murmansk: PINRO Publishing, 97 pp.

Mukhin V. A., Novikov V. Yu., Ryzhikova L. S. (2001b). A protein hydrolysate enzymatically produced from the industrial waste of processing Icelandic scallop *Chlamys islandica*. Applied Biochemistry and Microbiology, 37 (3), 292-296.

Mukhin V. A., Novikov V. Yu. (2002). Protein hydrolysates from processing waste of marine organisms. Ptitsevodstvo. 1, 21-23.

Mukhin V. A., Novikov V. Yu. (2005). Protein hydrolysates of sea origin as components for microbiological culture media. The FEBS Journal, 272 (Suppl. 1), 157-158.

Novikov V. Y., Mukhin V. A. (2003). Chitosan depolymerization by enzymes from the hepatopancreas of the crab Paralithodes camtschaticus. Applied Biochemistry and Microbiology, 39 (5), 464-468.

Mukhin V. A., Novikov V. Yu., Mukhina I. N. The Effect of Water Temperature on the Mortality Rate in Juveniles of Atlantic Salmon Salmo salar in Early Ontogenesis in the Conditions of Artificial Culture // Journal of Ichthyology.- 2003.- Vol. 43, No. 1.- P. 131–133.

Novikov V. Yu., Mukhin V. A. (2005). Detection of chitinolytic activity in digestive organs of hydrobionts from the Barents Sea. Journal of Evolutionary Biochemistry and Physiology, 41 (4), 473-475.

Novikov V. Yu., Mukhin V. A., Rysakova K. S. (2007). Properties of chitinolytic enzymes from the hepatopancreas of the Red King Crab (Paralithodes camtschaticus). Applied Biochemistry and Microbiology, 43 (2), 159-163.

Reissig J. L., Strominger J. L., Leloir L. F. (1955). A modified colorimetric method for the estimation of N-acetylamino sugars. The Journal of Biological Chemistry. 217 (2), 959-966.

Rysakova K. S., Novikov V. Yu., Mukhin V. A., Serafimchik E. M. (2008). Glycolytic activity of enzyme preparation from the Red King Crab (*Paralithodes camtschaticus*) hepatopancreas. Applied Biochemistry and Microbiology. 44 (3), 251-255.

Sakharov I. Yu. (1992). Extraction and research of enzymes from marine organisms and some aspects of their application. thesis for a Doctor's degree. Moscow. 47 pp.

Proceedings of the 10th International Chemical and
Biological Engineering Conference - CHEMPOR 2008
Braga, Portugal, September 4-6, 2008
E.C. Ferreira and M. Mota (Eds.)

Alkaline hydrolysis of chitin and chitosan

V. Yu. Novikov[1], I. N. Konovalova[2]
1 Knipovich Polar Research Institute of Marine Fisheries and Oceanography (PINRO), Murmansk, Russia.
2 The Murmansk State Techical University (MSTU), Murmansk, Russia

Keywords: chitin, chitosan, deacetylation, crystallinity
Topic: Advancing the chemical engineering fundamental.

Abstract

In this work process of alkaline hydrolysis of chitin and chitosan was studied. Structural properties of initial and reprecipitation samples of chitin and chitosan in dry and wet condition are investigated. It is established, that degree of crystallinity of the investigated samples renders considerably smaller influence on deacetylation rate, than an opportunity of formation of hydrated environment around macromolecules of polysaccharide. This interferes with nucleophilic attack by hydroxyl ion and retards reaction rate.

1 Introduction

Chitin is unique natural polysaccharide occupying the second place after cellulose. In the initial state it does not find wide application because of power solubility and small reactivity. Usually chitin is exposed to modification by various ways for reception of derivatives, in particular chitosan (Muzzarelli, 1977).

The alkaline hydrolysis of chitin and chitosan results to cleavage mainly acetamido linkages with formation of free amino groups and conservation polysaccharide chain. In result well soluble high molecular weight polysaccharide is formed. Chitosan is widely applied in medicine, cosmetics, agriculture and other (Goosen, 1997).

In this work we have studied a process of alkaline hydrolysis of chitin and chitosan. The basic purpose has consisted in an establishment of the mechanisms responsible for cleavage of amide linkage in an alkaline condition.

2 Experimental Methods

Deacetylation of chitin and chitosan, obtained on known technology (No and Meyers, 1995) from shells of crabs and shrimps, has been investigated with the help of chemical methods, IR-spectophotometry, X-ray crystallographic analysis.

Degree of deacetylation (DD) of chitin/chitosan was determined by potentiometric titration of 0.1% chitosan solution in 0.1N HCl by 0.1N NaOH. DD of chitin and chitosan was determined also by IR-spectophotometry. For estimation of degree of crystallinity we used X-ray analysis.

IR-absorption spectra in IR wrote down on infra-red spectrophotometer IR-420 ("Shimadzu", Japan) from 4000 to 400 cm_{-1}.

Researches of structural properties of chitin and chitosan samples have been carried out in the Kola Science Centre of the Russian Academy of Science on the X-ray diffractometer DRON-2 (NPO “Burevestnik”, USSR) by a method of X-ray phase analysis on CuKα radiation with Ni-filter in range of angles 2θ = 6-36°.

3 Results and Discussion

Research of alkaline deacetylation of chitin has shown, that at single-pass continuous carrying out of reaction DD does not achieve maximal value of 100 %. In the beginning there is fast increasing of DD, then the reaction rate falls and on the kinetic curve the flat plateau with DD 70-80 % is observed. After washing, drying and repeated alkaline processing recurrence of primary kinetics is observed: fast rise of DD and then formation of a flat plateau.

Features of deacetylation kinetics of chitin and chitosan are considered in works (Kurita et al., 1977; Mima et al., 1983; Tsaih and Chen, 2003).

Several possible explanations of decreasing of deacetylation rate during alkali treatment of chitin are offered: influence of heterogeneity of chitin crystalline structure, formation of solvate complexes of chitin or alkali, change of reagent concentrations during reaction, etc.

Authors of work (Kurita et al., 1977) explain deacetylation process specificity, first of all, by crystalline structure of natural chitin. This explanation is most recognized now.

The first fast field of the kinetic curve is caused by deacetylation of more available for alkali chitin moleculas in amorphous regions of a sample. The flat field describes kinetics of deacetylation of more dense crystalline regions. After washing there is a further amorphicity of a sample due to change of DD that results to recurrence of deacetylation kinetics.

Authors of work (Ottoy et al., 1996) investigated distribution of various fractions on DD in party deacetylated chitosan, having various acid solubility. Results obtained by them testify for the benefit of the diffusive mechanism of deacetylation reaction in which the rate of alkali diffusion inside of solids plays a basic role, and not division of polysaccharide on amorphous and crystalline regions.

In work (Chang et al., 1997) it is shown, that deacetylation rate depends on concentration of alkali: the constant of deacetylation rate increased with increase of NaOH concentration. Authors of this article assume, that rate of heterogenous deacetylation can be supervised both a chemical reaction, and a diffusion of a reagent and reaction product inside particles of polysaccharide.

Other idea consists in change of reactivity of reagents.

1. The form of the kinetic curve directs at the assumption of existence of reverse reaction of acetylation. But experimental results have not confirmed existence of such reaction in conditions of alkaline deacetylation.

2. It is suggested the change of alkaline reactivity due to the formation of solvate (hydrated) complexes. For example, in (Percot et al., 2004) a formation of hydrates of NaOH which are less active in chitin deacetylation reaction in comparison with unhydrated molecules is supposed.

3. A formation of low-activity solvate (hydrated) complexes of chitin which can be destroyed after washing and drying of deacetylated polysaccharide. In our early work we have assumed a formation of complexes OH^- with chitin (Novikov et al., 1990; Novikov, 2003; Novikov et al., 2005) and have shown, that reaction of deacetylation is described by two simultaneous reactions of the pseudo-first order, one of which consists in deacetylation, and another - in formation of chitin complex with hydroxyls ions:

deacetylation:

$$A_n + OH^- \rightarrow D_n + AcO^-,$$

formation of low-activity intermediate:

$$A_n + OH^- \rightarrow A_n \cdot OH^-_m.$$

where A_n - acetylated polysaccharide, D_n - deacetylated polysaccharide.

We have carried out a studying of alkaline deacetylation kinetics, variating crystalline structure of polysaccharide and a condition of hydration (Chebotok et al., 2007)
Crystallinity of different samples of chitin and chitosan are shown on fig. 1 and tab. 1.

The results in Table 1 and Figure 1a show that at reprecipitation the crystalline structure of chitin and chitosan is practically completely recovered. In samples of chitin, reprecipitated from NaOH X-ray diffraction patterns of restored structure have wider peaks, than a diffraction pattern of initial chitin, but positions of peaks practically coincide (not shown).

Obtained results are coordinated with data given in works (Kurita et al., 1977; Rege and Block, 1999).

Table 1. Degree of crystallinity ($\chi_{кр}$, %) of chitin and chitosan samples

Sample	$\chi_{кр}$, %
Chitin initial, dry	61.1
reprecipitated from NaOH solution, dry	55.5
reprecipitated from HCl solution, dry	60.7
reprecipitated from NaOH solution, wet	8.8
reprecipitated from HCl solution, wet	8.5
Chitosan initial, DD 82 %, dry	35.8
reprecipitated from HCl solution, DD 82 %, dry	37.5
reprecipitated from HCl solution, DD 82 %, wet	3.8

It is considered (Kurita et al., 1977), that after crystalline modification there is partially regeneration of structure of α-chitin, partially formation of other crystalline forms and amorphicity of chitin.

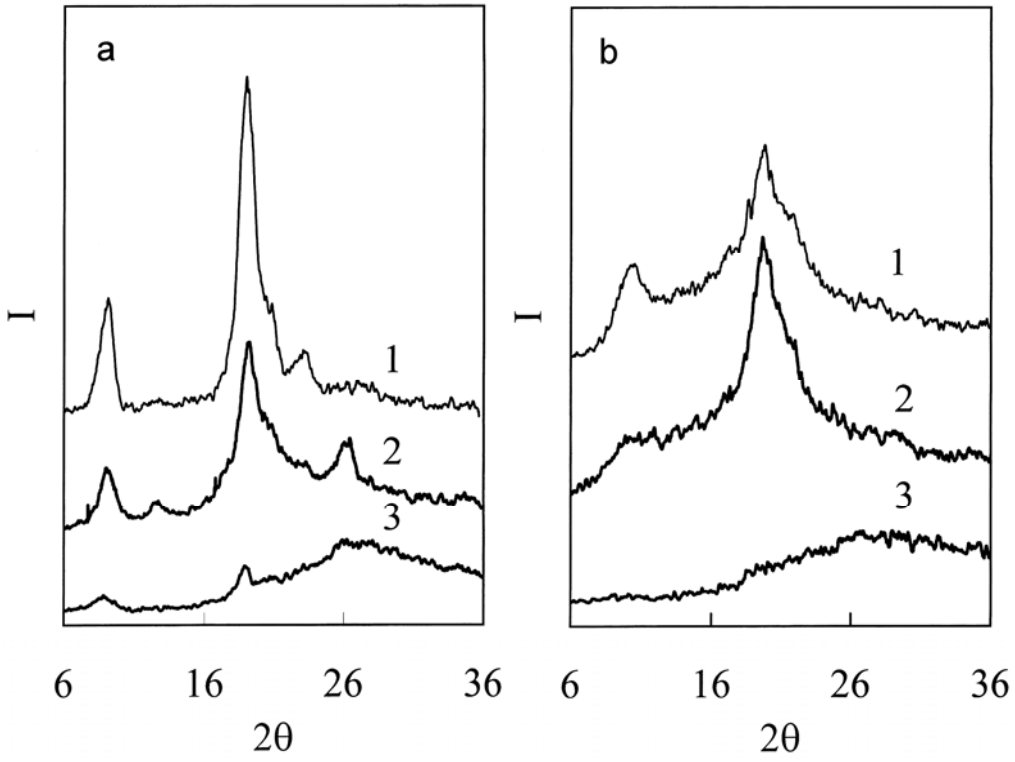

Fig. 1. X-ray diffraction pattern of chitin (a) and chitosan (b). Initial (1) and reprecipitation samples: dry (2) and wet (3).

In chitosan samples we also observed regeneration of crystalline structure (Fig. 1b) with some differences from initial structure of chitin. The positions of maximums of two basic peaks in chitosan sample is displaced concerning a positions of these peaks in a sample of α-chitin. In X-ray diffraction patterns of chitin with DD less than 71 % two peaks at 2θ 9.2° and 19.1° are observed. In chitosan (DD 95 %) these peaks are displaced and settle down at 2θ 11.2° and 20.1-20.4° accordingly. Our results d'not contradict the data of other researchers (Kurita et al., 1977; Gorbacheva et al., 1988; Rege and Block, 1999; Focher et al, 1992; Nud'ga et al., 1971).

We obtain X-ray diffraction patterns practically amorphous solids for reprecipitated wet samples of chitin and chitosan (fig. 1a, 1b).

1. Change of DD results in change of crystalline structure of polysaccharide at transferring from chitin to chitosan.

It is known, that at increasing of DD crystallinity of chitin drops, and then (after 90-95 %) the new crystalline structure of chitosan starts to form (Kurita et al., 1977; Focher et al., 1992).

If this fact takes place, with increasing of initial DD of chitin rate and depth of deacetylation should rise due to increasing of amount of amorphous regions. Taking into account such change, it is possible to expect, that the deacetylation kinetics of chitin/chitosan samples with various DD will differ. We have investigated the deacetylation kinetics of samples with initial DD 12, 66, 88 and 92 % (Fig. 2).

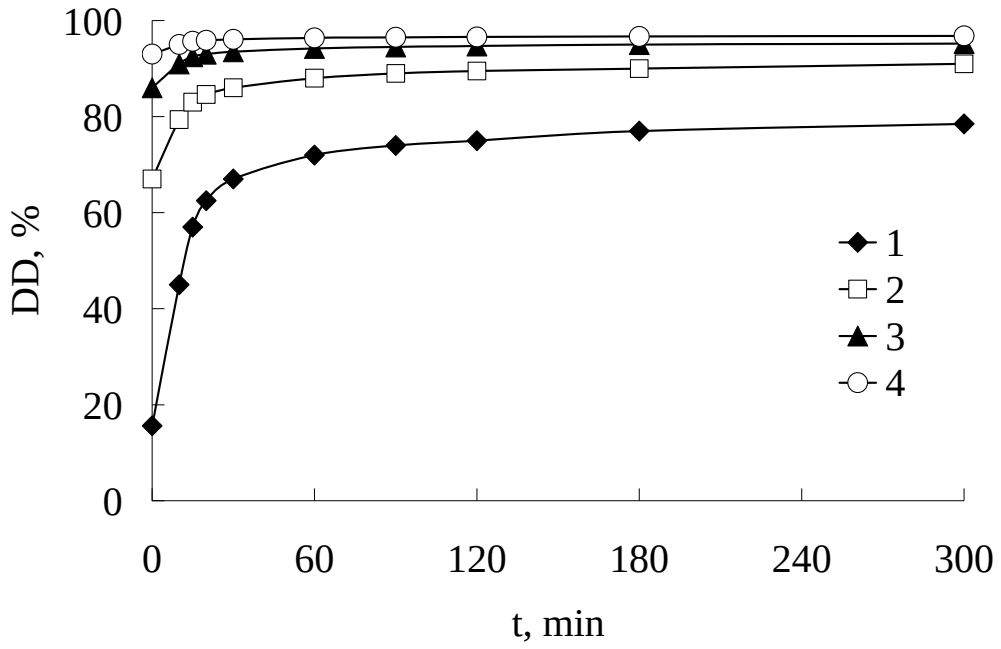

Fig. 2. Deacetylation kinetics curves of chitin/chitosan with initial DD 12 (1), 66 (2), 88 (3), and 92 % (4). Temperature 98 °C, 50 % NaOH.

Our results, have shown, that kinetic curves of deacetylation for normalized in relative values DD completely coincide. In other words, the deacetylation rate of chitin and chitosan does not depend on an initial DD. The form of kinetic curves appeared identical to chitin and chitosan with various initial DD, up to 95 % (Novikov et al., 1990; Novikov, 2003).

2. We have shown influence of crystallinity and a hydration of chitin molecules on deacetylation kinetics of dry and wet samples natural and reprecipitated chitin (Fig. 3) (Chebotok et al., 2007).

In our opinion, formation of solvated structures as a result of interaction of macromolecules of polysaccharides and low molecular weight electrolyte with solvent affects on deacetylation rate.

On Fig. 3 the kinetic curves of deacetylation of dry chitin (curve 1) and reprecipitated from solution NaOH of wet chitin (curve 2) are shown. From Fig. 3 it follows, that rate of deacetylation of wet reprecipitated sample ($\chi_{кр}$ = 4.0%) is much less than dry chitin ($\chi_{кр}$ = 59.0%). In NaOH solution, probably, the solvation (hydration) of chitin molecules takes place. Dipoles of water molecules are in appropriate way oriented around acetamidic and glycosidic linkages of macromolecules. According to the mechanism of reaction of deacetylation in an alkaline condition the hydrolysis of acetamidic linkage begins with nucleophilic attack by ions OH^- on carbonyl atom of acetamidic group. This hydrated environment complicates the nucleophilic attack that results in decrease of deacetylation rate.

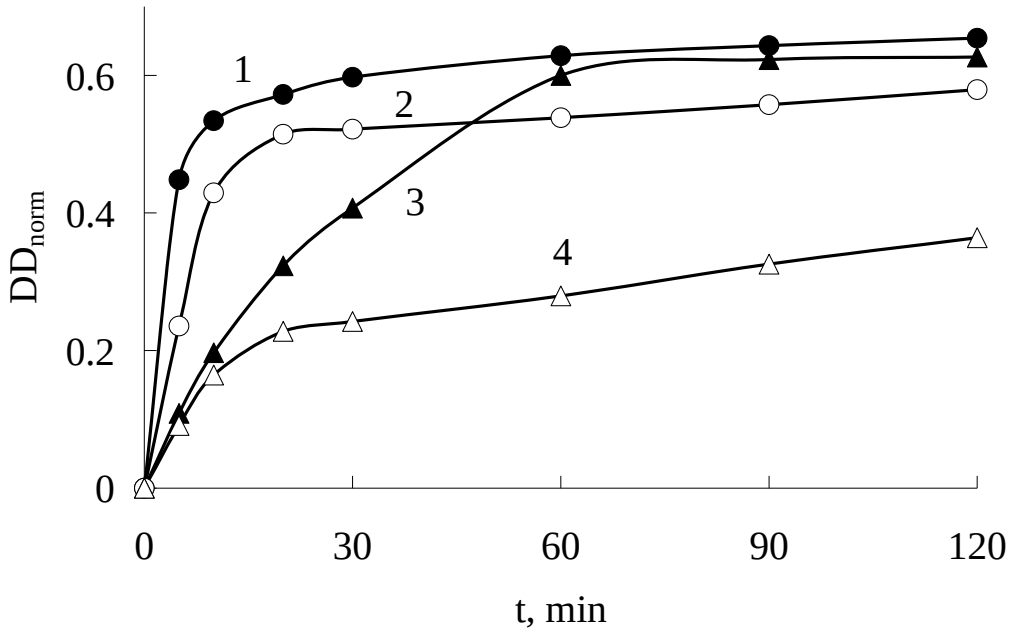

Fig. 3. Deacetylation kinetic curves of chitin: initial dry (1), initial wet (2), reprecipitated dry (3), and reprecipitated wet (4). Temperature 98 °C, 50 % NaOH. DD_{norm} – normalized DD, % (initial of each sample njrmalized to 0, upper DD - 100 %), t - time (min).

The decrease of reaction rate on the first part (0-30 mines) of deacetylation kinetics curve of reprecipitated dry chitin in comparison with dry and wet initial chitin can be explained by higher density of chitinous particles. In the initial samples obtained by consistent extraction of proteins and inorganic salts from the crab shell a particle of chitin are more porous. After crystallization of clear chitin from solution such pores are not formed for the account more density packing of molecules of polysaccharide.

Thus, obtained results allow to assume, that degree of crystallinity of the investigated samples renders considerably smaller influence on speed of deacetylation, than an opportunity of formation of a hydrated environment around of macromolecules of polysaccharide which interferes with nucleophilic attack of hydroxyl ion, retards reaction rate and stops reaction on fixed values of DD. The occurrence of two simultaneous reactions - deacetylations and formations of low-activity intermediate which is broken down at washing is possible.

References

Chang K. L. B., Tsai G., Lee J., Fu W.-R. (1997). Heterogeneous N-deacetylation of chitin in alkaline solution. Carbohydrate Research. 303, 327-332.

Chebotok E. N., Novikov V. Yu., Konovalova I. N. (2007). Kinetics of base deacetylation of chitin and chitosan as influenced by their crystallinity. Russian Journal of Applied Chemistry. 80 (10), 1753-1758.

Focher B., Naggi A. Torri G. Cosani A. Terbojevich M. (1992). Chitosans from Euphausia superba. 2: Characterization of solid state structure. Carbohydrate Polymers. 18 (1), 43-49.

Goosen M. F. A. (1997). Applications of Chitin and Chitosan. Lancaster, Pennsylvania, U.S.A.: Technomic Publishing Co., Inc.

Gorbacheva I. N., Ovchinnikov Yu. K., Gal'braykh L. S., Trofimov N. A., Majorov V. V. (1988). X-Ray studying of chitosan structure. Polymer Science, Ser. A**.** 30 (12), 2512-2515.

Kurita K., Sannan T. Iwakura Y. (1977). Studies on chitin, 4. Evidence for formation of block and random copolymers of N-acetyl-D-glucosamine and D-glucosamine by hetero- and homogeneous hydrolysis. Die Makromolekulare Chemie. 178 (12), 3197-3202.

Mima S., Miya M. Iwamoto R. Yoshikawa S. (1983). Highly deacetylated chitosan and its properties. Journal of Applied Polymer Science. 28 (6), 1909-1917.

Muzzarelli R. A. A. (1977). Chitin. Oxford, New York et al: Pergamon Press.

No H. K., Meyers S. P. (1995). Preparation and characterization of chitin and chitosan - a review. Journal of Aquatic Food Product Technology. 4 (2), 27-52.

Novikov V. Yu. (2003). Chemical hydrolysis of chitin and chitosan. Modern Perspectives in Chitin and Chitosan Studies: Proceedings of the VIIth International Conference (St. Petersburg - Repino, September 15-18, 2003). Moscow, VNIRO Publishing, 38-42.

Novikov V. Yu. (2005). The general relationships of chitin and chitosan chemical hydrolysis. Advances in Chitin Science. Vol. VIII. Ed. by H. Struszczyk, A. Domard, M. G. Peter, H. Pospieszny. Poznan, Poland: Institute of Plant Protection, 109-113.

Novikov V. Yu., Chebotok E. N., Gizatulina G. A., Konovalova I. N. (2005). Kinetic relationships of chemical deacetylation of chitin and chitosan. Vestnik MSTU. 8 (1), 179-182.

Novikov V. Yu., Orlova T. A., Voronina I. E. (1990). Kinetics of deacetylation reaction of chitin and chitosan. Izvestiya Vuzov. Food Technology. No. 5, P. 64-67.

Nud’ga L. A., Plisko E. A., Danilov S. N. (1971). Obtaining of chitosan and studying of its fractional composition. Zhurnal obschey khimii. 41 (11), 2555-2559.

Ottoy M. H., Varum K. M., Smidsrod O. (1996). Compositional heterogeneity of heterogeneously deacetylated chitosans. Carbohydrate Polymers. 29 (1), 17-24.

Percot A., Chaussard G., Sorlier P., Schatz C., Montembault A., Viton C., Domard A. (2004). Overall consideration on the evolution of the study of chitosan properties. Advances in Chitin Science. VII, 1-6.

Rege P. R., Block L. H. (1999). Chitosan processing: influence of process parameters during acidic and alkaline hydrolysis and effect of the processing sequence on the resultant chitosan's properties. Carbohydrate Research. 321, 235-245.

Tsaih M. L., Chen R. H. (2003). The effect of reaction time and temperature during heterogenous alkali deacetylation on degree of deacetylation and molecular weight of resulting chitosan. Journal of Applied Polymer Science. 88 (13), 2917-2923.

Proceedings of the 10th International Chemical and
Biological Engineering Conference - CHEMPOR 2008
Braga, Portugal, September 4-6, 2008
E.C. Ferreira and M. Mota (Eds.)

Application of surfactants to membrane separation processes

Gryzelda Poźniak*, Ryszard Poźniak, Kazimiera A. Wilk
Department of Chemistry, Wrocław University of Technology, 50-370Wrocław, Poland

Keywords: modified polyethersulfone, ultrafiltration, bovine serum albumin, cadmium
Topic: Sustainable process-product development through green chemistry

1. Introduction

Membrane separation processes, which are more environmentally friendly than conventional separation techniques, have been enjoying considerable interest in biotechnology and metallurgical industry. Among membrane processes ultrafiltration has deserved special interest. However, wider application of ultrafiltration has been hindered so far due to a detrimental effect of fouling, i.e. an irreversible process caused by solute sorption. In biotechnology, ultrafiltration membranes are commonly used for concentration and purification of protein solutions. Very often protein molecules block membrane pores which results in a decline of membrane flux. Most thermo-resistant polymers have adequate chemical and biological stability suitable for membrane formations but their strongly hydrophobic character accelerates sorption of proteins on the membrane surface. Polyethersulfone (PES) - popular membrane material - belongs to such polymers. There are several methods to protect the membrane from fouling: physical modification by surfactants [Jönsson and Jönsson, 1991] and introduction of ionic groups to the membrane materials by plasma [Poźniak et al., 2002] or chemical treatment [Poźniak et al., 1995, 2007].

The metallurgical industry, especially the electroplating and metal finishing sectors generate huge amounts of water containing heavy metal ions such as Cd(II). Ultrafiltration (UF) has proved to be an efficient way to remove from water high molar substances (polymers, proteins) - particles of a size ranging from 2 to 100 nm and M larger than 500 Da. In consequence, the pore size of UF membranes is too large to reject small molecules, like metal ions.

Micellar enhanced ultrafiltration (MEUF) is a surfactant-based separation process that has been used to remove heavy metal ions from dilute streams [Scamehorn et al., 1994, Poźniak et al., 2005]. In this process, an anionic surfactant at a concentration higher than its critical micelle concentration (cmc) is added to the aqueous stream containing dissolved solutes. Negatively charged micelles force the cations to bond to the micelle interface. Micelles (size above 10 nm) with the bonding cations are then separated by UF using membrane of suitable porosity, capable of retaining micelles.

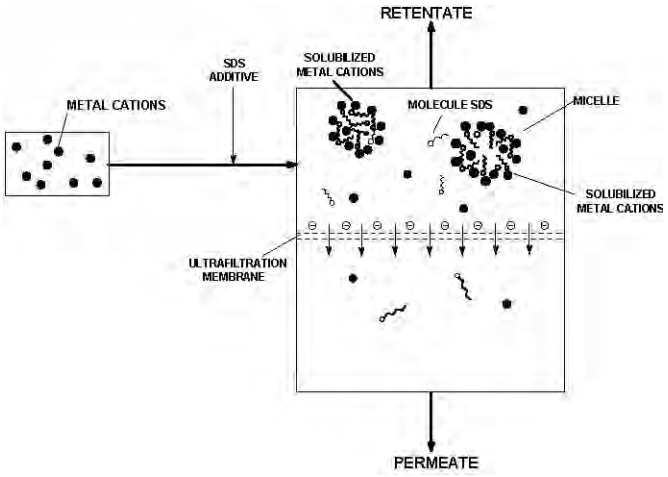

Fig. 1. Outline of metal cation separation by MEUF

To enhance selectivity in MEUF, ligand-modified micellar enhanced ultrafiltration (LM-MEUF) has been developed [Fillipi et al., 1997]. This method involves addition of an amphiphilic ligand and a surfactant to contaminated solution under conditions where most of the surfactant is present in the form of micelles. The ligand has a high degree of solubilization in the micelles and a tendency to selectively complexes the target metal on.

The goal of this paper is to show the effect of surfactant use for two membrane processes: ultrafiltration of protein and micellar enhanced ultrafiltration removal of Cd(II) ions. Polyethersulfone and sulfonated polyethersulfone UF membranes have been subjected to surfactant modification.

2. Experimental

2.1. Sulfonation of polyethersulfone and preparation of membranes

The polyethersulfone (PES ULTRASONE E-2020P from BASF) was sulfonated using a mixture of chlorosulfonic acid (CSA) and 1,2-dichloroethane (at room temperature, for 90 min). The initial molar ratio of CSA to PES was 3:1.

Three types of porous asymmetric membranes were formed by phase-inversion method from: (i) 13.5%-wt. solution of PES, (ii) mixture of 15%-wt. PES plus 10 %-wt. polyvinylpirrolidone (PVP 10 kDa) and (iii) 30%-wt. solution of sulfonated PSU in N,N-dimethylformamid (DMF). Water was used as coagulation medium.

2.2. Transport properties

The Amicon 8200 dead-end UF cell with membrane surface area of 19.6 cm^2 was used. The transmembrane pressure was set at 0.1 MPa.

Ultrafiltration of bovine serum albumin

The membranes formed from the mixture of PES and PVP were immersed in sodium dodecylsulfate, SDS (16.2 $mmol/dm^3$) or monoether dodecylpentaoxyethylene glycol, EDPEG (0.12 $mmol/dm^3$) solutions (24 hr). Additionally, the process was carried out in two cycles: the membrane was kept in SDS solution for 24 hr and then immersed in EDPEG solution for 5 min.

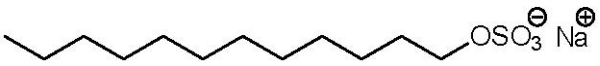

Sodium dodecylsulfate (SDS), cmc = 8.1 $mmol/dm^3$

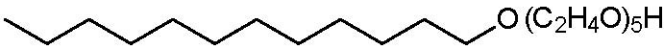

Monoether dodecylpentaoxyethylene glycol (EDPEG), cmc = 0.06 $mmol/dm^3$

The performance of surfactant modified membranes was determined with buffer of pH 8 and 0.1 M buffered solution of bovine serum albumin (BSA). The concentration of protein in the permeate was detected at 280 nm (Specord M-40, Carl Zeiss). From the flux values before and after protein filtration the transport parameters: fouling index (FI), reduction of the flux in filtration (RF) and solute rejection (R) were calculated according to our procedure [Poźniak et al., 2006]:

$$FI = [1 - (J_f/J_o)] \times 100 \quad (1)$$

$$RF = [1 - (J_p/J_o)] \times 100 \quad (2)$$

$$R = [1 - (C_p/C_o)] \times 100 \quad (3)$$

where:

J_o – is the flux of buffer through the freshly mounted membrane,

J_p - is the flux of buffered BSA through the same membrane,

J_f – is the flux of buffer through the membrane after BSA filtration,

C_p and C_o are concentrations of protein in the permeate and in the feed solution, respectively.

Micellar enhanced ultrafiltration of cadmium

Mixtures of SDS (8.1, 40.5 and 81 mmol/dm^3) and $CdCl_2$ (1 mmol/dm^3) and mixtures of SDS (4.0, 8.1 and 40.5 mmol/dm^3) and $CdCl_2$ (1 mmol/dm^3) with ligand 8-hydroxiquinoline, 8-HQ (4 mmol/dm^3) were filtrated through PES and SPES membranes. The concentrations of metal ions and SDS in the permeate were determined with an atomic adsorption spectrophotometer (AAnalyst 100, Perkin-Elmer).

To evaluate the filtration efficiency in removing the cadmium cations from the feed solution, we used the flux of permeate (J) and rejection (R) expressed as:

$$J = V/A\ t \qquad (4)$$

where:
V – is the volume of permeate,
A – is the membrane area,
t – is the time of ultrafiltration

$$R = [1 - (C_p/C_o)]x\ 100 \qquad (5)$$

where:
C_p and C_o – are the cation concentrations in the permeate and in the initial feed, respectively.

3. Results

The two systems were used to obtain more permeable membranes from polyethersulfone (PES):

(i) adsorption of surfactants: anionic (sodium dodecyl sulfate) and nonionic (monoether dodecylpentaoxyethylene glycol),

(ii) chemical introduction of sulfonate groups to polymeric chains.

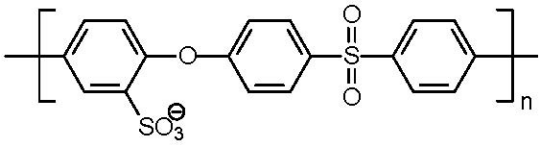

Three types of membranes were used in this study. Two of them we selected based on their similarities in physical structure; they differ in chemical composition only (PES and SPES, Table 1).

Membranes from PES+PVP system were used for hydrophilization by adsorption of surfactants. They have the greatest average pore diameter, because after physical modification of surfactants ultrafiltration of bovine serum albumin was performed.

Table 1. Characteristics of the used membranes

Membrane	Flux of water dm^3/m^{2}h	Total Porosity	Average pore diameter Nm	-SO_3 groups concentration mmol/g
PES+PVP	410	79	59	0.00
PES	53	72	13	0.00
SPES	76	79	18	0.79

Ultrafiltration of BSA

The effect of membrane hydrophilization by surfactants was monitored by evaluating the permeate fluxes and the resistance of the membrane to being fouled by bovine serum albumin. Hydrophilization was carried out according to different protocols: in one cycle by immersion in

surfactant solution and in two cycles by subsequent sorption of two surfactants - anionic and nonionic. It is well known that BSA molecules have negative charge at pH=8. Negative charge appeared also on a membrane modified with SDS, hence some repulsive effect was to be expected. With nonionic surfactant (EDPEG), the improvement in filtration indices was ascribed to the thick hydrophilic layer on the membrane surface which kept the protein molecules over the pore entrance [Chen et al., 1992]. The results of BSA ultrafiltration are shown in Table 2.

Table 2. Filtration indices of surfactant modified membrane PES+PVP

Surfactant	FI %	RF %	R %
SDS	21	33	95
EDPEG	15	28	96
SDS/EDPEG	6	15	98
NONE	58	77	91

In comparison with an unmodified PES membrane, the modified species show significant improvement of their performance in protein filtration. Fouling (FI) is less intensive and reduction of the flux in BSA filtration (RF) shows lower values. It is worth noting that the best results were obtained for BSA filtration through the membrane modified with consecutive sorption of SDS and EDPEG. That phenomenon can be explained by a combined effect of the nonionic surfactant that protects the membrane against deposition of BSA while the anionic surfactant reduces the fouling potential of BSA molecules which penetrate the first surfactant layer [Chen et al., 1992]. It is important to note here that the presence of surfactants on the membrane does not affect the separation properties of the membranes; the values of BSA rejection (R) are similar.

Micellar enhanced ultrafiltration of cadmium

The second reason for using surfactants in filtration processes is the phenomenon of enhanced removal of harmful species performed by micelles that are too large to penetrate the membrane pores. To check the effect of surfactant which is needed to remove Cd(II) ions, the MEUF processes were investigated. The results are shown in Tables 3 and 4.

Table 3. Cadmium flux and rejection in MEUF process

SDS concentration	PES membrane		SPES membrane	
mmol/dm^3	J dm^3/m^{2}h	R %	J dm^3/m^{2}h	R %
8.1	46	73	68	85
40.5	37	80	51	97
81.0	23	85	27	99

Table 4. Cadmium flux and rejection in LM-MEUF process

SDS concentration	PES membrane		SPES membrane	
mmol/dm^3	J dm^3/m^{2}h	R %	J dm^3/m^{2}h	R %
4.0	55	78	76	88
8.1	47	86	71	98
40.5	41	91	55	99

The highest rejection coefficient was observed for SDS concentration equal to 81 mmol/dm^3 in

MEUF and 40.5 mmol/dm^3 in LM-MEUF process. As usually, sulfonated polyethersulfone membrane worked more effectively that its off-charge analogue [Poźniak et al., 1995, Guan et al., 2005]. There is one more conclusion to be drawn from the presented data. The removal of divalent cations by means of MEUF and LM-MEUF hybrid systems is based on electrostatic binding of ions to oppositely charged micelles [Scamehorn et al. 1994]. After the addition of 8-HQ to SDS solution, the cmc is lower than without 8-HQ [Paulenová et al., 1996]. The evaluation of cmc for SDS in the investigated solution was about 10 times less than in distilled water (0.9 mmol/dm^3). Additionally, mixed micelles of ligand and surfactant with bound metal ions are more rigid and therefore the rejection of micelles is higher which is also favorable for cadmium recovery [Paulenová et al., 1996].

4. Conclusions

The hydrophilization of membranes from PES+PVP system by means of surfactant sorption improves membrane properties in the filtration of BSA. Polyethersulfone and sulfonated polyethersulfone membranes can be used for the separation of heavy metal ions by means of MEUF. However, charged membranes are more effective that their off-charge analogues. The best cadmium ions separations were observed for the LM-MEUF process.

References

Chen, D.V., Fane, A.G., Fell, C.J.D. (1992). The use of anionic surfactants for reducing fouling of ultrafiltration membranes: their effects and optimization. Journal of Membrane Science, 67, 249-257.

Fillipi, B.R., Scamehorn, J.F., Christian, S.D., Taylor, R.W. (1997). Selective removal of copper from aqueous solution using ligand-modified micellar-enhanced ultrafiltration using an alkyl-β-diketone. Separation Science and Technolology, 32, 2401-2412.

Guan, R., Zou, H., Lu, D., Gong, C., Liu, Y. (2005). Polyethersulfone sulfonated by chlorosulfonic acid and its membrane characteristics. European Polymer Journal, 41, 1554-1562.

Jönsson, A-S., Jönsson, B. (1991). The influence of nonionic and ionic surfactants on hydrophobic and hydrophilic ultrafiltration membranes. Journal of Membrane Science, 56, 49-76.

Paulenovà, A., Rajec, P., Ježikovà, M., Kučera, J. (1996). Micellar enhanced ultrafiltration of cadmium. Journal of Radioanalytical and Nuclear Chemistry, 208, 145-152.

Poźniak, G., Bryjak, M., Trochimczuk W. (1995). Sulfonated polysulfone membranes with antifouling activity. Die Angewandte Makromolekulare Chemie, 233, 23-31.

Poźniak, G., Gancarz, I., Bryjak, M., Tylus, W. (2002). N-butylamine plasma modifying ultrafiltration polysulfone membranes. Desalination, 146, 293-299.

Poźniak, G., Bryjak, M., Poźniak, R. (2005). Removal of metal ions from aqueous solutions by micellar enhanced ultrafiltration. Surfactants and Dispersed Systems in Theory and Practice, Ed. K.A. Wilk, 571-574.

Poźniak, G., Gancarz, I., Tylus, W. (2006). Modified poly(phenylene oxide) membranes in ultrafiltration and micellar enhanced ultrafiltration of organic compounds. Desalination, 198, 215-224.

Poźniak, G., Poźniak, R. (2007). Modified polyethersulfone membranes for micellar enhanced ultrafiltration of chromium. Proceedings of European Congress of Chemical Engineering (ECCE-6), Copenhagen, Denmark, pp. 7.

Scamehorn, J.F., Sherril, D.C., El-Sayed, D.A., Uchiyama, H. (1994). Removal of divalent metal cations and their mixtures from aqueous streams using micellar-enhanced ultrafiltration. Separation Science and Technology, 29, 809-830.

Proceedings of the 10th International Chemical and
Biological Engineering Conference - CHEMPOR 2008
Braga, Portugal, September 4-6, 2008
E.C. Ferreira and M. Mota (Eds.)

FUNCTIONALIZED NANO-MICROSTRUCTURES TO COMBAT BIOFILMS

Ferreira C., Pereira M. C., Bastos M.M.S.M., Nunes O.C., Coelho M. and Melo L. F.

LEPAE, Departamento de Engenharia Química, Universidade do Porto, Rua Dr. Roberto Frias, 4200-465 Porto, Portugal

carlaf@fe.up.pt

Keywords: micro- and nanoparticles, biofilms, biocides
Topic: Sustainable process-product development through green chemistry

Abstract

The present work suggests a new technological approach to minimize the use of antimicrobial agents, based on the principle of drug-delivery systems where the antimicrobial compounds are transported on nano-microparticles or in nano-micro-capsules. In this preliminary study, the efficacy of the method against biofilm of *Pseudomonas fluorescens* was assessed, using benzyldimethyldodecylammonium chloride (BDMDAC), which is a surfactant belonging to the family of benzalkonium chloride, as a biocide carried on microparticles (diameter: 4 μm). The latter were prepared using the layer-by-layer (LbL) self-assembly technique. The oppositely charged polyethyleneimine (PEI), sodium polystyrene sulfonate (PSS) and BDMDAC were assembled on polystyrene (PS) cores. The BDMDAC coated particles were observed by CryoSEM and their composition by X-ray microanalysis. Their size distribution (Coulter Particle Size Analyzer) and zeta potential (Nano Zetameter) were also determined. After nine days of the formation of biofilm, the coupons were collected and incubated for 30 min under two different conditions: i) saline solution; ii) solution of BDMDAC coated particles. In sterile saline solution (0.85% NaCl), the biofilm contained 1.6×10^7 CFU/mL. On the other hand, the biofilm exposed to the microparticles with biocide for 30 min contained no cultivable cells (determined by removing the biofilm from the coupon surface, diluting and spreading it on Plate Count Agar, followed by incubation at 30 ºC during 24 h).

Introduction

Layers of microorganisms and their extracellular polymers (“biofilms”) grow very easily on industrial cooling water tubes and heat exchanger channels, causing increased pressure drop and reduced heat transfer efficiency. These problems lead, ultimately, to an increase in the costs of the production and maintenance, as well as to public health problems and environmental impacts (Pereira et al, 2007). Often the layers build up in a non-uniform manner, with localized spots where thicker biofilms appear. Biofilm growth on surfaces is prevented by using biocides (e.g., chlorine) and detergents in the water stream in considerable large amounts. According to the E.U. Directive 98/8/EC, biocides are "chemicals with an active and in general toxic effect on living organisms, put up in the form in which they are supplied to the user, intended

to destroy, deter, render harmless, prevent the action of, or otherwise exert a controlling effect on any harmful organism" (Rasmussen et al, 1999). Such toxic chemicals are not totally consumed and their discharge into the environment or wastewater treatment plants is a source of serious problems.

Modern strategies to minimize fouling in industrial equipment (pipes, heat exchangers, etc.) focus on optimizing equipment design, developing new surfaces to reduce adhesion and applying efficient surface cleaning/disinfection methodologies, supported by on-line monitoring techniques. During the last 3 decades, a considerable amount of work has been reported on the effect of hydrodynamics on equipment performance and biofilm growth (Characklis *et al.*, 1990; Melo and Vieira, 1999) and although further advances are still possible on this aspect, the improvements will be generally marginal. High velocities have some drawbacks since, at the same time, they were shown to produce more compact deposits that are more difficult to remove from the surface (Melo and Vieira, 1999) both by mechanical actions and chemical methods (biocides find a higher resistance to diffusion in such compact structures). More recently, new low energy surfaces produced by surface bombardment to implant ions such as Mo and F, plasma sputtering and coatings with thin Ni-P-PTFE layers (Rosmaninho and Melo, 2006; Santos *et al.*, 2004) have been developed with an interesting potential for reducing deposit adhesion, but their application is much dependent on the relative costs of such expensive materials as compared to the costs associated to fouling. Applications to specific cases, such as tubing in medical purpose equipment, can be cost-effective, but this is not the case at industrial equipments. Additionally, it was shown that the major advantage of such surfaces is that they allow the production of deposits that are easier to clean (Santos *et al.*, 2004). Therefore, cleaning has increasingly become the crucial step in the optimization of these systems. There are, here, two interconnected issues: a) biofilms and other deposits do not attach uniformly along the surfaces; b) chemicals used to remove biofilms (such as biocides and dispersants) are carried as solutes by the bulk liquid and only a minor fraction does actually take part in the cleaning process, leaving a large amount in the discharge waters.

Nowadays, cleaning procedures are still highly inefficient processes that consume great amounts of water, chemicals and time. Large quantities of biocides are applied everyday to remove biofilms from power plant condensers (water flow rates above 2000 m^3/hour). Localized biofouling layers appear in different places of shell-and-tube heat exchangers and in plate heat exchangers, such as in the cooling section of milk pasteurizers (both in the process and in the water side). More efficient cleaning techniques are needed, that consume less water, fewer chemicals, less energy, less time and, simultaneously, are able to target the sites where the fouling layers develop. This will reduce the environmental burden (wastewater treatment) and minimize production losses caused by frequent stopping for cleaning.

The Layer-by-Layer (LbL) self-assembly of oppositely charged polyelectrolytes onto colloidal particles has been used to create novel nano- and microparticles with well controlled size and shape, finely tuned wall thickness and variable wall compositions (Decher, 1997; Donath *et al.*, 1998; Caruso *et al.*, 1998; Cordeiro *et al.* 2004). The original method was introduced in 1991 by Decher and co-workers for the construction of pure polymer multilayer

films on planar supports (Caruso, 2001).This technique uses electrostatic attraction and complex formation between polyanions and polycations to form supramolecular multilayer assemblies of polyelectrolytes. The first stage of shell fabrication involves step-wise deposition of polyelectrolytes from aqueous solutions. The polyelectrolyte multilayer film is formed by the alternate adsorption of oppositely charged layers on to the particle. After each adsorption step, the non adsorbed polyelectrolyte in solution is removed by repeated centrifugation or filtration and washing (Donath *et al*., 1998).

The goal was to develop and characterize microparticles with functionalized surfaces that act as carriers of biocide molecules. This will probably reduce the use of toxic chemicals and will minimize health and environmental risks of biocides.

The biocide benzyldimethyldodecylammonium chloride (BDMDAC) used in this work is a quaternary ammonium compound (QAC) and a component of benzalkonium chloride (BAC) that is normally used in re-circulating cooling water systems. BAC consists of a mixture of three alkyldimethylbenzlylammonium chlorides which differ only in the length of the alkyl side chains (C_{12}, C_{14} or C_{16}) (Bull *et al.,* 1998). BACs are surfactants with detergent and antimicrobial properties that are produced as industrial cleaners (Ferrer and Furlong, 2002) and are useful antiseptics and disinfectants. Quaternary ammonium compounds such as BDMDAC act by disrupting cell membranes and, depending on the their concentration, they can be either bacteriostactic or bactericidal (Ferrer and Furlog, 2001).

Materials and Methods

Particles Production Process

Polyethyleneimine (PEI – M_w 750 000) 50% (w/v) in water, Poly(sodium 4-styrenesulfonate) (PSS – M_w 70 000) and boric acid (SigmaUltra minimum 99.5%) were obtained from Sigma-Aldrich.
Benzyldimethyldodecylammonium chloride (BDMDAC – M_w 339.9) was obtained from Fluka. All chemicals were used without further purification.

Poly(styrene) (PS)-research particles 4.37 μm ± 0.07 μm 10% w/v aqueous solution were obtained from Microparticles GmbH.

The particles were prepared using the layer-by-layer (LbL) self-assembly technique as state above. The oppositely charged polyelectrolytes, PEI, PSS and BDMDAC, were assembled on polystyrene cores, in a process that comprises the following 3 steps according Figure 1. Polystyrene particles were allowed to interact with the PEI solution (1.0 mg/mL in borate buffer solution) for 20 min, and then washed in borate buffer solution 0.10 M pH 9 to remove the excess polymer. After this procedure the core was positively charged and was used for the deposition of the polyanion PSS, followed by the cation BDMDAC, both solutions of 1.0 mg/mL in borate buffer pH 9. The adsorption steps were carried by adding the polymer solution to the cores for 20 min, centrifuging at 4000 rpm for 4 min and resuspending them in borate buffer pH 9. This step was repeated twice.

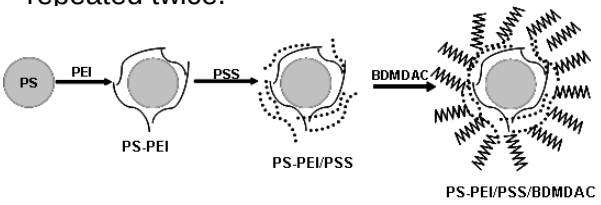

Figure 1: Schematic representation of the process of particles production.

The solvent used in the whole process

was borate buffer solution at pH 9. It was selected since the ionic strength of the solution as well as the pH value allows a better layer-by-layer process by promoting the right superficial charge for the different molecules intervening in the process.

Particle's Characterization

CryoSEM and X-ray Microanalysis The coated particle integrity was analysed by CryoSEM (model Gatan ALTO 2500) at CEMUP (Centro de Materiais da Universidade do Porto). Cryo preparation techniques for SEM have become essential for the observation of wet or "beam sensitive" sample. Using these techniques, the need for conventional preparation methods, such as critical point drying or freeze drying is removed. Besides, it allows observation of the sample in its natural hydrated state. CryoSEM is also a very rapid process, typically only a few minutes are needed. The X-ray microanalysis is an analytical technique for determination of the chemical composition of solid samples, thin layers or particles in electron microscopes like CryoSEM.

Size Distribution in Number and Volume. The size distribution of the particles was determined in a Coulter Particle Size Analyzer (model LS 230 – small volume module plus) by Laser Diffraction. The analysis of the particle size was considered as volume distribution and number distribution. A sample placed in the fluid module is circulated through a sample cell at a constant speed. A beam of laser light shone through the cell is diffracted by particles within the sample, and the forward scattered (or diffracted) light is collected by series of detectors. The distribution of light falling on the sensors enables the size distribution of the sample to be calculated.

Zeta Potential. The zeta potential of the particles was determined using a Nano Zetasizer (Malvern instruments, UK). Most particles dispersed in an aqueous system acquire a surface charge. These surface charges modify the distribution of surrounding ions, resulting in a layer around the particles that is different from the bulk solution. If the particle moves, this layer moves as part of the particle. The zeta potential is the potential at the point in this layer where it moves past the bulk solution. Zeta potential is a measure of one of the main forces that mediate interparticle interactions. Zeta potential is measured by applying an electric field across the dispersion. Particles within the dispersion with non-zero zeta potential will migrate toward the electrode of opposite charge with a velocity proportional to the magnitude of the zeta potential.

Microorganism and Growth Medium. Pseudomonas fluorescens was the microorganism used to produce biofilm. This microorganism is known to be a good biofilm producer (Melo and Vieira, 1999; Pereira et al. 2001; Simões et al., 2005). Their growth conditions were: T=27 ºC, pH=7 and glucose as carbon source. The optimum growth medium consisting in fifty milligram per litre glucose, 25 mg/L peptone, 12.5 mg/L yeast extract in phosphate buffer – pH 7. The medium was sterile (Pereira et al, 2007).

Biofilm Formation. A pure culture of *Pseudomonas fluorescens* was grown in a 4.0 L tank for 24 h, under optimal growth conditions (T = 27 ºC, pH = 7 and glucose as carbon source). After the incubation period, the suspension was diluted in 5.0 L of distilled and sterilized water that was put to recirculate between the fermenter and a flow cell where biofilm development on PVC coupons was monitored as the representation in Figure 2. The glucose concentration (determinated by

Dinitrosalicylic Colorimetric Method – DNS) was maintained at 20 ppm by pumping sterile medium into the system.

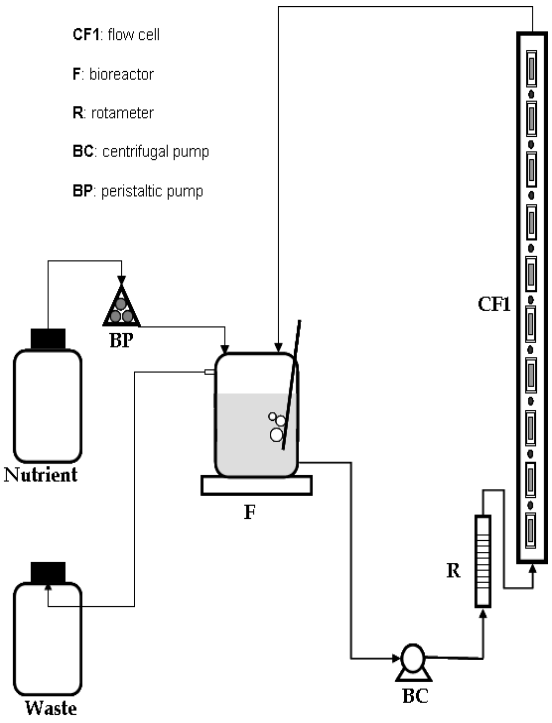

Figure 2: Schematic representation of the biofilm installation.

Biocidal properties of the BDMDAC coated particles. After nine days of the experience the coupons were collected, and incubated for 30 min at 27 ºC under different conditions: i) saline solution (0.85% NaCl); ii) solution of the BDMDAC coated particles. After this incubation time the biofilm was removed from the coupon surface, diluting and 100 μL of sample were spread on Plate Count Agar (PCA) with a sterilized glass rod and incubated for 24 h at 30 ºC. The viable cells were counted to assess the biocidal effect.

Results and Discussion

CryoSEM was used to visualize the morphology of the particles as well as the presence of the external layer (BDMDAC and/or PSS). The selection of this technique was mainly related to the fact that it allows the analysis of particles in the hydrated state. X-ray microanalysis coupled with CryoSEM was used to confirm the elemental constitution of the particles surface.

Cryo-SEM images of PS-PEI/PSS particles show that they are spherical and have a rough surface (see example in Figure 3).

The particles with an additional layer after contact with BDMDAC solution can be seen in Figure 3. X-ray microanalysis indicates that the external layer is mainly composed by C (carbon) and its content is considerably higher in PS-PEI/PSS/BDMDAC particles when compared with PS-PEI/PSS particles (Figures 3 and 4). This would be expected because BDMDAC has a very long carbon chain.

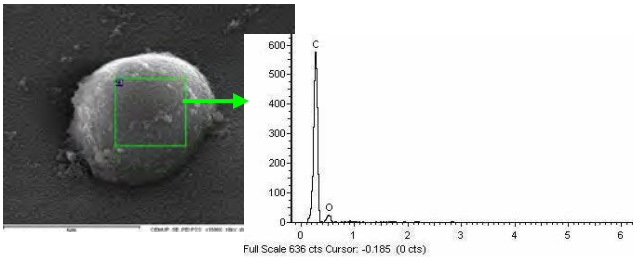

Figure 3: CryoSEM image (×15000, 10 kV) and X-ray microanalysis of PS-PEI/PSS particles.

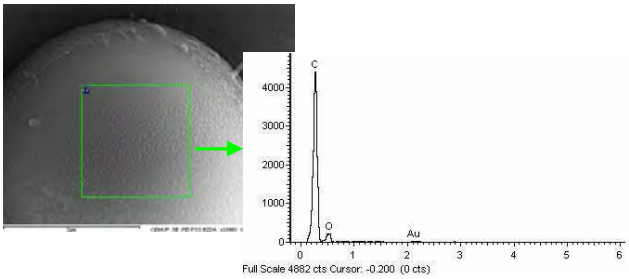

Figure 4: CryoSEM image (×30000, 10 kV) and X-ray microanalysis of PS-PEI/PSS/BDMDAC particles.

The size distribution of the particles is depicted in figure 5 and Figure 6. Three populations could be found for PS-PEI/PSS particles with an average size

of 3.0, 4.4 and 15.0 µm. In the case of PS-PEI/PSS/BDMDAC, again three populations were observed, but here two of them are well defined (3.0 and 4.4 µm), whereas a wider distribution could be seen between 6 µm and 20 µm (Figure 5). This can be related to particle aggregation due to the hydrophobic interactions between the carbon chains of BDMDAC. However, when considering the size distribution in number only the two populations of smaller diameters (3.0 and 4.4 µm) are observed, indicating that the number of particles of about 20 µm is not significant, for all type of particles (Figure 6).

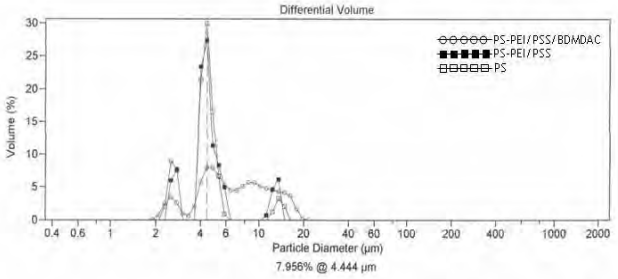

Figure 5: Volume distribution of the particles (PS, PS-PEI/PSS and PS-PEI/PSS/BDMDAC).

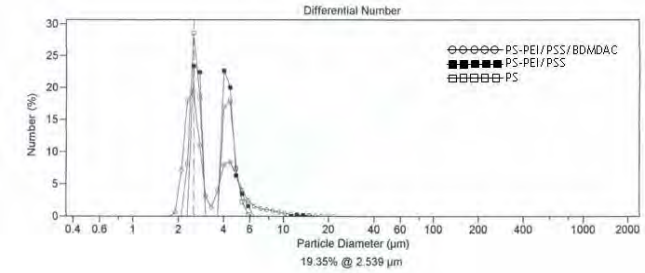

Figure 6: Size distribution of the particles in number (PS, PS-PEI/PSS and PS-PEI/PSS/BDMDAC).

The zeta potential of the particles PS-PEI/PSS at pH 9.0 in borate buffer solution is -34 ± 4 mV and the zeta potential of the particles PS-PEI/PSS/BDMDAC is -21 ± 5 mV.

After nine days, the coupons were collected and incubated for 30 min under two different conditions: i) saline solution; ii) solution of BDMDAC coated particles (2.3×10^8 particles/mL). In sterile saline solution (0.85% NaCl), the biofilm contained 1.6×10^7 CFU/mL. On the other hand, the biofilm exposed to the microparticles with biocide for 30 min contained no cultivable cells - see Figure 7.

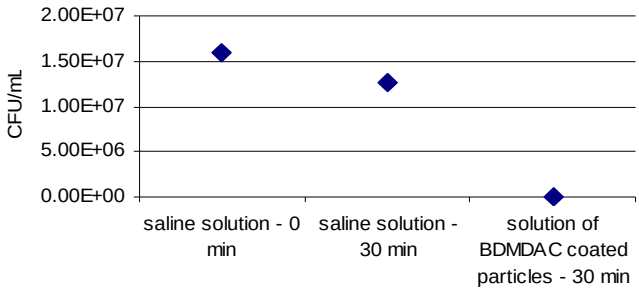

Figure 7: Number of bacteria colonies (CFU/mL) in biofilms subjected to different conditions.

We can see that the particles coated with biocide (BDMDAC) were effective against the biofilm formed by *P. fluorescens*.

Conclusions

The goal the work was to develop and characterize microparticles with functionalized surfaces that act as carriers of biocide molecules and test them against biofilm formed by *P. fluorescens*. The biocide used was benzyldimethyldodecylammonium chloride (BDMDAC) and the particle cores were polystyrene (PS, 4 µm). We can conclude that the particles coated with our biocide are active against biofilm of *P. fluorescens*.

The present work is the beginning of a study that will have, in the future, a potential impact in reducing environmental costs, a better control of the health risks associated with the use of biocides, a reduction in energy

consumption and a decrease in biocide costs in a large number of industrial plants.

References

Bull J. P., Serreqi A. N., Chen T. and Breuil C. (1998), Development of an Immunoassay for a Quarternary ammonium Compound Benzyldimethydodecylammonium Chloride, *Water Research*, 32, 3621-3630.

Caruso F., Caruso R.A., Möhwald H. (1998), Nanoengineering of Inorganic and Hybrid Hollow Spheres by Colloidal Templating, *Science*, 282, 1111-1114.

Caruso F. (2001), Generation of Complex Colloids by Polyelectrolyte-Assisted Electrostatic Self-Assembly, *Current Chemistry*, 54, 349-353.

Characklis, W.G. and Marshall, K.C. (1990), Biofilms, *John Wiley and Sons*, New York.

Cordeiro, A.L, Coelho, M., Sukhorukov, G.B., Dubreuil, F., Möhwald H. (2004), Effect of shear stress on adhering polyelectrolyte capsules, *Journal of Colloids and Interface Sciences*, 280, 68-75.

Decher, G. (1997), Fuzzy Nanoassemblies: Toward Layered Polymeric Multicomposites, *Science*, 277, 1232.

Directive 98/8/EC of the European Parliament and of the Council, concerning the placing of biocidal products on the market, EC Directive of 16 February 1998, *Official Journal of the European Communities*, L 123

Donath E., Sukhorukov G.B., Caruso F., Davis S.A., Möhwald H. (1998), Novel Hollow Polymer Shells by Colloid-templeted Assembly of Polyelectrolytes, *Angewandte Chemie International Edition*, 37, 2201-2205.

Ferrer I. and Furlong E. T. (2002), Accelerated Solvent Extraction Followed by on-Line Solid-Phase Extraction Coupled to Ion Trap LC/MS/MS for analysis of benzalkonium chlorides in Sediment Samples, *Analytical Chemistry*, 74, 1275-1280.

Ferrer I. and Furlong E. T. (2001), Identification of Alkly Dimethylbenzylammonium Surfactants in Water Samples by Solid-phase extraction followed by Ion Trap LC/MS and LC/MS/MS, *Environmental Science e Technology*, 35, 2583-2588.

Melo L.F., Vieira M.J. (1999), Physical stability and biological activity of biofims under turbulent flow and low substrate concentration, *Bioprocess engineering*, 20, 363-368.

Pereira A., Mendes J., Melo L.F. (2007), Using Nanovibrations to monitor Biofouling, *Biotechnology and Bioengineering*, 99, 1407-1415.

Pereira M. O. and Vieira M. J. (2001), Effects of the Interactions Between Glutaraldehyde and the polymeric Matrix on the Efficacy of the Biocide Against *Pseudomonas fluorescens* Biofilms, *Biofouling*, 1, 93-101.

Rasmussen K., Chemin P., Haastrup P. (1999), Regulatory Requirements for biocides on the market in the European union according to Directive 98/8/EC, *Journal of Hazardous Materials*, A67, 237-251.

Rosmaninho R., Melo L.F. (2006), Calcium Phosphate deposition from Simulated Milk Ultra-filtrate (SMUF) on different stainless steel-based surfaces, *International Dairy Journal*, 16, 81-87.

Santos O., Nylander T., Rosmaninho R., Rizzo G., Yiantsios S., Andritsos N., Karabelas A., Muller-Steinhagen H., Melo L., B._e-Petermann L., Gabet C., Braem A., Tragardh C., Paulsson M. (2004), Modified stainless steel surfaces targetted to reduce fouling – evaluation of fouling by milk components, *Journal Food Engineering*, 64, 63-79.

Simões M., Pereira M. O., Vieira M. J. (2005), Effect of mechanical stress on biofilms challenged by different chemicals, *Water Research*, 39, 5142-5152.

Proceedings of the 10th International Chemical and
Biological Engineering Conference - CHEMPOR 2008
Braga, Portugal, September 4-6, 2008
E.C. Ferreira and M. Mota (Eds.)

Synthesis and characterization of organic phase gold nanoparticles obtained through chloroaurate ions reduction with sodium citrate

Filcenco- 0lteanu Antoneta[1*], Radulescu Rozalia[1], Panturu Eugenia[1],
[1]Research & Development National Institute for Metals and Radioactive Resources-ICPMRR
70 Carol I Blvd., sector 2 , 020917 Bucharest , ROMANIA

Keywords: Gold, Nanoparticles, Organic phase, Sodium citrate.
Topic: Sustainable process-product development through green chemistry
Systematic methods and tools for managing the complexity

Introduction

Nanomaterials have a great importance in industrial applications due to their electronic, magnetic, optical [1] and catalyst [2] properties. Another important feature of nanoparticles is their large spectrum (range), an important characteristic in catalytic processes. Nanoparticle applications are found in communications, data storage [4,5], solar energy conversion [6]. It is well known that certain physical and mechanical properties of materials modify with the reduction of their particle size. Unfortunately, only a few synthesis methods of nanostructured powders are applicable at industrial scale.

Materials performance depend on their properties. Properties, in their turn, depend on the atomic structure, composition, microstructure, defects and interfaces, which are controlled by the synthesis kynetics and thermodynamics.

The synthesis of powders and their subsequent processing have a great influence over the final properties of the resulted materials. The selection of suitable processing methods determines, to a great extent, the results obtained for the final products.

At present, the obtaining of nanopowders for different practical applications uses nonconventional processing methiods, capable to offer better homogenity, increased purity, low sintherizing temperatures and a fine microstructure, with as small as possible grains.

Gold nanoparticles have raised the researchers' attention due to their numerous applications in catalytic processes [7] and in the DNA sequence determination [8].

Specialized literature presents a series of synthesis methods of different shapes [9] and size [10] gold nanoparticles which, by large, can be classified into two sections, function of their growth environment, i.e. polar (aqueous) or non-polar (organic) environment.

Generally, the gold hydrosols synthesis methods in aqueous phase suppose [1] the chloric-gold ions reduction with different reducing agents, such as: the citric acid [11], the sodium borohydride [12], the gold ion reduction by irradiation [13,14] and the sono-chemical reduction [15].

The synthesis of gold nanoparticles in nonpolar environments are based on the research performed by Burst &co. [16] who have managed to transfer the chloroaurate ions from the aqueous phase into the organic phase by using the tetraoctil ammonium bromide. After the phase transfer, the gold ions have been reduced and covered with alcanethiols[16]-alkylamines[17], thus obtaining stable monodispersed gold nanoparticles.

This paper presents the synthesis and characteristics of gold nanoparticles obtained in the organic phase with the use of sodium citrate. The gold nanoparticles characteristics were determined by in UV - visible spectoscopy (UV-Vis) and by electronic transmission microscopy (TEM).

* Corresponding author. Tel +040-213690467. E-mail:afilcenco@icpmrr.rot

Experimental

1. Materials and devices

Experiments were performed by using: the tetra-octilammonia, toluene, MERCK produced de-ionised water, Aldrich tetrachloroauric acid ($HAuCl_4$). Stirring was performed with a magnetic device.

2. Gold nanoparticles synthesis in the organic phase with sodium citrate

The aqueous solution of 0.011M tetrachloroauric acid was mixed with a 0.05M tetraoctil ammonium bromide solution in toluene for 10 minutes, to a 1:2.5 volume ratio at which the solution becomes orange. In order to obtain the desired size gold nanoparticles, a 10^{-2}M (1) and respectively $5x10^{-3}$M (2) sodium citrate solution was added by dripping under strong agitation, to a volume ratio between the mixed solution and the sodium citrate of 4:1. Stirring was maintained for 30 minutes at the environment temperature, the mixture being then transferred into a separating funnel. The reduction of gold metallic ions and the formation of nanoparticles has been evidenced by the modification of the solution colour, from orange to ruby red. After the phases separation, the organic ruby red phase which contains gold nanoparticles has been first washed with 2% hydrochloric acid for neutralization and several times with distilled water. After washing and phases separation, the organic phase has been kept into a dark colour glass bottle.

3. UV-Vis spectroscopic studies

The optical properties of gold colloidal solutions (1) and (2) have been characterized through UV-Vis spectrometry, by using a CECIL spectrophotometer within a wave length between 400 and 700 nm.

4. Electronic transmission microscopic measurements

The electronic transmission microscopy analysis (TEM) was made by using a CM12 Philips electronic microscope, with a 2Å resolution. The sample were prepared by placing a drop of gold colloidal solution on copper grid that has been covered with a very thin amorphous carbon layer. The examination has been made by electronic transmission microscopy in light fascicle (TEM-BF) and electron diffraction (SAED).

Results and discussions

The nanoparticle transfer mechanism from the aqueous solution into the organic solvent involves their hydrophobization. The aqueous solution containing the tetrachloroauric ions is mixed with the organic solvent which contains the coverage molecules (the tetraoctil ammonium bromide). Upon the mixture of the two phases, the coverage molecules will „wrap” the gold metallic nanoparticles, making them hydrophobic and thus facilitating their transfer into the organic solvent. The nanoparticle transfer from an aqueous environment into an organic one can be observed also by the change in the colour (from pale yellow to orange).

Figure 1 presents the UV-Vis spectra of gold colloidal solutions in the first experiment (10^{-2}M) and in the second experiment ($5x10^{-3}$M) respectively. Curve 3 corresponds to the $Oct_4N^+AuCl_4^-$ complex resulted from the mixture of the tetracloroauric acid with the tetraoctil ammonium bromide solution in toluene.

* Corresponding author. Tel +040-213690467. E-mail:afilcenco@icpmrr.rot

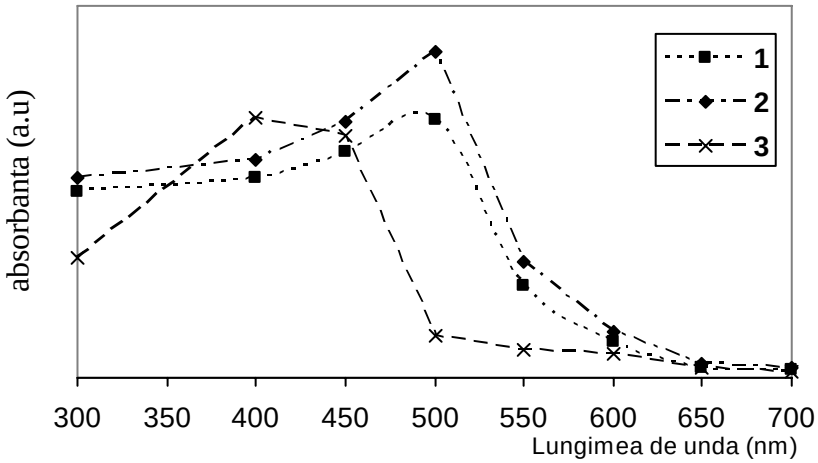

Figure 1. UV-Vis Spectrum of 10^{-2}M (curve 1), $5x10^{-3}$M (curve 2) gold colloidal solutions and of $Oct_4N^+AuCl_4^-$ complex (curve 3).

A strong absorbtion can be noticed in case of curve 3, around the 347nm value of the $Oct_4N^+AuCl_4^-$ complex resulted from the mixture of the tetracloroauric acid with the tetraoctil ammonium bromide solution in toluene. The absorbtion band is characteristic for the $AuCl_4^{6-}$ transfer band between the metal and the ligand.

The reduction of the $Oct_4N^+AuCl_4^-$ complex with sodium citrate leads to the formation of gold nanoparticles covered with the citrate ions, as illustrated by spectra 1 and 2 which reached their maximum around 530 nm. One can also notice that the absorbtion spectrum for curve 1 is flatter, which indicates a certain degree of aggregation of the obtained nanoparticles, in contrast to the sharper absorbtion spectrum registered for curve 2.

In spite of the fact that the samples exhibit a certain degree of aggregation, the colloidal gold solutions obtained in the organic phase with the aid of sodium citrate are stable for about 2 months, if preserved in a dark, constat temperature environment. A certain nanoparticle agglomeration is evident with time.

The electronic transmission microscopy enables to obtain qualitative data on the nanoparticle dimensions and on their distribution by size, as well as information on their microstructural and microcompositional morphology. The electronic transmission microscopy results (TEM) for the two samples are presented in Figures 2 and 3.

Figure 2 A presents the image obtained by electronic transmission microscopy of gold nano-particles obtained by the reduction of 0.011M tetrachloroauric acid with 10^{-2} M sodium citrate (**1**). A uniform gold nanoparticle distribution may be noticed. Figure B presents the distribution curve of nanoparticles dimensions. The continuous line overlapping the histogram is a Gaussian curve which gives information on the mean particle size, found to be in the range of 5-7 nm.

* Corresponding author. Tel +040-213690467. E-mail:afilcenco@icpmrr.rot

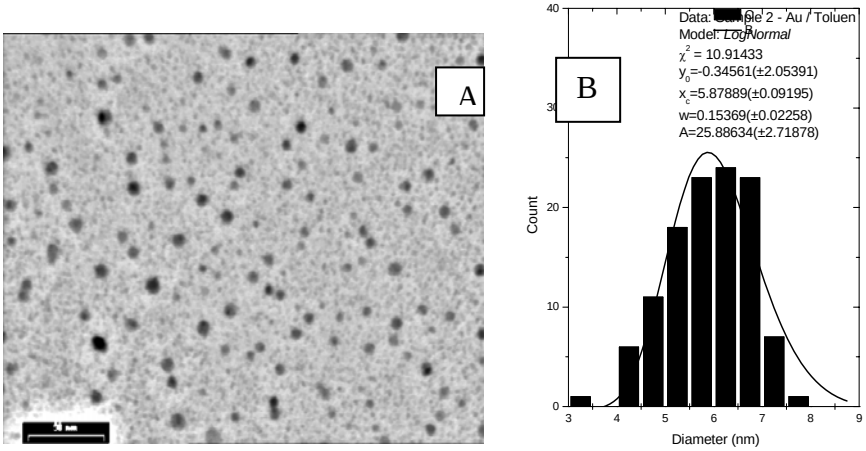

Figure 2. TEM image for A nano-particles obtained in the organic phase through 10^{-2} M sodium citrate reduction; B- Histogram of gold nanoparticle size distribution for the same sample.

Figure 3 A shows the image obtained through electronic transmission microscopy of gold nanoparticles obtained in the organic phase, using sodium citrate $5x10^{-3}$ M (2) solution as a reducing agent. An uneven distribution of gold nanoparticles is noticed; Figure B presents the nano-particle size distibution curve. The continuous line is a Gaussian fit to the histogram and gives information on the mean particles size, found to be in the range of 1-3 nm.

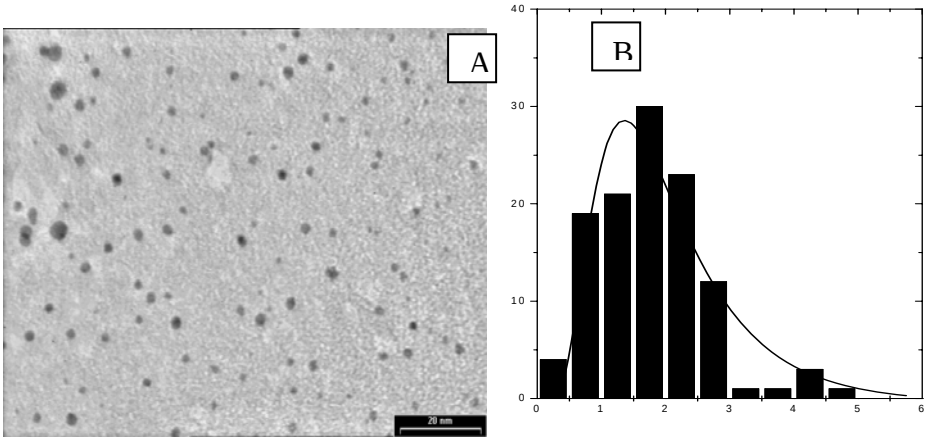

Figure 3. TEM image for A – nano-particles obtained in the organic phase by using a $5x10^{-3}$ M sodium citrate solution as a reducing agent; B - Histogram of gold nano-particle size distribution for the same sample.

The size of the obtained gold nanoparticles increases with the concentration of the sodium citrate solution. The results obtained through electronic transmission microscopy for these samples are consonant with those obtaine through UV spectroscopy.

Conclusions

This paper presented the organic phase synthesis of gold nanoparticles through the reduction of chloroauric ions with sodium citrate. In order to vary the nanoparticles dimensions, experiments were conducted with sodium citrate solutions of different concentrations: 10^{-2}M (1) and $5x10^{-3}$M (2). Following TEM investigations, the obtained nanoparticle sizes increased with the concentration of the reducing agent, all the other conditions remaining unchanged. Gold nanoparticle applications are found in solar energy conversion.

* Corresponding author. Tel +040-213690467. E-mail:afilcenco@icpmrr.rot

References

Wyatt P. McConnell, James P. Novak, Louis C. Brousseau, III, Ryan R. Fuierer, Robert C. Tenent, and Daniel L. Feldheim, *J.Phys.Chem.B 104 8925-8930*(2000)

M. Králik and A. Biffis, *J.Mol.Catal.A 177*,113-138(2001)

R.F.Marzke, *Cata. Rev.-Sci.Eng*.,1979,19,43.

Schmid,G. *Clusters and Colloids: From Theory to Application*; VCH; Weinheim,1994.

Ditlbacher,H.; Krenn J.R.; Lamprecht B.;Leitner A.; Aussenegg, F.R. Opt. Lett.2000, 25, 563.

Graetzel, *M. Electrochemistry in Colloids and Dispersions*; Raymond A. Mackay, John Texter;VCH;Weinheim,1992.

Baschong, W. and Wrigley, N. G., *J. Electron. Microsc. Tech.*, 1990, **14**, 313.

Elghanian, R., Storhoff, J. J., Mucic, R. C., Letsinger, R. L. and Mirkin, C. A., *Science*, 1997, **277**, 1078.

(a) Hayat M A 1991 *Colloidal gold* (San Diego, CA: Academic Press); (b) Bradley J S 1994 *Clusters and colloids* (Weinheim: VCH) pp 459–544

(a) Jana N R, Gearheart C and Murphy C 2001 *J. Phys. Chem.* **B105** 4065; (b) Dujardin S, Mann, S, Hsin L B and Wang C R C 2001 *Chem. Commun*. 1264; (c) Malikova N, Pastoriza-Santos I, Schierhorn M, Kotov N A and Liz-Marzan L M 2002 *Langmuir* **18** 3694; (d) Jin R, Cao Y, Mirkin C A, Kelly K L, Schatz G C and Zheng J G 2001 *Science* **294** 1901

Turkevich, J., Garton, G. and Stevenson, P. C., *J. Colloid Sci.*, 1954, **9**, 26.

Handley, D. A., *Colloidal Gold: Principles, Methods and Applications* (ed. Hayat, M. A.), Academic Press, San Diego, 1989, vol. 1, chap. 2.

Henglein, A., *Langmuir*, 1999, **15**, 6738.

Gachard, E., Remita, H., Khatouri, J., Keita, B., Nadjo, L. and Belloni, J., *New. J. Chem.*, 1998, 1257.

Mizukoshi, Y., Fujimoto, T., Nagata, Y., Oshima, R. and Maeda, Y., *J. Phys. Chem.*, 2000, **B104**, 6028.

(a) Brust M, Walker M, Bethell D, Schiffrin D J and Whymann R 1994 *J. Chem. Soc*., *Chem. Commun.* 801; (b) Fink J, Kiely C J, Bethell D and Schiffrin D J 1998 *Chem. Mater.* **10 922**
Leff D V, Brandt L and Heath J R 1996 *Langmuir* **12** 4723

* Corresponding author. Tel +040-213690467. E-mail:afilcenco@icpmrr.rot

Proceedings of the 10th International Chemical and
Biological Engineering Conference - CHEMPOR 2008
Braga, Portugal, September 4-6, 2008
E.C. Ferreira and M. Mota (Eds.)

Flexible silica based xerogels and aerogels for spatial applications

Luísa Durães[1*], Sofia Nogueira[1], Ana Santos[1], Carlos Preciso[1]
Jessica Hernandez[2], António Portugal[1]
[1] CIEPQPF–CEM group, Department of Chemical Engineering, University of Coimbra, Pólo II, Rua Sílvio Lima, 3030–790 Coimbra, Portugal
[2] Active Space Technologies, Rua Pedro Nunes, 3030–199 Coimbra, Portugal

Keywords: sol-gel synthesis, silica based xerogel/aerogel, flexible nanomaterial.
Topic: Sustainable process-product development through green chemistry: Nanotechnology.

Abstract

Flexible silica based xerogels and aerogels were synthesized via sol-gel technology with methyltrimethoxysilane (MTMS) precursor. A two-step acid-base catalyzed sol-gel process was used, followed by Ambient Pressure Drying or Supercritical Fluid Drying to produce the xerogels or the aerogels, respectively. The obtained materials have shown promising properties for aerospace applications, namely low density (40-100 kg/m^3), high surface area (~ 400 m^2/g), small pore size (~ 30 Å), high hidrofobicity (> 130º) and moderate flexibility.

1 Introduction

In the last few years, new synthesis technologies for advanced materials were developed. Commercial demand and environmental and energy restrictions have been the driving force for research on this area. The sol-gel technology is a good example of this trend, offering competitive advantages over traditional techniques: high homogeneity and purity of the product, low temperature required, preparation of new crystalline and noncrystalline solids and special products such as films and aerogels. By sol-gel technology, materials with improved and tailored properties may be prepared, as the product microstructure can be controlled during the synthesis and drying stages. Mainly, it is a wet technology, which starts from a homogeneous solution, that gives rise to a colloidal solution – sol, and evolves gradually to an integrated solid network – gel. In the end, a xerogel or an aerogel is obtained, if the gel is dried at ambient pressure or in supercritical conditions, respectively.

Silica aerogels synthesized with $Si(OR)_4$ precursors exhibit a nanostructured three-dimensional solid network with low density (~ 40 Kg/m^3), high surface area (~ 1000 m^2/g), low thermal conductivity (0.02 W/mK) and high transparency (~ 90 %). These unique properties allow their use in several applications, namely as thermal or acoustic insulators, dielectric or optical materials, filters and catalysts (Pierre and Pajonk, 2002, Rao *et al.*, 2006). However, they are brittle, absorb moisture and deteriorate with time. Flexible and hydrophobic aerogels would allow improved performance of these materials in particular applications, namely aerospace applications. An aerogel for applications in space should meet the targets/properties indicated in Table 1. The key property to tailorable aerogels for space is porosity: a high porous structure gives aerogels very low thermal conductivity and density, making them competitive with current space insulation materials. Also, if the application involves insulation from water, especially for electric components insulation, it is fundamental to have a material with high hydrophobicity. Aerogels in space have a wide range of applications, such as: thermal and structural insulators for re-entry and Mars vehicles, spacecraft components and cryogenic tanks; protection coatings for solar panels and thermal blankets; semi-flexible coatings for cables, ribbon Printed Circuit Boards (PCB's) and Multi Layer Insulation Blankets (MLI's) in space suits and spacecrafts; collection of

* Corresponding author. Tel + 351-239-798737. E-mail: luisa@eq.uc.pt

Table 1 Indicative values for the properties of a suitable aerogel for aerospace applications.

1. Low thermal conductivity	⇨ Thermal properties:	Thermal conductivity (air)	0.017 W/(m K)
		Thermal conductivity (vacuum)	0.004 W/(m K)
		Thermal tolerance	500 ºC
		Melting point	1200 ºC
		Coefficient of thermal expansion	2-4 x 10^{-6} K^{-1}
2. Low weight **3.** Flexibility **4.** High acoustic insulation	⇨ Physical and acoustic properties:	Density	2-350 kg/m^3
		Surface area, BET	400-1000 m^2/g
		Percent solids	0.13-0.15%
		Mean pore diameter	4-30 nm
		Primary particle diameter	2-5 nm
		Sound velocity through the medium	100 m/s
5. Robustness and strength	⇨ Mechanical properties:	Poisson's ratio	0.2
		Young's modulus	106-107 N/m^2
		Tensile strength	16 kPa
		Fracture toughness	0.8 kPa/m
		Compressive modulus	0.3 MPa
6. Tailorable electrical conductivity	⇨ Magnetic and electric properties:	Dielectric constant	0.14(18-40 GHz)
		Electrical resistivity	1015 Ω cm
		Electrical resistivity (carbon doped)	0.1-1 Ω cm
7. Tailorable optical properties	⇨ Optical properties:	Refractive index	1-1.05
		Colour	Translucent

space debris; reinforced composites for re-entry or low pressure atmospheres devices; acoustic insulators for spacecrafts and for the International Space Station (ISS); radiation shielding; windows and optical instruments (if translucent); *etc.*

Using methyltrimethoxysilane (MTMS) as precursor in sol-gel chemistry, as proposed by Rao *et al.* (2006), the obtained silica based aerogels can fulfil the major part of the targets listed above. In MTMS, one OR group of $Si(OR)_4$ is replaced by R, being R=CH_3. This group does not suffer hydrolysis during the synthesis and remains in the aerogel structure, providing the hydrophobicity and flexibility required (Rao *et al.*, 2006, Baghat *et al.*, 2007). The density, the surface area and porosity are also controlled by the drying technique, being the xerogels denser and less porous than aerogels. However, both have very low density, very high surface area and porosity, and consequently very low thermal and electric conductivities.

In this work, flexible silica based xerogels and aerogels were obtained via sol-gel technology with MTMS precursor. The materials were chemically and physically characterized, for assessment of their suitability to aerospace applications.

2 Materials and Methods

The applied sol-gel technology to synthesize the silica based xerogels and aerogels includes the sol-gel synthesis, which consists of a two-step acid-base catalyzed sol-gel process, pursued by ageing and drying stages. The overall experimental procedure followed the description of Rao, Baghat *et al.* (2006, 2007).

MTMS ($CH_3Si(OCH_3)_3$, 98 %, Aldrich), methanol (CH_3OH, 99.8 %, Riedel-de Haën), oxalic acid ($C_2O_2(OH)_2$, 99 %, Fluka) and ammonium hydroxide (NH_4OH, 25 % in water, Fluka) were used as precursor, solvent, acid and basic catalysts, respectively. At first, MTMS was diluted in methanol and then water was added, in the form of an oxalic acid solution (0.1 M), to promote the hydrolysis of MTMS (reaction 1) in acidic conditions (pH ≈ 2) – acid step.

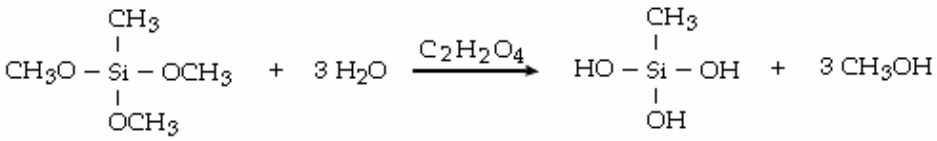

(1)

After 24 h, an ammonium hydroxide solution (10 M) was added, drop by drop, and the condensation of monomers began (reaction 2), forming a sol – basic step. As the first drops

were added, the pH increases sharply and the medium became alkaline. The pH after the total addition of the basic catalyst solution was ~ 12.

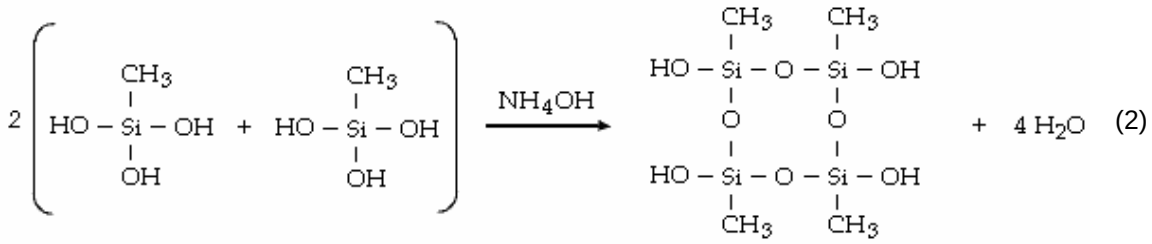

The acid and basic steps were carrying out at controlled temperature – 25 ºC, by means of a glass jacket with water as cooling agent (Fig. 1). In this work, the molar ratio of MTMS:methanol:acidic water:basic water tested was 1:35:4:[1.8-9.4].

The obtained sol was placed in an oven at 27 ºC and left for gelation. After 4-8 h, a gel was formed. In this stage, the alkaline conditions favours polycondensation reactions, resulting in the building of a tri-dimensional network of Si-O-Si (*cf.* hypothetical structure 3). The water produced in this inorganic polymerization may act as reactant in the hydrolysis and condensation reactions, increasing their completeness.

Figure 1 Experimental set-up for the synthesis stage.

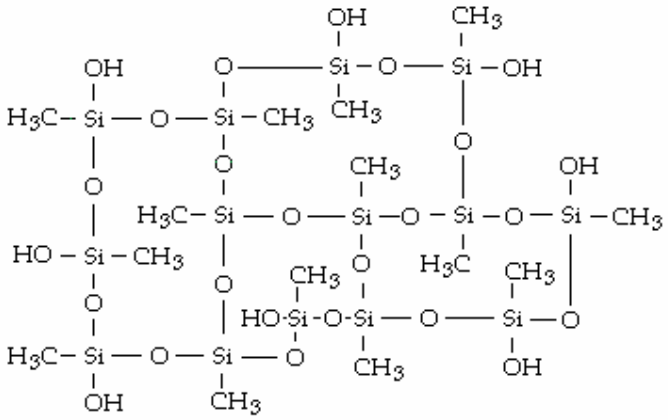

(3)

The resulting gel was aged for two days at 27 ºC. This ageing period promotes the cohesion of the solid network, because the polycondensation of monomers continues as long as neighbouring silanols are close enough to react. Besides this, syneresis and coarsening processes also occur during the ageing (Hench and Orefice, 1992).

To remove the liquid (methanol, water, catalysts), mainly methanol, entrapped in the solid network, the gel was dried in two different ways. Initially, Ambient Pressure Drying (APD) was used to produce xerogels. In this case, the gel was transferred to a ventilated oven, at atmospheric pressure, and submitted to a temperature cycle – 24 h at 60 ºC, followed by three stages, at 100 ºC, 150 ºC and 200 ºC, of one hour each – to evaporate the alcohol (T_b(methanol) = 65 ºC – Goodwin, 1987). This method leads to the shrinkage of the pores due to surface tension effects. Recently, aerogels have been produced using Supercritical Fluid Drying (SFD). To reach the supercritical point of the solvent (T_c(methanol) = 240 ºC and P_c = 80 bar – Goodwin, 1987), the gel was placed in an autoclave (Fig. 2), which was then filled up with methanol. After, the temperature of the autoclave was increased at constant volume, causing an increase in the pressure inside it. When the critical point of the methanol was exceeded, the liquid became a supercritical fluid and, from this condition, the gaseous solvent was released, at constant temperature, and, consequently, the pressure has decreased. Near the atmospheric pressure, the autoclave was flushed with nitrogen to remove the remaining solvent. In this process, the shrinkage is minimized because the liquid-gas saturation line is not crossed (Fig. 3).

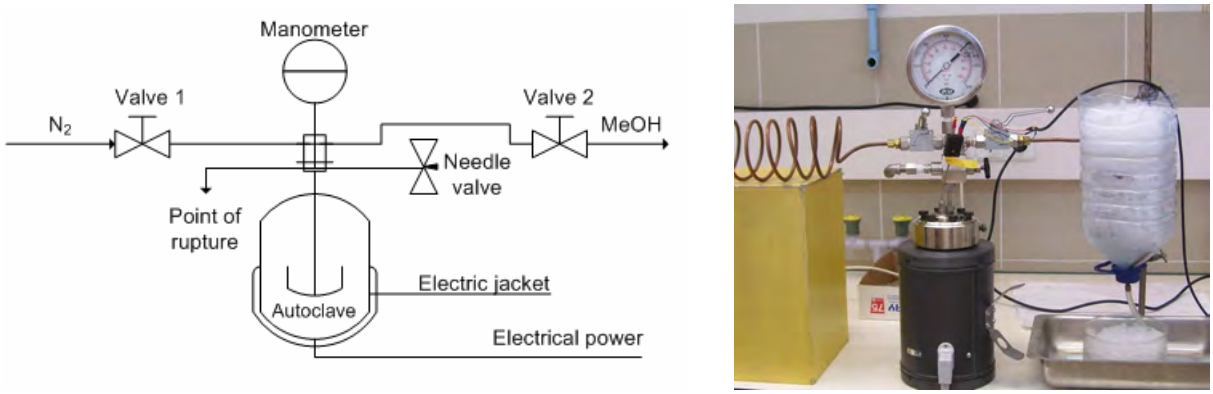

Figure 2 Experimental set-up for the SFD.

The elemental composition (C,H,N,O), chemical structure, surface area, density and contact angle of the xerogels and aerogels were accessed by elemental analysis (*EA 1108 CHNS-O*, *Fisons Instruments*), Fourier transform infrared spectroscopy (*Magna-IR™ System 750*, *Nicolet*), nitrogen gas adsorption (*ASAP 2000*, *Micromeritics*), weight-volume measurements and a contact angle technique (*Contact Angle System OCA 20*, *Dataphysics*), respectively.

3 Results and Discussion

During the basic step of the synthesis, a sharp pH increase from ~ 2 to ~ 9 was observed with the addition of the first 2-3 drops of the basic catalyst solution; then, the pH increased slowly towards its final value (pH = 10-11), depending this value on the total amount of the basic catalyst solution added (Fig. 4). The condensation reactions occurred extensively at the very beginning of the basic catalyst addition and the solution became cloudy and milky, proving that the main effect was achieved with a tiny amount of catalyst.

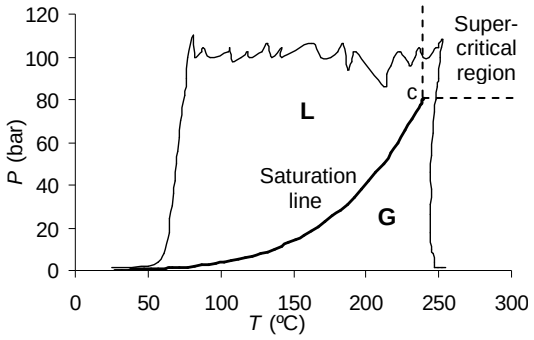

Figure 3 Typical *P-T* evolution in the SFD.

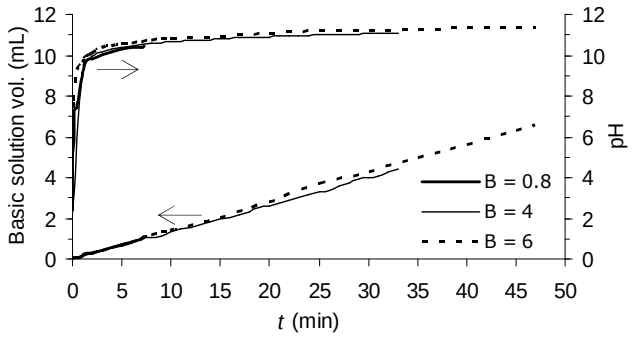

Figure 4 pH evolution during the basic catalysis step.

In a fully condensated material, the repetition units of the inorganic polymer have Si:O:C:H molar ratio of 1:~1.5:1:~3, neglecting the H atoms on the terminal groups (*cf.* structure 3). This corresponds to a theoretical C:O:H mass percent of 18.1:36.3:4.5. Comparing these values with the elemental analysis results – Table 2, it can be concluded that all the samples have only one CH_3 group per Si in its structural formula, since a good agreement for the % C is obtained. Therefore, the hydrolysis was complete. Also, the hypothesis of a fully condensed material is validated by this agreement, especially for samples in which B ≤ 6. This was expected, since the pH rise is accomplished by a small volume of the basic catalyst solution, as a consequence of its high concentration. The measured values for the % H are higher than 4.5 %, what can be explained by the contribution of H in OH terminal groups. The N content obtained in the experimental results proves the existence of impurity traces in the materials dried by APD or SFD, since only the basic catalyst had N atoms. The theoretical and experimental values for the % O in xerogels are very different, because the temperature used in the elemental analysis (1060 ºC) was not enough to break the Si-O bonds.

Table 2 Elemental compositions, surface areas, pore sizes, and contact angles of the obtained materials.

Molar ratios	Elemental analysis				Surface areas and pore size		Contact angle
B [a]	% C	% H	% O	% N	BET surface area (m^2/g)	BJH pore size [b] (Å)	
XEROGEL							
1.8	19.8	5.8	1.5	0.17	-	-	-
3.0	17.4	5.6	1.6	0.32	315.26 ± 4.53	32.5	152º
4.0	19.1	6.0	1.5	≤ 100 ppm	385.77 ± 6.61	32.3	141º
5.0	-	-	-	-	389,93 ± 8,28	29.8	-
6.0	19.5	5.8	1.5	0.14	388.46 ± 7.08	31.6	-
8.0	16.5	5.6	1.6	0.14	-	-	126º
9.4	15.4	5.4	1.5	≤ 100 ppm	-	-	-
AEROGEL							
1.8	17.1	5.3	-	0.07	-	-	137º
4.0	17.8	5.0	-	0.08	362.87 ± 6.75	29.8	135º

a) $B = (H_2O)_{Basic}/MTMS$; b) Based on desorption isotherms.

The FTIR results for the xerogel and aerogel, for B = 4, are shown in Fig. 5. Materials with different B ratios were also analyzed, but the obtained spectra were almost the same. This is also the case displayed in Fig. 5, being the little displacement between curves due to the intrinsic variability of the laser beam. The intense bands appearing around 760 cm^{-1} and between 1000 and 1100 cm^{-1} are due to symmetric and asymmetric stretching vibrations of Si-O-Si bonds, respectively (Hedge and Rao, 2007, Castro *et al.*, 2005). The band just after 500 cm^{-1} may possibly correspond to bending vibrations of the same bonds (Hedge and Rao, 2007). The bands at ~ 850 cm^{-1} and ~ 1270 cm^{-1} can be assigned to Si-C bonds (Hedge and Rao, 2007, Castro *et al.*, 2005). The little peaks observed at ~ 1400 cm^{-1} and near 3000 cm^{-1} are due to the bending and stretching of the C-H bonds, respectively (Becker *et al.*, 1997, Hedge and Rao, 2007). There are no significant bands between 1600 and 1700 cm^{-1} or after 3000 cm^{-1}, proving that the Si-OH bonds are not abundant, the solvent was properly removed and the adsorbed water is absent (Becker *et al.*, 1997, Hedge and Rao, 2007). These observations confirm that the condensation reactions were very extensive and the obtained materials have a silica based structure, with highly hydrophobic CH_3 groups inside.

A decrease in the density of the xerogels and aerogels with the increase of B is observed – Fig. 6. In the case of xerogels, this decrease is more pronounced up to the sample corresponding to B = 4. For higher B values, the variation is almost within the experimental uncertainty. As the xerogel became more powdery and weak with the increase of B (for B = 9.4, the xerogel was a powder), 4 was considered the optimum B value for the desired properties. Aerogels show considerably lower densities than xerogels. Furthermore, it seems that the stabilizing B value for density is now 3.

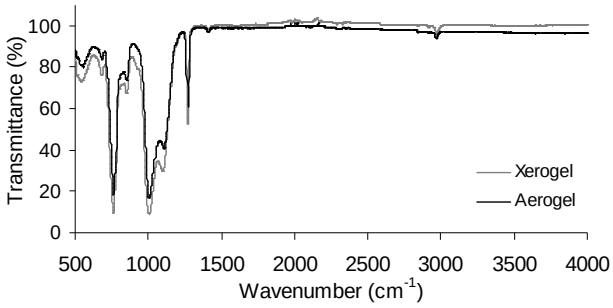

Figure 5 Typical FTIR results for the synthesized xerogels and aerogels.

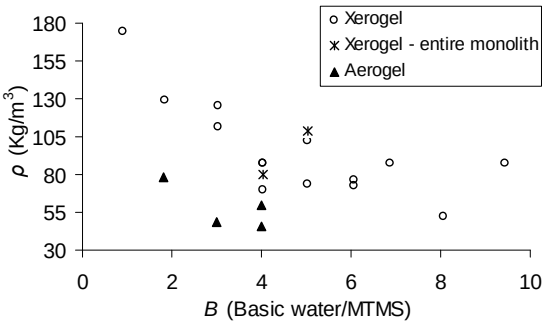

Figure 6 Densities of xerogels and aerogels for several B molar ratios.

Concerning the surface area results – Table 2, in the case of xerogels, the sample for B = 3 has lower surface area than the samples for B = 4-6. This was predictable, because the xerogels for B < 4 are more dense and rigid. The surface areas of the other three samples are comparable. For the aerogels, considering their density, higher BET surface area values were expected. For B = 4, the surface area value is lower then the one of the correspondent xerogel. This means that the results of surface area analysis should be completed and more replicas should be done. The pore sizes obtained for the xerogels and aerogels are consistent with a mesoporous structure, as they are in the interval 20-500 Å.

The contact angle values – Table 2 – confirm the high hydrophobicity of the obtained xerogels and aerogels and allow their classification as non wetting materials. Figures 7 and 8 show the flexibility characteristics of the synthesized xerogels and aerogels monoliths.

Figure 7 Xerogel monolith.

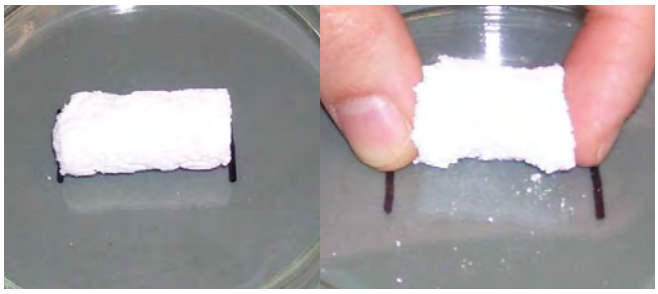

Figure 8 Aerogel monolith.

5 Conclusions

Flexible and hydrophobic silica based xerogels and aerogels were obtained, using MTMS as precursor in a two-step acid-base catalyzed sol-gel process, followed by drying at ambient pressure or at supercritical conditions. The synthesized materials showed suitable properties for aerospace applications, namely very low density (40-100 kg/m3), high surface area (~ 400 m2/g), small pore size (~ 30 Å), high hidrofobicity (> 130º) and moderate flexibility.

References

Becker, H. G. O., Berger, W., Domschke, G., Fanghänel, E., Faust, J., Fischer, M., Gentz, F., Gewald, K., Gluch, R., Mayer, R., Müller, K., Pavel, D., Schmidt, H., Schollberg, K., Schwetlick, K., Seiler, E., Zeppenfeld, G. (1997). *Organikum – Química Orgânica Experimental*, 2nd Ed., Fundação Calouste Gulbenkian, Lisboa.

Bhagat, S. D., Oh, C.-S., Kim, Y.-H., Ahn, Y.-S., Yeo, J.-G. (2007). Methytrimethoxysilane based monolith silica aerogels via ambient pressure drying. *Microporous and Mesoporous Materials,* 100, 350-355.

Castro, Y., Aparício, M., Moreno, R., Durán, A. (2005). Silica-zirconia sol-gel coatings obtained by different synthesis routes. *Journal of Sol-Gel Science and Technology*, 35, 2005, 41-50.

Goodwin, R. D. (1987). Methanol thermodynamic properties from 176 to 673 K at pressures to 700 bar. *Journal of Physical and Chemistry Reference Data*, 16, 799-892.

Hedge, N.D., Rao, A.V. (2007). Physical properties of methyltrimethoxysilane based elastic silica aerogels prepared by the two-stage sol-gel process. *Journal of Materials Science*, 42, 2007, 6965-6971.

Hench, L. L., Orefice, R. (1992). Sol-gel technology. In *Kirk-Othmer – Encyclopedia of Chemical Technology*, 4th Ed., Vol. 22, John Wiley & Sons, New York, 497-527.

Pierre, A.C., Pajonk, G.M. (2002). Chemistry of Aerogels and Their Applications. *Chemical Rev.*, 102, 4243-4265.

Rao, A.V., Bhagat, S.D., Hirashim, H., Pajonk, G.M. (2006). Synthesis of flexible silica aerogels using methyltrimethoxysilane (MTMS) precursor. *Journal of Colloid and Interface Science*, 300, 279-285.

Proceedings of the 10th International Chemical and
Biological Engineering Conference - CHEMPOR 2008
Braga, Portugal, September 4-6, 2008
E.C. Ferreira and M. Mota (Eds.)

Effect of operating conditions on the extraction of β-glucans from barley

O. Benito, S. Lucas, E. Alonso
Departamento de Ingeniería Química y Tecnología del Medio Ambiente. Prado de la Magdalena s/n. Facultad de Ciencias. Universidad de Valladolid (Spain)

Keywords: β-glucan, barley, extraction
Topic: Sustainable process-product development through green chemistry

Abstract

The aim of this work is to analyze the effect of operating parameters on the extraction of β-glucans from different varieties of barley. Several experiences have been carried out in batch extractors, with a reference experiment, in order to check the influence of temperature, pH, time, solvent and flour:solvent ratio. Time and temperature showed to have a strongly marked influence: the higher temperature, the higher extraction rate. Higher temperatures led to improve the extraction yield, increasing the amount of starch co-extracted. Extraction time was a critical factor up to 3 hours. Longer times did not increase the amount extracted. The influence of pH was not very remarkable, just generating a slight increase in extraction yield up to 8; beginning to decrease from that value. The use of alcohols (methanol and ethanol) as solvents, did not improve the extraction rate. On the other hand, it was observed an important decrease on the β-glucan solubility, greater the higher concentration of alcohol employed and the longer carbon chain. Finally, a extraction yield of 40-50% was obtained when operating at solvent:flour ratio from 7 to 12, at 55ºC, in almost all range of pH, when lasting the extraction process more than 2,5 hours.

1. Introduction

β-glucans are a kind of non-starchy polysaccharides (formed by the linkage of glucose units via β-(1→3) (approximately 30%) and β-(1→4)-glucosidic linkages) that can be found in several kinds of cereals, such as barley, oat or rye in concentrations from 2 to 12% in dry basis. In barley, β-glucans are minor components (up to 6-7%), located majoritary in the aleurone and endosperm cellwalls (Irakli *et al*, 2004) of the grain. They form part of the dietetic fibre (the same as other structural compounds of vegetals, such as cellulose and hemicelluloses), nevertheless β-glucans are soluble in water.

It is known that they have good properties for human health, if eaten. Among all these properties it is worth mentioning their implication in process of control of cholesterol and glucose concentration in blood (McIntosh *et al*, 1995; Bhatty, 1999; Brennan, 2005). These effects have been associated with the molecular weight of the polymers. Recently, FDA (Food and Drug Administration, USA) has included β-glucan in its list of products that contribute to lower the cholesterol level in blood, pointing out how to label the products that contain barley to remark its positive effect on health.

Extraction of β-glucans form cereals has to deal with several difficulties. A typical extraction process involves, at least, three stages (Bhatty, 1995; Laroche, 2007): inactivation of endogenous enzymes, extraction of β-glucans with a suitable solvent, and finally a purification-isolation stage, because other chemicals present in cereals (proteins, saccharides, or starch) can be co-extracted. All these stages increase the complexity of the overall process, increasing the economical costs, therefore. This is the most limiting factor for the extraction process.

When a solid-liquid extraction process is carried out, temperature, pH, extraction time and polarity of the solvent are some of the operating parameters that are to be taken into account. It is important to characterise the behaviour of the target compound when changing the operating variables, in order to improve the extraction process.

In this work a simple solid-liquid discontinuous extraction process from different waxy-type barley (H13-06 (hull-less) and D24-06) with hot water was proposed. The effect of most important operating parameters such as temperature, pH, extraction time and polarity of the solvent was checked in order to optimize the continuos extraction process. Moreover, a reference experience based on literature revision carried out at 55ºC, 3 hours, water as solvent, solid:liquid ratio 1:10 was chosen as a comparative tool (Papageorgiou *et al*., 2005).

2. Experimental section

Two different kinds of barley were used, both of them grown and harvested in Castilla y León (Spain): H13-06 and D24-06. These varieties correspond to the waxy-type barley, a specie of barley which has higher content in β-glucan and a lower in starch than common species. The main difference between those two kinds of barley is that grains of H13 are hulless, not presenting external hull covering the kernel. Barley was supplied by Instituto Tecnológico Agrario de Castilla y León (ITACYL). Table 1 summarizes the composition of both varieties:

Table 1. Chemical composition of the barley used as raw material

	H13-2006 (%)	D24-2006 (%)
Moisture	11,07	10,98
Fats	2,26	2,48
Ash	1,78	1,86
Proteines	4,9	4,3
Starch	52	44,8
Amilose/Amilopectine	10,22/89,78	9,05/90,95
β-Glucan	4,13	5,33
Dietic Fibre	13,85	18,7

Barley employed was milled and sieved through a 0,5mm sieve.

Initially, temperature, pH, time, solvent, flour:solvent ratio were defined as the factors that had to be tested. According to the literature, basic conditions (of temperature) for the initial experiments were selected: 55ºC, 3 hours, water as solvent, solid:liquid ratio 1:10 (these conditions constitue the basic experiment). In this reference experiment, pH of water was not modified, being around 6.

Barley flour was weighted and added to an erlenmeyer flask. Then water was added, being the flour suspended at high stirring rate. Temperature was kept constant in a water bath (Lauda Ecoline Staredition E100, Lauda, Germany). Stirring was obtained with a multistirrer plate (Fisher Scientific, USA), as shown in figure 1:

Once the extraction process was finished, solid:liquid separation was done by centrifugation (5500rpm, 10 minutes). Solid material was discarded and liquid (supernatant) was stored at 4ºC until the moment of being analysed.

All the experiments were conducted in duplicate.

Figure 1. Experimental set-up used for the extraction of β-glucans from barley

β-glucan determination was made at ITACYL, using the Megazyme Assay Kit for mixed linkage β-glucan analysis (*Megazyme*, Ireland). β-glucan concentration is expressed as % (weight) of the total sample.

Yield results shown in the following figures was calculated by dividing the amount of β-glucan in the extract generated and the total amount of β-glucans in the barley flour used in the extraction process.

3. Results

β-glucan extraction yield was 41,5±1,0% for D24 and 47,2±2,4% for H13 for the reference operating conditions This result, contrary to that expected, can be explained for the presence of interferences. H13 is a hulless barley, with a lower content in β-glucans. D24, despite of its higher content in this compound, is more difficult to extract them, probably due to the presence of the hull of the kernel. This problem can be solved by milling the barley in a industrial mill, that generates three milling fractions, with different compositions of β-glucans.

When the extraction process was divided in three stages (of one hour each), the amount of β-glucan extracted was around 60%, a 20% higher than when developing the process in one single stage.

Several experiments were carried out in order to check the influence of temperature, pH, time, solvent and flour:solvent ratio on β-glucans extraction, changing the study variable and keeping constant the remaining ones. The reference experiment was achieved at 55ºC, pH around neutrality (6), 3 hours of extraction time and with 1:10 solid:solvent ratio.

Temperature effect (35-75ºC): It was observed a costant increase in the extraction yield when increasing the temperature from 29% at 35ºC up to 56% at 75ºC. However when temperature is higher than 55ºC, operational problems connected with the higher suspension viscosity and the co-extraction of starch in the extract were observed (the amount of starch in the extract was increased dramatically, from 0,12% to 0,71%, which makes more difficult the subsequent purification, (Temelli, 1997)). For these reasons, the optimal extraction temperature was fixed in 55ºC (see Figure 2).

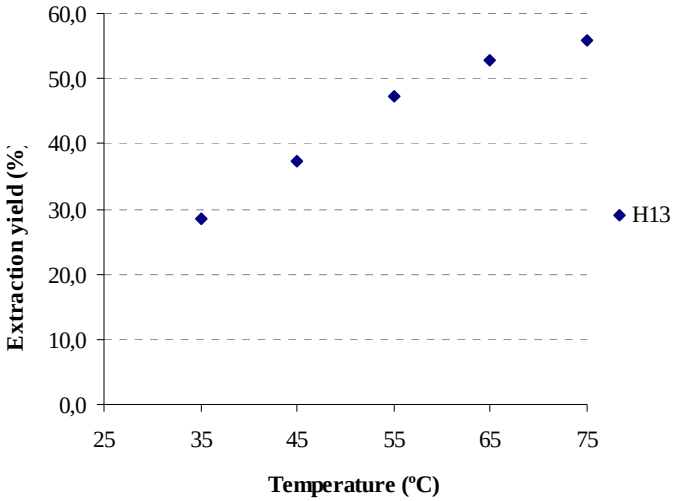

Figure 2. Temperature effect on the β-glucan extraction yield (H13 barley).

Extraction time effect (0.5-5 h). Times under 2,5 hours were found to be too short (yield fell down under 40%), but an extraction time of 5 hours did not entail a dramatic increase in the amount of β-glucan extracted, rather it kept constant (45-47%) after three hours of extraction. Extraction time of 3 hours is enough to ensure the equilibrium was reached and to get a high extraction yield (see Figure 3).

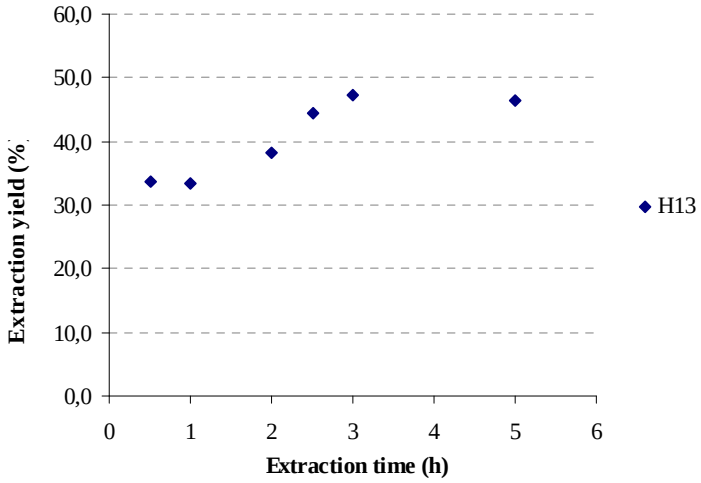

Figure 3. Effect of extraction time on the β-glucan extraction yield (H13 barley).

When the influence of pH (in the range 6-11) was studied (see Figure 4), a slight increase in extraction yield was produced. Water was weakly basified (pH 8) by addition of some drops of NaOH (6N). However, a further increase (pH 11), decreased the amount of β-glucans extracted. This decrease with pH was more marked in the case of H13 type. This could be due to the depolymerisation of our targed compounds. This result reveals that it is not necessary to increase the pH of the original water used as solvent (close to neutral pH).

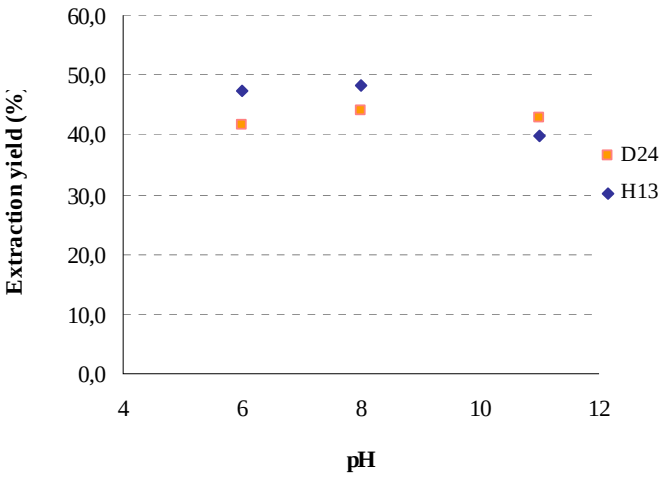

Figure 4. pH effect on β-glucan extraction yield (H13 and D24 varieties of barley).

Solid (flour):liquid ratio (in the range 5-15) was also tested for H13 variety. As it can be observed in Figure 5, an important change in extraction yield (over 50%) could be noticed when this ratio was shift from 5 to 10. The increase of this ratio to 15, did not produce a positive effect in the extraction of β-glucans. When using ratios of 8, 10 or even 12, it was observed a constant yield, around 47%. This result showed that it is possible to operate at lower solid:liquid rate (at 8), which is important taking into account a further purification step. Using less amount of solvent means simplifying the concentration of β-glucans.

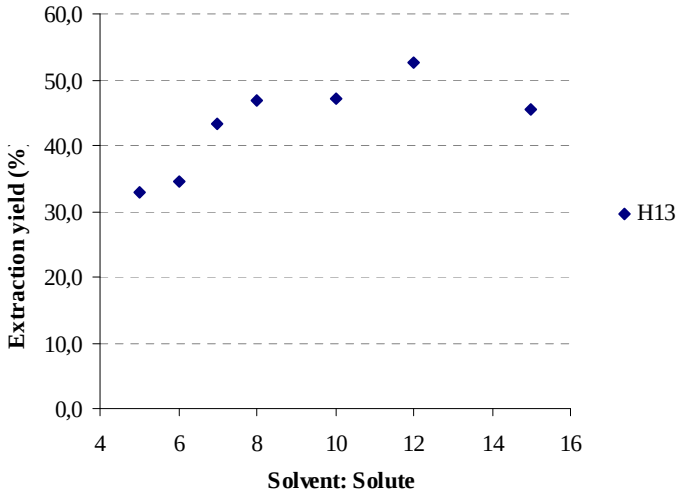

Figure 5. Effect of solvent:flour ratio on β-glucan extraction yield (H13 barley).

Polarity of the solvent can be classified as a critical parameter. This part of the study was developed using the D24 variety. The better results were obtained with water as solvent (yield was 41,5%). When an alcohol was used as solvent (5% in volume), the extraction yield decrease slightly to 41,4% in the case of the use of methanol and to 34,1% when ethanol was used. When the concentration of alcohol was increased (50% or 100%), it was not possible to extract β-glucans. The amount of polymer extracted in those cases was under the detection limit of the analysis method. According to this result, alcohols can not be used as co-solvents. This property would allow to the alcohols to be used to precipitate β-glucans, using the alcohols as anti-solvent.

4. Conclusions

Initial conditions fixed for discontinuous extraction of β-glucans from barley with water (55ºC, 3h and flour:solvent ratio of 8) are suitable to get extraction yields in the range 40-50% for both varieties of barley tested. Time and temperature showed to have a strongly marked influence: the higher temperature, the higher extraction rate. Longer times than 3 hours didn't increase the amount of β-glucans extracted. The influence of pH was not very remarkable, just generating a slight increase in extraction yield up to 8; beginning to decrease from that value. The use of alcohols (methanol and ethanol) as solvents, did not improve the extraction rate. The operation in 3 steps of one hour each one, allowed to increase the maximum amount of β-glucan up to 60%. This result shows that β-glucan extraction can be enhanced when increasing the number of extraction steps, which justifies the need to develop a continuos extraction process.

References

Bhatty R.S. (1995). Laboratory and pilot plant extraction and purification of β-Glucans from Hull-less Barley and Oat Brans. Journal *of Cereal Science*, 22, 163-170.

Bhatty R.S. (1999). The potential of hull-less barley. *Cereal Chemistry*, 76(5), 589-599.

Brennan, C.S.; Cleary, L.J. (2005). The potential use of cereal (1→3,1→4)-β-d-glucans as functional food ingredients. *Journal of Cereal Science*, 42(1), 1-13.

Irakli M., Biliaderis C.G., Izydorczyk M.S., Papadoyannis I.O. (2004). Isolation, structural features amd rheological properties of water-extractable β-glucans from different Greek barley cultivars. *Journal of the science of food and agriculture*, 84, 1170-1178.

Laroche, C.; Michaud, P. (2007). New developments and prospective applications for β-(1,3) glucans. *Recent Patents on Biotechnology*, 1, 59-73.

McIntosh, G.H., Newman, R.K., Newman, C.W. (1995). Barley foods and their influence on cholesterol metabolism plants. *Human Nutrition*, 77, 89-108.

Papageorgiou M, Lakhdara N, Lazaridou A, Biliaderis CG, Izydorczyk MS. (2005). Water extractable (1 → 3,1 → 4)-β-D-glucans from barley and oats: An intervarietal study on their structural features and rheological behaviour. *Journal of Cereal Science*, 42(2), 213-224.

Temelli, F. (1997). Extraction and functional properties of barley β-glucan as affected by temperature and pH. *Journal of Food Science*, 62(6), 1194-1197.

Proceedings of the 10th International Chemical and
Biological Engineering Conference - CHEMPOR 2008
Braga, Portugal, September 4-6, 2008
E.C. Ferreira and M. Mota (Eds.)

Alternative Route to Poly(Lactic Acid) Synthesis

Dina A. S. Marques[1*], S. Jarmelo[1,2], Cristina M. S. G. Baptista[1], M. H. Gil[1],
[1] CIEPQPF, Chemical Engineering Department, University of Coimbra, Pólo II, 3030-790 Coimbra, Portugal
[2] Department of Chemistry, University of Coimbra, Coimbra 3004-535, Portugal

Keywords: Poly(Lactic Acid), Biodegradable, Polycondensation, Molecular Weight, Sustainability
Topic: Sustainable process-product development through green chemistry

Abstract

In the present study the step-growth polymerization of lactic acid [HO−CH(CH_3)−COOH] in solution was studied. In order to attain a polymer with high molecular weight, the water formed during the polymerization reaction must be continuously removed. For that an organic solvent with high boiling point was added and the water was removed from the vapour phase with the help of drying agents. Moreover, higher molecular weights were achieved when pressure reduction in the reactor was implemented. This procedure allows to obtain poly(lactic acid) polymers (PLA) with a molecular weight up to 45 000 $g.mol^{-1}$ in a one single reaction stage. The polydispersity of the PLA polymers is satisfactory, nevertheless the results point out that, in the direct condensation of lactic acid, racemization reactions can be a limiting factor. Mainly, the small leaks in the reactor and the catalyst used are contributing for the racemization reactions. The specific rotation measurements, used in this work, showed to be a powerful technique to evaluate the racemization extent.

1 Introduction

An increasing effort in the development of sustainable alternatives to petrochemical origin materials has been recently registered, mainly due to environmental reasons (Bogaert and Coszack, 2000).

Poly(lactic acid), PLA, is an aliphatic polyester, biodegradable/compostable, biocompatible, and bioreabsorbable, obtained from a 100 % renewable raw material, the lactic acid. The possibility to tailor the lactic acid based polymers, with specific properties, allows to use them in many different aplications. Due to its hydrolytical instability and good biocompatibility, PLA can be used in biomedical, pharmaceutical and cosmetic industries, it is approved by the US Food and Drug Administration (FDA) (Garlotta, 2002). Moreover, PLA is also a promising substitute for conventional polymers, which leads to efforts to use PLA in large volume of applications. To be used as a commodity, lactic acid polymers need to have a high molecular weight and good mechanical properties. PLA, with high molecular weight, has mechanical properties similar to the conventional thermoplastics, like PET, and can find applications in important technological fields, as films for agriculture, fibers for the textile industry, packaging and composites (Bogaert and Coszack, 2000).

However, high molecular weights are difficult to reach, mainly due to the amount of water that is formed during the polymerization and its influence upon reactions´ equilibrium. High molecular weight PLA can be synthesized by two routes: ring opening polymerization (ROP)

* Corresponding author. Tel + 351-239-798793. E-mail:dinam3@eq.uc.pt

of the intermediate lactide or step-growth polymerization, also called polycondensation. The first mechanism is an effective and the most used method, but quite complex and an expensive process (Garlotta, 2002). The latter allows to obtain lactic acid polymers directly from the monomer. However, to obtain high molecular weight polymers, some weaknesses must be overcome. Due to the difficulty in removing water from a highly viscous medium, Ajioka *et al*., 1995*,* developed the polycondensation of lactic acid in solution*.* This method presents disadvantages for the environment, since it uses organic solvents with high boiling point as a reaction medium. However, it has proved to be effective allowing to achieve high molecular weight polymers by continuous removal of water. Nevertheless, other authors that used this technique for lactic acid polymerization were not able to achieve the results reported by Ajioka (Kim *et al*. 2002).

The limitations of the methods mentioned previously support the effort in developing new ways to obtain biodegradable lactic acid based polymers. In this study, the polymerization of lactic acid in solution by a step-growth mechanism has been investigated. Although, this technique is less developed, it is considered to be less complex, and there is room for improving the current reactions´ procedure, in order to reduce some of its disadvantages.

With the purpose to try to understand the relationship between the reaction conditions and the properties of the obtained polymers, these were subject to some characterization techniques: the molecular weight distribution was determined by size exclusion chromatography (SEC) and the stereoregularity was evaluated by optical rotation measurements and ^{1}H NMR spectroscopy.

2 Experimental Section

Reagents

All reagents were ordered from Sigma-Aldrich and used as received. L(+)-lactic acid aqueous solution 80 % was used as monomer and *m*-xylene (96%) was used as solvent. The catalysts tested were: tin (II) chloride dehydrate ($SnCl_2.2H_2O$) (98%), tin (II) octoate (Sn(II)Oct) (98%) and 4-dodecylbenzenesulfonic acid (DBSA) (90%). Molecular sieves, 3 Å beads, 8-12 mesh, absorption capacity of 21%, were used as drying agent.

Polycondensation of Lactic Acid Solution

The polymerization of L-lactic acid solution was carried out using an organic solvent with high boiling point, *m*-xylene, (Ajioka *et al.* 1995). The inicial concentration of monomer aqueous solution in the mixture was 20% (v/v). In a 2 L volume flask, equipped with a Dean-Stark trap and a mechanical stirrer, the reaction began with the distillation of the 80% L-lactic acid aqueous solution. Then, the catalyst was introduced (0.1% mol of catalyst) and the Dean-Stark trap was replaced by a tube packed with molecular sieves used as a drying agent. The polymerization was performed for several hours at the boiling point of the solvent, 140 ºC, using a bath to keep the temperature constant and under inert atmosphere (N_2). When the experiments were performed at reduced pressure, the pressure was decreased step by step till reaching the set-point. A cold trap was placed between the reactor and the vacuum pump to avoid the oil contamination. The final polymer is recovered as a white powder after dissolution in chloroform and precipitation in methanol. Table 1 summarizes the experimental conditions used in this study.

Characterization Techniques

The molecular weight distribution, average molecular weight (Mw) and polydispersity (PD) were determined using the SEC technique (Size Exclusion Chromatography), calibrated with

narrow polystyrene standards. The column set consists of a PL 5µm guard column (50x7.5mm) followed by one MIXED-D PL column (300x7.5mm, 10µm). The HPLC pump was set with a flow rate of 0.6 mL.min^{-1}. The eluent was chloroform and the experiments were carried out at 25 ºC with a sample concentration of ≈2 mg.mL^{-1}. Before the injection (≈100 µL) the samples were filtered through a PTFE membrane with a 0.45 µm pore. After column exclusion, the samples were analysed in a evaporative light scatttering detector, PL-EMD 960.

The ^{1}H NMR spectrum were recorded on a Varian 500-MHz spectrometer at 25 ºC, using CDCl3 as solvent containing 1% (v/v) of tetramethylsilane as an internal standard.

The specific rotation of lactic acid polymers $[\alpha]_{\lambda}^{T}$, was measured on a Optical Activity AA-5 electrical polarimeter at 25ºC, with a wavelenght of 589 nm and a concentration of 0.1 g.mL^{-1} in chloroform. The percentage of optical purity of lactic acid polymers (*OP%*) was calculated using the following relationship: $OP\% = [\alpha]_{589}^{25} / -156 \times 100$. Where -156 degree is the specific rotation of PLA with only L stereoisomer in its composition.

Table1: Operating conditions used in the experimental study and results.

Sample	Catalyst	Pres. set-point [bar]	Time [h]	Mw [g.mol^{-1}]	PD	OP [%]
PLA1	$SnCl_2.2H_2O$	1	30	3 163	1.5	83
PLA2	$SnCl_2.2H_2O$	1	24	7 900	1.0	83
PLA3	$SnCl_2.2H_2O$	0,3	40	45 356	-	54
PLA4	Sn(II)Oct	0,1	48	35 813	1.6	0
PLA5	DBSA*	0,3	48	17 536	1.5	83

*0,2 % (V/V)

3 Results and Discussion

Oligomerization

The reaction begins with the thermal dehydration of the initial 80% (v/v) lactic acid aqueous solution. At the end of the destillation the mixture has oligomers with a small polymerization degree. Fig. 1 shows a typical molecular weight distribution of the oligomers at the end of the destillation, oligomer4, and the final polymer at the end of polymerization, PLA4 (See Table 1 for polymer specifications). Unfortunately, due to the calibration restrictions, it is not feasible to use the SEC technique to determine the polymerization degree, neither the average molecular weight of these oligomers.

The initial lactic acid solution contains a carboxyl and an hydroxyl group resulting in a high polarity of the initial reaction mixture. The polarity of the medium decreases significantly with monomer convertion to the small oligomers during the initial thermal dehydration, which is self-catalysed by the carboxyl group of the monomer. The decrease in lactic acid concentration is followed by a decrease in the total amount of the carboxyl groups and a reduction on the reaction rate. As the self-catalysis by the carboxyl group does not allow reaching high molecular weight polymers a catalyst is added at the end of oligomerization. These results are confirmed by Moon *et al*. 2000, who reported that the polarity change can alter the catalyst activity.

Policondensation

The polymerization of lactic acid oligomers by step-growth was carried out under different reaction conditions and different strategies to remove the water from the reaction medium were explored. The polymerization was improved by screening catalyts and studying the influence of process variables on the quality of the final polymer. The results obtained are shown in Table 1. It is well-known that, for commodity aplications, PLA should have high molecular weight and high stereoregurarity (Garlotta, 2002). As these influence the mechanical properties, the crystallinity and the degradation rate, molecular weight and stereoregularity should be carefully controled to achieve polymers with required properties. Therefore, these two parameters were used for characterization.

Figure 2 shows the ^{1}H NMR spectrum of PLA1 (See Table 1 for polymer specifications). The bands at 1.6 and 5.2 ppm are due to the $-CH_3$ and $-CH$ groups present in PLA, thus confirming the synthesis of the desired polymer. The band at 7.3 ppm refers to the solvent used in the analysis, $CDCl_3$.

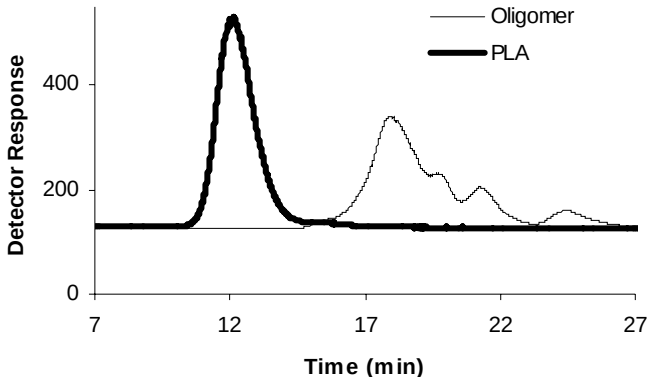

Figure 1: SEC curves for the oligomer4 and PLA4.

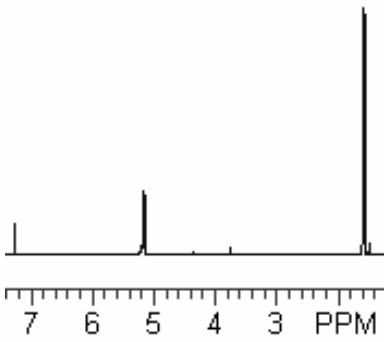

Figure 2: ^{1}H NMR spectrum for PLA1 in $CDCl_3$ at 500 MHz.

To control the water content in the reacting mixture, different procedures were applyied to the polymeric samples listed in Table 1. The water is a product of the esterification reaction (scheme A in Fig. 3). PLA1 was obtained at atmospheric pressure and during reaction the condensed water was not removed. The SEC curve (not here shown) indicates a low average molecular weight. In order to remove the water, in the second experiment, PLA2 (Table 1), a different approach was implemented. In this experiment, prior to condensation, the solvent vapour containing the condensed water passed through a tube packed with molecular sieves used as drying agent. This approach allowed a considerable increase on the final molecular weight, however, not reaching the target values. Thus, to facilitate water absorption by the drying agent, during the following experiments the pressure in the reactor was slowly decreased leading to high molecular weight polymers, PLA3, 4 and 5 (Table 1).

It is well known that esterifications are slow reactions and to increase the reaction rate a catalyst is required (Moon *et al*. 2000). Protonic acids, like H_2SO_4 or H_3PO_3, are usually used as catalysts. However, metal ions, as Lewis acids, can be more efficient for typical hydrogen ions (Roger and Long, 2003). The data in Table 1 show that the catalysts play a great influence on the molecular weight and optical purity of the final product. For the samples under analysis, the optical purity of the final product (polymer) decreased compared with that of the reagent (monomer), suggesting some racemization reactions. Moreover, the polymers obtained at reduced pressure show an optical purity that is drastically lower than those obtained at atmosferic pressure. Most probably, this is due to a small leak that disabled inertization, therefore allowing ester interchange reactions.

Tin (II) chloride dehydrate, $SnCl_2.2H_2O$, enabled achieving the highest molecular weight, near 45 000 $g.mol^{-1}$. It is a strong Lewis acid and largely used in direct polycondensation of lactic acid due to it high catalytic activity, although some ester interchange reactions have been reported (Hiltunen *et al.* 1997).

The mostly used catalyst in the lactide polymerization is tin (II) octoate, a strong Lewis acid, but the results show that it is not as efficient as tin (II) chloride dehydrate (Table 1). Concerning to the optical purity measured (0%) one can say that it proved to be a strong ester interchange catalyst promoting racemization reactions (Fig. 3 scheme C), *i.e.*, the PLA4 polymer has the same amount of L and D estereoisomers in the polymer chain.

The 4-dodecylbenzenesulfonic acid, DBSA, is a weak protonic acid with poor results in terms of molecular weight. However, it can be very efficient in terms of the polymer stereoregularity control (Table 1).

Other catalysts such as dibutyltin dilaurate, DBTL, and titanium (IV) butoxide were tested but the results were not encouraging.

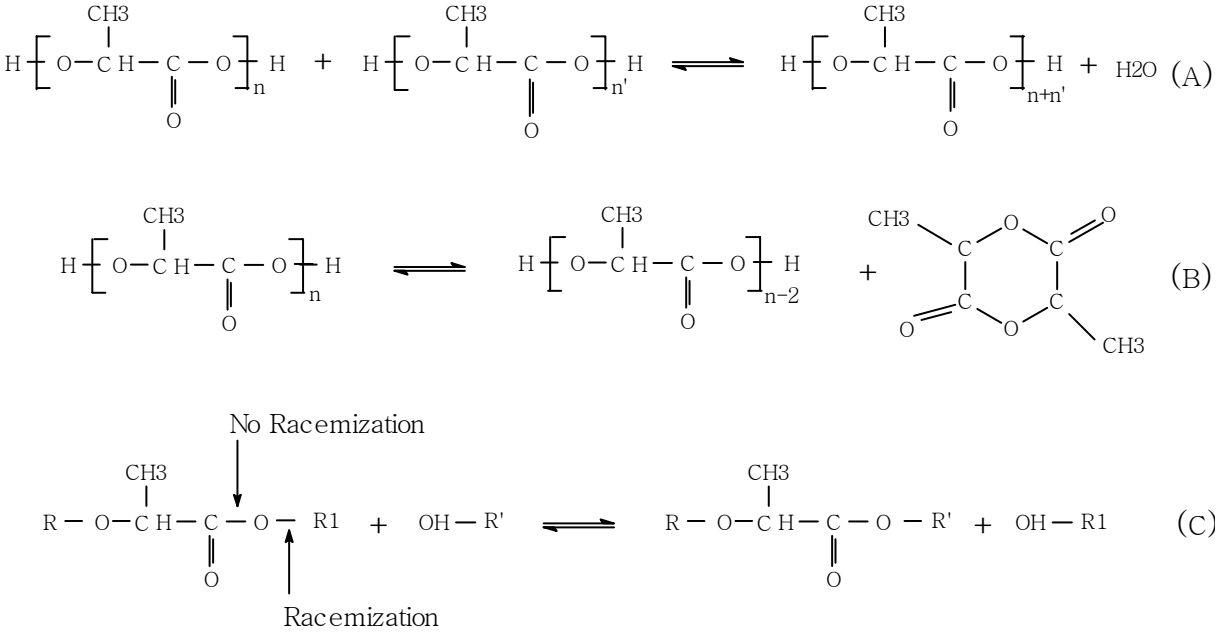

Figure 3: Reactions during lactic acid polycondensation: a) Dehydration, b) Ring-Chain c)Transesterification.

Reactions

The lactic acid polymerization by step-growth is an equilibrium system involving several reactions, the most important are represented in Fig. 3. Dehydration equilibrium, Fig. 3 A, is the most important reaction for attaining high molecular weight polymers. Lactic acid is an alpha-hydroxy acid, it has two functional groups, that reacts with himself by the condensation, realesing a water molecule. Efficient removal of the condensed water becomes the key point to obtaining high molecular weight polymers.

The ring-chain equilibrium, Fig. 3 B, involves the depolymerization of PLA into lactide. Under ideal reaction conditions, high temperature and high vacuum, the evaporation of lactide is favoured. However, with the use of organic solvents, the lactide is reintroduced into the reaction mixture and the depolymerization equilibrium is well controled.

Transesterification is a dynamic equilibrium of ester interchange reactions occurring between the polymer chains. These reactions can explain the introduction of D-lactyl units in the polymer chain. During the ester interchange reactions there are two ways in which ester linkage can cleave, Fig. 3 C. One is acyl-oxygen cleavage, which does not involve the chiral

carbon. The other is alkyl-oxygen cleavage, in which the covalent bond between oxygen and the chiral carbon breaks and subsequently reforms, this results in an inversion of the conformation and a decrease in optical purity (Hiltunen *et al*. 1997). The optical purity results, Table 1, indicate undoubtedly the racemization reactions occurence. According to the data analysis, racemization reactions are dependent on the reaction conditions and, mainly, on the catalyst used.

4 Conclusion

PLA polymer was successfully produced by direct condensation using a solvent with high boiling point to facilitate the continuous removal of water, a reaction side product, therefore increasing the extent of the polymerization reaction. The use of a drying agent combined with reduced pressure enabled to further improve the efficiency in water removal. This polymerization method allowed to obtain high molecular weight PLA in one single step, instead of the three steps required by the ROP method. From the economic point of view, it is of best interest to develop an efficient, effective and less expensive method to produce a promising polymer, Poly(lactic acid).

The change of L-lactyl units to D-lactyl units, suported by the optical results, is a major problem in PLA synthesis by polycondensation. Its control is essential and can be attained by a suitable catalyst. Protonic acids seem to be the best catalysts in order to avoid racemization reaction, therefore improving the optical purity of the polymer. More research work needs to be carried out to find the best catalyst to provide an enhanced molecular weight and a lower racemization extent.

5 References

Bogaert, J., Coszack, P. (2000). Poly(lactic acid): A potencial solution to plastic dilemma. *Macromol. Symp*., 153, 287-303.

Garlotta, D. (2002). A literature review of poly(lactic Acid). *Journal of Polymers and the Environment,* 9, 63-84.

Ajioka, M., Enomoto, K., Suzuki, K., Yamaguchi A. (1995). Basic Properties of Polylactic Acid produced by the Direct Condensation polymerization of Lactic acid. *Bull. Chem.Soc Jpn.,* 68, 2125-2131.

Kim, K., Woo S. (2002). Synthesis of high molecular weight poly(l-lactic acid) by direct polycondensation. *Macromol. Chem. Phys*., 203, 2245-2250.

Moon S., Lee C., Miyamoto M., Kimura Y. (2000). Melt Polycondensation of L-Lactic Acid Sn(II) Catalysts Activated by Various Proton Acids: A Direct Manufacturing Route to High Molecular Weight Poly(L-lactic acid), *Journal of Polymer Science*, 38, 1673 1679.

Roger M. E., Long T. E. (2003). Synthetic Methods in Step-Growth Polymers, *John Wiley&Sons, New Jersey*.

Hiltunen K., Seppala J., Harkonen M. (1997). Effect of catalyst polymerization conditions on the preparation of low molecular weight lactic acid polymers, *Macromolecules*, 30, 373-379.

Proceedings of the 10th International Chemical and
Biological Engineering Conference - CHEMPOR 2008
Braga, Portugal, September 4-6, 2008
E.C. Ferreira and M. Mota (Eds.)

Biodegradability of mixed plastics containing PVAL/Gellan and PVAL/Xanthan in soil environment

Martina Kopcilova[1*], Jaromir Hoffmann[1], Miroslava Tomalova[2], Pavol Alexy[3], Marketa Julinova[1] and Anna Nahalkova[3]

[1]Tomas Bata University in Zlin, Faculty of Technology, Department of Environmental Protection Engineering, nám. TGM 275, 762 72 Zlín, Czech Republic

[2] Regional Office Zlin, Department of Environment and Agriculture, T. Bati 21, 76190 Zlín, Czech Republic

[3]Slovak University of Technology, Faculty of Chemical and Food Technology, Department of Plastics and Rubber, Radlinského 9, 812 37 Bratislava, Slovakia

Keywords: biodegradation, PVAL, Gellan, Xanthan, gas-chromatography

Topic: Integration of life sciences & engineering

Abstract

Plastics represent one of the most important contemporary materials. Their features, easy workability and price far exceed classicality of metal, wood, glass etc. However, the long decomposition period of some polymeric materials as well as growing scores of plastic waste make a considerable problem. One of the possible solutions is development and production of biodegradable polymers which are more rapidly decomposed in biotic environment and thereby eliminated. Good examples of biodegradable materials are wraps, compostable bio-waste bags, agricultural mulch foils and protective painting and others.

Poly (vinyl)alkohol (PVAL) is considered to be relatively well biodegradable polymer. Hydrophile feature of PVAL makes its decomposition easier by using microorganisms but limits its range for practice application and that is why the PVAL is modified. Polymeric materials of biologic origin (biopolymers), for example proteins (colagen, protein hydrolyzate), polysacharides (starch), polyesters (e.g. poly-3-hydroxybutyrate, PHB) are often used for the purpose of modification. It is possible to use additives of extracellular polysacharides type such as Dextran, Xanthan and Gellan which are the most remarkable agents. These polysacharides can be added to the mixed polymers for the purpose of the increasing and accelerating of their biodegradability. Required feature low price can be limited factors.

The aim of the study was to review the impact of different Xanthan and Gellan proportion to biodegradability in soil environment of their mixtures with polyvinylalcohol (PVAL) and glycerol, with regard to mechanical properties of the mixtures (tensile stengh, fracture strain). Tested mixed granulates containing 10.5 %, 21 % and 42 % of Xanthan or Gellan were prepared on twin-screw thread extruder LABtech.

The tensile strengh of the mixtures was decreasing with increasing polysacharides content, in the tested range within cca 20 %, whereas the Gellan mixtures constantly showed lower values than Xanthan ones. The strain decreasing was more evident - between first two samples at cca 30 %, by the last mixtures (containing 42 % of polysacharides) the values approximated to zero. Obviously, the reaching of aplicable physicomechanical features will be compromising but eventually hardly achieved.

Mixed granulates biodegradation in soil environment was tested under aerobic conditions in reaction flasks [1,2]. The CO_2 production via gas – chromatography together with O_2 usage for aerobic conditions keeping control was monitored during all tests.

According to DCO_{2max} level of biodegradation, all the polymeric mixtures appeared as hardly degradable in the soil environment. The mixed granulate N/68/107 containing 10.5 % of

Gellan degraded the worst of all the set, respectively only of 17.9 %. Mixed granulates N/68/108 (21 % of Gellan) and N/68/109 (42 % of Gellan) degraded of 35.9 % and 39.6 %. Granulates N/68/110 (10.5 % of Xanthan), N/68/111 (21 % of Xanthan) and N/68/112 (42 % of Xanthan) degraded of 21.2%, 45.2% and 47.3%. These results showed that the polymeric mixtures containing Xanthan were better degradable than mixtures containing Gellan. It means that the kind and amount of used polysacharide had a significant effect over the biodegradation of polymeric mixtures but the biodegradability of PVAL itself was not influenced. The level of biodegradation was approximately in relation with content of degradable components (PVAL and glycerol).

1 Introduction

Development of new biodegradable polymeric materials, materials of shortened life, is an alternative in preventing “contamination” of the environment with non-degradable synthetic substances. A convenient solution may be in combining synthetic polymers with natural degradable polymers, for example, poly (vinyl)alcohol (PVAL) with current bacterial polysaccharides Xanthan and Gellan, assuming, of course, that required useful properties of the blends are met. Biodegradability of the substances themselves are by and large known [3,4,5], however, properties of their blends have been studied but very sporadically.

The concept of biodegradability is highly relative, depending on a whole number of factors and conditions under which the breakdown is studied. Action of the mentioned conditions and factors depends on where the polymeric products are degraded, whether in soil, natural water, biological treatment plant or in compost. In biodegradation testing, therefore, environmental conditions, if possible, should be kept standard and comparable to secure reliability and reproducibility of measured results.

Laboratory tests in a soil environment under aerobic conditions are affected by a whole number of factors: composition and structure of soil, particle size, soil origin (affecting occurrence and type of micro-organism settlement), also temperature (optimum for growth of soil micro-organisms is 25 – 27 ^{o}C), pH (5.5 - 6.5), moisture (50 – 70 %), aeration, presence of nutrients (C/N ratio within limits 10:1-40:1). The ratio of sample to soil substrate is also important – ISO standard 17556 [6] recommends ratio 1:1000. Duration of soil tests is highly variable – from 45 days to 6 months. The biodegradation progress may be assessed through changes of gaseous phase in an enclosed testing system [7] or through decrements in weight of tested samples – so-called burial tests [8]. Microbiological analysis may be a complementary criterion to these tests.

2 Experimental

Biological material

Soil substrates – mixtures of three soils – two kinds of commercial soils (garden substrate and grave substrate by the AGRO CS Co) and natural soil (taken at Holešov, Czech), ratio 2:1:1 (related to dry matter). Preparation was performed in accordance with ISO 17556 [6]. Soil substrates were kept at constant temperature 5 ^{o}C. Prior to test, soil substrate was disposed of coarse impurities by sieving through screen of approx. 5 mm mesh, dry matter was determined and basic analyses performed – pH 6.20, ignition loss 79.52 %, N content 0.5 %, P content 0.11 - 0.22 %, and TC 32.9 %.

Inert material

Material employed as inert was a product under trade name AGROPERLIT (hereafter Perlit, by AGRO CS Co). Perlit is an expanded volcanic rock. The mixture dosed into test bottles was soil/Perlit in a 1:1 ratio (related to soil dry matter). Perlit properties declared by manufacturer: water content max. 2.0 %, pH 6.0 - 7.5, particle size < 0.3 mm content max. 15%, < 1 mm max. 25 %, 1.0-4.0 mm max. 75 %, bulk density 200 kg m^{-3}.

Tested samples

Preparation and composition of blends

Samples based on PVAL, glycerol and bacterial exopolysaccharides Gellan and Xanthan were prepared at the Department of Rubber and Plastics, Chemical and Technological Faculty of Slovak Technical University in Bratislava, Slovakia. Preparation of samples on a twin-screw LABtech extruder was performed under thermal profile (feed hopper-extrusion head) 120/130/140/150/160/170/180/190/160/150 ^{o}C and 300 rpm. Blends containing Xanthan displayed processing properties superior to Gellan. Blend composition is presented in Tab.I.

Tab I.: Characteristics of polymeric blends

Sample	PVAL [%]	Saccharide [%]	GLY [%]	GLY v TPS	GLY v PVAL	Type of saccharide
N/68/107	74,8	10,5	14,7	4,5%	10,2%	GELLAN
N/68/108	61,6	21	17,4	9%	8,4%	
N/68/109	32,8	42	25,2	18%	7,2%	
N/68/110	74,8	10,5	14,7	4,5%	10,2%	XANTHAN
N/68/111	61,6	21	17,4	9%	8,4%	
N/68/112	32,8	42	25,2	18%	7,2%	

where:
GLY glycerol
TPS thermoplastic starch

Determining biodegradability

Soil tests were conducted according to own procedure, but reflecting requirements of standard ISO 17556 [6]. Quantities investigated were produced CO_2 and decrease in O_2 by means of gas chromatography. The tested sample served as sole external source of carbon and energy for soil micro-organisms. Biodegradation tests in all cases were carried out in gas-tight reaction bottles of approx. 1140 ml total volume [2,9].

At beginning of test, actual gaseous volume V_g of test bottles (around 980 ml) was determined. In all cases, soil substrate + Perlit (1:1) was dosed into test bottles, solutions of ammonium sulphate and sodium hydrogen phosphate (ratio C:N:P approx. 100:10:1) were added, water content in mixture was adapted to 50 % and tested samples were added (thoroughly “mixed in”). Bottles were enclosed gas-tight and incubated at 25^{o}C without access of light. Aeration frequency was based on performed analyses so that oxygen concentration would not go below approx. 6 % volume (1 to 2 weekly). Air for aerating bottles was disposed of CO_2 by washing in NaOH solution. Water content in blends was checked by gravimetry (weighing whole bottles) and kept at an approx. 50 % level.

Analysis of CO_2 and O_2 by gas chromatography

Gas-chromatographic analysis of CO_2 and O_2 on gas chromatograph was described in our other work [2,9].

Processing results

Daily and cumulated production of CO_2 were calculated, together with percentage of substrate removal

DCO_2 (actually produced quantity of CO_2 as related to theoretically producible quantity). Biodegradation dependencies were calculated by applying 1st-order kinetics. Description given in [2,9].

3 Results and discussion

Mechanical properties of samples

Specimens for determining mechanical properties were cut from strips prepared on a single-screw extruder (see Preparation and composition of blends). Mechanical properties were measured on Metrotest 5kN apparatus according to STN ISO 527 at jaw speed 1 mm/min in strain range 0-3 %, and 50 mm/min in strain range > 3 %, at room temperature. The working part of specimen was 10mm.

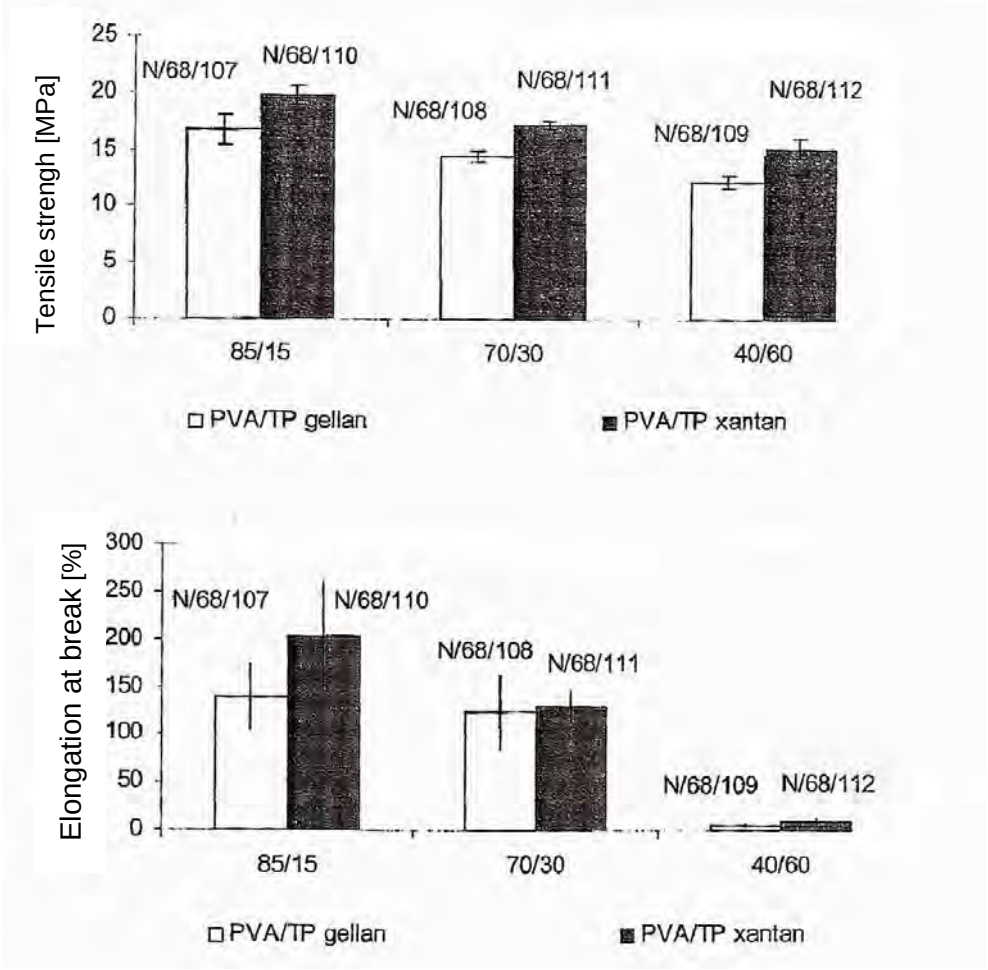

Fig. 1: Mechanical properties of samples

Blends containing Xanthan exhibited higher stress and strain values than blends containing Gellan. Tensile strength decreased with increasing concentration of polysaccharides, approx. 25 % for both sample series. The decrease in strain values was far more obvious, in the given series almost down to zero (blends with approx. 42 % Xanthan or Gellan), to practically inadmissible values.

Evaluation of soil test

Samples N/68/107 to N/68/109 contained polysaccharide Gellan and differed in percentual content of particular components in the blend, the same as samples N/68/110 to N/68/112 containing polysaccharide Xanthan. Duration of the test was 1145 hours (almost 48 days). Cumulative CO_2 production was calculated from read-off data together with percentage of substrate removal DCO_2. Dependencies were processed by formal 1st-order kinetics.

Figure 2 presents the biodegradation course of sample N/68/109 as an example.

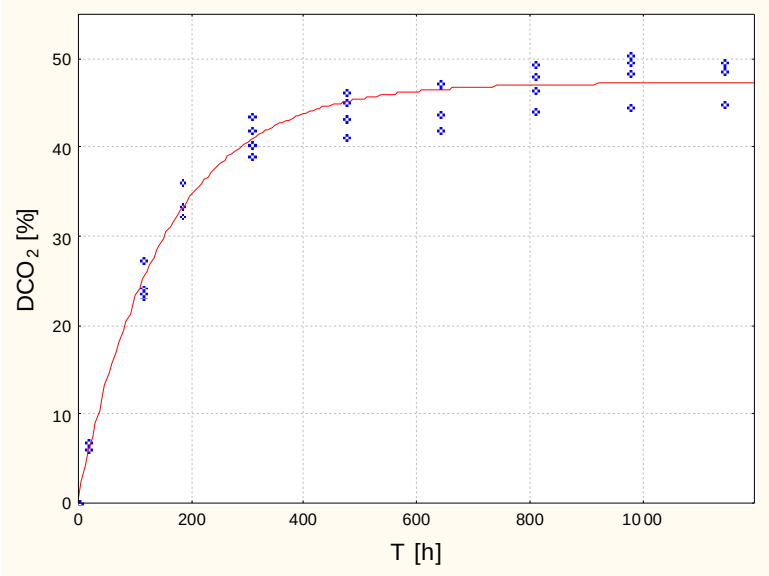

Fig.2: The biodegradation course of sample N/68/109

Viewed from CO_2 production, all tested samples appeared as poorly degradable, which followed from values of DCO_2max and from the graph spanning DCO_2max values (Fig.3). Sample N/68/107 with lowest Gellan content (10.5%) degraded worst and that by merely 17.86%. Sample N/68/109, containing four times more Gellan, degraded by 39.61%. The most readily degradable sample of the series, N/68/112 containing 42% Xanthan, degraded by 47.28%, sample N/68/110 containing 10.5% Xanthan degraded by only 21.21%. From the graphs above it is obvious that samples containing Xanthan were more readily degradable than samples containing Gellan.

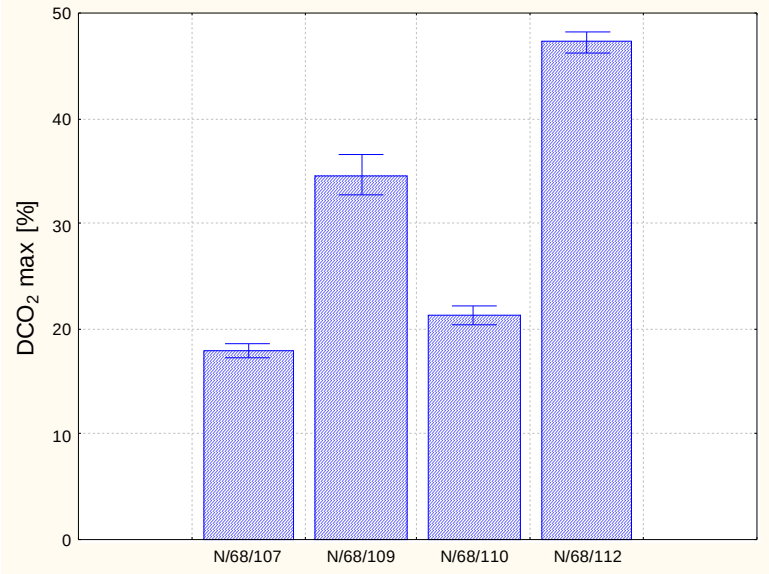

Fig.3: Blends DCO_2 values

The presented facts allow to admit that blends of given composition fail to meet the good biodegradability as required, levels of DCO_2max do not attain even 50 %. A greater addition of polysaccharide improves total degradability, which, however, is in no relation to addition volume.

4 Conclusion

The objective of this work was to evaluate biodegradability of a blend of poly (vinyl)alcohol (PVAL) with variable content of polysaccharides Xanthan and Gellan and glycerol in a soil environment, with respect to mechanical properties of the blend (tensile strength, elongation at break). Assessing biodegradability employed the so-called "bottle" test with a final determination employing gas chromatography for monitoring production of CO_2, which was designed and verified at our laboratory [2].

Based on test results, we may state the type as well as quantity of polysaccharide exerted significant influence on biodegradability and mechanical properties of investigated samples. Blends containing Xanthan exhibited superior mechanical properties and also degraded to greater extent than blends with Gellan. Despite that, from the viewpoint of CO_2 production, tested samples were poorly degradable in a soil environment and only the blend with highest Xanthan content approached 50% degradability. The "bottle" test turned out to be rather "comfortable" and offered credible results.

Acknowledgement

This work was supported by Research Project of the Ministry of Youth, Education and Sports of the Czech Republic, No. MSM7088352101.

References

[1] ISO 14855 (1999) : *Determination of the ultimate aerobic biodegradability and desintegration of plastic materials under controlled composting conditions – metod by analysis of evolved carbon dioxide*.

[2] Dřímal P., Hoffmann J., Družbík M.: *Evaluating the Aerobic Biodegradability of Plastics in Soil Environments through GC and IR Analysis of Gaseous Phase*. Polymer Testing 26, 2007, 729-741.

[3] Emo Chiellini, Andrea Corti, Salvatore D´Antone, Roberto Solaro: *Biodegradation of Poly (vinyl alkohol) based materials*. Prog. Polym. Sci 28 (2003) 963 – 1014.

[4] HAILI, L. et al.: *Biodegradation of xanthan by newly isolated Cellulomonas sp. LX, releasing elicitor-active xantho-oligosaccharides-induced phytoalexin synthesis in soybean cotyledons*; Process Biochemistry 40, 3701–3706, 2005

[5] SINGH, B. N., TROMBETTA, L. D., KWON, H. KIM: *Biodegradation Behavior of Gellan Gum in Simulated Colonic Media*; Pharmaceutical Development and Technology; Vol. 9, No. 4, pp. 399–407, 2004

[6] ISO 17556*: Plastics - Determination of the ultimate aerobic biodegradability in soil by measuring the oxygen demand in a respirometer or the amount of carbon dioxide evolved,* 2003

[7] GOVIND, R., GAO, Ch., LAI, L., TABAK, H. H.: *Continuous, automated and simulaneous measurement of oxygen uptake and carbon dioxide evolution in biological systeme,* Water Environment Research 69, ProQuest Agriculture Journals, pg. 73, 1997

[8] EUN-SOO PARK et al.: *Soil Burian Test for Poly(ethylene-co-vinyl alkohol)-graft-Polycaprolactone;* Journal of Applied Polymer Science, Vol. 96, 1064-1071, 2005

[9] Jaromír Hoffmann, Iva Kotasová, Pavel Dřímal, Markéta Julinová, Martina Kopčilová: *Biodegradation of Plastics in Composts – Laboratory Evaluation*, 34th International Conference of SSCHE, ISBN 978-80-227-2640-5

* Corresponding author. Tel +420 576 031 160. E-mail: kopcilova.m@seznam.cz

Proceedings of the 10th International Chemical and
Biological Engineering Conference - CHEMPOR 2008
Braga, Portugal, September 4-6, 2008
E.C. Ferreira and M. Mota (Eds.)

Development of Semi-Transparent Wood Polymer Composites

Paulo A. N. Dias; Marco S. Reis*; Maria H. Gil; José A. C. Alves
Chemical Engineering Department, University of Coimbra
Rua Sílvio Lima, 3030-790, Coimbra, Portugal

Keywords: Wood polymer composites; Acrylic polymers; Design of experiments; Free radical bulk polymerization

Topic: New materials & structured products

Abstract

We have developed a new material consisting of pieces of wood within a matrix of an acrylic polymer, resulting in a transparent or semi-transparent product. This material present quite appealing aesthetics features, opening new possibilities for innovation in decorative products.

Acrylic and methacrylic monomers are in the liquid state for temperature ranges including room temperature. Therefore, it is possible to introduce wood (in our case, walnut wood) in a mixture of acrylic (HPA – hydroxypropyl acrylate) and/or methacrylic monomers (MMA – methyl methacrylate and HEMA – 2-hydroxyethyl methacrylate) in the presence of a chemical initiator (benzoil peroxide). Introducing this reaction mixture along with pieces of wood in a mould, we obtained a transparent polymeric matrix with wood dispersed, through bulk free radical polymerization, i.e., a wood polymer composite.

A 2^{4-1} fractional factorial design was conducted, with the purpose of studying the importance of the composition of these materials in certain selected properties. The sheets produced were characterized by DMTA (to measure T_g), TGA (to assess thermal stability), tensile testing (determination mechanical properties under tensile loads) and HDT (heat-deflection temperature).

1 Introduction

The objective pursued in this work, was to develop a transparent or semi-transparent product with pieces of wood in it, presenting appealing aesthetics features, to be used in the production of furniture and decorative products. Acrylics (products based essentially on poly (methyl methacrylate) - PMMA), are known by their beauty and transparency, which is the reason why they were used in this work to produce the matrix where the pieces of wood were introduced.

The task of introducing a solid material (wood) into another solid (acrylic) can be quite challenging, from a technical point of view. A solution for producing such type of materials, is to make the acrylic suffer a state change that allows the introduction of wood pieces.

Acrylics are thermoplastic polymers and can be processed by injection molding and extrusion (Kirk-Othmer, vol. 19, 1996). Processing temperatures of PMMA in an injection molding process, are in the range of 200-250 ºC, and in an extrusion process are around 180-250 ºC. Wood does not resist to temperatures much higher than 180 ºC (Kirk-Othmer, vol. 25, 1996), and therefore it is not advisable to consider the use of such processes for addressing the goals of this work. Alternatively, one must think in the acrylic before it is produced. Acrylic

* Corresponding author. Tel + 351-239-798700. E-mail: marco@eq.uc.pt

and methacrylic monomers are in the liquid state for temperature ranges including room temperature. Therefore, it is possible to introduce wood (in our case, walnut wood) in a mixture of acrylic (HPA – hydroxypropyl acrylate) and/or methacrylic monomers (MMA – methyl methacrylate and HEMA – 2-hydroxyethyl methacrylate) in the presence of a chemical initiator (benzoil peroxide). Introducing this reaction mixture along with pieces of wood in a mould, we managed to obtained a transparent polymeric matrix with wood dispersed in it, through bulk free radical polymerization, i.e., a wood polymer composite (Kumar, 2006).

2 Experimental Design

In order to develop the new material, a 2^{4-1} fractional factorial design was conducted, where the impact of four factors in the relevant physical and chemical properties were systematically assessed. These factors were the presence of HEMA, HPA, dioctyl phthalate (DOP) and walnut wood. Two levels were adopted for each factor (Table 1): 0 and 10 w/w % for the first three factors and presence/absence for the fourth factor, the walnut wood. This experimental design as resolution IV, meaning that no main effect are aliased with any other main effect, or with any two-factor interactions, but two-factor interactions are aliased with each other (Montgomery, 2001). The composition of the samples was completed by adding MMA.

Table 1. Experimental design followed in this work

Test	**Design Factors**			
	***A* – HEMA (w/w %)**	***B* – HPA (w/w %)**	***C* – DOP (w/w %)**	***D* – Walnut**
1	0	0	0	Present
2	10	0	5	Present
3	0	10	5	Present
4	10	10	0	Present
5	0	0	5	Absent
6	10	0	0	Absent
7	0	10	0	Absent
8	10	10	5	Absent

The materials developed in this work are based in PMMA, an hydrophobic polymer with low polarity. Wood, on the other hand, is hydrophilic and polar (Jiang, 2004), due to the existence of hydroxyl polar groups (Castellano, 2004). This fact potentially conduces to weak adhesion in the interface between the polymeric matrix and wood (Jiang, 2004). The introduction of monomers HEMA and HPA in the reaction mixture, has the ability of introducing hydroxyl polar groups on the polymeric matrix, which may lead to higher levels of adhesion between the two phases.

In the literature, it is possible to find some references mentioning that polymers produced by methacrylic monomers (like MMA and HEMA) tend to be hard and brittle, whereas polymers produced by acrylic monomers (the case of HPA), tend to be soft (Kirk-Othmer, vol. 16, 1995). So, the introduction of HPA on the reaction mixture has the goal of promoting internal plasticization (Stevens, 1999), which can be compared with the external plasticization action promoted by the introduction of DOP.

3 Plates Preparation

In order to obtain the plates, one first needs to prepare the mold. Figure 1, presents a scheme with the main stages followed during mold preparation, namely:

(a) - Put in the hotte a glass plate on the horizontal. Apply a silicone spacer on the glass plate creating an open mould.

(b) - Introduce the walnut wood pieces on the mould.

(c) - Put the reaction mixture pre-polymerized on the mould. The pre-polymerization allows for a better temperature control of the exothermal polymerization reaction (Kirk-Othmer, vol. 16, 1995).

(d) - Cover the open mould with an additional glass plate.

(e) - Close the mould with adhesive tape and springs.

(f) – Put the mould on an oven, in the horizontal position. Maintain it at a temperature of 40 ºC for about 20 hours. Conclude the polymerization reaction at a temperature of 90 ºC for about 1 hour.

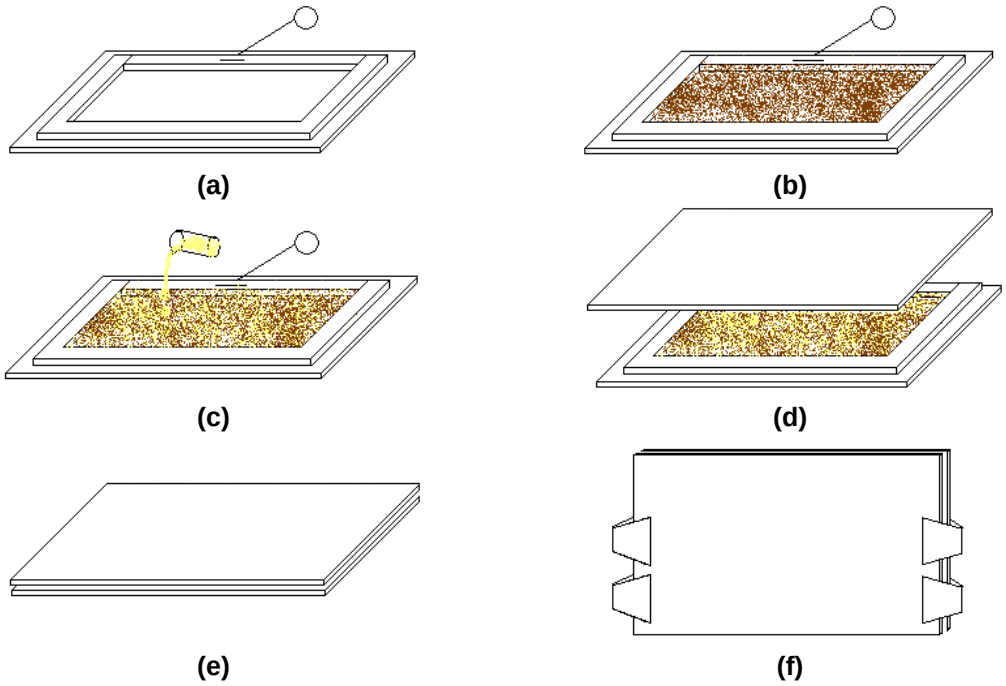

Figure 1. Scheme representing the main stages of preparation of a mold, for obtaining a wood polymer composite.

We have obtained 8 plates following this procedure, with dimensions of approximately 4x27x12 cm corresponding to the 8 runs of the experimental design. We have also produced an additional plate of PMMA, for comparison purposes. Figure 2 presents an example of a plate obtained (test #2 in Table 1).

Figure 2. A typical plate of wood polymer composite, produced in this work (test #2 in the experimental design).

4 Product Characterization

All samples produced were characterized by DMTA (determination of T_g), TGA (study of the thermal stability), tensile testing (determination of tensile mechanical properties) and HDT (heat-deflection temperature). All results obtained were properly analyzed through statistical methods.

DMTA

The tests were made for two frequencies: 1 and 10 Hz; the rate of heating was 2 ºC/min and the equipment was properly calibrated for these conditions. The samples analyzed had dimensions of about 15x8x2 mm. T_g was obtained using the maximum of the curve tan(δ) *versus* temperature.

TGA

The rate of heating was 10 ºC/min; an inert atmosphere of nitrogen was used, whose flow rate was of 10 ml/min. The equipment was correctly calibrated for such conditions, and the samples analyzed had a mass of approximately 10 mg.

Tensile Testing

The tests were made according to the ISO 527 standard, using test specimens of the 1B type and the appropriate equipment. The rate of elongation for the ultimate strength experiment was of 5 mm/min ± 1 mm/min, and for the modulus of elasticity experiment it was of 1 mm/min ± 0,2 mm/min. For the ultimate strength experiment, 3 measurements for each test were performed, and for the modulus of elasticity experiment, 2 measurements were made for each test. The mean values were used for estimating the regression models.

HDT

The heat-deflection temperature (HDT) is a useful indicator of the temperature limit above which polymers cannot be used for structural (load-supporting) applications (Fried, 1995). The tests were made according to the ISO 75 standard, for the method A. For each test of the experimental design, 2 experiments were made for specimens on the horizontal position. The mean values were used for estimating the regression models.

5 Results and Discussion

A summary table of the regression models obtained from the analysis of data collected during the experimental design runs, regarding the glass transition temperature (T_g), ultimate strength (σ_M), elongation at the ultimate strength (ε_M), modulus of elasticity (E_t) and heat-deflection temperature (HDT), can be seen in Table 2.

Table 2. Summary table with the regression models and their associated R^2 and P-values, for the properties: T_g, σ_M, ε_M, E_t and HDT.

Propriety	Regression Model	R^2	P-Value
Glass Transition Temperature (frequency 1 Hz), T_g	T_g (ºC) = 103,81 – 7,44 x **B** -7,61 x **C**	0,8195	0,0138
Ultimate Strength, σ_M	σ_M (MPa) = 40,22 + 18,46 x **D**	0,9497	0,0001
Elongation at the Ultimate Strength, ε_M	ε_M (%) = 2,74 + 1,77 x **D**	0,9447	0,0001
Modulus of Elasticity, E_t	E_t (MPa) = 1862,20 + 456,72 x **D** -324,38 x **BD**	0,8428	0,0098
Heat-Deflection Temperature, HDT	HDT (ºC) = 70,83 - 8,68 x **B**	0,7861	0,0033

As expected, the presence of HPA (internal plasticization) and DOP (external plasticization) in the reaction mixture, does promote the increase of the materials flexibility, because they cause a decrease in the values for T_g.

The TGA analysis determined that the materials produced in this work present a good thermal stability up to temperatures close to 200 ° C.

The introduction of monomers with -OH groups in the reaction mixture did not cause any significant increase in the ultimate strength (σ_M), which means that higher levels of adhesion between the polymeric and the wood phase were not achieved. Thus, the monomers to be used (even in the case of producing flexible materials, through the addition of acrylic monomers), can be chosen on the basis of cost, and not in terms of their polarity features.

The presence of HPA in the reaction mixture (internal plasticization) is the most important factor for determining the flexibility of new materials when subjected to load. Thus, if the intention is to develop materials showing flexibility when subjected to loads, attention should be focused on internal plasticization and not on the external plasticization.

6 Conclusions

We have developed a new material consisting of pieces of wood within a matrix of an acrylic polymer, resulting in a transparent or semi-transparent product. This material present quite appealing aesthetics features, opening new possibilities for innovative decorative products. The results obtained encourage further research in this topic, now focused on specific applications.

References

Castellano, M., Gandini, A., Fabbri, P., Belgacem, M.N. (2004). Modification Of Cellulose Fibres With Organosilanes: Under What Conditions Does Coupling Occur?, *Journal of Colloid and Interface Science*, 273, 505-511

Fried, J. R. (1995). *Polymer Science And Technology*, 1st ed., Prentice Hall PTR, Englewood Cliffs (N. J.).

Jiang, H., Kamdem, P. (2004). Development Of Poly(vinyl chloride)Wood Composites. A Literature Review. *Journal of Vinyl & Additive Technology*, 10, 59-69

Kirk – Othmer (1995). *Encyclopedia Of Chemical Technology*, vol. 16, 4th ed., John Wiley & Sons, New York.

Kirk – Othmer (1996). *Encyclopedia Of Chemical Technology*, vol. 19, 4th ed., John Wiley & Sons, New York.

Kirk – Othmer (1998). *Encyclopedia Of Chemical Technology*, vol. 25, 4th ed., John Wiley & Sons, New York.

Kumar, B., Zaidi, M.G.H., Rathore, S., Rai, A.K., Thakur, I.S., Sah, P.L. (2006). Optical, Morphological, Thermal, Mechanical, and Fungal Characterization of Wood Polymethyl Methacrylate Composites. *Instrumentation Science and Technology*, 34, 67-83

Montgomery, D.C. (2001). *Design and Analysis of Experiments*, 5th ed., John Wiley & Sons, New York.

Stevens, M. P. (1999). *Polymer Chemistry: An Introduction*, 3rd ed., Oxford University Press, New York.

Proceedings of the 10th International Chemical and
Biological Engineering Conference - CHEMPOR 2008
Braga, Portugal, September 4-6, 2008
E.C. Ferreira and M. Mota (Eds.)

SOLUBILITY OF SOME SULFATES IN SUPERCRITICAL WATER

Jesusa Rincón*, Isaac Asencio, Rafael Camarillo and Alicia Martín
Department of Chemical Engineering. Faculty of Environmental Science. University of Castilla-La Mancha. Avda. Carlos III, s/n. 45071 Toledo. SPAIN.

Keywords: catalysts regeneration, sulfates solubility, sub and supercritical water.
Topic: Sustainable process-product development through green chemistry

Abstract

The solubility of aluminium sulfate and sodium sulfate in water has been determined at supercritical temperatures ranging from 350–400°C and sub- and supercritical pressures varying from 150–290 bar. Measured aluminium sulphate and sodium sulfate concentrations ranged from 260–584 ppm and 5–802 ppm, respectively. In the experiments, water was saturated by continuously flowing it through a contacting cell contaning an aqueous salt solution of known concentration (0,5 g/L). The results for sodium sulfate agreed well with other studies which used continuous flow methods. Experiments with aluminium sulfate showed that its solubility in sub- and supercritical water was of the same order of magnitude of that reported in the literature for sodium sulfate at similar conditions.

1. Introduction

Despite the extended use of three-way catalysts in automobile industry for so many years, only a few attempts have yet been made aiming at expanding the durability of gasoline-driven aged three catalysts (TWCs) and in situ regenerating their catalytic performance after applying economically attractive and environmentally friendly techniques. Among these attempts are extraction of contaminants by using liquid solvents such as weak organic acids (e.g., acetic, oxalic, and citric acids) and employment of different combinations of thermal and chemical treatments by oxygen, hydrogen, and chlorine-containing gas mixtures or other chlorine-containing reagents (such us carbon tetrachloride, hydrochloric acid, etc.) to reverse thermal aging by redispersion of the large particles of catalysts noble metals.

However, all of these technologies present some objections, i. e., the efficiency of the process is not complete because of one or several reasons: only partial elimination of the impurities is achieved, there are exclusive treatments for specific pollutants, the recoveries of the catalytic activity and the oxygen storage capacity are limited and wastes streams are generated that need to be treated in order to yield a process environmentally benign. It is for this reason that we propose the use of sub and supercritical water to recycle the TWCs by extracting selectively the pollutants poisoning the catalysts surface. Data recently published (1, 2) suggest that the treatment could work.

Thus, the present study has been undertaken to investigate for the first time the possibility of using sub and supercritical water to improve the catalytic activity and oxygen storage capacity of aged TWCs. More specifically, the solubility in sub and supercritical water of TWCs pollutants such as aluminium sulfate and sodium sulfate is investigated in this work in order to optimize the experimental conditions to perform the extractions that would improve the catalytic and oxygen storage properties of the catalysts.

* Corresponding author. Tel + 34 - 925 265 708. E-mail:jesusa.rincon@uclm.es

2. Experimental

2.1 Experimental approach to determine the salt solubility

The goal in solubility studies is to achieve an equilibrium separation between the solvent media and the concentrated solute phase. A common method for determining solubility in sub and supercritical water involves passing water at such conditions through a salt bed and allowing the salt to saturate the water to its equilibrium concentration (3). The effluent from the salt bed is cooled, depressurized, and then analyzed for the salt. However, this method does not work with low-melting salts, since they have a tendency to be transported with the supercritical phase, contaminating the effluent samples and/or plugging the solubility apparatus (4).

As a result, we have developed a method to determine the solubility of salts that avoid these problems. The method takes advantage of the fact that nucleation and precipitation reactions can occur rapidly in SCW. Electolyte solutions of known composition are heated and compressed to conditions at which the solubility is to be determined and maintained at such conditions at an equilibrium cell, for 30 min, to ensure that equilibrium conditions are reached. After that time, water flows through the low flow velocity and long residence time equilibrium cell. The system pressure was maintained with a syringe pump. The equilibrium cell consisted of a 250 cm^3 cylinder. The saturated sub or supercritical water was depressurized through a metering valve. The dissolution of the inorganic salt in water at ambient pressure was collected in a bottle and the dissolved solute quantified by classical chemical SO_4^{2-} analysis. A schematic diagram of the apparatus is shown in Figure 1.

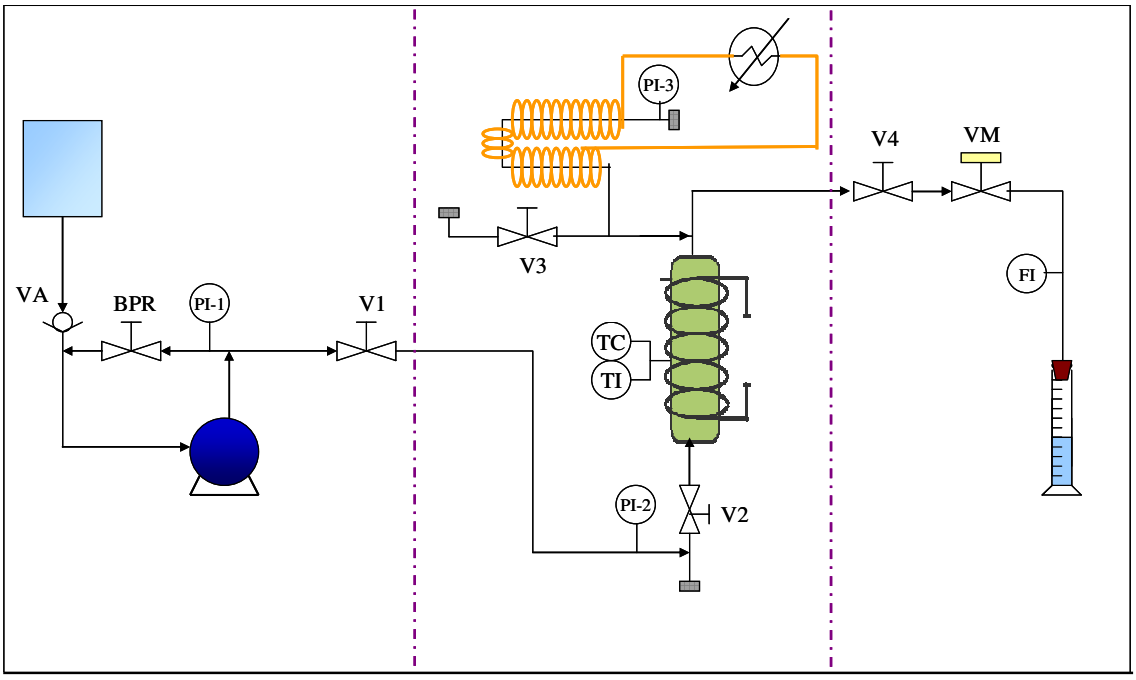

Figure 1. Schematic diagram of the solubility apparatus.

2.2 Materials

The sodium sulfate, Na_2SO_4, and the aluminium sulfate, $Al_2(SO_4)_3{\cdot}18H_2O$, were reagent grade chemicals manufactured by PANREAC. Both of them had a stated purity of 99 mass %. The water was laboratory distilled and deionized.

3. Results and Discussion

The reliability of the experimental procedure was first tested by measuring the solubility of sodium sulfate at two points and comparing it with values reported in the literature. Table 1 shows the results of these experiments. Since the measured solubilities are in good agreement with the literature values (Khan and Rogak, 2004) it may be stated that the experimental procedure for determining the solubility of sulfates is valid. Therefore, it may be used to determine the solubility of aluminium sulfate.

Table 1. Comparison of sodium sulfate solubilities from this work with those from the literature.

		Solubility (ppm)	
T (ºC)	P(atm)	This work	Khan and Rogak, 2004
382	244	802	850
397	243	5	4

For the investigation of the effect of pressure and temperature, the two variables affecting the aluminium sulfate solubility, a Central Composite Design was carried out. In this design there are five experimentation levels: +1, -1, +α, -α, and 0, where 0 corresponds to centre-point and $\alpha=2^{n/4}$, being n=number of variables=2.

For the purpose of analyzing the results, the factors were coded as X_1 and X_2 according to the following equations:

$$X_1 = (P - 218) / 50 \quad (1)$$

$$X_2 = (T - 374) / 20 \quad (2)$$

The 2-Factor Central Composite Design matrix and the values of the responses are shown in Table 2. As can be seen, 12 experiments were necessary: 2^n factorial experiments , 2n star point experiments and four experiments in the centre point. They were carried out in a random order according to the values given in Table 2.

Table 2. The 2-Factor Central Composite Design Matrix and the results for aluminium sulfate solubility.

Experiment Number	Experiment Order	Factor levels		Coded factors		Solublity (ppm)
		P (atm)	T (ºC)	X_1	X_2	
1	8	168	354	-1	-1	267
2	7	268	354	1	-1	486
3	5	168	394	-1	1	324
4	4	268	394	1	1	540
5	1	148	374	-1,41	0	260
6	2	288	374	1,41	0	420
7	12	218	346	0	-1,41	336
8	3	218	402	0	1,41	436
9	6	218	374	0	0	430
10	11	218	374	0	0	287
11	10	218	374	0	0	380
12	9	218	374	0	0	397

The use of the Central Composite Design permits us to express the cell concentration as a polynomial model of the form:

$$Y = a_0 + a_1X_1 + a_2X_2 + a_{11} X_1^2 + a_{22} X_2^2 + a_{12} X_1X_2 \quad (3)$$

where a_0 is the average value of the responses; a_1 and a_2, the temperature and the pressure main effects divided by 2, respectively; and a_{12}, half of the value of the pressure-temperature interaction.

Then, once calculated the parameters of Equation (3), the response funtion was obtained:

$$Y = 403,2 + 111,6\ X_1 + 31,6\ X_2 + 9,5\ X_1^2 - 8,3\ X_2^2 - 0,7\ X_1X_2 \quad (4)$$

where Y is the aluminium sulfate solubility (expressed in ppm), and X_1 and X_2 the coded values of the factors as given by Equations (1) and (2).

Equation (4) fits all data with an error less than 6.4%, indicating good agreement between experimental values and the empirical model.

The experimental solubility data are shown graphically as a funtion of temperature in Figure 2. It can be seen that the solubility of aluminium sulfate varies from 260 to 584 ppm for conditions ranging between 350–400°C and 150–290 atm. It can also be observed in such figure that the solubility increases with increasing pressure, at constant temperature, and with increasing temperature at constant pressure.

These results may be explained by considering that the solvent power of a supercritical fluid mainly depends on its density and that the effect of pressure and temperature on this variable is similar to that found for the salt solubility, i.e., it increases with increasing pressure, at constant temperature, and with increasing temperature at constant pressure.

Finally, it should be noticed that the experimental results obtained cover a wide range of experimental conditions and fill the gap in the information available in the literature. Very few measurements in the water critical region were found for sodium sulfate. Furthermore, the solubility of aluminium sulfate has been determined for the first time at conditions around the critical point of water.

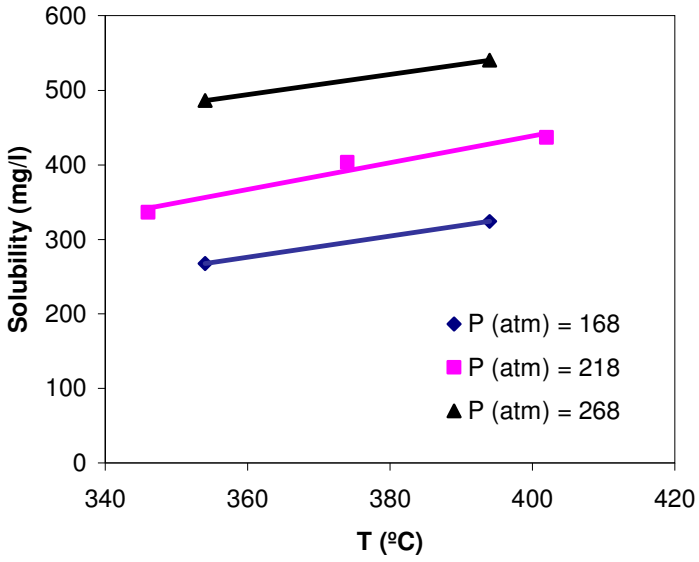

Figure 1. Solubility of aluminium sulfate as a function of temperature.

References

Doraiswami, L.K., Sharma, M.M. (1984). *Heterogeneous Reactions: Analysis, Examples and Reactor Design*, Volume 2, Wiley, New York.

Wang, J., Han, S., Wei, F., Yu, Z., Jin, Y. (1997). An axial dispersion model for gas-liquid reactors based on penetration theory. *Chemical Engineering and Processing* 36, 291-299.

Galobardes, J., Van Hare, D., Rogers, L. (1981) Solubility of sodium chloride in Dry Steam. *J. Chem. Eng. Data* 26, 363-366.

William, T.W., Gloyna, E.F. (1995) Solubility of Potassium Hydroxide and Potassium Phosphate in Supercritical Water J. Chem. Eng. Data 40, 968 – 973.

Khan, M.S., Rogak, S.N. (2004) Solubility of Na_2SO_4, Na_2CO_3 and their mixture in supercritical water. *J. of Supercrit. Fluids,* 30, 359-373.

Acknowledgements

The authors gratefully acknowledge to MMAM and MCyT financial support to this work through projects 096/2006/3-11.3 and CMT 2006-10105, respectively.

Proceedings of the 10th International Chemical and
Biological Engineering Conference - CHEMPOR 2008
Braga, Portugal, September 4-6, 2008
E.C. Ferreira and M. Mota (Eds.)

Generation of Pharmaceutical Cocrystals using Supercritical Fluid Technology

Luis Padrela, Miguel Rodrigues, Sitaram P. Velaga[1*], Henrique A. Matos, Edmundo Gomes de Azevedo[*]
Department of Chemical and Biological Engineering
Instituto Superior Técnico, Av. Rovisco Pais, 1049-001 Lisboa, Portugal
[1] Department of Health Science, Luleå University of Technology,
S-971 87 Luleå, Sweden.

Keywords: crystal engineering; supercritical fluids; microparticles; theophylline; pharmaceutical cocrystals
Topic: Sustainable process-product development through green chemistry.

Abstract

Supercritical fluid technology has been used together with crystal engineering approaches to produce cocrystals. Theophylline (TPL) cocrystals, using the FDA-approved sweetener saccharin (SAC) as a cocrystal former, were generated from ethanol and THF solutions by an Atomization and Anti-solvent (AAS) technique. In this process, high pressure N_2 and CO_2 have been used as supercritical media. The theophylline-saccharin (TPL-SAC) cocrystals morphology was analysed by SEM (Scanning Electron Microscopy) and the potential cocrystalline phase was characterized by DSC (Differential Scanning Calorimetry) and PXRD (Powder X-Ray Difraction) and Fourier Transform-Raman (FT-Raman).

1. Introduction

Bioavailability of an active pharmaceutical ingredient (API), the amount of the intact drug that reaches systemic blood circulation, relates to its aqueous solubility. Some fundamental strategies in improving the aqueous solubility or manipulation of technical properties of drugs include manipulation of solid state structure (polymorph changes or amorphous form), formation of a salt, for liquid drugs adjustment of pH of the solution. Drug delivery technologies, modifying chemical or mechanical environment surrounding the drug molecule, or physically altering the macromolecular characteristics of aggregated particles, have traditionally been considered for improving the solubility of drug substances.

Pharmaceutical cocrystallization is a relatively recent technology which has gained widespread attention for offering an alternative platform in improving the physicochemical properties of API's (e.g., solubility, hygroscopicity and tabletting properties) through the development of new class of crystalline solids, called pharmaceutical cocrystals (Almarsson and Zaworotko, 2004). Cocrystals, also referred as crystalline molecular complexes, may be defined as materials which contain two or more discrete molecular entities in the crystal lattice (Trask and Jones, 2005), incorporating pharmaceutically acceptable guest molecules along with the API. In cocrystals, the API's self-assemble *via* functional groups, such as amides and carboxylic acids, with complementary functional groups of a co-crystal former, resulting in new multi-component structural forms. The choice of pharmaceutical crystalline form can be used to optimize drug

[*] Corresponding author. Tel +46-920-493924. E-mail: sitaram.velaga@ltu.se.
[*] Corresponding author. Tel + 351-21 841 9394. E-mail: egazevedo@ist.utl.pt.

properties, like solubility and dissolution rate, and so cocrystals are emerging as new alternatives (Basavoju *et al.*, 2007).

Cocrystals are often prepared by grinding or using a traditional solution crystallization approaches such as solvent evaporation, cooling or anti-solvent addition. Specifically, in addition to these traditional means of preparing cocrystals, the use of SCF's (Supercritical Fluids) offers new platform that may enhance the rate of cocrystal formation and offers a solvent free product, allowing the single-step generation of microparticles that are difficult or even impossible to obtain by traditional techniques, particularly for substances with thermal sensitivity or structure instability (Rodrigues *et al.*, 2008).

The API under consideration in the current report is theophylline, a drug commonly used in the treatment of asthma and other respiratory diseases. Cocrystallization of theophylline with dicarboxylic acids (e.g., oxalic acid, malonic acid, etc.) had been shown to improve the stability of the drug towards moisture (Trask *et al.*, 2006).

In this work we address the ability of supercritical N_2 and CO_2 for the synthesis of a recently reported theophylline-saccharin cocrystal (Lu *et al.*, 2008), using theophylline as the API and saccharin as the cocrystal former (see Figure 1).

(a) (b)

Figure 1: Chemical structures of theophylline (a) and saccharin (b).

2. Experimental

2.1. Materials

Theophylline (minimum 99% chemical purity) was purchased from BioChemika (USA) and saccharin (99.9%) from Sigma Aldrich (Sweden). Absolute ethanol (99.5%) was supplied by Panreac, THF (99.9%) by Reidel-de Haën, and carbon dioxide and nitrogen (99.998%) by Ar Líquido (Portugal).

2.2. Feed solution preparation

For TPL particle production, 50 mg (0.28 mmol) of theophylline was dissolved in 10 g of ethanol.

For TPL-SAC cocrystal production, a 1:2 mixture of theophylline (22.5 mg, 0.14 mmol) and saccharin (48.6 mg, 0.27 mmol) was dissolved in 10 g of ethanol or THF.

2.3. Particle production

The AAS apparatus was configured for the co-crystallization as described schematically in Figure 2.

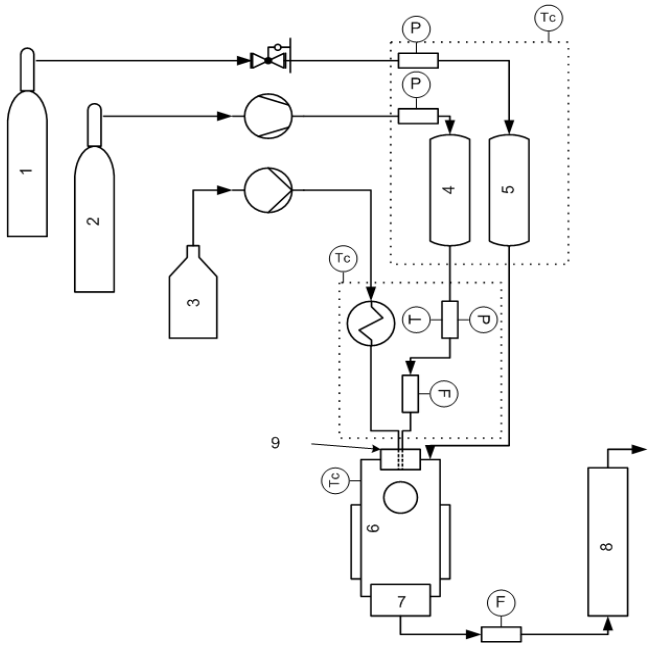

Figure 2: Schematic diagram of the AAS apparatus. 1: N_2 cylinder; 2: CO_2 cylinder; 3: liquid solution flask; 4: temperature controlled CO_2 storage cylinder; 5: temperature controlled N_2 storage cylinder; 6: precipitator; 7: filter; 8: solvent trap; 9: nozzle cap.

The solution containing both substances (theophylline and saccharin) is pumped (by a TSP metering pump, model 2396-74) through a coaxial nozzle (where it mixes with the supercritical fluid in a small mixing chamber prior to its depressurization into a precipitator vessel. The gas (N_2 or CO_2) is compressed by a Newport Compressor (model 46-13421-2).

Gas flows through the nozzle are measured by a Rheonik flowmeter (model RHM007) and pressures are measured by PX603 transducers from Omega. Temperatures are controlled in an air chamber or in a water bath by T-type thermocouples and Ero Electronic controllers (model LDS). A secondary current of dry gas (N_2) is fed into the precipitator to enhance the solvent extraction from the particles. The particles are collected in a filter at the precipitator exit.

A smaller nozzle orifice was used for CO_2 processing to limit the CO_2 flow rate and nozzle freezing due to strong depressurizations. A nozzle with a 200 μm orifice was used in the experiments with N_2 whereas a nozzle with a 80 μm orifice was used in the experiment with CO_2.

2.4. Particle characterization

The particle size and morphology were examined by SEM (Philips XL30, The Netherlands). Particles of representative samples were gold sputtered in an argon atmosphere at room temperature before the examination.

Thermal analyses (DSC) of the samples were performed on a Thermal Advantage DSC Q1000 V9.8 (TA instruments-Waters, LLC) which was calibrated for temperature and cell constants using indium and sapphire. Samples (1-2 mg) were crimped in non-hermetic aluminium pans and scanned at 10°C/min under a dry nitrogen purge (50 ml/min).

The PXRD patterns were collected on a Siemens DIFFRACplus 5000 powder diffractometer (tube voltage 40 KV and current 40 mA) with Cu Kα radiation (1.54056 Å). Each sample was

scanned between 5º and 50º 2θ with a step size of 0.01º. The instrument had previously been calibrated using a silicon standard.

The Raman analysis (Perkin Elmer NIR FT-Raman 1700X spectrometer equipped with InGaAs detector) was also performed. However, the results are not presented here.

3. Results and discussion

3.1. Particle morphology

The morphology of the processed particles showed some differences between theophylline and TPL-SAC cocrystals: the former having plate-shape morphology and the latter with a more spherical form (Figure 3). However, the morphology of TPL-SAC cocrystals was not affected by the varying processing conditions in AAS (Table 1).

Table 1. Experimental conditions for particle production. *P* is the pressure before the nozzle; *t* is the temperature in the mixing chamber; *R* is the volumetric flow-rate ratio of the aqueous feed to the supercritical fluid; t_{max} is the sample melting point; $\Delta_{fus}h$ is the enthalpy of fusion. TPL sample corresponds to the pure processed theophylline; TPL-SAC 1 to 5 correspond to processed theophylline-saccharin cocrystals under different experimental conditions.

Reference samples	Supercritical Fluid	*P* (MPa)	*t* (ºC)	Solvent	*R* (mL/NL)*	Melting Point t_{max} (ºC)	$\Delta_{fus}h$ (J/g)
TPL	N_2	12.8	60	Ethanol	0.11	272.6 ± 0.1	155.2 ± 7.2
TPL-SAC 1	N_2	8.0	50	Ethanol	0.04	197.7 ± 0.2	133.9 ± 12.0
TPL-SAC 2	N_2	8.0	50	THF	0.04	197.8 ± 0.2	124.5 ± 4.1
TPL-SAC 3	N_2	11.8	50	Ethanol	0.06	197.8 ± 0.3	129.0 ± 3.5
TPL-SAC 4	N_2	12.0	50	THF	0.06	197.6 ± 0.1	129.7 ± 3.1
TPL-SAC 5	CO_2	8.0	50	THF	0.07	197.5 ± 0.1	110.0 ± 11.7

*NL = Normal Liter (1 L of CO_2 at 1 atm and 293 K or 1.8 g of CO_2).

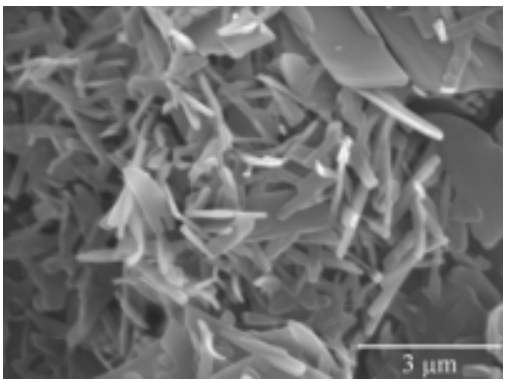

(a)

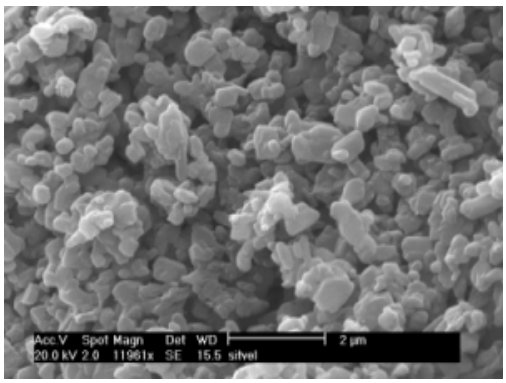

(b)

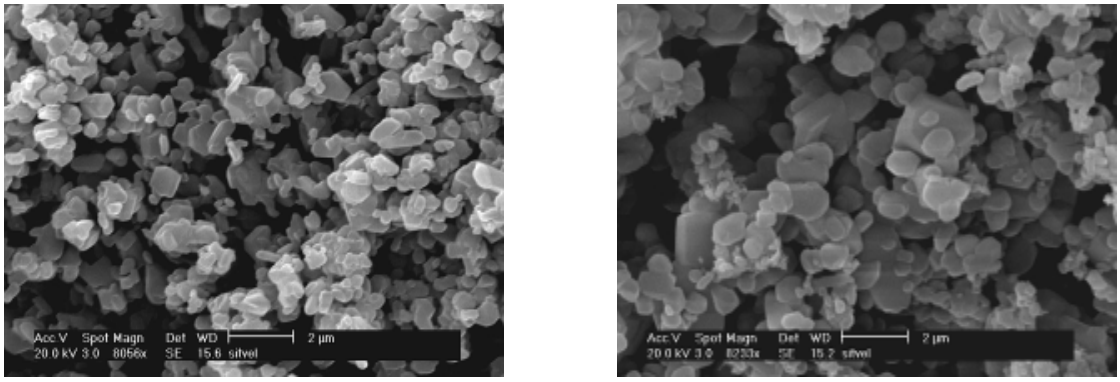

(c) (d)

Figure 3: SEM images of AAS processed samples: (a) TPL; (b) TPL-SAC 1; (c) TPL-SAC 2; (d) TPL-SAC 5.

3.2. Cocrystalline solid state characterization

Cocrystalline phase characterization and identification was carried out using classical solid state characterization techniques such as DSC, PXRD and Raman (not presented). As can be seen in Figure 4, TPL-SAC cocrystals have a single melting transition at ~197.6ºC that is different from those of the corresponding pure components and TPL-SAC cocrystals (1:1) (produced by solvent crystallization), suggesting a new cocrystalline phase formation.

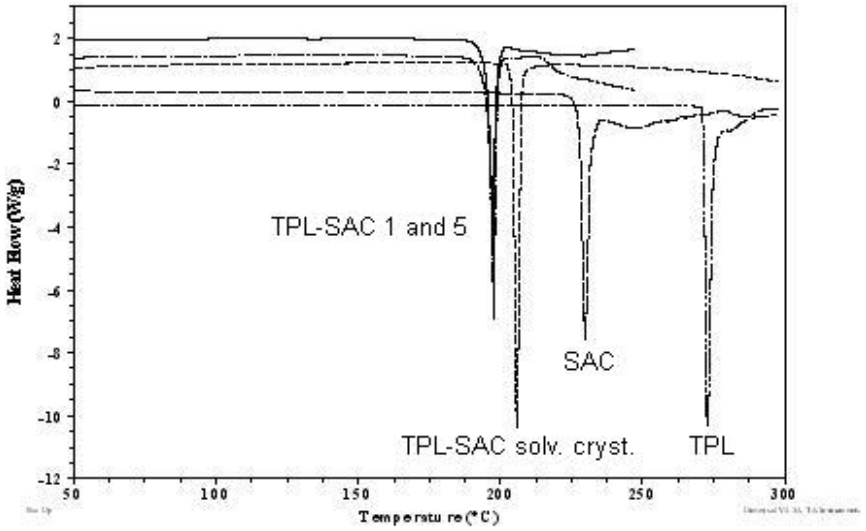

Figure 4: DSC heating curves of pure theophylline (TPL), pure saccharin (SAC), and TPL-SAC cocrystals produced by solvent crystallization and TPL-SAC cocrystal samples 1 and 5.

The powder X-ray diffraction (PXRD) pattern of TPL-SAC cocrystals (TPL-SAC sample 1) showed distinct peaks compared to the crystalline TPL (anhydrate or hydrate), SAC and reported TPL-SAC cocrystals (1:1). PXRD analysis together with FT-Raman (not presented) strongly suggests the formation of a new cocrystalline (possibly with 1:2 stoichiometry) or polymorphic form of 1:1 TPL-SAC cocrystal. Our current efforts in obtaining pure crystals of this new phase and a follow-up single crystal X-ray study (including the simulated XPRD pattern) will hopefully confirm the true nature of the cocrystalline phase.

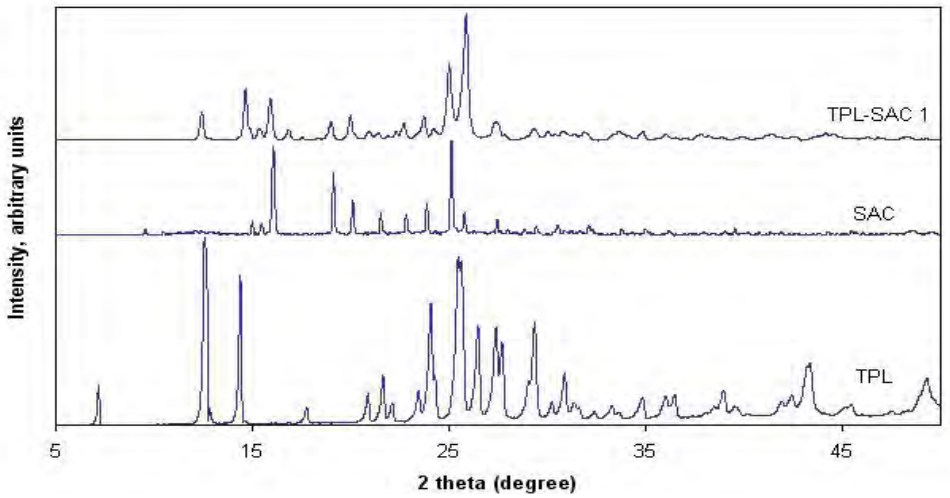

Figure 5: PXRD pattern of pure theophylline (TPL), saccharin (SAC) and TPL-SAC 1 cocrystal sample.

4. Conclusions

Pharmaceutical cocrystal micro- and nanoparticles can be produced using SCF's by AAS process and to our knowledge this is a first report on the topic. The cocrystal formed between theophylline and saccharin using a 1:2 molar ratio, is most likely a new cocrystalline phase with a distinct morphology compared to the pure processed theophylline.

Further work is currently in progress for extensive characterization of this cocrystal and analysis of its physicochemical properties, particularly its stability under relative humidity conditions. In addition, other cocrystal systems are under investigation towards an in-depth understanding of the cocrystal formation mechanism in supercritical fluids.

Acknowledgements

The authors are grateful for financial support to FCT (Project PPCDT/EQU/55911/2004) and E.U. Program FEDER. S. P. V. is thankful to Swedish Research Council (VR) and Kempestiftelserna for financial support and instrumental grant, respectively.

References

Almarsson, O., Zaworotko, M. J. (2004). *Crystal engineering of the composition of pharmaceutical phases. Do pharmaceutical co-crystals represent a new path to improved medicines?*, Chem. Comm., 17: 1889-1896.

Basavoju, S., Bostrom, D., Velaga, S. P. (2007). *Indomethacin-saccharin cocrystal: design, synthesis and preliminary pharmaceutical characterization*, Pharm. Res., 25: 530-541.

Lu, E., Rodríguez-Hornedo, N., Suryanarayanan, R. (2008). *A rapid thermal method for cocrystal screening*, Cryst. Eng. Comm., 10: 665-668.

Rodrigues, M. A., Padrela, L., Li, J., Almeida, A., Matos, H. A., Azevedo, E. G. (2008). *Anti-solvent effect in the production of lysozyme nano- and microparticles by supercritical fluid-assisted atomization processes*, J. Supercrit. Fluids, submitted.

Trask, A. V., Jones, W. (2005). *Crystal engineering of organic cocrystals by the solid-state grinding approach*, Top. Curr. Chem., 204: 41-70.

Trask, A. V., Motherwell, W. D. S., Jones, W. (2006). *Physical stability enhancement of theophylline via cocrystallization*, Int. J. Pharm., 320: 114-123.

Proceedings of the 10th International Chemical and
Biological Engineering Conference - CHEMPOR 2008
Braga, Portugal, September 4-6, 2008
E.C. Ferreira and M. Mota (Eds.)

CO_2 capture with CaO / MCM-41 materials

Josefa Fernández*, Fernando González, Carmen Pesquera, Carmen Blanco and Mª Josefina Renedo
Chemical Engineering and Inorganic Chemistry Department, ETSIIyT, University of Cantabria, Avda. de los Castros s/n, 39005 Santander, Spain

Keywords: CO_2 capture, CaO, MCM-41, Temperature Programmed Desorption (TPD)
Topic: Sustainable process-product development through green chemistry.

Abstract

CaO / MCM-41 sorbents (2.5, 5 and 10% in weight of CaO) were prepared by mixing raw materials in water at room temperature and they were characterized and tested as CO_2 adsorbents at low temperature (50ºC). TPD experiments carried out after exposition of the sorbents to CO_2 showed that the sorbents capture CO_2 at this low temperature, and that gas is mainly desorbed near 200ºC (CO_2 adsorbed). The gas retention at this low temperature is slow, being necesary near 18 hours to achieve the maximum capture, that is obtained with the 2.5% CaO / MCM-41 sorbent (9.8 mg CO_2 / g sorbent). The maximum CO_2 capture at 200ºC decreases at values of 1.3 to 2.1 mg CO_2 / g depending on the sorbent used. Five cycles of adsorption at 50ºC and desorption up to 550ºC were carried out with all the sorbents, founding reproducibility in the capture higher than 85%, better than that obtained with CaO, which normally captures CO_2 at higher temperatures as $CaCO_3$ and experiments a much higher loss-in-capacity.

Introduction

In the short term, fossil fuels will continue to be the main energy supply, and technologies associated with CO_2 capture and storage are increasingly considered to achieve these emission reductions (IPPC Special Report, 2005). Developed post-combustion technology consists in the flue gas absorption in an aqueous solutions with amines. Adsorption at low temperatures is considered one of the potential alternatives to absorption processes, with added advantages, and the development of adsorbents with a high CO_2 selectivity and adsorption capacity is needed. Modified carbons, zeolites, mesoporous materials, metal oxides and amines supported have been tested as adsorbents, but no work has been done by using calcium bases supported on MCM-41 materials.

The aim of this work was to study the carbon dioxide adsorption of sorbents prepared by aqueous mixture at room temperature of CaO and a MCM-41 support. Temperature-programmed desorption (TPD) analysis of these materials previously treated with CO_2 was used. The influence of time of contact, percentage of CO_2 in the flow gas and temperature of contact in the adsorption were studied. The behaviour in consecutive adsorption-desorption cycles was also tested in order to check the stability of the adsorbents, comparing to a commercial CaO adsorbent.

Materials and methods

MCM-41 material used as support was prepared with two silicon sources, heated under reflux and calcined at 550ºC (Blanco et al., 2004). The molar composition of the gel was: 1.00 SiO_2: 0.25 Na_2SiO_3: 0.25 CTMABr:0.10 TMAOH:100 H_2O. The CaO /MCM-41 sorbents were prepared at the same conditions that CaO/smectite sorbents (Renedo et

* Corresponding author. Tel + 34-42-202026. E-mail:fernandj@unican.es

al., 2006) by mixing at room temperature CaO with distillate water, adding the MCM-41 support and stirring for 30 minutes, filtering and drying at 110ºC to constant weight. The weight percentage of CaO /support in the sorbents prepared was 2.5%, 5% and 10% and the water to solid ratio was 10.

The prepared sorbents were characterized by determining their BET specific surface area and pore size distribution by N_2 adsorption in a Micromerics ASAP-2000 apparatus.

Experiments of CO_2 adsorption and desoption were performed by using an AutoChem II 2920 equip. Initially, the sample was outgassed in He flow by thermal treatment from room temperature to 550ºC. After being cooled to the temperature at which adsorption was carried out (50 to 200ºC) the adsorbent material was contacted to a mixture of CO_2 in He (10% normally, but 50% was also checked) for times varying from 30 minutes to 24 hours. The reversible adsorbed CO_2 was removed by treatment of the sample in He flow, normally for 30 minutes at the adsorption temperature. Then, Temperature Programmed Desorption (TPD) experiments were carried out by heating the sample with a ramp of 10ºC/min until 550ºC in a constant He flow. The signals obtained with a Thermal Conductivity Detector (TCD) after the TPD experiment were integrated in order to obtain the amounts of CO_2 desorbed, previous calibration of the device. To study the regenerability of the adsorbents, after holding the sample temperature at 550ºC during 30 minutes, the temperature was decreased to the initial value and the adsorption-desorption cycle repeated.

Results and Discussion

BET specific surface area of the sorbents showed a drastic reduction with respect to the MCM-41 support when $Ca(OH)_2$ (formed by hydration of the CaO) was added. This area decreased gradually as the $Ca(OH)_2$ increased (from 1085 m^2/g of the MCM-41 support to 204, 196 and 159 m^2/g in sorbents with 2.5%, 5% and 10% CaO /support respectively) The pore size distribution also evidence that the $Ca(OH)_2$ produces the closure of the pores in the mesopore range, as can be seen in figure 1, with data of the accumulated pore volume.

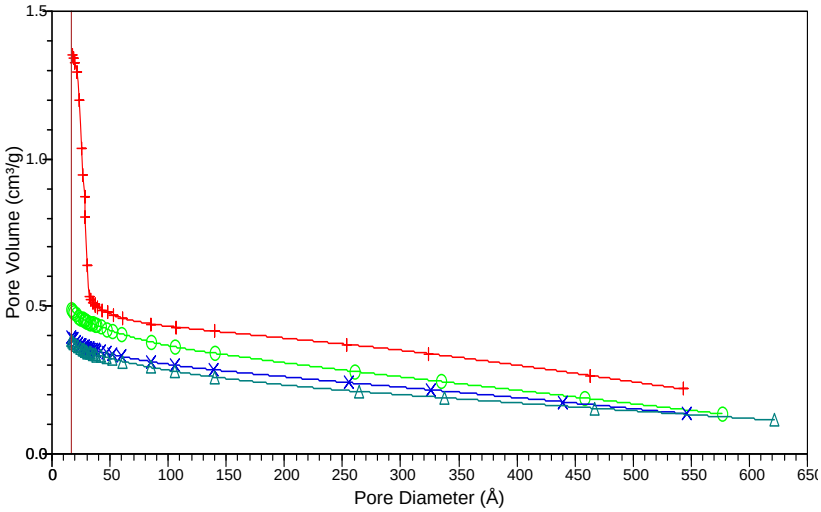

----o----2.5% CaO/MCM-41 -----Δ---- 5 % CaO/MCM-41
----x----10% CaO/MCM-4 ------¡--- MCM-41 support

Figure 1. Accumulated Pore Volume for the prepared sorbents and the MCM-41 support.

In order to maintain the structure of the support, prepared by calcination at 550ºC, sorbents were treated in Helium flow up to 550ºC. It was proved previously that CO_2 is not retained in these sorbents as $CaCO_3$, which decomposes at 625ºC.

Figure 2 shows the results of TPD experiments obtained with 2.5% CaO / MCM-41 sorbent over five cycles, after 30 minutes exposition to a 10% CO_2 in He flow. Three peaks are showed, with maximums at 100ºC, 200ºC and 550ºC, being the most important peak centered at 200ºC. Similar profiles were observed by using the 5% or 10% CaO / MCM-41 sorbents, indicating that the CO_2 is adsorbed, because the desorption takes place mainly near 200ºC, at temperatures much lower than 625ºC.

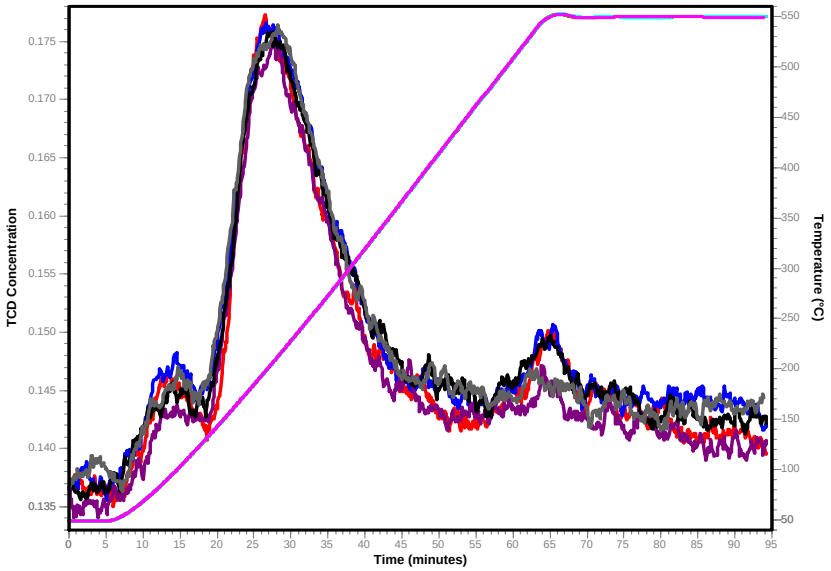

Figure 2. TPD results after adsorption for 30 minutes with 10% CO_2 in He for 2.5% CaO / MCM-41 sorbent during 5 cycles.

Data of the CO_2 amount desorbed in the different peaks for 2.5% CaO / MCM-41 sorbent, identified by the temperature of the peak maximum (100ºC, 200ºC and 550ºC) are presented in figure 3. This figure shows that the CO_2 desorption values are quite similar in the five cycles tested, mainly the peaks desorbed with maximum at 200ºC.

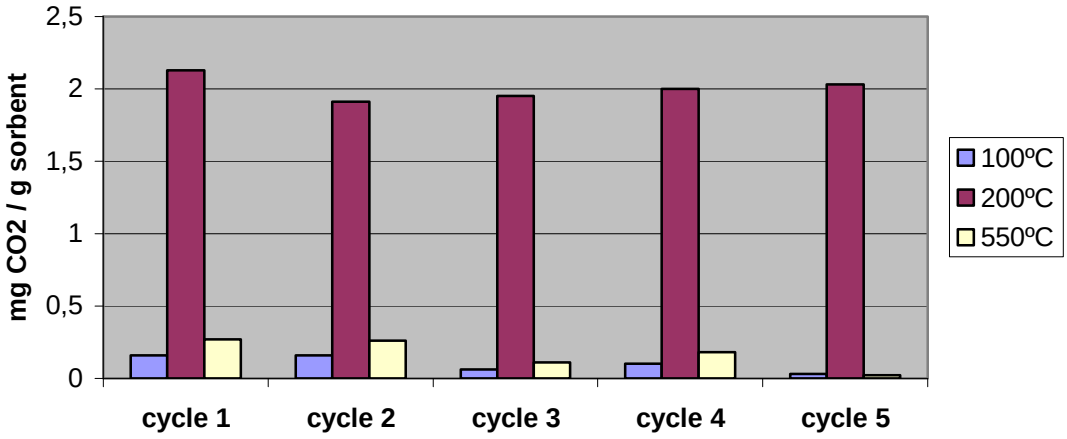

Figure 3. Milligrams of CO_2 desorbed per gram of sorbent in the different peaks for 2.5% CaO / MCM-41 sorbent during five cycles after adsorption at 50ºC with 10% CO_2 for 30 minutes.

To study the influence of the CO_2 concentration and the time of contact with CO_2 in the retention of this gas, several experiments were performed. An experiment of five cycles with a gas flow of 50% CO_2 in He for 30 minutes at 50ºC was carried out and results were compared with those obtained with 10% of CO_2 in He for 10% CaO / MCM-41 sorbent. The same value, 3.2 mg CO_2 captured / g of sorbent, was obtained in the first cycle for both conditions, being the differences in the values in the rest of the cycles lower than 2%. Therefore, no influence of the CO_2 concentration in the retention values was found.

After the exposition of 10% CaO / MCM-41 sorbent to 10% CO_2 at 50ºC in consecutive cycles for times varying from 30 to 1440 minutes (24 hours), TPD experiments were performed with reversible desorption times of 30 minutes. The time of reversible desorption was also checked, varying from 30 to 480 minutes, in the same experiment. Table 1 shows the values of the variables programmed in each cycle in this experiment.

Cycle number	Adsorption time (min)	Desorption time (min)
1	30	30
2	120	30
3	240	30
4	480	30
5	480	120
6	480	240
7	480	480
8	960	30
9	1440	30
10	30	30

Table 1. Times of adsorption and reversible desorption planned in each cycle for the experiment carried out with 10% CaO / MCM-41 sorbent, Temperature of adsorption 50ºC.

Results obtained are showed in figure 4. No influence of the reversible desorption time (cycles 4, 5, 6 and 7) is observed, being 30 minutes time enough to eliminate the reversible CO_2 adsorbed. Nevertheless the retention of CO_2 in the sorbent increases as the contact time does, as can be seen in figure 4, cycles 1 to 4, 8, 9 and 10, reaching approximately the equilibrium near 18 hours, which indicates the slow retention rate of CO_2 in the basic sorbent.

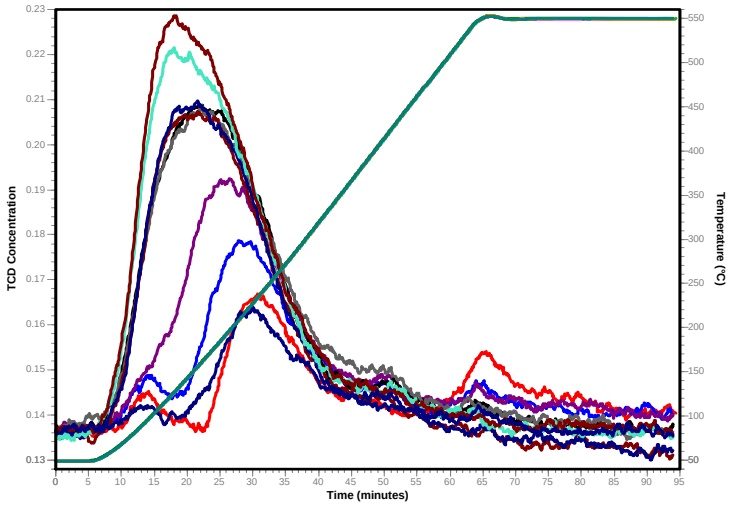

-----TCD Concentration-TPD-CO_2-10C/min(cycle 1)
-----TCD Concentration-TPD-CO_2-10C/min(cycle 2)
-----TCD Concentration-TPD-CO_2-10C/min(cycle 3)
-----TCD Concentration-TPD-CO_2-10C/min(cycle 4)
-----TCD Concentration-TPD-CO_2-10C/min(cycle 5)
-----TCD Concentration-TPD-CO_2-10C/min(cycle 6)
-----TCD Concentartion-TPD-CO_2-10C/min(cycle 7)
-----TCD Concentration-TPD-CO_2-10C/min(cycle 8)
-----TCD Concentration-TPD-CO_2-10C/min(cycle 9)
-----TCD Concentration-TPD-CO_2-10C/min(cycle 10)
-----Temperature TPD-CO_2-10C/min

Figure 4. Results of CO_2 desorption corresponding to the programmed cylces for the experiment showed in Table 1 for 10% CaO / MCM-41 sorbent after 10% CO_2 adsorption at 50ºC.

Table 2 shows the desorption values for the three sorbents prepared, obtained after 30 minutes of CO_2 adsorption at 50ºC, and the results after CO_2 adsorption at 50ºC during 18 hours, obtained in consecutive cycles for each sorbent. It can be seen that after 30 minutes of CO_2 adsorption, the 10% CaO / MCM-41 sorbent captures more CO_2 than the other sorbents. Results of the maximum CO_2 adsorption capacity (measured by the desorption data obtained in the TPD experiments after adsorption during 18 hours) show that an important increase in the CO_2 captured takes place, being the sorbents with less CaO content (2.5%) that obtain the highest capacity of capture (9.8 mg CO_2 / g). This is an important result in order to optimize the preparation of these sorbents with the minimum cost.

	CO_2 desorbed after 30 minutes of exposition to CO_2 at 50ºC (mg CO_2 / g sorbent)	**CO_2 desorbed after 18 h of exposition to CO_2 at 50ºC (mg CO_2 / g sorbent)**	**CO_2 desorbed after 18 h of exposition to CO_2 at 200ºC (mg CO_2 / g sorbent)**
2.5% CaO / MCM-41-2	2.6	9.8	1.3
5% CaO / MCM-41-2	2.8	8.6	1.6
10% CaO / MCM-41-2	3.2	8.0	2.1

Table 2. Data of the CO_2 desorbed, in mg CO_2 / g sorbent, obtained in TPD experiments after flow of 10% CO_2 in He at the temperatures and times indicated. Values at 200ºC were obtained after the cycle at 50ºC for 18 hours.

To study the influence of the temperature in the CO_2 captured, a consecutive cycle of adsorption at 200ºC during 18 hours was performed in each sorbent, after the first

exposition at 50ºC during 18 hours and desorption. Results of the TPD are also showed in Table 2. They indicate, according to the desorption profile of these sorbents, that an enormous reduction in the CO_2 retained takes place.

Figure 5 shows the desorption results obtained over five consecutive cycles of 30 minutes at 50ºC with all the prepared CaO / MCM-41sorbents. It can be observed that the reproducibility in the capture was higher than 85%. When commercial $Ca(OH)_2$ was used as sorbent, without support, CO_2 retention values were higher than those obtained with the prepared sorbents. After 30 minutes of exposition to CO_2 at 50ºC, 22 mg CO_2 / g commercial $Ca(OH)_2$ was desorbed and after 18 hours of exposition to CO_2 at 50ºC, the value was 29 mg CO_2 / g. But desorption was done up to 800ºC. These desorption values in commercial $Ca(OH)_2$ correspond mainly to the decomposition of the $CaCO_3$ formed, over 600ºC, and the loss-in-activity found was 42% in the fifth cycle of 30 minutes and 27% after the third cycle of 18 hours.

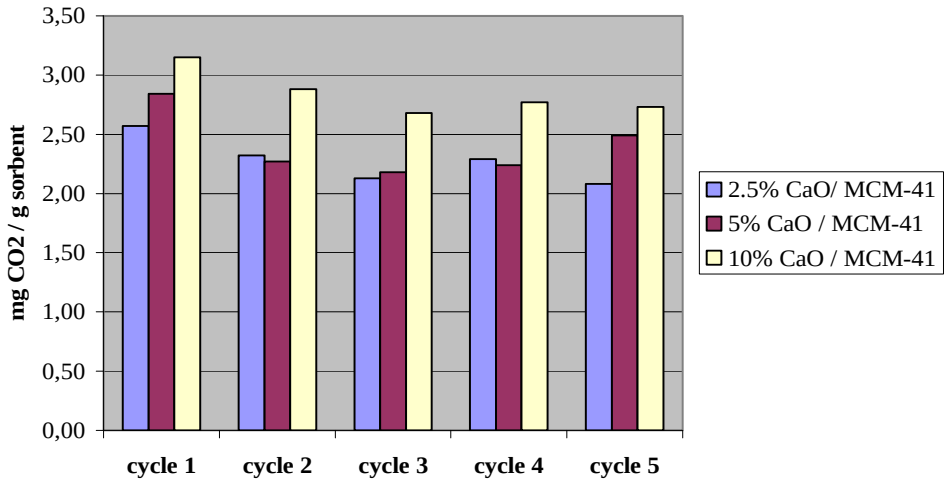

Figure 5. Desorption results (mg CO_2 / g) obtained during five consecutive cycles of 30 minutes of exposition to CO_2 at 50ºC in all the CaO / MCM-41sorbents prepared.

Apart from the slight reduction in the total CO_2 desorbed after the first cycle, the values obtained with the CaO /MCM-41 sorbents are approximately constant. This results confirm, as other author did (Feng et al., 2006) that the good distribution of CaO particles in an inert porous framework does not present the problem of loss in capacity that normally suffers calcium oxide after cycles of carbonation / decarbonation, that is an obstacle for its use in cyclic processes.

Acknowledgment
Our acknowledgment to M.C. y T. for financial support of this work under Project MAT 2006-03683.

References

IPPC Special Report on carbon dioxide capture and storage (2005). Intergovernmental panel on climate change. Cambridge University Press**.**

Blanco, C.; Pesquera C.; González, F. (2004). Synthesis and characterization of MCM-41 with different Si/Al molar ratios and different silicon sources. *Studies in Surface Science and Catalysis*, 154, 432.

Renedo, M.J.; González, F.; Pesquera, C.; Fernández, J. (2006). Study of sorbents prepared from clays and CaO or $Ca(OH)_2$ for SO_2 removal at low temperature. *Ind. Eng. Chem. Res.*, 45, 3752.

Feng, B.; Liu, W.;Li, X.; An, H. (2006). Overcoming the Problem of Loss in Capacity of Calcium Oxide in CO_2 Capture. *Energy & Fuels*, 20, 2417.

Proceedings of the 10th International Chemical and
Biological Engineering Conference - CHEMPOR 2008
Braga, Portugal, September 4-6, 2008
E.C. Ferreira and M. Mota (Eds.)

Preparation of mesoporous carbons using a porous clay heterostructured as template

Clara Santos[1], Angela Martins[1*], Ruben Elvas Leitão[1], João Pires[2], Cristina Freire[3], Ana Paula Carvalho[2]

[1]Departamento de Engenharia Química, CIEQB, Instituto Superior de Engenharia de Lisboa, Rua Conselheiro Emídio Navarro, 1, 1959-007 Lisboa, Portugal

[2]Departamento de Química e Bioquímica, CQB, Faculdade de Ciências da Universidade de Lisboa, Campo Grande C8, 1749-016, Lisboa, Portugal.

[3]REQUIMTE, Departamento de Química, Faculdade de Ciências da Universidade do Porto, Rua do Campo Alegre, 687, 4169-007, Porto, Portugal.

Keywords: Mesoporous carbons, Template synthesis, Porous Clay Heterostructure, Furfuryl alcohol.
Topic: Sustainable process product development through green chemistry (New materials & structured products).

Abstract

In this work two mesoporous carbon replicas were prepared using a porous clay heterostructure - obtained from a Portuguese natural motmorillonite - as template and furfuryl alcohol as carbon source. The samples where characterized by X-ray powder diffraction, scanning electron microscopy and N_2 adsorption at low temperature. The ash content and the pH at the point of zero charge were also determined. The previous acidification of the surface revealed to be not important since the samples prepared with and without the previous impregnation with *p*-toluenesulfonic acid presented the same textural, structural and morphological characteristics. The surface chemistry properties must also be similar since the carbons present the same pH at the point of zero charge.

1 Introduction

The extensive use of porous carbons is the natural consequence of their properties, such as high specific surface areas, large pore volumes, chemical inertness and good mechanical stability. Most carbons are primarily microporous, however there are numerous potential applications for which materials with wider pores, preferably in mesopore range, would be advantageous (Lee, 2006). In this sense, since the pioneer work of R. Ryoo *et al.* (1999), much effort has been made concerning the preparation of Ordered Mesoporous Carbons (OMCs). Such materials are important for applications in emergent areas such as energy storage in double-layer supercapacitors, in addition to the common applications as adsorbents and catalyst supports (Lee, 2006).

The synthesis of OMCs is generally made by the templating approach. The main steps are: i) infiltration of the porous structure of a mesostructured inorganic material (template) by the carbon precursor (usually a polymer or pre-polymer); ii) polymerization of the infiltrated substance; iii) carbonization of the nano-composites formed and iv) elimination of the template. Depending on the type of mesostructured silica used as template, carbons with different structures and pore sizes can be prepared (Fuertes, 2004).

Although silicas of MCM and SBA families have been extensively employed as templates, the use of other inorganic matrixes has also been envisaged. In fact, in the literature there are some studies where clay based solids or zeolite frameworks were used, as is the case of the work developed by D. Nguyen-Thanh and T.J. Bandosz (2006) that, to our knowledge, is

* Angela Martins. Fax nº: 003518317267, e-mail: amartins@deq.isel.ipl.pt

the only study were the potentialities as template of a porous clay heterostructured (PCH) for mesoporous carbons preparation were evaluated.

In the present study a new approach of templated synthesis of mesoporous carbons was tried, using a PCH as inorganic matrix and furfuryl alcohol as carbon precursor. The preparation procedure was monitorized by the results of nitrogen adsorption at – 196 ºC. The carbons were also characterized by X-ray powder diffraction, scanning electron microscopy, quantification of the ash content and evaluation of the pH of the point of zero charge.

2 Experimental

The PCH used was prepared from a natural Portuguese montmorillonite from Benavila (Alentejo, Portugal). Briefly, the preparation procedure consisted in the intercalation of cetyltrimethylammonium bromide (Aldrich) and decylamine (Aldrich, 95%) to direct the interlamelar hydrolysis of tetraethylortosilicate (Aldrich, 98%), that will form the pillars in the galleries of the modified clay. The clay:amine:TEOS proportion used was 1:20:150. Finally, the sample was calcined at 650 ºC for 5 h with a ramp of 1 ºC min^{-1}.

Two carbon samples were prepared, CF and CF-TS, differing only in the fact that in the preparation of CF-TS a previous impregnation of the PCH with p-toluenesulfonic acid (Carlo Erba, 99%) was made. Following the conditions reported in Kim (2006), we used the proportion 4.3 mg of *p*-toluenesulfonic acid *per* g of furfuryl alcohol to be impregnated in the matrix. The purpose of this procedure was to increase the surface acidity of the solid which will catalyse the polymerization process of the carbon precursor, that is, furfuryl alcohol. The infiltration of this organic compound onto the PCH porosity was carried out by incipient wetness at room temperature, using a volume of alcohol equal to the total pore volume of the matrix. The material was then placed in a covered recipient and heated overnight at 95 ºC, after what it was carbonized in a horizontal tubular oven (Thermolyne, model 21100) at 700 ºC for 1 h, under nitrogen flow (6.7 cm^3 s^{-1}). The obtained composites are designated as CF/PCH and CF-TS/PCH. After removing the inorganic template using HF, the samples were thoroughly washed with distilled water until pH 7.

The porosity modifications promoted by the samples preparation methodology were studied by N_2 adsorption at low temperature, using an automatic apparatus ASAP2010. Before the essays the samples were outgassed at 300 ºC for 2 h under vacuum better than 10^{-2} Pa.

The ash content of the carbons was estimated by the mass residue left after the combustion of the samples in air, according to a procedure adapted from the Spanish Norm UNE 32 111. Approximately 1 g of dried carbon was heated in a furnace equipped with a Eurotherm 2416 controller according to the temperature regime: from room temperature to 500 ºC in 10 min, kept for 30 min at this temperature and then to 815 ºC in 15 min and kept for 2 h 30 min. After cooling, the residue was weighted (Mettler AE 240 analytical balance) and the ash content (mean of three essays) was estimated by dried mass of carbon. The pH of the point of zero charge (pH_{PZC}) was determined by reverse mass titration, following the method proposed by Noh and Schwarz (1989). The pH of several carbon slurries in distilled water (in %) up to 10 was measured after stirring for, at least, 24 h. The pH_{PZC} corresponds to the pH of the plateau of the curve obtained plotting the equilibrium pH as a function of solid weight fraction.

X-ray powder diffraction (XRD) patterns were obtained in a D8 Advance Bruker diffractometer with automatic data acquisition, using Cu$K\alpha$ graphite-monochromatised radiation. Data were acquire by step scanning from 0.7º to 6º 2θ, with a step size of 0.03º 2θ, a time per step of 4 s and 40 kV and 40 mA in the X-ray tube. The morphological characterization was made by scanning electron microscopy (SEM) in a Jeol Model JSM –

6301F microscope using electron secondary beams at 15 kV with samples coated with gold (coating chamber: Jeol JFC-1200).

3 Results and discussion

The determination of the ash content of carbon replicas is very important since it is an expedite method to check the matrix removal. The results obtained demonstrated that the procedure used efficiently removed the PCH since the ash content found were in the order of 0.4 %.

The N_2 isotherms at -196 ºC displayed in Fig. 1a) exemplify the evolution of porosity observed using either of the two samples preparation strategies used in this study. The curves obtained with PCH and carbon samples exhibit an important uptake at low pressures indicating the presence of a developed microporosity, associated with a mesoporous structure responsible for the continuous increase of the N_2 uptake that occurs at high relative pressures and the hysteresis loops observed. The isotherm of the carbon obtained using *p*-toluenesulfonic acid, CF-TS/PCH (not shown) practically overlaps that of CF/PCH. The composites obtained after carbonization present curves very close to a isotherm of type I according to the IUPAC classification (IUPAC, 1984). This result reveals that a fraction of the PCH microporosity, and all of its mesoporous structure, is filled with carbon after the carbonization of furfuryl alcohol. It is interesting to note that, after the removal of the inorganic matrix by HF treatment, the sample exhibits an adsorption capacity higher than that presented by the PCH used as template.

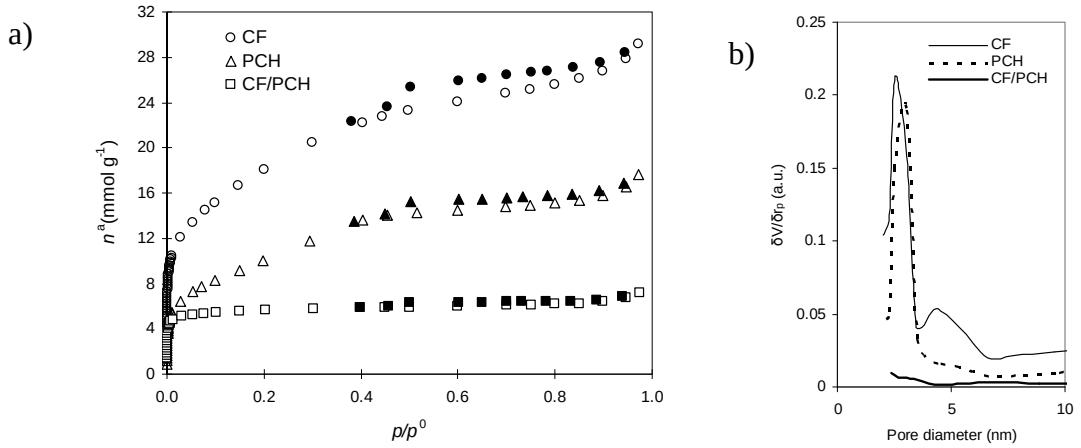

Figure 1 - Nitrogen adsorption-desorption isotherm at – 196 ºC for the samples indicated (a) and respective mesopore size distribution (b).

Table 1 presents the apparent specific surface area, S_{BET}, assessed applying the BET equation (in the range $0.05<p/p^0<0.15$) and the microporous volume, V_{micro}, obtained using the α_s method, taking as reference the isotherm reported in Rodríguez-Reinoso et al. (1987). In Table 1 the values of the the total porous volume, V_{total}, estimated from the amount of N_2 adsorbed at $p/p^0=0.95$ and the values of the mesoporous volume, V_{meso}, obtained by the difference between V_{total} and V_{micro} are also listed.

Table 1 - Textural characteristics of the samples.

Sample	S_{BET} m^2 g^{-1}	V_{micro} (α_s method) cm^3 g^{-1}	V_{meso} cm^3 g^{-1}	V_{total} (p/p^0 = 0.95) cm^3 g^{-1}
PCH	818	0.44	0.14	0.58
CF/PCH	452	-	-	0.24
CF	1469	0.64	0.34	0.98
CF-TS/PCH	428	-	-	0.24
CF-TS	1433	0.64	0.35	0.99

In line with the previous discussion based on the isotherms configuration, the values reported in Table 1 show that, the preparation of the composite materials, CF/PCH and CF-TS/PCH, resulted in the loss of 50 % of the apparent surface area and of the porous volume estimated for the template. The removal of the template leads to a very important increase of all the parameters assessed. The two carbon replicas are texturally identical and their S_{BET} and V_{total} are almost double than those presented by the starting PCH. The gain of V_{total} results of the increase of both micro and mesoporous volumes. Although in the overall process a more accentuated development of the mesoporous structure is observed, the porosity of the carbons materials is formed by, approximately, 60 % of microporores and 30 % of mesopores.

These results are different from those obtained by of D. Nguyen-Thanh and T.J. Bandosz (2006) focussed on the preparation of carbon replicas from PCH templates using sucrose as carbon source. In fact, the carbons replicas obtained by these authors present a higher mesoporous volume than that of the template used, and a smaller microporous volume. These different results seem to point out the potentialities of PCH structures to derive carbon replicas with distinct textural characteristics that can be tailored to a specific application. It must also be noted that the carbon materials obtained in the present study have both micro and mesoporous volumes higher than those reported by D. Nguyen-Thanh and T.J. Bandosz (2006)

The mesopore size distribution was made according the Broekhoff-de Boer method, in a version simplified (Lukens, 1999) with the Frenkel-Halsey-Hill equation (BdB-FHH). The curves displayed in Fig.1b show that the methodology followed permitted the preparation of carbons presenting a by-modal mesoporous size distribution, the smallest mesopores being slightly narrow than those of the PCH.

The textural characteristics of the carbons prepared with and without surface acidification (samples CF and CF-TS in Table 1) allow us to conclude that the surface acidity of the PCH is sufficient to catalyze the furfuryl alcohol polymerization and the methodology followed permitted that the replicas maintain the layered structure of the matrix in some extension.

However, this inherit of the templated structural features was not revealed in the X-ray diffraction analysis, as can be verified in the patterns shown in Fig. 2. SEM images of the PCH and the two carbon replicas prepared (Fig. 3) also show morphological changes upon the materials preparation. The particles dimensions of the carbon materials are smaller than those of the template.

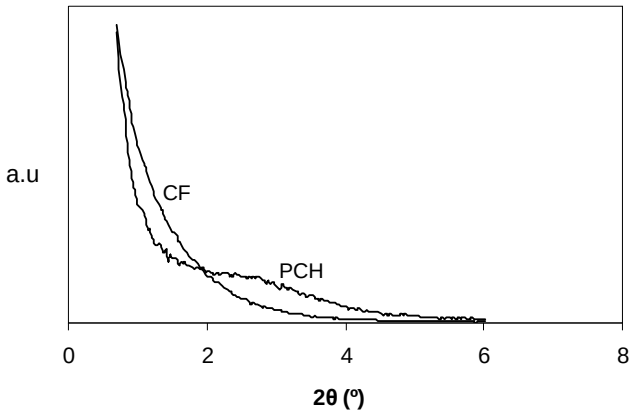

Figure 2 – XRD patterns for PCH silica template and carbon sample CF.

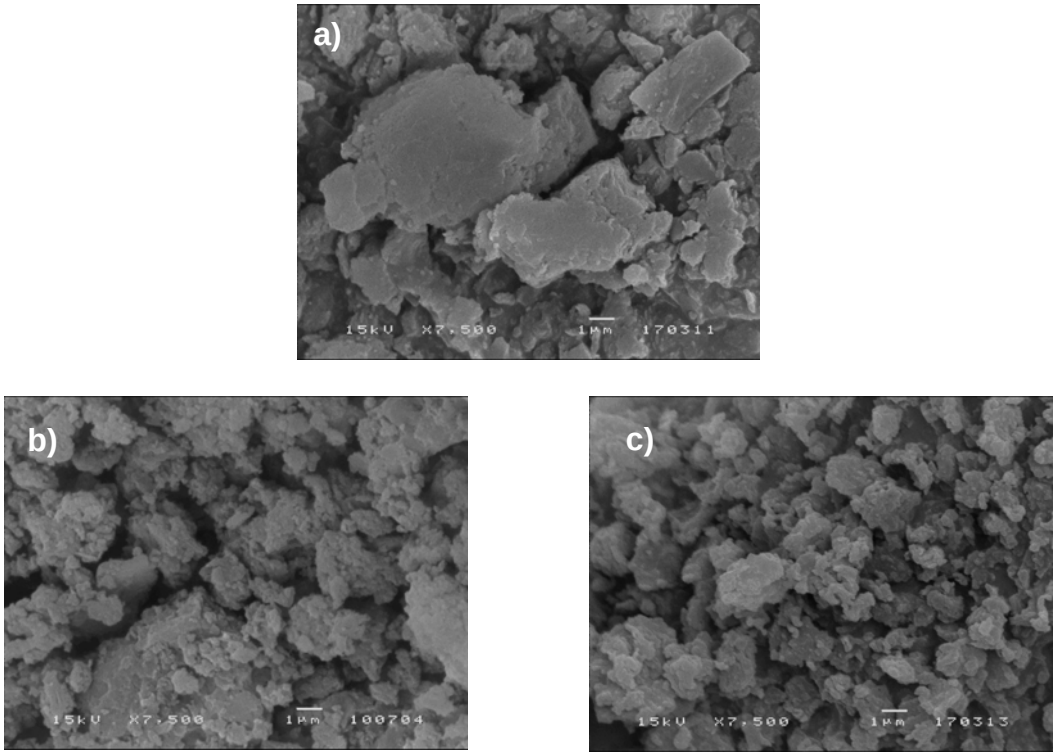

Figure 3 – Scanning electron microscopy images of: a) PCH; b) CF and c) CF-TS.

To have a first assess of the surface chemistry properties, the pH_{PZC} of the carbons was determined. No difference between the two samples was observed, since both presented a pH_{PZC} of 3.5, that is, both are acidic carbons. This result reveals once again that the previous impregnation with *p*-toluenesulfonic acid is not reflected in the carbons characteristics. The acidic properties of the surface are important for several applications, namely as adsorbents, and is usually obtained only after post-preparation treatments, what permits to envisage a large number of potential applictions for these materials.

4 Conclusions

The results obtained in this study reveal that the surface acidity of the PCH was sufficient to catalyze the furfuryl alcohol (carbon precursor) polymerization. In fact, none of the characteristics evaluated distinguished the carbon replica prepared with the previous acidification of the matrix surface from that where the furfuryl alcohol was directly impregnated. The samples obtained are characterized by an acid surface and a developed microporosity associated to a triple mesoporous volume than that presented by the starting PCH. A bi-modal mesoporous size distribution was obtained; the smallest mesopores being slightly narrow than those of the PCH. The textural and surface chemistry properties of the carbon prepared make them very promising materials, not only for adsorption purposes but also as catalysts or catalysts supports. In this sense, in the near future these materials could be used as supports for homogeneous catalysts.

Acknowledgments

This work was supported by 'Fundação para a Ciência e Tecnologia' (Portugal) through project PTDCI/CTM/65718/2006

References

Fuertes, A.B., (2004). Synthesis of ordered nanoporous carbons of tunable mesopore size by templating SBA-15 silica materials. Microporous and Mesoporous Materials, 67, 273-281.

Gregg, S.J., Sing, K.S.W., (1982). Adsorption Surface Area and Porosity. Academic Press: London.
IUPAC (1994). Recommendations for the characterization of porous solids, Pure and Applied Chemistry, 66, 1739-1758.
Lee, J., Kim, J., Hyeon, T., (2006). Recent progress in the synthesis of porous carbon materials. Advanced Materials, 18, 2073-2094.
Lukens Jr., W.J., Schimidt-Winkel, P, Zhao, D., Feng, J. Stucky, G.D., (1999). Evaluating pore sizes in mesoporous materials:a simplified standard adsorption method and a simplified Brokhoff-de Boer method. Langmuir, 15, 5403-5409.
Kim, T.-W., Solovyov, X(?)(2006). Synthesis and characterization of large-pore ordered mesoporous carbons using gyroidal silica template. Journal of Materials Chemistry, 16, 1445-1455.
Mestre, A.S., Pires, J., Nogueira, J.M.F., Carvalho, A.P., (2007). Activated carbons for the adsorption of ibuprofene. Carbon, 45, 1979-1988.
Nguyen-Thanh, D., Bandosz, T.J., (2006). Metal-loaded carbonaceous adsorbents templated from porous clay heterostructures. Microporous and Mesoporous Materials, 92, 47-55.
Noh, J.S., Schwarz, J.A., (1989). Estimation of the point of zero charge of simple oxides by mass titration. Journal of Colloid and Interface Science, 130, 157-164.
Rodríguez-Reinoso, F., Martin-Martinez, J.M., Prado-Burguete, C., McEnaney, B., (1987). A standard adsorption isotherm for the characterization of activated carbons. Journal of Physical Chemistry, 91, 515-516.
Ryoo, R., Joo, S.H., Jun, S., (1999). Synthesis of highly ordered carbon molecular sieve via template-mediated structural transformation. Physical Chemistry B, 103, 7743-7746.
Spanish Norm (1995) UNE 32 111 of October.

Proceedings of the 10th International Chemical and
Biological Engineering Conference - CHEMPOR 2008
Braga, Portugal, September 4-6, 2008
E.C. Ferreira and M. Mota (Eds.)

Influence of the preparation methodologies in the performance of Pd-Cu/AC and Pt-Cu/AC catalysts for nitrate reduction with hydrogen

Olívia Salomé G. P. Soares, José J. M. Órfão, Manuel F. R. Pereira*
Laboratório de Catálise e Materiais (LCM), Laboratório Associado LSRE/LCM,
Departamento de Engenharia Química, Faculdade de Engenharia, Universidade do Porto,
Rua Dr. Roberto Frias, 4200-465 Porto, Portugal

Keywords: nitrate reduction, activated carbon, bimetallic catalysts, water treatment.
Topic: Sustainable process-product development through green chemistry.

Abstract

The influence of calcination and reduction temperatures on the catalytic properties of Pd-Cu and Pt-Cu bimetallic catalysts supported on activated carbon for the reduction of nitrates was studied. The catalysts were prepared according to different methodologies and the respective activities and selectivities for the reduction of nitrate in water with hydrogen were assessed. It was found that the different preparation conditions lead to different catalytic activities and selectivities. For all the catalysts, the activity decreases by increasing calcination and reduction temperatures, whereas the effect on the selectivity is not uniform. In all the preparation conditions tested the Pd-Cu pair seems to be more selective for the transformation of nitrate into nitrogen.

1 Introduction

Nitrate concentrations in surface water and especially in groundwater have increased in many locations in the world, including in Europe. The catalytic reduction with hydrogen has been suggested in the literature as a promising method for nitrate removal from water without the drawbacks of the conventional methods (Pintar, 2003; Prusse and Vorlop, 2001). This process was reported for the first time by Vorlop and Tacke (1989) and consists in the reduction of nitrate towards nitrogen over bimetallic catalysts in the presence of a reducing agent. Nitrite as intermediate and ammonium as by-product are considered the main disadvantages of this process (Pintar, 2003). The activity and selectivity of the bimetallic catalysts are highly dependent on the preparation method, on the way the noble metal is promoted, on the metal/promoter ratio and on the operation conditions (Matatov-Meytal and Sheintuch, 2005). Alloying of metals may result in important changes in their activity and selectivity in catalytic reactions (Epron et al., 2002). The selection of the support is also important for this process since it has been shown that the support affects the catalysts activity and selectivity (Matatov-Meytal and Sheintuch, 2005).

2 Experimental

The active metals were supported on a commercial activated carbon NORIT GAC 1240 PLUS (ACo). The catalysts were prepared by incipient wetness co-impregnation, from aqueous solutions of the corresponding metal salts (H_2PtCl_6, $PdCl_2$, $Cu(NO_3)_2$). Then, the samples were dried at 100 ºC for 24 h. Different temperatures were selected for calcination (T_{Cal}) under a nitrogen flow for 1 h and reduction (T_{Red}) with hydrogen for 3 h. No calcined and no reduced catalysts (N_{Cal} N_{Red}) were also evaluated. The contents of noble and

* Corresponding author. Tel +351 225 081 468. E-mail: fpereira@fe.up.pt

promoter metals were maintained constant at 1%wt and 0.3%wt, respectively. The catalysts were characterized by N_2 adsorption at 77 K, XRD, TEM and XPS.

The catalytic tests were carried out in a semi-batch reactor, at room temperature and pressure, with an initial nitrate solution of 100 ppm and using hydrogen as reducing agent. CO_2 was used as a buffer (pH 5.5). In standard tests, the catalysts were in contact with an hydrogen flow during 15 min before introducing the nitrate solution in the reactor. Nitrate and nitrite concentrations were simultaneously determined by HPLC. The concentrations of ammonium ions were quantified using a convenient selective electrode. pH values were also measured.

3 Results and Discussion

3.1. Catalysts characterization

The BET surface area of the support is 869 m^2/g. Two samples, with 2%Pd-1%Cu and with 2%Pt-1%Cu (a total metal loading higher than that used in the samples tested in this work), were also characterized by N_2 adsorption, and it was verified that the textural parameters remained almost unchanged compared to the unloaded activated carbon. Therefore, it was assumed that the surface areas of the supported metal catalysts are not significantly different from the original activated carbon.

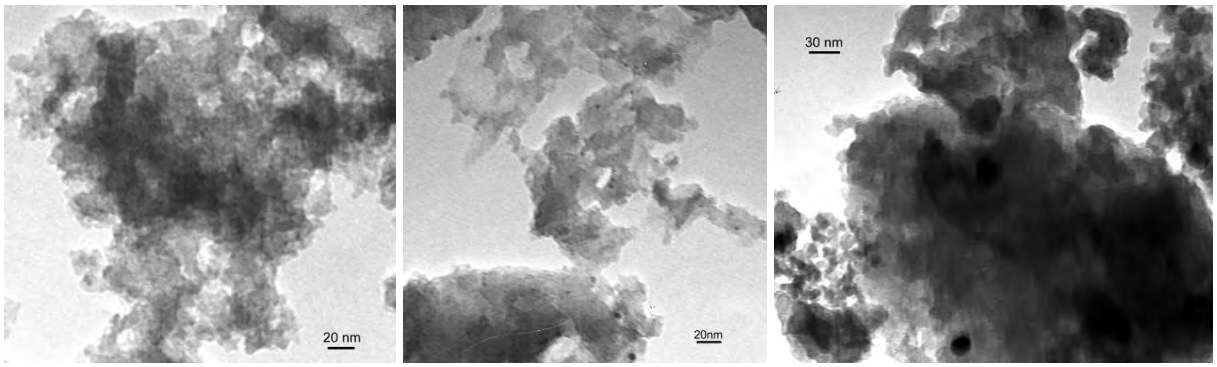

a) b) c)

Figure 1. TEM images of 1%Pd-0.3%Cu_ACo catalysts a) T_{Cal}=200ºC N_{Red}, b) T_{Cal}=200ºC T_{Red}=100ºC and c) T_{Cal}=400ºC T_{Red}=400ºC.

TEM images of the samples revealed that particle size depends on the preparation conditions. In both series (Pd-Cu and Pt-Cu) the evolution of the particle size with the temperatures used during calcination/reduction presents a similar trend (see the Pd-Cu series as an example in Figure 1). No major differences were observed in the morphology of the catalysts neither calcined nor reduced; in fact in this sample no particles can be detected, probably due to the fact that this catalyst was not heat treated and consequently no metal particles were generated. For the catalyst T_{cal}=200ºC N_{red} (Figure 1 a) a few not well defined particles can be observed. In the case of 1%Pd-0.3%Cu_ACo T_{cal}=200ºC T_{red}=100ºC (Figure 1 b) it is already possible to see some well defined particles. These observations suggest that metals are well dispersed on the support. From the distribution particle size it was observed that these catalysts mainly present particle sizes between 3 and 4 nm. For the 1%Pd-0.3%Cu_ACo catalyst with T_{cal}=400ºC T_{red}=400ºC (Figure 1 c) TEM analysis shows the presence of not only small particles in the range of 5-6nm, but also larger particles. Summarizing, from TEM images it can be concluded that an increase in the calcination and reduction temperatures causes an increase in the particle size of the crystallites.

All the catalysts were analyzed by XRD to determine the metal particle size and to identify if the metals were isolated or forming alloys. In 1%Pd-0.3%Cu_ACo and 1%Pt-0.3%Cu_ACo catalysts, XRD of the catalysts do not show any intense peak of both metals, which could be due to the low amount of metal loaded and, on the other hand, could be taken as an indication of a good metal dispersion on the support. TEM images support this conclusion. Only in the XRD spectra of the catalysts 1%Pd-0.3%Cu_ACo and 1%Pt-0.3%Cu_ACo with T_{cal}=400ºC T_{red}=400ºC significant peaks of the metals can be observed, which is also indicative that these catalysts present larger particles than those treated at lower temperatures. In addition, in these XRD spectra it can be observed that the peaks of Pd and Pt are slightly displaced to the right, which is indicative of the formation of alloys.

3.2. Catalytic tests

The effects of calcination and reduction temperatures on the catalysts activity and selectivity during the reduction of nitrates were studied.

As can be seen in Figure 2 and Figure 3 the reduction of nitrate is quite different depending on the supported metal and the preparation conditions. For all the catalysts the activity decreases by increasing the calcination and reduction temperatures. This effect is more pronounced for the pair Pd-Cu. For high calcination and reduction temperatures the Pt-Cu catalysts are more active than the Pd-Cu catalysts. However, using a low reduction temperature or not carrying out the reduction step, the Pd-Cu catalysts are the most active. The order of activity for both catalysts is similar: T_{Cal} = 200ºC N_{Red} > N_{Cal} N_{Red} > T_{Cal} = 200ºC T_{Red} = 100ºC > T_{Cal} = 200ºC T_{Red} = 200ºC > T_{Cal} = 400ºC T_{Red} = 400ºC, with nitrate conversion values after 5h of 93, 85, 79, 35 and 25%, and 77, 73, 64, 57 and 53%, respectively for the Pd-Cu and the Pt-Cu catalysts. Epron et al. (2002) studied the influence of oxidizing and reducing procedures on the activity of a Pt-Cu bimetallic catalysts supported on alumina, and also observed that the poorest activity was achieved when the catalyst was oxidized and reduced at 400 ºC. They concluded that this lower activity results from the destruction of the interactions between copper and platinum, and a subsequent migration of copper towards the alumina support. Therefore, an enrichment of platinum in the surface was noticed. This eventually decreases the catalytic activity. In the present work, the results obtained by XPS confirm an increase of the Pd content on the surface of the catalyst with the increase of calcination and reduction temperatures.

The nitrite concentration goes through a maximum (Figures 2b and 3b) and the ammonium concentration increases with the nitrate conversion (Figures 2c and 3c), indicating the occurrence of consecutive/competitive reactions. The reduced catalysts give rise to similar nitrite concentrations, which, particularly in the case of the Pt-Cu catalysts, are much lower than the concentrations obtained with the non-reduced catalysts. This can be explained by the fact that for the catalysts only calcinated or not heat treated the active sites for nitrite reduction are not completely formed. As can be seen by TEM images, no particles were observed for these catalysts, indicating a good dispersion of the metals or, most probably, that the metal is still in its salt form (especially for the non heat treated sample). Therefore, in these conditions, the metal could not be very active for nitrite reduction. It is well assumed that nitrite reduction occurs principally on monometallic sites (Epron et al., 2001; Prusse and Vorlop, 2001). A similar trend is observed for ammonia, but in this case the highest concentrations were measured for the Pd-Cu catalysts, probably because the conversion for these catalysts is higher than for the Pt-Cu catalysts.

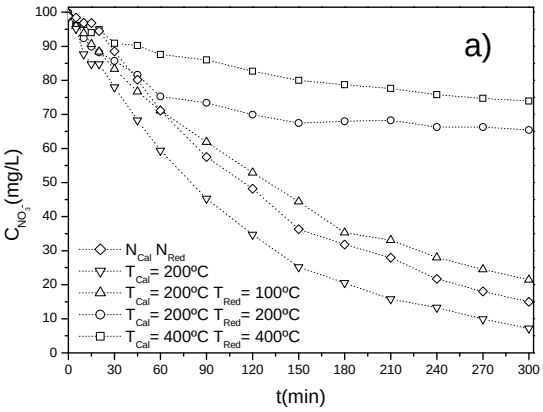

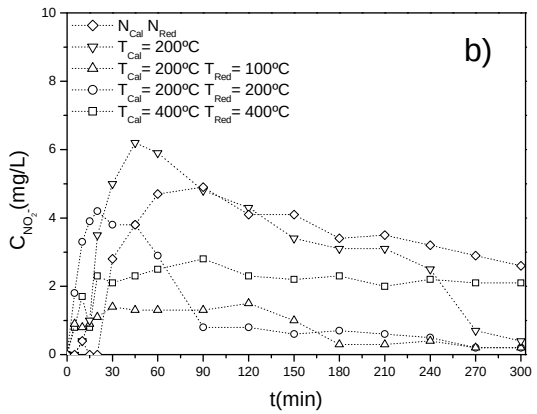

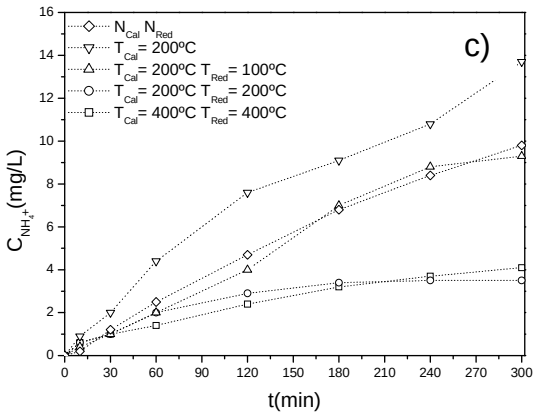

Figure 2. a) NO_3^-, b) NO_2^- and c) NH_4^+ concentrations as a function of time during nitrate reduction in the presence of 1%Pd-0.3%Cu_ACo catalysts ($C_{NO3\text{-}i}$ = 100 mg/L, catalyst = 0.5 g/L, pH = 5.5, Q_{H2} = 100 Ncm^3/min, Q_{CO2} = 100 Ncm^3/min, T = 25 ºC).

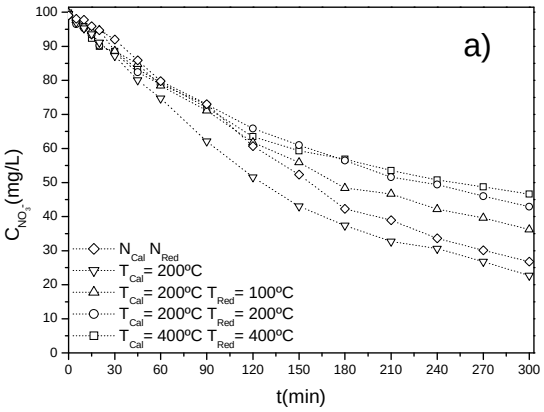

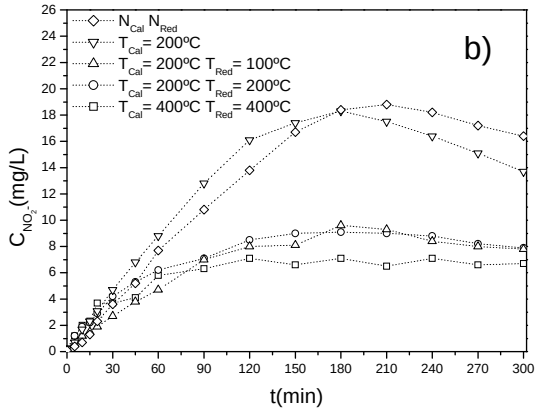

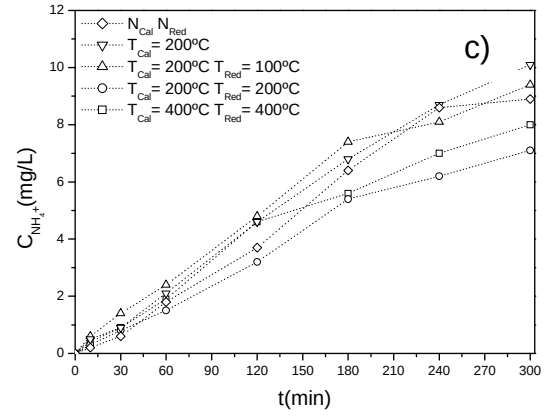

Figure 3. a) NO_3^-, b) NO_2^- and c) NH_4^+ concentrations as a function of time during nitrate reduction in the presence of 1%Pt-0.3%Cu_ACo catalysts ($C_{NO3\text{-}i}$ = 100 mg/L, catalyst = 0.5 g/L, pH = 5.5, Q_{H2} = 100 Ncm^3/min, Q_{CO2} = 100 Ncm^3/min, T = 25 ºC).

Considering that these catalysts have the same amount of metals, the different performances should be related to the metal dispersion and/or active sites. Calcination and reduction at high temperatures lead to a decrease in the nitrate conversion in comparison with the catalysts treated at low temperatures; this can be explained by the metal surface area decreasing due to alloying and/or sintering. Preparation of the catalysts at higher temperatures results in larger metal particles with an overall loss of catalytic activity.

For both catalysts the highest nitrogen selectivities were observed for the catalysts T_{Cal} = 200 ºC T_{Red} = 200 ºC, being the catalysts T_{Cal} = 400ºC T_{Red} = 400 ºC the most selective into ammonium. Nevertheless, for the Pt-Cu catalysts, the selectivities into nitrogen were not too different from sample to sample. The two catalysts corresponding to T_{Cal} = 400 ºC T_{Red} = 400 ºC present different nitrate conversions but similar high selectivities into ammonia. According to Sá et al. (2005) the decrease in the selectivity of the process with the increase of the reduction temperature, can be attributed to alloying of the metal. Yoshinaga et al. (2002) suggested that a dilution of Pd faces takes place during alloying. This leads to an increment in the number of isolated Pd atoms, which are suggested to be active sites for the ammonium formation. The pair Pd-Cu is more selective into nitrogen than the pair Pt-Cu, which presents higher selectivity into ammonia. The pair Pd-Cu is the most active but is also the most selective into nitrogen, which is the desirable end product.

To investigate the influence in the activity and in the oxidation state of the catalyst of passing a hydrogen flow during 15 min before the introduction of nitrates in water, the catalytic reduction of nitrates was performed in different conditions than those normally used. For that purpose, the catalyst (sample 1%Pd-0.3%Cu_ACo T_{Cal} = 200 ºC N_{Red}) was introduced in the reactor together with the concentrated nitrate solution, i.e. after 15 min of flowing water with hydrogen. Figure 4 shows the evolution of nitrate reduction in this experiment.

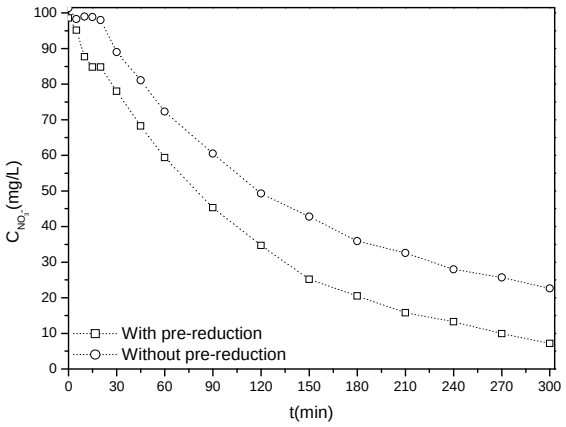

Figure 4. NO_3^- concentration as a function of time during nitrate reduction in the presence of 1%Pd-0.3%Cu/AC catalysts with and without a pre-reduction in situ (C_{NO3^-i} = 100 mg/L, catalyst = 0.5 g/L, pH = 5.5, Q_{H2} = 100 Ncm^3/min, Q_{CO2} = 100 Ncm^3/min, T = 25 ºC).

Figure 4 shows that, for the experiment without pre-reduction in situ, the reaction only begins after a period of 20 min, and a displacement in the corresponding curve relative to the observed for the experiment with pre-reduction was observed. With the exception of this initial lag, the performance of the catalysts in these experiments is similar. This induction period can be explained by the time necessary to reduce in-situ the catalyst with hydrogen and, probably, the presence of hydrogen in water allows a rearrangement of the metal phase. To confirm this hypothesis, a XPS analysis of the catalyst was carried out after and before being in contact with hydrogen during 15 min. The XPS results lead to the conclusion that the contact with hydrogen in water changes significantly the surface composition of the

catalyst. A decrease of the metal surface ratio (Pd/Cu) is observed probably due to a palladium migration towards the support and/or a migration of copper to the top of palladium. The results obtained permits to conclude that the catalyst can be reduced in-situ by hydrogen (avoiding the ex-situ reducing step).

4 Conclusions

The reduction of nitrate is quite different depending on the supported metal and the preparation conditions. For all the catalysts, the activity decreases with the increase of calcination and reduction temperatures, whereas the effect on the selectivity is not uniform. The calcination and reduction at high temperatures are inadequate due to the formation of higher metal particles. The contact with hydrogen in water has an important effect in the catalysts activity. The performance of the catalysts is maximised for low calcination and reduction temperatures. For all the preparation conditions tested the Pd-Cu pair seems to be more selective in the transformation of nitrate into nitrogen.

Acknowledgments

This work was carried out with the support of Fundação para a Ciência e a Tecnologia (FCT) under programme POCTI/FEDER (POCTI/1181) and research fellowship BD/30328/2006.

References

Epron, F., Gauthard, F., Pineda, C.,Barbier, J. (2001). Catalytic reduction of nitrate and nitrite on Pt-Cu/Al_2O_3 catalysts in aqueous solution: Role of the interaction between copper

Epron, F., Gauthard, F.,Barbier, J. (2002). Influence of oxidizing and reducing treatments on the metal-metal interactions and on the activity for nitrate reduction of a Pt-Cu bimetallic catalyst. *Applied Catalysis A-General*, 237, 253-261.and platinum in the reaction. *Journal of Catalysis*, 198, 309-318.

Matatov-Meytal, U.,Sheintuch, M. (2005). Activated carbon cloth-supported Pd-Cu catalyst: Application for continuous water denitrification. *Catalysis Today*, 102, 121-127.

Pintar, A. (2003). Catalytic processes for the purification of drinking water and industrial effluents. *Catalysis Today*, 77, 451-465.

Prusse, U., Vorlop, K. D. (2001). Supported bimetallic palladium catalysts for water-phase nitrate reduction. *Journal of Molecular Catalysis A-Chemical*, 173, 313-328.

Sá, J., Gross, S.,Vinek, H. (2005). Effect of the reducing step on the properties of Pd-Cu bimetallic catalysts used for denitration. *Applied Catalysis A-General*, 294, 226-234.

Vorlop, K. D.,Tacke, T. (1989). 1st Steps towards noble-metal catalyzed removal of nitrate and nitrite from drinking-water. *Chemie Ingenieur Technik*, 61, 836-837.

Yoshinaga, Y., Akita, T., Mikami, I.,Okuhara, T. (2002). Hydrogenation of nitrate in water to nitrogen over Pd-Cu supported on active carbon. *Journal of Catalysis*, 207, 37-45.

Proceedings of the 10th International Chemical and
Biological Engineering Conference - CHEMPOR 2008
Braga, Portugal, September 4-6, 2008
E.C. Ferreira and M. Mota (Eds.)

Modification of zeolite porosity by alkaline treatments

Viviana Paixão[1], Ana Paula Carvalho[2], Angela Martins[1]*
[1]Departamento de Engenharia Química, CIEQB, Instituto Superior de Engenharia de Lisboa, Rua Conselheiro Emídio Navarro, 1, 1959-007 Lisboa, Portugal
[2]Departamento de Química e Bioquímica, CQB, Faculdade de Ciências da Universidade de Lisboa, Campo Grande C8, 1749-016, Lisboa, Portugal.

Keywords: Zeolites, Alkaline Treatment, Desilication, Mesoporosity, Acidity.
Topic: Sustainable process product development through green chemistry (New materials & structured products).

Abstract

In this work a set of MOR, BEA, MFI and FER zeolites were submitted to alkaline treatment in order to extract silicon from the framework, resulting in the generation of mesoporosity inside the zeolite crystals. The samples where characterized by X-ray powder diffraction and scanning electron microscopy. The textural properties were studied by N_2 adsorption at low temperature. The effect of the desilication treatment on the acidity was evaluated by the model reaction of catalytic craking of n-heptane and by pyridine adsorption followed by infrared spectroscopy.

1 Introduction

Zeolites are crystalline aluminosilicates with a unique combination of properties, such as, high surface area, well-defined microporosity, high thermal stability and intrinsic acidity. These materials have been widely used in catalysis as well as in separation and purification fields (Yousheng, 2006).

The modification of the purely microporous character of zeolites is an important aspect that can be explored. In fact, a more efficient performance of zeolites as catalysts can be envisioned upon enhanced accessibility to the active sites and shortening of the diffusion path length in the micropores (Groen, 2006).

The traditional dealumination treatments, in steam or acidic medium, generally induce limited mesoporosity in zeolites and directly impact on the acidic properties due to depletion of Brönsted acidity (Groen 2006). Recently, the controlled extraction of framework silicon in alkaline medium, referred to as desilication treatment, was proposed by Groen *et al.*(2004). This treatment has resulted in a promising methodology to produce extended mesoporosity in zeolites crystals, without impacting on the acidity (Groen, 2006). In recent years, several publications on this subject have emerged, especially focused on MFI type zeolite.

2 Experimental

MOR, BEA, MFI and FER zeolites, supplied by Zeolyst, with a Si/Al ratio of 10, 12.5, 25 and 27.5, respectively, were desilicated using the optimised experimental conditions described by Groen *et al.* (2004). For example, approximately 2.64 g of MFI zeolite sample was vigorously stirred in 80 mL of 0.2 M NaOH solution at 65 ºC for 30 min. The suspension was then centrifuged and washed with distilled water. The alkaline-treated samples were converted into the H-form by three consecutive exchanges with 1 M NH_4NO_3 solution for 3 h. Then the suspension was filtered, the solid was dried overnight, and finally calcined in air flow at 500 ºC for 3 h. The samples were characterized by X-ray powder diffraction (XRD) in a Philips PW 1710 diffractometer with automatic data acquisition (APD Philips (v3.6B) software) and scanning electron microscopy (SEM) in a Jeol Model JSM – 6301F microscope

Angela Martins. Fax nº: 003518317267, e-mail: amartins@deq.isel.ipl.pt

using electron secondary beams at 15 kV and samples coated with gold (coating chamber: Jeol JFC-1200). The porosity modifications were studied by N_2 adsorption at low temperature, performed in an automatic apparatus ASAP2010. Before the essays the samples were outgassed at 300 ºC for 3 h under vacuum better than 10^{-2} Pa. The possible changes in the acidity were evaluated by the model reaction of n-heptane cracking. The reaction was performed in a continuous flow reactor at 350 ºC under a total pressure of 1 bar. The catalysts were pre-treated at 500 ºC *in situ* for 10 h under nitrogen flow of 36 L h^{-1} g^{-1}. Experiments were made for 90 min using a flow of 3 mL h^{-1} of n-heptane (molar ratio N_2/n-C_7=9) and WHSV=20.5 h^{-1}. The reaction products were analysed by an on-line gas chromatograph Hewlett-Packard 6890 series with a flame ionisation detector (FID), using a capillary column PLOT-Al_2O_3/KCl. The surface acidity of selected samples was also characterized by adsorption of pyridine followed by infrared (IR) spectroscopy. Before the experiments, the self-supported wafers were outgassed at 300 ºC for 2 h under vacuum better than 10^{-2} Pa. To estimate the strength of the acid sites, after pyridine chemisorption the samples were successively outgassed for 1.5 h at 200, 300 and 400 ºC. After each treatment the IR spectrum was registered in a Nicolet 6700 FTIR spectrometer.

3 Results and discussion

The XRD patterns of the parent and treated samples (Fig. 1) do not evidence significant losses of cristallinity during the alkaline treatment. The preservation of the long-range crystal ordering is especially evident in the case of MFI structure since the diffractograms of the parent and the treated samples are practically coincident. These results are in line with that reported by Groen *et al.* (2004) although in our study a less accentuated decrease in the peaks intensity was observed.

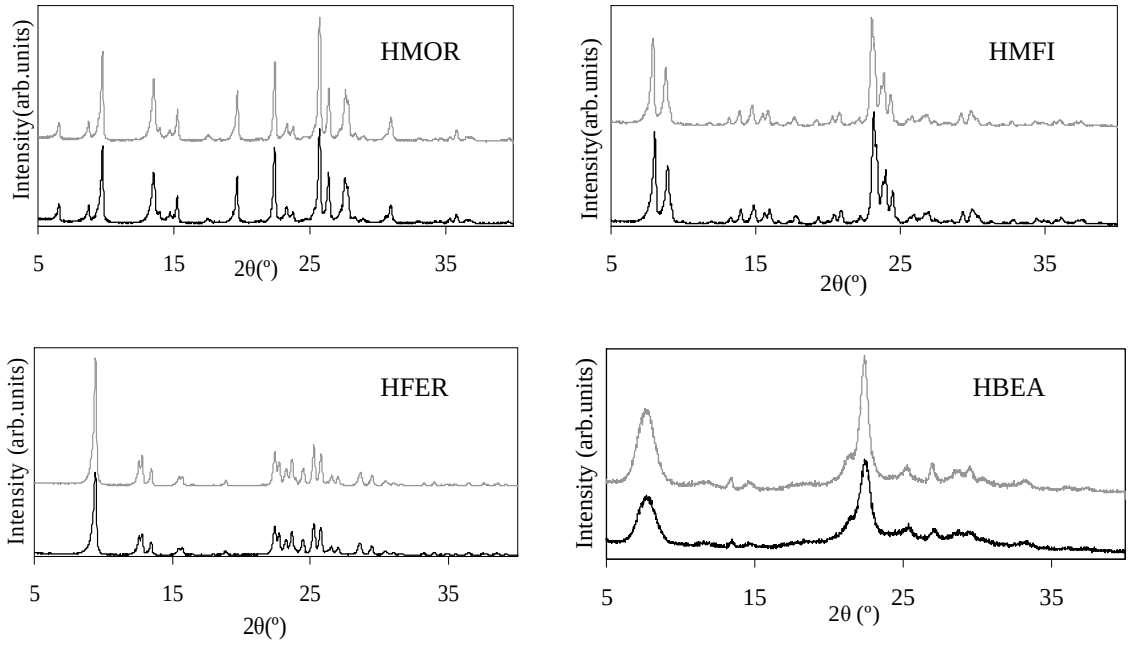

Figure 1 – XRD patterns for parent (grey lines) and alkaline treated samples (back lines).

The nitrogen adsorption/desorption isotherms displayed in Fig. 2 show that for all the starting structures a sharp rise in uptake at low pressure is observed, confirming the predominant microporous character of solids. The presence of a significant mesoporous structure is observed only for BEA. For the majority of the essayed structures, the alkaline treatment

results in the development of mesoporosity that is evidenced by the increase of the nitrogen uptake at high relative pressures and the presence of a more or less pronounced H4 type hysteresis loop. In the case of BEA the treatment did not promote any change in the zeolite structure since the isotherms of the parent and treated samples are coincident in the overall range of relative pressures.

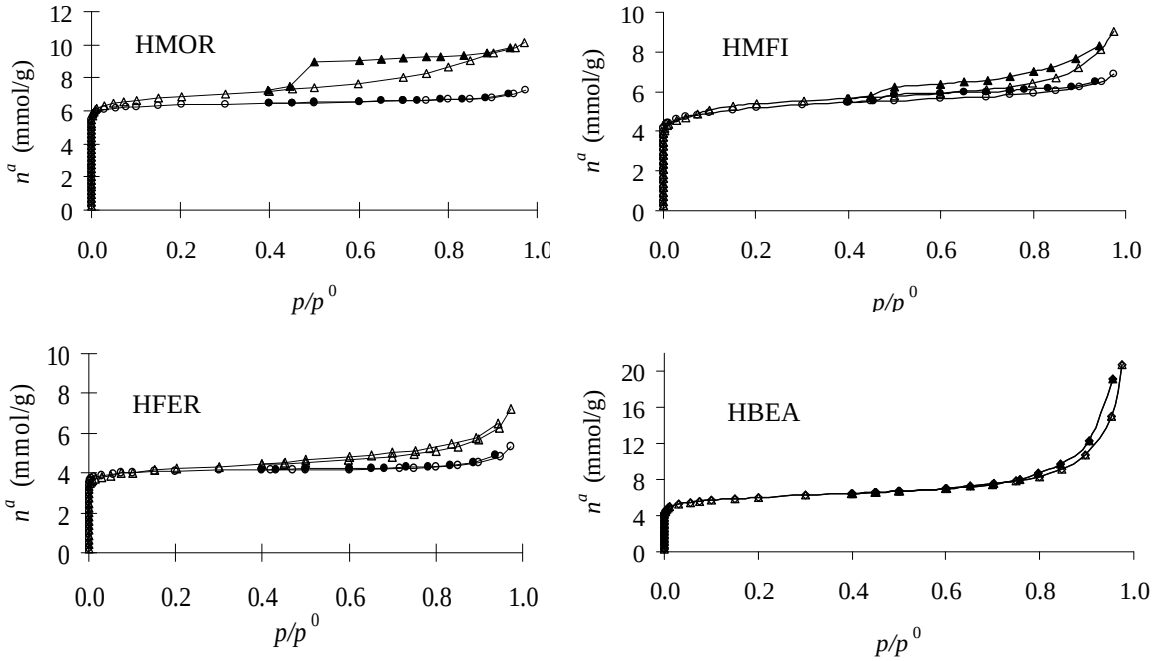

Figure 2 – N_2 adsorption/desorption isotherms at -196 ºC for parent (circles) and alkaline treated (triangles) zeolites. Open and closed symbols represent adsorption and desorption points, respectively.

From adsorption data the micropore (V_{micro}), mesopore (V_{meso}) and total porous volumes (V_T), as well as the external surface area (A_{ext}), were calculated. The results are listed in Table 1, where treated samples are named according with the convention: parent zeolite-des.

Table 1 – Textural properties of the parent and alkaline treated HMOR zeolites; micropore (V_{micro}) by t-method, mesopore (V_{meso}) by subtracting the microporous volumes from the total pore volume at $p/p^0 \sim 0.95$ (V_T) and external surface area (A_{ext}).

Zeolite	V_{micro} (cm^3g^{-1})	V_{meso} (cm^3g^{-1})	V_T (cm^3g^{-1})	A_{ext} (m^2g^{-1})
HMOR	0.21	0.04	0.25	16
HMOR-des	0.19	0.15	0.34	101
HMFI	0.16	0.07	0.23	56
HMFI-des	0.16	0.13	0.29	61
HFER	0.14	0.03	0.17	13
HFER-des	0.13	0.10	0.23	51
HBEA	0.16	0.40	0.56	123
HBEA-des	0.16	0.40	0.56	123

In line with the discussion made by the analysis of the isotherms configuration, the values reported in Table 1 show that, except in the case of BEA, the alkaline treatment lead to an important development of the mesoporosity. For instance, HMOR-des and HFER-des present a V_{meso} more than triple of that observed for the correspondent parent structures. Associated with the mesoporosity development a small fraction of the inherent microporous structure was destroyed. In the most unfavourable case, HMOR, the loss corresponds to only 10 % of the initial microporous volume. It is interesting to note that, in disagreement with the

data reported by Groen *et al.* (2004), the V_{micro} of the HMFI sample did not change after the desilication treatment and curiously this is the structure where V_{meso} showed the smallest increase. The results obtained with BEA were also unexpected because, according to the literature, among all the essayed structures this is the one that should lead to an easiest Si extraction, as a result of both less stable framework and the relatively large interconnected channels, which permits an adequate transport of hydroxyl ions through the channels for hydrolysis of Si-O-Si bonds (Groen, 2004). These results are most likely related with the fact that we used BEA and MFI structures with much smaller Si/Al ratios than those of the structures essayed by Groen *et al.* (2004). In fact, in other study, focused on MFI type zeolites, these authors found out that the mesoporous structure development depends of the framework Si/Al ratio, being particularly important for high values (Groen, 2005). On the other hand, the BEA zeolite used in the present study has a much lower V_{micro} than that of the structure used by Groen *et al.(*2004), suggesting that our sample was less crystalline, what could also influence the desilication process. The mesopore size distribution was made according the Broekhoff-de Boer method, in a version simplified (Lukens, 1999) with the Frenkel-Halsey-Hill equation (BdB-FHH). The very broad size distribution curves obtained (not shown) reveal that the mesopores created upon the alkaline treatment have openings covering all the mesoporosity range.

SEM images of the parent zeolites (Fig. 3) show that in all the cases the crystals are very small. HBEA image reveals not only the presence of the smallest crystallites but also an high degree of aggregation, what justifies the important mesoporous volume detected for this zeolite, that most probably comes from the pores that are formed in the spaces resulting of the crystallites aggregation. The small sizes of the crystallites prevent a global conclusion about morphological changes due to the alkaline treatment. In fact, only in the case of HFER-des a partial dissolution of the outer surface of the crystals could be detected (Fig. 3e).

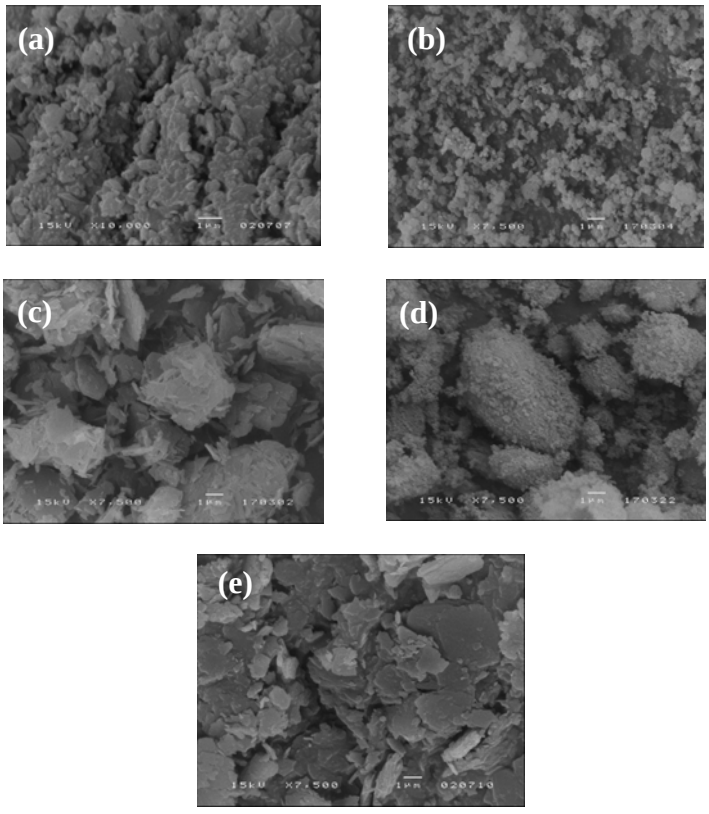

Figure 3 – SEM images of HMOR (a), HMFI (b), HFER(c), HBEA (d), and HFER-des (e).

n-Heptane cracking was used as a model reaction to characterize the acidity of the samples and, in this sense, evaluate possible changes in acidity after desilication treatments. The main reaction products are hydrocarbons (olefins and paraffins) with three and four carbon atoms (C_3 and C_4). Some isomerization and aromatization products and also light products, with one and two carbon atoms (C_1 and C_2) are also detected in small amounts. After desilication all samples show identical catalytic behaviour as the parent ones. In Table 2 the main parameters related to n-heptane cracking for the parent and desilicated zeolite samples are quoted.

Table 2 – Main parameters for n-heptane cracking at 350 ºC after 5 min. of time-on-stream.

Sample	Conversion (molar %)	O/P (C_4)	B/L (C_4)	Deactivation (%)
HMOR	31.39	0.2	2.3	85.3
HMOR-des	24.28	0.2	2.7	83.2
HMFI	28.15	0.7	0.9	3.3
HMFI-des	29.36	0.7	0.9	5.7
HFER	1.92	0.8	2.3	43.8
HFER-des	0.92	1.7	0.7	20.7
HBEA	33.90	0.2	4.0	62.7
HBEA-des	39.19	0.2	3.7	50.7

The alkaline treated samples show a slightly lower initial activity but a similar deactivation, except for FER and BEA samples. The olefin/paraffin (O/P) ratio measures the hydrogen transfer ability of the catalysts. An O/P ratio, lower than 1, indicates a consumption of olefins for the formation of heavy carbonaceous compounds during hydrogen transfer reaction (Poutsma, 1976). As this reaction follows a bimolecular mechanism, it is favoured by a high density of acid sites. The O/P ratio remains constant after desilication for all samples, except for HFER-des, where it increases, indicating that in the majority of the cases the acid sites density is not modified. The branched/linear (B/L) ratio is related not only with the catalyst acidity but also with the space available inside the porous structure. HMOR-des is the only sample that presents higher B/L ratio, meaning that the desilication treatment enlarged the zeolite pores, increasing the formation of branched products. This result is in agreement with the textural characterisation, since if we do not consider the unusual values found for BEA samples, this is the sample that presents the highest values of V_{meso} and A_{ext}. The B/L ratio remains practically unchanged after alkaline treatment for HBEA and HMFI catalysts. HFER based samples show a distinct behaviour with very small conversions, indicating the occurrence of catalytic reactions mainly at the external surface, due to difusional limitations inside the narrow porous structure of this zeolite. After alkaline treatment higher O/P and low B/L values are observed, what is in agreement with the partial dissolution of the crystal surface detected by SEM.

Infrared spectra of pyridine after desorption at temperatures between 200 and 400 ºC, in the range 1400-1700 cm^{-1}, are shown in Fig. 4 for HMOR and HMOR-des samples. The interaction between pyridine and the zeolite acid sites results in the appearance of bands characteristic of pyridine adsorbed to Brönsted acid sites around 1544 and 1636 cm^{-1}, to Lewis acid sites at 1622 and 1455 cm^{-1} (Guadurier and Lefebvre, 1988) The presence of both types of acid sites was detected in the parent and in the treated sample. To estimate the relative site population for Brönsted acid sites the integral intensity of the bands characteristic of pyridine coordinated to these centers were normalized against the structure Si-O combination band, at 1860-1800 cm^{-1}. The results are designated as N.I. (normalized integral intensities) and are displayed in Fig. 5.

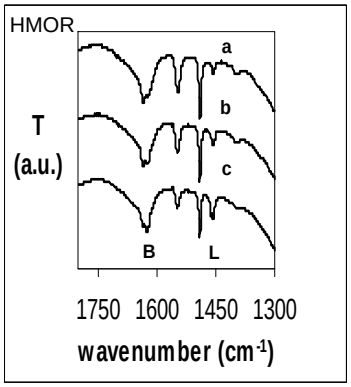

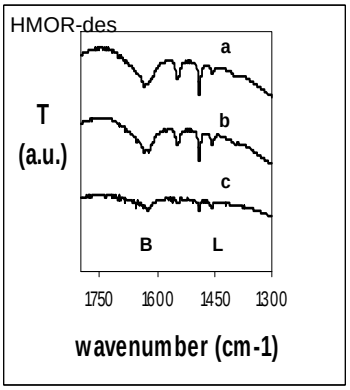

Figure 4 – IR spectra of pyridine adsorbed on HMOR and HMOR-des after outgasing at 200 (a), 300 (b) and 400 ºC (c). B and L indicate the bands related to Brönsted and Lewis acid sites, respectively.

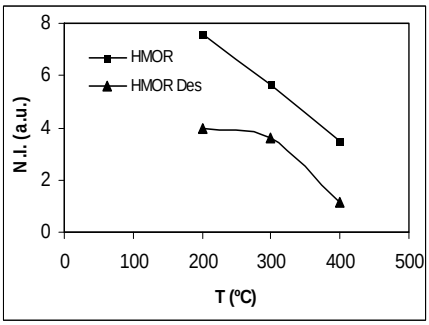

Figure 5 – Normalised integral intensities (N.I.) of pyridine adsorbed on Brönsted acid sites versus desorption temperature.

The estimation of Brönsted site density for HMOR-des shows a decrease of about 50% in all the range of temperature, when compared with the parent zeolite. This result is in agreement with some decrease in conversion observed for the alkaline treated sample in n-heptane cracking. Nevertheless is does not seem to affect the O/P ratio, meaning that the remaining acid sites are enough to ensure the occurrence of bimolecular reactions in the same extent as in the parent material.

References

Gaudurier, G. F., Lefebvre in Imélik, B, Védrine, J.C. (1988) Les Techniques Physiques d'Études des Catalyseurs, Chap.2, Editions TECHNIP, Paris.

Groen, J.C., Peffer, L. A. A., Moulijn, J.A., Pérez-Ramírez, J., (2004). On the introduction of intracrystalline mesoporosity in zeolites upon desilication in alkaline medium. Microporous and Mesoporous Materials, 69, 29-34.

Groen, J.C., Moulijn, J.A., Pérez-Ramírez, J., (2005). Decoupling mesoporosity formation and acidity modification in ZSM-5 zeolites by sequential desilication-dealumination. Microporous and Mesoporous Materials, 87, 153-161.

Groen, J.C., Moulijn, J.A., Pérez-Ramírez, J., (2006). Desilication: on the controlled generation of mesoporosity in MFI zeolites. Journal of Materials Chemistry, 16, 2121-2131.

Lukens Jr., W.J., Schimidt-Winkel, P, Zhao, D., Feng, J. Stucky, G.D., (1999). Evaluating pore sizes in mesoporous materials:a simplified standard adsorption method and a simplified Brokhoff-de Boer method. Langmuir, 15, 5403-5409.

Poutsma, M.I. in Rabo, J.A. (1976), Zeolite Chemistry and Catalysis, ACS Monograph 171, American Chemical Society, Washington DC.

Yousheng, T., Hirofumi, K., Katsumi, K., (2006). Developments and structures of mesopores in alkaline-treated ZSM-5 zeolites. Adsorption, 12, 309–316.

Proceedings of the 10th International Chemical and
Biological Engineering Conference - CHEMPOR 2008
Braga, Portugal, September 4-6, 2008
E.C. Ferreira and M. Mota (Eds.)

The kinetics of ampicillin release from hydroxyapatite porous for bones regeneration

Silvio V. Albuquerque[1], Caroliny G. Oliveira[2], Giovanilton F. Silva[2], Andrea L.O. Ferreira[2*], Ricardo E.F.Q. Nogueira[1]

[1] LDMC – Laboratório de Desenvolvimento de Materiais Cerâmicos, Departamento de Engenharia Mecânica, Universidade Federal do Ceará, Campus do Pici, Bloco 720, Pici, 60455-760 Fortaleza, Brasil.
[2] GPBIO – Grupo de Pesquisa em Processos Biotecnológicos, Departamento de Engenharia Química, Universidade Federal do Ceará, Campus do Pici, Bloco 709, Pici, 60455-760 Fortaleza, Brasil

Keywords: Antibiotic release, Hydroxyapatite, Ampicillin, Kinect study.
Topic:

Abstract

Semi-synthetic beta-lactam antibiotics are the most important class of antibacterial agents. Ampicillin (6-[2-amino-2-phenylacetamide] penicillanic acid) is in the penicillin group of which penicillin proper was the first antibiotic to be used in therapy (Bruggink et al., 2001; Pessina et al., 1988). There is a growing need for developing bioactive implants, due biomaterials are biocompatible, resorbable, and present osteoconductive properties. Advantages of implantable drug delivery tools can include high release efficiency, precise dose control, low toxicity, and allow to overcome disadvantages connected with conventional methods (Uhrich et al., 1999). In this respect, hydroxyapatite (HA) is an elective material. It enables to produce architectures similar to those of real bones. Here we studied a kinetic model to describe ampicillin release from HA. In the course of the release experiment, ampicillin was dissolved in phosphate buffer to make a stock solution, maintained at 30 ºC and shaken at 60 strokes/minute. Samples were withdrawn periodically for analysis and then returned to the mixture. Adsorbed amounts were measured by the difference of the concentration of the antibiotics before and after adsorption using UV adsorption at 225 nm.

1 Introdution

Semi-synthetic beta-lactam antibiotics are the most important class of antibacterial agents. Their use in veterinary and human medicine is in continuous expansion. Some examples of semi-synthetic penicillins and cephalosporins are: amoxicillin, ampicillin, cephalexin, cefadroxil, cefazolin, among many others. They have in common the presence of the beta-lactam ring, responsible for their anti-microbial activity. They irreversibly inhibit the last step of the bacterial cell wall biosynthesis.

The beta-lactam antibiotics can be described in terms of a beta-lactam nucleus with a side-chain (see Figure 1). Many different nuclei and side-chains are found in the antibiotics that are in use today. Different combinations of side-chains and nuclei form antibiotics with distinctive properties; for example, replacing the phenylacetic acid side-chain of penicillin G with D-phenylglycine (PG) results in the beta-lactam antibiotic ampicillin, which in contrast to penicillin G, is orally stable (Cole, 1969; Bruggink et al., 1998; Wegman et al., 2001; Ribeiro et al., 2005). Ampicillin (6-[2-amino-2-phenylacetamide] penicillanic acid) is in the penicillin group of which penicillin proper was the first antibiotic to be used in therapy (Bruggink et al., 2001; Pessina et al., 1988). It is one of most widely used semi-synthetic beta-lactam antibiotics (Ospina et al., 1996). It has an estimated market of 20,000 ton/year (Bruggink et al., 2001).

* Corresponding author. Tel +55 85 3366 9611. E-mail:andrea@ufc.br

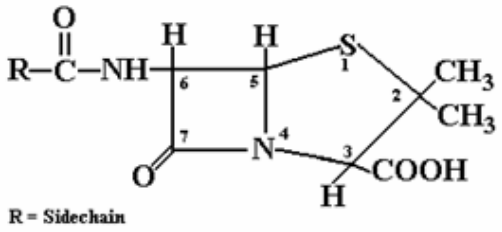

Figure 1: General structure of beta-lactam antibiotics.

There is a growing need for developing bioactive implants, due biomaterials are biocompatible, resorbable, and present osteoconductive properties. It is known that the use of bone substances has many inherent disadvantages in practical applications, and it is linked to many surgical problems (Suchanek and Yoshimura, 1998).

Advantages of implantable drug delivery tools can include high release efficiency, precise dose control, low toxicity, and allow to overcome disadvantages connected with conventional methods (Uhrich et al., 1999). In this respect, hydroxyapatite (HA) is an elective material. It enables to produce architectures similar to those of real bones. Here we studied a kinetic model to describe ampicillin release from HA. HA analogous to the mineral component of bones, its properties make it desirable as implant materials and delivery agents of drugs. This paper describes the ampicillin adsorption and release profiles of HA material. The aim of this work was to evaluate its application as ampicillin delivery carrier.

2 Materials and methods

2.1 Materials

Ampicillin was from Aldrich Chem. Co., USA. All other chemicals were of laboratory grade from different commercial suppliers.

2.2 Antibiotic loaded HA samples

Ampicillin was used as drug molecules. HA were impregnated with 25 mM of antibiotic buffer solution at 30 ºC for 48 h. Ampicillin adsorbed in the HA has been quantified by spectophotometric analysis. In the course of the release experiment, ampicillin was dissolved in phosphate buffer to make a stock solution, maintained at 30 ºC and shaken at 60 strokes/minute. Kinetic experiments to determine the amount of ampicillin adsorbed as a function of contact time were conducted by stirring. Samples were withdrawn periodically for analysis and then returned to the mixture. Adsorbed amounts were measured by the difference of the concentration of the antibiotics before and after adsorption using UV adsorption at 215 nm.

2.3 HA synthesis

HA was synthesized by the aqueous precipitation method from CaO and H_3PO_4 as the reagents, and used as a carrier for charging ampicillin. In this study, apatite nanoparticles were produced by aqueous precipitation. The starting solution was 0.3 M H_3PO_4, 0.5 M $Ca(OH)_2$, 1M CH_3CHCO_2HOH. The pH value of the solution was adjusted to pH 8 by NH_4OH additon. The suspensions were left overnight for ageing. The suspension was then vacuum filtered and washed in deionised water to remove NH_4OH. The powders were dried in an oven at 100 ºC overnight. The powders were analysed by X-ray diffraction (XRD) and then sintered. Sintered powders were again analysed by XRD to assess the final phase composition (Albuquerque et al., 2003).

2.4 Solubility experiments

Solubility of ampicillin was determined following Gude et al., 1996. The samples were prepared gravimetrically. Glass-flasks with screw caps filled with the samples were immersed

into a thermostated water bath and stirred. All samples were stirred for at least 4 h. Subsequently, the mixture was allowed to settle. The samples were taken with syringes with an attached 0.2 μm filter to avoid entrainment of solids. The compositions of the liquid phases were analyzed by HPLC.

2.5 Analysis

Concentrations of ampicillin were determined using HPLC to analyze if antibiotic degraded during the assays: C18 column (Waters Nova-Pack, C18, 60 Å, 4 μm, 3.9 × 150 mm); eluent: 35% acetonitrile, 2‰ SDS (lauryl sodium sulphate), 10 mM H3PO4, 5 mM K2H2PO4, with a flow of 1 mL/min at 25 °C and λ = 225 nm.

2.6 Adsorption performance:

Ampicillin adsorption performance (*AP*) was defined as follows:

$$\%AP = \left(1 - \frac{C^*}{C^{initial}}\right) \times 100$$

Where *C** is the concentration of ampicillin (mM) and, $C^{initial}$ is the concentration of ampicillin at the beginning of the assays (mM).

3 Results

3.1 Solubility Studies

The solubility of ampicillin was measured for pHs in the range 7.0-8.0, at 30ºC. The selected range of pHs for the solubility studies was bracketed by stability of antibiotic. The obtained results, which are shown in Figure 2, are similar to the ones obtained by other authors (Diender et al., 1998; Rudolph et al., 1999; Youshko et al., 2000).

Ampicillin solubility increases with the pH. This behavior can be explained by its determined values of the acid group pK (2.66) and amine group pK (7.24) and calculated of its isoelectric point (4.95). Hence, above the pH correspondent to its isoelectric point the number of ampicillin molecules with a neutral charge (which is the most insoluble form) decreases, leading to higher solubility values. This effect becomes more important for pH above 7.0.

Our aim is to perform the ampicillin adsorption with its separation from HA at 37ºC, what implies to working at sorption conditions where the solubility of AMP is the highest possible. Therefore, the obtained results indicate that for higher pH the performance of the ampicillin release might be better. However, the best value for pH is a trade-off between AMP solubility and temperature.

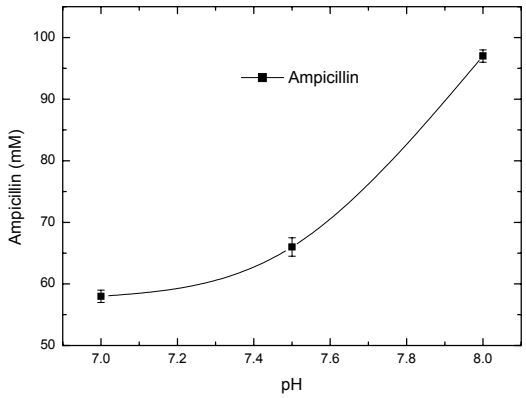

Figure 2: Solubility of ampicillin as function of pH at 30ºC.

Temperature effects on the solubility of all compounds were also evaluated by determining the compounds solubility at pH 7.0 and 8.0, at 37ºC. The antibiotic solubility slightly increases at 37ºC. Most of the solubility values at 37ºC were around 11% higher than

those at 30ºC. However, operation of the system at 37ºC implies to much lower adsorption rates than at 30ºC. It is believed that a increase of 11 % in the ampicillin solubility is not big enough to justify the operation at such a high temperature. Anyway, these experiments aimed at only indicating the range of adsorption conditions for studying the kinetic of the process.

3.2 Equilibrium time

In order to properly evaluate the adsorption process of ampicillin, the equilibrium curves were determined experimentally. Equilibrium time depends on adsorption rate, i.e., affinity between antibiotic and HA and, temperature of assay. Figure 3 shows the results to ampicillin adsorption at 30 and 37 ºC, respectively. It can be observed that equilibrium state was obtained at 8 hour. At 37 ºC, adsorption rate higher than at 30 ºC can be explained due to increasing of mass transfer, because adsorption is not favor at higher temperatures.

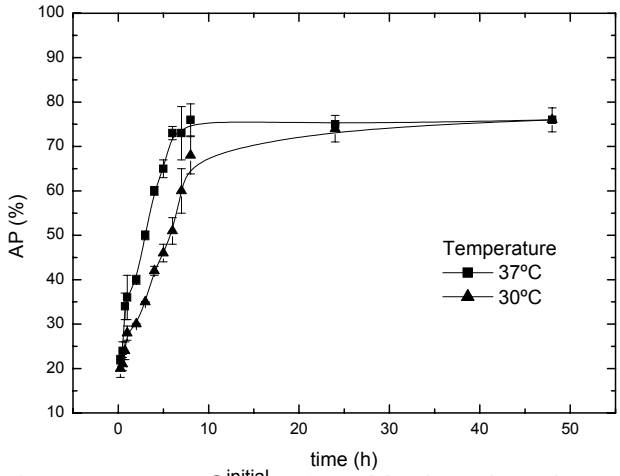

Figure 3: Equilibrium assays at $C^{initial}$ = 25 mM, phosphate butter 10 mM, pH 7.5.

3.3 pH effect at adsorption isotherms

Figure 4 shows the effect of pH at adsorption performance of ampicillin. It can be observed that AP decreases when pH increases. The amino group of ampicillin is not protoned when pH increases, so less antibiotic can be adsorbed on HA. Therefore, ampicillin adsorption slightly improves when pH decreases.

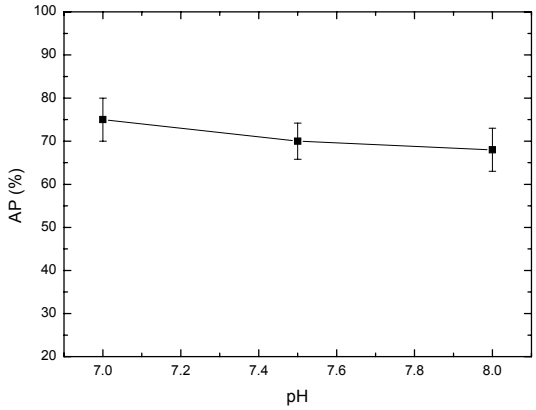

Figure 4: pH effect on adsorption ampicillin at 30 ºC.

Adsorption isotherms of ampicillin on HA at 30 ºC and pH 7.0 were shown in Figure 5. The adsorption isotherms were further correlated to the Freudlich equation:

$$q = KC^{1/n}$$

Where *q* is the equilibrium adsorption capacity (mg/g_{HA}), *C* is the initial concentration of ampicillin (mg/mL), *K* is the Freundlich parameter and, *n* is the Freundlich parameter related to the magnitude of adsorption driving force. Some assumptions were made to adsorption model: the process operated under isothermal conditions, HA porosity was constant and homogeneous along as the particle. The data plotted according to the Freundlich isotherm were K = 52.51 ± 3.48, n = 1.758 ± 0.036 and, R^2 = 0.980. The results indicate that Freundlich isotherm can represent the isotherm data of HA appropriately in the given concentration range.

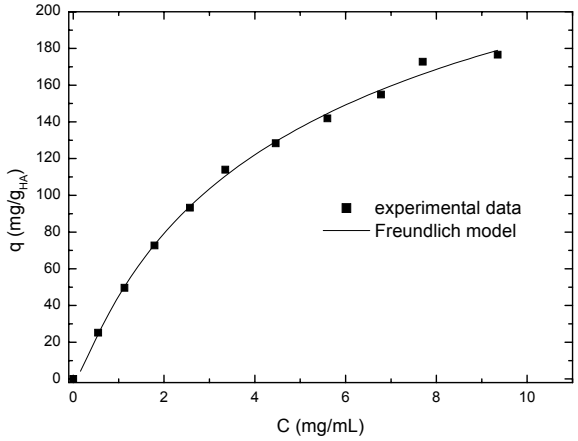

Figure 5: Adsorption isotherm of ampicillin on HA at 30 ºC, pH 7.0

4 Conclusions

Ampicillin solubility was studied at different pH. Higher pH improved ampicillin solubility. The equilibrium state was obtained at 8 hour of assay. At 37 ºC, adsorption rate was higher than at 30 ºC. The best results of adsorption performance were obtained when pH decreased (7.0). The relation between the adsorption capacity and the equilibrium solute concentration was analyzed. Freundlich isotherm was used and provided good fit for data.

References

Albuquerque, J.S.V., Neto, J.V.F., Junior, J.I.L.A., Lima, D.O., Nogueira, R.E.F.Q., Prado da Silva, M.H. (2003). Porous bioceramics produced with calcium phosphate nanoparticles. *Key Eng. Mat*., 240, 23-26.

Bruggink, A., Ross, E.C., Vroom, E. (1998). Penicillin Acylase in the industrial production of beta-lactam antibiotics. *Org Proc Research & Development*, 2(2), 128-133.

Bruggink, A., Roy, P.D., Sheldon, R.A., van Rantwijk, F., Wegman, M.A., Cao, L., Janssen, M.H.A. (2001). Synthesis of beta-lactam antibiotics. *Dordrecht:Kluwer Academic Publishers*, pp. 102-205.

Cole, M. (1969). Penicillins and other acylamino compounds synthesized by cell-bound penicillin acylase of Escherichia coli. *Biochem J,* 115, 747-756.

Diender, M.B., Straathof, A.J.J., van der Wielen, L.A.M., Ras, C., Heijnen, J.J. (1998) Feasibility of the thermodynamic controlled synthesis of amoxicillin. *J. Mol. Catal. B: Enzym.*, 5, 249- 253.

Ospina, S., Barzana, E., Ramírez, O.T., López-Munguía, A. (1996). Effect of pH in the synthesis of ampicillin by penicillin acylase. *Enzyme Microb. Technol*. 19, 462-469.

Pessina, A., Lüthi, P., Luisi, P.L. (1988). Amide-bond synthesis catalyzed by penicillin acylase. *Helvetica Chimica Acta*, 71, 631-641.

Ribeiro, M.P.A., Ferreira, A.L.O., Giordano, R.L.C., Giordano, R.C. (2005). Selectivity of the enzymatic synthesis of ampicillin by E. coli PGA in the presence of high concentrations of substrates. *J Mol Catal B Enzym*, 33, 81-86.

Rudolph, E.S.J., Zomerdijk, M., Luyben, K.C.H.A.M., Van der Wielen, L.A.M. (1999).

Correlating the phase behaviour of semi-synthetic antibioics and their precursors in water + 1-butanol mixtures. *Fluid Phase Equilibrium*, 160, 903-912.

Suchanek, W., Yoshimura, M. (1998). Functionally graded SrTiO3-BaTiO3 thin films prepared by the hydrothermal-electrochemical method under flowing solution. *J. Mater. Res*, 13, 94-117.

Uhrich, K.E., Cannizzaro, S.M., Langer, R.S., Shakesheffe, K.M. (1999). Polymeric systems for controlled drug release. *Chem. Rev*. 99 (11), 3181-3198.

Wegman, M.A., Janssen, M.H.A., van Rantwijk, F. (2001). Towards biocatalytic synthesis of beta-lactam antibiotics. *Adv Synth Catal*, 343 (6-7), 559-576.

Youshko, M.I., Langen, L.M., Vroom, E., Moody, H.M., Rantwijk, F., Sheldon, R.A., Svedas, V.K (2000). Penicillin acylase-catalyzed synthesis of ampicillin in “aqueous solution-precipitate” systems. High substrate concentration and supersaturation effect. *J. mol. Catal. B: Enzym*, 10, 509-515.

Proceedings of the 10th International Chemical and
Biological Engineering Conference - CHEMPOR 2008
Braga, Portugal, September 4-6, 2008
E.C. Ferreira and M. Mota (Eds.)

Solvent Effect on the Antioxidant Activity of Extracts of *Myrtus communis* L. leaves

Idalino Manuel Costa Faísca, M. Gabriela Bernardo-Gil*, José Abecassis Empis, M. João Cebola, Paula Gomes Pereira

Centre for Biological and Chemical Engineering, IBB, DEQB, IST,
Av. Rovisco Pais, 1049 – 001 Lisboa, Portugal

Keywords**:** Myrtle, *Myrtus communis*, antioxidant activity, extraction, Rancimat
Topic: Multi-scale and/or multi-disciplinary approach to process-product innovation

Abstract

Myrtle (*Myrtus communis* L.) leaves, from plants originated from the Centre region of Portugal, were subjected to different treatments to obtain extracts with antioxidant activity.

The sample leaves were submitted to hydrodistillation (Clevenger distillation) and the deodorised solid residues were solvent extracted. The solvents tested were hexane, diethyl ether, isobutyl acetate, ethyl acetate, acetone, isopropyl alcohol, butanol, ethanol, and methanol. The largest extract yields were obtained with methanol, followed by ethanol.

The antioxidant activity of the extracts was evaluated by Rancimat against the sunflower oil. All the extracts presented very high protection factors (PF), the highest being the extract obtained by using ethyl acetate (PF = 2.58). When both the yields and the PF were compared, the isopropyl alcohol extract presented the best values (PF = 1.8; Yield = 25 g extract / 100 g deodorised solid residue).

1. Introduction

Oxidative stress is involved in the pathogenesis of numerous diseases. On the other hand, lipid oxidation is responsible for deterioration of fats and oils resulting in colour, flavour and nutritive value changes. One of the main practices in order to retard oxidation is the addition of antioxidants in fats and fatty foods and cosmetics. The antioxidants can be of synthetic or natural origin. The use of synthetic antioxidants is restricted in several countries, because of their undesirable long-term toxicological effects, including carcinogenicity (Gazzani *et al.*, 1998). For instance, butylated hydroxytoluene (BHT) had little effect on mutagenicity at low concentrations, but significantly increased their mutagenicity at high concentrations (Shahidi and Wanasundara, 1992). A number of studies have reported that BHT may cause internal and external haemorrhaging at high doses that is severe enough to cause death in some strains of mice and guinea-pigs (Chen *et al.*, 1992). As a result, there is a great interest in finding antioxidants from natural sources for food and medicinal applications.

Extracts obtained from herbs and spices have been found to present antioxidant activity, and their use instead of synthetic antioxidants is becoming increasingly popular. Several works show that the majority of antioxidant active substances occur in extracts, but some essential oils were also studied to analyse their antioxidant activity, namely essential oil containing thymol and carvacrol, and other phenolic compounds, which exhibit high antioxidative activity. Esquível *et al.* (1999) evaluated the antioxidant

* Corresponding author: M. Gabriela Bernardo-Gil
Email: gbernardo.gil@ist.utl.pt;
phone: +351.21.841.7582; Fax: +351.21.841.9176

activity of savoury extracts. Ribeiro *et al.* (2001) studied the antioxidant activity in supercritical fluid extracts residues. Reddy *et al.* (2005) determined the antioxidant activity of amla, drumstick leaves, and raisins. Rubilar *et al.* (2006) evaluated murta leaves as a source of antioxidant polyphenols. Pellegrini *et al.* (2007) studied the efficiency of extraction of a sequence of solvents of some fruit and vegetable foods, in order to evaluate their antioxidant capacity. Ali *et al.* (2007) studied several Indian medicinal herbs as sources of antioxidants. Yanishlieva *et al.* (2006) presented a review with results on the stabilization of lipids and lipid-containing foods with different herbs and spices (ground materials and extracts). Although many plants has been investigated, only rosemary and sage are commercially available as flavourless, odourless, and colourless antioxidant extracts.

Myrtle (*Myrtus communis* L.) belongs to the Myrtaceae family. It is an evergreen shrub which grows wild in the Mediterranean area under different conditions of light availability that has been used since ancient times for medicinal, food and spice purposes (Mendes *et al.* 2001). The leaves contain tannins, flavonoids such as quercetin, catechin and myricetin derivatives and volatile oils, the fruits are mostly composed of volatile oils, tannins, sugars, flavonoids and organic acids such as citric and malic acid, and leaves and fruits have been used as an antiseptic and for healing wounds as well as in the treatment of urinary diseases, in folk medicine. The essential oil is also important in perfumery (Cakir, 2004). Tuberoso *et al.* (2006) determined the compositions of essential oils and alcoholic extracts of myrtle leaves and berries collected in Sardinia (Italy), and Jamoussi *et al.* (2005) studied the effect of harvest time on the yield and composition of Tunisian myrtle oils. Messaoun *et al.* (2005) showed that there is strong variability of the essential oil composition in natural populations of *Myrtus communis* in Tunisia. Farah *et al.* (2006) studied the effect of fractional distillation on the chemical composition of Moroccan myrtle essential oils.

Owing to the differing antioxidant potential of compounds with different polarities in complex whole foods, all methods for assessing the antioxidant activity of food samples are strongly affected by the solvents that were used during extraction (Pellegrini *et al.*, 2007). Romani, Pineli *et al.* (1999), and Romani *et al.* (2004) identified polyphenols in leaf extracts of *Myrtus communis* L. Demo *et al.* (1999) used hexane to obtain extracts of several plants including myrtle, and they found that their antioxidant activity could be correlated to the α-tocopherol content. Appendino *et al.* (2002) obtained extracts from myrtle by using acetone, and observed that the extracts presented strong antioxidant activity. Silva *et al*. (2007) studied the extraction of phenolics from *Inga edulis* leaves by using different proportions of the mixture ethanol + water, at various temperatures and at several liquid-to-solid ratios.

There are several methods for the evaluation of antioxidant action on fats and oils (Frankel and Meyer, 2000; Becker, Nissen and Skibsted, 2004). The Rancimat method has some advantages such as a quick answer, and allowing the stability evaluation at high temperatures, which are important factors for the use of the antioxidants in food processing. Dessi *et al*. (2001) studied the antioxidant activity of methanol extracts from several plants growing in Sardinia, having used the oxidation of linoleic acid as oxidation trials. Pizzale *et al.* (2002) studied the antioxidant activity by using the Rancimat apparatus of methanolic extracts of sage and oregano.

The objective of this work was to obtain extracts from the solid residues of the hydrodistillation of myrtle leaves, by using several solvent, and to study their antioxidant activity.

2. Materials and Methods

Materials

Wild myrtle was collected in the Centre of Portugal region, at pre-floral and post-floral stages. Leaves were naturally air-dried in darkness. The remaining humidity was 12.3 %. Before extraction, leaves were milled. The particle diameter after size reduction was

determined by using a Retsch KS 1000 sieving machine, the medium particle dimension being calculated as 0.8 mm.

Standards were purchased from Sigma Aldrich, and all the other chemicals were obtained from Merck, at the highest purity available.

Extraction of essential oils

The essential oils of *Myrtus communis* were obtained by using a modified Clevenger apparatus during 3 hours. The amounts of recovered oils were measured gravimetrically.

Solvent extraction

The solid residues of Clevenger distillation were used for preparation of extracts with eventual antioxidant activity, by using two solvent extraction methods: solid-liquid extraction at solvent boiling temperature with the solid immersed in solvent, and Soxhlet method. Hexane (Hex), diethyl ether (Diet), isobutyl acetate (iBtAc), ethyl acetate (EtAc), acetone (Acet), isopropyl alcohol (iPrOH), butanol (BtOH), ethanol (EtOH), and methanol (MeOH) were used as solvents. After the extraction, the solvent was evaporated by using a rotary evaporator (Heidolph VV2000).

Analysis of essential oils

The essential oils were analysed by gas chromatography on a Hewlett-Packard 5890 Series II chromatograph equipped with a FID detector and a DB5 column (5% phenyl, 95% dimethylpolysiloxane), 0.32 mm id x 50m, film thickness 0.17 μm. The column temperature was programmed to hold at 60 ºC for 10 minutes, then heated to 180 ºC at a slope of 2 ºC/min, with a final isothermal hold at 180 ºC for 30 minutes. Injector and detector temperatures were 200 and 250ºC, respectively. Carrier gas, N_2 was adjusted to a linear velocity of 2 ml/min. The samples were injected using the split mode (split ratio 1:20) being the injection volume 0.2 μl.

The sample components were identified by comparing the retention times with those of chromatographic standard of the compounds. Peak areas were determined using a Hewlett-Packard 3396 Series II integrator. For quantitative analyses, the peak areas were converted to absolute values using response factors estimated from the standard compounds. Results were compared to those obtained by GC-MS.

Rancimat method

The Rancimat method is commonly used to evaluate the antioxidant activity of extracts and is based on the increase of electrical conductivity due to the formation of volatile dicarboxylic acids as a result of lipid oxidation. Metrohm Rancimat 679 was used.

Samples of extract were dissolved in 7.0 g of sunflower oil, so that the concentration in extracts was 5000 ppm, and were heated at 110 ºC. A continuous air stream (20 L/h) was passed through the heated samples, and the volatile compounds were absorbed in a conductivity cell. Conductivities were continuously monitored until a sudden rise signified the end of induction period. Protection factors were determined by the ratio between the induction period found for the sunflower oil with a certain quantity of extract and the induction time obtained for sunflower oil with no addition of extract.

3. Results and Discussion

In Table 1 components of myrtle essential oils (EO) obtained from plants harvested in Centre – Portugal (sample 1 – pre-floral and sample 2 – post-floral) are presented. Results are medium values of five replicates.

The main components are 1,8-cineole followed by α-pinene and myrtenyl acetate. No evident differences occurred between compositions of pre-floral and post-floral myrtle leaves essential oils.

Table 1. Chemical composition (wt %) of *Myrtus communis* essential oils

Compound	Sample 1	Sample 2
α-Tujene	0.18	0.15
α-Pinene	33.5	34.1
Camphene	0.06	-
β-Pinene	0.32	0.29
Myrcene	0.09	0.09
α-Phellandrene	0.34	0.34
α-Terpinene	0.12	0.14
p-Cymene	0.14	0.04
Limonene	13.1	9.74
1,8-Cineole	25.4	26.7
Camphor	0.05	0.07
γ-Terpinene	0.16	0.14
Terpinolene	0.09	0.13
Linalool	3.91	6.62
Linalyl acetate	0.36	0.53
Cis-Verbenol	0.10	-
Terpinene-4-ol	0.12	0.16
α-Terpeniol	1.44	2.33
Borneol	0.51	0.53
Myrtenol	0.22	0.37
Nerol	0.04	-
Geraniol	0.40	1.03
Tymol	0.10	0.17
Myrtenyl acetate	5.74	9.84
Methyl eugenol	0.10	0.34
Eugenol	0.04	0.09
Geranyl acetate	0.72	1.71
Verbenone	0.83	1.42
β-Caryophyllene	0.08	0.27
α-Humulene	0.04	0.16
Iso-eugenyl acetate	0.17	0.39
Caryophellene oxide	0.14	0.20

In Figure 1, the extraction yields obtained from solid residues of hydro-distillation, with different solvents, at 2h of extraction time are presented. The higher yields were obtained for extracts obtained by using Soxhlet apparatus, when alcohols were used as solvents, and the highest was obtained with methanol (29.8 %), but similar values (about 26 %) were obtained by using ethanol, butanol and iso-propanol. Pizzale *et al.* (2002) obtained yields of about 20 % and 26 % when methanol was used to produce extracts of *Sage officinalis* and *Sage fruticosa*, respectively.

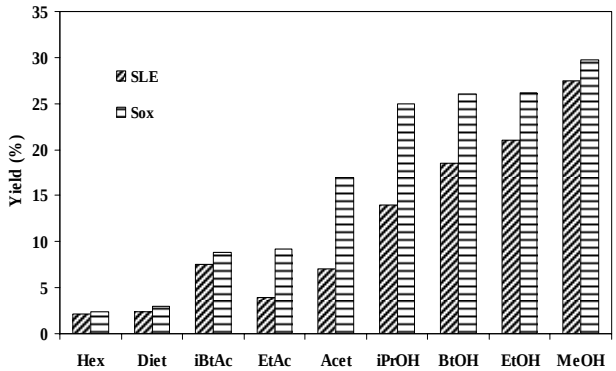

Fig. 1. Extraction yields obtained from solid residues of hydro-distillation, with different solvents, after 2h of extraction time. SLE – solid-liquid extraction at solvent boiling temperature with the solid immersed in solvent; Sox – Soxhlet method.

Protection Factors of extracts obtained from solid residues of Clevenger distillation of sample 2, at 2h of extraction time, with different solvents, are presented in Figure 2. The extraction method did not affect significantly the antioxidant activity of the extracts. The higher values of protection factors were obtained with solvents of intermediate polarity, such as ethyl acetate (PF=2.58) and diethyl ether (PF=2.23). However, alcoholic extracts also presented high antioxidant activity.

Silva *et al*. verified that the high values of phenolics contents were obtained by using the mixture ethanol + water, 86.8 % (v:v), at 58.2 ºC. The protection factors obtained by Pizzale *et al.* (2002) for methanolic extracts of sage and oregano are of the same magnitude of methanolic extracts of Myrtle obtained in this work.

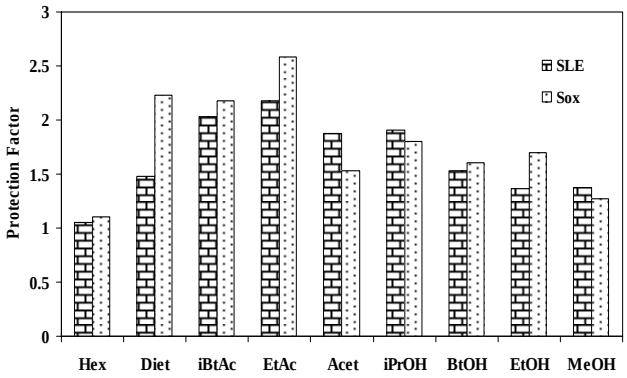

Fig. 2. Protection Factors of extracts (5000 ppm, total extract) obtained from solid residues of hydro-distillation, with different solvents, after 2h of extraction time. SLE – solid-liquid extraction at solvent boiling temperature with the solid immersed in solvent; Sox – Soxhlet method.

When both the yields and the protection factor were compared, the best solvent was isopropyl alcohol (yield = 25 % and PF = 1.8).

Conclusions

The obtained results shows that *Myrtus communis* leaves have a high potential for the production of extracts with high antioxidant activity.

Deodorised solid residues were extracted by using several solvents, and the results point towards the alcohols as being the solvents producing the best yields. But a good yield does not mean that the solvent is selective. And that seems to be what is happening with the alcohols, because when observing the results of the antioxidant activity, the best protection factors were obtained with ethyl acetate and diethyl ether, although alcoholic extracts also evidenced high antioxidant activity.

When both the yields and the protection factor were compared, the best solvent was the isopropyl alcohol.

References

Ali, S. S., Kasoju, N., Luthra, A., Singh, A., Sharanabasava, H., Sahu, A., & Bora, U. (2007). Indian medicinal herbs as sources of antioxidants. *Food Research International*, doi: 10.1016/j.foodres.2007.10.001.

Appendino, G., Bianchi, F., Minassi, A., Sterner, O., Ballero, M., & Gibbons, S. (2002). Oligomeric Acylphloro glucinols from myrtle (*Myrtus communis*). *Journal of Natural Prodducts, 65*, 334-338.

Becker, E. M., Nissen, L. R., & Skibsted, L. H. (2004). Antioxidant evaluation protocols: food quality or health effects. *European Food Research and Technology, 219*, 561-571.

Cakir, A. (2004). Essential oil and fatty acid composition of the fruits of *Hippophae rhamnoides* L. (Sea Buckthorn) and *Myrtus communis* L. from Turkey. *Biochemical Systematics and Ecology, 32*, 809-816.

Chen, C. H., Pearson, A. M., & Gray, J. I. (1992). Effects of synthetic antioxidants (BHA, BHT and PG) on the mutagenicity of IQ-like compounds. *Food Chemistry, 43*, 177–183.
Demo, A., Petrakis, C., Kefalas, P., & Boskin, D. (1999). Nutrient antioxidants in some herbs and Mediterranean plant leaves. *Food Research International, 31*, 351-354.
Dessi, M., Deiana, M., Rosa, A., Piredda, M., Cottglia, F., Bonsignore, L., Deidda, D., Pompei, R., & Corongiu, P. (2001). Antioxidant Activity of Extracts from plants growing in Sardinia. *Phytotherapy Research. 15*, 511-518.
Esquível, M. M., Ribeiro, M. A., & Bernardo-Gil, M. G. (1999). Supercritical extraction of savory oil: study of antioxidant activity and extract characterization. *Journal. Supercritical Fluids, 14*, 129-138.
Farah, A., Afifi, A., Fechtal, M., Chhen, A., Satrani, B., Talbi, M., Chouch, A. (2006) Fractional distillation effect on the chemical composition of Moroccan myrtle (*Myrtus communis* L.) essential oils. *Flav. Frag. J.* 21, 351–354.
Frankel, E. N., & Meyer, A. S. (2000). The problems of using one-dimensional methods to evaluate multifunctional food and biological antioxidants. *Journal Science Food Agriculture, 80*, 1925–1941.
Gazzani, G., Papetti, A., Massolini, G. & Daglia M. (1998). Anti- and prooxidant activity of water soluble components of some common diet vegetables and the effect of thermal treatment. *Journal of Agricultural and Food Chemistry, 46*, 4118–4122.
Jamoussi, B., Romdhane, M., Abderraba, A., Hassine, B.B., Gadri, A.E. (2005) Effect of harvest time on the yield and composition of Tunisian myrtle oils *Flav. Frag. J*. 20, 274–277.
Mendes, M. M., Gazarini, L. C., Rodrigues, M. L. (2001). Acclimation of *Myrtus communis* to contrasting Mediterranean light environments — effects on structure and chemical composition of foliage and plant water relations. *Environmental and Experimental Botany, 45*, 165–178.
Messaoud, C., Zaouali, Y., Salah, A.B., Khoudja, M.L., Boussaid, M. (2005) *Myrtus communis* in Tunisia: variability of essential oil composition in natural populations. *Flav. Frag. J.* 20, 577–582.
Pellegrini, N., Colombi, B., Salvatore, S., Brenna, O. V., Galaverna, G., Del Rio, D., Bianchi, M., Bennett, R. & Brighenti, F. (2007). Evaluation of antioxidant capacity of some fruit and vegetable foods: efficiency of extraction of a sequence of solvents. *Journal Science Food and Agriculture, 87*, 103–111.
Pizzale, L., Bortolomeazzi, R., Vichi, S., Uberegger, E., Conte, L. S. (2002). Antioxidant activity of sage (*Salvia officinalis* and *S fruticosa*) and oregano (*Origanum onites* and *O indercedens*) extracts related to their phenolic compound content. *Journal Science Food and Agriculture*, 82, 1645–1651.
Reddy, V., Urooj, A., Kumar, A. (2005). Evaluation of antioxidant activity of some plant extracts and their application in biscuits. *Food Chemistry, 90*, 317-321.
Ribeiro, M. A., Bernardo-Gil, M. G., & Esquível, M. M. (2001). *Melissa Officinalis* L.: Study of antioxidant activity in supercritical residues. *Journal Supercritical Fluids, 21*, 51-60.
Romani, A., Pineli, P., Mulinacci, N., Vincieri, F. F., & Tattini, M. (1999). Identification and quantification of polyphenols in leaves of *Myrtus communis* L.. *Chomatographia, 49*, 17-20.
Romani, A., Coinu, R., Carta, S., Pinelli, P., Galardi, C., Vincieri, F., & Franconi, F. (2004). Evaluation of Antioxidant Effect of different extracts of *Myrtus communis* L.. *Free Radical Research 38*, 97-103.
Rubilar, M., Pinelo, M., Ihl, M., Scheuermann, E., Sineiro, J., & Nuñez, M.J. (2006). Murta Leaves (*Ugni molinae* Turcz) as a Source of Antioxidant Polyphenols *Journal Agricultural Food Chemistry, 54*, 59-64.
Shahidi, F., & Wanasundara, P. D. (1992). Phenolic antioxidants. *Critical Reviews Food Science Nutrition 32*, 67–103.
Silva, E. M., Rogez, H., Larondelle, Y. (2007). Optimization of extraction of phenolics from *Inga edulis* leaves using response surface methodologies. *Separation and Purification Technology* 55, 281–387.
Tuberoso, C.I.G., Barra, A., Angioni, A., Sarritzu, E., Pirisi, F.M. (2006) Chemical Composition of Volatiles in Sardinian Myrtle (*Myrtus communis* L.) Alcoholic Extracts and Essential Oils *Agric. Food Chem.* 54, 1420–1426.
Yanishlieva, N. V., Marinova, E., & Pokorný, J. (2006). Natural antioxidants from herbs and spices. *European Journal Lipid Science Technology, 108*, 776–793.

Proceedings of the 10th International Chemical and
Biological Engineering Conference - CHEMPOR 2008
Braga, Portugal, September 4-6, 2008
E.C. Ferreira and M. Mota (Eds.)

Selection of a suitable adsorbent for decoloring sugar solutions from beet industry with ion exchange resins

M. Teresa García*, Mónica Coca, Silvia Mato, Irene Mediavilla, Gerardo González

Univ. Valladolid, Dep. Chemical Engineering and Environmental Technology, Pº Prado de la Magdalena s/n, 47011 Valladolid, Spain.

Keywords: Sugar technology; Color removal; Melanoidins; Resins; Size exclusion chromatography
Topic: Food Engineering

Abstract

Decolorization processes based on ion exchange resins have been applied for removing colorants present in sugar beet thin juices, in order to obtain a higher quality juice, without colored impurities that may reduce the efficiency of the crystallization stage. Molecular size distribution of coloring impurities in sugar beet juices was also studied to follow the evolution of colorants during the decolorization process. The color reduction percentages achieved were about 84-87% using decolorization processes based on one single stage. No considerable differences were observed between styrenic and acrylic resins. Dry matter content, purity and pH remained virtually constant during the decolorization process. The color reduction percentages slightly increased up to 91-92% using two beds in series. Size exclusion chromatography (SEC) of sugar beet thin juices confirmed the presence of colorants with molecular masses of 100-50 kDa and 2-3 kDa. The colorants with molecular mass of 100-50 kDa were completely removed whereas components 2-3 kDa presented lower removal efficiencies, showing lower affinity for the resins, especially for the acrylic resin.

1 Introduction

Juices and syrups formed during sugar beet processing contain impurities that impart yellow or brown color to white sugar. The origins of colorants are very diverse. These compounds are mainly formed through beet processing as a result of sugar degradation reactions, pH changes, thermal effects and reactions between amino compounds and carbohydrates (Maillard reaction). Despite their small quantities, colorants have a great impact on sugar quality. High molecular weight colorants may be occluded within sugar crystals, causing a negative effect on quantity and quality of white sugar. To meet standards of whiteness, it is necessary to undertake efforts to reduce color levels in the end product. The use of sulphur dioxide that inhibits non-enzymatic browning reactions or the adsorption with activated carbon is some of decolorization methods employed in industry. However, at usually process pH conditions, the colorants in beet sugar juices are mainly anionic compounds that may be removed by adsorption using ionic exchange resins (Broughton et al., 1991; García Agudo et al., 2002). Acrylic resins are commonly used to decolorize refined sugar solutions. These resins show low adsorption selectivity but can be easily regenerated. Polystyrenic resins show high decolorization efficiencies but its regeneration is more difficult than acrylic resins. The extent of adsorption of colored impurities depends on their molecular weight, type of charge, pH and character hydrophobic/hydrophilic (Bento, 1997). Most of resin applications in decolorization have been made in cane sugar industry (Bento, 1992, 1997; Godshall,

* Corresponding author. Tel +34 983 423 166; Fax: +34 983 432 013; E-mail: maite@iq.uva.es.

1999). Decolorization by ion exchange resins has not been employed in the beet sugar industry to the same extent as in cane sugar processing. The aim this work was to remove colored compounds present in sugar beet thin juice. Styrenic and acrylic resins were used in order to select a suitable decolorization scheme based on a single bed or two resin columns placed in series. Analysis by size exclusion chromatography coupled with diode array detection was chosen to yield information about the evolution of high molecular weight colorants in the decolorization stage.

2 Material and Methods

- *Adsorbent*: Three resins have been tested: the strong styrenic resins Lewatit S 6368 and Lewatit S 6328 A (Bayer) and the acrylic resin Lewatit VP OC 1074. Prior to being used, resins were regenerated with sodium hydroxide (4%w/w) and then washed with distilled water.
- *Adsorbate*: Sugar beet solutions containing 17-18% dry matter, pH 8.5-9.0, purity 96-97% and 3000-3300 IU were used in all experiments. Sugar solutions were prepared by diluting thick juice from a Northern beet sugar factory in Spain**.**
- *Experimental set up*: Experiments were carried out in duplicate in jacketed columns operating in parallel. Each column held 207 mL of resin (1 Bed Volume). Decolorization experiments were performed at 60 ºC feeding the thin juice at a flow rate of 11 BV/h in down flow direction. The cycle length was prolonged up to reduce about 90% of color. Decolorization was followed measuring absorbance at a wavelength of 420 nm, according to ICUMSA methods (ICUMSA, 1994). Two decolorization procedures were studied. First, decolorization in one bed (styrenic or acrylic resin) and then, decolorization in two beds connected in series. Two different types of resins were used in the columns. The experimental setup is shown in Figure 1.

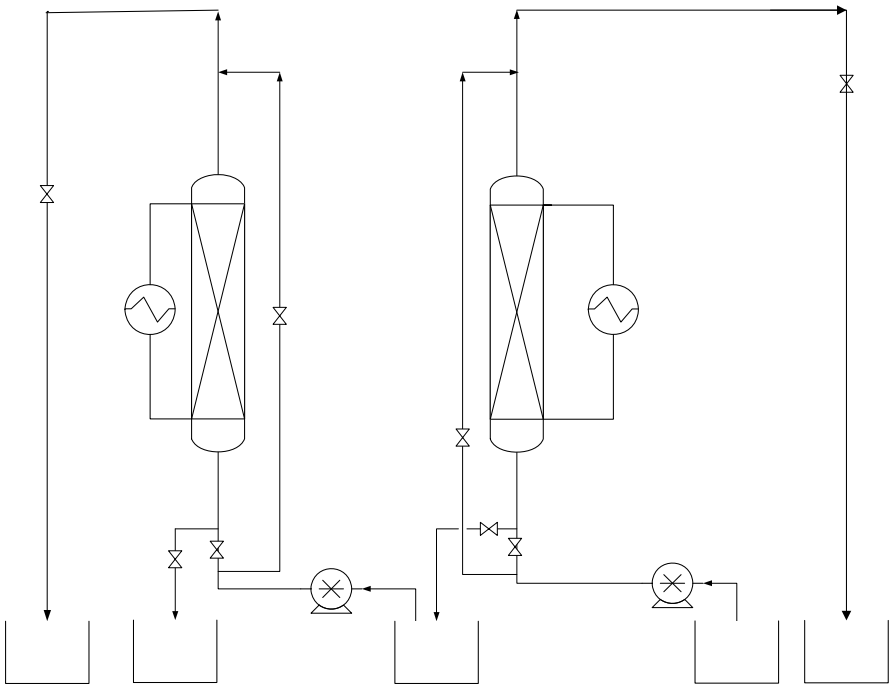

Figure 1: Experimental set up. Decolorization using two adsorbents in series.

After decolorization, resins were washed with 9 BV/h of distilled water in up flow mode until the outlet stream had almost no sugar in solution (0 to 1% dry matter). Resin regeneration was achieved with an alkaline calcium saccharate (Bento, 1999) solution containing $CaCl_2$ (25 g/L), CaO (5 g/L) and sucrose (120 g/L). Regenerant was fed

through the resin in down flow at 2.3 BV/h and 60 ºC. Finally, the resin was washed with distilled water at 9 BV/h in up flow mode until a value of dry matter content in the effluent lower than 5%. Washings were performed at room temperature. All the experiments were carried out in duplicate and mean values are presented.

- *Analytical procedures*: Color, dry matter content, pH and purity were determined according to ICUMSA methods (ICUMSA, 1994). The molecular masses of colored compounds were estimated by size exclusion chromatography (SEC). Separation was achieved in an Ultrahydrogel™ 250 column. Identification was achieved by using a Waters 996 Photodiode Array Detector. Samples were filtered through a 0.22 μm membrane before injecting onto the column.

3 Results and Discussion

Decolorization experiments were carried out feeding 5.5 BV (bed volume) at 11 BV/h. The volume of regenerant was 6.9 BV, fed during 180 min for achieving the release of adsorbed colorants. Table 1 compares the mean decolorization percentages attained using one decolorization bed or two decolorization beds in series. Color load adsorbed was calculated according to references (Bento, 1997).

Table 1: Decolorization efficiencies using ion exchange resins.

Resin	Decolorization, %	Adsorbed color load, %
S 6328A	84.4 ± 2.7	84.7 ± 2.7
S 6368	87.1 ± 3.8	88.6 ± 2.2
VP OC 1074	87.0 ± 0.1	87.4 ± 0.1
VP OC 1074 + S 6368	91.8 ± 0.8	95.3
S 6368 + VP OC 1074	91.5 ± 1.5	95.5

Dry matter content, purity and pH remained almost constant during the experimental runs. From the experimental results shown in Table 1, it can be concluded that there were no considerably differences among the resins studied. The styrenic resin S6368 provided slightly higher color removal percentages, a mean value about 87.1% was obtained, which corresponded to an adsorbed color load about 88.6%. As can be seen from Table 1, the decolorization percentages slightly increased using two beds in series. The acrylic resin followed by the styrenic resin (S 6368) provided the higher decolorization percentages, about 91.8%, which an adsorbed color load of 95.3%. The combination styrenic-acrylic resins provided a similar color reduction percentage, 91.5%.

Size exclusion chromatograms (Figure 2) showed that the colorants of higher molecular masses, 100-50 kDa, were more efficiently removed than the colorants of lower molecular weigh (about 2-3 kDa). As can be seen in Figure 2, colorants of higher molecular masses were almost completely removed whereas the reduction of 2-3 kDa colorants was considerably lower. Colorants of higher molecular mass are likely to be related to melanoidins (Coca et al., 2004). SEC chromatograms also confirmed that both styrenic resins were more efficient in removing lower molecular weight colorants than the acrylic resin VP OC 1074.

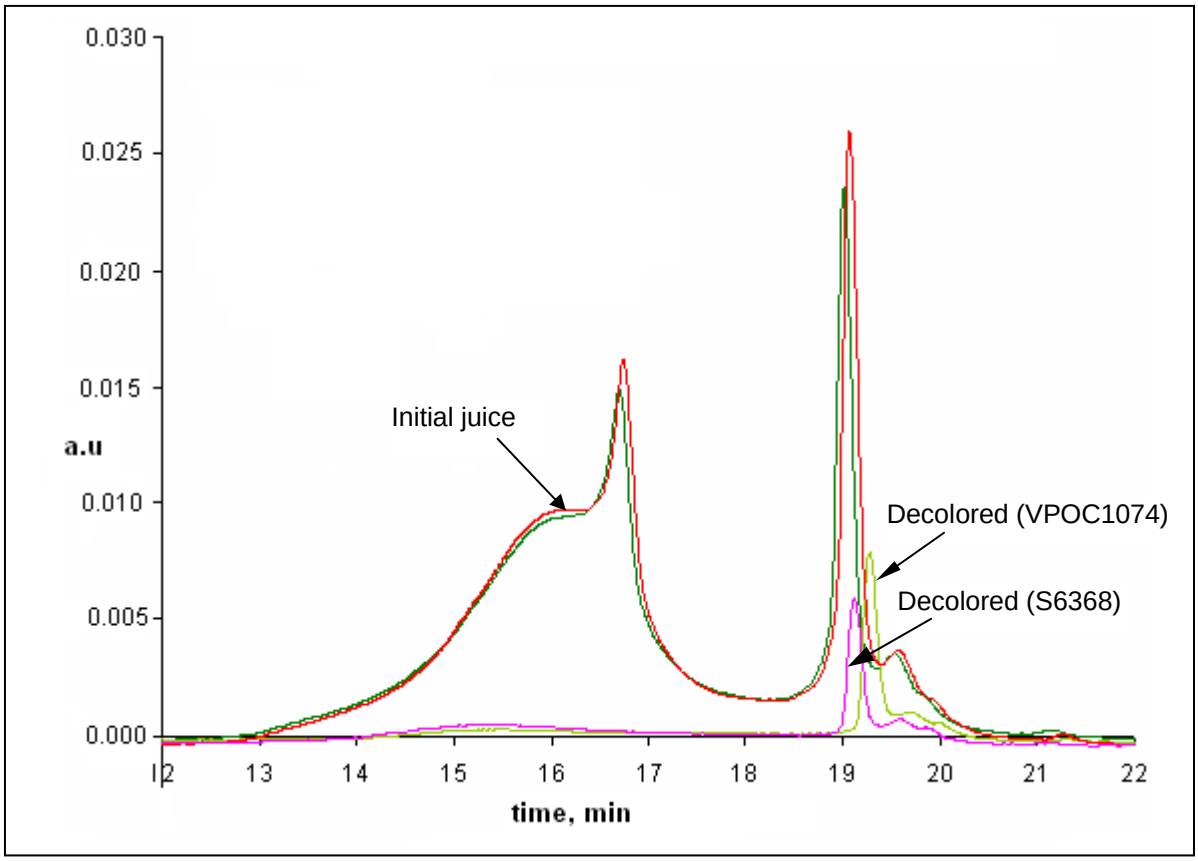

Figure 2: Decolorization of thin juice. Chromatograms run at 420 nm; a.u. absorbance units

4 Conclusions

In this work, a decolorization process using ion exchange resins has been studied for removing colored impurities in sugar solutions. The experimental results showed that decolorization using ion exchange resins is a suitable process for removing high molecular weight colorants in thin juices. The styrenic and acrylic resins tested showed similar results. Decolorization using two beds in series did not increase considerably the color reduction percentages. However, ion exchangers suffer the disadvantage of requiring regeneration. Therefore, this study must be improved with an optimization of the regeneration stage regarding the reduction of chemicals consumption and effluent disposal.

Acknowledgements

The authors acknowledge the financial support of this research to the Ministery of Science and Technology (MCyT, PPQ2000-0270-P4-02) and the company Azucarera Ebro, S.L. for its contribution to the development of the project.

References

Bento, L.S.M. (1992). Sugar Liquor Decolourization by Ion Exchange Resins. In Proceedings of SPRI Conference, New Orleans, USA

Bento, L.S.M. (1997). Ion exchange resins for sugar liquors decolourization. In Proceedings of SIT Conference, Montreal, Canada. Symposium A: Sugar Colour.

Bento, L.S.M. (1999). Utilisation of calcium chloride in an alkaline calcium saccharte solution to regenerate ion exchange resins for cane sugar liquors decolourisation. In Proceedings of CITS 21st General Assembly. Antwerp, 25-28.

Broughton, N.W., Sargent, D., Jones, G.C., Brown, B.W. (1991). Resin decolorization of beet sugar factory juices. In Proceedings of CITS, 477-502.

Coca, M., García, M.T., González, G., Peña, M., García, J.A. (2004). Study of colored components formed in sugar beet processing. Food Chemistry, 86, 421-433.

García Agudo, J.A., García Cubero, M.T., González Benito, G., & Peña Miranda, M. (2002). Removal of colored compounds from sugar solutions by adsorption onto anionic resins: equilibrium and kinetic study. *Separation and Purification Technology* 29, 199-205.

Godshall, M.A. (1999). Removal of colorants and polysaccharides and the quality of white sugar. In *Proceedings of 6º Symposium Association AVH*, Reims, 28-35

Proceedings of the 10th International Chemical and
Biological Engineering Conference - CHEMPOR 2008
Braga, Portugal, September 4-6, 2008
E.C. Ferreira and M. Mota (Eds.)

Kinetics of Kraft Pulp Brightening with Hydrogen Peroxide in a Final ECF Stage

Pedro E.G. Loureiro[1*], Dmitry V. Evtuguin[2], M. Graça V.S. Carvalho[1]
[1] CIEPQPF, Dep. Chemical Engineering, University of Coimbra, 3030-790 Coimbra, Portugal
[2] CICECO, Dep. Chemistry, University of Aveiro, 3810-193 Aveiro, Portugal

Keywords: Hydrogen Peroxide, Kinetics, Final bleaching stage, Brightness, Eucalyptus
Topic: Advancing the chemical and biological engineering fundamentals

Abstract

An industrial ECF partially bleached kraft pulp (DED) was further bleached in the laboratory with a final hydrogen peroxide stage in order to study its brightening kinetics. DTPA was used as additive since the preliminary study showed its usefulness on reducing peroxide consumption and on preserving pulp intrinsic viscosity. A novel approach was used to separate the peroxide consumption in pulp brightening reactions from the amount wasted in decomposition reactions. A negative effect of temperatures higher than 70 ºC was observed on peroxide decomposition, reaching half of its total consumption at 90 ºC. Furthermore, residence times greater than 120 min are not advisable for temperatures greater than 70ºC.

1 Introduction

Elemental chlorine free (ECF) sequences are presently the most used technology in wood pulp bleaching. The consolidation of this multistage pulp bleaching technique still needs better coordination between bleaching stages and target brightness, enhanced flexibility and higher washing efficiency, within the so-called concept of minimum impact mill. Regarding eucalyptus bleached pulps, there is an ever-increasing market demand, mainly for printing and writing paper grades. These specific products demand high strength pulps bleached to high brightness levels and exhibiting low brightness reversion. In this context, the final bleaching stage plays a key role in determining the quality of a market end-product.

The final stage in a chemical pulp bleaching sequence is a truly brightening stage to gain the difficult brightness points with the destruction of the chromophores remaining in pulp. The origin of many of these chromophores has been recently assigned to quinone type structures (Rosenau et al., 2007), thus justifying the final bleaching stage with hydrogen peroxide, which degrades these kinds of structures. Under alkaline conditions the brightening agent is considered to be the hydrogen peroxide anion (HOO^-), a strong nucleophile that reacts preferentially with carbonyl and conjugated carbonyl groups (Lachenal, 1996). However, besides chromophores destruction, the waste of hydrogen peroxide in decomposition reactions should be also considered. These competitive reactions are rather complex being base- and metal-catalysed. They involve distinct pathways, being water, oxygen and the intermediates hydroxyl ($HO\cdot$) and superoxide anion ($O_2\cdot^-$) radicals, the decomposition products. The reactions catalysed by transition metals, such as Mn, Fe and Cu, are the most detrimental due to the production of unselective radical species that can attack polysaccharides, thus reducing the pulp quality and/or yield. That is why a hydrogen peroxide bleaching stage always needs a metals control in the bleach plant which is carried out by using a previous selective chelation stage in a dedicated tower or by an unselective acid wash stage. The use of magnesium (as $MgSO_4$), which counteracts the detrimental effect of the transition metals, and/or chelants (e.g., EDTA and DTPA) as additives in the peroxide stage is common as well.

* Corresponding author. Tel + 351-239-798 700. E-mail: ploureiro@eq.uc.pt

The replacement of the final chlorine dioxide stage (D) in a conventional bleaching sequence, such as DEDD, by a hydrogen peroxide stage (P) is now well recognized to be advantageous in terms of pulp beatability and paper quality, with a particular emphasis on a lower brightness reversion (Parthasarathy and Colodette, 2007, Carvalho et al., 2008; Loureiro et al., 2008a). Accordingly, this shift in the last stage demands a kinetic study to find the optimal conditions to run the final P stage and also to provide a comprehensive comparison of the brightening and decomposition reactions rates, which is the aim of this paper. Our ultimate goal will be the development of mathematical kinetic models that could ensure efficient process control and optimization in a mill situation and, whenever possible, some mechanistic insights on reaction phenomena.

2 Experimental

An industrial sample of *Eucalyptus globulus* kraft pulp was collected in a conventional ECF bleach plant, DEDED, before entering in the last stage. The DED pulp was then thoroughly washed in the laboratory. This pulp had an ISO brightness of 87.5% and an intrinsic viscosity of 1066 dm^3/kg. In a preliminary study, the best stabilizing system was studied by using $MgSO_4$ and the sodium salt of diethylenetriaminepentaacetate (DTPA) and ethylenediaminetetraacetate (EDTA) as additives - Table 1. As for the kinetic studies, the pulp was bleached with hydrogen peroxide according to the conditions summarized in Table 1, at the reaction times of 1, 5, 15, 30, 60, 120, 180 and 240 min. The components of the bleaching system were pre-heated in an agitated thermostatic water bath to the desired temperature, as follows: the pulp was mixed with DTPA and NaOH solutions at 13% consistency in a polyethylene bag; in a glass flask, the H_2O_2 solution was added to the equivalent amount of water needed to attain a final consistency of 10%. After the pre-heating period, the hydrogen peroxide solution was added to the pulp suspension, setting the beginning of the reaction. The hydrogen peroxide decomposition kinetics were studied also according to the conditions in Table 1, using a highly bleached pulp (ISO brightness of 93.4 %) produced with the same DED pulp by applying a P stage twice at 8.0% odp H_2O_2, 1.1% odp NaOH, 0.05% odp DTPA, 90ºC for 60 min, with standard pulp washing in between.

Table 1. Ranges of bleaching conditions used in the final P stage.

Bleaching variable*	Preliminary study	Kinetic study
H_2O_2 (% odp)	1.0	0.5 – 2.0
NaOH (% odp)	0.60	0.6 – 0.8
DTPA (% odp)	0.05-0.20	0.05
EDTA (% odp)	0.05-0.20	---
$MgSO_4$ (% odp)	0.025-0.100	---
Temperature (ºC)	70	60 – 90
Time (min)	30	0 – 240

* - odp – oven dried pulp; consistency: 10%; 20 g of pulp (on a dry basis) were used in all experiments.

After each batch experiment, the pulp was vacuum filtered and the collected filtrate was used for the determination of chemicals residuals after its cooling in an ice bath. The pulp was also cooled with distilled water (~4ºC) and then washed with three litres of distilled water (~35ºC) divided into three equal portions. Hydrogen peroxide residual was determined by iodometric titration with standardized sodium thiosulphate solution while sodium hydroxide residual was determined by titration until pH 8.6 with standardized hydrochloric acid solution after barium chloride addition and filtration.

The ISO brightness and intrinsic viscosity were measured according to ISO 2470 and ISO 5351, respectively. Handsheets for optical properties determination were prepared using the standard procedure described in ISO 3688. The pulp metals content was determined by

atomic absorption spectroscopy in accordance with TAPPI T266-om. All the experimental procedures were performed twice and the results presented are the mean values.

3 Results and Discussion

The results of the preliminary study about peroxide stabilization are presented in Table 2. The positive effects of the additives on peroxide consumption, pulp ISO brightness and pulp intrinsic viscosity confirms their importance towards an economical and efficient brightening response. In fact, for the same ISO brightness level of 90±0.5%, the hydrogen peroxide consumption is much higher when no additives are introduced, as well as the loss in the viscosity, compared to the other bleaching systems. The reduction on peroxide consumption is most significant with DTPA, being a small charge of 0.05% odp quite enough. This is linked to the well established role of the transition metals on catalysing hydrogen peroxide decomposition reactions. Therefore, the results show that these competitive reactions can be minimized if efficient additives are introduced in the stage. The calcium, magnesium, iron and manganese contents of some bleached pulp samples is depicted in Figure 1. The use of chelants (EDTA and DTPA) led to a reduction in transition metals content, in particular Mn, which is the most detrimental ion in catalyzing hydrogen peroxide decomposition. The highest values of the Mg/Mn ratio, greater than 170 (much higher than the critical value of 30), are reached with the use of DTPA alone (both charges) or combined with $MgSO_4$ and with the use of EDTA+$MgSO_4$. Therefore, in the following kinetic studies a DTPA charge of 0.05% odp was used.

Table 2. Effect of different stabilizing systems on the performance of the final P stage of a $DE_{OP}DP$ bleaching sequence.

Additive charge (% odp)			DEDP pulp		
$MgSO_4$	DTPA	EDTA	H_2O_2 consumed (%)	ISO brightness (%)	Intrinsic viscosity (dm^3/kg)
---	---	---	42	90.2	979
0.025	---	---	21	89.9	1002
0.100	---	---	31	90.0	1056
---	0.050	---	9	90.1	1051
---	0.200	---	9	89.8	1065
0.025	0.050	---	15	89.9	1018
0.100	0.100	---	19	89.9	1049
---	---	0.050	22	90.0	1000
---	---	0.200	15	89.7	1001
0.025	---	0.050	14	89.9	1050
0.100	---	0.100	19	89.7	1035

The pulp ISO brightness evolution throughout the bleaching process is presented in Figures 2 and 3. In all experiments, there is a fast brightness gain in the first minutes of reaction which slows down afterwards. In some cases, asymptotic levels are attained and in others a negative evolution is even observed. These results suggest that a kinetic model to be developed may comprise two phases with different kinetics parameters due to the presence of chromophoric structures with dissimilar reaction rates. The brightness evolution is faster as hydrogen peroxide charge and/or the temperature increases. The moderate temperature of 70ºC renders a continuous evolution of brightness values for several hydrogen peroxide charges. In fact, even with the lowest charge, a brightness ceiling is not attained (Figure 2). Although an initial higher development of pulp brightness as temperature raises is observed (Figure 3), for temperatures greater than 70ºC, all hydrogen peroxide is consumed after

nearly 60 min (Figures 4 and 5) which leads to a slight pulp darkening for longer times. Therefore, 70ºC – 80ºC is a recommended range for the pulp used and residence times greater than 120 min are not advisable for greater temperatures. The recommended value is quite lower than the optimum reported in related literature, 90 ºC (Anderson and Amini, 1996). However, as shown in a complementary study (Loureiro et al., 2008b) the brightening kinetics of a final P stage strongly depends on pulp history, therefore no straightforward conclusions can be drawn without mention the pulp nature.

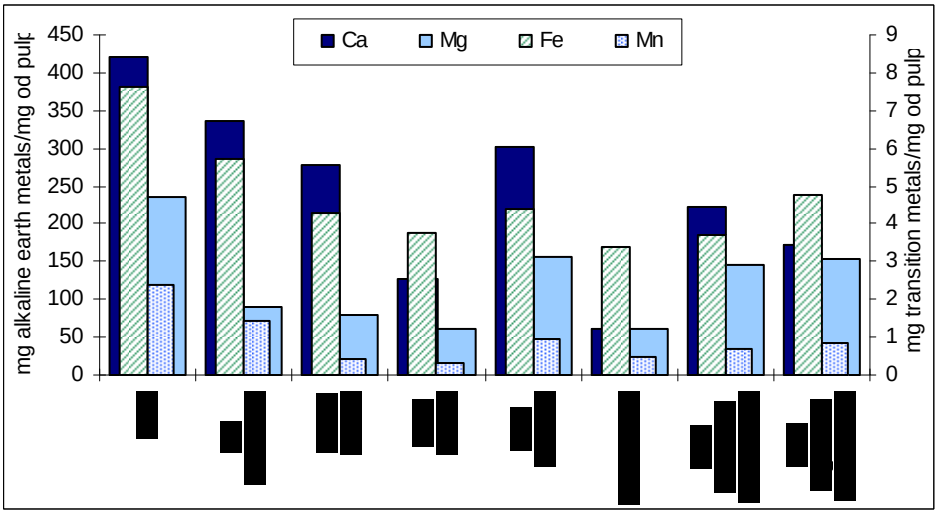

Figure 1. Ca, Mg, Fe and Mn contents of the $DE_{OP}DP$ bleached pulps using different stabilizing systems in the final P stage.

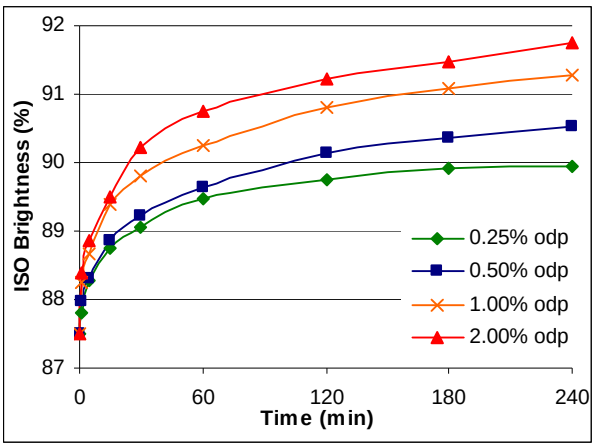

Figure 2. Brightening kinetics at 70 ºC with different hydrogen peroxide charges.

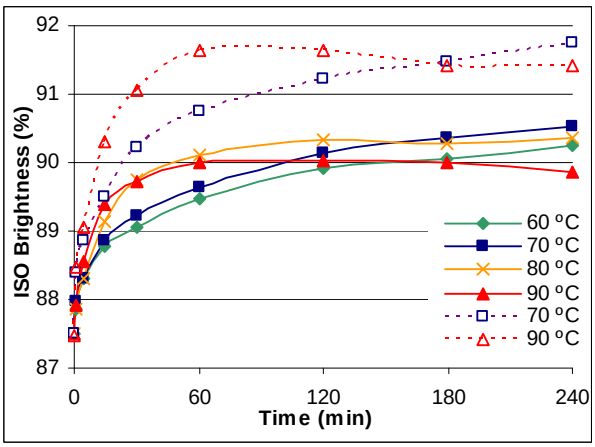

Figure 3. Effect of temperature on the brightening kinetics. H_2O_2 charges of 0.5 (filled symbols) and 2.0 % odp (empty symbols).

In terms of sodium hydroxide consumption, a continuous trend is seen only for temperatures greater than 70 ºC, while at 70 ºC the profile is by floors - Figures 6 and 7. Its consumption increases with temperature.

To assess the hydrogen peroxide consumed in the parallel reactions, other than brightening reactions, the same industrial pulp was used but bleached to very high brightness (with negligible chromophores content). A comparison between the total hydrogen peroxide consumed in the final P stage and the fraction consumed in decomposition reactions is presented in Figures 8 and 9 where a strong dependence on the temperature is perceived.

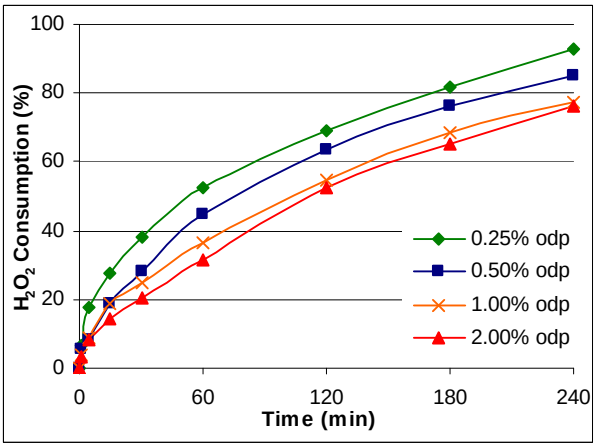

Figure 4. Hydrogen peroxide consumption kinetics at 70 ºC with different H_2O_2 charges.

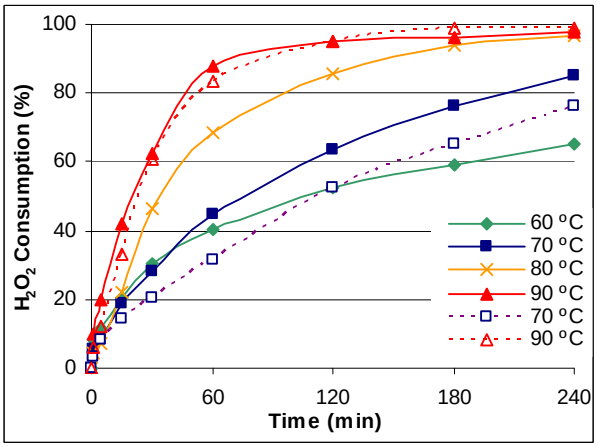

Figure 5. Effect of temperature on H_2O_2 consumption. H_2O_2 charges of 0.5 (filled symbols) and 2.0 % odp (empty symbols).

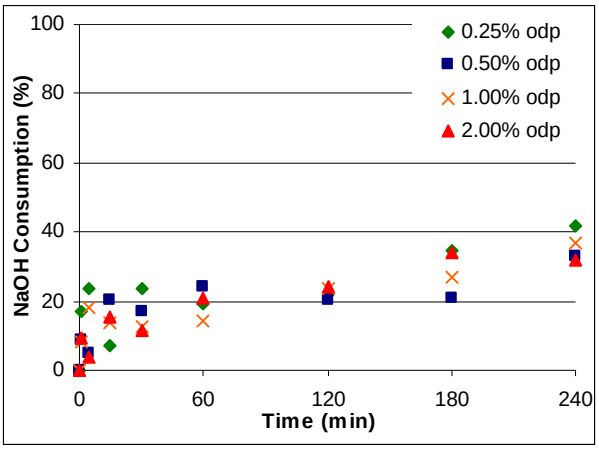

Figure 6. Sodium hydroxide consumption kinetics at 70 ºC with different H_2O_2 charges.

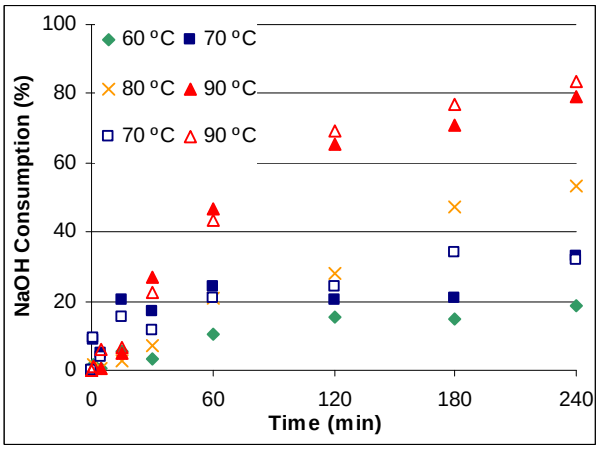

Figure 7. Effect of temperature on sodium H_2O_2 kinetics. H_2O_2 charges of 0.5 (filled symbols) and 2.0 % odp (empty symbols).

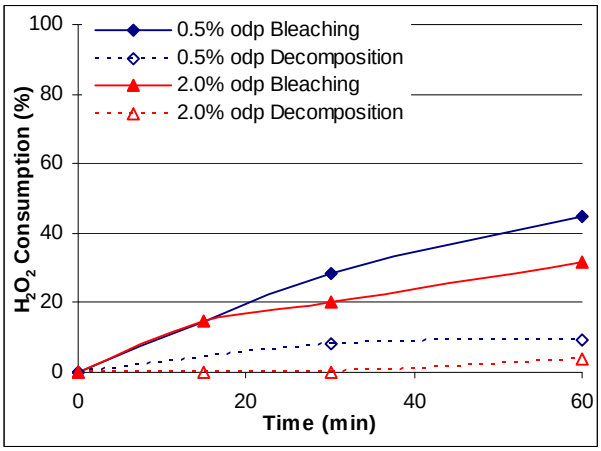

Figure 8. Comparison of H_2O_2 decomposition kinetics with total consumption kinetics in the P stage at 70 ºC with different H_2O_2 charges.

.

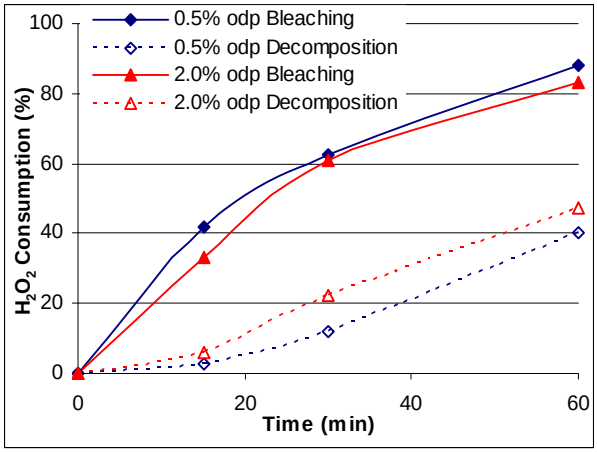

Figure 9. Comparison of H_2O_2 decomposition kinetics with total consumption kinetics in the P stage at 90 ºC with different H_2O_2 charges.

.

At 70ºC the H_2O_2 decomposition is minimal while at 90ºC the rate is enhanced. At 90ºC, the ratio between both consumptions increases with reaction time in favour of decomposition, reaching after 60 min near 50%, which is therefore wasted in non-brightening reactions.

In an earlier work by Stevens and Hsieh (1997), using an oxygen delignified softwood kraft pulp post-chelated, the peroxide decomposition was measured in a different way by monitoring the pressure rise in a CRS reactor. However, the majority of the experiments were conducted at very low consistency (0.5%) and keeping constant the chemicals concentration. In their additional experiments at 5 and 10% consistency, they did not find significant differences in the pulp brightness and peroxide consumption, despite being difficult to keep a medium homogeneous using a stirred reactor at such higher levels of consistency. Nevertheless, they also pointed out that the rate of decomposition is substantially increased at high temperatures, mostly under transition metal catalysis. Even with the addition of DTPA in our trials, it is expected that at high temperatures its metal trapping efficiency is impaired, not avoiding decomposition reactions.

4 Conclusions

It is important to minimize transition metal catalyzed reactions through the use of efficient additives in the final P stage, otherwise hydrogen peroxide is wasted in non-brightening reactions and at the same time impairing pulp intrinsic viscosity. A low charge of DTPA was quite enough to fulfil these requirements, at least at 70ºC. Residence times greater than 120 min are not advisable for temperatures greater than 70ºC for the pulp used.

Comparing the hydrogen peroxide decomposition kinetics with total peroxide decomposition kinetics, it was shown the importance of temperature in the decomposition rate. At 90ºC it reached half of the total hydrogen peroxide consumption after 60 min of reaction.

Acknowledgements

To RAIZ (Instituto de Investigação da Floresta e Papel) for the laboratorial assistance and to FCT (Fundação para a Ciência e Tecnologia) for the PhD scholarship granted to P. Loureiro.

References

Anderson, J.R., Amini, B. (1996). Hydrogen Peroxide Bleaching. In: Dence, C.W., Reeve, D.W. (eds). *Pulp Bleaching: Principles and Practice*, TAPPI PRESS, Atlanta, 411-442.

Carvalho, M.G.V.S., Carvalho, N.M.V, Loureiro, P.E.G. (2008). Performance of a Final Hydrogen Peroxide Stage in the ECF Bleaching of Eucalypt $D_0E_{OP}D_1$ Kraft Pulps. *Tappi Journal* (accepted).

Lachenal, D. (1996). Hydrogen Peroxide as a Delignifying Agent. In: Dence, C.W., Reeve, D.W. (eds.), *Pulp Bleaching – Principles and Practice*, TAPPI PRESS, Atlanta, 347-361.

Loureiro, P.E.G., Ferreira, P.J., Evtuguin, D.V., Carvalho, M.G.V.S. (2008a). Effect of the Final ECF Bleaching Stage on the Eucalyptus Kraft Pulp Properties – A Comparison between Hydrogen Peroxide and Chlorine Dioxide. *Proceedings of the International Pulp Bleaching Conference*, Québec City, 259-263.

Loureiro, P.E.G., Antunes, J.M.C., Gando-Ferreira, L.M., Evtuguin, D.V., Carvalho, M.G.V.S. (2008b). Comparison of brightening kinetics in the final hydrogen peroxide stage of $DE_{OP}DP$ and OQ(PO)DP bleaching sequences. *ABTCP 2008 - 41st International Pulp and Paper Congress*, São Paulo (accepted).

Parthasarathy, V.R., Colodette, J. (2007). Influence of Final Bleaching Stage on ECF Brightness Development, Refineability and Pulp Properties, *Proceedings of the International Colloquium on Eucalyptus Pulp*, Belo Horizonte, 1-15.

Rosenau, T., Potthast, A., Kosma, P., Suess, H., Nimmerfroh, N. (2007). Isolation and Identification of Residual Chromophores from Aged Bleached Pulp Samples. *Holzforschung*, 61(6):656-661.

Stevens, J.A., Hsieh, J.S. (1997). Achieving Maximum Peroxide Bleaching Response through Proper Selection of pH – a comparison of decomposition and bleaching reaction rates. *Proceedings of the Tappi Pulping Conference*, San Francisco, 765-773.

Proceedings of the 10th International Chemical and
Biological Engineering Conference - CHEMPOR 2008
Braga, Portugal, September 4-6, 2008
E.C. Ferreira and M. Mota (Eds.)

A Case Study of an Absorption Process for Flue Gas Treatment

Isabel M.B. Pereira[1*], M. Teresa Sena Esteves[1], Vitorino M. Beleza[1], Fernando Martins[2]

[1]CIETI, Instituto Superior de Engenharia do Porto, R. Dr. António Bernardino de Almeida, 431, 4200-072 Porto, Portugal

[2]Group PORTUCEL SOPORCEL, Cacia, Aveiro, Portugal

Keywords: Flue gas, Absorption, Bubble Columns, CO_2, SO_x, NO_x
Topic: Environmental engineering & management or Sustainable & clean technologies

Abstract

The use of alkaline industrial effluents as liquid absorbents is an attractive solution for flue gases treatment, when both currents are produced in the same plant.

The present work studies the removal of CO_2, SO_2 and NO from mixtures with similar composition to those of flue gases. The experimental essays were performed in a bubble column (inside diameter of 0.14 m, total height of 0.70 m), operated in counter current flow, at atmospheric pressure and ambient temperature. Two different types of absorbents were used: an alkaline industrial effluent and synthetic alkaline aqueous solutions (Na_2CO_3:NaOH).

The main conclusions were that both the industrial and the synthetic alkaline effluents with maximum pH of 12.6 were effectively neutralised to 7.0 < final pH <9.5, the removal values of CO_2 from the gaseous current were up to 25% and SO_2 was completely removed. The absorption of NO, significantly less effective, still claims further work.

1 Introduction

Fossil fuels combustion remains one of the greatest threats for air pollution. As energy demand keeps growing, environmental concerns increase and legal restrictions are more and more exigent. This justifies all the research work made within last decades in order to improve the efficiency of technologies used for the abatement of pollutants produced by fossil fuels combustion. All measures taken to improve the efficiency of combustion units are of prime importance for emissions reduction and good results are obtained with those preventive strategies in many power generation units. However, even in these cases, the removal of pollutants in flue gases by end of line technologies is normally necessary to meet legal standards.

Special attention has been devoted to the removal of SO_x, NO_x and more recently CO_2, due to its effect on global warming. Wet scrubbing, semidry and dry processes for SO_x removal, selective non-catalytic or catalytic reduction of NO_x are used for emissions treatment. Costs associated with these technologies are significant, mainly for the budget of small and medium size industrial units. Absorption processes used to eliminate acid gases from flue gases are widely described in the literature as wet scrubbing. They are considered the most efficient for SO_x removal, but usually more expensive. The equipment includes spray towers, plate columns or packed towers. Bubble columns are not fully explored. Typical absorbents are aqueous solutions of lime, limestone and sodium carbonate. Simultaneous removal of NO_x is less efficient but recent developments brought new results.

The selection of integrated procedures that take the industrial process as a whole is a quite recent concept. The replacement of common absorbents by alkaline effluents produced in

* Corresponding author. Tel + 351 228 340 500. E-mail: imp@isep.ipp.pt

situ is an attractive solution, as the neutralisation of both currents may be accomplished in a single step. In many industries (Portuguese industrial plants included) both kind of effluents are effectively produced. This study was designed under this perspective, bearing in mind the optimisation of absorption processes. This is considered in the literature an important aspect to be developed.

In the frame of this project and with the objective of studying real cases, a privileged cooperation protocol was established with an industrial Portuguese company: Group PORTUCEL SOPORCEL (Plant of Cacia, Aveiro, Portugal).

2 Experimental procedure

A schematic drawing of the experimental setup is presented in figure 1. The experiments were performed in a bubble column (1, in Figure 1) with inside diameter of 0,14 m and total height of 0,70 m. The column was operated in counter current flow at atmospheric pressure and ambient temperature (16±2ºC), with partial liquid recirculation. The liquid, coming from a feed tank (2, in Fig.1) was dispersed at the top of the column. The approximate volume of liquid in the column was 7 litres, in each experiment, and the total liquid average flowrate in the column was 200 L/h, with 80% recirculation. The gas entered the bottom of the column either through a perforated plate (with 24 holes of 5 mm diameter and one central hole of 2 cm diameter, PP) or through a perforated tube (with 9 holes of 2 mm diameter; PT2 or of 3 mm diameter, PT3).

As gaseous phase, mixtures of CO_2 and air were tested, as well as gaseous mixtures simulating flue gases composition. For these, two synthetic calibrated gas mixtures were used, one containing SO_2, NO and N_2 and the other CO_2, O_2 and N_2.

Experiments were carried out at different total gas flowrates (between 200 and 360 cm^3/s, 20ºC, 1bar) and different gas compositions ($8\%<CO_2<12\%$, $0<SO_2<980ppmv$, $0<NO<720ppmv$).

For every experiment, gas and liquid flowrates were regulated and measured inline (4 and 5 in fig. 1). The pH of the liquid outlet was monitored during each experiment. Except for the initial set of experiments, where the gaseous mixture only contained CO_2 and air, the gas composition at the inlet and outlet of the column has been continuously monitored by means of a gas analyser (Horiba PG 250, 6 in figure 1), in terms of O_2, SO_2, NO_x and CO_2. Data were acquired and stored by means of the analyser software.

All experiments were run until a stable value of pH in the column liquid outlet was reached. At this time, the gas analyser (when used) also provided stable values for the column gas outlet composition.

In a first set of experiments, an industrial effluent from Cacia paper pulp plant ($10.2<pH<11.7$, total alkalinity between 1.2 and 1.6 g $CaCO_3$/L) was used as the liquid phase. Being an industrial effluent, it showed some variability of pH and other characteristics in different dates of sampling. To minimize these differences, the industrial effluent was collected in Aveiro plant and transported to Porto (60 km) in large quantities (300 L or more) so that the largest number of experiments could be performed with no significant change of liquid properties. From these experiments, it was possible to characterize the absorption behaviour of the effluent, for a set of operating conditions.

To overcome the difficulties found with experimental reproducibility and effluent availability, and in order to simplify the experimental planning, the following step was to select a synthetic effluent with similar behaviour to that of the industrial one. Some aqueous solutions of Na_2CO_3:NaOH (in different proportions, meq/L, total concentration of 1.5 g/L as $CaCO_3$) were tested for the same experimental conditions as the industrial effluent.

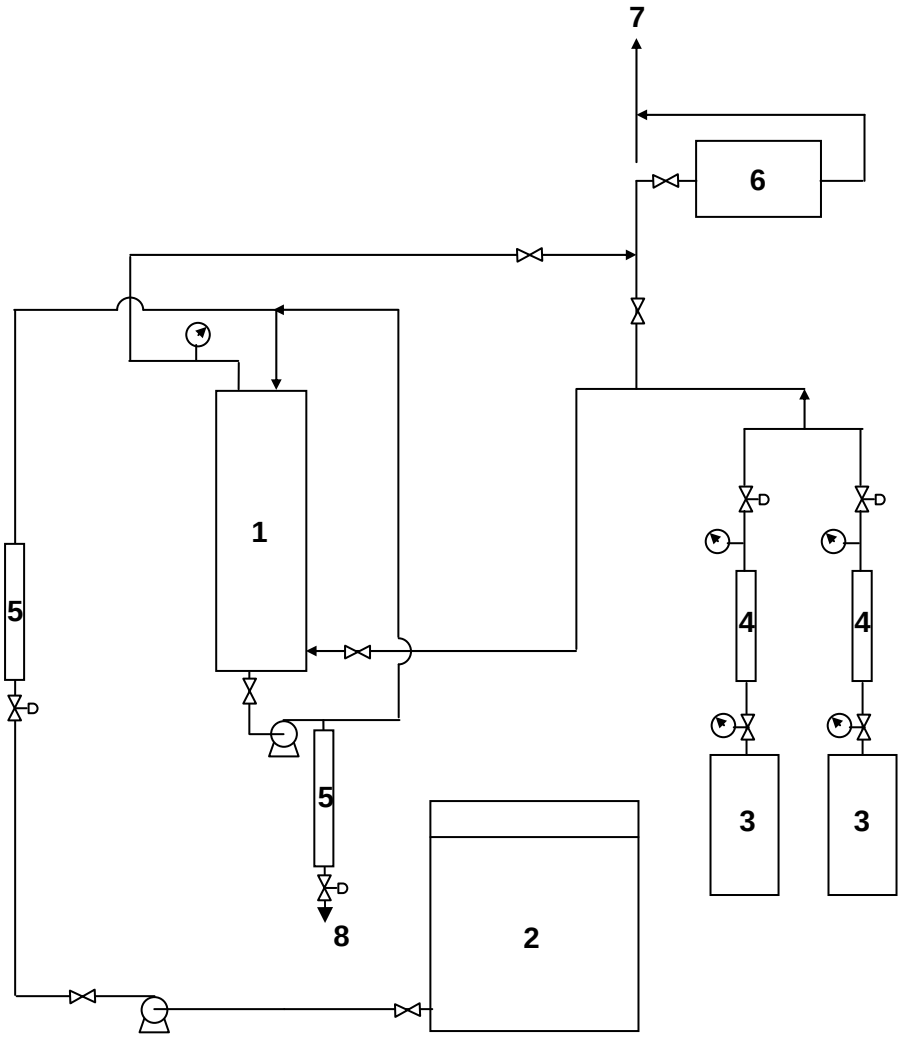

Legend

1 – bubble column
2 – liquid tank
3 – gas cylinder
4 – gas flowmeter
5 – liquid flowmeter
6 – Horiba gas analyser
7 – exhaustion
8 – liquid purge

- on-off valve
- flow regulation valve
- gauge manometer
- pressure reducer
- centrifugal pump

Figure 1 – Experimental setup for absorption experiments in a bubble column

3 Results and discussion

Industrial effluent absorption behaviour and selection of a synthetic effluent

The results presented in figure 2 were obtained for a total gas flowrate of 200 cm^3/s (1bar, 20ºC), using the perforated plate (PP) as gas distributor, and for two different inlet gas compositions (12% and 8% CO_2 in air).

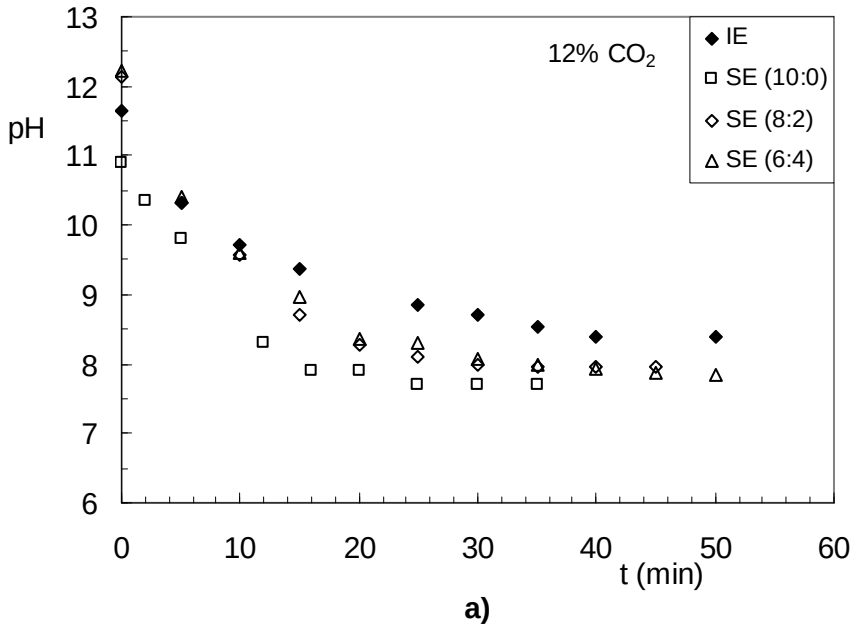

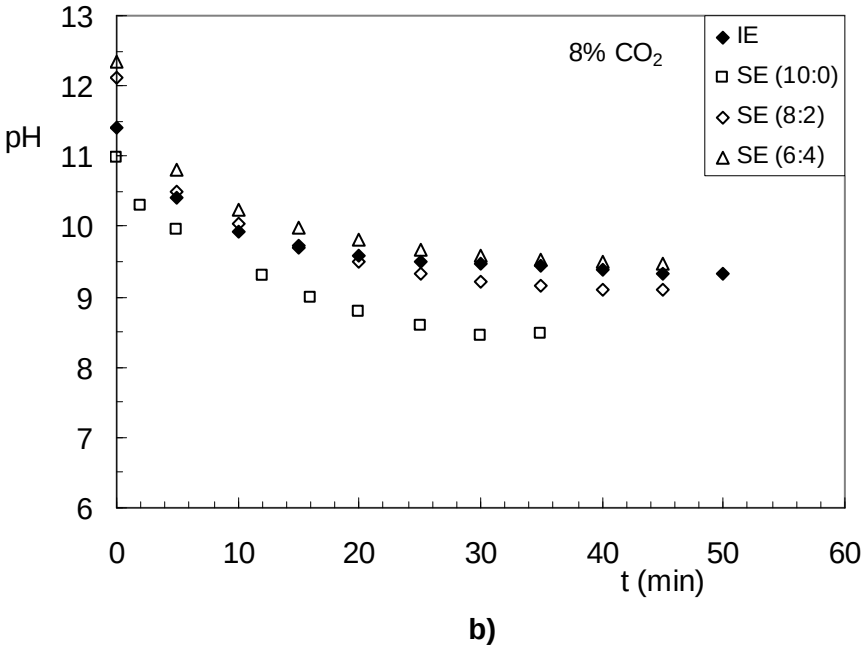

Figure 2 – Evolution of pH in the liquid column outlet with time, for absorption experiments with two different CO_2-air mixtures (a) 12% CO_2; b) 8% CO_2), where industrial effluent (IE) or synthetic effluent (SE) with 3 different proportions (meq/L) of Na_2CO_3:NaOH (1.5 g/L as $CaCO_3$) were used (total gas flowrate: 200 cm^3/s, 20ºC, 1bar; total liquid flowrate: 200 L/h; liquid purge: 42 L/h)

From figure 2, it may be observed that the neutralisation of the industrial effluent (initial pH around 11.5) was accomplished in both experiments, with final pH values of 8.4 (12%CO_2) or 9.3 (8% CO_2).

A similar behaviour was found when the gas phase included SO_2 and NO (9.0% CO_2, 714 ppmv NO, 975 ppmv SO_2). For these experiments, the industrial effluent used had an initial pH of 10.5, leaving the column, in final steady state conditions, with a pH of 7.0.

When comparing the behaviour of the industrial effluent (IE) to that of the synthetic effluents (SE), in both graphs of figure 2, the conclusion is that for the 3 proportions Na_2CO_3:NaOH tested, the one that better approximates the IE behaviour is the 6:4. This concentration was selected to continue the absorption study.

At this stage of the experimental work, the gas analyser was not yet available. Quantifying the removal of CO_2 from the gas phase was only possible by a liquid phase balance to the CO_2 in solution. The validity of this analytical method would be tested later in time, by comparison with gas balance results. The values obtained show that the removal percentages calculated by the liquid balance are systematically higher than those obtained by the gas balance, and with significant differences mainly for high initial values of pH of the liquid. Due to these discrepancies, the only conclusion about CO_2 removal for all the conditions tested (200 < total gas flowrate < 360 cm^3/s, 20ºC, 1bar, 8% < inlet CO_2 < 12%), in this first set of experiments (where CO_2-air was used), the percentage removed from the gaseous current was always less than 17%.

Absorption experiments using typical flue gas compositions

In table 1 some results of CO_2 removal efficiencies are presented, using gas compositions similar to those of flue gases. The CO_2 removal efficiency (as % of inlet CO_2) was calculated from a gas balance, based on the measured values of the gas inlet and outlet composition, in steady state conditions, and on the measured value of the inlet gas flowrate. The outlet gas flowrate was not experimentally measured but could be estimated, from the other known parameters.

Table 1 – Values of CO_2 removal efficiency, for different types of gas distributor, different gas flowrates and compositions; absorbent: aqueous solution of Na_2CO_3:NaOH (6:4, in meq/L), 1.5g/L as $CaCO_3$; liquid flowrate: 200 L/h

Inlet gas phase						Liquid phase		CO_2 removal efficiency (% of inlet)
Gas distributor*	Total gas flowrate (cm^3/s, 20ºC, 1bar)	CO_2 (%)	SO_2 (ppmv)	NO (ppmv)	O_2 (%)	inlet pH	outlet pH	
PP	272	9.40	416	326	9.20	12.0	7.9	14.8
PP	302	9.45	373	291	9.25	11.9	7.7	13.0
TP3	201	8.84	974	714	8.56	12.0	9.5	24.7
TP3	266	9.30	474	348	9.00	12.4	8.4	18.6
TP3	302	9.37	398	292	9.07	12.3	8.0	16.9
TP2	201	8.84	974	714	8.56	12.1	9.0	24.1
TP2	266	9.30	474	348	9.00	12.1	8.0	20.5

*PP – perforated plate; TP3 – perforated tube with 3mm holes; TP2 -– perforated tube with 2mm holes

The results of table 1 show that the perforated tubes allow higher CO_2 removals, without a significant difference between the two (TP2 and TP3), for identical flowrates. For the same gas distributor (TP3, TP2 or PP), the higher values of CO_2 % removal efficiency are obtained

for the lowest gas flowrate. This is probably due to a predominance of the effect of gas contact time in the column, when compared to the effect of higher turbulence for higher gas flowrates. For smaller flowrates, it also may be expected that the specific surface area might be somewhat higher as smaller bubbles are formed.

For the other relevant pollutants, SO_2 and NO, the removal efficiencies were calculated in a similar way. SO_2 was completely removed, as expected. For NO, the percentual removals varied between 0 and 16%.

4 Conclusions

Both the industrial and the synthetic alkaline effluents were effectively neutralised to 7.0< final pH <9.5.

An aqueous solution of Na_2CO_3:NaOH (6:4, in meq/L) with total concentration of 1.5 g/L as $CaCO_3$ was found to reproduce very reasonably the behaviour of the industrial effluent with pH of 11.5 and total alkalinity around 1.5 g/L as $CaCO_3$.

The efficiency values for the removal of CO_2 from the gaseous current were up to 25% (related to the inlet). SO_2 was completely removed, for every experiment and the absorption removal efficiency for NO was not higher than 16% and still claims for further work.

References

Beér, J.M. (2000). Combustion technology developments in power generation in response to environmental challenges. *Progress in Energy and Combustion Science*, 26, 301-327

Chien, T.W., Chu H. (2000). Removal of SO_2 and NO from flue gas by wet scrubbing using an aqueous $NaClO_2$ solution*. Journal of Hazardous Materials*, B80, 43-57

Jaber, J.O. (2002). Future energy consumption and greenhouse gas emissions in Jordanian industries. *Applied Energy*, 71, 15-30

Meikap, B.C. et al. (2002). Modelling of a novel multistage bubble column scrubber for flue gas desulphurisation. *Chemical Engineering Journal*, 86, 331-342

Radojevic, M. (1998). Reduction of nitrogen oxides in flue gases. *Environmental Pollution*, 102, S1, 685-689

Sedman, C.B. (1999). Controlling emissions from fuel and waste combustion-Newer methods look to remove multiple contaminants. *Chem. Engineering*, Jan, 82-88

Acknowledgements

This work was carried out with the financial support of the European Community Fund FEDER through the FCT, *Fundação para a Ciência e a Tecnologia*. (Approved Project in the frame of POCTI – Programa Operacional Ciência, Tecnologia e Inovação, do Quadro Comunitário de Apoio III)

The research team acknowledges the cooperation of Group Portucel Soporcel (and specifically of Cacia staff), which was of prime importance for the fulfilment of this project.

A special acknowledgement is given to all students from the Chemical Engineering Department/ISEP that participated for limited periods of time in the experimental work herein presented and/or all previous tests needed for the absorption setup and experimental procedure optimisation: Bruno Pereira, Eduarda Pina, Joaquim Correia, Marlene Eira, Pedro Costa, Renato Teixeira, Ricardo Lima, Sandra Marinho, Sara Barros, Vitor Fonseca.

Proceedings of the 10th International Chemical and
Biological Engineering Conference - CHEMPOR 2008
Braga, Portugal, September 4-6, 2008
E.C. Ferreira and M. Mota (Eds.)

Influence of nitrogen oxides on ozone concentrations at urban and remote areas

Sofia I.V. Sousa*, Maria C. Pereira, Fernando G. Martins, Maria C.M. Alvim-Ferraz

LEPAE – Laboratory for Process, Environmental and Energy Engineering, Department of Chemical Engineering, Faculty of Engineering, University of Porto, Rua Dr. Roberto Frias, s/n, 4200–465 Porto, Portugal.

Keywords: ozone, nitrogen oxides, urban area, remote area
Topic: Sustainable process-product development through green chemistry— Environmental engineering & management.

Abstract

High concentrations of near-surface ozone are known to have negative impacts on human health, especially among risk groups such as persons with respiratory problems, children and elderly. The purposes of this work were to compare ozone concentrations at remote areas with urban ones influenced by traffic and to evaluate how nitrogen dioxide influences ozone concentrations in both, urban and remote areas. For that, the concentrations of ozone and of its precursors at remote areas were assessed and compared with those observed at an urban area influenced by traffic. Measurements using passive samplers were compared with those performed with continuous monitors and it was possible to conclude that measurements with passive samplers had satisfactory reproducibility and precision. Comparing with one urban site, the results obtained at remote sites showed significantly lower concentrations of nitrogen dioxide (12 to 20 times) and volatile organic compounds (2 to 8 times) and higher ozone concentrations (2 to 3 times). It was inferred that the lower concentrations of nitrogen dioxide had determinant influence on the higher ozone concentrations found at the remote sites.

1 Introduction

High concentrations of superficial ozone have negative impacts on human health, vegetation, materials, climate and atmosphere composition (WHO, 2000). It is a particular threat to both, people suffering from respiratory problems, especially children and elderly, and those who exercise outdoors. Health effects include reduced pulmonary function, pulmonary inflammatory processes and increased airway permeability. Long-term exposure to high levels of ozone may lead to irreversible effects on lung function (WHO, 2005). Considering the harmful effects of this pollutant, standards that should not be exceeded were legislated by the European Union: i) information threshold (IT) - 180 $\mu g\ m^{-3}$ (1-hour average); ii) alert threshold (AT) - 240 $\mu g\ m^{-3}$ (1-hour average); and iii) target value for the protection of human health (TVPHH) - 120 $\mu g\ m^{-3}$ (8-hour running average) (EC Directive, 2002).

It is currently accepted that tropospheric ozone is a problem of international dimension, being one of the most important atmospheric pollutants for the twenty-first century (EEA, 1998). Five main factors control tropospheric ozone levels: i) photochemical production; ii) chemical destruction; iii) atmospheric transport; iv) surface dry deposition on vegetation, water and other materials; and v) stratospheric-tropospheric exchanges. In rural areas, ozone is removed mainly through dry deposition, whilst in urban areas the chemical destruction has the most important role (Sienfeld and Pandis, 1998).

* Corresponding author. Tel + 351-22-5081976. E-mail:sofia.sousa@fe.up.pt

Photochemical ozone is formed by reactions involving solar radiation and anthropogenic pollutants (methane, non-methane volatile organic compounds, carbon monoxide) in the presence of nitrogen oxides.

Ozone concentrations are strongly influenced by meteorological factors and their typical seasonal variation shows maximum values during spring and summer and minimum values during winter (Alvim-Ferraz et al., 2006). Several studies have concluded that the ozone concentrations are clearly higher at rural areas than at urban areas (Bayer-Oglesby et al., 2004; Dueñas et al., 2004).

In National Air Quality Monitoring Networks, ozone concentrations are measured with monitors working continuously. Data are collected via modem through specific software to calculate and store 15 minute averages. These measurements are costly and essentially designed for measuring at urban and suburban areas. The use of such equipment at remote areas is very difficult, reason why the values of ozone concentrations at remote areas are almost unknown (Manes et al., 2003; Sanz et al., 2007). Therefore, fpr monitoring at remote areas, alternatives were developed aiming to perform ozone measurements. A low-cost alternative and/or complement to continuous monitors is the use of passive samplers. These samplers require no power, are simple to assemble and operate and do not require calibration on the field (Bernard, et al., 1999; Krupa and Legge, 2000; Manes et al., 2003; Sanz et al., 2007).

The purposes of this work were to compare ozone concentrations at remote areas with urban ones influenced by traffic and to evaluate how nitrogen dioxide influences ozone concentrations in both, urban and remote areas.

2 Methodology

The study here reported was based on data measured at one urban site influenced by traffic in Oporto (PO) and at six remote sites: five at Bragança district (BG_1, BG_2, BG_3, BG_4 and BG_5) and one at Vila Real district, Lamas d'Olo (LO). PO site is located in a roundabout with several traffic streets, being considered an urban site mainly influenced by traffic. BG_1, BG_2, BG_3, BG_4, BG_5 and LO sites were located in natural environments not directly influenced by anthropogenic pollution sources and were, therefore, considered background remote sites.

Pollutant concentrations were measured with passive samplers (provided by Gradko International Ltd, England). To test their performance, the passive samplers were co-located with continuous monitors, at sites PO and LO. Those continuous monitors belong to the Air Quality Monitoring Network that is managed by *Comissão de Coordenação e Desenvolvimento Regional do Norte* (CCDR-N), under the responsibility of the Ministry of Environment. According to specified requirements, the sampling tubes were protected from sunlight and heat before and after exposure as well as during storage and transportation. Samplers were placed in an open field at a height of 2-2.5 m and were protected from rain and wind by appropriate shelters. Sampling tubes were simultaneously kept without exposure to be used as blanks for future analyses.

Pollutant concentrations were measured with passive samplers in two periods during the summer of 2006: 1st period - between 28/07/2006 and 10/08/2006 for PO and LO sites and between 27/07/2006 and 09/08/2006 for the other sites; and 2nd period - between 10/08/2006 and 05/09/2006 for PO and LO sites and between 09/08/2006 and 05/09/2006 for the other sites. The pollutants measured were ozone (O_3) and its precursors (recommended by the Directive 2002/3/EC): nitrogen dioxide (NO_2), total VOC and some specific VOC, namely, benzene, 1,2,4-trimethylbenzene, 1,3,5-trimethylbenzene, m/p-xylene, o-xylene and toluene. O_3, NO_2, and VOC determination on diffusion tubes was performed, respectively, by ion chromatography, UV spectrophotometry and Gas Chromatography-Mass Spectrometry (GC-MS).

O_3 and NO_2 concentrations were also continuously monitored using, respectively, UV-

absorption photometry and chemiluminescence methods. The equipment for continuous monitoring was submitted to a rigid maintenance program being periodically calibrated.

3 Results and Discussion

3.1 Comparison between Passive and Continuous Monitoring

The accuracy of passive samplers was evaluated by comparing the O_3 and NO_2 data obtained using continuous monitors with those using passive samplers at sites PO and LO. Comparison of VOC concentrations was not possible since they were not continuously measured.

It was possible to observe that the differences between both measurements were very low. Table 1 shows the mean concentrations of O_3 and NO_2 measured using passive sampling and continuous monitoring and the respective modules of the absolute and relative differences calculated for both sites and periods.

Table 1. Mean concentrations of ozone and nitrogen dioxide measured with passive sampling and continuous monitoring and the respective modules of the absolute and relative differences calculated for both sites and periods.

Pollutant	Period	Site	Passive Sampling ($\mu g.m^{-3}$)	Continuous Monitoring ($\mu g.m^{-3}$)	Absolute Difference ($\mu g\ m^{-3}$)	Relative Difference (%)
O_3	1st	PO	51.04	54.00	2.96	5.5
		LO	87.09	89.52	2.43	2.7
	2nd	PO	40.90	44.83	3.93	8.8
		LO	113.21	109.11	4.10	3.8
NO_2	1st	PO	39.13	38.24	0.89	2.3
		LO	3.22	2.44	0.78	31.8
	2nd	PO	50.94	45.67	5.27	11.6
		LO	2.83	3.38	0.55	16.2

For O_3, the comparison of both methods showed a maximum absolute difference of 4.1 $\mu g.m^{-3}$ and relative differences lower than 8.8%. The maximum absolute difference for NO_2 was 5.3 $\mu g.m^{-3}$ and the relative differences were higher than 12% only for very low concentrations (2-3 $\mu g.m^{-3}$). These results indicated satisfactory reproducibility and precision of the measurements made using passive samplers.

3.2 Influence of Nitrogen Oxides and Volatile Organic Compounds on Ozone Concentrations

Figure 1 shows the O_3 concentrations measured at all sites, for both 1st and 2nd periods of passive sampling.

The lowest concentrations of O_3 were observed at the PO site being 51.0 $\mu g\ m^{-3}$ and 40.9 $\mu g\ m^{-3}$ for the 1st and 2nd periods, respectively. From all remote sites analysed, BG_4 was the one with the highest concentrations during both periods (97.9 $\mu g\ m^{-3}$ and 122.0 $\mu g\ m^{-3}$, respectively). As expected, during the period of passive sampling the exceedances of IT, AT, and TVPHH were greater at the LO site than at the PO site, being, approximately, 5, 8, and 2 times greater, respectively.

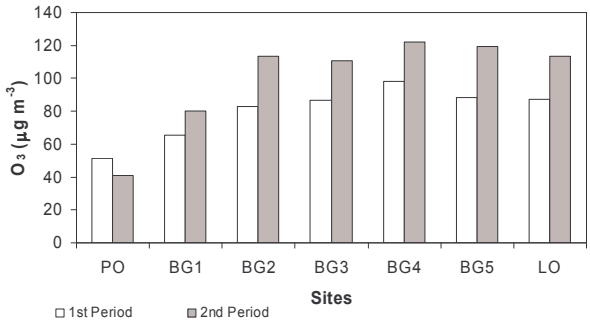

Figure 1. Ozone concentrations measured at all sites, during both 1st (around 305 h) and 2nd (around 640 h) periods of passive sampling.

It could be observed for PO site a typical profile of an urban area where O_3 formation was controlled by VOC concentrations, leading to a decrease on O_3 concentrations when NO_2 concentrations increased.

The NO_2 concentrations measured at all sites for both 1st and 2nd periods of passive sampling are presented in Figure 2.

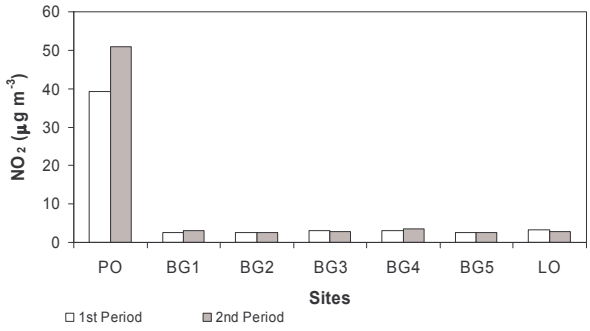

Figure 2. Concentrations of nitrogen dioxide measured at all sites during both 1st (around 305 h) and 2nd (around 640 h) periods of passive sampling.

NO_2 concentrations at PO site were, from 12 to 20 times higher than those at remote sites, due to the influence of traffic emissions. At remote sites, the concentrations were very low, being on average around 3 $\mu g\ m^{-3}$.

The total VOC concentrations during the periods of passive sampling are shown in Figure 3.

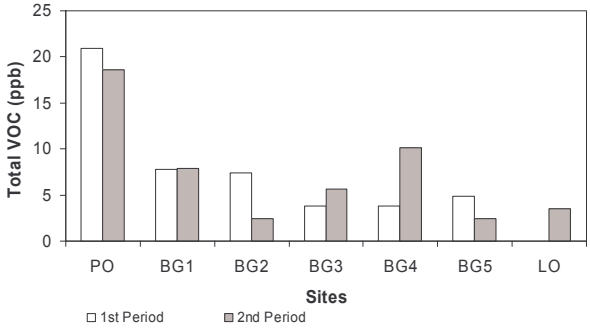

Figure 3. Concentrations of total volatile organic compounds measured at all sites during both 1st (around 305 h) and 2nd (around 640 h) periods of passive sampling.

The VOC concentrations were also considerably high at PO site, being from 2 to 8 times higher than at remote sites, again confirming the traffic influence. The total VOC concentrations observed at remote sites were very low varying from 2.5 ppb to 10.1 ppb.

The concentrations of NO_2 and VOC were very low at remote sites, therefore confirming the absence of anthropogenic emission influence. However, it was simultaneously observed at these sites the highest concentrations of O_3 which can be explained through the competition between VOC and NO_2 for the OH radical. When [VOC]/[NO_2] is low, typical of urban areas, OH reacts predominantly with NO_2, retarding O_3 formation; thus, an increase of NO_2 concentrations leads to a decrease on O_3 concentrations. For higher [VOC]/[NO_2], typical of rural areas, OH reacts predominantly with VOC, accelerating O_3 formation: in this situation, an increase of NO_2 concentrations leads to an increase on O_3 concentrations (Seinfeld and Pandis, 1998).

Figure 4 shows a daily profile of 8-hour running averages at PO site for: (a) one day belonging to the period of passive sampling; and (b) the average values for all the period of passive sampling.

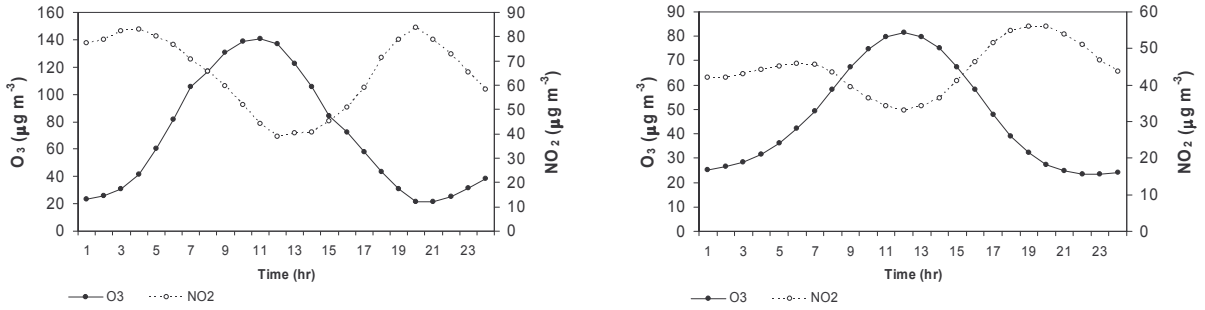

(a) (b)

Figure 4. Daily profile of 8-hour running averages at PO site for: (a) one day belonging to the period of passive sampling; and (b) the average for all the period of passive sampling.

For PO site, a typical profile of an urban area was observed where O_3 formation was controlled by VOC concentrations, leading to a decrease on O_3 concentrations when NO_2 concentrations increased.

Figure 5 shows a daily profile of 8-hour running averages at LO site for: (a) one day belonging to the period of passive sampling; and (b) the average values for all the period of passive sampling. For LO site, a typical profile of a rural area was observed where O_3 formation was controlled by NO_2 concentrations and therefore a decrease on O_3 concentrations led to a decrease in NO_2 concentrations.

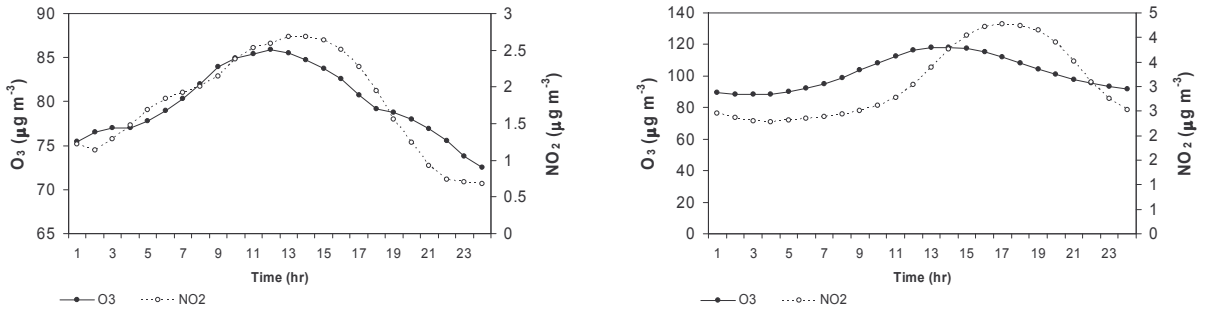

(a) (b)

Figure 5. Daily profile of 8-hour running averages at LO site for: (a) one day belonging to the period of passive sampling; and (b) the average for all the period of passive sampling.

These results showed that [VOC]/[NO_2] were relatively high at LO site because of the relatively quicker removal of NO_x from distant sources compared to that of VOC, coupled with the absence of NO_x local sources. Concluding, the absence of anthropogenic sources at remote areas, led to very low concentrations of NO_2, that had determinant influence on the high concentrations of O_3.

4 Conclusions

At the urban site, ozone formation was controlled by volatile organic compound concentrations, leading to a decrease in ozone concentrations when nitrogen dioxide concentrations increased. At the remote sites, ozone formation was controlled by nitrogen dioxide concentrations, due to its very low level. Accordingly, a decrease on ozone concentrations was observed when nitrogen dioxide concentrations decreased.

References

Alvim-Ferraz, M.C.M., Sousa, S.I.V., Pereira, M.C., Martins, F.G. (2006). Contribution of anthropogenic pollutants to the increase of tropospheric ozone levels in Oporto Metropolitan Area, Portugal since the 19th century. *Environmental Pollution*, 140, 516-524.

Bayer-Oglesby, L., Briggs, D., Hoek, G., Hoogh, K., Janssen, N., Jantunen, M., Sram, R., Urbanus, J. (2004). Air-Pollution and Risk to Human Health-Exposure Assessment. *Airnet work group 1*. Available at http://airnet.iras.uu.nl/.

Bernard, N.L., Gerber, M.J., Astre, C.M., Saintot, M.J. (1999). Ozone measurement with passive samplers: validation and use for ozone pollution assessment in Montpelier, France. *Environmental Science & Technology*, 33, 217-222.

Dueñas, C., Fernández, M.C., Cañete, S., Carretero, J., Liger, E. (2004). Analyses of ozone in urban and rural sites in Málaga (Spain). *Chemosphere*, 56, 631-639.

EC Directive. (2002). *2002/3/EC of the European Parliament and the Council relating to ozone in ambient air*. Off J Eur Commission, L67, 14–30.

EEA. (1998). *Tropospheric ozone in the European Union-the consolidated report*. Topic report nº 8/1998, European Environment Agency, Copenhagen.

Krupa, S.V., Legge, A.H. (2000). Passive sampling of ambient, gaseous air pollutants: an assessment from an ecological perspective. *Environmental Pollution*, 107, 31-45.

Manes, F., De Santis, F., Giannini, A., Vazzana, C., Capogna, F., Allegrini, I. (2003). Integrated ambient ozone evaluation by passive samplers and clover biomonitoring mini-stations. *Science of the Total Environment*, 308, 133-141.

Sanz, M.J., Calatayud, V., Sánchez-Peña, G. (2007). Measures of ozone concentrations using passive sampling in forests of South Western Europe. *Environmental Pollution*, 145, 620-628.

Seinfeld, J.H., Pandis, S.N. (1998). Atmospheric Chemistry and Physics – from Air Pollution to Climate Changes, A Wiley-Interscience Publication, USA.

WHO. (2000). *Air Quality Guidelines*, World Health Organization Regional Office, Copenhagen.

WHO. (2005) *The effects of air pollution on children's health and development: a review of the evidence*. WHO Regional Office, Bonn.

Proceedings of the 10th International Chemical and
Biological Engineering Conference - CHEMPOR 2008
Braga, Portugal, September 4-6, 2008
E.C. Ferreira and M. Mota (Eds.)

Influence of tobacco smoke on carcinogenic content of indoor particulate matter

Klara Slezakova, Maria C. Pereira, Maria C. Alvim-Ferraz
LEPAE, Departamento de Engenharia Química, Faculdade de Engenharia, Universidade do Porto, R. Dr. Roberto Frias, 4200-465 Porto, Portugal.

Keywords: PM_{10}, $PM_{2.5}$, PIXE, tobacco smoke, carcinogenic elements
Topic: Suitable process-product development trough green chemistry—Environmental engineering & management.

Abstract

Tobacco smoking is one of the greatest sources of the indoor inhalable (PM_{10}) particles. In past, the studies conducted on indoor particulates were mostly related to PM_{10}, however in the last decade respirable particles ($PM_{2.5}$) and even smaller particles (PM_1) began to be more important as they penetrate deeper in the respiratory system, causing severe health effects. Therefore, more information on fine particles should be provided. Aiming a further evaluation of the tobacco smoke impact on public health, this work evaluates the influence of tobacco smoke on the characteristics of PM_{10}, $PM_{2.5}$, and PM_1 considering concentration and elemental composition. Samples were collected at sites influenced by tobacco smoke, as well as at reference sites, using low-volume samplers; the element analyses were performed by Proton Induced X-ray Emission (PIXE).

It was found that tobacco smoke increased the total concentrations of five carcinogenic elements (Cr, Ni, As, Cd and Pb) 1100-2400% for PM_{10} and 840-2200% for $PM_{2.5}$. The analysis of elemental ratios confirmed that tobacco smoking mainly influenced the composition of the fine fraction of particles; as these smaller particles have a strong influence on health, these conclusions are relevant for the development of strategies to protect public health.

1 Introduction

Tobacco smoking (TS), a world wide habit, is certainly one of the greatest sources of the indoor inhalable particles, not only for the smokers but also for all those who are somehow exposed to it. Voluminous literature and public media linked the active tobacco smoking to lung and heart diseases and to cancers of various organ systems. However, passive smoking, i.e., exposure to secondhand tobacco smoke, also called environmental tobacco smoke (ETS), has also became an important health issue. It increases the risk and frequency of respiratory symptoms (wheeze, cough, breathlessness and phlegm) (WHO, 1999), being a proven cause of respiratory diseases of the lower airways (croup, bronchitis, bronchiolitis, pneumonia) in childhood and probably also during adulthood (Skorge et al., 2005). In 1993, the US Environmental Protection Agency (US EPA) classified ETS as a ‘‘Class 1’’ human carcinogen (EPA, 1993); accordingly, the International Agency for Research on Cancer unanimously stated that ETS is carcinogenic to humans (IARC, 2002). Over 4000 different chemicals have been identified in tobacco smoke that is a complex mixture of gaseous components including carbon monoxide, benzene, formaldehyde, toluene, and of particles of different sizes (Paoletti et al., 2006) mainly constituted by carbonaceous compounds, aromatic hydrocarbons with high molecular number, nicotine, and heavy metals; as most of particle components have known impacts on health, the exposure to particles represents serious risk to human health.

In the past years, many epidemiological studies (Alvim-Ferraz et al., 2005) showed a strong association between the exposure to PM_{10} (particles with aerodynamic diameter smaller than 10 μm) and especially to $PM_{2.5}$ (particles with aerodynamic diameter smaller than 2.5 μm) and the increase of morbidity and mortality rates, caused by pulmonary and cardiovascular diseases. The size of particles is an important characteristic because it determines the place of particle deposition in the respiratory systems, the smaller the particles, the deeper the penetration. While coarse particles deposit mainly in the nose and throat, fine particles can penetrate in the deeper parts of the lungs and they are able to reach the alveoli. Therefore, recent attention has been focused on $PM_{2.5}$ and PM_1 (particles with aerodynamic diameter smaller than 1 μm). It is still not clear though, whether the particles mass concentration itself accounts for the majority of the adverse health effects, as it is commonly belief that chemical composition may also significantly contribute to health effects of PM.

Despite several studies conducted on tobacco smoking, there is still information missing, mainly related to detailed physical-chemical characteristics of tobacco smoke particles. To further understand the impact of tobacco related particulate matter on public health, this study evaluated the influence of tobacco smoke on the characteristics of PM_{10}, $PM_{2.5}$ and PM_1, considering concentration and elemental composition of five carcinogenic elements (Cr, Ni, As, Cd and Pb).

2 Methods

The monitoring of PM_{10}, $PM_{2.5}$ and PM_1 was conducted during summer-autumn 2006 at four sites situated in Paranhos district of Oporto city in Portugal: two directly influenced by tobacco smoke, one office (Ts_1) and one cafeteria (Ts_2), and two homes not directly influenced by tobacco smoke, reference sites Rf_1 and Rf_2. At each site the sampling was conducted for 28 consecutive days. The number of occupants during sampling as well as other characteristics, such as the presence and use of electronic and cooking devices, cleaning activities and room ventilation were observed. Mechanical ventilation did not exist at the motoring sites; natural ventilation was provided by opening windows as occupants thought necessary.

Samples of indoor PM were daily collected for 12-h in order not to over-load filters for consequent chemical analysis. Sampling was done using TCR TECORA Bravo H2 constant flow samplers, combined with PM EN LVS sampling heads in compliance with the norm EN12341, using an air flow rate of 38.3 L min^{-1}. Inlets were placed 1.5 m above the floor and about 1 m from the walls, without obstructing the normal usage of the rooms. In order to perform different chemical analysis, two types of filter media were used; in alternating days PM_{10} and $PM_{2.5}$ were collected on polytetrafluoroethylene (PTFE) membrane filters with polymethylpentene support ring (2 μm porosity, Pall Life Science Teflon™), or on quartz fiber filters (∅47mm Schleicher & Schuell). PM_1 were collected on quartz fibre filters only as the respective sampler did not allow different filters.

PM masses were determined gravimetrically by subtracting the initial average mass of the blank filter from the final average mass of the sampled filter; the difference was then divided by the total volume of air that passed through filter (at 25°C and 101.3 kPa).

The elemental compositions of PM_{10} and $PM_{2.5}$ were determined by Proton Induced X-ray Emission (PIXE), which provided analysis for elements from magnesium trough uranium. For elemental analysis the PTFE filters were cut in half. One half was analysed while the other part was kept for possible replicates and other analysis. The analyses were performed at the ITN van de Graaff accelerator. As PM_1 were collected on quartz fibre filters it was not possible to determine the respective elemental composition.

For the data treatment, the Student's t-test was applied to determine the statistical significance ($P<0.05$, two tailed) of the differences between the determined means.

3 Results and discussions

At sites influenced by tobacco smoke, PM_{10} concentrations ranged from 21.3 to 220 μg m^{-3} (mean of 107 μg m^{-3}) and from 111 to 242 μg m^{-3} (mean of 156 μg m^{-3}), the corresponding $PM_{2.5}$ concentrations ranged from 17.6 to 202 μg m^{-3} (mean of 103 μg m^{-3}) and from 95.0 to 213 μg m^{-3} (mean of 132 μg m^{-3}). The reference sites exhibited lower values of PM, ranging from 8.4 to 58.8 μg m^{-3} (mean of 29.3 μg m^{-3}) and 6.8 to 44.8 μg m^{-3} (mean of 23.6 μg m^{-3}) for PM_{10} concentrations; the corresponding $PM_{2.5}$ concentrations ranged from 6.9 to 58.2 μg m^{-3} (mean of 24.6 μg m^{-3}) and from 6.1 to 40.5 μg m^{-3} (mean of 16.9 μg m^{-3}). PM_1 concentrations ranged from 17.1 to 153 μg m^{-3} (mean of 84.2 μg m^{-3}) and from 69.3 to 181 μg m^{-3} (mean of 110 μg m^{-3}) at the sites influenced by tobacco smoke; at the references sites PM_1 ranges were 5.5 to 44.7 μg m^{-3} (mean of 17.3 μg m^{-3}) and 3.6 to 30.2 μg m^{-3} (mean of 13.4 μg m^{-3}). In general, the results showed that tobacco smoke increased concentrations 270-560% for PM_{10}, 320-680% for $PM_{2.5}$ and 390-720% for PM_1. The statistical analysis of these results indicated that: i) as expected, PM_{10}, $PM_{2.5}$ and PM_1 concentrations were significantly higher at the sites influenced by tobacco smoking than at the reference ones; ii) the differences observed between PM_{10} means at sites Ts_1 and Ts_2 were statistically significant; iii) the differences observed between $PM_{2.5}$ means (as well as between PM_1) at sites Ts_1 and Ts_2 were not statistically significant; iv) the differences observed between PM_{10} means at sites Rf_1 and Rf_2 were statistically significant; v) the differences observed between $PM_{2.5}$ means (as well as between PM1) at sites Rf_1 and Rf_2 were not statistically significant; vi) PM_{10} and $PM_{2.5}$ means were significantly different at sites Ts_2 and Rf_2 but not at sites Ts_1 and Rf_1. In general, the results showed that tobacco smoke increased concentrations 270-560% for PM_{10}, 320-680% for $PM_{2.5}$ and 390-720% for PM_1. These results allowed concluding that tobacco smoke strongly increased PM concentrations, this increase being clearly higher for smaller particles.

To further understand the influence of tobacco smoke on public health, the elemental composition of PM was analysed with more detail. The elements listed as human or animal carcinogens are chromium (Cr), nickel (Ni), arsenic (As), cadmium (Cd) and lead (Pb), beryllium (Be), cobalt (Co) and mercury (Hg) (ATSDR, 2003). Of these Cr, Ni, As, Cd and Pb were reported to be the carcinogenic elements in ETS (Smith et al., 1997). In total, 25 elements were determined using the PIXE technique to characterize PM_{10} and $PM_{2.5}$ sampled at the two sites influenced by tobacco smoke and at the two reference sites, of these five elements were the carcinogenic ones: Cr, Ni, As, Cd and Pb. The mean concentrations of these carcinogenic elements (ng m^{-3}) in PM_{10} and $PM_{2.5}$ are presented in Figure 1.

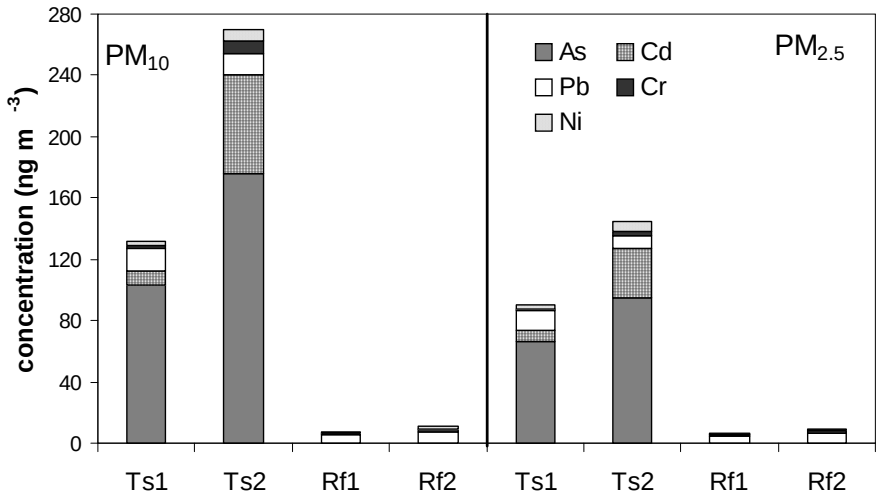

Figure 1. Comparison of mean concentrations of carcinogenic elements at two sites influenced by tobacco smoke (Ts1, Ts2) and two reference sites (Rf1, Rf2).

The obtained results showed that: i) at both sites influenced by tobacco smoke the levels of Cr, Ni, As, Cd and Pb in both fractions were significantly higher than at the reference sites; ii) the highest levels of Cr, Mn, Ni, As, Cd and Pb in both fractions were recorded at site Ts_2. From this figure it is also clear that at sites influenced by tobacco smoke, As was the most abundant element in both PM (ranging from 103 to 176 $\mu g\ m^{-3}$ and from 66 to 95 $\mu g\ m^{-3}$ in PM_{10} and $PM_{2.5}$, respectively). As and Cd occurred only in PM of sites with tobacco smoking, showing its strong influence on the presence of carcinogenic elements in indoor air. Pb concentrations at these sites were 110-180% and 30-190% higher than at the reference sites for PM_{10} and $PM_{2.5}$, respectively. Cr and Ni exhibited lower concentrations than As, Cd and Pb, mainly for the reference sites. Still, at the sites influenced by tobacco smoke, Cr and Ni concentrations in PM_{10} were 15-680% and 15-480% higher, respectively; the concentrations in $PM_{2.5}$ were 20-250% and 10-490% higher for Cr and Ni, respectively. The obtained results showed that by tobacco smoke increased 1100-2400% and 840-2200% the total concentrations of five carcinogenic elements (Cr, Ni, As, Cd and Pb) in PM_{10} and $PM_{2.5}$, respectively.

To understand better the distribution of elements between both PM fractions, the elemental concentrations of particles with sizes between 2.5 and 10 μm were calculated ($PM_{2.5-10}$). Figure 2 presents the mean ratios of elemental concentrations (expressed in $\mu g\ g^{-1}$) in $PM_{2.5}$ versus $PM_{2.5-10}$ for the sites influenced by tobacco smoking.

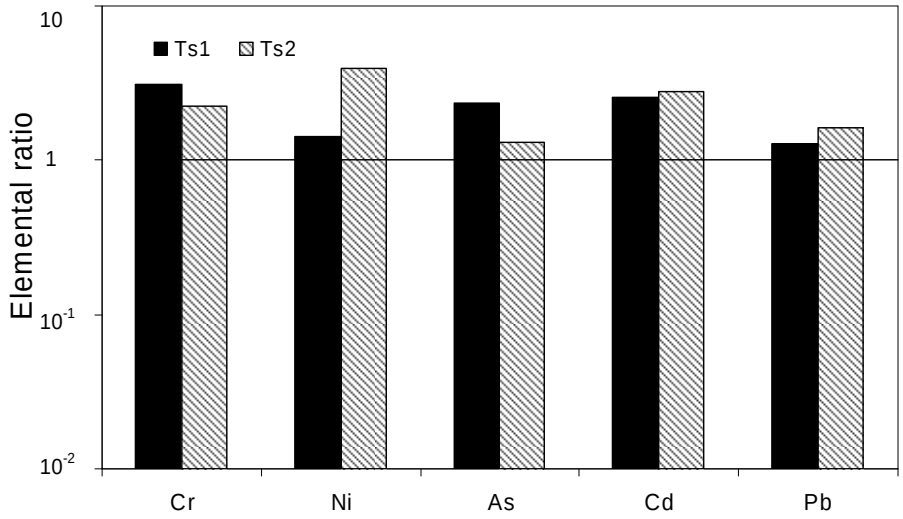

Figure 2. Mean ratios of elemental concentrations ($\mu g\ g^{-1}$) in $PM_{2.5}$ versus $PM_{2.5-10}$ at sites influenced by tobacco smoke.

At both sites influenced by tobacco smoking Cr, Ni, As, Cd and Pb exhibited ratios higher than 1 being the highest for Cr and Ni at Ts_1 and Ts_2, respectively. Thus, $PM_{2.5}$ was clearly the most important fraction for these five carcinogenic elements. Justifying the observed values, tobacco smoking was responsible for emissions of Cr, Ni, As, Cd, Pb present the mostly in the fine fraction.

The mean ratios of the elemental composition in $PM_{2.5}$ versus $PM_{2.5-10}$ at the references sites (Figure 3) showed that the behaviour of the background sites were different from those of the sites influenced by tobacco smoking. At both references sites only Ni exhibited the ratios higher than 1 showing that it was predominantly present in $PM_{2.5}$. For the other elements $PM_{2.5-10}$ was the prevailing fraction.

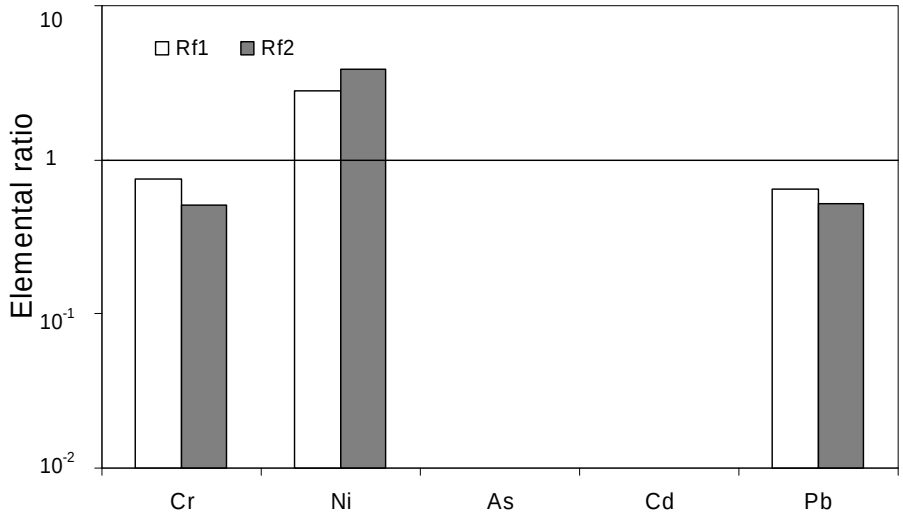

Figure 3. Mean ratios of elemental concentrations ($\mu g\ g^{-1}$) in $PM_{2.5}$ versus $PM_{2.5-10}$ at the reference sites.

4 Conclusions

Tobacco smoke strongly increased PM concentrations, this increase being clearly higher for smaller particles: 270-560% for PM_{10}, 320-680% for PM2.5 and 390-720% for PM_1. Levels of Cr Ni, As, Cd and Pb in PM_{10} and $PM_{2.5}$ reached values higher when influenced by tobacco smoke. Namely, for these five carcinogenic elements the total increase was 1100-2400% and 840-2200% for PM_{10} and $PM_{2.5}$, respectively. Cr concentrations were 15-680% and 20-250% higher in PM_{10} and $PM_{2.5}$, respectively. Ni concentrations were 15-480% and 10-490% higher in PM_{10} and $PM_{2.5}$, respectively. As and Cd occurred only in PM of sites with tobacco smoking. Pb concentrations were 110-180% and 30-190% higher than at the reference sites for PM_{10} and $PM_{2.5}$, respectively. These carcinogenic elements were predominantly present in the fine fraction. Thus, tobacco smoking mainly influenced the composition of the fine fraction of particles; as these smaller particles have a strong influence on health, these conclusions are relevant for the development of strategies to protect public health.

References

Alvim-Ferraz, M. C., Pereira, M. C., Ferraz, J. M., Almeida e Mello, A. M. C., Martins, F. G., (2005). European directives for air quality: Analysis of the new limits in comparison with asthmatic symptoms in children living in the Oporto Metropolitan area, Portugal. *Human and Ecological Risk Assessment*, 11, 607-616.

ATSDR, (2003). *Agency for Toxic Substances and Disease Registry. Toxicological profile information sheet*, http://www.atsdr.cdc.gov/toxprofiles.

EPA, (1993). *EPA Designates Smoking a ''Class 1'' or Known Human Carcinogen*. Available from: /http://www.epa.gov/history/smoke/01.htmS.

IAARC, (2002). *Involuntary smoking (Group 1).* Available from: /http://monographs.iarc.fr/htdocs/monographs/vol83/02/involuntary.htmlS.

Paoletti L., De Berardis B., Arrizza L., Granato V., 2006. Influence of tobacco smoke on indoor PM10 particulate matter characteristics. *Atmospheric Environment*, 40, 3269-3280.

Smith, C. J., Livingston, S. D., Doolittle, D. J., (1997). An international literature survey of "IARC Group I carcinogens" reported in mainstream cigarette smoke. *Food Chemistry and Toxicology*, 35, 1107-1130.

WHO, (1999). *International consultation on environmental tobacco smoke (ETS) and child health.* Available from:/http://www.who.int/tobacco/research/en/ets_report.pdfS.

Proceedings of the 10th International Chemical and
Biological Engineering Conference - CHEMPOR 2008
Braga, Portugal, September 4-6, 2008
E.C. Ferreira and M. Mota (Eds.)

Mechanized separation of plastics from municipal solid waste: evaluation of the separation efficiency by selective dissolution and Infrared Spectroscopy

Liliana R. Santos[1*], M. Conceição Paiva[2], Ana V. Machado[2], M. Teresa Carvalho[3]
[1] PIEP – Innovation in Polymer Engineering, University of Minho, 4800-058 Guimarães, Portugal
[2] I3N/IPC – University of Minho, Department of Polymer Engineering, 4800-058 Guimarães, Portugal
[3] CERENA, Instituto Superior Técnico, Av. Rovisco Pais, 1049-001 Lisboa, Portugal

Keywords: Polymer recycling, Polymer separation, Polymer analysis, Selective Dissolution, Fourier Infrared Spectroscopy
Topic: Sustainable process-product development through green chemistry.

Abstract

The work reported herein is part of a larger project aiming at developing a technology for the mechanical separation of plastics waste from drop-off-points. It uses analytical methods to characterize ternary mixtures of polymers that are difficult to separate by gravity techniques. Model mixtures of recycled PET/PVC/PS were separated using a method developed by G. Pappa et al (2001) and Nauman (1994) and were analyzed using solubility tests, thermogravimetry and infrared spectroscopy. Two approaches to this method were studied, one using the selective dissolution with flash evaporation (SD/FE) of the solvent and the other using selective dissolution with reprecipitation (SD/R) of the dissolved polymer. The solubility tests showed that the plastics in the ternary mixture could be separated in two steps. First, PS could be separated by dissolution in toluene, which does not dissolve PVC and PET at room temperature, and second, PVC could be separated from the remaining binary mixture using tetrahydrofuran as it does not dissolve PET at room temperature, remaining as the non dissolved plastic. TGA proved to be a very useful technique to assess PVC contamination, allowing the detection and quantification of small amounts of PVC in mixtures with other polymers. Infrared spectroscopy was used as a tool to detect the presence of polymers in mixtures, when they presented distinct characteristic IR bands. These analytical methods were used to determine the composition of plastic waste mixtures obtained through physical separation techniques developed in this project.

1 Introduction

Due to the increase of waste production in the last decades, the recycling of plastics and other materials is no longer seen as an option but as an obligation of the concerned society we are living in. It is the government's responsibility not only to develop the legislation for waste management and recycling activities, but also to support research and technologies in this area.

The plastics found in Municipal Solid Waste (MSW), originated mainly from packaging, became a serious environmental problem and a source of pollution because of their short life time and fast discard. The recycling of these plastics is a difficult problem to solve due to the level of contamination and the presence of a large variety of plastics. The recycling of heterogeneous mixed plastics must be preceded by their separation, due to the physico-

* Corresponding author. Tel + 351-253-510065. E-mail: liliana.rosa@piep.pt

chemical incompatibility of the different plastics and thus the difficulty in obtaining recycled materials with good mechanical properties directly from their mixtures.

There are two main types of plastics separation. The first is based on the separation by one physico-chemical property (Agante et al, 2004, Falconer, 2003, Dodbiba and Fujita, 2004), such as a difference in density, tribological separation, or use of infrared spectroscopy, and the second is the separation based on differences in solubility. The processes based on solubility are an alternative path for secondary recycling by type of plastic, and implicates the dissolution of the waste plastic with solvents and their subsequent recovery (Poulakis and Papaspyrides, 1995, 1997 and 2001).

The separation processes based on solubility include dissolution of a number of incompatible polymers in a common solvent, at different temperatures, or in different solvents, separating each polymer at a time. The polymer can be recovered either by fast evaporation of the solvent, using selective dissolution, or by the addition of an appropriate non-solvent (NS), that precipitates the polymer. The application of these methods to the separation of plastic waste, however, cannot be used because it would cause environmental problems due to the use of large amounts of solvents (Pappa et al, 2001).

The work reported here is part of a project under development in Portugal for the implementation of a pilot plant for the mechanical separation of granulated plastics from packaging waste. The project SEMEC, financed by Sociedade Ponto Verde (SPV), aims at the development of a low-cost, environmentally friendly methodology for the separation of the different plastics occurring at drop-off-points. The partners of the project are CERENA (a research center of Instituto Superior Técnico), PIEP (a research center at Minho University), Tratolixo (a solid waste management company, responsible for the collection of solid wastes in an area nearby Lisbon), and Selenis-Ambiente (a Portuguese PET recycling company). The partners from CERENA are involved in the development of separation technologies, while the PIEP/DEP partners are involved in the development of analytical methods for the characterization of the composition of the separated plastics.

The analysis of the plastic mixtures from MSW before and after separation was based on a selective dissolution method (Nauman and Lynch, 1994). The method used for selective dissolution tests in model mixtures of recycled plastics involved the following steps: (a) addition of a solvent to selectively dissolve only one of the polymers, under certain conditions; (b) filtration to remove the non dissolved polymers; (c) solvent evaporation to recover the dissolved polymer and for reuse of the distilled solvent (in the SD/FE method) or addition of a non-solvent (NS) to precipitate the dissolved polymer (in the SD/R method); (d) application of the same procedure for each polymer in the mixture.

In practice, for the mixtures from MSW the plastics were washed and the polyolefin fraction separated by density difference, in a water tank. The remaining plastics were constituted mostly by polystyrene (PS), polyvinyl chloride (PVC) and polyethylene terephthalate (PET). These were the plastics used in the dissolution process for mixtures quantification.

This analytical method allowed the systematic characterization of the fractions of MSW plastics separated by different mechanized methods, and to assess the interest and possible applications of the separated plastics according to the degree of purity or type of contaminations measured.

2 Experimental

Materials and Solvents

The materials used in the model mixtures of PET, PVC and PS were sent by *CERENA* and the plastics from Municipal Solid Waste (MSW), were collected by *Tratolixo.*

The solvents used were general reagent grade chemicals; toluene 28701, tetrahydrofuran Rectapur 28552 and methanol 20903, from VWR BDH Prolabo.

Polymer Recovery by the Selective Dissolution Process

The selective dissolution process consists in dissolving one polymer, in a mixture of polymers, using a solvent that dissolves that polymer at room temperature but doesn't dissolve the others. The recovery of the dissolved polymer can be made either by fast evaporation of the solvent or by the addition of a non-solvent (NS) that precipitates the polymer.

In order to test the selective dissolution/fast evaporation process (SD/FE), the ternary mixtures of plastics (PET/PS/PVC), in the form of granules, were weighed and stirred in toluene, at room temperature, with a magnetic stirrer. At room temperature, toluene dissolves PS but not PET or PVC. The PS solution was transferred to a flask, the solvent was evaporated and the PS was recovered. The procedure was repeated for the remaining PET/PVC binary mixture using tetrahydrofuran (THF) as a solvent. THF dissolves PVC at room temperature but not PET. The PVC solution was evaporated and the remaining PVC was recovered. PET was obtained as the remaining solid fraction.

For selective dissolution/reprecipitation (SD/R) the process was similar from the described above, but instead of evaporating the solvent, a non-solvent (methanol) was added to precipitate the dissolved polymers (PS in toluene and PVC in THF).

The separated plastics were then dried in a vacuum oven during 6 hours at 120 ºC for PS and PVC and at 160 ºC for PET. After drying, all the samples were identified by infrared spectroscopy (FTIR) and some of them were characterized by thermogravimetry (TGA).

The described methods were applied to ternary model mixtures of polymers, to evaluate the separation efficiency of the techniques, in order to be used later for the quantification of polymers in mixtures sampled from MSW, studied in the aim of the project SEMEC.

Fourier Transform Infrared Spectroscopy (FTIR)

The identification of the separated plastics was carried out on a FTIR Perkin Elmer 1610 instrument. Thin films of the samples were prepared in a hot press at 200 ºC for PS and PVC and at 290 ºC for PET and the FTIR spectra was acquired between 4400 and 450 cm^{-1}.

Thermogravimetry (TGA)

A thermogravimetric balance TA Instruments Q500 was used for the quantification of PVC in binary and ternary mixtures. Sample weights were approximately 10 mg, and the heating rate was 10 ºC/min from 100 ºC to 600 ºC, under nitrogen atmosphere.

3 Results and Discussion

Polymer Recovery by the Selective Dissolution Process

Model ternary mixtures of PET/PS/PVC were used to test the selective dissolution process and establish the best conditions for the laboratory procedure. The polymers separated by this process were dried, weighed, and identified by FTIR. The composition of the polymer mixtures before recovery and the weight % of the individual polymers recovered after solvent selective dissolution is presented in Table 1.

It was observed that, for the SD/FE process, the amount of material recovered by dissolution in toluene was higher than the amount of PS incorporated in the model mixture. This was mostly due to the solubility of the plasticizers contained in PVC that were partially dissolved in toluene. This was confirmed by FTIR of the residue obtained after solvent evaporation of PVC/toluene suspensions prepared in similar conditions as for PS dissolution. Other types of additives may also dissolve in toluene, but they were present in trace amounts.

Table 1 Weight percent composition of the polymer mixtures before separation and after recovery by selective dissolution/fast evaporation (SD/FE) and by selective dissolution/reprecipitation (SD/R).

Sample	PS (%)		PVC (%)		PET (%)		Total weight % of plastic recovered
	Before	***After***	***Before***	***After***	***Before***	***After***	
SD/FE	5.04	5.39	10.03	9.63	84.93	83.74	98.75
Stand. Dev.	0.04	0.11	0.02	0.12	0.05	0.48	0.47
SD/R	5.02	4.51	10.05	8.91	84.94	84.55	97.97
Stand. Dev.	0.03	0.21	0.02	0.29	0.04	0.06	0.34

In order to evaluate the typical amount of additives dissolved in toluene and THF, suspensions of PVC and of PET in toluene, and of PET in THF, were prepared in similar conditions as those used for the dissolution of PS and PVC. For the samples studied it was observed that toluene dissolved 3.54±0.12% of the initial weight of PVC, and 0.04±0.00% of the PET, and that THF dissolved 0.12±0.01% of the initial weight of PET. The solubility of PET additives in toluene is very low, and also relatively low in THF. PVC presents much higher weight loss due to the high amount of plasticizers usually incorporated in this polymer. This amount will vary from batch to batch, depending on the composition of the PVC waste present in the MSW.

The results obtained by reprecipitation of the polymer (SD/R) showed slightly higher losses in the polymer recovery but provided a more accurate estimate for the polymer mixture composition, since it was free from the interference of the soluble additives.

A typical sample from MSW was obtained from Tratolixo. At CERENA the sample was washed, the polyolefins separated from the other plastics by density difference, in water, and the remaining plastics mixture was analyzed at PIEP using the SD/FE method. The composition obtained for the MSW sample is presented in Table 2.

Table 2 Weight percent composition of the polymer mixtures obtained from MSW, determined by selective dissolution/fast evaporation (SD/FE)

Sample	Initial weight (g)	PS (%)	PVC (%)	PET (%)	Total weight % of plastic recovered
SD/FE	4.87	2.31	5.14	92.30	99.75
Stand. Dev.	0.29	0.78	1.03	1.58	0.16

Fourier Transform Infrared Spectroscopy (FTIR)

The different polymer fractions separated by selective dissolution were analyzed by FTIR. The spectra obtained identified the presence of pure PS, PET and plasticized PVC, indicating an efficient separation of the mixed polymers by selective dissolution, as shown in Fig. 1. For the PVC, the esther bands observed in the FTIR spectra are due to the presence of plasticizers, usually phtalates. Most of the plasticizers can be removed by Sohxlet extraction with ether (Fig. 1).

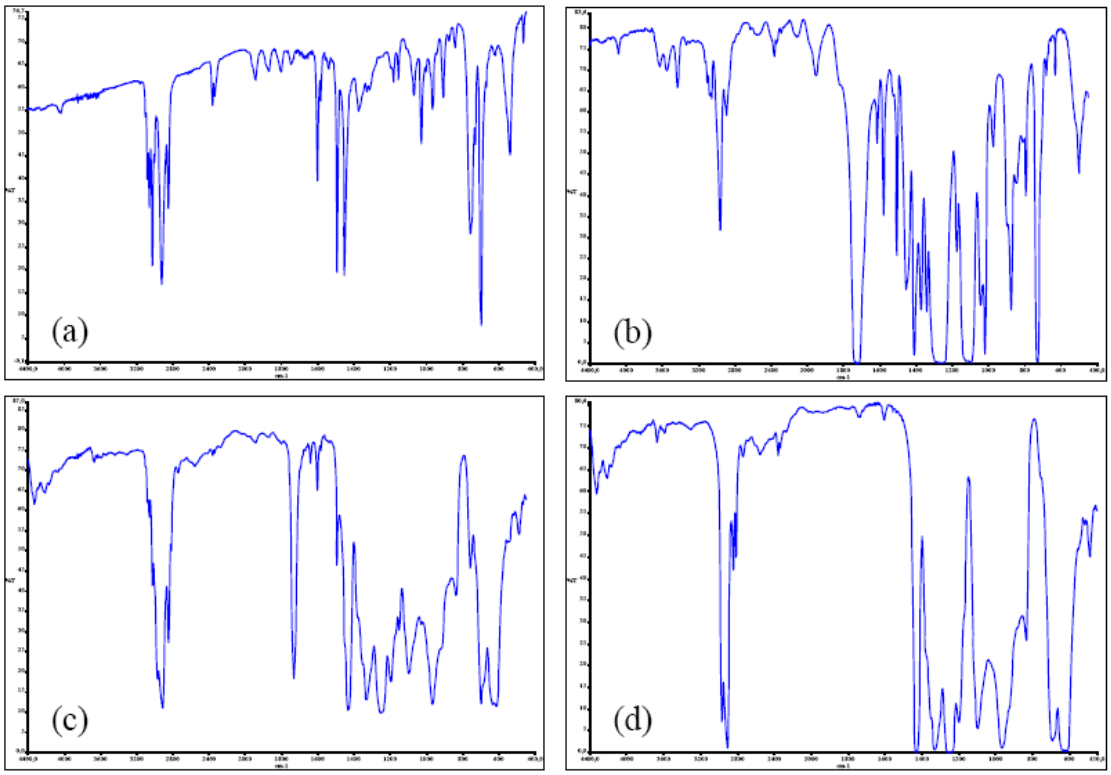

Figure 1 Infrared spectra of recovered samples: (a) PS, (b) PET, (c) PVC with plasticizer and (d) PVC without plasticizer.

Thermogravimetry (TGA)

The thermal degradation of PET and PS, in nitrogen, follows a very similar path, presenting one degradation step above 400ºC. The thermal degradation of PVC is different from the other polymers, presenting two degradation steps. The first step appears at a relatively low temperature (above 270ºC), corresponding to the elimination of HCl, and the second at a higher temperature, corresponding to the degradation of the carbonaceous backbone. This first dehydroclorination step of PVC is a characteristic step that can be used to quantify the amount of PVC present in polymer mixtures, at a concentration level not lower than approximately 1%. Thus, the weight loss observed in the first degradation step, above 270ºC, will correspond to approximately 58.3% of the PVC present in the sample. Figure 2 represents the TGA curve obtained for pure PVC (a) and for a mixture of polymers containing approximately 5% in weight of PVC (b).

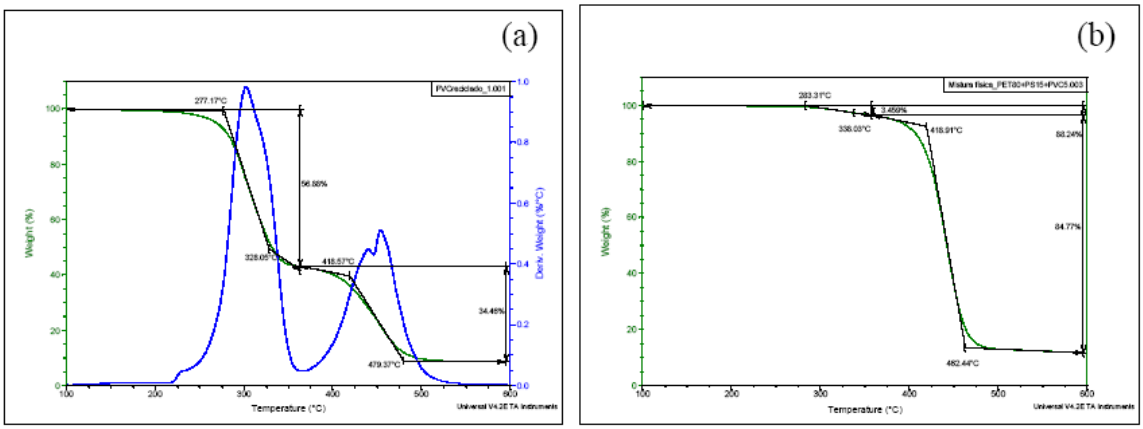

Figure 2 Thermograms of samples containing: (a) 100% of PVC; (b) 80% of PET, 15% of PS and 5% of PVC, obtained by heating at 10 ºC/min under N_2.

4 Conclusions

The conditions used in the selective dissolution/fast evaporation (SD/FE) and in the selective dissolution/reprecipitation (SD/R) methods described were efficient in the separation of plastics in model mixtures. The separated plastics were recovered with higher yield in the SD/FE method and with higher purity in the SD/R method. For fast and low cost quantification of the plastics present in the mixtures the SD/FE method was preferred, although there may be contamination from additives of the other plastics in the solution. The SD/R method was better suited for the separation of pure plastics, or when there is an interest in reusing the recovered plastics, but this method revealed to be more expensive and time consuming.

Small amounts of PVC in plastic mixtures could be quantified by TGA, for PVC contents higher than approximately 1 %.

The SD/FE method was used with success for the characterization of the MSW sample.

Acknowledgements: The authors gratefully acknowledge the financial support of Sociedade Ponto Verde through the project “Separação Mecanizada de Granulados de Plásticos da Recolha Selectiva”.

References

Pappa, G., Boukouvalas, C., Giannaris, C., Ntaras, N., Zografos, V., Magoulas, K., Lygeros, A., Tassios D. (2001). The selective dissolution/precipitation technique for polymer recycling: a pilot unit application. *Resources, Conservation and Recycling*, 34, 33-44

Nauman, E. B., Lynch, J. C. (1994). U. S. Patent 5,782,282

Agante, E., Carvalho, M. T., Durão, F., Bártolo T. (2004). *Proceedings do Global Symposium on Recycling, Waste Treatment and Clean Technology* (REWAS`04), Madrid – Spain, 26-29/09/2004

Falconer, A. (2003). Gravity separation: Old technique/new methods. *Physical Separation in Science and Engineering*, 12, 1, 31-48.

Dodbiba, G., Fujita, T. (2004). Progress in separating plastic materials for recycling. *Physical Separation in Science and Engineering*, 13, 3-4, 165-182.

Poulakis, J. G., Papaspyrides, C. D. (1995). The Dissolution/Reprecipitation Technique Applied on High-Density Polyethylene : I. Model Recycling Experiments. *Advances in Polymer Technology*,14, 3, 237-242

Poulakis, J. G., Papaspyrides, C. D. (1997). Recycling of polypropylene by the dissolution/reprecipitation technique : I. A model study. *Resources, Conservation and Recycling*, 20, 31-41

Poulakis, J. G., Papaspyrides, C. D. (2001). Dissolution/Reprecipitation: A Model Process for PET Bottle Recycling. *Journal of Applied Polymer Science*, 81, 91-95

Proceedings of the 10th International Chemical and
Biological Engineering Conference - CHEMPOR 2008
Braga, Portugal, September 4-6, 2008
E.C. Ferreira and M. Mota (Eds.)

Photo-degradation studies of polypropylene geotextiles

José Ricardo Carneiro[1*], Inês Maria Valente[2], Paulo Joaquim Almeida[2], Maria de Lurdes Lopes[1]

[1] Department of Civil Engineering, Faculty of Engineering, University of Porto,
Rua Dr. Roberto Frias, 4200-465 Porto, Portugal.

[2] Department of Chemistry, Faculty of Science, University of Porto,
Rua do Campo Alegre, 687, 4169-007 Porto, Portugal

Keywords: Geotextiles, Durability, Photo-degradation, Chimassorb 944, FTIR, HPLC.
Topic: Sustainable process-product development through green chemistry.

Abstract

In this work, non-woven geotextiles, made from polypropylene fibres stabilised with different amounts of the additive Chimassorb 944 (0%, 0.2% and 0.4%), were exposed to ultraviolet radiation (different radiant exposures) in a laboratory weatherometer. The photo-degradation suffered by the geotextiles was studied by infrared spectroscopy and by scanning electron microscopy. Simultaneously, the level of Chimassorb 944 on the geotextiles was monitored by liquid chromatography with spectrophotometric detection.

1 Introduction

Geotextiles (GTXs) are polymeric materials widely applied in the construction of infrastructures (such as, landfills, roads, railways, tunnels, dams and reservoirs) due to economical, technical and environmental advantages. In those applications, the GTXs can be exposed to several degradation agents (ultraviolet radiation and other weathering agents, atmospheric oxygen, high temperatures, chemicals and microorganisms), that may decrease their durability.

Among all the degradation agents, exposure to sunlight is considered one of the most damaging for the GTXs. The solar radiation that reaches the earth surface has wavelengths between 295 nm and 3000 nm. However, only the ultraviolet (UV) radiation (between 295 nm and 400 nm) is sufficiently energetic to initiate the polymeric degradation of the polymers used on the production of GTXs (polypropylene and polyester are the most used ones). The high-energetic UV radiation can promote the formation of high-reactive free radicals and, in the presence of oxygen, it is possible the occurrence of photo-degradation of the polymeric chains of the GTXs, according to the following reaction (Suits and Hsuan, 2003):

$$RH + O_2 + h\nu \rightarrow R\bullet + ROO\bullet + RO\bullet + \bullet OH$$

where RH is the polymer chain, *hv* is the energy supplied by UV radiation and R•, ROO•, RO• and •OH are free radicals formed during the degradation process. Hydroperoxides are successively formed and then decomposed during the photo-degradation of polyolefins (Commereuc *et al.*, 1997). The presence of carbonyl groups (resultant from the decomposition of hydroperoxides) in a degraded polymer indicates that oxidation has occurred (Kaci *et al.*, 2000). The degradation mechanism induced by UV radiation will continue until all free radicals are transformed into non-reactive species (for example, by the action of an antioxidant). This degradation process is usually accelerated by high temperatures and by the existence of high moisture contents on the materials.

* Corresponding author. Tel + 351225081613. E-mail:rcarneir@fe.up.pt

The simplest way to protect the GTXs against photo-degradation is by avoiding exposing them to sunlight. However, the elimination of all exposition to sunlight is in the majority of the cases impossible and, in some situations, the GTXs can be exposed during long periods of time (months or even years). In order to retard and/or inhibit the photo-degradation process, chemical stabilisers (such as UV stabilisers, antioxidants and pigments) are often added to the GTXs composition.

Nowadays, many techniques are available for evaluating the photo-degradation suffered by polymeric materials. For instance, chemical changes arising from exposing materials to UV radiation can be investigated by infrared spectroscopy, while changes on the materials surface can be characterised by microscopic techniques; mechanical tests are available for determining changes on the mechanical properties of the materials. Several analytical methods are also described in literature for the determination of many chemical additives often present in polymeric materials.

2 Experimental description

In this work, we studied three non-woven GTXs (mass per unit area of 500 $g.m^{-2}$) made from polypropylene (PP) fibres stabilised with different amounts (0%, 0.2% and 0.4%, *w/w*) of the additive Chimassorb 944 (C944). C944 is an additive widely used in the stabilisation of polyolefins against the damaging effects of oxygen and UV radiation.

The GTXs were exposed to UV radiation, at the temperature of 60 ºC, in a laboratory weatherometer – the QUV (Q-Panel Lab Products, model QUV/spray). Fluorescent UV lamps (type UVA-340) were used as the UV radiation source (these lamps provide a very good simulation of the UV radiation emitted by sunlight). The GTXs were exposed to different total UV (290-400 nm) radiant exposures of 35 $MJ.m^{-2}$, 69 $MJ.m^{-2}$, 104 $MJ.m^{-2}$ and 138 $MJ.m^{-2}$.

The degradation suffered by the PP fibres was studied by Fourier transform infrared spectroscopy (FTIR) and by scanning electron microscopy (SEM). The infrared analyses were performed in a spectrometer from Perkin-Elmer (model Spectrum RXI FT-IR system). PP fibres (mass of about 5 mg) were grinded and then crushed in a mechanical press to form translucent pellets. SEM analysis was used to characterise the microscopic changes occurred on the PP fibres during the exposition to UV radiation.

A simple methodology was developed for the determination of C944 on the PP fibres. This methodology can be divided in two main steps: (1) ultrasonic extraction with chloroform at 60 ºC for removing C944 from the samples; (2) separation and determination of the additive by liquid chromatography with detection at 244 nm. The ultrasonic extractions were performed in an ultrasonic bath from Bandelin Sonorex (model TK52, frequency of 35 kHz). For the chromatographic analyses, a Jasco HPLC equipment was used, consisting of a flow pump Jasco (model PU-2089 Plus), a Rheodyne (model 7725(i)) injection valve with a 20 μL loop, a spectrophotometric detector Jasco (model UV-2070 Plus) and an interface box Jasco LC-Net II/ADC. A pre-column Kromasil NH_2 (10 mm x 4 mm, 5 μm particle size) and a column Kromasil NH_2 (250 mm x 4.6 mm, 5 μm particle size) from Hichrom were used. Isocratic elution was used with a flow of 1 $mL.min^{-1}$ of chloroform. In these conditions, C944 had a retention time of about 5 minutes.

3 Main results

The UV-exposure tests caused serious damages on the GTX without the additive C944. Indeed, just after an exposure of 35 $MJ.m^{-2}$ of UV radiation, this GTX was reduced into small pieces or powder (the unstabilised PP fibres depolymerised completely). The exposition to higher amounts of UV radiation (69, 104 and 138 $MJ.m^{-2}$) resulted in similar damages for this material.

The GTXs stabilised with 0.2% and 0.4% of C944 were not completely destructed after the exposition to 35 $MJ.m^{-2}$ of UV radiation, which showed the importance of C944 on the protection of the materials against photo-degradation. However, after the exposition to 104 $MJ.m^{-2}$ of UV radiation, both GTXs were releasing small pieces of depolymerised fibres (almost powder), which indicated the existence of serious damages on their polymeric structure. After exposition to 138 $MJ.m^{-2}$ of UV radiation, the GTX with 0.2% of C944 was near complete destruction (less than 5% of its original tensile strength, data not shown), while the GTX with 0.4% of C944 continued to release high amounts of damaged fibres.

SEM analysis showed the degradation suffered by the PP fibres during the UV-exposure tests (Figure 1). After exposition to 35 $MJ.m^{-2}$ of UV radiation, no microscopic damages were found on the GTXs with 0.2% and 0.4% of C944. However, after the exposition to 69 $MJ.m^{-2}$ of UV radiation, both GTXs presented visible signs of degradation, such as transversal fissures along their fibres. As the total UV radiant exposure increased, more damages were continuously found on the PP fibres. For the same total UV radiant energy, the fibres with 0.2% of C944 were always more damaged than the fibres with 0.4% of C944. SEM analysis was not performed for the GTX without C944 (this material was completely destructed).

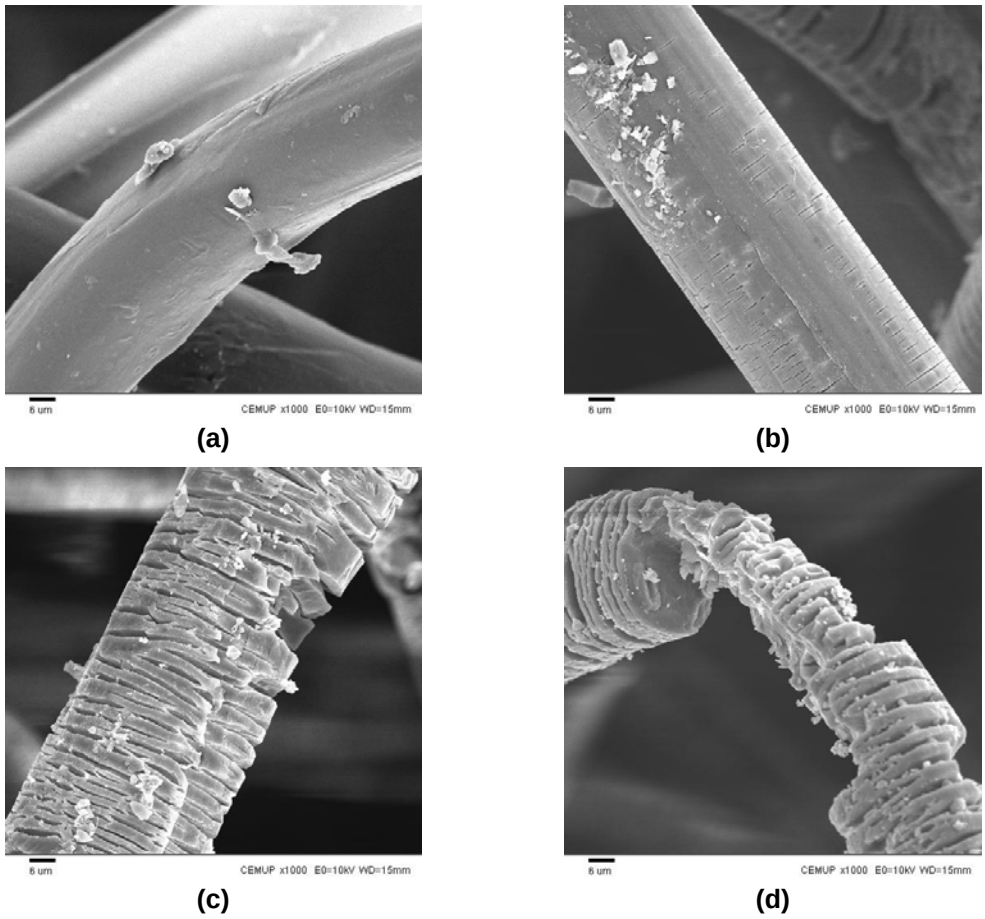

Figure 1 – SEM photographs (x 1000) of the PP fibres stabilised with 0.2% of C944 before (a) and after the exposition to 35 $MJ.m^{-2}$ (b), 69 $MJ.m^{-2}$ (c) and 104 $MJ.m^{-2}$ (d) of UV radiation.

FTIR analysis showed the appearance of a new band (centred at 1720 cm^{-1}) on the infrared spectra of the exposed GTXs (Figure 2). This band, inexistent on the spectra of the reference GTXs (without any UV exposure), indicates the presence of carbonyl groups resulting from the photo-degradation process of PP. The photo-degradation suffered by the GTXs was evaluated by the height of this band (Figure 3).

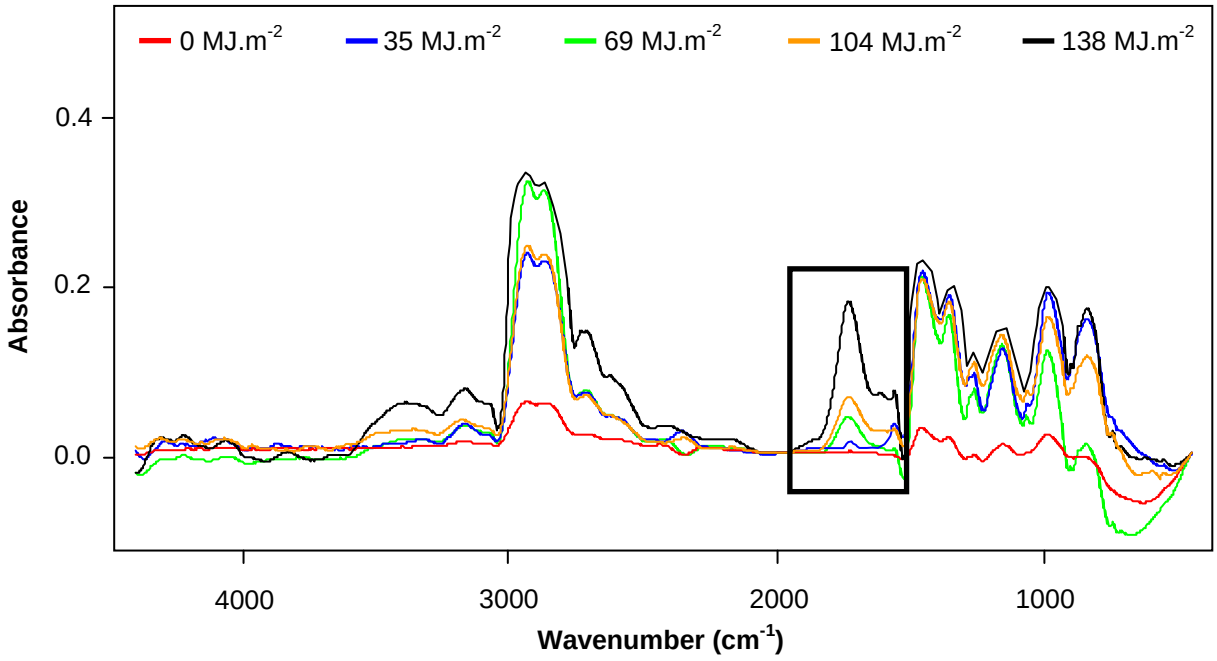

Figure 2 – Infrared spectra of the PP fibres with 0.2% of C944 before and after exposition to UV radiation.

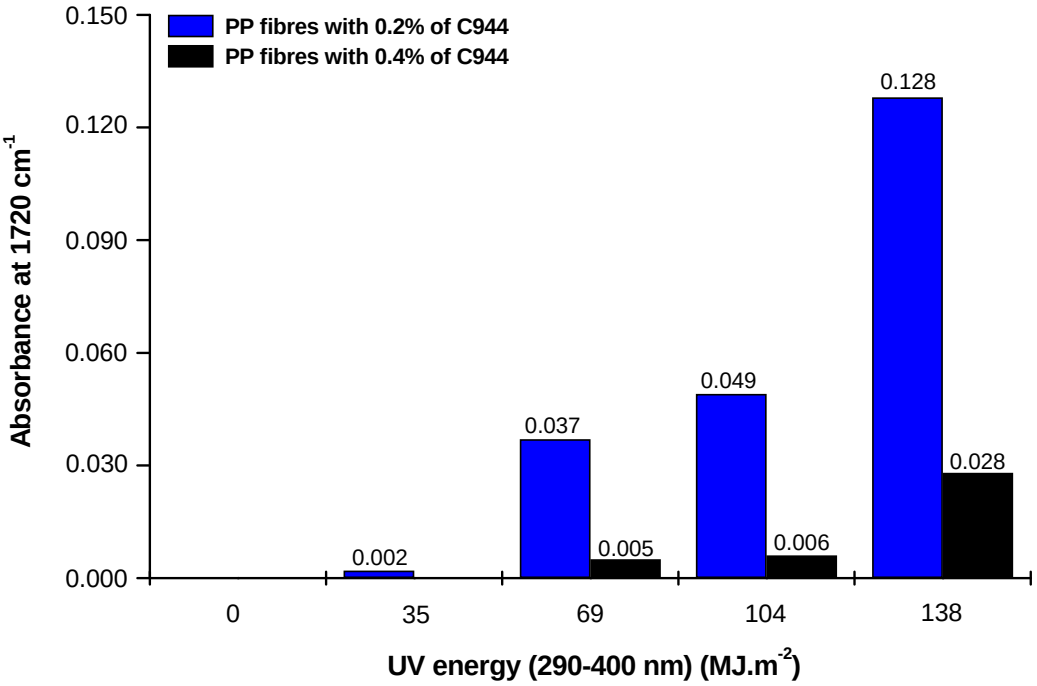

Figure 3 – Evolution of the absorbance (measured at 1720 cm^{-1}) as the PP fibres stabilised with 0.2% of C944 and 0.4% of C944 were exposed to higher total UV radiant exposures.

A small band (absorbance of 0.002 at 1720 cm^{-1}) appeared on the infrared spectra of the PP fibres with 0.2% of C944 after exposition to 35 $MJ.m^{-2}$ of UV radiation. As it can be seen in Figure 3, the intensity of this band increased as the total UV radiant exposure increased. After the exposition of the GTX with 0.2% of C944 to 69 $MJ.m^{-2}$ of UV radiation, this band had already an absorbance of 0.037 at 1720 cm^{-1}, while after 138 $MJ.m^{-2}$ of UV radiation it had an absorbance of 0.128 at 1720 cm^{-1}.

The development of the band centred at 1720 cm^{-1} was more pronounced for the GTX with 0.2% of C944 than for the GTX with 0.4% of C944, showing that the degree of degradation was higher for the fibres with less C944. This way, a better protection of the PP fibres against the damaging effects of UV radiation can be achieved by including a higher amount of C944 on their composition. After exposition to 138 $MJ.m^{-2}$ of UV radiation, the PP fibres with 0.4% of C944 had an absorbance of only 0.028 at 1720 cm^{-1} (in the same conditions, the PP fibres with 0.2% of C944 had an absorbance of almost 4.5 times more).

The results found by infrared spectroscopy were in agreement with the damages observed by SEM and with mechanical results obtained by tensile tests (data not shown). Mechanical results about the resistance of PP GTXs against artificial and natural weathering can be found in Carneiro *et al.* (2006) and in Carneiro *et al.* (2008), respectively.

From the previous results it was possible to conclude that C944 had a very important paper on the protection of the PP fibres against UV radiation. A methodology was developed for the determination of this additive in order to try to understand what happens to C944 while protecting the materials against photo-degradation. Figure 4 shows the evolution of the level of C944 (on the PP fibres with 0.4% of C944) as the total UV radiant exposure increased (the FTIR data is also plotted in the same figure for comparison purposes).

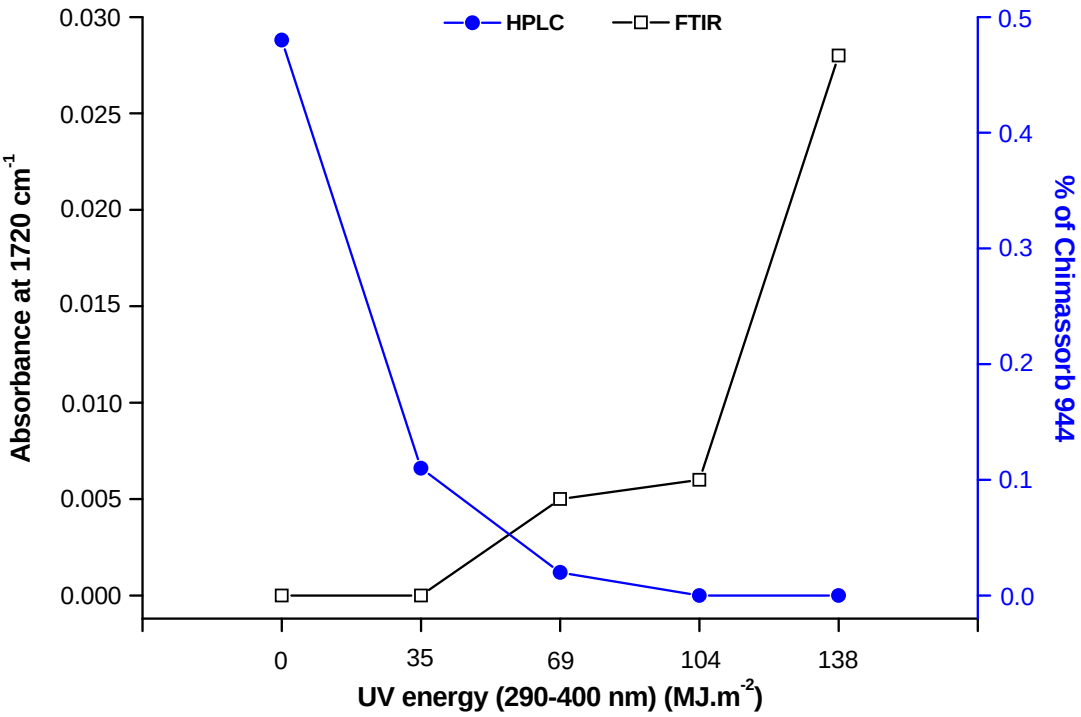

Figure 4 – Evolution of the level of C944 found on the PP fibres *versus* the FTIR absorbance at 1720 cm^{-1} (results for the PP fibres stabilised with 0.4% of C944).

As it can be seen in Figure 4, the level of C944 decreased as the GTX was consecutively exposed to higher amounts of UV energy. After exposition to 35 $MJ.m^{-2}$ of UV radiation, the level of C944 on the PP fibres decreased from 0.48% down to 0.11%, while after 69 $MJ.m^{-2}$ the percentage of C944 present on the fibres was only 0.02%. After exposition to 104 $MJ.m^{-2}$ of UV radiation, the presence of C944 on the PP fibres was not detected. These results indicate that C944 was consumed and/or lost while protecting the GTXs against the harmful effects of UV radiation.

By comparing the FTIR results with the chromatographic results, it was possible to establish a correlation between the degradation suffered by the GTX with 0.4% of C944 and the evolution of the level of the additive on the fibres of this material. As the total UV radiant exposure increased, the level of C944 decreased (leaving the PP fibres successively more vulnerable to suffer UV degradation) and the absorbance at 1720 cm^{-1} increased (indicating successively the existence of more damages on the materials).

4 Conclusions

The durability of the PP GTXs was seriously affected by the exposition to UV radiation; the GTX without C944 was completely destructed (transformed into small pieces or powder), while the GTXs stabilised with 0.2% and 0.4% of C944 suffered serious damages on their structure. SEM analysis showed the appearance of transversal fissures on the PP fibres. As the total UV radiant exposure increased more damages were found on the GTXs stabilised with C944. The GTX with 0.2% of C944 was always more damaged than the GTX with 0.4% of C944, showing that a higher concentration of C944 resulted in a better protection of the materials against UV radiation.

FTIR analyses showed the development of a new band (centred at 1720 cm^{-1}) on the infrared spectra of the PP fibres. This band was used to evaluate the degree of degradation of the PP fibres. By chromatographic analyses, it was possible to observe that the level of C944 on the PP fibres decreased as the total UV radiant exposure increased. C944 was consumed and/or lost while protecting the PP fibres against the damaging effects of UV radiation.

References

Carneiro, J.R., Almeida, P.J., Lopes, M.L. (2006). Durability of polypropylene geotextiles exposed to artificial weathering conditions. *5th ICEG Environmental Geotechnics: Opportunities, Challenges and Responsibilities for Environmental Geotechnics – Proceedings of the ISSMGE 5th International Congress*, Volume I, 399-406, Thomas Telford, London.

Carneiro, J.R., Almeida, P.J., Lopes, M.L. (2008). Ageing of polypropylene geotextiles under natural weathjering conditions, *Proceedings of the Fourth European Geosynthetics Conference – EUROGEO 4*, *paper in press*.

Commereuc, S., Vaillant, D., Philippart, J.L., Lacoste, J., Lemaire, J., Carlsson, D.J. (1997). Photo and thermal decomposition of iPP hydroperoxides. *Polymer Degradation and Stability,* 57, 175-182.

Kaci, M., Sadoun, T., Cimmino, S. (2000). HALS stabilisation of LDPE films used in agricultural applications. *Macromolecular Materials and Engineering,* 278, 36-42.

Suits, L.D., Hsuan, Y.G. (2003). Assessing the photo-degradation of geosynthetics by outdoor exposure and laboratory weatherometer. *Geotextiles and Geomembranes,* 21, 111-122.

Acknowledgements

The authors want to thank CARVALHOS (Lousã, Portugal) for producing the polypropylene fibres and the geotextiles studied in this work.

This paper reports research developed under financial support provided by “FCT – Fundação para a Ciência e a Tecnologia”, Portugal (Research Project PTDC/ECM/67547/2006).

Proceedings of the 10th International Chemical and
Biological Engineering Conference - CHEMPOR 2008
Braga, Portugal, September 4-6, 2008
E.C. Ferreira and M. Mota (Eds.)

Biosorption kinetic of orange II dye with non living leaves of *Posidonia oceanica*

J.F. Ortuño*, V. Meseguer, N. Murcia, M.I. Aguilar, M. Lloréns, J. Sáez, A.B. Pérez-Marín
Chemical Engineering Department, University of Murcia, Campus of Espinardo
30071 Murcia, Spain.

Keywords: Biosorption, orange II, dyes, *Posidonia oceanica*
Topic: Sustainable process-product development through green chemistry. Environmental engineering & management

Abstract

Batch sorption experiments were carried out to remove orange II from aqueous solutions using *Posidonia oceanica* non living leaves. The effect of sorbent particle size, biosorbent dose and pH on the dye uptake was studied. The kinetics of orange II adsorption have been investigated at different temperatures. Sorption data were fitted to pseudo-first order, pseudo-second order and Elovich kinetic models. The results showed that no significant differences in adsorption capacity exit with particle size from <0.15 to 2.5-3.2 mm. When the adsorbent dose increased the percentage of dye sorption increased accordingly. Color removal was maximum at an acid pH of 1, and decreased when pH value rised. The kinetic data were found to follow pseudo-second order kinetic and revealed that the sorption capacity increased when the temperature decreased from 40ºC to 10ºC.

1 Introduction

Synthetic dyes are extensively used in many industries such as textile, paper, printing, leather tanning, food technology, hair colorings, etc. There are over 100000 commercially available dyes and two per cent of dyes produced are discharged directly in aqueous effluent. The presence of very small amounts of dyes in wastewater is highly visible, and many of these dyes are toxic, carcinogenic and present a serious hazard to aquatic living organisms (Aksu, 2005).

Several physical, chemical and biological methods for dye removal have been reported: coagulation-flocculation, membrane separations, oxidation process, ion-exchange, adsorption, etc. Activated carbon adsorption is an extended procedure, but this sorbent is expensive. In last years many non-conventional low cost adsorbents, including natural materials, have been used for dyes removal (Crini, 2006).

In this work the adsorption potential of dead biomass of *Posidonia oceanica* (inexpensive material abundant in the beaches of the Mediterranean Sea) for orange II removal is evaluated. The effect of sorbent particle size, biosorbent dose and pH on the dye uptake was studied. The kinetics of orange II adsorption have been investigated at different temperatures. Sorption data were fitted to pseudo-first order, pseudo-second order and Elovich kinetic models

2 Materials and methods

2.1. Biosorbent material

Non living leaves of *Posidonia oceanica* were collected from the beaches of Mediterranean Sea at the Region of Murcia, washed repeatedly with tap water to

* Corresponding author. Tel:+34 968367360. E-mail: jfortuno@um.es

remove sand and salt and dried in an oven at 50-60ºC. This material was ground and sieved to obtain various size fractions.

2.2. Dye and chemicals

An azo dye, orange II (Acid orange 7) provided by Sigma, was used without further purification and stock solution of 1000 mg·L^{-1} was made with distilled water. Experimental solutions were prepared by diluting the stock solution with distilled water when necessary. HNO_3 and NaOH used to adjust pH were of analytical grade and supplied by PANREAC.

2.3. Sorption experiments

Batch sorption experiments were carried out in glass flasks at desired temperature, using a constant temperature bath. Biomass and orange II solutions of known concentrations were brought into contact by magnetic stirring. The pH of the solutions was controlled using HNO_3 or NaOH dilute solutions. After the desired contact time, samples were collected and then centrifuged. The dye residual concentration in the supernatant solutions was determined using a UV spectrophotometer (Shimadzu UV-1603) measuring their absorbance at maximum absorbance wavelength (λ= 485 nm). Calibration curve was obtained with standard solutions. The amount of dye adsorbed was found by mass-balance procedure.

2.3.1. Effect of sorbent particle size

In this study 50 mL of dye solution of 100 mg·L^{-1} was agitated with 0.2 g of biosorbent (adsorbent dose 4 g·L^{-1}) at pH 2 and 25ºC. The used sorbent particle sizes were: < 0.15 mm, 0.15-0.3 mm, 0.3-0.5 mm, 0.5-0.8 mm, 0.8-1.0 mm, 1.0-1.5 mm, 1.5-2.5 mm, 2.5-3.2 mm and 0.5-2.5 mm. Agitation was made for 24 h which is more than sufficient to reach equilibrium.

2.3.2. Effect of sorbent dosage

Different quantities of biomass (particle size fraction 0.5-2.5 mm), from 0.025 to 1.0 g, were shaken for 24 h, at 25ºC and pH 2, with 100 mL of dye solution (100 mg·L^{-1}).

2.3.3. Effect of pH

The effect of pH on amount of color removal was analyzed over the pH range from 1 to 12. The pH was adjusted using NaOH and HNO_3 dilute solutions. 50 mL of dye solution of 100 mg·L^{-1} was agitated with 0.2 g of biosorbent at 25ºC. The particle size fraction used was 0.5-2.5 mm. The contact time was 24 h.

2.3.4. Sorption kinetics

Batch kinetic experiments were carried out by agitating 500 mL of dye solution (initial concentration 100 mg·L^{-1}) with 2 g of biosorbent in 1 L glass beakers. Samples were pipetted out at different time intervals, centrifuged and analyzed for residual dye concentration. Experiments were performed at the desired temperature (10, 25 and 40ºC) using particle size of 0.5-2.5 mm and pH 2.

The prediction of batch sorption kinetics is necessary for the design of industrial sorption equipments. Several kinetics models have been proposed in order to predict the mechanism involved in the sorption process. Kinetic experimental data have been adjusted to pseudo-first order, pseudo-second order and Elovich kinetics models (Ho and McKay, 1998) by non linear regression.

Pseudo-first order equation

The pseudo-first order equation is generally expressed as follows:

$$\frac{dq}{dt} = k_1 \cdot (q_e - q)$$

After integration and applying the boundary conditions, for q=0 at t=0 and q=q at t=t, the equation becomes:

$$q = q_e \cdot (1 + e^{-k_1 \cdot t})$$

where q_e and q ($mg \cdot g^{-1}$) are the amount of dye sorbed at equilibrium and at time t, respectively, and k_1 (min^{-1}) is the rate constant of pseudo-first order equation.

Pseudo-second order equation

The pseudo-second rate order equation is expressed as:

$$\frac{dq}{dt} = k_2 \cdot (q_e - q)^2$$

Integrating this equation for the boundary conditions, gives:

$$q = \frac{t}{\frac{1}{k_2 \cdot {q_e}^2} + \frac{t}{q_e}}$$

where k_2 is the pseudo-second order rate constant ($g \cdot mg^{-1} \cdot min^{-1}$) and $h = k_2 \cdot {q_e}^2$ where h ($mg \cdot g^{-1} \cdot min^{-1}$) is the initial sorption rate.

Elovich equation

Elovich equation is of general application to chemisorption kinetics. The equation has been applied satisfactorily to some chemisorption processes and has been found to cover a wide range of slow adsorption rates. The same equation is often valid for systems in which the adsorbing surface is heterogeneous, and is formulated as:

$$\frac{dq}{dt} = \alpha \cdot e^{-\beta \cdot q}$$

Integrating this equation for the boundary conditions, gives:

$$q = \frac{1}{\beta} \cdot \ln(\alpha \cdot \beta) + \frac{1}{\beta} \cdot \ln t$$

where α ($mg \cdot g^{-1} \cdot min^{-1}$) is the initial sorption rate and β is related to the extend of surface coverage and activation energy for chemisorption ($g \cdot mg^{-1}$).

3 Results and discussion

3.1. Effect of sorbent particle size

In Figure 1 can be observed that no significant differences in adsorption capacity (q_e) for orange II exit with particle size fractions from <0.15 to 2.5-3.2 mm (q_e varies between 9.8 – 11.7 $mg \cdot g^{-1}$ adsorbent). This fact may be due to the small thickness of the *Posidonia oceanica* leaves, which favours diffusion processes.

3.2. Effect of sorbent dosage

Figure 2 shows the effect of biosorbent dose on the percentage of color removal and on biomass sorption capacity. As can been expected, the percentage of dye removal increased with the increasing biomass concentration. Thus, an increase in the dose of adsorbent from 0.25 to 4 g/L increased appreciably the removal of orange II from 8% to 55%. A greater dose increases the removal of dye in lower extent. However, the adsorption capacity (q_e) decreased with the increasing in biomass concentration.

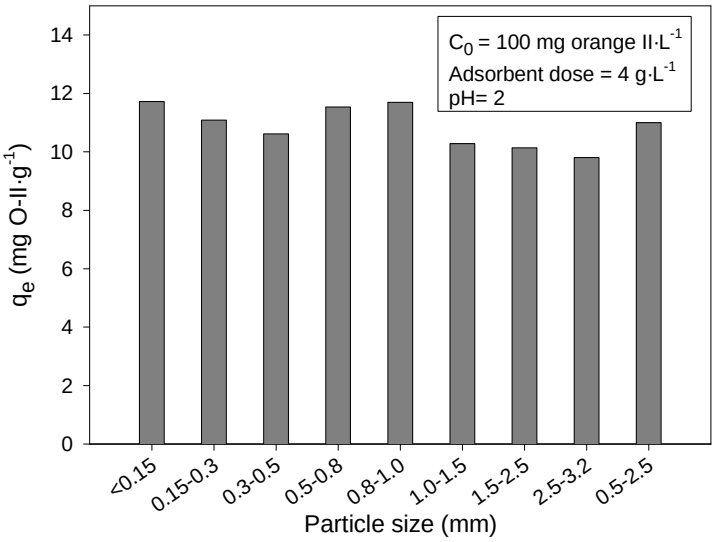

Figure 1.- Effect of particle size

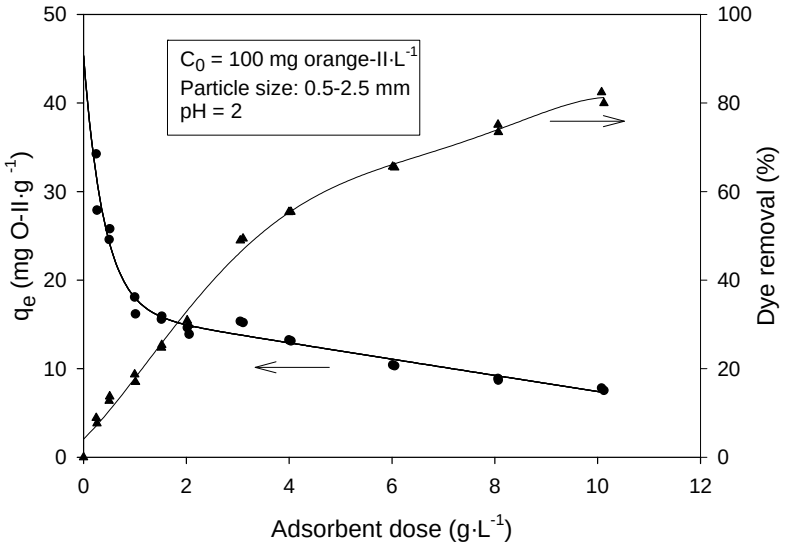

Figure 2.- Effect of adsorbent dose

3.3. Effect of pH

The pH is one of the most important factors controlling the adsorption of dye onto biosorbent. Figure 3 shows the extent of dye removal at different pH values from 1 to 12. The removal of dye was the greatest at pH 1 (q_e=16 mg·g^{-1}) and decreased significantly when pH increased from pH 1 to 12. At pH>6 the q_e value was small (< 5 mg·g^{-1}), and was near 0 at pH 12. At acidic pHs the sorbent surface acquire positive charge due to the excess of protons in solution. Thus, the electrostatic attraction between the negatively charged adsorbate species and the positively charged adsorbent particles increases.

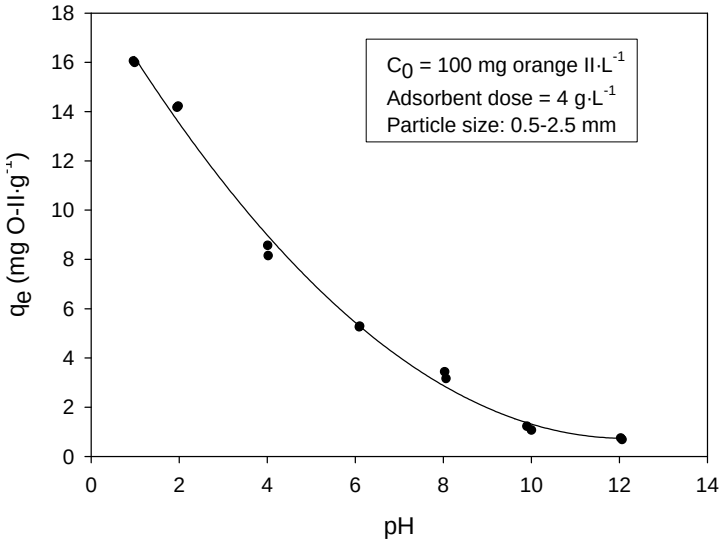

Figure 3- Effect of pH

3.4. Sorption kinetics

Figure 4 shows a plot of the amount of dye adsorbed (q, mg·g^{-1}) versus contact time for different experimental temperatures (10, 25 and 40ºC). The removal of orange II by adsorption on *Posidonia oceanica* leaves increased with contact time at all temperatures. A two-staged kinetic behavior is evident: a rapid initial adsorption occurred during the first hours, followed by a long period of much slower uptake. The higher sorption rate at the initial period (first 120 min) may be due to the great number of surface vacant sites available at this stage. Therefore, the concentration gradient between adsorbate in solution and adsorbate in the adsorbent surface is high. As time proceeds this gradient is reduced due to the accumulation of dye in the sorption sites, leading to a decrease in sorption rate at later stage. The equilibrium was reached before 24 h of contact time at all temperatures studied.

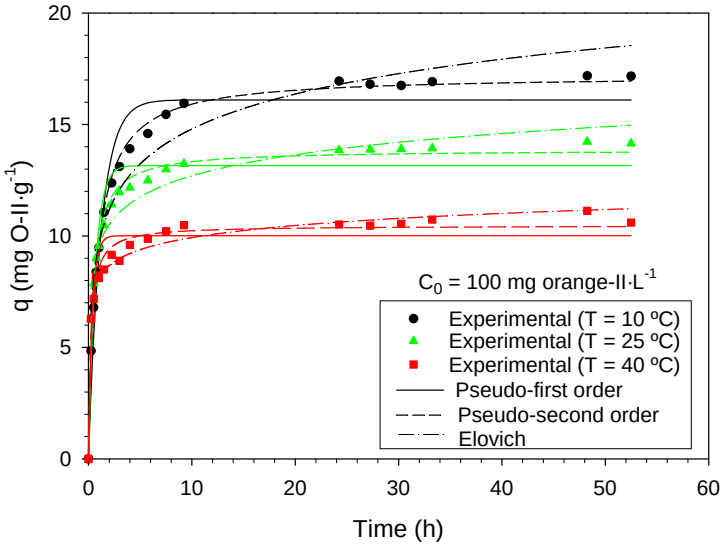

Figure 4.- Kinetics of orange II adsorption

The temperature dependence of orange II sorption is shown in Figure 4. The results revealed that the sorption capacity decreased from 17 to 11 $mg \cdot g^{-1}$ when the temperature of dye solutions increased from 10 to 40ºC. However, the sorption initial rate increased from 0.36 to 0.77 $mg \cdot g^{-1} \cdot min^{-1}$ when the temperature increased from 10 to 40ºC.

Figure 4 shows the theoretical curves obtained by fitting experimental data to pseudo-first order, pseudo-second order and Elovich kinetic models by non linear regression. The characteristic parameters of the different kinetic models employed to study the dynamic of the orange II uptake are tabulated in Table 2. The pseudo-second order equation provides the best correlation for all of the experimental data

Table 1. Characteristic parameters of the different kinetic models

		Temperature (ºC)		
		10	**25**	**40**
Pseudo-first order	**q_e ($mg \cdot g^{-1}$)**	15.8	13.0	10.0
	k_1 (min^{-1})	0.016	0.029	0.044
Pseudo-second order	**q_e ($mg \cdot g^{-1}$)**	17.3	13.9	10.5
	k_2 ($g \cdot mg^{-1} \cdot min^{-1}$)	0.001	0.003	0.007
	h ($mg \cdot g^{-1} \cdot min^{-1}$)	0.36	0.58	0.77
Elovich equation	**α ($mg \cdot g^{-1} \cdot min^{-1}$)**	1.75	19.9	421
	β ($mg \cdot g^{-1}$)	0.41	0.72	1.28

Acknowledgements: *The authors gratefully acknowledge the economic support to the "Fundación SENECA" (Comunidad Autónoma de la Región de Murcia).*

References

Aksu, Z. (2005). Application of biosorption for the removal of organic pollutants: a review. *Process Biochemistry* 40, 997-1026

Crini, G. (2006) Non-conventional low-cost adsorbents for dye removal: A review. *Bioresource Technology* 97, 9, 1061-1085.

Ho, Y.S., McKay, G. (1998) *Transactions of the Institution of Chemical Engineers*, 76 (Part B), 332-340.

Proceedings of the 10th International Chemical and
Biological Engineering Conference - CHEMPOR 2008
Braga, Portugal, September 4-6, 2008
E.C. Ferreira and M. Mota (Eds.)

Continuous biosorption of methylene blue in packed bed of *Posidonia oceanica* leaves

V. Meseguer, J.F. Ortuño*, S. Calvo, M.I. Aguilar, M. Lloréns, J. Sáez, A.B. Pérez-Marín
Chemical Engineering Department, University of Murcia, Campus of Espinardo, 30071 Murcia, Spain.

Keywords: Biosorption, methylene blue, packed bed, *Posidonia oceanica*
Topic: Sustainable process-product development through green chemistry. Environmental engineering & management

Abstract

A continuous up-flow fixed bed study was carried out by using *Posidonia oceanica* non living leaves as a biosorbent for the removal of methylene blue (MB) dye from aqueous solution. The effect of process variables, such as bed depth (6.64, 11.6 and 18 cm) and solution flow rates (11.5, 16.5 and 21.5 $mL \cdot min^{-1}$), on the sorption characteristics of sorbent was investigated. The experimental breakthrough curves were obtained. Experimental data confirmed that the breakthrough time and amount of sorbed dye increased with increasing the bed depth and decreased with increasing flow rate. Bed depth service time (BDST), Thomas, Clark and Yoon-Nelson models were used to describe the breakthrough curves and to determine the characteristic parameters of the column, useful for process design. All these models showed a good correlation between the experimental data and the model-calculated breakthrough curves.

1 Introduction

For decades, dyes and pigments have been used for coloring in the industry. Several types of dyes are available for usage with various types of materials. Among these many types, cationic dyes, commonly known as basic dyes, are widely used in acrylic, nylon, silk and wool dying. In textile dying processes, a large volume of dye-contaminated effluents are discharged, and it was estimated that 10-15% of the dye is lost in the effluent. The presence of dyes in the effluents could be highly undesirable. Consequently, the removal of these compounds from effluents is required to decrease their impact on the environment. This is usually achieved through physico-chemical means, since dyes are relatively resistant to microbial degradation due to their complicated structures. Activated carbon adsorption is an extended removal procedure, but this sorbent is expensive. In last years many non-conventional low cost adsorbents, including natural materials, have been used for dye removal (Aksu, 2005).

Results obtained in previous studies carried out in batch mode showed that *Posidonia oceanica* non living leaves biomass was able to remove methylene blue from aqueous solutions by biosorption (Ortuño et al., 2006). The biomass contains, among others, phenolic, carboxylic and hydroxyl functional groups, useful for binding dyes.

Fixed-bed adsorption systems are widely used to remove contaminants from wastewater because present numerous advantages. It is simple to operate, can provide continuous treatment with a long breakthrough time, gives high yields and can be easily scaled up from laboratory experiments, often used to obtain design information and to predict column performance. The performance of packed beds is usually described by means of breakthrough curves, where the ratio of the effluent concentration to the influent

* Corresponding author. Tel +34 968367360. E-mail: jfortuno@um.es

concentration is plotted against the service time of the column.

The aim of this study was to investigate the influence of flow rate and bed depth on the performance of methylene blue biosorption onto *Posidonia oceanica* non living leaves in an up-flow packed bed column. Several simplified models were applied to the experimental data to simulate the breakthrough curves in order to predict the scale-up of a unit plant.

2 Materials and methods

2.1. Biosorbent material

Posidonia oceanica non living leaves were collected from the beaches of Mediterranean Sea at the Region of Murcia (southeast Spain). They were washed with tap water to remove impurities and dried in an oven at 60ºC. Dry biomass was crushed and sieved to a particle size of 0.5–2.5 mm.

2.2. Chemicals

The column feed solution of methylene blue (20 mg MB·L^{-1}, pH = 6.0) was prepared by dissolving the neccesary quantity of MB-trihydrated, provided by Sigma-Aldrich, in distilled water.

2.3. Column

Continuous-flow sorption experiments were conducted in a fixed bed column packed with biosorbent material. The column was made of a methacrylate tube of 2.2 cm internal diameter. At the bottom of the column, a plastic sieve was fixed, then a layer of glass balls (3 mm diameter) was placed in order to provide a uniform inlet flow of solution into the bed. A weighed amount of adsorbent, depending on the bed depth (6.64, 11.6 or 18 cm), was put within the column between teflon adsorbent-retaining sieves, and then an upper layer of glass balls was placed on top of the bed. The ratio sorbent weight/bed depth was 0.6 g·cm^{-1} (0.158 g·cm^{-3}).

2.4. Experimental procedure

The dye solution was pumped by a peristaltic pump (Watson Marlow 505 Du) vertically upward through the column to avoid channeling due to gravity and to enhance uniform distribution of solution throughout the bed. The desired flow rate (11.5, 16.5 or 21.5 mL·min^{-1}) was maintained constant during each experiment and checked periodically by collecting solution at the outlet for a given time and weighing the amount collected. Samples from column effluent were collected periodically by an automatic fraction collector until the dye concentration exceeded a value of 19.9 mg·L^{-1}. The dye concentrations were determined using a UV-VIS spectrophotometer (Shimadzu UV-1603) by measuring the absorbance of solutions at their maximum absorbance wavelength (664 nm) and using a calibration curve. This procedure enabled the breakthrouhg curves to be obtained. The pH values of the effluent samples were recorded.

2.5. Modeling of column data

The performance of packed beds is described through the breakthrough curve. Several characteristic parameters, determined by using the breakthrough curve may be used to evaluate the performance of the fixed bed. Breakthrough and exhaustion times were defined at relative effluent concentration C/C_0 of 0.05 and 0.95, respectively. The quantity of dye retained in the column, represented by the area above the breakthrough curve, was obtained through numerical integration. Sorption capacity (q_{ads}) was defined as total amount of dye sorbed per gram of sorbent at the end of total flow time.

Several simplified fixed bed models have been developed to predict the behaviour of the adsorption bed and to describe the breakthrough curves. Bed depth service time (BDST), Thomas, Clark and Yoon-Nelson models (Aksu and Gönen, 2004) are used in this work (Table 1).

Table 1. Simplified fixed-bed breakthrough curve models.

Mathematical models	Equation	Parameters
BDST	$\frac{C}{C_0} = \frac{1}{\left(e^{\left(K_a N_0 H / v\right)} - 1\right) \cdot e^{-K_a C_0 t} + 1}$	K_a, kinetic constant ($L \cdot mg^{-1} \cdot h^{-1}$). N_0, volumetric sorption capacity of bed ($mg \cdot L^{-1}$)
Thomas	$\frac{C}{C_0} = \frac{1}{1 + \exp\left(\frac{K_{Th}}{Q}\left(q_0 \cdot X - C_0 \cdot V_{eff}\right)\right)}$	K_{Th}, kinetic constant ($L \cdot mg^{-1} \cdot h^{-1}$) q_0, equilibrium sorption capacity, ($mg \cdot g^{-1}$) X, sorbent amount in the column
Clark	$\frac{C}{C_0} = \left(\frac{1}{1 + A \cdot e^{-r \cdot t}}\right)^{\frac{1}{n-1}}$	A, constant of the Clark model r, adsorption rate (h^{-1}) n, Freundlich adsorption constant
Yoon-Nelson	$\ln\left(\frac{C}{C_0 - C}\right) = K_{YN} \cdot t - \tau \cdot K_{YN}$	K_{YN} , kinetic constant (h^{-1}) τ, time when $C = 0.5 \cdot C_0$ (h)

Experimental column data were fitted, by non linear regression, to each model equation. The model parameter values were determined by minimising the average relative error (ARE) function using the Solver add-in with Microsoft spreadsheet, Excel. The ARE function is described as follow, where *n* is the number of experimental data to fit:

$$ARE\ (\%) = \frac{100}{n} \sum_{i=1}^{n} \left| \frac{\left(\left(C/C_0\right)_{\exp} - \left(C/C_0\right)_{calc}\right)}{\left(C/C_0\right)_{\exp}} \right|$$

3 Results and discussion

Experimental breakthrough curves are shown in Figure 1. Breakthrough time (t_b) and sorption capacity of fixed bed (q_{ads}) were evaluated from experimental data and they are included in Table 2.

3.1. Effect of flow rate

The effect of flow rate (11.5, 16.5 and 21.5 $mL \cdot min^{-1}$) was studied for constant bed height (11.6 cm) (Figure 1a and Table 2). As the flow rate through the bed increases, the breakthrough curve becomes steeper and the breakthrough time decreases. Usually, the adsorption capacity decreases at higher flow rates, because MB biosorption is affected by insufficient residence time of the solute in the column (insufficient contact time between the dye and the sorbent) and because the diffusion of the solute into the pores of biosorbent is limited. An increase in the flow rate reduces the volume treated efficiently until breakthrough point and therefore decreases the service time of the bed.

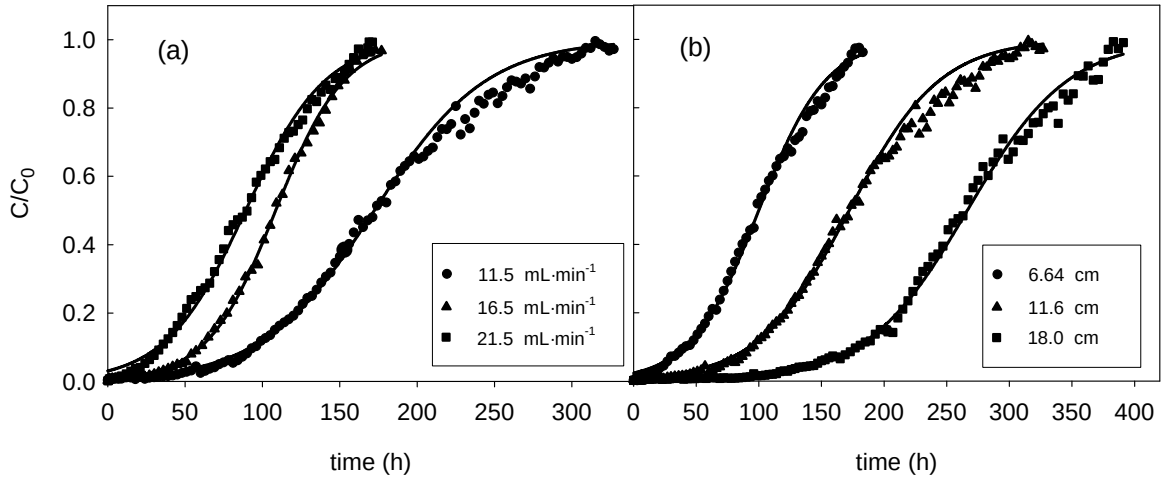

Figure 1. Breakthrough curves. Experimental data (symbols) and predictect by BDST model (lines) (C_0 = 20 mg/L, pH_0 = 6.0). (a) H = 11.6 cm; (b) Q = 11.5 mL/min.

Table 2. Experimental and models parameters. (Units: Q: $mL \cdot min^{-1}$; H: cm; t_b and τ: h; q_{ads} and q_0: $mg \cdot g^{-1}$; K_a and K_{Th}: $L \cdot mg^{-1} \cdot h^{-1}$; N_0: mg/L; r and K_{YN}: h^{-1}).

		Experimental		BDST		Thomas		Clark		Yoon-Nelson	
Q	H	t_b	q_{ads}	$K_a \cdot 10^3$	$N_0 \cdot 10^{-3}$	K_{Th}	q_0	r	A	K_{YN}	τ
	6.64	25	337	1.87	54.1	1.87	345	0.022	0.226	0.037	100.0
11.5	11.6	72	341	1.38	53.1	1.36	341	0.016	0.367	0.027	172.9
	18	146	387	1.24	52.8	1.24	368	0.014	0.950	0.025	266.5
11.5		72	341	1.38	53.1	1.36	341	0.016	0.367	0.027	172.9
16.5	11.6	45	288	2.26	47.94	2.26	307	0.025	0.368	0.045	108.5
21.5		23	314	1.94	51.67	1.94	328	0.024	0.182	0.039	89.1

3.2. Effect of the bed height

Figure 1b shows the breakthrough curves for different bed depths. As expectable, breakthrough time (t_b) and dye sorbed quantity are higher as the bed height increases (Figure 1b and Table 2) due to the increase in adsorbent amount in larger beds, which provide greater service area and adsorption sites.

3.3. Modeling of column data

The four simplified models showed in Table 1 were applied to experimental data for the description of the beakthrough curves and to determine the model parameters. The values of the model parameters, calculated by non-linear regression, are given in Table 2. The average relative error (ARE), between the experimental and model predicted values of C/C_0, was used to compare the goodness of the theoretical models to describe experimental data. All of these models provide good approximations to the experimental behaviour (ARE values lower than 11%), describing adequately the experimental breakthrough curves. Figure 1 shows experimental (points) and BDST model predicted (lines) breakthrough curves.

In order to compare the experimental and model calculated values of breakthrough time (t_b), the time at which $C = 0.5 \cdot C_0$ (t_0) and sorption capacity (q_{ads}), calculated values of t_b, t_0 and q_{ads} were plotted vs experimental ones. It was observed that the experimental values of these parameters do not differ significantly from model calculated ones.

3.4 Column effluent pH

Effluent pH values were recorded at the exit of the column. As shown in Figure 2, outlet pH values were, initially, higher than those in feed solution and later decrease until the inlet value. This may be explained as sorption of hydrogen ions on sorbent surface or because of the dissolution of alkaline compounds from the sorbent.

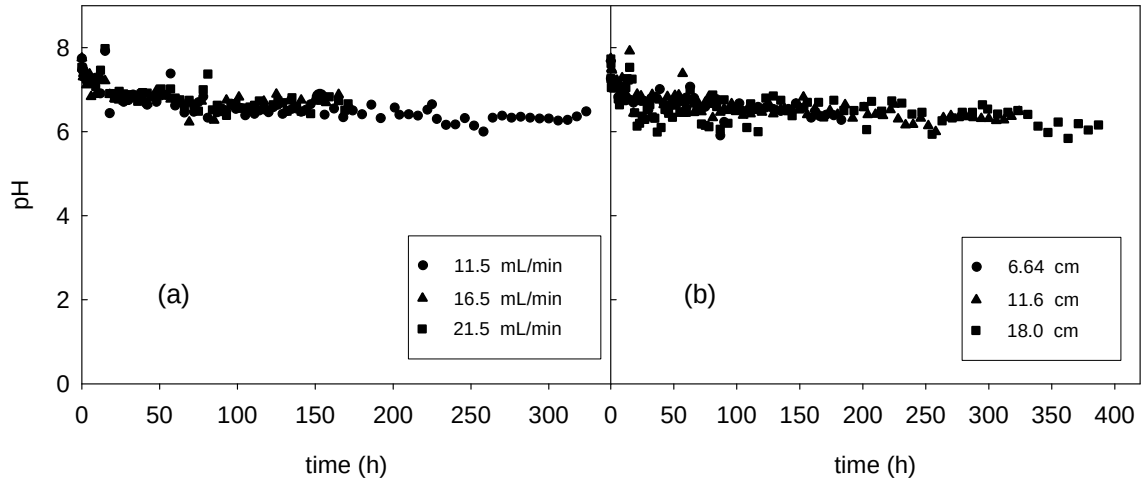

Figure 2. Effluent pH values (C_0 = 20 mg/L, pH_0 = 6.0). (a) H = 11.6 cm; (b) Q = 11.5 mL/min.

4 Conclusion

The sorption of methylene blue by *Posidonia oceanica* non living leaves in a fixed-bed column was studied. The experimental results showed that this biomass removes the dye effectively and its adsorption capacity depends on the column operating parameters (flow rate and bed height). The experimental breakthrough curves can be predicted adequately using the BDST, the Thomas, the Clark and the Yoon-Nelson models. These models can be used to simulate the scaling-up of a unit plant.

Acknowledgements: *The authors gratefully acknowledge the economic support to the "Fundación SENECA" (Comunidad Autónoma de la Región de Murcia).*

References

Aksu, Z. (2005). Application of biosorption for the removal of organic pollutants: a review. *Process Biochemistry* 40, 997-1026

Aksu, Z., Gonëm, F. (2004). Biosorption of phenol by inmovilized activated sludge in a continuous packed bed: prediction of breakthrough curves. *Process Biochemistry*, 39, 599 – 613.

Ortuño, J.F., Aguilar,M.I., Pascual, M., Meseguer, V.F., Sáez, J. and Sánchez-Pina, J. (2006). Sorption of methylene blue by non living leaves of *Posidonia oceanica*. *6th International Congress of Chemistry "Chemistry and sustainable development".* Puerto de la Cruz (Spain). Abstracts book, Vol. 2 T4-59 , 507-508.

Proceedings of the 10th International Chemical and
Biological Engineering Conference - CHEMPOR 2008
Braga, Portugal, September 4-6, 2008
E.C. Ferreira and M. Mota (Eds.)

Optimization of Chromium adsorption upon chitosan by surface response analysis

Andelib Aydın*, Nuran Deveci Aksoy, Bayram Andak
ITU – Istanbul Technical University, Chemical Engineering Department, Ayazaga Campus, 34469 Istanbul, Turkey.

Keywords: Chromium adsorption, Experimental design, Optimization, Chitosan
Topic: Sustainable process-product development through green chemistry

Abstract

The adsorption of Cr^{6+} upon chitosan flakes was investigated as function of pH, adsorbent dose and initial concentration. The effects of these factors were studied in the ranges 1.5-9.5, 1.8-24.2 g/L and 15-95 mg/L, respectively. Surface response methodology was involved in the design of experiments and also optimization studies. Maximum removal was attained from a solution as concentrated as 30 ppm at pH 3 with an adsorbent dosage of 13 g/L. The adsorption capacity of chitosan flakes was determined as 22.09 mg/g. Adsorption data was found to correlate best with Freundlich isotherm with 99.5% consistency. The Freundlich isotherm parameters K_F and n were calculated as 2.79 and 1.7, respectively.

1 Introduction

The continuously increasing demand for the commodities produced by chemical industries has triggered heavy metals accumulation in the ecosystem. Chromium is discharged to the environment, well above trace limits, as a result of electroplating, leather tanning, cement preservations, paints, pigments, textile, steel fabrication and canning industries. There exist two stable oxidation states for Chromium in nature, Cr^{3+} and Cr^{6+}. The latter of species is known to be highly mobile in soil and aquatic system, and is also more toxic, mutagenic and carcinogenic (Dubey and Gopal, 2007).

Conventional methods applied for Cr^{6+} removal are chemical precipitation, oxidation/reduction, filtration, ion exchange, membrane separation and adsorption. Chemical precipitation produces great amounts of mud, whilst ion exchangers and membrane separation are relatively of very high cost (Nomanbhay and Palanisamy, 2005). Therefore, adsorption is the most frequently applied technique owing to its advantages such as variety of adsorbent materials and high efficiency at a relatively lower cost (Babel and Kurniawan, 2003). Recently, the removal of metals, compounds, and particulates from solution by biological material is recognized as an extension to adsorption and is named as biosorption (Boddu et al., 2003). Many biosorbents such as algae (Gupta et al., 2001), seaweeds (Kratochvil et al., 1998) and biopolymers (Bailey et al., 1998) have been utilized in the removal of heavy metals from wastewater.

Chitosan, the major derivative of chitin, and second abundant biopolymer in nature after cellulose, is a good scavenger for metal ions owing to the amine and hydroxyl functional groups in its structure (Zhao et al., 2007). The formerly conducted studies considering the adsorption of Cr^{6+} have proved that the process parameters, namely, pH, initial concentration, temperature, adsorbent dose and particle diameter influence the removal efficiency immensely (Rojas et al., 2005). This influence can be realized by inspection of the reported values for Cr^{6+} adsorption capacity of chitosan which varies from 27.3 mg Cr^{6+}/g (Bailey et al., 1999) to 273 mg Cr^{6+}/g (Babel and Kurniawan, 2003). The confusion about adsorption capacity could be overcome by optimization of the parameters involved. Therefore, this study aimed to investigate the effects of process parameters on the Cr^{6+}

* Corresponding author. Tel + 90-212-2856878. E-mail:erdoganyas@itu.edu.tr

adsorption capacity of chitosan and to determine the set of parameters leading to maximum Cr^{6+} removal. The effects of pH, initial concentration and adsorbent dose were studied, while the efffects of temperature and particle diameter were excluded intentionally. Surface responce methodology was utilized for optimization studies.

Classical methods of optimization involve the change of one variable at a time which is quite time consuming especially when a large number of variables are considered. Alternatively, response surface methodology aims to optimize the response surface shaped under the influence of the process parameters.

2 Materials and Methods

2.1 Reagents

Chitosan flakes (low molecular weight) of deacetylation degree of minimum 85.0% were obtained from Sigma. Extra pure potassium dichromate, 37.0% pure HCl, and analysis grade 1,5-diphenyl carbazide were purchased from Merck. Sodium hydroxide (≥98.0%), nitric acid (65.0%), and sulphuric acid (95-97%) were obtained from Fluka. Acetone (99.0%) used in preparation of 1,5-diphenyl carbazide solution was purchased from Carlo Elba. Deionized water was involved in preparation of all solutions as well as rinsing of glassware.

2.2 Design of Experiments

Central composite design was employed in the experimental design procedure. The total number and sequence of experimental runs were determined using the MINITAB software. According to this design, 20 experiments were conducted with three replications each to ensure the accuracy of the results. The effects of process parameters pH, ion concentration and adsorbent dosage were investigated at five levels as summarized in Table 1. Significance level (α) was chosen as 0.05.

Table 1. Lower and upper bounds of the parameters

Parameters	Coded Value				
	-1.6	**-1**	**0**	**1**	**1.6**
pH	1.5	3	5.5	8	9.5
Initial concentration (mg/L)	15	30	55	80	95
Adsorbent Dose (g/L)	1.8	6	13	20	24.2

Surface plots were constructed by using MINITAB. Main effects and interactions of the factors were determined by fitting a second order polynomial equation (Eq.1) and by interpretation of the ANOVA table. A variable is considered significant when the calculated probability value (p) is smaller than the chosen significance level. In case of insignificance the variable is omitted from the model.

$$y = \beta_0 + \sum_{i}^{k} \beta_i x_i + \sum_{i}^{k} \beta_{ii} x_i^2 + \sum_{i} \sum_{j} \beta_{ij} x_i x_j + \varepsilon \quad (1)$$

Here, y is the predicted response, i and j take value from 1 to the number of independent process variables. The β values are coefficients predicted by the method of least squares, ε is the error of prediction and x_i and x_j are the level of the independent process variables (Palanikumar and Karthikeyan, 2006). The responce surface plots constructed by the aid of predictive model were used in determination of the optimum values of the process variables leading to maximum removal percentage.

2.3 Adsorption Experiments

Stock Cr^{6+} solution of 500 ppm was prepared using $K_2Cr_2O_7$ with deionized water. For further experiments, solutions of 50 mL volume were prepared by dilution of this stock. Batch tests were conducted in 100 mL stoppered flasks in a water bath kept at 298K. Agitation rate was

held constant at 120 rpm. The required time to reach equilibrium was determined as 24 hours by preliminary experiments. The pH of the solutions were regulated by micro additions of 0.2N H_2SO_4 and 0.1N NaOH. For the development of isotherms, 5 g/L beads were placed in chromium solutions of varying concentration. Diphenyl carbazide method was used for analysis of Cr^{6+} concentration of solutions.

3 Results and Discussion

3.1 Data Analysis and Construction of Model

The sequence of experiments and summary of the results are given in Table 2. The removal percentages listed in the fifth column are averages of three parallel experiments and they are calculated according to Eq.(2).

$$\text{Removal \%} = \frac{C_0 - C_e}{C_0} * 100 \quad (2)$$

where C_0 and C_e are the initial and equilibrium concentration of solutions (mg/L), respectively. Removal percentage values were recorded as the responce of the system and the values were used in creating the surface plots as shown in Figures 1-3.

Table 2. Calculated results for adsorption of Cr(VI) on chitosan.

Experiment No.	Initial Concentration	Adsorbent Dose	pH	Removal (%)
1	-1.0	-1.0	-1.0	84.18
2	1.6	0.0	0.0	88.47
3	0.0	1.6	0.0	78.42
4	0.0	0.0	0.0	93.12
5	0.0	0.0	0.0	76.89
6	0.0	0.0	0.0	93.36
7	0.0	0.0	1.6	84.71
8	-1.6	0.0	0.0	59.99
9	0.0	0.0	-1.6	85.52
10	-1.0	1.0	-1.0	72.38
11	1.0	1.0	1.0	84.98
12	-1.0	-1.0	1.0	64.42
13	0.0	-1.6	0.0	96.07
14	0.0	0.0	0.0	80.69
15	0.0	0.0	0.0	59.77
16	1.0	1.0	-1.0	92.81
17	-1.0	1.0	1.0	96.56
18	1.0	-1.0	1.0	82.84
19	1.0	-1.0	-1.0	64.11
20	0.0	0.0	0.0	82.03

Variance analysis conducted for full quadratic model including all linear, square and interaction terms proved that the interaction and square terms other than the square effect of pH had very poor effect on the adsorption of Cr^{6+}. Although the regression coefficient of this model was quite high (0.93), a large difference was observed with the adjusted regression coefficient (0.86). When insignificant terms were excluded from the model, the regression coefficient happened to drop to 0.90; however, adjusted regression coefficient increased to 0.87. Both the narrowed gap between the regression coefficients and the decreased standard deviation were accepted as indications of enhanced strength of the model. The ANOVA table for the final model given in Eqn. 3 is provided in Table 3.

$$\text{Removal (\%)} = 83.555 - 11.783*\text{pH} - 3.55*C_0 + 3.353*\text{Adsorbent dose} - 3.795*\text{pH}^2 \quad (3)$$

Table 3. Analysis of Variance for the final model.

Source	DF	Seq SS	Adj SS	Adj MS	F	P
Regression	4	2314.31	2314.31	578.578	32.80	0.000
Linear	3	2134.32	2134.32	711.441	40.33	0.000
Square	1	179.99	179.99	179.988	10.20	0.006
Residual Error	15	264.61	264.61	17.640	8.82	0.013
Lack-of-Fit	10	250.41	250.41	25.041		
Pure Error	5	14.20	14.20	2.840		
Total	19	2578.92				

The outcomes of variance analysis were used to evaluate the intensity of the effects of process conditions. The probability values were calculated as 0.000, 0.008, and 0.011 for pH, initial concentration and adsorbent dosage, respectively. Since all p values were lower than significance level, all parameters were effective on the extent of adsorption at main effect levels. However, the order of effectiveness for main effects was determined as pH>initial concentration>adsorbent dose.

3.2 Surface and Contour Plots

Surface and contour plots were used in determination of the optimum set of process conditions. The surfaces constructed under the combined effect of process parameters are shown in Figures 1-3.

The combined effect of pH and initial concentration is shown in Figure 1. Accordingly, when pH was held in the acidic region, preferably below pH<3, over 90% removal was attained for solutions concentrated up to 70 mg/L.

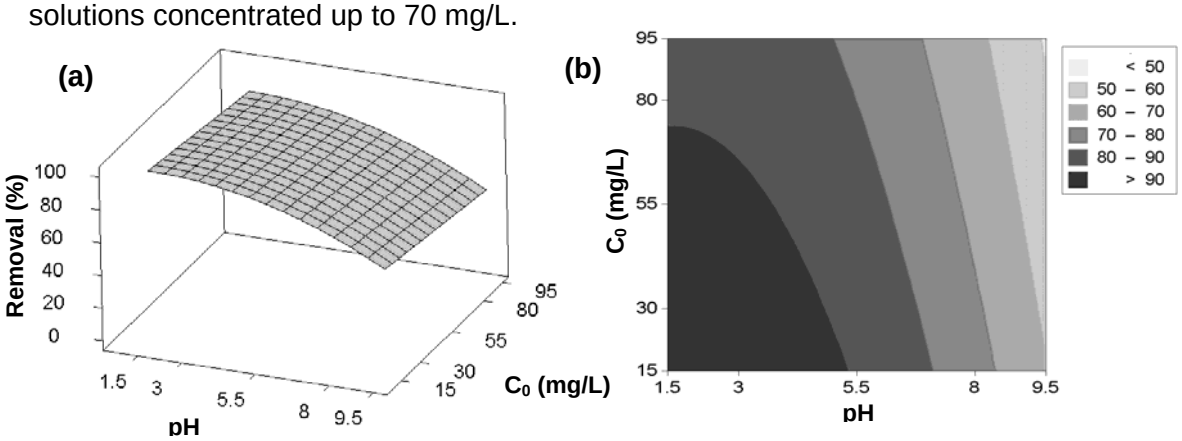

Figure 1. (a) Surface, **(b)** contour plot for pH-initial concentration pair (ads. dose= 13 g/L).

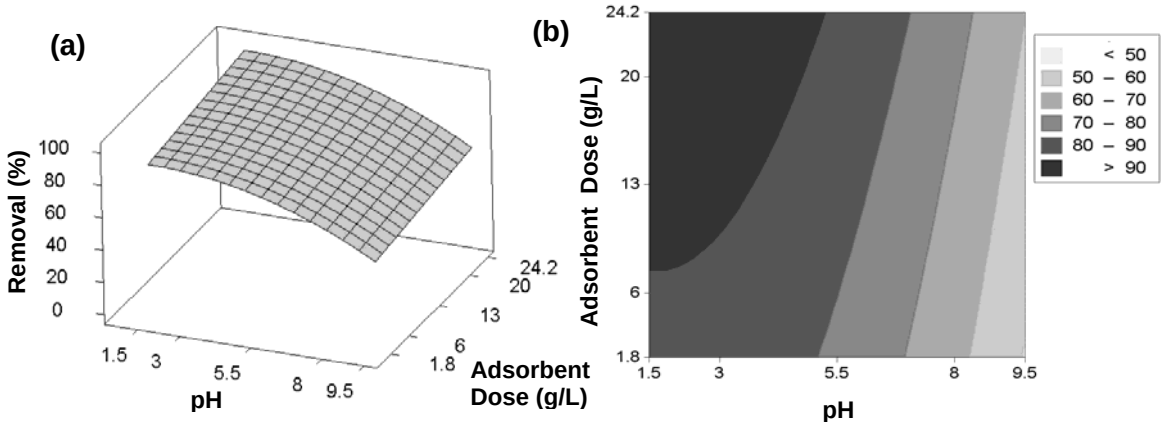

Figure 2. (a) Surface, **(b)** contour plot for pH-adsorbent dose pair (C_0= 55 mg/L).

The surface and contour plots showing the combined effect of pH and adsorbent dose is given in Figure 2. Although both plots exhibited enhanced Cr^{6+} removal at higher adsorbent doses, the improvement of removal percentage was not sufficiently high to justify excessive use of adsorbent and the related costs. When pH was held below pH 3, an adsorbent dose of 7 g/L was sufficient to ensure >90% Cr^{6+} removal 55 mg/L. For lower initial concentrations, even 2 g/L would be efficient at significantly acidic pH.

Initial concentration implied a considerable effect on the extent of Cr^{6+} removal. The combinational effect of initial concentration and adsorbent dose is shown in Figure 3. Accordingly, by utilization of 1.8g/L chitosan, at least 70% removal was attained from solutions as concentrated as 95 mg/L at pH 5.5. Higher extent of removal (>90%) was attained at relatively lower initial concentrations by using 15 g/L or more chitosan.

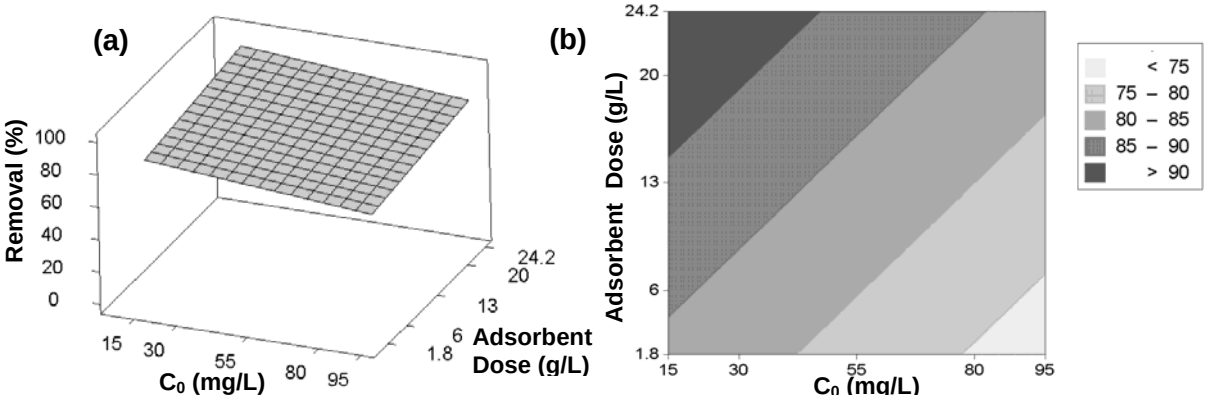

Figure 3. (a) Surface, **(b)** contour plot for initial concentration-adsorbent dose pair (pH=5.5).

The optimum set of process variables were predicted as pH 3, initial concentration of 30 mg/L and 24.2 g/L adsorbent dose by the model. At those conditions, the model predicted 100% Cr^{6+} removal. Experiments were conducted to check the accuracy of the optimum set of parameters and the resulting removal percentage was compared to the output of the model. Experimental results showed that only 89.2% removal could be attained at those conditions. Further experiments proved that the optimum adsorbent dose was 13 g/L, by which 92.9% Cr^{6+} removal was achieved.

3.3 Equilibrium Isotherms

The relationship between adsorbed metal concentration and concentration of the solution at equilibrium is described by isotherm models, of which Langmuir and Freundlich are the most widely referred equations. Whilst Langmuir isotherm model is representative of monolayer adsorption occurring on a homogeneous surface, Freundlich model is an empirical equation describing the adsorption on a heterogeneous surface. Both models are transformed into linear relationships so that the corresponding constants can be computed. Mathematical expressions for non-linear and linear forms of Freundlich model are given in eqn. 4 and 5.

$$q_e = K_F C_e^{1/n} \tag{4}$$

$$\ln q_e = \ln K_F + \frac{1}{n} \ln C_e \tag{5}$$

Here, q_e represents the mg amount of adsorbate adsorbed on unit amount of adsorbent and C_e is the equilibrium concentration of solution. K_F and n are constants for Freundlich isotherm (Dubey and Gopal, 2007).

Both Langmuir and Freundlich equations were involved in the interpretation of data obtained from experiments. Although the data fitted reasonably well to linearized forms of both models, the regression coefficient for Freundlich model was significantly higher, *i.e* 0.995.

The plot of ln q_e vs. ln C_e is shown in Figure 4. The Freundlich isotherm parameters K_F and n were calculated as 2.79 and 1.7, respectively.

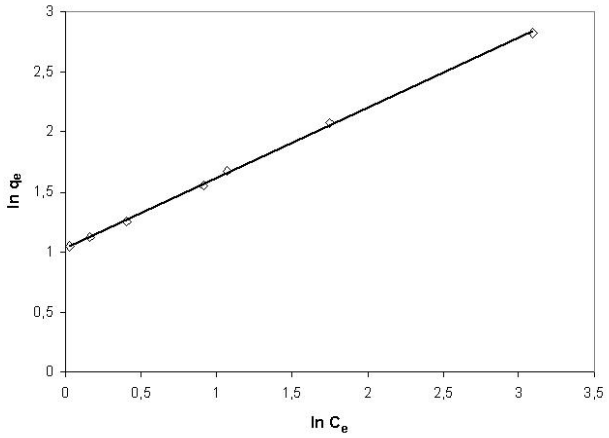

Figure 4. Linearized form for Freundlich isotherm model.

4 Conclusions

Chitosan has been found to be an effective adsorbent for Cr^{6+} removal from wastewater (Rojas et al., 2005), however several values have been reported for adsorption capacity and optimum process conditions. In this study, the optimum set of process parameters were determined as pH 3, initial concentration of 30 mg/L and 13 g/L adsorbent dose by surface responce methodology. The adsorption capacity of chitosan was calculated as 22.09 mg/g at these conditions. pH was determined to be the most effective parameter, followed with initial concentration and adsorbent dose, respectively.

References

Babel, S., Kurniawan, T.A. (2003). Low-cost adsorbents for heavy metals uptake from contaminated water: a review. *Journal of Hazardous Materials*, B97, 219–243.

Bailey, S.E., Olin, T.J., Bricka, R.M., Adrian, D.D. (1999). A review of potentially low-cost sorbents for heavy metals. *Water Research*, 33*,* 2469-2479.

Boddu, V., Abburi, K., Talbott, J.L., Smith, E.D. (2003). Removal of hexavalent Chromium from wastewater using a new composite chitosan biosorbent. *Environmental Science and Technology*, 37, 4449-4456.

Dubey, S.P., Gopal, K. (2007). Adsorption of chromium(VI) on low cost adsorbents derived from agricultural waste material: a comparative study. *Journal of Hazardous Materials*, 145, 465–470.

Gupta, V.K., Shrivastava, A.K., Jain, N. (2001). Biosorption of Chromium(VI) from aqueous solution by green algae *Spirogyra* species. *Water Research*, 35, 4079–4085.

Kratochvil, D., Pimentel, P., Volesky, B. (1998). Removal of trivalent and hexavalent chromium by seaweed biosorbent. *Environmental Science and Technology*, 32, 2693–2698.

Nomanbhay, S.M., Palanisamy, K. (2005). Removal of heavy metal from industrial wastewater using chitosan coated oil palm shell charcoal. *Electronic Journal of Biotechnology*, 8, 43-53.

Palanikumar, K., Karthikeyan, R. (2006). Optimal machining conditions for turning of particulate metal matrix composites using Taguchi and response surface methodologies. *Machining Science and Technology*, 10, 417–433.

Rojas, G., Silva, J., Flores, J.A., Rodriguez, A. (2005). Adsorption of chromium onto cross-linked chitosan. *Separation and Purification Technology*, 44, 31–36.

Zhao, F., Binyu, Y., Yue, Z., Wang, T., Wen, X., Liu, Z., Zhao, C. (2007). Preparation of porous chitosan gel beads for copper(II) ion adsorption. *Journal of Hazardous Materials*, 147, 67-73.

Proceedings of the 10th International Chemical and
Biological Engineering Conference - CHEMPOR 2008
Braga, Portugal, September 4-6, 2008
E.C. Ferreira and M. Mota (Eds.)

Influence of different cations of N3 dyes on their photovoltaic performance and stability

Luísa Andrade[1], Shaik M. Zakeeruddin[2], Mohammed K. Nazeeruddin[2], Michael Graetzel[2], Helena Aguilar Ribeiro[1], Adélio Mendes[1*]

[1] LEPAE - Department of Chemical Engineering, Faculty of Engineering at the University of Porto, 4200-465 Porto, Portugal

[2] Laboratory of Photonics and Interfaces, Swiss Federal Institute of Technology – 1015 Lausanne, Switzerland

Keywords: dye-sensitized solar cells, solar energy, photovoltaics
Topic: Sustainable process-product development through green chemistry

Abstract

In the present work, the N3 dye was modified by substituting two of its protons by potassium or sodium cations. The performance and stability of DSC devices incorporating the new dyes were evaluated under light soaking (1000 $W \cdot m^{-2}$) at 50 ºC. Photocurrent measurements demonstrated that proton substitution by potassium cations rends the system more stable. Further characterization of the potassium-based devices was performed by electrochemical impedance spectroscopy, to investigate the charge transfer phenomena occurring at the different interfaces of the cells.

1. Introduction

Nowadays, a particular interest in the development of alternative energy sources arises, especially motivated not only by the need of reducing the dependency on fossil fuel resources, but also for providing the reduction of the CO_2 emissions. An attractive strategy in order to overcome the present energy problem is using renewable energy sources, such as the direct solar radiation, for producing clean energy. In this sense, the direct conversion of sunlight into electricity by means of photovoltaic systems makes an important contribution to this energy contend in an environmentally friendly way (Grätzel, 2001; Zweibel 2008). In conventional solar cells, the charge separation occurs at the interface of two materials of different conduction mechanisms, exploiting the photovoltaic effect (Grätzel, 2003). More recently, a new generation of cells emerged, the Dye-sensitized Solar Cells (DSC). DSCs are considered very promising since they use low cost, abundant and environmentally safe raw materials and they show relatively high-energy efficiency (Grätzel, 2001).

A DSC is made of a nanoparticulated titania film coated with an adsorbed dye monolayer. This thin film is applied on a glass substrate coated with a transparent conducting oxide (TCO) that collects the electrons. A back electrode consists of the same conducting glass coated with platinum. This serves as a catalyst for the redox reaction occurring in the electrolyte present in between the two electrodes (figure 1).

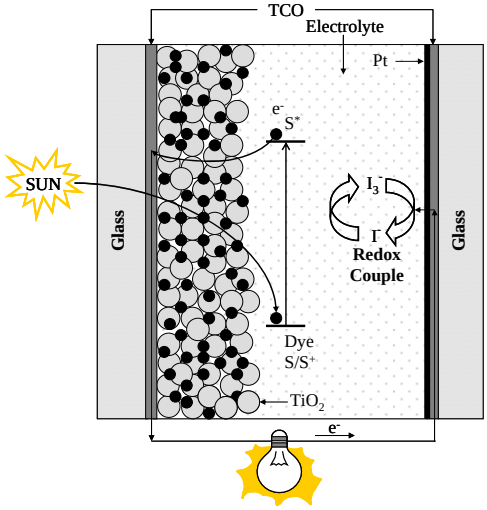

Figure 1 - Schematic representation of a dye-sensitized solar cell.

In DSCs, the dye is a crucial component to achieve high overall photoelectric conversion efficiency. Up to now, ruthenium complexes have been widely investigated

due to their advantageous spectral properties, photostability in the final device and high conversion efficiency (Amadelli *et al*., 1990). An example of these ruthenium polypyridine complexes with better performance as sensitizer is the cis-dithiocyanatobis(4,4'-dicarboxilic acid-2,2'-bipyridine)Ruthenium(II), commonly known as N3 (Nazeeruddin *et al*., 1993). Since the development of the N3 dye in 1993 (Nazeeruddin *et al*., 1993), its tetrabutylammonium (TBA) salt N719 has been used as the standard red dye because of its unmatched performances. Similarly to the N719 dye, new dyes were developed bearing in mind that the number of protons in the dye influences the open-circuit potential and the short circuit current of the DSC (Nazeeruddin *et al.*, 2003). In this work we modified the N3 dye by partially substituting its protons with different cations, namely sodium and potassium. The modified dyes where subsequently incorporated in final DSC devices, which were then submitted to accelerated thermal/light soaking aging tests for performance and stability evaluation. The cells were subjected to full sunlight irradiation at 50 ^{o}C for about 1000 h, during which time their photovoltaic parameters were periodically monitored. Electrochemical impedance spectroscopy (EIS) was used to investigate the charge transfer phenomena occurring at the different interfaces of the DSC. The charge-transfer resistance at the TCO layer, the charge-transfer resistance at the counter-electrode/electrolyte interface and the charge-transfer resistance at TiO_2/dye/electrolyte interface were obtained by fitting the EIS results to an appropriate equivalent electrical circuit (Fabregat-Santiago *et al.*, 2007).

2. Experimental section

N719 dye was synthesized as reported earlier (Nazeeruddin *et al.*, 1999). The dipotasium [$2K^{+}$(N3, $2H^{+}$)] and disodium [$2Na^{+}$(N3, $2H^{+}$)] dyes were prepared as follows. First N719 dye was dissolved in acetonitrile solvent and to this an excess amount of potassium triflate or sodium triflate in acetonitrile was added, and immediately the respective counter ion containing complex was precipitated, filtered and washed with acetonitrile and dried under vaccum.
Composition of electrolyte A: 0.1 M iodine, 0.5 M N-methylbenzimidazole in a mixture of BMII; PMITFSI; g-BL (2; 3 ;1) vol/vol.

Fabrication of DSC devices: The mesoscopic TiO_2 films used as photoanodes consisted of double layers of TiO_2 (7-μm thick transparent layer of 20 nm TiO_2 anatase nanoparticles and 5-μm thick scattering layer of 400 nm anatase TiO2 particles). The detailed method of TiO_2 film preparation and cell assembling was reported elsewhere (Kuang *et al.*, 2006).

Photovoltaic Measurements: All photovoltaic measurements were performed under a 450 W xenon light source able to provide 1000 W·m^{-2} sunlight equivalent irradiation (AM 1.5). *I - V* curves were obtained by applying an external bias to the cells and measuring the respective photocurrent response with a digital source meter (Keithley Instruments Inc.®, Model 2400). The incident photon-to-current conversion efficiency (IPCE) was recorded by a data-collecting system as a function of excitation wavelength. The incident light from a 300 W xenon lamp (ILC Technology, USA) was focused through a Gemini-180 double monochromator (Jobin Yvon., UK) onto the cell under test. No white light bias was applied and the dc photocurrents were in a domain where their response to light intensity was linear.

Electrochemical Impedance Measurements: Impedance experiments were carried out with a computer-controlled potentiostat (EG&G M273) equipped with a frequency response analyzer (EG&G M1025). The frequency range was 0.005 Hz-100 kHz and the magnitude of the modulation signal was 10 mV. All the measurements were performed at room temperature in the dark at -0.75 V bias. The EIS spectra were fitted to an appropriate electrical analogue by means of the Z View® software (v2.5b, Scribner Associates Inc.).

Stability Tests: Hermetically sealed cells were used to check the long-term stability under visible light soaking at 50 ^{o}C. The light soaking experiments employed a polymer film of 50-μm

thickness (Preservation Equipment Ltd, UK), eliminating UV light. Cells were exposed at open circuit to a Suntest CPS lamp (ATLAS GMBH, 100 mW·cm^{-2}, 50 ^{o}C) over a period of 1000 h. The cells were taken out at regular intervals to record the photocurrent-voltage curve.

3. Results and Discussion

Figure 2a) shows the photocurrent density-voltage curves under AM 1.5 simulated sunlight (1000 W·m^{-2}) for the DSCs prepared with [2K^{+}(N3, 2H^{+})], [2Na^{+}(N3, 2H^{+})] and N719 dyes in association with electrolyte A. The cells were labelled as device A, B and C, respectively.

Comparing the three systems under study, device C shows the best initial photovoltaic performance. In fact, it is already known by its unmatched performance. On the basis of cations' substitution in the N3 dye, the anchoring groups of the adsorbed sensitizer transfer most of its protons to the semiconductor surface, charging it positively. This change in the TiO_2 surface enhances the adsorption of the anionic ruthenium complexes and favours electron injection from the excited state of the dye into the conduction band of the semiconductor, resulting in higher photocurrents. Nevertheless, this positive shift of the Fermi level induced by surface protonation leads to a low open-circuit potential. In fact, if the sensitizer has no protons, it is expected to obtain high open-circuit potential and low photocurrents, and the other way round if sensitizer is fully protonated. So, an optimal degree of protonation of the sensitizer should be considered to reach maximum overall conversion efficiency (Nazeeruddin et al., 2003). In this study we observed that the sodium-based system (device B) presents higher values of short-circuit current, J_{sc}, and open-circuit voltage, V_{oc}, than cells with the potassium based system (device A). However, the latter system has higher overall power conversion efficiency, η, due to a higher value of the fill factor, *FF.* This fact is explained by a reduction in the series resistance of the cell with potassium salt dye.

In Figure 2b) the incident photon-to-current conversion efficiency (*IPCE*) for devices A, B and C can be compared. The *IPCE* is plotted as a function of the excitation wavelength. In line with the better photovoltaic performance, device C shows the highest *IPCE*: maximum of about 67 % at 530 nm. At the same wavelength, device A reaches a maximum of 63 %, while device B reaches approximately 54 %.

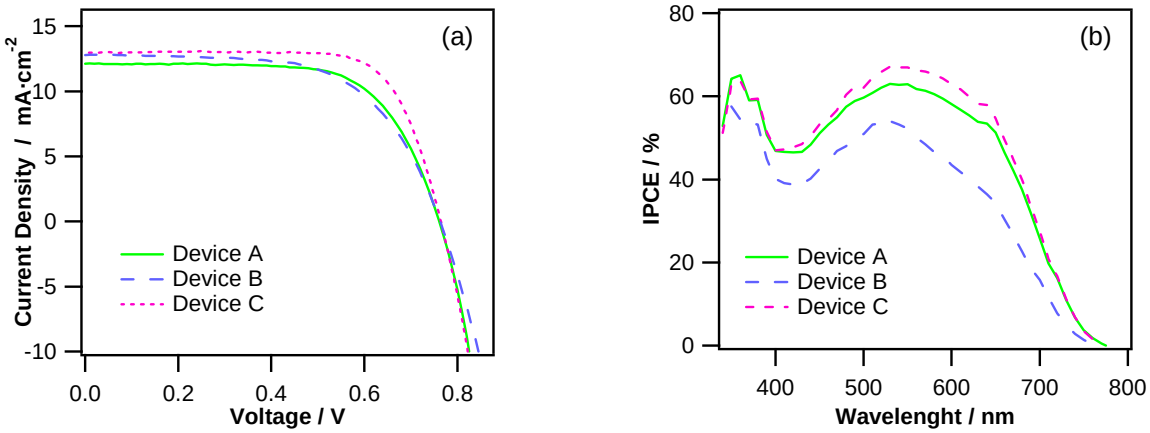

Figure 2 - a) Photocurrent intensity-voltage characteristics for devices A, B and C, measured at 1 sun (1000 W·m^{-2}), AM 1.5 global sunlight illumination. b) Photocurrent action spectra of the same devices.

Besides efficiency, the long-term stability is also a key issue regarding the industrial development and commercialization of DSCs. Thus, an intimate relation between photovoltaic performances and stability should be achieved. The evolution of the photovoltaic performances throughout the aging process of the three systems under study is presented in Figure 3. Device

A reveals a very good stability when compared with the two other systems. Actually, this device kept close to 90 % of its initial performance after 1000 h of light soaking at 50 ºC. In contrast, devices B and C showed a drop in efficiency of about 23 % and 25 %, respectively. The higher stability of device A is mainly due to increase in the photocurrent (6 %) during the first week of aging and latter it was maintained at the same level for the rest of the aging period. Additionally, this system shows a quite stable evolution of the *FF* values, indicating constancy in series resistance during the aging process. Despite its high photovoltaic performance as a fresh cell, the N719 system was unstable, exhibiting a marked decrease in J_{sc} and V_{oc} soon after the first week. This may be due to desorption of dye from the TiO_2 surface. Moreover, the sodium salt containing device B doesn't rend the system very stable, as suggested by the strong oscillation in all photovoltaic parameters of device B.

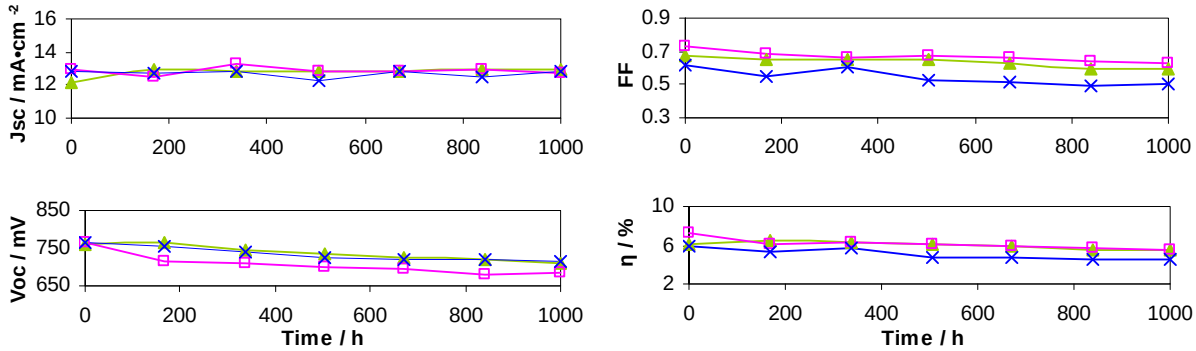

Figure 3 - Evolution of photovoltaic parameters for device A (▲), device B (x) and device C (□). The cells were kept under one sun visible-light soaking at 50 ºC for approximately 1000 h.

Bearing in mind the promising results in terms of performance and long-term stability of potassium-based DSC, a deeper characterization of the system was performed. In this sense, the effect of the aging process in the overall performance of device A was analysed by means of electrochemical impedance spectroscopy. This technique allows us to determine the charge-transfer resistances at the platinum counter-electrode and at the TiO_2/dye/electrolyte interface, as well as to determine the Nernstian diffusion of I^-/I_3^- ions within the electrolyte (Fabregat-Santiago et al., 2007). The Bode and Nyquist (*Z''*-imaginary part of impedance vs. *Z'*-real part of impedance) plots for the potassium system, before and after the aging process, are shown in Figure 4.

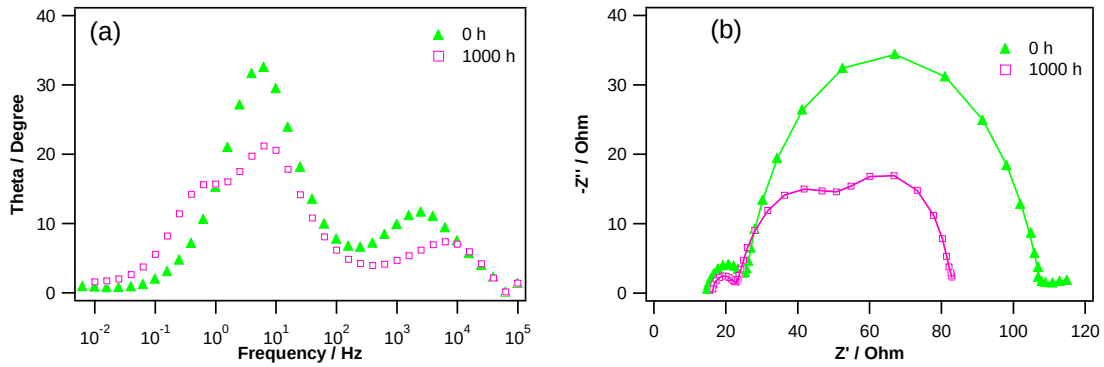

Figure 4 - Bode (a) and Nyquist (b) diagrams obtained for device A before and after 1000 h under thermal/light soaking stress. In the Nyquist diagram, symbols correspond to the impedance data obtained experimentally in the dark under -0.75 V bias, while solid lines represent the fittings (Wang et al., 2006).

Several physical models have been developed in an effort to understand all the complex charge-transfer processes that take place in DSCs (Wang et al., 2006; Bisquert et al., 2000; Adachi et al., 2006). Actually, the electron transport and charge recombination in nanocrystalline TiO_2 films have been widely studied by Bisquert et al. (Bisquert et al., 2000), who suggested an infinite transmission line model to describe the charge-transfer phenomena occurring at the TiO_2/electrolyte. Based on this model, the charge transfer resistance related to recombination of electron at the TiO_2/electrolyte interface (R_k) and the electron transport resistance (R_w) can be extracted as shown in Table 1 (Wang et al., 2006). Also the information about charge transfer at the counter electrode/electrolyte and the diffusion of iodide and triiodide within the electrolyte can also be obtained by using this model (Wang et al., 2006). Besides the determination of R_k and R_w, the effective rate constant for recombination (k_{eff}), the effective electron diffusion length ($L_e = d\sqrt{R_k/R_w}$ where d is the TiO_2 film thickness) and the effective diffusion coefficient of electrons in the TiO_2 semiconductor (D_{eff}) were also calculated.

Table 1. Parameters of device A determined by EIS, according to the procedure developed by Adachi et al (Adachi et al., 2006).

Exposure time / h	R_k / Ω	L_e / μm	k_{eff} / s^{-1}	D_{eff} / $cm^2 \cdot s^{-1}$
0	66.1	14.1	2.5	1.5×10^{-5}
1000	32.3	22.2	4.0	5.8×10^{-5}

Table 1 shows that L_e is much higher than unity in both fresh and aged cells, which suggests that the recombination resistance of electrons is much larger than the diffusion resistance in the TiO_2 layer, as expected. The increased J_{sc} for the aged sample can be attributed to the longer electron diffusion length compared to the fresh sample. As shown in Fig. 4a), the middle frequency peak position of the aged sample was slightly shifted to higher frequency, revealing a decrease in the electron lifetime, which is in line with k_{eff} in Table 1. The decrease of electron lifetime explains the drop of V_{oc} observed in aged devices. The decreased electron lifetime is mainly ascribed to a major decrease in R_k (in Table 1) for the aged sample compared to the fresh one. This means that electrons recombine more easily with the electrolyte upon aging. The same conclusions can be drawn from the significant decrease of the intermediate semicircle in Figure 4(b), which corresponds to a lower value of the charge-transfer resistance (R_k) at this interface. The increased electron diffusion coefficient was probably due to the positive shift of the conduction band energy level edge.

Finally, a decrease in the redox charge transfer resistance at the platinum counter electrode was observed upon aging. This explains the decrease of the left-hand side semicircle in the Nyquist diagram. This semicircle corresponds to the high-frequency peak in the Bode plot, which has moved towards larger values (meaning lower electron lifetimes and shorter redox reaction times). Additionally, an overlap between the photoelectrode impedance (middle semicircle) and that related to the Nernstian diffusion within the electrolyte (right-hand semicircle) can be noticed, probably due to a larger over potential for the I^-/I_3^- redox reaction on the platinum electrode for the aged sample, accompany with a fill factor problem (*FF* decreases from 0.67 to 0.59 upon aging).

4. Conclusion

Two N3-based dyes were synthesized bearing in mind that the number of protons in the sensitizer influences the open-circuit potential and the short circuit current of the DSC. Potassium and sodium cations were used to substitute two protons of the N3 dye and the resulting dyes were compared with the well-known N719 dye that contains two TBA (tetrabutylammonium) cations. Despite presenting the highest initial photovoltaic performance,

the N719 system was rather unstable, exhibiting a strong decrease in J_{sc} and V_{oc} upon aging, which might be due to the dye desorption. In addition, sodium substitution in place of TBA does not help to enhance the stability of devices, whereas substitution with potassium salt revealed better stability compared to the other two systems. In fact, this system kept close to 90% of its initial performance after 1000 h of light soaking at 50 ºC.

References

Grätzel, M. (2001). Molecular photovoltaics that mimic photosynthesis. *Pure Appl. Chem.*, 73, 459-467.

Zweibel, K., Mason, J., Fthenakis V., (2008). By 2050 solar power could end U.S. dependence on foreign oil and slash greenhouse gas emissions, *Scientific American*, January, 64-73.

Grätzel, M., (2003). Dye-sensitized Solar Cells. *J. Photochemistry and Photobiology C: Photochemistry Reviews*, 4, 145-153.

Grätzel, M. (2001). Photoelectrochemical cells, *Nature*, 414, 338-344.

Amadelli, R., Argazzi, R., Bignozzi, C. A., Scandola, F. (1990). Design of Antenna-Sensitizer Polynuclear Complexes. Sensitization of Titanium Dioxide with $[Ru(bpy)_2(CN)_2]_2Ru(bpy(COO)_2)^{2-}_2$. *J. Am. Chem. Soc.*, 112, 7099-7103.

Nazeeruddin, M. K., Kay, A., Rodicio, I., Humphry-Baker, R., Müller, E., Liska, P., Vlachopoulos, N., Grätzel, M. (1993). Conversion of light to electricity by cis-X_2bis(2,2'-bipyridyl-4,4'-dicarboxylate)ruthenium(II) charge-transfer sensitizers (X = Cl^-, Br^-, I^-, CN^-, and SCN^-) on nanocrystalline titanium dioxide electrodes, *J. Am. Chem. Soc.*, 115, 6382-6390.

Nazeeruddin, M. K., Humphry-Baker, R., Liska, P., Grätzel, M. (2003). Investigation of Sensitizer Adsorption and the Influence of Protons on Current and Voltage of a Dye-Sensitized Nanocrystalline TiO_2 Solar Cell, *J. Phys. Chem. B*, 107, 8981-8987.

Nazeeruddin, M. K., Zakeeruddin, S. M., Humphry-Baker, R., Jirousek, M., Liska, P., Vlachopoulos, N., Shklover, V., Fisher, C. H., Grätzel, M. (1999). Acid-Base Equilibria of (2,2¢-Bipyridyl-4,4¢-dicarboxylic acid)ruthenium(II) Complexes and the Effect of Protonation on Charge-Transfer Sensitization of Nanocrystalline Titania. *Inorg. Chem.,* 38, 6298-6305.

Fabregat-Santiago, F., Bisquert, J., Palomares, E., Otero, L., Kuang, D., Zakeeruddin, S., Grätzel, M. (2007). Correlation between Photovoltaic Performance and Impedance Spectroscopy of Dye-Sensitized Solar Cells Based on Ionic Liquids. J. Phys. Chem. C., 111, 6550-6560.

Kuang, D., Ito, S., Wenger, B., Klein, C., Moser, J.-E., Humphry-Baker, R., Zakeeruddin, S. M., Grätzel, M. (2006). High Molecular Extinction Coefficient Heteroleptic Ruthenium Complexes for Thin Film Dye-sensitized Solar Cells. *J. Am. Chem. Soc.*, 128, 4146-4154.

Q. Wang, S. Ito, M. Grätzel, F. Fabregat-Santiago, I. Mora-Sero, J. Bisquert, T. Bessho, H. Imai (2006). Characteristics of high Efficiency Dye-sensitized Solar Cells. *J. Phys. Chem. B*, 110, 25210-25221

Bisquert, J., Garcia-Belmonte, G., Fabregat-Santiago, F., Ferriols, N. S., Bogdanoff, P., Pereira, E. C. (2000) Doubling Exponent Models for the Analysis of Porous Film Electrodes by Impedance. Relaxation of TiO_2 Nanoporous in aqueous Solution. *J. Phys. Chem. B*, 104, 2287-2298.

M. Adachi, M. Sakamoto, J. Jui, Y. Ogata, S. Isoda (2006). Determination of Parameters of Electron Transport in Dye-sensitized Solar Cells *using Electrochemical Impedance Spectroscopy. J. Phys. Chem. B*, 110, 13872-13880.

Proceedings of the 10th International Chemical and
Biological Engineering Conference - CHEMPOR 2008
Braga, Portugal, September 4-6, 2008
E.C. Ferreira and M. Mota (Eds.)

Membrane charge effects on the recovery of Fe-EDTA species in aqueous solution by nanofiltration

Xavier Bernat[1], Frank Stüber[1], Agustí Fortuny[2], Christophe Bengoa[1], Azael Fabregat[1], Josep Font[1*]

[1] Departament d'Enginyeria Química, ETSEQ, Universitat Rovira i Virgili, Av. Països Catalans 26, 43007 Tarragona, Catalunya, Spain

[2] Departament d'Enginyeria Química, EPSEVG, Universitat Politècnica de Catalunya, Av. Víctor Balaguer s/n, 08800 Vilanova i la Geltrú, Barcelona, Catalunya, Spain

Keywords: Nanofiltration, iron, EDTA, speciation, membrane charge
Topic: Advancing the chemical engineering fundamentals — Membranes and membrane science.

Abstract

Nanofiltration has been found to be an efficient treatment for the recovery of metals from aqueous streams. However, mechanisms involved in the removal of species by nanofiltration are still unclear. Thus, experimental studies are needed to know the features of nanofiltration membranes in removing specific substances. The nanofiltration of iron chelates by means of three commercial membranes, NF, NF270 and NF90 (from Dow-Filmtec), is presented. The effect of the pH on the chelates removal is investigated, finding that it affects both the chemistry of the solution and the membrane surface charge. Therefore, the retentions observed are strongly correlated to sieving but also to charge attraction/repulsion between the membrane and the iron chelates. All the membranes are able to be used at mid-acid pH (around 4.3) as their retentions are nearly 98% for all them. Also at slight basic pH of about 8.4, NF membrane still allows 95% iron retention whilst NF270 an NF90 show high iron retention of 99%. Finally, at the lowest tested pH (around 2.5), NF and NF270 membranes exhibit acceptable iron retention of 90% and 95%, respectively, however NF90 has found to be more sensitive to low pH and the retention observed with this membrane was only 53%.

1 Introduction

Membrane processes are being widely studied as useful technologies to recover contaminants from polluted waters. Nanofiltration is a promising membrane technology that allows the recovery of small size organic compounds as well as multivalent metal ions from aqueous streams. Nanofiltration mechanisms allowing the retention of such compounds are based on electrostatic interactions between the charged molecules (or ions) and sieving mechanisms due to the molecular weight cut-off of the membranes and the molecular weights of the targeted compounds (Van der Bruggen et al., 1999). Thus, it is of high importance to control both the chemistry of the solutions to be filtered as well as the membrane properties for correctly predicting the retention mechanisms involved in the separation process.

Nanofiltration membranes have been used for the recovery of a wide variety of organic compounds such as dyes (Van der Bruggen et al., 2001), herbicides (Plakas et al., 2006), aromatic compounds (Zhang et al., 2006), etc. In addition, nanofiltration has been used for the recovery of metal ions such as copper (Tanninen et al., 2006a), chromium (Frenzel et al., 2006), or cobalt (Choo et al., 2006) among many others.

* Corresponding author. Tel + 34 977559646. E-mail:jose.font@urv.cat

Nowadays, chelating agents, such as ethylenediaminetetraacetic acid (EDTA), are broadly used in fertilizers, herbicides, detergents, as effective agents to remove metals from contaminated industrial containers, and even as promoters of the oxidation (Fenton-like processes) of biorefractory organic compounds when iron is also present in the reactive media. For the latter, the homogeneous catalytic pair (in this case, Fe-EDTA) leaves the oxidation reactor together with the partially-treated effluent, increasing the costs associated to the treatment and also adversely affecting the environment. Thus, the recovery of the complex Fe-EDTA is mandatory for solving the abovementioned problems.

In this study, nanofiltration is presented as a successful process for recovering Fe-EDTA chelates from synthetic wastewater. In addition, as Fe-EDTA complexes change in nature when the pH of the solutions is modified, the sieving and electrostatic effects involved in their retention have been investigated in connection with pH.

2 Materials and methods

Nanofiltration experiments were performed in a commercial batch filtration cell (Sterlitech Corporation, model HP4750) with a total capacity of 250 mL and an available filtration area of 14.6 cm^2. The cell is equipped with a controlled speed magnetic stirrer, (Selecta, model Agimatic REV-S). NF, NF90 and NF270 polymeric flat-sheet membranes were selected for this study. These membranes were manufactured and supplied (free of charge) by Dow Chemical Co. Iron (III) nitrate nonahydrate (Riedel-de Haën, purity 98%) and EDTA disodium salt dihydrate (Panreac, purity 99%) were used to prepare the solutions to be filtered. These solutions were always prepared by dissolving the stoichiometric amounts of Fe (III) and EDTA (1:1) in deionised water. The concentration of Fe(III) in the solutions was always 0.9 mM. Concentrated hydrochloric acid solution (Fluka, 37%) and sodium hydroxide (Sigma, purity 98%) were used to adjust the solutions to be filtered to the desired pH.

A typical filtration experiment started cutting the membrane sample in the adequate size. Then, the membrane was rinsed with deionised water and subsequently left overnight in deionised water. After this, the membrane was placed in the filtration cell and compacted with deionised water at 12 bar for one hour. The transmembrane pressure (TMP) was fixed thanks to the connexion of the cell with a nitrogen gas cylinder, a backpressure valve and a manometer. After the compaction step, 250 mL of solution to be filtered were added to the cell and a 10-mL sample was withdrawn for iron analysis, as explained below. After fixing the TMP at 6 bar and the magnetic stirrer at 300 rpm, the system was left to permeate until around 200 mL of initial solution had permeated. Thus a Volume Reduction Factor (initial volume/non-filtered volume) of 6 was achieved in the experiments. Permeate samples were periodically withdrawn for iron analysis to obtain the evolution of the iron retention percentage (%R) along the time. The %R was calculated as follows.

$$\%R = 100 \cdot \left(1 - \frac{C_P}{C_r}\right) \quad (1)$$

where C_P is the iron concentration in the permeate and C_r is the concentration in the retentate. The C_P and the initial iron concentration in the initial solution to be filtered were analysed by Atomic Absorption Spectrometry (Perkin Elmer, model 3100). As the filtration experiments were performed in batch mode, C_P changed along the time due to the continuous concentration of the original solution. This concentration was estimated from the mass balance supposing that no iron adsorption on the membrane took place. However, although the stirring does in principle decrease the concentration polarisation phenomenon and, in consequence, the extent of the iron adsorption impact, it has to be taken into account.

3 Results

3.1. Chemical speciation diagram

The formation of metallic chelates is strongly affected by the chemical conditions, such as pH, concentration of chelate and metal, ionic strength and so on. Thus, it is of great importance to know the exact species expected in the solutions to be filtered. Thus, the correlation between the filtration features and the chemical properties of the solutions could be more accurate. The chemical speciation diagram of a 0.9 mM Fe (III) – 0.9 mM EDTA solution, shown in Figure 1, was obtained with a freely available software (Puigdomènech, 2004) designed for this purpose.

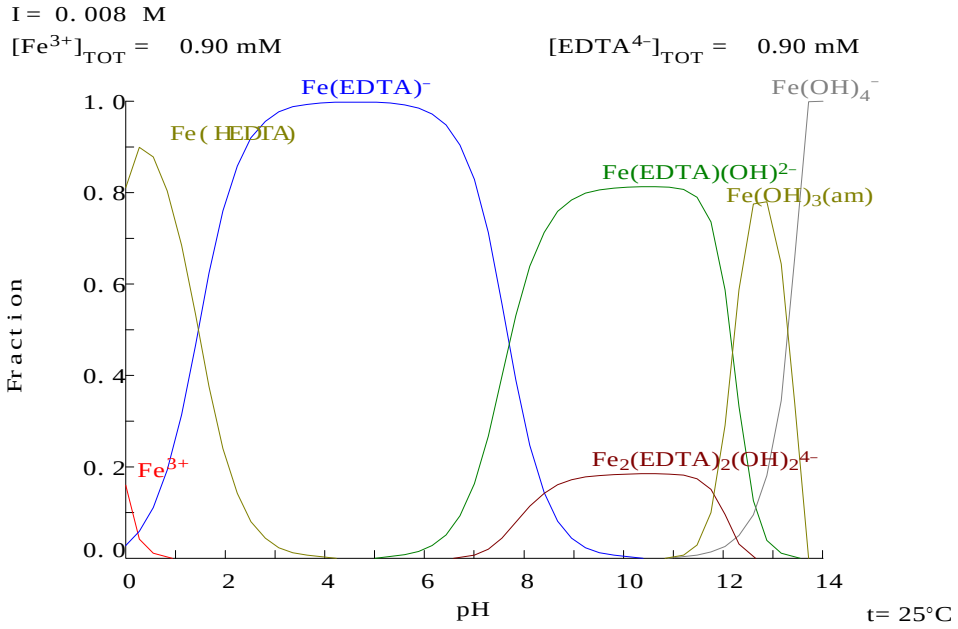

Figure 1. Chemical speciation diagram of the solution to be filtered.

As Figure 1 shows, the pH has a significant effect on the speciation of iron, concretely on the charge of the iron chelates formed. As the pH of the solution increases up to around 5, the fraction of Fe(HEDTA) and free Fe(III) decreases and that of $Fe(EDTA)^-$ increases until 100% of this species is achieved. Beyond this pH, the fraction of $Fe(EDTA)^-$ starts to decrease and $Fe(EDTA)OH^{2-}$ and $Fe_2(EDTA)_2(OH)_2^{4-}$ increase. The latter species is a clear example of the importance of the pH on the properties of the solution. This species has a higher molecular weight and presents a higher negative charge, which can affect the iron retentions obtained by nanofiltration. At pH 11, iron precipitate appears, indicating that chelation no longer occurs.

3.2. Filtration results

In this section, the iron retentions obtained with the three nanofiltration membranes are presented. The TMP was fixed at 6 bar for all the experiments and every membrane was tested at three different pH in order to test the effects of the speciation of the Fe-EDTA chelates on the iron retention efficiency.

Figure 2 shows the iron retention obtained with the NF membrane at several pH. NF membrane has the isoelectric point (iep) at around pH 5.1 (Tanninen et al., 2006b). Thus, at a pH lower than 5.1, the membrane surface is positively charged whilst at pH higher than the iep, the membrane is negatively charged. Thus, at pH 2.5 and 4.2, the membrane is positively charged. Figure 1 shows that the species present at these pH are negatively charged. Thus, the retention of the chelates at these pH is probably due to sieving effects. However, at pH 2.5, the retention is lower than at pH 4.2 because, at this pH, the membrane has a lower charge density than at higher pH, causing higher attraction, therefore decreasing

the iron retention. At pH 8.2, where both the membrane and the chelates exhibit negative charges, the retention may be due to both sieving effects and repulsive forces.

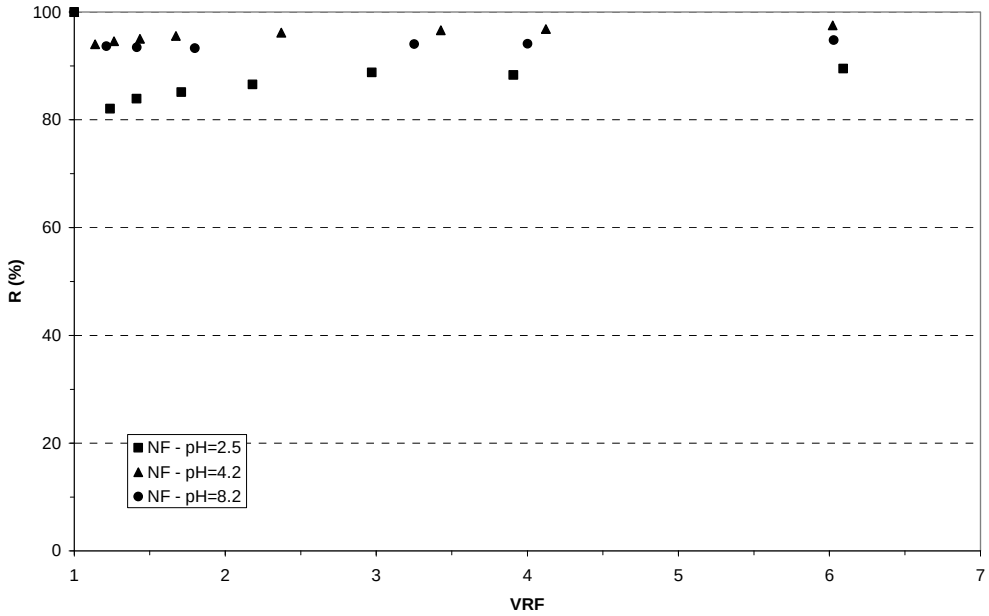

Figure 2. Effect of the pH on the iron retention by NF membrane.

Similarly to the NF membrane, iron retentions obtained with NF270 membrane are strongly correlated with the solution pH because it significantly affects the membrane charge as well as the iron chelate speciation. NF270 membrane has an iep of around 3.3 (Tanninen et al., 2006b). Figure 3 shows the effect of the pH on the iron retention when filtering with NF270 membrane.

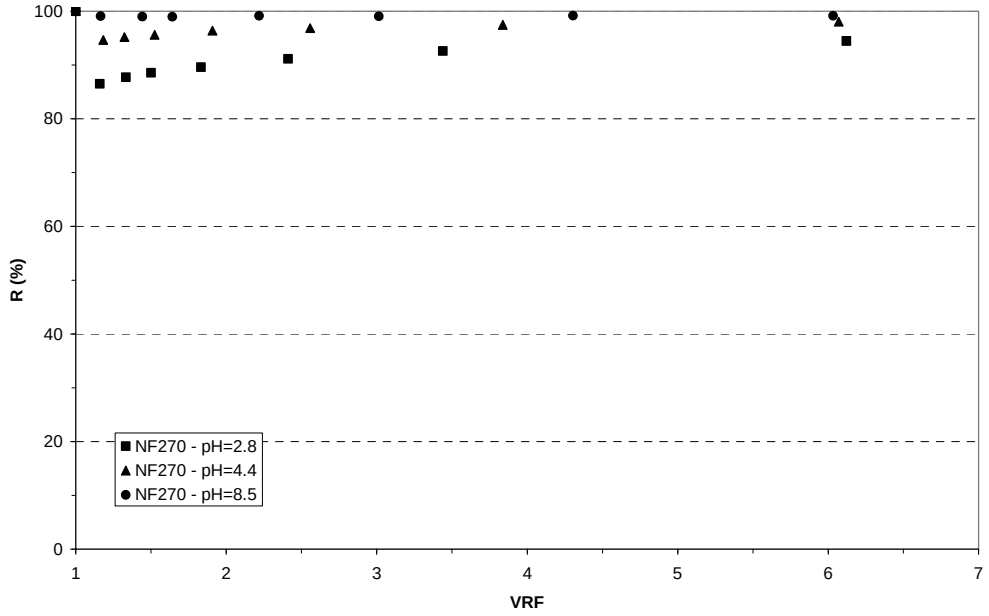

Figure 3. Effect of the pH on the iron retention by the NF270 membrane.

As it can be seen in Figure 3, at pH 2.8, the lowest retention is achieved. This result may be attributed to the low charge repulsion phenomena between the chelates and the membrane surface charge as the pH is very close to the membrane iep, decreasing the membrane charge. However, as with NF membrane, the retention in these conditions may be still due to sieving. At pH 4.4 and 8.5, where the membrane is negatively charged, the retentions

achieved are higher, being a little bit higher at pH 8.5. This behaviour could be assigned to the fact that at the highest pH, the membrane has a higher negative charge density, causing a slight increase on the iron retention due to the higher charge repulsion between the membrane and the chelated. In addition, at this pH, the presence of a small fraction of binuclear iron chelates, as shown in Figure 1, might also contribute to the increase on the iron retention.

Finally, the NF90 membrane was also tested for the recovery of iron chelates. NF90 membrane has an iep at pH 4.5 (Nghiem et al., 2005). As shown by Figure 4, at pH 2.4, the membrane also shows the lowest iron retention. However, in this case, the iron retention is much more lower (53% at a VRF around 6) than with NF and NF270 membranes. NF90 membrane exhibits higher positive charge at pH 2.4 than NF270 does (Nghiem et al., 2005). Thus, due to a higher attraction between the membrane and the positively-charged chelates occurring at pH 2.4 (see Figure 1), NF90 retention is lower than when for the other membranes. In addition, as with NF and NF270, at the lowest tested pH, the iron retentions significantly increased as the VRF did. Therefore, the iron retention increased from 27% to 53% when the VRF passed from 1.1 to 6.1. This trend may indicate that some adsorption phenomena are actually taking place and, in consequence, contributing to the iron retention. At pH 4.3 and 8.4, the retentions are higher than at pH 2.4 and comparable to those obtained with NF and NF270 membranes. A small difference between the iron retentions at pH 4.3 and 8.4 can be observed in Figure 4. At pH 4.3 the iron retention is 98% whilst at pH 8.4 is 99%. This could be a result of the almost no charge of the membrane at pH 4.3, because of the pH vicinity to the membrane iep (pH 4.5), thus decreasing the repulsions membrane-negative chelate, and consequently lowering the iron retention.

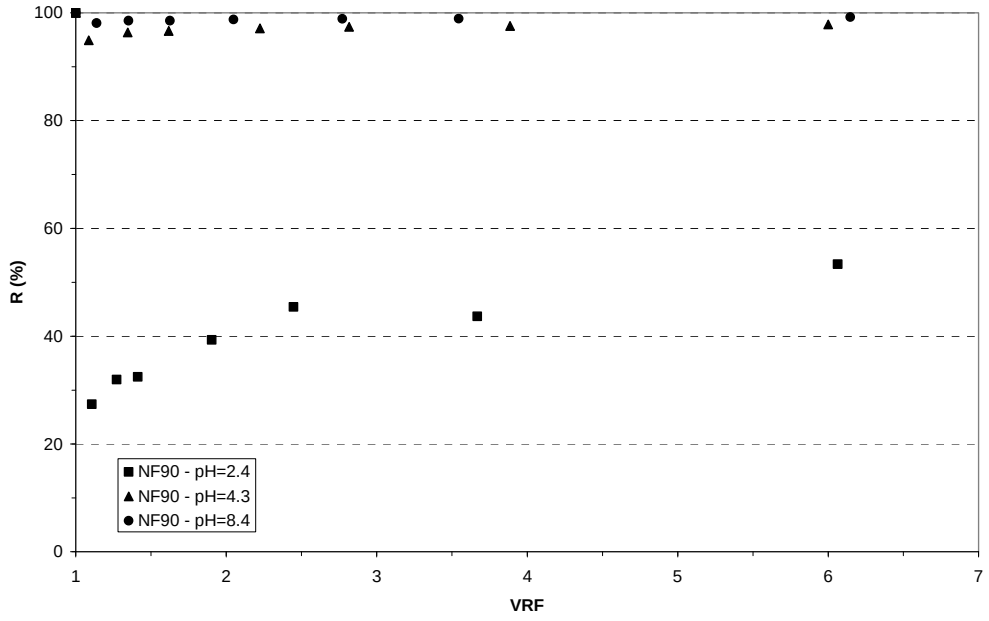

Figure 4. Effect of the pH on the iron retention by the NF90 membrane.

4 Conclusions

The removal of iron chelates by using nanofiltration membranes can be successfully achieved. However, the removal efficiency is strongly related to the chemistry of the solutions to be filtered and to the membrane properties. Particularly, the pH is found to be a crucial variable on the retention mechanism as it affects both the membrane charge (and charge density) as well as the speciation of the iron chelates. In general, the lowest retentions are obtained at the lowest tested pH (around 2.5), where all the membranes are positively charged and the chelates are negatively charged. This favours the attraction between the

charged species and the membrane surface, lowering the retention and also increasing the adsorption of chelated species onto the membrane. The iron retentions of NF, NF270 and NF90 at the lowest pH and at a VRF of around 6 have been found to be 90%, 95% and 53%, respectively. At the middle tested pH (around 4.3), the iron retentions at a VRF of about 6 were 98% for all the tested membranes. At the highest tested pH (around 8.4), the iron retentions at a VRF of around 6 were 95% for NF and 99% for both NF270 and NF90.

Acknowledgements

This work was funded by the Spanish Ministry of Education and Science (research grant CTM2005-01873/TECNO). We are also indebted to the Rovira i Virgili University for providing a fellowship to one of the authors. Dow Chemical Co. is gratefully acknowledged for offering membrane samples free of charge.

References

Choo, K.-H., Kwon, D.-J., Lee, K.-W., Choi, S.-J. (2002). Selective removal of cobalt species using nanofiltration membranes. *Environmental Science & Technology,* 36, 1330-1336.

Frenzel, I., Stamatialis, D.F., Wessling, M. (2006). Water recycling from mixed chromic acid waste effluents by membrane technology. *Separation and Purification Technology,* 49, 76-83.

Nghiem, L.D., Schäfer, A.I., Elimelech, M. (2005). Pharmaceutical retention mechanisms by nanofiltration membranes. *Environmental Science & Technology,* 39, 7698-7705.

Plakas, K.V., Karabelas, A.J., Wintgens, T., Melin, T. (2006). A study of selected herbicides retention by nanofiltration membranes – The role of organic fouling. *Journal of Membrane Science,* 284, 291-300.

Puigdomènech, I. (2004). Medussa Software, www.kemi.kth.se/medusa.

Tanninen, J., Mänttäri, M., Nyström, M. (2006a). Nanofiltration of concentrated acidic copper sulphate solutions. *Desalination,* 189, 92-96.

Tanninen, J., Mänttäri, M., Nyström, M. (2006b). Effect of salt mixture concentration on fractionation with NF membranes. *Journal of Membrane Science,* 283, 57-64.

Van der Bruggen, B., Schaep, J., Wilms, D., Vandecasteele, C. (1999). Influence of molecular size, polarity and charge on the retention of organic molecules by nanofiltration. *Journal of Membrane Science,* 156, 29-41.

Van der Bruggen, B., Daems, B., Wilms, D., Vandecasteele, C. (2001). Mechanisms of retention and flux decline for the nanofiltration of dye baths from the textile industry. *Separation and Purification Technology,* 22-23, 519-528.

Zhang, Y., Causserand, C., Aimar, P., Cravedi, J.P. (2006). Removal of bisphenol A by a nanofiltration membrane in view of drinking water production. *Water Research,* 40, 3793-3799.

Proceedings of the 10th International Chemical and
Biological Engineering Conference - CHEMPOR 2008
Braga, Portugal, September 4-6, 2008
E.C. Ferreira and M. Mota (Eds.)

Sorption Isotherms of organic-inorganic hybrids

Vânia Dias, Dmitry Evtyugin, Inês Portugal*
Chemistry Department and CICECO - University of Aveiro, Campus de Santiago,
3810-193 Aveiro, Portugal

Keywords: Cellulose/Silica hybrids, O/I hybrids, Water Sorption, Isotherms
Topic: Sustainable process-product development through green chemistry.

Abstract

Water-vapour sorption of cellulose/silica hybrids was studied at different temperatures in the range 20 - 40 ºC using a static gravimetric method. Several isotherm models were tested to fit the multilayer type II isotherms obtained for these new hybrids. Best results were obtained with the BET equation for water activity ≤ 0.45 and the GAB equation for water activity ≤ 0.9. GAB model parameters were used to determine the difference between molar sorption enthalpies of the monolayer and the multilayer, ΔH_c = 18 kJ/mol, and the difference between molar sorption enthalpies of the bulk liquid and the multilayer, ΔH_k = -11 kJ/mol.

1 Introduction

Organic–inorganic hybrids (OIHs) are promising composite materials compiling in a synergetic way the properties of the starting components depending on the synthesis mode. Cellulose/Silica hybrids (CSHs) are an example of such materials (Sequeira *et al*. 2007) fitting well in the concept of green chemistry.

Cellulose is the most abundant biodegradable, recyclable and renewable natural polymer. The incorporation of silica in cellulose at the nanometer scale was accomplished by a mild sol–gel process, involving hydrolysis and polycondensation of tetraethoxysilane (TEOS) used as silica precursor. The reactions were performed at room temperature, using solid acid catalysts and benign solvents such as water and alcohol (co-solvent). The advantage of this sol–gel process is that silica particles are generated *in situ* and evenly dispersed in the polymeric host matrix (i.e. cellulose), bounding to the polymer through hydrogen or covalent bonds thus forming a three-dimensional network with -O-Si-O-Si- linkages on the cellulose surface (Sequeira *et al*. 2007).

The combination of nanoscale inorganic moieties with organic polymers, such as cellulose, has high potential for future applications. When compared to the starting materials these new OIHs exhibit improved thermal and mechanical stability, excellent heat and acoustic insulation properties, and improved dimensional stability to humidification (Sequeira *et al.* 2008). Altogether these properties render these materials suitable for insulation or packaging purposes.

The efficient processing and storage of cellulose/silica hybrids and the appropriate modeling and optimization of the drying process require the knowledge of moisture sorption isotherms at different temperatures. These isotherms describe the equilibrium relationship between moisture content and water activity at constant temperatures and pressures.

The most common procedures for obtaining water sorption isotherms are the gravimetric and the hygrometric methods. In the gravimetric method the air temperature and water activity are kept constant until the moisture content of the sample attains a constant equilibrium value. This technique involves the use of

* Corresponding author. Tel + 351-234 370 708 . E-mail:inesport@ua.pt

saturated salt or sulphuric acid solutions to maintain a constant relative humidity. The air may be circulated at constant flow (dynamic methods) or stagnant (static methods). In the hygrometric method the material's moisture content is kept constant until the surrounding air attains a constant equilibrium value, then the air-water activity is measured via hygrometer or manometer (Mujumdar *et al*. 2006).

The IUPAC classification of gas-solid adsorption isotherms (Fig. 1), based on the work of Brunauer *et al.* (1940), includes among others:

- Type I isotherms are typical of microporous solids and chemisorption;
- Type II isotherms are typical of finely divided non-porous solids and hydrophilic polymers such as natural fibers;
- Type III isotherms are typical of vapor adsorption i.e. water vapor on hydrophobic materials; for example rubbers, plastics and synthetic fibers (Mujumdar *et al*. 2006).

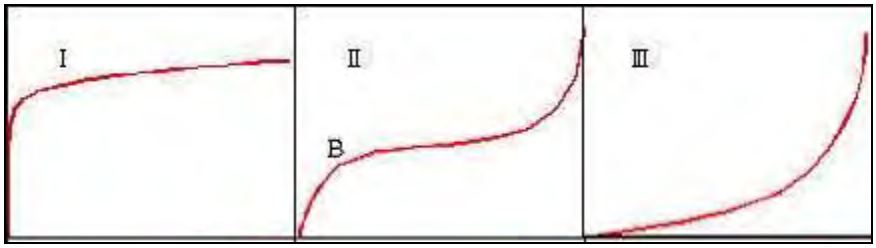

Figure 1- IUPAC classification of adsorption isotherms (Brunauer, 1940).

Several mathematical models exist to describe adsorption isotherms. Available models suitable to describe moisture sorption isotherms can be divided into several categories: kinetic models based on monolayer adsorption (BET model) or multilayer adsorption and condensed film (GAB model), semi-empirical models (Henderson and Halsey models) and empirical models (Smith and Oswin models).

The Brunauer-Emmet-Teller (BET) model represents a fundamental milestone in the interpretation of monolayer sorption isotherms, particularly types II and III (Krupinska *et al.* 2007) but this model is generally restricted to values of water activity (a_w) below 0.45 because of the assumptions used in the derivation of the equation.

The BET model is represented by equation (1)

$$Xeq = \frac{MCa_w}{(1-a_w)(1-a_w+Ca_w)} \quad \textbf{(1)}$$

where, where Xeq is the equilibrium moisture content expressed as grams of sorbate per gram of adsorbant, a_w is the water activity, M and C are the model's constants. Theoretically, M (g water/g dry solids) is the monolayer moisture content and C is a constant related to the heat of adsorption.

The Guggenheim-Anderson-deBoer (GAB) model represents an extension of the BET model valid for $a_w \leq 0.9$. In this model, represented by equation (2), a third constant K is introduced to describe the modified properties of the sorbate in the multilayer region in relation to the sorbate in the monolayer and in the bulk liquid (Timmermann, 2003).

$$Xeq = \frac{MCKa_w}{(1-Ka_w)(1-Ka_w+CKa_w)} \quad \textbf{(2)}$$

where Xeq, a_w and M are as above mentioned, C is a constant related to the first layer heat of sorption and K is a factor related to the multilayer adsorption heat. The influence of temperature on GAB parameters C and K can be expressed by Arrhenius type equations (3) and (4)

$$C = C_0 \exp\left(\frac{\Delta H_c}{RT}\right), \quad \text{with} \quad \Delta H_c = h_m - h_n \tag{3}$$

$$K = k_0 \exp\left(\frac{\Delta H_k}{RT}\right), \quad \text{with} \quad \Delta H_k = h_i - h_n \tag{4}$$

where C_0 and k_0 are entropic accommodation factors; ΔH_c and ΔH_k are functions of the water heat of sorption; h_m, h_n and h_i are sorption enthalpies (J/mol) of the monolayer, the multilayer and the bulk liquid (heat of condensation of water vapour), respectively; R (J/mol K) is the ideal gas constant and T (K) is the absolute temperature (Telis *et al.* 2000).

The monolayer moisture content, determined with the BET model (for $a_w \leq 0.4$) or GAB model (for $a_w \leq 0.9$), is related to the solid's surface area according to equation (5)

$$S = M \frac{N_A A_m}{M_w} \tag{5}$$

where S is the solid surface area (m^2/g dry solids), M is the monolayer moisture content (g water/g dry solids), M_w is the molecular weight of water (18 g/mol), N_A is Avogadro's number (6×10^{23} molecules/mol) and A_m is the projected area of a water molecule (1.06×10^{19} m^2) (Togrul *et al.* 2006).

The objectives of this study were to obtain the sorption isotherms of cellulose/silica hybrids (CSHs) based on *Eucalyptus globulus* kraft pulp, to select a suitable isotherm model and to determine the characteristic thermodynamic parameters.

2 Experimental procedure

Sorption isotherms of CSHs containing 34% of silica were determined by a static-gravimetric method at different temperatures, in the range 15 - 40 ºC, using an experimental setup similar to that presented in Fig. 2.

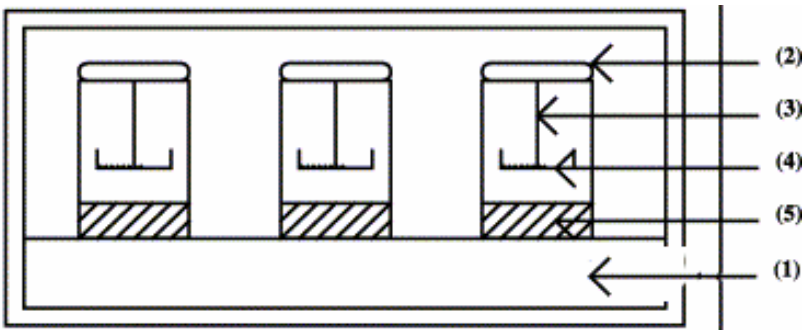

Figure 2: Experimental setup: (1) thermostatic bath, (2) closed flasks, (3) sample holder, (4) CHSs samples, (5) saturated salt solution (adapted from Lahsasni *et al.* 2003).

Saturated aqueous salt solutions of KOH, CH_3COOK, $MgCl_2.6H_2O$, K_2CO_3, $Mg(NO_3)_2$, KI, $(NH_4)_2SO_4$ and KNO_3 were used to control the atmosphere's moisture content (RH, %) in the range 7% to 95% (Greenspan *et al*. 1977; WebbTech). Excess salt was maintained in each solution.

CSHs samples (≈ 1 g) were oven-dried overnight at 105 ºC, dehydrated over P_2O_5 during 8 days, weighted and placed in flasks containing the saturated salt solutions. The flasks were closed and placed in a shaking water bath (Julabo SW23) at controlled temperature (± 1 ºC) and weighted regularly (Mettler toledo, sensitivity ± 0.0001g) until

reaching a constant weight (≈ 15 days). Experiments were stopped when the difference between two successive weightings in different days was less than 0.001g.

3 Results and discussion

The experimental results for CHSs water sorption isotherms in the range of 20-40 ºC are presented in Fig. 3. These results are consistent with type II isotherms (IUPAC classification) and clearly reveal that the amount of adsorbed water decreases with temperature, indicating that CHSs becomes less hygroscopic at higher temperatures.

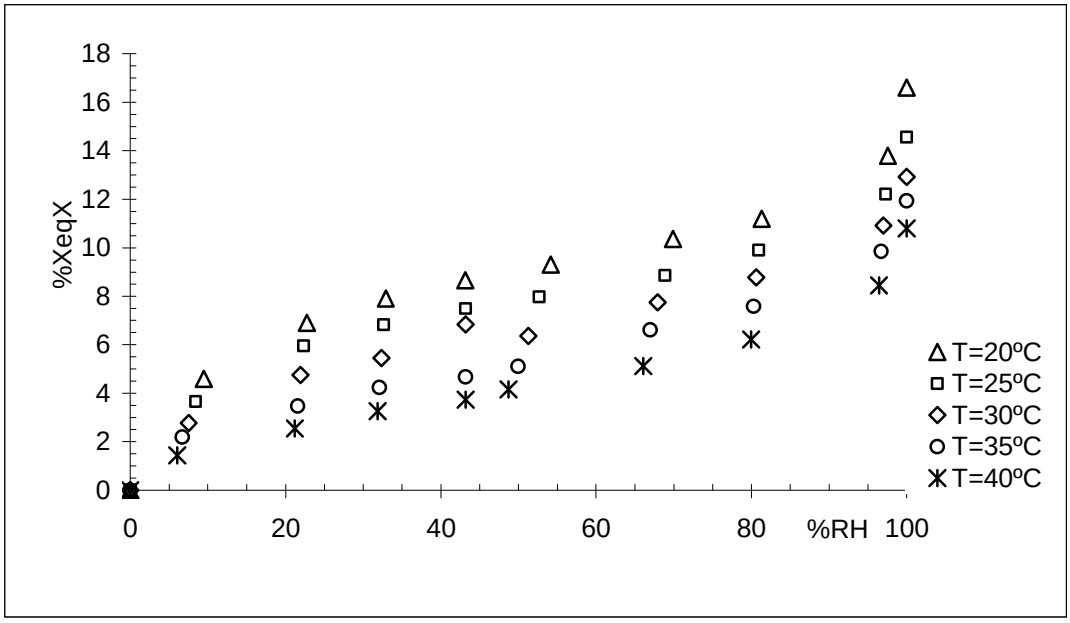

Figure 3: Experimental data (equilibrium water content –Xeq, *versus* relative humidity – %RH) for celulose/silica hibrids at temperatures in the range of 20 - 40 ºC.

In the region of low and intermediate water activities, also known as multilayer sorption region, the moisture content increases linearly with a_w, whereas at high water activity levels, designated as capillary condensation region, the water content rapidly increases with a_w. A possbile explanation for the behaviour at low water activities is the occurrence of physical adsorption of water on strongly active sites such as surface –OH groups of cellulose/silica hybrids.

Several sorption isotherm equations (GAB, BET, Oswin, Halsey) were tested to model the experimental data for CSHs water sorption at 25ºC, using nonlinear regression analysis. Goodness of fit was evaluated by the mean relative percentage deviation, P, defined by equation (6).

$$P = \frac{100}{N}\sum_{i=1}^{N}\frac{\left|Xeq_{\exp-i} - Xeq_{calc-i}\right|}{Xeq_{\exp-i}} \qquad \textbf{(6)}$$

The GAB model was found to be the most suitable for describing the sorption data but the BET model (for $a_w < 0.45$) was also selected for further analysis for it is recommend by IUPAC for solids characterization (Timmermann, 2003). The experimental results and the GAB and BET sorption isotherms at 25ºC are shown in Fig. 4.

Throughout the entire range of water activity and temperature the fitness of the GAB model was better than the BET model. Parameters for both models (C, M, K) are presented in Table 1 together with the mean relative percentage deviation (P) and specific surface area (S).

The value of the monolayer moisture content (M) obtained by GAB and BET models is an important parameter for it is a measure of the sorption capacity of a solid material

and an indicator of available polar sites for water vapour binding (Mihoubi *et al.* 2006). M values of CSHs decrease with increasing temperature which indicates that the sorption capacity is lower at higher temperatures. As temperatures rises so does the kinetic energy of water vapour molecules surrounding the CHSs samples and thus the monolayer moisture content is reduced (Mihoubi *et al.* 2006). The value of M is sistemathically lower for the BET model as stated by Timmermann (2003).

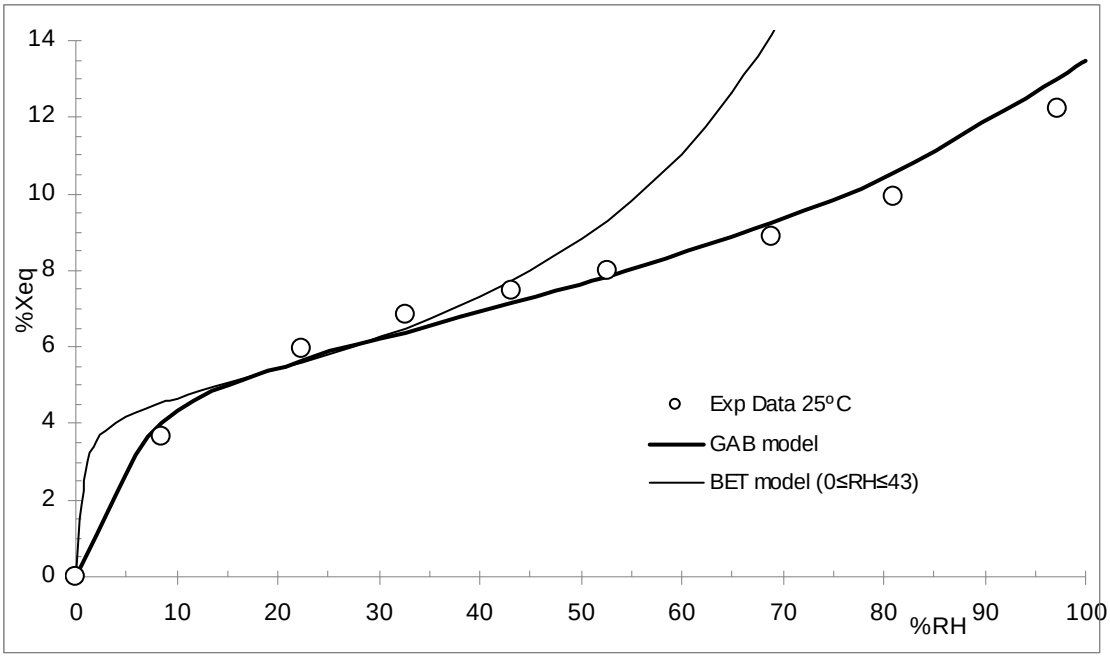

Figure 4: Experimental data (equilibrium water content –Xeq, *versus* relative humidity – %RH), GAB and BET model fitting for celulose/silica hibrids at 25ºC.

Table 1: Estimated GAB and BET model parameters, mean relative percentage deviation (P) and estimated surface area (S) at different temperatures.

Model	parameters	Temperature (ºC)				
		20	25	30	35	40
GAB	M (g water/g dry solids)	0.0665	0.0577	0.0467	0.0353	0.0267
	C	42.5	38.2	35.3	31.5	26.0
	K	0.572	0.581	0.617	0.694	0.742
	P(%)	5.2	5.3	6.2	2.6	4.3
	S (m^2/g dry solids)	235	204	165	125	94.3
BET	C	224	146	53.1	128	56.7
	M (g water/g dry solids)	0.0511	0.0444	0.0391	0.0283	0.0219
	P(%)	6.3	7.6	5.9	7.0	5.8
	S (m^2/g dry solids)	180	157	138	99.9	77.3

The values of the GAB parameter K, a correction factor related to properties of the multilayer adsorption, are lower than 1 (Table 1). This suggests that water adsorption on CSHs involves multilayers. Furthermore, the fact that K increases with temperature is related to the negative effect of temperature on adsorption. As K aproaches unity the GAB model aproaches the BET model that accounts only for monolayer adsorption.

The values for total surface area (S) obtained with the GAB model and with the BET model are quite different and the BET model underestimates S values (Timmermann, 2003). However, in both models the effect of temperature is consistent indicating that the total surface area available for hydrophilic bonding decreases with temperature.

The effect of temperature on the GAB model's parameters was analyzed using equations (3) and (4). The resulting thermodynamic parametes are shown in Table 2. The difference between molar sorption enthalpies of the monolayer and the multilayer, $\Delta H_{c,}$ is = 18 kJ/mol and ΔH_k, the difference between molar sorption enthalpies of the bulk liquid and the multilayer is -11 kJ/mol. The large positive value of $\Delta H_{c,}$ is due to the strong interaction of water vapour with the sorption sites of CSHs. The negative value of ΔH_k indicates an exothermic interaction of water vapour with CSHs and confirms the tendency to multilayer reduction when temperature rises as mentioned earlier (Togrul *et al*. 2006).

Table 2: Estimated GAB parameters.

Monolayer Parameters		Multilayer Parameters	
C_0	0.0277	k_0	42.7
ΔH_c (KJ/mol)	17.9	ΔH_k (J/mol)	-10.6

References

Brunauer S., Deming L.S., Deming W.S., Teller E., (1940). On a theory of the van der Waals adsorption of gases, J. Am. Chem Soc. 62, 1723-1732

Greenspan L. (1977). Humidity fixed points of binary saturated aqueous solutions. *Journal of Research of the National Bureau of Standards*, 81a, 89–112.

Krupinska B., Strommen I., Pakowski Z., Eikevik T.M., (2007). Modeling of Sorption Isotherms of Various Kinds of Wood at Different Temperature Conditions. *Drying Technology*, 25,1463-1470.

Lahsasni S., Kouhila, M., Mahrouz, M., Fliyou, M. (2003). Moisture adsorption-desorption isotherms of prickly pear cladode (*Opuntia ficus* indica) at different temperatures. *Energy Conversion and Management*, 44, 923-936

Marinos-Kouris D., Maroulis Z.B. (2006) Transport properties in the drying of solids in *Handbook of Industrial Drying* , Mujumdar A.S., Mujumdar A.M.S. Eds., CRC Press. (on line access 1-07-2008, http://books.google.pt).

Mihoubi D., Bellagi A. (2006), Thermodynamic analysis of sorption isotherms of bentonite. *J. Chem. Thermodynamics*, 38, 1105–1110

Sequeira S., Evtuguin D., Portugal I. (2007). Synthesis and characterization of cellulose/silica hybrids obtained by heteropoly acid catalyzed sol–gel process. *Materials Science and Engineering*, C 27, 172–179.

Sequeira S., Evtuguin D., Portugal I. (2008). Thermal and Mechanical Properties of Cellulose/Silica Hybrid Materials (*in press)*

Telis V.R.N., Gabas A.L., Menegalli F.C., Telis-Romero J. (2000). Water sorption thermodynamic properties applied to persimmon skin and pulp. *Thermochimica Acta.* 343, 49-56

Timmermann O. (2003). Multilayer sorption parameters: BET or GAB values?. *Colloids and Surfaces A: Physicochem. Eng. Aspects,* 220, 235-260.

Togrul H., Arslan N. (2006), Moisture Sorption Behaviour and Thermodynamic Characteristics of Rice stored in a Chamber under Controlled Humidity. Biosystems Engineering 95 (2), 181-195

WebbTech - http://www.users.bigpond.com/webbtech/salt.html (on line access 12-12-2007) Last modified: 09-Jul-2008

Proceedings of the 10th International Chemical and
Biological Engineering Conference - CHEMPOR 2008
Braga, Portugal, September 4-6, 2008
E.C. Ferreira and M. Mota (Eds.)

Solar evaporation of produced and potable water in Teflon trays

Magna A.S.B. Sousa[1], Andréa O. Nunes[1], Matheus C. Borges[1], Henio N.S. Melo[1], Josette L.S. Melo[1*]

[1] DEQ – Departamento de Engenharia Química, Centro Tecnológico, UFRN, Campus Universitário, CEP: 59072-970, Natal/RN, Brasil.

Keywords: Solar evaporation, Produced water, Steam pressure, Salting effect, Boiling point

Topic: Advancing chemical and biological engineering fundamentals.

Abstract

Produced waters are a complex mixture of water, salts, oil, microorganisms and traces of heavy metals. Owing to this complexity, the conventional techniques used to treat these waters are onerous and a suitable final destination for them must also be found. It is desirable and beneficial to study new alternatives for the treatment and final disposal of these effluents. This study was to investigate the variation in solar evaporation of samples of potable water and produced water, in aluminum trays coated with commercial Teflon. The work was developed in the city of Natal, whose solar radiation is around 5000 W/m^{2}d. The trays used were made of commercial Teflon with a capacity of 2.8 L. The experiment consisted of placing 1 L of sample from each tray and exposing them to the sun for an equal period of time: from 10 to 14 h. Temperature was monitored using a mercury thermometer and the amount that evaporated from each tray was measured at the end. The results demonstrate that there were no significant temperature variations between the trays, which remained between 39°C and 40°C during the experiment. The average volumes evaporated in this interval were 400 mL for potable water and 403 mL for produced water. These results show that evaporation output varied between 34% and 40%, and it should be pointed out that the evaporation rates in this case are influenced by temperature, pressure, wind and solar radiation. The incident solar radiation peaks on the experimental days varied between 1061.30 and 844.40 W/m^2, corresponding to the highest and lowest output, respectively. This study highlights the importance of a more thorough knowledge of the solar evaporation process of produced water, given industry requirements of returning the water to the hydrologic cycle with the least environmental damage possible and collecting the salt for more adequate disposal.

1 Introduction

Water, considered the universal solvent, is undoubtedly one of the most important substances for maintaining life on Earth. Its presence for the survival of live beings and for the performance of human activities is indispensable.

In addition to acting as a solvent and raw material in industrial processes, water acts as an input in the heating or cooling of systems and is even a subproduct of a number of processes such as oil production. Regardless of its use, legislation, which is increasingly restrictive, requires that the effluents generated be treated and disposed of properly.

Understanding and predicting the behavior of aqueous systems is useful and necessary in every sense, be it optimizing its industrial use (minimizing waste), be it improving the

* Corresponding author. Tel + (55)3215-3757-(209). E-mail:josette@eq.ufrn.br

treatment systems of effluents and their final disposal or reuse (Bezerra, 2004).

Among the industrial operations performed with water, the evaporation processes stand out. In many industrial processes a highly saline effluent is produced and in these cases the water must be separated from the salts and solar evaporation may be a viable alternative to perform this operation, both for allowing the reuse of the salts and as a way to return the water to the environment.

Pure water boils at 100°C at atmospheric pressure and although the water on Earth is not pure, owing mainly to its power of solvency, this temperature may vary in real systems, depending on the elements that this mixture contains.

Water evaporation, however, begins at zero degrees. In the so-called triple point the three states of matter coexist (Van Ness, 1980). When temperature rises in an isobaric system, the evaporation rate also rises, reaching the boiling point at around 100°C. It is known that saline solutions raise the boiling point (bp) of water by reducing its water pressure. On the other hand, volatile organic compounds increase water vapor pressure and consequently its evaporation rate.

Produced waters are a complex mixture of water, salts, oil, microorganisms and traces of heavy metals (Azevedo, 1998). Due to this complexity these waters may have their boiling point moved up or down and this displacement is defined by their individual characteristics, which are quite inconstant, varying from one producing field to another and depending on the treatment used to extract the petroleum. According to Schulli (2003), evaporation towers have been used to desalinate produced water using electrical energy.

2. Objectives

The aim of the present study was to study the variation in solar evaporation of potable water (groundwater) and produced water (low organic concentration) samples at the same pressure, in aluminum trays coated with commercial Teflon.

3. Methodology

The work was carried out in the city of Natal, Northeast Brazil (5º 47’ 42” S 35º 12’ 32” W), whose mean solar radiation is around 5000 W/m^{2}d. The 2.8 L trays were made of commercial Teflon. The experiment consisted of placing 1L of each sample type in the corresponding tray and exposing them to the sun for an equal period of time: from 10 to 14 h. Temperature was monitored using a mercury thermometer and the amount that evaporated from each tray was measured at the end. Figure 1 shows the configuration of the experiment.

Figure 1: Teflon trays for sample evaporation

The conductivity and pH of the samples were measured. The results are shown in Table 1.

Table 1: Characteristics of the sample before the experiments (average values)

Parameters	Potable water	Produced water
pH	8.8	8.7
Conductivity (μS/cm)	357	3,500

4. Results and discussion

The results demonstrate that there were no significant temperature variations among the trays, which remained between 39°C and 40°C during the experiment. The average volumes evaporated in this interval were 400 mL for potable water and 403 mL for produced water, which was also not significant. The largest difference was for the tray with potable water, which evaporated 340 mL, whereas the tray with produced water evaporated 330 mL. These findings indicate that, for the samples with these characteristics, the effects tend to cancel each other out, in contrast to the results of conventional distillation tests, which point to a higher T_{bp} at 100°C, showing in this case, the effect of the salt.

It was found that the evaporation output varied between 34% and 40% and it should be pointed out that the evaporation rates in this case are influenced by temperature, pressure, wind and solar radiation. A comparison of solar radiation values showed that the largest outputs were obtained when the highest radiations occurred and the smallest outputs at the lowest radiations, which were 1061.30 and 884.40 W/m^2, respectively.

5. Conclusions

The study highlights the importance of a more thorough knowledge of the solar evaporation process of produced water, given industry requirements of returning the water to the hydrologic cycle with the least environmental damage possible and collecting the salt for more adequate disposal.

6. Acknowledgements

The authors wish to thank Petrobras as well as CNPq and FINEP for their support.

References

Azevedo, E. B. Aplicação da fotocatálise para a degradação de poluentes das águas de produção de petróleo. 1998. 94f. Dissertação (Mestrado em Ciências em Engenharia Química), COPPE, Universidade Federal do Rio Grande do Norte, Rio de Janeiro.

Bezerra, M. A. dos S. Desenvolvimento de um Destilador Solar para Tratamento de Águas de Produção de Petróleo com Vistas a sua Utilização na Agricultura e Geração de Vapor. 2004. 105p. Dissertação (Mestrado em Engenharia Química) – Centro Tecnológico, Departamento de Engenharia Química, Programa de Pós-Graduação em Engenharia Química, Universidade Federal do Rio Grande do Norte, Natal, RN.

SCHUHLI, Juliana Bregenski. Previsão de Equilíbrio Líquido-Vapor de misturas contendo água-hidrocarboneto-sal. 2007. 67p. Dissertação (Mestrado em Engenharia Química) – Programa de Pós-Graduação em Engenharia, COPPE, Rio de Janeiro, RJ.

van Ness, H. C. and SMITH, J. M. Introdução a Termodinâmica da Engenharia Química. Editora Guanabara Koogan S. A. Rio de Janeiro, RJ, 1980.

Wang, J., Han, S., Wei, F., Yu, Z., Jin, Y. (1997). An axial dispersion model for gas-liquid reactors based on penetration theory. *Chemical Engineering and Processing,* 36, 291-299.

Proceedings of the 10th International Chemical and
Biological Engineering Conference - CHEMPOR 2008
Braga, Portugal, September 4-6, 2008
E.C. Ferreira and M. Mota (Eds.)

An innovative biological system to treat wastewater: A year of operation of the first wastewater treatment plant in real scale.

A.B. Pérez Marín*, M. Lloréns, J. Sáez, J.F. Ortuño, V.F. Meseguer, M.I. Aguilar
Chemical Engineering Department, University of Murcia, Campus of Espinardo
30071 Murcia, Spain.

Keywords: wastewater, symbiotic treatment, wetland, nitrification/denitrification
Topic: Sustainable process-product development through green chemistry. Environmental engineering & management

Abstract

The first wastewater treatment plant of an innovative biological treatment, named symbiotic depuration (Golftrat, 2007), was constructed at the Campus of Espinardo (University of Murcia), supported by the successful experience assays carried out in pilot scale (Llorens et al., 2004). The cited technology combines a natural and subterranean treatment with the generation of green areas over the surface of the plant. It is a promising technology, when comparing with conventional systems, due to the simple operational and maintenance procedures and the high depuration rates. The removal efficiency is up to 86 % for COD, 94 % for BOD, and 81 % for suspended solids, with an average nitrogen and phosphorus removal of 86 % and 84 %, respectively. Besides, an increasing in dissolved oxygen is obtained along the treatment with the consequent increase in nitrates concentration. With the final treatment in the wetland an important level of denitrification is achieved. The overall treatment plant provides an effluent with adequate quality for reuse as garden irrigation waters.

Introduction

Rapid population growth and industrial development have put extreme pressure on future demands for water. Additional human activities (household cleaning, industrial uses, hospitals, business, and schools) cause the deterioration of water resources. So, an adequate management and conservation of water resources is required.

There is a great quantity of conventional wastewater treatment systems, nevertheless they require high construction and operational costs. Nowadays, priority has been given to those technologies which have a minimum cost, with simple operational and maintenance procedures, and which guarantee efficiency and a high level of inertia when faced with large fluctuations in the flow and the effluent load to be treated, and which simplify sludge handling processes.

An innovative technology, named “symbiotic plant®” (Golftrat, 2008), was selected for this purpose. It is a clean and ecological technology, and has as its main characteristic the existence of two well-distinguished areas, the depuration area and the cultivation area. The water is applied by means of underground drippers to a gravel bed over which a green area is situated. So, the evaporation losses are minimal, the green areas can be used even during irrigation and direct contact of users of such areas with residual waters is prevented.

After carrying out diverse assays at pilot scale and verifying the suitability of the cited technology for treating the wastewater from the university installations and a nearby housing development (Lloréns et al., 2004), ESAMUR (Wastewater Treatment

* Corresponding author. Tel + 34 968 367515. E-mail: abelenpm@um.es

Organisation of Murcia) had provided the economic support to carry out the construction and the scientific study of “An Experimental Symbiotic Wastewater Treatment Plant” in the Campus of Espinardo (University of Murcia). This paper shows the results of the physico-chemical control of this pioneering plant, during the first year of operation, in order to demonstrate the success of this system to treat the wastewater generated at the University of Murcia and the possibility of applying this technology to the wastewater generated in small villages.

Materials and methods

Experimental wastewater treatment plant of the University of Murcia

The wastewater treatment plant, designed by Golftrat, S.L. for treating 500 m^3/d, is integrated by a physical treatment and the symbiotic treatment. A flowsheet of the plant can be shown in Figure 1.

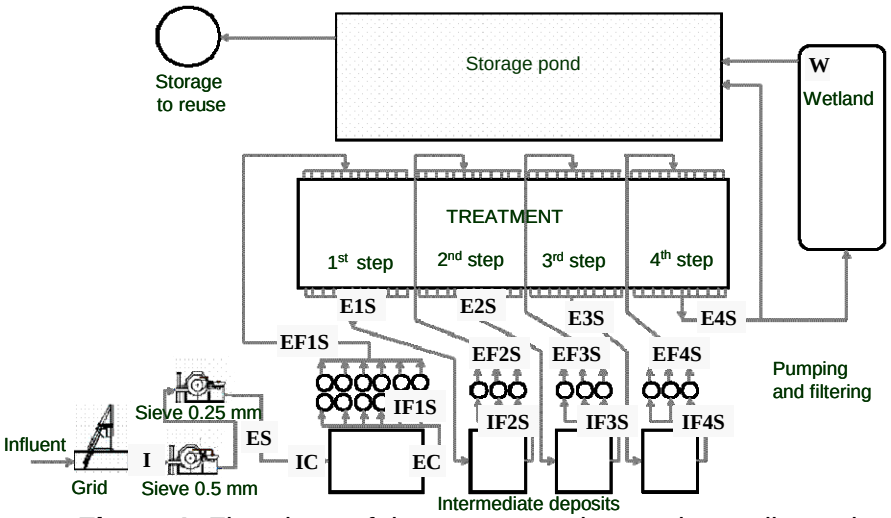

Figure 1. Flowsheet of the treatment plant and sampling points.

The wastewater is pretreated before entering the symbiotic plant. The pretreatment consists of two subsequent rotary sieves with 0.5 and 0.25 mm sieve openings, respectively, a clarifier (recentely installed in order to reduce the inlet solid content to filters) and a series of twelve 50 µm mesh ring filters.

Pretreated wastewater enters the biological treatment, which consist in four symbiotic stages placed in series. Each symbiotic stage consists of a depuration area, 120 cm thick of gravel bed, which is isolated from the ground by a waterproof layer. A network of subterranean drippers, placed directly on the gravel, is used to apply the wastewater. The cultivation area is situated over this area and is composed by approximately 30 cm of sandy substrate. Each stage provides a filtering surface of 205 m^2/stage.

Pretreated wastewater enters the first stage of the symbiotic plant through the drippers falling by gravity through the gravel bed until it reaches the bottom waterproof layer. The effluent is collected in a deposit and then filtered through a series of three 75 µm size mesh filters before being pumped to the next stage. The effluent from the fourth stage falls by gravity into an artificial wetland or a storage pond. Treated water is reused as irrigation water.

The clarifier, situated after the pretreatment, collects the small amounts of sludge generated by sloughed off biofilm from the surface of the gravel bed and the wash water from cleaning filters and drippers. Nine daily sludge purges of two minutes each one are made. The total volume purged is 1.35 m^3/d (≅ 4.5 kg/d) and the sludge purged is used for composting.

Sampling and methods

Physico-chemical analysis was made of samples collected from: influent (IS) and

effluent (ES) of the rotatory sieves, influent (IC) and effluent (EC) of the clarifier, influent (IFnS) and effluent (EFnS) of each filter battery and inlet (InS) and outlet (EnS) of each one of the four treatment stages (n = number of stage). Samples were also collected in the wetland (W) to asses the improvement in the water quality after this final treatment. Samples were analysed to follow-up several pollution parameters according to the treatment: total suspended solids (TSS), chemical oxygen demand (COD), biochemical oxygen demand (BOD_5), total Kjeldahl nitrogen (TKN), ammonia nitrogen ($N\text{-}NH_4^+$), nitrates, total phosphorus (TP) and phosphates. pH, conductivity and dissolved oxygen (DO) were also measured. All water samples were analysed in accordance with the Standard Methods for Examination of Water and Wastewater (APHA, 1995).

Results and discussion

In this section, box plot are used to evaluate the experimental results. The upper and lower box indicate 25th and 75th percentile, the whiskers are the 5th and 95th percentile, the symbols represent the outliers, the solid line is the median and the dashed line is the mean.

Characterization of wastewater

As can be seen in Figure 2, there is a great variation in the influent composition. The raw wastewater is comparable to a domestic wastewater with high strength (Metcalf&Eddy, 1995).

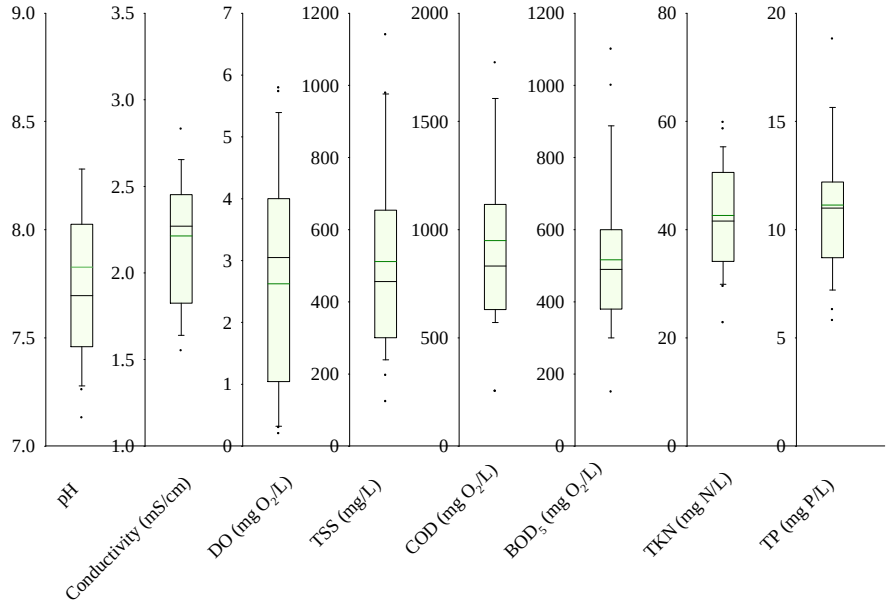

Figure 2. Influent composition.

Evolution of different parameters along the treatment

According to the obtained results, pH values fall well within the optimum range for the growth of the microorganisms for digesting organic matter (6.6-8.5). The conductivity remains almost constant along the depuration process and its value oscillate between 1.7 and 2.8 mS/cm.

The dissolved oxygen is one of the most important parameters in this system. As it can be seen (Figure 3.a.), an increase in the concentration of dissolved oxygen along the steps of the symbiotic plant was observed. The gravel bed remains unsaturated at all times, so the water which irrigate the gravel bed is always in contact with air, and so that depuration is carried out in aerobic conditions. The highest concentrations of dissolved oxygen are achieved within the wetland. The oxygen supply is via the air-water surface exchange and the photosynthesis of the phytoplankton and algal biofilms

attached to the surface of the emergent aquatic macrophytes present in the wetland.

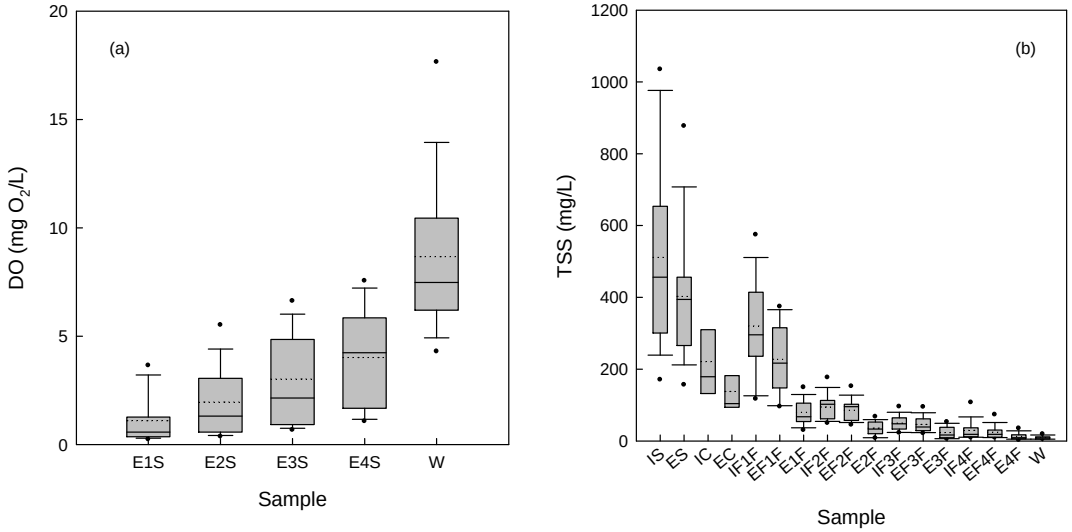

Figure 3. Box plot of the evolution in dissolved oxygen (a) and in total suspended solids (b) through the depuration process.

An important decrease in total suspended solids is achieve with the treatment (Figure 3b). The sieves, the clarifier, the filters and the symbiotic bed of the first stage give the major contribution to the removal of suspended solids. It is neccesary to point up that, after the pretreatment, symbiotic beds rather than filters accounts for the main contribution to TSS removals. The small amounts of sludge generated by sloughed off biofilm from the surface of the gravel beds, settle down rapidly in the deposits of treated wastewater of each stage and they were carried to the clarifier without pass to the filters. Filters of the three last stages do not provide a significant decrease in this parameter.

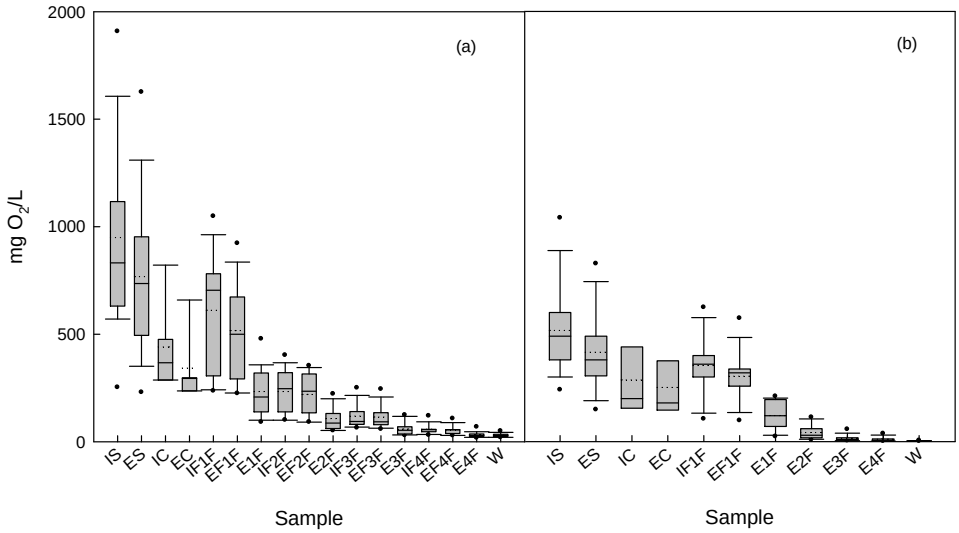

Figure 4. Box plots of the evolution in organic mater (COD and BOD_5) through the depuration process.

The concentration of organic matter (COD and BOD_5) gradually decrease throughout the depuration process (Figure 4). The reduction in organic matter could be due to the retention of suspended solids of organic nature in the filter, in the clarifier and in the gravel bed, and also to the biodegradation of the organic matter by the living organisms on the gravel bed. A biofilm is generated over the gravel surface which is the main cause of the removal in soluble organic matter in each one of the symbiotic stages.

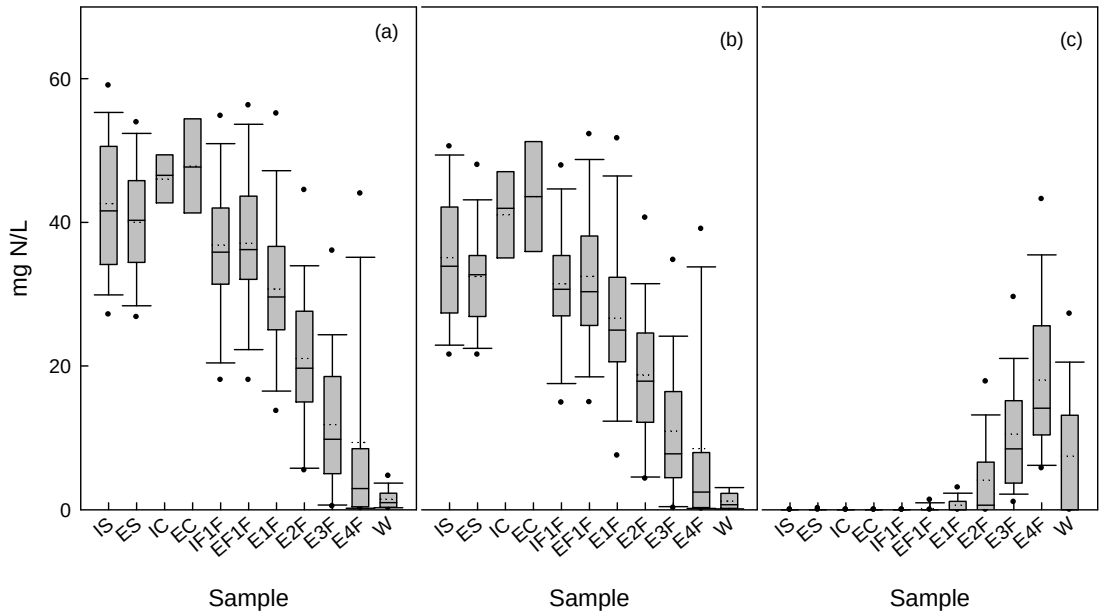

Figure 5. Box plots of the evolution in TKN a), N-NH_4^+ (b) and nitrates (c) through the depuration process.

TKN and N-NH_4^+ decrease along the depuration process (Figures 5a and 5b). A great similitude between both parameters in the last stage of symbiotic tretment is obtained, due to the descomposition by microorganisms of organic nitrogen to ammonia nitrogen. The overall ammonium removed is transformed to nitrates (Figure 5c). The aerobic conditions and the low level of organic matter in the last symbiotic beds favoured the nitrification. In most of the cases, the symbiotic system shows a high removal of ammonia. However, removal of total nitrogen would be very low because of nearly zero denitrification. With the final treatment in the wetland an important level of denitrification is achieved.

The main contribution to phosphorus removal was obtained in the first stage of the symbiotic treatment (Figure 6a). It could be due to the phosphorus retention in filters and gravel bed and also by the microorganisms assimilation of dissolved phosphate in the wastewater. No significant differences were obtained in the amount of phosphates (Figure 6b) through the symbiotic treatment stages (transformation of organic phosphorus to phosphates is equilibrated with phosphates assimilation by microorganisms).

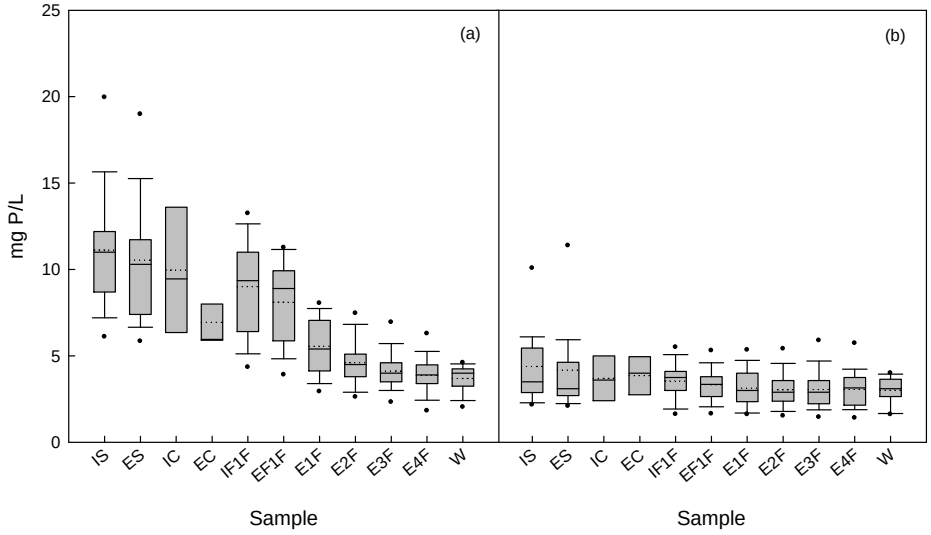

Figure 6. Box plots of the evolution in TP (a) and phosphates (b) through the depuration process.

Characterization of effuent

Table 1 shows the minimum, maximum and average value (parenthesis) of each one of the parameters studied for the effluent of the fourth treatment phases, as well as the percentage removal. The effluent complies with the Directive 91/271/ECC effluent requeriments of $\leq$ 35 mg/L TSS, $\leq$ 125 mg/L COD and $\leq$ 25 mg/L BOD_5. High removal efficiencies were obtained for TSS, COD and BOD_5. In the case of nitrogen and phosphorus species, there is a great variability on the percentage removal, maybe due to the high sensibility of the microorganisms, responsible of their elimination, to variations of their environmental conditions.

Table 1.- Characteristics of wastewater at the outlet of the plant and percentage removal.

	Outlet	Removal (%)
pH	6.8-8 (7.24)	-
Conductivity (mS/cm)	1.62-3.02 (2.31)	-
DO (mg O_2/L)	1-8.02 (4.20)	-
T (ºC)	14-29.3 (19.98)	-
TSS (mg/L)	2-31 (13.2)	80.8-99.5 (96.0)
COD (mg O_2/L)	16-63 (32.5)	85.6-98.7 (95.6)
BOD_5 (mg O_2/L)	0-22 (6.24)	94.4-100 (98.7)
TKN (mg N/L)	0.2-45.8 (7.68)	35.8-99.7 (85.6)
$N\text{-}NH_4^+$ (mg N/L)	0.1-40 (6.86)	27.7-99.8 (83.8)
Nitrates (mg N/L)	4.4- 43.4(18.2)	-
TP (mg P/L)	1.1-7.7 (4.02)	6.1-85.5 (60.9)
$P\text{-}PO_4^{3-}$ (mg P/L)	0.5-6.57 (3.27)	-

Conclusions

Considering the experimental results, before more than a year of operation of the cited wastewater treatment plant, it can be concluded that the treatment plant installed at the University of Murcia is able to treat high fluctuations in influent load and provide an effluent that complies with the Directive 91/271/ECC effluent requeriments. Besides, with the observation of the plant operation, a quick stars-up of the process, a great simplicity of operation and maintenance, no umpleasant odours and low generation of sludge were observed. So, symbiotic depuration could be considered a promissing alternative to conventional wastewater treatment systems.

Acknowledgements

The authors gratefully acknowledge the economic support to ESAMUR and the technical support provided by Golftrat, S.L.

References

APHA (1995). Standard Methods for the Examination of Water and Wastewater. 19th edition. American Public Health Association, Washington, D.C.

Golftrat, S.L. (2008) [Internet]: Spain. Available from:<http://www.golftrat.com> [Accessed June 2008]

Lloréns, M., Portero, S., Sáez, J., Aguilar, M.I., Ortuño, J.F. and Meseguer, V.F. (2004); "Una alternativa para el tratamiento de aguas residuales urbanas de pequeños núcleos de población: la depuración simbiótica". Tecnología del Agua, 246, 38-44.

Metcalf & Eddy, INC. (1995). Ingeniería de Aguas Residuales. Tratamiento, Vertido y Reutilización, 3ª ed. McGraw-Hill, New York.

Proceedings of the 10th International Chemical and
Biological Engineering Conference - CHEMPOR 2008
Braga, Portugal, September 4-6, 2008
E.C. Ferreira and M. Mota (Eds.)

Denitrification in an anoxic rotating biological contactor under two carbon/nitrogen ratios

Susana Cortez*, Pilar Teixeira, Rosário Oliveira, Manuel Mota
IBB – Institute for Biotechnology and Bioengineering, Centre of Biological Engineering,
University of Minho, Campus de Gualtar, 4710–057 Braga, Portugal.

Keywords: anoxic rotating biological contactor, C/N ratio, denitrification
Topic: Environmental engineering and management

Abstract

The aim of the present work was to compare the performance of an anoxic bench-scale rotating biological contactor (RBC), in terms of the denitrification process, applied to treat synthetic wastewater under two carbon/nitrogen (C/N) molar ratios (1.5 and 3). The average removal efficiency in terms of nitrogen-nitrate was of about 90.4% at a C/N=1.5 lowering to 73.7% at a C/N=3. Considering carbon-acetate removal an overall efficiency of 82.0% and 63.6% was attained at a C/N ratio of 1.5 and 3, respectively. These results evidence that, for the tested conditions, the use of C/N=1.5 is advantageous.

The increase of nitrogen-nitrate and carbon-acetate influent concentrations, keeping C/N constant, and the decrease of hydraulic retention time (HRT) had a slight negative effect in terms of substrate removal.

The accumulation of nitrite was observed in both experiments, which could probably be lowered with an increase in phosphorus influent concentration.

Results show that an anoxic RBC using acetate as a carbon source is a convenient and reliable process for the removal of nitrate from wastewater.

1 Introduction

Nowadays, the presence of nitrate in wastewater is considered a critical problem. The processes used for treating nitrate-rich wastewater include reverse osmosis, ion exchange, electrodialysis and biological nitrate reduction (denitrification). Denitrification has been shown to be more economical and practical and the most promising and versatile approach among all (Mateju et al., 1992). In this process, microorganisms first reduce nitrate (NO_3^-) to nitrite (NO_2^-) and then produce nitric oxide (NO), nitrous oxide (N_2O), and, finally, nitrogen gas (N_2), in the absence of dissolved oxygen (DO) or under limited DO concentrations (Tchobanoglous and Burton, 1991).

Most denitrification processes rely on heterotrophic bacteria so, when the wastewater does not contain biodegradable organic carbon compounds, these have to be added (Beaubien et al., 1995). Acetate has been reported to give high denitrification rates in most cases (Hallin et al., 2006).

Cervantes et al. (1999) reported that for high denitrifying efficiencies the carbon to nitrogen ratio was the main parameter of control to achieve a dissimilative respiratory process.

A rotating biological contactor is an attached growth bioreactor that offers an alternative technology to the conventional activated sludge process and is used for both municipal and

* Corresponding author. Tel + 351-253-604400. E-mail:susana_cortez@deb.uminho.pt

industrial wastewater treatment. A RBC unit typically consists of a series of closely spaced discs that are mounted on a common horizontal shaft and are partially or completely submerged in wastewater. The shaft continually rotates and a biofilm is established onto the entire surface area of the media, which metabolizes the organic materials contained in the wastewater. Due to its advantages: simplicity of operation, short hydraulic retention time (HRT), low land area requirement, low operating and maintenance cost and high biomass concentration per reactor volume, RBCs constitute a very unique and superior alternative technology for carbon oxidation, nitrification, denitrification and phosphorus removal. Although in the last decade RBCs tightly closed to avoid air entrance have started to be used for denitrification, few studies have still been conducted with anoxic RBCs (Cortez et al. 2008).

In this study the denitrification efficiency of an anoxic bench-scale RBC was followed under two carbon/nitrogen (C/N) molar ratios: 1.5 and 3, with acetate as carbon source.

2 Materials and methods

2.1 Anoxic rotating biological contactor and operation

The anoxic RBC single-stage system consisted of 8 polymethylmethacrylate (PMMA) discs (diameter = 130 mm, thickness = 3 mm, 20 mm interspace) mounted on a horizontal shaft, having a working volume of 2.5 L. The rotating biological contactor was operated at a rotational speed of 4 rpm and the temperature was maintained at 28 ºC by means of a heating jacket. The submergence of the discs was 93.5%. Prior to continuous operation the reactor was inoculated with microorganisms, acclimatized to acetate and nitrate, collected from an activated sludge tank from a wastewater treatment plant. Microbial attachment onto the discs was allowed to occur in batch mode and a visible attachment of biomass on the discs was noticed after 4 days of inoculation. On day 6, the anoxic RBC mixed liquor was removed, the reactor was re-filled and started to be fed continuously with synthetic wastewater. The time “zero” of operation was considered when the hydraulic retention time was adjusted to 10 hours. Two days after that, samples started to be collected.
The synthetic wastewater contained nitrate, acetate as carbon source, a phosphorus concentration of 10 mg P/L and trace elements.
To evaluate the reactor efficiency, during the assay, nitrogen-nitrate concentration was doubled at the 8th day of operation and carbon-acetate concentration was adjusted to keep the ratio C/N constant (according to the experiment, C/N=1.5 or C/N=3). In both experiments the hydraulic retention time was also changed and reduced from 10.00 h to 5.68 h, as shown in Table 1.

Table 1. Operation parameters of the anoxic RBC.

Days of operation	HRT (h)	N-NO_3^- (mg/L)
0 - 8	10.00	50
8 - 15	10.00	100
15 - 22	6.84	100
22 – 28	5.68	100

The study was conducted for a period of 28 days (for each C/N ratio). The nitrogen-nitrate range selected is typical of concentrations found in agricultural and industrial wastewaters (Bickers and Oostrom, 2000).

2.2 Sampling and analysis

During the course of continuous operation, samples of the RBC influent and effluent were collected routinely and analysed for various parameters such as nitrate, acetate and nitrite. In order to remove interfering suspended particles samples were filtered over a 0.2 µm membrane filter. Nitrate and acetate concentrations were measured by HPLC in an organic

acids column (*Varian Metacarb*, type 67H, 9 µm, 300 mm long, 6.5 mm internal diameter). Nitrite was determined by a colorimetric method using N-(1-naphthyl)-ethylene-diamine, according to the standard methods (APHA, 1989). Periodically, gas samples were analysed by gas chromatography.

3 Results and discussion

Variations in the removal efficiencies of nitrogen-nitrate ($N\text{-}NO_3^-$) and carbon-acetate ($C\text{-}CH_3COO^-$) as a function of operating time are shown in Figure 1 (a) and (b), respectively.

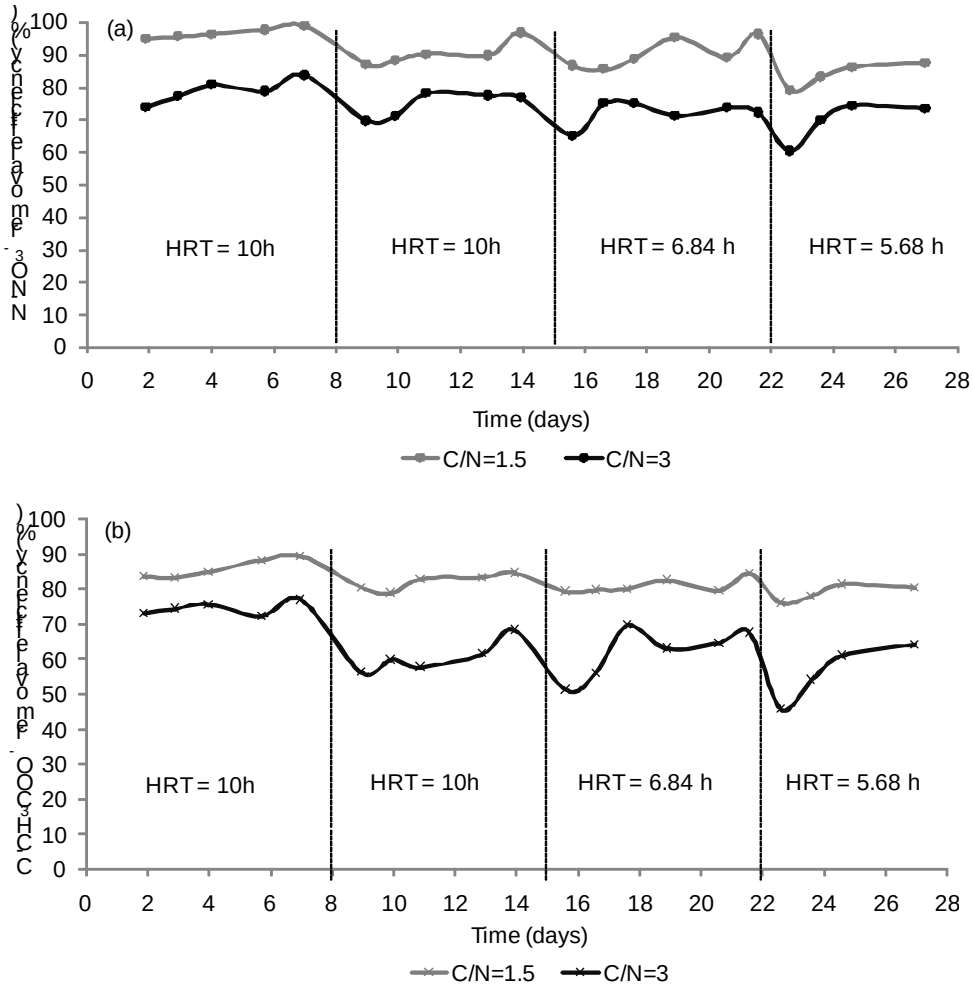

Figure 1. Nitrogen-nitrate (a) and carbon-acetate (b) removal efficiency along the time at two C/N ratios: 1.5 and 3.

The bench-scale RBC showed a high nitrate removal percentage in both experiments. $N\text{-}NO_3^-$ overall efficiency was of about 90.4% at a C/N=1.5 lowering to 73.7% at a C/N=3 (Figure 1 (a)). Considering carbon-acetate removal (Figure 1 (b)), an overall efficiency of 82.0% and 63.6% was attained at a C/N ratio of 1.5 and 3, respectively. These results evidence that, an increase in the C/N ratio from 1.5 to 3 was accompanied by a decrease in substrate removal efficiencies. Consequently, in the experiment at C/N=3 the biomass present in the anoxic RBC did not metabolize all the substrates and as a result they were accumulated along the time. For economical and environmental reasons the use of C/N=1.5 is advantageous.

The maximum substrate removal efficiencies were obtained in the first period of operation, with an influent nitrogen-nitrate concentration of 50 mg $N\text{-}NO_3^-$/L and a hydraulic retention

time of 10 h. The removal efficiencies were slightly lowered by a twofold increase in nitrate and acetate loading rate and a decrease in HRT.

Data presented in Figure 2 show the accumulation of nitrogen-nitrite ($N\text{-}NO_2^-$). Accumulation of nitrite has been frequently found in biological denitrification processes. Several factors such as oxygen concentration, pH, temperature, biofilm composition, toxic substances, influent nitrate concentration, available and type of carbon source and carbon to nitrogen ratio influence nitrite accumulation (Moreno et al., 2005). It is very important to avoid nitrite accumulation because it can lead to inhibition of bacterial development. Moreover, high nitrite concentration is highly undesirable once nitrite is more toxic than nitrate (Hunter, 2003).

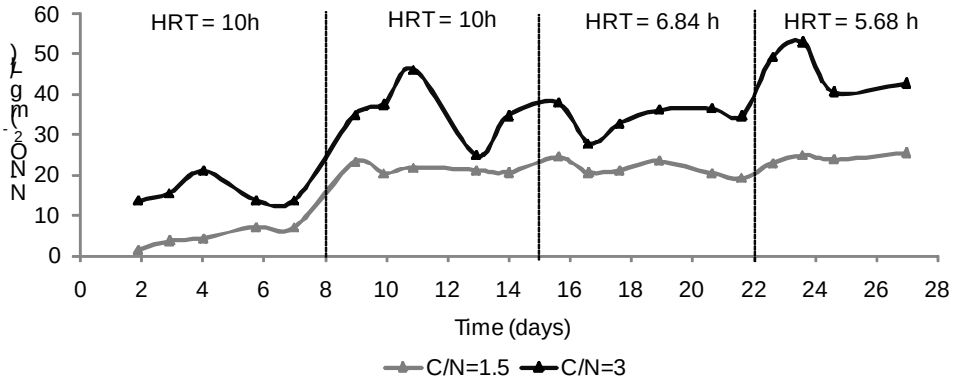

Figure 2. Nitrogen-nitrite effluent concentration along the time at two C/N ratios: 1.5 and 3.

An insufficient phosphate level also leads to nitrite accumulation (Reisinger et al., 1989). In order to reduce the formation of nitrite, Teixeira and Oliveira (2000) increased the phosphorus concentration tenfold (from 2 mg P/L to 20 mg P/L) which resulted in a drastically decrease in the accumulation of nitrite and induced a good RBC performance. It can be speculated that the influent phosphate concentration limited the conversion of nitrite to nitrogen gas. Alternatively, the accumulation of nitrite can result from the microbial population present inside the RBC rich in nitrate reducing bacteria.

4 Conclusions

The RBC had a very good performance at C/N=1.5, using acetate as carbon source, attaining a nitrate removal of about 90%, that could probably be enhanced with an increase in phosphorus concentration. As a general conclusion, the RBC proved to be very robust in coping with high nitrate loads and shock loads.

Acknowledgments

Susana Cortez and Pilar Teixeira fully acknowledge the financial support provided from Fundação para a Ciência e Tecnologia (FCT) through the grants SFRH/BD/24715/2005 and SFRH/BPD/26803/2006, respectively.

References

APHA (1989). *Standard Methods for the Examination of Water and Wastewater*, 17th ed., American Public Health Association/Water Environment Federation, Washington DC.

Beaubien, A., Bellahcen, H., Urbain, V., Chang, J. (1995). Monitoring metabolic activity of denitrification processes using gas production measurements. *Water Research*, 29, 2269-2274.

Bickers, P.O., van Oostrom, A. J. (2000). Availability for denitrification of organic carbon in meat-processing wastestreams. *Bioresource Technology*, 73, 53-58.

Cervantes, F., Monroy, O., Gómez, J. (1999). Influence of ammonium on the performance of a denitrifying culture under heterotrophic conditions. Applied Biochemistry and Biotechnology, 81, 13-21.

Cortez, S., Teixeira, P., Oliveira, R., Mota, M. (2008). Rotating biological contactors: a review on main factors affecting performance. *Reviews in Environmental Science and Biotechnol*ogy, 7, 155-172.

Mateju, V., Cizinska, S., Krejei, J., Janoch, T. (1992). Biological water denitrification: a review. *Enzyme and Microbial Technology*, 14, 170-183.

Moreno, B., Gomez, M., Gonzalez-Lopez, J., Hontoria, E. (2005). Inoculation of a submerged filter for biological denitrification of nitrate polluted groundwater: a comparative study. *Journal of Hazardous Materials*, 117, 141-147.

Hallin, S., Throbäck, I., Dicksved, J., Pell, M. (2006). Metabolic profiles and genetic diversity of denitrifying communities in activated sludge after addition of methanol or ethanol. *Applied and Environment Microbiology, 72*, 5445-5452.

Hunter, J. (2003). Accumulation of nitrite in denitrifying barriers when phosphate is limiting. *Journal of Contaminant Hydrology*, 66, 79-91.

Reisinger, C., Braun, R., Moser, A. (1989). Cybernetic and technical aspects for advanced biological drinking water treatment. In *Workshop – Strategies for Closed Cycle Production, Department of Biotechnology, Technology*, Technical University of Graz, Austria, p.10.

Tchobanoglous, G., Burton, F.L. (1991). *Wastewater Engineering: Treatment, Disposal and Reuse*. Metcalf & Eddy, 3rd ed., McGraw-Hill International Editions, New York.

Teixeira, P., Oliveira, R. (2000). Denitrification by *Alcaligenes denitrificans* in a closed rotating biological contactor. *Biotechnology Letters*, 22, 1789-1792.

Proceedings of the 10th International Chemical and
Biological Engineering Conference - CHEMPOR 2008
Braga, Portugal, September 4-6, 2008
E.C. Ferreira and M. Mota (Eds.)

INTEGRATION OF ADVANCED AND BIOLOGICAL OXIDATION PROCESSES: ENHANCING BIODEGRADABILITY OF PHENOL SOLUTIONS

F. C. N. Sassano [1]; J. E. F. Moraes [2,3]; C. A. O. Nascimento [1,3]

[1] Departamento de Engenharia Química, Escola Politécnica, Universidade de São Paulo, CEP: 05508-900, São Paulo, Brasil.
[2] Escola Paulista de Engenharia Química, Universidade Federal de São Paulo, CEP: 09972-270, Diadema, Brasil.
[3] Centro de Capacitação e Pesquisa em Meio Ambiente (CEPEMA-USP), Universidade de São Paulo, CEP: 11525-970, Cubatão, Brasil.
Email: sassano@pqi.ep.usp.br

Abstract – Phenol and phenolic compounds have been listed as priority-pollutants by Environmental Protection Agency (EPA – USA). They are often found in industrial effluents such as from pulp and paper, plastics and synthetic polymer, pharmaceutical, pesticide, oil and petrochemical industries. Most of the traditional wastewater treatments have shown inefficiency against high phenol concentrations. This work aims to treat phenol solution via Advanced Oxidation Processes (AOP´s) to enhance medium biodegradability and using it as an effluent in a continuous activated sludge biological process. The purpose of the pre-treatment is to modify the phenol structure leading it to its byproducts such as aromatics compounds and carboxylic acids. The experiments have shown the effectiveness of the pre-treatment by the biodegradability parameter BOD_5/COD which was achieved 0.35 at 30 min of Fenton reaction in the following experimental conditions: $[phenol]_0$ = 1000 $mgC.L^{-1}$; $[FeSO_4]$ = 1 mM and H_2O_2 was added, along 2 hours of reaction, with a constant flow of 0.1 $L.h^{-1}$ (8.33 $mmol.min^{-1}$).

KEYWORDS: wastewater, phenol, process integration, activated sludge, advanced oxidation process and synthetic polymer, pharmaceutical, pesticide, oil and petrochemical industries.

. INTRODUCTION

Due to the toxic nature of some phenolic compounds the Environmental Protection Agency (EPA-USA) has set a water purification standard of less than 1 part per billion (ppb) of phenol in surface waters (Melo *et al*., 2005). They are often found in industrial effluents such as from pulp and paper, plastics

Conventional oxidative methods for the wastewater treatment utilize the combination of biological, physical and chemical treatments. Biotreatment processes tend to be very large due to the slow rate of the biological reactions; physical methods generally transfer waste components from one phase to another; chemical treatment, such as chlorination, can result in the formation of chlorinated phenols and their byproducts which are as toxic and non-

biodegradable as the original medium (Kusic and Koprivanac, 2006).

Advanced Oxidation Processes (AOP´s) have been used as one of the most effective processes to remove organic pollutants from aqueous solutions containing soluble organic compounds that are either toxic or non-biodegradable. AOP´s involve the generation of the hydroxyl radical (•OH), which has a very high oxidation potential and is able to oxidize almost all organic pollutants (Esplugas *et al*., 2002; Moraes, *et al*, 2004; Kusic and Koprivanac, 2006). Although these processes have shown high efficiency for water and wastewater treatment, they have high costs related to investment (complex installations) and operation (high consumption of energy and/or reagents), according to Esplugas *et al.*, 2002.

A promising alternative to complete oxidation of biorecalcitrant wastewater is the use of an AOP as pre-treatment to convert the highly toxic organic compounds to readily biodegradable intermediates (Devlin and Harris, 1984), followed by biological oxidation of these intermediates to biomass and water (Hsu *et al*, 2004; De Morais and Zamora, 2005; Al Momani, 2006).

The ratio (BOD_5/COD) has been used as a biodegradability paramerter, representing a fraction of organic material easily assimilate microorganisms. Solutions with ratio DBO_5/DQO > 0.4 has been considered as organic matter thoroughly biodegradable (Chamarro *et al*., 2001).

Fenton's reaction may be recommended as a pre-treatment process to enhance later microbial transformation, lowering the operational costs, by increasing its biodegradability, generally through the cleavage of large organic compounds into smaller ones (Walling , 1975; Chamarro *et al*., 2001; Zazo *et al*, 2005).

2. MATERIAL AND METHODS

The reagents used in the pre-treatments runs were carried out via Fenton and photo-Fenton processes were 1000 $mgC.L^{-1}$ of phenol (C_6H_5OH), 8.33 $mmol.min^{-1}$ of hydrogen peroxide (H_2O_2; 30% m/m), 1 $mg.L^{-1}$ of ferrous sulphate heptahydrate ($FeSO_4.7H_2O$) and sulfuric acid concentrated (H_2SO_4). A solution 0,1M of sodium hydroxide (NaOH) was prepared to stop the reaction of the samples to be analyzed. All the reagents were analysis grade. A peristaltic pump (Ismatec, model IPC-4) was used to add the hydrogen peroxide (H_2O_2; 30% m/m) with a constant flow of 0.1 $L.h^{-1}$ (8.33 $mmol.min^{-1}$).

The apparatus used were a photochemical reactor that consists of an inox cylinder with mirrored wall presenting 12 black light fluorescent lamps (Sylvania, 40 W each) connected in it. At the center of this reactor is attached a borosilicate glass tube (inner diameter = 3 cm; length = 100 cm), through which flows the effluent to be treated (upper flux). The upper part of the reactor is kept a exhaust system to refrigerate the internal part from the heat of the lamps. The reactor is attached to 20L mixing tank connected to a centrifuge pump for the effluent recirculation (200 $L.h^{-1}$).

The procedure was initially, filling the mixing tank with 9.4 L of distillated water. Afterwards, the centrifuge pump (200 $L.h^{-1}$) and the 12 fluorescent lamps were switched on. It was been added the phenol aqueous solution (C_6H_5OH; 13.25 g in 500 mL of distillated water). The pH of the reactor solution was adjusted to 3.0 (without further control) with concentrated sulfuric acid (H_2SO_4). After 5 min of recirculation, the first sample was collected them the time begun with the addiction of both ferrous sulphate solution ($FeSO_4.7H_2O$; 2.82 g in

250 mL of distillated water) and H_2O_2 was added via a persitaltic pump (Ismatec, model IPC-4) with a constant flow of 0.1 $L.h^{-1}$ (8.33 $mmol.min^{-1}$), along 2 hours of reaction. All runs were carried out at room temperature (≈ 29 ºC).

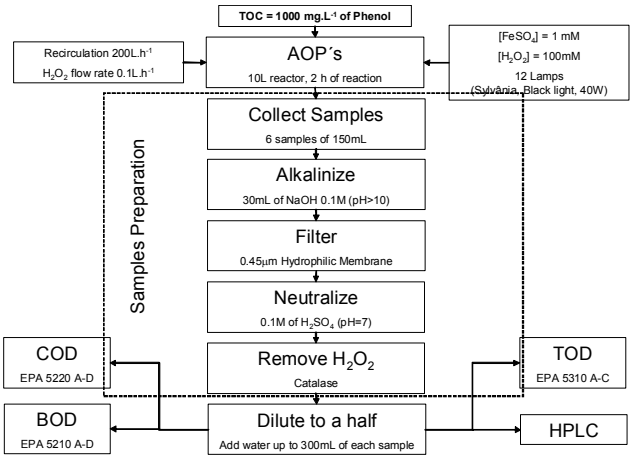

Figure 1: Procedure of sample preparation

The sample´s preparation were as follows: pH ajust to 10.0 using 0.1 M NaOH solution to stop the reaction. Afterwads, the samples were filtered with 0.45 μm hydrophilic membrane (Durapore, Millipore) to remove ions ferrous precipitaed (Zazo *et al*., 2007), added 0.1 M sulfuric acid to neutralize the samples and, finally, enzyme catalase to remove H_2O_2 residual from the samples to be analised, as observed in Figure 1.

All samples were diluted to a half to simulate the condition of the input effluent in the pos-treatment (biological processs), because, in previous experiments (Sassano *et al*., 2007), the wastewater was fed, simultaniously, with the same flow as the nutrients (1:1). A scheme of the integrated processes (photochemical and biological reactors) can be seen in Figure 2.

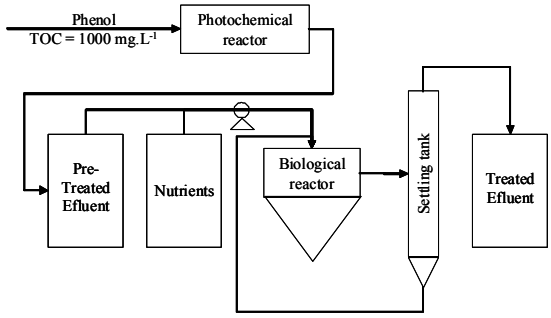

Figure 2: Scheme of the integrated processes

The analytical determinations were as follows:

Biological Oxygen Demand (BOD_5) through a manometric BOD measurement device (OxiTop 12 WTW). Measurement is based on pressure measurement in a closed system: microorganisms in the sample consume the oxygen and form CO_2. This is absorbed by NaOH, creating a vacuum which can be read directly as a measured value (US Standard Methods 5210 D).

Total Organic Carbon (TOC) performed by total organic carbon analyzer TOC-5000A (Shimadzu) resulting from a diference of Total Carbon (TC) ande Inorganic Carbon (IC) based on catalyst combustion method (TC) and acidification method (IC).

Chemical Oxygen Demand (COD) through a COD solution A+B (Merck). The water sample is oxidized with a hot sulfuric solution of potassium dichromate, with silver sulfate as catalyst. Chloride is masked with mercury sulfate. The concentration of unconsumed yellow $Cr_2O_7^{2-}$ ions or, respectively, of green Cr^{3+} ions is then determined photometrically (EPA 410.4, US Standard Methods 5220 D, and ISO 6060).

High Performance Liquid Chromatography (HPLC) equipped with software LCMS Solutions, liquid chromatograph LC-10ADvp, degasser DGU-14A, UV-VIS detector SPD-10AV vp , system controller SCL-10A vp

and column Supelco C18 (Shimadzu). The mobile fase used was water (A) and acetonitrile (B) with a gradient from B to A: 0min, 18%; 3 min, 18%; 15 min, 58%; 17 min, 58%; 19 min, 18% at 0.7 mL.min^{-1} and wavelength of 270 nm. The time retentions of phenol, cathecol and hydroquinone were 14.5, 8.0 and 5.0 min respectively.

3. RESULTS AND DISCUSSION

3.1 Pre-treatment: Fenton Reaction

In the Fenton's experiment the 12 fluorescent lamps were switched off. Considering the dilution step (1:1), the TOC values were almost constant (460 mgC.L^{-1}), showing that the organic matter remained at the solution along the 30 min of time reaction.

By the HPLC analysis, it could be observed the decay of phenol concentration by 76%, the formation of 1.13 mmol.L^{-1} of cathecol and 0.64 mmol.L^{-1} of hydroquinone at 30 min of reaction as byproducts of the degradation, as observed in Figure 3.

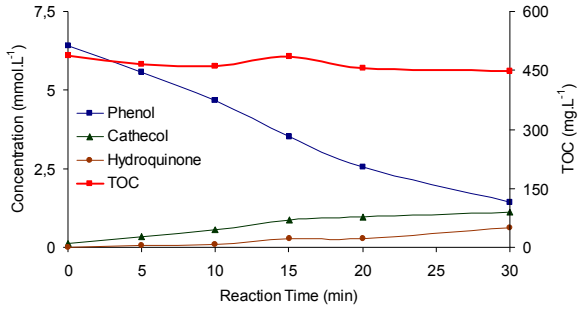

Figure 3: TOC, [phenol], [cathecol] and [hydroquinone] from diluted samples (1:1) along Fenton reaction ([phenol$_0$] = 1000 mgC.L^{-1}, [Fe^{2+}] =1 mg.L^{-1}, H_2O_2 rate feed = 8.33 mmol.min^{-1} and pH$_0$ = 3.0).

The COD results have shown a decrease of the initial value from 2024 mgO_2.L^{-1} to 634 mgO_2.L^{-1} in 30 min of reaction, representing 69% removal of COD.

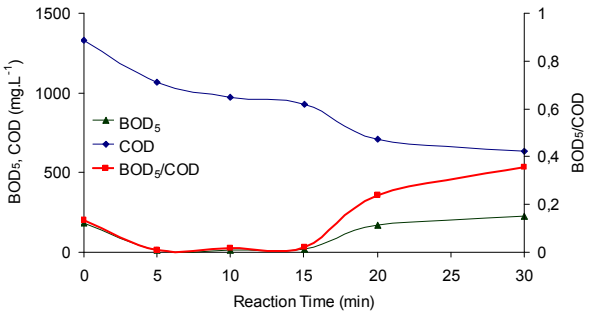

Figure 4: COD and BOD_5 along Fenton reaction, [COD_0] = 2024 mgO_2.L^{-1}.

From BOD analysis, it could be observed only at zero, 20 and 30 min using the same scale factor for the manometric device, showing that the BOD values from samples 5, 10 and 15 min were lower than the BOD expected value that refers to a chosen factor. The higher BOD value was 225 mgO_2.L^{-1} for the 30 min sample.

The best biodegradability factor BOD_5/COD for the samples of the Fenton experiment was 0.35 at 30 min of reaction, indicating the technical feasibility of the pre-treatment, as observed in Figure 4.

3.2 Pre-Treatment: photo-Fenton Reaction

For the photo-Fenton experiment, considering the dilution step (1:1), the TOC values were almost constant in 500 mgC.L^{-1}, showing that the organic matter remained at the solution along the 30 min of time reaction.

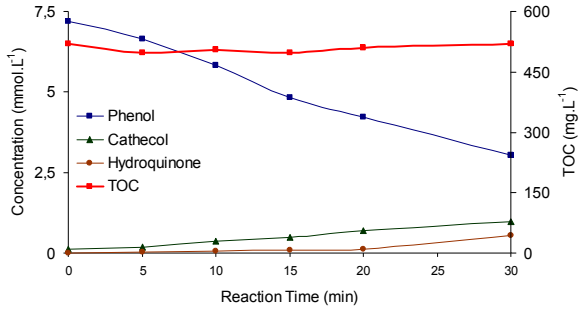

Figure 5: TOC, [phenol], [cathecol] and [hydroquinone] from diluted samples (1:1) along photo-Fenton reaction ([$phenol_0$] = 1000 $mgC.L^{-1}$, [Fe^{2+}] =1 $mg.L^{-1}$, H_2O_2 rate feed = 8.33 $mmol.min^{-1}$ and pH_0 = 3.0).

By the HPLC analysis, it could be observed the concentration reduction of phenol by 57%, the formation of 0.69 $mmol.L^{-1}$ of cathecol and 0.55 $mmol.L^{-1}$ of hydroquinone at 30min of reaction, showing the production of byproducts, as observed in Figure 5.

The DOC results have shown a decrease of the initial value from 1333 $mgO_2.L^{-1}$ to 1017 $mgO_2.L^{-1}$ in 30 min of reaction, representing 24% removal of DOC.

From BOD analysis, it could be observed only at zero, 5, 20 and 30 min using the same scale factor for the manometric device, showing that the BOD values from samples 10 and 15 min were lower than the BOD expected value that refers to a chosen factor. The higher BOD value was 195 $mgO_2.L^{-1}$ for the 30 min sample.

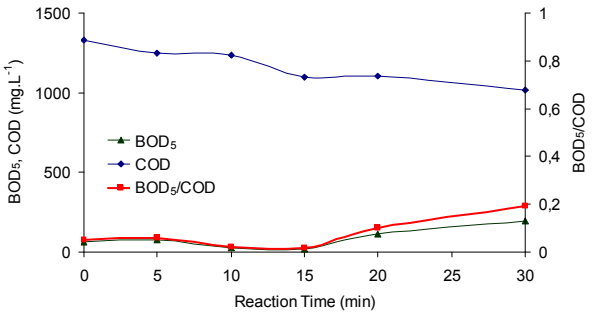

Figure 6: COD and BOD_5 along photo-Fenton reaction, [COD_0] = 1333 $mgO_2.L^{-1}$.

The best biodegradability factor BOD_5/COD for the samples of the photo-Fenton experiment was 0.19 at 30min of reaction, showing the enhancement of the pre-treatment, as observed in Figure 6.

4. CONCLUSIONS

The Fenton and photo-Fenton conditions used in the experiments have shown values of TOC constants along 30 min of reaction, keeping the organic matter at the media.

From HPLC results we could observe decay of phenol concentration (76%) and formation of byproducts such as cathecol (1.13 $mmol.L^{-1}$) and hydroquinone (0.64 $mmol.L^{-1}$) at 30 min of Fenton reaction, showing structure modification from the initial compound into its derivates.

Both Fenton and photo-Fenton processes have shown high efficiency in forming intermediates that were much easier assimilated by the activated sludge (BOD_5 = 225 $mgO_2.L^{-1}$) and an organic matter decay oxidize chemically (69% COD removal), representing biodegradability values of 0.35 (BOD_5/COD) at the same 30 min of Fenton's reaction, this value is very close to 0.4, indicating that this effluent could be considered biodegradable (Chamarro *et al.*, 2001).

The experimental results show that a wastewater containing 1000 $mgC.L^{-1}$ of phenol can be pre-treated via Fenton reaction, along short time (around 30 min), allowing an integration with a conventional biological process (activated sludge, for example), reducing energy and material costs.

Further studies to identify more byproducts from phenol degradation via HPLC, could be interesting as much as the use of bioreactors that enable the pH and DO (Dissolved Oxygen) control., letting a much favor medium for microbial action, allowing kinetics parameters optimization for the continuous biological system, increasing the process efficiency and costs reduction.

5. ACKNOWLEDMENTS

The authors appreciate financial support from FAPESP, CAPES, FUSP and CEPEMA.

6. REFERENCES

AL MOMANI, F. Impact of photo-oxidation technology on the aqueous solutions of nitrobenzene: Degradation efficiency and biodegradability enhancement. *J. Photochem. Photobiol a-Chemistry*, v.179, n.1-2, Apr, p.184-192, 2006b.

ALNAIZY, R. e A. AKGERMAN. Advanced oxidation of phenolic compounds. *Adv. Environ. Res.*, v.4, n.3, Aug, p.233-244, 2000.

CHAMARRO, E., A. MARCO, *et al*. Use of Fenton reagent to improve organic chemical biodegradability. *Water Res.*, v.35, n.4, p.1047-1051, 2001.

DE MORAIS, J. L. e P. P. ZAMORA. Use of advanced oxidation processes to improve the biodegradability of mature landfill leachates. *J. Hazard. Mater.*, v.123, n.1-3, Aug, p.181-186, 2005.

DEVLIN, H. R. e I. J. HARRIS. Mechanism of the oxidation of aqueous phenol with dissolved-oxygen. *Ind. Eng. Chem. Fundam.*, v.23, n.4, p.387-392, 1984.

ESPLUGAS, S., J. GIMENEZ, *et al*. Comparison of different advanced oxidation processes for phenol degradation. *Water Res.*, v.36, n.4, Feb, p.1034-1042, 2002.

GOGATE, P. R. E A. B. PANDIT. A review of imperative technologies for wastewater treatment I: oxidation technologies at ambient conditions. *Adv. Environ. Res.*, v.8, n.3-4, Mar, p.501-551, 2004a.

HSU, Y. C., H. C. YANG, *et al*. The enhancement of the biodegradability of phenolic solution using preozonation based on high ozone utilization. *Chemosphere*, v.56, n.2, Jul, p.149-158, 2004.

KAVITHA, V. e K. PALANIVELU. The role of ferrous ion in Fenton and photo-Fenton processes for the degradation of phenol. *Chemosphere*, v.55, n.9, Jun, p.1235-1243, 2004.

KUSIC, H., N. KOPRIVANAC, *et al*. Photo-assisted Fenton type processes for the degradation of phenol: A kinetic study. *J. Hazard. Mater.*, v.136, n.3, Aug, p.632-644, 2006a.

MELO, J. S., S. KHOLI, *et al*. Effect of oxygen transfer limitations in phenol biodegradation. *Process Biochem.*, v.40, n.2, Feb, p.625-628, 2005.

MORAES, J.E.F., QUINA, F.H., NASCIMENTO, C.A.O., SILVA, D.N. and Chiavone-Filho, O. Treatment of Saline Wastewater Contaminated with Hydrocarbons by

the Photo-Fenton Process, *Env. Sci. Technol.*, 38, 1183, 2004.

SASSANO, F. C. N.; VIEIRA, J. A.; TEIXEIRA, A. C. S. C.; MORAES, J. E. F.; NASCIMENTO, C. A. O. Integração entre os processos fotoquímico e biológico no tratamento de efluentes industriais contendo fenóis. *IV EPOA: Encontro sobre aplicações ambientais de processos oxidativos avançados*. Cubatão/SP: CEPEMA-Centro de Capacitação e Pesquisa em Meio Ambiente, 2007.

WALLING, C. Fenton´s reagent revisited. *Acc. Chem. Res.*, v.8, n.4, p.125-131, 1975.

ZAZO, J. A., J. A. CASAS, *et al*. Chemical pathway and kinetics of phenol oxidation by Fenton's reagent. *Environ. Sci. Technol.*, v.39, n.23, Dec, p.9295-9302, 2005.

ZAZO, J. A., J. A. CASAS, *et al*. Evolution of ecotoxicity upon Fenton's oxidation of phenol in water. *Environ. Sci. Technol.*, v.41, n.20, Oct, p.7164-7170, 2007.

Proceedings of the 10th International Chemical and
Biological Engineering Conference - CHEMPOR 2008
Braga, Portugal, September 4-6, 2008
E.C. Ferreira and M. Mota (Eds.)

Impact of Operational Parameters in Activated Sludge System treating Persistent Industrial Wastewater

A. V. Ribeiro, M. A. Z. Coelho, M. C. Cammarota
Department of Biochemical Engineering, School of Chemistry, Federal University of Rio de Janeiro, Rio de Janeiro, Brazil, ZIP 21.949-900, E-mail:alice@eq.ufrj.br

Keywords: activated sludge, persistent compounds, biodegradability
Topic: Sustainable process-product development through green chemistry

Introduction

Despite of the employment of physical-chemical and biological processes, some industries have difficulty to adequate the treated effluents to the discharge standards established by local environmental legislation such as the fine chemicals industry of this study. The referred industry is an all-purpose plant, with chemical synthesis being carried in a batch mode, where most processes occur in aqueous phase, some of them using organic solvents. There are three main lines of products: stilbene compounds, whitening agent DSBP (Tinopal CBS), finishing and textile processing products. The wastewater generated in the production of stilbene compounds are the main source of chemical oxygen demand (COD) being diluted in the WWTP with less concentrated effluents from other production processes. The complex structure of these constituents, having stilbene as the molecule base (trans-1,2-diphenylethylene) replaced with amine and sulfate groups (high MW, many ramifications, presence of HSO_3^- groups), high salinity (12,000 mg NaCl/L, on average) and the high variability on the wastewater composition, providing to the influent of the WWTP high recalcitrance or low biodegradability characteristics (Stoll et al., 1998).

The treatment system is based on a sequence of coagulation/flocculation processes (with the addition of aluminum sulfate and flocculating agent Magnafloc 155) and activated sludge (operating with hydraulic retention time of approximately 48 h), producing a treated wastewater with COD value (800 mgO_2/L, on average) higher than the discharge limit established by local legislation (250 mg O_2/L). The industry is seeking to reach this COD value without success. So, the objective of the present study was to evaluate the impact of operational parameters in the performance of the activated sludge system of the WWTP to improve its performance and to attain lower COD values.

Material and Methods

Kinetic model: a descriptive kinetic model of the organic matter removal process, based on Monod type functions, was employed to estimate kinetic parameters from WTP and posterior evaluation of the response sensibility of the biological system to variations in the operational conditions and estimated kinetic parameters. The kinetic model employs two variables of state (carbonaceous substrate and biomass concentrations) and four kinetic parameters necessary for the description of the organic matter removal in WWTP. To develop the model some hypotheses were considered in the mass balance calculation, for both substrate and biomass concentrations, such as continuous system where all biomass is recycled to aeration tank, i.e., does not have any discard of excess sludge; the cell growth rate is proportional to the substrate concentration (expressed as COD) and the dissolved oxygen concentration in the aeration tank; cell lysis generates biodegradable material and this rate is proportional to the cell quantity in the aeration tank; and the influent (of the aeration tank) and the treated effluent (from settler) streams do not contain biomass.

The equations 1 and 2 refer to the mass balance for each component. These equations resulted in a system of ordinary differential equations that describes the organic matter consumption rate and cells production rate.

Mass balance for biomass:

$$\frac{dX}{dt} = \frac{1}{V}\left(F_2 X_R - F_3 X\right) + \mu_{\max} X \frac{S}{\left(K_S + S\right)} \frac{OD}{\left(K_{OD} + OD\right)} \quad (1)$$

Mass balance for substrate:

$$\frac{dS}{dt} = \frac{1}{V}\left(F_1 S_a + \left(F_2 - F_3\right)S\right) - \mu_{\max} X \frac{S}{\left(K_S + S\right)} \frac{OD}{\left(K_{OD} + OD\right)} + m X \quad (2)$$

where:
dX/dt – biomass variation with the time (mg VSS/d.L); dS/dt – substrate variation with the time (mg COD/d.L); X – biomass concentration into reactor (mg VSS/L); X_r – biomass concentration in the settler bottom (mg VSS/L); V – reactor volume (L); S_a – influent substrate concentration (mg COD/L); S – substrate concentration into reactor (mg COD/L); F_1 – reactor influent feed rate (L/d); F_2 – recycle feed rate (L/d); F_3 – reactor effluent feed rate (L/d); OD – dissolved oxygen concentration into reactor (mg O_2/L); μ_{max} – maximum specific growth rate (d^{-1}); K_s – half saturation coefficient for carbonaceous substrate (mg COD/L); K_{OD} – dissolved oxygen coefficient (mg O_2/L); *m* – parameter related to the biodegradable material production from cellular lysis, proportional to cell concentration (mg COD/ mg VSS.d).

Data sets (including information about X, Xr, Sa, S, OD, V, F1, F2 and F3) obtained along 16 months (June 2004 to September 2005) of WWTP operation were used to determine the model parameters. Parameter estimation was conducted with MATLAB Optimization Toolbox (The Mathworks Inc.) by the minimization of squared residual error between experimental and estimated values (Eq. 3) through Nelder and Mead type simplex search method (Edgar and Himmenblau, 1988). A maximum of 10% in the experimental deviations were accepted for the parameter estimation.

$$Fobj = \sum_{i}^{ne} \sum_{j}^{np} w_1 \left(\left[S\right]_{\exp} - \left[S\right]_{calc}\right)^2 + w_2 \left(\left[X\right]_{\exp} - \left[X\right]_{calc}\right)^2 \quad (3)$$

where:
ne – experimental number; np – experimental data number in the experiment *I*; w_i – respective error for concentration measurement.

Model Sensibility: a study to consider the impact of kinetic parameters on process' performance prediction was carried considering variations (δ) of $\pm$ 5% in the initial value (base). The influence of the parameter p(i) on the component C concentration is given by Eq. 4.

$$\frac{dC_{(i)}}{dp} = \frac{C_{(i+\delta)} - C_{(i)}}{\delta} \quad (4)$$

The effects of these variations were analyzed on carbonaceous substrate and biomass concentrations. The sensibility was normalized by the maximum concentration value achieved by each component C, in the base case.

The model sensibility to the variations in the operational conditions, with variations (δ) of $\pm$ 5%, was evaluated in a similar way. In the WWTP sensibility analysis, the operational parameters were selected according to the influence it will exert on carbon removal and cell growth. Indeed, some of these parameters were variables of the system, such as: reactor influent flow (F_1), recycle flow (F_2), reactor effluent flow (F_3), substrate concentration into feed stream (S_a), dissolved oxygen concentration into reactor (OD), reactor volume (V) and biomass concentration into recycle from settler for reactor (X_R).

Pilot plant: the pilot plant employed in this study simulated the biological step of the WWTP. The plant was installed and operated in the industry, being continuously fed with effluent from industrial physical-chemical step added of sewage (generated in the industry) to supply essential nutrients (nitrogen and phosphorus) for the microorganisms. Indeed, phosphoric acid was also regularly added as extra nutrient source to obtain the recommended COD:N:P ratio (100:5:1).

The pilot unity was composed by an equalization tank (with usable volume of 800 L) and an aeration tank (180L), both of amiante coated with resin to avoid deterioration of the material and contamination of the effluent during the operation. The reactor tank was aerated by mechanical agitator and membrane tubular diffusers disposed in the bottom. This configuration leads to a continuous stirred tank reactor with perfect mixture (CSTR). After the aeration tank, there was a circular secondary settler (50L) of fiberglass of which left a recycle line of settled sludge, stabilizing biomass concentration inside the aeration tank. This pilot unit operated along 9 months with different hydraulic retention times (24, 48, 72 and 96 h). During these four regimes, sludge discharges were periodically made (around 6 L at alternated days) to stabilize the solids concentration in the reactor around 4500 mg/L and to renew the microbial flora. The feed stream of the pilot plant (effluent of the physical-chemical phase) had its pH adjusted with soda to values of 6.6 ± 0.4.

The performance of the plant in each HRT was evaluated through analysis of pH, COD (influent and effluent), VSS (into reactor) and turbidity (effluent). The F/M (feed to microorganism) ratio and SVI (sludge volumetric index) were also determined along the operation. The analytical methods were carried according the procedures described in Standard methods (APHA, 1992).

Results and Discussion

Table 1 shows the values obtained in the model identification using data collected in the industrial WWTP along 16 months. The data were divided in three phases, according temperature variation along the year, as the estimative of a unique set of parameters for the whole period was not representative of the WWTP experimental operation.

Table 1. Values estimated for the kinetic parameters.

Period	μ_{max} (d^{-1})	K_S (mgCOD/L)	K_{OD} (mgO_2/L)	m (mgCOD/ mg VSS.d)
Jun. 2004 to Oct. 2004	0.59	1112.9	0.000	0.25
Nov. 2004 to May 2005	0.18	344.7	0.026	0.40
Jun. 2005 to Sept. 2005	0.34	1185.9	0.000	0.29

The kinetic parameters presented in Table 1 indicate that from June to September/October, period in which the environment temperature is lower, the cells present high μ_{max} values. These results indicate that in these conditions a better cell replication occurs, independent of the dissolved oxygen concentration ($K_{OD} = 0$). The values obtained for the parameter *m* reveal a concordant behavior, indicating higher cellular lysis in the period with higher temperature (November to May). In this period, the cell growth rate is influenced by dissolved oxygen concentration. It may be considered that dissolved oxygen solubility in the aqueous phase diminishes with increasing temperature, reducing the availability of this nutrient to the cells.

A sensibility analysis of the variations (± 5%) in the WWTP operational conditions indicates similar impact for both + 5% and - 5%. It was observed that the state variables were influenced by different operational conditions, in descending order, the influent flow (F_1), the COD in feed (S_a) and the reactor volume (V). Considering that hydraulic retention time (HRT) is defined as the ratio between influent feed rate and reactor volume, there are an indirect influence of the HRT on COD removal that is also related with the load fed to the system. The operational conditions that more influenced cell growth were, in descending order, the reactor volume (V) and the effluent feed rate (F_3), indicating the possible occurrence of washout. In minor degree, the recycle flow rate (F_2) and

the COD influent concentration (S_a) also show some influence on the cell growth profile. An analysis using ±10 and ±50% of deviation did not result in a worse WWTP performance, being an indicative that the industrial system operates in its maximum limit: ± 5% variation would be so harmful than ± 50%.

Fig. 1 shows COD values in the influent and effluent streams of the activated sludge pilot plant along time of operation. It is observed that in none regime studied the COD attained the maximum value established by legislation (250 mg O_2/L). In the regimes operated with HRT of 24h and 48 h, it is verified a great fluctuation in influent COD values, probably due to little period of equalization of the influent. It caused an impact on microbial flora because there was not sufficient time to adaptation to variation of organic load. This fact is proven by high effluent COD values, mainly in the first regime (HRT of 24 h). In the regime operated with HRT of 48 h, the microorganisms had sufficient time to adapt to peaks of organic load and effluent COD values were less dispersed. In the other hand, in the regimes operated with HRT of 72 and 96 h, the relation between feed flow and equalization tank volume was sufficient to obtain a feed stream with more homogeneous organic load, improving consequently the stability and performance of the experimental system.

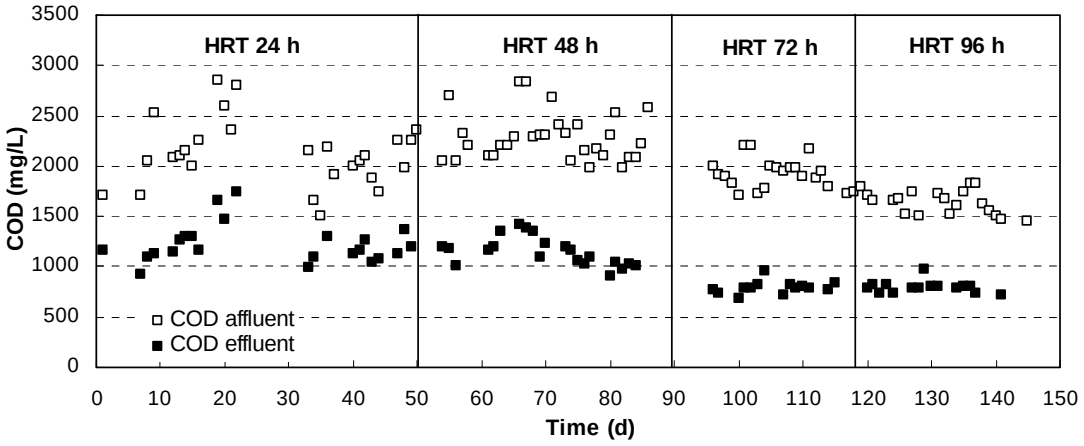

Fig. 1. Influent and effluent COD values along time of operation of the activated sludge pilot plant.

During pilot plant operation, it was observed that the increase of the HRT until 72 h improved the COD removal efficiency (Fig. 2). The COD removal efficiency varied in the first regime (30 to 55 %), increased in the second regime, attaining values up to 60 %, stabilizing around of this value in the third regime and decreasing in the last regime to 53 % on average.

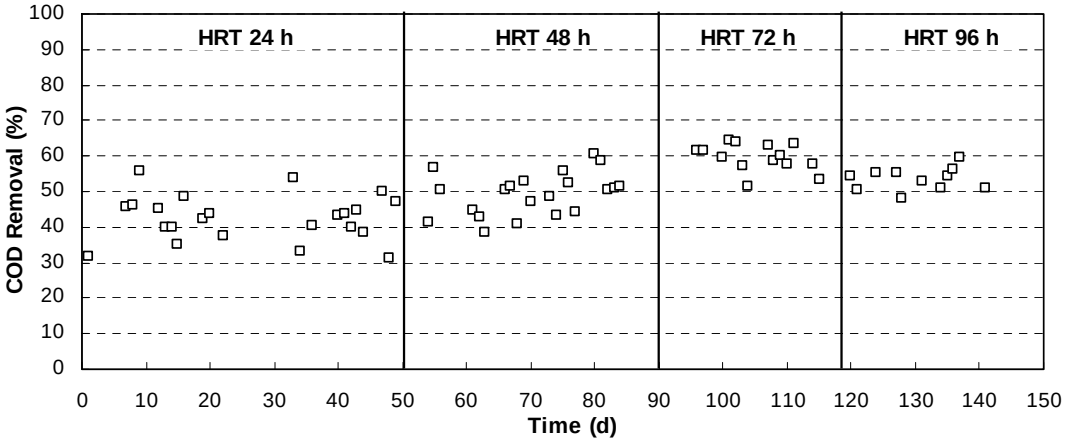

Fig. 2. COD removal efficiencies along time of operation of the activated sludge pilot plant.

Fig. 3 presents VSS concentration into aeration tank along time of operation. There was a great fluctuation of the VSS concentration, mainly in the 1st regime (HRT 24h), in which the biological system was more affected by variation of the influent stream. According Meltcalf and Eddy (1991), in an activated sludge conventional system the typical VSS concentration is in the range of 1500-3000 mg/L. Meanwhile, in extended aeration activated sludge systems the typical value is in the range of 3000-6000 mg/L. Analyzing the results can be concluded that, except for 1st regime, all other three regimes operated as extended aeration systems, because the VSS values stayed always above 3000 mg/L (4266 mg/L on average).

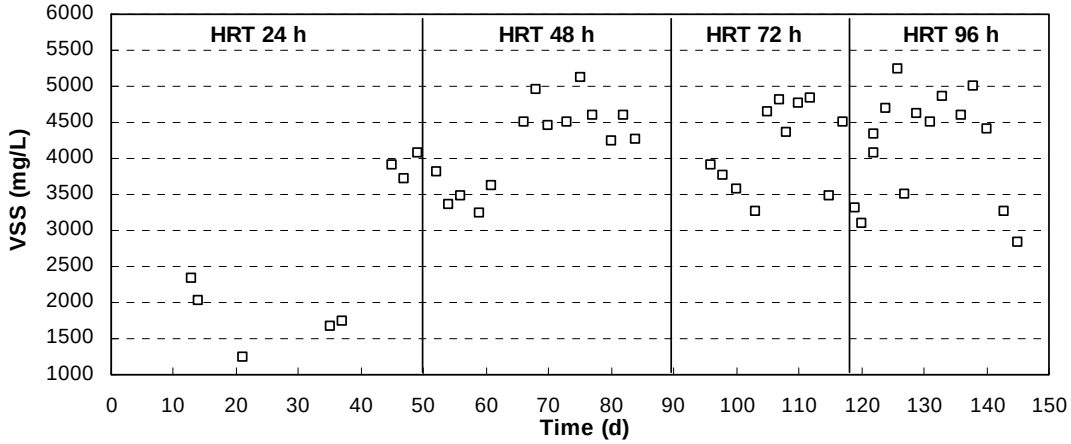

Fig. 3. VSS concentrations into aeration tank along time of operation of the activated sludge pilot.

Turbidity was measured in the final effluent to evaluate the system's behavior in relation to characteristics of the biomass. Fig. 4 illustrates the turbidity values obtained in the period studied. It was observed a great fluctuation in the 1st regime, probably due to washout of cells in the effluent stream and to bad operation of the system in this period. In the other regimes, the majority of the turbidity values were below of 30 NTU, indicating that follow to 1st regime, the system developed a biomass with better characteristics of flocculation and sedimentation. In relation to SVI, the majority of the values obtained were above of the range recommended in the literature for a good sedimentation (≤ 100 mL/g, Tchobanoglous et al., 2003). The regime operated with HRT of 72 h presented better results in terms of SVI, with more stable values varying between 109 and 135 mL/g.

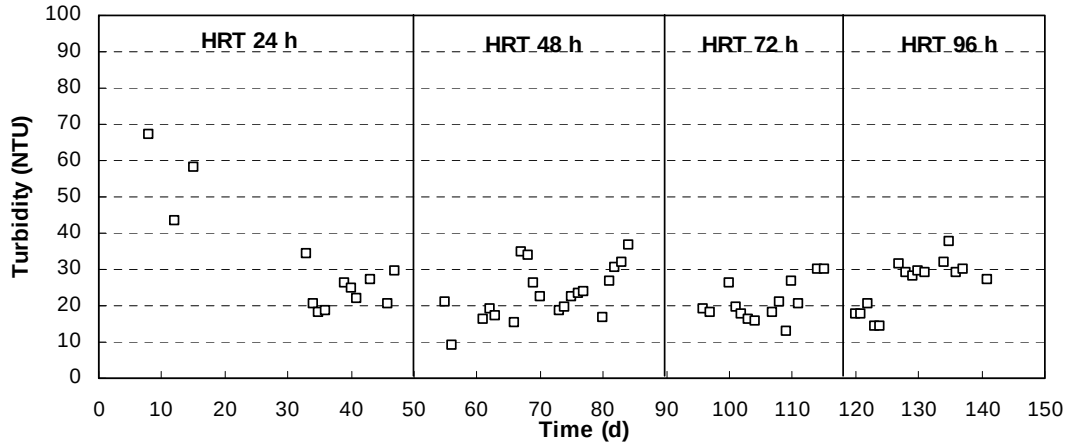

Fig. 4. Turbidity values in the effluent of the activated sludge system along time of operation.

The F/M ratio relates the available organic load with the quantity of biomass presents in the system, for a uniform substrate removal. When the substrate concentration diminishes, the search of food by microorganisms increases and consequently the organic matter removal efficiency also increases. The F/M values obtained along time of operation, except those for 1st regime (0.2 – 0.8 d^{-1}), were inside in the range recommended in the literature (0.08 – 0.15 d^{-1}) for extended aeration systems (Tchobanoglous et al., 2003).

Another important parameter evaluated was the temperature, measured daily into aeration tank. The temperature did not vary much along experimental runs, presenting values of (28 ± 2)ºC, (30 ± 1)ºC, (29 ± 1)ºC e (26 ± 2)ºC, in the regimes with HRT of 24, 48, 72 and 96 h, respectively. This parameter was appointed by mathematic model as of great influence in the WWTP performance. In fact, more stable values for temperature in the pilot plant resulted in values equally stable for COD removal efficiencies, mainly in the last two regimes (Fig. 2).

In representative absorption's spectra of the regimes operated with HRT of 48 and 72 h it was verified a little reduction of the absorbance after biological treatment. However, in the regimes with HRT of 24 and 96 h practically equal spectra were obtained for raw and treated effluents. These results are according with COD removals obtained, that were also higher in the regimes with HRT of 48 and 72 h. All spectra presented absorption's peaks in wavelengths of 210, 265 e 345 nm. Comparing the absorbance values in the wavelength of 265 nm for influent and effluent streams of the activated system it can estimate the optical brighteners' removal (22 and 45% for HRT of 48 and 72 h, respectively). Again, higher values were obtained in the regime operated with HRT of 72 h, confirming previous results obtained for COD removal. These results indicate that part of these compounds is removed in the activated sludge system, but it does not indicate necessarily that there was biodegradation because they can be removed by adsorption to sludge flocs.

Conclusions

Based on results obtained from sensibility analysis of operational conditions and kinetic parameters it can be concluded that the temperature is a control parameter that affects considerably the WWTP performance. In the sensibility study of kinetic parameters, m and μmax presented greater influence on analyzed variables (COD and biomass concentration). The saturation constants K_S and K_{OD} presented minor impact on response variables. In the sensibility study of operational conditions of WWTP, a variation of ± 5% was so harmful how much variations of 10 and 50%. Effluent COD was influenced by influent flow, influent COD and reactor volume, and consequently the HRT had indirect influence. Biomass concentration was influenced by reactor volume, effluent flow, recycle flow and influent COD. In the pilot plant operation, the HRT of 72h presented better results (COD removal efficiencies of 60%). These results show that other factors indeed temperature are important for the WWTP performance such as recalcitrance of the compounds present in the effluent.

Acknowledgments

The authors are thankful to CAPES, CNPq and FAPERJ.

References

APHA (1992). *Standard Methods for the Examination of Water and Wastewater.* 18th Ed. Washington, DC. American Public Health Association.

Edgar, T. F., Himmenblau, D. M. (1988). *Optimization of Chemical Processes*. McGraw-Hill Book Company. New York. USA.

Tchobanoglous, G., Burton, F., Stensel, H. (2003). *Wastewater Engineering – Treatment, Disposal and Reuse*. McGraw-Hill International Editions. New York. 4th Ed.

Stoll, J.-M. A., Giger, W. (1998). Mass balance for detergent-derived fluorescent whitening agents in surface waters of Switzerland. *Water Research*, 32, 2041-2050.

Proceedings of the 10th International Chemical and
Biological Engineering Conference - CHEMPOR 2008
Braga, Portugal, September 4-6, 2008
E.C. Ferreira and M. Mota (Eds.)

Influence of the reactor contents recirculation on methane production - anaerobic digestion of fruits, vegetables and grass waste feedstocks

M. T. Santos[1], L. M. Amaral[2], J. V. Prata[1*]
[1] Centro de Estudos de Engenharia Química and Departamento de Engenharia Química, Instituto Superior de Engenharia de Lisboa, Instituto Politécnico de Lisboa, R. Conselheiro Emídio Navarro 1, 1959-007 Lisboa, Portugal.
[2] Departamento de Ciências e Engenharia do Ambiente, Faculdade de Ciências e Tecnologia, Universidade Nova de Lisboa, Quinta da Torre, 2829-516 Caparica, Portugal

Keywords: Anaerobic digestion, Fruits, Vegetables, Grass, Recirculation
Topic: Sustainable process-product development through green chemistry - Environmental engineering & management.

Abstract

The present work was undertaken, in order to evaluate the influence of the reactor contents recirculation on anaerobic digestion of biodegradable solid wastes like fruits, vegetables and grass. For that propose two reactors (R1 and R2) were tested with the same mixture of substrates (50% of fruits, vegetables and 50% of grass), at mesophilic range, having reactor R2 recirculation of its contents. Maximum specific methane production was 41.54 and 223.24 mL $CH_4.g^{-1}VS$ for reactors R1 e R2 respectively. The methane (%) presented in biogas was significantly higher for reactor R2 (70% CH_4) than for reactor R1 (45% CH_4). The recirculation had a considerably positive effect in methane production, which corresponds to better and higher energy recovery.

1 Introduction

Anaerobic digestion of solid waste is a topic of increasing interest throughout the world, because it is an effective method for the treatment of many biodegradable wastes, with three main advantages: production of biogas, what is considered a renewable energy source; production of compost that can be used as a soil fertilizer and the assurance of a lower contribution to greenhouse gases effects in comparison with other technological solutions.

Anaerobic digestion of waste is complex, because it involves several bacterial groups and many simultaneous degradation and product forming reactions catalysed by those microorganisms. There are several diagrams to represent the anaerobic digestion. Gujer and Zehnder (1983) presented a complex diagram with five simultaneous steps: hydrolysis, acidogenesis, acetogenesis, aceticlastic methanogenesis and hydrogenotrophic methanogenesis.

In Europe, the study of anaerobic digestion of solid wastes only started in the 1980's (Mata-Alvarez, 2002). After the energy crises of the 1970's and the global environmental considerations, such as greenhouse effect, anaerobic digestion process had a significant development. In 1998, only 13% of the anaerobic digestion capacity available in Europe was designed for digestion of residual municipal waste, but by the end of 2006 that capacity had reached more than 52% (De Baere, 2008). Nowadays, the construction of anaerobic digestion plants for municipal solid waste is about 2/3 for residual waste and 1/3 for source separated biowaste on digestion capacity (De Baere, 2006).

* Corresponding author. Tel + 351-21-8317172. E-mail:jvprata@deq.isel.ipl.pt

Another benefit associated with the anaerobic digestion is the possibility to reduce the amount of waste sent to landfill, which is a way to achieve the targets of European Directive 1999/31/CE for landfills.

Fruits and vegetables wastes represent potential energy resources (Gunaseelan *et al.*, 2004). This kind of waste is produced in great quantity from markets, restaurants, agriculture and others domestic activities. Also grass is a waste produced in significant quantities from golf clubs, stadiums and gardens.

In Portugal, the first anaerobic digestion plant for waste was constructed only in the last years. In order to fully evaluate the overall anaerobic digestion process, particular attention should be devoted to the study of specific waste characteristics and process parameters. In fact, the ability to manage a biological process is deeply related to substrate biodegradability and proper control and operational conditions of the process.

The anaerobic digestion process depends on several environmental factors such as substrate concentrations, temperature, organic volatile acids, pH, alkalinity, inoculum and others. The recirculation of the content of reactors is one of the modes to promote de complete mixture of reactors, but this operation consumes enormous amounts of energy. Complete mixed reactors, usually, produces higher quantities of biogas and so this work aims to evaluated the effect of recirculation step in the performance of anaerobic digestion of biodegradable solid wastes like fruits, vegetables and grass.

2 Materials and methods

2.1 Apparatus

The experiments were carried out on two reactors with 10 L capacity. Schematic configuration and a view of reactors are shown in Figure 1. There reactors were operated in batch mode at mesophilic range. The content of reactor R2 was collected in the bottom and it was recycled to the top, with a peristaltic pump. Both reactors were mixed once per day, before the biogas collection. Experiments were run during 35 days. The biogas production and the others parameters were registered and estimated along the experimental running.

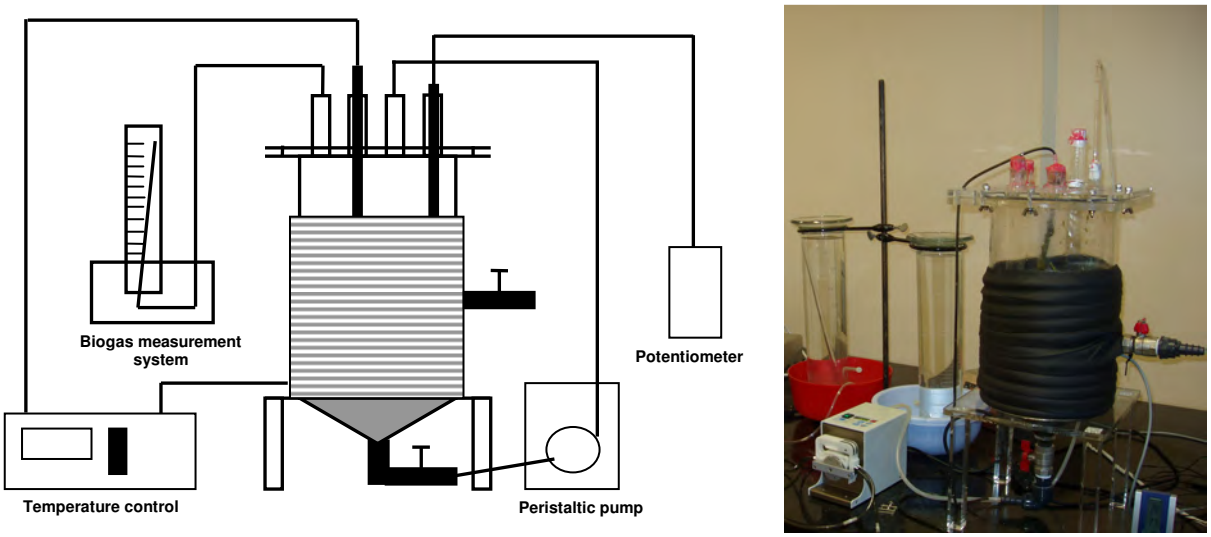

a) b)

Figure 1 Pilot reactor a) schematic configuration and b) view

2.2 Analytical procedure

Total and volatile solids (TS and VS) were measured as described in Standard Methods (APHA, 1998). The chemical oxygen demand (COD) was done in accordance with the open reflux method as described in Standard Methods (APHA, 1998). The samples for the analysis of soluble COD were prepared by filtration. The pH was measured with an ORION electrode. Gas production was determined with a glass syringe by the volume displacement. The biogas composition was measured with a Shimadzu 14B gas chromatograph fitted with Porapak Q packed column (0.32 mm ID and 2 m length) and a thermal conductivity detector (TCD). Helium was used as a carrier gas. Injector, oven and detector temperatures were 60ºC, 30ºC and 90ºC, respectively.

2.3 Inoculum

The inoculum used in experiments (sludge) was taken from an anaerobic digester in a wastewater treatment plant. After collection, the inoculum was adapted for several weeks, in a 10L reactor, with increasing substrate concentrations until achieving concentrations near the ones of the assays, and reaching a stable biogas production. During that period, the inoculum was fed with glucose and nutrient medium, prepared in accordance with Owen *et al*. (1979).

2.4 Substrates

The substrates used were fruits and vegetables manually sorted from municipal solid waste and grass. In order to get a more homogeneous mixture, fruits and vegetables were blended with a domestic blender. Table 1 shows the composition of the substrates used in this study.

Table 1. Characterization of substrates

Biodegradable Solid Wastes	TS (%)	VS (%)	pH
Vegetables and fruits	11	84	4.3
Grass	29	88	6.5

3 Results and Discussion

The average methane content in the biogas produced was 45 % and 70 % for R1 and R2 respectively (Figure 2). Assuming the heat potential of CH_4 as 35 880 $kJ.m^{-3}$, (Lastella *et al*., 2002) the heat potentials of biogas produced by reactors R1 and R2 were 16 146 and 25 116 $kJ.m^{-3}$. In accordance with Lastella *et al*. (2002) the biogas produced by reactor R2 represents a good potential energy recovery. The CH_4 percentage present in biogas produced by reactor R2 was comparable with values reported by Sosnowski *et al*. (2003) which achieved values greater than 60% and with those presented by Misi e Foster (2002) (between 60 and 64%). The value achieved by the reactor R1 it's similar only to the values reported by Gómez-Lahoz *et al*. (2007), which presents also lower methane production (0.100 $m^3CH_4.kg^{-1}VS$).

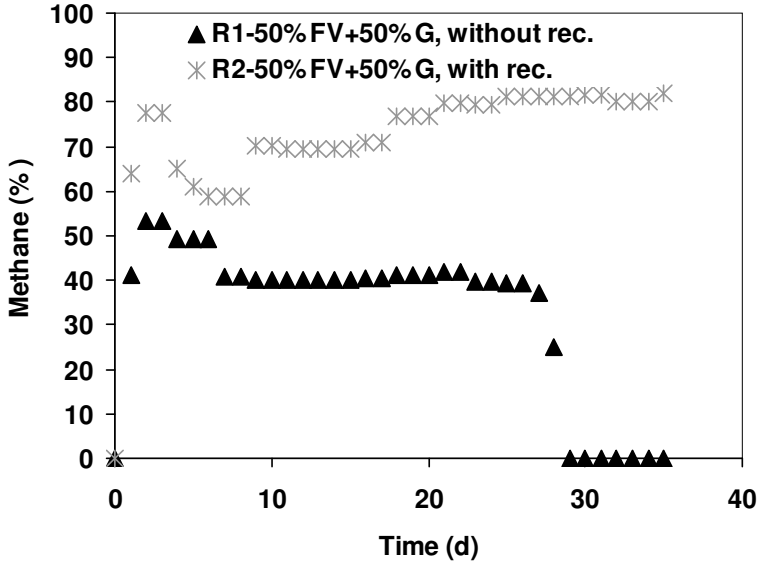

Figure 2. Methane content in biogas for reactor R1 e R2.

The methane production for both reactors is shown in Figure 3. Maximum specific methane production was achieved after 5 days for R1 and in after 15 days for R2. R2 presents a greater methane production (223.24 mL $CH_4.g^{-1}VS$) than R1 (41.54 mL $CH_4.g^{-1}VS$). The methane production achieved by reactor R2 was lower than the literature data on methane production from fruits and vegetables (0.409 – 0.529 $m^3CH_4.kg^{-1}VS$) and grass (0.342 – 0.420 $m^3CH_4.kg^{-1}VS$) (Gunaseelan, 1997). The value presented by reactor R1 it's only comparable with studies with very low methane production caused by a possible inhibition problem under anaerobic conditions (Agdag e Sponza, 2005, Gómez-Lahoz *et al.*, 2007). The methane volumetric productions achieved during the experiments were 0.2 and 1.1 m^3CH_4 per m^3 of reactor, for R1 and R2 respectively (Table 2). The problem with reactor R1 is possible caused by the poor contact between substrate and microorganisms.

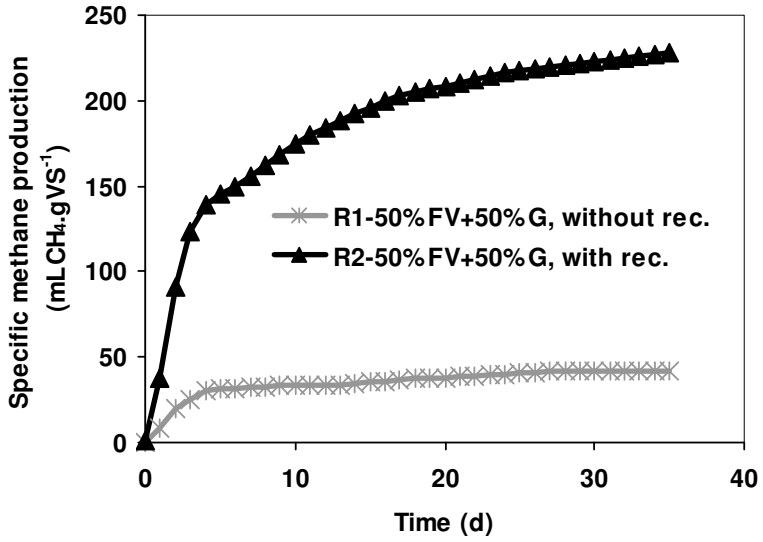

Figure 3. Specific methane production for reactor R1 and R2.

In both reactors, and during all the period of incubation, the pH (Table 2) of the digestion mixture did not need to be adjusted externally, because it was kept in the adequate range for anaerobic digestion 6.5 – 7.5 (Cecchi *et al.*, 2002), except for reactor R2 which presents a value of 7.65 at the initial stage, but quickly achieved values lower than 7.5 in the course of the digestion.

Table 2. pH and maximum specific methane production for R1 and R2

Reactor	pH initial	pH final	Methane volumetric production (m^3/m^3)	Maximum specific methane production (mL $CH_4.g^{-1}VS$)
R1	7.42	7.38	0.2	41.54
R2	7.65	7.49	1.1	223.24

The COD total (CODt) and soluble (CODs) were monitored during the experiments as an indicative parameter of organic matter removal. Both COD decreased rapidly in the first 25 days for reactor R1 and R2; reactor R2 presented COD values lower than R1, especially in CODs.

The rate methane production was calculated from the specific methane production (Table 3).

Table 3. Maximum rate methane production for reactor R1 and R2

Reactor	Time (d)	Maximum rate methane production (mL $CH_4.gVS^{-1}.d^{-1}$)
R1 (50%FV+50%G, without rec.)	2	10.87
R2 (50%FV+50%G, with rec.)	2	53.05

As was expected, the maximum methane rate production was much greater for reactor R2, clearly pointing to the importance of the recirculation in the overall methane production. Both reactors achieved the maximum value in 2 days.

4 Conclusions

The overall volume of methane produced was much higher in R2 than R1. This is probably due to the recirculation system which ensures a good homogenization of the reactor contents. Similar results were presented by Sponza and Agdag (2004).

The recirculation had a considerably positive effect in methane production, which corresponds to better energy recovery.

Further work will follow to determine the effect of different recirculation ratios on methane production, in order to maximize the energy recovery.

References

APHA-AWWA-WEF, (1998) *Standard methods for the Examination of Water and Wastewater.* 20th ed. American Public Health Association, Washington, DC.

Cecchi, F., Traverso, P.; Pavan, P., Bolzonella, D., Innocenti, L. (2002). *Characteristic of the OFMSW and behaviour of the anaerobic digestion process*, Biomethanization of the

organic fraction of municipal solid wastes, IWA Publishing, Edited by Mata-Alvarez, UK.
De Baere, L., (2006). Will anaerobic digestion of solid waste survive in the future?, *Wat. Sci. Tech.*, 53 (8), 187-194.
De Baere, L., (2008). Partial stream digestion of residual municipal solid waste, *Wat. Sci. Tech.*, 57 (7), 1073-1076.
Gomez-Lahoz, C., Fernández-Giménez, B., Garcia-Herruzo, F., Rodriguez-Maroto, J. M., Vereda-Alonso, C. (2007). Biomethanization of mixtures of fruits and vegetables solid wastes and sludge from a municipal wastewater treatment palnt. *Journal of Environmental Science and Health*, Part A, 42 (4), 481-487.
Gujer, W. & Zehnder, A. J. B. (1983). Conversion processes in anaerobic digestion. *Wat. Sci. Tech.*, 15, 127-167.
Gunaseelan, V. N. (2004). Biochemical methane potential of fruits and vegetable solid waste feedstocks. *Biomass & Bioenergy,* 26, 389-399.
Lastella, G., Testa, C., Cornacchia, G., Notornicola, M., Voltasio, F., Sharma, V. K. (2002). Anaerobic digestion of semi-solid organic waste: biogas production and its purification. *Energy Conversion and Management*, 43, 63-75.
Mata-Alvarez, J. (2002). *Fundamentals of the anaerobic digestion process*, Biomethanization of the organic fraction of municipal solid wastes, IWA Publishing, Edited by Mata-Alvarez, UK.
Misi, S. N., Forster, C. F. (2001). Batch co-digestion of multi-component agro-wastes. *Bioresource Techonology*, 80, 19-28.
Owen, W. F., Stuckey, D. C., Healy Jr, J. B., Young, L. Y., McCarty, P. L. (1979). Bioassay for monitoring biochemical potential and anaerobic toxicity, *Water Reasearch*, 13, 485-492.
Sosnowski, P., Wieczorek, A., Ledakowwicz, S. (2003). Anaerobic co-digestion of sewage sludege and organic fraction of municipal solid wastes, *Advances in Environmental Research*, 7, 609-616.
Sponza, D. T., Agdag, O. N. (2004). Impact of leachate recirculation and recirculation volume on stabilization of municipal solid wastes in simulated anaerobic bioreactors. *Process Biochemistry*, 39 (12), 2157-2165.

Acknowledgements
We thank Instituto Politécnico de Lisboa (project IPL/12/2003) for partial financial support. M. T. Santos thanks Ministério da Educação and Instituto Superior de Engenharia de Lisboa for a PhD fellowship (PRODEP III–05.03/LTV/00181.013/03).

Proceedings of the 10th International Chemical and
Biological Engineering Conference - CHEMPOR 2008
Braga, Portugal, September 4-6, 2008
E.C. Ferreira and M. Mota (Eds.)

Comparison of different control cascade strategies for anaerobic digesters using ADM1

Carlos Garcia Dieguez[1*], Francisco Molina[2], Eugenio F. Carrasco[1], J. M. Lema[1], Enrique Roca[1]

[1] USC - University of Santiago de Compostela, Department of Chemical Engineering/School of Engineering. Rua Lope Gomez de Marzoa s/n, 15782 Santiago de Compostela, Spain.
[2] Faculty of Engineering, University of Antioquia, A.A. 1226, Medellin, Colombia.

Keywords: Anaerobic digestion, ADM1, control, modeling, wastewater treatment.
Topic: Systematic methods and tools for managing the complexity — Process control & operations.

Abstract

In this work, different configurations of robust cascade controllers applied to anaerobic wastewater treatment are evaluated by simulation with ADM1 according to benchmark recommendations. Two of the controllers are already available in literature (Alvarez-Ramirez et al., 2002; Liu et al., 2004). In addition, a novel cascade controller approach is presented and compared with the others. This new approach, unlike the other two, is a multi-objective one. It considers two operational objectives in the same simple control structure: a.- the control on the effluent quality for fulfilling with the environmental regulations; and b.- the control on the maximum methane production rate. It requires two measured variables as inputs: the methane flow rate (Q_{CH4}) and the concentration of volatile fatty acids (VFA) expressed as acetic acid. The advantages and disadvantages of the controllers are discussed in detail.

1 Introduction

Anaerobic digestion processes consist of a set of conversions of organic matter into methane and carbon dioxide, occurring in absence of oxygen (Lettinga, 1995). Most of the organic effluents and wastes coming from industrial, municipal or agricultural activities can be effectively processed by anaerobic wastewater treatment (AWT) plants. The following are some of the reasons why AWT has gained importance in the last years (van Lier et al., 2001): a.- use of methane as an energy source; b.- the low production of sludge; and c.- its ability to treating wastewater with medium to high organic loads. However, AWT has classically been regarded as a difficult process to be controlled and managed. Different disturbances can affect the performance of an anaerobic reactor and the recovery of the normal conditions can be long and expensive. Therefore, the selection of an accurately control system could give important advantages in the management of these reactors helping to minimize the operational cost and maintain the plant under safe conditions.

The range of possible control systems is quite broad, and its application has been quite limited. In this sense, it is necessary to have a standard tool that allows different controllers performance to be compared. Several researchers have been working to standardize the use of models in wastewater treatment processes (Copp, 2002; Vrecko et al., 2006; Jeppsson et al., 2007). Particularly, with regard to anaerobic digestion models, Rosen et al. (2006) discussed about a number of research works with the Anaerobic Digestion Model Nº1 (ADM1 - Batstone et al., 2002) during COST/IWA Benchmark Simulation Model (BSM2). The BSM2 is a control benchmark for plant wide modeling. Complex models such as ADM1 are a good

* Corresponding author. Tel +34 981-563100 Ext.: 16742. E-mail:carlos.garcia.dieguez@usc.es

choice to evaluate controllers competitively, and develop operational strategies (Batstone & Steyer, 2007).

In this work, ADM1 was used, according to benchmark recommendations, for comparing the performance of three different configurations of robust cascade controllers for anaerobic wastewater treatment (AWT) of vinasses.

2 Model description and problem statement

2.1. *IWA Anaerobic Digestion Model no. 1 (ADM1) and AWT plant*

ADM1 (Batstone et al., 2002) is a complex model of the multistep anaerobic process transformations. This tool is adequate for predictions of enough accuracy to be useful in process development, optimization and control. ADM1 incorporates processes such as hydrolysis of particulates, acidogenesis, acetogenesis and methanogenesis, and it includes 26 dynamic state concentration variables, 19 biochemical kinetic processes, 3 gas-liquid mass transfer kinetic processes, and 8 implicit algebraic variables per liquid vessel.

A modified version of ADM1 (Batstone et al., 2002) incorporating ethanol degradation pathways and calibrated for a heavily instrumented USBF reactor of 1.15 m^3 (Ruiz-Filippi et al., 2004) was used. In this ADM1 version, an additional group of ethanol degraders was included as well as a new state variable for ethanol concentration. The extension for ethanol not only considers the hydrogen and acetate pathways but also takes into account other pathways of interest in controller design as volatile fatty acids (VFA) pathways (in particular for propionate and butyrate) by means of the stoichiometry. Thus, VFA evolution, including responses against overloads or transitions between steady states, is adequately predicted.

2.2. *New controller approach*

The block diagram describing the structure of the new cascade controller approach proposed here is shown in Figure 1. Basically, this control system consists of two loops in cascade. The inner loop (Slave Controller) uses the methane production rate as state variable as well as the output of the Master Controller as reference. The outer loop (Master Controller) compares the measured VFA concentration with the VFA set-point as input error.

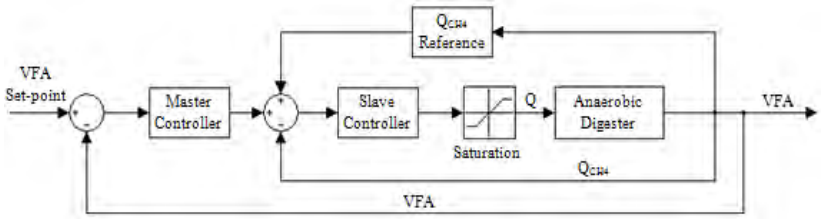

Figure 1. Block diagram of the new approach cascade controller. Note that Q_{CH4} reference signal provides the set-point to the inner control loop.

The parameters of the new approach had been optimized, and the applied values are given in Table 1, where K_c, K_I and K_d are the proportional gain, the integral factor and the derivative factor for each PID controller, respectively.

Parameters	Slave	Master
K_c	0.0172	0.38
K_I	$7.2 \cdot 10^{-7}$	0
K_d	0.0006	0

Table 1. Parameters of the new cascade controller approach.

The methane reference signal (Q_{CH4} reference) was established as a function of the chemical oxygen demand in the influent (COD_{in}) through an empirical correlation. This empirical correlation is different for each control objective. In this case, it was obtained by means of simulations. In the case of cascade controller, the simulations consist of optimizing in pseudo steady-state the methane production rate for different concentrations of COD_{in} that accomplished the requirement of spillage (150 mg Ac/l). For the inner loop controller, the simulation consists of obtaining the maximum methane production rate vs. COD_{in}.

The feed flow rate (Q) is constrained by a saturation function (according to physical restrictions on manipulated variable). The minimum feed flow rate is zero and the maximum feed flow rate was established using the criterion of minimum hydraulic retention time (HRT) of 9 hours for preventing undesired wash-out of biomass. Furthermore, the speed of variation (increase or decrease) of the feed flow rate (ΔQ) was limited to 0.5 l/h each 15 minutes.

3 Controllers comparison

The three types of cascade controllers were properly tuned as a previous step to the comparative evaluation of their performance. For this task, a sequential quadratic programming (SQP) combined with ethanol modified ADM1 for parameter optimization was required for the new cascade controller approach. The time required for this optimization was approximately 12 min in an Intel Core Duo E6550 233GHz and 2 Gb of RAM running Matlab® 7.0 (R14). In the other cases, an extensive manual tuning from the original parameters was employed. The parameters of the new controller were already shown in Table 1. The parameters used for the Liu controller were K_{pm} = 33 (master controller proportional gain), K_{ps} = 2 (slave controller proportional gain), D_{min} = -0.3 (lower limit for D, which represents the difference between the methane flow rate and its set-point) and D_{max} = 0.1 (upper limit for D in the supervisor system), being those for the Alvarez-Ramirez et al. controller K_{Im} = 3 (integral factor of the master controller) and K_{ps} = 0.5 (slave controller proportional gain).

3.1. *Alvarez-Ramirez et al. controller versus new approach*

The controller of Alvarez-Ramirez et al. (2002) only controls the outlet concentration of VFA and it was not designed to achieve automatic restart-up in a wastewater treatment system. On the other hand, one of the main advantages of the new controller approach is that it offers total control over an automatic restart-up of the system. The response of both controllers to a severe organic overload by a 50% of increase of input COD from 10 g COD/l to 15 g COD/l, is shown in Figure 2. Considering a quality effluent control criterion, the new approach cascade controller had a greater speed of response against organic overload perturbations than the Alvarez-Ramirez et al. controller. The new controller approach can stabilize the treatment system, in a very reasonable time, taking into account the magnitude of the perturbation and the low error permitted for the controlled variable. Thus, the controller of Alvarez-Ramirez et al. presents more oscillations, having a tendency to destabilize if other perturbations take place at the same time. This fact can be visualized through the error on the controlled variable (VFAs).

The variables selected for the Alvarez-Ramirez et al. controller do not take advantage of the difference between the dynamics of the liquid and gas phases for improving its response. Besides, the measurement times for this controller are very low compared with the response times of the control variables (VFAs and COD). In the work of Alvarez et al. large oscillations, considering the magnitude of the perturbations applied can be observed.

Therefore, if the treatment system suffers important concentration disturbances in the influent, this controller could not be the most appropriate. In addition, the best option for on-line monitoring COD and VFAs would be to use infra-red spectrometry. This choice is more

expensive than on-line monitoring of VFAs by means of a titrimetric smart sensor (Molina et al. 2008).

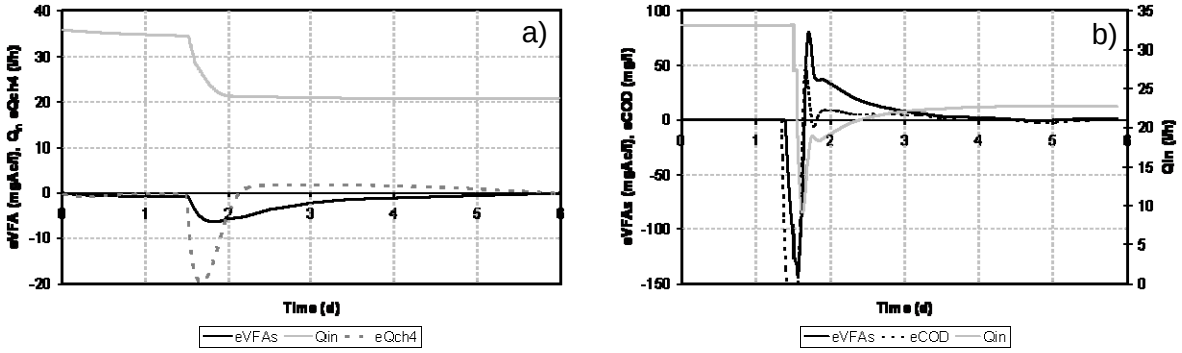

Figure 2.Comparison during a severe organic overload (from 10 to 15 g COD/l): a) New controller approach, b) Alvarez-Ramirez et al. controller.

3.2. *Liu et al. controller versus new approach*

The Liu et al. (2004) controller, unlike that of Alvarez-Ramirez et al. (2002), does not take into account the effluent quality, because its objective is the maximization of methane production. In this regard, it has been compared with the new controller approach presented here. The new controller approach can lead to the system up to the maximum treatment capacity, if the external control loop is disconnected, and set up the methane reference signal that corresponds with this objective. The results obtained with both controllers during an automatic restart-up experiment (COD_{in} constant and equal to 10 g COD/m^3) are shown in Figure 3. According to Molina et al. (2007), a treatment capacity equal to 12 kg COD/m^3·d was considered for the USBF reactor.

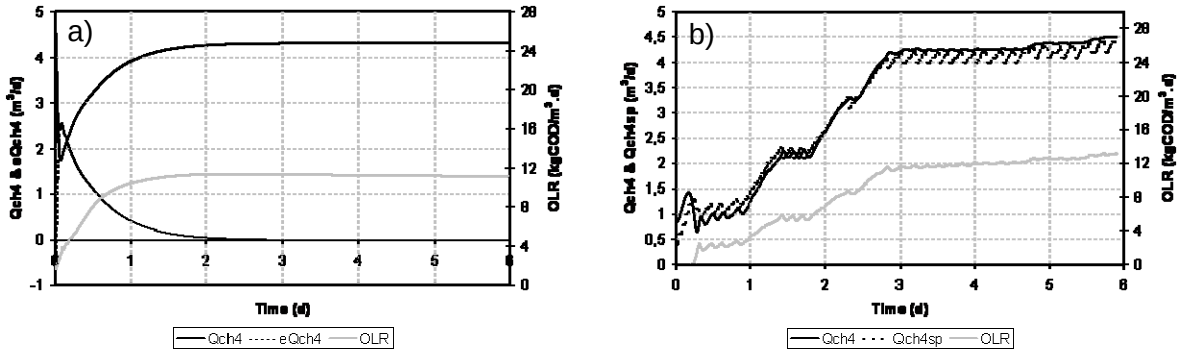

Figure 3. Restart-up of the USBF reactor using the new cascade controller approach and the Liu et al. controller: a) New cascade controller approach; b) Liu et al. controller.

In terms of maximum methane production rate criterion, the Liu et al. controller and the new controller approach presented a reasonably similar performance. However, the new approach reaches an organic loading rate (OLR) equivalent to the maximum production capacity of methane earlier than Liu et al. controller. Furthermore, the Liu et al. controller does not take into account the effluent quality. Besides, this controller uses the pH in the inner-loop, generating a series of difficulties in its industrial scale application: 1. The location of pH sensor that can be able to capture the appropriate information; 2. A pH sensor for an industrial application does not have enough resolution for a properly function of the control system; 3. The simulations reveal that set-point reached by the controller is highly dependent

of the alkalinity added and the selected parameters. This controller required a great consumption of bicarbonate for fulfilling alkalinity needs and maintaining the reactor in a stable operation. These seem to be the main drawbacks for its application at industrial scale. On the other hand, the new controller approach requires to be tested in closed loop experiments at pilot scale to confirm the hypothesis. The main advantage of Liu et al. controller is that already uses available variables in all anaerobic industrial plants, while the new approach requires the use of a relatively low-cost sensor for measuring VFAs, which is already available on the market (Molina et al, 2008).

4 Discussion

The difference between the evaluated controllers owes principally to the different variables used to define the control strategy or the control law. The selection of the properly inner-loop variable determines the performance of cascade structures, as the inaccurately cancellation of the error in the inner-loop affects the cascade efficiency. An internal suitable variable must fulfill with a series of criteria or requirements. The most relevant ones are listed in Table 2 together with the variables, indicating a qualitative degree of fulfillment for the development of a controller in cascade for an AWT plant.

Criterion	Q_{CH4}	$\%CH_4$	Q_{gas}	$\%CO_2$	**CO**	H_2
Secondary variable is available	A	A	Y	O	A	A
Indicates a key disturbance	Y	O	Y	N	N	Y
Causal relationship with the controlled variable	Y	N	Y	N	N	N
Secondary dynamic faster than primary	Y	Y	Y	Y	Y	Y

Table 2. Evaluation criteria for inner-loop variables suitability. (Y-Yes; N-No or Not appreciable; N/A- Not applicable; A-Advanced instrumentation; O- In occasions; S-Similar).

As it can be seen in Table 1, the methane flow rate (Q_{CH4}) and the biogas flow rate (Q_{gas}) were the best inner-loop variables. The liquid phase variables are supposed to present higher response times than the gas phase variables. Therefore, bear in mind this criterion an inner control loop with a secondary variable from the liquid phase does not seem to be the most appropriate. In addition, with the same criterion, a combination between variables in the gas and liquid phases will allow the controller to take advantage of the difference between the dynamic of both phases. Thus, the best choice seems to be the use of a variable of the liquid phase (slow response) as control variable in the external loop, and a variable of the gas phase (fast response) as control variable in the inner loop.

In this way, Alvarez-Ramirez et al. controller uses two variables of the liquid phase (VFA and COD_{out}) as process variables, which would delay the response of this control system. The Liu et al. controller uses pH, as state variable. This variable does not enable a fast and appropriate control action unless a fine control on the addition of alkalinity was also available, especially at a full-scale reactor.

5 Conclusions

In this paper, the performance of a new controller in cascade for anaerobic wastewater treatment plants was compared with two other controllers in cascade already available in literature (Alvarez et al., 2002 and Liu et al., 2004) by means of simulations. The model used for this work was the Anaerobic Digestion Model N°1 (ADM1), implemented according to the BSM2. This tool has allowed the performance of these controllers to be tested under the same conditions of operation, obtaining as main conclusion that the selection of the inner-loop control variable affect the performance of the controllers studied here. The promising

new controller requires a further and extensive validation in closed-loop for checking its suitability working in pilot and industrial scale systems.

Acknowledgements

Authors wish to acknowledge to Spanish National R&D Program and European Regional Development Fund (ERDF) for the Project ANACOM CTQ2004-07811-C02-01.

References

Alvarez-Ramirez, J., Meraz, M., Monroy, O., and Velasco, A. (2002) Feedback control design for an anaerobic digestion process. *Journal of Chemical Technology and Biotechnology* 77 (6), 725-734.

Batstone, D.J., Keller, J., Angelidaki, I., Kalyuzhny, S., Pavlostathis, S.G., Rozzi, A., Sanders, W., Siegrist, H., and Vavilin, V.A. Anaerobic Digestion Model No. 1 (ADM1). [Report No. 13]. 2002. London, IWA Publishing.

Batstone, D.J. and Steyer, J.P. (2007) Use of modelling to evaluate best control practice for winery-type wastewaters. *Water Science and Technology* 56 (2), 147-152.

Copp, J.B. (2002) *The COST Simulation Benchmark — Description and Simulator Manual*., Office for Official Publications of the European Communities, Luxembourg.

Jeppsson, U., Pons, M.N., Nopens, I., Alex, J., Copp, J.B., Gernaey, K.V., Rosen, C., Steyer, J.P. and Vanrolleghem, P. (2007) Benchmark simulation model no 2: general protocol and exploratory case studies. *Water Science and Technology* 56 (8), 67-78.

Lettinga, G. (1995) Anaerobic digestion and wastewater treatment systems. *Antoine van Leeuwenhoek. International Journal of general and molecular microbiology* 67 (1), 3-28.

Liu, J., Olsson, G. and Mattiasson, B. (2004) Monitoring and Control of an Anaerobic Upflow Fixed-Bed Reactor for High-Loading-Rate Operation and Rejection of Disturbances. *Biotechnology and Bioengineering* 87 (1), 43-53.

Molina, F., Ruiz-Filippi, G., Garcia, G., Roca, E., Lema, J.M. (2007) Winery effluent treatment at an anaerobic hybrid USBF pilot plant under normal and abnormal operation. *Water Science and Technology* 56 (2), 25-31.

Molina, F., Ruiz-Filippi, G., Garcia, G., Lema, J.M., Roca, E. (2008) Validation at pilot scale of a new sensor for on-line analysis of volatile fatty acids and alkalinity in anaerobic wastewater treatment plants. *Environmental Engineering Science* (under review).

Rosen, C., Vrecko, D., Gernaey, K.V., Pons, M.N. and Jeppsson, U. (2006) Implementing ADM1 for plant-wide benchmark simulations in Matiab/Simulink. *Water Science and Technology* 54 (4), 11-19.

Ruiz-Filippi, G., Rodriguez, J., Roca, E. and Lema, J.M. Modification of the IWA-ADM1 for application to anaerobic treatment of ethanolic wastewater from wine factories. 1341-1344. 2004. Anaerobic Digestion 10th World Congress Anaerobic Bioconversion for Sustainability. 29-8-2004.

van Lier, J., Tilche, A. Ahring, B., Macarie, H., Moletta, R., Dohanyos, M., Hulshoff Pol, L., Verstraete, W. (2001) News perspectives in anaerobic digestion. *Water Science and Technology* 43 (1), 1-18.

Vrecko, D., Gernaey, K.V., Rosen, C. and Jeppsson, U. (2006) Benchmark Simulation Model No 2 in Matlab-Simulink: Towards plant-wide WWTP control strategy evaluation. *Water Science and Technology* 54 (8), 65-72.

Proceedings of the 10th International Chemical and
Biological Engineering Conference - CHEMPOR 2008
Braga, Portugal, September 4-6, 2008
E.C. Ferreira and M. Mota (Eds.)

Treatment of waters contaminated with diesel fuel by electrocoagulation

Adžamić, Tamara[1]; Jukić, Ante[1]; Sertić-Bionda, Katica[1]; Bobić, Vedranka [2]

[1]Faculty of Chemical Engineering and Technology, Marulićev trg 19, HR-10000 Zagreb
[2]INA - Oil refinery, Lovinciceva b.b., HR-10000 Zagreb

Keywords: water, diesel fuel, emulsion, electrocoagulation, modeling
Topic: Sustainable process – product development through green chemistry

Abstract

Electrocoagulation (EC) is one of the promising contaminated water treatments, where impurities are removed by coagulation and flotation, while coagulant is added *in situ* by electrochemical oxidation of the suitable anode material. EC is possible alternative to the metal salts or polymers and polyelectrolyte addition, for the stable emulsion breaking, adsorption, as well as the metal, colloids and soluble inorganic impurities removing.

In this work, efficiency of electrocoagulation process for hydrocarbon removing from the water emulsion was investigated. As model solution, emulsion of diesel fuel in distillate water with addition of sorbitan monooleate as the emulsifier was used. Process was conducted in the batch reactor with the aluminum electrodes, with addition of the NaCl for the increase of electrical conductivity of the emulsion. Inlet parameters were NaCl and diesel fuel concentrations in emulsion, current density and reaction time. Outlet parameters were total organic carbon (TOC), filtrate volume and mass loss of the anode material. Experiments were conducted in two sets, each with 16 treatments, settled by two level factorial design (TLFD) method. Quantitative influence of each factor, inlet parameters and their interactions on the main responses were calculated, and presented with mathematical correlations.

Obtained results indicated very high efficiency of the electrocoagulation process, for the hydrocarbon removal from water emulsion, ranging from 98.9 to 99.5 %, calculated in respect to the total organic carbon content in water, while current efficiency was in the range from 17 to 78 %. Water phase after the EC process was odorless, tasteless and colorless. As expected, it is proven that the current efficiency is increasing with increase of the electric conductivity of the emulsion and with decrease of the current density. High TOC removal was obtained even for the short periods of reaction time (5 minutes), meaning that higher current efficiencies are possible with lower current densities at prolonged reaction times.

1. Introduction

Petroleum and its derivates are one of the most used substances in the world today. Generally, they are very complex mixtures of various compounds, mostly hydrocarbons. These compounds are usually categorized as alkanes, naphtenes and aromatic hydrocarbons. Motor fuels, lubricants and other oil derivates contain these groups of hydrocarbons in different ratios. Most hydrocarbon compounds are not soluble in water. Nevertheless, if the spill out occurs, there is a danger of emulsion formation. There is also a danger of gradual hydrocarbon dissolution from sediments that are formed because of the oil spill. One of the nature purging mechanisms of the contaminated water is hydrocarbon compounds sedimentation, i.e. deposition to the bottom; cca 10 to 30 mas.% of the total amount is deposited, depending on the conditions that dominate at that area and water depth[1].

Today, varieties of the water purification methods that include biological and physico-chemical treatments are well known and available. New methods that do not include different chemicals and reagents addition will become very popular in the near future. Some of those methods are electrocoagulation, electroflotation, electrodecantation[2]. Coagulation is phenomena were charged particles in colloid suspension are neutralized by negatively charged ions, followed by agglomeration and then sedimentation. Coagulant is added in the form of an appropriate chemical substance. In electrocoagulation coagulant is added in situ by electrochemical oxidation, i.e. appropriate anode material dissolving. This process is carried out in three successive phases: the first phase is coagulant formation by anode oxidation, followed by contamination and suspension destability and emulsion breaking. The last phase is an unstable phase aggregation and flocs formation, followed by electro flotation / electro precipitation[3]. The best anode materials are iron and aluminum because they have high charge ions. Aluminum ions are especially unstable; with release from the electrode surface they react with hydroxyl ions and are adsorbed on the colloid particle surface. With electrochemically dissolution of the anode (aluminum electrode) cation monomer species like Al^{3+} and $Al(OH)^{2+}$ are produced under low pH values, that with the rise of the pH values become $Al(OH)_3$ and finally polymerized $Al_n(OH)_{3n}$ by following reaction pathway[4]:

$$Al \rightarrow Al^{3+}(aq) + 3e^- \qquad E^o = -1.66\ V \qquad (1)$$

$$Al^{3+}(aq) + 3H_2O \rightarrow Al(OH)_3 + 3H^+ \qquad (2)$$

$$nAl(OH)_3 \rightarrow Al_n(OH)_{3n} \qquad (3)$$

Simultaneously, hydrogen is forming on cathode by following reaction pathway:

$$2H_2O_{(l)} + 2e^- \rightarrow H_2(g) + 2OH^-(aq) \qquad E^o = -0{,}83\ V \qquad (4)$$

At the last few years electrocoagulation has proven itself as an effective method of treatment and purification for various contaminated waters, such as waters contaminated with mineral and vegetable oils, organic dyes, as well as waters from metallurgic, paper and leather industry, etc[4]. In this paper effect of current density and reaction time, in electrocoagulation process, on the diesel /water emulsion breaking is investigated. Efficiency of the process is monitored through total organic carbon (TOC), filtrate volume and mass loss of the anode material[5].

2. Experimental

Materials

Emulsions used in this research were prepared by mixing appropriate masses of diesel and redistilled water with addition of the NaCl for the electrical conductivity increase. Non-ionic surfactant, sorbitan monolaurate, Span 80 having an 4.3 HLB (hydrophilelipophile balance) (Fluka), was used as the stabilising agent at concentration of 0.5 wt.%. A sample of commercial diesel was obtained from INA d.d. Croatian Oil Company. The main properties of

the diesel are listed in Table 1.

Table 1. Physical and chemical properties of the diesel fuel

Property	Value
Cetane number	51.0
Density at 15°C (kg m^{-3})	845.0
Total sulfur (mg kg^{-1})	50
Polycyclic aromatic hydrocarbons (wt.%)	11
Kinetic viscosity at 40°C (mm^2 s^{-1})	2.0
End of distillation (°C)	360

Process and methods

Emulsions were prepared in vessel with variable speed-controlled impeller. Redistilled water and Span 80 were mixed at 400 rpm for a mixing time of 1h. Thereafter, diesel and NaCl were added to the emulsion and continued with mixing for 1 hour, until stabile emulsion was formed. Electrocoagulation process was conducted in batch reactor, in glass cell with aluminum electrodes (anode and cathode). The electrocoagulation apparatus and electric circle scheme is presented in Fig 1. The anode and the cathode surface were 50 cm^2 each and the distance between them was 5 cm. All measurements were conducted under constant stirring rate (400 rpm) and controlled temperature (25.0 °C). Effect of current density and time on the emulsion separation efficiency was investigated. EC efficiency was monitored through measurements of electrode mass loss, filtrate volume and TOC values in the separated aqueous phase. TOC values of the samples were measured using Total Organic Analyzer (Shimadzu, TOC-V_{CPN}).

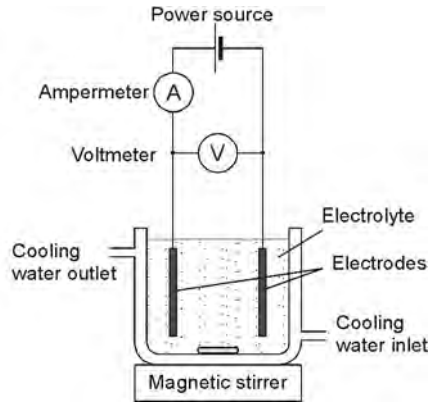

Figure 1. The electrocoagulation apparatus and electric circle scheme

Hydrocarbon separation efficiency from aqueous phase is given by equation:

$$U_{TOC} / \% = (TOC / TOC_0) \times 100 \quad (5)$$

Current efficiency , η_{el}, for the production of dissolved Al^{3+} is given by equation:

$$\eta_{el} / \% = (m_{teor} / m_{exp}) \times 100 \quad (6)$$

where m_{exp} is the weight loss of the aluminium electrodes during the experiment and m_{teor} the theoretical amount of aluminium consumed according to Faraday's law given by equation:

$$m_{teor} / g = [I (A) \times t (s) \times M (g\ mol^{-1})] / [z \times F (A\ s\ mol^{-1})] \quad (7)$$

where *I* (A) is the current density, *t* (s) the experiment duration, *M* (g mol^{-1}) the molar mass of aluminium and *F* (A s mol^{-1}) the Faraday constant.

Statistical study

A statistical study was performed by applying a 2^4 full factorial design[6]. According to this design, 32 runs were made during which 4 parameters: diesel fuel concentration (X_1), NaCl concentration (X_2), current density (X_3) and time (X_4) were varied over the 2 levels. The levels of the parameters with their actual and coded factors are presented in Tab 2. The coded values of the two levels were designed so 1 represents the higher value and 0 the lower value. Experimental runs were carried out randomly, with one replicate of each run. Described design was carried out to determine which parameter have important effect on response and possible interactions between parameters, which couldn't be seen by variation of only one parameter, leaving others constant. The statistical calculations were performed using software tool Design-Expert (State Ease, Inc.).

Table 2. Designed levels of the parameters with their actual and coded factors

Parameter	Value	
	Lower level (0)	Higher level (1)
X_1: Diesel fuel concentration, *c* (DF) [mas. %]	4	15
X_2: NaCl concentration, *c* (NaCl) [mas. %]	1	2.5
X_3: Current density, *I* [A]	0.5	1
X_4: Time, *t* [min]	5	30

3. Results and discussion

2^4 full factorial design with coded factors and experimentally obtained data is presented in Tab. 3. Determination of the most significant influences on the EC process response was made by half normal probability of main effects and their interaction analysis. Chosen significant effects were additionally validated with F-test, which value below 0.05 implied that effect is significant and can be implemented into the mathematical model of the process. With multiple regression analysis of the obtained data, performed with Design-Expert software, mathematical description of EC batch process was expressed with statistical model (Eq. 8).

$$y = \beta_0 + \beta_A X_1 + \beta_B X_2 + \beta_C X_3 + \beta_D X_4 + \beta_{AB} X_1X_2 + \beta_{AC} X_1X_3 + \beta_{AD} X_1X_4 + \beta_{BC} X_2X_3 + \beta_{BD} X_2X_4 + \beta_{CD} X_3X_4 + \beta_{ABC} X_1X_2X_3 + \beta_{ACD} X_1X_3X_4 + \beta_{ABD} X_1X_2X_4 + \beta_{BCD} X_2X_3X_4 + \beta_{ABCD} X_1X_2X_3X_4 \quad (8)$$

where; y is the response, X_1, X_2, X_3 and X_4 are variables, β_0 is the constant coefficient, β_j´s, β_{jj}´s and, β_{jjj}´s are interaction coefficients. The experimental results were evaluated and coefficients of main variables for investigated responses obtained with the least square method and are given in the Tab. 4.

Coefficients values are representing impact of that factor, i.e. interaction, on the response of the process. It can be seen from the Tab. 4 that the most significant factor for TOC and electrode mass loss was time (X_4) with constant coefficients of 14.31 and 0.11. For the filtrate volume most significant factor was inlet diesel concentration (X_1) with constant coefficient of 0.66. The most significant interaction for TOC and filtrate volume was between inlet diesel concentration in emulsion and current density with interaction coefficient of 8.83 and 0.21. For electrode mass loss interaction between NaCl concentration and time, and current density and time, were almost equal and were 0.02 and 0.03.

Table 3. 2^4 full factorial design and results of experiments.

Run no.	Coded Value				TOC (mg kg^{-1})	Δm_A (g)	V_f (mL)	η (%)	U_{TOC} (%)
	X_1	X_2	X_3	X_4					
1	1	1	1	0	146.7	0.074	188	37.84	99.77
2	0	0	1	0	121.2	0.038	35	73.68	99.30
3	0	1	0	0	119.0	0.050	27	28.00	99.31
4	1	0	1	0	123.9	0.072	210	38.89	99.81
5	0	0	0	1	116.5	0.242	90	34.71	99.33
6	1	1	0	1	118.5	0.137	197	61.31	99.82
7	1	0	1	1	106.3	0.279	136	60.22	99.84
8	0	1	1	1	105.1	0.278	64	60.43	99.39
9	1	0	0	0	190.8	0.045	177	31.11	99.71
10	1	0	0	1	130.8	0.155	120	54.19	99.80
11	1	1	0	0	184.7	0.082	96	17.07	99.72
12	0	1	1	0	127.9	0.098	28	28.57	99.26
13	0	0	1	1	118.6	0.398	95	42.21	99.32
14	0	0	0	0	134.9	0.028	18	50.00	99.22
15	0	1	0	1	124.9	0.158	35	53.16	99.28
16	1	1	1	1	112.0	0.228	234	73.68	99.83
17	0	1	1	0	138.4	0.094	35	29.79	99.20
18	1	1	0	1	129.1	0.121	183	69.42	99.80
19	0	0	1	0	123.5	0.046	38	60.87	99.29
20	0	1	1	1	100.5	0.269	59	62.45	99.42
21	0	0	1	1	106.8	0.264	100	63.64	99.38
22	0	0	0	1	107.3	0.108	88	77.78	99.38
23	1	1	1	0	118.0	0.077	200	36.36	99.82
24	1	0	1	1	93.8	0.247	130	68.02	99.86
25	0	1	0	0	120.0	0.060	27	23.33	99.31
26	1	0	1	0	119.7	0.075	243	37.33	99.82
27	1	0	0	0	186.7	0.062	179	22.58	99.71
28	0	0	0	0	123.8	0.053	28	26.42	99.29
29	1	1	0	0	176.5	0.053	80	26.42	99.73
30	1	0	0	1	108.9	0.163	143	51.53	99.83
31	1	1	1	1	103.7	0.282	245	59.57	99.84
32	0	1	0	1	115.1	0.169	47	49.70	99.34

Table 4. Calculated values of coefficients for Eq. 8 for responses: TOC, Δm_A i V (filtrate).

	β_0	β_A	β_B	β_C	β_D	β_{AB}	β_{AC}	β_{AD}
TOC	126.68	7.71	0.83	-10.04	-14.30	-	-8.82	-7.19
Δm_A	0.35	-3.0×10^{-3}	4.3×0^{-3}	0.04	0.11	-	-	-
V (filtrate)	4.45	0.66	-0.07	0.15	0.22	0.08	-	-0.21
	β_{BC}	β_{BD}	β_{CD}	β_{ABC}	β_{ACD}	β_{ABD}	β_{BCD}	β_{ABCD}
TOC	1.58	0.41	3.53	-	6.41	-	3.34	-
Δm_A	-	-0.02	0.03	-	-	-	-	-
V (filtrate)	-	0.04	-	-	-	0.19	-	-

With mathematical model it is possible to predict most important responses of the EC process in the range of the chosen inlet parameters values. In Figs. 2a-c three-dimensional dependences of TOC values vs. inlet diesel concentration, NaCl concentration, current density and time for EC separation of diesel emulsion, are presented in the form of response surfaces. In this way it is easy to see influence of parameters and their interactions on chosen response. On Figs. 2a and 2b it can be seen that response surfaces are curved

which means that influences of X_1X_3 and X_1X_4 on TOC are significant. Response surface on Fig. 2c is almost plane, meaning that X_3X_4 interaction on TOC is less significant.

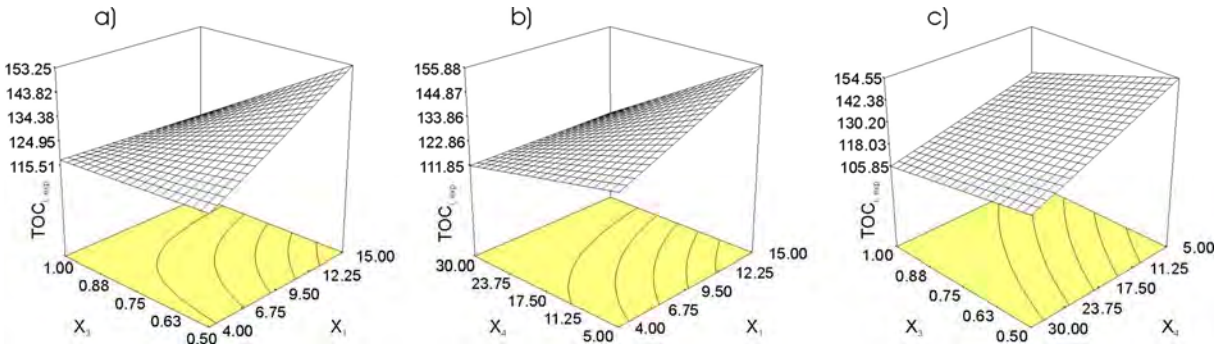

Figure 2. Response surfaces and contour plots of TOC values for EC process

From presented TOC dependences, it can be seen that all experimentally obtained TOC values after EC process are very small. Slightly higher TOC values were obtained for higher diesel fuel concentrations, while lower TOC values were obtained with increased current density and longer reaction time. Still, these differences are very small for given parameters in researched range of values. With current density increase, reaction time for diesel separation is decreasing, same as current efficiency for anode reaction of aluminum dissolution. As hydrocarbon separation efficiency do not change significantly with current density and it is easy to control kinetics and electrical energy consumption of the EC process.

4. Conclusion

With electrocoagulation process successful separation of diesel from aqueous emulsion was achieved, with efficiencies higher than 99%. Obtained filtrate was colorless, odorless and clear, with sludge that could be easily separate from the solution. EC process was empirically described with suitable mathematical model, in which experimentally obtained TOC value do not differ much from values predicted by model.

Obtained results showed a great potential of the EC process as a treatment method for waters contaminated with oil. EC process doesn't require use of any chemicals, allow separation of smallest colloid particles and it is easy to control with low maintenance of the equipment. Limitations of EC process are required high electrical conductivity of the emulsion and relatively short lifetime of the sacrificed anode.

References

1. Fingas, M. F., Charles, J. (2001). *The basics of oil spill cleanup*, Lewis Publishers.
2. Mohammad, Y.A., Morkovskyb, P., Gomesc, J.A.G., Kesmezc, M., Pargad, J., Cockec, D.L. (2004) Fundamentals, present and future perspectives of electrocoagulation. *Journal of Hazardous Materials*, B114, 199-210.
3. Yousuf, M., Mollah, A., Schennach, R., Parga, J.R., Cocke, D.L. (2001) Electrocoagulation (EC)-science and applications. *Journal of Hazardous Materials*, B84, 29-41.
4. Chen, X., Chen, G., Yue, P.L. (2000) Separation of pollutants from restaurant wastewater by electrocoagulation. *Separation and Purification Technology*, 19, 65-76.
5. Timothy B. Spruill, (1988) Use of total organic carbon as an indicator of contamination from an oil refinery, south-central Kansas. *Ground water monitoring review*, 8 (3), 36.
6. Douglas C. Montgomery, (2001) *Design and Analysis of Experiments*, John Wiley & Sons, USA

Proceedings of the 10th International Chemical and
Biological Engineering Conference - CHEMPOR 2008
Braga, Portugal, September 4-6, 2008
E.C. Ferreira and M. Mota (Eds.)

Application of coagulation systems coupled with adsorption on powdered activated carbon to textile wastewater treatment

Franciele R. Furlan, Laís G. M. da Silva, Antônio A. Ulson de Souza, Ayres F. Morgado, Selene M. A. Guelli Ulson de Souza*
UFSC, Universidade Federal de Santa Catarina, Departamento de Engenharia Química e Engenharia de Alimentos, Campus Universitário Trindade, 88040-900, Florianópolis, Santa Catarina, Brasil.

Keywords: Coagulation, Adsorption, Reactive dyes, Aluminum chloride, Reactivation
Topic: Sustainable process-product development through green chemistry.

Abstract

The aim of the present study was to investigate the removal of reactive dyes, Black 5 and Orange 16, through a combined coagulation/adsorption process on activated carbon. A coconut-based powdered activated carbon was used as an adsorbent and aluminum chloride was chosen as the coagulant. In order to obtain the best removal conditions for these dyes, the influence of the following parameters were investigated: coagulant dosage, aqueous solution pH, addition of sodium chloride and the application of increased temperature plus sodium chloride. Adsorption results for the reactive dyes were analyzed by Langmuir and Freundlich isotherm models and showed good correlation. The presence of sodium chloride in the mixture resulted in significant adsorption improvement. The influence of increased temperature plus sodium chloride on the dye removal from aqueous solution showed the feasibility of adsorption and its endothermic nature. Through the reactivation experiments it was verified that the adsorbent can be reused three times, consecutively, after the first adsorption with the virgin carbon. For the final evaluation of the effluent, obtained after the coagulation and adsorption process, acute toxicity tests were carried out with *Daphnia magn*a, and the results obtained showed that the final effluent was not toxic. The combined coagulation/adsorption process was found to be an excellent option for the removal of reactive dyes.

1 Introduction

The removal of dyes from industrial effluents is an extremely complex problem due to the different dye structures and properties and, more importantly, to the majority having a non biodegradable nature (Jain *et al*., 2002). However, many physical, chemical and biological treatment processes have been used for dye removal in order to achieve a better quality effluent. The choice of one or the combination of two or more techniques is dependent on the potential of each technique and on the mechanisms involved in the reduction of the contaminant of interest (Papic *et al.,* 2004, Chakraborty *et al*., 2005, Solmaz *et al*., 2007).

The adsorption of organic compounds on activated carbon is one of the most important technologies used for the treatment of industrial effluents. This adsorbent has a high surface area and a variety of functional groups at its surface (Duan *et al*., 2002, Guilarduci *et al*., 2006).

Many of the materials present in a textile effluent cannot be removed by simple physical separation. In these cases, when the treatment is unsatisfactory, other processes are necessary (Tomaszewska *et al*., 2004).

2 Materials

In this study, a synthetic wastewater was prepared to simulate the characteristics found in textile effluents, with the objective of controlling the effluent composition during the

experimental investigation. Initially, a concentrated solution (2000 mg/L) was prepared from the mixture of the quantities of dyes established and distilled water. All the other solutions used experimentally were obtained through careful dilution of this solution. Next, the pH of the diluted solutions was adjusted with a pH meter to the levels selected with addition of NaOH and 0.1 M HCl.

The experiments were carried out with two non-hydrolyzed reactive dyes, Black 5 (λ =598 nm) and Orange 16 (λ =491 nm). A coconut-based powdered activated carbon with a surface area of 734 m^2/g was used as the adsorbent.

Aluminum chloride ($AlCl_3.6H_2O$ – 99.5 % purity) was used as the coagulant having a molecular mass of 241.43 g/mol. The dye concentration was evaluated using spectrophotometry (Shimadzu Model: UV-1240) at the wave of maximum absorbance.

3 Methods

The chemical coagulation experiments were carried out in static reactors (*Jar test*) using 1 L of solution in each reactor at a temperature of 25 ± 1ºC. The samples were allowed to settle for a period of 1h after 1 min 40 s of rapid mixing (175 rpm) and 10 min of slow mixing (15 rpm). At the end of the sedimentation period aliquots were removed at 2 cm below the surface of the effluent for the determination of the residual color. The optimum dosage of coagulant and pH of the mixture in the coagulation process were determined.

The experimental adsorption tests were carried out with the pre-treated synthetic effluent using the activated carbon adsorbent. Kinetic and equilibrium data were determined and the influence of pH, salt addition (NaCl) and increased temperature plus salt addition on the dye removal using the adsorption process was investigated.

In the preparation of the reactivated carbon, the material precursors of successive adsorptions were dried in an oven for 4 hours and then prepared for carbonization before subsequent chemical activation with acetic acid 1M. After the pore activation stage, the activated carbon was dried in an oven at 110ºC for a period of 4 hours.

The experimental data on the variation of the solute concentration adsorbed in the solid phase (adsorbent) as a function of the equilibrium concentration in the fluid phase were adjusted using the Langmuir and Freundlich models.

The tests with the bioindicator *Daphnia magna* were carried out according to the ABNT standard (1993), and results were expressed as the Factor of Dilution (FD). The FD represents the first of a series of sample dilutions at which acute toxic effects to the test organism are no longer observed (FATMA, 2002). The time for which the test organism was exposed to the effluent was 48 hours, after which the number of immobile organisms was observed and recorded. According to the legislation (article n°017/02 of FATMA), the maximum dilution factor for an effluent of textile origin is two (FATMA, 2002).

4 Results

4.1 Coagulation Tests: Optimum pH and Coagulant Dosage

In the Jar Test experiments the pH values were varied from 4 to 12 in order to obtain the most favorable pH for the color removal. The best results were obtained in the acid region of pH 4 to 7, the greatest removal percentage being obtained at pH 6 for the two dyes under study, as shown in Figure 1a. Similar results were reported by Kim *et al*. (2004) for a chemical treatment by coagulation with removals of 71.7% at pH 6 and 93.9% at pH 5, for dyes Blue 106 and Yellow 54, respectively. The subsequent experiments were thus carried out at the pre-determined pH value of 6, varying the coagulant dosage from 150 mg/L to 750 mg/L. The dye removal as a function of the coagulant concentration is shown in Figure 1b. The removal efficiency for both dyes increased with an increase in the coagulant dosage up to a certain dosage and then remained constant for the dye Black 5 and reduced gradually for Orange 16. The maximum efficiency of color removal was for a coagulant dosage of 200

mg/L, for Black 5 and for Orange 16 the maximum removal was obtained with 250 mg/L of coagulant.

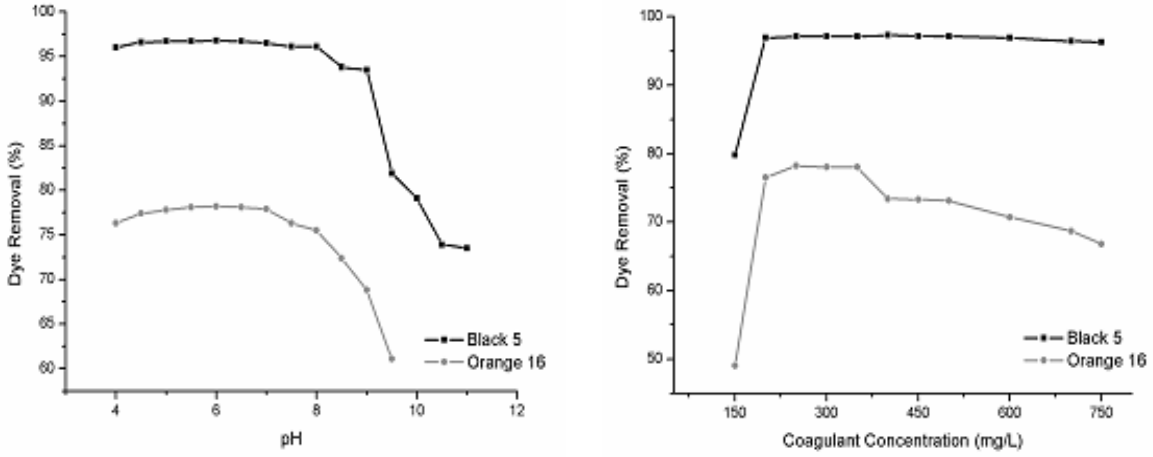

(a) (b)

Figure 1: Optimization of the parameters in the pre-treatment stage for reactive dye removal: (a) pH (b) coagulant concentration

4.2 Influence of pH on the adsorption process

The influence of pH on the dye adsorption on activated carbon was analyzed through data on the adsorption kinetics and isotherms, in order to select the most favorable pH for the adsorption of the dye by the carbon. Through the kinetic experiments it was verified that the time to reach equilibrium was approximately 380 minutes, for all the pH values investigated. The kinetics data allowed the construction of the adsorption isotherms, shown in Figure 2, for the pH values of 2, 3, 4 and 7, respectively. The maximum adsorption capacity, as shown in Figure 2, increased from 16.6 to 19 mg/g with an increase in the pH from 2 to 3. However, it decreased to 5.8 mg/g with a pH of pH 7. Thus, it can be concluded that pH 3 is the optimum pH for the color removal process.

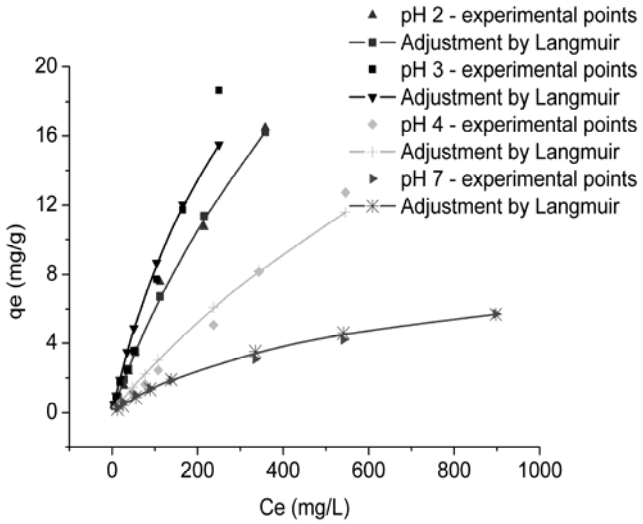

Figure 2: Langmuir isotherms for the different pH values.

4.3 Influence of the Addition of Sodium Chloride

Identical solutions were used for the kinetic experiments, varying only the values of sodium chloride between 0, 1, 3, 6 and 10% (by mass). Equilibrium was reached in approximately

340 minutes for solutions containing salt. In the case of solutions without salt, the adsorption was a little slower and equilibrium was reached in 380 minutes for both dyes. The values for the Langmuir parameters ($q_{máx}$) were calculated from the isotherms for addition of different quantities of sodium chloride to Black 5 and Orange 16. It was found that the maximum adsorption capacity increased from 19 to 87.7 mg/g with an increase in the quantity of sodium chloride from 0% to 6%. However, it decreased to 43.7 mg/g with an increase in the quantity of sodium chloride to 10%. In relation to the dye Orange 16, it was verified that the adsorption capacity increases from 27.5 to 74.1 mg/g with an increase in the quantity of sodium chloride from 0% to 1%.

Thus, 6 and 1% of sodium chloride appear to be the optimum quantities to improve the color removal process for the dyes Black 5 and Orange 16, respectively.

According to Guelli U. Souza *et al*. (2008), the presence of salt promotes the adsorption of positive charges when compared with experiments in its absence. This may indicate that the salt cations neutralize the negative charge on the surface of the carbon, increasing the adsorption of molecules.

4.4 Influence of increased temperature plus Salt Addition

Increased temperature combined with sodium chloride addition (6% of the aqueous solution mass for the dye Black 5 and 1% for Orange 16) was found to improve the adsorption process. The time required for equilibrium to be reached was approximately 300 minutes, for the two dyes under study. On analyzing the Langmuir parameters, it was verified that the maximum adsorption capacity increased with the increase in the temperature from 87.7 mg/g at 25ºC to 95 mg/g at 70°C for the dye Black 5, and from 73.5 mg/g at 25ºC to 99.7 mg/g at 70°C, for Orange 16. These results indicate the endothermic behavior of this adsorption process. This result is consistent with that reported by Senthilkumaar *et al*. (2006), where the capacity for adsorption of the dye Crystal Violet increased by 40% when the temperature was increased from 28 to 48 °C.

4.5 Reactivated Carbon Tests

Through the reactivation experiments, it was found that the adsorbent can be reused three times, consecutively, after the first adsorption with the virgin carbon. The time for the solutions with reactivated adsorbent to reach equilibrium was approximately 340 min; in the case of the solution with the virgin carbon, the equilibrium adsorption was reached in 300 min. Figure 3 shows the Langmuir isotherms obtained for the cases of adsorption with the virgin carbon and its respective reactivations. It is possible to verify in Figure 3 that the values for the maximum adsorption capacity, q_m, were 95, 80, 44.4 and 28 mg/g for the virgin carbon and the first, second and third reactivations, respectively.

For the four pH values studied, R_L varies between 0.206 and 0.976 ($0 < R_L < 1$), and the Freundlich coefficient, n, varies between 0.671 and 0.939 ($0 < n < 1$), confirming conditions favorable for adsorption.

For the cases of sodium chloride addition, R_L varied between 0.283 and 0.976 ($0 < R_L < 1$), and the Freundlich coefficient, n, between 0.756 and 0.918 ($0 < n < 1$).

For the three reactivation cases, R_L varied between 0.292 and 0.940 ($0 < R_L < 1$), and the Freundlich coefficient, n, between 0.836 and 0.867, confirming conditions favorable for adsorption ($0 < n < 1$).

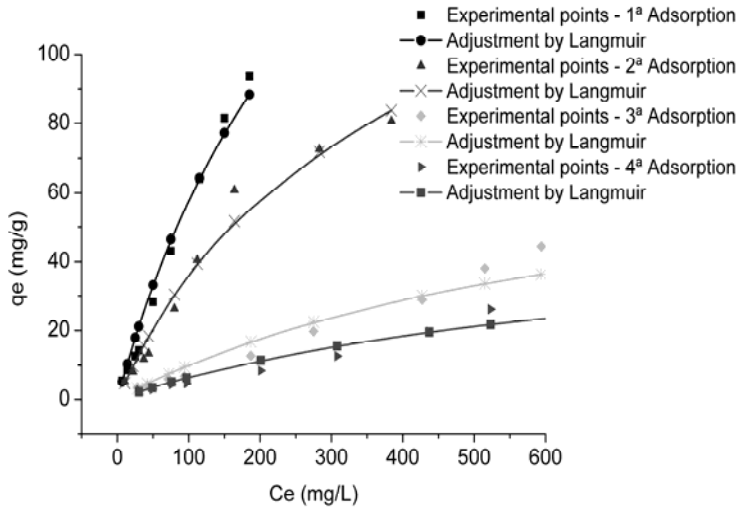

Figure 3: Langmuir isotherms for the adsorption with the virgin carbon and three reactivations.

4.6 Acute Toxicity Tests

The results with the bioindicator *Daphnia magna* showed that the dilution factor for the untreated effluent was 256, which is still higher than the maximum value allowed for textile industry effluent, indicating that it is necessary to carry out treatment before the effluent can be discarded to water bodies in compliance with the legislation in force. The toxicity of the solution reduced considerably after pre-treatment with coagulation/flocculation, with a dilution factor of 16. It is evident that the dye under study (Reactive Black 5) has a toxic effect on the test organism. After the complete treatment process it was verified that the effluent was not toxic (dilution factor = 1), indicating that, in achieving the complete removal of color, the chemical products used during the pre-treatment stage do not increase the effluent toxicity at the end of the process.

5 Conclusions

The aluminum chloride coagulant demonstrated good results, and is suitable for the treatment of aqueous solutions containing reactive dyes. The best dosage found was 200 mg/L for Black 5 and 250 mg/L for Orange 16.

The pH had a strong influence on the medium under study; the color removal process was favored in the acid region, pH 6 and 3 showing high efficiency for coagulation and adsorption, respectively. The use of this adsorbent in final wastewater treatment processes is not recommended in cases where it is necessary to neutralize the effluent to comply with environmental legislation, considering that for the best adsorbent performance acid solutions are required.

The addition of sodium chloride to the synthetic wastewater favored the adsorption process, and the influence of increased temperature plus salt addition had an endothermic nature.

The reactivation experiments revealed that the adsorbent could be reused three times, consecutively, after the first adsorption with the virgin carbon.

In the evaluation of the acute toxicity with the bioindicator *Daphnia magna* as the test organism, the complete treatment process, besides having a good dye removal efficiency, reduces the toxicity of the final effluent.

6 References

Associação Brasileira de Normas Técnicas (ABNT) (1993). NBR 12713: *Água–ensaio de toxicidade aguda com Daphnia sp.* (Crustacea, Cladocera). Rio de Janeiro.

Chakraborty, S., De, S., Basu, J.K., Dasgupta, S. (2005). Treatment of a textile effluent: application of a combination method involving and nanofiltration. *Desalination*, 174, 73-85.

FATMA (2002). *Limites máximos de toxicidade aguda para efluentes de diferentes origens***.** Portaria nº 017/02 – 18 abril.

Duan, J., Wilson, F., Graham, N., Tay, J.H. (2002). Adsorption of humic acid by powdered activated carbon in saline water conditions. *Desalination*, 151, 53–66.

Guelli U. Souza, S.M.A., Peruzzo, L.C., Souza, A.A.U. (2008). Numerical study of the adsorption of dyes from textile effluents. *Applied Mathematical Modelling*, 32, 1711-1718.

Guilarduci, V.V.S., Mesquita, J.P., Martelli, P.B., Gorgulho, H.F. (2006). Adsorção de fenol sobre carvão ativado em meio alcalino. *Revista Química Nova*, 29, 1226-1232.

Jain, A. K., Suhas, Bhatnagar, A. (2002). Methylphenols removal from water by low-cost adsorbents. *Journal of Colloid and Interface Science*, 251, 39–45.

Kim, T., Park, C., Shinb, E., Kim, S. (2004). Decolorization of disperse and reactive dye solutions using ferric chloride. *Desalination,* 161, 49-58.

Papic, S., Koprivanac, N., Bozic, A.L., Metes, A. (2004). Removal of some reactive dyes from synthetic wastewater by combined Al(III) coagulation/carbon adsorption process. *Dyes and Pigments*, 62, 291-298.

Senthilkumaar, S., Kalaamani, P., Subburaam, C.V. (2006). Liquid phase adsorption of Crystal violet onto activated carbons derived from male flowers of coconut tree. *Journal of Hazardous Materials,* B136, 800-808.

Solmaz, S.K.A., Üstün, G.E., Birgül, A., Tasdemir Y. (2007). Treatability studies with chemical precipitation and ion exchange for an organized industrial district (OID) effluent in Bursa, Turkey. *Desalination*, 217, 301-312.

Tomaszewska, M., Mozia, S., Morawski, A.W. (2004). Removal of organic matter by coagulation enhanced with adsorption on PAC. *Desalination*, 161, 79–87.

Acknowledgements

The authors are grateful to CAPES for the financial support given by way of the scholarship and to FINEP for financing the project INOTEXTIL, in partnership with the Brazilian textile companies: Buettner, Coteminas, Brandili and Tapajós.

Proceedings of the 10th International Chemical and
Biological Engineering Conference - CHEMPOR 2008
Braga, Portugal, September 4-6, 2008
E.C. Ferreira and M. Mota (Eds.)

Treatment of Wastewater Polluted with Urea by Counter-current Thermal Hydrolysis in an Industrial Urea Plant

M. M. Barmaki, **M. R. Rahimpour***, **A. Jahanmiri**

Department of Chemical Engineering, School of Engineering, Shiraz University, P.O. Box 71345, Shiraz, Iran

Keywords: Urea thermal hydrolysis, Liquid non-ideality, Nakamura equation state, Modeling,
Topic: Industrial case studies & Environmental and food process and product modeling.

Abstract

In this work, the removal of urea from industrial wastewater by thermal hydrolysis is studied. The features of our model are (1) the use of Nakamura equation state and UNIQUAC equation for describing vapor and liquid equilibrium, (2) the use of multistage well-mixed for liquid and vapor flows with non-ideal rate-based, (3) the reaction assumed to take place in liquid phase. The model incorporates reaction rate of urea hydrolysis and takes into account the effects of solution non-ideality and back-mixing on the reactor performance. The rate of reaction is written in terms of activity of reactants which are determined using a thermodynamic framework for system of NH_3–CO_2–H_2O–urea mixture.

The model provides temperature and concentration distribution of different components in liquid and vapor phases along the height of reactor. Also the effects of key parameters on the performance of urea hydrolyser such as the steam flow rate and the temperature of wastewater has been examined. The result of this work shows that an increasing of inlet temperature of wastewater and steam flow rate improves the urea removal efficiency. The predicted data of the model are consistent with the plant data indicating the validity of the model.

Introduction & Process

A urea plant produces water as well as urea. This water, which is contaminated, mainly by entrainment from the evaporation section, requires treatment if it is to be reused again. This process condensate generally contains about 2 to 9 percent by weight ammonia, 0.8 to 6 percent by weight carbon dioxide and 0.3 to 1.5 percent by weight urea.

It is now recognized by both the urea industry and the responsible governmental agencies that having urea-containing effluent streams may create possible environmental hazards. Therefore, several processes have been suggested for treating these urea-containing streams due to environmental restrictions. Which in the past decade, 100 ppm of urea was considered acceptable, but today's requirements mostly call for a maximum concentration of 10 ppm (Rahimpour, 2004).

A modern wastewater treatment consists mainly out of a first desorber column, which reduces the ammonia and carbon dioxide contents. For the next column, the hydrolyser, it is important that the ammonia and carbon dioxide concentrations at the inlet are sufficiently low, in order, not to reach the chemical equilibrium. Under these conditions the hydrolisation reaction proceeds towards the ammonia and carbon dioxide side, reducing the urea content to virtually zero.

* Corresponding author, Phone: +987112303071, Fax: +987116287294;
E-mail: rahimpor@shirazu.ac.ir (Prof. M. R. Rahimpour)

Contrary to other commercial hydrolysers, this hydrolyser is operated as a counter-current bubble column to improve the efficiency; water with urea meets continuously relatively clean vapours during its way through the column from the top to the bottom. The urea outlet of the hydrolyser is decreased to ppm level. In the second desorber column again operating at low pressure, the ammonia and carbon dioxide content are also decreased to ppm level.

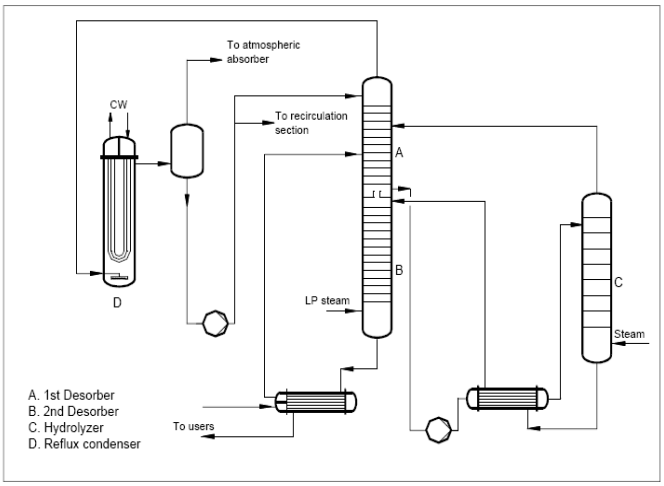

There is no information available in the literature regarding the modeling and simulation of an industrial urea removal process by counter-current thermal hydrolysis method. Therefore, we decided to study more thoroughly the phenomenon of urea removal from industrial wastewater (Rahimpour and Azarpour, 2005).

Figure 3. Process Water Treatment System (khorasan petrochemical complex, 2008)

Reaction Scheme:

The urea first reacts with water to generate ammonium and carbamate ions, then ammonium and carbamate ions react to yield carbon dioxide and ammonia liquid:

$$NH_2CONH_2(l) + H_2O(l) \Leftrightarrow H_2NCOO^- + NH_4^+ \qquad \Delta H_{298} = -23 \ \frac{kJ}{mol} \qquad (1)$$

$$H_2NCOO^- + NH_4^+ \Leftrightarrow 2NH_3(l) + CO_2(l) \qquad \Delta H_{298} = 84 \ \frac{kJ}{mol} \qquad (2)$$

Reaction (1) is slow and exothermic, while reaction (2) is endothermic and fast in both directions, so that it could be considered at equilibrium under the conditions found in industrial thermal hydrolyser (Isla, Irazoqui, and Genoud, 1993). Therefore reaction (1) is the rate controlling step and its rate is considered as the overall rate of urea hydrolysis. For chemical reactions in thermodynamically non-ideal systems, as shown elsewhere (R.J. Madon and E. Iglesia, 2000), the rate becomes:

$$R = k_f\left(a_1a_2 - \frac{1}{K_{e,1}}a_3a_4\right) = k_f\left[(\gamma_1C_1)(\gamma_2C_2) - \frac{1}{K_{e,1}}(\gamma_3C_3)(\gamma_4C_4)\right] \qquad (3)$$

Where k_f is the forward reaction rate constant *($k_f=k_0\ exp(-E/RT)$)* and $K_{e,1}$ is the equilibrium constant of reaction (1). The experimental values of the preexponential factor and the activation energy in the Arrhenius expression of k_f are k_0 =3.75×10^7 *m^3/kmolh* and E =87780.3 *kJ/kmol* respectively (Aoki et al, 1999).The equilibrium constant for reactions (1) and (2) are defined as follows:

$$K_{e,j}(T) = K_{X,j}(X)K_{\gamma,j}(T,X); \quad j = 1,2 \qquad (4)$$

The following functional form:

$$\ln K_j(T) = \left(\frac{U_{1,j}}{T}\right) + U_{2,j}\ln T + U_{3,j}\,T + U_{4,j} \qquad (5)$$

was adopted to describe the temperature dependence of the *r* reaction equilibrium constant (Anderson et al, 1978). In the above equation, U_j is a constant related to reaction of number j where tabulated in Table 1.

Thermodynamic modeling

Table 1.	parameters			
function	U_1	U_2	U_3	U_4
$\ln K_{e,1}$	-31363	-64.26	-0.0595	482.11
$\ln K_{e,2}$	-11046	-5.19	0.01115	51.47

Urea processes are challenging to model from a thermodynamic point of view. In this study, the thermodynamic framework to describe liquid activity coefficients of molecular species in NH_3–CO_2–H_2O–urea system is based on the model developed by Isla et al. The liquid phase contains physically dissolved and chemically combined components that are mainly present as ions and molecules, namely H_2O(1), H_2NCONH_2(2), H_2NCOO^-(3), NH_4^+(4), CO_2(5), NH_3(6). The volatility of urea and ammonium carbamate are negligible and ions cannot leave from liquid phase to vapor phase, so there are only three molecular components including H_2O, NH_3, and CO_2 in the vapor phase.
In this work because of existence of gaseous mixture containing highly polar molecules (ammonia, water) and nonpolar molecule (carbon dioxide), a semiempirical equation of state (perturbed-hard-sphere (PHS) equation of state) is proposed which provides accurate estimates of thermodynamic properties for this gas mixture (Nakamura, Bread, and Prausnitz,1975).

Model development

The feed to the urea thermal hydrolysis reactor consists of liquid (water rich) stream entering from the top and pure high pressure steam stream entering from the bottom as the stripper. The movement of bubbles through the liquid phase causes mixing in the liquid phase. Moreover, there are several perforated plates at different levels inside the reactor in order to prevent back mixing and further mixing between the two phases. In this way a substantially zigzagging flow path of the liquid is created which crosses the substantially vertical flow path of the gaseous phase.
Therefore, for simulation purposes it will be approximated as a series of continuous multi-stage stirred tank reactors (CSTRs). Rahimpour et al. (2004) considered the whole co-current urea thermal hydrolysis reactor as a sequence of continuously stirred tank reactor (CSTRs). The same approach has been adopted in the present study for the hydrodynamic behavior of the counter-current urea hydrolysis reactor. The CSTRs in sequences will be referred to as stages, numbered from top to bottom. Stage 0 and 14 are index of specifications of liquid feed and steam streams respectively. The reaction kinetics is appropriately incorporated in the component balances. The enthalpy balances are expressed in terms of enthalpies of formation, which excludes the need for reaction enthalpies in these balances.

$$M_{i,j} \equiv V_{j+1}y_{i,j+1} + L_{j-1}x_{i,j-1} + \alpha_{i,1}H_j r_j + \alpha_{i,2}w - V_v y_j - L_j x_j = 0 \qquad \mathrm{i}=1,\ldots,\mathrm{M} \qquad \mathrm{j}=1,\ldots,\mathrm{N} \qquad (6)$$

$$H_j \equiv \sum_i^M V_{i,j+1}H_{i,j+1}^v + \sum_i^M L_{i,j-1}H_{i,j-1}^l - \sum_i^M V_{i,j+1}H_{i,j+1}^v - \sum_i^M L_{i,j}H_{i,j}^l = 0 \qquad \mathrm{j}=1,\ldots,\mathrm{N} \qquad (7)$$

$$E_{i,j} \equiv K_{i,j}x_{i,j} - y_{i,j} = 0 \qquad \mathrm{i}=1,\ldots,\mathrm{M} \qquad \mathrm{j}=1,\ldots,\mathrm{N} \qquad (8)$$

$$S_j^x \equiv \sum_i^M x_{i,j} - 1 = 0 \quad , \quad S_j^y \equiv \sum_i^M y_{i,j} - 1 = 0 \qquad \mathrm{j}=1,\ldots,\mathrm{N} \qquad (9)$$

$$P_j \equiv p_{j+1} - \Delta p_j - p_j = 0 \qquad \mathrm{j}=1,\ldots,\mathrm{N}\text{-}1 \qquad (10)$$

Model validation

The validation of steady state model was carried out by comparison of model results with the plant data under the design specifications and input data. The model results and the

corresponding observed data of the plant are presented in Table 2. It was observed that, the steady state model performed satisfactorily well under industrial conditions and a good agreement was obtain between plant data and simulation data which confirm that the proposed model can be considered suitable and reliable.

Comparison of calculated results with the observed plant data under the design specifications and input data (khorasan petrochemical complex, 2008)

Table 2.	Liquid phase output			Vapor phase output		
	observed	model	Error	observed	model	Error
Temperature (°C)	207	207.6	+0.3%	194.2	193.3	0.5%
Component molar rate ($kmol/h$)						
Water	2066.7	2070.5	+0.2%	48.15	44.37	-7.8%
Urea	<10ppm	7ppm	-	0	0	0
CO_2	0.15	0.14	-6.7%	10.18	10.16	-0.2%
NH_3	33.63	33.33	-0.9%	3.91	4.19	+7.1%
Total ($kmol/h$)	2100.48	2103.97	+0.2%	62.24	58.72	-5.6%

Result & discussions

The simulation results were plotted as profiles of the dependent parameters versus independent variables. In addition, the effects of different parameters on the urea removal performance were investigated.

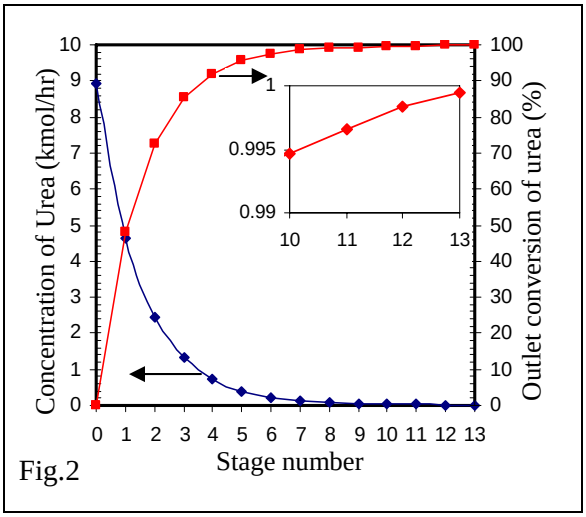

Fig.2

Figure 2 shows conversion and concentration of urea along the hydrolyser. It should be noted that the outlet urea content of the hydrolyser is virtual zero due to hydrolysis reaction and conversion is approximately complete. As liquid moves from top to bottom of the hydrolyser, it undergoes changes in temperature, which is shown in Fig. 3. It can be seen that there are two parts in this figure. At the first segments of hydrolyser, the temperature of reacting material decreases owing to the endothermic reaction, then increases by the injection of high pressure steam as demonstrated in. Figures 4-6 show the concentration profiles of ammonia, carbon dioxide and water along the reactor in the liquid and vapor phases. As can be seen in figure 4 and 5, concentrations of the ammonia and carbon dioxide increase in the liquid phase. These profiles clearly show the production of these components due to reaction as liquid moves down the hydrolyser. Inlet temperature of wastewater has an influence on the removal performance as demonstrated in figure 7. This figure indicates the increasing the inlet temperature of wastewater improves the removal performance due to endothermic reaction. The role of steam mass flow rate in urea removal for a specified inlet wastewater temperature is shown in Figure 8. As can be seen from this figure, higher steam mass flow rate maintains a higher temperature level in the reactor which would cause changes in liquid temperature profile and in extent of hydrolysis reactions. In addition, enhances the urea removal efficiency.

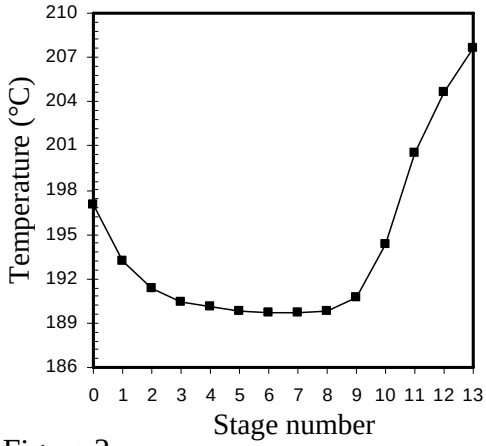

Figure 3

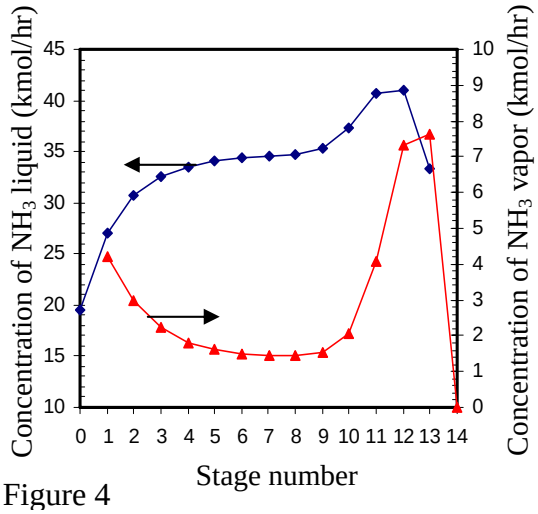

Figure 4

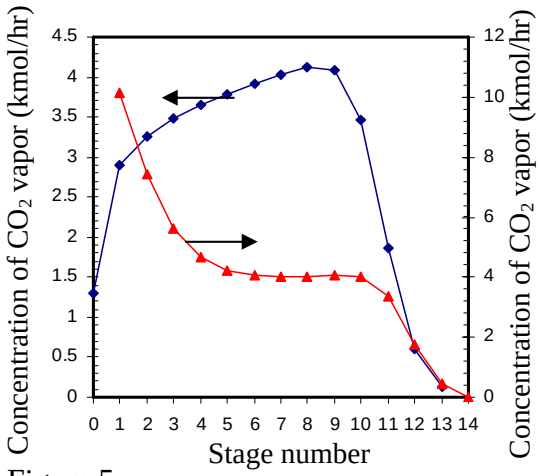

Figure 5

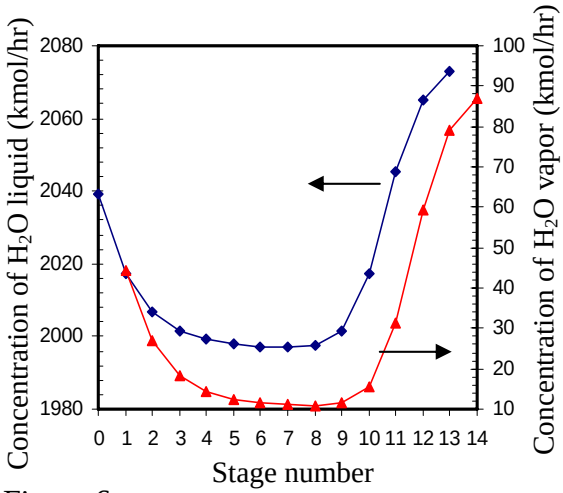

Figure 6

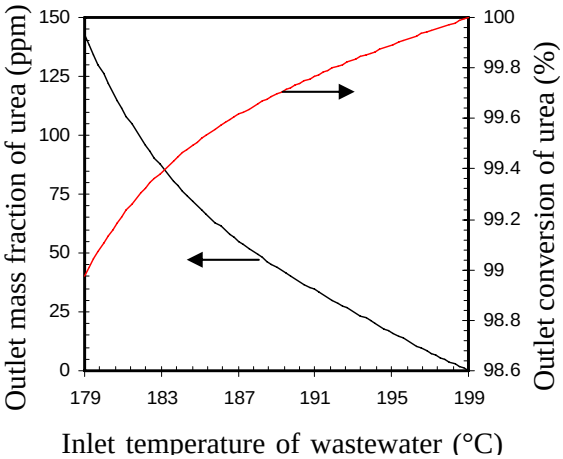

Figure 7

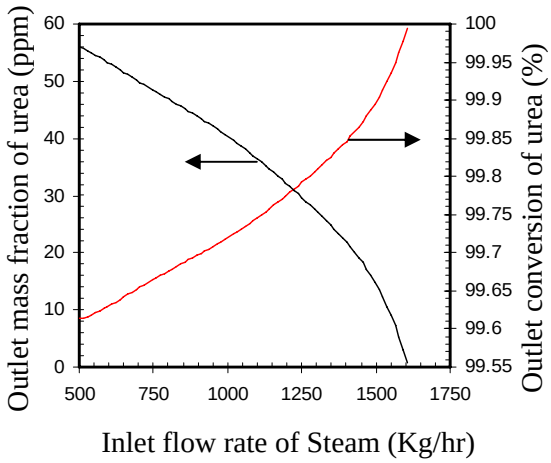

Figure 8

Conclusion

Urea thermal hydrolyser can remove urea from waste stream effectively, so that all components including the water can be recycled and reused in the plant. The model could be used to study the effects of process variables, such as temperature of wastewater and flow rate of steam on the reactor performance. It is also useful for a better control of the currently operating units and in the design of new hydrolysis plants.

Nomenclature

C_i	concentration of component i (kmolm^{-3})
E	activation energy (kJ kmol^{-1})
F_i	molar flow rate of component i (kmol h^{-1})
H_i	Liquid holdup in stage j (m^3)
$H_{i,j}^{v}$	Enthalpy of component i in vapor phase in stage j (kj/kmol)
$H_{i,j}^{l}$	Enthalpy of component i in liquid phase in stage j (kj/kmol)
ΔH	heat of reaction (kJ kmol^{-1})
i	component number
j	stage number
$K_{i,j}$	the equilibrium constant
K_0	pre-exponential factor of urea hydrolysis rate constant (m^3 kmol^{-1} h^{-1})
$K_{e,1}$	the equilibrium constant of reaction 1
K_f	the forward reaction rate constant (m^3 kmol^{-1} h^{-1})
$K_{x,j}$	equilibrium constant of reaction j dependent on temperature and mole fraction
$K_{\gamma,j}$	equilibrium constant of reaction j dependent on mole fraction
L_j	mole flow rate of liquid in stage j (kmol h^{-1})
M	Number of components
N	Number of stages
$L_{i,j}$	liquid mole flow rate of component i in stage j (kmol h^{-1})
P_j	Peressure of stage j (bar)
ΔP_j	pressure drop (bar)
r	overall rate of reaction (kmolm^{-3} h^{-1})
T	temperature (K)
U	constant Eq.5
V_j	mole flow rate of vapor in stage j (kmol h^{-1})
$V_{i,j}$	vapor mole flow rate of component i in stage j (kmol h^{-1})
w	consumption molar flow rate of carbamate in reaction (2) (kmol h^{-1})
x_i	mole fraction of component i in liquid phase
y_i	mole fraction of component i in vapor phase

Greek letters

$\alpha_{l,1}$	stoichiometric coefficient of species i in reaction 1
$\alpha_{l,2}$	stoichiometric coefficient of species i in reaction 2
γ_i	activity coefficient of component i

Reference

Rahimpour, M. R., Azarpour, A. (2005). Simulation of a Urea Thermal Hydrolysis Reactor, Chem. Eng. Comm., 192: 155–167

Rahimpour, M.R. (2004). A non-ideal rate-based model for industrial urea thermal hydrolyser, Chem. Eng and Processing 43 ,1299–1307

Isla, M. A., Irazoqui, H. A., Genoud, C. M. (1993). Simulation of a urea synthesis reactor. Part 1. Thermodynamic framework, Ind. Eng. Chem. Res. 32, 2662–2670

Khorasan Petrochemical Complex, Urea Plant, Operating Data of Urea Thermal Hydrolysis Process, 2008.

R.J. Madon, E. Iglesia, (2000). Catalytic reaction rates in thermodynamically non-ideal systems, J. Mol. Catal. A: Chem. 163, 189–204.

H. Aoki, T. Fujiwara, Y. Morozumi, T. Miura, (1999). in: Proceedings of the Fifth International Conference on Technologies and Combustion for a Clean Environment, Lisbon, pp. 115–118.

T.F. Anderson, D.S. Abrams, E.A. Grens, (1978). Evaluation of parameters for nonlinear thermodynamics models, AICHE J. 24, 20–29.

Nakamura, R. C., Bread, V. J. F., & Prausnitz, J. M. (1975). Thermodynamic representation of gas mixtures containing common polar and nonpolar components. *Industrial and Engineering Chemistry, Product Research and Development*, *15*, 557.

Proceedings of the 10th International Chemical and
Biological Engineering Conference - CHEMPOR 2008
Braga, Portugal, September 4-6, 2008
E.C. Ferreira and M. Mota (Eds.)

Tertiary Treatment of Slaughterhouse Wastewater using Ferric Coagulation Followed by UV or UV/H_2O_2 processes

Danielle B. Luiz[1*], Aziza K. Genena[1], Humberto J. José[1], Regina F. P. M. Moreira[1], H.Fr. Schröder[2]

[1] LEMA – Laboratory of Energy and Environment, Chemical and Food Engineering Department, Technology Center, Federal University of Santa Catarina, 88040-900 - C.P. 476, Florianópolis, Brazil

[2] ISA – Institute of Environmental Engineering, Environmental Analytical Laboratory, RWTH Aachen University, Krefelder Str. 299, D-52070 Aachen, Germany

Keywords: Hydrogen peroxide (H_2O_2), Kinetics, UV radiation, Slaughterhouse, Water reuse.
Topic: Sustainable process-product development through green chemistry.

Abstract

Guidelines and regulations, with respect to the use and reuse of water or wastewater in the food industry, have been created which accepted or do not restrict the use of non-potable water as process water or water treated for direct reuse as drinking water. However, careful analysis is needed in each case based on a complete knowledge of the risk involved for the safety of the food production and the health of the consumers. Advanced oxidative processes (AOP) increasingly are studied to provide treated water as a source of indirect reuse with or without characteristics of drinking water, however, excluding any risk to product integrity, environment and health of distributers and consumers in household and industry. To ensure that these topic will be reached our objectives in this study were to evaluate the kinetics of the degradation of wastewater constituents, e.g., especially compounds with aromatic structures using UV or UV/H_2O_2, in order to achieve the characteristics for a subsequent water reuse.

1 Introduction

The necessity to save water as the most important food stuff of man is crucial because of the finite nature of this resource. Therefore, the sustainable use of water demands the direct reuse of water. The consumption of water in many parts of the world is increasing in household, agrarian and industrial activities. Confronted with these issues, agencies world-wide have recognized and stimulated the implementation of techniques to treat wastewater to such an extent that characteristics of drinking water quality will be reached to make a direct or indirect wastewater reuse possible according to the Codex Alimentarius (2001). Advanced biological treatment techniques in combination with physicochemical and/or chemical treatment steps were performed. Thus advanced oxidation processes (AOP) have developed as a powerful tool to degrade organic pollutants via oxidation transforming the vast majority of organic contaminants in carbon dioxide, water and inorganic ions when applied after an effective biological treatment. The degradation reactions involve transitional oxidants such as hydroxyl radicals (●OH). These radicals can be generated by reactions involving strong oxidants such as ozone (O_3) and hydrogen peroxide (H_2O_2), ultraviolet radiation (UV), and semiconductors such as titanium dioxide and zinc oxide.

The reaction mechanism of hydrogen peroxide photolysis by UV radiation and degradation of organic compounds (RH) by the action of hydroxyl radicals are divided into four stages of reactions (eq. 1-8): Initiation, propagation, termination and decomposition (Alfano et al., 2001):

* Corresponding author. Tel + 55 48 37219448, r. 240. E-mail: danielledebem@yahoo.com.br

Initiation: (1) $H_2O_2 \xrightarrow{h\nu} 2 \bullet OH$

Propagation: (2) $H_2O_2 + \bullet OH \xrightarrow{k_2} HO_2 \bullet + H_2O$

(3) $H_2O_2 + HO_2 \bullet \xrightarrow{k_3} \bullet OH + H_2O + O_2$

Termination: (4) $2 \bullet OH \xrightarrow{k_4} H_2O_2$

(5) $2HO_2 \bullet \xrightarrow{k_5} H_2O_2 + O_2$

(6) $\bullet OH + HO_2 \bullet \xrightarrow{k_6} H_2O + O_2$

Decomposition: (7) $RH + \bullet OH \xrightarrow{k_7} \text{products}$

(8) $RH + HO_2 \bullet \xrightarrow{k_8} \text{products}$

However, when natural water matrices (e.g., superficial, ground water or wastewater) are used, natural organic matter and alkalinity are the main ●OH scavengers and in addition amplify light scattering. These effects influence the degradation effectiveness for organic compound (Chen et al. 2007). However, the presence of nitrate, iron (III) and organic matter in low concentration can increase the degradation rate due to photo-oxidation of these compounds using UV or other AOP steps in combination with UV, e.g., UV/H_2O_2. Nitrate ions absorb UV light, acting as an internal filter to UV light and in parallel can form hydroxyl radicals (●OH) by the mechanism presented below (eq. 9-13) (Neamtu and Frimmel, 2006).

(9) $NO_3^- \xrightarrow{h\nu} NO_2^- + O$

(10) $NO_3^- \xrightarrow{h\nu} NO_2 \bullet + O \bullet^-$

(11) $NO \bullet + H_2O \longrightarrow NO_2^- + NO_3^- + 2H^+$

(12) $O + H_2O \longrightarrow 2HO \bullet$

(13) $O \bullet^- + H_2O \longrightarrow HO \bullet + HO^-$

At wavelengths larger than 300 nm, aqueous ferric ion complexes can provide ferrous ions and hydroxyl radical undergo photolysis by an internal transfer of electrons (eq. 14) (Espinoza et al., 2007).

(14) $Fe(OH)^{2+} \xrightarrow{h\nu} Fe^{2+} + \bullet OH$

Dissolved organic matter absorbs UV light and can generate reactive radicals such as singlet oxygen, superoxide anions (●O^{2-}), hydroxyl radicals (●OH) and peroxyl radicals (ROO●). These reactive transients can degrade the organic pollutants following different pathways; consequently, they would not be degraded only by direct photolysis (Chin et al., 2004, Neamtu and Frimmel, 2006).

The main objective of this study was to evaluate the degradation kinetics of aromatic compounds applying UV or UV/H_2O_2 in order to achieve the characteristics for water reuse considering the restrictions imposed by Brazilian legislation and hygiene concerns in particular to food industry. Therefore, following those regulations, water reuse must be applied in processes without contacting food product.

2 Materials and methods

2.1 Sample collection and their analysis

Four treated wastewater samples representative of the effluents of the wastewater treatment plant (WWTP) of a Brazilian poultry and swine slaughterhouse were sampled in 2007. The samples were kept in darkness at 4°C to preserve their physicochemical characteristics. The samples differed in their characteristics, as shown in Table 1. The compounds resistant to biological treatment processes were detected and identified by LTQ orbitrap mass spectrometer (Thermo Electron, Germany) applying electrospray ionization (ESI) after liquid chromatography (LC) applying high-resolution mass and tandem mass spectrometry (LC-(HR)MS and -MS^n). Nonylphenols (NP), octylphenols (OP), linear alkylbenzene sulfonates (LAS) and ibuprofen were detected in negative ion mode. In the positive ion mode the precursor compounds of NP and OP, nonylphenol ethoxylates (NPEO), octylphenol ethoxylates (OPEO) and polyethylene glycols (PEG) besides erythromycin, sulfamethoxazole and sulfadimidine were detected and identified.

Table 1 Concentration ranges of the treated wastewater from slaughterhouse

	Range	***DW[a]***
Apparent Color, Pt/Co units	-	15.0
Chemical Oxygen Demand, mg L^{-1}	18.9-95.0	-
Chloride, mg L^{-1}	120.0-150.0	250.0
Nitrate, mg L^{-1}	10.2-17.4	-
pH, at 25°C	7.3-7.6	6.0– 9.5
Real color, mg L^{-1} Pt-Co	33.5-62.2	-
Total coliforms, CFU/100 mL	1000-58000	none
Total iron, mg L^{-1}	3.5-7.0	0.3
Turbidity, FTU	3.8-30.0	5.0
UV_{254} absorbance, m^{-1}	15.2-18.4	-

[a] Limitations for water to be used as drinking water in Brazil.

2.2 Treatments and kinetics

Two different treatment methods were evaluated in order to achieve the drinking water parameters that are required to water reuse in food industry: (A) ferric coagulation followed by UV radiation; and (B) ferric coagulation followed by UV/H_2O_2 treatment. Color, turbidity, total organic carbon (TOC), chemical oxygen demand (COD), total coliforms and aromatic compound content (UV_{254}) were the parameters followed to evaluate the performance of UV and UV/H_2O_2 processes they were measured before and after each treatment step. The combined treatment of coagulation followed by UV aimed to remove turbidity to facilitate UV efficiency in mineralization of pollutants and disinfection.

The optimization of the ferric coagulation process (FC) was performed in jar tests. The stock solution of ferric sulphate was 5 g Fe^{3+} L^{-1}. The volume of wastewater samples used for each beaker in jar test was 300 mL applying an iron concentration in the range of 5 – 25 mg L^{-1} in combination with a pH in the range of 4.5 – 7.0, adjusted by NaOH or H_2SO_4 addition. The experiment using a Fe(III) concentration of 16 mg L^{-1} and a neutral pH resulted in a maximum turbidity removal and therefore, was chosen as optimized condition.

The wastewater in the UV batch reactor (Trojan UV MaxTM, Model E) was radiated by a UV-lamp (15W) with a light intensity of 2.64 $x10^{-3}$ einstein min^{-1}. For radiation UV light with wavelengths between 300 and 410 nm and a maximum in radiation at 355 nm. The UV photolytic treatment was carried out in triplicate at pH 7.0 and ambient temperature. For UV/H_2O_2 treatment a pH of 4.0 and an ambient temperature was chosen. The initial concentration of hydrogen peroxide was given by the Cruncher number ([H_2O_2]/COD = 2).

The sampling for determination of degradation kinetics under UV_{254} was performed till absorbance reached 1.0 m^{-1}. The time necessary to reach that concentration is the reaction time (t_r).

2.3 Analytical methods

Apparent and real color, COD and $COD_{dissolved}$, suspended solids, UV_{254} absorbance were analyzed according the Standard Methods (1998). Apparent and real colors were determined by spectrophotometric detection at wavelength 455 nm. These two types of color were determined by the presence of turbidity in the sample: with "apparent color" colloidal and dissolved compounds that cause color and larger particles that cause turbidity were recorded, while the real color determination recorded dissolved compounds responsible for color after a removal of turbidity. COD and $COD_{dissolved}$ were determined by "Closed Reflux, Colorimetric Method" while UV_{254} absorbance was determined using an UV spectro-photometer at wavelength 254 nm (Shimadzu 1650C UV).

Nitrate, total coliforms and total iron were measured using reagents and instructions of HACH and the measurements were made by HACH spectrophotometer DR/2000. Turbidity and pH were measured by a turbidimeter (Instrutherm TD-200) and pH-meter (Micronal B474 and Lutron PH-206). Total coliforms were determined using ColiGel™ Test. Each ColiGel™ bag can detect a single microorganism in 100 mL water sample and uses X-gal indicator to produce an indigo blue positive reaction.

3 Results and Discussion

The efficiency of each treatment is presented in Table 2. Ferric coagulation showed high removal of COD and TOC, but low efficiency to remove turbidity and aromatic compounds. The irradiation with UV light diminished the aromatic compound content and turbidity, because UV decomposes organic matter by double bonds cleavage (Benitez et al., 2003). This removal can also be due to the formation of ●OH radicals by UV photolysis of natural compounds found in water and also present in treated effluents: nitrate, iron (III) and dissolved organic matter such as fulvic and humic acids as mentioned above. The addition of H_2O_2 was also efficient to remove aromatic compounds. The reaction time (t_r) to reach UV_{254} = 1.0 m^{-1} decreased from 600 or 840 min to 265 min by UV treatment or UV/H_2O_2 treatment, respectively.

Table 2 Removals rates under different treatment methods

	A*	***B****	***C****		***A****	***B****	***C****
TOC	85.4±5.4	89.7±5.7	95.9	$COD_{dissolved}$	33.3±33.3	54.2±20.8	78.2
$Coliforms_{total}$	99.4±0.1	100.0	100.0	Total Iron	83.1±9.1	-	-
Real colour	21.4±7.1	100.0	100.0	Turbidity	34.1±11.3	71.0±6.5	68.9
COD	85.7±5.7	89.5±5.5	91.6	UV_{254}	31.8±6.8	94.3±0.4	94.3

*) **A** (FC): Wastewater after ferric coagulation, pH_{final} = 7.1. **B** (FC+UV): Wastewater treated by ferric coagulation followed by UV treatment (t_r = 600-840 min UV exposure), pH_{final} = 7.3. **C** (FC+UV/H_2O_2): Wastewater treated by ferric coagulation followed by UV/H_2O_2 treatment (t_r = 100 min UV exposure), pH_{final} = 7.4.

The microbiological parameter "total coliforms" was diminished by coagulation treatment and AOP treatment. FC treatment yielded an efficient removal of 99.4% by direct sedimentation of microorganisms as by adsorption onto flakes. The removal efficiency was better than the limit of removal disclosed by Achilleos et al. (2005) which varied between 40 and 80% of removal of bacteria during coagulation. During the application of AOP treatment steps UV

and UV/H_2O_2 the removal of 100% of total coliforms may not be due only to the bactericidal action of UV light, but also by the presence of ferric ions added in coagulation treatment. If Fe(III) was added, there might be two more ways for disinfection. The first way is the formation of ●OH radicals by photolysis of complex ferrous dissolved in water (eq. 14). The second possibility is due to the formation of intracellular processes induced by Fenton and Photo-Fenton. Hydroxyl radicals (●OH), superoxide anions and hydrogen peroxide cause oxidative stress resulting in the damage to proteins, nucleic acids and cell membranes (Rincón and Pulgarin, 2006).

The kinetics of aromatic content removal showed that the addition of hydrogen peroxide increased the rate of aromatic compounds decomposition and both processes following a pseudo-first order kinetic model (Figure 1). The pseudo-first order constants and the time required to reduce half of the initial concentration of aromatic pollutants (half-life time) by UV were: $k_{UV_{254}}$ = 0.0056 min^{-1} and $t_{½,UV_{254}}$ = 123.8 min while for the treatment UV/H_2O_2: $k_{UV_{254}}$ = 0.0306 min^{-1} and $t_{½,UV_{254}}$ = 22,6 min.

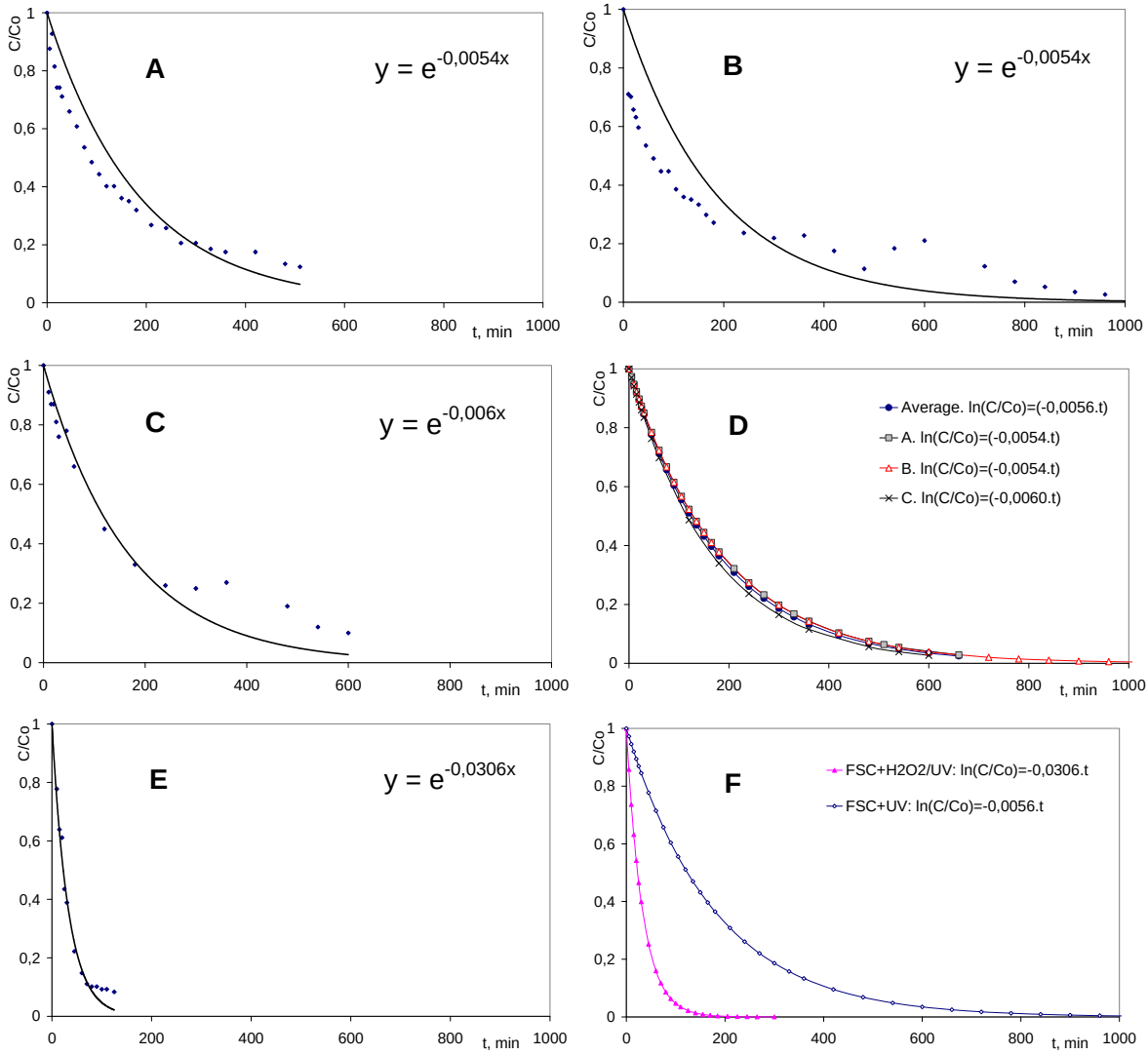

Figure 1 (A, B, C) Pseudo-first order degradation kinetics of UV_{254} absorbance: FC + UV: experiments; (D) Optimized and averaged curves of (A, B, C); (E) FC + UV/H_2O_2; (F) Combined and optimized curves of (E) and (D).

The expected raise of the UV_{254} degradation rate by adding H_2O_2 could not be observed. One explanation may be due to the reduction of ●OH radicals in the steady-state due to the

scavenger effect of natural compounds found in wastewater and also present in sewage treatment plant effluents. Chen et al. (2007) indicated that total organic carbon present in the wastewater effluents consumed ≥ 70% of ●OH radicals generated in natural water.

3 Conclusions

In conclusion, both AOP methods tested were able to degrade organic compounds contained in slaughterhouse wastewater after biological treatment. The combined treatment using ferric coagulation followed by UV/H_2O_2 in the degradation of aromatic compounds, however, was 5.2 times faster than ferric coagulation in combination with UV treatment. Therefore this method can be assumed to be an efficient and economical alternative in the treatment of biologically treated slaughterhouse wastewater to reach drinking water parameter quality enabling indirect and direct water reuse in slaughterhouse industry.

References

Alfano, O.M., Brandi, R. J., Cassano, A. E. (2001). Degradation kinetics of 2,4-D in water employing hydrogen peroxide and UV radiation. *Chemical Engineering Journal*, 82, 209-218.

Benitez, F.J., Acero, J.L., Real, F.J., García, J. (2003). Kinetics of photodegradation and ozonation of pentachlorophenol. *Chemosphere*, 51 (8), 651-662.

Chin, Y.-P., Miller, P. L., Zeng, L., Cawley, K., Weavers, L. K. (2004). Photosensitized Degradation of Bisphenol A by Dissolved Organic Matter. *Environental Science & Technology*, 38 (22), 5888-5894.

Chen, L., Zhou, H-Y., Deng, Q.-Y. (2007). Photolysis of nonylphenol ethoxylates: The determination of the degradation kinetics and the intermediate products. *Chemosphere*, 68 (2), 354-359.

Codex Alimentarius (2001). Codex Alimentarius Commission: Codex Committee on Food Hygiene. Proposed Draft Guidelines for the Hygienic Reuse of Processing Water in Food Plants. *Joint FAO/WHO Food Standards Programme*, 34th Session, Bangkok, Thailand.

Espinoza, L.A.T., Neamțu, M., Frimmel, F.H. (2007). The effect of nitrate, Fe(III) and bicarbonate on the degradation of bisphenol A by simulated solar UV-irradiation. *Water Research*, 41 (19), 4479-4487.

Neamtu, M., Frimmel, F.H. (2006). Photodegradation of endocrine disrupting chemical nonylphenol by simulated solar UV-irradiation. *Science of The Total Environment*, 369 (1-3), 295-306.

Standard Methods for the Examination of Water and Wastewater (1998). 20th edn, *American Public Health Association/American Water Works Association/Water Environment Federation*, Washington DC, USA.

Proceedings of the 10th International Chemical and
Biological Engineering Conference - CHEMPOR 2008
Braga, Portugal, September 4-6, 2008
E.C. Ferreira and M. Mota (Eds.)

Membrane bioreactor and advanced oxidation processes applied to wastewater containing non-steroidal anti-inflammatory drugs (NSAIDs)

José L. Tambosi[1,2*], Rênnio F. Sena[1,2], Wilhelm Gebhardt[2], Regina F.P.M. Moreira[1], Humberto J. José[1] and Horst Fr. Schröder[2].

[1] Department of Chemical Engineering and Food Engineering - Federal University of Santa Catarina - Campus Universitário – Trindade – 88040-970 – Florianópolis – SC –Brazil.

[2] Institute of Environmental Engineering - RWTH Aachen University - Templergraben 55 - D-52056 Aachen – Germany.

Keywords: Elimination, Mass spectrometry (MS), Membrane bioreactor (MBR), NSAIDs.
Topic: Sustainable process-product development through green chemistry.

Abstract

Pharmaceutical compounds such as non-steroidal anti-inflammatory drugs (NSAIDs) have been detected in treated wastewater, aquatic environment and even in drinking water in many parts of the world. Although health effects of the consumption of pharmaceuticals at low concentration levels are not yet completely elucidated, drinking water should not contain such compounds. Membrane bioreactors (MBRs) in combination with different physicochemical and advanced oxidation processes (AOPs) have been developed as promising technologies for the complete elimination of polar and persistent pollutants of high concern, especially pharmaceutical compounds. However, available information on the performance of MBRs regarding removal of pharmaceuticals is currently limited. This paper evaluates the treatment of three NSAIDs of large consumption worldwide (acetaminophen, ketoprofen and naproxen) by MBR combined with AOP. The identification and quantification of the compounds along the different treatment steps applied during the study was performed with liquid chromatography coupled with high resolution mass spectrometry (LC-MS).

1 Introduction

The occurrence of pharmaceutically active substances in the environment has become an important issue in the last few years. These drugs, their metabolites and bacterial transformation products, which can be even more harmful than the parent compound, are continuously released into the environment. Recent improvements in substance specific analytical techniques today allow the detection of trace levels of pharmaceuticals in wastewater effluents, surface and ground waters as well as drinking waters (Gebhardt and Schröder, 2007).

Non-steroidal anti-inflammatory drugs (NSAIDs) belong to a class of pharmaceuticals that are extensively used worldwide and their consumption only in developed countries is estimated to be higher than several hundred of tons per year (Daughton and Ternes, 1999). To obtain the desired therapeutic results the drugs are designed to resist degradation while in parallel for renal excretion after use they are equipped with polar structures, which may be responsible for their incomplete elimination during conventional biological wastewater treatment thus reaching the environment via wastewater discharges.

These compounds of concern may induce toxic effects to aquatic organisms disturbing the ecological balances, e.g., leading to the development of multi-resistant strains of bacteria. To eliminate these compounds of concern it is necessary to improve wastewater treatment because sewage treatment plant (STP) discharges are well known as predominant point sources for these drugs (Andreozzi et al., 2003). For this purpose, membrane bioreactor (MBR) and advanced oxidation processes (AOPs) have been presented as promising technologies towards the degradation of polar persistent compounds, especially pharmaceuticals.

* Corresponding author. Tel + 55-48-37219448. E-mail:jltambosi@enq.ufsc.br

In this study, three NSAIDs with worldwide large consumption rates (acetaminophen, ketoprofen and naproxen) were selected to monitor their fate and their removal efficiency during MBR and AOP treatment. The detection, identification and quantification of the drugs along the different treatment techniques applied during this study were performed using liquid chromatography coupled with high resolution mass and tandem mass spectrometry (LC-(HR)MS and -MS^n).

2 Material and methods

2.1 Chemicals

Ultra-pure water used in all treatments or as LC eluent component was prepared using a Milli-Q system (Millipore, Milford, MA, USA). All solvents used as mobile phases, for desorption of the pharmaceuticals and their potential degradation products extracted by solid phase extraction (SPE) were Nanograde solvents purchased from LGC Promochem (Wesel, Germany). All other chemicals used were of “Analytical Reagent” or of “Residue Analysis” purity grade with the exception of hydrogen peroxide solution 30% (H_2O_2) applied in AOP examinations was of "medical extra pure" grade (Merck, Darmstadt, Germany). All gases applied were products of Linde, Germany, and were of 99.99% purity with the exception of oxygen with the purity “medical grade” which was used for the O_3 generation applying an ozone generator from Sander (Uetze-Eltze, Germany).

2.2 Pharmaceuticals

The three NSAIDs acetaminophen, ketoprofen and naproxen were purchased from Sigma-Aldrich. Relevant information about these pharmaceuticals is given in Table 1. Concentrated stock solutions were prepared in methanol for analytical determination and for spiking purposes. To avoid degradation during the test period solutions were kept at -18°C.

Table 1. Name, CAS N°, sum and structural formula, pK_a and log K_{OW} of NSAIDs under research (Jones et al., 2002; Khan and Ongerth, 2004; Urase and Kikuta, 2005; Ternes et al., 2007).

Name	CAS N°	Formula	Chemical structure	Acid, base or neutral	pK_a	Log K_{ow}
Acetaminophen	103-90-2	$C_8H_9O_2N$	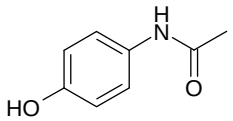	N	9.39	0.46
Ketoprofen	22071-15-4	$C_{16}H_{14}O_3$	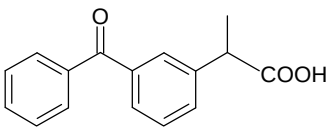	A	4.45	3.12
Naproxen	22204-53-1	$C_{14}H_{14}O_3$	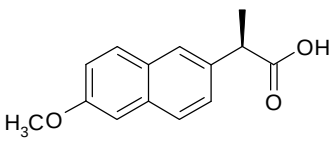	A	4.15	3.18

2.3 Membrane bioreactor (MBR) pilot plants

Wastewater used as feed for the MBR pilot treatment plants was taken continuously from the effluent of the pre-settling tank of the municipal STP of Aachen, Germany. MBR treatment was performed over a period of 4 weeks. The sludge retention time (SRT), sludge concentration (SC) and the hydraulic retention time (HRT) of the pilot-plants were 15d, 12 g/L and 9h for MBR-15, and 30d, 12 g/L and 13h for MBR-30, respectively. Both MBRs used in this study were equipped with 1.43 m^2 of hollow-fiber ultrafiltration (UF) membranes (PURON, KMS Germany). The nominal pore size and material of the membranes were 0.04 µm and polyethersulfone (PES), respectively. A steady-state was reached over 6 months before the tests started. The pharmaceutical compounds were spiked into the feed of each MBR to reach a steady-state concentration of 50 µg/L. During the week spiking was performed by the addition of 2/3 (33.33 µg/L) of the total daily spiking quantity in the morning (10:00 a.m.) and 1/3 (16.67 µg/L) in the afternoon (04:00 p.m.). Spiking during the weekend was performed by the addition of the total amount of 50 µg/L at 04:00 p.m. in the afternoon. Every day at 03:00 p.m. in the afternoon samples of 500 mL of each MBR and of permeates were taken. In parallel, 16L (MBR-15) or 8L (MBR-30) of excess MBR sludge were discharged in order to keep the sludge concentration (SC) in both MBRs constant.

2.4 UV radiation, O_3 and AOP experiment

The advanced treatment techniques applied in this study were H_2O_2/UV, H_2O_2/Fe^{2+} (Fenton), H_2O_2/Fe^{2+}/UV (photo-Fenton), UV radiation and ozone. Solutions of NSAIDs (100µg/l of each one in Milli-Q water or in MBR permeate), isolated or as a mixture, were prepared prior the AOP treatments from the standard solutions. All treatments were performed at room temperature and the pH was adjusted to 3.0 for a better comparison of the results. The experiments applying H_2O_2/UV, Fenton, photo-Fenton and UV radiation were performed in a glass cylindrical reactor system (500 mL) along 30 min. A 15 W medium pressure mercury lamp (Heraeus, Hanau, Germany), surrounded by a quartz thimble, was used when necessary as UV source. The quartz thimble was double-walled and water was used in a cooling circuit to maintain a constant temperature. The agitation of the system was realized by a magnetic bar. Ferrous sulfate heptahydrate was used as font of iron for the Fenton and photo-Fenton process. Iron concentration of 3.4 mg/L and hydrogen peroxide concentration (30%) of 17 mg/L were used in the experiments. For ozonation experiments Milli-Q water contained in a glass reactor was brought to ice bath temperature prior to saturation with ozone. For this purpose ozone generated from oxygen was fed into the reactor using a sintered glass plug located at the botton of the reactor. After time intervals of 1,2,5,10,20 and 30 min, a 1 mL of aliquot of O_3–saturated water was taken and added to flasks containing 1 mL of a solution of 100 µg/L of selected drugs, dissolved in Milli-Q water or in MBR permeates. After a reaction time of 30 min the samples then were analyzed without further sample preparation by LC/MS and MS^n in order to get qualitative, quantitative and structural information about ozone degradation products.

2.5 Sampling preparation

The pharmaceuticals and their metabolites present in the MBR permeates were concentrated using commercially available solid phase extraction (SPE) cartridges (1 ml) filled with 100 mg of Isolute ENV+ material from IST (Mid Glamorgan, UK). Prior to use they were handled as prescribed by the manufacturer. After the SPE procedure, the cartridges were rinsed with ultra-pure water to remove salts before they were dried in a gentle stream of nitrogen at 30°C. The pharmaceuticals adsorbed were desorbed by the addition of 6 x 1 mL of methanol. STP eluates were brought to dryness in a gentle stream of nitrogen at 60°C. The dry residues containing the pharmaceuticals were reconstituted in 1 mL of methanol/water (1:1) and were used for injection during LC-MS and -MS^n analyses.

2.6 Analytical procedures

Sodium chloride (NaCl) was applied as a tracer compound to ensure an ideal mixing in the MBRs. Its monitoring was performed using a conductivity probe. Identification and quantification of spiked pharmaceuticals in MBR permeates were performed by means of a LTQ Orbitrap mass spectrometer (Thermo Electron, Bremen, Germany) applying electrospray ionization (ESI), both in the positive (for acetaminophen) and in negative (for ketoprofen and naproxen) mode as described by Gerhardt and Schröder (2007). To calculate the efficiency of the pharmaceutical removal from the spiked wastewater, the concentrations in the MBR permeates were determined quantitatively using LC-MS after SPE. Metabolites present in permeates after MBR treatment and degradation products after AOP treatment were determined by extraction of selected mass traces from TICs recorded under high resolution MS (HRMS) and identified by LC-MS^n.

2.7 Liquid chromatographic and MS data

LC-separations were carried out with a Hypersil GOLD aQ column (RP5, 5 µm, spherical; 150 x 2.1 mm I.D.) equipped with a Hypersil GOLD aQ pre-column (10 x 2.1 mm I.D.), also filled with 5 µm, spherical material (Thermo Electron). Gradient elution by means of (A) methanol/water 90:10 (v:v) in combination with (B) Milli-Q-purified water/methanol 90:10 (v:v) was applied both containing 2 mM of ammonium acetate. The gradient was programmed as follows: Starting with 20% A/80% B the concentration was increased linearly to 90% A/10 % B within 12 min. Up to 20 min the composition was kept constant. The overall flow rate was 0.2 ml/min. Instrument control, data acquisition and data processing were performed using Xcalibur 2.0 software (Thermo Electron, USA).

3 Results and discussion

3.1 Removal of pharmaceutical compounds applying MBR-treatment

Figure 1 shows the mean removal rates for pharmaceutical compounds applying MBR treatment during 4 weeks. The compound acetaminophen showed the highest removal efficiency (about 100 %), due to its hydrophilic nature (log K_{ow} < 1) and also due to its less complex chemical structure, however, elimination could be cleared up as a biodegradation. Nevertheless these results are in agreement with the results reported by Kim et al. (2007) who obtained a 99% acetaminophen removal during the treatment of municipal sewage in a MBR pilot plant. Concerning the ketoprofen behaviour, an almost complete removal of the precursor drug can be observed for this compound in both MBRs (cf. Fig. 1). The compound ketoprofen has a hydrophobic nature (log K_{ow} > 3) and acidic character. According to Quintana et al. (2005), for polar compounds like acidic pharmaceuticals, microbial degradation is the most important removal process in activated sludge wastewater treatment while the retention by hydrophobic adsorption onto the membrane will not reduce concentration. Kimura et al. (2005) compared ketoprofen removal through MBR pilot plant and conventional activated sludge treatment (CAST) in municipal sewage effluent and reported a concentration of 300 ng/L of ketoprofen after CAST, while the concentration after MBR treatment was approx. 10 ng/L. The compound naproxen has similar physicochemical properties as ketoprofen, however, naproxen removal in both MBRs was lower than ketoprofen removal, and this partially can be explained by its more stable chemical structure (naphthalene ring system). According to the study by Quintana et al. (2005) on microbial degradation of pharmaceuticals, the degradation of naproxen was low with approximately 60% of transformation in 28 days and only one metabolite could be detected. Kimura et al. (2005) compare the removal of naproxen in municipal sewage effluents using either MBR pilot plant or CAST with the result that CAST led to a concentration of 50 ng/L of ketoprofen, while a concentration of approximately 20 ng/L after MBR was reached. Kim et al. (2007) reported a 41% removal of naproxen from domestic sewage after treatment in a pilot scale MBR.

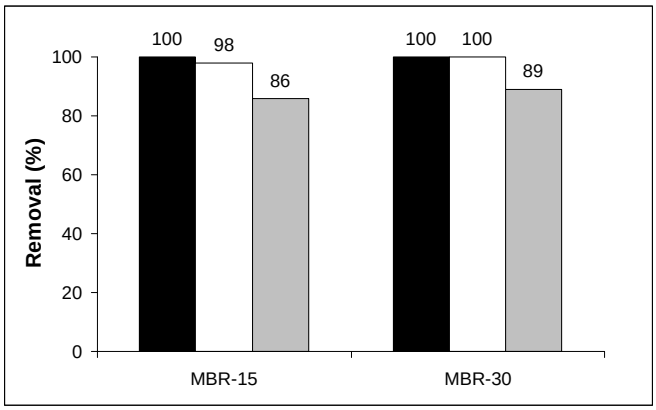

Figure 1 - Elimination rates of NSAIDs during 4 weeks applying MBR treatment with SRT of 15 (MBR-15) or 30 (MBR-30) days (acetaminophen ■ , ketoprofen ❑ , naproxen ▩).

3.2 Removal of NSAIDs by UV radiation, O_3 and different AOP treatment steps

Figure 2 shows the elimination of the pharmaceutical compounds after 30 minutes applying UV radiation, O_3 and AOP treatments. With regard to acetaminophen, Andreozzi et al. (2003) reported that at pH 2.0 and 7.0, 800 mg/L of acetaminophen could be completely degraded within 20 min using an large excess of O_3 (72 g/h) while slightly lower oxidation rates were observed with 170 mg/L of H_2O_2/UV at pH 5.5 applied to 1.51 mg/L acetaminophen resulting in an elimination rate of > 90% combined with a TOC removal of 40%. Comparing these results with the data reported here, we recognized that the efficiency of H_2O_2/UV for the reachable oxidation of acetaminophen was lower. Only 66.3% were degraded within 30 min. Concerning ketoprofen removal, it can be observed in Fig. 2 that ketoprofen is a compound that has a high sensitivity to UV light, although the mechanisms and the possible pathways are still under investigation. Nakajima et al. (2005) studied the photodynamic action of ketoprofen, determining the generation of free radicals and active oxygen species by photo-irradiation, as well as the identification of 3 different degradation products. In our results, UV radiation induced a high destruction rate of ketoprofen already within the first minute, which led to the complete elimination of the parent compound during this short reaction period. Few data were available about the degradation of naproxen, the third NSAID compound, as well as the formation of degradation products. According to Isidori et al. (2005), phototrans-formation appears to be its main elimination process in the environment, where naproxen in water can be partly transformed by irradiation into different photoproducts. From our results it was recognizable that O_3 besides photo-Fenton seemed to be the most efficient oxidation treatment step for naproxen, reaching elimination of 100 or > 90 %.

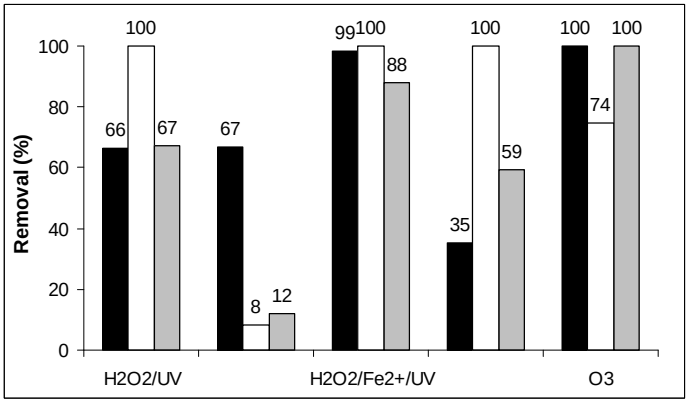

Figure 2 – Mean elimination rates of NSAIDs by UV radiation, O_3 and AOPs over a period of 30 min to MBR permeates (acetaminophen ■ , ketoprofen ❑ , naproxen ▩).

4. Conclusions

The performance of two MBR pilot plants with submerged membranes, operated with different SRTs, for the removal of selected drugs, could be examined in this study. The effect of sludge retention time (SRT) on the removal efficiency of the compounds was slightly higher in MBR with SRT of 30 days (MBR-30) compared to SRT of 15 days (MBR-15). The compounds acetaminophen and ketoprofen exhibited highest removal efficiencies, while naproxen resisted microbial attack with lower removal rates in both MBRs. Concerning the potential mechanisms responsible for the removal of the target pharmaceuticals in MBRs (sludge sorption + biodegradation + membrane retention), it was not possible to determine exactly to what extent each mechanism contributed to the removal efficiency. Membrane retention using ultrafiltration membranes can be neglected, biodegradation, however, played an important role, since higher removal efficiencies were obtained for higher SRTs. Nevertheless, elimination by MBR treatment using ultrafiltration was only partially successful and therefore, persistent pharmaceuticals in small concentrations and their metabolites were discharged with the wastewater into the environment. Concerning those results obtained with an advanced treatment, it can be concluded that oxidation method using O_3 would be a powerful tool for a complete elimination of the target compounds. In conclusion, results indicated the importance to investigate the environmental fate of NSAIDs and their mainly unknown polar metabolites. Therefore additional research is overdue first to recognize the parent drugs and their metabolites and then to assess the effect of these pollutants to the environment.

References

Andreozzi, R., Marotta, R., Paxéus, N. (2003). Pharmaceutical in STP effluents and their solar photodegradation in aquatic environment. *Chemosphere*, 50, 1319-1330.

Daughton, C.G.,Ternes, T.A. (1999). Pharmaceuticals and personal care products on the environment: agents of subtle change? *Environ. Health Perspect.*, 107, 907-938.

Gebhardt, W., Schröder, H.Fr. (2007). Liquid chromatography-(tandem) mass spectrometry for the follow-up of the elimination of persistent pharmaceuticals during wastewater treatment applying biological wastewater treatment and advanced oxidation. *J. Chromatogr. A*, 1160, 34-43.

Jones, O.A.H., Voulvoulis, N., Lester, J.N. (2002). Aquatic environmental assessment of the top 25 English prescription pharmaceuticals. *Water Res.*, 36, 5013-5022.

Isidori, M., Lavorgna, M., Nardelli, A., Parrella, A., Previtera, L., Rubino, M. (2005). Ecotoxicity of naproxen and its phototransformation products. *Science of the Total Environment* , 348, 93-101.

Khan, S.J., Ongerth, J.E. (2004). Modelling of pharmaceutical residues in Australian sewage by quantities of use and fugacity calculations. *Chemosphere*, 54, 355-367.

Kim, S.D., Cho, J., Kim, I.S., Vanderford, B.J., Snyder, S.A. (2007). Occurrence and removal of pharmaceuticals and endocrine disruptors in South Korean surface, drinking, and waste waters. *Water Res.*, 41, 1013-1021.

Kimura, K., Hara, H., Watanabe, Y. (2005). Removal of pharmaceutical compounds by submerged membrane bioreactors (MBRs). *Desalination*, 178, 135-140.

Nakajima, A., Tahara, M., Yoshimura, Y., Nakazawa, H. (2005). Determination of free radicals generated from light exposed ketoprofen. *Journal of Photochemistry and photobiology A: Chemistry*; 174, 89-97.

Quintana, J.B., Weiss, S., Reemtsma, T. (2005). Pathways and metabolites of microbial degradation of selected acidic pharmaceutical and their occurrence in municipal wastewater treated by a membrane bioreactor. *Water Res.*, 39, 2654-2664.

Ternes, T.A., Bonerz, M., Hermann, N., Teiser, B., Andersen, H.R. (2007). Irrigation of treated wastewater in Braunschweig, Germany: An option to remove pharmaceuticals and musk fragrances. *Chemosphere*, 66, 894-904.

Urase, T., Kikuta, T. (2005). Separate estimation of adsorption and degradation of pharmaceutical substances and estrogens in the activated sludge process. *Water Res.*, 39, 1289-1300.

Proceedings of the 10th International Chemical and
Biological Engineering Conference - CHEMPOR 2008
Braga, Portugal, September 4-6, 2008
E.C. Ferreira and M. Mota (Eds.)

Basic Dyestuffs Removal from Textile Wastewaters Using Almond Hulls: Equilibrium and Kinetic studies

M. L., Ávila, C. F. Farinha, S. A. Figueiredo*
REQUIMTE / Instituto Superior de Engenharia do Instituto Politécnico do Porto
Rua Dr. António Bernardino de Almeida, 431, 4200 – 072 Porto - Portugal

Keywords: Adsorption, Equilibrium, Dyestuffs, Kinetics, Textile wastewater
Topic: Sustainable process-product development through green chemistry

Abstract

In this work a natural waste from almond production was used. Its culture is widespread in Mediterranean climate areas, namely in some regions of Portugal, so these wastes are easily available. This waste was tested for removal of basic dyestuffs from textile wastewaters.

The basic dyestuff Red Astrazon FBL 200% (CI basic red 46), from Dystar is an azo dye and was selected for this study based on preliminary tests. Batch equilibrium and kinetic studies were performed for the selected system.

Langmuir or Freundlich models can fit equilibrium batch studies. It is observed an increase of adsorption capacity with temperature, from 15±3 to 30±11 mg/g, indicating that adsorption is rather favoured at 41 than at 20ºC. The pH influence was tested in t he range 4.5 to 9 and was not considered significant, under testing conditions. The presence of auxiliary dyeing agents, as occurs in a real effluent, gave rise to the development of microrganisms along the 13 days of contact time.

The kinetic experiments were well described by the pseudo-second order model, using a experimental equilibrium concentration of 2.44 mg/g and a 80 ±14 g/(g min) kinetic constant.

1 Introduction

It is nowadays well known that there is a need of treating textile wastewaters, not only concerning primary and secondary treatments for organic matter and suspended solids removal, but also a tertiary treatment, mostly for residual colour removal.

Textile dyestuffs should be removed from wastewaters because they can cause reduction in the primary production that will affect the aquatic ecosystem, and also for aesthetical reasons. Besides, some of them may also be toxic.

Activated carbon is one of the most widely used adsorbents for colour removal in wastewater treatment. However, this treatment needs a high investment and leads to high operation costs, due to the high price of the activated carbon and to the high wastewater flow rate always involved, which can be greatly increased when there are no regeneration units nearby, as in the case of Portugal.

Research has recently been directed towards alternative adsorbents, namely low cost adsorbents, including natural and waste materials. Many research works studying valuable alternatives to activated carbon for dyestuffs removal appeared, using: inorganic adsorbents such as, sepiolite (Santos and Boaventura, 2008) and natural zeolites (Meshko et al., 2001); natural adsorbents from vegetal source, like hardwood (Asfour et al., 1985), and from animal source, like Anodonta shell, Squid and Sepia pen (Figueiredo et al., 2005).

* Corresponding author. Tel + 351-22-8340500. E-mail:saf@isep.ipp.pt

In this work a natural waste from almond production was used. Its culture is widespread in Mediterranean climate areas, namely in some regions of Portugal, so these wastes are easily available. This waste was tested for removal of basic dyestuffs from textile wastewaters.

Basic dyestuffs are water-soluble cationic dyes that can be applied to acrylic fibres, wool, silk, leather and modified cotton (Venkataraman, 1972). Their use has been increasing due the increment of acrylic fibres production especially in Asia, where most of the textile industries are located (Dobson, 2001).

According to Anliker et al. (1988), basic dyes have been classified as toxic colorants; they are considered as one of the more problematic classes of dyes by some authors (El Quada et al., 2008). Moreover, the basic dyestuff selected for this study is an azo compound; their metabolites (such as aromatic amines) might be either carcinogenic or cancer suspect agents (Reife and Freeman, 1996).

2 Methods

2.1 Dyestuff preparation

The basic dyestuff Red Astrazon FBL 200% (C.I. basic red 46), kindly supplied by Dystar, was selected for this study; it is an azo dye and its structural formula is presented in figure 1. Dyestuff solutions were prepared with distilled water, with a 25 ppm concentration, and were boiled for 30 min for complete dissolution. The final pH was adjusted to the desired value with acetic glacial acid or sodium hydroxide. These solutions were also prepared containing one of the industrial dyeing auxiliary agents, glacial acetic acid or trisodium phosphate; the simulated wastewater prepared contained both products.

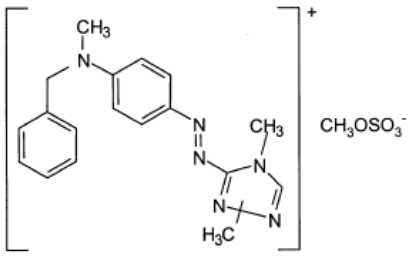

Figure 1 Chemical structure of Astrazon Red FBL 200% - C.I. Basic Red 46 (Martin et al., 2003)

2.2 Adsorbent preparation

The almond hulls were ground and sieved. All experiments were performed with particles of grain size between 0.710 and 1.190 mm.

2.3 Equilibrium batch studies

The equilibrium adsorption isotherms were determined, at 20 and 41ºC, using an orbital P-Selecta Rotabit shaker into a refrigerated incubator P-Selecta Hotcold-M. A set of 100 mL erlenmeyers (with cap) containing 50 mL of dyestuff solution and different amounts of adsorbent were shaken at 100 rpm during 13 days, contact time necessary to reach equilibrium. A blank test was run, at the same conditions.

At the end, the adsorbent was separated using a Centrifuge Sartorius, Sigma 2-16. The dyestuff concentration of each sample was obtained by measuring its absorbance in a Jenway 6100 spectrophotometer at the maximum absorbance wavelength (525 nm). Initial and pH final values were also evaluated using a Metro HM-632 meter.

2.4 Kinetic studies

The kinetic experiments were performed in a batch continuously stirred vessel (1.2 L) with 4 g of adsorbent, at 20ºC. The shaft stirring rate was 400 rpm. The 3 mL samples were

collected using a syringe, allowing the determination of the dyestuff concentration and pH histories.

3 Results and discussion

Adsorption isotherms were determined at different pH and temperature and the influence of the presence of some auxiliary dyeing agents was also evaluated. Both Langmuir and Freundlich models can fit the experimental results and the model parameters can be consulted in tables 1 and 2, respectively, together with the experimental conditions. Freundlich constant, n, is always greater than 1, indicating favourable adsorption.

To study the influence of temperature, isotherms at 20 and 41ºC (experiments 1 and 2), and pH 6, were performed. The experimental results and their Langmuir and Freundlich fits are shown in figure 2. Comparing the Langmuir maximum adsorption capacities, presented in table 1, it is observed an increase with temperature, from 15±3 to 30±11 mg/g, respectively. This increase might be explained (Asfour *et al.*, 1985) by an increase of pore size diameter due to the swelling of the almond hulls caused by heating at 41ºC, allowing the dyestuff molecules to penetrate further in the adsorbent pore structure than at 20ºC.

Table 1 Experimental conditions and Langmuir model [$q = q_s.k_L.C/(1+k_L.C)$] parameters, respective confidence intervals, square correlation to model (r^2) and variance (s^2) for each experiment.

Experiment	pH initial	pH final	T (ºC)	q_s (mg/g)	k_L (L/g)	r^2	s^2
1	6.09	6.85	20	15±3	0.31±0.14	0.979	$3.42x10^{-7}$
2	6.04	6.49	41	30±11	0.084±0.047	0.986	$3.09x10^{-7}$
3	9.05	7.31	20	16±6	0.18±0.13	0.943	$6.96x10^{-7}$
4	4.5	6.52	20	13±3	0.199±0.100	0.979	$2.33x10^{-7}$
5	4.95	5.39	20	23±26	0.033±0.054	0.896	$9.35x10^{-7}$

Table 2 Experimental conditions and Freundlich model [$q = k_F.C^{(1/n)}$] parameters, respective confidence intervals, square correlation to model (r^2) and variance (s^2) for each experiment.

Experiment	pH initial	pH final	T (ºC)	k_F $(mg/g)(L/g)^{1/n}$	n	r^2	s^2
1	6.09	6.85	20	3.7±0.6	2.13±0.38	0.982	$2.90x10^{-7}$
2	6.04	6.49	41	2.7±0.7	1.43±0.25	0.983	$4.05x10^{-7}$
3	9.05	7.31	20	2.9±0.7	1.88±0.40	0.971	$3.36x10^{-7}$
4	4.5	6.52	20	2.6±0.3	2.03±0.23	0.993	$6.79x10^{-8}$
5	4.95	5.39	20	1.0±0.8	1.34±0.57	0.886	$1.02x10^{-6}$

To evaluate the influence of pH, isotherms at three different initial pH values, 4.5 (adjusted with acetic glacial acid, an auxiliary dyeing agent), 6 and 9 (adjusted with sodium hydroxide), at 20ºC, were performed (experiments 4, 1 and 3, respectively). The experimental results and the Langmuir and Freundlich model adjusts are presented in figure 3. Comparing the Langmuir maximum adsorption capacities, in table 1, there is an intersection of confidence intervals, indicating no significant effect of pH, which could be related to the fact that final pH

was almost the same in both cases, ranging from 6.5 to 7.3. The buffer effect observed might be related with acid-base reactions with substances leached by the almond hulls.

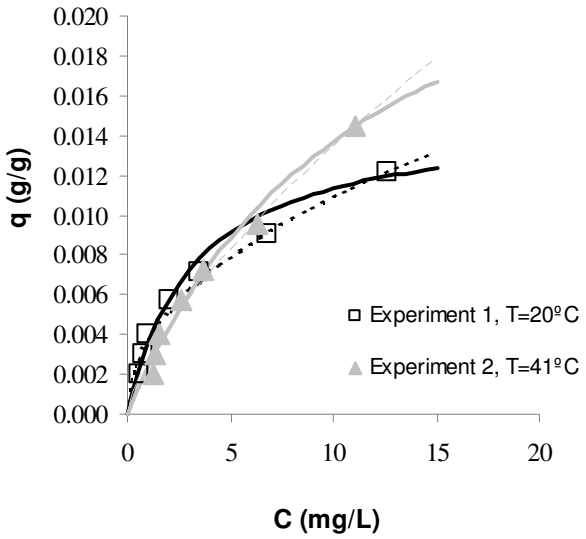

Figure 2 Experimental equilibrium isotherms, at 20 and 41ºC, and respective fits to Langmuir (continuous lines) and Freundlich models (dashed lines).

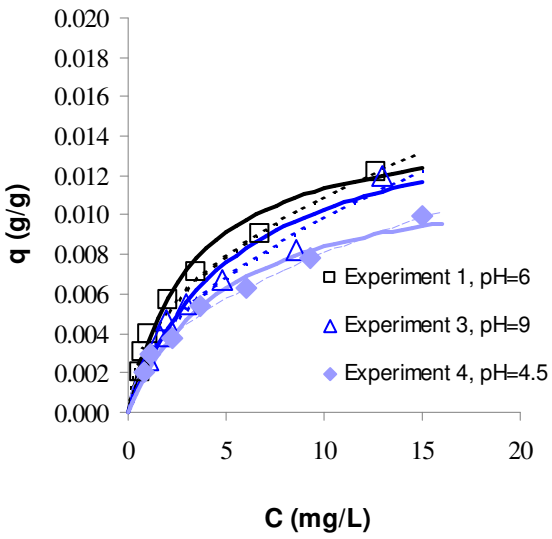

Figure 3 Experimental equilibrium isotherms, at different initial pH values, and respective fits to Langmuir (continuous lines) and Freundlich models (dashed lines).

In order to approach real situations, isotherms were also performed with a simulated effluent (experiment 5), containing acetic glacial acid, used for acidification to a 5 pH, and 0.5 g/L of trisodium phosphate. These auxiliary dyeing agents are always used for dyeing acrylic fibres and their concentrations belong the range of typical values. Usually acetic acid is added to the dye bath to help the take up of the dye onto the fibre. The salt is used as an electrolyte and has also a buffer effect in the dyeing bath. Consequently the final pH of this experiment, 5.4, was similar to the initial value.

The experimental results obtained with this simulated wastewater and respective Langmuir and Freundlich adjusts were compared with the ones obtained for the dyestuff solution without addition of other chemicals (experiment 1) and with the dyestuff solution prepared with glacial acetic acid (experiment 4), as auxiliary dyeing agent, in figure 4. A reduction of adsorption is observed when the dyestuff solution complexity increases, as it was expected however this is not clear due to the results dispersion in experiment 5 caused by the growth of microrganisms (detected visually). The presence of organic matter, nitrogen (present in the dyestuff) and phosphorus (present as trisodium phosphate) at moderate pH, gave rise to the development of microrganisms along the 13 days of contact time. The simultaneous occurrence of biological degradation and adsorption are considered advantageous (Figueiredo *et al.*, 2000), allowing longer operation times that delay, or avoid, the replacement of the spent adsorbent.

Although equilibrium studies are important to known the maximum amount that can be removed by a given material, the kinetic of the process limits the rate at which equilibrium state can be reached, what is usually the critical point in operation conditions.

A kinetic study was also performed with the same synthetic wastewater of experiment 5, at 20ºC, and 400 rpm shaft stirring rate. Under these conditions equilibrium was reached after 120 min and the experience lasted for 180 min. This period of time is smaller than the equilibrium time used for isotherms determination because agitation rate is higher. It was not enough to allow microrganisms growth, so the equilibrium adsorption isotherm obtained with simultaneous biogradation was consider no longer valid.

Pseudo-first order and pseudo-second order models were adjusted to the experimental results and are presented in figure 5; the adjusted parameters are shown in table 3. The best fit was obtained for pseudo-second order model, using a experimental equilibrium concentration of 2.44 mg/g in the solid phase and a 80 ±14 g/(g min) kinetic constant. If the equilibrium concentration in the solid phase was calculated using the Langmuir Model (the best model fit obtained) a 10.4 mg/g value would be obtained, indicating that there was a strong contribution of biodegration (77%) to the dyestuff removal from the synthetic textile wastewater.

Pseudo-second order kinetics are often verified for biomaterials, namely in agricultural wastes (Mckay and Ho, 1999). The model parameters obtained can be used for comparison with different systems or different experimental conditions.

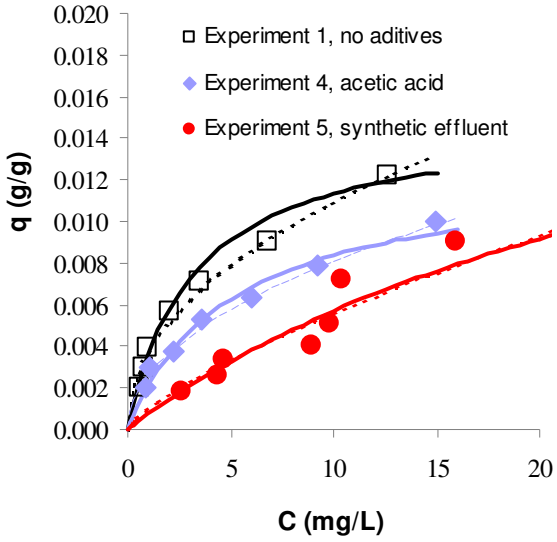

Figure 4 Experimental equilibrium isotherms for different compositions of dyestuff solution and respective fits to Langmuir (continuous lines) and Freundlich models (dashed lines).

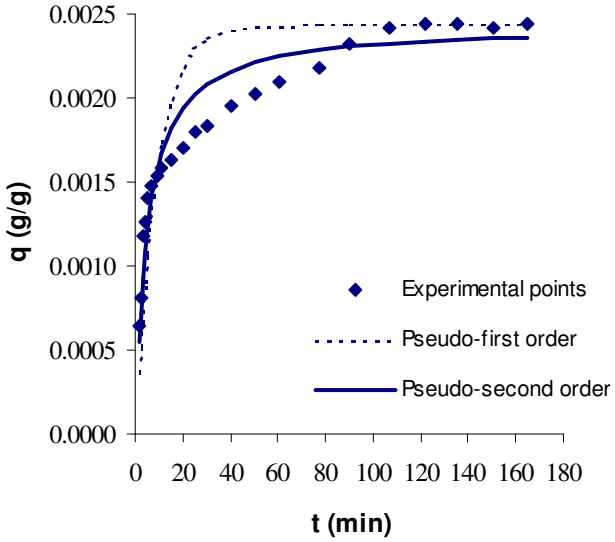

Figure 5 Experimental points of the kinetic study and pseudo-first and pseudo-second order model fits.

Table 3 Experimental conditions, pseudo-first and pseudo-second order model parameters, kinetic constants (k) and experimental equilibrium solid phase (q_e), respective confidance intervals, square correlation to model (r^2) and variance (s^2).

Model	pH initial	pH final	T (ºC)	k	q_e (mg/g)	r^2	s^2
Pseudo-first order	4.95	5.39	20	0.11±0.03	2.44	0.862	9.92×10^{-8}
Pseudo-second order	4.95	5.39	20	80±14	2.44	0.934	2.42×10^{-8}

Although the equilibrium capacities of almond hulls are much lower than those obtained for activated carbon for basic dyes (El Qada et al., 2008) the cost of this industrial adsorbent is also much higher. Besides the valorization of almond huks, an easy available waste, the material shows a significative uptake of dyestuff.

This affinity can be attributed (Mckay et al, 1987; Laszlo and Dintzis, 1994) to the columbic interaction of the cellulosic surface, negatively charged in aqueous solution, with cationic species, like the basic dyestuff studied. However there are still ways of improving the

performances of this adsorbent, such as by chemical treating of the natural material (Gong *et al*., 2005).

4 Conclusions

Almond hulls, a natural waste are easily available, were tested in order to remove the basic dyestuff Red Astrazon FBL 200% (CI basic red 46), from Dystar.

The kinetic experiments were well described by the pseudo-second order model. Langmuir or Freundlich models can fit equilibrium batch studies. The equilibrium results show a slight influence of temperature, indicating that adsorption is rather favoured at 41 than at 20ºC. The pH influence was not significant under testing conditions.

The increase of complexity of the dyeing solution decreased the dyestuff removal. However, the presence of auxiliary dyeing agents, as occurs in a real effluent, gave rise to the development of microrganisms along the 13 days of contact time. The simultaneous occurrence of biological degradation and adsorption are considered advantageous (Figueiredo *et al*., 2000), allowing longer operation times that delay, or avoid, the replacement of the spent adsorbent. The results obtained suggest a possible application of almond hulls, a cost effective solution that may contribute to the sustainability of the environment.

References

Anliker, R., Dürig, G., Steinle, D., Moriconi, E.J. (1988). List of colorants to be classified as toxic, *Journal of the Society of Dyers and Colourists*, 104, 223–225.

Asfour, H. M., Fadali, O. A., Nawar, M. M., El Geudi, M. S. (1985). Equilibrium studies on adsorption of basic dyes on hardwood. *J. Chem. Tech. Biotechnol.*, 35A, 21-27.

Dobson, S. (2001). Manmade Fibers Fuel - Growth of Nonwovens. Volume 16, Number 1, TECNON, UK.

El Qada, E. N., Allen, S. J., Walker, G. M. (2008). Adsorption of basic dyes from aqueous solution onto activated carbons. *Chemical Engineering Journal*, 135, 174–184.

Figueiredo, S.A., Boaventura, R.A., Loureiro, J.M. (2000). Color removal with natural adsorbents: modeling, simulation and experimental. *Sep. Pur. Tech.*, 20, 129-141.

Figueiredo, S. A., Loureiro, J. M., Boaventura, R. A. (2005). Natural waste materials containing chitin as adsorbents for textile dyestuffs: Batch and continuous studies. *Water Research* 39, 4142–4152.

Gong, R., Sun, Y., Chen, J., Liu, H., Yang, C. (2005). Effect of chemical modification on dye adsorption capacity peanut hull. *Dyes and Pigments*, 67, 175-181.

Laszlo, J. A., Dintzis, F. R. (1994). Crop residues as ion-exchange materials: Treatment of soybean hull and sugar beet fiber (pulp) with epichlorohydrin to improve cation-exchange capacity and physical stability. *Journal of Applied Polymer Science.* 52, 531-538.

Martin, M.J., Artola, A., Balaguer, M.D., Rigola, M. (2003). Activated carbons developed from surplus sewage sludge for the removal of dyes from dilute aqueous solutions. *Chemical Engineering Journal*, 94, 231-239.

McKay, G., El Geundi, M., Nassar, M. M. (1987). Equilibrium studies during the removal of dyestuffs from aqueous solutions using Bagasse pith. *Water Research*, 21,1513-1520.

Mckay, G., Ho, Y. S. (1999). Pseudo-second order model for sorption processes. *Process Biochemistry*, 34, 451-465.

Meshko, V., Markovska, L., Minceva, M. ,Rodrigues, A. E. (2001). Adsorption of basic dyes on granular activated carbon and natural zeolite. *Water Research,* 35(14), 3357-3366.

Reife, A. , Freeman, H. S. (1996). Environmental chemistry of dyes and pigments, Wiley Interscience, New York, USA.

Santos, S. C. R., Boaventura, R. A. R. (2008). Adsorption modelling of textile dyes by spiolite. *Applied Clay Science*, doi:10.1016/j.clay.2008.01.002.

Venkataraman, K. (1972). The Chemistry of Synthetic Dyes, Volume VI, Academic Press, Inc., New York, USA.

Proceedings of the 10th International Chemical and
Biological Engineering Conference - CHEMPOR 2008
Braga, Portugal, September 4-6, 2008
E.C. Ferreira and M. Mota (Eds.)

INTEGRATION OF EMERGENT PROCESSES FOR THE TREATMENT OF WASTEWATER FROM NITROCELLULOSE INDUTRY: TREATMENT WITH *ASPERGILLUS 2BNL1* FUNGUS AND TIO_2/UV

Marcio Barreto-Rodrigues; João V. B. Souza; Érica S. Silva; Flávio T. Silva; Teresa C. B. Paiva*
Biotechnology Department, University of São Paulo – USP, Lorena School of Engineering
Estrada Municipal do Campinho, s/n, 12.602-810, C. P. 116, Lorena, SP, Brazil
teresa@debiq.eel.usp.br

Keywords: delignification effluent; fungus treatment; combined processes; alginate beads
Topic: Integration of life sciences & engineering

Abstract

The aim of this work was to characterize the delignification effluent from nitrocellulose industry, evaluate the activity of immobilized catalyst (TiO_2) in alginate beads for photocatalysis and evaluate the combination of fungus treatment and photocatalytic treatment (catalyst immobilized in Ca-alginate beads), for the treatment of this effluent. The delignification effluent has proven harmful to the environment because it presents high color (3516 CU), total phenol (876 mg/L) and TOC (1599 mg/L) and also highly toxic even at in low concentration. The results of photocatlysis with catalyst were 11, 25 and 13 % higher for reductions in color, total phenol and TOC, respectively than the parallel processes (photolysis + adsorption). The combined treatments presented benefits when compared to the non-combined ones. Fungus and photocatalysis in combination showed to be the best treatment, reducing the color, total phenol, toxicity (inhibition of Escherichia coli growth) and TOC by 99.5 %, 95.4%, 64% and 56 %, respectively.

1 Introduction

During the production of nitrocellulose, an important polymer for the inks, lac and explosives industries, effluents are also produced. Delignification effluent results from the alkaline treatment of cotton fibers. This effluent has dark color, a large amount of organic matter and is highly toxic (Paiva *et al*., 2001; Tran *et al*., 2006).

Since 1977, several studies or the treatment of effluents originating from the cellulose industry have indicated fungi as an alternative method. This is because fungi are able not only metabolize lignin and its derivatives, but also reduce the effluent's color, organic matter and toxicity (Malaviya *et al*., 2007; Souza *et al*., 2005; Rao *et al*., 2006).

Heterogeneous photocatalysis is based on the activation of semicondutor material by solar or artificial light. The literature shows several works employing immobilized catalyst since this technique allows the catalyst recovery after the reaction and also operation in a continuous mode (Peralta-Zamora et al., 1998; Silva *et al*., 2002).

The use of integrated processes could be a promising alternative for the treatment of these kind of effluents. This kind of combination process is attractive for cellulose industry effluents, since the photocatalytic process could be employed in the biological process for the degradation of recalcitrant, toxic and inhibitory compounds, increasing the effluent biodegradability. On the other hand, the biological process, when employed as a pre-treatment, could remove the biodegradable fraction, decreasing this way the use of energy and reagents in the photocatalysis process (Oller et al., 2007; Bandala et al., 2008; Pedroza *et al*., 2007; Beek *et al*., 2007).

The aim of this work was to characterize the delignification effluent from nitrocellulose industry, evaluate the activity of immobilized catalyst in alginate beads for photocatalysis and evaluate the combination of fungus treatment and photocatalytic treatments, as a possible effluent treatment.

2 Material and methods

2.1 Effluent characterization

Delignification effluent: All the experiments were carried out employing a delignification effluent originating from the alkaline pulping (NaOH) of the nitrocellulose producted by an industry that uses cotton as the raw material. The original pH value of the cotton delignification effluent was adjusted to five and the effluent was always diluted 10 times before it was used in the treatment tests.

Color measurement: Color was measurement as described by CPPA (1975). In all cases the effluent were previously centrifuged at 3.500 rpm for 5 minutes.

Total phenol: Total phenol was measured following the standard procedures described by APHA (1989).

Total organic carbon (TOC): Total organic carbon was measured according to the standard procedures described by ISO (1987).

Acute toxicity test: The effluent acute toxicity test was carried out by determining the growth inhibition of *Escherichia coli*, modifying a method previously described by Jardim *et al*., (1990). *E. coli* cultures were contaminated with different concentrations of effluent and their growth was quantified using spectrophotometry (400 nm).

2.2 Reactor system

The photocatalytic reactor used in this study has a 9.5 cm^{-1} diameter cylinder (250 mL working volume). The irradiation in the photoreactor was obtained using 125 W (λ= 254 nm) low pressure Phillips mercury lamp (without the glass cover), positioned inside the reactor. The temperature was controlled by water circulation through the annular jacket surrounding the reaction zone. During the irradiation, the solution was magnetically stirred to ensure proper mixing and air was bubbled at an air flow rate of 90 mL/min.

2.3 Catalyst free and immobilization in alginate beads

Catalyst free: A TiO_2 Degussa P25 catalyst provided by Degussa Company was used throughout this work without further modification. It has the following main physical characteristics: BET surface area 55 $\pm$ 15 $m^2.g^{-1}$, average primary particle size around 30 nm, purity above 97% and with 80:20 anatase to rutile.

Catalyst immobilization: A 3% w/v solution of alginate was employed as support, and TiO_2 was added in the ratio of 10 g/L of gel. The catalyst beads, about 2 mm in diameter, were produced in a syringe, which was used to drip this mixture into a stirred solution of $CaCl_2$ (2%) at 4^oC. Afterward, the beads were stored in $CaCl_2$ solution during 24 h for stabilization.

Photolysis/adsorption: The photocatalytic activity of the immobilized catalyst in the alginate beads was evaluated by an experiment using catalyst without catalytic activity (TiO_2 ink industry - amorphous). A total of 10 g of immobilized catalyst per 100 mL of effluent was used and the irradiation time was 120 min. The TiO_2 concentration in the beads was of 0,1g (w/w).

2.4 Treatments

2.4.1 Fungus treatment

The fungus used in this work was isolated from activated sludge and identified as *Aspergillus* 2BNL1. This strain was selected after screening a group of fungi for their ability to decolorize delignification effluent. *Aspergillus* 2BNL1 was grown in Potato Dextrose Agar (PDA) medium in Petri dishes for 72 h at 28 ^{o}C and the spores were then suspended in sterile water, as described by Souza *et al*. (2002). Each flask (1000 mL) containing 250 mL of culture medium was inoculated with $1x10^5$ spores/mL culture medium (Malt Broth - MB). After 72 h, the pre-inoculum medium was filtered and the fungus biomass (20g) was transferred to 250 mL of the diluted delignification effluent (10 %, v/v), pH 5, without extra carbon source, and the effluent was treated for 24 h.

2.4.2 Photocatalytic treatment

A total of 100 mg of free anatase TiO_2 were added to 250 mL of effluent in reactor equipped with water refrigeration and magnetic stirrer, as described in items 2.2.1. The water evaporation was corrected by restoring the initial volume with distilled water. These conditions were previously optimized for Peralta-Zamora (1998) for the treatment of black liquor of a paper and cellulose Industry.

3 Results and discussion

3.1 Effluent characterization

The effluent presented a deep and even diluted color (3516 CU). This value is very high and if this effluent was released into the environment, even at low concentrations, it would impede light from penetrating the water, hindering the algae photosynthesis and consequently damaging the aquatic environment.

The total phenol content was 59.2 mg/L. The literature correlates the presence of compounds quantified by the Folin-Ciocalteus reagent with the effluent color (CPPA, 2007; APHA, 1989) and with the depolymerization of high molecular mass lignin derivatives.

The TOC content of the delignification effluent was 1599 mg/L. This TOC value is three times higher than that of domestic wastewater (Chan, 2004). The release of this effluent into water can cause an increase consumption of dissolved oxygen, damaging the aquatic environment. However, the effluent recalcitrance and toxicity most likely present a more significant problem.

3.2 Activity of immobilized catalyst in photocatalysis

The photocatalityc activity is defined as the difference between the parallel processes (photolysis + adsorption) and the photocatalytic degradation process.

In order to evaluate the photocatalytic activity of the immobilized catalyst in the alginate beads two experiments were carried: one using catalyst with photocatalytic activity (TiO_2 – Degussa-P25) and another one employing the catalyst without photocatalytic activity (TiO_2 ink industry - amorphous). The results are shown in Table 1.

Table 1- Parameters for evaluation of the catalyst activity

	Color Reduction (%)	Total Phenol Reduction (%)	TOC Reduction (%)
Photocatalysis	94.4 ± 0.3	83 ± 1	16 ± 0.8
Photolysis + adsorption *	83.4 ± 0.4	58 ± 1	3 ± 0.3

*Alginate beads doped with TiO_2 (amorphous) without catalyst activity.

The photocatalityc activity improved the reductions of color, total phenol and TOC in 11, 25 and 13 % respectively, that the immobilized catalyst was effective in its.

It is important to observe that the parallel processes of photolysis and adsorption were significant (mainly for the parameters of color and total phenol reductions), but contributed to the global process of photocatalytic degradation. The alginate beads doped with TiO_2 gather physical properties (absorption and adsorption) and chemistries (photocatalytic degradation) that can contribute in a combined way to the effluent purification.

Another important issue that should be investigated is the possible increase in TOC due to the degradation of the alginate support. This degradation is expected and the viability of the use of alginate as the support depends on the degradation rate of the substrate (effluent) in relation to the alginate degradation, that should be as highest as possible.

COMBINED AND NON-COMBINED TREATMENTS

The major problems presented by the delignification effluent are the color and the presence of lignin-derived phenolic compounds.

All the treatments reduced the effluent color significantly (86-99 %). The best treatment was the combination of fungus and photocatalysis treatment. This result can be explained by the increased efficiency of the photocatalytic treatment due to the reduction in chromophore compounds caused by the fungus treatment. Photocatalytic treatments were more efficient for the effluents with low color due to the increased transmittance and photonic efficiency (Tariq *et al*., 2008). This same explanation can be used to justify the other positive results obtained through this association.

A correlation between color reduction and total phenol concentrations was observed (r^2 = 0.9979). This same result was previously reported by Souza *et al*. (2004) and demonstrates that there was a correlation between the compounds quantified by the Folin-Ciocalteu reagent and the chromophores present in the effluent. The best treatment for this parameter once again was the combination of Fungus treatment and Photocatalysis treatment (95 %reduction).

The TOC reduction after the combined and non-combined treatments was studied. The photocatalytic treatment reduced TOC by 16 % while fungal treatment reduced it by 10 %. This low efficiency of the photocatalysis and fungal treatment in terms of reducing organic matter was justified by the high medium opacity and TOC content.

The combined treatments showed an increased reduction of organic matter in relation to the non-combined ones. The reductions revealed a high synergic effect of the combined treatments. In this context, the fungus + photocatalysis combination was more efficient (56%) than the photocatalysis + fungus combination (46%). Possible explanations for these results could be related to the following factors: 1-Phototratability elevation for the reduction in organic matter and opacity of the medium, increasing the photonic efficiency; 2-Reduction in the recalcitrant compounds, for the fungus biodegradation, after the photocatalytic treatment.

The untreated effluent, even at low concentrations, presented high toxicity, inhibiting 70% of *E. coli* growth (20 h) at the concentration of 5% (v/v).

All the treatments reduced the inhibition caused by the untreated effluent. The best non-combined treatment was Photocatalysis (19 % inhibition) and the best combined treatment was fungus + photocatalysis (6.7 % inhibition). In general, the treatments in which photocatalysis was sole or the last treatment applied produced results.

4 Conclusion

The delignification effluent has proven harmful to the environment because it presents high color, total phenol and TOC and is also highly toxic even in low concentration.

The results of photocatlysis with catalyst were higher for reductions in color, total phenol and TOC, than the parallel effects (photolysis and absorption).

The combined treatments presented benefits when compared with the non-combined ones. Fungus in combination with photocatalysis proved to be the best treatment, reducing color, total phenol, toxicity and TOC.

Acknowledgments

The authors are grateful to FAPESP, CNPq and CAPES for financial support. We also thank Lúcia A. B. A. Castro for technical assistance.

References

APHA- American Public Health Association. (1989), *Standard Methods for the examination of water and wastewater*. 17, 5-68.

Bandala, E. R.; Pelaez, M. A.; Garcia-López, A. J.; Salgado, M. J.; Moeller, G. (2008). *Photocatalytic decolourisation of synthetic and real textile wastewater containing benzine-based azo dyes*. Chem. Eng. Process., 47, 169-176.

Beek , T. A. V.; Kuster, B,; Claassen, F. W.; Sierra-Alvarez, R. (2007). *Fungal bio-treatmen of spruce wood with Trametes versicolo for pitch control: influence on extractive contents, pulping process parameters, paper quality and effluent toxicity,* Bioresour. Technol., 98, 302-311.

CPPA., Technical Section Standart Method H5P (1975).

ISO – International Organization For Standarization (1987). Water Quality Guidelines for the Determination of Total Organic Carbon (TOC) ISO 8245.

Jardim W. F.; Pasquini C.; Guimarães J. R.; Faria L. C. (1990). *Short-term toxicity test using Escherichia coli: monitoring CO2 production by flow injection analysis*. Wat. Res., 24, 351-354.

Malaviya, P.; Rathore, V. S. (2007). *Bioremediation of pulp and paper mill effluent by a novel fungal consortium isolated from polluted soil*. Bioresour. Technol., 96, 3647-3651.

Oller, I.; Malato, S.; Sanchez-Perez, J. A.; Maldonato, M. J.; Gassó, R. (2007). *Detoxification of wastewater containing five common pesticides by solar AOPs-biological coupled system.* Catal. Today, 129, 69-78.

Pedroza, A. M.; Mosqueda, R.; Alonso-Vante, N.; Rodriguez-Vazquez, R. (2007). *Seqüencial treatment via Trametes versicolor and UV/TIO_2/Ru_xSe_y to reduce contaminants in wastewater resulting from the bleaching process during paper production*. Chemosphere, 67, 793-801.

Paiva, T. C. B.; Silva, R. C.; Santos, L. F.; Moraes, S. G.; Durán N.; Silva F. T. (2001). *Characterization of the pulping and bleaching effluents from a nitrocelulose industry and their environmental impact*. 11TH INTERNATIONAL SYMPOSIUM ON WOOD AND PULPING CHEMISTRY, Nice- França, Proceedings, 391-396.

Peralta-Zamora.; Moraes S. G.; Pelegrini R.; Freire M.; Reyes J.; Mansilla H.; Durán N. (1998). *Evaluation of ZnO, TiO2 and supported ZnO on the photoassisted remediation of black liquor, cellulose and textile mill efluents*. Chemosphere, 36, 2119-2133.

Rao, R. N.; Venkateswarlu, N. (2006). *Removal of amino and nitro-substituted stilbenesulfonic acids from aqueous environment: biosorption and biodegradation by isolated Aspergillus awamori*. Process. Biochm., 1097-1105.

Silva, E. S.; Souza, J. V. B.; Paiva, T. C. B. (2002). *Evaluation of Lentinus edodes UEC 2019 efficiency in the bioremediation of an ECF effluent.* In: CONGRESO IBERO AMERICANO DE INVESTIGACION EM CELULOSA Y PAPEL, Campinas, Programas e Trabalho completo. SP.

Souza, J. V. B.; Silva, E. S.; Silva, F. T.; Paiva, T. C. B. (2005). *Fungal treatment of a delignification effluent from a nitro cellulose industry*. Bioresour. Technol., 96, 1936-1942.

Souza, J. V. B.; Barreto-Rodrigues, M.; Silva, E. S.; Silva, F. T.; Paiva, T. C. B. (2004). T*reatment of a delignification effluent with Aspergillus 2BNL1 and optimization of biomass production.* J. Food, Agric., Environ., 2, 391-394.

Tariq, M. A.; Faisal, M.; Saquib, M.; Muneer, M. (2008). *Heterogeneous photocatalytic degradetion of na anthraquinone and a triphenylmethane dye derivative in aqueous suspensions of semicondondutor*. Dyes Pigments, 76 358-365.

Tran, A. V. (2006). *Decreasing effluent loads through bleaching modification*. Waste Res., 40 487-494.

Proceedings of the 10th International Chemical and
Biological Engineering Conference - CHEMPOR 2008
Braga, Portugal, September 4-6, 2008
E.C. Ferreira and M. Mota (Eds.)

Olive mill effluents treatment by physical-chemical integrated processes

Rui C. Martins, Nádia C. Costa, Cátia M. Augusto, Margarida J. Quina, Licíno M. Gando-Ferreira, Rosa M. Quinta-Ferreira*
GERSE, Group on Environment, Reaction and Separation Engineering
Department of Chemical Engineering, Faculty of Sciences and Technology Pólo II
University of Coimbra, 3030-790 Coimbra, Portugal

Keywords: Agro-industrial wastewaters, Fenton process, Ozonation, Ultrafiltration, Process integration
Topic: Sustainable process-product development trough green chemistry

Abstract

Olive Mill Wastewaters (OMW) are known by the recalcitrant character to biological treatments, therefore, with the aim to find technological solutions for the environmental problems related with the OMW, the efficiency of two chemical oxidations systems was tested. The effect of the main operating parameters in Fenton's process (pH, hydrogen peroxide concentration and iron concentration) was analysed. This process showed high efficiency for the degradation of the effluent phenolic content for all the conditions in use. The highest COD removal was 78.5%. Ozonation revealed higher difficulty in COD degradation with 17.6% removal after 180 min for the best conditions tested (high ozone inlet gas concentration and acidic pH). The effect of ozone gas inlet concentration and pH in the process efficiency was investigated. Moreover, preliminary results showed the efficiency of ultrafiltration, a refining treatment of OMW subjected to Fenton's process followed by ozonation.

1 Introduction

Sustainable development is related with a good management of the effluents produced during the industrial processes. In general, the agro-industries are characterized by small familiar companies spread all over the country where the management and depuration of the final effluents is not usually efficient. Nevertheless, the growing public concern around environmental problems related to the disposal of such wastewaters brought up more restrictive legislation that is being progressively applied. In this context, the operation license of the companies is dependent on the environmental certificate which implies the use of adequate wastewater treatment technologies.

Mediterranean Sea area countries are the world main producers of olive oil with an estimated production volume of 2.5 millions of ton correspondent to almost 98% of the global production. Within this scenario, Olive Mill Wastewaters (OMW) are of special concern to these countries. It is estimated that each year 30 million m^3 of olive mill effluents are produced. Even if the characteristics of those wastewaters vary widely with regard to the oil extraction method and the region, the following general characteristics can be attributed: dark brown to black colour; strong smell; high organic content; low biodegradability; acidic character; high concentration in phenolic compounds and high solid content (Azbar *et al.*, 2004).

Due to the presence of several toxic compounds (as is the case of phenolic substances) allied with the seasonal character of these effluents, since the mills only operate during a few months each year (normally the olives collection and oil extraction only takes place during the winter months, starting in November and finishing in February), the application of the

* Corresponding author. Tel + 351-239-798723. E-mail:rosaqf@eq.uc.pt (R. M. Quinta-Ferreira), martins@eq.uc.pt (R. C. Martins)

traditional active sludges treatment leads to inefficient depuration levels. Therefore, alternative methods have to be tested and implemented to minimize the ambient impact and/or allow to water recycling in the olive oil production. In this context, the application of physico-chemical processes appears to be a suitable alternative, which may have higher implementation and operational costs when compared with the traditional biological processes. Nevertheless, the application of integrated systems involving several treatment processes seems to be a suitable alternative concerning both organic content degradation and operational costs. Some studies involving physico-chemical and/or biological treatment processes integration for the depuration of OMW are found in the literature. Gomec *et al.* (2007) used Fenton process to treat OMW after acid cracking, polyelectrolyte and lime flocculation obtaining a final Chemical Oxygen Demand (COD) < 2000 mgO_2/L. Bedoui *et al.* (2008) achieved almost 90% of COD removal using UV radiation coupled with hydrogen peroxide. Andreozzi *et al.* (2008) concluded that, even for long experimental times, the different combinations between centrifugation, ozonation, solar photolysis and photo Fenton were only able to lead to a maximum of 74.7% of COD removal. Photo-Fenton process reduced the effluent toxicity allowing to a more efficiency pos-anaerobic digestion (Khoufi *et al.*, 2007). Also ozonation coupled with anaerobic treatment showed good results in OMW depuration (Beltran-Heredia and Garcia, 2005). Some work was done in the application of ultrafiltration for the treatment of OMW. Akdemir and Ozer (2008) used a Box-Wilson statistical experiment design method to optimize the operational condition of an ultrafiltration unit in a raw OMW. Turano *et al.* (2002) integrated centrifugation with ultrafiltration while Drouiche *et al.* (2004) tested the applicability of an oxidant system UV/H_2O_2 to finish the treatment of the permeate after the ultrafiltration process. The aim of this research is to study the efficiency of the combination of the oxidation processes Fenton and ozonation and the separation technique in the treatment of OMW in order to achieve an effluent suitable to be discharged in municipal wastewater treatment plants. In Fenton process the oxidant power of hydrogen peroxide is enhanced by the presence of the iron catalyst, whereas ozonation is based on the oxidant ability of ozone which reacts quickly with high electronic density molecules as phenolic compounds. The ultrafiltration is a membrane process suitable for separating dissolved macromolecules in solution on the basis of size and is usually used as a refining process of the other treatment technologies.

2 Experimental

The effluent from the olive oil extraction was collected during the month of February from a mill in the Extremadura region of Spain.

2.1 Experimental Procedure

2.1.1 Fenton process

The tests involving the Fenton reagent were performed in a *Jarr-Test* unit provided with baffles paddles. The reactors were filled with 300 mL of effluent and the stirring speed was set at 200 rpm. $FeSO_4.H_2O$ was added as catalyst in a concentration range of 1520 – 15200 ppm on iron. Hydrogen peroxide was added in batch mode with a range of concentration between 7000 and 34000 ppm. When the influence of the initial pH was studied, a solution of H_2SO_4 was used. Samples were periodically withdrawn (3 mL) and the reaction stopped by the addition of NaOH (1.75 M), for further analysis. The iron sludge formed was removed by filtration before the application of the several analytical procedures.

2.1.2 Ozonation

Ozonation was performed in a semi-batch glass reactor (500 mL) provided with two gas diffusers as described elsewhere (Martins *et al.*, 2008). Ozone was generated in a 802N BMT ozone generator by means of an oxygen stream (500 cm^3/min). Ozone gas inlet concentration was set in the range 40-120 g/m^3 (BMT 963 vent BMT ozone gas analyzer). When the effect of pH was studied (In the study of the effect of pH on the process efficiency), a solution of NaOH (1.75 M) was used to set this parameter in the desired value. Samples were periodically withdrawn for analysis.

2.1.3 Ultrafiltration

In the ultrafiltration tests, which were operated in total recirculation mode, the effluent was stored in a stirred reservoir and pumped to a hollow fiber membrane module (Minikros, *Sepctrum*). The membrane studied had a molecular weight cut-off of 50 kDa and an area of 400 cm^2. Two manometers, one before and other after the module ~~membrane~~ allowed to measure and control the pressure drop in the module. The liquid flow was established by means of two valves and one rotameter. The liquid flow was first stabilized and along the experiments different pressure drops in the membrane were tested. Permeate samples were taken for analyses.

2.2 Analytical methods

Due to the wide variety of compounds present in OMW, it is useful to characterize the effluent in terms of lumped parameters, such as Total Organic Carbon (TOC), Chemical Oxygen Demand (COD), Biological Oxygen Demand (BOD) and Total Phenolic Content (TPh). TOC was measured in a *Shimadzu 5000 TOC* analyzer, which operates based on combustion/non-dispersive infrared gas analysis method (NDIR). COD was measured by the dichromate method; the samples were digested at 148ºC in a *WTW CR3000* thermoreactor and COD measured in a *WTW MPM3000* photometer. BOD after 5 days (BOD_5) was obtained by the method described in the Standard Methods (1985) measuring the dissolved oxygen (*Multi-parameter Analyser CONSORT C863*) before and after 5 days of incubation of a population of microorganisms obtained from a garden soil suspension. TPh was determined using a Folin-Ciocalteau reagent in a *T60 U PG instruments* spectrophotometer by the procedure described elsewhere (Martins *et al.*, 2008). Total Suspended Solids (TSS) and Total Dissolved Solids (TDS) were determined according to the Standard Methods (1985).

3 Results and discussion

In this section the effluent characterization is firstly presented. The laboratorial results addressing Fenton's process and ozonation are then discussed and afterwards the application of ultrafiltration as refining process to an Olive Mill Wastewater treated by Fenton followed by ozonation in an industrial unit is analysed.

3.1 Effluent Characterization

The effluent characterization was mainly performed in terms of the lumped parameters shown in Table 1.

Table 1. Characterization of industrial effluent

pH	TOC (mgC/L)	COD (mgO_2/L)	BOD5 (mgO_2/L)	BOD5/COD	TPh (mgeq. gallic acid/L)	TSS (mg/L)	TDS (mg/L)
4.7	368±23	1485±15	216±24	0.14	106.4±5	40	1160

The effluent shows acidic character (pH=4.7) typical of OMW, yet the organic content of the wastewater, measured as TOC, COD or BOD_5, is low when compared with the range of values present in the literature (Azbar *et al.*, 2004). Nevertheless, this sample had already suffered sedimentation which explains also the low TSS value and also the wastewater results from the mixture of the process effluent with the washing waters. A ratio between BOD_5 and COD lower than 0.3 means an effluent with low biodegradability (Farré *et al.*, 2007). This was expected since OMW is known by the presence of several organic compounds toxic to the microorganims as is the case of phenolic substances here quantified by the equivalent gallic acid concentration (106.4 mgeq. gallic acid/L). These substances are usually quickly removed by chemical oxidation processes and therefore the applicability of Fenton reagent and ozonation was tested.

3.2 Fenton stage

The Fenton process is based in the oxidant power of hydroxyl radicals produced by the catalytic decomposition of hydrogen peroxide in the presence of iron at acidic conditions. The influence of the operating parameters, hydrogen peroxide initial concentration, ferrous iron initial concentration and pH was investigated. Figure 1a despites the COD normalized concentration during the Fenton experiments. In all the experiments, a high COD decrease occurred for the first minutes of reaction followed by a lag period with low oxidation rates. The increase in the initial concentration of H_2O_2 from 7000 to 34000 ppm largely improved the process efficiency with COD removal increasing from 52.5% to 78.5%. The growth in H_2O_2 concentration leads to the formation of more hydroxyl radicals enhancing oxidation, while an excess of this reactant in solution may also act as radical scavenger which reduces the process performance (Ahmadi *et al.*, 2005). Also the increase of the initial iron concentration from 1520 to 15200 ppm (with all the other variables constant) improves the process efficiency in terms of COD removal in 16% after 120 min of reaction. Nevertheless, the impact of this variable is not as important as the hydrogen peroxide initial concentration. In fact, from an optimization process based on an experiment design and response surface methodology (results not shown) it was concluded that among the process parameters tested only H_2O_2 initial concentration had statistical relevance for the treatment efficiency in terms of COD removal. The Fenton's process efficiency is highly affected by pH, being generally acidic media (pH between 2 and 4) more favourable (Rivas *et al.*, 2001). In our studies, COD removal increased when pH increased from 2.5 to 4.7 (62.3% and 78.5%, respectively). Nevertheless, it should be pointed out that the pH suffered a quick self adjustment to 2.8 after the reactants introduction, regardless the initial value. Due to the effluent toxicity related with the phenolic content it is important to evaluate the efficiency of the treatment technology on the removal of these compounds. For every experimental conditions tested, total phenolic degradation was achieved in the early minutes of reaction.

3.3 Ozonation stage

The effect of pH and ozone inlet gas concentration was tested in the efficiency of ozonation process for the treatment of OMW. The first observation taken from the results in Figure 2 is that ozonation leads to lower COD removal efficiency than the Fenton's process for all the experimental conditions under study.

The increase of ozone inlet gas concentration (for the same pH value) from 40 g/m^3 to 120 g/m^3 allowed higher degradation levels with COD removal raising from 10.6% to 17.6%. This was expectable, since a higher amount of ozone was available for reaction. pH is an important parameter in aqueous ozone chemistry since it controls the oxidant double action. At low pH values ozone attacks selectively organic molecules characterized by high electronic density. For alkaline pH values ozone is decomposed into highly reactive hydroxyl radicals, which will correspond in general to a higher depuration level. Nevertheless, comparing the results achieved for the experiments conducted at pH = 3.4 and 9.2 (for the same inlet ozone gas concentration of 120 g/m^3), one can observe a decrease in ozonation efficiency with the increase of pH with COD removal of 17.6% and 8.8%, respectively. In fact, in real wastewaters the presence of inorganic compounds, like carbonates that act as radical scavengers may interfere with the treatment, which can explain the decrease in the degradation for the experiment with alkaline pH.

3.4 Ultrafiltration process for Fenton – Ozonation pre-treated effluent

Within the previous results for the individual Fenton and Ozonation treatments of OMW, the applicability of Ultrafiltration as refining process for an effluent previously submitted to Fenton followed by ozonation in an industrial plant was examined. The pre-treated OMW was characterized by a COD value of 883 mgO_2/L. The effect of the operating variables (feed flow rate and pressure drop) on the ~~(~~COD removal efficiency and permeate flux - J is given in Figure 2. As expected, J shows a linear behaviour with the transmembrane pressure (Figure 2a). Moreover, for a constant pressure, J increases with the recycling flow rate. In fact, higher cross-flow velocity results in the increasing of the transport of the solutes from the membrane surface to the bulk feed; therefore the concentration polarization is reduced which

increases the permeate flux (Akdemir and Ozer, 2008). As observed in Figure 2b, COD removal in ultrafiltration process is in the range of 11.1% and 31.5%. Contrarily to what was expected, the increase of the COD removal efficiency increased with the recycling flow rate for constant pressure, for example for 0.5 bar COD reduction changes from 31.5% to 11.1% for the cross-flow rate of 0.12 and 0.06 m/s, respectively. It should be also noticed that, while for higher cross-flow rates (0.12 and 0.09 m/s) COD removal is almost constant with transmembrane pressure, for the lowest cross-flow rate the efficiency decays with pressure. These phenomena can be attributed to the fact that the fouling layer was not totally formed and, therefore steady state was not reached yet.

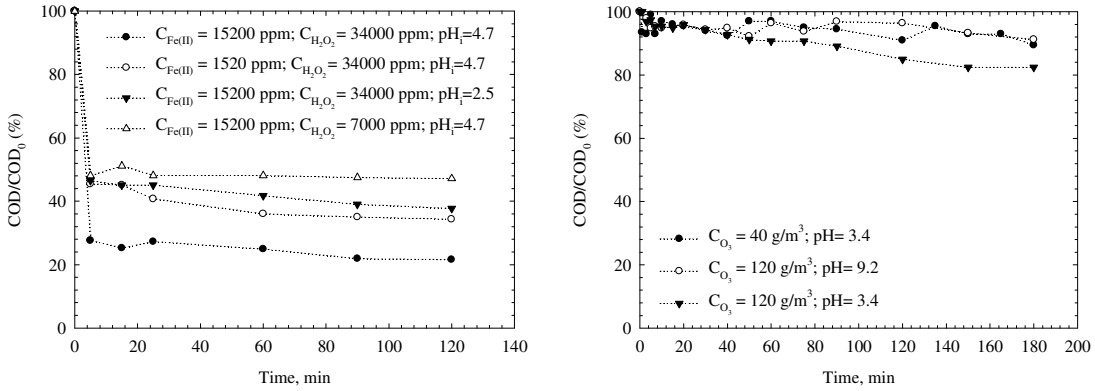

Figure 1. COD removal along **a)** Fenton's process at several experimental conditions and **b)** ozonation.

Figure 1. Evolution of the COD removal at different experimental conditions: a) Fenton treatment and b) Ozonation process.

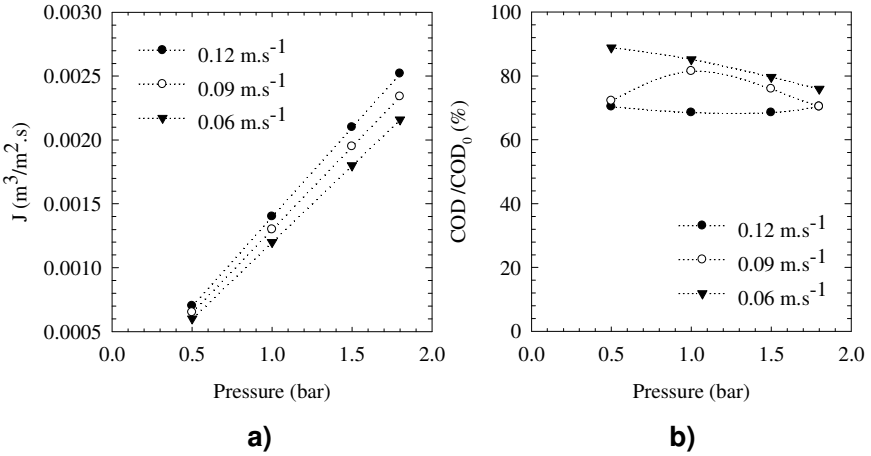

Figure 2. Permeate flux (a) and COD removal (b) as function of the transmembrane pressure at different recirculation velocities.

4 Conclusions

OMW constitutes a major environmental problem due to the bio-refractory character and seasonability. Therefore it is a technological issue of main importance the finding of suitable technologies to safely treat these effluents. Within this objective, the chemical oxidation by Fenton's reagent and ozonation were tested for the depuration of a real OMW. Fenton's process efficiency was on the range of 52.5 and 78.5% of COD removal depending on the

operating conditions (initial pH, concentration on hydrogen peroxide and iron). Among those operational variables the main effect on the process efficiency was caused by the concentration on hydrogen peroxide with an improvement of 26% on COD degradation when this value rises from 7000 to 34000 ppm. Ozonation showed lower efficiency in the mineralization of this effluent, with COD removals between 8.8 and 17.6%. The increase on ozone inlet gas concentration improved the process whereas the increase of the pH reduced the treatment efficiency probably due to the presence of inorganic radical scavenger on the effluent composition. Preliminary tests involving ultrafiltration of a pre-treated OMW by Fenton's reagent followed by ozonation on an industrial plant enhanced the applicability of this physical separation process as a refining treatment on OMW depuration. Within our results, ultrafiltration led to colourless effluent and for the best experimental conditions reduced 31.5% of the COD.

Acknowledgements

Rui C. Martins gratefully ackonwledes *Fundação para a Ciência e Tecnologia*, Portugal for the finantial support under the PhD grant (BD/28854/2006).

References

Ahmadi, M., Vahabzadeh, F., Bonakdarpour, B., Mofarrah, E., Mehranian, M. (2005). Application of the central composite design and response surface methodology to the advanced treatment of olive oil processing wastewater using Fenton's peroxidation. *Journal of Hazardous Materials*, B123, 187-195.

Akdemir, E., Ozer, A. (2008). Application of a statistical technique for olive oil mill wastewater treatment using ultrafiltration process. *Separation and Purification Technology*. 62, 222-227.

Andreozzi, R., Canterino, M., Di Somma, I., Lo Giudice, R., Marotta, R., Pinto, G., Pollio, A. (2008) Effect of combined physico-chemical processes on the phytotoxicity of olive mill wastewaters. *Water Research*. 42, 1684-1692.

Azbar, N., Bayram, A., Filibeli, A., Muezzinoglu, A., Sengul, F., Ozer, A. (2004). A review of waste management options in olive oil production. *Critical reviews in environmental science and technology*, 34, 209-247.

Bedoui, A., Sindi, K., Bensalah, N. (2008). Treatment of refractory organics contained in actual agro-industrial wastewaters by UV/H2O2. *Clean*, 36(4), 373-379.

Beltran-de-Heredia, J., Garcia, J. (2005). Process integration: continuous anaerobic digestion – ozonation treatment of olive mill wastewater. *Industrial & Engineering Chemistry Research*. 44, 8750-8755.

Drouiche, M., Le Mignot, V.; Lounici, H.; Belhocine, D.,Grib, H., Pauss, A., Mameri, N. (2004). A compact process for the treatment of olive mill wastewater by combining UF and UV/H_2O_2 techniques. *Desalination*, 169, 81-88.

Farré, M., Franch, M, Ayllón, J., Domènech, X. (2007). Biodegradability of treated solutions of biorecalcitrant pesticides by means of photocatalytic ozonation. *Desalination*, 211, 22-33.

Gomec, C., Erdim, R., Turan, I., Aydin, A., Ozturk, I. (2007). Advanced oxidation treatment of physico-chemically pre-treated olive mill industry effluent. *Journal of Environmental Science and Health part B.*, 42, 741-747.

Khoufi, S., Aloui, F., Sayadi, S. (2006). Treatment of olive oil mill wastewater by combined process electro-Fenton reaction and anaerobic digestion. *Water Research*, 40, 2007-2016.

Martins, R., Leal, H., Quinta-Ferreira, R. (2008). Single and catalytic ozonation for phenolic wastewaters remediation, in: *Current themes in Engineering Technology,* American Institute of Physics, New York.

Turano, E., Curcio, S., De Paola, M., Calabrò; V., Iorio, G. (2002). An integrated centrifugation-ultrafiltration system in the treatment of olive mill wastewater. *Journal of Membrane Science*, 209, 519-531.

Proceedings of the 10th International Chemical and
Biological Engineering Conference - CHEMPOR 2008
Braga, Portugal, September 4-6, 2008
E.C. Ferreira and M. Mota (Eds.)

Removal of formaldehyde by oxidation from phenolic resin plant effluents

Shiva Agarwal, Ana E. Ferreira, Licínio M. Ferreira, M. Teresa A. Reis, Remígio M. Machado, Jorge M. R. Carvalho*
Centre for Chemical Processes, Department of Chemical and Biological Engineering,
Instituto Superior Técnico
Av. Rovisco Pais, 1049-001 Lisboa – Portugal

Keywords: Phenolic resin plant effluent, formaldehyde, chemical oxidation, Fenton
Topic: Sustainable process-product development through green chemistry – Environmental engineering & management

Abstract

In the present work, formaldehyde, which left in phenolic resin plant effluent after removal of phenol, has been treated with hydrogen peroxide in alkaline medium and also in acidic medium (Fenton process). In alkaline medium, formaldehyde was oxidized with hydrogen peroxide to formate ion, which was tried to recover by liquid-liquid extraction. The oxidation of formaldehyde with Fenton process was also studied under different initial pH, mole ratio of hydrogen peroxide to formaldehyde, pressure and temperature. It was found that ratio H_2O_2:HCHO 7 provided 97% removal of total organic carbon (TOC) after 2 h and larger amounts of H_2O_2 were necessary to mineralize around 90% HCHO in 1 h, at atmospheric pressure and 25 ºC. The combination of pressure and high temperature strongly increased the kinetics of the process.

1 Introduction

Phenol and formaldehyde are the main pollutants discharged by phenolic resin producing industries. Since exposure of these chemicals has potential toxic effect on living being, these chemicals must be removed from effluent before releasing it in the environment. The usual treatments of phenolic effluent are biodegradation, thermal decomposition, extraction and adsorption [Kibret *et al.*, 2000; Mollah and Robinson, 1996; Yu and Savage 2000]. Among them, biological treatment is limited to only less concentrated phenolic effluent (< 3000 mg/L) [Kibret *et al.*, 2000] because microorganisms can not survive in higher concentration of organic compounds. On the other hand, thermal decomposition and adsorption proved high energy consuming and costly methods [Mollah and Robinson, 1996; Yu and Savage 2000]. But solvent extraction method finds some advantages in treating concentrated phenolic wastewater. This is justified with the work published in literature [Li *et al.*, 2004]. Our research group also studied the removal of C_6H_5OH and HCHO from phenolic resin plant effluents by using solvent extraction [Correia and Cravalho, 2005; Correia *et al.* 2007]. The studies revealed that Cyanex 923 was found more selective extractant for C_6H_5OH than other tested extractants and also extraction of formaldehyde (present in the solution with phenol) was almost nil. So the objective of the present work is to remove formaldehyde after the separation of phenol. In literature, several methods are cited to obtain this objective like liquid-liquid extraction, polymerization with urea, oxidation in alkaline medium, oxidation in acidic medium (Fenton process), photo-Fenton process, treatment with active charcoal and conversion to easily biodegradable formaldehyde disulfide.

The liquid-liquid extraction of formaldehyde with 1-decanol was already tested [Correia *et al.*, 2007], but the kinetics of the extraction was very slow. Equilibrium was reached in more than 6 h. Therefore, oxidation of formaldehyde in alkaline and acidic medium (Fenton process) were studied and the results are presented here. In presence of base, formaldehyde was

* Corresponding author. Tel: +351 218417311. E-mail: jcarv@ist.utl.pt

oxidized with hydrogen peroxide to formate according to the following chemical equation (Walker, 1975).

$$2\ HCHO_{(aq)} + H_2O_{2\ (aq)} + 2\ NaOH_{(aq)} \longrightarrow 2\ NaHCOO_{(aq)} + 2H_2O_{(aq)} + H_{2(g)}$$

After oxidation, the resultant formate was acidified to formic acid. Further the recovery of formic acid was carried out by liquid-liquid extraction with Cyanex 923 and Alamine 336. In literature, some other works are also published related to formic acid extraction using phosphate containing extractants [Wisniewski and Pierzchalska, 2005; Cai et al., 2001] and tertiary amines [Hu and Adeyiga, 1997]. Also oxidation of formaldehyde with Fenton process in different experimental conditions were carried out and the results are discussed here.

2 Experimental

Formaldehyde oxidation studies

The experiments of chemical oxidation in alkaline medium were carried out at 22 °C using 130 Vol. hydrogen peroxide (José Manuel Gomes dos Santos LDA), sodium hydroxide (Panreac, p.a.) and potassium hydroxide (MERCK, p.a.). The experiments of chemical oxidation of formaldehyde, using Fenton reagent, at 25 °C, were carried out in 2 L Pyrex glass insulated reactor with agitation. This reactor could withstand 0.6 bar external pressure. The experiments with high temperature and under pressure were conducted in a 1.5 L stainless steel 316 AISI insulated reactor with agitation. It is coated with Hypalon and a high temperature of 200 °C and 15 bar pressure can be maintained in this reactor. pH was adjusted by using dilute sulphuric acid. Heptahydrated ferrous sulphate, $FeSO_4.7H_2O$ (MERCK, p.a.) was used as catalyst.

Liquid-liquid extraction studies

The organic phases were prepared by diluting the extractant in aliphatic diluents viz., Shellsol T (Shell Chemical Ltd.) and Exxsol D80 (ExxsonMobil, Spain). In the present study, the extractant Cyanex 923 was used as such as obtained from Cytec, Netherlands. Another extractant Alamine 336 (Cognis) was also tested but along with the modifier 1-decanol (Acros Organics, Belgium). Before use, Alamine 336 was washed with acidified water and then with water to remove impurities. 3 M NaOH was used to strip loaded formic acid.

Analytical methods

Formaldehyde analysis was done by the Hantzsch reaction colorimetric method [ASTM, 1999]. A double beam ultraviolet/visible spectrophotometer Hitachi U2000 was used for the analysis. Formate ion was analyzed by potentiometric titration in a Metrohm 682 Titroprocessor. Total organic carbon was determined by Dohrmann Carbon analyzer. pH was measured by a Metrohm 827 pH meter with a Metrohm combined electrode.

3 Results and discussion

Oxidation of formaldehyde in alkaline medium and recovery of formate

The phenolic effluent, after removal of phenol, contains mainly formaldehyde which was treated with hydrogen peroxide in alkaline medium. The concentration of formaldehyde oxidized, by hydrogen peroxide in presence of either KOH or NaOH, was 41 g/L. The results showed that reaction is independent of nature of base as nearly 100% stoichiometric conversion of formaldehyde to formate was obtained in both the cases. Further, kinetic study revealed that the reaction was over in less than 5 min.

The extraction of formate ion, obtained after oxidation, with tertiary amine and Cyanex 923 was tried but extraction was lower than 5%, so extraction of formate ion in the form of formic acid was tried. This is also supported by the work of Hu and Adeyiga [1997] who used CO_2 to convert formate to formic acid before extraction with tertiary amines. Since the oxidation was performed in alkaline medium, the pH of the resultant solution was as high as 12. Therefore, the resultant formate solution was first acidified with concentrated sulphuric acid and for that a reasonable amount of acid was used. To adjust the pH around 2.0 of the 1500 mL formate

solution, 60 mL concentrated sulphuric acid was required. This data shows that the removal of formaldehyde in the form of formic acid from waste water ought not to be very economical for industrial purpose. Nevertheless, bench scale studies were carried out to explore the potential of extraction and concentration. The extraction of formic acid with Alamine 336 has been already studied by our research group [Correia *et al.*, 2005]. In those studies Alamine 336 was protonated before using it for extraction of formic acid. Here two extractants i.e. Cyanex 923 and Alamine 336 again but in unprotonated form are used. The preliminary experiments of extraction of formic acid using Cyanex 923 with diluents Shellsol T and Exxsol D80 were carried out at 25 ºC. The results showed that extractive performance of Cyanex 923 remained almost the same with both diluents. Shellsol T was used as diluent in all the subsequent studies. The extraction of 61 g/L formic acid was then tried with 0.6 M and 1.0 M Cyanex 923 and the extraction capacity increases with the increase in concentration of extractant as also obtained with Alamine 336. In case of extraction with Alamine 336, 10% 1-decanol was used as modifier. The equilibrium curve for the extraction of 61 g/L formic acid solution with 1.0 M Cyanex 923 was compared with that obtained with 1.0 M unprotonated Alamine 336 and presented in Fig. 1.

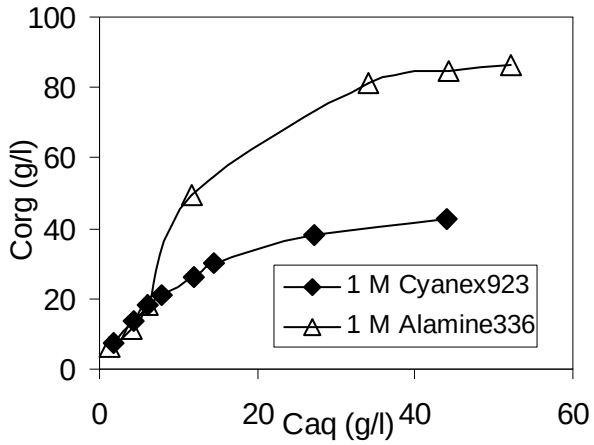

1.0 M Cyanex 923			1.0 M Alamine 336		
C_{aq} (g/L)	C_{org} (g/L)	D	C_{aq} (g/L)	C_{org} (g/L)	D
1.8	7.5	4.2	1.4	5.9	4.4
4.2	13.6	3.2	4.1	11.4	2.8
6.1	18.1	2.9	6.1	18.3	2.9
7.9	21.2	2.7	11.8	49.4	4.2
12.0	26.0	2.2	34.1	81.3	2.4
14.5	30.2	2.1	44.3	84.4	1.9
27.2	38.1	1.4	52.1	86.5	1.6
44.1	42.4	1.0			

Fig. 1. Comparison of equilibrium curves for the extraction of 61 g/L formic acid solution with 1.0 M Cyanex 923 and 1.0 M Alamine 336 at 25 °C. D – distribution ratio.

From results it is clear that the extraction with Cyanex 923 did not seem very promising in case if extraction of a higher concentration of formic acid i.e. 61 g/L was performed. While unprotonated Alamine 336 provided much better extraction than Cyanex 923. Except few preliminary stripping studies with loaded Cyanex 923, rest of the stripping studies were carried out with 0.6 M and 1.0 M loaded unprotonated Alamine 336 as shown in Fig. 2.

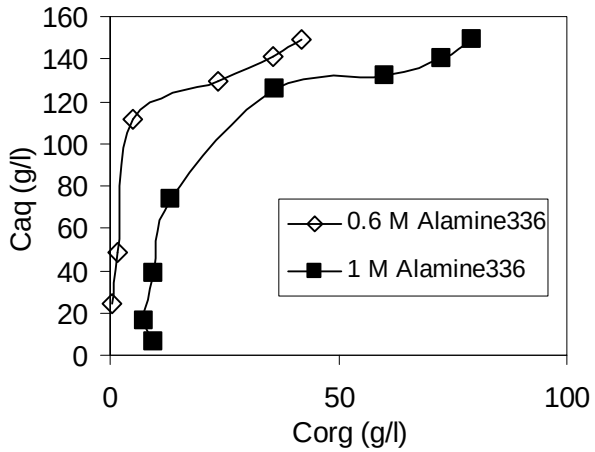

Fig. 2 Comparison of equilibrium isotherms for the stripping of formic acid from loaded Alamine 336 (0.6 M loading=49.6 g/L, 1 M loading=86.6 g/L) with 3 M NaOH at T=25 °C.

From the equilibrium data presented, it can be concluded that Alamine 336 allows concentration of formic acid in the form of formate by liquid-liquid extraction. However, the concentration ratio obtained was about 2 times. Moreover, as mentioned, a reasonable amount of sulfuric acid was required to adjust the pH before extraction. Therefore, some of these uneconomical aspects of the previous studies prompted us to try the removal of formaldehyde with Fenton process.

Oxidation of formaldehyde in acidic medium

The oxidation of formaldehyde in acidic medium using Fenton reagent was also carried out. Kajitvichyanukul et al. [2006 and 2008] also studied formaldehyde degradation using Fenton and photo-Fenton processes. They obtained almost complete removal of total organic carbon (TOC) content in 4 h. However, for industrial purposes 4 h reaction time seems long enough so the aim of the present study was to try other conditions to degrade formaldehyde in less time. Therefore, in all the experiments carried out, the reaction time was limited to 2 h only.

Usually phenolic resin plants discharge different concentrated effluents and for instance a Portuguese phenolic resin company discharges effluents namely 'Low' and 'High' containing 0.4-3 g/L and 10-40 g/L formaldehyde respectively. So some preliminary experiments were carried out with varying initial concentration of formaldehyde and it was found that initial concentration of formaldehyde did not effect much on the % removal of TOC if all other conditions were kept same. On the basis of these results, a low initial concentration of formaldehyde i.e. 2 g/L was selected for all subsequent studies.

The effect of pH on degradation of formaldehyde was studied at initial pH 1.6, 2.5 and 3.5 at different mole ratio of hydrogen peroxide to formaldehyde. The results are depicted in Fig. 3.

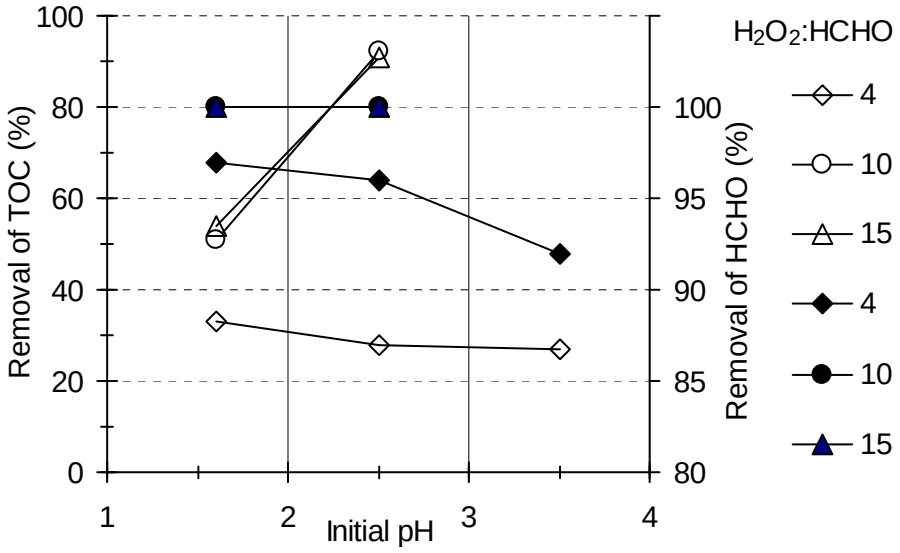

Fig. 3 Effect of initial pH on degradation of HCHO with Fenton process for mole ratio H_2O_2:HCHO 4, 10 and 15; [HCHO]=2 g/L (0.067 M), [Fe^{2+}]=0.013 M, T=25 °C, (open symbols: TOC removal, solid symbols: HCHO removal).

From Fig. 3, initial pH 2.5 allowed highest removal of TOC in case of ratio H_2O_2:HCHO 10 and 15. So in all further experiments initial pH 2.5 was adjusted. It is worth mentioning that pH 3.5 decreased to 2.5 after 2 h, whereas pH 2.5 decreased less than 0.1. Concerning the removal of formaldehyde, almost 90-100% was achieved in all cases. This data indicates that formation of intermediates during the course of oxidation are more resistent to degradation than the parent compound. Moreover, the usual presence of methanol in the solution of formaldehyde also inhibits the complete mineralization. These results are consistent with that observed by Kajitvichyanukul et al. [2006, 2008]. In all the experiments mole ratio HCHO:Fe^{2+} 5 was used and this data was taken from literature [Kajitvichyanukul et al., 2008].

Further, the influence of amount of hydrogen peroxide on mineralization of formaldehyde was also studied and the results of % of TOC removal in variation with H_2O_2:HCHO ratio after 1 h and 2 h are shown in Fig. 4. As observed, with ratio H_2O_2:HCHO 6, around 91% of TOC removal was achieved but only after 2 h, whereas 33 % TOC was removed after 1 h. It was found that a high amount of H_2O_2 (ratio H_2O_2:HCHO 10 and 15) was necessary to mineralize around 90% HCHO only in 1 h.

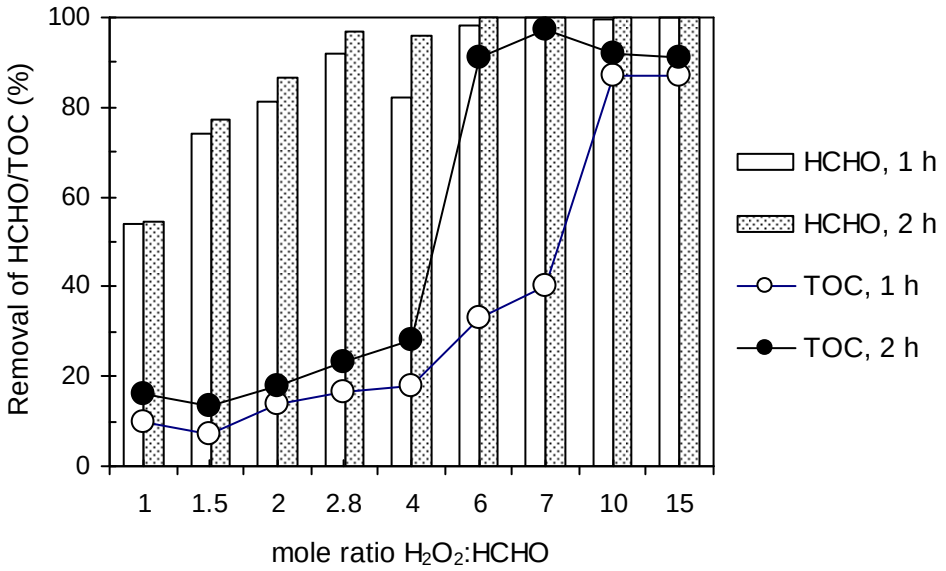

Fig. 4. Effect of amount of H_2O_2 on degradation of HCHO with Fenton process; [HCHO]= 2 g/L (0.067 M), [Fe^{2+}]= 0.013 M, T= 25 °C, initial pH 2.5.

Some experiments were then carried out under pressure and a higher temperature to try to avoid the use of such a large excess of hydrogen peroxide. The results are presented in Fig. 5. It is evident that under relative pressure of 0.5 bar, % TOC removal was higher than that obtained under atmospheric pressure, which indicates that pressure can be an important parameter in Fenton process. Besides, under pressure, augment in temperature was allowed without significant problems in decomposition of hydrogen peroxide.

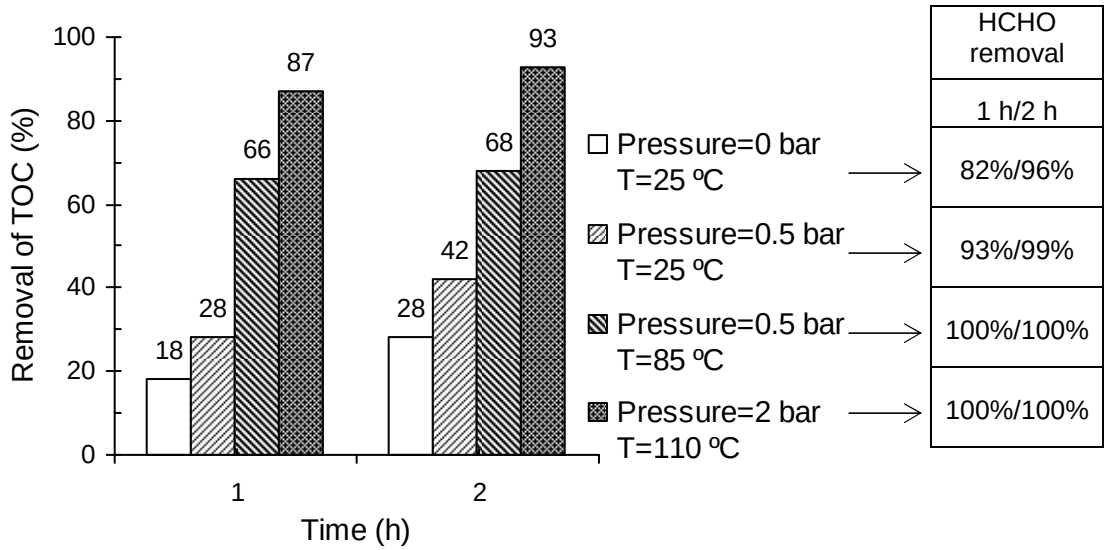

Fig. 5 Effect of pressure and temperature on degradation of HCHO with Fenton process; [HCHO]= 2 g/L (0.067 M), [Fe^{2+}]= 0.013 M, mole ratio H_2O_2:HCHO=4, initial pH 2.5.

As shown in Fig. 5, the combination of high temperature and pressure strongly enhance the kinetics of the process. The removal of TOC increased to about 70 % (relative pressure 0.5

bar and T= 85 °C) and 90 % (relative pressure 2.0 bar and T= 110 °C) after 1 h. Since the results are very promising, the influence of these parameters should be explored and optimized. Therefore, some more studies with pressure and high temperature are still in progress.

4 Conclusions

The oxidation of formaldehyde with hydrogen peroxide in alkaline medium allowed stoichiometric conversion of formaldehyde into formate ion, which could be recovered by liquid-liquid extraction. Cyanex 923 and unprotonated Alamine 336 were used as extractants and with latter better results were achieved. It is possible to concentrate about 120 g/L of formate using 3 M NaOH as stripping phase. In continuation of oxidation of formaldehyde, Fenton process was also investigated by varying some parameters at atmospheric pressure and 25 ºC like pH and amount of hydrogen peroxide. The removal of formaldehyde was very high in most cases. It was found that ratio H_2O_2:HCHO 7 provided 97% removal of TOC after 2 h and larger amounts of H_2O_2 were necessary to mineralize around 90% HCHO in 1 h. The combination of pressure and high temperature strongly increased the kinetics of the process.

5 Acknowledgements

The financial support of AdI/PRIME through the AMBIRES project is acknowledged. Shiva Agarwal acknowledges FCT for her post PhD financial assistance (SFRH/BPD/32429/2006).

6 References

ASTM (1999), Standard Test Method for Formaldehyde in water. In: *1999- Annual Books of ASTM Standards*, ASTM, Philadelphia, Vol. 11, pp. 1007-1011.

Correia, P.M.M., Carvalho, J.M.R. (2005). Salt effects on the recovery of phenol by liquid-liquid extraction with Cyanex 923. *Sep. Sci. Technol.*, 40, 3365-3380.

Correia, P.F.M.M., Ferreira, L.M., Reis, M.T.A., Carvalho, J.M.R. (2007). A study on the selective recovery of phenol and formaldehyde from phenolic resin plant effluents by liquid-liquid extraction. *Solvent Extr. Ion Exch.*, 25, 485-501.

Correia, P.F.M.M., Sampaio M.A.P., Reis, M.T.A., Carvalho, J.M.R. (2005). Removal of phenol and formaldehyde from phenolic resin plant effluents, *Chempor'2005*, Coimbra, Portugal.

Hu, L., Adeyiga, A.A. (1997). Extraction of formic acid from sodium formate. *Ind. Eng. Chem. Res.*, 36, 2375-2379.

Jiang, H., Fang, Y., Fu, y, Guo, Q-.X. (2003). Studies on extraction of phenol in wastewater. *J. Hazard. Mater. B*, 101, 179-190.

Kajitvichyanukul, P., Lu, M.C., Liao, C.H., Wirojanagud, W., Koottatep, T. (2006). Degradation and detoxification of formaline wastewater by advanced oxidation processes. *J. Hazard. Mater. B*, 135, 337-343.

Kajitvichyanukul, P., Lu, M.C., Jamroensan, A. (2008). Formaldehyde degradation in the presence of methanol by photo.Fenton process. *J. Environ. Manag.*, 86, 545-553.

Kibret, M., Somitch, W., Robra, K-.H. (2000). Characterization of a phenol degrading mixed population by enzyme assay. *Wat. Res.*, 34, 1127-1134.

Li, Z., Wu, M., Jiao, Z., Bao, B., Lu, S. (2004). Extraction of phenol from wastewater by n-octanoylpyrrolidine, *J. Hazard. Mater. B*, 114, 111-114.

Mollah, A.H., Robinson, C.W. (1996). Pentachlorophenol adsorption and desorption characteristics of granular activated carbon-I.isotherms. *Wat. Res.*, 30, 2901-2907.

Walker, J.F. (1975). *Formaldehyde*, 3rd. Ed., Robert E. Krieger Publishing Co., New York, 483-660.

Wisniewski, M., Pierzchalska, M. (2005). Recovery of carboxylic acids C_1-C_3 with organophosphine oxide solvating extractants, *J. Chem. Technol. Biotechnol.*, 80 , 1425-1430.

Yu, J., savage, P.E. (2000). Phenol oxidation over CuO/Al_2O_3 in supercritical water. *App. Catal. B: Environmental*, 28, 275-280.

Proceedings of the 10th International Chemical and
Biological Engineering Conference - CHEMPOR 2008
Braga, Portugal, September 4-6, 2008
E.C. Ferreira and M. Mota (Eds.)

Removal of Linoleic Acid From Ethanolic Solutions Using Ion Exchange Resin

Ana C. Morelli[1], Erika C. Cren[1], Antonio J.A. Meirelles[1*]
[1] FEA – Faculdade de Engenharia de Alimentos, Departamento de Engenharia de Alimentos, Unicamp, 13083-862 Campinas, Brazil.

Keywords: Ion Exchange Resin, Linoleic Acid, Langmuir Isotherm, Oil Refining, Equilibrium
Topic: Advancing the chemical and biological engineering fundamentals.

Abstract

Adsorption isotherms for the removal of linoleic acid from ethanol + water solutions using a strong anion exchange resin (Amberlyst A26 OH) were experimentally determined. The equilibrium data were correlated using the Langmuir model by adjusting the parameters q_m, maximum content that can be adsorbed on solid phase (g acid/g dry resin), and K_d, equilibrium constant (g acid/g solvent). In this way the behavior and the capacity of the resin to remove the fatty acid from the liquid phase were evaluated at different experimental conditions: the water content in ethanol was varied within the range (0 to 15) mass % and the temperature was constant 25^{o}C. It was observed that the water content in ethanol does not significantly influence the equilibrium behavior. It was also observed that the strong anion exchange resin (Amberlyst A26 OH) has a good performance in the removal of the fatty acid from the ethanolic phase.

1 Introduction

The most important step of the edible oil refining process is the removal of free fatty acids. The traditional refining methods, physical and caustic refinings, are not appropriate for crude oils with high free fatty acids content, like cotton oil as other ones. They are sensible to the severe conditions that these oils are submitted when employed the traditional refining. These oils can present large losses of neutral oil and in their nutritional value.

The interest in cotton oil is increasing because it is rich in linoleic acid, an essential fatty acid. For these reasons several investigations are performed in order to develop alternative refining methods.

The oil deacidification by liquid-liquid extraction with an appropriate solvent is one of those alternative methods. This process uses solvent for the extraction like methanol, ethanol (Batista et al., 1999), and employs mild operational conditions concerning temperature and pressure. This technology has the possibility of restricting the loss of neutral oil and nutraceutical compounds by an adequate selection of the water content in the ethanolic solvent. This technology lso allow an easy stripping of the residual solvent from the refined oil as a consequence of the very high volatility difference between ethanol and neutral oil (Rodrigues et al., 2004; Gonçalves et al., 2003).

The liquid-liquid extration generates two streams: a stream of desacidified oil (refinated), and a stream rich in solvent and free fatty acids (extract).

But the recovery of the solvent and the essential fatty acid from the extract phase was still not investigated. So the possibility of using anion exchange resins in order to adsorb fatty acids from the extract phase, allowing the recovery of the solvent and the essential fatty acid,

* Corresponding author. Tel + 551935214037. E-mail:tomze@fea.unicamp.br

was investigated in the present work. In this case the use of ion exchange resins could be considered as a complement of the whole liquid-liquid extraction process.

Actually a prior work has already investigated the treatment of the extract stream of the liquid-liquid extraction, using ion exchange resin, but in the case of oleic acid removal (Cren and Meirelles, 2005).

Nowadays, the use of ion exchange resins is very well established as a unit operation. However, investigations using ion exchange resins in fatty systems are still rare (Latip et al., 2001, Ibanez Gonzalez, et al., 2001). In this way, the study of adsorption isotherms and ion exchange mechanism in these conditions is important in order to develop new purification techniques for organic solutions.

2 Material and Methods

Material. The chemicals used in the work were commercial grade linoleic acid, Anhydrous and azeotropic ethanol and sodium hydroxide (Merck). The ethanolic solutions were prepared in mass, by adding demineralized water to anhydrous ethanol. The corresponding water concentrations were: (0,5 $\pm$ 0,01) mass % (anhydrous ethanol), (3,23 $\pm$ 0,06) mass %, (6,79 $\pm$ 0,03) mass % (azeotropic ethanol), (8,22 $\pm$ 0,04) mass % and (15,27 $\pm$ 0,27) mass %. The strong anionic resin used in the experiments was Amberlyst A26 OH (Rohm and Haas).

Methods. Equilibrium experiments were conducted in equilibrium cells, connected to a thermostatic bath, with a proportion of 1:3 of resin and solutions with different linoleic acid initial concentrations, (9,0 to 6,0) mass %. Before performing each equilibrium experiment, the resin was preconditioned, according to the procedure described by Cren and Meirelles, 2005.

The system resin + ethanolic solutions were stirred, until equilibrium was achieved (5 h). At the end of this period, the solutions were removed from each cell with the help of a syringe. The acid concentration in the solutions was determined using titration.

As usual in experiments for determining adsorption isotherms, the equilibrium concentration in the solid phase was calculated by mass balance. The mass balance was performed on a solute (linoleic acid) free basis, taking into account the initial and final oleic acid concentrations and the solvent carried by the resin into the cell. The equilibrium concentrations were also expressed on a solute free basis, as q* (g of linoleic acid/g of dry resin) versus C* (g of linoleic acid/g of solvent).

In this way the influences of water content in ethanolic solutions could be investigated.

3 results and discussion

The experimental equilibrium data obtained for each system investigated, corresponding to the counterion (linoleic acid) concentration in the solution (C*), and the concentration of counterion (linoleic acid) adsorbed in the resin (q*), are shown in Figure 1 and Figure 2.

As can be observed in these Figures, the resin can adsorb high amounts of linoleic acid. In fact, the equilibrium concentrations in the liquid phase are in most cases very low, indicating that most part of the linoleic acid dissolved in the initial solutions was transferred to the solid phase. Figure 1 shows the whole set of experimental data and Figure 2 the data obtained at low linoleic acid concentrations.

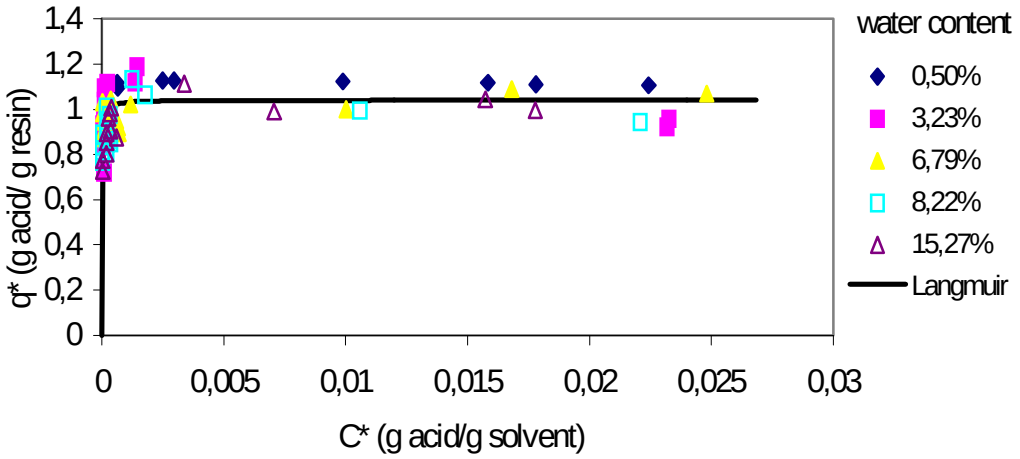

Figure 1 - Equilibrium isotherms for all experiments.

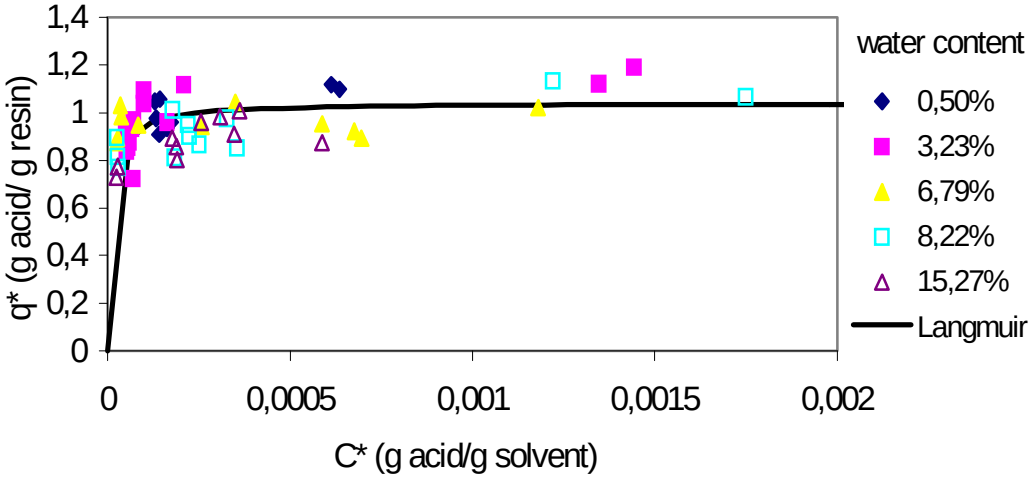

Figure 2 - Equilibrium isotherms at low linoleic acid concentrations.

The experimental data were correlated by the Langmuir equilibrium model, given in Eq. (1) below:

$$q^* = \frac{q_m \cdot C^*}{K_d + C^*} \qquad (1)$$

Where C* (g linoleic acid/g solvent) is the equilibrium concentration of the counterion in the liquid phase, q* (g linoleic acid/g dry resin) is the equilibrium concentration of the counterion adsorbed in the resin, q_m indicates the maximal adsorption capacity of the resin, K_d represents the equilibrium constant. K_d is usually interpreted as the ratio of the desorption (k_2) and adsorption (k_1) rate constants, the constants of the reversible equilibrium reaction on which the Langmuir model is based.

Most works in the literature use the Langmuir and Freundlich model for description of the equilibrium behavior using ion exchange resins (Cao et al., 2002; Antonio de Lucas et al., 1997; Anasthas and Gaikar, 1999).

The parameters of the Langmuir model varied within the range 1,00 ± 0,04 to 1,12 ± 0,02 (g acid/g resin) for q_m parameter and 1,0 ± 0,2 x 10^{-5} to 1,5 ± 0,4 x 10^{-5} for K_d parameter, considering the different water contents in the solvents.

The Average Absolute Deviations (AAD) between the experimental (q^*_{exp}) and calculated (q^*_{calc}) data were evaluated according to Eq. (2).

$$AAD = \frac{1}{m} \cdot \sum_{i=1}^{m} \left| \frac{q^*_{exp,\,i} - q^*_{calc,\,i}}{q^*_{exp,\,i}} \right| x\,100 \qquad (2)$$

Where m is the total number of experimental data. The AAD varied within the range values (0,42 to 1,26) %.

The fitting results indicate that the Langmuir model describe very well the experimental data. The K_d-values are much lower than 1, reflecting the fact that the equilibrium isotherms are favorable to the removal of the linoleic acid by the ion exchange resin and that their curvatures are convex-upward (Brunauer et al., 1940).

Taking into account the q_m and K_d-values and their standard deviations, it can be concluded that the water content in the solvent does not have a significant influence on the equilibrium behavior, at least in the range of values selected for the present work. For this reason a unique set of parameters can be adjusted to the whole set of experimental data. The following results were obtained: q_m (g linoleic acid/g dry resin) = (1,04 ± 0.01), K_d (g linoleic acid/g solvent) = (1,00 ± 0,16) x 10^{-5}, AAD = 5,74 %.

The small value obtained for the equilibrium constant, K_d, indicates that the adsorption rate constant (k_1) is much higher than the desorption rate constant (k_2), expressing the preference of the solute for the solid phase. Such result is also reflected in the high slope of the curve in the first part of the isotherm (Figures 1 and 2).

The q_m values indicate the maximal resin capacity. Taking into account the resin initial moisture, its maximal capacity can be converted to a wet basis, as it is usually reported in the literature. In this case the q_m (g acid/g dry resin) value (1,04) corresponds to 0,274 (g acid/g wet resin). Considering the bulk apparent density of the resin, this value can be further expressed as 0,65 eq/l. This result is a little lower than the capacity reported by the manufacturer (> 0.8 eq/l).

Finally it can be concluded that the water content in the solvent did not significantly influence the equilibrium isotherms. The experimental data were well correlated by the Langmuir model with low deviations between experimental and calculated data. The anionic resin presented a very good performance in the removal of linoleic acid from ethanolic solutions.

References

Anasthas, H. M., Gaikar, V. G. (1999). Adsorptive Separation of Alkylphenols Using Ion Exchange Resins. *React. Funct. Polym*., *39*, 227.

Antonio de Lucas, J. L., Cañizares, P., Rodriguez, J. F., Garcia, I. (1997). Potassium Removal from Water – Polyol Mixtures by Ion Exchange on Amberlite 252. *Chem. Eng. J.*, *66*, 137.

Batista, E., Monnerat, S., Kato, K., Stragevitch, L., Meirelles, A.J.A. (1999). Equilibrium For Systems Of Canola Oil, Oleic Acid And Short-Chain Alcohols. *J. Chem. Eng. Data,* 44, 1360-1364.

Brunauer, S., Deming, L. S., Deming, W. E., Teller, E. J. (1940). On a Theory of the van der Waals Adsorption of Gases. *J. Am. Chem. Soc*., *62*, 1723.

Cao, X., Yun, H. S., Koo, Y. (2002). Recovery of L - (+) Lactic Acid by Anion Exchange Resin Amberlite IRA – 400. *Biochem. Eng. J., 11*, 189.

Cren, E.C., Meirelles, A.J.A. (2005). Adsorption Isotherms for Oleic Acid Removal from Ethanol + Water Solutions Using the Strong Anion – Exchange Resin Amberlyst A26 OH. *J. Chem. Eng. Data,* 50, 277-283.

Gonçalves, C.B., Batista, E., Meirelles, A.J.A. (2002). Liquid – Liquid Equilibrium Data for the System Corn Oil + Oleic Acid + Ethanol + Water at 298.15 K. *J. Chem. Eng. Data,* 47, 416-420.

Ibanez G., M.J., Robles M.A., Esteban C.L., Camacho P.B., Jimenez, A., Molina G.E. (2001). Adsorption Equilibria Of Fatty Acids Between Metanol/ Water And Reserved Phase Chromatographyc Adsorvents. *J. Am. Oil Chem. Soc*., 78, 277-283.

Latip, R.A., Baharin, B.S., Chen Man, Y.B., Rahman, R.A. (2001). Effect Of Adsorption And Solvent Extraction Process On The Percentage Of Caroteno Extracted From Crude Palm Oil. *J. Am. Oil Chem. Soc*., 78, 83-85.

Rodrigues, C.E.C., Pessoa Filho, P.A., Meirelles, A.J.A. (2004). Phase Equilibrium For The System Rice Bran Oil + Fatty Acids + Ethanol + Water + Γ-Orizanol + Tocols. *Fluid Phase Equilibria,* 216, 271-283.

Proceedings of the 10th International Chemical and
Biological Engineering Conference - CHEMPOR 2008
Braga, Portugal, September 4-6, 2008
E.C. Ferreira and M. Mota (Eds.)

Oleic acid Removal of Isopropanol Solutions Using Strong Anion Exchange Resin Amberlyst A 26OH

Natália P. Macedo[1], Erika C. Cren[1], Antonio J. A. Meirelles[1*]
[1] FEA – Faculdade de Engenharia de Alimentos, Departamento de Engenharia de Alimentos, Unicamp, 13083-862 Campinas, Brazil.

Keywords: Breakthrough Curves, Ion Exchange resin, Organic Solutions, Oleic Acid
Topic: Advancing the chemical and biological engineering fundamentals.

Abstract

The traditional refining methods, physical or caustic refining, are not appropriate for some crude oils. In the case of such oils, both processes cause high losses of neutral oil and nutraceutical compounds, the physical refining is energy intensive and the chemical refining generates high amounts of soapstock. The liquid-liquid extraction is an alternative method for deacidification of crude oils, and has the advantage of using mild operational conditions concerning temperature and pressure and the possibility of restricting the loss of neutral oil and nutraceutical compounds. The liquid-liquid extraction generates two streams: the deacidified oil (raffinate), and a stream rich in solvent and free fatty acids (extract), but this process has the disadvantage of requiring the treatment of the out put streams, specially the extract stream. The solvent used in the process could be recovered and reutilized again in the process. Ion exchange resin can be employed as a complement of the whole liquid-liquid extraction process, in order to adsorb fatty acids from the extract phase, allowing the recovery of the solvent for a new liquid-liquid deacidification step. The applicability of ion exchange resins in industrial processes has steadily grown up, and generally the adsorption process uses a fluid that flow continuously through the column bed. In this way, the adsorption process investigation in a bed column allows a better understanding of the ion exchange behavior in organic media. Breakthrough curves for the uptake of oleic acid from isopropanol solutions, on anion exchange resin (Amberlyst 26A OH), at different temperatures and oleic acid concentration were studied. The breakthrough data were obtained by a study using an experimental factorial design (2^2) with surface response analysis.

1 Introduction

The deacidification of crude oils is the most important step of refining process, and is essential to convert crude oil in to an edible one. An alternative method to the conventional methods of deacidification (physical and chemical) is the liquid-liquid extraction that uses solvents for the extractions. This process has been investigated for a long time and has a good acceptance because employs mild operation conditions, minimizing the losses and damages to the refined oil (Rodrigues et al., 2004; Gonçalves et al., 2003). Some vegetable oils were investigated using the liquid-liquid extraction, like soy oil, rice oil, and the solvents generally used in this process are the short chain alcohol, like methanol, ethanol, etc (Batista et al., 1999).

However, few studies have been made for the treatment of exit streams of this process. Actually the treatment of the extract streams of the liquid-liquid extraction has been studied, using ion exchange resin (Cren and Meirelles, 2005). This streams needs treatment once it is the effluent of the process.

* Corresponding author. Tel + 551935214037. E-mail:tomze@fea.unicamp.br

This last study may help the liquid-liquid process to become viable, since the liquid-liquid extraction step was already extensively investigated. The present work investigated the possibility to use anion exchange resins in order to remove fatty acids from the extract phase and to recover the solvent

Some resin applications in process with fatty systems were found in the literature, but such studies are still scarce. For example, it can be mentioned the separation of carotene from crude palm oil using resins (Latip et al., 2001), the separation of mixture of fatty acids, of fatty esters, and of triglycerides (Adolf and Emken, 1981), and adsorption of fatty acids from metanol/ water solutions. (Ibanez Gonzalez, et al., 2001).

The advantage of using ion exchange resins to complement the liquid-liquid extraction is related to its low energy consumption, to the possibility of regeneration and rense of the resin and to the recovery of the fatty acids and other nutraceutical compounds that can be adsorbed by the resin.

2 Material and Methods

Material. Commercial grade oleic acid, isopropanol (Ecibra) and sodium hydroxide (Merck), strong anionic resins Amberlyst A26 OH (Rohm and Haas).

Methods. The experiments were conducted in a glass column with dimensions 66,5 cm (high) x 4,5 cm (diameter), aproximately 100 ml of resin previously conditioned in water and afterwards in the solvent (isopropanol), were used as adsorption media.

The resin was put in contact (continuous system) with isopropanol solutions containing oleic acid. The different oleic acid solutions concentrations were prepared in mass. The flow rate was constant at 4 bed-volume or 7 ml/min. Samples were collected in the column exit at different times. They were analyzed by titration to determine the oleic acid content. The results were analyzed by statistical method of surface response to optimize the operation parameters (temperature and initial concentration of oleic acid in solution) in the process of oleic acid removal by the resin. Figure 1 shows the squematic layout of the experiments.

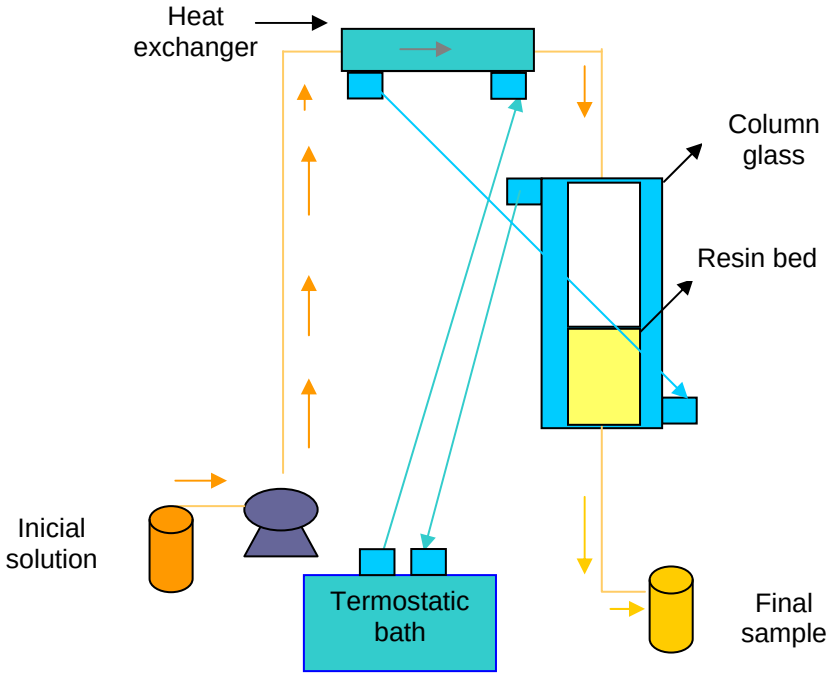

Figure 1 – Squematic breakthrough experiments.

3 Results and Conclusion

In the column study, the breakthrough curves were expressed by the adimentional concentration (C/Co) versus time (minutes). Figure 2 shows some experimental breakthrough curves.

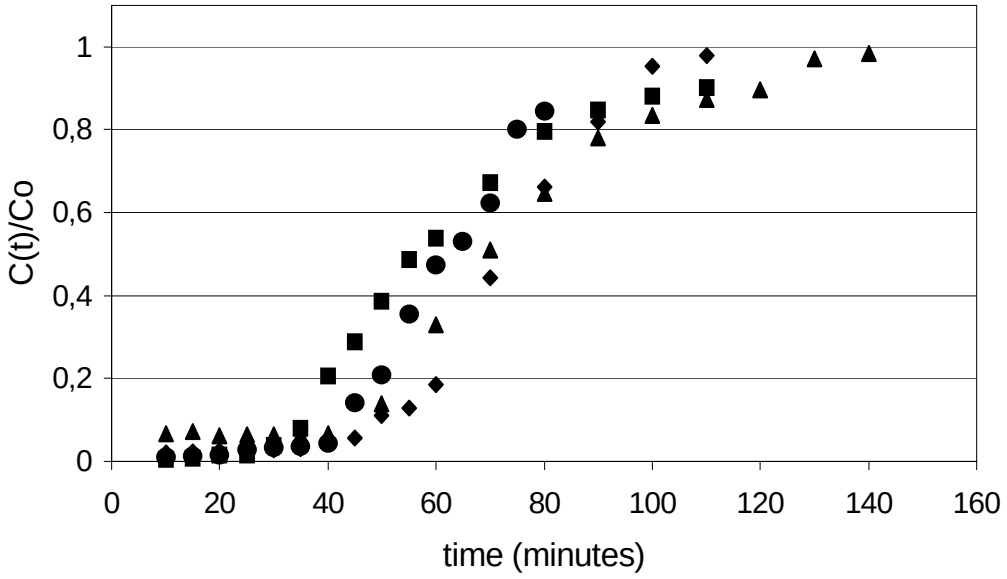

Figure 2 – Breakthrough curves (♦) 50 ^{o}C and Co = 6,5 %; (●) 46,5 ^{o}C and Co = 9,0 %; (▲) 37,5 ^{o}C and Co = 6,5 %; (■) 28,5 ^{o}C and Co = 9,0 %.

In Figure 2 above it can be noted that for a higher initial concentration the breakthrough point is reached more quickly. This fact occurs because at high concentrations the resin sites are quickly occupied, and at low concentrations the breakthrough curve become more disperse because the occupation of the sites occurs more slowly.

At the same concentration the higher is the temperature, slower the breakthrough point is reached and faster the saturation time is reached. This occurs because at high temperature the viscosity is lower, so the ions have better accessibility to the sites. In this way the sites are occupied efficiently and faster.

The breakthrough data for the isopropanol solutions were obtained using an experimental factorial design (2^2) with surface response analysis. At these experiments 2 factors were studied, the temperature (25 to 50 ^{o}C) and oleic acid concentration in isopropanol solution (3 to 10 mass %). The objective was to analyse the effects of the parameters in the efficiency of oleic acid removal by the resin.

The efficiencies are defined in Equations 1 and 2 (see Figure 3) in terms of different areas represented in the breakthrough curve. They were obtained by integration of the areas using the rectangular method (Shidhar et al., 1994).

$$Er = \frac{m_s \cdot Co \cdot \left(t_b - \int_0^{t_b} \frac{C(t)}{Co} dt \right)}{m_s \cdot Co \cdot t_b} = \frac{A1}{A1 + A2} \quad (1)$$

$$EF = \frac{m_s \cdot Co \cdot \left(t_b - \int_0^{t_b} \frac{C(t)}{Co} dt \right)}{m_s \cdot Co \cdot \left(t_f - \int_0^{t_f} \frac{C(t)}{Co} dt \right)} = \frac{A_1}{A_1 + A_3} \quad (2)$$

Where Er = efficiency of solute recovery, EF = efficiency of resin utilization, A1 = capacity of the resin efficiently used (g solute) (area above the curve until the breakthrough point (0,1.Co)), A2 = total amount of solute contained in the effluent (g solute) (area beneath the curve until the breakthrough point), A3 = capacity of the resin not efficiently used (g solute) (area above the curve after the breakthrough point and before the saturation (≥0,9.Co)).

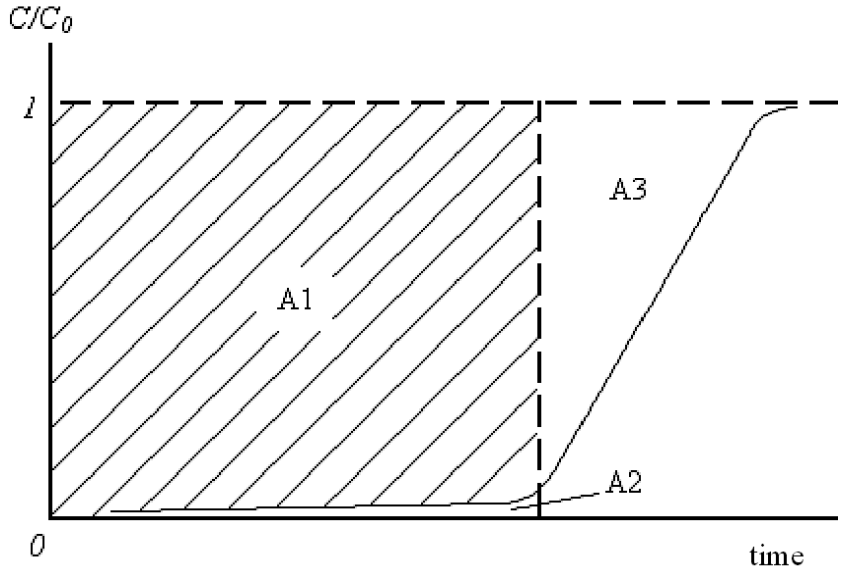

Figure 3. Breakthrough curve and the different areas associated to the process.

The efficiency of solute recovery (Er) was always larger than 78%, and was not influenced by temperature but positively influenced by the oleic acid concentration (higher the oleic acid concentration higher is the efficiency of recovery). The efficiency of resin utilization (EF) varied in the range of 21% to 66%, and was influenced positively by the oleic acid concentration as by temperature. The mainly effect is attributed to changes in oleic acid concentrations. The experimental data for breakthrough curves were analyzed by the response surface methodology, in order to maximize the response function, that is the efficiency of resin utilization, considering the parameters temperature and initial oleic acid concentration. Figure 4 shows the surface response obtained from the model by the statistical study using the data of the experimental design.

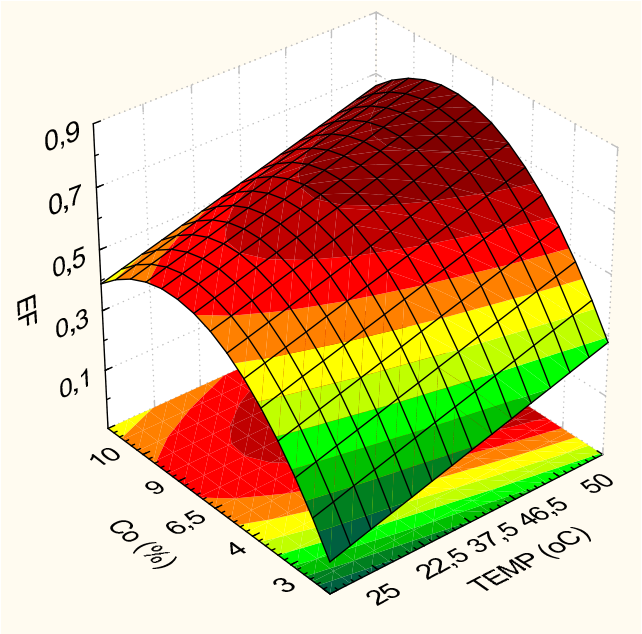

Figure 4 - Surface response, effects of temperature and concentration on the efficiency of utilization.

Figure 4 shows that the maximum efficiency occurs at high temperatures and high concentrations, and the maximum value was around 66%. So higher the concentration of oleic acid in solution and the temperatue, higher is the response function (EF), more oleic acid is removed efficiently by the column. In this way, the parameters have a positive influency in the efficiency of utilization.

From these experimental data, a good efficiency of recovery was obtained for all experiments, (78 to 98 %). This fact indicates that a high capacity of oleic acid removal was achieved.

Generally it could be concluded that the ion exchange resin shows good capacity of removing oleic acid from ethanolic solutions.

References

Adolf, R.O., Emken, E.A. (1981). Partial argentation resin chromatography (PARC): III. The Efects Of Sodium Ion Incorporation And Solvent On The Separation Of Mixture Of Fatty Acids, Of Fatty Esters, And Of Triglycerides. *J. Am. Oil Chem. Soc.,* 2, 99-101.

Batista, E., Monnerat, S., Kato, K., Stragevitch, L., Meirelles, A.J.A. (1999). Equilibrium For Systems Of Canola Oil, Oleic Acid And Short-Chain Alcohols. *J. Chem. Eng. Data,* 44, 1360-1364.

Cren, E.C., Meirelles, A.J.A. (2005). Adsorption Isotherms for Oleic Acid Removal from Ethanol + Water Solutions Using the Strong Anion – Exchange Resin Amberlyst A26 OH. *J. Chem. Eng. Data,* 50, 277-283.

Gonçalves, C.B., Batista, E., Meirelles, A.J.A. (2002). Liquid – Liquid Equilibrium Data for the System Corn Oil + Oleic Acid + Ethanol + Water at 298.15 K. *J. Chem. Eng. Data,* 47, 416-420.

Ibanez G., M.J., Robles M.A., Esteban C.L., Camacho P.B., Jimenez, A., Molina G.E. (2001). Adsorption Equilibria Of Fatty Acids Between Metanol/ Water And Reserved Phase Chromatographyc Adsorvents. *J. Am. Oil Chem. Soc*., 78, 277-283.

Latip, R.A., Baharin, B.S., Chen Man, Y.B., Rahman, R.A. (2001). Effect Of Adsorption And Solvent Extraction Process On The Percentage Of Caroteno Extracted From Crude Palm Oil. *J. Am. Oil Chem. Soc*., 78, 83-85.

Rodrigues, C.E.C., Pessoa Filho, P.A., Meirelles, A.J.A. (2004). Phase Equilibrium For The

System Rice Bran Oil + Fatty Acids + Ethanol + Water + Γ-Orizanol + Tocols. *Fluid Phase Equilibria,* 216, 271-283.
Shidhar, P., Satri, N.V.S., Modak, J.M., Mukherjee, A.K. (1994). Mathematical Simulation of Bioseparation in an Affinity Packed Column. *Chem. Eng. Technol*., 17, 422-429.

Proceedings of the 10th International Chemical and
Biological Engineering Conference - CHEMPOR 2008
Braga, Portugal, September 4-6, 2008
E.C. Ferreira and M. Mota (Eds.)

Chromium removal by constructed wetlands: evaluating the effects of chromium rich industrial effluents

Dina M.R. Mateus*, Ângela Leonardo, Filipe Pequeno, Henrique J.O. Pinho
Escola Superior de Tecnologia de Tomar, Instituto Politécnico de Tomar, Estrada da Serra, Quinta do Contador, 2300-313 Tomar, Portugal.

Keywords: chromium removal, wastewater treatment, constructed wetlands
Topic: Sustainable process-product development through green chemistry

Abstract

Two constructed subsurface flow pilot wetlands, normally used for nutrients removal from a secondary treated urban wastewater, were monitored for trivalent chromium removal efficiency and for its impact over the nutrients removal primary function of this pilot plant. Cr(III) solutions were pulse injected in the pilot wetlands inflow, and wetlands outflow collected and analysed for this metal by a colorimetric technique. A total chromium removal was obtained by the wetland with macrophyte plants, and a minor removal of nearly 65% by the control wetland without plants. Under the conditions applied, no negative effects were detected over the nutrient removal capacity of both pilot wetlands resulting from chromium presence.

1 Introduction

Contamination of natural waters by heavy metals is of great concern due to its toxicological effects. The presence of heavy metals in the environment results normally from anthropogenic activities. To reduce the emissions, the industrial metal rich effluents should be subject to adequate treatments before their discharge, which can be extremely expensive. Usually these wastewaters are joined to domestic waters, after some initial physicochemical treatment, resulting in the so-called urban wastewaters, which are further treated at municipal facilities. This practice may cause problems since municipal treatment plants are as a rule designed for domestic wastewaters, and consequently the heavy metals removal is usually scarce.

Constructed wetlands (CW) may complement or replace the typical secondary treatment operations, but its efficiency concerning metals removal from wastewater and the effects of the metal pollutants over these complex environments should be addressed.

Chromium has been selected for the present study, as an example of this problem, with regard to its industrial use and potential pollution impact. This pollutant typically occurs in the trivalent or hexavalent form. The late is the most toxic, and the most common specie in industry, but is relatively unstable and was normally converted to the trivalent form at industrial localized wastewaters plants. For that, the trivalent chromium is the dominant form in the inflow of municipal treatment plants.

Wastewaters from tannery, metal plating and many other industries contain high chromium concentrations, namely hexavalent chromium (Nriagu and Niober, 1988). Common treatment of industrial chromium rich effluents conducted at industrial plants consists mainly in physicochemical processes that transform Cr(VI) into Cr(III) with subsequent precipitation

* Corresponding author. Tel + 351-249323160. E-mail:dinamateus@ipt.pt

(Abass et al, 2005; Chang, 2001; Eary and Ray, 1988). However, these processes are not totally effective, since they often still leave high chromium levels in the water discharged.

The use of CW for urban wastewater treatment is a rapidly growing practice, due to its economical and environmental advantages (Kadlec and Knight, 1996). CW specially dedicated to industrial wastewaters remediation have also been studied and implemented, with examples of application to heavy metals pollutants cited in the literature (Knight et al., 1999; Mant et al., 2006; Mitsch and Wise, 1998; Scholes et al., 1998; Vymazal, 2005). The effects of heavy metals in CW, used as secondary or tertiary treatment at municipal wastewater treatment plants dedicated mainly to common urban waters, are less reported. It should be considered that both Cr(VI) and Cr(III) have been identified as plant toxics, in particular to *Phragmites australis*, species commonly used in CW (Mant et al., 2006; Shanker et al., 2005).

The aim of this work was to evaluate the effects of sporadic chromium discharges on the performance of CW normally operated for nutrients removal.

2 Materials and methods

The CW pilot plant consists of two tanks with a working volume of 240 L, filled with lightweight aggregate (expanded clay). Tank A was planted with the emergent macrophyte *Phragmites australis*. Tank B, without plants, serves for control purposes.

To simulate sporadic discharges of industrial chromium polluted effluents on the public frameworks using CW, small volumes of Cr(III) solutions (1 L 0,005 M $CrCl_3 \cdot 6H_2O$) were injected in the pilot CW plant feed line. The CW effluents were collect and analysed for chromium concentration.

To check the chromium removal capacity of the filter media by itself, 5g-samples of the expanded clay, first washed and dried, were shaken for 24 h with 100 mL 0,010 M Cr(III) solutions, and the liquid phase analysed for chromium concentration after solids separation by filtration.

The chromium concentration was determined by the colorimetric method (Greenberg et al, 1992). Total phosphorus was quantified by the ascorbic acid method, after the samples digestion with persulfate, and total nitrogen was quantified by the 2,6-dimethylphenol spectrometric method, also after persulfate digestion of the samples (Greenberg et al, 1992). COD was determined by the titrimetric method (Greenberg et al, 1992).

3 Results and discussion

The pilot plant has been operated continuously for more than six years, performing the treatment of a typical secondary effluent. CW A average removal efficiencies were about 50% for total phosphorus, 75% for total nitrogen and 70% for COD. CW B, unplanted, showed an average removal efficiency of 30%, 50% and 55%, respectively for total phosphorus, total nitrogen and COD.

After chromium injection, the tanks outflows have been monitored to pH, temperature and volumetric flow rate. The volumes collected were sampled and analysed for chromium contents. Mass balances calculations were performed to evaluate chromium removal. Figure 1 shows the chromium concentration at CW outflow over time.

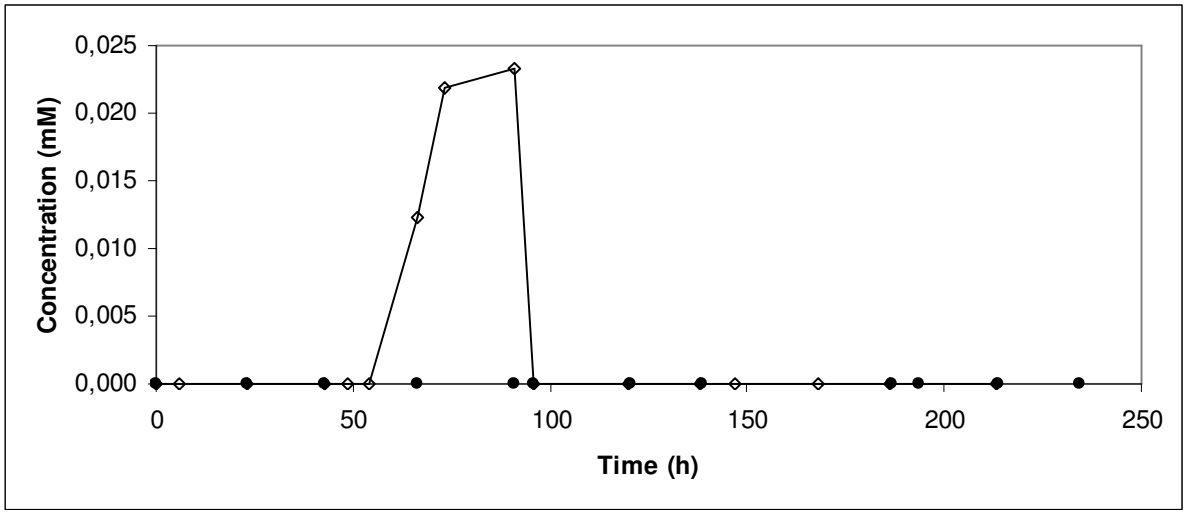

Figure 1 – Chromium concentration at pilot constructed wetlands outflow over time, after a pulse injection of a 5 mM Cr(III) solution (• tank A, planted; ◊ tank B, without plants).

Chromium removal by CW A, with plants, was verified to be 100%. The CW B, without plants, shows a lower removal capacity, near 65%. The lab tests demonstrate an only residual chromium removal by the filter media itself. From these results, we can infer a contribution of plants for the chromium removal near 35%.

To evaluate the effects of the chromium presence over the normal operation of the pilot CW, the efficiency for total phosphorus removal, total nitrogen removal and COD removal within the period of chromium experiments was compared with the efficiencies obtained at the precedent year (2006) in the same period, to contemplate the usual seasonal efficiency variations observed in these systems (Figure 2).

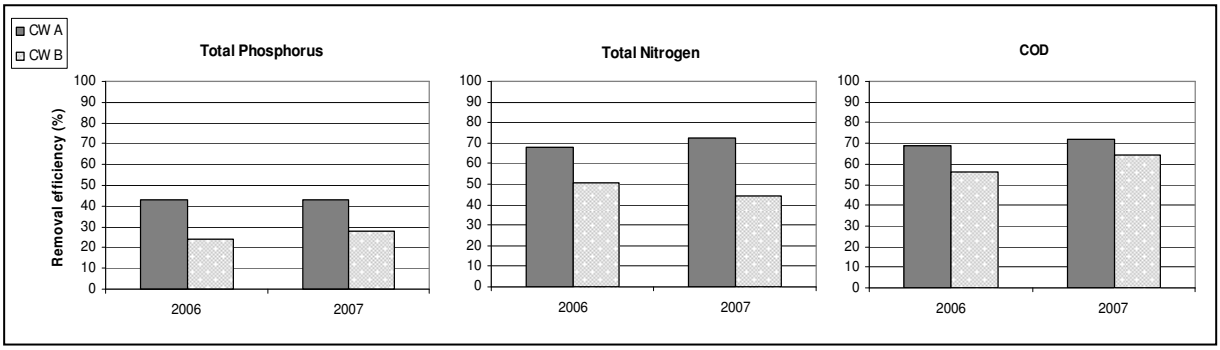

Figure 2 – Total phosphorus, total nitrogen and COD removal efficiencies of the two pilot constructed wetlands: at 2007 in the period of tests with chromium; at 2006 in the same period, before chromium experiments.

From figure 2, dismissing small variations due to the complexity of removal phenomena at CW, it can be concluded that the removal of nutrients seems not to be disturbed by the presence of the chromium in the inflow water.

4 Conclusions

The results suggest a potential chromium depuration capacity of CW, which can be attributed mainly to the action of the filter media microcosms, while plants uptake and adsorption to their roots and rhizomes contributes with 35% of the chromium removal capacity.

For the reason that the chromium removal may occur by plants uptake and, primarily, by accumulation into the filter media microcosms – sediments, humic substances and microorganisms present – concerns may be taken about the end use of filter media and the harvested plant materials.

Under the conditions experimented, the CW didn't show any efficiency loss with respect to COD and nutrients removal function. Future experiments should be conducted to evaluate the long term effects of continuous chromium feed to the CW, and to access the sustainability of chromium concentration reduction with time.

References

Abass, E., Alireza, M., Reza, V. (2005). Chromium (III) removal and recovery from tannery wastewater by precipitation process. *American Journal of Applied Sciences*, 2 (10), 1471-1473.

Chang, L.-Y. (2001). Chrome reduction and heavy metals removal from wastewater – a pollution prevention approach. WM'01 Conference, February-March 2001, Tucson. http://www.wmsym.org/abstracts/2001/21D/21D-45.pdf

Eary, L.E., Rai, D. (1988). Chromate removal from aqueous wastes by reduction with ferrous ion. *Environmental Science & Technology*, 22, 972-977.

Greenberg, A.E., Clesceri, L.S. and Eaton, A.D., Ed. (1992). *Standard Methods for the Examination of Water and Wastewater*, 18 ed., A.P.H.A, A.W.W.A., W.E.F., Washington.

Kadlec, R.H., Knight, R.L. (1996). *Treatment wetland*. CRC Press/Lewis Publishers, Boca Raton.

Knight, R.L., Kadlec, R.H., Ohlendorf, H.M. (1999). The use of treatment wetlands for petroleum industry effluents. *Environmental Science & Technology*, 33, 973-980.

Mant, C., Costa, S., Williams, J., Tambourgi, E. (2006). Phytoremediation of chromium by model constructed wetland. *Bioresource Technology*, 97, 1767-1772.

Mitsch, W.J., Wise, K.M. (1998). Water quality, fate of metals, and predictive model validation of a constructed wetland treating acid mine drainage. *Water Research*, 32, 1888-1900.

Nriagu, J.O., Nieboer, E. (1988). *Chromium in the natural and human environments*, John Wiley & Sons, New York.

Scholes, L., Shutes, R.B.E., Revitt, D.M., Forshaw, M., Purchase, D. (1998) The treatment of metals in urban runoff by constructed wetlands. *Science of the Total Environment*, 214, 211-219.

Shanker, A.K., Cervantes, C., Loza-Tavera, H., Avudainayagam, S. (2005). Chromium toxicity in plants. *Environment International*, 31, 739-753.

Vymazal, J. (2005). Removal of heavy metals in a horizontal sub-surface flow constructed wetland. *Journal of Environmental Science and Health,* 40, 1369-1379.

Proceedings of the 10th International Chemical and
Biological Engineering Conference - CHEMPOR 2008
Braga, Portugal, September 4-6, 2008
E.C. Ferreira and M. Mota (Eds.)

Recovery of heavy metals by hybrid membrane processes

Gryzelda Poźniak*, Ryszard Poźniak, Kazimiera A. Wilk
Department of Chemistry, Wrocław University of Technology, 50-370Wrocław, Poland

Keywords: modified poly(phenylene oxide), ultrafiltration, dialysis, zinc, copper
Topic: Sustainable process-product development through green chemistry

1. Introduction

Metallurgical industry, especially electroplating and metal finishing sectors, generate huge amounts of water containing heavy metal ions. For attempts to recover and concentrate these valuable components as well as for removal of undesired toxic ions from waste the application of membrane separation processes is very useful. This well consolidated technology has become the central focus of industry interest due to its low operational costs, conceptual simplicity, modularity, flexibility to the quality of treated water, and productivity in relation to other separation techniques [Mulder, 1991].

In order to separate ions, reverse osmosis (RO) or nanofiltration (NF) is commonly used. However, the permeating fluxes in RO and NF are not so high and both processes require the use of high transmembrane pressure. That operation turns them into more expensive membrane processes. The other pressure-driven process - ultrafiltration (UF) – needs smaller transmembrane pressure and its operational cost is not so high. It has been shown that ultrafiltration is efficient in the removal of larger molar substances (polymers, colloids) whose size ranges from 2 to 100 nm and whose molecular weight is larger than 500 Da. However, the pore size of any ultrafilter is too large to reject small molecules like inorganic ions.

The polymer enhanced ultrafiltration (PEUF) [Cãnizares et al., 2002] and micellar enhanced ultrafiltration (MEUF) [Juang et al., 2003, Poźniak et al., 2007], hybrid (non-conventional) processes, have been shown to be promising methods of removing low levels of toxic heavy metal ions from industrial effluents.

PEUF and MEUF constitute a combination of two phenomena; binding ~~of~~ metal ions to a water soluble polymer (complexation) or solubilizing by surfactant micelles, respectively, and ultrafiltration. Since the pore size of ultrafiltration membranes is not suitable for separating heavy metal ions, water soluble polymers are used to form macromolecular complexes with metal cations or anionic surfactant micelles are used to solubilize cations. Ultrafiltration membranes with pores smaller than both the polymeric agents and surfactants (above the critical micelle concentration, cmc) are employed; thus, the polymer-metal complexes or the micelle-solubilized metal can be retained while simple (non-binding or non-complex) ions pass through the membrane.

Dialysis is the oldest membrane process for removing metal ions from water in which the ions move across nonporous ion-exchange membranes, based on the Donnan equilibrium principle [Donnan, 1924]. Dialysis is a diffusion phenomenon which is governed by a difference in metal concentration on both sides of the nonporous ion-exchange membrane. The solute flux is stopped when the concentrations are equal in both compartments. The amount of metal passing through the membrane can be increased by modifying the chemical potential of the metal in one of the two compartments. If some complexion polymer is added to the feed compartment, a decrease in free metal ion concentration will lead to a decrease in the transfer rate of metal ions to the receiving compartment [Wang, 2004].

In contrast, if the complexion polymer is added to the receiving compartment, the interaction of the metal ions with polymer (polymer-metal complex formation) should be responsible for an increase in the amount of metal ions transferred. In the case of stable complex formation, it should be possible to recover the total amount of metal ions in the receiving compartment

[Marty et al., 2000, Poźniak, 2006a]. In the PED a porous membrane is used. The transport rate through the porous membrane is significantly larger than the rate through a solid membrane – this is another benefit resulting from the application of the PED process.

Poly(phenylene oxide) (PPO) is frequently used as a membrane material due to its good mechanical strength, thermo-, biological, and chemical stability, and film-forming properties. Hydrophobicity, the shortcoming of the PPO membrane, can be counterbalanced by introduction of ionic functional groups to the polymer chain. The porous ion exchange membranes form a new category of filtration media. They proved to be very useful in the filtration of charge-bearing solutes [Bryjak et al., 2004; Poźniak et al., 1995, 2002, 2006b].

The goal of this paper is to evaluate a possibility to prepare membranes from aminated and sulfonated poly(phenylene oxide) and to determine the usefulness of porous ion exchange membranes in the hybrid separation processes for removal of Zn(II) and Cu(II) ions from aqueous media.

2. Experimental

2.1. Amination of poly(phenylene oxide)

PPO (M_v=27,000, from Aldrich Chemie) was chloromethylated using a mixture of methyl chloromethyl ether (8 mole per mer PPO) with $SnCl_4$ (0.1 mole per mer PPO) in a solution of 1,2-dichloroethane (10 wt. %). The reaction was conducted for 1 h at room temperature. Membranes were formed from the chloromethylated product.

Aminolysis of chloromethylated membranes was performed in 50 vol. % solution of N,N-dimethylaminetanol in 1:1 (vol.) mixture of water and methanol. The reaction was completed within 24 h at room temperature. The sample symbol is APPO.

2.2. Sulfonation of poly(phenylene oxide)

PPO was sulfonated in a solution of chlorosulfonic acid and chloroform at room temperature for 2 h. The concentration of PPO in chloroform was 10 wt. % and the molar ratio of chlorosulfonic acid to polymer was 0.25:1. The sample was called SPPO.

2.3. Preparation of membranes

Porous asymmetric membranes were formed by means of the phase-inversion method from: native PPO, chloromethylated PPO and sulfonated PPO. The concentration of all polymers in a mixture of chloroform and nonyl alcohol (8:2 ratio by weight) was 10 wt. %. Methanol was used as a coagulation medium.

2.4. Transport properties of membranes

The dead-end UF apparatus (Amicon 8200) with membrane filtration surface area of 19.6 cm^2 was used for determination of water flux and filtration of 1 mM solution of $ZnCl_2$ and $CuCl_2$. Transport measurements were run under the transmembrane pressure of 0.05 MPa in MEUF and PEUF. Sodium dodecyl sulfate, SDS, (critical micelle concentration, cmc = 8.1 $mmol/dm^3$) in MEUF, and polyethyleneimine, PEI, (M_w=25,000) in PEUF were applied.

The dialysis cell was divided into two identical compartments (35 cm^3) separated by the SPPO membrane. One of them contained the metal salt ($CuCl_2$) and the other the poly(acrylic acid-co-maleinic acid) (M_w=50,000).

The concentration of metal cations was determined with AAS (AAnalyst 100, Perkin-Elmer). To evaluate the filtration efficiency in removing the zinc and copper cations from the feed solution, we used the rejection (R) expressed as:

$$R = [1 - (C_p/C_o)] \times 100$$

where:
C_p and C_o – are the cation concentrations in the permeate and in the initial feed, respectively.

3. Results

It is known that amination of a polymer results in the introduction of positive charges on the membrane surface while sulfonation results in the introduction of negative ones.

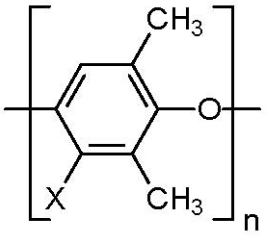

$$X = -SO_3^- \text{ or } -CH_2N^+(CH_3)_2C_2H_4OH$$

The properties of obtained membranes are shown in Table 1.

Table 1. Properties of porous ion exchange membranes

Membrane	Ion exchange capacity mmol/g	Porosity %	Average pore diameter nm
PPO	0.00	72	12
APPO	0.94	73	23
SPPO	1.45	83	21

For each evaluated membrane, the transport enhanced species was selected. The selection criterion was to keep the same charge on both bodies: the membrane and the species. For Zn(II) and Cu(II) cations recovery, APPO membrane with PEI was used in PEUF mode while SPPO membrane for MEUF mode with SDS as the surfactant.

It is predictable that ion removal according to the PEUF mode should be strongly related to the pH of the solution. To see that effect the process was evaluated at pH=3, 5 and 7 keeping the same molar ratio of salt to PEI, namely 1:4 – Figure 1.

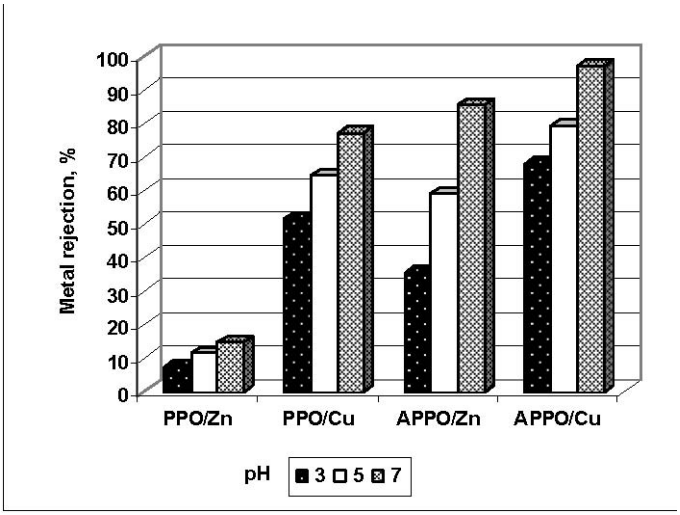

Fig. 1. Dependence of Zn(II) and Cu(II) rejection on pH and type of membrane – PEUF process

In the case of MEUF mode, the sorption of cations is mostly related to the surfactant concentration. For the purpose of this work SDS concentration was set at 8.1 and 40.5 mmol/dm^3, that is equivalent to 1 and 5 x critical micelle concentration, cmc) – Figure 2.

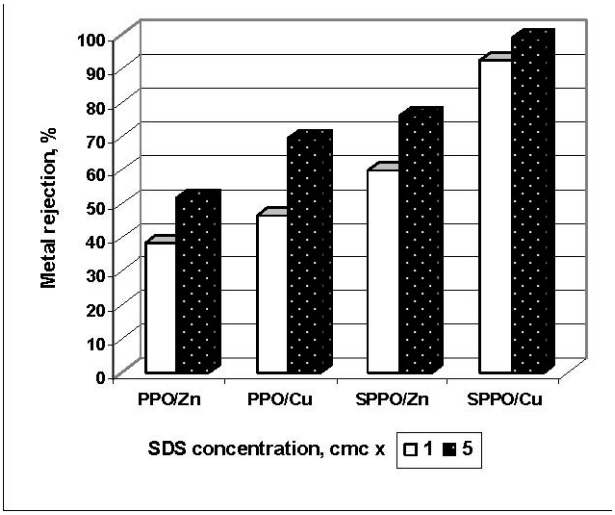

Fig. 2. Dependence of Zn(II) and Cu(II) rejection on SDS concentration and type of membrane - MEUF process

When comparing the degree of metal rejection in PEUF and MEUF processes one may note the positive effect of the presence of ionogenic groups. In both processes zinc and copper are better separated by modified PPO membranes. In PEUF and MEUF, stronger effect of Cu(II) interaction with PEI and better solubilization with SDS micelle were observed.

An ordinary dialysis of Cu(II) was also compared to the PED process. It is predictable that ion flux depends on the molar concentration ratio of the polymer to the cation and on the pH of the receiving phase [Marty et al., 2000]. In our experiments, the concentration of Cu(II) in the feed solution was kept as 10^{-3} mole/dm^3 and the concentration of the polymer in the receiving solution was equal to 10^{-2} mole/dm^3 while pH = 7. The course of metal ions concentration in the feed and receiving compartments along with the time of dialysis is presented in Figure 3.

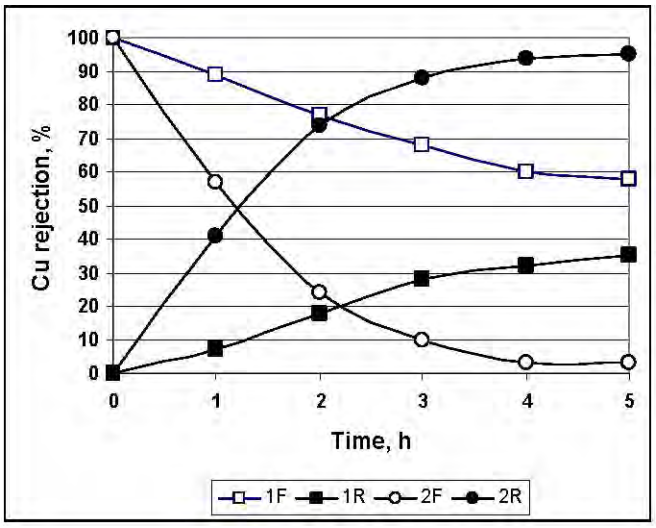

Fig. 3. Cu(II) concentration in the feed and in the receiving solution in the absence (1F, 1R) and presence (2F, 2R) of poly(AA-coMA) for SPPO membrane – PED process

For runs without the polyelectrolyte, natural dialysis of the metal ions is observed; the concentration of Cu(II) in the receiver is lower than 50% (curve 1R). The interaction of metal ions with poly(AA-co-MA) is mainly due to electrostatic forces and the formation of coordinating bonds. Hence, in the presence of polyelectrolyte, the concentration of metal ions in the receiving solution (curve 2R) increased to 100%.

4. Conclusions

1. Zn(II) and Cu(II) ions can be removed from aqueous solutions in the PEUF process with APPO membranes as well as in the MEUF process with SPPO membrane. In the first case polyethyleneimine should be used as a complexion agent while the second process should be assisted by a micelle formed by SDS.
2. Dialysis enhanced by poly(AA-co-MA) can recover nearly 100% of Cu(II).
3. The sulfonated and aminated poly(phenylene oxide) membranes worked more effectively than the neat membrane from poly(phenylene oxide) in all investigated processes (the positive effect of the presence of ionogenic groups).

References

Bryjak, M., Poźniak, G., Gancarz, I., Tylus, W. (2004). Microwave plasma in preparation of new membranes. Desalination, 163, 231-238.

Cãnizares, P., Pérez, Á., Camarillo, R. (2003). Recovery of heavy metals by means of ultrafiltration with water-soluble polymers: calculation of design parameters. Desalination, 144, 279-285.

Donnan, F.G., (1924). Theory of membrane equilibrium. Chem. Rev., 1, 73-89.

Juang, R.S., Xu, Y.Y., Chen, C.L. (2003). Separation and removal of metal ions from dilute solutions using micellar-enhanced ultrafiltration. Journal of Membrane Science, 218, 257-267.

Marty, J., Persin, M., Sarrazin, J. (2000). Dialysis of Ni(II) through an ultrafiltration membrane enhanced by polymer complexation. Journal of Membrane Science, 167, 291-299.

Mulder, M., (1991). Basic principles of membrane technology. Kluwer Academy Pub., Dordrecht, Holland.

Poźniak, G., Bryjak, M. and Trochimczuk, W., (1995). Sulfonated polysulfone membranes with antifouling activity. Die Angewandte Makromolekulare Chemie, 233, 23-31.

Poźniak, G., Gancarz, I., Bryjak, M., Tylus W. (2002). N-butylamine plasma modifying ultrafiltration polysulfone membranes. Desalination, 146, 293-302.

Poźniak, G. (2006a). Ultrafiltration membranes from polysulfone and sulfonated polysulfone in metal ion dialysis enhanced by polyelectrolyte. Ars Separatoria Acta, 4, 50-56.

Poźniak, G., Gancarz, I., Tylus, W. (2006b). Modified poly(phenylene oxide) membranes in ultrafiltration and micellar-enhanced ultrafiltration of organic compounds. Desalination, 198, 215-224.

Poźniak, G., Poźniak, R., (2007). Modified polyethersulfone membranes for micellar enhanced ultrafiltration of chromium. Proceedings of European Congress of Chemical Engineering (ECCE-6), Copenhagen, Denmark, pp. 7.

Wang, J-K., (2004). Preferential transport behaviors of ternary system ferric-cupric-nickel ions through cation exchange membrane with a complex agent by dialysis. Desalination, 161, 277-285.

Proceedings of the 10th International Chemical and
Biological Engineering Conference - CHEMPOR 2008
Braga, Portugal, September 4-6, 2008
E.C. Ferreira and M. Mota (Eds.)

Removal of Dyes from the Textile Industry by Adsorption in Fixed Bed columns – A Sustainable Process

Andressa R. Vasques [1], Selene M. Guelli U. de Souza[1], José A. B. Valle[2], Antônio A. Ulson de Souza[1]*

[1] UFSC, Federal University of Santa Catarina, Chemical Engineering and Food Engineering Department, Campus Universitário Trindade, 88040-900, Florianópolis, Santa Catarina, Brazil.

[2] FURB, Chemical Engineering Department, Regional University of Blumenau, Campus II, Blumenau, Santa Catarina, Brazil.

Key words: Adsorption, Dyes, Textile Industry, Fixed bed, Activated Sludge.
Topic: Sustainable process-product development through green chemistry.

Abstract

The capacity and mechanism of mono and bi-functional reactive dye adsorption utilizing a new adsorbent obtained from the dried residual sludge (~10% w.w.) of a textile wastewater treatment system was studied. With the focus on determining the efficiency of the adsorbent in the dye removal, the adsorption isotherms were determined for the reactive dyes RR2 and RR141, at different temperatures and salt concentrations. The experiments were carried out in fixed bed adsorption columns, which were defined as the best adsorption experimental condition for both of the dyes through the parameter q_m (mg/g), obtained by the adjustment of Langmuir isotherms. Breakthrough curves for the dyes RR2 and RR141 were obtained varying the height to which the fixed bed columns were packed with adsorbent (15, 30 and 45 cm) and varying the adsorbate feed rate in the column (8, 12 and 16 mL/min). For the dye RR2 the maximum adsorption capacity was 53. 48 mg/g and for the dye RR141 it was 78.74 mg/g.

1 Introduction

There is no single process capable of adequate mineralization of colored effluents, mainly due to their complex nature (Jain *et al*., 2002). Thus, a final refining treatment is required, usually involving oxidative processes, with ozone, Fenton's reactant, or hydrogen peroxide + UV radiation, membrane separation or adsorption (Órfão *et al*., 2006).

In adsorption processes, activated carbon is widely used, and it can be employed in fixed bed columns (Órfão *et al*., 2006). Due to the high cost of some conventional adsorbents, researches have been directed to the use of alternative adsorbents, like bottom ash, sludge, red mud, etc. (Calvo *et al*., 2001; Jain *et al*., 2002). Throughout this essay, a new adsorbent developed from the dried residual sludge of a textile wastewater treatment system (Ulson de Souza *et al*., 2007) is studied. With the goal of determining the efficiency of this adsorbent in dye removal, the adsorption isotherms were determined for the reactive dyes RR2 and RR141, at different temperatures and salt concentrations. Defined as the best experimental adsorption condition for both dyes, through the parameter q_m (mg/g) obtained by the adjustment of the Langmuir isotherm, we carried out the experiments in fixed bed adsorption columns.

* Corresponding author. Tel (48) 37219448. E-mail:augusto@enq.ufsc.br

2 Materials and Methods

2.1 Preparation of samples

The absorbent under study is a dried residual sludge of a textile industry wastewater treatment system with approximately 10% w.w., obtained from a textile processing factory in the region of Blumenau, SC, Brazil. The adsorbent was obtained after the residual sludge passed through a thermal treatment step followed by chemical treatment, as described by Ulson de Souza *et al*., 2007. The thermal treatment step occurred at 500°C and after heating the sample was chemically activated with 1M acetic acid.

The two dyes used as the adsorbates were CI Reactive Red 2 (monoazo) and CI Reactive Red 141 (diazo). The chemical structures and properties of these dyes are described in Netpradit *et al*., 2004. The standard solutions of the dyes were prepared from stock solutions of 2000 mg/L as per the methodology given in Netpradit *et al*., 2004. The spectrophotometrical analysis was performed at the wavelength of maximum adsorption (λ_{max}), with a spectrophotometer UV-Vis (Cary 50, Varian). When necessary, the pH of solutions was adjusted with 0.1M acetic acid or 0.1M sodium hydroxide.

2.2 Adsorbent Characterization

The surface area values were calculated as per the method described by Brunauer-Emmett-Teller, BET (Brunauer *et al*., 1938) using a Quantachrome Autosorb - 1C instrument. To obtain a micrograph of the physical structure of the adsorbent, and to carry out the EDS analysis, scanning electron microscopy (SEM) (Philips, Model XL30) was used.

2.3 Equilibrium Studies

The adsorption isotherms were determined through batch experiments where 100 mL of solution containing different adsorbate concentrations (100 to 2000 mg/L – pH 4.0) were transferred volumetrically to 250 mL Erlenmeyer flasks containing 1g of adsorbent, which remained under agitation for 6h in a shaker.

The data obtained from the adsorption experiments were adjusted according to the Langmuir isotherm which is based on the hypothesis that the forces of interaction among the molecules adsorbed are negligible and that each site can be occupied by only one molecule – Equation 1 (Órfão *et al*., 2006, Kumar and Sivanesan, 2006, Fernandes, 2005).

$$q_{eq} = \left(q_m K_L C_{eq}\right) / \left(1 + K_L C_{eq}\right) \quad (1)$$

where q_m is the maximum quantity of dye adsorbed per unit adsorbent mass (mg/g), K_L, is Langmuir equilibrium constant, (l/g); C_{eq} is the adsorbate concentration in equilibrium, mg/L.
The essential characteristics of a Langmuir isotherm can be expressed in terms of a separation factor non dimensional constant, commonly called the equilibrium parameter, R_L. The value of R_L indicates the type of adsorption isotherm, as reported by Ciola, 1981.

2.4 Experiments in fixed bed column

The experiments were carried out in adsorption columns with dimensions of 1.43 cm diameter and 36 cm height, to investigate the influence of the process parameters on the removal of mono and bi-functional reactive dyes. The feed dye concentration in the adsorbate solution used in the continuous experiments was 500 mg/L, and this was acidified with acetic acid 0.1M (pH 4.0) and for the adsorbate RR141, 10% sodium chloride (NaCl) (% in mass) was added. Breakthrough curves for the dyes RR2 and RR141 were obtained varying the packed height of the fixed bed columns with 15, 30 and 45 cm of adsorbent and varying the adsorbate feed rate in the column to 8, 12 or 16 mL/min.

Also, the adsorption capacity in equilibrium (column saturation) for the different operational conditions previously described was determined. Due to the high adsorption capacity of the

adsorbent, the breakthrough curves were obtained until the concentration of adsorbate in the outlet of the column reached 80% of the feed concentration (C/Co=0.8).

3 Results

3.1 Adsorbent Characterization

The adsorbent has a B.E.T surface area (Brunauer *et al*., 1938) of 137.61 m^2/g, total pore volume of 2.76 x 10^{-1} cm^2/g, and pore diameter of 8.032 $\mathring{A}$. The chemical composition of the adsorbent is: carbon (21.38%), oxygen (21.61%), sodium (0.72%), manganese (1.6%), aluminum (19.06%), silica (17.88%), phosphorus (10.8%), potassium (1.22%) and calcium (5.73%).

The image analysis and determination of the chemical composition of the adsorbent were carried out by SEM. Figure 1 shows images of the surfaces at a magnification of 1000X for the adsorbent under study as well as for a commercial adsorbent [activated carbon Fitrasorb 200 – Calgon, USA] (Chen and Chu, 2002).

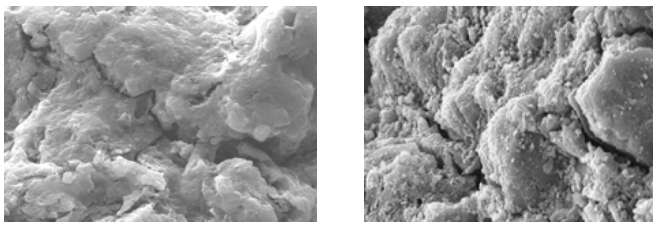

(a) (b)

Figure 1 - Microscopic surface of adsorbents (a) adsorbent under study (thermally and chemically activated residual sludge) (b) commercial activated carbon Fitrasorb 200.

The structure of the adsorbent is comparable to that of a commercial activated carbon sample (Fitrasorb 200) (Figure 1 (b)).

3.2 Equilibrium Studies

Table 2 shows the Langmuir isotherm equilibrium parameters for different experimental conditions. It can be observed that the maximum adsorption capacity of the adsorbent, (q_m), decreased while the temperature of the adsorption experiments increased, for both dyes. With the addition of different concentrations of sodium chloride to the solution with adsorbate RR2, q_m reduced as the concentration of this salt is increased. For the experiments carried out with the addition of sodium chloride, for both dyes, good correlation coefficients were obtained (0.907 to 0.987).

When different masses of sodium sulfate were added to the solution with the adsorbate RR2, q_m increased in relation to the addition of NaCl. For the dye RR141 there was a small reduction in q_m when compared to the adsorption experiments in the presence of NaCl. In Table 2 it is possible to identify the best adsorption conditions (highest q_m value (mg/g)). For the dye RR2, the best adsorptive condition is at 25°C with a complete absence of salt in the solution, but for the dye RR141, the best adsorptive condition was at 25°C in the presence of 10% (by mass) of sodium chloride in the solution. There was a 58.81% reduction in the adsorption capacity of dye RR2 when 10% of sodium chloride was added to the solution and there was a 15.33% reduction for dye RR141 when 10% of sodium sulfate to was added to the adsorbate.

Table 2 - Langmuir isotherm equilibrium parameters for the different experimental conditions.

Dyes	Temperatures (°C)	Langmuir parameters		
		K_L(L/mg)	q_m(mg/g)	R^2
RR2	25	0.113	53.476	0.928
	40	0.275	31.746	0.872
	60	0.077	24.876	0.954
RR141	25	0.209	66.670	0.997
	40	0.199	65.789	0.976
	60	0.117	51.020	0.984
	NaCl Concentration (% mass)			
RR2	1	0.104	45.450	0.907
	5	0.366	30.120	0.930
	10	0.409	22.026	0.931
RR141	1	0.210	44.248	0.987
	5	0.091	47.619	0.967
	10	0.077	78.740	0.984
	Sodium Sulphate Concentration (% mass)			
RR2	1	0.051	47.393	0.985
	5	0.291	39.850	0.965
	10	0.191	39.526	0.991
RR141	1	0.347	52.356	0.912
	5	0.750	40.161	0.862
	10	0.004	66.667	0.960

(*)The experiments with salt were carried out at 25°C.

For the best adsorption conditions, for both dyes, R_L varied from 0.02 to 0.75 as shown in Table 3, indicating that these isotherms are favorable (Ciola, 1981).

In Table 3 the removal percentages for dyes RR2 and RR141 for the best adsorption experimental conditions and with initial dye concentrations of 100 and 500 mg/L are shown.

Table 3 - Removal percentage for dyes RR2 and RR141 for the best adsorption conditions with initial concentrations of 100 to 500 mg/L.

Adsorbate	Temp. (°C)	Co (mg/L)	Ce (mg/L)	qe (mg/g)	%Removal	R_L
RR2	25	500	57.14	44.29	88.57	0.1313
		100	0.274	9.97	99.73	0.9693
RR141 with 10% (by mass) of sodium chloride	25	500	21.37	47.86	95.72	0.3783
		100	47.86	2.798	97.20	0.8230

From the removal percentage data given in Table 3, the great effectiveness of the color removal by the adsorbent for both dyes studied can be verified.

3.3 Continuous Experiments

Breakthrough curves were obtained for dyes RR2 and RR141 under the best adsorption conditions shown in Table 2. The porosity of the packed bed has a value ε=0.42. The curves in continuous experiments were obtained for dye RR2 at the operation temperature of 25°C with different bed heights and flow rates and for dye RR141 at the temperature of 25°C with addition of 10% (w:w) of sodium chloride (NaCl) to the column feed solution, also using different feed rates and bed heights. The breakpoints for these conditions are shown in Table 4.

Table 4 – Breakpoint (t_b) and amount of dye removed by the adsorbent in equilibrium for the dyes RR2 and RR141.

Dye	Feed rates (mL/min)	Bed heights(cm)	t_b(min)	q_{eq} (mg/g)	Dye	Feed rates (mL/min)	Bed heights (cm)	t_b (min)	q_{eq} (mg/g)
RR2	8	15	170	13.70	RR141	8	15	320	38.69
		30	290	19.00			30	530	48.56
		45	430	19.55			45	820	57.70
	12	15	100	16.41		12	15	210	41.73
		30	165	27.20			30	360	49.25
		45	210	21.51			45	490	44.70
	16	15	55	13.42		16	15	160	39.98
		30	100	17.08			30	290	45.82
		45	190	18.60			45	330	42.37

For the dye RR2 the column saturation time, when operated with a fixed bed height of 15 cm and flow of 16 mL/min, was only 55 min and for a flow of 8 mL/min it was 3.1 times greater. For the dye RR141 the saturations time under the same conditions were 160 and 320 min, respectively. When the column operated with a solution of dye RR2 the operation time was shorter than with the dye RR141, for the different flows studied, as a consequence of the magnitude of the values obtained for q_m, 53.48 and 78.74 mg/g, for the dyes RR2 and RR141, respectively.

Guelli U. Souza *et al*., 2008, studied the adsorption of the dye Basic Green 4 in fixed bed columns packed with granular activated carbon for different feed rates. For a feed rate of 3.2 mL/min the breakpoint occurred in twice the time compared to a feed rate of 6.0 mL/min

Figure 2 shows the breakthrough curves for the dyes a) RR2 and b) RR141 for different bed heights and a feed rate fixed at 16 mL/min.

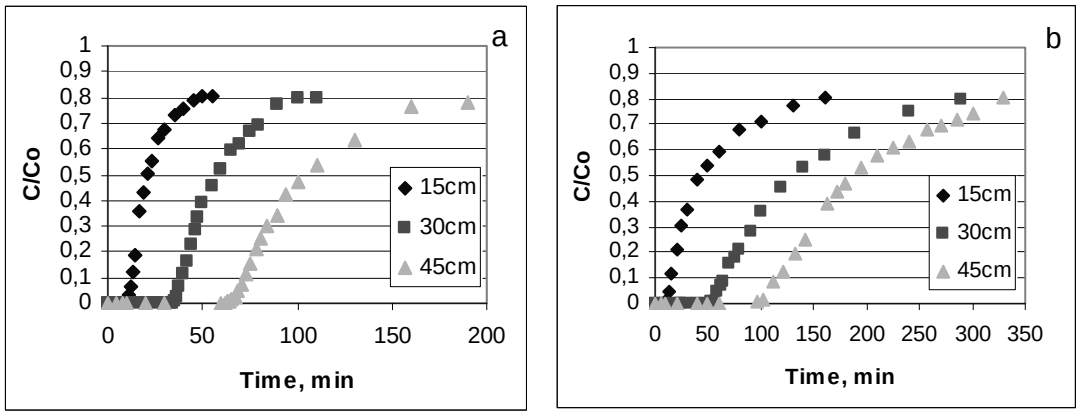

Figure 2 - Breakthrough curves for the dyes a) RR2 (T=25°C) and b) RR141 (T=25°C-10% NaCl) with different bed heights for a feed rate of 16 mL/min.

According to Figure 2, it can be observed that an increase in the critical bed height leads to a slower column saturation, due to the larger quantity of adsorbent, which increases the time of the column operation. For a bed height of 45 cm and fixed feed rate of 12 mL/min, the saturation time for the dye RR2 was 52.38% greater, when compared to a bed height of 15 cm and for the dye RR141 under the same conditions the saturation time was 57.14% greater when compared to the bed height of 15 cm. The adsorption capacity in equilibrium increased with the increase in the height of packed column from 15 to 30 cm and for the feed rate increase there were no significant variations in this parameter.

The experimental results were compared with data given in the literature showing a higher adsorption capacity of the adsorbent under study. The adsorbent here investigated represents as a very promising alternative in terms of an environmentally correct process,

focusing on a reduction in the environmental impact of dyes from the textile industries on water sources.

4 Conclusions

The great effectiveness of the absorbent was verified through the color removal for both dyes studied, where the percentage removal for the dyes RR2 and RR141 under the best adsorption conditions, with initial concentrations of 100 and 500 mg/L, were 88.57% and 99.73%, respectively, for the dye RR2 and 95.72% and 97.20% respectively for the dye RR141. The presence of salt in the system is a factor which interferes in the adsorption performance, according to the quantity and the chemical species.

The parameters determined in the continuous experiments will be used for the design of prototype columns in industrial scale. The adsorption capacity in equilibrium increased with an increase in the packed column height from 15 to 30 cm and there was no variations with the feed rate increase.

The use of this new adsorbent can be recommended for the final stage of the wastewater treatment process, where neutralization is required by the environmental legislation, considering that the best performance of the adsorbent occurs in an acid environment.

References

Brunauer, S., Emmett, P.H., Teller, E. (1938). Adsorption of Gases in Multimolecular Layers. *Journal of the American Chemical Society*, 60, 309-319.

Calvo, L. F., Otero, M., Morán, A., García, A. I. (2002) Upgrading sewage sludges for adsorbent preparation by different treatments. *Bioresource Technology*, 80, 143-148.

Ciola, R. (1981). *Fundamentos de catálise*. 1. ed. São Paulo: Editora da USP.

Chen, K.M., Chu, H.C. (2002). Reuse of activated sludge biomass: I. Removal of basic dyes from wastewater by biomass. *Process Biochemistry*, 37, 595-600.

Fernandes, R. (2005). Adsorventes alternativos para remoção de fenol em solução aquosa. *Dissertação de Mestrado*. Santa Catarina. Universidade Federal de Santa Catarina.

Guelli U. Souza, S. M. A., Peruzzo, L. C., Ulson de Souza, A. A., (2008).Numerical study of the adsorption of dyes from textile effluents. *Applied Mathematical Modelling*, 32, 1711-1718.

Jain, A. K., Suhas, Bhatnagar, A. (2002). Methylphenols removal from water by low-cost adsorbents. *Journal of Colloid and Interface Science*, 251, 39–45.

Kumar, K. V., Sivanesan, S. (2006). Equilibrium data, isotherm parameters and process design for partial and complete isotherm of methylene blue onto activated carbon. *Journal of Hazardous Materials*, B134, 237–244.

Netpradit, S., Thiravetyan, P., Towprayoon, S (2004). Adsorption of three azo reactive dyes by metal hydroxide sludge: effect of temperature, pH and electrolytes. *Journal of Colloid and Interface Science*, 270, 255–261.

Órfão, J. J. M. Silva, A. L. M., Pereira, J. C. V., Barata, S. A., Fonseca, I. M., Faria, P. C. C., Pereira, M. F. R. (2006). Adsorption of a reactive dye on chemically modified activated carbons—influence of pH. *Journal of Colloid and Interface Science*, 296, 480–489.

Ulson de Souza, A. A, Vasques, A. R., Guelli U. Souza, S. M. G. U. de, Valle, J. A. B. (2007). *Composto adsorvente, processo para sua preparação e processo para tratamento de efluentes.* Pedido de patente no INPI sob depósito n° 017070001291/2007.

Proceedings of the 10th International Chemical and
Biological Engineering Conference - CHEMPOR 2008
Braga, Portugal, September 4-6, 2008
E.C. Ferreira and M. Mota (Eds.)

Activated carbon from coconut shells as catalyst for CWAO of phenol in a trickle bed reactor

Maretva Baricot[1], Geoffrey Fowler[2], Agustí Fortuny[3], Frank Stüber[1], Christophe Bengoa[1], Azael Fabregat [1] and José Font [1*]

[1] Departament d'Enginyeria Química, ETSEQ, Universitat Rovira i Virgili, Av. Països Catalans, 26, Campus Sescelades, 43007 Tarragona, Catalunya, Spain

[2] Department of Civil and Enviromental Engineering, Skempton Building, Imperial College of London, London SW7 2AZ, United Kingdom

[3] Departament d'Enginyeria Química, EPSEVG,, Universitat Politècnica de Catalunya, 08800 Vilanova I la Geltrú, Catalunya, Spain

Keywords: activated carbon, steam activation, catalytic oxidation, phenol
Topic: Sustainable process-product development through green chemistry

ABSTRACT

Nowadays, the access to clean water is more and more difficult. Therefore, the detoxification of polluted water and its recycling when possible is mandatory for a sustainable and sustained development. For wastewater containing organic compounds at low to medium load, Catalytic Wet Air Oxidation (CWAO) yields satisfactory results, with the advantage that relatively mild operating conditions are needed, leading to lower investment and operation costs in comparison to non-catalytic WAO or other Advanced Oxidation Processes. Some activated carbons (AC) have been successfully used as catalyst in the CWAO of phenol in a trickle bed reactor (TBR) configuration. However, the reason for the catalytic activity of AC in CWAO is not yet completely understood. The aim of this research work was to fully characterising a coal-based commercial activated carbon (ME) with proven catalytic properties in the CWAO of phenol, and later, the manufacturing of an activated carbon tailored to have similar characteristics, so that it was expected to show the similar catalytic activity. Coconut shells were used as raw material for the preparation of the activated carbon by physical activation using steam (MCS). In order to increase the metal content (specifically iron) of this carbon, iron was added during the activation procedure (MCSFe). The results confirm the hypothesis that mineral matter, specifically iron, is mainly responsible for the catalytic behaviour of activated carbons in the CWAO of phenol. However, the presence of iron does not guarantee to be catalytically active in this reaction. It seems to be necessary iron to be actually available in the carbonaceous matrix and in an appropriate state.

1. Introduction

Activated carbon is a very well-known material widely used as adsorptive material for the removal of organic compounds. It has also been used for supporting catalytic metals for dedicated processes, due to its thermal and mechanical stability. Depending on the raw material used for its manufacturing and the type of activation applied (physical or chemical), some characteristics of the activated carbon, such as surface chemistry and textural properties, could be adjusted to improve its performance as adsorbent or as catalyst support. Lillo-Ródenas et al. (2005), for instance, applied activated carbons, made from Spanish anthracite through chemical and physical activation, for the adsorption of benzene and toluene. The carbons obtained had different porosity and surface chemistry, and the tests demonstrated that those with low content in oxygen surface groups have the best adsorption capacity. On the other hand, modification of manufactured activated carbons can be conducted in order to change the performance of these materials. Dastgheib et al. (2004) modified two commercial activated carbons by either acid wash, heat treatment under inert atmosphere, anhydrous ammonia treatment, or iron impregnation. All samples were tested in the adsorption of dissolved organic matter (DOM). Overall, acid wash dramatically decreased

the adsorption capacity due to significant increases in the carbon surface acidity. Heat treatment, ammonia treatment of oxidised carbons and iron impregnation increased the DOM adsorption. These latter treatments increased the carbon basicity and the accessible surface area, in addition they promoted a favourable chemistry, which resulted in an improvement of the activated carbon performance.

Another interesting and yet not widely explored application of the activated carbon is as catalyst by itself. Fortuny et al. (1998) and Tukac et al. (1998) demonstrated that some activated carbons possess catalytic activity towards the aqueous oxidation of phenol both in batch and in continuous reactors. However, actual parameters responsible for this catalytic behaviour have not been yet fully identified. According to some investigations, carbonyl type oxygen surface groups could be responsible for the catalytic activity shown by activated carbon in some reactions, for instance in the oxidative dehydrogenation of ethyl benzene (Pereira et al., 1999). On the other hand, an increase in the amount of acidic surface functionalities after nitric acid wash demonstrated to decrease the catalytic activity shown by a commercial activated carbon in the catalytic wet air oxidation (CWAO) of phenol (Santiago et al., 2005).

The aim of this study is fully characterising a coal-based commercial activated carbon (ME, Merck ref. 2514) with proven catalytic properties in the CWAO of phenol, and the subsequent manufacturing of an activated carbon tailored to have similar characteristics, so that it is to be expected to give the comparable catalytic activity. Coconut shells were used as raw material for the preparation of the activated carbon by physical activation using steam (MCS). In order to increase the metal content (specifically iron) of this carbon, iron was added during the activation procedure (MCSFe).

2. Materials and Methods

For the preparation of AC from coconut shells, one-step pyrolysis/activation with steam was conducted. Based in the results collected in the review made by Ioannidou and Zabaniotou (2007) and with the purpose of obtaining a microporous material, a high temperature was selected for the activation. Thus, the activation was done at 1000ºC in an oven. The coconut shells were heated at 10ºC/min to final temperature under nitrogen flow (500 ml/min). Once 1000ºC was reached, the inert atmosphere was replaced by a mixture of steam/nitrogen by injecting distilled water through a calibrated peristaltic pump, which was set to work at a constant flow of 0.812 ml/min. These conditions were kept for 1 hour and then the steam flow was stopped and the carbon cooled under nitrogen.

The iron-containing AC made from coconut shells was prepared in two steps. First, the raw material was heated under nitrogen up to 450ºC in order to produce a char free from volatile species and condensable oils. This char was then impregnated with a $FeCl_2 \cdot 4H_2O$ 0.1 M solution for 24 hours, and then filtered and dried overnight at 105ºC. Once moisture free, it was heated up to 1000ºC in an oven and kept at this temperature for 1 hour under a mixture of steam/nitrogen as previously described. Finally, the water flow was stopped and the AC was cooled under just nitrogen.

The coconut shell-based activated carbons and the commercial ME were crushed and sieved. Later, the 0.3-0.7 mm (50-25 mesh) size particle range was separated. The above fraction was repeatedly washed to remove all fines and oven-dried overnight at 105ºC. Then, it was stored in amber bottles until use. All samples were characterised by determining its typical physico-chemical characteristics. Surface area and porosity of the activated carbons were estimated from nitrogen isotherms at 77 K. Surface area was determined from BET equation, total pore volume from the near saturation nitrogen uptake at the relative pressure of 0.98, and micropore volume from the Dubinin-Radushkevich equation. Volume of meso- plus macropores was obtained from subtracting the micropore volume from the total pore volume. Mass titration method was used to determine the point of zero charge of each

sample. Boehm titration was carried out to determine the content and the distribution of the acidic surface functional groups. For measuring the iron concentration, samples were digested in concentrated nitric acid by a microwave digestion equipment. Dilute solutions were later analysed by AAS. The phenol adsorption isotherms were obtained at 20ºC (± 2ºC) in oxic conditions. Specifically, solutions with phenol concentrations ranging from 0.5 to 7 g/l were left in contact with 0.25 g of adsorbent. The catalytic performance was assessed for the CWAO of 5 g/l phenol solutions in a trickle bed reactor in downflow co-current at 140ºC, 0.2 MPa of oxygen partial pressure and 0.12 h of space time. The detailed description of the equipment and experimental procedure has been given elsewhere (Suarez-Ojeda et al., 2005).

3. Results

Table 1 summarises the liquid and solid products rendered during the manufacture of the activated carbons. The liquid product yield in sample MCS, made from coconut shells and by one-step pyrolysis activation, was higher than that obtained for MCSFe. This is attributed to the carbonisation step that was conducted before the iron impregnation step and the activation. In the manufacturing of the chars that were later used in the iron impregnation, the liquid products yield was about 70%. For that reason, after the iron impregnation and the activation with steam, the liquid product yield was only about 10%, because most of the organic material that is later released as oils was already eliminated in the char production step.

Table 1. Yields obtained in the manufacturing of activated carbons.

Sample	Solid product (% wt)	Liquid product (% wt)	Gas + losses (% wt)
MCS	19.0	35.4	45.6
MCSFe	56.4	10.4	33.2

The physical characterisation of both coconut-based activated carbons, MCS and MCSFe are listed in Table 2. MCS is a highly microporous carbon since 96% of its total porosity is in the micropore range. The surface area is also relatively high, which indicates that steam was effective as activating agent promoting the formation of micropores. Sample MCSFe, on the contrary, showed a surface area 40% lower than MCS and also 47% lower micropore volume. Despite the iron is supposed to enhance the gasification of the carbon, thus promoting the porosity, in this case the iron impregnated on the char made from the coconut shells could have prevented the water and the char from interacting and thus from reacting. As a result, development of the surface area and microporosity were suppressed and only superficial reactions, typically producing mesoporosity, promoted. Actually, some increase in the mesopore volume, from 4% to 9%, was observed in sample MCSFe (Marsh and Rodríguez-Reinoso, 2006; Alcañiz-Monge et al., 2007).

Table 2. Physical properties of tailored activated carbons.

Sample	SA_{BET} (m^2/g)	V_{mic} D-R (cm^3/g)	$V_{mes+mac}$ (cm^3/g)	V_{tot} (cm^3/g)
ME	1261	0.473	0.137	0.610
MCS	830	0.369	0.014	0.383
MCSFe	493	0.194	0.020	0.214

The surface oxygen content measured by Boehm titrations, the pH_{pzc} and the iron content of the manufactured carbons are collected in Table 3. The coconut based carbons show not detectable amount of carboxylic functionalities. Also, the content of other functional groups like lactones and phenolics is lower than the content of commercial ME. This could be explained by the fact that, after the activation, the samples were left to freely cool from 1000ºC until room temperature under just the nitrogen flow, so most of the acidic surface functionalities were probably decomposed into CO and CO_2 during cooling.

Table 3. Chemical properties of tailored activated carbons.

Sample	Phenolics (meq/g)	Lactones (meq/g)	Carboxyls (meq/g)	pH_{pzc}	Fe content (%wt)
ME	0.097	0.123	0.031	7.36	0.40
MCS	0.059	0.033	0.000	10.82	0.00
MCSFe	0.017	0.042	0.000	10.52	0.20

The phenol adsorption isotherms of the tailored carbons are presented in Figure 1. Sample MCS showed high adsorption capacity at bulk phenol concentration values higher than 5000 mg/L , whereas for lower values it is in the same order than the commercial ME. However, sample MCSFe gave a considerable decrease in the phenol adsorption capacity, i.e. a loss of 74% in its original adsorption capacity. As it has been reported in the literature (Dabrowski et al., 2005), surface chemistry is determinant in the activated carbon performance as adsorbent for phenol. Low content of acidic surface functionalities lowers the hydrophilicity of the carbon surface, avoiding the formation of water clusters and improving the interaction of the phenol molecules with the carbonaceous structure. All these effects enhance the phenol adsorption on activated carbons. Since MCS and MCSFe have very similar oxygen content (see Table 3), the decrease of the adsorption capacity should be attributed to the considerable difference in both the surface area and the micropore volume as seen in Table 2.

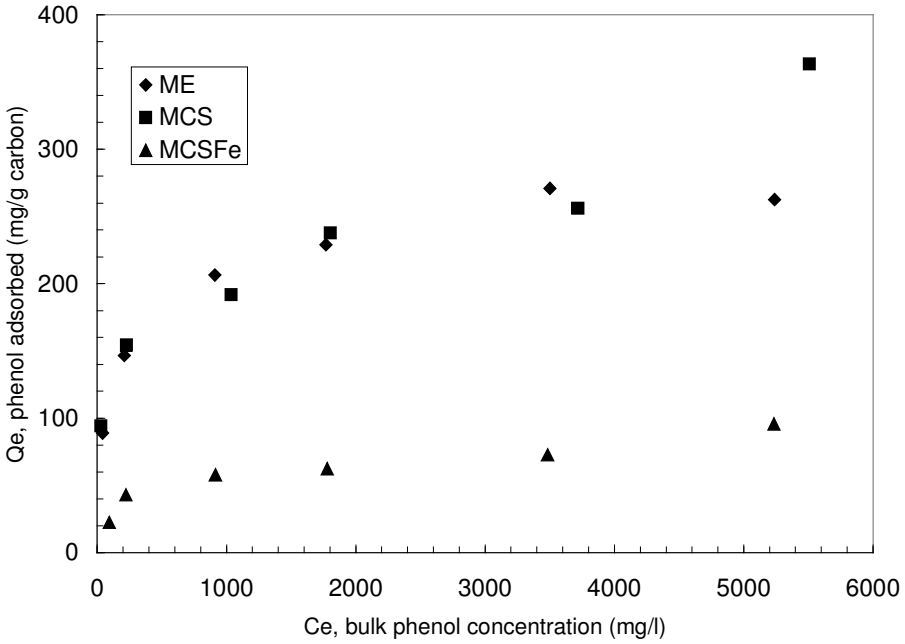

Figure 1. Phenol adsorption isotherms over tailored activated carbons at 20ºC.

The phenol conversions obtained with these tailored carbons in the TBR tests are shown in Figure 2. Regardless of the iron content of sample MCSFe, which is half that of ME (see Table 3), the conversion achieved with MCSFe is considerably much more lower, only 10% compared to 45% given by ME. The poor catalytic activity exhibited by MCSFe could be attributed to the very low value of both surface area and micropore volume developed during its activation. Actually, the value of phenol conversion obtained with MCSFe is practically the same observed for MCS, which suggests that both MCS and MCSFe are affected by serious problems of surface availability. When measuring the amount of acidic compounds formed as intermediates from the phenol oxidation with these carbons as catalysts, some noticeable observations can be made. With carbon MCS, 33% of the intermediates were acids. This is a quite low mineralisation that correlates with its poor catalytic performance. However, the amount of acidic intermediates considerably increased when iron was incorporated to the carbon, MCSFe, up to 88%, for which the increase of phenol conversion, compared to MCS, is only from 8% to 10%. Commercial ME also shows a high selectivity towards acidic intermediates, thus 94% of the compounds in the exited effluent are acidic.

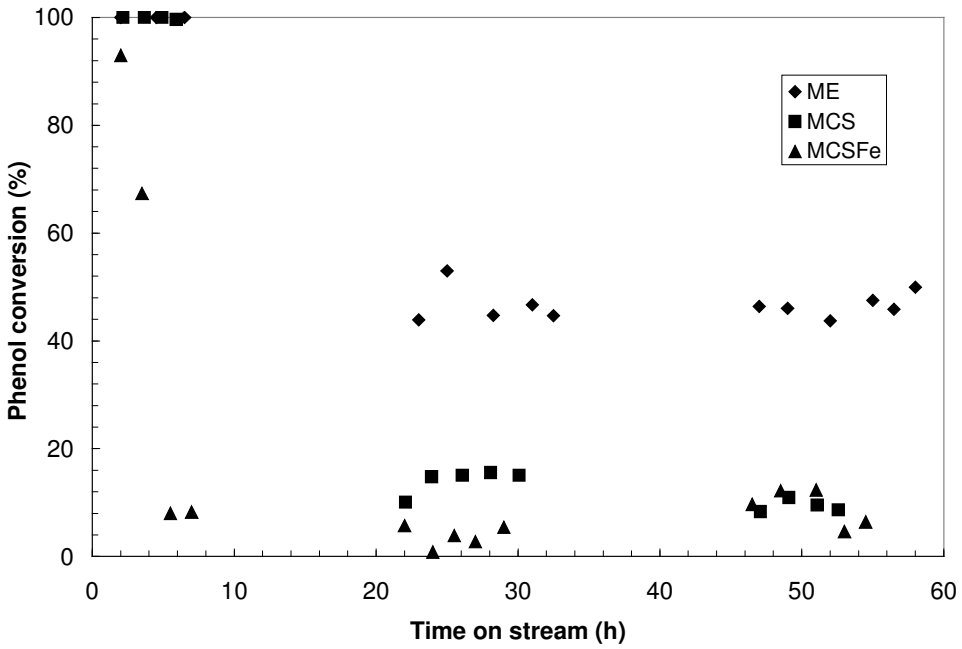

Figure 2. Phenol conversion in TBR using tailored manufactured samples, at 140ºC, 2 bar of oxygen partial pressure and 0.12 h of space time.

Leaching of iron was found for ME and MCSFe. The iron content in the used activated carbons after 55 hours on stream are listed in Table 4. As well, the weight gained by the AC bed, ΔW, of all three carbons, the pH and the iron concentration in the exited effluent at the end of the run are given. The leaching was about 80% for sample MCSFe. Since the iron in the liquid is measured in the last sample taken from the reactor, and the value measured in the case of MCSFe is very low compared with the one measure in the liquid when using ME, which in contrast only lost 22% of its original iron, it is possible to think that most of the leaching could be occurring during the first hours of operation. Zhu et al. (1997) proposed that during carbonisation step, iron atoms migrate from the surface to the inner part of the bulk of carbon particles. This migration depends on the temperature of the carbonisation. Also time could be affecting the iron migration in the carbon, however the effect of this parameter has not been reported. For MCSFe, the iron impregnation was done before the activation, but after the carbonisation step. The textural properties of the char could be affecting the proposed iron migration, remaining most of it on the surface, where it probably cannot be properly fixed in the carbonaceous matrix, which facilitates leaching. The ΔW after

55 hours of operation can probably be assigned to the deposition of phenolic polymers over AC surface due to condensation by oxidative coupling. Also, the oxidative coupling products could be responsible for the increase observed in ΔW.

.

Table 4. Weight difference in ME and tailored manufactured samples after operation in TBR and final pH of liquid stream.

Sample	ΔW (g)	Final pH	Fe in the outlet effluent (mg/L)	Fe content after use (% wt)
ME	2.519	2.13	9.9	0.31
MCS	2.900	3.85	0.0	0.00
MCSFe	2.051	2.96	0.3	0.04

4. Conclusions

One-step pyrolysis procedure was effective to manufacture activated carbon from coconut shells, MCS, achieving high values of surface area and well developed porosity, although most of the porous being in the range of microporosity. MCS carbon, despite having 34% lower surface area, shows the same adsorption capacity than commercial carbons like ME made from coal. However, due to the absence of mineral matter in the raw coconut shells, carbon MCS did not show little catalytic activity for CWAO of phenol. Sample MCSFe, made also from coconut shells but with an additional iron impregnation step included before the activation, also showed poor catalytic behaviour. This indicates that the iron in sample MCSFe is not catalytically active. In conclusion, the presence of iron in the carbonaceous materials does not always guarantee catalytic activity, probably due to the position or even the crystalline phase in which it is present.

References

Alcañiz-Monge, J., Lillo-Ródenas, M., Bueno-López. A. and M. Illán-Gómez, (2007) The influence of iron chloride addition to the precursor pitch on the formation of activated carbon fibers. *Microporous Mesoporous Mater.*, 100, 202-209.

Dastgheib, S., Karanfil, T., Cheng, W. (2004). Tailoring activated carbons for enhanced removal of natural organic matter from natural waters. *Carbon*, 42, 547-557.

Dabrowski, A., P. Podkoscielny, Z. Hubicki and M. Barczak, (2005) Adsorption of phenolic compounds by activated carbon - a critical review. *Chemosphere*, 58, 1049-1070.

Fortuny, A., J. Font, Fabregat, A. (1998). Wet air oxidation of phenol using active carbon as catalyst. *Applied Catalysis B*, 19, 165-173.

Lillo-Ródenas, M.A., Cazorla-Amorós, D., Linares-Solano, A. (2005). Behaviour of activated carbons with different pore size distributions and surface oxygen groups for benzene and toluene adsorption at low concentrations. *Carbon*, 43, 1758-1767.

Marsh, H. and F. Rodríguez-Reinoso, (2006) *Activated Carbon*, Elsevier Ltd.

Pereira, M.F.R., Orfao, J.J.M., Figueiredo, J.L. (1999) Oxidative dehydrogenation of ethylbenzene on activated carbon catalysts. I. Influence of surface chemical groups. *Applied Catalysis A*, 184, 153-160.

Santiago, M., Stuber, F., Fortuny, A., Fabregat A, Font J. (2005) Modified activated carbons for catalytic wet air oxidation of phenol. *Carbon*, 43, 2134-2145.

Suarez-Ojeda, M.E., Stuber, F., Fortuny, A., Fabregat A., Carrera J., Font, J. (2005) Catalytic wet air oxidation of substituted phenols using activated carbon as catalyst. *Applied Catalysis B*, 58, 105-114.

Tukac, V., Hanika, J. (1998) Catalytic wet oxidation of substituted phenols in the trickle bed reactor. *Journal of Chemical Technology and Biotechnology*, 71, 262-266.

Zhu, Z., Liu, Z. and Y. Gu, (1997) Formation of N_2 during carbonisation of polyacrylonitrile using iron catalyst. *Fuel*, 76, 155-163.

Proceedings of the 10th International Chemical and
Biological Engineering Conference - CHEMPOR 2008
Braga, Portugal, September 4-6, 2008
E.C. Ferreira and M. Mota (Eds.)

Use of chemical modification to determine the binding of Cd(II), Zn(II) and Cr(III) ions by orange waste

A.B. Pérez Marín*, J.F. Ortuño, M.I. Aguilar, V.F. Meseguer, J. Sáez, M. Lloréns
Chemical Engineering Department, University of Murcia, Campus of Espinardo
30071 Murcia, Spain.

Keywords: orange waste, functional groups, sorption, FTIR and ^{13}C-NMR
Topic: Sustainable process-product development through green chemistry. Environmental engineering & management

Abstract

This study focuses on the roles played by three major functional groups (amine, carboxyl and hydroxyl) in the orange waste biomass for sorption of three heavy metals (Cd^{2+}, Zn^{2+} and Cr^{3+}). The biosorbent was chemically modified to block the mentioned functional groups in order to determine their contribution to the adsorption of metals. Fourier transform infrared (FTIR) and solid state carbon-13 nuclear magnetic resonance (^{13}C-NMR) spectroscopy were used to investigate the chemical modification. Additionally, batch biosorption tests were carried out with the different biosorbents in order to determine the possible reduction in metal uptake with the chemically modified biosorbent. Blocking of the COOH groups by chemical esterification resulted in an important reduction in metal binding. Nevertheless, no significant modification in metal removal was observed with acetylated and methylated orange waste.

Introduction

The increase in industrial activities has intensified environmental pollution and the deterioration of some ecosystems, with the accumulation of pollutants such as heavy metals, synthetic compounds, etc. The pollution by heavy metals is of great corcern due to potential health hazard caused by these compounds to the environment.

Therefore, an adequate treatment of the polluted wastewater are required. Traditional treatment techniques include chemical precipitation, membrane filtration, electrolysis, ion exchange, carbon adsorption and co-precipitation/adsorption. Nevertheless, the application of such processes is sometimes restricted because of technical or economic constraints.

The search for new technologies involving the removal of toxic metals from wastewaters has directed attention to biosorption, based on the metal binding capacities of various biological materials. Among these materials, fruit waste materials are tipically generated in large quantities by the fruit juice industry as a waste by-product and they have demonstrate their ability to remove heavy metals in solution. Pectin has been identified as an important component of citrus wastes and has been found to have great affinity for metal ions.

Even though orange waste has been recently used as adsorbent in many studies, the biomass–metal binding mechanisms are not well understood. In order to investigate the adsorption mechanism, chemical modifications to orange waste were performed to indirectly determine the ligands on the biomass responsible for metal binding. Sorption test, with the different biomass, in combination with FTIR spectrometric and ^{13}C-NMR studies were carried out to investigate the participating functional groups.

* Corresponding author. Tel + 34 968 367515. E-mail: abelenpm@um.es

Materials and methods.

Biomass conditioning

The orange waste used as adsorbent was obtained from orange juice industry. The material was cut into small pieces, was extensively washed with tap water and was oven-dried at 50-60 ºC until constant weight. The washed and dried material was crushed and sieved to obtain a particle size lower than 1.5 mm.

Chemical modification of the biomass

The following treatments (Kapoor and Viraraghavan, 1997) were carried out on orange waste:

Chemical esterification. The carboxyl group of the biomass was methanol esterified. Esterification was carried out by heating 9 g of biomass in 633 mL of 99.9% pure methanol and 5.4 mL of concentrated hydrochloric acid (HCl), given a final acidic concentration of 0.1 M HCl, under reflux for 48 h. Then the esterified biomaterial was thoroughly washed with distilled water, filtered and dried. The general reaction scheme of this treatment is:

$$RCOOH + CH_3OH \xrightarrow{H^+} RCOOCH_3 + H_2O$$

Chemical methylation. The modification of amino group was made by shaking, at ambient temperature, 9 g (dry weight) of the raw biomass in 180 mL of formaldehyde (HCHO) and 360 mL of formic acid (HCOOH) for 6 h at 125 rpm. Then the treated biomaterial was thoroughly washed with distilled water, filtered and dried. This treatment resulted in methylation of amino group. The general reaction scheme is:

$$RNH_2 + 2HCHO + 2HCOOH \longrightarrow RN(CH_3)_2 + 2CO_2 + 2H_2O$$

Chemical acetylation. Total acetylation of amino and hydroxyl groups of the sorbent was carried out by refluxing the biomass suspension in acetic anhydride at 80 ºC for 10 h. Then the acetylated biomaterial was thoroughly washed with distilled water, filtered and dried. The general reaction scheme of this treatment is:

$$RNH_2 + CH_3COOH \longrightarrow RNHCOCH_3 + H_2O$$

$$RCH_2OH + CH_3COOH \longrightarrow RCH_2OCOCH_3 + H_2O$$

Sorption assays

Adsorption studies were carried out by batch process. 0.2 g of biomass were added to glass flasks containing 50 mL solution of metal ion (Cd^{2+}, Zn^{2+} or Cr^{3+}) of the desired concentration. The mixture was stirred magnetically for the time neccesary to reach equilibrium (3 h for Cd^{2+} and Zn^{2+}, and 3 days for Cr^{3+}). The pH of solutions was adjusted to 4, by adding small amounts of dilute solutions of HNO_3 and NH_3. After the contact time, the biosorbent was removed by filtration through glass fibre prefilters (Millipore AP40) and the filtrates were analysed for residual metal concentration by atomic absorption spectrophotometry (Perkin Elmer model AA300). Batch experiments were performed by varying the initial concentration of metal from 0 to 300 mg/L. All experiments were conducted in duplicate. The metal percentage removal and the biomass sorption capacity were calculated in each case.

Cd^{2+}, Zn^{2+} and Cr^{3+} sorption equilibrium data onto raw orange waste were fitted to Langmuir isotherm in order to obtain the maximum sorption capacity and to be able to compare the sorption properties of this material with other adsorbents in bibliography.

FTIR spectra and ^{13}C-NMR study

FTIR and ^{13}C-NMR spectra were used to analyse the functional groups in the raw as well as chemically modified biomass. FTIR spectra were recorded in a Fourier transform infrared spectrophotometer (Perkin Elmer 16F PC) with the samples prepared as KBr discs. ^{13}C-NMR spectra were recorded at the Complutense University of Madrid, Spain, on a Bruker WB-400 spectrometer.

Results and discussion.

FTIR analysis results

FTIR spectra of raw and chemically modified orange waste (OW) are shown in Figure 1.

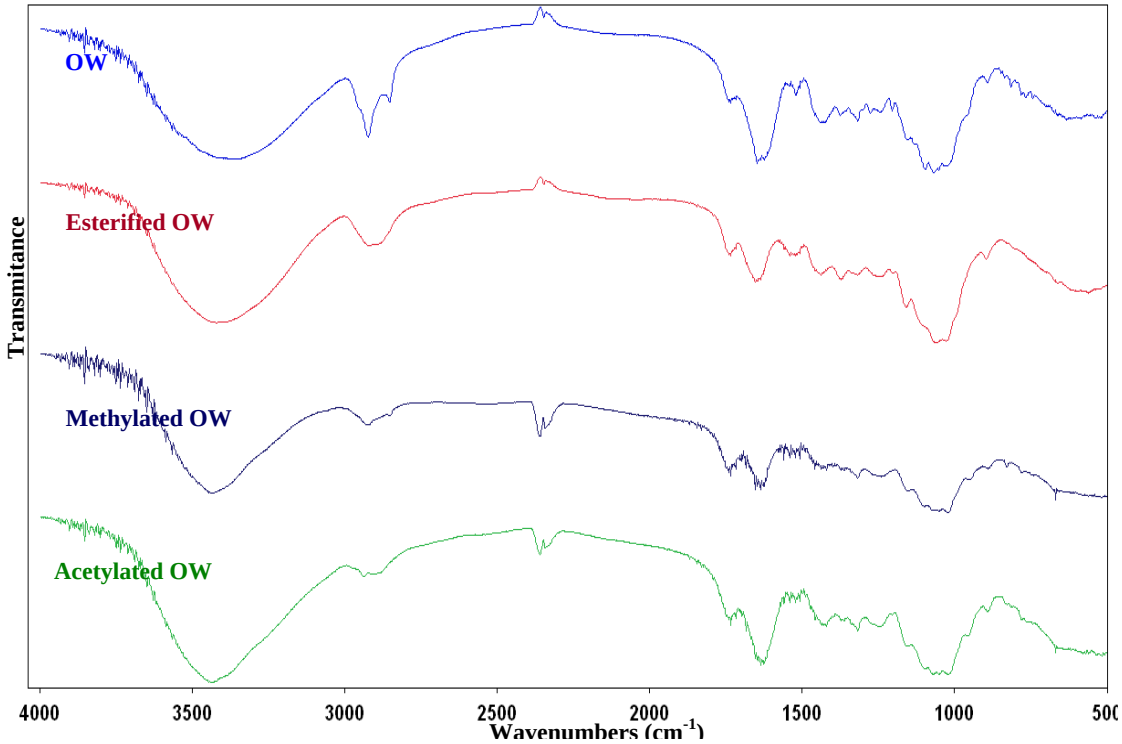

Figure 1. FTIR spectra of raw and chemically modified orange waste.

The spectra of orange waste display a number of adsorption peaks, indicating the complex nature of the material examined. The FTIR spectra of raw biomass exhibits a broad peak between 3200 cm^{-1} and 3600 cm^{-1} which is indicative of the existence of macromolecular assotiation (cellulose, pectin, etc.) and might be the indication of both amine and bonded OH groups. The finger print region of 1000-1200 cm^{-1} exhibits the characteristic peaks of cellulose. Bands around 1647 cm^{-1} and 1736 cm^{-1} are indicative of free and esterified carboxyl groups, respectively, which may be useful in identifying pectins.

The shift in wavenumbers at 1636 cm^{-1} in esterified biomass corresponds to a change in bonding energy associated with a modification in carboxyl groups on cellulose or pectin chains.

The band observed at 3357 cm^{-1} in raw material got widened in acetylated and methylated biomass. It suggests changes in the amine groups present in the biomass and, in the case of acetylated orange waste, the change could be also due to hydroxyl groups. The increase in the band at 1716 cm^{-1} in methylated biomass indicates the presence of formic acid.

^{13}C-NMR analysis results

Figure 2 shows the ^{13}C-NMR spectrum of raw material and chemically modified biomass.

^{13}C-NMR spectrum of raw material are similar to those obtained for other authors for this type of material (Javis et al., 1996). The characteristic bands at 105 ppm (C-1), 84 ppm (C-4), 72-75 ppm (C-2, C-3 and C-5) and 65 ppm (C-6) are assigned to cellulose. Related to hemicellulose signal at 101 ppm (C-1), 89 ppm (C-4) and 62 ppm (C-6) are observed and peaks at 101 ppm (C-1), 80 ppm (C-4) and 71 ppm (C-2, C-3) are attributed to pectins. Besides these peaks, signals attributed to carboxyl groups in

their ionized (177 ppm) and esterified (165 ppm) form, methoxyl carbon (56 ppm), methylene carbon (33 ppm), acetyl carbon (23 ppm) and methyl carbon (19 ppm) were also obtained.

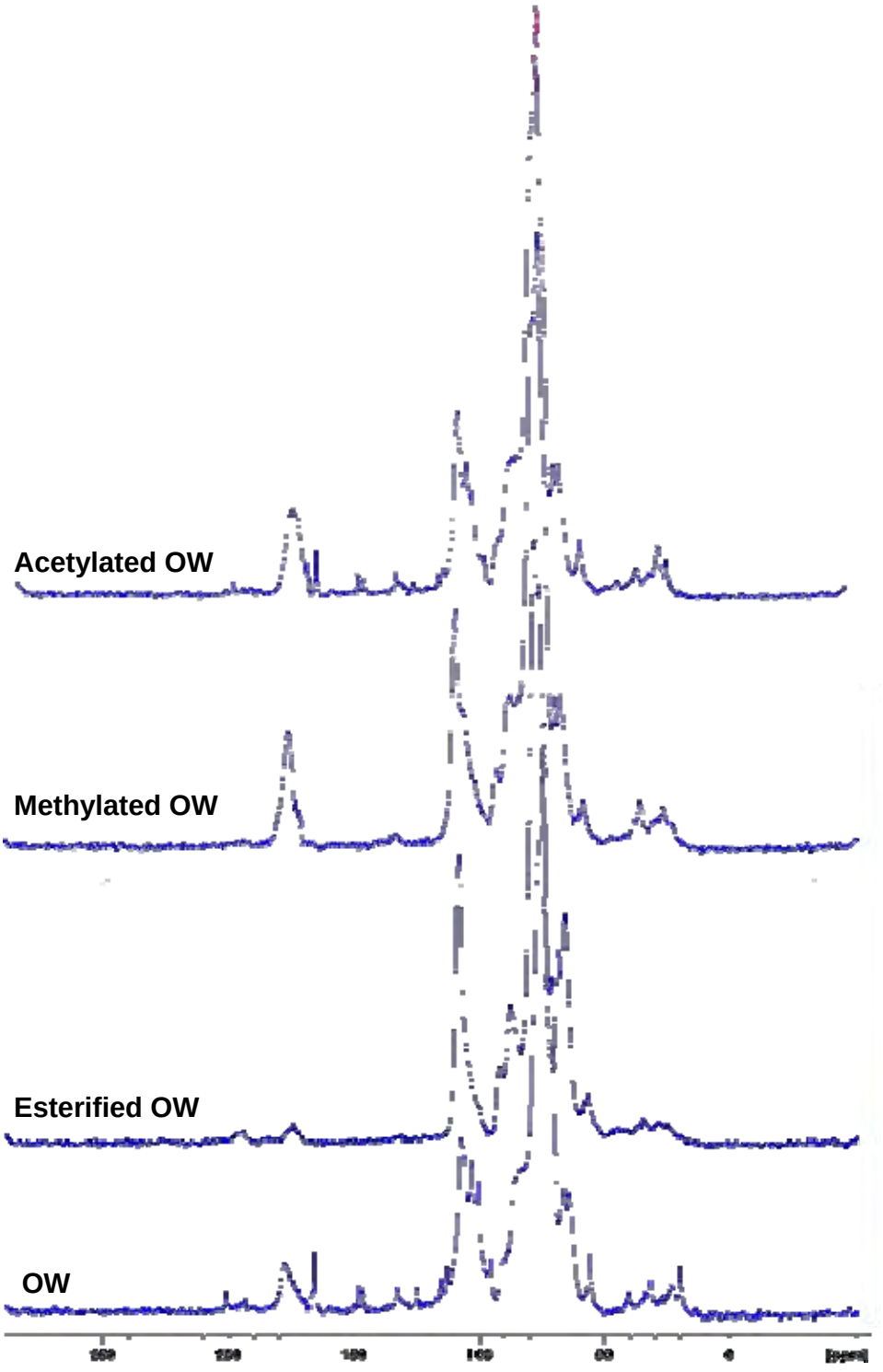

Figure 2. ^{13}C-NMR spectra of raw and chemically modified orange waste.

After esterification treatment, signal at 177 ppm disappears and, contrary to that we expected, the band at 165 ppm is considerably reduced. This unexpected result could be explained by the pectins extraction, and consequently the disappearance of carboxylic groups present in them, with this treatment. In fact, several authors have

studied the extraction of pectin by heating in acid conditions (May, 1990).

An increase in peaks at 38 ppm and 23 ppm was obtained with the methylation and acetylation treatments, respectivately. This fact is indicative of the presence of amine and hydroxyl groups.

Thus, correlating the data obtained from FTIR and ^{13}C-NMR spectra it could be concluded that carboxyl, amine and hydroxyl groups are present in the studied biomass and they have been modified chemically. So, all these groups might be responsible of metal uptake.

Sorption assays

Batch sorption tests were carried out with both, raw and chemically modified biomass, to compare the biosorption efficiency and hence the contribution of active compounds existing on the biomass. The sorption uptake by raw biomass and modified biomass are compared in Figure 3

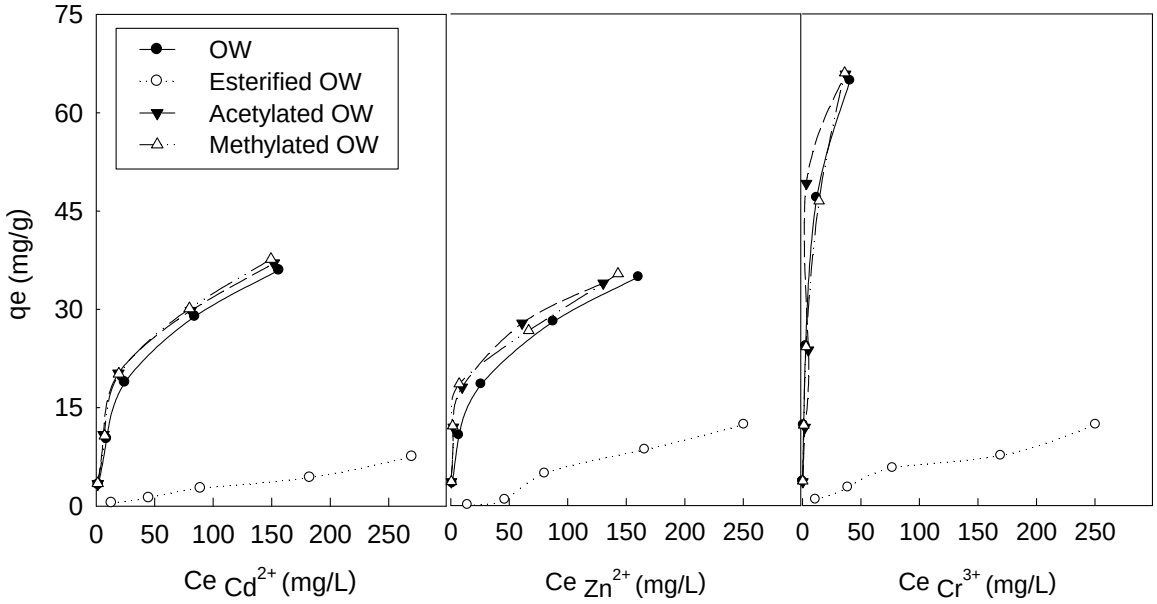

Figure 3. Effect of chemical modification of orange waste on Cd^{2+}, Zn^{2+} and Cr^{3+} biosorption.

As it can be seen, the lowest metal uptake was obtained with esterified biomass. Biosorption of cadmium, zinc and chromium was almost inhibited with the esterification treatment, when pectins were extracted from raw materials and carboxyled groups were esterified, thus indicating the important role played by pectins and carboxyl groups in the biosorption of heavy metals onto orange waste. The reductions in percentage removal of metals with the esterification treatment, in comparison with raw material, were higher than 79%, 66% and 82% for Cd, Zn and Cr, respectively. No significant modification in biosorption were observed in acetylated and methylated biomass, so these functional groups do not seems to be involved in metal uptake by orange waste.

A good correlation of equilibrium data for raw material was obtained by Langmuir isotherm. The maximum sorption capacity are 41.2 mg/g, 40.9 mg/g and 72.5 mg/g for Cd^{2+}, Zn^{2+} and Cr^{3+}, respectively. These values are within the range of other materials that have been described in bibliography as promissing biosorbent for removal heavy metals (Table 1).

Table 1. Maximum sorption uptake for different materials (Volesky, 2004).

Material	Metal	Maximum sorption uptake ($mg \cdot g^{-1}$)
Bacillus biomass	Cr^{3+}	118
Rhizopus arrhizus	Cr^{3+}	31
Candida tropicalis	Cr^{3+}	4.6
Sargassum species	Zn^{2+}	70
Candida tropicalis	Zn^{2+}	30
Bacillus sp.	Zn^{2+}	3.4
Sargassum natans	Cd^{2+}	135
Candida tropicalis	Cd^{2+}	60
Rhizopus arrhizus	Cd^{2+}	19

Conclusions

Modification of orange waste biomass was performed using various kinds of chemical reagents in order to verify the contribution of different functional groups on the biosorption of Cd^{2+}, Zn^{2+} and Cr^{3+}. FTIR and ^{13}C-NMR analysis of raw and modified orange waste disclosed the existence of carboxylic, amine and hydroxyl functional groups and pectins on the biomass. Sorption studies demonstrated that the esterification treatment resulted in the decrease of biosorption capacity of the biomass, which suggested that the eliminated pectins and the carboxylic groups existed in the biomass are major component and functional groups involved in biosorption process. They play an important role in the biosorption of studied metal onto orange waste. The acetylated or methylated biomass do not provided significant differences in sorption uptake, when comparing with raw biomass, which indicates that amine and hydroxyl groups have negligible effect on metal sorption onto orange waste at the studied experimental conditions. The biosorption process of raw biomass has been described by Langmuir isotherm and it has been demonstrated that maximum sorption capacity of orange waste are within the range of other materials that have been previously described in bibliography as promissing biosorbents for heavy metals removal.

Acknowledgements
The authors gratefully acknowledge to the Ministry of Science and Technology of Spain (REN2002-02030) for this economic support.

References

Kapoor, A.; Viraraghavan, T. (1997) Heavy metal biosorption sites in *Aspergillus niger*. *Bioresource Technology* 61, 221-227.

Jarvis, M.C.; Fenwick, KM.; Apperley, DC. (1996) Cross-polarisation kinetics and proton NMR relaxation in polymers of Citrus cell walls. *Carbohydrate Research* 288, 1-14.

May, C.D. (1990) Industrial pectins: Sources, production and applications. *Carbohydrate Polymers* 12 (1), 79-99.

Volesky, B. (2004) Sorption and biosorption. Ed. BV Sorbex. Montreal.

Proceedings of the 10th International Chemical and
Biological Engineering Conference - CHEMPOR 2008
Braga, Portugal, September 4-6, 2008
E.C. Ferreira and M. Mota (Eds.)

Mercury removal from solutions with low metal levels: ETS-4 and activated carbon comparison

Cláudia B. Lopes[1], Marta Otero[1], Zhi Lin[2], Carlos M. Silva[2], João Rocha[2], Eduarda Pereira[1], Armando C. Duarte[1]

[1] CESAM & Chemistry Department, University of Aveiro, Campus de Santiago, 3810 – 193 Aveiro, Portugal

[2] CICECO & Chemistry Department, University of Aveiro, Campus de Santiago, 3810 – 193 Aveiro, Portugal

Keywords: Mercury, Removal, ETS-4, Activated carbon
Topic: Sustainable process-product development through green chemistry

Abstract

ETS-4 titanosilicate and activated carbon were investigated and compared for removal of trace amounts of mercury (II) from contaminated aqueous solutions. Isothermal batch stirred experiments were performed using a batch factor of 250 mL mg^{-1} and an initial Hg^{2+} concentration of 50 µg L^{-1}. ETS-4 titanosilicate exhibited much higher mercury removal capacity (~12 mg g^{-1}) than activated carbon (~5 mg g^{-1}). However, Hg^{2+} removal by activated carbon is faster, which was confirmed by pseudo first-order and pseudo second-order rate models. This study revealed that the removal of Hg^{2+} by ETS-4 titanosilicate and activated carbon from solutions with low metal levels is quite different and that ETS-4 titanosilicate is more efficient.

1 Introduction

Considered by EPA and by the European Water Frame Directive as a priority pollutant, mercury (Hg) is one of the most hazardous heavy metals present in the environment. Due to its toxic effects on aquatic life, human beings and environment, increasing attention has been given to the removal of Hg from effluents, in such a way to satisfy the actual strict environmental regulations.

Microporous titanosilicates are novel materials which were found to have valuable properties for the decontamination of mercury (II) polluted waters (Lopes et al., 2007). The question is: are they good enough to replace typically used adsorbents in water purification processes such as commercially available activated carbon?

Activated carbon is perhaps one of the most common and widely used adsorbents for uptaking noxious substances from water. Several studies have reported the successful application of activated carbons to remove pollutants from waters and wastewaters (e.g. Mohan et al., 2001; Krishnan and Anirudhan, 2002; K. Ranganathan, 2003; Jusoh et al., 2007; Vreysen et al., 2008).

The main objective of this study is to assess and compare the Hg^{2+} removal capacity of ETS-4 titanosilicate and activated carbon from solutions with low metal levels, in order to evaluate if microporous materials, such as ETS-4 are competitive with respect of commercial adsorbents, such as activated carbon.

2 Experimental

[1] Corresponding author. Tel + 351-234-370737. E-mail: claudia.b.lopes@ua.pt

All chemicals reagents used in the work were of analytical reagent grade and obtained from chemical commercial suppliers, without further purification. The certified standard stock solution of mercury (II) nitrate (1000 mg L^{-1} Hg^{2+}) was purchase from BDH Chemicals Ltd.

ETS-4 titanosilicate was synthesised according to the procedure described in Lopes et al. (2007, 2008) and the activated carbon (*Chemviron Pulsorb FG4 type*) was kindly supplied by *Chemviron Carbon*. The characteristic properties of these materials are depicted in Table 1. The particle size of ETS-4 was determined from the scanning electron microscope images obtained by a Hitachi S-4100 microscope and the pore size was calculated from the framework data. The activated carbon characteristics shown in Table 1 are those given by the *Chemviron* product bulletin.

Table 1. Properties of ETS-4 titanosilicate and activated carbon (*Chemviron Pulsorb FG4 type*).

	ETS-4	Chemviron Pulsorb FG4 type
Formula	$[(Na)_9Ti_5Si_{12}O_{38}(OH).12H_2O]$	---
Physical form	white powder	black powder
Surface area (N_2BET method*)	---	800
Density (g cm^{-3})	2.2	0.45
Particle diameter (µm)	0.5-0.9	30
Pore size (nm)	0.4	---

**Brunauer, Emmett and Teller, 1938. J. Am. Chem. Soc., 60: 309.*

In order to compare ETS-4 titanosilicate and activated carbon efficiencies on Hg^{2+} removal from solutions with low metal levels, batch stirred sorption experiments were isothermally (21±1ºC) carried out. Each batch experiment was performed using 8 mg of material (ETS-4 or activated carbon *Chemviron Pulsorb FG4 type*) and 2 L of 50 µg L^{-1} Hg^{2+} solution. The solution-powder suspension was magnetically stirred at 1000 rpm. In order to determine the mercury concentration in solution along time, samples were withdrawn at increasing times, filtered through a Millipore membrane (0.45 µm), acidified to pH<2 with HNO_3 "Hg free", and then analysed by cold vapour atomic fluorescence spectroscopy (CV-AFS), on a PSA cold vapour generator, model 10.003, associated with a Merlin PSA detector, model 10.023, and using $SnCl_2$ as reducing agent. A Hg^{2+} control solution (50 µg L^{-1}) was always run in parallel under the same experimental conditions.

For each material, the concentration curves of the remaining mercury in solution versus time were obtained. The amount of mercury removed by the materials at a given time, q_t (mg g^{-1}), was calculated by the mass balance:

$$q_t = (C_0 - C_t)\frac{V}{M} \quad (1)$$

where C_0 (µg L^{-1}) is the initial concentration of mercury in the liquid-phase and confirmed by the control solution, C_t (µg L^{-1}) is the mercury liquid-phase concentration at a certain time (t), V the volume of the solution (L) and M the material dry mass (mg).

In order to compare the kinetic performance of both materials, the experimental results were fitted with pseudo first-order Lagergren (Lagergren, 1898) and the pseudo second order kinetic equations (Ho and McKay, 1999). These are empirical rate equations commonly used to describe the kinetics of sorption (Ho and McKay, 1999; Reddad et al., 2002; Zhang et al., 2005), which are based on the overall sorption rate.

The Lagergren rate expression is generally expressed as follows (Lagergren, 1898):

$$\frac{dq_t}{dt} = k_1(q_e - q_t) \tag{2}$$

where q_t (mg g^{-1}) is the amount of mercury sorbed onto the material at time t (h), and k_1 (h^{-1}) is the rate constant of first-order sorption. After integrating and applying boundary conditions, t=0 to t=t and q_t=0 to q_t= q_e, one obtains:

$$\log(q_e - q_t) = \log q_e - \frac{k_1}{2.303}t \tag{3}$$

The validity of the model is shown by the linear trend observed when graphing experimental $log\ (q_e - q_t)$ as a function of t, so the rate constant (k_1) may be found from the corresponding slope and the intercept should match the q_e value previously introduced.

The pseudo second-order equation, as the pseudo-first order one, is also based on the sorption capacity of the solid phase and, in contrast with the first model, it usually predicts the behaviour over the whole range of adsorption (Namasivayam et al., 1998; Ho and McKay, 1999) and no parameter has to be known beforehand:

$$\frac{dq_t}{dt} = k_2(q_e - q_t)^2 \tag{4}$$

where k_2 (g mg^{-1} h^{-1}) is the second-order sorption rate constant. For the boundary conditions, t=0 to t=t and q_t=0 to q_t= q_e, the integrated form of Eq. (4) is:

$$\frac{t}{q_t} = \frac{1}{k_2 q_e^2} + \frac{1}{q_e}t \tag{5}$$

If the second-order kinetics model is applicable, the plot of t/q_t versus t should be linear and k_2 and q_e may be found from the corresponding intercept and slope.

3 Results and discussion

The concentration of mercury in solution along time (C_t) and the corresponding amount of mercury removed by each material (q_t) are shown in Figure 1.

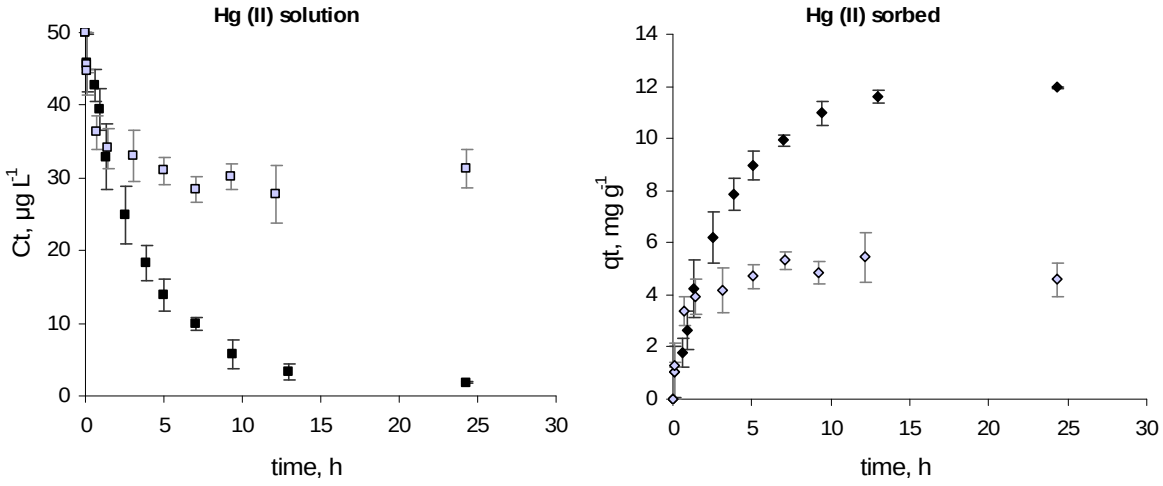

Figure 1: Mercury concentration in the liquid phase (C_t) and removrd (q_t) by ETS-4 (black symbols) or on activated carbon (grey symbols) as function time.

For both materials the Hg^{2+} concentration in the liquid phase decreases with time until the equilibrium, from when mercury concentration in solution remains the same. However, it is

clear that the two materials have distinct ability to remove Hg^{2+} under the current experimental conditions. For the initial Hg^{2+} concentration of 50 µg L^{-1}, which is the limit value for discharges from industrial sectors other than the chlor-alkali electrolysis industry, in accordance with Directive 84/176/EEC, and using only 8 mg of material, ETS-4 has demonstrated to have much higher capacity to remove Hg^{2+} from solutions than activated carbon. At the equilibrium, the amount of Hg^{2+} removed by ETS-4 is almost three times higher than onto activated carbon (Table 2). Moreover, at the equilibrium, after 24 hours treatment with ETS-4, it was possible to get clean water, of drinking quality since the residual Hg^{2+} concentration (Table 2) was below of the allowable limits for mercury ([Hg] ≤ 2 µg L^{-1}) (http://www.inspect-ny.com/water/levels.htm). In contrast, when using activated carbon *Chemviron Pulsorb FG4 type* the Hg^{2+} concentration remaining in solution was quite above the limits of clean drinking water (Table 2).

Table 2. Hg^{2+} concentration in solution at the equilibrium (C_e, µg L^{-1}), experimental sorption capacity (q_e, mg g^{-1}) and removal percentage (%) after 24h.

Material	C_e, µg L^{-1}	q_e, mg g^{-1}	% removal
ETS-4	1.79 ± 0.11	12.0 ± 0.1	96.4 ± 0.2
Activated carbon	31.4 ± 2.6	4.6 ± 0.6	37.2 ± 5.2

The first-order rate constant (k_1) and the second-order rate constant (k_2) were calculated from the plots shown in Figure 2. The corresponding kinetic sorption rate constants k_1 and k_2 together with the R-squared (R^2) of fittings, which indicate the quality of the regressions, are depicted in Table 3 together with the experimental and calculated q_e.

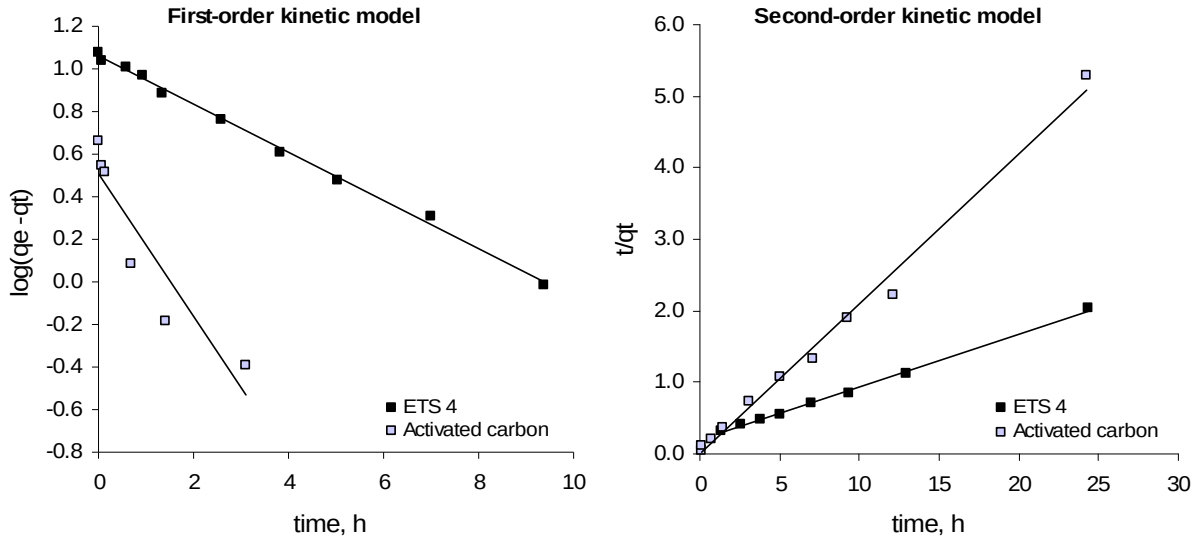

Figure 2. Pseudo first-order Lagergren and pseudo second-order plots for the removal of mercury from solution by the ETS-4 (black symbols) and by activated carbon (grey symbols).

For ETS-4 the correlation coefficients are the same for the two models (Table 3), which indicates that both of them describe the experimental kinetic results of the Hg^{2+} removal appropriately. However, there is a better agreement between the experimental q_e value and the value given by the first-order kinetic model. For activated carbon the sorption kinetic is better described by the second-order model, supported by the correlation coefficient and by the comparison between the experimental and fitted q_e values.

As it may be seen by the kinetic constants, activated carbon displayed faster mercury sorption kinetics than ETS-4. Although the equilibrium was reached in a shorter time when using activated carbon than ETS-4, both the fitted and experimental q_e obtained by using ETS-4 are higher than those obtained by the activated carbon.

Table 3: Kinetic sorption rate constants, k_1 (pseudo first-order Lagergren) and k_2 (pseudo second-order), together with experimental and calculated q_e, and the corresponding R-squared (R^2) of the fittings.

		First-order kinetics			Second-order kinetics		
	q_e-exp (mg g^{-1})	k_1 (h^{-1})	R^2	q_e-fitted (mg g^{-1})	k_2 (g mg^{-1} h^{-1})	R^2	q_e-fitted (mg g^{-1})
ETS-4	11.95	0.260	0.997	11.48	0.03	0.997	13.51
Activated carbon	4.60	0.772	0.858	3.22	5.46	0.992	4.78

4 Conclusions

The behavior of ETS-4 and activated carbon when removing mercury (II) from solutions with low metal levels has been evaluated and compared. According with the results obtained in this study both materials are able to remove Hg^{2+} from solution, even at low initial concentrations, although they display different uptake capacity. ETS-4 titanosilicate is much ore efficient than activated carbon as it is able to remove more than 96% of mercury from solution (C_0 = 50 µg L^{-1}) and to remove around 12 µg mg^{-1} of mercury after 24 hours. Activated carbon has a lower sorption capacity (~ 5 µg mg^{-1}) but a faster mercury sorption kinetics. It is worth to highlight that ETS-4 allows to purify Hg^{2+} contaminated water up to drinking quality water, so this material may be considered as a very efficient cleaning agent.

References

Directive 84/176/EEC, COUNCIL DIRECTIVE of 8 March 1984 on limit values and quality objectives for mercury discharges by sectors other than the chlor-alkali electrolysis industry. Official Journal of the European Communities, No L 74/49.

Ho, Y.S., McKay, G. (1999). Pseudo-second order model for sorption processes. *Process Biochemistry*, 34, 451-465.

Jusoh, A.,Shiung, L.S., Ali, N., Noor, M.J.M.M. (2007). A simulation study of the removal efficiency of granular activated carbon on cadmium and lead. *Desalination*, 206. 9-16.

Krishnan, K.A., Anirudhan, T.S. (2002). Removal of mercury(II) from aqueous solutions and chlor-alkali industry effluent by steam activated and sulphurised activated carbons prepared from bagasse pith: kinetics and equilibrium studies. *Journal of Hazardous Materials*, B92, 161-183.

Lagergren, S. (1898) Zur theorie der sogenannten adsorption geldster stoffe. *Handlingar*, 24, 1-39.

Lopes, C.B., Otero, M., Coimbra, J., Pereira, E., Rocha, J., Lin, Z., Duarte, A.C. (2007). Removal of low concentration Hg2+ from natural waters by microporous and layered titanosilicates. *Microporous and Mesoporous Materials,* 103, 325-332.

Lopes, C.B., Coimbra, J. Otero, M., Pereira, E., Duarte, A.C., Lin, Z., Rocha, J. (2008). Uptake of Hg2+ from aqueous solutions by microporous titano- and zircono-silicates. *Quimica Nova,* 31, 321-325.

Mohan, D., Gupta, V.K., Srivastava, S.K., Chander, S. (2001). Kinetics of mercury adsorption from wastewater using activated carbon derived from fertilizer waste. *Colloids and Surfaces*, 177, 169-181.

Namasivayam, C., Senthilkumar, S. (1998). Removal of arsenic(V) from aqueous solution using industrial solid waste: Adsorption rates and equilibrium studies, *Industrial and*

Engineering Chemistry Research, 37, 4816-4822.
Ranganathan, K. (2003). Adsorption of Hg(II) ions from aqueous chloride solutions using powdered activated carbons. *Carbon*, 41, 1087-1092.
Reddad, Z., Gerente, C., Andres, Y., Le Cloirec, P. (2002). Adsorption of several metal ions onto a low-cost biosorbent: kinetic and equilibrium studies. *Environmental Science & Technology*, 36, 2067-2073.
Vreysen, S., Maes, A., Wullaert, H. (2008). Removal of organotin compounds, Cu and Zn from shipyard wastewaters by adsorption – flocculation: A technical and economical analysis. Marine Pollution Bulletin, 56, 106-115.
Zhang, F.-S., Nriagu, J.O., Itoh, H. (2005). Mercury removal from water using activated carbons derived from organic sewage sludge. *Water Research,* 39, 389-395.
http://www.inspect-ny.com/water/levels.htm - Table of Allowable Limits of Water Contaminants. Drinking Water Contaminant Levels - New York State Maximum Allowed (last consulted 03.07.2008).

Proceedings of the 10th International Chemical and
Biological Engineering Conference - CHEMPOR 2008
Braga, Portugal, September 4-6, 2008
E.C. Ferreira and M. Mota (Eds.)

Selection of indigenous acidophilic bacteria for the bioleaching of two Somincor concentrates

Susana M. Paixão, Maria C. Sàágua*, Lina Baeta-Hall, Carlos Nogueira, Paula Sá-Pereira, José C. Duarte, Ana M. Anselmo
INETI – Instituto Nacional de Engenharia, Tecnologia e Inovação,
Estrada do Paço do Lumiar 22, 1649-038 Lisboa, Portugal

Keywords: bioleaching, acidophiles, chalcopyrite, lead concentrates
Topic: Integration of life sciences & engineering

Abstract

Biometallurgy can be defined as the field of applications resulting for the control of natural (biochemical) processes of interactions between acidophilic bacteria populations and minerals to recover valuable metals. This work concerns to the screening of the bioleaching potential of a indigenous microbial consortium (Achada Sludge – AS), collected at the abanboned S. Domingos copper mine, for using on metals bioleaching and recovery of two different mineral concentrates: a rich copper concentrate (chalcopyrite) and a lead concentrate (Pb-concentrate). For copper concentrate, the highest metals recoveries were found for 1% chalcopyrite with 41% Fe, 30% Cu and 75% Zn after 1 week of enrichment, reaching a recovery of 92% Fe, 92.5% Cu and 100% Zn after 1 month of enrichment. The best bioleaching results for Pb-concentrate were obtained for 2% substrate, with a % metals recovery of 44% Fe, 22% Cu and 100% Zn after 2 weeks of enrichment, and reaching a recovery of 65% Fe, 82% Cu and 100% Zn after 2 months of enrichment. Microbial population characterization was performed using 16S rRNA approach.

1 Introduction

Application of microbial processes by the mineral industry - biohydrometallurgy - predates the understanding of the role of microorganisms in metals extraction, commonly referred to as bioleaching (Olson et al., 2003). Biohydrometallurgy, an interdisciplinary field involving geomicrobiology, microbial ecology, microbial biochemistry, and hydrometallurgy, it is now a well biotechnology alternative for treating specific mineral ores with distinctive advantages over traditional mining (Valenzuela et al., 2006).

Bioleaching exploits the ability of microbes that thrive in high acid environments, require inorganic food and energy sources and frequently display resistance to heavy metals. These unique chemoautotrophic bacteria have the primary roles in acceleranting sulfide mineral dissolution (Ghauri et al., 2007) and are extensively used for industrial applications. The costs associated with maintenance of sulfide bioprocessing microorganisms are minimal because many gain energy from the redox reactions, utilize carbon dioxide from the air as C source and obtain their phosphorus, nitrogen, potassium and micronutrients from the bioleach environment (Watling, 2006).

Two different bacteria types (mesophilic and thermophilic) are most important in bioleaching of sulphide metals. Currently, these two types of bacteria have been playing a major role in industrial bioleaching applications. The mesophilic iron- and/or sulphur-oxidising bacteria, notably *Acidithiobacillus ferrooxidans*, *Acidithiobacillus thiooxidans* and *Leptospirillum ferrooxidans* are the most extensively used microorganisms within the mining and metallurgical industries for the oxidation of sulphide minerals. These bacteria derive the energy required for their growth and other metabolic functions from the oxidation of inorganic materials such as sulphide ores/concentrates (Akcil, 2004).

Commercial bioleaching initially involved copper concentrates; however, new processes have been developed for the extraction of other metals. It has been shown that

microorganisms can extract cobalt, nickel, cadmium, antimony, zinc, lead, gallium, indium, manganese, copper, and tin from sulphur-based ores (Rawlings, 2002, 2005;Rodríguez et al., 2003; Olson et al., 2003; Ndlovu, 2008).

Somincor (Sociedade Mineira de Neves-Corvo SA, Portugal) showed interest in testing metals recovery from copper concentrates and evaluation of technical and economical feasibility of using biological processes for that purpose. Recently, Somincor has a zinc concentrator and is responsible by the production of a zinc concentrate by treating a sulphide ore with 3.5% Zn and a considerable lead grade. During this process is produced a lead concentrate with high grade of secondary elements (average composition 30% Pb, 8% Zn and 7% Cu), which is a byproduct difficult to commercialize. For Somincor it would be interesting to investigate its possible valorization routes. So, the main objective of this work was to evaluate the bioleaching potential of indigenous microbial consortium (Achada Sludge – AS) from S. Domingos abandoned mine, for metals recovery of two different mineral concentrates: a rich copper concentrate (chalcopyrite) and a lead concentrate (Pb-concentrate).

2 Materials and Methods

2.1 Mineral concentrates

Somincor (Sociedade Mineira de Neves-Corvo SA, Portugal) has being producing for many years a rich copper concentrate as the major product of its operation. This concentrate contains about 25% Cu, 31% Fe, 1.3% Zn, 0.4% Sn and 0.3% Pb. Phase analysis by X-ray diffraction showed the presence of chalcopyrite ($CuFeS_2$) (71%) and pyrite (FeS_2) (20%) as main mineralogical species.

Recently, Somincor started a new zinc plant where a lead concentrate contaminated with zinc and copper (Pb-concentrate) is produced as by-product. This concentrate was essentially composed of lead, zinc, iron and copper sulphides. Its chemical analysis showed: 27% Pb, 8% Zn, 19% Fe, 7% Cu, 29% S, 0.5% As and 0.13%Sb. X-ray diffraction analysis of the concentrate showed galena (PbS) as the major component (32%), followed by pyrite (FeS_2) (28%), chalcopyrite ($CuFeS_2$) (28%) and sphalerite (ZnS) (12%).

2.2 Microbial inoculum

A microbial inoculum, Achada Sludge (AS), was collected at the abandoned cupric pyrite mine (S. Domingos Mine, Southeast Alentejo, Portugal) and was used in the bioleaching tests. This inoculum was enriched and maintained routinely in ferrous sulphate liquid medium (Johnson, 1995).

2.3 Bioleaching assays

The bioleaching assays were carried out in 500 ml Erlenmeyer flasks containing 200 ml of autotrophic basal medium (Johnson, 1995), using 0.5 to 4% (w/v) of metal concentrates (Pb-concentrate or chalcopyrite) as substrate, and 10% (w/v) of inoculum. The initial pH was adjusted to 1.8-2.0, using H_2SO_4 10 N, and then the flasks were kept at 30ºC or 35ºC, under stirring in a thermostated rotary shaker at 150 rpm.

These batch assays were monitored by measuring soluble metal content concentrations (Fe, Zn, Cu) and pH during time (daily/weekly). Simultaneously, blank tests were also carried out in the same operating conditions but without inoculum, and monitored.

2.4 Genetic characterization of microbial population

The AS inoculum is being genetically characterized, in the time course of the leaching process, to identify the microbial community responsible for the bioleaching of the two different metal concentrates (Pb-concentrate or Chalcopyrite). The separation of whole DNA from samples of different bioleaching stages was performed using UltraClean soil DNA isolation Kit (MO BIO). After isolation of gDNA, PCR was done using 16S rDNA primers for bacteria and archaea, primers 1510R and 1492R respectively, (Hugenholtz and Goebel, 2001). The amplicons were inserted in pJET plasmid (CloneJET PCR cloning kit, Fermentas) and a metagenomic library was constructed with recombinant DH5α cells with clones with

partial 16S rDNA gene that were sequenced by an ABI PRISM 310 sequencer (Applied Biosystems). In order to assess the effect of combined contamination of heavy metals on bacterial communities a genetic community fingerprinting by 16S rDNA profiles is being performed.

The sequencing data was analyzed as follows: (i) assembly of the reverse and forward sequences into a consensus sequence, (ii) editing of the consensus sequence to resolve discrepancies between the two strands by evaluation of the electropherograms, and (iii) comparison of the consensus sequences with GenBank sequences by using Ribosomal Database Project (RDP-II; Michigan State University, East Lansing) (Maidak et al., 2001) and the basic local alignment search tool (BLAST) (Benson et al., 2002).

3 Results and Discussion

3.1 Bioleaching results

In this study a inoculum (AS) from S Domingos mine was tested for its ability to bioleach two sulfide concentrates: a copper concentrate (chalcopyrite) and a Pb-concentrate.

The results obtained in the screening batch assays for chalcopyrite bioleaching with 1% pulp density at two different temperatures, 30ºC and 35ºC, are presented in Fig. 1. An augment of 5ºC in the incubation temperature (30ºC to 35ºC) led to a significant increase in the % metals recovery: ΔFe - 45% (39.3 to 57.0%), ΔCu – 76.6% (26.9 to 47.5%) and ΔZn – 29.4% (48.6 to 62.5%).

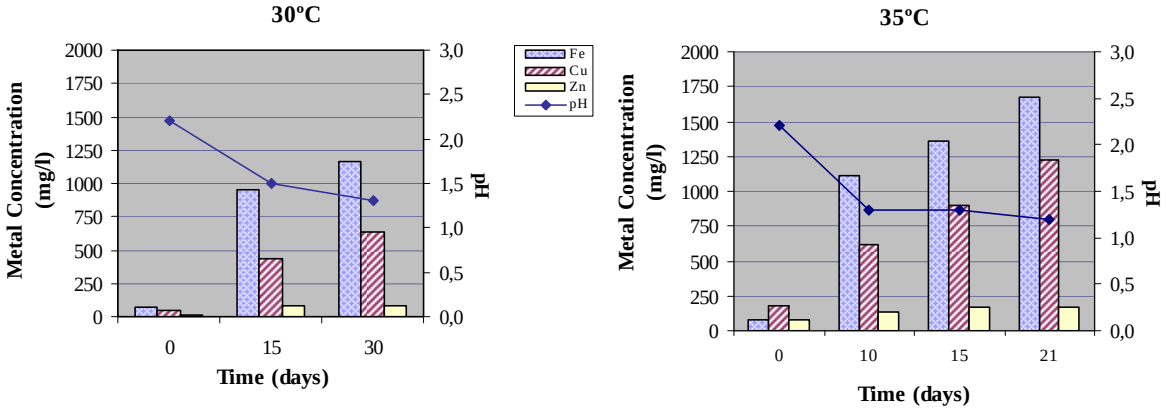

Fig. 1. Bioleaching results obtained in chalcopyrite (1%) for AS inoculum at 30ºC and 35ºC.

Based in these results, the effect of pulp density concentration (1, 2 and 4% chalcopyrite) was evaluated at 35ºC and the percentages of metal recovery by AS inoculum are presented in Table 1. Data showed that the highest % metals recovery: Fe – 92%, Cu – 92.5% and Zn – 100% was obtained at 1% chalcopyrite after 1 month of incubation time. Blank tests showed a % of metal recovery ranged from 5.9% (Fe) to 27.7% (Cu).

It was clear that the increase of the chalcopyrite concentration from 1% to 4% (w/v) resulted in decreased numbers of metals recoveries: Fe - 92.0 (1% Chalc.) to 61.8% (4%

Table 1. Percentage of metals recovery by AS inoculum in bioleaching batch assays with different concentrations of chalcopyrite (1 to 4%).

Sample	Bioleaching Time (days)	% Metals Recovery		
		Fe	Cu	Zn
AS + 1% Chalcopyr.	7	9.8	18.5	24.9
	15	80.4	25.7	52.1
	30	**92.0**	**92.5**	**100**
AS + 2% Chalcopyr.	7	17.7	11.8	42.0
	15	41.0	29.6	75.0
	30	**77.3**	**76.3**	**91.7**
AS + 4% Chalcopyr.	7	8.8	11.0	31.4
	15	34.4	17.7	33.9
	30	**61.8**	**43.1**	**50.9**

Chalc.), Cu – 92.5 (1% Chalc.) to 43.1% (4% Chalc.) and Zn – 100.0 (1% Chalc.) to 50.9% (4% Chalc).

This decrease in AS bioleaching potential suggests the need of a previous enrichment technique with sucessive increasing of substrate concentration to improve inoculum aclimatization to chalcopyrite and selected metals leading an optimi-zation of the bioleaching process.

Relatively to the AS ability to bioleach Pb-concentrate the results obtained in a first screening assay, carried out during 2 months with concentrations of 0.5-2.0% Pb-concentrate, showed that AS was able to recover 65% Fe, 82% Cu and 100% Zn for 2% concentrate (Table 2). In blank assays the % of metal recovery ranged from 0% (Cu, Fe) to 10% (Zn).

Table 2. Percentage of metals recovery by AS inoculum in bioleaching batch assays with different concentrations of Pb-concentrate (0.5 to 2%).

Sample	Bioleaching Time (days)	% Metals Recovery		
		Fe	Cu	Zn
MI + 0.5% Pb Conc.	30	30.4	57.6	100
	45	**31.4**	**78.5**	**100**
	60	23.1	69.7	100
MI + 1% Pb Conc.	30	38.9	59.6	100
	45	40.9	82.1	100
	60	**40.1**	**88.2**	**100**
MI + 2% Pb Conc.	30	50.4	48.9	100
	45	45.7	65.7	100
	60	**65.1**	**82.2**	**100**

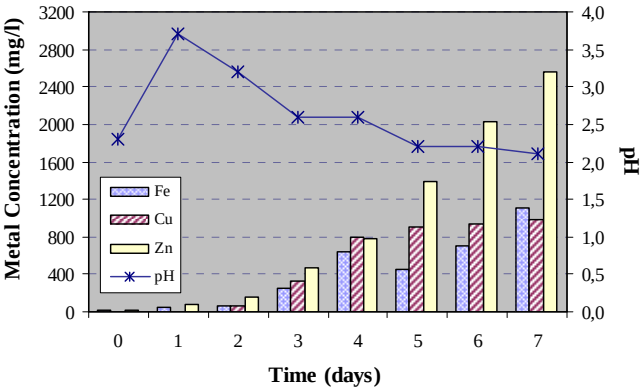

Fig. 2. Metals removal (Fe, Zn, Cu) during bioleaching process by AS, for 4% Pb-concentrate, at pH 1.8-2.0.

In order to verify the previous results, a set of assays with successive increasing pulp density (2 to 4%) was carried out with AS inoculum to evaluate its adaptative potential to higher levels of Pb and to improve its bioleaching potential increasing Zn dissolution.

The results obtained for metal recovery from 4% Pb-concentrate are presented in Fig. 2. The biological activity is confirmed by the pH trend during the leaching process, remaining at low values (pH ≈2.0), and by the increase in the % metals recovery reaching to about 80% of zinc recovery from the Pb-concentrate in 7-days.

During Pb-concentrate bioleaching the adaptative potential of AS microbial population was clearly showed in the successive enrichments with increasing pulp density, with an improvement of zinc removal from 1720 mg/l in 1-month (2% Pb-concentrate) to 2719 mg/l in only 7-days (4% Pb-concentrate).

In conclusion, LA consortium presented an high bioleaching potential for metal-recovery from both mineral concentrates tested. Biometallurgy processes applied for Cu-recovery in copper concentrate (chalcopyrite) and for Zn-recovery in Pb-concentrate can be an interesting tool to improve the added value of products. In the case of Cu concentrate this process would allow the implementation of a copper bio- hydrometallurgy to produce copper cathodes instead of selling a concentrate. For the Pb-concentrate, this type of treatment could improve the economic interest of products, which constitutes a residual stream.

3.2 Genetic characterization of microbial population

A first screening of the indigenous microbial consortium (AS), collected at the abanboned S. Domingos copper mine, using 16S rRNA genes sequencing allowed the identification of the more representative microbial strains present in the original inoculum. A total of 558 clones

were grouped into 5 operational taxonomic units (OTUs). These preliminary results indicates, according to the expected, that in this consortium are present strains like *Leptospirillum ferroxidans*, *Thiobacillus* sp, *Acidithiobacillus ferroxidans*, *Sulfobacillus* sp, *Acidithiobacillus albertensis and Acidithiobacillus thiooxidans*.

Acknowledgements
This study was partially supported by the European Commission project BioMinE – Biotechnology for Metal bearing materials in Europe (Project No.: 500329).

References

Akcil, A. (2004). Potential bioleaching developments towards commercial reality: Turkish metal mining's future. *Minerals Engineering*, 17, 477-480.

Benson, D. A., Karsch-Mizrachi, I., Lipman, D. J., Ostell, J., Rapp, B. A., Wheeler, D. L. (2002). GenBank. *Nucleic Acids Research*, 30, 17-20.

Ghauri, M.A., Okibe, N., Johnson, D.B. (2007). Attachment of acidophilic bacteria to solid surfaces: The significance of species and strain variations. *Hydrometallurgy*, 85, 72-80.

Johnson, D.B. (1995). Selective solid media for isolating and enumerating acidophilic bacteria. *Journal of Microbiological Methods,* 23, 205-218.

Maidak, B.L., Cole, J.R., Lilburn, T.G., Parker, Jr., C.T., Saxman, P.R., Farris, R.J., Garrity, G.M., Olsen, G.J., Schmidt, T.M., Tiedje J.M. (2001). The RDP-II (Ribosomal Database Project). *Nucleic Acids Research*, 29, 173-174.

Ndlovu, S. (2008). Biohydrometallurgy for sustainable development in the African minerals industry. *Hydrometallurgy*, 91, 20-27.

Olson, G.J., Brierley, J.A., Brierley, C.L. (2003). Bioleaching review part B: Progress in bioleaching: applications of microbial processes by the minerals industries. *Applied Microbiology and Biotechnology*, 63, 249-257.

Rawlings, D.E. (2002). Heavy metal mining using microbes. *Annual Reviews of Microbiology*, 56, 65-91.

Rawlings, D.E. (2005). Characteristics and adaptability of iron- and sulfur-oxidizing microorganisms used for the recovery of metals from minerals and their concentrates. *Microbial Cell Factories*, 4, 13-28.

Rodríguez, Y., Ballester, A., Blázquez, M.L., González, F., Munoz, J.A. (2003). New information on the sphalerite bioleaching mechanism at low and high temperature. *Hydrometallurgy*, 71, 57-66.

Valenzuela, L., Chi, A., Beard, S., Orell, A., Guiliani, N., Shabanowitz, J., Hunt D.F., Jerez, C.A. (2006). Genomics, metanogenomics and proteomics in biomining microorganisms. *Biotechnology Advances*, 24, 197-211.

Watling, R.H. (2006). The bioleaching of sulphide minerals with emphasis on copper sulphides - A review. *Hydrometallurgy*, 84, 81-108.

*Corresponding author, E-mail: ceu.sampaio@ineti.pt

Proceedings of the 10th International Chemical and
Biological Engineering Conference - CHEMPOR 2008
Braga, Portugal, September 4-6, 2008
E.C. Ferreira and M. Mota (Eds.)

Kinetic constants of phenolic compounds oxidation by Fenton's reagent

Marco S. Lucas[1], Joaquín R. Domínguez[2], José A. Peres[1*]
[1]Departamento e Centro de Química, Universidade de Trás-os-Montes e Alto Douro, Apartado 1013, 5001-801 Vila Real, Portugal.
[2]Departamento de Ingeniería Química y Química Física, Universidad de Extremadura, Edificio J.L. Sotelo, Avda. de Elvas s/n, 06071 Badajoz, Spain.

Keywords: Fenton reagent, kinetic constants, phenolic compounds, Advanced Oxidation Processes (AOPs).
Topic: Sustainable process-product development through green chemistry.

Abstract

Phenolic compounds are present in several types of wastewater but with special incidence in the agro-industries effluents. The knowledge of the kinetic parameters is of main importance to design and optimize the reactors where will occur the treatment of these wastewaters. Hence, with this work a competitive method is applied to calculate and compare kinetic constants of the phenolic compounds oxidized by Fenton's reagent process. The phenolic compounds studied were: *p*-coumaric, caffeic, veratric, ferulic, protocatechuic, vanillic, syringic, β-resorcylic, 3-(4-hydroxyphenyl)-propionic and 3,4,5-trimethoxybenzoic acids.

1. Introduction

Pulp and paper industries, wine production, distillery industries, olive-oil extraction and table olive production are examples of industries and agro-industries that produce highly contaminant wastewaters. These wastewaters are characterized for being rich in organic substances (phenols, polyphenols, organic acids), high COD values and a remarkable recalcitrant character due to the presence of phenolic compounds.

As result of this situation and the more restrictive legislation concerning effluents released into rivers and streams, new technologies have been developed to reduce these refractory contaminants. For example, Fenton's reagent oxidation is a homogeneous catalytic oxidation process based on the generation of very reactive oxidising free radicals, especially hydroxyl radicals, through the combination of hydrogen peroxide and ferrous ions. The oxidation mechanism of Fenton's reagent is complex, but could be resumed in the following reaction (Parsons, 2004):

$$Fe^{2+} + H_2O_2 \rightarrow Fe^{3+} + HO^- + HO\bullet \qquad (1)$$

Hence, the main objective of this study is to calculate and compare the kinetic constants of the Fenton's reagent oxidation process of phenolic compounds normally present in industrial wastewaters using a competitive kinetic model. The comparison is made with a phenolic compound which constant kinetic is known: the *p*-hydroxybenzoic acid, with a value of is 2.2 x 10^9 $M^{-1}s^{-1}$ (Haag and Yao, 1992). The 10 phenolic

* Corresponding author. Tel + 351-259-350227. E-mail:jperes@utad.pt

compounds studied were: *p*-coumaric, caffeic, veratric, ferulic, protocatechuic, vanillic, syringic, β-resorcylic, 3-(4-hydroxyphenyl)-propionic and 3,4,5-trimethoxybenzoic acids.

2. Materials and methods

Analytical grade phenolic acids (Figure 1) were obtained from Sigma. Hydrogen peroxide (30% w/w) and ferrous sulphate heptahydrate were obtained from Merck.

The reactor consisted in a 1 L glass cylinder provided with the necessary elements (inlets for stirring, sampling and measuring the temperature) for the development of the experiments. This reactor was kept at the desired temperature within ±0.5°C. Initially, the reactor was loaded with 500 mL in all cases, and the initial concentration of each phenolic compound was 100 mg/L.

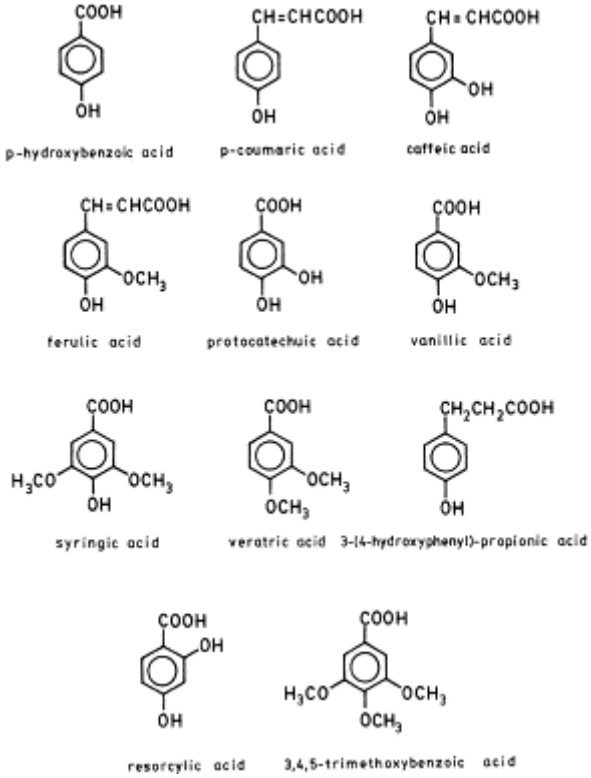

Figure 1 - Phenolic compounds

At regular times of reaction, samples were withdrawn to determine the phenolic acids remaining. These samples were analysed by HPLC, using a Waters chromatograph with a 996 photodiode array detector and a Nova-Pak C18 Column. Detection was at 280 nm with a mobile phase composed of a methanol:water:acetic acid mixture (15:82.5:2.5 in volume) at a flow rate of 1 mL/min.

3. Results and discussion

A series of experiments were developed to determine the rate constants for the reaction between each individual phenolic compound and hydroxyl radicals generated in Fenton process. These determinations were performed under certain specific conditions, by means of a competitive kinetic model. In this case, was used a mixture of a reference compound (R), *p*-hydroxybenzoic acid, and another phenolic compound (B).

In all the decomposition experiments of phenolic compounds by Fenton's reagent a progressive decrease of the different compounds is appreciated with reaction time. As an example Figure 2 shows the disappearance curves of some phenolic compounds: β-resorcylic acid, 3-(4-hydroxyphenyl)-propionic acid, ferulic acid and the reference compound p-hydroxybenzoic acid.

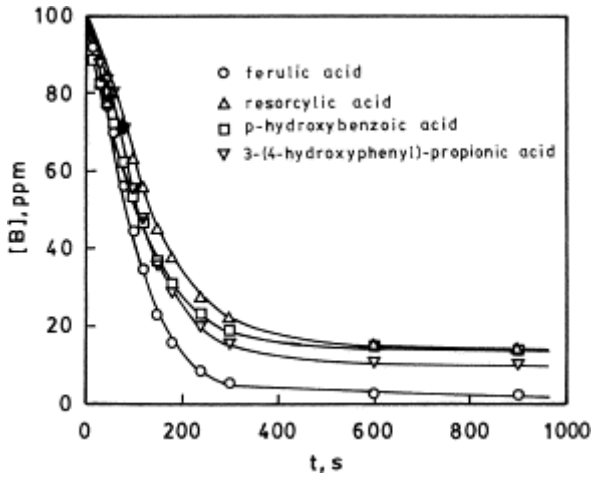

Figure 2 – Evolution of the concentration of phenolic compounds along the oxidation experiments: ferulic, resorcylic, p-hydroxybenzoic and 3-(4-hydroxyphenyl)-propionic acids.

The process of oxidation by ·OH radicals could be carried out in a system containing a mixture of compound B and a reference compound R, whose rate constant is known. The equation of the reaction between each organic B and the ·OH radical can be expressed by the reaction (2):

$$B + {}^{\cdot}OH \rightarrow B_{ox} \qquad (2)$$

Assuming a first-order reaction with respect to the radical concentration and the phenolic acid concentration, the reaction rate can be expressed as:

$$-\frac{d[B]}{dt} = k_B [B][HO\bullet] \qquad (3)$$

where k_B is the rate constant of reaction for every compound B with hydroxyl radical. Similarly to the Eq. (3), the reference compound presents the following rate equation:

$$-\frac{d[R]}{dt} = k_R [HO\bullet][R] \qquad (4)$$

By dividing both (3) and (4) it is obtained:

$$\frac{d[B]}{d[R]} = \frac{k_B}{k_R}\frac{[B]}{[R]} \qquad (5)$$

and integrating between t=0 and t=t:

$$\ln\frac{[B]_0}{[B]} = \frac{k_B}{k_R}\ln\frac{[R]_0}{[R]} \qquad (6)$$

In this expression k_R is the rate constant for the reference compound, i.e., p-hydroxybenzoic acid with $k_R = 2.2 \times 10^9$ L/(mol.s) at 30 ºC and k_B is the rate constant for each one of the phenolic compounds. A plot of $\ln([B]_0/[B])$ versus $\ln([R]_0/[R])$ yields a straight line, whose slope is the ratio of rate constants k_B/k_R, as showed as an example in Figure 3.

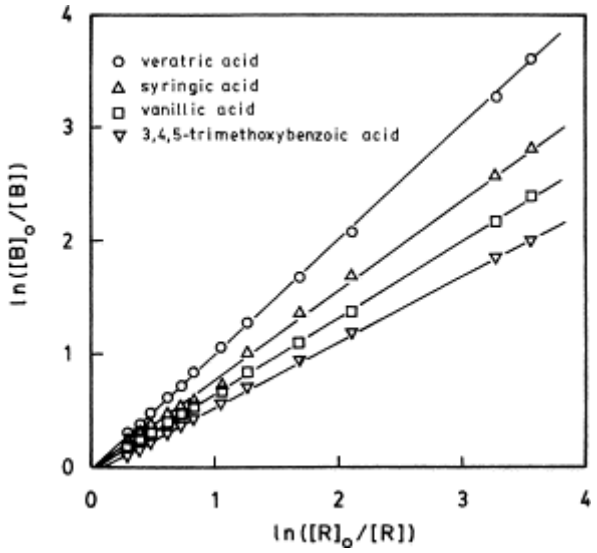

Figure 3 - Plot of $\ln([B]_0/[B])$ versus $\ln([R]_0/[R])$ for some phenolic compounds: veratric, syringic, vanillic and 3,4,5-trimethoxybenzoic acids.

Figure 3 shows this plot as an example of different phenolic compounds: veratric, syringic, vanillic and 3,4,5-trimethoxybenzoic acids. As can be seen, the excellent alignment of the points around straight lines confirms the goodness of the described method. After regression analysis, the slope k_B/k_R for each compound was deduced, and using the known k_R, the rate constants k_B for the remaining phenolic compounds are determined. The values are exposed in Table 1.

Table 1 - k_B/k_R and k_B values for each phenolic compound

Phenolic compound	**k_B/k_R**	**$k_B \times 10^{-9}$** (L/mol.s)
Ferulic acid	1.754	3.8
3-(4-hydroxyphenyl)-Propionic acid	1.172	2.6
p-Coumaric acid	1.155	2.5
Veratric acid	1.011	2.2
***p*-Hydroxybenzoic acid** (reference)	**1.000**	**2.2**
β-Resorcylic acid	0.991	2.2
Caffeic acid	0.821	1.8
Syringic acid	0.791	1.7
Vanillic acid	0.672	1.5
3,4,5-Trimethoxybenzoic acid	0.567	1.2
Protocatechuic acid	0.307	0.7

It is possible to deduce that cinnamic acids, with 9 atoms of carbon (C_6-C_3) like ferulic, veratric and caffeic acids have, in general, kinetic constants higher than the benzoic acids with 7 carbon atoms (C_6-C_1).

These values are concordant with the deduced values for hydroxyl radical rate constants in aqueous solution for other similar compounds in an order of 10^9 L/(mol.s) (Abad *et al.*, 2007) and moving closer to the limit the reaction controlled by diffusion.

Note that in the case of extremely fast reactions, with reaction times very short, such as the reactions of phenolic acids with hydroxyl radical, it is sometimes difficult to distinguish between "physical" and "chemical" changes. Bimolecular reactions, like in this case, consist of at least two steps: the approach of the two species, controlled by diffusion and real chemical transformation. Second-order (or pseudo-1st order) constants cannot, therefore, exceed those for the diffusion process. This limits the maximum attainable to around 10^9-10^{11} $M^{-1}s^{-1}$.

Comparing kinetic reaction of the different phenolic compounds with the Fenton's reagent shows that variations between the compounds studied are small, which may suggest, in a first analysis, that substitute groups have a small effect on the attack to benzenic ring by Fenton's reagent. Indeed, the hydroxyl radical, which is the basis of Advanced Oxidation Processes, is very reactive, but not very selective.

In the case of attacks by free radicals there should be no major differences regarding reactivity of aromatic compounds having electrons acceptors or electrons donors groups. However, it is generally accepted that high density electronics in the ring tends to inhibit the oxidation by free radicals.

For example, the reactivity of monosubstitutes phenols by a nitro group or by a halogen atom (both electrons acceptors) is similar to that of phenol (Vella, 1992). The unstabilizing effect becomes more important with multissubstitution, as it happens with the acid 3,4,5-trimetoxibenzoic acid.

For Lipczynska-Kochany (1991), the influence of substitute groups in the reactivity of $HO^{\cdot}$ radical with aromatic compounds, showed that the $HO^{\cdot}$ mechanisms' attack to an aromatic compound is similar to the reaction of electrophilic substitution. For example, the presence of donor groups of electrons, as the groups –OH or -OCH_3 in aromatic ring, is known to activate the ring in reactions of electrophilic substitution (Table 2).

Table 2 – Effect of substituints on electrophilic aromatic substitution (Solomons and Fryhle, 2000).

Functional group	Group characteristics	Director
-OH	Strongly activating	Ortho-para
-COOH	Moderately deactivating	Meta
-CH=CHCOOH	Weakly activating	Ortho-para
-OCH_3	Moderately activating	Ortho-para
-CH_2COOH	Weakly activating	Ortho-para

There are small differences in reactivity between the phenolic compounds, although, sometimes, there are not very significant structural differences between them. This means that the presence of certain substituents groups (hydroxy, di-hydroxy, methoxy) in specific positions of the aromatic ring influence the efficiency of the reaction. In general, the electrophilic substitution reactions are delayed by the presence of acceptors groups of electrons and promoted by donors groups of electrons.

4. Conclusions

The application of a competitive method allows to calculate the rate constant for 10 phenolic compounds based on the rate constant previously known of the reference compound *p*-hydroxybenzoic acid. The phenolic compounds studied were: *p*-coumaric, caffeic, veratric, ferulic, protocatechuic, vanillic, syringic, β-resorcylic, 3-(4-hydroxyphenyl)-propionic and 3,4,5-trimethoxybenzoic acids. The deduced values for hydroxyl radical rate constants in aqueous solution for these phenolic compounds are in the range of (0.7 – 3.8) x 10^9 $M^{-1}s^{-1}$.

References

Abad, L.V., Saiki, S., Kudo, H., Muroya, Y., Katsumura, Y., de la Rosa, A.M. (2007). Rate constants of reactions of k-carrageenan with hydrated electron and hydroxyl radical. *Nuclear Instruments and Methods in Physics Research B,* 265, 410-413.

Haag, W.R., Yao, C.C.D. (1992). Rate constants for reaction of hydroxyl radicals with several drinking water contaminants. *Environ. Sci. Technol.*, 26, 1005-1013.

Lipczynska-Kochany, E., (1991). Degradation of aqueous nitrophenols and nitrobenzene by means of the Fenton reaction. *Chemosphere*, 22 (5-6), 529-536.

Parsons, S. (2004). *Advanced Oxidation Processes for water and wastewater treatment*, IWA, UK.

Solomons, G., Fryhle, C. (2000). *Organic Chemistry*, 7th edition, John Wiley & Sons, New York.

Vella, P.A., Munder, J.A., (1992). Uses of $KMnO_4$, H_2O_2, and ClO_2 in wastewater applications. *Proceedings of Chemical Oxidation: Technologies for the Nineties*. Eckenfelder, W.W., Bowers, A.R., Roth, J.A. (Eds.), 222-238.

Proceedings of the 10th International Chemical and
Biological Engineering Conference - CHEMPOR 2008
Braga, Portugal, September 4-6, 2008
E.C. Ferreira and M. Mota (Eds.)

Model-Based Optimization of a Semi-Batch Industrial Polymerization Process

Teodora Miteva[1*], Nadja Hvala[1], Rodrigo Alvarez[2], Dolores Kukanja[3]
[1] Jožef Stefan Institute, Department of Systems and Control, Jamova 39, SI-1000 Ljubljana, Slovenia
[2]UPC, Enginyeria Quimica, Avda. Diagonal 647, Pab. G-2, E-08028, Barcelona, Spain
[3] MITOL d.d., Sežana, Partizanska cesta 78, SI-6210, Slovenia

Keywords: vinyl acetate, polymerization, modeling, control
Topic: Systematic methods and tools for managing the complexity: Process control & operations

Abstract

The research work presented in this paper considers polymerization process in MITOL, a chemical factory in Sezana, Slovenia. The challenge is to increase the production rate while keeping the quality parameters at the desired values. A possible approach to reach that goal is by applying better control strategies that will decrease the batch time. For this purpose a model consisting of differential and algebraic equations (DAE) has been already constructed and is extended in this paper with the energy balance model to simulate the reactor temperature as a function of reacting chemicals. The model will be used for control design and in the search for more optimal plant operation. Model simulation results based on real plant data, derived in gPROMS environment, are presented.

1 Introduction

Emulsion polymerization of vinyl acetate is an important process in the chemical industry. Efforts have been made to determine the mechanism of the reaction. A good number of comprehensive models of vinyl acetate with different theories and approaches could be found in the literature. In 1992, Urquiola et al.[1][2][3] wrote a series of papers about the polymerization of vinyl acetate using a polymerization surfactant.

The research work presented in this paper considers the polymerization process in MITOL factory, Sezana, Slovenia. This is the leading glue manufacturer in the country with production rate more than 90% of its capacity. The production process is semi-batch polymerization with initiator and monomer added during the batch. The current batch control is done by following a recipe derived from experience. Monomer is added at a constant flow, while initiator addition is performed manually and is used to control the temperature in the reactor. The challenge we are facing now is to design optimal control actions required to reach the final product with specified quality parameters in as short time as possible. The large quantities of raw materials and equipment resources involved in the batch prevent us from performing experiments for batch optimisation directly on the plant. Therefore we need a good predictive model for controlling the temperature and also the addition of the initiator and monomer. The already constructed model [4] provides estimates of four outputs: conversion, solid content, viscosity and particle size diameter. In this paper we extend the model using first principle modelling based on energy balance to observe the reactor temperature as a function of the concentration of reacting chemicals. Having temperature we are able to design and test control strategies for shortening the batch duration with initiator and monomer addition as control variables.

* Corresponding author. Tel + 386-1-477 3606. E-mail:Nadja.Hvala@ijs.si

2 Process description

The process presented hereby is a polymerization of vinyl acetate by using potassium persulfate (KPS) as initiator and polyvinyl alcohol as a protective colloid. The production process is semi-batch polymerization. In the beginning initial amounts of initiator and monomer as added in the reactor as well as the whole amount of water and polyvinyl alcohol (PVOH). The reactor is closed and the heating starts. When the temperature of the reactor reaches approximately 70˚C, the operator stops the hot water through the heating jacket (Figure 1). The exothermic reaction and the heat of the remaining water filling the heating coat continue to rise the temperature. After the reactor temperature reaches a certain level, the remaining fixed amount of monomer starts to be pumped into the reactor with a constant flow. The monomer flow rate is controlled by a PID controller acting on the pump. The temperature of the added monomer is the outdoors temperature.

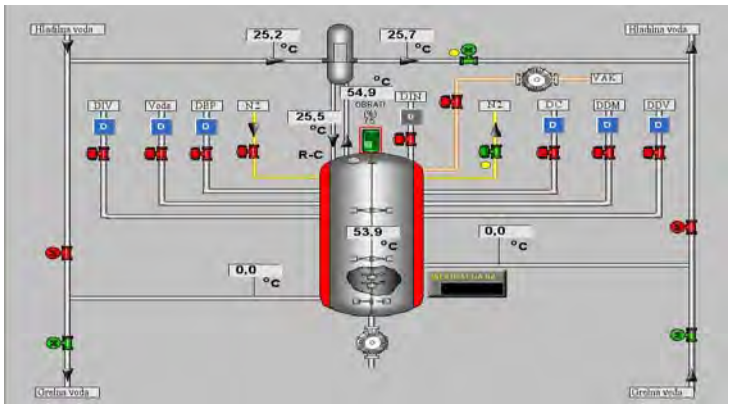

Figure 1. *Scheme of polymerization reactor in MITOL*

For emulsion polymerization processes it is very important to keep the temperature in certain limits. For vinyl acetate those limits are 75-80°C. Therefore every time the temperature starts to decrease a determinate amount of initiator is added in the system so that the temperature starts increasing. When all the monomer is added into the reactor a larger amount of initiator is added in order to terminate the reaction. The temperature is then allowed to increase up to 90°C. The reaction is considered as finished when the temperature starts to decrease again.

The main variables affecting the duration of the reaction and possibly used in batch optimization are: the reactor temperature, flow rate of the monomer and the addition of the initiator.

The quality of the product is defined by the following parameters: conversion into polymer, particle size distribution, viscosity and solid content.

3 The Model

The current model is based on a model described in previous papers [4][5]. For control purposes we estimate the temperature profile from an energy balance model. The energy balance model is based on reaction heat capacity and the energy produced and consumed during the reaction. The latter include the following:

- Heating of the reactor through the heating jacket,
- Producing the heat in the exothermic reaction,
- Heating the incoming monomer to the reactor temperature,
- Cooling the reactor by the reflux,
- Heat losses to the surroundings.

Reaction heat capacity (K_R) accounts for the heat capacities of the reactor ingredients - monomer, converted into polymer monomer, water and polyvinyl alcohol. It also depends of their mass and specific heat capacities. It is given by the equation:

$$K_R = M\ MW_m\ Cp_{mon} + M_{conv}\ MW_m\ Cp_{pol} + W\ Cp_{water} + PVOH\ Cp_{pol} \quad (1)$$

The energy balance model is divided into three parts, depending of the stage of the process and the reaction. The first part of the modelled temperature profile starts when we close the reactor and start heating it up with hot water through the heating jacket, and ends when we stop the hot water and wait till the temperature in the reactor reaches around 80°C. In that first part we take into account the monomer enthalpy, the heating produced due to the exothermic reactions and heating though the heating jacket. This is mathematically expressed as follows:

$$K_R \frac{dT_R}{dt} + T_R \frac{dK_R}{dt} = Q_m MW_m Cp_{mon} T_{mon} - \Delta H_r r_{pol} - C_3 \Delta H_{jacket} \quad (2)$$

The left side of the equation accounts for the changes in the internal energy of the reactor, which is due to the change of the reactor temperature (first term) and the change of its heat capacity (second term). The heating through the heating jacket (ΔH_{jacket}) is given by:

$$\Delta H_{jacket} = 0.00018(T - T_{jacket})K_R \quad (3)$$

The second part of the model starts at the end of the first part and ends at the first initiator addition during the batch. In that part the reactor is no more heated through the heating jacket, the losses are negligible, as well as the flow through the condenser because the reaction has just been started. The energy balance model includes only monomer enthalpy and the reaction heat:

$$K_R \frac{dT_R}{dt} + T_R \frac{dK_R}{dt} = Q_m MW_m Cp_{mon} T_{mon} - C_4 \Delta H_r r_{pol} \quad (4)$$

The energy balance for the third last part of the modelled temperature profile takes into account also the reflux through the condenser and heat losses. The equation has the following form:

$$K_R \frac{dT_R}{dt} + T_R \frac{dK_R}{dt} = Q_m MW_m Cp_{mon} T_{mon} - C_5 \Delta H_r r_{pol} - Q_{cond} - C_6 Q_{loss} \quad (5)$$

Here the energy loss through the condenser (Q_{cond}) is calculated by the following equation:

$$Q_{cond} = Q_{FC} Cp_{Cout} (T_{Cout} - T_{Cin}) - Q_{FC} \lambda \quad (6)$$

where λ is the vaporization heat and it is:

$$\lambda = -0.00281 T_{Cout}^2 - 0.32738 T_{Cout} + 408.178 \quad (7)$$

Losses through the surroundings are given by:

$$Q_{loss} = 0.95(T - T_{ext}) \quad (8)$$

Model parameters in the equations (1-8) are taken from the literature [6] (MW_m, Cp_{pol}, Cp_{mon}, Cp_{out}, ΔH_r) or estimated based on real plant data (C_3, C_4, C_5, C_6) so that a satisfactory agreement between the process and the model was obtained. The values of model parameters are given in Table I.

Parameter	*Value*
MW_m [gmol^{-1}]	86.09
Cp_{pol} [kJ kg^{-1} K^{-1}]	1.77x10^{-2}
Cp_{mon} [kJ kg^{-1} K^{-1}]	1.77x10^{-2}
Cp_{out} [kJ kg K^{-1}]	1.17
Cp_{water} [kJ kg K^{-1}]	4.18x10^{-2}
T_{ext} [K]	283.15
ΔH_r [kJ mol^{-1}]	-87.5
C_3 (dimensionless)	0.50
C_4 (dimensionless)	0.35
C_5 (dimensionless)	0.60
C_6 (dimensionless)	Depending on the batch

5 Results

The presented model was simulated using gPROMS modeling tool [7][8]. Model simulations were performed based on real plant data. The flow rates of the added monomer and initiator during the batch were calculated from the weight change of the monomer and initiator dozing tanks. Examples of reactor temperature, initiator and monomer flow rates during the batch are shown in Figure 3.

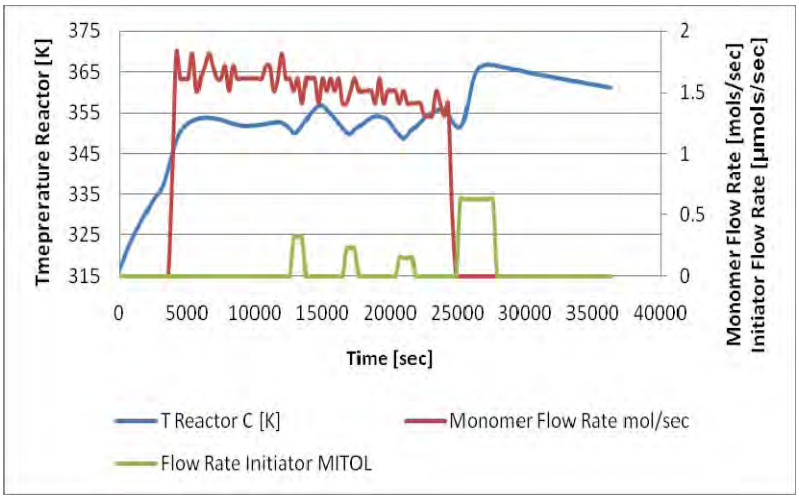

Figure 3. *Initiator addition, monomer flow rate and temperature profile during the batch*

With the presented energy balance model we are able to get relatively good estimates of the reactor temperature. From Figure 4 it can be seen that the estimated profile follows the dynamics of the real one. Not so good estimates are obtained at the beginning and at the end of the batch. At the beginning of the batch, the most influential part of the model is the heating of the reactor through the heating jacket. So most probably, the corresponding model parameters still need to be estimated more precisely. The agreement of the model is also not good in the last part of the estimated profile. This is when the whole amount of monomer has been already added in the reactor and a larger amount of initiator is put to finish the reaction. A possible reason is that in this part the actual heat losses are higher than estimated.

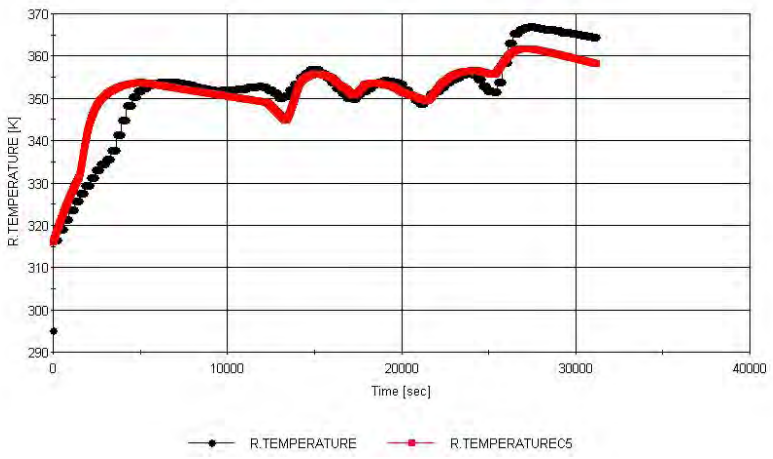

Figure 4. *Estimated and real plant temperature profile*

The overall model was also used to calculate the product quality parameters. Table II shows the validation of model on 5 batches. For the viscosity and the solids content, laboratory analyses were performed at the end of the reaction. These measurements are normally performed after mixing several batches and therefore no individual data is available.

Table II *Output variables – real plant data and estimated data*

Batch No.	Conversion (%)		Solids Content (%)		Viscosity (Brookfield 200C, 50rpm), (mPas)	
	Real Data	Modelled Data	Real Data	Modelled Data	Real Data	Modelled data
1192	99.95	99.79	46.4	45.84	37520	33723
1203	99.90	99.74	45.9	45.86	31200	36324
1214	99.89	96.17	45.4	43.88	25040	32697
1253	99.13	99.36	46.9	45.97	34000	35486
1256	99.37	99.45	46.4	45.61	30160	33343

From the table we can see that the model output variables are in good agreement with real plant data. To obtain these results it was necessary to adjust the C_6 parameter for each batch. This could be attributed to the variable and increased fouling of the reactor walls between cleaning periods. The average model error for conversion and solids content is around 2% and for the viscosity around 15%. Some bigger deviations can be noticed for batch 1214 for all output variables.

6 Conclusion

A model for polymerization of vinyl acetate has been developed. The model has two inputs – flow rate of monomer and flow rate of initiator addition. The outputs of the presented model are four – conversion, particle size diameter, solid content and viscosity. The overall model has thirteen differential equations, sixty-three algebraic equations and nine adjustable parameters. In this model we are able to observe temperature profile and based on it apply the control of the initiator addition and estimate more precisely the sufficient amount of initiator which needs to be added during the batch. The model has been validated on data of five batches taken from the real plant. The presented temperature profile is quite satisfactory and also the model output variables are in the range. The work continues with the design and testing of initiator and monomer control strategies.

7 Acknowledgment

The support of the European Commission in the context of the 6th Framework Programme (PRISM, Contract No. MRTN-CT-2004-512233) is greatly acknowledged.

Numeclature

T_R	Temperature in the reactor	[K]
K_R	Reaction heat capacity	kJ kg K^{-1}
Q_m	Flow rate of monomer	mol s^{-1}
MW_m	Molecular weight of monomer	$gmol^{-1}$
Cp_{mon}	Specific heat capacity of monomer	kJ kg K^{-1}
Cp_{pol}	Specific heat capacity of polymer	kJ kg K^{-1}
Cp_{out}	Specific heat capacity of the monomer going in and out of the reactor	kJ kg K^{-1}
T_{mon}	Temperature monomer	[K]
ΔH_r	Heat of polymerization	kJ mol^{-1}
r_{pol}	Polymerization reaction rate	-
ΔH_{jacket}	Heating through the heating jacket	kJ mol^{-1}
Q_{cond}	Reflux through the condenser	kJ kg K^{-1}
Q_{loss}	Heat losses to the surroundings	[K]

References

1. Urquiola M. B., Dimonie V. L., Sudol E. D., El-Aasser M. S., (1992) *Journal of Polymer Science: Part A: Polymer Chemistry, 30, 12, 2631-2644*
2. Urquiola M. B., Dimonie V. L., Sudol E. D., El-Aasser M. S., (1992) *Journal of Polymer Science: Part A: Polymer Chemistry, 30, 12, 2619-2629.*
3. Urquiola M. B., Dimonie V. L., Sudol E. D., El-Aasser M. S., (1992) *Journal of Polymer Science: Part A: Polymer Chemistry, 31, 6, 1403-1415.*
4. Aller F. al al., Modeling of semibatch vinyl acetate emulsion polymerization in an industrial reactor, *CHISA 2006, 27-31 August 2006, Prague - Czech Republic*
5. Miteva T., Alvarez R., Hvala N., Kukanja D., Modeling of Polyvinyl Acetate Polymerization Process for Control Purposes, *ESCAPE18, 1-4 June 2008, Lyon, France*
6. Berger K.C. and Meyerhoff G., *Polymer handbook, 3th edition, Wiley, New York (1989)*
7. Process Systems Enterprise Ltd., 2004, gPROMS Industry User Guide
8. Process Systems Enterprise Ltd., 2004, gPROMS Advanced user Guide

Proceedings of the 10th International Chemical and
Biological Engineering Conference - CHEMPOR 2008
Braga, Portugal, September 4-6, 2008
E.C. Ferreira and M. Mota (Eds.)

Reacting media models building optimization

Chernykh I.G.[1], Stoyanovskaya O.P.[2,3], Zasypkina O.A.[2,3]
[1]Institute of Computational Mathematics and Mathematical Geophysics SB RAS, Lavrentjeva ave., 6, Novosibirsk, 630090, Russia.
[2]Boreskov Institute of Catalysis SB RAS, Lavrentjeva ave., 5, Novosibirsk, 630090, Russia.
[3]Novosibirsk State University, Novosibirsk, Pirogova str. 2, Novosibirsk, 630090, Russia.

Keywords: Chemical Kinetics, Catalysis, Reaction Engineering, CFD & chemical engineering

At present, mathematical modeling is successfully used to support decision making in the development and modernization of chemical processes and reactors. Note that modernization of chemical processes and reactors is the interdisciplinary problem, which requires the involvement of experts in physics, chemistry and mathematical modeling. Determination of kinetic scheme of chemical reactions is a key stage in devising a mathematical model of reactor. Such a scheme includes the proposed reaction mechanism and the values of rate constants for individual reaction steps. It was shown elsewhere that different kinetic schemes used to describe a certain reactive flow with the same gas-dynamic parameters lead to radically different simulation results. In the literature, a process can be described by alternative schemes due to the prevalence of semiempirical models of chemical kinetics, with stoichiometric equations being used instead of elementary steps. Although semiempirical representations are of limited use, the development of such kinetic schemes is quite topical, as they provide a model of reactive medium, which is adequate in a specified range of conditions. The development of semiempirical models and determination of rate constants for individual reaction steps are based on the full-scale and computational experiments. The computational experiment aimed at determination of kinetic scheme is the iterative process including the following stages: advancement of a postulated reaction scheme; generation and solution of a stiff nonlinear set of ordinary differential equations that describes chemical transformations of substances within the proposed scheme; and comparison of numerical and experimental data on the reaction kinetics.

Note that a correct comparison of the calculated and experimental data is not a trivial task, since each time it is necessary to evaluate the roughness of numerical model and the accuracy of measurements. Thus, to determine the parameters of elementary steps in relatively simple kinetic schemes, it is reasonable to use a detailed two-dimensional model taking into account the diffusion, heat conduction and heterogeneous reactions on the reactor walls in combination with the in situ spectral diagnostics. The development of semiempirical schemes for more complicated processes (e.g., pyrolysis of hydrocarbons) permits the use of more rough models due to technical limitations of experimental diagnostics. Analysis and selection of kinetic schemes can be performed with any software package that solves the primal problem of chemical kinetics, i.e., determines changes in the composition of reacting mixture that occur with time. However, most of them are not intended for the search of kinetic schemes. Besides, in many cases, the proposed scheme can be evaluated only in the context of its energy effects or design features of the reactor where the experiments are carried out. Such analysis should be based on spatial models of the reactive medium. Thus, program packages intended for research and engineering work (HYSYS, ReactOp, CARAT, etc.) were suggested for reactor optimization and kinetic model development. Employing the library of reactor models, a user can make computations with these models using different kinetic schemes entered via the package interface. For instance, the ReactOp library comprises 30 types of single reactors with liquid and gaseous reactants, and seven types of cascade reactors. FORTRAN codes implementing the numerical models of these reactors are extensible, which allows a user to modify them. This approach is convenient when working with the most-used reactor designs, since all the stages of chemical process simulation and optimization can be performed within a

single software product. However, this approach has some limitations: the development of mathematical models for new type reactors will require a considerable extension of each library; and the search problem using a full model of reactor will be highly time-consuming. When searching for an adequate kinetic scheme, the most simple (one-dimensional) reactor models will be used, and simulation will be performed for a wide range of temperatures and pressures. Then the chosen kinetic scheme can be included in computations by the three-dimensional models implemented in commercial or special-purpose CFD packages. The modeling results can be obtained quite rapidly due to a rational use of computational tools at the stage of kinetic scheme development and through an orderly division of labor of the specialists involved in the simulation process and computations.

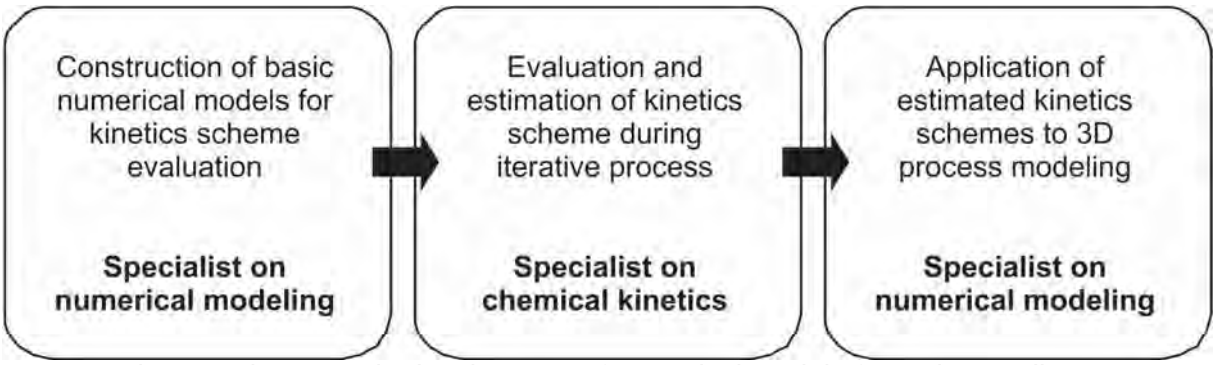

Fig. 1. Main stages in development of numerical model of reactive medium.

Figure 1 shows three main stages necessary for the development of numerical model of reactive medium. At the first stage, basic numerical models of reactive medium are constructed and codes for evaluation of kinetic schemes are chosen. This work can be operated by the specialists in mathematical modeling and chemical kinetics. The second stage consists in evaluation and estimation of the kinetic scheme during the iterative process. This work can be operated by the specialists in chemical kinetics using the efficient chemical kinetics software. At the third stage, the estimated kinetic schemes are applied to three-dimensional simulation of the reactive medium (CFD + chemical reactions, etc.). This work can be operated by the specialists in mathematical modeling. For the first two stages, a new software package ChemPAK was developed by the authors. ChemPAK can be operated by a specialist in chemical kinetics without any knowledge on mathematical modeling. ChemPAK can work with the systems of chemical reactions stored in the network database or obtained via the package interface. Then the program automatically generates a numerical model of the chemical reaction system and makes the computations. Thus, a user of ChemPAK can obtain the results of numerical modeling, adjust the chemical kinetic scheme, and promptly evaluate the resulting scheme.

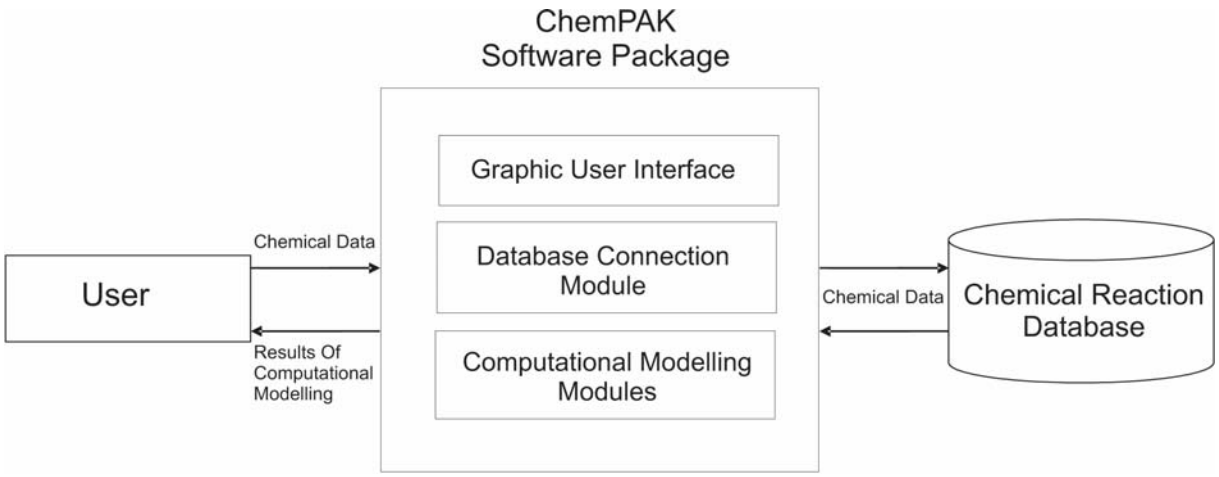

Fig. 2. The architecture of ChemPAK.

Figure 2 shows architecture of ChemPAK software package. ChemPAK consists of network database, computational modules and visual interface. User can create and edit systems of chemical equations with unlimited number of equations with easy-to-use interface, translate systems of chemical equations to systems of ODE, add some new equations to the translated system and solve this system by using one of ChemPAK computational modules. ChemPAK can work with the systems of chemical reactions stored in the network database or obtained via the package interface. Then the program automatically generates a numerical model of the chemical reaction system and makes the computations. Thus, a user of ChemPAK can obtain the results of numerical modeling, adjust the chemical kinetic scheme, and promptly evaluate the resulting scheme.

ChemPAK was tested on different tests. Main tests are the problem of modeling kinetics of Butlerov reaction in circumstellar disk and the problem of homogenous pyrolysis of C2-C3 hydrocarbons under CO2-laser-induced heating. The problem of modeling kinetics of Butlerov reaction consists of 44 reversible chemical equations. Reaction scheme for homogenous pyrolysis of C2-C3 hydrocarbons consists of more than 100 chemical equations. These problems are fully described in referenced works.

This work was supported by the Russian Foundation for Basic Research (grant No. 07-03-12149-ofi, 08-01-00615), the RAS Presidium Program "Origin and Evolution of the Biosphere"(grant No. 18-2, 2006), the RF Education Ministry Program" Development of Scientific Potential in High School" (Project RNP.2.1.1.1969)

References

Chernykh I.G., Zasypkina O.A. (2007). Computer simulation of the sugar synthesis of Butlerov reaction in a circumstellar disk. II International Conference "Biosphere Origin and Evolution", Abstracts, Greece, 187.

Chernykh I.G., Stoyanovskaya O.P. (2006). Homogenous pyrolysis of C2-C3 hydrocarbons under CO2-laser-induced heating. 4th EFCATS School on Catalysis ‘Catalyst Design - from Molecular to Industrial Level’, Russia, 165.

Proceedings of the 10th International Chemical and
Biological Engineering Conference - CHEMPOR 2008
Braga, Portugal, September 4-6, 2008
E.C. Ferreira and M. Mota (Eds.)

Multiobjective optimization of the benzene nitration process

Paula A. G. Portugal[1 2] * Marco S. Reis[1], Cristina M. S. G. Baptista[1]
[1]CIEPQPF, Chemical Engineering Department, University of Coimbra, Pólo II, Rua Sílvio Lima, 3030–790 Coimbra, Portugal.
[2]Chemical Engineering and Environment Department, High Scholl of Technology of Tomar, Polytechnics Institute of Tomar, Quinta do Contador, Estrada da Serra, 2300-313 Tomar, Portugal.

Keywords: Multiobjective Optimization, Goal Attainment Method, Benzene Nitration
Topic: Systematic methods and tools for managing the complexity

Abstract

The nitration of benzene with mixed acid is an important chemical process where liquid-liquid reactions take place, whose degree of conversion to mononitrobenzene (MNB) and selectivity depend on a wide range of parameters. Santos (2005), studied this system in a pilot plant under operating conditions in the range of those used in the industrial process. The experimental data thus collected are here used in order to set up a strategy for establishing an adequate trade-off between two conflicting objectives: to maximize the MNB concentration while minimizing by-products (di- and trinitrophenol – DNP and TNP) formation. The methodology consisted in searching for the optimum noninferior solutions, by establishing a multiobjective optimization problem (MOOP) bound to be solved by the Goal Attainment Method (GAM). A statistical multivariate analysis approach was adopted to develop empirical models for estimating the DNP and TNP concentrations, and the predictions are in good agreement with the experimental data. The definition of the feasible region for the optimum search had in consideration the intrinsic relationships in the operating conditions found in data. A Pareto front in the feasible region was identified, showing that a reduction in by-products concentration can only be achieved for lower MNB concentrations. The multiobjective optimization results obtained are expected to assist process engineers in the selection of the operating conditions according to theirs production targets.

1 Introduction

In the continuous adiabatic benzene nitration process to produce MNB, the DNP and TNP are by-products that have to be removed from the final product. As they represent a serious menace to the aquatic ecosystems their disposal must follow strict criteria. Aware of this in Santos (2005) an important contribution was given to understand this system and how operating conditions influence yield and the extent of secondary reactions. The present work aims at using the same experimental data to develop an optimization framework in order to properly rationalize and quantify trade-offs between two conflicting objectives: to maximize the concentration of MNB while minimizing by-products formation, thus reducing the environmental footprint of the process.

If a MOOP is well formed, there should not be a single solution that simultaneously minimizes each objective to its fullest (Censor, 1977). In each case, we are looking for a solution for which each objective has been optimized to the extend that, if we try to optimize it any further, then the other objective(s) will suffer as a result. Finding such a solution, and quantifying how much better this solution is compared to the others, is the goal to be attained in MOOP. Pareto solutions (or noninferior solutions) are then, those for which improvement in one objective can only occur with the worsening of at least another objective. A design

* Corresponding author. Tel + 351-239-798793. E-mail:pagp3@eq.uc.pt

point x* in the objective space, X, is termed Pareto optimal if there is not any another feasible design objective vector, x, such that $x_i \le x_i^*$ for all $i \in \{1,2,...,n\}$, and $x_j \le x_j^*$ for at least one index of $j \in \{1,2,...,n\}$.

In order to find the Pareto front, a scalar method was used, the goal attainment method (GAM) developed by Gembicki (1974, 1975). GAM is a highly effective method for obtaining the best balanced solution to multiobjective problems and, unlike the basic weighted sum of objective functions method, it is not subject to convexity limitations of any kind (Collette and Siarry, 2003). A vector of goals, $g = [g_1,...g_n]^T$, to be attained by a set of objectives, $F(x) = \{f_1(x),...,f_n(x)\}$, is specified in GAM. The relative degree of under or overattainment of the desired goals is controlled by a vector of weights, $w = [w_1,...w_n]^T$, that defines the direction for search from g (*Figure 1*) to the feasible objective space, $\Lambda(\phi)$. The best compromise solution is found by solving the following problem:

$$\begin{aligned} &\text{Min} \quad \phi \\ &\text{S. t.} \quad F(x) - \phi w \le g, \\ &\qquad x \in X, \quad w \in \Re^n \end{aligned} \tag{1}$$

where ϕ is an unrestricted scalar variable, called degree of under, or overattainment of the goals, and X represents a feasible solution region. The term ϕw introduces a degree of slackness into the problem, which would otherwise impose the goals to be rigidly met. The weight vector w enables the decision maker (DM) to express quantitatively the tradeoffs between the objectives. The smaller $|w_i|$, the less the function value of the i^{th} objective, and to make an objective function greater than the corresponding goal value, w_i must be set to be positive.

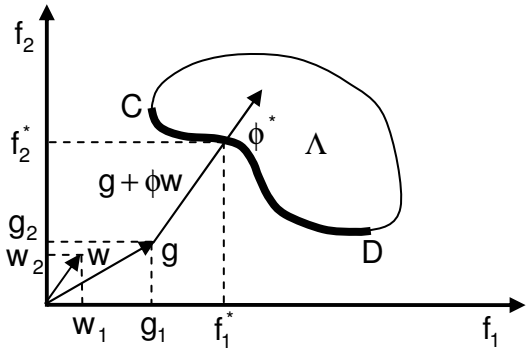

Figure 1 –Graphic representation of the Goal Attainment Method with two objectives.

Given the vectors g and w, the direction of the vector $g + \phi w$ can be determined. Therefore, the problem in (1) is equivalent to finding a feasible solution which is nearest g, but that falls in the line spanned by this vector. The best noninferior solution for this problem will be the first point, ϕ^*, where $g + \phi w$ intersects the feasible region, Λ, in the objective space. During the optimization, ϕ is varied, changing the size of the feasible region. A negative ϕ implies that the goal of the DM is attainable, and an improved solution will be obtained. Otherwise, $\phi > 0$ and the DM goal is unachievable. The attainment method has the advantage that it can be posed as a nonlinear programming problem, which can be solved by classical optimization approaches, such as the sequential quadratic programming (SQP).

Formulating the correct MOOP requires establishing the feasible solution region X which means developing mathematical models for the relationships that constrain the model input

variables. For these relations, a Mahalanobis distance approach (Chatterjee, 1991) was adoped. The squared Mahalanobis distance, MD, is essentially a covariance weighted distance to the centroid, μ, where the covariance is computed from experimental data.

$$MD^2 = (x-\mu)^T \Sigma^{-1} (x-\mu) \qquad (2)$$

Points with MD less than a given threshold belong to an ellipsoid cluster, whose axis ratio depends on the covariance matrix (*Figure 2*). So, unlike an absolute distance measurement, it takes into account the shape of the cluster. For instance, although points A and B appear to be equidistant from the center, in terms of MD, A is much closer, and therefore more likely to be a member of the cluster.

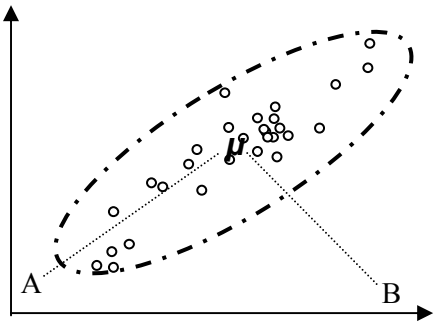

Figure 2 – Geometric interpretation of the Mahalanobis distance.

The threshold is set with resource to the Hotelling's T^2 statistic, which describes the variability of the MD for a multivariate normal distribution, where F stands for the F-distribution for a defined confidence level, α, usually 0,05.

$$T^2 \sim \frac{p(n-1)}{(n-p)} F_\alpha (p, n-p) \qquad (3)$$

This multiobjective optimization approach was used for establishing quantitatively the trade-offs, and the optimum process variables set points that will allow to relate the production of MNB and the concentration of both DNP and TNP, providing essential information for the DM in setting the operating conditions for the benzene nitration process.

2 Problem formulation and results

The reaction mechanisms involved in the production of nitrophenols are complex, and the physical and chemical data required for the development of mechanistic models are scarce. Therefore, a statistical multivariate analysis approach was adopted to develop data-driven empirical models to predict the formation of these compounds. The models in Quadros (2005) were improved, using the same experimental data sets and the multivariate linear regression (MLR) methodology (Chatterjee, 1991) with the forward stepwise variable selection method, implemented in the Statistica® software. The procedure followed is mainly the one described in Quadros, 2005.

The variables chosen as potential regressors were: T, F_B/F_N, NA, SA, *a* and θ. The regressors selection was driven by the aim of developing models that remain valid over a wide range of conditions and hopefully not dependent on the reactor size. Two of the

variables, *a* and T, are not process inputs and can not be set independently from the others. Nevertheless, it is known (Santos, 2005) that *a* is related to the ratio of organic to acid phases, here represented by F_B/F_N, and to the physical properties of the liquid-liquid mixture, which, in turn, are both sensitive to T. By checking the matrix of scatter plots, a relationship between *a*, F_B/F_N and T was established creating a feaseable elliptic cluster based on the concept of MD. A similar procedure was followed for modelling the relationship between NA and SA, since they are concentrations in the mixed acid, and therefore cannot be set independently. This elliptic cluster is shown in *Figure 3*.

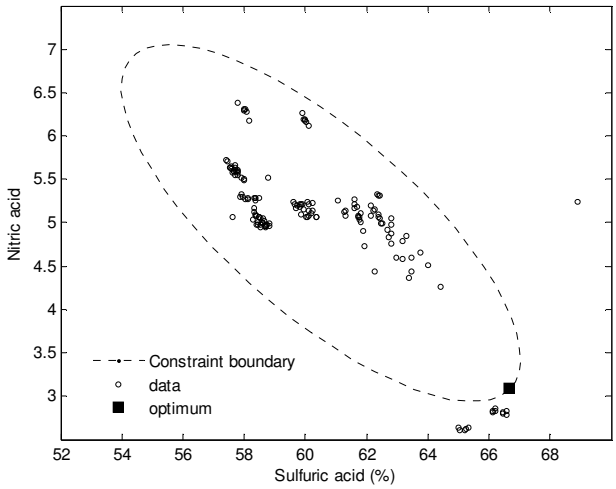

Figure 3 – Data scatter plot relating the concentrations of SA and NA in the mixed acid, showing the constraint cluster and the optimum value.

The problem formulation is then as:

Min ϕ

$x \in \Re^n \quad \phi \in \Re$

$$S.\ t. \quad x_i - w_i\phi \le g_i \quad i = \{1,6,8\} \qquad (4)$$

$$x_i - H(x_j) = 0 \quad i = \{1,6,8\} \quad j = \{2,3,4,5,7\} \qquad (5)$$

$$MD_k^{\,2} = (x_i - \mu_i)^T \Sigma_k^{\,-1} (x_i - \mu_i) \quad k \text{ is the number of the constrain based on the MD} \qquad (6)$$

$$k = 1 \Rightarrow i = \{3,4\}, \quad k = 2 \Rightarrow i = \{2,5,7\}$$

$$lb_i \le x_i \le ub_i \quad i = \{1,\ldots,8\} \qquad (7)$$

Where *(5)* are the set of predictive models for MNB, DNP and TNP, and *(6)* comprehend two restrictions based upon the MD. With the exception of θ, all the upper and lower limit bounds, ub and lb, were relaxed so that they were not active constraints in the optimization process, therefore allowing the constraints *(6)* to freely play their role. Due to the fact that θ is not implicitly limited in constraints *(4)* to *(6),* its upper bound, ub_8, could not be relaxed; as, such upper bound happened to be an active constraint, it must be kept within the range found in collected data (2 to 5 minutes).

Goals were set as $g_i = \{100,0,0\}$, meaning that 100% of MNB and 0 ppm for DNP and TNP were sought.

The problem was solved by the GAM implemented in the *fgoalattain* routine from the Optimization Toolbox of Matlab®. Using this routine implicated adapting the weight values, w_i. Due to the way *fgoalattain* was built, the "opposite rules" were considered, which means that w_i was set lower for the more important objectives, and negative to make an objective function greater than the goal. Setting up the weights requires having in mind the industrial targets, where it is undoubtedly far more critic to reach 100% of MNB than 0 ppm of DNP and TNP. Accordingly, and after an iterative sensitivity study, the weights for MNB were set in the range $1x10^{-8}$ to 0.03, while the weights for DNP and TNP were kept constant and equal to -1.

As expected, it can be seen in *Figure 4* that when MNB increases the by-products formation also increases. In *Figure 5* the results are presented for TNP and we can clearly verify that the major contributor for the nitrophenols (NP's) is DNP. As a matter of fact, for the optimum solutions obtained, TNP can be considered negligible. The results for the other process variables T, *a* and F_B/F_N are similar to the pattern in Figure 4. For a fixed residence time it is clear that to achieve a lower NP's formation with consequent MNB reduction, T, *a* and F_B/F_N must decrease, which means that lower values of these variables reduce the extension of the main and side reactions. Moreover the magnitude of these process variables decreases for increasing residence time.

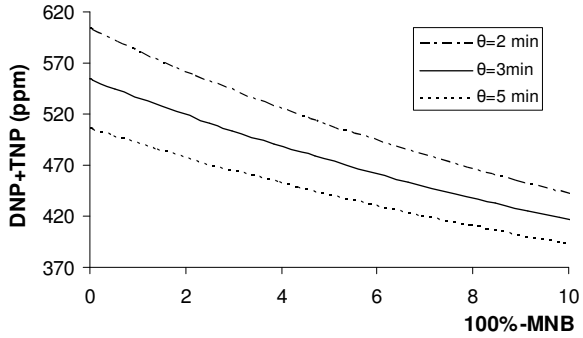

Figure 4 – Pareto front for the total NP's in the interest region of MNB>90% as a function of the θ upper limit constraint.

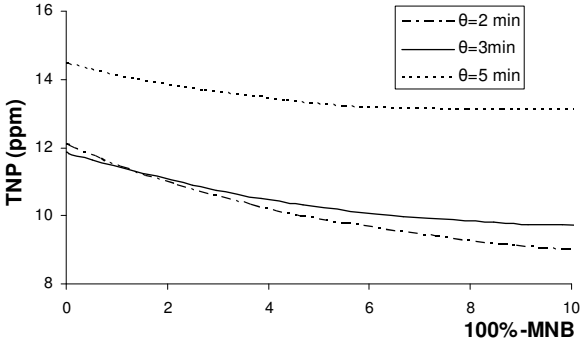

Figure 5 – Pareto front for the TNP in the interest region of MNB>90% as a function of the θ upper limit constraint.

NA and SA optimum values are constant and equal to 3.1% and 66.6% respectively, as it was already observable in the scatter plot in *Figure 3*. The residence time contribution to the optimum values can be wrongly interpreted if we only consider selectivity. In fact, for a higher residence time the same MNB concentration is achieved with fewer secondary products. Nevertheless the MNB production is lower for a higher residence time.

3 Conclusions

In this work we presented an optimization framework for addressing the achievement of adequate trade-off evolution for the benzene nitration process in terms of the concentrations of the main and by-products. In particular, it puts at the disposal of a decision maker a set of Pareto fronts in an interest region of MNB concentration greater than 90%, providing optimum solutions in a granted feasible region. The results obtained can be further exploited by introducing economical information in the tradeoffs formulations.

Acknowledgments

Financial support from FCT for Ph.D. Grant SFRH/BD/27398 /2006 is aknowledged.

Notation

a	interfacial area between the organic and acid phases (m^2/m^3)
DNP	DNP concentration in the outlet organic stream (ppm)
F	objective functions
g	vector of the goals to be attained by the objective functions
F_B/F_N	ratio of the inlet molar flow rates of benzene and nitric acid
H	vector of the MLR models obtained for MNB, DNP and TNP
lb	vector of the lower bounds for the process variables
MD	Vector of the squared Mahalanobis distances
MNB	MNB weight percentage in the outlet organic stream after excluding the benzene excess (%)
n	number of observations (experiments)
NA	nitric acid inlet weight fraction in the acid phase
p	number of regressors
SA	sulfuric acid inlet weight fraction in the acid phase
T	temperature in the reactor (ºC)
TNP	TNP concentration in the outlet organic stream (ppm)
ub	vector of the upper bounds for the process variables
x	matrix of the process variables {MNB,a, SA, NA, T, DNP, F_B/F_N , TNP, θ }
w	vector of the weights for the relative under or over attainment of the objectives
θ	residence time (min)
ϕ	degree of attainment - GAM parameter to be minimized
μ	vector of the means of the process variables
Σ	matrix of the covariances of the process variables

References

Censor, Y. (1977) *Pareto optimality in multiobjective problems*. *Appl. Math. Optimiz.*, Vol. 4, 41-59.

Chatterjee, S., Price, B. (1991). *Regression analysis by example*. John Wiley & Sons, 2nd ed., New York.

Collette, Y., Siarry, P. (2003). *Multiobjective optimization – Principles and case studies*. Springer-Verlag, 1st ed., Germany

Gembicki, F.W. (1974) *Vector optimizatrion for control with performance and parameter sensitivity indices*. PhD Thesis, Case Western Reserve Univ. Cleveland, Ohio.

Gembicki, F.W. (1975) *Approach to performance and sensivity multiobjective optimization: The goal attainment method*. IEEE Trans. on Automatic Control, December, 769-771.

Quadros, P. A., Reis, M. S., Baptista, C. M. S. G. (2005) *Different modelling approches for a heterogeneous liquid-liquid reaction process. Ind. & Eng. Chem. Res.*, 44, 9414-9421.

Santos, P. A. (2005). *Nitração de compostos aromáticos: transferência de massa e reacção química*. PhD Thesis, University of Coimbra, Portugal.

Proceedings of the 10th International Chemical and
Biological Engineering Conference - CHEMPOR 2008
Braga, Portugal, September 4-6, 2008
E.C. Ferreira and M. Mota (Eds.)

Dynamic Optimization of Fed-Batch Alcoholic Fermentation

Patricia C.S. Borges[1], Adriene A. Pfeifer[2], Fran S. Lobato[3], Eloízio J. Ribeiro[4], Valéria V. Murata[5] *

[1,2,4, 5] Faculdade de Engenharia Química, [3]Faculdade de Engenharia Mecânica
Universidade Federal de Uberlândia, Campus Santa Mônica,
Av. João Naves de Ávila 2121, Uberlândia - MG.

Keywords: Alcoholic Fermentation, Direct Method, Fed-Batch Process, Optimal Control Problem, Switching Times.
Topic: Integration of life sciences & engineering

Abstract

The numerical solution of dynamic optimization problems has been intensively investigated through indirect and direct methods, genetic algorithms, dynamic programming and hybrid methodologies. Several experimental studies confirm the yield and productivity increments of ethanol in the fed-batch fermentation but the results are highly dependent of the microorganism and substrate, filling times, feeding strategy and substrate concentration and are applicable to restrict conditions (Xiong & Zhang, 2003; Bravo *et al*., 2000; Carvalho *et al*., 1993, 2005; Laopaiboon *et al*., 2007). In this paper the optimal feeding strategy to maximize ethanol production from sugarcane is calculated considering conditions and constraints representative of Brazilian industrial conditions. The parameters of the Andrews kinetic model (1968) were estimate by Differential Evolution for high fed substrate concentrations using S*accharomyces cerevisiae* from batch and fed-batch experiments. The resulting differential-algebraic dynamic optimization problem is solved by the control and state parameterization method trough Dircol code (von Stryk, 1999). The control and state variables profiles are presented and the influences of factors like substrate concentration and filling rate on the optimal profiles are evaluated.

1 Introduction

Modak et al. (1986) classified the fermentative processes according to the form of the specific rates of growth of cells and formation of product, from the analysis of the maximum points. The optimal sequence of the phases was determined in function of the specific rates and the initial conditions of the process. Srinivasan et al. (2003) focuses on interpreting the various arcs that constitute the optimal solution in terms of the path and terminal objectives of the optimization problem, such as the cost, constraints and sensitivities.

The Dircol code is a set of FORTRAN subroutines to solve multi-phase Optimal Control Problems (OCP) described by differential equations subject to inequality and/or equality constraints on the state and/or control variables. The parameterization of state and control variables is done by direct collocation, transforming the OCP into a NLP which is solved through dense Sequential Quadratic Programming (SQP) by NPSOL code (Gill et al., 1986).

The main goal of this paper is to apply the Pontryagin's Minimum Principle (PMP) to identify the singular control strategy and to use the Direct Method implemented in Dircol code (von Stryk, 1999) to maximize the ethanol production for *Saccharomyces cerevisae* fed-batch fermentation from sugarcane. Previous studies are related to *Zymomonas mobilis* or adopt operational restrictions and kinetic models that do not represent the conditions adopted by Brazilian industries, some of them presenting yield higher than 0.511[g/g] for glucose as substrate, justified by less accurate kinetic models (Hong, 1986; Chen & Hwang, 1990; Xiong & Zhang, 2003). The challenge to solve a singular problem with differential index fluctuation

*Corresponding author. Tel +55 (02134) 3239-4292 Ramal 229. e-mail: valeria@ufu.br

is added to the development of accurate and simple enough mathematical models of a nonlinear process with complex metabolism, for control and optimization purposes.

This paper is presented as following. Section 2 presents the mathematical model of fed-batch reactor. Section 3 presents the necessary conditions for optimality and optimal feeding strategy. In Section 4 one case study is presented and finally the conclusions are summarized in Section 5.

2 Problem Formulation for Fed-Batch Fermentation

In fed-batch fermentation, the process is represented by the following mass balance equations:

$$\frac{d(XV)}{dt} = \mu XV; \quad X(0) = X_0 \qquad (2.1) \qquad \frac{d(SV)}{dt} = FS_f - \sigma XV; \quad S(0) = S_0 \qquad (2.2)$$

$$\frac{d(PV)}{dt} = \pi XV; \quad P(0) = P_0 \qquad (2.3) \qquad \frac{dV}{dt} = F; \quad V(0) = V_0 \qquad (2.4)$$

where X, S and P stand for the concentration of cell mass, substrate, and product respectively; F stands for the substrate feed rate; S_f is the feed substrate concentration; V is the bioreactor volume; and μ, σ, π are the specific rates of growth, substrate consumption and product formation, respectively. X_0, S_0, P_0 and V_0 are the initial conditions. Constraints are imposed on the final bioreactor volume and on the substrate feed rate (Eq. 2.5 and 2.6):

$$V(t_f) \le V_{max} \qquad (2.5) \qquad 0 = F_{min} \le F \le F_{max} \qquad (2.6)$$

The objective is to determine the optimal feed profile, F, which maximize the Objective Function $\Phi \equiv PV(t_f)$ with free final time t_f. Let the amounts of cells, substrate, and product be denoted by $x_1=XV$, $x_2=SV$, $x_3=PV$, and be $x_4=V$. If t_f appears explicitly, as in this case, and additional state variable, x_5, is introduced (with $dx_5/dt=1$ and $x_5(0)=0$). Then $x_5(t_f)= t_f$ and the original system is given by:

$$\frac{d}{dt}\begin{bmatrix} x_1 \\ x_2 \\ x_3 \\ x_4 \\ x_5 \end{bmatrix} = \begin{bmatrix} \mu x_1 \\ -\sigma x_1 \\ \pi x_1 \\ 0 \\ 1 \end{bmatrix} + \begin{bmatrix} 0 \\ S_f \\ 0 \\ 1 \\ 0 \end{bmatrix} F \quad \Rightarrow \quad \dot{x} = a(x) + bF; \quad x(0) = x_0 \qquad (2.7)$$

3 Necessary Conditions for Optimality and Optimal Feeding Strategy

The system to be solved is described by Eq. (2.7) subject to Eq. (2.5) and Eq. (2.6). Defining the Hamiltonian as:

$$H \equiv \lambda^T a(x) + \lambda^T bF = \psi(x,\lambda) + \phi(\lambda)F \qquad (3.1)$$

where the adjoint vector must satisfy the following:

$$\frac{d\lambda}{dt} = -\frac{\partial H}{\partial x} = -\left[\frac{\partial a}{\partial x}\right]^T \lambda; \quad \lambda_i = -\frac{\partial \Phi}{\partial x_i} \qquad (3.2)$$

Since control F appears linearly in the Hamiltonian, the optimal control which minimizes the Hamiltonian can be determined examining the sign of ϕ:

$$F = \begin{cases} F_{\max} & if \ \phi < 0 \\ F_{sing} & if \ \phi = 0 \\ F_{\min} & if \ \phi > 0 \end{cases} \tag{3.3}$$

Thus, the optimal feed rate sequence may consist of nonsingular intervals and singular intervals. According Bryson and Ho (1975), since on a singular interval ϕ is identically zero over a finite interval, all of its time derivatives must also vanish:

$$\phi = 0 \tag{3.4}$$

$$\frac{d\phi}{dt} = 0 \tag{3.5}$$

$$\frac{d^2\phi}{dt^2} = 0 \tag{3.6}$$

For the case where μ, σ and π are functions of substrate concentrations, the Hamiltonian is given by:

$$H \equiv \psi + \phi F = (\lambda_1 \mu - \lambda_2 \sigma + \lambda_3 \pi) x_1 + \lambda_5 + (\lambda_2 S_f + \lambda_4) F \tag{3.7}$$

The adjoint equations are given by:

$$\dot{\lambda}_1 = -(\lambda_1 \mu - \lambda_2 \sigma + \lambda_3 \pi) = -(\psi - \lambda_5)/x_1 \tag{3.8}$$

$$\dot{\lambda}_2 = -(\lambda_1 \mu' - \lambda_2 \sigma' + \lambda_3 \pi') x_1 / x_4 \tag{3.9}$$

$$\dot{\lambda}_3 = 0 \tag{3.10}$$

$$\dot{\lambda}_4 = (\lambda_1 \mu' - \lambda_2 \sigma' + \lambda_3 \pi') x_1 x_2 / x_4^2 \tag{3.11}$$

$$\dot{\lambda}_5 = 0 \tag{3.12}$$

On the singular interval $\phi = 0$ and thus $\psi = H^*$. Using the equations (3.4), (3.5) and (3.8) yields three equations in five adjoint variables, which must be satisfied on the singular arc:

$$\lambda_1 \mu - \lambda_2 \sigma + \lambda_3 \pi = (H^* - \lambda_5)/x_1 \tag{3.13}$$

$$\lambda_2 S_f + \lambda_4 = 0 \tag{3.14}$$

$$\lambda_1 \mu' - \lambda_2 \sigma' + \lambda_3 \pi' = 0 \tag{3.15}$$

Equation (3.15) may be substituted into Eq. (3.9) and Eq. (3.11) to obtain:

$$\dot{\lambda}_2 = \dot{\lambda}_4 = 0 \tag{3.16}$$

which implies that λ_2 and λ_4 are constant on the singular arc. The singular control is obtained from Eq. (3.6):

$$(\lambda_1 \mu'' - \lambda_2 \sigma'' + \lambda_3 \pi'') \dot{S} + \dot{\lambda}_1 \mu' = 0 \tag{3.17}$$

Equation (3.17) may be solved by $\dot{S}$:

$$\dot{S} = -\dot{\lambda}_1 \mu' / (\lambda_1 \mu'' - \lambda_2 \sigma'' + \lambda_3 \pi'') = (H^* - \lambda_5) \mu' / [x_1 (\lambda_1 \mu'' - \lambda_2 \sigma'' + \lambda_3 \pi'')] \tag{3.18}$$

For free time problems in which the objective function is independent of the final time have $H^* = 0$ and $\lambda_5 = 0$, thus the feed rate on singular interval is:

$$\dot{S} = (H^* - \lambda_5) \mu' / [x_1 (\lambda_1 \mu'' - \lambda_2 \sigma'' + \lambda_3 \pi'')] = 0 \Rightarrow F_s (S_f - S)/V - \sigma x / V = 0 \tag{3.19}$$

Equation (3.19) shows that the substrate concentration may be kept constant on singular arc. This constant value of substrate concentration (*S**) can be obtained solving equations (3.13) and (3.15):

$$\frac{\pi'\sigma - \sigma'\pi}{\mu'\sigma - \sigma'\mu} = -\frac{\lambda_1}{\lambda_3} \tag{3.20}$$

As $H^* = 0$ and $\lambda_5 = 0$, this implies that λ_1 is constant from beginning of singular arc until final time. Thus we may write $\lambda_1(t) = \lambda_1(t_f)$ and $\lambda_3(t) = \lambda_3(t_f)$, since λ_3 is constant over entire optimal control path. Hence, Eq. (3.19) may be rewritten as:

$$\frac{\pi'\sigma - \sigma'\pi}{\mu'\sigma - \sigma'\mu} = -\frac{\lambda_1(t_f)}{\lambda_3(t_f)} = -\frac{0}{-\dfrac{\partial\Phi}{\partial x_3}} = 0 \tag{3.21}$$

Thus, switching to the singular arc is possible only when the substrate concentration in the bioreactor satisfies Eq. (3.21).

In this way, in the previous established strategy control consists in the following phases with constant-singular-constant control:

- *First phase*: as the initial substrate concentration is zero, $F = F_{max}$ to rapidly increase the substrate concentration to $S=S^*$ (calculated by equation (3.21));
- *Second phase*: when *S** is reached this constant substrate concentration must be maintained so that the control variable F is calculated to satisfy $dS/dt=0$, until the maximum volume of the reactor is reached;
- *Third phase*: when the constraint in maximum volume is satisfied, the singular phase arrives to end and $F = F_{min}$ (batch phase).

4 Results and Discussion

The dimensionless parameters of Andrews's kinetic model given by Eq.(4.1) were estimated by Differential Evolution and the values μ_{max}, K_S, K_i and M_S are, respectively, 0.3135, 0.1199, 0.5949 and 0.05523. Equations (4.2) and (4.3) define the specific rates substrate consumption and product formation as function of yields Y_{xs} and Y_{ps}.

$$\mu = \mu_{max}\left(\frac{S}{K_S + S + \dfrac{S^2}{K_i}}\right) \quad (4.1) \qquad \sigma = \left(\frac{1}{Y_{XS}}\mu + M_S\right) \quad (4.2) \qquad \pi = \frac{Y_{PS}}{Y_{XS}}\mu \quad (4.3)$$

Table 4.1 presents the singular substrate concentration, the switching times t_{s1} and t_{s2} which identify each phase, the final fermentation time and the objective function for two different feed substrate concentration and considering two maximum values of control variable F. The results were obtained through Dircol code with tolerance 10^{-5}, five grid points by phase and assuming the following range for switching and final times: $0< t_{s1}<4$, $4< t_{s2}<7$ and $7< t_f <18$. It can be observed that the increasing of F_{max} value have no significative influence on final fermentation time and product formation, resulting in a light decreasing of time and increasing of *pV*. As expected, the first phase becomes short-range with decreasing of t_{s1} values and consequent increasing of singular phase.

Table 4.1 Switching times, final time and objective function.

s_F (g/L)	*S** (g/L)	F_{max} (L/h)	t_{s1} (h)	t_{s2} (h)	t_f (h)	*pV* (g)
216.6	57.8610	0.6598	2.7208	5.9115	12.6110	386.0925
		1.6500	0.4431	5.7373	12.5067	386.1175
285.1	76.1433	0.6598	1.7125	7.4970	16.6181	461.3241
		1.6500	0.4116	7.3553	16.4593	461.3525

Otherwise, the product formation pV increases significantly with S_f associated with the increase of final time fermentation. Figures 1 to 10 present the simulated cells, substrate, product, volume and control profiles, where the three mentioned phases may be clearly identified.

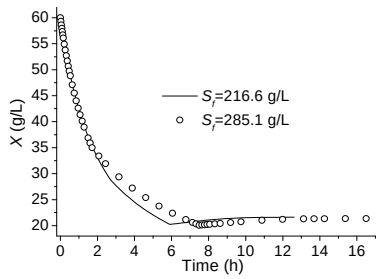

Figure 1: Cells concentration profiles (u_{max}=0.6598 L/h).

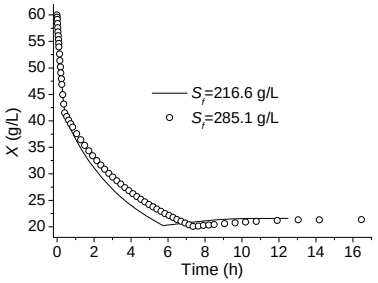

Figure 2: Cells concentration profiles (u_{max}=1.6500 L/h).

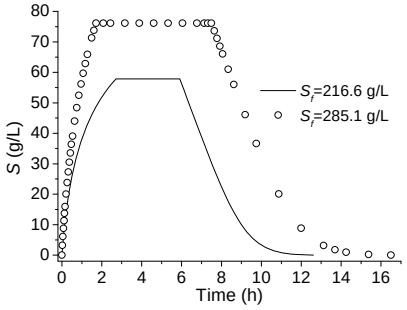

Figure 3: Substrate concentration profiles (u_{max}=0.6598 L/h).

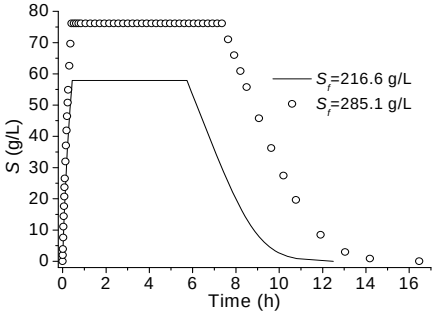

Figure 4: Substrate concentration profiles (u_{max}=1.6500 L/h).

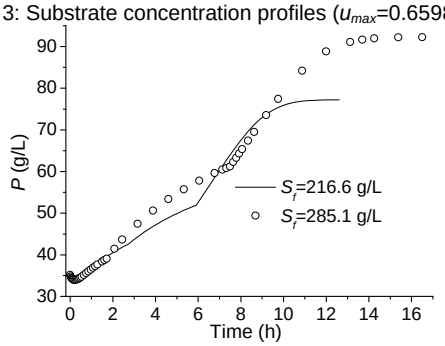

Figure 5: Product concentration profiles (u_{max}=0.6598 L/h).

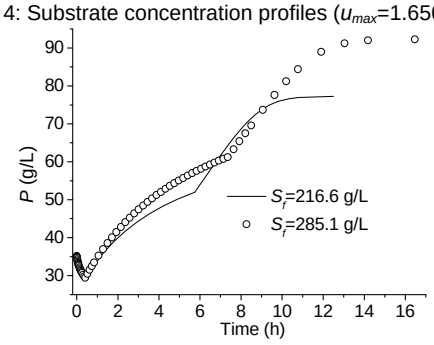

Figure 6: Product concentration profiles (u_{max}=1.6500 L/h).

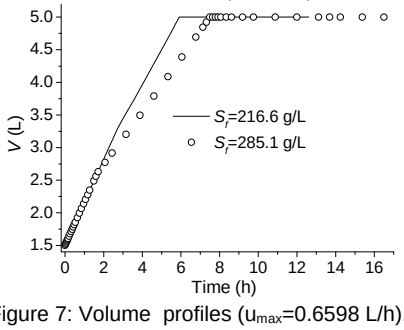

Figure 7: Volume profiles (u_{max}=0.6598 L/h).

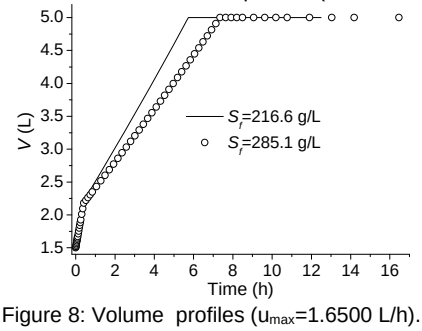

Figure 8: Volume profiles (u_{max}=1.6500 L/h).

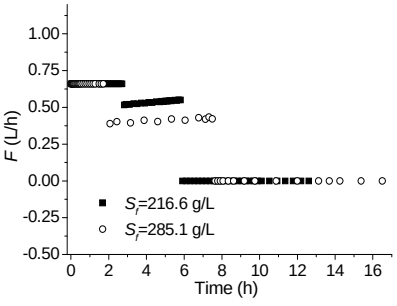

Figure 9: Control variable profiles (u_{max}=0.6598 L/h).

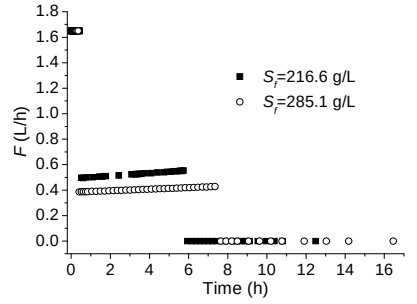

Figure 10: Control variable profiles (u_{max}=1.6500 L/h).

5 Conclusions

The methodology presented consists in the application of PMP to define the characteristics of singular arc in each phase and use of control and state parameterization though Dircol code to maximize de productivity of fed batch ethanol fermentation from sugarcane. It was shown that at singular arc the substrate concentration should be maintained constant at value S*. The increasing of S_f causes the decreasing of first switching time, shortening the range of the first phase and lengthening the singular phase with consequent increasing on final fermentation time and productivity. It should be observed that the proposed methodology is based on the process operating conditions and optimization goals to define the sequence of events. It is also dependent of the characteristics of the model equations, which in its final formulation should be necessary well posed.

Acknowledgments

The authors wish to acknowledge CAPES (Coordenação de Aperfeiçoamento de Pessoal de Nível Superior), a Federal Agency, for the financial support to this work.

References

Andrews J. F. (1968). *A mathematical model for the continuous culture of microorganisms utilizing inhibitory substrates.* Biotechnol. Bioengng 10, 707-723.

Bravo, S., Mahn, A. and Shene, C. (2000). *Effect of feeding strategy on Zimomonas mobilis CP4 fed-batch fermentations and mathematical modeling of the system.* Applied Microbiol. Biotech., 43, 487-493.

Bryson, A. E., Ho, Y. C. (1975). *Applied Optimal Control*. S.I.: Hemisphere Publishing Washington.

Carvalho, J.C.M, Aquarone, E., Sato, S., Brazzach, M.L., Almeida, K.A. and Borzani, W. (2005). *Influence of exponentially decreasing feeding rates on fed-batch ethanol fermentation of sugar cane blackstrap molasses.* Biotechnology Letters, 12 (10).

Carvalho, J.C.M., Aquarone, E., Sato, S., Brazzach, M.L., Moraes, D.A., Borzani, W. (1993). *Fed-batch alcoholic fermentation of sugar cane blackstrap molasses: influence of the feeding rate on yeast yield and productivity.* Appl. Microbiol. Biotechnol, 38,596-598.

Chen, C., Hwang, C. (1990). Optimal on-off control for fed-batch fermentation processes. *Industrial Engineering Chemical Research*, v. 29, 1869-1875.

Gill, P. E., Murray W.; Saunders, M. A. (1986) *User's Guide for NPSOL: a Fortran package for nonlinear programming*.

Hong, J. (1986). Optimal substrate feeding policy for a fed batch fermentation with substrate and product inhibition kinetics. *Biotechnol. and Bioeng.*, 28, 1421-1431.

Laopaiboon, L., Thanonkeo, P., Laopaiboon, P. J. (2007). *Ethanol production from sweet sorghum juice in batch and fed-batch fermentations by Saccharomyces cerevisiae.* World J. Microbiol Biotechnol, 23, 1497–1501.

Modak, J. M., Lim, H. C., Tayeb, Y. J. (1986). *General characteristics of optimal feed rate profiles for various fed-batch fermentation process.* Biotechnology and Bioengineering, 28, 1396-1407.

Srinivasan, B., Palanki, S., Bonvin, D (2003). *Dynamic optimization of batch process I: characterization of the nominal solution*. Computer and Chemical Engineering, 27, 1-26.

von Stryk, O. (1999). *User's Guide for DIRCOL - a Direct Collocation method for the numerical solution of optimal control problems*. Technische Universitat Darmstadt, Fachgebiet Simulation und Systemoptimierung (SIM).

Xiong, Z. and Zhang, J. (2003). Modelling and optimal control of fed-batch processes using a novel control affine feed forward neural network. *Proceedings of the 2002 American Control Conference*, Anchorage, AK, USA, 5025-5030.

Proceedings of the 10th International Chemical and
Biological Engineering Conference - CHEMPOR 2008
Braga, Portugal, September 4-6, 2008
E.C. Ferreira and M. Mota (Eds.)

Selection of controlled Variables for Complex Distillation Column with Heat Pump

M. Ebrahiminejad ,R. Eslamloueyan*
Petroleum and Chemical Engineering Department, Shiraz University, Shiraz, Iran

Keywords: Controlled variable selection, Distillation column, Heat-integrated, self-optimizing control
Topic: Systematic methods and tools for managing the complexity (Process control & operations)

Abstract

A complex distillation column with heat pump that separates propylene and propane is considered for control configuration selection. The column is an industrial C3 splitter used for producing polymer grade propylene. The overhead vapour is compressed so that it can condense in the shell side of the column reboiler and produce the needed boilup at the bottom. The method of self optimizing control is employed for selection of controlled variables. The proposed strategy is based on selecting the most economical controlled variables according to steady state condition of the process. The controlled variables are those output variables that when kept at their constant setpoints cause the disturbed process to stay near an economic optimum. The results show that the ratio of the boilup rate to reflux flowrate has the least loss, from the view point of self optimizing strategy.

Introduction

Distillation columns used for highly pure separations of close boiling mixtures are extremely energy consuming. Low relative volatilities and high product purity lead to very large reflux ratios and subsequently large amount of energy consumption in the column condenser and reboiler. In addition, if the components being processed have low boiling points then cooling water cannot be used in the condenser and expensive low temperature refrigeration system have to be installed. Some improvement methods have been recommended for such columns to decrease cost of energy. These modifications are mainly based on optimizing the process in steady state conditions so, if they were applied on the process then the control and operation of the column would become very difficult. Using a heat pump is one of the heat integration methods to reduce the consumption of energy in the distillation columns. It is usually applied in the columns when the temperature difference between the overhead and the bottom is small. Propylene and propane splitters, being used to produce polymer grade propylene, are placed in this category of columns. Several types of heat pumps have been suggested and used for C3 splitter in the industry. Direct vapor recompression is the most frequent heat pump system in propylene-propane separation when the distillate is a good refrigerant.

Finco and Luyben (1989) studied the control of a conventional distillation column with low relative volatilities used for separation of propylene and propane. They performed both dynamic and steady state modeling. In the case of dual composition control, they examined several control structure. Based on the Relative Gain Array (GRA), they concluded the reflux flow rate and bottom flow rate (R, B) should be used as manipulated variables. Muhrer et al. (1990) studied the control of vapour recompression distillation columns with reference to C3 splitter and ethanol/water

* Fax:+98-711-6287294 , Email: eslamlo@shirazu.ac.ir ; reslamloueyan@yahoo.com

separation. They stated that the control system used on these two specific vapour recompression columns could be the same as the control system of conventional columns. They replaced heat input control by compressor control. Papastathopoulou and Luyben (1991) did a comprehensive study of the dynamics and control of a large industrial column with 190 trays and a high reflux ratio. They used a steady state model to calculate steady state gains for a large number of alternative controls. Several control indices were calculated, such as the Morari resiliency index (MRI), the Relative Gain Array (RGA), the Niederlinski index (NI). They showed that the most effective control structure depends on the control objectives. Gokhale, Hurowitz, and Riggs (1995) compared dual composition control performance for a diagonal proportional integral PI controller and several advanced controllers. They observed significant improvement in performance for the multivariable controllers over the PI controller for a periodic variation in feed composition. Hurowitz et. al. (1998) studied a propylene and propane column on Distillation control configuration selection. They found that the reflux flow rate and bottom flow rate (R,B) and the reflux flow rate and boilup flow rate to bottom flow rate ratio (R,V/B) configurations were the best control configurations. They also observed that the distillate flow and bottom flow rates (D,B) configuration with tight level control provided roughly equivalent results. Enagandula and Riggs (2006) presented a technique to evaluate control configuration selection for distillation columns by developing closed-loop Bode plot using a linear dynamic tray-to-tray model of the process. They concluded based on the results for the product variability prediction, the ratio of reflux to distillate flow rates and boilup flow rate (R/D, V), the ratio of reflux to distillate flow rates and the ratio of boilup to bottom flow rates (R/D, V/B) and the distillate flow rate and bottom flow rate (D, B) (with tight level control) configurations provided the best overall control performance. Olujic et. al. (2006) introduced internally heat integrated (HIDiC) version of a state of the art propylene-propane splitter as an economically attractive option for new designs, provided the barriers related to increased design complexity could be overcome.

A self-optimizing control method (Skogestad, 2000) presents a mathematical procedure for selection of controlled variables. In this method, a cost or profit function is formulated as quality of operation that would be minimized or maximized. The optimum value of cost function is calculated in normal condition of the process when no disturbances exist in the process. A set of controlled variables are selected and kept constant at their setpoint values. The disturbances are introduced to the process for each group of controlled variables in the set and, the cost functions are estimated for each group separately. The difference between the cost function of disturbed process and optimum nominal value of cost function is called loss function. That group of variables having the least value of loss function is considered as the variables being controlled. Mathematical definition of the concept gives:

$$L(cs,d)=J(cs,d)-J(opt) \quad (1)$$

As a result with proper selection of controlled variables there is an acceptable loss without a need to repeat the optimization again. The feature of the self-optimizing control method is that the control scheme is obtained based on the steady state simulation of the .

Industrial C3 Splitter with Heat Pump

Fig. 1 shows flowsheet of the industrial C3 splitter studied in this work. The distillation heat pump (DHP) system consists of a vapor compression cycle loop. The type of the condenser/reboiler heat exchanger is shell and tube. The compressor has a variable speed motor.

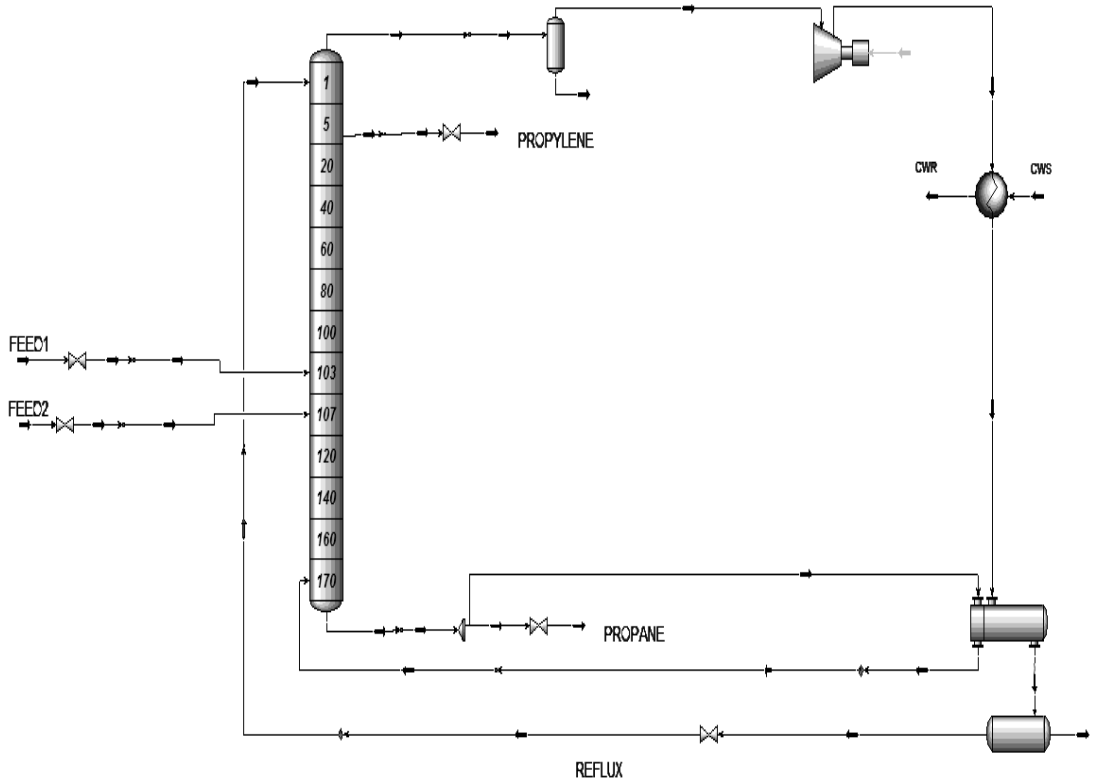

Fig. 1 flowsheet of the process

TABLE 1
Steady state data

Variable	Variable description	Steady state value
F_1	First feed flow rate	61.63 (kmol/hr)
z_{F1}	First feed composition	0.9556
q_{F1}	First feed liquid fraction	1.0
F_2	Second feed flow rate	259.86 (kmol/hr)
z_{F2}	Second feed composition	0.9200
q_{F2}	Second feed liquid fraction	1.0
D	Top product flow rate	300.0 (kmol/hr)
B	Bottom product flow rate	21.5 (kmol/hr)
x_D	Top product composition	0.995
x_B	Bottom product composition	0.1
N_{tot}	Total number of trays	170
P_{top}	Column pressure	10 (barg)
N_{F1}	First feed tray location	103
N_{F2}	Second feed tray location	107

The discharge vapor of the compressor is desuperheated by cooling water in a cooler before entering the shell side of the condenser/reboiler exchanger. Overhead vapor is compressed to a higher pressure, to prepare heat duty for boiling bottom liquid. In this way condenser and reboiler duties are coupled and, then the cooling water consumption of for separation is reduced. The Steady state data of the column are reported in Table 1. The process was simulated by Hysys simulator.

Self optimizing control method

The self-optimizing method has the following six steps:

A. Determination of degrees of freedom

In this step, the number of manipulated variables are considered as the degree of

freedom. The distillation plant in Fig. 1 has 7 control degrees of freedom: two feedrates, reflux flowrate, distillate and bottom product flowrates, compressor speed, and cooling water flowrate. For distillation column case study there are two holdups in the reboiler/condenser heat exchanger that have to be stabilized then two degrees of freedom are consumed. If it is assumed that two feedrates are fixed then it leaves three degrees of freedom for optimization.

B. Definition of cost function and constraint

In the second step, the cost function is formulated as the operating cost defined by the following equation.

$$P = -J = (p_D D + p_B B - p_{F_1} F_1 - p_{F_2} F_2 - p_s W_s - p_{cw} V_{cw}) \quad (2)$$

Where W_s and V_{cw} are the power consumption of the compressor and volumetric flow rate of the cooling water, respectively With given feedrates, F1 and F2 are fixed and, the related terms have no effect on the cost function. After the economic objective is defined, the system constraint must be determined. The following two constraints were specified:

- The pressure of column should be greater than or equal to 10 bar.
- The product purity of the distillate should be above or equal to 99.5%.

Table 2. Loss calculation results

Var.	Variable description	F1-20%	F1+20%	F2-20%	F2+20%	F2-20%	z_{F1}-10%	z_{F1}-10%
V	Boilup rate	4.08573	7.44458	0.44375	20.043	21.1896	11.0859	10.7154
L	Reflux rate	4.05064	17.7547	0.40665	20.043	17.9273	10.9953	11.8629
V/L	Boilup to Reflux rate	1.31519	4.91015	0.40665	2.43012	13.3021	6.23499	4.76654
D/L	Distillate to Reflux rate	6.72135	3.81979	5.92583	4.96206	16.9095	20.6957	9.83905
V/F	Boilup to 1'st feed rate	6.38827	3.59944	5.95306	4.50379	14.9243	11.3559	7.78746
L/F	Reflux to 1'st feed rate	6.32581	3.73325	5.96455	4.45376	14.8795	11.2732	7.18482
Ws/F	Compressor work to feed rate	5.75363	11.5910	2.44328	30.8421	16.2709	14.1709	12.2284
Q/F	Heat primary exchanger duty to feed rate	6.17157	3.88984	6.19230	4.30151	14.8440	11.0043	8.30179
Ws/L	Compressor work to reflux rate	4.90015	7.29700	0.40665	18.6870	17.9273	10.9953	10.0355
Q/L	Heat primary condenser duty to Reflux rate	11.3535	0.41506	2.69549	3.83057	15.8939	17.2597	8.57475
B/L	Bottom to Reflux rate	5.14098	5.08775	7.37214	6.15289	6.50461	22.3334	8.76530
V/B	Boilup rate to bottom rate	5.22683	5.08775	7.33895	6.11001	6.37226	22.0659	8.7003
DT	Two products temperature difference	4.05832	9.37510	0.40568	18.6923	14.7031	11.0317	9.71106
T	130'tray temperature	4.05879	9.37510	0.40559	18.6923	14.7975	11.0325	9.72699
xD	Distillate product composition	4.05733	3.53556	5.91343	2.90518	12.9534	9.31361	6.44642

C. Identification of important disturbances

The most important disturbances are ±20% variation in each of the two feed flowrates,

10% decrease in each of two feed composition.

D. Steady state optimization

After simulation, the optimization problem is done to determine nominal steady state operating point, when there are no disturbances. The values of optimal operating point are chosen as setpoint of candidate controlled variables. Optimization is repeated when the disturbances occurring to obtain optimum cost function.

E. Identification of sets of candidate controlled variable

As it is mentioned, there are four constraints that should be controlled at their setpoints: the pressure of the column, the purity of the distillate product, and two holdups in reboiler/condenser heat exchanger. Therefore one of the degrees of freedom remains for self optimizing control. The alternative controlled variables, considered in this study, are shown in Table 2.

F. Evaluation of the loss

To determine the best controlled variable, the losses were calculated for each candidate controlled. The results of the loss evaluation are presented in Table 2.

The comparison of economic losses in Table 2 suggests that the best controlled variable is V/L and, the other controlling candidates are operationally feasible.

Conclusion

In this paper the primary controlled variable is selected based on self-optimizing method for a distillation column with heat pump. The software Hysys is used both to simulating and optimizing the process. For the distillation column case study there are five degrees of freedom. Four of them are consumed for two holdups and two active constraint, i.e. column pressure and distillate product purity. A number of alternative controlled variables were compared with respect to their calculated losses. Based on the loss calculation, the ratio of boilup rate to reflux rate is found as the best controlled variable for the remaining degree of freedom.

References

Enagandula, S., Riggs, J. B., (2006). Distillation control configuration selection based on product variability prediction, *Controll Engineering Practice,* 14, 743-755.

Finco, M. V., Luyben, W. L., Polleck, R. E. (1989). Control of distillation columns with low relative volatilities. *Industrial and Engineering Chemistry Research*, 28, 75–84.

Gokhale, V., Hurowitz, S., Riggs, J. B., (1995). A comparision of Advanced distillation control technique for a poppylene/propane Splitter, *Industrial Engineering Chemistry Research*, 34, 4413-4419.

Hurowitz, S. E., Anderson, J., Duvall, M., & Riggs, J. B. (2003). Distillation control configuration selection. *Journal of Process Control*, 13, 357–362.

Muhrer, C., Collen, M., Luyben, W., Control of vapor recompression distillation columns, *Industrial and Engineering Chemistry Research*, 29, 59-71 (1990).

Olujic, Z., Sun, L., de Rijke, A., Jansens, P. J, (2006). Conceptual design of an internally heat integrated propylene-propane splitter, *Energy,* 31, 3083-3096.

Papastathopoulou, H., Luyen, W., Control of binary sidestream distillation column, *Industrial and Engineering Chemistry Research*, 30, 705-713 (1991).

Skogestad, S., (2000). Plantwide control: the search for the self-optimizing control structure, Journal of Process Control, 10, 487-507.

Proceedings of the 10th International Chemical and
Biological Engineering Conference - CHEMPOR 2008
Braga, Portugal, September 4-6, 2008
E.C. Ferreira and M. Mota (Eds.)

An SPC inspired MPC formulation for quality variables

Belmiro P.M. Duarte[1,2]*, **Nuno M.C. Oliveira**[2], **João F.M. Gândara**[3,2]

[1]Department of Chemical and Biological Engineering, ISEC
Polytechnic Institute of Coimbra, R. Pedro Nunes, 3030–199 Coimbra, Portugal.

[2] GEPSI, CIEPQPF, Department of Chemical Engineering
University of Coimbra, Pólo II, Pinhal de Marrocos, 3030–790 Coimbra, Portugal.

[3] Department of Food Science and Technology, ESAC,
Polytechnic Institute of Coimbra, Bencanta, 3040–316 Coimbra, Portugal.

Keywords: MPC, state-space models, stochastic optimization, quality costs.
Topic: Subject area — Systematic methods and tools for managing the complexity.

Abstract

This paper describes a new Model Predictive Control (MPC) algorithm inspired on Statistical Process Control (SPC) paradigms, to handle systems represented by linear state-space models with stochastic disturbances. It is considered that a linear discrete-time process model is identified based on operational data, and employed to propagate states and outputs within the control horizon. The uncertainty of the states due to model parameters is also projected, taking into account model realization and innovation terms described by normal probability distribution functions (pdfs). The optimal sequence of actions is formulated as a non-linear programming problem whose objective function accounts for the probabilistic cost of quality variables falling outside the product specifications. The strategy proposed is demonstrated with a system comprising two inputs and two quality variables, representing the dynamics of a precipitated calcium carbonate plant.

1 Introduction

Model Predictive Control is an approach nowadays highly disseminated at the industrial level and well studied by the research community, especially when dealing with complex units. Additionally, model robustness has become a fundamental topic in the design of Model Predictive (MP) controllers. This property, assessing the stability properties of the closed-loop system in the presence of plant-model mismatches, has been extensively studied for unconstrained systems (Morari and Zafiriou, 1989). Similar analysis relative to MPC constrained systems has also been addressed in a number of works (e.g, Michalska and Maine (1993)). A classic approach to address the problem of robust MPC considers worst-case scenarios (Lee and Yu, 1997): however, this strategy often leads to conservative performance. Therefore, practical solutions require often better performance in the presence of stochastic disturbances, for systems described by uncertain parameters. This is particularly relevant when the purpose is to control quality variables subject to market specifications.

The monitoring of modern plants involve the acquisition of thousands of signals, later stored in large databases. This source of knowledge might be employed to build process data-driven models. Several tools devoted to this task have received significant attention in recent years, and are nowadays common at the industrial level. For example, linear discrete state-space models offer a simple representation of

*Corresponding author. Tel. +351-239-790720. E-mail: bduarte@isec.pt.

system dynamics incorporating stochastic components to describe either uncertainties in the parameters or non-stationary features (Durbin and Koopman, 2001).

An MPC formulation accounting for the two sources of uncertainty (parameters uncertainty and inflows variability) has emerged in the later years as a framework able to provide MPC with the ability to incorporate probabilistic constraints in the so-called chance-constrained MPC (Schwarm and Nikolaou, 1999; Li et al., 2008). Here we exploit the ideas behind the chance-constrained MPC formulation to determine optimal controllers able to cope with uncertainty. However, such a formulation treats the probabilistic features as constraints, aiming to address the problem of robustness when stochastic inputs appear. Here, the classic optimization MPC problem is reformulated to incorporate the probabilistic cost of failing to fulfill the quality specifications, thus explicitly evaluating the effects of uncertainties in the objective function. This modification relies on the conceptual paradigms of SPC, where probabilistic quality losses represent potential costs (Alwan, 2000). Moreover, it is also in close agreement with the MPC formulation of Batina et al. (2002), to handle linear systems subject to stochastic disturbances, with state and input constraints.

2 An SPC inspired MPC formulation

Let us consider a process represented by a discrete state space model

$$x(t+1|t) = A\,x(t|t) + B\,u(t|t) + K\,e(t|t) \tag{1a}$$

$$y(t|t) = C\,x(t|t) + D\,u(t|t) + e(t|t) \tag{1b}$$

where $x \in \mathbb{R}^{\mathrm{s}}$ is the process state, $u \in \mathbb{R}^{\mathrm{u}}$ are the input variables, $y \in \mathbb{R}^{\mathrm{y}}$ the output variables, and $e \in \mathbb{R}^{\mathrm{s}}$ represents the stochastic component. A, B, C, D and K are time independent parameter matrices, and $x(t+1|t)$ represents the forecast of the states at the discrete instant $t+1$ given the value at t. The input variables include disturbances, here designated as d, with $d \in \mathbb{R}^{\mathrm{d}}$, and manipulations, designated as $c \in \mathbb{R}^{\mathrm{c}}$, with $\mathbb{R}^{\mathrm{u}} \equiv \mathbb{R}^{\mathrm{d+c}}$. The vector of outputs includes quality variables $q \in \mathbb{R}^{\mathrm{q}}$ and non-controlled outputs $\bar{q} \in \mathbb{R}^{\bar{\mathrm{q}}}$, with $\mathbb{R}^{\mathrm{y}} \equiv \mathbb{R}^{\mathrm{q}+\bar{\mathrm{q}}}$. Thus:

$$\begin{bmatrix} q(t|t) \\ \bar{q}(t|t) \end{bmatrix} = \begin{bmatrix} C_q \\ C_{\bar{q}} \end{bmatrix} x(t|t) + \begin{bmatrix} D_q \\ D_{\bar{q}} \end{bmatrix} u(t|t) + \begin{bmatrix} e_q(t|t) \\ e_{\bar{q}}(t|t) \end{bmatrix} \tag{2}$$

The identification of model (1) based on process data, considering missing observations, was discussed by Gândara et al. (2006). The uncertainty affects the inputs with the innovation for each state described by a normal pdf $\mathcal{N}(0, \sigma^2)$. The joint pdf is represented by $\mathcal{N}(0, \Sigma)$, where $\Sigma = \mathrm{Cov}(e)$ is the variance-covariance matrix of states uncertainty. The MPC formulation derived above, based on time-discrete models, can be easily extended to first principles models including uncertain parameters.

Figure 1 presents the classic model-based control scheme for a SISO system when uncertainty is explicitly considered, and when joint/individual pdfs describing the controlled quality variables are evaluated by means of their moments, at each discrete time instant. The process states and outputs are forecasted within the control horizon employing equations (1), without the stochastic component. One may see that the quality variables at any time instant $t+i$ are influenced by the process state at time t and all control actions implemented $u_{t+j},\ 0 \le j \le i$.

On the other hand, the uncertainty is also projected in the control horizon employing the discrete-time model. Here, $\epsilon(t+i|t)$ represents the prediction error of the quality variables at time instant $t+i$, when t is the present instant. Thus

$$\epsilon(t+i|t) = \left[C \left(\sum_{j=0}^{i-1} A^j \right) K + I \right] e(t|t) + C\,A^{i-1}\,e_{x0} \tag{3}$$

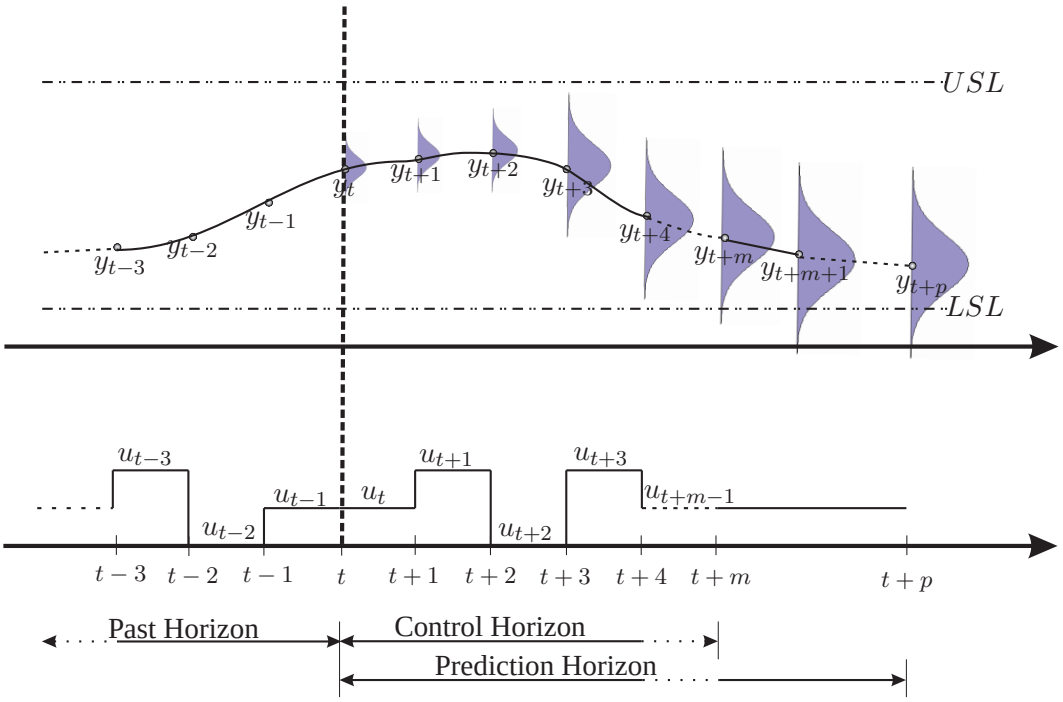

Figure 1: MPC representation for models including parameter uncertainty.

where e_{x0} stands for the uncertainty of the process state at time t. The prediction error variance, $\chi(t+i|t),\ 0 \leq i \leq p$, where p is the dimension of the prediction horizon, is to be estimated employing the propagation formulas developed by Seppala (1998):

$$\chi(t+i|t) = [\Psi(t+i|t) \bullet \Psi(t+i|t)]\ \mathrm{Cov}(e) + [\Omega(t+i|t) \bullet \Omega(t+i|t)]\ \mathrm{Cov}(e_{x0}) \tag{4a}$$

$$\Psi(t+i|t) = \begin{cases} C\ \sum_{j=0}^{i-1} A^j\ K + I & \text{if} \quad i > 0 \\ I & \text{if} \quad i = 0 \end{cases} \tag{4b}$$

$$\Omega(t+i|t) = \begin{cases} C\ A^{i-1} & \text{if} \quad i > 0 \\ I & \text{if} \quad i = 0 \end{cases} \tag{4c}$$

where $[\Psi \bullet \Psi]$ stands for the Hadamard product of matrices Ψ. Those equations allow the analytical determination of the joint pdf of the quality variables, considering the linear characteristics of the system, under the assumption that for each time instant the pdf is given by a q-dimensional normal distribution. The matrix $\chi(t+i|t)$ is formed by four-block matrices, with $\chi_{q,q}(t+i|t)$ used to represent the uncertainty of the quality variables:

$$\chi(t+i|t) = \begin{bmatrix} \chi_{q,q}(t+i|t) & \chi_{\bar{q},q}(t+i|t) \\ \chi_{q,\bar{q}}(t+i|t) & \chi_{\bar{q},\bar{q}}(t+i|t) \end{bmatrix} \tag{5}$$

where $\chi_{q,q}(t+i|t)$ stands for the variance-covariance matrix of the prediction error of quality variables q at discrete time instants $t+i$.

The probabilistic cost of producing out of specification is defined by the hyperplane of values θ belonging to the space $\Re^{\mathrm{q}}$, with $\{\theta : \theta \leq [LSL^1, \cdots, LSL^{\mathrm{q}}]^{\mathrm{T}} \wedge \theta \geq [USL^1, \cdots, USL^{\mathrm{q}}]^{\mathrm{T}}\}$, where LSL and USL are lower and upper quality specifications, respectively. The probability of failure at each time instant is determined by the joint pdf, considering the state and error variance estimates:

$$p_f(t+i|t) = 1 - \int_{LSL^1}^{USL^1} \int_{LSL^2}^{USL^2} \cdots \int_{LSL^{\mathrm{q}}}^{USL^{\mathrm{q}}} \frac{1}{\sqrt{2\,\pi}\ |\chi_{q,q}(t+i|t)|} \times$$
$$\times \exp[-(\theta - q(t+i|t))^{\mathrm{T}}\ \chi_{q,q}^{-1}(t+i|t)\ (\theta - q(t+i|t))]\ \mathrm{d}\theta^1\ \mathrm{d}\theta^2 \cdots \mathrm{d}\theta^{\mathrm{q}} \tag{6}$$

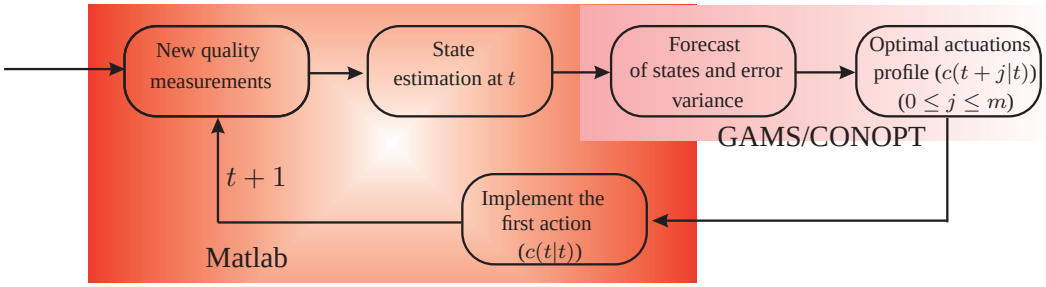

Figure 2: Stochastic MPC information flows.

The analytical evaluation of the q-dimensional integral included in Equation (6) has obvious advantages over numerical approaches based on Hammersley sampling (Diwekar and Kalagnanam, 1997) and cubature formulas (Bernardo et al., 1999). However, such a strategy cannot be applied for non-linear models, since the joint pdf is non-gaussian and its evaluation consequently rather complex.

The MPC optimal control problem falls into the class of non-linear programming (NLP), and is solved with the GAMS/CONOPT solver using a formulation

$$\min_{c} \sum_{i=1}^{m} p_f(t+i|t) \tag{7a}$$

$$\text{s.t.} \quad \text{Equations (1, 4, 6)} \tag{7b}$$

$$c^L \leq c(t+i|t) \leq c^U, \qquad \forall i,t \tag{7c}$$

where c^L and c^U are lower and upper boundaries of the manipulation variables. The problem (7) is solved at each time instant, and the first action, $c(t|t)$, implemented (see Figure 2). Then the prediction horizon is updated to start at the next time instant, new quality variables measured, the problem is solved again and another action is implemented. The estimate of the process state at time instant t is performed based on the observations of the past horizon and on the process model. The window employed for state estimation is updated at every discrete time to account for new observations. A Matlab-based interface is used to re-iterate the calculation sequence.

3 Application

Here we consider the control of a precipitated calcium carbonate (PCC) production plant. The quality variables controlled are the average diameter, designated as quality variable 1, and the specific surface area of the PCC particles, named quality variable 2, resulting from the reaction between lime particles and CO_2. The main disturbance is the granulometry of the lime particles that flows into the reactor, quantified by its average diameter and represented as d_1, and the variable employed for controlling the process is the flow of CO_2, represented as c_1. The time discrete model was identified from process data after convenient variable scaling, and time-independent parameter matrices are presented below. It is noticeable that the model obtained, optimal regarding the Akaike's criterion, includes four process

states, with $u = \begin{bmatrix} d_1 & c_1 \end{bmatrix}^{\mathrm{T}}$:

$$A = \begin{bmatrix} 0.1366 & 0.0811 & -0.0052 & -0.0203 \\ 0.0129 & 0.9631 & -0.2474 & -0.1023 \\ 0.0005 & 0.1386 & 0.6645 & -0.3611 \\ 0.0431 & 0.0516 & 0.2792 & -0.0684 \end{bmatrix}, \qquad B = \begin{bmatrix} -0.0002 & 0.0234 \\ 0.0020 & -0.0020 \\ -0.0206 & 0.0010 \\ 0.0085 & -0.0004 \end{bmatrix}$$

$$C = \begin{bmatrix} 16.5016 & 2.3803 & -0.1114 & -0.0979 \\ 0.0223 & 4.2695 & 0.2905 & 0.1180 \end{bmatrix}, \qquad K = \begin{bmatrix} 0.0076 & 0.0110 \\ 0.0605 & 0.1399 \\ 0.0424 & 0.0118 \\ 0.0149 & -0.0038 \end{bmatrix}$$

$$\mathrm{Cov}(e) = \begin{bmatrix} 0.0023 & 0.0008 \\ 0.0008 & 0.0016 \end{bmatrix}, \qquad \mathrm{Cov}(e_{x0}) = 8.33 \times 10^{-4}\, I_{4\times 4}, \qquad D = 0_{2\times 2}$$

$$LSL = \begin{bmatrix} -1.0000 & -0.7500 \end{bmatrix}^{\mathrm{T}}, \qquad USL = \begin{bmatrix} 1.0000 & 0.75000 \end{bmatrix}^{\mathrm{T}}$$

$$c^L = \begin{bmatrix} -1.0 \end{bmatrix}^{\mathrm{T}}, \qquad c^U = \begin{bmatrix} 1.0 \end{bmatrix}^{\mathrm{T}}$$

The process involves two quality variables and a single manipulated variable, corresponding to the second component of u. Although there exists a certain degree of correlation between the quality variables, captured by a previous time series analysis of the data, the structure will lead to a non-perfect controller. Indeed, the optimal manipulations profile trade-off the quality variables losses, which means that the objectives of each one could not be exactly reached. The forecasting horizon is set to 10, the past horizon dimension is 20, and all signals available in the past horizon (quality variables and inputs) are used to update the process state, x_t. The optimal control problem is solve to a relative tolerance of 10^{-6}, and the limits of the manipulated variable are presented above.

Figure 3(a) presents the manipulations and the disturbance profiles for a window comprising 30 sequential discrete time instants. The disturbance dynamics was simulated employing the normal pdf identified from original process data, $d_1 \approx \mathcal{N}(0, 0.35)$. The value of the disturbance is maintained constant in the prediction horizon. Figure 3(b) presents the dynamics of quality variables. One may see that the manipulation variable reaches the saturation limit at the beginning of the run, as a result of the process state in the first instants being totally determined by past data. It is also shown that the second quality (specific area) is tightly controlled, while the first one exhibits larger variations. This behavior is partially due to the inability of the controller to achieve an optimal performance for both qualities simultaneously, since a single manipulation variable is available. The manipulation actions are chosen to primarily stabilize the second quality variable, which could result in larger probabilistic losses. The propagation of the uncertainty of this variable leads to broad expectation distributions, which can be seen comparing the columns of the matrix K, providing that the values of the $\mathrm{Cov}(e)$ are of the same order of magnitude. Thus, the control of the quality variable 2 is more accurate than the control of quality 1; however, in the optimal solution the probabilistic quality losses due to the latest become similar to the losses due to the former.

4 Conclusions

This paper describes a new MPC formulation inspired by the SPC paradigm, to account for the uncertainty of model parameters. The basic formulation stands on linear state-space discrete time models identified from process data, but can be extended to other model families. The model is employed to propagate states and quality variables within the prediction horizon. The uncertainty, described by the pdf of predictions, is represented by a multi-dimension normal distribution, and propagated taking into account the model innovations. The optimal control problem is then formulated aiming to minimize the loss of quality associated to quality forecasting, falling into the class of NLP problems. The determination of the probability of failure is handled analytically by integrating the normal pdf representing the

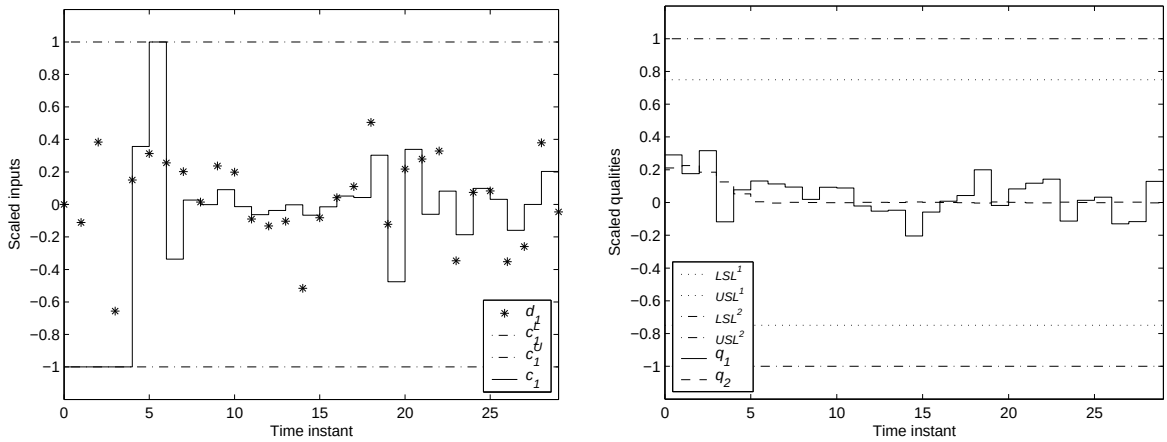

(a) (b).

Figure 3: Simulation results: (a) Inputs profiles; (b) Quality variable profiles.

qualities expectation. The approach presented is demonstrated by controlling a process with two quality variables, four states, and two inputs (one manipulated variable and a disturbance), representing the model of a plant devoted to the production of PCC. The MPC algorithm introduced can be extended to trade-off the costs of failure with the costs of the manipulation actions and the costs of measuring discretely the qualities to assess additional information to reduce the uncertainty of the forecasts. To address these problems the basic approach presented only requires a reformulation of the objective function of the optimal control problem. Another aspect to look at is the use of sampling algorithms to numerically determine the quality loss, which allow us to broaden the application of this approach to non-linear models and non-gaussian uncertainty forms.

References

Alwan, L.C. (2000). *Statistical Process Analysis*, Irwin-McGraw Hill, New York.

Batina, I., Stoorvogel, A.A., Weiland, S. (2002). Optimal control of linear, stochastic systems with state and input constraints, in *Proceeding of the 41st IEEE Conference on Decision and Control*, 1564–1569.

Bernardo, F.P., Pistikopoulos, E.N., Saraiva, P.M. (1999). Integration and computational issues in stochastic design and planning optimization problems, *Ind. Eng. Chem. Resear.*, 38, 3056–3068.

Diwekar, U.M., and Kalagnanam, J.R. (1997). Efficient sampling techniques for optimization under uncertainty, *AIChE Journal*, 43(2), 440–447.

Durbin, J., Koopman, S.J. (2001). *Time series analysis by State Space models*, Oxford University Press, Oxford.

Gândara, J.M., Duarte, B.P.M., Oliveira, N.M.C. (2006). Dynamic estimation and uncertainty quantification for Model-Based Control of discrete systems, in *Proceedings of AdChem 2006*, 585–590.

Lee, J.H., and Yu, Z. (1997). Worst-case formulation of Model Predictive Control for systems with bounded parameters, *Automatica*, 33(5), 765–781.

Li, P., Arellano-Garcia, H., Wozny, G. (2008). Chance constrained programming to process optimization under uncertainty, *Comp. & Chem. Eng.*, 32, 24–45.

Michalska, H., and Maine, D.Q. (1993). Robust receding horizon control of constrained nonlinear systems, *IEEE Trans. Autom. Control*, 38(11), 1623–1633.

Morari, M., and Zafiriou, E. (1989). *Robust Process Control*, Prentice Hall, Englewood Cliffs, NJ.

Schwarm, A.T., and Nikolaou, M. (1999). Chance-constrained Model Predictive Control, *AIChE Journal*, 45(8), 1743–1752.

Seppala, C.T. (1998). *Dynamic Analysis of Variance Methods for Monitoring Control System Performance*, PhD Thesis, Queen's University.

Proceedings of the 10th International Chemical and
Biological Engineering Conference - CHEMPOR 2008
Braga, Portugal, September 4-6, 2008
E.C. Ferreira and M. Mota (Eds.)

The Importance of the Simulation in Refinery Processes

Fernando G. Martins[1*], Marta I. M. S. Cruz[1], Manuel L. Tavares[2], Manuel A. N. Coelho[1]

[1] LEPAE – Chemical Engineering Department, Faculty of Engineering, University of Porto, Rua Dr Roberto Frias s/n, 4200-465 Porto, Portugal.

[2] Petrogal Porto Refinery, Leça da Palmeira, Portugal.

Keywords: Simulation, Process simulators, Performance models

Topic: Systematic methods and tools for managing the complexity

Abstract

The main tool of the computer aided process engineering is the process simulation (Biegler, 1989). One of the main objectives of the simulation is allowing the creation of models in steady-state or in transient regime of the performance of a plant, under defined conditions and through the development of process material and energy balances (Glasscock and Hale, 1994).

The study, here reported, corresponds to the use of a process simulator to develop a model of the distillation unit of the fuel plant of the Petrogal Porto Refinery. The results of the studies performed with the process simulator demonstrated that this tool allows developing models applied to the reality that are very useful to evaluate different operational scenarios.

1 Introduction

In mathematical point of view, a simulation problem corresponds to obtain a solution of a high number of equations which represents the performance of the unit operations and the behaviour of the chemical compounds.

The simulation is very relevant in several working areas of the refinery processes, such as:

Conception/Design – Study of different design alternatives and determination of the operation values, to determine good solutions, using economic drivers, safety rules and/or environment control requirements;

Start up – Prediction of operational conditions during the starting up of the processing units;

Operation – Study of limit operation conditions attending to safety rules and the possible modifications in the project specifications;

Optimization – Modification of the operational values with the objective to evaluate the operational conditions which minimizes the economic, energy and environmental requirements. In this case, the simulation has been demonstrated as a good strategy to maximize the profit through the reduction of consumption and/or by increasing the production, for the installed equipment.

The main steps in simulation are: i) the problem definition; ii) the development of the process model; iii) the collection of additional data; iv) the resolution of the model equations, and finally v) the analysis of the results.

One simulation problem is defined through a sequence of steps which are: i) the selection of components, ii) the selection of the appropriate unit operations, iii) the creation of the process flow diagram, iv) the selection of the correlations to evaluate the thermodynamic

* Corresponding author. Tel + 351-22-5081974. E-mail:fgm@fe.up.pt

properties, and iv) the introduction of the information related with streams, equipment and operation.

The distillation unit of the Petrogal Porto fuel plant consists in three main sections, focused on three distillation columns (T3001, T3004 and T3005). Figure 1 presents a schematic diagram of the installation. The column T3001 is the principal column which separates the crude oil into different fractions. The T3004 (naphtha splitter) separates the heavy naphtha into gasoline (bottom product) and a top product, which is fed to the T3005 column. This column (debutanizer) has as products the gases (top product) and light gasoline (bottom product).

Crude oil is heated previously through 7 heat exchangers and a furnace (H3001), forming the heating system. The temperature of crude oil at the entrance of the main column of atmospheric distillation is a crucial variable, very important for the performance of the total plant.

The principal heating supplier to the column T3001 is the furnace (H3001). Additionally, there are also several streams of steam injected to the columns T3001, T3002 and T3003 which allow to introduce heat in system and to rectify kerosene, diesel and residue. The three columns (T3001, T3002 and T3003) are designated by the topping unit. This group has a total of 4 products. The top product (naphtha) is fed to the T3004 column. The bottom product (residue) from T3001 column is for storage. The remaining 2 products are the lateral products of the T3002 and T3003 columns, corresponding to kerosene and diesel, respectively.

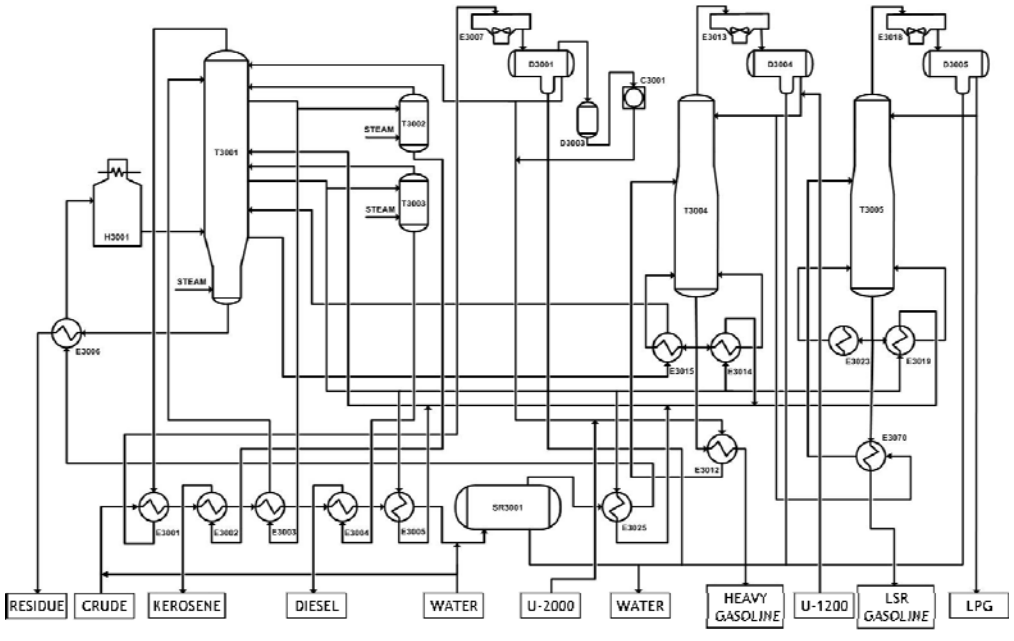

Figure 1 – Diagram of the fuel plant distillation unit.

The software used was the PRO/II which is a steady-state simulator. This software performs rigorous mass and energy balances for a wide range of processes. PRO/II combines the data resources of a large chemical component library and extensive thermodynamic property prediction methods with advanced and flexible unit operations techniques. PRO/II runs in an interactive Windows®-based GUI environment (http://www.simsci-esscor.com, 2008)

2. The procedure

The study, here reported, was developed in two phases: i) in the first phase, the objective was to obtain a performance model for the unit, comparing the results obtained by simulation with the operational values; and ii) in the second phase, some modifications in equipment were introduced, to evaluate the global performance of the unit for processing of a light crude oil.

The topping unit was designed, many years ago, to separate heavy crude oils. However, nowadays the crude oils are more light and as consequence the current plant is not well prepared to manipulate these types of crudes oils. Thus, it is very important to evaluate the performance of the plant, after installing new equipment that allows the separation of these new crudes oils.

Figure 2 (a, b, c and d) shows the current topping unit with three modifications which corresponds to three different scenarios:

Scenario 1 - the introduction of a drum to remove the light fractions of crude oil, being the top product of this column fed to the main column (Figure 2b);

Scenario 2 - the introduction of a pre-flash column, instead of a drum, to remove the light fractions of crude oil being the top product of this column fed to the main column (Figure 2c);

Scenario 3 - the introduction of a pre-flash column to remove the light fractions of crude oil, being the top product of this column fed the column T3004 (Figure 2d).

The main objective was to evaluate the impact of theses scenarios on the increase of the diesel yield and on the reduction of energy consumption.

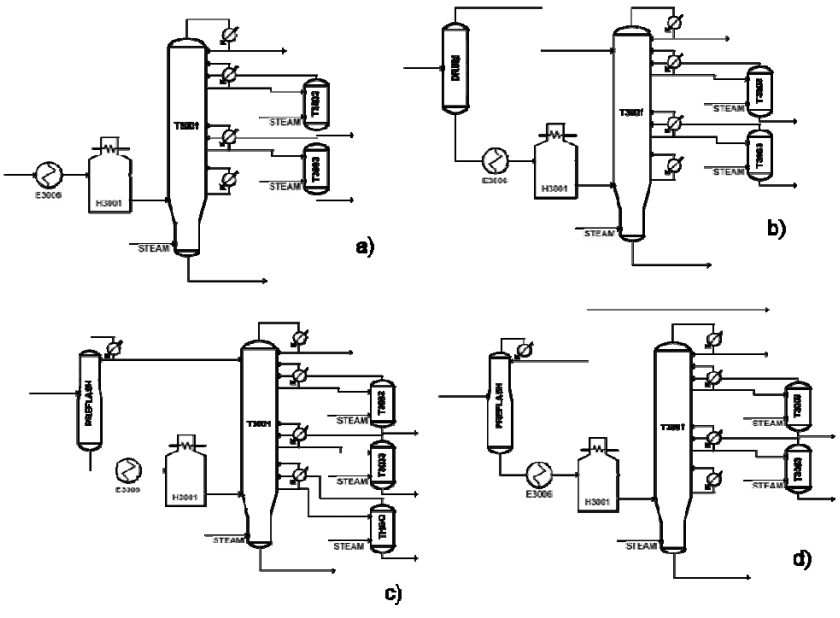

Figure 2 - Study cases with modifications of installed equipment.

It was also analysed the impact of the production of an additional product (heavy diesel) in the diesel yield, using the operational configurations suggested before. Figure 3 presents the different equipment configurations with the additional lateral product.

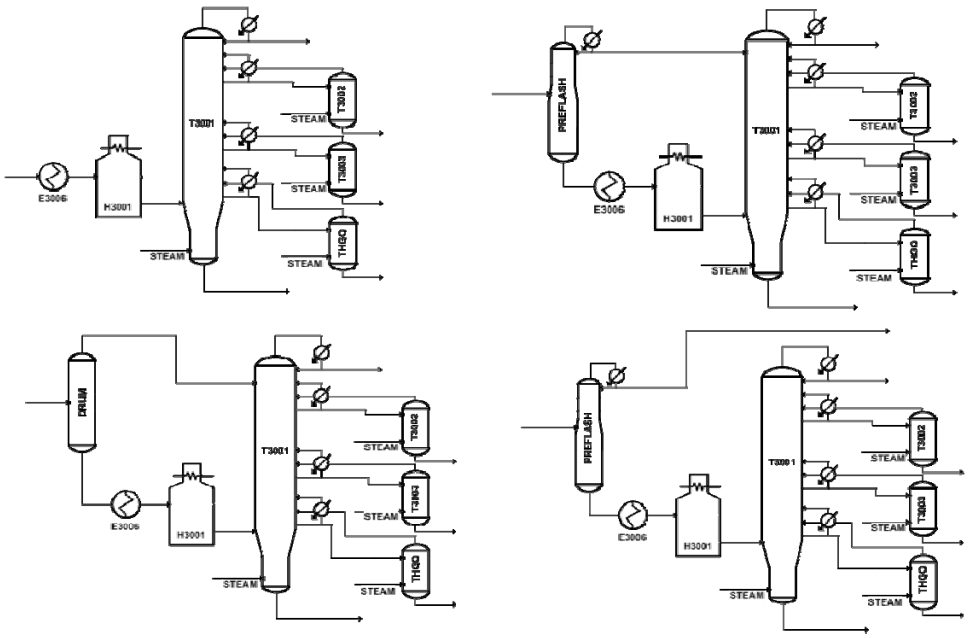

Figure 3 – Equipment configurations with the additional lateral product (heavy diesel).

3. Results and discussion

Figure 4 presents real data and the results obtained by simulation for the topping unit. As can be seen, the model adjusted clearly the real data.

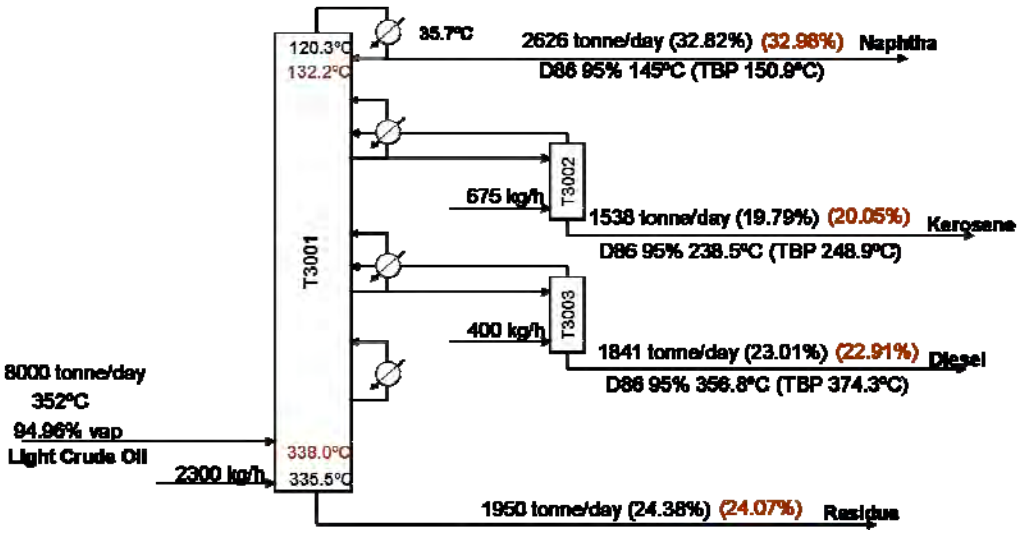

Figure 4 – Real data and results obtained by simulation (color values) for the topping unit.

Concerning the heating system, Figure 5 shows also that the model is able to simulate this system.

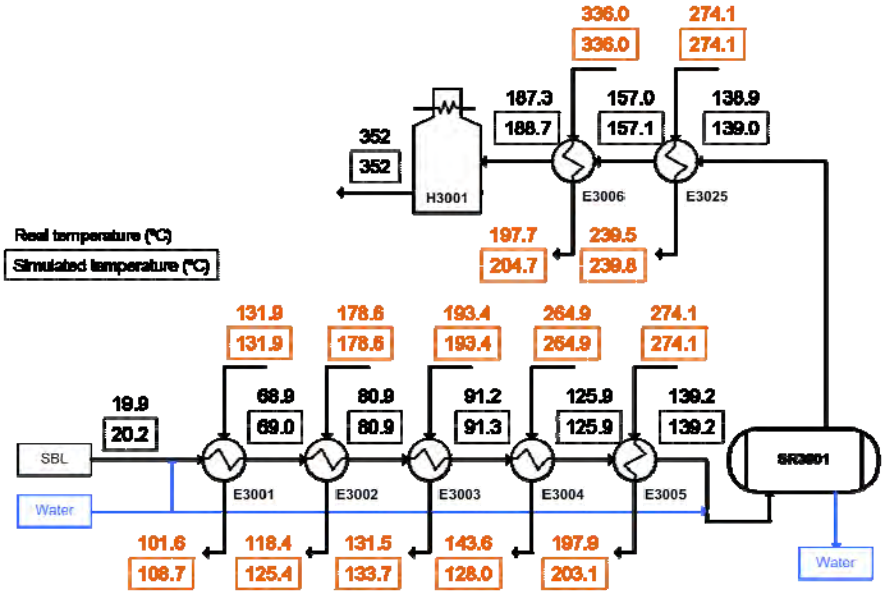

Figure 5 – Heating system (real data versus simulated results).

Table 1 shows the results obtained by the incorporation of new equipment in the plant, corresponding to the three scenarios describe before, using a light crude oil. The results allowed to conclude that the main impact of the introduction of a drum or a preflash in the unit is the decrease of duty of furnace H3001. Is was possible to verify that there wasn't no significant differences between the utilization of a drum or a preflash unit.

Table 1 – Results obtained for a light crude oil for the the diferent equipment scenarios.

	Base	**Drum**	**PreFlash**	**PreFlash with bypass**
Duty H3001 (Gcal/h)	49.76	40.71	41.94	42.81
Vapour at H3001 outlet (%)	94.96	90.71	91.22	91.50
Duty Condenser T3001 (Gcal/h)	32.62	28.94	23.74	23.91
Yield Naphtha (%)	32.82	32.85	32.10	21.33(*)
Yield Kerosene (%)	19.79	19.16	20.09	19.62
Yield Diesel (%)	23.01	23.26	23.10	23.15
Yield Residue (%)	24.38	24.74	24.71	24.68

(*) This value corresponds to the top product of T3001. The top product of the *Preflash* had a yield of 11.21%.

In what concern the production of an additional lateral product (heavy diesel). Table 2 presents the results obtained with the actual plant and the three scenarios described before, for a production a 15 m^3/h of heavy diesel, manipulating a light crude oil. The results indicated that all configurations obtained identical results. However, it was not possible to obtain a product with the target quality limits (heavy diesel TBP 5% and heavy diesel TBP 5% approximately equal to 380 ^oC and 420 ^oC, respectively).

Table 2 – Results obtained with the incorporation of an additional product (heavy diesel).

	Base	***Drum***	***PreFlash***	***PreFlash* with *bypass***
Yield Naphtha (%)	32.82	32.70	32.41	20.54 (*)
Yield Kerosene (%)	19.80	19.35	19.69	19.59
Yield Diesel (%)	23.15	23.34	23.33	23.30
Yield Heavy Diesel (%)	3.99	3.98	3.98	3.98
Yield Residue (%)	20.25	20.65	20.6	20.61
Diesel TBP 95% (ºC)	377.7	377.7	377.7	377.7
Heavy Diesel TBP 5% (ºC)	304.5	300.1	300.6	300.5
Heavy Diesel TBP 95% (ºC)	455.8	458.8	458.8	458.7
Residue TBP 5% (ºC)	360.9	357.9	358.9	358.8

(*) This value corresponds to the top product of T3001. The top product of the *Preflash* had a yield of 11.98%.

4. Conclusions

For the simulations performed for this plant, it was possible to conclude that:

1. The existing plant presents limitations to manipulate light crude oils because some columns are pratically at the flooding conditions;
2. The pre-separation can be beneficial by reducing the energy consumption of the furnace and for cooling at the top of T3001. However, this strategy is dependent of the type of the crude oil, being suggested for light crudes;
3. The studies developed with the inclusion of an heavy diesel lateral product demonstrated that the amount of this product is very low if the product is obtained within the specifications. So, it is not a relevant modification to be implemented for the processing of the light crude oil studied.

The results obtained by the simulations performed in this work demontrated that simulation is a very usefull tool to help analyzing possible revampings in refinery processes.

Acknowledgements

This work was supported by ADI (Agência de Inovação), under project GALPORTOID.

References

Doraiswami, L.K., Sharma, M.M. (1984). Heterogeneous Reactions: Analysis, Examples and Reactor Design, Volume 2, Wiley, New York.

Wang, J., Han, S., Wei, F., Yu, Z., Jin, Y. (1997). An axial dispersion model for gas-liquid reactors based on penetration theory. Chemical Engineering and Processing, 36, 291-299.

http://www.simsci-esscor.com, accessed on June 2008

Proceedings of the 10th International Chemical and
Biological Engineering Conference - CHEMPOR 2008
Braga, Portugal, September 4-6, 2008
E.C. Ferreira and M. Mota (Eds.)

Dynamic Simulation of CO_2 absorption from post combustion gases

Greer T.[3], Bedelbayev, A.[3], Igreja, J.M.[1], Gomes, J. F.[1,2*], Anastácio, P[1], Lie, B.[3]
[1] ISEL – Instituto Superior de Engenharia de Lisboa, Chemical Engineering Department. R. Conselheiro Emídio Navarro 1, 1959 – 007 Lisboa, Portugal
[2] IST – Instituto Superior Técnico, CEBQ/IBB, Av. Rovisco Pais, 1049-001 Lisboa, Portugal
[3] Telemark University College, Postboks 203, N-3901 Porsgrunn, Norway

Keywords: CO_2 capture ; gas absorption ; dynamic simulation
Topic: Sustainable process-product development through green chemistry

Abstract

CO_2 capture from combustion flue gases is currently an issue of main interest due to the high taxes being imposed on industrial companies as a measure to achieve CO_2 emissions abatement. CO_2 capture can be efficiently achieved by gas absorption using amines, namely Monoethanolamine (MEA). Based on henrys law, validated with previously published experimental work, this study considers the development of a dynamic model of an absorption column for post combustion CO_2 capture. A dynamic model of the temperature swing de-absorption process was developed with the integration of both models for absorption and de-absorption (with the introduction of heat exchangers, pumps and other ancillary equipment). A control system for the process was also devised, comprising the pertinent sensors, and various control structures for the absorption column were tested and compared, such as single loop PID controllers (including the pairing problem) and MPC.

1. Introduction

CO_2 emissions result from a chemical reaction when fossil fuels are combusted to release stored chemical potential energy. This is, nowadays, the predominant source of world energy (about 86%) and has resulted in a marked increase on the CO_2 levels in the terrestrial atmosphere from 280 ppm in 1000, to 295 ppm in 1900 and about 377 ppm in 2004. CO_2 is not particularly toxic but is a major contributor to the greenhouse effect, which is most likely the cause of the climate change and increasing global heating over the Earths surface. Bearing in mind this situation, three main options arise to reduce total CO_2 emission into the atmosphere: i) to reduce energy intensity (which can be obtained by the efficient use of energy), ii) to reduce carbon intensity (which requires switching to using non-fossil fuels such as hydrogen and renewable energy), iii) to enhance the sequestration of CO_2. This third option involves the development of technologies to capture and sequester more CO_2.
There are, currently, many options for CO_2 separation and capture, and these include adsorption, absorption, membrane separations and biotechnology. The absorption/stripping process, using amine solutions such as monoethanolamine (MEA), is a commercialized technology used in natural gas industry for 60 years and is regarded as the most mature process and the CO_2 recovery rate can be as high as 98%. Nevertheless, the stability of the amines and the energy consumption of the stripping process, as well as the overall process control, have large room for further improvement.

2. Developed model

The typical process flow diagram for CO_2 removal process is shown in Figure 1. In this process, absorption of CO_2 by MEA takes place in the absorption column A, whereas stripping, for MEA recovery and recycling into the process takes place in stripper B. Other equipment consists of pumps, heat exchangers and, particularly, a reboiler E to supply stripping steam to increase the amine temperature reversing the chemical reactions and reducing the solubility of CO_2 in the liquid, thus releasing the CO_2 as a concentrated gas.

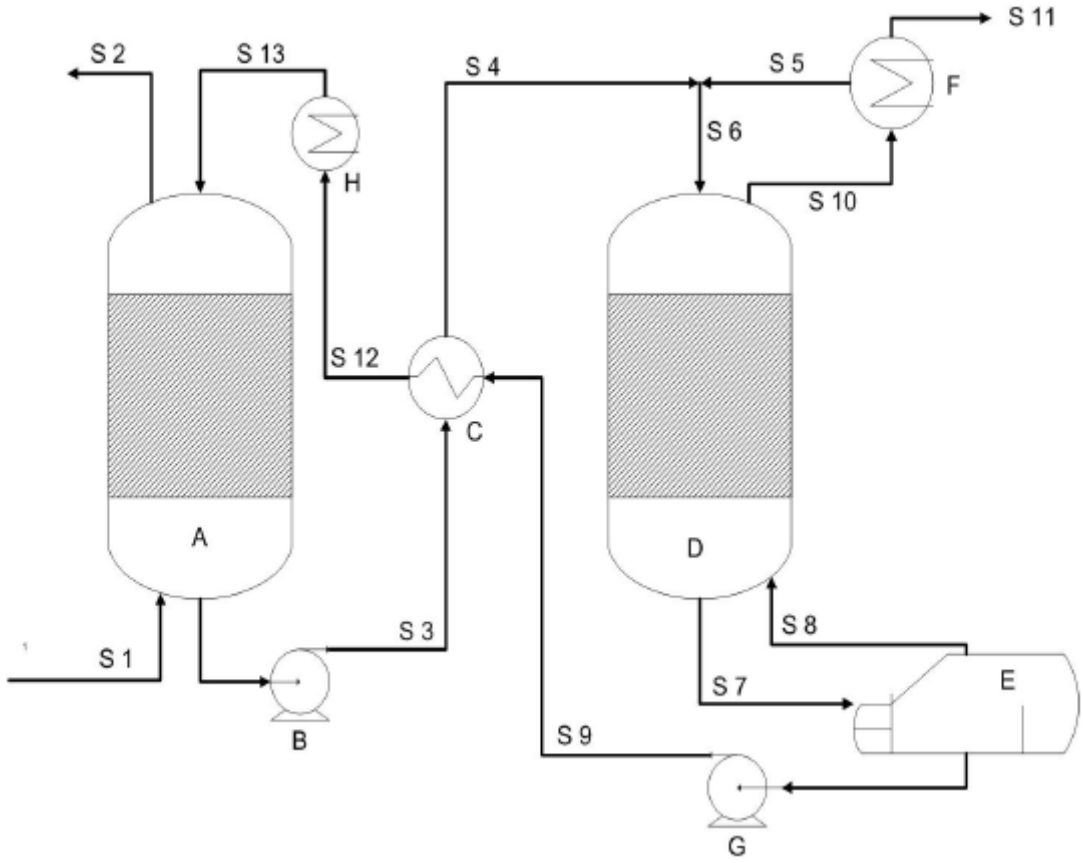

Figure 1. Process flow diagram of CO2 removal process using Monoethanolamine (MEA)

The model was constructed as a boundary condition PDE using Matlab and comprised a set of 6 chemical reactions occurring within the process and also the estimate of appropriate kinetics and thermo chemical properties such as density, viscosity, heat capacity, diffusivities and vapour liquid equilibrium. A schematic calculation flow sheet is presented in Figure 2.

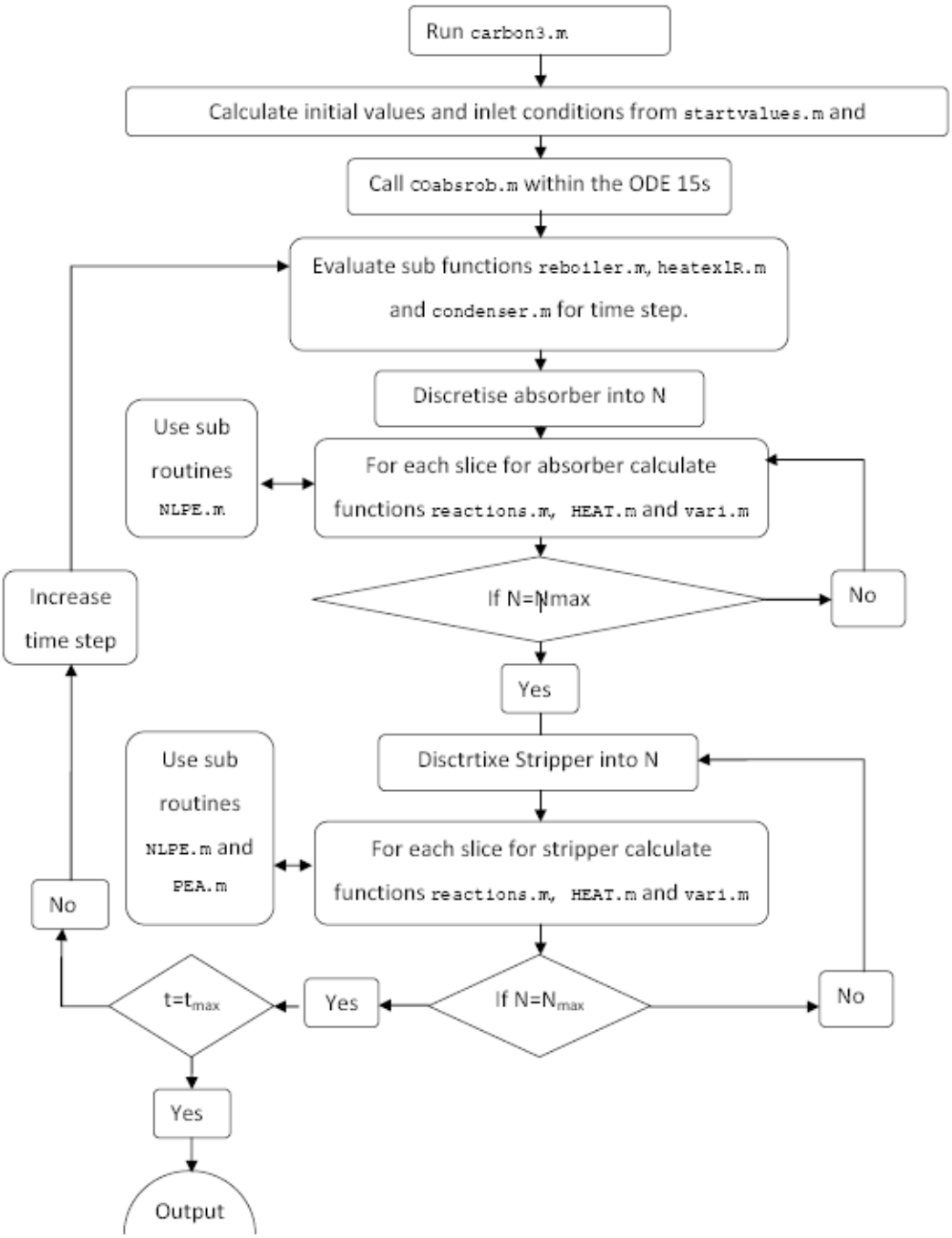

Figure 2. Calculation flow sheet

3. Results and discussion

The obtained results were generated by simulation with 35 discretised volumes so that the accuracy is increased. It allowed a graphical representation of the concentrations of the several chemical species involved as shown in Figure 3 regarding CO_2 in the absorber. This plot clearly shows that the CO_2 is depleted from the entrance at the bottom of the absorption column until it leaves at the top. The removal percentage is estimated at 88%, which is the range estimated from literature. As expected the removal rate is higher at the bottom of the tower, decreasing as the concentration in the gas approaches zero. The height of the tower has a large effect on the removal rate as the higher the tower, the higher the retention time of the liquid and the gas phases. Other obtained plots were the temperature of the vapour and liquid phases as well as the other species in both phases such as H_2O, N_2, MEA, O_2 and the chemical species formed when CO_2 reacts with MEA.

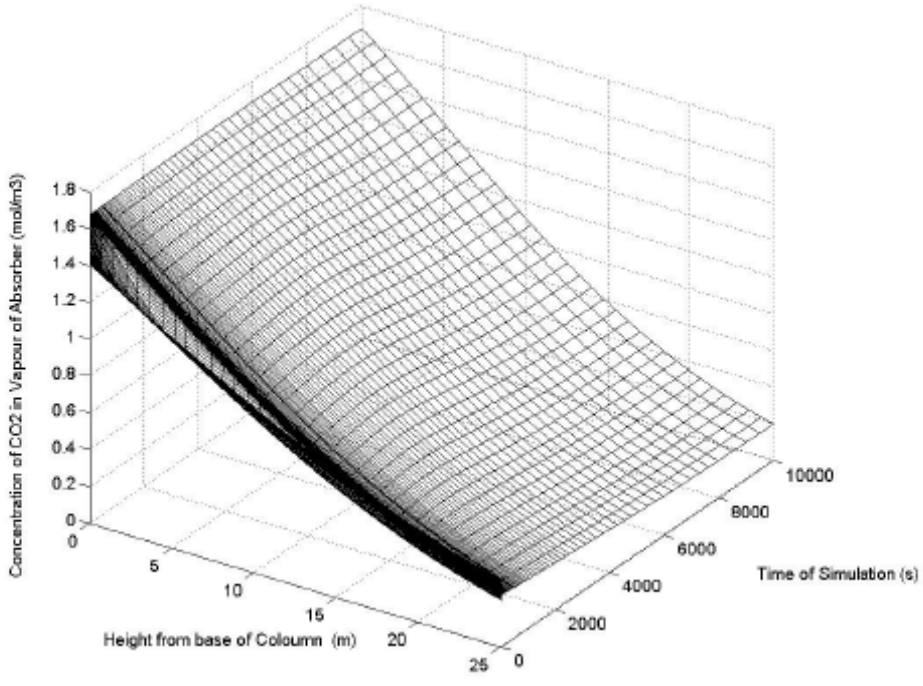

Figure 3. Obtained profile of CO_2 concentration in the absorption column

The developed model allowed for a sensitivity analysis of several operational and design parameters on the system. Table 1, shows some introduced variations ("perturbations") of the model from its baseline case. It is interesting to note the values for the CO_2 removal, energy consumption per kg of absorbed CO_2, cleaned gas composition and CO_2 loading for different parameters and inputs. The perturbations were run with 5 slices in the towers so that the results are not as accurate as with more slices, but do allow a quick overview of the controlling influences.

Table 1. Results of sensitivity analysis

	Base case	Perturbation	CO_2 removal rate (%)	Energy consumed (MJ/kg CO_2)	Cleaned gas (%)			CO_2 Loading (mol CO_2/mol MEA)	
					CO_2	MEA	H_2O	Lean	Rich
Base case			***78.7***	***4.02***	***37.6***	***0.16***	***62.2***	***0.257***	***0.416***
Absorber height (m)	**25**	*30*	83.5	3.90	38.4	0.16	61.4	0.253	0.425
Absorber diameter (m)	**16**	*13*	72.3	4.25	35.9	0.17	63.8	0.252	0.40
Stripper height (m)	**15**	*10*	78.6	4.05	36.7	0.17	63.1	0.253	0.416
Stripper diameter (m)	**5**	*7*	78.4	3.82	40.1	0.15	59.4	0.255	0.418
Amine solution volume flow rate (m^3/s)	**0.8**	*0.6*	70.3	3.41	39.8	0.14	60.0	0.257	0.453
Heat exchanger ΔT (K)	**10**	*5*	78.4	3.92	34.8	0.18	64.9	0.255	0.415
Inlet gas temperature (absorber	**313**	*333*	77.4	4.03	37.3	0.16	62.5	0.254	0.415
Inlet liquid temperature (absorber) (K)	**318**	*333*	78.3	3.95	38.7	0.16	61.1	0.258	0.423
Condenser reflux rate (%)	**10**	*30*	78.9	4.05	43.2	0.15	56.6	0.251	0.413
Reboiler temperature	**394.2**	*394.5*	84.9	6.37	18.5	0.31	81.2	0.198	0.366
Pressure reboiler (Pa)	**20000**	*190000*	88.7	28.47	3.6	0.51	95.8	0.15	0.31
Temperature liquid exiting condenser (K)	**380**	*330*	78.7	4.02	37.6	0.16	62.2	0.253	0.416
Packing used	**Montz**	Pall	66.1	4.52	34.3	0.19	65	0.253	0.38

Some important results could be noted, as follows:
i) absorber height: increasing the absorber height from 25 to 30 m, increases the removal rate from 78.7 to 83.4%, the energy required per kg removed is decreased by 2.5% and the cleaned gas has a higher proportion of CO_2. The main disadvantage is the increased capital cost.

ii) absorber diameter: decreasing the absorber diameter from 16 to 13 m, reduces the cross sectional area from 196 to 136 m^2, increasing the vapour and liquid velocities and reducing also the fluid retention time in the tower. The net result is a drop in the removal efficiency of 6% and an increase in the energy used per kg recovered of 6%. The advantage is that the capital cost is lower.
iii) stripper height: decreasing the stripper height from 15 to 10 m drops the removal rate slightly and increases the removal cost per kg also. The reactions and mass transfer take place more quickly at the elevated temperature of the stripper and, therefore, the controlling factor in the stripper is the equilibrium constants which dictate how much aqueous CO_2 is released from the bound CO_2 in other ions.
iv) stripper diameter: increasing the stripper diameter from 5 to 7 m, increases the cross sectional area of the stripping column from 20.5 to 37 m^2, effectively halving the fluid velocities. The longer retention time results in removing a larger amount of CO_2, increasing the cleaned gas proportion and decreasing the energy requirements by 5%. This is obtained at the expense of increased capital cost.
v) reboiler temperature: increasing the reboiler temperature increase the amount of vapour that is flashed in the reboiler. A higher vapour load decreases the lean loading as more of the MEA is regenerated. This results in an increased CO_2 removal percentage and a higher energy cost. It can be noted that increasing the temperature by only 0.3 K increases the removal rate by 2.5% and the energy consumed by 12%. The outlet from the condenser also contains a larger proportion of water vapour.

Also a typical control philosophy that could be implemented is:

a) rich amine pump B controls volumetric liquid flow rate to a given set point
b) lean pump G is controlled to keep a constant level in the bottom of the stripper
c) stream 13, the inlet liquid to the absorber, is controlled to a temperature set point by heat exchanger H
d) the de-absorption condenser F is used to control the temperature of S5 back to the stripper and the captured gas composition
e) the temperature and heat load to the reboiler E sets the temperature and flow rate of stream S8 which is the stripping steam.
f) with an MPC control philosophy the system can be optimised to find the minimum energy requirements but still remove the desired amount of CO_2

4. Conclusions

A dynamic model of CO_2 removal from a post combustion process was developed within this work, based on chemical absorption in MEA solution. The model comprises an absorption tower, de-absorption tower, reboiler, condenser, heat exchangers and pumps. Allowing for chemical reactions in the film with an enhancement factor is the easiest and least computational demanding method.
The residence time of the liquids in the absorption tower has a large effect on the results as the rate of CO_2 transfer is strongly dependent of the amount of surface area available for transfer. Increasing the absorption tower diameter and height produce a higher removal rate as the volume of inside packing is increased.
The de-absorption process is controlled by the equilibrium constants which dictate how much soluble CO_2 is released from the bound CO_2. At the elevated temperature in the stripper, the reactions proceed faster, the enhancement factor is greater and the diffusion process is increased.
The heat of reaction in the absorber adds heat to the liquid and gas phase increasing the temperature. In the stripper, the reactions are reversed and require energy as are endothermic. The higher the MEA concentration, the lower the energy requirements as less energy is required to heat the bulk fluid to a temperature to reverse the chemical reactions.
It was also noted that the overall system is very nonlinear with very fast reaction rates through to much slower diffusion rates and temperature transfer making the model computationally demanding. There are many parameters and inputs which affect the results

and finding an optimal solution is a challenging task especially if one includes the balance between capital and operational cost. A significant amount of H_2O and MEA leaves the system with the exhaust gas and the purified stream. The addition of a water wash, post capture dehydration and MEA and water make up should also be included. Finally it should be noted that the model of a absorption and de-absorption process using amine solution is a complex problem with many interactions. In the developed model, many assumptions and simplifications have been made but the results are still reasonable.

References

Figueroa, J. et al., Int. J. Greenhouse Gas Control, **2** (2008), 9-20

Frequin, S., Rochelle, G.T., AICheJ, **49** (2003)

Yang, H. et al., J. Env. Sciences, **20** (2008), 14-27

Proceedings of the 10th International Chemical and
Biological Engineering Conference - CHEMPOR 2008
Braga, Portugal, September 4-6, 2008
E.C. Ferreira and M. Mota (Eds.)

Three-dimensional gas-solid fluidized bed simulation based on the kinetic theory of granular flow

Fábio Marini[1], Maria G. E. Silva[1], Milton Mori[1*]
[1]University of Campinas, School of Chemical Engineering, Department of Chemical Processes, P.O. Box 6066, 13083-970, Campinas-SP, Brazil

Keywords: Fluidized bed, CFD, Multiphase flow, Kinetic theory
Topic: CFD & Chemical Engineering.

Abstract

In this study, a three-dimensional two-phase flow model based on the kinetic theory of granular flow (KTGF) was used to predict the behavior of a gas-solid fluidized bed. The model is based on a Eulerian description of the two phases, gas and particles, and is composed of a set of mass conservation and momentum equations for each phase. In this model, the k-epsilon turbulence model and multiphase mixture are used. In order to describe the behavior of several particles in a continuum, the kinetic theory of granular flow was used.

The geometry and numerical mesh were generated using ANSYS ICEM CFD software and the set of partial differential equations was discretized and solved using CFX. Simulation data were verified against data found in Samuelsberg and Hjertager (1996), who used a cold flow laboratory circulating fluidized bed and simulated a two-dimensional model. Results using this model show that the model agrees with the experimental data and predicts a flow behavior similar to that found experimentally. It predicts the core annulus flow, which is known from the literature.

1 Introduction

Fluidized beds are widely used in many operations in chemical, metallurgical, energy generation and especially petrochemical industries. Major applications are fluid catalytic cracking (FCC) risers and CFB combustor systems. Although fuidized beds are successfully and widely used in commercial industrial operations, much remains to be done due to the complexity of the gas-solid flow. No analytical tools that describe the influences of complex geometries, chemical reaction, internal reflux and heat transfer on the flow pattern in fluidized beds are available. With the increased availability of computers, mathematical models have been applied to predict the behavior of a fluidized bed and several models have been proposed. Gidaspow *et al.* (2004) carried out an extensive review of the models developed for the fluidized bed reactors and Peirano and Leckner (1998) reviewed turbulent gas-solid flow modeling in circulating fluidized beds.

Gas-particle two-fluid models, which treated the particle phase as a continuous fluid based on the Eulerian method, were widely employed in modeling gas-solid flow in the past several decades. A fundamental problem encountered in modeling the hydrodynamics of a gas-solid fluidized bed by the two-fluid method is how to include the stress of the particle phase in the particulate momentum equation. In the more recent two-fluid models, for the particle phase in dense gas-particle flow, the kinetic theory of granular flow has received attention and its use in Eulerian simulations has increased (Jenkins and Savage, 1983; Ding and Gidaspow, 1990; Gidaspow, 1994; Hrenya and Sinclair, 1997; Samuelsberg and Hjertager, 1996). The kinetic theory of granular flow is based on the kinetic theory of gases, first developed by

* Corresponding author. Phone + 55-19-3521-3963. E-mail:mori@feq.unicamp.br

Chapman and Cowling (1970). In this theory, the inter particle interactions are taken into account by adding the contribution of collisions between particles (Jenkins and Savage, 1983), which are the main mechanism of transport due to particulate phase properties.

The present study aims to simulate a three-dimensional two-phase flow model, based on the kinetic theory of granular flow (KTGF), to predict the behavior of a gas-solid fluidized bed, using a computational fluid dynamics technique.

2 Mathematical model

Based on Eulerian description of the phases, a multiphase computational fluid dynamics model for turbulent gas-solid flow is presented. The Eulerian approach considers the two phases, gas and solid, as a continuum. The conservation equations for the solid phase are based on the kinetic theory for granular flow (Gidaspow, 1994).

The governing equations for transient three-dimensional gas-solid flow are presented as follows:

The continuity equation for phase i (= g,s):

$$\frac{\partial}{\partial t}\left(\varepsilon_i \rho_i\right) + \nabla \cdot \left(\varepsilon_i \rho_i \vec{\upsilon}_i\right) = S_i^{\rho} \tag{1}$$

where the subscript i can denote gas or solid phase, ε is the volume fraction, ρ is the density, t is the time, $\vec{\upsilon}$ is the velocity vector and S^{ρ} is the source term for mass transfer between the phases. Hence, no mass transfer is allowed between the phases.

The gas phase momentum equation:

$$\frac{\partial}{\partial t}\left(\varepsilon_g \rho_g \vec{\upsilon}_g\right) + \nabla \cdot \left(\varepsilon_g \rho_g \vec{\upsilon}_g \vec{\upsilon}_g\right) = -\varepsilon_g \nabla p_g + \nabla \vec{\tau}_g + \varepsilon_g \rho_g \vec{g} + \beta_{gs}^{m}\left(\vec{\upsilon}_s - \vec{\upsilon}_g\right) \tag{2}$$

where $\vec{g}$ is the gravity vector, p is the pressure and β_{gs}^{m} is the two-phase drag coefficient.

The stress tensor of the gas phase can be written as

$$\vec{\tau}_g = \varepsilon_g \mu_g \left(\left(\nabla \vec{\upsilon}_g + \left(\nabla \vec{\upsilon}_g\right)^T\right) - \frac{2}{3}\left(\nabla \cdot \vec{\upsilon}_g\right)\vec{I} \right) \tag{3}$$

Here, μ is the shear viscosity.

The gas phase turbulence is modeled with the k-epsilon model.

The solid phase momentum equation:

$$\frac{\partial}{\partial t}\left(\varepsilon_s \rho_s \vec{\upsilon}_s\right) + \nabla \cdot \left(\varepsilon_s \rho_s \vec{\upsilon}_s \vec{\upsilon}_s\right) = \nabla \vec{T}_s + \varepsilon_s \rho_s \vec{g} + \beta_{gs}^{m}\left(\vec{\upsilon}_g - \vec{\upsilon}_s\right) \tag{4}$$

where the solid stress tensor, $\vec{T}_s$, is the sum of a collisional part and a kinetic part and may be formulated as

$$\vec{T}_s = \left(-p_s + \lambda_s \nabla \cdot \vec{\upsilon}_s\right)\vec{I} + \mu_s \left(\left(\nabla \vec{\upsilon}_s + \left(\nabla \vec{\upsilon}_s\right)^T\right) - \frac{2}{3}\left(\nabla \cdot \vec{\upsilon}_s\right)\vec{I} \right) \tag{5}$$

where λ_s is the solid phase bulk viscosity.

The total solid phase pressure, p_s, consists of two terms; one of them, p_s^{k+t}, is determined from Lun *et al.* (1984) and includes both kinetic and collisional pressures, as follows:

$$p_s^{k+t} = \rho_s \varepsilon_s \left[1 + 2(1+e)\varepsilon_s g_o\right]\theta \tag{6}$$

where e is the coefficient of restitution and g_o is the radial distribution function.

The other term, p_s^f, is caused by friction and collisions in the solid phase due to highly dense flow, as proposed by Johnson and Jackson (1987), as follows:

$$P_s^f = Fr\frac{\left(\varepsilon_s - \varepsilon_{s,min}\right)^n}{\left(\varepsilon_{s,max} - \varepsilon_s\right)^p} \tag{7}$$

where the values of the constants in Equation (7) are Fr = 0.05, n = 2, p = 3 and $\varepsilon_{s,min}$ = 0.55, as suggested by Van Wachen (1998).

The total solid phase pressure is then given by

$$P_p = P_p^{k+t} + P_p^f \tag{8}$$

The radial distribution function, adopted by Lun and Savage (1986), is

$$g_o = \left(1 - \frac{\varepsilon_s}{\varepsilon_{s,max}}\right)^{-2.5\varepsilon_{s,max}} \tag{9}$$

where $\varepsilon_{s,max}$, the maximum particle packing chosen is 0.62.

Equation (9) is appropriate for dilute flow.

In Equation (6), θ is the granular temperature related to the kinetic turbulent energy of the particle motion. Ding and Gidaspow (1990) proposed the following equation for granular temperature:

$$\theta = \frac{1}{15(1-e)} d_p^2 \left(\frac{1}{2}\left(\nabla \vec{v}_s + \left(\nabla \vec{v}_s\right)^T\right)\right) \tag{10}$$

where d_p is the particle diameter.

Solid phase bulk viscosity, λ_s, due to particle collisions (Lun *et al.*, 1984) and solid phase shear viscosity, μ_s, for dense and dilute flow (Hrenya and Sinclair, 1997) are given by the following equations:

$$\lambda_s = \frac{4}{3}\varepsilon_s^2 \rho_s d_s g_o (1+e)\sqrt{\frac{\theta}{\pi}} \tag{11}$$

$$\mu_s = \frac{5\sqrt{\pi\theta}}{96}\rho_s d_s \left[\left(\frac{1}{1+\frac{\lambda_{mfs}}{R}}\frac{1}{\eta g_o} + \frac{8\varepsilon_s}{5}\right)\left(\frac{1+\frac{8}{5}\eta(3\eta-2)\varepsilon_s g_o}{2-\eta}\right) + \frac{768}{25\pi}\eta\varepsilon_s^2 g_o\right] \tag{12}$$

where λ_{mfs} and η are given by

$$\lambda_{mfs} = \frac{d_p}{6\sqrt{2}\varepsilon_s} \tag{13}$$

$$\eta = \frac{1}{2(1+e)} \tag{14}$$

The gas-solid drag coefficient for $\varepsilon_g \le 0.8$ is based on the Ergun equation and is given by

$$\beta_{gs}^m = 150\frac{\varepsilon_s^2 \mu_g}{\varepsilon_g d_p^2} + 1.75\frac{\left|\vec{v}_s - \vec{v}_g\right|\varepsilon_s \rho_g}{d_p} \tag{15}$$

And for $\varepsilon_g > 0.8$, based on the Wen and Yu equation:

$$\beta_{gs}^{m} = \frac{3}{4} C_D \frac{\left|\vec{\upsilon}_s - \vec{\upsilon}_g\right| \varepsilon_s \rho_g}{d_p} f\left(\varepsilon_g\right) \tag{16}$$

where $f\left(\varepsilon_g\right) = \varepsilon_g^{-2.65}$, as used by Gidaspow and Ettehadieh (1983).

The drag coefficient, C_D, is related to the Reynolds number as follows:

$$C_D = \varepsilon_g^{-2.65} \max\left[\frac{24}{Re_p\, \varepsilon_g}\left(1 + 0.15\left(Re_p\, \varepsilon_g\right)^{0.687}\right)\right] \text{ for } Re_p < 1000 \tag{17}$$

$$C_D = 0.44 \text{ for } Re_p \geq 1000 \tag{18}$$

$$Re_p = \frac{\left|\vec{\upsilon}_s - \vec{\upsilon}_g\right| \rho_g d_p}{\mu_g} \tag{19}$$

3. Results and discussion

In order to validate the present numerical results, we compared them with the experimental results of Samuelsberg and Hjertager (1996). Then the simulations were carried out for the riser section of a circulating fluidized bed similar to that used by Samuelsberg and Hjertager (1996) and Mathiesen *et al.* (2000), shown in Figure 1 (a). In this study, just the riser section was simulated. The riser section is 1m high with an inner diameter of d = 0.032m. A secondary air supplier, positioned 0.05m above the gas inlet, feeds the solid back into the riser. The secondary gas inlet and the gas outlet have a diameter of 0.008m (Figure 1 (b)).The initial bed height is 0.05m and the initial solid volume fraction is 0.61. The system properties are defined in Table 1.

The riser section, as shown in Figure 1 (b), is modeled and simulated in a three-dimensional Cartesian coordinate system. Numerical predictions were obtained using the finite volume approach through the CFX-10 code, a CFD software developed by ANSYS, and the ICEM CFD code to generate the numerical grid, shown in Figure 1 (b). Numerical tests were conducted in order to optimize the computational grid. A grid of 300,000 control volumes was considered satisfactory considering the precision of the results (10^{-4}) and the computation time consumed. The time step used in all simulations was 10^{-3}s. The boundary conditions are summarized in Table 2.

At the primary gas inlet, the superficial gas velocity, V_{sup}, was 0.71m/s. At the secondary gas inlet, the gas velocity and volume fraction were 0.05m/s and 0.6, respectively, and the particle volume fraction was 0.4. In order to permit all particles at the outlet back into the riser at the secondary gas inlet, a subroutine was implemented in the CFX code. At the outlet, atmospheric pressure was prescribed. At the walls, no-slip conditions were used for the solid phase as well as the gas phase.

The simulation results were computed through time-averaged distribution of flow variables. All the simulations were run for 7s of real time. To compute the granular temperature, solid-phase pressure and solid-phase bulk and shear viscosity must be programmed into the CFD codes due to the fact that the models used in this study were not presents in the CFX-10.

Figure 2 shows a comparison of the experimental results of Samuelsberg and Hjertager (1996) and the present numerical results to the solid radial velocity profiles for heights of 0.16, 0.32 and 0.48m in the riser section and superficial gas velocity, V_{sup}, of 0.71m/s at the primary gas inlet. Other simulations were performed to superficial gas velocities of 0.36 and 1.42m/s. All results presented the same trends.

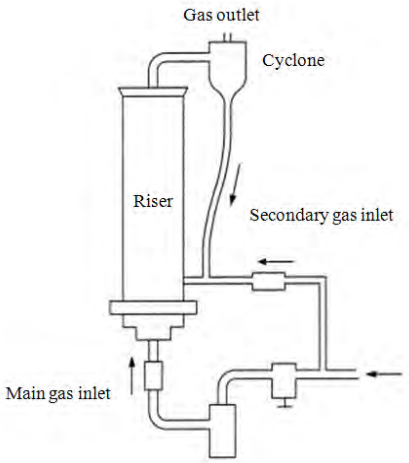

(a)

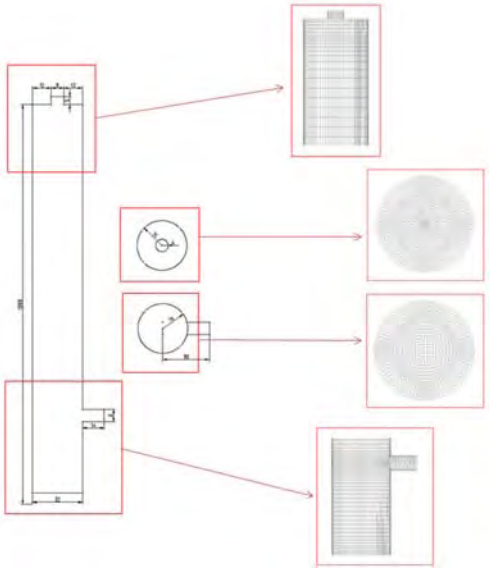

(b)

Figure 1 – (a) Geometry of Mathiesen *et al.* (2000). (b) Calculation domain and grid nodes

Table 1 – System properties

Gas density	1.185kg/m^3
Particle density	1600kg/m^3
Particle size	60μm
Gas viscosity	1.831x10^{-5}kg/m s
Maximum solids volume fraction	0.62
Particle-particle restitution coefficient	0.95

As can been seen in Figure 2 (b) and (c), the agreement is very good in the central region for all heights. The particles move upward in the central part of the riser and downward near the walls, a behavior well known from the literature, which is typical of core-annulus flow. However, in Figure 2 (a), for the height of 0.16m, the agreement between the curves differs significantly. These differences can probably be attributed to the region, at the height of 0.16m, being so close to the secondary inlet, causing large perturbations in the flow. In Figure 2, a significant difference can be observed in the wall region for all results compared. This result may indicate that the no-slip wall boundary condition for both phases is not correctly used when employing KTGF.

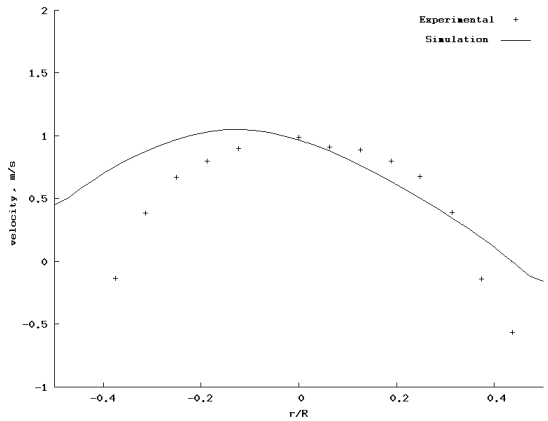

(a) Height of 0.16m

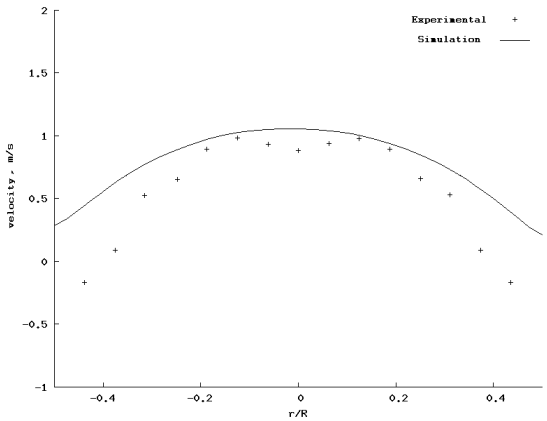

(b) Height of 0.32m

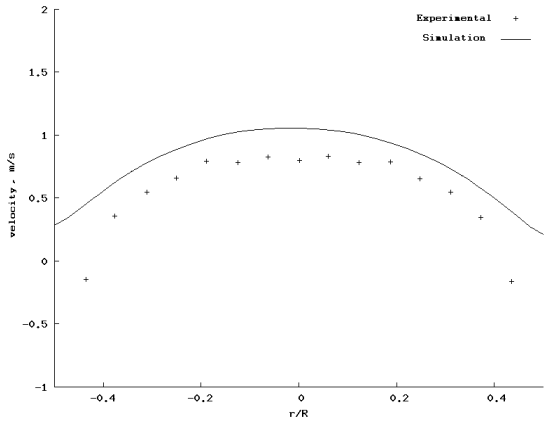

(c) Height of 0.48m

Figure 2 – A comparison of the experimental data of Samuelsberg and Hjertager (1996) and computed solid velocity profiles at different heights in the riser section and superficial gas velocity, V_{sup}, of 0.71m/s.

4. Conclusions

A three-dimensional two-phase flow model based on the kinetic theory of granular flow (KTGF) was used to predict the behavior of a gas-solid fluidized bed. The numerical results are compared against the experimental results of Samuelsberg and Hjertager (1996). The agreement is found to be satisfactory in the riser central region. However, in the wall region, the numerical results indicated a significant difference between all results compared.

References

Chapman, S., Cowling, T.G. (1970). *The Mathematical Theory of Non-Uniform Gases*, Cambridge University Press, London.

Ding, J., Gidaspow, D. (1990). A bubbling fluidization model using kinetic theory of granular flow. *AICHE J.*, 36, 523-538.

Gidaspow, D. (1994). *Multiphase Flow and Fluidization*, Academic Press, London.

Gidaspow, D., Ettehadieh, B. (1983). Fluidization in two-dimensional beds with a jet. 2. hydrodynamic modeling. *Industrial and Engineering Chemistry Fundamentals*, 22, 193-201.

Gidaspow, D., Jung, J., Singh, R.K. (2004). Hydrodynamics of fluidization using kinetic theory: an emergin paradigm 2002 flour-daniel lecture. *Powder Technology*, 148, 123-141.

Hrenya, C.M., Sinclair, J.L. (1997). Effects of particle-phase turbulence in gas-solids flows. *AIChE Journal*, 43, 853-869.

Jenkins, J.T., Savage, S.B. (1983). A Theory for the rapid flow of identical, smooth, nearly elastic, spherical particles. *AIChE Journal*, 42, 1536-1546.

Johnson, P.C., Jackson, R. (1987). Frictional-collisional constitutive relations for granular materials, with application to plane shearing. *Journal of Fluid Mechanics*, 176, 67-93.

Lun, C.K.K., Savage, S.B. (1986). The effects of an impact velocity dependent coefficient of restitution on stresses developed by sheared granular materials. *Acta Mechanica*, 63, 15-44.

Lun, C.K.K., Savage, S.B., Jeffrey, D.J., Chepurniy, N. (1984). Kinetic theories for granular flow: inelastic particles in couette flow and slightly inelastic particles in a general flowfield. *Journal of Fluid Mechanics*, 140, 223-256.

Mathiesen, V., Solberg, T., Hjertager, B.H. (2000). An experimental and computational study of multiphase flow behavior in a circulating fluidized bed. *International Journal of Multiphase Flow*, 26, 387-419.

Peirano, E., Leckner, B. (1998). Fundamentals of turbulent gas-solid flows applied to circulating fluidized bed combustion. *Progress Energy Combustion Science*, 24, 259-296.

Samuelsberg, A., Hjertager, B.H. (1996) Computational modeling of gas/particle flow in a riser. *AIChE Journal*, 42, 1536-1546.

VanWachen, B.G.M. (1998). *Derivation, Implementation and Validation of Computer Simulation Models for Gas-Solid Fluidized Beds*, PhD Thesis - Delft University.

Proceedings of the 10th International Chemical and
Biological Engineering Conference - CHEMPOR 2008
Braga, Portugal, September 4-6, 2008
E.C. Ferreira and M. Mota (Eds.)

Writing a software package for simulation of the three-dimensional structure of paper

Eduardo L.T. Conceição*, António A.T.G. Portugal
CEM Group, Department of Chemical Engineering, University of Coimbra
Rua Sílvio Lima – Pólo II, 3030-790 COIMBRA, Portugal.

Keywords: Modeling of the three-dimensional structure of paper, Cellular automata, Implementation.
Topic: Systematic methods and tools for managing the complexity.

Abstract

Almost everyone agrees that numerical models for simulating the microstructure of paper can bring tangible benefits to experiments. Nonetheless, after more than 20 years very few standard software packages at an affordable price were provided. This article explains the software implementation on key features of a three-dimensional random fiber deposition model. The approach was implemented as a prototype for a forthcoming MATLAB toolbox.

1 Introduction

Although theoretical paper models have existed in the literature for over two decades, most experimental research work encountered in the field of pulp and paper is mainly of empirical nature. One of the primary reasons that have hindered the generalized use of modeling in this area is the lack of easy understood models and available computational implementations.

Paper has a network structure of cellulosic fibers that lie roughly horizontal. It turns out that even for a thin material as paper it appears necessary to develop a three-dimensional (3D) structure model to be able to predict various properties consistent with experimental data (Alava and Niskanen, 2006). Simulation models which can grow networks of finite thickness are traced to the work of Niskanen and Alava (1994), who featured a 3D stacking of bendable fibers resembling real paper.

In this context, we aim to render the barrier to the use of modeling less binding by describing key building blocks of a MATLAB implementation for the KCL-PAKKA model (Nilsen et al., 1998). This is a simple 3D random sedimentation model to generate disordered fiber networks. We assume the reader has some familiarity with the MATLAB language.

In the next section we briefly review the basics for the sedimentation-like process. Besides the standard KCL-PAKKA we also discuss an extension of this model to incorporate a formation control parameter. Section 3 is the core of the paper. We present the prominent design features and discuss its MATLAB-specific implementation.

*Corresponding author. Tel.: (+351) 239 798 748. E-mail: etc@eq.uc.pt.

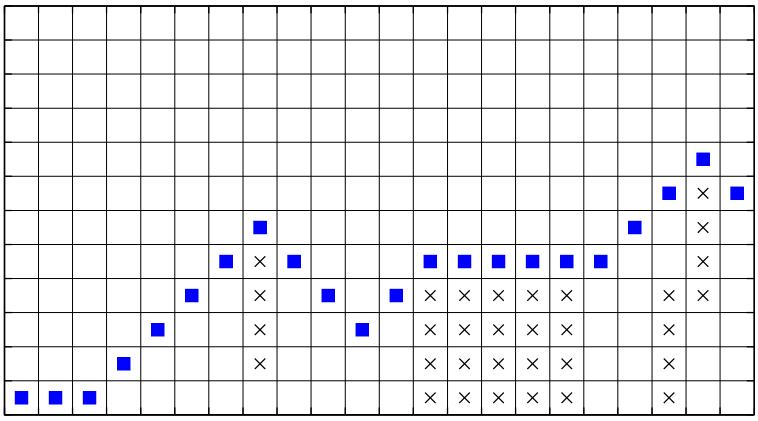

Figure 1: Bending mechanism of fiber generated by computational simulation. The crosses represent parts of previously deposited fibers and the squares denoting the bottom layer of the bending fiber. Bending flexibility $F = 1$.

2 Brief description of the handsheet formation model

To form a paper web, *flexible* straight fibers are laid down, one at a time, onto a flat substrate. Fibers are positioned and oriented at random in the in-plane (x and y) directions and placed parallel to the substrate on top of the underlying network. Thereafter the parts of the fiber that do not touch the network beneath them undergo bending in the vertical direction (or z direction) such that they either do contact with previous adjacent fibers or the largest deflection allowed by the bending stiffness of fibers is reached. In the latter case, free spaces arise between the fibers in the thickness direction because their stiffness prevents them from adjusting to the top surface roughness.

Flexing rule. Space is discretized into a Cartesian *uniform* grid of cells so that each fiber in the model is represented by a single vertical planar strip one cell wide and thickness of m vertical cells. Any two nearest neighboring cells on the fiber can make at most the maximum F vertical lattice steps allowed. We remark that this result depends only on the behavior of the bottom surface layer. It may be written as:

$$|z_{\mathrm{B}}(j) - z_{\mathrm{B}}(j')| \leq F,$$

where $z_{\mathrm{B}}(j)$ and $z_{\mathrm{B}}(j')$ are the elevations of two nearest neighbor cells j and j' covered by the surface bottom of a fiber and F can be any positive integer $\leq m$. Figure 1 shows what the deformed fibers look like in 2D.

Fiber interactions. The tendency of fibers in the suspension to concentrate around drainage sinks (those parts of the deposit that have less fibers per unit area) leads to a smoothing mechanism of a paper sheet. This effect is simulated by the particle deposition rule of Provatas and Uesaka (2003) which works over the *rejection model* introduced by Provatas et al. (2000). The operation works as follows: A candidate fiber lands on a section of the web whose mean height is compared with a fraction of its counterpart of the entire paper. If the following condition is fulfilled, the attempt is always accepted:

$$h \leq \alpha H,$$

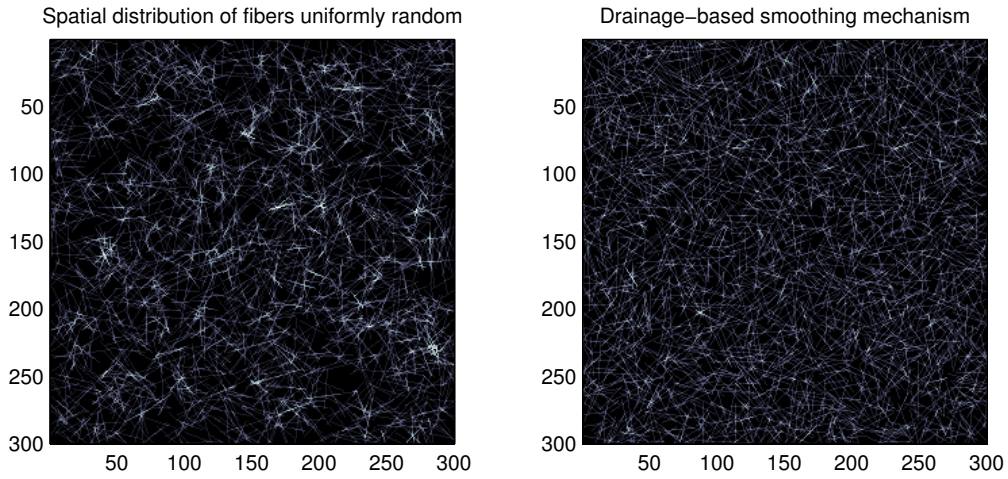

Figure 2: Simulated X-ray image of the (x,y) plane for paper handsheet as generated from the deposition rule, with formation control parameters set to $p = 1$, $\alpha = 1$ (left) and $p = 0.01$, $\alpha = 0.94$ (right).

where h is the average thickness of the paper over the projected area of the trial fiber, $0 \leq \alpha \leq 1$ is a constant, and H is the average thickness of the entire paper. Otherwise, the attempt is accepted only with a probability $0 \leq p \leq 1$, called the *acceptance probability*.

In the limit $p = 1$ produces uniformly random networks for all values of α. However, for $p \to 0$ the model tend to enhance mass density uniformity by favoring deposition into valleys within the web. Two configurations of fibers are shown in Figure 2.

3 Some implementation aspects

This section outlines the most essential implementation aspects. We list the relevant code and present a brief walkthrough. We restrict ourselves to only one type of fiber for the sake of simplicity and emphasize that the code is purely illustrative.

To summarize, our generation process of a 3D fiber network consists of the following steps:

1. Generation of a fiber in the in-plane directions.
2. Testing particle deposition rule. If the fiber is not accepted, the generation trial is repeated.
3. Extraction of the out-of-plane slice from the 3D network where the bending procedure occurs.
4. Fiber bending simulation for the bottom surface.
5. Filling up the remaining $m-1$ cell layers and then the 3D network is updated.

Generation of a fiber. Each straight fiber is built by randomly placing the center within the boundaries of a flat surface represented by the rectangle $[0,L_x] \times [0,L_y]$ such that both position and orientation are uniformly distributed. This corresponds to the case of laboratory handsheets. Fibers length is characterized by a Poisson distribution following Provatas and Uesaka (2003). After this the fiber is discretized to a chain of square cells of size w onto a discrete lattice $[1,N_x] \times [1,N_y]$. They are defined by the *Bresenham's line drawing algorithm* (Agoston, 2005, pp. 38–40). Fiber length in lattice units is a multiple of w. Parts of fibers that exceeds the lattice limits are cut. In MATLAB this can be done with

```
XMIN = 1; YMIN = 1; XMAX = Nx; YMAX = Ny;
midpoint = unifrnd([0 0], [Lx Ly], 1, 2);
orientation = unifrnd(-1, 1, 1, 2);
orientation = orientation / norm(orientation);
half_fiber_length = poissrnd(mean_fiber_length) / 2;
startPt = midpoint - half_fiber_length*orientation; % Start point of segment.
endPt = midpoint + half_fiber_length*orientation;   % End point of segment.
% Transforming from continuous to discrete coordinates.
startPt = floor(startPt.*[(Nx-1)/Lx (Ny-1)/Ly] + 1);
endPt = floor(endPt.*[(Nx-1)/Lx (Ny-1)/Ly] + 1);
% Draw the discrete fiber segment using Bresenham algorithm.
[fiber_xcoord, fiber_ycoord] = bresline(startPt, endPt);
% Restrict the fiber segment to the rectangle [1,Nx] x [1,Ny].
clip = fiber_xcoord < XMIN | fiber_xcoord > XMAX | ...
       fiber_ycoord < YMIN | fiber_ycoord > YMAX;
fiber_xcoord(clip) = [];
fiber_ycoord(clip) = [];
```

Extracting an out-of-plane slice from the 3D network. The region under consideration is divided into $N_x \times N_y \times N_z$ cells in the form of a square parallelepiped. The array web of dimension N_z-by-N_x-by-N_y is used to store the 3D grid of discrete locations. Once the (x,y) coordinates of the fiber have been obtained our task is to extract the two-dimensional vertical slice in the volume web at the points in the column vectors fib_xcoord and fib_ycoord. The sedimenting fiber bends around structures along this planar surface. The following is one possible way to do this:

```
z_extent = firstVPos:lastVPos;
height = length(z_extent);
width = length(fib_xcoord);
X = repmat(fiber_xcoord, height, 1);
Y = repmat(fiber_ycoord, height, 1);
Z = repmat(z_extent', 1, width);
web_idx = sub2ind([Nz Nx Ny], Z, X, Y);
bending_slice = web(web_idx);
```

This will generate the (i,j,k) subscripts of web comprising the particular slice. We then use the function sub2ind to convert to one-dimensional subscripting and this can be used to index into web.

Fiber bending simulated using a cellular automata framework. The spatial discretization allow us to exploit the potential of *cellular automata* (see the book by Schiff, 2008). A cellular automaton is a spatial discrete time model. Each cell can exist in different states chosen from a finite set. At each time step each cell changes its state based on a set of rules or *transition functions* that represent the allowable physics of the phenomena.

The discrete space for the automaton maps onto the bending plane and is represented in the matrix bending_slice. For each cell, (i,j), at time t there are three states which represent the presence or absence of fiber particles, namely:

Moving Deforming particle covers cell.

Idle Stopped particle covers cell.

Empty The cell is unoccupied.

As time goes on, the new state of each cell $s_{t+1}(i,j)$ is then updated according to the following rules:

$$\begin{aligned} s_{t+1}(i,j) = \text{idleCell} \leftarrow s_t(i,j) = \text{movingCell} \wedge (s_t(i-F, j-1) = \text{idleCell} \vee \\ s_t(i+1,j) \neq \text{emptyCell} \vee \\ s_t(i-F, j+1) = \text{idleCell}) \end{aligned}$$

$$\left.\begin{aligned} s_{t+1}(i,j) = \text{emptyCell} \\ s_{t+1}(i+1,j) = \text{movingCell} \end{aligned}\right\} \leftarrow s_t(i,j) = \text{movingCell} \wedge \neg (s_t(i-F, j-1) = \text{idleCell} \vee$$
$$s_t(i+1,j) \neq \text{emptyCell} \vee$$
$$s_t(i-F, j+1) = \text{idleCell})$$

$$s_{t+1}(i,j) = \text{idleCell} \leftarrow s_t(i,j) = \text{idleCell}$$
$$s_{t+1}(i,j) = \text{emptyCell} \leftarrow s_t(i,j) = \text{emptyCell} \wedge (s_t(i-1,j) = \text{emptyCell} \vee s_t(i-1,j) = \text{idleCell})$$

where i and j are the row and column indices and the negation of a given statement P is denoted by $\neg P$. Via the preceding rules, particles can move only in the downward (increasing time) direction at most one cell at each time step t, so that the cell states are updated *asynchronously* by a line-by-line sweep of each row sequentially. An example of code that would implement this behavior might look like this:

```
bending_slice = ...
    [repmat(EMPTY,height,1) bending_slice repmat(EMPTY,height,1)];
stop = false(1, width+2);
run = [false true(1, width) false];
j = 2:width+1;
for i = startInd:height-1
    stop(j) = bending_slice(i-F, j-1) == IDLE | ...
                bending_slice(i+1, j) ~= EMPTY | ...
              bending_slice(i-F, j+1) == IDLE;
    bending_slice(i, run & stop) = IDLE;
    run = run & ~stop;
    if all(~run), break, end % Fiber bending stops.
    bending_slice(i, run) = EMPTY
    bending_slice(i+1, run) = MOVING;
end
bending_slice( end, bending_slice(end, :) == MOVING ) = IDLE;
bending_slice(:, [1 end]) = [];
```

In the first part of the code the lattice is augmented by a column vector of fictitious cells having the pre-assigned value EMPTY at the extreme left and right sides, so that the corresponding neighborhood is completed. The loop, **for** i = startInd:height−1, drives the line-by-line sweep. We use logical vector run & stop to pick out those js at which particles moving terminate given the i current value. We then compute the vector run & ~stop whose true elements specify the moving particles left. On leaving the **for** loop we restore the lattice of cells to the original dimensions in the assignment bending_slice (:, [1 **end**]) = [];.

Copying the plane back into the 3D network. Finally, having defined the vertical coordinates z_j describing the location of the bottom surface, it is time to filling up the remaining $m-1$ cell layers stacked one on top of the other through each point of the fiber. All we need now is to carry out the updating of the 3D network. This can be done by

```
zPos = find(bending_slice == IDLE);
bottom_idx = sub2ind([height width], zPos, 1:width);
stack_idx = bsxfun(@minus, bottom_idx, 0:m-1);
bending_slice(stack_idx) = fiberID;
web(web_idx) = bending_slice;
```

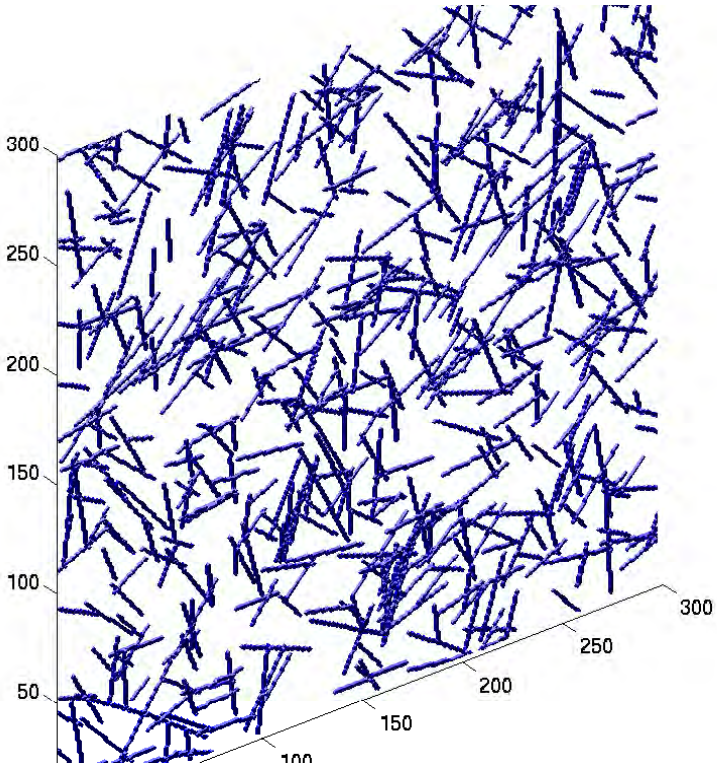

Figure 3: Simulated 3D fiber network.

Figure 3 shows an example of a 3D fiber network constructed with the prototype implementation.

4 Conclusion

There are huge gains to be had by simulating paper webs. This article is intended to serve as an illustration of the cellular automata framework to your coding work. We choose to use cellular automata since through the use of interactive components parts the high-level bending behavior *emerges* as a result of rules fairly straightforward to implement.

References

Agoston, M. K. (2005). *Computer Graphics and Geometric Modeling: Implementation and Algorithms*, Springer-Verlag, London.

Alava, M., Niskanen, K. (2006). The physics of paper, *Reports on Progress in Physics*, 69(3), 669–723.

Nilsen, N., Zabihian, M., Niskanen, K. (1998). KCL-PAKKA: a tool for simulating paper properties, *TAPPI Journal*, 81(5), 163–166.

Niskanen, K. J., Alava, M. J. (1994). Planar random networks with flexible fibers, *Physical Review Letters*, 73(25), 3475–3478.

Provatas, N., Haataja, M., Asikainen, J., Majaniemi, J., Alava, M., Ala-Nissila, T. (2000). Fiber deposition models in two and three spatial dimensions, *Colloids and Surfaces A: Physicochemical and Engineering Aspects*, 165, 209–229.

Provatas, N., Uesaka, T. (2003). Modelling paper structure and paper–press interactions, *Journal of Pulp and Paper Science*, 29(10), 332–340.

Schiff, J. L. (2008). *Cellular Automata: A Discrete View of the World*, Wiley, New Jersey.

Proceedings of the 10th International Chemical and
Biological Engineering Conference - CHEMPOR 2008
Braga, Portugal, September 4-6, 2008
E.C. Ferreira and M. Mota (Eds.)

3D simulation of multiphase flow in large-scale venturi scrubbers

Ângela M. Silva[1*], Senhorinha F.C.F. Teixeira[1], José C.F. Teixeira[2]
[1] Department of Production and Systems, School of Engineering, University of Minho, Campus de Azurém, 4800–058 Guimarães, Portugal.
[2] Department of Mechanical Engineering, School of Engineering, University of Minho, Campus de Azurém, 4800–058 Guimarães, Portugal.

Keywords: Venturi, Multiphase flow, CFD
Topic: Advancing the chemical and biological engineering fundamentals.

Abstract

Venturi scrubbers are efficient and effective devices for gas cleaning. In addition, they may be used for cooling and humidification processes, which are major requirements in some industries.

Using computational fluid dynamics techniques, the multiphase flow behaviour of a venturi scrubber has been modelled. The simulations were carried out using Fluent, which is based in the finite volume method. The gas flow is simulated using the Eulerian approach solving the Navier-Stokes equations and a Lagrangian procedure has been taken describing the motion of the liquid droplets.

The results obtained have been validated with experimental work in a large scale venturi scrubber. Different air and liquid flow rates were tested. Very good agreement has been obtained, making this approach very useful in testing new geometries.

1 Introduction

Venturi scrubbers are very attractive devices for gas cleaning in industrial environments and are applicable from small scale textile plants up to large scale power plants. They combine a simple and robust construction with high efficiency for small, micron size, particles. Furthermore, they can be used for other purposes such as gas absorption and cooling.

They have been extensively studied in order to foster their understanding and modelling. The flow of gas and water in a venturi scrubber can be described as annular two-phase flow with further complexities due to the venturi geometry. Different models have been proposed in the literature and they range from simple correlations to more complex models (Azzopardi et al., 1991; Cruz et al., 1997; Ananthanarayanan and Viswanathan, 1999, Pak and Chang, 2006).

Pressure drop is a major parameter in assessing the performance of venturi scrubbers as the energy costs associated with gas pumping are the main drawback of these systems. It has been observed that an improvement in the efficiency of the equipment is always related to this parameter (Gamisans et al., 2002).

In this study, a computational fluid dynamics (CFD) model for the flow in a large-scale venturi scrubber has been developed using the Fluent software. This is based upon the finite volume method to solve the conservation equations. The effect of the turbulence models on pressure drop and axial velocity is analyzed. Predictions concerning the local and overall pressure drop are compared with data from an experimental facility for a wide range of operating conditions. An Eulerian-Lagrangian approach has been taken in simulating the two-phase flow.

* Corresponding author. Tel + 351-253-510344. E-mail:asilva@dps.uminho.pt

2 CFD Model

Because of the geometry the two-phase flow inside the venturi is a very complex one. The gas entering the venturi accelerates in the convergent section. It reaches the higher pressure drop at the end of the throat and the pressure recovery in the diffuser must take into account the gas boundary layer growth.

The water is injected upstream of the convergence section by a set of a set of radial spray nozzles equally distributed around the venturi perimeter. The liquid jet penetrates into the gas core and is atomized into drops of varying size by the high velocity air stream.

In the present model, the gas is treated as a viscous incompressible, Newtonian fluid and the flow is considered turbulent. The loading ratio of the liquid droplets is very low and so, the discrete-phase model of Fluent is used to study the droplet transport.

An Eulerian (continuous-phase)-Lagrangian (discrete-phase) approach is employed in the present model. The droplet trajectories are calculated using a Lagrangian formulation that includes the discrete phase inertia and hydrodynamic drag.

As both phases are at ambient conditions, there is no heat or mass transfer between the discrete and the continuous phases and the droplets are defined in the model as inert. The dispersion of droplets due to turbulence in the gas phase is predicted by using stochastic particle tracking. Fluent predicts the turbulent dispersion of particles by integrating the trajectory equations for individual particles, using the instantaneous fluid velocity along the particle path during integration.

2.1 Mathematical Model

The governing equations for the continuous phase are the continuity, the momentum and the turbulence equations. The mass conservation equation, often called the equation of continuity, is:

$$\frac{\partial u_i}{\partial x_j} = 0 \tag{1}$$

For the resolution of the velocity field, the Navier-Stokes equations are solved. These equations describe the momentum conservation:

$$\rho u_j \frac{\partial u_i}{\partial x_j} = -\frac{\partial p}{\partial x_i} + \frac{\partial}{\partial x_j}\left[\mu\left(\frac{\partial u_i}{\partial x_j} + \frac{\partial u_j}{\partial x_i} - \frac{2}{3}\delta_{ij}\frac{\partial u_l}{\partial x_l}\right)\right] + \frac{\partial}{\partial x_j}\left(-\rho\overline{u_i' u_j'}\right) + S_D \tag{2}$$

where u_i is the air phase velocity components, p is the static pressure, ρ is the air density, μ is the air viscosity, $-\rho\overline{u_i' u_j'}$ is called the turbulent stresses and the last term represents the source terms due to the presence of particles/droplets.

Due to the importance and complexity of the turbulence flow, an appropriate turbulence model must be chosen. The turbulence kinetic energy, k, and its rate of dissipation, ε, are obtained from the following transport equations, based on the Renormalization Group (RNG) k-ε model:

$$\rho\frac{\partial}{\partial x_i}(k u_i) = \frac{\partial}{\partial x_j}\left[\alpha_k \mu_{eff}\frac{\partial k}{\partial x_j}\right] + G_k - \rho\varepsilon \tag{3}$$

$$\rho\frac{\partial}{\partial x_i}(\varepsilon u_i) = \frac{\partial}{\partial x_j}\left[\alpha_\varepsilon \mu_{eff}\frac{\partial \varepsilon}{\partial x_j}\right] + G_{1\varepsilon}\frac{\varepsilon}{k}G_k - C_{2\varepsilon}.\rho.\frac{\varepsilon^2}{k} - R_\varepsilon \tag{4}$$

In Fluent, the trajectories of a discrete phase particle (droplet) are predicted by integrating the force balance on the particle which is written in a Lagrangian reference frame, for the x-direction in Cartesian coordinates, as:

$$\frac{du_D}{dt} = F_D(u - u_D) + g_x \frac{\rho_D - \rho}{\rho_D} + F_x \tag{5}$$

where u_D is the particle (droplet) velocity and ρ_D is the droplet density. The first term in the right side of equation (5) accounts for the drag force and F_D is the drag force, given by:

$$F_D = \frac{18\mu}{\rho_D d_D^2} \frac{C_D \,\mathrm{Re}}{24} \tag{6}$$

where μ is the molecular viscosity of the fluid and d_D is the droplet diameter.

The second term in the right side of equation (5) accounts for the gravity effects and F_x includes additional forces such as thermophoretic force, Brownian force, Saffman's lift force which can be important only in certain circumstances. However, provided that the particles meet the condition that $\rho_D \geq \rho$, these two terms can be neglected.

2.2 Boundary conditions

The air velocity is used as the inlet condition, and an outflow condition is considered at the venturi outlet. Outflow boundary conditions are used to model flow exits where the details of the flow velocity and pressure are not known prior to the solution of the flow problem. They are appropriate where the exit flow is close to a fully developed condition, as the outflow boundary condition assumes a zero normal gradient for all flow variables except pressure.

The turbulence model requires parameters that estimate *k* and ε at the inlet and outlet. The turbulence intensity and the hydraulic diameter approach are used to specify *k* and ε at inlet and outlet of the venturi. The diameter of venturi is used as the hydraulic diameter and the turbulence intensity is predicted using the relation for fully developed flow (Fluent user's guide, 2005).

2.4 Solution Procedure

The SIMPLE (Semi-Implicit Method for Pressure-Linked Equations) algorithm is used by Fluent, to couple the momentum and continuity equations for the gas phase. In the momentum and turbulence equations discretization, the second order implicit method was applied.

Fluent solves the continuity and momentum equations in every control volume of the domain. The turbulence parameters are then calculated. Once convergence has been achieved, the particle trajectories are determined and after these calculations the continuous phase source terms are updated, in a two-way coupling approach.

3 Results

The experimental validation of these more complex models is always important but experimental data, in large-scale venturi scrubbers, are scarcely available in the literature.

A large scale cylindrical venturi was built for measuring the most relevant operating parameters for industrial applications and to provide a reliable experimental data base that can be used for model validation. The experimental measurements include: the pressure drop along the venturi (Silva et al., 2008a), the droplet size, measured by a laser diffraction based instrument (Silva et al., 2008b), and the performance of the venturi scrubber in the

collection of fine powder (Silva et al., 2007), for different operating parameters such as gas velocity and liquid flow rates. The liquid mass flows tested are from 0.013 to 0.075 kg/s and the throat gas velocity varied between 34 and 70 m/s.

The geometric details of the scrubber used in the present work are presented in Figure 1.

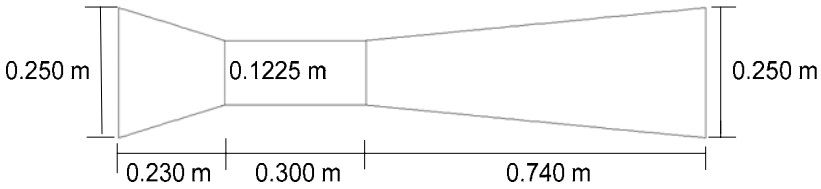

Figure 1 – Schematic of venturi scrubber used.

For the domain discretization, flow symmetry is assumed along the cross sections of the scrubber. Hence only one-fourth of the scrubber volume is modeled. The resulting grid is defined using a Hexahedral/Wedge Cooper mesh generation algorithm in Gambit. The 3D final mesh results in 15229 hexahedral elements (Figure 2).

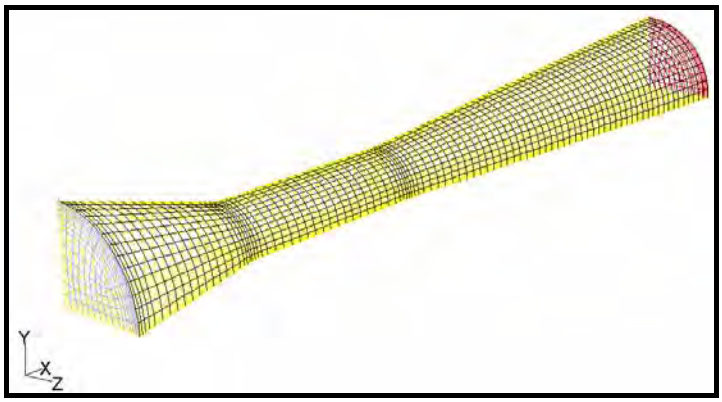

Figure 2 – Computational grid for the domain (Gambit).

In order to test the gas phase calculations, the various gas throat velocities (Vg) have been simulated. Convergence and grid independence of the results have been reached and Figure 3 shows the pressure drop along the venturi, relatively to that at the venturi inlet.

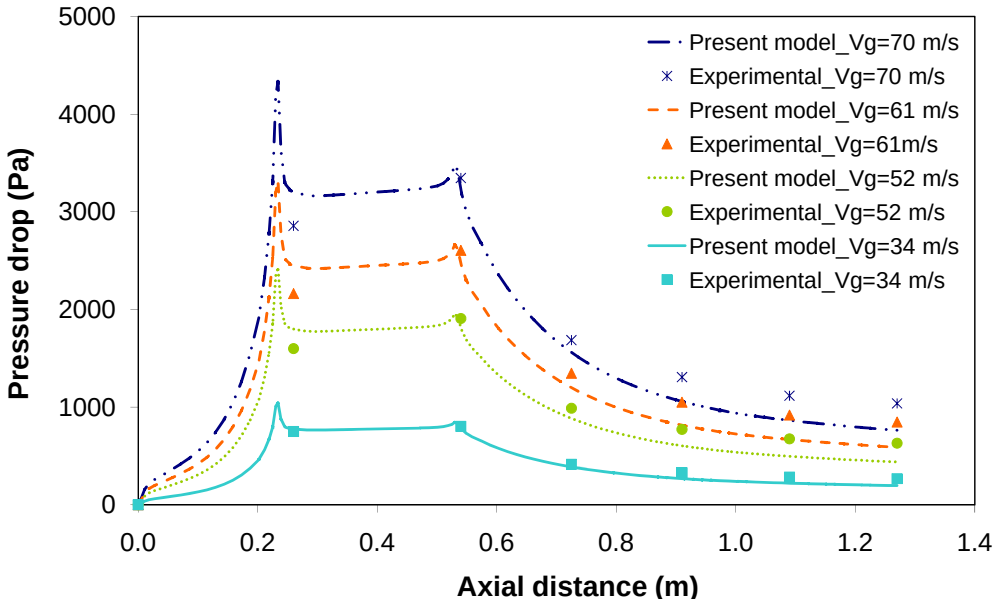

Figure 3 – Experimental and numerical single-phase pressure drop for various air velocities.

The sharp peaks in the predicted pressure drop values represent the losses at the sudden transitions between the throat and the converging and diverging sections. The experimental entrance of the throat, although some differences can be observed in this region.

These small discrepancies between the experimental data and the model simulations are more evident for higher velocities.

The effect of the dispersed phase was then simulated. The liquid mass flow rate was introduced through the spray nozzles at the venturi entrance. The droplet size distribution is within the range from 15 to 1504 μm for all the operating conditions simulated.

The data for a liquid mass flow rate of 0.038 kg/s and throat gas velocity of 70 m/s case are presented in Figure 4. The results for pressure drop along the venturi geometry show a very good agreement with the experimental data.

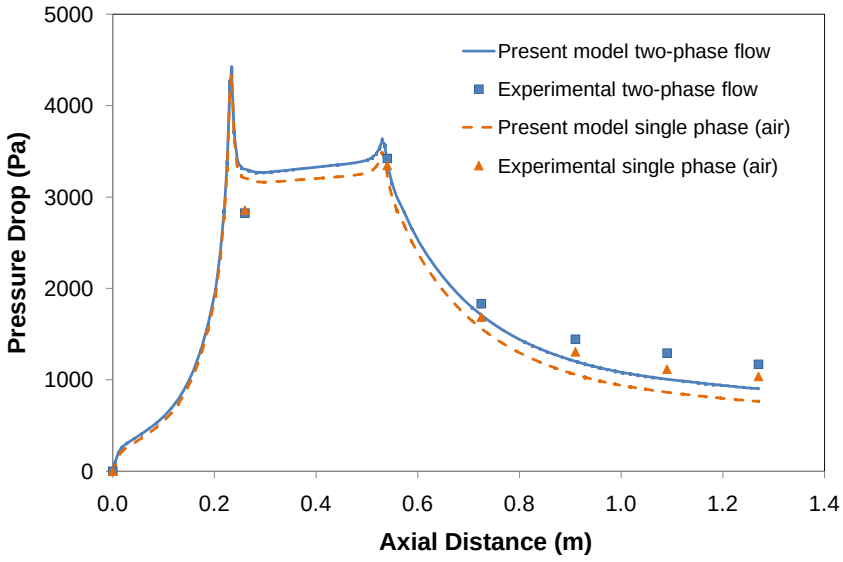

Figure 4 – Comparisons between experimental and predicted pressure drop along venturi.

The predicted pressure drop in the converging section, in the converging and throat sections and the total pressure drop are plotted against the available experimental data on Figure 5. The results are very encouraging.

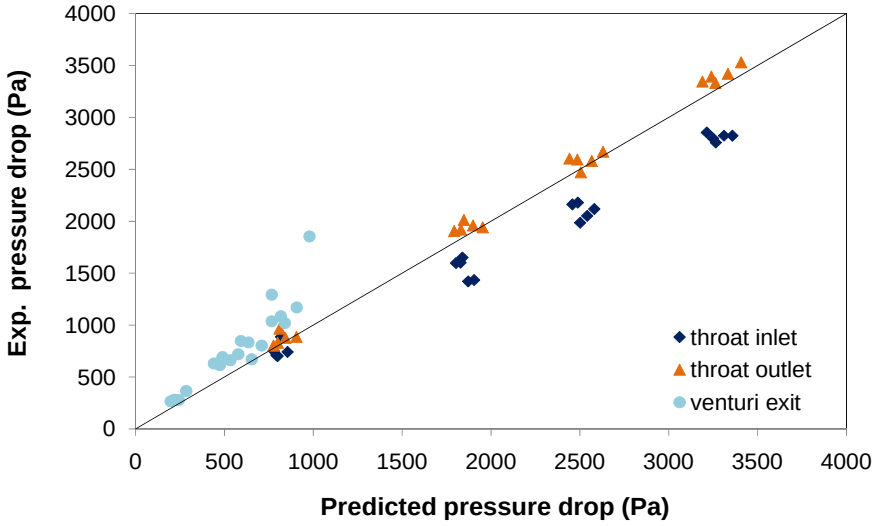

Figure 5 – Experimental versus numerical pressure drop results for the available data.

It can be observed that for the beginning of the throat the predicted values are higher that the experimental ones. At the end of the venturi the opposite behavior is observed, that means the numerical model predicts higher pressure recovery than the experimental tests. At the end of the throat section, the numerical and experimental results present a perfect agreement.

4 Conclusions

A new two-phase model was developed to predict pressure drop along a venturi scrubber, using the CFD code Fluent. An Eulerian-Lagrangian approach was used and a liquid droplet distribution has been considered. The model was tested against experimental data and very good results have been obtained.
Annular flow features are not included in the present work which can explain some discrepancies. This study shows that CFD models could be useful on the optimization of venturi scrubbers configurations.

Acknowledgment

The author A. Silva expresses her gratitude to the Portuguese Foundation for the Science and Technology (FCT) for the scholarship awarded. Ref: SFRH/BD/11195/2002.

References

Ananthanarayanan, N.V., Viswanathan S. (1999). Effect of nozzle arrangement on venturi scrubber performance. *Ind. Eng. Chem. Res*., 38, 4889-4900.

Azzopardi, B. J., Teixeira S.F.C.F., Govan A.H., Bott T.R. (1991). An improved model for pressure drop in venturi. *Trans. Inst. Chem. Eng.*, 69, 55-64.

Cruz, T.M.S., Teixeira S.F.C.F., Teixeira J.C.F (1997). The role of droplets in scrubbing combustion flue gases, *Proc. 4th Int. Conf. on Technologies and Combustion for a Clean Environment*, 67-71.

FLUENT INC. (2005). Chapter 11 – Modeling Turbulence. In: User's Guide, Lebanon, New Hampshire.

Gamisans X., Sarra M., Lafuente F. J., Azzopardi B. J.(2002). The hydrodynamics of ejector-venturi scrubbers and their modelling by annular flow/boundary layer model. *Chemical Engineering Science*, 57, 2707-2718.

Pak S.I., Chang, K.S. (2006). Performance estimation of a Venturi scrubber using a computational model for capturing dust particles with liquid spray. *Journal of Hazardous Materials*, B138, 560-573.

Silva A. M., Teixeira J.C.F., Teixeira S.F.C.F. (2008a). Experiments in large scale venturi scrubber Part I: Pressure Drop. *Chemical Engineering and Processing* (In press).

Silva A. M., Teixeira J.C.F., Teixeira S.F.C.F. (2008b). Experiments in large scale venturi scrubber Part II: Pressure Drop. *Chemical Engineering and Processing* (In press).

Silva, A. M., Teixeira, J. C. F., Teixeira,S. F. C. F. (2007). Performance of a large scale venturi scrubber with 2D boundary layer. *Proc. of IASTED Int. Conf. on Applied Simulation and Modelling*, Palma de Mallorca, Espanha, paper nº 581-167.

Proceedings of the 10th International Chemical and
Biological Engineering Conference - CHEMPOR 2008
Braga, Portugal, September 4-6, 2008
E.C. Ferreira and M. Mota (Eds.)

Numerical Simulation of Supercritical Extraction Processes

Carlos M. Silva[1], Claudia P. Passos[1], Manuel A. Coimbra[2], Francisco A. Da Silva[1*]

[1] University of Aveiro, Department of Chemistry, CICECO, 3810-193 Aveiro, Portugal
[2] University of Aveiro, Department of Chemistry, 3810-193 Aveiro, Portugal

Keywords: supercritical extraction, method of lines, finite differences.
Topic: Systematic Methods and Tools for Managing the Complexity.

Abstract

A mathematical model with two different methods to represent the mass transfer in the biomass matrix, (series and parallel), is proposed to simulate a supercritical fluid extraction unit. The model is solved using the method of lines and finite differences with flow correction. Experimental data is fitted fairly well by both models with equivalent accuracy. Two operating regimes were detected in the selected experimental conditions: equilibrium and mass transfer controlled. The last one is more difficult to simulate, requiring specific mass transfer parameters for series and parallel alternatives, for its accurate representation.

1 Introduction

The supercritical fluid extraction (SFE) of natural compounds using CO_2 is a promising separation technique for the recovering of high added value products with minimum degradation, environmentally friendly solvents, and higher selectivities. An important related task is the SFE modelling and subsequent determination of the key parameters involved, in order to simulate the process and finally optimize the interested operating conditions. This work focus on the modeling of SFE of grape seed oil, and the numerical solution of the corresponding differential equations. The model comprehends a set of coupled material balances distributed into three control volumes: one mass balance to the fluid phase (extractor bed), another one to the freely available oil in the seed, and a third mass balance to the tied oil existent inside the core of the seed. Several authors propose different mechanisms for the transport kinetic in the solid particle, as mass transfer in parallel or in series (Marrone *et al.*, 1998; Sovová, 2005). Both approaches are analyzed and compared. The solutions obtained are compared with experimental data provided in terms of extraction curves, i.e. extraction yield *versus* time. The concentration wave fronts inside the extractor are compared and computation time reported.

2 Model Description

The matematical modelling of a SFE unit to carry out the extraction of natural products with supercritical (SC) CO_2 has been an important target of study in the last two decades. Frequently, the column is considered isothermal, and both pressure drop and axial dispersion are neglected in the moving phase while, in the biomass matrix, several approaches have been used to describe the interaction between the SC fluid and the solid particle containing the natural product to be extracted. Several alternatives have been considered for these interactions, most of them altering the type of equilibrium relationships and particle modelling (Sovová, 2005). While the mass balance to the moving phase is well understood, the hardest task has been an amainable representation of the biomass matrix. This is a complex region structured on cavity arrays where in their interior are placed the oil bearing units

* Corresponding author. Tel +351-234 401 549. E-mail:fsilva@ua.pt

(Sineiro *et al.*, 1998). Figure 1 shows a simplified preview of the extraction column. At the grain scale, all its internal details were smoothed in two regions, accessible (η fraction) and non direct accessible ($1-\eta$ fraction). This concept was introduced to take into account some biological morphology (Sovová, 1994). Looking to the main SFE unit, it can be envisioned as composed by two main regions: a) a moving phase occupying the bulk void fraction ε, where the SC solvent is collecting the natural products from biomass; b) a fixed biomass composed region, occuping the void fraction $1-\varepsilon$, where the oil is initially retained in two types of regions: b.1) An oil free region, occuping the particle volume fraction η, where the solute is extracted with minor transfer resistance; b.2) an oil non-free zone, occuping the particle volume fraction $1-\eta$, where the solute is obtained with higher mass transfer resistance or even inaccessible.

Figure 1, shows schematically the extraction column identifying each zone and two plausible mass transfer options tagged as Series (Sovová, 2005) and Parallel (Marrone *et. al.*, 1998). A particle model is considered a "series model" due to the form how the mass transits from the non-free oil from inside seed cavities or tied to the internal structure to the free oil region of the seed, broken cavities or pore particles, and from here to the external fluid. Another way to model this system is by assuming that both free and non-free regions are exposed directly and simultaneously to mass transfer to the moving fluid but at different rates. Based on the control volumes of the extractor unit depicted in Figure 1 two mathematical models have been implemented, one for series and another one for parallel mass transfer. Table 1 presents the set of partial diferential equations, initial and boundary conditions which conforms the models.

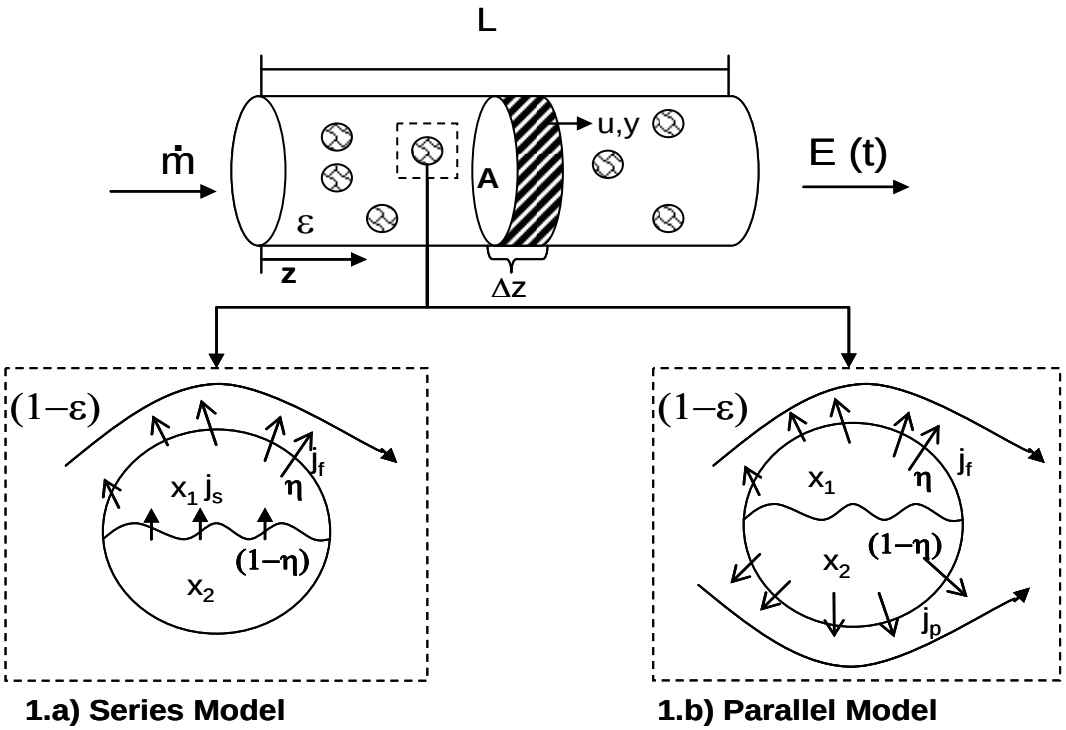

Figure 1: Scheme of the extractor column. Main control volumes used, and mass tranfer options considered: a) Flowing phase, y, occupying the void volume fraction, ε; b) biomass fraction, $(1-\varepsilon)$; where two zones are identified: free available oil, x_1; non-free oil, x_2.

Two mass transfer model options are represented in terms of: **1.a)** $j_f / \bar{j}_s$ for the series model case, and **1.b)** $j_f / \bar{j}_p$ with parallel model alternative.

A set of partial differential equations of the hyperbolic type results, which can be solved by classical numerical techniques: the Method of Lines (Shiesser, 1994) and Method of Characteristics (Acrivos, 1956; Aris and Amundson, 1973; Perrut et al., 1997). In this work, the method of lines was adopted with axial spatial coordinate discretization using upwind finite differences. Additionally, the library due to Shampine (2005) is used for solving the same model, based on central finite differences with flux correction, a variant of Lax-Wendroff scheme with a non-linear filter (SLxW), which is a versatile and specialized numerical library for hyperbolic systems of equations. All these libraries and routines are implemented in Matlab. Single extraction curves were obtained numerically spending between 2 to 6 CPU minutes, with 50 segments in the axial coordinate, running in Pentium IV 3Ghz computers.

3 Extraction Curves

The extraction curve is obtained from experimental runs by registering the mass flow of solvent fed, $\dot{m}$, normally constant, and the natural product retired from the column as a function of time. From the model, it can be readily calculated as $E(t) = \dot{m}\int_0^t y(L)dt$.

Table 1: SFE mathematical model considering two type of particle mass transfer models in alternatives.

	Mass Balances	Initial and Boundary Conditions
	Particle Series Model	
Free Oil Region	$\eta\rho_s \frac{\partial \bar{x}_1}{\partial t} = j_s - \bar{j}_f$	$\bar{x}_1(0) = x_{1,o}$
Non-Free Oil Region	$(1-\eta)\rho_s \frac{\partial \bar{\bar{x}}_2}{\partial t} = -\bar{j}_s$	$\bar{\bar{x}}_2(0) = x_{2,o} \approx x_u$
	Particle Parallel Model	
Free Oil Region	$\eta\rho_s \frac{\partial \bar{x}_1}{\partial t} = -j_f$	$\bar{\bar{x}}_1(0) = x_{1,o}$
Non-Free Oil Region	$(1-\eta)\rho_s \frac{\partial \bar{x}_2}{\partial t} = -\bar{j}_p$	$\bar{\bar{x}}_2(0) = x_{2,o} \approx x_u$
	Mass balance in Moving phase	
Moving phase	$\varepsilon\rho_f \frac{\partial y}{\partial t} = -u\rho_f \frac{\partial y}{\partial z} + (1-\varepsilon)(j_f + \bar{j}_p)$	$y(0,z) = y_o$ $y(t,0) = 0$
	Equilibrium, mass transfer, initial closure restriction and extraction curve	
Equilibrium	$y^*(\bar{x}_1) = y_s(T,P), \bar{x}_1 > x_t$ $y^*(\bar{x}_1) = K(T,P)\bar{x}_1, \bar{x}_1 \le x_t; Kx_t < y_s$	
Mass tranfer	$j_f = \rho_f k_f a_f (y^*(\bar{x}_1) - y))$ $\bar{j}_s = \rho_s k_s a_s (\bar{\bar{x}}_2 - \bar{x}_1)$ $\bar{j}_p = \rho_f k_s a_s (y^*(\bar{\bar{x}}_2) - y)$	

Initial closure restriction	$(1-\varepsilon)\rho_s x_u = \varepsilon\rho_f y_0 + (1-\varepsilon)\rho_s(\eta x_{1,0} + (1-\eta)x_{2,0})$
Extraction Curve	$E(t) = \dot{m}\int_0^t y(L)dt$

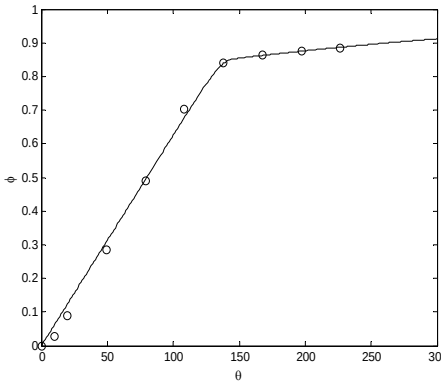

Figure 2: A dimensionless extraction curve fitted to the experimental data using the series model using upwind differences. Experimental data is from an oil grape seed extraction operating at 200 bar, 40ºC.

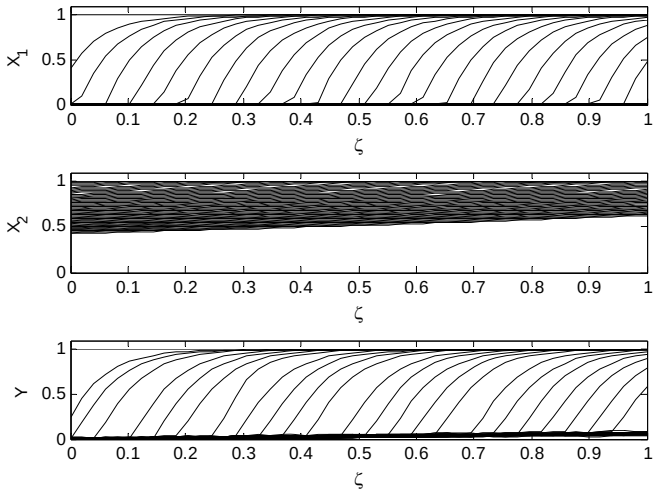

Figure 3: Axial profiles predicted in the interior of a SFE unit as a function of dimensionless time, θ, in intervals of $\Delta\theta = 6$, for dimensionless free (X_1), non-free (X_2) and solute concentration in the solvent, (Y).

In Figure 2 it is shown an experimental dimensionless extraction curve, $\Phi(\theta) = \dfrac{E(t)}{\text{Total extractable oil}}$, against dimensionless time, $\theta = \dfrac{t}{\tau}$, fitted with the mass transfer particle model and model parameters: $\varepsilon = 0.22$, $\eta = 0.796$, $x_u = 0.149$ kg/kg, $x_t = 0$ kg/kg, $x_{1,0} = 0.148$kg/kg, $y_0 \approx y_s = 0.0027$, $\tau =$,122s, $u = 0.033$ cm/s, $k_f a_f = 0.03$ s^{-1}, $k_s a_s =$ 3.6 .10^{-6}s^{-1}, $\rho_s = 688$ kg/m^3, $\rho_f = 840$ kg/m^3. The experimental extraction curve is reproduced fairly well, showing clearly two behaviors, first an equilibrium controlled regime followed by a mass transfer controlled step, after 150 dimensionless units. Figure 3 shows the progress prediction with dimensionless time of axial concentration profiles in the interior of the column for the same case, in terms of non-dimension variables, $X_1 = \dfrac{x_1}{x_{1,0}}$, free oil, $X_2 = \dfrac{x_2}{x_{1,0}}$, non free oil and $Y = \dfrac{y}{y_o}$ solute concentration in solvent gas against the spatial coordinated, $\zeta = \dfrac{z}{L}$. The two mass transfer regimes are detected again in the moving fluid phase. At the beginning, the X_1 and Y waves run together, and at the end, the Y collapses at the bottom, defining the mass transfer controlled period, where the non free oil, represented by the X_2 is the main source of the natural product. Figure 4 and 5 compares

the extraction curve and the evolution of axial profiles obtained with three different numerical methods: upwind finite differences, tank series and smoothed Lax-Wendroff (SLxW). In the equilibrium regime, all extraction curves solutions are equivalent, showing differences in the last part which reveals to be more sensible to differences in the axial profiles predicted in the interior of extractor column. They are more dispersive in tank series and more abrupt with

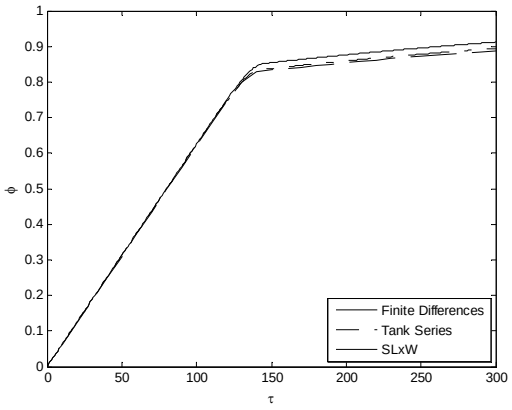

Figure 4: A dimensionless extraction curve obtained with different numerical methods: upwind finite differences, tank series (Sovová, 2005) and smoothed Lax-Wendroff (SLxW option, Shampine 2005). Modeling parameters are the same as Figure 2.

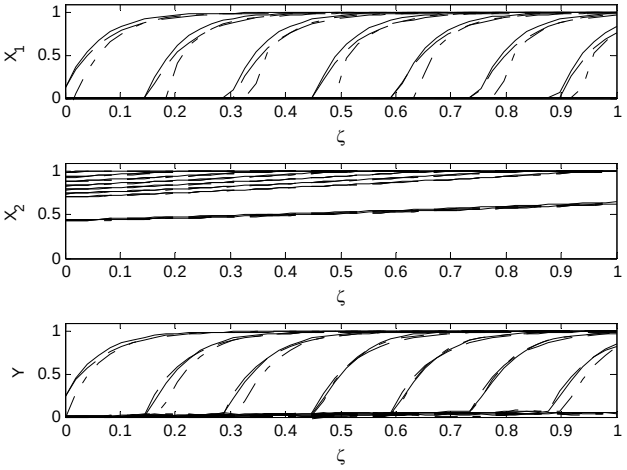

Figure 5: Dimensionless axial profiles with series model, using upwind finite differences (—), tank series (---) and SLxW (-.-) methods compared at $\theta =$ 10, 30, 50,…,130, 290 and 300.

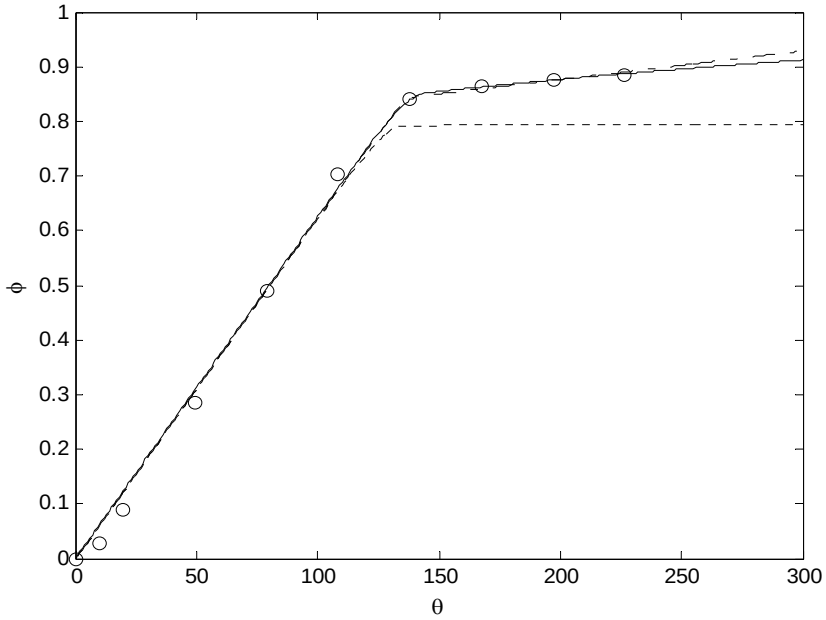

Figure 6: Extraction curve obtained with series model (—), parallel model with $k_f a_f$ =0.03s^{-1}, $k_s a_s$ = 3.6 .10^{-6}s^{-1} (---), and parallel fitted with $k_f a_f$ =0.048 s^{-1}, $k_s a_s$ = 2.7.10^{-4}s^{-1}(—·—).

the SLxW numerical option. Standard central differences of second order are not recommended because huge oscillations are obtained, damaging the axial profile and extraction curve simulation. Figure 6 compares the solutions obtained with the series model with the parallel option, using the same set of mass transfer parameters and those fitted with the parallel model. It is observed that the same set of parameters coming from the series model are not applicable to the parallel case, but this model can be easily fitted to the same experimental extraction curve, only modifying the mass transfer parameters.

4 Conclusions

A mathematical model with two alternatives for the particle mass transfer was proposed to simulate a SFE unit, solved using the method of lines with finite differences with flow correction. An experimental extraction curve is well fitted with both series and parallel mass transfer particle models only modifying the mass transfer coefficients. Two different operating regimes are detected upon the operating conditions of selected experimental data: and equilibrium and mass transfer controlled regimes. The most sensible zone of extraction curve was the mass transfer controlled regime at the end of the experiment, both to the numerical method used to discretize the axial coordinate in the column and the mass transfer approach used to represent the particle dynamic.

Acknowledgments

The authors gratefully acknowledge the financial support from Programa Operacional “Ciência, Tecnologia, Inovação” QCA III and FEDER, project POCTI/EQU/46055/2002.

References

Acrivos, A. (1956) Method of Characteristics Technique. Application to Heat and Mass Transfer Problems, *Ind. and Eng. Chem.*, 48(4), 703-710.

Aris, R., Amundson, N. R., (1973), *Mathematical Methods in Chemical Engineering. Vol.2 – First Order Partial Differential Equations with Applications*, Prentice-Hall, USA.

Marrone, C., Poletto, M., Reverchon, E. and Stassi, A., (1998), Almond oil extraction by supercritical CO2: experiments and modeling, *Chemical Engineering Science*, 53(21), 3711-3718.

Perrut, M., Clavier, J. Y., Poletto, M., Reverchon, E. (1997), Mathematical Modeling of Sunflower Seed Extraction by Supercritical CO2, *Industrial and Engineering Chemical Research*, 36, 430-435.

Shampine, L. F., (2005), *Solving Hyperbolic PDEs in Matlab*, Mathematics Department, Southern Methodist University, Dallas, TX.

Shiesser, W. E., (1994), *Computational Mathematics in Engineering and Applied Science*, CRC Press, Boca Raton, FL.

Sovová, H., (1994), Rate of the vegetable oil extraction with supercritical CO2. I. Modelling of extraction curves, Chem. Eng. Sci., 49, 409-414

Sovová, H., (2005), Mathematical model for supercritical fluid extraction of natural products and extraction curve evaluation, *Journal of Supercritical Fluids*, 33, 35-52.

Proceedings of the 10th International Chemical and
Biological Engineering Conference - CHEMPOR 2008
Braga, Portugal, September 4-6, 2008
E.C. Ferreira and M. Mota (Eds.)

Influence of a heated brine spray system on the dynamic model of an integrated recrystallization industrial process

Raquel D. Moita[1], Henrique A. Matos[1*], Cristina Fernandes[1], Clemente P. Nunes[1], Mário J. Pinho[2]

[1] Instituto Superior Técnico – DEQB, Av. Rovisco Pais, 1049-001, Lisboa, Portugal.
[2] Grupo CUF, Quinta da Indústria, 3864-755 Estarreja, Portugal.

Keywords: Dynamic modelling, Simulation, Process integration, Industrial case study, Cogeneration, Spray system, Crystallization process.
Topic: Systematic methods and tools for managing the complexity.

Abstract

The aim of this study is to perform a dynamic modelling and simulation of a Portuguese industrial integrated system in order to analyse the integration and feasibility of the different units, maximizing its efficiency and minimizing its environmental damage, and to study the effect of some operational and atmospheric conditions on the system.

For that purpose, a distributed dynamic model was built using *gPROMS 2.3.7* language for the integrated Process including a cogeneration system, a set of plate heat exchangers and a salt recrystallization process.

Thus it was analysed the effect of the heated brine spray system on the integrated process by considering a new three-dimensional dynamic mathematical model, which is based on the ballistic theory, and includes material and energy balances, and that allows to predict the spray system behaviour. It was studied its effect on the integrated process by comparing the global performance of the system with and without sprays. Due to air drift issues, quasi-random time daily profiles for the allowed operation of the spray system (on-off working time periods) were used. Using three distinctive atmospheric scenarios, several ponds sprays distributions schemes were analysed. A sensibility analysis of the salt production was considered by changing the fraction of the flow rate that enters in the ponds through taps and through sprays.

1 Introduction

The main goal of this study is to achieve the best operational conditions of an open air industrial integrated system including three processes, by exploiting different atmospheric scenarios, in order to maximize its global energy efficiency and to minimize the environmental impact, reducing the primary energy supply and the raw materials usage. This integrated system, located at Carriço, Pombal (Portugal), includes the following three separated processes: a natural gas storage built inside salt caverns owned by Transgás, a gas turbine cogeneration system owned by Galp Power, and a salt recrystallization process owned by Renoeste. The integration of these three independent units, improves the global system efficiency (Moita et al., 2004).

2 Dynamic modelling and simulation of the integrated system

The model of the whole integrated process was built through algebraic and differential equations taking into account the phase equilibrium thermodynamics: solid, liquid and gas phases. The integrated system includes the cogeneration system, the five plate heat

* Corresponding author. Tel + 351-21-8417639. E-mail:henrimatos@ist.utl.pt

exchangers and the salt recrystallization process. This involves, mainly, a maximum of six recrystallization ponds, a feed tank and a collecting channel.

The plate heat exchangers (PHE) are the physical connecting link between the cogeneration system and the recrystallization process. The PHE set was included using its design equation and heat balances at both sides. The mass and heat balances are axially distributed providing the expected profile inside the ponds (30 elements). The salt saturation concentration depends on brine density and salt solubility values, which vary with brine temperature.

The water evaporation rate is a function of the salt concentration, of the temperature in the brine solution and of the atmospheric conditions (air temperature, humidity and wind velocity). Both for the water evaporation rate and for the convection energy loss it was considered the maximum value obtained between natural and forced convection (mixed laminar-turbulent flow), given the importance of accounting for natural convection, specially at lower wind velocities (Moita et al., 2006).

The thermal power (TP) values are given by the cogeneration system operation. The solar energy contribution absorbed through the brine in the recrystallization ponds is the diffuse part and a fraction of the direct solar energy, which is dependent on the brine pond level.

A new heated brine spray distribution system model was also accounted for, that is an extension of the model previously presented (Moita et al., 2005), in order to study its effect on the integrated system by dynamic simulation. So, for that purpose, a three-dimensional dynamic mathematical model for the hereinabove mentioned heated brine spray system was built (Moita et al., 2008). Two models were developed: one for a single drop and the other for the spray system. The single drop model, which is based on the ballistics theory and includes material and energy balances, allows for the calculation of the trajectory and velocity of the drop once catapulted from a nozzle, as well as its temperature, salt concentration, and volume during the flight. The spray system model accounts for the effect of all the drops hits, released from a single full-cone spray-nozzle, by considering a set of random defined drops, through statistical distributions.

Some global variables for the entire spray system are determined by accounting the results for each drop i obtained with the dynamic model herein developed. For instance, it is possible to calculate the total spray volume (V_{sp}) and brine mass ($M_{brine,sp}$) obtained by unit of brine volume sent to the nozzle:

$$V_{sp} = \frac{\sum V_{drop,i}}{\sum V_{drop,i}\Big|_{t=0}} \tag{1}$$

$$M_{brine,sp} = \frac{\sum m_{brine,i}}{\sum V_{drop,i}\Big|_{t=0}} \tag{2}$$

The mean spray temperature T_{sp} is calculated through an energy balance in which the effect of all falling drops is accounted for. The total water evaporated by unit volume of the entering brine ($M_{evap,sp}$), during the spraying time, is given by:

$$M_{evap,sp} = \frac{\sum \int M_{evap,i}\, dt}{\sum V_{drop,i}\Big|_{t=0}} \tag{3}$$

The global evaporative spray efficiency (E_{ff}), which considers the convection and radiation energy losses to the open air, is determined by:

$$E_{ff} = \frac{\sum \int E_{evap,i}\, dt}{\sum \int \left(E_{evap,i} + E_{conv,i} + E_{rad,i}\right) dt} \qquad (4)$$

Using this new model the effect of several variables on the spray system behaviour was analysed. Based on the simulated results, multi-linear correlations for the water evaporation rate ($M_{evap,sp}$) and for the mean spray temperature (T_{sp}) were determined as a function of the heated brine temperature, air humidity and temperature, wind velocity and nozzle height, for a given operating pressure.

The effect of the spray system is included in the integrated system model by considering spray material and energy balances, using the mentioned correlations. A maximum of ten sprays were considered in each pond entering through its length, that is, in the axial elements of the pond model (around 30% of the total length).

The whole integrated system was modelled through the general-purpose modelling, simulation and optimization tool gPROMS 2.3.7, of the Process System Enterprise, Ltd. A flow diagram illustrating the dynamic model structure implemented in this software is shown in Figure 1. There are five sub-models, including the algebraic and differential equations needed to describe each system. Some variables are used as connecting sub-models information, such as brine flow rate (Q), concentration (X), temperature (T) and density (ρ).

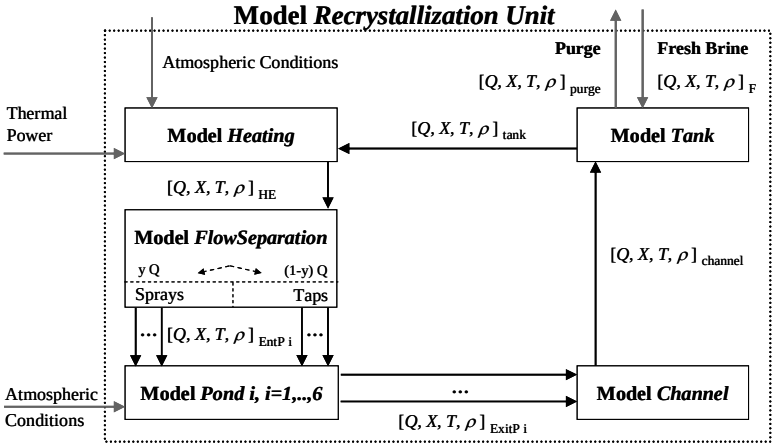

Figure 1. Structure of the dynamic model of the integrated process in gPROMS 2.3.7.

For this model the main state variables are: the number of ponds in service, the atmospheric conditions (wind velocity, air temperature and humidity), the fresh brine flow rate and concentration, the flow rate of the brine pumped into the plate heat exchangers, the thermal power profile and the solar energy input (Moita et al., 2005).

3 Influence of the brine spray system

The effect of the sprays system on the integrated process was analysed, by comparing its performance with and without sprays, using different operational and atmospheric scenarios.

Due to brine air drift issues for some wind directions the use of the spray system is prohibitive, and therefore on-off sprays working time periods must be defined. Using atmospheric data obtained from the industrial site, corresponding to 10 months (from August 2005 to May 2006), and by analysing the wind directions values, it was specified the allowed

time periods for the sprays operation. Then, for each month, it was calculated the mean hourly time percentage of allowed spray use, that is, by accounting the time intervals that sprays can be turned on in each hour of the day, and using all the data concerning that month. Using these mean hourly time percentages, it was calculated the total mean time percentage for the allowed operation of the sprays for the whole month. Based on these values, two scenarios were defined: a winter scenario, based on October to January total mean values; and a summer scenario, accounting monthly mean values of February to May, August and September. A third intermediate scenario was also considered (Moita et al., 2007).

For each scenario the global time percentage of spray use is constant. It was created a quasi-random time daily profile for the allowed operation of the sprays, which is repeated through the simulation time and respects the fixed global time percentage of spray use defined in each scenario (Table 1).

Table 1. Atmospheric conditions ($T_{air,}$ humidity, wind velocity V, solar energy E), global time percentage and random time daily profile of allowed sprays operation, for each scenario.

Scenario	**Winter**	**Intermediate**	**Summer**
Duration (h)	2830	1420	4250
Tair (ºC)	10	17	20
Humidity (%)	75	75	68
V (m/s)	1.3	3.0	2.3
E (kWh/m^2/day)	2.6	4.0	5.5
% Spray use	30%	45%	62%
Daily Profile	1W1S1W1S1W3S 2W5S1W5S1W2S	3S1W1S2W3S1W1S 3W2S1W2S1W1S2W	1S1W2S3W2S3W1S 4W1S2W1S2W1S

nS = n hours with sprays Stopped (turned off);
mW = m hours with sprays Working.

Table 2 presents the salt production predicted by simulation, when sprays are turned on, using as a comparison the case of operation without sprays with 3 ponds in service (100 units of mass per year). The cogeneration system requires the water temperature T_2 within the operational interval of: 90± 1ºC. In order not to exceed this temperature it is not possible to work only with two ponds. The use of the spray system leads to a reduction of the ponds brine temperature, due to the cooling of the brine as the drops are sent from the nozzle to the open air. Therefore, the (v1 + v2) number of sprays can be useful since they allow operating with only two ponds, and still respect the mentioned temperature limits. For that purpose, it is required to use a 4+0, 8+0 and 10+0 ponds spray distributions in the winter, intermediate and summer scenarios, respectively. This operation scheme leads to a salt increase of almost 2%. Alternatively, the equivalent operation modes 2+2, 4+4 and 5+5 could be used.

Table 2. Salt production obtained without and with sprays for all the scenarios (um/year).

Scenario	**3P_(0+0+0)**	**2P_(0+0)**	**2P_(v1+v2)**
Winter	28.7	30.7	30.5 [a]
Intermediate	16.6	17.1	16.9 [b]
Summer	54.7	54.7	54.2 [c]
Total (u.m./year)	100.0	102.5	101.6

nP_(v_1+v_2+v_3) = n ponds, with v_1, v_2 and v_3 sprays entering in the first, second and third pond;
■ – Water temperature T_2 is higher than its upper limit (91ºC);
a: 2P_(4+0); b: 2P_(8+0); c: 2P_(10+0).

An operation scheme with 3 ponds, such as 3P_(2+0+0), could also be used. However, this leads to water temperatures values lower than its desirable lower limit. To avoid this, a brine flow rate distribution in the ponds and in the spray system should be used. Consider the heated brine flow rates distribution in the ponds and spray system illustrated in Figure 2, where y is the flow rate fraction sent to the sprays and x_n (n=2,3) is the fraction of the flow rate that was not sent to the sprays entering by taps in pond 2 or 3.

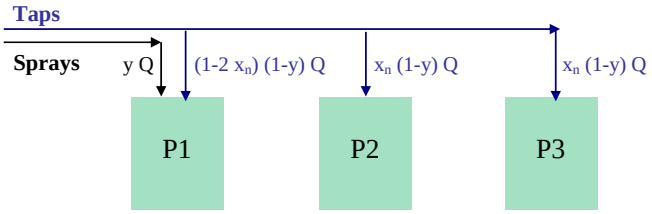

Figure 2. Brine flow rate distribution in the ponds and spray system.

Using as an example the intermediate scenario, and considering the mentioned 3P_(2+0+0) operation scheme, x_n values from 0.1 to 0.5 were considered. Reducing x_n to 0.1 increases the brine flow rate entering through the taps in the first pond, and decreases it in the two other ponds. When x_n is increased the opposite occurs, where a x_n value of 0.5 corresponds to an extreme situation in which the first pond only receives brine when the sprays are turned on, otherwise works as a “solar pond” (Figure 3).

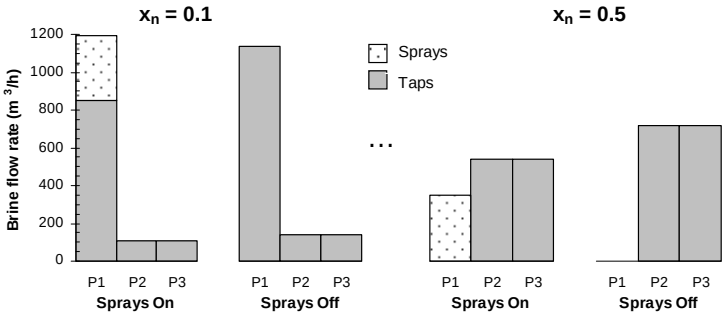

Figure 3. Flow rate distribution in (P_1, P_2, P_3) ponds with sprays on and off, considering x_n=0.1 and x_n=0.5.

Figure 4 shows the simulation results obtained from the sensibility analysis of the x_n value, namely, the hot and cold water cogeneration temperatures (T_2 and T_1), heated brine temperature and salt increase when compared to the base operation scheme (no sprays, 3 ponds).

In order to maintain the hot water temperature within the defined operational temperature interval, x_n should be between 0.15 and 0.2, or between 0.45 and 0.48, corresponding to a salt increase between 1.5 and 0.7%, or between 1.5 and 3.8%, respectively. Using the smaller values of x_n means large values of the brine flow rate in the first pond, while increasing x_n leads to a higher water temperature oscillation, due to the non-constant flow rate entering in the ponds.

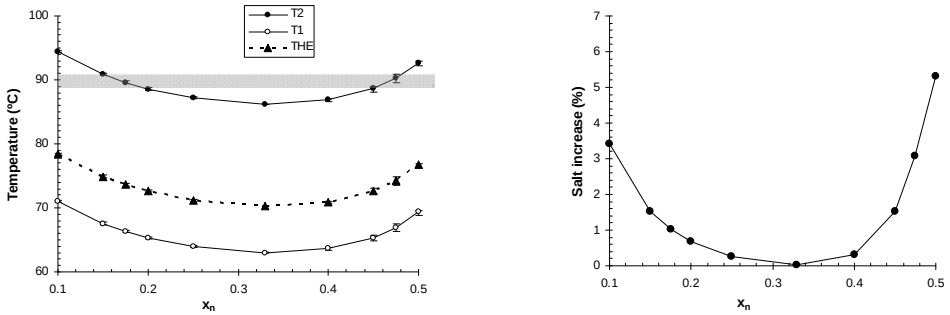

Figure 4. Hot and cold water temperatures (T_2, T_1), heated brine temperature (T_{HE}) and % of salt increase compared to the base operation (no sprays and 3 ponds), for x_n from 0.1 to 0.5; ■ – Hot water temperature (T_2) operational window.

4 Conclusions

The effect of the spray system on the integrated process was analysed through the use of a new dynamic mathematical model, by comparing its performance with and without the use of sprays. Due to air drift issues, on-off sprays working time periods were defined, by using quasi-random time daily profiles for the allowed spray operation. Using three characteristic atmospheric scenarios, several ponds sprays distributions were analysed. In order to respect the operational intervals of the temperature of the water circulating in the cogeneration system, and to work with only two ponds, the best option is to operate using two ponds with a (4+0), (8+0) and (10+0) spray system installed for the winter, intermediate and summer scenarios, respectively. This leads to a salt increase of almost 2%, if we compare with the base case of 3 ponds without sprays. Alternatively, a 3 ponds scheme with sprays can be used. For instance in the case of the intermediate atmospheric scenario, and considering that it operates with three ponds with two sprays in one of them, a heated brine flow rate ponds distribution should be implemented to increase the salt production up to 4%.

Acknowledgements

The authors gratefully acknowledge financial support from Renoeste and from the Portuguese agency FCT – grant SFRH/BDE/15 533/2004.

References

Moita, R. D., Matos, H. A., Fernandes, C., Nunes, C. P., Prior, J. M., Santos, D. A. (2004). Process integration of a dynamic industrial system. In A. Barbosa-Póvoa & H. Matos (Eds.), *Escape 14 – Computer Aided Chemical Engineering*, Volume 18, 445-450, Elsevier, Amsterdam.

Moita, R. D., Matos, H. A., Fernandes, C., Nunes, C. P., Prior, J. M. (2005). Dynamic modelling and simulation of a cogeneration system integrated with a salt recrystallization process. *Computers and Chemical Engineering,* 29, 1491-1505.

Moita, R. D., Matos, H. A., Fernandes, C., Nunes, C. P., Pinho, M. J. (2006). Studies of evaporative efficiency by dynamic simulation of an open integrated industrial system. In A. G. Bruzzone, A. Guasch, M. Piera & J. Rozenblit (Eds.), *EMSS – 2006 Procedings*, 441-450, Barcelona.

Moita, R. D., Matos, H. A., Fernandes, C., Nunes, C. P., Pinho, M. J. (2007). Influence of brine spray system on the thermal salt recrystallisation process by dynamic simulation. In V. Plesu & P. S. Agachi (Eds.), *Escape 17 – Computer Aided Chemical Engineering*, Volume 24, 479-484, Elsevier, Amsterdam.

Moita, R. D., Matos, H. A., Fernandes, C., Nunes, C. P., Pinho, M. J. (2008). Dynamic modelling and simulation of a heated brine spray system. *Computers and Chemical Engineering*, submitted.

Proceedings of the 10th International Chemical and
Biological Engineering Conference - CHEMPOR 2008
Braga, Portugal, September 4-6, 2008
E.C. Ferreira and M. Mota (Eds.)

Non isothermal phenomenological model of an enological fermentation: modelling and performance analysis

Pablo M. Aballay[1], Gustavo J.E. Scaglia[1], Martha D. Vallejo[2]
Oscar A. Ortiz[1*]
[1] Instituto de Ingeniería Química. Universidad Nacional de San Juan.
[2] Instituto de Biotecnología. Universidad Nacional de San Juan. Av. Libertador San Martín Oeste 1109, J5400ARL - San Juan, Argentina.

Keywords: Non-isothermal model, Enological fermentation, Killer yeasts, Performance Analysis.
Topic: Systematic methods and tools for managing the complexity.

Abstract

The grape juice fermentation constitutes the core of the winemaking process. In this stage, complex physical, chemical and biological changes occur. Also, the presence of non-constant parameters and high non-linearities produce complex dynamic responses of the bioprocess. In this work, a non-isothermal phenomenological model for a batch alcoholic fermentation is proposed. The model predicts the main process state variables: viable cells, substrate (sugar) and ethanol concentrations, carbon dioxide released, and the bioreactor temperature. It is based on the model developed by Scaglia *et al.* (2008) which is excellent for isothermal fermentations. In this case, the main model objective has been posed on temperature, due to its control is critical to produce high quality wines and to reduce the winery cooling requirements. The model combines mass and energy balances coupled by the Arrhenius equation that describes the temperature influence on the cell growth rate. Due to the temperature inside the bioreactor must be maintained at 23±1 ºC to avoid the quality product decrease, a wide performance analysis with the model proposed was carried out. The obtained results from simulation show acceptable agreement with own experimental and published data. Therefore, the acceptable model performance will allow its application in advanced optimization and control strategies.

1 Introduction

High-quality wines are the market segment that offers the best advantages for wine production in Cuyo (Argentina). Usually, fermenters are operated in batch mode with limited control. Therefore, a strict process monitoring and control in winemaking is required (Vallejo *et al.*, 2005; Ortiz *et al.*, 2006). Also, some of the selected strains possess killer properties, which represent a guarantee for their implantation in the fermentation (Zagorc *et al.,* 2001).

The alcoholic fermentation in winemaking is characterized by complex physical, chemical and biological changes, the presence of non-constant parameters and high non-linearities, which produce complex dynamic responses of the bioprocess and determine the final quality of wine. Although many of these problems have been widely studied (Boulton *et al.*, 1996; Fleet, 1993), it still exist several that need to be solved.

In this work, a non-isothermal model for a batch alcoholic fermentation is presented. The model couple mass and energy balances predicting the behavior of the main state process variables: viable cells, substrate (sugar) and ethanol concentrations, carbon dioxide released, and the bioreactor temperature. The proposed model is based on the one developed by Scaglia *et al.* (2008), that possesses a good performance for isothermal fermentations. In this case, the main model objective has been posed on temperature, due to

* Corresponding author. E-mail: rortiz@unsj.edu.ar

its control is critical to produce fine wines with constant quality and to reduce the winery cooling requirements (Aballay *et al.*, 2006).

The proposed non-isothermal kinetic model consists of a set of ordinary differential equations (ODE) for the balances mentioned, including the heat transferred between the reactor and its cooling jacket. Balances have been coupled by means of the Arrhenius equation which describes the temperature influence on the cell growth rate (Aballay *et al.*, 2006; Phisalaphong *et al.*, 2006).

Kinetic parameters were adjusted using experimental data obtained from anaerobic lab-scale cultures of *Saccharomyces cerevisiae* (killer), and/or *Candida cantarelli* yeasts in Syrah must (grape juice) (Toro and Vazquez, 2002). In the case of the specific parameters in Arrhenius expression, they were adjusted by the least-square method (Aballay *et al.*, 2006).

Due to in practice, the temperature in the bioreactor must be maintained constant at 23±1 ºC to avoid the quality product decrease, a performance analysis by using the dynamic model developed was carried out. The most frequently found disturbances in real plants are applied on the main manipulated process variable, and the corresponding responses of the state process variables considered are showed.

Results from the proposed model simulation and its performance analysis are shown. They report acceptable agreement with own experimental and published data, predicting fermentation evolution without appreciable delays what allows to take proper control actions on the process.

The paper is organized as follow. First, the non-isothermal kinetic modeling of the bioprocess from a previously developed isothermal model is presented. Second, the experimental data from laboratory tests and, the simulation results are exhibited. Third, the model performance analysis is developed. Fourth, a discussion about the application of the obtained model in advanced optimization and control strategies and conclusions are exposed.

2 Modelling

The reductive metabolic pathway characterizes the yeast population growth in anaerobic conditions as: $S \rightarrow X + P + CO_2$

In this equation, X, S, P and CO_2 correspond to viable cells, carbon source (glucose and fructose) and ethanol concentrations, and carbonic dioxide released [kg m^{-3}], respectively.

The formation ethanol reaction from glucose is: $C_6H_{12}O_6 \rightarrow 2CH_3CH_2OH + 2CO_2$ (1)

The metabolite accumulation in the extra cellular medium has been modelled by a set of ODE based on mass balances on X, S, P and CO2 like in the isothermal model of Scaglia et al. (2008), which can be seen for further details. All the mentioned variables depend on cells concentration evolution in time t [h] and the kinetics for cell growth is mainly subject to μ_m,

$$\left\{\frac{dX}{dt}, \frac{dS}{dt}, \frac{dCO_2}{dt} and\ \frac{dP}{dt}\right\} = f(X), \text{ and } \frac{dX}{dt} = f(\mu_m) \quad (2)$$

The non-isothermal kinetic model proposed here is constituted by the previous mass balances and the energy balance in the reactor and its cooling jacket. These balances were coupled by means of Arrhenius equation that describes the main influence of the temperature on cell growth rate (Aballay *et al.*, 2006; Phisalaphong *et al.*, 2006; Coleman *et al.*, 2007). Since, in this case, a typical alcoholic fermentation in a representative operating temperature range is modelled (20~30 ºC); the effect of temperature on cellular death and other parameters like ethanol production or sugar consumption, which are significant at higher temperatures, were neglected. This latter can be observed in experimental yeast population curves vs. temperature in the winemaking fermentations of Torija *et al*. (2003). Other mass balance parameters of the model proposed by Scaglia *et al.* (2008), including pH, were supposed constant in the fermentation temperature range considered.

Taking account Eq. (2), the effect of fermentation temperature on the maximum specific cellular growth rate, μ_m, has the following form, $\mu_m = \gamma . \frac{T \cdot e^{-\frac{E_a}{R \cdot T}}}{1 + e^{-\frac{\Delta G_d}{R \cdot T}}}$ (3)

γ is the maximum cellular growth rate per Kelvin degree [$h^{-1}K^{-1}$], E_a is the activation energy [kJ $kmol^{-1}$] and ΔG_d [kJ $kmol^{-1}$] is Gibbs free energy change of the fermentation reaction. Both of the mentioned parameters were adjusted by the least-square method, using experimental data obtained from anaerobic lab-scale cultures of *Saccharomyces cerevisiae* (killer) and *Candida cantarelli* yeasts, with Syrah must in batch mode (Toro and Vazquez, 2002). The fermentation temperature is T [K] and R is general gases constant [kJ $kmol^{-1}$ K^{-1}].

In the energy balance (Eq. 4), the assumptions are: heat losses due to CO_2 evolution, water evaporation and ethanol and flavor losses were neglected; the average grape juice-wine density and all physical properties are uniform in the fermenting mass bulk. They are constant with temperature and time as well. Heat transfers by radiation and conduction are negligible. The balance for the energy accumulation in the bioreactor is,

$$\frac{d\left(\rho_r \cdot V_r \cdot Cp_r \cdot T\right)}{dt} = Y_{H/CO_2} \cdot V_r \cdot \frac{dCO_2}{dt} - Q \quad (4)$$

In Eq. (4), ρ_r [kg m^{-3}], V_r [m^3] and Cp_r [W-h kg^{-1} K^{-1}] are density, volume and specific heat of the fermenting mass in the bioreactor. Y_{H/CO_2} [W·h produced/kg CO_2 released] is the energy due to the carbon dioxide released by the bioreaction. It was obtained by stoichiometry (Eq. 1) from $Y_{H/S}$, the likely energetic yield on substrate consumed. At last, Q [W] is the exchanged heat between the fermenting mass and the cooling jacket,

$$Q = F_w \cdot Cp_w \cdot \left(T_{w,out} - T_{w,in}\right) \quad (5)$$

Where, F_w is the cooling water flow rate [kg h^{-1}] and Cp_w is specific heat of water [W-h kg^{-1} K^{-1}]; the cooling water temperature in the jacket inlet is $T_{w,in}$ [K] and in the jacket outlet is $T_{w,out}$ [K] (Perry *et al.*, 1997), $T_{w,out} = T - \frac{T - T_{w,in}}{e^{\frac{U \cdot A_t}{F_w \cdot Cp_w}}}$ (6)

Heat exchange area is A_t. Global heat transfer coefficient, U [W m^{-2} K^{-1}], mostly depends on: convective heat transfer coefficient of fermentation mass, which is assumed constant (Colombié *et al.*, 2007); and the heat transfer coefficient for forced convection of water in the cooling jacket. This one was assumed as an annulus (Kern, 2001) and it is function of F_w. Water properties variations and the fouling factor inside the jacket were neglected. Geometry of the bioreactor, equivalent heat transfer diameter of the cooling jacket annulus and fermentation mass height in the bioreactor were considered by their impact on U (Colombié *et al.*, 2007). Finally, water physicochemical properties are required: density, viscosity and thermal conductivity.

3 Simulations

First, the non-isothermal phenomenological model proposed was tested via simulation in the same nominal experimental conditions of two typical winemaking fermentations FER1 and FER2 at laboratory scale. Toro and Vazquez (2002) have described further details about experimental procedures and analytical determinations used here.

The experimental data set used was attained from cultures carried out in 5 liters capacity containers with: an effective must volume of 3 liters; a temperature control at 23 +/-1°C (296+/-1 K) during the cellular growth phase by means of a cooling water jacket; and weight loss detection. Figure 1 and 2 show two experimental fermentations and the corresponding modelled curves for temperature, viable cells and CO_2 and μ_m evolution.

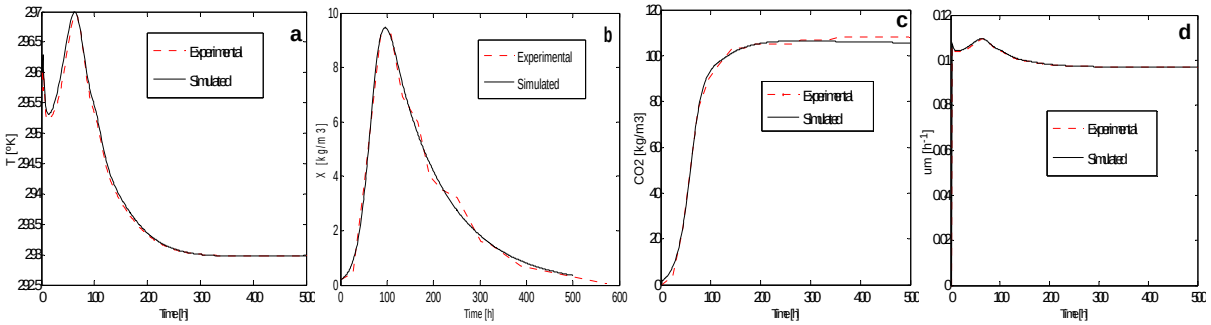

Figure 1. Experimental and modelled curves for fermentation FER1. (a) Fermentation temperature. (b) Viable cells. (c) Carbon dioxide released. (d) Maximum specific growth rate. Experiment at initial (X_0 = 2x10^6 CFU ml^{-1}, S_0 = 208.5 kg m^{-3}, P_0 = $CO_{2,0}$ = 0 kg m^{-3}, T_0 = 296 K) and operating conditions ($F_{w,nominal} \cong$ 0.448 kg h^{-1}, $T_{w,in}$ = 293 K) with *Saccharomyces cerevisiae and/or Candida cantarellii yeasts* inocculated in Syrah must.

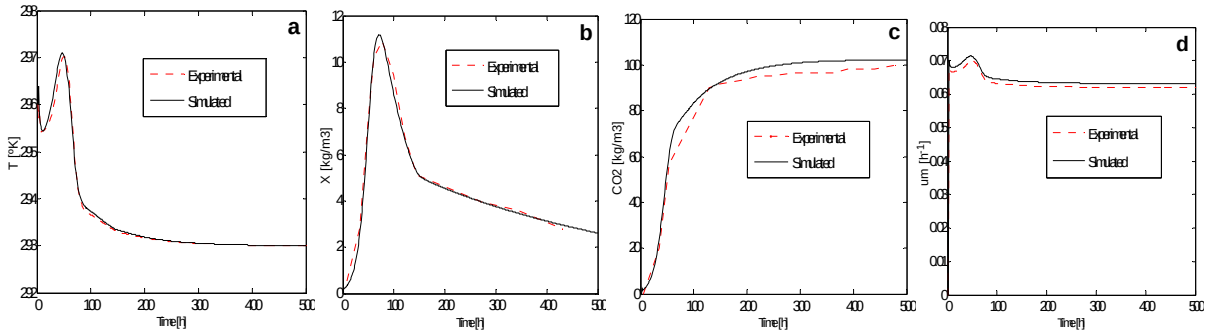

Figure 2. Experimental and modelled curves for fermentation FER2. (a),(b),(c),(d), Idem than Fig. 1. Experiment at similar initial conditions (S_0 = 213.5 kg m^{-3}), same yeasts and must than FER1, with operating conditions ($F_{w,nominal} \cong$ 0.403 kg h^{-1}, $T_{w,in}$ = 293 K).

Second, the model validation was carried out by simulation using different experimental data sets at different constant values of cooling water flow rate and temperature.

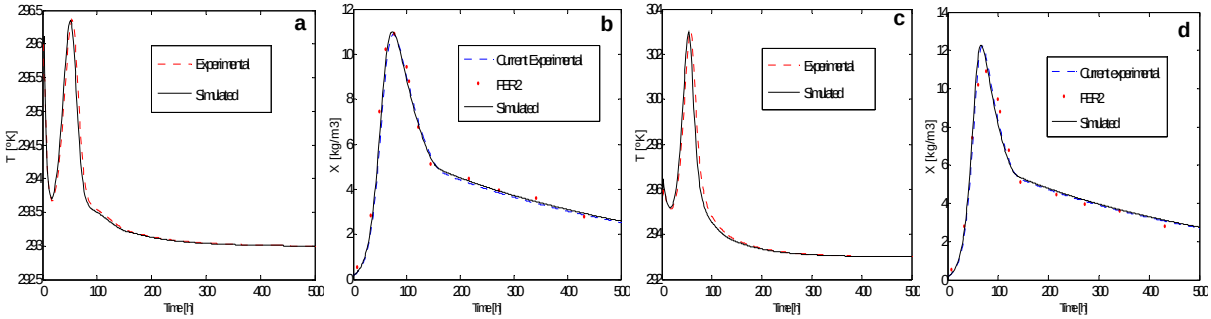

Figure 3. Experimental and modelled curves for fermentation FER3. (a) and (c) Fermentation temperature. (b) and (d) Viable cells concentration. Experiment at same initial conditions, yeasts and must than FER2, but with operating conditions: $T_{w,in}$=293 K in all cases. (a) and (b), F_w = 0.475 kg h^{-1}= constant. (c) and (d), F_w = 0.171 kg h^{-1}= constant.

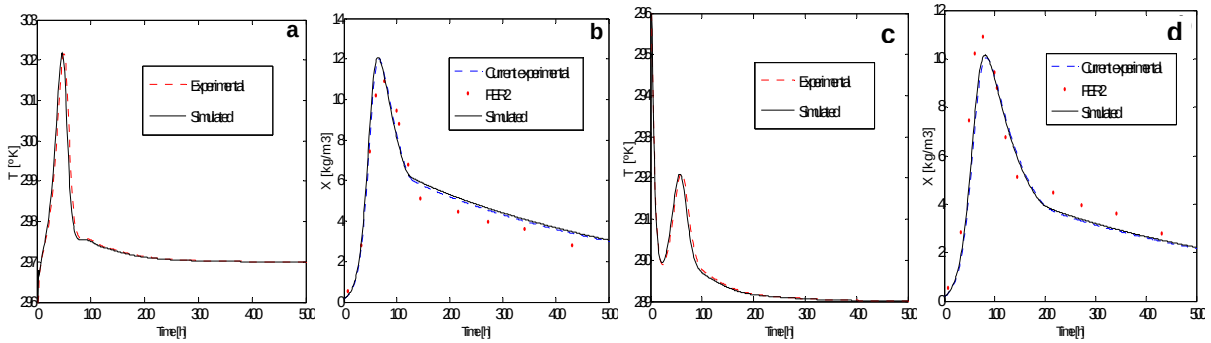

Figure 4. Experimental and modelled curves for fermentation FER4. (a) and (c) Fermentation temperature. (b) and (d) Viable cells concentration. Experiment performed with the same initial conditions, yeasts and must than FER2, but with operating conditions: F_w = 0.403 kg h^{-1} in all cases. (a) and (b) with $T_{w,in}$ = 297 K = constant. (c) and (d) with $T_{w,in}$ = 289 K = constant.

Figures 1 to 4 show the approximation between the experimental and simulated curves for T, X, CO_2 and μ_m. As can be seen, the model proposed has a satisfactory prediction of up to 4 hours in advance regarding experimental fermentation temperature. In addition, all figures reveal that the model is suitable because its error is into an acceptable maximum limit of 3% in respect of variables data ranges, which is compensated with an experimental measurement error of around the same value. Also, all simulations agree with the experimental variables behavior. On the other hand, a fermentation temperature increase occurs due to using a lower flow rate (-60%) or a higher temperature of cooling water (+20%), (Fig. 3c, 3d or 4a, 4b) and vice versa (Fig. 3a, 3b or 4c, 4d) if this is compared with nominal conditions. Finally, the previous considerations are in agreement with experimental published data (Coleman *et al.*, 2007; Colombié *et al.*, 2007; Martínez *et al.*, 1999).

4 Performance analysis

The non-isothermal model was studied in presence of disturbances. Steps changes on most probable manipulated variable in practice, such as the cooling water flow rate, were introduced. A decrease or a shut-down in the cooling water flow can affect the most critical state variable for wine quality, the fermentation temperature. Then, the model performance was evaluated considering responses of μ_m, fermentation temperature and CO_2 evolution (key fermentation measure) to negative step changes, -33% and -70% of nominal F_w (Fig. 5).

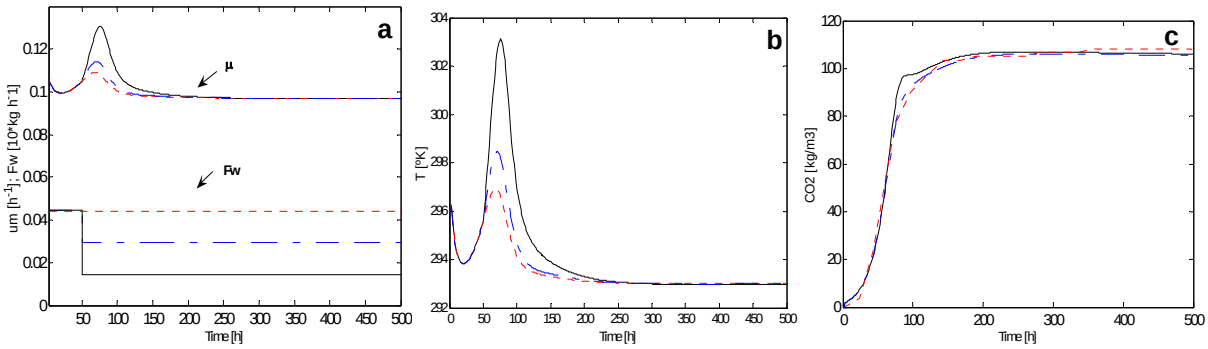

Figure 5. Model responses to steps on the cooling water flow rate. $F_{w,nominal}$ = 0.448 kg h^{-1} (- - -); $F_{w,}$ = 0.30 kg h^{-1} (— - —); $F_{w,}$ = 0.143 kg h^{-1} (—). (a) Maximum specific growth rate and water flow rate. (b) Fermentation temperature. (c) Carbon dioxide released.

In Figure 5, responses to more negative steps on water flow rate each time, up to -70%, can be seen. They produce a positive increase on: maximum growth rate (up to +20%), (a), and maximum fermentation temperature (up to +25%), (b). Moreover, an early positive increase in carbon dioxide released (+14%) at t = 88 hours can be observed, (c); then, a come back to the typical CO_2 trajectory (d). At last, F_w step responses on μ_m and fermentation temperature have a delay of up to 8 hours in both cases, and 14 hours for CO_2 = 86.0 kg m^{-3}. All cases are referred to the nominal simulation with F_w = 0.448 kg h^{-1}; $T_{w,\,in}$ = 293 K was kept constant.

5 Conclusions

An accurate non-isothermal phenomenological model for alcoholic fermentation in winemaking conditions has been presented in this contribution. It is based on a previously developed for the mass balances in isothermal conditions; these were coupled with an energy balance in the bioreactor and its cooling jacket by means of Arrhenius expression. In this sense, cellular growth rate dependence on temperature, at usual operating conditions for typical fermentations, has been considered to improve the prediction. These latter was done to predict key state variables as: viable cells, substrate (sugar) and ethanol concentrations, CO_2 released, and the bioreactor temperature as well. Even so, some model limitation such

the prediction of mentioned variables at fermentation temperatures higher than 30ºC, must be still enhanced.

The proposed model has been adequately validated via simulation with published and own experimental data, showing a suitable behavior and leading to predict in advance the fermentation evolution. Also, a satisfactory performance analysis has been carried out. This allows disposing of a reliable model to approximate state variables trajectories and take suitable control actions on the bioprocess. Hence, its use in different control algorithms can be promising and will be addressed in next works.

References

Aballay, P.M., Vallejo, M.D., Ortiz, O.A. (2006). Temperature control system for high quality wines using a hybrid model and a neural control system. *Proceedings of XVI Congresso Brasileiro de Engenharia Química-COBEQ,* 1153-2429.

Boulton, R., Singleton, V.L., Bisson, L., Kunkee, R. (1996). *Yeast and Biochemistry of Wine Fermentation. In Principles and Practices of Winemaking*. Chapmann & Hall, 102-181.

Coleman, M.C., Fish, R., Block, D.E. (2007). Temperature-dependent kinetic model for nitrogen-limited wine fermentations. *Applied and Environmental Microbiology,* 73 (18), 5875–5884.

Colombié, S., Malherbe, S., Sablayrolles, J.M. (2007). Modeling of heat transfer in tanks during wine-making fermentation. *Food Control*, 18, 953–960.

Fleet, G. (Editor). (1993). *Wine Microbiology and Biotechnology*. Harwood Academic Publishers.

Kern, D.Q. (2001). *Procesos de Transferencia de Calor (Process Heat Transfer)*. Compañía Editora Continental (CECSA) – México/McGraw-Hill Book Co., Inc. (1965), 132-138.

Martínez, G., López, A., Esnaoz, A., Vírseda, P., Ibarrola, J. (1999). A new fuzzy control system for white wine fermentation. *Food Control,* 10*,* 175-180.

Ortiz, O.A., Aballay, P.M., Vallejo, M.D. (2006). Modelling of the killer yeasts growth in an enological fermentation by means of a hybrid model. *Proceedings XXII Interamerican Congress of Chemical Engineering and V Argentinian Congress of Chemical Engineering. Innovation and Management for Sustainable Development.* Buenos Aires. Argentina. A. 13b-224, 451-452.

Perry, R.H., Green, D.W., Maloney, J.O. (1997). *Perry's Chemical Engineers' Handbook. 7TH Edition.* McGraw Hill.

Phisalaphong, M., Srirattana, N., Tanthapanichakoon, W. (2006). Mathematical modeling to investigate temperature effect on kinetic parameters of ethanol fermentation. *Biochemical Engineering Journal,* 28, 36–43.

Scaglia, G.J.E., Aballay, P.M., Vallejo, M.D., Ortiz, O.A. Improved phenomenological model for an isothermal winemaking fermentation. *Food Control*, *Paper under review (January 2008).*

Torija, M.J., Rozès N., Poblet M., Guillamón J. M., Mas A. (2003). Effects of fermentation temperature on the strain population of *Saccharomyces cerevisiae*. *International Journal of Food Microbiology, 80,* 47-53.

Toro, M.E., Vazquez, F. (2002). Fermentation behavior of controlled mixed and sequential cultures of *Candida cantarellii* and *Saccharomyces cerevisiae* wine yeasts. *World Journal of Microbiology & Biotechnology,* 18, 347- 354.

Vallejo Herrera, M.D., Aballay, P.M., Toro, M.E., Vázquez, F., Suárez, G.I., Ortiz, O.A. (2005). Hybrid modeling and neural prediction of the wild killer yeast fermentation performance in a winemaking process. *2nd Mercosur Congress on Chemical Engineering. 4th Mercosur Congress On Process Systems Engineering. ENPROMER 2005. Rio de Janeiro. Brasil. Abstracts ENPROMER 2005. E-Papers (Editors). ISBN: 85-7650-042-6.* Paper code 230*,* 79-92.

Zagorc, T., Maráz, A., Cadez, N., Povhe Jemec, K., Péter, G., Resnik, M., Nemanic, J., Raspor, P. (2001). Indigenous wine killer yeasts and their application as a starter culture in wine fermentation. *Food Microbiology,* 18, 441-451.

Proceedings of the 10th International Chemical and
Biological Engineering Conference - CHEMPOR 2008
Braga, Portugal, September 4-6, 2008
E.C. Ferreira and M. Mota (Eds.)

Model aided design of gas-lift reactor for oxidation reaction with fast reversible catalyst deactivation

Zuzana Gogová*, Jiří Hanika
Institute of Chemical Process Fundamentals, AS CR, v.v.i., Rozvojová 135/2, 165 02 Prague 6 - Suchdol, Czech Republic

Keywords: Gas-lift reactor, Model, Glucose, Palladium, Catalyst deactivation
Topic: Process synthesis & design

Abstract

Tanks-in-series based model was applied to aid design of gas-lift reactor (GLR), where oxidation reaction along with catalyst reversible deactivation proceeds.

Heterogeneously catalyzed wet air oxidation of glucose dissolved in aqueous alkaline solution served as model reaction. Commercial 2.8% Pd/C catalyst was used in this study. Its advantage is activity at mild conditions with high selectivity towards salt of gluconic acid. But it gets deactivated by the action of oxygen quickly during the reaction course.

Multifunctional gas-lift reactor allows the desired reaction, as well as the catalyst reactivation. Optimal design of the gas-lift reactor makes it possible to keep high and stable activity of the catalyst.

1 Introduction

The model reaction

Glucose (Glc) wet air oxidation is used as the model reaction. It takes place in three-phase medium. The overall reaction can be schematically drawn as follows:

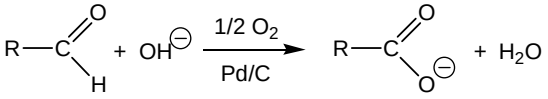

Palladium on activated carbon was used as the catalyst in this study. Results of the model system kinetics study can be found in ref. [1]. The palladium catalyst advantage is the ability to catalyze the reaction at mild conditions selectively towards gluconic acid (Glcac). Its drawback is fast deactivation during the oxidation reaction. This is due to oxidation of the active component surface when oxygen penetrates to Pd subsurface layer [2, 3]. Typically, in one hour the catalyst activity can drop to less than 40% of its original value depending on the reaction conditions. Although the deactivation was proved reversible [4], the rate it takes would present a crucial problem for industrial implementation of the process.

Activation and reactivation of the catalyst is based on reduction the catalyst active sites. Any substance ready to offer its hydrogen can be used for this purpose [5]. Depending on the reductive properties of the particular chemicals to be oxidized in the process, these can be used for the catalyst activation under inert atmosphere. Glucose is good reduction agent to pre-reduce the catalyst.

Solution to the catalyst deactivation problem

Solution to the problem with the catalyst fast reversible deactivation is offered by employment of multifunctional gas-lift reactor (GLR). In GLR, the main reaction, as well as

* Corresponding author. Tel + 420 220 390 349. E-mail:gogova@icpf.cas.cz

the catalyst reactivation proceeds within one reactor unit. In principle, GLR operation is based on spontaneous circulation of catalyst dispersion in liquid, which results from difference in apparent density of the reaction mixture present in riser and downcomer of the reactor. Therefore, if complete separation of the gas phase is ensured after the reaction media passes the riser where the main reaction (and the catalyst deactivation) takes part, the downcomer serves as reactivation zone of the reactor.

The goal of this study was to design a target GLR with optimal geometry for given input conditions, so that the highest possible reactor productivity can be achieved.

2 Theoretical

Mathematical model of gas-lift reactor

GLR mathematical model was derived and applied to aid the target reactor design. Gas-lift reactor is not a simple unit; the GLR mathematical model therefore takes into account that the overall reactor performance is a sum of contributions of each section: the riser, the gas separator, the downcomer and the bottom of the reactor. Each of these sections has its distinct hydrodynamics and its own specific chemistry that is a consequence of different media coming into contact in them. Therefore, the GLR model, as previously introduced by the authors (see reference [6] for more details), consists of two main parts – the first one (hydrodynamics iteration cycle) is to calculate hydrodynamics and optimal geometry based on input adjustable parameters, and second part (reactor performance iteration cycle) uses the results of the first part and calculates the actual GLR performance.

Tanks-in-series model (Figure 1) was employed in the second part of the GLR mathematical model to grasp the way of mixing in real GLR. Every single tank of the tanks-in-series model was described by a set of equations combining hydrodynamics and chemistry that are supposed to hold for the individual section of GLR reactor. The number of tanks that form each section (the riser and downcomer mainly) in the tanks-in-series model corresponds to the extent of axial dispersion in these sections [7, 8], and is set as one of input parameters.

The GLR model was used to firstly aid the target GLR design for given input conditions, and secondly to predict either steady state characteristics of the target reactor, or to find out about transient characteristics as a response to disturbances of its control parameters. Therefore, set of either NAE or ODE is used to mathematically describe the tanks-in-series model [6] depending on the desired outcome from the modelling.

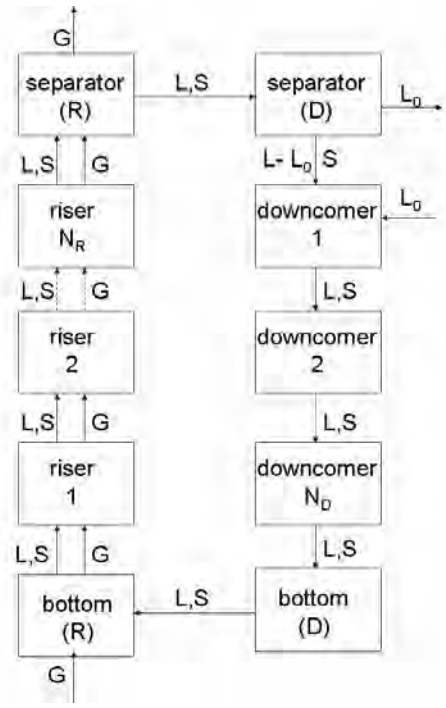

Figure 1: Scheme of tanks-in-series model employed in the "reactor performance iteration cycle" of the GLR mathematical model (see the text above). It enables combining the hydrodynamics and chemistry that are supposed to hold for the individual sections of gas-lift reactor. The tanks-in-series model is employed in continuous mode of operation See the ref. [6] for the GLR model detailed description.

The GLR model parameters

The GLR model parameters form two categories: adjustable operating parameters and non-adjustable parameters. The input adjustable parameters are: degree of Glc conversion, feed (and start-up) concentrations, amount of the catalyst, superficial gas velocity, number of tanks in series, kinetics parameters [1], temperature (30℃), operation pressure (atmospheric). Basic geometrical parameters were adopted from GLR, volume 40L (see [7, 9-11]). This particular reactor has been a source of many correlations employed in the model. Following the procedure described in detail in ref. [6], the input adjustable parameters form a basis to calculate the non-adjustable parameters.

The GLR model assumptions

1) The GLR operates in the region of homogeneous bubbly flow.
2) The downcomer gas hold-up is zero; this can be achieved by appropriate design of separator [12].
3) The number of tanks that form riser and downcomer corresponds to the extent of axial dispersion in these sections. Plus, there are two tanks for each – the bottom and the separator. In the latter two tandems, the sizes of the individual twin tanks vary depending on the respective volumes taken up by either liquid (then they become functional part of downcomer) or G-L dispersion (and then act as a part of riser).
4) Each of the tanks in series operates isothermally at 30℃ and is perfectly mixed.
5) The mathematical model combines description of the GLR hydrodynamics with the kinetics of the glucose oxidation reaction and the catalyst deactivation and reactivation.
6) The reactor operates at low Glc conversions so that 100% selectivity towards gluconic acid can be presumed; based on conclusions of Kunz and Recker [13].
7) The Pd/C catalyst particles (size about 45 μm) are assumed to be homogeneously dispersed in liquid phase. Then it is feasible, for the mathematical description purpose, to accept a concept of pseudo-liquid reaction phase.
8) Constant liquid volumetric flow rate within the reactor sections is assumed i.e. liquid density is constant – independent on the conversion.

3 Results and discussion

The task was to design a target GLR with optimal geometry for given input conditions, so that the highest possible reactor productivity can be achieved. The GLR model was used for this purpose. The presented simulations were run by using commercial software Matlab.

For each set of the input adjustable parameters the location of optimum geometry shifts as a consequence of change in deactivation extent of the catalyst after it passes riser of the GLR. For any deactivation extent always an optimum activation time exists. If the reactivation time is lower, the reactivation process is insufficient. If the reactivation time exceeds its optimum, the time the main reaction could have proceeded is wasted and the reactor productivity drops down. In Figures 2 and 3 the effects of superficial gas velocity and concentration of reactants on the GLR optimum geometry location is shown. The geometrical coordinate is represented by the downcomer-to-riser cross sectional area ratio, A_D/A_R. The GLR productivity is represented by cycle-time-averaged reaction rate, $\bar{\dot{\xi}}_w$, that reaches maximum in the point of the GLR optimal geometry.

During the model reaction kinetics study [1] it was found that the reaction rate is inhibited by oxygen. Moreover, oxygen affects the extent of the catalyst deactivation. The variation range of oxygen concentration is therefore limited in gas feed stream to the GLR. Figure 2 covers major part of the target GLR operational window in terms of U_{GR} and $Y_{OG\text{-}feed}$. It can be seen from Figure 2, that change in $Y_{OG\text{-}feed}$ is compensated to large extent by change in A_D/A_R and the reaction rate responds only slightly to it. In the case of increasing Glc con-

centration (Figure 3), the GLR productivity increases significantly (in the point of the GLR optimal geometry). This is in agreement with the observations from the model reaction kinetics study [1]. As the Glc concentration rises up, the rate of the catalyst reactivation increases as a result of quicker consumption of oxygen. Consequently, the downcomer zone of GLR required for the catalyst reactivation shrinks, too.

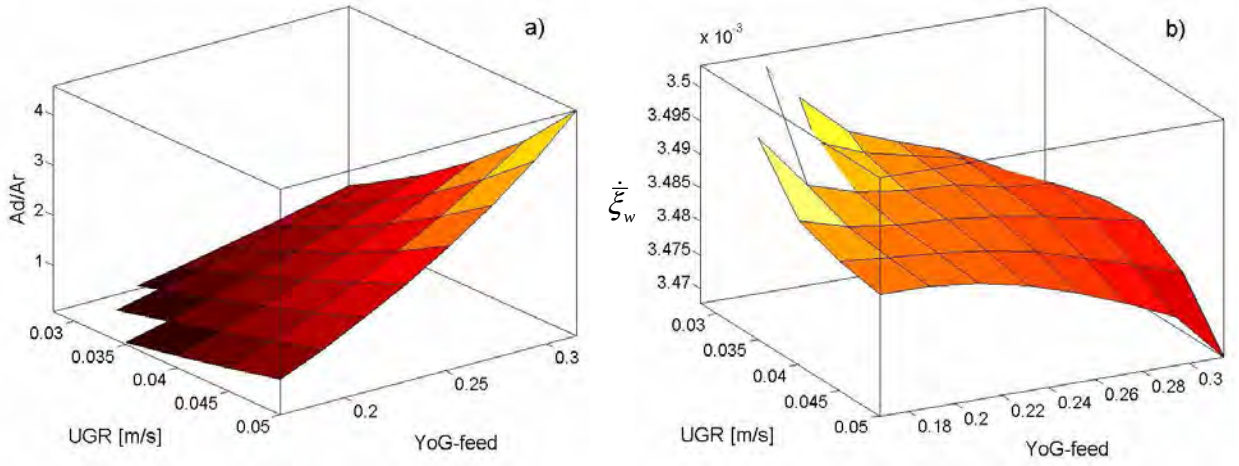

Figure 2: Influence of oxygen concentration in the gas feed ($Y_{OG\text{-}feed}$) stream at various U_{GR} levels on **a)** location of the target GLR optimum geometry; **b)** cycle-time-averaged reaction rate in the point of optimal geometry. Conditions: $C_{Glc\text{-}feed}$=100mol/m^3; $C_{Glcac\text{-}feed}$=0; X_{Glc}=2%.

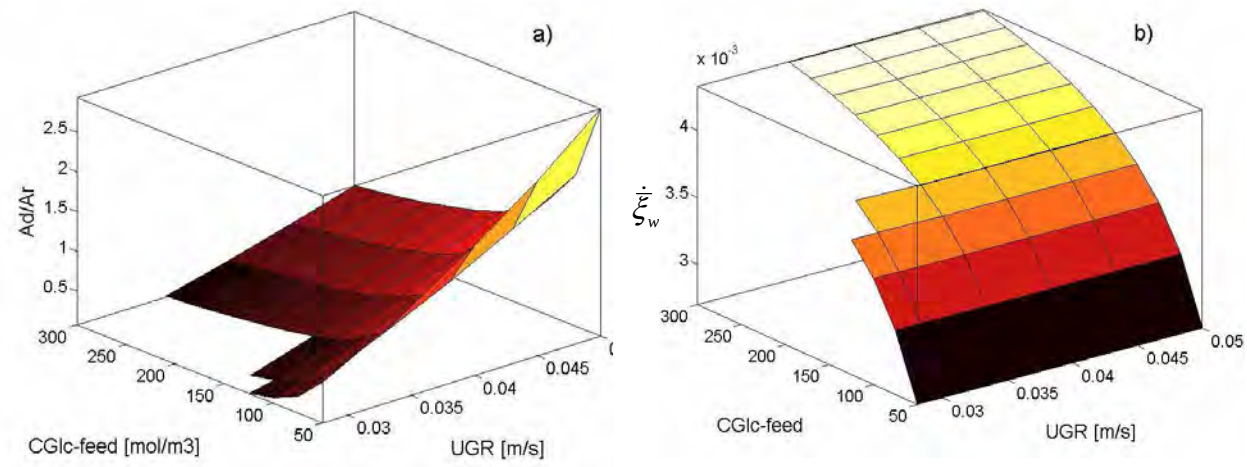

Figure 3: Effect of glucose concentration in the liquid feed stream at various U_{GR} levels on **a)** location of the target GLR optimum geometry; **b)** cycle-time-averaged reaction rate in the point of optimal geometry. Conditions: $Y_{OG\text{-}feed}$=0.21; $C_{Glcac\text{-}feed}$=0; X_{Glc}=2%.

For the input parameters given by the points on the U_{GR}-C_i coordinates in Figures 2a and 3a, the 3D-plane of solutions represents the optimum geometry with the only possible reaction-reactivation time-share to achieve the highest possible cycle-time-averaged reaction rate in the target GLR. Every geometrical solution either above or below the optimum plane would lead to either too long or too short reactivation time, respectively. Any of these two deviations from the optimum geometry result in lower cycle-time-averaged reaction rate than the one achieved in GLR of optimal geometry (Figures 2b and 3b).

In Figure 4, profiles of the actual concentrations and reaction rates along the tanks-in-series are presented for given set of input parameters. Depending on the input conditions the

optimum reaction-reactivation time-share varies and so do the profiles of the reaction rate and the concentrations along the tanks of the tanks-in-series model. As mentioned before, the target GLR operates continuously and these profiles are linked with the points of inlet and discharge from the reactor (see Figure 1). Change in the catalyst fractional coverage by inactive oxygen species, θ_{so}, in Figure 4 indicates change in the catalyst activity. The higher the θ_{so} is, the more the catalyst's activity drops. For more explanation see ref. [1].

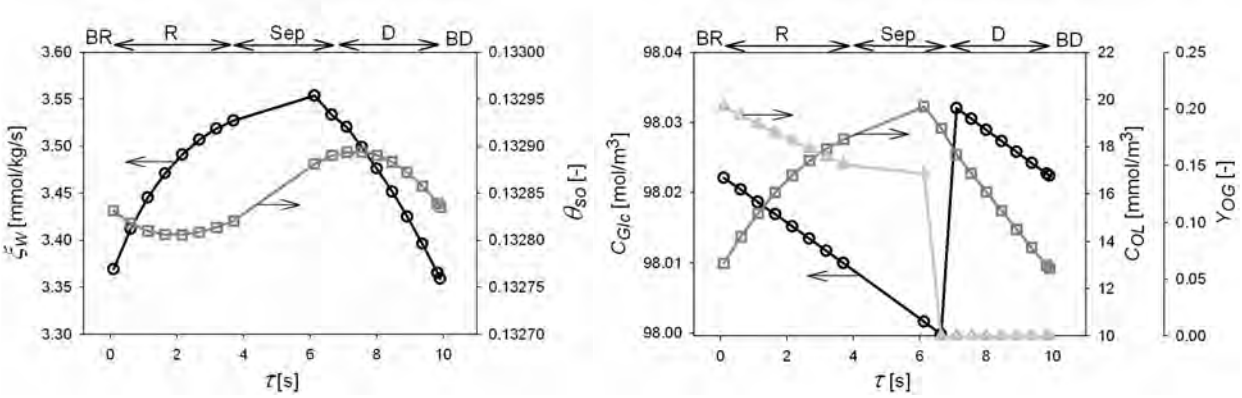

Figure 4: Profiles of the actual reaction rates (circles) and fractional coverage by inactive oxygen (squares) – **left**; Glc (circles) and dissolved oxygen concentrations (squares) and molar fraction of oxygen in the gas phase (triangles) – **right**; in the tanks of the tanks-in-series model (see Figure 1 and the text above for more explanation). Conditions: $C_{Glcac\text{-}feed}$=0; $C_{Glc\text{-}feed}$=100mol/m^3; $Y_{OG\text{-}feed}$=0.21; X_{Glc}=2%; U_{GR}=0.04 m/s; N_R=N_D=7; N_{Sep}=N_B=2; W=80%.

4 Conclusions

GLR mathematical model was used to aid design of target reactor for reaction of heterogeneously catalyzed glucose oxidation. The derived model helps to overcome the problem of the catalyst's fast reversible deactivation by appropriate calculation of the target GLR geometry for any given input conditions.

Nomenclature

0	inlet, start-up	*R*	riser
A	area (m^2)	*S*	solid
B	bottom of reactor	*Sep*	separator
BD	downcomer portion of the bottom	*SepD*	downcomer portion of the separator
BR	riser portion of the bottom	*SepR*	riser portion of the separator
C	concentration (mol/m^3)	τ	space time (s)
D	downcomer	*U*	superficial velocity (m/s)
feed	feed	*W*	volumetric portion of separator that is taken up by G-L dispersion and becomes a functional part of riser (%)
G	gas		
Glc	glucose		
Glcac	gluconic acid	*X*	conversion (%)
GLR	gas-lift reactor	$\dot{\xi}_w$	specific reaction rate (mol/kg/s)
L	liquid	$\dot{\bar{\xi}}_w$	cycle-time-averaged specific reaction rate (mol/kg/s)
N	number of tanks (-)		
O	oxygen	*Y*	molar fraction (-)
θ_{so}	fractional coverage by inactive oxygen species (-)		

Acknowledgement:

Supported by Grant Agency of Czech Republic (grant No.: 203/08/H032).

References

1. Gogová, Z., M. Fujasová, and J. Hanika. *Kinetics and modelling of glucose wet air oxidation over Pd/C catalyst*. in *34th International Conference of SSCHE*. 2007. Tatranské Matliare, Slovakia.
2. Ketteler, G., D.F. Ogletree, H. Bluhm, H. Liu, E.L.D. Hebenstreit, and M. Salmeron, *In Situ Spectroscopic Study of the Oxidation and Reduction of Pd(111).* J.Am.Chem.Soc., 2005. **127**: p. 18269-18273.
3. Lundgren, E., G. Kresse, C. Klein, M. Borg, J.N. Andersen, M. De Santis, Y. Gauthier, C. Konvicka, M. Schmid, and P. Varga, *Two-Dimensional Oxide on Pd(111).* Physical Review Letters, 2002. **88**(24).
4. Vleeming, J.H., B.F.M. Kuster, and G.B. Marin, *Selective Oxidation of Methyl α-D-Glucopyranoside with Oxygen over Supported Platinum: Kinetic Modeling in the Presence of Deactivation by Overoxidation of the Catalyst.* Ind. Eng. Chem. Res., 1997. **36**: p. 3541-3553.
5. Mallat, T. and A. Baiker, *Oxidation of alcohols with molecular oxygen on platinum metal catalysts in aqueous solutions.* Catalysis Today, 1994. **19**: p. 247-284.
6. Gogová, Z. and J. Hanika. *Purpose tailored design of gas-lift reactor*. in *35th International Conference of SSCHE*. 2008. Tatranské Matliare, Slovakia.
7. Sikula, I. and J. Markoš, *Modeling of enzymatic reaction in an airlift reactor using an axial dispersion model.* Chemical Papers, 2008. **62**(1): p. 10-17.
8. Schuller, L., *Diplomová práca: Určovanie axiálnych disperzných koeficientov v airlift reaktoroch s vnútornou cirkuláciou*. 2007, ÚChEI FChPT STU Bratislava.
9. Blažej, M., M. Juraščík, J. Annus, and J. Markoš, *Measurent of mass transfer coefficient in an airlift reactor with internal loop using coalescent and non-coalescent liquid media.* J Chem Technol Biotechnol., 2004. **79**: p. 1405-1411.
10. Juraščík, M., M. Blažej, J. Annus, and J. Markoš, *Experimental measurements of the volumetric mass transfer coefficient by the dynamic pressure-step method in an internal loop airlift reactors of different scale.* Chemical Engineering Journal, 2006. **125** p81-87.
11. Blažej, M., M. Kiša, and J. Markoš, *Scale influence on the hydrodynamics of an internal loop airlift reactor.* Chem. Eng. and Processing, 2004. **43**: p. 1519-1527.
12. Gogová, Z., V. Čamaj, M. Hronec, and F. Stanček, *Patent No.: WO2004047980 (PP SK 1676-2002), Device for conditions of chemical technologies and its application, (also published as: EP1569747, RU2005120243, AU2003222562)*.
13. Kunz, M. and C. Recker, *A new continuous oxidation process for carbohydrates.* Carbohydrates in Europe, 1995. **13**: p. 11-15.

Proceedings of the 10th International Chemical and
Biological Engineering Conference - CHEMPOR 2008
Braga, Portugal, September 4-6, 2008
E.C. Ferreira and M. Mota (Eds.)

A new hybrid modeling methodology based on delayed differential equations: Application to antibody expression by Pichia pastoris

M. von Stosch[1], R. Oliveira[2], J. Peres[1], S. Feyo de Azevedo[1*]
[1] LEPAE, Departamento de Engenharia Química, Faculdade de Engenharia, Universidade do Porto, Rua Dr. Roberto Frias s/n, 4200-465 Porto, Portugal
[2] REQUIMTE/CQFB, Departamento de Quimica, Faculdade de Ciências e Tecnologia, Universidade Nova de Lisboa, 2829-516 Caparica, Portugal

Keywords: Hybrid Modeling, Biosystem Dynamics, Delay Differential Equation, AR(X)
Topic: Systematic methods and tools for managing the complexity

Abstract

In this paper a novel methodology for biosystems dynamic modelling is presented in which discrete time series, namely AutoRegressive (eXogenous) models are incorporated in the traditional parametric/nonparametric hybrid modelling framework. This results in a set of Delay Differential Equations (DDE) which describe the material balances of a bioreactor system in which dynamic kinetics are mimicked by a parametric/nonparametric submodel. The idea is to display better consistency with the nature of biological systems by associating the dynamics of a cellular metabolism to a parametric/nonparametric subsystem. The proposed hybrid structure is evaluated with fed-batch experimental data taken from a process for antibody expression by recombinant *Pichia pastoris* in addition to two simulation case studies. The first of these assumes a discrete time delay and the second assumes a distributed delay between kinetics. In this paper, it is shown that the proposed hybrid model is capable of modelling discrete and distributed delays between kinetics and outperforms the standard hybrid modelling methods with static kinetic models.

1 Introduction

Time delays have been observed in many bioprocesses and, as is well known, they can be source of instabilities and oscillations. In most cases, however, only a certain time delay between the substrate uptake, biomass growth and product formation is observed such as the case of the growth phase of fed-batch *Saccharomyces cerevisiae* or the *Pichia pastoris* cultivations (Ren et al, 2003). Many phenomenological models that consider discrete delays (Wolkowicz et al, 1997), distributed delays (Daugulis et al, 1997, Wolkowicz and Xia, 1997), ordinary differential equations (ODE) of kinetic rates (Ren et al, 2003) or other time delay considering techniques have been reported. They are usually based on the general mathematical concept of Retarded Functional Differential Equations (RFDE), Bocharov and Rihan (2000). On the one hand, these models are capable of explaining stability of processes and are suitable for the estimation of process key variables. However, on the other hand, their application to other cell systems is limited and their development is cost expensive. In contrast, hybrid modelling has been reported to be a suitable, cost effective alternative capable of being applied to a number of cell systems, Oliveira (2004). Hybrid models combine mechanistic knowledge and process knowledge in form of mechanistic models and data-base nonparametric models. Mechanistic and nonparametric models can be arranged in two possible manners: parallel or serial. In the serial structure, which has been applied in this study, the process dynamics are described by time differentials of process classifying variables and the cell system is mimicked by a parametric/nonparametric submodel. However, until now, cell system dynamics have not been taken into account by these submodels, but it is known that cell systems are sources of time delays. Thus, in this paper, the dynamics of the cell system will be ascribed to the parametric/nonparametric

* Corresponding author. Tel + 351-22-508-1694. E-mail: sfeyo@fe.up.pt (S.F. de Azevedo)

submodel. Similar techniques as in the case of phenomenological models could be used, for example discrete delays or distributed delays of state variables in the kinetics or differential equations of the kinetics. The latter is not appropriate, because both the kinetic function and the kinetic values remain unknown. Therefore, a solution or estimation of the kinetics is not a straightforward process. Distributed delays are also rather unlikely to be used, due to the fact that a mathematical postulation of arbitrarily large delays for unknown weighting functions of the delayed variable would have to be assumed and this mathematical convenience is in limit biologically unrealistic (Bocharov and Rihan, 2000). Instead, the use of discrete delays in the hybrid model estimated values and in additional measurements, when available, is proposed in this paper. This is analogous to the application of discrete time series, namely AR(X) models. Whereas, in theory, an endless number of time lagged values of one variable can be used as inputs to the nonparametric function, in practice this would lead to long training times and to identification problems of the network structure and parameters (Haykin (1999)). Hence an optimal number of time lagged values exists which represent the proportion between redundancy and the additional gain of information in the inputs. This has been neglected by this paper and instead it has been shown that a limited number of time lagged variable values significantly enhances the prediction capacity of the model and that time lags and the number of time lags have been chosen by trial, which was for example also the case of Parlos et al (2000).

The remainder of the paper is organized as follows. Section 2 presents the embedding of discrete time series into the hybrid parametric/nonparametric structure proposed by Oliveira (2004) along with the changes to the sensitivity equations. The evaluation of the structure which has been presented through the analysis of two simulation cases in addition to experimental fed-batch data of a *Pichia pastoris* process is carried out in section 3. Finally, conclusions are presented in section 4.

2 Hybrid Model Structure

The serial parametric/nonparametric hybrid model structure presented in this paper is shown in figure 1. The structure is based on the originally proposed model by Oliveira (2004). However, in this paper, discrete time series, namely AR(X), are incorporated into the hybrid framework, resulting in a set of DDE for the bioreactor system. Then, the identification of the parameters of the nonparametric function is carried out.

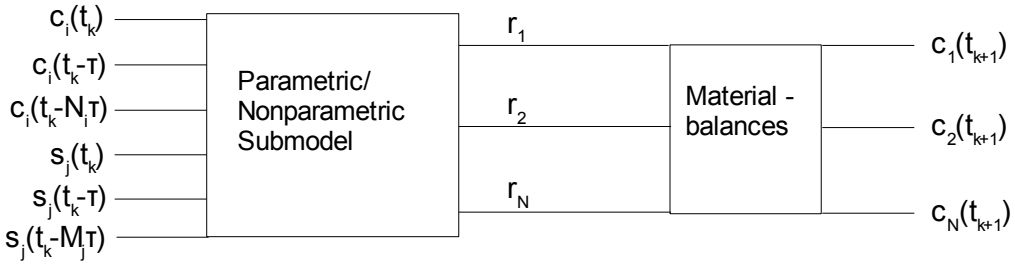

Figure 1: Structure of the proposed serial parametric/nonparametric hybrid model structure

2.1 General hybrid parametric/nonparametric structure

A bioreactor model can be expressed through a set of material balance equations, which describe the dynamics of state variables such as biomass, substrate, product, etc.,

$$\frac{dc}{dt} = r - D \cdot c + u \,. \qquad (1)$$

Here c is a vector of state variables, D is the dilution rate, u is a vector of volumetric control inputs, and r is the kinetic rate vector. The vector of kinetic rates combines, when available, first principle knowledge with nonparametric functions and according to Oliveira (2004) is:

$$r(c,w) = K(\psi_j(c) * \rho_j(X,w)) \,, \qquad (2)$$

where K is a $n \times m$ yield coefficient matrix, ψ_j are m kinetic functions from mechanistic knowledge and where ρ_j are m unknown kinetic functions which have been modelled with nonparametric techniques, X stands for the vector of inputs and w represents the vector of parameters. Nonparametric techniques have the ability of accounting for nonlinear mappings between inputs and outputs. Yet, this nonparametric modelling of the kinetic functions has barely taken the dynamics of the cell system into account, i.e. the input vector only contemplated the current concentration values $c(t)$ and/or the current exogenous inputs $s(t)$. In this study, and in analogy to the AR(X) models, discrete past values of the model outputs and the exogenous input are also contemplated as inputs to the nonparametric function, resulting in the following equation

$$X = \begin{bmatrix} c_i(t), c_i(t-\tau_i), c_i(t-2\cdot\tau_i), \ldots, c_i(t-N_i\cdot\tau_i), \\ s_j(t), s_j(t-\tau_j), s_j(t-2\cdot\tau_j), \ldots, s_j(t-M_j\cdot\tau_j) \end{bmatrix} . \quad (3)$$

In this equation c_i represents the i[th] value of vector c, τ_i is the associated time lag, N_i defines the number of time lags assumed for each value c_i of vector c, s_j is the j[th] exogenous input, τ_j the associated time lag and its lag number is defined by M_j. Note that the time lags and the numbers of time lags, τ_i, τ_i, N_i, and M_j have been chosen by trial as was previously referred to in the introduction. The nonparametric model adopted here is a three layer back propagation ANN with hyperbolic tangent activation function formulated as ρ_j:

$$\rho_j(X, w) = w_2 \cdot g(w_1 \cdot X + b_1) + b_2 , \quad (4)$$

where w is the vector form of the weights and biases, w_1, w_2, and b_1, b_2, respectively. The hyperbolic tangent activation function $g(\cdot)$ is,

$$g(x) = \frac{2}{(1+\exp(-2\cdot x))} - 1 . \quad (5)$$

By merging Equations (1) – (5) it becomes clear that these model equations which describe a bioreactor system with intracellular dynamics are DDEs as “retarded” or “lagged” phenomena are accounted by the nonparametric submodel.

2. The identification of the parameters of the nonparametric submodel

In this study, a least squares criteria of residual concentrations has been adopted to identify the nonparametric model parameters vector w through process data. This criteria is formulated by the following expression:

$$min\left(E = \frac{1}{P \times n} \sum_{l=1}^{P} \sum_{i=1}^{n} \frac{(c_{m,i}(t) - c_i(t, w))^2}{c_{max,i}} \right) , \quad (6)$$

where P represents the number of measured patterns, n is the number of state variables, $c_{m,i}$ are measured state variables, $c_i(w, t)$ represent calculated state variables and $c_{max,i}$ are the scaling factors. The serial hybrid structure of ANN and material balances has been proven to be trained most effectively when using sensitivity approach along with analytical gradients, Oliveira (2004). The analytical gradients are obtained differentiating equation (1) with respect to w while taking the time lagged differential variables into consideration which reads as follows,

$$\frac{d}{dt} \cdot \frac{\partial c}{\partial w} = \sum_{k=0}^{N_i} \left(\frac{\partial (K \cdot \psi \cdot \rho)}{\partial c(t-k\cdot\tau)} \cdot \frac{\partial c(t-k\cdot\tau)}{\partial w} \right) + \frac{\partial K \cdot \psi \cdot \rho}{\partial w} + D \cdot I_n . \quad (7)$$

This least square problem is solved by using the “lsqnonlin” Matlab function which uses a subspace trust region method and is based on the interior-reflective Newton method (Matlab Optimization toolbox) and which favours analytical gradients. The sensitivity equation (7) is integrated along with the delay differential model equations (1)–(5). For integration the differential equations are linearly approximated which results in a time inexpensive algorithm. Unfortunately, some error has been introduced due to this simplification, but if average kinetic rates are estimated for each time step, the error is significantly minimized. Initial

values of sensitivity equations are $(\partial c/\partial w)_{t=0}=0$, as the initial state variables are independent of w and as the gradients $(\partial c/\partial w)_{t<0}=0$ for $t<0$. The residual gradients are then obtained by using the corresponding sensitivity values. It is important to stress that the lagged values of either state variables and exogenous inputs are assumed to be equal to the initial values for all $t-\upsilon\cdot\tau<0$.

3 Results and Discussion

The evaluation of the original and the proposed (DDE) Hybrid Model has been carried out through the analysis of two fed-batch simulation cases in addition to fed-batch experimental data of a *Pichia pastoris* fermentation.

3.1 Simulation cases

In both simulation cases the bioreactor system is modelled by material balances, resulting in a set of differential equations of biomass, substrate and product concentrations and also of the reactor volume, in which the kinetics are expressed as follows. The substrate uptake rate is modelled with Monod kinetics and depends on the current substrate concentration. Specific growth is composed from some bias which accounts for maintenance and the Monod kinetics of a lag variable. Product formation depends linearly on the specific biomass growth. For the lag variable two different approaches have been adopted. The first, was inspired by Wolkowicz and Xia (1997), and it considers a discrete time lag in the substrate concentration as the lag variable. The second, which was inspired by Daugulis et al (1997), Wolkowicz et al (1997), considers distributed delays in the substrate concentration to be the lag variable. The substrate feeding in both cases is linearly controlled in regards to user desired set points of substrate concentrations.

For the evaluation of the DDE hybrid structure, three sets of data, namely training, validation and test data, have been used. This data consist of simulated fed-batches in which concentrations of biomass, substrate and product, the reactor volume and as well the feeding concentration are assumed to be the measured data.

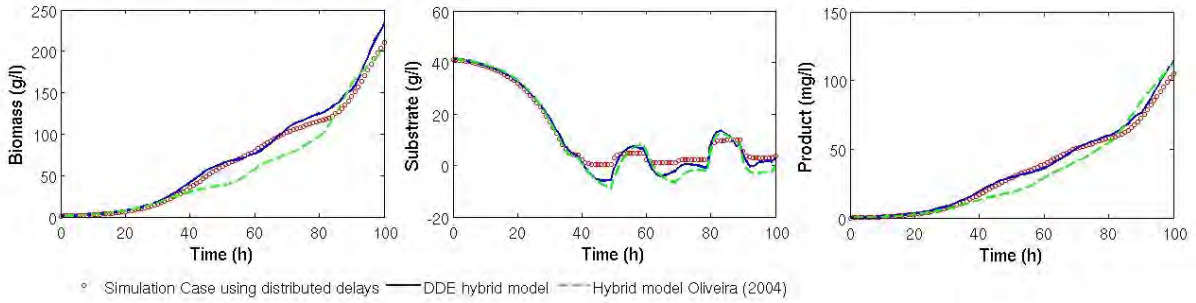

Figure 2: Plot of concentrations over time for data obtained with the DDE hybrid model (solid line, blue), the hybrid model Oliveira (2004) (dashed line, green) and the true simulation using the distributed delay model (o, no line, red)

3.1.1 Hybrid Model Structures

The standard hybrid model structure (Oliveira (2004)) and the DDE hybrid model structure describe three state variables: biomass, product and substrate concentration. The kinetics of each of them are estimated by training an Artificial Neural Network (ANN) with the training set. The estimated substrate concentration, in the standard hybrid model, is the only input to the Artificial Neural Network. In contrast, a series of time delays in the estimated substrate concentrations are considered as being inputs to the ANN for the DDE hybrid model.

The training and identification of the best network structure is carried out according to the best value, namely the greatest value, for the Bayesian Information Criteria (BIC) (Burnham and Anderson (2004)), obtained for the validation set. The test set is used to explore the model generalization capabilities.

3.1.2 Results of Simulation Cases

In Table 1 a selection of the best results obtained for both simulation cases with the standard and the DDE hybrid model are presented. The BIC values for the DDE hybrid model are found to be better than those of the standard hybrid model for both simulation cases. The consistency of all the BIC values obtained for different model structures is elevated although it is not presented here. In fact, the enhancement in model prediction has also been reflected in plots of estimated concentrations and "true" concentrations over time, as being exemplary shown for predictions of a fed-batch considering distributed delays in Fig. 2. Therefore, it is possible to conclude that the proposed DDE hybrid model is capable of accounting for all kinds of time delays observed in process by allowing series of time lagged values of state variables as inputs to the nonparametric model. Thus, a significant enhancement is to be expected for the modelling of experimental data.

3.2 Experimental data of antibody expression of recombinant *Pichia pastoris*

Pichia pastoris fermentation finds application here, as time delays between substrate uptake, biomass growth and product formation have been observed (Ren et al (2003)). Data of Temperature, pH, biomass and product concentrations and the accumulated mass of glycerol and methanol were measured as described in Cunha et al (2004). The bioreactor system is modelled by differential equations of biomass and product concentrations and of the reactor volume while other measurements are considered for the identification of kinetics.

3.2.1 Hybrid Model Structure

In total, four data sets of fed-batch fermentations have been recorded, three of which are used for the training of the hybrid model and the last which is used for its validation. Biomass and product concentrations and the reactor volume are used as state variables. Substrate concentrations, ie glycerol and methanol concentrations have unfortunately not been measured, but instead measurements of accumulated mass of feeding of glycerol and methanol were available. The estimated biomass concentration along with measurements of substrates, such as the sum of mass of glycerol and methanol, temperature and pH, at time t, are inputs for the standard hybrid model. It was assumed that the accumulated mass of feeds along with the estimated biomass concentration could compensate for the lack of substrate concentrations. However measured glycerol and methanol concentrations might have lead to an even more accurate representation of the complexity of the system under analysis. For partial compensation of time delayed substrate concentrations, a time delay in the biomass concentration was taken into account. This is due to the assumption that the delay appearing in the cell metabolism is somewhat similar to a time delay of the cell. Such, in addition to the standard hybrid model, the influences of time lags in the estimated biomass concentration and the measuring of temperature, pH, the sum of mass of glycerol and of methanol on the DDE model estimates have been studied separately and subsequently, a joint delay model for the most significant variables and time delays was studied, namely biomass concentration, temperature and the accumulated mass of glycerol and methanol. The identification of the best network structure was carried out as before.

3.2.2 Results for experimental data

A selection of results is presented in Table 1, revealing the best BIC values for the standard hybrid model and the best BIC values of the DDE hybrid model for lagged inputs of biomass concentration, pH and temperature. The influence of time lags on the estimates, when each variable was studied separately, did not result in significant enhancements of the BIC values in comparison to the standard hybrid model and have therefore not been presented here. The BIC values for the combinations of delayed variables, namely biomass concentration, pH and temperature have been found to be significantly better than the ones of the standard hybrid model, see Table 1. The enhancement of combinations of delayed variables in comparison to the separate delayed variables can be explained by the complexity of the system under study. The state of a system is generally characterized by a set of variables. The time delays in the kinetics are provoked by the cell metabolism which experiences a

change of the state of the system with time. Therefore, combinations of time delays in state characterizing variables lead to better BIC values in contrast to when they are analysed separately. In addition they are also biologically more realistic. However it has been clearly demonstrated that the use of some time lagged values of concentration estimations and exogenous measurements significantly enhances the hybrid model's process predictions.

Simulation Case	Model	NN	Time lag (h)	N_i	BIC train	BIC valid	BIC test
Discrete Delays	Standard hybrid model	2	-	-	-12332	-3256	-3399
Discrete Delays	DDE hybrid model	3	5	1	-11115	-2883	-2882
Distributed Delays	Standard hybrid model	2	-	-	-18942	-5127	-5149
Distributed Delays	DDE hybrid model	4	2	5	-17020	-4552	-4587
Experimental Data	Standard hybrid model	7	-	-	-43373	-13755	-
Experimental Data	DDE hybrid model	3	2	2	-42549	-12890	-
Experimental Data	DDE hybrid model	4	2	2	-42909	-13545	-

Table 1: Best BIC results of both simulation cases and experimental data for the standard and DDE hybrid model, where NN is the number of nodes in the hidden layer of the ANN

4 Conclusions

In order to account for dynamics in the cell metabolism, discrete time series have been incorporated into the hybrid model originally proposed by Oliveira (2004), leading to Delayed Differential Equations (DDE). More accurate prediction qualities of the DDE hybrid model than those obtained through the standard hybrid model have been achieved when applied to two simulation cases containing either discrete or distributed delays between the kinetics. Therefore, it has been concluded that the DDE hybrid model is capable of accounting for all the time delays observed in bioprocess systems. Expectations in regards to the application to the antibody expression of recombinant *Pichia pastoris* have been met, where a significant enhancement of process prediction has been achieved, in which a limited number of time lagged values of predicted concentration and exogenous measurements have been used.

References

Bocharov G.A., Rihan F.A., (2000), Numerical modelling in biosciences using delay differential equations, J. of Computational and Appl. Math., **125,** 183-199.

Burnham K.P., Anderson D.R., (2004), Multimodel inference - understanding AIC and BIC in model selection, Social Methods & Research, **33**, 261-304

Cunha A.E., Clemente J.J., Gomes R., Pinto F., Thomaz M., Miranda S., Pinto R., Moosmayer D., Donner P., Carrondo M.J.T., (2004), Methanol Induction Optimization for scFv Antibody Fragment Production in Pichia pastoris, Biotech. and Bioeng., **86**, 458-467

Daugulis A.J., McLellan P.J., Li J., (1997), Experimental Investigation and Modeling of Oscillatory Behaviour in the Continuous Culture of Zymomonas mobilis, Biotech. and Bioeng., **56**, 99-105

Haykin S. (1999), Neural Networks – A Comprehensive Foundation 2nd edition, Prentice Hall Inc., Upper Saddle River, New Jersey, America

Oliveira R., (2004), Combining first principles modelling and artificial neural networks: a general framework, Computers & Chemical Engineering, **28,** 755-766.

Parlos A.G., Rais O.T., Atiya A.F., (2000), Multi-step-ahead prediction using dynamic recurrent neural networks, Neural Networks, **13**, 765–786

Ren H.T., Yuan J.Q., Bellgardt K.H., (2003), Makrokinetic model for methylotrophic Pichia pastoris based on stoichiometric balance, J. of Biotech., **106**, 53-68

Wolkowicz G.S.K., Xia H.,(1997), Global Asympotic Behavior of Chemostat Model with Discrete Delay, J. Appl. Math., **57**,1019-1043

Wolkowicz G.S.K., Xia H., Ruan S., (1997), Competition in Chemostat: A Distributed Delay Model and its Global asymptotic Behaviour, J. Appl. Math., **57**, 1281-1310

Proceedings of the 10th International Chemical and
Biological Engineering Conference - CHEMPOR 2008
Braga, Portugal, September 4-6, 2008
E.C. Ferreira and M. Mota (Eds.)

Adaptive evolutionary design of extractants for the separation of organic compounds from aqueous streams by liquid extraction

Juan Carlos Serrato B. [1*], Jonatan Gómez P. [2], Luis A. Caicedo M. [1]
[1] Chemical and Biochemical Process Group, Chemical Engineering Laboratory, National University of Colombia, Bogotá, Colombia
[2] Systems Engineering Department, National University of Colombia, Bogotá, Colombia

Keywords: Genetic algorithms, molecular design, Unifac, CAMD, extraction agents.
Topic: Systematic methods and tools for managing the complexity

Abstract

Industry poses different separations problems for diverse compounds recovery. Separation stage is very important for the product cost; it is especially true for the biotechnological products. Liquid-liquid extraction is a widely used separation operation; however it requires separation agents that must fulfill conditions such as low toxicity, high distribution coefficient and selectivity, among others. Therefore, different approaches have been developed to tackle this problem, being computer aided molecular design the most promising alternative. It is an optimization process looking for the best group combination to successfully perform some objective in a given process, including some physical, feasibility and process restrictions. To solve this problem we present a new genetic algorithm that does not show some limitations present in earlier works.

1 Introduction

Computer aided molecular design is an inverse engineering methodology, it has been successfully used by some authors for the generation of different molecules. The molecular design could be understood as an optimization process with various kinds of restrictions: physical, structural properties, etc; defined in function of the molecule structural groups. The CAMD methodology is based on different property estimation methods coupled with an optimization method. In despite of their limitations, the more used alternative for property estimation are group contribution methods.

The optimization problem involved in molecular design is formulated as a mixed integer non linear programming model (MINLP) (Churi & Achenie, 1996, Duvedi & Achenie, 1996, Stefanis, et al., 1996, Hostrup, et al., 1999), but some authors use non linear programming. Due to the high level of complexity, deterministic methods not always find the global optimum and are very susceptible to get trapped in local minima. In contrast, stochastic methods have a greater possibility to find the global optimum and their form of use is very flexible. These are reasons that lead to use of genetic algorithms in this work.

Thanks to the advantages of the genetic algorithms over the other stochastic methods, authors as van Dyk (van Dyk & Nieuwoudt, 2002), Venkatasubramanian (Venkatasabrumanian, et al., 1994) and Xu (Xu & Diwekar, 2005) has used them for solvent design. However, their implementations have some limitations: a) the molecules representation is diverse and often allows the construction of molecules with a low complexity (due to the representation itself and the low maximum number of groups that form the molecule); additionally, almost in all cases the representation permits multiple molecules b) there is a non uniform use of the restrictions of the problem, especially the structural feasibility restrictions, and it is unknown the effect of the problem formulation on the results, c) in despite of the genetic operators used are similar, their probability of use in the algorithm is a parameter to be adjusted by the user, no warranting convergence nor optimality, and d)

* Corresponding author: Tel: + 57 - 1 - 3165000 Ext: 14029. E mail: jcserratob@unal.edu.co, serratojc@yahoo.com

the use of different property estimation methods makes difficult the results evaluation and introduces a high uncertainty level in the problem that could change the results.
This work presents an alternative software that aims to alleviate the aforementioned difficulties.

2 Solvent Design

The CAMD software for solvent design is divided in the following way: a routine to construct molecules structurally feasible, another to estimate properties, and a final that encompasses the others and makes the optimization. Every part is described in the following lines.

2.1 Molecule's Construction

The required molecules to initialize the software are constructed in the following way: once the user has defined how many groups are allowed in a molecule (Np), the software chooses the number of terminal groups randomly. That number varies between 1 and Np/2. Terminal groups have a valence of 1. Then, other group with a valence higher than 1 is selected randomly and is connected to some terminal groups according to its valence, leaving a number of bonds free. These connected groups are joined with other random selected groups up to the molecule valence is zero.
For aromatic and cyclic compounds a special routine is used. The software determines the cycle size randomly and it is constructed using only special cyclic groups. For aromatics construction the cycle size is fixed to 6 and it is constructed using only aromatics groups. When appears a cyclic-aliphatic or aromatic-aliphatic group, the aliphatic branch is constructed by the same random selection used before and it is finished with a terminal group. The maximum number of functional groups is restricted to three, considering easy of synthesis heuristic. Constructed molecules must fulfill the Odele-Machietto restrictions (GANI and BRIGNOLE 1983).

2.2 Properties Estimation

The principal properties needed for the estimation of solvent performance are distribution coefficient and selectivity. Melting point, boiling point, Gibbs free energy, solvent loss and density are also included in the design.

2.2.1. Activity coefficient Distribution coefficient, selectivity and solvent loss are functions of activity coefficients. These coefficients are calculated using the Unifac-Dortmund model (Gmehling et al. 1993; Gmehling et al. 2002). In this method, the activity coefficients are estimated as the sum of residual and combinatorial contributions.

$$\ln\gamma_{\mathrm{i}} = \ln\gamma_{\mathrm{i}}^{\mathrm{C}} + \ln\gamma_{\mathrm{i}}^{\mathrm{R}}$$

The combinatorial contribution considers compounds with very different sizes and forms, and it is calculated as:

$$\ln\gamma_{\mathrm{i}}^{\mathrm{C}} = 1 - V_i^{'} + \ln V_i^{'} - 5q_i\left(1 - \frac{V_i}{F_i} + \ln\left(\frac{V_i}{F_i}\right)\right)$$

The parameters $V^{'}_{i,}$ V_i, q_i, r_i y F_i are calculated by the following equations and are functions of the relative van der Waals volumes and areas (R_k y Q_k) for the different groups:

$$V_i^{'} = \frac{r_i^{3/4}}{\sum_j x_j r_j^{3/4}} \qquad V_i = \frac{r_i}{\sum_j x_j r_j} \qquad F_i = \frac{q_i}{\sum_j x_j q_j}$$

$$r_{\mathrm{i}} = \sum \upsilon_k^{(i)} R_k \qquad q_{\mathrm{i}} = \sum \upsilon_k^{(i)} Q_k$$

The residual contribution is calculated as:

$$\ln \gamma_i^R = \sum_k \upsilon_k^{(i)} \left(\ln \Gamma_k - \ln \Gamma_k^{(i)}\right)$$

$$\ln\Gamma_k = Q_k\left(1 - \ln\left(\sum_m \theta_m \Psi_{mk}\right) - \sum_m \frac{\theta_m \Psi_{km}}{\sum_n \theta_n \Psi_{nm}}\right)$$

The group area fraction (Φ_m) and the group mole fraction (X_m) are given by the following equations:

$$\theta_m = \frac{\theta_m X_m}{\sum_n \theta_n X_n} \qquad X_m = \frac{\sum_j \upsilon_m^{(j)} x_j}{\sum_j \sum_n \upsilon_n^{(j)} x_j}$$

The group interaction parameters are temperature dependent by the following expression:

$$\Psi_{nm} = \exp\left[-\frac{\left(a_{nm} + b_{nm}T + c_{nm}T^2\right)}{T}\right]$$

The relative van der Waals volumes and areas, and some group interaction parameters can be found in literature (Gmehling et al. 1993; Gmehling et al. 2002; Weidlich and Gmehling 1987).

2.2.2 **Other estimated properties** Melting and boiling points, density and Gibbs free energy are used as restrictions in the design process. For its estimation the last version of the GCVOL method for density (Ihmels and Gmehling 2003) and the Constantinou and Gani methods for melting point, boiling point and Gibbs free energy are used. To include these restrictions in the design, the method of fitness function penalization is used. Sigmoidal and Gaussian functions were utilized to normalize the constraints. These functions included a special form to take into account the uncertainty on the evaluated properties.

2.3 Genetic Algorithm

For the solution of the problem, an adaptive genetic algorithm called HAEA [42] was used. Genetic search methods have their basis in Darwinian models of natural selection and evolution. Introduced by Holland, the general idea behind genetic algorithms is the evolutionary creation of a new population of individuals from an earlier generation through genetic processes, such as crossover and mutation, and by passing on the better offsprings to the next generation. In general, individuals that are better adapted to their environment will have a better chance of survival and thus pass on their genetic material to the succeeding generations. This approach is expected to lead to generations that become more and more fitted through evolution thus achieving the desired design objective.

2.3.1. Fitness Function Distribution coefficient is the fundamental property studying liquid-liquid extraction; it shows how a compound is distributed between two phases. However, generally a solvent with good extraction capacity shows low selectivity, and the inverse relation is also true. Therefore in this work, the fitness function for solvent design is the product of the distribution coefficient and the selectivity. Selectivity is calculated with the equation suggested by Pretel [41]:

$$\beta = \frac{\gamma_{B,S}^{\infty}}{\gamma_{A,S}^{\infty}} \frac{MW_A}{MW_B}$$

The distribution coefficient is calculated by the following equation:

$$k = \frac{\gamma^{\infty}_{A,B}}{\gamma^{\infty}_{A,S}} \frac{MW_B}{MW_S}$$

Both properties are functions of activity coefficients and molecular weights. The former property is calculated by the Unifac method described above.

2.3.2. Representation Every population individual or molecule is represented in two ways, genotype and phenotype. A tree representation for molecule genotype is employed; in it every node represents a group and the branches, the bonds of every group with other groups. An array of groups of the same molecule is utilized as phenotype; it is used for the genetic operators. Phenotype is an array of groups of the same molecule; it is employed for properties estimation. For example, lactic acid whose structure is CH3CH(OH)COOH, is represented by its genotype (figure 1):

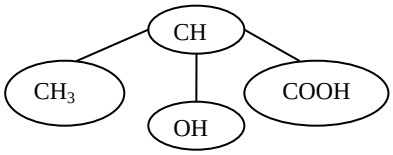

Figure 1. Lactic acid representation

Its phenotype is given by the array (1, 3, 15, 43), where the numbers are the corresponding groups codes (Gmehling et al. 1993).

2.3.3. Population An initial population of 100 individuals was used. The molecules have variable length and a maximum length of 10 groups. In order to achieve a good diversity of the initial population, 10 % of the molecules created are cyclic, 10 % aromatics, and the others aliphatic.

2.3.4. Reproduction For the generation of new individuals four genetic operators were used: mutation, crossover, group insertion y deletion. The operator's probabilities were adjusted with the problem using the adaptive algorithm HAEA.

2.3.4.1. Mutation Initially the program chooses a parent individual randomly, then choose the mutation point and the group to insert according to the residual valence of the fragment (randomly) and make the interchange. Figure 2 shows an example.

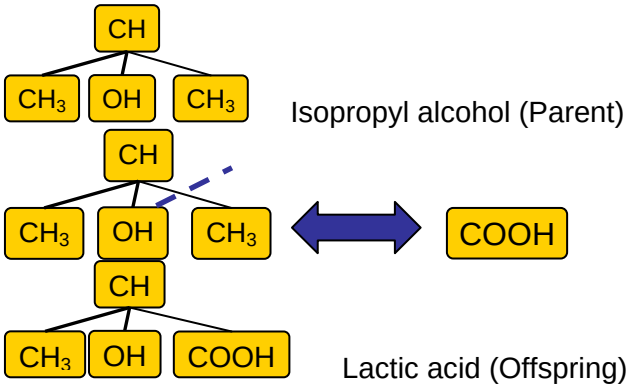

Figure 2. Molecule's mutation example.

2.3.4.2. Cross To do a cross, the program chooses randomly two parent individuals by their fitness and two operation points, one for molecule. Then it makes the fragment interchange, to construct the new molecules. An example is given in figure 3:

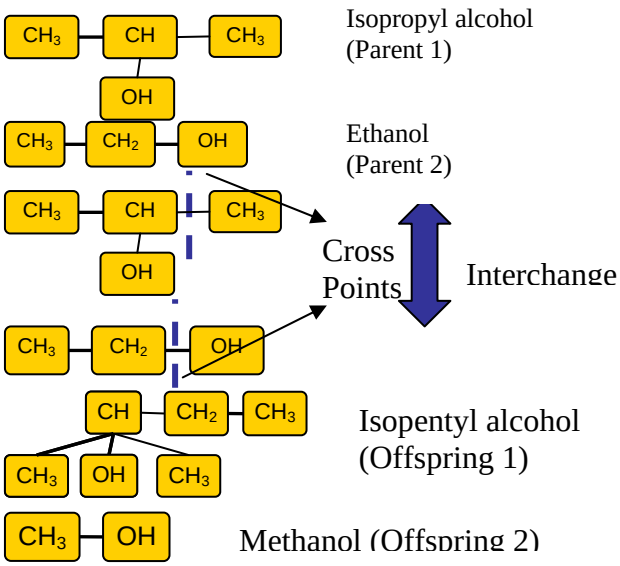

Figure 3. Molecules cross example.

2.3.5. Selection The individual's selection was performed by tournament.

3 Results and Analysis

The design of extractants for acetic acid from an aqueous solution as model problem, and for lactic acid as a biotechnological application was done. The results depicted in figures 4 and 5 are the best compounds obtained in 50 runs of the solvent design problem for each case.

In acetic acid solvent design problem, the designed molecules with the best fitness contain esters, ethers and very often chloride groups. These results are in agreement with the results of Wang and Achenie (Wang and Achenie 2002), Kim Diwekar and Tomazi (KIM et al. 2004) (Kim and Diwekar 2002), and are oxygenated groups such as the groups suggested by Harper (Harper et al. 1999). However, it is clear that a higher number of functional groups into a molecule would give a higher fitness value. Our program does not limit the number of functional groups into a molecule; therefore our solvents are more complex than methyl dimethyl ester and diisobutyl ketone reported previously. However, our molecules have the right groups. Normally, the authors exclude the chloride groups for the design due to their well-know toxic properties. Although we did not exclude these groups, our results indicate a strong affinity between the acetic acid and this kind of compounds. In a future publication we will exclude these groups to design more environmental friendly solvents.

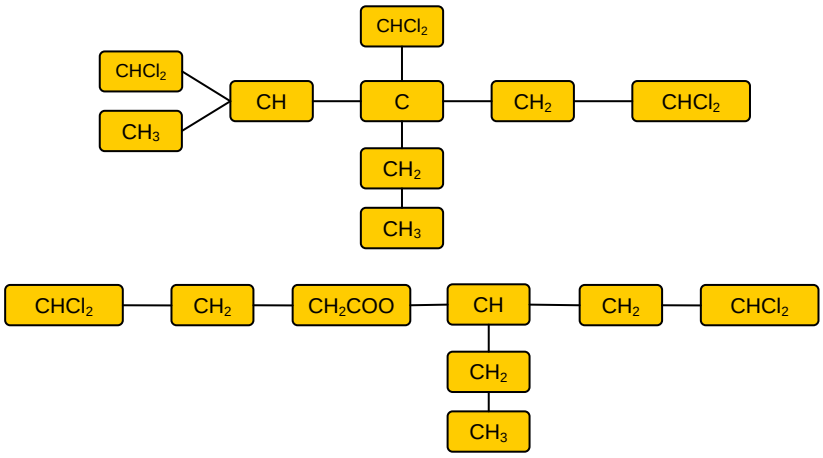

Figure 4. Designed solvents for acetic acid

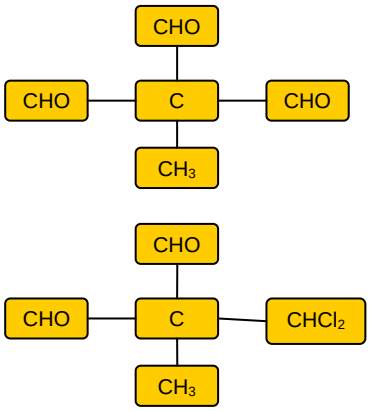

Figure 5. Designed solvents for lactic acid

To our knowledge these are the first published compounds for the extraction of lactic acid. It is apparent that the aldehyde and chloride groups are important part of good solvent molecules. Experimental verification of these results is under development.

4 Conclusions

A solvent design program was constructed and evaluated using two problems.
Our results for acetic acid shows the inclusion in the designed solvents of groups already reported in the literature. The chloride groups are important for this application but its toxic properties excluded them from further consideration.
We present new solvents for lactic acid extraction, they include aldehyde and chloride groups as the most important groups in the design.
New runs of our program without toxics groups are necessary to find better solvents.

References

GANI R, BRIGNOLE EA. 1983. Molecular Design of Solvents for Liquid Extraction Based on UNIFAC. Fluid Phase Equilibria 13:331-340.

Gmehling J, Li J, Schiller M. 1993. Modified UNIFAC model. 2. Present parameter matrix and results for different thermodynamic properties. Industrial and Engineering Chemistry Research 32(1):178-193.

Gmehling J, Wittig R, Lohmann J, Joh R. 2002. A modified UNIFAC (Dortmund) model. 4. Revision and extension. Industrial and Engineering Chemistry Research 41(6):1678-1688.

Harper PM, Gani R, Kolar P, Ishikawa T. 1999. Computer-aided molecular design with combined molecular modeling and group contribution. Fluid Phase Equilibria 158-160:337–347.

Ihmels EC, Gmehling J. 2003. Extension and Revision of the Group Contribution Method GCVOL for the Prediction of Pure Compound Liquid Densities. Ind. Eng. Chem. Res. 42: 408-412.

Kim K-J, Diwekar UM. 2002. Efficient Combinatorial Optimization under Uncertainty. 2. Application to Stochastic Solvent Selection. Ind. Eng. Chem. Res. 41:1285-1296.

KIM K-J, DIWEKAR UM, TOMAZI KG. 2004. Entrainer Selection and Solvent Recycling in Complex Batch Distillation. Chem. Eng. Comm. 191:1606-1633.

Wang Y, Achenie LEK. 2002. Computer aided solvent design for extractive fermentation. Fluid Phase Equilibria 201(1):1-18.

Weidlich U, Gmehling J. 1987. Modified Unifac Model. 1. Prediction of VLE, h**E, and gamma ** infinity. Industrial and Engineering Chemistry Research 26(7):1372-1381.

Proceedings of the 10th International Chemical and
Biological Engineering Conference - CHEMPOR 2008
Braga, Portugal, September 4-6, 2008
E.C. Ferreira and M. Mota (Eds.)

Heuristic methods to scheduling operations in parallel machines

José A.V. Oliveira[1*]
[1] DPS – Department of Production and Systems Engineering, University of Minho, Campus de Gualtar, 4710–057 Braga, Portugal.

Keywords: Parallel Machines, Scheduling, Heuristics, Dyeing
Topic: Systematic methods and tools for managing the complexity.

Abstract

This paper presents a study about scheduling a set of tasks in a set of parallel machines. The tasks have setup times that are dependent of the sequence. The problem of planning parallel machines is frequent in the textile industry and this particular case arises in the dyeing section.

This paper presents a constructive algorithm and also a local search procedure. This study also addresses the neighbourhood schemes developed for the problem. Computational results obtained with adapted public instances are presented and discussed.

1 Introduction

Processing in parallel machines is frequent in the textile industry, particularly in the dyeing sector. Figure 1 presents a set of identical parallel dye machines that is a common situation in the textile industry.

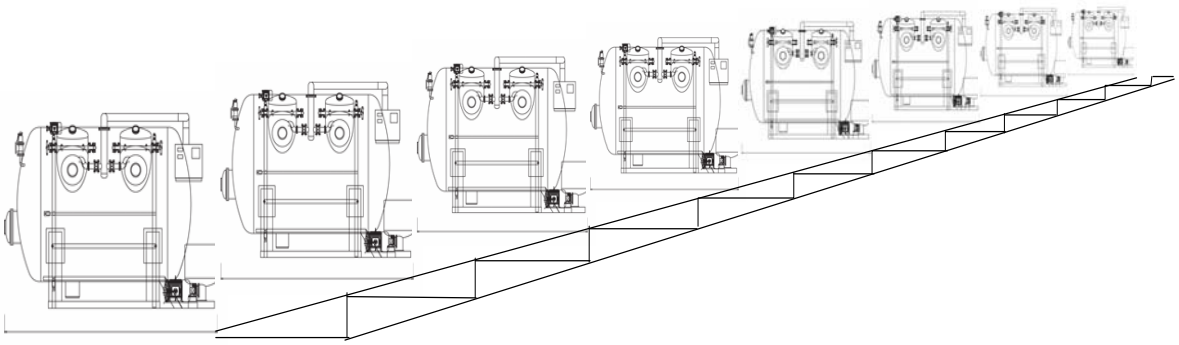

Figure 1 – Dyeing machines

In this paper, a scheduling problem of identical parallel machines is presented in that the orders, with due dates, have different processing times and different priorities. It is still considered the existence of dependent setup times of the sequence. The objective is to minimize the total weighted tardiness of delivering the orders.

This is a difficult problem to solve. It belongs to the NP-hard problems. By that, the use of heuristic methodology is justified. The objective of this study is to test and evaluate the efficiency and the effectiveness of the heuristic methods developed specifically for this problem, and to extend their use in general situations.

* Corresponding author. Tel + 351-253-604763. E-mail:zan@dps.uminho.pt

2 Model Description

The problem of scheduling parallel machines is defined by the set of tasks T to be processed and by the set of machines M available for their processing. Let be:

- the set of *n* tasks, $T = \{t_1, t_2, \ldots, t_i, t_j, \ldots, t_n\}$
- the set of *m* machines, $M = \{M_1, M_2, \ldots, M_k, \ldots, M_m\}$

In this problem the aim is to find a solution that assigns the tasks in T to a machine in M in such a way to complete their processing while respecting the set of imposed constraints. Scheduling problems have the following two main constraints to respect: (1) a machine can only process one task at a time; and (2) a task can be processed only in one machine at a time. Also, it is assumed when a task is started, their processing cannot be interrupted until completed.

The machines are identical and parallel; they perform the same type of operations and have equal processing speed.

At every time it is possible to obtain the following information about the machines:

- the set of instants when the machines M_k became available, represented by the vector $A = [a_1, a_2, \ldots, a_k, \ldots, a_m]^T$;
- the set of tasks that are being processed on the machines M_k, represented by the vector $B = [b_1, b_2, \ldots, b_k, \ldots, b_m]^T$.

The vectors A and B form the matrix $F[A, B, k]$.

The set of tasks T is characterized by the following data:

- the set of processing times, that is necessary to complete the set of tasks t_j, is represented by the vector $P = [p_1, p_2, \ldots, p_j, \ldots, p_n]^T$;
- the set of due dates, that is necessary to delivery the set of tasks t_j without being delayed, is represented by the vector $D = [d_1, d_2, \ldots, d_j, \ldots, d_n]^T$.
- the set of weights that describes the importance of tasks t_j is represented by the vector $W = [w_1, w_2, \ldots, w_j, \ldots, w_n]^T$.

The vectors P, D and W are integrated in the matrix $E = [P, W, D, j]$.

Depending on the sequence of processing the set of tasks, there are different setup times to prepare the machines. The set of setup times is given by the matrix $S = [s_{1j}, s_{2j}, \ldots, s_{nj}]$, for $j = 1, 2, \ldots, n$, where s_{ij} is the setup time of the machine, if the task j follows immediately the task i in terms of sequence. When a task j uses the same dyeing process of task i, $s_{ij} = 0$, i.e. there is no need to prepare the machine. When a task j uses a different dyeing process of task i, $s_{ij} = K$. K represents the amount of time that is necessary to clean the dye machine to be ready for the next task.

Aiming the simplification, this paper considers that all relevant data are integer values, all tasks are available at instant 0, and the processing of the task j is independent of the processing of the task i.

For each task can be calculated the following values:

- instant of conclusion of the processing of the task j, C_j;
- lateness of task j, $L_j = C_j - d_j$;
- tardiness of task j, $T_j = \max\left(0, C_j - d_j\right)$.

With these variables it is built the objective function that represents the total weighted tardiness:

$$\min \sum_{j=1}^{n} w_j T_j$$

3 Constructive Algorithm

In this work, a heuristic of constructive type is presented, that is based in the processing list that assigns the tasks in sequential order to the machines that are available earlier. This list is an ordering of all tasks. Sequentially, the tasks will be assigned one by one to the machine that is available earlier by attending to the ordering defined in the list of processing. In this constructive algorithm, the processing list is defined by the dispatch rule Earliest Due Date (EDD).

Constructive Algorithm

0. Define the processing vector. Use the EDD rule to order the tasks.
1. Choose the task with minimum due date; select a machine that will be available earlier, i.e. a machine with the minimum a_k. Let be j the selected task, k the selected machine, and i the last task processed by k;

   Do:

   $$C^{(n)} = p_j^{(n)} + a_k^{(n)} + s_{ij}^{(n)}$$

   $$L^{(n)} = C^{(n)} - d_j^{(n)}$$

   $$T^{(n)} = w_j^{(n)} \times \max\left(0, L^{(n)}\right)$$

2. Rewrite the line in the matrix F corresponding to the machine k;

   $$F^{(n)} = \left[C^{(n)} \quad j^{(n)} \quad k^{(n)} \right];$$

3. Construct the matrix sol:

   $$sol = \begin{bmatrix} C^{(1)} & j^{(1)} & k^{(1)} & T^{(1)} \\ \vdots & \vdots & \vdots & \vdots \\ C^{(n)} & j^{(n)} & k^{(n)} & T^{(n)} \end{bmatrix}$$

4. Add $T^{(n)}$.

End

4 Local Search

To improve the quality of the results obtained by the constructive algorithm, a local search procedure is implemented. Starting from an initial complete solution, replacing the current

solution by the best solution existing in the neighbourhood of the current solution will be tried iteratively.

The initial solution is obtained by the constructive algorithm based in EDD rule. Starting from the current solution, a swap process is initiated within the list by which the tasks are assigned to the machines. The swap procedure consists in changing the order of two consecutive tasks in the processing list. From this swap results a new solution that is evaluated by the constructive algorithm. Now, instead of using the EDD rule, the tasks are sequenced by the new order defined in the list that respects the operations exchange.

Given a current solution, all solutions that are possible to be obtained by the sway procedure are generated. The solution that produces the lowest value of total weighted tardiness becomes the current solution if it is better than the actual current solution; if not, the search ends, giving the current solution as the local optimum solution. When a current solution is replaced by a new one, the procedure for a generation of a new set of solutions is initiated. This strategy is defined as the best improvement. The adoption of this strategy is justified by the number of new solutions that is possible to be generated by the swap procedure of consecutive tasks. This strategy allows obtaining acceptable computing times.

5 Computational Results

Instances were used based in the instances for the single machine problem available in OR Library from J.E. Beasley. The information for the setup times was added using random values based on the following proportions: 75% of tasks use common chemist processes to clean the dyeing machine; and 25% of tasks use a different process that takes more time to setup the machine, and it was used $K = 24$.

The due date information was updated, dividing by the number of parallel machines. This option intends to keep the same level of congestion that exists in the single machine instances. There were selected instances of size 40, 50, and 100 tasks with different levels of congestion. Also, a small instance with 6 tasks was added. In all greatest instances, it was considered 6 parallel machines; and only 2 machines for the smallest one.

The experiments were performed into two computers. One computer has a CPU Intel Pentium M, processor 760 (2.0 GHz, 533 MHz FSB, 2 MB L2 cache) with 1,00 GB of RAM; the other computer has a CPU Intel Pentium D, processor 3,0 GHz and 0,99 GB of RAM. Both computers use the operative system Microsoft Windows XP with SP2. The results are presented at Table 1.

Table 1 – Computational results

	Constr. Algorithm			Local Search				Constr. Algorithm				Local Search		
Tasks	Solution	P1	P2	Solution	P1	P2		Tasks	Solution	P1	P2	Solution	P1	P2
6	622	0	0	183	0	31		50	1934	0	0	24	0	16
40	3495	0	0	2260	0	0		50	1980	0	0	516	0	0
40	267775	0	0	131619	0	16		50	8603	0	0	2560	15	16
40	54804	0	16	50951	16	16		50	10723	0	0	7502	0	16
40	110	0	0	0	0	0		50	18390	0	0	11842	0	15
40	737	0	0	31	0	16		100	29637	0	15	24476	46	47
40	1197	0	0	988	0	16		100	8653	0	0	3938	36	47
40	160	0	0	0	0	16		100	229729	0	0	213085	47	47
40	75	0	0	0	0	0		100	614	0	15	0	16	15
40	5039	0	0	1657	13	16		100	0	0	0	0	16	16
40	8498	0	0	5521	16	15		100	2191	0	0	150	0	32
50	14644	0	0	8364	0	16		100	5059	0	0	1237	47	47
50	18275	0	0	16817	16	15		100	442	16	16	0	32	15
50	68604	0	0	56338	16	31		100	26589	0	15	12056	62	63
50	2002	0	0	751	16	16		100	62423	0	0	46836	47	46
50	6951	0	0	1085	0	16								

The columns “Solution” present the objective function for each algorithm. The columns “P1” present the computational times in milliseconds for the computer with the CPU Intel Pentium M. The columns “P2” present the computational times in milliseconds for the computer with the CPU Intel Pentium D.

Table 2 details the obtained solution with the Constructive Algorithm for the first instance with 40 tasks. The objective function is 3495.

Table 2 – Constructive Algorithm Solution

Sequence	*P*	*w*	*d*	*j*	*M*	*S*	*C*	*wt*
1st	90	4	247	18	0	0	90	0
2nd	30	7	257	34	0	0	120	0
3rd	64	7	264	16	0	0	184	0
4th	67	3	273	9	0	0	251	0
5th	29	10	285	14	0	0	280	0
6th	46	10	296	3	0	0	326	300
7th	27	7	306	17	0	0	353	329
1st	52	3	252	21	1	0	112	0
2nd	73	3	261	6	1	0	185	0
3rd	40	3	274	13	1	0	225	0
4th	94	4	277	15	1	24	343	264
5th	74	2	307	7	1	24	441	268
1st	95	5	252	25	2	0	107	0
2nd	55	7	260	19	2	0	162	0
3rd	86	7	267	10	2	0	248	0
4th	32	10	282	4	2	24	304	220
5th	50	3	302	39	2	0	354	156

Sequence	*P*	*w*	*d*	*j*	*M*	*S*	*C*	*wt*
1st	9	10	241	37	3	0	9	0
2nd	68	7	250	35	3	0	77	0
3rd	12	5	255	33	3	24	113	0
4th	49	1	263	38	3	0	162	0
5th	24	10	270	1	3	24	210	0
6th	44	7	275	30	3	0	254	0
7th	79	9	289	2	3	0	333	396
8th	28	4	306	31	3	0	361	220
1st	70	5	247	36	4	24	94	0
2nd	46	3	257	11	4	0	140	0
3rd	26	1	265	0	4	0	166	0
4th	86	4	271	29	4	0	252	0
5th	14	10	288	8	4	0	266	0
6th	35	5	295	20	4	0	301	30
7th	69	4	299	23	4	24	394	380
1st	35	4	248	5	5	0	40	0
2nd	36	5	252	22	5	0	76	0
3rd	85	9	254	24	5	0	161	0
4th	14	2	266	26	5	0	175	0
5th	39	9	271	32	5	0	214	0
6th	78	8	276	27	5	24	316	320
7th	37	10	304	28	5	0	353	490
8th	78	1	309	12	5	0	431	122

Table 3 details the obtained solution with the Local Search procedure for the same instance presented before. The objective function is 2260.

Table 3 – Local Search Solution

Sequence	*P*	*w*	*d*	*j*	*M*	*S*	*C*	*wt*
1st	90	4	247	18	0	0	90	0
2nd	30	7	257	34	0	0	120	0
3rd	64	7	264	16	0	0	184	0
4th	67	3	273	9	0	0	251	0
5th	94	4	277	15	0	0	345	272
1st	52	3	252	21	1	0	112	0
2nd	73	3	261	6	1	0	185	0
3rd	40	3	274	13	1	0	225	0
4th	32	10	282	4	1	0	257	0
5th	79	9	289	2	1	0	336	423
6th	78	1	309	12	1	0	414	105
1st	95	5	252	25	2	0	107	0
2nd	55	7	260	19	2	0	162	0
3rd	86	7	267	10	2	0	248	0
4th	29	10	285	14	2	0	277	0
5th	37	10	304	28	2	0	314	100
6th	69	4	299	23	2	0	383	336

Sequence	*P*	*w*	*d*	*j*	*M*	*S*	*C*	*wt*
1st	9	10	241	37	3	0	9	0
2nd	68	7	250	35	3	0	77	0
3rd	12	5	255	33	3	24	113	0
4th	49	1	263	38	3	0	162	0
5th	24	10	270	1	3	24	210	0
6th	44	7	275	30	3	0	254	0
7th	46	10	296	3	3	0	300	40
8th	27	7	306	17	3	0	327	147
9th	74	2	307	7	3	0	401	188
1st	70	5	247	36	4	24	94	0
2nd	46	3	257	11	4	0	140	0
3rd	26	1	265	0	4	0	166	0
4th	86	4	271	29	4	0	252	0
5th	14	10	288	8	4	0	266	0
6th	35	5	295	20	4	0	301	30
7th	50	3	302	39	4	0	351	147
1st	35	4	248	5	5	0	40	0
2nd	36	5	252	22	5	0	76	0
3rd	85	9	254	24	5	0	161	0
4th	14	2	266	26	5	0	175	0
5th	39	9	271	32	5	0	214	0
6th	78	8	276	27	5	24	316	320
7th	28	4	306	31	5	0	344	152

Figure 2 shows the Gantt charts of the solutions presented in Table 2 (Constructive Algorithm) and in Table 3 (Local Search).

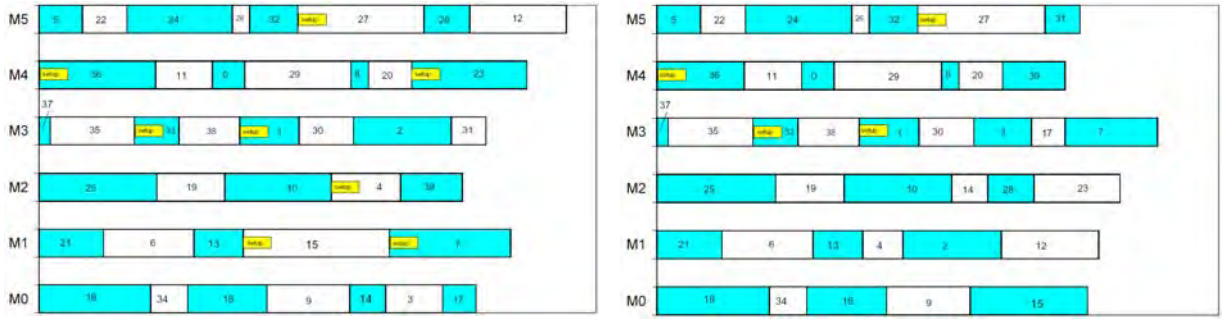

(Constructive Algorithm) (Local Search)

Figure 2– Gantt charts

6 Conclusions

This paper proposes two efficient heuristics to minimise the total weighted tardiness of a set of tasks with known processing times, due dates, weights and family types for identical parallel machines. The exact methods are not appropriate to solve large instances of this problem. The alternative is the use of efficient heuristics methods.

On average, for the used instances, the local search procedure allows for 56% of the total weighted tardiness to be reduced; and for some instances, the local search obtained the optimum solution. Furthermore, the increasing in computation time was not significant.

For this problem it is possible to develop meta-heuristics to improve the objective function values of the solutions. This kind of methods necessarily involves an increase of the computational efforts that can be compensated with the quality improvement of the solutions. As a further work, a genetic algorithm with random keys will be developed.

References

Beasley, J.E. (1990). OR-Library: distributing test problems by electronic mail. *Journal of the Operational Research Society,* 41, 1069-1072.

Brucker, P., Knust, S. (2003). *Complexity results for scheduling problems*. University of Osnabrück.

French, S. (1982). *Sequencing and Scheduling - An Introduction to the Mathematics of the Job-Shop*. Ellis Horwood Limited, Chicester.

Michalewicz, Z., Fogel, D. (2000). *How to Solve It: Modern Heuristics.* Springer-Verlag.

Morton, T.E., Pentico, D.W. (1993). *Heuristic scheduling systems.* John Wiley & Sons, New York.

Oliveira, J.A. (2001) *Aplicação de Modelos e Algoritmos de Investigação Operacional ao Planeamento de Operações em Armazéns*. Ph.D. thesis, Universidade do Minho.

Proceedings of the 10th International Chemical and
Biological Engineering Conference - CHEMPOR 2008
Braga, Portugal, September 4-6, 2008
E.C. Ferreira and M. Mota (Eds.)

Multiproduct Pipeline with Inventory Management: the CLC's Case Study

Susana Relvas[1*], Ana Paula F.D. Barbosa-Póvoa[1], Henrique A. Matos[2]
[1] CEG – IST, UTL, Av. Rovisco Pais, 1049-001 Lisboa, Portugal
[2] CPQ – IST, Av. Rovisco Pais, 1049-001 Lisboa, Portugal

Keywords: Pipeline, Inventory Management, MILP, Decision Support System
Topic: Systematic methods and tools for managing the complexity

Abstract

The oil supply chain has a large impact on world wide economics. Therefore, the optimization of each operation in the supply chain will cause impact on the final profit margin. One of the final operations of this chain is the distribution of products, which makes products available to the consumer markets. Thus, it is a challenge to provide an efficient and cost effective distribution so as to enhance the operation profit value as well as the global supply chain value. Such operation often involves pipelines as a reliable and cost effective equipment to transport the final products but, on the other hand, their scheduling appears as a complex problem to be solved so as to answer to market demands coping with transportation and quality approval timings. This work considers an oil products distribution system comprising a refinery, one pipeline and a distribution centre. The objective is to develop a pipeline schedule from a continuous time MILP model that answers to local market demands and distribution centre's conditionings. The prototype of a decioson support tool is presented. This was applied to a real world scenario of Companhia Logística de Combustíveis.

1 Introduction

Supply chain management has continually attracted much attention from several service and industry organizations; due to the fact that companies are constantly looking for new opportunities to cut costs, improve profit margins while maintaining customer satisfaction. Being the oil supply chain one of the most important entities in world wide economy, it is crucial to develop advanced decision support tools to efficiently manage such system. This chain comprises several types of operations, several sites and several workers, at different levels. If, on the one hand, integrated planning and scheduling provides solutions with a wide vision, on the other hand such management tool would be rather complex to build and to use over the complete chain.

Several authors have proposed methodologies addressing different business areas within this chain, from exploration to distribution. Refinery operations remain as the core field, but the left over functions are crucial to take the maximum benefit from the chain. One of these cases is the logistics operations that play an important role in the definition of an efficient flow of goods, services and information.Within such operations, pipelines are widely used in distribution between chain nodes, being reliable equipment for oil and oil products transportation, with reduced costs for a long term solution. Pipeline transportation scheduling has been addressed by some authors through both continuous and discrete mathematical programming models, such as Rejowski and Pinto (2008), Magatão *et al.* (2004), Cafaro and Cerdá (2008). In these works, pipelines are already fairly represented, but no effort has been done to represent tank farms with all physical tanks and mandatory inventory management procedures, which was first proposed by Relvas *et al.* (2006).

* Corresponding author. Tel +351 214 233 550. E-mail: susanaicr@ist.utl.pt

Furthermore, the complexity of this type of systems also includes a high level of uncertainty. In this sense, scheduling plans must be flexible to accommodate unforeseen situations that dictate new restrictions. Reactive scheduling procedures have been proposed for general production plants and situations, having a significant gap to be applied to pipeline systems. Within this context, Relvas *et al.* (2007) proposed a reactive scheduling procedure for pipeline systems, tackling several specific situations that are likely to happen. These situations were modelled through a Mixed-Integer Linear Programming (MILP) formulation.

In order to tackle an effective inventory management, a detailed MILP model was developed, which uses as basis the model develop by Relvas *et al.* (2006). In this way, individual tanks are represented rather than aggregated storage capacities. Finally, being the approach directed for real world applicability, it was necessary to develop a sequencing heuristic that provides pumping sequences of products so as to reduce model complexity.

In this work, it is proposed a framework for a decision support tool that defines pipeline operations and inventory management at final distribution centres, combining the MILP model proposed by Relvas *et al.* (2006) and the reactive scheduling approach proposed by Relvas *et al.* (2007), being validated by Companhia Logística de Combustíveis case study.

2 Problem Characteristics

This work addresses the system described in Figure 1, comprising a pipeline transporting several oil products between one refinery and one distribution centre positioned in a local market. The transportation within the pipeline has to respect possible sequences of products and flowrate constraints. At the distribution centre each tank as fixed product service. Each new batch discharged from the pipeline has to settle for a minimum amount of time, varying with the product. Clients are satisfied on site and forecasts are available on a daily basis. The pipeline schedule should accomplish the availabilities at the distribution centre, and satisfy the complete set of demands.

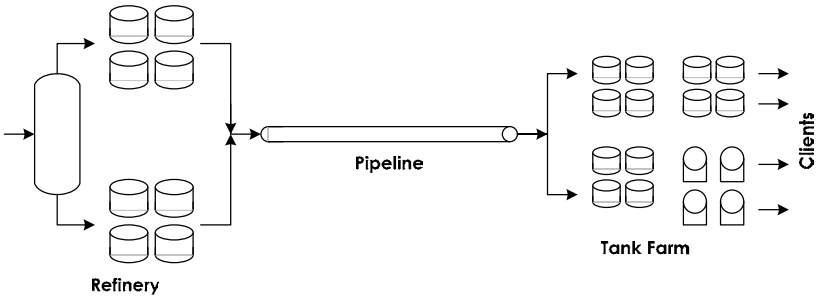

Figure 1 – Operating system

Given: a) the number of products to be transported, b) the matrix of possible/forbidden sequences between pairs of products in pipeline transit, c) the allocation of products to tanks, d) the maximum storage capacity for each product and for each tank, e) the pipeline capacity, f) the pumping rate limits, g) the minimum settling period for each product, h) the time horizon extent and the total number of days to be considered, i) the maximum number of allowable batches to be pumped to the pipeline during the time horizon, j) the initial inventory of each product in each tank, k) the initial state of each tank, l) the daily clients' demands for each product, m) the planned pipeline stoppages;

It is desired to determine: 1) the optimal pipeline schedule, with sequence of products, batches' volumes, pumping rates and pumping/discharging timings and 2) the inventory management at the distribution centre, including daily volume balances by product/tank, monitoring of arrivals, settling and approving tasks and satisfaction of daily clients' demands.

Subject to: an objective function that optimizes operational variables, such as minimising medium flowrate, maximising pipeline usage and the product with lowest final inventory level.

3 MILP Models

To tackle the problem defined above two models have been developed. The model develop by Relvas *et al.* (2006, 2007) adopts a strategy of aggregating storage capacity, i.e., each product is stored in a single tank that has a capacity equal to the total capacity available in the real tanks. This model is referred as Aggregated Tanks' Formulation (ATF). On the other hand, if a detailed inventory management representation is required, a second model developed from the ATF is proposed where each real thank is a single model entity. This is the Disaggregated Tanks' Formulation (DTF).

The main characteristics of these models remain in the time and volume scales, demand and settling period representations. Both models use a continuous time and volume representations. The time scale is build from the sequencing variables that represent the pumping sequence. The volume scale is updated at each time interval where each product located inside of the pipeline moves towards the pipeline end in an amount equal to the volume of the most recent pumped product.

The demand is usually provided on a discrete basis. Thus, it is necessary to translate this information in continuous form. This is done through a time operator that compares both time scales, allocating discrete time points to continuous time intervals.

The settling period is one if the system conditions that restricts the pipeline operation. Settling periods are mandatory for each new batch that is discharged from the pipeline to the tank farm. Within this time intervals, product quality is improved due to settling and meanwhile product approval is obtained.

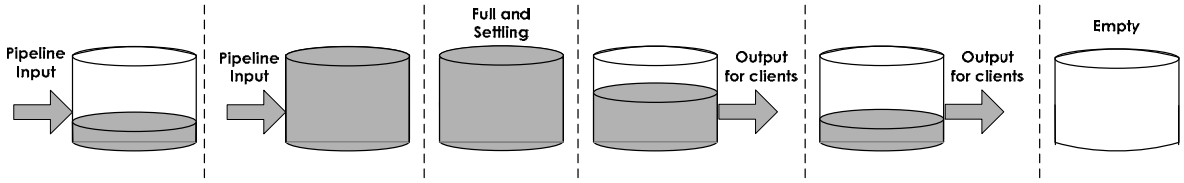

Figure 2 - Individual tank's operational cycle

The approach used to represent the settling period differs between the ATF and the DTF. In the ATF it is mandatory that the fraction of product that corresponds to new batch is maintained in settling (not suitable for clients' demands fulfilment) until the minimum period is reached. On the other hand, as the DTF undertakes individual tank representation, the receiving tank is kept settling until the minimum amount of time is reached.

The DTF uses binary variables that represent and control tank states, which are detailed in Figure 2. A regular tank cycle is composed by a period of pipeline input that fulfils tank capacity. At this point the tank starts to settle until the minimum settling period is reached. At this point it is ready to fulfil market demands until it is totally empty, returning to the starting point. Despite being a more complex model, the detail level of the DTF enables an efficient inventory management at the distribution centre, enabling schedulers precise information of tanks states and how to operate the pipeline reception and product delivery operations.

4 Support Tools: Reactive Scheduling Procedure and Sequencing Heuristic

The implementation of such models in real world scenarios requires attention on two essential points: system dynamics and to obtain results in real time. System dynamics motivates the development of a reactive scheduling procedure that receives an unforeseen situation and integrates it in a new schedule with minimum deviation from the previous one. Six possible causes for rescheduling are presented in Table 1, which have been typified through the analysis of real plant occurrences. These situations are modelled through a MILP representation. Whenever a situation occurs, the corresponding formulation is included in the model formulation. The objective is to readjust the current schedule and incorporate the new situation minimising the amount of changes required. This is a critical step because it

ensures to the refinery production that the changes required are minimal and accommodated in the current plant production and storage profiles.

On the other hand, to obtain results in real time it is essential to explore support techniques that reduce complexity, minimising the solution search effort, such as an initialization heuristic. This heuristic is used prior to model run and reduces the search space. The heuristic receives as input the initial inventory and market demands. The objective is to find the product that would stock out in first place if no pipeline discharges occur. In this way, priorities are established and a sequence of products is developed, corresponding to the given scenario. A second result can be obtain from this heuristic. Given market demands and medium batch volume by product, it can be obtained in advance the number of batches to pump from each product so as to restore product inventory levels.

Table 1 – Rescheduling situations

Situation		Description
S1	Clients' demands	Adjustments on demands on a periodic basis, e.g. weekly.
S2	Imposition on products' sequence	Due to inventory management reasons (at the refinery or tank farm).
S3	Unpredicted pipeline stoppages	Due to product shortage at the refinery or operational conditions (at the refinery or tank farm).
S4	Lots' volumes changes	Mainly due to refinery imposition (e.g. product shortage).
S5	Flowrate adjustments	Mainly due to answering quickly to an unexpected client demand.
S6	Variation on maximum storage capacity	Due to tanks' maintenance, which take place when the tank is empty.

5 Decision Support Framework

The integration of the current models with the proposed supporting tools enables the development of the decision support system architecture presented in Figure 3. Information can be used in a shared way to take advantages from the synergies between modules.

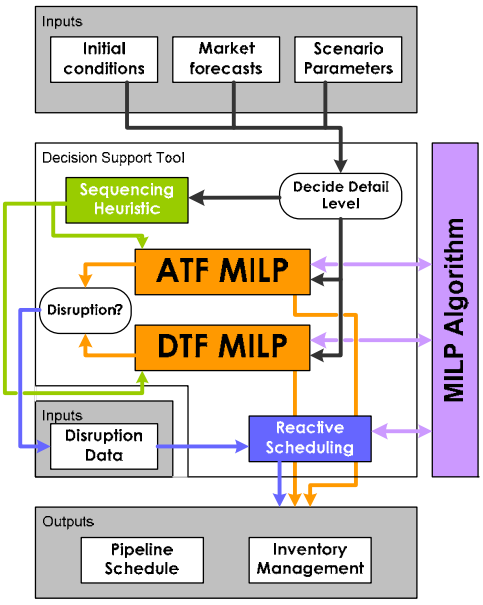

Figure 3 – Decision Support System Architecture

Inputs required are initial conditions (inventory, tank states, pipeline contents), market forecasts and scenario parameters (e.g. flowrate limits, time horizon) while outputs are the pipeline schedule and tank management prodedures with two different levels of detail.

Before running the model, it is necessary to define whether the sequencing heuristic is used and which level of detail is required. The ATF is suitable for medium term horizons, providing

pipeline schedules for refinery production plans and giving an overview for chain management. The DTF detail has high interest to the distribution schedulers, combining the pipeline schedule with an effective inventory management between available individual tanks being suitable for short-term periods. Whenever a disruption occurs, the reactive scheduling procedure is activated, providing a new schedule that incorporates the new occurences. Both MILP models are run in a MILP algorithm.

6 Model Implementation and Results

The real world scenario of CLC – Companhia Logística de Combustíveis has been used as a case study. This company transports six oil products (P1-P6) from Galpenergia Sines' Refinery and distributes them in the central region of Portugal. The distribution centre comprises 29 tanks, whose product service is fixed. The MILP models were implemented in GAMS/CPLEX and results were obtained for medium and short term horizons. The reactive scheduling has been used to address several types of occurrences, while a sequencing heuristic provides valid pumping sequences, which are given to the model as parameters.

As scenario it will be taken the month of July 2007, where several studies were made i) develop several pumping sequences using the sequencing heuristic and implement them in the ATF model, ii) the chosen sequence will be used in the pipeline schedule, giving origin to a detailed inventory management for the first week with the DTF model and iii) the reactive scheduling procedure so as to face unforeseen situations occurring during July 2007.

- When implementing the sequencing heuristic it was verified that product P2 was the one with highest priority to be pumped. In this way, pumping sequences were developed placing this product as earlier as possible in the pipeline transportation schedule. The termination criteria is to finish the monthly schedule with the pipeline filled up with P1. Five sequences were developed, being the final decision taken over the operational indicators results as presented in Table 2. Sequence 5, with a total of 41 batches, was the selected candidate due to fact that operational results are the most consistent (lowest medium flowrate or flexible minimum inventories by product).

Table 2 – Operational indicators by sequence candidate

Sequence	2	3	4	5	CLC
Medium Flowrate (m^3/h)	510.63	511.04	511.04	**510.49**	557.59
∆Inventário (m^3)	+380	+680	+680	**+280**	+19580
Pipeline Usage (%)	**98.66**	**98.66**	**98.66**	**98.66**	94.97
Total Final Inventory (%)	55.34	**55.50**	**55.50**	55.29	65.46
Minimum global inventory (%, product)	16.40 (P3)	18.44 (P3)	18.80 (P3)	**21.19 (P3)**	5.31 (P3)
Minimum Final Inventory (%, product)	51.67 (P1)	**52.53 (P1)**	**52.53 (P1)**	**52.53 (P1)**	20.51 (P3)
Time of computation (min)	**8.7**	120.5	120.5	120.5	-

- The comparison between the ATF and DTF models can be done through the model statistics presented in Table 3, where it is clearly shown the different model sizes and computational effort when considering the first week of operation of July 2007 and the optimal solutions. For the same problem, the number of binary variables increases significantly as well as the computational effort. On the other hand it is obtained a broader set of results comprising specific and detailed procedures for inventory management.

Table 3 – Model statistics

Model	DTF	ATF
# Continuous Variables	3112	3190
# Binary Variables	2199	890
# Equations	11474	7273
# Nodes	3533	0
Time of computation (s)	310.875	0.312

- The reactive scheduling procedure was applied in five situations during the month, where one or more situations can be combined in the same reschedule. CLC's schedulers developed six schedule revisions. Table 4 presents the operational results after the last revision undertaken. The model managed to return a lower medium final inventory while using a larger portion of the total time horizon to pump products. However, the balance between inputs and outputs is higher than the one achieved by CLC's schedulers. The number of interfaces inside of the pipeline when pipeline stoppages occurs is an important factor, because it is likely to decrease adjacent product quality.

Table 4 – Reactive scheduling results

Approach	Revision 5 (ATF)	Revision 6 (CLC)
Medium Flowrate (m^3/h)	508.32	518.17
∆Inventário (m^3)	+8899	+3477
Pipeline Usage (%)	96.91	93.66
Total Final Inventory (%)	59.85	56.98
Minimum global inventory (%, product)	23.63 (P6)	10.09 (P6)
Minimum Final Inventory (%, product)	28.21 (P3)	31.97 (P4)
# Interfaces while pipeline is stopped	1	2

7 Conclusions and Further Work

In this paper it was presented a framework composed of several tools developed to improve the scheduling and management tasks of an oil products distribution centre with pipeline feed. From the real world implementation at CLC, the set of approaches has shown significant improvements in achieving optimal schedules and inventory management plans, while offering a wide range of solutions to explore.

As future work it is proposed to enhance the mathematical formulation of the DTF, reducing model complexity by describing real and complete tank operations in the model formulation. Furthermore, it is proposed to develop a decomposition framework that uses both MILP models in a rolling horizon procedure.

This framework is currently under improvement and testing, through a technological cooperation between Instituto Superior Técnico (IST) and CLC where the main objective is the development of a user-ready software for daily operations management at CLC.

Acknowledgments

The authors gratefully acknowledge the case study and financial support provided by Companhia Logística de Combustíveis.

References

Cafaro, D., Cerdá, J. (2008). Dynamic scheduling of multiproduct pipelines with multiple delivery due dates. *Computers & Chemical Engineering*, 32, 728-753.

Magatão, L., Arruda, L.V.R., Neves, Jr F. (2004). A Mixed Integer Programming for Schedulling Commodities in a Pipeline. *Computers & Chemical Engineering*, 28, 171-185.

Rejowski, Jr. R., Pinto, J.M. (2008). A novel continuous time representation for the scheduling of pipeline systems with pumping yield rate constraints. *Computers & Chemical Engineering*, 32, 1042-1066.

Relvas, S., Matos, H.A., Barbosa-Póvoa, A.P.F.D., Fialho, J., Pinheiro, A. S. (2006). Pipeline Scheduling and Inventory Management of a Multiproduct Distribution Oil System. *Industrial & Engineering Chemical Research*, 45, 7841-7855.

Relvas, S., Matos, H.A., Barbosa-Póvoa, A.P.F.D., Fialho, J. (2007). Reactive Scheduling Framework for a Multiproduct Pipeline with Inventory Management. *Industrial & Engineering Chemical Research*, 46, 5659-5676.

Proceedings of the 10th International Chemical and
Biological Engineering Conference - CHEMPOR 2008
Braga, Portugal, September 4-6, 2008
E.C. Ferreira and M. Mota (Eds.)

WATER USE OPTIMIZATION IN WINE INDUSTRY. DESIGN OF THE WATER AND THE WASTEWATER TREATMENT NETWORK

Patricia Oliver[1], Rosa A. Rodriguez[1*], Stella M. Udaquiola[1]
(1) Instituto de Ingeniería Química -Facultad de Ingeniería -Universidad Nacional de San Juan
Libertador 1109 (O) CEP 5400, San Juan, Argentina

Keywords: winery industry, effluent treatment, integer linear programming, water pinch
Topic: Sustainable process-product development through green chemistry

Abstract

In San Juan, Argentina, one of the main industrial activities is the wine production. Wineries use large quantities of fresh water for cleaning tasks especially during the wine vintage. This study presents two parts: the design of the water and wastewater network. These proposals have been carried out in a winery of San Juan, Argentina. The results proved that a water reduction of 30 % can be achieved, approximately.
The second part of this work attempts to demonstrate that a distributed effluent treatment network leads to reduction of the effluent flowrate to be treated in order to fulfill the permitted contaminant level for discharging in the sewage or a natural water course. The present work combines this technology with an equation system that leads to design a distributed effluent treatment network for batch processes. The obtained network reduces the global treatment flowrate by collecting streams in different groups according to their contaminant concentrations and processing them separately.

1. Introduction

Nowadays water has become a very valuable resource, not only in those regions where it is scarce, but also in those where water is abundant. The origin problem is due to the contamination of natural water sources. In this context it is necessary to develop tools to allow for the design of urban and industrial water networks that optimize water use. If the water requirements are minimized, the water effluent generation will decrease and natural water course contamination will be reduced. That is to say the best way to minimize treatment costs is beginning the analysis at the water input to the industrial plant instead of applying end of pipe methods. In San Juan, Argentina, one of the main industrial activities is the agroindustry, producing olive oil, wine, dried fruits, sweetmeats and canned goods. All of them are seasonal activities, characterized by multibatch processes, with peaks of water and energy requirements. This work presents two parts: the design of the water and wastewater network. These proposals have been carried out in a winery of San Juan, Argentina. Wineries use large quantities of fresh water for cleaning tasks especially during the wine vintage, the season in which the largest amount of water is consumed in the entire region takes place. This work presents a combination of the water pinch technology, which is a graphical tool, with the mathematical modelling, to synthesize the winery water network. Taking into account the wastewater and the results obtained in the previous work, in a centralized treatment system, even if two streams require different treatment operations, they are combined, and both streams undergo each treatment, increasing both capital and operating costs. In a distributed effluent treatment system, in contrast, the streams are segregated and treated separately (Mann G. and Liu Y., 1999). The present work combines this technology with an equation system that leads to design a distributed effluent treatment network for batch processes. The obtained network reduces the global treatment flowrate by collecting streams in different groups according to their contaminant concentrations and processing them separately.

2. Minimum Pure Water Flowrate Determination for an Integrated Process with Reuse

The limiting contaminants are the ones that restrict the reuse possibilities. The selection is made based on the wastewater characteristics of the industry under study, so that its concentration allows to determine if the output of some water using operation can be reused at the input of others. The chemical oxygen demand (COD) and the total suspended solids (TSS) are important water quality parameters. They do not indicate if there are toxic compounds or pathogen microorganisms in water but, given that the main water use in wineries is cleanliness, they have been considered sufficiently representative of the water quality. In the context of this work, the word "contaminant", refers to the parameters mentioned above. The data provided is based on actual site measured data using measuring instruments and are average values based on readings taken throughout the day and/or several tests carried out in a big winery in San Juan Capital.

The input and output water flowrate of every water-using operation is considered constant and independent of the input concentration. This means there are no flowrate changes caused by process operations, only changes in the limiting contaminant concentration. The equations for the calculation presented by Mann G.; Liu Y (1999) are the following:

$$\Delta m_{i,tot} = \frac{f_i}{\left(C^{w}_{i,out} - C^{w}_{i,in}\right)} * \frac{1}{10^3} \qquad (1) \qquad C^{\lim}_{i,out} = C^{\lim}_{i,in} + \frac{\Delta m_{i,tot}}{f_i} * 10^3 \qquad (2)$$

Where $C^{w}_{i,in}$ y $C^{w}_{i,out}$, are the contaminant concentrations of the water supply and water stream that leaves operation i, respectively; f_i, is the water flowrate required by operation i; $C^{lim}_{i,in}$ y C^{lim}_{out},, are the limiting contaminant concentrations at the input and output of operation i, respectively; and $\Delta m_{i,tot}$, is the total contaminant mass load transferred from operation i. The reuse possibilities are determined considering all the water using operations of the process simultaneously and, water reuse is preferred instead of freshwater use in each stage. The effluent of a water using operation can be reused into another only if the contaminant level of the first one does not interfere with the second one. In those systems where two contaminants are considered for the analysis, the mass transfer between them is considered proportional as Eq. (3) points out.

$$\frac{C_{iA,n} - C_{iA,in}}{C_{iAout} - C_{iAin}} = \frac{C_{iB,n} - C_{iBin}}{C_{iB,out} - C_{iB,in}} \qquad (3)$$

Where $C_{i,A,in}$, $C_{i,A,out}$, and $C_{i,A,n}$, are the contaminant A concentrations of operation i at the input, at the output and, at the concentration interval n, respectively. The concentration interval boundaries are determined from the limiting inlet and outlet concentrations for each water using operation from the limiting process data. The same definitions apply for contaminant B. The flowrates determined above are apparent minimum freshwater flowrates since they have been determined without considering the contaminants influence on each other. The solution of the following equation system for every concentration interval leads to the determination of reuse flowrates and limiting contaminants concentrations of each water using operations.

$$f^{*}_{i,n} = \theta_{i,n} f_i \qquad \text{(Necessary water flowrate for operation } i\text{)} \qquad (4)$$

Where $f^{*}_{i,n}$, is the actual flowrate of operation i at the concentration interval boundary n; $\theta_{i,n}$, is a fraction from 0 to 1 and; f_i, is the limiting flowrate of operation i.

Global water balance in interval *n*.

$$f^{*}_{i,n} = T_{i,n} + q_{li,m \le n} + F_{i,n} = \theta_{i,n} f_i \qquad (5) \qquad \text{where } \theta_{i,n} = \max_j \left[\frac{C_{ij,n+1} - C_{ij,n}}{C_{ij,n+1} - \overline{W}_{ij,n}} \right] \qquad (6)$$

Flowrate-weighted average concentration of the three sources of water considered in the global balance.

$$\overline{W}_{ij,n} = \frac{T_{i,n}W_{ij,n} + \sum_{l} q_{li,m\leq n}W_{lj,m\leq n}}{T_{i,n} + \sum_{l} q_{li,m\leq n} + F_{i,n}} \quad (7)$$

In Eq. (5) to (7), $T_{i,n}$, is the flowrate of water available for reuse within operation i at concentration interval boundary and $W_{ij,n}$ is the correponding concentration of contaminant j; $q_{li,m\leq n}$, is the flowrate of water from operation i at the concentration interval boundary n that is reused from operation l at concentration interval boundary m smaller than n and $W_{lj,m\leq n}$ is the correponding concentration of contaminant j; $F_{i,n}$, is the flowrate of freshwater supplied to operation i at concentration interval boundary n. The water network obtained after applying the water pinch analysis could be used only if storage tanks are utilized. In this case, 26 storage tanks are necessary; an extremely high number considering the cost implied.

3. Mathematical Optimization. Batch process

To achieve the real water network for a batch process on the industrial scale, water storage tanks must be included in the network. This would allow water supply in due form and time to each water-using operation depending on the quantity and quality requirements.The objective function could be expressed by the following equation:

Objective Function $\min \sum_{i} F_i$ (8)

In order to design a water network for discontinuous process in relation to water use, some constraints must be included in the mathematical model:

1. If the output of operation j can be reused by operation i, then stream j will direct to storage tank t. If operation j' admits water reuse from operation i, then operation j' will be supplied by tank t, which is sink of stream i.
2. Water using operation can be supplied only by a single tank. If water available by tank t for operation i is insufficient, then the lacking flowrate will be supplied with freshwater, Fi. This additional freshwater flowrate, previously, will enter tank t.
3. The excess flowrate available for reuse coming from operation i that is stored in tank t is sent to effluent treatment. There are no streams from tank to tank.

Water mass balances. Input/output balances on operation i

$$F_i + \sum_{j} f_{j,i} + f_{t,i} = f_i^{in} \text{ (Real Mixing Node)} \quad (9)$$

$$E_i + \sum_{j'} f_{i,j'} + f_{i,t'} = f_i^{out} \text{ (Real Splitting Node)} \quad (10) \qquad f_i^{in} = f_i^{out} = f_i \quad (11)$$

Input/output balances on tank t

$$\sum_{i} f_{i,t} + F_t + f_{k,t} = f_t^{in} \text{ (Imaginary Mixing Node)} \quad (12)$$

$$E_t + \sum_{i'} f_{t,i'} + f_{t,k'} = f_t^{out} \text{ (Imaginary Splitting Node)} \quad (13) \qquad f_t^{in} - f_t^{out} = f_{Ac} \quad (14)$$

$$x_{i,t} = \frac{f_{i,t}}{f_t^{in}} \quad (15) \qquad x_t^{w} = \frac{F_t}{f_t^{in}} \quad (16)$$

$$x_{t,i'} = \frac{f_{t,i'}}{f_t^{out}} \quad (17) \qquad x_t^{ww} = \frac{E_t}{f_t^{out}} \quad (18)$$

$$\sum_{i} x_{i,t} + x_t^{w} = 1 \quad (19) \qquad \sum_{i'} x_{t,i'} + x_t^{ww} = 1 \quad (20)$$

Contaminant mass balances. Balances on operation i

$$f_i * c_i^{in} = \sum_j \left(f_{j,i} * c_{j,i}^{out} \right) + f_{t,i}^{out} * c_{t,i}^{out} \quad (21) \qquad f_i * c_i^{out} = f_i * c_i^{in} + \Delta m_i \quad (22)$$

$$\Delta m_i = f_i^{fixed} * \left(c_i^{out,\max} - c_i^{in,\max} \right) \quad (23)$$

Balances on tank t

$$c_t^{out} = c_t^{in} = c_t \quad (24) \qquad f_t^{in} * c_t^{in} = \sum_i \left(f_{i,t} * c_i^{out} \right) \quad (25)$$

Restrictions

$$f_i \geq f_i^{fixed} \quad (26) \qquad c_{j,i}^{out} \leq c_i^{in,\max} \quad \forall i \neq j \quad (27)$$

$$c_{t,i}^{out} \leq c_i^{in,\max} \quad (28) \qquad c_t = \max \left(c_{j,t}^{out}, c_k \right)_t \quad \forall k \neq t \quad (29)$$

$$c_i^{in} = \max \left(c_j^{out}; c_t \right)_i \quad \forall j \neq i \quad (30)$$

Fig. 1 shows the water network obtained considering the discontinuous use of water in the wine industry.

4. Minimum Treatment Flowrate

The treatment cost is optimized minimizing the inlet flowrate to the treatment process. The effluent flowrate is assumed to be constant. To begin with the analysis, the following heuristics have been considered.

1. Those effluent streams with contaminant concentration higher than that of the treatment pinch are only partially-treated, and those effluent streams with contaminant concentration equal to that of the treatment pinch must be treated completely.
2. Those effluent streams with contaminant concentration lower than that of the treatment pinch can bypass the treatment.
3. The treatment cost is proportional to the effluent flowrate to depurate. The treatment process that admits the highest contaminant concentration at the input must be the first one. The least expensive treatment must be run at the maximum possible flowrate. Physical and chemical treatments must come before the biological ones.The easiest treatment to control must be run at the maximum possible flowrate.

Input/output concentrations, removed contaminant mass loads and treatment flowrates, are determined solving the following equation system:

$$f^I = máx \left(\frac{m_i}{\Delta c_i} \right) \quad (38) \qquad c_{in}^I = c_e + \left(\frac{\Delta m_{total}}{f^I} \right) * 10^3 \quad (39)$$

$$c_{out}^I = c_{in}^I * \left(1 - r^I \right) \quad (40)$$

$$\Delta m^I = \frac{f^I * \left(c_{in}^I - c_{out}^I \right)}{10^3} \quad (41) \qquad c_{in}^{II} = c_{out}^I \quad (42)$$

$$c_{out}^{II} = c_{in}^{II} * \left(1 - r^{II} \right) \quad (43) \qquad c_{i,out}^I = c_{i,in}^I * \left(1 - r^I \right) \quad (44)$$

$$c_{i,in}^{II} = c_{i,out}^I \quad (45) \qquad c_{i,out}^{II} = c_{i,in}^{II} * \left(1 - r^{II} \right) \quad (46)$$

The ratio of stream i that can bypass treatment II is determined solving equation 10 iteratively up to $f_{(n-x)}^{II} < f_{(n-x)}$, which means until one stream has to be divided into two smaller ones, one of which is processed by the two available treatments and the other one, just by treatment I.

$$c_e = \left[\frac{f_1^{II} * c_{1,out}^{II} + f_2^{II} * c_{2,out}^{II} + \ldots + f_{(n-2)}^{II} * c_{(n-2),out}^{II} + \left(f_{(n-2)} - f_{(n-2)}^{II}\right) * c_{(n-2),out}^{I} + f_{(n-1)} * c_{(n-1),out}^{I} + f_n * c_{n,out}^{I}}{\sum_{i=1}^{n} f_i} \right] \quad (47)$$

In multiple contaminants and multiple treatment process systems, for a given treatment process h, a good estimate of the minimum flowrate is the maximum flowrate among the minimum treatment flowrates for all contaminants, that is(Mann G. and Y. A. Liu, 1999):

$$f_{\min}^{h} = \max_{k}\left(f_{k,\min}^{h}\right) \quad \text{(minimum treatment flowrate for treatment process h and contaminant k)} \quad (48)$$

The following results correspond to the second part of a study to optimize the water use, made in a winery in San Juan, Argentina. The maximum concentrations permitted for discharging in a natural water course are: TSS: 40 ppm and COD: 75 ppm. The starting point to design a multiple treatment network is the synthesis of subnetworks for each contaminant according to the minimum flowrates determined above. Then, these subnetworks are merged and once all simplifications are made, the optimal treatment network design is achieved. Fig. 2 shows the resulted network.

5. Conclusions

An approach to synthesize the optimal water network for batch processes has been developed. The new formulation combines the water pinch technology, to determine the minimum water requirement, with the mathematical modelling, to design the water network for batch processes that satisfies the minimum water requirement and requires the minimum amount of tanks. The percentages in which the freshwater flowrates can be reduced compared with those of the actual situation of the plant is 30.22%. With regard to the effluents, it has been proved that optimizing the treatment network the treatment flowrates are minimized. These reductions, besides to make smaller the treatment installations, facilitate the treatment because, the smaller the flowrate to depurate, the easier the treatment.The methodology applied in this work is a feasible and useful tool to implement in the processing plants that generate several effluents that vary greatly in their contaminant concentrations.The distributed effluent treatment network offers the advantage of determining in which treatment unit will be each effluent stream processed so that, in case those that should be treated in the same device were not generated, the corresponding unit operations would not be operated.

References

Yang Y., Lou H., Huang Y., 1999. *Synthesis of an optimal wastewater reuse network.* Waste Management 20 (2000) 311-319.

Savelski M., Bagajewicz M. 2000. *On the optimality conditions of water utilization systems in process plants with single contaminants.* Chem. Eng. Science 55 (2000) 5035-5048.

Tan Y., Manan ZainuddinA., FOO C. 2003. *Water minimization by pinch technology – Water cascade table for minimum water and wastewater targeting.* Universiti Teknologi Malaysia 81310 Skudai, Johor, Malaysia.

Majozi T., 2005. *Wastewater minimization using central reusable water storage in batch plants*. Computers and Chemical Engineering 29 (2005) 1631 – 1646.

Mann G.; Liu Y.*Industrial Water Reuse and Wastewater Minimization*. Editorial Mc Graw-Hill, 1999.

Oliver P; Rodriguez R.; Udaquiola S. 2007. *Water use optimization in batch process industries. P1. Design of the water network.* 2007. Journal of Cleaner Prod. In press.

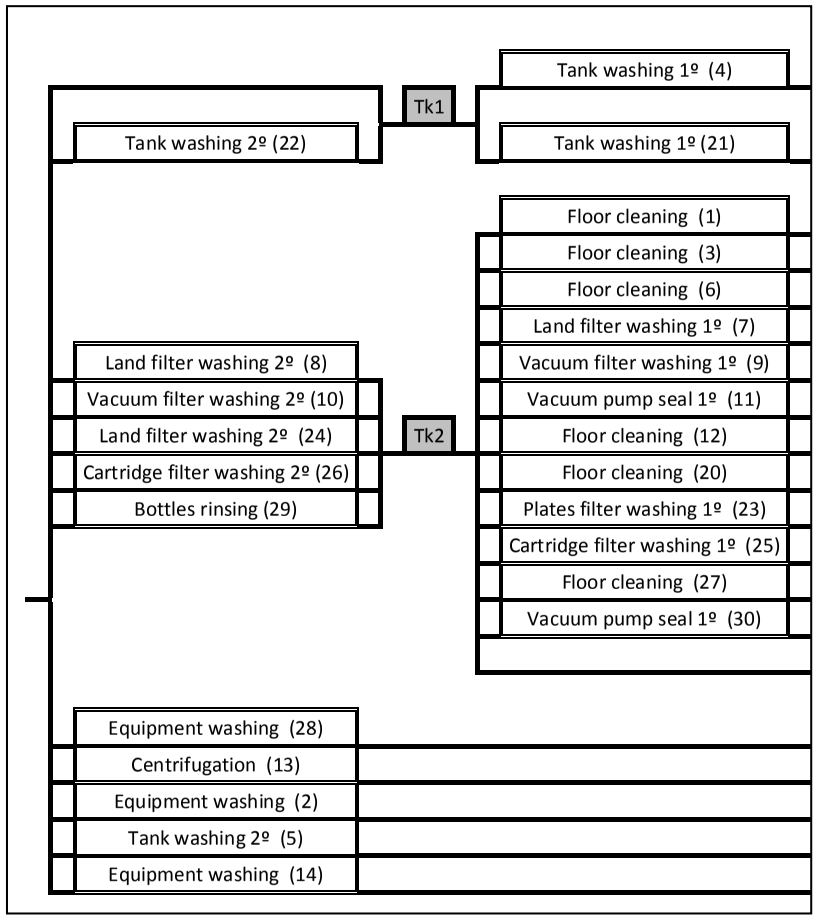

Fig. 1. Winery water network

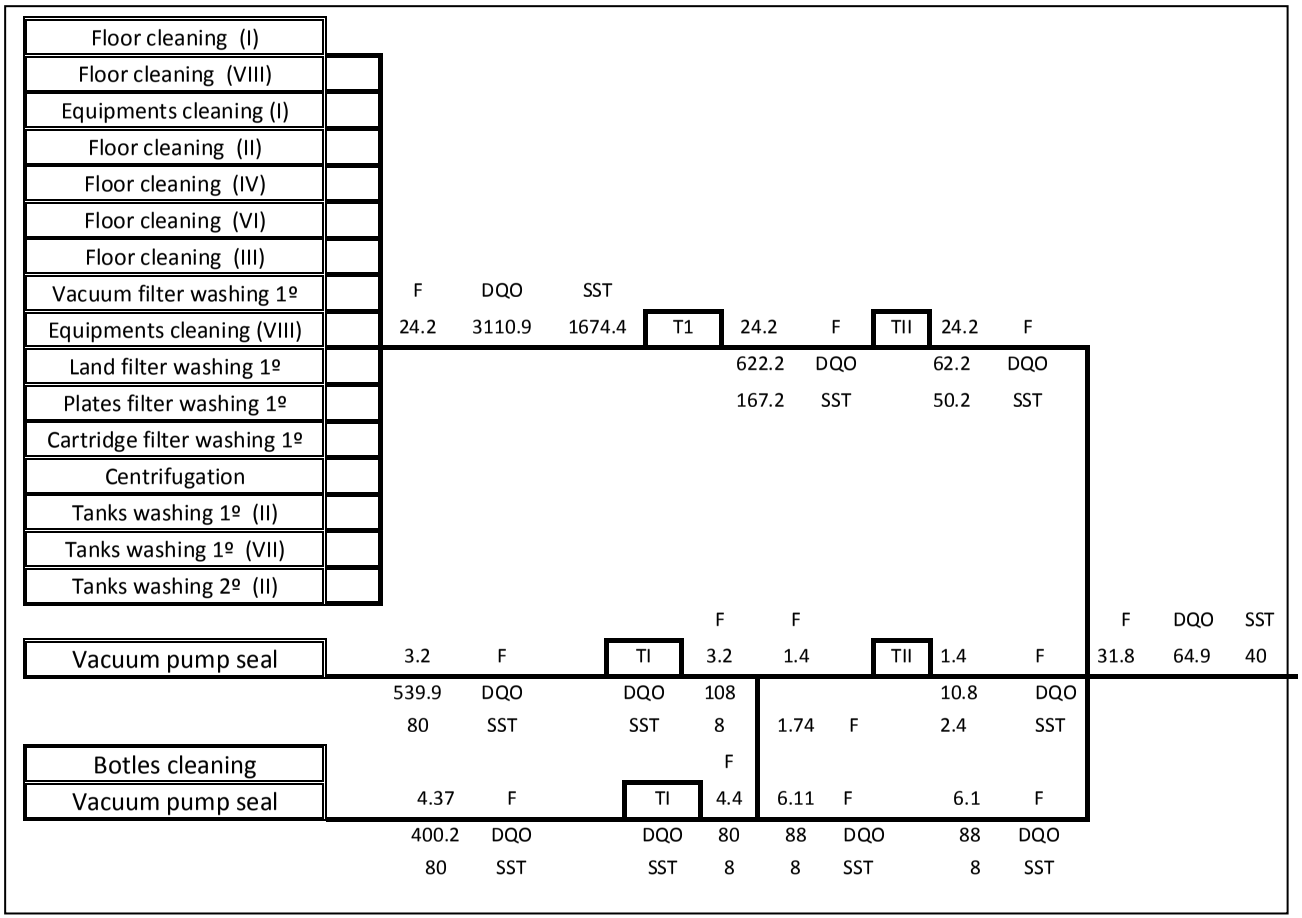

Fig. 2. Resulted treatment network.

Proceedings of the 10th International Chemical and
Biological Engineering Conference - CHEMPOR 2008
Braga, Portugal, September 4-6, 2008
E.C. Ferreira and M. Mota (Eds.)

Optimal Heat Exchanger Network Synthesis Including the Detailed Equipment Design Using Particle Swarm Optimization

M. A. S. S. Ravagnani[1], A. P. Silva[1,2], E. C. Biscaia Jr[2]. and J. A. Caballero[3]
[1]Chemical Engineering Department – State University of Maringá – Maringá – Brazil
[2]PEQ/COPPE - Federal University of Rio de Janeiro – Rio de Janeiro – Brazil
[3]University of Alicante – Alicante – Spain

Keywords: Heat exchanger network, particle swarm optimisation, Superstructure model, shell and tube heat exchangers design, Bell-Delaware method
Topic: Systematic methods and tools for managing the complexity.

Abstract

Many studies and methodologies to the Heat Exchanger Network (HEN) synthesis were proposed to make possible the energy recovery between process streams, minimizing the utilities consumption and the number of heat transfer equipment.

Most of these formulations assume constant heat-transfer coefficients and counter current arrangement for all stream matches, which can lead to non-optimal results. In the present contribution an optimisation model for the synthesis of HEN that includes a detailed design for each heat exchanger in the network is proposed.

Particle Swarm Optimisation approach has been applied to determine the HEN that minimizes the total annual cost, considering capital costs of heat exchangers, energy costs for utilities and pumping duties. The algorithm combines two distinct models, a superstructure simultaneous optimization model for the HEN synthesis considering stream splitting and a model for the detailed equipment design following rigorously the standards of TEMA.

One example from the literature were used to show the application of the proposed algorithm, and the results confirm the achievement of the optimum HEN configuration with the detailed heat exchangers design using little computational effort.

1 Introduction

One of the most frequent problems in industrial plants is the excessive energy consumption. Heat Exchanger Network (HEN) synthesis has been a well-studied subject over the past decades to solve these problems. Many studies and methodologies were proposed to make possible the energy recovery between process streams, minimizing the utilities consumption, the number of heat transfer equipment and the gaseous and liquid pollutant emissions from the combustible burn and water usage.

Furman and Sahinidis (2002) published a complete review on HEN synthesis. The majority of published papers in HEN synthesis consider constant heat transfer coefficients and countercurrent arrangement for all stream matches. This consideration can achieve solutions very far from the point of view of industrial application because heat transfer coefficients are strongly influenced by the heat exchanger geometry and operational constraints.

A few papers incorporate the design of the heat exchangers in the HEN synthesis. Ravagnani, et al. (2003) presented a methodology for the synthesis of HEN including the thermo-hydraulic design of the heat exchangers. The HEN synthesis is accomplished by using Pinch Analysis. After the synthesis, the network equipment are designed considering pressure drops and fouling with the Bell-Delaware method (Taborek, 1983) for the shell side.

Mizutani et al. (2003b) developed a model for the synthesis of HEN based on a heat exchanger design model (Mizutani et al., 2003a). To the network synthesis, the logic based outer approximation method of Turkay and Grossmann (1996) was used.

Ravagnani and Caballero (2007a) proposed a mathematical model to find the best shell-and-tube heat exchanger configuration, using the Bell-Delaware method for the shell side thermal-hydraulic calculation and following rigorously the standards of the Tubular Exchangers Manufacturers Association (TEMA, 1998).

In this contribution, an optimization procedure for the synthesis of HEN including a detailed design for each heat exchanger in the network is proposed, as presented in Silva et al. (2008). The model takes into account the optimization of the equipments and their geometric and operational constraints from the synthesis stage. Shell and tube pressure drops and fouling are considered, as well as mechanical aspects, like shell and tube bundle diameters, internal and external diameter of tubes, number of tubes, number of baffles, baffles spacing, number of shells, tube length, tube pitch, tube arrangement and the fluid allocation in the heat exchanger.

The approach is based on the use of Particle Swarm Optimization to determine the HEN that minimizes the total annualized cost, accounting for capital costs of heat exchangers and the energy costs for utilities and pumping duties, following the model proposed by Ravagnani et al. (2008). The algorithm combines two distinct models: a superstructure simultaneous optimization model for the HEN synthesis considering stream splitting and by-pass without isothermal mixing similar to the proposed by Yee and Grossmann (1990); and a model for the detailed equipment design, following rigorously the standards of the TEMA.

Mechanical design features and thermal-hydraulic variables (heat, area, individual and global heat transfer coefficient, shell and tube pressure drops and fouling) are variables to be optimized. The equipments are designed under pressure drop and fouling limits. The great contribution of this paper is the incorporation of the equipment detailed design and the achievement of optimal mechanical and thermo-hydraulical variables and the warrantee of the use of the standards of TEMA.

One example from the literature were used to show the application of the proposed method, and the results confirm the achievement of the optimum HEN configuration with the detailed heat exchangers design, following the TEMA standards.

2 Problem Definition

The problem consists of finding the HEN that minimizes the total annual investment plus operating costs. The investment term includes the cost of exchangers and pumps, and the operating costs comprise the energy for utilities and pumps.

Given a set of hot and cold streams with their supply and target temperatures, flowrates and physical properties (density, viscosity, heat capacity and thermal conductivity), pressure drop and fouling limits, as well as hot and cold utilities with their temperatures and corresponding costs, the objective is to find the best HEN configuration with the detailed heat exchangers design concerning the minimum global annual cost, considering utility, area and pumping costs.

For the HEN synthesis an algorithm similar to the stage-wise superstructure representation of Yee and Grossmmann (1990) is proposed. Heaters and coolers are placed at the ends of the streams. This algorithm (main problem) is combined with the heat exchangers design model presented in Ravagnani and Caballero (2007b) for each network equipment, to find the minimum global annual cost, comprising area, utilities and pumping costs. The design of heat exchangers is solved as an inner optimisation loop.

At the HEN optimization problem an objective function to minimize global annual cost is proposed, presented at Eq. (1). The constraints are the thermodynamics restrictions of the heat exchanges, showed in Eq. (2).

The problem to be formulated as an optimisation problem is the design of the optimum shell and tube equipment to exchange heat between a cold and a hot stream. The objective is to find the heat exchanger that presents the minimum cost including exchange area and pumping costs, following the TEMA standards constrained to allowable pressure drops and fouling limits, Eq. (3) and (4).

Minimize: $$C_{GLOBAL} = C_{utilities} + \sum_{k}^{unit} (C_{total})_k \quad (1)$$

Subject to: $$\begin{cases} (Th_{in})_k > (Tc_{out})_k \\ (Th_{out})_k > (Tc_{in})_k \end{cases} \quad k=1,\ldots,\text{number of heatexchangers} \quad (2)$$

Where, k are the heat transfer equipments; Th_{in} and Th_{out} are the inlet and outlet temperatures of the hot streams; Tc_{in} and Tc_{out} are the inlet and outlet temperatures of the cold streams.

Minimize: $$C_{total} = C_{area} + C_{pump} \quad (3)$$

Subject to: $$\Delta P_t \le \Delta P_{max};\ \Delta P_s \le \Delta P_{max};\ r_d \ge r_{d,design};\ F_t \ge 0.75 \quad (4)$$

3 Particle Swarm Optimization

The proposed HEN synthesis problem is solved with Particle Swarm Optimisation (PSO). PSO is a stochastic optimisation technique developed by Kennedy and Elberhart (2001), inspired in the social behaviour of bird flocking or fish schooling. PSO as an optimisation tool provides a population-based search procedure in which individuals called particles change their position (state) with time. In a PSO system, particles fly around a multidimensional search space. During flight, each particle adjusts its position according to its own experience, and according to the experience of a neighbouring particle, making use of the best position encountered by itself and its neighbour.

In the last years, PSO has been successfully applied in many research and application areas. One of the reasons that PSO is attractive is that there are few parameters to adjust. In this work, it was used a PSO proposed by Vieira and Biscaia (2002). The particles and the velocity of each particle are actualized according to Eq. (3) and (4).

$$v_{k+1}^{(i)} = \omega_k v_{k+1}^{(i)} + c_1 r_1 \left(p_k^{(i)} - x_k^{(i)}\right) + c_2 r_2 \left(p_k^{global} - x_k^{(i)}\right) \quad (5)$$

$$x_{k+1}^{(i)} = x_k^{(i)} + v_{k+1}^{(i)} \quad (6)$$

Where $\boldsymbol{x}_k^{(i)}$ and $\boldsymbol{v}_k^{(i)}$ are, respectively, position and velocity vectors of the particle *i*, ω_k is the inertia weight, c_1 and c_2 are constants, r_1 and r_2 are two random vectors, $\boldsymbol{p}_k^{(i)}$ is the position with the best result of particle *i* and $\boldsymbol{p}_k^{global}$ is the position with the best result of the group. In above equations subscript *k* refers to the iteration number.

In a HEN synthesis problem, the variables considered independents are randomly generated at the optimization beginning and are modified in each iteration by the Eqs. (5) and (6). At the main optimisation, each particle is formed by the follow variables: fraction of hot stream splitting, fraction of cold stream splitting, number of stages and heat exchanged in each equipment. At the inner optimisation, each *particle* is composed by the variables: tube length,

hot fluid allocation, position in the TEMA table (that automatically defines the shell diameter, tube bundle diameter, internal and external tube diameter, tube arrangement, tube pitch, number of tube passes and number of tubes).

After the generation of the particle, the heat exchangers areas are calculated, as well as the hot and cold utilities demand. This is done to all particles even they are not a problem solution. The objective function value (global cost of the HEN) is obtained. If the particle is not a solution of the problem (any restriction is violated), the objective function is penalized.

The PSO parameters used in this work are presented in Table 1.

Table 1. PSO Parameters

c1	c2	w	Npt
1.0	1.0	0.5	50

4 Illustrative Example

An example, first used in Castillo et. Al (1998), is presented to illustrate the applicability of the proposed methodology. Six hot and five cold process streams are considered, as well as a hot and a cold utility. Streams, utilities and cost data are shown on Table 2. Physical properties of the streams and utilities and pumping cost data are not presented to the authors, so they are ficticious.

The value of the HEN global annual cost without the detailed heat exchangers design is 139,675 $/year. By applying the proposed methodology, the HEN cost is 152,120 $/year considering the pumping cost. The cost considering just the area and utilities cost is 137,466 $/year, that is smaller than that with no design is considered. The optimal network configuration obtained is presented in Fig. 1. Table 3 presents the details of the equipments design. Also, the designed heat exchangers are in accordance with TEMA standards. Table 4 shows the comparison with literature.

Table 2 – Streams and Cost Data

Stream	T_{in} (K)	T_{out} (K)	m (kg/s)	μ (kg/ms)	ρ (kg/m3)	Cp (J/kgK)	κ (W/mK)	ΔP (kPa)	r_d (W/mK)
H1	1113	313	2,033	2.4 E-4	634	2454	0.114	68.95	1.7 E-4
H2	349	318	1,909	2.4 E-4	634	2454	0.114	68.95	1.7 E-4
H3	323	313	0.315	2.4 E-4	634	2454	0.114	68.95	1.7 E-4
H4	453	350	0.249	2.4 E-4	634	2454	0.114	68.95	1.7 E-4
H5	453	452	119.28	2.4 E-4	634	2454	0.114	68.95	1.7 E-4
H6	363	318	1,249	2.4 E-4	634	2454	0.114	68.95	1.7 E-4
C1	297	298	134.39	2.4 E-4	634	2454	0.114	68.95	1.7 E-4
C2	298	343	0.219	2.4 E-4	634	2454	0.114	68.95	1.7 E-4
C3	308	395	1,519	2.4 E-4	634	2454	0.114	68.95	1.7 E-4
C4	363	453	0.248	2.4 E-4	634	2454	0.114	68.95	1.7 E-4
C5	353	454	1051.79	2.4 E-4	634	2454	0.114	68.95	1.7 E-4
UQ	503	503							
UF	293	313							

Area cost=9094 + 485$A^{0.81}$, A in m^2. Pumping cost = 0.7 ($\Delta P^t m^t/\rho^t + \Delta P^s m^s/\rho^s$), ΔP in Pa, m in kg/s and ρ in kg/m^3. Hot utility cost = 110 $/kW year. Cold utility cost = 15 $/kW year.

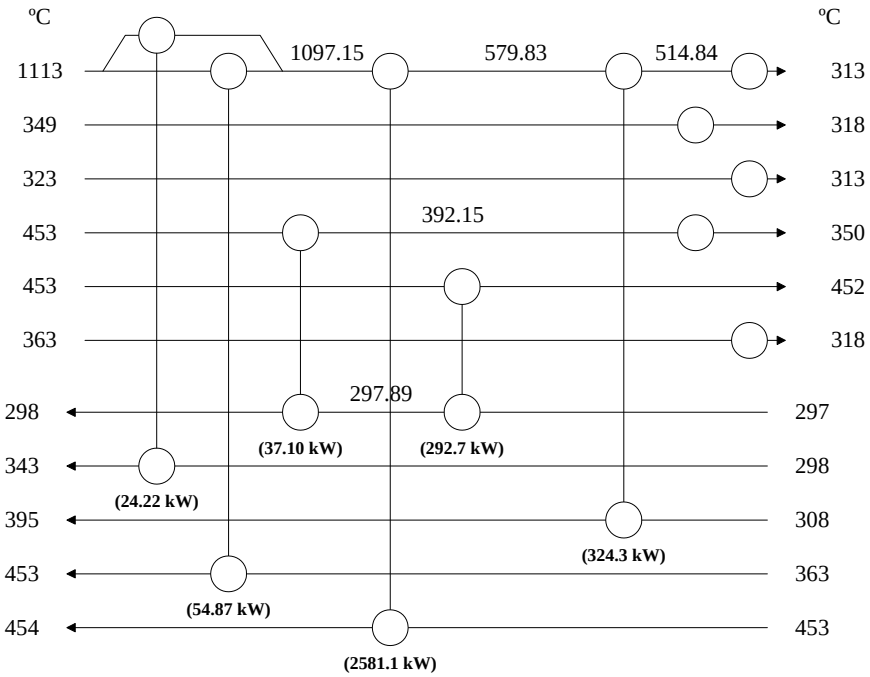

Figure 1 – Optimal HEN

5 Conclusions

In the present paper an algorithm for the synthesis of HEN including the detailed design of the equipments is proposed. It is based in a model similar to the stage-wise superstructure considering stream splitting and by-pass and a model for the optimal design of a shell and tube heat exchanger design, following rigorously the TEMA standards. The global annual cost objective function takes into account investment and utility costs.

An example were used to describe the algorithm applicability. The final results obtained in this paper are consistent with the presented in the literature and lower than those showed for Castillo et. al (1998) when considering no equipment design. The problem was optimised with PSO method, which is a reliable way compared with other methods, because it suits well to MINLP problems. Although with a very reasonable computational time of 540 minutes, the results are better and more realistic than the presented in literature.

Table 3 - Detailed equipment design

	E1	**E2**	**E3**	**E4**	**E5**	**E6**
Area (m^2)	0.23	0.27	2.88	6.79	3.31	0.36
L (m)	2.438	2.438	2.438	2.438	2.438	3.048
D_s (m)	0.205	0.205	0.489	0.686	0.533	0.205
N_t	16	14	148	349	170	20
d_{ex} (m)	0.0191	0.0254	0.0254	0.0254	0.0254	0.0191
d_{in} (m)	0.0142	0.0193	0.0221	0.0225	0.0221	0.0142
hs ($W/m^2 K$)	243.81	238.14	81.38	244.81	4074.85	1016.41
ht ($W/m^2 K$)	1939.92	2395.75	2800.81	2724.39	2326.12	2399.69
U_c ($W/m^2 K$)	190.66	191.96	76.14	204.46	878.05	501.30
U_d ($W/m^2 K$)	13.20	28.96	10.58	120.84	57.13	454.76
ΔP_t (kPa)	38693.30	67766.48	17078.80	16194.09	10861.74	47523.62
ΔP_s (kPa)	3.58	3.91	0.45	13.83	30509.97	168.78
r_d (m^2 KW)	7.048E-02	2.931E-02	8.133E-02	3.384E-03	1.636E-02	2.041E-04
Arrangement	1	1	2	1	2	2

Hot fluid allocation	1	1	2	2	2	2

Table 4 - Final results

	Castillo et. al (1998)	Present paper Without Design	Present paper With Design
Global annual cost ($/year)	141554.88	139675.40	152120.31
Area cost ($/year)	121699.02	119820.60	117611.64
Pumping cost ($/year)	--	--	14653.86
Utility cost ($/year)	19855.86	19854.80	19854.80
CPU time (min) @ Pentium IV 170 GHz	--	~ 80	~540

References

Castillo, E., Acevedo, L. and Reververi, A., Cleaner Production of Nitric Acid by Heat Transfer Optimization: A case study, Chem. Biochem. Eng., 12, 157 – 165, 1998.

Furman, K. C., and Sahinidis, N. V. *A critical review and annotated bibliography for heat exchanger network synthesis in the 20th century*. Industrial and Engineering Chemistry Research, 41, 2335–2370. 2002.

Kennedy, J. and Eberhart, R.; Swarm Intelligence. Academic Press, London, 2001.

Mizutani, F. T., Pessoa, F. L. P., Queiroz, E. M., Hauan, S., & Grossmann, I. E. (2003a). *Mathematical programming model for heat exchanger network synthesis including detailed heat eschanger designs. 1. Shell-and-tube heat exchanger design*. Industrial and Engineering Chemistry Research, *42*, 4009–4018.

Mizutani, F. T., Pessoa, F. L. P., Queiroz, E. M., Hauan, S., & Grossmann, I. E. (2003b). *Mathematical programming model for heat exchanger network synthesis including detailed heat exchanger designs. 2. Network synthesis*. Industrial and Engineering Chemistry Research, *42*, 4019–4027.

Ravagnani, M. A. S. S., Silva, A. P., Caballero, J. A., and Biscaia Jr., E. C., *Shell and Tube Heat Exchanger Design Using Particle Swarm Optimization*, Proceedings of the Brazilian Congress of Chemical Engineering, paper to appear, 2008.

Ravagnani, M. A. S. S.; Caballero, J. A., (2007a). Optimal design of shell and tube heat exchangers. *Chemical Engineering Research & Design*, 85 (A10) 1–13.

Ravagnani, M. A. S. S.; Caballero, J. A., (2007b). Optimal heat exchanger network synthesis with the detailed heat transfer equipment design *Computers and Chemical Engineering*, 31, 1432-1448.

Ravagnani, M. A. S. S., Silva, A. P., and Andrade, A. L. *Detailed equipment design in heat exchanger networks synthesis and optimization*. Applied Thermal Analysis, 23, 141–151. 2003.

Taborek, J. (1983). *Shell-and-tube heat exchangers,* Section 3.3. Heat exchanger design handbook. Hemisphere Publishing.

TEMA. (1988). *Standards of the tubular heat exchanger manufacturers association* (7th ed.). New York: Tubular heat exchanger manufacturers association.

Turkay, M., and Grossmann, I. E. Logic-based MINLP algorithms for the optimal synthesis of process networks. Comput. Chem. Eng., 208, 959–978. 1996.

Silva, A. P., Ravagnani, M. A. S. S. and Biscaia Jr., E. C., *Particle Swarm Optimisation in Heat Exchanger Network Synthesis Including Detailed Equipment Design*, Proceedings of the 18th European Symposium on Computer Aided Process Engineering – ESCAPE 18, 2008.

Vieira, R. C. and Biscaia Jr., E. C., Métodos Heurísticos De Otimização. Notas De Aula Da Escola Piloto Virtual Do Peq/Coppe/Ufrj. Available Under Consultation: biscaia@peq.coppe.ufrj.br, 2002.

Yee, T. F., and Grossmann, I. E. Simultaneous optimization models for heat integration. II. Heat exchanger network synthesis. Comput. Chem. Eng., 14, 1165. 1990.

Proceedings of the 10th International Chemical and
Biological Engineering Conference - CHEMPOR 2008
Braga, Portugal, September 4-6, 2008
E.C. Ferreira and M. Mota (Eds.)

Using Neural Network Predictive Control for Riser- Slugging Suppression

R. Eslamloueyan [*], **E. Hosseinzadeh** [†]
Petroleum and Chemical Engineering Department, Shiraz University, Shiraz, Iran

Keywords: Slug Flow, Neural Network, Nonlinear Model, Control Structure Design
Topic: Systematic methods and tools for managing the complexity (Process control & operations)

Abstract

Riser-slugging is a flow regime that can occur in multiphase pipeline-riser systems, and is characterized by severe flow and pressure oscillations. Reducing undesired slugging effects can have great economic benefits. Recently, control methods have been proposed to conquer slugging flow problems in pipeline risers. The advantages of using a control system are that it can be installed on existing oil and gas production facilities with no need to expensive equipment and that no significant pressure drop is imposed to the system.

In this work, a predictive control system based on Neural Network (NN) model of process is developed for handling and suppressing riser-slugging. An ANN model of the plant is used to predict future response of the nonlinear process. Storkaas dynamic model (Storkaas and Skogestad,2002) is employed for process simulation. Comparison of the results of this research to that of other works, indicates a significant improvement in setpoint tracking.

1 Introduction

Riser-slugging produce a cyclic variation of flow and pressure in pipeline risers. This phenomenon can be divided into four stages. At the first stage, slug begins to form because of low velocity of gas. During this period, the liquid is no longer carried over by the gas and begins to fall down and to make blockage in the riser bottom. The pipeline pressure increases until the liquid level in the riser reaches to the top. The second stage, which is called slug production, starts when the liquid level reaches the top of the riser, and the liquid slug is produced until the gas reaches the riser base. At the third stage, i.e. bubble penetration, gas permeates the liquid in the riser, so the hydrostatic pressure decreases and gas flow rate increases. The fourth stage is called gas blowdown. If the gas produced at the riser base reaches the top then the pressure is minimum and the liquid is no longer gas-lifted. The liquid downfall is repeated and a new cycle begins (Mokhatab et al.,2007).

The challenge of handling intermittent flow with liquid slugs followed by gas pockets in multiphase flow lines becomes more important when the number of production wells increases. Oil, gas and water are transported from the offshore wells through long pipelines (several kilometres) along the seabed and go up through a riser to the production platform. Slugging may have undesirable effects on the oil and gas production process. Severe slugging will cause fluctuations in the inlet separator liquid level. This may lead to poor separation or even in some cases to separator flooding. The oscillating pressure can increase the wear and tear in the processing equipment and will reduce the lifetime and increase the maintenance costs (Godhavn et al.,2005). Designing the topside facilities to tolerate these disturbances may involve large and expensive slug catchers as well as compressor packages with fast responding control systems. Hence, using a simpler

[*] Fax:+98-711-6287294 , Email: eslamlo@shirazu.ac.ir ; reslamloueyan@yahoo.com
[†] E-mail: elham_hosssienzadeh@yahoo.com

preventive system to alleviate or eliminate severe slugging phenomenon becomes very essential. Control systems have been widely proposed to tackle the slugging problem in pipeline risers. For a complete review of current technologies for severe slugging remediation, see Mokhatab et al. (2007).

Fard et al.(2003) show that a cascade-control strategy with feedback from bottom pressure and flow rate at the top of the riser is adequate to suppressing the slugs. However this control strategy requires pressure measurements at the bottom of the riser. Storkaas and Skogestad (2002) developed a simple dynamic nonlinear model for riser-slugging in pipeline-riser system and presented controllability analysis and conventional controller design for linearized model around equilibrium point. Hardy B. Siahaan proposed a state feedback design method for attenuating severe slugging in multiphase flow pipeline-riser systems. The algorithm is designed based on the input output linearization method, and incorporates the saturation effect on the input. The designed state feedback can suppress the slugging phenomenon provided some conditions are satisfied.

The nonlinearity of the slugging cycle in pipeline risers can motivate researchers to use nonlinear model based controllers. Nonlinear model predictive control (NMPC) allows direct consideration of a nonlinear process model as well as state and input constraints. Thus NMPC seems to be well suited for this kind of processes. MPC have been used for control of various systems including process industries (Findeisen et al., 2001; Majanne, 2005). The term MPC does not specify a specific controller but a wide range of control strategies which use a model of process to obtain the optimum values of manipulated signals by minimizing an objective function. Most predictive control algorithms are based on a linear model of the process. However, industrial processes usually contain complex nonlinearities and a linear model may be acceptable only when the process is operating around an equilibrium point. If the process is highly nonlinear a nonlinear model will be necessary to describe the behaviour of the process. Recently, neural networks have been used in some predictive control algorithms that utilize nonlinear process models. In this work, the process model of the proposed MPC is a non stationary neural network with one hidden layer. The following section is devoted to the process model and Neural Network MPC method.

2 Process Model

A simple nonlinear model with only three dynamic states was developed by Storkaas and Skogestad (2002) to simulate the dynamic behaviour of slug formation in pipeline risers. This model covers both riser-slugging, and, more importantly, the unstable but preferred non-oscillatory flow regime that exists at the same boundary condition. Conservation equations are given in equation 1.

$$\begin{aligned} \frac{d}{dt} m_L &= \dot{m}_{L,in} - \dot{m}_{L,out} \\ \frac{d}{dt} m_{G_1} &= \dot{m}_{G,in} - \dot{m}_{G_1} \\ \frac{d}{dt} m_{G_2} &= \dot{m}_{G_1} - \dot{m}_{G,out} \end{aligned} \tag{1}$$

The three-state model is well suited for analysis and controller design because of its limited complexity and its ability to predict the essential system characteristics for control purposes, and can be used for designing anti-slug controllers. Figure 1 illustrates pipeline-riser system at the situation of riser-slugging. The model has only three dynamic states: the gas and liquid holdups in the riser (i.e. m_L, m_{G_2}), and the holdup of gas in the upstream pipeline(m_{G_1}).The most important adjustable parameters are the ”valve constant” for the flow of gas into the riser and two parameters describing the fluid distribution in the riser. For the details of modelling see Storkaas and Skogestad (2002).

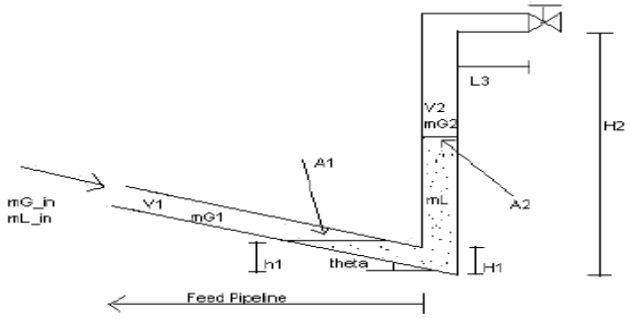

Figure 1- Illustration of pipeline-riser system

3 NN Predictive Controller Design

Neural networks have been applied very successfully in the identification and control of dynamic systems. The universal approximation capabilities of the multilayer perceptron make it a popular choice for modelling nonlinear systems and for implementing general-purpose nonlinear controllers. The progress in computer technology has made a significant advancement in neural network research. Artificial neural network (ANN) is an mathematical expression of the neural aspect of the human brain. The process of learning in ANN's is based on experience and repetition rather than the application of rule-based principles and formulas. ANN provides capabilities such as learning, self-organization, generalization (response to new problems using incomplete information), and training (Hagan et al.,1996).
Two steps are carried out when using neural networks for control:
- System Identification
- Control Design

In the system identification step, a neural network model of the plant is developed. In the control design stage, the neural network model is used to design (or train) the controller.

For the model predictive control, the plant model is used to predict future behaviour of the plant, and an optimization algorithm is used to select the control input that optimizes future performance. The fundamental idea in predictive control is to predict the vector of future tracking errors and minimize its norm over a given number of future control horizons. It is therefore clear that predictive controller design mainly consists of two parts: prediction and minimization. An optimization algorithm computes the control signals that optimize future plant performance. The neural network plant model is trained offline, using one of the training algorithms based on backpropagation.The controller, however, requires a significant amount of on-line computation, since an optimization algorithm is performed at each sample time to compute the optimal control input.

3.1 System Identification

The first stage of model predictive control is to train a neural network to represent the forward dynamics of the plant. The prediction error between the plant output and the neural network output is used as the neural network training signal. The process is represented in figure 2. A neural network consists of layers of simple processing units coupled by weighted interconnections. The neural network plant model uses previous inputs and previous plant outputs to predict future values of the plant output. The structure of the neural network plant model is given in figure 3.

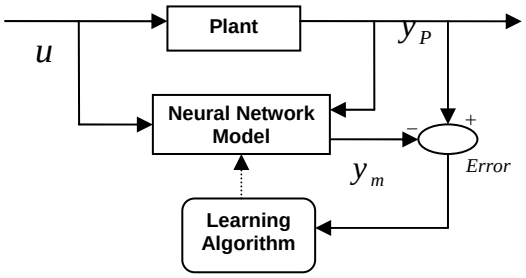

Figure 2- System identification with neural network

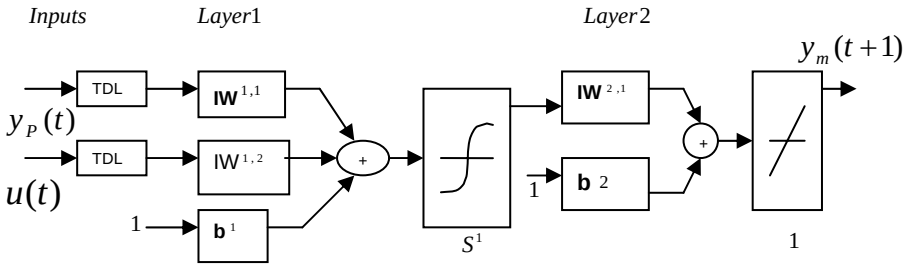

Figure 3- Structure of the neural network plant model

This multi layer perceptron (MLP) network can be trained offline in batch mode, using data collected from the operation of the plant. Any of the training backpropagation algorithms can be used for network training.

The plant model neural network has one hidden layer with 7 neurons. Levenberg-Marquardt algorithm was used for training the network. The application of Levenberg-Marquardt to neural network training is described by Hagan et al. (1996). Tangent sigmoid transfer functions were selected for neurons. The required training data was generated by by applying a series of random step inputs to the process simulation.

3. 2 Predictive Control

The model predictive control method is based on the receding horizon technique (Soloway and Haley,1996). The neural network model predicts the plant response over a specified time horizon. The predictions are used by a numerical optimization program to determine the control signal that minimizes the following performance criterion over the specified horizon.

$$J = \sum_{j=N_1}^{N_2} (y_r(t+j) - y_m(t+j))^2 + \rho \sum_{j=1}^{N_u} (u'(t+j-1) - u'(t+j-2)) \quad (2)$$

Where N_1, N_2 and N_u define the horizons over which the tracking error and the control increments are evaluated. The variable u' is the tentative control signal, y_r is the desired response and y_m is the network model response. The value ρ determines the contribution that the sum of the squares of the control increments has on the performance index. Figure 4 illustrates the block diagram of the model predictive control process. The controller consists of the neural network model and the optimization block. The optimization block determines the values of u' that minimize J, and then the optimal u is input to the plant. Backtracking technique was used as a linear search routine for optimization algorithm. It searches in a given direction with search parameter α to locate the minimum of the performance function in that direction (Dennis et al., 1983).

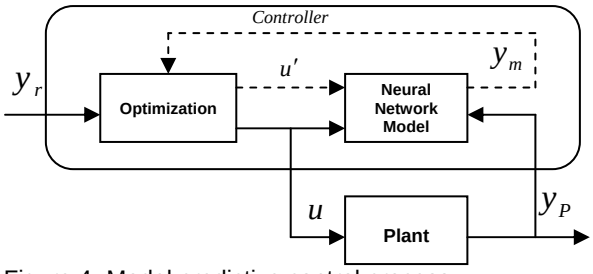

Figure 4- Model predictive control process

The controller horizons N_2 and N_u. (N_1 is fixed at 1, $N_2 > N_u$) and weighting parameter can be defined based on optimization algorithm.

4 Results

As shown in Fig. 5, the control objective is to maintain flow regime at desired condition to avoid pressure oscillations by manipulating the valve opening at top of the riser. The controlled variable is P1, the pressure of feed-pipeline, and the manipulated variable is the percentage of valve opening.

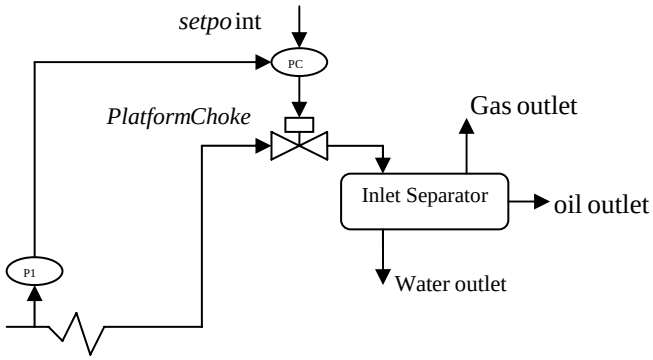

figure5- control structure with feedback from pressure at the bottom

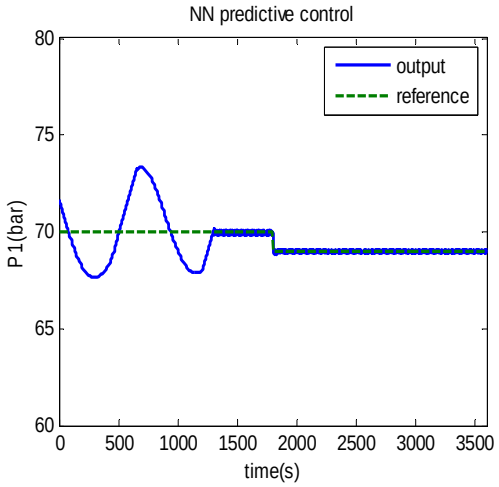

Figure 6- simulation result for NN predictive control

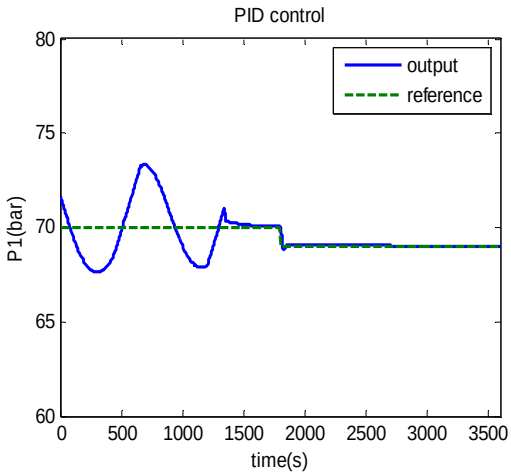

Figure 7- simulation result for PID control

The closed loop responses of the developed NN-MPC and a conventional PI controller are indicated in Fig. 6 and 7 respectively. The controllers are triggered after 1200 seconds and a unit step decrease in reference signal is introduced after 1800 seconds. The tuning parameters of Storkaas were used for the PI controller. In another scenario, while both controllers are active, a unit step change in reference signal is introduced after 60 seconds. Figures 8 and 9 illustrate the responses of the controllers in this case.

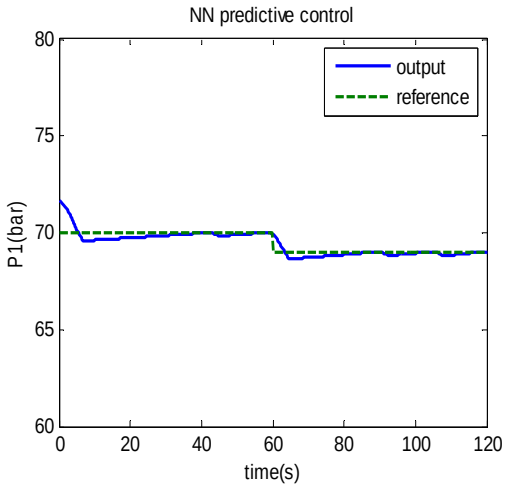

Figure 8- detailed result for NN predictive control

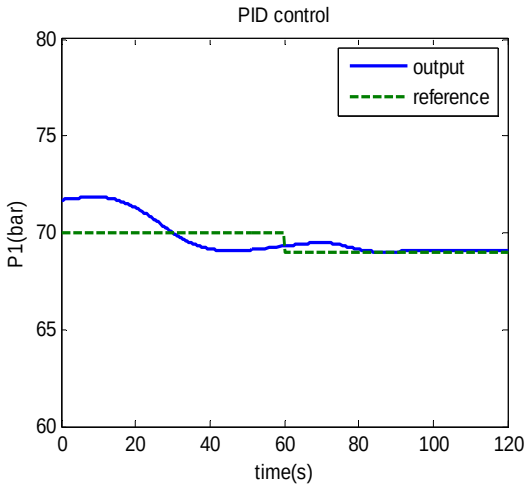

Figure 9- detailed result for PID control

The integral of absolute errors (IAE) for the NN MPC and the PI controller are respectively, 22.9 and 72.6. Figures 6-9 and IAE performance index indicate that the response of NN MPC is considerably better than that of the PI controller.

5 Conclusion

This paper introduced NN predictive control for handling flow regime in pipeline-riser systems to avoid riser-slugging phenomenon. In comparison with conventional control, NN predictive control acts early with better set point tracking. Simulation proved that in case of higher step change or reversing the change direction, the capability of the developed NN predictive control in comparision to the PI controller becomes much more apparent.

References

Storkaas, E., Skogestad, S. (2002). Stabilization of severe slugging based on a low-dimensional nonlinear model. *AIChE Annual meeting*, Paper 259e.

Mokhatab, S., Towler, B. F., Purewal, S. (2007). A review of current technologies for severe slugging remediation. *Petroleum Science and Technology*, 25:10, 1235 -1245.

Godhavn, J. M., Mehrdad, P. F., Fuchs, P. (2005). New slug control strategies, tuning rules and experimental results. *Journal of Process Control* ,15, 547-577.

Fard, M., Godhavn, J. M., Sagatun, S. (2003). Modeling and slug control within OLGA. *SPE* 84685.

Hardy B. Siahaan, Ole M. Aamo, Bjarne A. Foss . (2005). Suppressing riser-based slugging in multiphase flow by state feedback. *Proceedings of the 44th IEEE Conference on Decision and Control, and the European Control Conference 2005.* 452-457.

Rolf Findeisen, Frank Algower ,Mortiz Diehl, H. George Bock, Johannes P. Schloder, Zoltan Nagy.(2001).Efficient nonlinear model predictive control. *Proceedings of Chemical Process Control* ,6,pp 454 -460.

Yrjo Majanne.(2005). Model predictive pressure control of steam networks. *Control Engineering Practice*, 13, 1499-1505.

Martin T. Hagan, Howard B. Demuth, Mark Beale. (1996). *Neural Network Design*, PWS publishing co..

Soloway, D., P. J. Haley.(1996). Neural Generalized Predictive Control. *Proceedings of the 1996 IEEE International Symposium on Intelligent Control*, pp. 277-281.

Dennis, J. E., R. B. Schnabel.(1983). *Numerical Methods for Unconstrained Optimization and Nonlinear Equations*, Englewood Cliffs, NJ: Prentice-Hall.

Proceedings of the 10th International Chemical and
Biological Engineering Conference - CHEMPOR 2008
Braga, Portugal, September 4-6, 2008
E.C. Ferreira and M. Mota (Eds.)

USE OF KOHONEN NEURAL NETWORK IN THE SENSORIAL ANALYSIS OF *Malpighia glabra* L. WINES

Cleber Gustavo Dias[1], José Carlos Curvelo Santana[1, 2], Santana; Roberto Rodrigues de Souza[3], Elias Basile Tambourgi[2*]

[1]Department of Exact Sciences (DCE), Nine of July University (UNINOVE), São Paulo, Brazil. [2*]Department of Engineering of Chemical Systems, School of Chemical Engineering, State University of Campinas, Post Cod: 6066, Zip Code: 13083-970, Barão Geraldo, Campinas, SP, Brazil. [3]Department of Chemical Engineering, Federal University of Sergipe, Brazil.

Key-words: neural network, wines, sensorial analysis, Kohonen algorithm, *Malpighia glabra* L.
Topic: Integration of life sciences & engineering

Abstract: This paper presents an approach of artificial neural networks to predict the sensorial quality of wines. A Kohonen network has been used as a software tool in order to increase the human skills in this kind of application. An initial prototype was implemented using the artificial neural networks technology, together with the Visual Basic software from Microsoft, for evaluation of sensorial qualities of seven samples of acerola (*Malpighia glabra* L.) wine. 50 consumers chosen to perhaps had been used to obtain the sensorial data using a hedonic scale of 1-9 times. Sensorial values of flavor, aroma and appearance obtained of the hedonic dating were compared. The characteristic of wine, as flavor and color were similar to the acerola fresh fruit. The consumers evaluated the wines as very good, all sensorial qualities were more than 5 in hedonic scale. Results showed that Kohonen network classified the acerola wines in distinct group, for frequency among yours sensorial responses. Kohonen network results were similar or better than statistical classification, this shows that the use of Kohonen algorithm in the sensorial analysis of wines is valid. Kohonen algorithm is very good in clustering of acerola wine samples and it uses in sensorial analyses of wines is promises.

1. Introduction

The wine commercialization undergoes long and traditional trajectories until it arrives at the table for consumption. However, the product undergoes stabilization treatments and packaging that transforms it into a quality product although at many times, turns it to be quite original and personalized. Thus being, the wines should constant improvements in its characteristics and these must be perfectly stabilized and submitted to severe rules which assure product protection against frauds, whereby guarantee the consumer (Delanoe et al., 1989).

Although the wines better appreciated are made from grapes yet other fruits could be utilized as raw material for the manufacture of wines. These fruits could be orange, pineapple, strawberry, acerola, cashew apple and other exotic fruits such as cupuacu (Freitas et al., 2001; Garrutti, 2001). Generally, the wines made from these fruits result in flavor and aroma characteristics of the original fruit utilized and if due care is taken, could last for long time storage.

Evaluations of sensorial analysis are made, commonly, by statistical methods. These methods are wide used to evaluate the consumer acceptance on the food qualities, as: the appearance, aroma, color and flavor of several products. In fruit wines these methods had be also applied. Costa et al. (2006) had made a sensorial analysis with 30 consumers to compare statistically the

* Author for correspondence, E-mail: eliastam@feq.unicamp.br Phone: 55+19+35213952

wine from cashew apple (*Anacardium occidentale* L.) against the peach and grape wines. Severo Júnior et al. (2007) had made the statistical sensorial evaluation of wines produced from cajá (*Spondias mombin L.*) pulp; to evaluate the effects of clarification methods, one by sedimentation and other by membrane separation process.

Artificial neural networks technology had been applied in simulation and optimization of several industrial processes (Kohonen, 1989). Actually, Kohonen algorithm was applied to help in the pediatrics diagnosis area, considering particular issues noticed in newborns and suckling, usually with non-specific clinical trial (Dias and Radonsky, 2003). This paper presents an approach of artificial neural networks to predict the sensorial quality of wines. A Kohonen network has been used as a software tool in order to increase the human skills in this kind of application. An initial prototype was implemented using the artificial neural networks technology, together with the Visual Basic software from Microsoft, for evaluation of sensorial qualities of seven samples of acerola (*Malpighia glabra* L.) wine.

2. Material and Methods

2.1 Preparation of Must

The acerola fruit at stage of maturity were selected, cleaned with chlorine (2 ppm of active Cl_2) water and triturated in mixer, thus obtaining the pulp which was stored in a refrigerator. For the preparation of must, the pulp quantity of acerola fruits and total soluble solids (°Brix) content were varied according to the experimental planning design of 2^2, presented in Table 1. The inorganic nutrients were added in the concentrations of 1 g/L of $NH_4H_2PO_4$ and 0.1 g/L of $MgSO_4$. The pH of the medium was later corrected in the range of 4 to 5 with Na_2CO_3. Fractions of total volume of these were separated in different flasks, from the principal vat as being to approximately 4 L, 500 ml and 10 ml, which were denominated as vessels. These were pasteurized by heating in an autoclave and cooling rapidly in running water having the sole objective of sterilization of medium (Delanoe et al., 1989; Garruti, Evangelista et al., 2005; 2001).

In order to better evaluate the effect of total solids (°Brix, g sugar/l00 mL of must) and fruit pulp mass (%Mass, kg acerola pulp/ liter of must) on the wines acceptability in relation to flavor, color and aroma.

Table 1. Experimental conditions of manufacture of acerola wines.

Wine samples	Factors	
	°Brix (g sugar/100mL)	% Mass (kg acerola pulp/liter of must)
A	22	1/6
B	26	1/6
C	22	1/3
D	26	1/3
E	24	¼
F	24	¼
G	24	¼

2.2 Preparation of wines

Fermentation: the yeast *Saccharomyces cerevisiae* was inoculated in the lowest volume of vessel at a concentration of 70 to 80 g/L, where it remained between 20 - 24 h for adaptation of the medium. It was later transferred to the next vessel and maintained for 48 h, after which it was transferred to the principal vat, in which it remained for the final days of its fermentation. After fermentation, the wines were clarified by added of bentonit clay at 1% solution. Later

filtration for complete separation of the two phases (liquid and solid) was achieved, resulting in a clear wine (Delanoe et al., 1989; Garruti, 2001; Lima et al., 2001). The wines were packed in amber-colored bottles of 1.0 L capacity which were sealed with cork. The closed wine bottles were pasteurized by heating in an autoclave at 115°C and 1.5 kg/cm^2 for 15 min, cooled later in running water and stored in refrigerator at 5°C for a period of 6 months for posterior evaluation of its quality (Gava, 1986).

2.3. Sensory analyses

The acceptability of samples of fermented musts were evaluated using sensory affective tests, comparing with the aroma of sparkling wine. The samples were served to the 50 consumers in codified tulip-shaped glasses covered with watch glasses, using a monadic presentation and a hedonic scale distributed on 9-times. The consumers also registered their purchasing intentions for each sample on the same score sheet, using a five-point attitude scale (Mamede et al., 2005; Teixeira et al., 1987). Sensorial characteristics such as flavor, color and aroma of wines were evaluated. The experimental research on quantitative basis was undertaken wherein a standard form for sensorial analysis was used and random sampling was applied for each of the above attributes using a hedonic scale (1-9 times). Based on frequency of responses, the sensorial data were compared by average values and Kohonen neural network.

2.4. Wine classification by Kohonen algorithms

An initial prototype was implemented using the artificial neural networks technology, together with the Visual Basic software from Microsoft, for evaluation of sensorial qualities of seven samples of acerola (*Malpighia glabra* L.) wine. Similarities among wine samples were classified into groups by Kohonen algorithms. The sensorial values attributed by consumers to the same wine samples were cataloged in tabled form, as it showed in Table 2. The subscript index ap, ar and fl are corresponding respectively to the appearance, aroma and flavor sensorial qualities from A, B, C, D, E, F and G wine samples. The Kohonen neural network makes a screen of the lines and columns of this table, clustering the sensorial values of one sample against the sensorial values of other samples (Dias and Radonsky, 2003; Kohonen, 1989).

Table 2. Example of the weight distribution (Wn) to screen of sensorial values by Kohonen neural network.

Samples	W1	W2	…….	W50
Aar	2	9	.....	9
Bar	3	8	.....	7
Car	4	7	.....	8
Dar	5	6	.....	8
Ear	6	5	.....	2
Far	7	7	.....	3
Gar	8	6	.....	1

3. Results and Discussion

The wines obtained in this work had color, aroma and flavor characteristics from acerola fruit and it was classified as suave. Its alcoholic gradation was approximately 11 °GL and had all other physical-chemical characteristics within the norms specified by Brazilian legislation.

The sensorial analysis demonstrated that there was no significant difference among the various wines manufactured and their mean acceptance was about 6 point. It showed that the wines

which were produced with the must of higher °Brix and lower quantity of pulp mass were more acceptable by panel members.

Figure 1 shows the results obtained for clustering of the sensorial quality, appearance. Sensorial values for some wine samples after comparison were grouping by similarity via Kohonen neural network and its average values (statistic method). It notes that the groups obtained by Kohonen methods are identical to the statistical method group.

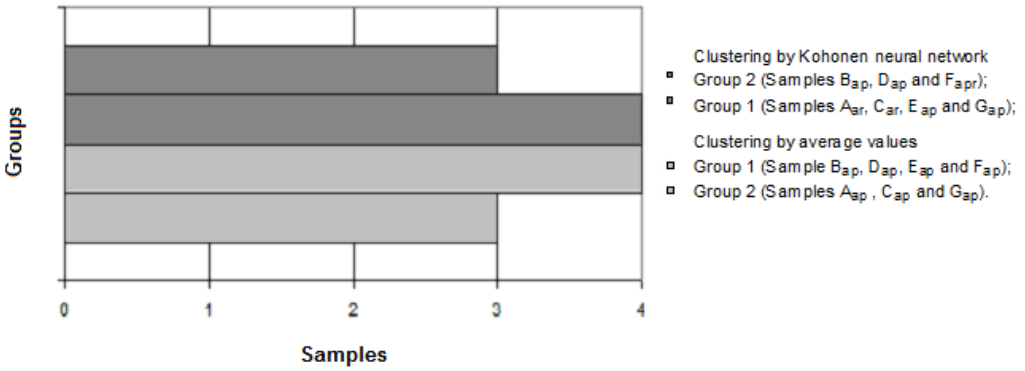

Figure 1. Classification for grumping by the similarity among wine samples; for the appearance sensorial quality.

Figure 2 shows the results obtained for clustering of the sensorial quality, flavor. It notes that Kohonen neural network had obtained four groups and statistical method (average values) only three groups. Kohonen neural network had find difference among the samples of statistic Group 2; and re-grouping in two new Groups (Kohonen Group 2 and 4). This occurred due to Kohonen algorithm found smaller differences among samples. Also, there were similarities among Kohonen Group 1 to the statistical Group 3 and Kohonen Group 3 to the statistical Group 1; and difference among the others.

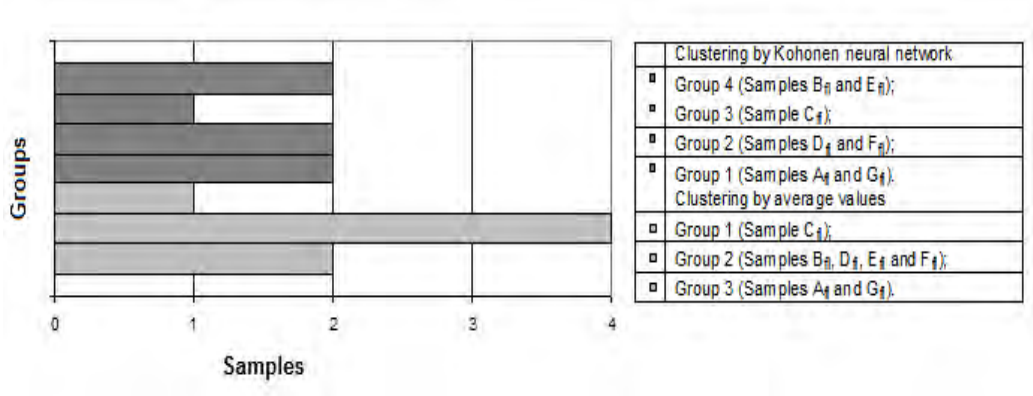

Figure 2. Classification for grumping by the similarity among wine samples; for the flavor sensorial quality.

Figure 3 shows the results obtained for clustering of the sensorial quality, aroma. It notes that Kohonen neural network had obtained three groups and statistical method (average values) only

two groups. Kohonen neural network had find differences among all statistical Groups. From statistical Group 1, Kohonen neural network had separated E_{ar} sample in one Group (Kohonen Group 3); from statistical Group 2, Kohonen neural network had separated Aar, while it was grouping in Kohonen Group 1. The other samples were similar. It emphasizes that Kohonen neural networks can be evaluate a conjunct of great quantities of values and finding differences among its samples; this is torn a good tool to clustering of beverage samples by sensorial comparison.

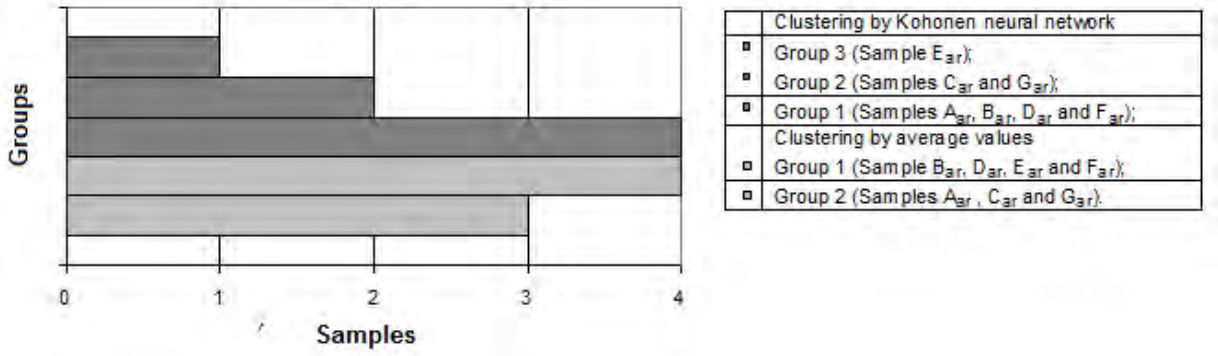

Figure 3. Classification for grumping by the similarity among wine samples; for the aroma sensorial quality.

4. Conclusions

The wines obtained in this work had color, aroma and flavor characteristics of acerola and it was classified as suave. Its alcoholic gradation was approximately 11 °GL and had all other physical-chemical characteristics within the norms specified by Brazilian legislation. Their mean acceptance was about 6 point in hedonic scale. Wines which were produced with the must of higher °Brix and lower quantity of pulp mass were more acceptable by panel members.

Kohonen network classified the acerola wines in distinct group, for frequency among yours sensorial responses. Kohonen network results were similar or better than statistical classification, this shows that the use of Kohonen algorithm in the sensorial analysis of wines is valid. Kohonen algorithm is very good in clustering of acerola wine samples and it uses in sensorial analyses of wines is promises.

References

Costa. A. G. B. F.; Severina. C. O.; Lopes. F. L. G.; Souza. R. R.; Santana. J. C. C. (2006). Cashew apple wine: preparation and sensorial analysis. *Revista SODEBRAS* (On Line), v.10, n.1.

Delanoe. D.; Maillard. C. & Maisondieu. D. (1989). *O vinho da analise à elaboração.* Col. EUROAGRO. Porto – Pt: Europa-América Ltda, 230p.

Dias, C.G. and Radonsky, V. (2003). *The development of an auxiliar system to help in the pediatrics diagnosis using artificial neural*. *Exacta*, v.1, 89-95.

Evangelista, A.F.; Almeida, S.S; Santana, J.C.C, Souza, R.R. (2005). RSM evaluation of factors that influencing to acerola wine production. *Brazilian Journal of. Food Technology*., 5th SIPAL, march, 8-13.

Freitas. R. F.; Schwan. R. F.; Dias. D. R. & Oliveira. R. L. (2001). Elaboração e caracterização de vinho de cupuaçu (*Theobroma grandiflorum* - Will ex. Spreng: Schum). XXI Congresso Brasileiro de Microbiologia. Foz do Iguaçu. PR. Brazil. *Proceedings: XXI Congresso Brasileiro de Microbiologia.* Microbiologia dos Alimentos: AL-120, pp.396.

Garrutti. D. S. (2001). *Comportamento de Voláteis e qualidade de aroma do vinho de caju*. Campinas: School of Food Engineering. State University of Campinas,220p. (PhD Thesis).

Gava. A. J. (1986). *Princípios de tecnologia de alimentos*. 7ª ed., São Paulo: Editora Nobel, p.25.

Kohonen, T. (1989). *Self-Organization and Associative Memory*. Berlin: Springer-Verlag.

Lima.U. A.; Borzani.; Aqarone. E. and Schimidel. W. (2001). *Biotecnologia Industrial: Processos Fermentativos***.** Vol.3, 1ª ed., São Paulo – SP: Ed. Blucher Ltda, 598 p.

Mamede. M. E. O.; Cardello. H. M. A. B. and Pastore. G. M. (2005). Evaluation of an aroma similar to that of sparkling wine: Sensory and gas chromatography analyses of fermented grape musts. *Food Chemistry,* vol.89, pp.63–68.

Severo Júnior, J. B.; Almeida. S. S.; Narain. N.; Souza. R. R.; Santana J. C. C.; Tambourgi. E. B. (2007). Wine Clarification from *Spondias mombin L.* Pulp by Hollow Fiber Membrane System. *Process Biochemistry,* doi:10.1016/j.procbio.2007.08.003.

Teixeira. E.; Meinert. E. M.; Barbetta. P. A (1987). *Análise Sensorial de Alimentos*. Série Didática. Florianópolis – SC: EDUFSC. 1987, p.18-102.

Proceedings of the 10th International Chemical and
Biological Engineering Conference - CHEMPOR 2008
Braga, Portugal, September 4-6, 2008
E.C. Ferreira and M. Mota (Eds.)

Study of Aromatic Recovery by Extractive Distillation

Mariana A. N. Moreira[1], Helena M. M. Campos[1], Sónia C. F. Santos[1], Ana R. Marques[2], Manuel L.C. Tavares[2], Paula C. P. Silva[1], Luísa A.C.N.Gomes[1]

[1] Chemical Engineering Department, Instituto Superior de Engenharia, IPP, P4200-072 Porto, Portugal.

[2] Technology Dept, Galp Energia, Apartado 3015, 4451-852 Leça da Palmeira, Portugal.

Keywords: Sulfolane, Extractive distillation, Aspen Plus, NRTL, Aromatics
Topic: Systematic methods and tools for managing the complexity

Abstract

The feasibility to use an extractive distillation process to replace liquid-liquid extraction unit (Arosolvan) at Galp Energia plant in Leça da Palmeira was studied. The simulations were performed using Aspen Plus® simulation modules, and NRTL model was used to predict thermodinamic data. Simulation results allowed to conclude that aromatics recovery increases comparatively to actual operation data. An economic study was performed determining the investiment and operating costs.

Introduction

Nowadays, Chemical and Petrochemical industries are facing a growing need for cheaper and higher quality raw materials. Aromatic compounds, such as benzene and toluene, are examples of such important feedstocks. Traditionally, these substances are produced from petroleum distillation cuts by liquid-liquid extraction, which was, for many years,the first choice for the mentioned industries to recover aromatic compounds, due to the fact that the available solvents were not suitable for the separation processes based in extractive destillation.

However, the technology for producing new solvents has suffered an improvement and the availability of new solvent mixtures makes more profitable the implementation of extractive distillation for aromatic recovery.

Extractive distillation is the state of art of distillation since it allows to optimize the production and purity of the required products at low operation costs. The main difference between this technology and liquid–liquid extraction is the addition of a third component, a highly selective solvent that changes the separation caracteristics between the substances by increasing relative volatility values.

Aromatics can be produced through the reformate, which is a mixture of aromatic and aliphatic hydrocarbons. This is a complex and very difficult mixture to separate in different compounds due to the existence of components with volatility nearly the same as azeotropic components. In extractive distillation the addition of a solvent alters the relative volatilities of the components, thus increasing the difference between them and thereby promoting their separation (Wankat, 2007). These interations occur mainly in the liquid phase, being the solvent continuosly added close to the top of the extractive column, allowing that a significant amount is present in the liquid phase on all trays. The reformate is added near the middle of the column and the component with greater volatility (non-aromatic compounds) is taken overhead as a quite pure distillate. This causes the solvent to go downwards in the column while the non-aromatics travels upwards, and on each tray both phases are closely contacted and re-separated as shown in Figure 1.

Non-aromatic compounds are removed on the top of the column and condensed, constituting the raffinate product. A portion of the condensate liquid is refluxed to the column and this reflux determinates also the ratio of separation. The aromatics and the solvent leave

the bottom of the column and are sent to the solvent recovery column. In this column the aromatics are separated from the solvent by a simple distillation process. Aromatic vapors from the solvent recovery column are condensed and this liquid is the extract product. The bottom product of this column is aromatic-free solvent and returns to the extractive distillation column, passing through an heat exchanger. The efficiency of the solvent recovery column is a very important factor, not only because of the quantity and purity of the produced aromatics, but also because of the recovered solvent. This allows to minimize the fresh solvent needs (Ko *et al.*, 2002).

Beside the improvement of new solvent production technology, extractive distillation systems now use better heat integration, enhanced mass transfer devices, as a way to maximize production capacities with reduced operation costs and lower environmental impacts.

The purpose of this project was to verify the aplicability of extractive distillation in Arosolvan Unit at the Aromatics Plant of Leça da Palmeira's refinery (Galp Energia), using Aspen Plus® simulator. A comparison between simulator and operating data from the refinery was also performed.

Following this study, an economic analysis was performed, to assess the investment needed in the replacement of the liquid-liquid extraction plant by a extractive distillation unit. The number of years of return of investment was also determined.

Simulation

The implementation of a extractive distillation process begins with the choice of an appropriate solvent. The parameters to consider are its selectivity, stability and toxicity, cost effectiveness to use in commercial operation and compatibility with plant operations. After a literature review, the solvent Sulfolane was chosen. This solvent is already used by UOP company (www.uop.com) and it has the particularity of promoting a good separation at acceptable costs for an industrial application (Choi *et al.,* 2002).

Sulfolane solvent was developed in the early 1960's but it still remains as one of the most efficient solvent available for aromatics recovery. Studies (Gentry *et al.*, 2004) made, using this solvent to separate the binary mixture C-7/benzene, which is a rough approach to the feed conditions, revealed that it alters the relative volatility of the components by a margin large enough to obtain a successful result. This solvent is easy separable from the bottom product and doesn't react chemically with none of the components in the reformate, or causes corrosion in the equipment.

The extractive distillation was designed and simulated using Aspen Plus® simulator, one of AspenONE ™ Process Engineering modules, developed by AspenTech. The thermodynamic model used was the Non-Random-Two-Liquid (NRTL), found to give a better aproach to a real system (Ko *et al.*, 2002).

The basic configuration of a extractive distillation process, as shown in Figure 1, requires two separation columns, while the existing liquid–liquid extraction unit (Arosolvan) has three columns.

The first column is the Extractive Distillation column, where the separation between the aromatics and non-aromatics occurs. The second column is the Solvent recovery column, where the separation of the solvent from the aromatics occurs, producing the main product and clean solvent.

As a way to design the extractive distillation column, Distl and DSTWU models were used. These two models are used in simple distillations, differing only in the method of calculation, the first one uses the Winn-Underwood-Gilliland method and the second one the Edmister method. Both models consider one column with just one feed and two exit products, as well as a total or partial condenser.

Thereby, the DSTWU model was used to estimate the operating conditions and on the basis

of these results we simulated the desired conditions in RadFrac model.

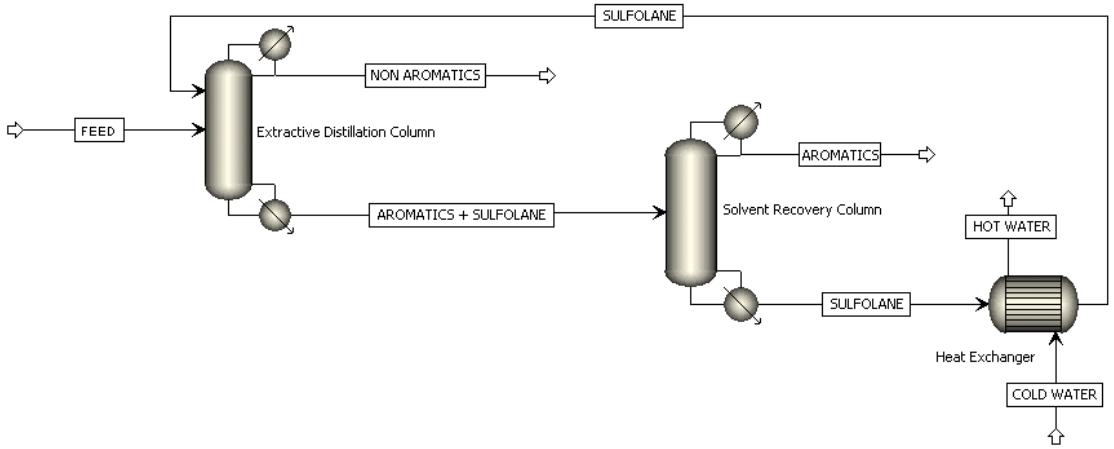

Figure 1 – Flowsheet of the extractive distillation unit, with *Sulfolane* solvent.

The feed conditions were defined based on data obtained from Galp Energia plant, and after several simulations the extractive distillation column which presented the best results was a column with 40 stages and a reflux ratio of 1.4.

In this type of simulation, the operation conditions on the column can be predicted, as well as the composition of the exit products. This data can be recovered through the program report, however all the informations are available on the Aspen Plus result window.

In these simulated conditions, the reboiler needs 14133 kW of power consumption, at 418.2 K and 0.431 mass reflux. It was selected a total condenser, which needs 5152 kW of cooling power at 372.2 K, and 1.4 reflux ratio.

One of the factors related to the power needs of the reboiler and the condenser is the reflux ratio. When the reflux ratio increases, the power needs of the two equipments also increases. The higher the reflux ratio used, the greater the amount of liquid introduced, increasing the need of energy at the reboiler. Furthermore, the greater the amount of liquid added, the greater will be the production of vapor at the top of the column, increasing the energy needed by the condenser.

The RadFrac model estimates, for each stage, the molar and mass volumes of the liquid and vapor, plus the temperature and composition profiles of the components in the mixture.

Figure 2 shows the mole fraction profiles of the components in the liquid phase for the extractive distillation column. The Sulfolane composition suffers two major changes near stages 5 and 10, where the feed enters. With the exception of these two points, the proportion of solvent remains constant. While these changes occur in Sulfolane composition, it can be verified that the n-heptane changes its physical state, passing from the liquid phase to the gas phase. On the other hand, benzene and toluene profiles are graphically similar, as expected, because they leave the column together.

As it can be seen in Figure 3, there is no Sulfolane in the vapor phase along the entire column. The changes in the profiles occur after the introduction of the feed and solvent streams. The top stream of the column consists essentially of n-heptane, while the bottom stream of the column is rich in benzene, toluene and Sulfolane

The Solvent Recovery Column was designed following the same methodology of the extractive distillation column, originating similar charts to previous ones (Figure 2 and 3). For this column the best results were obtained with 30 stages and a reflux ratio of 1.2. The reboiler and condenser's conditions are shown in Figure 4.

Aspen Plus doesn't give only the information about the power needs for the equipment, but

also gives information about the composition and physical properties of the liquid and vapour at any stage. From the computed results, the aromatics recovery was calculated and compared to actual data from the refinery. Table 1 shows the recovery fractions.

Table 1 – Recovery fractions.

Compound	Total Recovery [%]	
	Actual	Proposed alterations
Toluene	90,026	99,996
Benzene	88,215	99,339
N-heptane	57,062	99,138

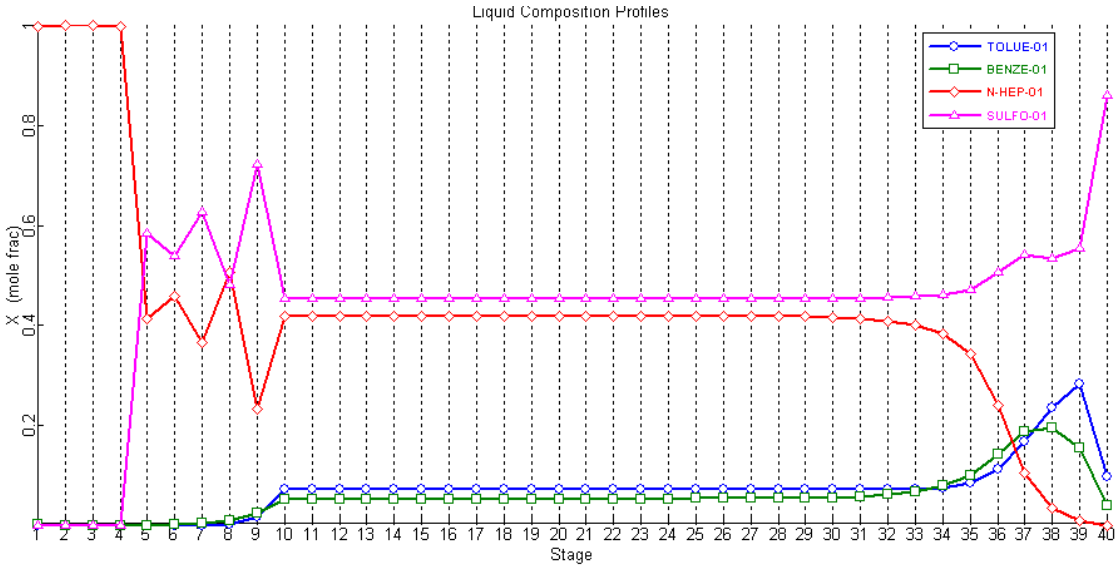

Figure 2 – Liquid composition profilles of the Extractive Distillation Column.

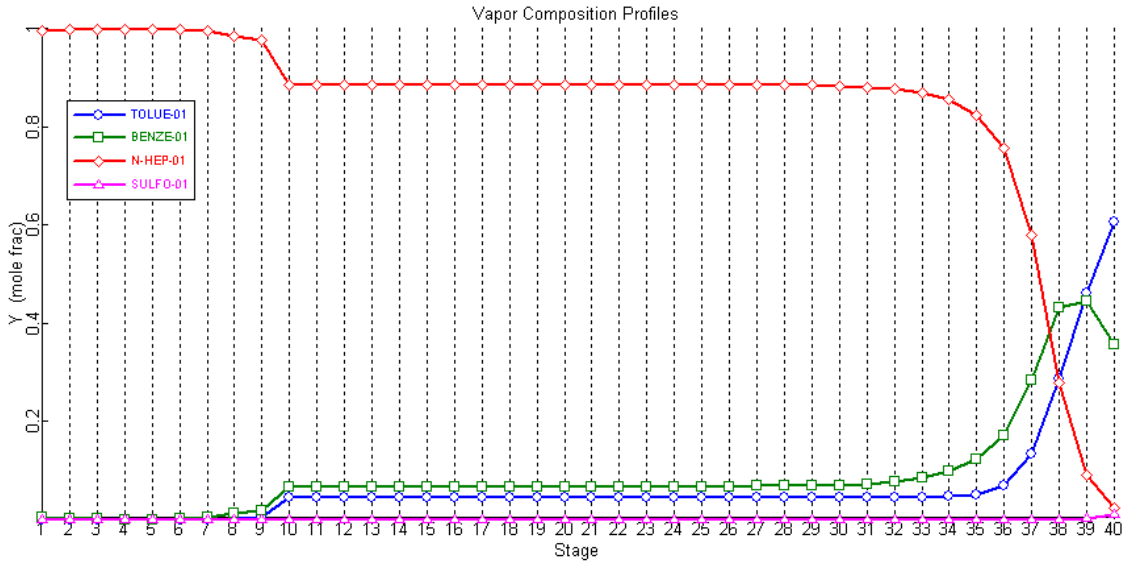

Figure 3 – Vapor composition profilles of the Extractive Distillation Column.

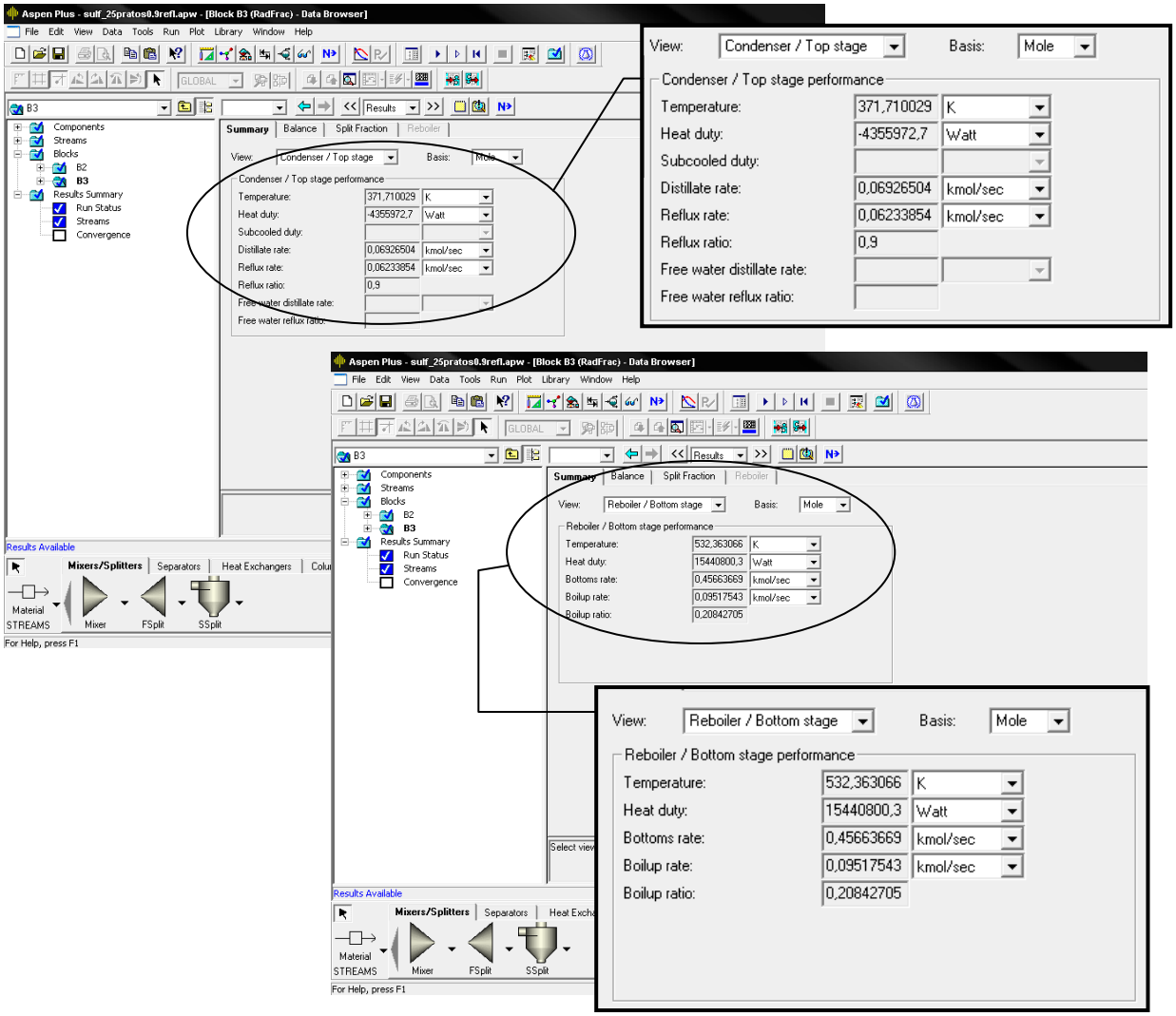

Figura 4 – Window of the Aspen Plus simulator, with reboiler and condenser's operating conditions.

In order to complete the study of this unit, the transfer area needed in the heat exchanger was determined, resulting in the value of 275 m^2.

An economic study was conducted, taking into account the necessary equipment, operating costs and the profits due to the achieved improvements, and considering a discount rate of 10%.

To implement the extractive distillation unit, and taking into consideration the existing plant, it was necessary to acquire only one new column. The real size of the columns, was calculated taking into account that the trays implemented would have an efficiency of 80%.

The operating costs were determined considering the expenditure necessary to ensure a year production and the energy consumption associated to the process.

The main profits of this project come from the additional amount of benzene and toluene which will be produced.

Therefore, after the necessary calculations, it was determined that for a facility with this scale it will be required around 6 000 000 euros (values referred to 2007), resulting in a return of capital employed of 5 years.

Conclusions

The extractive distillation process has many advantages compared to liquid-liquid extraction process. The basic configuration of liquid-liquid extraction requires four units, while extractive distillation only needs two, making the investment costs lower in ED. Apart from using new solvent formulas, the extractive distillation system uses also better heat integration. Another advantage is the improvement of the operation conditions, leading to an enhanced control of the system.

The Sulfolane process was simulated with Aspen Plus, a sequential modular simulation software, using NRTL model. With the proposed process we achieved a 99% compounds recovery with a total investment amounting to 6 000 000 euros (values refered to 2007).

Acknowledgment

This work was carried out under the gratefully support and cooperation of Galp Energia.

References

Choi, Y.J., Cho, K.W., Cho, B.W., Yeo, Y.K. (2002). Optimization of the Sulfolane Extraction Plant Based on Modeling and Simulation. Industrial & Engineering Chemistry Research, 41, 5504-5509.

Gentry, J. C., Kumar S. (2004). Use extractive distillation to simplify petrochemical processes. Hydrocarbon Processing, 83, (6).

Ko, M., Na, S., Kim, H. (2002). Simulation of the Aromatic Recovery by Extractive Distillation. Korean Journal of Chemical Engineering, 19(6), 996-1000.

Wankat, P. C. (2007). *Separation Process Engineering*, 2nd edition, Prentice Hall.

Proceedings of the 10th International Chemical and
Biological Engineering Conference - CHEMPOR 2008
Braga, Portugal, September 4-6, 2008
E.C. Ferreira and M. Mota (Eds.)

Drop distribution determination in a liquid-liquid dispersion by image processing

Brás, L.M.R.[1], Gomes E.F. [1,2*], Ribeiro M. M. M.[1,2], Guimarães M. M. L.[2]
[1] Instituto Superior de Engenharia do Porto, Rua Dr. António Bernardino de Almeida, 431, Porto, Portugal.
[2] SIPROM-CIGAR - Centro de Investigação Geo-Ambiental e Recursos, Porto, Portugal.

Keywords: liquid-liquid systems, image processing, drop size distributions

Topic: Systematic methods and tools for managing the complexity

Abstract

Image processing is a very relevant area of computer science with applications in many domains. Quantitative analysis and interpretation of digitized images is currently an important tool in several scientific domains.

Namely in multiphase systems modelling in Chemical Engineering, the acquisition and treatment of images of particulate phases become essential for the calculation of particle size and shape distributions. In the modelling of liquid-liquid systems these are of major importance either for hydrodynamic and mass transfer (with or without chemical reaction) modelling and validation. From these arise simulation, interpretation and performance predictions of multiphase reactors

Often, such a treatment is undertaken by visual/manual techniques which imply high costs, intensive labour, weariness build-up and consequent high error rates, while a fully automated computational approach has a definite potential for better performance.

The aim of the present work is the development of shape discrimination and size classification algorithms for liquid drops in monochromatic digitized frames.

1 Introduction

Image frames were obtained at our SIPROM (Modelling and Simulation of Multiphase Systems) Laboratory with a digital video camera + microscope + illumination set-up from a dispersion of toluene in water within a transparent mixing vessel (Ribeiro, 2002).

Experimental conditions (mainly phase ratio and agitation speed) led to frames of deeply focused fields with partially overlapping drops and high background noise, as we can see in Figure 1. In this figure we show two images, the first one is what we consider a better quality image whereas the second image is very difficult to process. Since non-invasive image acquisition and lighting were our uncompromising starting option, no significant improvements were obtained although all available image acquisition and cleaning techniques were used within this fundamental constraint. Thus, partial images and ill-defined drop boundaries led to all low-cost, market-available image processing software packages requiring a high number of frames in order to secure statistically significant drop samples which, again, made for greatly time-consuming, unreliable procedures.

* Corresponding author. Tel + 351-228340500. E-mail:efg@isep.ipp.pt

This led us to develop our own software for which a preliminary test and calibration stage was performed on archive images previously obtained with a semi-automated procedure (Ribeiro et al. 2004). We have developed a promising approach, implemented in *Matlab*, which, given one of these photographic images of a dispersion, automatically identifies the contour of existing drops and classifies them according to their diameter.

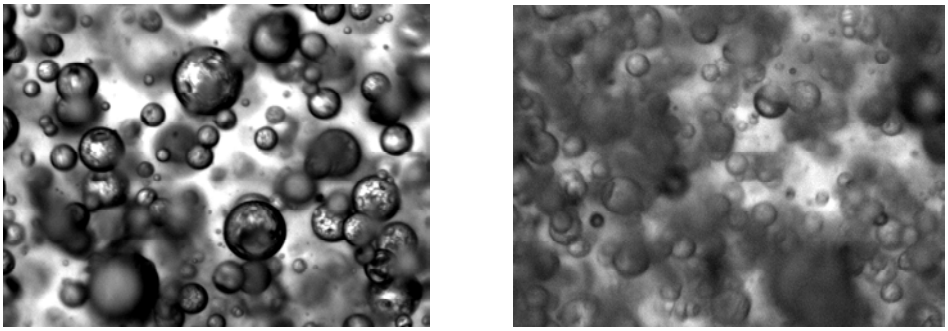

Figure 1: Examples of images, the leftmost is a very good image and the rightmost is a difficult image.

2 Description of the method

In our approach, implemented in Matlab (Gonzalez and Woods 2004), given one of the photographic images of dispersion, automatically identifies the contour of existing drops and classifies them according to their diameter.

This work for the detection of the drops in an image was done in two distinct steps. In the first step, we detect the edges of the drops in the original image, manipulating the gradient and the descending thickness and creating an output image with those contours. In the second phase, we detect the drops in this contour image, using the Hough Transform (Russ 2006). This transform is widely used in image processing to detect lines and also to detect circles.

2.1 Edges detection

In Figure 2 we show the phases of the detection process of the drops. Thus, starting from the original image (leftmost), we detect the edges (centre) and, in the next step, we detect the contours of the drops using the Hough transform (rightmost).
In our images, of poor quality, the drops have, in majority, dark edges.

Figure 2: Original image, the edge detection and the detection of the drop using the Hough transform.

To reduce the noise, the image is smoothed using a Gaussian filter. This eliminates some false contours and reduces the detection of false drops.

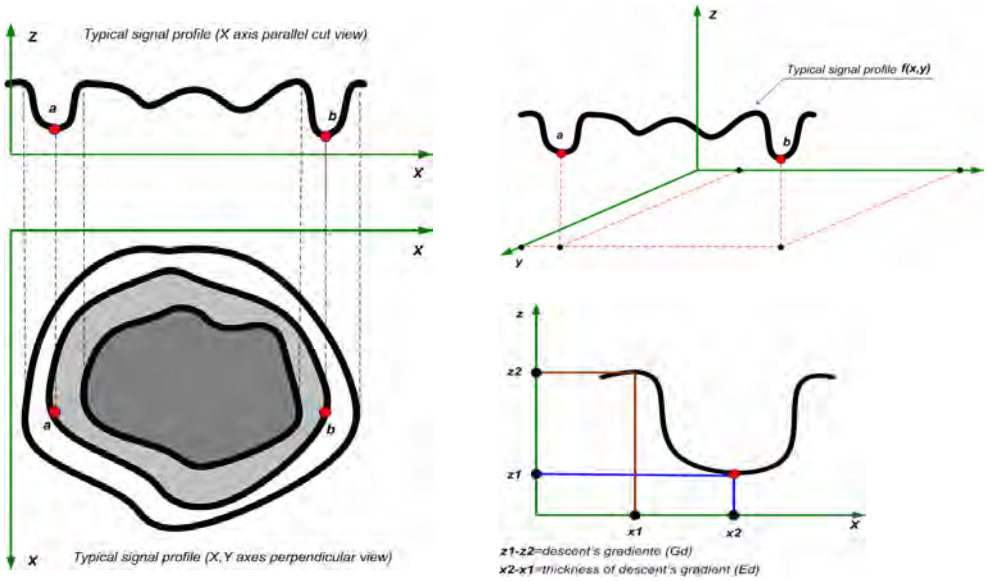

Figure 3: Typical signal profile

Using the typical profile of the signal, edge detection is made by evaluating the relation between the gradient's descent (Gd) and its respective thickness (Ed), shown in Figure 3.

The filtered image (If) is derived, with kernels of convolution, indicated below, originating two matrices, Ix and Iy (see Eq. (1)) corresponding to the partial derivatives dz/dx and dz/dy:

$$Ix = If * \begin{bmatrix} 1 & -1 \end{bmatrix} \quad Iy = If * \begin{bmatrix} 1 \\ -1 \end{bmatrix} \tag{1}$$

From the images Ix and Iy we obtain the average and the standard deviation of the descending gradient (μg, σg) and the average and the standard deviation of the descending thickness (μe, σe). The edge detection threshold is defined by the combination of Gd and Ed, where Gd takes negative values and Ed positive. In processing of each descent (negative derivative) from its origin to inflexion point, if Ed>μe-σe/2 and Gd<μg+σg/2, then the pixel of this point is considered an edge pixel. From the matrix Ix we obtain the partial contour matrix Ia, and from Iy the matrix Ib. The sum of Ia and Ib yields the contour image Ic, shown in Figure 4.

Preliminary experiments with other known methods for contour detection such as Sobel, Canny and Marr Hildreth showed that these degrade the results of the Hough Transform in the detection of the drops. They introduce additional information that causes the detection of false drops.

2.2 Detection of drops in the contour image

In the second step of the work, we applied the Hough transform to the contour image Ic (Figure 4 a) to detect the contour of the drops for different radius.

We consider, as we can see in (Figure 4 b), that the contour of each drop can be represented as one object with irregular form, centred in a point and with a radius that varies from $r1$ to $r2$.

The Hough transform is widely used to detect lines and also to detect circles. To find circles using a Hough transform, each edge element votes for all the points x, y which are centres of the circles with radius r that it could lie on. This transform allows determining the centre of the drop through the identification of the most voted zone. It has the inconvenience of, for each useful vote, generating $2 \times \pi \times r - 1$ noise votes. In an image with many drops, this could

cause the detection of inexistent drops.

a) b)

Figure 4: Drop contour – a) the resulting contour image; b) representation of the drop contour as an irregular object.

In the second step of the process we applied the Hough transform to the contour image Ic taking into account the relative deformation (*k*) of the drops. For a maximum deformation of radius *r*2 the minimum deformation will be *r*1=*r*2×(1-*k*). Votes will be generated from the successive application of the Hough Transform to the range *r*1:*r*2.

This procedure is repeated for all the radii considered as maximum deformation, in order to process all the contours of all dimensions of the drops. The voting window (centre of Figure 5Figure 6) has a dimension of 3x3 pixels for radii above 15 and dimension of 1x1 otherwise. To reduce the number of noise points we considered half of the voting amplitude (two quadrants). For that we analyse the signal of the partial derivatives according to the partial contour matrix, Ia or Ib, related to the edge pixel.

Figure 6 illustrates the detection quadrant voting procedure for an edge pixel related to matrix Ia. If the drop was a regular solid, it would be possible to determine the correct quadrant, by analysing the gradient's angle variation, *β*. In our case, it is only possible to determine a pair of possible voting quadrants (A, C or B, D), by analysing the partial derivative's signal. The similar process is used for the edge pixels related to matrix Ib.

The detection process starts with the set of drops with radii between 17 and 48 pixels because these are the most frequent. This detection is accomplished with the erosion of the contour image to avoid the false drops with a higher radius. Then we treat the drops with at least 48 pixels of radius. Finally we process the drops with radius between 8 and 16 pixels.

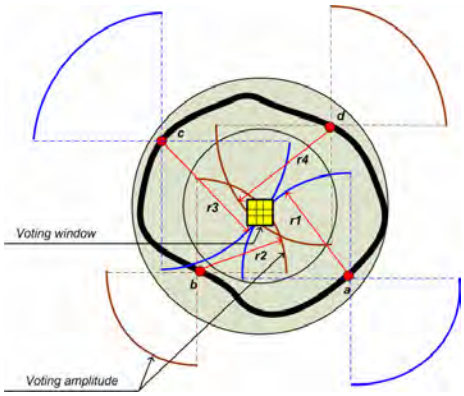

Figure 5: Voting window and voting amplitude.

Processing the drops with higher radius first, reduces the probability of detecting false drops with a lower radius, caused by agglomerates of pixels in the contour of the drops. However, the detection is not efficient for radii below 8 pixels.

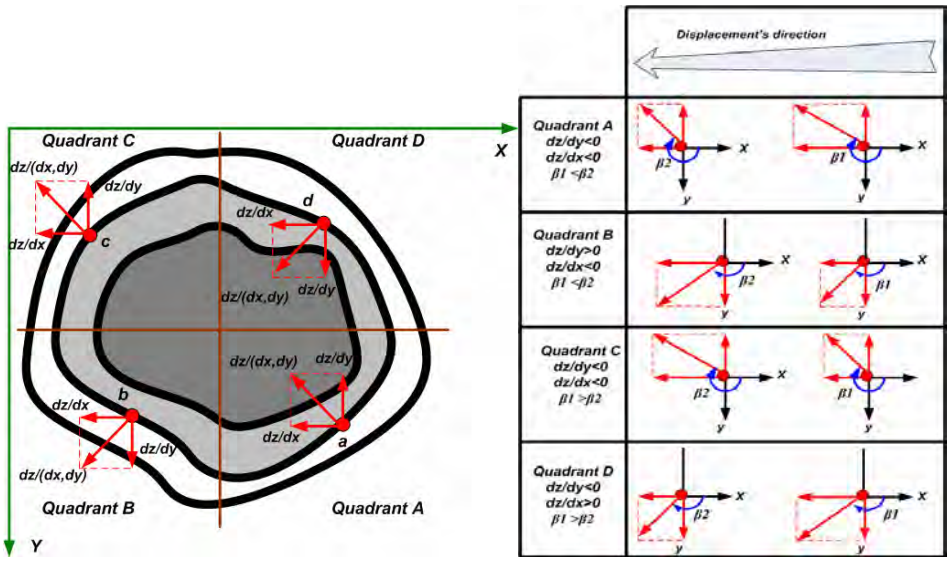

Figure 6: Detection of the quadrant voting across the X axis

In Figure 7 we can see the results obtained for a radius between 5 and 46 pixels.

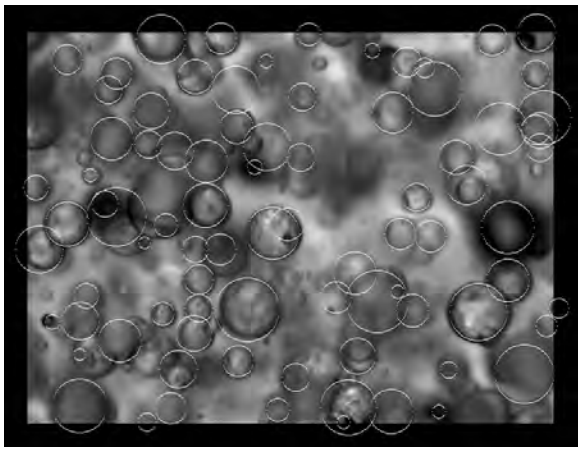

Figure 7: the drops detected by our program. Each detected drop is marked with a white circle on top of the original image.

3 Results

To evaluate more objectively our approach we have chosen two images with different levels of photographic quality, and compared the sets of drops obtained automatically with the drops manually identified by us. In Table 1 we show the results obtained with two of the images in terms of recall and precision values. We have calculated those values as defined in Eq. (2) where *TP* is the true positives (number of drops correctly identified by the program), *FN* the false negatives (actual drops not identified by the program) and *FP* the false positives (drops incorrectly identified by the program). In other words, recall measures the proportion of existing drops that the program was able to identify correctly, whereas precision is the proportion of drops identified by the program that are truly correct.

$$recall = \frac{TP}{TP + FN} \qquad precision = \frac{TP}{TP + FP} \tag{2}$$

In the case of the first image, we have obtained the following results. For a radius less then 7 pixels the program cannot find any drop. For the radius 10, not in the table because recall=0

and precision not defined, we have *TP*=0, *FP*=0 and FN=3. For the radius 12, also not in the table, because recall=0 and precision not defined, we have a *TP*=0, *FP*=0 and *FN*=1. For the other values of the radius not represented in the table, we have *TP*=0, *FP*=0 and *FN*=0. As final results, taking into account all the values of radius, we have for this image a recall of 0.71 and a precision of 0.89.

Table 1: Precision and Recall for different radii on two images

First image						Second image					
Radius (pixels)	Recall	Precision	Radius (pixels)	Recall	Precision	Radius (pixels)	Recall	Precision	Radius (pixels)	Recall	Precision
7	0.25	1.00	17-19	1.00	0.90	7	0.44	0.80	16	0.57	1.00
8	0.50	1.00	20	0.75	1.00	8	0.50	1.00	17	0.77	1.00
9	0.57	1.00	21	0.60	0.60	9	0.40	1.00	18	0.57	1.00
11	1.00	0.67	22	0.60	1.00	11	0.25	1.00	19	0.50	1.00
13	0.67	1.00	23	0.67	1.00	12	0.25	1.00	20	0.50	0.60
14	0.80	1.00	24	0.33	1.00	13	0.25	0.50	22	0.25	0.33
15	0.67	1.00	25-26	1.00	0.75	14	0.57	0.57	23	0.75	1.00
16	0.75	0.75	28-44	1.00	1.00	15	0.57	1.00	24-44	1.00	1.00

For the second image, which has a lower photographic quality, we have worse results, having a total 0.55 for recall and 0.87 for precision. Nevertheless we have, for many values of radius in the image, maximum recall and precision. For several values of radius from 7 to 23 and for radius equal to 35, 40 and 45, recall and precision are not shown in the table, for the same reasons as in the previous image. We believe the cause for these worse results with respect to the previous image is the lower quality of this second image.

4 Conclusions

In this paper we have presented a method for the automatic identification of drops in images taken from agitated liquid-liquid dispersion. The results obtained with two images lead to the conclusion that our program is able to detect a good percentage of the drops. In the case of a better quality image, the program recognized 71% of the drops. For the other image, with lower quality, only 55% were detected. We have also observed that the approach is less efficient for smaller values of the radius, since very small drops can be easily mistaken by noise.

References

Ribeiro, M. M. M., Guimarães, M. M. L., Madureira, C. M. N., Cruz-Pinto, J. J. C, (2004). *Non-Invasive System and Procedures for the Characterization of Líquid-Líquid Dispersions*. Chemical Engineering Journal. Vol 97, 173-182,

Ribeiro, M. M. M., (2002). *Medição e Interpretação do Comportamento Hidrodinâmico de Dispersões Líquido - Líquido em Vaso Agitado em Regime Contínuo e Descontínuo*. Tese de Doutoramento em Engenharia Química, Universidade de Aveiro.

Gonzalez, C.R. Woods R.E. Digital Image Processing Using MATLAB. Prentice Hall. ISBN 0130085197 (2004).

Russ, J.C. Image Processing handbook. CRC Press. ISBN 0-8493-1142-X (2006).

Proceedings of the 10th International Chemical and
Biological Engineering Conference - CHEMPOR 2008
Braga, Portugal, September 4-6, 2008
E.C. Ferreira and M. Mota (Eds.)

Bright field versus phase contrast microscopy in activated sludge image acquisition methodologies

D. P. Mesquita[1], O. Dias[1], A. L. Amaral[1,2], E. C. Ferreira[1*]
[1] IBB – Institute for Biotechnology and Bioengineering, Centre of Biological Engineering, University of Minho, Campus de Gualtar, 4710–057 Braga, Portugal.
[2] Instituto Superior de Engenharia de Coimbra, Instituto Politécnico de Coimbra, Rua Pedro Nunes, Quinta da Nora, 3030-199 Coimbra, Portugal

Keywords: Activated sludge, image analysis, bright field, phase contrast, aggregates, filaments
Topic: Integration of life sciences & engineering

Abstract

Monitoring activated sludge processes by microscopic observations and image analysis methodologies is a well established technique with the utmost importance for microbial community characterization. Furthermore, image processing and analysis is currently considered a powerful tool to identify and quantify biomass morphological and physiological changes. In the present work, image processing and analysis methodologies were used to determine aggregates and protruding filaments contents and morphology using both bright field and phase contrast microscopy. The obtained results showed that the simpler and less expensive bright field microscopy also provided the best overall results.

1 Introduction

An activated sludge system includes a complex ecosystem composed of different types of microorganisms such as protozoa, metazoan and filamentous, zoogleal and other bacteria. A good balance between the different types of microorganisms is essential to guarantee good settling properties and a clear supernatant which can be performed by visual inspection under an optical microscope coupled to automated image analysis methodologies. As a matter of fact, in recent years, activated sludge processes have been already monitored through microscopic observations for aggregates contents and morphology and protruding filamentous bacteria contents determination (da Motta *et al*., 2001, Amaral and Ferreira, 2005, Jenné *et al*., 2007).

Automated image analysis is considered to be a feasible method to characterize quantitatively both aggregated and filamentous bacteria, with two image acquisition methodologies standing out: phase-contrast microscopy as proposed in the works of Cenens *et al*., 2002 and Jenné *et al*., 2007 among others; and bright field microscopy as in the works of da Motta et al., 2001, and Amaral and Ferreira, 2005. In comparison, bright field microscopy is the cheapest and simplest activated sludge examination methodology, whereas the phase-contrast microscopy requires more expensive equipment and a skilled operator. Furthermore, the inner nature of the phase contrast microscopy causes the aggregates borders to become ill-defined, as the objects hallo hinders the assessment of their boundaries. However, this methodology presents the advantage of a more precise determination with respect to the protruding filamentous bacteria contents. As a matter of fact, the high transparency of the filamentous bacteria poses a contrast problem in bright field microscopy acquisition, opposite to the clear filaments/background distinction in phase contrast microscopy. Therefore, it comes as no surprise that studies have already been

* Corresponding author. Tel + 351-253-604407. E-mail: ecferreira@deb.uminho.pt

performed using bright field acquisition methodologies to survey aggregated biomass and phase contrast acquisition for filamentous bacteria assessment (Amaral, 2003).

In order to determine the best image analysis acquisition methodology of activated sludge samples, the present work aims to determine both protruding filamentous bacteria and aggregated bacteria contents using, on one hand, bright field microscopy and, on the other, phase contrast microscopy.

2 Material and Methods

Experimental study

The biomass used in this study was collected from the aeration basins of seven wastewater treatment plants, treating domestic effluents, located in the North of Portugal. Samples were taken to perform microscopic observations, in order to estimate the contents of the microbial aggregates and protruding filamentous bacteria by image acquisition and analysis. For each sample, the biomass content (TSS) was determined by dry weight (APHA *et al*., 1989).

Image Acquisition

A volume of 25 µL was placed on a slide and covered with a 20x20 mm cover slip for visualization and image acquisition in bright field and phase contrast microscopy. Roughly 200 images were acquired per sample to obtain significant data for both acquisition methodologies.

Bright field microscopy: Images were acquired in a Leitz Laborlux S optic microscope (Leitz, Wetzlar), with 100x magnification, coupled to a Zeiss AxioCam (Zeiss, Oberkochen). Image acquisition was performed in 1300 x 1030 pixels and 8-bit format through the commercial software Axio Vision 3.1 (Zeiss, Oberkochen).

Phase contrast microscopy: Images were acquired in a Diaphot 300 microscope (Nikon Corporation, Tokyo) with 100x magnification, coupled to a Sony CCD AVC–D5CE (Sony, Tokyo) grey scale video camera. The images were acquired in 768×576 pixels and 8-bit format by a Data Translation DT 3155 (Data Translation, Marlboro) frame grabber using the commercial software package Image Pro Plus (Media Cybernetics, Silver Spring).

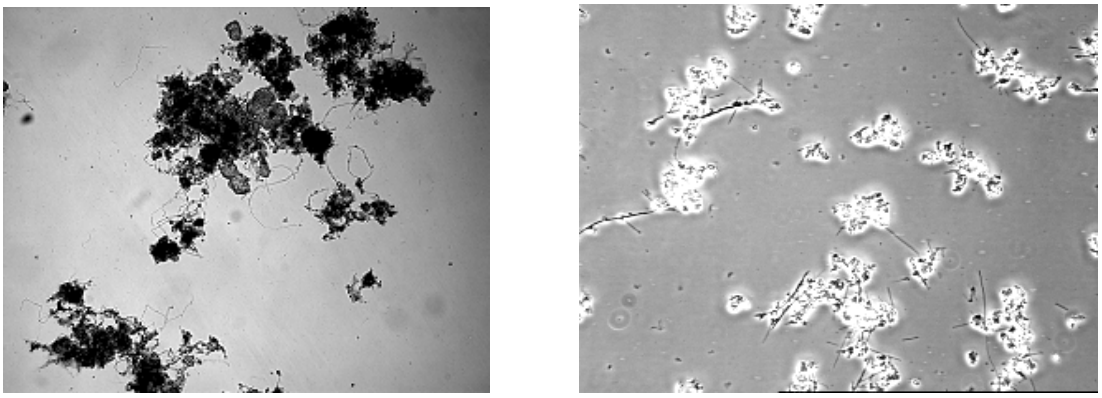

Figure 1. Bright field and phase contrast images.

Calibration from pixels to the metric unit dimensions was performed by means of a micrometer slide.

Image Processing and Analysis Methodology

The aggregates and filaments contents and morphological descriptors were determined by means of image processing and analysis methodologies developed in Matlab 7.3 (The Mathworks, Inc., Natick) language adapted from a previous program developed by Amaral and Ferreira (2005).

The image processing and analysis methodology is divided into two stages. Primarily, the image processing program determines and saves both the aggregated and protruding filamentous biomass binary images. Secondly the image analysis program proceeds to the aggregates and filaments contents and morphological parameters determination.

Image Analysis Parameters

Supported on the previous study of Amaral and Ferreira (2005) 4 parameters were determined, either directly from the image analysis program, either in association with the sludge physical properties, for a total of 131 different samples. Total aggregates area (TA), total filaments length (TL), total filaments length per volume (TL/Vol), total aggregated area per volume (TA/Vol), and total filaments length per total aggregates area (TL/TA) were determined alongside the total filaments length per total suspended solids (TL/TSS) characterizing the aggregates and filaments dynamics. Those parameters were used to establish the best acquisition methodology for both aggregated and protruding filamentous bacteria. A more detailed description of each parameter can be found in Amaral and Ferreira (2005).

3 Results and Discussion

The results herein depicted in Figure 2 revealed a similar trend for both acquisition methodologies with respect to the four studied parameters. However, it is also notorious some differences regarding the absolute value of the TA/Vol (Figure 2a) and TL/TA (Figure 2c) throughout the whole of the data points and in TL/Vol (Figure 2b) and TL/TSS (Figure 2d) in some samples.

Analyzing the aggregated biomass contents, in terms of TA/Vol (Figure 2a), throughout the data points the values obtained for the phase contrast methodology were higher than for the bright field methodology. As a matter of fact, the full data set revealed a 42% increase on the TA/Vol values for the phase contrast acquisition. Given the poorer representation of the objects boundaries in phase contrast microscopy, it seems safe to conclude that this methodology overestimated the aggregated biomass contents considerably.

With respect to the protruding filamentous bacteria contents, in terms of TL/Vol (Figure 2b), for a significant part of the analyzed data, phase contrast and bright field methodology provided similar results. However, for most of the data points there seems to take place a slight overestimation for the bright field microscopy. This fact resulted in an 18% increase on the TA/Vol values for the bright field acquisition. Given the better filaments/background contrast obtained by the phase contrast microscopy, these results were not expected. However, these results may be explained by the fact that the activated sludge samples analyzed in this work presented low protruding filamentous bacteria contents, and that the aggregates area is overestimated in phase contrast. That being the case, the filaments true length would be shortened by the halo of the aggregates in phase contrast, which is a pressing matter in the studied activated sludge, which presented low (and short) protruding filamentous bacteria.

The difference between bright field and phase contrast acquisition is also quite clear when observing the TL/TA (Figure 2c) which comprises only image analysis information (expressing filaments per aggregates area). Bright field microscopy seems to provide higher results than phase contrast which is due to the highest recognition of filaments and lowest aggregates detection. Therefore, it comes as no surprise that, the analysis of the full data set revealed TL/TA values for the phase contrast acquisition that were half of the bright field values.

According to Schuler and Jassby (2007), expressing filaments contents per mass (TL/TSS) is probably the most useful way for comparing filaments contents data from different studies and/or from samples with different biomass concentrations. Given the fact that such concentrations can vary greatly from one system to the other this approach normalizes filaments contents to biomass. Regarding this parameter behavior (Figure 2d) with biomass

normalization, a similar trend between the bright field and phase contrast methodologies arises when compared to the TL/Vol analysis. The main difference relies on the fact that the phase contrast TL/TSS ratio underestimation slightly increased to 22% instead of 18%.

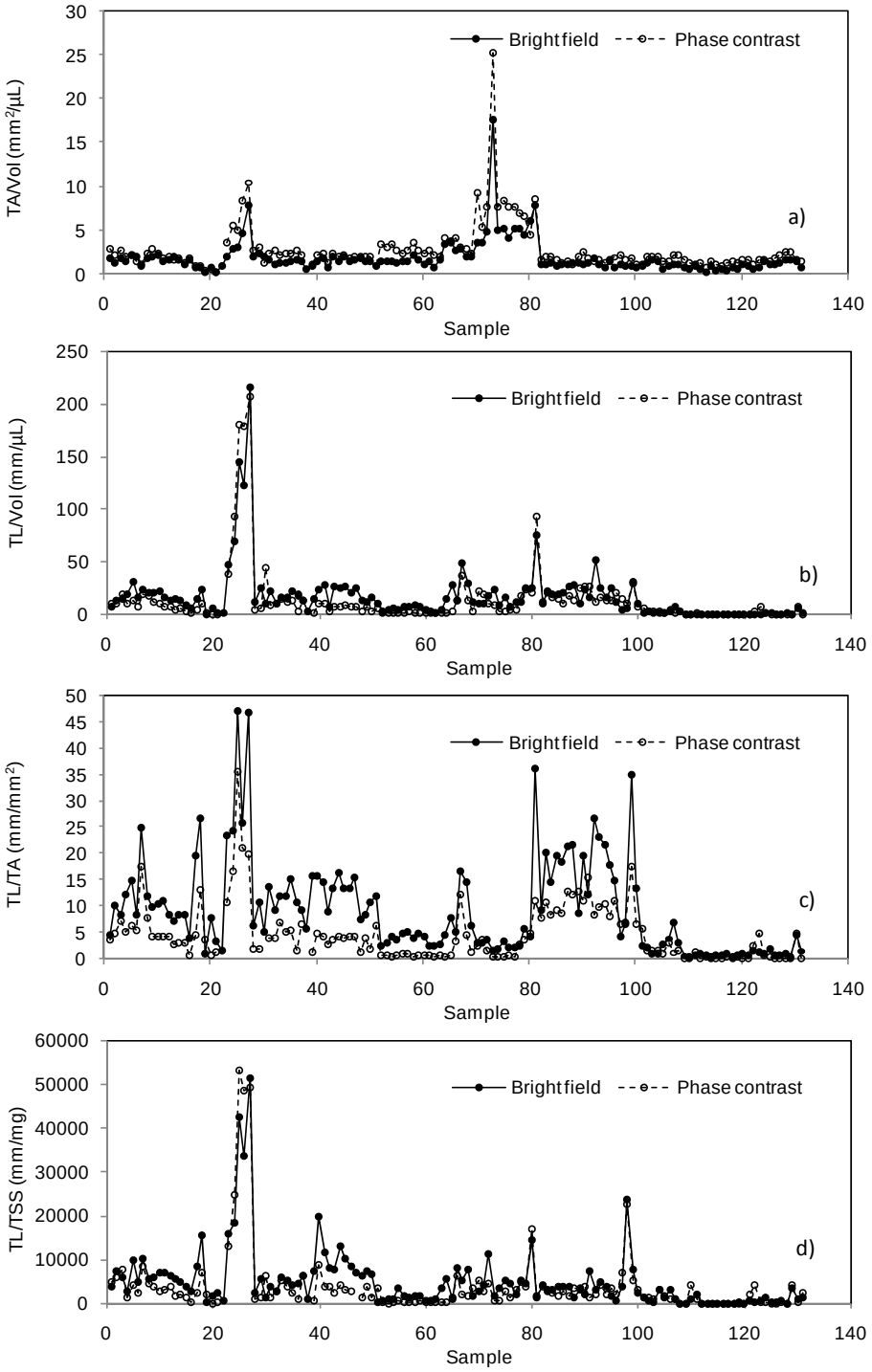

Figure 2. Bright field and phase contrast results for TL/Vol (a), TA/Vol (b), TL/TA (c) and TL/TSS (d) considering 131 samples.

Regarding the behaviors presented in Figure 2, it seems clear the existence of a correlation between the results for bright field and phase contrast microscopic acquisition. Bearing this in mind, were seek the relationships between the bright field and phase contrast results, in order to establish the best acquisition methodology for both aggregated and protruding

filamentous bacteria. Figure 3 represents the obtained relationships between bright field and phase contrast methodologies.

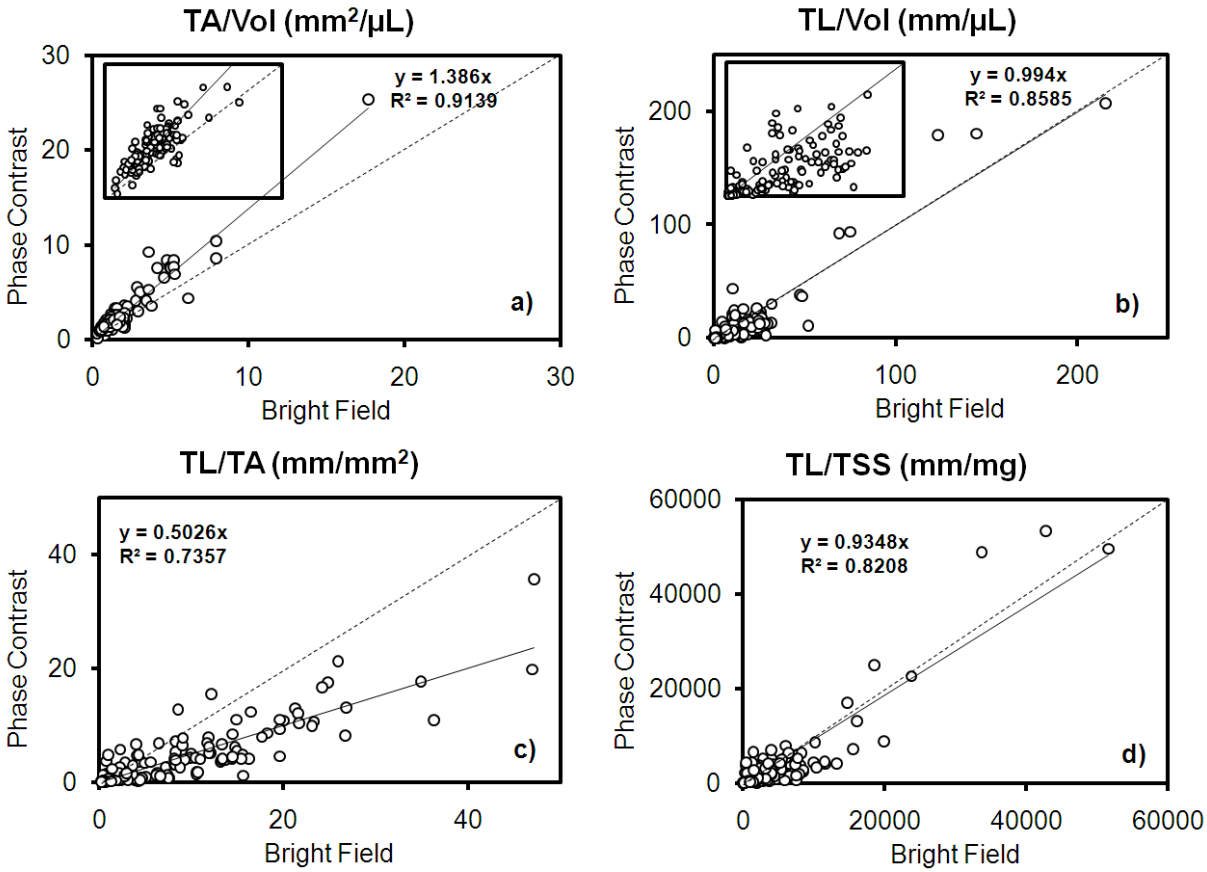

Figure 3. Bright field and phase contrast regressions for TL/Vol (a), TA/Vol (b), TL/TA (c) and TL/TSS (d).

The results herein reported in Figure 3a, revealed a satisfactory correlation coefficient (0.956) for the TA/Vol between bright field and phase contrast assessment. Again, it was possible to infer that the phase contrast methodology overestimated the aggregates detection with respect to the bright field acquisition method. Furthermore, the obtained trend line for the TA/Vol estimation points towards a global overestimation around 39% which is not far apart from the 42% obtained in the previous point to point analysis.

With respect to the protruding filamentous bacteria recognition (Figure 3b), the obtained correlation (0.927) was not as satisfactory as for the TA/Vol and a higher dispersion between bright field and phase contrast assessment was noticed. Furthermore, the trend line pointed to a global correspondence between the two methodologies against the phase contrast underestimation of 18% in the point to point analysis. The reason between such discrepancies may be attributed to the importance of the larger TL/Vol points with respect to the correlation determination. As a matter of fact, the lower values on larger filaments contents of the bright field methodologies, compensates, at some extent, the larger values obtained for smaller contents. It should be noted that, in larger filaments contents, the advantage of the phase contrast methodology on filamentous bacteria recognition is less hindered by the ill defined aggregates borders, leading to a more precise (and higher) filaments determination. All things considered, the correspondence found between the two methodologies allows inferring that the bright field acquisition does not lead to overall significant errors with respect to the protruding filamentous bacteria determination. However care should be taken in analyzing the results of bright field acquisition from activated sludge with high filamentous contents.

Observing Figure 3c, a considerable dispersion between bright field and phase contrast assessments was detected and a poor 0.858 correlation coefficient for the TL/TA ratio was achieved. This result might be due to the cumulative sum of impreciseness both in terms of TL and TA, resulting also in a strong underestimation of this parameter in phase contrast acquisition. This conclusion is further emphasized by the 0.50 slope obtained. This results in a global 50% underestimation of the TL/TA ratio by the phase contrast methodology which is in accordance with the 50% reduction in the previous point to point analysis.

Regarding the TL/TSS ratio results (Figure 3d), a non completely satisfactory correlation coefficient of 0.906 was obtained meaning a global underestimation for the phase contrast of 7% (0.93 slope). Again, a discrepancy was found between the 7% underestimation pointed by the trend between the two methodologies against the phase contrast underestimation of 22% in the point to point analysis. The reason for this behavior is directly related to the protruding filamentous bacteria estimation differences found in the two methodologies, and the same caution must be applied in the TL/TSS ratio as in the TL/Vol assessments.

4 Conclusions

This study clearly demonstrated that, with respect to the protruding filamentous bacteria, the bright field acquisition results mimic, at a certain extent, the phase contrast results. However, the inverse relationship does not hold true for the aggregated biomass contents assessment for the phase contrast acquisition. In fact, it was found that this methodology overestimates by approximately 40% the results obtained by the bright field approach. Thus, considering the advantages and disadvantages of each acquisition methodology and the obtained results, the bright field microscopy proved to be not only more simple and inexpensive but also provided the best overall results.

Acknowledgments

The authors gratefully acknowledge the financial support to Daniela Mesquita and Oscar Dias through the grant SFRH/BD/32329/2006 and the project POCI/AMB/57069/2004, respectively, provided by Fundação para a Ciência e Tecnologia (Portugal). The authors express their gratitude to AGERE (*Empresa de Águas, Efluentes e Resíduos de Braga, Portugal – EM*) and Rui Gonçalves for their cooperation.

References

APHA, AWWA, WPCF. (1989). *Standard Methods for the Examination of Water and Wastewater*. 17th Ed., American Public Health Association, Washington D.C.

Amaral A.L. (2003). *Image Analysis in Biotechnological Processes: Applications to Wastewater Treatment*. PhD. Thesis, University of Minho - (http://hdl.handle.net/1822/4506).

Amaral, A.L., Ferreira, E.C. (2005). Activated sludge monitoring of a wastewater treatment plant using image analysis and partial least squares regression. *Analytica Chimica Acta*, 544, 246-253.

Cenens, C., Jenné, R., Van Impe, J.F. (2002). Evaluation of different shape parameters to distinguish between flocs and filaments in activated sludge images. *Water Science and Technology*, 45(4-5), 85-91.

da Motta, M., Pons, M.N., Roche, N. (2001). Automated monitoring of activated sludge in a pilot plant using image analysis. *Water Science and Technology*, 43(7), 91–96.

Jenné, R., Banadda, E.N., Smets, I.Y., Deurinck, J., Van Impe, J.F. (2007). Detection of Filamentous Bulking Problems: Developing an Image Analysis System for Sludge Composition Monitoring. *Microscopy and Microanalysis*, 13, 36-41.

Schuler, A., Jassly, D. (2007) Filament content threshold for activated sludge bulking: Artifact or Reality? *Water Research*, 41, 4349-4356.

Proceedings of the 10th International Chemical and
Biological Engineering Conference - CHEMPOR 2008
Braga, Portugal, September 4-6, 2008
E.C. Ferreira and M. Mota (Eds.)

Screening of a metagenomic library obtained from soils and water of S. Domingo's mine.

Paula Sá-Pereira*, Susana M. Paixão, Lina Baeta-Hall, Maria C. Sàágua, Ana M. Anselmo, José C. Duarte

INETI – Instituto Nacional de Engenharia, Tecnologia e Inovação, Estrada do Paço do Lumiar 22, 1649-038 Lisboa, Portugal.
*paula.sapereira@gmail.com

Keywords: metagenome, heavy-metal resistance, 16S rDNA
Topic: Systematic methods and tools for managing the complexity

Abstract

The composition of microbial populations of tailings waste at the abandoned São Domingo's copper mine was investigated, and the ability of pure and mixed cultures of indigenous microorganisms to reduce sulphates was examined. Average grades of the exploited material range from 1.25% Cu (10% Cu maximum), 2-3% Zn and Pb (14% Zn and Pb, maximum). Massive pyrite grades average in the range from 45- 48% in sulphur, and in addition to pyrite there are subordinate amounts of chalcopyrite, sphalerite, galena and other rarer sulphides (Webb, 1958).
These approaches revealed new genes and gene products that may have a major role in biomining processes.

1 Introduction

Despite the dominance of microorganisms in the biosphere, relatively little is known about the majority of environmental microorganisms, largely because of their resistance to culture under standard laboratory conditions. As such, alternative approaches are required to assess the large amount of information in the environmental metagenome.
An often-cited estimate is that as much as 99% or more of microbial life remains unculturable, and therefore cannot be studied and understood in a way that microbial ecologists have become accustomed to over the past century. Although the portrait of the microbial world was revolutionized by analysis of 16S rRNA genes, such studies yielded only a phylogenetic description of community membership, providing little insight into the genetics, physiology, and biochemistry of the members. Metagenomics provides a second tier of technical innovation that facilitates study of the physiology and ecology of environmental microorganisms. A variety of chemolithotrophic and heterotrophic microorganisms are responsible for the solubilization of metals from sulfide minerals in acidic environments.

2 Materials and Methods

Samples of soil and water from an abandoned cupric pyrite mine (Mina de S. Domingo's, Southeast Alentejo, Portugal) were used in batch assays to study the dynamics of AMD mesophilic population in presence of iron and plumb. The inoculum (34) (200 ml) was

grown 15 days in (g l^{-1}): 1.2 Na_2SO_4; 0.16 $CuSO_4.5H_2O$; 1.245 $FeSO_4.7H_2O$; 0.33 $ZnSO_4.7H_2O$; 0.3 $Na_3C_6H_5O_7$, pH 6.0, final volume 600ml (34). This culture (200 ml) was then subjected to a double concentration of the metals (same volume) used previously, during 1.5 months (29) and sub-cultivation was dome with supplementation of culture medium with 2% (w/v) Pb (35) and 4% (w/v) Pb (36).
Separation of whole DNA from samples of each batch assay including original inoculum (34, 29, 35, 36) was performed using UltraClean soil DNA isolation Kit (MO BIO).
After isolation of gDNA, PCR was performed using 16S rDNA primers for bacteria and archaea, primers 1510R and 1492R respectively, (Hugenholtz and Goebel, 2001). The amplicons were inserted in pJET plasmid (CloneJET PCR cloning kit, Fermentas) and a metagenomic library was constructed with recombinant DH5a cells with clones with partial 16S rDNA genes that were sequenced by an ABI PRISM 310 sequencer (Applied Biosystems). In order to assess the composition of microbial population in what concers the most representative genera, it was study the presence of *Acidiphilium* sp., *Leptospirillum* sp., *Sulfobacillus* sp., (De Wulf-Durand et al., 1997) and *Thiobacillus caldus*, *T. ferrooxidans* and *T. thiooxidans* belonging to *Acidithiobacillus* gen. nov. sp. genus. (Kelly and Wood, 2000). The 16S rDNA PCR products (from universal primers) were used as templates in PCR with 12 specific 16S rDNA primers for typical AMD communities.

3 Results and Discussion

Primers based on 16S rRNA sequences were designed to be specific for bacterial groups and clones described in bioleaching environments. The 16S rRNA sequence data was obtained from the EMBL and GenBank databases.
The 16S rRNA genes specific for each strain were cloned from acidophilic bacteria obtained from enrichment cultures (Figure 1).

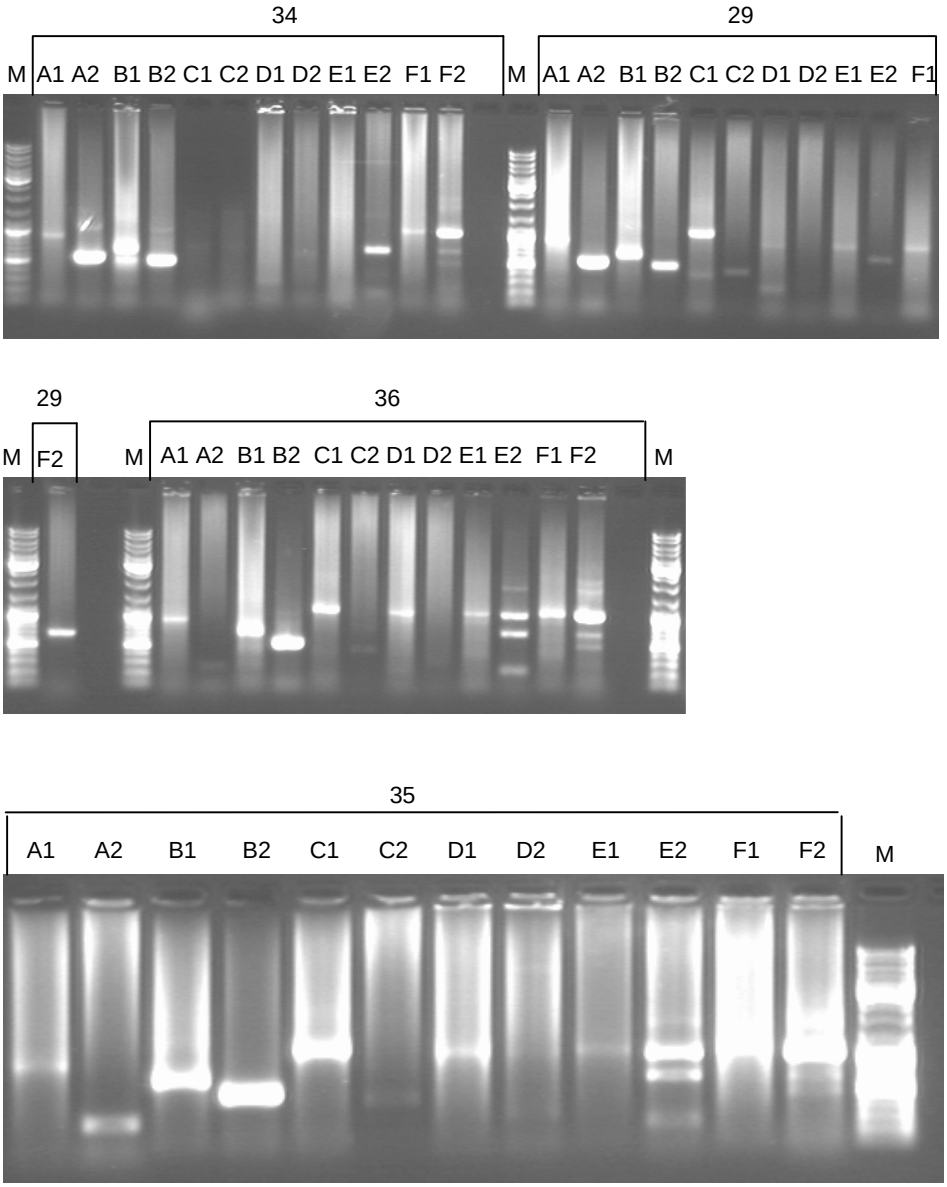

Fig 1. PCR amplifications with AMD specific primers, which templates were the 16S rDNA PCR products amplified with 1510R and 7F universal primers.
A12 – *Acidiphilium* sp., B12 – *Leptospirillum* sp. C12 – *Sulfobacillus* sp., D12 – *Thiobacillus caldus*, E12 – *Thiobacillus thiooxidans,* F12 – *Thiobacillus ferrooxidans.*

The sequence data was compared with 16S rRNA sequences deposited in public databases by using the BLAST search program. The 16S rRNA gene sequences of various bacteria (including those closely related to the unknown sequences, as indicated by the BLAST search) obtained from the GenBank database (Figure 2).

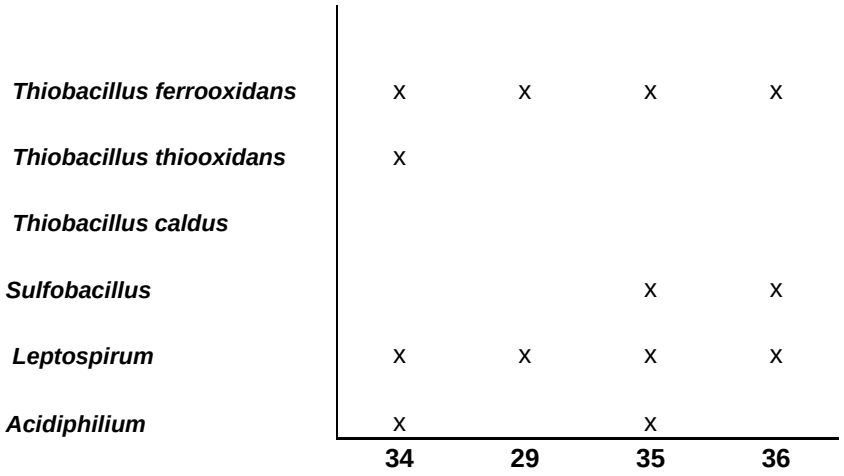

Fig 2. Dynamics of bioleaching population. 34, 29 (presence of copper, iron and zinc) 35 (2% Pb), 36 (4% Pb).

A combination of cultivation-based and molecular-based approaches was used to reveal the culturable and molecular diversity of the microbes inhabiting an open-dumped Pb/Zn mine tailings Analysis the sequences obtained from the metagenomic library constructed with each pool of DNA revealed that microbial population suffers adaptive events that can be explained by the effect of selective pressure caused by metal concentration of culture media, in the dynamics of microbial population. The introduction of Pb in culture media, revealed the presence of *Sulfobacillus* sp., that is a thermophilic iron oxidizing bacterium, usually present in the sphalerite (ZnS) concentrate associated to chalcopyrite that revealed to be important in Pb bioleaching.

Acknowledgements

This study was partially supported by the European Commission project BioMinE – Biotechnology for Metal bearing materials in Europe (Project No.: 500329).

References

De Wulf-Durand, P., Bryant, L.J., Sly, L.L. (1997) PCR-mediated detection of acidophilic, bioleaching-associated bacteria, *Applied and Environmental Microbiology,* 63(7): 2944–2948.

Hugenholtz, P. & Goebel, B. M. (2001). The polymerase chain reaction as a tool to investigate microbial diversity in environmental samples. In *Environmental Molecular Microbiology: Protocols and Applications*, pp. 31–42. Edited by P. A. Rochelle. Wymondham, UK: Horizon Scientific Press 2001

Kelly DP and Wood PA (2000) Reclassification of some species of *Thiobacillus* to the newly designated genera *Acidithiobacillus* gen. nov., *Halothiobacillus* gen. nov. and

Thermithiobacillus gen. nov. *International Journal of Systematic and Evolutionary Microbiology* 50, 511–516.

Webb, J. (1958) Observations on the geology and origin of the S. Domingos Pyrite deposits, Portugal. *Com. Serv. Geol. Portugal*, Lisboa. T. 42, pp.129-143.

Proceedings of the 10th International Chemical and
Biological Engineering Conference - CHEMPOR 2008
Braga, Portugal, September 4-6, 2008
E.C. Ferreira and M. Mota (Eds.)

Equilibrium and kinetics modelling of separation of Cr(III) from industrial effluents by a chelating resin

Licínio M. Gando-Ferreira*, Margarida M. Quina, Sofia A. Cavaco and Rosa Quinta-Ferreira
GERSE - Group on Environment, Reaction and Separation Engineering, Chemical Engineering Department, University of Coimbra, Pólo II, 3030–790 Coimbra, Portugal

Keywords: Equilibrium; Langmuir; Chromium; Breakthrough curves; Multicomponent adsorption
Topic: Advancing the chemical engineering fundamentals.

Abstract

In this study, a chelating resin containing iminodiacetic acid group (Diaion CR 11) was investigated to separate chromium(III) and copper from synthetic effluents. To determine single-component equilibrium isotherms for the two species, batch experiments were performed at 25 ^{o}C. On basis of these results, it was found that the resin exhibited better selectivity for Cu over Cr (III). The Langmuir model enabled a good description of the ion-exchange equilibrium data. To study the dynamic behaviour of the process, column tests were performed for monocomponent - Cr(III)/Diaion CR11 and multicomponent - Cr(III)/Cu^{+2}/Diaion CR 11 adsorption systems. A mathematical model considering dispersed plug flow for the liquid phase, intraparticle mass transfer by pore diffusion and external mass-transfer resistance at the pore/wall interface enabled a reasonable description of the experimental breakthrough curves.

1. Introduction

The environmental contamination with heavy metals may create acute or chronic toxicity problems, which should be avoided when ever is possible. Indeed, although heavy metals could be found naturally in soils, sediments, water and even in living organisms, anthropogenic releases can increase its concentration to higher levels. The electroplating processes is an example of an industry that may create serious problems, since their wastewaters may contain large number of heavy metals, including chromium, copper, nickel, zinc, manganese and lead. The specific contaminants addressed in our work were chromium and copper.

The chromium was selected mainly due to its high concentration in electroplating effluents, commercial value and also based on health concerns (hexavalent chromium is potentially carcinogenic when inhaled). Copper is in general a heavy metal of serious concern because of its toxicity to aquatic life.

The ion exchange process showed to be a promising alternative technique to the traditional methods of precipitation coupled with filtration, for removal and recovery Chromium. The chelating resins are commonly employed as ion-exchange materials, once their ligands can selectively bind to certain metallic ions. Recent studies (Cavaco *et al*. 2007; Gode *et al*. 2003; Kabay *et al.* 1998, 2003) have shown that these resins could be used for the selective removal and recovery of chromium (III). In this work the performance of a chelating exchange resin (Diaion CR11) was evaluated for a system with two species: Cr(III) and Cu. In order to assess the sorption capacity of the resin some equilibrium experiments were carried out, as well as transient column tests for understanding the kinetic behaviour of the process. The experimental results were very motivating, and are now complemented with the modelling approach, since it allow the enhancement and the understanding of the global process.

* Corresponding author. Tel + 351-239-798700. E-mail: lferreira@eq.uc.pt

2 Theory

2.1 Adsorption equilibrium model

In order to quantitatively describe the adsorption experimental data obtained by the batch technique, the Langmuir equation was used:

$$q_i = \frac{q_{\max i}\, k_{Li}\, C_i}{1 + k_{Li}\, C_i} \tag{1}$$

where q_i correspond to the adsorbed mass of component i (mg/g wet resin) and C_i is the equilibrium concentration of component i (Cr and Cu^{2+}) in the liquid phase (mg/L). K_{Li} and q_{maxi} are the Langmuir model parameters.

2.2 Dynamic Model for Fixed Bed Adsorption and Parameter Estimation

A model was developed to describe the dynamic behaviour of the system during the saturation step, namely regarding the species concentrations in the solution at the outlet of the column as a function of time (breakthrough curve). The model includes pore diffusion, mass transfer resistance in the film and axial dispersion. Dimensionless model equations are:

Mass balance for the fluid phase

$$\frac{\partial \mathrm{X_i}\,(z^*,\theta)}{\partial \theta} = \frac{1}{\mathrm{Pe}} \frac{\partial^2 \mathrm{X_i}\,(z^*,\theta)}{\partial z^{*2}} - \frac{\partial \mathrm{X_i}\,(z^*,\theta)}{\partial z^*} - \mathrm{N_{fi}}\,(\,\mathrm{X_i}\,(z^*,\theta) - \mathrm{Xp_i}\,(1,z^*,\theta)\,) \tag{2}$$

where i = 1(Cr(III)), 2 (Cu^{2+}).

Mass balance inside particles

$$\frac{\rho_h}{C_{E_i}} \frac{\partial q_i\,(u^*,z^*,\theta)}{\partial \theta} + \varepsilon_p \frac{\partial Xp_i\,(u^*,z^*,\theta)}{\partial \theta} = N_{Di}\,(\frac{\partial^2 X_{p_i}\,(u^*,z^*,\theta)}{\partial u^{*2}} + \frac{2}{u^*} \frac{\partial Xp_i\,(u^*,z^*,\theta)}{\partial u^*}) \tag{3}$$

Multicomponent Equilibrium Adsorption pore / wall interface described by the extended Langmuir model

$$q_i = \frac{q_{\max_i}\, k_{Li}\,(C_{Ei}\, X_{Pi} / \eta_i)}{1 + \sum_{j=1}^{2} k_{Lj}\,(C_{Ej}\, Xp_j / \eta_j)} \tag{4}$$

where the q_{maxi}, k_i are given by the individual Langmuir (eq. 1), and the η_i are the interaction terms to quantify the competitive adsorption in multicomponent systems.

Initial conditions

$\theta = 0$ $\quad X_i\,(z^*,0) = Xo_i$ and $Xp_i(u^*,z^*,0) = Xo_i$ (5)

Boundary conditions

$u^*=0$ $\quad \frac{\partial Xp_i\,(u^*,z^*,\theta)}{\partial u^*}\Big|_{u^*=0} = 0$ (6)

$$u^*=1 \quad N_{fi}\,(\,X_i(z^*,\theta) - Xp_i(1,z^*,\theta)\,) = 3\frac{1-\varepsilon}{\varepsilon} N_{Di}\,\frac{\partial Xp_i(u^*,z^*,\theta)}{\partial u^*}\Big|_{u^*=1} \qquad (7)$$

The equations of the model are written in terms of dimensionless variables: $X_i = C_i/C_{Ei}$, $Xp_i = Cp_i/C_{Ei}$ are the dimensionless concentrations of the species i in the bulk liquid phase and in the liquid inside particle pores, respectively; $\theta = t/\tau$ is a reduced time, where τ is the bed space time; z* = z/L is the reduced axial coordinate, where L is the fixed bed length; u* = r/R is the reduced particle radial coordinate, in which R is the adsorbent particle radius.

The dimensionless groups are the Peclet number $Pe = uL/(\varepsilon D_{ax})$ (D_{ax} is the axial dispersion coefficient), the number of mass transfer units by pore diffusion for species i, $N_{Di} = \tau\varepsilon_P D_{Pi}/R^2$ ($D_{pi} = D_{mi}/\tau_p$ is the effective diffusivity for the species i and τ_P is tortuosity factor) and the number of film mass transfer units for species i, $N_{fi} = 3(1-\varepsilon) k_{fi} \tau / (\varepsilon R)$, where k_{fi} is the film mass transfer coefficient for species i. The axial dispersion was calculated from the Butt correlation (Buts, 1980): $(u d_p/D_{ax}) = (0.2 + 0.011 Re^{0.48})$, where $Re = u \rho d_p / \varepsilon \mu$.

Numerical solutions of eqs (2) – (7) were performed by discretizing eq. (3) in the radial direction using orthogonal collocation in NE finite elements with cubic Hermite polynomials as basis functions. This led to a new boundary value problem of N_{comp} (2NE +1) [N_{comp} is the number of components] parabolic PDE's in the independent variables z* and θ that was numerically integrated with the PDECOL package.

3 Experimental Methods

Before the experiments, the resin Diaion CR11 was supplied by Mitsubishi Chemical Corporation and was pretreated by repeated washings with 2M HCl and 2M NaOH solutions to remove solvents and other preparation chemicals. The last step of the conditioning consisted in percolating a solution of HCl through the column in order to convert the resin to H^+ form. The resin matrix is polystirenic and contains the iminodiacetic acid as chelating group. For all the experiments, synthetic effluent samples were prepared by dissolving an appropriate amount of chromium salt $Cr(NO_3)_3$ and copper salt $Cu(NO_3)_2$ in distilled water.

Equilibrium isotherms were determined through batch tests, where 40 mL of a synthetic solution at different initial concentrations of the metal were added into a flask with 1 g of preconditioned resin. The flasks were sealed and kept in a shaker at 25ºC for 24h. The resin was separated by filtration and some aliquots of liquid were analyzed using flame atomic absorption spectrophotometry in order to determine the total concentration of Cr (III) and Cu in solution.

In the column tests, a glass tube with 1.6 cm of internal diameter and 20 cm height, packed with approximately 5 g of resin was used. The experimental conditions for these tests (Run 1 to Run 3) are summarized in Table 1. A peristaltic pump was utilized to percolate 10 mL/min through the column of a synthetic solution containing Cr (III) and Cu^{2+} ions. Several samples were collected at the column outlet and the concentrations of both metals were analysed along the time as described above.

Table 1 – Experimental conditions for fixed bed experiments

	$C_{Cr(III)}$	C_{Cu+2}	Feed pH	Resin Properties	Bed Properties	Flow conditions
Run 1	484 mg/L	-	3.26	ε_p = 0.66	ε = 0.35 L = 4.0 cm	Q = 10 mL/min τ = 0.28 min
Run 2	240 mg/L	160 mg/L	3.30	ρ_h = 1015 g/L	ε = 0.40 L = 5.0 cm	Q = 10 mL/min τ = 0.40 min
Run 3	230 mg/L	70 mg/L	3.11	d_p = 0.536 mm	ε = 0.40 L = 5.0 cm	Q = 10 mL/min τ = 0.40 min

4 Results and discussion

The single-isotherms equilibrium data for Diaion / Cr (III) and Diaion /Cu^{+2} are illustrated in Fig. 1a and Fig. 1b, respectively. These data show that the resin exhibits higher sorption capacity for copper than for the trivalent chromium, this means that Cu^{+2} forms a stronger chelate complex with the functional group (iminodiacetic acid) of the resin.

The metal sorption of both metals leads to a decrease in the equilibrium pH of the solution with respect to initial pH from approximately 5 to 2. This pH variation is a consequence of the hydrogen ions release from the resin, in the H^+ form, since those ions are exchanged with the metallic ions in solution.

The Langmuir model fits very well the equilibrium experimental data, for the conditions tested and for both metals (Cr and Cu). The values found for the parameters are: $K_L = 8.47x10^{-3}$ *L/mg* and $q_{max} = 10.68$ *mg/g*$_{resin}$ for Cr(III); $K_L = 5.97x10^{-2}$ *L/mg* and $q_{max} = 31.75$ *mg/g*$_{resin}$ *for* Cu^{+2}.

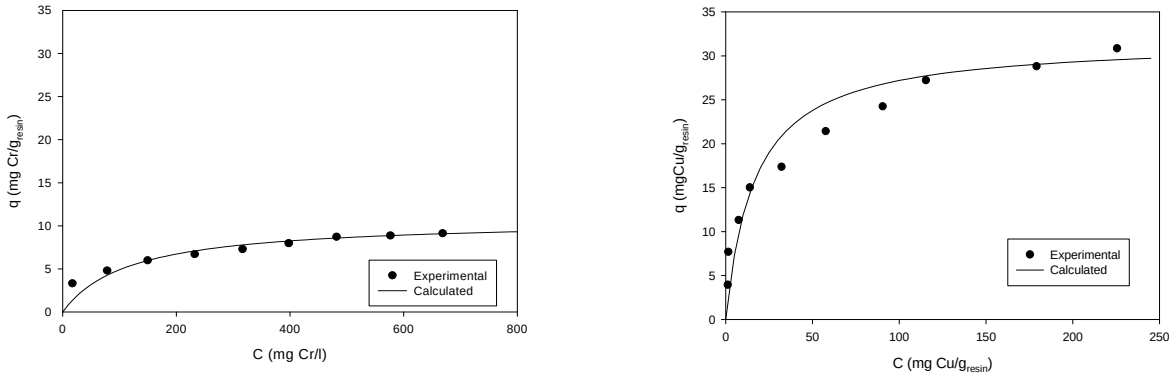

(a) (b)

Figure 1- Adsorption equilibrium isotherms. Experimental data and model predictions using the Langmuir equation: (a) – Diaion / Cr(III) ; (b) – Diaon / Cu^{+2}.

Experimental and simulated breakthrough curves plotted as metal concentration at column outlet against time are depicted in Figs. 2 – 5.

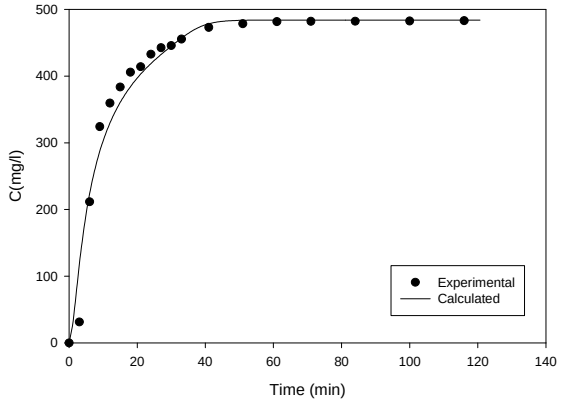

Figure 2 – Breakthrough curve of Cr (III) sorption on Diaion Cr 11 – Run 1.

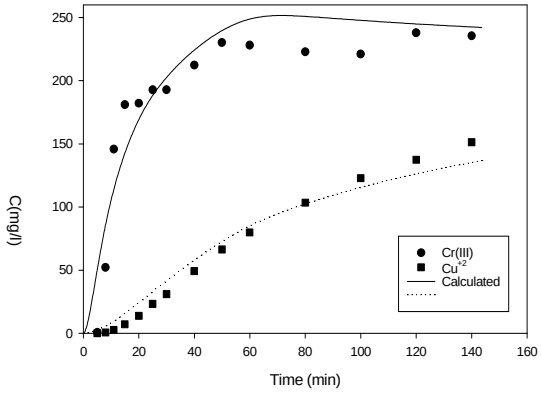

Figure 3 – Breakthrough curves for sorption of the mixture Cr (III) and Cu^{+2} on Diaion Cr 11 – Run 2.

A reasonable agreement is observed between experimental and calculated breakthrough curves, being the model solution achieved with the parameter values indicated in the Table 2. The Peclet values demonstrate a intermediate effect of axial dispersion on the hydrodynamic conditions of the fixed bed, while the $N_{D,i}$ ones enable to conclude that the mass transfer is controlled by the intraparticle resistance. Regarding the N_f parameter, high values were used in the simulations for neglecting external mass transfer resistance.

Table 2 – Parameter values used in the simulations of the saturation step.

	Pe	$N_{D,cr}$	$N_{D,Cu}$
Run 1	33.0	0.04	-
Run 2	52.3	0.06	0.09
Run 3	49.3	0.06	0.09

In the case of multicomponent system, corresponding to the Runs 2 and 3, the equilibrium isotherm for each species took into account the following interaction factors adjusted: η_1 = 1.11 for Cr(III) and η_1 = 0.5 for Cu^{+2}. The breakthrough curves of these runs (Figs 3 and 4), in which the copper concentration in the feed was decreased, show that copper emerges later since this metal is strongly adsorbed by the resin, confirming so the equilibrium studies. It should be noted that the change of the initial copper concentration had effect on the breakthrough time of the saturation curve for this metal. Higher initial concentration leads to faster saturation of the resin and consequently the breakthrough curve emerges at column outlet earlier. The chromium behaviour is little affected by the change of copper concentration feed.

Figure 5 illustrates the effect of the flowrate on the breakthrough curves obtained by simulation. As expected, at low flow rates, a longer contact between the solid and liquid phase is promoted and this leads to the retardation in the saturation curve.

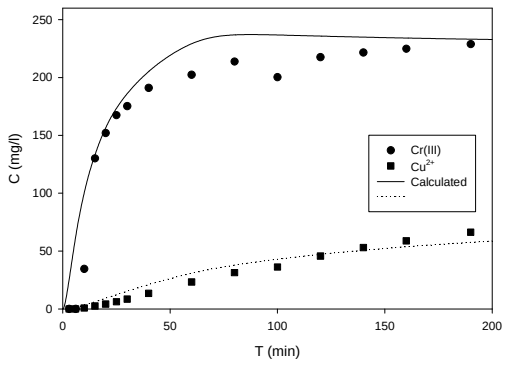

Figure 4 – Breakthrough curves for sorption of the mixture Cr (III) and Cu^{+2} on Diaion Cr 11 – Run 3.

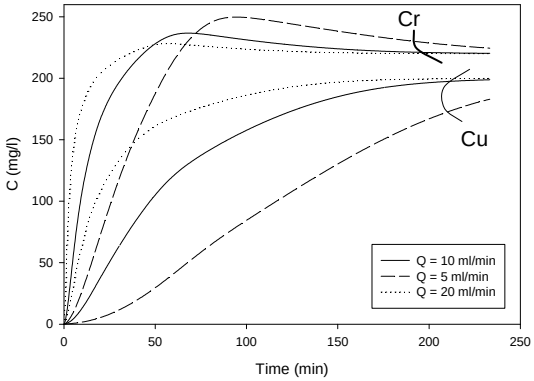

Figure 5 – Effect of the flowrate on the breakthrough curves for sorption of the mixture Cr (III) and Cu^{+2} on Diaion Cr 11.

5 Conclusions

The chelating ion-exchange resin Diaion CR 11, in the hydrogenium form, have been tested for separating chromium (III) and copper from synthetic effluents. The equilibrium isotherms showed that the resin have strong affinity to the copper ions than for chromium. The experimental data were well described by the Langmuir model.
The breakthrough curves resulting from the saturations in fixed bed enabled to study the dynamic behaviour of the process for the monocomponent - Cr(III)/Diaion CR11 and multicomponent - Cr(III)/Cu^{+2}/Diaion CR 11 adsorption systems. A mathematical model considering dispersed plug flow for the liquid phase, intraparticle mass transfer by pore diffusion and external mass-transfer resistance at the pore/wall interface was used to simulate the saturation curves. The model yields results in reasonable agreement with the experimental data and seems to be a suitable approach for the design of industrial systems directed to the treatment of effluents from electroplating processes.

Acknowledgement

We would like to thank FCT (Foundation for Technology and Science) for its financial support for this work (*Project: POCTI/EQU/58149/2004*).

References

Butt, S (1980). . In: *Reaction Kinetics and Reactor Design* Prentice-Hall, Englewood Cliffs, NJ

Cavaco, S.A., Fernandes, S., Quina, J.Q. and Ferreira, L.F (2007). Removal of chromium from electroplating industry effluents by ion-exchange resins. *Journal of Hazardous Materials*, 144, 634-638.

Gode, F. Pehlivan E. (2003). A comparative study of two chelating ion-exchange resins for the removal of chromium (III) from aqueous solution. *Journal of Hazardous Materials B100 , 231-243.*

Kabay, N., M. Demircioğlu, H. Ekinci, M. Yüksel, M. Sağlam, M. Akçay, M. Streat (1998). Removal of Metal Pollutants (Cd(II) and Cr(III)) from phosphoric acid solutions by chelating resins containing phosphonic or diphosphonic groups. Ind. Eng. Chem. Res. 37,2541-2547.

Kabay, N., Gizli, N., Demircioğlu, M.,Yŭksel, Jyo, A., Yamabe, K. and Shuto, T. (2003). Cr (III) removal by macroreticular chelating ion exchange resins. *Chem. Eng. Comm., 190, 813-822.*

Proceedings of the 10th International Chemical and
Biological Engineering Conference - CHEMPOR 2008
Braga, Portugal, September 4-6, 2008
E.C. Ferreira and M. Mota (Eds.)

Hydrogen production from methane steam reforming: parametric and gradient based optimization of a membrane reactor

L. C. Silva; V. V. Murata; C. E. Hori; A. J. Assis[1*]

Keywords: Modeling and simulation, sensitivity analysis, reforming reactions, hydrogen, DIRCOL
Topic: Advancing the chemical engineering fundamental.

Abstract

In this work, the effects of five important parameters, as well as, the use of two different intrinsic kinetics available on the model developed were evaluated. The influence of the parameters, inlet reactor pressure (PR0), methane feed flow rate (FCH40), sweep gas flow rate (FI), external reactor temperature (TW) and steam to methane feed flow ratio (M), on methane conversion (X_{CH_4}) and hydrogen recovery (Y_{H_2}) was parametrically evaluated through simulations. In addition, a gradient based method (DIRCOL) was used to perform the optimization of the sum of methane conversion and hydrogen recovery. High methane conversions and H_2 recoveries were reached by parametric optimization, but, disdaining the interactions between the variables. Due to numeric problems in the optimization using DIRCOL, the lower value of methane feed that allowed the optimization was $1 \cdot 10^{-4} mol/s$. It was possible to reach a methane conversion around 96% and a hydrogen recovery of 91%.

1 Introduction

Nowadays, methane steam reforming is the main route for hydrogen production. Methane steam reforming reactions are endothermic and reversible, which implies on the conventional technology, in high operating temperatures to reach satisfactory conversions. Since the maximum conversion that could be achieved is the equilibrium conversion, the membrane technology is an alternative process that can overcome this limitation. Membrane reactors are generally constituted by concentric tubes in which one of them is the membrane. The membrane is usually made of Palladium or an alloy of Palladium-Silver that is only permeable by hydrogen. Therefore, in a membrane reactor, hydrogen is continuously removed from the reaction zone, displacing the chemical equilibrium and enabling operation at moderate temperatures. Satisfactory conversions are dependent on many factors such as the operating parameters. Several studies (Lin et al. 2003, Shu et al. 1994, Falco et al. 2006) have studied the influence of the factors such as operating pressure, methane feed flow rate, operating temperature, sweep gas flow rate, area of permeation, etc., on the methane conversions. In this work a combination of a parametric optimization and a gradient based optimization is made to provide an insight about the choice of some parameters that maximize the hydrogen recovery and the methane conversion for a small scale reactor.

2 Mathematical modeling

In accordance with Froment and Xu (1989) the reactions among methane, water, monoxide of carbon, carbon dioxide and hydrogen that present greater probability to occur during methane steam reforming are:

$$CH_4 + H_2O \leftrightharpoons CO + 3\,H_2 \qquad -\Delta H_{298K} = -206.1\,kJ/mol \tag{1}$$

$$CO + H_2O \leftrightharpoons CO_2 + H_2 \qquad -\Delta H_{298K} = 41.15\,kJ/mol \tag{2}$$

$$CH_4 + 2\,H_2O \leftrightharpoons CO_2 + 4\,H_2 \qquad -\Delta H_{298K} = -165.0\,kJ/mol \tag{3}$$

*Corresponding author. Tel. +55-34-3239-4292. E-mail: ajassis@ufu.br

The reactor modeled is schematically represented in Fig. 1. The inner tube is the Pd-based membrane and the outer one is the shell. The catalyst is packed in the annular region. The inert or sweep gas passes into the inner tube in co-current flow mode.

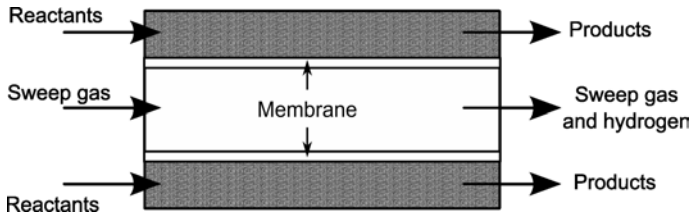

Figure 1: Membrane reactor scheme considered in this work.

The model is summarized by the equations in Table 1. Where, for $\Psi = 0 \Rightarrow i = CH_4, CO, CO_2, H_2O$

Table 1: Model equations

Mass balance in the reaction chamber $\frac{dF_i}{dZ} = W\left(\sum_{j=1}^{3}\nu_{ij}r_j\right) - \Psi J_{H_2} A_m$	Molar flux of hydrogen through the membrane $J_{H_2} = \frac{A_0 e^{\left(\frac{E}{RT_m}\right)}}{\delta}\left((p_{H_2})^{0.5} - (p_{H_2p})^{0.5}\right)$
Energy balance in the reaction chamber $\rho_r C_{v_r} \underline{v_r} \cdot \frac{dT_R}{dZ} = T_R \left.\frac{\partial P}{\partial T}\right\|_V \frac{dv_r}{dZ} + \frac{1}{V_{an}}\left(Q_1 - Q_2 + W\sum_{j=1}^{3}(-\Delta H_j)\, r_j - H_{H_2} J_{H_2} A_m\right)$	
Mass balance in the permeate side $\frac{dF_{H_{2p}}}{dZ} = J_{H_2} A_m$	Heat exchanged in the reactor $Q_1 = U_1 A_1 (T_w - T_R) \quad ; \quad Q_2 = U_2 A_2 (T_R - T_P)$
The pressure drop in the catalytic bed $\frac{dP_R}{dZ} = -f\frac{\rho_r u_s^2}{d_p}$	Friction factor (Ergun's equation) $f = \frac{1-\varepsilon}{\varepsilon^3}\left(a + \frac{b(1-\varepsilon)}{Re}\right)$

and for $\Psi = 1 \Rightarrow i = H_2$.

The mathematical model considered real gases for thermodynamic properties calculations. Additional hypotheses adopted in the model development were: nonisothermal/nonisobaric, pseudo-homogeneous model, steady-state operation, plug-flow behavior was adopted for the permeate and reaction zone, nonexistence of boundary layer on the membrane and hydrogen diffusion in the membrane is the rate-determining step for hydrogen permeation.

The reactor dimensions used in this work were taken from Shu et al. (1994). All thermodynamic mixture properties were calculated using the Virial equation of state, with van der Waals mixing rules. The gases and the gaseous mixture viscosities were calculated by Chung's method (Poling 2004). The values of constants a and b of Ergun's equation are 150 and 1.75 respectively (Froment 1990). Other catalyst properties used were taken from Froment and Xu (1989).

Methane conversion and hydrogen recovery were defined as:

$$X_{CH_4} = \frac{F^0_{CH_4} - F_{CH_4}}{F^0_{CH_4}} \quad ; \quad Y_{H_2} = \frac{F_{H_{2p}}}{F_{H_{2p}} + F_{H_2}} \tag{4}$$

3 Results and discussion

3.1 Model Validation

Two different intrinsic kinetics available for the reactions of methane steam reforming were used. The first one is reported by Froment (1990) and it is the oldest and widely used. The second one, by Hou e Hughes (2001) is more recent and there is no reference about its use in a reactor model. The basic difference between them is that the first one was developed for catalysts of $Ni/MgAl_2O_4$ and only one of the products, the hydrogen, adsorbs on the surface. The second one was developed for catalysts of Ni/Al_2O_3 in which two products, hydrogen and carbon monoxide, adsorb on the surface. These two

kinetics were evaluated during the validation of the model, in this work. The validation of each model was carried out using given experimental data of a Pd-based membrane reactor reported by Shu et al. (1994) with the same design and operating conditions. Methane conversions obtained by the model were compared with the experimental ones reported by Shu et al. (1994). Methane conversions were evaluated for different steam to methane feed flow ratio, different operating temperatures and different operating pressures, and in this paper only a sample of the results are presented (Fig. 2 A)).

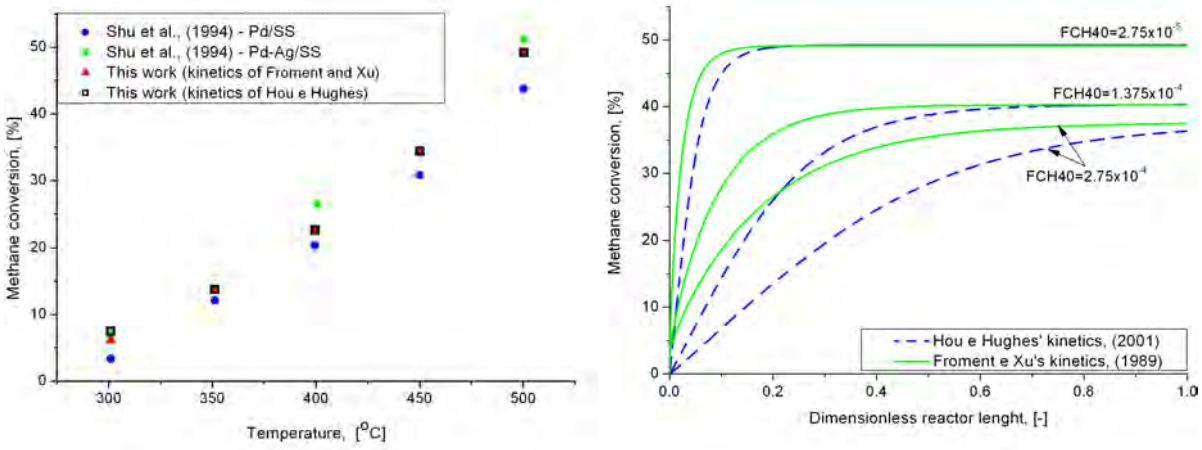

A) B)

Figure 2: Model validation. A) Methane conversions versus reactor temperature. B) Methane conversion profiles along the reactor.

The agreement between the simulated results and the experimental ones was good as it can be seen in the Fig. 2 (A). Moreover, the two available kinetics leads to similar results. The difference between them resides on their behavior along the reactor. As it can be seen in the Fig. 2 (B), methane conversion has an abrupt rise at the reactor beginning. This behavior is somewhat different when Hou's kinetics was used, and this difference increases as the methane feed flow rate increases. In other words, Froment's kinetics predicts an abrupt change for the composition at the reactor beginning, whereas the Hou's kinetics foresees a less sudden change. As it will be discussed further, molar methane feed flow rate less then $1 \cdot 10^{-4}\, mol/s$ cause dramatic changes the compositions at the reactor beginning, and as a result, the optimization using the gradient based optimization could not be performed for values smaller than $1 \cdot 10^{-4}\, mol/s$ of methane feed.

3.2 Parametric and gradient based optimization

At first, Froment's kinetics was chosen due to two mainly reasons. This kinetics is widely known and used, and also because it implies in less mathematical problems. Both kinetics demand products feed, the Froment's kinetics requires hydrogen feed and Hou's kinetics requires hydrogen and carbon monoxide feed. These problems are caused by the presence of the partial pressure of these components in the denominator of the rate equations. Therefore, low values were used ($1.0 \cdot 10^{-4}$) as initial conditions for these products. However, during the optimization using a gradient based method, the use of the Froment's kinetics cause failure of the algorithm. In this case, the lower admissible value for methane feed flow rate was $1.0 \cdot 10^{-4}\, mol/s$ and using the Hou's kinetics only.

To perform the optimization, a standard or reference operational condition for membrane reactors in methane steam reforming were taken according to Shu et al. (1994): PR0 = 136000 Pa, TW = 773.15 K, M = 3, FI = $2.75 \cdot 10^{-5}$ mol/s and FCH40 = $2.75 \cdot 10^{-5}$ mol/s.

3.3 Parametric optimization

In order to try to maximize methane conversion and hydrogen recovery, defined by Eqs. 4, different values around the standard parameters reported by Shu et al. (1994) were adopted. The lower and upper bounds were chosen based on operating characteristics of the membrane reactors and on the Shu's work. The upper and lower bounds are shown in Table 2. As it is shown in Fig. 3 A and B, an increase in

pressure, temperature and sweep gas flow cause an increase in methane conversion and hydrogen recovery. Conversely, an increase in methane conversion and hydrogen recovery is caused by a decrease in methane inlet flow. Particularly, an increase in steam to methane feed flow ratio (M) has an opposite effect on the methane conversion and hydrogen recovery. However, an increase in M causes an increase in the sum ($X_{CH_4} + Y_{H_2}$). Therefore, it can concluded that the use of the upper values of pressure, temperature and sweep gas and the lower methane feed value leads to the maximal methane conversion and hydrogen recovery, regardless of the interactions among the parameters. On the other hand, analyzing methane conversion and hydrogen recovery sum (Fig. 3 C), it can be noticed that the highest value for this parameter leads to the maximal methane conversion + hydrogen recovery. Indeed, the gain obtained in methane conversion, keeping the others parameters in the considered best conditions, is less than the setback obtained in the hydrogen recovery. Therefore, depending on the values of the other parameters, the trend of this effect change from an increase to a decrease in the objective (methane conversion plus hydrogen recovery). In other words, the interactions between the parameters are important in the optimization. Even so, high conversions (from 99.92 to 99.99%) and high recoveries (from 96.82 to 99.28%) could be achieved varying the steam to methane feed ratio and keeping the pressure, temperature and sweep gas at the highest values and the methane feed at the lowest value.

3.4 Optimization by a gradient based method (DIRCOL)

Having in mind the importance of the interaction between the parameters, it is imperative to perform the optimization taking into account these interactions. In order to carry out this task a gradient based algorithm of optimization (DIRCOL) was used (Von Stryk 2002). The optimization was performed directly from the differential equation by discretization. Therefore, the optimization problem was posed as:

Maximize: $X_{CH_4} + Y_{H_2}$,

Subject to:

- Model equations from Table 1;
- Parameters bounds from Table 2;
- Bounds of the state variables (for all state variables, the range is between 0 and 1 due to a normalization).

Due to a numerical instability in the optimizer's code the methane feed was kept in $1 \cdot 10^{-4} mol/s$, and the others parameters (PR0, TW, M and FI) were taken as variable decision. The optimization was carried out using the following input information supplied by the user: optimal tolerance and nonlinear feasibility tolerance equal $1.0 \cdot 10^{-3}$, *iscale* equal 0, initial grid points equal 15, with equidistant grid points, initial estimates for the parameters equal $PR0 = 506625.0\,Pa$, $FI = 1.375 \cdot 10^{-4}\,mol/s$, $TW = 873.15\,K$ e $M = 2.5$. The initial estimates for the state variables were based on a non linear fit on the integrated model. To avoid reaching local maxima, other initial estimates for the parameters were used, but all converged to the same values. The best parameters values are shown in Table 2. These parameters lead to a methane conversion of 96.27% and a hydrogen recovery of 91.26%, that are higher than 41.57% and 11.90% obtained in the adopted standard conditions changing methane feed from $2.75 \cdot 10^{-5}$ to $1.0 \cdot 10^{-4} mol/s$. It is important to emphasize that values lower than $1.0 \cdot 10^{-4} mol/s$ cause numerical instability, probably because the dramatic change in composition in the reactor beginning achieved for low values of methane feed, as can be seen in Fig. 3 D. This figure also shows the profiles of methane conversion along the reactor. It is also import to cite that this optimization could be carried out only with the Hou's kinetics, probably due to the fact that the Froment's kinetics lead to a more dramatic change in composition than the Hou's kinetics.

4 Conclusions

Comparing methane conversion obtained by the developed model using two available kinetics for methane steam reforming, it can be conclude that both characterize a good representation of the real reactor. However, the conversion profile obtained using Hou's kinetics describes smoother concentration profiles along the reactor. By parametric optimization, it was possible to obtain high conversions and recoveries (more

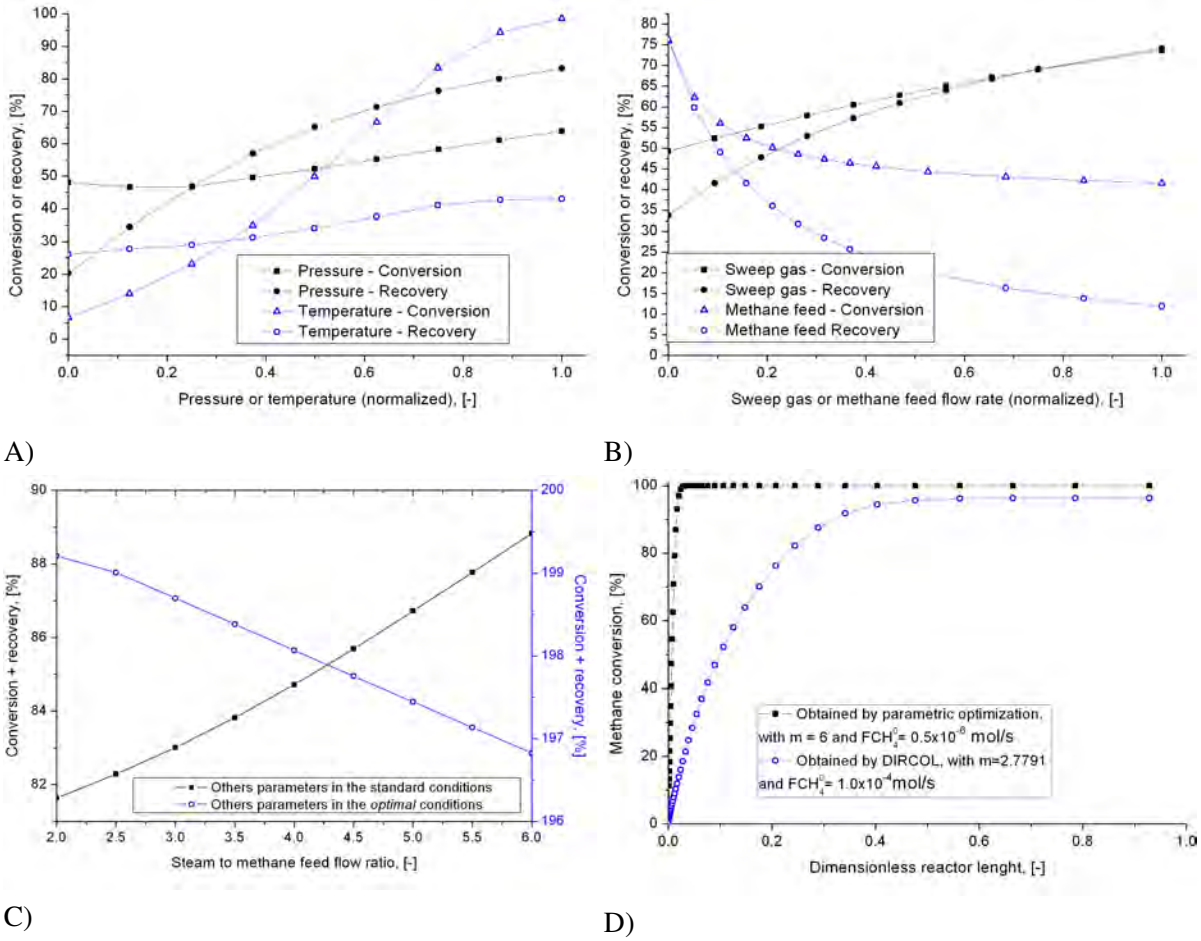

Figure 3: Parametric study (Graphics A-C) and profiles along the reactor obtained by parametric optimization and optimization with DIRCOL (D)

than 99 and 96 %) but, the best value could not be evaluated with assurance. The use of the DIRCOL to perform the optimization could only be possible with the use of Hou's kinetics in the model, even so for a value of methane feed of $1 \cdot 10^{-4} mol/s$. This value is about three times the standard value. A methane conversion of 96.27% and hydrogen recovery of 91.26% were obtained for the best parameters choice.

Table 2: Lower, upper bounds and best values of the parameters

	Parametric optimization			Optimization with DIRCOL		
Parameters	lower bound	upper bound	best value	lower bound	upper bound	best value
Pressure (Pa)	101325	506625	506625	101325	506625	506625
Temperature(K)	573.15	873.15	873.15	573.15	873.15	873.15
FI (mol/s)	$2.75 \cdot 10^{-5}$	$1.375 \cdot 10^{-4}$	$1.375 \cdot 10^{-4}$	$2.75 \cdot 10^{-5}$	$1.375 \cdot 10^{-4}$	$1.375 \cdot 10^{-4}$
m	2.5	6	2.5 to 6 *	2.5	6	2.7791457
$FCH4$0 (mol/s)	$5 \cdot 10^{-6}$	$1 \cdot 10^{-4}$	$5 \cdot 10^{-6}$		Fixed=$1 \cdot 10^{-4}$	

* not conclusive.

5 List of symbols

a - Constant in Ergun's equation $[-]$

A_0 - Pre-exponential factor $\left[\frac{N}{LT}\left(\frac{T^2 L}{M}\right)^{0.5}\right]$

A_1, A_2 - Area of heat transfer $\left[L^2\right]$

A_m - Permeation area of membrane $\left[L^2\right]$

b - Constant in Ergun's equation $[-]$

Cv - Specific heat at constant volume $\left[\frac{M\,L^2}{T^2 N\,\Theta}\right]$

dp - Equivalent diameter of catalyst particle $[L]$

u_s - Gaseous velocity $\left[\frac{L}{T}\right]$

U_1, U_2 - Overall heat transfer coefficient $\left[\frac{M}{T^3\Theta}\right]$

v - Mean velocity of the gaseous mixture $\left[\frac{L}{T}\right]$

V_{an} - Annular volume $\left[L^3\right]$

V_{pe} - Permeate volume $\left[L^3\right]$

X_{CH_4} - Methane conversion $[-]$

W - Catalyst mass $[M]$

E - Activation energy $\left[\frac{M\,L^2}{T^2 N}\right]$
f - Friction factor $[-]$
$FCH40$ - Methane feed flow rate $\left[\frac{N}{T}\right]$
F_i - Molar flow rate of component $\left[\frac{N}{T}\right]$
FI - Molar flow rate of inert or sweep gas $[mol]$
H_{H_2} - Hydrogen enthalpy $\left[\frac{M\,L^2}{T^2 N}\right]$
J_{H_2} - Hydrogen permeation flux $\left[\frac{N}{L^2 T}\right]$
L - Reactor length $[L]$
M - Steam to methane feed flow ratio H_2O e CH_4 $[-]$
p_{H_2} - Hydrogen partial pressure $\left[\frac{M}{T^2 L}\right]$
Q_1, Q_2 - Heat exchanged $\left[\frac{M\,L^2}{T^2}\right]$
r_j - Rate of the reaction j $\left[\frac{Kmol}{Kg_{cat}h}\right]$
R - Universal gas constant $\left[\frac{M\,L^2}{T^2 N\,\Theta}\right]$
Re - Reynolds' number $[-]$
T - Temperature $[\Theta]$
T_w - External temperature $[\Theta]$
Y_{H_2} - Hydrogen recovery $[-]$
Z - Axial position $[-]$

Greek letters

δ - Membrane thickness $[L]$
ΔH_j - Heat of the reaction j $\left[\frac{M\,L^2}{T^2 N}\right]$
ε - Void fraction $[-]$
ν_{ij} - Stoichiometric coefficient $[-]$
ρ_p - Permeate density $\left[\frac{M}{L^3}\right]$
ρ_r - Reaction density $\left[\frac{M}{L^3}\right]$

Subscripts

i = CH_4, CO, H_2, H_2O, CO_2.
j = 1, 2, 3 (reactions 1,2,3)
k = CH_4, CO, H_2, H_2O.
m= refer to membrane
p = refer to permeate side
R or r= refer to reaction side

Acknowledgement

This work has been supported by Brazilian funding agency CNPq (Grant n. 475934/2006-7).

References

Falco, M. D. T.; Di Paola, L.; Marrelli and Nardella, L.(2006) Simulation of large-scale membrane reformers by a two-dimensional model, *Chemical Engineering Journal*, 128, 115-125.

Froment, K. and Bischoff, K. B.(1990) *Chemical Reactor Analysis and Design*. John Wiley, New York.

Gallucci, F.; Paturzo, L.; Fama, A.; Basile, A.(2004) Experimental Study of the Methane Steam Reforming Reaction in a Dense Pd/Ag Membrane Reactor, *Industrial and Engineering Chemistry Research* , 43, 928-933.

Hou, K. ; Hughes, R. (2001): The kinetics of methane steam reforming over a $Ni/\alpha - Al_2O_3$ catalyst, Chemical Engineering Journal, v. 82, p.311-328.

Lin, Y.-M.; Liu, S.-L.; Chuanga, C.-H. and Chub, Y-T.(2003). Effect of incipient removal of hydrogen through palladium membrane on the conversion of methane steam reforming: experimental and modeling, *Catalysis Today*, 82, 127-139.

Ogden, J. M.(2001) Review of small stationary reformers for hydrogen production, *Report No. IEA/H2/TR-02/002*. Princeton, USA: Princeton University.

Ohmori, W. Y. T.; YU, W.; Yamamoto, A.; Endo, A.; Nakaiwa, M.; Hayakawa, T. and Itoh, N.(2005) Simulation of a porous ceramic membrane reactor for hydrogen production, *Int. J. Hydrogen Energy*, 30(10), 1071-1079, .

Poling, B. E.; Prausnitz. M. J.; O'Connell, J. P.(2004) *The Properties of Gases and Liquids*, 5th ed., McGraw-Hill.

Shu, J.; Grandjean, P. A. and Kaliaguine, S.(1994) Methane steam reforming in asymmetric Pd- and Pd-Ag/porous SS membrane reactors, *Applied Catalysis A: General*, 119, 305-325.

Sjardin, M.; Damen, K. J. and Faaij, A. P. C.(2006) Techno-economic prospects of small-scale membrane reactors in a future hydrogen-fuelled transportation sector, *Energy*, 31, 2523-2555.

Tong, J.; Matsumura, Y.; Suda, H. and Haraya, K.(2005) Experimental Study of Steam Reforming of Methane in a Thin (6 μM) Pd-Based Membrane Reactor, *Ind. Eng. Chem. Res.*, 44, 1454-1465.

Von Stryk O.(2002) User's Guide for DIRCOL - A Direct Collocation Method for the Numerical Solution of Optimal Control Problems, Version 2.1 of November 1999 (Updated: April 2002).

Xu, J. and Froment, G. F.(1989) Methane Steam Reforming, Methanation and Water-Gas Shift: I. Intrinsic Kinetics, *AIChE Journal* , 35(1), 88-96.

Proceedings of the 10th International Chemical and
Biological Engineering Conference - CHEMPOR 2008
Braga, Portugal, September 4-6, 2008
E.C. Ferreira and M. Mota (Eds.)

Evaluation of redundant measurements on the air quality monitoring network of Lisbon and Tagus Valley

José C.M. Pires, Fernando G. Martins[1], Maria C.M. Alvim-Ferraz, Maria C. Pereira
LEPAE, Departamento de Engenharia Química, Faculdade de Engenharia, Universidade do Porto, Rua Dr. Roberto Frias, 4200-465 Porto, Portugal.

Keywords: Principal component analysis, air quality, monitoring networks
Topic: Sustainable process-product development through green chemistry.

Abstract

The aim of this study was to evaluate redundant measurements in the air quality monitoring network (AQMN) of Lisbon and Tagus Valley (LTV). With this purpose, the minimum number of monitoring sites that should operate was achieved using principal component analysis (PCA). The air pollution data were colected in twenty monitoring sites during the period from January to December 2006. The air pollutants analysed were CO, NO_2, PM_{10} and O_3.

In this study, a different criterion for selection of the number of principal components (PCs) was applied. The PCs were selected representing at least 95% of the original data variance. Using this criterion, the PCs have more information about the air pollution data, increasing the confidence in the PCA results.

The PCA results showed that, from twenty studied monitoring sites, only ten for CO, eleven for NO_2, five for O_3 and nine for PM_{10} were needed to characterize the region. The air pollutant analysers corresponding to the redundant measurements can be installed in non-monitored regions, allowing the enlargement of the air quality monitoring network.

1 Introduction

The concerns about the negative effects of air pollution led to increased efforts to prevent and control the air pollution. As a consequence, the directives 1999/30/EC (EC Directive, 1999) and 2002/03/EC (EC Directive, 2002) defined the location of sampling points for the measurement of air pollutant concentrations. According to these directives, monitoring sites should be placed to provide data: (i) in areas within zones and agglomerations, where the population is likely to be directly or indirectly exposed to high concentrations (limit and target values were established as references); (ii) in other areas within zones and agglomerations which are representative of the general population exposure. However, redundant measurements of air pollutant concentrations should be avoid minimizing the costs relative to the management of the air pollutant analysers. Thus, the identification of the redundant measurements is an important task to be done for all AQMNs.

Principal component analysis (PCA) is a statistical method used for classification and regression tasks. It is a way of identifying patterns in data, finding their similarities and differences. The procedure started with the evaluation of the eigenvalues and eigenvectors of the covariance matrix of the standardized variables. The eigenvalues and eigenvectors are determined through the Equations 1 and 2, respectively.

$$\left|\mathbf{C}-\boldsymbol{\lambda}\mathbf{I}\right|=0 \tag{1}$$

$$\left(\mathbf{C}-\boldsymbol{\lambda}\mathbf{I}\right)\mathbf{T}=0 \tag{2}$$

[1] Corresponding author. Tel + 351-225081974. E-mail:fgm@fe.up.pt

where **C** is the covariance matrix of variables, **λ** is the vector of the eigenvalues, **I** is the identity matrix and **T** is the standardized weight values of each variable in the PCs (the eigenvectors). The PCs are then obtained, multiplying the original data set by the weights. Thus, PCs are linear combinations of the original variables and are orthogonal and uncorrelated to each other. They are obtained in such a way that the first PC explains the largest fraction of the original data variability, the second PC explains a smaller fraction of the data variance than the first one and so forth (Abdul-Wahab et al., 2005; Sousa et al., 2007; Wang and Xiao, 2004). To better clarify the influence of each original variable on the PCs, Varimax rotation is a rotational algorithm commonly applied to obtain the rotated factor loadings that represent the contribution of each variable on a specific PC.

PCA was recently applied for the identification of redundant measurements of air pollutant concentrations (Pires et al., 2008a, 2008b). Pires et al. (2008a, 2008b) applied PCA to identify similar air pollution behaviours in the AQMN of Oporto Metropolitan Area. According to these studies, only one monitoring site should operate in a region defined by a specific air pollution behaviour. Five air pollutants monitored at twelve sites were analysed. The results showed that only six monitoring sites should measured SO_2 concentrations, three for CO and NO_2 concentrations, and two for PM_{10} and O_3 concentrations.

The aim of the presented study was to evaluate redundant measurements in the air quality monitoring network (AQMN) of Lisbon and Tagus Valley (LTV), applying PCA to CO, NO_2, PM_{10} and O_3 concentrations data.

2 Data

The air quality data was collected from the monitoring sites integrated in the AQMN of LTV, managed by the Regional Commission of Coordination and Development of LTV, under the responsibility of the Ministry of Environment. The analysed air pollutants were CO, NO_2, PM_{10} and O_3 monitored in twenty monitoring sites: Alfragide (S1), Arcos (S2), Avenida da Liberdade (S3), Beato (S4), Camarinha (S5), Cascais (S6), Chamusca (S7), Entrecampos (S8), Escavadeira (S9), Laranjeiro (S10), Lavradio (S11), Loures (S12), Mem-Martins (S13), Odivelas (S14), Olivais (S15), Paio Pires (S16), Quebedo (S17), Quinta do Marquês (S18), Reboleira (S19) and Restelo (S20). Table 1 shows the main monitoring site characteristics, including the type and the main pollution sources associated to them (QualAr, 2008). The period considered was from January 2006 to December 2006. CO concentrations were obtained through non-dispersive infrared spectrometric method; NO_2 concentrations were monitored through chemiluminescence; PM_{10} concentrations were obtained through beta radiation attenuation; and O_3 concentrations were monitored by UV-absorption photometry (EC Directive, 1999, 2002). The monitoring was continuous and hourly averages were

Table 1. Site characteristics of the air quality monitoring network of Lisbon and Tagus Valley

Site	Type	Main pollution source	Site	Type	Main pollution source
S1	Urban	(Background)	**S11**	Urban	Industrial
S2	Urban	(Background)	**S12**	Urban	(Background)
S3	Urban	Traffic	**S13**	Urban	(Background)
S4	Urban	(Background)	**S14**	Urban	Traffic
S5	Urban	(Background)	**S15**	Urban	(Background)
S6	Urban	Traffic	**S16**	Suburban	(Background)
S7	Rural	(Background)	**S17**	Urban	Traffic
S8	Urban	Traffic	**S18**	Urban	(Background)
S9	Urban	Industrial	**S19**	Urban	(Background)
S10	Urban	Traffic	**S20**	Urban	(Background)

(concentrations expressed in μg m^{-3}). All the equipments were submitted to a rigid maintenance program, being periodically calibrated.

The data were organized in such a way that each column had the hourly average concentrations of a specific air pollutant at a specific monitoring site. To be possible to apply the PCA, the pollutant concentrations must be available at the same time in all monitoring sites. Thus, the lines with missing data were removed from the analysis. Concentrations were Z standardized to have zero mean and unit standard deviation.

3 Results and Discussion

PCA was applied as a classification method to group monitoring sites with redundant measurements of air pollutant concentrations during the analysed period. The first step to apply this method is the selection of the number of PCs. Kaiser criterion, which selects PCs with eigenvalues greater than 1, is commonly used for this purpose (Yidana et al., 2008); as this criterion do not usually achieve 95% of the original data variance (Mendiguchía et al., 2004; Pires et al., 2008a, 2008b), in this study, a different criterion (ODV_{95}) was also used, aiming to select PCs representing at least 95% of the original data variance; this procedure allowed to obtain more information about original data contained in the selected PCs and to increase the confidence in the PCA results.

Table 2 shows, as an example, the main results (rotated factor loadings, eigenvalues, variance and cumulative variance) of PCA application to PM_{10} concentrations data. Considering ODV_{95} criterion, the first nine PCs need to be taken into account for analysing the PM_{10} concentrations. The factor loadings represented both how the original variables are weighted for each PC and the correlation between the original variables and the PCs. Varimax rotation was the rotation algorithm used to maximize the squared loadings of the columns, obtaining the rotated factor loadings. Therefore, each PC presents high loadings for some variables and low loadings for others, facilitating the interpretation of the PCs in terms of the original variables. The rotated factor loadings in bold indicate the original variables that mostly influence the correspondent PC. Thus, PC1 had important contributions of S8, S10, S14 and S15 sites, while PC6 was heavily loaded by S5 and S17 sites. PC8 had important contributions of S13, S18 and S19 sites. S11, S7, S6, S3, S12 and S9 sites were significantly associated with PC2, PC3, PC4, PC5, PC7 and PC9, respectively. The monitoring sites grouped in the same PC presented redundant measurements. Thus, only nine monitoring sites should measure the PM_{10} concentrations.

Figure 1 shows the location of the monitoring sites and the results of the PCA application to the concentrations of all air pollutants. The groups of monitoring sites with redundant measurements can be explained by the location of emission sources and the variability of the wind direction as it was explained in our previous studies (Pires et al., 2008a, 2008b). As a rural site, S7 presented a specific pollution behaviour. Thus, it was not coupled with other sites. The monitoring sites in Setúbal city (S2, S5 and S17) presented redundant measurements due to their proximity. Thus, the geographic location of the monitoring sites was also important in the formation of the groups of monitoring sites. Despite the geographic proximity to other monitoring sites, S3 site presented different air pollution behaviour for NO_2 and PM_{10}. This site is highly influence by traffic, presenting the highest concentrations of these air pollutants.

Concluding, from the twenty studied monitoring sites, only ten for CO, eleven for NO_2, five for O_3 and nine for PM_{10} were needed to characterize the region. The air pollutant analysers corresponding to the redundant measurements can be installed in non-monitored regions, allowing the enlargement of the air quality monitoring network.

Figure 1. Location of monitoring sites and the PCA results using: (a) CO concentrations data (CO concentrations were not measured at S7 site); (b) NO_2 concentrations data (S19 site did not present 75% of the annual data); (c) PM_{10} concentrations data (PM_{10} concentrations were not measured at S2, S4 and S16 sites; S1 and S20 sites did not present 75% of the annual data); (d) O_3 concentrations data (O_3 concentrations were not measured at S3, S6, S11 and S17 sites).

Table 2. Main results of the PCA application to PM_{10} concentrations data

Site	PC1	PC2	PC3	PC4	PC5	PC6	PC7	PC8	PC9
S3	-0.403	-0.203	-0.145	0.269	**0.725**	-0.238	-0.150	0.252	0.185
S5	-0.241	-0.310	-0.422	0.245	0.170	**-0.626**	-0.064	0.285	0.186
S6	-0.252	-0.108	-0.131	**0.863**	0.168	-0.182	-0.151	0.256	0.091
S7	-0.173	-0.222	**-0.876**	0.122	0.093	-0.203	-0.118	0.215	0.138
S8	**-0.761**	-0.184	-0.136	0.280	0.248	-0.225	-0.161	0.275	0.154
S9	-0.270	-0.440	-0.229	0.131	0.187	-0.225	-0.168	0.200	**0.702**
S10	**-0.535**	-0.276	-0.355	0.200	0.225	-0.346	-0.053	0.327	0.316
S11	-0.198	**-0.845**	-0.251	0.116	0.136	-0.209	-0.111	0.198	0.225
S12	-0.343	-0.201	-0.211	0.348	0.182	-0.254	**-0.611**	0.368	0.199
S13	-0.318	-0.261	-0.310	0.290	0.134	-0.267	-0.156	**0.683**	0.065
S14	**-0.519**	-0.190	-0.233	0.313	0.224	-0.178	-0.306	0.456	0.187
S15	**-0.585**	-0.235	-0.291	0.224	0.223	-0.313	-0.223	0.393	0.188
S17	-0.336	-0.216	-0.212	0.214	0.206	**-0.683**	-0.256	0.310	0.176
S18	-0.336	-0.186	-0.260	0.365	0.233	-0.301	-0.114	**0.595**	0.259
S19	-0.395	-0.177	-0.188	0.232	0.236	-0.287	-0.319	**0.590**	0.240
Eigenvalue	11.09	0.92	0.56	0.40	0.33	0.31	0.24	0.20	0.19
Variance (%)	73.94	6.13	3.76	2.68	2.23	2.05	1.57	1.35	1.29
Cumulative variance (%)	73.94	80.07	83.83	86.51	88.74	90.80	92.37	93.71	95.00

4 Conclusions

This study aims the identification of redundant measurements in AQMN of LVT through the application of PCA. PCA was applied as a classification method, coupling the monitoring sites with redundant measurements.

The results showed that, from twenty studied monitoring sites, only ten for CO, eleven for NO_2, five for O_3 and nine for PM_{10} were needed to characterize the region. The air pollutant analysers corresponding to the redundant measurements can be installed in non-monitored regions, allowing the enlargement of the air quality monitoring network.

Acknowledgements

Authors are grateful to *Comissão de Coordenação da Direcção Regional de Lisboa e Vale do Tejo* for kindly providing the air quality data. This work was supported by *Fundação para a Ciência e Tecnologia* (FCT). J.C.M. Pires also thanks the FCT for the fellowship SFRD/BD/23302/2005.

References

Abdul-Wahab, S.A., Bakheit, C.S., Al-Alawi, S.M. (2005). Principal component and multiple regression analysis in modelling of ground-level ozone and factors affecting its concentrations. *Environmental Modelling & Software*, 20(10), 1263-1271.

EC Directive (1999). Council Directive 99/30/EC, relating the limit values for sulphur dioxide, nitrogen dioxide and oxides of nitrogen, particulate matter and lead in ambient air. *Official Journal of the European Communities*, L163, 41-60.

EC Directive (2002). Council Directive 2002/3/EC, relating to ozone in ambient air. *Official Journal of the European Communities*, L67, 14-30.

Mendiguchía, C., Moreno, C., Galindo-Riaño, M.D., García-Vargas, M. (2004). Using chemometric tools to assess anthropogenic effects in river water: A case study: Guadalquivir River (Spain). *Analytica Chimica Acta*, 515, 143-149.

Pires, J.C.M., Sousa, S.I.V., Pereira, M.C., Alvim-Ferraz, M.C.M., Martins, F.G. (2008a). Management of Air Quality Monitoring using Principal Component and Cluster Analysis – Part I: SO_2 and PM_{10}. *Atmospheric Environment*, 42, 1249-1260.

Pires, J.C.M., Sousa, S.I.V., Pereira, M.C., Alvim-Ferraz, M.C.M., Martins, F.G. (2008b). Management of Air Quality Monitoring using Principal Component and Cluster Analysis – Part II: CO, NO_2 and O_3. *Atmospheric Environment*, 42, 1261-1274.

QualAr (2008). Environmental Institute database for air quality website. http://www.qualar.org/ (acessed February 2008)

Sousa, S.I.V., Martins, F.G., Alvim-Ferraz, M.C.M., Pereira, M. C. (2007). Multiple linear regression and artificial neural networks based on principal components to predict ozone concentrations. *Environmental Modelling & Software*, 22, 97-103.

Wang, S., Xiao, F. (2004). AHU sensor fault diagnosis using principal component analysis method. *Energy and Buildings*, 36(2), 147-160.

Yidana, S.M., Ophori, D., Banoeng-Yakubo, B. (2008). A multivariate statistical analysis of surface water chemistry data — The Ankobra Basin, Ghana. *Journal of Environmental Management*, 86, 80-87.

Proceedings of the 10th International Chemical and
Biological Engineering Conference - CHEMPOR 2008
Braga, Portugal, September 4-6, 2008
E.C. Ferreira and M. Mota (Eds.)

Comparison of dynamic data reconciliation estimators and gross errors detection strategies

Andrea C. Farias, Ricardo G. Duraiski, Argimiro R. Secchi, Jorge O. Trierweiller
Chemical Engineering Department, Federal University of Rio Grande do Sul (UFRGS)
R. Luis Englert, s/n. Campus Central. CEP: 90040-000 - Porto Alegre - RS - BRAZIL

Keywords: Data reconciliation, Kalman filters, MHE approach, Gross Error Detection
Topic: Systematic methods and tools for managing the complexity.

Abstract

The purpose of this work is to compare dynamic data reconciliation estimators and algorithms for detecting gross errors. Also is proposed a methodology for measure the performance of the algorithms. The problem of dynamic data reconciliation is treated using five different Kalman filters formulations and a moving horizon estimator approach. The estimators are compared using a nonlinear dynamic example, in transient scenarios. The problem of gross error detection and bias estimation is also treated using two different algorithms combined with the global test: The Generalized Likelihood Ratio (GLR), proposed by Narashiman and Mah (1988), and a bias detection method, proposed by McBrayer and Edgar (1995). The data reconciliation results show there are not significant differences in quality of the reconciled states obtained by the different estimators. On the other hand, the time spent in the data reconciliation step differs significantly among the estimators. The implementation of the proposed gross error detection strategies shows the GLR is simpler and less computation time spending than the algorithm proposed by McBrayer and Edgar. In this work is showed an alternative implementation of the combined use of the global test and the GLR which consists in evaluating the global test for a finite number of times and not in a cumulative way, as proposed in the original GLR.

1. Introduction

A real-time on-line optimization provides set-points to the distributed control system and therefore maintains the process near its optimum operating conditions. This optimization requires an accurate process model and reconciled process data needful to specify the current status of the plant model and to estimate model parameters for plant-model matching. The main goal of data reconciliation is to adjust process measurements with random errors by having them satisfy material and energy balance constraints. During the data reconciliation it is natural to assume the presence of random, normally distributed errors with zero mean and known variances, to be present in the process data. However, a different type of error – gross error – sometimes is present in the data. The presence of gross error invalidates the statistical basis of data reconciliation procedure. When flawed information is used for state estimation and process control, the state of the system is misrepresented and the resulting control performance may be poor and can lead to suboptimal and even unsafe process operation because the reconciled values will exhibit '*smearing*' when compared with the true values (Liebman, Edgar & Lasdon, 1992). The elimination of less-frequent gross errors is achieved by gross error detection techniques. The purpose of this work is to compare dynamic data reconciliation estimators and algorithms for detecting gross errors. The problem of dynamic data reconciliation is treated using five different Kalman filters formulations and a Moving Horizon Estimator (MHE) approach. The estimators are compared using a nonlinear dynamic example, in transient scenarios. The Kalman filters formulations are (Salau et al., 2007): Extended (EKF), Constrained Extended (CEKF), Discrete Extended (DEKF), Modified Discrete Extended (MDEKF), and Continuous Extended (CtEKF). The MHE formulation is similar to a nonlinear model-predictive control (NMPC). The main difference between those algorithms is the NMPC optimizes and predicts forward in time,

while MHE optimizes and smoothes backward in time. Additionally, in the MHE, the estimates of the past measured state and input variables over finite history horizon are adjusted to optimally satisfy the modeling equations. The problem of gross error detection (GED) and bias estimation is also treated using two different algorithms combined with the global test: The GLR, proposed by Narashiman and Mah (1988), and a bias detection method, based on the moving horizon strategy, proposed by McBrayer and Edgar (1995). The algorithms were compared using the five different Kalman formulations. Moreover, an alternative implementation of the combined use of the global test and the GLR, which consists in evaluating the global test for a finite number of times and not in a cumulative way, as proposed in the original GLR, is presented.

2. Problem Formulation

Consider the dynamic systems represented by nonlinear differential-algebraic equations as shown below:

$$\dot{x}(t) = f[x(t), u(t), t, p(t)] + w(t) \qquad y(t) = h(x(t), u(t), t) + v(t)$$

Where x denotes the states, u the deterministic inputs, p the model parameters, and y the vector of measured variables. The process-noise vector, w(t), and the measurement error, v(t), are assumed to be a white Gaussian random process with zero mean and covariance Q(t) and R(t), respectively.

In the formulations, the matrices Q and R are the tuning parameters for reconciling the model with the process measurements and their statistical significance are a measure of confidence in the model and in the process sensors, respectively.

3. The Estimators formulations

The extended Kalman filter has been the most widely-used technique for nonlinearly-constrained weighted least-squares estimation problems. The EKF formulations (Table 1) use local linearization to extend the scope of the Kalman filter to systems described by nonlinear ordinary differential equations. The advantages of the EKF formulations are their simplicity, the recursivity of the algorithms, and their modest computational load. These formulations are suitable for real-time industrial-scale applications (Becerra et al., 2001). On the other hand, the main advantages of the moving-horizon approach over the extended Kalman filter are its capability of handling path constraints on the variables and its flexibility with respect to the choice of the estimation criterion. Its disadvantage is, for on-line implementation, the high computational load for large estimation horizons.

Table 1. EKF and MHE formulations

	Prediction	**Correction**
EKF	$\hat{x}_k^- = \hat{x}_{k-1}^+ + \int_{k-1}^{k} f(\hat{x}, u, t)dt$ $P_k^- = P_{k-1}^+ + \int_{k-1}^{k} \left[F(t)P(t) + P(t)F(t)^T + Q(t)\right]dt$	$\hat{x}_k^+ = \hat{x}_k^- + K_k[y_k - \hat{y}_k] \quad K_k = P_k^- H_k^T [H_k P_k^- H_k^T + R]^{-1}$ $P_k^+ = [I - K_k H_k]P_k^-[I - K_k H_k]^T + K_k R K_k^T$
CtEKF	$\hat{x}_k^- = \hat{x}_{k-1}^+ + \int_{k-1}^{k} f(\hat{x}(t), u, t)dt$ $P_k^- = P_{k-1}^+ + \int_{k-1}^{k} \left[\begin{array}{l} F(t)P(t) + P(t)F(t)^T - \\ - P(t)H(t)R^{-1}H(t)P(t) + Q \end{array}\right]dt$	$K_k = P_k^- H_k^T [H_k P_k^- H_k^T + R]^{-1}$ $\hat{x}_k^+ = \hat{x}_k^- + K_k[(y_k - \hat{y}_k)]$
CEKF	$\hat{x}_k^- = \hat{x}_{k-1}^+ + \int_{k-1}^{k} f(\hat{x}, u, t)dt$	$\min_{\hat{w}_{k-1}} \left\{\psi_k = \hat{w}_k \left(P_{k-1}^+\right)^{-1} \hat{w}_k^T + \hat{v}_k (R_d)^{-1} \hat{v}_k^T\right\}$ $\hat{x}_k^+ = \hat{x}_k^- + \hat{w}_k, \quad y_k = h(\hat{x}_k^+, k) + \hat{v}_k, \quad \hat{x}_{min} \le \hat{x}_k^+ \le \hat{x}_{max}$ $P_k = Q_d + \varphi_k P_{k-1} \varphi_k^T - \varphi_k P_{k-1} H_k^T [H_k P_{k-1} H_k^T + R_d]^{-1} H_k P_{k-1} \varphi_k^T$

DEKF	$\hat{x}_k^- = \hat{x}_{k-1}^+ + \int_{k-1}^{k} f(\hat{x},u,\tau)d\tau$, $P_k^- = \varphi_k P_{k-1}^+ \varphi_k^T - Q_d$	$K_k = P_k^- H_k^T [H_k P_k^- H_k^T + R_d]^{-1}$, $P_k^+ = P_k^- [I - K_k H_k]$ $\hat{x}_k^+ = \hat{x}_k^- + K_k [y_k - \hat{y}_k]$
MDEKF	$\hat{x}_k^- = \hat{x}_{k-1}^+ + \int_{k-1}^{k} f(\hat{x},u,\tau)d\tau$	$K_k = P_k^- H_k^T [H_k P_k^- H_k^T + R_d]^{-1}$ $\hat{x}_k^+ = \hat{x}_k^- + K_k [y_k - \hat{y}_k]$ $P_k = Q_d + \varphi_k P_{k-1} \varphi_k^T - \varphi_k P_{k-1} H_k^T [H_k P_{k-1} H_k{}^T + R_d]^{-1} H_k P_{k-1} \varphi_k^T$
MHE	$\hat{x}_i^- = \hat{x}_{i-1}^+ + \int_{t_{i-1}}^{t_i} f(\hat{x},u,t)dt = F(x_{i-1},u_{i-1})$ Where i=(k-N),..K $x(0) = x_0$ $\hat{y}_i^- = h(\hat{x}_i^-)$	$\min_{\hat{w}_{k-N-1},..\hat{w}_k,\hat{v}_{k-N},..,\hat{v}_k} \left\{ \psi_k = \left(\hat{w}_{k-N-1}^+\right)^T \left(P_{k-N}^-\right)^{-1} \left(\hat{w}_{k-N-1}^+\right) + \right.$ $\left. + \sum_{j=k-N}^{k} \left(\hat{v}_j^+\right)^T R^{-1} \left(\hat{v}_j^+\right) + \sum_{j=k-N}^{k} \left(\hat{w}_j^+\right)^T Q^{-1} \left(\hat{w}_j^+\right) \right\}$ St to: $\hat{x}_{k-N}^+ = \hat{x}_{k-N}^- + \hat{w}_{k-N-1}$, $\hat{x}_{j+1}^+ = F(\hat{x}_j^+) + \hat{w}_j$ $j = k-N,..,k-1$ $y_j = h(\hat{x}_j^+) + \hat{v}_j$, $\hat{x}_{min} \le \hat{x}_j^+ \le \hat{x}_{max}$ $j = k-N,..,k$

4. Gross Error Detection Strategies

The treatment of gross errors can be divided into three stages. In the first stage, gross error detection is performed to certify whether gross errors are present in the measurements or not. If the presence of gross errors is detected, the next stage is the identification of the sources of those errors. The final stage is the elimination of the gross errors. The global test was introduced by Ripps (1965) and its conclusion that no bias is present obviates the identification of gross error location. The global test was used combined with the GLR strategy, as the first indicative of the presence of gross error. The complete algorithm can be found in Narashiman and Jordache (2000). The GLR is based on the maximum likelihood ratio principle used in statistics. The main advantage is the GLR test is capable of identify different types of gross errors. The complete algorithm can be found in Narasimhan and Mah (1988). Another algorithm used in the present work was tailored for using with MHE approaches. The gross error detection and estimate are made by a different data reconciliation problem. The objective function includes the gross error as a parameter. The complete algorithm can be viewed in McBrayer and Edgar (1995), which has a questionable assumption by using the criterion of 30% difference between the base case and the measurements.

5. Case of study

The case of study presented in this work is a reactor where an exothermic irreversible reaction is taking place in a continuous stirred tank reactor. The modeling equations in dimensionless form are given by (Limqueco and Kantor, 1990). The nominal parameter values are shown in Table 2**Error! Reference source not found.**.

$$\frac{dx_1}{d\tau} = -\phi x_1 k(x_2) + q(x_{1f} - x_1) \qquad \frac{dx_2}{d\tau} = \beta \phi x_1 k(x_2) - (q+\delta)x_2 + \delta u + q x_{2f}$$

Where x_1 is the dimensionless concentration, x_2 is the dimensionless temperature and u is the dimensionless cooling jacket temperature.

Table 2. Model Parameters

Parameter	ϕ	β	δ	γ	q	x_{1f}	x_{2f}	x_{1S} (ss point)	x_{2S} (ss point)
Value	0.072	8	0.3	20	1.0	1.0	0	0.856	0.885

The algorithms and the simulations were implemented in MATLAB 5.3. The integration algorithm was *ode*15*s* and the nonlinear optimization was solved by using the function *fmincon*.

6. Results and Discussion

Initially, the performances of the estimators were compared. The model was subjected to disturbances in the input concentration x_{1f}. The disturbances and the simulated outputs,

without noise, can be viewed in the Figure 1. After the simulation, white random noises, with known variances were added to the outputs and then given as the measurements for the estimators. The used estimators' parameters are listed in Table 3.

Table 3. Estimators parameters

$$Q = \begin{bmatrix} 1e\text{-}4 & 0.2e\text{-}4 \\ 0.2e\text{-}4 & 0.2e\text{-}4 \end{bmatrix} \qquad R = \begin{bmatrix} 2.4e\text{-}4 & 0 \\ 0 & 2.4e\text{-}4 \end{bmatrix}$$

Parameter	Sample Time (Δt)	Qd	Rd	White noise variance	MHE horizon
Value	0.25	(Q × Δt)	(R / Δt)	2.4×10^{-4}	5

The results were obtained after a set of 10 runs, with different random noises added into each run. The data reconciliation results for all estimators are shown in Figure 2 and Figure 3.

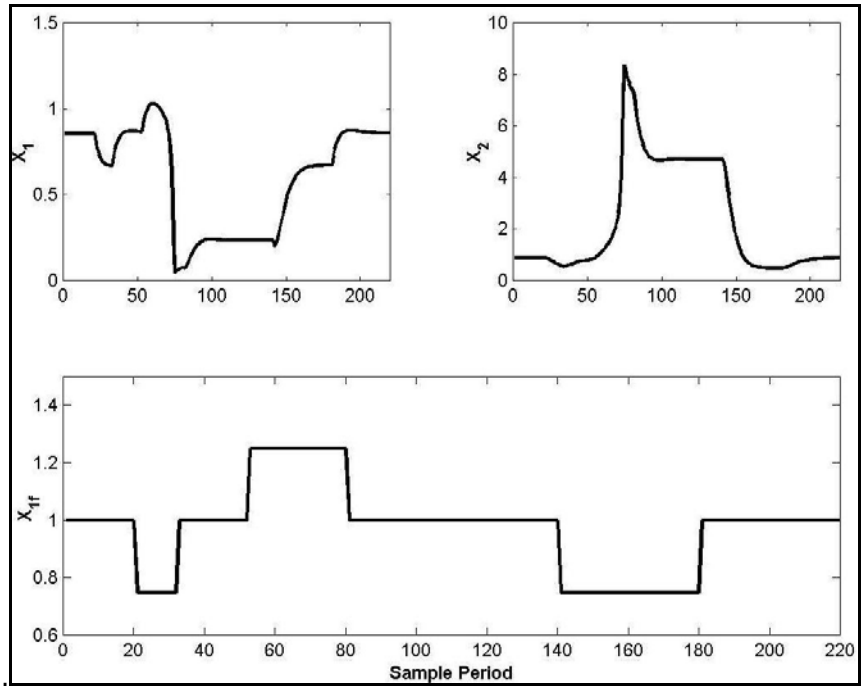

Figure 1. Input disturbances in X_{1f} and Outputs simulated variables

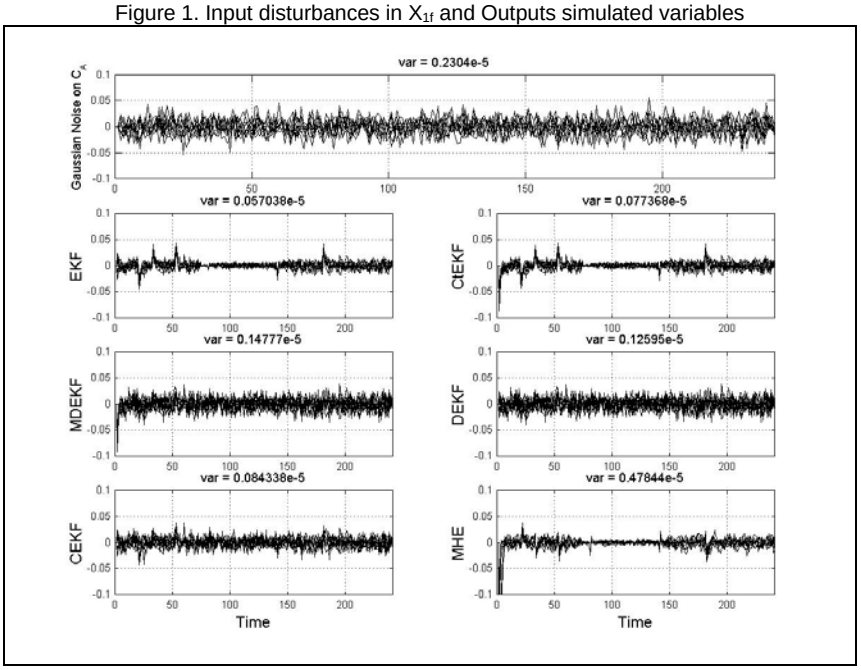

Figure 2. Difference between the reconciled variable X_1 and the measured variable X_1, for all estimators.

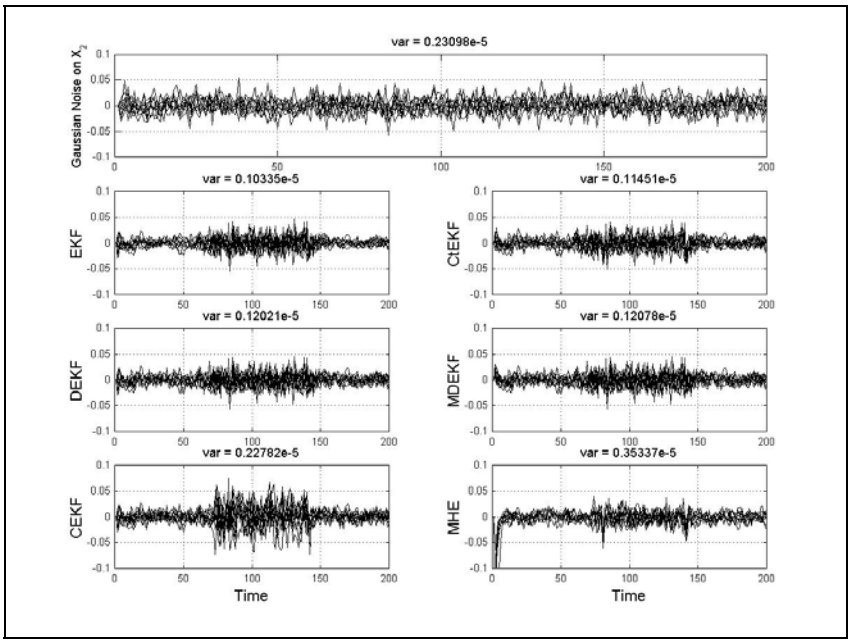

Figure 3. Difference between the reconciled variable X_2 and the measured variable X_2, for all estimators

All estimators, excluding MHE, have shown different attenuation degrees, which can be proved by the variance shown in each figure. Comparing among all estimators, the EKF have shown the best performance based on noise attenuation. The noise variance has been reduced in 75% for concentration and 55% for temperature. In Table 4, the noise attenuation percentages related to the measured variables are shown. It is important to notice that exist a relationship between the nonlinearity of the model (in different operation points) with the quality of the reconciliation in each variable. Hence, there is a variable attenuation degree related with the operating point. The estimators which strongly have shown this behavior are: EKF, CEKF, CtEKF, and MHE. The estimators MDEKF and DEKF have shown stability related to this behavior with a small modification in the noise variance to different regions. This is due to the discrete form of prediction of the error covariance matrix in these two formulations.

The gross error detection tests were performed for scenario where a bias of -0.08 was added in x_1. The confidence degree of the global test was 95% and the bias value was chosen to ensure that this value would be out of this region. The MHE was not tested due to its high computational time.

Table 4. Noise attenuation percentage for all estimators

Estimator	Attenuation on x_1	Attenuation on x_2
EKF	75.24	55.26
CtEKF	66.42	50.43
CEKF	63.39	1.37
DEKF	45.33	47.96
MDEKF	35.86	47.71
MHE	-107.66	-16.77

Table 5. Computing time for all estimators

Estimator	Proposed GLR	McBrayer and Edgar
EKF	57.39	452.95
CtEKF	56.12	448.12
CEKF	70.23	474.71
DEKF	50.41	408.18
MDEKF	50.32	391.93

The implementation of the proposed gross error detection strategies shows the GLR is simpler and less computation-time spending than the algorithm proposed by McBrayer and Edgar (1995). In Table 5 is shown the comparison of computing time between all the sets (estimators + detector algorithms). The set MDEKF + GLR has presented the best performance. Figure 4 shows the result for the gross error detection problem with a bias in x_1.

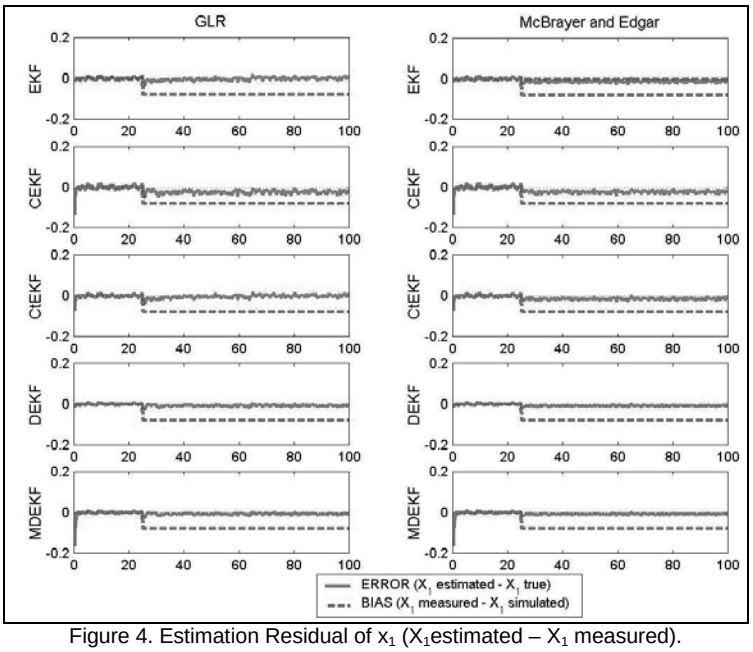

Figure 4. Estimation Residual of x_1 (X_1estimated – X_1 measured).

It can be observed in Figure 4 that all the sets have presented similar good results, eliminating the bias and providing good reconciled values. Only the CEKF have presented a biased estimative.

7. Conclusions

- The EKF is the best formulation to reduce noise variance and MDEKF presents the best cost/benefit because its easy implementation and stability related with the linearization and
- The MHE did not present noise attenuation and has excessively high computational time to be used with on-line applications.
- GLR was the best GED strategy based on the criterion: performance versus computing time and Global test is useful and should be included in the McBrayer and Edgar's algorithm replacing the criterion of difference between the base case and the measurements to detect gross errors.
- Both gross error detection and estimation algorithms have obtained a good estimate of the bias.

8. References

Abu-el-zeet, Z. H., Becerra, V. M., Roberts, P. D., (2002). Combined bias and outlier identification in dynamic data reconciliation. *Comp. and Chem. Engng*., 26 (2), 921– 935.

Becerra, M., Roberts D., Griffiths W. (2001). Applying the extended Kalman filter to systems described by nonlinear differential-algebric equations. *Control Eng. Pract.*,9, 267-281.

Liebman, M. J., Edgar, T. F., Lasdon, L. S. (1992). Efficient data reconciliation and estimation for dynamic processes using nonlinear programing techniques. *Comp. and Chem. Engng*, 16 (10/11), 963–986.

Limqueco L. C., Kantor J. C. (1990). Nonlinear output feedback control of an exothermic reactor. *Comp. and Chem. Engng* 14, 427

McBrayer, K., Edgar, T. F. (1995). Bias detection and estimation in dynamic data reconciliation. *Journal of Process Control*, 5 (4), 285–289.

Narasimhan, S., Mah, R. S. H. (1988). Generalized likelihood ratios for gross error identification in dynamic processes. *AIChE J.*, 34 (8), 1321

Narashiman S., Jordache C. (2000). Data Reconciliation and Gross Error Detection, *Gulf Publis. Company.*

Ripps, D. L. (1965). Adjustment of experimental data. Chemical Engineering Progress *Symposium Series*, 61, 8.

Salau, N. P., Secchi, A. R., Trierweiler, J. O. (2007). Five formulations of extended kalman filter: Which is the best for D-RTO? *in Proceedings of the ESCAPE 17*, paper T3-486.

Proceedings of the 10th International Chemical and
Biological Engineering Conference - CHEMPOR 2008
Braga, Portugal, September 4-6, 2008
E.C. Ferreira and M. Mota (Eds.)

Risk estimation of compost application in agriculture: evaluating metal accumulation and biotransfer

Millic Gil[1*], Marta Herva[1], Amaya Franco[2], Enrique Roca[1]

[1] Dept. of Chemical Engineering, School of Engineering, University of Santiago de Compostela, Campus Sur, 15782 Santiago de Compostela, Spain.
[2] Process Engineering Group, Marine Research Institute IIM-CSIC Eduardo Cabello, 6 - 36208 Vigo, Spain.

Keywords: Compost; Metals; Accumulation; Exposure; Risk assessment.
Topic: Sustainable process-product development through green chemistry.

Abstract

Composting is an attractive technology for diverting solid organic waste from landfill disposal. Furthermore, compost allows the improvement in nutrients content and soil structure. However, different quality compost can be obtained depending on the origin of its raw materials (urban residues, grass and forest residues, sludge, etc.). In some cases, the presence of heavy metals may become a source of risk in a long-term scenario of compost application for crop production.

In this work, an environmental risk assessment of compost application for agricultural crop production was carried out considering the heavy metal (Cu, Cr, Cd, Pb, Ni and Zn) content of different types of compost (green, green mixed with sewage sludge wood residues, organic urban waste, etc). Accumulation and biotransfer of heavy metals to the food chain, as well as the final human exposure by different pathways, was estimated by a multicompartmental model considering a number of temporal horizons (5 to 100 years) of compost application. In general, the hazard indexes (HI) obtained for the considered scenarios were quite low. Thus, it can not be considered as a direct risk source to human health. However, in some cases HI reached values around 0.5, what suggested that a more precautionary attitude should be adopted towards this practice, specially bearing in mind that soil pH has an important contribution to uncertainty, so this behaviour could be modified if compost was applied in other scenarios with different soil characteristics and pluviometry.

1 Introduction

Composting can be defined as a humification process of the organic matter under controlled conditions and in absence of soil resulting in compost. Compost acts as a bearer of nutrients to the soil, improving its structure and helping to reduce the erosion and the absorption of water and nutrients by plants. It offers a number of advantages in comparison with other mechanisms of elimination of residues. However, European legislation has become more restrictive with the priority pollutants content in residues that can be used as raw materials in the production of fertilizers (European Commission, 1999; European Commission, 2001). The restrictions stated regarding the quality of raw materials employed for the compost manufacture, and the compost itself, affects the use of compost as fertilizer in agriculture, as well as the kind of raw material that can be used.

Nowadays, there are diverse types of compost, which are characterized by the origin of its raw materials: urban residues, grass and forest residues, wastewater treatment sludge, other organic residues, and mixtures of them. Depending on the raw material, the presence of

* Corresponding author. Tel + 34-981-563100 Ext. 16772. E-mail: millicg@usc.es

potentially toxic elements (PTEs) for the human health and the environment (persistent organic pollutants – POPs - or heavy metals) may become important (Rojas, 2004).

Variations in some toxic metal concentrations contained in compost (Cd, Cr, Pb, Ni, Zn, Cu among others) have been detected, in some cases exceeding the thresholds values for these parameters (Greenway and Song, 2002). Consequently, in a long-term application scenario, compost for the production of agricultural crops must be controlled by certain procedures. The presence of high concentrations and the possible chemical and physical associations occurring in natural systems can cause the accumulation of heavy metals in soil, and it may pose a risk since they can be transferred to the food web. Environmental Risk Assessment could help on establishing safety conditions for compost application for agricultural crops and pasture production (Franco et al, 2006). In this sense, the considered mechanisms of transfer, accumulation and exposure take great importance in the estimation of human exposure to heavy metals transferred from the applied compost.

In this work, an incremental environmental risk assessment for the application of different types of compost for agricultural crop production was carried out considering the heavy metals (Cu, Cr, Cd, Pb, Ni and Zn) content. Exposure doses were calculated applying a multicompartmental model and later compared to reference doses to obtain the corresponding hazard quotient for the considered scenarios. A sensitivity analysis was also carried out to evaluate the contribution of the different variables considered in the model to uncertainty.

2 Materials and Methods

Characterization of the Scenario

The Environmental Risk Assessment (ERA) for the application of compost containing heavy metals as fertilizer in the production of agricultural crops (corn and garlic) and pasture was carried out. A conceptual model for the scenario of application of compost can be seen in Figure 1.

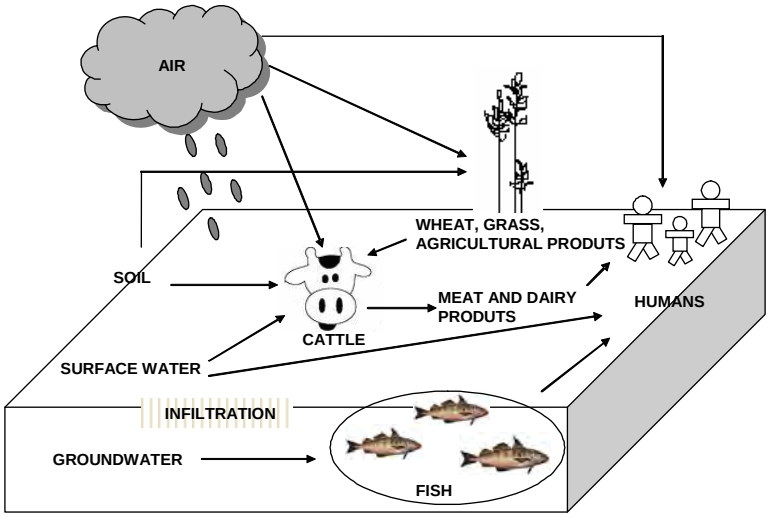

Figure 1. Conceptual model for the Environmental Risk Assessment.

Fertilizers of different characteristics (five types of compost, mineral-N as fertilizer and a mixture of 50% mineral-N with 50% of compost) found in the literature (Greenway and Song, 2002; Rosal et al, 2007) were used for this risk assessment, as well as reference limits from Spanish legislation for different compost quality (A, B and C). They have been named as C1 (Grass and Leaves), C2 (Mixture of Green and Sludge Waste), C3 (Vegetable Waste), C4

(Wood Waste), C5 (Municipal Solid Waste MSW), C6 (N-Mineral) and C7 (50% C5 – 50% C6). Table 1 shows heavy metal content in the different fertilizers and precipitation rates in the studied area.

Table 1. Heavy metal content in compost and precipitation rates for the considered scenarios

Compost / Law thresholds	Excessive precipitation (m^3/year)	Precipitation rate (m^3/year)	Heavy metal concentration (mg/kg)					
			Cd	Cu	Cr	Ni	Pb	Zn
C1 (Grass and Leaves) [(a)]	0.945		1.5	50.2	23.9	15.0	117.2	220.4
C2 (Green and Mixed Waste Sludge) [(a)]		2.7	3.2	140.3	30.3	16.5	133.5	354.6
C3 (Vegetable Waste) [(a)]		2.7	0.20	10.8	9.0	5.8	13,7	25.9
C4 (Wood Waste) [(a)]		2.7	0.18	10.7	8.6	5.7	17.3	35.8
C5 (Municipal Solid Waste – MSW -) [(b)]	0.1857	2.7	1.5	25	32	20	42	33
C6 (N-Mineral) [(b)]		0.58	1.3	20	29	20	39	28
C7 (50C – 50M) [(b)]		0.58	1.5	24	21	22	36	32
RD 824/2005-A [(c)]	0.945	2.7	0.7	70	70	25	45	200
RD 824/2005-B [(c)]		2.7	2	300	250	90	300	500
RD 824/2005-C [(c)]		2.7	3	400	300	100	200	1000

(a) Greenway and Song (2002)
(b) Rosal et al (2007)
(c) Spanish Government (2005)

Composts C5 to C7, were applied in agricultural soils in which rotatory crops of wheat-garlic-wheat were cultivated.

Apart from heavy metal concentration in compost, other data are necessary to carry out an environmental risk assessment of the application of compost, like soil properties or application rates (Table 2). Thus, using the information provided by the studies above mentioned, potential risks on human health (including possible carcinogenic effects) derived from the presence of various metals were assessed. The analysis was carried out in different temporal horizons (3, 5, 10, 50 and 100 years). Different exposure pathways like intake of meat, milk, wheat and water, inhalation and skin contact were considered, as well as other influencing factors like the exposure time.

To predict metal concentrations in soil, three equations were employed for each metal: a mass balance model for the proper estimate of metal accumulation in soil, and two multi-correlation models to estimate the uptake by plants from soil and the free metal concentration in soil solution. The exposure model was constituted by six equations, two of them being food-chain models for the estimation of metal concentration in the meat and milk of cattle. The remaining equations were employed to assess human exposure through the pathways considered: 1) ingestion of cattle meat and milk, 2) ingestion of soil, 3) inhalation of soil, 4) dermal contact with soil, and 5) ingestion of wheat. The latter route was considered only for the data of Rosal et al (2007).

Table 2- General characteristics regarding compost application.

Compost		**Source**
- Application rate	7.5 m^3/ha·year	Rosal et al, (2007)
Soil		
- Initial HM concentration	0.23 mg/kg	Franco et al, (2006)
- O.M.	36%	Rosal et al, (2007)

Estimation of Hazard Quotients

The quantification of the potential non-carcinogenic risk was obtained through the determination of a Hazard Quotient (HQ), which was calculated dividing the individual doses of each metal by its Reference Dose (RfD). Carcinogenic effects were evaluated multiplying the estimated dose by a Slope Factor. In this study, the oral, inhalation and dermal routes were considered. However, studies involving different routes of exposure were not always available. Thus, route-to-route extrapolations were needed when no specific dose-response data were present. Values of the HQ lower than 1.0 are considered as indicative of acceptable risk.

The HQ was calculated using equation [1]:

$$HQ = ExpD / RfD \quad [1]$$

where ExpD represents the individual estimated exposure dose for each metal. When aggregating the HQ corresponding to the different metals, the Hazard Index (HI) is obtained for each compost.

Biotransfer model

For estimates regarding the biotransfer of metals, equation [2] was applied:

$$Cx = (Cp \cdot PIRx \cdot fm + Cs \cdot SIRx + Cw \cdot WIRx) \cdot BTFx \quad [2]$$

where Cx is the concentration of metals accumulated in meat or milk ($mg \cdot kg^{-1}$). Cp is metal concentration in crops ($mg \cdot kg^{-1}$), PIRm is crops ingestion rate ($kg \cdot day^{-1}$), fm is the fraction of food that comes from the area, Cs is metal concentration in soil, SIRm is soil ingestion rate ($kg \cdot day^{-1}$), Cw is metal concentration in water ($mg \cdot l^{-1}$), WIRm is water ingestion ($l \cdot day^{-1}$) and BTFm is a biotransfer factor for meta or milk ($day \cdot kg^{-1}$), which is specific for each metal (U.S.EPA, 1989).

Sensitivity analysis

Monte Carlo simulations, a technique that allows a numerical simulation propagating the uncertainty of the parameters under the distributions stated, were done using the software Crystal Ball (5000 iterations employed). In this was, the appraisal of the influence of the different variables in the hazard index estimate was carried out.

3 Results

In Figure 2 the estimated HI is represented for the considered composts and scenarios. According to this figure, it can be noticed that compost made from vegetable waste (C3) and wood waste (C4) present the lowest HI in all cases. On the other side, the HI calculated for composts C5 to C7 were significantly higher and even exceeded the limits permitted by the Spanish legislation when compost was applied during 50 or 100 years. These results can be

attributed to the high content of heavy metals present in these types of compost. Thus, it was observed that the application of compost manufactured with green raw materials would be safer than employing those made from MSW.

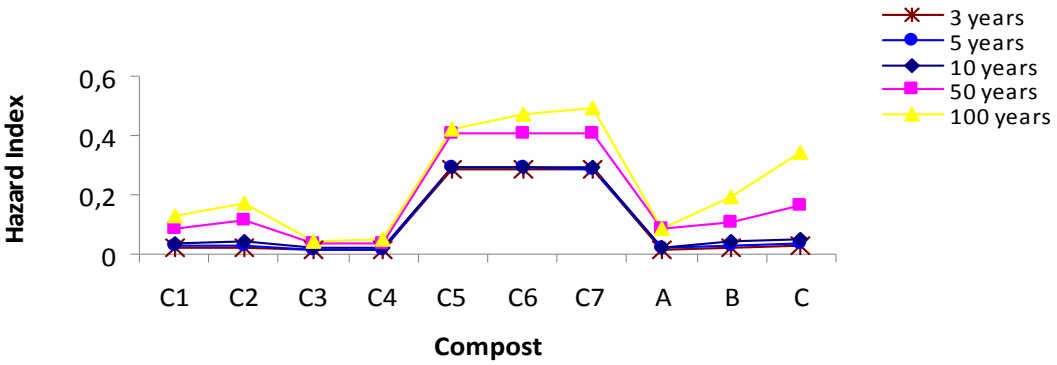

Figure 2. Hazard Index estimates.

Table 3 summarizes the main results obtained in the sensitivity analysis of the HI associated to the application of MSW compost (C5). The compost application rate presents the major influence in the variability of the HI. The pH and organic matter content in soil also showed an important contribution. Organic matter serves as an important ligand to metals. In particular, dissolved organic matter (DOM), being the most mobile and biologically active soil organic fraction, increases the bioavailability and mobility of trace elements in the soil, while insoluble organic complexes can effectively remove metals from the solution and thus reduce their ecotoxicity (Strobel et al, 2005). Low pH favours solubility, and hence mobility, and in addition, complexation by OM may enhance the solubility of heavy metals and thus its transfer to the food chain, increasing the HI. This is in accordance to the results obtained in the sensitivity analysis.

Table 3. Sensitivity analysis: main contributions to uncertainty in HI for the scenario of MSW compost (C5).

Parameter	**%**
Application rate	19.8
Time	12.8
Soil pH	-8.5
Initial heavy metal concentration in soil	3.3
O.M.	3.2
Precipitation rate	2.9

4 Conclusions

The application of compost as organic fertilizer for agriculture is promoted for the reduction of solid waste and chemical fertilizers use. The application of compost to agricultural crops is an ecological alternative; however, in some cases, the metals present in the compost can be released into the soil, water and plants and therefore they can be biotransfered to livestock and subsequently being a source of environmental risk. The sensitivity analysis gave as main result that compost application rate, pH and OM had an important influence in the HI obtained. Therefore, the definition of the scenario parameters is a key factor in determining the final fate of metals and thus, extrapolation may lead to important errors.

Acknowledgements

This work has been supported by the Dirección Xeral de I+D (Xunta de Galicia) (Project FARIA, PGDIT05TAM00201CT).

References

Efroymson, R., A., Sample, B.E., Suter II, G.W. (2001). Uptake of inorganic chemicals from soil by plant leaves: regressions of field data. *Environmental Toxicology and Chemistry*, 20, 2561-2571.

European Commission. (1999). Council Directive 1999/31/EC of 26 April 1999 on the landfill of waste. Official Journal of the European Communities, No. L 182, 16 July 1999, 1-19.

European Commission (2001). DG Environment. Biological Treatment of Biowaste. Working Document. Brussels. http://europa.eu.int/comm/ environment/waste/facts_en.htm.

Franco, A., Schuhmacher, M., Roca, E., Domingo, J.L. (2006). Application of cattle manure as fertilizer in pastureland: estimating the incremental risk due to metal accumulation employing a multicompartment model. *Environment International*, 32, 724-732.

Greenway, G.M., Song, Q.J. (2002). Heavy metal speciation in the composting process. Journal of Environmental Monitoring, 4, 300–305.

Haug, R.T. (1993). The practical handbook of compost engineering. Lewis Publishers. ISBN 0-87371-373-7, pp717.

Rojas, J. (2004). EGMASA, Ministry of Environment, Government of Andalusia. Solid waste and assimilated. Spain (in spanish).

Rosal, A., Perez, J., Bows, M., God, M. (2007). The incidence of Heavy Metals in Urban Solid Waste Compost and its use in agronomy in Spain. Información Tecnológica, Vol. 18 Nº 6. University of Cordoba, Spain (in Spanish).

Sauvé, S., Hendershot, W., Herbert, E.A. (2000). Solid-Solution Partitioning of Metals in Contaminated Soils: Dependence on pH, Total Metal Burden and Organic Matter. *Environmental Science and Technology*, 34(7), 1125-1131.

Spanish Government. (2005). RD 824/2005, 8th July, about fertilizing products.

Strobel, B.W.,.Borggaard, O.K., Hansen, H.C.B, Andersen, M.K., (2005). Raulund-Rasmussen, K. Dissolved organic carbon and decreasing pH mobilize cadmium and copper in soil *European Journal of Soil Science*, 56, 189–196.

U.S.EPA. Exposure Assessment Methods Handbook, EPA/600, Exposure Assessment Group, Office of Health and Environmental Assessment, Washington, D.C.; 1989.

Proceedings of the 10th International Chemical and
Biological Engineering Conference - CHEMPOR 2008
Braga, Portugal, September 4-6, 2008
E.C. Ferreira and M. Mota (Eds.)

IN WHAT WAY MAY RECENT LAWS ON CHEMICAL SUBSTANCES PROMOTE SCIENTIFIC RESEARCH

Carlos Lopes, Patrícia Correia, Carla Raminhos, João Lourenço *
INETI – Instituto Nacional de Engenharia e Tecnologia Industrial, Estrada do Paço do Lumiar, 22, 1649-038 Lisboa, Portugal.

Keywords: REACH, Chemical risk, Safety, QSAR's
Topic: Systematic methods and tools for managing the complexity.

The European Parliament approved on the 16th of December 2006 the Regulation (EC) No. 1907/2006 concerning the Registration, Evaluation, Authorisation and Restriction of Chemicals commonly known as the REACH regulation.

The REACH text took about 6 years before its final shape, all of them full of intense discussions and polemic. Today, it represents a dramatic change in the way the risk from chemical substances to the human health and the environment is approached by the authorities and the enterprises in the European Union, having replaced more than 40 directives.

But besides its strict regulamentary purpose, REACH has the objectives stated in its Article 1(1) of promoting "alternative methods of assessment of hazards of substances" and "enhancing competitiveness and innovation".

For these objectives to be attained it is useful to know REACH if not in detail at least in its general structure and processes, understanding in which directions the legislation points needing new developments and better knowledge.

REACH besides contributing to the collection of an huge amount of data for later exploitation, will provide through its dissemination of information mechanism an early alert that can be useful to focus research efforts on specific substances, on its characteristics and uses.

We will explain in what ways REACH will promote those goals and what are the concerned areas of scientific research, among them the replacement of substances of very high concern by safer new ones, the development of new testing methods and the use of QSARs.

Introduction

The European Parliament approved on the 16th of December 2006 the Regulation (EC) No. 1907/2006 concerning the Registration, Evaluation, Authorisation and Restriction of Chemicals commonly known as the REACH regulation.

This Regulation represents an important change in the EU policy for chemical substances moving to those who produce and to those who place the chemical substances on the market the responsibility and the burden for making evidence that human health and environment are protected.

This is done through the registration of each substance that each enterprise manufactures or imports above 1 ton/yr. To make the registration the enterprises will have to provide scientifically founded information on the intrinsic properties of the substance and - taken in consideration the hazardous ones - on the risk management measures taken to control the risk.

The Regulation come out in the middle of an intense discussion mainly derived from the fact that the costs for gathering the information and making the tests to obtain them whenever

* Corresponding author. Tel + 351-21-0924758. E-mail:joao.lourenco@ineti.pt

they are not available will lay upon the enterprises together with a fee that has to be paid with the registration.

The more important enterprises under the umbrella of their european associations, namely the CEFIC for the chemical industry, stimulated by the systematic consultations that took place during the development of the law, understood their interest in cooperating with the European Commission in order to obtain a final balanced text.

Innovation driven Regulation

Besides its strict regulamentary purpose, REACH states as objectives in its Article 1(1) promoting “alternative methods of assessment of hazards of substances” and “enhancing competitiveness and innovation”.

As a matter of fact several dispositions of the law invite the scientific community to be attentive to the evolution of the tools and methodologies involved in REACH and to the needs arised by changes and threats in the market caused by the enforcement of the Regulation.

Alternative methods of assessment of hazards of substances

Some Regulation related obligations are stated in its text that encourage the development of new methods of assessment of hazardous substances. In REACH those obligations are the ones derived from the objective of avoiding as much as possible the sacrifice of vertebrates associated to some tests as explicitly stated in its Article 13. This is done not only through the mechanisms implied in the registration that make mandatory sharing registration data and submit testing proposals with vertebrates to the Agency before their execution, but by the use of *in vitro* methods, qualitative or quantitive structure-activity relationship models ((Q)SARs) or from information from structurally related substances (grouping or read-across) to estimate the substance properties.

Also improvement of testing methods seeking that they are exact and accurate as well as low cost and effective contributors for the main goal of identifying and assessing the hazards of the substances is a continuously open field for research of new methods and revision of existing ones.

At the present about 40 testing methods are currently under development or revision. New methods that may be proposed in a near future are, among others, vapour pressure determinations, determinations of the partion coefficient n-octanol/water using a HPLC, hydrolysis a function of pH and biodegradation in surface waters[(a)].

Methods to be used with nano materials represent also an increasingly challenge.

Where tests on substances are required to generate information on intrinsic properties of substances they shall be conducted in accordance with the test methods laid down in a Commission Regulation or in accordance with other international test methods recognised by the Commission or the European Chemicals Agency. Some test methods useful to REACH are not yet implemented in the current legislation and will be published later. But the great majority will be transferred straightforwardly from the Annex V of the Directive 67/548/EC where the legally binding EU standardised methods according to which a substance can be classified as dangerous are indicated. In the Table I tests that may be needed for registration in REACH according to the tonnage associated to a manufacture or import are schematically indicated not regarding adaptation rules that may be applied.

Innovation pushed by the market threats and changes

It is expected that this Regulation will force a redraw of the market because of the withdrawl of substances no longer profitable particularly small volumes produced or imported.

TABLE I

TESTS FOR THE REGISTRATION OF SUBSTANCES AS REQUIRED BY THE REACH REGULATION

TONNAGE CLASS	PHYSICOCHEMICAL PROPERTIES
≥ 1 ton./yr	State of the substance state at 20ºC and 101,3 kPa
	Melting/Freezing point
	Boiling point
	Relative density
	Vapour pressure
	Surface tension
	Water solubility
	Partition coefficient n-octanol/water
	Flash-point
	Flammability
	Explosive properties
	Self-ignition temperature
	Oxidising properties
	Granulometry
≥ 100 ton./yr	Stability in organic solvents and identity of relevant degradation products
	Dissociation constante
	Viscosity
	TOXICOLOGICAL INFORMATION
≥ 1 ton./yr	Skin Irritation or skin corrosion : data assessment; acid or alkaline reserve assessment; tests *in vitro*
	Eye irritation
	Skin sensitisation
	Mutagenicity : *In vitro* gene mutation of bacteria
	Acute toxicity: by oral
≥ 10 ton./yr	Skin Irritation : *in vivo*
	Eye irritation : *in vivo*
	Mutagenicity: cytogenicity in mammalian cels *in vitro* or *in vitro* de micronucleus study
	Acute toxicity: by inhalation, by dermal route
	Repeated dose toxicity: short-term dose toxicity (28 days) one species, male and female
	Reproductive toxicity: screening for reproductive/developmental toxicity one species
	Toxicokinetics
≥ 100 ton./yr	Repeated dose toxicity: sub-chronic toxicity (90 days), one species, rodent, male and female
	Reproductive toxicity: pre-natal developmental toxicity, one species; Two-generation reproductive toxicity, one species, male and female
≥ 1000 ton./yr	Carcinogenecity study
	ECOTOXICOLOGICAL INFORMATION
≥ 1 ton./yr	Aquatic toxicity: short-term test on invertebrates (preferred on *Daphnia*)*;* growth inhibition of aquatic plants (algae preferred)
	Degradation: biotic, ready biodegradability
≥ 10 ton./yr	Aquatic toxicity: short-term test on fish; activated sludge respiration inhibition testing; Two-generation reproductive toxicity, one species, male and female
	Degradation: abiotic, hydrolysis as a function of pH
	Fate and behaviour in the environment: adsorption/desorption screening
≥ 100 ton./yr	Aquatic toxicity: Fish early-life stage (FELS); Short-term toxicity test on embryo and sac-fry stages; Juvenile growth test on fish
	Degradation: biotic, simulation on ultimate degardation on surface water; Soil simulation; Sediment simulation; Identification of degradation products
	Fate and behaviour in the environment: Bioaccumulation in aquatic species, preferably fish
	Effects on terrestrial organisms: short-term toxicity to invertebrates and plants; effects on soil micro-organisms
≥ 1000 ton./yr	Fate and behaviour in the environment: Long-term toxicity to sediment organisms; Long-term or reproductive toxicity to birds

But mainly substances of very high concern (SVHC[1]) will be put under a continuous pressure to withdraw the market as a consequence of an Authorisation process created in REACH with the purpose of ensuring a good functioning of the internal market while assuring that the risks from those substances are properly controlled. From another perspective this will be also a challenge to the research community help solving the problems raised by the disappearance or anticipated disappearance of substances from the market.

The substances identified as SVHC are first included in a list of substances that are candidates to be part od Annex XIV of REACH – the Annex that lists the substances that will need an authorisation to be used. According to a prioritisation criteria this list is ordinated and by that order the substances will be put in the work programme of the European Chemicals Agency (ECHA). The Agency will recommend then to the European Commission – the responsible for the final political decision - the inclusion of the substance in the Annex XIV of REACH. Once in this Annex manufacturers importers and downstream users will need to submit an application to the Agency whenever they want to use the substance.

The public in general and the scientific community may early alerted to the probability of a substance to became part of Annex XIV because of the publication of a notice on the website of the Agency that a dossier has been prepared for the identification of a substance as SVHC (Article 59(4)). Being positively identified as such the Agency there is another opportunity to spot the substance because of the obligation of the Agency to make a public consultation before sending the Comission a recommendation for the decision of inclusion. This consultation spans for three months after the date of publication and asks in particularly for the indication of uses that should be exempt from the authorisation requirement.

Once the substance included in the Annex XIV by the Commission the application for an auhorisation is clearly a burden on the use – besides the obligation for the applicant to pay a fee he needs to provide with the application and among other information a chemical safety report on the substance (unless already submitted as part of the registration), an analysis of the alternatives to the substance considering their risks and the technical and economic feasability of a substitution, including also, if appropriate, any relevant R&D activities by the applicant. If the analysis shows that there are suitable alternatives available the applicant will inform about a substitution plan for the substance and if appropriate information about any relevant R&D activities involved. And it should also be considered that authorisation will be subjected to time-limited reviews (Article 60(8)).

The substances on Annex XIV are then a problem for human health for environment and also for the enterprises who rely on them for their business.

So what is the advantage of the scientific community to early spot them as we previously pointed out? With the possibility to address a problem already identified as affecting the human health and the environment the scientific groups interested in those substances and its uses may start also to push their efforts to a solution and use themselves or through convenient partners the presentation of solutions to the substituition of the uses under authorisation , proposing either new substances or instead new technologies related with the uses and with its risk management measures. The presentation and arguing about the merits of the proposals will have an institutional european forum through the possiblity offered by the obligation of the Agency to make available information on its web-site whenever an authorisation is applied on its uses and receiving information on alternative substances or technologies submitted by third parties (Article 64(2)). This information will be analysed by the Committees for Risk Analysis and Socio-economic Analysis of the Agency who will draft an opinion on the application taking in consideration all the received information before a decision of the Commision on the granting of an authorisation, Summaries of the Commision

[1] Substances of very high concern in REACH are substances that are carcinogenic or mutagenic or toxic to the reproduction (CMR substances) or persistent, bioccumulative and toxic (PBT substances) or very persistent and very biaccumulative (vPvB substances). Others may raise equivalent concern – as for instance endocrin disruptors – and be subject of the same procedures under the regulation.

decisions including reasons for the decision, in particular when suitable alternatives exist, shall be published on the Official Journal of the European Union (Article 64(9)).

QSARS a research field of main importance to REACH

QSAR's (**Q**uantitative **S**tructure-**A**ctivity **R**elationship) are mathematical models useful to predict a particular endpoint based on the structural and chemical information of substances.

The use of QSAR's in the context of the REACH legislation becomes of great interest since it avoids the use of *in vivo* testing in vertebrates, and it also contributes to minimize the cost of gathering information for a specific chemical substance. Images like the ones seen on Draize's tests for eye irritation, where the substance to be tested is applied directly in the eye of a rabbit (or other mammallian) while it's reaction is visually monitored for large periods of time in which the animal is left suffering without any kind of relief of it's symptoms, are images that appeal to the development of new alternatives to this kind of testing.

Nevertheless the use of QSAR's should be applied bearing in mind the need to assure that it's capability of predicting a certain endpoint (avoiding vertebrate testing) is still compatible with the same level of protection of human and environmental health as before (Lilienblum *et al* 2008). This way, testing on vertebrates could be used only for substances that are predicted as non-irritant and non corrosive by the model, avoiding the use of *in vivo* testing for the ones already predicted as irritant or corrosive.

The OECD (**O**rganisation for **E**conomical **C**o-operation and Development) principles for QSAR validation (accepted for regulatory purposes under REACH legislation) stated that a QSAR should be associated with (Gramatica, 2007):

(P1) – a defined endpoint

(P2) –an unambiguous algorithm

(P3) – a defined domain of applicability

(P4) – appropriate measures of goodness-of-fit, robustness and predictivity

(P5) – a mechanistic interpretation (if possible).

The need for a defined endpoint it's in itself obvious since this is the prime goal of a QSAR. The last principle is limited by the knowledge one has about the mechanism and the way that a specific property or descriptor is responsible for the predicted endpoint. The concept of descriptor appears in QSAR's as an entity that exists in the system to be modulated (for example, the shape of the molecular orbitals, the molecular weight or the acidity of the molecule) and can be associated with a certain endpoint (for example, acidity it's related to skin corrosion).

A brief review concerning (P2), (P3) and (P4) is made outlining some important guidelines on QSAR use under the scope of REACH legislation (Annex XI).

The unambiguous algorithm that (P2) refers to, should also be able to accurately predict a certain endpoint for any chemical substance that falls within the domain of applicability. Included in the algorithm is not only the mathematical method of calculation, but also the specific molecular descriptors required in the model. Almost all the developed QSAR's use certain physicochemical properties as molecular descriptors for the model.

Benfenati *et al.* (2003) pointed out that commonly used molecular descriptors, may be calculated or experimentally determined mixing different methodologies with a strong effect on the output of the QSAR in use. For example, the use of a QSAR model based on *log* K_{OW} (logarithm of the octanol/water partition coefficient) as the molecular descriptor for nonpolar narcosis in fish, expressed as:

$$\log (LC_{50}) = -0{,}846 \log K_{OW} - 1{,}39$$

can't be used to give a reliable prediction unless care is taken to ensure that *log* K_{OW} is obtained using the same methodology than the one used in obtaining this correlation. Although *log* K_{OW} is well defined by thermodynamics, and this descriptor is well known,

several methodologies are accepted to it's determination, resulting in different values.

The domain of applicability referenced in (P3) is a theoretical region in chemical space, defined by the model descriptors and modeled response obtained during the use of the training set.

It's important to note that even a validated QSAR can't be expected to give a good prediction if any chemical substance that doesn't fall within it's domain of applicability is tested. Care should be taken on which substances to include in the training set and in the test set (Eriksson *et al.* 2003).

The goodness-of-fit, robustness and predictivity of the model are included in (P4). The R^2 (R^2 = (1- RSS/TSS), where RSS is the Residual Sum of Squares and TSS is the Total Sum of Squares] is the most widely used measure of the goodness-of-fit of a QSAR, and usually no attention is taken upon robustness (insensibility of the model to the uncertainties in the experimental measures) and predictivity.

The most commonly used approach to assess model predictivity is cross validation in which, statistical techniques are applied to evaluate the effect of iteratively removing different proportions of the training set (Q^2_{LOO} known as Leave One Out approach). A detailed discussion upon these parameters can be found in Gramatica (2007).

As an example of the possible usage of QSAR's under the REACH scope is the capability they provide for predicting eye and skin irritation/corrosion (needed for substances which are produced in a range of 1 to 10 ton/year, as seen in Table 1).

The mechanisms for skin and eye irritation are diverse and not fully understood. Some of the parameters accepted as influencing this kind of phenomena are: the acid or basic properties of the substance, its capability of penetrating the skin (function of hydrophobicity and molecular size) and cytotoxicity.

The use of QSARs in this field of application is in the origin of some good expert systems for assessing irritation and corrosion (some of them available as an application software corresponding to the gathering of several QSARs and their descriptors). Several reviews can be found in literature, comparing each software and its functionality. Examples of this software are:

DEREK (for windows) – Deductive Estimation of Risk from Existing Knowledge[(b)]

MultiCASE – Multiple Computer Automated Structure Evaluation[(c)]

TOPKAT – Toxicity Prediction by Komputer-Assisted Technology[(d)]

An extended review on the use of QSARs to predict eye and skin irritation/corrosion is available in Saliner *et al.* (2008).

Although there is a great amount of published QSARs and studies developed for several endpoints, the applicability of each one for the purpose of REACH regulation should be made under the OECD principles of validation for QSARs and each case should be treated with precaution. For some of these studies difficulties are expected in its use for regulatory purposes, but this should be interpreted as an incentive for further development in this particular area of knowledge.

The development of global databases searchable and accessible by any parameter of interest (endpoint, applicability domain, etc) is a future demand, and efforts are already being made for this goal.

References

Lilienblum, W., Dekant, W., Foth, H., Gebel, T., Hengstler, J. G., Kahl, R., Kramer, P.-J., Schweinfurth, H., Wollin, K.-M. (2008). Alternative methods to safety studies in experimental animals: role in risk assessment of chemicals under the new European Chemicals Legislation (REACH), *Archives of Toxicology*, 82, 211-236.

Benfenati, E., Gini, G., Piclin, N., Roncaglioni, A., Varý, M. R. (2003). Predicting log*P* of

pesticides using different software, *Chemosphere*, 53, 1155-1164.
Eriksson, L., Jaworska, J., Worth, A. P., Cronin, M. T. D., McDowell R. M., Gramatica P., (2003). Methods for Reliability and Uncertainty Assessment and for Applicability Evaluations of Classification- and Regression-Based QSARs, *Environmental Health Perspectives*, 111, 1361-1375.
Gramatica, P., (2007). Principles of QSAR models validation: internal and external, *QSAR & Combinatorial Science* 26, 5, 694-701.
Saliner, A. G., Patlewicz G., Worth, A. P, (2008). A review of (Q)SAR models for skin and eye irritation and corrosion. *QSAR & Combinatorial Science*, 1, 49-59.
(a) http://ecb.jrc.it/testing-methods/, in 14th July 2008.
(b) http://www.lhasalimited.org/index.php?cat=2&sub_cat=64#top, in 9th July 2008.
(c) http://www.multicase.com/products/prod01.htm, in 9th July 2008.
(d) http://accelrys.com/products/discovery-studio/toxicology/, in 9th July 2008.

Proceedings of the 10th International Chemical and
Biological Engineering Conference - CHEMPOR 2008
Braga, Portugal, September 4-6, 2008
E.C. Ferreira and M. Mota (Eds.)

Simulation optimizes feedback control on the temperature of a heterogeneous batch reactor

M. Çetin Koçak *
Chemical Engineering Department, Engineering Faculty, Ankara University, Tandoğan 06100, Ankara, Turkey

Keywords: Dynamic simulation, Feedback control, Heterogeneous batch reactor, MATLAB, SIMULINK
Topic: Systematic methods and tools for managing the complexity

Abstract

This work is a SIMULINK® application using its non-linear S-function block to solve a feedback control problem posed by Franks (1972). The controller's task is to raise the temperature of a heterogenous batch reactor to a certain level as rapidly as possible, with minimum overshoot, and maintain it there for the remainder of the reaction. The research required a thorough study of DYFLO (Franks, 1972), development of a mini package in MATLAB® environment, model adaptation with suitable modification, open-loop verification by comparison with the original, construction of a SIMULINK® diagram including a single S-function block housing both the reactor and the newly added temperature control loop, open-loop verification again, and finally closed-loop experimentation with controller settings.

1 Introduction

Many dynamic models can be compactly represented in vector form by a set of algebraic equations $\underline{0} = \underline{g}(t, \underline{x}, \underline{a}, \underline{c})$ coupled to a set of differential equations $\underline{x}' = \underline{f}(t, \underline{x}, \underline{a}, \underline{c})$ where t, $\underline{x}$, $\underline{a}$, and $\underline{c}$ respectively denote the independent variable time, state variables, algebraic variables, and constants. Further, the prime $(')$ indicates differentiation with respect to t.

Simulation almost always means a series of small steps of numerical integration because analytical solution is either unavailable or intractable. Design and optimization may require several simulation runs starting from $t = 0$ and advancing to a pre-specified time or state, producing output at regular intervals. Boundary conditions and/or some constants may vary from one run to the next.

Simulators usually offer a set of different driver routines each one handling the chores of a particular numerical integration method. Triggered after appropriate data initialization, these solvers can supervise a run calling upon the nominated model function as often as necessary. They expect this function to solve $\underline{0} = \underline{g}(t, \underline{x}, \underline{a}, \underline{c})$ for $\underline{a}$ at the current time and state prior to calculating and returning fresh derivatives. Figure 1 shows a typical simulation run.

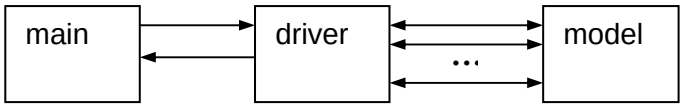

Figure 1. Typical simulation run.

Simulators may be classified as equation-oriented or modular. When the model partly or wholely partitions the algebraic and differential equation sets between sequential modules as in the famous DYFLO (Franks, 1972) care must be taken to preserve simultaneity. ACES

* Tel + 90 312 212 67 20 Ext.1330. E-mail:kocak@eng.ankara.edu.tr

(Koçak, 1980) pioneered true simultaneous modularization by twice-round execution of modules. DYFLO and ACES are both Fortran-based, modular chemical engineering simulators without a preprocessor.

MATLAB® is a highly convenient simulation environment with many integrators, e.g. ode23, ode45, and ode15s functions. The latter is a driver for stiff models. SIMULINK® is far useful than the standard MATLAB® package for control system simulation. SIMULINK® enables the rapid construction and simulation of control block diagrams (Bequette, 2003). Its library offers many linear and nonlinear blocks as icons which can be dragged and dropped into a model workspace. Block parameters and coefficients may be entered here by double-clicking on the icon. Its easy to connect the blocks by arrows. Standart input functions such as step and ramp are supplied. The simulation parameters can be changed by going to the Simulation pull-down menu and modifying the stop time or the integration solver method.

The S-function icon is in the nonlinear library of SIMULINK®. When simulations are performed, the equations in the m-file named by the S-function block are claimed to be solved simultaneously with other blocks in the diagram.

2 The Model

The heterogenous batch reactor whose temperature is to be controlled has three phases, where several phenomena occur simultaneously, making manual calculations virtually intractable. An organic compund A is hydrogenated to compound C via an intermediate B, i.e. $A + H_2 \rightarrow B,\ B + H_2 \rightarrow C$. This reaction occurs on the surface of a metal catalyst in the form of loose particles, the reagents diffusing from the liquid phase to the catalyst surface, reacting and returning to the liquid phase. A degree of control over the internal temperature can be achieved by a series of cooling coils contacting the liquid phase. The reaction is highly exothermic, which will cause a significant rise in the temperature and pressure during the course of the reaction, monitored by suitable instrumentation. A significant exchange of material between the liquid and vapor phases occurs as the reaction proceeds with the simultaneous division of heat energy. However, all phases will have the same temperature since the agitation has sufficient violence to maintain equilibrium.

For this reactor, Franks (1972) developed a dynamic model with five components by writing mole and heat balances considering the reaction system as a whole. As depicted in Figure 2, a flash calculation involving trial-and-error established the vapour-liquid split as well as the equilibrium temperature and pressure. Ideal behaviour is assumed throughout.

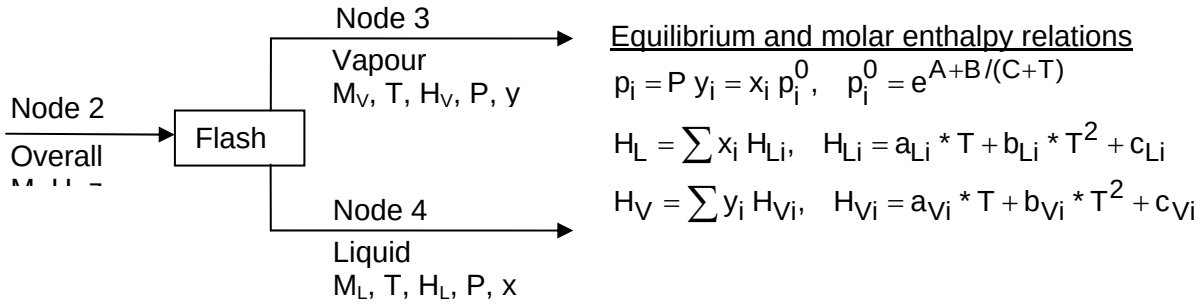

Figure 2. Flash calculation.

For lack of space, description of the model will be brief. The reaction system loses heat to the vessel and the coils at the rates Q_W and Q_C respectively:

$$Q_W = UA_W\,(T - T_W),\quad Q_C = UA_C\,(T - T_C),\quad HT = Q_W + Q_C \tag{1}$$

The subscripts G and S respectively denote the hydrogen gas and the solvent. Suppose W is the catalyst weight. Let

$$R_1 = \frac{k_1 x_A W}{den}, \quad R_2 = \frac{k_5 W^2 x_B x_G}{den^2}, \quad den = 1 + K_4 x_B + K_2 x_G + K_6 x_C \tag{2}$$

The dynamic mole balances are as follows:

$$\frac{dM_A}{dt} = -R_1, \quad \frac{dM_B}{dt} = R_1 - R_2, \frac{dM_C}{dt} = R_2, \frac{dM_G}{dt} = -R_1 - R_2, \frac{dM_S}{dt} = 0, \quad \frac{dM}{dt} = -R_1 - R_2 . \tag{3}$$

The accompanying heat balances are

$$\frac{d(M\ H)}{dt} = R_1(-\Delta H_1) + R_2(-\Delta H_2) - HT , \tag{4}$$

$$\frac{dT_W}{dt} = \frac{Q_W}{MC} . \tag{5}$$

Consider the control loop now. The reactor temperature is measured with a thermal system having a first-order time constant of 0.4 minutes, so

$$\frac{dT_M}{dt} = (K_M * T - T_M)/\tau_M, \quad K_M = 1, \quad \tau_M = 0.4 . \tag{6}$$

The temperature of the coolant through the coils is obtained by mixing two fluids with temperatures of 130º C and 70º C. The mixing is assumed to be linear with valve position X_v. The valve response to the control signal CO can be simulated with a first-order time constant of 0.05 minutes. Thus,

$$\frac{dX_V}{dt} = (K_V * CO - X_V)/\tau_V, \quad K_V = 1, \quad \tau_V = 0.05 , \tag{7}$$

$$T_C = 70 + X_V * (130 - 70) \tag{8}$$

The task of the controller is to raise the reactor temperature to $T_{SET} = 120^{\circ}$ C as rapidly as possible, with minimum overshoot, and maintain it at this level for the remainder of the reaction. Let

$$ERR = T_{SET} - T_M \tag{9}$$

The output of a P type controller is

$$CO = CO_0 + K_C * ERR \tag{10}$$

If

$$ERRINT = \int ERR\, dt , \tag{11}$$

then the output of a PI type controller are

$$CO = CO_0 + K_C * (ERRINT/\tau_I + ERR) . \tag{12}$$

The simulation part of this work is organised as follows:

1) The file “hb_sfun0.m” is triggered from the command window of MATLAB®.

2) After some preliminaries, this file calls SIMULINK® driver function “sim” which activates “hb_sfun_sim.mdl” shown in Figure 3. Easily constructed, this diagram simply indicates that the S-function block is asscociated with the “hb_sfun.m” file and outputs M, T, H, and P values. (These pertain to the liquid phase.)

3) SIMULINK® sets a flag to 0, 1 or 3 to signal that dynamic blocks in “hb_sfun_sim.mdl” should enter their own initialization, derivative calculation or output sections respectively.

4) When the run is over, “sim” returns the time and state profiles to the place it was triggered. The output profiles are made available in the workspace. Note that SIMULINK® window allows the user to select the integration driver and specify the run interval as well as output times.

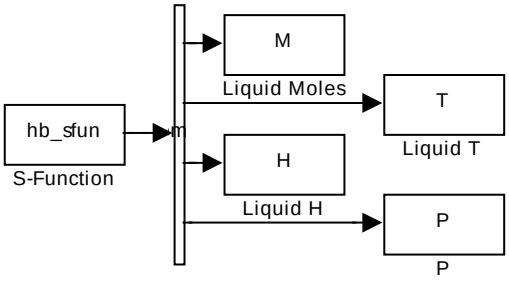

Figure 3. SIMULINK® diagram with an S-Function block.

Now, the only dynamic block in this set up is an S-function associated with the “hb_sfun.m” file given in Figure 4. (Note: Any workspace containing a global statement has permission to read and modify the objects it names. This statement helps shorten argument lists.) The X argument denotes the state vector here. Notice that state variables are in fact plant values forwarded as X0 on the first entry ($flag = 0$) and back-transferred on each subsequent call. The DX vector holds the state derivatives. The model with a PI controller has a total of 11 state variables in the order zz(2,1), zz(2,2), zz(2,3), zz(2,4), zz(2,5), HHOLDM(2), eenmpm(2), TW=TT(5), TM=TT(7), XV, and ERRINT. (For open-loop study, the last three derivatives (DX(9), DX(10), and DX(11)) are reset to zero.)

```
function [sys,X0,str,ts]=hb_sfun(t,X,u,flag)
global AANT EENTL EENTV TT PP zz eenpm HHOLDM HHOLDE FFM FFE tabs rbv hw hc W…
    MCP NC KM TAUM KV TAUV XV TCSET CO0 KC TAUI ERRINT
switch flag
   case 0 % initilization
      X0=[zz(2,:) HHOLDM(2) eenpm(2) TT(5) TT(7) XV ERRINT]'; [m,n]=size(X0);
      sizes=simsizes; sizes.NumContStates=m; sizes.NumDiscStates=0; sizes.NumOutputs=4;
      sizes.NumInputs=0; sizes.DirFeedthrough=0; sizes.NumSampleTimes=0;
      sys=simsizes(sizes); str=[ ]; ts=[ ];
   case 1 % derivatives
      DX=X; % dimension DX
      zz(2,:)=X(1:NC)'; HHOLDM(2)=X(NC+1); eenpm(2)=X(NC+2); TT(5)=X(NC+3); TM=X(NC+4);
      XV=X(NC+5); ERRINT=X(NC+6);
      [PP,R,zz(4,:),HHOLDM(4),TT(4),eenpm(4),zz(3,:),HHOLDM(3),TT(3),eenpm(3)]=...
         PPflash(tabs,rbv,0,zz(2,:),HHOLDM(2),TT(4),eenpm(2),PP,AANT,EENTL,EENTV);
      [RX, RXTM,RXTQ]=react(W,TT(4),zz(4,:));
      TT(6)=70+XV*(130-70); FFE(1)=hw*(TT(4)-TT(5)); FFE(2)=hc*(TT(4)-TT(6));
      HT=-(FFE(1)+FFE(2));
      DX=bbatch(HT,zz(2,:),HHOLDM(2),eenpm(2),RX,RXTM,RXTQ)'; DX(NC+3)=FFE(1)/MCP;
      ERR=TCSET-TM;
      % The control signal below is for PI type. For P type change signal to CO=CO0+KC*ERR.
      CO=CO0+KC*(ERR+ERRINT/TAUI); % PI controller
      DX(NC+4)=(KM*TT(4)-TM)/TAUM; DX(NC+5)=(KV*CO-XV)/TAUV; DX(NC+6)=ERR;
      % For open-loop response activate the line below by removing the leading %
      %DX(9:11)=0;
      sys=DX;
   case 3 % outputs
      zz(2,:)=X(1:NC)'; HHOLDM(2)=X(NC+1); eenpm(2)=X(NC+2); TT(5)=X(NC+3); TM=X(NC+4);
      XV=X(NC+5); ERRINT=X(NC+6);
      [PP,R,zz(4,:),HHOLDM(4),TT(4),eenpm(4),zz(3,:),HHOLDM(3),TT(3),eenpm(3)]=...
         PPflash(tabs,rbv,0,zz(2,:),HHOLDM(2),TT(4),eenpm(2),PP,AANT,EENTL,EENTV);
      sys=[HHOLDM(4) TT(4) eenpm(4) PP];
   case {2,4,9}
      sys=[ ];
end
```

Figure 4. The hb_sfun.m file.

When $\text{flag} = 1$ the entry is for DX values. The call to the PPflash function establishes the vapour-liquid split. Equations (1) through 2 to (4) are complete on exit from the bbatch function. Equation (5) corresponds to DX(NC+3)=FFE(1)/MCP. Equations (9) and (12) are easily recognised. As indicated in the listing, the changed from PI to P type is achieved simply by tailoring (12) to (10). Equations (6), (7) and (11) appear on the line containg (12). Finally, in order to obtain an open-loop response, just activate the statement $DX(9:11) = 0$ by removing the leading % sign. When $\text{flag} = 3$ the entry is for output estimation. This short section needs no explanation.

Activated from the command window, the script file "hb_sfun0.m" attends to pre-initialisation tasks like filling pysical property database, giving the reactor's first charge, and specifying controller parameters to be tested before calling the SIMULINK® driver (sim function) and passing over the name "hb_sfun.m" as the model file. As seen in Figure 5, the call to sim function returns tt and XX as the collected values of time and state respectively.

```
global AANT EENTL EENTV TT PP zz eenpm HHOLDM HHOLDE FFM FFE tabs rbv hw hc W…
    MCP NC KM TAUM KV TAUV XV TCSET CO0 KC TAUI ERRINT
AANT=[10.5 -2955 273;  10.5 -3010 273; 11.2 -3400 273; 10.5 -2750 273; 13.0 -4600 273];
EENTV=[16 0 5805; 19 0.1 8060; 22 0.2 9726; 6.9 0.05 2600; 33 0.06 12174];
EENTL=[24 0 0; 30 0.03 0; 33 0.02 0; 22 0.1 0; 41 0 0];
tabs=273; rbv=0.007; hw=200; hc=100; W=100; MCP=600; NC=5;
KM=1; TAUM=0.4; KV=1; TAUV=0.05; CO0=0.5;  TCSET=120;
KC=0.25; TAUI=50; XV=0.5; ERRINT=0;
TT=[85 85 85 85 75 100 85]; %   T0 T2 T3 T4 TW TC TM
PP=7; zz=zeros(4,5); zz(2,:)=[0.185 0 0 0.445 0.37]; zz(4,:)=[0.18 0 0 0.4 0.42];
HHOLDM(2)=27; eenpm(2)=eenthm(TT(2),zz(2,:),EENTL);
[PP,R,zz(4,:),HHOLDM(4),TT(4),eenpm(4),zz(3,:),HHOLDM(3),TT(3),eenpm(3)]=...
   PPflash(tabs,rbv,0,zz(2,:),HHOLDM(2),TT(4),eenpm(2),PP,AANT,EENTL,EENTV);
[tt,XX]=sim('hb_sfun_sim');
```

Figure 5. The hb_sfun0.m file.

Table 1 compares the open-loop response of the reactor with the original (Franks, 1972). The harmony is reasonable considering the changes of organisation, integration driver, iteration techniques, and accuracy criteria.

Table 1. Open-loop response of the batch reactor.

	$t = 0$ min		$t = 10$ min	
Liquid Phase	This work	Franks, 1972	This work	Franks, 1972
M (moles)	23.9192	23.92	12.2237	12.19
T (º C)	77.4336	77.43	153.274	153.6
H (PCU)	2579.9	2580	6020.0	6034
P (atm)	7.5574	7.557	18.5488	18.76
x_1	0.1840	0.1840	0.0068	0.0073
x_2	0.0000	0.0000	0.0486	0.0503
x_3	0.0000	0.0000	0.1806	0.1776
x_4	0.4045	0.4045	0.1099	0.1116
x_5	0.4115	0.4115	0.6540	0.6532

Many PI settings were tested but only two results were selected for display in Figure 6 together with the open-loop response. Both seem satisfactory considering the assignment. Possibilities for future work include formal optimization of controller settings, segregation of the model into several S-function blocks without spoiling simultaneity, and combination with built-in linear elements of SIMULINK®.

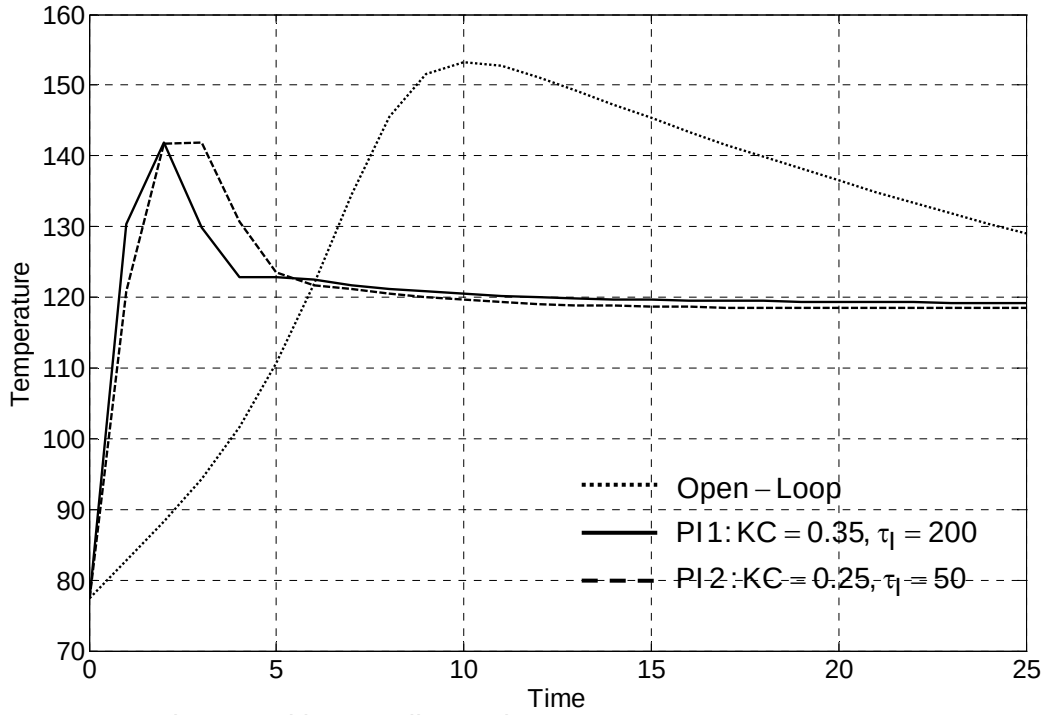

Figure 6. Experiments with controller settings.

References

Franks, R.G.E. (1972). Modeling and Simulation in Chemical Engineering, Wiley-Interscience, New York.

Koçak, M.Ç. (1980). Dynamic simulation of chemical plant, Ph.D. thesis, University of Aston in Birmingham, England.

Bequette, B.W. (2003). Process Control: Modeling, Design and Simulation, Pearson Education, Inc., Upper Saddle River, New Jersey.

Proceedings of the 10th International Chemical and
Biological Engineering Conference - CHEMPOR 2008
Braga, Portugal, September 4-6, 2008
E.C. Ferreira and M. Mota (Eds.)

Study of volumetric oxygen transfer coefficient in a Taylor vortex flow bioreactor

Patrícia Ap. Santiago[1]*, **Cláudio A. T. Suazo**[1], **Roberto C. Giordano**[1]
[1]Department of Chemical Engineering, Federal University of São Carlos,
P.O. Box 676, Post Code 13565-905, São Carlos, SP, Brazil.

Keywords: Taylor vortex flow, mass transfer, volumetric oxygen transfer coefficient (K_La), animal cell culture, bioreactor.
Topic: Integration of life sciences and engineering.

Abstract

In biochemical processes involving cultivation of animal cells, the supply of oxygen in culture medium is an extremely important parameter in the project of bioreactors and its operation. An inadequate transfer of oxygen can lead to rapid changes in cell physiology, metabolism, productivity, product quality and cell death. In this work, the global volumetric transfer coefficient of oxygen (K_La) is evaluated in a Taylor vortex flow bioreactor (TVFB) and a correlation of mass transfer, of this equipment, is proposed. The experimental conditions employed in TVFB were: rotational Reynolds number between 244 and 2928, airflow rates varying from 80 mL.min^{-1} to 550 mL.min^{-1} and used culture medium DMEM in liquid phase. The results of this study suggest that Taylor-vortex flow regimes provide an effective oxygen transport required for long-term cell culture.

1 Introduction

In the last 20 years, there have been rapid increase and progress in the development and use of large-scale animal cell cultivations for the commercial production of therapeutic and diagnostic biochemicals, as viral vaccines, monoclonal antibodies and recombinants proteins (Ma et al., 2002). Nowadays, for commercial production, cells are often cultured in large scale stirred bioreactors. Within of that equipment, the fluid dynamic environment may be used to enhance delivery of oxygen and other chemical species (as nutrients) to cells through forced convective transport (Curran and Black, 2005). The supply of oxygen to production cultures during scale-up is an important part of bioprocess design (Butler, 2004). At high cell densities ($>10^6$ cells.mL^{-1}) or at high volume cultures ($>$10L) gas diffusion in this kind of bioreactor is not adequate to meet the metabolic demands of the cells (Konz et al., 1998). A constant oxygen supply is required because of its low solubility in water (7.8 mg.L^{-1} at 25°C), and even lower in culture media, depending on the composition. Nevertheless, the conventional methods of agitation and aeration generally used in microbial culture bioreactors are difficult to apply due to the physiological characteristics of animal cells. The absence of cell walls in mammalian cells and their relatively large size make them particularly sensitive to shear forces. The cell damage caused by bubble bursting were performed by Hand-Corrigan et al. (1989), Kunas and Papoutsakis (1990), Chalmers and Bavarian (1991), Wu (1995), Camacho et al. (2000), among others.

As it can be observed in the literature, the oxygen transfer is a limiting factor on the bioreactor design. Therefore, the main objective of this work is to assess the potential use of a Taylor vortex flow bioreactor (TVFB) designed and built at the Department of Chemical Engineering of São Carlos Federal University, for cultivation of animal cells. The overall volumetric oxygen mass transfer coefficient (K_La) and mass transfer correlation was estimated under Taylor vortex flow regimes. TVFB has a non-conventional configuration, when compared to other bioreactors like stirred tank and airlift, it consists of two concentric

*Corresponding author. Tel. +55 16 81461351. E-mail: patriciaapsantiago@hotmail.com.

cylinders, one internal rotating cylinder and the other external stationary. Taylor vortices are secondary flow patterns that appear above a critical rotation, determined by the critical Taylor number, in the gap between inner (rotating) and outer (rotating or stationary) cylinder (Taylor, 1923). The vortex is capable of fulfilling the gap between the two cylinders in a stable and reproductive way that provides an efficient mixture of the medium, ensuring favorable conditions of pH, temperature, nutrients and a less aggressive agitation of the medium for the cells inside the bioreactor (Moore, 1994, Giordano et al., 1998, 2000a and b; Resende, 2002). Taylor vortex flow is more appropriate in cell cultures involving shear sensitiveness, as animal cells, because the transition from the previous flow, known as Couette, for Taylor produces the reduction in shear, as an overall effect. The decrease of shear stress (tangential) is due to decomposition by the vortex of tension applied by internal cylinder in three components: axial, radial and tangential. When working with anchorage dependent animal cells, in a heterogeneous system, the rotation of the inner cylinder is an additional operating variable that may facilitate particle fluidization. In order to reduce hydrodynamic shear damage in the cell culture due to bubble breakup, a silicone tubular membrane around all inner cylinder was used. This system allows the diffusion of gases in the culture medium, through the membrane, without the formation of air bubbles.

2 Materials and methods

2.1 Equipment

The experiments were performed in a Taylor vortex bioreactor with a useful volume of 800mL. The photograph of TVFB is illustrated in Figure 1. The TVFB is composed of two concentric cylinders, where the internal one is rotating and manufactured in polypropylene, while the external is stationary and is manufactured in glass and stainless steel. The outer cylinder has a heat exchanger which is responsible for maintaining the temperature inside the equipment in the desired value using a water closed loop allied to an external water heater. The electrodes used to monitor and control the pH, dissolved oxygen and temperature are introduced by appropriate holes in the base of the outer cylinder. Aeration of the culture medium was achieved by a silicone tubular membrane, which has an outer diameter of 4.4 mm and a wall thickness of 0.55 mm.

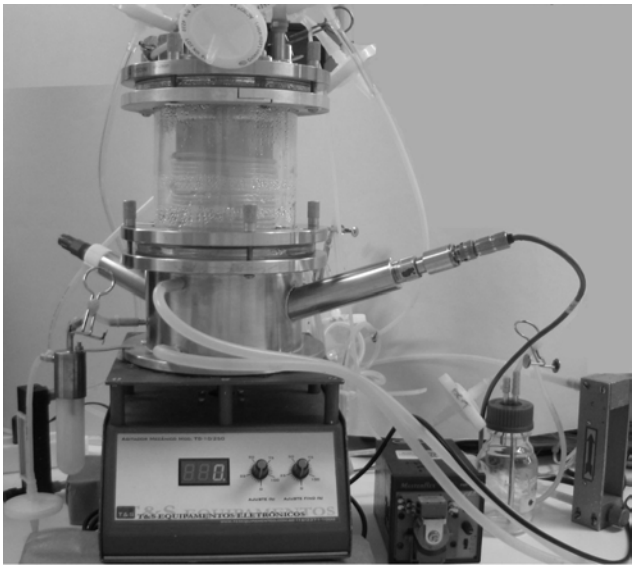

Figure 1: Photograph of the Taylor vortex flow bioreactor (TVFB) used in the experiments.

2.2 Measurement of the overall volumetric oxygen transfer coefficient (K_La)

The measurement of the overall volumetric oxygen mass transfer coefficient (K_La) is based on the dynamic gassing-out method using an oxygen electrode. Equation 1 is used for evaluation of K_La.

$$\frac{dC}{dt} = K_L a(C^*_{O_2} - C_{O_2}) \tag{1}$$

where, $K_L a$ is the overall volumetric oxygen mass transfer coefficient, and a is interfacial area of the mass transfer per unit volume, in this case the area is the surface of the tubular silicone membrane; C_{O_2} is the oxygen concentration in the medium (mmol.L^{-1}), $C^*_{O_2}$ is the oxygen concentration in the medium in equilibrium with air (mmol.L^{-1}) (Blanch and Clark, 1997).

The method consists in provoking abrupt changes of dissolved oxygen concentration between two known steady states. It is possible by gassing it with nitrogen within the bioreactor, eliminating all dissolved oxygen. After the elimination of oxygen inside the bioreactor, the aeration is turned on at the conditions desired for that experiment (agitation and air flow rate), which is equivalent to the application of a step function of aeration in the system. The experiments were carried out in the TVFB of 1L (0.8L working volume), operated in the absence of cells, at 37°C, containing culture medium DMEM ($Dulbeco's Modified Eagle's Medium$ - Cultilab). The experimental conditions were: inner cylinder rotation rate varying from 25 to 300 rpm with aeration varying from 80 mL.min^{-1} to 550 mL.min^{-1}. The dissolved oxygen concentration was measured by a sterilizable electrode (Mettler-Toledo, model INPRO 6100/120/S/N) bearing a Teflon membrane (Mettler Toledo, model InPro T-96). The data acquisition, control equipment and sensor transmitters are manufactured by Autsens Industry, model SIMAD. All data was collected from the process, stored in its internal memory and, after the experiment, transferred to personal computer by a RS232 interface.

2.3 Mass transfer correlation of TVFB

Mass transfer is one of the most intensively investigated aspects of Taylor vortex flow. Mass transfer characterization typically employed dimensional analysis to correlates a mass transfer parameter (Sherwood number) to experimental data. Sherwood number which represents the ratio of actual convective mass transfer to purely diffusive transfer, is given by (2).

$$Sh = \frac{k_L \cdot d}{D} \tag{2}$$

where d corresponds gap between concentric cylinders; D is the oxygen diffusion coefficient in the liquid phase and k_L that corresponds mass transfer coefficient of liquid film.

In order to evaluate Sh, the mass transfer coefficients must be determined for each experimental vortex flow regime. In this study, other non-dimensional parameters were selected, as the rotational Reynolds number defined by (3) which corresponds to the ratio of viscous to centrifugal forces.

$$R_{e\theta} = \frac{\omega r_{in} d}{\nu} \tag{3}$$

where ω is the velocity of inner cylinder rotation, d corresponds the gap width between the cylinders, r_{in} is the inner radius and ν is the kinematic viscosity of fluid medium, in this case culture medium DMEM, at 37°C.

The air Reynolds number ($R_{e_{air}}$), defined by (4), which represents the ratio between the air rate flow and the product of membrane diameter by air viscosity. This dimensionless number equation was deduced exclusively for this work.

$$R_{e_{air}} = \frac{4}{\pi} \frac{Q}{d_{in} \nu_{air}} \tag{4}$$

where Q is the entry of airflow in equipment, d_{in} is the inner diameter of silicone tubular membrane and ν_{air} is the kinematic viscosity of air at 37°C.

So, the mass transfer correlation takes the following general form:

$$Sh = aR_{e\theta}^{b}R_{e_{air}}^{c} \tag{5}$$

where a, b and c are constants (Santiago, 2007).

3 Results and Discussion

Figure 2 illustrates the values of K_La in TVBF according to the rotational Reynolds number ($R_{e\theta}$) for each airflow rate that flows by the tubular silicone membrane (80 to 550mL.min^{-1}).

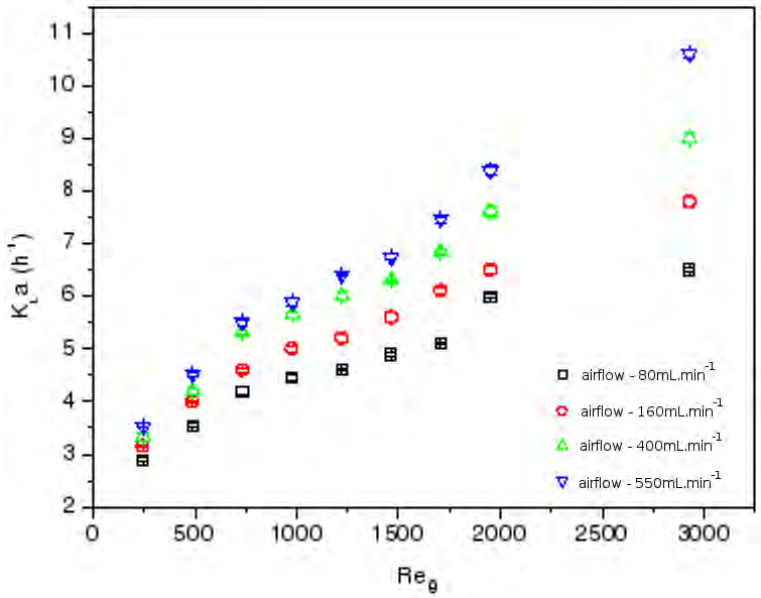

Figure 2: Experimental values of K_La as a function of rotational Reynolds number ($R_{e\theta}$) on TVFB. The experiments were made in cell-free media, at 37°C, containing culture medium DMEM and different airflow rates. The error bars correspond to the standard deviation of experiments performed in triplicates.

The results of K_La in the TVFB ranged from 3.0 to 10.7h^{-1}, which can be considered high when compared to other conventional rotating wall and other kinds of bioreactors used for animal cell culture, as the stirred tank. In this graph, the increase of Reynolds dimensionless number ($R_{e\theta}$) and the airflow rate contributed to a greater oxygen transfer to the liquid medium. Curran and Black (2005) performed experiments to determine K_La in Taylor vortex flow bioreactors, called DC-25R and using aeration in the surface, where the obtained results were: 0.6h^{-1} for $R_{e\theta}$=203 and 0.78h^{-1} to $R_{e\theta}$=1018. Values considered small because it is difficult to increase the scale of equipment.

In experiments performed in agitated tank bioreactors, employing tubular silicone membrane for aeration of the culture medium, values obtained from K_La were: 2 to 3h^{-1} (Tonso, 2000, Qi et al., 2003). In these works, the lengths of membranes ranged between 50 and 80 meters and its dimensions were similar to those used in membrane TVFB. Comparing the results of K_La in TVBF, operated under conditions similar to this bioreactors, it can be noted that the equipment enables an efficient oxygen transfer and mixture of medium, with a smaller length of the membrane, only 7m.

3.1 Mass Transport Correlation

In the experimental range of the used parameters, $R_{e\theta}$ between 244 and 2928 and airflow rates varying from 80 mL.min^{-1} to 550 mL.min^{-1} ($37 < R_{e_{air}} < 254$), the overall volumetric oxygen mass transfer

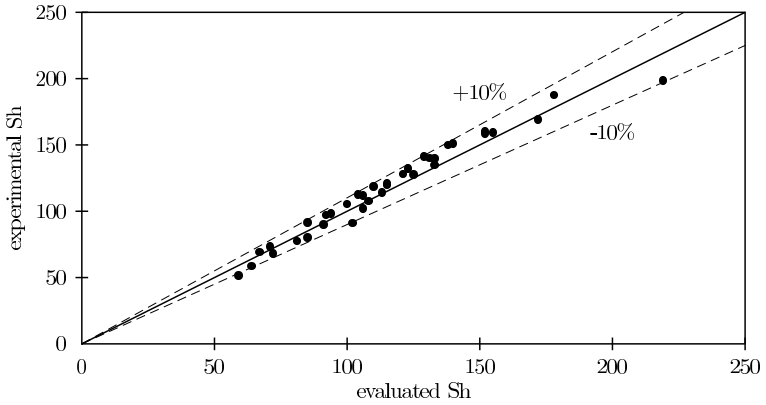

Figure 3: Comparison between calculated (Eq. 6) and experimental data of the Sh.

coefficient (K_La) varied from 3.0 to 10.7 h^{-1}. This leads to the mass transfer correlation of TVFB shown in Equation 6.

$$Sh = 2.97 R_{e\theta}^{0.4} R_{e_{air}}^{0.18} \tag{6}$$

The values of the parameters were obtained considering a confidence interval of 95%, and a correlation coefficient value (R^2) of 0.96, which ensures that the proposed model adequately describes the experimental data. The exponent of $R_{e\theta}$ (a) is around 0.5, since this value corresponds to the majority of correlations found in the literature for the case of Taylor vortex flow bioreactors with narrow gap ratios ($b/r_{in} < 0.5$) and small or zero axial flow (Moore, 1994).

Figure 3 shows a comparison between the experimental values of Sh and the values calculated for Sh by equation 6. It can be observed the difference between the experimental and calculated values of Sh are lower than 10%. As expected, the effects of increasing $R_{e\theta}$ and $R_{e_{air}}$ on K_La are positive, as shown by the exponent signals.

4 Conclusions

These results suggest that the TVFB has been identified as a competitive solution for animal cell culture in bioreactors, once it provides an effective means for oxygen transport. Membrane-aeration offers a convenient means of supplying oxygen to mammalian cell bioreactors with minimal introduction of shear, because it avoids the disruption of air bubbles in the gas-liquid interface. The mathematical model presented in this study allows estimation of the mass transfer in TVFB, considering the overall volumetric oxygen transfer coefficient (K_La), the operating conditions and the geometry of the bioreactor.

Acknowledgements

The authors thank the financial support provided by the brazilian foundations “Fundação de Amparo a Pesquisa do Estado de São Paulo” (Fapesp) and “Conselho Nacional de Desenvolvimento Científico e Tecnológico” (CNPq).

References

Blanch, H.W., Clark, D.S. (1997). *Biochemical Engineering.* New York: M. Dekker Inc. cap.5, 343-452.

Butler, M. (2004). *Mammalian cell culture and technology.* 2nd edition. Oxford: Bios Scientific. 256 p.

Camacho F, Gomez A, Sobczuk T, Grima E. (2000). Effects of mechanical and hydrodynamic stress in agitated, sparged cultures of Porphyridium cruentum. *Process Biochemistry*, 35, 1045-1050.

Chalmers J., Bavarian F. (1991). Microscopic visualization of insect cell-bubble interactions II: The bubble film and bubble rupture. *Biotechnology Progress*, 7, 151-158.

Curran, S.J., Black, R.A. (2005). Oxygen transport and cell viability in an annular flow bioreactor: Comparison of laminar coquette and Taylor-vortex flow regimes. *Biotechnology and Bioengineering*, 89, 7, 766-774.

Giordano, R.C., Giordano, R.L.C., Prazeres, D.M.F., Cooney, C.L. (1998). Analysis of a Taylor-Poiseuille vortex flow reactor I: flow patterns and mass transfer characteristics. *Chemical Engineering Science*, 53, 20, 3635-3652

Giordano, R.C., Giordano, R.L.C., Cooney, C.L (2000a). Performance of a continuous Taylor-Couette-Poiseuille vortex flow enzymatic reactor with suspended particles. *Process Biochemistry*, 35, 1093-1101.

Giordano, R.C., Giordano, R.L.C., Prazeres, D.M.F., Cooney, C.L. (2000b). Analysis of a Taylor-Poiseuille vortex flow reactor II: reactor modeling and performance assessment using glucose-fructose isomerization as test reaction. *Chemical Engineering Science*, 55, 3611-3626.

Hand-Corrigan A., Emery A.N, Spier R.E. (1989). Effect of gas-liquid interfaces on the growth of suspended mammalian cells: Mechanisms of cell damage by bubbles. *Enzyme Microbial Technology*, 11, 230-235.

Konz, J.O., King, J., Cooney, C.L. (1998). Effects of oxygen on recombinant protein expression. *Biotechnology Progress*, 14, 393-409.

Kunas, K., Papoutsakis, E. T. (1990). Damage mechanisms of suspended animal cells in agitated bioreactors with and without bubble entrainment. *Biotechnology and Bioengineering*, 36, 5, 476-483.

Ma, N., Koelling, K.W., Chalmers, J.J. (2002). Fabrication and use of a transient contractional flow device to quantify the sensitivity of mammalian and insect cells to hydrodynamic forces. *Biotechnology and Bioengineering*, 80, 428-437.

Moore, C. (1994). *Characterization of a Taylor-Couette vortex flow reactor.* 239 p. Ph.D. thesis, Massachusetts Institute of Technology, Cambridge, MA, USA.

Qi, H.N., Goudar, C.T., Michaels, J.D., Henzler, H., Jovanovic, G.N.; Konstantinov, K.B. (2003). Experimental and theorical analysis of tubular membrane aeration for mammalian cell bioreactors. *Biotechnology Progress*, 19, 1183-1189.

Resende, M.M. (2002). *Proteálise enzimática de soro de queijo em reator de Taylor-Couette-Poiseuille.* Ph.D. thesis – Department of Chemical Engineering, Federal University of São Carlos, São Carlos, SP, Brazil

Ruffieux, P.A, von Stockar, U, Marison, I.W. (1998). Measurement of volumetric (OUR) and determination of specific (qO2) oxygen uptake rates in animal cell cultures. *Journal of Biotechnology*, 63, 85-95.

Santiago, P.A. (2007). *Uma nova proposta de biorreator de escoamento em vártices de Taylor (BEVT) para cultivo de célula animal: o caso da célula CHO-K1 ancorante.* Ph.D. thesis – Department of Chemical Engineering, Federal University of São Carlos, São Carlos, SP, Brazil.

Taylor, G.I. (1923). Stability of a Viscous Liquid Contained Between Two Rotating Cylinders. *Philosophical Transactions of the Royal Society A*, 223, 289-343.

Tonso, A. (2000). *Monitoramento e operação de cultivos de células animais em sistemas de perfusão.* Ph.D. thesis – Department of Chemical Engineering, Escola Politécnica da Universidade de São Paulo, São Paulo, SP, Brazil.

Proceedings of the 10th International Chemical and
Biological Engineering Conference - CHEMPOR 2008
Braga, Portugal, September 4-6, 2008
E.C. Ferreira and M. Mota (Eds.)

Studies on synthetic medium composition for continuous production of clavulanic acid by *Streptomyces clavuligerus*

L. C. G. Domingues[1], J. C. Teodoro[2], C. O. Hokka[2], A. C. Badino Junior[2], M. L. G. C. Araujo[1*]

[1]Instituto de Química, Universidade Estadual Paulista
P.O.Box 355, ZIP Code 14801-970 Araraquara SP, Brasil
[2] Department of Chemical Engineering
Universidade Federal de São Carlos
P.O Box 676, ZIP Code 13565-905 São Carlos SP, Brasil

Keywords: clavulanic acid, synthetic media, *Streptomyces clavuligerus*, continuous culture, ornithyne
Topic: Integration of life sciences & engineering

Abstract

Amino acids are well metabolized during the clavulanic acid, CA, production process by *Streptomyces clavuligerus* cultivation with glycerol as carbon and energy source. However only some amino acids, such as arginine and ornithine, are favorable to CA biosynthesis. The aim of this work was to optimize the glycerol:ornithine molar ratio in the feed medium to enhance CA production in continuous cultivation. Factorial design experiments showed that a glycerol: ornithine molar ratio of 40:1, in the feed medium, resulted in the the highest CA concentration. Fermentor runs, under the optimized conditions, resulted in CA concentration enhancement above twice the value observed during the factorial design experiments with shake flasks.

1 Introduction

Clavulanic acid (CA) is commercially produced by *Streptomyces clavuligerus* in rich media containing glycerol as the main C and energy source, and complex nitrogen sources, such as soybean flour or soybean cake, that yield high CA production. These complex nitrogen sources, however, usually contain also undesirable components that interfere with microbial metabolism. In this way, amino acids and soluble components such as protein extracts and hydrolizates produce broths less viscous and more homogeneous, enhancing mass and heat transfer, facilitating monitoring and control of process variables, as well as it can make simpler the separation and purification steps (Elander, 2003). Despite that the great majority of amino acids are well metabolized by the microorganism, only some of them are favorable to CA biosynthesis. Such is the case of arginine and ornithine, precursors of CA molecule (Romero et al, 1984). However, Romero et al. (1984, 1986) observed that supplementary arginine in the medium may lead to intracellular accumulation of glutamate that, according to these authors, affects negativelly the production of CA. Ives and Bushell (1997) fed a continuous culture with single amino acids belonging to the main carbon flux of the biosynthetic pathway of CA; they observed that the addition of leucine, isoleucine, serine or valine, but not arginine, led to production rate increase. In another recent work, Bushell et al. (2006) evaluated the carbon fluxes working with media limited by phosphate, nitrogen or carbon utilizing Metabolic Flux Analysis techniques. These authors observed no significant correlations between reactions which fluxes are linked directly to arginine. This fact is in agreement with the work of Kirk et al (2000), suggesting that the biosynthesis of this amino acid is saturated in CA production process under phosphate-limited conditions. Chen et al.

* Corresponding author. Tel + 55-16-33016710. E-mail:mlaraujo@iq.unesp.br

(2003) observed that feeding ornithine in fed-batch culture not only provided an adequate supply of arginine for CA production, but also inhibited the glycerol-utilizing cephamycin biosynthesis. These results made clear that ornithine, rather than arginine, enhances effectively CA production if the amount of C3 precursor (glycerol) is sufficient. Thus, the aim of this work was to optimize the molar ratio between glycerol and ornithine in the feed medium making use of Factorial Experimental Design (Box et al, 1978) in order to achieve higher CA concentration.

2 Materials and Methods

Streptomyces clavuligerus ATCC 27064 used throughout this work was stored in the form of vegetative cells (8.0 $g.L^{-1}$ dry weight) at −70°C in cryotubes, utilizing glycerol 20% (w/v). Inoculum medium was composed of (in g/L) glycerol (15.0), soybean protein isolate (Soytone) (15.5), yeast extract (1.0), Malt extract (10.0), K_2HPO_4 (0.8), $MgSO_4.7H_2O$ (0.75), 1.0 mL/L of salt solution containing: (in g/L) $MnCl_2.4H_2O$ (1.0), $FeSO_4.7H_2O$ (1.0) e $ZnSO_4.7H_2O$ (1.0). Production medium had the same composition except that malt extract was not added. The media were supplied with 21 g/L of MOPS, and initial pH was adjusted to 6.8.

Fermentation was carried out in shake flasks (250 rpm, 28ºC) and in bench scale fermentor (News Brunswick Bioflo 2000, 5L working volume), experiments were carried out with automatic control of pH (6.8±0.2), temperature (28 ºC) and DO level (approximately 40% saturation by varying agitation speed), 1 vvm aeration rate. In both casesm shake flasks and fermentor, after 48 h cultivation, broth withdrawal and medium feeding were accomplished at $D = 0.005\ h^{-1}$. The feed medium was composed of tap water 5%, MOPS (21 g/L) and several combination of glycerol and ornithyne concentrations. Same medium and dilution rate were utilized for a 5 L bioreactor run (DO controlled above 40% saturation). CA was determined by the method described by Bird et al. (1982), cell mass was determined as dry weight and glycerol by the method described by Lambert and Neish (1950).

Concentration range for the independent variables – glycerol (x_1) and ornithyne (x_2) – were defined based on the literature, setting the response variable as CA concentration (mg/L), at 144 h cultivation. Romero *et al.* (1986) observed that glycerol concentration of 165 mM inhibited CA synthesis while ornithine (ca. 5 mM) exerted a positive effect. A central composite factorial design was performed, with x_1 e x_2 from –1 to +1 (coded units), and added star (x_1 e x_2 from $-\sqrt{2}$ to $+\sqrt{2}$) (Box et al., 1978).

3 Results and Discussion

In all experiments biomass concentration was assumed constant, around 8 g/L, and the residual glycerol concentration was practically zero despite its addition through the feed medium (Figure 1).

Statistical analysis resulted in a response surface adjusted at 95% confidence level and 0.91, determination coefficient. The resulting response surface, fitted by Equation 1 (x_1 and x_2 in coded units) with the significant parameters, predicted maximum CA concentration (mg/L) at a molar ratio glycerol to ornithyne of 40, corresponding to 87 mM and 2.12 mM, respectively, in the flask at the moment of each addition (Figure 2). The statistical evaluation of data indicated that CA production decreases whenever there is any minor change in glycerol or ornithine concentration around the values of the optimized ratio.

$$C_{AC} = 472.4\ (\pm 18.0) - 20.8\ (\pm 12.8)\cdot x_1 - 68.6\ (\pm 14.4)\cdot x_1^2 - 89.2\ (\pm 14.2)\cdot x_2^2 \qquad \text{(Eq. 1)}$$

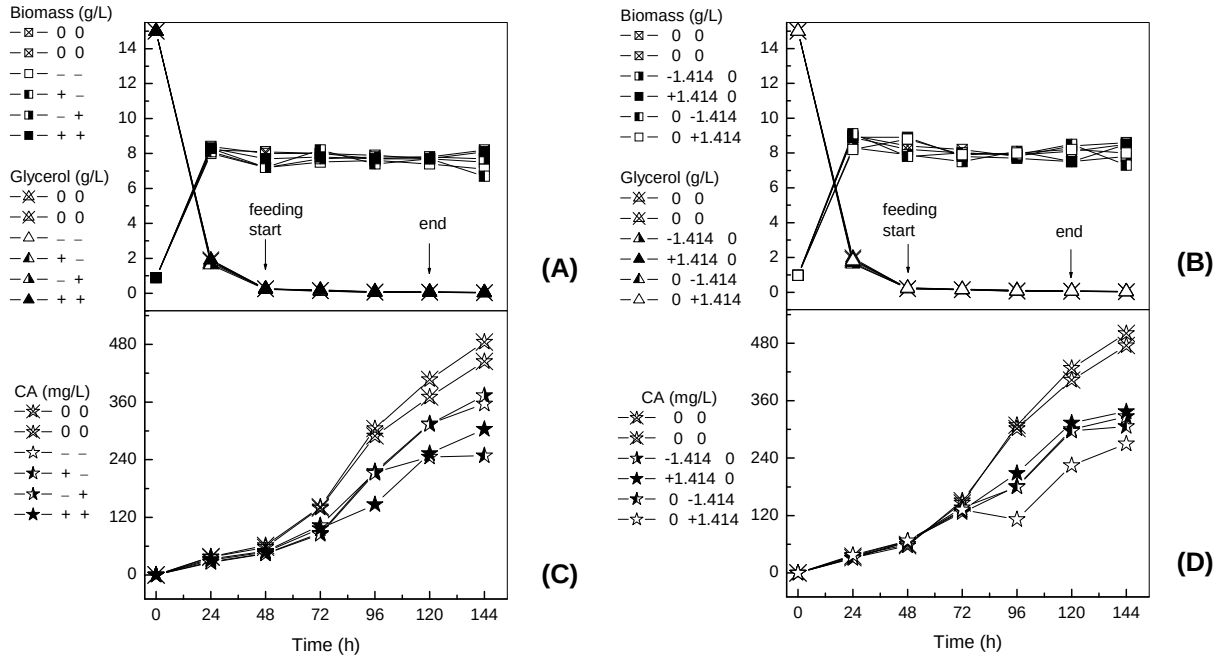

Figure 1 – Central composite factorial design with added star – time course of biomass and glycerol (A and B), and CA (C and D)

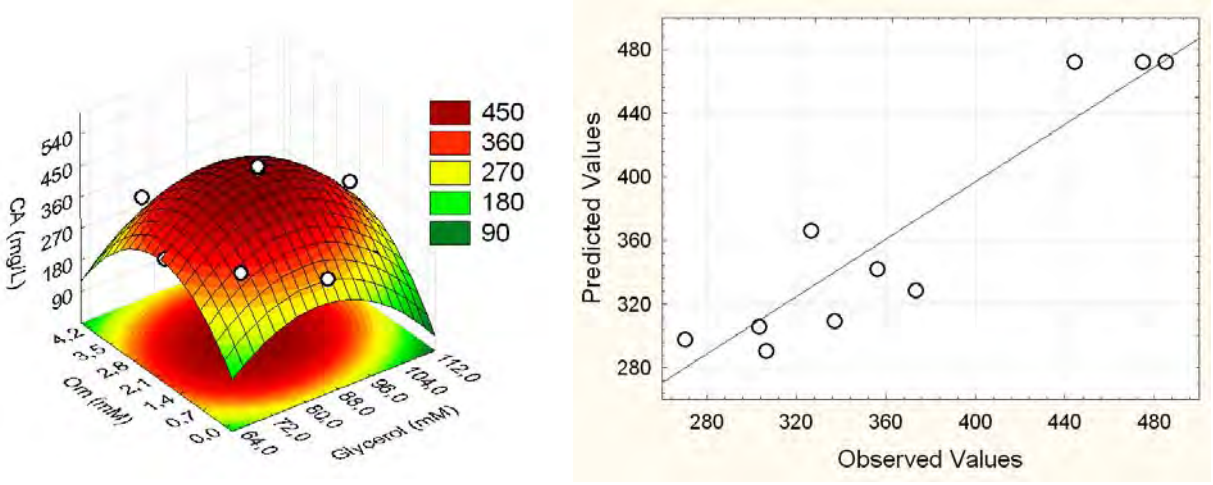

Figure 2 – Fitted response surface (0.91 determination coefficient at 95% confidence level) (A) and observed vs. predicted values of CA (mg/L) obtained at 144 h of continuous process in shake flasks (D = 0.005 h^{-1}) (B)

The optimized molar ratio was tested in a feed medium containing 70.7 mM glycerol and 1.72 mM ornithine. These concentrations are ca. 20% lower than that utilized originally (Figure 3). Under these conditions, CA production has stabilized at levels 25% greater than previously, after 72 h. The optimized molar ratio was then utilized in a experiment with a 5 L bioreactor provided with agitation and aeration, at the same dilution rate as that utilized in shake flasks, D = 0.005 h^{-1}. The process behaviour is illustrated in Figure 3. As it can be observed, in the bioreactor, the CA concentration achieved a value 60% higher than that in shake flasks which in turn, with the optimized ratio, reached a value 25% higher than that the control run.

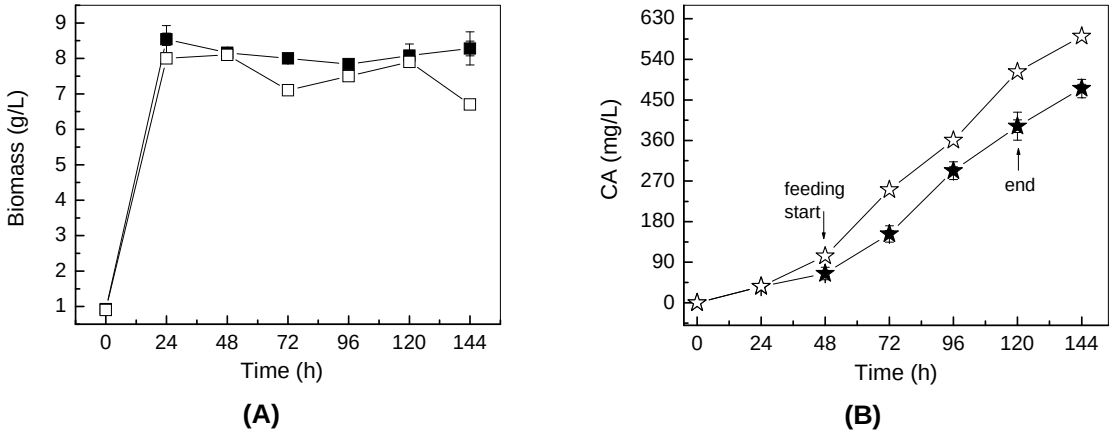

Figure 3 – (A) Biomass (□, ■) and (B) CA (☆, ★) obtained in continuous process in shake flasks (D = 0,005 h^{-1}) with glycerol:ornithine ratio 40 (glycerol 70.7 mM and Orn 1.72 mM – open symbols; glycerol 87 mM and Orn 2.12 mM – closed symbols, concentrations in the flask, at the moment of each addition).

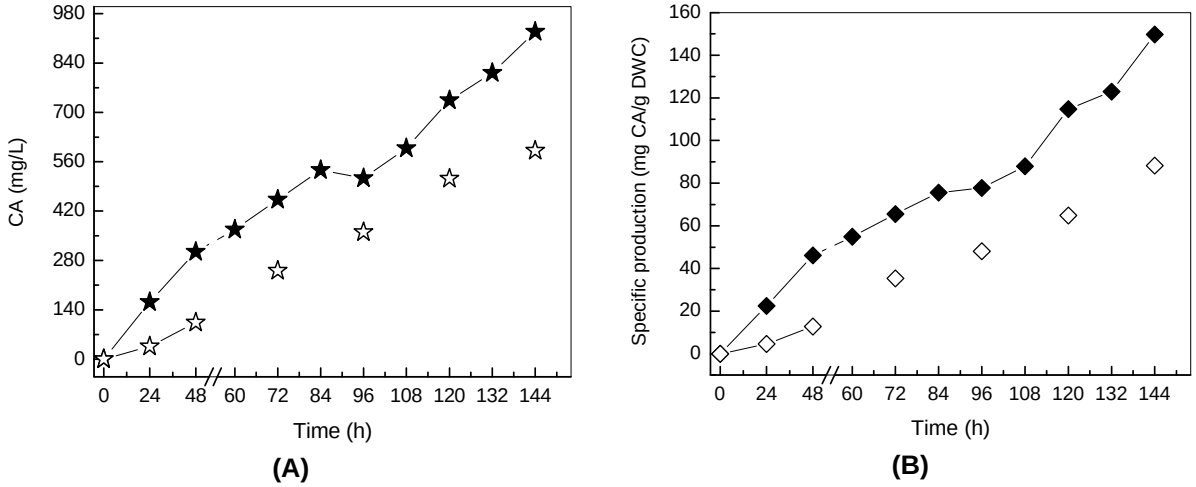

Figure 4 – Time course of (A) CA concentration and (B) specific yield in shake flasks (open symbol) and in agitated and aerated bioreactor (filled symbols), constant volume, D = 0.005 h^{-1}, glycerol:ornithine molar ratio = 40, with 70.7 mM glycerol and 1.72 mM ornithine in the flask, at the moment of each addition.

The final CA yield, in regards to glycerol consumption during the idiophase, was 3.3 mg CA/g glycerol, i.e., 57% higher than that obtained in shake flasks under the same conditions of glycerol and ornithine concentrations and 140% higher than that produced in shake flasks under the optimal concentrations evaluated from the conditions pointed out by the analysis of the factorial design results.

References

Bird, A. E.; Bellis, J. M.; Gasson, B. C. (1982). Spectrophotometric assay of clavulanic acid by reaction with imidazole. *Analyst,* 107, 1241-1245.

Bushel, M. E.; Kirk, S.; Zhao, H-J.; Rosa, C. A. (2006). Manipulation of the physiology of clavulanic acid biosynthesis with the aid of metabolic flux analysis. *Enzyme Microbial Technology*, 39,149-157.

Box , G. E. P.; Hunter, W. G.; Hunter, J. S. Statistics for experimenters (1978). New York: John Wiley and Sons, 655p.

Chen, K-C.; Lin, Y-H.; Wu, J-Y.; Hwang S-C. J. (2003) Enhancement of clavulanic acid production in Streptomyces clavuligerus with ornithine feeding. *Enzyme Microbial Technology*, 32, 152-156.

Elander, R. P. (2003). Industrial production of β-lactam antibiotcs. *Applied Microbiology and Biotechnology*, 61, 385-392,

Ives, P. R.; Bushell, M. E. (1997). Manipulation of the physiology of clavulanic acid production in Streptomyces clavuligerus. *Microbiology*, 143, 3573-3579.

Kirk, S.; Avignone-Rossa, C. A.; Bushell M. E. (2000). Growth limiting substrate affects antibiotic production and associated metabolic fluxes in *Streptomyces clavuligerus*. *Biotechnology Letters*; 22, 1803–1809.

Lambert, M.; Neish, A. C. (1950). Rapid method for estimation of glycerol in fermentation solution. *Canadian Journal of Research*, 28, 83-89.

Romero, J.; Liras, P.; Martín, J. F. (1984). Dissociation of cephamycin and clavulanic acid biosynthesis in *Streptomyces clavuligerus. Applied Microbiology Biotechnology*, v.20, p.318-325.

Romero, J.; Liras, P.; Martin, J. F. (1986). Utilization of ornithine and arginine as specific precursors of clavulanic acid. *Applied and Environmentall Microbiology* 52, 892-897.

Proceedings of the 10th International Chemical and
Biological Engineering Conference - CHEMPOR 2008
Braga, Portugal, September 4-6, 2008
E.C. Ferreira and M. Mota (Eds.)

Effect of physicochemical properties of solvents on clavulanic acid extraction from fermentation broth

L. M. Brites[1], J. H. Oliveira[1], C.O.Hokka[1], M.Barboza[1*]

[1] Department of Chemical Engineering

Federal University of Sao Carlo

P.O Box 676, ZIP Code 13565-905 Sao Carlos SP, Brazil

Keywords: clavulanic acid, extraction, organic solvent, dissociation constant, purification

Topic: Integration of life sciences & engineering

Abstract

A study was made of the effect of the physicochemical properties of organic solvents on the extraction of clavulanic acid, from fermented broth, including its concentration and purification. The extraction were carried out at room temperature, at pH values of 2.0, 3.0, 4.0 and 5.0. It was observed that extraction with butanol leads to a higher Distribution Coefficient than ethyl acetate. The optimal condition with ethyl acetate occurs at pH 1.63, yielding an extraction factor of 35.6% with a distribution coefficient of 0.73.

Introduction

The isolation of clavulanic acid, CA from fermentative broth requires a series of steps due to the high contents of various contaminants that are typical in bioprocesses involving complex media. At the end of fermentation, the broth is clarified by filtration or centrifugation to eliminate mycelia, cell debris and insoluble particles, after which it is subjected to the primary extraction or direct extraction from clarified broth with organic solvent, producing an organic phase containing CA, which is subsequently isolated (Butterworth, 1982; Nabais & Cardoso, 1995). Several patents describe the extraction of clavulanic acid onto organic solvents (Cole *et al.*, 1978; Cardoso, 1998). These patents explain that CA can be extracted from fermentation broth by different procedures, and that CA is isolated when its corresponding potassium salt is formed. This salt is produced by reacting CA with potassium 2-ethylhexanoate in the solvent-rich phase, i.e., after cell removal, the resulting clarified broth is acidified to reach pH values between 2 and 3. The CA is then extracted using organic solvents such as ethyl acetate, n-butanol, methyl isobutyl ketone (MIK), n-butyl acetate, and others, and the salt is formed. Care should be taken, since clavulanic acid is highly unstable depending on the pH of the medium (pH lower than 6.2 and higher than 7.0), the presence of ammonium compounds, and the temperature (Bersanetti, *et al.* 2005). On the other hand, clavulanic acid forms unstable hygroscopic oil which cannot be used as a pharmaceutical compound (Cardoso, 1998); therefore, this purification step requires special attention to ensure an efficient process. The extraction of CA onto organic solvents is strongly affected by physicochemical properties such as solubility, polarity and dielectric constant.

* Corresponding author. Tel + 55-16-33518713. E-mail:marlei@ufscar.br

This paper discusses the conditions, procedure and results obtained in the extraction of clavulanic acid from fermented broth using different organic solvents. The effect of physicochemical properties on the CA distribution coefficient, D, in the aqueous media-solvent system was determined with different organic solvents, namely, butyl acetate, ethyl acetate, methyl-isobutyl-ketone, 2-butanol and n-butanol. In addition, the effect of each solvent's physicochemical properties on the values of D was examined.

Materials and methods

Materials

Streptomyces clavuligerus ATCC 27064 fermentation broth according to Rosa *et al*. (2005). The CA was determined using the HPLC method proposed by Foulstone & Reading (1982). The concentration of contaminants was determined by spectrophotometric analysis at 280, disregarding the influence of clavulanic acid at that wavelength.

Assuming that no CA molecule is charged during the extraction and that the extraction process takes place in a perfectly stirred tank, the distribution coefficient in equilibrium can be given by Equation 1.

$$D = \frac{C_{OP1}}{C_{AP1}} \quad (1)$$

where C_{OP1} is the solute concentration in the light phase, OP (organic phase), and C_{AP} is the solute concentration in the heavy phase, AP (aqueous phase). Figure 1 illustrates the extraction process schematically.

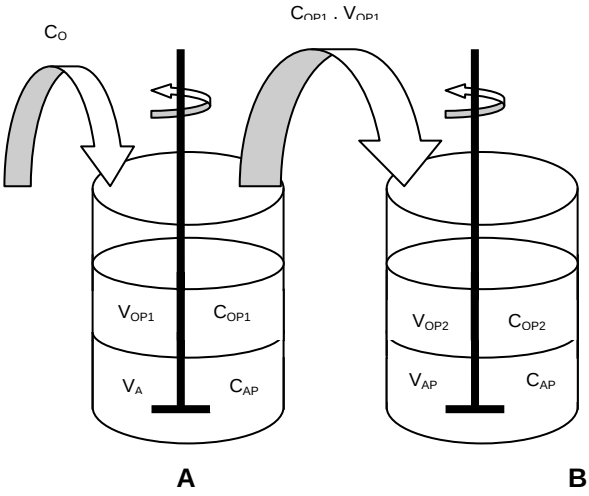

Figure 1. Scheme of the batch extraction process for clavulanic acid. A): extraction step, and B) back-extraction step

The mass balance of the extraction process can yield:

$$C_O \cdot V_{AP1} = C_{AP1} \cdot V_{AP1} + C_{0P1} \cdot V_{0P1} \quad (2)$$

$$C_{OP1} \cdot V_{OP1} = C_{AP2} \cdot V_{AP2} + C_{OP2} \cdot V_{OP2} \quad (3)$$

where C_O: clavulanic acid concentration in feed stream ($g.L^{-1}$), C_{FA1}: solute concentration of the first aqueous phase ($g.L^{-1}$), $C_{FO\ 1}$: solute concentration of the first organic phase ($g.L^{-1}$), , V_{FA1} : volume of the first aqueous phase (L), $V_{FO\ 1}$: volume of the first organic phase (L), C_{FA2} : solute concentration of the second aqueous phase ($g.L^{-1}$), $C_{FO\ 2}$: solute concentration of the second organic phase ($g.L^{-1}$), V_{FA2} : volume of the second aqueous phase (L), $V_{FO\ 2}$: volume of the second organic phase (L).Assuming

that all the CA molecules become charged during the back-extraction with neutral aqueous solution, the concentration in the organic phase becomes negligible (C_{OP2}=0). Hence, Equation 3 becomes

$$C_{OP1} = \frac{C_{AP2} \cdot V_{AP2}}{V_{OP1}} \quad (4)$$

Equation 1 can be combined with equation 4, leading to equation 5:

$$\frac{C_{AP2}}{C_{AP1}} = D \cdot \frac{V_{OP1}}{V_{AP2}} \quad (5)$$

The distribution coefficient (D) was calculated from Equation 5 for different volume and concentration ratios.The performance of the process can be analyzed in terms of such important parameters as yield Y, purification factor PF and concentration factor CF. PF is the ratio between the CF (C/C_o) of the CA and the CF of contaminants (C_T/C_{To}), according to Barboza *et al.*, 2002 and Almeida *et al.* 2003. At low pH, beta-lactam antibiotics, including clavulanic acid, usually have a protonated carboxylate group causing its low solubility in water and can be readily extracted into an organic solvent. At higher pH values the carboxylate group is deprotonated and charged, rendering the CA water soluble. The neutral concentration can be expressed according to Equation 6

$$\mathrm{Cn} = \frac{\mathrm{Co}}{(1+10^{(\mathrm{pH}-\mathrm{pKa})})} \quad (6)$$

where Cn is the concentration of the neutral form of CA and Co is the initial concentration. This equation allows for calculation of the clavulanic acid concentration in the neutral form, which remains in the heavy aqueous phase.

Results and discussion

Table 1 presents the experimental values together with each solvent's pertinent properties such as the dielectric constant, polarity, solubility in water and its molecular weight.

Table 1 Clavulanic acid distribution coefficient in different solvents and relevant properties of the solvents

Solvent	D (-)	Dielectric constant (d) (ε vacuum^{-1})	Solubility (S) (g/100g H_2O)	Molecular Weight (MW)
Butyl acetate	0.19	5.01	0.7	116.60
Ethyl acetate	0.56	6.02	8.5	88.10
Methyl isobuthyl ketone	0.32	13.11	1.9	100.16
2-butanol	0.91	15.80	9.0	74.12
n-butanol	1.38	17.51	12.5	74.12

The effects of the physicochemical properties of the organic solvents on the CA extraction are listed in Table 1. The degree of extraction is intrinsically affected by these properties. The first influence observed was on the organic solvent molecular weights. Figure 2 shows that D is inversely related to the solvent's molecular weight, i.e., the higher the MW the lower the distribution coefficient. The extraction of CA with 2-butanol and n-butanol, representing the low MW solvents, was considerably higher than with the other solvents. As for the effect of the dielectric constant on D, there is no simple or theoretical function able to relate these two variables, as indicated in Figure 3. However, if the data are divided into two regions, two directly proportional

relationships are observed. The first region encompasses the results obtained with butyl and ethyl acetate, while the second region involves the other three solvents, with a dielectric constant higher than 10. The discontinuity of the tendency for the linear increase of D with the dielectric constant is intrinsically related to the molecular structure of each solvent, particularly with regard to the functional ketone group, and with the solubility of these solvents in water. CA contains two hydroxyl groups in its structure, allowing for interactions between molecules through hydrogen bonds. The dissolution of substances like CA is favored in polar solvents in which hydrogen bonds are formed, such as alcohols. Solvents like ethyl acetate and other esters present weaker intermolecular interaction (dipole-dipole) when compared with hydrogen bonds, leading to a low dielectric constant and a weak interaction between solute (CA) and solvent, despite their higher polarity. The composition of the medium strongly affects the thermodynamic properties, which in turn affect the intermolecular interaction between the solvent and CA, producing different yields and purification factors. Figure 4 illustrates the behavior of D with solubility, S, and their relationship. The third point shown in this figure, corresponding to ethyl acetate, deviates from the linear behavior shown by the other solvents, i.e., although the solubility of ethyl acetate is nearly the same as that of 2-butanol, the dielectric constant of 2-butanol is much higher than that of ethyl acetate. However, as Figure 5 indicates, there is a well defined direct proportionality between D and the product of the dielectric constant and solubility, dxS, showing that this product can be used as a criterion to investigate other possible solvents to extract CA from aqueous media.

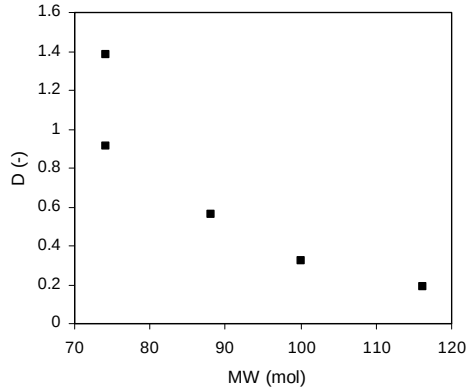

Figure 2. Relation between distribution coefficient and molecular weight

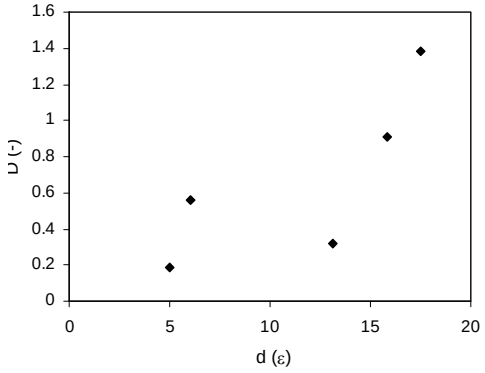

Figure 3. Relation between distribution coefficient and the dielectric constant

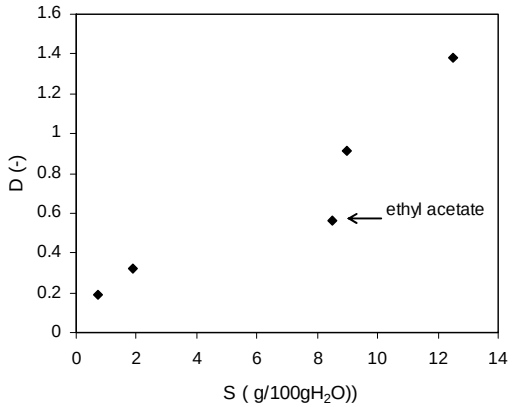

Figure 4. Relation between distribution coefficient and solubility of solvent in water

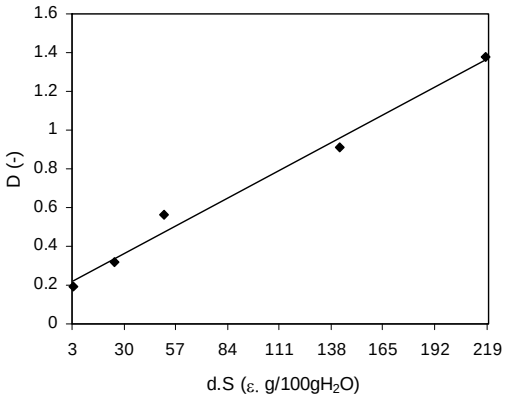

Figure 5. Linear relation between distribution coefficient and the product of solubility and the dielectric constant (dxepsilon): Correlation obtained: $D = 0.0053\ d\ \varepsilon + 0.2045$ with $r^2 = 0.9881$

Table 2 lists the results of yield, purification factor and concentration factor for CA

extraction from the clarified broth, while Table 3 presents these results for ethyl acetate and n-butanol.

Table 2. Extraction of clavulanic acid with ethyl acetate

C_{CAi} ($mg.L^{-1}$)	C_{CAf} ($mg.L^{-1}$)	CT_i (-)	CT_f (-)	CF (-)	PF (-)	Vi (mL)	Vf (mL)	Y (%)
184.1	352.6	3.3	2.0	1.9	3.1	300.0	40.0	25.5
269.3	271.7	3.3	1.3	1.0	2.4	300.0	104.0	35.0
191.6	291.9	2.0	1.1	1.5	2.7	300.0	65.0	33.0
161.9	173.6	1.7	0.4	1.1	5.3	100.0	34.0	36.5

Table 3 Extraction of clavulanic acid with n-butanol

C_{ACi} ($mg.L^{-1}$)	C_{ACf} ($mg.L^{-1}$)	CT_i (-)	CT_f (-)	CF (-)	PF (-)	Vi (mL)	Vf (mL)	Y (%)
171.7	448.6	2.3	1.1	2.6	5.4	250.0	40.0	41.8
179.7	511.1	*	*	2.8	*	250.0	50.0	56.9
217.5	493.7	2.3	1.5	2.3	3.5	225.0	50.0	50.4
225.4	612.6	2.3	1.5	2.7	4.2	210.0	37.0	47.9

* not determined

The solvent n-butanol produces better results than ethyl acetate in terms of its ability to concentrate the CA solution, because n-butanol is more water-soluble than ethyl acetate; CA, in turn, is highly water-soluble, improving the extraction. The values of the concentration factor were found to decrease when ethyl acetate was used to extract CA, due to its low solubility in water. Although n-butanol presents a higher distribution coefficient for CA, the fact that it is more water-soluble actually hinders the purpose of the purification process, which is to trigger the precipitation reaction in this solvent. This is a decisive factor in choosing the most adequate solvent for the process. Therefore, ethyl acetate is potentially the solvent of choice to purify CA from fermentation broth.

In order to increase the value of the distribution constant, experiments were conducted to determine the pH at which all the CA was in the dissociated form. The results in Figure 6 indicate the pH at which the maximum CA extraction is achieved, i.e., the pH corresponding to the lowest neutral CA (clavulanate form) concentration. The neutral concentration is zero at pH 1.63; in this condition the extraction factor is 35.6% with a distribution coefficient of 0.73. Figure 7 presents the relation between D and CA in the neutral form (clavulanate), in the extraction with ethyl acetate. Therefore, at zero level of Cn, the maximum D value is 0.73.

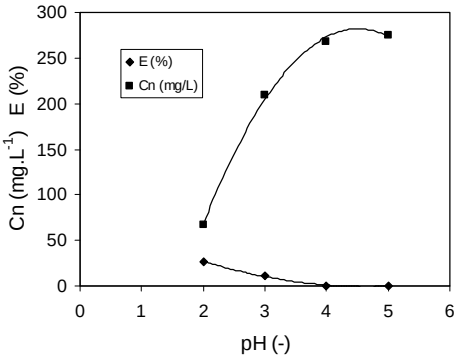

Figure 6. Variation of neutral concentration and the extraction factor, with pH, for ethyl acetate.

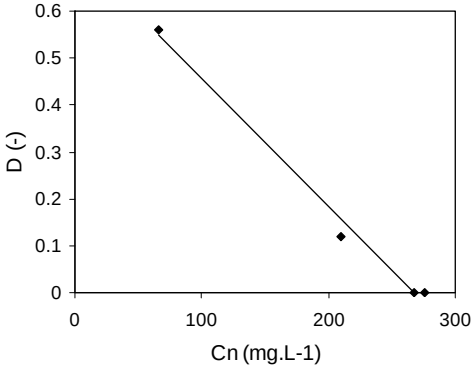

Figure 7. Distribution coefficient for clavulanic acid in ethyl acetate as a function of the neutral concentration and initial concentration.

The use of n-butanol is very attractive because it produces a high, but in this case, the use of a desiccant substance or dehydrating material is mandatory in order to withdraw water solubilized in n-butanol. The cost of removing water from the process should be a decisive factor in the choice between n-butanol and ethyl acetate as the solvent. During the extraction of clavulanic acid by organic solvents such as ethyl acetate and other esters, dipole-dipole type interactions occur. These are weak interactions, e.g., hydrogen bonding. Despite the higher polarity of some organic solvents, they usually have a low dielectric constant, which affects the CA extraction, and a weak solute-solvent interaction. These interactions may be stronger or weaker, depending on the components in the solution which are able to promote changes in the thermodynamic properties of the mixture, affecting the purification factor and yield. The extraction of clavulanic acid with n-butanol is better than with ethyl acetate, but the higher solubility of water in n-butanol impairs the final precipitation of CA.

The optimal condition for the extraction of clavulanic acid with ethyl acetate is at pH 1.63, which provides an extraction factor of 35.6% with a distribution coefficient of 0.73.

In addition, the distribution coefficient is linearly related to the product dxS, which could be used to investigate other solvents to extract CA or other beta-lactam antibiotics from fermentation broth.

Acknowledgements:The authors gratefully acknowledge the financial support of FAPESP (Grants 04/16056-6, 04/15540-1 and 05/55079-4) and the CNPq scholarship granted to L. M. Brites.

References

Almeida, R. M. R. G; Barboza, M.; Hokka, C. O. (2003) Continuous clavulanic acid adsorption process. *App. Bioch. and Biotech.*, **105** 867-879.

Barboza, M.; Almeida, R. M. R. G.; Hokka, C. O. (2002). Kinetic studies of clavulanic acid recovery by ion exchange chromatography. *Biosep.*, **10** 221-227.

Bersanetti, P. A., Almeida, R. M. R. G., Barboza, M., Aaraujo, M. L. G. C., Hokka, C. O. (2005) Kinetics studies on clavulanic acid degradation. *Bioch.l Eng. J.l.* , **23** 31-36.

Butterworth, D. (1984) Clavulanic Acid: Properties, Biosynthesis and Fermentation. In: Vandamme, E. J. *Biotech. of Ind.l Antib.*. New York, Marcel Deckker. **22** 225-235.

Cardoso, J.P. (1998) Process for the isolation of a pharmaceutically acceptable alckali metal salt of clavulanic acid. EP 0 867 515 A1

Cole, M.; Howarth, T.T.; Reading, C. (1978) Process of Production Of Clavulanic Acid. USP 4110165.

Foulstone, M. e Reading, C. (1982), Assay of Amoxicilin and Clavulanic Acid, the Components of Augmentin, in Biological Fluids with High-Performance Liquid Chromatography. *Antim. Ag. and Chemoth.*. 753-762.

Nabais, A. M. A.; Cardoso, J. P. (1995) Ultrafiltration of Fermented Broths and Solvent Extraction of Antibiotics. *Biop. Eng.,* **13** 215-221.

Rosa, J.C.; Baptista-Neto, A.; Hokka, C.O.; Badino, A.C. (2005) Influence of dissolved oxygen and shear conditions on clavulanic acid production by Streptomyces clavuligerus. *Biop. and Biosys. Eng..* **27** 99-104

Proceedings of the 10th International Chemical and
Biological Engineering Conference - CHEMPOR 2008
Braga, Portugal, September 4-6, 2008
E.C. Ferreira and M. Mota (Eds.)

Kinetic production of the antioxidant ellagic acid by fungal solid state culture

Juan S. Hernández[1], Antonio F. Aguilera-Carbó[2], Raúl Rodríguez-Herrera[1], José L. Martínez[1], Cristóbal N. Aguilar[1]*

[1] Food Research Department. School of Chemistry. Universidad Autónoma de Coahuila. Blvd. Venustiano Carranza PO BOX 252. ZIP 25000, Saltillo, Coahuila, México.

[2] Department of Food Science, Technology and Engineering. Universidad Autónoma Agraria Antonio Narro Buenavista Satillo.

Keywords: solid state culture, polyphenols, ellagic acid, ellagitannins, *Punica granatum*
Topic: Integration of life science & engineering.

Abstract

The solid-state bioprocess for microbial production of potent antioxidants is an emerging promissory biotechnology. Ellagic acid (EA) is a potent antioxidant with important physiological and functional properties. In this study EA was produced by solid state fermentation (SSF) using pomegranate husk as support and nutrient source. *Aspergillus niger* GH1 was used to release ellagic acid from ellagitannins present into pomegranate residues. SSF was kinetically monitored during 168 h. Polyphenolic content was evaluated during the fermentation, EA released was measured by HPLC. Obtained results demonstrated high rates of biodegradation of the hexahydroxydiphenic group from the ellagitannins. The highest EA accumulation was reached at the 96 h of culture (12.3 mg per gram of substrate). A yield of 0.3 g EA per g of substrate was obtained. EA formation specific rate was of $1.92x10^{-4}$ g product per g biomass per hour and the productivity of $1.29x10^{-4}$ g EA per g support per hour. SSF is an excellent alternative bioprocess for bio treatment of pomegranate residues to produce ellagic acid

1. Introduction

Ellagic acid (EA) and ellagitannins (ET´s) are naturally occurring phenolic compounds widely distributed in plants, the importance of this compound is due its diverse properties reported as potent antioxidant, anti-inflammatory, anti'-tumoral, anti-microbial, anti-viral and anti-proliferative capacities (Aguilera-Carbo et al. 2007). Major ellagitannins source are wood oak (*Quercus sp*), chesnut (*Castanea sp*) and myrobalan (*Terminalia chebula*) and some fruits like strawberry, raspberry, blueberry, cranberry, pecan and walnut.(Clifford and Scalbert, 2000). Chemically, ellagitannins consist of glucose esterified with hexahydroxidiphenic acid, gallic acid and their derivates (Shi et al., 2005). For industrial EA production from ET's, the acidic hydrolysis is the common method, however, it is an expensive and low-yield procedure (Saavedra et al. 2005). Recently, several studies on biotechnological production of EA from several plant materials have been published (Huang et al. 2007a, b, c, d; Robledo et. al. 2008; Aguilera-Carbo et al., 2008; Aguilar et al., 2008).

Our group, previously reported the first findings on fungal EA production through SSF (Aguilera-Carbó et al., 2008; Robledo et al. 2008) demonstrating that the pomegranate husk residue is an excellent alternative for EA production. Also, a biodegradation process of ET's for EA production has been proposed (Aguilera-Carbo et al. 2007). SSF is one of the most attractive alternative to management of agro industrial by-products, in this case the residues of pomegranate husk contain an interesting profile of nutrients such as large amounts of insoluble carbohydrates, small amount of protein, minerals and some remaining juice and other soluble substances favoring a rapid microbial growth. These properties can be approached for the production of high value-added metabolites. In this study we evaluated the kinetic parameters of EA production by *Aspergillus niger* GH1 using a pomegranate husk residues as support of SSF

2 Materials and methods

Powder of pomegranate husk. The samples of pomegranate fruits were collected from a rustic orchat in Sabinas, Coahuila, México. The pomegranate fruits were cleaned with water and separated in husk and seed, the husk were dried in a funnel dryer, at 60 ºC for 48 h. The dried husk was pulverized and sifted to a 30 mesh particle size in an industrial homogenizer (5 L, model LP12 Series 600-182, JR Maquinaria para mercado S.A. de C.V., México) and stored in dark and dry conditions. The material obtained was called powder of pomegranate husk (PPH).

Microorganism strain. Aspergillus niger GH1, was provided by Food Research Department collection (Universidad Autónoma de Coahuila, in Saltillo, Coahuila, México). This was previously isolated from a native plant of a semidesert zone, and selected to grow in high tannin concentrations (Cruz-Hernandez et al., 2005).

Propagation, composition media and culture conditions. The mycophill agar medium was used for propagation of fungal inoculum. The culture broth for SSF was PPH medium composed with (gL^{-1}) $NaNO_3$ 6.0, KH_2PO_4 2.4, $MgSO_4$ 1.2, KCl 1.2 and inoculated with $2x10^7$ spores per gram of PPH (support). The fermentation was carry out in tray reactors under moisture of 70 % at 30 ºC by seven days. SSF was analyzed in triplicates.

Pre treatment of material fermented for the determination. Fermented PPH was resuspended with water (30 mL) and shacked in a RIVAL immersion blender (model IB901 MX) during two cycles of 30 s, the material was transfered at 50 mL conic tubes and these were immersed in a vibrating sonic bath for 30 min (Bransonic, Model 2510R-MTH, Branson Corp, CT, USA). The material was centrifuged at 6000 rpm by 30 min, decanted and the liquid fraction was recovered (Aguilera-Carbo et al. 2007a).

Analytical methods. The biomass content was indirectly evaluated by spectrophotometry using the glucosamine content determination (Boone-Villa et al., 2008). Substrate consumption (total polyphenols content) was evaluated using the methodology reported by Makkar (1993).

Sample Preparation of ellagic acid determination and quantification by HPLC. The PPH fermented was resuspended with 30 mL of ethanol and homogenized in a submerged blender by two cycles of 30 s, the material was transfered at 50 mL conic tubes and immersed into a vibrating sonic bath by 30 min, the mixed material, an aliquot of 1.5 mL was transferred into an eppendorff tube and centrifuged at 6000 rpm (3600g) by 20 min. The supernatant was decanted and the precipitate was resuspended in ethanol. The sample was immersed into a vibrating sonic bath again for 30 min and the solution was transferred into clean test tubes and filled up to a 5 mL with ethanol and reimmersed into vibrating sonic bath for 2 h. The suspended material was filtered through 0.45 μm nylon membrane and injected into HPLC. The EA recovered was quantified by HPLC method previously reported by our group (Aguilera-Carbo et al., 2008a), The HPLC Varian Pro Star systems with a photodiode array detector (PDA Pro Star 330) was used Separation was carried out with a Prodigy ODS column (5 m; 250 x 4.6 mm, Phenomenex) and temperature of 25°C. A gradient profile of mobile phase, consisting of acetonitrile (solvent A) and 0.3% acetic acid in water (v/v) (solvent B), 7-20% A (0-7 min), 20-30% B (7-12 min), 30% B (12-18 min), 30-60% B (18-20 min), 60-100% B (20-23 min), 100% B (23-30 min) y 7% B (30-31)and 7 min for baseline stabilization was applied at a flow rate of 0.6 mL/min. The sample injection was of L. A wavelength of 254 nm was used.

Mathematical models

Biomass production was adjusted with the Velhurst-Pearl logistic equation, originally developed for population growth.

$$\frac{dX}{dt} = \mu_M \left[1 - \frac{X}{X_{\max}} \right] X \qquad (1)$$

where X is biomass density (g per L, per cm^2 or per kg), μ_M the maximum specific growth rate (h^{-1}) and X_M the equilibrium level of X for which, dX/dt = 0 for X > 0. Solution of the above equation can be written as follows:

$$X = \frac{X_{\max}}{1 + \left(\frac{X_{\max} - X_0}{X_0} \right) e^{-\mu_M t}} \tag{2}$$

where X_0 is the initial condition for X. Eq. (2) is useful to fit experimental data by Eq. (1), finding the least value of the sum of squared errors as a function of parameters, X_0, X_M and μ_M.

Substrate consumption was modeled using a two-term expression proposed by Viniegra-Gonzalez et al. (2003) as follows:

$$-\frac{dS}{dt} = \frac{1}{Y_{X/S}} \frac{dX}{dt} + mX \tag{3}$$

where S is the substrate concentration (g per L, per cm^2 or per kg), $Y_{X/S}$ the biomass yield coefficient (g X/g S) and m the maintenance coefficient (g S/g X h). Solution of Eq. (3) can be obtained as a function of X as follows:

$$S(t) = S_0 - \left(\frac{X - X_0}{Y_{X/S}} \right) - \left(\frac{X_{\max} * m}{\mu} \right) \ln \left[\frac{X_{\max} - X_0}{X_{\max} - X} \right] \tag{4}$$

where S_0 is the initial condition for substrate level, S. Eq. (4) helps to test the importance of the maintenance coefficient, m, because a state plot of $S(t)$ vs. $X(t)$ will yield a straight line with slope, $1/Y_{X/S}$, whenever m is negligible. Otherwise, a logarithmic correction will appear with coefficient, mX_M/μ_M.

Kinetics of product formation can be modeled using the equation as proposed by Aguilar et al. (2001) as follows:

$$\frac{dP}{dt} = Y_{P/X} \frac{dX}{dt} + kX \tag{5}$$

where P is the product concentration, $Y_{P/X}$ the product yield in terms of biomass (units of product per unit of biomass) and k the secondary coefficient of product formation or destruction. Eq. (5) is similar to Eq. (3), but here the coefficient k can be negative, zero, or positive, since product formation or destruction is not necessarily related to growth. Again it is possible to solve Eq. (5) as a function of biomass

$$P(t) = P_0 + Y_{P/X}(X - X_0) + \frac{kX_M}{\mu_M} \ln \left[\frac{X_M - X_0}{X_M - X} \right] \tag{6}$$

The specific growth rate (μ) was obtained by the growth plot linearization and, the slope obtention was from the straight line by minimal square regression. The specific production rate of enzyme, q_P, was defined as follows:

$$q_P = \mu_M \cdot Y_{P/X} \tag{7}$$

The specific substrate uptake rate, q_S, was defined as follows:

$$q_S = \mu_M / Y_{X/S} \tag{8}$$

$Y_{P/X}$ and $Y_{X/S}$ were estimated from the linear correlation between the ellagic acid and biomass concentration, and biomass and pomegranate husk powder, respectively.

Basic model for metabolite productivity

Enzyme productivity for fermentation systems can be expressed in different ways. In this paper it is chosen to define productivity, *Γ*, for every *t>0* as *P*(*t*)/*t*, within the overall culture medium. For example, if the porosity and the liquid content of a given SSF are known, productivity, in terms of reaction volume, can be corrected by corresponding proportional factors. Also, if enzymes are excreted to the medium and leached out at the end of the fermentation, final productivity can be estimated by taking into account the dilution factor. However, in all cases, the initial figure, related to microbial physiology is productivity defined as follows:

$$\Gamma_{\max} = \text{maximum of} \left[\frac{P}{t} \right] \quad (9)$$

That is, for a given fermentation curve, Γ_{max}, will be the maximum of the ratio between the product level per liquid broth volume, *P*, added to the system and divided by the fermentation time, *t*. In most cases, Γ_{max} will be evaluated at the peak of metabolic activities production, but, this is not always the case because of the time factor involved and the asymptotic nature of end fermentation points.

In particular, there is a term named as reference productivity ($_{Ref}$), which helps to identify the major physiological factors involved in productivity of a given experimental system that in some cases can be corrected by otter two parameters.

$$\Gamma_{Ref} = \mu_M Y_{P/X} X_{\max} \quad (10)$$

Results and discussion

In this study we evaluated the kinetic parameters of EA production by *Aspergillus niger* GH1 using a pomegranate husk residues as support of SSF. Figure 1 shows the biomass production where it was observed a lag phase during the first 50 hours of culture, After this time, the exponential growth was permanent reaching the maximal biomass concentration (0.45gg^{-1}) at 120 hours. *A. niger* GH1 grew faster and higher in comparison with the same strain grown on creosote bush leaves (Aguilera-Carbo et al., 2008). In a similar study, Vatem and Shetty (2002) reported the growth of *Rhizopus oligosporus* during the SSF of cranberry pomace for antioxidant production, where the fungus reached its maximum growth after 240 h of culture. Consumption of THP from PPH, to the first 24 hours we observed an increase on THP concentration around 20%, can must to THP solubility on the culture media, More than 40 % (0.061 gg-1) of THP were consumed at the 48 hours, while the following days polyphenols concentration remained constant, this behavior could be due to the THP degradation and the generation and consumption of polyphenols monomers. Figure 1 shows that the *A. niger* GH1 strain is capable to degrade the THP from pomegranate husk powder, in a great manner mainly due to the material chemical composition. THP content reported in pomegranate husk are monomeric ET's, such punicalagin, vascalagin and some glycosides of ellagic acid (with hexoses, pentoses, ramnoses, etc.) which are potential sources of EA (Seeram et al. 2005).

The results for EA accumulation are showed in figure 1 where it is possible to observe that during the fermentation time the maximal ellagic acid concentration was reached at 96 hours with an amount of 12.3 mgg-1 in comparison with 1.5 mgg-1 EA present at initial time (EA free present in pomegranate husk powder). These results suggest that the ET's fraction from THP, are degraded by enzymes from *A. niger* GH1 strain.

After 96 hours of fermentation it was observed a decrement in the ellagic acid concentration, have it in end of the culture 2 mgg-1.This behavior appear may be caused by interaction of EA with proteins, some metals or well, to be consumed by the fungus, but does not exist reports about the ellagic acid consumption by microorganism, It is important to consider that EA has been mentioned as inhibitor of microbial growth (Aguilera'Carbo et al. 2007). Values found in the present research for EA production are higher than those reported by Vattem

and Shetty (2003) using *Lentinus edodes* fermenting cranberry pomace (320 μgg^{-1} in extracts with ethanol at time of fermentation of 120 hours in SSF).

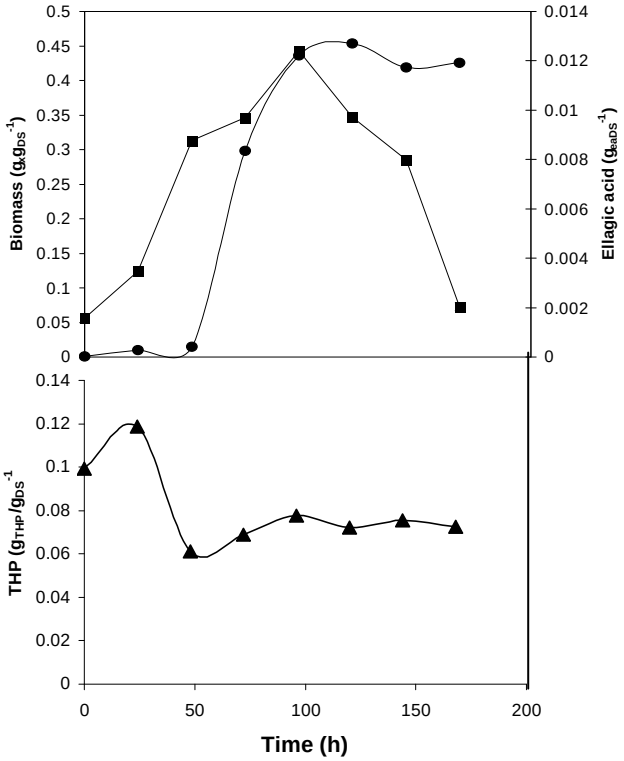

Figure 1. Mycelial growth (●), EA production (■) and THP consumption (▲).

Important advances in EA production from ellagitannins have been reported in submerged co-cultures by Huang et al. (2007a, b, c). Recently, high EA yields (24%) were obtained after optimization of the co-culture of *A. oryzae* with *Trichoderma reesei* using acorn cups extract containing up to 62% ellagitannins as substrate (Huang et al., 2007c). However, in SSC the information is limited to those studies reported by Vattem & Shetty 2002; Vattem & Shetty 2003, using cranberry pomace as support and source of ellagitannins with very low EA yields. Huang et al. (2007c) suggested for the first time, the presence of ellagitannin acyl hydrolase as the enzyme responsible of the EA accumulation, which indicates that a new tannase is involved in the biodegradation ellagitannins. Also, they reported that such enzyme had an synergistic activity with other enzymes as xylanase and cellulase to enhance the EA accumulation. However, further studies are needed to define the catalytic role and properties of this new EHA or ellagitannin acyl hydrolase detected. Aguilera-Carbo et al. (2008) reported that the SSF of *A. niger* GH1 using creosote bush ellagitannins impregnated in polyurethane foam could remarkably enhance EA accumulation.

The kinetic parameters estimated under evaluated conditions are showed in Table 1. It is important to note that a yield of 0.024 grams of EA per gram of biomass produced can be reached, however the experimental value was 6 times lower than that value. SSF of pomegranate husk can yield 0.323 grams of EA per gram of substrate, but the experimental value was of 0.299. These kinetic parameters demonstrated that it is necessary to optimize the SSF bioprocess to enhance the EA production.

Table 1 kinetics parameters on EA production in SSF

Parameter	Yx/s	Yp/x	Yp/s	Qs	Qp	P
Experimental	0.378	0.024	0.323	0.021	$1.92x10^{-4}$	$1.29x10^{-4}$
Calculated	0.357	0.004	0.299	0.279	$4.87x10^{-4}$	$8.51x10^{-5}$

Conclusions

Biotechnological EA production is a interesting field where is necessary more studies on exploration of a novel sources, byproducts carry out of optimization in EA production. The kinetic evaluation of EA production by *Aspergillus niger* GH1 using a pomegranate husk residues as support it allows kinetics parameters involved under production if this metabolite were calculated and can be considerate for the optimization of EA in SSF.

References

Aguilar, C.N., Augur, C., Favela-Torres, E. and Viniegra-González, G. 2001. Production of tannase by Aspergillus niger Aa-20 in submerged and solid state fermentations: influence of glucose and tannic acid. *Journal of Industrial Microbiology and Biotechnology*. 26(5): 296-302.

Aguilar CN, Aguilera-Carbo A, Robledo O, Ventura J, Belmares R, Martinez D, Rodríguez R and Contreras JC (2008). Production of antioxidant-nutraceuticals by solid state cultures of pomegranate residues (*Punica granatum*) and creosote bush (*Larrea tridentata*). *Food Technology and Biotechnology*. 46(2); 216-220.

Aguilera-Carbo AF, Augur C, Prado-Barragan LA, Favela-Torres E and Aguilar CN (2007). Microbial production of ellagic acid and biodegradation of ellagitannins. *Applied Microbiology and Biotechnology*. 78: 189-199.

Aguilera-Carbo A, Hernandez-Rivera JS, Prado-Barragán LA, Augur C, Favela-Torres E, Aguilar CN (2007a) Ellagic acid production by solid state culture using a *Punica granatum* husk aqueous extract as culture broth. Proceedings of the 5th International Congress on Food Technology. Thessaloniki, Greece.

Aguilera-Carbo A, Hernandez JS, Augur C, Prado-Barragan LA, Favela-Torres E and Aguilar CN (2008).. Ellagic acid production from biodegradation of creosote bush ellagitannins by Aspergillus niger in solid state fermentaton. *Food and Bioprocess Technology*. DOI: 10.1007/s11947-008-0063-0.

Aguilera-Carbo AF, Augur C, Prado-Barragan LA, Aguilar CN and Favela-Torres E (2008a). Extraction and analysis of ellagic acid from novel complex sources. *Chemical Papers*. 62 (4): 440-444.

Boone-Villa VD, Contreras-Esquivel JC, Rodriguez-Herrera R, Aguilar CN (2004) Comparison of cellular components analysis techniques to estimate fungal growth in cultures on inert supports. Proceedings of the First Food Science and Food Bitechnology in Developing Countries, Durango, Dgo. México.. FE15.

Clifford MN, and Scalbert A. (2000), Review: Ellagitannins-nature, occurrence and dietary burden. *Journal of the Food Science and Agriculture*. 80: 1118-1125.

Cruz-Hernández M, Contreras-Esquivel JC, Lara F, Rodríguez R & Aguilar CN (2005) Isolatation and Evaluation of Tannin-degrading Fungal Starins from the Mexican Desert. *Z. Naturforsch*. 60, 844-848.

Huang W, Niu H, Gong G, Lu Y, Li Z & Li H (2007a). Individual and combined effects on physicochemical parameters on ellagitannin acyl hydrolase and ellagic acid production from ellagitannin by *Aspergillus oryzae. Bioprocess Biosystems Engineering*, 30, 281-288.

Huang W, Niu H, Li Zm Lin W, Gong G & Wang W (2007b). Effect of ellagitannin acyl hydrolase, xylanase and cellulase on ellagic acid production from cups extract of Valona acorns. *Process Biochemistry*, (in press: DOI: 10.1016/j.procbio.2007.06.013).

Huang W, Niu H, Li Z, He Y, Gong W & Gong G (2007c). Optimization of ellagic acid production from ellagitannins by co-culture and correlations between its yield and activities of relevant enzymes. *Bioresource Technology,* (in press, doi: 10.1016/j.biortech.2007.01.032).

Huang W, Niu H, Li Z & Wang W (2007d). Ellagic acid from acorn fringe by enzymatic hydrolysis and combined effects of operational variable and enzymes on yield of the production. *Bioresource Technology*, (in press: doi:10.1016/j.biortech.2007.04.026).

Robledo A, Aguilera-Carbo A, Rodríguez R, Martinez JL, Garza Y & Aguilar CN (2007) Ellagic acid production by *Aspergillus niger* in solid state fermentation of pomegranate residues. *Journal of Industrial Microbiology and Biotechnology* (In press: DOI 10.1007/s10295-008-0309-x).

Saavedra G, Couri S, Ferreira S, Sousa de Brito E (2005) Tannase: concepts, products ande applications (in portuguese). B. CEPPA Curitiba 23:435-462.

Seeram N, Lee R, Hardy M, Heber D (2005) Rapid large scale purification of ellagitannins from pomegranate husk, a by-product of the commercial juice industry. *Separation and Purification Technology*, 41:49–55.

Shi B, He Q, Yao K, Huang W, Li Q (2005) Production of ellagic acid from degradation of valonea tannins by *Aspergillus niger* and *Candida utilis. Journal of Chemical Technology and Biotechnology*, 80:1154-1159.

Vattem DA, Shetty K (2002) Solid state production of phenolic antioxidant activity from cranberry pomace by Rhizopues oligosporum. *Food Biotechnology*, 16:189-210.

Vattem Dam Shetty K (2003) Ellagic acid production and phenolic antioxidant activity in cranberry pomace (*Vaccinium macrocarpon*) mediated by *Lentinus edodes* using a solid-state system, *Process Biochemistry,* 39:367-379.

Viniegra-González, G., Favela-Torres, E., Aguilar, C.N., Romero-Gómez, S.J., Díaz-Godínez, G. and Augur, C. 2003. Advantages of fungal enzyme production in solid state over liquid fermentation systems. *Biochemical Engineering Journal,* 13, 157-167.

Proceedings of the 10th International Chemical and
Biological Engineering Conference - CHEMPOR 2008
Braga, Portugal, September 4-6, 2008
E.C. Ferreira and M. Mota (Eds.)

Bioprocessing of Spent Sulphite Liquor for Production of Single Cell Protein

Ana S.N. Pontes[1], Mariana F. Correia[1], Ana M.R.B.Xavier[1*], Dmitry Evtyugin[1], António Prates[2]

[1] CICECO – Departamento de Química, Universidade de Aveiro, Campus Universitário de Santiago, 3810-193 Aveiro, Portugal.

[2] CAIMA , Indústria de Celulose S.A., Constança, Portugal

Keywords: Xylose Fermentation, Sulphite Spent Liquor, Single Cell Protein, Sulphite Pulping, Lignosulphonate

Topic: Integration of life sciences & engineering

Abstract

The Sulphite Spent Liquor (SSL) is the by-product from acidic sulphite pulping of wood. Besides dissolved sulphonated lignin (lignosulphonates), SSL normally contains notable proportion of sugars, arisen during the pulping, which can be a valuable raw material for bioprocessing. Single cell protein (SCP) is known as valuable relatively cheap product with wide applications in human and animal food staffs, as texture providing agents and flavour enhancers among others. Sugars-free SSL, from another side, may be considered as the value added product for a multipurpose utilization. In this work the possibility of single cell protein production from SSL of acidic sulphite pulping of *Eucalyptus globulus* wood (CAIMA Pulp Mill, Constancia) has been investigated employing the fungus *Paecilomyces variotii* and *Kluyveromyces fragilis* and *Candida utilis* yeasts. Different batch fermentations for SCP production were carried out with the fungus and the yeasts on both Malt Extract Medium (ME) and Yeast Medium (YM), with different concentrations of sulphite liquor. The results indicate that the fungus has a high capacity to metabolize the SSL available carbon sources for cell growth and exhibit high tolerance to the present inhibitors. Yeasts showed much lower yields on biomass production being strongly inhibited at 80% liquor medium. Fungus biomass analysis was performed and a protein content of 67 – 70% and a nucleic acid content of 17% were presented. These levels are according to requirements for SCP feed/food staffs.

1 Introduction

The shortage of protein-rich food and global existence malnourished people has forced mankind to search for alternative protein sources. Single Cell Protein (SCP) seams to be a promising alternative. SCP is the protein extracted from cultivated microbial biomass. Bioconversion of agricultural and industrial wastes to microbial protein has an additional benefit of making the final product cheaper and of representing a contribution to the environment. More over, it would make food production less dependent upon land and reduce the pressure on agriculture. Currently SCP is produced from many species of microorganisms, namely fungi and yeasts. Their rapid growth and high protein content made them excellent sources of SCP. The final product should not only be nutritious but also pass all toxicity tests to be commercialized as a food product (Anupama and Ravindra, 2000).

The Hardwood Spent Sulphite Liquor (HSSL) is the waste by-product of the pulp and paper industries that produce bleached pulps by acidic sulphite pulping of *Eucalyptus globulus* wood. After the pulping, HSSL is burned for reagents and energy recovering. HSSL contains essentially sulphonated lignin (lignosulphonates) and sugars from degraded hemicelluloses, mainly pentoses. Xylose is the main pentose present. HSSL can be used as a substrate for different bioconversion products with market value.

* Corresponding author. Tel + 351-234-370716. E-mail:abx@ua.pt

Yeasts usually exhibit a high capacity to assimilate sugar substrates through specific transport mechanisms and oxide-reductive metabolism, thus promoting a fast rate of growth (Ugalde and Castrillo, 2002).

Morphological properties of pellet and flocculated fungus biomass products could lead to relatively easy and cheap harvesting compared with yeasts or bacteria (Jin et al., 1999)

Candida utilis is especially suitable because it has a high tolerance for sulphite, can convert both hexoses and pentoses and has been used for production of several industrial products both for human and animal consumption (Rajoka et al, 2006).

Kluyveromyces fragilis has been found to have a high specific growth rate and it has been used for industrial purposes due to its physiological characteristics and bioproduct yields, in particular hydrolytic enzymes and food biomass (Schultz et al., 2006).

Paecilomyces variotii is a fungus that can be used to produce microbial protein due to its optimal performance in highly polluted residues, such as sulphite liquor. Besides monosaccharides it consumes also acetic acid of spent sulphite liquor. Protein produced by this fungus meets the aminoacids requirements for humans and animals (Almeida e Silva et al., 2003).

In this work the ability of SSL as a substrate for SCP bioproduction has been studied and a comparison between *Paecilomyces variotii*, *Candida utilis and Kluyveromyces fragilis* has been done in order to evaluate their industrial implementation.

2 Materials and Methods

Industrial thin spent sulphite liquor (SSL) was supplied by Caima Cellulose Company S.A.. SSL was prepared for the fermentation process by the addition of NH_4OH to adjust the liquor pH to 5.5 and to supplement it with a source of nitrogen. SSL was oxygenated and vacuum-filtered through glass fibre membrane filters with 1 µm pores (Filtrac.Herzberg, Ahlstrom). The liquor was analysed for dry solids (105 Cº), ash (cacinations at 525 ºC), sugars composition, acetic acid, furfural and lignosulphonate (LS) contents. Sugars analysis as alditol acetate derivatives were carried out using GC after Saeman hydrolysis of SSL. The quantification of LS was done by UV spectroscopy at 273 nm (Hitachi 2000 UV/Vis spectrophotometer). The analyse of furfural was carried out on Knauer HPLC system (Pump Mode K-1001 equipped with dynamic mixer K-1500; detector – UV fast scanning K-2600 operating at 280 nm wavelength; column – 8 µm PL Hi-PlexH 300 x 7.7 mm; eluent – water, 0.6 mL/min, 65 ºC) using phenol as an internal standard. The analysis of acetic acid was carried out on Gilson HPLC system (Pump Gilson 307; detector - refractive index Gilson 131; column - 10 µm Eurokat®; eluent - H_2SO_4 0,01N, 0.4 mL/min). Total reducing sugars concentration was analyzed by DNS method (Miller, 1959).

Paecilomyces variotii NRRL 1115 and the yeasts *Kluyveromyces fragilis* PYCC 3886 and *Candida utilis* PYCC 2541 were kept on malt extract and yeast medium (YM) agar slants at 5 ºC, respectively, and renewed every month. For the inoculum preparation, the fungus was transferred to 500 mL Erlenmeyer flasks containing 250 mL of 60% liquor and 40% malt extract medium (ME) and it was carried out for 2,3 and 6 days. For the preparation of yeasts inoculum, yeasts were transfered to 100mL Erlenmeyer flasks containing 50mL of yeast medium (YM) and the cultivation was carried out for 20h. Batch fermentations for SCP production were carried out with the fungus and the yeasts on both malt extract medium and yeast medium, with different concentrations of sulphite liquor (40, 60, 80 and 100%) at 29 ºC and 180 rpm. ME and YM pH was not adjusted – pH ~ 6.5.

Xylose, glucose and acetic acid contents were determined by referred Gilson HPLC system. Yeasts optical densities (OD) were measured using UV/Vis spectrophotometer Shimadzu at 620nm for *K.fragilis* and 640nm for *C. utilis*. Calibration curves OD versus

dry cell weight allowed to quantify biomass concentration.The fungus biomass formed during the fermentation process was assayed by direct weighing because this is an heterogeneus culture. A 0.044 mm opening sieve was used to separate the microrganism from the medium. The mycelia was washed in flowing distilled water to eliminate the residual fermentation medium, dried at 105 ºC at atmospheric pressure and weighed. After cells were freezed-dried, the crude protein content of cells was determinated with the powdered fungus by the Kjeldahl nitrogen method (N x 6.25) (Clesceri et al., 2001). Lowry method (Harris et al., 1989) was used to determine true protein content after cell disruption by sonication technique. Nucleic acids were quantified according to Sambrook et al. (1989).

3 Results and discussion

The general chemical composition of eucalypt SSL has been analysed and its composition is shown in Table 1.

Table 1. The chemical composition of SSL from acidic sulphite pulping of eucalypt wood.

Component	Concentration (gL^{-1})
Lignosulphonates	78,2 ± 0,6
Acetic acid	9,6 ± 0,1
Furfural	Traces
Ash	15,1 ± 0,2
Dry solids	150,3 ± 0,8
pH	3,4 ± 0,1
Reducing sugars	44,7 ± 0,4
D-xylose	20,5 ± 0,7
D-mannose	8,5 ± 0,3
L-arabinose	7,8 ± 0,2
D-galactose	4,5 ± 0,5
D-glucose	2,3 ± 0,1
L-rahmnose	1,6 ± 0,3
L-fucose	0,4 ± 0,2

Besides lignosulphonates, SSL contained remarkable amounts of acetic acid and sugars from degraded hemicelluloses, mainly pentoses. In particular, a high concentration of xylose was detected, which can be used as substrate for growth of biomass in order to increase the industrial profit. In addition to xylose, the acetic acid may be considered to be a suitable source of carbon for the fungus growth.

As SSL has such diverse composition certainly associated to any growth inhibition, inoculate have been made with 60% of liquor and 40% of ME. Time of inoculation has been studied making a set of equal batch fermentations assays to choose the best innoculation time between 2, 3 and six days. After these times biomass was transfered to 100% of liquor and one flask sample was analysed at day 0, 4^{th}, 7^{th} and 11^{th} from each experience. Results are presented on Figure 1.

Paecilomyces variotii grows consuming pentoses, hexoses and acetic acid and best results were reached with a 2 days inoculum where a 4 fold biomass increase was atteined: biomass production at the end of the 11 days fermentation time was 39,3 g/L.

A batch experiment with direct inoculation from Petri dish to 100% liquor was carried out and results are presented in Figure 2.

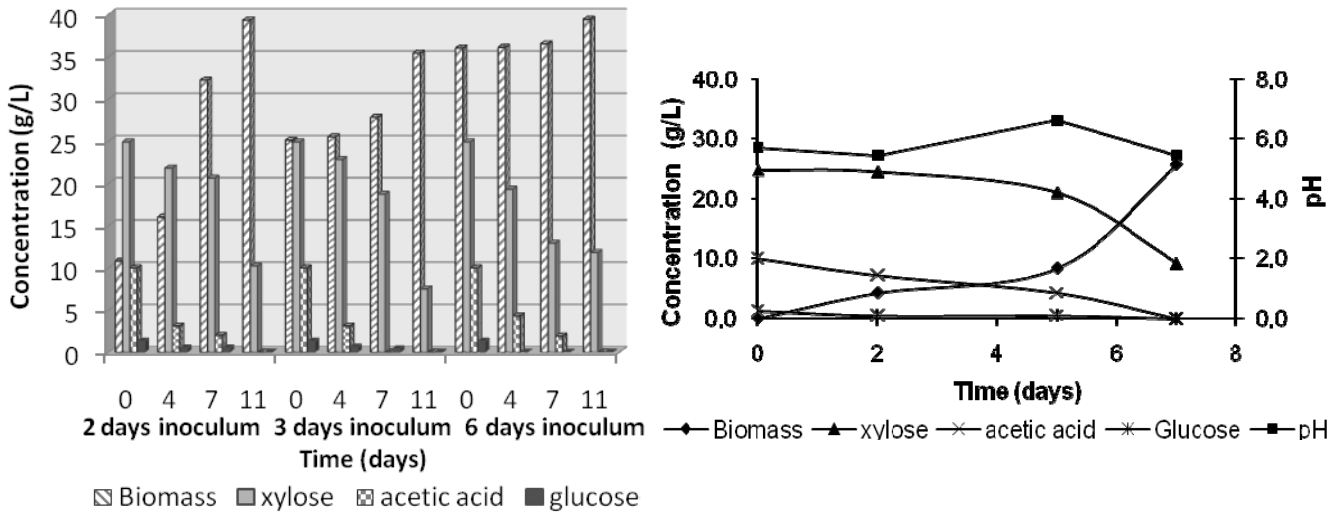

Figure 1 - *Paecilomyces variotii* 100% liquor medium fermentations.

Figure 2 - *Paecilomyces variotii* growth time course at 100% liquor medium, 0 days inoculum.

Acetic acid was completely consumed with the highest consumption rate and a low sugar consumption was verified until the 7th day. Without previous inoculum *P. variotii* showed a huge capacity to metabolize the SSL available carbon sources for cell growth and exhibit high tolerance to the traditional inhibitors acetic acid between others.

Some protein production yields (based on sugars and acetic acid carbon sources only) exceeded 100% and these results stand for the hypothesis that phenolic compouds present in the liquor such as: pyrogallol, syringic, galli and, ellagic acids represent another aditional carbon source for the fungus. *P. variotii* biomass has a high true protein content as well as crude protein that might be considered as the sum of real protein and the nucleic acids content what means the total nitrogen content (Table 1).

Table 1 - *Paecilomyces variotii* biomass analysis.

Analysis method	Kjeldahl	Lowry	Nucleic acids
	80.0%	68.1%	17.8%

Batch tests for biomass production have been carried out with *K. fragilis* with three different liquor concentrations (Table 2).

Table 2 – *Kluyveromyces fragilis* growth parameters analysis.

Medium (% Liquor)	μ_{max} (h^{-1})	$Q_{p\,max}$ (g/L/h)	$Y_{x/s\,max}$ (g/g)	Biomass (g/L)
40	0.19	0.13	0.39	3.1
60	0.19	0.07	0.94	1.0
80	0.14	0.04	0.27	0.5

It is clear that liquor has some component that is responsible for yeast growth inhibition: much lower yields on biomass production were obtained with liquor contents higher than 80%. Liquor is strongly inhibitory for yeasts.

Candida utilis was tested on 60% liquor and results are presented on Figure 3.

A growth curves comparison was established for both yeasts at the same conditions (Figure 4).

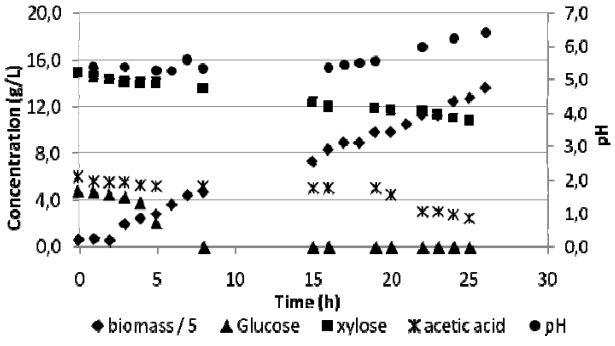

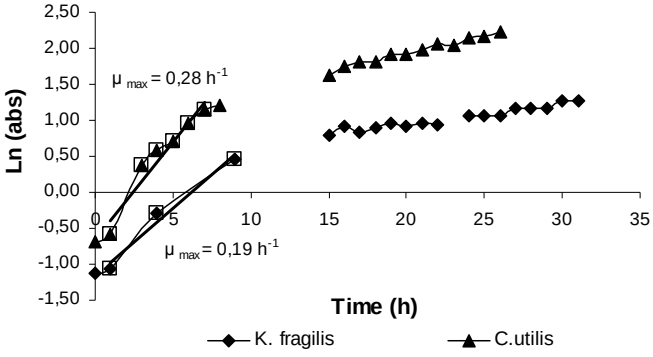

Figure 3 – Time course for *C. utilis* fermentation – medium: 60% liquor + YM.

Figure 4 - *C. utilis* and *K. fragilis* specific growth rates; medium: 60% liquor + YM**.**

The diferences in behaviour concerning sugars consumption and specific growth rates indicate that *K. fragilis* and *C.utilis* exhibit different degrees of tolerance for toxic components, such as acetic acid and phenolic compounds. *C. utilis* showed better results: 3 times more biomass than *K. fragilis* at the same conditions and 42% acetic acid consumption. Acetic acid was suggested to be a strong inhibitor for *K. fragilis*.

The potential of spent sulphite liquor as a substrate for SCP was demonstrated. After the optimization of biomass production, the resulting protein will be analysed in order to evaluate its composition, susceptibility to food and feed applications and process feasibility for the industrial implementation.

References

Almeida e Silva, J. B., Lima, U. A., Taqueda, M. E. S., Guaragna, F. G. (2003). Use of responce surface methology for selection of nutrient levels for culturing *Paecilomyces variotii* in eucalyptus hemicellulosic hydrolyzate. *Bioresource Technology*, 87, 45-50.

Anupama, Ravindra, P. (2000). Value-added food: Single Cell Protein. *Biotechnology Advances*, 18, 459-479.

Clesceri, L., Greenberg, A., Eaton, A. (2001). *Standard Methods for the Examination of Water and Waste Water*, 20th Edition, APHA, Washington.

Harris, E. L. V., Angal, S. (1989). *Protein purification methods: a practical approach*, Oxford University Press.

Jin, B., Leeuwen, J. H., Yu, Q., Patel, B. (1999). Screening and selection of microfungi for microbial biomass protein production and water reclamation from starch processing wastewater. *Journal of Chemical Technology and Biotecnology*, 74, 106-110.

Miller, G. L. (1959). Use of dinitrosalicylic acid reagent for determination of reducing sugar. *Analytical Chemistry*, 31, 426-428.

Rajoka, M.I., Khan, S.H., Jabbar, M.A., Awan, M.S., Hashmi, A.S. (2006). Kinetics of batch Single Cell Protein production from rice polishings with *Candida utilis* in continuously aerated tank reactors. *Bioresource Technology*, 97, 1934-1941.

Sambrook, J., Fritsch, E. F., Maniatis, T. (1989). *Molecular cloning – a laboratory manual*, 2nd Edition, Coldspring Harbor Laboratory Press, New York.

Sarkanen, K.V., Ludwig, C.H. (1971). *Lignins. Occurrence, formation, structure and reactions.* Wiley-Interscience, New York.

Schultz, N, Chang, L., Hauck, A, Reuss, M., Syldatk, C. (2006). Microbial production of single-cell protein from deproteinized whey concentrates. *Applied Microbiology and Biotechnology*, 69, 515-520.

Ugalde, U. O., Castrillo, J. I. (2002). Single Cell Proteins from Fungi and Yeasts. *Applied Mycology and Biotechnology*, 2, 123-149.

Proceedings of the 10th International Chemical and
Biological Engineering Conference - CHEMPOR 2008
Braga, Portugal, September 4-6, 2008
E.C. Ferreira and M. Mota (Eds.)

Enzymatic interesterification of milkfat with soybean oil using lipases from different sources immobilized on polysiloxane–polyvinyl alcohol hybrid matrix

Ariela V. Paula, Gisele F. M. Nunes, Josiane L. Silva, Heizir F. Castro, Júlio C. Santos*
*University of São Paulo, Engineering School of Lorena,
P.O.Box 116, 12602-810- Lorena, SP, Brazil.

Keywords: lipases, enzymatic interesterification, milkfat modification, enzyme immobilization, polysiloxane–polyvinyl alcohol hybrid matrix
Topic: Biotechnology applied to production of new and better quality food

Abstract

Two food grade commercial preparations of lipases from *Rhizopus oryzae* and *Candida rugosa* were evaluated in relation to their potential to perform milkfat interesterification with vegetable oil. Both lipases were immobilized on polysiloxane–polyvinyl alcohol (POS-PVA) activated with sodium metaperiodate and used to catalyze the interesterification in a solvent free medium containing milkfat (80%) and soybean oil (20%). Reactions were monitored by the formation of free fatty acids using acid-base titration and the profile of triacylglycerols (TAG) analyzed by gas chromatography. Starting materials and interesterified products were analyzed in terms of saponification and iodine indexes determined by standard methods, and consistency. Both lipases resulted in changes on the triacylglycerols profile with a decrease on the TAGs concentration having C_{38} and C_{54} acyl-carbon numbers and an increase in the TAGs concentration containing C_{26}–C_{32} and C_{46}–C_{48}. It was also observed that the decrease in the concentration of the TAG C_{38}, characteristic of milkfat, was more pronounced using *Candida rugosa* lipase. On the other hand, the use of *Rhizopus oryzae* lipase resulted in higher reduction in the concentration of the TAG C_{54}, characteristic of soybean oil. The consistency expressed as yield value, decreased 27.67 and 21.12% after the interesterification catalyzed by *R. oyzae* and *C. rugosa* lipases, respectively. These results showed the potential of the selected immobilized lipases to change the TAGs profile of the milkfat-soybean oil blend, with a correspondent decrease in the consistence similar for both lipases, meaning a better spreadability of the product after the reaction.

1 Introduction

Milkfat is a very complex food, constituted by a broad range of long and short chain fatty acids in the form of triglycerides. This complexity is responsible for its unique physical and organoleptical characteristics. Nevertheless, the consumption of milkfat has been declined due to its high degree of saturation, price and high percentage of hypercholesterolemic fatty acids (Balcão and Malcata, 1998). An alternative to overcome such drawbacks was to replace milkfat by partial hydrogenated vegetable oils, in the form of margarines and spreads. However, vegetal oil hydrogenation process generates also high amount of *trans* fatty acids as by-product. The ingestion of these fatty acids has been found to increase both the low density lipoprotein cholesterol (LDL-cholesterol), known as “bad” cholesterol, and decrease the high density lipoprotein cholesterol (HDL-cholesterol) known as “good” cholesterol. This has motivated the food industry to reformulate products that could take advantage of the beneficial effects of milkfat as conjugated linoleic acids (Haug et al., 2007).

An interesting approach is to blend milkfat with vegetable oils either in the presence (interesterification reaction) or without catalyst (physical mixture). The former yielded a product with better spreadability properties and can be catalyzed by chemical or enzymatic routes. Enzymatic interesterification is advantageous in comparison to chemical

* Corresponding author. Tel + 55-1231595149. E-mail:jsant200@yahoo.com.br

interesterification because enzymes (lipases) allow carrying out processes under mild reaction conditions (temperature and pressure) that results better preservation of the milkfat flavor (Rodrigues and Gioielli, 2003).

To fully exploit the technical and economical advantages of lipases, it is recommended to use them in an immobilized form to reduce the cost and the poor stability of the soluble form. There are many methods available for biocatalyst immobilization that span from binding on prefabricated carrier materials to incorporation into in situ prepared carriers. Recently, the potential of using a hybrid matrix of Polysiloxane-Polyvinyl Alcohol (POS-PVA) obtained by sol-gel process for lipase immobilization has been demonstrated in our laboratory (Paula et al., 2008).

Thus, in this work, two food grade commercial preparations of lipases from *Rhizopus oryzae* and *Candida rugosa* were evaluated in relation to their potential to perform milkfat interesterification with soybean oil. Both lipases were immobilized on POS-PVA activated with sodium metaperiodate and used to catalyze the interesterification of a solvent free medium containing milkfat (80%) and soybean oil (20%).

2 Materials and Methods

2.1 Materials

Food grade commercial lipase samples from *Rhizopus oryzae* (Lipomod L036P) and *Candida rugosa* (Lipomod L034P) were kindly donated by Biocatalysts (Cardiff, Inglaterra). Lipase samples were immobilized on POS-PVA activated with sodium metaperiodate. Milkfat was obtained from complete fusion, in microwaves oven, from commercial butter (Paulista Extra without salt, purchased in a local market) at temperatures from 50 to 65°C, to disperse the emulsion, followed by centrifugation and separation of the aqueous phase. Commercial soybean oil (Liza Type 1 Extra filtered 5 times, purchased in a local market) was utilized without additional treatment. Other reagents were tetraethoxysilane (TEOS), acquired from Aldrich Chemical Co. (Milwaukee, WI, USA); polyvinyl alcohol (PVA, MW 72,000) and polyethylene glycol (PEG, molecular weight 1500), supplied by Reagen (Rio de Janeiro, RJ, Brazil). All other chemicals were of analytical grade.

2.2 Support synthesis, activation and immobilization procedure

The polysiloxane-polyvinyl alcohol (POS-PVA) hybrid composite was prepared by sol-gel technique according to the methodology described by Paula et al. (2008). The resulting POS-PVA particles was activated with sodium metaperiodate (Cunha et al., 1999) and used to immobilize both lipases at fixed loading (0.20 g of lipase per gram of support). Aqueous polyethylene glycol (PEG) 1500 solution (5 mg/mL) was added together with the enzyme at a fixed amount (5mg/g of support). Lipase-support system was maintained in contact for 24h at 4^{o}C. Immobilized lipase derivatives were filtered and thoroughly rinsed with hexane.

2.3 Interesterification of milkfat with soybean oil

The interesterification reactions were performed in duplicate under inert nitrogen atmosphere, in cylindrical glass reactors (100mL), containing 50g of milkfat and soybean oil blends at proportions of 80:20. Mixtures were incubated with immobilized derivatives on POS-PVA at proportions of 10% (w/w) in relation to the total weight of reactants involved in the reaction media. Reactions were carried out for a maximum period of 72h, in a rotary shaker (170 rpm) at 45ºC. The progress of the reaction was followed by the determination of the saponification and iodine indexes, triacylglycerols (TAGs) composition and consistency of the interesterified products.

2.4 Free fatty acids and indexes of saponification and iodine

The content of free fatty acids was determined according to standard method Cd 3d-63 (American Oil Chemists' Society, 2004). The saponification and iodine indexes were determined by the standard methods Cd 3-25 and Cd 1b-87, respectively (American Oil Chemists' Society, 2004).

2.5 Determination of the triacylglycerols (TAGs) profile in interesterification reactions

The determination of the TAGs was carried out using a gas chromatography (Varian - Model 3800), with a column packed 3% OV1 SILPT-WBM 100/120 MESH in Silco Var, Restek (purchased from the Frankel Commerce of Ltd Analytic Instruments, São Paulo, SP), operating under conditions previously established (Paula, 2008).

2.6 Hydrolysis degree (H, %)

The hydrolysis degree was calculated according to the equation 2.1:

$$H(\%) = \frac{AG_f}{AG_t} \cdot 100 \qquad (2.1)$$

where: AG_f = total concentration of fatty acids formed in the reaction (mM); AG_t = total concentration of fatty acids that would be liberated, considering the total hydrolysis of triacylglycerols in the reaction medium (mM).

2.7 Interesterification Degree (I, %)

The interesterification degree was calculated according to the equation 2.2:

$$I(\%) = \frac{\sum (TAG_I)_t - \sum (TAG_I)_0}{\sum (TAG_D)_0} \cdot 100 \qquad (2.2)$$

where: TAG_I = concentration (mM) of the triacylglycerols in which concentration increased during the reaction; TAG_D = concentration (mM) of the triacylglycerols in which concentration decreased during the reaction. The index "t" and (0) represent the concentrations of TAG in any time of reaction and in the initial reaction mixture, respectively.

2.8 Consistency

The consistency of the raw materials and interesterified products were determined utilizing a texture analyzer (Model QTS-25 Brookfield, Middleboro, MA, USA) controlled by the Texture Pro software v. 2.1. Samples were heated in microwave oven (55–62ºC) for the fusion of the crystals, and conditioned in cubic silicone forms (edge of 25mm) during 48h, at 10ºC. The probe TA15 was used, corresponding to an acrylic cone with angle of 45º. Tests were under the following conditions: total of cycles 1, distance = 10mm, speed = 120mm/min, time = 5s; determination of the force in compression (gf), in duplicate.

The results were used to calculate the "yield value", defined according to Equation 2.3 (Deman and Deman, 2002):

$$C = K \cdot \frac{W}{p^{1.6}} \qquad (2.3)$$

where: C = "yield value" (gf/cm); K = a constant depending on cone angle (4700 for 45º); W = maximum compression force (gf), for 5s; p = penetration depth (in 0.1mm).

3 Results and discussion

Table 1 shows the saponification and iodine indexes for the interesterified products obtained in the reactions catalyzed by lipases from *R. oryzae* (L036P) and *C. rugosa* (L034P). Values for pure milkfat and physical blend of milkfat with soybean oil are also shown in Table 1.

As can be noted, similar saponification indexes (218.91 and 218.29 mgKOH/g) were found for both interesterified products. Such results can be understood by considering that the interesterification reaction is responsible for changes in the fatty acids positions but cannot afford alterations on the molecular weight of the raw materials.

Table 1. Saponification and iodine indexes for pure milkfat, milkfat and soybean oil mixture (80%:20%) and interesterified products.

Index	Milkfat	Mixture	Interesterified Products	
			L036P (*R. oryzae*)	L034P (*C. rugosa*)
Saponification (mgKOH/g)	230.17	209.29	218.91	218.29
Iodine (gI_2/100g)	34.41	49.61	49.27	50.59

Interesterified products showed iodine indexes higher than the one observed for pure milkfat (34.41 gI_2/100g). This can be explained by the fatty acids composition of soybean oil which has more unsaturated fatty acid proportions than milkfat and, therefore, the mixture of these two components resulted in higher iodine index. Besides this, values for interesterified products were similar to the one given by the physical raw materials blend (49.10 gI_2/100g). As already mentioned, the interesterification reaction is responsible only for changes in fatty acids positions, resulting in products that present the same fatty acids composition.

Figure 1 shows the composition profile in TAGs for the interesterified products, pure milkfat and raw materials blend. As can be observed, the addition of soybean oil to milkfat resulted in a reduction of TAGs C_{28}–C_{46} concentrations and an increase in long chain TAGs (C_{52} and C_{54}) concentrations, which are presented in the soybean oil in high amounts. The comparison between the composition of the interesterified products with the initial raw materials blend (Figure 1) showed a decrease in the triacylglycerols level with a long chain (C_{54}) and increase in the content of the triacylglycerols C_{26}–C_{32} and C_{46}–C_{48}, after the process. A decrease in the TAG C_{38} concentration, characteristic of the milkfat, was observed mainly for *Candida rugosa* lipase, whereas for the lipase from *Rhizopus oryzae* higher reduction was noted for TAG C_{54} concentration, characteristic of soybean oil.

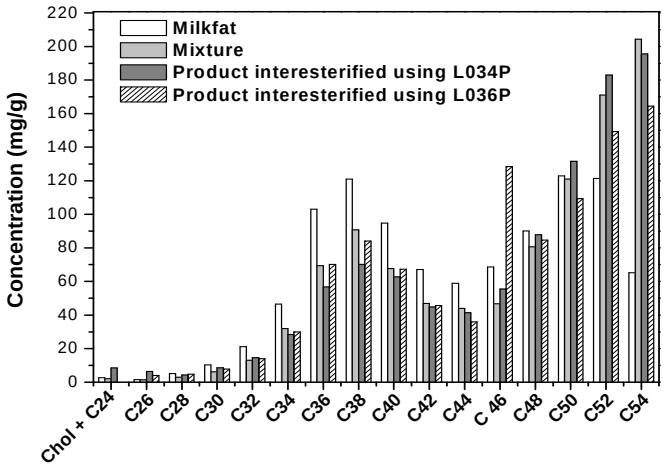

Figure 1. Comparison between TAGs composition for interesterified products, pure milkfat and raw materials blend (TAGs were identified by the sum of the number of carbons in the fatty acid residues).

From the TAGs profile, the interesterification degree (%) was calculated according to equation 2.2, and this result was compared to the hydrolysis degree (%), as shown in Figure 2. As observed, the enzymes L034 (Figure 2.a) and L036 (Figure 2.b) resulted in a maximum interesterification degree of 9 and 14 %, in 72 and 48 h, respectively.

To achieve high yields in the interesterification reactions the water content in the bulk liquid phase should be kept as low as possible. Although a small amount of water is needed for

maintenance of the enzymatic activity (Lamboursain et al., 1996), high levels of water may lead to the formation of free fatty acids, mono and diglycerides, instead of TAGs redistribution. In this work, immobilized derivatives containing 10% of water were used and this fact can explain the hydrolysis degree (about 5 %) obtained in the reactions catalyzed by L034P and by L036P, as observed in Figure 2. This may suggest that additional strategy should be taken into consideration to control the water content aiming to avoid the undesirable hydrolysis of the TAGs.

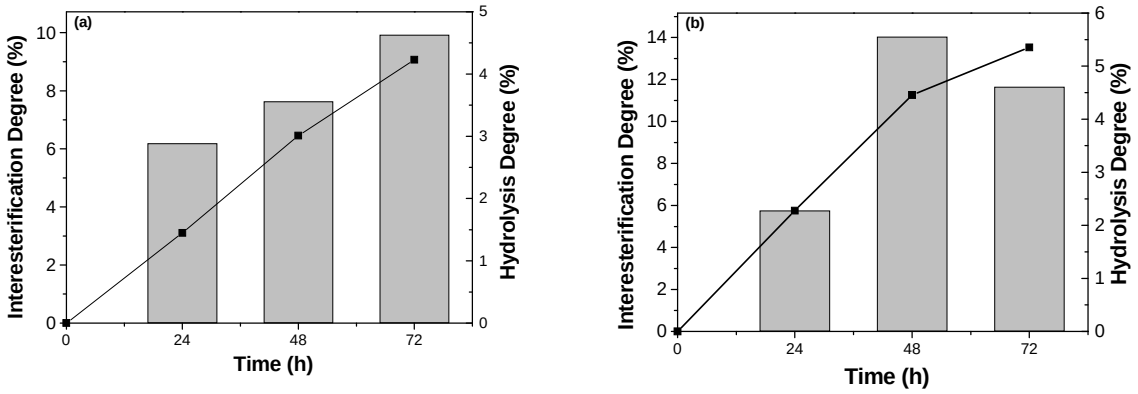

Figure 2. Interesterification (bars) and Hydrolysis (●) Degree for interesterification reactions catalyzed by lipases from *Candida rugosa* (a) and *Rhizopus oryzae* (b).

The consistency values for the interesterified products, pure milkfat and raw materials blends, measured at 10ºC are displayed in Figure 3. These results indicated that a reduction higher than 50% can be achieved by simply adding soybean oil to the pure milkfat. Rodrigues et al. (2003) also described similar behavior for milkfat and corn oil blends and explained this assuming that the addition of liquid oil to the milkfat dilute the fat crystals, giving, as a consequence, a more fragile structure.

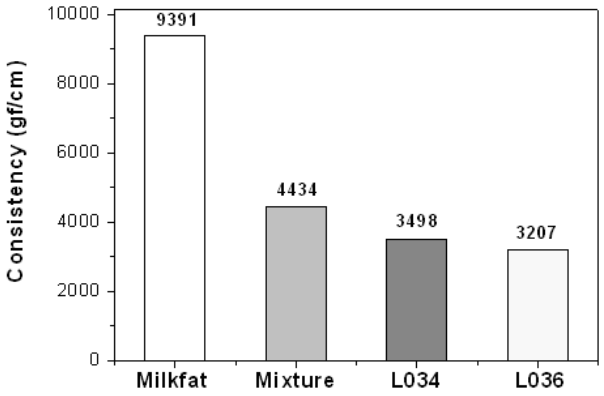

Figure 3. Consistency of the interesterified products compared to the milkfat and the mixture of the raw materials

In relation to the consistency of the physical raw materials blend, the interesterification reactions catalyzed by *R. oyzae* and *C. rugosa* lipases provided a decrease in the consistency in the order of 28 and 21%, respectively. Such reductions can be explained either by the incorporation of the unsaturated fatty acids present in the soybean oil in the TAGs of the milkfat or by the presence of small amounts of mono and diglycerides, which can behave like emulsifiers and can modify the texture products (Kaewthong et al., 2005).

4 Conclusions

Results showed the potential of the evaluated lipases for the interesterification of milkfat with soybean oil. The use of these enzymes resulted in the modification of the triglycerols composition and the interesterified products presented a reduction of 27.67 and 21.12% in the consistency values for reactions catalyzed by *R. oyzae* (L036P) and *C. rugosa* (L034P) lipases, respectively. Therefore, the feasibility of using these lipases to reduce the milkfat consistency and turning the milkfat more spreadable under cooling temperature has been demonstrated.

5 Acknowledgments

The authors acknowledge the financial assistance from Fundação de Amparo à Pesquisa do Estado de São Paulo (FAPESP), CAPES (Coordenação de Aperfeiçoamento de Pessoal de Nível Superior) and Conselho Nacional de Desenvolvimento Científico e Tecnológico (CNPq). The authors also acknowledge Biocatalysts for the enzyme samples.

6 References

American Oil Chemists' Society. (2004). *Official Methods and Recommended Practices of the AOCS*. 5th Edition, AOCS Press.

Balcão, V.M., Malcata, F.X. (1998). Lipase catalyzed modification of milkfat. *Biotechnology Advances*, 16, 309-341.

Carneiro-da-Cunha, M. G., Rocha, J. M. S., Garcia, F.A.P., Gil, M.H. (1999). Lipase immobilization on to polymeric membranes. *Biotechnology Techniques*, 13, 403-409.

Deman, J.M.; Deman, L. (2002). Texture of fats. In: MARANGONI, A.G.; NARINE, S.S. Physical Properties of Lipids. New York: Marcel Dekker, Inc, Cap7, p.191–217.

Haug, A., Høstmark, A.T., Harstad, O.M. (2007). Bovine milk in human nutrition – A review. *Lipids in Health and Disease*, 6, 25.

Kaewthong, W., Sirisansaneeyakul, S., Prasertsan, P. (2005). Continuous production of monoacylglycerols of palm olein with immobilized lipase. *Process Biochemistry*, 40, 1525-1530.

Lamboursain, L., Marty, A., Kermasha, S., Condoret, J. S., Combes, D. (1996). Enzymatic transesterification of a triacylglycerol mixture: Application to butterfat modification. *Annals of the New York Academy of Sciences*, 678-682.

Paula, A. V. Seleção de preparações comerciais de lipase para interesterificação da gordura do leite com óleo de soja. 2008. 110f. Dissertação (Mestrado em Engenharia Química) - Escola de Engenharia de Lorena, Universidade de São Paulo, Lorena/ SP.

Paula, A.V., Moreira, A.B.R., Fonseca, M.M., Braga, L.P., Bruno, L.M., Castro, H.F (2008). Comparação do desempenho da lipase de *Candida rugosa* imobilizada em suporte híbrido de polissiloxano-polivinilálcool empregando diferentes metodologias. *Química Nova*, 31, 35-40.

Rodrigues, J.N., Gioielli, L.A. (2003). Chemical interesterification of milk fat and milk fat-corn oil blends. *Food Research International*, 36,149–159.

Rodrigues, J.N., Gioielli, L.A., Anton, C. (2003). Propriedades físicas de lipídios estruturados obtidos de misturas de gordura do leite e óleo de milho. *Ciência e Tecnologia de Alimentos*, 23, 226-233.

Proceedings of the 10th International Chemical and
Biological Engineering Conference - CHEMPOR 2008
Braga, Portugal, September 4-6, 2008
E.C. Ferreira and M. Mota (Eds.)

Enzymatic Hydrolysis of Buriti (*Mauritia vinifera*) Oil for Obtainment of Beta-Carotene

Bernardo Dias Ribeiro[1], Maria Alice Z. Coelho[1*], Daniel W. Barreto[2]
[1] BIOSE (Biological System Engineering Group), Biochemical Engineering Department, Federal University of Rio de Janeiro (UFRJ), 21941-900, Rio de Janeiro, Brasil.
[2] Organic Processes Department, UFRJ, Rio de Janeiro, Brasil

Keywords: Lipase, Beta-Carotene, Buriti, Enzymatic hydrolysis, Vegetable Oil
Topic: Clean Technology, Valorization of Amazonic Products
Presentation Format: Poster

Abstract

The present work involves enzymatic hydrolysis of crude buriti oil, for further extraction and concentration of β-carotene. In the hydrolysis process, the performance of commercial lipase Lipozyme TL IM was evaluated. The analyzed parameters in the hydrolysis process were temperature, enzyme quantity (enzymatic activity) and ratio of buriti oil / water. The experimental conditions were established based on an experimental design in order to set the maximum free fatty acids contents and the minimum loss of carotenoids.

The results were analysed for the free fatty acids content using titration; total carotenoids through spectrophotometry and its composition by HPLC, employing a YMC ODS-A column with a mobile phase of acetonitrile/methanol/THF (50/45/5). The optimized conditions of the enzymatic hydrolysis were 31.2°C (temperature), 25 U (enzymatic activity in 8 mL of mixture volume), 2.33 (ratio oil/water), at 300 rpm, during 4 hours of reaction. After the hydrolysis of the oil, some methods were tested to separate the formed fatty acids from the carotenoids, as partition with ethanol and winterization, increasing the β-carotene concentration in the final product.

1 Introduction

β-carotene is the main source of provitamin A and is widely used as a food colorant and nutritional supplier. The global market for carotenoids, which was of US$ 887 millions in 2005 and has been growing at an yearly rate of 3%, is estimated to surpass US$ 1 billion in 2009, being β-carotene responsible for almost 30% of this market (Fraser & Bramley, 2004).

Most of the β-carotene sold in the world is produced by chemical synthesis from β-ionone, but a small amount is manufactured using biotechnological processes, based on different microorganisms, such as fungi (*Blaskelea trispora* and *Phycomyces blaskeleeanus*), yeasts (*Rhodotorula glutinis*), bacteria (*Flavobacterium multivorum*) and microalgae (*Dunaliella salina* and *D. bardawil*) (Bhosale & Bernstein, 2004; Dufossé *et al*, 2005; Kuzina & Cerdá-Olmedo, 2007; Maldonade *et al*, 2008).

Some oleaginous fruits, such as palm (*Elaeis guineensis*) and buriti (*Mauritia vinifera*), present high concentrations of carotenoids, specially β-carotene. Buriti is a palm tree that grows wild in different areas of Brazil, and has been traditionally used for the preparation of beverages and candies in the Amazon area. The recent interest about other natural sources of β-carotene stimulated the development of processes to extract the carotenoid-rich oil of the buriti fruit. Most processes, however, are still based on the conventional technologies for pulps, including drying and pressing the oil off the pulp (Rodriguez-Amaya, 2001; Santos, 2005).

* Corresponding author. Tel + 55-21-25627572. E-mail:alice@eq.ufrj.br

Due to similarity between the physical properties (solubility, polarity, molar massr) of carotenoids and triglycerides, besides low selectivity of most physical separation methods currently used for carotenoids extraction, as well as irreversible structural alterations caused by chemical methods, the search for more specific and mild methods to the extraction of carotenoids contained in vegetable oils is a great challenge (Güçlü-Üstündag & Temelli, 2004).

The present work consists in a bioprocess development by enzymatic hydrolysis of crude buriti oil using commercial lipase Lipozyme TL IM, for further extraction and concentration of β-carotene.

2 Materials and Methods

The crude buriti oil RF3800 was gently provided by Beraca Sabará®. The commercial lipase utilized was Lipozyme TL IM from *Thermomyces lanuginosus* from Novozymes®, which presented 690,24 ± 6 kU/kg of lipolytic activity, measured as Meirelles (1997).

Some conditions for the enzymatic hydrolysis were initially constant as reaction time (4 h), agitation speed (200 rpm), reaction volume (8 mL) and amount of alumina, used as fatty acid adsorbent, (10 % w/v). Others parameters, like temperature, enzyme quantity (activity) and ratio buriti oil/ water, were evaluated (Table 1) with a central composite experimental design with 3 levels and 3 central points.

Table 1 – Value range utilized for parameter optimization of enzymatic hydrolysis

Parameters	-1,68	-1	0	+1	+1,68
Temperature (°C)	25	29	35	41	45
Enzymatic Activity (U)	1	10,7	25	39,9	50
Ratio Oil/Water	1/1 (1)	7/5 (1.4)	2/1 (2)	13/5 (2.6)	3/1 (3)

For achieving higher yiels in free fatty acids content, additional tests were realized, which the conditions (temperature and ratio oil/water) obtained in the experimental design were maintained, but considering enzyme activity within small intervals (5, 15, 25, 35, 45, 55 and 65 U), besides agitation speed (200, 300 and 400 rpm) and reactional time (0,5, 1, 1.5, 2, 3, 4, 6 and 8 h). After this, the organic phase (carotenoids and oil) were separated from the other components (water, glycerol, lipase, saturated fatty acids and alumina). Then, desacidification and concentration were tested by partition with ethanol (Gonçalves *et al*, 2007) and winterization.

The results were analyzed for the free fatty acids contents using potentiometric titration (Kanicky & Shah, 2002; Osawa & Gonçalves, 2006); and total carotenoids using spectrophotometry (Rodriguez-Amaya, 2001).The samples were also analyzed according to the composition of carotenoids in HPLC. The separation was carried out with a 100 x 4.6 i.d. mm YMC-Pack ODS-A column (5 mm particle size), using as mobile phase acetonitrile/methanol/THF (50/45/5 v/v/v), with addition of 0.05% triethilamine to methanol. The flow rate was 1.0 mL/min, and the absorbance was detected on 450 nm. The standards used was obtained by open column chromatography separation, in which activated magnesium oxide – diatomaceous earth mix was employed. Initially was added the unsaponifiable fraction of crude buriti oil to the column, and then eluted with petroleum ether in concentrations varying from 4 to 20 of diethyl ether. The fractions obtained were α-carotene, β-carotene and γ-carotene. These carotenoids were confirmed by scanning in the visible spectre in DR400 UV Hach spectrophotometer (Godoy & Rodriguez-Amaya, 1995; Rodriguez-Amaya, 2001; Ribeiro, 2008). The results of experimental design were analyzed employing software STATISTICA 6.0.

3 Results and Discussion

The crude buriti oil presented a high content of unsaturated fatty acids, mainly oleic acid (75%), and carotenoids, about 1800 ppm (Table 2), which carotenoids composition can be observed in Figure 1 (Ribeiro, 2008).

Table 2 – Major components in crude buriti oil

Components	%
Fatty acids	
Saturated	22.2
Unsaturated	77.8
Carotenoids	
β-carotene	76.8
α-carotene	8.8
γ-carotene	4.5

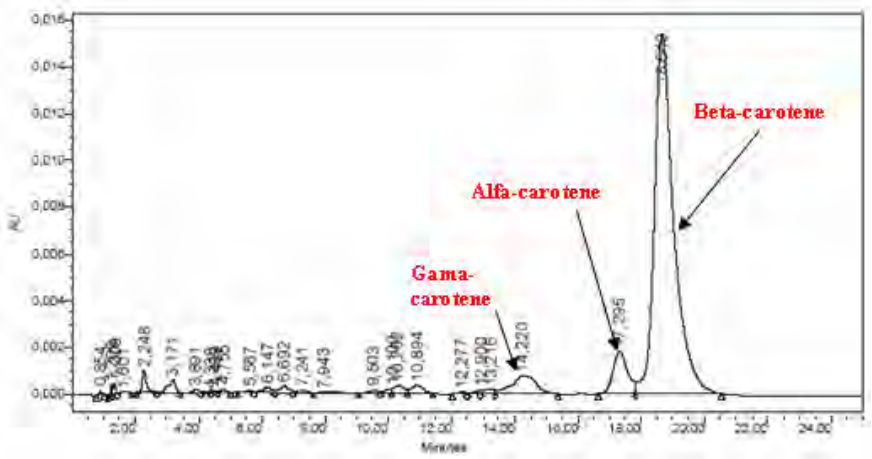

Figure 1 – Carotenoid composition profile of crude buriti oil

The results obtained in the central composite experimental design referred to the enzymatic hydrolysis with Lipozyme TL IM were decpited in the Table 3. The optimized conditions obtained were: 31.2 °C (temperature), 21.6 U (enzymatic activity) and 2.33 (ratio oil/water), which using the regression coefficients, the variables free fatty acid and carotenoids could be calculated, resulting in 6.48% and 1749 ppm, respectively.

Table 3 – Results of enzymatic hydrolysis of crude buriti oil using central composite design

Assays	T(°C)	Activ(U)	Oil/Water	%FFA	Carot. (ppm)
1	29.0	10.7	1.4	62.89	1539
2	29.0	10.7	2.6	56.58	1810
3	29.0	39.9	1.4	73.61	1561
4	29.0	39.9	2.6	73.04	1732
5	41.0	10.7	1.4	62.53	1580
6	41.0	10.7	2.6	52.83	1692
7	41.0	39.9	1.4	**76.46**	1609
8	41.0	39.9	2.6	61.20	1609
9	25.0	25.0	2.0	60.11	1547
10	45.0	25.0	2.0	66.06	1570
11	35.0	1.0	2.0	18.78	1814
12	35.0	50.0	2.0	72.00	1602
13	35.0	25.0	1.0	64.24	1631
14	35.0	25.0	3.0	67.86	1596
15 (C)	35.0	25.0	2.0	66.06	1728
16 (C)	35.0	25.0	2.0	62.61	1746
17 (C)	35.0	25.0	2.0	68.87	1720

High free fatty acids yield could be explained by tridimensional structure of lipase active site (Gutierrez-Ayesta *et al*, 2007) or also by possible hiperactivation generated by immobilization method used in the production of Lipozyme TL IM, which could leave the active site always exposed and activated (Cunha, 2007). Devos *et al* (2006) performed a comparation between 12 lipases in the hydrolys of algal phospholipids, showing that Lipozyme TL IM also generated free fatty acids yields of 75%, although using higher reaction time (24 h), agitation speed (800 rpm), enzyme quantity (1% w/v) and ratio between organic and aqueous phases (1/10).

Since the enzymatic activity was the only parameter statistically significant in the oil hydrolysis, it was tested in small intervals, which determined that better condition was 25 U (0,47% w/v), without great carotenoids loss (Figure 2).

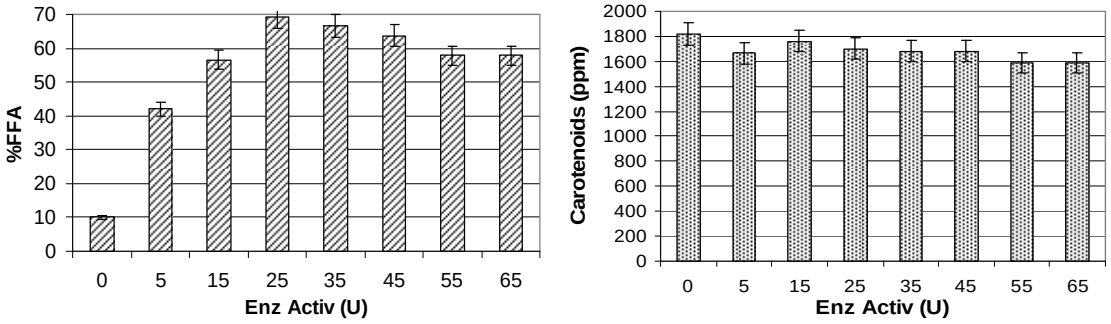

Figure 2 – Optimization of enzyme quantity in the enzymatic hydrolysis of buriti oil

Still objecting a higher oil hydrolysis, different agitation speed were tested in the system to increase the interfacial area and facilitate lipase action. The chosen speed was 300 rpm due to the increased free fatty acids yields (about 75%), with carotenoid loss slightly lower than obtained in 40 rpm (Figure 3).

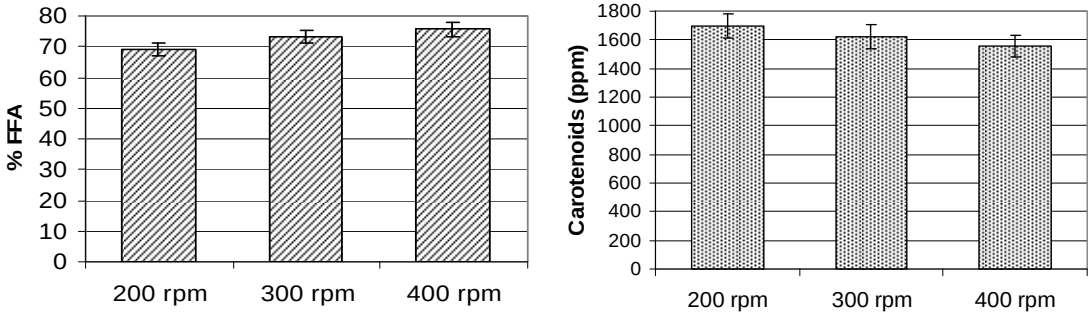

Figure 3 – Evaluation of agitation speed in the enzymatic hydrolysis of buriti oil

Maintaining all the previous conditions, the reaction hydrolysis kinetics was evaluated, and then observed that, in 4 h of reaction, the oil hydrolysis was stabilized (Figure 4). Probably, the free fatty acids yields remained about 75% due to pH alteration, which reached values near to 5, leading to a possible lipase inhibition.

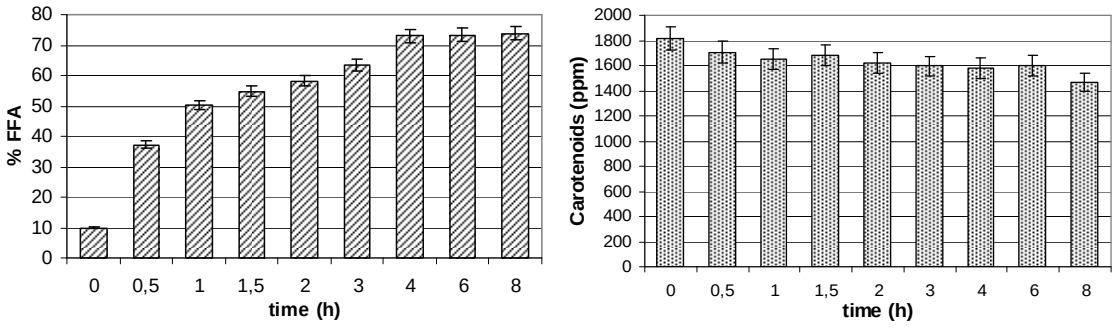

Figure 4 – Optimization of reactional time in the enzymatic hydrolysis of buriti oil

After phase separation, two methods of carotenoids concentration were tested. First was the partition with ethanol, which, in 15 min, the fatty acid concentration in alcoholic phase was 10%. Gonçalves & Meirelles (2004) reached concentration of 53%, but in their work was included stand-by step of 24 h to equilibrate the system, and the quantity of fatty acids in the sample was near to 4%.

In relation to carotenoids, just 2% were distributed to ethanolic phase when crude buriti oil was used. Gonçalves et al (2007) verified the carotenoids of palm oil distribute to the alcoholic phase between 1.6 a 2.7%, which could increase if the water quantity in the system was lower, for example with anhydrous ethanol the carotenoids partition rise to 13%. In Figure 5, the variation of free fatty acids and carotenoids was observed since the ending of enzymatic process (1), the separation of organic and aqueous phases (2), and the sucessive extraction of organic phase with ethanol (3).

In this process, the carotenoid loss was of 4.4%, and practically duplicating the total quantity after the sucessive extraction. The fatty acids was reduced to 30%, indicating that more extraction will be needed.

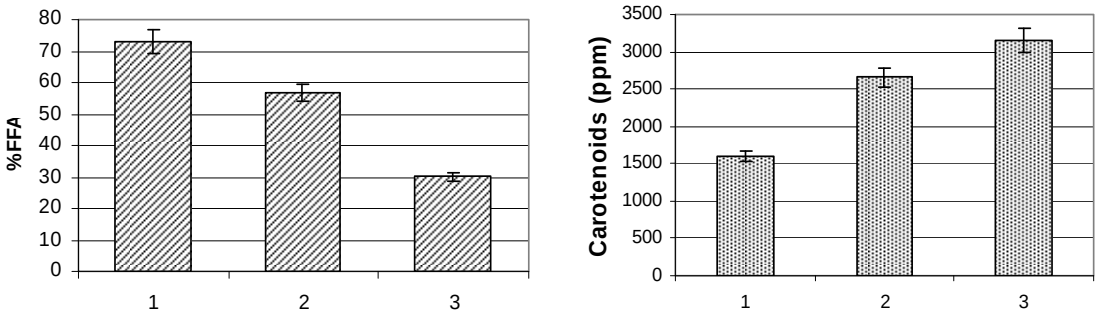

Figure 1 – Evaluation of free fatty acids and carotenoids during the post-processing of buriti oil

In winterization process, two phases were obtained: the first solid with 43% of free fatty acids and 3186 ppm of carotenoids, while the other liquid with 26% of free fatty acids and 3910 ppm of carotenoids (Figure 6).

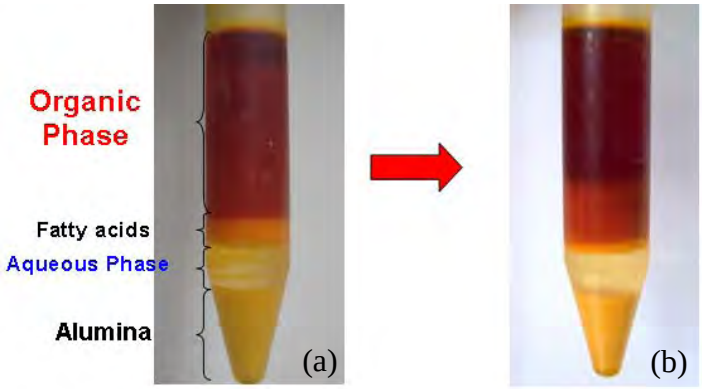

Figure 6 – (a) Before and (b) after the winterization of buriti oil

4 Conclusions

The enzymatic hydrolysis followed by partition with ethanol or winterization demonstrated to be a feasible method for extraction and concentration of carotenoids. This could facilitate a generation of food products rich in carotenoids, reducing the problems of hipervitaminose A in the world.

Acknowledgements

The authors are grateful for the financial support given by CNPq, FAPERJ and CAPES.

References

Bhosale, P.; Bernstein, P.S. (2004). β-Carotene production by *Flavobacterium multivorum* in the presence of inorganic salts and urea. *Journal of Industrial Microbiology and Biotechnology***,** 31, 565-571.

Cunha, A. G.; *Purificação e imobilização de lipases microbianas em suportes com diferentes graus de hidrofobicidade***.** Dissertação (Mestrado), Programa de Bioquímica, Instituto de Química, UFRJ, 2007.

Dufossé, L.; Galaup, P.; Yaron, A.; Arad, S.M.; Blanc, P.; Murthy, K.N.C.; Ravishankar, G.A. (2005). Microorganisms and microalgae as sources of pigments for food use: a scientific oddity or an industrial reality? *Trends in Food Science & Technology***,** 16, 389-406.

Devos, M.; Poisson, L.; Ergan, F.; Pencreac'h, G.; Enzymatic hydrolysis of phospholipids from *Isochrysis galbana* for docosahexaenoic acid enrichment. *Enzyme and Microbial Technology***,** 39, 548-554, 2006.

Fraser, P.D.; Bramley, P.M. (2004). The biosynthesis and nutritional uses of carotenoids. *Progress in Lipid Research***,** 43, 228-265.

Godoy, H.T.; Rodriguez-Amaya, D.B.; Buriti (*Mauritia vinifera* Mart.), uma fonte riquíssima de pró-vitamina A. *Arquivos de Biologia e Tecnologia***,** 38 (1), 109-120, 1995.

Gonçalves, C.B.; Meirelles, A.J.A.; Liquid-liquid equilibrium data for the system palm oil + fatty acids + ethanol + water at 318.2 K. *Fluid Phase Equilibria***,** 221, 139-150, 2004**.**

Gonçalves, C.B.; Pessoa Filho, P.A.; Meirelles, A.J.A.; Partition of nutraceutical compounds in deacidification of palm oil by solvent extraction. *Journal of Food Engineering,* 81, 21-26, 2007.

Güçlü-Üstündag, Ö.; Temelli, F.; Correlating the solubility behavior of minor lipids components in supercritical carbon dioxide. *Journal of Supercritical Fluids***,** 31, 235-253, 2004.

Gutiérrez-Ayesta, C.; Carelli, A.A.; Ferreira, M.L.; Relation between lipase structures and their catalytic ability to hydrolyse triglycerides and phospholipids. *Enzyme and Microbial Technology***,** 41, 35-43, 2007.

Kanicky, J.R.; Shah, D.O.; Effect of degree, type, and position of unsaturation on the pK_a of long-chain fatty acids. *Journal of Colloid and Interface Science,* 256, 201-207, 2002.

Kuzina, V.; Cerdá-Olmedo, E. (2007). Ubiquinone and carotene production in the *Mucorales Blakeslea* and *Phycomyces*. *Applied Microbiology and Biotechnology***,** 76, 991-999.

Maldonade, I.R.; Rodriguez-Amaya, D.B.; Scamparini, A.R.P. (2008). Carotenoids of yeasts isolated from the Brazilian ecosystem. *Food Chemistry***,** 107, 145-150.

Meirelles, F.V.P.*; Produção de lipases por Yarrowia lipolytica (IMUFRJ50682).* Tese (Doutorado), Programa de Bioquímica, Instituto de Química, UFRJ, Rio de Janeiro, 1997.

Osawa, C.C.; Gonçalves, L.A.G.; Titulação potenciométrica aplicada na determinação de ácidos graxos livres de óleos e gorduras comestíveis. *Química Nova***,** 29 (3), 593-599, 2006.

Ribeiro, B.D.; *Aplicação de Tecnologia Enzimática na Obtenção de β-Caroteno a partir de Óleo de Buriti (Mauritia vinifera)***.** Dissertação (Mestrado), Programa de Pós-Graduação de Tecnologia de Processos Químicos e Bioquímicos, EQ, UFRJ, 2008.

Rodriguez-Amaya, D.B. (2001). *A Guide to Carotenoid Analysis in Food***.** ILSI Press, Washington.

Santos, L.M.P. (2005); Nutritional and ecological aspects of buriti or aguaje (*Mauritia flexuosa* Linnaeus filius): a carotene-rich palm fruit from Latin America. *Ecology of Food and Nutrition***,** 44, 1-14.

Proceedings of the 10th International Chemical and
Biological Engineering Conference - CHEMPOR 2008
Braga, Portugal, September 4-6, 2008
E.C. Ferreira and M. Mota (Eds.)

Enzymatic inulin hydrolysis using PVA-based matrices

Pedro Fernandes*, Stefano Cattorini, Joaquim M.S. Cabral
IBB – Institute for Biotechnology and Bioengineering, Centre for Biological and Chemical Engineering, Instituto Superior Técnico, Av. Rovisco Pais, 1049-001 Lisboa, Portugal.

Keywords Hydrogels, polyvinyl alcohol, inulin hydrolysis, inulinase, encapsulation
Topic: Integration of life sciences & engineering.

Abstract

Inulinase form *Aspergillus niger* was immobilized into poly(vinylalcohol) hydrogel lens-(Lentikats®) and hemispherical-shaped capsules, based on LentiKat® liquid. Temperature and pH profiles, as well as kinetic constants were determined, for both free and immobilised enzyme. A broader-shaped curve was observed for the pH-activity profile when immobilized forms were matched to the free form. The K_M of inulinase increased roughly 2-fold upon immobilization, suggesting diffusion limitations of inulin inside the gel. Long term operation with immobilized enzymes is not viable given the decay of mechanical strength of the support above 55ºC. The hemispherical form of the immobilized enzyme displayed long-term operational stability in repeated batch-mode runs, for it allowed for 20 runs at 50ºC, with a final decay of product yield in 20%. When Lentikats® were used, similar decay was roughly of 70%.

1 Introduction

Inulin is a linear-linked fructose polymer that occurs as reserve substrate in Jerusalem artichoke, chicory or dahlia tubers. This polymer is an acknowledged source for the production of fructose syrups, in alternative to the multi-enzymatic starch hydrolysis or the less favored inverted sugar production (Ricca et al., 2007). Inulin hydrolysis can be performed chemically, but this approach leads to unwanted by-products and colored compounds, shortcomings that can be overcome if the enzymatic route, performed by inulinases, is used (Vandamme and Derycke, 1983). The enzymatic approach is further favored if a suitable immobilization method can be used. In the food industry this requires for a readily available support and simple immobilization procedures, to comply with the need to cut down costs and complexity (Walsh, 2007). Immobilization of inulinase for fructose production has mostly relied in covalent and ionic binding methods, although entrapment into alginate, chitin and casein has also been reported (Gill et al. 2006, Ricca et al., 2007) Polyvinyl alcohol is a synthetic polymer that can be used to form hydrogels, and combines the biocompatibility of natural polymers with high mechanical strength (Angelova and Hunkeler, 1999). Several methods have been developed to produce PVA capsules. One of the most recent relies on the controlled drying of a PVA based hydrogel (LentiKat® liquid), and subsequent chemical stabilization, leading to lens-shaped particles (Vorlop and Jekkel, 1999). This methodology has been applied to the hydrolysis of di- and oligosaccharides (Rebros et al., 2006, 2007), but not to polysaccharides such as inulin. In the present work two procedures of inulinase immobilization for inulin hydrolysis to fructose, based in the use of LentiKats® liquid, were evaluated: gelation of PVA by controlled drying, yielding lenticular shaped particles, and a novel approach where PVA is extruded into polyethylene glycol (PEG), where gelification occurs instantaneously in the form of hemisphere-like capsules. The kinetic parameters, pH and temperature profiles of free and both forms of immobilized inulinase were matched and the long term stability of the two forms of the immobilized enzyme was evaluated.

* Corresponding author. Tel + 351-218-419065. E-mail: pedro.fernandes@ist.utl.pt

2 Materials and methods

Fructozyme L, a commercial preparation of inulinase from *Aspergillus niger*, was provided by Sigma, polyethylene glycol (PEG) 600 was from Fluka, LentiKat® liquid, a PVA-based material, and LentiKat® stabilizer were from GeniaLab and inulin from chicory (Fibruline Instant) was a kind gift from Cosucra. All other chemical were of analytical grade from various suppliers.

Inulinase immobilization

Entrapment of inulinase in Lentikats® was performed according to the protocol provided by GeniaLab (http://www.geniaLab.de/download/tt-english.pdf). Briefly, the LentiKat® liquid was heated at 95ºC and then cooled to 40ºC. The enzyme suspension (0.5 ml of a ten-fold, 100 mM acetate buffer, pH 4.5, diluted commercial preparation) was added to 10 ml of the LentiKat® liquid and thoroughly mixed. The liquid was extruded through a needle (Therumo, 20 G x 2") into Petri dishes to form small drops. These were left at room temperature, until roughly 28% of the initial mass remained. LentiKat® stabilizer was then poured into the Petri dish, and after 2-3 minutes, the suspension was transferred to a flask, about a 10-fold volume of stabilizer further added, and the whole stirred for 2 hours. The lens-shaped particles, with 3-4 mm diameter, were harvested, thoroughly washed with acetate buffer, and soaked in the buffer for two hours, harvested and weighed after removal of excess buffer with qualitative filter paper, and either immediately used for bioconversion runs or stored at 4ºC until use. Alternatively, immobilized biocatalyst particles were prepared by extruding drop-wise the LentiKat® liquid containing inulinase into stirred 150 ml of PEG 600. After a 2-hour period, the hemispherical capsules formed were harvested, thoroughly washed with acetate buffer, weighed after removal of excess buffer with qualitative filter paper, and either immediately used for bioconversion runs or stored at 4ºC until use. Immobilization yield was determined as the ratio between the specific activity of immobilized inulinase and that of the soluble inulinase, in a 30 minutes run. Runs were performed in 1.5 ml screw-capped magnetically stirred (500 rpm) reactors, filled with 1.0 ml of 100 mM acetate buffer (pH 4.5), containing 5.0% (w/v) of inulin.

Determination of temperature and pH profiles and of kinetic parameters

Experiments were performed at the intended pH (4–6) and temperature (40–65ºC), in inulin (5.0 % w/v, unless stated otherwise) dissolved in 1 ml of acetate buffer (100 mM), containing 50 mg of immobilized inulinase or 20 μl of a 40-fold diluted preparation of free inulinase. Runs were performed in 1.5 ml screw caped vessels and agitation (500 rpm) was promoted by magnetic stirring. Samples (10 μl) were taken after 30 minutes and immediately assayed for reducing sugars. All runs were performed in triplicates, at least. Kinetic parameters were determined using the commercial software Leonora (Cornish-Bowden,1995)

Repeated batch hydrolysis

Reactions were performed in 1.5 ml screw-capped magnetically stirred (500 rpm) reactors at 50ºC or 55ºC, in 1.0 ml of 100 mM acetate buffer (pH 4.5), containing 5.0% (w/v) of inulin and 50 mg of immobilized inulinase. Throughout each cycle (24-hours run), 10 μl samples were collected and assayed for reducing sugars. After each cycle the immobilized biocatalyst was harvested, thoroughly washed with acetate buffer and used for the next run. All runs were performed in triplicates, at least.

Analytical methods

Quantification of reducing sugars was performed by the DNS method (Miller, 1959). Quantification of protein was performed by the BCA method (Smith et al., 1985) using a commercial kit from Pierce. Particles of immobilized biocatalyst were dissolved in distilled water heated at 70ºC, prior to protein quantification. Liquid supernatants resulting form the immobilization procedures were also assayed for protein levels. The standard deviation from these determinations did not exceed 8%, except if stated otherwise.

3. Results and discussion

Depending on the nature of the procedure for the formation of the production of the PVA-encapsulated inulinase, different shapes were obtained (Figure 1).

Figure 1. Typical shapes of PVA capsules obtained according to the standard Genialab methodology to yield lens-shaped particles, Lentikats® (a); or following extrusion into PEG 600, to yield hemispherical particles (b).

Lentikats® allowed slightly higher enzyme loading and activity retention upon immobilization when compared to hemispherical beads, but the differences are not significant (Table 1). No traces of protein were observed in the supernatants resulting from the immobilization procedures, hence the difference in enzyme loading may be ascribed to the differences in overall weight of the particles obtained. Given the mild methodology used for immobilization, immobilization yields are most likely affected by diffusion limitations. Still, roughly full conversion of a 5.0 % (w/v) solution of inulin is obtained after a 24-hour biotransformation period, as reflected by the final product concentration, which is similar to the result obtained with the free enzyme, and clearly highlights the potential of this approach.

Table 1. Immobilization of inulinase in Lentikat®-liquid based matrices.

Immobilized biocatalyst	**Relative mass of the capsules (%)**	**Enzyme loading (mg $g^{-1}_{support}$)**	**Immobilizaton yield (%)**	**Final product concentration (g l^{-1})[a]**
Lentikats®	80	0.20 ± 0.05	34 ± 5	46 ± 3
Hemispherical capsules	100	0.13 ± 0.02	37 ± 4	47 ± 2
Free enzyme	-	-	-	49± 4

[a] Determined after a 24-hour biotransformation run using a 5.0 % w/v inulin solution in 100 mM acetate buffer, pH 4.5 and using similar amount of enzyme.

The activity retention upon immobilization in PVA matrices compares favorably or at least matches data from other authors for immobilization of inulinase in gelatin (Bajpai and Margaritis, 1985), casein (Kochhar et al., 1998), activated charcoal, porous silica beads, gelatin and gelatin-citrate (Paula et al., 2007), alginate and Dowex (Gill et al., 2006).

Effect of pH and temperature in enzyme activity

The influence of pH on the initial activity of free and immobilized inulinase was evaluated in the pH range 4.0–6.0 at 50 ºC (Figure 2a).

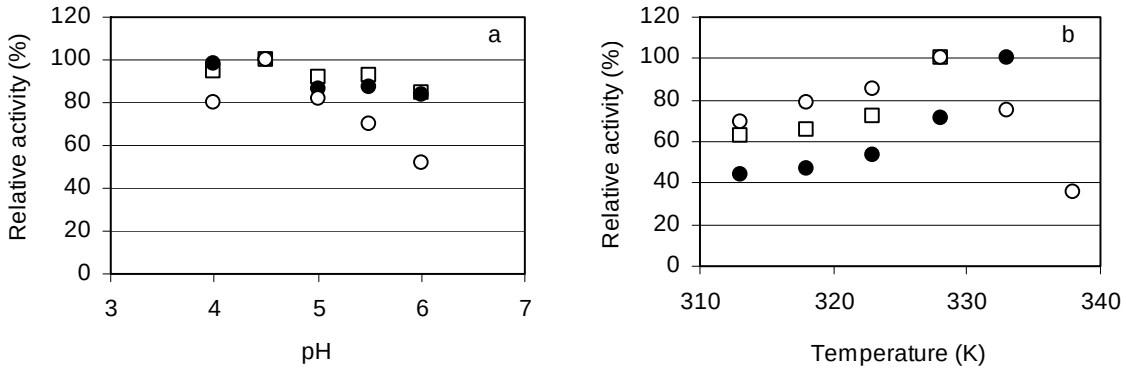

Figure 2. pH (a) and temperature (b) profiles of free inulinase (open dots), inulinase immobilized in Lentikats® (open squares) and inulinase immobilized in hemispherical particles (closed dots). Reactions were performed in 100 mM acetate buffer containing 5.0 % (w/v) of inulin, at 50ºC (a) and pH 4.5 (b).

Both free and immobilized forms of the enzyme show an optimum pH for catalytic activity at 4.5. A much broader-shaped curve was observed for the two immobilized forms of the biocatalyst, when compared to the free form, particularly in the more acidic range. This can be advantageous, for operation at lower pH values reduces the risk of microbial contamination. A broadened pH range upon immobilization was also reported for inulinase immobilization in Amberlite (Rocha et al., 2006), but was not observed for immobilization in DEAE-Sephacel or in QAE-Sephadex (Gill et al., 2006). This effect was also reported for invertase immobilization in Lentikats®, and was tentatively ascribed to secondary interactions between the polymer and the enzyme and polymer matrix throughout the immobilization process (Rebros et al., 2007).

The free inulinase displayed the maximum activity at 55 ºC. The activity of the inulinase immobilized in Lentikats® steadily increased up to 55 ºC, but above this temperature the PVA-based matrix was shown to be unstable and tended to melt, a feature that effectively took place almost immediately once the lens-shaped particles were incubated at 60 ºC. Such behavior, that clearly prevents the useful application of Lentikats® above 55 ºC, was previously reported by Rebros and co-workers (2007), while evaluating the use of immobilized invertase for sucrose hydrolysis. Hemispherical shaped particles displayed slightly enhanced mechanical stability, for temperature activity profile could be evaluated up to 60ºC, with biocatalytic activity also consistently increasing with temperature. Above 60 ºC, however the trend towards melting was also observed, hence 60 ºC was determined as the temperature for maximum activity for the latter immobilized biocatalyst. Particle formation through extrusion into PEG seems thus to slightly enhance mechanical stability at the higher temperatures tested, and therefore increase the optimum temperature for immobilized inulinase activity, when matched to the free form.

Effect of immobilization in kinetic parameters

The trials for the evaluation of the kinetic constants for the Michaelis-Menten type kinetics of inulin enzymatic hydrolysis (Rocha et al., 2006), were performed at pH 4.5 and 50 ºC. Kinetic constants were determined from experimental data using Leonora software (Cornish-Bowden, 1995). The K_M for both forms of the immobilized enzyme was roughly 2-fold higher than that of the free inulinase (Table 2). Such increase can be most likely ascribed to the impaired accessibility of the bulky inulin molecule to the active site of the immobilized enzyme due to the diffusion barrier created by the matrix. Although the thin nature of the lenticular particles would be likely to lower diffusion hindrances, when compared to hemispherical particles, that effect was not significantly noticeable, given the similarity of the data. An increase in K_M upon immobilization by entrapment in gelatin (Bajpai and Margaritis,

1985) or adsorption in porous supports (Gupta et al., 1992) has also been reported. Immobilization also affected V_{max} was also affected by immobilization, a roughly 4-fold decease was observed, irrespective of the immobilization strategy, as compared to the free enzyme (Table 2).

Table 2. Kinetics constants obtained for inulin hydrolysis with free and immobilized inulinase.

Biocatalyst	**K_M (g l^{-1})**	**V_{max} ($g_{fructose}$ g^{-1}_{enzyme} s^{-1})**
Free enzyme	26 ± 3	2.7± 0.1
Lentikats®	46 ± 8	1.1 ± 0.2
Hemispherical	53 ± 5	0.71 ± 0.02

Biocatalyst reuse

The feasibility of the application of an immobilized enzyme system in a large scale process clearly depends on its operational stability. In order to evaluate this key parameter, repeated batch hydrolysis runs were performed at 50 ºC and 55 ºC, using both immobilized biocatalysts (Figure 3). Reuse of the immobilized biocatalyst at 55 ºC proved unfeasible due to mechanical instability of the supports. This effect was also somehow noticed in Lentikats® at 50 ºC, which seemed furthermore relatively sensitive to stress from magnetic stirring. Hemispherical beads were successfully used at 50 ºC throughout 20 cycles, displaying a final decrease in the relative product yield of roughly 20%.

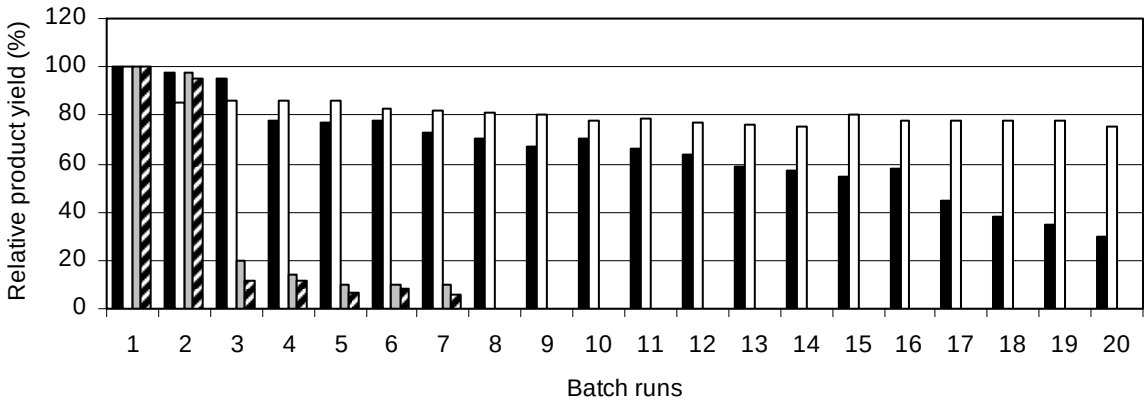

Figure 3. Effect on the final product yield of the repeated use of inulinase immobilized in Lentikats® (closed and grey bars) and in hemispherical beads (open and stripped bars), for the hydrolysis of a 5% (w/v) inulin solution. Batch runs (24 h) were performed at 50 ºC (closed and open bars) and 55 ºC (grey and stripped bars), at pH 4.5. Final fructose concentration in the first cycle was 50 g l^{-1}.Standard deviation did not exceed 10%.

4. Conclusions

Inulinase was effectively immobilized polyvinyl alcohol particles, either as LentiKats® or in hemispherical beads obtained through extrusion of LentiKat® liquid into PEG 600. Immobilization broadened the pH-activity profile paving the way for operation under relatively acidic conditions. The activity of free and LentiKats® immobilized enzyme reached a maximum at 55 ºC, which was shifted to 60 ºC when hemispherical beads were used. Still in

both immobilized preparations a significant decay in mechanical strength was observed above 55ºC, which limits to 50 ºC their application in long term operation. Diffusion limitations were observed as a result of entrapment. Hemispherical beads were successfully used throughout 20 consecutive batch runs with no apparent mechanical changes in the matrix and no significant decrease in the final product yield, which highlight the potential of inulinase immobilized in PVA-based particles obtained through extrusion into PEG as a suitable biocatalyst for application in large scale processes for fructose production through inulin hydrolysis.

References

Angelova, N., Hunkeler, D. (1999) Rationalizing the design of biomaterials. *Trends in Biotechnology*, 17, 409-421.

Bajpai, P., Margaritis, A. (1985) Immobilization of *Kluyveromyces marxianus* cells containing inulinase activity in open pore gelatin matrix. 1. Preparation and enzymatic properties. *Enzyme and Microbial Technology*, 7, 459–461.

Cornish-Bowden, A., 1995. *Analysis of Enzyme Kinetic Data*. Oxford Science Publications, Oxford.

Gill, P. K., Manhas, R. K., Singh, P. (2006) Hydrolysis of inulin by immobilized thermostable extracellular exoinulinase from *Aspergillus fumigatus*. *Journal of Food Engineering*, 76, 369–375.

Kochhar, A., Kaur, N., & Gupta, A. K. (1998). Immobilization of inulinase from Aspergillus versicolor for preparing fructose from inulin. *Journal of Scientific Industrial Research*, 57, 184–187.

Miller, G. L. (1959). Use of dinitrosalicylic acid reagent for determination of reducing sugar. *Analytical Chemistry*, 31, 426–428.

Paula, F. C., Cazetta, M. L., Monti, R., Contiero, J. (2006) Screening of supports for *Kluyveromyces marxianus var. bulgaricus* inulinase immobilization. Current Trends in Biotechnology and Pharmacy, 1, 34-40.

Rebros, M., Rosenberg, M., Mlichová, Z., Kristofıkova, L., Paluch, M. (2006) A simple entrapment of glucoamylase into LentiKats® as an efficient catalyst for maltodextrin hydrolysis. *Enzyme and Microbial Technology*, 39, 800-804.

Rebros, M., Rosenberg, M., Mlichová, Z., Kristofıkova, L. (2007) Hydrolysis of sucrose by invertase entrapped in polyvinyl alcohol hydrogel capsules. *Food Chemistry*, 102, 784-787.

Ricca, E., Calabrò, V., Curcio, S., Iorio, G. (2007) The State of the Art in the Production of Fructose from Inulin Enzymatic Hydrolysis. *Critical Reviews in Biotechnology*, 27, 129–145.

Rocha, J. R., Catana, R., Ferreira, B. S., Cabral, J. M. S., & Fernandes, P. (2006). Design and characterisation of an enzyme system for inulin hydrolysis. *Food Chemistry*, 95, 77–82.

Smith, P. K., Krohn, R. I., Hermanson, G. T., Mallia, A. K., Gartner, F. H., Provenzano, M. D., Fujimoto, E. K., Goeke, N. M., Olson, B. J., Klenk, D. C. (1985) Measurement of protein using bicinchoninic acid. *Analytical Biochemistry,* 150, 76–85.

Vandamme, E.J., Derycke, D.G. (1983) Microbial inulinases: fermentation process, properties, and applications. *Advances in Applied Microbiology*, 29, 139–176.

Vorlop, K.-D., Jekkel, M. (1999) Process for producing a polyvinyl alcohol gel and mechanically highly stable gel produced by this process. Patent WO 99/67320.

Walsh, M.K. (2007) Immobilized enzyme technology for food applications, In: *Novel enzyme technology for food applications*. Rastall, R. (ed.), Woodhead Publishing Ltd., Cambridge, England, 60-83.

Proceedings of the 10th International Chemical and
Biological Engineering Conference - CHEMPOR 2008
Braga, Portugal, September 4-6, 2008
E.C. Ferreira and M. Mota (Eds.)

Kinetic study of enzymatic biodiesel production from macauba acid oil using *Candida antarctica* B lipase immobilized in coconut fiber

Rafaella F. Nascimento[1], Ana I. S. Brígida[1], Carla C. C. M. Silva[1], Maria H. Rocha-Leão[1], Luciana R. B. Gonçalves[2], Maria A. Z. Coelho[1], Suely P. Freitas[1]*

[1] Escola de Química, Centro de Tecnologia, Universidade Federal do Rio de Janeiro, Cidade Universitária, 21941–909 Rio de Janeiro, Brasil.

[2] Departamento de Engenharia Química, Universidade Federal do Ceará, Campus do Pici, 60455-760 Fortaleza, Brasil

Keywords: Biodiesel, Macaúba acid oil, Green coconut fiber, *Candida antarctica* B lipase, Immobilized enzyme
Topic: Integration of life sciences & engineering

Abstract

Biodiesel production from acids oils is considered as a step up of recycling waste oil and has a positive environmental impact. In this study the biodiesel production from macauba high acid oil using *C. antarctica* B lipase (CALB) immobilized in green coconut fiber was investigated. The results showed that the conversion rate of a reaction catalyzed by CALB immobilized in coconut was similar to Novozyme 435. Maximum conversion (82.91%) was obtained at 50ºC, amount of catalyst of 10% w/w of oil and macauba acid oil: ethanol ratio of 3:1 w/w. The viscosity of this biodiesel from macauba acid oil (2.75 cSt, at 40ºC) is smaller than reported values in the literature.

1 Introduction

Biodiesel is defined by American Society for Testing and Materials (ASTM) as monoalkyl esters of long chain fatty acids derived from a renewable lipid feedstock, such as vegetable oil or animal fat. It is a renewable and sustainable substitute of the diesel fuel traditionally obtained from petroleum (MARCHETTI *et al*., 2008). Actually, one of the biggest disadvantages of the use of biodiesel is its high cost in comparison with petroleum-based fuel. Feedstock oil is responsible for 60-75% of the cost (TAMALAMPUDI *et al*., 2008). Thus, to provide biodiesel at a reasonable price, not only refined vegetable oils but mainly crude, waste materials and by-products should be used.

Brazil has a vegetable rich variation that can be used as oil source, as castor-bean, palm, macauba, sunflower, babassu, soy, and others. From these vegetables, macauba (*Acrocomia aculeata*) has potential to produce up to 5 ton of palmitic oil and 1.4 ton of lauric oil giving a total productivity of 6.4 ton of oil/ha (CLEMENTE *et al*., 2005). This feature highlights this palm tree as a good source of oil. Another characteristic of this fruit is that its oil presents high content of free fatty acids few weeks after raw fruit harvest. This occurs due to the high content of unsaturated fatty acids and the endogenous enzymes in the macauba pulp.

In biodiesel production studies, several researches have been attempt to acid oils. Biodiesel production from acids oils is considered as a step up of recycling waste oil and has a positive environmental impact. However, using alkaline catalyst, there is a significant drop in the ester conversion when free fatty acids are beyond 2% (SHARMA *et al*., 2008). Thus, to apply chemical catalysis is necessary to perform a pretreatment in order to reduce the free fatty acids. In this case, use of immobilized lipases for biodiesel production eliminates the disadvantages of the homogeneous process by producing of very high purity product without pretreatment and with less or no downstream operations.

Therefore, the aim of this study was to investigate the kinetic of enzymatic esterification and transesterification reaction of macauba high acid oil for biodiesel production using *C. antarctica* B lipase immobilized in green coconut fiber. In this work, the biodiesel fuel was produced by the enzyme-catalyzed esterification and transesterification from high acid value macauba oil and ethanol. The selected routes are able to use less expensive feedstocks that cannot be converted to biodiesel by conventional methods which use strong base, such as sodium hydroxide.

2 Material and Methods

Raw-material: Macauba acid oil utilized in this study was purchased from rural producers at Minas Gerais State, Brazil. Free fatty acids in the oil were determined by AOCS Official Method. The sample was diluted in a neutralized solvent, followed by titration with a standard NaOH solution (0.1N), in the presence of phenolphthalein as indicator (AOCS, 2004).

Immobilized biocatalyst production: CALB was immobilized by adsorption on green coconut fiber, at room temperature, through the enzyme - support contact for 2 h. For each gram of dry support, 10 mL of lipase solution (1000 U/L), in 25 mM sodium phosphate buffer, were used. After immobilization, the biocatalyst was separated by filtration, rinsed with phosphate buffer and dried at vacuum for 10 min.

Biodiesel synthesis: A batch small-scale reaction was performed in a thermostatized bath from a mixture of macauba acid oil and ethanol (3:1 w/w) using lipase type B from *C. antarctica* immobilized in coconut fiber as catalyst. The enzyme was added in the proportion of 10% to the oil weight and the alcoholysis was carried at 35^{o}C and 30 rpm during 96h (FUKUDA *et al*., 2001). The mixture was filtered under vacuum. The enzyme was recovered in filter paper and glycerin was easily separated by gravity. Experiments, carried under same experimental conditions, were performed with a commercial immobilized lipase (Novozym 435) to compare with the coconut immobilized lipase performance.

Additionally, the hydroesterification using the macauba acid oil was carried out in two steps for comparison purposes: hydrolysis of the oil at 300^{o}C and 1000 psi, followed by acid-catalyzed methanolysis performed at 190^{o}C and 500 psi using niobic acid (NB-340 CBMM) as catalyst at concentration of 10 wt% relative to FFA

Yield: The conversion efficiency to methyl esters was accomplished by colorimetric method at intervals of 24 h. Determination of free glycerol in biodiesel was performed measuring the absorbance at 500 nm (ARANDA and ANTUNES, 2004).

Statistical analysis: A 2^3 complete factorial design was adopted to evaluate the effects of three operational parameters on biodiesel conversion from *C. antarctica* immobilized in coconut fiber: catalyst concentration in relation to oil mass (5-10 %), temperature (35-50^{o}C) and oil:ethanol weight ratio (3:1-6:1). Those selected levels were based on preliminary experiments. The standard deviation was evaluated from triplicate experiments carried out at the center-point and the experiments were carried out in a randomized order. The experimental data obtained were analyzed by the response surface regression procedure to fit a non linear first order model as follows: $Y = \lambda_0 + \sum \lambda_i X_i + \sum \lambda_{ij} X_{ij}$ (1)

where Y is the predicted response variable, λ_o, λ_i, λ_{ij} are regression coefficients of the model, and X_i, X_j represent the independent variables in the form of coded values. Statistica software version 7.0 was used for variance analysis.

Rheology: The biodiesel viscosity was determined in a cone-plate rheometer (Brookfield Ultra/DVD III). The variation of kinematic viscosity (η) with temperature was represented by equation: $\eta = e^{(A+B/T+C/T^2)}$ (2)

3 Results

The macauba acid oil presented 27 to 30% of free fatty acids, expressed as oleic acid. This oil have higher free fatty acid levels: 2 and 12 fold compared to jatropha and karanja oil for example (SHARMA *et al.*, 2008). Viscosity is another important property of vegetable oil and biodiesel. The average viscosity of vegetable oil is in ranger of 23.2 to 53.0 cSt at ~40ºC (DEMIRBAS, 2008). For macauba acid oil, the viscosity value is 26.82 cSt at 40ºC. Another characteristic is the molecular weight of waste oil, 858.7, which was calculated from fatty acid composition of macauba oil (FREITAS *et al*., 2008).

A preliminar test was realized to compare the effect of reaction time on the conversion of macauba oil in fatty acids ethyl esters when catalyzed by CALB immobilized in coconut fiber or by Novozyme 435 (Figure 1). The reaction conditions were T=35ºC, amount of catalyst of 10% w/w of oil and macauba acid oil: ethanol ratio of 3:1 w/w. The lipase immobilized in coconut fiber reached biodiesel conversion of 53±1.61% after 24 h and for reaction catalyzed by Novozyme 435, after 24 h, the conversion was 52.33±0.58%. The maximum conversion (82±3.0 %) was reached after 72 h in a reaction catalyzed by Novozyme 435, however this value is only slightly superior at CALB immobilized in coconut fiber. In this way, we selected the CALB immobilized in coconut fiber as catalysis for operational parameters analysis on biodiesel conversion.

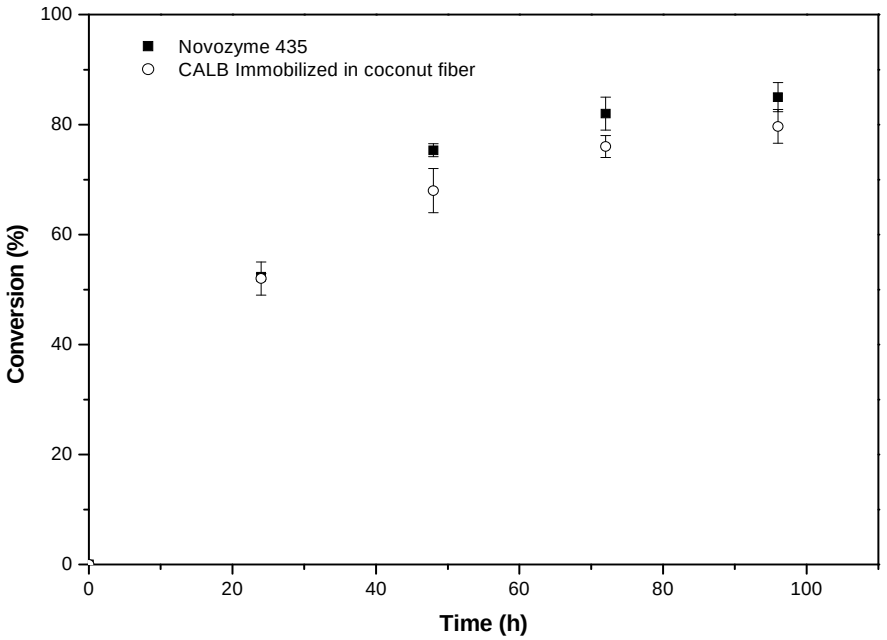

Figure 1. Kinetic of conversion of macauba oil in fatty acids ethyl esters using CALB immobilized in coconut fiber and commercial enzyme (Novozyme 435).

The results of the 2^3 complete factorial design are shown in Table 1. Maximum conversion (82.91%) was obtained at 50ºC, amount of catalyst of 10% w/w of oil and macauba acid oil: ethanol ratio of 3:1 (w/w). This value is comparable to the conversion obtained when the reaction was catalyzed by Novozyme 435 (82±3.0 %), after 72 h (Figure 1). For researches where ethanol was the nucleophile, after 24h, maximum conversion for Novozyme 435 was 86 % (HERNÁNDEZ-MARTÍN and OTERO, 2008), a value near to obtained in this study for CALB immobilized in coconut fiber.

The results of experimental design were analyzed via multiple regressions. The coefficients of a full model were evaluated via regression analysis and tested for significance, leading to the best model fiited. This showed that only the linear coefficients (X_1, X_2, X_3) were

significant. The ANOVA analysis for response surface, considering only the significant coefficients, is provided in Table 2.

Table 1 - 2^3 complete factorial design matrix and the responses of the dependent variable

Run	X_1	X_2	X_3	Y predicted	Y experimental
1	35 (-1)	5 (-1)	3 (-1)	54.48	59.7
2	50 (1)	5 (-1)	3 (-1)	72.42	64.9
3	35 (-1)	10 (1)	3 (-1)	74.52	72.1
4	50 (1)	10 (1)	3 (-1)	92.46	**82.9**
5	35 (-1)	5 (-1)	6 (1)	54.44	57.5
6	50 (1)	5 (-1)	6 (1)	59.38	64.4
7	35 (-1)	10 (1)	6 (1)	61.48	59.3
8	50 (1)	10 (1)	6 (1)	79.42	72.3
9	43 (0)	7.5 (0)	4.5 (0)	66.95	66.7
10	43 (0)	7.5 (0)	4.5 (0)	66.95	70.0
11	43 (0)	7.5 (0)	4.5 (0)	66.95	66.7

Table 2 – Analysis of variance for the fitted model for predict the conversion rate

Source	Sum of square	d.f.	Mean square	F value
Regression	447.25	3	149.08	12.60
Residual	82.81	7	11.83	
Lack of fit	75.55	5	15.11	4.16
Pure erro	7.26	2	3.63	
Cor total	530.07	10	53.01	
$R^2 = 0.844$	Adj. $R^2 = 0.777$			

The final estimative response model equation by which the conversion rate of macauba oil to biodiesel was estimated was as follows: $Y = 66.95 + 8.97X_1 + 10.02X_2 - 6.52X_3$ (3).

From this model, we can to conclude that, for the experimental range analyzed, the enzyme concentration was the most relevant parameter affecting the transesterification, followed by temperature and oil:ethanol ratio. As expected, this factor has a positive influence, but the enzyme cost should be considered as the main limitation to increase enzyme concentration in the process.

Using the conditions where maximum conversion was reached, 50ºC, amount of catalyst of 10% w/w of oil and macauba acid oil: ethanol ratio of 3:1 (w/w), lipase-based biodiesel was used in some product analyses. First, the variation of kinematic viscosity (η) with temperature for lipase-based biodiesel and macauba acid oil were evaluated (Figure 2). The constants (A, B, C) and the regression coefficients (R^2) for each regression shown in Figure 2 are presented in Table 3. The viscosity of the biodiesel obtained from macauba acid oil (2.75 cSt, at 40ºC) is in accordance with biodiesel standards outlined in EN 590 and it is smaller than reported values in the literaturature (2.83 to 5.12 cSt, at 40^{o}C) (DEMIRBAS, 2008).

Although the transesterification time using lipase is higher, bioconversion appears as a cleaner technology to biodiesel production. Furthermore, glycerin can be easily recovered, biodiesel presented lower viscosity and better quality due to very low temperature of enzymatic reaction (35^{o}C).

In parallel, the hydroesterification process with niobic acid has been studied for a comparison with biocatalyzed reaction. The hydroesterification processes reached 78±2.0 % and 22±0.5% of conversion in a very smaller reaction time (60 minutes) for systems with methanol and ethanol, respectively (Figure 3). And regarding the lipase-based biodiesel the viscosity decrease of 5.4 cSt at 20°C to 2.2 cSt at 40°C (Ea/R = 4108 K) while to hidroesterification-based biodiesel the viscosity decrease of 10.6 cSt at 20°C to 5.34 cSt at 40°C (Ea/R = 3117 K).

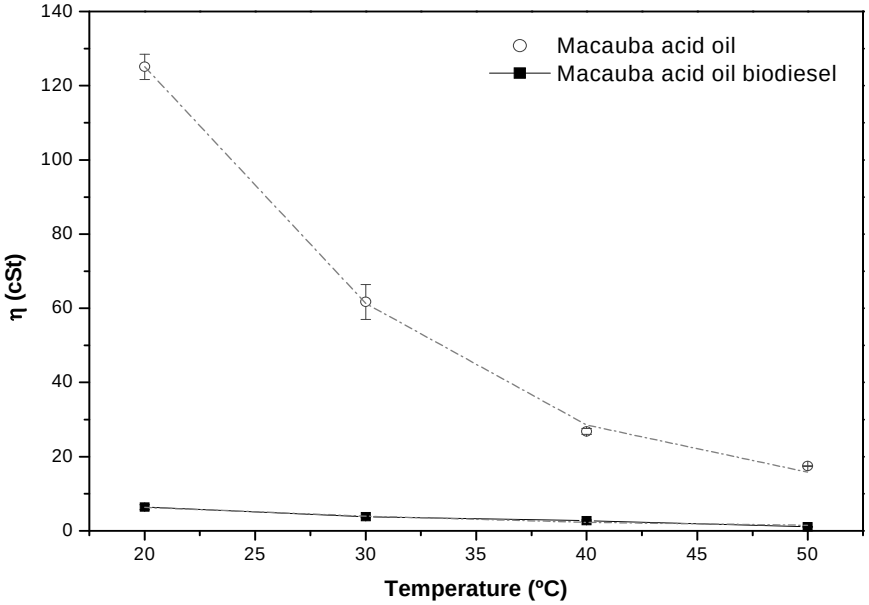

Figure 2. Variation of macauba acid oil and biodiesel kinematic viscosity with temperature.

Table 3 – Regression parameters for viscosity

Fuel type	Regression equation $\eta = e^{(A+B/T+C/T^2)}$			
	A	**B**	**C**	**R^2**
Macauba acid oil	-0.57232	205.81453	-1955.5515	0.9992
Macauba acid oil biodiesel	-2.03205	150.96777	-1467.13455	0.97319

Conclusions

Candida antarctica B lipase immobilized in coconut fiber was found to be an active enzyme catalyzing the conversion of high acid value waste oil to biodiesel. For only one cycle, the conversion rate of a reaction catalyzed by CALB immobilized in coconut was similar to Novozyme 435. And, however studies of hydroesterification had shown smaller reaction time, easier separation and purification steps and better viscosity value were observed using enzymatic process. These results are an indicative that CALB immobilized in coconut fiber can be a cheap alternative catalyst to biodiesel production. To confirm this, more studies analyzing CALB immobilized in coconut operational stability, biodiesel characteristics and others are being performed.

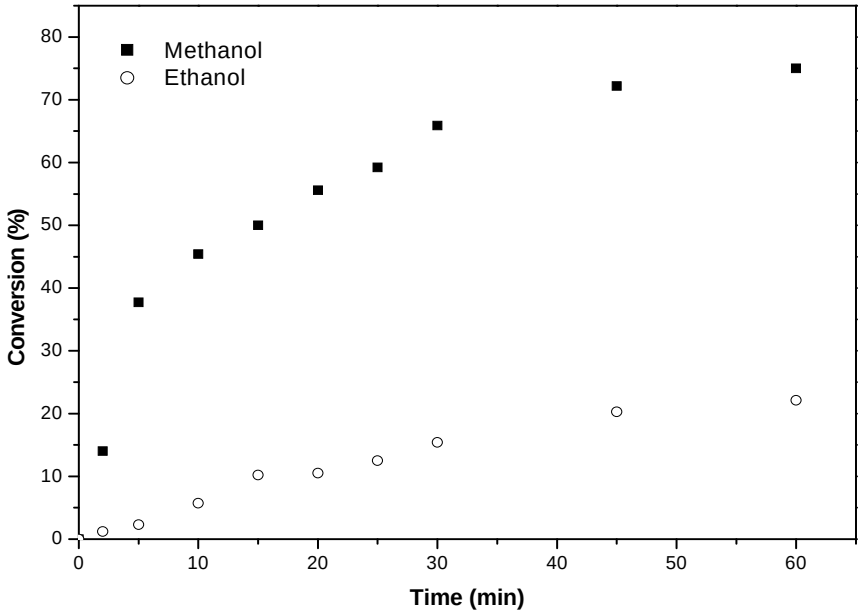

Figure 3. Hidroesterification of macauba fatty acids using niobic acid as catalyst

Acknowledgements

The authors are grateful for the financial support given by CNPq, FAPERJ and CAPES.

References

AOCS (2004). Official methods and recommended practices of the American Oil Chemists' Society. American Oil Chemists' Society, Champaign.

Aranda, D.A.G., Antunes, O.A.C (2004) Catalytic process to the esterification of fatty acids present in the acid grounds of the palm using acid solid catalysts, WO 2004096962.

Clement, C.R., Lleras Pérez, E., van Leeuwen, J. (2005). O potencial das palmeiras tropicais no Brasil: acertos e fracassos das últimas décadas. *Agrociências*, 9, 67-71.

Demirbas, A. (2008) Relationships derived from physical properties of vegetable oil and biodiesel fuels. *Fuel*, 87, 1743-1748.

Freitas, S. P., Silva, C.C.M., Aranda, D.A.G., Mariano, R.G.B., Couri, S. (2008) Potential for biodiesel synthesis from macauba (*Acrocomia aculeata*) pulp oil with a high content of free fatty acids. In: 30th *Symposium on Biotechnology for Fuels and Chemicals*, New Orleans, LA, 1, 68-68.

Fukuda, H., Kondo, A., Noda, H. (2001) Biodiesel fuel production by transesterification of oils. *Journal of Bioscience and Bioengineering*, 92, 405-416.

Hernández-Martín, E., Otero, C. (2008) Different enzyme requirements for the síntesis of biodiesel: Novozym®435 and Lipozyme® TL IM. *Bioresource Technology*, 99, 277-286.

Marchetti, J.M., Miguel, V.U., Errazu, A.F. (2008) Techno-economic study of different alternatives for biodiesel production. *Fuel Processing Tecnology*, 9.

Sharma, Y.C., Singh, B., Upadhyay, S.N. (2008) Advancements in development and characterization of biodiesel: A review. *Fuel*, 87, 2355-2373.

Tamalampudi, S., Talukder, M.R., Hama, S., Numata, T., Kondo, A., Fukuda, H. (2008) Enzymatic production of biodiesel from Jatropha oil: A comparative study of immobilized-whole cell and commercial lípases as a biocatalyst. *Biochemical Engineering Journal*, 39, 185-189.

Proceedings of the 10th International Chemical and
Biological Engineering Conference - CHEMPOR 2008
Braga, Portugal, September 4-6, 2008
E.C. Ferreira and M. Mota (Eds.)

Enzymatic resolution and separation of *sec*-alcohols based on sustainable acylating agents

Carlos M. Monteiro[1], Nuno M. T. Lourenço[2], Carlos A. M. Afonso[1,*]
[1] CQFM – Centro de Química-Física Molecular and IN – Institute of Nanoscience and Nanotechnology, Instituto Superior Técnico, Av. Rovisco Pais, 1049-001 Lisboa, Portugal
*carlosafonso@ist.utl.pt
[2] IBB: Institute for Biotecnology and Bioengineering, Centre for Biological and Chemical Engineering, Instituto Superior Técnico, Av. Rovisco Pais, 1049-001 Lisboa, Portugal

Keywords: Secondary alcohols, lipases, enzymatic kinetic resolution, green chemistry
Topic: Sustainable process-product development through green chemistry

Introduction

The synthesis of enantiomeric pure chiral compounds, became one of the most important fields of chemistry investigation due to their significance in the pharmaceutical industry. Chiral secondary alcohols are usually used as synthetic intermediates or chiral auxiliaries in the synthesis of different drugs (Stecher & Faber, 1997). The demand for attainment one or, in certain cases, both enantiomers alcohols with pharmacological value, lead to the development of strategies to access such chiral compounds, namely enzymatic resolution (Wang *et al.*, 1988), asymmetric hydrogenation of ketones (Noyori *et al.*, 1995), Corey-Bakshi-Shibata borane reduction (Corey *et al.*, 1987), kinetic resolution of epoxides (Tokunaga *et al.*, 1997), ketone reduction (Goldberg *et al.*, 2007) and fermentation (Suzuki *et al.*, 1996).

Several different techniques have been developed to achieve the resolution of enantiomers. Some of these techniques take advantage of the chemical or physical properties differences in each enantiomer, such as crystallization, chromatography, distillation, membranes technology (Maier *et al.*, 2001).

Enzymatic kinetic resolution of racemic alcohols is a well-established method and often the unique and/or most practical route for the preparation of enantiomerically enriched precursors (Ghanem, 2007; Patel, 2001). The enzymes present real advantages in view of the fact that they catalyse reactions under mild conditions with high enantio- or diasteroselectivity, high efficiency and offer the possibility of working with organic solvents (Kazandjian & Klibanov, 1985), supercritical fluids or ionic liquids (Rasalkar *et al.*, 2004). On the other hand, some limitations are observed, specifically the need of large excess of acylating agent and in what concern to the separation step. The chromatography techniques usually used on the separation of enantiomers are a drawback at large scale. More elegant methods of separation have been report to improve the separation of the alcohol from the acylating agent, such as, by using fluorous solvent (Luo *et al.*, 2002), ionic liquids (Lourenco & Afonso, 2007), membrane or PEG (Nogawa et al., 2006).

The selection of the acylating group is an important issue for the separation and to achieve irreversible esterification. The utility of vinyl esters and isopropenyl esters as acylating reagents in this enzymatic reactions was reported since 1987, but present some restrictions like formation of side products (Hanefeld, 2003). New acylating agents are being developed in order to oppose those limitations, namely succinic anhydride (Gutman *et al.*, 1993; Vaidyanathan *et al.*, 2007) and carbonates (Pozo *et al.*, 1992).

The production of enantiomerical enriched secondary alcohols at large (Negishi *et al.*, 1997) or lab (Irimescu *et al.*, 2003) scale by enzymatic esterification or transesterification using

ester from fatty acids was claimed. These reactions were carried out without organic solvents and continuous removal of water or volatile alcohol under vacuum.

Herein we present the progress achieved for irreversible enzymatic kinetic resolution of secondary alcohols in the presence of fatty esters without solvents under vacuum; utilization of the same enzyme for recover of the other enantiomer by transesterification; and application of low pressure distillation as a green separation technique.

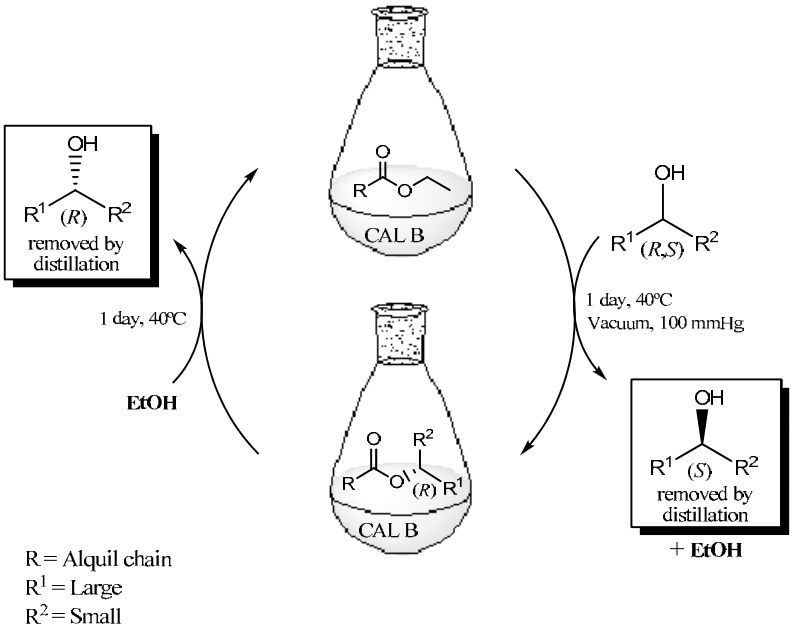

Scheme 1 - Enzymatic transesterification for the resolution of *rac-sec*-alcohols

Results and discussion

On course of previously work developed in this laboratory, where ionic liquids and ionic acylating agents were applied, it was reported a simple, robust, reliable, reusable and efficient preparative methodology for the one pot resolution-separation of *sec*-alcohols based on the enzymatic resolution with CAL B as biocatalyst. It was also demonstrated by this strategy the possibility to separate both enantiomers only by enzymatic resolution and extraction, without need or chromatographic separations techniques.

The acylating agent and the alcohol for this study were selected based on their chemical and physical properties. The fatty esters are stable liquid compounds, which are easily prepared in high yield and high purity, that present good properties as a solvent and acylating agent, avoiding the use of organic solvents. The alcohol tested was the 1-phenylethanol, a compound formed by a bulky phenyl and a small methyl group that can be used as model in the studies of enantioselective catalysts for alcohol conversion.

The conditions used were optimized with the aim of control and shift to products formation. In this way the reaction was performed under vacuum (100 mmHg) during 24 hours at 40ºC. Under these conditions the evaporation of the alcohol is minimal and we obtained better conversions.

From the results obtained (Table 1) we can observe that the efficiency of the enzyme is retained for the two cycles since minimal erosion of yield and enantioselectivity was observed for each transesterification step. Further, the lose of 3-7% yield in each step is due to product lost during the distillation process.

Table 1. Results for enzymatic resolution of (*rac*)-1-Phenylethanol following the method described on scheme 1.

Cycle	*(S)*-1-phenylethanol		*(R)*-1-phenylethanol	
	Yield (%)	ee (%)[a]	Yield (%)	ee (%)[a]
1	47	89	44	86
2	43	87	44	80

[a] enantiomer excess analyzed by GC

Conclusions

A more sustainable method for efficient enantiomeric kinetic resolution and enantiomer separation of secondary alcohols is demonstrated based on: 1) use of fatty esters as acylating agents, by removal of the unreacted enantiomer alcohol by distillation, while the other enantiomer stay in the form of less volatile fatty ester; 2) second enzymatic reaction to generate the other enantiomer and the acycling agent ready for the next cycle.

Experimental

General procedure for enzymatic kinetic resolution and separation of sec-alcohols: CALB (Novozym 435; 500 mg) and racemic 1-phenylethanol (10.35 mmol) were added to a stirred ethyl myristate (10.35 mmol). The reaction mixture was stirred for 24 hours under reduced pressure (100 mmHg) at 40ºC in a thermostatic bath. After this time, the reaction mixture was filtrated and the enzyme washed with hexane (3 x 15 mL). The solvent was then evaporated and destilated under reduced pressure (1mmHg, 60ºC) to give the *(S)*-1-phenylethanol.

The enzyme was dried under reduced pressure (20 mmHg) for 2 h.

After distillation, ethanol (2.5 equiv) and the recovered enzyme were added and the mixture was stirred for 24 hours at 40ºC in a thermostatic bath.

Then, the reaction mixture was filtrated again and the enzyme washed with hexane (3 x 15 mL). The solvent was then evaporated and destilated under reduced pressure (1mmHg, 60ºC) to give the *(R)*-1-Phenylethanol.

Reuse experiment: The enzyme was dried under reduced pressure (20 mmHg) for 2 h and added to recovered ethyl myristate, then more racemic 1-phenylethanol (10.35 mmol) was added to the mixture, and the reaction was performed as described above.

The GC analysis of 1-phenylethanol was performed using Trace Focus Unicam, FID detection, using capillary column astec chiraldex^{TM} G-TA (30m $\times$0.25mm $\times$ 0.12µm). t_R (*S*) = 12.78 min.; t_R (*R*)-25= 13.45 min.

Acknowledgments

We thank Fundação para a Ciência e Tecnologia (POCI 2010) and FEDER (POCI/QUI/60175/2004 and SFRH/BPD/41175/2007) for financial support

References

Corey, E. J., Bakshi, R. K., & Shibata, S. (1987). Highly enantioselective borane reduction of ketones catalyzed by chiral oxazaborolidines - mechanism and synthetic implications. *Journal of the American Chemical Society*, 109, 5551-5553.

Ghanem, A. (2007). Trends in lipase-catalyzed asymmetric access to enantiomerically pure/enriched compounds. *Tetrahedron*, 63, 1721-1754.

Goldberg, K., Schroer, K., Lutz, S., & Liese, A. (2007). Biocatalytic ketone reduction - a powerful tool for the production of chiral alcohols - part i: Processes with isolated enzymes. *Applied Microbiology and Biotechnology*, 76, 237-248.

Gutman, A. L., Brenner, D., & Boltanski, A. (1993). Convenient practical resolution of racemic alkyl-aryl alcohols via enzymatic acylation with succinic anhydride in organic solvents. *Tetrahedron: Asymmetry*, 4, 839-844.

Hanefeld, U. (2003). Reagents for (ir) reversible enzymatic acylations. *Organic & Biomolecular Chemistry*, 1, 2405-2415.

Irimescu, R., Saito, T., & Kato, K. (2003). Enzymatic kinetic resolution of secondary alcohols by esterification with fa under vacuum. *Journal of the American Oil Chemists Society*, 80, 659-663.

Kazandjian, R. Z., & Klibanov, A. M. (1985). Regioselective oxidation of phenols catalyzed by polyphenol oxidase in chloroform. *Journal of the American Chemical Society*, 107, 5448-5450.

Lourenco, N. M. T., & Afonso, C. A. M. (2007). One-pot enzymatic resolution and separation of sec-alcohols based on ionic acylating agents. *Angewandte Chemie-International Edition*, 46, 8178-8181.

Luo, Z. Y., Swaleh, S. M., Theil, F., & Curran, D. P. (2002). Resolution of 1-(2-naphthyl)ethanol by a combination of an enzyme-catalyzed kinetic resolution with a fluorous triphasic separative reaction. *Organic Letters*, 4, 2585-2587.

Maier, N. M., Franco, P., & Lindner, W. (2001). Separation of enantiomers: Needs, challenges, perspectives. *Journal of Chromatography A*, 906, 3-33.

Negishi, S., Shirasaw, S. E., Susuki, J. Y., & Yukie, M. 1997. Optical resolution for production optically active alcohol: Smuldersm Theodorus A.H.J. et al.

Nogawa, M., Shimojo, M., Matsumoto, K., Okudomi, M., Nemoto, Y., & Ohta, H. (2006). Kinetic resolution of poly(ethylene glycol)-supported carbonates by enzymatic hydrolysis. *Tetrahedron*, 62, 7300-7306.

Noyori, R., Tokunaga, M., & Kitamura, M. (1995). Stereoselective organic-synthesis via dynamic kinetic resolution. *Bulletin of the Chemical Society of Japan*, 68, 36-55.

Patel, R. N. (2001). Enzymatic synthesis of chiral intermediates for drug development. *Advanced Synthesis & Catalysis*, 343, 527-546.

Pozo, M., Pulido, R., & Gotor, V. (1992). Vinyl carbonates as novel alkoxycarbonylation reagents in enzymatic-synthesis of carbonates. *Tetrahedron*, 48, 6477-6484.

Rasalkar, M. S., Potdar, M. K., & Salunkhe, M. M. (2004). Pseudomonas cepacia lipase-catalysed resolution of racemic alcohols in ionic liquid using succinic anhydride: Role of triethylamine in enhancement of catalytic activity. *Journal of Molecular Catalysis B-Enzymatic*, 27, 267-270.

Stecher, H., & Faber, K. (1997). Biocatalytic deracemization techniques: Dynamic resolutions and stereoinversions. *Synthesis-Stuttgart*, 1-&.

Suzuki, T., Idogaki, H., & Kasai, N. (1996). Production of (s)-4-chloro-3-hydroxybutyronitrile using microbial resolution. *Bioorganic & Medicinal Chemistry Letters*, 6, 2581-2584.

Tokunaga, M., Larrow, J. F., Kakiuchi, F., & Jacobsen, E. N. (1997). Asymmetric catalysis with water: Efficient kinetic resolution of terminal epoxides by means of catalytic hydrolysis. *Science*, 277, 936-938.

Vaidyanathan, R., Hesmondhalgh, L., & Hu, S. H. (2007). A chemoenzymatic synthesis of an androgen receptor antagonist. *Organic Process Research & Development*, 11, 903-906.

Wang, X. Y., Liao, M. L., Hung, T. H., & Seib, P. A. (1988). Liquid-chromatographic determination of l-ascorbate 2-polyphosphate in fish feeds by enzymatic release of l-ascorbate. *Journal of the Association of Official Analytical Chemists*, 71, 1158-1161.

Proceedings of the 10th International Chemical and
Biological Engineering Conference - CHEMPOR 2008
Braga, Portugal, September 4-6, 2008
E.C. Ferreira and M. Mota (Eds.)

Enhanced Production of Recombinant Staphylokinase: An Experimental Design Approach

Arshad Jawed, K. L. Dikshit, Debendra K. Sahoo*
IMTECH - Institute for Microbial Technology, Sector 39A, Chandigarh, INDIA, 160 036

Keywords: Staphylokinase, Response surface methodology, Central composite design, Optimization, *Escherichia coli*
Topic: Integration of life sciences & engineering.

Abstract

Aiming at large-scale production of staphylokianse we cloned and intracellularly expressed staphylokinase in plasmid pET-9b using *Escherichia coli* as host in soluble form. Initial optimization studies, carried out for increasing SAK expression using defined medium resulted in a cell concentration of 1.15 g DCW/L and staphylokinase production of 84.5 mg SAK/L. Further optimization was carried out by using statistical methods, namely Response Surface Methodology (RSM). RSM was employed with 4 variables at 5 levels of concentrations using Central Composite Design (CCD), with glucose, KH_2PO_4, $(NH_4)_2HPO_4$ and various organic nitrogen sources in separate experiments and also in combination by D-optimal design. Optimized medium resulted in cell concentration of 1.97 g DCW/L and staphylokinase expression level of 83.0 mg SAK/g DCW corresponding to 163.86 mg SAK/L. The results obtained were validated at fermentation of scale of 5 L, with final cell concentration of 5.8 g DCW/L and staphylokinase production exceeding 415 mg SAK/L in batch mode. Fed-batch fermentation strategy with nutrient (substate) feeding resulted in 24.4 g DCW/L with 1290 mg of SAK/L at 5L and the process was scaled up and validated at 20L scale.

1. Introduction

Thrombolytic therapies aim at early dissolution of the blood clot that causes occlusive thrombosis and results in heart attack. The 15.5 kDa bacterial protein staphylokinase (SAK) isolated from *Staphylococcus aureus* is one such molecule that forms a stochiometric protein-protein complex with plasmin (-ogen) in the plasma millieu and the complex thus formed is capable of dissolving the blood clots (Collen and Lijnen, 1991). The SAK-plasmin(ogen) complex is fibrin specific and is strongly inhibited by α_2-antiplasmin and recycles staphylokinase in its active form (Collen,1998; Lijnen *et al*. 1991; Silence *et al*. 1993).

Owing to the market potential, we aimed for development of a process for production of staphylokinase, especially with a significantly increased product titer. Process development cannot be generalized for every protein or expression sytem or a combination there off as the requirements for maximum growth and productivity are highly case specific and are unique in terms of promoter systems, host-vector interaction, amino acid sequences and the characteristics of the recombinant protein (Shin *et al*. 1997). The effect of parameters such as medium composition, nutrient concentration and availability, dissolved oxygen concentration, specific growth rate, concentration of inducer and antibiotic (selection pressure), plasmid stability, formation of inhibitory by-products etc., varies from case to case and have to be studied in detail for each process and expression host (Lee, 1996).

* Corresponding author. Tel + 91 – 172 – 2636680 extn. 3314. E-mail:debsahoo@imtech.res.in

2. Materials and Methods

2.1 Bacterial strain and plasmid

The strain used was *Escherichia coli* BL 21, transformed with plasmid pET 9b, containing gene for staphylokinase, that was placed downstream of the T7 RNA promoter regulated by the control of *lac* promoter in pET-series expression vector. A kanamycin resistance gene present in the plasmid acts as a selection marker. The culture was maintained in glycerol stocks at –70 ^{0}C in an ultra-low freezer.

2.2 Culture medium

The staphylokinase production medium for initial screening included LB medium, a defined (synthetic) medium and a defined medium supplemented with yeast extract (semi-synthetic). The defined (synthetic) medium consists of glucose 10 gL^{-1} (carbon source), KH_2PO_4, 1.33 gL^{-1}, $(NH_4)_2HPO_4$, 4 gL^{-1}, $MgSO_4.7H_2O$, 0.40 gL^{-1} and trace metal solution. The staphylokinase production medium consisted of varied concentrations of carbon source (Glucose), nitrogen source (yeast extract / tryptone / peptone), KH_2PO_4), $(NH_4)_2HPO_4$ and $MgSO_4.7H_2O$, 0.04 gL^{-1} and trace metals as per experimental plan. The initial pH of the medium was adjusted to 6.8 by 1N NaOH or 1N HCl.

2.3 Inoculum preparation and culture conditions

LB agar plates (containing Kanamycin, 30 µg/ml) streaked with a loopful of culture from frozen glycerol stock (kept at -70^{O}C) were incubated overnight at 37 ^{0}C. A single isolated colony, picked from this plate, was used to inoculate 10 ml LB medium (as pre-inoculum) and incubated in a rotary shaker at 37 ^{0}C at 200 rpm for 8 h. It was used to inoculate 90 ml of LB medium taken in 500 ml flask and the flask was incubated in a rotary shaker at 200 rpm and 37 ^{0}C for 8 h to be used latter as inoculum for the production medium. After inoculation, the flasks were added with kanamycin (30 µg/ml) to maintain plasmid stability and after 4 h of incubation at 37 ^{0}C and 200 rpm, the culture was induced with Iso-Propyl-Thio-Galactoside (IPTG), 0.5 mM for staphylokinase expression.

2.4 Analytical methods

Samples were taken from the culture broth after 4 h of induction with IPTG, and centrifuged at 10,000 rpm for 15 minutes. The settled cell mass from one tube was dissolved in sterile saline and was used to estimate cell growth by measuring cell density at 600 nm using a spectrophotometer. (One absorbance unit corresponds to 0.46 gDCW OD^{-1} L^{-1}). The cells settled in other tubes were lysed to release intracellular proteins, using multiple sample buffer (containing urea and β-mercaptoethanol). The lysate was directly loaded onto 12 % SDS-Poly-acrylamide gel. The protein concentration was obtained by densitometry with Bovine serum albumin (BSA) as standard on a gel documentation system using GENE SNAP and GENE TOOLS (Syngene Inc., USA).

2.5 *Design of experiments*

Response surface methodology, a powerful tool for understanding complex processes and for describing factor interactions in multi-factor systems, has been used for designing the experiments. In our study, a fractional factorial design, using Design Expert Software (Stat Ease Inc., Minneapolis. U.S.) was employed. The optimum levels for growth and staphylokinase production by the recombinant strain, with respect to carbon source, nitrogen source and phosphates were obtained by response surface methodology. Using response surface methodology, the relationship among the variables, i.e. Carbon source, Nitrogen source, KH_2PO_4, $(NH_4)_2HPO_4$, were expressed mathematically in the form of a polynomial model, which gave the response as a function of relevant variables. The present work was based on Central

Composite Design (CCD) utilized to obtain the experimental data, which would fit an empirical second order polynomial model representing the response surfaces over a relatively broad range of parameters.

A second order RSM design with 5 levels CCD was used to explore the effect of various medium ingredients on growth and formation of product. Each factor was studied at five different levels (-2, -1, 0, 1, 2). The test variables chosen in this study were KH_2PO_4, $(NH_4)_2HPO_4$, glucose and nitrogen sources (yeast extract / tryptone / peptone) in separate experiments. After obtaining the optimum results, the effect of a combination of the three nitrogen sources was checked by D-optimal design. The optimal concentrations of the critical medium components were obtained by solving the regression equation and also by analyzing the response surface contour plots.

3. Results and Discussion

Luria-Bertini is one of the widely used undefined mediums for production of recombinant proteins. The medium suffers with the major drawback of quality and varying nutrient contents, leading to high batch-to-batch variation and less reproducibility at fermentations scale (Lee, 1996) and has a number of limitations for use in fed-batch fermentation. On the other hand, the synthetic medium provides better controllability with respect to nutrients and other parameters, but may result in lower product formation. So, many times synthetic medium needs supplementation with complex complex organic nitrogen sources to yield better productivity.

3.1 RSM with Tryptone as nitrogen source

Central composite design (CCD) with glucose, tryptone, KH_2PO_4 and $(NH_4)_2HPO_4$ were chosen as independent variables and for each run, the experimental responses, namely cell growth and staphylokinase expression were obtained at 4 h of induction with IPTG or at 8 h of incubation. ANOVA was required to test the significance, adequacy and accuracy of the model. Emphasis was given on maximizing both the responses namely cell growth and staphylokinase expression. The statistical analysis of the data showed that the level of significance for the model was above 95 % (with p-value <0.001). A *p*-value less than 0.05 indicate the adequacy of the model and less than 0.1 indicates the adequacy of the interaction.

By applying multiple regression analysis on experimental data, the experimental results fitted into quadratic model, with R^2 value of 0.98, for *Escherichia coli* cell growth and R^2 value of 0.99 for staphylokinase production. Both the models showed high value of regression coefficient and it was also suggested that the second order polynomial equation was accurate and capable of representing the model selected within the experimental domain. A low probability value, P<0.001 was obtained for both cell growth and staphylokinase production. The components showed good interactions with *p*-value lower than 0.1 in almost all the individual and interaction terms. The mathematical regression model for growth of cells and production of staphylokinase in the form of factors in their coded terms are given in Table 1, where the terms A, B, C and D are coded values of the variables glucose, tryptone, KH_2PO_4 and $(NH_4)_2HPO_4$. The optimum values for maximum cell growth and staphylokinase production were 4.53 gDCW and 61.89 mg SAK/g DCW (Table 2). The predicted values by the program and the actual values were found to be very close to each other.

3.2 RSM with peptone as nitrogen source

In the second case peptone was used as sole organic nitrogen source in semi-synthetic medium to investigate the region of response surface in the neighborhood of the optimum, an experimental design with more than two levels of each variable is required, so that a second order approximation to the response surface can be developed. A central composite design (CCD) with glucose, peptone, KH_2PO_4 and $(NH_4)_2HPO_4$ were chosen as independent variables and the statistical analysis of the data showed that the significance level for the model was above 95 % (with p-value <0.001).

Glucose, peptone, KH_2PO_4 and $(NH_4)_2HPO_4$ were taken as variables for analysis and optimization of parameters for maximum growth and staphylokinase production. The values obtained after experiments were considered in terms of responses and were fitted into a suitable model. By applying multiple regression analysis on experimental data, the experimental results were fitted with a second order polynomial equation and R2 value of 0.99 for *Escherichia coli* cell growth and R2 value of 0.99 for staphylokinase production were obtained. Both the models showed high value of regression coefficient and it also suggested that the second order polynomial equation was accurate and capable of representing the model selected within the experimental domain. A low probability value, $P < 0.001$ was obtained for both cell growth and staphylokinase production. The mathematical regression model for cell growth and production of staphylokinase in the form of factors in their coded terms are given in Table 1, where the terms A, B, C and D are coded values of the variables glucose, peptone, KH_2PO_4 and $(NH_4)_2HPO_4$. The optimum values for maximum cell growth and staphylokinase production were 1.86 g DCW and 73.5 mg SAK/gDCW (Table 2). The predicted values by the program and the actual values were found to be very close to each other.

3.3 RSM with Yeast extract as nitrogen source

Central Composite Design experiment was set up with the four independent variables, namely glucose, yeast extract, KH_2PO_4 and $(NH_4)_2HPO_4$. The statistical analysis of the data showed that the level of significance for the model was above 95 % (with p-value <0.01).
Glucose, yeast extract, KH_2PO_4 and $(NH_4)_2HPO_4$ were taken as variables for analysis and optimization of parameters for maximum growth and staphylokinase production. The values obtained after experiments were considered in terms of responses and were fitted into a suitable model. By applying multiple regression analysis on experimental data, the experimental results were fitted with a second order polynomial equation. In this case the results were fitted into quadratic model, with R2 value of 0.99, for *Escherichia coli* cell growth and R2 value of 0.98 for staphylokinase production. Both the models showed high value of regression coefficient and it also suggested that the second order polynomial equation was accurate and capable of representing the model selected within the experimental domain. A low probability value, $P < 0.001$ was obtained for both cell growth and staphylokinase production. The mathematical regression model for cell growth and production of staphylokinase in the form of factors in their coded terms are given in Table 1, where the terms A, B, C and D correspond to the variables glucose, tryptone, KH_2PO_4 and $(NH_4)_2HPO_4$. The optimum values for maximum cell growth and staphylokinase production were 1.70 gDCW and 71.50 mgSAK/gDCW (Table 2). The predicted values by the program and the actual values were found to be very close to each other.

As indicated by the results obtained from central composite designs by running the variables glucose, KH_2PO_4, $(NH_4)_2HPO_4$ and tryptone / peptone / yeast extract separately as the sole organic nitrogen source, it could be argued that none of the nitrogen sources had a substantial advantage over the others in enhancing cell growth or staphylokinase production. Therefore, a new set of experiment with a combination of these three organic nitrogen sources to a final concentration of 1 % (w/v) was set up using D-optimal design to investigate the effect of a combination of these three organic nitrogen sources on staphylokinase expression. The parameters were used were varied each at 5 levels (-2, -1, 0, +1, +2), with a final sum (combination of all three nitrogen sources) equal to 1 % (w/v), which was constant throughout the experiment.

3.4 D-optimal design for a combination of tryptone / peptone /yeast extract

A combination all three nitrogen sources was tried using D-optimal design with the three nitrogen sources namely, tryptone, yeast extract and peptone. The three components were locked at the maximum level of 1 % (w/v) and were varied from 0 – 1 % (w/v) at 5 levels coded as (-2, -1, 0, +1 and +2). By applying the regression analysis on the experimental data obtained, the

experimental results were fitted with a second order polynomial equation. Thus a mathematical regression model for growth of cells and staphylokinase production in the form of coded variables could be easily defined (Table 1). The experimental data fitted in the quadratic model yielded R2 value of 0.98 for cell growth and R2 value of 0.90 for staphylokinase production.

The different organic nitrogen sources showed good interactions with each other for staphylokinase expression but the interaction between tryptone and yeast extract was not found to be very significant (p-value >0.1). The optimization results showed the maximum cell growth (1.974 gDCW) along with higher expression of staphylokinase (83.01 mg SAK/g DCW) when tryptone, 0.76 (% w/v) and yeast extract, 0.24 (% w/v) were taken (approximate ratio of 3:1) and validated the use of RSM as a useful tool for the optimization of recombinant protein expression in *E. coli.*

3.5 Batch and fed-batch fermentation

Batch and fed-batch fermentation runs were performed for validation of the fermentation medium obtained by RSM and D-optimal design. Cell growth was found to be 5.9 g/L of the fermentation broth with SAK expression mounting to 480 mg SAK/L of fermentation broth, while in fed-batch mode cell growth increased to 24.4 gDCW/L and SAK expression went up to 1200 mg SAK/L of fermentation broth.

4. Conclusion

The ultimate aim of any optimization process is maximization of the yield of target product and reduction of input. Our investigation showed glucose, tryptone, yeast extract, potassium di-hydrogen phosphate and di-ammonium hydrogen phosphate to have significant effect on staphylokinase expression. The optimization work resulted in the reduction in concentration of medium components and increase in staphylokinase yield under experimental conditions. This demonstrated that the statistical approach described in this work could be successfully applied for optimization of media components in case of a recombinant therapeutic protein like staphylokinase and result in the saving of material, labor and time.

References

Collen D. Lijnen H. R. (1991). Basic and Clinical Aspects of Fibrinolysis and Thrombolysis. *Blood*, 78, 3114-3124.

Collen D. (1998). Staphylokinase: a potent, uniquely fibrin-selective thrombolytic agent. *Nature Medicine*, 4, 279-284 .

Lee J. (1996). High cell density cultures of *Escherichia coli*. *TIBTECH*, 14, 98 – 105.

Lijnen H. R. VanHoef B. DeCock F. Okada K. Ueshima S. Matsuo O. Collen D. (1991). On the mechanism of fibrin-specific plasminogen activation by staphylokinase. *Journal of Biological Chemistry*, 266, 11826-11832.

Shin C. S. Hong M. S. Bae C. S. Lee J. (1997). Enhanced production of mini-proinsulin in fed-batch culturesat high cell density of *Escherichia coli* BL21 (DE3) [pET-3aT2M2]. *Biotechnology Progress*, 13, 249 – 257.

Silence K. Collen D. Lijnen H. R. (1993). Interaction between staphylokinase, plasmin(ogen), and alpha 2-antiplasmin. Recycling of staphylokinase after neutralization of the plasmin-staphylokinase complex by alpha 2-antiplasmin. *Journal of Biological Chemistry*, 268, 9811-9816.

Table 1 Model equation for cell growth and staphylokinase production

With tryptone as nitrogen source

Growth (gDCW) = *1.393632 + 0.261299 * A +0.188638 * B +0.015506 * C + 0.237544 * D + 0.151769 * A * B - 0.045 * A * C + 0.044113 * A * D + 0.227576 * B * D + 0.017958 * A^2 – 0.03023 * B^2*

SAK production (mg/gDCW) = *51.373 -2.372 * A +12.264 * B -0.145 * C +0.431 * D -2.895 * A * B +2.494 * A * C +10.080 * A * D -3.706 * B * C -6.621 * B * D -2.419 * C * D +2.473 * A^2 +2.231 * B^2 -4.448 * C^2 -6.343 * D^2*

With peptone as nitrogen source

Growth (gDCW) = *1.696079 + 0.195625 * A + 0.301821 * B + 0.05048 * C + 0.205406 * D + 0.055006 * A * B + 0.170221 * A * D + 0.031125 * B * D - 0.05709 * A^2 - 0.0305 * B^2 - 0.01638 * C^2 - 0.09614 * D^2*

Staphylokinase (mg/gDCW) = *75.65152 - 1.94138 * A + 0.041622 * B + 0.903997 * C + 2.10787 * D - 7.20588 * A * B + 3.830372 * A * D - 2.48013 * B * D - 7.36548 * A^2 - 7.36371 * B^2 - 7.39023 * C^2 - 6.33311 * D^2*

With yeast extract as nitrogen source

Growth (g DCW) = *1.610635 + 0.165894 * A + 0.195327 * B + 0.071203 * C + 0.163219 * D + 0.091219 * A * B + 0.01575 * A * C +0.091827 * A * D +0.04725 * B * C +0.057894 * B * D - 0.00225 * C * D -0.1009 * A^2 -0.0834 * B^2 -0.06749 * C^2 -0.11204 * D^2*

Staphylokinase (mg/gDCW) = *67.98879 - 4.74418 * A + 12.75235 * B + 0.539619 * C + 0.607255 * D - 2.55232 * A * B + 4.837455 * A * D - 2.55319 * B * C - 3.24418 * B * D - 5.10136 * A^2 - 5.93635 * B^2 - 5.93635 * D^2*

With a combination of tryptone, peptone and yeast extract (as nitrogen sources)

Growth (gDCW) = *1.691213*A + 1.66292*B + 1.485202*C - 0.08241*A* B + 0.318058 *A*C - 0.3351*B*C*

Staphylokinase (mg/gDCW) = *46.37732 * A + 77.48137 * B + 70.24089 * C + 71.25321 * A * B + 78.85035 * A * C – 111.785 * B * C*

Table 2 Optimum condition for cell growth and maximum production of staphylokinase

Glucose (%-w/v)	Nitrogen Source (%-w/v)	KH_2PO_4 (%-w/v)	$(NH_4)_2HPO_4$ (%-w/v)	Cell Growth (gDCW)	SAK Production (mg/gDCW)
1.00	Tryptone(1.00)	0.80	0.70	4.53	61.89
0.70	Peptone (1.1)	0.70	0.67	1.86	73.80
0.73	Yeast extract (0.75)	0.66	0.56	1.70	71.50

Table 3 Optimum condition for cell growth and production of staphylokinase

Tryptone (%-w/v)	Yeast extract (%-w/v)	Peptone (%-w/v)	Cell Growth (g DCW)	SAK Production (mg/gDCW)
0.76	0.24	0.0	1.974	83.01

Proceedings of the 10th International Chemical and
Biological Engineering Conference - CHEMPOR 2008
Braga, Portugal, September 4-6, 2008
E.C. Ferreira and M. Mota (Eds.)

Biocatalysis in organic media by using calixarene-myoglobin complex with pseudoactivity of peroxidase

Magda C. Semedo, Amin Karmali[1]*, Patrícia D. Barata and José V. Prata

CIEQB - Chemical Engineering and Biotechnology Research Center and Department of Chemical Engineering of Instituto Superior de Engenharia de Lisboa
Rua Conselheiro Emídio Navarro, 1959-007 Lisboa, Portugal

Keywords: Calixarenes; Liquid-liquid protein extraction; myoglobin; biocatalysis in organic media; pseudoactivity of peroxidase
Topic: Advancing the chemical and biological engineering fundamentals.

ABSTRACT

The present work involves the use of *p-tert*-butylcalix[4,6,8]arene carboxylic acid derivatives for selective extraction of myoglobin. All three calixarenes were found to extract this haemoprotein to organic phase, exhibiting extraction parameters higher than 0.90. Myoglobin-^{t}butyl[6]CH_2COOH complex revealed pseudoactivity of peroxidase which catalysed the oxidation of seryngaldazine in the presence of hydrogen peroxide in organic medium containing chloroform. The effect of pH, protein and substrate concentrations was investigated in biocatalysis by using myoglobin-^{t}Butil[6]CH_2COOH complex. The highest specific activity of myoglobin was 1.37×10^{-1} U. mg protein^{-1} at initial pH of 6.5 in organic medium. Apparent kinetic parameters ($V'_{máx}$, K'_m, k'_{cat} e k'_{cat}/K'_m) for the pseudo-activity of peroxidase were determined in organic media for different pH values by Michaelis-Menten. Furthermore, the stability of the protein-calixarene complex was investigated for different initial pH values and $t_{1/2}$ values were obtained in the range of 3.5 – 5.2 days. Myoglobin-calixarene complex present in organic medium was recovered in fresh aqueous solutions at alkaline pH, with a recovery of pseudo-peroxidase activity of over 100 %. The results strongly suggest that the use of calixarene derivatives is an alternative technique for protein extraction and solubilisation in organic media for biocatalysis.

INTRODUCTION

Protein recognition by synthetic molecules is a highly challenging field both in academic and applied research (Ludwig, 2005). The use of calix[n]arenes has attracted an increasing interest in the last two decades as a tool for biochemical recognition and separation of biological macromolecules such as proteins (Ludwig, 2005 and Shimojo *et al.*, 2007). Calix[n]arenes are macrocyclic structures which consist of phenol rings connected by methylene bridges. These compounds consist of cup-shaped molecules which can form host-guest complex with a wide range of guest molecules by introducing several functional groups either at the upper or lower rim (Gutsche, 1995).

Recently, Oshima *et al.* (2002 and 2005), have reported that a calix[6]arene carboxylic acid derivative (^{t}Oct[6]CH_2COOH) exhibited high affinity for cationic proteins such as cytochrome *c* by promoting its extraction in organic media. Besides the extraction of cytochrome c to organic phase by using such calixarenes, they observed pseudoactivity of peroxidase in organic solvents. Biocatalysis in non-conventional media is an important field in enzyme engineering

[1]* Corresponding author. E-mail: akarmali@deq.isel.ipl.pt

because there several advantages over the aqueous media such as change in substrate specificity, selectivity and biocatalyst´s stability (Gupta and Roy, 2004 and Aires-Barros, 2000).

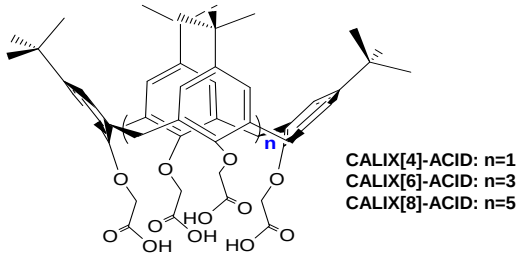

Figure 1 - Structure of *p-tert*-butylcalix[n]arene acid derivates.

The present work involves the use of lower rim substituted acid derivatives of *p-tert*-butylcalix[4,6,8]arenes, CALIX[4,6,8]-ACID (Figure 1) for selective extraction of myoglobin (Mb) which was used as a model protein.

Myoglobin is a multifunctional hemeprotein involved in several key physiological roles in animals as well as it exhibits peroxidase-like activity by catalyzing the oxidation of phenolic compounds in the presence of hydrogen peroxide (Carlsen *et al.*, 2003). The present work is concerned with extraction of myoglobin with CALIX[4,6,8]-ACIDs in organic media and biocatalysis of Mb-CALIX[6]-ACID complex which catalysed the oxidation of syringaldazine in the presence of hydrogen peroxide in organic medium.

MATERIALS AND METHODS

Materials

The structures and abbreviations of the extractants used in the present work are show in the Figure 1. The *p-tert*-butylcalix[n]arenes (n=4, 6 and 8) used as starting materials were prepared according to the Gutsche's procedures (Gutsche and Iqbal, 1990, Gutsche *et al.*, 1990 and Munch and Gutsche, 1990). These were in turn etherified with ethyl bromoacetate in the presence of anhydrous potassium carbonate in refluxing dry acetone for several hours (25h-72h, TLC control) (Iwamoto and Shinkai, 1992, Arnaud-Neu *et al.*, 1989). After appropriated work-up, the products were recrystallised from ethanol (*tetraethyl p-tert-butylcalix[4]arene tetraacetate, 1a*) or ethanol-dichloromethane (*hexaethyl p-tert-butylcalix[6]arene hexaacetate***,** *1b* and *octaethyl p-tert-butylcalix[8]arene octaacetate, 1c*), yielding the corresponding esters in moderate to good yields. Treatment of 1a-c with aqueous 10% tetramethylammonium hydroxide under reflux for 24h, afforded the calixarene acids CALIX[4,6,8]-ACID, after acidic workup (Chang and Cho, 1986).

Myoglobin from horse heart (Mb *c*) was obtained from Sigma Chemical Co. (USA) and all other chemicals were of analytical grade.

Methods

Extraction of Mb c With Calixarenes in Organic Solvents

Mb *c* solutions (14.7 μM) were prepared in buffers with different pH (see Table 1) as reported previously with some modifications (Oshima *et al.* 2002 and 2005). Calixarenes (CALIX[4,6,8]-ACID) were prepared either in chloroform or dichloromethane at a concentration range of 0.1 - 3.0 mM. The two phases (2, 3 and 5 mL), were mixed in stoppered glass

Table 1 - Experimental conditions for Mb *c* extraction.

Aqueous Phase	**Volume (mL)**	2, 3 and 5
	[Protein] (μM)	14.7
	pH	4.5 – 9.0 (10mM citrate buffer, 50mM phosphate buffer and 10mM glycine buffer)
Organic Phase	**Volume (mL)**	2, 3 and 5
	Solvent	CH_2Cl_2 and $CHCl_3$
	Extractant	**CALIX[4,6,8]-ACID**
	[Calixarene] (mM)	0.1, 0.2, 0.5, 1.0, 2.0 and 3.0
Temperature (ºC)		28
Contact Time (h)		0.5, 0.75 and 1

test tube and gently shaken for about 0.5 – 1 hr at 28 ºC. Phases were separated and protein concentration was measured by the absorbance of the Soret band peak (407 – 410 nm, Li and Mabrouk, 2003) both in aqueous and organic phases and the extractability was determined by the degree of extraction (E = 1 – [Mb c]$_{aq,eq}$/[Mb c]$_{aq,ini}$).

Protein Assay

Protein concentration in aqueous solutions was determined by Coomassie blue dye binding method by using BSA as the protein standard (Sedmak and Grossberg, 1977).

Biocatalysis

Pseudoperoxidase Activity of Mb c

The pseudoperoxidase activity of Mb *c* was assayed by using syringaldazine (Syr) and H_2O_2 as substrates as described previously (Goldberg *et al.*, 1983). The assay of pseudoactivity of Mb *c* in aqueous phase was carried out by using 15 μL of 1mM Syr dissolved in ethanol, 3 μL of 0.8 mM H_2O_2, 262 μL of 50 mM phosphate buffer pH 6.5 and 50 μL of Mb *c* solution (14.7 μM). The enzyme reaction was followed in a microtiter plate reader (Bio-Rad 680) at 550 nm due to oxidation of Syr to corresponding quinone at room temperature. The assay of pseudoperoxidase activity of Mb *c* – CALIX[6]-ACID complex in chloroform was performed by using a reaction mixture containing 100 μL of Syr 1mM dissolved in chloroform, 3 μL of 0.8 mM H_2O_2, 127 μL of chloroform and 100 μL of Mb *c* – CALIX[6]-ACID complex. One enzyme unit is defined as the amount of either Mb *c* or Mb *c* – CALIX[6]-ACID complex required to convert one μmole substrate into product per min under these experimental conditions.

Optimum pH of Pseudoactivity of Mb c

Mb *c* (14.7 μM) was prepared in different buffers as follows: 50 mM phosphate buffer pH 6.5, 50 mM citrate buffer pH 3.5 – 5.5 and 10 mM glycine buffer pH 7.5 – 9.0. Such initial Mb *c* solutions were extracted with CALIX[6]-ACID in organic medium and pseudoperoxidase activity of Mb *c* – CALIX[6]-ACID complex was determined as described above.

Kinetic Parameters

Specific activity of Mb *c* – CALIX[6]-ACID complex was determined by using aqueous initial solutions of Mb *c* (0.2 – 4.8 μM) in different buffer systems which was extracted with CALIX[6]-ACID in organic medium and pseudoperoxidase activity of Mb *c* – CALIX[6]-ACID complex was determined as described above. Apparent kinetic parameters (V'_{max}, K'_{cat} and K'_m) of the reaction catalysed by Mb *c* – CALIX[6]-ACID complex were determined by both Michaelis-Menten and Lineweaver-Burk plots by using the software Enzyme Kinetics – SigmaPlot v.10.0 (Systat Software, Inc.). All enzyme assays were carried out in triplicates by varying the concentration of Syr (0.01 – 0.6 mM) in the reaction medium as described previously.

Recovery of Mb c from organic phase to fresh aqueous solution

Mb *c* was recovered from organic phase to fresh aqueous solution by using buffers with different pH values (3.5 – 14.0) in order to disrupt the non-covalent Mb *c* – CALIX[6]-ACID complex. Therefore, equal volumes (1 mL) of organic phase containing the complex and aqueous solutions of buffer with different pH, were mixed in an end over end mixer, for about 2 min and phases were separated by centrifugation at 10,000 rpm for 2 min. UV-Vis spectra of both phases were carried out and degree of recovery (E') was determined by E' = [Mb c]$_{aq,eq}$/[Mb c]$_{org.ini}$ as described by Oshima *et al.,* 2005. Pseudoperoxidase activity of Mb *c* was assayed in both organic and aqueous phases in order to determine the recovery of pseudoactivity of Mb *c*.

RESULTS AND DISCUSSION

The extraction of Mb *c* at initial aqueous pH of 5.1 was investigated by using increasing concentrations of C4, C6 and C8 in chloroform as shown in Figure 1. As far as the degree of

extraction (*E*) is concerned, the highest value of 0.92 was obtained by using 3 mM CALIX[6]-ACID. However, regarding the A_{Soret} in organic phase, it was observed an increase in the following order: C8 > C6 > C4 (Figure 2).

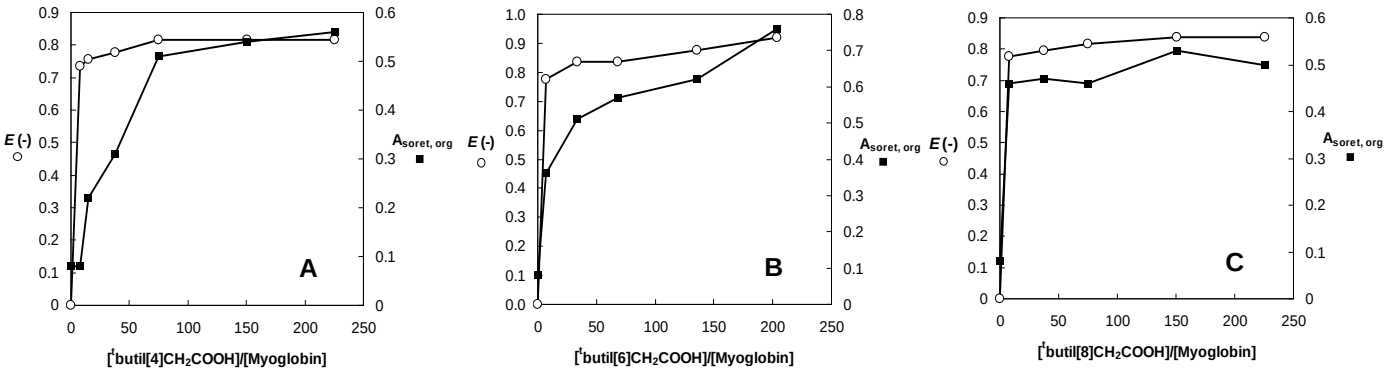

Figure 2 – *Effect of stoichiometric ratio of p-tert*-butylcalix[n]arenes acid derivatives: Mb c on the extraction Mb *c*, with $[Mb\ c]_{ini}$= 14.7μM at pH_{ini} = 5.1: A – extraction with CALIX[4]-ACID; B – extraction with CALIX[6]-ACID; C – extraction with CALIX[8]-ACID.

The structural changes of Mb *c* - CALIX[6]-ACID complex in chloroform were investigated by UV-Vis spectroscopy compared with the free Mb *c* in aqueous medium which revealed significant changes at Soret band peak as well as in Q band peaks (Figure 3).

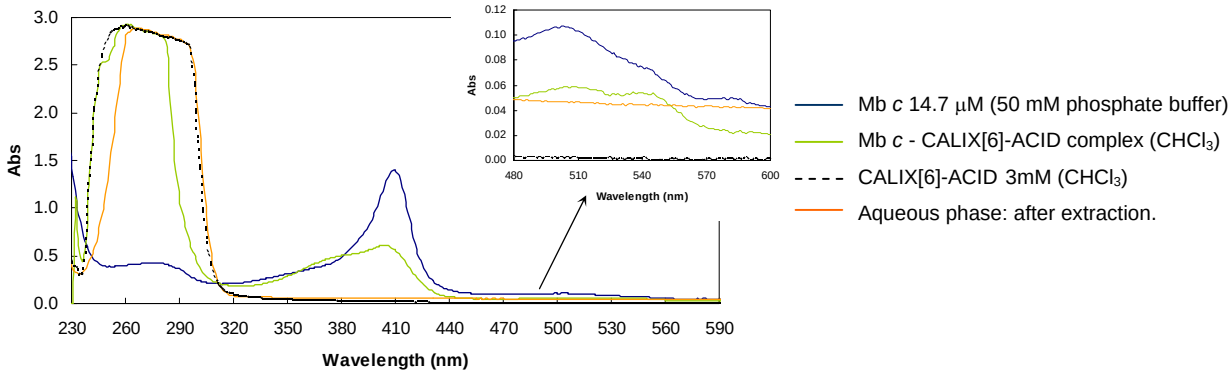

Figure 3 – UV-Vis spectra (230-590nm) of Mb *c* 50mM phosphate buffer pH 6.5, Mb *c* - CALIX[6]-ACID complex in $CHCl_3$ and aqueous phase after extraction.

Wiwatchaiwong *et al*. (2006) also reported similar changes in the Soret band of Mb *c* which was chemically modified with poly(ethylene oxide) in organic solvents. The effect of initial pH of Mb *c* solutions on degree of extraction was also investigated with CALIX[6]-ACID which revealed that protein extraction occurred in a wide range of pH values (4.5 – 9.0) (Figure 4). These data strongly suggest that there are several interactions involved between Mb *c* and CALIX[6]-ACID such as electrostatic and hydrophobic. On the other hand, protein extraction was observed at pH value higher than its pI which suggests apparently that at these pH values electrostatic interactions are not involved since the protein and CALIX[6]-ACID are charged negatively and therefore other interactions may play a role in protein extraction process in organic media.

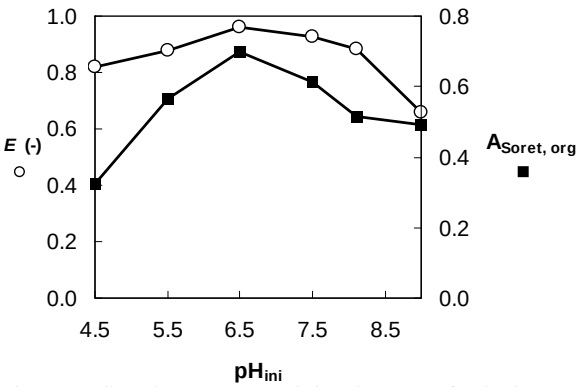

Figure 4 – Effect of pH_{ini} aqueous solution of 14.7 μM **Mb *c*** for the degree of extraction (*E*), with 3mM **CALIX[6]-ACID** in $CHCl_3$.

As far as biocatalysis is concerned, Mb *c* - CALIX[6]-ACID complex exhibited peroxidase-like activity (Figure 5 a) in chloroform and there is a linear relationship between [Mb *c* - CALIX[6]-ACID complex] and initial velocity of peroxidase activity (Figure 5 b). The effect of initial pH of Mb *c* solutions on peroxidase activity was also investigated which revealed that the highest specific activity was obtained at pH 6.5 (Figure 6). Apparent kinetic parameters (K'_m, V'_{max} and K'_{cat}) were determined for the reaction catalysed by Mb *c* - CALIX[6]-ACID complex which are presented in Table 2.

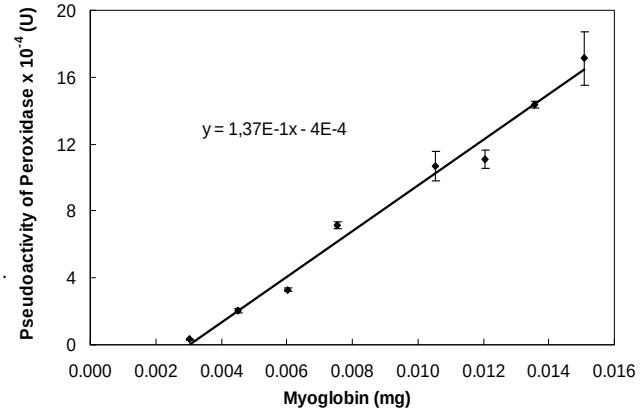

Figure 5 a – The effect of Mb *c* - CALIX[6]-ACID complex concentration on the pseudoperoxidase activity in organic medium (Mb *c* pH_{ini}=6.5).

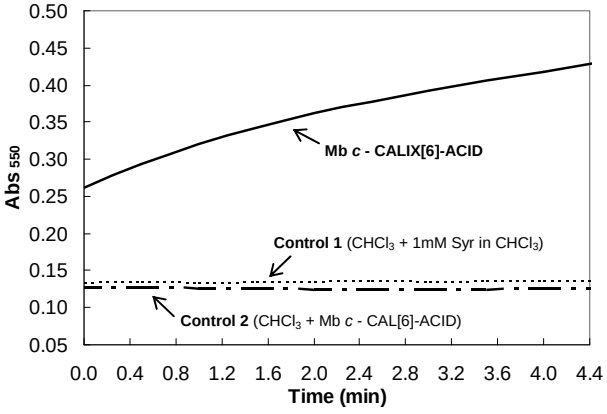

Figure 5 b – Progress curve of the Syr oxidation reaction in organic medium, catalyzed with Mb *c* - CALIX[6]-ACID complex (4.5 μg protein in $CHCl_3$).

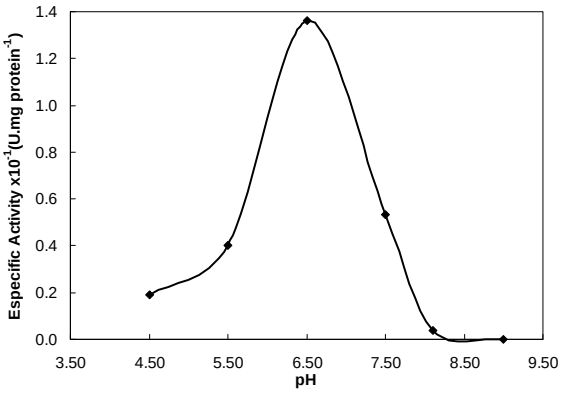

Figure 6 – The effect of pH_{ini} aqueous solution of Mb *c* on the specific activity of Mb *c* - CAL[IX6]-ACID complex in organic medium.

Table 2 – Apparent kinetic parameters of Mb *c* - CALIX[6]-ACID complex by using Syr as the substrate, by Michaelis-Menten Plot.

	MICHAELIS-MENTEN			
pH	4,5	5,5	6,5	7,5
Kinetic Parameters				
K'_m (mM)	$3,83\times10^{-1} \pm 1,12\times10^{-2}$	$6,35\times10^{-1} \pm 1,56\times10^{-2}$	$4,55\times10^{-2} \pm 2,09\times10^{-3}$	$5,41\times10^{-2} \pm 3,23\times10^{-3}$
k'_{cat} (s^{-1})	$7,00\times10^{-3} \pm 1,03\times10^{-3}$	$1,59\times10^{-2} \pm 2,45\times10^{-3}$	$1,51\times10^{-2} \pm 1,14\times10^{-3}$	$6,40\times10^{-3} \pm 6,68\times10^{-4}$
V'_{max} (U.mg $protein^{-1}$)	$2,48\times10^{-2} \pm 3,66\times10^{-3}$	$5,64\times10^{-2} \pm 8,66\times10^{-3}$	$5,33\times10^{-2} \pm 4,03\times10^{-3}$	$2,26\times10^{-2} \pm 2,36\times10^{-3}$
k'_{cat} / K'_m ($mM^{-1}\ s^{-1}$)	$1,83\times10^{-2} \pm 9,19\times10^{-3}$	$2,51\times10^{-2} \pm 2,50\times10^{-3}$	$3,31\times10^{-1} \pm 5,45\times10^{-3}$	$1,18\times10^{-1} \pm 2,07\times10^{-3}$

Subsequently, Mb *c* was recovered from organic phase to fresh aqueous solution by using buffers with different pH values (3.5 – 14.0) as shown in Figure 7. The degree of recovery (*E'*)

was found to be highest at pH 9.5 suggesting that alkaline pH was required to disrupt the Mb *c* - CALIX[6]-ACID complex. However, peroxidase activity of free Mb *c* in fresh aqueous solution exhibited the highest value at pH 10.5 and the recovery of enzyme activity was about 300 % compared with the initial aqueous solution of Mb *c*. Such recoveries of peroxidase activity higher than 100 % may be due to structural and conformational changes in Mb *c* molecules during this recovery process.

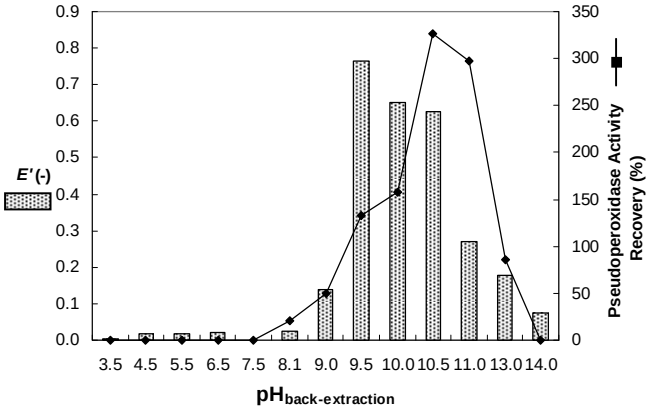

Figure 7 – Degree of back –extraction and pseudoperoxidase activity recovery of Mb *c* in an fresh aqueous solution.

ACKNOWLEDGEMENTS

We acknowledge partial financial support from Instituto Politécnico de Lisboa, Portugal (Research project Nº. 25/2003) and Fundação para a Ciência e a Tecnologia (Unit 702).

REFERENCES

Aires-Barros, M.R. (2002) Biocatálise em solventes orgânicos. *Boletim de Biotecnologia*, 72, 2-12.

Carlsen, C.U., Skovgaard, I.M., Skibsted, l. H. (2003) Pseudoperoxidase activity of myoglobin: kinetics and mechanism of the peroxidase cycle of myoglobin with H_2O_2 and 2,2-Azino-bis(3-ethylbenzthiazoline-6 sulfonate) as substrates. *J. Agric. Food Chem.,* 51*,* 5815-5823.

Chang, S. and Cho, I., (1986) New Metal Cation-Selective Ionophores Derived from Calixarenes: Their Syntheses and Ion-Binding Properties. *J. Chem. Soc. Perkin Trans. I*, 211-214.

Goldberg, R., Catesson, A.-M., Czaninski, Y. (1983) Some properties of syringaldazine oxidase, a peroxidase specifically involved in the lignification processes. *Z.Pflanzenphysiol Bd.*, 110, 267–279.

Gupta, M., Roy, I. (2004) Enzymes in organic media – Forms, functions and applications. *Eur. J. Biochem.*, 271, 2575-2583.

Gutsche, C.D. (1995) Calixarenes. *Aldrichimia Acta*, 28, 3-9.

Gutsche, C.D., Iqbal, M. (1990) *p-tert*-Butylcalix[4]arene. *Org. Synth.*, 68, 234-237.

Gutsche, C.D., Dhawan, B.,Leonis, M., Stewart, D.(1990) *p-tert*-Butylcalix[6]arene*. Org.Synth*, 68, 238-242.

Iwamoto, K., Shinkai, S., Syntheses and ion selectivity of all conformational isomers of tetrakis((ethoxycarbonyl)methoxy)calix[4]arene. (1992) *J. Org. Chem.*, 57, 7066-7073.

Li, Q.C., Mabrouk, P.A. (2003) Spectroscopic and electrochemical studies of horse myoglobin in dimethyl sulfoxide. *J. Biol. Inorg. Chem.*, 8, 83–94.

Ludwig, R. (2005) Calixarenes for biochemical recognition and separation. *Microchim Acta*,152, 1–19.

Munch, J.H. and Gutsche, C. D. (1990) *p-tert*-Butylcalix[8]arene. *Org. Synth*, 68, 243-246.

Arnaud-Neu, F., Collins, E. M., Deasy, M., Ferguson, G., Harris, S., Kaitner, B., Lough, A., McKervey, M., Marques, E., Ruhl, B., Weill, M., Seward, E., (1989) Synthesis, X-ray crystal structures, and cation-binding properties of alkyl calixaryl esters and ketones, a new family of macrocyclic molecular receptors. *J. Am. Chem. Soc.*, 111, 8681-8691.

Oshima, T., Goto, M., Furusaki, S. (2002) Complex formation of cyt *c* with a calixarene carboxylic acid derivate: A novel solubilization method for biomolecule in organic media. *Biomacromolecules*, 3, 438-444.

Oshima, T., Higuchi, H., Ohto, K., Inoue, K., Goto, M. (2005) Selective extraction and recovery of cyt *c* by liquid-liquid extraction using a calix[6]arene carboxylic acid derivative. *Langmuir*, 21, 7280-7284.

Sedmak, J.J., Grossberg, S.E. (1977) A rapid, sensitive, and versatile assay for protein using Coomassie brilliant blue G250, *Anal. Biochem*., 79, 544-552.

Shimojo, K., Oshima, T., Naganawa, H., Goto, M. (2007) Calixarene-assisted protein refolding via liquid-liquid extraction. *Biomacromolecules*, 8, 3061-3066.

Wiwatchaiwong, S., Nakamura, N., Ohno, H. (2006) Spectroscopic characterization and electrochemistry of poly(ethyleneoxide)-modified myoglobin in organic solvents. *Biotechnol. Prog.*, 22, 1276-1281.

Proceedings of the 10th International Chemical and
Biological Engineering Conference - CHEMPOR 2008
Braga, Portugal, September 4-6, 2008
E.C. Ferreira and M. Mota (Eds.)

Immobilization of Lecitase® Ultra in XAD 2 and XAD 4 under Ultrasound Irradiation

Karen M. Gonçalves[1]*, Rodrigo O. de Souza[1], Octavio A. C. Antunes[1], Enrique G. Oestreicher[2]

[1] Instituto de Química, Universidade Federal do Rio de Janeiro, Centro de Tecnologia, Bloco A, Cidade Universitária, 21945-970 Rio de Janeiro, Brazil

Keywords: Lecitase® ultra, amberlite XAD 2 and XAD 4, ultrasound irradiation

Abstract

Several immobilization conditions of Lecitase® ultra on amberlite XAD 2 and XAD 4 resin were investigated. The immobilization by adsorption led to an improved enzyme activity and recyclability. Using this approach, soy oil hydrolysis furnished linoleic acid in 12.4 and 11.9% in XAD 2 and XAD 4 respectively.

1. Introduction

Lipases (glycerol ester hydrolases; EC 3.1.1.3) are enzymes that catalyze the hydrolysis of triglycerides to glycerol and fatty acids. They are the most used enzymes in organic chemistry and its versatility leads to multiple industrial applications (Polaina J. and MacCabe A. P., 2007). Moreover, these enzymes may also catalyze the hidrolysis of phospholipids.

Lecitase® ultra, a new enzyme preparation with phospholipase A1 activity, was patented and made commercially available (Schroder, Novozymes A/S, 200). This enzyme is a preparation obtained from the fusion of the genes from lipase *Thermomyces lanuginosus* and phospholipase *Fusarium oxysporum*. Lecitase® ultra was initially developed for degumming process. However, it can be used as enantioselective biocatalyst in fine chemistry (Jose M. Guisan *et al.,* 2007).

Phospholipases have been described to undergo interfacial activation, similarly to lipases. Due to the nature of Lecitase® ultra, some authors found similarities between this enzyme and lipases, as it is hyper-activated by some detergents and it is able to recognize different esters (Jose M. Guisan *et al.,* 2007).

Although lipases and phospholipases present multiple industrial applications, they are often easily inactivated and are difficult to be separated from the reaction system for reuse. The ordinary method to enhance the operational lifetime, stability, recovery, reuse and continuous operation of lipase is to immobilize it on solid supports. The most commonly used immobilization approach is the adsorption because of its easy use and the reduced costs.

In this work, we disclose our results concerning the lipase activity of Lecitase® ultra supported onto hydrophobic amberlite XAD 2 and XAD 4 under different conditions, including ultrasound irradiation.

The ultrasound at low intensity levels favours the mass transfer because it enhances the movement of the liquid medium. However this phenomenon promote high local increases of

*Corresponding author. Tel + 55-21-25627248. E-mail: karen.goncalves@yahoo.com.br

temperature and pressure that can inactivate the enzyme, affecting its secondary structure (Sinisterra J.V., 1992).

Knowing that many beneficial effects in prevention of atherosclerosis, different types of cancer, hypertension and also improvement of immune function has been attributed to.CLA or Conjugated Linoleic acid, the preparations with best activities, after the optimization of immobilization procedures and the study of the effects of ultrasound irradiation, were applied on hydrolysis of soy oil intending to produce it and oleic acid. Which fatty acids are used as food supplements (Gabriel Fernandes *et al.*, 2006).

2. Materials and methods

2.1. Materials

Lecitase® ultra was obtained from Novozymes, amberlite XAD 2 and XAD 4 resin were purchased from Supelco. Acetone and *n*-hexane were obtained from Vetec and were used as received. The ultrasonic source was an ultrasonic bath Branson 2210 operating at 47 kHz. pH measurements were performed using Biocristal pH-stat and pH eletrod Quimis.

2.2. Immobilization of lipase

Crude Lecitase® ultra (16 mg of protein) was dissolved in 6 mL of buffer solution (sodium phosphate 0.1 M, pH 7.0) and mixed with 2 g of amberlite XAD 2 or XAD 4. Then 30 mL of cold acetone or hexane were added and the mixture was stirred under mechanical (*shaker*) or ultrasonic irradiation for 1 h at the immobilization temperature of 10.5°C. The immobilized lipase was collected by filtration, washed twice with *n*-hexane and the solvent was evaporated under reduced pressure. The immobilized lipase was then lyophilized for 1 h (Chwen-Jen Shieh *et al.*, 2007).

2.3. Enzyme activity assay

Lipase activity was checked by hydrolyzing a stabilized olive oil emulsion as proposed by Freire *et al*., (1997). The methodology was modified to determine the activity of the solid biocatalyst. The enzyme (1 mL for the enzyme solution or 0.1 g for the immobilized one) was feeded in a reactor, which contained 19.0 mL olive oil emulsion (5.0% w/v), a buffer (sodium phosphate 0.1 M, pH 7.0) and arabic gum solution (10.0% w/v). After the specified time (15 min), the reaction was quenched by adding 20 mL of acetone:ethanol solution (1:1). Control reactions were performed without the addition of the enzyme. Titration with NaOH 0.05 N were performed until pH 11. One unit of activity was defined as the amount of enzyme required to release 1 μmol of product per minute under the conditions described above.

2.4. Protein assay

Protein concentration was determined by the Bradford method (M.M. Bradford, 1976).

2.5. Immobilization efficiency

The immobilization efficiency was evaluated using the following parameters:
Lipase activity (U/g)
Specific activity (U/mg-protein)

$$\text{Protein loading ratio (\%)} = \frac{\text{amount of protein loaded}}{\text{amount of protein introduced}} \times 100\%$$

$$\text{Activity yield (\%)} = \frac{\text{specific activity of imobilized lipase}}{\text{specific activity of free lipase}} \times 100\%$$

2.6. Hydrolysis of soy oil

The optimized immobilized preparations were applied on soy oil hydrolysis as follows: 2.0 g of soy oil and 0.344 mL of distilled water (1:3) and 0.6 g of immobilized preparations (5 mg of protein) were mixed and the mixture was stirred at 300 rpm at 50°C for 6 h. The hydrolysis

yield was quantified by titration with NaOH 0.05 N using phenolphthalein as indicator and ethanol:ether solution (1:1) as a solvent. The quantification of fatty acids was performed using the following parameters:

- Acidity: Mililiters of NaOH solution to neutralize 100 g of sample: $\frac{V \times N \times f \times 100}{w}$

- Acidity on linoleic acid: Amount of fatty acids represented by linoleic acid:

$$\frac{V \times N \times f \times 100 \times 0{,}280}{w}$$

Where: V = volume of sample
N = normality of NaOH solution
f = correction factor of NaOH solution
w = weight of sample

3. Results and discussion

Lecitase® ultra presented significant activity for all immobilized preparations, however as shown in Table 1, the use of acetone and pre-treated XAD 2 (Table 1, Entry 7), shows better results than the same procedure without previous treatment (pre-treatment consisted of washing resins with distilled water followed by methanol) of XAD 2 (Table 1, Entries 2). The use of ultrasound as an activating source does not lead to any improvement on lipase activity and the temperature of ultrasound bath has not a significant influence on the enzymatic activity as shown in entries 5 and 10 (Table 1).

The use of *n*-hexane as solvent for the Lecitase® ultra immobilization gave interesting results (Table 1, Entry 9) for the reaction with XAD 2 without pre-treatment, leading to a specific activity close to the best result obtained with acetone (Table 1, Entry 7). Again, ultrasound does not enhance the lipase activity under the conditions used in this work.

The difference between protein loading ratios was not significant on protocols used, not including the case that a solvent was not used (Table 1, Entry 1).

Table 1: Results obtained for the Lecitase ® Ultra immobilization in XAD 2:

Entry	Solvent	Stirring	Temperature	Activity (U/g)	Specific activity (u/mg de ptn)	Protein Loading ratio (%)	Activity yield (%)[d]
1 [a]	-	300 rpm	10.5°C	26.6	7.97	41,5	107.41
2 [a]	Acetone	300 rpm	10.5°C	103.74	13	99,3	175.2
3 [a,c]	Acetone	-	24- 44°C	17.38	2.18	99,4	36.33
4 [a,c]	Hexane	-	24- 44°C	46	7.2	79,8	120
5 [b,c]	Acetone	-	24- 44°C	62.36	7.75	99,9	129.17
6 [b,c]	Hexane	-	33 – 50°C	62.69	8.13	95,8	135.5
7 [b]	Acetone	300 rpm	10.5°C	136.12	16.96	100,0	249.41
8 [b]	Hexane	300 rpm	10.5°C	30	3.77	98,8	55.44
9 [a]	Hexane	300 rpm	10.5°C	105.68	13.35	98,5	222.5
10 [b,c]	Acetone	-	14 – 17°C	73	9.26	97,9	136.18

[a] XAD 2 was used without previous treatment [b] XAD 2 was washed with methanol and water before immobilization
[c] Ultrasound was used
[d] Activity yield **(%) =** Specific activity of immobilized lipase **x** 100 / Specific activity of free lipase

The best conditions obtained were applied for XAD 4 resin and the results are summarized in Table 2. As shown in Table 2, conversely to the results obtained for XAD 2, the use of

ultrasound improved the specific lipase activity when compared to the same reaction profile under only mechanical stirring (Table 2, Entries 1, 2 and 3).

Table 2: Results obtained for the Lecitase ® Ultra immobilization in XAD 4

Entry	Solvent	Stirring	Temperature	Activity (U/g)	Specific activity (U/mg of ptn)	Protein Loading ratio (%)	Activity yield (%)[d]
1 [a]	Acetone	300 rpm	10.5°C	77.87	9.72	99.4	142.94
2 [b]	Acetone	300 rpm	10.5°C	95.87	11.94	99.6	175.59
3 [a,c]	Acetone	-	14-17°C	103.17	13.71	93.4	201.62

[a] XAD 4 was washed with methanol and water before immobilization [b] XAD 4 was used without previous treatment
[c] Ultrasound was used
[d] Activity yield **(%) =** Specific activity of immobilized lipase **x** 100/Specific activity of free lipase

The amount of protein immobilized on amberlite XAD 4 under sonication (Table 2, Entry 3) was lower than the others, however its specific activity increased, probably because of difusional limitations were reduced.

3.1. Storage stability at 4°C

The storage stability of the immobilized preparations which presented the best specific activities (Table 1, entries 7 and 9) to amberlite XAD 2 resin and to amberlite XAD 4 resin (Table 2, entry 3) were observed during several days (Figure 1). This could be observed in terms of lipase activity.

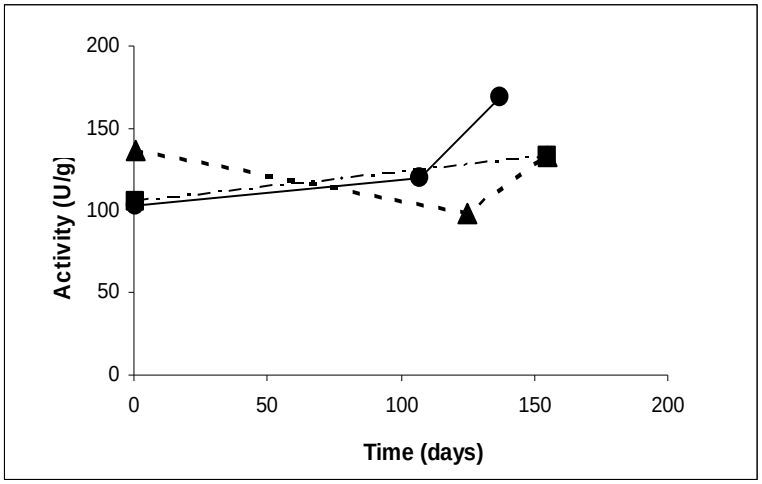

Figure 1. Storage stability.
Immobilized preparation on XAD 2 resin: 7(- - -▲- - -), 9 (– –■– –).
Immobilized preparation on XAD 4 resin: 3 (—●—)

As shown in Figure 1, the enzyme activity was slightly higher after 150 days of storage at 4°C, which could indicate that the enzyme can be used after almost 6 months without loose of activity. This increase in enzymatic activity could be a normal zone of variation, depending on the enzyme used, however it has to be investigated.

3.2. Hydrolysis of soy oil

On the hydrolysis of soy oil the acidity obtained for the reaction catalyzed by XAD 2 (Table 1, Entry 7) and XAD 4 (Table 2, Entry 3) was 44.3% and 42.4%, respectively. When the acidity was quantified based on amount of linoleic acid, the results obtained were 12.4 and 11.9% to XAD 2 and XAD 4, respectively.

4. Conclusions

The different conditions applied on immobilization of Lecitase® ultra showed that the use of *n*-hexane as solvent offers better results when amberlite XAD 2 is not pre-treated. Probably the hydrophobic nature of this solvent facilitates the enzymes access to the support against the other organic substances in the resin. However, when acetone was used, amberlite needed to be pre-treated.

The ultrasound irradiation does not improve the hydrolysis activity of Lecitase® ultra on XAD 2. However, difference between the amounts of protein adsorbed is observed. While the ultrasound irradiation improves the adsorption of protein when XAD 2 was not pre-treated (Table 1, Entries 4 and 6), the lipase activity has not significant alterations. In case of XAD 4, ultrasound improves the activity with acetone as solvent.

Therefore, Entries 7, 9 (Table 1) and 3 (Table 2) are the best conditions to immobilize Lecitase® ultra on amberlite XAD 2 and XAD 4. The immobilized preparations (Table 1, Entry 7 and Table 2, Entry 3) present interesting results on hydrolysis of soy oil, made it available to produce fatty acids as linoleic and oleic acids, important food supplements.

References

Polaina J. and MacCabe A. P. (2007), *Industral Enzimes: Structure, Function and Applications*, Springer

Schroder, Novozymes A/S, Denmark. PCT International application WO2000/32758, 2000

Gloria Fernandez-Lorente, Jose M. Palomo, Jose M. Guisan, Roberto Fernandez-Lafuente *Journal of Molecular Catalysis B: Enzymatic* 47 (2007) 99-104

Sinisterra J.V. (1992), Application of ultrasound to biotechnology: an overview, *Ultrasonics*, 30, n3 180-185

Arunabh Bhattacharya, Jameela Banu, Mizanur Rahman, Jennifer Causey, Gabriel Fernandes (2006), Biological effects of conjugated linoleic acids in health and disease, *Journal of Nutritional Biochemistry,* 17, 789–810

Shuo-Fen Chang, Shu-Wei Chang, Yue-Horng Yen, Chwen-Jen Shieh (2007), *Applied Clay Science,* 37, 67–73

D.M.G. Freire, E.M.F. Teles, E.P.S. Bon, G.L. Sant'Anna Jr. (1997), *Applied Biochemistry and Biotechnology,* 63, 409–421.

M.M. Bradford (1976), *Analytical Biochemistry*, 72, 248-254

Proceedings of the 10th International Chemical and
Biological Engineering Conference - CHEMPOR 2008
Braga, Portugal, September 4-6, 2008
E.C. Ferreira and M. Mota (Eds.)

Use of molecular biology techniques to assess the bacterial community diversity of a lab-scale biofilter and an industrial biotrickling filter treating high loads of H_2S

Roger Rovira[1], Juan P Maestre[1], Xavier Gamisans[2], Javier Lafuente[1], Jordi Mas[3], David Gabriel[1]*

[1]Department of Chemical Engineering. Universitat Autònoma de Barcelona. Edifici Q. Campus de Bellaterra. 08193 Bellaterra, Barcelona, Spain
[2]Department of Mining Engineering and Natural Resources, Universitat Politècnica de Catalunya, Bases de Manresa 61-73, 08242 Manresa, Spain
[3] Department of Genetics and Microbiology. Universitat Autònoma de Barcelona. Edifici C. Campus de Bellaterra. 08193 Bellaterra, Barcelona, Spain

Keywords: Industrial Biotrickling filter, lab-scale biotrickling filter, Hydrogen sulfide, Bacterial Community diversity, Clone library
Topic: Integration of life sciences & engineering.

Abstract

The bacterial diversity in a lab-scale and an industrial biotrickling filter treating high loads of hydrogen sulfide (H_2S) were assessed by using molecular biology techniques. Both reactors were operating for more than 6 months with sustained elimination capacities above 90% when samples were withdrawn. In both cases the same experimental procedure was applied, 16S rRNA gene clone libraries were created and clones were clustered into operational taxonomic units (OTUs) for further analysis. The different operational conditions as well as other significant factors like sampling or DNA extraction induced unexpected results in the industrial reactor clone library. Whereas the lab-scale clone collection showed high percentage of sulfur oxidizing bacteria (45%), the industrial bioreactor clone library did not have clones affiliated to any genera of sulfur oxidizers. As a result, industrial library obtained is believed not to be completely representative of the diversity existing in the reactor. Although industrial scale bioreactor showed higher number of OTUs, nearly all the sequences were related to the non sulfur related family Enterobacteriaceae. In contrast, the lab-scale bioreactor clone library demonstrated to have less differentiated OTUs but widely distributed phylogenetically, which indicates the higher representativeness of this collection. Experimental factors which led to these results are analyzed and better knowledge on the implementation of molecular techniques when investigating industrial scale bioreactors is obtained.

1 Introduction

Biogas, that contains secondary components like hydrogen sulfide (H_2S), is produced in the anaerobic treatment of wastewater treatment plant sludge. H_2S is a corrosive, toxic and odorous gas, which has been successfully degraded in biotrickling filters (Fortuny et al. 2008).

A comprehensive study of the communities in these biologic reactors has been shown to be critical to the understanding of the whole biodegradation process (Borin et al., 2006). The

* Corresponding author. Tel + 34935811587. E-mail: david.gabriel@uab.es

methods used in the traditional culture-dependent approach for assessing the microbial community are often biased since it has been estimated that less than 1% of all microorganisms are cultivable by standard methods (Amann et al., 1995). Nevertheless, techniques used in the novel molecular approach targeting the small subunit rRNA-encoding genes, can solve this bias problem. Thus, a more representative picture of the microbial populations could be obtained.

Several studies have been reported analyzing lab-scale as well as industrial bioreactors communities by using molecular tools (Sakano and Kerkhof, 1998; Friedrich et al., 2002; Sercu et al., 2006). In this study the cloning and sequencing methodology have been successfully applied in a lab-scale biotrickling filter (LSBTF) treating high concentrations of H_2S. However, several problems arose when applying lab-scale molecular biology procedures to the industrial scale biotrickling filter (ISBTF). To our knowledge, this is the first research to study the microbial communities of an industrial scale biotrickling filter degrading high loads of H_2S and to analyze the factors influencing negatively on the coverage of the clone library obtained.

2 Materials and Methods extensive

Experimental setups.

In this work, two biotrickling filters (BTFs) were studied. The start-up in both bioreactors was carried out using sludge from the same municipal WWTP as inoculum. Both BTFs were continuously operated for six months at an empty bed residence time 180 s for gas treatment with inlet concentrations of 2000 ppm_v of H_2S (55.6 g H_2S m^{-3} h^{-1}). Details of the LSBTF can be found elsewhere (Fortuny et al., 2008). It was designed with a single compartment and packed with 3 L of polypropylene HD Q-PAC (Lantec) with a 4 x 4 mm grid opening. The pH was controlled between 6.5 and 7.5 by adding acid or base. The bioreactor worked at room temperature. On the other hand, the ISBTF, located in a wastewater treatment plant, was designed as 4 separated modules with a bed volume of 5.2 m^3 packed with 1" Pall rings. The pH of the ISBTF was set between 2 and 3, and the temperature was allowed to fluctuate according to environmental conditions, from 0 to 20 ºC. In order to keep the pH at the fixed setpoint, a flow of make–up water (effluent from the WWTP containing the following average values: BOD 5 mg l^{-1}, TKN 7 mg l^{-1} and P_{total} 7 mg l^{-1}) was introduced at a flow rate of 30 m^3 d^{-1}.

Under these conditions, elimination capacities around 50 g H_2S m^{-3} h^{-1} were achieved for nealy the whole experimental period. In the LSBTF, metered amounts of H_2S, N_2 and air (0.2, 77.3 and 22.4 % respectively) were used to simulate a controlled biogas inflow whereas in the ISBTF, H_2S laden biogas was obtained directly from the biogas storage tanks of the anaerobic sludge treatment produced in the WWTP. On average, industrial biogas composition was 69% CH_4, 29% CO_2, 1% N_2, and others (including H_2S). In the lab-scale reactor N_2 was used instead of CH_4 for security reasons. More details of the LSBTF, the mineral medium used as make-up water, other operational conditions and analytical methods can be found elsewhere (Fortuny et al., 2008).

DNA isolation and 16S rRNA gene amplification.

In the lab-scale case, biomass samples were withdrawn on day 189 of operation from two sampling ports situated at different heights in the reactor, 17 cm and 34 cm. Both biomass samples were mixed in a 1:1 ratio (w/w) and DNA extraction was carried out. Similarly, in the ISBTF each module was sampled. Separated DNA extractions were carried out for biomass from each module. DNAs from ISBTF modules were mixed prior to PCR amplification according to the DNA concentration obtained to have the same quantity of DNA of every module in the resulting mixture. DNA was tested and preserved as described elsewhere (Chihua and Banks, 2006).

The small subunit (SSU) rRNA gene was polymerase chain reaction (PCR) amplified from

genomic DNA extracted from the environmental samples using the universal bacterial primers 8F and 926R (Molbiol, Germany). PCR reactions were performed as described elsewhere (Chihua and Banks, 2006) but containingd 100 ng of template DNA.Then, 16S rRNA gene fragments were cloned with the TOPO TA Cloning® Kit for Sequencing (Invitrogen, CA, USA) according to the manufacturer's instructions.

Sequencing and phylogenetic reconstruction.

One hundred clone inserts were sequenced for each clone library. In the LSBTF case, clones were sequenced in full with pUC/T3-T7 primers by Macrogen (Korea) wheras in the ISBTF clones were sequenced only with T3 primer, obtaining partial sequences. All sequences were checked for chimeric artifacts by using the CHIMERA_CHECK program of the Ribosomal Database Project (Maidak et al., 2000) and for similar sequences with the ClustalW program. Sequences (approximately 1500bp in LSBTF case or around 800pb in the ISBTF collection) were compared with similar sequences of the reference organisms by a BLAST search (Altschul et al., 1997). Sequences with the same first accession number were grouped into OTUs. Thus, the clustering process was based on the BLAST results obtained for every clone. Similarity between clones within the same OTU was studied by sequence comparison using ClustalW.

Rarefaction analysis.

The rarefaction analysis was calculated using the defined OTUs. The software Analytic Rarefaction (version 1.3, S.M. Holland, http://www.uga.edu/~strata/software/) was used to perform rarefaction analysis. The 16S rRNA gene sequences of the clones have been submitted to the Genbank /EMBL/DDBJ to obtain the corresponding accession numbers. The coverage of the clone library was calculated according to the following equation: $C= 1 - (n/N) * 100$, where n is the number of unique clones and N is the total number of clones examined (Ravenschlag et al., 1999).

3 Results and Discussion

Microbial populations are predictable to be determined by the operational conditions set in the bioreactors, that is, by the microenvironments created by gradients of pH, temperature, O_2 concentration and pollutant concentration, among other factors. Thus, dissimilar sulfur oxidizing communities were expected among the LSBTF and the ISBTF just because of the pH differences. Conversely microbial community collection obtained for the ISBTF was found to be biased and not to represent the whole bacterial community of the reactor.

Assesment of bacterial communities.

In the present work, microbial communities of two BTFs, lab-scale and industrial scale, degrading high loads of H_2S were investigated. Accordingly with the pollutant being degraded, sulfur-oxidizing bacteria were expected to be predominant in both clone collection of both BTFs. In the LSBTF, neutrophilic bacteria were predictable whereas in the ISBTF, acidic communities were likely the most predominant. Biodiversity in the reactors are influenced by operational conditions such us packing material, pollutant load, pH, etc. Both BTFs have inert packing material which could diminish biological diversity in comparison to organic materials. Also, extreme H_2S concentrations may affect the presence of specific groups of bacteria like sulfur oxidizing bacteria (SOB). In spite of these factors, biomass grows forming biofilms in this sort of reactors what creates microenvironments and favors variety of ecological conditions and consequently increase bacterial assortment.

In this work, the molecular approach was selected to overcome culture-techniques problems and to obtain representative results of the microbial communities present in the reactors. Despite 16S rRNA gene approach also have biases such as preferential DNA extraction or PCR amplification; it would cover most of the populations existing in the biological sample. Such biases emerged during the molecular procedure could modify population relative abundances in the clone collection, indicating that this cloning-sequencing methodology

cannot be considered quantitative. Nevertheless, if good practices are applied results obtained in clone libraries are expected to be directly related to communities present in the bioreactors.

Although results obtained in both clone collections showed that there is a high bacterial diversity in this kind of bioreactors, the industrial scale library demonstrated to have more number of differentiated OTUs (62) but less widely distributed phylogenetically than the lab-scale collection (24). The quantity of OTUs was likely determined by the fact that industrial scale collection was obtained by sequencing only with T3 primer, thus only partial sequences of 750-850 bp were acquired. This could reduce the specificity of the sequences leading to find more OTUs in the clone collection. Conversely, LSBTF's 16S rRNA gene clone library was constructed with near full-length 16S rRNA gene sequences (1500 bp). Although the number of OTUs determines some of the regular analysis usually carried out in this type of studies, it was not a particular issue in the analysis of the ISBTF collection.

Rarefaction analysis demonstrated that the LSBTF clone library constructed was enough representative of the bacterial diversity (curve not shown). ISBTF collection was less suitable describing the specific bacterial richness in terms of species. Nevertheless, concerning ribosomal data project (RDP) genera classification, only 3 genera (Kluyvera, Citrobacter and Enterobacter) comprised the 84% of the clones showing that in terms of genera the community was theoretically less diverse. Coverage percentage was higher in the LSBTF clone library (nearly 68%). In the industrial case coverage was only 29%, lower that values found in literature for industrial bioreactors (Friedrich et al.,2002), demonstrating that an important fraction of microbial diversity is not covered and consequently, clone collection obtained could not be sufficiently representative.

A wide variety of OTUs were found to be SOB in the LSBTF (Table 1), including 45% of the clones. They were closely related to various SOB species such as: *Thiothrix Lakustris*, *Thiothrix sp. CT3*, *Sulfurimonas denitrificans*, *Thiobacillus denitrificans*, *Thiobacillus sajanensis* and *Thiobacillus plumbophylus*. Unexpectedly, only one clone out of 87 could be related to a SOB genera in the ISBTF collection. One clone is affiliated to an uncultured *Pseudomonas spp*. Some *Pseudomonas spp.* have been previously related to sulphur oxidation (Shibata and Kobayashi, 2006) or found in sulfur oxidizing biofilms (Ferrera et al., 2004). None of the typical SOB genera such us Acidithiobacillus was found in the bioreactor.

In table 1 is possible to observe the most abundant clones found in both libraries. Only OTUs comprising more than 3 clones are showed. ISBTF presented species affiliated with Kluyvera, Enterobacter and Rahnella among other genera within the Enterobacteriaceae family.

Table 1. Phylogenetic affiliation of the most abundant clone sequences retrieved in both clone libraries: L: lab-scale, I: industrial scale. OTUs composed by more than 3 clones are represented. Cn: clone number, , S: Similarity

OTU nº	*Nº clones*	*Closest match (accession number)*		*S (%)*	*Cultured closest match (accession number)*		*S (%)*
			Lab-scale biotrickling filter				
OTU-L1	29	Thiothrix lakustris strain BL	EU642572	96-99	Thiothrix lakustris strain BL	EU642572	96-99
OTU-L12	13	Uncultured Bacteroidetes bacterium	AJ318142	89-97	Haliscomenobacter hydrossis	AJ784892	85-87
OTU-L3	3	Sulfurimonas denitrificans DSM 1251	CP000153	99	-	CP000153	99
OTU-L5	3	Uncultured bacterium	AB181499	97-98	Sulfurimonas denitrificans DSM 1251	CP000153	95-98
OTU-L23	3	Uncultured bacterium	AB186831	91-98	Denitratisoma oestradiolicum strain AcBE2-1	AY879297	90-93
			Industrial scale biotrickling filter				
OTU I-12	7	Uncultured bacterium	EF515371.1	96-99	Kluyvera ascorbata strain CDC	AF176567.1	95-99
OTU I-15	4	Uncultured Enterobacteriaceae bacterium	EU530475.1	96-98	Enterobacter aerogenes, strain RW9516	AM933751	96-98
OTU I-2	3	Kluyvera sp. IAL9558/98 16S	AF176564.1	94-99	-	AF176564.1	94-99
OTU I-3	3	Kluyvera ascorbata strain CDC	AF176567.1	94-99	-	AF176567.1	94-99
OTU I-7	3	Enterobacter sp. 9B_2 16S	AY689062.1	93-99	-	AY689062.1	93-99
OTU I-11	3	Uncultured bacterium	EF402397.1	97-99	Enterobacter aerogenes, strain RW9516	AM933751	97-99
OTU I-13	3	Uncultured bacterium	EF551862.1	95-96	Rahnella sp. BIHB 783	DQ885948	94-96
OTU I-16	3	Uncultured Enterobacteriaceae bacterium	EU530479.1	97-99	Enterobacter aerogenes, strain RW9516	AM933751	96-99

High removal efficiencies achieved in the reactor in long term operation (over six months) indicated that SOB must be present in the bioreactor in enough number to degrade the high loads of H_2S treated. The scarce representation of SOB in the industrial library could be caused by different factors affecting concomitantly.

Causes of low representation of SOB.

As previously stated, the representativeness of the clone library obtained for the industrial bioreactor is uncertain. Acidic SOB are supposed to be degrading hydrogen sulphide at high rates inside the ISBTF and were not found in the collection of clones. Several causes could be not only influencing the relative abundance of the species but also diminishing the presence of some groups of bacteria to the extent that some of them do not appear in the collection. Methodological aspects when applying the same procedure used to construct the lab-scale clone collection might have been key factors to make SOB not predominant and even present in the library.

First of all, representativeness is influenced by the sampling technique. In the lab-scale biofilters samples were withdrawn at two heights, representing the sample volume almost 20% of the total reactor volume. However, ISBTF was sampled for the 4 modules but the total volume sampled represented less than 5% of the total volume due to the technical difficulties when sampling this industrial scale plug flow bioreactor. The 4 modules were sampled and individual DNA extractions were carried out. According to the quantity of elemental sulfur found in the modules, H_2S oxidation is supposed to be accomplished in the two first modules of the bioreactor and mainly in the first one. In the rest of the bioreactor, other types of bacteria would be predominant since almost no source of sulfur would be available. As a result, the vast majority of SOB bacteria could be settled in these parts of the reactor. Prior to PCR amplification, DNA from each module was mixed taking into account the DNA concentration obtained. This could lead to a drastic reduction of the SOB DNA in the resulting sample and consequently in the clone collection.

Another factor affecting the molecular procedure is the elemental sulfur found in the biological samples. The presence of sulfur is thought to be responsible of the low DNA quantities obtained from the industrial bioreactor. Conversely, in the LSBTF, almost no elemental sulfur was found in the samples. In spite of the similar operational conditions, in the lab-scale biofilters oxygen could be distributed in a better way so less elemental sulfur was produced. Thus, the grid used as packing material could be more suitable and favor O_2 transference in front of the Pall rings used in the ISBTF.

As previously stated, pH is a key factor determining populations in the bioreactor. LSBTF was kept at neutral conditions during the whole experimental period. Normally, in lab-scale setups pH is controlled by adding HCl or NaOH. In the industrial case, it would be expensive to control pH in the same way so make-up water is used for that purpose. Make-up water used in this case comes from the wastewater treatment plant effluent, which still contains microorganisms (most of them enteric bacteria, a normal part of the gut flora found in the intestines of humans) as well as BOD, nitrogen and phosphorous. Make-up water average rate used for pH control was 30 $m^3\ d^{-1}$, so this constant addition of microorganisms and nutrients could result in a regular re-inoculation of the reactor. These non sulfur oxidizing bacteria could become predominant in those parts of the reactor where H_2S was not significant, that was likely in the 3^{rd} and 4^{th} module. Moreover, Enteriobacteriaceae are facultative anaerobes so oxygen requirements were not decisive for them, resisting the low levels of oxygen that existed in the reactor. This could considerably explain why Enterobaceriaceae family is so predominant in the clone library obtained.

4 Conclusions

In this study, a molecular approach has been used to characterize the microbial diversity in an industrial as well as in a lab-scale biotrickling filter. Clone libraries potentially representing most abundant species present were created. Whereas lab-scale library was representative

of the bacterial richness present in the reactor, the industrial clone library did not show any SOB. That led to conclude that the collection obtained could not have enough representativeness. Some key factors were identified as possible causes of this lack of fidelity between the real community present in the reactor and the diversity obtained in the clone library. Total sample volume, the presence of sulfur when extracting the DNA as well as the mixture of each volume DNA could have distorted the relative abundances of bacteria in the collection.

Finally, the continuous re-inoculation effect caused by passing through the reactor a high flow rate current of make-up water containing enteric bacteria from the effluent of the WWTP could also determine the high abundance of this group in the industrial clone library.

References

Altschul, S.F., Madden, T.L., Schaffer, A.A., Zhang, J., Zhang, Z., Miller, W., and Lipman, D.J. (1997). Gapped BLAST and PSI-BLAST: a new generation of protein database search programs. *Nucleic Acids Res.* 25, 3389-3402.

Amann,R.I., Ludwig,W., and Schleifer,K.H. (1995). Phylogenetic identification and in situ detection of individual microbial cells without cultivation. Microbiology and Molecular Biology Reviews 59, 143-169.

Borin,S., Marzorati,M., Brusetti,L., Zilli,M., Cherif,H., Hassen,A., Converti,A., Sorlini,C., and Daffonchio,D. (2006). Microbial Succession in a Compost-packed Biofilter Treating Benzene-contaminated Air. Biodegradation 17, 79-89.

Chi-hua, H. and Banks, M.K. (2006). Degradation of Polycyclic Aromatic Hydrocarbons in the Rhizosphere of Festuca arundinacea and Associated Microbial Community Changes. *Bioremediation Journal* 10, 93-104.

Ferrera,I., Massana,R., Casamayor,E.O., Balague,V., Sanchez,O., Pedros-Alio,C., and Mas,J. (2004). High-diversity biofilm for the oxidation of sulfide-containing effluents. Appl.Microbiol.Biotechnol. 64, 726-734.

Fortuny, M., Baeza, J.A., Gamisans, X., Casas, C., Lafuente, J., Deshusses, M.A., and Gabriel, D. (2008). Biological sweetening of energy gases mimics in biotrickling filters. *Chemosphere* 71, 10-17.

Friedrich, U., Prior, K., Altendorf, K., and Lipski, A. (2002). High bacterial diversity of a waste gas-degrading community in an industrial biofilter as shown by a 16S rDNA clone library. *Environ.Microbiol.* 4, 721-734.

Maidak,B.L., Cole,J.R., Lilburn,T.G., Parker,C.T., Jr., Saxman,P.R., Stredwick,J.M., Garrity,G.M., Li,B., Olsen,G.J., Pramanik,S., Schmidt,T.M., and Tiedje,J.M. (2000). The RDP (Ribosomal Database Project) continues. Nucleic Acids Res. 28, 173-174.

Ravenschlag,K., Sahm,K., Pernthaler,J., and Amann,R. (1999). High bacterial diversity in permanently cold marine sediments. Appl.Environ.Microbiol. 65, 3982-3989.

Sakano,Y. and Kerkhof,L. (1998). Assessment of changes in microbial community structure during operation of an ammonia biofilter with molecular tools. Appl.Environ.Microbiol. 64, 4877-4882.

Sercu,B., Nuñez,D., Aroca,G., Boon,N., Verstraete,W., and Van Langenhove,H. (2005). Inoculation and start-up of a biotricking filter removing dimethyl sulfide. Chemical Engineering Journal 113, 127-134.

Shibata,H. and Kobayashi,S. (2006). Characterization of a HMT2-like enzyme for sulfide oxidation from Pseudomonas putida. Can.J.Microbiol. 52, 724-730.

Proceedings of the 10th International Chemical and
Biological Engineering Conference - CHEMPOR 2008
Braga, Portugal, September 4-6, 2008
E.C. Ferreira and M. Mota (Eds.)

Production and chromatographic behaviour of polygalacturonase from *Pleurotus ostreatus* on immobilized metal chelates

Maria do Rosário Freixo[1,2], Amin Karmali[2*], José Maria Arteiro[1]
[1] Department of Chemistry, Universidade de Évora,
Rua Ramalho Ortigão Nº59, Évora, Portugal
[2] Chemical Engineering and Biotechnology Research Center of Instituto Superior de Engenharia de Lisboa, Rua Conselheiro Emídio Navarro 1950-062 Lisboa, Portugal.
[*] corresponding author

Keywords: Tomato pomace; Immobilized Metal Affinity Chromatography; polygalacturonase; lignocellulosic enzymes; *Pleurotus ostreatus*.
Topic: Multi-scale and/or multi-disciplinary approach to process-product innovation

Abstract

A strain of *Pleurotus ostreatus* was grown in submerged culture in tomato pomace as sole carbon source for production of polygalacturonase. The culture of *P. ostreatus* revealed a peak of polygalacturonase activity (2181 U/L) on 4th day with specific activity of 42.8 U/mg protein. Differential chromatographic behaviour of polygalacturonase, xylanase and laccase from *P. ostreatus* was investigated on immobilized metal chelates. The effect of ligand concentration, pH, the length of spacer arm and the nature of metal ion was studied for enzyme adsorption on immobilized metal affinity chromatography (IMAC). The presence of imidazole in the equilibration buffer abolished the adsorption of the enzymes to immobilized metal chelates. A one-step purification of polygalacturonase from *P. ostreatus* was devised by using a column of Sepharose 6B-EPI 30-IDA-Cu(II). Purified enzyme exhibited a specific activity of about 1600 U/mg protein, final recovery of enzyme activity of 80% and a purification factor of about 65. The purified enzyme preparation was analysed by SDS-PAGE as well as by *in situ* detection of enzyme activity. Purified preparation of polygalacturonase exhibited a pH and temperature optima of activity at 7.0 and at 50ºC, respectively. The kinetic parameters (V_{max}, K_m, K_{cat}, and K_{cat}/K_m) of purified enzyme were found to be 5530.8 ± 260.7 U/mg of protein, 13.23 ±2.79 mg/ml of polygalacturonic acid, 5553.01 ± 261.7 $s^{-1}$and 419.72 $s^{-1}.mg^{-1}$, respectively. Purified enzyme exhibited a half life (t ½) of 60 ± 7.45 min and 35 ± 0.37 min at 50ºC and at pH 6.0 and 7.0, respectively.

1 Introduction

Food processing industries and agriculture produce annually a huge amount of wastes that are both a disposal and an environmental problem. During tomato processing, a huge amount of the starting raw product represents solid waste material which is known as tomato pomace. It consists of tomato peel, seeds as well as some pulp. The chemical composition of tomato pomace includes proteins, lipids, carbohydrates, amino acids, caratenoids and minerals (Alvarado, Pacheco-Delahaye, Hevia, 2001; Knoblich, Anderson, Latshaw, 2005; Valle, Cámara, Torija, 2006).

Pectinases or pectinolytic enzymes are a group of enzymes that catalyse altogether the degradation of pectic substances present in vegetable cells. Microbial pectinases play an important role in biotechnological applications, namely in food industry (fruit juice extraction, coffee and tea fermentation, oil extraction, improvement of chromaticity and stability of red wines), textile industry (bioscouring of cotton fibers), paper and pulp industry and in waste water treatment. On the other hand, pectinases are used in novel applications such as the purification of plant viruses (Jayani,

Saxena, Gupta, 2005; Gummadi, Panda, 2003) However, industrial production of pectinolytic enzymes makes use almost exclusively of *Aspergillus niger* strains.
Polygalacturonases (EC 3.2.1.15 and EC 3.2.1.67) are pectinolytic enzymes that catalyse the hydrolytic cleavage of the polygalacturonic acid chain with the introduction of water. These enzymes are of industrial interest since they are used in specific applications, such as in baby and functional foods [8]. There is only one report in the literature about the production of endo and exo-polygalacturonases (EC 3.2.1.15 and EC 3.2.1.67, respectively) from *Coriolus trogii* (Levin, Forchiassin, 1998). To our knowledge, the production of such enzymes from *P. ostreatus* has not been reported in the literature.
Since this enzyme is secreted extracelularly by white-rot fungi as well as other lignocellulosic enzymes, it is of great interest to devise a simple and cheap separation method for these enzymes in order to be used in different industrial applications. Immobilized metal affinity chromatography (IMAC) has been used for purification of wild-type and recombinant proteins. The interactions between accessible coordination sites of metal ions and electron-donating groups present on the protein surface are responsible for retention of proteins in IMAC. Several factors affect the adsorption process, such as the nature of metal ion involved in coordination, the matrix, the length of spacer arm, the ligand concentration, the pH and buffer used (Porath, 1992; Gutiérrez, Valle, Galán, 2007).
The present work is concerned with the production of polygalacturonase from *P. ostreatus* by using tomato pomace as sole carbon source in culture medium. Subsequently, the chromatographic behavior of this enzyme as well as other lignocellulosic enzymes (i.e xylanase and laccase) on immobilized metal chelates will be investigated as a function of ligand concentration, pH, length of spacer arm and nature of metal ion. The selective adsorption of polygalacturonase on immobilized metal chelates will be carried out for purification of this enzyme with high yield and purity and kinetic characterization of the purified enzyme will be presented.

2 Methods

2.1 Growth and maintenance of fungal strain

The strain of *P. ostreatus* was grown and maintained in solid potato dextrose agar (PDA). For enzyme production, the strain was grown on liquid media, containing carbon source (either 20 g/L of tomato pomace or 10 g/L of pectin), 1 g/L of $(NH_4)_2SO_4$, 0.125 g/L of $CaCl_2$, 1 g/L of $NaH_2PO_4.H_2O$ and 0.5 g/L of $MgSO_4.7H_2O$. The pH was adjusted to 5.5 prior to autoclaving.

2.2 Fungal growth conditions

Fungal growth conditions were described as reported previously (Freixo , Karmali, Arteiro, 2008).

2.3 Enzyme assays

Enzymatic assays were performed as described in the literature (Freixo, Karmali, Arteiro, 2008).

2.4 Preparation of chromatographic matrices

Chromatographic matrices were prepared as described in the literature (Freixo, Karmali, Arteiro, 2008).

2.5 Adsorption tests of polygalacturonase, xylanase and laccase on metal chelates

As previously described (Martins, Andrade, Karmali, Serralheiro, 2006), a rapid batch method carried out in ELISA microtiter plates was used to study the adsorption of polygalacturonase, xylanase and laccase on the following Cu(II), Ni(II), Zn(II) and Co(II) metal chelate supports: Sepharose 6B- BDGE-30-IDA- M(II), Sepharose 6B- EPI-30-IDA- M(II) and Sepharose 6B- EPI-10-IDA- M(II).

2.6 Purification of polygalacturonase from *P. ostreatus*
Based on the results of the batch mode on ELISA microtiter plates, a set of experimental conditions were selected to purify polygalacturonase from this fungal strain, as described in the literature (Freixo, Karmali, Arteiro, 2008).

2.7 Kinetic characterization of purified polygalacturonase from *P. ostreatus*
Kinetic characterization of purified polygalacturonase from *P. ostreatus* was performed as described in the literature (Freixo, Karmali, Arteiro, 2008).

3 Results and Discussion

3.1 Production of polygalacturonase and protein content in culture supernatants
The cultivation of *P. ostreatus* on tomato pomace medium was followed for 14 days (Fig.1) and displayed a bell-shaped curve for protein content as well as for polygalacturonase activity. Pectinlyase activity in the fermentation broth was also determined during the cultivation process and no activity was detected in culture supernatants. The culture of *P. ostreatus* revealed a peak of polygalacturonase activity (2181U/L of fermentation broth) on the 4th day of culture with a specific activity of 42.8U/mg protein (Fig. 1). This data revealed that at 3rd day of incubation, polygalacturonase activity reached a maximum value and then it exhibited a decrease in activity. This change in enzyme activity may be due to the accumulation of microbial metabolites in the fermentation broth.

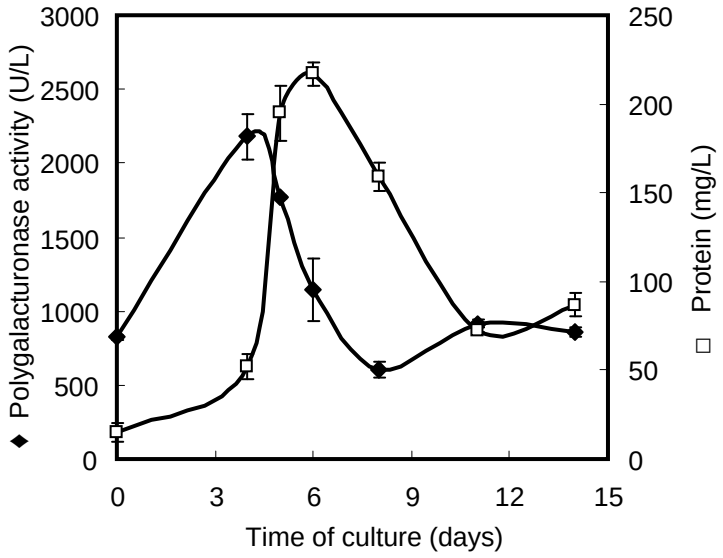

Figure 1 – Total protein content and polygalacturonase activity in shaken cultures of *P. ostreatus* by using tomato pomace as a carbon source which was assayed in culture supernatant of fermentation broth. ♦- Polygalacturonase activity and □ – Protein content.

3.2 Chromatographic behaviour of polygalacturonase, xylanase and laccase on immobilized metal chelates
The chromatographic behaviour of these lignocellulosic enzymes is summarized in Table 1, for different stationary phases (Sepharose 6B-BDGE 30 – IDA, Sepharose 6B-EPI 30–IDA, Sepharose 6B–EPI 10–IDA) as well as for different immobilized metal ions.

Table 1 – Results from adsorption tests of lignocellulosic enzymes from *Pleurotus ostreatus* on immobilized metal chelates.

	pH	Stationary phase	Cu(II)	Ni(II)	Zn(II)	Co(II)
Xylanase	6	BDGE 30, EPI 30, EPI 10	–	–	–	–
	7	BDGE 30, EPI 30, EPI 10	±	–	–	–
	8	BDGE 30, EPI 30, EPI 10	±	–	–	–
Polygalacturonase	6	BDGE 30, EPI 30, EPI 10	+	–	–	–
	7	BDGE 30, EPI 30, EPI 10	+	±	–	–
	8	BDGE 30, EPI 30, EPI 10	+	±	–	–
Laccase	6	BDGE 30, EPI 30, EPI 10	–	–	–	–
	7	BDGE 30, EPI 30, EPI 10	±	–	–	–
	8	BDGE 30, EPI 30, EPI 10	+	–	–	–

3.3 Purification of polygalacturonase by using imidazole in equilibration buffer

The combination of tailor-made stationary phases for IMAC and a correct choice of the adsorption conditions permitted to design a one-step purification procedure for polygalacturonase from *P. ostreatus*. The chromatographic behaviour of polygalacturonase on Sepharose 6B – EPI 30 – IDA-Cu(II) colum at pH 6.0 (Fig.2b) resulted in partially purified enzyme according to the electrophoretic analysis (data not shown). However, the presence of 1mM imidazole in the equilibration buffer abolished the adsorption of several protein contaminants to Sepharose 6B – EPI 30 – IDA- Cu(II) column including laccase and xylanase (data not shown). Hence, polygalacturonase was desorbed from the column with a linear gradient of imidazole (Fig. 2c) with a specific activity of about 1600 U/mg protein, a final recovery of enzyme activity of about 80% and a purification factor of about 65 (Table 3). The purity of chromatographic fractions from Sepharose 6B – EPI 30 – IDA- Cu(II) was analysed by SDS-PAGE which revealed that the purified fractions exhibited two protein bands with Mr of 60 and 70 kDa which was coincident with an activity band of polygalacturonase with Mr of 65 kDa.

Table 3 – Purification of polygalacturonase from *Pleurotus ostreatus* by Immobilized Metal Affinity Chromatography on Sepharose 6B – EPI 30 – IDA - Cu(II) column at pH 6 in the mobile phase containing 1mM imidazole.

	Purification Steps	Total protein (mg)	Total activity (IU)	Specific activity (IU/mg protein)	Recovery (%)	Purification factor
1.	Culture supernatant	0.881	21.24	24.109	100	1
2.	EPI 30-Cu (II) column eluate	0.0109	17.3	1587.1	81.4	65.8

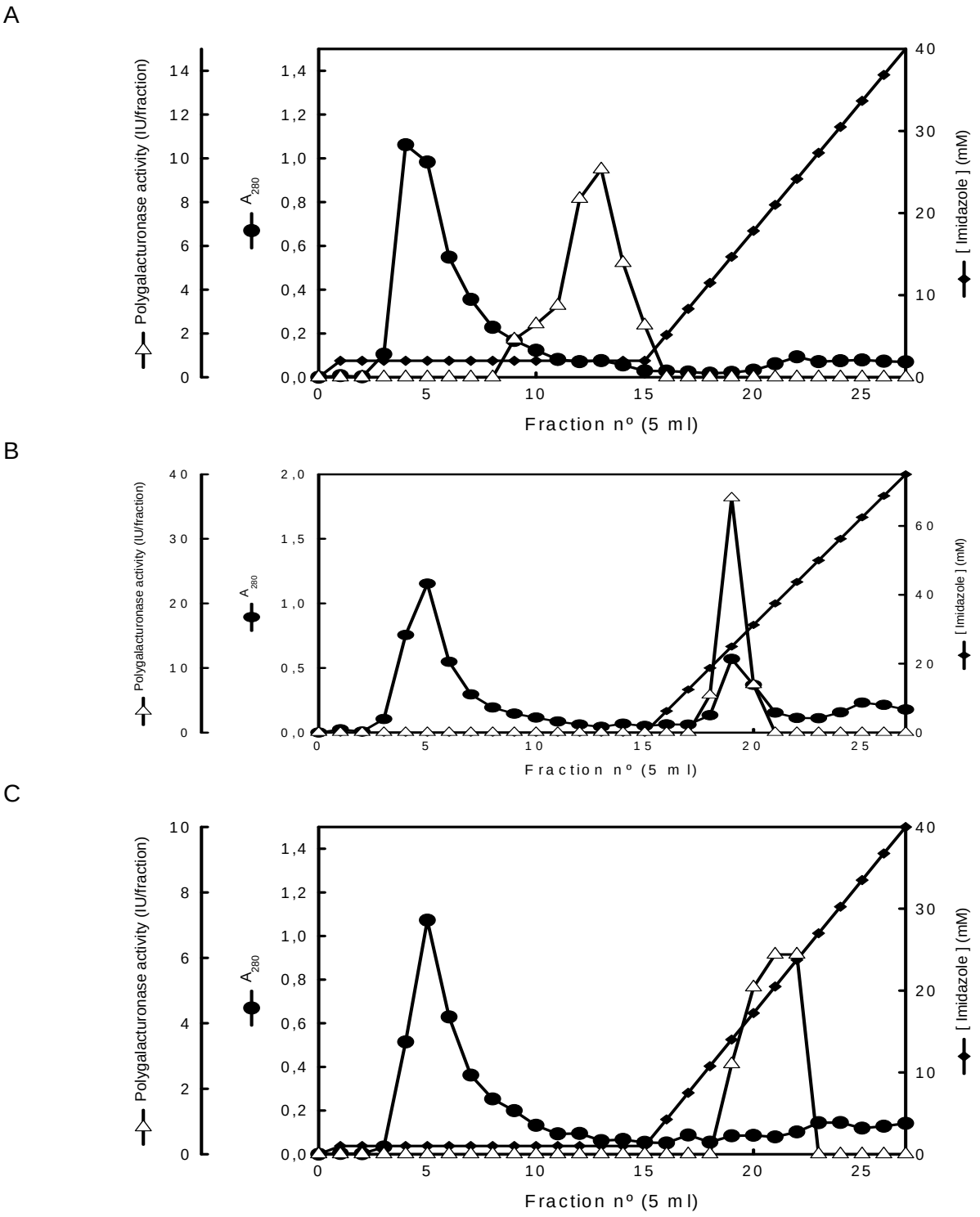

Figure 2 - Chromatographic behaviour of polygalacturonase from *P. ostreatus* on a Sepharose 6B–EPI-30–IDA-Cu(II) column at pH 6.0, as described in Materials and Methods. A- 2mM imidazole in the mobile phase (i.e equilibration buffer); B- No imidazole in the mobile phase and C- 1mM imidazole in the mobile phase.

3.4 Kinetic characterization of purified enzyme

The purified preparation of polygalacturonase exhibited an optimum pH of activity at pH 7.0, in both MES and citrate buffer. On the other hand, the optimum temperature of activity for this enzyme

was found to be at 50ºC in MES buffer at pH 7.0. As far as literature is concerned, in general, fungal polygalacturonases exhibited optimum pH in the acidic range of 3.8 – 4.6 and optimum temperature in the range of 40-60˚C. Therefore, polygalacturonase from *P. ostreatus* exhibited a higher optimum pH of activity than other enzymes from different microbial sources and moreover it is catalytically active at slightly alkaline pH which may be of great advantage for some industrial applications of this enzyme in biocatalysis.

The thermal stability of the purified enzyme was investigated at 50ºC both in citrate buffer at pH 6 as well as in MES buffer at pH 7 which revealed half life ($t_{½}$) values of 60 ± 7.45 min and 35 ± 0.37 min, respectively. These data are within the values reported in the literature for fungal polygalacturonases.

The kinetic parameters (V_{max}, K_m, K_{cat}, and K_{cat}/K_m) of the purified enzyme were found to be 5530.8 ± 260.7 U/mg of protein, 13.23 ±2.79 mg/ml of polygalacturonic acid, 5553.01 ± 261.7 s^{-1} and 419.72 $s^{-1}.mg^{-1}$, respectively at 50˚C in MES buffer and pH 7. The Km values for polygalacturonic acid for the enzymes from *Aspergillus níger* are usually lower in the range of 0.15 - 7.2 mg/ml whereas polygalacturonases from other fungal strains exhibited higher values, namely 5.77 and 11.55 mg/ml from *Sclerotium rolfsii* and 2.3 mg/ml from *Trichosporon penicillatum* SNO-3. As far as V_{max} values are concerned, a range of 828 - 24900 IU/mg protein have been reported in the literature for the enzyme from *Aspergillus níger* and *Trichosporon penicillatum,* respectively.

Acknowledgements

MRF is grateful to Évora University for finantial support and the authors thank FCT for partial financial support (Research Unit 702, POCTI/EQU/48812/2002) as well as Instituto Politécnico de Lisboa (Research Grant No. 25/2003).

References

Alvarado, A., Pacheco-Delahaye, E., Hevia, P. (2001). Value of a tomato byproduct as a source of dietary fiber in rats. Plant Foods for Hum Nutr, 56, 335-348.

Knoblich, M., Anderson, B., Latshaw, D. (2005). Analyses of tomato peel and seed byproducts and their use as a source of carotenoids. J Sci Food Agric, 75, 1166-1170.

Valle, M.D., Cámara, M., Torija, M.E. (2006). Chemical characterization of tomato pomace. J Sci Food Agric, 86, 1232-1236.

Jayani, R.S., Saxena, S., Gupta, R. (2005). Microbial pectinolytic enzymes: A review. Process Biochem, 40, 2931-2944.

Gummadi, S.N., Panda, T. (2003). Purification and biochemical properties of microbial pectinases – a review. Process Biochem, 38, 987-996.

Levin, L., Forchiassin, F. (1998). Culture conditions for the production of pectinolytic enzymes by the white-rot fungus *Coriolus troggi* on a laboratory scale. Acta Biotechnological, 18, 157-166.

Porath, J. (1992). Immobilized metal ion affinity chromatography. Protein Expr Purif;, 3, 1-7.

Gutiérrez, R., Valle, E.M.M., Galán, M.A. (2007). Immobilized Metal-Ion Affinity Chromatography: Status and Trends. Separation & Purification Reviews, 36, 71-111.

Martins, S., Andrade, J., Karmali, A., Serralheiro, M.L. (2006). Screening of suitable immobilized metal chelates for adsorption of monoclonal antibodies against mutant amidase from *Pseudomonas aeruginosa*. J Mol Recognit, 19, 340-347.

Freixo, M.R., Karmali, A., Arteiro, J.M. (2008). Production and chromatographic behaviour of polygalacturonase from *Pleurotus ostreatus* on immobilized metal chelates. Process Biochem, 43:531-539.

Proceedings of the 10th International Chemical and
Biological Engineering Conference - CHEMPOR 2008
Braga, Portugal, September 4-6, 2008
E.C. Ferreira and M. Mota (Eds.)

Procyanidin Average Degree of Polymerization

Cláudia P. Passos[1*], Susana M. Cardoso[3], António S. Barros[2], Carlos M. Silva[1], Manuel A. Coimbra[2]

[1]CICECO, Departamento de Química, Universidade de Aveiro, 3810-193 Aveiro, Portugal

[2] Departamento de Química, Universidade de Aveiro, 3810-193 Aveiro, Portugal

[3] CIMO/Escola Superior Agrária, Instituto Politécnico de Bragança, Campus de Santa Apolónia, 5301-854 Bragança, Portugal

Keywords*:* Procyanidins, DPn, FT-IR spectroscopy, O-PLS, PLS1, grape seed.

Topic: Integration of life sciences & engineering.

Abstract

In this work, procyanidins were extracted with methanol and acetone/water from seeds of white and red grape varieties. A fractionation by graded methanol/chloroform precipitations permitted to obtain 28 samples that were characterised using thiolysis as pre-treatment followed by HPLC-UV detection; and by FT-IR spectroscopy within the region of 1300-800 cm^{-1}. By applying Orthogonal Projection to Latent Structures (O-PLS) as a generic data pre-treatment in tandem with a PLS1 regression, a robustness model for the prediction of the DPn of procyanidins is presented.

1. Introduction

Grape seeds are known as an abundant rich source of procyanidins formed by both (+)-catechin and (-)-epicatechin monomers (Escribano-Bailon et al., 1992), as well as by more polymerized fractions containing type-A and type-B procyanidin linkages (Passos et al., 2007) (**Figure 1**).

* Corresponding author. Tel + 351-234-401549. E-mail: cpassos@ua.pt

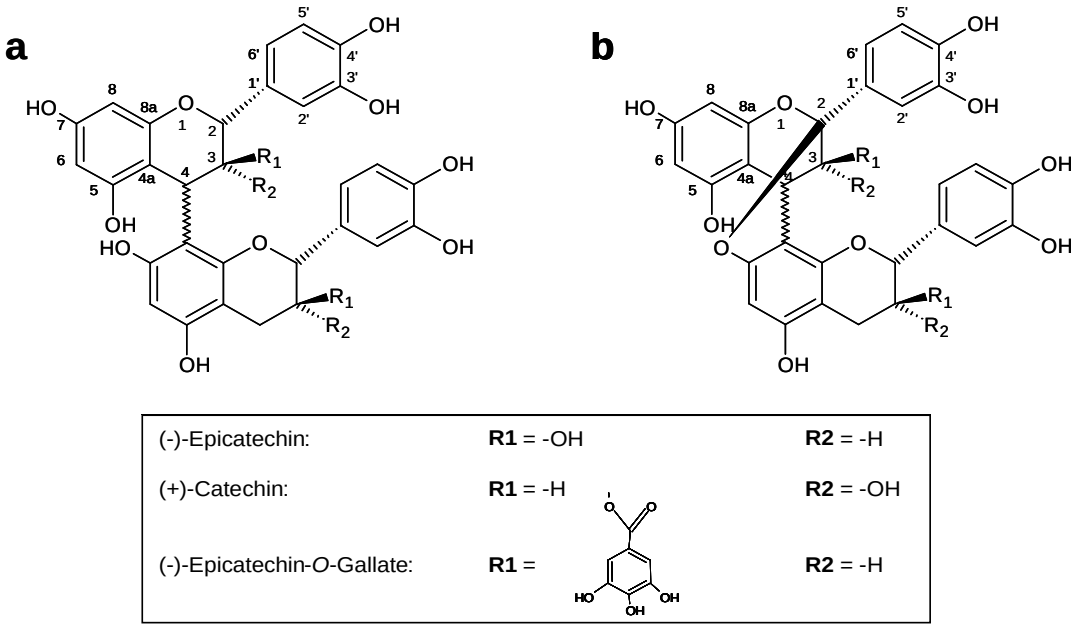

Figure 1. Structure of procyanidin dimers: (a) type-B,containing (C4-C8) interflavanic linkage and (b) type-A containing (C4-C8) interflavanic linkage (Passos et al., 2007).

Although the polymerized fractions represent more than 70% of all procyanidins, they have been only easily quantified up to tetramers (Monagas et al., 2003) . The interest upon the knowledge of their degree of polymerization has influenced the application of conventional experimental methods to assess them. For the calculation of DPn, the polymerized compounds are converted into monomers corresponding to the terminal and extension composing units of the polymer. This calculation however, is complex as it relies in previous preparation methods, (the most commonly used based on acid-catalysed degradations in the presence of nucleophilic agents), followed by characterization on reverse-phase HPLC with UV detection at 280nm (Guyot et al., 1998).

At the same time, growing interest is focused upon the development of faster, cheaper and cleaner methodologies. Nowadays, infrared spectroscopy appears as a very useful tool to accomplish a rapid evaluation, being a widespread technique in food components. Chemometric methods allow the extraction of useful information from high complex samples, among which the multivariate regression methods are widely used to build calibration models. Partial Least Squares (PLS) regression (Wold et al., 1983) is one of the most adopted. The PLS algorithm is based on a bilinear model, where the information contained in the *X* data matrix is projected over a small number of "latent" variables known as PLS components. The interpretation of the relationships between the *X* and *Y* data is simplified to the relationships between the smaller number of PLS components (Barros et al., 2004), (Guillen et al., 2005).

2. Experimental

2.1. Plant Material.

Seeds were collected from grapes (*Vitis vinifera* L.) of the white variety 'Chardonnay' at technological maturity, in Bairrada Appellation, from an experimental vineyard (Estação Vitivinícola da Bairrada, Anadia, Portugal), during transfer of the musts for wine fermentation.

A mixture of red grape varieties 'Touriga Nacional', 'Touriga Francesa' and 'Tinta Roriz', were also provided by wine producers of Adega Cooperativa de Pinhel (Pinhel, Portugal). The remaining pulp and skins were separated from seeds by decantation and sieving (pore size <2.8 mm diameter). The seeds were then submitted to several wash cycles with water (200 g/L) under gentle stirring with a magnetic bar at 4 ºC during a minimum of 3 days, with two water exchanges a day, until a minimum turbidity was constant, assuring that no remaining adherent tissues were present. The purified seeds were then washed with ethanol, air dried at room temperature, and stored at 4 ºC until further analysis.

2.2. Procyanidin Extracts.

Seeds were immersed into liquid nitrogen, milled in a domestic coffee mill and sieved (pore size <0.75 mm diameter). The extraction methodology was adapted from Guyot et al., (1998), followed by a methanol/chloroform graded precipitations according to the proposed by Saucier et al., (2001) and presented in **Scheme 1**.

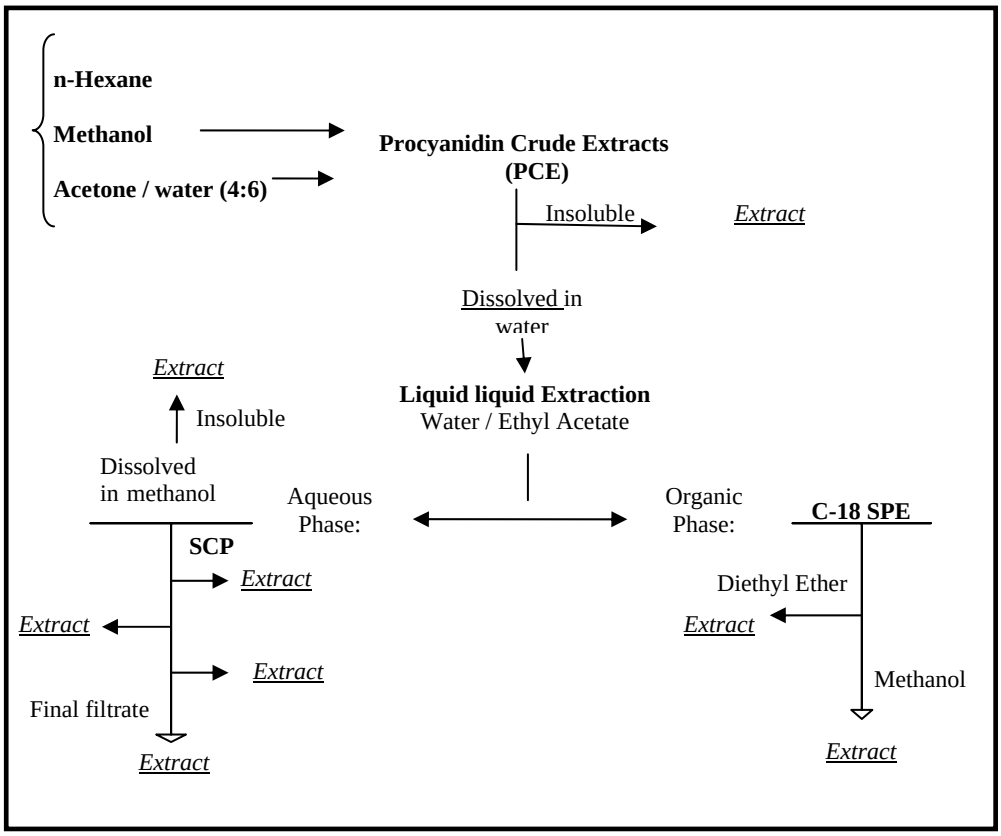

Scheme 1- Extraction and fractionation of grape seed flavan-3-ols. SPE: Solid Phase Extraction; SCP: Sequential Chloroform Precipitations.

Seed powder was extracted three times with *n*-hexane to remove the lipids. It was then treated three times with methanol containing 5% acetic acid to extract the phenolic compounds. The phenolic extracts were combined and filtered through a G3 sintered glass filter, and rotary-evaporated under vacuum at 40 ºC. The resultant concentrated aqueous solutions were submitted to the same treatment as for the methanol extraction but now using 5% acetic acid in an acetone/water (4/6) solution, combined the several parts, filtered with G3 glass filter, rotary-evaporated and freeze-dried as explained.

The PCE extracts from white and red grape seeds were then fractionated by dissolving the PCE powder (10 g/L) in 5% acetic acid. The undissolved material was removed by centrifugation and the supernatant was submitted three times to a liquid-liquid extraction with ethyl acetate, using a water/ethyl acetate ratio of 6:4 (v/v), resulting in an organic phase and an aqueous phase. The organic phase was concentrated, and submitted to a C18 solid phase extraction column (SPE-C18, SPE, Supelco-Discovery – 5g) by eluting with diethyl ether and methanol. The aqueous phase was evaporated to dryness and redissolved in methanol (10 g/L). The supernatant was submitted to successive additions of chloroform until the formation of a new precipitate, and then collected by centrifugation, rotary-evaporated and freeze-dried.

2.3. HPLC-UV analysis

HPLC analysis followed the conditions described by Peng et al., (2001). The HPLC apparatus used was from Perkin Elmer (series 200), with UV-Vis Detector (785A UV-VIS Detector). Samples were loaded at 30 ºC into a C_{18} column (LichroCart 250-4 Superspher 100 RP-18) equipped with a C_{18} guard cartridge with the same packing material equilibrated with 0.2% (v/v) formic acid (eluent A). Phenolic compounds were eluted by a gradient with 82% (v/v) acetonitrile and 0.04% (v/v) formic acid (eluent B) from 0 to 15% eluent B in the first 15 min; 15 to 16% from 15 to 40 min; 16 to 17% from 40 to 45 min; 17 to 43% from 45 to 48 min; 43 to 52% from 48 to 49 min, held isocratic at 52% from 49 to 56 min, reduced from 52 to 43% from 56 to 57 min, reduced from 43 to 17% from 57 to 58 min, and reduced from 17 to 0% from 58 to 60 min. Samples were loaded, at least, in duplicate. Peaks were detected at 280 nm and the monomers and procyanidin B2 dimer were identified by comparison of their retention times with standards. The epicatechin thioderivative was identified by comparison with the retention time of the products of procyanidin B2 dimer after thiolysis; the catechin and epicatechin-*O*-gallate thioderivatives were identified by their retention times and abundance and confirmed by analysis of their mass spectra. The average degree of polymerization was calculated as the ratio of all the flavan-3-ols units areas (thioether adducts plus terminal units) to the sum of the areas of catechin, epicatechin and epicatechin-*O*-gallate, corresponding to terminal units.

2.4. FT-IR spectroscopy and multivariate analyses

The FT-IR spectra were obtained using a Golden Gate single reflection diamond ATR system in a Bruker IFS-55 spectrometer. The spectra were recorded at the absorvance mode from 4000 to 400 cm^{-1} (mid infrared region) at the resolution of 8 cm^{-1}. Five replicate spectra (140 co-added scans) were collected for each sample. The measured spectra were transferred via a JCAMP.DX format into the data analysis software developed in the Institut National Agronomique Paris-Grignon in collaboration with the University of Aveiro (1999). The multivariate calibration was applied in the 1300-800 cm^{-1} region. Each spectrum was previously SNV (Standard Normal Deviates) corrected.

In order to build the calibration model for the quantification of DPn parameter a Monte Carlo cross-validation (Xu and Liang, 2001) framework was used. The dataset was split into a calibration (learning set) and a validation (external) set to assess the predictive power of the DPn model. The dimensionality of the calibration model was assessed by internal-cross validation at each iteration level, with the leave-5-out procedure. Then these models were used to predict the parameters of interest from the external set, expressed as root mean square error of prediction (RMSEP).

3. Results and discussion

3.1. Characterisation of grape seed procyanidin extracts

The dataset of procyanidin samples used in this study were composed by 28 samples from seeds of white and red grapes. The flavan-3-ols samples are constituted by monomers of catechin, epicatechin and epicatechin-*O*-gallate, and procyanidins (oligomers, and polymers) with the same constituting units. The samples, resulting from the fractionation process (according to the **Scheme 1**), resulted in a range of DPn from 1 to 11; while the chloroform graded precipitations (apparently related to a decrease in the DPn range) decreasing from DPn 10 to 1 with increasing chloroform percentage in the precipitation scheme. The region to be considered for the flavan-3-ols characterization, is represented as the region between 1300-800 cm^{-1} were substitution of the aromatic ring appears (Ramos-Tejada et. al., 2002).

3.2. Calibration models for procyanidin DPn in grape seed extracts

Using the 1300 and 800 cm^{-1} region of the FT-IR spectra, a PLS1 regression procedure has been applied to 140 FT-IR spectra (five spectra per sample) of procyanidin rich extracts for the estimation of DPn. It was necessary to have a calibration model with 12 Latent Variables (LVs), using an internal-cross validation (leave-5-out) procedure, to have a predictive power of the model using the PLS1 for the estimation of the DPn parameter. However, the relative high number of LVs introduces difficulties in the interpretation of the **b** vector profile, which may reveal a weakness of the model In these cases, it is a common approach to use different data pre-treatments to reduce the effect of variability non related to the factor of interest. One of the most powerful data pre-treatment used for removing unwanted variations is the O-PLS (Orthogonal Projections to Latent Structures) (Trygg, 2002). It resulted in a predictive O-PLS1 model with 1 LV, giving a RMSECV of 14.0%, with a R^2 of 0.89 and a RMSEP of 2.1. The final results exhibit a good linear relationship as Figure 2 points out, where the relationship between measured and estimated DPn values is plotted.

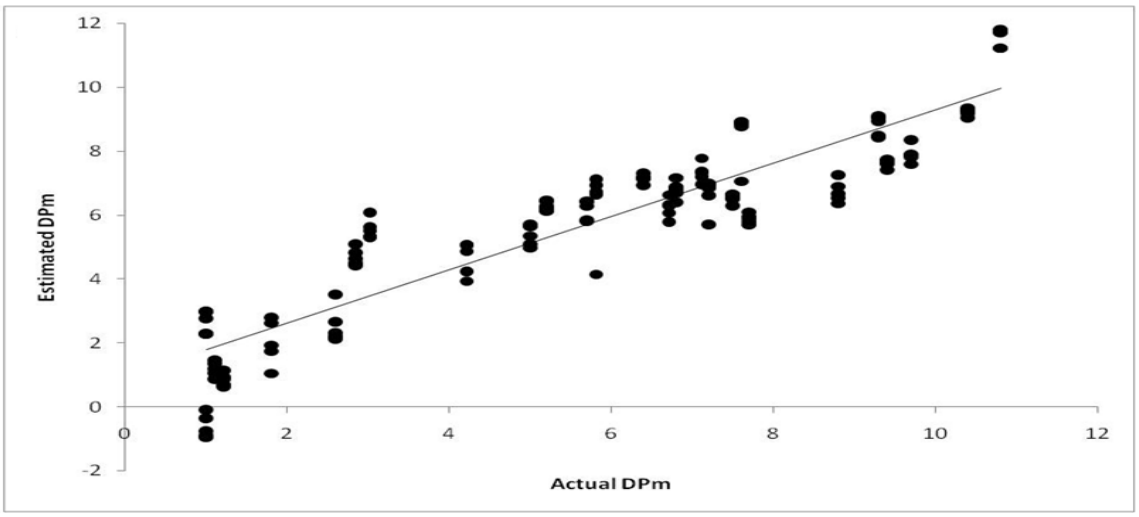

Figure 3-: Relationship between measured *versus* estimated DPn values (Regression model using O-PLS).

4. Concluding remarks.

The need for testing fast and cheap but reliable methodologies has been the base of the present work. The fractionation methodology gave the number and representative samples required to build a FT-IR model for the DPn determination. Using the resulting calibration curve it is possible to characterize grape seed procyanidins in terms of DPn.

References

Escribano-Bailon, T., Gutierrez-Fernandez, Y., Rivas-Gonzalo, J.C., Santos-Buelga. C. (1992). Characterization of procyanidins of Vitis vinifera variety Tinta del Pais grape seeds. *Journal of Agricultural and Food Chemistry*, 40, 1794-1799.

Passos, C.P., Cardoso, S.M., Domingues, M.R.M., Domingues, P., Silva, C.M., Coimbra, M.A. (2007). Evidence for galloylated type-A procyanidins in grape seeds. *Food Chemistry,* 105, 1457-1467.

Monagas, M. , Gomez-Cordoves, C., Bartolome, B., Laureano, O., Ricardo da Silva. J.M. (2003). Monomeric, Oligomeric, and Polymeric Flavan-3-ol Composition of Wines and Grapes from *Vitis vinifera.* L. Cv. Graciano, Tempranillo, and Cabernet Sauvignon. *Journal of Agricultural and Food Chemistry*, 51, 6475-6481.

Guyot, S., Marnet, N., Laraba, D., Sanoner, P., Drilleau, J.F. (1998). Reversed-Phase HPLC following Thiolysis for Quantitative Estimation and Characterization of the Four Main Classes of Phenolic Compounds in Different Tissue Zones of a French Cider Apple Variety (Malus domestica Var. Kermerrien). *Journal of Agricultural and Food Chemistry*, 46, 1698-1705.

Wold, S., Martens, H., Wold, H. in: Ruhe, A., Kagstrom, B. (Eds.) (1983), *Lecture Notes in Mathematics 1983.* Proceedings of the Conference Matrix Pencils, March 1982, Springer Verlag, Heidelberg, p. 286.

Barros, A.S., Rutledge, D.N. (2004*).* Principal components transform-partial least squares: a novel method to accelerate cross-validation in PLS regression. *Chemometrics and Intelligent Laboratory Systems*, 73, 245-255.

Guillen, D.A., Palma, M., Natera, R., Romero, R., Barroso, C.G. (2005). Determination of the Age of Sherry Wines by Regression Techniques Using Routine Parameters and Phenolic and Volatile Compounds. *Journal of Agricultural and Food Chemistry,* 53, 2412-2417.

Saucier, C., Mirabel, M., Daviaud, F., Longieras, A., Glories, Y. (2001). Rapid Fractionation of Grape Seed Proanthocyanidins. *Journal of Agricultural and Food Chemistry,* 49, 5732-5735.

Peng, Z., Hayasaka, Y., Iland, P.G., Sefton, M., Hoj, P., Waters, E.J. (2001). Quantitative Analysis of Polymeric Procyanidins (Tannins) from Grape (Vitis vinifera) Seeds by Reverse Phase High-Performance Liquid Chromatography*. Journal of Agricultural and Food Chemistry,* 49, 26-31.

Barros, A.S. (1999). Contribution à la sélection et la comparaison de variables caractéristiques. *Institut National Agronomique Paris-Grignon*, France, p. Chapter 1.

Xu, Q.-S., Liang, Y. Z. (2001). Monte Carlo cross validation. *Chemometrics and Intelligent Laboratory Systems*, 56, 1-11.

Ramos-Tejada, M.M. Duran, J.D.G. Ontiveros-Ortega, A. Espinosa-Jimenez, M. Perea-Carpio, E. Chibowski, Colloids and Surfaces B: Biointerfaces, 24 (2002) 297.

Johan Trygg, S. S.W. Orthogonal projections to latent structures (O-PLS). *Journal of Chemometrics*, (2002), 16, 119-128.

Proceedings of the 10th International Chemical and
Biological Engineering Conference - CHEMPOR 2008
Braga, Portugal, September 4-6, 2008
E.C. Ferreira and M. Mota (Eds.)

One-step purification of hemoglobin from human erythrocytes by using a novel chromatographic matrix based on polymer-bound calix[6]arenes

Magda C. Semedo, Amin Karmali[1]*, Patrícia D. Barata and José V. Prata

CIEQB - Chemical Engineering and Biotechnology Research Center and Department of Chemical Engineering of Instituto Superior de Engenharia de Lisboa
Rua Conselheiro Emídio Navarro, 1959-007 Lisboa, Portugal.

Keywords: Chromatographic matrix; *p-tert*-butylcalix[6]arene; polymer; purification of hemoglobin; human erythrocytes; pseudoactivity of peroxidase.
Topic: Integration of life sciences & engineering.

ABSTRACT

Calixarenes are host molecules which exhibit molecular recognition towards a wide range of guest bioactive substances such as amino acids, proteins and carbohydrates. Calix[n]arenes consist of cavity-shaped architecture which can form host-guest complex with a wide range of guest molecules by introducing several functional groups either at the upper or lower rim.
The present work involves the use of a novel chromatographic matrix based on repeating units of *p-tert*-butylcalix[6]arene carboxylic acids for one-step isolation of haemoglobin from human erythrocytes. The red cell lysate was applied to a column packed with this matrix which was previously equilibrated in phosphate buffer. The adsorbed proteins were eluted from the column with a linear gradient of Na_2CO_3 pH 11.0 and the column fractions were analysed for protein and pseudo-activity of peroxidase. Human haemoglobin was purified in a one-step procedure with a recovery of pseudo-activity of about 35% and a purification factor of about 12. The purified haemoglobin was analysed both by SDS and native PAGE which exhibited single proteins bands with Mr of 16.0 and 61.0 kDa, respectively. Furthermore, the single protein band observed in native PAGE was coincident with the pseudo-activity of peroxidase band detected *in situ* on this gel. Protein adsorption on this novel chromatographic matrix involved several interactions such as electrostatic and hydrophobic and other parameters affected this process such as protein size, pI, pH, ionic strength and nature of buffer.

These results strongly suggest that this novel chromatographic matrix presents some advantages over other matrices as far as selectivity is concerned for protein purification.

INTRODUCTION

Calix[n]arenes are one of the major classes of macrocyclic host compounds in supramolecular chemistry, which exhibit molecular recognition towards a wide range of bioactive molecules such as amino acids, peptides and proteins, lectins, enzymes, nucleotides, saccharides and steroids. (Shimojo *et al.*, 2007 and Ludwig, 2005). These host compounds can be synthesized with a large choice of functional groups which exhibit differential affinity for guest molecules. Calixarenes are widely used in several applications namely as sensor devices, in nuclear waste treatment, as catalyst in synthetic reactions, biocatalysis and in liquid crystals (Gutsche, 1995 and Barata, 2004).

The unit operations involved in downstream processing of recombinant proteins and monoclonal antibodies are extremely expensive since they account for about 80 - 90% of total production cost. Therefore, there is a great interest to synthesize novel chromatographic

[1*] Corresponding author. E-mail: akarmali@deq.isel.ipl.pt.

matrices for protein purification in a single step with a high recovery of biological activity and purity. The complexing abilities exhibited by calixarenes has stimulated their potential use as molecular and biomolecular receptors immobilized on an existing polymeric matrix, for which appropriate grafting methods have been developed (Barata *et al.*, 2004). Therefore, the present work involves the use of a novel chromatographic matrix based on a polymer-bound acid derivative of *p-tert*-butylcalix[6]arene for one-step isolation of haemoglobin from human erythrocytes.

MATERIALS AND METHODS

Materials

The chromatographic matrix based on a Merrifield's resin containing units of acid derivative of *p-tert*-butylcalix[6]arene (Figure1) was synthesised according to procedures described previously (Barata, 2004). The blood was collected from one of the authors of this work and all other chemicals were of analytical grade.

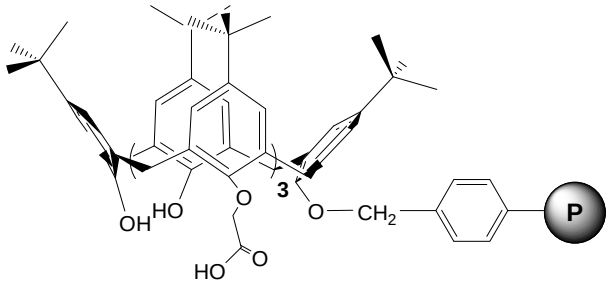

Figure 1 – Merrifield's resin containing units of acid derivative of *p-tert*-butylcalix[6]arene (PC6) structure.

Methods

Initial Treatment of Human Blood

Human blood was collected and stored at 4ºC for about 16 h. The erythrocytes were separated and washed as described by Karmali (1983) and the red cells (5 mL) were lysed with 4 volumes of deionised water and the pH of the mixture adjusted to 5.8 with 0.1N HCl and the stroma was removed by centrifugation at 15000 rpm for 30 min at 4ºC.

Purification of Hb A from human erythrocytes on Polymer-bound Acid Derivative of p-tert-Butylcalix[6]arene

Polymer-bound acid derivative of *p-tert*-butylcalix[6]arene (501 mg) was used as chromatographic matrix which was prepared by adding 6mL of $CHCl_3$. After stirring for 45 min, the solvent was removed and the chromatographic support was washed with 50 mM phosphate buffer at pH 6.5 (12 mL).

The column (1 × 5 cm) containing 2 mL of chromatographic matrix, was equilibrated with 50 mM phosphate buffer pH 6,5 (10 volumes)m and red cell lysate (diluted 1:10) was applied to the column at a flow rate of 16 mL/h. The column was washed with the same buffer system until A_{280} was less than 0,05 and adsorbed proteins were eluted from the column with 100 mM Na_2CO_3 pH 11.0, at a flow rate of 25 mL/h. The eluted fractions (0.75 mL) were collected in test tubes containing previously 50 mM citrate buffer pH 3.5 in order to adjust the pH to 7.0. The fractions were analysed for protein and pseudoperoxidase activity and those fractions exhibit enzyme activity were pooled and concentrated by ultrafiltration with a P10 membrane at 4ºC.

Electrophoretic Analysis

SDS-PAGE of red cell lysate and purified Hb A was carried out as described previously (Laemmli, 1970) and stained for protein with silver nitrate (Sasse and Gallagher, 2003).

Native PAGE of protein samples was performed as reported previously (Hames, 1990) and stained for protein with silver nitrate. The specific detection of pseudoactivity of peroxidase of Hb A *in situ* in native PAGE was carried out by using syringaldazine and hydrogen peroxide (Semedo, 2008).

Protein Assay

Protein concentration was determined by Coomassie blue dye binding method by using BSA as the protein standard (Sedmak and Grossberg, 1977).

Assay of Pseudoperoxidase Activity of Hb A

The pseudoperoxidase activity of Hb A was assayed by using syringaldazine (Syr) and H_2O_2 as substrates as described previously (Renaldo *et al.*, 1981 and Goldberg *et al.*, 1983). The assay of pseudoactivity of Hb A was carried out by using 15 μL of 1mM Syr dissolved in ethanol, 3 μL of 0.8mM H_2O_2, 262 μL of 50 mM phosphate buffer pH 6.5 and 50 μL of Hb A samples. The enzyme reaction was followed in a microtiter plate reader (Bio-Rad 680) at 550 nm due to oxidation of Syr to corresponding quinone at room temperature. One enzyme unit is defined as the amount of Hb A required to convert one μmole substrate into product per min under these experimental conditions.

RESULTS AND DISCUSSION

Hb A from human erythrocytes was purified in a single step procedure on a column packed with PC6 chromatographic matrix. The protein was desorbed from the column with 0.1 M Na_2CO_3 pH 11 (Figure 2) since buffers with neutral pH were not effective as elution agents (data not shown).

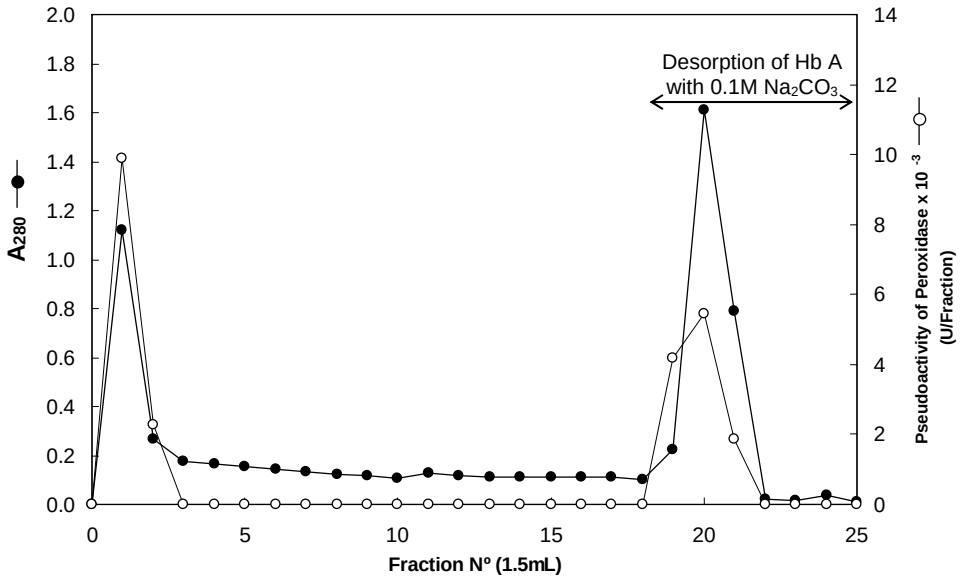

Figure 2 – Purification of Hb A from human erythrocytes, applied to a column packed with PC6.

Hb A was purified human red lysate with a final recovery of enzyme activity of about 40%, specific activity of 0.06 U/mg protein and a purification factor of 33 (Table 1).

Table 1 – One-step purification of Hb A from human blood by using a chromatographic matrix of polymer containing units of acid derivative of *p-tert*-butylcalix[6]arene.

PURIFICATIONS STEPS	TOTAL PROTEIN (mg)	TOTAL ACTIVITY (U)	SPECIFIC ACTIVITY (U/mg protein)	RECOVERY (%)	PURIFICATION FACTOR
1. Blood lysate	16.45	3.00×10^{-2}	1.82×10^{-3}	100	1
2. Column eluate	0.19	1.14×10^{-2}	6.00×10^{-2}	38	33

However, significant pseudoperoxidase activity was detected in washing fractions which suggests saturation of the chromatographic matrix. On the other hand, the purification factor obtained in the present work is apparently high since Hb A represents about 75% of total red cell protein. This discrepancy may be due to the fact that the purification factor was calculated as a function of pseudoperoxidase activity of Hb A and not as a function of Hb A concentration as reported in most of research work on Hb A in the literature. Therefore, these data may be explained by either of the following phenomenon or a combination of several factors: a - pseudoactivity of Hb A in red cell lysate may be inhibited due to the presence of metabolites in human erythrocytes; b - HbA may exhibit changes in conformation in red cell lysate with low peroxidase activity and c - the desorption of Hb A from column promoted changes in conformation of the protein which may enhance the pseudoactivity of Hb A compared with red cell lysate.

Based on these explanations, the specific activity of peroxidase of Hb A in red cell lysate exhibited a low value which resulted in a high purification factor (Table 1). Inhibition of enzymes or monoclonal antibodies either in cell-free extract or red cell lysate has been reported by several research workers (Karmali, 1983, Cruz, 1995 and Martins *et al.*, 2007).

As far as data presented in Table 1, it is not possible to compare this data with the literature because there are no reports of purification of Hb A from red cell lysate by using pseudoperoxidase activity of Hb A.

The purified Hb A was analysed by SDS-PAGE which revealed a single protein band with a Mr of 16 kDa which represents the Mr of Hb A subunits (Figure 3). However, native PAGE exhibited a single protein band with a Mr of 58 kDa which was coincident with peroxidase activity band *in situ* (Figure 4).

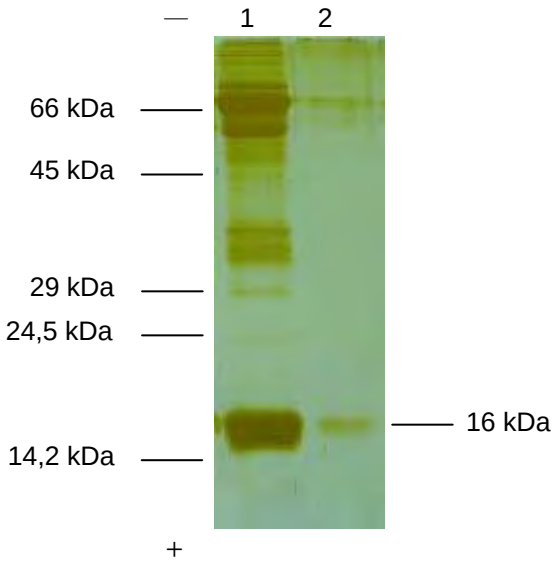

Figure 3 – SDS-PAGE of purified Hb A using a 12.5% separating gel. Lanes: 1 – Lysate blood (14.7 μg); 2 – Fractions Nº 19 to 21 (1.7 μg). The molecular weight of protein markers are presented on the left margin.

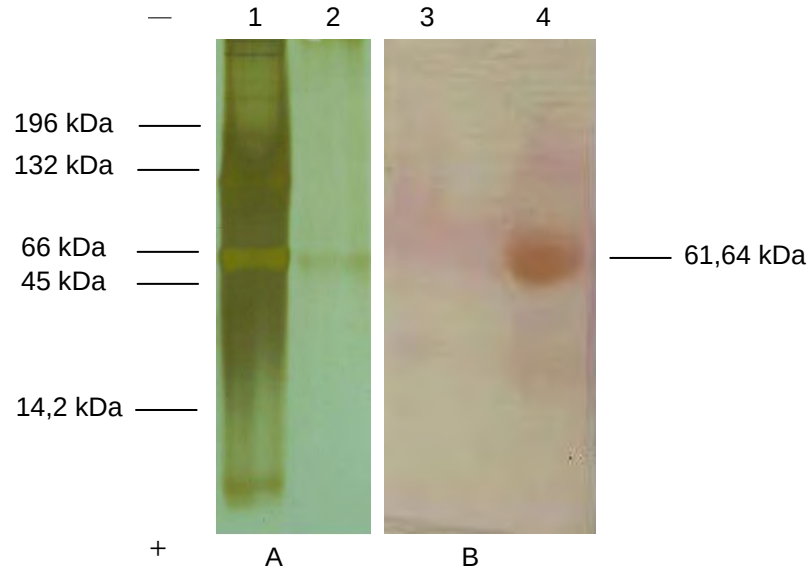

Figure 4 – Native PAGE of purified Hb A using a 7.5% separating gel. A - stained for protein with silver nitrate; B - pseudoactivity of peroxidase of Hb A *in situ*. Lanes: 1 – Lysate blood (3.7 μg); 2 – Fractions Nº 19 to 21 (1.7 μg); 3 - Fractions Nº 19 to 21 (1.67 μg); 4 - Lysate blood (52.8 μg). The molecular weight of protein markers are presented on the left margin.

The results presented in this work strongly suggest that such novel chromatographic matrices are potentially useful as far as protein purification is concerned.

ACKNOWLEDGEMENTS

We acknowledge partial financial support from Instituto Politécnico de Lisboa, Portugal (Research project Nº. 25/2003) and Fundação para a Ciência e a Tecnologia (Unit 702).

REFERENCES

Barata, P. (2004) Polímeros Funcionais Contendo Calixarenos – Síntese e Aplicações. *M.Sc.* Thesis (FCT-UNL, Portugal).

Barata, P. D., Costa, A.I., Granja, P., Prata, J. V. (2004) The synthesis of novel polymer-bound calix[4]arenes. *Reactive & Functional Polymers*, 61, 147-151.

Cruz, F. (1995) Purificação e Caracterização Parcial de Amidase de uma Estirpe Mutante (Ph 1) de *Pseudomonas aeruginosa*. *M.Sc.*Thesis (IST-UTL, Portugal).

Goldberg, R., Catesson, A.-M., Czaninski, Y. (1983) Some properties of syringaldazine oxidase, a peroxidase specifically involved in the lignification processes. *Z. Pflanzenphysiol Bd.*, 110, 267–279.

Gutsche, C.D. (1995) Calixarenes. *Aldrichimia Acta*, 28, 3-9.

Karmali, A. (1983) The Properties of D-Ribulose 5-Phosphate 3-Epimerase from Human Erythrocytes. Ph. D. Thesis (University of London, UK).

Laemmli, U.K. (1970) Cleavage of structural proteins during the assembly of the head of bacteriophage T4. *Nature*, 227, 680 – 685.

Ludwig, R. (2005). Calixarenes for biochemical recognition and separation. *Microchim Acta*,152, 1–19.

Martins, S., Lourenço S., Karmali, A. and Serralheiro, M. L. (2007) Monoclonal antibodies recognize conformational epitopes on wild-type and recombinant mutant amidases from *Pseudomonas aeruginosa*. *Mol. Biotechnol.*, 37, 136-145.

Renaldo, A.F., Bailey, D.T., Nagel, G.M. (1981) Multiple forms of peroxidase from *Narcissus pseudonarcissus*. *Phytochemistry*, 20, 591–595.

Sasse, J., Gallagher, S.R. (2003) Current Protocols in Molecular Biology – Laboratory Manuals. John Wiley & Sons, Inc., New York.

Sedmak, J.J., Grossberg, S.E. (1977) A rapid, sensitive, and versatile assay for protein using Coomassie brilliant blue G250, *Anal. Biochem*., 79, 544-552.
Semedo, M. C. (2008) Utilização de Derivados de Calixarenos no Isolamento de Proteínas e Biocatálise em Solventes Orgânicos. *M.Sc.*Thesis (FC-UL, Portugal).
Shimojo, K., Oshima, T., Naganawa, H., Goto, M. (2007) Calixarene-assisted protein refolding via liquid-liquid extraction. *Biomacromolecules*, 8, 3061-3066.

Proceedings of the 10th International Chemical and
Biological Engineering Conference - CHEMPOR 2008
Braga, Portugal, September 4-6, 2008
E.C. Ferreira and M. Mota (Eds.)

Kinetic resolution of 1,2-epoxyhexane by whole cells of *Rhodotorula glutinis* in a two-liquid phase system

Michiaki Matsumoto*, Takashi Sugimoto, Naoya Wada, Kazuo Kondo
[1] Department of Chemical Engineering and Materials Science, Doshisha University, Kyotanabe, Kyoto 610-0321 JAPAN

Keywords: kinetic resolution, epoxide, two-phase, whole cell, organic solvent
Topic: biochemical engineering.

Abstract

In this research, we examined kinetic resolution of *rac*-epoxides by epoxide hydrolase from *Rhodotorula glutinis* for preparing enantio-pure diol in the presence of organic solvent. Epoxide hydrolase from *Rhodotorula glutinis* ATCC 201718 shows high catalytic activity without being extracted from whole cells, and good enantioselectivity for R-enantiomer was confirmed. The experimental data was explained well by Michaelis Menten model, including distribution of substrate and product inhibition. We examined the effect of organic solvent, initial reaction rates were correlated with the hydropohbicity of organic solvent and enatiometric ratio were correlated with the solubilty parameter. We succeed to improve enantiomeric exess by using inhibition effect of 1-heptanol. These results show possibility of preparing enantiopure diol without complicated chemical treatment.

1 Introduction

Epoxides and diols are important intermediates for pharmaceutical and organic synthetic chemistry, because each enantiomer shows different biological activity. The preparation method for enantiopure epoxides is composed to asymmetric synthesis and kinetic resolution. For the production of enantiopure epoxides, some chemocatalytic and biocatalytic routes have successfully been developed. Recently enzymatic enantioselective degradation of racemic epoxides using epoxide-hydrolases, which are relatively cheap, has been recognized as an alternative to these synthetic routes. The productivity of this biocatalytic route is limited by the low solubility of hydrophobic epoxides to aqueous solution and inhibition of enzymatic reaction at high diol concentration. To resolve these problems, the organic solvent forming two-liquid phase has been used. Decane and octane were selected in resolution of 1,2-epoxyhexane (Choi *et al*., 1999) and styrene oxide (Baldascini *et al.,* 2001), respectively.
In this paper, we examined the kinetic resolution of racemic 1,2-epoxyhexane under the two-liquid phase system. We described the kinetic analysis of this system using dodecane and examined the effect of organic solvent on the initial reaction rate and enatiometric ratio, *E*.

2 Experimental

The yeast, *Rhodotorula glutinis* ATCC201718, was cultivated for 48 h in the medium described previously (Choi *et al.*, 1999) at 30ºC. The cells were harvested by centrifugation and washed with the buffer. Hydrolysis of 1,2-epoxyhexane was conducted in screwed capped bottles sealed with rubber septa. Ten ml cell suspension of *R. glutinis* (0.9 g-drycell/ml) and 10 ml organic solvent containing 1,2-epoxyhexane were added in the bottles. Samples were taken periodically from the organic and aqueous solutions. Organic samples were analyzed by chiral GC. Aqueous samples were extracted with an equal volume of ethylacetate and then analyzed by chiral GC.

* Corresponding author. Phone/Fax + 81-774-656655. E-mail:mmatsumo@mail.doshisha.ac.jp

3 Results and discussion

Figure 1 shows typical results of the time-courses of epoxides and diols in the presence of dodecane. It clearly appeared that *R. glutinis* prefentially hydrolyzed (R)-epoxide and produced (R)-diol.

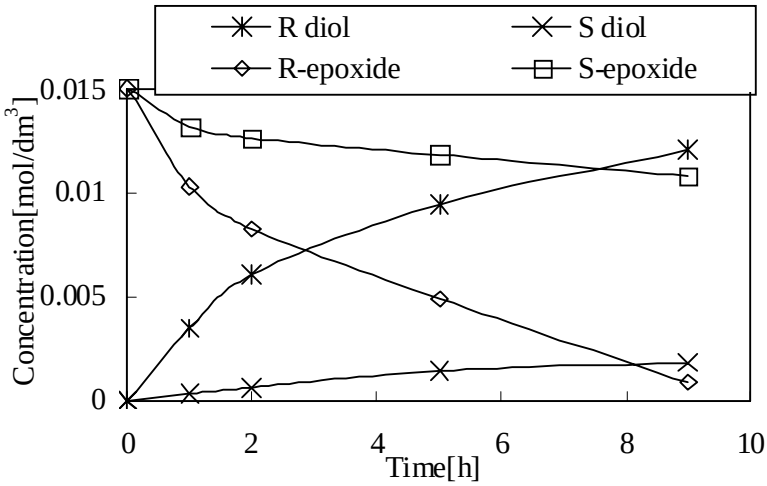

Figure 1 Kinetic resolution of *rac*-1,2-epoxyhexane by *Rhodotorula glutinis* in the presence of n-dodecane

3.1 Kinetics of hydorlysis of 1,2-epoxyhexane in the presence of dodecane

Rates of the enzymatic conversion of both enatiomers in the aqueous solution can be described as equations (1) and (2) by considering competitive Michaelis-Menten kinetics and competitive product inhibition in the view of distribution equilibrium of epoxides.

$$r_{R_0} = \frac{{V_{\max}}^{R}[R]_0}{(1+D){K_m}^{R} + \left(1+\frac{{K_m}^{R}}{{K_m}^{S}}\right)[R]_0 + (1+D){K_m}^{R}\left(\frac{[D_S]_0}{{K_I}^{D_S}} + \frac{[D_R]_0}{{K_I}^{D_R}}\right)} \quad (1)$$

$$r_{S_0} = \frac{{V_{\max}}^{R}[S]_0}{(1+D){K_m}^{S} + \left(1+\frac{{K_m}^{S}}{{K_m}^{R}}\right)[S]_0 + (1+D){K_m}^{S}\left(\frac{[D_S]_0}{{K_I}^{D_S}} + \frac{[D_R]_0}{{K_I}^{D_R}}\right)} \quad (2)$$

We determined the parameters included in above equations by kinetic experiment in the absence and presence of diols in the initial organic solution, and distribution experiment and parameters obtained were shown in Table 1. Unlike in the case of hydrolysis of styrene oxide by *Agrobacterium radiobacter* AD1 (Rink and Janssen, 1998), preference of (R)-enantiomer was caused by the large difference in the maximum velocities of enatiomers.

Table 1 Kinetic parameters

Parameter	Value
${V_{max}}^{R}$	3.41×10^{-2} mol $dm^{-3}h^{-1}$
${V_{max}}^{S}$	1.20×10^{-3} mol $dm^{-3}h^{-1}$
${K_m}^{R}$	6.90×10^{-3} mol dm^{-3}
${K_m}^{S}$	4.25×10^{-3} mol dm^{-3}
${K_I}^{D_R}$	1.80×10^{-2} mol dm^{-3}
${K_I}^{D_S}$	7.33×10^{-1} mol dm^{-3}
D	36 -

3.2 Effect of organic solvents on the reaction rate and enatiometric ratio

We examined the effect of organic solvents on the initial velocities of (R)-enatiomer, r_{R0} and enantiometric ratio, *E*.

Figure 2 shows the relationships between r_{R0} and log *P* of organic solvents. The more hydrophobic solvents, such as dodecane, isooctane gave the higher reaction rate. Hydrophilic alcohols such as hexanol, heptanol were storongly inhibitory to epoxide hydrolase of *R. glutinis*.

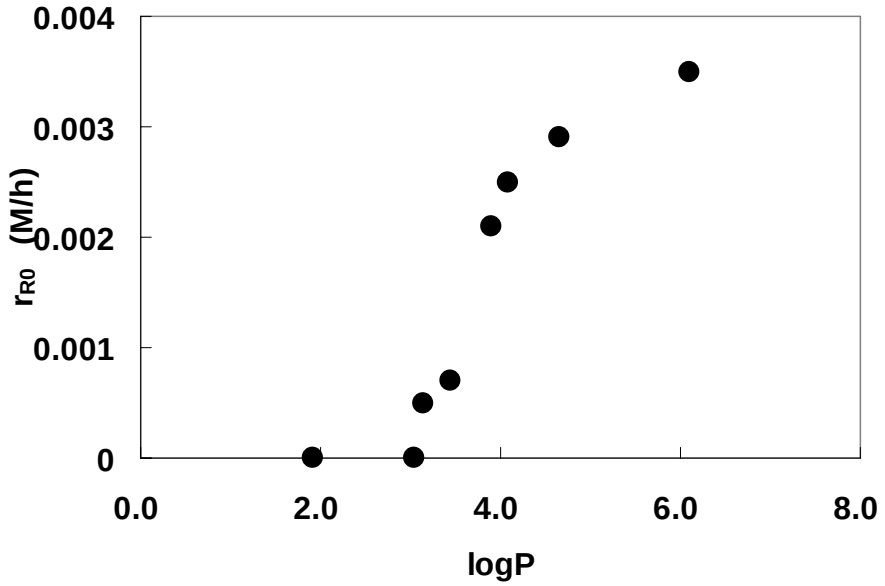

Figure 2 Relationship between r_{R0} and log *P* of organic solvent

Figures 3 shows the relationships between enatiometric ratio *E* and solubility parameters. Enationmetric ratio is defined as following equation.

$$E = \frac{\ln\left[1-\zeta\left(1+ee_p\right)\right]}{\ln\left[1-\zeta\left(1-ee_p\right)\right]} \qquad ee=\frac{R-S}{R+S} \tag{3}$$

where *E* is enantiomeric ratio, ζ is yield, *ee* is enantiomeric exess , and R and S are concentrations of *R*- and *S*- enantiomers, respectively. Solubility parameter δ provides a numerical estimate of the degree of interaction between the solvents and 1,2-epoxyhexane(δ=9.18). Solvents having high solubilty parameters such as higher alcohol, carboxylic acid did not give the high enatioselectivity because of the strong interaction between the solvent and substrate.

For the further improvement of the enantiometric ratio, we examined the effect of addtion of inhibitory compound, 1-heptanol, on the kinetic resolution in the presence of dodecane. Figure 4 shows the relationship between initial production rate of (R,S)-1,2-hexanediol and sustrate concentration. Control denotes the experiment in the presence of dodecane. By adding 1-hexanol (0.017 mol/dm^3), initial production rate of R-1,2-hexanediol a little bit reduced, while it was not detected S-1,2-hexanediol in the reaction mixture, indicating that enatiometric ratio is infinitely large.

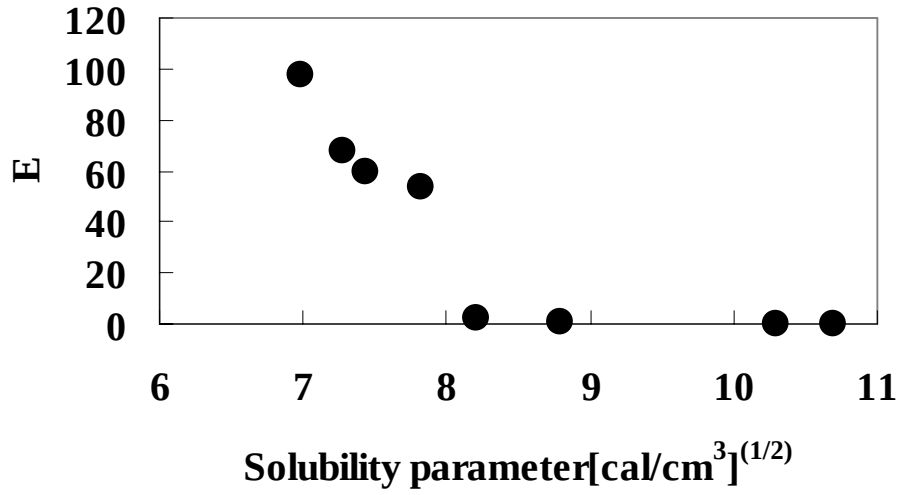

Figure 3 Relationship between enatiometric ratio *E* and solubility parameter of organic solvent

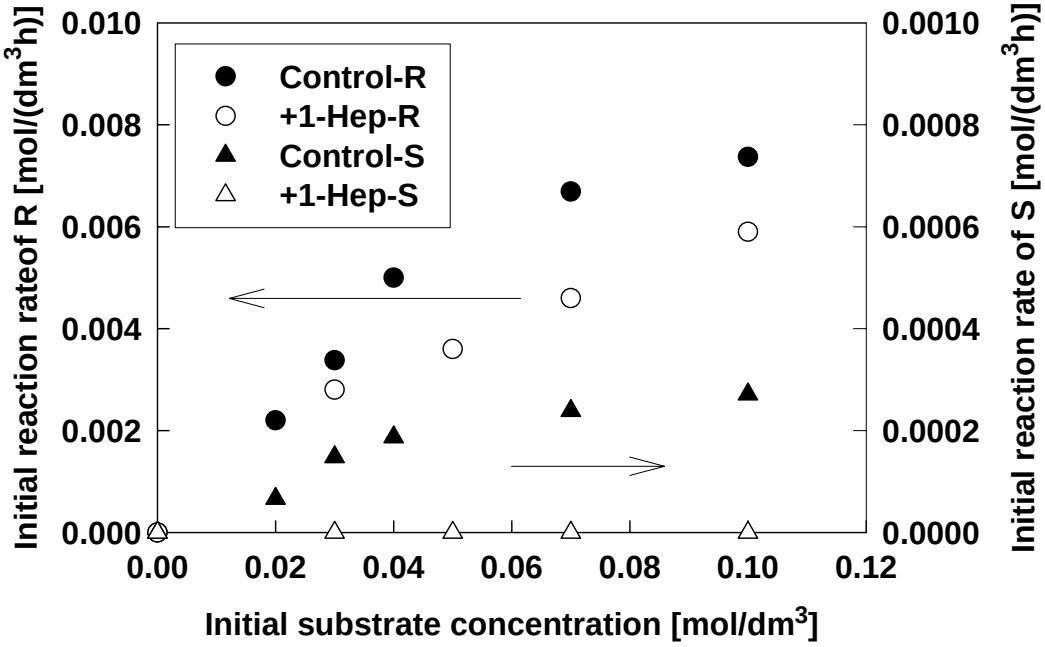

Figure 4 Effect of 1-heptanol on kinetic reslution of epoxyhexane

References

Baldascini, H., Ganzeveld, K.J., Janssen, D.B., Beenackers, A.A.C.M.(2001). Effect of mass transfer limitations on the enzymatic kinetic resolution of epoxides in a two-liquid-phase system. *Biotechnol. Bioeng.*, 73, 44-54.

Choi, W.J., Choi, C.Y., de Bont, J.A.M., Weijers, C.A.G.M. (1999). Resolution of 1,2-epoxy-hexane by *Rhodotorula glutinis* using a two-phase membrane bioreactor. *Appl. Microbial. Biotechnol*., 53, 7-11.

Rink, R., Janssen, D.B. (1998). Kinetic mechanism of the enantioselective conversion of styrene oxide by epoxide hydrolase from *Agrobacterium radiobacter* AD1. *Biochemistry,* 37, 18119-18127.

Proceedings of the 10th International Chemical and
Biological Engineering Conference - CHEMPOR 2008
Braga, Portugal, September 4-6, 2008
E.C. Ferreira and M. Mota (Eds.)

A multipurpose hydrogel system for biocatalyst immobilization

P. Fernandes[1*], Stefano Cattorini[1], Filipe Carvalho[1], Marco P.C. Marques[1], Susana Bernardino[1,2], Filipa Maduro[1], Sara Badenes[1], Dragana Barros[1], Carla C.C.R. Carvalho[1],Luis P. Fonseca[1], Joaquim M.S. Cabral[1]

[1] IBB – Institute for Biotechnology and Bioengineering, Centre for Biological and Chemical Engineering, Instituto Superior Técnico, Av. Rovisco Pais, 1049-001 Lisboa, Portugal. [2] Escola Superior de Tecnologia do Mar de Peniche, Instituto Politécnico de Leiria, Portugal

Keywords: Hydrogels, polyvinyl alcohol, immobilization of enzymes and cells, biotransformations, encapsulation
Topic: Integration of life sciences & engineering.

Abstract

Inulinase, penicillin G acylase, cutinase, *Mycobacterium* sp. NRRL B-3805 and *Rhodococcus erythropolis* DCL14 cells were immobilized in PVA-based hemispherical-shaped capsules, obtained through extrusion into polyethylene glycol, according to a novel method. The immobilized biocatalysts obtained were tested for sucrose hydrolysis, penicillin G hydrolysis, caproic acid esterification with ethanol, sitosterol side-chain cleavage and limonene-1,2-epoxide hydrolysis, respectively. The effect of immobilization in overall biotransformation rate was assessed, as well as the feasibility of biocatalyst reuse. Mass transfer and partition effects were evident upon immobilization, more so in the three latter systems, where an organic phase was used as substrate reservoir/product sink. Immobilized inulinase and penicillin G acylase were effectively reused in 10 consecutive batch runs with no noticeable decay in performance. In the remaining systems tested decay of activity was observed, more noticeably in whole cell systems, as immobilized cutinase was effectively used in three consecutive runs.

Hydrogels are suitable materials for biocatalyst immobilization and concomitant application in biotransformation systems of relevance in important industrial areas, such as food and feed, pharmaceutical, fine chemicals, renewable energy sources and bioremediation (Guisan, 2006). Hydrogels typically present biocompatibility, low coefficient of friction, and high water content. Still, most hydrogels, namely those from natural polymers, have low mechanical stability (Willaert and Baron, 1996) and are furthermore prone to enzyme leakage (Cao, 2005). Polyvinyl alcohol-based matrices have been shown to lead to particles with considerable mechanical stability, and thus present a suitable alternative to overcome the drawbacks of natural polymers while retaining the benefits inherent to their use (Schlieker and Vorlop, 2006). Several methods have been developed to form hydrogels from polyvinyl alcohol (PVA). In the present work a modified procedure for the encapsulation of biocatalysts in PVA capsules from LentiKats® liquid (GeniaLab, Germany) is presented. In this method, the PVA based hydrogel is extruded to low molecular weight polyethylene glycol (PEG) or polypropylene glicol (PPG), where gelification occurs instantaneously, in the form of spherical-like capsules. The procedure is quite simple and the PEG or PPG can be recycled for several times. The feasibility of the method was evaluated through immobilization of enzymes (cutinase, penicillin acylase, inulinase) and whole cells (*Mycobacterium* spp. and *Rhodococcus* spp.), currently used in our laboratory, and the resulting biocatalysts were tested in their corresponding applications. These include sucrose hydrolysis (inulinase), penicillin G hydrolysis (penicillin acylase), and esterification of caproic acid with ethanol (cutinase), sitosterol side-chain cleavage to

* Corresponding author. Tel + 351-218-419065. E-mail: pedro.fernandes@ist.utl.pt

yield androstenedione, AD (*Mycobacterium* spp.) and conversion of limonene-1,2-epoxide to limonene-1,2-diol (*Rhodococcus* spp.) No enzyme leakage was observed, during immobilization procedure, even for the low molecular weight cutinase (21 kDa), although during bioconversion runs some leakage of cutinase has occured. Biocatalytic activity was maintained following immobilization, although diffusion limitations occurred. Nevertheless all immobilized biocatalysts were effectively used in aqueous or organic media, if the latter was more appropriate. PVA capsules maintained their integrity even in the presence of magnetic stirring and immobilized inulinase and penicillin acylase were used in consecutive batch runs without activity loss. A decrease in activity was observed when immobilized cutinase was used along five consecutive runs. A marked decay in activity was observed when either of the immobilized cell systems was reused. Since a similar decrease was observed for free cells, this could be ascribed to intrinsic loss of catalytic activity and not to biocatalyst leakage

The method developed proved nevertheless promising, particularly for applications in aqueous systems, since it displayed favorable mass transfer and partition features. In the overall it is quite easy to implement, is relatively cheap and can be easily scaled-up, thus providing a suitable alternative to currently used approaches

2 Materials and methods

Fructozyme L, a commercial preparation of inulinase from *Aspergillus niger*, penicillin G acylase (PGA) solution (26.6 mg ml^{-1}) from *Escherichia coli* were obtained from Sigma, *Fusarium solani pisi* cutinase wild-type was produced by recombinant *S. cerevisiae* SU50 strain as described by Calado and co-workers (Calado et al.,2002). *Mycobacterium* sp. NRRL B-3805 cells with sitosterol side-chain cleavage activity were obtained as described elsewhere (Staebler et al, 2004). *Rhodococcus erythropolis* DCL14 present a limonene epoxide hydrolase activity were obtained as described by de Carvalho and co-authors (2000) Ethyl caproate and caproic acid were obtained from Sigma-Aldrich, ethanol 96 % form AGA, penicillin G was obtained from Fersinca Gb, β-sitosterol was from Acros, androstenedione (AD), and progesterone were obtained from Sigma, polyethylene glycol (PEG) 600 and polypropylene glycol (PPG) 425 and 2000 were from Fluka, LentiKat® liquid, a PVA-based material, was from GeniaLab and inulin from chicory (Fibruline Instant) was a kind gift from Cosucra. all other chemical were of analytical grade from various suppliers.

Biocatalyst immobilization

Entrapment of biocatalyst in PVA based capsules was performed as follows. The LentiKat® liquid was heated at 95ºC for melting and then allowed to cool to 35ºC - 40ºC. Individual Enzyme or whole cell preparations were added to 10 ml of the LentiKat® liquid and thoroughly mixed. The resulting liquid was extruded through a needle (Therumo, 20 G x 2'') into stirred 150 ml of PEG 600 at room temperature. In the case of inulinase immobilization, the use of PPG 425 and PPG 2000 were also evaluated. After a 2-hour period, the hemispherical capsules formed, with roughly 3 mm diameter, were harvested, thoroughly washed with adequate buffer, weighed after removal of excess buffer with qualitative filter paper, and immediately used for bioconversion runs.

Enzyme solution or whole cell suspensions added to LentiKat® liquid were as follows: for inulinase, 0.5 ml of a ten-fold, 100 mM acetate buffer, pH 4.5, diluted commercial preparation were used; for cutinase, 0.5 ml of cutinase solution (61.2 mg ml^{-1}) in 50 mM phosphate buffer, pH 7.0, were used; for PGA, 75 μL of enzyme preparation were used; for mycobacterial cells, 2.5 ml of a 400 mg ml^{-1} suspension (wet cell weight) in 100 mM phosphate buffer, pH 7.0 were used; for *Rhodococcus* cells a 200 mg ml^{-1}

suspension (wet cell weight) in mineral medium. Capsules were washed using buffer solution used in enzyme/cell preparations.

Bioconversion runs

Sucrose hydrolysis to reducing sugars was performed in 24-hour runs, in 1.5 ml screw-capped magnetically stirred reactors at 50ºC, in 1.0 ml of 100 mM acetate buffer, pH 4.5, containing 10.0% (w/v) sucrose and 50 mg of immobilized inulinase. Penicillin G hydrolysis was performed in 10 minutes runs in a small batch stirred reactor, using 5.0 g of biocatalyst and 25 ml of a 4% (w/v) penicillin solution in 20 mM phosphate buffer, pH 8.0, at 37ºC. Esterification was carried out at 30ºC, in 24-hour runs, in isooctane (containing 20 mM n-decane) as organic solvent in 10 ml magnetically stirred flasks capped with EPDM stoppers, black (Sigma.Aldrich) and filled with 7 ml reaction medium, containing 0.2 M ethanol and 0.1 M caproic acid, and 3.3 g capsules. AD production was performed in 24-hour runs, at 30ºC, in 250 rpm shaken 15 ml screw-capped cylindrical flasks, filled with 1.0 g of biocatalyst. and 5 ml of a 1:1 organic–aqueous volumetric phase ratio medium, composed of phosphate buffer and a 12 mM solution of β-sitosterol in dioctyl phthalate. The hydrolysis of limonene-1,2-epoxide to limonene-1,2-diol, with 3.0 g of immobilized *R. erythropolis* cells, was performed in magnetically stirred 100 ml cylindrical flasks closed with rubber bungs, at 30ºC, containing 20 ml of a 1:5 organic–aqueous volumetric phase ratio medium, composed of mineral medium and a 50 mM (referred to the aqueous phase) solution of limonene-1,2-epoxide in dodecane or *iso*-octane. After each bioconversion run, the immobilized biocatalysts were washed with buffer, except immobilized cutinase, which was washed with isooctane, and used for further runs. Bioconversion runs were also performed with free biocatalysts, in concentrations that matched those corresponding to the immobilized biocatalyst. Free biocatalysts were also challenged for reuse. In all cases, samples were periodically collected for substrate/product analysis.

Analytical methods

Quantification of reducing sugars formed during sucrose hydrolysis was performed by the DNS method (Miller, 1959). Quantification of penicillin G hydrolysis was performed by the pH STAT method, based on automatic pH correction. The concentration of ethanol, caproic acid, and ethyl caproate was determined by gas chromatography, in a Hewllet-Packard model 5890 gas chromatography (GC) equipped with a flame ionization detector (FID) and a WCOT Fused Silica coating CP Chirasil- Dex CB column, 25m x 0.25mm, DF=0.25 (Varian Inc.). n-Decane present in the reaction medium was used as internal standard. AD concentration was determined by HPLC as described elsewhere (Staebler et al., 2004). The concentration of limonene-1,2-diol was determined by GC (de Carvalho et al., 2000). Quantification of protein was performed by the BCA method (Smith et al., 1985) using a commercial kit from Pierce, or by monitoring of aqueous liquid phases at 280 nm.

3. Results and discussion

Hemispherical capsules with catalytic activity for sucrose hydrolysis were obtained following extrusion of PVA based liquid into both PEG 600 and PPG 425. Extrusion into PPG 2000 failed to allow the formation of stable, individualized particles. Since the former allowed for slightly higher specific activity yields (Table 1), the former polyether was chosen for further trials. No biocatalyst leakage was observed during the immobilization process (data not shown).

Table 1. Effect of polyether used for capsule formation in the relative specific activity of inulinase

Polyether	PPG 425	PPG 2000	PEG 600
Relative specific reaction rate	0.92	Capsules not formed	100

Immobilization of the biocatalyst brought along mass transfer hindrance, which were particularly noticeable when non-purely aqueous systems were used. In these systems, involving the use of relatively hydrophobic chemicals, partition effects are most likely to also have to be accounted for (Table 2).

Table 2. Effect of immobilization on the reaction rate of the different bioconversion systems trialed.

Bioconversion	Sucrose hydrolysis	Penicillin G hydrolysis	Ethyl caproate synthesis	AD production	Limonene-1,2-diol production
Relative reaction rate [a]	0.40	0.25	0.05	0.08	0.15

[a] Determined as the ratio of the specific reaction rate using immobilized and free biocatalyst

The evaluation of the effect of immobilization in the overall reaction rate of a given bioconversion system plays a significant role when assessing the feasibility of the system trialed. Along with it, the possibility of biocatalyst reuse plays also a key role, as it contributes to the economical feasibility of the process. In the different systems evaluated, PVA capsules performed best in sucrose and penicillin G hydrolysis, where several consecutive runs were performed with no decrease in product yield or in biocatalyst activity, respectively (Figure 1). A decrease in product yield was on the other hand observed for immobilized cutinase, partly due to enzyme leakage from the capsules, given some residual activity observed in the supernantant

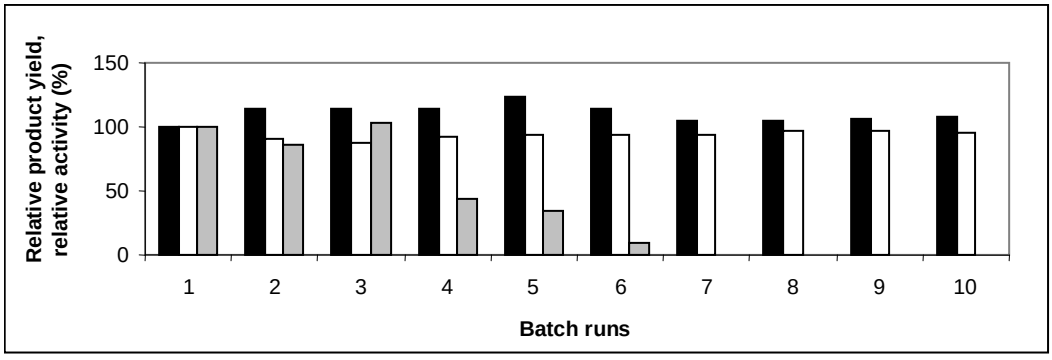

Figure 1. Effect on the final product yield and relative activity of the repeated use of inulinase, PGA and cutinase immobilized in hemispherical beads (open, closed and grey bars, respectively), for sucrose and penicillin G hydrolysis and ethyl caproate synthesis. Initial product yield for sucrose hydrolysis was of 100 g l^{-1} reducing sugars, initial activity was of 200.4 U, where U is defined as the amount of enzyme required to produce 1 μmol of 6-Amino Penicillanic Acid per minute, and initial product yield for esterification corresponded to 60% conversion yield, based on caproic acid.

As for the feasibility of reusing immobilized mycobacterial or *Rhodococcus* cells in the selected bioconversion systems, PVA capsules effectively retained biomass, particularly in the case of mycobacterial cells, although considerable loss of biocatalytic activity was observed upon reuse (Figure 2). Still a similar pattern was observed when free cells were used, which suggests that the decay of catalytic activity is an intrinsic cell feature, possible related to lack of adequate maintenance requirements, as already suggested (Fernandes et al., 1998)

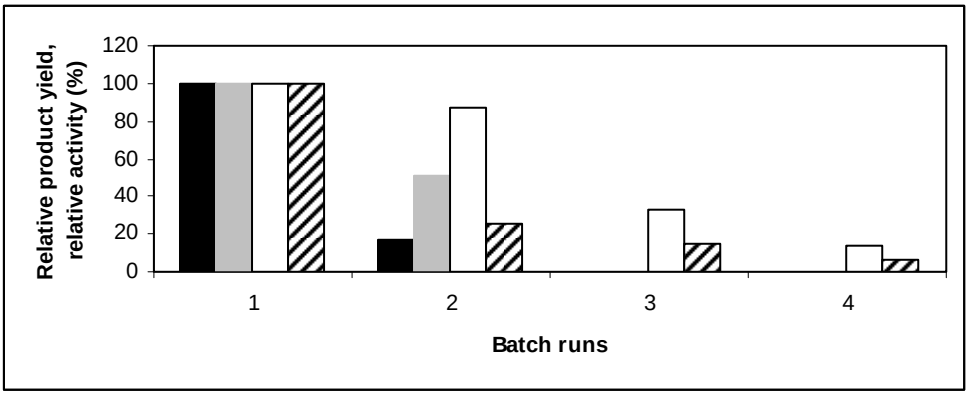

Figure 2. Effect on the final product yield and relative activity, respectively, of the repeated use of mycobacterial (open and striped bars) and *Rhodococcccus* cells (closed and grey bars) either free (closed and open bars) or immobilized in hemispherical beads (grey and striped bars) for AD and limonene-1,2-diol production.

4. Conclusions

A new methodology to obtain PVA based capsules from LentiKat® liquid was used to immobilize enzymes and whole cells, specifically inulinase, PGA, cutinase, *Mycobacterium* sp. NRRL B-3805 and *R. erythropolis* DCL14 cells. The performance of the immobilized biocatalysts was evaluated in well known bioconversion systems, by assessing the effect of immobilization on overall reaction rate and biocatalyst reuse. Promising results were obtained for inulinase and PGA, for mass transfer limitations were not most relevant and biocatalysts were effectively reused in ten consecutive batch runs. In the remaining systems enzyme and biomass were immobilized and catalytic activity retained but mass transfer limitation were significant, possibly given the hydrophobic nature of chemicals and solvents in these systems. Still, immobilized cutinase was effectively recycled in three consecutive batch runs. On the other hand, a marked decay in catalytic activity was observed, when either free or immobilized cells were reused, suggesting lack of maintenance requirements.

References

Calado, C. R. C., Mannesse, M., Egmond, M., Cabral, J. M. S., Fonseca, L. P. (2002) Production of Wild-Type and Peptide Fusion Cutinases by Recombinant *Saccharomyces cerevisiae* MM01 Strain. *Biotechnology and Bioengineering*, 78, 692-698.

Cao, L. (2005) Carrier-bound Immobilized Enzymes - Principles, Application and Design, Wiley-VCH, Weinheim.

de Carvalho, C.C.C.R., van Keulen, F., da Fonseca, M.M.R. (2000) Biotransformation of Limonene-1,2-epoxide to Limonene-1,2-diol by *Rhodococcus erythropolis* Cells. An Introductory Approach to Selective Hydrolysis and Product Separation. *Food Technology and Biotechnology*, 38, 181-185.

Fernandes, P., Cabral, J.M.S., Pinheiro, H.M. (1998) Stability of free and immobilized

Mycobacterium sp. cells in aqueous and organic media, in: *Progress in Biotechnology 15 - Stability and Stabilization of Biocatalysts*. Ballesteros, A., Plou, F. J., Iborra, J.L., Halling, P. J. (eds.), Elsevier Science B.V., Amsterdam, pp. 625-630.

Guisan, J.M. (ed.) (2006). *Immobilization of Enzymes and Cells, 2nd ed.*, Humana Press, Totowa, New Jersey.

Miller, G. L. (1959). Use of dinitrosalicylic acid reagent for determination of reducing sugar. *Analytical Chemistry*, 31, 426–428.

Schlieker, M., Vorlop, K.-D. (2006) A novel immobilization method for entrapment Lentikats, in *Immobilization of Enzymes and Cells, 2nd ed.* (Guisan, J.M. ed.) Humana Press, Totowa, New Jersey.

Smith, P. K., Krohn, R. I., Hermanson, G. T., Mallia, A. K., Gartner, F. H., Provenzano, M. D., Fujimoto, E. K., Goeke, N. M., Olson, B. J., Klenk, D. C. (1985) Measurement of protein using bicinchoninic acid. *Analytical Biochemistry,* 150, 76–85.

Staebler, A., Cruz, A., van der Goot, W., Pinheiro, H. M., Cabral, J. M. S., Fernandes, P. (2004) Optimization of androstenedione production in an organic-aqueous two-liquid phase system. *Journal of Molecular Catalysis B: Enzymatic*, 29, 19-23.

Wiegant, W.M., de Bont, J.A.M. (1980) A new route for ethylene glycol metabolism in *Mycobacterium* E44, *Journal of General Microbiology*, 120, 325-331.

Willaert, R.G., Baron, G.V. (1996) Gel entrapment and micro-encapsulation: mathods, applications and engineering principles. *Reviews in Chemical Engineering*, 12. 1-205.

Proceedings of the 10th International Chemical and
Biological Engineering Conference - CHEMPOR 2008
Braga, Portugal, September 4-6, 2008
E.C. Ferreira and M. Mota (Eds.)

The Effects of Operation Parameters on the Electrodialysis Recovery of Citric Acid from Dilute Solutions

Altan Güvenç, Beyhan Hacıoğlu

Eskişehir Osmangazi University,Chemical Engineering Department, Meşelik, Eskişehir, TURKEY
Tel: +90 222 2393750-3274
e-mail: aguvenc@ogu.edu.tr

Abstract

The purpose of this study was to investigate the effect of influential parameters on the recovery of citric acid from dilute solutions by using electrodialysis which is one of the effective membrane processes. The laboratory-scale experimental setup consisted of a three compartment perspex cell, a power supplier and three peristaltic pumps. The cathode and anode compartments were separated from the center compartment with ion exchange membranes. The effects of applied potential, feed solution concentration, feed flow rate and feed solution pH values on the recovery rate of citric acid, current efficiency and specific energy consumption were examined. High levels of citric acid recovery were achieved (up to 99.5%) in 270 minutes with higher current efficiency (~97%) and lower energy consumption (~6.5 kWh/kg) values. It was found that these values were obtained by applying the optimum operating conditions of 15 V, 2.6 $mL.s^{-1}$, 8 $g.L^{-1}$ and 3 as voltage, flow rate, feed concentration and pH, respectively. The results have indicated that electrodialysis is an effective method for recovery of citric acid which is already employed in the food industry.

Keywords: Electrodialysis; Citric acid; Ion exchange membranes; Current efficiency; Energy consumption.

2.1 Introduction

Citric acid (H_3Cit) is of paramount industrial importance because it is a useful product which has been widely used in dairy, medicine and biochemical industries (Chen, 1991). In particular, there is an increasing use of sodium citrate in washing formulations. Sodium citrate is used as builder and buffering agent in liquid detergents to replace the tetrapotassium pyrophosphates, which has become a global concern for the environment (Rohr et all., 1983). The production of citric acid is normally accomplished by fermentation whereby the separation from the fermenter broth is achieved by a chemical method. This traditional process causes a large amount of water effluent as well as solid residue. Electrodialysis (ED) is an environmentally friendly alternative to the technology which is currently in use. Electrodialysis has been developed not only for the recovery of useful components, but also for recycled use of water.

Voss (1986) compared three ED designs to deacidification of citric acid using both monopolar and bipolar membranes. His results indicated that ED using combination of anion-exchange membranes and bipolar membranes gave the best performance.

Xu and Weihua (2002) investigated the effect of cell configurations on the performance of citric acid production by a bipolar membrane ED and suggested the optimum cell configuration. They used three basic cell arrangements and discussed these configurations in view of cell voltages, bipolar potential drop, current efficiency and energy consumption. They suggested that the arrangement of cation exchange membrane – bipolar membrane – cation exchange membrane seemed to be the favorable cell configuration for the production of citric acid.

Nikbakht et al. (2006) investigated the effects of some influential factors such as pH, voltage, flow rate, temperature and feed concentration on the performance of an ED experimental setup by using Taguchi method. According to their final results, all factors have some effects on the response while effects of pH and voltage on the mean response are more significant than those of flow rate and temperature.

The aims of this paper were to recover the citric acid from dilute solutions using the Ionac MA-3470 and MC-3475 ion-exchange membranes, to test the separation efficiency of the ion-exchange membranes for the process and to obtain the fundamental data for the development of electrodialysis process taking the current efficiency and energy consumption into consideration.

2. Experimental

2.1 Experimental Setup

The experimental setup consisted of an ED cell, a DC power supplier, three solution tanks (each was with the capacity of 250 mL) with peristaltic pumps. The ED cell was composed of three compartments separated a pair of ion exchange membranes (cation and anion). Carbon fiber and stainless steel were used as an anod and a cathode, respectively. The experiments have been performed in batch recycle mode at ambient temperature (Hacıoğlu, 2006).

2.2 Membrane And Material

Ionac MA-3475 anion exchange membrane and MC-3470 cation exchange membrane (Sybron chemicals Inc.) were employed. The chemical and physical properties of ion exchange membranes are presented in Table 1. Effective area of each of the membranes and electrodes was 19 x 4 cm^2 while thickness of center compartment was 1 cm^2 and the thickness of each electrode compartment was 0.5 cm. All chemicals used were analytical grade.

Table 1
Main characteristics of ion-exchange membranes

	Ionac MC-3470	Ionac MA-375
Type of membrane	Cationic	Anionic
Ionic form, as shipped	Sodium	Chloride
Permselectivity	96	99
Area resistance, Ohm/cm (0,1 N NaCl)	25	50
Mullen Burst Test, min. (psi)	150	150
Temperature Stability, max. (C°)	80	80
Exchange capacity (Meq/g)	1.4	0.9
Water permeability (ml/hr/ft^2) @ 5 psi	25	25
Thickness (mils)	15	16
Chemical Stability, pH	1 to 10	1 to 10

2.3 Experimental Procedures

During all the experimental studies, 0.05 M sodium chloride solution was circulated through the electrode compartments at flow rate of 0.5 $mL.s^{-1}$ and pH of 6.5. The changes in the citric acid conc. in the feed solution tank were determined at each ten minutes and the experiments were ended when the (99±0.5)% recovery of citric acid reached. Volumetric

method was applied to determine the concentration of citric acid using 0.1 M sodium hydroxide solution. The potentiostatic mode was chosen in ED experiments taking our previous study into consideration (Güvenç and Karabacakoğlu, 2005).

The experiments can be summarized as follows:

- To investigate the effect of cell voltage, the trials were carried out at constant feed solution concentration of 8.0 $g.L^{-1}$, feed flow rate of 2.60 $mL.s^{-1}$ and feed solution pH of 3, by applying the voltages of 7.5, 15, 30 and 45 V.
- To investigate the effect of feed flow rate, the trials were carried out at constant feed solution concentration of 8.0 $g.L^{-1}$, pH of 3 and cell voltage of 15 V, by applying 1.00, 2.60 and 6.80 $mL.s^{-1}$ flow rates.
- To investigate the effect of feed concentration, the trials were carried out at constant cell voltage of 15 V, flow rate of 2.60 mLs^{-1} and pH of 3, by using the concentrations of 8 $g.L^{-1}$ and 16 $g.L^{-1}$.
- To investigate the effect of pH, the trials were carried out at the constant feed solution concentration of 8.0 $g.L^{-1}$, feed flow rate of 2.60 $mL.s^{-1}$ and voltage of 15 V, by employing the pH values of the feed solutions as 3 and 4

3. Results and Discussion

3.1 Current-Voltage Curves

The amount of ions transported through the membrane is directly proportional to the current or current density. İncreasing the current density leads to an increase in the number of ions transferred. The relation of current-voltage characteristics of the ion-exchange membrane for the different citric acid conc. was investigated. As shown in Fig.1, the current reached a plato when the lower conc. of citric acid solutions were used. This is the region of the limiting current density where all the available ions are transferred. If the ionic conc. of citric acid increased then the limiting current density increased as well but the plato value became less pronounced. When the voltage increased further, no ions are available anymore to transfer the charge and water splitting will occur to generate ions related to the overlimiting current (Mulder, 1998).

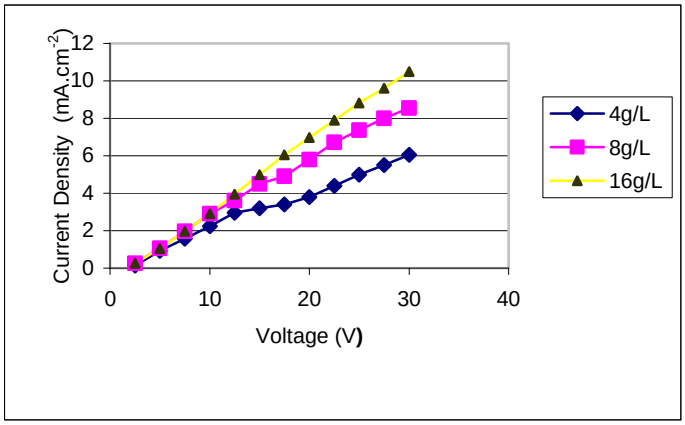

Fig 1. Experimental I-V curves at different concentrations of citric acid

To interprete the results obtained from the experimental studies, the current efficiency and energy consumptions, which were the electrochemical performance factors, were calculated and discussed.

- The current efficiency ŋ was calculated using Eq.(1)

$$\eta = \frac{(C_O - C_t)VF}{NIt} \quad (1)$$

where C_0 and C_t are the conc. of citric acid at time 0 and t, respectively. V is the circulated volume of feed solution, I the current, F the Faraday constant and N is the number of cell triplets. The current efficiency is determined by various time intervals from the beginning and therefore it is dependent of time.

- The energy consumption E (kWh/kg) was calculated using Eq. (2)

$$E = \int \frac{UIdt}{C_t VM} \quad (2)$$

where U is the potential across the cell (V), M is the molar weight of citric acid (192 $g.mol^{-1}$).

3.2 Influence of cell voltage

Cell voltage is an important parameter because it is related to energy consumption associated with the recovery of citric acid. The voltage drop, which refers to the variation taking place in the ED cell, mainly includes the Donnan Potential at all solution-membrane interface and diffusional potential both in the ion-exchange membrane and in the solution. In the study, the ranging of cell voltages were 7.5, 15, 30 and 45 regarding the relation of current-voltage curve as given in Fig. 2-3. The results obtained by applying 7.5 and 15 Volts showed that the current efficiency and energy consumption values were nearly similar in both cases. However, since the recovery of citric acid took more time in the case of 7.5 V applied voltage, the 15 V applied voltage value was chosen as optimum by considering membrane fouling. This was also supported by Fig. 1 where the available ions were transferred between the 10-20 voltages. On the other hand, the 30 V and 45 V applied voltages could not be considered as optimum values due to the lower current efficiencies and higher energy consumptions.

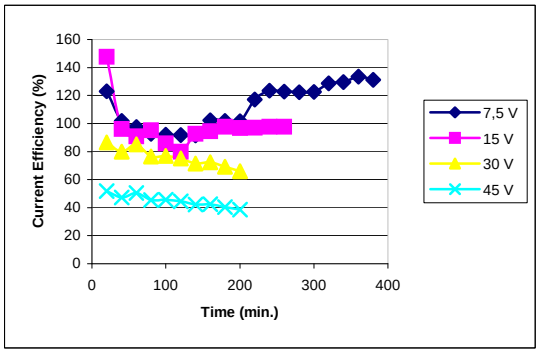

Figure 2. Variation of current efficiency with removal time for a range of applied voltages (The conc. of the feed solution: 8.0 $g.L^{-1}$; pH: 3; flow rate of solution: 2.60 $mL.s^{-1}$)

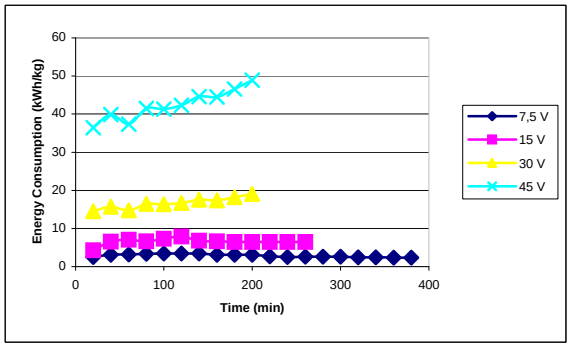

Figure 3. Variation of energy consumption with removal time for a range of applied voltages (The conc. of the feed solution: 8.0 $g.L^{-1}$; pH: 3; flow rate of solution: 2.60 $mL.s^{-1}$)

3.3 Influence of flow rate

The use of lower flow rate (1 $mL.s^{-1}$) was not advantageous for economy of treatment since it allowed the increase in the time of treatment and it may also give rise membrane fouling. (Fig.-4.5) Increasing the flow rate up to 6.8 $mL.s^{-1}$ decreased the recovery of citric acid duration due to residence time reduction. As a matter of fact, increasing the residence time is equivalent to enhancing the effective membrane contact area. From the engineering point of view, the flow rate of 2.6 $mL.s^{-1}$ can be chosen as an optimum value with higher current efficiency, lower energy consumption and also with the proper duration of ED.

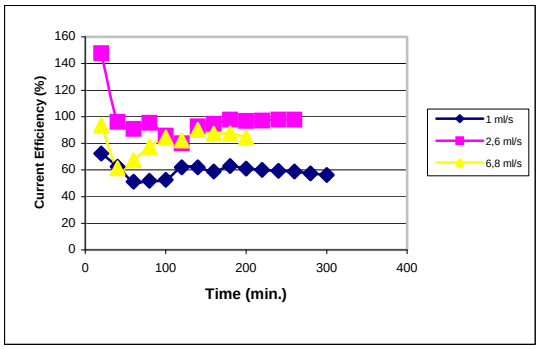

Figure 4. Variation of current efficiency with removal time for a range of applied flow rates (The conc. of the feed solution: 8.0 $g.L^{-1}$; pH: 3; applied voltage:15V)

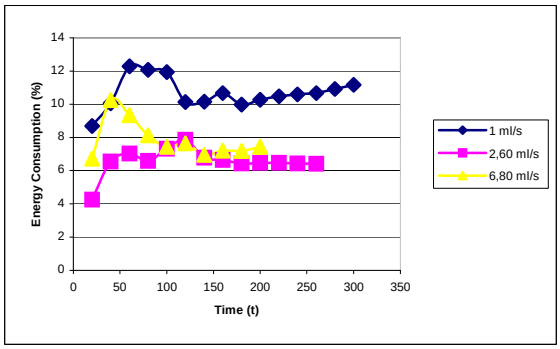

Figure 5. Variation of consumption with removal time for a range of applied flow rates (The conc. of the feed solution: 8.0 $g.L^{-1}$; pH: 3; applied voltage:15V)

3.4 Influence of feed concentration

In the case of higher conc. of feed solution, ED cell use higher current owing to the presence of higher charged ions since the solution conc. is related to the current density. The conductivity of solution increases as the solution conc. increases (resistance decrease). In this case, the electric current increases by Ohm's law. As can be seen from Fig. 6-7, when we used higher conc. of citric acid (16 $g.L^{-1}$), lower current efficiency and higher energy consumption were obtained according to the Eq. 1 and 2 and the duration of ED reached 100 min. After this time, the variation of current efficiency and energy consumption showed similar trends for both higher and lower conc. of citric acid due to the decreasing of conc. diference between the solutions.

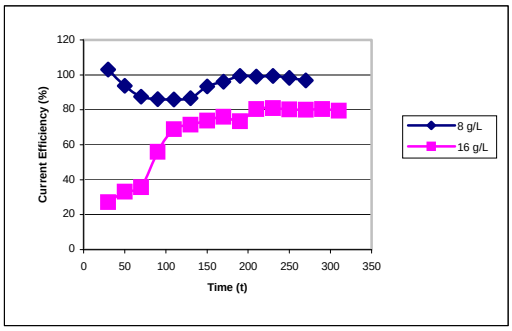

Figure 6. Variation of current efficiency with removal time for the different conc. of the feed solution (Applied voltage: 15 V; pH: 3; flow rate: 2.60 $mL.s^{-1}$)

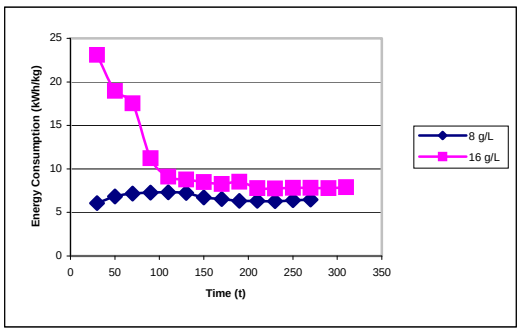

Figure 7. Variation of energy consumption with removal time for the different conc. of the feed solution (Applied voltage: 15 V; pH: 3; flow rate: 2.60 $mL.s^{-1}$)

3.5 Influence of pH

Citric acid is a weak acid and its dissociation depends on pH. Vera et al. (2007) declared that at the initial pH of clarified tropical fruit juices, close to 3, the dissociation of citric acid is higher than that of malic acid and they concluded that the ED performances were not affected by the final pH up to 7.9. We have also studied the feed solution of pH 3 which is close to the original pH value of the diluted solution (8 $g.L^{-1}$). The experiments were also carried out at pH 4 in order to observe the effect of initial pH of the feed solution.

As shown in Fig. 8-9, when the different pH values of feed solution were compared in view of current efficiency and energy consumption, it can be seen that the trends are just opposite. For example, in the case of pH 4, the higher energy consumption corresponds to the lower current efficiency while the lowest energy consumption corresponds to the highest current efficiency in the case of pH 3. Finally, it was concluded that starting the experimental studies with the feed solution pH value of 3 was suitable for the applied experimental conditions.

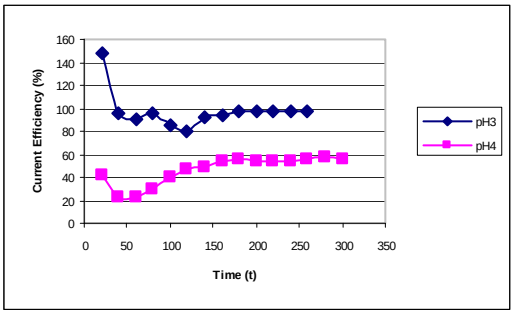

Figure 8. Variation of current efficiency with removal time for different pH values of the feed solution (Applied voltage: 15 V; flow rate: 2.60 mL.s^{-1}; conc. of the feed solution: 8g.L^{-1})

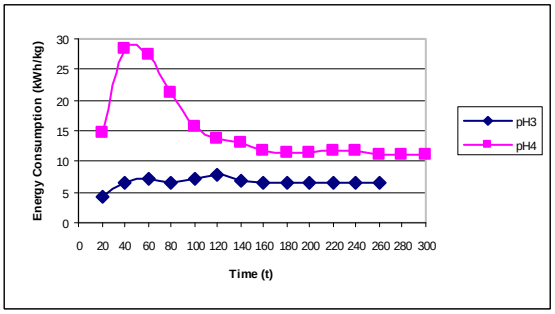

Figure 9. Variation of energy consump. with removal time for different pH values of the feed solution (Applied voltage: 15 V; flow rate: 2.60 mL.s^{-1}; conc. of the feed solution: 8g.L^{-1})

4. Conclusion

- ED with ion Exchange membrane used in this study provides a convenient way to recover the citric acid from dilute solutions .
- The results of this work can also serve as a basis for the laboratory and pilot scale studies on the treatment of whey, juices and wine.

References

Chen, J.S. (1991), The Technology Of Organic Acid by Fermentation, Press of Chemical Industry,120-168, Beijing.

Güvenç, A., Karabacakoğlu, B. (2005). Use of electrodialysis to remove silver ions from model solutions and wastewater. Desalination, 172,7-17.

Hacioğlu, B. (2006). Recovery ofcitric acid from model method. Master thesis, Eskişehir Osmangazi University, Eskişehir, Turkey.

Mulder, M. (1998). Basic Principles of Membrane Technology, 382-386., Enschede, The Netherlands.

Nikbakht, R., Satrzadeh, M., Mohammadi, T. (2007). Effect of parameters on concentration of electrodialysis, Journal of Food Enginnering, 83,596-604.

Rohr, M., Kubicek, C.P., Kominek, J. (1983). Citric, Acid, in:H.J. Rehm, G. Reed (Eds.), Biotechnology., pp. 419., Verlag Chemie, Weinheim.

Xu, T., Weihua, Y. (2002a). Citric acid production by electrodialysis with bipolar membranes. Chemical Engineering and Processing, 41, 519-524.

Xu, T., Weihua, Y. (2002b). Effect of cell configurations on the performance of citric acid production by a bipolar membrane electrodialysis. Journal of Membrane Science, 203(1-2) 145-153.

Vera, E., Sandeaux, J., Persin, F., Pourcelly, G., Dornier, M., Ruales, J. (2007). Deacidification of clarified tropical fruit juices by electrodialysis. Part I. Influence of operating conditions on the process performances. Journal of Food Engineering, 78,1427-1438.

Voss, H. (1986). Deacidification of citric acid solutions by electrodialysis. Journal of Membrane Science, 27(2), 165-171.

Proceedings of the 10th International Chemical and
Biological Engineering Conference - CHEMPOR 2008
Braga, Portugal, September 4-6, 2008
E.C. Ferreira and M. Mota (Eds.)

Influence of operational fed-batch strategies on heterologous *Rhizopus oryzae* lipase production in *Pichia pastoris* system using mixed substrates.

Carolina Arnau, Ramón Ramón and Francisco Valero.

Departament d'Enginyeria Química. ETSE. Universitat Autònoma de Barcelona (Bellaterra, Barcelona) Spain. (Francisco.Valero@uab.cat)

Keywords: *Pichia pastoris*, ROL, mixed substrate co-feeding, sorbitol, fed-batch cultivation, heterologous protein.

Topic: Bioprocess Engineering.

Introduction

The methylotrophic yeast *Pichia pastoris* has become a well-established host system for heterologous protein production (Macauley-Patrick et al., 2005).

There are three types of *P. pastoris* host strains available that vary with regard to their ability to utilize methanol. The wild type or methanol utilization plus phenotype (Mut^+), and those resulting from deletions in the *AOX1* gene, methanol utilisation slow (Mut^S), or both *AOX* genes, methanol utilisation minus (Mut^-). An important advantage of Mut^S strains is that the culture is not as sensitive to residual methanol in the cultivation media relative as Mut^+ strains, and hence the process of scale up can be easier (Stratton et al., 1998). However, the lower maximum specific growth rate of wild type Mut^S strains compared with wild type Mut^+ strains limits the productivity of the process.

To increase cell density and process productivity, as well as to reduce the induction time, a typical approach is the use of a multicarbon substrate in addition to methanol (Files et al., 2001). It has proved to be a straightforward strategy to increase the energy supply to recombinant cells (Zhang et al., 2003). This strategy has been mostly employed for fermentations using Mut^S strains because of their genetically reduced capacity to assimilate methanol, which results in long induction times (above 100 h).

Sreekrishna et al., (1997) successfully implemented the use of sorbitol/methanol mixtures in fed-batch fermentations for matrix metalloproteinases (MMP-2) production. Moreover, Thorpe et al., (1999) compared methanol/glycerol and methanol/sorbitol fed-batch mixed-feed strategies maintaining the residual methanol concentration between 1-2 $g \cdot l^{-1}$. Although cell yields are lower on sorbitol, this is compensated by higher specific product formation rates, which results in comparable recombinant protein levels at lower final cell concentrations. Inan and Meagher (2001) compared different carbon sources in terms of their ability to support growth and expression of an *AOX1-lac Z* fusion in shake flasks studies of a *P. pastoris* Mut^- strain confirming sorbitol as an excellent non-represive carbon source.

The production of the heterologous *Rhizopus oryzae* lipase (ROL) has been shown to have a negative effect on *P. pastoris* growth (Minning et al., 2001). This effect was even more drastic when ROL gene dosage was increased, particularly when using a Mut^S host strain growing on methanol as a sole carbon source in fed-batch cultures (Cos et al., 2005). Thus, sorbitol co-feeding should be an excellent approach to bypass this problem.

Ramon et al., (2007) showed that mixed substrate strategy applied to a Mut^S ROL fed-batch culture at a low residual methanol concentration set-point (0.5 $g \cdot l^{-1}$) allowed to increase the production of heterologous protein in Mut^S phenotype, avoiding the drastic reduction of the specific production rate observed after the start of the induction phase when methanol is used as a sole carbon source. This fact, together with the higher specific growth rate

achieved resulted in a significant increase of the bioprocess volumetric and specific productivities. Recently, Jungo et al., (2007) has published an excellent article about the influence of different mixed feed of methanol and sorbitol working under limited conditions on the recombinant avidin production. However, for our knowledge, there are not studies about the influences of different methanol set-points and specific growth rates on heterologous protein production with this two mixed substrates.

The objective of this work is a systematic study of the influence of methanol set-point and sorbitol feeding rate in fed-batch operation with Mut^S phenotype producing heterologous ROL.

Materials and methods

Strains

P. pastoris KM71 (*arg4 his4 aox1Δ::SARG4 AOX2*, derived Mut^S strains having single copy of the ROL gene and its histidine auxotrophy reverted have been described in Cos et al., (2005).

Fed-batch cultivation set up and operational conditions

The basal salt synthetic medium for fed-batch cultivations contained per litre of distilled water: H_3PO_4 (85%) 26.7 ml, $CaSO_4$ 0.93 g, K_2SO_4 18.2 g, $MgSO_4 \cdot 7H_2O$ 14.9 g, KOH 4.13 g, glycerol 40 g, and 4.35 ml of PTM1 solution. Also 0.1 $ml \cdot l^{-1}$ of antifoam agent (Mazu DF 7960) –a polyoxyalkylene glycol- was added.

Cells were cultured in a 5 litre Braun Biostat B bioreactor (Braun Biotech, Melsungen, Germany). The cultivation conditions were: stirring rate 900 rpm, temperature 30 ºC, pH controlled at 5.5 by adding NH_4OH 30 % (v/v), dissolved oxygen above 30 % with a constant air flow rate of 1.5 $l \cdot min^{-1}$.

The cultivation started with a 40 $g \cdot l^{-1}$ of glycerol batch phase (BP). After that, a pulse of sorbitol and methanol was added to achieve a concentration of 10 $g \cdot l^{-1}$of sorbitol and 5 $g \cdot l^{-1}$of methanol into the bioreactor as a transition phase (TP).

For the induction phase (IP) a feeding medium containing per litre 300 grams of sorbitol and 7.5 ml of trace salts solution was used in a pre-programmed exponential feeding rate strategy at a selected specific growth rate; maximum specific growth rate (0.02 h^{-1}) and a half of maximum specific growth rate (0.01 h^{-1}) .

Methanol addition rate was programmed by a control algorithm developed (Cos et al., 2006) attempting to maintain a 0.5 $g \cdot l^{-1}$ or 2 $g \cdot l^{-1}$ constant methanol concentration adding a solution of pure methanol with 12 $ml \cdot l^{-1}$ of PTM1. Methanol was analyzed on-line by a Methanol detector and sensor unit (Raven Biotech Inc., Vancouver, Canadà). Both carbon sources were also added in the production phase by an automatic microburette MicroBU-2031 from Crison Instruments (Alella, Barcelona, Spain).

Biomass Analysis

Biomass was expressed as dry cell weight (Ramon et al., 2007).

Glycerol, Sorbitol and methanol determination

Off-line glycerol, sorbitol and methanol determination was made as reported elsewhere (Ramon et al., 2007).

Lipolytic activity assay

Lipolytic activity determination was carried out using the Lipase colorimetric assay (LIP kit, reference no. 1821792, from Roche Diagnostics, Mannheim, Germany), as described in Ramon et al., (2004). Extracellular lipolytic activity was measured after removing cells from cultivation samples by centrifugation in a microcentrifuge at 12,000 g.

Results and discussion

In previous Mut^S fed-batch experiments using methanol as sole carbon source it was observed that the highest secretion levels were detected at the lowest methanol set-point tested (0.5 g·l^{-1}). However, the specific production rate profile under those conditions showed a maximum value soon after the start of the induction phase, followed by an abrupt decrease to almost zero values after 20 h of induction. (Cos et al., 2006). Under these conditions, the negative effect of ROL production on cell growth is combined with the reduced methanol assimilation capacity of Mut^S cells. This effect became more striking when attempting to grow the prototrophic Mut^S ROL multi copy strain in fed-batch cultures, as growth on methanol during the fed-batch induction phase did not progress for more than 24 hours.

Preliminary studies of Ramon et al., (2007) showed that mixed substrate (sorbitol-methanol) strategy applied to a Mut^S ROL fed-batch culture at a low residual methanol concentration set-point (0.5 g·l^{-1}) allowed to increase the production of heterologous protein in Mut^S phenotype, avoiding the drastic reduction of the specific production rate observed after the start of the induction phase when methanol is used as a sole carbon source. This fact, together with the higher specific growth rate achieved resulted in a significant increase of the bioprocess volumetric and specific productivities.

Remarkably, sorbitol co-feeding in Mut^S ROL multi copy strain batch cultivations allowed sustained cell growth and lipase productivity, strongly suggesting that cells growing on mixed substrates can –at least partially- overcome the stress caused by ROL overexpression in Mut^S cells. Furthermore, this observation reveals that the (stress) cellular response to heterologous protein overexpression and secretion is interconnected with the energetic state of the cells.

To make a systematic study of the influence of methanol set-point and sorbitol feeding rate in fed-batch operation with Mut^S phenotype, four experiments were made at a constant methanol set-point of 0.5 g·l^{-1} and 2 g·l^{-1} controlling by a predictive control algorithm (Cos et al., 2006) with two different sorbitol feeding rate to assure a constant specific rate of μ_{max} and $\mu_{max}/2$ by means of a pre-programmed exponential feeding rate strategy.

The experiment showed that methanol set-point is the key parameter to optimize production, productivity and specific productivity of the bioprocess. Low influence of specific growth rate on productivity and specific productivity was observed.

For this reason only the fermentations at constant specific growth rate of $\mu_{max}/2$ and methanol set-point of 0.5 g·l^{-1} and 2 g·l^{-1} are presented. The evolution of biomass, lipolytic activity, methanol and sorbitol for a methanol set-point of 0.5 g·l^{-1} are presented in figure 1, and the same parameters at methanol set-point of 2 g·l^{-1}, are presented in figure 2.

An accurate pre-programmed exponential feeding rate strategy for sorbitol concentration (open-loop control) was reached; specific growth rate was maintained practically constant at set-point value of 0.01 h^{-1} without sorbitol accumulation. Thus, sorbitol was limited substrate.

On the other hand, methanol closed-loop control strategy using the predictive control algorithm previously developed was also effective. The two methanol set-points were maintained with minimal deviations along the fermentation.

The efficient of control strategies for both substrates permits an accurate study of the effect of both parameters on the productivities of the ROL production bioprocess, and it reveals the importance of PAT (process analytical technology) to obtain reproducible bioprocesses.

Biomass levels were very similar in both bioprocesses. It reveals that practically all biomass production is related with sorbitol consumption and the effect of different methanol set-points on biomass production is negligible.

Also the influence of ammonium addition in the induction phase was tested. Basal salt medium has only ammonium to reach a biomass concentration around 30-40 g·l^{-1}.The lack of ammonium has a negative effect on microorganism growth and protein production, also it

starts the proteolytic processes. One pulse of ammonium during the induction phase showed, in some fermentations, a negative influence on *Pichia* growth and protein production as it has been also revealed in a drastic depletion of CO_2 production rate (data not shown). Although growth and production was recovered after a lag phase of some hours, obviously this strategy is not applicable. The best strategy to avoid these problems was to feed ammonium jointly with sorbitol in their stoichiometric relation during the induction phase.

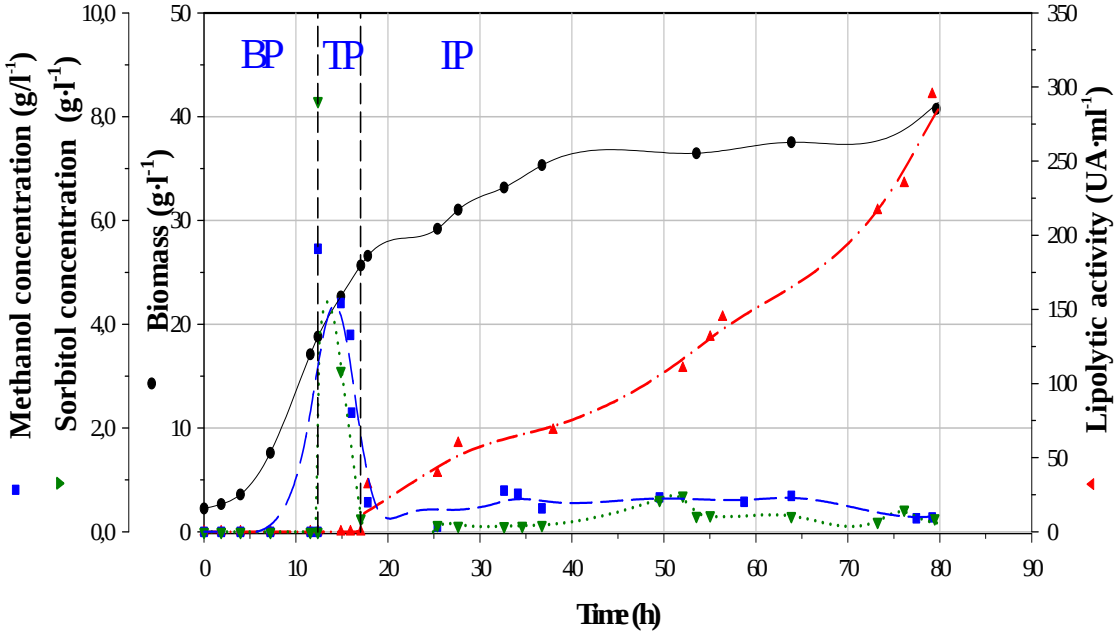

Figure 1.- Time evolution of biomass, methanol, sorbitol and lipolytic activity for a methanol set-point of 0.5 g·l^{-1} at a specific growth rate of 0.01 h^{-1} (μ_{max}/2).

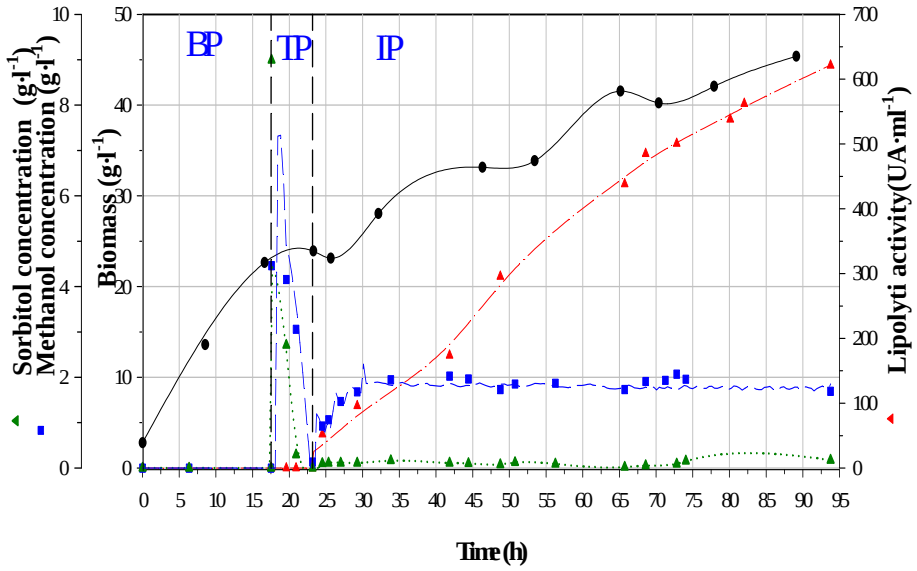

Figure 2.- Time evolution of biomass, methanol, sorbitol and lipolytic activity for a methanol set-point of 2 g·l^{-1} at a specific growth rate of 0.01 h^{-1} (μ_{max}/2).

A different behaviour was observed when lipolytic activity was compared. At methanol set-point of 2 $g \cdot l^{-1}$, lipolytic activity was 2.4 fold higher than methanol set-point of 0.5 $g \cdot l^{-1}$. It shows the importance of methanol set-point on heterologous protein production in *Pichia pastoris* and the pressing need to get an accurate control of substrate inductor (methanol).

The evolution of specific production rates of both bioprocesses were also quite different (Figure 3). Heterologous protein production starts at the beginning of the induction phase. Both methanol set-points reached a maximum of specific production rate during the first ten hours of the induction phase, and did not fall downs abruptly as observed when cells was grown on methanol as sole carbon source at the same point of 0.5 $g \cdot l^{-1}$ (Cos et al., 2006). The maximum specific production rate reached at methanol set-point of 2 $g \cdot l^{-1}$ was 2.8 fold higher than methanol set-point of 0.5 $g \cdot l^{-1}$.

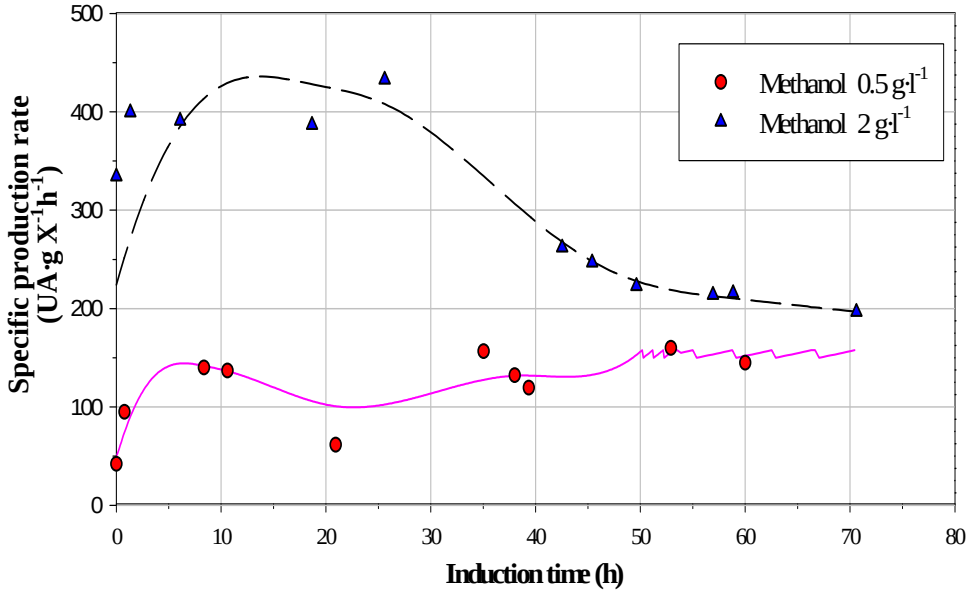

Figure 3.- Time evolution of specific production rates at methanol set-points of 0.5 and 2 $g \cdot l^{-1}$ at a specific growth rate of 0.01 h^{-1} ($\mu_{max}/2$).

At a low methanol set-point, specific production rate was maintained practically constant along the fermentation (around 150 $UA \cdot gx \cdot h^{-1}$). However, at high methanol set-point, the maximum (around 425 $UA \cdot gx \cdot h^{-1}$) was maintained only during 25 hours decreasing previous to stabilize at 200 $UA \cdot gX \cdot h^{-1}$, a value little bit higher than observed at low methanol set-point.

It has been shown that methanol set-point is the key fermentation parameter in the modulation of heterologous protein production in *Pichia pastoris*. On the other hand, the modulation of transcriptional level and the use of a co-substrate such as sorbitol minimizes the negative impact of high-level protein expression on cell physiology and growth rate reduction.

References:

Cos, O., Serrano, A., Montesinos, J.L., Ferrer, P., Cregg, J.M., and Valero, F. (2005). Combined effect of the methanol utilization (Mut) phenotype and gene dosage on recombinant protein production in *Pichia pastoris* fed-batch cultures. J. Biotechnol. 116, 321-335.

Cos, O., Ramon, R., Montesinos, J.L., and Valero, F. (2006). A simple model-based control for Pichia pastoris allows a more efficient heterologous protein production bioprocess. Biotechnol. Bioeng. 95, 145-154.

Files, D., Ogawa, M., Scaman, C.H., and Baldwin, S.A. (2001). A *Pichia pastoris* fermentation process for producing high-levels of recombinant human cystatin-C. Enzyme Microb. Technol. 29, 335-340.

Inan, M. and Meagher, M.M. (2001). Non-represing carbon sources for alcohol oxidase (*AOX1)* promoter of *Pichia pastoris*. J. Biosci. Bioeng. 92, 585-589

Jungo, C., Schenk, J., Pasquier, M., Marison, I.W., and von Stockar, U. (2007). A quantitative analysis of the benefits of mixed feeds of sorbitol and methanol for the production of recombinant avidin with *Pichia pastoris*. J. Biotechnol. 131, 57-66.

Macauley-Patrick, S., Fazenda, M.L., McNeil, B., and Harvey, L.M. (2005). Heterologous protein production using the *Pichia pastoris* expression system. Yeast, 22, 249-270.

Minning, S., Serrano, A., Ferrer, P., Sola, C., Schmid, R.D., and Valero, F (2001). Optimization of the high-level production of *Rhizopus oryzae* lipase in *Pichia pastoris*. J. Biotechnol. 86, 59-70

Ramón R., Ferrer, P. and Valero F. (2007). Sorbitol co-feeding reduces metabolic burden caused by the overexpression of a *Rhizopus oryzae* lipase in *Pichia pastoris.* J. Biotechnol. 130, 39-46.

Sreekrishna, K., Brankamp, R.G., Kropp, K.E., Blankenship, D.T., Tsay, J-T., Smith, P.L., Wierschke, J.D., Subramaniam, A., and Birkenberger, L.A. (1997). Strategies for optimal synthesis and secretion of heterologous proteins in the methylotrophic yeast *Pichia pastoris.* Gene, 190, 55-62.

Stratton, J., Chiruvolu, V., and Meagher, M.M. (1998). High cell-density fermentation. In:Higgins DR, Cregg JM, editors. Methods in molecular biology. Totowa, NJ: Humana Press. 103, 107-120.

Thorpe, E.D., d'Anjou, M.C., and Daugulis, A.J. (1999). Sorbitol as a non-represing carbon source for fed-batch fermentation of recombinant *Pichia pastoris.* Biotechnol. Lett. 21, 669-672.

Zhang, W.H., Potter, K.J., Plantz, B.A., Schlegel, V.L., Smith, L.A., and Meagher, M.M. (2003). *Pichia pastoris* fermentation with mixed-feeds of glycerol and methanol: growth kinetics and production improvement. J. Ind. Microbiol. Biotechnol. 30, 210-215.

Acknowledgements:

This work was supported by grants from the Spanish program on Chemical Science and Technology (CTQ2007-60347/PPQ), 2005-SGR-00698 (Generalitat de Catalunya). Chemical Engineering Department of the UAB constitutes the Biochemical Engineering Unit of the Reference Network in Biotechnology (XRB) from the DURSI (Generalitat de Catalunya),

Proceedings of the 10th International Chemical and
Biological Engineering Conference - CHEMPOR 2008
Braga, Portugal, September 4-6, 2008
E.C. Ferreira and M. Mota (Eds.)

Adaptive control of glycerol & methanol feeding in recombinant *Pichia pastoris* cultures: Impact on antibody titre

Filipe Ataíde[1], Ana R. Ferreira[2], João J. Clemente[2], António E. Cunha[2], Rui Oliveira[1,2*]
[1]CQFB/REQUIMTE, Departamento de Química, Faculdade de Ciências e Tecnologia,
Universidade Nova de Lisboa, P-2829-516 Caparica, Portugal
[2]IBET/ITQB Instituto de Biologia Experimental e Tecnológica /
Instituto de Tecnologia Química e Biológica, Apartado 12, P-2781-901 Oeiras, Portugal

Keywords: Aerobic cultivation processes, Dissolved oxygen control, Adaptive control, Recombinant *Pichia pastoris*
Topic: Systematic methods and tools for managing the complexity.

Abstract

P. pastoris processes for heterolougous protein expression are typically run in three phases: a batch phase, an exponential feeding fed-batch phase and a long oxygen transfer limitation (OTL) phase. The final protein titer is often limited by the oxygen availability in the OTL phase. In this paper, a direct adaptive controller is designed for the OTL phase. The controller was validated in pilot *P. pastoris* cultivations expressing a single chain antibody fragment (ScFv). This work shows that the proposed controller can regulate the dissolved oxygen tension (DOT) at very low levels (5 %) with high stability by manipulating the glycerol feeding rate, thereby enhancing the oxygen transfer at high cell density, which finally leads to a higher antibody titre.

1 Introduction

Pichia pastoris is currently viewed as a very promising host for heterologous protein expression (Cereghino and Cregg, 2000) since it can be easily manipulated at molecular genetic level, it has the ability to express high levels of proteins, either intra or extracellularly and it has the capability to perform eukaryotic post-translational modifications such as glycosylation, disulfide bond formation and proteolytic processing (Cereghino and Cregg, 2000; Cereghino et al., 2002).

In recent studies, *P. pastoris* has been genetically engineered to secret human glycoproteins, such as rEPO, with homogeneous fully complex terminally sialylated N-glycans (Hamilton et al., 2003, 2006; Choi et al., 2003; Bobrowicz et al., 2004). These studies open new perspectives for the production of therapeutic proteins in yeast cell cultures with advantages such as reducing both fermentation and development (from gene to protein) times, lower operating costs, chemically defined media, higher protein titers and no viral contamination.

P. pastoris is normally cultivated in fed-batch mode in order to limit the amount of substrate in the reactor. It can tolerate wide pH variations but it doesn't seem to increase its cell productivity with pH changes, although achieving different protease activities (Shi et al., 2003).

This yeast is able to grow at very high cell densities with massive oxygen uptake requirements, being the oxygen transfer capacity, a critical limitation factor. Charoenrat et al. (2006) concluded that high cell productivity could be improved by increasing oxygen transfer rate.

*Corresponding author. Tel: +351 21 2948303 E-mail: rui.oliveira@dq.fct.unl.pt

Once the maximum oxygen transfer rate is reached, regulation of DOT at very low values by manipulating the carbon source feeding has been proposed by several authors. Oliveira et al. (2005) developed two indirect adaptive control algorithms, based on dissolved oxygen (for both algorithms) and oxygen transfer rate (for one of the algorithms) measurements. It was shown that off-gas measurements did not improve the controller performance since responses by estimator and controller were being caused by the measurement delays.

In this paper, a direct adaptive controller is derived and tested in *P. pastoris* cultivations. The production is highly sensitive to the specific methanol feeding in the methylotrophic strains. A controller that can maintain constant specific feedings on the basis of DO control would be of extremely high value.

2 Process control feeding strategy

The control of *P. pastoris* cultivation is based on carbon source limitation, i.e through glycerol feeding. The process starts with a glycerol batch (GB) phase, where the cultivation is carried out in batch mode for 9 hours with initial glycerol concentration of approximately 40 g/l. Then follows the glycerol fed-batch Phase (GFB) according to an exponential profile,

$$F = F_0 e^{\mu t} \tag{1}$$

with F the glycerol feeding rate in g/h, F_0 the initial feeding rate (10.35 g/h) and μ the desired specific growth rate, set to 0.16 h^{-1} in this work.

In GB and GFB phases, dissolved oxygen concentration is controlled in cascade mode, first by overhead pressure between 80 and 500 mbarg to regulate dissolved oxygen level to 95 % of saturation and, as second control loop, agitation rate between 320 and 1000 rpm to regulate the dissolved oxygen level to 50 % of saturation. At the end of the GFB, the stirrer speed reaches the maximum value of 1000 rpm and DO starts to drop thereby signaling the beginning of oxygen transfer limitation phase. In this latter phase an adaptive DO-stat feeding controller was implemented.

3 Adaptive DO-stat glycerol feeding controller

3.1 System description

To describe the dissolved oxygen dynamics in the liquid phase, the following material balance equation holds when glycerol accumulation in the liquid phase is negligible:

$$\frac{\mathrm{d}C_O}{\mathrm{d}t} = -\frac{F}{V} S_0 Y_{O/S} + k_L a \left(C_O^* - C_O\right) \tag{2}$$

with C_O the dissolved oxygen concentration, F the glycerol solution feed rate, V the broth volume, S_0 the glycerol concentration in the feed solution, $Y_{O/S}$ the observed oxygen/glycerol yield, that may change in time, $k_L a$ the oxygen mass transfer coefficient, C_O^* is the saturation dissolved oxygen concentration at working conditions. Equation (2) can be rearranged in the following equations:

$$\frac{\mathrm{d}x}{\mathrm{d}t} = -a_p x + k_p F \tag{3a}$$

with

$$x = 100 - DOT \tag{3b}$$

$$k_p = \frac{S_0 Y_{O/S} 100}{V C_O^*} \tag{3c}$$

$$a_p = k_L a \tag{3d}$$

It should be noted that due to the time-varying nature of $Y_{O/S}$, k_La, V and C_O^*, equations (3a)-(3d) form a linear time-varying dynamical system. Nevertheless, the dynamics of k_p and a_p are expected to be much slower than x. Thus this system can be classified as a linear quasi time-invariant system. (Narendra and Annaswamy, 1989).

3.2 Controller design

The goal is to derive a control law for x by manipulating the glycerol feed rate and by considering k_p and a_p as piecewise time-varying unknown parameters. A model reference design was adopted in which the process dynamics is forced to follow a linear reference model:

$$\frac{\mathrm{d}x}{\mathrm{d}t} = \frac{x^* - x}{\tau_c} \tag{4}$$

with x^* the desired set-point for x and τ_c a first order time constant. Combining (3a) and (4), results in the following controller equation:

$$F = \theta\left(t\right) x + K\left(t\right) x^* \tag{5a}$$

with

$$\theta\left(t\right) = \frac{a_p\left(t\right) - \dfrac{1}{\tau_c}}{k_p\left(t\right)} \tag{5b}$$

$$K\left(t\right) = \frac{1}{\tau_c k_p\left(t\right)} \tag{5c}$$

If a_p and k_p are unknown and time-varying then stability can only be garanteed through on-line adaptation of θ^* and K^*. The following adaptation laws were adopted:

$$F = \hat{\theta}\left(t\right) x + \hat{K}\left(t\right) x^* \tag{6a}$$

$$\frac{\mathrm{d}\hat{x}}{\mathrm{d}t} = \frac{x^* - \hat{x}}{\tau_c} \tag{6b}$$

$$\frac{\mathrm{d}\hat{\theta}}{\mathrm{d}t} = \frac{\mathrm{d}\left(\hat{\theta} - \theta\right)}{\mathrm{d}t} = -\gamma x e \tag{6c}$$

$$\frac{\mathrm{d}\hat{K}}{\mathrm{d}t} = \frac{\mathrm{d}\left(\hat{K} - K\right)}{\mathrm{d}t} = -\gamma x^* e \tag{6d}$$

with

$$e = x - x^* \tag{6e}$$

$\hat{\theta}$ and $\hat{K}$ are estimates of θ and K respectively, γ is a tuning parameter. It may be shown that this system is uniformly stable in the Lyapunov sense.

4 Results and discussion

4.1 Typical process dynamics

A constitutive *P. pastoris* strain expressing ScFv was cultivated in a pilot bioreactor. Figure 1 illustrate the process dynamics.

From Figure 1(a), it can be seen that the control cascade worked as expected. In the first control step, pressure was kept constant at 100 mbarg – at the end of this phase, cell density was still low (∼80 gWCW/l); when DO dropped to 50 %, the stirrer speed increased up to 1000 rpm (achieving high cell density of around 600 gWCW/l), remaining at this value until the end of the fermentation. For the last phase, the adaptive DO-control was initiated, regulating DO steadily at 5 % saturation.

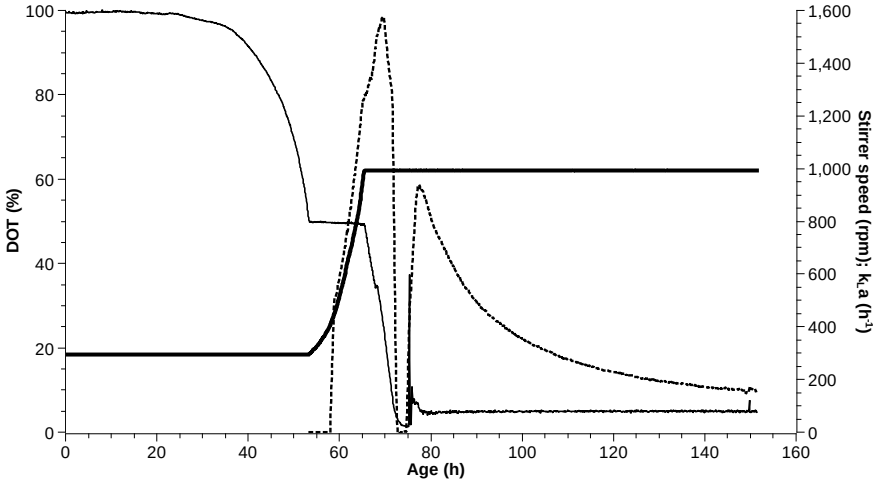

(a)

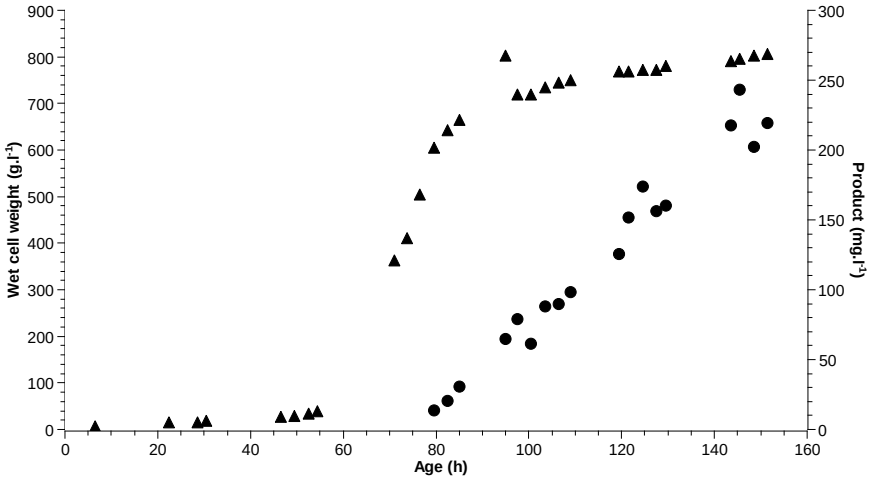

(b)

Figure 1: Fermentation variables' profiles: (a) stirrer speed (bold line), DOT (medium line) and k_La (dotted line); (b) wet cell weight (▲) and product (●).

Table 1: The effect of different factors on productivity

DOT (%)	pH	Medium	Starting biomass (g/l)	Productivity (mg/l)
5	5	Defined	503.8	219.0
5	5		575.8	187.0
5	5	Complex	153.1	238.1
5	4		238.5	325.9
10	5		92.3	440.9
30	5		132.3	252.4

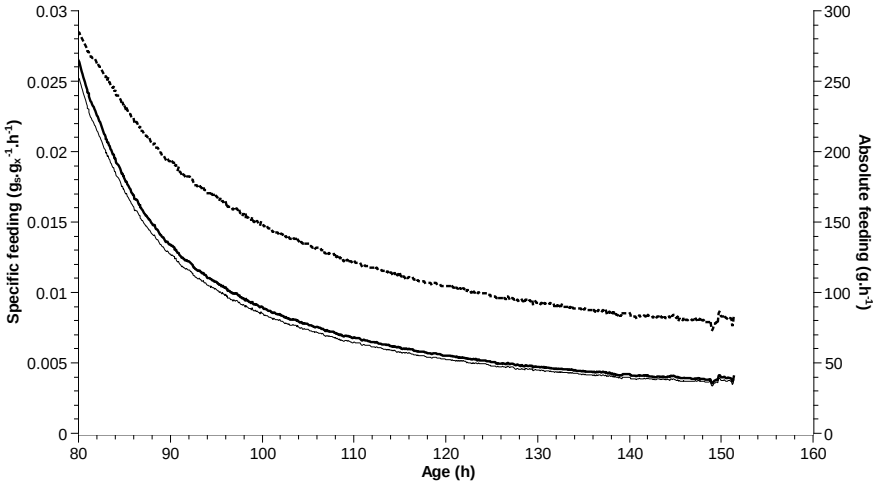

Figure 2: Absolute feeding (dotted line) and specific glycerol feeding for DOT set point of: 5 % (normal line) and 0 % (bold line).

4.2 Factors affecting productivity

In the present analysis, four factors were hypothesized to affect productivity, namely pH, DO concentration, medium composition and starting biomass concentration, which are shown in Table 1.

In what concerns pH, there seems to be an increase in productivity when pH is decreased, which comes accordingly with a previous study (Jahic et al., 2003), due to inhibition of proteolysis. As for DO concentration, when the DO set point is decreased (during OTL), an increase in productivity is usually observed. When DOT is lowered, the driving force of oxygen transfer rate (OTR) is increased and consequently, the OTR is also increased. With an increased OTR, there will be a higher supply of oxygen to cells which is critical for high productivity. Defined medium shows an inferior productivity when comparing to complex medium, most likely because important constituents may be missing in the medium. For the influence of initial biomass concentration on productivity no visible correlation seems to apply.

4.3 Effect of controller on productivity

As stated previously, having a controller that can maintain a constant and low DOT is a valuable tool in *P. pastoris* cultivation. In Figure 1(a) it is shown that the adaptive controller was robust and stable in regulation DOT to 5 %. Another benefit of this controller is that it can maintain its specific feeding close to the theoretical maximum, which would be if for DOT = 0 % (Figure 2). Therefore, with this

controller it is expected to increase productivity when comparing with previous fermentations, without such control.

5 Conclusions

In this work, an adaptive controller was derived that proved to regulate the DOT at a very low levels ($\sim$5 %) in a *P. pastoris* cultivation process with high accuracy. With the presented controller, it was possible to limit the carbon source availability such that the oxygen mass transfer is maximised. As a result,the process productivity and final antibody fragment titre could be increased.

6 Acknowledgments

This work was supported by the Portuguese Fundação para a Ciência e Tecnologia through a Ph.D. grant SFRH/BD/36285/2007.

References

Bobrowicz, P., Davidson, R. C., Li, H., Potgieter, T. I., Nett, J. H., Hamilton, S. R., Stadheim, T. A., Miele, R. G., Bobrowicz, B., Mitchell, T., Rausch, S., Renfer, E., Wildt, S. (2004). Engineering of an artificial glycosylation pathway blocked in core oligosaccharide assembly in the yeast *Pichia pastoris*: production of complex humanized glycoproteins with terminal galactose, *Glycobiology*, 14, 757–766.

Cereghino, G. P. L., Cereghino, J. L., Ilgen, C., Cregg, J. M. (2002). Production of recombinant proteins in fermenter cultures of the yeast *Pichia pastoris*, *Current Opinion in Biotechnology*, 13, 329–332.

Cereghino, J. L., Cregg, J. M. (2000). Heterologous protein expression in the methylotrophic yeast *Pichia pastoris*, *FEMS Microbiology Reviews*, 24, 45–66.

Charoenrat, T., Ketudat-Cairns, M., Jahic, M., Veide, A., Enfors, S.-O. (2006). Increased total air pressure versus oxygen limitation for enhanced oxygen transfer and product formation in a *Pichia pastoris* recombinant protein process, *Biochemical Engineering Journal*, 30, 205–211.

Choi, B.-K., Bobrowicz, P., Davidson, R. C., Hamilton, S. R., Kung, D. H., Li, H., Miele, R. G., Nett, J. H., Wildt, S., Gerngross, T. U. (2003). Use of combinatorial genetic libraries to humanize n-linked glycosylation in the yeast *Pichia pastoris*, *Proceedings of the National Academy of Sciences*, 100, 5022–5027.

Hamilton, S. R., Bobrowicz, P., Bobrowicz, B., Davidson, R. C., Li, H., Mitchell, T., Nett, J. H., Rausch, S., Stadheim, T. A., Wischnewski, H., Wildt, S., Gerngross, T. U. (2003). Production of complex human glycoproteins in yeast, *Science*, 301, 1244–1246.

Hamilton, S. R., Davidson, R. C., Sethuraman, N., Nett, J. H., Jiang, Y., Rios, S., Bobrowicz, P., Stadheim, T. A., Li, H., Choi, B.-K., Hopkins, D., Wischnewski, H., Roser, J., Mitchell, T., Strawbridge, R. R., Hoopes, J., Wildt, S., Gerngross, T. U. (2006). Humanization of yeast to produce complex terminally sialylated glycoproteins, *Science*, 313, 1441–1443.

Jahic, M., Gustavsson, M., Jansen, A.-K., Martinelle, M., Enfors, S.-O. (2003). Analysis and control of proteolysis of a fusion protein in *Pichia pastoris* fed-batch processes, *Journal of Biotechnology*, 102(1), 45–53.

Narendra, K. S., Annaswamy, A. M. (1989). *Stable adaptive systems*, 494, Prentice-Hall, Inc.

Oliveira, R., Clemente, J. J., Cunha, A. E., Carrondo, M. J. T. (2005). Adaptive dissolved oxygen control through the glycerol feeding in a recombinant *Pichia pastoris* cultivation in conditions of oxygen transfer limitation, *Journal of Biotechnology*, 116, 35–50.

Shi, X., Karkut, T., Chamankhah, M., Alting-Mees, M., Hemmingsen, S. M., Hegedus, D. (2003). Optimal conditions for the expression of a single-chain antibody (scFv) gene in *Pichia pastoris*, *Protein Expression Purification*, 28, 321–330.

Proceedings of the 10th International Chemical and
Biological Engineering Conference - CHEMPOR 2008
Braga, Portugal, September 4-6, 2008
E.C. Ferreira and M. Mota (Eds.)

Yarrowia lipolytica as biocatalyst for crude oil degradation

Roberta R. Ribeiro[1], Tatiana F. Ferreira[1], Priscilla F. F. Amaral[1], Maria Alice Z. Coelho[1*], Maria Helena M. Rocha-Leão[1]

[1]Departamento de Engenharia Bioquímica, Escola de Química, Universidade Federal do Rio de Janeiro, 21941-909, Brazil.

Keywords: *Yarrowia lipolytica*, biodegradation, crude oil.
Topic: Integration of life sciences & engineering.

Abstract

In the present work, the degrading potential of an aerobic alkane assimilating yeast, *Yarrowia lipolytica* IMUFRJ 50682, isolated from tropical estuarine water, is evaluated. Even showing a greater potential to degrade aliphatic hydrocarbons*, Y. lipolytica* was evaluated in terms of crude oil degradation. An experimental design was performed varying the initial cell concentration (0.1 - 1.0 mg/ml), initial petroleum concentration (0.1 - 1.0% (v/v)), agitation speed (70 - 160 rpm) and glucose concentration (0 - 1.0 mg/ml). The results show the microorganism great potential to degrade crude oil. *Y. lipolytica* was capable assimilating hydrocarbons up to 20 carbons.

Introduction

Oil spills pose a great hazard for terrestrial and marine ecosystems. The total annual influx of oil into the sea is estimated to be approximately 5.2 million tones, and in productive areas it is almost unavoidable (Leahy and Colwell, 1990). Therefore, a search for new technologies to clean up oil-polluted environments is urgent.

Many microorganisms have the ability to utilize hydrocarbons as sole carbon sources of energy and carbon. Biodegradation is a microbial process whereby the petroleum is used as an organic carbon source, resulting in the breakdown of petroleum components to compounds of lower molecular weight or the transformation of petroleum components to more polar compounds of a carbon number equal to the parent compound. Naturally occurring microorganisms in a contaminated site are already biodegrading the pollutant. Addition of microorganisms in these sites may enhance contaminant removal (Aldrett *et al.*, 1997). The growth of microorganisms on hydrocarbons is often accompanied by the emulsification of the insoluble carbon source in the aqueous phase (Reddy *et al.*, 1982). In some cases, this has been due to the production of extracellular emulsifying agents during hydrocarbons breakdown (Ilori *et al.*, 2005).

Yarrowia lipolytica is an unique strictly aerobic yeast with the ability to degrade very efficiently hydrophobic substrates such as n-alkanes, fatty acids, fats and oils for which it has specific metabolic pathways (Fickers *et al.*, 2005). Kim *et al.* (1999) isolated yeast from an industrialized oil polluted area and verified it was capable to removed 94% of aliphatic hydrocarbons. Analyzing the genetic material of this microorganism concluded it was *Yarrowia lipolytica*. Analyzing 6 different yeast species for crude oil degradation, Zinjarde and Pant (2002) concluded that *Yarrowia lipolytica* was the best degrader utilizing 78% of the aliphatic fraction of Bombay High crude oil.

In the present work, yeast isolated from an estuarine in Guanabara Bay in Rio de Janeiro, Brazil, *Y. lipolytica* IMUFRJ 50682, was evaluated for its crude oil degradation ability. This strain has shown unique surface characteristics such as a high hydrophobicity (Amaral *et al.*, 2006a), which facilitates the contact with the oil phase, and also production of a bioemulsifier (Amaral *et al*., 2006b).

Materials and methods

Materials

Peptone and yeast extract were obtained from Oxoid (Hampshire, UK) and glucose from Reagen (Rio de Janeiro, Brazil).

The crude Oil was provided by *Petróleo Brasileiro* S.A. (PETROBRAS, Brazil), Marlin petroleum: 18,93 ºAPI; asphaltenes = 3,1%; resins/asphaltenes = 8.1; saturated hydrocarbons/aromatic hydrocarbons = 1.6; 2.66% of N, S and O.

Strain, Media and Culture Conditions

A wild type strain of *Yarrowia lipolytica* (IMUFRJ 50682) was selected from an estuarine in the vicinity of Rio de Janeiro, Brazil (Hagler and Mendonça-Hagler, 1981) and maintained at 4ºC on YPD-agar medium. Cells from a preculture, cultivated for 48 h in YPD medium (w/v: Yeast Extract, 1%; Peptone (from casein), 2%; Dextrose, 2%) at 160 rpm, in stationary phase of growth, were centrifuged and used to inoculate 250 mL shake flasks containing 100 mL of mineral medium (g/L: NaCl, 3.5; K_2HPO_4, 0.7; KNO_3, 2.1; $NH_4H_2PO_4$, 0.1; $(NH_4)_2SO_4$, 0.1; $MgSO_4.7H_2O$, 0.02) and the crude oil. To study the influence of glucose, some experiments were realized with 1% (w/v) of glucose in the mineral medium.

Crude oil degradation studies

Before inoculating the cells in the mineral medium, the crude oil was added to the medium. The control experiment was performed without the crude oil. The control experiment was performed without the crude oil. Cells were cultivated at 28ºC in a rotary shaker at 70, 155 and 160 rpm.

Analytical Methods (in aqueous phase)

Cell Growth: Cell growth was followed by optical density measurements at 570 nm converted to mg/ml using a factor previously established. When mentioned in the text, cell growth was determined by plate counting on YPD Agar of susceptive diluted cell suspension, after incubation of 48 h at 28ºC.

Glucose: Extracellular glucose concentration was determined by glucose oxidase method (Enzymatic Colorimetric Glucose Assay Kit, HUMAN GmbH - Germany).

Determination of crude oil degradation

To analyze crude oil degradation, an extraction of the oil phase was performed with chloroform (1:1) in flasks from the beginning (control) and at the end of the crude oil degradation studies. After that, the chloroform solution with extracted crude oil was diluted (when needed) and was analyzed in a spectrophotometer (DR4000UV (HACH)) by a wavelength scan. A solution of crude oil in chloroform in concentration of 9.55 g/l was prepared and some dilutions were performed. For each dilution a wavelength scan was performed in order to show a relation between petroleum concentration and absorbance.

Experimental design and optimization

A 2^2 full-factorial design with two levels leading to a set of 16 experiments was performed more three central points totaling 19 experiments. The range and the levels of the variables here in investigated are given in Table 1. The maximum biomass concentration ($\Delta X_{máx}$) and maximum specific growth rate ($\mu_{máx}$) were taken as the dependent variables or response of the designed experiments. 'Statistica' (version 6.0) software was used for regression and graphical analyses of the obtained data. The statistical significance of the regression coefficients was determined by Student's t-test.

Table 1. The experimental range and levels of the independent variables

Factor	Symbol	Range and levels		
		-1	0	1
Agitation speed (rpm)	Agitation	70	115	160
Initial cell concentration (mg/ml)	[Cells]	0.1	0.55	1.0

Initial crude oil concentration (%, v/v)	[Crude Oil]	0.1	0.55	1.0
Initial glucose concentration (mg/ml)	[Glucose]	0	0.5	1.0

Gas Chromatographic analysis of Crude Oil

Gas chromatographic analyses (GC-MS) were carried out on a Hewlett-Packard Model 6890 Plus equipped with automatic sampler Agilent 7673. Separations were achieved using a capillary column coated with DB-5 (J&W Scientific, 25 m x 0.25 mm i.d., 0.25 μm film thickness) and flame ionization detection (FID). The column temperature for analyses was programmed from 60 ºC to 320 ºC at a rate of 6 ºC min^{-1} and held at 320 ºC for 20 min. The injector was heated at 290 ºC and the flame ionization detector at 340ºC. Helium was used as carrier gas. The samples were injected in splitless mode, injection volume of 1 μL.

Results and Discussion

Crude oil degradation

In order to verify *Y. lipolytica*'s degradation potential of crude oil, the variables studied were: initial cell concentration (0.1, 0.5 and 1.0 mg/ml), initial petroleum concentration (0.1, 0.55 and 1.0% (v/v)), system agitation speed (70, 115 and 160 rpm) and presence of glucose (0, 0.5 and 1.0 g/L), in a full factorial design with three replicates in the central point.

A reduction in biomass concentration was observed in the beginning of the experiments. Figure 1 shows microscopic observations depicting cell adhesion to the crude oil. This phenomena seems to occur because of the amphiphilic surface of this *Y. lipolytica* strain (Amaral et al., 2006a). Therefore cell concentration measurements in aqueous phase were underestimated.

Figure 1. Optic Microscopy of *Yarrowia lipolytica* (1000X)

The first step in the process of seeking optimum conditions is to identify the input variables that have the greatest influence on the experimental response. Figure 2 shows all the variables and their effect in ΔXmáx (Fig. 2-A) and μmáx (Fig. 2-B). The variables with P-values inferior to 0.05 are not statistically significant at the 95% confidence level. It is possible to observe that the individual variable that most influences ΔXmáx and μmáx is the initial cell concentration, followed by the system agitation speed. The initial petroleum and glucose concentration are the variables that have minor influence in cell growth (ΔXmáx and μmáx).

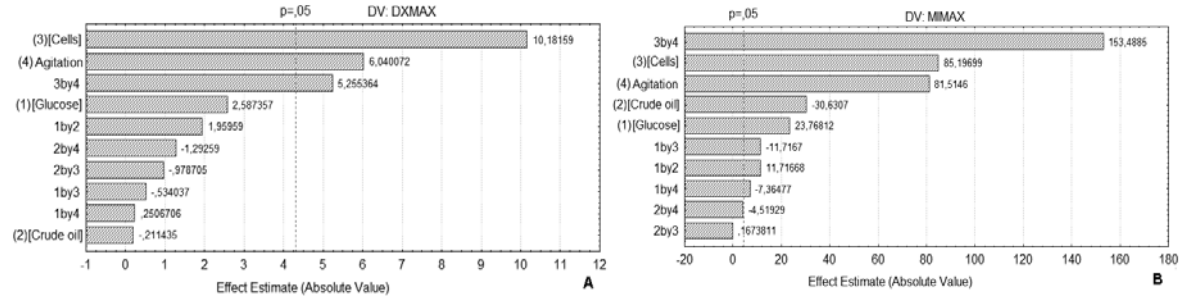

Figure 2. Pareto Chart – Effect of the dependent variables in maximum biomass produced per volume (ΔXmáx) (A) and the maximum specific growth rate (μmáx) (B).

The cells grow faster when the system agitation speed is higher in the presence of higher initial cell concentration. Jobson et al. (1972) worked with several cultures isolated from contaminated soil and the growth rate was not affected by raising aeration. However, *Y. lipolytica* is a strictly aerobic yeast and its growth and metabolites production are influenced by oxygen availability (Amaral et al., 2006b, Alonso et al., 2005). Therefore, higher agitation speed promoted a higher system oxygenation and, consequently, a higher biomass yield.

In the presence of high petroleum concentration, glucose is needed to obtain higher cell production. Kim et al. (1999) also detected increasing *Y. lipolytica*'s cell number as oil concentration raised. Glucose is degraded in the beginning of the experiment as Figure 3 depicts. Being an easily degradable carbon source, glucose is readily consumed producing higher cell concentration that will degrade petroleum. When initial the cell concentration is higher the presence of glucose becomes unnecessary, which indicates that the crude oil compounds assimilation is not associated to cell growth, but related only to cell concentration. However, it is possible to notice that the microorganism grows slightly after glucose starvation, indicating that part of the crude oil assimilation may be designated to cell growth (Fig. 3).

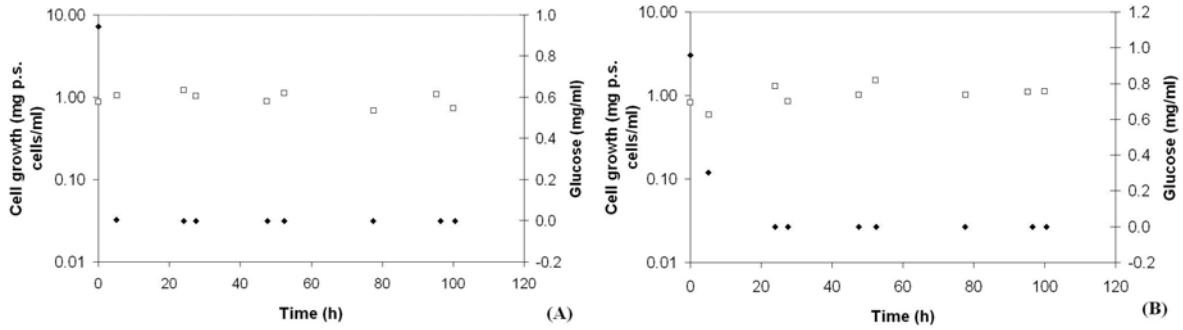

Figure 3. Cell growth profiles (□) and glucose concentration (♦) during crude oil biodegradation. Conditions: 160 rpm agitation speed, with 1.0 mg/ml of glucose, and 1.0 mg/ml initial cell concentration. Initial Crude Oil concentration: (A) 0.1% (v/v); (B) 1.0% (v/v).

Through those results some of the significant conditions to crude oil degradation were chosen: 160 rpm agitation speed and 1.0 mg/ml initial cell concentration. Subsequent experiments with these conditions were performed with cell growth analysis through Colony forming units (CFU), and extraction of oil phase to analyze crude oil degradation. Table 2 shows the results obtained for those experiments. Such results demonstrate that crude oil is used as carbon source for cell growth (experiments without glucose). On the other hand, the presence of this raw material seems to have an inhibitory effect on cell growth when glucose is present, since the number of cells (UFC/ml) obtained in the presence of glucose and petroleum was inferior to that with glucose only. This fact indicates that the cells may need a significant adaptation period to alternate between the consumption of an easily degraded carbon source (glucose) to the crude oil utilization.

Table 2. Colony-Forming Units (UFC) from initial (0 h) and end (120 h) of experiments of crude oil degradation in flasks agitated at 160 rpm. Initial cell concentration: 1.0 mg/ml.

Conditions		UFC/ml	
		Initial	Final
Glucose (mg/ml)	Petroleum (%, v/v)	(x 10-12)	(x 10-15)
0	0.1		1.32
1.0	0.1		0.57
0	1.0	2.32	8.50
1.0	1.0		0.95
1.0	0		1.48

The scanning of the crude oil at UV demonstrated that Marlin petroleum absorbed mostly at three wavelengths: 208, 266 and 388 nm (data not shown). The elevated absorption at 208 nm is due the presence of olefins. Aromatics compounds absorb at 255-275 nm being responsible for the absorption at 266 nm. Paraffins absorbed near VIS being probably responsible for the peak at 388 nm (Silverstein *et al.*, 1991).

Table 3 shows these observations, presenting the crude oil removal for selected wavelengths, which is calculated by Eq. (2):

$$\text{Crude oil removal} = \frac{\text{Abs}_{0h} - \text{Abs}_{120h}}{\text{Abs}_{0h}} * 100 \quad (2)$$

where Abs_i is the absorbance of the sample at the wavelength chosen at i hour of the experiment.

Table 3. Crude oil removal from initial (0 h) and end (120 h) of experiments of crude oil degradation in flasks agitated at 160 rpm. Initial cell concentration: 1.0 mg/ml.

Conditions		Removal (%)		
Glucose (mg/ml)	Crude oil (%, v/v)	208 nm	266 nm	388 nm
0	0.1	5.6	8.2	45.4
1.0	0.1	5.1	7.5	38.0
0	1.0	54.5	59.7	89.0
1.0	1.0	36.8	29.7	80.4

It is possible to notice that crude oil removal by biodegradation is higher for compounds that absorb light in wavelength near 388 nm. Kim *et al*. (1999) has shown 94% degradation rate of saturated aliphatic components in crude oil by *Y. lipolytica*. In the presence of higher crude oil concentration and absence of glucose it is possible to remove more than 50% of crude oil for all selected wavelengths (Table 3).

Gas Chromatographic analysis of Crude Oil

Figure 4 shows the chromatography of the remaining crude oil extracted in the end (Fig. 4-B) of *Y. lipolytica*'s biodegradation tests and in the beginning (Fig. 4-A).

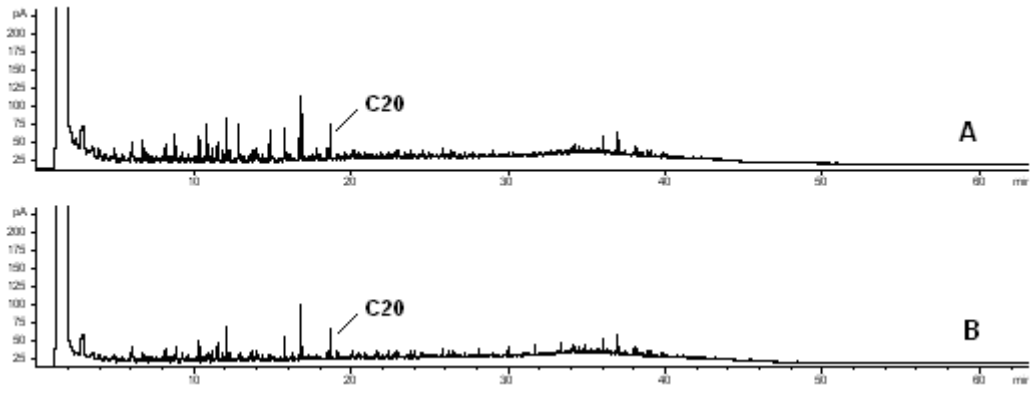

Figure 4. Chromatography of remaining crude oil in the end (B) of of *Y. lipolytica*'s biodegradation tests and in the beginning (A).

Comparing Fig. 4-A with Fig. 4-B it is possible verified that *Y. lipolytica* is capable to assimilate hydrocarbons up to 20 carbons. Some peaks, that are presented before C20 at the chromatography of crude oil in the beginning (Fig. 4-A), do not appear at chromatography of crude oil in the in the end (Fig. 4-B). Also, other peaks before C20 are minors at Fig 4-B indicating that these compounds are less concentrated after biodegradation.

Conclusions

The results here in obtained indicate that *Y. lipolytica* IMUFRJ 50682 has crude oil biodegrading potential, being capable to assimilate hydrocarbons up to 20 carbons. The system agitation that most favored cell growth was 160 rpm due to the aeration rate raise. In flasks containing higher crude oil concentration the observed biodegradation was higher, showing the potential to use this microorganism in crude oil contaminated sites.

The presence of glucose was not positive for the cell growth or crude oil biodegradation, which is an important result for its employment in contaminated sites that may not usually have glucose presence.

References

Aldrett, S., Bonner, J.S., Mills, M.A., Autenrieth, R.L. and Stephens, F.L. (1997). Microbial degradation of crude oil in marine environments tested in a flask experiment. Waters Research, 31, 2840-2848.

Alonso, F.O.M, Oliveira, E.B.L., Dellamora-Ortiz, G.M. and Pereira-Meirelles, F.V. (2005). Improvement of lipase production at different stirring speeds and oxygen levels. Brazilian Journal of Chemical. Engineering, 22(1), 9-18.

Amaral, P.F.F., Lehocky, M., Barros-Timmons, A.M.V., Rocha-Leão, M.H.M., Coelho, M.A.Z. and Coutinho, J.A.P. (2006a). Cell Surface Characterization of *Yarrowia lipolytica* IMUFRJ 50682. Yeast, 23, 867–877.

Amaral, P.F.F., Lehocky, M, da Silva, J.M., Marrucho, I.M., Barros-Timmons, A., Coelho, M.A.Z., Coutinho, J.A.P. (2006b). Production and Characterization of a Bioemulsifier from *Yarrowia lipolytica.* Process Biochemistry, 41, 1894-1898.

Fickers, P., Benetti, P.-H., Waché, Y., Marty, A., Mauersberger, S., Smit, M.S., Nicaud, J.-M. (2005). Hydrophobic substrate utilisation by the yeast *Yarrowia lipolytica* and its potential applications. FEMS Yeast Research 5, 527–543.

Hagler, A.N., Mendonça-Hagler, L.C. (1981), Yeasts from Marine and Estuarine Waters with Different Levels of Pollution in the State of Rio de Janeiro, Brazil. Applied Environmental. Microbiology, 41(1), 173-178.

Ilori, M.O., Amobi, C.J., Odocha, A.C. (2005). Factors affecting biosurfactant production by oil degrading *Aeromonas* spp. isolated from a tropical environment. Chemosphere, 61(7), 985-992.

Jobson, A., Cook, F.D. and Westlake, D.W.S. (1972). Microbial Utilization of Crude Oil. Applied Environmental Microbiology., 23(6), 1082-1089.

Kim, T.H., Lee, J.H., Oh, Y.S., Bae, K.S. and Kim, S.J. (1999). Identification and Characterization of an Oil-degrading Yeast, *Yarrowia lipolytica* 180. The Journal of Microbiology, 37(3), 128-135.

Leahy, J.G. and Colwell, R.R. (1990). Microbial degradation of hydrocarbons in the environment. Microbiology. and Molecular Biology Reviews. 54(3): 305-315.

Reddy, P.G., Singh, H.D., Roy, P.K. and Buruah, J.N. (1982). Predominant role of hydrocarbon solubilization in the microbial uptake of hydrocarbons. Biotechnology and Bioengineering. 24, 1241-1269.

Silverstein, R.M., Bassler, G.C. and Morril, T.C. (1991). Identificação espectrométrica de compostos orgânicos. Rio de Janeiro, RJ.

Zinjarde, S.S. and Pant, A.A. (2002). Hydrocarbon degraders from tropical marine environments. Marine Pollution Bulletin, 44(2), 118-121.

Proceedings of the 10th International Chemical and
Biological Engineering Conference - CHEMPOR 2008
Braga, Portugal, September 4-6, 2008
E.C. Ferreira and M. Mota (Eds.)

Hyperbaric bioreactors use with Yarrowia lipolytica cultures: cellular adaptation to hyperbaric conditions

Marlene Lopes[1], Nelma Gomes[1], Manuel Mota[1], Isabel Belo[1*]
[1] IBB – Institute for Biotechnology and Bioengineering, Centre of Biological Engineering, University of Minho, Campus de Gualtar, 4710–057 Braga, Portugal.

Keywords: hyperbaric bioreactor, pressure, cell concentration, *Yarrowia lipolytica*, oxidative stress
Topic: Suitable conference topic — Integration of life sciences & engineering.

Abstract

Increase air pressure for aeration of microbial cell cultures can prevent oxygen limitation but cause oxidative stress and consequently affect cell physiology. A pressurized bioreactor was used for *Y. lipolytica* batch cultivation under increased air pressure up to 6 bar and no inhibition of cell growth was observed. Moreover, an increase of 6-fold led to a 3.4-fold increase in specific growth rate under atmospheric pressure. The antioxidant enzyme superoxide dismutase was induced by the air pressure raise, which indicates that the defensive mechanisms of the cells were effective and cells could cope with increased pressure. The extracellular lipase activity increased from 22.3 to 43.7 U/l using a 5-bar air pressure instead of air at 1 bar pressure.

1 Introduction

Y. lipolytica is a non-conventional yeast, non-toxic, that can grow to very high densities. It has a haploid genome and sexual life cycle, and therefore is amenable to both classical and molecular analysis (Juretzek et al., 2001; Barth and Gaillardin, 1996). It is also advantegeous in studies of the biodegradative pathways for a variety of hydrophobic compounds including alkanes, oils, and fatty acids and thus for its capacity to produce lipid-degrading enzymes, such as lipases.

The amount of oxygen available to *Y. lipolytica* seems to be an important parameter since that strain is strictly aerobic. Many efforts have been made to overcome the oxygen limitation in the culture medium and previous work demonstrated that hyperbaric air could be successfully applied to yeast cultivation, as a way of improving the oxygen transfer rate to aerobic cultures (Lopes et al., 2008; Aguedo et al., 2005; Belo et al., 2003).

In industrial bioreactors, levels and gradients of total and partial pressures are considerably higher than on the laboratory scale. Thus, cells in bioreactors are often exposed to O_2 partial pressures higher than 210 mbar (corresponding to air at 1 bar). In many cases, increased O_2 partial pressure (higher than approx. 1 bar) is toxic to aerobic cultures and inhibits microbial growth and product formation (Onken and Liefke, 1989). During the reduction of molecular oxygen to water through acceptance of four electrons, active oxygen species such as superoxide anion radical ($O_2\cdot^-$), hydrogen peroxide (H_2O_2), and hydroxyl radical ($HO\cdot$) are generated. These active oxygen species may give rise to damage of enzymes, nucleic acids, or lipids (Izawa et al., 1995). To counter oxidative stress, cells constitutively express enzymes that detoxify the reactive oxygen species and repair the damage caused by them. In addition, yeast cells have adaptive responses to elevated levels of oxidative stress, indicating that these cells sense increased levels of reactive oxygen species and transduce the signal into increased expression of defence activities (Storz and Imlay, 1999). Antioxidant enzymes, such as catalase and superoxide dismutase (SOD), constitute the primary

* Corresponding author. Tel + 351-253604413. E-mail:ibelo@deb.uminho.pt

defences of the cells because they are responsible to transform these reactive oxygen species into nonreactive ones (Moradas-Ferreira et al., 1996).

High pressure is typically viewed as a denaturing factor (Dong et al., 2007), however there is a little report about the effects of slight increased air pressure on the growth and metabolism of microbe cells. The aim of this work is to investigate whether increasing air pressures may lead to increasing biomass yields of *Yarrowia lipolytica* W29, without giving rise to oxidative stress. This paper also reports an investigation into the influence of a pre-adaptation phase of cells to hyperbaric conditions on the lipase production by *Y. lipolytica* cells.

2 Materials and Methods

Yarrowia lipolytica W29 (ATCC 20460) was grown in YPD medium. The medium for lipase production was YNB/olive oil as described in Lopes et al. (2008).

Yeast cells were pregrown in 250 ml Erlenmeyer flasks filled with 100 ml of the YPD medium at 140 rpm, 27 ºC of temperature and for 24 h. Batch cultivations were carried out using a 600 ml stainless steel stirred tank bioreactor (Parr 4563, Parr Instruments, USA), with 400 ml of YPD media, at 27 ºC and 400 rpm in order to asses the effect of pressure in cellular growth and on antioxidant enzymes induction. Compressed air was continuously sparged into the culture at a flow rate of 1 vvm. The values of air pressure studied were 1 bar to 6 bar. An experiment in an Erlenmeyer flask (500 ml) with 200 ml of YPD medium, under atmospheric pressure (1 bar) and an agitation rate of 140 rpm was used as a control. With the aim of investigate the influence of a pre-adaptation phase of cells to hyperbaric conditions on the lipase production by *Y. lipolytica* cells, experiments were conducted in the pressurized bioreactor in which the lipase production phase (YNB/olive oil medium, 400 rpm, at 27 ºC for 48 h, Lopes et al. 2008) was preceded by a 24 h growth in YPD medium at 1 bar or 5 bar of total air pressure.

Culture samples were collected for analysis of cell concentration (optical density at 600 nm and cell number and converted to g cell dry/l), total soluble protein, glucose consumption and enzymatic assays. Total soluble protein was obtained by Bradford's method. Glucose was determined using the 3,5-dinitrosalycilic acid (DNS) method. Extracellular lipase was measured in the samples supernatant using *p*-nitrophenyl-butirate (pNPB) in sodium acetate buffer 50 mM at pH 5.6 as a substrate, at 37 ºC for 15 min. One unit of activity was defined as the amount of enzyme that produces 1 µmol of *p*-nitrophenol per minute under assay conditions. Protease in cell-free samples was quantified as described in Lopes et al. (2008). The antioxidant enzymes were measured after dialysis of the cell extracts, which were obtained as described in Pinheiro et al. (2000). Catalase was assayed using the method described by Beers and Sizer (1952) and superoxide dismutase (SOD) was quantified by the method of Marklund and Marklund (1974).

3 Results and Discussion

Air effects on cell growth

Typical batch growth curves and glucose consumption profiles for the experiments under increased air pressure and atmospheric pressure are shown in Figure 1.The application of 6 bar stimulated cell growth compared to the atmospheric conditions.

Pressure increase had a clear positive effect on this yeast metabolism, since the biomass production increased and reached its maximal value for an air pressure of 6 bar. An increase of the cell dry weight at 6 bar of 3.5- and 5-fold was obtained compared with the experiments under atmospheric pressure in the control and in the bioreactor, respectively.

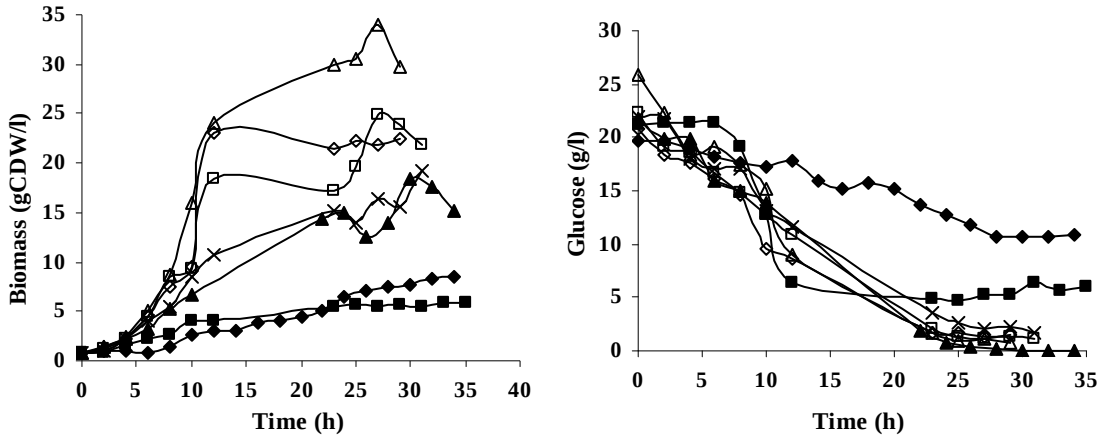

Fig. 1 Batch growth and glucose consumption of *Yarrowia lipolytica* at atmospheric pressure (♦) and in hyperbaric reactor under pressures of 1 bar (■), 2 bar (▲), 3 bar (×), 4 bar (□), 5 bar (◊) and 6 bar (Δ).

The results described above are in accordance with the previous work of Lopes et al. (2008), in which no cellular activity inhibition by pressure was detected in batch cultures of *Y. lipolytica* in culture media without glucose. Also, Belo et al. (2005) observed for semi-continuous cultures of *Saccharomyces cerevisiae* that an increase of pressure up to 10 bar had no metabolic impact in the cells. Aguedo et al. (2005) reported that the application of 5 bar air pressure stimulated the cell growth of *Y. lipolytica* W29 comparatively to atmospheric growth conditions.

In experiments under atmospheric pressure and 1 bar of air pressure, glucose was not totally consumed. The raise of air pressure up to 6 bar led to a completely consumption of glucose.

The use of pressure might be exploited to improve the biomass productivity of *Y. lipolytica* W29 (Table 1). An increase of air pressure up to 6 bar led to a 4.1-fold improvement in biomass productivity comparatively to atmospheric pressure. This result is in accordance with previous work of Pinheiro et al. (2000), in which the productivity in biomass of *K. marxianus* CBS 7894 was increased with the increase in air pressure up to 6 bar. Also, Charoenrat et al. (2006) observed that the cell mass productivity of *Pichia pastoris* can be improved by application of increased air pressure. However, for *S. cerevisiae*, Pinheiro et al. (1997) reported that an increase of 6-bar air pressure led to a decrease on biomass productivity for a batch mode of operation. This shows that microorganisms react differently to the air pressure rise, depending also on other culture conditions.

Table 1 Changes in biomass yield, specific growth rate and productivity with air pressure in batch experiments.

Pressure (bar)	$Y_{x/s}$ (g biomass/g glucose) (%)	μ (h^{-1})	P (g biomass/l·h)
Control	53.3	0.09	0.25
1	34.7	0.18	0.17
2	70.2	0.19	0.45
3	96.7	0.23	0.62
4	104.1	0.26	0.71
5	117.9	0.28	0.77
6	121.1	0.31	1.02

The specific growth rate of *Y. lipolytica* was clearly enhanced by the increase of air pressure. An increase of 6-bar led to a 3.4- and 1.7-fold increase in specific growth rate under atmospheric pressure and 1 bar, respectively. Due to the high oxygen mass transfer rate, the cells have more oxygen in the medium giving higher growth rates, and less time is necessary to obtain maximum cell concentration. Belo et al. (2005) reported that an increase of air pressure up to 6 bar led to a 1.8-fold improvement in the specific growth rate of *S. cerevisiae*.

Also, Pinheiro et al. (2000) observed that an increase of 4-bar led to a high increase in specific growth rate for *K. marxianus*.

Biomass yield was also enhanced by air pressure rise. With 6 bar air pressure biomass yield was 121.1 % whereas at 1 bar it was 34.7 %. At values of air pressure up to 2 bar glucose was not totally consumed, probably due to oxygen limitation. An increase of the yield at 6 bar of 56 % and 71 % was obtained compared with the experiments under atmospheric pressure and 1 bar, respectively.

It is clear from these results that pressure had no inhibitory effects on the growth of this yeast strain. An increase of air pressure up to 6 bar might successfully be applied to the improvement of the biomass production of *Y. lipolytica* W29.

Yeast cells were observed by optical microscopy and was noted that the cells displayed a typical oval form in all assays up to 6 bar (data not shown). The results demonstrated that cell exposure to increased air pressure did not induce hyphae formation.

Pressure effect on antioxidant enzyme activities

To examine the effects of oxygen toxicity on yeast cells, with the increase in oxygen partial pressure, the changes of cellular antioxidant enzyme activities under different air pressures were determined. Figure 2 presents the data of the catalase and SOD specific activities, measured at the end of the cell cultivation under hyperbaric conditions.

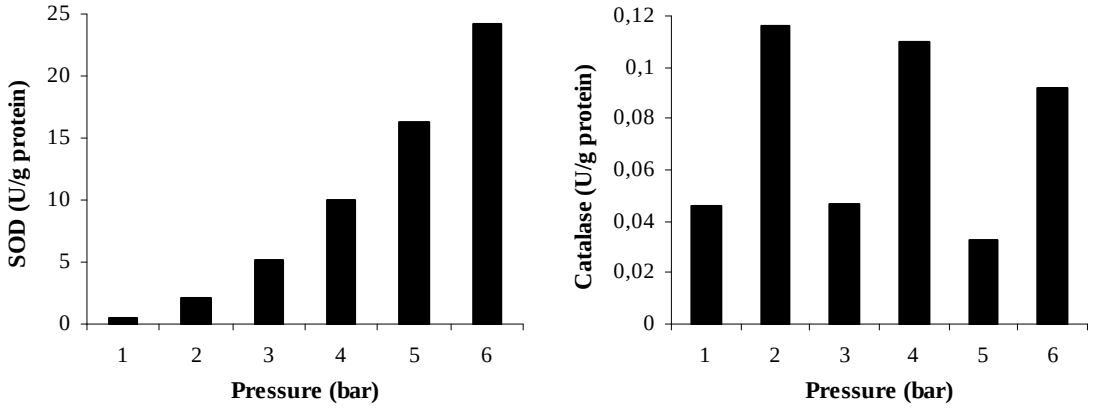

Fig. 2 Effect of air pressure on superoxide dismutase and catalase specific activities, in the final batch cell cultures (approximately 30 h of growth).

Superoxide dismutase specific activity was induced by hyperbaric air to a maximum of 6 bar. An increase of the SOD specific activity at 6 bar of 53.4-fold was obtained compared with the experiments under 1 bar. This shows the ability of *Y. lipolytica* cells to respond to the increase of reactive oxygen species formation because of hyperoxygenation. The SOD induction showed the cell sensitivity to high oxygen concentrations. However, as no cell growth inhibition was observed under pressurized conditions, it is quite safe to state that the cells of the strain used can cope with air pressure values up to 6 bar.

The influence of total air pressure on the catalase activity is not clear, thus it seems that this enzyme plays a minor role in the defensive mechanisms against the oxidative stress, for *Y. lipolytica*.

These results demonstrate that the raise of air pressure could be also applied to SOD production, once it is most induced.

Pressure effect on lipase production and pre-adaptation

In order to investigate the influence of a pre-adaptation phase of cells to hyperbaric conditions on the lipase production by *Y. lipolytica* cells under increased pressure, assays

were conducted in the pressurized bioreactor in which cells were pregrown on the bioreactor at normal and increased pressure following by a lipase production phase at normal and increased pressure.

The increase of total air pressure influences enzymatic activity, as demonstrated by previous work of Lopes et al. (2008). The authors observed that an increase of OTR by raising air pressure up to 8 bar resulted in an increase of the lipase production by *Y. lipolytica* cells grown at atmospheric pressure. In this work, an increase of the lipase activity and lipase productivity at 5 bar of 1.8-fold and 3.7-fold, respectively, was obtained compared with the experiments under 1 bar, independently of the pressure conditions used in the inocullum preparation (Fig. 3A).

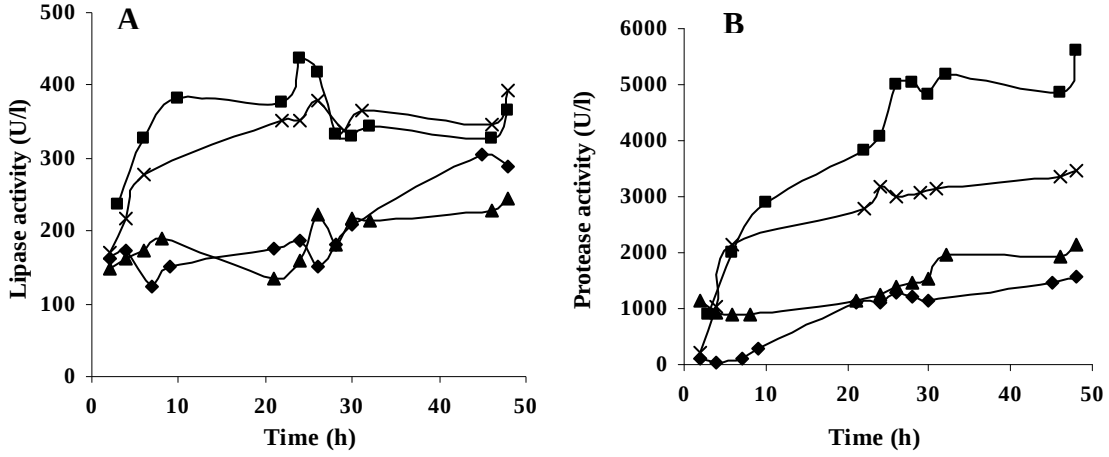

Fig. 3 Extracellular lipase (A) and protease (B) activities profiles by *Yarrowia lipolytica* in the pressurized reactor at different air pressures of growth and production, respectively: 1 bar and 1 bar (♦), 1 bar and 5 bar (■), 5 bar and 1 bar (▲) and 5 bar and 5 bar (×).

For the range of air pressure values applied, the pre-adaptation phase of cells to hyperbaric conditions did not improve the lipase production. The lipase production at 5 bar with cells pregrown at the same air pressure was similar to the obtained with grown cells under atmospheric pressure. Therefore, it can be concluded that the *Y. lipolytica* cells can quickly respond and adapt to hyperbaric conditions and no need of long phases of hyperbaric stress adaptation is needed.

Besides lipase production, the production of other enzymes, such as proteases, by *Y. lipolytica* strains has been reported (Puthli et al., 2006). Figure 3B shows the results of monitoring protease secretion along time, using azocasein as substrate. During the first hours of culture the protease activity was low, increasing gradually until the end of the cultivation time, suggesting that the decrease of the medium pH (data not shown) favours the production of an acid protease by yeast.

The highest value of protease production was found for the 5 bar assays, whereas in the experiments carried out under 1 bar its concentration in the medium was lower. The presence of protease in culture medium can influence the production kinetics of lipases since the prolonged time of fermentation can lead to the loss of product due to its decomposition. However, in this work, highest value of protease production was reached at the same air pressure (5 bar) that the maximum lipase productivity was obtained. Probably, lipase activity might be improved even more if protease secretion into the medium is inhibited by a chemical agent.

4 Conclusions

For the experimental conditions used in this work, air pressure rise up to 6 bar proved to be applicable to the batch cultivation of *Yarrowia lipolytica* W29. It has been demonstrated that the use of air pressure has positive effects on the growth behaviour of yeast and that air

pressure may be a way of increase the specific growth rate, leading to high biomass productivity. For *Y. lipolytica*, an increase of air pressure up to 6 bar led to a 4.1-fold improvement in biomass productivity comparatively to atmospheric pressure.
To protect against the damage caused by oxidative stress, cells possess a number of antioxidant enzymes and repair activities, most of which are expressed al low levels during normal growth. In spite of the SOD induction, air pressure rise did not inflict oxidative stress to the cells. Yarrowia lipolytica W29 adapt rapidly to hyperbaric conditions, thus this conditions can be imposed to cultures of this strain was a way of preventing oxygen limitation to cell growth and as a mean of several enzymes production improvement such as lipases, proteases and SOD.

References

Aguedo, M., Gomes, N., Garcia, E.E., Waché, Y., Mota, M., Teixeira, J.A., Belo, I. (2005). Decalactone production by *Yarrowia lipolytica* under increased O_2 transfer rates. *Biotechnol Lett* 27, 1617-1621.

Barth, G., Gaillardin, C. (1996). The dimorphic fungus *Yarrowia lipolytica*. In: Wolf K, ed. *Nonconventional Yeasts in Biotechnology*, Berlin, Germany: Springer-Verlag, pp 313-388.

Beers, R.F., Sizer, I.W. (1952). A spectrophotometric method for measuring breakdown of hydrogen peroxide by catalase. *J Biol Chem* 195, 276-287.

Belo, I., Pinheiro, R., Mota, M. (2005). Morphological and physiological changes in *Saccharomyces cerevisiae* by oxidative stress from hypebaric air. *J Biotechnol* 115: 397-404.

Belo I, Pinheiro R, Mota M (2003) Fed-batch cultivation of Saccharomyces cerevisiae in a hyperbaric bioreactor. *Biotechnol Prog* 19, 665-671.

Charoenrat, T., Ketudat-Cairns, M., Jahic, M., Veide, A., Enfors, S-O. (2006). Increased total air pressure versus oxygen limitation for enhanced oxygen transfer and product formation in a *Pichia pastoris* recombinant protein process. *Biochem Eng J* 30, 205-211.

Dong, Y., Yang, Q., Jia, S., Qiao, C. (2007). Effects of high pressure on the accumulation of trehalose and glutathione in the *Saccharomyces cerevisiae* cells. *Biochem Eng J* 37, 226-230.

Izawa, S., Inoue, Y., Kimura, A. (1995). Oxidative stress response in yeast: effect of glutathione on adaptation to hydrogen peroxide stress in *Saccharomyces cerevisiae*. *FEBS Lett* 368, 73-76.

Juretzek, T., Le Dall, M., Mauersberger, S., Gaillardin, C., Barth, G., Nicaud, J. (2001). Vectors for gene expression and amplification in the yeast *Yarrowia lipolytica*. *Yeast* 30, 97-113.

Lopes. M., Gomes, N., Gonçalves, C., Coelho, M.A.Z., Mota, M., Belo, I. (2008). *Yarrowia lipolytica* lipase production enhanced by increased air pressure. *Lett Appl Microbiol* 46, 255-260.

Marklund, S., Marklund, G. (1974). Involvement of the Superoxide Anion Radical in the Autoxidation of Pyrogallol and a Convenient Assay for Superoxide Dismutase. Eur J Biochem 47(3), 469-474.

Moradas-Ferreira, P., Costa, V., Piper, P., Mager, W. (1996). The molecular defenses against reactive oxygen species in yeast. *Mol Microbiol* 19, 651-658.

Onken, U., Liefke, E. (1989). Effect of total and partial pressure (oxygen and carbon dioxide) on aerobic microbial processes. Adv Biochem Eng Biotechnol 40, 137-169.

Pinheiro, R., Belo, I., Mota, M. (1997). Physiological behaviour of *Saccharomyces cerevisiae* under increased air and oxygen pressures. *Biotechnol Lett* 19(7), 703-708.

Pinheiro, R., Belo, I., Mota, M. (2000). Air pressure effects on biomass yield of two different Kluyveromyces strains. Enz Microbiol Technol 26, 756-762.

Puthli, M.S., Rathod, V.K., Pandit, A.B. (2006). Optimization of lipase production in a triple impeller bioreactor. *Biochem Eng J* 27, 287-294.

Storz, G., Imlay, J.A. (1999). Oxidative stress. *Curr Opin Microbiol* 2, 188-194.

Proceedings of the 10th International Chemical and
Biological Engineering Conference - CHEMPOR 2008
Braga, Portugal, September 4-6, 2008
E.C. Ferreira and M. Mota (Eds.)

Development of bioprocesses based in biphasic media involving the yeast *Yarrowia lipolytica*

Nelma Gomes, Cristiana Gonçalves, Marlene Lopes, Mário Aguedo, José A. Teixeira, Manuel Mota, Isabel Belo*

IBB – Institute for Biotechnology and Bioengineering, Centre of Biological Engineering, University of Minho, Campus de Gualtar, 4710–057 Braga, Portugal.

Keywords: Biphasic media, *Yarrowia lipolytica*, lipase, castor oil, OMW
Topic: Suitable conference topic — Integration of life sciences & engineering

Abstract

Yarrowia lipolytica has been intensively used in our research group to develop different bioprocesses based in the ability of this yeast to use hydrophobic substrates. Work has been focused in the optimization of the production of γ-decalactone and lipase, and to degrade and detoxify olive oil wastewater producing simultaneously high-value compounds, such as enzymes. Studies of the oxygen mass transfer phenomenon in biphasic media was also conducted and applied to select the most adequate oxygenation conditions for bioprocesses. Application of increased air pressures has also been proven to be an effective mean to improve oxygen transfer rate into *Y. lipolytica* cultures.

1 Introduction

The ascomycetous yeast *Yarrowia lipolytica* is a natural dimorphic fungus, which forms yeast cells, pseudohyphae and septate hyphae. The morphology is determined both by growth conditions (aeration, carbon and nitrogen sources, pH, etc) and by the genetic background of the strain (Barth and Gaillardin, 1997).

Y. lipolytica is one of the more intensively studied non-conventional yeast species. This microorganism is not only of interest for fundamental research, but also for biotechnological applications (Barth and Gaillardin, 1997). As it is considered as non-pathogenic and as GRAS by the American Food and Drug Administration, this yeast has been used in several industrial applications like production of single cell protein, peach flavour and citric acid (Beckerich et al., 1998). The range of substrates used by *Yarrowia lipolytica* include alkanes, fatty acids, organic acids, proteins and some sugars, which also contributes to the interest of this yeast (Fickers et al., 2005).

In our laboratory we have been exploring the abilities of this yeast in three main different fields: optimization of a peach-like aroma compound production; optimization of lipase production using hyperbaric conditions; and valorization of olive mill wastewater (OMW) by producing high-value compounds while degrading this waste.

2 Aroma production

γ-Decalactone is a peach-like aroma compound well known in several food and beverages, reason why the food industry has a high interest in its biotechnological production. One of the better known applications is the biotransformation of ricinoleic acid catalysed by yeasts with GRAS status, conferring a natural label to the aroma, which is very important, considering the increasing health- and nutrition-conscious lifestyles.

* Corresponding author. Tel + 351-253604413. E-mail:ibelo@deb.uminho.pt

Ricinoleic acid (12-hydroxy-octadec-9-enoic acid) is a hydroxylated C_{18} fatty acid that in its esterified form is the major constituent (about 86%) of castor oil, making it an abundant compound.

The yeast *Yarrowia lipolytica* is able to carry out the biotransformation of ricinoleic acid into γ-decalactone. This process involves the substrate degradation through the peroxisomal β-oxidation (Figure 1), leading to the formation of 4-hydroxydecanoic acid, which cyclises into γ-decalatone (Blin-Perrin et al., 2000).

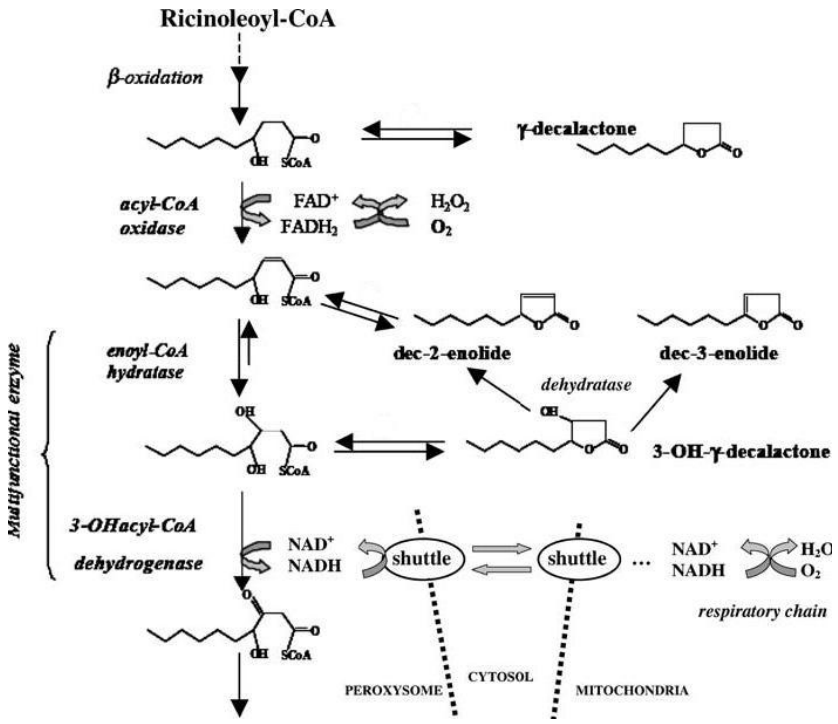

Figure 1 - β-Oxidation cycle from 4-hydroxydecanoic acid (the direct precursor of γ-decalactone) during the degradation of ricinoleoyl-CoA.

The production of γ-decalactone has been intensively investigated in order to better understand the all process and optimize it (Aguedo, 2002; Waché et al., 2001). Oxygen availability in the medium is a determining factor in the process, intervening in the control of the peroxisomal β-oxidation pathway. Thus, work has focused in the optimization and modelization of oxygen mass transfer in this complex multi-phase system composed by an aqueous and an organic phase as well as a gaseous and a solid phase (Gomes et al., 2007).

Oxygen mass transfer in the biphasic system

Oxygen transfer rate (OTR) in a system is a function of the oxygen volumetric mass transfer coefficient (k_La) and the oxygen solubility in the medium. For a specific bioreactor and medium, it is possible to increase k_La and, consequently, OTR, using high agitation and aeration rates. However, this causes high power consumption, significantly increasing operation costs. The addition of a second, water-immiscible phase, in which oxygen has a higher solubility, has been proposed by several authors as an alternative mean of OTR improvement. Usually, experiments described in the literature use a hydrocarbon or a perfluorocarbon (PFC) as an inert dispersed phase in the aqueous medium. In the system herein described, the organic phase is the substrate used by the cells and not an inert compound used with the only purpose of increasing OTR. The effects of adding a second liquid organic phase on k_La may change (k_La values may increase, decrease, or remain constant) depending on the nature of the organic compound and the operating conditions (Dumont and Delmas, 2003). So, in order to take into account, not only the effect of the

organic phase, but also the effect of surfactant and operating conditions (agitation and aeration rates) on k_La, an empirical correlation was proposed, assuming that the two liquid phases behave as a single homogeneous phase (Eq. 1).

$$k_L a = 243 \cdot \left(\frac{P_g}{V}\right)^{0.6} \cdot (v_s)^{0.6} \cdot (1 - X_{RM})^3 \cdot (1 - X_{Tween})^{-141} \quad \text{Eq. (1)}$$

Where P_g represents the power input of the aerated bioreactor; V, the bioreactor working volume; v_s, the superficial gas velocity through the bioreactor; X_{ORG}, the fraction of the organic phase; X_{Tween}, the fraction of surfactant; and δ, α, β and γ are numerical constants.

This correlation enables the prediction of k_La as a function of operating conditions and organic phase composition for the biotransformation system (Gomes et al., 2007).

An interaction effect between the organic phase and the surfactant was found: the organic phase increased k_La in the absence of the surfactant but had an opposite effect when Tween 80 was available in the medium. This is due to a change in the surfactant at the gas-liquid interface because when an organic phase is added to aqueous solutions with Tween 80, a new distribution of surfactant between interface and bulk phases is originated. The presence of surfactant inhibits the mass transfer because its accumulation at the gas-liquid interface causes a decrease in the liquid surface elements renewal (turbulence near the interface) and it implies that oxygen concentration in the liquid phase zone, near to the gas-liquid interface, is higher than the oxygen concentration in the bulk of the liquid phase. Therefore, the driving force of the absorption process decreases producing the same decrease in the absorption rate (Goméz-Díaz et al., 2008).

Influence of oxygen transfer rate on the aroma production

The influence of k_La on γ-decalactone production by the biotransformation of methyl ricinoleate (ricinoleic acid source) was proven through the performance of several experiments at different operating conditions, in a 2-L stirred bioreactor. A maximal aroma compound production (141 ± 21 mg L^{-1}) was achieved for a k_La of 70 h^{-1}, obtained at 27ºC with agitation and aeration rates of 400 rpm and 0.6 vvm, respectively, 1% (v/v) methyl ricinoleate and a cellular density of 1.4×10^8 cells mL^{-1}.

Previous works in the group have demonstrated that hyperbaric air can be successfully applied to yeast cultivation as a way of improving the OTR to aerobic cultures (Belo et al., 2003). Based on this, the effect of increased air pressures on the oxygen mass transfer improvement for the production of γ-decalactone was studied (Aguedo et al., 2005). Essays were carried out in a 600-mL stainless steel high-pressure bioreactor. Air pressures of 1 bar (atmospheric pressure), 5 bar and 10 bar were applied on the cell growth and on the biotransformation of ricinoleic acid. The application of 5 bar accelerated cell growth, compared to the atmospheric conditions. However, when 10 bar was used, growth was inhibited after 10 h exposure, suggesting hyperbaric stress on the cells.

Besides γ-decalactone, also other compounds (3-hydroxy-γ-decalactone, dec-2-en-4-olide and dec-3-en-4-olide) proceeding from the direct precursor of γ-decalactone (4-hydroxydecanoic acid) were analyzed (Figure 1).

Results revealed that oxygen plays an important role on the enzymes that control the β-oxidation metabolic pathway. Low oxygen concentrations in the medium induced the control of the β-oxydation pathway by acyl-CoA oxidase and therefore, an accumulation of γ-decalactone occured. On the contrary, when higher oxygen levels were used, the control of the pathway was carried out by 3-hydroxyacyl-CoA dehydrogenase, resulting in an accumulation of 3-hydroxy-γ-decalactone.

Effect of two different substrates and its concentrations on the aroma production

Since oxygen is more soluble in the organic phase than in the aqueous phase, increasing oil concentration leads to an oxygen mass transfer improvement.

We investigated the influence of two different ricinoleic acid sources (castor oil and methyl ricinoleate) at several concentrations, on the production of γ-decalactone by *Y. lipolytica* (Gomes et al., 2008). Experiments were carried out in 500-mL flasks. The highest amounts of γ-decalactone (around 2 gL^{-1}) were achieved with oil concentrations of 3% and 5% (v/v) for each substrate, but as the process was quite long, the productivity of the process was small (10 to 14.5 mg L^{-1} h^{-1}). In order to improve this, experiments with 3% (v/v) methyl ricinoleate were carried out in a 2-L stirred bioreactor, under different agitation and aeration rates. The highest concentration and productivity achieved for the aroma production was approximately 1 g L^{-1} and 87.6 mg L^{-1} h^{-1}, respectively, with an agitation rate of 600 rpm and 5 L min^{-1} of aeration (Figure 2). However, contrary to the essays in flask, in bioreactor, high concentrations of 3-hydroxy-γ-decalactone were produced for all conditions tested, reaching a maximal value of 8 g L^{-1}, using 600 rpm and 5 L min^{-1} of agitation and aeration rates, respectively. The accumulation of this compound and of γ-decalactone were directly proportional to the increase of OTR in the medium. Work now proceeds in the optimization of the OTR conditions to improve the overall process.

3 Lipase production

Lipases, triacylglycerol hydrolases, are an important group of biotechnologically relevant enzymes finding vast applications in food, dairy, detergent and pharmaceutical industries.

Due to the facility of single cell use and to the high secretion ability, *Yarrowia lipolytica* has revealed to be an interesting and alternative organism to be used in lipase production (Pignede, 1998).

The increase of lipase productivity during the fermentation process is of great importance since lower costs of production could promote new industrial applications. The extracellular lipase production is affected by different environmental factors such as pH, temperature, medium composition, aeration, agitation and proteases present in the medium. Moreover, the presence of some compounds (i.e. fatty acids, triglycerides and surfactants) has often shown to induce lipase secretion (Dalmau et al., 2000).

Effect of medium composition and pH on lipase production

Lipase production by the strain *Y. lipolytica* W29 was previously studied through a experimental 2^{4-1} fractionated factorial design (Lopes et al., 2007). A culture medium composed by YNB without aminoacids, at pH 7.2, with an arabic gum concentration of 0.5% (w/v) promoted the highest values of lipase activity (247 U L^{-1}) and productivity (10.7 U L^{-1} h^{-1}). The presence of Tween 80 revealed to have a negative effect on lipase activity. Contrary to other studies (Dalmau et al., 2000; Fickers et al., 2003), the increase of olive oil concentration did not improve lipase activity and the presence of glucose did not inhibit the enzyme production.

Effect of increased air pressures on cell growth and morphology and on lipase production

The amount of available oxygen to *Y. lipolytica* is an important parameter since this strain is strictly aerobic. In order to obtain a further insight on the influence of moderate total air pressure both on yeast growth and on lipase production, *Y. lipolytica* was grown in 300-mL cylindrical stainless steel pressurized bioreactor where the variation of OTR with pressure could be modeled (Lopes et al., 2008). Despite the OTR increase of 2.3-fold when the pressure varied from 4 bar up to 8 bar, no differences were observed in the cellular growth.

An increase of the lipase activity at 8 bar (550 U L^{-1}) of 5.5-fold and 2.3-fold was obtained compared with the experiments under atmospheric pressure and 4 bar, respectively. The rise of the total air pressure from 1 bar up to 8 bar, led to a 4.8-fold improvement in the lipase productivity (11 U L^{-1} h^{-1}). Besides lipase production, protease secretion into the medium was also observed. Its activity was inhibited by air pressure of 8 bar, indicating that pressure has different effect on lipase and protease activities.

Simultaneously, the effect of hyperbaric air in the morphology of this dimorphic yeast has been investigated using an automatic image analysis technique. It was observed that cell exposure to increased air pressure did not induced hyphae formation but led to a cell size decrease for the 8 bar cultures (Lopes et al., 2008).

Lipase induction by castor oil and methyl ricinoleate

Besides olive oil, other compounds can be used to induce lipase activity in *Y. lipolytica*. This is the case of the oils used in the biotransformation process of aroma production mentioned above. Lipase activity was detected in experiments with different concentrations of both ricinoleic acid sources, castor oil (CO) and methyl ricinoleate (MR) (Table 1).

Table 1 – Maximum lipolytic activity obtained for different operating conditions.

Experiments	[Substrate] (% v/v)	Maximum lipolytic activity (U L^{-1})
w/ washed cells	[MR] = 3	19 ± 3.9 (169.5 h)
w/o washed cells	[MR] = 3	105 ± 4.8 (271.5 h)
	[CO] = 3	42 ± 7.1 (192 h)

Methyl ricinoleate seemed to be more adequate than castor oil to induce lipase production, since the lipolytic activity was 2.5-fold higher with MR than with CO, for the conditions tested. Moreover, the enzyme production seems to be significantly affected by the hydrophobic characteristics of the cell, since a higher lipase activity was found when the biotransformation was carried out with cells that did not suffer the washing pre-treatment.

4 Olive mill wastewater

The ability of hydrophobic substrates use by *Yarrowia lipolytica* strains has been used not only to develop industrial biporocesses but also to solve environmental problems, such as bioremediation and lipidic wastewaters treatment (Fickers et al., 2005). Olive mill wastewater (OMW) is an example of those environmental problems resulting from the olive mill industry. OMW is a dark-colored stable emulsion effluent, characterized by a high polluting load.

The organic fraction of OMW includes sugars, tannins, polyphenols, polyalcohols, pectins and lipids, resulting in high values of chemical oxygen demand (COD). Thus, OMW can represent a possible renewal resource that might be a basis for fermentation processes.

Yeast species such as *Yarrowia lipolytica* can grow well in OMW media, consume the organic material and, simultaneously, produce biomass and other valuable products like enzymes and organic acids (D'Annibale et al., 2006), contributing for the valorization of OMW, which is the aim of the current investigation in our laboratory. Thus, in a first stage, work focused on the potential use of OMW as a culture medium for different *Yarrowia lipolytica* strains; i.e. their ability to grow and to produce high-value compounds, such as enzymes (e.g.: lipases), while degrading and detoxifying this waste was evaluated. For this purpose, different OMW from different regions of Portugal have been collected and characterized. Although all strains were able to grow in OMW based media without dilution, to consume almost all of the sugars present in the media and to significantly reduce COD values, the most adapted strains were selected.

Investigation now proceeds on the optimization of OMW fermentation process on a lab-scale bioreactor.

References

Barth, G.; Gaillardin, C. (1997) Physiology and genetics of the dimorphic fungus *Yarrowia lipolytica*. FEMS Microbiology Review, 19:219-237.

Beckerich, J.-M.; Baudevin, A. B.; Gaillardin, C. (1998) *Yarrowia lipolytica*: a model organism for protein secretion studies. International Microbiology, 1:123–130.

Fickers, P.; Benetti, P.-H.; Waché, Y.; Marty, A.; Mauersberger, S.; Smit, M. S.; Nicaud, J.-M. (2005) Hydrophobic substrate utilisation by the yeast *Yarrowia lipolytica*, and its potential applications. FEMS Yeast Research, 5:527-543.

Blin-Perrin, C.; Molle, D.; Dufosse, L.; Le-Quere, J.-L. ; Viel, C. ; Mauvais, G. ; Feron, G. (2000) Metabolism of ricinoleic acid into γ-decalactone: β-oxidation and long chain acyl intermediates of ricinoleic acid in the genus *Sporidiobolus* sp. FEMS Microbiology Letters, 188:69-74.

Aguedo, M. (2002) Biotransformation de lipides en arômes par *Yarrowia lipolytica*: interactions avec le substrat, excrétion et toxicité des métabolites produits. PhD Thesis, Université de Bourgogne, Dijon, France.

Waché, Y.; Aguedo, M.; Choquet, A.; Gatfield, I.; Nicaud, J.-M., Belin, J.-M. (2001) Role of β-oxidation enzymes in γ-decalactone production by the yeast *Yarrowia lipolytica*. Applied and Environment Microbiology, 67(12): 5700-5704.

Gomes, N., Aguedo, M., Teixeira, J.A., Belo, I. (2007) Oxygen mass transfer in a biphasic medium: Influence on the biotransformation of methyl ricinoleate into γ-decalactone by the yeast *Yarrowia lipolytica*. Biochemical Engineering Journal, 35, 380-386

Dumont, E., Delmas, H. (2003) Mass transfer enhancement of gas absorption in oil-in-water systems: a review. Chemical Engineering Process, 42:419-438.

Gómez-Díaz, D., Gomes, N., Teixeira, J.A., Belo, I. (2008) Oxygen mass transfer to emulsions in a bubble column contactor. Submitted to Chemical Engineering Journal.

Belo, I., Pinheiro, R., Mota, M. (2003) Fed-batch cultivation of *Saccharomyces cerevisiae* in a hyperbaric bioreactor. Biotechnology Progress, 19, 665-671.

Aguedo, M., Gomes, N., Garcia, E.E., Waché, Y., Mota, M., Teixeira, J.A. (2005) Decalactone production by *Yarrowia lipolytica* under increased O_2 transfer rates. Biotechnology. Letters, 27, 1617-1621.

Gomes, N., Aguedo, M., Teixeira, J.A., Belo, I. (2008) Production of γ-decalactone from two different ricinoleic acid sources by *Yarrowia lipolytica*: effect of substrate concentration, oxygen and role of extracellular enzymes. Process Biochemistry (submitted).

Pignede, G., Fudalej, F., Nicaud, J.M., Gaillardin, C., Seman, M. (1998) French Patent 98899.

Dalmau, E., Montesinos, J.L., Lotti, M., Casas, C. (2000) Enzyme and Microbial Technology, 26, 657-663.

Lopes, M. (2007) Produção de Lipase por *Yarrowia lipolytica*: Optimização da Composição do Meio e Condições de Arejamento. MsC Thesis, Universidade do Minho, Braga, Portugal.

Fickers, P., Nicaud, J. M., Destain, J., Thonart, P. (2003) Overproduction of lipase by *Yarrowia lipolytica* mutants. Applied Microbiology and Biotechnology, 63, 136–142.

Lopes, M., Gomes, N., Gonçalves, C., Coelho, M.A.Z., Mota, M., Belo, I. (2008) *Yarrowia lipolytica* lipase production enhanced by increased air pressure. Letters of Applied Microbiology, 46, 255-260.

D'Annibale, A., Sermanni, G., Federici, F., Petruccioli M. (2006) Olive-Mill Wastewaters: a promising substrate for microbial lipase production. Bioresource Technology, 97, 1828-1833.

Proceedings of the 10th International Chemical and
Biological Engineering Conference - CHEMPOR 2008
Braga, Portugal, September 4-6, 2008
E.C. Ferreira and M. Mota (Eds.)

Image analysis to investigate electrochemical stress in lipase production by *Yarrowia lipolytica*

André A. C. de Oliveira, Priscilla F.F. Amaral, Maria Alice Z. Coelho, Ofelia Q.F. Araújo*

Escola de Química, Universidade Federal do Rio de Janeiro, CT, Bl. E, Cidade Universitária, 21949-900, Rio de janeiro, Brazil. Email:ofelia@eq.ufrj.br

Keywords: stress, *Yarrowia lipolytica*, electric field, metabolism, yeast
Topic: Integration of life sciences & engineering

Abstract

Biochemical processes important to cell viability depend on the electric potential through cell membrane. The application of an electric field to a living cell might promote metabolic responses and modification of cell membrane potential. In this work the effects of the application of electric field in the yeast *Yarrowia lipolytica* was investigated analyzing its physiology (cell growth, glucose consumption and lipase activity) and population morphology through digital image analysis. Electrical potential promoted increased lipase productivity formation of hyphaes and maintained cells viability.

1 Introduction

Yarrowia lipolytica is an aerobic microrganism capable of producing important metabolites with an intense secretory activity, which justifies efforts to use it in industrial processes (as a biocatalyst), in molecular biology and in genetics studies. It has been considered an adequate model for dimorphism studies in yeasts, since it has an efficient system for genetic engineering transformation, and it is easy to distinguish between its morphological forms, in contrast to *S. cerevisiae*, which does not produce true filaments and exhibits pseudo-hyphae growth under nitrogen-limited conditions. The yeast-to-mycelium transition is associated with unipolar growth, asymmetric division, large polarly located vacuoles and repression of cell separation after division (Cruz *et al*, 2000).

Responses of living cells to electrical signals have been used, for example, in biotechnology (Bartlett et al., 1997), bioanalytical techniques (Lötzbeyer et al., 1996; Ci et al., 1997; Gheorghiu and Asami, 1998) and medical purposes (Chen et al., 1998; Veiga et al., 2005). Araujo et al. (2004) reported oscillation on culture of *S. cerevisiae* when electrical potential was imposed to a batch culture. Additionally, visual observation of cells using optical microscopy indicated smaller cell sizes in cultures submitted to pulsing electrical potential as compared to control experiments.

The aim of this work is to investigate the effects of the application of an electric field in the yeast *Yarrowia lipolytica* analyzing its population physiology (cell growth, glucose uptake and lipase activity) and morphology (monitored by digital image analysis and fluorescence microscope).

2 Experimental Methods

2.1 Strain, media, culture and experimental conditions

A wild type strain of *Yarrowia lipolytica* (IMUFRJ 50682) was employed and kept at 4ºC on YPD-agar medium. For growth conditions, cells were cultivated at 28ºC in a rotary shaker at 160 rpm, in flasks containing YPD medium (w/v: yeast extract (Oxoid) 1%; peptone (Merck),

* Corresponding author. Tel + 55-21-2562-7637. E-mail:ofelia@eq.ufrj.br

2%; glucose (Isofar), 2%). The cells were inoculated in a bioelectrochemical reactor containing modified YPD medium (0.64% peptone, 1% yeast extract, 2% glucose).

The bioreactor (Multigen, New Brunswick Scientific Co., EUA), with volume of 2 l, contains aeration system, magnetic stirring and control of temperature, provided with two turbines and two baffles. An oxygen probe (Lutron DO-5510, Lutron Electronics Co., Inc) was used to measure the concentration of dissolved oxygen in the bioreactor. The supply of oxygen was conducted with filtered air (Advantec, Toyo Roshi Kaisha, Japão with porosity 0,2 μm) using a system of submerged aeration through 12 holes in the agitation shaft with 7 mm in diameter located 1.82 cm from the vessels' bottom. Stirring speed of 550 rpm and airflow rate (Q) of 1.5 $dm^3.min^{-1}$ were used.

In cell growth experiments, the value of applied potential was 0.75 V_{SCE}, based on Araujo *et al.* (2004). To apply this eletrical potential, a potentiostat (PG-01 Ohnimetra Instruments) was used with working electrode and counter-electrode of platinum, and reference electrode (SCE).

2.3 Biochemical Methods

- Cell growth was followed by optical density measurements at 570 nm. Absorbance values were converted to mg d.w./mL using a factor previously determined experimentally.

- Lipase activity was estimated by variations on absorbance at 410nm in spectrophotometer (Hach, DR4000UV) due to oxidation of p-nitrophenyl laurate (p-NFL) (supplied by SIGMA) with a concentration of 0.162 mg / mL in potassium phosphate buffer (0 , 05M), pH 7.0 (Pereira-Meirelles, 1997).

- Glucose comsumption: Glucose was quantified by the method of glucose oxidase (enzyme kit, Human GmbH, Germany).

2.4 Microscopic Methods

- Morphological analysis

Cell morphology was observed along the batch run using a Nikon optical microscope with 1,000 X magnification, in both control and stress conditions. Traditional tools generally used for image enhancing were employed. The RGB image was decomposed into its respective channels, and the green channel was employed in the image treatment steps (Kawasse *et al.*, 2003). A grayscale intensity image was created and a combination of bottom and top hat filtering was used to enhance image contrast. A binarization step was performed followed by the elimination of border structures and a hole-fill procedure was carried out. Application of morphological operations, such as erosion (to remove small debris) and reconstruction, gave the final image. This image treatment was performed in MATLAB v.6.1 (The Mathworks Inc., The Mathworks Inc.) environment.

In order to extract cells' individual properties, their characteristics were determined using image analysis of the labeled objects: *area* is the area of the projected surface of the object on the plane of vision; *hyphal length* and *hyphal width* were determined as the maximum Feret diameter (FMax) and minimum Feret diameter (FMin), respectively. The Feret diameter is given by the distance between two parallel tangents in any given direction (Kawasse *et al.*, 2003). Elongation is given by the ratio between *hyphal length* and *hyphal width*:

$$Elongation = \frac{F_{Max}}{F_{Min}}$$

- Viability analysis

Fluorescent dye of acridine orange was used for the simultaneous distinction of live and dead cells (dead cells give out red or orange fluorescence and living cells yellow-green; 180 µM AO, pH 6). Cell counting was done in a Nikon optical microscope with 1,000 X magnification.

The procedure for the treatment of the cells consists in two washes of cells with phosphate buffer (0,05M) followed by resuspension of cells in 0.5 ml of phosphate buffer (0,05M) with 0.5 ml of acridine orange(0,5M). The cells were kept in darkness for 20 minutes.

3 Results and Discussions

3.1 Biochemical Responses

Table 1 presents the results of maximum specific growth rate (µ) and glucose consumption rate ($-dS/dt$) of both stress and control conditions.

Table 1: Specific growth rate (µ) and glucose consumption ($-dS/dt$) of *Y. lipolytica* cultivated with and without electrochemical potential.

Stress	µ (h^{-1})	$-dS/dt$ (g/l/h)
No	0.32±0.04	0.63±0.04
Yes	0.30±0.04	1.03±0.04

It is possible to observe that µ values are similar for both experiments (with and without electrochemical stress). However, substrate consumption ($-dS/dt$) increases around 61% with application of electrochemical potential. It is proposed that the applied electrical potential increases cell's metabolism and the consumed glucose might have been directed to another metabolite.

Figure 1 presents lipase prodution by *Y. lipolytica* under eletrochemical stress conditions and control conditions (no stress).

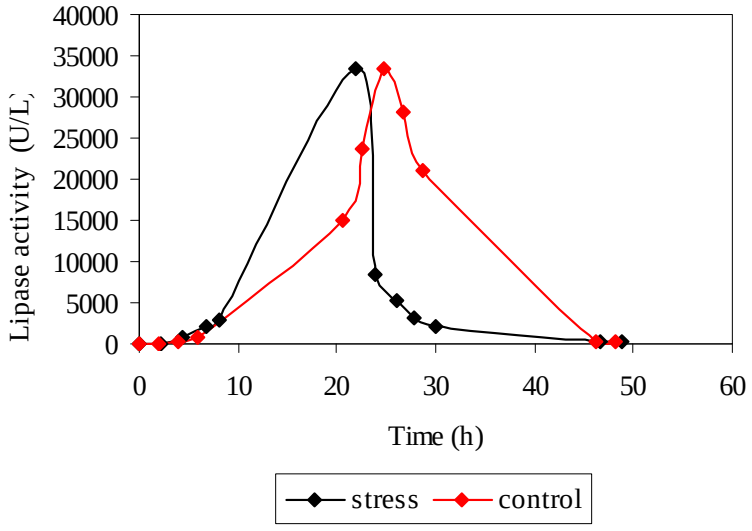

Figure 1. Lipase production with and without electrochemical stress.

It is possible to observe that the activity peaks were very close in intensity, but the application of electrical stress advanced lipase's activity peak (peak value was reached

earlier). Therefore, the lipase productivity, calculated in Table 2, is 13% higher with electrochemical potential application.

Table 2: lipase productivity by *Y. lipolytica* with and without electrochemical stress.

Stress	Produtivity (U/l*h)
No	1353.5
Yes	1526.4

3.2 Morphological Responses

The morphological response of cell exposure to electrochemical stress is displayed in Figure 2. There is a subtle tendency for the formation of more elongated cells, or hyphaes, with the application of electric potential. This tendency might be the result of the cell defence system to the stress condition implyed to the cells.

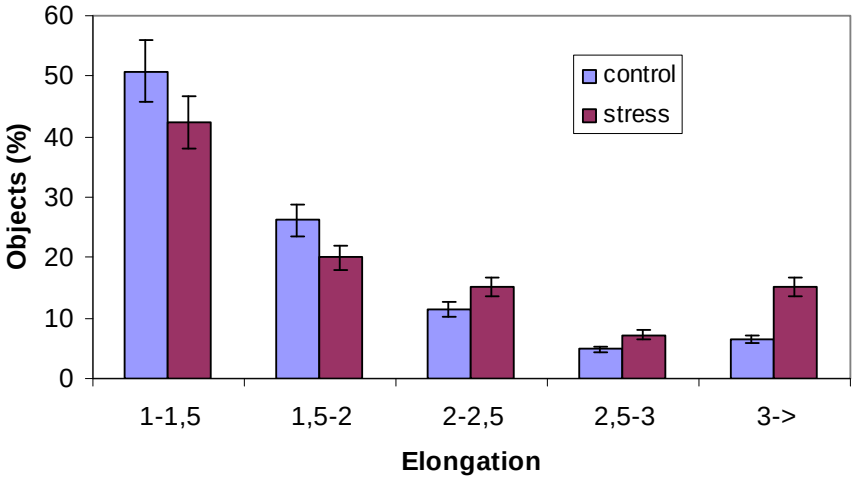

Figure 2. Elongation factor distribution for control and stressed experiments.

In order to evaluate if the stress condition had also affected the viability of cells, a staining method distinguishing dead and living cells was performed. Figure 3 presents the results during control and stress experiments.

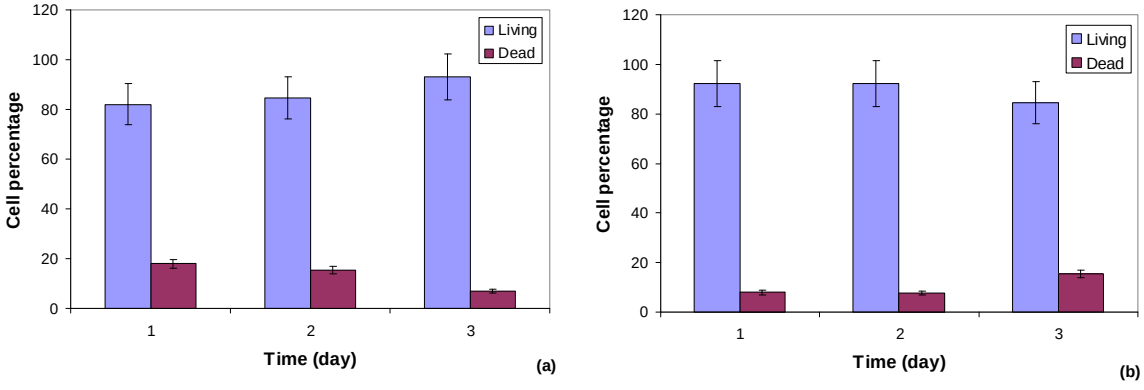

Figure 3. Percentage of living and dead cells during the experiments: (a)control and (b) under stress.

According to Figure 3, it is possible to notice that when cells are subjected to electrical stress there is no significant difference in their viability as compared to a control experiment. The maintenance of-cell's viability increases the interest in this type of stress.

4 Conclusions:

This work reports the evaluation of physiological and morphological effects of applied electrical potential to a culture of *Yarrowia lipolytica*. Specific growth rates (μ) are similar for experiments with and without electrochemical stress, but substrate consumption (-dS/dt) increases around 61% with application of electrochemical potential.

Electrochemical stress advanced time of lipase's activity peak and its productivity increased 13%. A cell's viability study indicates that there is no significant difference of viability when cells are subjected to electrochemical stress when compared to the control conditions, showing that this stress condition does not compromise the cells. On the other hand, the application of this stress modified cell morphology, giving a more elongated aspect. Such response is attributed to cell's defense system.

References

Alonso, F.O.M., Oliveira, E.B.L, Dellamora-Ortiz, G.M., Pereira-Meirelles, F.V. (2005). Improvement of lipase production at different stirring speeds and oxygen levels. *Brazilian Journal of Chemical Engeneering*, 22, 1, 9-18.

Amaral, P.F.F., Rocha-Leão, M.H.M., Marrucho, I., Coutinho, J.A.P, Coelho, M.A.Z., (*2006*). Improving Lipase Production using a Perfluorocarbon as Oxygen Carrier. *Journal of. Chemical Technology Biotechnology*, 81, 8, 1368-1374.

Araújo, O.Q.F., Coelho, M.A.Z., Margarit, I.P., Vaz-Junior, C.A., Rocha-Leão, M.H.M. (2004). Electrical Stimulation of *Saccharomyces cerevisiae* Cultures, *Brazilian Journal of Microbiology*, 35, 97-103.

Bartlett, P.N.; Pletcher, D.; Zeng, J. (1997). Aprroaches to the integration of electrochemistry and biotechnology, *Journal of Electrochemical Society*, 144, 11, 3705-370.

Chen, W.; Han, Y.; Chen, Y.; Xie, J.T. (1998). Field-induced electroconformational damages in cell membrane proteins: a new mechanism involved in electrical injury, *Bioelectrochemistry and Bioenergetics*, 47, 237-245.

Ci, Y.; Feng, J.; Jiang, Z.; Luo, D. (1997). The voltammetric behavior of *Saccharomyces cerevisiae*. *Bioelectrochemistry and Bioenergetics*, 43, 293-296.

Gheorghiu, E.; Asami, K. (1998). Monitoring cell cycle by impedance spectroscopy: experimental and theoretical aspects, *Bioelectrochemistry and Bioenergetics*, 45, 139-143.

Kawasse, F.M., Amaral P.F., Rocha-Leao M.H.M., Amaral A.L., Ferreira E.C., Coelho M.A.Z. (2003). Morphological analysis of Yarrowia lipolytica under stress conditions through image processing. Bioprocess, *Biosystem and Engenniering*, 25, 371-375.

LötzbeyeR, T.; Schuhmann, W.; Schmidt, H. (1997). Minizymes. A new strategy for the development of reagentless amperometric biosensors based on direct electron-transfer processes. *Bioelectrochemistry and Bioenergetics*, 42, 1-6.

Münch, T., Sonnleitner, B., Fiechter, A. (1992). New insights into the synchronization mechanism with forced synchronous cultures of *Saccharomyces cerevisiae*. Journal of Biotechnology, 24: 299-314.

Pereira-Meirelles, F.V., Rocha-Leão, M.H. e Sant'Anna, G.L. (1997). A stable lipase from *Candida lipolytica*-cultivation conditions and crude enzyme characteristics. Applied. Biochemistry and Biotechnology, 63-65, 73-85.

Veiga, V.F.; Nimrlchter, L.; Teixiera, C.A.; Morales, M.M.; Alviano, C.S.; Rodrigues, M.L.; Holandino, C. (2005). Exposure of human leukemic cells to direct electric current, *Cell Biochemistry and Biophysics*, 42, 61-74.

Proceedings of the 10th International Chemical and
Biological Engineering Conference - CHEMPOR 2008
Braga, Portugal, September 4-6, 2008
E.C. Ferreira and M. Mota (Eds.)

Liquid-liquid extraction in the presence of electrolytes of nisin and green fluorescent protein (GFPuv)

Priscila Gava Mazzola[1], Angela Faustino Jozala[1,2], Pérola de Oliveira Magalhães[3], Adalberto Pessoa Jr. [1], Thereza Christina Vessoni Penna[1]

[1]Department of Biochemical and Pharmaceutical Technology, School of Pharmaceutical Sciences, University of São Paulo, Avda. Prof. Lineu Prestes, 580, Bl. 16, 05508-900, São Paulo, Brazil.
[2]IBB - Institute for Biotechnology and Bioengineering, Centre of Biological Engineering, Universidade do Minho, Braga, Portugal.
[3]School of Health Sciences, University of Brasília, Campus Universitário Darcy Ribeiro,70910-900, Brasília, DF, Brazil.

Keywords: Liquid-liquid extraction, green fluorescent protein, nisin
Topic: Integration of life sciences & engineering

Abstract

In the biotechnology field, it has been suggested that extractions in two-phase aqueous complex-fluid systems can possibly be used instead of, or as complementary processes to, the more typical chromatographic operations, to reduce the cost of the downstream processing of many biological products (Lam et al., 2004; Mazzola et al., 2006). This method offer attractive conditions to be applied in this study, thereby two-phase systems can be exploited in separation science for the extraction/purification of desired biomolecules directly on the culture medium (Mazzola et al., 2008). This study aimed to evaluate the aqueous two phase system (ATPS) composed by a nonionic surfactant, Triton X-114 (TX), in presence or absence of electrolytes, to separate two interesting biomolecules: nisin and recombinant green fluorescent protein (GFP). Results indicated that nisin partitions preferentially to the micelle rich-phase, with significant antimicrobial activity increase (up to 10-fold). GFP partitioned evenly between the phases in TX system without electrolytes.

1 Introduction

The industrial production of proteins and other biomolecules depend significantly on the extraction/purification processes. The development of techniques and methods for separation and purification of proteins has been essential for many advances in biotechnology (Wilcheck et al., 1999). In this sense, one of the techniques that can be considered promising is liquid-liquid extraction. Various liquid-liquid extraction methods that use different types of two-phase aqueous complex-fluid systems have been proposed to address a wide variety of separation needs in the chemical, biotechnological, and environmental fields. In general, these methods offer the possible advantages of versatility, scalability, cost effectiveness, and environmental friendliness compared to the conventional methods that they may replace. In the biotechnology field, it has been suggested that extractions in two-phase aqueous complex-fluid systems can possibly be used instead of, or as complementary processes to, the more typical chromatographic operations, to reduce the cost of the downstream processing of many biological products (Lam et al., 2004; Mazzola et al., 2006).

In particular, two-phase aqueous micellar systems, formed by some surfactants at certain conditions, have been proposed as an attractive option, to be used in bioseparations (Liu et al., 1998). In these systems an aqueous surfactant solution, under the appropriate solution conditions, spontaneously separates into two predominantly aqueous, yet immiscible, liquid phases, one of which has a greater concentration of micelles than the other (Liu et al., 1998).

The difference between the physicochemical environments in the micelle-rich phase and in the micelle-poor phase forms the basis of an effective separation and makes two-phase aqueous micellar systems a convenient and potentially useful method for the separation, purification, and concentration of biomaterials (Liu et al., 1996).

This method offer attractive conditions to be applied in this study, thereby two-phase systems can be exploited in separation science for the extraction/purification of desired biomolecules directly on the culture medium (Mazzola et al., 2008).

Nisin is an extracellular antimicrobial peptide, discovered in 1928, its utilization are approved by Food and Drugs Administration (FDA) (Hansen, 1994; Vessoni Penna and Moraes, 2002), meeting the requirements of safe food with fewer chemical additives (Chol et al., 2000). This peptide has large antimicrobial activity spectrum against Gram-positive bacteria and their spores (Delves-Broughton et al., 1996). Other applications of nisin include dental care products (Turner et al., 2004), pharmaceutical products such as stomach ulcers and colon infection treatment and potential birth control (Aranha et al., 2004; Dubois, 1995). Recently the optimization of nisin production has been reported. Jozala and co-workers (2005, 2007) and Vessoni Penna and co-workers (2005, 2006) studied nisin expression using different media compounds based on skimmed milk diluted with synthetic media (MRS and M17) and with nutrients added. Diluted skimmed milk was observed to be the best culture media for nisin production and activity by *L. lactis*.

The GFP, expressed by *Escherichia coli* DH5-α, is widely applied with as biossensor and can be detected by spectrofluorometry or using hand UV lamp, it has became a versatile tool for a variety of biotechnological uses and as a potential biological indicator, for preservation of manufactured and processed products (Vessoni Penna et al., 2004). GFP is an excellent biosensor due to its ability to be easily monitored in a wide variety of applications. Enzymes and proteins have been used as biological indicators to evaluate the immediate efficacy of industrial procedures, such as blanching, pasteurization, and disinfection treatments, as well as to monitor the satisfactory preservation of a product subjected to disinfection or sterilization.

This study aimed to evaluate the aqueous two phase system (ATPS) composed by a nonionic surfactant, Triton X-114 (TX), in presence or absence of electrolytes, to separate two interesting biomolecules: nisin and recombinant green fluorescent protein (GFP).

2 Materials and Methods

The biomolecules were obtained from commercial and produced way, standard nisin was provide by Nisin™ (Sigma, St. Louis, MO) and GFP expressed by transformed *E. coli*; produced nisin was skimmed milk fermented by *L. lactis* and GFP was complex media fermented by *E. coli* DH5-α. The system was composed by 2% w/w TX with and without $MgSO_4$ or $(NH4)_2SO_4$. The phase diagram of the TX in buffer was obtained by the cloud-point method. Buffered solutions of the 2%TX with or without electrolytes, each with a total volume of 3 mL, were prepared in graduated 10-mL test tubes. Each solution was placed in a thermo-regulated device set at a temperature of 36.2ºC for 2h to attain partitioning equilibrium. Nisin activity was determined by agar diffusion with *L. sakei* as bioindicator. GFP concentration was determined by fluorimetry.

The biomolecules were purchased and biosynthesized, standard nisin was provides by Sigma (St. Louis, MO) and GFP was expressed by modified *E. coli* and purified; produced nisin was skimmed milk fermented by *L. Lactis*. The initial concentration of nisin in each system was 3 log AU/mL, and the initial concentration of GFP was 18µg/mL.

The system was composed by 2% w/w TX with and without $MgSO_4$ or $(NH4)_2SO_4$. The phase diagram of the TX in buffer was obtained by the cloud-point method. Buffered solutions of the 2%TX with or without electrolytes, each with a total volume of 3 mL, were prepared in graduated 10-mL test tubes. Each solution was placed in a thermo-regulated device set at a

temperature of 36.2ºC for 2h to attain partitioning equilibrium. After 2h the two coexisting micellar phases formed were withdrawn separately and the biomolecules concentration was determined in each micellar phase. Nisin activity was determined by agar diffusion with *Lactobacillus sakei* as bioindicator. GFP concentration was determined by fluorimetry.

3 Results

Since it is often observed that the phase behavior of aqueous micellar solutions can be sensitive to the presence of electrolytes and impurities (Balzer and Lüders, 2000), it was first necessary to study how the TX/buffer phase diagram, that is, the temperature versus TX concentration coexistence curve, changes in the presence of these components. The phase diagram of the TX/buffer system in the presence of the different electrolytes was therefore mapped, and the results are presented in Figure 1. The experimentally measured coexistence curve, in the absence of any extra components, was and is also presented for comparison purposes.

As can be seen, the coexistence curves in the presence of the electrolytes have considerably shifted when compared to the TX/buffer curve in the absence of salts.

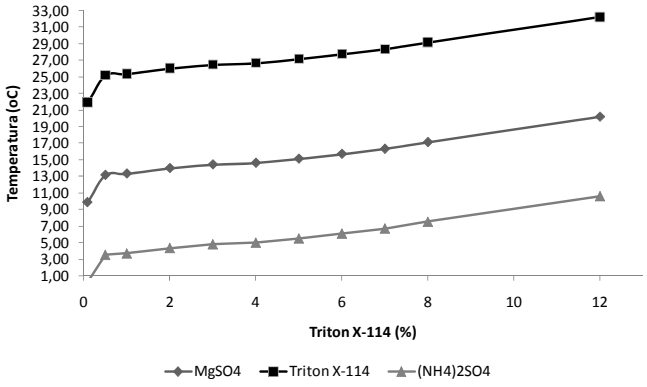

Figure 1. Phase diagram of Triton X-114/buffer system in the absence and in the presence of eletroctrolytes. The squares (■) represent the addition of $MgSO_4$; the losangles (♦) represents the coexistence curve for TX/buffer and the triangles (▲) represent the addition of $(NH_4)_2SO_4$.

The addition of salts in an ATPMS promotes a stronger electrostatic interaction between the water molecules compared to the hydrogen bonds between the head and the tail of the surfactant monomers. This phenomenon drives the water molecules to solvate the ions from the salts and the amphiphilic molecules interact more intensely, if compared to the absence of electrolytes (Carale, 1993).

The ions, such as sulphate, phosphate and chlorine, can increase the water structure and stabilize the structure of proteins, in this case they are called cosmotropic ions. On the other hand, there are some ions (perchlorite, thiocyanate, i.e.) which decrease the structure of the water and destabilizing the structure of proteins, being called chaotropic. The micelle formation is also changed by the presence of salts, once the critical micellar concentration (CMC) and the aggregation number (number of monomers in each micelle) are dependent on the solvation of ions (Anacker, Ghose, 1963; Tonova, Lazarova, 2005), also, the binding of the ions to the micelles affects the the organization and the electrostatic interaction between the polar heads and the tails of the surfactant monomers (Quina, Chaimovich, 1979; Brochsztain et al., 1990).

After the determination of the coexistence curves, systems containing nisin or GFP in the presence and in the absence of electrolytes were prepared and placed in a transparent thermo-regulated device whose temperature was controlled to within 0.02^{o}C.

In initial partitions, nisin was driven to the micelle-rich phase in the TX/buffer system, in the presence of the electrolytes similar behavior was observed, but the presence of $MgSO_4$ enhanced the most the partition of nisin to the micelle-rich phase (Figure 2). Results indicated that nisin partitions preferentially to the micelle rich-phase, with significant antimicrobial activity increase (up to 10-fold).

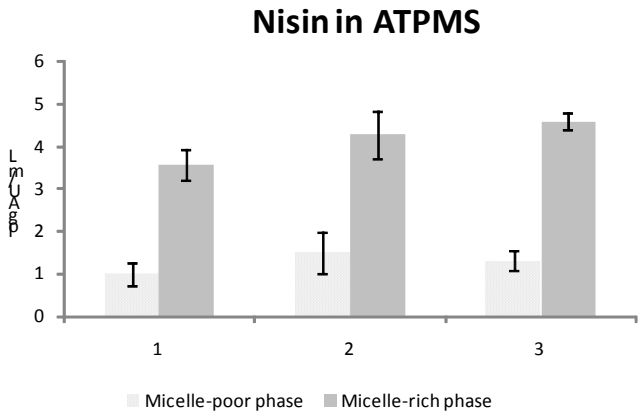

Figure 2. Nisin activity in the micelle-poor phase (gray and white bars) and in the micelle-rich phase (solid gay bars), after partitioning in ATPMS. (1) TX/buffer system; (2) TX/buffer and $(NH_4)_2SO_4$; (3) TX/buffer and $MgSO_4$. The error bars represent 95% confidence limits for the measurements.

The green fluorescent protein, in the TX/buffer system partitioned evenly between the phases, while in the presence of both salts GFP partitioned extremely to the micelle-poor phase (Figure 3).

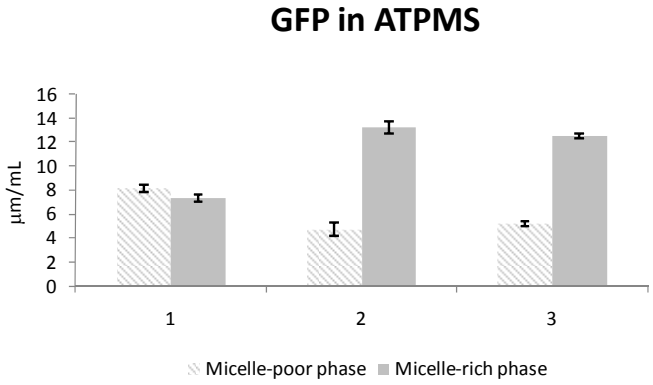

Figure 3. Green fluorescent proteins concentration in the micelle-poor phase (gray and white bars) and in the micelle-rich phase (solid gay bars), after partitioning in ATPMS. (1) TX/buffer system; (2) TX/buffer and $(NH_4)_2SO_4$; (3) TX/buffer and $MgSO_4$. The error bars represent 95% confidence limits for the measurements.

Different proteins are not soluble in water, but their solubility increases in the presence of electrolytes reaching a limit that can vary according to the protein and the chosen salt, this is called salting-in and can be explained by the interaction of the ions (positive and negative) in

the solution with the charged sites on the protein molecule, softening the interaction amongst them. For this reason, the electrostatic effect provided by diluted solutions containing salts is an important factor to the increase of solubility of proteins.

When the salt concentration is increased, some of the water molecules are attracted by the salt ions, decreasing the number of water molecules available to interact with the proteins. As a result of the increased demand for solvent molecules, the protein-protein interactions are stronger than the solvent-solute interactions; the protein molecules coagulate by forming hydrophobic interactions with each other. This process is known as salting out, and is caused by the presence of di or trivalent ions ($(NH_4)_2SO_4$, Na_2SO_4, i.e.)

The addition of salt, even milimolar concentrations, influences the partitioning of charged molecules. Although the ions partitions quite evenly between the phases, the small difference in their behavior in the phases creates a dielectrical potential that affects the biomolecules partition (SARUBBO et al., 2000). The addition of salts in ATPMS containing Triton X-114 influences the partitioning of both nisin and GFP, being a good strategy for extracting and purification of these biomolecules from the fermentation broth where they are biosynthesized.

The successful implementation of protein partitioning from a mixture containing the target biomolecule and other compounds, in a two-phase aqueous micellar system, presented in this work, represents an important step towards developing a novel separation method for proteins of interest.

4 Conclusions

The partitioning behavior of the biomolecules, nisin and GFP, in aqueous two-phase micellar systems in presence of electrolytes was investigated experimentally, showing that the target biomolecules can be extracted from respective media, either commercially available or produced by our research group. Increasing in activity of nisin and GFP concentration, after partitioning encourages further researches aiming to optimize the biomolecules extraction using simple tools as temperature variations, amongst others. In conclusion, the successful implementation of proteins partitioning, directly from a suspension containing the biomolecules and other unknown compounds, in a aqueous two-phase micellar system, presented in research, represents an important step towards developing a cost-effective separation method, and more generally, for other biomolecules of interest.

Acknowledgments

This research was supported by grants from CAPES (Coordenação de Aperfeiçoamento de Pessoal de Nível Superior, Brazil), CNPq (Conselho Nacional de Desenvolvimento Científico e Tecnológico, Brazil) and FAPESP (Fundação de Amparo à Pesquisa do Estado de São Paulo, Brazil).

References

Wilchek, M., Miron, T. (1999). Thirty years of affinity chromatography. *Reactive and. Functional Polymers*. 41, 263-268.

Lam, H., Kavoosi, M., Haynes, C.A., Wang, D.I.C., Blankschtein, D. (2004). Affinity-enhanced protein partitioning in decyl beta-d-glucopyranoside two-phase aqueous micellar systems. *Biotechnology and Bioengineering*, 89, 381–392.

Mazzola, P.G., H. Lam, H., Kavoosi, M., Haynes, C.A., Pessoa Júnior, A., Vessoni Penna, T.C., Blankschtein, D. (2006). Affinity-tagged green fluorescent protein (GFP) extraction from a clarified E. coli cell lysate using a two-phase aqueous micellar system., Biotechnology and Bioengineering, 93, 998–1004.

Liu, C.L., Kamei, D.T., King, J.A., Wang, D.I.C., Blankschtein, D. (1998). Separation of proteins and viruses using two-aqueous micellar systems. *Journal of Chromatography B*,

711, 127–138.
Liu, C.L., Nikas, Y.J., Blankschtein, D. (1996). Novel bioseparations using two-phase aqueous micellar systems, *Biotechnology and Bioengineering*, 52, 185–192.
Mazzola, P.G., Lopes, A.M., Hasmann, F.A., Jozala, A.F., Vessoni Penna, T.C., Magalhaes, P.O. Rangel-Yagui, C.O., Pessoa Júnior, A. (2008). Liquid-liquid extraction of biomolecules: an overview and update of the main techniques. *Journal of Chemical Technology and Biotechnology,* 83, 143-157.
Hansen, J.N. (1994). Nisin as a model of food preservative. *Critical Reviews in Food Science and Nutrition*, 69–93.
Vessoni Penna, T.C., Moraes, D.A. (2002). Optimization of nisin production by Lactococcus lactis. *Applied Biochemistry and Biotechnology*, 98-100, 775-789.
Chol, H.J., Cheigh, C.I., Kim, S.B., Pyun, Y.R. (2000). Production of a nisin-like bacteriocin by Lactococcus lactis subsp. lactis A164 isolated from Kimchi. *Journal of Applied Microbiology*, 88, 563-57.
Delves-Broughton, J., Blackburn, P., Evans, R.J., Hugenholtz, J. (1996). Applications of the bacteriocin, nisin. *Antonie Leeuwenhoek*, 69(2), 193-202.
Turner, S.R., Love, R.M., Lyons, K.M. (2004). An in-vitro investigation of the antibacterial effect of nisin in root canals and canal wall radicular dentine. *Internacional Endodontic Journal,* 37, 664–671.
Aranha, C., Gupta, S., Reddy, K.V.R. (2004). Contraceptive efficacy of antimicrobial peptide Nisin: in vitro and in vivo studies. *Contraception: An Internacional Journal*, 69, 333–338.
Dubois, A. (1995). Spiral bacteria in the human stomach: the gastric Helicobacter, Emerging *Infection Diseases Journal*, 1(3), 79–88.
Jozala, A.F, Novaes, L.C.L., Cholewa, O., Moraes, D., Vessoni Penna, T.C. (2005). Increased of Nisin Produced by Lactococcus lactis in Different Media. *African Journal of Biotechnology*, 4(3), 262-265.
Jozala, A.F, Andrade, M.S., Arauz, L.J., Pessoa Júnior, A., Vessoni Penna, T.C. (2007). Nisin production utilizing skimmed milk aiming to reduce process cost. *Applied Biochemistry and Biotechnology*, 136, 515-528.
Vessoni Penna, T.C., Jozala, A.F, Novaes, L.C.L., A. Pessoa Júnior, A., Cholewa, O. (2005). Production of nisin by Lactococcus lactis in media with skimmed milk. *Applied Biochemistry and Biotechnology*, 121–124, 1–20.
Vessoni Penna, T.C., Jozala, A.F, Gentille, T.R., Pessoa Júnior, A., Cholewa, O. (2006). Detection of nisin expression by Lactococcus lactis using two sensitive bacteria to associate the effects of nisin with EDTA, *Applied Biochemistry and Biotechnology* , 121–124, 334–346.
Carale M.T.R. *Salt effects on micellization, micellar growth, and phase behavior of aqueous solutions of nonionic surfactants*. Cambridge, 1993. 189p. Tese de Doutorado - Massachusetts Institute of Technology.
Anacker, E.W.; Ghose, H.M. (1963). Counterions and micelle size. 1. Light scattering by solutions of dodecyltrimethylammonium salts. *Journal of Physical Chemistry*, 67, 8, 1713-1716.
Tonova K, Lazarova Z. (2005). Influence of enzyme aqueous source on RME-based purification of α-amylase. *Separation and Purification Technology*, 47, 43-51.
Quina, F.H.; Chaimovich, H. (1979). Ion-exchange in micellar solutions. 1. Conceptual-framework for ion-exchange in micellar solutions. *Journal of Physical Chemistry*, 83, 14, 1844-1850.
Brochsztain, S., Berci, P., Toscano, V.G., Chaimovich, H., Politi, M.J. (1990). Ion binding and selectivity in zwitterionic micelles. *Journal of Physical Chemistry*, 94, 17, 6781-6785.
Sarubbo, L.A., Oliveira, L.A., Porto, A.L.F., Duarte, H.S., Carneiro-Leão, A.M.A., Lima Filho, J.L., Campos-Takaki, G.M., Tambourgi, E.B. (2000). New aqueous two-phase system based on cashew-nut tree gum and poly(ethylene glycol). *Journal of Chromatography, B*, 743, 1/2, 79-84.

Proceedings of the 10th International Chemical and
Biological Engineering Conference - CHEMPOR 2008
Braga, Portugal, September 4-6, 2008
E.C. Ferreira and M. Mota (Eds.)

Analysis of production of recombinant wild-type amidase from *Pseudomonas aeruginosa* in *Escherichia coli*

Patrícia A.T. Borges[1], Rita Pacheco[1*], Amin Karmali [1]

[1] Chemical Engineering and Biotechnology Research Center and Department of Chemical Engineering of Instituto Superior de Engenharia de Lisboa,
Rua Conselheiro Emídio Navarro, 1, 1959-007 Lisboa, Portugal

Keywords: Recombinant amidase; *Escherichia coli*; inclusion body; Ethanol effect; arginine.

Topic: Integration of life sciences & engineering

Abstract

This work reports on the optimization of a recombinant *Pseudomonas aeruginosa* amidase (E.C.3.5.1.4) production in an *Escherichia coli* strain. The effect of several parameters such as temperature incubation, IPTG induction and ethanol shock on the enzyme aggregation *in vivo* was investigated. The results have demonstrated the formation of inclusion bodies at all the experimental conditions with the highest yield of soluble amidase relatively to other proteins obtained for the condition at 37ºC using 0.40 mM IPTG to induce growth with ethanol. Our findings showed that the addition of ethanol in LB ampicillin culture medium at 25ºC allowed the production of high levels of amidase but which aggregated quantitatively in a biological active form and exhibited a four-fold higher specific activity when compared with the soluble form of the enzyme. Nondenaturing solubilization of the aggregated amidase was achieved using L-arginine with the highest yield of enzyme solubilization obtained when using a concentration of 2 M. Conversely GdnHCl did not succeed in the denaturing solubilization of amidase inclusion bodies.

1- Introduction

The bacteria *Escherichia coli* is often the first choice of host in recombinant DNA technology for reasons of speed and simplicity (Middelberg, 2002) however a disadvantage is the formation of inclusion bodies when protein is overexpressed. High levels of expression of recombinant proteins often result in aggregation and accumulation in inclusion bodies which prevents the production of soluble protein at high yields.

Inclusion bodies are dense aggregates of misfolded polypeptide formed intracellularly due to the protein aggregation characteristics or possibly the inability for the cell processes to ensure that the expressed protein is correctly folded and soluble (Lilie *et a*l, 1998). Though the formation of inclusion bodies could facilitate protein purification refolding into biological active forms often is a complicated procedure which results in poor recovery being the major cost in production of recombinant proteins (Thomas and Baneyx, 1997).

Thus, it is desirable to avoid or at least reduce inclusion body formation producing the recombinant proteins in a soluble form *in vivo* and to purify the active polypeptide chains by conventional techniques.

* Corresponding author. Tel + 351-21-8317000 ext.1229. E-mail:rpacheco@deq.isel.ipl.pt

There have been numerous reports on inclusion bodies and considerable research has addressed the mechanisms by which cells avoid forming aggregates of certain protein. The reduction of the cultivation temperature is known to increase the amount of soluble protein due to a decrease in the rate of protein biosynthesis. Another possibility of increasing soluble protein is to limit the induction of gene expression by the promoters which can be controlled by the inducer concentration such as isopropylthio-β-D-galactoside (IPTG) (Garcia-Junceda *et al*, 1995). Moreover, have also reported that supplementation of the grown medium with 3% ethanol can improve the solubility of some recombinant proteins (Thomas and Baneyx 1997).

Here we report the optimized production of a recombinant *Pseudomonas aeruginosa* amidase (E.C. 3.5.1.4.) overproduced in an *E coli* strain. In this study we inspect the combination of parameters such as cultivation temperature of LB ampicillin supplemented medium, IPTG concentration and ethanol shock in the prevention of the *in vivo* aggregation of this protein. However, repeatedly the literature reports on proteins aggregated in inclusion bodies which retain their biological activity and for such cases mild solubilization has proved to be the key for high recovery of bioactive protein from inclusion bodies in comparison to solubilization using a high concentration of a chaotropic agent (Tsumoto *et al*, 2003 Lilie *et al*, 2005). The present work also reports on the attempt to renaturate biologically active amidase inclusion bodies under nondenaturing conditions, using L-arginine, and strongly denaturing conditions, with guanidine hydrochloride (GdnHCl).

2- Materials and Methods

Culture Conditions

Recombinant *E.coli* JM 109 cells containing cloned amidase gene from wild-type strain 8602 of *Pseudomonas aeruginosa* amidase gene (Pacheco *et al*, 2000) were grown in Luria-Bertani (LB) medium, with 100 µg/ml ampicillin (Sigma Aldrich) at 37ºC or 25ºC, suplemented or not with 3% (v/v) ethanol and using different IPTG (Sigma Aldrich) concentrations for induction, ranging from 0.1 mM to 1mM.

Soluble and Insoluble cell fraction preparation

Cells grown at the different conditions mentioned above were collected by centrifugation, washed, and frozen when the absorbance of the culture at 600 nm was approximately 1 or higher (stationary phase). Frozen cells (15 mg) of each condition were suspended in 1 ml of 10 mM sodium phosphate buffer as pH 7.2 and broken by sonication with 3 bursts of 5 seconds at 150W. Part of this suspension (0.5 ml) which represents total cell extract (T) was collected and the remaining was centrifuged during 30 min at 13400 rpm at 4ºC in order to separate soluble (S) and insoluble (IS) cell fractions. Total cell, soluble and insoluble fractions for each of the tested conditions were assayed for amidase activity and protein concentration and analysed by electrophoresis.

Enzyme activity assay

Amidase transferase activity was determined using a modification of the method developed by Brammar and Clarke (Brammar and Clarke, 1964) using a solution of $FeCl_3$ 6% (w/v) in HCl 2%(w/v). The amidase activity was followed by measuring the formation of acetohydroxamic acid, using acetamide and hydroxylamine as substrates. The synthesis of acetohydroxamic acid was detected by formation of a brown colour complex, which absorbs at 490 nm (ε=0.026 $mM^{-1}.cm^{-1}$), when adding to the reaction mixture two volumes of $FeCl_3$ 6% (w/v) in HCl 2%(w/v) solution at several time intervals during the reaction.

A unit of enzymatic activity (UI) is defined as the amount of enzyme required to form 1 µmol acid acetohydroxamic per minute under the conditions of the reaction.

Protein assay and Electrophoretic analysis

Protein concentration was determined by Coomassie blue dye binding method using bovine serum albumin as the protein standard (Bradford, 1976).

Native polyacrylamide gel electrophoresis (PAGE) and SDS-PAGE with 8M Urea of T, S and IS cell fractions for all the tested conditions were carried out as described elsewhere and stained with silver staining (Hames, 1981). A method was also developed for the *in situ* detection of enzyme activity in native gels based on the amidase transferase activity. S and IS cell fractions containing amidase were subjected to 7.5 % native PAGE.

Subsequently the gel was cut in two, so that each half contained one of the samples of each cell fractions. Amidase transferase activity was detected by incubating at 25 ºC for 15 minutes one half of the gel with a reaction mixture containing equal amounts of 400 mM acetamide and 2 M hydroxylamine pH 7.0 in Tris-HCl buffer 75 mM at pH 7. Afterwards the formation of hydroxamic acid upon amidase reaction *in situ* was detected by overlaying filter paper soaked in a solution of $FeCl_3$ 6% (w/v) in HCl 2% (w/v) solution.

Brown bands indicated the position of the enzyme in the native gel relatively to the same position of the bands in the other half of the gel which was subjected to silver staining.

Solubilization of protein in inclusion bodies

In order to evaluate the capacity of L-arginine and guanidine hydrochloride (GdnHCl) in the successful solubilization of amidase aggregates obtained at the different tested conditions, IS cell fractions were suspended in L-arginine solutions and GdnHCl solutions at different concentrations, ranging from 0 to 1.5M of L-arginine and 0 to 3M GdnHCl. The mixture was incubated at room temperature with orbital shaking for 24 hours. After such period the sample was extensively washed with 10 mM sodium phosphate buffer as pH 7.2 in order to eliminate residues of solubilizing agent and centrifuged at 13400 rpm during 30 min at 4ºC separating S from IS solubilized fraction. The collected fractions were assayed for amidase transferase activity and protein concentration.

3- Results and Discussion

In order to determine the influence of parameters such as growth temperature, IPTG concentration and alcohol shock with ethanol in the beneficial production of native amidase, recombinant *E.coli* JM 109 cells containing the wild-type amidase gene from *P.aeruginosa* were grown at 37ºC or 25ºC in LB medium supplemented or not with 3% ethanol. The synthesis of the enzyme was also induced by addition of different concentrations of IPTG to the culture during the middle exponential phase. Culture cells harvested at stationary phase were disrupted into S and IS cell fractions as described. Figure 1 summarizes the results in enzyme yield for the effect of the different growth conditions to which the strain was subjected. It was evident that the cultures submitted to suboptimal growth condition, 25ºC, demonstrated an increased expression levels of recombinant amidase as referred in the literature (Thomas and Baneyx, 1997) except for 0.7 M IPTG. Moreover as expected this situation was verified in general also for conditions with ethanol shock as higher amidase specific activity was obtained in ethanol presence. The highest amidase specific activity was obtained for the S fraction of cells grown at 37ºC in ethanol presence with 0.40 mM IPTG induction. Cells grown in ethanol presence produce the maximum yield of soluble and insoluble amidase specific activity. The higher specific activity was found in the inclusion bodies obtained at 25ºC with ethanol. These results clearly demonstrate that all the conditions produce biologically active inclusion bodies.

Figure 2 shows the SDS-PAGE analysis of the produced proteins in T,S and IS cell fractions of the cultures induced with 0.7 mM IPTG subjected to different growth conditions as

representative of identical profile obtained when other IPTG concentrations were used. The insoluble fractions at 25ºC always showed the presence of amidase as the main component of all the protein which accumulated in the cell in the form of inclusion bodies (Lane 2 and 5) as opposed to the conditions at 37ºC in which others proteins expressed by the strain also aggregated (Lanes 9 and 12). The presence of a single protein band in IS fractions for all the tested conditions at 25ºC indicates homogenous inclusion bodies mainly constituted of amidase which offers the possibility of a facilitated recovery when compared with the inclusion bodies obtained 37ºC. The presence of amidase subunits was identified through its molecular weight, approximately 36 000Da, corresponding to the arrow shown at Figure 2.

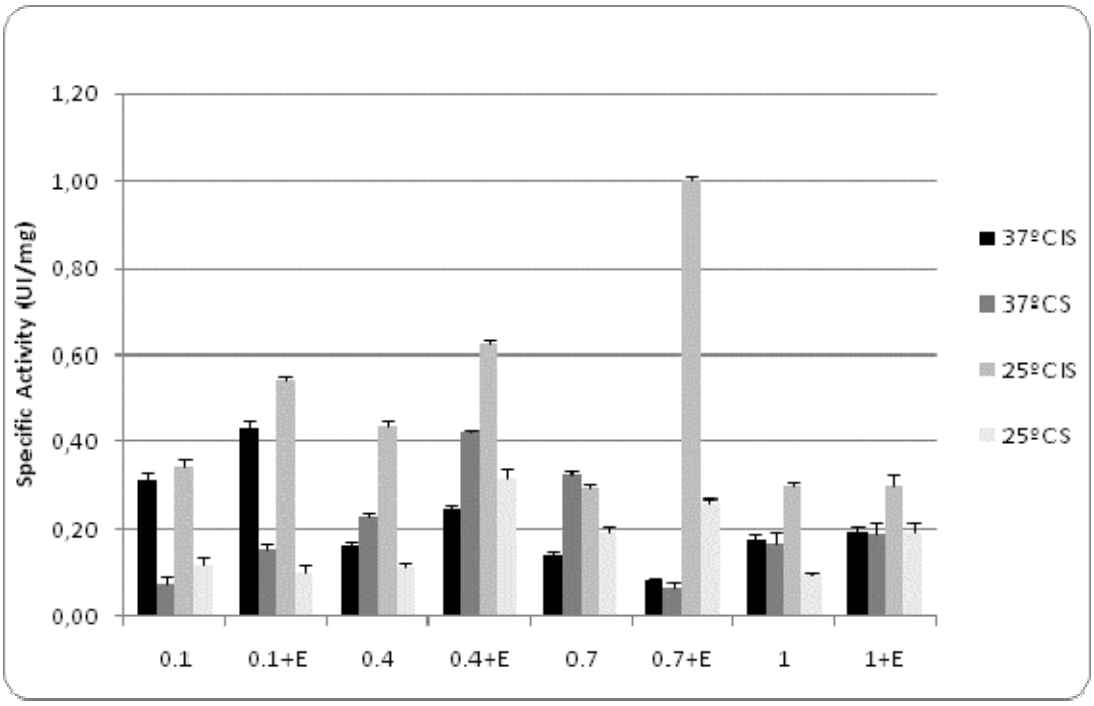

Figure 1- Effect of temperature, IPTG concentration and 3% ethanol supplementation (+E) on specific activity for amidase obtained in the soluble (S) and insoluble (IS) of cells submitted to different conditions.

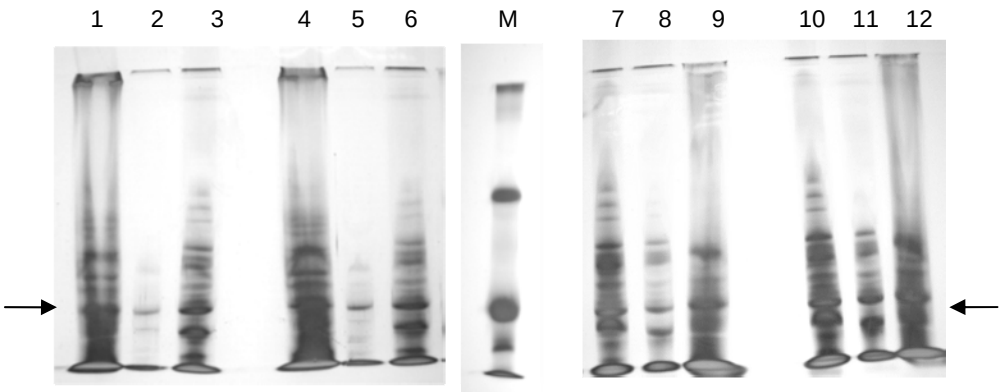

Figure 2- SDS-PAGE with urea analysis of amidase produced from *E.coli* recombinant strain under different growth condition in LB ampicilin medium using 0.7 mM IPTG. **Lanes: 1-** 25ºC+ 3% ethanol, total cell extract; **2-** 25ºC+ 3% ethanol, insoluble fraction; **3-** 25ºC+ 3% ethanol, soluble fraction; **4-** 25ºC, total cell extract; **5-** 25ºC, insoluble fraction; **6-** 25ºC, soluble fraction; **7-** 37ºC+ 3% ethanol, total cell extract; **8-** 37ºC+ 3% ethanol, soluble fraction; **9-** 37ºC+ 3% ethanol, insoluble fraction; **10-** 37ºC, total cell extract; **11-** 37ºC, soluble fraction; **12-** 37ºC, insoluble fraction; **M-** Molecular weight markers: 66000, 45000 and 24500 from top to bottom. The position of amidase subnunits is indicated by arrows.

In order to confirm the electrophoretic profile of the samples and the amidase activity of the cell fractions obtained for each condition, amidase transferase activity was performed *in situ* in a native PAGE as can be seen in Figure 3. The development of a brown colour in the gel lanes is indicative of the enzyme expression and the intensity of the formed colour is proportional to the quantity of expressed enzyme. The dark brown obtained in lanes 13-16 for 25ºC demonstrate an overall higher amidase activity when compared with 37ºC (lanes 1-4) as expected. Again the highest amidase specific activity was obtained for 25ºC with ethanol induced with 0.7 mM IPTG (lane 16).

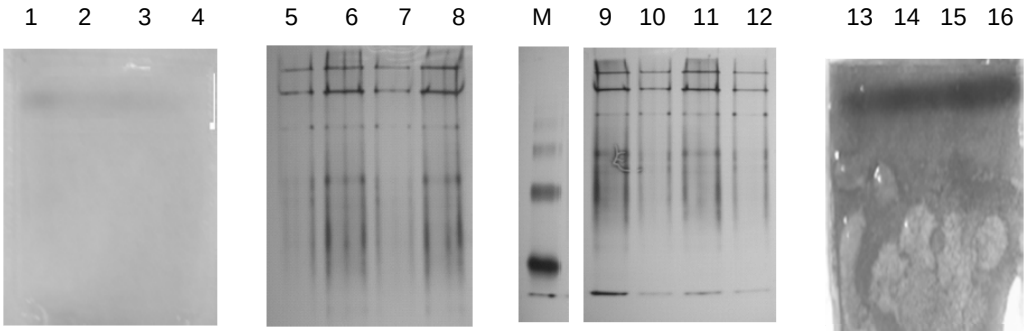

Figure 3 – Native PAGE analysis of amidase produced from *E.coli* recombinant strain under different growth condition in LB ampicilin medium using 0.7 mM IPTG. **Lanes: 1, 5 -** 37ºC, soluble fraction; **2, 6-** 37ºC, insoluble fraction; **3, 7-** 37ºC + 3% ethanol, soluble fraction; **4, 8-** 37ºC + 3% ethanol, insoluble fraction; **9, 13-** 25ºC, soluble fraction; **10, 14-** 25ºC, insoluble fraction; **11, 15-** 25ºC + 3% ethanol, soluble fraction; **12, 16-** 25ºC + 3% ethanol, insoluble fraction; **M-** Molecular weight markers: 132000, 66000, 45000 and 17800 from top to bottom.

The IS cell fractions obtained for each condition were subjected to solubilization using L-arginine solutions or guanidine hydrochloride at different concentrations. Addition of 0.25, 0.5 and 1 M L-arginine demonstrated a high increase in amidase yield in its bioactive and soluble form with the best results achieved when using 1 M L-arginine. When considering L-arginine concentration of 1.25 and 1.5 M the results are not as promising probably due to high concentration of L-arginine resulting in enzyme inactivation. The recovery of soluble protein was higher for the condition at 37ºC with 0.7mM IPTG and ethanol, with a recuperation of approximately 400 fold of amidase specific activity in the soluble fraction subjected to solubilization with L-arginine.

As opposed to the results obtained with L-arginine there was no amidase specific activity in S solubilized fractions obtained after solubilization with guanidine hydrochloride possibly due to the denaturing properties of guanidine hydrochloride and the incapacity for the enzyme to renaturate and restore its activity.

Nevertheless, a smaller increase (approximately 75 fold) in amidase activity for S solubilized fractions in the absence of L-arginine and guanidine hydrochloride (0 M) was verified in general for all conditions which suggest the importance of agitation in the solubilization of aggregated enzyme.

The effect of L-arginine is often attributed to the ability of arginine to suppress aggregation of proteins in which aggregates formed have native-like conformation probably showing biological activity (Tsumoto *et al*, 2003 Lilie *et al*, 2005). Our results seem to be consistent with such assumption however Fourier Transform Infrared Spectroscopy (FTIR) can be used in order to evaluate the secondary structure of the aggregates obtained and the effect of the used solubilization agents.

4 - Conclusions

Results have shown that all of growth conditions tested produced amidase aggregated in the form of inclusion bodies with the conditions at 25ºC showing inclusion bodies constituted by amidase as the single protein. For the overall of the tested conditions higher specific activity of soluble amidase was obtained at 37ºC in the presence of 3% ethanol. Nevertheless the highest specific activity was found at the inclusion bodies when the cells were grown at 25ºC in the presence of ethanol using 0.7mM IPTG for induction.

A method was developed in order to solubilize the aggregated amidase obtained in all the tested conditions using L-arginine as a non denaturing agent as opposed to GdnHCl that should be avoided. The efficiency of L-arginine in the non denaturing solubilization of amidase from inclusion bodies is being evaluated in a consistent FTIR analysis of aggregates structure which is already in progress.

References

Bradford, M.M. (1976). A rapid and sensitive method for quantification of microgram quantities of protein utilizing the principle of protein-dye binding. *Anal. Biochem.,* 101, 200-203.

Brammar, W.J. and Clarke, P.H. (1964). Induction and repression of *Pseudomonas aeruginosa* amidase. *J. Gen Microbiol.,* 37, 307-319.

Garcia-Junceda, E., Shen, G.J., Sugai, T., Wong, C.H. (1995). A new strategy for the cloning, overexpression and one step purification of three DHAP-dependent aldolases:rhamnulose-1-phosphate aldolase, fuculose-1-phosphate aldolase and tagatose-1,6-diphosphate aldolase. *Bioorg. Med. Chem.,* 3, 945-953.

Hames, B.D. and Rickwood, D. (1990). *Gel Electrophoresis of Proteins- A practical Approach*, Second Edition, The Practical Approach Series, New York.

Lilie, H., Schwarz, E., Rudolph, R. (1998). Advances in refolding of proteins produced in *E.coli*. *Current Opinion in Biotechnology,* 9, 497-501.

Lilie, H., Reddy, R.C., Rudolph, R., Lange, C. (2005). L-Arginine increases the solubility of unfolded species of hen egg white lysozyme*. Protein Science,* 14, 929-935.

Middelberg, A.P.J. (2002). Preparative protein refolding. *Trends in Biotechnology,* 20, 437-443.

Pacheco, R., Martins, S., Faurnaud, S., Pacheco, V., Karmali, A., Tata, R. and Brown, P.R. (2000). Differential Behaviour of recombinant wild-type and altered amidases on immobilized metal-ion affinity chromatography. *Int. J.C.B.,* 5, 111-129.

Thomas, J.G., Baneyx, F. (1997). Protein divergent effects of chaperone overexpression and ethanol supplementation on inclusion body formation in recombinant *E.coli*. *Protein Expression and purification,* 11, 289-296.

Tsumoto, K., Umetsu, M., Kumagai, I., Ejima, D., Arakawa, T. (2003). Solubilization of active green fluorescent protein from insoluble particles by guanidine and arginine*. Biochemical and Biophysical Research Communications,* 312, 1383-1386.

Proceedings of the 10th International Chemical and
Biological Engineering Conference - CHEMPOR 2008
Braga, Portugal, September 4-6, 2008
E.C. Ferreira and M. Mota (Eds.)

Mathematical modeling of recombinant *Escherichia coli* aerobic batch fermentations

Rafael Costa, Isabel Rocha and Eugénio C. Ferreira*

IBB – Institute for Biotechnology and Bioengineering, Centre of Biological Engineering
University of Minho, Campus de Gualtar, 4710–057 Braga, Portugal.

Keywords: Mathematical modelling, GFP production, acetate inhibition kinetics, recombinant *Escherichia coli*, parameter estimation
Topic: Integration of life sciences & engineering

Abstract

In this work, three competing unstructured mathematical models for the biomass growth by recombinant *E. coli* strains with different acetate inhibition kinetics terms were evaluated for batch processes at constant temperature and pH.
The models considered the dynamics of biomass growth, acetate accumulation, substrate consumption, Green Fluorescence Protein (GFP) production and three metabolic pathways for *E. coli*. Parameter estimation and model validation was carried out using the Systems Biology toolbox for Matlab (The Mathworks) with different initial glucose concentrations (5g/kg to 25g/kg) in a 5dm^3 bioreactor. Model discrimination was based on the two model selection criterion (Akaike's information criterion and normalized quadratic difference between the simulated and experimental data criterion). The first model described by Jerusalimsky approach is an approximation to the non-competitive substrate inhibition. Cockshott approach describes the inhibition at high acetate levels and Levenspiel considers the critical inhibitory acetate concentration that limits growth. Within the studied experimental range, Jerusalimsky model provided a good approximation between real and simulated values and should be favored. The model describes the experimental data satisfactorily well.

1 Introduction

Acetate, when present in *Escherichia coli* fermentations during aerobic growth on glucose is a major obstacle to cell growth and recombinant protein production (Jensen and Carlsen 1990,Nakano *et al.* 1997) and a detailed documentation of acetate production becomes important.
Many different mathematical models were reported in the literature to describe the kinetics of primary metabolites and the acetate overflow metabolism from *E. coli* (Varma and Palsson 1994,Xu *et al.* 1999, Akesson *et al.* 1999). However, there have been few studies focused on the recombinant proteins (GFP) production multi-route models with acetate inhibition kinetics. Lee and Ramirez (1992) used a simple and unstructured model to simulate recombinant protein production that include inducer effect on cell growth and recombinant protein production. A similar model was used by Chae and co-workers (2000) with introduction product inhibition term on the specific growth rate. However, models from previous works for recombinant proteins production are based usually on simplified Monod kinetics description and have neglected the influence of inhibition effect of acetate on *E. coli* growth and glucose uptake although it is known that this play an important role.
The models evaluated here take into account three specific substrate uptakes kinetics with different acetate inhibition terms for the representation of the growth of recombinant *E. coli* strain HMS174AcGFP1. In this work, a set of batch data on fermentations of glucose has been also collected for a better understanding of the environmental effects (glucose concentration) of the acetate overflow phenomenon and

GFP production. The aim of this study was to test three well-established kinetic models for their suitability to describe recombinant *E. coli* growth using batch fermentations data. Subsequently, the best kinetic model can be applied to fed-batch processes in order to determine optimal operation conditions.

2 Material and Methods

Pre-cultures and batch cultures
E. coli HMS174(DE3)pet28aAcGFP1 strains were obtained originally from the stock centre and were used throughout the present study. In these strains, GFP proteins are induced by isopropyl-β-D-thiogalactopyranoside (IPTG). Cells from a glycerol stock culture stored at -80ºC were reactivated by inoculating a frozen aliquot (1ml) into 1L Erlenmeyer flasks with 300 ml of a defined inoculum media with kanamicin (0.03 g kg^{-1}). Flasks were then incubated at 37ºC and 150 rpm until the culture reached exponential phase. Finally, the culture was then transferred into the reactor, containing 3 L from defined medium as described previously in Rocha and Ferreira (2002) to give an initial optical density at 600nm (OD_{600}) in the bioreactor of 0.20-0.25.

Medium and Fermentation Conditions
Cells were grown in a defined medium, with kanamicin and ampicilin as described above. The different initial glucose solution (5.0, 10.0, and 25.0 g kg^{-1}) and the mineral solution were sterilized separately by autoclaving and were later added to the reactor together with a sterile filtered solution containing $MgSO_4$, $CaCl_2$, trace elements, vitamins and thiamine prior to inoculation.
All fermentations were carried out in batch-mode in a 5 L fermenter from B. Braun Biotech (Germany) with a working volume of 3 L equipped with a digital control unit (DCU). In addition, temperature, pH, dissolved O_2 and CO_2 sensors were connected to this DCU and to a data acquisition system. All the cultures were run at ca. 25h and with controlled temperature (at 37ºC) and dissolved oxygen (above 30% to maintain aerobic condition of growth at all times). Silicone (Merck) was used as antifoam reagent.

Analytic Methods
Cell growth was monitored by measuring the OD at 600nm on a UV-visible Jasco V-560 spectrophotometer. The OD_{600} unit was converted to the cell dry weight based on the relation: OD_{600} = 0.21 g kg^{-1}. Samples for acetate and the glucose measurements during the course of the batch fermentations were collected at regular intervals and centrifuged at 10000g in a microcentrifuge for 10 min. After filtration through a 0.2 mm syringe filter the samples were stored at -20ºC for subsequent analysis. Glucose and acetate concentration in samples were detected and measured by high performance liquid chromatography (HPLC) with a Metacarb 87H, 300x7.8mm column (Varian, Palo Alto, CA), a UV detector (Jasco) with a detection wavelength of 210 nm and a refractive index detector (Knauer). The mobile phase used was 0.01N H_2SO_4 with a flow rate of 0.7ml min^{-1} and at a column temperature of 60ºC. The glucose concentration was also measured using commercial enzymatic kits according to the manufacturer's instructions (Spinreact, Sant Esteve de Bas, Spain).

Kinetic Model Development
The presented model combines terms for cell growth, substrate consumption, acetate accumulation and green fluorescence protein (GFP) production for fed-batch cultures with constant pH and temperature. Glucose was assumed to be the only carbon source used for the oxidation and fermentation processes needed for biomass growth and GFP production (eq. 1 and 2). The oxidation of acetate is considered as well (eq. 3) but the oxygen and carbon dioxide dynamic are not. The potential effect of the induction with isopropyl-beta-Dthiogalactopyranoside (IPTG) on the decrease of the growth rate

and yield coefficients was not contemplated in the model. The substrate inhibition was also not considered in the kinetic model.

The reformulated model was based from Bastin and Dochain (1990) and considers three main metabolic pathways:

Oxidation of glucose,

$$k_1 S \xrightarrow{\mu_1} X + k_5 P \qquad \text{if } qs < qs_{cr} \text{ and } A > 0 \qquad (1)$$

fermentation of glucose,

$$k_2 S \xrightarrow{\mu_2} X + k_3 A \qquad \text{if } qs < qs_{cr} \text{ and } A \leq 0 \qquad (2)$$

oxidation of acetate,

$$k_4 A \xrightarrow{\mu_3} X \qquad \text{if } qs > qs_{cr} \text{ and } A > 0 \qquad (3)$$

and the following four ordinary differential equations (4-6), capable of describing glucose fermentation by *E. coli*:

The biomass growth is given by,

$$\frac{dX}{dt} = (\mu_1 + \mu_2 + \mu_3)X - \left(\frac{F}{W}\right)X \qquad (4)$$

and the substrate concentration by,

$$\frac{dS}{dt} = (-\mu_1 k_1 - \mu_2 k_2 - m_S)X - \frac{((\mu_1 + \mu_2 + \mu_3)k_5 + \beta)X}{K_6} - \left(\frac{F}{W}\right)(S_0 - S) \qquad (5)$$

that included the substrate conversion to product formation, maintenance and cell growth.

Finally, the acetate accumulation and product formation is described by equations 6 and 7 respectively,

$$\frac{dA}{dt} = (\mu_2 k_3 - \mu_3 k_4)X - \left(\frac{F}{W}\right)A \qquad (6)$$

$$\frac{dP}{dt} = (\mu_1 + \mu_2 + \mu_3)k_5 X + \beta X - \left(\frac{F}{W}\right)P \qquad (7)$$

where P (GFP production) includes a growth and non-growth associated term. The variable X, S, A and P represents biomass, substrate, acetate and product concentrations, respectively (g kg^{-1} and mg kg^{-1} for product); F and W are the mass flow feed rate and weight of the fermentation broth, respectively (for cultures operated in batch mode F is zero; the k_i are the yield coefficients; β, non-growth associated product constant; m_s maintenance coefficient and μ_i the specific growth rates.

As described in the introduction, it is known that acetate accumulation limits the productivity of the fermentation process. For this reason, three alternative equations for the specific substrate uptake rates (q_s) with different acetate inhibition terms tested in this study at initial glucose concentration 5 g kg^{-1}. Model I, according to Jerusalimsky (Roels, 1983) is an approximation to the non-competitive substrate inhibition. Model II (Cockshott and Bogle 1999) describes the inhibition at high acetate levels and model III (Han and Levenspiel 1988) considers the critical inhibitory acetate concentration that limits growth.

3 Results and Discussion

Parameter estimation and model evaluation

The simulated data are obtained by solving the differential equations (1-4), and the experimental state variables were taken from the experimental studies described in the Materials and Methods section. The kinetic parameters were estimated by fitting the experimental data using the simulated annealing algorithm from the Systems Biology toolbox running in Matlab v.7.1.0 (The Mathworks). For model discrimination, Akaike's information criterion (AIC) and normalized quadratic difference between the simulated and experimental data criterion (*dif*) were used.

Batch fermentations using *E. coli* for HMS174pacGFP strain were performed for estimation and validation of model parameters. Observation of the experimental data revealed that acetate was not metabolized (Figure 1). In this way, the metabolic pathway for the acetate oxidation (μ_3) was not considered in the developed model. Initial estimates for the yield parameter (k_5) were first calculated using the experimental data obtained from the batch fermentations. The initial estimates for the remaining parameters were taken from the literature for *E. coli* on a single substrate. Subsequently, some of the parameters were set to the values described on Table 1 (k_1, k_2, K_s, m_s, β_1, n, and A_{crt}), while all the others parameters were fitted using the experimental data.

Table 1. Initial parameter values (kinetics and yield coefficients) for the growth of *E. coli* K12 taken from the literature and determined from experimental data.

Parameter	Values	Units	Reference (s)
k_1	1.88	($g_S\ g_X^{-1}$)	(Galvanauskas *et al.* 1998)
k_2	20	($g_S\ g_X^{-1}$)	(Rocha, 2003)
$\boldsymbol{k_3}$	14	($g_A\ g_X^{-1}$)	(Rocha, 2003)
k_4	-	($g_A\ g_X^{-1}$)	-
$\boldsymbol{k_5}$	9.22	($mg_P\ g_X^{-1}$)	determined
$\boldsymbol{k_6}$	50	($mg_P\ g_S^{-1}$)	(Aucoin *et al.* 2006a)
$\boldsymbol{qs_{max}}$	1.8	($g\ g^{-1}\ h^{-1}$)	(Galvanauskas *et al.* 1998)
K_s	0.1	($g\ kg^{-1}$)	(Galvanauskas *et al.* 1998)
$\boldsymbol{K_{ai}}$	15.5	($g\ kg^{-1}$)	(Galvanauskas *et al.* 1998)
$\boldsymbol{qs_{cr}}$	0.15	($g\ g^{-1}\ h^{-1}$)	(Akesson *et al.* 1999)
m_s	0.02	($g\ g^{-1}\ h^{-1}$)	(Galvanauskas *et al.* 1998)
β	0.1	($mg\ g^{-1}\ h^{-1}$)	(Aucoin *et al.* 2006b)
A_{crt}	0.9	($g\ kg^{-1}$)	(Aristidou *et al.* 1999)
n	1.41	-	(Théodore and Panda 1999)

The estimated parameters are showed in Table 2. The parameters obtained from the experimental data fitting were in relatively agreement to the values observed in the literature reports for model I, contrary to the model II and III. However, the value estimated from the parameter k_3 and qs_{cr} was higher in comparison to the literature data. This discrepancy might be attributed not only to different operating conditions and/or *E. coli* strains, but also to different modeling strategies to parameter fitting.

The proposed Jerusalimsky and Cockshott approaches (models I and II, respectively) describe very well the experimental data for the time courses of glucose, acetate, biomass growth and GFP concentration (Figure 1). However, the model III curves were in significant disagreement with the experimental data for the acetate concentration. These observations can be confirmed by comparing the statistical analysis from selection models criterions AIC and *dif*. According to the Table 2, models I has the lowest AIC and *dif* values. As a consequence, it was favoured and selected for further analysis.

Table 2. Estimated values of parameters for the model I obtained by fitting the experimental data with 5 g kg^{-1} initial glucose concentration.

Parameter	Model I	Model II	Model III
k_3	33.45	69.89	70.00
k_5	12.78	12.73	12.02
k_6	51.95	25.73	25.00
qs_{max}	0.97	0.89	7.50
K_{ai}	7.75	7.75	25.60
qs_{cr}	0.61	0.63	0.63

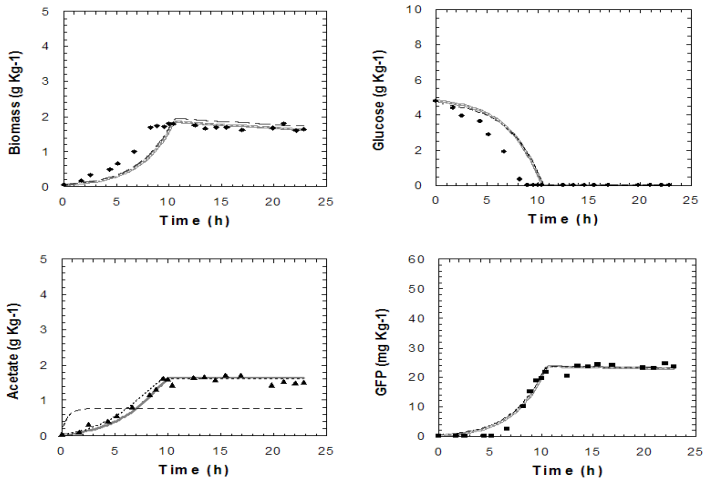

Figure 1. Comparison between experimental and simulated data (a) biomass growth, (b) glucose, (c) acetate and (d) GFP concentration in batch fermentation by HMS174AcGFP1 at 5g kg^{-1} initial glucose concentration. Solid lines represent the simulation data from model I, depicted lines the model II and dashed lines the model III, using the fitted parameters (Table 2). Lines from model I, II and III for glucose and GFP are overlapped for biomass, glucose and GFP concentrations.

Table 3. Model selection criterion Akaike's (AIC) and normalized quadratic difference between the simulated and experimental data (*dif*) at 5.0 g Kg^{-1} initial glucose concentration for model I, II and III.

Criterion	Model I	Model II	Model III
AIC	201.28	221.52	243.14
dif	2.32	2.34	3.45

* AIC and *dif* are the average values from the variable states

To validate the developed model it is necessary to use other experimental data set than that applied to identify initial parameters. Therefore, the selected kinetic model (model I) was validated and tested using the fitted parameters values with different fermentation conditions. Figure 2 compares the experimental data profiles and simulation data 10 g kg^{-1} concentration.

The better fitting with this initial glucose concentration to the experimental biomass, acetate and GFP concentration is observed and demonstrates the applicability of the presented kinetic model. However, the model was unable to predict the experimental data with 25.0 g kg^{-1} glucose concentration (data not shown). Additionally, the simulated glucose concentration at 10 g kg^{-1} glucose concentration was considerably lower than the one obtained by experimental methods, probably because there is a substrate consumption inhibition phenomenon that is not considered in the model.

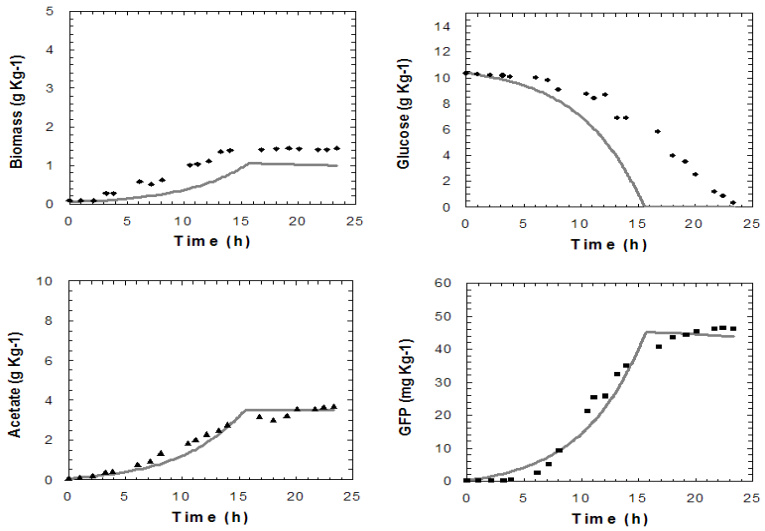

Figure 2 Comparison between experimental and simulated data (a) biomass growth, (b) glucose, (c) acetate and (d) GFP concentration in batch fermentation by HMS174AcGFP1 at 10g kg^{-1} initial glucose concentration.

4. Conclusions

A mathematical unstructured model describing the recombinant protein production (GFP) in *E. coli* HMS174AcGFP1 using acetate inhibition kinetics was developed for batch fermentations. The model considers the inhibition of recombinant cultures by acetate inhibition. Using this modelling approach a satisfactory prediction was achieved (5-10 g Kg^{-1}), with the parameter obtained by experimental data fitting. Within the range of the model, the Jerusalimsky and Cockshott approaches should be favoured.

References

Akesson,M., Karlsson,E.N., Hagander,P., Axelsson,J.P., and Tocaj,A. (1999) *Biotechnology and Bioengineering* **64** (5), 590-598.
Andrews,J.F. (1968). *Biotechnology and Bioengineering* **10** (6), 707-&.
Aristidou,A.A., San,K.Y., and Bennett,G.N. (1999). *Biotechnology Progress* **15** (1), 140-145.
Aucoin,M.G., Murray-Beaulieu,V., Poulin,F., Boivin,E.B., Chen,J.K., Ardelean,F.M., Bastin,G. and Dochain,D. (1990). Amsterdam.
Chae,H.J., DeLisa,M.P., Cha,H.J., Weigand,W.A., Rao,G., and Bentley,W.E. (2000) *Biotechnology and Bioengineering* **69** (3), 275-285.
Cockshott,A.R. and Bogle,I.D.L. (1999) *Bioprocess Engineering* **20** 83-90.
Galvanauskas,V., Simutis,R., Volk,N., and Lübert,A. (1998) *Bioprocess Engineering* **18** 227-234.
Han,K. and Levenspiel,O. (1988) *Biotechnology and Bioengineering* **32** (4), 430-437.
Jensen,E.B. and Carlsen,S. (1990) *Biotechnology and Bioengineering* **36** 1-11.
Kleman,G.L. and Strohl,W.R. (1994) *Applied and Environmental Microbiology* **60** (11), 3952-3958.
Lee,J. and Ramirez,F. (1992) *Biotechnology and Bioengineering* **39** 635-646.
Nakano,K., Rischke,M., Sato,S., and Markl,H. (1997) *Applied Microbiology and Biotechnology* **48** (5), 597-601.
Rocha,I. (2004) European symposium on computer-aided process engineering, 14, Lisbon.
Rocha,I. and Ferreira,E.C. (2002) *Analytica Chimica Acta* **462** (2), 293-304.
Roels,J.A. (1983) *Energetics and kinetic in Biotechnology*.
Théodore,K. and Panda,T. (1999) *Bioprocess Engineering* **20** 309-311.
Varma,A. and Palsson,B.O. (1994) *Applied and Environmental Microbiology* **60** (10), 3724-3731.
Xu,B., Jahic,M., and Enfors,S.O. (1999) Biotechnology Progress 15 (1), 81-90.

Proceedings of the 10th International Chemical and
Biological Engineering Conference - CHEMPOR 2008
Braga, Portugal, September 4-6, 2008
E.C. Ferreira and M. Mota (Eds.)

Overproduction of protein-bound polysaccharides from a *Coriolus versicolor* strain by submerged fermentation

José M. Santos Arteiro[1,2], M. Rosário Martins[1,3], Cátia Salvador [1], Fátima B. Candeias[1,3], Sónia Martins[4], Amin Karmali[4], A. Teresa Caldeira[1,2 *]

[1]Chemical Department, University of Évora, 7000 - 671 Évora, Portugal
[2]CQE, University of Évora, 7000 - 671 Évora, Portugal
[3] ICAM, University of Évora, Ap. 94 7002 - 554 Évora Portugal
[4] CIEQB, ISEL,1950-062 Lisboa

Keywords: Protein-bound polysaccharides, *Coriolus versicolor*, submerged fermentation, edible mushrooms
Topic: Integration of life sciences & engineering

Abstract

Some mushroom strains are able to synthesize polysaccharopeptides with antitumoral and immunostimulating properties. The aim of this study was to define experimental conditions to optimize the production of protein-bound polysaccharides by *Coriolus versicolor*. In order to evaluate and to optimize the production of these compounds, submerse cultures were performed with four different carbon sources: glucose, maltose, sucrose and mannitol. Additionally, aiming for a clean process and to reduce the medium cost, two kinds of agro-industrial residues were used: tomato pomace and beet wastes.

The highest polysaccharide concentration was achieved with tomato pomace as agro-industrial residue corresponding to the 14th day of culture. Based on these results *C. versicolor* was cultivated in a basal medium plus tomato pomace in a stirred bioreactor. Endocellular and exocellular protein-bound polysaccharides were quantified. The concentration of the polysaccharide compounds was higher in the supernatant than in mycelia and supernatant complex has higher protein content. The main protein-bound polysaccharides produced by *C. versicolor* ranged between molecular weights of $1.3x10^3$-$8.9x10^4$ Da.

The comparison of the results obtained in this study with those reported in the literature, let us to confirm the interest of this selected culture medium with tomato pomace, in order to maximise the production of complexes protein-polysaccharides by *C. versicolor*. Besides, this clean process allows valuing the agro-industrial residues with a low cost and a higher production of polysaccharide compounds.

1. Introduction

Several species of mushrooms have been valued as edible and medicinal resources. Polysaccharides mushroom-derived have shown medicinal effects such as blood pressure and cholesterol lowering, liver protection, anti-fibrotic, anti-inflammatory, anti-diabetic and anti-viral activities. Additionally, some strains are able to synthesize new polysaccharopeptides with antitumoral and immunostimulating properties (Cui *et al*., 2007; Li *et al*., 2008). Protein-bound polysaccharides or polysaccharopeptides produced by the white rot fungus, *C. versicolor*, are effective immunopotentiators used to supplement the chemotherapy and radiotherapy of cancers and various infectious diseases (Cui and Chisti, 2003).

Polysaccharopeptide Krestin (PSK) and polysaccharopeptide PSP are the best known commercial polysaccharopeptide preparations obtained from *C. versicolor* mycelium (Cui and

* Corresponding author: Tel + 351-266745313. E-mail:atc@uevora.pt

Chisti, 2003). In fact, most of the reported studies referred polysaccharides isolated from mycelium (IPS), however few studies on exopolysaccharides (EPS) from *C. versicolor* have been reported (Kim *et al.,* 2002; Tavares *et al*., 2005). Really, polysaccharides represent the major constituent that establishes the rigidity and morphological properties of the fungal cell wall and, depending on the culture conditions, they can be excreted to the medium. In this work, endo and exo protein-bound polysaccharides produced by *C. versicolor* will be investigated in flasks and stirred-tank bioreactor cultures.

2. Material and Methods

Microorganism and inoculum

C. versicolor was isolated from *Quercus suber* and kindly provided by ISEL. The culture was maintained on PDA, transferred to a fresh agar plate every month, and grown at 28 °C for approximately 7 days. Mycelia of *C. versicolor* on the media surface were cut and transferred to culture flasks.

Cultures

Cultures were prepared in shake-flask with a basal media comprised by the following ingredients per liter: yeast extract 2 g, KH_2PO_4 0.8 g, $MgSO_4.7H_2O$ 0.5 g, $Na_2HPO_4.2H_2O$ 0.25 g, NH_4NO_3 1 g, pH 6.0. Four different carbon sources were provided at 10 g L^{-1} in the basal medium: glucose, maltose, sucrose and mannitol. Additionally two kinds of agro-industrial residues were used: tomato pomace and beet wastes. The different carbon sources were added one by one to the basal medium. Flasks were incubated at 28°C, for 20 days using an orbital shaker at 150 rpm. Samples were collected periodically along the twenty days of the assays.

Fermentations in the bioreactor were carried out in batch mode, using glucose or tomato pomace, at an agitation speed of 145 rpm and air flow rate of 2 vvm, for approximately 20 and 14 days respectively, at 28ºC. Sterilized water was added to the fermented broth to compensate the loss of moisture every 24 h and maintained at 1,3L fill level.

Biomass and Glucose concentration

The culture broth was filtered through Whatman nº 1 filter paper, washed with distilled water and the retained biomass was dried at 60 ºC for 48 h for the determination of the biomass dry weight. Glucose concentration in the supernatant of cultures was determined using an enzymatic Kit with glucose oxidase (D-Glucose, Roche)

Polysaccharide recovery

Isolation and quantification of extracellular and intracellular polysaccharides

EPS were isolated from supernatant of cultures, adding four volumes of 95% ethanol and kept at 4 °C for 12 h, centrifuged at 1350×g for 15 min at 4 °C. Precipitate was resuspended with equal volume of 75% ethanol and centrifuged again as described above. Polysaccharide precipitated were dried at 60 °C to remove residual ethanol and the residues were dissolved in an equal volume of distilled water (Lin and Sung, 2006).

The mycelial biomass pellets were heated in water (90ºC) for 2 h to release the IPS, filtered through Whatman filter paper and the extract was collected (Lee *et al*., 2006). The IPS in the extract was recovered using the same procedure as the EPS recovery.

The EPS and IPS concentration were determined by phenol–sulphuric method (Dubois *et al*., 1956) using glucose as a standard curve.

The polysaccharide protein contents were determined by Lowry method with bovine serum albumin as the standard (Lowry *et al*., 1951).

Polysaccharide molar mass

Weight-average molecular weights (Mw) of the polysaccharides were determined using size-exclusion chromatography (SEC) coupled to UV (280 nm) and RI detectors, using a HPLC system. Mobile phase, ultrapure water containing 0.05% NaCl, was pumped at a flow rate of

0.6 ml/min. Compounds detection was simultaneously performed on the UV and RI detector. Standards of polyethylene glycol (1.5, 3, 6 and 20 kDa, Sigma Chemical Co., MO, USA) were used for determination of biopolymers molecular weight.

3. Results and Discussion

Effect of carbon sources in cultures

Four different defined carbon sources were provided in the basal medium (glucose, maltose, sucrose and mannitol), to examine the effect of carbon sources on mycelial growth and exobiopolymer production. As shown in Table 1-A, high levels of mycelial biomass were obtained with sucrose or mannitol, whereas higher levels of EPS and IPS were obtained for sucrose and glucose as the sole carbon source. Additionally, intending for a clean process and to reduce the medium cost, two kinds of agro-industrial residues were used: tomato pomace and beet wastes. The biomass formed in cultures with agro-industrial residues was higher than cultures with defined carbon sources, mainly in beet wastes (Table 1-B).

Table 1 Effect of carbon sources on mycelial biomass, final pH, EPS and IPS production in shake flask cultures of *C. versicolor*[a]

	Mycelial biomass ($g.L^{-1}$)	EPS ($g.L^{-1}$)	IPS ($g.L^{-1}$)	Final pH
A				
Glucose	2,01 ± 0,02	$17,83x10^{-2} \pm 4,01x10^{-2}$	$2,03x10^{-2} \pm 0,76\ x10^{-4}$	6,84 ± 0,01
Sucrose	2,38 ± 0,02	$15,80x10^{-2} \pm 1,07x10^{-2}$	$1,05\ x10^{-2} \pm 2,46\ x10^{-4}$	6,44 ± 0,04
Maltose	1,62 ± 0,02	$7,49\ x10^{-2} \pm 1,80x10^{-2}$	$0,78\ x10^{-2} \pm 0,92\ x10^{-4}$	7,27 ± 0,04
Mannitol	2,53 ± 0,01	$8,38\ x10^{-2} \pm 2,84x10^{-2}$	$1,15\ x10^{-2} \pm 0,65\ x10^{-4}$	4,73 ± 0,02
B				
Beet wastes	6,45 ± 0,01	$18,30x10^{-2} \pm 2,45x10^{-2}$	$1,56\ x10^{-2} \pm 1,42\ x10^{-4}$	7,27 ± 0,01
Tomato pomace	4,82 ± 0,01	$55,05x10^{-2} \pm 3,40x10^{-2}$	$2,50\ x10^{-2} \pm 7,21\ x10^{-4}$	7,23 ± 0,02

[a]Fermentations were carried out for 20 days at 28ºC with initial pH 6. Values are mean of triple determination with standard deviation. A- Defined carbon sources. B- Agro-industrial residues used as carbon sources.

Maximal protein-bound polysaccharide (EPS) concentration obtained in batch cultures ranged between 0.15-0.90 $g.L^{-1}$ (Fig. 1) and IPS concentration, at the end of cultures, ranged between 0.01-0.03$g.L^{-1}$ (Table 1). The highest polysaccharide concentration was achieved with tomato pomace as agro-industrial residues corresponding to the 14^{th} day (Fig. 1).

Fig 2 shows some aspects of cultures performed with agro-industrial residues. The pellets formed in tomato pomace cultures were smaller than those formed in beet wastes cultures (Fig. 2-a,b). Mycelial morphology (Fig.2-c) illustrate the homogeny of pellets developed, however, their size and hairiness were different according to the substrate used. The gelatinous appearance of the pellets, in part due to the presence of exopolysaccharides adhered to the mycelia can led to an overestimation of the biomass and the underestimation of exopolysaccharides concentration (Gern *et al*., 2008).

C. versicolor was cultivated in a basal medium plus glucose in a stirred bioreactor aiming the optimization of EPS and IPS production. Fig. 3 shows the dynamic changes of glucose utilization, EPS production, dissolved O_2 (%) and pH during 20 days of culture. Dissolved oxygen (DO_2) concentration also fell rapidly during the exponential growth phase of fermentation (Fig. 3-b). This may be due to the rapid increase of biomass concentration observed in this period, simultaneously, a decrease of glucose was observed. pH value increased afterwards 10 days of culture, when glucose on the medium is residual. The yield of exobiopolymer formation from substrate ($Y_{P/S}$) was 0.0297 at the final of culture however the highest EPS concentration (0,445 g/L) was produced after 15 days. EPS concentration in bioreactor was increased around 1.5 times comparatively to flask cultures, on the same culture medium. The consumption of these polymers during the process was observed in our study and could be attributed to the existence of residual glucose in the culture medium,

starting from the 15th day of culture (Fig. 3), this phenomenon was observed in all cultures (Fig. 1, 3) and is also referred by other authors (Rosado *et al.*, 2002; Wisbeck *et al.*, 2005).

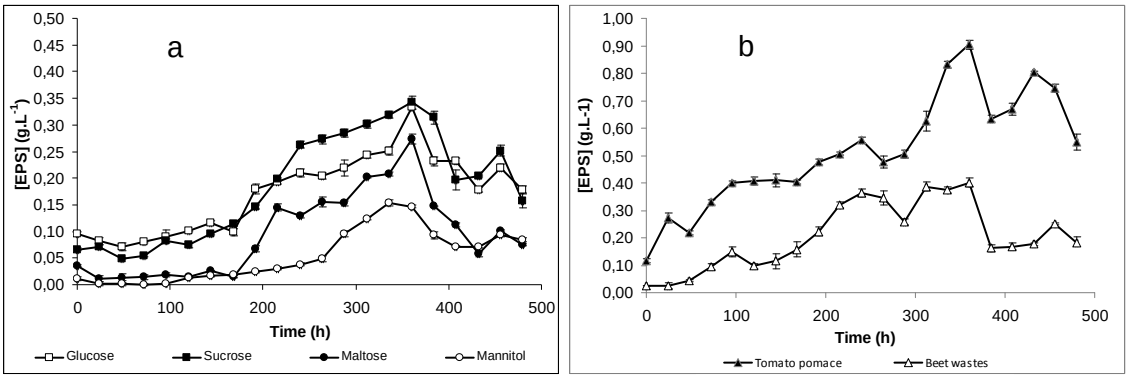

Figure 1- Dynamic changes of EPS production in shake flask *C. versicolor* cultures: a- Defined carbon sources. b- Agro-industrial residues.

Fig.2: Aspects of *Coriolus versicolor* cultures on tomato pomace (a) and beet wastes (b) Mycelial morphology observed with 6X enlargement (c)

Agitation could be benefit to the growth and performance of microorganisms, in fact agitation promote a better mixing of the fermentation broth, allowing to maintain a concentration gradient between the interior and the exterior of the cells and also favours oxygen supply. This is important for high biomass concentration, moreover, mycelial morphology can also be affected (Gern *et al*., 2008). In this work, a decrease in the size of the pellets was observed on stirred bioreactor, comparatively to flask cultures. Agitation and aeration cause probably damage to the stability of the pellets, affecting mycelial morphology.

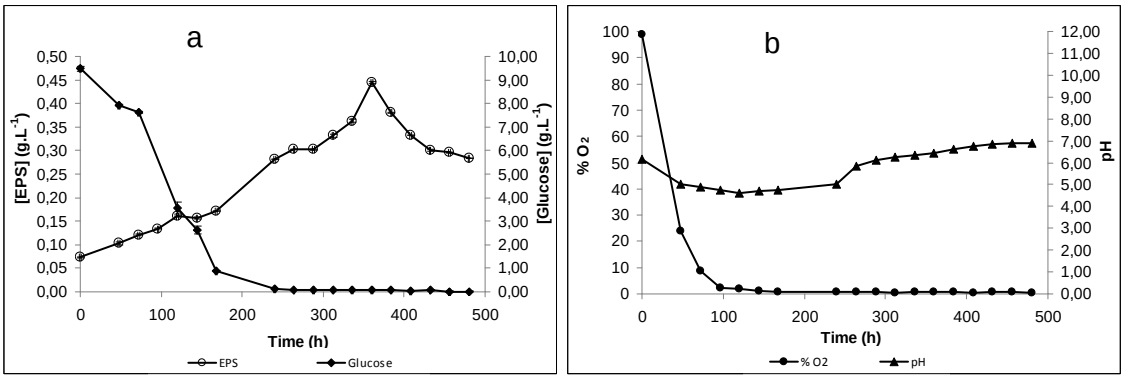

Figure 3- Dynamic changes of glucose utilization and EPS production (a), % O_2 dissolved and pH (b) during 20 days of *C. versicolor* culture, in bioreactor.

In order to enhance the production of protein-bound polysaccharides, *C. versicolor* was cultivated in a stirred bioreactor during 14 days, using tomato pomace. The EPS and IPS protein-bound polysaccharides were extracted, giving concentrations of about 1.7 $g.L^{-1}$ and 0.08 $g.L^{-1}$ respectively. This approach allows the increase of EPS production 1.9 times. The supernatant complex has a protein concentration 40 times higher than mycelia complexes, however the relationship polyssacharide/bounded proteins is two times higher in mycelium than in supernatant, revealing a different protein-bound polysaccharides production by *C. versicolor.*

Molecular weights of EPS and IPS

EPS and IPS produced in all cultures were separated by HPLC using a size exclusion column. Table 2 summarizes the molecular weights (Mw) of the main compounds isolated. The largest molecular weight fraction of EPS compounds (>10^4) were isolated in mannitol, maltose, tomato pomace and beet wastes, but the highest M_w EPS (>1,0x10^5 Da) was produced in maltose cultures. Molecular weight fraction of IPS was quite similar to the EPS produced for each carbon source, however, the highest M_w IPS (>1,0x10^5 Da) were produced in maltose, mannitol, tomato pomace and beet cultures. Nevertheless these IPS polymers were present in lower concentrations than EPS.

Table 2- Average molecular weights of EPS and IPS fraction separated by size exclusion chromatography

		Molecular weight (Da)			
		Peak 1	Peak 2	Peak 3	Peak 4
EPS	Tomato pomace	<1,0x10^3	1,3x10^3	2,9x10^3	1,7x10^4
	Beet waste	<1,0x10^3	3,5x10^3	9,8x10^3	8,9x10^4
	glucose	<1,0x10^3	1,3x10^3	2,9x10^3	
	sucrose	<1,0x10^3	1,4x10^3	3,5x10^3	7,6x10^3
	maltose	<1,0x10^3	3x10^3	3,5x10^3	>1,0x10^5
	mannitol	1,0x10^3	1,7x10^3	3,1x10^3	1,1x10^4
IPS	Tomato pomace	<1,0x10^3	5x10^3	>1,0x10^5	
	Beet wastes	<1,0x10^3	5x10^3	>1,0x10^5	
	glucose	1,3x10^3	5x10^3	9,0x10^3	2,6x10^4
	sucrose	1,3x10^3	1,2x10^4	2,6x10^4	
	maltose	<1,0x10^3	5x10^3	1,2x10^4	>1,0x10^5
	mannitol	1,3x10^3	5x10^3	1,2x10^4	>1,0x10^5

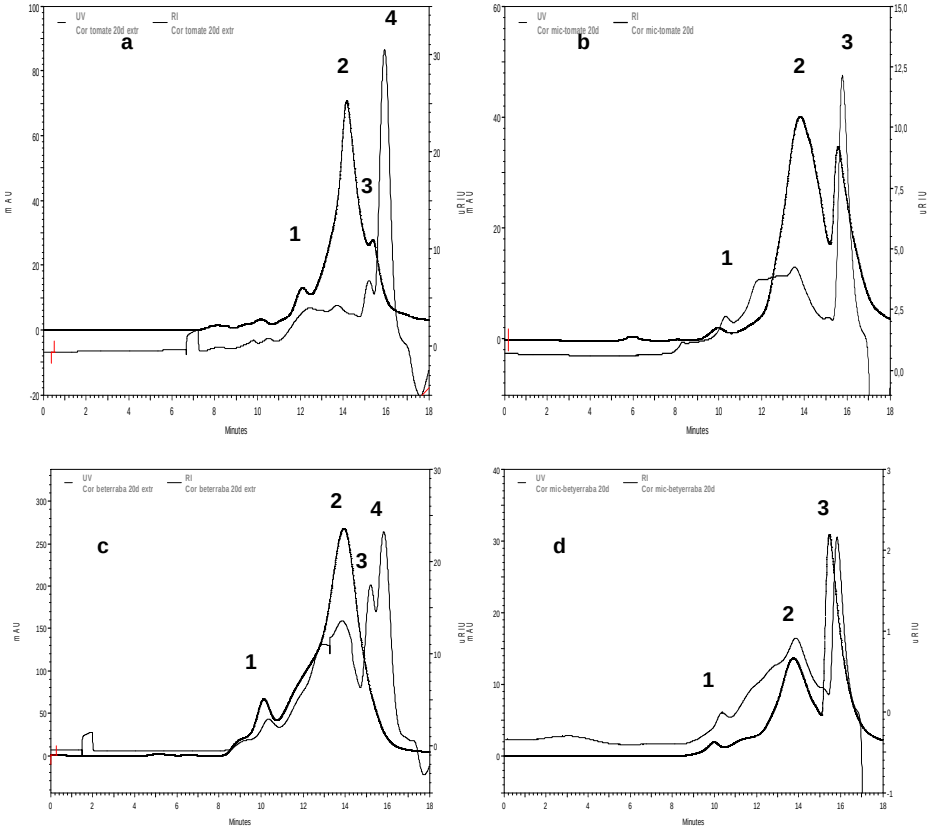

Figure 4- Chromatogram obtained from HPLC showing RI signal (line) and UV signal (dot) plotted as a function of retention time for *Coriolus versicolor* cultures using tomato pomace (a – supernatant; b – mycelium) or beet wastes (c – supernatant; d – mycelium)

Figure 4 shows chromatogram profiles obtained by HPLC with RI and UV signal for the EPS and IPS compounds produced by *C. versicolor* in tomato pomace or beet wastes cultures. IPS chromatograms of the two cultures had very close profile (Fig. 4 b, d), but it must be noted that very similar molar mass range does not imply similar molecular structure and molecular conformation. From EPS chromatograms it is evident that the largest molecular weight fraction was present at a very low concentration (< 3%) compared to the other molecular weight fractions (Fig. 4 a, c). In both cultures, peak 2 of EPS had a nearly molecular weight (~3 x10^3 Da).

Some authors related the production of EPS and IPS compounds by mushrooms. Sakagami *et al.* (1991) reported sub-fractions found in PSK whose the largest fraction is >2.0 x 10^5 Da. Wang *et al.* (1996) compared EPS with IPS using a gel permeation column and they found that IPS and EPS contained two high molecular weight fractions (2.8 x 10^4 Da from IPS; 1.5 x 10^4 Da from EPS) and a lower molecular fraction of ~3.5 x 10^3 Da. Tavares *et al* (2005) found that the molar mass of EPS obtained by gel permeation chromatography was ~6.7 x 10^4 Da. J-Y Oh *et al* (2007) produced exobiopolymer with molecular weight ranging 1.4 10^3 - 27 x 10^3 Da, using submerged culture of *Cordyceps sphecocephala.* Cui *et al*, (2007) reported molecular weight sub-fractions ranging from 3 x 10^3 to 2 x 10^6 Da isolated in EPS and IPS from *C. versicolor*, using size-exclusion chromatography coupled to a multi-angle laser light scattering device.

Results obtained in this study let us to confirm the interest of this selected culture medium, using tomato pomace, in order to maximise the production of protein-polysaccharide complexes by *C. versicolor.* Besides, this clean process allows valuing the agro-industrial residues with a low cost and a higher production of these polysaccharides compounds. The different polysaccharide concentration in endocellular and exocellular complexes shows that this *C. versicolor* strain produces different protein-bound polysaccharides, so further studies are being done in order to isolate and identify different *C. versicolor* complexes and investigate its bioactivity.

References

Cui, J., Chisti, Y. (2003). Polysaccharopeptides of *Coriolus versicolor*: physiological activity, uses, and production. *Biotechnology Advances*, 21, 109 - 122.

Cui, J., Goh, K., Archer, R., Singh, H. (2007). Characterisation and bioactivity of protein-bound polysaccharides from submerged-culture fermentation of *Coriolus versicolor* Wr-74 and ATCC-20545 strains. *Journal of Industrial Microbiology and Biotechnology,* 34, 393–402.

Dubois, M., Gilles, K., Hamilton, J., Rebers, P., Smith, F. (1956). Colorimetric method for determination of sugars and related substances. *Analitycal Chemistry*, 28, 350 - 356.

Gern, R., Wisbeck, E., Rampinelli, J., Ninow, J., Furlan, S. (2008). Alternative medium for production of *Pleurotus ostreatus* biomass and potential antitumor polysaccharides. *Bioresource Technology*, 99, 76–82.

Jung-Young Oh , Eun-Jae Cho , Sung-Hee Nam , Jang-Won Choi , Jong-Won Yun (2007) Production of polysaccharide–peptide complexes by submerged mycelial culture of an entomopathogenic fungus Cordyceps sphecocephala Process Biochemistry 42, 352–362.

Kim, S., Hwang, H., Park, J., Cho, Y., Song, C., Yun, J. (2002). Mycelial growth and exo-biopolymer production by submerged culture of various edible mushrooms under different media. *Letters in Applied Microbiology,* 34, 56-61.

Lee, C., Yang, X., Wan, J. (2006). The culture duration affects the immunomodulatory and anticancer effect of polysaccharopeptide derived from *Coriolus versicolor*. *Enzyme and Microbial Technology*, 38, 14–21.

Li, S., Wang, D., Tian, W., Wang, X., Zhao, J., Liu, Z., Chen, R. (2008). Characterization and anti-tumor activity of a polysaccharide from *Hedysarum polybotrys* Hand.-Mazz. *Carbohydrate Polymers*.

Lin, E., Sung, S. (2006). Cultivating conditions influence exopolysaccharide production by the edible Basidiomycete *Antrodia cinnamomea* in submerged culture. *International Journal of Food Microbiology*, 108, 182–187.

Lowry, O., Rosebrough, N., Farr, A., Randall, R. (1951). Protein measurement with the folin phenol reagent. *J Biochem*,193, 265–75.

Rosado, F., Carbonero, E., Kemmelmeier, C., Tischer, C., Gorin, P., Iacomini, M. (2002). A partially 3-O-methylated (1→4)-linked β-D-galactan and β-D-mannan from *Pleurotus ostreatoroseus* Sing. *FEMS Microbiol. Lett.*, 212, 261–265.

Sakagami, H., Aoki, T., Simpson, A., Tanuma, S. (1991). Induction of immunopotentiation activity by a protein-bound polysaccharide, PSK (review). *Anticancer Res,* 11, 993–999.

Tavares, A., Agapito, M., Coelho, M., Silva, J., Barros-Timmons, A., Coutinho, J., Xavier, A. (2005). Selection and optimization of culture medium for exopolysaccharide production by *Coriolus* (Trametes) *versicolor*. *World Journal of Microbiology & Biotechnology*, 21,1499–1507.

Wang, H., Ng, T., Liu, W., Ooi, V., Chang, S. (1996). Polysaccharide-peptide complexes from the cultured mycelia of the mushroom *Coriolus versicolor* and their culture medium activate mouse lymphocytes and macrophages. *Int J Biochem Cell Biol*, 28, 601–607.

Wisbeck, E., Furlan, S., Ninow, J. (2005). Efeito da concentração inicial de glicose e do pH na produção de exopolissacarídeos de potencial antitumoral por *Pleurotus ostreatus* DSM 1883. *Health Environ. J.*, 6 (2), 19–22.

Proceedings of the 10th International Chemical and
Biological Engineering Conference - CHEMPOR 2008
Braga, Portugal, September 4-6, 2008
E.C. Ferreira and M. Mota (Eds.)

Production, purification and partial characterization of protein – bound polysaccharides from *Pleurotus ostreatus* and *Lentinula edodes*

S. Silva, S. Martins and A. Karmali*
Chemical Engineering and Biotechnology Research Center and Department of Chemical Engineering of Instituto Superior de Engenharia de Lisboa,
Rua Conselheiro Emídio Navarro Nº.1, 1950-072 Lisboa, Portugal
*Corresponding author: email – akarmali@deq.isel.ipl.pt

Keywords: Protein-bound polysaccharides; *Pleurotus ostreatus* and *Lentinula edodes;* Batch and continuous cultures; HPLC and FTIR; gel filtration chromatography.

Abstract

The medicinal power and the nutritional value of some mushrooms are widely known. However, only in the last decades of the last century that it was possible to isolate and partially characterize some biologically active anti-cancer substances.

The therapeutic properties of mushrooms are attributed mainly to their polysaccharide content which has exhibited immunomodulatory properties such as anti-cancer, anti-viral and anti-bacterial activities. Protein-bound polysaccharides are macromolecules which consist of a central core protein to which are attached a number of polysaccharide chains and PSP and PSK from *Coriolus versicolor* are the most widely studied protein-bound polysaccharides.

Although protein-bound polysaccharides from mushrooms exhibit important medicinal properties, there is little information in the literature about their biological and physico-chemical properties.

Therefore, the aim of this work consists of production, purification and partial characterization of these protein-bound polysaccharides from *Pleurotus ostreatus* and *Lentinula edodes*.

The fungal strains were grown in several culture media such as whey permeate supplemented with glucose, yeast extract and suitable salts. The cultures were grown in agitated and aerated bioreactors at pH 5.5 and 27ºC, with pH and temperature control for 10 days and suitable daily samples were removed from the reactor. These samples were centrifuged and intracellular and extracellular protein-bound polysaccharides were extracted from the biomass and culture supernatant, respectively. Subsequently, these polysaccharides were purified by gel filtration chromatography on a Sephacryl S-300-HR column and fractions were analysed for protein, superoxide dismutase (SOD) activity and polysaccharides. Fractions containing protein-bound polysaccharides were characterized by HPLC which revealed UV and RI peaks with retention times of 6 and 13 min., respectively. On the other hand, FTIR analysis of these polysaccharide preparations revealed absorption peaks at 910, 989, 1078, 1644, 2335, 2363 and 3115 cm^{-1} which are characteristics of such macromolecules. Moreover, purified polysaccharides exhibited SOD activity which is in agreement with the data published in the literature.

The results presented strongly suggest that these basidiomycete strains produce high levels of free and protein-bound polysaccharides which exhibit similar physico-chemical properties compared with the data in the literature as far as HPLC and FTIR analysis are concerned.

Introduction

Mushrooms have been known to exhibit medicinal properties for thousands of years. Higher basidiomycete mushrooms have been used in clinical nutrition because they

exhibit antitumour, immune modulating, cardiovascular and anti-microbial activities (Parris, 2000). The benefits of mushroom nutrition on these clinical conditions has attracted great interest in the scientific community in the last decade in order to understand the molecular mechanism responsible for their action (Peng *et. al*., 2003).

There are several reports in the literature about production of free and protein-bound polysaccharides from basidiomycete strains such as *Coriolus versicolor*, *Letinula edodes* and *Ganoderma lucidum* (Parris, 2000). However, the physico-chemical properties of such polysaccharides are poorly investigated as far as pI, Mr, amino acid sequence of the protein portion and the nature of carbohydrate residues (Wang *et.al*. 2007: Cho *et. al*., 2006).

Moreover, it has been reported that polysaccharides exhibiting different structures have revealed different biological activities. On the other hand, hyperbranched polysaccharides have been poorly investigated as far as structure and function are concerned (Wang *et.al*. 2007: Cho *et. al*., 2006).

The use of agro-industrial residues (i.e tomato pomace, whey milk and rice husks) have not been studied in detail as carbon and nitrogen sources for production of these complex polysaccharides from basidiomycete strains in submerged fermentation. Therefore, the aim of this work consists of production, purification and partial characterization of these protein-bound polysaccharides from *Pleurotus ostreatus* grown by submerged fermentation.

Materials and Methods

Materials

Chemicals

Potato Dextrose Agar (PDA) medium and yeast extract were purchased from Oxoid (Hampshire, England). Milk whey was supplied from a local manufacturer. Glucose, benzamidine, phenol, Coomassie Blue G-250, urease, xanthine, nitro-blue tetrazolium were supplied by Sigma Chemical Company (S. Louis, MO, USA). Sephacryl S-300HR was purchased from Amersham Biotech (Sweden). Shodex Ohpak SB-804 HQ HPLC column was supplied from Showa Denko K.K. (Tokyo, Japan). Hemoglobin, peroxidise and xanthine oxidase were obtained from Biozyme Laboratories (Gwent South Wales, UK). All other reagents used were of analytical grade.

Microorganism

Pleurotus ostreatus was isolated from old growth forests of the Olympic Peninsula in Port Townsend, Washington (USA).

Methods

Production of polysaccharides from Pleurotus ostreatus

Pleurotus ostreatus was first grown on PDA and then transferred into the seed culture medium. The seed culture was grown in 250 mL flasks containing 50 mL of culture medium as follows: 2 % (w/v) glucose, 0.6 % (w/v) yeast extract, 0.3 % (w/v) $(NH_4)_2SO_4$, 0.2 % (w/v) KH_2PO_4, 0.05 % (w/v) $MgSO_4.7H_2O$ and 0.05 % (w/v) KCl and aqueous solution of milk whey 50 % (v/v) at 28 ºC on an orbital shaker at 200 rpm for 10 days as described previously (Cui *et al.*, 2007, Cho *et al.*, 2006). Biomass growth, protein and polysaccharides production were followed by taking aliquots of 50 mL of fermentation broth on the 4^{th}, 7^{th} and 10^{th} days of fermentation.

Isolation of extracellular and intracellular protein-bound polysaccharides

Mycelial biomass was separated from the fermentation broth by suction in a Buchner funnel as described previously (Cui *et al.*, 2007). Four volumes of 95 % (v/v) ethanol were added to the filtrated to precipitate the extracellular polysaccharides (EP). The EP were recovered by centrifugation (30 min, 10 000 rpm) and the precipitate was suspended in a minimum volume of 50 mM phosphate buffer pH 6.5 containing 1mM

benzamidine. The mycelial biomass suspension was incubated at 100 ºC for 2.5 h to release the intracellular polysaccharides (IP). The mixture was filtered by suction and the filtrate containing IP were recovered the same way as the EP recovery.

Protein and polysaccharide assays

EP and IP levels were quantified by phenol/sulphuric acid method using the polygalacturonic acid as a standard and protein quantification was carried out by the Comassie blue method.

Purification of polysaccharides by gel filtration chromatography

IP and EP were purified by gel filtration chromatography on Sephacryl S-300-HR column (1x100 cm) which was eluted with 50 mM phosphate buffer pH 7.0 at a flow rate of 40 mL/h. Column factions were analyzed for polysaccharides and protein contents and those fractions containing polysaccharides were selected to measure superoxide dismutase (SOD) activity.

The molecular weight of the protein-bound polysaccharides was also determined by gel filtration chromatography on a Sephacryl S-300-HR (detection range of molecular weight: $1 \times 10^4 - 1.5 \times 10^6$) column as described previously (Kim *et al.*, 2003). Urease, amidase, hemoglobin and peroxidase were used as protein standards.

HPLC analysis of polysaccharides

HPLC analysis was carried out by using Shodex column with 0.01 % (w/v) sodium azide as the solvent at a flow rate of 1 mL/min and at 80 ºC. Intracellular and extracellular polysaccharides extracted as described above, were injected (20 μL) and peak analysis was carried by UV and RI detectors.

SOD assay

Superoxide dismutase (SOD) assay was carried out at room temperature and the reaction mixture consisted of 0.1 M phosphate buffer containing 1.3 mM EDTA pH 8.0, xanthine, xantine oxidase and nitro-blue tetrazolium (NBT) and a suitable aliquot of polysaccharide was added to the sample and reaction was followed at 550 nm as described previously (Beuchamp and Fridovich, 1971). One unit of SOD is defined as the amount of SOD required to inhibit the rate of reduction of nitroblue tetrazolium by 50 % in a coupled system, using xanthine and xanthine oxidase at pH 7.8 at 25 °C in a final volume of 0.3 mL of reaction mixture. The xanthine oxidase concentration should produce an initial (uninhibited) rate of 0.005 per minute.

FTIR analysis of polysaccharides

Infrared spectra were recorded in a Bruker Tensor 27 FTIR spectrometer at 4 cm^{-1} resolution. Polysaccharide sample (40 μL) was transferred into a CaF_2 infrared cell, fitted with 25 μm path-length Teflon spacers and placed into the spectrometer.

Effect of heating on SOD activity and FTIR analysis

The column fractions exhibiting SOD activity were used to investigate the effect of heating on SOD activity. Suitable samples of SOD were placed in a water bath at 100 ºC and aliquots at suitable time intervals were removed from the water bath to an ice bath. SOD activity as well as FTIR analysis were determined as described in this paper.

Results and Discussion

Polysaccharides were produced by growing *Pleurotus ostreatus* in milk whey for 10 days, at 28 ºC in agitated flask at 200 rpm. Figure 1 presents the increase of biomass formation throughout the fermentation process as well as the increase in protein and polysaccharide concentration. As far as extracellular polysaccharides are

concerned, it is clear that there is a decrease in protein and polysaccharide concentrations after the 4th day of culture.

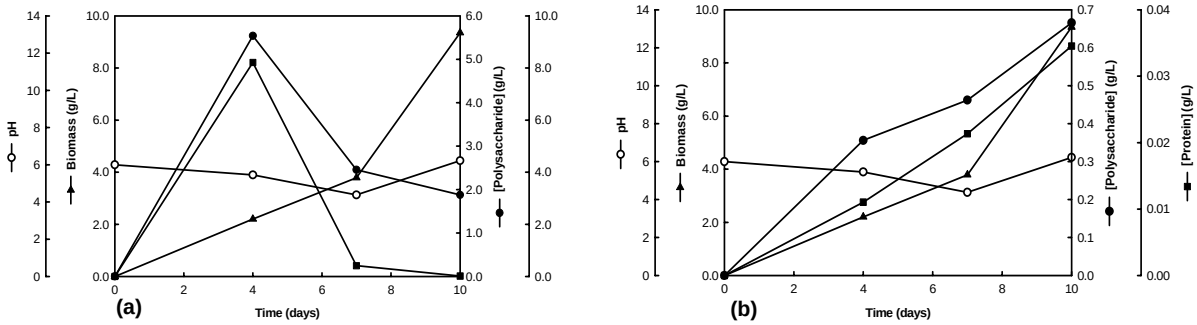

Fig. 1 – Fermentation profile showing variations of biomass growth, pH, polysaccharide and protein concentrations:. **(a)** Extracellular polysaccharides from *Pleurotus ostreatus;* **(b)** Intracellular polysaccharides from *Pleurotus ostreatus*

Fractions containing protein-bound polysaccharides were characterized by HPLC which revealed UV and RI peaks with retention times of 6 and 13 min., respectively (Figure 2).

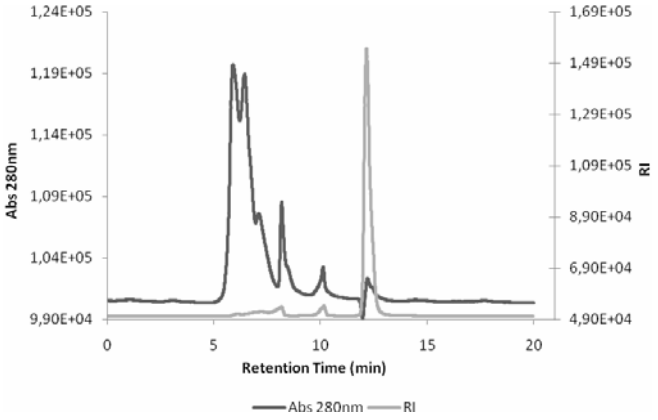

Fig. 2 – HPLC analysis of extracellular polysaccharides from *Pleurotus ostreatus.*

Extracellular polysaccharides were isolated by precipitation with alcohol and were purified by gel filtration chromatography on Sephacryl S-300-HR column (Fig. 3). According to this figure, there are several polysaccharide peaks whose Mr were determined by gel filtration chromatography (Table 1). Since there is a report in the literature that polysaccharides mimic SOD activity (Wang *et. al.,* 2007), some column fractions were selected to assay for SOD activity (Fig. 4). There is a correlation between SOD activity and polysaccharide content in such column fractions as shown in Fig. 4.

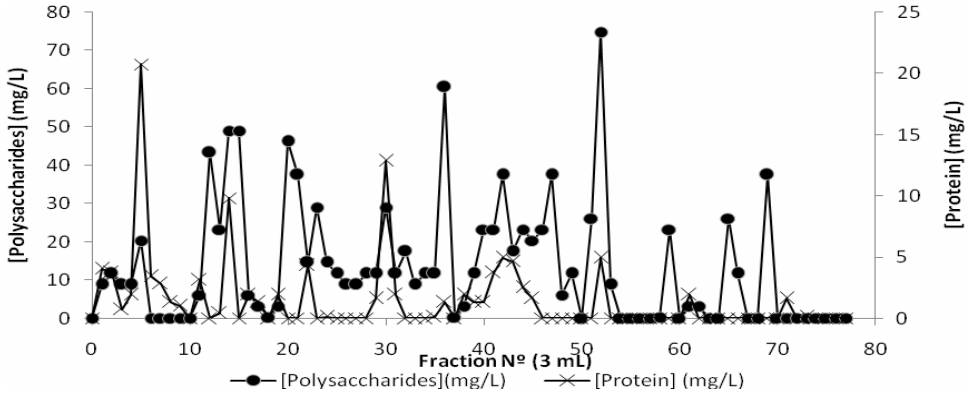

Fig. 3 – Chromatographic behavior of extracellular polysaccharides from *Pleurotus ostreatus* on Sephacryl S-300-HR column.

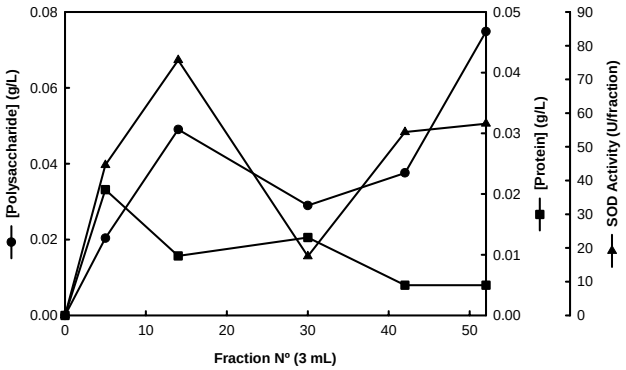

Fig. 4 – SOD activity of some selected fractions from gel filtration chromatography exhibiting protein and polysaccharide contents Concentration variation of protein and polysaccharides in relation to SOD activity in selected gel filtration chromatography fractions.

Fraction Nº.	[Protein] (mg/L)	[Polysaccharide] (mg/L)	Mr (kDa)
5	20.4	20.7	848.7
14	49.0	9.8	517.7
30	29.0	12.8	215.0
42	37.6	5.0	111.2
52	74.8	5.0	64.2

Table 1 - Polysaccharide and protein concentration as well as Mr values for some selected fractions of gel filtration chromatography.

In order to investigate the nature of SOD mimicking activity of these polysaccharides, we studied the effect of heating on some selected column fractions exhibiting SOD activity. Surprisingly, the heating at 100 ºC of polysaccharide fractions exhibited an increase in SOD mimicking activity as shown in Fig. 5. Moreover, the effect of time of heating of such polysaccharide fractions on SOD activity was also investigated which revealed that there was an increase in SOD mimicking activity with time of heating (Fig. 6).

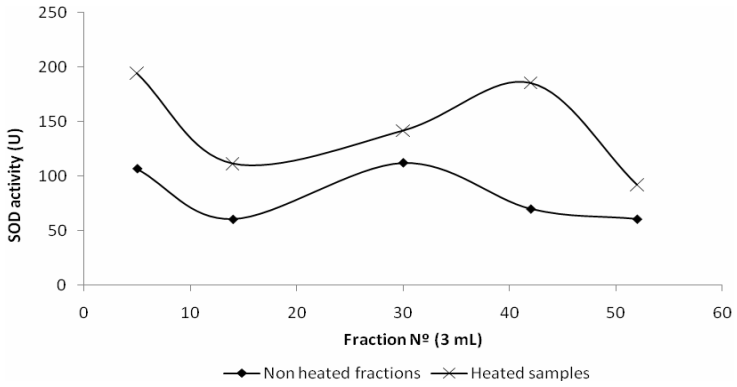

Fig. 5 – Variation of the SOD activity in selected fractions of gel filtration chromatography submitted to heat treatments. (- non-heated.; - heated at 100°C for 15 minutes).

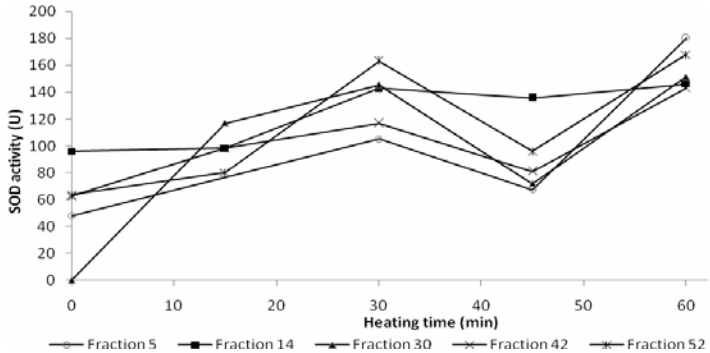

Fig. 6 – Variation of the SOD activity in selected fractions of gel filtration chromatography submitted to heat treatments. (- non-heated.; - heated at 100°C for 15 minutes).

Moreover, the increase in SOD mimicking activity was also investigated by FTIR analysis which exhibits an increase in absorption of several peaks at 910, 989, 1078, 1644, 2335, 2363 and 3115 cm^{-1} (Fig 7).

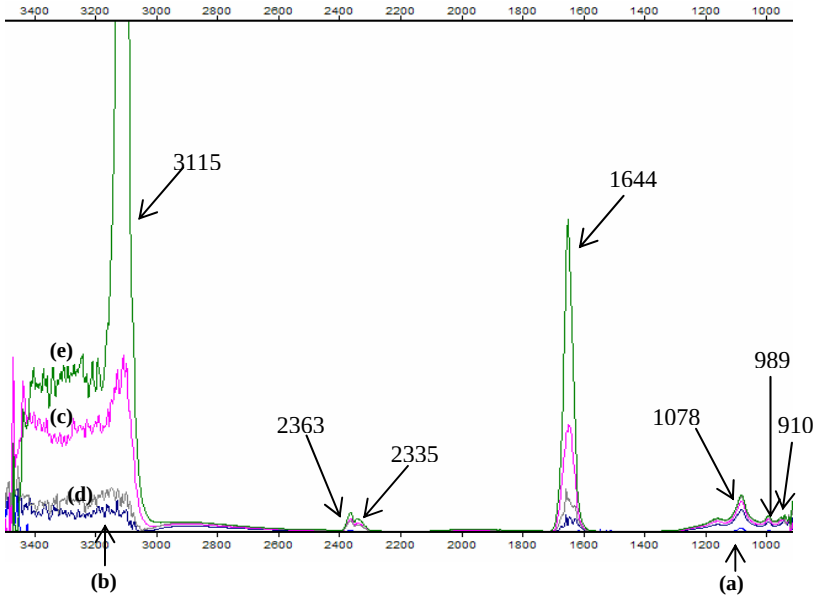

Fig. 7 – FTIR spectrum of a column fraction exhibiting SOD activity. Effect of heating time of a column fraction at 100 ºC on FTIR spectrum (**(a)** non- heated sample; **(b)** 15 minutes; **(c)** 30 minutes; **(d)** 45 minutes; **(e)** 60 minutes).

Acknowledgements

We acknowledge financial support from Fundação para a Ciência e a Tecnologia (Unit 702, PTDC/AGR-AAM/74526/2006).

References

Beuchamp, C. Fridovich, I. (1971) Superoxide dismutase: Improved assays and an assay applicable to acrylamide gels. Anal. Biochem., 44, 276-287.

Caili, F., Haijun, T., Tongyi, C., Yi, L., Quanhong, L., (2007) Some properties of an protein-bound polysaccharide from the fruit of pumpkin. Food Chemistry 100, 944 -947.

Cho, E.J., Oh, J.Y., Chang, H. Y., Yun, J. W. (2006) Production of exopolysaccharides by submerged mycelial culture of a mushroom *Tremella fuciformis*. J. Biotechnology 127, 129–140.

Cui, J., Goh, K.K.T., Archer, R., Singh, H., (2007) Characterization and bioactivity of protein-bound polysaccharides from submerged-culture fermentation of *Coriolus versicolor* Wr-74 and ATCC-20545 strain. J Ind Microbiol Biotechnol 34, 393-402.

Kim, G., Park, H., Nam, B., Lee, S., Lee, J., (2003) Purification and characterization of acidic proteo-heteroglycan from the fruiting of *Phellinus linteus (Berk.& M. A. Curtis) Teng.* Bioresource Technology 89, 81-87.

Parris, M. Kidd, (2000) The use of mushroom glucans and proteoglycans in cancer treatment. Alternative Medicine Review 5, 4-27.

Peng, Y., Zhang, L., Zeng, F., Xu, Y. (2003) Structure and antitumor activity of extracellular polysaccharides from mycelium. Carbohydrate Polymers 54, 297-303.

Wang, H., Jiang, X., Mu, H., Liang, X., Guan, H. (2007) Structure and protective effect of exopolysaccharide from *P. Agglomerans* strain KFS-9 against UV radiation. Microbiological Research 162, 124-129.

Proceedings of the 10th International Chemical and
Biological Engineering Conference - CHEMPOR 2008
Braga, Portugal, September 4-6, 2008
E.C. Ferreira and M. Mota (Eds.)

Headspace - SPME as a screening system for yeast metabolic compounds - A case study

Margarida Martins,[1] Mariana Henriques,[1] Joana Azeredo,[1] Rosário Oliveira[1*]
[1] IBB – Institute for Biotechnology and Bioengineering, Centre of Biological Engineering, University of Minho, Campus de Gualtar, 4710–057 Braga, Portugal.

Keywords: HS - SPME, GC - MS, *Candida* species, isoamyl alcohol, 2-phenylethanol
Topic: Integration of life sciences & engineering

Abstract

Aim: This study aimed to identify and quantify the fusel alcohols secreted by the opportunistic yeasts *Candida albicans* and *Candida dubliniensis* to further get insights into the amino acid catabolism of those two organisms.

Methods and Results: Fusel alcohols were screened in cell - free supernatants of yeasts cultivated in RPMI medium. For simultaneous identification and quantification of these alcohols, a Headspace - Solid Phase Micro Extraction (HS - SPME) coupled with gas chromatography - mass spectrometry (GC - MS) methodology, previously developed to analyse the volatile composition of fruits, was followed (Coelho et al. 2006). Results obtained show that both *C. albicans* and *C. dubliniensis* produced isoamyl alcohol and 2-phenylethanol, end – products of the catabolism of the amino acids leucine and phenylalanine, respectively.

Significance and Impact of the study: The HS – SPME used herein allows the simultaneous identification and quantification of compounds, requires small sample volume, has high sensitivity and reproducibility, is simple and rapid and is solvent free. This revealed to be a powerful tool for the screening system of yeast metabolic compounds.

1 Introduction

The recognition that the catabolism of amino acids to their respective fusel alcohols plays an important role in (off-) flavour and aroma of yeast fermented products motivated the scientific interest in this field. Whereas in most eukaryotes the carbon skeletons derived from amino acids enter the tricarboxylic acid cycle, in the yeast *Saccharomyces cerevisiae* the degradation of the aromatic amino acids (tryptophan, phenylalanine and tyrosine) and the branched-chain amino acids (valine, leucine and isoleucine) occur through the Ehrlich pathway (recently reviewed by Hazelwood et al. 2008). This pathway comprises an initial step of transamination of the amino acid to the corresponding α-keto acid, followed by its decarboxylation to the respective aldehyde and the reduction of the aldehyde to form the corresponding fusel alcohol. Research developed so far aimed to identify (1) the end - products of amino acids catabolism, (2) the enzyme(s) involved in the metabolic process and (3) the bioactivities of fusel alcohols (Dickinson 1996;Dickinson et al. 1997;Dickinson et al. 2003).

Despite the efforts done to identify metabolites in yeast/ fungal extracts, there is a scarce knowledge concerning the metabolism of amino acids in *Candida albicans* and *Candida dubliniensis*, two closely related opportunistic fungal pathogens. A number of techniques have been employed for fungal metabolites profiling including paper chromatography, thin layer chromatography, capillary electrophoresis and the mainly applied high performance

* Corresponding author. Tel +351 253 604 409. E-mail:roliveira@deb.uminho.pt

liquid chromatography (HPLC) and gas chromatography - mass spectrometry (GC – MS) (Frisvad et al. 2008). Although chromatographic methods are very sensitive and selective their major disadvantage is the need of sample preparation. Traditional methods used for sample concentration and purification are time consuming, expensive and require a large volume of hazardous organic solvents (Lanças 2003). However, in the beginning of the last decade solid phase microextraction (SPME) technology was introduced to overcome some of these difficulties. SPME is a microextraction technique based in a equilibrium partition of the compounds between the sample matrix and the extracting phase, a polymer-coated fused fiber and can be directly coupled with HPLC or GC - MS (Arthur and Pawliszyn 1990). This technique was successfully applied for polar and non - polar compounds in gas, liquid and solid samples from environmental or biological sources (Ulrich 2000).

The objective of this work was to identify and quantify the fusel alcohols: isoamyl alcohol and 2-phenylethanol, secreted by *C. albicans* and *C. dubliniensis*, using headspace - SPME coupled with GC – MS, to further get insights into the amino acid catabolism of those two microorganisms.

2 Material and Methods

Chemicals. Standard alcohols were obtained from Sigma. Isoamyl alcohol stock solution was prepared in water whereas the 2-pheneylethanol was prepared in methanol.

Organisms. Two *Candida* species were used in this study: *C. albicans* CECT 1472 (Colección Española de Cultivos Tipo, Spain) and *C. dubliniensis* CBS 7987 (Centraalbureau voor Schimmelcultures, Germany).

Media and culture conditions. Prior to each experiment, both *Candida* species were maintained at 37°C in Sabouraud dextrose agar. After, cells were grown in Sabouraud dextrose broth at 37°C for 24 h on a mechanical shaker at 130 rpm. Subsequently, cells were washed twice with ultrapure water and counted in a hematocytometer. Standardized cell suspensions were prepared at a cell density of 1×10^6 cells/ml in 1×RPMI 1640 medium (Sigma) buffered with morpholinepropanesulfonic acid (MOPS– Sigma) (final concentration 0.165 M for pH 7.0). For culture supernatants preparation, 120 ml of standardized cell suspensions were inoculated in 300 ml flasks and incubated at 37°C, 130 rpm. After 24 h cell – free supernatant fractions were filter sterilized (0.22 µm) and stored at 4°C.

Biomass dry weight measurements. At the end of incubation, 1 ml of the planktonic culture was filtered through pre-weighted filters (0.45 µm) and washed three times with ultrapure sterilized water. Filters were dried at 60°C until constant weight and cell dry weight (CDW) was determined. This was repeated at least four times.

Supernatant alcohols analyses. Supernatant fusel alcohols were extracted using HS - SPME and analysed by GC - MS using a method adapted from Coelho et al. (2006). Supernatant fractions (20 ml) were introduced into a 60 ml bottle, together with 4 g of NaCl and a 20 × 5 mm stirring bar. After sealing the vial with a teflon septum and an aluminium cap, it was placed in a water bath at 40±0.1 ºC for a period of 15 min (200 rpm) to transfer the compounds from the sample to the headspace. The headspace volatiles were extracted along 45 min with a SPME carbowax-divinylbenzene fused silica fibre (CW-DVB, 65 µm- Lot P334957) (Supelco). The GC - MS parameters were established according to Coelho *et al*. (2006). *Candida* fusel alcohols were identified by comparison of their mass spectra and retention times with those of data system library (Wiley 275) and of reference substances. A control analysis was done with growth medium. Compounds quantification was performed by preparation of RPMI solutions containing pure standards and using the same conditions applied to samples. For each compound appropriate concentration ranges were chosen in order to include sample concentrations. All measurements were made with, at least, two

replicates. Blanks, corresponding to the analysis of the coating fibre not subjected to any extraction procedure, were run between sets of three analyses. Alcohols analyses were carried out in duplicate for each sample with results agreeing within ≤ 15 %.

3. Results and Discussion

RPMI 1640 medium was chosen as growth medium. This medium contains all 20 amino acids and nitrate but not ammonium ions. This combination may force *Candida* cells to get its nitrogen from amino acids and in the process secrete fusel alcohols such as isoamyl alcohol (from leucine) and 2-phenylethanol (from phenylalanine). Establishment of the HS - SPME methodology for the identification and quantification of these compounds in *C. albicans* and *C. dubliniensis* cell – free supernatants will be presented and discussed below.

Establishment of the HS - SPME GC - MS methodology

Fiber selection. The fiber polarity, porosity and surface area are critical parameters in SPME, thus several types of coating fibers with different film thicknesses are commercially available (1998b). In this study, a 65 µm CW - DVB fused silica fibre was used. The CW - DVB coating fibre is recommended for small and polar molecules (molecular weight between 40 and 275). The CW - DVB coating fibre was selected because it is a mixed coating that contains a liquid polymer and solid particles. This type of coating combines the absorption properties of the liquid polymer with the adsorption properties of porous particles, which are composed of macro (>500 Å), meso (20-500 Å) and microporous (2-20 Å). The mutually synergetic effect of adsorption and absorption to the stationary phase promotes a high retention capacity and, consequently, a higher sensitivity than fibres based on absorption only (Kataoka et al. 2000).

Extraction mode. Compounds extraction can be achieved exposing the fiber in the headspace (vapour phase) surrounding the sample, headspace (HS) - SPME, or introducing it directly in the sample matrix, direct immersion (DI) - SPME (Zhang and Pawliszyn 1993). In HS - SPME mode equilibrium is attained more rapidly and the prevention of the fiber direct contact with the sample minimizes background noise and can extend the fiber life time. Additionally, HS - SPME is more sensitive for the analysis of volatile compounds of complex matrices (Kataoka et al. 2000). In this work the HS - SPME mode was used. In a three system analysis (sample – headspace – CW - DVB coating fiber), the transference occurs from the liquid matrix to the headspace, and from that to the coating fiber, which promote the sorption of the compounds in the coating fiber.

Extraction conditions and sample modification. In general, sample volumes used in SPME extraction range from 4 to 120 ml (Krutz et al. 2003). In contrast, traditional techniques such as the described by Hornby et al. (2001) for the purification of farnesol from *C. albicans* cell – free supernatant require larger sample volume, specifically five litres. In SPME the amount of compound extracted and/or the extraction time can be increased by manipulation of some parameters. First, stirring liquid samples facilitates the transfer of the compounds to the coating fiber. Second, as a typical guideline, sample modification by the addition of a soluble salt such as NaCl or Na_2SO_4 decreases compound solubility in the matrix, favouring its extraction onto the fiber due to the salting – out effect. Third, for HS - SPME the compound concentration in the vapour phase is dependent on the extraction temperature, and samples are usually heated (Kataoka et al. 2000). Thus, over this study, all samples were extracted using a magnetic stirring for agitation that was maintained at 200 rpm, after the addition of 4 g of NaCl of 20 ml of sample and in a water bath operating at 40±0.1 ºC. In order to achieve accurate and precise analyses, sampling parameters such as sampling time, vial size, magnetic bar size and sample volume were kept constant (see Material and Methods section) intra and inter assays. The extraction procedure was completed within one hour/ sample, demonstrating that SPME is a rapid technique.

Fusel alcohols discrimination. Prior to sample analysis, the methodological approach described was tested using a standard mixture containing isoamyl alcohol and 2-phenylethanol (Figure 1). Under the GC - MS conditions used (Coelho et al. 2006), the signal (total ion current) obtained exhibited resolved peaks at 9.5 min for isoamyl alcohol (Figure 1, I) and at 55.7 min for 2-phenylethanol (Figure 1, II), demonstrating that this is a rapid screening procedure for the simultaneous extraction and identification of these compounds.

.External standardization. The quantitation approach when using SPME is dependent on the sample matrix, its complexity and extraction method being used. In the case of a liquid and simple sample an external standard calibration is recommended (1998a). Standard mixtures were prepared in a clean matrix sample (RPMI medium) and analysed under the same conditions as those of samples. This allows the GC peak area data to be used as an indirect approach to estimate the relative content of each compound. Standard curves were generated for GC - MS peak areas versus concentration of each compound (R^2>0.98). Estimated limit of quantification (LOQ) and limit of detection (LOD) were: 0.08 mg/l and 0.02 mg/l for isoamyl alcohol and 0.04 mg/l and 0.01 mg/l for 2-phenylethanol. Thus, using quantitative HS – SPME GC – MS a linear response was obtained for a wide range of concentrations and the LOD levels were found suitable for the analysis (see below).

HS - SPME GC - MS *Candida* sample analyses

Qualitative analysis. The growth medium was analysed for possible interference and was shown to have no interfering compounds into or near the retention times of those compounds (Figure 2, I). Figure 2 (II) shows a typical chromatogram obtained for *C*. *albicans* and *C. dubliniensis*. Comparison of GC retention times and mass spectra of pure standard compounds (such as those presented in Figure 1) allowed the identification of isoamyl alcohol and 2-phenylethanol in these two samples, showing that these two fusel alcohols are produced and secreted into the extracellular medium by *C. albicans* and *C. dubliniensis*.

Quantitative analysis. The detector response from the sample was compared to the response from the target compounds in the calibration curve. Values were standardized against cell dry weight. In *C. albicans* cell - free supernatants isoamyl alcohol was found at 5.65 mg/ g of CDW and 2-phenylethanol at 0.90 mg/ g of CDW. For *C. dubliniensis*, fusel alcohols concentrations (mg/ g of CDW) were: 6.06 for isoamyl alcohol and 1.88 for 2-phenylethanol. This evidences that quantitative HS – SPME GC – MS using matrix-matched calibration curves allowed determination of both fusel alcohols in *Candida* spp samples.

Conclusion

The HS - SPME is a microextraction technology that combines sample preparation and pre-concentration into one single step. The HS – SPME strengths include: (i) the simultaneous identification and quantification of compounds, (ii) small sample volume requirements, (iii) high sensitivity and reproducibility, (iv) simplicity, (v) speed, (vi) no solvent needs. Moreover, it is compatible with compound separation and detection by several systems and it can be automated. This sampling technology revealed to be a powerful tool for the screening system of yeast metabolic compounds.

References

(1998a) A practical guide to quantitation with solid phase microextraction. Sigma-Aldrich Co.
(1998b) Solid phase microextraction: theory and optimization of conditions. Sigma-Aldrich Co.

Arthur,C. and Pawliszyn,J. (1990) Solid phase microextraction with thermal desorption using fused silica optical fibers. *Analytical Chemistry* 62, 2145-2148.

Coelho,E., Rocha,S.M., Delgadillo,I. and Coimbra,M.A. (2006) Headspace-SPME applied to varietal volatile components evolution during *Vitis vinifera* L. cv. 'Baga' ripening. *Analytica Chimica Acta* 563, 204-214.

Dickinson,J.R. (1996) 'Fusel' alcohols induce hyphal-like extensions and pseudohyphal formation in yeasts. *Microbiology* 142, 1391-1397.

Dickinson,J.R., Lanterman,M.M., Danner,D.J., Pearson,B.M., Sanz,P., Harrison,S.J. and Hewlins,M.J. (1997) A ^{13}C nuclear magnetic resonance investigation of the metabolism of leucine to isoamyl alcohol in *Saccharomyces cerevisiae*. *J Biol Chem* 272, 26871-26878.

Dickinson,J.R., Salgado,L.E. and Hewlins,M.J.E. (2003) The catabolism of amino acids to long chain and complex alcohols in *Saccharomyces cerevisiae*. The *Journal of Biological Chemistry* 278, 8028-8034.

Frisvad,J.C., Andersen,B. and Thrane,U. (2008) The use of secondary metabolite profiling in chemotaxonomy of filamentous fungi. *Mycological Research* 112, 231-240.

Hazelwood,L.A., Daran,J.M., van Maris,A.J., Pronk,J.T. and Dickinson,J.R. (2008) The Ehrlich pathway for fusel alcohol production: a century of research on *Saccharomyces cerevisiae* metabolism. *Applied and Environmental Microbiology* 74, 2259-2266.

Hornby,J.M., Jensen,E.C., Lisec,A.D., Tasto,J.J., Jahnke,B., Shoemaker,R., Dussault,P. and Nickerson,K.W. (2001) Quorum sensing in the dimorphic fungus *Candida albicans* is mediated by farnesol. *Applied and Environmental Microbiology* 67, 2982-2992.

Kataoka,H., Lord,H.L. and Pawliszyn,J. (2000) Applications of solid-phase microextraction in food analysis. *Journal of Chromatography A* 880, 35-62.

Krutz,L.J., Senseman,S.A. and Sciumbato,A.S. (2003) Solid-phase microextraction for herbicide determination in environmental samples. *Journal of Chromatography A* 999, 103-121.

Lanças,F.M. (2003) The role of the separation sciences in the 21th century. *Journal of the Brazilian Chemical Society* 14, 183-197.

Ulrich,S. (2000) Solid-phase microextraction in biomedical analysis. *Journal of Chromatography A* 902, 167-194.

Zhang,Z. and Pawliszyn,J. (1993) Headspace Solid-Phase Microextraction. *Analytical Chemistry* 65, 1843-1852.

A B

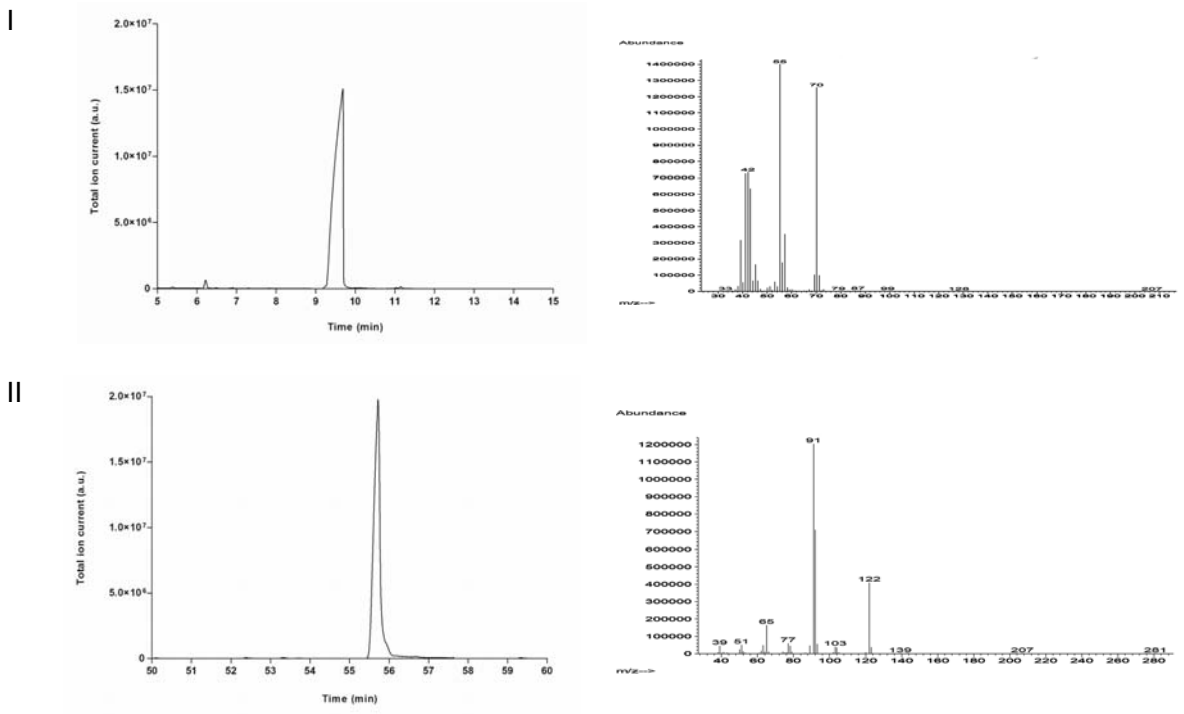

Figure 1: Discrimination of fusel alcohols using HS - SPME GC - MS. Typical chromatograms (total ion current) (A) and mass spectrum (B) of isoamyl alcohol (I) and 2-phenylethanol (II) obtained for a standard solution.

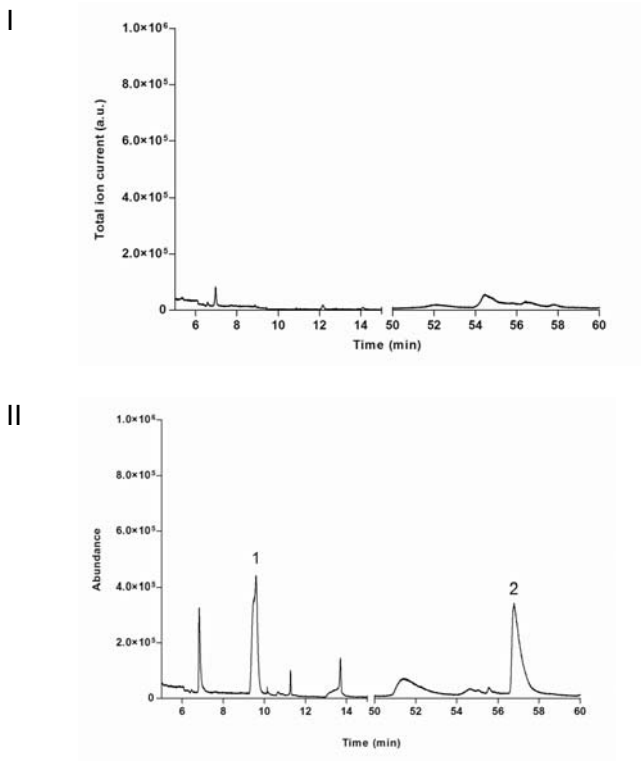

Figure 2: Typical HS - SPME-GC – MS chromatograms (total ion current) for the determination of the fusel alcohols 1, isoamyl alcohol and 2, 2-phenylethanol in *C. albicans* and *C. dubliniensis* samples inoculated in RPMI medium showing no interfering peaks at fusel alcohols retention times (I) and a cell - free supernatant sample (II).

Proceedings of the 10th International Chemical and
Biological Engineering Conference - CHEMPOR 2008
Braga, Portugal, September 4-6, 2008
E.C. Ferreira and M. Mota (Eds.)

Model-Based iterative design of dynamic experiments in modeling for Optimization of a Bioprocess for a Recombinant Protein Production

Mariano CRISTALDI[1] , Ricardo GRAU[1] and Ernesto MARTINEZ[2]

[1]INTEC (CONICET/UNL), Guemes 3450, 3000 Santa Fe, Argentina.
[2]INGAR (CONICET/UTN), Avellaneda 3657, S3002 GJC Santa Fe, Argentina

Keywords: Modeling, Optimization, Biotechnology, Dynamic Experiments.
Topic: Biological Process System Engineering.

Abstract

Finding optimal operating conditions fast with a scarce budget of experimental runs is a key problem to speed up the development and scaling up of innovative bioprocesses. In this paper, a novel iterative methodology for model-based design of dynamic experiments in modeling for optimization is developed and successfully applied to the optimization of the production of interleukin-11 (IL-11) whose DNA sequence has been cloned in an *Escherichia coli* strain. At each iteration, the proposed methodology resorts to a library of models to increasingly bias operating conditions by selecting the *'most informative'* model for designing the next dynamic experiment consisting of an improved operating policy and optimal sampling times. Model selection is done by computing an error measure which distinguishes between parametric and structural uncertainty to selectively bias data gathering towards optimal operation. Parametric uncertainty is iteratively reduced using Global Sensitivity Analysis (GSA) to pinpoint which parameters are key for estimating the objective function. Results obtained after just three iterations are very promising.

1 Introduction

Today, many pharmaceuticals and high-value specialty products are obtained using genetically modified microorganisms. Since the first gene cloning in the beginning of the 1970s, it is possible to modify a microorganism to produce a desired substance, often a protein. To cope with a steadily increasing demand for biotech products along with fierce worldwide competition issues such as lowering downstream costs, shorten time to market of new products and improving productivity of installed capacity and culture broth should be addressed.

Bioprocess modeling and optimization is a challenging task due to the complexity of both of metabolic regulation and organism's reactions that follow to changes in the cell environment as a consequence of the implementation of an operating policy. As a result, several modeling strategies have been proposed which have different characteristics; for example, it can be found from purely statistical modeling methods to highly structured ones. Although those approaches are very valuables, many of them have shown inherent failures derived from basic assumptions done in model building and in some cases their detailed development could be costly and very time consuming. Keeping above considerations in mind, a new point of view called *modeling for optimization*, which has been developed for batch processes in general, is being now explored for fast experimental optimization of bioreactor operation.

2 Methodology

Modeling for Optimization is a systematic approach for biasing data gathering using one or several first-principles models of a given process with the explicit objective of improving its operating condition. Taking advantage of a library of first-principles models this method reduces uncertainty in extrapolation when the process is driven to unknown operating regimes. In this contribution, a methodology for iterative design of dynamic experiments in modeling for optimization methods will be presented using a case study related to the production of a recombinant peptidic hormone rIL-11. For each iteration, a dynamic experiment is designed using a selected model. This selection is based on a novel uncertainty measure in which both structural and parametric model uncertainty is computed using Global Sensitivity Analysis (GSA) (Saltelli *et al.*, 2004). The designed dynamic experiment consists of an operation policy $\hat{\wp}(\hat{w},t)$ and optimal sampling times ψ^{opt} along a modeling run. The experiment is carried out and new data is collected. Before proceeding to (re)estimate model parameters, the sensitivity of the performance index with respect to model parameters is assessed using GSA. This allows using new data more effectively to reduce parametric uncertainty in the subset of model(s) parameters which is the most relevant for policy improvement. A complete iteration of the proposed approach for integrating model development with dynamic optimization using a sequence of designed experiments is shown in the Fig. 1.

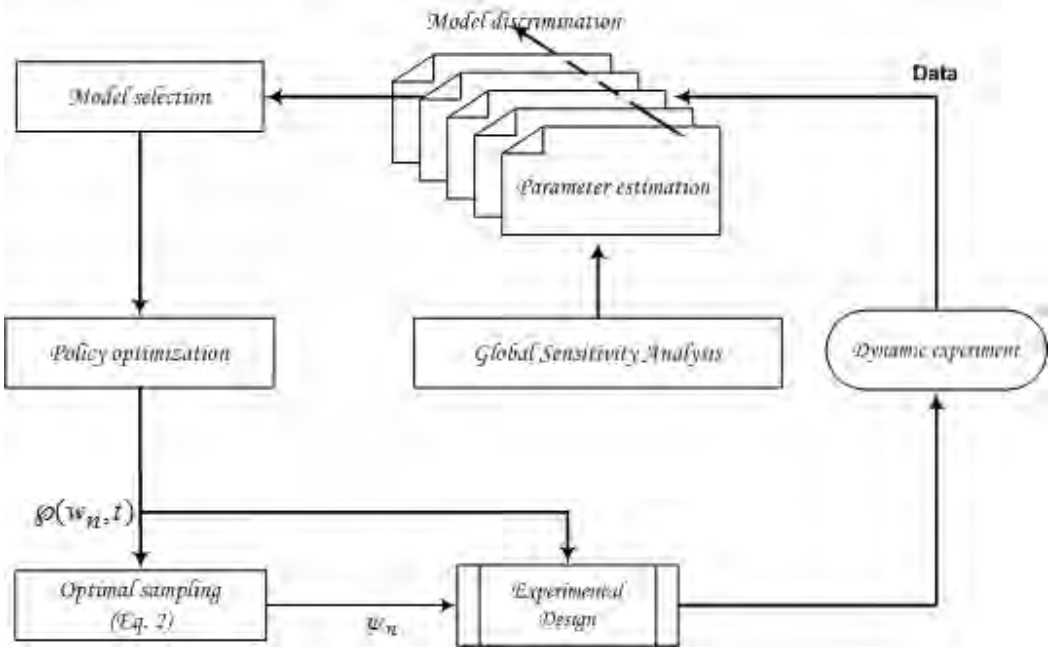

Figure 1. Iterative Model-based Design of Dynamic Experiments for Optimization

Given a set of ℓ alternative models for the process defined as

$$\frac{dx}{dt} = f_\ell(x(t), \wp_k(w,t), \theta^\ell, t),\ J(t_f) = h(x(t_f), \wp_k(w,t), t),\ \ell = 1,...,M \qquad (1)$$

where $x(t)$ are the state variables, $\wp_k(w,t)$ is the operating policy at the *kth* iteration defined upon a set of parameters *w* and time *t* where θ^{ℓ} are parameters of the ℓth model whose uncertainty is characterized by Θ^{ℓ} and J is the objective function to be optimized.
To improve the current operating policy, experimental data (dynamic experiment) is needed to suitably reduce parametric uncertainty in each model. To this end, it is important to determine when along the run each of the n_{sp} sampling times should be located in order to obtain the sampling points times $\psi^{opt} \in \Psi$ which are the most informative in modeling for optimization in the face of uncertainty. Optimal sampling is formulated as the following optimization problem:

$$\psi^{opt} = \max_{\psi \in \Psi} \left| M(\hat{\theta}, \wp_k, \psi) \right|, \; M = Q^T Q$$
$$Q = \begin{pmatrix} S_{11} & \cdots & S_{1n} \\ \vdots & \ddots & \vdots \\ S_{m1} & \cdots & S_{mn} \end{pmatrix} \tag{2}$$

where the entries of the matrix Q , S_{ij}, measure the sensitivity of the performance index J at the *ith* sampling time with respect to *jth* policy parameter. Once sample data from the dynamic experiment is available, the first question is how to selectively improve parameter precision of alternative models. To address this issue, GSA techniques (Saltelli *et al.*, 2004) are used to identify for each model the subset of parameters to which the objective function J is most sensitive. Having reduced parametric uncertainty, for improving the operating policy a model must be selected.

In this work, model selection is based on distinguishing between parametric uncertainty and structural errors in performance prediction using alternative models. For the *rth* realization of model parameters, the corresponding simulated trajectory of process performance is $\hat{J}_r$. At each sampling point, a sample average $\left\langle \hat{J} \right\rangle$ of different realizations can be used to characterize parametric uncertainty for each model as follows (Asprey 2000; Asprey and Machietto, 2002; Chen and Asprey, 2003):

$$\varepsilon_{\hat{J}_i \to \left\langle \hat{J}_i \right\rangle} = \frac{1}{n_{sp} n_{\rho}} tr\left[\left(\frac{\hat{J}_{ir} - \left\langle \hat{J}_i \right\rangle}{\left\langle \hat{J}_i \right\rangle} \right)^T W_{ir} \left(\frac{\hat{J}_{ir} - \left\langle \hat{J}_i \right\rangle}{\left\langle \hat{J}_i \right\rangle} \right) \right]; i = 1,2,..., n_{sp}; r = 1,2,..., n_{\rho} \tag{3}$$

where W_{ir} is weighting matrix. As parametric uncertainty is iteratively reduced the importance of structural errors in each model regarding performance predictions are more evident when the operating condition is change in the search for policy improvement. As a measure of structural uncertainty, the average performance trajectory $\left\langle \hat{J}_i \right\rangle$ is compared at *ith* sampling point to the actual trajectory J_i to define the structural error:

$$\varepsilon_{\left\langle \hat{J} \right\rangle \to J} = \frac{1}{n_{sp}} tr\left[\left(\frac{\left\langle \hat{J}_i \right\rangle - J_i}{J_i} \right)^T W_{ii} \left(\frac{\left\langle \hat{J}_i \right\rangle - J_i}{J_i} \right) \right]; i = 1,2,..., n_{sp}; W_{ii} : weighting \;\; matrix \tag{4}$$

The total error of the ℓth model can be expressed as a weighted sum of errors in (3) and (4). Model selection may simply be done so that the model whose total error is the lowest is chosen for policy optimization. More elaborated strategies for model selection can also be developed. For example, initially model selection may emphasize reducing parametric uncertainty and as more data are gathered model selection is based on structural errors.

3 Case of study

To illustrate the proposed methodology, results obtained in the optimization of fed-batch fermentation process for the recombinant protein **rIL-11** using a genetically modified *E. coli* strain are presented. A structured kinetic model proposed by Tang *et al*. (2007) which describes state variables trajectories such as: biomass (*X*), substrate (*S*), intracellular recombinant protein concentration (*P*) will be used as an *in silico* bioreactor. Four unstructured models which differ in their biomass growth kinetics are used as guidelines for optimization so that the mismatch between "real" bioprocess and alternative models of the bioreactor is accounted for. Also, the operation policy has been defined based on the substrate feeding rate and induction time as the main components subject to optimization, including the initial culture condition. The basic model equations and the alternative biomass growth kinetics are:

$$\frac{dX}{dt} = \mu X; \quad \frac{dS}{dt} = -\frac{\mu}{Y_{xs}} X - f(X,t); \quad \frac{dP}{dt} = r_P - \mu P \tag{5}$$

$$r_P = \begin{Bmatrix} 0, & t \geq t_{ind} \\ K_P^{\max}\left(\frac{S}{K_s + S}\right)\left[\frac{1}{1+\left(\frac{P}{KI_P}\right)^5}\right], & t \geq t_{ind} \end{Bmatrix}$$

$$\text{Pr } imer\ orden: \quad \mu = \mu_{\max} S; \qquad f(X,t) = 0$$

$$Monod: \quad \mu = \mu_{\max} \frac{S}{K_S + S}; \qquad f(X,t) = 0$$

$$Contois: \quad \mu = \mu_{\max} \frac{S}{K_X X + S}; \qquad f(X,t) = 0$$

$$Manteinance: \quad \mu = \mu_{\max} \frac{S}{K_S + S}; \qquad f(X,t) = mX$$

Based on experimental data provided by Tang et al. (2007), a rough estimation of each model parameters was made and referred to as "initial values" in Table 1. Due to the significant level of parametric uncertainty a ±50% confidence interval around these initial values for each parameter is assumed for the first iteration. Moreover, a uniform distribution over its confidence interval is assumed for each parameter. In Table 2, parametric and structural errors for each model are given for the first two iterations. The total error is calculated by providing the same weight to parametric uncertainty and structural errors. It is worth noting that parametric uncertainty is so high at the beginning of the study that structural errors are almost no informative until an actual performance trajectory is available which is clear in the 2nd and 3rd iterations.

According to Table 2 the *Monod* model should be chosen for designing the first dynamic experiment since it exhibits the minimum parametric and structural errors. The optimal operation policy is computed by assuming the following feeding time profile:

$$F(t) = A\frac{t'}{1 + Bt' + Ct'^2}; \quad t' = t - t_{feed} \tag{6}$$

where upper and lower bounds for policy parameters A, B and C have been defined so that the total fed volume to the bioreactor does not exceed 10L while minimizing the correlation among them. The optimized policies obtained for the three iterations are shown in Table 3.

Table 1: Model Parameter (re)Estimation

		Initial values				Re-estimation			
		Model				Model			
Parameter	Unit	1st Order	Monod	Contois	Manteinance	1st Order	Monod	Contois	Manteinance
μ_{max}	h^{-1}	0.2000	0.6301	0.5607	0.5261	$0.397^{c} \pm 7.10^{-3}$	$0.4391^{c} \pm 1.2.10^{-4}$	$0.568^{c} \pm 7.10^{-3}$	$0.415^{a} \pm 3.10^{-3}$
K_S	$g\ L^{-1}$	2.0184	1.4956	-	0.7190	$2.25^{c} \pm 0.04$	-	-	-
Y_{xs}	$g_{biomass}\ g_{substrate}^{-1}$	0.3982	0.4506	0.4826	0.4464	$0.346^{a} \pm 7.10^{-3}$	$0.411^{a} \pm 4.10^{-3}$	$1.42^{a} \pm 0.02$	$0.452^{a} \pm 0.015$
K_P^{max}	$g\ L^{-1}$	0.0759	0.0629	0.0557	0.0536	$0.166^{b} \pm 3.10^{-3}$	$0.04109^{c} \pm 1.10^{-4}$	$0.0853^{b} \pm 1.7.10^{-3}$	$0.0508^{c} \pm 7.10^{-4}$
KI_p	$g\ (L\ h)^{-1}$	0.0877	0.0609	0.0627	0.0600	$0.0559^{b} \pm 1.1.10^{-4}$	$0.0617^{b} \pm 2.10^{-4}$	$0.0668^{b} \pm 1.3.10^{-4}$	$0.0525^{b} \pm 6.10^{-4}$
K_x	$g_{substrate}\ g_{biomass}^{-1}$	-	-	1.7291	-	-	-	-	-
m	h^{-1}	-	-	-	0.0100	-	-	-	-

Re-estimation in the: [a] 1st iteration; [b] 2nd iteration; [c] 3rd iteration.

Table 2: Errors for different models (initial process condition)

Model	Initial Condition			1st iter			2nd iter		
	$E_{\hat{J}_i \to \langle \hat{J} \rangle}$	$E_{\langle \hat{J} \rangle \to J}$	E_{total}	$E_{\hat{J}_i \to \langle \hat{J} \rangle}$	$E_{\langle \hat{J} \rangle \to J}$	E_{total}	$E_{\hat{J}_i \to \langle \hat{J} \rangle}$	$E_{\langle \hat{J} \rangle \to J}$	E_{total}
1st Order	0.4748	0.0149	0.4896	0.1529	0.5976	0.7506	0.0174	0.3730	0.3904
Monod	0.3352	0.0037	**0.3388**	0.1915	0.3441	0.5356	0.1159	0.0156	**0.1315**
Contois	0.4469	0.0033	0.4502	0.6558	0.3804	1.0362	0.0432	0.2287	0.2719
Manteinance	0.3382	0.0075	0.3457	0.0891	0.3018	**0.3909**	0.0343	0.5499	0.5842

Optimal sampling times for designed dynamic experiments in each iteration were:

$$\psi_{1st}[h] = [1.83,\ 2.33,\ 3.33,\ 4.00,\ 5.00,\ 5.50,\ 7.33,\ 11.33,\ 11.83,\ 12.33,\ 13.67,\ 15.67]$$
$$M = 1.93 \cdot 10^{-20}$$

$$\psi_{2nd}[h] = [0.17,\ 0.83,\ 1.33,\ 2.00,\ 3.50,\ 4.17,\ 5.33,\ 5.83,\ 11.17,\ 11.83,\ 12.33,\ 13.17]$$
$$M = 1.61 \cdot 10^{-24}$$

$$\psi_{3rd}[h] = [1.00,\ 2.50,\ 3.83,\ 4.33,\ 5.00,\ 6.00,\ 8.00,\ 12.17,\ 12.66,\ 13.33,\ 13.83,\ 14.33]$$
$$M = 1.91 \cdot 10^{-22}$$

Normalized Global Sensitivity Indexes for models parameters after each experimental run have been computed and later the most uncertain were re-estimated using experimental data from *in silico* bioreactor (data not shown). Re-estimated values for parameters and their 95% confidence intervals are shown in Table 1.

Table 3: Optimun Operation Policies for E. coli culture for rIL-11

Parameter	Units	Minimum	Maximum	Initial	1st run	2nd run	3rd run
A	$L\ h^{-2}$	$2\ 10^{-3}$	1.1	-	0.0569	0.0545	0.0569
B	h^{-1}	$3\ 10^{-4}$	0.1	-	$3\ 10^{-4}$	$3\ 10^{-4}$	$3\ 10^{-4}$
C	h^{-2}	$3\ 10^{-4}$	0.1	-	$3\ 10^{-4}$	$3\ 10^{-4}$	$3\ 10^{-4}$
S_f	$g\ L^{-1}$	5	30	-	30	30	30
t_{feed}	h	0	5	-	0	0	0
t_{ind}	h	3	7	-	4	4	4
t_f	h	8	16	10	16	16	16
V_0	L	5	10	8	5	5.30	5
X_0	$g\ L^{-1}$	0.01	0.1	0.05	0.1	0.1	0.1
S_0	$g\ L^{-1}$	2	7	5	7	3	6.5
			$J(g)$	**1.09**	**7.12**	**6.44**	**7.10**
			std(J)[g]		0.32	0.12	0.09

The iterative improvement methodology has been finished after the 3rd dynamic experiment since, as shown in Table 3, no further improvement is gained and the operating policy converges. Furthermore, it can easily be seen that the method deals very well with the objective of improving the final amount of rIL-11 obtained in a single run. Furthermore, the uncertainty in the objective function prediction has been significantly reduced by selectively re-estimating model parameters after each experiment.

4 Concluding remarks

A systematic methodology for designing optimally informative dynamic experiments in modeling for optimization based on several approximate models have been proposed. Results obtained in the production of interleukin-11 (IL-11) case study are very promising and industrial applications in the development of novel specialty-chemicals and bioprocesses are currently underway.

References

Asprey, S. M., S. (2000). Statistical tools for optimal dynamic model building. *Computers and Chemical Engineering,* 24, 1261-1267.

Asprey, S., Machietto, S. (2002). Designing robust optimal dynamic experiments. *J. of Process Control,* 12, 545-556.

Chen, B. H., Asprey. S. P. (2003). On the design of optimally informative dynamic experiments for model discrimination in multiresponse nonlinear situations." *Industrial Engineering Chemical Research*, 42, 1379-1390.

Saltelli, A.,Tarantola, S., Campolongo, F., Ratto, M. (2004). *Sensitivity Analysis in Practice: A Guide to Assessing Scientific Models*. John Wiley & Sons Ltd, Chichester, England.

Tang, S., Chen, J., Zhang, Z. (2007). Structured models for recombinant human interleukin-11 fermentation. *Biochemical Engineering J.*, 35, 210-217.

Proceedings of the 10th International Chemical and
Biological Engineering Conference - CHEMPOR 2008
Braga, Portugal, September 4-6, 2008
E.C. Ferreira and M. Mota (Eds.)

KINETIC MODELS EVALUATION FOR FED-BATCH ALCOHOLIC FERMENTATION

Patricia C.S. Borges[1], Fran S. Lobato[2], Eloízio J. Ribeiro[3], Valéria V. Murata[4 *]
[1, 3, 4] Faculdade de Engenharia Química, Universidade Federal de Uberlândia, Bloco K do Campus Santa Mônica, Av. João Naves de Ávila 2121, Uberlândia-MG.
[2] Faculdade de Engenharia Mecânica, Universidade Federal de Uberlândia, Bloco M do Campus Santa Mônica, Av. João Naves de Ávila 2121, Uberlândia-MG.

Keywords: Alcoholic Fermentation, Fed-Batch Process, Ethanol, Differential Evolution, Parametric Sensitivity.
Topic: Integration of life sciences & engineering

Abstract

This paper presents experimental observations and a theoretical study of the dynamic behavior of the fed-batch alcoholic fermentation for ethanol production, utilizing the *Saccharomyces cerevisiae* Y904 yeast and operational conditions equivalent to the adopted in Brazilian industries. The influence of substrate concentration and feeding rate on yield and productivity is discussed and the parameters estimation of two kinetic models through an Differential Evolution algorithm associated to the correlation and parametric sensitivity analysis are presented. The first model (Tosetto, 2002) considers the inhibition effects by substrate and product and the second is the classical Monod model. The parameters μ_{max} and K_S present the highest sensitivities. The Monod model was validated to a fed-batch fermentation with sucrose concentration and feeding rate 277.0 g/L and 1.166 L/h respectively with good results.

1 Introduction

The biofuels production has increased significantly in the last years. In 2006 the global production was about 40 M ton. of ethanol, being Brazil the major producer of alcohol from sugarcane, produced on 1% of the Brazilian arable land. There is no competition between ethanol and food segment in the country and besides it its energy balance is highly positive.

The fermentation processes can be operated in batch, fed-batch or continuous mode. The fed-batch operation is preferable when high substrate levels inhibit the product formation and there is production of undesired components. In these circumstances changes in the feeding rate of the substrate affect the productivity and the yield of the desired product so that the determination of the feeding policy that maximizes the ethanol production becomes a priority (Arpornwichanop and Shomchoam, 2007; Xiong *et al.*, 2007). The definition of the reaction kinetic is dependent of the operation mode used (Baltes *et al*.,1994; Pertev *et al.*, 1997; Wang and Sheu, 2000) and its determination in equivalent conditions to that utilized industrially is fundamental for the modeling, simulation and dynamic optimization of these processes. However, the parameter estimation from experiments still remains as an obstacle for a major advancement in biochemical processes (Rodriguez-Fernandez *et al.*, 2006).

In this paper the *Saccharomyces cerevisiae* Y904 yeast was used for fermentation with different combinations of sucrose concentrations and feeding rates to study the dynamic behavior of the fed-batch alcoholic fermentation for ethanol production. Despite recent studies which demonstrate that *Zymomonas mobilis* bacteria supplies a major yield when compared with the *S. cerevisiae* yeast (Lin and Tanaka, 2006; Bai *et al.*, 2008), this bacteria presents constraints about the substrates utilized (Bai *et al.*, 2008) and is not economically

*Corresponding author. Tel +55 (02134) 3239-4292 Ramal 229. E-mail: valeria@ufu.br

competitive with the yeast. So, its generalized application in Brazilian industries is not expected. The parameter estimation of the non-structured kinetic model proposed by Tosetto (2002) and of the classical Monod model was obtained through the Differential Evolution algorithm of Storn and Price (1996), available at http://www.ICSI.Berkeley.edu/~storn/code.html, considered more competitive for the global optimization despite demands a major number of evaluations of the Objective Function (Rodrigues-Fernandes *et al.*, 2006). The parametric sensitivity analysis and the estimate of the correlation matrix were realized through DDASPK code of Petzold *et al.* (2000) and of the methodology proposed by Sanz and Voss (2006), respectively.

2 Materials and Methods

The yeast used was the *Saccharomyces cerevisiae* Y904 strain. The composition of the cultivate medium consisted of sucrose with concentrations in the range 217 - 285 g/L; KH_2PO_4 (5 g/L); $MgSO_4.7H_2O$ (1 g/L); NH_4Cl (5 g/L); KCl (1 g/L) and yeast extract (6 g/L). The temperature, pH and agitation were set at 32 ºC, 4.50 and 200 rpm. The fermentations were performed using a 5 L bioreactor (New Bioflo 110 Brunswick Scientific CO). The inoculum volume was 1.5 L and corresponded to 30% of the bioreactor volume with initial cell and ethanol concentrations about 86 g/L and 4% (v/v) respectively. The ethanol and biomass concentrations were determined by dry biomass and spectrophotometric methods (Steckelberg, 2001) and the glucose concentration by glucoseoxidase test.

The Equations 2.1-2.4 present the dimensionless balances of cells (X), substrate (S), product (P) and volume (V) for the fed-batch bioreactor, where the characteristic scales were the initial and maximum values of the state variables (x_0, s_F and v_{max}), the ethanol concentration where there is greater cellular growth inhibition (p_{max} = 115 g/L, Ferreira, 1998) and the total fermentation time (Dutta *et al.*, 2001; Popova and Boyadjiev, 2007). The unstructured kinetic model presented in Eq. 2.5 was developed by Ghose and Thyagi (1979) and modified by Tosetto (2002) and considers the parabolic inhibition by both substrate and product with the power n different of one. Eq. 2.6 presents the classical Monod model.

$$\frac{dX}{d\tau} = -\frac{F_a}{V}X + \mu X \qquad (2.1)$$

$$\frac{dS}{d\tau} = \frac{F_a}{V}(S_F - S) - \left(\frac{1}{Y_{XS}}\mu + M_S\right)X \qquad (2.2)$$

$$\frac{dP}{d\tau} = -\frac{F_a}{V}P + \frac{Y_{PS}}{Y_{XS}}\mu X \qquad (2.3)$$

$$\frac{dV}{d\tau} = F_a \qquad (2.4)$$

$$\mu = \mu_{max}\left(\frac{S}{K_S + S + \frac{S^2}{K_i}}\right)\left(1 - \frac{P}{P_{max}}\right)^n \qquad (2.5)$$

$$\mu = \mu_{max}\left(\frac{S}{K_S + S}\right) \qquad (2.6)$$

The Differential Evolution algorithm was performed ten times for each set of estimated parameters, with population size 20, 300 iterations, disturbance rate 0.8 and crossing probability 0.8.

The Ddaspk.f code (Petzold *et al.*, 2000) was utilized to solve the sensitivity (*se*) equations given by Eq. 2.7, where $y \in \mathrm{IR}^n$ and $b \in \mathrm{IR}^n{}_b$, for relative and absolute error tolerances equal to 10^{-6}.

$$F(t, y, y', b) = 0 \qquad \frac{\partial F}{\partial y}se_i + \frac{\partial F}{\partial y'}se_i' + \frac{\partial F}{\partial b_i} = 0, i = 1, \ldots, n_b \qquad se_i = \frac{dy}{db_i} \qquad (2.7)$$

The correlation between the model parameters was carried out as proposed by Sanz and Voss (2006), through association of parametric sensitivity and statistical parameters correlation and covariance (Eq. 2.8).

$$cor(b_i, b_J) = \frac{cov(b)_{iJ}}{[cov(b)_{ii}\, cov(b)_{JJ}]^{1/2}} \qquad cov(b) = \sigma^2 (se^T \omega se)^{-1} \qquad (2.8)$$

where σ^2 is the variance of errors in observations and ω is the matrix of weights.

3 Results and Discussion

The Table 3.1 presents the experimental results for cell yield (y_{xs}), ethanol yield (y_{ps}), ethanol productivity (Q_p) and final product concentration (p_f) for three different feeding rates F (L/h), also considering the effect of sucrose concentration (s_F) of the feeding flow.

Table 3.1 Experimental results: yields, productivity and final ethanol concentration

F (L/h)	1.166			0.872			0.670		
s_F (g/L)	218.4	245	277	218	245	285	217	241.4	285
y_{xs} (g/g)	0.007	0.018	0.020	0.026	0.027	0.018	0.024	0.021	0.018
y_{ps} (g/g)	0.415	0.415	0.408	0.450	0.431	0.404	0.445	0.418	0.413
Q_p(g/Lh)	4.8	4.9	4.6	6.2	5.1	4.38	5.3	4.5	4.8
p_f (g/L)	74.3	81.8	89.2	77.4	84.0	89.2	77.6	81.2	91.5

The increase of s_F resulted in increase of p_f without noticeable cellular growth. Considering the variations of the feeding rate for $s_F \approx 218$, $s_F \approx 245$ g/L and $s_F \approx 285$ g/L, the feeding flows F ≈ 0.872, 0.872 L/h e 0.670 L/h, respectively, supplied higher productivities and ethanol yields. The ethanol yields did not diminish linearly with feeding rate and the increase of feeding velocity resulted in smaller fermentation time, unlike the results obtained by Andrietta *et al.* (2003) which considered higher values of F and s_F in the range 230 - 254.8 g/L.

The Table 3.2 shows the dimensionless estimated parameters of kinetic models of Tosetto (Eq. 2.5) and of Monod (Eq.2.6) with respective Objective Function (OF) values.

Table 3.2 Estimated Dimensionless Parameters of Tosetto and Monod Kinetic Models

Parameter values	Tosetto Model	Monod Model
μ_{max}	0.3031	0.1971
K_S	0.08550	0.04764
K_i	1.166	------
P_{max}	0.8007	------
N	0.1832	------
M_S	0.03508	0.06038
OF	0.020946	0.025992

The parametric sensitivity profiles for $s_F \approx 241.4$ g/L can be seen in Fig. 3.1. The sensitivity profiles of cell concentration are similar to the ethanol concentration but with a smaller range of variation of the sensitivities, between -0.112 and 0.141. The parameters μ_{max} and K_S present the highest sensitivities. The sensitivity of the inhibition term power (n) is more evident at final time while for the cellular maintenance constant (M_S) it arises when sucrose concentration diminished reflecting the need of more nutrients by the cells. The sensitivity for P_{max} was relatively small along the time, being more significant when the ethanol concentration was more accentuated. The sensitivity of cellular growth inhibition constant by substrate (K_i) was the less significant. This sensitivity analysis indicates that a classical Monod model may accurately predict the kinetic of fermentation considering these operation conditions.

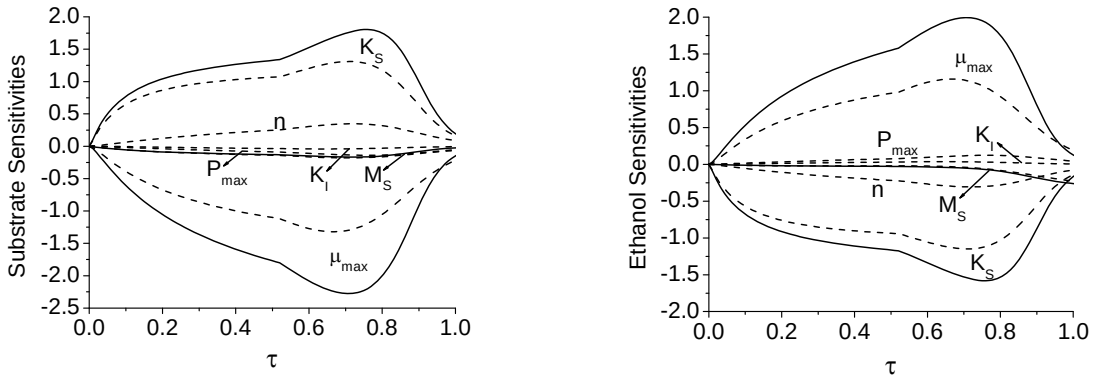

(a) (b)

Figure 3.1 (a) Sucrose and (b) ethanol concentration sensitivity profiles for s_F = 241,4 g/L regarding the parameters of the (---) Tosetto (2002) and (—) Monod models.

The correlations between the parameters of the Tosetto model are shown in Tab. 3.3 for s_F = 241.4 g/L. The majority of the parameter pairs exhibit high correlations. The parameters μ_{max} and K_S in Fig. 3.1, for example, presented similar profiles and opposite sign for all the variables S, X and P and model types indicating a positive correlation, while K_S and n presented similar profiles and equal sign indicating a negative correlation.

Table 3.3 Tosetto (2002) model parameter pair correlations for s_F = 241.4 g/L.

S	μ_{max}	K_S	K_i	P_{max}	n	M_s
μ_{max}	1.0	0.99	-0.99	-0.95	0.98	-0.99
K_S		1.0	0.97	0.94	-0.97	0.98
K_i			1.0	-0.95	0.98	-0.98
P_{max}				1.0	0.99	-0.98
N					1.0	0.99
M_s						1.0

X	μ_{max}	K_S	K_i	P_{max}	n	M_s
μ_{max}	1.0	0.99	-0.99	-0.95	0.98	0.45
K_S		1.0	0.97	0.94	-0.97	-0.44
K_i			1.0	-0.95	0.98	0.42
P_{max}				1.0	0.99	0.62
n					1.0	-0.53
M_s						1.0

P	μ_{max}	K_S	K_i	P_{max}	n	M_s
μ_{max}	1.0	0.99	-0.99	-0.95	0.98	0.45
K_S		1.0	0.97	0.94	-0.97	-0.44
K_i			1.0	-0.95	0.98	0.42
P_{max}				1.0	0.99	0.62
n					1.0	-0.53
M_s						1.0

The parameter pairs μ_{max}, K_S, K_i, P_{max} and n with M_S exhibit low correlations for the ethanol and cell concentrations and high correlations for the sucrose concentration for both models. This analysis confirms the behavior of previous sensitivity profiles where the pair [μ_{max}; M_S], for example, exhibit different profiles for P and similar profiles for S due to the low and high correlation, respectively.

The Figure 3.2 exhibits experimental and simulated results using the kinetic models of Tosetto and Monod for $s_F \approx$ 217 and $s_F \approx$ 285 g/L, where moderate deviations are observed in the sucrose concentration profile for $s_F \approx$ 285 g/L.

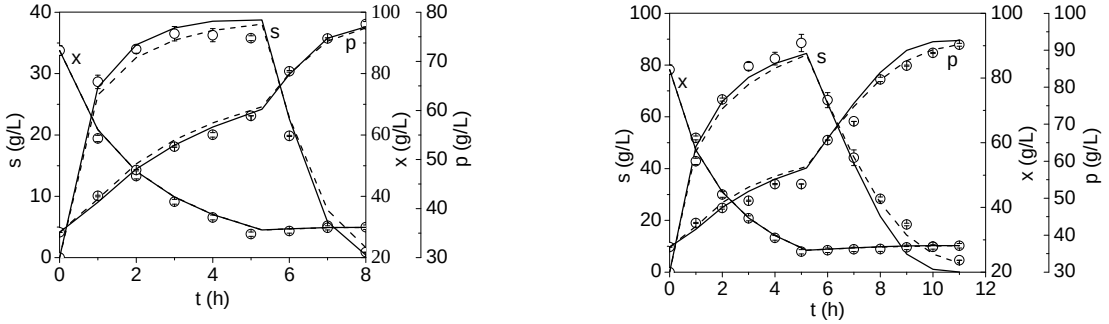

(a) (b)

Figure 3.2 Sucrose, cell and ethanol concentration profiles for (a) s_F = 217 g/L and (b) s_F = 285 g/L with F=0.670 L/h (○) Experimental data. (---) Simulated with the Tosetto model. (—) Simulated with the Monod model.

The Figure 3.3 presents the experimental validation of the Monod model for s_F = 277 g/L and F = 1.166 L/h proving its good capacity of prediction.

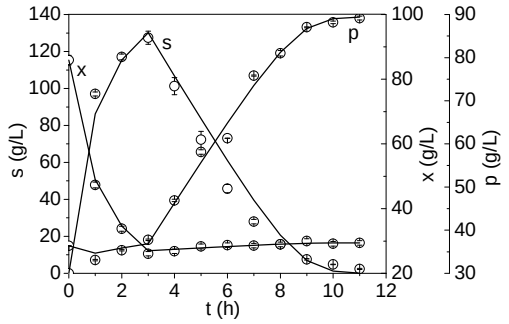

Figure 3.3 Sucrose, cell and ethanol concentration profiles for s_F = 277 g/L and F= 1.166 L/h (○) Experimental data. (—) Simulated with the Monod model.

4 Conclusions

The influence of the feeding rate and fed substrate concentration in the fed-batch alcoholic fermentation using sucrose and considering operational conditions representative of industrial conditions was shown. The influence of the parameters μ_{max} and K_S is the greatest amongst all the parameters considered while the influence of the cellular growth inhibition constant by substrate (K_i) is irrelevant. The cell concentration is less affected than product and substrate concentrations by parameters variations in the operation range considered. The parameters of Tosetto and Monod models were estimate using Differential Evolution. The analysis of correlation matrix between parameters, which exhibit high correlation for both models, confirmed the previous parametric sensitivity analysis. The Monod model was validated against experimental values with good results and due to its simplicity is appropriate for the modeling, simulation and optimization of the fed-batch process.

Acknowledgements

The partial support of CAPES (Coordenação de Aperfeiçoamento de Pessoal de Nível Superior) is gratefully acknowledged.

References

Andrietta, S. R., Ferreira, E., Andrietta, M. G. (2003). Avaliação da Influência da Velocidade de Alimentação sobre o Rendimento e Produtividade dos Processos de Produção de

Etanol Operando em Batelada Alimentada. *Anais do Sinaferm 2003*. Faculdade de Engenharia Química, Universidade Estadual de Campinas. Campinas, 7 p.

Arpornwichanop, A., Shomchoam, N. (2007). Studies on optimal control approach in a fed-batch fermentation. *Korean J. Chem. Eng.*, 24, 11-15.

Bai, F.W., Anderson, W.A., Moo-Young, M. (2008). Ethanol fermentation technologies from sugar and starch feedstocks. *Biotechnology Advances*, 26, 89–105.

Baltes, M., Schneider, R., Sturm, C., Reuss , M. (1994). Optimal Experimental Design for Parameter Estimation in Unstructured Growth Models. *Biotechnology Progress*, 10, 480-488.

Dutta, S., Chowdhury, R., Bhattacharya, P. (2001). Parametric sensitivity in bioreactor: an analysis with reference to phenol degradation system. *Chemical Engineering Science,* 56, 5103-5110.

Ferreira, A. A. (1998). Simulação da Fermentação Alcoólica de Meios à Base de Glicose por *Saccharomyces cerevisiae*. Uberlândia, 98p. Dissertação (Mestrado em Engenharia Química) – Faculdade de Engenharia Química, Universidade Federal de Uberlândia.

Ghose, T.K., Thyagi, R.D. (1979). Rapid Ethanol Fermentation of Cellulose Hydrolysate. II Product and Substrate Inhibition and Optimization of Fermentor Design. *Biotechnology and Bioengineering*, 21, 1401-1420.

Lin, Y., Tanaka, S. (2006). Ethanol fermentation from biomass resources: current state and prospects. *Applied Microbiology Biotechnology*, 69, 627-642.

Pertev, C., Türker, M., Berber, R. (1997). Dynamic modeling, sensitivity analysis and parameter estimation of industrial yeast fermenters. *Computers Chemical Engineering*, 21, 739-744.

Petzold, L. R., Brown, P. N., Hindmarsh, A. C., Li, S. (2000). Code DDASPK. Copyright. University of California, 1-206.

Popova, P., Boyadjiev, C. (2007). Hierarchical Approach for Parameter Identification of Multiparameter Models. *Biochemical Engineering Journal*, 39, 397-402.

Rodriguez-Fernandez, M., Egea, J.A., Banga, J.R. (2006). Novel metaheuristic for parameter estimation in nonlinear dynamic biological systems. *BMC Bioinformatics*, 7, 483.

Sanz, E., Voss, C. I. (2006). Inverse modeling for seawater intrusion in coastal aquifers: Insights about parameter sensitivities, variances, correlations and estimation procedures derived from the Henry problem. *Advances in Water Resources*, 29, 439-457.

Steckelberg, C. (2001). Caracterização de leveduras de processos de fermentação alcoólica utilizando atributos de composição celular e características cinéticas. Tese (Doutorado em Engenharia Química) – Universidade Estadual de Campinas, Campinas-SP. 215p.

Storn, R., Price, K. (1996). Differential Evolution – A simple and efficient adaptive scheme for global optimization over continuous spaces. International Computer Science Institute, Berkeley, 1-15.

Tosetto, G. M. (2002). Influência da matéria-prima no comportamento cinético de levedura na produção de Etanol. Dissertação (Mestrado em Engenharia Química) – Universidade Estadual de Campinas, Campinas-SP. 82p.

Wang, F., Sheu, J. (2000). Multiobjective parameter estimation problems of fermentation processes using a high ethanol tolerance yeast. *Chemical Engineering Science*, 55, 3685-3695.

Xiong, Z., Xu, Y., Zhang, J., Dong, J. (2007). Batch-to-batch control of fed-batch processes using control-affine feedforward neural network. *Neural Comput & Applic*. DOI 10.1007/s00521-007-0142-6.

Proceedings of the 10th International Chemical and
Biological Engineering Conference - CHEMPOR 2008
Braga, Portugal, September 4-6, 2008
E.C. Ferreira and M. Mota (Eds.)

Production Costs of Wheat Straw-Based Ethanol in Mexico. A Parametric Analysis

Hector Gutierrez-Murillo[1], **Gabriela Magaña**[1], **Arturo Sanchez**[1*]
[1]Centro de Investigación y Estudios Avanzados (CINVESTAV) Unidad Guadalajara.
31-438, 45015 Guadalajara, México.

Keywords: Bioethanol production, lignocellulosic ethanol.
Topic: Integration of life sciences and engineering.

Abstract

This work presents a parametric analysis of total production costs of wheat straw-based ethanol for a hypothetical facility located in Mexico. Using the Net Present Value (NPV) method the ethanol price (USD/kg) was estimated as a function of plant size (feedstock flowrate) and feedstock cost, interest, investment period and equity percentage taking into consideration local economy conditions. The analysis is based on a standard process flowsheet incorporating novel technology for pretreatment and separation operations. Steady state mass balances calculations were made employing separation and reaction factors taken from "state-of the-art" literature for second generation biofuels. The resulting total costs are within competitive margins for this geographical region. For our base case, feedstock (34%) and production costs (28%) are the main contributors for the ethanol price. Therefore, process efficiency and technologies for diminishing production costs are alternatives worth exploring.

1 Introduction

First generation biofuels are currently in full commercial exploitation worldwide with production carried out using mature technologies. Following the steps of the US, the Mexican government has recently decided to incorporate in the short term biofuels as part of the transport fuel commercialized nationwide by the state-owned company Pemex. Therefore, it is highly probable that this substitution will be carried out with biofuel imports from large producer countries such as the US and Brazil and with the participation of players with large investing capacities and foreign technologies. Therefore, upper generation biofuels can be alternatives for local providers to participate in satisfying part of the transport fuel demand in a socially and environmentally sensible way. It is well accepted that raw matter contributes up to 40% to production costs and better process technology is currently is under development. Therefore, in order to study conditions for a feasible production in Mexico, this paper presents a parametric analysis of total production costs of wheat straw-based ethanol for a hypothetical facility. The wheat-straw was chosen as raw matter because the amounts and prices available in certain regions in Mexico as well as its secondary applications appear to be adequate for this exercise. Taking into consideration local economy conditions, the ethanol price (USD/kg) is estimated using the Net Present Value (NPV) method as a function of plant size (feedstock flowrate) and feedstock cost, interest, investment period and equity percentage as financial parameters. Results seem to indicate that production can be financially sound.

Plant related information (i.e. equipment size and process flows) is obtained from a steady state model of a modified process flowsheet (Aden et al. 2002) as discussed in section 2. Five main processing stages are considered: pretreatment, saccharification-fermentation, separation, services and cogeneration. Water treatment is considered part of the services stage due to its environmental relevance. The cogeneration stage includes both electricity and steam generation. Steady state mass balances were built

*Corresponding author. Tel. +52-33-37773600. E-mail: arturo@gdl.cinvestav.mx.

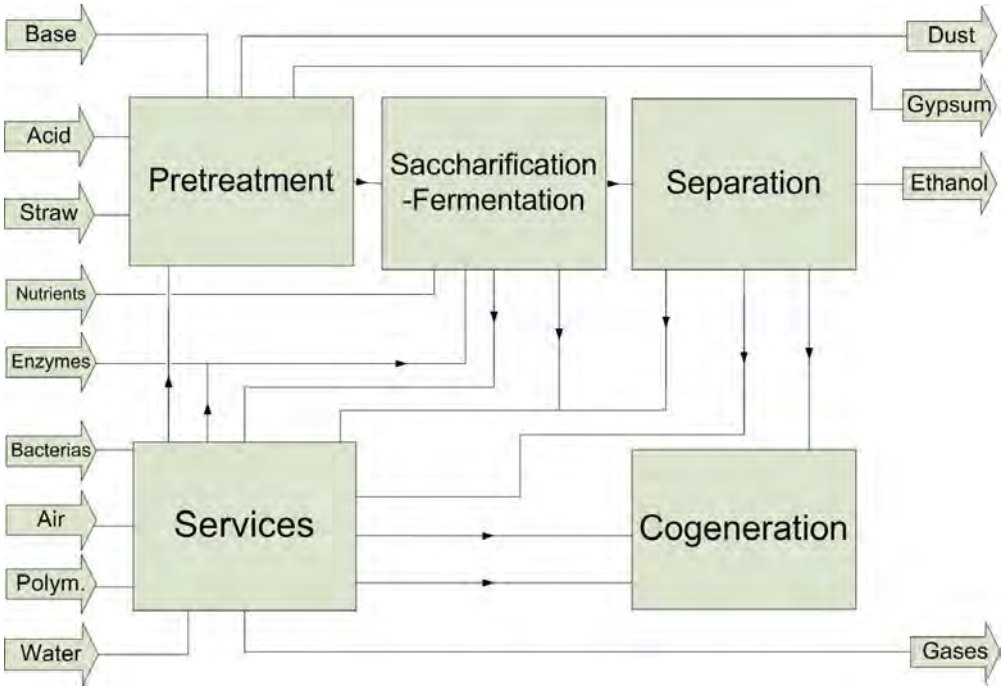

Figure 1: Process Flowsheet

for each stage. Section 3 presents the modelling strategy. Calculations for each stage were carried out employing separation and reaction factors taken from the "state-of the-art" literature (Aden et al. 2002), (Saha et al. 2005), (Thomsen et al. 2006) as well as from our own experience. Equipment cost calculations for each stage as well as total capital investment and total product costs were carried out using a standard conceptual design approach. Local economic conditions are taking into consideration. The ethanol price is estimated in section 4 employing the Net Present Value (NPV) technique. Using a base case of 200ton/day of wheat-straw, the resulting price is 0.75 USD/kg of ethanol. Feedstock (34%)and production costs (28%) are the main contributors, followed by equipment (21%) and other capital costs (18%). Therefore, improving process efficiency or technologies for diminishing production costs are alternatives worth exploring. The sensitivity of the model is explored for different feedstock flowrates and prices. Results show that if plant capacity is increased to manageable amounts, total costs are substantially reduced reaching feasible production costs. In the final part, the paper discusses crop and market conditions in Mexico and, in the light of these results, the relevance of urgently exploring other alternative sources for bioethanol production.

2 Plant Description

The process flowsheet is a modification of a standard model for ethanol production using corn stover (Aden et al. 2002). Five main processing stages are considered: pretreatment (size reduction and thermochemical treatment), saccharification and fermentation (polysaccharide's conversion to monosaccharide and ethanol production), separation (distillation to azeotropic point and molecular sieves), services (waste water treatment) and cogeneration (electricity and steam generation) (Aden et al. 2002), (Saha et al. 2005). Novel process technologies were incorporated for pretreatment and separation operations. A counterflow reaction system (Thomsen et al. 2006) is employed for the hydrolysis and molecular sieves for ethanol dehydration (Aden et al. 2002). The five main stages and the principal flowrates of the process are shown in Figure 1. Due to space limitations, flowsheets of each stage are not presented in this paper. Table 1 lists relevant process equipment separated by stages involved in this hypothetical ethanol plant.

Pretreatment			
Vibrating screen, 2 decks	2	Dust collector	1
Soaking tank	1	Acid mixer tank	1
Conveyor reactor	1	Ph mixer tank	1
Pneumatic conveyor	1	Base mixer tank	1
Hammer mill	1	Pre saccharification tank	1
		Rotary drum vacuum filter	1
Sacch.-Ferm.		**Separation**	
Saccharification tank	3	Beer column	1
Fermentor tank	3	Rectification column	1
Mixer tank	1	Molecular sieve	2
Services		Triple effect evaporator	1
Anaerobic reactor	1	Pressure leaf filter	2
Aerobic reactor	1	**Cogeneration**	
Clarifier	1	Boiler	1
Scrubber	1	Steam turbine	1
Mixer tank	1		
Rotary drum vacuum filter	1		

Table 1: Main process equipment

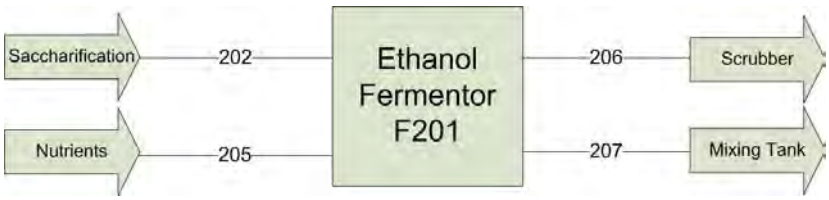

Figure 2: Fermentor flowsheet

3 Steady State Process Modelling

Steady state mass balances were built for each equipment. The model is written in terms of the total mass flowrates, component mass fractions and separation and reaction factors. Values for the last two types of parameters are taken from the "state-of the-art" literature (Aden et al. 2002), (Saha et al. 2005),(Thomsen et al. 2006). The complete model comprises 315 algebraic equations.

As an example of the model building strategy, the mass balance corresponding to the fermentation battery in the saccharification-fermentation stage is shown in Figure 2. Nomenclature is given in table 2. The mass balance comprises equations 1 to 5. Equation 1 represent the ethanol general balance in the ethanol fermenter (F201), $M_{207}X_{207ET}$ and $M_{106}X_{206ET}$ (the ethanol mass flow in streams 207 and 206) are the variables to solve. Equation 2 symbolizes the ethanol mass produced in F201 which is determined by equations 3 and 4. These equations correspond to the mass flowrates of glucose and pentose converted to ethanol and equation 5 describes the ethanol flowrate in the stream 206. $M_{202}X_{202ET}$ is the result of a previous balance not showed in this paper.

$$M_{202}X_{202ET} = M_{207}X_{207ET} + M_{206}X_{206ET} - r_{F201ET} \tag{1}$$

$$r_{F201ET} = \alpha + \beta \tag{2}$$

$$\alpha = \frac{2Z_{F201ETA}(M_{202}X_{202GL})PM_{ET}}{PM_{GL}} \tag{3}$$

$$\beta = \frac{5}{3}Z_{F201ETB}PM_{ET}(\frac{M202X_{202XY}}{PM_{XY}} + \frac{M_{202}X_{202AR}}{PM_{AR}}) \tag{4}$$

$$M_{206}X_{206ET} = Z_{F202033}(r_{201ET} + M_{202}X_{202ET}) \tag{5}$$

Variable	Description	Units	Factors	Description	Units
M202	Mass flow rate in 202	kg/h	ZF201Eta	Glucose molar fraction converted to ethanol in 201	-
M206	Mass flow rate in 206	kg/h	ZF201Etb	Glucose and Arabinose molar fraction converted to ethanol in 201	-
M207	Mass flow rate in 207	kg/h	ZF201ET	Ethanol fraction gone in 206	-
X202ET	Ethanol fraction in 202	-	PMAR	Arabinose molecular weight	kg/kmol
X206ET	Ethanol fraction in 206	-	PMET	Ethanol molecular weight	kg/kmol
X207ET	Ethanol fraction in 207	-	PMGL	Glucose molecular weight	kg/kmol
X202GL	Glucose fraction in 202	-	PMXY	Xylose molecular weight	kg/kmol
X202XY	Xylose fraction in 202	-	α	Glucose flow converted to ethanol	kg/kmol
X202AR	Arabinose fraction in 202	-	β	Xylose flow converted to ethanol	kg/kmol
rF201ET	Ethanol mass produced in f201	kg/h			

Table 2: Parameters corresponding to ethanol fermentor (F201)

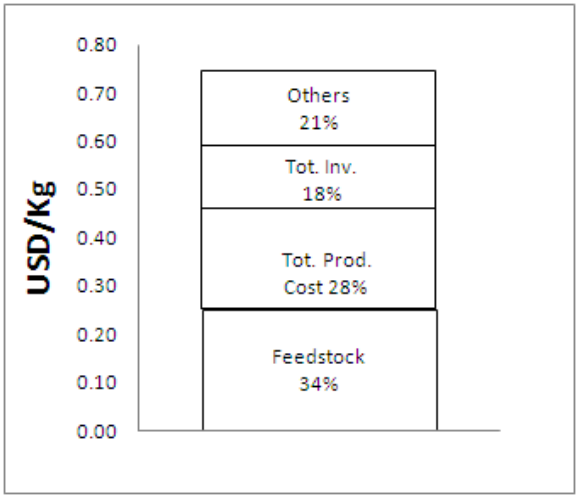

Figure 3: Contributions to ethanol cost

The mass balance results were employed to determined the equipment size of each stage (Seider et al. 2004) and a standard conceptual design procedure (Seider et al. 2004), (Douglas 1988) was employed to calculate, for each stage, the equipment costs and for the complete facility, total investment, total production costs, feedstock costs and annual cash flow using a base case (200 ton/day feedstock, 10 years life period, 9% discount rate, equity 30% and 0.07USD/kg for wheat straw price). The construction period was established in 2.5 years (Aden et al. 2002). The energy produced in the cogeneration stage was discounted to the utilities costs.

4 Net Present Value (NPV) Analysis

The NPV is the difference between the present values of the annual cash flows and the initial required investment. If $NPV = 0$ the discount rate i is understood as the return on investment (ROI). Equation 6 represents the standard NPV with ACF as the annual cash flow, n is the life period, I is the total investment, WC is the working capital. ACF, WC, I expresions were obtained based on Douglas (1988).

$$NPV = ACF\frac{(1+i)^n - 1}{(1+i)^n i} + \frac{WC}{(1+i)^n} - I \tag{6}$$

The NPV method and the base case mentioned previously were used to calculate the ethanol price. Best and worst case scenarios were established as boundaries for the sensitivity analysis. The price composition of the ethanol for the base case is shown in Figure 3. Total production cost (28%) and the raw material cost (34%) are the main contributions. Total investment (18%) and others (taxes, equity and general expenses) (21%) complete the ethanol price. Table 3 shows the resulting ethanol prices.

Sensitiviy analysis for ethanol price			
Factor	Best case	Base case	Worst case
Wheat straw flow rate (ton/day)	2,000	200	20
Wheat straw price (USD/kg)	0.03	0.07	0.07
Discount rate (%)	7	9	12
Life period (years)	15	10	5
Equity (%)	0	30	100
Ethanol price (USD/kg)	0.14	0.75	2.69

Table 3: Best and worst cases for ethanol price calculations

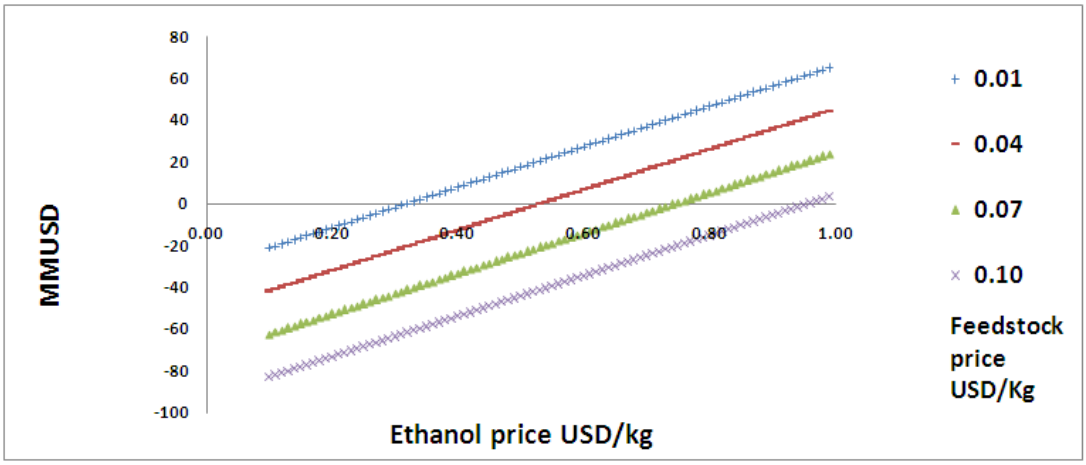

Figure 4: VPN vs Ethanol price for different feedstock prices

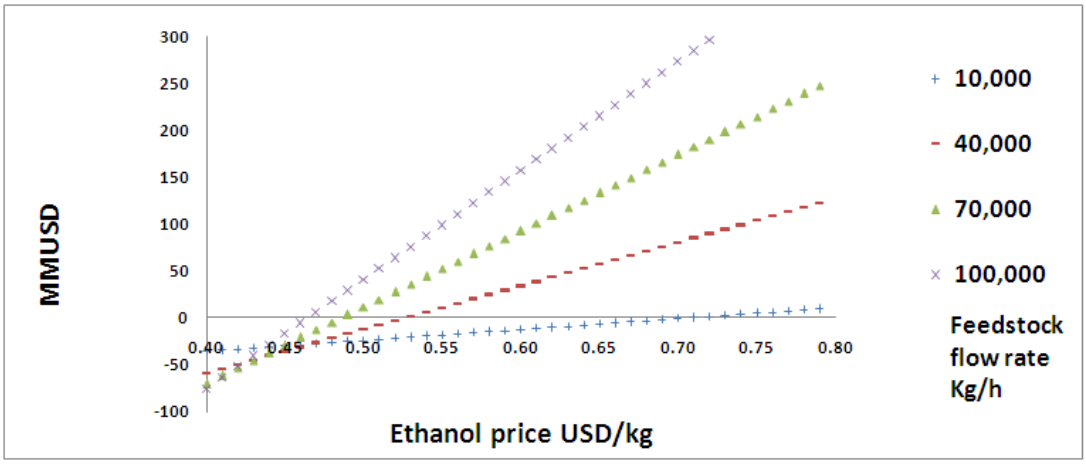

Figure 5: VPN vs Ethanol price for different feedstock flow rates

In this paper, results are presented for variations on feedstock price (Figure 4) and flowrate (Figure 5). The values for the rest of the independent variables were maintained as in the base case. Figure 4 indicates that the relation of feedstock price and the ethanol price is lineal. More interesting, figure 5 shows a negative exponential dependence of the ethanol price with the feedstock flowrate. This is because the feedstock flowrate is a function of the equipment price equations that have a logarithmic form. Therefore, the feedstock flowrate could be increased (e.g. 4 times the base case flowrate) in order to be in a "good design zone" .

5 Conclusion

The results obtained in this exercise are similar in order of magnitude to others previously published using different second generation feedstocks (Aden et al. 2002). Since the main contributors to ethanol price are feedstock and total production costs, alternative sources of lignocellulosic materials as well as process efficiency and new technologies are important aspects worth exploring. Results show that competitive ethanol prices can be achieved with plant sizes and feedstock amounts suitable to be handled within the local economy. However, it is important to take into consideration possible pressures originated from the large installed production capacity of first generation ethanol and financial factors in other countries as well as the lack of policies in Mexico regarding this matter. For instance, the US currently employs more than 10 % of its maize production (which represents three times the national maize consumption) to serve an industry with important tax exception programs and demanding to duplicate feedstock available for producing first generation ethanol. Moreover, Mexico is highly dependent on basic crops from foreign suppliers (30% and 50% of its maize and wheat consumption is imported) and maize and wheat stover are important sources of food for livestock. Thus, they must be cautiously employed for ethanol production.

References

Aden, A., Ruth, M., Ibsen, K., Jechura, J., Neeves, K., Sheehan, J. & Wallace, B. (2002), Lignocellulosic biomass to ethanol process design and economics utilizing co current dilute acid prehydrolysis and enzymatic hydrolysis for corn stover, Technical report, National Renewable Energy Laboratory.

Douglas, J. M. (1988), *Conceptual Design of Chemical Processes*, McGraw Hill.

Saha, B. C., Iten, L. B., Cotta, M. A. & Wu, Y. V. (2005), 'Dilute acid pretreatment enzymatic saccharification and fermentation of wheat straw to ethanol', *Process Biochemistry* **40**, 3693–3700.

Seider, W. D., Seader, J. D. & Lewin, D. R. (2004), *Product and Process Design Principles*, WILLEY.

Thomsen, M. H., Thygesen, A., Jorgensen, H., Larsen, J., Christensen, B. H. & Thomsen, A. B. (2006), 'Preliminary results on optimization of pilot scale pretreatment of wheat straw used in coproduction of bioethanol and electricity', *Applied Biochemistry and Biotechnology* **129**(132), 448–460.

Proceedings of the 10th International Chemical and
Biological Engineering Conference - CHEMPOR 2008
Braga, Portugal, September 4-6, 2008
E.C. Ferreira and M. Mota (Eds.)

Optimization of Process Variables and Kinetics of the Xanthan Gum Biosynthesis Using Sugar Cane Broth

S. Faria[1], M. M. Resende[1], E. J. Ribeiro[1], F. P. de França[2*] and V. L. Cardoso[1]
[1] Faculty of Chemical Engineering, Universidade Federal de Uberlândia, Caixa Postal 593, CEP: 38.400-902, Uberlândia – MG, Brazil.
[2*]School of Chemical, Universidade Federal do Rio de Janeiro, Bloco E, CEP: 21949-900, Rio de Janeiro - RJ, Brazil.

Keywords: study kinetic, xanthan gum, optimization, sugar cane broth
Topic: Integration of life sciences & engineering

Abstract
Biopolymers are produced commonly by submerged fermentation and among those with high commercial value is xanthan gum. Acting as thickening, stabilizing excellent, suspension and emulsifying agent this gum possesses many advantages due to its superior rheological characteristics. Studies of process variables optimization and kinetic profile using sugar cane broth in the xanthan gum biosynthesis have not been reported by the literature. Due the mentioned relevance, this work was developed with the purpose of optimizing agitation speed and aeration level in the xanthan production using sugar cane broth diluted, as well as to evaluate the kinetic behavior in the optimum condition by Weiss and Ollis model. Therefore, the conversion and viscosity obtained were (0.607 $g.g^{-1}$) and (23,002 cP) using sucrose concentration (27.0 g/L), yeast extract (2.0 g/L), ammonium nitrate (0.8 g/L), 750 rpm, and 0.35 vvm.

1 - Introduction
Xanthan gum is a natural polysaccharide and an important industrial biopolymer, is classified as a ramified, anionic hetero-exopolysaccharide, and is produced by fermentation using the bacterium *Xanthomonas*. The main producers of xanthan are Merck, Kelco, and Pfizer in the United States; Rhône Poulenc, Mero-Rousselot-Santia, and Sanofi-Elf in France; Saidy Chemical in China; and Jungbunzlauer in Austria (García-Ochoa et al. 2000; Pradella, 2006). World production of xanthan gum is 30,000 tons/year (Skaracis et al. 2003; Pradella, 2006), while its consumption in the United States has an annual growth rate between 5-10% (Harcum et al., 1999). Xanthan has an actual market of approximately US$ 270 million, and is expected to reach US$ 400 million with a production of 80,000 tons/year in 2015 (Pradella, 2006). Xanthan production is usually modeled by unstructured models as described by Moraine and Rogovin (1971), De Vuyst et al. (1987) and Pons et al. (1990). García-Ochoa et al. (1995) and Letisse et al. (2003) have proposed and applied unstructured kinetic models describing biomass, carbon source, nitrogen source, and dissolved oxygen evolution. Rosalam and England (2006) in yours review to the xanthan gum production reported also the characteristics of the unstructured and structured kinetics models emphasizing the kinetics behavior has been described by García Ochoa et al. (1995) and Weiss and Ollis (1980) models. Since Brazil is a major producer of sugar cane, it is advantageous for researchers there to create new biotechnological processes using cane broth as the raw material for the production of xanthan gum. The purpose of this study was to optimize the process variables of sucrose, yeast extract, ammonium nitrate concentrations, agitation speed and aeration. Response surface methodology was used for optimization, and the kinetic parameters (μ_{max}, X^*, m, λ, α, and β) regarding the bioprocess were obtained by applying the unstructured kinetic model.

* Corresponding author. Tel 55 21 25627620. E-mail: fpfranca@eq.ufrj.br

2 - Materials and methods

In previous studies, the nitrogen source was selected and a central composite design of sixteen experiments, defined three quantitative variables to represent the optimum composition of the medium inside of researched range: sucrose concentration (27.0 g/L), yeast extract (2.0 g/L) and ammonium nitrate (0.8 g/L). Na_2HPO_4 (2.5 g/L) and KH_2PO_4 (2.5 g/L) were also added in the medium as buffer agent. In the described conditions, a factorial project 3^2 was idealized with the objective of discovering the influence of the agitation speed (500, 750 and 1,000 rpm) and aeration (0.25; 0.5 and 0.75 vvm) in the process, once that their costs are considerable and happens directly in the final price of the product. Concisely, the adopted procedure consisted in the accomplishment of two different stages: the fermentative process and the recovery of the gum. The fermentations were carried out in a 2.0 L Biostat-B bioreactor by *Xanthomonas campestris pv. campestris* NRRL B-1459 at constant temperature and pH of 28 ± 1^oC and 7.5, respectively, for 24 hours. The working volume was 1.5 L. The monitored responses were: substrate conversion to product ($Y_{P/S}$) and gum viscosity in solution 1% using 0.75 s^{-1}. The sucrose, after acidic hydrolysis, was assayed by the enzymatic method using glucose-oxidase and the viscosities were measured by the Brookfield RVDVIII rheometer. The measurements of dissolved oxygen for determination of the Oxygen Transfer Coefficient (K_La) were done in the absence of the inoculum. The recovery and the purification of the polymeric were done as suggested by the literature. The fermented broth was diluted 1:1 with deionized water and centrifuged in a Beckman Coulter Avanti J-25 centrifuge at 18,900x*g* for 40 min to remove cells. The supernatant was filtered and treated with a saturated solution of KCl; the polymer was recovered by precipitation with ethanol (Ramírez et al., 1988). The unstructured kinetic model used in this investigation expresses the growth rate only as a function of the biomass, by utilization of the Verhulst-Pearl equation [Eq. (1)] and the Luedeking-Piret equations [Eqs. (2) and (3)] (Luedeking and Piret, 1959).

$$\frac{dX}{dt} = \mu_{max} X \left(1 - \frac{X}{X_{max}} \right) \quad (1)$$

$$\frac{dP}{dt} = m \frac{dX}{dt} + \lambda X \quad \text{where} \quad m = \frac{1}{Y_{X/P}} \quad (2)$$

$$-\frac{dS}{dt} = \alpha \frac{dX}{dt} + \beta X \quad \text{where} \quad \alpha = \frac{1}{Y_{X/S}} \quad (3)$$

The kinetic parameters ($\mu_{max.}$, $X_{max.}$, m, λ, α and β) of the Weiss and Ollis (1980) model were obtained by non-linear regression using a multiresponse algorithm.

3 - Results and discussion

Table 1 presents the obtained results for the factorial project 3^2 executed. In this way, in agreement with the response surface methodology (RSM), the agitation speed and the aeration of 750 rpm and 0.35 vvm produced experimentally the most expressive responses for the conversion (0.607 $g.g^{-1}$) and the viscosity (23,002 cP) inside of the investigated optimization region. These results showing that the process costs are smaller when compared to the agitation speed (800 rpm) and aeration (0.5 vvm) fixed in the first central composite design for the sixteen assays. All of the experiments were accomplished in duplicate and the optimized point was confirmed.

Table 1 – Effect of the independent variables, agitation speed and aeration, in the responses $Y_{P/S}$ and viscosity.

Runs	Agitation speed [rpm] X_1	Aeration [vvm] X_2	K_La [h^{-1}]	$Y_{P/S}$ [$g.g^{-1}$]	Viscosity 0.75 s^{-1} [cP]
1	500	0.25	24.978	0.486	18,200
2	500	0.50	30.966	0.479	19,000
3	500	0.75	41.034	0.435	18,000
4	750	0.25	40.614	0.600	23,470
5	750	0.50	58.65	0.633	24,000
6	750	0.75	66.66	0.577	23,400
7	1,000	0.25	51.858	0.615	22,900
8	1,000	0.50	69.678	0.607	23,100
9	1,000	0.75	78.558	0.544	21,680
10	750	0.50	57.921	0.637	24,300
11	750	0.50	59.235	0.641	24,500

Experiments 5, 10 and 11 were done with the values of the variables set at the central point (Table 1). The central point represents the best conditions obtained for the responses, $Y_{P/S}$ (0.641 $g.g^{-1}$), and viscosity of the gum solution at 1% concentration (24,500.0 cP). Statistical analysis using the response surface technique confirmed that the maximum point was close to the central point. For statistical analysis of the responses, the parameters with significance levels larger than 10%, using a t-Student hypothesis test, were not considered relevant.

Figure 1 represents the contour plots for X_1 and X_2 considering $Y_{P/S}$ (A), and viscosity (B), while, Figure 2 illustrates the response surface for the Oxygen Transfer Coefficient. Figure 1 is very important because shows the optimum range of operation (black area) for agitation speed and aeration rate, furthermore, it is evident from these figures that we can find a desirable combination of X_1 and X_2 for increased the xanthan production and viscosity of the gum solution. Equations 4, 5, and 6 refer to the effects of the isolated variables X_1, and X_2 and the quadratic interactions effects that compose the adjusted statistical models.

The optimized conversion $Y_{P/S}$ calculated from the Equation 4 was 0.634 $g.g^{-1}$ when the maximum point (750 rpm, and 0.35 vvm) was substituted, while, the optimized viscosity and K_La calculated from the Equations (5, 6) were 24,117 cP and 49.736 h^{-1}, respectively.

$$Y_{P/S} = 0.632 + 0.0611X_1 - 0.0805(X_1)^2 - 0.0241X_2 - 0.0352(X_2)^2 \qquad (r^2) = 0.98 \qquad (4)$$

$$Y_{Viscosity} = 24{,}272 + 2{,}080X_1 - 3{,}229(X_1)^2 - 248X_2 - 844(X_2)^2 - 255(X_1X_2) \qquad (r^2) = 0.99 \qquad (5)$$

$$Y_{KLa} = 56.616 + 17.186X_1 - 7.104(X_1)^2 + 11.467X_2 \qquad (r^2) = 0.97 \qquad (6)$$

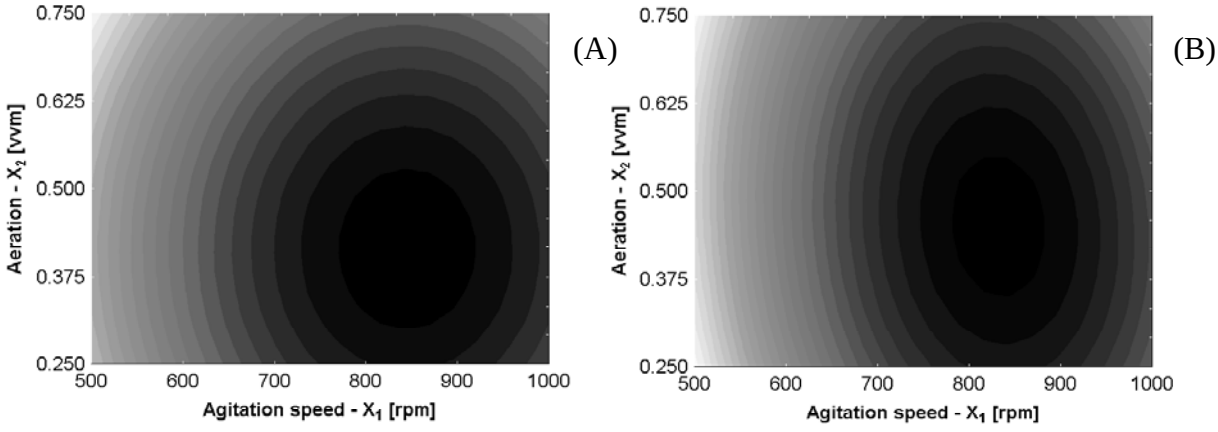

Figure 1 – Contour plot considering X_1 (agitation speed) and X_2 (aeration): (A) $Y_{P/S}$ response, (B) Viscosity response. It was found for region of the optimum (black area), maximum conversion and viscosity of 0.61 $g.g^{-1}$ and 24,000 cP, respectively.

Figure 2 shows the variation of Oxygen Transfer Coefficient for different combinations of X_1 and X_2. It should be noted that higher K_La can be obtained by increasing the agitation speed and aeration. A second ordered polynomial model was fitted and optimum conditions were estimated (Equation 6). Furthermore, the magnitudes of coefficients indicated that the agitation has more positive linear influence than the aeration.

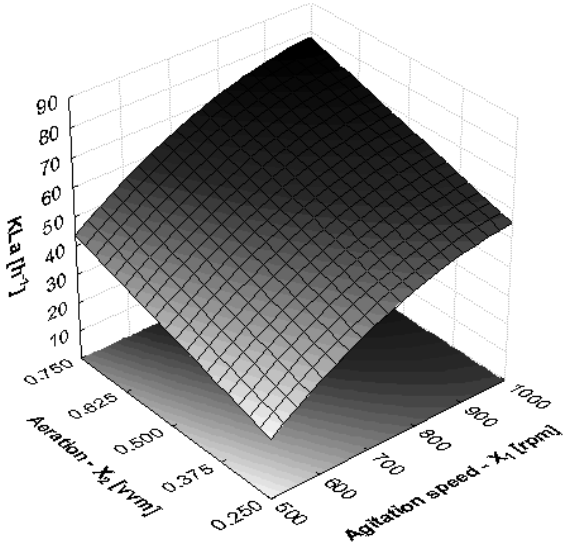

Figure 2 – 3D Plots of response surface optimization experiment results: the effect of agitation speed and aeration on the Oxygen Transfer Coefficient (K_La).

Figure 3 represents a typical correlation graph of the amount of oxygen dissolved with the time for different agitation speeds and aeration rates. The angular coefficient of the straight lines gives the K_La value for each assay.

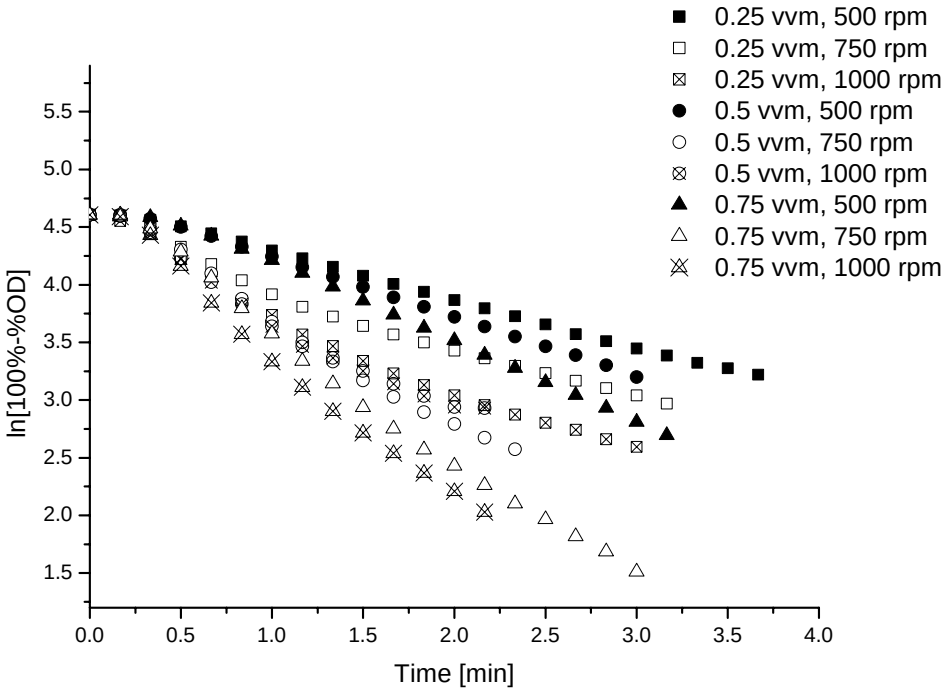

Figure 3 – Oxygen Transfer in function of the aeration rate (0.25, 0.50, 0.75 vvm) and agitation speed (500, 750, 1,000 rpm).

Table 2 shows the kinetic parameters determined in the optimized conditions of aeration and agitation speed in the factorial project 3^2. The variability between the studies can be explained hypothetically by differences in correlated factors, including the strain selected,

C/N relationship, nitrogen source, agitation speed, aeration rate, pH control in the medium, and the use of complex mediums, such as sugar cane broth. In addition, it is difficult to characterize complex fermentation processes.

Table 2 – Comparison of kinetic constant values from modeling and the literature.

Parameters	Assay in the optimized condition	Weiss & Ollis (1980)	Pinches & Pallent (1986)	García-Ochoa et al. (1990)	Serrano-Carreón et al. (1998)	Letisse et al. (2003)
μ_{max} [h^{-1}]	0.429 ± 0.037	0.152	0.29	0.110	0.25	0.38
X_{max} [g/L]	2.665 ± 0.094	2.450	2.15	1.790	4.42	3.30
α [gS/gX]	0.334 ± 0.091	2.00	1.24	14.286	3.03	3.23
β [gS(gX h)$^{-1}$]	0.529 ± 0.067	0.284	0.24	0.120	0.26	0.36
m [gP/gX]	0.120 ± 0.055	1.830	0.47	10.00	2.00	0.50
λ [gP(gX h)$^{-1}$]	0.342 ± 0.041	0.155	0.13	0.003	0.25	0.23

The kinetic study was accomplished for the point found experimentally by design. A fourth order Runge-Kutta algorithm was coupled to the non-linear regression method to derive the solutions for the differential equations 1, 2, and 3. The kinetic parameter values determined in this study were within the ranges reported in the literature, as shown in Table 2. Except α (associated growth terms), the others parameters were closest to those cited by Letisse et al. (2003). In the Figure 4, when the experimental data are compared to the quantitative responses predicted by the Weiss and Ollis model, there is a high degree of correspondence suggesting a good model fit.

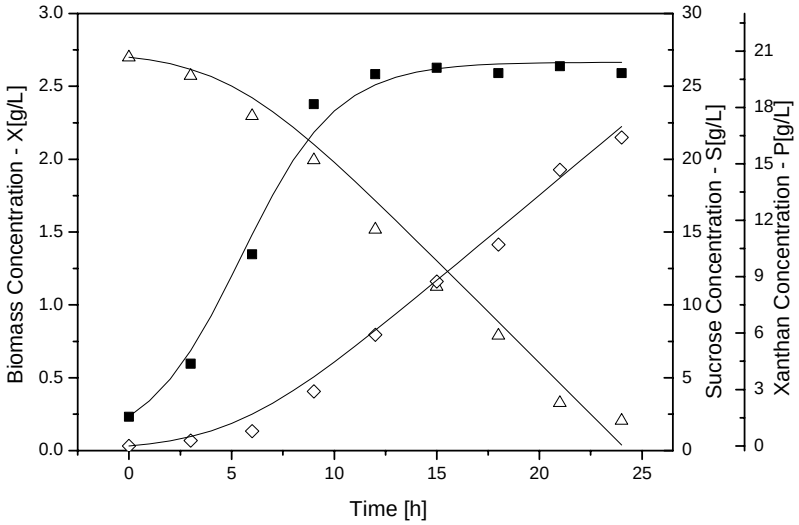

Figure 4 – Change in the concentration of microbial biomass (■), sucrose (Δ), and xanthan gum (◇). Symbols represent the experimental results; lines represent the Verhulst-Pearl (V-P) and Luedeking-Piret (L-P) kinetic model data.

4 - Conclusion

Therefore, this paper goal the optimization of the process variables in the xanthan gum biosynthesis from the sugar cane broth. The adjusted statistical models for the studied responses represented the experimental data accurately. The results show that higher levels of xanthan gum can be produced on the central point and optimum region of operation when the variables evaluated were agitation speed and aeration. Regarding the kinetic study, the Weiss and Ollis model adjusted the experimental data satisfactorily for the cellular growth, the substrate consumption and the product formation.

References

De Vuyst, L., Vermiere, A., Van Loo, J. & Vandamme, E. J., (1987). Nutritional, physiological and process technological improvements of xanthan fermentation process. *Met. Fat. Lundbouww. Rijkuniv. Genr.*, 52, p. 1881 – 1900.

García-Ochoa, F., García-León, M. A., Romero, A., (1990). Kinetic modeling of xanthan production from sucrose. *Chemical and Biochemical Engineering*, 4, 15 – 20.

García-Ochoa, F., Santos, V. E., Alcon, A., (1995). Xanthan gum production: An unstructured kinetic model, *Enzyme and Microbial Technology,* 17, 206 – 217.

García-Ochoa, F., Santos, V. E., Casas, J. A., Gómez, E. (2000). Xanthan gum: production, recovery, and properties – Research review paper, *Biotechnology Advances* 18, p. 549 – 579.

Harcum, S. W., Yoo, S. D. (1999). Xanthan gum production from waste sugar beet pulp, *Bioresource Technology*, v. 70, 105 – 109; short communication.

Letisse, F., Lindley, N. D. & Roux, G. (2003). Development of a phenomenological modeling approach for prediction of growth and xanthan gum production using *Xanthomonas campestris*. *Biotechnology Progress*, 19, 822 – 827.

Luedeking, R., Piret, E. L., (1959). A kinetic study of the lactic acid fermentation: batch process at controlled pH. *Journal of Biochemistry, Microbiology and Technological Engineering*, 1, 393 – 412.

Moraine, R. A. & Rogovin, P. (1971). Xanthan biopolymer production at increased concentration by pH control. *Biotechnology Bioengineering,* 13, 381 – 391.

Pinches, A., Pallent, L. J., (1986). Rate and yield relationships in the production of xanthan gum by batch fermentations using complex and chemically defined growth media. *Biotechnology Bioengineering,* 28, 1484 – 1496.

Pons, A., Dussap, C. G., Gros, J. B., (1990). Xanthan batch fermentation: compared performances of a bubble column and a stirred tank fermentor. *Bioprocess Engineering*, 5, 107 – 114.

Pradella, J. G. C., (2006) Biopolímeros e Intermediários Químicos, Centro de Gestão e Estudos Estratégicos, Relatório Técnico nº 84 396–205, Laboratório de Biotecnologia Industrial - LBI/CTPP, São Paulo, 119p.

Ramírez, M. E., Fucikovsky, L., García-Jiménez, F., Quintero, R., Galindo, E. (1988). Xanthan gum production by altered pathogenicity variants of *Xanthomonas campestris*. *Applied Microbiology and Biotechnology*, 29, 5 – 10.

Rosalam, S., England, R. 2006. Review of xanthan gum production from unmodified starches by *Xanthomonas comprestris sp*. *Enzyme and Microbial Technology* 39 (2), 197 – 207.

Serrano-Carreón, L., Corona, R. M., Sánchez, A., Galindo, E. (1998). Prediction of xanthan fermentation development by a model linking kinetics, power drawn and mixing. *Process Biochemistry*, 33 (2), 133 – 146.

Skaracis, G. N., Kalogiannis, S., Iakovidou, G., (2003). Optimization of xanthan gum production by *Xanthomonas campestris* grown in molasses, *Process Biochemistry* 39, 249 – 256.

Weiss, R. M. & Ollis, D. F. (1980). Extracellular microbial polysaccharides. Substrate, biomass, and product kinetics equation for batch xanthan gum fermentation. *Biotechnology Bioengineering*, 22, 859 – 873.

Acknowledgments: The authors wish to thank the CNPq, FAPERJ and FAPEMIG - Brazil for its financial support.

Proceedings of the 10th International Chemical and
Biological Engineering Conference - CHEMPOR 2008
Braga, Portugal, September 4-6, 2008
E.C. Ferreira and M. Mota (Eds.)

A new strategy for xylanase production using wheat straw autohydrolysis liquor as substrate

Michele Michelin[1,2], Maria de Lourdes T. M. Polizeli[2], Denise S. Ruzene[1], Daniel P. Silva[1], António A. Vicente[1], João A. Jorge[2], Héctor F. Terenzi[2], José A. Teixeira[1*]

[1] IBB - Institute for Biotechnology and Bioengineering, Centre of Biological Engineering, University of Minho, Campus de Gualtar, 4710-057 Braga, Portugal.
[2] Department of Biology, Faculty of Philosophy, Sciences and Letters of Ribeirão Preto, University of São Paulo, 14040-901 Ribeirão Preto-SP, Brazil.

Keywords: Xylanase, Wheat straw, Wheat bran, Autohydrolysis liquor, Fermentation
Topic: Multi-scale and/or multi-disciplinary approach to process-product innovation

Abstract

Agro-industrial residues are lignocellulosic materials with a high content of cellulose, hemicellulose and lignin. If such residues can be produced in bioprocesses (e.g. xylanase production) there is an attractive possibility of their integral use in biotechnological processes. In general, xylanase biosynthesis is induced by its substrate – xylan, but the high xylan content of some wastes such as corn cobs and wheat bran makes them an accessible and cheap source of inducers. Another alternative to improve the xylanase production, which is the main goal of this work, is the treatment of lignocellulosic materials in autohydrolysis processes which, under optimized conditions, lead to the solubilization of hemicelluloses (liquid phase, liquor) that may be favorable to xylanase production. The inclusion of these components in the nutrient medium composition can be a strategy to optimize the microbial xylanase biosynthesis. The best conditions for xylanase production were observed when the microorganism was cultivated in birchwood xylan for 6 days; however, satisfactory results were obtained using a combination of 1% wheat bran with 2% or 10% autohydrolysis liquor, for 5 days fermentation, once the xylanase production was around 86-87% of production with xylan. Besides, the obtained production with 100% wheat straw autohydrolysis liquor was also interesting, once after 7 days of cultivation, the xylanase production was higher than the ones obtained with wheat bran or by the combination of wheat bran and liquor.

1 Introduction

The hemicelluloses are a large group of high molecular polysaccharides, insoluble in water but soluble in alkaline solutions. These polysaccharides are associated with cellulose and lignin and play an important structurally-supportive role in building up of plant cell walls (Nakamura, 2003). The composition of hemicelluloses, includes branched heteropolymers of pentoses (xylose, arabinose), hexoses (mannose, galactose, glucose), and uronic acids. Xylan is the major constituent of hemicellulose and the second most abundant renewable resource with a high potential for degradation to useful end-products. Microbial xylanases (1,4-β-D-xylan xylanohydrolase, EC 3.2.1.8) are the preferred catalysts for xylan hydrolysis due to their high specificity, negligible substrate loss and side product generation. During the last decades, xylanases have attracted considerable research interest because of their potential industrial applications (Chen et al., 1997; Yuan et al., 2004).

* Corresponding author. Tel +351-253-604406. E-mail: jateixeira@deb.uminho.pt

The enzyme hydrolysis of xylan lies in the basis of its utilization as an energy source in animal feed or in different biotechnological processes (Coughlan and Hazlewood, 1993; Kulkarni et al., 1999; Subramanyan and Prema, 2002). The partial enzyme hydrolysis of xylan changes its physical and chemical properties, which concerns the quality of different products of the food and flavour industry. Xylanase finds applications in fruit juices and wines clarifying (Colins et al., 2005; Coughlan and Hazlewood, 1993). In brewing, xylanase is applied in filtering improvement (Yin et al., 2005). The utilization of xylanase in bread-making significantly improves the desirable texture, loaf volume and shelf life of bread (Courtin and Delcour, 2002). Xylanase enzyme preparations are also widely used in bio-bleaching in paper industry. They facilitate the delignification of the plant pulp in the production of high-quality paper. In that way, the chlorine-containing bleaching agents, that are a serious ecological problem, can be reduced (Gupta et al., 2000).

The industrial production of xylanase preparations is based on a microbial biosynthesis. Most often industrial xylanase producing strains moulds of the species *Aspergillus sp.* and *Trichoderma sp.*, as well as bacterial strains of the species *Bacillus sp.*, are used. There are two possibilities for cultivation of microbial enzyme producing strains: solid-state and submerged cultivation (Gawande and Kamat, 1999). At the present moment, the submerged cultivation is more widely used, allowing a higher degree of processes intensification and a better level of automation. Xylanases from moulds are extracellular, inducible enzymes. That determines the great significance of nutrient medium selection. The xylanase biosynthesis is induced by its substrate – xylan (Subramanyan and Prema, 2002; Kulkarni et al., 1999). The high xylan content of some of the wastes such as corn cobs and wheat bran makes them an accessible and cheap source of inducers. Annually about seven million tonnes of wastes are deposited from the member-countries of the EU, in the form of corn and wheat bran (Bonnin et al., 2001). The inclusion of these components in the nutrient media composition is the main strategy in microbial xylanase biosynthesis (Davidov and Atev, 1996).

Besides, treatments of lignocellulosic materials in aqueous media (autohydrolysis or hydrothermal treatments) under optimized conditions lead to the solubilisation of hemicelluloses, leaving a solid phase enriched in both cellulose and lignin (Garrote et al., 1999). This solid phase can be subjected to further processing to obtain a variety of commercial products, e.g. enzymatic hydrolysis and further fermentation of hydrolyzates (Rivas et al., 2004), allowing an integrated use of the raw material; in turn, the liquid phase can be used to optimize the microbial biosynthesis of enzymes. Thus, in this work, the performance of wheat straw autohydrolysis liquor as adjunct in medium containing wheat bran for xylanase production in submerged cultivation of the strain *Aspergillus terricola* was evaluated.

2 Materials and methods

Material

Wheat residues (wheat bran and wheat straw) were kindly supplied by a local farmer (Portugal). The wheat bran stored at room temperature and the wheat straw (material for autohydrolysis in this work), after being dried at 40 ºC in an oven for 12 h, was cut into small pieces (1-3 cm), milled in a knives mill to pass through a 0.4 mm screen (for chemical composition) and 1.0 mm (for hydrothermal pre-treatments).

Liquor obtaining: wheat straw autohydrolysis treatment

Wheat straw samples and water were mixed in a closed and pressurized vessel in order to obtain a liquid/solid ratio of 10:1 w/w. The system was heated to 200 ºC during 30 min. The liquid phase or liquor (hemicelluloses rich fraction) was separated from the solids by filtration. The hemicelluloses were then precipitated with three volumes of 95% ethanol (20 °C, 24 h) and dried for yield determination (4.9%), or used directly as liquid substrate.

Microorganism and fermentation runs

The microorganism used in this work was the fungal strain *Aspergillus terricola* Marchal. This fungus was colleted on *campus* Ribeirão Preto of São Paulo University (Brazil), in an area near to laboratory of Microbioly and Cellular Biology, on Biology department of Faculty of Philosophy, Sciences and Letters for Michele Michelin, and identified by the fungal collection of Pernambuco Federal University (Brazil). This fungus was maintained at 30 °C, on slants of solid PDA media (Difco). Conidia from 7- day-old cultures, with cell concentration of 2×10^7 cells.mL^{-1}, were inoculated into 250 ml Erlenmeyer flasks containing 50 ml of the liquid medium described by Vogel et al. (Vogel et al., 1964), pH 6.0, containing the carbon source: 1% (w/v) birchwood xylan; 1% (w/v) wheat bran; 100% (v/v) wheat straw autohydrolysis liquor; combination of 1% (w/v) wheat bran and 2% (v/v) wheat straw autohydrolysis liquor; and combination of 1% (w/v) wheat bran and 10% (v/v) wheat straw autohydrolysis liquor. The cultures were incubated at 30 °C, for 100 rpm, a maximum of seven days. During fermentations, samples were taken in specified intervals and both the mycelia and residues were removed by centrifugation at 10000 g for 15 minutes. The filtrates were used as the source of crude extra-cellular xylanase and β-xylosidase.

Figure 1 shows a scheme for the production of wheat straw autohydrolysis liquor, extraction of hemicelluloses from ground wheat straw.

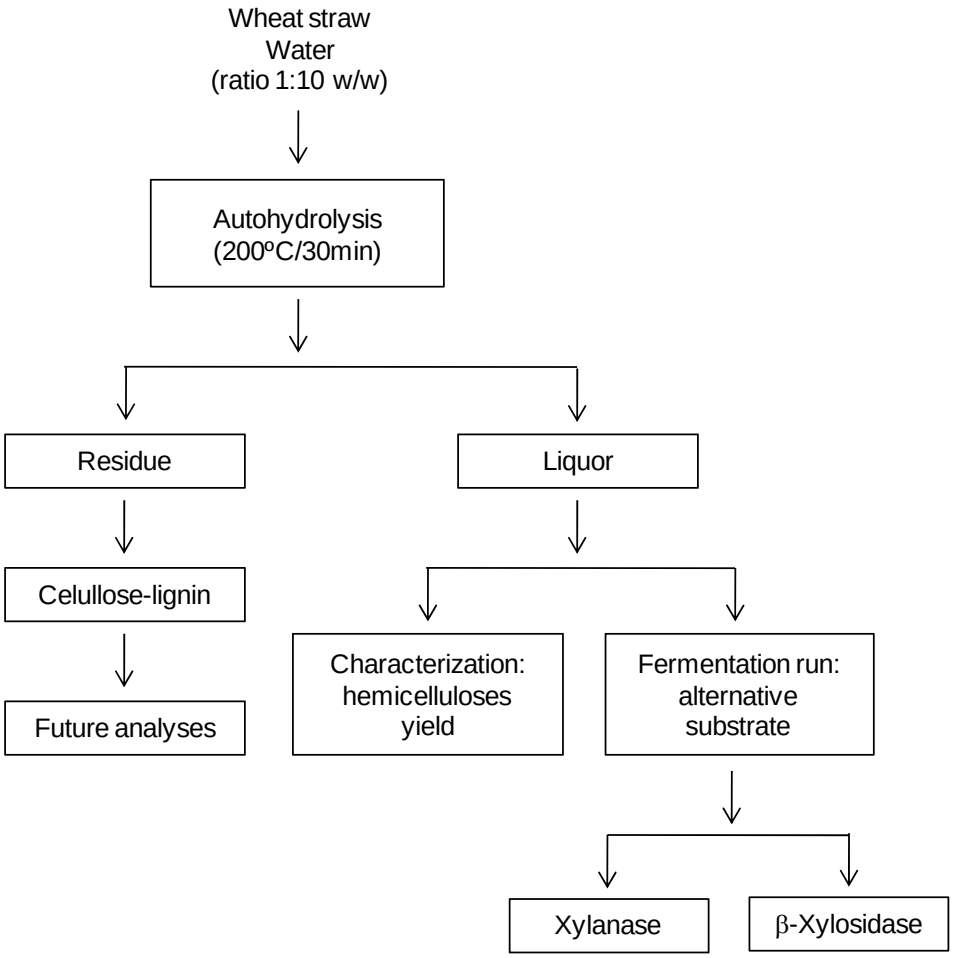

Figure 1. Scheme for extraction of hemicelluloses from ground wheat straw

Activity determinations

Xylanase activity was assayed using 1% (w/v) of birchwood xylan (Sigma, St. Louis, MO, USA) as substrate. Reaction mixtures contained 0.2 ml enzyme and 0.2 ml 1% xylan solution in citrate-phosphate buffer, pH 6.0 (Vilela et al.,1973). The mixture was incubated at 60ºC, and after predetermined periods the released reducing sugars were estimated with 3,5-dinitrosalicylic acid (DNS), using xylose as standard (Miller, 1959). One unit of xylanase activity was defined as the amount of enzyme that released 1 μmol product per minute under the conditions of the assay.

β-Xylosidase activity was assayed using 0.25% (w/v) of *p*-nitrophenyl-β-D-xylopyranoside (PNP-xyl) as substrate. Reaction mixtures containing 0.2 ml enzyme, 0.15 ml citrate-phosphate buffer, pH 4.5 (Vilela et al., 1973) and 0.05 ml 0.25% PNP-xyl in distilled water. The mixture was incubated at 70ºC, and after predetermined periods the released *p*-nitrophenolate were estimated with saturated sodium tetraborate solution, using *p*-nitrophenol as standard. One unit of β-xylosidase was defined as the amount of enzyme that released 1 μmol of product per minute under the conditions of the assay.

3 Results and discussion

Several fungal industrial production processes use complex media, consisting of agricultural byproducts as corn steep liquor, peanut flour, sugar beat molasses, pharma medium, etc. These media are inexpensive and yield much higher productivity than synthetic ones. The particular polymer (cellulose, hemicellulose, starch, protein), which often forms a suspension in the complex cultivation medium, serves as an inducer for the formation of hydrolyzing enzymes. This is the case for the production of xylanase, which is induced by xylan, an integral component of wheat bran (Adolph et al., 1996).

In our work, and according to Figure 2, the best conditions for xylanase production were observed when the microorganism was cultivated in birchwood xylan during 6 days of incubation. However, when on industrial level, this substrate become impracticable because of its high cost. In this context, the use of residues as well as its subproducts become very atractive. Besides, the use of wheat bran as inducer for xylanase production was very good (around 82% of production verified with xylan). However, the use of combinations of wheat bran and wheat straw autohydrolysis liquor, as well as only autohydrolysis liquor was superior that obtained with only wheat bran, once that with 5 days of fermentation the production obtained with combinations of wheat straw autohydrolysis liquor was of 86-87% when compared with birchwood xylan; and the prodction of xylanolytic enzymes using 100% liquor as adjunt on fermentation during seven days was 88% of production obtained with xylan

The fermentation process was conducted during 7 days; however in this period the xylanase production was still being induced by the wheat straw autohydrolysis liquor. Thus, with this result two conclusions were taken: (i) xylanase production can be improved in periods longer than 7 days when using autohydrolysis liquor; and (ii) it is possible that the induction of xylanases using wheat straw autohydrolysis liquor, produced under different conditions of time and temperature, can be more favorable for xylanase production, once the enzymic production started with 5 days of incubation (Figure 2). These results suggest the presence of short xylooligosaccharides on wheat straw autohydrolysis liquor, being that the use of wheat straw autohydrolysis liquor that posses xylooligosaccharides higher perhaps can be more favorable to xylanase induction.

Thus, by temperature control and reaction time it is possible to influence characteristics of the xylo-oligosaccharides such as the acetyl content and the molar mass distribution (Nabarlatz et al., 2004, 2005), but the nature of the raw material has also a significant role.

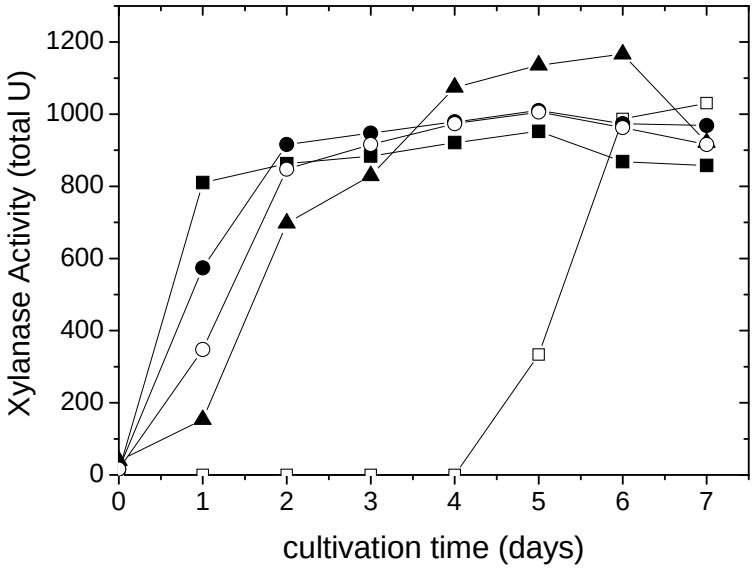

Figure 2. Performance of *A. ochraceus* during fermentation for xylanase production using different carbon sources: 1% (w/v) birchwood xylan (-▲-), 1% (w/v) wheat bran (-■-), 100% (v/v) wheat straw autohydrolysis liquor (-□-), combination of 1% (w/v) wheat bran and 2% (v/v) wheat straw autohydrolysis liquor (-●-), and combination of 1% (w/v) wheat bran and 10% (v/v) wheat straw autohydrolysis liquor (-○-)as adjunct. The microorganism was cultivated at 30ºC, 100 rpm.

4 Conclusion

Wheat straw autohydrolysis liquor showed to be promising as adjunct in xylanase and β-xylosidase production processes by filamentous fungi. This suggests that studies of liquor preparation under more convenient times and temperatures can result in a liquor more appropriated to the production of xylanolytic enzymes. This process is very attractive due to the use of residues (such as wheat straw) and also due to its low cost, therefore adding value to final product.

Acknowledgements

Biota FAPESP (Brazil); FCT (Portugal).

References

Adolph, S., Muller, S., Siedenberg, d., Jager, H.L., Schugerl, K., Giuseppin, M. (1996). Cultivation of *Aspergillus awamori* on wheat bran: Ultrastructural description of growth and localization of xylanase by immunogold labeling. Journal of Biotechnology, 46:221-234.

Chen, C., Chen, J.L., Lin, T.Y. (1997). Purification and characterization of a xylanase from *Trichoderma longibrachiatum* for xylooligosaccharide production. Enzyme and Microbial Technology, 21:91–96.

Bonnin, E., Brunel, M., Gouy, Y., Lesage-Meesen, L., Asther, M., Tribault, J.F. (2001). *Aspergillus niger* I-1472 and *Pycnoporus cinnabarinus* MUCL 39533, selected for the biotranformation of ferulic acid to vanilin, are also able to produce cell wall polysaccharidedegrading enzymes and feruloyl esterases. Enzyme and Microbial Technology, 28:70–80.

Colins, T., Gerday, C., Feller, G. (2005). Xylanases, xylanase families and extermophilic xylanases. FEMS Microbiology Letters, 29:3–23.

Coughlan, M., Hazlewood, G. (1993). β-1,4-D-xylan-degrading enzyme systems: biochemistry, molecular biology and applications. Biotechnology and Applied. Biochemistry, 17:259–289.
Courtin, C.M., Delcour, J.A. (2002). Arabinoxylans and endoxylanases in wheat flour bread-making. Journal of Cereal Science, 35:225–243.
Davidov, E.R., Atev, A. (1996). Method for production of enzyme preparation. Patent number Ru 2057179 C1.
Garrote, G., Domínguez, H., Parajó, J.C. (1999). Hydrothermal processing of lignocellulosic materials. Holz Roh Werk., 57:191–202.
Gawande, P., Kamat, M. (1999). Production of *Aspergillus* xylanase by lignocellulosic waste fermentation and its application. Journal of Applied Microbiology, 87:511–519.
Gupta, S., Bhushan, B., Hoondai, G.S. (2000). Isolation and characterization of xylanase from *Staphylococcus sp.* SG-13 and its application in biobleaching of kraft pulp. Journal of Applied Microbiology, 88:325–334.
Kersters-Hilderson, H., Claeyssens, M., Doorslaer, E.V., Saman, E., Bruyne, C.K (1982). β-D-xylosidase from *Bacillus pumilus*. Methods in Enzymology, 83: 631-639.
Kulkarni, N., Shendye, A., Rao, M. (1999). Molecular and biotechnological aspects of xylanases. FEMS Microbiology Letters, 23:411–456.
Lowry, O.H., Rosebrough, N.J., Farr, A.L., Randall, R.J. (1951). Protein measurement with the folin phenol reagent. Journal of Biological Chemistry, 193:265-275.
Miller, G. L. (1959). Use of dinitrosalicylic acid reagent for determination of reducing sugar. Analytical Chemistry, 31:426-428.
Nakamura, S. (2003). Structure and function of a multiplidomain alkaline xylanase from alkaliphilic *Bacillus sp.* strain 41M-1. Catalysis Surveys from Asia, 7:157–164.
Nabarlatz, D., Farriol, X., Montané, D. (2004). Kinetic modeling of the autohydrolysis of lignocellulosic biomass for the production of hemicellulose-derived oligosaccharides. Industrial and Engineering Chemistry Research, 43:4124-4131.
Nabarlatz, D., Farriol, X., Montané, D. (2005). Autohydrolysis of almond shells for the production of xylooligosaccharides: product characteristics and reaction kinetics. Industrial and Engineering Chemistry Research, 44:7746–7755.
Rivas, B., Moldes, A.B., Domínguez, J.M., Parajó, J.C. (2004). Lactic acid production from corn cobs by simultaneous saccharification and fermentation: a mathematical interpretation. Enzyme and Microbial Technology, 34:627–634.
Subramanyan, S., Prema, P. (2002). Biotechnology of microbial xylanases: Enzymology, molecular biology and application. Critical Reviews in Biotechnology, 22:33–64.
Villela, G.G., Bacila, M., Tastaldi, H. (1973). Técnica e experimentos de bioquímica. Ed. Guanabara Koogan, p.523.
Vogel, H.F. (1964). Distribution of lysine pathways among fungi: evolutionary implications. American Naturalist, 98:435-446.
Yin, L., Jian, L., Guoxian, G., Zhonping, S., Zhongui, M. (2005). Studies on water-extractable arabinoxylans during malting and brewing. Food Chemistry, 93:33–38.
Yuan, Q.P., Zhang, H., Qian, Z.M., Yang, X.J. (2004). Pilot-plant production of xylo-oligosaccharides from corncob by steaming, enzymatic hydrolysis and nonofiltration. Journal of Chemistry and Technology Biot., 79:1073–1079.

Proceedings of the 10th International Chemical and
Biological Engineering Conference - CHEMPOR 2008
Braga, Portugal, September 4-6, 2008
E.C. Ferreira and M. Mota (Eds.)

Approach Model for Simulation of the Starch Hydrolysis by α-Amylase and Alcohol Production from Manioc Root Starch

José Carlos Curvelo-Santana[1, 2], André Felipe H. Librantz[1], Elias Basile Tambourgi[2*]

[1]Department of Exact Sciences (DCE), Nine of July University (UNINOVE), São Paulo, Brazil. [2]Department of Engineering of Chemical Systems, School of Chemical Engineering, State University of Campinas, University Campus "Zeferino Vaz", Av. Albert Einstein, 500, Post Code: 6066, Zip Code: 13081-970, Barão Geraldo,Campinas, SP, Brazil.

Key-words: starch, manioc roots, alcohol, kinetic model.
Topic: Integration of life sciences & engineering

Abstract: This work shows optimal conditions of using the amylases from *A. niger* in starch hydrolysis and alcohol production from manioc root starch. Bioreactors contained manioc starch at 10 and 20 g/L of concentration on temperatures of 35 and 55°C, at pH 4.8 were made for evaluation of effects of starch concentration and temperature on hydrolysis yield. New models for starch hydrolysis kinetic were fitted; for substratum dependence ([S]) to the hydrolysis time (t) and hydrolysis rate (V) dependence with the substratum concentration ([S]). Results showed that exponential models fitted more than other models. Fitting model were $[S] = e^{-kt}$ and $V = e^{\frac{V_{max}}{K_M}[S]}$, while k, V_{max} and K_M are kinetic constant, maxim velocity and Michaelis-Menten constant, respectively. These models possible to simulate the hydrolysis process by amylases and its scale-up of this process. On starch hydrolysis, it perceived that in optimal condition the mean yield got 70%. After fermentation an alcohol yield above of 45% was gotten (the theoretical is 51.1%). This work showed as to obtain alcohol of manioc root starch, as alternative to the substitution of the sugar-cane juice in alcohol production.

1 Introduction

The hydrolysis of starch to products with low molecular weight, catalyzed by amylases, is the most important commercial enzyme process. The hydrolyzed products are widely applied in food, paper, and textile industries (Konzula and Liakopoulon-Kyriakides, 2004). Because of the increasing demand for these enzymes in various industries, there is enormous interest in developing enzymes with better properties, such as raw starch degrading amylases suitable for industrial applications and their cost-effective production techniques.

Being a renewable fuel and a lower pollutant when compared with petroleum fuels, ethylic alcohol is a combustible car fuel widely used in Brazil, and is desired by various countries. Recently, a search for new energetic sources was unleashed after the pronounced governing of various countries on a possible energetic crisis. At present, Brazil is in search of methods that will increase the ethanol offer by production of the combustible alcohol (Oliveira and Vasconcelos, 2006). Starch, the main reserve carbohydrate of several crops, is highly abundant in nature and can be easily extracted with high purity and at low cost (Cereda et al., 2001). Recently, a search for new energetic sources was unleashed after the pronounced governing of various countries on a possible energetic crisis.

Thus, it shows the optimal conditions to produce fermentable syrup from manioc starch and as a potential substitute to sugarcane in alcohol production. The food industry is using starch for a long time as ingredient because of its functional properties.

* Corresponding author, E-mail: eliastam@feq.unicamp.br, Phone: 55+19+ 3521-3952

Modeling and optimization of processes are good tools for knowing and reducing of costs of industrial processes. Thus, in this work aimed to make a new model to simulate the hydrolysis processes by amylases from *Aspergillus niger* for alcohol production from manioc root starch

2 Material and Methods

2.1 Making of Bioreactors

Bioreactors contained 10 and 20 g/L of Starch concentration, at pH 4.8 and temperatures of 35 and 55°C were made, for evaluation of effects of starch concentration and temperature on hydrolysis yield. Total volumes of bioreactors were of 25 mL and they are heated on water bather. After temperature equilibrium had got in bioreactor, 0.5 mL of α-amylases (Forilase NTL®) from *Aspergillus niger* provided by Cognis (São Paulo, Brazil) were added. Total protein contents of Forilase NTL® measured by Bradford (1976) was of 11,214 mg/mL, so, total protein content on bioreactor, $[E]_0$ was of 0.2243 mg/mL or 0.2243 g/L. Glucose concentration released was measured time to time by DNS method (Miller, 1959).

2.2 Hydrolysis scale-up

Optimal condition of starch concentration and processing temperature from micro-scale study was used in hydrolysis scale-up. The experiment of starch degradation was assayed in a bioreactor with 2 L of total volume, with mechanic agitator for mixing, and a jacket for heating at operation temperatures. Bioreactors were operated in boat-load, contained 1 L of manioc starch solution, and 20 mL of Forilase NTL® enzymatic solutiont, at constant agitation of 70 rpm and pH 4.8, as it is shown in Figure 1 (Ferreira et al., 2005; Konzula and Liakopoulon-Kyriakides, 2004; Marshal et al., 1999). The glucose concentration ($C_{Glucose}$, g/L) released into bioreactor was measured by DNS method (Miller, 1959). Theoretical glucose concentration ($C_{Starch\ glucose}$, g/L) contained in manioc starch is given in Equation 1 and the hydrolysis yield (Y, %) is given in Equation 2, as follows:

$$C_{Starch\ \ glu\cos e} = \left(\frac{180}{162}\right) * C_{Starch} \qquad (1) \text{ and } Y = \left(\frac{C_{Glu\cos e}}{C_{Starch\ \ glu\cos e}}\right) * 100 \qquad (2)$$

Where 162 and 180 are molecular masses of dextrin monomers and glucose, respectively, and C_{Starch} is the starch concentration into bioreactor (Ferreira et al., 2005; Sleiman and Venturi Filho, 2004).

Figure 1. Bioreactor photo used in hydrolysis assays of manioc starch by amylases from maize malt.

2.2 Modeling of process

New models for starch hydrolyses can be proposed, with base in Michaelis-Menten model for first order kinetics. It uses some considerations to M-M model, showing into Equations 3 and 4, and they were fitted by non linear methods using Origin 6.0 ® software.

Following model had been adjusted to simulate the dependence of [S], the starch, to hydrolysis time (t):

$$[S] = [S]_{eq} + ([S]_0 - [S]_{eq}) * e^{-kt} \qquad (3)$$

While: $[S]_{eq}$ and $[S]_0$ are equilibrium and initial substratum concentrations, and *k* is the kinetic constant of product formation.

To simulate the dependence of conversion rate of starch to reduced sugar (-d[S]/dt = V) the following model was used:

$$V = e^{\frac{V_{max}}{K_M}[S]} \qquad (4) \qquad \text{and} \qquad V_{max} = k * [E]_0 \qquad (5)$$

Being V_{max} and K_M and $[E]_0$ are maxim velocity, Michaelis-Menten constant and initial enzyme concentration, respectively.

2.3 Alcohol production

Starch manioc syrup of optimal hydrolysis assay was used in must manufacture; where it was added and mixed 1 g of $(NH_4)H_2PO_4$, 0.1 g of $MgSO_4$ and sugar mass until obtaining of 50 g/L of total reduce sugar content. The pH was adjusted at 4.5. Fractions of approximately 10 mL, 100 mL and 1 L from the principal vat were distributed among different flasks, referred to as vessels. These were heated in an autoclave and cooled rapidly in running water with the sole objective of sterilization of the medium. *Saccharomyces cerevisae* yeast (Flashmman, Jundiaí -SP, Brazil) at 1 g/L was added into the first vessel (10 mL) and the fermentation process occurred for one day. The total volume of fermented was transferred to the second vessel (500 mL) and the fermentation process occurred for one day. After the end of fermentation in the second vessel, the fermented was transferred to the principal vessel (1 L) until full fermentation of must. All fermentation occurred at 27°C and samples were collected daily for alcohol, total and reducer sugar determinations (Cadogan and Hanks, 1995; Ferreira et al., 2005).

3 Results and Discussions

3 Hydrolysis study

From Table 1 note a hydrolysis yields were above to 45% and in the best condition (55°C and 10 g of starch/L) a yield of about 70% had been finding. According to Lima *et al.* (2001) a full starch hydrolysis is not possible by use of α and/or β-amylases, due these enzymes cannot braking of 1,6 binding of amilopectins. The yields obtained in this work were higher than others research works. For example, Ferreira *et al*. (2005 and 2006) cited yields of about 30% of starch hydrolysis in your work using maize malt amylases at 65°C. Neves *et al*. (2006) observed that increasing the temperature there was a reducing on the hydrolysis yield for trigo starch using microbial amylases. They found yields of about 27.3% at 55 °C and of 14.8% at 75 °C. Leonel and Cereda (2000) obtained a hydrolysis yield of manioc starch similar to Ferreira et al (2005 and 2006).

Table 1 Results of starch hydrolysis yields by amylases at pH 4.8.

Assays	C_{Starch} (g/L)	T (°C)	Y (%)
1	10	35	46.341
2	20	35	45.623

3	10	55	69.636
4	20	55	59.452

Table 2 and 3 show the parameters to the fitting models for knowing the dependence of substratum concentration on influence of reaction time and the dependence of conversion rate on influence of substratum concentration, respectively. As the correlations (R) are about 1.0, there are a good fitting of model to the experimental data, it the model may be used to predict the variation of substratum and glucose concentration into bioreactor in a scale-up of starch hydrolysis process.

Table 2 Parameters of fitting models for describe the dependence of substratum concentration with the hydrolysis time, for starch hydrolysis process by *A. niger* amylases at pH 4.8.

Assays	$[S]_{eq}$ (g/L)	$[S]_0$-$[S]_{eq}$ (g/L)	k (min^{-1})	R
1	5.3005	4.0040	46.950	0.9663
2	10.066	9.3453	53.998	0.9756
3	2.5592	5.7952	40.658	0.9322
4	8.3988	10.647	19.437	0.9726

Values of V_{max} were obtained from $[E]_0$ (0.2243 g/L) and k values substituted into Equation 5 and 4, as showing in Table 3. It observed an increase in *k* and V_{max} values to the starch concentration at 35°C and at 55°C, this behavior was inversed, due to the enzyme inactivation for long exposition time at high temperature. Minor K_M introduces a high affinity of enzyme to the substratum, it was found at 55°C (Forgaty and Kelly, 1979; Lima et al., 2001; Reguly, 2000; Wiseman, 1987).

Table 3 Parameters of fitting models for describe the dependence of conversion rate with the substratum concentration, for starch hydrolysis process by *A. niger* amylases at pH 4.8.

Assays	A	V_{max}/K_M	V_{max}	K_M	R
1	5.10^{-5}	1.0580	10.530	9.9528	0.8649
2	1.10^{-3}	0.3350	12.110	36.152	0.9964
3	3.10^{-4}	0.8461	9.1187	10.777	0.9556
4	$6.1.10^{-3}$	3.2610	4.3594	1.3368	0.9624

Figures 2 and 3 show the experimental and simulated starch hydrolysis processes at 35 and 55°C, respectively. It notes that the predicted and experimental data had similar behavior, it shows a good adjust of proposed models.

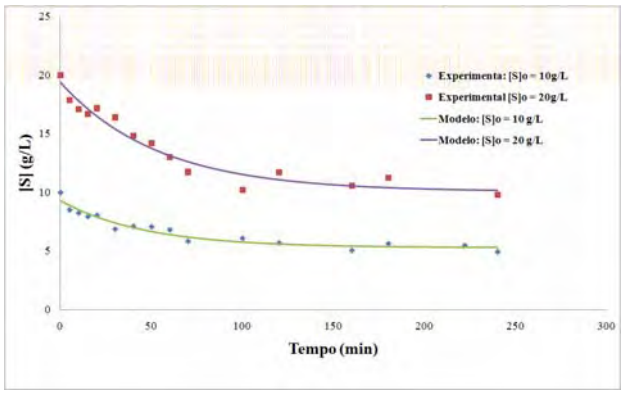

a

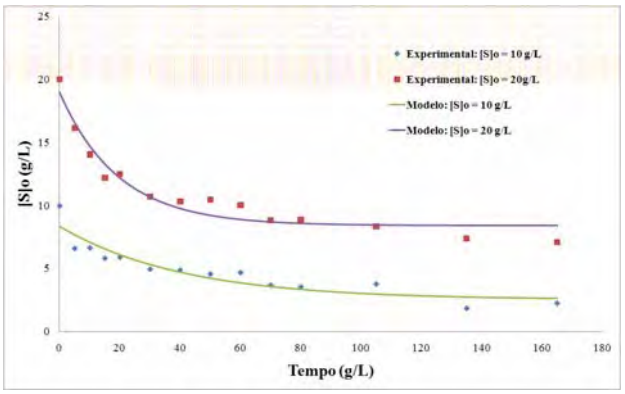

b

Figure 2. Experimental and simulated data, of behavior of substratum concentration ([S]) on influence of reaction time (t) at pH 4.8. a) at 35°C and b) at 55°C.

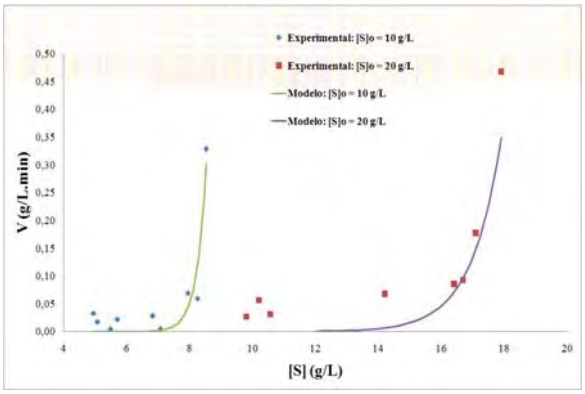

A

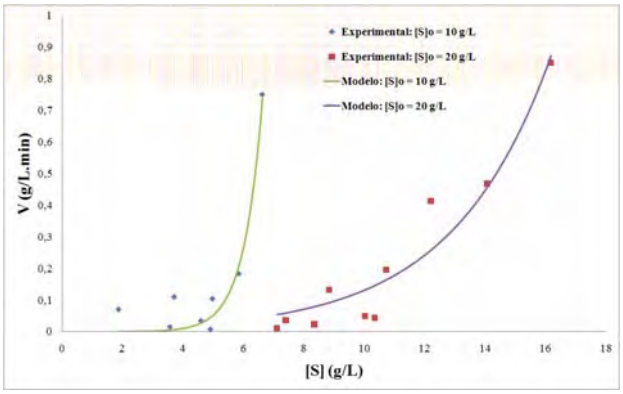

B

Figure 3. Experimental and simulated data to observe the behavior of conversion rate (V) on influence of starch concentration ([S]) at pH 4.8. a) at 35°C and b) at 55°C.

3.2 Fermentation

Figure 4 show the alcohol and reduce sugar varying to fermentation time, for the syrup must fermentation by S. cerevisae. After end fermentation process, an alcohol content of 3.4°GL and alcohol yield of 45% had found. This yield is high, for the maxim alcohol yield is of 51.11%, according to Ferreira et al. (2005 and 2006), Lima et al. (2001) and Reguly (2000). There was starch hydrolysis by amylase during the fermentation process, for the sugars produced of starch hydrolyses (amylase inhibitors) were consumed during fermentation time (Forgaty and Kelly, 1979; Lima et al., 20001; Reguly, 2000)

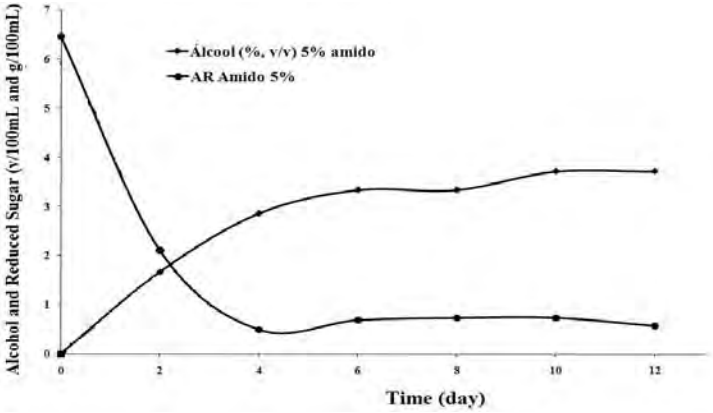

Figure 4. Curves of fermentation of manioc must.

Alcohol yield was more than 39% obtained by Ferreira *et al* (2005 and 2006) and more than 27% obtained by Neves et al. (2006).

4 Conclusions

Results showed that exponential models fitted more than other models. These models possible to simulate the hydrolysis process by amylases and its scale-up of this process. On starch hydrolysis, it perceived that in optimal condition the hydrolysis yield got 80%. After fermentation an alcohol yield above of 45% was gotten (the theoretical is 51.1%). This work showed as to obtain alcohol of manioc root starch, as alternative to the substitution of the sugar-cane juice in alcohol production.

References

Bradford, M. M. (1976). A rapid and sensitive method for the quantitation of microgram quantities of protein. Utilizing the principle of protein-dye binding. *Anal. Biochem.* 72, 248-254.

Cadogan, A. and Hanks, J. (1995) *Microbiology & Biotechnology: Biology Advances Studies*. 1st ed., Croacia: Ed. Nelson.

Cereda, M.P.; Franco, C.M.L.; Daiut. E.R. (2001). *General properties of Starch*, first edition, v.1, Fundação Cargill, Campinas, Brazil.

Ferreira, G. B.; Melo, V. V.; Almeida, J.B.O.; Evangelista, A. F.; Souza, R. R. (2005). Characterizing of obtaining process of a manioc spirit. *Braz. J. Food Technol*., 9, special issue, 2-7.

Ferreira, G.B; Melo, V. V.; Lopes, F. L. G.; Souza, R. R.; Santana, J. C. C.; Tambougi, E. B. (2006). Produção de Álcool a partir da Hidrólise do Amido de Mandioca por Amilases do Malte de Milho. *Revista SODEBRAS*, 10 (on line).

Fogarty, W. M. & Kelly, C. T. *Topics in Enzyme and Fermentation. Biotechnology*. Vol.3, J. Wiley and Sons, 1979.

Leonel, M. and Cereda, M. P. (2000). Avaliação da concentração de pectinase no processo de hidrólise-sacarificação do farelo de mandioca para obtenção de etanol. *Ciênc. Tecnol. Aliment*., 20, 2, on line.

Lima, U. A.; Aquarone, E. Borzani, W. E; Schmidell, W. (2001). *Processos Fermentativos e Enzimáticos.* Vol.3. 1ª ed., Série Biotecnologia Industrial. São Paulo: Ed. Edgard Blücher Ltda.

Miller, G. L. (1959). Use of dinitrosalicylic acid reagent for determination of reducing sugar. *Analytical Chemistry*, 31, 3, 426-428.

Neves, M. A.; Kimura, T.; Shimizu, N.; Shiiba, K. (2006). Production of alcohol by simultaneous saccharification and fermentation of low-grade wheat flour. *Brazilian Archives of Biology and Technology*, 49, 3, 481-490.

Oliveira, M. and Vasconcelos, Y. (2006). Revolução no canavial. *Pesquisa FAPESP* 122, 62-70.

Reguly, J. C. (1996). *Biotecnologia dos Processos Fermentativos,* Vol.1, EDUFPel.

Reguly, J. C. (2000) *Biotecnologia dos Processos Fermentativos: Produção de enzimas e Engenharia das fermentações*. Vol.2, Pelotas: EDUFPel.

Sleiman, M. and Venturi Filho, W. G. (2004). Utilização de extratos de malte na fabricação de cervejas: Avaliação físico-química e sensorial. *Braz. J. Food Tech.,* 7, 2, 145-153.

Wiseman, A. (1987). *Handbook of Enzyme Biotechnology*. 2ª ed., John Wiley Sons, New York, EUA.

Proceedings of the 10th International Chemical and
Biological Engineering Conference - CHEMPOR 2008
Braga, Portugal, September 4-6, 2008
E.C. Ferreira and M. Mota (Eds.)

RSM OPTIMIZATION OF FRACTIONAL PRECIPITATION AND CHARACTERIZING OF AMYLASE FROM MAIZE MALT

Joana Paula Menezes Biazus[1], Taís Ramaiana Silva Guimarães[1], José Carlos Curvelo Santana[2, 3], Santana; Roberto Rodrigues de Souza[1], Elias Basile Tambourgi[3*]

[1]Department of Chemical Engineering, Federal University of Sergipe, Brazil. [2]Department of Exact Sciences (DCE), Nine of July University (UNINOVE), São Paulo, Brazil. [3*]Department of Engineering of Chemical Systems, School of Chemical Engineering, State University of Campinas, Post Code: 6066, Zip Code: 13083-970, Barão Geraldo, Campinas, SP, Brazil.

Keywords: maize malt, purification, amylases, alcohol, acetone.
Topic: Integration of life sciences & engineering Suitable.

Abstract: This work aimed to purify the amylases from maize (*Zea mays*) malt by solvent precipitation and it biochemistry characterization. A 2^3 factorial planning was making to study the effects of pH, temperature and concentration and type solvent (alcohol or acetone) on the enzymes purification index. Malt was obtained by maize seed germination for five days on controlled home conditions. Larges recovery index were found for alcohol precipitation. Square model was the best fitting to description of amylase purification from maize malt by alcohol precipitation process. RSM showed that optimal condition to amylase precipitation was obtained at 10°C, on a pH 7 and 0.7 (w/w) of alcohol concentration, while a purification factor of 10 times was obtained. Optimal pH was obtained between 4.5 and 6.5 and optimal temperatures were of 50°C for β-amylase and 90°C for α-amylase and the values of K_M and V_{max} constants was of $7.69.10^{-2}$ g/L and $7.69.10^{2}$ g/L.min, respectively.

1 Introduction

The enzymes α-amylase (EC 3.2.1.1, α-1,4 glucan 4-glucanhydroxylase) and β-amylase (EC 3.2.2.1 α-1,4 glucan 4-malthydrolase) with a molecular weight of about 50 kDa, are exoenzymes that simultaneously degrade starch to produce glucose, maltose and boundary dextrins, which are much utilized in food industries (Aguilar et al., 2000; Biazus et al., 2005). Their optimum pH is 4.8 and 5.4 and optimum temperature is 75 °C and 55 °C, respectively. According to Sigma (1996), the price of amylases enzymes is about U$ 1,500/gram of purified material.

The partition coefficients of hydrolytic enzymes, α- and β-amylases and glucoamylase, of high purity, have been determined in PEG/dextran (Furuya et al., 1995 and 1996), PEG/$MgSO_4$ (Blásquez et al., 1998) and PEG/$CaCl_2$ (Curvelo-Santana, 2003) batch aqueous two-phase systems (ATPS). The influence of polymer, salt and initial enzyme concentration on partition was investigated in these studies. The experimental and correlated amylase concentration by method Flory-Huggins equation into PEG/dextran and PEG/$MgSO_4$ were measured between 0.04 and 0.97. Curvelo-Santana (2003) had concentred in 5-fold the α- and β-amylases from maize malt into PEG/$CaCl_2$ ATPS, and Gu and Glantz (2007) had concentrated in 3-folds for corn protein into PEG/NaCl ATPS. Nirmala and Muralikrishna (2003) had purified the amylase from malt of *Finge millet* by gel chromatography and 3-folds of recovery index had been found.

This work aimed to purify the amylases from maize (*Zea mays*) malt by solvent precipitation and it biochemistry characterization. A 2^3 factorial planning was making to study the effect of pH, temperature and solvent (alcohol or acetone) concentration on the enzymes recovery index.

2 Material and Methods

* Corresponding author, E-mail: eliastam@feq.unicamp.br, Phone: 55+19+ 3521-3952

2.1 Making of the maize malt

The maize seeds were selected, their weight was measured, and the seeds washed. The seeds were soaked in water until water absorption was 40–45% (w/w), and germinated in laboratory. The germination time was between 4–5 days. The maize malt was dried at 55°C and tritured. A 2% maize malt solution in phosphate buffer had been made (Biazus et al., 2005; Curvelo-Santana, 2003).

2.2 Enzyme assays

Amylase activities were measured according to DNS method (Miller, 1959). 20 mL of 2 % soluble starch at pH 4.8 (0.1 M acetate buffer) were hydrolyzed by 500µL of enzyme sample in 10 min at 30±2 °C (Biazus et al., 2005; Reguly, 1996). Total protein concentration was determined according to the dye binding method of Bradford (1976) with BSA as protein standard. One unit of enzyme activity was defined as µmol of glucose released per min under the assay conditions. The specific activity was calculated as activity for mg protein.

2.3 Fractional precipitation

Enzyme precipitations were released with alcohol or acetone solvents on controlled pH and temperature; at home pressure. For pH and temperature controls the 0.1M phosphate buffer and thermal batch had been used. Into assay tubes, volumes of maize malt solution and solvent were placed until a 10 mL of total volume had been got. Volumes of maize malt and solvents had been varied in the volumetric proportion (v/v) of according factorial design of Table 1. Activity and total protein were measured in crude and purified samples (Luccarini et al., 2005; Teotia et al., 2003).

2.4 Recovery index (IR)

Pirification eficience was measured using the recovery index (IR) calculated from theEquation 1.

$$\mathrm{IR} = \frac{\mathrm{SA}_{\mathrm{phase}}}{SA_{crude}} \qquad (1)$$

where $SA_{purified}$ is the specific activity (U/mg of protein) in the evaluated purified sample and SA_{crude} is the specific activity in *Zea mays* malt (U/mg of protein).

2.5 Experimental design

Orthogonal experimental designs by modified star methods was used in the optimization of amylase purification from maize malt by frational precipitation with alcohol or acetone solvents. Three factors were used: solvent concentration (x_1), precipiting temperature (x_2) and precipiting pH (x_3), and one response, the recovery index (IR). The assays are shown in Table 1; the level changed as follows: –1, 0, +1, and α = ± 1.414, with three repetitions in the center point (Barros Neto et al., 2001; Biazus et al., 2005).

$$x_1 = \frac{C_S - 0.5}{0.2} \qquad (2); \qquad x_2 = \frac{T - 20}{10} \qquad (3) \text{ and } x_3 = pH - 6 \qquad (4).$$

Where C_S and T are solvent concetration and precipiting temperatore.

The evaluation of the empiric models was performed by variance analysis (ANOVA) and optimization by response surface methodology (RSM) in the program Statistics for Windows 7.0 (Barros Neto et al., 2001). The planning design used to obtain the optimal condition for recovery of amylases from maize malt by fractional precipitation is shown in Table 1.

2.6 Enzyme characterization

The optimum pH of the enzyme was determined by measuring its activity, after 10 min of reaction, in the pH range varying among 3.0–10.0 at 30±2 °C. The optimum temperature was obtained by measuring its activity after 10 min, among 10 at 95±2°C,

using some soluble starch solution in 0.1 M acetate buffer at pH 4.8. Initial rates of starch hydrolysis were determined at various substrate concentrations (0.01–20 mg/mL). The kinetic constants K_m and V_{max} were estimated by Lineweaver–Burk method (Aguilar et al., 2000; Biazus et al., 2005; Nirmala and Muralikrishna, 2003; Reguly, 1996).

3 Results and Discussion

Table 1 shows experimental design used in this work, so as, its results for alcohol and acetone precipitation. It notes that the purification factors of alcohol precipitation were more than acetone precipitation, and only three assay of amylase purification by acetone precipitation had been effective. Thus, the RSM optimization will be make for alcohol precipitation, only.

Table 1 Experimental design and results to optimize the maize malt amylase precipitation.

Assays	C_S (v/v)	*T* (ºC)	*pH*	x_1	x_2	x_3	$IR_{Alcohol}$	$IR_{Acetone}$
1	0.3	10	5	-1	-1	-1	0.2867	0
2	0.7	10	5	1	-1	-1	3.0243	0
3	0.3	30	5	-1	1	-1	0	0
4	0.7	30	5	1	1	-1	0	4.0733
5	0.3	10	7	-1	-1	1	3.9617	5.9685
6	0.7	10	7	1	-1	1	9.6337	0.7446
7	0.3	30	7	-1	1	1	2.7312	0
8	0.7	30	7	1	1	1	0	0
9	0.5	20	6	0	0	0	1.0349	0
10	0.5	20	6	0	0	0	0	0
11	0.5	20	6	0	0	0	0	0
12	0.2	20	6	-1.682	0	0	0	0
13	0.8	20	6	1.682	0	0	3.0458	0

Where: C_S is solvent concentration, T and pH are precipitating temperature and pH, respectively, and $IR_{Alcohol}$ and $IR_{Acetone}$ are recovery index for alcohol and acetone solvents.

ANOVA results showed multiple correlation (R^2) was about 1.0. Calculated F were higher than 2 times and minor than 3 times of the tabled F; these introduce that model had been fitted to the experimental data (Barros Neto et al., 2001).

Table 2 Anova to evaluation of the model for optimization of alcohol precipitation of amylase from maize malt

R^2	0.9313
Test F_1*	2.1932
Test F_2*	0.2825

*F test = calculated F/Tabled F

Square model was the best fitting among the models tested. Fitted model for alohol precipitation are shown at follown.

$$IR = 0.8161 + 0.7908.C_{Alcohol} - 1.7719.T + 1.6269.pH + 1.6386.T^2 - 1.3926.C_{Alcohol}.T - 0.0254.C_{Alcohol}.pH - 0.9441.T.pH \quad (5)$$

Figures 1.a, 1.b and 1.c are the response surfaces to obtain the best conditions of

amylase purification from maize malt by alcohol precipitation. By RSM optimization, the best condition to amylase purification from maize malt by alcohol precipitation are: 10°C on a pH of 7 and an alcohol concentration of 0.7 (v/v). In this condition a recovery index of about 10 times is obteined. This index is more than found by Furuya et al (1995 and 1996), by Blázquez et al. (1998) Gu and Glantz (2007), Nirmala and Muralikrishna (2003) and Curvelo-Santana (2003).

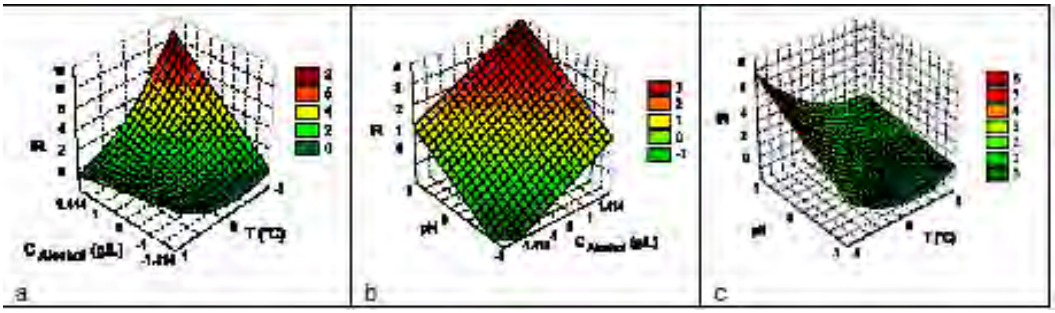

Figure 1. Response surfaces to know effects of factores on recovery index (IR) of amylase from maize malt. a) Effects of alcohol concentration and temperature; b) Effects of pH and alcohol concentration and c) Effects of pH and temperature.

Figure 2.a shows that the maize malt amylases kept 80% of the activity in a pH range between 4.5 and 6.5. Figure 2.b shows that there are two optimum temperatures: one at 50 °C, due to β-amylase activity and the other at 90 °C, due to that of α-amylase. Figure 2.c shows the derivation of the K_m, and V_{max} constants using Lineweaver–Burk method; their values were 7.69×10^{-2} g/L and 7.69×10^{2} g/L.min (or 2.48×10^{4} U/mg), respectively.

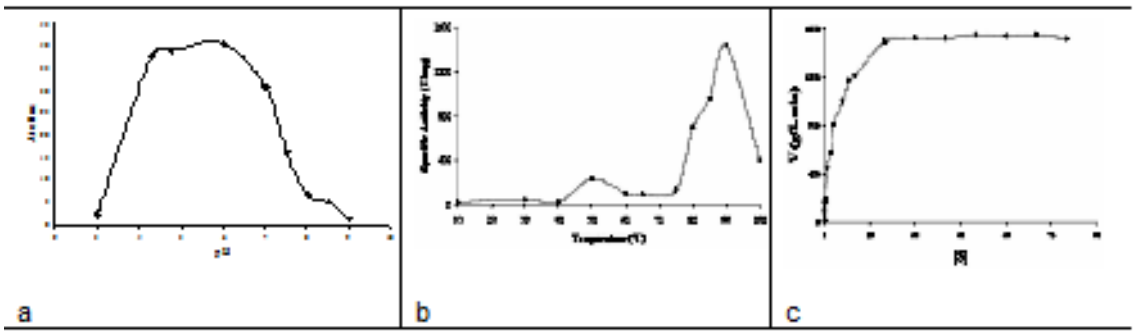

Figure 2. Enzyme characterization of amylase from maize malt. a) Effect of pH; b) Effect of temperature and c) Starch hydrolysis kinetic.

4 Conclusion

Alcohol is the best solvent to the amylase precipitation from maize malt than acetone. A square model was the best fitting to description of amylase purification from maize malt by alcohol precipitation process. RSM shows that optimal condition to amylase precipitation was obtained at 10°C, on a pH 7 and 0.7 (v/v) of alcohol concentration, while a purification factor of 10 times was obtained. Enzyme characterization showed an optimal pH was obtained between 4.5 and 6.5 and optimal temperatures were of 50°C for β-amylase and 90°C for α-amylase and the values of K_M and V_{max} constants was of $7.69.10^{-2}$ g/L and $7.69.10^{2}$ g/L.min, respectively.

References

Aguilar, G. Morlon-Guyot, M. Trejo-Aguilar, B. Guyot, J. P. (2000). Purification and characterization of an extracellular α-amylase produced by *Lactobacillus manihotivorans* LMG 18010^{T}, an amylolytic lactic acid bacterium. *Enzyme and*

Microbial technology, 27, 406-413.

Barros Neto, B.; Scarminio, I. S. E Bruns, R. E. (2001).*Como Fazer Experimentos: Pesquisa e Desenvolvimento na Ciência e na Indústria.* Vol. 1, 1ª edição, Livros - Textos, EDUNICAMP, Campinas – SP.

Biazus, J. P. M., Souza, A. G.; Santana, J. C. C.; Souza, R. R. And Tambourgi, E. B. (2005) Optimization of Drying Process of *Zea Mays* Malt to Use as Alternative Source of Amylolytics Enzymes. *Brazilian Archives of Biology and Technology*.48, Special issue, pp.185-190.

Blásquez, G.; Camacho, F.; González-Tello, P. and Alarcón, F.J. (1998). Partition coefficients of α-amylase in aqueous two-phase systems PEG+$MgSO_4$.$7H_2O$ at 298 K, *Biochimica et Biophysica Acta,* 1379: 191-197.

Bradford, M. M. (1976). A rapid and sensitive method for the quantitation of microgram quantities of protein. Utilizing the principle of protein-dye binding. *Anal. Biochem.* 72, 248-254.

Curvelo-Santana, J.C. (2003). *Recuperação das enzimas α e β - amilases em sistema bifásico aquoso PEG / $CACL_2$ para uso como biocatalizador de amiláceos*. Campinas-SP, FEQ/UNICAMP. (Dissertação de Mestrado)

Gu Z. and Glantz, C.E. (2007). Aqueous two-phase extraction for protein recovery from corn extracts. *Journal of Chromatography B* 485:1, 38-50.

Furuya, T.; Iwai, Y; Tanaka, Y; Uchida, H.; Yamada, S. and Arai, Y. (1995). Measurement and correlation of partition coefficients of hydrolytic enzymes for dextran+poly(ethylene glycol)+water aqueous two-phase systems at 20°C. *Fluid Phase Equilbria* 110, 115-128.

Furuya, T.; Yamada, S.; Zhu, J.; Yamaguchi, Y.; Iwai, Y. and Arai, Y. (1996). Measurement and correlation of liquid-liquid equilibria and partition coefficients of hydrolytic enzymes for DEX T500+PEG20000+water aqueous two-phase systems at 20°C. *Fluid phase Equilibria* 125: 89-102.

Luccarini, A. C.; Kilikian, B. V.; Pessoa Jr., A. (2005). Precipitação. In: *Purificação de produtos biotecnológicos*. A. Pessoa Jr. & B. V. Kilkian (Coord). Vol.1. Ed. Manole, Barueri-SP.

Miller, G.L. (1959). Use of dinitrosalicylic acid reagent for determination of reducing sugar. *Analytical Chemistry*, 31:3, 426-428.

Nirmala, M. and Muralikrishna, G. (2003). Three α-amylase from malted finger millet (Ragi, *Eleusine coracana*, Indaf-15) - Purification and partial characterization. *Phytochemistry* 62, 21-23.

Reguly, J. C. *Biotecnologia dos Processos Fermentativos.* Vol.1. Pelotas – RS: EDUFPel, 1996, 330p.

Sigma Chemical Company, Cataloge. (1996). *Biochemicals Organic Compounds and Diagnostic Reagents*, p.116-117.

Teotia et al. (2001). Purification of β-amylases of sweet-potato by precipitation affinity with alginate. *Enzyme and Microbial Technology,*.28, 792-795.

Proceedings of the 10th International Chemical and
Biological Engineering Conference - CHEMPOR 2008
Braga, Portugal, September 4-6, 2008
E.C. Ferreira and M. Mota (Eds.)

Hydrothermal treatments of corn cob and hemicelluloses extraction

Denise S. Ruzene[1*], Elif Yagiz[1, 2], Dilek Marangoz[1, 2], Daniel P. Silva[1], António A. Vicente[1], José A. Teixeira[1]

[1] IBB - Institute for Biotechnology and Bioengineering, Centre of Biological Engineering, University of Minho, Campus de Gualtar, 4710-057 Braga, Portugal.
[2] Chemical Engineering Department, Engineering Faculty, Ege University, 35100 Bornova/İzmir, Turkey.

Keywords: Autohydrolysis, Extraction, Hydrothermal treatments, Hemicelluloses, Xylan
Topic: Integration of life & engineering

Abstract

Corn cob samples were treated with water (autohydrolysis reaction) using a liquid to solid ratio of 10:1 w/w. The optimal condition for extraction of hemicelluloses was found at 185ºC for 30 min. This resulted in the release of 9.7% of hemicelluloses (% dry starting material), corresponding to the dissolution of 27.9% of the original hemicellulose. Chemical composition and physico-chemical properties of the samples were elucidated by a combination of sugar analyses and thermal analysis. The results showed that the treatment was effective on the extraction of hemicelluloses from corn cob and that the TGA analysis of xylan from birch wood was found to be initially degraded at about 220 ºC whereas hemicelluloses from corn cob would be degraded at about 225 ºC.

1 Introduction

Agricultural wastes are mainly of lignocellulosic nature (with cellulose, hemicelluloses and lignin as structural components). Chemically, about 35-55% of the dry material is the glucose polymer cellulose, much of which is in a crystalline structure; while another 25-35% is hemicellulose, an amorphous polymer. The remainder is mostly lignin plus less amounts of minerals, waxes, and other compounds (Sun and Cheng, 2002). Cellulose is formed by β(1-4) glucosyl linkages in a linear backbone, whereas hemicelluloses are branched polymers composed of several monosaccharides (Fengel and Wegener, 1989).

Treatments of lignocellulosic materials in autohydrolysis processes (or hydrothermal treatments), under optimized conditions, lead to the solubilisation of hemicelluloses, leaving a solid phase enriched in both cellulose and lignin. These aqueous processes, when used in mild conditions, are an environmentally friendly technology for biomass utilization (Garrote et al., 1999).

On the other hand, corn is the one of the most widely planted crops in the World. According to the Food and Agriculture Organization of the United Nations (FAO, 2008), the annual production worldwide is about 695×10^9 kg. The major production regions are the American continent (53%), Asia (29%), and Europe (11%). In particular, corn cob is an important by-product of this industry: for every 100 kg of corn grain approximately 18 kg of corn cobs are produced (Torre et al., 2008). A large quantity of corn cobs remains unused as lignocellulosic waste or used as animal feed. Owing to their chemical composition, corn cobs show great potential as a renewable raw material for producing a variety of added-value chemicals (Rivas et al., 2004).

* Corresponding author. Tel + 351-253-604400. E-mail: ruzeneds@hotmail.com

The hemicelluloses fraction of corncobs has a comparatively high content of acetylated xylan (a polymer made up of xylose units with acetyl substituents). When corn cobs are contacted with water and heated, the hydronium ions coming from water autoionisation cause both xylan depolymerisation (sugar oligomers and sugars) and cleavage of acetyl groups (to give acetic acid, which increases the hydronium concentration in the reaction medium) (Garrote, 2002). Autohydrolysis solid residues which contain mainly cellulose and lignin can be subjected to further chemical or biotechnological processing and can also be used as substrate for conversion into a variety of marketable end-products (Parajó et al., 1994).

The aim of this work is to assess the effect of the autohydrolysis treatment of corn cob on the hemicelluloses yield with particular emphasis on the further applications of the extracted fractions.

2 Materials and Methods

Materials

Corn residues (corn cob) were kindly supplied by a local farmer (Portugal). After being dried at 40 ºC in an oven for 12 h, the corn cob was cut into small pieces (1-3 cm), milled in a knives' mill to pass through a 0.4 mm screen (for chemical composition) and 1.0 mm (for hydrothermal pre-treatments), and stored at room temperature. All chemicals used were of analytical or reagent grade. Experiments were performed in triplicate and yields are given on a dry weight (untreated corn cob) basis.

Chemical composition of corn cob

Two grams of ground corn cob were treated with 10 mL of 72% H_2SO_4 under stirring at 45 °C for 7 min. The flask was autoclaved for 30 min at 1.05 bar for the complete hydrolysis of oligomers. After filtration through a Sep-Pak C18 cartridge to remove aromatic compounds, the hydrolysate was analyzed in a MetaCarb 67H column at 45 °C using a Shimadzu chromatograph with refractive-index detector. The mobile phase was 0.005 mol/L H_2SO_4 at 0.6 mL/min flow rate. Sugar concentrations, reported as glucan and xylan, were determined from calibration curves obtained with pure compounds. Lignin was determined by gravimetric analysis (Rocha, 2000). All experiments were performed in triplicate.

Hydrothermal treatments

Corn cob samples and water were mixed in a closed and pressurized vessel in order to obtain a liquid/solid ratio of 10:1 w/w, taking into account the moisture content of the sample. The reactor was heated to the desired temperature (165-195 ºC) by periods ranging from 10 to 60 min. After each treatment, the liquid phase was separated from the solids by filtration. The hemicelluloses were then precipitated by pouring the concentrated supernatant fluid with three volumes of 95% ethanol (20 °C, 24 h). The precipitates were recovered by filtration, washed with 70 % ethanol and dried (30 ºC). All experiments were performed in triplicate.

Thermogravimetric Analyzer

The thermal stability of the samples was evaluated using thermogravimetric analysis (TGA) on a thermal analyzer (TGA-50 Shimadzu, Japan). The apparatus was continually flushed with nitrogen. The samples weighed between 10 and 12 mg and were run from room temperature to 580 °C at a rate of 10 °C/min.

3 Results and Discussion

The compositional data of the corn cob samples used as raw material (average of three replicates) are shown in Table 1. The results are expressed as glucan, hemicelluloses and lignin. Thus, lignocellulosic materials can be defined by their contents of glucan (corresponding to cellulose), xylan (measured as xylose equivalent, which forms the main polymer backbone), xylan substituents (arabinose units, reported as arabinan expressed in sugar equivalent, and acetyl groups), and total lignin (measured as soluble lignin and Klason lignin). As can be seen from Table 1, xylan and xylan substituents (hemicelluloses) accounted jointly for 34.7% of corn cobs (in oven-dryed basis).

Samples of corn cob were subjected to hydrothermal treatments in aqueous media under conditions leading to maximal hemicellulose yield. Figure 1 shows that the treatment of corn cob released 0.28 - 9.68 % hemicelluloses (in respect to dry starting material), corresponding to the dissolution of 0.8 and 27.9 % of the original hemicelluloses, respectively. These results revealed that autohydrolysis of the corn cob was effective, and that the highest extraction yield was obtained with 30 min and 185 ºC (27.9% of the total available hemicelluloses).

Table 1. Chemical composition of corn cob

Chemical Components	Composition (%)
Glucan	31.8 ± 0.8
Hemicelluloses	34.7 ± 1.1
Xylan	29.4 ± 0.2
Arabinan	1.1 ± 0.2
Acetyl group	3.1 ± 0.4
Total lignin	27.9 ± 0.4
Soluble lignin	11.3 ± 0.2
Klason lignin	16.6 ± 0.4
Total Composition	93.3 ± 0.9

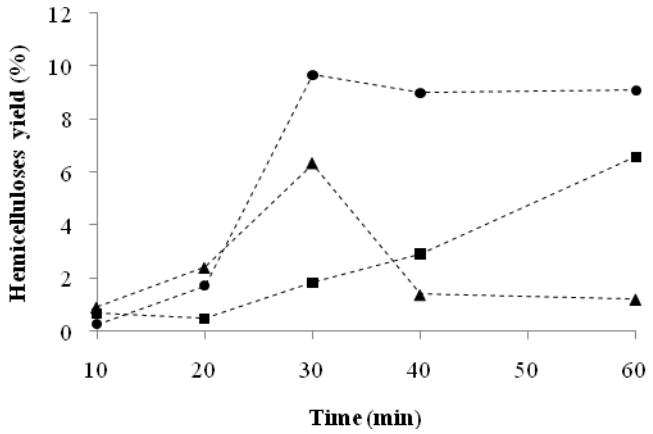

Figure 1. Hemicelluloses yield (%) at temperatures of (■) 165 ºC, (●) 185 ºC and (▲) 195 ºC.

In this work, the thermal properties (Figure 2) of xylan from birch wood (line 1), hemicelluloses from corn cob at 165ºC/60 min (line 2), 185ºC/30 min (line 3) and 195ºC/30 min (line 4) were studied by TGA. Figure 2 and Table 2 show the TGA results obtained of xylan from birch wood and hemicellulose from corn cob. There is distinction between the amounts of the residues remaining after heating of 560 ºC heating. All samples have a residual weight between 4.4 and 16.5% at 560 ºC (Table 2).

Table 2. Degradation characteristics of the xylan from birch wood, hemicellulose from corn cob at 165ºC/60 min, 175ºC/40 min, 185ºC/30 min and 195ºC/30 min.

Samples	Onset of degradation (ºC)	Residue after 560 ºC (%)
Xylan from birch wood	270	16.5
165 ºC/60 min	250	10.9
185 ºC/30 min	240	4.4
195 ºC/30 min	240	11.9

Samples of xylan from birch wood were found to be initially degraded at about 220 ºC whereas hemicelluloses from corn cob at 165ºC/60 min, 185ºC/30 min and 195ºC/30 min would be degraded at about 225 ºC. Maximum rates of weight loss were observed between 230 and 320 °C. As observed, samples were stable up to 200 °C. Beyond these temperatures, thermal degradation takes place. As can be seen (Figure 2), for a 30% weight loss, the decomposition temperatures of the degraded samples occurred at 220 °C (lines 2-4) and 280 °C (lines 1). No thermal events were observed at temperatures higher than 560ºC.

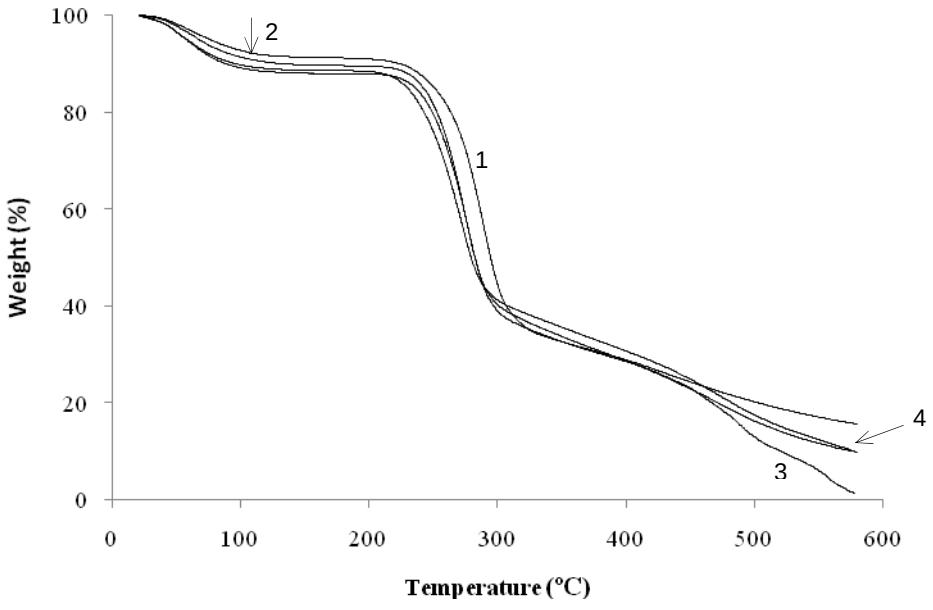

Figure 2. TGA curves of commercial xylan from birch wood (line 1), hemicelluloses from corn cob at 165ºC/60 min (line 2), 185ºC/30 min (line 3) and 195ºC/30 min (line 4).

4 Conclusion

The autohydrolysis treatment of corn cob was effective for the hemicelluloses extraction, and it was shown that the best conditions of extraction were at 185ºC and 30 min, obtaining 27.9% of the total available hemicelluloses. Degradation characteristics of hemicellulose (185ºC/30min): onset of degradation at 240 ºC and residue after 560 ºC of 4.4 %.

Acknowledgements

Fundação para a Ciência e a Tecnologia/FCT (Portugal) and Erasmus Programme (Turkey).

References

FAO, Food and Agriculture Organization of the United Nations (2008). FAOSTAT statistics database http://faostat.fao.org/site/567/DesktopDefault.aspx?PageID=567 (last updated 08 July 2008).

Fengel, D., Wegener, G. (1989). Wood chemistry, ultrastructure, reactions p. 613. Berlin: Walter de Gruyter.

Garrote, G., Domínguez, H., Parajó, J.C. (1999). Hydrothermal processing of lignocellulosic materials. Holz Roh Werk. 57, 191-202.

Garrote, G., Domínguez, H., Parajó, J.C. (2002). Autohydrolysis of corncob: study of non-isothermal operation for xylooligosaccharide production. Journal of Food Engineering, 52, 211-218.

Rivas B., Domınguez J.M., Domınguez, H., Parajo, J.C. (2004). Bioconversion of posthydrolysed autohydrolysis liquors: an alternative for xylitol production from corn cobs. Enzyme Microbiology Technology, 31, 431-438.

Rocha, G.J.M. (2000). PhD. Thesis, São Carlos/Universidade de São Paulo, Brazil.

Sun, Y., Cheng, J. (2002). Hydrolysis of lignocellulosic materials for ethanol production: a review. Bioresource Technology, 83, 1-11.

Torres, P., Aliakbarian, B., Rivas, B., Domínguez, J.M., Converti, A. (2008). Release of ferulic acid from corn cobs by alkaline hydrolysis. Biochemestry Engineering Journal, In Press.

Proceedings of the 10th International Chemical and
Biological Engineering Conference - CHEMPOR 2008
Braga, Portugal, September 4-6, 2008
E.C. Ferreira and M. Mota (Eds.)

Bioconversion of xylose from lignocellulose wastes in raw materials for biochemical syntheses

Beata Abraham[1], Alexandru Szep[1], Ildiko Miklossy[1], Emese Both[1], Maria Palfi[1], Szabolcs Lanyi[1*]

[1] SHUT – Sapientia Hungiarian University of Transylvania, Department of Bioengineering, Campus Miercurea Ciuc, 530104 Miercurea Ciuc, Romania.

Keywords: Bioconversion, xylose, fixed bed reactor, phosphoketolase
Topic: Integration of life sciences & engineering.

Abstract

The primary aim of the presented study was design of an enzymatic reaction cascade on which an industrially applicable process can be based on, implying the enzymes xylose isomerase, xylulose kinase and phosphoketolase, which convert xylose derived from lignocellulolsic wastes into a high-value-added product, glyceraldehyde-3-phosphate. The xylose conversion to gliceraldehyde 3-phosphate was carried out by a dynamic reactor-cascade system, made up of three modules each of them containing a substrate conditioning element, a fixed-bed reactor and an adequate storage tank. The modular form permitted analysis of each of the enzymatic processes, assuring at the same time, separation of the obtained products.

Introduction

For the sustainable use of lignocellulose-containing wastes produced by paper industry, both chemical and biotechnological procedures are used; chemical procedures represent in many cases a high environmental hazard and less valuable products. The biotechnological procedures are more effective and have reduced environmental impact; these procedures being conducted based on bioconversions performed by enzymes of different microorganisms, as well as by whole-cell systems, which function as biocatalysts. By the aid of these processes the lignocellulosic biomass and its derivatives can be converted to ethanol or other organic raw materials for the chemical industry. However, these procedures have been applied as bases of industrial technologies only at a low level. Processing of industrial and agricultural byproducts with high lignocellulosic contents can be achieved in the first phase by hidrolysis carried out eighter by chemical or by enyzmatic reactions, the free sugars resulted by these processes can be further utilized for obtaining different products.

Xylose conversion had been studied extensively in order to achieve obtention of high-value added products by processes which can easily been scaled-up. Fermentative processes have been studied more in detail in both the case of yeasts and bacteria (Kuyper et al., 2005; Taniguchi et al., 2004), genetically modified strains, as well as metabolic engineering approaches had been used (Nyyssola et al., 2005). In fermentation approaches, xylose utilization as a sole carbon source has been a limiting factor, as even recombinant micrroganisms require additional sugar source for their growth (Krishnan et al., 1999). Xylose metabolism in bacteria has been described for a wide array of microorganisms including *Escherichia coli* (Lawlis et al., 1984)

[*] Corresponding author. Tel + 40745.100.924. E-mail:lanyiszabolcs@sapientia.siculorum.ro

Lactobacillus ssp (Bor et al., 1992), *Staphylococcus xylosus* (Sizemore et al., 1991) and *Lactococcus lactis* (Erlandson et al., 2000). Xylose metabolism involves gene products of the *xylA, xylB* genes in the first phase, which yields xylulose-5 phosphate, a common intermediate for reactions of the pentose metabolism. During heterofermentative degradation in lactic acid bacteria, xylulose-5 phosphate is further converted via the phosphoketolase pathway. We designed an enzymatic reaction cascade on which an industrially applicable process can be based on, implying the enzymes xylose isomerase, xylulose kinase and phosphoketolase, which convert xylose derived from lignocellulolsic wastes into a high-value-added product, glyceraldehyde-3-phosphate. The figure below illustrates the enzymatic process yielding a high added-value product starting from xylose derived from lignocellulose, which is converted to glyceraldehyde-3-phosphate in three metabolic steps. The partial enzymatic reactions can be found in several microbial organisms, different organisms having slightly different enzymes for the three reactions and require specific conditions for optimal activity.

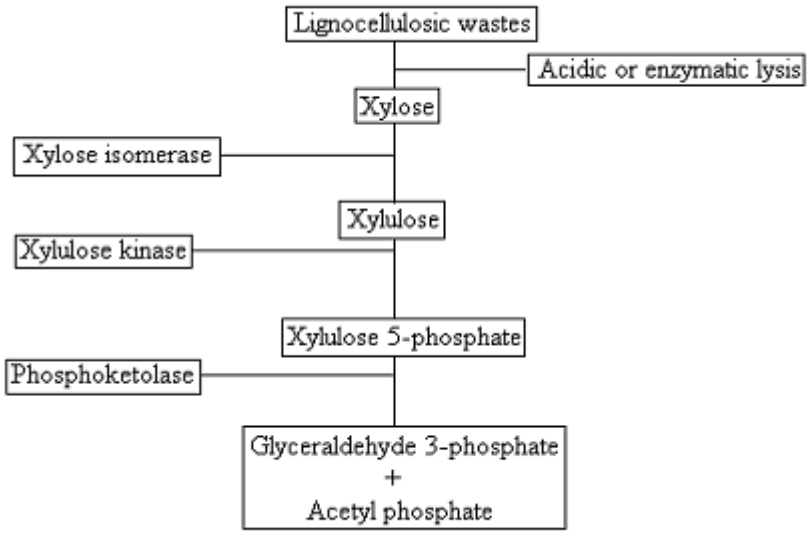

Figure 1. Conversion of xylose into glyceraldehyde-3-phosphate.

Realization of a bioprocess with such a complexity, even at a laboratory or small-scale level requires a reliable chemical, biochemical and technological background. Even if the biochemical and enzymatic part is solved, the technological scale-up raises many problems, particularly if continuous systems are to be used.

The first reaction is known to work well in industrial applications at high concentrations, but the second and third reactions, working with millimolar concentrations have not been optimized yet at larger scale. The overall yield of the process is limited by the second reaction, which results in xylulose-5-phosphate, as coupling to the first isomerization reaction presents difficulties due to the different scales. Standard biochemical experiments work with material quantities of µg or mg order of magnitude, whereas scaling-up of enzymatic bioconversions usually requires materials in a quantity with at least one order of magnitude higher; methods for recombinant enzymes obtained at laboratory scale thus present a disadvantage when used in prefabricated bioreactors. By this we considered design of a unique reactor system to conduct the studied process.

Materials and methods

Enzymes

To perform the first isomerization reaction, immobilised xylose isomerase commercialized as Sweetzyme was used (Novo Nordisk). Recombinant plasmids containing the coding regions for xylulose kinase (pET28a(+)-*XylB*) and xylulose 5-phosphate phosphoketolase (pHAT2-*PK*) used for heterologous expression of the enzymes were obtained as a courtesy of Stefan Szedlacsek, Department of Enzymology, Institute of Biochemistry (Bucharest).

Obtention of the enzymes xylulose-kinase and phosphoketolase was carried out by modified protocols after by Sambrook, J. (1989). For the enzyme D-xylulose-5-phosphokinase, as expression host the *E.coli* strain BL21 (DE3) pLysS was used, whereas in the case of phosphoketolase derived from *Leuconostoc mesenteroides*, the recombinant protein was obtained in *E. coli* strain BL21(DE3)RIL.

Immobilization of both xylulose kinase and phosphoketolase was carried out taking the advantage of the N-terminal 6XHis tags present as fusion partners of the expressed enzyme preparates. One step purification and immobilization of the obtained proteins was achieved by binding to the chelating matrix Porfinity IMAC Ni^{2+} Charged Resin (BioRad), which was found to be the optimal matrix from the point of view of binding capacity and reduced cation leakage.

In the first reaction, xylose was converted to xylulose in an equilibrium reaction by the immobilized xylose isomerase derived from *Streptomyces murinus*, having its temperature optimum at 60 °C, by which a conversion rate of 25% was obtained. As the reaction product raised the problem of the presence of xylose, which inhibits phosphoketolase activity required in the last phase of the transformation; the resulted mixture was separated in xylose and xylulose. Xylulose was phosphorilated by the heterologuosly expressed enzyme D-xylulose-5-phosphokinase in the presence of ATP in a subsequent reaction, in which a conversion rate of 90% was achieved. The expressed xylulose 5-phosphate phosphoketolase was used to carry out the final step of the xylose conversion reaction. The final reaction performed by the obtained phosphoketolase was conducted at 37 °C, in the presence of inorganic phosphate as well as of the cofactor Mg2+ and

Product separation and determination of catalytic efficiency

Activity assays of the xylose isomerase and xylulose kinase, respectively were realized with a Varian Pro Star HPLC, detector RI Varian Pro Star 350, on a Supercosil LC NH2 column, using 0,01 N sulfuric acid as elution agent at a 0,5 ml/min flow rate. The first reaction was performed starting from 1 M xylose and the resulted product was separated on boric acid (2 ml, Sigma). For separation, the product mixture was diluted to contain 0,01 mM xylulose. The second reaction was fed with the separated xylulose and 4 mM ATP.

Characterization of catalyitic properties of the obtained phosphoketolase was carried out by determination of conversion of xylulose 5-phosphate to glyceraldehide 3-phosphate under optimized conditions, showing a specific activity of 0.5-0.6 U/mg.

The conversion in glyceraldehyde 3-phosphate was followed by indirect determination by coupled reactions with the enzymes triose isomerase (TIM) and glyceraldehyde dehydrogenase (GDH), measuring the decrease in NADH concentration. The auxiliary implicated enzymes were added to the system in excess, so that the reaction rate only depended on phosphoketolase activity.

Reactor

The xylose conversion to glyceraldehyde 3-phosphate was carried out by a dynamic reactor-cascade system, set up of three modules each of them containing a substrate conditioning element, a fixed-bed reactor and an adequate storage tank. The modular form permitted analysis of each of the enzymatic processes, assuring at the same time, separation of the obtained products. With the modular design the separation of the different processes can be solved and by changing the reactor charge, the separation

of products can be achived as well. The modules are equipped with thermostats and product collector tanks.
Materials that make up the reactos were chosen in order to prevent microbial contamination of the reactor system, which inhibit biofilm formation and can easilly be disinfected.

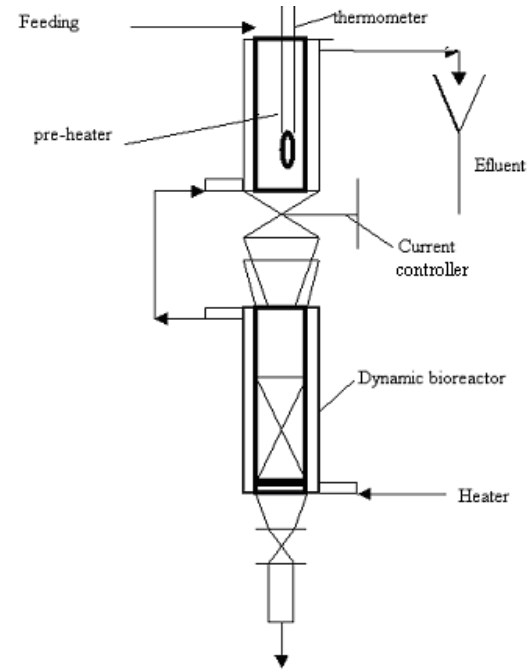

Figure 2. Module of the bioreactor system.

Results and discussion

Xylose conversion to xylulose. The chromatogram below referres to the reaction products of the first enzymatic conversion products, the xylose/xylulose mixture, according to which a 70-30% conversion rate can be observed.

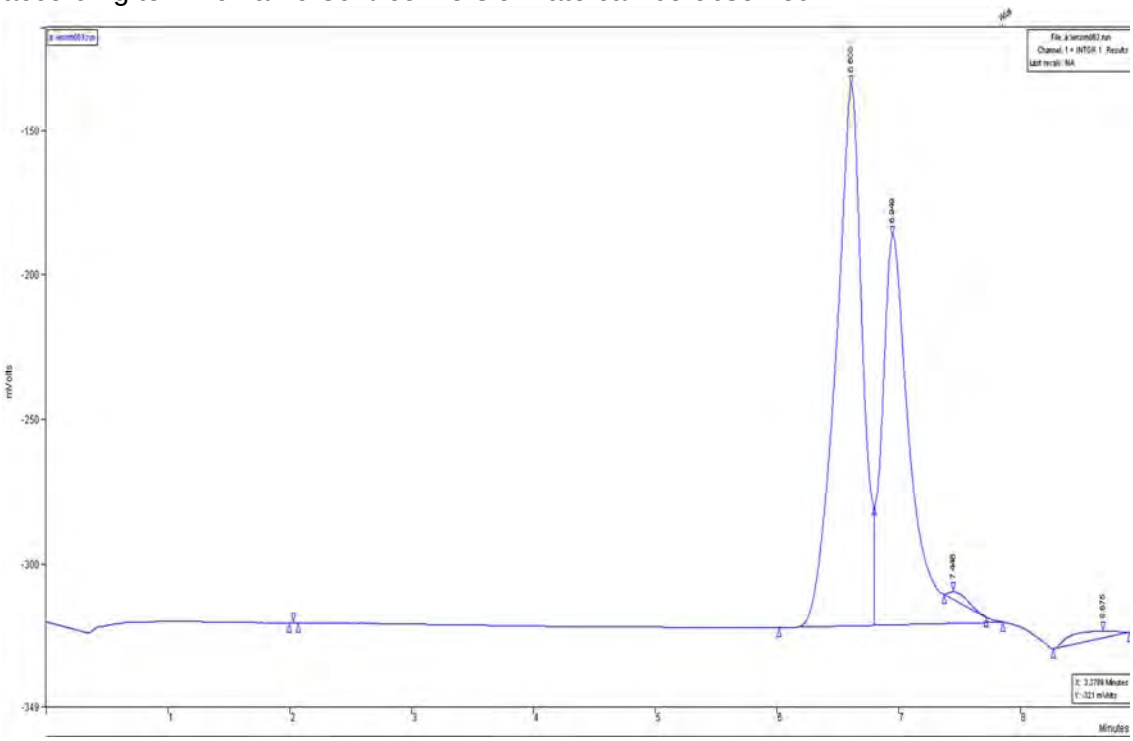

Chromatogram 1. The xylose-xylulose conversion reaction products.

Xylulose-xylulose-5-phosphate conversion. Regarding the xylulose phosphorylation step, the HPLC separation of the resulted reaction products indicates a 90% conversion yield, the 10% difference containing errors of concentration determinations. The chromatogram presented below illustrates separated products of the xylulose-xylulose-5-phosphate conversion, catalyzed by the obtained xylulose kinase.

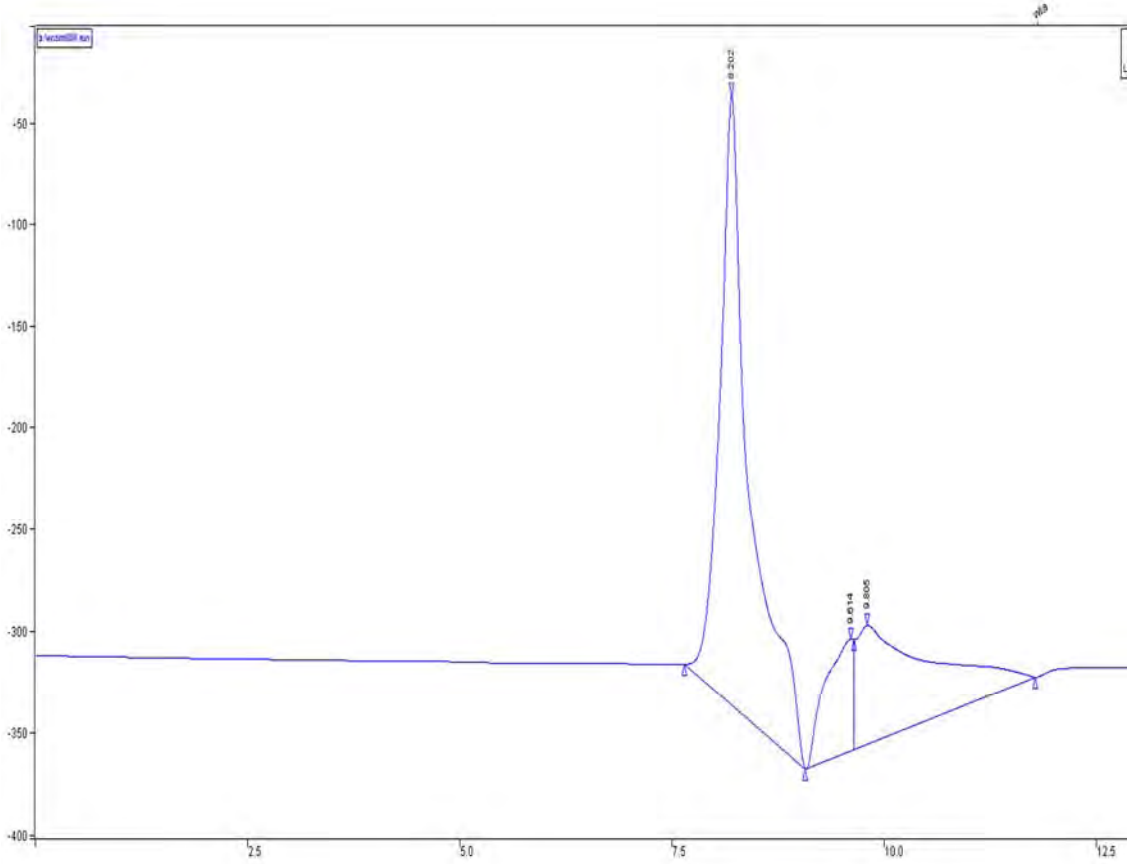

Chromatogram 2. Reaction products of the xylulose- xylulose-5-phosphate conversion.

Obtention of glyceraldehyde-3-phosphate. In case of the third reaction, the obtained phosphoketolase was assayed for activity in both free and immobilized form, as presented in tables 1. and 2., a 15%-20% activity decrease being observed in the case of the immobilized form.

The reaction performed in the designed reactor system did not achieve the yield presented by the free enzyme; enzyme stability of the expressed phosphoketolase needs to be correctly correlated in order to achieve better conversion yield, optimization studies of the third reaction are in progress.

Free phosphoketolase	Probe 1.	Probe 2.	Probe 3.
ΔA/Δt	0,089	0,086	0,112
Activity U/mg	0,541	0,523	0,681

Table 1. Activity of the free enzyme.

Immobilized phosphoketolase	Probe 1.	Probe 2.	Probe 3.
ΔA/Δt	0,069	0,067	0,057
Activity U/mg	0,419	0,407	0,346

Table 2. Activity of the immobilized enzyme.

Conclusions

Despite the rather low conversion rate achieved by the designed reactor system; it can be a solution for lignocellulosic waste utilization and processing after optimization.
The study has a demonstrative importance regarding viable possibilities of replacing chemical procedures with enzymatic and biotechnological solutions.

References

Kuyper M, Toirkens MJ, Diderich JA, Winkler AA, van Dijken JP, Pronk JT. (2005) Evolutionary engineering of mixed-sugar utilization by a xylose-fermenting Saccharomyces cerevisiae strain. FEMS Yeast Res.

Nyyssola A, Pihlajaniemi A, Palva A, von Weymarn N, Leisola M. (2005) Production of xylitol from d-xylose by recombinant Lactococcus lactis. J Biotechnol. 2;118(1):55-66.

Krishnan MS, Ho NW, Tsao GT. (1999) Fermentation kinetics of ethanol production from glucose and xylose by recombinant Saccharomyces 1400(pLNH33). Appl Biochem Biotechnol. Spring; 77-79:373-88.

Lawlis VB, Dennis MS, Chen EY, Smith DH, Henner DJ. (1984) Cloning and sequencing of the xylose isomerase and xylulose kinase genes of Escherichia coli. Appl Environ Microbiol.; 47(1):15-21.

Bor YC, Moraes C, Lee SP, Crosby WL, Sinskey AJ, Batt CA. (1992) Cloning and sequencing the Lactobacillus brevis gene encoding xylose isomerase. Gene.; 114(1):127-32.

Erlandson KA, Park JH, Wissam, El Khal, Kao HH, Basaran P, Brydges S, Batt CA. (2000) Dissolution of xylose metabolism in Lactococcus lactis. Appl Environ Microbiol.; 66(9):3974-80.

Sizemore C, Buchner E, Rygus T, Witke C, Gotz F, Hillen W. (1991) Organization, promoter analysis and transcriptional regulation of the Staphylococcus xylosus xylose utilization operon. Mol Gen Genet.; 227(3):377-84.

Proceedings of the 10th International Chemical and
Biological Engineering Conference - CHEMPOR 2008
Braga, Portugal, September 4-6, 2008
E.C. Ferreira and M. Mota (Eds.)

Optimization of ethanol production from cheese whey powder by *Kluyveromyces fragilis* using factorial design and response surface methodology

Giuliano Dragone[1,2*], Solange I. Mussatto[1], João B. Almeida e Silva[2], José A. Teixeira[1]

[1] IBB – Institute for Biotechnology and Bioengineering, Centre of Biological Engineering, University of Minho, Campus de Gualtar, 4710–057 Braga, Portugal.

[2] Department of Biotechnology, Engineering College of Lorena, University of São Paulo, Estrada Municipal do Campinho s/n, 12602-810, Lorena/SP, Brazil.

Keywords: Cheese whey, Ethanol, *Kluyveromyces fragilis*, Response surface methodology.
Topic: Integration of life sciences and engineering.

Abstract

The individual and combined effects of initial lactose concentration, temperature and inoculum concentration on ethanol production from cheese whey powder by *Kluyveromyces fragilis* were investigated. A 2^3 full-factorial central composite design (CCD) and response surface methodology (RSM) were employed in order to determine the optima conditions that maximize the ethanol production. Statistical analysis of results showed that, in the range studied, only the initial lactose concentration had a significant effect on ethanol production. Response surface data showed maximum ethanol production at inoculum concentration between 1 and 3 g/L and temperature between 25 and 35ºC when the initial lactose concentration was 150 g/L.

1 Introduction

The dairy industry represents an important part of the food processing industry and contributes significant liquid wastes that can be used for the production of ethanol (Ghaly and El-Taweel, 1997). Cheese whey (CW), a by-product of the cheese manufacturing process whose major components are lactose (44-52 g/L), proteins (6-8 g/L) and mineral salts (4-9 g/L), constitutes an inexpensive and nutritionally rich raw material for the production of ethanol by fermentation. However, the production of ethanol from unconcentrated CW is not economically feasible because the levels of ethanol obtained at the end of fermentation reach only about 2%, making the distillation process too expensive. Otherwise, costs are significantly reduced with the increase of lactose concentration up to about 100-120 g/L lactose (González Siso, 1996). Therefore, dry cheese whey powder (CWP) may be an attractive raw material for ethanol production. CWP is a dried and concentrated form of CW and contains lactose in addition to nitrogen, phosphate and other essential nutrients (Kargi and Ozmihci, 2006). The use of CWP instead of CW for ethanol fermentations has significant advantages such as elimination of costly ultrafiltration processes to concentrate lactose before fermentation, compact volume, long-term stability and high concentrations of lactose and other nutrients yielding high ethanol concentrations by fermentation (Ozmihci and Kargi, 2007a).

Optimization of fermentation conditions by the classical method involves changing one independent variable while fixing all others at a fixed level. This is extremely time-consuming and expensive for a large number of variables (Adinarayana et al., 2003) and also may result in wrong conclusions (Oh et al., 1995). Response surface methodology (RSM) is a collection of statistical techniques for designing experiments, building models, evaluating the effects of

* Corresponding author. Tel + 351-239- 604400 ext. 605413. E-mail:gdragone@deb.uminho.pt

factors, and searching optimum conditions of factors for desirable responses (Li et al., 2001). Although this method was successfully applied in many areas of biotechnology, there is no report in the literature describing the influence of process parameters on the production of ethanol from CWP through RSM.

The present study aimed to optimize the conditions for ethanol production from CWP through RSM designed with composite central design (CCD). Three factors were selected as process (independent) parameters: initial lactose concentration, temperature and inoculum concentration, while ethanol concentration was selected as response (dependent parameter).

2 Material and Methods

2.1 Microorganism and inoculum preparation

The yeast strain *Kluyveromyces fragilis* (Kf 1) used in this work was obtained from the culture collection of the Centre of Biological Engineering, University of Minho (Portugal) and maintained on YPD agar plates at 4ºC.

The inoculum culture was prepared by transferring a loopful of cells from a freshly grown culture (incubated at 30ºC for 30 h) into 500 mL Erlenmeyer flasks containing 100 mL sterile CWP solution (50 g/L lactose). Incubation was carried out on a rotary shaker (200 rpm) at 30ºC for 24 h.

2.2 Fermentation conditions

Batch experiments were performed in 500 mL Erlenmeyer flasks containing 100 mL of medium composed by CWP solution with initial pH adjusted to 5 with citric acid (1 M). The flasks were maintained in an orbital shaker at 150 rpm for 44 h. The initial lactose concentration, temperature and inoculum concentration were considered according to the experimental design showed in Table 1. All experiments were performed in duplicate.

2.3 CWP solutions preparation

Cheese whey powder (CWP) was kindly supplied by Lactogal (Porto/Portugal). Deproteinization was carried out by heat treatment (115ºC, 15 min) of acidified (pH 5) CWP solutions with different initial lactose concentrations. The precipitates were removed by centrifugation at 8500 rpm and 10ºC for 15 min and the supernatant was used as fermentation medium.

2.4 Analytical methods

The fermented media samples were centrifuged at 4000 rpm for 10 min and the supernatant was used to quantify the lactose and ethanol concentrations. Remaining solid was washed once with distilled water and centrifuged and then, diluted with distilled water for analysis of biomass. The biomass concentration was monitored spectrophotometrically at 600 nm and estimated from a biomass dry weight vs. absorbance calibration curve obtained previously. The lactose and ethanol concentrations in the supernatant were quantified by high-performance liquid chromatography (HPLC), using a Jasco chromatograph equipped with a refractive index (RI) detector (Jasco 830-RI) and a Chrompack column (300 x 6.5 mm) at 60ºC, using 5 mM sulfuric acid as the eluent at a flow rate of 0.5 mL/min and a sample volume of 20 μl.

2.5 Experimental design

In order to optimize process parameters, a central composite design (CCD) with three factors at three levels was performed. Experimental results of the CCD were fitted with a second-order polynomial equation by a multiple regression analysis. The quadratic model for predicting the optimal point was expressed as follows:

$$Y = C_0 + \sum_{i=1}^{3} C_i x_i + \sum_{i=1}^{3} C_{ii} x_i^2 + \sum_{i=1}^{3} \sum_{j<i} C_{ij} x_i x_j \quad (1)$$

where Y is the response (ethanol concentration), C_0, C_i, C_{ii}, and C_{ij} are constant coefficients, and x_i and x_j are the coded independent factors. The independent factors were coded according to the following equation:

$$x_i = \frac{X_i - X_0}{\Delta X_i} \quad (2)$$

where x_i is the coded value of the ith independent variable, Xi the real value of the ith independent variable, X_0 the original value of the ith independent variable at the center point, and ΔXi the step change value (50 for initial lactose concentration, 5 for temperature and 1 for inoculum concentration).

The quality of the fitted polynomial model was expressed by the coefficient of determination R^2, and its statistical significance was checked by the F-test. The significance of the regression coefficients was tested by t-value. Results were analyzed by the Experimental Design Module of the Statistica 5.0 software (Statsoft, USA). The model permitted evaluation of the effects of linear, quadratic and interactive terms of the independent variables on the chosen dependent variable.

3 Results and Discussion

A central composite design for the three factors (initial lactose concentration, temperature and inoculum concentration), each at three levels and three replicates at the center (to account for pure internal error), was applied for optimizing ethanol production in shake flasks. The design matrix for these factors in the optimization runs is noted in Table 1.

The results presented in Table 1 for ethanol production were subjected to analysis of regression and analysis of variance (ANOVA) (Table 2). After applying the ANOVA statistical test, it was found that, in the range studied, only the linear and quadratic effect of initial lactose concentration had a significant effect on ethanol production at 95% confidence level. The lack-of-fit test was insignificant (p = 0.066), and the regression equation obtained presented a R^2 value of 0.968 (R^2 > 0.75 indicates the aptness of the model), suggesting that a second-order model accurately represents the data in the experimental region studied, explaining 96.8% of the variability in the response. The following regression equation was obtained:

$$Y = 27.5 + 17.9\, x_1 + 3.8\, x_1^2 \quad (3)$$

where Y is the ethanol concentration (response) and x_1 is the initial lactose concentration (coded independent factor). The significance of each coefficient was determined by Student's t-test and p-values, which are listed in Table 2. The larger the magnitude of the t-value and smaller the p-value, more significant is the corresponding coefficient.

Table 1. Coded levels (C) and real values (R) of the variables in central composite design: lactose (X_1, g/L); temperature (X_2, ºC); inoculum (X_3, g/L); ethanol (Et); ethanol per biomass yield factor ($Y_{P/X}$); ethanol yield factor ($Y_{P/S}$).

Run	Design matrix						Experimental results		
	X_1		X_2		X_3		Et (g/L)	$Y_{P/X}$ (g/g)	$Y_{P/S}$ (g/g)
	C	R	C	R	C	R			
1	-1	50	-1	25	-1	1	12.7	3.21	0.25
2	-1	50	-1	25	+1	3	13.4	3.39	0.26
3	-1	50	+1	35	-1	1	12.0	2.65	0.27
4	-1	50	+1	35	+1	3	13.4	3.04	0.35
5	+1	150	-1	25	-1	1	48.2	7.49	0.34
6	+1	150	-1	25	+1	3	47.0	7.43	0.36
7	+1	150	+1	35	-1	1	48.5	7.57	0.35
8	+1	150	+1	35	+1	3	41.5	8.80	0.28
9	-1	50	0	30	0	2	10.3	2.22	0.22
10	+1	150	0	30	0	2	55.9	8.01	0.37
11	0	100	-1	25	0	2	28.8	4.78	0.33
12	0	100	+1	35	0	2	24.5	4.51	0.28
13	0	100	0	30	-1	1	32.4	4.91	0.33
14	0	100	0	30	+1	3	28.8	4.62	0.29
15	0	100	0	30	0	2	26.1	3.96	0.30
16	0	100	0	30	0	2	25.6	3.98	0.30
17	0	100	0	30	0	2	23.8	3.68	0.29

Table 2. Analysis of variance (ANOVA) and coefficient estimates for second-order model.

Source of variation	Degree of freedom	Sum of squares	Mean square	*F*-value	*p*-value
X_1	1	3214.849	3214.849	2196.936	0.000*
X_1^2	1	39.105	39.105	26.723	0.035*
X_2	1	10.404	10.404	7.110	0.117
X_2^2	1	18.526	18.526	12.660	0.071
X_3	1	9.409	9.409	6.430	0.127
X_3^2	1	4.671	4.671	3.192	0.216
X_1X_2	1	2.531	2.531	1.730	0.319
X_1X_3	1	13.261	13.261	9.062	0.095
X_2X_3	1	3.251	3.251	2.222	0.275
Lack of fit	5	106.254	21.251	14.522	0.066
Pure error	2	2.927	1.463		
Total	16	3422.749			

Factors	Degree of freedom	Regression coefficient	Standard error	*t*-value	*p*-value
Mean/Intercept	1	27.5	0.52	53.16	0.000
X_1	1	17.9	0.38	46.87	0.000
X_1^2	1	3.8	0.74	5.17	0.035
X_2	1	-1.0	0.38	-2.67	0.117
X_2^2	1	-2.6	0.74	-3.56	0.071
X_3	1	-1.0	0.38	-2.54	0.127
X_3^2	1	1.3	0.74	1.79	0.216
X_1X_2	1	-0.6	0.43	-1.32	0.319
X_1X_3	1	-1.3	0.43	-3.01	0.095
X_2X_3	1	-0.6	0.43	-1.49	0.275

$R^2 = 0.968$

* Values significant at 95% confidence level

The relation between factors and response can best be understood by examining surface plots as a function of two factors at a time and holding the other factor at fixed level. The three-dimensional response surface curves were then plotted (Fig. 1). Figure 1 shows that increasing initial lactose concentration resulted in higher ethanol production, with maxima values (≥41.5 g/L) at maximum concentration tested (150 g/L). Previous report on ethanol production from cheese whey powder found that the ethanol concentration was proportionally increased with the increase in initial sugar concentration up to 75 g/L (Ozmihci and Kargi, 2007b). The maxima ethanol amounts produced in the present study were higher than those obtained by direct fermentation of crude (nonconcentrated) cheese whey (Zafar and Owais, 2006) or cheese whey powder (Ozmihci and Kargi, 2007b).

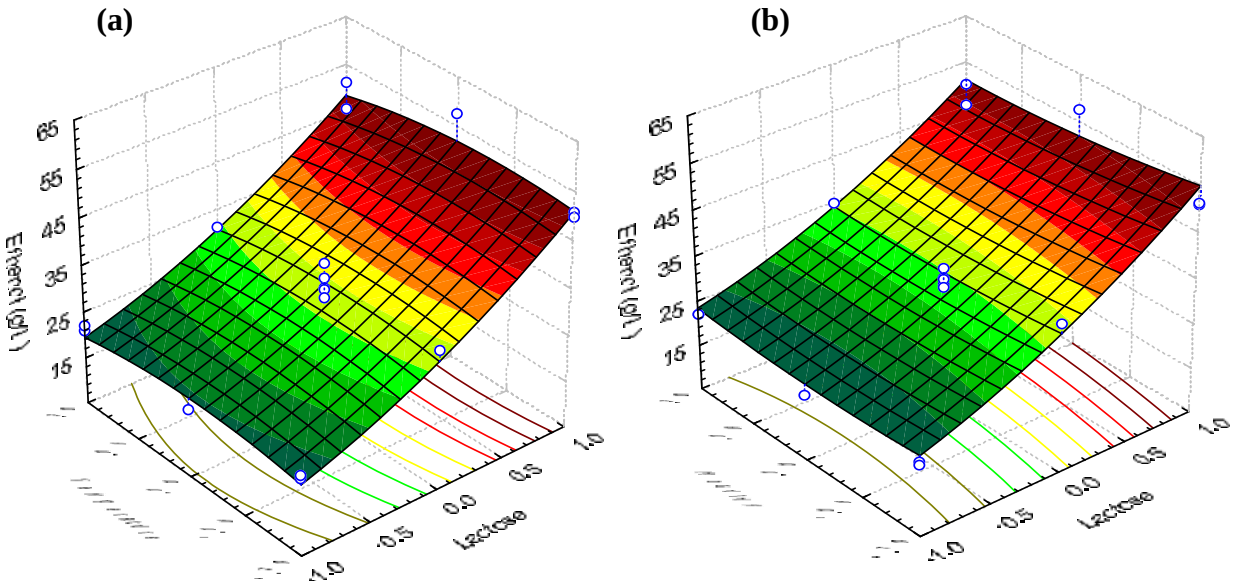

Figure 1. Response surface of ethanol production from cheese whey powder by *K. fragilis* as a function of: (a) initial lactose concentration and temperature, (b) initial lactose and inoculum concentrations.

4 Conclusions

The initial lactose concentration of cheese whey powder affected the production of ethanol by *K. fragilis* (Kf 1) (p<0.01).

The response surface analysis of the central composite design results indicated that, in the range studied, the optima conditions for maximum ethanol production (≥41.5 g/L) consisted in using an initial lactose concentration of 150 g/L, temperature between 25 and 35ºC, and inoculum concentration between 1 and 3 g/L.

The results proved the feasibility of using cheese whey powder as substrate to produce higher ethanol concentrations than those obtained by direct fermentation of nonconcentrated cheese whey.

Acknowledgements

The authors acknowledge the financial support from CAPES/Grices (BEX2150/07-7) and Lactogal for supplying cheese whey powder.

References

Adinarayana, K., Ellaiah, P., Srinivasulu, B., Devi, R.B., Adinarayana. G. (2003). Response surface methodological approach to optimize the nutritional parameters for neomycin production by *Streptomyces marinensis* under solid-state fermentation. *Process Biochemistry*, 38, 1565–1572.

Ghaly, A.E., El-Taweel, A.A. (1997). Kinetic modelling of continuous production of ethanol from cheese whey. *Biomass and Bioenergy*, 6, 461-472.

González Siso, M.I. (1996). The biotechnological utilization of cheese whey: A review. *Bioresource Technology*, 57, 1-11.

Kargi, F., Ozmihci, S. (2006). Utilization of cheese whey powder (CWP) for ethanol fermentations: Effects of operating parameters. *Enzyme and Microbial Technology*, 38, 711–718.

Li, C., Bai, J., Cai, Z., Ouyang, F. (2001). Optimization of a cultural medium for bacteriocin production by Lactococcus lactis using response surface methodology. *Journal of Biotechnology*, 93, 27–34.

Oh, S., Rheem, S., Sim, J., Kim, S., Baek, Y. (1995). Optimizing conditions for the growth of *Lactobacillus casei* YIT 9018 in tryptone-glucose medium by using response surface methodology. *Applied and Environmental Microbiology*, 61, 3809–3814.

Ozmihci, S., Kargi, F. (2007a). Continuous ethanol fermentation of cheese whey powder solution: effects of hydraulic residence time. *Bioprocess and Biosystems Engineering*, 30, 79–86.

Ozmihci, S., Kargi, F. (2007b). Kinetics of batch ethanol fermentation of cheese-whey powder (CWP) solution as function of substrate and yeast concentrations. *Bioresource Technology*, 98, 2978–2984.

Zafar, S., Owais, M. (2006). Ethanol production from crude whey by *Kluyveromyces marxianus*. *Biochemical Engineering Journal*, 27, 295–298.

Proceedings of the 10th International Chemical and
Biological Engineering Conference - CHEMPOR 2008
Braga, Portugal, September 4-6, 2008
E.C. Ferreira and M. Mota (Eds.)

APPLICATION OF NORMALIZED WEIBULL MODEL FOR DESCRIBING THE AIR DRYING OF MANGO SLICES AT DIFFERENT MATURITY STAGES

Otoniel Corzo[1*], Nelson Bracho[2], Carlos Alvarez[1]
[1] Department of Food Technology, Universidad de Oriente, Nucleo de Nueva Esparta. Guatamare. Venezuela.
[2]Program of Statistic, Universidad de Oriente, Núcleo de Nueva Esparta, Guatamare, Venezuela.

Keywords: Moisture content, water diffusion coefficient, simulation
Topic: Multi-scale and/or multi-disciplinary approach to process-product innovation: Food Engineering.

Abstract

Application of Weibull model was investigated for describing the thin layer drying of green and half-ripe mango slices and determining the water effective diffusion coefficient (D_e), respectively. Mango fruits at green and half-ripe stages were cut into slices with an average thickness of 3.0 x10^{-3} m. The air drying was carried out at four air temperatures of 50, 60, 70 and 80 ºC and two air velocities of 1.80 and 1.91 m/s. The high regression coefficients (R^2 > 0.99), low asymptotic standard errors for derive parameters and chi-square indicated the acceptability of normalized Weibull model for determining D_e. The values of D_e ranged approximately from 1.76 x 10^{-10} to 3.14 x 10^{-10} m^2/s, and from 2.30 x 10^{-10}.

1. Introduction

Developing drying models and determining moisture transport parameters are of particular interest for efficient mass transfer analysis and reproducibility of quality-controlled products. Fick's law of diffusion, based on effective diffusivity approach, has been used to describe the moisture diffusion process for food products by many researchers. Although this model provides insights into mechanistic relevance of an observed phenomenon, it frequently sacrifices the precision of the representations due to overlooked existence of uncertainties. On the other hand, the development of empirical models requires considerably less effort. They are able to overcome any inaccuracies of mechanistic models caused by the existence of uncertainties among the empirical models. The probabilistic Weibull model has been used to describe the behavior of rehydration kinetics (García-Pascual et al., 2006), water loss during osmotic dehydration (Cunha et al., 2001), and mass transfer during vacuum osmotic dehydration (Corzo and Bracho, 2008). The Weibull distribution model is described by two parameters, the scale parameter and the shape parameter. The scale parameter (α) defines the process rate constant, and the shape parameter (β) is related to velocity of the mass transfer at the beginning. Many attempts were made in order to utilize the scale parameter of the Weibull distribution function as an indicator of the mechanism (i.e. diffusion, external resistance and matrix relaxation) of liquid uptake during rehydration. The Weibull distribution model was normalized by Marabi *et al*. (2003) to describe water uptake during rehydration of food particulates (Marabi *et al*., 2003, 2004). Internal diffusion, external resistance and relaxation processes could be described with a normalized Weibull distribution. There is little information available in the literature about using Weibull model to describe the air drying of fruit products. The objectives of this study were the determination of the applicability of normalized Weibull model in describing the thin layer drying of green and

half-ripe mango slices, and determining the water effective diffusion coefficient of mango slices.

2. Materials and methods

Sample preparation

Green and half-ripe mango fruits (*Mangifera indica*, variety Hilacha) were acquired from same crop grown in Margarita Island, Venezuela. Ten mango fruits of given maturity stage (N = 80) were used for each experimental condition. Samples were washed by a tap water, peeled and cut into slices with an average large of 45.2 $x10^{-3}$ m, average width of 34.4 $x10^{-3}$ m, and average thickness of 3.0 $x10^{-3}$ m. The determination of moisture content for fresh mango was carried out in four replicates.

Air drying

The air drier used mainly consists of three basic units, a fan providing desired drying air velocity, heat exchanger using resistance coil controlling the temperature of drying air and drying chamber. The mango slices were uniformly spread in a drying pan as thin layer. The drying experiments were carried out at air velocity of 1.80, or 1.91m/s and temperature of 50, 60, 70 or 80 ºC. The air humidity was 0.018 ± 0.001 kg/kg dry air. Changes in weight of slices were monitored at 10 min intervals by a digital balance of 0.01 g accuracy. The drying was continued until there is no large variation in the weight. Drying experiments were repeated twice.

The normalized Weibull model

The Weibull model was modified and the rate parameter was normalized with a characteristic dimension for the thickness:

$$\frac{X_w - X_{we}}{X_{w0} - X_{we}} = MR = \exp\left[-\left[\frac{t}{\alpha_n}\right]^{\beta}\right] = \exp\left[-\left[\frac{t\,D}{L^2}\right]^{\beta}\right] \quad (1)$$

where X_{wo}, X_w and X_{we} are the initial, at a time t, and at equilibrium moisture content respectively, α is the scale parameter of the Weibull model, β is the shape parameter (dimensionless), D is the calculate water diffusion coefficient, L is the half-thickness of the slices for drying from both top and bottom sides, and t is the drying time.

The effective diffusion coefficient (D_e) can be calculated by following equation:

$$D_e = \frac{D}{R_g} \quad (2)$$

where (R_g) is the geometric factor.

Simulation

To establish the adequate parameter (R_g) to be utilized for the implementation of the normalized Weibull, the solution of Fick's second law for diffusion from a flat plate have been used (Crank, 1975):

$$MR = \frac{8}{\pi^2}\sum_{n=0}^{n=\infty}\frac{1}{(2n+1)^2}\exp\left[-\frac{(2n+1)^2\,\pi^2\,D_e\,t}{L^2}\right] \quad (3)$$

In order to simulate realistic conditions, a set of random errors taken from a population with normal distribution with zero mean and different values of standard deviation (i.e., noise's span) was introduced (Azevedo *et al*., 1998):

$$MR_{noise} = MR_{theoretical}\left[1 + SD\ x\ Zn\right] \quad (4)$$

where *SD* is the standard deviation (%) and *Zn* is the random number with standard normal distribution, *Zn* ~ (0.1).The noise span of 2.5% was utilized to depict experimental error expected in air drying process.

For simulation the range of the effective diffusion coefficient was taken as 10^{-10} to 10^{-12} m^2/s describing typical values expected for dehydrated foods. The moisture ratio data at the different drying conditions were derived from simulation using the first three terms of the serie in the analytical solution of the Fickian diffusion model. Then, the normalized Weibull model was fitting to data derived from simulation and the geometric factor (R_g) was

determined.

Statistical analysis

Non linear regression using Levenberg-Marquandt method was diffusion coefficient and used for fitting experimental moisture ratio data to Esq. 1. Normalized Weibull model was used to compare predicted moisture ratio during drying to that of experimental moisture ratio data. The performance of the model was determined using the determination coefficient (R^2) of the non linear regression, and the chi-square (χ^2).

3. Results and discussion

Moisture content changes

The initial moisture content of green and half-ripe mango slices were observed to be 6.673 ± 0.112 and 6.015 ± 0.231 kg water/kg db, respectively. The equilibrium moisture content ranged from 0.136 ± 0.011 to 0.325 ± 0.018 kg water/kg db for green mango slices and from 0.105 ± 0.008 to 0.313 ± 0.016 kg water/kg db for half-ripe mango slices. An analysis of variance showed that moisture ratio decreased ($p < 0.05$) with increasing drying time and air temperature and velocity for all maturity stages. In general, towards the end of drying the influence of both air temperature and velocity on moisture ratio changes are lower than at the beginning. Similar results were found during convective drying of figs (Piga et al., 2004), plum (Goyal et al., 2007), peach (Kingsly et al., 2007) and cherry laurel (Kaya and Aydin, 2008).

Simulation

The moisture content data at the different drying conditions were derived from simulation using the first four terms of the serie in the analytical solution of the Fickian diffusion model. Results of fitting normalized Weibull model to data derived from simulation are shown in Table 1. The high coefficients of determination ($R^2 > 0.98$) and the low asymptotic standard errors (ASE) for derive parameters (D and β) indicated the goodness of fit.

Table 1. Effect of theoretical D_e on derived parameter (β) and geometric factor (R_g) of normalized Weibull model.

D_e (m^2/s)	β	ASE	R_g	R^2
1.0×10^{-10}	0.83	0.01	13.1	0.999
1.0×10^{-11}	0.80	0.01	13.2	0.997
1.0×10^{-12}	0.76	0.01	13.2	0.994

Table 1 shows that: 1) the calculate diffusion coefficient was one order of magnitude lower than used theoretical diffusion coefficient; 2) derived R_g value was maintained practically constant; and 3) β values increased with increasing the theoretical diffusion coefficient. Similar results were found for rehydration of food particulates (Marabi *et al*., 2003).

Application of normalized Weibull model

The high coefficients of determination ($R^2 > 0.99$), the low asymptotic standard errors for D and β, the low chi-square (χ^2) values (Table 2) and no pattern evident with the residuals across the range of diffusion coefficient (non shown) indicated the goodness of fit of experimental data to Eq. (1). The value of effective diffusion coefficient (D_e) was calculated by Eq. 8 using R_g equal 13.1 (Table 2). The D_e values ranged approximately from 1.76×10^{-10} to 3.14×10^{-10} m^2/s, and from 2.30×10^{-10} to 3.25×10^{-10} m^2/s for green and half-ripe mango, respectively. Similar values were finding by using Fick's second law of diffusion (Corzo *et al*. 2008). These values fell within the normally expected range of D_e (10^{-8} to 10^{-12} m^2/s) for dehydrated foods (Zogzas *et al*., 1996).

Values of β ranged from 0.76 to 0.80 and from 0.79 to 0.80 for green and half-ripe mango, respectively. The shape parameter is related to velocity of the mass transfer at the beginning, e.g., the lower is the β value, the faster the water loss rate at the beginning. Marabi *et al*. (2003) reported that the β value could be used to classify and differentiate between the various mechanisms involved during process. From the derived value of the β parameter (≈ 0.80) it follows that the mango slices followed a diffusion mechanism during air drying.

Table 2. Water effective diffusion coefficient (D_e) and shape parameter (β) of mango slices during air drying at different air velocities (V) and temperatures (T).

T (ºC)	V (m/s)	D x10^9 (m^2/s)	ASE x10^9	β	*ASE*	R^2	D_e x10^{10} (m^2/s)	χ^2
			Green mango slices					
50	1.80	2.31	0.05	0.76	0.02	0.993	1.76 ± 0.01	0.00032
	1.91	2.92	0.05	0.78	0.02	0.993	2.23 ± 0.01	0.00033
60	1.80	2.73	0.04	0.78	0.02	0.994	2.08 ± 0.01	0.00038
	1.91	3.55	0.04	0.80	0.02	0.994	2.71 ± 0.01	0.00039
70	1.80	3.26	0.08	0.79	0.02	0.994	2.49 ± 0.01	0.00034
	1.91	4.01	0.08	0.80	0.023	0.994	3.06 ± 0.01	0.00032
80	1.80	3.92	0.10	0.80	0.03	0.994	2.99 ± 0.02	0.00036
	1.91	4.11	0.10	0.80	0.03	0.994	3.14 ± 0.02	0.00034
			Half-ripe mango slices					
50	1.80	3.01	0.04	0.79	0.02	0.994	2.30 ± 0.01	0.00029
	1.91	3.29	0.08	0.79	0.03	0.992	2.51 ± 0.01	0.00035
60	1.80	3.23	0.05	0.79	0.02	0.996	2.46 ± 0.01	0.00038
	1.91	3.80	0.08	0.80	0.03	0.994	2.90 ± 0.01	0.00031
70	1.80	3.66	0.04	0.80	0.03	0.994	2.79 ± 0.01	0.00035
	1.91	4.02	0.05	0.81	0.02	0.995	3.07 ± 0.01	0.00032
80	1.80	4.08	0.04	0.80	0.03	0.995	3.11 ± 0.01	0.00036
	1.91	4.26	0.11	0.81	0.03	0.996	3.25 ± 0.02	0.00032

ASE = asymptotic standard error
χ^2 = chi-square

4. Conclusions

The normalized Weibull model describes the air drying of green and half-ripe mango slices at different air temperatures and velocities. Also, it allows calculates the water effective diffusion coefficient during process. The water effective diffusion coefficient values found were comparable with those obtained with Fick second law. The results of the analysis of variance test showed significant effects of air temperature and velocity on the water effective diffusion coefficient.

References

Azevedo, I.C.A, Oliveira, F.A.R. Drumond, M.C. (1998). A study on the accuracy and precision of external mass transfer and diffusion coefficients jointly estimated from pseudo-experimental simulated data. Mathematical Computation Simulation, 48(1), 11–22.

Corzo, O., Bracho, N. (2008). Application of Weibull distribution model to describe the vacuum pulse osmotic dehydration of sardine sheets. Lebensmittel-Wissenschaft und-Technolgie, 41(6), 1108-1115.

Corzo, O., Bracho, N., Alvarez, C. (2008). Water effective diffusion coefficient of mango slices at different maturity stages during air drying. Journal of Food Engineering, 87(4), 479-484.

Crank, J. (1975). The mathematics of diffusion. (2nd ed.). pp 24-25. Clarendon Press, Oxford.

Cunha, L.M., Oliveira, F.A.R., Aboim, A.P., Frías, J.M. (2001). Stochastic approach to the modelling of water losses during osmotic dehydration and improved parameter estimation. Int. Journal of Food Science and Technology, 36, 253-262.

García-Pascual, P., Sanjuán, N., Melis, R., Mulet, A. (2006). *Morchella esculenta* (morel) rehydration process modeling. Journal of Food Engineering, 72, 346-353.

Goyal, R.K., Kingsly, A.R. P., Manikatan, M.R., Ilyas, S.M. (2007). Mathematical modeling of thin layer drying kinetics of plum in a tunnel dryer. Journal of Food Engineering, 79(1), 176-180.

Kaya, A., Aydin, O. (2008). Experimental investigation of drying kinetics of cherry laurel. Journal of Food Processing and Engineering, 31, 398-412.

Kingsly, R.P., Goyal, R.K., Manikantan, M.R., Ilyas, S.M. (2007). Effects of pretreatments and drying air temperature on drying behaviour of peach slice. International Journal of Food Science and Technology, 42(1), 65-69.
Marabi, A., Jacobson, M., Livings, S., and Saguy, I.S. (2004). Effect of mixing and viscosity on rehydration of dry food particulates. European Food Research Technology, 218, 339–344.
Marabi, A., Livings, S., Jacobson, M., Saguy, I.S. (2003). Normalized Weibull distribution for modeling rehydration of food particulates. European Food Research Technology, 217, 311-318.
Piga, A., Pinna, I., Ozer, K.B., Agabbio, M., Aksoy, U. (2004). Hot air dehydration of figs (*Ficus carica* L.): drying kinetics and quality loss. Int. Journal of Food Science and Technology, 39, 793–799.
Zogzas, N.P., Maroulis, Z.B., Marinos-Kouris, D. (1996). Moisture diffusivity data compilation in foodstuffs. Drying Technology. 14(10), 2225–2253.

Proceedings of the 10th International Chemical and
Biological Engineering Conference - CHEMPOR 2008
Braga, Portugal, September 4-6, 2008
E.C. Ferreira and M. Mota (Eds.)

DETERMINATION OF SUITABLE THIN LAYER MODEL FOR AIR DRYING OF MANGO SLICES

Otoniel Corzo[1], Nelson Bracho[2*] Carlos Alvarez[1]
[1] Department of Food Technology, Universidad de Oriente, Núcleo de Nueva Esparta. Guatamare. Venezuela.
[2]Program of Statistic, Universidad de Oriente, Núcleo de Nueva Esparta, Guatamare, Venezuela.

Key words: Midilli and Kucuk model, green and half-ripe mango slices.
Topic: Multi-scale and/or multi-disciplinary approach to process-product innovation: Food Engineering.

Abstract

An air dryer was used for thin layer drying process of green and half-ripe mango and moisture ratio at any drying time were compared by ten models (Newton, Page, Henderson and Pabis, modified Henderson and Pabis, logarithmic, two-term, two-term exponential, Wang and Singh, Verma *et al*. and Midilli and Kucuk). The Midilli and Kucuk model satisfactorily described the drying behaviour of mango slices at different maturity stages with highest R^2 values and lowest χ^2. air drying was carried out at four air temperatures of 50, 60, 70 and 80 ºC and two air velocities of 1.80 and 1.91 m/s. Temperature sensitivity of parameter *k* and *n* for green mango decreased ($p<0.05$) with increasing air velocity from 1.76 m/s to 1.80 m/s and then increased with increasing velocity to 1.91 m/s. Temperature sensitivity of parameter *k* for half-ripe mango increased ($p<0.05$) with increasing air velocity, at 1.91 m/s and was found to be the most temperature sensitive while that at 1.76 was the least temperature sensitive. Temperature sensitivity of parameter *n* for half-ripe mango increased ($p<0.05$) with increasing air velocity from 1.76 m/s to 1.80 m/s and then decreased with increasing velocity to 1.91 m/s.

1 Introduction

Thin layer drying studies form the basis of understanding the drying characteristics of food since every food is unique. Numerous mathematical models (theoretical, semi-theoretical or purely empirical) available in the literature for explaining thin layer drying characteristics of agricultural products have been used. Among semi theoretical thin layer drying models, the Newton model, the Henderson and Pabis mode, the modified Henderson and Pabis model, the Page model, the modified Page model, the logarithmic model, the two term, the two term exponential, the Verma *et al*., the Midilli and Kucuk and Singh models are used widely. Mathematical models have proved to be very useful in the design and analysis of the mass and heat transfer processes during drying. All parameters used by simulation models are directly related to the drying conditions. Little information is available about research on thin layer drying of mango in literature (Goyal *et al*., 2006). Therefore, the objectives of this study were to determining the suitable model for predicting the thin layer drying kinetics of green and half-ripe mango slices at different drying air temperature and velocity conditions, and analyze the effects of temperature and velocity on the constants of the suitable model.

2 Materials and methods

Sample preparation

Green and half-ripe mango fruits (*Mangifera indica*, variety Hilacha) were acquired from same crop grown in Margarita Island, Venezuela. Ten mango fruits of given maturity stage (N = 80) were used for each experimental condition. Samples were washed by a tap water, peeled and cut into slices with an average large of 45.2 $x10^{-3}$ m, average width of 34.4 $x10^{-3}$ m, and average thickness of 3.0 $x10^{-3}$ m. The determination of moisture content for fresh

mango was carried out in four replicates.

Air drying

The air drier used mainly consists of three basic units, a fan providing desired drying air velocity, heat exchanger using resistance coil controlling the temperature of drying air and drying chamber. The mango slices were uniformly spread in a drying pan as thin layer. The drying experiments were carried out at air velocity of 1.80, or 1.91m/s and temperature of 50, 60, 70 or 80 ºC. The air humidity was 0.018 ± 0.001 kg/kg dry air. Changes in weight of slices were monitored at 10 min intervals by a digital balance of 0.01 g accuracy. The drying was continued until there is no large variation in the weight. Drying experiments were repeated twice. This procedure was followed for each experiment corresponding to the conditions according to a 4x3x2 factorial design where the air temperature, velocity, and maturity were 50, 60, 70 and 80 ºC, 1.76, 1.80 and 1.91 m/s, and green and half-ripe mango, respectively.

Drying models

Moisture ratio of samples during drying was expressed as:

$$MR = \frac{X_t - X_e}{X_0 - X_e} \quad (1)$$

where X_t is the moisture content at any time t, X_e and X_0 are equilibrium and initial moisture contents (dry matter).

To select a suitable model for describing the drying process of mango slices, drying curves were fitted with eight theoretical and semi-theoretical models:

1. Exponential or Newton model $MR = \exp(-k\,t)$ (2)

2. Henderson and Pabis model $MR = a \exp(-k\,t)$ (3)

3. Modified Henderson and Pabis model

$$MR = a \exp(-k\,t) + b \exp(-g\,t) + c \exp(-h\,t) \quad (4)$$

4. Page model. $MR = \exp(-k\,t^n)$ (5)

5. Two term model. $MR = a \exp(-k_0\,t) + b \exp(-k_1\,t)$ (6)

6. Two term exponential model. $MR = a \exp(-k\,t) + (1-a) \exp(-k\,a\,t)$ (7)

7. Logarithmic model. $MR = a \exp(-k\,t) + c$ (8)

8. Verma et al. model. $MR = a \exp(-k\,t) + (1-a) \exp(-g\,t)$ (9)

9. Midilli and Kucuk model. $MR = a \exp(-k\,t^n) + b\,t$ (10)

10. Wang and Singh model. $MR = 1 + a\,t + b\,t^2$ (11)

where *n, a, b, c, g, h, k, k_0, and k_1* are constant of models, and *t* is the drying time.

Statistical analysis

Non linear regression using Levenberg-Marquandt method (Bates & Watts, 1988) was used to fit experimental moisture ratio data to different models. Analysis of variance was carried out to find effects ($p<0.05$) of air temperature and velocity on the constants of selected models. The different models were used to compare predicted moisture content during drying to that of experimental moisture content data. The performance of the models was determined using the coefficient of determination (R^2) of the non linear regression, and the reduced chi-square (χ^2) between the values predicted from the model and the experimental

3. Results and discussion

Evaluation of the Models

The values of coefficient of determination (R^2), and reduced chi-square (χ^2) for proposed models are presented in Table 1.For all experiments, all models gave R^2 values greater than 0.92 and low χ^2 values indicating a good fit. The results showed that highest values of R^2 and lowest values of χ^2 for both maturity stages were obtained with the Midilli and Kucuk model. Similar results were obtained by some authors on drying of fruits and vegetables (Doymaz, 2005; Akpinar, 2006; Menges and Ertekin, 2006; Togrul, 2006). The constants for Midilli and Kucuk model at different conditions and maturity stages are shown in Table 2. The analysis of variance (ANOVA) showed that constants *k*, *n* and *b* for Midilli and Kucuk model were significant different ($p<0.05$) for both maturity stages and were affected by air velocity and

temperature and its interactions

Table 1. Statistical results obtained from the proposed models for mango slices

Model	Velocity (m/s)	Temperature (ºC)	Green mango		Half-ripe mango	
			R^2	χ^2	R^2	χ^2
Newton	1.76	50	0.989	0.00042	0.994	0,01755
		60	0.987	0.00030	0.976	0,09342
		70	0.994	0.00014	0.935	0,03698
		80	0.990	0.00044	0.980	0,09267
	1.80	50	0.993	0.00012	0.997	0,01154
		60	0.990	0.00031	0.967	0,14206
		70	0.981	0.00730	0.956	0,02531
		80	0.969	0.00021	0.982	0,09300
	1.91	50	0.977	0.00091	0.947	0,03693
		60	0.998	0.00434	0.991	0,04202
		70	0.972	0.00019	0.989	0,04260
		80	0.994	0.00092	0.953	0,02514
Page	1.76	50	0.991	0.00015	0.997	0,00177
		60	0.995	0.00041	0.994	0,00424
		70	0.997	0.00016	0.989	0,00093
		80	0.999	0.00010	0.997	0,00011
	1.80	50	0.997	0.00031	0.998	0,00013
		60	0.998	0.00021	0.995	0,00042
		70	0.997	0.00016	0.996	0.00040
		80	0.999	0.00010	0.999	0.00012
	1.91	50	0.997	0.00021	0.980	0.00144
		60	0.993	0.00029	0.996	0.00042
		70	0.995	0.00042	0.999	0.00011
		80	0.995	0.00093	0.997	0.00027
Henderson And Pabis	1.76	50	0.973	0.00042	0.990	0.00068
		60	0.976	0.00027	0.994	0.00042
		70	0.982	0.00018	0.994	0.00250
		80	0.981	0.00021	0.997	0.00482
	1.80	50	0.985	0.00081	0.996	0.00047
		60	0.975	0.00141	0.994	0.00636
		70	0.964	0.00295	0.992	0.00154
		80	0.976	0.00152	0.994	0.00930
	1.91	50	0.942	0.00907	0.995	0.02557
		60	0.992	0.00068	0.991	0.02718
		70	0.927	0.00242	0.998	0.04200
		80	0.936	0.00297	0.993	0.01489
Modified Henderson and Pabis	1.76	50	0.991	0.00044	0.986	0.00099
		60	0.994	0.00042	0.982	0.00012
		70	0.994	0.00134	0.957	0.00036
		80	0.987	0.00137	0.982	0.00091
	1.80	50	0.996	0.00019	0.955	0.00042
		60	0.994	0.00042	0.977	0.00082
		70	0.992	0.00042	0.975	0.00025
		80	0.994	0.00047	0.991	0.00090
	1.91	50	0.995	0.00422	0.955	0.00047
		60	0.992	0.00045	0.977	0.00014
		70	0.998	0.00097	0.989	0.00013
		80	0.973	0.00172	0.988	0.00010
Logarithmic	1.76	50	0.999	0.00085	0.994	0.00041
		60	0.995	0.00019	0.996	0.00040
		70	0.997	0.00021	0.995	0.00044
		80	0.994	0.00042	0.995	0.00043
	1.80	50	0.998	0.00019	0.998	0.00013
		60	0.997	0.00016	0.997	0.00031

		70	0.999	0.00017	0.996	0.00014
		80	0.999	0.00016	0.997	0.00016
	1.91	50	0.999	0.00021	0.997	0.00013
		60	0.995	0.00042	0.998	0.00016
		70	0.996	0.00024	0.998	0.00021
		80	0.994	0.00045	0.995	0.00048
Two term	1.76	50	0.996	0.00015	0.988	0.00091
		60	0.984	0.00182	0.985	0.00099
		70	0.996	0.00021	0.963	0.00036
		80	0.989	0.00131	0.987	0.00013
	1.80	50	0.992	0.00043	0.996	0.00024
		60	0.995	0.00042	0.987	0.00014
		70	0.993	0.00046	0.979	0.00017
		80	0.995	0.00040	0.992	0.00042
	1.91	50	0.994	0.00044	0.962	0.00036
		60	0.995	0.00040	0.981	0.00145
		70	0.991	0.00052	0.991	0.00098
		80	0.977	0.00164	0.990	0.00093
Two term exponential	1.76	50	0.999	0.00041	0.997	0.00031
		60	0.995	0.00047	0.993	0.00042
		70	0.997	0.00029	0.986	0.00113
		80	0.999	0.00856	0.997	0.00016
	1.80	50	0.991	0.00552	0.998	0.00011
		60	0.996	0.00037	0.996	0.00042
		70	0.999	0.00016	0.995	0.00042
		80	0.999	0.00093	0.999	0.00010
	1.91	50	0.997	0.00081	0.979	0.00145
		60	0.995	0.00044	0.996	0.00042
		70	0.994	0.00090	0.999	0.00019
		80	0.995	0.00096	0.997	0.00017
Wang and Singh	1.76	50	0.991	0.00048	0.996	0.00042
		60	0.985	0.00096	0.995	0.00043
		70	0.981	0.00142	0.996	0.00019
		80	0.989	0.00112	0.998	0.00041
	1.80	50	0.997	0.00023	0.992	0.00045
		60	0.992	0.00047	0.994	0.00047
		70	0.992	0.00058	0.998	0.00014
		80	0.995	0.00045	0.991	0.00010
	1.91	50	0.997	0.00130	0.991	0.00015
		60	0.994	0.00043	0.989	0.00016
		70	0.989	0.00139	0.988	0.00044
		80	0.991	0.00052	0.995	0.00010
Verma *et al*.	1.76	50	0.995	0.00042	0.991	0.00012
		60	0.998	0.00160	0.975	0.00252
		70	0.996	0.00028	0.996	0.00364
		80	0.978	0.00140	0.989	0.00134
	1.80	50	0.998	0.00016	0.995	0.00042
		60	0.993	0.00042	0.986	0.00013
		70	0.992	0.00053	0.979	0.00025
		80	0.993	0.00143	0.991	0.00052
	1.91	50	0.992	0.00045	0.963	0.00365
		60	0.995	0.00042	0.983	0.00014
		70	0.991	0.00052	0.988	0.00144
		80	0.978	0.00141	0.985	0.00142
Midilli and Kucuk	1.76	50	0.999	0.00005	0.996	0.00018
		60	0.995	0.00255	0.996	0.00042
		70	0.997	0.00016	0.996	0.00041
		80	0.999	0.00011	0.997	0.00012
	1.80	50	0.998	0.00019	0.998	0.00013
		60	0.997	0.00028	0.997	0.00016

	70	0.999	0.00006	0.998	0.00015
	80	0.999	0.00010	0.999	0.00010
1.91	50	0.997	0.00011	0.986	0.00012
	60	0.995	0.00029	0.995	0.00042
	70	0.997	0.00016	0.999	0.00011
	80	0.994	0.00042	0.997	0.00020

The constants for Midilli and Kucuk model at different conditions and maturity stages are shown in Table 2. Analysis of variance (ANOVA) showed that constants *k*, *n* and *b* for Midilli and Kucuk model were significant different ($p<0.05$) for both maturity stages and were affected by air velocity and temperature and its interactions. ANOVA showed that constant *k* increased ($p<0.05$) with increasing air temperature while constant *n* decreased ($p<0.05$). There are not trends in constants *k* and *n* with increasing velocity. There are not trends in constant *b* with increasing temperature and velocity. The *k* values are higher for half-ripe mango while the *n* an *b* values are higher for green mango.

Table 2. Values of constant of Midilli and Kucuk model for green and half-ripe mango at different air temperature (T) and velocity (V).

V (m/s)	T (°C)	Green mango					Half-ripe mango				
		a	k x10^2	n	bx10^4	R^2	a	k x10^2	n	bx10^4	R^2
1.76	50	1.00	1.17	1.17	-1.3	0.999	1.00	0.72	1.24	-0.5	0.997
	60	1.01	1.53	1.15	-2.1	0.998	1.00	0.98	1.23	-4.0	0.998
	70	1.00	2.04	0.96	-1.2	0.997	0.99	1.21	1.22	-7.9	0.986
	80	0.99	2.05	0.89	-0.5	0.999	0.99	1.37	1.19	-0.5	0.997
1.80	50	1.00	1.01	1.18	-0.5	0.998	0.99	0.53	1.29	-0.5	0.998
	60	1.01	1.13	1.15	-1.2	0.997	0.99	0.68	1.26	-3.5	0.986
	70	1.00	1.24	1.13	-1.8	0.999	0.99	0.78	1.23	-3.1	0.997
	80	1.00	0.71	1.10	-4.1	0.998	0.99	1.15	1.19	-0.5	0.998
1.91	50	1.01	1.08	1.11	-0.5	0.997	0.99	0.53	1.22	-6.5	0.986
	60	1.01	1.47	0.99	-0.5	0.999	1.00	0.65	1.21	-0.5	0.996
	70	1.00	1.75	0.94	-8.0	0.998	1.00	1.06	1.18	-1.3	0.998
	80	0.99	2.05	0.87	-12.6	0.997	0.99	1.25	117	-0.5	0.986

Modeling Effects of Temperature on the Midilli and Kucuk Model Constants

Dependence of the Midilli and Kucuk model constants with the temperature is represented by the Arrhenius equation:

$$A = A_0 \exp\left(-\frac{E_a}{R\,T}\right) \tag{12}$$

where A_0 is the frequency factor (min^{-1}), E_a s the activation energy (kJ/mol), R the universal gas constant (8.314 J/mol K) and T is the absolute temperature (K). Non linear regression pooling all data was applying to determine the constants and Arrhenius parameters. The results of the non-linear regression used to fitting data to Eq. (12) are shown in Table 3. The high coefficients of determination ($R^2 > 0.93$) indicate that the constants *k* and *n* of Midilli and Kucuk model as a function of air temperature followed an Arrhenius relationship for all the air velocity (Table 3). Temperature sensitivity of parameter *k* and *n* for green mango decreased ($p<0.05$) with increasing air velocity from 1.76 m/s (E_{ak} = 20.994 J/mol and E_{an} = 9,685 J/mol) to 1.80 m/s (E_{ak} = 28.656 J/mol and E_{an} = 2.188 J/mol) and then increased with increasing velocity to 1.91 m/s (E_{ak} = 20.053 J/mol and E_{an} = 7.662 J/mol). Temperature sensitivity of parameter *k* for half-ripe mango increased ($p<0.05$) with increasing air velocity, at 1.91 m/s was found to be the most temperature sensitive (E_{ak} = 29.451 kJ/mol) while that at 1.76 was the least temperature sensitive (E_{ak} = 20.451 kJ/mol). Temperature sensitivity of parameter *n* for half-ripe mango increased ($p<0.05$) with increasing air velocity from 1.76 m/s (E_{an} = 1.361 J/mol) to 1.80 m/s (E_{an} = 2.363 J/mol) and then decreased with increasing velocity to 1.91 m/s (E_{an} = 1.632 J/mol).

Table 3. Activation energy (E_a) and natural logarithm of frequency factor (*ln (ko, n_0)*) values for for *k* and *n* constants of Midilli and Kucuk model at different drying conditions.

Parameter	1.76 m/s		1.80 m/s		1.91 m/s	
	Estimate	Standard Error	Estimate	Standard Error	Estimate	Standard Error
			Green mango			
$-ln\ (k_o)$	3.564*	0.682	1.367*	0.152	2.973*	0.638
E_{ak} (KJ/mol)	-20.994*	1.872	-8.656*	0.427	-20.053*	1.788
$-ln\ (n_o)$	3.416*	0.446	0.151*	0.052	2.756*	0.183
E_{an} (KJ/mol)	9.685*	1.251	2.188*	0.149	7.662*	0.515
R^2	0.955		0.983		0.947	
			Half-ripe mango			
$-ln\ (k_o)$	2.716*	0.573*	3.380*	0.853	5.619*	1.015
E_{ak} (KJ/mol)	-20.451*	1.607	-23.229*	2.385	-29.264*	2.848
$-ln\ (n_o)$	0.228*	0.049	0.624*	0.084	0.404*	0.065
E_{an} (KJ/mol)	1.361*	0.138	2.363*	0.237	1.632*	0.182
R^2	0.958		0.936		0.937	

* p–value < 0.001

4. Conclusion

Acording to the results of thin layer drying of green and half-ripe mango slices, Midilli and Kucuk model could be used to predict the moisture content of the product at any time of drying process with high ability between drying air temperatures of 50 and 80 ºC and velocities of 1.76 and 1.91 m/s.

References

Akpinar, E.K. (2006).Determination of suitable thin layer drying curve model for some vegetables and fruits. Journal of Food Engineering, 73, 75-84.

Bates, D.M., Watts, D.G. (1988). Nonlinear regression and its applications, Wiley, New York.

Doymaz, I. (2005). Sun drying of figs: an experimental study. Journal of Food Engineering, 71(4), 403-407.

Goyal, R.K., Kingsly, A.R.P., Manikantan, M.R., Ilyas, S.M. (2006). Thin-layer drying kinetics of raw mango slices. *Biosystems Engineering*. 95(1), 43-49.

Menges, H.O., Ertekin, C. (2006). Mathematical modeling of thin layer drying of Golden apples. Journal of Food Engineering, 77(1), 119-125.

Togrul, H. (2006). Suitable drying model for infrared drying of carrot. Journal of Food Engineering, 77(3), 610-619.

Proceedings of the 10th International Chemical and
Biological Engineering Conference - CHEMPOR 2008
Braga, Portugal, September 4-6, 2008
E.C. Ferreira and M. Mota (Eds.)

Analysis of Cellular Tissue of Chestnuts during Drying and Rehydration Process

R. Moreira*, F. Chenlo, L. Chaguri
Departamento de Enxeñaría Química, Escola Técnica Superior de Enxeñaría (ETSE), Universidade de Santiago de Compostela, Rúa Lope Gómez de Marzoa, s/n 15782 Santiago de Compostela, España.

Keywords: Microstructure, Convective drying, Shrinkage, Swelling, Size distribution
Topic: Food engineering.

Abstract

Analysis of changes in microstructure is very important in order to understand mass transfer processes in biological systems and to evaluate the quality of fresh and processed food materials. In this study, chestnuts (*Castanea sativa*) were dried by hot air at 65ºC and rehydrated at 25ºC. The cellular superficial tissue of fresh and processed chestnut at different moisture contents was characterized by optical microscopy. The results show that during drying the size of chestnut cells decreased and shape was changed. During rehydration the cells recoved size and the most of shape parameters.

1. Introduction

Food processing involves different operations such as dehydration and rehydration that involve changes in the structural characteristics of the cell tissue. These changes are directly related to heat and mass transfer gradients that take place during these processes (Prothon et al., 2001). The type and magnitude of these gradients depend on the process conditions and dehydration technique (convective, osmo-convective, freeze drying, etc). Microscopy techniques (optical, scanning electron, transmission electron) are important visualization tools of the cell structure and therefore, are used to improve the knowledge of the dehydration and rehydration processes (Aguilera and Stanley, 1999). Optical microscopy is a simple technique that allows the observation of the presence of damages on the cell tissue.

The main aim of this work is to characterize the cell tissue of fresh chestnut (no data can be found in the bibliography) and, additionally, monitoring the changes in size and shape of chestnut cells during drying and rehydration processes.

2. Materials and Methods

Experiments of optical microscopy have been carried out with cell tissue of chestnuts at different moisture contents: fresh, dried and rehydrated. Experimental conditions during convective drying were at 65 ºC and 30 % of relative humidity at different times. After drying, samples of chestnuts were rehydrated employing distilled water at 25 ºC during different times. In order to visualize cells by microscopy, thin slabs were cut using a razor blade. These samples were put on a thin glass plate under the objective (10x). One side of the slab was stained with toluidine solution (0.1 % during 15 s). In this way, samples were ready for observation under the light microscope (Zeizz Axioskop 40). A digital camera (Nikon D70) was attached to the microscope to take images of cells structures and transfer them to a computer. Images were calibrated with a micrometer of 10 mm length and divisions of 0.1 mm interval (Zeiss). The images were analysed using “Image Tool” (free software available from University of Texas). Several geometrical parameters (area, external perimeter, Feret diameter, roundness,

* Corresponding author. Tel + 34-981-563-100. E-mail:eqmoncho@usc.es

elongation and compactness) of cells were determined. These parameters were previously considered by other authors for other food materials (Reeve, 1953; Lewicki and Pawlak, 2003; Mayor et al., 2005).

3. Results

Figure 1 shows a image of the microstructure of chestnut superficial cellular tissue. As can be observed, the cells present different sizes and shapes. Some of them are round, others more elongated or polygonal. It can be observed the presence of intercellular spaces, which contain the gas phase of the tissue and some of them can be filled with and aqueous solution.

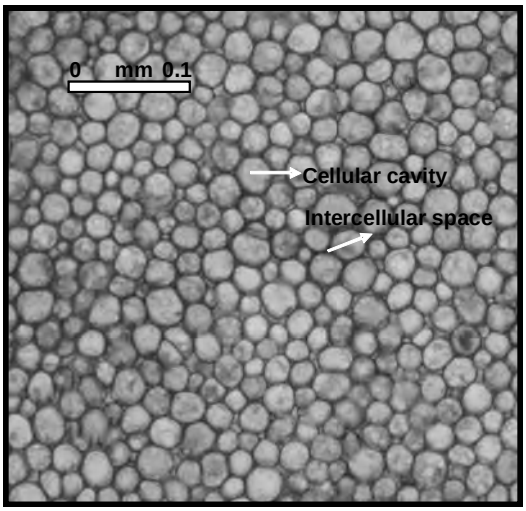

Figure 1 Microscopy image of fresh chestnut cellular tissue

Table 1 shows average values, corresponding deviations and the range of experimental data for the geometric parameters obtained from fresh samples. The characterization of the size and shape parameters for cells of fresh chestnuts with different ripeness was developed analysing more than 500 cells and the results indicated that values vary in a wide range. Average area value (876 μm^2) was less than values obtained for other products, such as apple and pumpkin (Lewicki y Porzecka-Pawlak, 2005; Mayor et al., 2005). By other hand, in the case of shape parameters the range was similar to pumpkin cells.

Table 1 Size and shape parameters for fresh chestnut cells.

Parameters	Average	Range
Area (10^{-3} mm^2)	0.8761 ± 0.0311	0.5000-1.9500
Perimeter (mm)	0.1394 ± 0.0280	0.0841-0.2009
Feret diameter (mm)	0.0329 ± 0.0057	0.0232-0.0571
Elongation	1.2311 ± 0.1369	1.0067-1.6793
Roundness	0.5736 ± 0.1656	0.1977-0.8755
Compactness	0.8499 ± 0.0632	0.6066-0.9585

The size distribution of fresh chestnuts cells can be observed in Figure 2 and showed the highest quantity (74 %) was in the range from 500 to 1050 μm^2.

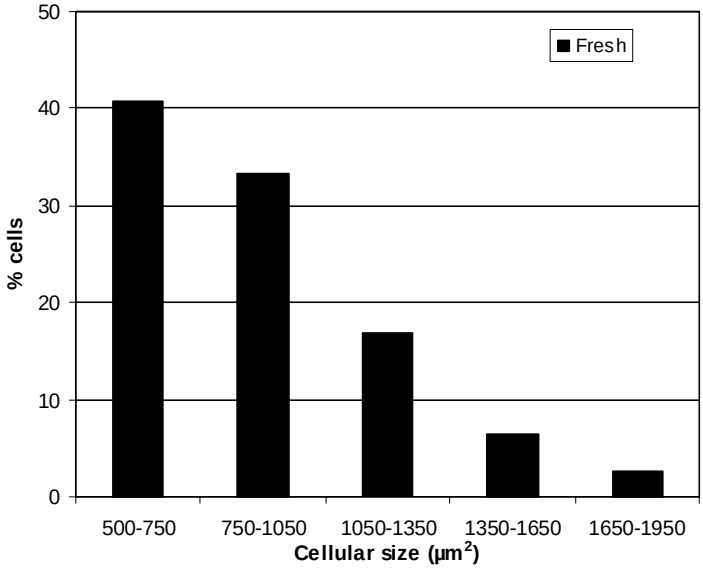

Figure 2 Cell size distribution of fresh chestnuts

Figure 3 shows images of cell tissue of the same sample of chestnut, selected as example, obtained by microscopy during diferent convective drying times at 65 ºC. The fresh chestnut cells (Figure 3a) are larger and with high values of roundnes than drying chestnuts during 0.5, 1.5 and 4 hours (Figure 3b,c,d). By other hand, chestnut structure does not present significant changes like internal ruptures and shrinkage that were found during drying of carrot (Kerdpiboon and Devahastin, 2007), red pepper (Vega-Gálvez et al., 2008) and apple (Mayor et al., 2005).

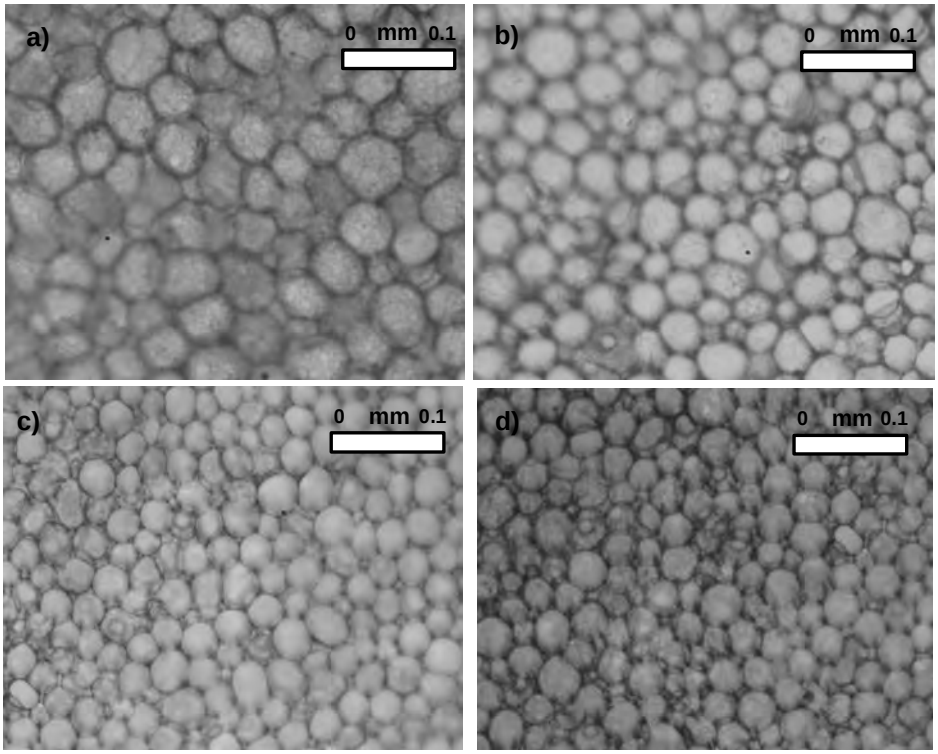

Figure 3 Cells of chestnut tissue after drying at 65 ºC: a) 0h; b) 0.5h; c) 1.5; d) 4h

The results obtained of size distribution of chestnuts cell during drying process can be observed in Figure 4. The results showed a relevant increase (from 0 to 62 %) in the minor size range (from 100 to 400 μm^2) and the cells population corresponding to the largest sizes (from 750 to 1350 μm^2) decreased (from 35 to 18 %) (Figure 4a,d). The changes were more important during first hours (0.5 and 1.5 h) (Figure 4b,c), period in which drying rates are also higher.

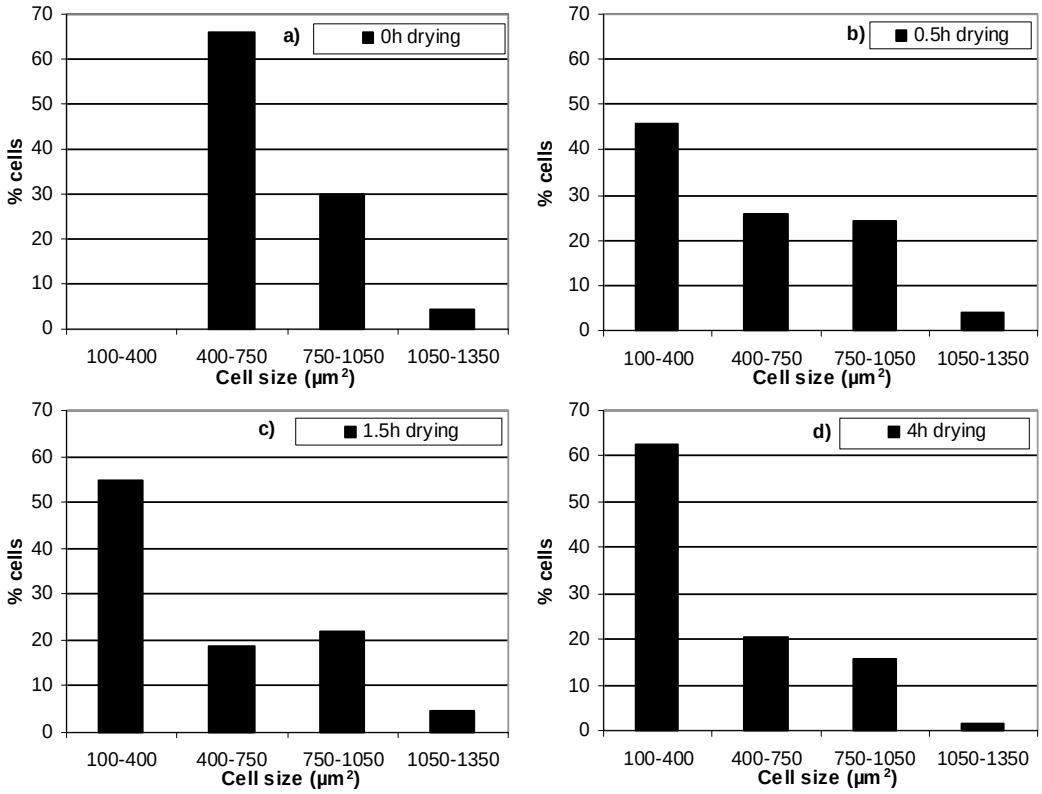

Figure 4 Chestnut cells size distribution after drying at 65ºC: a) 0h; b) 0.5h; c) 1.5; d) 4h

Concerning chestnut cell size parameters, these values reduced with drying time. After 1.5h of process, values of area, perimeter and Feret diameter did not change significantly regard as chestnuts dried until 4h. Cellular shape changed during drying and these parameters are shown in Table 2. The cells roundness and compactness decreased and became more elongated (typical behaviour of cells during food materials drying).

Table 2 Chestnut cell shape parameters after drying at 65 ºC

t (h)	Average	Range
	Elongation	
0	1.2324 ± 0.1624	1.1072-1.5760
0.5	1.2892 ± 0.2133	1.0242-2.1849
1.5	1.4124 ± 0.1950	1.0746-1.8590
4	1.5547 ± 0.3063	1.1487-2.2144
	Roundness	
0	0.4814 ± 0.1449	0.1936-0.8169
0.5	0.5459 ± 0.1382	0.2140-0.8295
1.5	0.4041 ± 0.1091	0.1442-0.6013
4	0.3160 ± 0.1309	0.1176-0.5906
	Compactness	
0	0.8682 ± 0.0532	0.6752-0.9572
0.5	0.8472 ± 0.0710	0.5856-0.9579
1.5	0.7888 ± 0.0787	0.5797-0.8929
4	0.7058 ± 0.0951	0.4952-0.8455

Figure 5 shows images of cell tissue obtained by microscopy of chestnut that was previously dried at 65 ºC until 4 h and after rehydrated during diferent times at 25 ºC. The images of surface cells during rehydration indicated that size increases strongly in a short period of time.

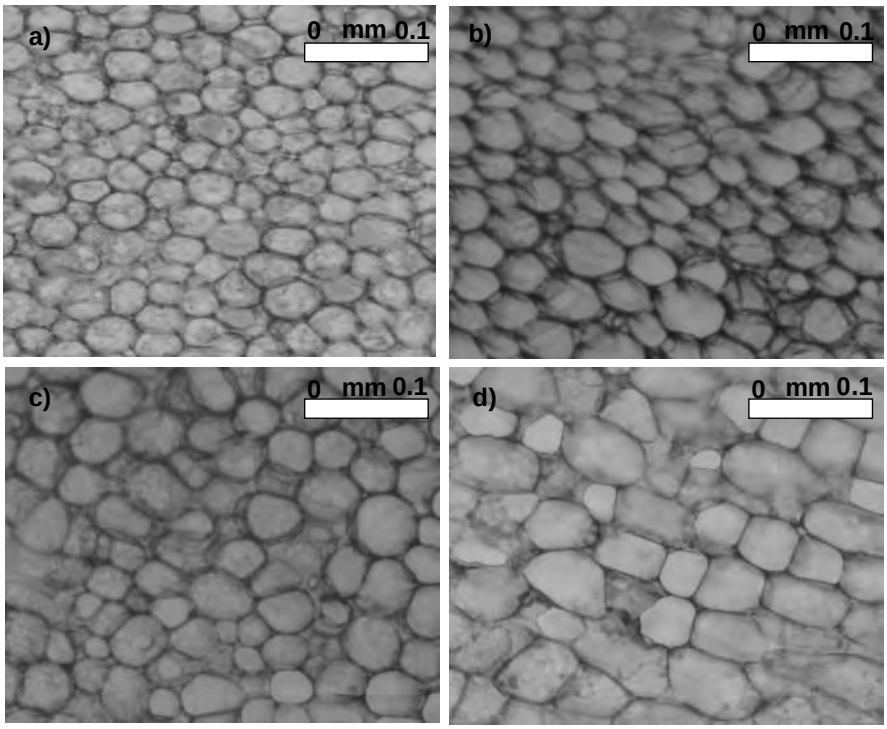

Figure 5 Cells of chestnut tissue after rehydration at 25 ºC: a) 10min; b) 30 min; c) 60 min; d) 120 min

Figure 6 shows the corresponding distribution cell size during rehydration of chestnuts. The relative population of smaller cells (from 100 to 750 μm^2) decreased and population (from 1050 to 2350 μm^2) corresponding to larger sizes increased during rehydration process. A great number of cells achieved size values higher than the corresponding cells of fresh chestnut.

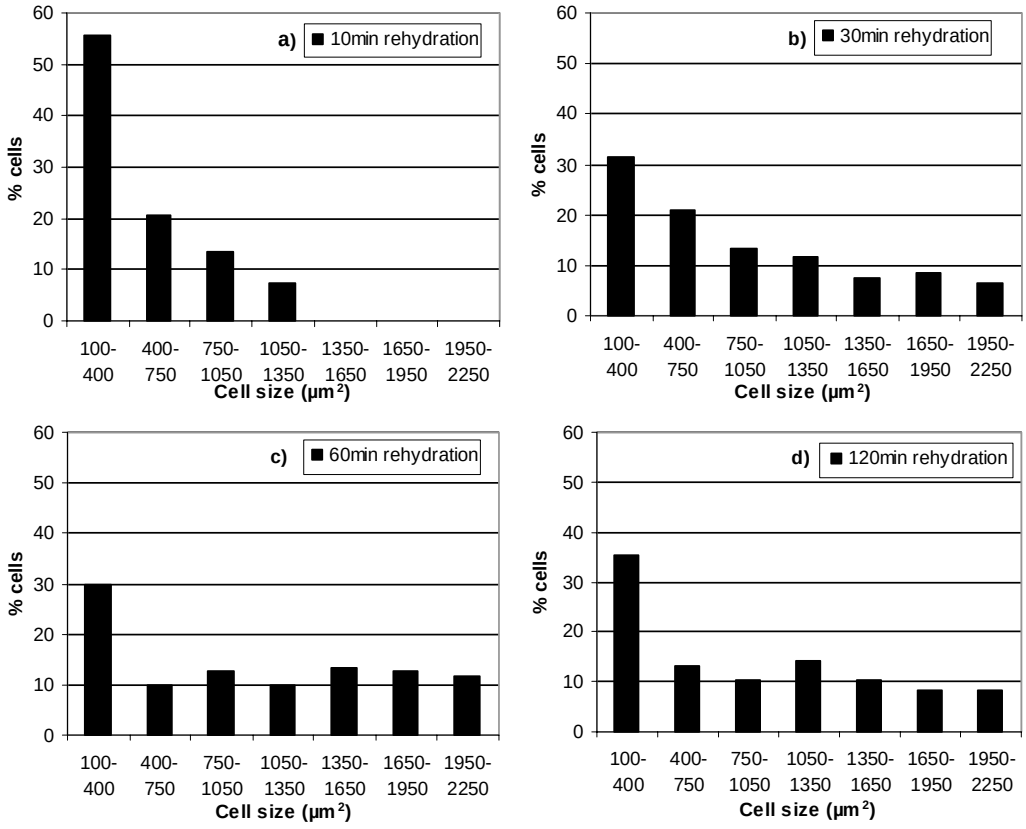

Figure 6 Chestnut cell size distribution after rehydration at 25ºC a) 10min; b) 30min; c) 60min; d) 120min

The size parameters (area, perimeter and Feret diameter) after 30 minutes at 25 ºC were similar to the corresponding of fresh chestnut. Table 3 shows shape parameters (elongation, roundness and compactness) during rehydration time. Elongation decreases, roundness and compactness parameters increase up to 10 min of rehydration. These parameters became constants after this time. Shape parameters were slightly lower than fresh chestnuts at the end of rehydration process.

Table 3 Chestnut cell shape parameters after rehydration at 25 ºC

t (min)	Average	Range
	Elongation	
10	1.6639 ± 0.4326	1.0515-2.9380
30	1.2689 ± 0.1570	1.0234-1.6482
60	1.2596 ± 0.1241	1.0297-1.4599
120	1.2626 ± 0.1253	1.0293-1.5165
	Roundness	
10	0.3818 ± 0.1536	0.1022-0.6922
30	0.4139 ± 0.1424	0.1079-0.6507
60	0.4233 ± 0.1221	0.1427-0.6371
120	0.4622 ± 0.1134	0.1707-0.6419
	Compactness	
10	0.7076 ± 0.0986	0.4460-0.8808
30	0.7849 ± 0.0940	0.4968-0.9048
60	0.7602 ± 0.0908	0.5179-0.8951
120	0.7705 ± 0.0724	0.4945-0.8677

4. Conclusions

Changes in size and shape of chestnut cells were determined during drying and rehydration processes. Shrinkage and swelling of cells were observed during both processes being recovered the fresh samples values of size, roundness and elongation after rehydration. Finally, these results indicate that the analysis by microscopy is an interesting tool to link macroscopic processes with microscopic phenomena and to improve the knowledge of mass transfer processes in cellular tissues.

References

Aguilera, J.M., Stanley, D.W. (1999). *Microstructural Principles of Food Processing and Engineering*, Aspen Publishers, Gaithersburg.

Kerdpiboon, S., Devahastin, S. (2007). Fractal characterization of some physical properties of a food product under various drying conditions. *Drying Technology*, 25, 135-146.

Lewicki, P.P., Pawlak, G. (2003). Effect of drying on microstructure of plant tissue. *Drying Technology*, 21, 657-683.

Lewicki, P.P., Porzecka-Pawlak, R. (2005). Effect of osmotic dewatering on apple tissue structure. *Journal of Food Engineering*, 66, 43-50.

Mayor, L., Silva, M.A., Sereno, A.M. (2005). Microstructural changes in during drying of apple slices. *Drying Technology*, 23, 2261-2276.

Prothon, F., Ahrné, L.M., Funebo, T., Kidman, S., Langton, M., Sjöholm, I. (2001). Effects of combined osmotic and microwave dehydration of apple on texture, microstructure and rehydration characteristics. *Lebensmittel-Wissenschaft und-Technologie*, 34, 95-101.

Reeve, R.M. (1953). Histological investigations of texture in apples. II Structure and intercellular spaces. *Food Research*, 18, 604-617.

Vega-Gálvez, A., Lemus-Mondaca, R., Bilbao-Sáinz, C., Fito, P., Andrés, A. (2008). Effect of air drying temperature on the quality of rehydrated dried red bell pepper (var. Lamuyo). *Journal of Food Engineering*, 85, 42-50.

Proceedings of the 10th International Chemical and
Biological Engineering Conference - CHEMPOR 2008
Braga, Portugal, September 4-6, 2008
E.C. Ferreira and M. Mota (Eds.)

Molecular Biomarkers to characterize *Amanita ponderosa* Mushrooms

A. Teresa Caldeira[1,2], Cátia Salvador[1], Fátima Pinto[1], José M. Arteiro[1,2], M. Rosário Martins[1,3] *

[1]Chemical Department, University of Évora, 7000 - 671 Évora, Portugal
[2]CQE, University of Évora, 7000 - 671 Évora, Portugal
[3] ICAM, University of Évora, Ap. 94 7002 - 554 Évora Portugal

Keywords: *Amanita ponderosa*, edible mushrooms, M13-PCR, RAPD
Topic: Integration of life sciences & engineering

Abstract

Amanita ponderosa strains are wild mushroom, edible, with a high exportation potential. This specie grows spontaneously in some microclimates in Iberian Peninsula, due to its Mediterranean characteristics, namely in Alentejo and Andaluzia. Due to the great diversity of wild mushrooms, it is essential be able to differentiate and identify the several edible mushrooms species. RAPD markers have been used as a valuable tool to distinguish different genotypes in edible mushrooms; however, it's a new approach, for *Amanita ponderosa* strains.

In the present study six *Amanita ponderosa* strains were compared with others Basidiomycetes (*Pleurotus ostreatus*, *Lactarius deliciosus* and *Coriolus versicolor*) and one Ascomycete strain (*Tuber* sp.) in order to establish different genetic fingerprintings profiles between strains.

Molecular profiles were analyzed by RAPD-PCR using eight micosatelites primers and by MSP-PCR using the M13. Results showed that different patterns were generated for each nine strains tested. RAPD analysis enabled to differentiate at species and strain level, however, the degree of discrimination by means of RAPD-PCR depends highly on the primers used. The MSP-PCR is a fast method to amplified DNA polymorphic sequences, with high reproducibility and similarity for the same specie that allow to characterise the genetic profile of the edible mushrooms *Tuber* sp., *Lactarius deliciosus*, *Pleurotus ostreatus* and *Amanita ponderosa*. Moreover, constitute a valuable tool to distinguish the different genotypes of *Amanita ponderosa* strains, allowing to identify at specie level and to differentiate *A. ponderosa* strains from each origin sites.

1. Introduction

Mushrooms are exhaustively known for its high nutritive value, gastronomic and medicinal proprieties. Consequently, the consumption of the eatable mushroom comes increasing. Most *Amanita* species are obligatorily ectomycorrhizal and play a significant role in forest ecosystems.

The south of Portugal, due to its climatic conditions and flora diversity, is one of the European regions with a high predominance of wild edible mushrooms *Amanita ponderosa*, specie with great gastronomic relevance because of their high consumption by the rural population and their economic value in the gourmet markets, of Spain and Portugal. A profound knowledge is therefore required for this specie, only few studies are described in the literature, relating mineral content (Moreno-Rojas *et al*., 2004) and molecular phylogenetic analysis (Moreno *et al*., 2008). Genetic profiles and polymorphic sequences can constitute important tools for a fast and effective characterization, namely in certification processes. Literature related a range of molecular approach based on RAPD and ITS

* Corresponding author: Tel + 351-266745313. E-mail: mrm@uevora.pt

analyses in order to characterize and identified edible mushrooms (Moncalvo *et al*., 2000; Firenzuoli *et al*., 2007; Pacioni *et al*., 2007; Ro *et al*., 2007), MSP-PCR fingerprinting was also used to study genetic variability in yeasts and filamentous fungi species (Godoy *et al*., 2004; Alves *et al*., 2007; Lopes *et al*., 2007), showing that these methodologies have a great potential as diagnostic tools. However a lack of information to *A. ponderosa* mushrooms is verified, only one study is reported to distinguish *A. curtipes* and *A. ponderosa* species sequencing the D1-D2 domains of the 28S rRNA gene and ITS1-5.8S-ITS2 region (Moreno *et al*., 2008).

The aim of this study is to characterise *A. ponderosa* mushrooms with molecular biomarkers, by RAPD and MSP-PCR, in order to establish different genetic profiles, between wild edible mushrooms. This work is a new approach for the *A. ponderosa* species from Portugal, since until now any study was performed concerning molecular identification of these specie.

2. Material and Methods

Samples

Fruiting bodies of the *Amanita ponderosa* mushrooms were collected in Spring from 6 different locations area, in the southwest of the Iberian Peninsula, namely Évora, Beja, Mina de São Domingos, Santo Aleixo da Restauração and Vila Nova de São Bento (Alentejo, Portugal) and from Cabeza Rubia (Andalusia, Spain). For the molecular study, the *A. ponderosa* strains were compared with others Basidiomycetes (*Pleurotus ostreatus* and *Lactarius deliciosus*) and with one Ascomycete strain (*Tuber sp*.). The mushrooms are deposited in Biotechnology Laboratory, Chemistry Department, University of Évora (Portugal).

Molecular analyses

The genomic DNA extraction from the small fragments of fruiting bodies was performed by the modified microsfers method (Sambrook *et al*., 1989; Martins, 2004).

DNA was quantified and diluted to a final value of 0,1 ng/L for PCR assays. The RAPD-PCR was performed with the microsatellite primers OPF-1 (5'-ACGGATCCTG-3'); OPF-6 (5'-GGGAATTCGG-3'); OPF-9 (5'-CCAAGCTTCC-3'); OPF-13 (5'-GGCTGCAGAA-3'); OPG-2 (5'-GGCACTGAGG-3'); OPG-3 (5'-GAGCCCTCCA-3'); OPH-2 (5'-TCGGACGTGA-3'); OPH-4 (5'-GGAAGTCGCC-3'). The M13 primer (5'- GAGGGTGGCGGTTCT-3') were used for MSP-PCR. The PCR conditions consisted of an initial denaturing step of 5 min at 94 ºC followed by 40 cycles of 1 min at 94 ºC, 1 min at 50°C and 72 ºC for 1 min. The reaction was completed with a final extension at 72 ºC for 5 min and then cooled and held at 4 ºC. PCR samples were separated in a 1.5% agarose gel and visualized on a UV transilluminator (Bio-Rad) using the Quantity One 1-D Analysis software (Biorad).

Statistical analysis

Phylogenetic tree was generated by UPGMA method, using the Dice coefficient of similarity, based on the fingerprinting profile of *A. ponderosa* and other Basidiomycetes and Ascomycetes strains.

3. Results and Discussion

Fruiting bodies of the *Amanita ponderosa* mushrooms were collected since February to April 2007 in the region of Évora, Beja, Mina de São Domingos, Santo Aleixo da Restauração and Vila Nova de São Bento (Alentejo, Portugal) and from Cabeza Rubia (Andalusia, Spain).

Samples were collected in different sites, growing on acidic soils in forests of *Quercus ilex* ssp. ballota and *Cistus ladanifer* and *C. laurifolius*. *A. ponderosa* mushrooms analysed were obtained in the same development stage to eliminate the interference of size. *A. ponderosa* is

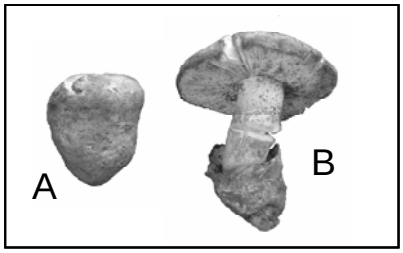

Figure 1- Some macroscopic aspects of *A. ponderosa* Mushrooms.
A - Young mushrooms.
B - Mushrooms in maturity.

characterized by large and robust basidiomata, with a cap 8–17 cm in diameter, with a hemispheric morphology when young and plane-convex in maturity, with a slight depression in the centre (Fig. 1).

Molecular fingerprinting profile of six *A. ponderosa* strains was compared with other edible mushrooms: *Pleurotus ostreatus*, *Lactarius deliciosus* and *Tuber* sp. It is important to emphasize that our aim was not to screening pathogenic species of the genus *Amanita*, indeed several studies are reported for the detection and quantification of toxins, but to provide a rapid method to screening enable strains, namely the Mediterranean specie *A. ponderosa*.

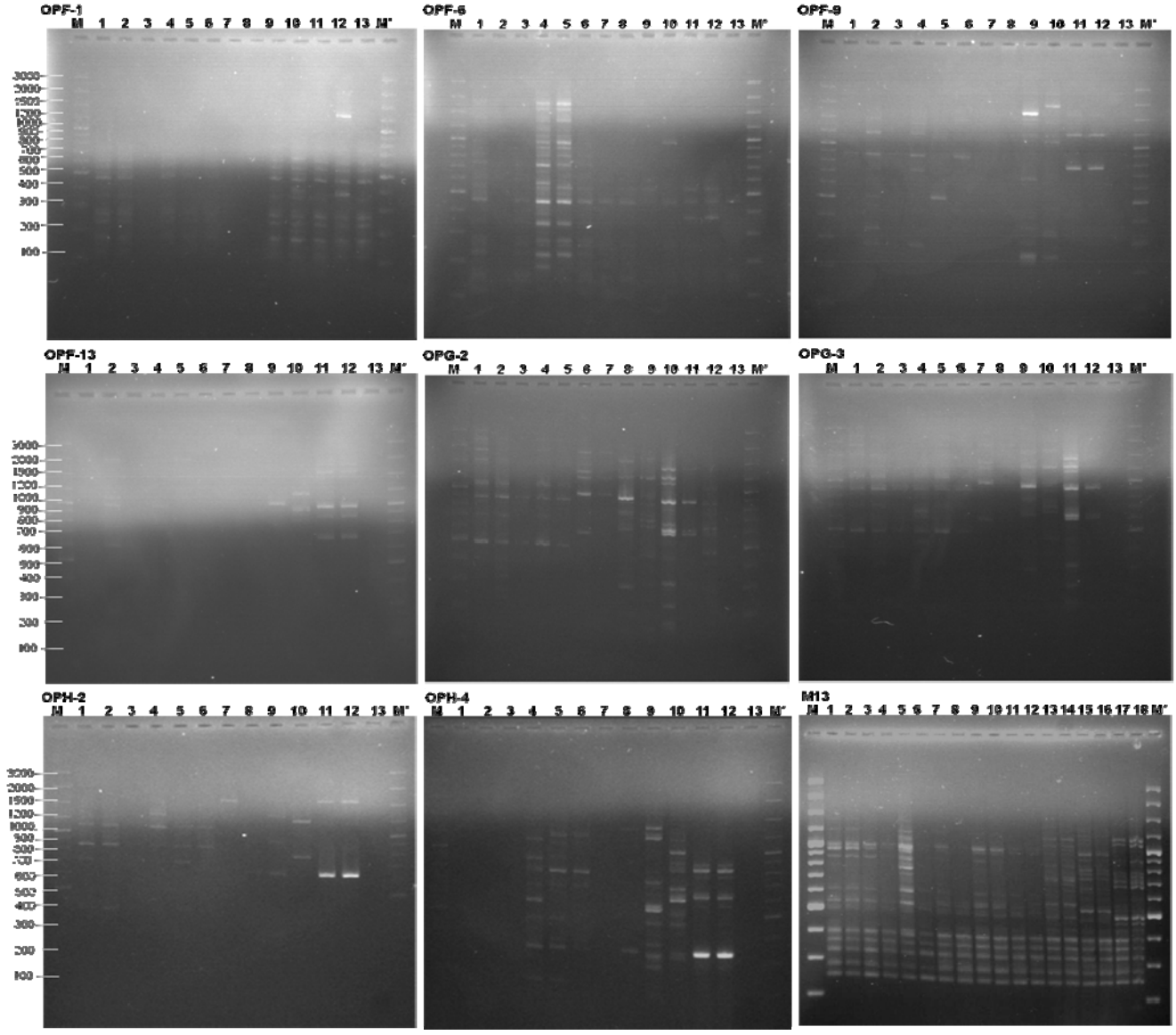

Figure 2- Fingerprinting patterns obtained with *Tuber* sp., *L. deliciosus*, *P. ostreatus* and *A. ponderosa* mushrooms collected from different located area.

Legend – RAPD primers
M e M' – DNA molecular ladder 100 bp plus (Fermentas)
1 – *A. ponderosa* (Évora)
2 – *A. ponderosa* (Cabeza Rubia)
3 – *A. ponderosa* (V. Nova S. Bento)
4 – *A. ponderosa* (Mina S. Domingos)
5 – *A. ponderosa* (Beja)
6 – *A. ponderosa* (Sto Aleixo R.)
7 – *C. versicolor*
8, 9 – *P. ostreatus*
10 – *L. deliciosus*
11,12 - *Tuber* sp. 13- control

Legend - M13 primer
M e M' – DNA molecular ladder 100 bp plus (Fermentas)
1 , 2 – *A. ponderosa* (Beja)
3 , 4 – *A. ponderosa* (V. Nova S. Bento)
5 , 6 – *A. ponderosa* (Mina S. Domingos)
7 , 8 – *A. ponderosa* (Évora)
9 , 10 – *A. ponderosa* (Cabeza Rubia)
11, 12 – *A. ponderosa* (Sto Aleixo R.)
13, 14 – *L. deliciosus*
15, 16 – *P. ostreatus*
17, 18 – *Tuber* sp.

Fig. 2 shows the fingerprinting profiles obtained by RAPD-PCR using OPF-1, OPF-6, OPF-9, OPF-13, OPG-2, OPG-3, OPH-2, OPH-4 and by M13 primer. Table 1 summarizes the band profile obtained in this study. Results showed that different patterns were generated for each ten strains tested. RAPD assays have produced polymorphism in all the studded strains, except for *C. versicolor*, showing 2-14 bands ranging from 0.1 to 2.4 kb. The amplification using M13 primer has generated a profile with 9-20 bands ranging from 0.2 to 1.3 kb.

Table1- Band profile obtined with different primers

Primers	Strains	*A. ponderosa* (Beja)	*A. ponderosa* (V. N. S. Bento)	*A. ponderosa* (Mina S. Domingos)	*A. ponderosa* (Évora)	*A. ponderosa* (S^{to} Aleixo R.)	*A. ponderosa* (C. Rubia)	*L. deliciosus*	*P. ostreatus*	*C. versicolor*	*Tuber* sp.
OPF-1	Bands (n)	8	8	8	8	8	8	9	7	0	8
	bp	118 - 738	118 - 738	118 - 738	118 - 738	118 - 738	118 - 738	166 -1539	118 - 591	--	166-661
OPF-6	Bands (n)	13	6	13	9	7	6	2	3	2	3
	bp	166 - 1763	166 - 532	166 - 1763	166 - 1763	166 -932	166 - 532	376 - 584	509 - 584	259 - 445	368 - 532
OPF-9	Bands (n)	5	4	6	4	4	6	6	7	0	3
	bp	274 - 948	274 - 948	274 - 1236	274 - 948	342 - 948	274 - 1236	229 -1855	24 -1945	--	727-1310
OPF-13	Bands (n)	2	2	2	2	2	3	4	2	2	6
	bp	946 - 1900	946 - 1900	946 - 1900	946 - 1900	946 - 1900	586 - 1900	803 -1117	744 - 984	657-1362	653-1552
OPG-2	Bands (n)	8	8	8	8	8	8	9	8	8	14
	bp	486 - 2317	486 - 2317	486 - 2317	486 - 2317	486 - 2317	486 - 2317	429-1520	285 -1520	559-1706	150-1520
OPG-3	Bands (n)	8	8	8	8	8	8	9	7	7	8
	bp	434 - 2354	434 - 2354	434 - 2354	434 - 2354	434 - 2354	434 - 2354	432 -1563	272 -1563	606-1873	225-1439
OPH-2	Bands (n)	5	5	5	5	5	5	4	3	1	4
	bp	413 -1339	413 -1339	413 -1339	413 -1339	413 -1339	413 -1339	644 -1193	621 -1299	1621	619-1621
OPH-4	Bands (n)	12	6	11	7	10	5	12	10 - 13	1	11
	bp	210 - 1069	210 - 1069	210 - 1069	210 - 1069	246 - 1069	210 - 1069	322 -1532	210 -1293	1248	322-1185
M13	Bands (n)	13	11	15	9	9	13	18	20	--	16
	bp	237 - 1189	237 - 1001	237 - 1189	237 - 1001	237 –1001	237 - 1189	237 -1140	237 -1299	--	237-1154

Among all RAPD primers tested, the OPF-6, OPG-2 and OPG-3 allow to distinguish the Basidiomycetes than Ascomycetes strains, presenting clusters, for all Basidiomycetes, with a similarity of 30%, 25% and 20% respectively. The fingerprinting profile obtained with M13 primer also allowed differentiate *Tuber* sp. from the studied Basiodiomycetes with 44% of similarity. That is coherent, once *Tuber* sp. is ectomycorrhizal ascomycetes that produce subterranean ascomata known as truffles, while all other studied strains were basidiomycetes. OPF-6, OPG-2 and OPG-3 RAPD markers and M13-PCR allowed differentiate at specie and strain level. However, the degree of discrimination by RAPD-PCR depends highly on the primers used, generating different fingerprintings profiles. *A. ponderosa* strains formed clusters with 65% of similarity for OPF-6 and OPG-2 primers and 80% of similarity with OPG-3 primer. In M13-PCR fingerprinting profile, *A. ponderosa* strains were grouped in a cluster with a similarity of 67% (Figure 3).

RAPD analyses have been used as a valuable tool to distinguish different genotypes in edible mushrooms such as *Ganoderma lucidum* (Hseu *et al.*, 1996), *Lentinula edodes* (Zhang and Molina, 1995), *Agaricus bisporus* (Khush *et al.*, 1992) and *Pleurotus ostreatus* (Lee *et al.*, 2000) and to evaluate the genetic similarities (Andrade *et al.*, 2006). However, it's a new approach, for *Amanita ponderosa* strains. The second fingerprinting approach, using the minisatelite M13 makes use of the occurrence of high copy numbers of interspersed repeats motifs in most genomes, and has been used successfully to amplify hypervariable repetitive DNA sequences with high reprodutibility (Martin *et al.*, 1998; Lopes *et al*., 2007).

In this study, MSP-PCR has been used as a fast method to amplify DNA polymorphic sequences, with high reproducibility and similarity for the same specie that allow to characterise the genetic profile of the edible mushrooms *Tuber* sp., *Lactarius deliciosus*, *Pleurotus ostreatus* and *Amanita ponderosa*. Moreover, constitute a valuable tool to distinguish the different genotypes of *Amanita ponderosa* strains, allowing to identify at specie level and to differentiate *A. ponderosa* strains from each origin sites.

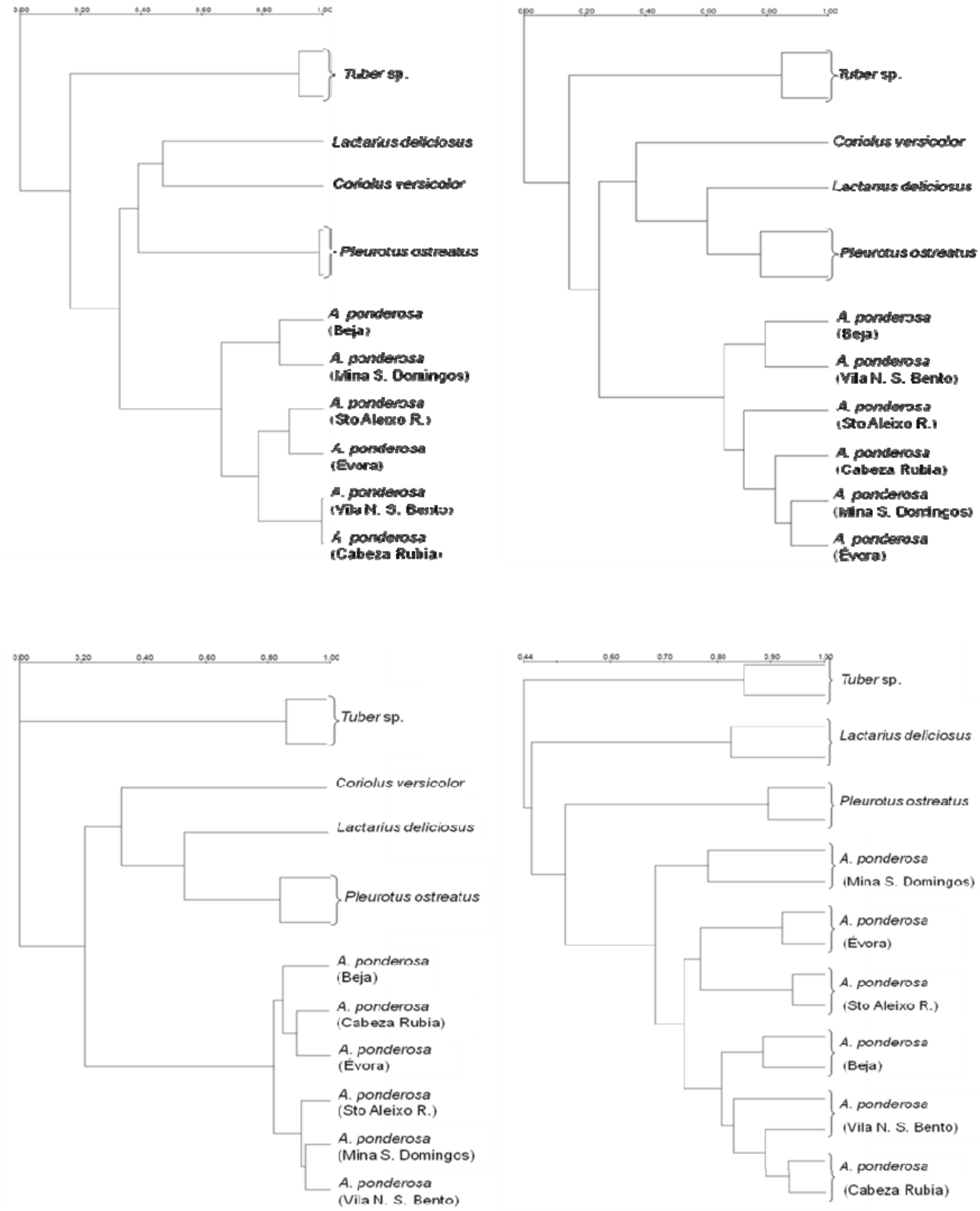

Figure 3- Dendogram analysis based on the RAPD- PCR using OPF6, OPG2 and OPG3 and M13-PCR fingerprinting patterns for different strains of *A. ponderosa* and for *L. deliciosus*, *P. ostreatus* and *Tuber* sp. The distance values between branches are reported as percentage of similarity (0– 100%).

In conclusion RAPD-PCR and MSP-PCR analysis establish different genetic profiles between *Tuber sp., P. ostreatus, L. deliciosus* and *A. ponderosa* strains. Additionally, the amplified DNA polymorphic sequences using OPF-6, OPG-2, OPG-3 and M13 primers allowed differentiate *Amanita ponderosa* strains collected from the different places. For maximum discriminatory power of these types of fungi, both methods RAPD-PCR and MSP-PCR should be used to categorize wild edibles mushrooms species usually found in Mediterranean ecosystems. Results clearly showed that the geographical collecting site influences the molecular fingerprint profile of *A. ponderosa strains*. A greater number of wild enable mushrooms should be analysed more often in Alentejo region (Portugal) with respect to molecular characterization.

References

Alves, A., Phillips, A., Henriques, I., Correia, A. (2007). Rapid differentiation of species of Botryosphaeriaceae by PCR fingerprinting. *Research in Microbiology*, 158, 112 – 121.

Andrade, M., Rodríguez, M., Sánchez, B., Aranda, E., Córdoba, J. (2006). DNA typing methods for differentiation of yeasts related to dry-cured meat products. *International Journal of Food Microbiology,* 107, 48 – 58.

Firenzuoli, F., Gori, L., Lombardo, G. (2007). The Medicinal Mushroom *Agaricus blazei* Murrill: Review of Literature and Pharmaco-Toxicological Problems. *Advance Access Publication*, 5(1), 3–15.

Godoy, J., Negro, J., Hiraldo, F., Donázar, J. (2004). Phylogeography, genetic structure and diversity in the endangered bearded vulture (*Gypaetus barbatus* , L.) as revealed by mitochondrial DNA. *Molecular Ecology*, 13, 371–390.

Hseu, R., Wang, H., Wang, H., Moncalvo, J. (1996). Differentiation and grouping of isolates of the *Ganoderma lucidum* complex by random amplified polymorphic DNA-PCR compared with grouping on the basis of internal transcribed spacer sequences. *Appl. Environ. Microbiol*., 62, 1354.

Khush, R., Becker, E., Wach, M. (1992). DNA amplification polymorphisms of the cultivated mushroom *Agaricus bis-porus*. *Appl. Environ. Microbiol*., 58, 2971.

Lee, Y., Changa, H., Kima, J., Kima, J., Lee, K. (2000). Lignocellulolytic mutants of *Pleurotus ostreatus* induced by gamma-ray radiation and their genetic similarities. *Radiation Physics and Chemistry*, 57, 145-150.

Lopes, M., Silva, D., Freitas, G., Tenreiro, R. (2007). Simultaneous identification and typing of Candida species by MSP-PCR and AFLP: Study of clinical isolates from a Portuguese pediatric hospital. *Journal de Mycologie Médicale*. 17, 157—167.

Martin, . Costa, G, Delaruelle, C, Diez, J. (1998). Genomic Fingerprinting of Ectomycorrhizal Fungi by Micorsatellite-Primed PCR.

Martins, M. (2004). Degradação Biológica de Fungicidas em Amostras de Solo, Tese de Doutoramento, Departamento de Química, Universidade de Évora, Évora, pp 140-142.

Moncalvo, J., Drehmel, D., Vilgalys, R. (2000). Variation in Modes and Rates of Evolution in Nuclear and Mitochondrial Ribosomal DNA in the Mushroom Genus Amanita (Agaricales, Basidiomycota): Phylogenetic Implications. *Molecular Phylogenetics and Evolution,* 16, 8–63.

Moreno, G., Platas, G., Peláez, F., Bernedo, M., Vargas, A., Daza, A., Santamaría, C., Camacho, M., de la Osa, L., Manjón, J. (2008). Molecular phylogenetic analysis shows that *Amanita ponderosa* and *A. curtipes* are distinct species. *Mycol Progress*, 7, 41–47.

Moreno-Rojas, R., Díaz-Valverde, A., Moreno-Arroyo, B., González, T., Capote, C. (2004). Mineral content of gurumelo (*Amanita ponderosa*). *Food Chemistry*, 85, 325–330.

Pacioni, G., Leonardi, M., Aimola, P., Ragnelli, A., Rubini, A., Paociolli, F. (2007). Isolation and characterization of some mycelia inhabiting *Tuber* ascomata. *Mycological Research*, 111, 1450-1460.

Ro, H., Kim, S., Ryu, J., Jeon, C., Leed, T., Le, H. (2007). Comparative studies on the diversity of the edible mushroom *Pleurotus eryngii*: ITS sequence analysis, RAPD fingerprinting, and physiological characteristics. *Mycological Research III*, 710-715.

Sambrook, J., Feitsch, E., Maniatis, T. (1989). Molecular Cloning: a Laboratory Manual. Cold Spring Harbor Laboratory Press, Cold Spring Harbor, NewYok.

Zhang, Y., Molina, F. (1995). Strain typing of *Lentinula edodes* by random amplified polymorphic DNA assay. *FEMS Microbiology Letters*, 131, 17-20.

Proceedings of the 10th International Chemical and
Biological Engineering Conference - CHEMPOR 2008
Braga, Portugal, September 4-6, 2008
E.C. Ferreira and M. Mota (Eds.)

Structural and kinetics effects of *Pseudomonas aeruginosa* amidase encapsulation in reversed micelles

Ana Fragoso[1], Rita Pacheco[1*] and Amin Karmali[1]
[1]Chemical Engineering and Biotechnology Research Center, Departmento de Engenharia Química do Instituto Superior de Engenharia de Lisboa – Rua Conselheiro Emídio Navarro, 1, 1950-062 Lisboa, Portugal

Keywords: Reversed micelles, *Pseudomonas aeruginosa* amidases; acetohydroxamic acid; water content; stability.
Topic: Advancing the chemical and biological engineering fundamentals

Abstract

The present work involves the entrapment of either cell-free extract or whole cells from both *Pseudomonas aeruginosa* L10 and AI3 in a reversed micellar system composed of cationic surfactant tetradecyltrimethyl ammonium bromide (TTAB) in heptane/octanol (80/20%). The reaction used to study the effect of the encapsulation was a transamidation reaction catalysed by the enzyme amidase (E.C. 3.5.1.4) which is expressed by both bacteria. The effect of micellar water content (w_0) in the enzyme activity was also evaluated. The results demonstrated a major increase in the activity of acetohydroxamic acid synthesis in reverse micelles when compared with the conventional aqueous system. Furthermore when micelles water content was changed a bell-shaped profile was obtained for amidase specific activity in both cell-free extract and whole cells with a maximum activity exhibited at ω_0 =10. The study of storage stability of whole cell and cell free extract when entrapped in reverse micelles at 24ºC revealed a half-life of respectively 17 days and 26 days for *Pseudomonas aeruginosa* AI3 strain and 11 days and 8.5 days for *Pseudomonas aeruginosa* L10.

1-Introduction

Aliphatic amidases (E.C. 3.5.1.4) catalyse the hydrolysis of amide bonds in small aliphatic amides. As can be seen in Figure 1 this enzyme has also the capacity to catalyse the transfer of acyl groups to amines what enlarged the possibility of synthesising different compounds with amide bonds in a transamination reaction (Pacheco *et al*, 2005 a). Hydroxamic acid derivatives, with the general formula R–CO–NHOH, are products of transamidation reaction when the acyl acceptor is hydroxylamine.

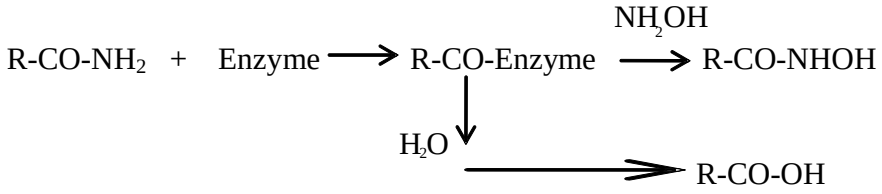

Figure 1-Aliphatic amidase catalyses the hydrolysis and transamidation reactions of amides.

* Rita Pacheco. Tel +351-21-8317000 ext. 1229 . E-mail: rpacheco@deq.isel.ipl.pt

Amidases which we are in concern have been isolated mainly from wild-type *Pseudomonas aeruginosa* 8602 but the use of mutagenic agents has allowed the isolation of several constitutive mutants producers of amidases such as L10 and AI3 (Domingos *et al* 1989). Although mutant L10 strain exhibited no difference in substrate specificity compared with wild-type amidase, in mutant strain AI3, the *amiE* gene mutation T103I is responsible for the amidase activity towards *p*-nitroacetanilide and acetamide (Karmali *et al* 2001).

Amidase from *Pseudomonas aeruginosa* has been used for studying the hydrolysis and synthesis of several compounds either in conventional medium (Pacheco *et al* 2005 a), or with reverse micelles for the synthesis of acetohydroxamic acid (Pacheco *et al*, 2005 b). These hydroxamic acids derivatives have a wide spectrum of application Hydroxamic acids are chelating agents which are known to inhibit enzymes often associated to several human diseases. These compounds are used in a number of applications since they are constituents of growth factors, antibiotics, antibiotic antagonists, tumor inhibitors and antifungal agents. On the other hand, hydroxamic acids can also be applied in food industry and waste-water treatment. (Fournaud *et al.* 1998).

Reverse micelles are spherical waterdroplets surrounded by one layer of closely packed surfactant molecules dispersed in a solvent of low polarity. The polar heads of the surfactant are in contact with only a few water molecules in the interior of the micelle and the surfactant hydrophobic tails are in contact with the surrounding organic solvent (Gómez –Puyou *et al*, 2007). Regarding the reaction scheme showed in Figure 1 the amidase transamidation reaction could be successfully performed comparatively to the hydrolysis reaction at low water content. Hence a reversed micellar system is a medium containing organic solvents with reduced quantity of water appropriate to such synthesis.

In this work *Pseudomonas aeruginosa* whole cells and cell free extract of strains L10 and AI3 containing amidase were encapsulated in reverse micelles of the cationic surfactant tetradecyltrimethyl ammonium bromide (TTAB) dissolved in heptane/octanol (80/20 %). The effect of the water content of the system on the amidase acetohydroxamic acid activity was analysed and compared with the reaction in aqueous solution. Moreover results on the whole cell and cell free extract storage stability when encapsulated in such conditions are shown in order to demonstrate the potential of such immobilization systems in numerous applications.

2-Materials and methods

Bacterial strain

Pseudomonas aeruginosa L10 and AI3 were used as the source of amidase (Domingos *et al* 1989).

Cell and cell free extract production

Pseudomonas aeruginosa strains were grown as described previously (Karmali *et al* 2001; Brown and Clarke 1972). The cell culture was harvested by centrifugation when absorbance at 600 nm was approximately 1. Cell pellet was washed twice, centrifuged and stored at .-20ºC. Frozen cells of each strain were suspended in 2 volumes of 20mM Tris-HCl buffer, pH 7.2 containing 1mM β-mercaptoethanol, 1mM EDTA, 10% V/V glycerol and 1 mM benzamidine (TMEGB buffer). Part of this suspension was used as the source of amidase and represents the whole cell of each strain. The remaining cell suspension was broken by sonication five times at 150 W for 20 s in an ice bath and centrifuged at 13400 rpm for 30 min at 4ºC, the supernatant was used as the source of amidase and represents the cell free extract of each strain.

* Rita Pacheco. Tel +351-21-8317000 ext. 1229 . E-mail: rpacheco@deq.isel.ipl.pt

Protein concentration was determined by the Coomassie blue dye binding method (Bradford, 1976) for the whole cells and cell free extract samples of each strain.

Reversed micellar system

The reverse micellar system was prepared by injecting hydroxylamine 15 mM and 30 µl of whole cell or cell free extract in TMEGB buffer into a solution of 200 mM tetradecyltrimethyl ammonium bromide (TTAB) in heptane/octanol (80/20 % v/v) under constant agitation.

Acetamide in TMEG buffer (20 mM Tris buffer pH 7.2 containing 1mM EDTA, 1mM β-mercaptoethanol, 10% glycerol) was injected to initiate the reaction in order to give a final concentration of 7.5 mM in the reverse micelles solution. The water content in the system, usually defined through the parameter w_0 = $[H_2O]/[surfactant]$ was controlled by adjusting the TMEG buffer volumes added in order to be established in the range of 3.5 to 11.5.

Analysis of storage stability for each strain whole cell and cell free extract when encapsulated was determined in a reversed micellar system prepared by injecting solely whole cell or cell free extract into a solution of 200 mM TTAB in heptane/octanol (80/20 % v/v) and the w_0 kept to a final value of 10 by adjusting the TMEG buffer volume added. This mixture was left at 24ºC during several days. Amidase activity was determined during this period, at several time intervals, by injecting to aliquots of this mixture hydroxylamine 15 mM and acetamide 7.5 mM in TMEG buffer in order to initiate the reaction.

Enzymatic activity

The amidase transferase activity associated to whole cell or cell free extract inside the reverse micelles and in aqueous solution were determined using a modification of the method developed by Brammar and Clarke (1964) using a solution of $FeCl_3$ 6% (w/v) in HCl 2%(w/v). The amidase activity was followed by measuring the formation of acetohydroxamic acid, using acetamide and hydroxylamine as substrates. The synthesis of acetohydroxamic acid was detected by formation of a brown colour complex, which absorbs at 490 nm, when adding to the reaction mixture two volumes of $FeCl_3$ 6% (w/v) in HCl 2%(w/v) solution at several time intervals during the reaction.

A calibration curve was produced for determining both concentration of hydroxamic acid inside reverse micelles and in aqueous solution at each time interval in the reaction mixture. For these calibration curves values of 0.021 $mM^{-1}cm^{-1}$(R^2= 0.9971) and 0.0889 $mM^{-1}cm^{-1}$(R^2= 0.9936) were obtained for the extinction coefficient ε, respectively, for aqueous solution and reverse micelles.

A unit of enzymatic activity (U) is defined as the amount of enzyme required to form 1 µmol acid acetohydroxamic per minute under the conditions of the reaction.

3-Results and discussion

Whole cells or cell free extract *Pseudomonas aeruginosa* L10 and AI3 were used as the source of amidase and encapsulated in a reversed micellar system of TTAB in heptane/octanol. The effect of water content w_0 was evaluated in a range from 3.5 to 11.5 by measuring amidase activity of acetohydroxamic acid synthesis resulting from a transamidation reaction.

* Rita Pacheco. Tel +351-21-8317000 ext. 1229 . E-mail: rpacheco@deq.isel.ipl.pt

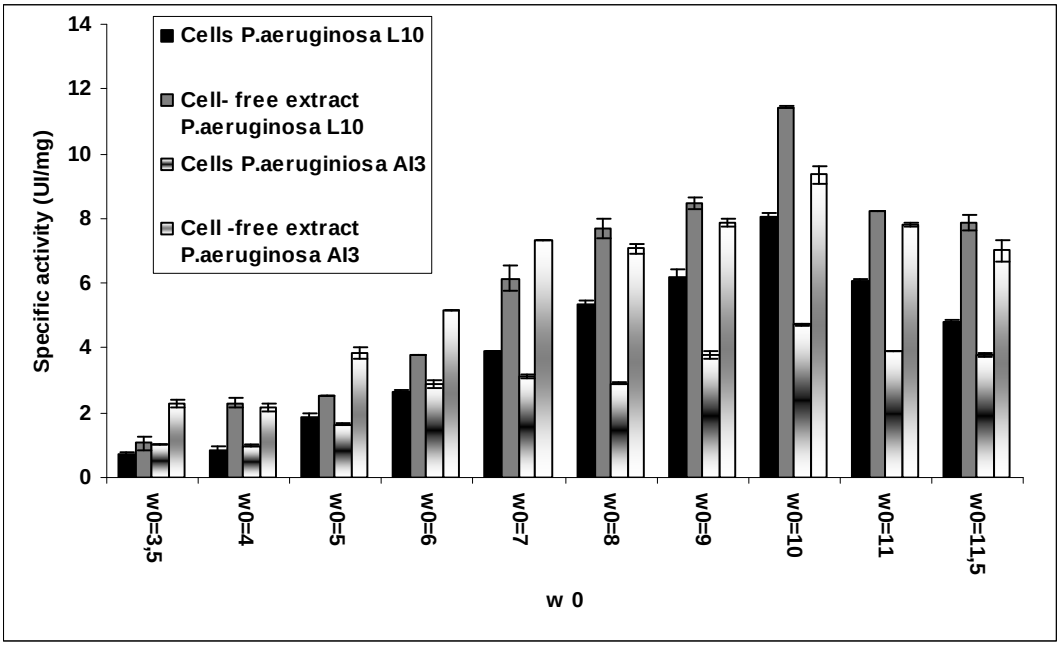

Figure 2- Influence of water content in acetohydroxamic acid synthesis for both strains

The obtain results are shown in Figure 2 and reveal a bell shape profile with a maximum in amidase activity obtained for $w_0 = 10$ in both strains. The water content of the micelles is often associated to the variation in the micelle diameter which will lead to a condition more favourable to the fitting of the enzyme inside this structure and affecting its activity (Biasutti *et all* 2008).Work is already in progress in order to evaluate the micelle internal diameter by Light Scattering and to associate such variations with amidase structure analyzed by FTIR.

As can be also seen from Figure the highest amidase activity was obtained for *P.aeruginosa* L10 cell free extract. A similar situation was also found for *P. aeruginosa* AI3 cell free extract when compared with the strain whole cells. Such difference is probably due to different diffusional resistances which occur on the transportation of the substrates from the micro environment inside the micells to the enzyme catalitic centre (Cabral *et al* 2003). This effect is much more noticeable in whole cells that in cell-free extract since in the former the biocatalyst is shielded inside the bacteria cell. Nevertheless whole cells can be also be successfully used in acetohydroxamic acid synthesis inside reversed micelles. Results shown in Figure 3 illustrate the fact that for such reaction when performed in conventional aqueous media the enzyme specific activity is considerably lower than in reversed micelles presumably due to the elevated content of water in the medium which favours the amidase hydrolysis reaction. These results are according to the literature (Pacheco *et al*, 2005 b).

The effect of encapsulation of whole cells and cell free extract on the amidase storage stability at 24ºC was analysed and results are presented in Figure 4. This analysis has as main objective to determine the amidase half life when encapsulated. Such parameter becomes extremely important when considering the significance of enzymes as biocatalysts in several industrial processes. As can be observed in Figure 4 both strains whole cells and cell-free extract exhibit the same progression profile of decrease in enzyme activity over time. Inactivation constant (k) were determined for whole cells and cell free extract and the results were respectively 0.0017 and 0.0011 h^{-1} for whole

* Rita Pacheco. Tel +351-21-8317000 ext. 1229 . E-mail: rpacheco@deq.isel.ipl.pt

cells and cell-free extract of *P. aeruginosa* AI3 and 0.0027 and 0.0034 h^{-1} for whole cells and cell-free extract of *P. aeruginosa* L10. As amidase half life ($t_{1/2}$) is concern the results were 17 and 26 days for whole cells and cell-free extract of *P. aeruginosa* AI3 and 11 and 8.5 days for whole cells and cell-free extract of *P.aeruginosa* L10 respectively. Such results demonstrate that althoug *Pseudomonas aeruginosa* L10 had overall a higher amidase specific activity is has lower storage stability than *P.aeruginosa* AI3 which makes it suitable for more robust industrial applications.

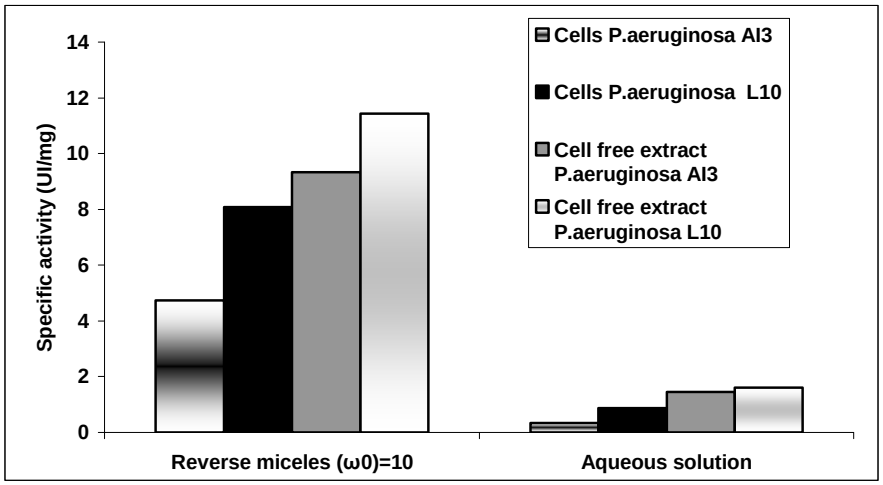

Figure 3- Acetohydroxamic acid synthesis in aqueous solution and at $w_0 = 10$ for both strains

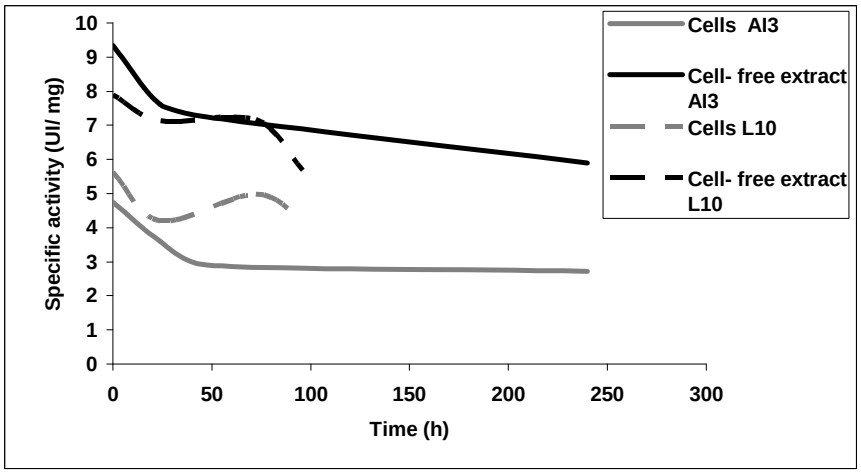

Figure 4-Study of stability for whole cells and cell free extract at 24ºC in reversed micelles

4-Conclusions

The reversed micellar system of TTAB in heptane/octanol seemed adequate to encapsulate whole cells and cell free extract with preservation and displaying an increase amidase activity of acetohydroxamic acids when compared with the conventional aqueous media. By choosing the appropriate water content w_0=10 transamidation reactions can be carried out in these systems with high performance. These changes in amidase activity can be explained by the diameter of the micelle possibly associated to a change in the enzyme secondary structure when entrapped

* Rita Pacheco. Tel +351-21-8317000 ext. 1229 . E-mail: rpacheco@deq.isel.ipl.pt

inside reversed micelles. Work is already in progress in order to understand such behaviour by Light Scatering and FTIR analysis.

Our preliminary studies of storage stability revealed a higher half-life for *Pseudomonas aeruginosa* AI3 than for *Pseudomonas aeruginosa* L10. The enzyme stability is very important parameter due to enzyme application as biocatalysts therefore the studies about this parameter will continue and also performance stability in reverse micelles and in aqueous solution in order to determine the optimal conditions of production of such important products such as hydroxamic acids.

References

Pacheco R., Karmali A., Serrallheiro M.L.M., Haris P.I. (2005 a). Application of Fourier transform infrared spectroscopy for monitoring hydrolysis and synthesis reactions catalyzed by a recombinant amidase. *Analytical Biochemistry* 346, 49-58

Domingos, A., Karmali, A. ,Brown, P.R. (1989). One-step affinity purification of amidases from mutant strains of *Pseudomonas aeruginosa. Biochimie* 71, 1179-1184

Karmali, A., Pacheco, R., Tata, R., Brown, P. (2001) Substitutions of Thr-103-Ile and Trp-138-Gly in amidase from Pseudomonas aeruginosa are responsible for altered kinetic properties and enzyme instability .*Molecular Biotechnology*, 17, 201- 212

Pacheco, R., Karmali, A., Matos-Lopes, M. L. Serralheiro, M.L. (2005 b). Amidase encapsulated in TTAB reversed micelles for the study of transamidation reactions. *Biocatalysis and Biotransformation* 23, 407- 414

Fournand, D., Vaysse, L., Dubreucq, E., Arnaud, A., Galzy P. (1998).Monohydroxamic acid biosynthesis.*J. Mol. Catalysis B: Enzymatic*, 5, 207-211

Gómez –Puyou, M.T, Gómez –Puyou, A.,(1998). Enzymes in low content of water. *Critical Reviews in Biochemistry and Molecular Biology*, 33, 53 – 89

Brown, P.R., Clarke, P.H. (1972), Amino acid substitution in an amidase produced by an acetanilide-utilizing mutant of *Pseudomonas aeruginosa*, *J. Gen. Microbiol.* 70 **,**287–298.

M.M. Bradford, M.M, (1976). A rapid and sensitive method for the quantitation of microgram quantities of protein utilizing the principle of protein-dye binding, *Anal. Biochem.* 72 **,**248–254

Brammar W.J. , Clarke P.H., (1964). Induction and repression of Pseudomonas aeruginosa amidase, J. Gen Microbiol. 37 ,307-319.

Biasutti, M.A., Abuin, E.B, Silber, J.J., Mariano Correa, N. , Lissi, E.A. (2008).Kinetics of reactions catalyzed by enzymes in solutions of surfactants. *Advances in colloid and interface science,* 136, 1-24

Cabral, J.M.S., Aires-Barros, M. R., Gama, M., (2003) Engenharia Enzimática, Lidel - Edições Técnicas, Lda.,

* Rita Pacheco. Tel +351-21-8317000 ext. 1229 . E-mail: rpacheco@deq.isel.ipl.pt

Proceedings of the 10th International Chemical and
Biological Engineering Conference - CHEMPOR 2008
Braga, Portugal, September 4-6, 2008
E.C. Ferreira and M. Mota (Eds.)

Identification and evaluation of fungal strains with fucoidan degradation potential

Rosa María Rodríguez Jasso [1], Cristobal Noé Aguilar Gonzalez [2], Lorenzo Pastrana [3], Jose A. Couto Teixeira [1*]

[1] IBB – Institute for Biotechnology and Bioengineering, Centre of Biological Engineering, University of Minho, Campus de Gualtar, 4710–057 Braga, Portugal.

[2] Food Research Department, Universidad Autonoma de Coahuila, 25001, Saltillo, Coahuila, Mexico

[3] Departamento de Bioquimica, Genetica e Inmunologia, Universidad de Vigo, Ourense 32004, Galicia, Spain.

Keywords: Fungal strains, Fucoidan, Fucoidanases, Screanning
Topic: Integration of life sciences & engineering.

Abstract

Ten fungal strains isolated of Mexican semi-desert were screened for ability to hydrolyze fucoidan in order to search microorganism capable to produce sulfated fucans-degrading enzymes. Plate assay and liquid fermentation experiments were carried out using *Laminaria japonica* fucoidan as only carbon source, testing three nitrogen sources. Growth was observed only in *Aspergillus niger* PSH, *Mucor sp*., and *Penicillum purpurogenum* GH2 in fucoidan-urea medium. The activity of fucoidanases was determined by reduced sugars. *Aspergillus niger* PSH showed the highest activity titles. This research indicate that filamentous fungi, using specific medium, are sources enable to induce active metabolism that act toward this class of polysaccharide.

1 Introduction

Fucoidan is a sulfated fucose hetero-polysaccharide, found in cell walls of brown algae with a wide variety of biological activities including anticoagulant, antithrombotic, antitumoral and antiviral being the most relevants against hepatitis, herpes and human immunodeficiency (AIDS) viruses (Berteau and Mulloy, 2003; Ellouali et al., 1993; McClure et al., 1992). Morever, preparations of polysaccharides with standard characteristics as well as medicines and supplements from these biopolymers also include enzymatic treatments. Although, scientific and practical interest of studying the relation between structure and biological activity has been studied, a detailed chemical structure of fucoidan elucidation remains unknown.

Specific (Glycosylhydrolases) enzymes capable to tailored fucoidan sulfated matrix are important tools for establish the structural characteristics and biological functions of this class of polysaccharide. Endo- and exo- fucoidanases have been principally found in marine bacteria as *Vibrio* sp. (Furucawa et al., 1992), *Pseudoalteromonas citrea* (Bakunina et al, 2002) *Pseudomonas sp.*, *Alteromonas sp.* (Sakai et al., 2004), *Flavobacteriaceae* sp., (Urvantseva et al., 2006), and marine invertebrates as *Haliotis* sp., *Mizuhopecten yessoensis* mollusks and *Strongylocentrotus nudus* sea urchin (Giordano et al., 2006).

There are any reports of terrestrial and neither fungal microorganism that hydrolyzes fucoidan. For that reason, the aim of the present work was to identify fungal strains that can growth over fucoidan medium as sources of active fucoidanases, and to evaluate enzymes excretion capacity over minimal conditions.

* Corresponding author. Tel + 351-253604406. E-mail: jateixeira@deb.uminho.pt

2 Materials and methods

Fucoidan of *Laminaria japonica* (molecular weight 100,000 Da) was obtained from Rizhao Jiejing Ocean Biotechnology Development Co.,Ltd.

The filamentous fungus studied in the present work were isolated from Northeast Mexican desert (Cruz-Hernandez et al., 2005), collected during scientific expeditions realized by the Fermentation Group of Food Research Department, Universidad Autonoma de Coahuila, (Saltillo, Mexico). Strains identification was carried out in the Micoteca of Universidade do Minho (MUM, Braga, Portugal). Five *Aspergillus*: *A. ustus* PSS, *A. niger* ESH, *A. niger* PSH, *A. niger* AA20, *A. niger* GH1; four Penicillium: *P. pinophilum* EH2, *P. pinophilum* EH3, *P. purpurogem* GH2, *P.* ESS; and one *Mucor sp.* were used.

The screening methodology was carried out preparing agar plates (60x15 mm petri dish) with fucoidan-peptone, fucoidan-urea and fucoidan-sodium nitrate medium. The concentration used were: carbon source 5 gL^{-1}, nitrogen source 2 gL^{-1} and agarose 10 gL^{-1} in 100 mM acetate buffer (pH 4.5). Each strain was tested by the tree different treatments; inoculation was realized in the center of the plate and incubation was at 30ºC for ten days (experiments were made by duplicate). The presence of growth were measured each 24 h.

Submerged fermentation was realized in 250 mL Erlenmeyer flask using a minimal medium of fucoidan and urea, 10 and 5 gL^{-1}, respectively. Culture medium was sterilized by microfiltration with membranes filter of 0.2 µm. Inoculum was prepared by transferring fungal spores to potato dextrose agar medium, incubated at 30 °C for 5 days. Spores were scraped into 0.01% Tween 80 solution and counted in a Neubauer chamber. The culture conditions used were: $1x10^6$ spores mL^{-1} of inoculum concentration, 30°C, 140 rpm, initial pH 5.0 and incubation time of 96h.

For biomass determination the mycelium obtained after filtration (membrane filter 0.45 µm, 47 mm) was dried at 150 W for 10 -20 min. Total sugar quantification was carried out using phenol-sulfuric acid method (Dubois et al., 1956). The protein concentration in fungal extracts was determined using Coomasie (Bradford) protein assay kit (Pierce).

Enzymatic activity was measured by the dinitrosalicylic acid technique (Miller, 1959) to estimate the release of reducing sugars using the following reaction: 900 µL of sustrate (fucoidan 10 gL^{-1} in 200 mM acetate buffer, pH 4.5) and 100 µL of enzyme extract incubated for 24 h at 37ºC. One unity (U) of enzyme was defined as the amount of enzyme able to releases 1 µmol of reducing sugars per minute. All data correspond to triplicates of independent experiments.

3 Results and discussion

Filamentous fungus have the ability to growth over complex substrates behind minimal conditions as well as their capacity to produce a wide range of commercially interesting metabolites. Due to their exceptional high capacity to express and secrete proteins, filamentous fungi have become indispensable for the production of enzymes.

Growth fungal evaluation over fucoidan was carried out with the purpose of found terrestrial microorganism able to depolimeryzate this complex polysaccharide. From the ten strains assesed, testing three diferent mediums, only *Aspergillus niger* PSH, Penicillum *purpurogenum* GH2 and *Mucor sp*., showed mycelium presence in fucoidan-urea plates (Fig. 1) after 24 h of inoculation. However, any strain growth in fucoidan-peptone and fucoidan-sodium nitrate complex. Mucor sp. and *A. niger* PSH colonies cover completely the agar plate after six days of incubation. On the contrary, peripheral growth zone of *P. purpurogenum* GH2 was only a small part of the agar.

The presence of fungal colonies can evidence that these microorganisms are capable to excrete metabolites able to hydrolyze the branched structure of fucoidan, consisting of 1,2-linked fucose residues with sulfate at C-4.

Aspergillus niger PSH | *Mucor sp* | *Penicillum purpurogem* GH2

Figure 1. Microorganism with growth presence over fucoidan-urea dishes

Submerged fermentation experiments were realized comparing the strains that showed growing capacity over fucoidan. Urea was selected as the nitrogenum source applied in the culture medium. The morphological form observed during the submerged culture where dispersed mycelial filaments. The particular form exhibited is determined not only by the genetic material of the fungal species but also by the nature of the inoculum as well as the chemical and physical culturing conditions (Papagianni, 2004).
Higher biomass production was 0.84 gL^{-1} with *Mucor sp.* and 0.49 gL^{-1} with *A.* PSH, after 72h (Figure 2a). As was observed in agar plates experiments *P*. GH2 biomass only reach values closed to 0.2 gL^{-1}. Substrate consumption was approximately 3.5 gL^{-1} of total sugars.

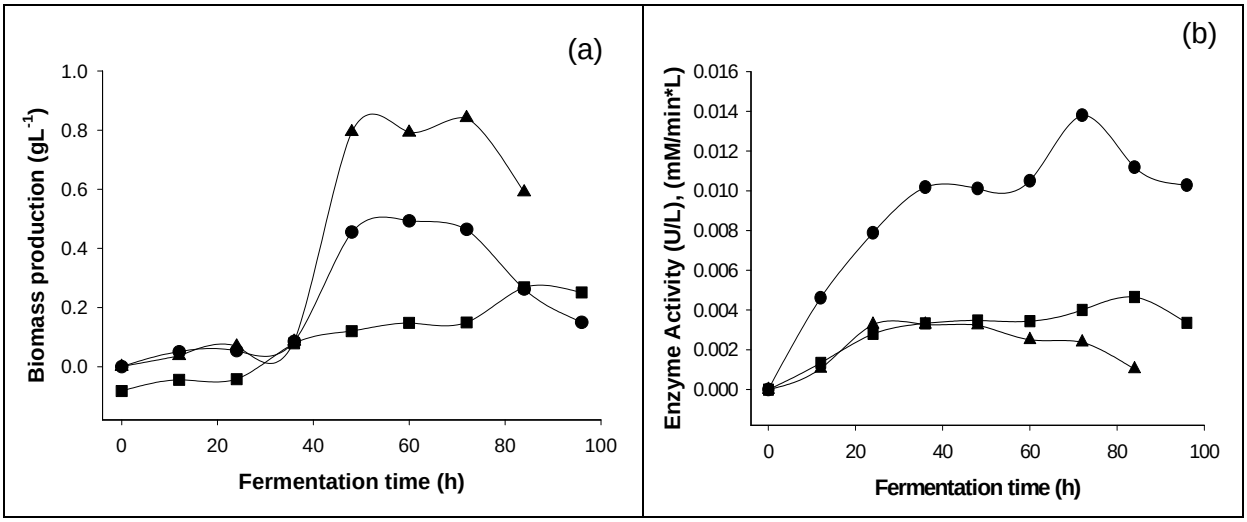

Figure 2. Submerged fermentation with fucoidan-urea medium of *Aspergillus niger* PSH (–●–), *Mucor sp*., (–▲–) and *Penicillium purpurogenum* GH2 (–■–): a) Biomass production; b) Enzyme activity.

Fucoidan activity (Fig. 2b) obtained by fungal strains was highest with *A.* PSH with values oscillating from 0.0102 to of 0.0138 UL^{-1} after 36h of fermentation. Mucor sp. and *P.* GH2 activities were 0.005 and 0.004 UL^{-1}. The enzymatic activity may be underestimated because active proteases were founded at the first 36 h of fermentation, principally in experiments with *P.* GH2.
Despite of enzyme activity were lower, there are any reports of fungal fucoidanases by induction procedure. Morever, fucoidan hydrolases reported by Alexeva et al*.,* (2002), Burtseva et al., (2000) and Bakunina et al., (2000) with marine bacteria and invertebrates exhibited weak catalysis.

The present study suggest that fungal strains from the genus *Aspergillus, Penicillium* and *Mucor* have the capacity for synthesize fucoidan hydrolytic enzymes, being potential microbiology tools for used in fermentation process, looking for the optimization in order to obtain higher titles under different processes.

References

Alexeeva, Y.V., Ivanova, E.P., Bakunina, I.Y., Zvaygintseva, T.N., Mikhailov, V.V. (2002). Optimization of glycosidases production by *Pseudoalteromonas issachenkonii* KMM 3549, *Letters in Applied Biotechnology*, 35, 343-346.

Bakunina, I.Y., Shevchenko, L.S., Nedashkovskaya, O.I., Shevchenko, N.M., Alekseeva, S.A., Mikhailov, V.V., Zvyagintseva, T.N. (2000). Screening of marine bacteria fro fucoidanases. *Microbiology*, 69 (3), 303-308.

Bakunina, I.Y., Nedashkovskaya, O.I., Alekseeva, S.A., Ivanova, E.P., Romanenko, L.A., Gorshkova, N.M., Isakov, V.V., Zvyagintseva, T.N., and Mikhailov, V.V. (2002). Degradation of fucoidan by the marine proteobacterium Pseudoalteromonas citrea, *Mikrobiologiya*,71 (1), 49–55.

Berteau, O., Mulloy, B. (2003). Sulfated fucans, fresh perspectives: structures, functions, and biological properties of sulfated fucans and an overview of enzymes active toward this class of polysaccharide. *Glycobiology* 13: 29R–40R.

Burtseva, Yu. V., Kusikin, M. I., Sova, V.V., Shevchenko, N.M., Skobun, A.S., Zvyagintseva, T.N. (2000). Distribution of fucoidán hydrolases and some glycosidases among marine invertebrates. *Russian Journal of Marine Biology*, 26(6), 453-456.

Cruz-Hernandez, M., Contreras-Esquivel J. C., Lara, F., Rodriguez, R., Aguilar, C. N. (2005) Isolation and evaluation of tannin-degrading fungal strains from the Mexican Desert. Z. Naturorsch, 60: 844-848.

Dubois, M., Gilles, K.A., Hamilton, J., Rebers, P.A., Smith, F. (1956). Colorimetric method for determination of sugar relates substances. *Analytical Chemistry*, 28, 350–356.

Ellouali, M., Boisson-Vidal, C., Durand, P., Jozefonvicz, J. (1993). Antitumor activity of low molecular weight fucans extracted from brown seaweed Ascophyllum nodosum. *Anticancer Reseach,* 13(6A), 2011-2019

Furukawa, S., Fijikawa, T., Koga, D., Ide, A. (1992). Purification and some properties of exo-type fucoidanases from *Vibrio* sp. N-5. *Japan Society fro Bioscience, Biotechnology and Agrochemistry*, 56(11), 1829-1834.

Giordano, A., Andreotti, G., Tramice, A., Trincone, A. (2006). Marine glycosyl hydrolases in the hydrolysis and synthesis of oligosaccharides, *Journal of Biotechnology*, 1, 511–530.

Miller, G.L. (1959). Use of dinitrosalicylic acid reagent for determination of reducing sugar, *Analytical Chemistry*, 31, 426–428.

McClure, M. O., Moore, J. P., Blanc, D. F., Scotting, P., Cook, G. M. W., Keynes, R. J., Weber, J. N., Davies, D., Weiss, R. A. (1992) Investigations into the mechanism by which sulfated polysaccharides inhibit HIV infection *in vitro*. AIDS Research and Human Retroviruses, 8, 19–26.

Papagianni, M. 2004. Fungal morphology and metabolite production in submerged mycelial processes. *Biotechnology Advances*, 22(3),189-259.

Sakai, T., Kawai, T., and Kato, I. (2004). Isolation and characterization of a fucoidan-degrading marine bacterial strain and its fucoidanase. *Marine Biotechnology*, 6(4), 335–346.

Urvantseva, A. M., Bakunina, I. Y., Nedashkovskaya, O. I., Kim, S. B., Zvyagintseva, T. N. (2006). Distribution of Intracellular Fucoidan Hydrolases among Marine Bacteria of the Family Flavobacteriaceae. *Applied Biochemistry and Microbiology*, 42 (5), 484–491.

Proceedings of the 10th International Chemical and
Biological Engineering Conference - CHEMPOR 2008
Braga, Portugal, September 4-6, 2008
E.C. Ferreira and M. Mota (Eds.)

Modeling and Experimental Evaluation of Poly(3-hydroxybutyrate) Production in *Bacillus megaterium*

Débora Jung Luvizetto Faccin[1], Ivana Martins[1], Nilo Sérgio Medeiros Cardozo[1], Rosane Rech[2], Marco Antônio Záchia Ayub[2], Tito Lívio Moitinho Alves[3], Rossano Gambetta[4], Argimiro Resende Secchi[3*]

[1]Departamento de Engenharia Química, Universidade Federal do Rio Grande do Sul, R. Eng. Luis Englert, s/n. Campus Central. CEP: 90040-040 – Porto Alegre – RS – Brasil
[2]Instituto de Ciência e Tecnologia de Alimentos, Universidade Federal do Rio Grande do Sul, Porto Alegre – RS – Brasil
[3]Universidade Federal do Rio de Janeiro (COPPE/ UFRJ) – Programa de Engenharia Química, Rio de Janeiro – RJ – Brasil
[4]Quattor S/A, Mauá – SP

Keywords: Biopolymers, Poly(3-hydroxybutyrate), Modeling, Optimization.
Topic: Integration of life sciences & engineering.

Abstract

The aim of this research was the optimization of poly(3-hydroxybutyrate) – P(3HB) – production obtained in submerged cultures of *Bacillus megaterium* in a mineral medium, using sucrose as carbon source and the nitrogen as the limiting substrate. A bench-scale bioreactor was used in order to obtain experimental data for phenomenological modeling of the biopolymer production, microbial growth, and substrate consumption. From an experimental design, which was carried out in shaker at 30°C and 160 rpm, it was evaluated the best initial sucrose concentration and carbon-to-nitrogen ratio in order to maximize the biomass accumulation and biopolymer production. It was observed the P(3HB) accumulation in bacteria without the need of nitrogen limitation and a strong correlation between accumulated P(3HB) and pH. Bench-scale bioreactor experiments were carried out and showed the importance of a control pH strategy. The proposed model was implemented in the EMSO process simulator and its parameters were estimated using this tool and the experimental data from the bioreactor. The simulation results showed good agreement with the experimental data.

1 Introduction

Plastics have been regarded as ideal materials for the production of various consumer products because of their durability and inherent resistance to degradation. However, these same qualities are sources of environmental and waste management problems. These problems have created much interest in the development of biopolymer. In addition, biopolymers can be obtained from agriculture or from biotechnological processes and are therefore, in principle, available from renewable resources (Luengo et al., 2003; Reddy et al., 2003).

Polyhydroxyalkanoates (PHAs) biopolymers are polyesters synthesized by numerous bacteria and are accumulated on inclusion bodies in the cytoplasm of the cells as energy storage. They are produced from renewable carbon sources and, generally, with limiting nutrient; and their main characteristic is the biodegradability (Lee, 1996b; Madison and Huisman, 1999). Poly(3-hydroxybutyrate) (P(3HB)) is the most characterized PHA, partially crystalline polymer, and with material properties similar to polypropylene (Lee, 1996a; Sudesh et al., 2000).

The aim of this research was the optimization of poly(3-hydroxybutyrate) – P(3HB) – production obtained in submerged cultures of *Bacillus megaterium* in a mineral medium, using sucrose as carbon source and the nitrogen as the limiting substrate.

* Corresponding author. Tel +55-21-2562-8301. E-mail:arge@peq.coppe.ufrgs.br

2 Materials and methods

2.1 Microorganism and culture medium: The bacterium used in this study was *Bacillus megaterium*, DSM 32^T. The mineral medium is the same used in Wang and Lee (1997).

2.2 Design of experiments: Shaker experiments were carried out, according to a central composite design with three repetitions in the central point, in order to evaluate the best initial sucrose concentration (S) and carbon-to-nitrogen ratio (C:N) for increasing cell concentration and accumulated polymer. In Table 1, it was shown the concentration of sucrose and source of nitrogen (SN) to give the desired carbon-to-nitrogen ratio. Batch fermentations were carried out in 250 mL Erlenmeyer flasks containing 50 mL of culture medium with initial pH = 7. The flasks were inoculated and maintained at 30°C and 160 rpm for the requested time. Samples were collected in 4, 8, 12, 16, 20 and 24 hours.

Table 1: Design of experiments

EXP	X1 (S)	X2 (C:N)	S (g·L^{-1})	C:N	SN (g·L^{-1})
1	1	1	44	22	2.00
2	1	-1	44	8	5.50
3	-1	1	16	22	0.73
4	-1	-1	16	8	2.00
5	0	$-\sqrt{2}$	30	5	6.00
6	0	$\sqrt{2}$	30	25	1.20
7	$-\sqrt{2}$	0	10	15	0.67
8	$\sqrt{2}$	0	50	15	3.33
9a	0	0	30	15	2.00
9b	0	0	30	15	2.00
9c	0	0	30	15	2.00

2.3 Bench-scale bioreactor: For larger scale production, a 5 L bioreactor was used containing 4 L of the culture medium. The initial substrate concentration (16 g·L^{-1} of sucrose and 2 g·L^{-1} of ammonium sulphate) was chosen according to the optimal point of the surface response curve from the design of experiments.

Bench-scale bioreactor experiments were carried out with dissolved oxygen and pH control. Cultivations parameters were as follows: pH, 7; temperature, 30°C; aeration, 4 L/min; stirred speed, 200-700 rpm. The dissolved oxygen (pO_2) was controlled changing the stirred speed in order to keep the value of dissolved oxygen above 40%. Bench-scale bioreactor experiments without pH control, but keeping the other conditions unchanged, were also carried out.

2.4 Analytical procedures: Total biomass was evaluated by dry weight, from 40-10 mL of culture broth. The cell suspension was centrifuged at 3500 rpm for 20 min at 4°C, washed with distilled water, transferred to pre-weighed vials and dried in an oven at 80°C till constant weight. P(3HB) amount was determined by propanolysis of monomers according to the method of Riis and Mai (1988). Residual biomass was calculated total biomass less biopolymer amount, once biopolymer was accumulated into the cell. The sucrose was analyzed according to Dubois et al. (1956) and by HPLC using a Rezex-RHM (300 mm x 7.8 mm) column at 80°C and RI detector. Nitrogen was determined by the phenol-hypochlorite reaction according to Weatherburn (1967).

2.5 Modeling: Different mathematical models for microbial growth, biopolymer production and substrate consumption were analyzed (Khanna and Srivastava, 2005; Raje and Srivastava, 1998). A new model which is a improved version of the Khanna-Srivastava model presenting a lower number of parameters. This model is shown in Table 2. All models were implemented in the EMSO process simulator (Soares and Secchi, 2003) and their parameters were estimated using this tool and the experimental data from the bioreactor.

Table 2: Equation of the modified model

Residual Biomass(X_R):	$\frac{dX_R}{dt} = (\mu - k_d) \cdot X_R$
Specific grow rate (μ):	$\mu = \mu_m \left(\frac{S}{K_{SS} + S} \right) \cdot \left(\frac{N}{K_{NS} + N} \right)$
Biopolymer (P):	$\frac{dP}{dt} = (k_1 \cdot \mu + k_2) \cdot X_R$
Sucrose(S):	$\frac{dS}{dt} = -(\alpha \cdot \mu + \gamma) \cdot X_R$
Nitrogen (N):	$\frac{dN}{dt} = -\frac{\mu}{Y_{RN}} \cdot X_R$

3. Results and discussion

3.1 *Design experiments*

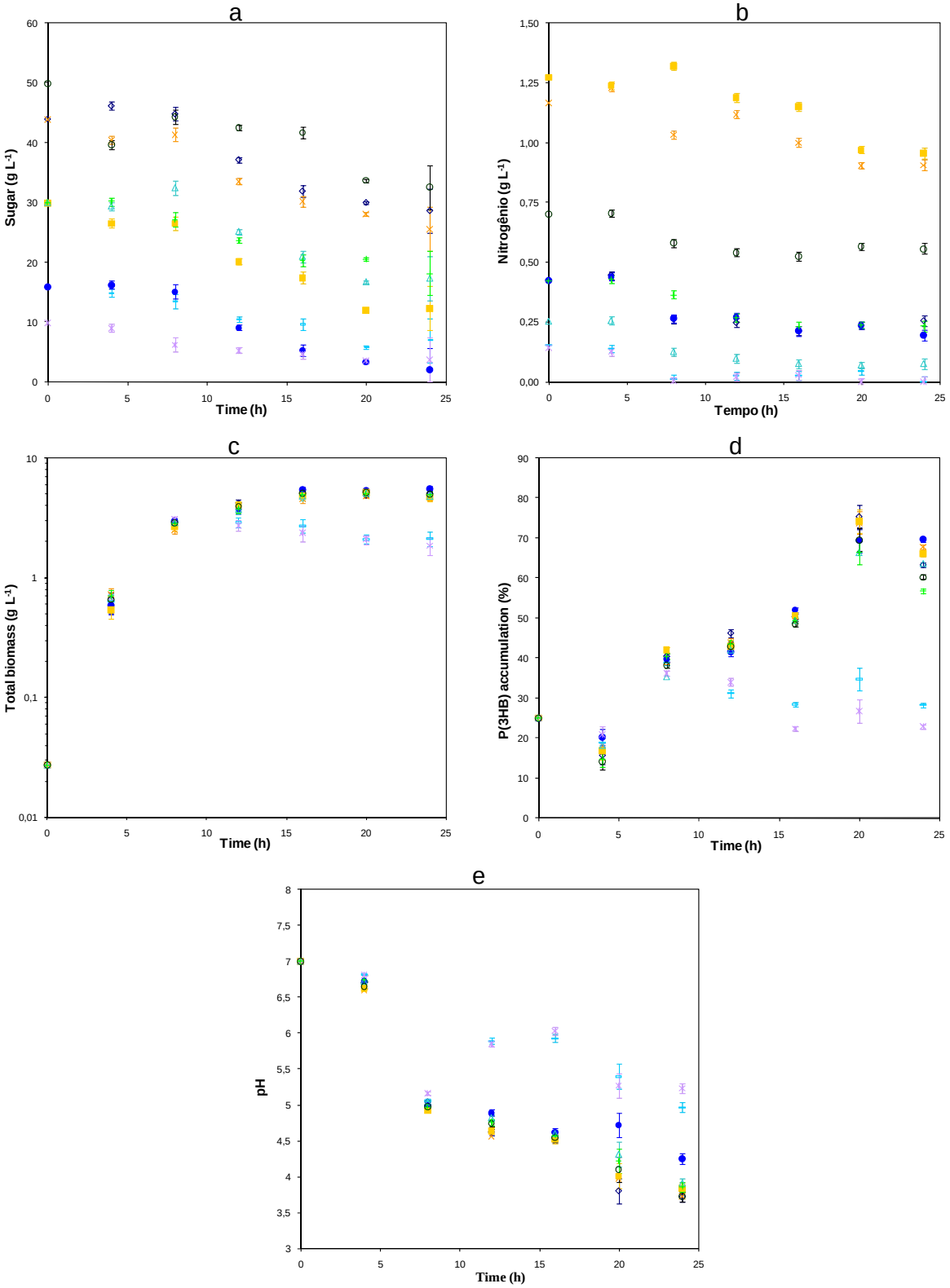

Figure 1: Time evolution of sugar concentration (a), nitrogen concentration (b), total biomass concentration (c), polymer accumulation (d) and pH (e) throughout the culture.

In the experiments, P(3HB) was accumulated in the cell about 75% at 20 hours of culture. In most of the cases, there was no limitation in the sucrose or nitrogen (Figure 1a and 1b) but a decreasing in P(3HB) accumulation after 20 h could be seen (Figure 1c) and no more increasing in the biomass could be detected (Figure 1d). The pH decreased with the time (Figure 1e) and it was observed a strong correlation between accumulated P(3HB) and pH of the medium.

It is observed that *B. megaterium* shows different behavior from bacteria commonly used on biopolymer production, like *R. eutropha*, since it is able to produce large amounts of P(3HB) without nitrogen limitation. Similar results are found in Omar et al. (2001) and Maccol et al. (1996).

The results of the design of experiments were analyzed using surface response for biomass, polymer accumulated, and residual sucrose. With the fitted equations from this surfaces it was constructed an objective function to determine the best condition to maximize the biomass accumulation and biopolymer production and also to minimize the residual sucrose.

This objective function is shown in equation (1) and also in Figure 2 with weight w = 0.2. The optimal point was found to be close to the experiment number 4 (S = 16 g·L^{-1} e C:N = 8), which was then chosen to carry out the experiments in bench-scale bioreactor.

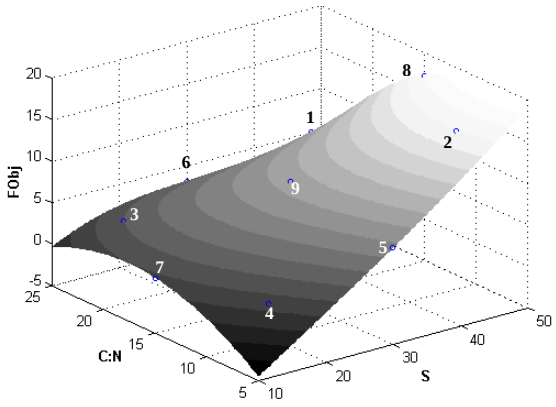

$$F_{Obj}(S,C:N) = (1-w)\cdot S_R(S,C:N) - w\cdot\left(\frac{P(S,C:N)\cdot X_T(S,C:N)}{100}\right) \quad (1)$$

Figure 2: Plot of the objective function and the equation that represents this function.

3.2 *Bench-scale bioreactor*

The experiments without pH control (SCPH) and with pH control (CCPH) were done in duplicate in the bench-scale bioreactor. The results (medium values of duplicates) are shown in Figure 3. The SCPH experiment was finished earlier than the CCPH, after 12 h, because the dissolved oxygen came back to 100% (Figure 3e).

Comparing the results from bench-scale bioreactor with those from shaker we could observe that the polymer accumulation is much lower in the bioreactor, even without pH control, which is the condition corresponding to the shaker process. This decrease in the P(3HB) accumulation compared with shaker was also observed in Omar et al. (2001).

In Figure 3a, it can be observed that total biomass (Xt) and residual biomass (Xr) were lower in SCPH than in CCPH experiments, although the P(3HB) amount was similar. Therefore, P(3HB) accumulation (%) into the cell in SCPH experiments was higher than the CCPH (Figure 3b). As in SCPH experiments there was no limitation either in sucrose or in nitrogen, the cells growing interruption could be attributed to the final pH was very low. These results show that: i) the use of a pH based control strategy is very important and ii) maintaining pH = 7 during the whole process, as in CCPH experiments, is not the most adequate control strategy.

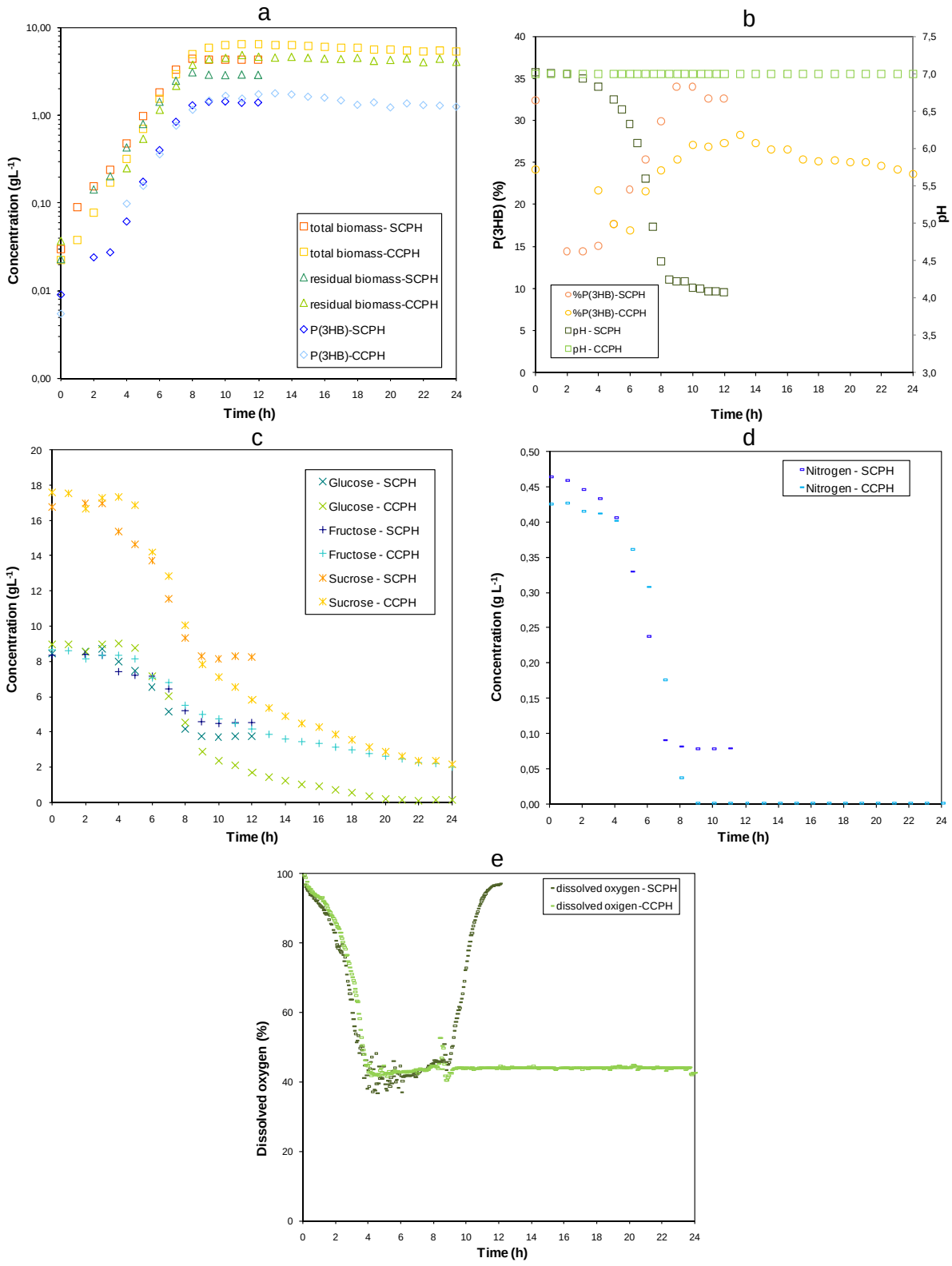

Figure 3: Time evolution of total biomass concentration, biopolymer accumulation and residual biomass (a), biopolymer accumulated and pH (b) sugar concentration (c), nitrogen concentration (d) and dissolved oxygen (e) throughout the culture without control pH (SCPH) and pH controlled (CCPH).

The values of parameters estimated using experimental data from the bioreactor with pH control are shown In Table 3. The simulation results showed good agreement with the experimental data, as pointed by the low value of the objective function.

Table 3: Parameter values for CCPH experiment.

Parameter	Unit	Values
α		2,0606
γ	1/h	0,0849
k_1		0,4053
k_2	1/h	-0,0079
k_d	1/h	0,0073
K_{SS}	g/L	0,1928
K_{SN}	g/L	0,0447
μ_m	1/h	0,7979
Y_{RN}		10,6314
Objective function		**0,1575**

5. Conclusions

Results of shaker experiments shown that *Bacillus megaterium* is able to produce large amounts of P(3HB) without nitrogen limitation. Results of shaker and bench-scale experiments realized the importance of a programmed pH control strategy, different from the used in CCPH experiment.

Therefore, more experiments need to be done in order to test new strategies for pH control in specific ranges (like as from 5 to 7), that can be able to generate similar results of P(3HB) accumulated in cells as the ones obtained in the shaker experiments.

6. Acknowledgements

The authors wish to thank MCT/CNPq for the financial support.

7.References

Khanna, S.; Srivastava, A. K. (2005). A Simple Structured Mathematical Model for Biopolymer (PHB) Production. Biotechnol. Prog., 21, 830-838.

Lee, S. Y. (1996a). Bacterial Polyhydroxyalkanoates. Biotechnology and Bioengineering, 49,1-14.

Lee, S. Y. (1996b). Plastic bacteria? Progress and prospects for polyhydroxyalkanoate production in bacteria. Tibtech, 14, 431-438.

Luengo, J. M.; García, B.; Sandoval, A.; Naharroy, G.; Oliveira, E. R. (2003). Bioplastics from microorganisms. Current Opinion in Microbiology, 6, 251–260.

Madison, L. l.; Huisman, G. W. (1999). Metabolic Engineering of Poly(3-Hydroxyalkanoates): from DNA to Plastic. Microbiology and Molecular Biology Reviews, 63, 1, 21-53.

Mccool, G. J.; Fernandez, T.; LI, N.; Cannon, M. C. (1996). Polyhydroxyalkanoate inclusion-body growth and proliferation in Bacillus megaterium. FEMS Microbiology Letters, 138, 41-48.

Omar, S.; Rayes, A.; Eqaab, A.; Voß, I.; Steinbüchel, A. (2001). Optimization of cell growth and poly(3-hydroxybutyrate) accumulation on date syrup by a *Bacillus megaterium* strain. Biotechnology Letters, 23, 1119-1123.

Raje, P.; Srivastava, A. K. (1998). Updated mathematical model and fed-batch strategies for poly-β-hydroxybutyrate (PHB) production by *Alcaligenes eutrophus*. Bioresource Technology, n. 64, p. 185-192.

Reddy, C. S. K.; Ghai, R.; Rashmi; kalia, V. C. (2003). Polyhydroxyalkanoates: an overview. Bioresource Technology, 87, 137-146.

Riis, V. and Mai, W. (1988). Gas chromatographic determination of poly-β-hydroxybutyric acid in microbial biomass after hydrochloric acid propanolysis. Journal of Chromatography, 445, 285-289.

Soares, R.P.; Secchi, A.R. EMSO: A New Environment for Modeling, Simulation and Optimization, Proceedings 13th European Symposium on Computer Aided Process Engineering, p. 947–952, Lappeenranta (2003)

Sudesh, K.; Abe, H.; Doi, Y. (2000). Synthesis, structure and properties of polyhydroxyalkanoates: biological polyesters. Progress in Polymer Science, 25, 1503-1555.

Wang, F. e Lee S. Y. Poly(3-Hydroxybutyrate) Production with High Productivity and High Polymer Content by a Fed-Batch Culture of Alcaligenes Latus under Nitrogen Limitation. Applied and Environmental Microbiology, 63, 3703-3706 (1997).

Weatherburn, M. W. (1967). Phenol-Hypoclorite Reaction for Determination of Ammonia. Analytical Chemistry, 39 (8), 971-974.

Proceedings of the 10th International Chemical and
Biological Engineering Conference - CHEMPOR 2008
Braga, Portugal, September 4-6, 2008
E.C. Ferreira and M. Mota (Eds.)

Statistical analysis of oxygen effect on the culture of *Bacillus thuringiensis*

Azam Najafloo[1], Mohammad H. Sarrafzadeh[1*], Abbas Gerami[2]
[1]Department of Chemical Engineering, College of Engineering, University of Tehran, P.O. Box 11155-4563, Tehran, Iran.
[2]School of Mathematics, Statistics and Computer Science, University of Tehran, Tehran, Iran

Keywords: Biological fight; *Bacillus thuringiensis*; Dissolved oxygen; Statistical analysis; Sporulation

Topic: Integration of life sciences & engineering.

Abstract

Oxygen supply is known to be an important constraint on the growth of the aerobic sporeforming bacteria (Liu et al. 1994). However, the effects of oxygen on sporulation of these bacteria have been limited studied. In *Bacillus thuringiensis* (Bt), sporulation is associated with production of an entomocidal parasporal crystalline toxin, also known as δ-endotoxin, which is generally the most important feature of this bacterium (Aronson, 1993; Sarrafzadeh et al. 2005). Thus the effect of oxygen in relation to toxicity must be considered too. The actual disagreements between reports show that oxygen role is far from to being completely understood (Avignone-Rossa and Mignone. 1995). Statistical analysis could be a very powerful tool to interpret the diverse results at this situation (Montgomery et al. 2001). In this work, attempts are made to study the effect of dissolved oxygen (DO) on sporulation development of Bt. investigations have been carried out involving fed-batch cultivation of *Bacillus thuringiensis* H14 followed by a batch culture after 24 h at different DO concentration. The sporulation in three different levels of DO (0, 50 and 100%) was followed by using microscopic methods and on-line measurements. The viability decreasing due to sporulation was also monitored. Statistical analysis of the effect of oxygen in sporulation was performed using a regression method and with the help of Minitab as the available software. The results showed a significant effect ($P < 0.05$) of oxygen not only on total spore formation but also on mature spore liberation. The statistical models were proposed to show the relations between sporulation development and oxygen levels. These statistical models were able to predict satisfactory the sporangium and mature spore formation at different levels of DO.

1) Introduction

The potential of *Bacillus thuringiensis* for use as a control agent of insects has provided a promising natural insecticide which can be an alternative to the chemical insecticides or as a part of integrated pest management system (Rowe & Margaritis 1987; Feitelson et al. 1992). *Bacillus thuringiensis* is a large gram-positive and spore-forming bacterium that produces, concomitantly with sporulation, an entomocidal parasporal crystalline protein, also known as δ-endotoxin (Aronson 1993, 2002; Agaisse & Lereclus 1995). *B.*

* Corresponding author. Tel + 982161112185. E-mail: sarrafzdh@ut.ac.ir

thuringiensis serotype H14 is the most effective microbial control agent available to date, against the larvae of dipterans such as mosquitoes and blackflies (de Barjac 1978). Large quantities of spores with high insecticidal activity are required for practical applications. Therefore, an engineering approach is needed to ensure a suitable environment for growth and δ-endotoxin synthesis. Oxygen is necessary for all aerobic fermentation. Maintaining the appropriate concentration of dissolved oxygen has been pointed out as an important factor in the fermentation of *B. thuringiensis* (Avignone-Rossa & Mignone 1995; Morris et al. 1996; Flores et al. 1997) Although there is a considerable amount of literature available in relation to the effects of oxygen on the biomass concentration (Liu et al. 1994) and toxin synthesis (Foda et al. 1985). The research was invariably carried out under constant aeration conditions, all along the culture, in flasks or laboratory fermenters. However the oxygen demands of culture are not the same all along the culture and depend strictly on the dominant physiological state of the microbial population in the culture. For this reason, there is no a general agreement between all authors and the reports are very diverse. Statistical analysis is a good tool in this situation to make clear the real requested conditions for aeration. Statistical analysis is used not only to optimize fermentation conditions but also it could be used to describe and predict the culture behavior (Montgomery et al. 2001). The aim of our work was to study the production of the spore of Bacillus *thuringiensis* H14 and statistical analysis of it. We decided to use regression analysis to determine the correlations between the total spore, mature spore and sporangium with dissolve oxygen percent during the time.

2) Materials and methods

Microorganism and media

Bacillus thuringiensis H14 (Ecautec, Tahiti) was used. A preculture flask containing 500 ml of medium was incubated at 30 °C on an orbital shaker for 9 h and used to inoculate the fermentor. The composition of the culture medium was (g/l): glucose, 5; hydrolysed casein, 4.5; yeast extract, 0.5; ammonium sulphate, 6; K_2HPO_4, 1.4; KH_2PO_4, 1.4; $MgSO_4$. 7 H_2O, 0.61; $CaCl_2$, 0.332; $MnSO_4$. 7 H_2O, 0.006. A concentrated medium, containing (g/l): glucose, 240; hydrolysed casein, 155; yeast extract, 25, was added during fed-batch phase. The pH of the medium was adjusted to 6.8 by 3 M NaOH (Sarrafzadeh et al. 2005).

Fermentation procedure

The fermenter (Biolafitte) had a maximum working volume of 15 l in which 9 l of culture medium were sterilized in situ. three fermentations were initiated under identical conditions in batch mode at 30 °C. Fed-batch cultures were started from 4 to 24 h of fermentation at a constant feed rate of 150 ml/h. Dissolved oxygen (DO) was monitored continuously and maintained above 20% of saturation during the growth period. During the sporulation phase a different oxygenation level was maintained. The three oxygen concentration performed were 0%, 50% and 100% which we define as interrupted, non-limited and saturated, respectively. The latter was carried out using pure oxygen which replaced air after 24 h of culture. The pH was maintained at 6.8 during the growth phase by 3 M NaOH but its increase during the sporulation phase was not controlled.

Sporulation, cell lysis and crystal formation

Sporulation, formation of inclusion bodies and cell lysis were monitored using a phase contrast microscope (Olympus Bx60). Cell counts (vegetative and sporulated cells) were

carried out using this microscope and a Thoma chamber. Unlysed sporulated cells were counted as spores. Sporulation was determined as the ratio of lysed and unlysed sporulated cells, which were distinguished due to their refractile nature, over the total cell count. The percentage of sporulated lysed cells vs. the total cell count has also been calculated as a mature spore count (Sarrafzadeh et al. 2005).

Statistical treatment

Regression analysis of the data obtained and three statistical models explaining the effects of the studied parameters establishing the optimal conditions of the parameters studied for total spore, mature spore and sporangium production were carried out using Minitab package for personal computers.

3) Results and discussion

A set of fermentation experiments, for determining the values for total spore, mature spore and sporangium at the different levels of dissolve oxygen (0%, 50% and 100%) were carried out. The data obtained were statistically analyzed. First, a second order model with all terms included was tested. The analysis of variance indicated that the model should be reduced in order to obtain better significance of the individual parameters. The reduced models obtained were as follows:

$$S_1 = -28.328+2.641t+0.952\times O-0.0034O^2-0.0237tO \quad (1)$$

$$S_2 = -102.488+4.281t+0.895\times O-0.032tO \quad (2)$$

$$S_3 = 74.435-1.637t+0.0098O-0.0029O^2+0.0080tO \quad (3)$$

Where S_1 refers to total spore percent; S_2 refers to mature spore percent; S_3 refers to sporangium; O refers to the oxygen percent of saturation; and t refers to time (h). These statistical models were able to predict satisfactory the total spore, mature spore and sporangium formation at different levels of dissolved oxygen during the time.

All the terms included in the presented statistical model were found to be significant at 95% level of significance, and the models were found to explain 88.9%, 94.2% and 89.3% of the experimental data, respectively.

Statistical analysis showed that the dissolve oxygen and time has the significant effect ($P<0.05$) on the total spore and mature spore. The dissolve oxygen has insignificant effect ($P>0.05$) on the sporangium but oxygen is not omitted of third model because square of oxygen and interaction of oxygen and time have the significant effect on the sporangium.

Figure 1, Figure 2 and Figure 3 provide two-dimensional views where all points that have the same total spore, mature spore and sporangium, respectively, are connected to produce contour lines of constant responses. Figure 1 and Figure 2 show that with decrease of oxygen at the constant time total spore and mature spore percent increase. Figure 3 show that sporangium production is independent of oxygen percent.

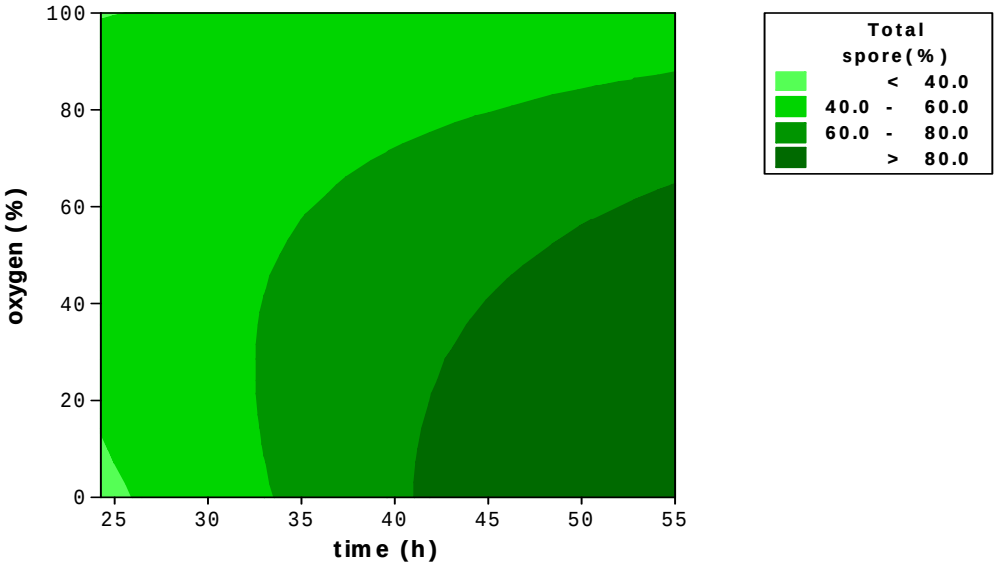

Figure 1. Contour plot for total spore production by *Bacillus thuringiensis* H14 at different levels of oxygen (% of saturation) and time.

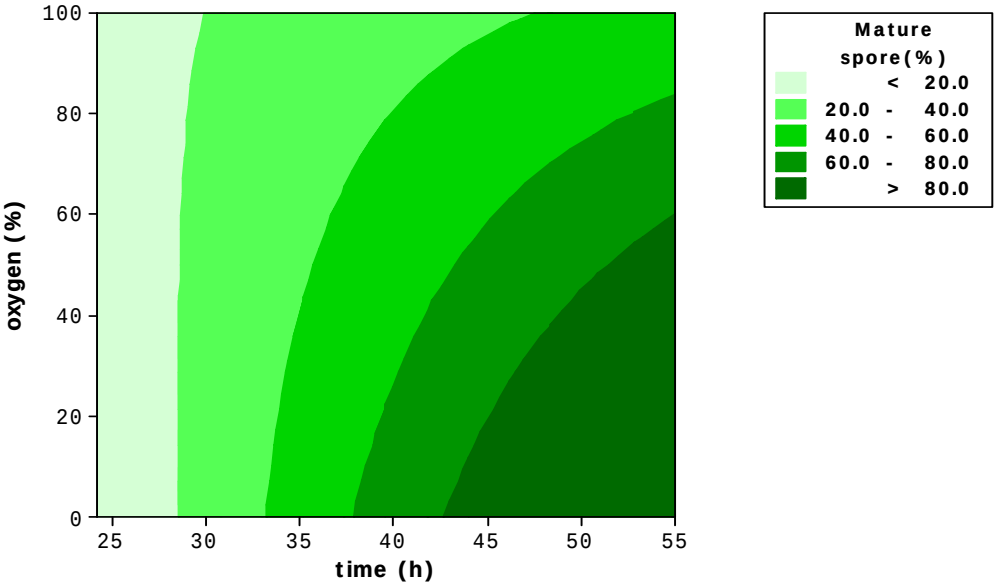

Figure 2. Contour plot for mature spore production by *Bacillus thuringiensis* H14 at different levels of oxygen (% of saturation) and time.

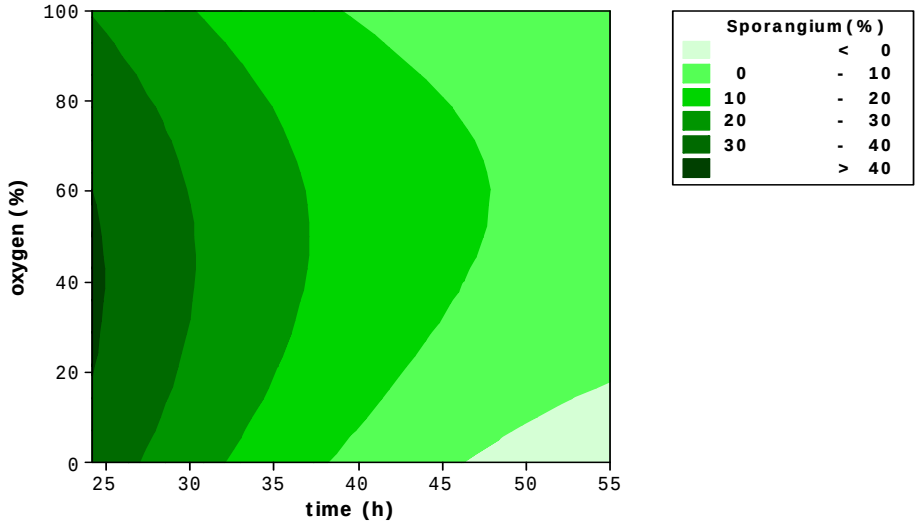

Figure 3. Contour plot for sporangium production by *Bacillus thuringiensis* H14 at different levels of oxygen (% of saturation) and time.

References

Agaisse, H. & Lereclus, D. (1995). How does *Bacillus thuringiensis* produce so much insecticidal crystal protein? Journal of Bacteriology 177, 6027–6032.

Aronson, A. (2002). Sporulation and δ-endotoxinsynthesis by *Bacillus thuringiensis*. Cellular and Molecular Life Sciences 59, 417–425.

Aronson, A.I. (1993). The two faces of Bacillus thuringiensis – insecticidal proteins and postexponential survival. Molecular Microbiology 7, 489–496.

Avignone-Rossa, C. & Mignone, C.F. (1995). *Bacillus thuringiensis* growth and toxicity – basic applied considerations. Molecular Biotechnology 4, 55–71.

de Barjac, H. (1978). Une nouvelle variete de *Bacillus thuringiensis* tres toxique pour les moustiques: *B. thuringiensis israelensis* serotype 14. Comptes Rendues des Seances de l'Academie des Sciences de Paris, ser D 286, 797–800.

Feitelson, J.S., Payne, J. & Kim L. (1992). *Bacillus thuringiensis*: insects and beyond. Bio/Technology 10, 271–275.

Flores, E.R., Perez, F. & De la Torre, M. (1997). Scale-up of *Bacillus thuringiensis* fermentation based on oxygen transfer. J. Ferment. and Bioeng. 83, 561–564.

Foda, M.S., Salama, H.S. & Selim, M. (1985). Factors affecting growth physiology of *Bacillus thuringiensis*. Applied Microbiology and Biotechnology 22, 50–52.

Liu W, Bajpai R, Bihari V (1994). High-density cultivation of sporeformers. Ann. N.Y. Acad. Sci. 721: 310–325.

Montgomery, D.C., Peck, E.A., Vinning, G.G., (2001). Introduction to linear regression analysis. 3rd Ed., Wiley. pp 205.

Morris, O.N., Converse, V., Kanagaratnam, P. & Davies, J.S. (1996). Effect of cultural conditions on spore-crystal yield and toxicity of *Bacillus thuringiensis* subsp *aizawai* (HD133). Journal of Invertebrate Pathology 67, 129–136.

Rowe, G.E. & Margaritis, A. (1987). Bioprocess developments in the production of bioinsecticides by *Bacillus thuringiensis*. CRC Critical Reviews in Biotech. 6, 87– 27.

Sarrafzadeh, M.H., Guiraud, J.P., Lagneau, C., Gaven, B., Carron, A. & Navarro, J.M. (2005). Growth, sporulation, δ-endotoxinsynthesis and toxicity during culture of *Bacillus thuringiensis* H14 Current Microbiology 51, 75–81.

Proceedings of the 10th International Chemical and
Biological Engineering Conference - CHEMPOR 2008
Braga, Portugal, September 4-6, 2008
E.C. Ferreira and M. Mota (Eds.)

Characterization of phenolic compounds of OMW: toxicity and degradability by yeasts.

Cristiana Gonçalves[1], João P. Ferreira[1], Marlene Lopes[1], Soraia Falcão[2], António M. Peres[2,3], Susana M. Cardoso[2], Isabel Belo[1*]

[1] IBB – Institute for Biotechnology and Bioengineering, Centre of Biological Engineering, University of Minho, Campus de Gualtar, 4710–057 Braga, Portugal.

[2] CIMO, [3] LSRE - Agrarian Superior School, Institute Polytechnic of Bragança, P-5301-855 Bragança, Portugal.

Keywords: Lipolytic yeasts, phenolic compounds, respirometry OMW
Topic: Suitable conference topic — Integration of life sciences & engineering

Abstract

The characterization of Olive Mill Wastewaters (OMW), focusing the phenolic compounds, is one of the aims of the present work. As a first approach to characterize the phenolic compounds of OMW, the extraction methods used were: a liquid-liquid extraction by acidified ethyl acetate and a solid-liquid extraction with acidified methanol. The analysis of these extracts by reversed phase liquid chromatography confirmed that hydroxytyrosol was the most abundant phenolic compound in OMW, and that this compound was more efficiently recovered by the solid-liquid extraction technique. It was also a goal of this work to study the phenolic compounds toxicity to some yeast strains. Among the phenolic compounds tested catechol is the most inhibitory one to the cells. The phenols degradation was quite difficult, particularly when more easily degradable carbon source is still present in the medium.

1 Introduction

The olive oil consumed in the world is mainly produced in the Mediterranean area. The three -phase extraction system is the most common technology used in these countries, with exception of Spain, the most important producer, that mostly uses the two-phases process. These technologies differ in the water requirements. The three-phase extraction process requires large amounts of water, resulting in a large amount of effluent, known as Olive Mill Wastewater (OMW). OMW represents a major environmental problem due to its high organic content.

OMW is often characterized by a strong acidic smell and an intensive brown to dark color due to the presence of biodegradable and recalcitrant compounds (such as polyphenolic compounds). The phytotoxicity of the olive mill wastewaters can be attributed to the phenolic compounds (Lanciotti et al, 2005). In fact, the olive pulp is very rich in phenolic compounds (Cardoso et al, 2005), but only 2% of the total phenolic content of the olive fruit passes in the oil phase, while the remaining amount is lost in the OMW (approximately 53%) and in the pomace (approximately 45%) (Rodis et al., 2002).
Due to their instability, OMW phenols tend to polymerize during storage into condensed high-molecular-weight polymers that are difficult to degrade (Crognale et al, 2006). Thus, uncontrolled OMW disposal can create severe risks to water and soil quality. OMW is currently concentrated by evaporation in open pools, but this method is not satisfactory because it only reduces the volume of waste without treating the pollutants and a black foul-smelling sludge, difficult to remove, is produced. The research on OMW valorization is focused on the recovery or on the degradation of the phenolic compounds since its presence

* Corresponding author. Tel + 351-253604413. E-mail:ibelo@deb.uminho.pt

is considered to be the limiting step in the biotreatment of OMW (Tsioulpas et al, 2002).

Instead of disposal solutions an approach of using this waste as a resource to be valorized is of greater interest. OMW contains sugars, lipids, mineral elements and phenolic compounds (10 % of the organic matter) that could be either directly recovered by chemical extraction and subsequent purification, or utilized as a basis for fermentative processes. Thus, the extraction and purification of biologically active compounds (namely biophenols) turns OMW into a source of natural antioxidants. These compounds are object of growing interest in pharmaceutical and food industries since reactive oxygen species are involved in the onset of several human diseases and in the oxidative degradation of food (De Marco et al, 2007).

One of the aims of the present investigation was the characterization of different OMW, from north of Portugal, focusing the phenolic compounds identification. Subsequently to this identification it was also a goal of this work to study its toxicity to yeast strains that are under investigation for potential use of OMW as culture media.

2. Materials and Methods

Characterization of phenolic compounds in OMW

Extraction of phenolic compounds

The olive oil mill wastewater was collected in a continuous three phases olive oil factory in the north of Portugal and stored at -80 ºC right after arrival to the lab. The phenolic compounds were extracted from the OWM by two distinct extraction methods: (1) a liquid-liquid extraction by acidified ethyl acetate, according to the procedure of De Marco et al. (2007) and (2) a solid-liquid extraction with acidified methanol. For the solid-liquid procedure, an OWM sample was lyophilized and 2 g of the resulting freeze-dried material was defatted 3 times with 20 mL of *n*-hexane, and the residue was extracted 5 times with 20 mL of methanol at pH 2. The methanolic extracts were filtered, combined, concentrated under vacuum and the dry residue was dissolved in 10 mL of methanol.

Colorimetric and HPLC analysis of the phenolic extracts

The total concentration of phenolic compounds in the phenolic extracts was determined by an adaptation of the Folin-Ciocalteu method (Singleton and Rossi, 1965), using tyrosol as a reference.

HPLC analysis was performed on a HPLC apparatus from Knauer equipped with a Smartline 1000 bomb, an automatic Smartline Manager 5000 degassing unit, a Smartline 2500 UV/Vis detector and a JASCO automatic sampler, model AS-2057. The column (Nucleosil 100-5 C18 Macherey-Nagel, 250×4.6 mm) was kept at 30ºC using a Gecko 2000 oven. The results were recorded and processed using a Knauer Claritychrom software, version 2.4.4.80. The mobile phase was (A) formic acid 0.1% and (B) acetonitrile containing 0.1% formic acid. The solvent gradient started with 97% A and 3% B reaching 91% A at 4 min, 85% A at 15 min, 84% A at 25 min, 60% A at 70 min, 10% A at 80 min followed by an isocratic plateau for 5 min and return to initial conditions. Hydroxytyrosol in the phenolic extracts was identified and quantified by the comparison of the retention time of the peak and the correlation of its area to the retention time and to the calibration curve of the standard, respectively.

Phenolic compounds toxicity to lipolytic yeast strains

Two OMW's samples (A and B) with the composition shown in Table 1 where used. Chemical Oxygen Demand (COD), Solids (total, volatile and dissolved), Nitrogen (Kjeldahl) were determined according to Standard Methods (APHA et al., 1989). Reducing sugars were measured by DNS method. Samples collected through fermentations were analyzed for COD, sugars, total phenols and by the methods above described.

Table 1. Characterization of OMW's used

Parameter [a]	Olive Mill Wastewater	
	A	B
pH	4.71	4.93
COD/(g·L^{-1})	99 ± 1	191 ± 2
Total Solids/(g·L^{-1})	148± 3	119.6 ± 0.2
Total Volatile Solids/(g·L^{-1})	117 ± 6	84 ± 42
Nitrogen (Kjeldhal) /(mg·L^{-1})	192 ±17	-
Phenols (Tyrosol)/(g·L^{-1})	5.5 ± 0.1	12.1 ± 0.2
Reducing Sugars/(g·L^{-1})	12.9 ± 0.7	34.4 ± 0.9
Total protein/(g·L^{-1})	1.2 ± 0.2	1.3 ± 0.0

[a] Data are mean values ± standard deviation (n=20)

Phenolic compounds toxicity and biodegradability

The phenolic compounds degradation and toxicity tests were carried out in microplates for 4 days and 6 yeast strains were used: *C. rugosa* PYCC 3238, *C. cylindracea* CBS 7869, *C. rugosa* CBS 2275, *Y. lipolytica* CBS 2073, *Y. lipolytica* W29 ATCC 20460 and *Y. lipolytica* IMUFR. Cells were pre-grown in YPD medium, for 24 h. After that, 20 µL of cells suspension were transferred to each microplate well with the sterilized phenolic medium. The phenolic mediums were composed of YPD medium (10 fold diluted) with different phenolic compounds (commonly found in OMW), such as tyrosol, hydroxytyrosol, cafeic acid, cathecol, oleuropein, syringic acid and vanillic acid.

In order to evaluate the induction of phenolic metabolism in yeast strains, assays with pre-adaptation to phenolic compounds were carried out. Cells were pre-grown in YPD medium by 24 h, harvested (12225 g, 5 min), re-suspended in the phenolic medium (YP and phenolic solution in phosphate buffer pH 7.2, 0.1 M) and grown for 24 h in this conditions. After this pre-adaptation phase, cells were transfered to OMW mediums (A and B). Batch cultures were carried out in 500 mL Erlenmeyer baffled flasks filled with 200 mL of OMW sterilized medium, supplemented with ammonium chloride at a concentration corresponding to 10% (w/w) of the COD value and yeast extract (40% of the NH_4CL added).

Respiratory activity assays were carried on a Biological Oxygen Monitor System (YSI 5300A) with a stirred thermostatic bath. *Y. lipolytica* W29 culture with, approximately, 22 h of growth was harvested, washed and ressuspended in sodium phosphate buffer in order to obtain a final suspension with an optical density of 0.3 (λ = 600 nm). This suspension was aerated for 30 min to ensure the oxygen saturation and after this time was placed in the temperature-controlled vessel at 27 ºC. The vessels were closed and the decrease in air saturation percentage was monitored over time. The linear decrease observed between time zero and carbon source addition corresponds to the endogenous respiration rate. To determine the oxygen uptake rate due to substrate oxidation, different volumes of a glucose solution (10 g·L^{-1}), phenolic solution (tyrosol, oleuropein, syringic acid and gallic acid 2.5 g·L^{-1} each and hydroxytyrosol 1.25 g·L^{-1}) or OMW (COD 115 g·L^{-1}) were injected into the vessel. The slope of the linear decrease in the air saturation percentage immediately after carbon source injection corresponds to the total respiration rate. In order to calculate the influence of exposition of the yeast suspension to catechol solution, the cell suspension was incubated with a catechol solution (0.3 g·L^{-1}) for 30 min with aeration. After the required contact time, the cell suspension was placed in the vessels in order to assess the metabolic state of the yeast culture by respiratory activity as described above.

3. Results and discussion

Characterization of phenolic compounds in OMW

The total amount of phenolic compounds recovered from the OMW by the solid-liquid extraction procedure was approximately three times higher than that obtained by the liquid-liquid extraction methodology (5.1 mg/mL and 1.7 mg/mL, respectively). For the two extracts, the main phenolic chromatographic peak was eluted at 8.9 min (Figure 1), and this corresponded to hydroxytyrosol. The recovery of this compound accounted for 0.81 mg/mL and 0.06 mg/mL of OMW, for the solid-liquid and the liquid-liquid extraction procedures, respectively.

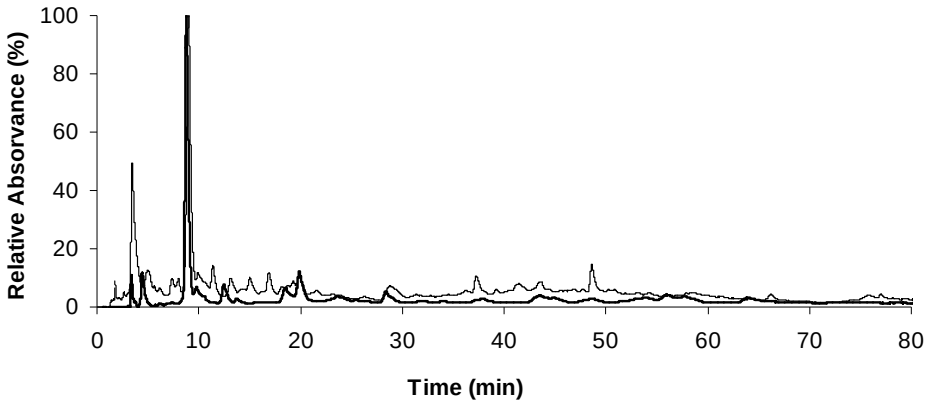

Figure 1. Chromatographic profiles of phenolic extracts of OMW at 280 nm obtained by liquid-liquid extraction (▬) and solid-liquid extraction (▬) procedures.

Phenolic compounds toxicity and biodegradability

The effect of different phenolic compounds on each yeast strain growth was evaluated by the assays in microplate. Typical batch growth curves profile for the experiments with *Y. lipolytica* W29 and C. *rugosa* CBS strains are shown in Figure 2.

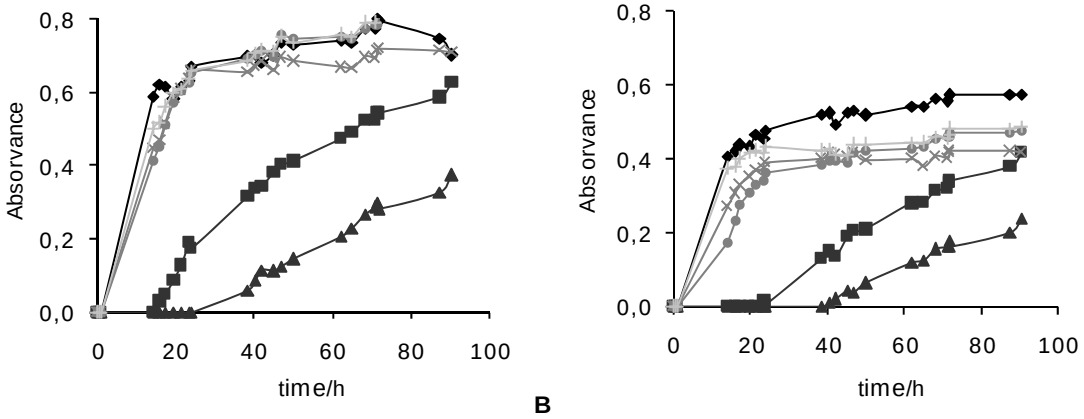

Figure 2. Batch growth profile of *Yarrowia lipolytica* W29 (A) and *Candida rugosa* CBS (B) in YPD medium (♦) and phenolic mediums: Catechol (▲), Hydroxityrosol (●), Caffeic Acid (■), Tyrosol (×) and Oleuropein (+).

For the phenolic concentrations used (1 $g \cdot L^{-1}$), it was observed that the final biomass concentration decrease in phenolic mediums comparatively to YPD medium for all strains used, except for *Yarrowia lipolytica*. Beside this difference, it was verified that the cells still grown in the presence of phenolics. However, in the presence of catechol the cell growth (for all strains) decreased substantially. An adaptation phase is noticed for catechol and caffeic

acid. In all the assays no phenolic compounds degradation was observed, particularly when more easily degradable carbon source, such as glucose, is still present in the medium.

In order to investigate the influence of a pre-adaptation phase of cells to a phenolic medium, assays were conducted in Erlenmeyer flasks, as described above. It was observed that the phenolic compounds degradation was not improved, suggesting that the pre-adaptation phase used was not efficient to induce the metabolism of *C. cylindracea* CBS, *Y. lipolytica* W29 and *C. rugosa* CBS strains.

Respirometric assays

The toxicity of phenolic compounds and OMW on the activity of *Y. lipolytica* cells was evaluated through respiratory activity. The measurement of the oxygen uptake rate due to carbon source oxidation gives the fraction of the cells that are active. Figure 3 shows an example of the respiratory profiles of a cellular suspension with and without an injection of carbon source. The slope of linear decrease in the air saturation percentage represents the OUR.

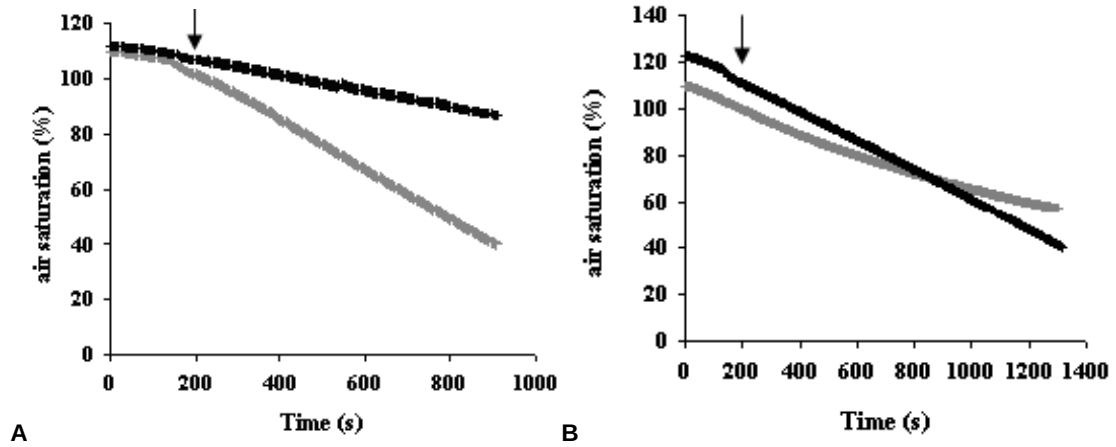

Figure 3. A - Air saturation percentage curves of a *Y. lipolytica* suspension (+) and cellular suspension with injection (+) of OMW (A) or catechol (B). The arrow represents the injection of carbon source.

The injection of a carbon source in cell suspension increase the oxygen uptake rate comparatively to that found in the assay without this addition, as proved with the injection of OMW. However, the addition of catechol to *Y. lipolytica* suspension leads to an inhibitory effect in the respiratory activity of this strain. The respiratory activity factor (RAF) for the different carbon sources was also determined and it was defined as a ratio between the total and the endogenous respiration rate (Table 2).

Table 2. *Y. lipolytica* respiratory activity factor (RAF) with different carbon sources

	Glucose	Phenolic solution	OMW (COD)	Catechol
Concentration/($g \cdot L^{-1}$)	0.48	0.83	3.8	0.63
RAF	2.01	2.24	3.09	0.82

It was observed that the injection of OMW and phenolic solution, without catechol, improved the total respiration rate even more than glucose. However, catechol injection leads to a respiratory activity inhibition.

The loss of activity factor was determined for assays with 30 min of catechol incubation and injection of glucose. The loss of activity obtained was, approximately, 99.6% for a concentration of catechol of 0.32 $g \cdot L^{-1}$.

Conclusions

The phenolic extracts obtained from the OMW have a large number of phenolic compounds, but these are mainly rich in hydroxytyrosol. The recovery of this important compound is improved in the solid-liquid extraction procedure, compared to that obtained by the liquid-liquid extraction methodology.

The less toxic compound, hydroxityrosol, is the most abundant in both OMW but there was no significant inhibition by the other phenolic compounds existing in the OMW. Thus the OMWs collected could be used by the lipolytic strains studied (*C. rugosa* PYCC 3238, *C. cylindracea* CBS 7869, *C. rugosa* CBS 2275, *Y. lipolytica* CBS 2073, *Y. lipolytica* W29 ATCC 20460 and *Y. lipolytica* IMUFR).

From the studied concentrations, no evidences of *Y. lipolytica* respiratory activity inhibition, by OMW and it's phenolic compounds, was observed. However, the results for catechol solution proved that exist considerable inhibition to yeast culture by this compound.

Acknowledges

The authors acknowledge the financial support provided by "Fundação para a Ciência e Tecnologia" (Project PTDC/AMB/69379/2006; grant SFRH/BD/27915/2006).

References

APHA, AWWA, WPCF, 1989, Standard methods for the examination of water and wastewater, 17th Ed. Washington D.C.

Cardoso, S. M., Guyot, S., Marnet, N., Lopes-da-Silva, J. A., Renard, C. M. G. C., Coimbra, M. A., (2005). Characterisation of phenolic extracts from olive pulp and olive pomace by electrospray mass spectrometry, *Journal of the science of food and agriculture*, 85, 21-32.

Crognale, S., D'Annibale, A., Federici, F., Fenice, M., Quaratino, D., Petruccioli, M., (2006). Olive oil mill wastewater valorisation by fungi, *Journal of Chemical Technology & Biotechnology*, 81, 1547 – 1555.

De Marco, E., Savarese, M., Paduano, A., Sacchi, R. (2007). Characterization and fractionation of phenolic compounds, *Food Chemistry*, 104, 858–867.

Lanciotti, R., Gianotti, A., Baldi, D., Angrisani, R., Suzzi G., Mastrocola, D., Guerzoni, M.E., (2005). Use of *Yarrowia lipolytica* strains for the treatment of olive mill wastewater, *Bioresource Technology*, 96 , 317-322.

Leonardis, A., Macciola , Lembo, G., Aretini, A., Nag, A., (2007). Studies on oxidative stabilisation of lard by natural antioxidants recovered from olive-oil mill wastewater, *Food Chemistry*, 100, 998-1004.

Rodis, P. S., Karathanos, V. T., & Mantzavinou, A. (2002). Partitioning of olive oil antioxidants between oil and water phases. *Journal of Agricultural and Food Chemistry*, 50, 596–601.

Singleton, V. and Rossi, J. A. (1965). Colorimetry of total phenolics with phosphomolybdic-phosphotungstic acid reagents. *American Journal of Enology and Viticulture*, 16, 144-158.

Tsioulpas, A., Dimou, D., Iconomou, D., Aggelis G., (2002). Phenolic removal in olive oil mill wastewater by strains of Pleurotus spp. in respect to their phenol oxidase (laccase) activity, *Bioresource Technology*, 84, 251–257.

Proceedings of the 10th International Chemical and
Biological Engineering Conference - CHEMPOR 2008
Braga, Portugal, September 4-6, 2008
E.C. Ferreira and M. Mota (Eds.)

CHANGES IN THE WASTEWATER BACTERIAL COMMUNITY OF OIL REFINERY DURING PHENOL SHOCK LOADINGS

Fernanda R. Pinhati[1], Aline F. Viero[2], Eduardo M. Del Aguila[1], Ana Paula R. Torres[3], Joab T. Silva[1], Vânia M. F. Paschoalin[1*]

[1]Instituto de Química, Centro de Tecnologia, Bloco A, Sala 545, Universidade Federal do Rio de Janeiro, Rio de Janeiro, RJ, Brazil.
[2]COPPE, Universidade Federal do Rio de Janeiro, Rio de Janeiro, RJ, Brazil.
[3]Petrobrás – CENPES, Gerência de Biotecnologia e Ecossistemas, Rio de Janeiro, RJ, Brazil

Keywords: oil refinary wastewater, phenol removal, bacterial community, 16S rDNA, PCR-DGGE

Topic: Integration of life sciences and engineering

Abstract

The stability of the bacterial community of an oil refinery treatment system was monitored over the course of 34 days, along with phenol shock loading. Changes in the bacterial community were monitored by denaturing gradient gel electrophoresis (DGGE) of polymerase chain reaction (PCR) that amplified 16S rRNA gene fragment. It was used a submerged membrane bioreactor (SMBR) operating with constant flux. During the operation, long-term high organic loading rates were applied in the SMBR by feeding blends of the oily stream with a high strength phenolic wastewater, also generated in petroleum refineries. During the operation, long-term high phenol loading rates were applied in the SMBR. Initially it was applied a high phenolic load (mean value of 85 mg L^{-1}) for a period of 18 days and a subsequent period of 16 days with low phenolic load (mean value of 15 mg L^{-1}). A quality of the effluents from phenol shock loadings was consistently high with respect to phenol ($\leq$ 85 mg L^{-1}) indicating efficient removal of 98%, along to the operation process. The analysis by PCR-DGGE indicated that the bacterial community has been able to adapt to the changes in environmental conditions and showed a relative stability, despite of the changes during the process in its microbial diversity that showed a coefficient of similarity exceeding 57% (Cs = 57%) throughout the process. The efficiency of phenol removal in SMBR (over 98%) associate to the stability of bacterial community, mainly in the ultimate phase of the process, was decisive to confirm that the bacterial community of sludge in SMBR was able to adjust in response to perturbations to sustain high effluent quality.

1 Introduction

Petroleum refinery wastewaters have a wide range of chemical compounds that are toxic to the environment. Phenolic compounds have remarkable importance as pollutants in refinery wastewater, since they are highly toxic for human beings, fishes and also impair several biochemical functions. Development of methods for phenol removal from industrial wastewaters has generated significant interest since phenols and other aromatic compounds play an important role as sole carbon and energy source of several microorganisms. The phenol concentration can be accepted as an indicator of the removal efficiency of pollutants

* Corresponding author. Tel + 55 21 2562 7362. E-mail: paschv@iq.ufrj.br

compounds from industrial wastewater, in particular, effluent of refinery (Margesin et al. 2005).

Although the conventional wastewater treatment plants normally produce good results, the conventional activated sludge processes involved are unlikely suitable to tackle with drastic flow rate and/or large composition variation. For those reasons, biological treatment of phenol is generally preferred to physical or chemical treatments mainly due to lower costs and the possibility of complete mineralization *(*Jiang et al. 2004). Activated sludge of aerobic wastewater treatment plants consists of a complex mixture of microorganisms that are either generalists or specialists. For years, researchers have examined the microbial populations of these activated sludge communities in order to understand their specific biological processes (Amann et al.1998).

Development of cost-effective manufacturing of membranes and increasingly stringent regulations for the discharge of effluents has accelerated the application of membrane technology of wastewater treatment and reuse. Membrane bioreactors (MBR), due to their higher biomass concentration, are able to deal with shock loadings and also to produce permeate suitable for reuse (Qin et al. 2007).

Studies on the effects of shock loadings in MBR treating industrial wastewaters are rarely reported in the literature, especially considering oil refinery wastewater treatment. Even for other activated sludge processes, there are few works concerning shock loading effects, although some studies reported phenolic wastewater degradation (Hsien and Lin*,* 2005). Viero et al. (2008) studied the effects of organic shock loadings regarding to the organic matter, ammonia-nitrogen, and phenols removal efficiencies. The results proved the ability of the SMBR to tackle with high strength feed during long-term exposition achieving high phenols and ammonia-nitrogen removal efficiencies, even in such complex feed.

Recently, numerous cultivation-independent techniques have been developed in order to analyze bacterial community structures without the inherent biases of cultivation. These cultivation-independent techniques for bacterial community structure analysis have revealed extremely complex communities within wastewater treatment bioreactors (Amann et al. 1998).

In this study, we investigated the bacterial community structure in SMBR treating oil refinery wastewater during long-term phenol shock loadings. We used the denaturing gradient gel electrophoresis (DGGE) of PCR-amplified 16S ribosomal RNA (RNAr) gene fragments for this purpose. During the process the changes in bacterial community structure were evaluated concomitantly with the SMBR performance regarding to the removal efficiencies of phenol.

2 Material and methods

SMBR plant and refinery wastewater

The submerged membrane bioreactor (SMBR) used in this work was described previously and it was used in the same operated conditions (Viero et al., 2008). In brief the reactor consisted of a cylindrical acrylic tank with working volume of 4.4 L, where a membrane skein with $2.78\times10^{-2}m^2$ area and a porous stone diffuser were inserted. Operation was conducted by alternating filtration with air backwashing to maintain permeate flux constant. Activated sludge for seeding was collected in an oil refinery wastewater treatment plant, in São José dos Campos, Brazil, and sediment to reach total suspended solid concentrations around 10 g L^{-1}. The sludge was acclimatized for 33 days in the SMBR. The reactor was operated in three different conditions regarding to the wastewater. The first one refers to the adaptation of the sludge to the operational condition, where the average concentration of phenol in the feed was around $15mgL^{-1}$ and was always less than 35 mg L^{-1}. In the second and third phases, average feed contained phenol concentrations of 85 and 15 mg L^{-1}, respectively.

Activated sludge samples

The SMBR was sampled throughout a 93-day period, with more frequent sampling from the 34 to 90 day. In the day 34, a sample of the activated sludge was collected to characterize the 'native' sludge (NS) acclimatized to the SMBR. During the high loading rate shock, activated sludge samples were collected every day and at the last phase, when the loading rate feed in the process was low, activated sludge samples were taken every two days. Samples for PCR-DGGE were colleted by centrifugation at 2,000 X *g* for 15 min and the pellet stored at -20^{o}C for DNA extraction.

Removal of phenol

The permeate values of phenol concentration were evaluated with the R-8012 kits used as recommended by the manufacturer (Chemetrics, Inc.).

DNA extraction from sludge samples

Genomic DNA from sludge samples was extracted according to the method described by Melvin and Hobson (1994) with some modifications. DNA was extracted from 0.5g (wet weight) sludge pellet that was resuspended in 1mL of TESC buffer (10mM Tris; 0.1mM EDTA; 0.1mM NaCl pH8.3). After 2 h incubation at –80ºC, 5 µL of DMSO (dimetyl sulfoxide) were added to the suspension and incubated again at room temperature for 1min. Subsequently, 500 µL of guanidine thiocyanate 5M and 500 µL of phenol:chloroform:isoamyl alcohol (25:24:1; v/v) were added. After centrifugation, the aqueous phase was transferred to a new tube and 30 µL of sodium acetate 3M was added. Total nucleic acid was precipitated from the aqueous extract with 2.5 volumes of 100% ethanol (-20ºC), dried, resuspend in sterile double distilled water and then stored at –20ºC.

PCR-DGGE analysis

Primers used in the PCR reactions were 968F (Nubel et al. 1996) and 1401R (Heuer et al. 1997) to amplify the V3 region of the Bacterial 16S rRNA gene. A GC-rich sequence attached to the 5'-end of primer 968F prevented the PCR products from completing melting during separation via DGGE. The PCR mixture contained 50pmol of the forward and reverse primers, 5µl of 10X PCR buffer, 0.2mM of deoxynucleoside triphosphates, 100ng of DNA template, 5U Taq DNA polymerase (Invitrogen), 0.1µM $MgCl_2$, and sterile deionized water to a final volume of 50 µL. PCR was performed following the program: an initial denaturation at 94ºC for 7 min, 25 cycles of 94ºC for 1 min, 60ºC for 1 min and 72ºC for 1 min, and final single extension at 72ºC for 7 min. PCR products were visualized by electrophoresis on 1.2% agarose gel after ethidium bromide staining. Amplicons of approximately 433bp were obtained and were analyzed by DGGE.

DGGE was carried out using a BioRad D-Code Universal Mutation Detection System. Samples containing approximately equal amounts of PCR amplicons were loaded onto 6% (w/v) polyacrylamide gels (38,9:1,1, acrylamide : bisacrylamide) in 1 X TAE buffer (20 mM Tris, 10 mM acetate, 1 mM EDTA, pH 7,4) using a denaturing gradient ranging from 45% to 65% (100% denaturant contains 7M urea and 40% (v/v) formamide). Electrophoresis was performed at 60ºC at 50V for 14h. Following electrophoresis, the gel was stained for 60 min with SYBR Green I nucleic acid gel stain (1:10.000 dilution; Molecular Probes, USA) and visualized/documented under UV light with the MiniBisPro (BioAmerica Inc.). DGGE fingerprints were manually scored by the presence or absence of co-migrating bands, independent of intensity. A dendrogram was constructed using the un-weighted pair group method with arithmetic averages (UPGMA). For these analyses, the NTSYS software package (version 2.02, Exeter Software, Setauket, NY, USA) was used. Pairwise community similarities were quantified using the Dice index (Cs) as: $C_s = 2\,j\,/\,(a + b)$, where *j* is the number of bands common to the samples **A** and **B**, and *a* and *b* are the number of bands in samples **A** and **B**, respectively.

3 Results and Discussion

Phenol removal and efficiency of reactor

Generally, the average phenol removal was higher than 98% for all phases of the operation; therefore when the feed had concentrations of less than 15mgL^{-1}, namely in the last phase, the phenol removal was superior to 99.3%. The efficiencies of phenol removal were similar to those reported in the literature, although the influent had significant concentrations of NH_4^+-N that could produce toxic effects and, then, reduce phenols and also organic matter removal efficiencies. Notwithstanding, the removal efficiencies were high considering the hydraulic retention time employed.

The results for phenol concentration in the permeate are under the limits specified by the Brazilian law for discharge of effluents (0.5mgL^{-1}) (CONAMA, 2005).

Bacterial communities analysis

Prominent bands were observed in the sludge samples during the overall process (Fig. 1). The pattern observed in the DGGE analysis indicates a presence of a wide variety species in the samples.

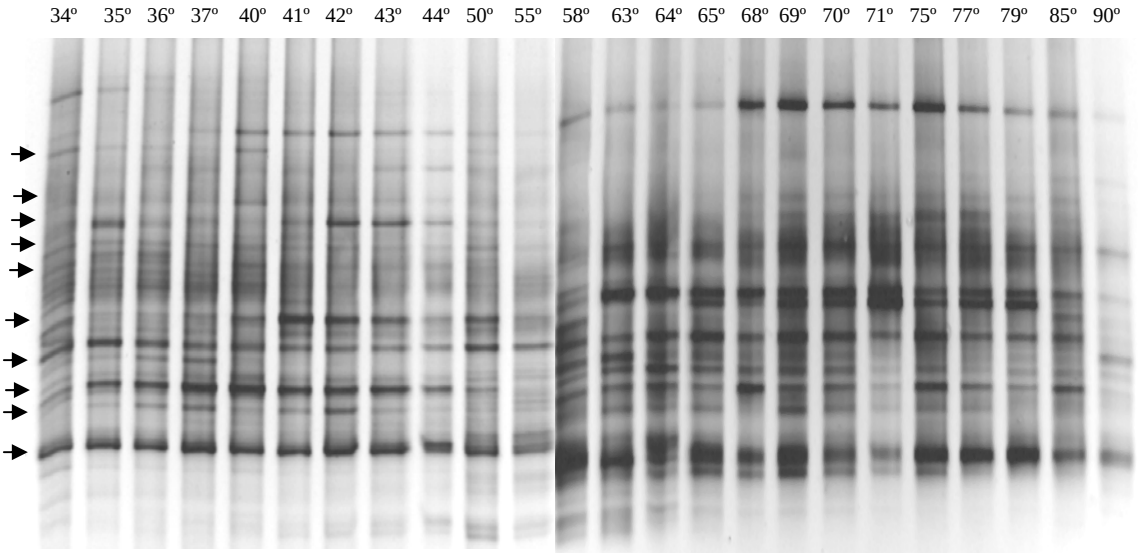

Figure 1: DGGE of PCR-amplified region 968F to 1401R of 16S rDNA from the SMBR bacterial communities. Lane labels along the top show sampling time (days) from startup of the shock loading process where high phenol shock loading were performed from 35 to 58 days (mean value of 85 mg L^{-1}) and low phenol shock loading, from 63 to 90 days (mean value of 15 mg L^{-1}). Solid black arrows identify bands found along the 90-days sampling.

It was identified 28 different bands along the samples, which were distributed in different forms in the sampling days. Analysis of DGGE profiles revealed changes in the bacterial community exposed to different concentrations of phenol. The diversity of the bacterial community was higher during the high loading rate shock (85 mg L^{-1}phenol) when compared the low loading rate shock (15 mg L^{-1}phenol), demonstrated by showing a superior number of bands.

The 'native' sludge sample and the 37 day's sample showed a higher number of bands, containing 89% of the total 28 detected bands. Some communities were preserved during the two phenol shock loadings as observed from the 35 to the 90 day. The high and the low phenol shock loadings samples showed an average of 72.9% and 51.5%, respectively, from the total number of bands. Although the samples collected during the 15 mg L^{-1}phenol shock rate loading (from 63 to 90-day samples) showed reduced number of bands, they should represent the most adapted microorganisms since they maintained their growth for the whole phenol shock loading periods.

Ten DGGE bands were found along the 90-days sampling (Fig.1). These bands may represent the long-term community structure with high stability and may have been responsible by the success of the SMBR, ensuring the efficiency of phenol degradation. Individual persistent species responsible for these bands would be likely candidates for

incorporation into a seed culture in order to improve bioreactors performance, particularly during startup of wastewater treatment

Other bands were found only at the first days of the phenol shock loading, demonstrating the toxic effects of phenol for certain microorganisms.

The hierarquical grouping of bacterial communities was performed by the NTSYS and is illustrated by the dendrogram in Figure 2. The bacterial communities from 'native' sludge and from the two-phenol shock loadings grouped in three different main clusters. The bacterial community structure during high phenol shock loading was divided in two clusters (I and II). They had similar community structures when compared to each other (Cs = 77%). The third cluster had slightly lower Cs value compared to the first one (Cs = 57%).

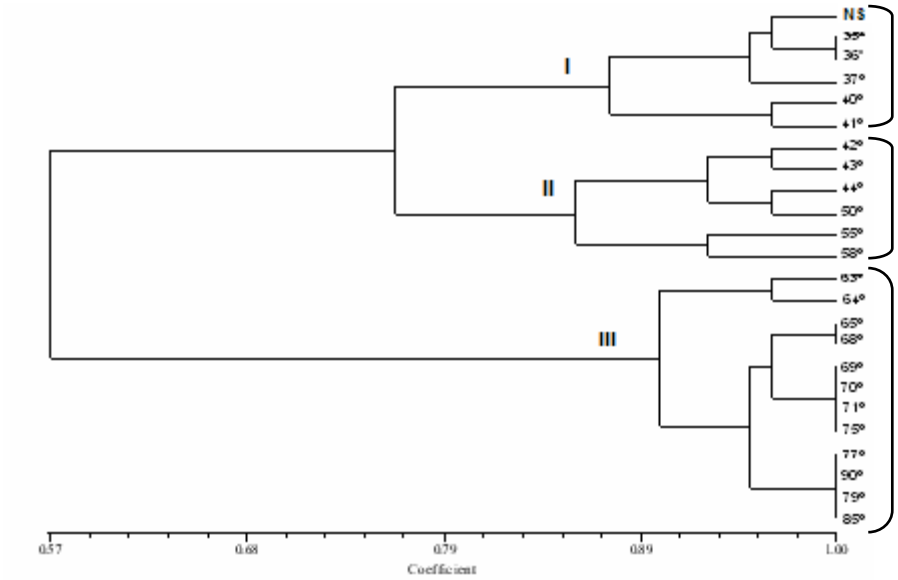

Figure 2: UPGMA analysis dendrograms of bacterial community DGGE fingerprints. Arabic numerals show the sample time (days), and roman numerals indicate major clusters.

Comparing the Cs index of the 'native' sludge with the last day of each phenol shock loading phase it may be noted that the community showed small shifts during the process. Thes last day during the high phenol shock loading (58 day) and a sample collected during the low phenol shock loading (90 day) presented a Cs regarding the 'native' sludge of 76.1% and 56.4%, respectively. At long of the whole period of high phenol shock loading, compounding 12 samples of sludge, it was obtained an index superior to 82.7%. The community stability between the 69th day and 70, 71, 75 and 77 days, and also between the 75th day and 79, 85 and 90 days may be evaluated by analyzing the Cs index, that was 100% for these days. These high Cs values confirmed the stability of the community on overall process, and showed the ability of the bacterial community to adapt to long-term phenol shock loading. During the high phenol shock loading it was observed a diminishment in the bacterial community diversity, and this may be explained as the proper toxicity of phenol towards microorganisms (Barrios-Martinez et al. 2006).

Conclusions

This work presents the tracking of bacterial community from an oil refinery wastewater treatment during phenol shocks, using PCR-DGGE analysis of the V3 region of the 16SrRNA gene. As observed, the bacterial community could adapt to environmental condition changes, a desirable characteristic, since the flexibility relationated to the bacterial community structure leads to more stable process performance (Fernández et al., 2000).

Functionally stable wastewater treatment reactor was maintained in response to varying effluent wastewater characteristics by a microbial community that adapted its structure to

sustain high effluent quality. The phenol efficiency removal was higher than 98%. PCR-DGGE can be considered a useful tool to evaluate microbial community structures in biological wastewater treatment reactors, indicating the changes on the microbial communities during the process and which communities is still presented along the entire operation. The persistent species in the long-term operation should be identified to be used as seed culture to improve bioreactors performance, particularly during startup of wastewater treatment.

References

Amann, R., Lemmer, H., Wagner, M. (1998). Monitoring the community structure of wastewater treatment plants a comparison of old and new techniques. *FEMS Microbiology Ecology*, 25, 205-215.

Barrios-Martinez, A., Barbot, E., Marrot, B. Moulin, P. Roche, N. (2006). Degradation of synthetic phenol-containing wastewater by MBR. *Journal of Membrane Science*, 281, 288-296.

CONAMA, (2005) Resolução 357, *Diário Oficial da União*, 53, 58-63.

Fernández, A., Huang, S., Seston, S., Xing, J., Hickey, R., Criddle, C., Tiedje, J. (2000). How stable is stable? Function versus community composition. *Applied Environmental Microbiology*, 65, 3697-3704.

Heuer, H., Krsek, M., Baker, P., Smalla, K., Wellington, E. M. H. (1997). Analysis of actinomycete communities by specific amplification of genes encoding 16S rRNA and gel-electrophoresis separation in denaturing gradients. *Applied Environmental Microbiology*, 63, 3233-3241.

Hsien, T.-Y., Lin, Y.-H. (2005). Biodegradation of Phenolic Wastewater in a Fixed Biofilm Reactor. *Biochemical Engineering Journal*, 27 95-103.

Jiang, H-L., Tay, J.-H., Maszenan A. M., Tay, S. T.-L. (2004). Bacterial diversity and function of aerobic granules engineered in a sequencing batch reactor for phenol degradation. *Appl. Environ. Microbiol*, 70, 6767-6775.

Margesin, R., Fonteyne, P. A., Redl, B. (2005). Low-temperature biodegradation of high amounts of phenol by Rhodococcus spp. and basidiomycetous yeasts. *Research in Microbiology* 156, 68-75.

Melvin, W. T., Hobson, P. N. (1994). Identification of anaerobic digester bacteria using a polymerase chain reaction method. *Bioresearch Technology*, 47, 73-80.

Nubel, U., Engelen, B., Felske, A., Snaidr, J., Wieshuber, A., Amann, R. I., Ludwig, W., Backhaus, H. (1996). Sequence heterogeneities of genes encoding 16S rRNAs in Paenibacillus polymyxa detected by temperature gradiente gel eletrophoresis. *Journal of Bacteriology*, 178, 5636-5643.

Qin, J.-J., Oo, M. H., Tao, G., Kekre, K. A. (2007) Feasibility study on petrochemical wastewater treatment and reuse using submerged MBR. *Journal Membrane Science*, 293, 161-166.

Viero, A. F., Melo, T. M., Torres, A. P. R., Ferreira, N. M., Sant'Anna Jr., G. L., Borges, C. P., Santiago, V. M. J. (2008) .The effects of long-term feeding of high organic loading in a submerged membrane bioreactor treating oil refinery wastewater. *Journal of Membrane Science*. 319, 223-230.

Proceedings of the 10th International Chemical and
Biological Engineering Conference - CHEMPOR 2008
Braga, Portugal, September 4-6, 2008
E.C. Ferreira and M. Mota (Eds.)

Degradation of acid, basic and reactive dye mixture in a continuous bioreactor

Palma, C., Contreras, E., Sepúlveda, L., Carvajal, A.[1]
Department of Chemical Engineering. University of Santiago de Chile.
Alameda 3363, Estación Central, Santiago de Chile.

Keywords: Fungal, decolourization and textile dyes
Topics: Integration of Life Sciences & Engineering

Abstract

The increasing global scarcity of water it is imperative to develop technologies that permit to treat wastewater for its subsequent reutilization. The treatment of coloured wastewater from some manufacturing processes is a challenge due to the complex contaminants involved. White-rot filamentous fungi have shown their capacity to degrade molecules with high molecular weight that are analogous to their natural substrate, i.e., lignin, which are present in the effluents from wood pulp and paper mills, sugar refineries and olive oil plants, among others. The degradation mechanism is based on the action of extra-cellular enzymes that are synthesized and secreted by fungi during the secondary metabolism stage under limiting nutrient conditions. This ligninolytic system has also been successfully used in the degradation of synthetic dyes (1, 2).
The purpose of this study is to quantify the action of the extracellular oxidation system of *Phanerochaete chrysosporium* over multi-component coloured solutions in order to establish the potential degrading capacity in the effluent from a textile plant. Previous studies (3) determined, by means of screening, that the ligninolytic system of this fungus has a greater affinity for those azoic dyes containing naphthalene rings in their molecules. Based on these results, mixtures were prepared by selecting dyes for which the enzymatic system has shown a different affinity. This strategy would also lead to the prospect of evaluating possible synergic effects between substrates. For this purpose, fixed-bed bioreactors were used with immobilized biomass and feed with bi-component mixtures of textile dyes: acid (Acid Black 1 and Acid Orange 6), basic (Basic Violet 4 and Basic Blue 24) and reactive (Reactive Blue 19 and Reactive Orange 16). The biological unit was feed in increasing steps with equimass mixtures at varied concentrations.

Introduction

Environmental pollution caused by hazardous waste containing recalcitrant xenobiotic chemicals has become one of the major ecological problems. Unlike the naturally occurring organic compounds that are readily degraded upon their discharge into the environment, some of these synthetic chemicals are extremely resistant to biodegradation by native microorganisms. In particular, synthetic dyes are extensively used for textile dyeing, paper printing and colour photography, and as additives in petroleum products. During the dyeing process, 10–15% of dye is discharged into the effluent. Approximately half of all well-known dyes are azoic, representing the largest group of synthetic colorants. Azo dyes and their pigments are versatile and are therefore the synthetic colorants that are most released into the environment. Their structural modification is also possible and they can be caused to bind with most synthetic and natural textile fibres.
Studies related to biodegradability of dyes using white rot fungi (WRF) are extensive and include reports on living and dead cells. In the case of living cells, the major mechanism is the biodegradation caused by the lignin-modifying enzymes (LME) which mineralize synthetic lignin or dyes. For dead cells, the mechanism is biosorption, which involves physical-chemical interactions, such as adsorption, deposition, and ion-exchange (4).
WRF produces a variety of extracellular lignin-modifying enzymes (LiP and MnP) (5, 6, 7) and phenol-oxidase enzymes such as laccase (8) which are related to the degradation of lignin. A new peroxidase, called versatile peroxidase (VP), was found in active lignin-degrading strains of *Pleurotus eryngii*. This peroxidase combines catalytic properties observed in LiP and MnP of *Phanerochaete chrysosporium* (9).
Numerous researches have been reported regarding the decolorizing and/or degradation of dyes with different chemical structures as well as, using diverse treatment alternatives. In particular it has been proved the capacity of degradation *in vivo* and *in vitro* of *Phanerochaete chrysosporium*, using static, agitated and continuous systems (10, 11, 12, 13, 14). In the continuous systems the analyzed substrata are diverse and the used microorganisms are fundamentally fungi. The studied dyes are

[1] Corresponding author. Tel + 562-7181835. E-mail:andrea.carvajal.g@gmail.com

triphenylmethane, azoic, ftalocianine, anthraquinone as well as also, textile effluents (14, 15). In more recent studies (3) promissory results have been obtained using continuous reactors with biomass immobilized in foam of polyurethane to decolorizing and/or to degrade azoic dyes.
The later application of this technology for the treatment of the industrial effluent must have in consideration that the waste water contains varied pollutants. In particular in those originated in the textile processes there is more than one dye. From this perspective it is important to establish the effect that the different dyes of the mixture might have on the degradation (decolorization) of each of them. In this context the goal of present study is to analyze the degradation of mixture of dyes of acid, basic and reactive type in the bioreactor with immobilized *Phanerochaete chrysosporium*.

Materials and Methods

Microorganism: *Phanerochaete chrysosporium* BKM-F-1767 (ATCC 24725) was kept at 4ºC in malt extract plates (16).
Dyes: The dyes selected for the study, of analytic quality and given by Sigma S.A., as well as their characteristics are presented in the Table 1.

Table 1. Characteristics of dyes

Dye	Cromophore	λ (nm)	Structure
Acid Black 1 (AB1)	Diazoic	618.5	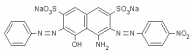
Acid Orange 6 (AO6)	Azoic	390.0	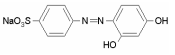
Basic Violet 4 (BV4)	Triphenylmethane	595.0	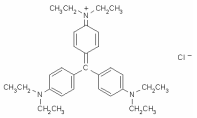
Basic Blue 24 (BB24)	Thiazine	633.0	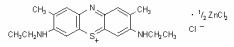
Reactive Blue 19 (RB19)	Anthraquinone	592.5	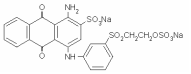
Reactive Orange 16 (RO16)	Azoic	493.0	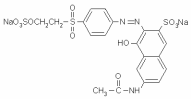

Culture immobilized: The preinoculate was prepared in a Fernsbatch (2 l) which contained 10-12 plugs (5mm in diameter) as an inoculate with 100ml of culture medium, and was incubated at 37ºC for 2d. The medium composition was $10g \cdot l^{-1}$ of glucose, 2.2mM of ammonium tartrate, and $100ml \cdot l^{-1}$ of BIII mineral medium (17) in sodium acetate (20mM) as a buffer (pH 4.5). The medium was autoclaved and then a filter-sterilized thiamine solution ($400mg \cdot l^{-1}$) was added ($5ml \cdot l^{-1}$). The mycelium that formed on the surface was homogenized and inoculated in a 10%(v/v) proportion in Erlenmeyer flasks (250ml) which contained 81ml of culture medium (described above) and 1.8g of immobilization support. These support consisted of polyurethane foam cubes of $0.125cm^3$ with a density of $20kg \cdot m^{-3}$. The cultures were incubated at 37ºC in an orbital agitator, at 150r.p.m. After inoculation and every 24h afterward, the cultures were oxygenated with pure O_2 for 3min using a pressure of 0.8bar. After 3 or 4d two Erlenmeyer flasks with the colonized foam were transferred as inoculate to the bioreactor.
Bioreactor operation: The medium feed to the bioreactor consisted of: $5.75g \cdot l^{-1}$ glucose, $0.0144g \cdot l^{-1}$ ammonium tartrate, $16.4g \cdot l^{-1}$ sodium acetate as buffer (pH 4.5), $0.0056g \cdot l^{-1}$ Mn^{+2} as $MnSO_4 \cdot H_2O$, $100ml \cdot l^{-1}$ BIII and $5ml \cdot l^{-1}$ Tween 80 (15, 17). This culture media was supplemented by the previously sterilized mixture of dyes, with the global concentration varying from 20 to 160; 20 to 240 and 10 to 60 $mg \cdot l^{-1}$ for acid, reactive and basic dyes, respectively. The bioreactor was operated with a hydraulic retention time of 24h (18) and flow rate of $8.4ml \cdot h^{-1}$. The system was oxygenated by a pulsed flow of gaseous O_2 applied with a frequency of $0.0625s^{-1}$. The temperature was kept at 37°C by water circulating at the jacket of the bioreactor. Two samples of the culture media were taken every 24h, the first at the bottom and another at the top of the column during the whole operation period.
Enzyme activity and analytical assays: MnP activity was measured by the oxidation of 2.6-dimethoxyphenol at 468nm (19). LiP activity was assayed against veratryl alcohol as was described by Tien and Kirk (1988).

Dye decolourization was monitored by the reduction absorbance spectrum of the mixture dyes between 380 and 750nm. The spectrum was adjusted to a polynomial equation using the Curve Expert v1.3® program. Integration of this function permitted to estimate the decolourization degree reached day by day. The absorbance spectra of each of the three formulated dye mixtures are shown in Figure 1.

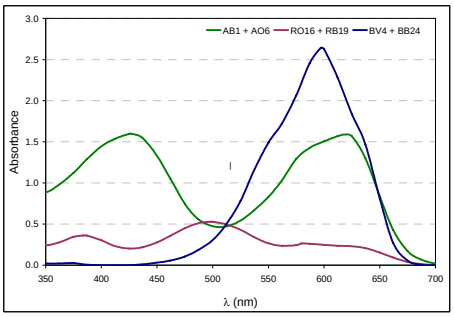

Figure 1. Absorbance Spectra of Mixture Dyes.

Results

Figure 2 shows the results obtained to the operation of bioreactor with the mixture of dyes. In all of them is observed that after 8 days of continuous operation, the feeding of the bioreactor was supplemented with dye. For the basic dyes (Figure 2a) the decolourization assay began with a total concentration of mixture of dyes of 10mg·l^{-1} and an average level of activity of 60U·l^{-1}, which droops temporarily after the injection. From day 15 the value of specific activity doubled, when the amount of dye was also doubled. Later the activity shows a continuous increase observing peaks in days 19 and 25 (240U·l^{-1}) in circumstances that the system is operating with a dye concentration of 40mg·l^{-1}. Finally a dye concentration of 60mg·l^{-1} caused the drop of the expression of MnP activity up to zero, inhibiting completely the enzyme production. On the other hand, the monitoring of the decolourization process began the day 14, reaching an absorbance reduction of 91%. This value stays practically constant until the day 25. Later, from the day 32 a continuous decrease of the decolourization was observed up to 40%.

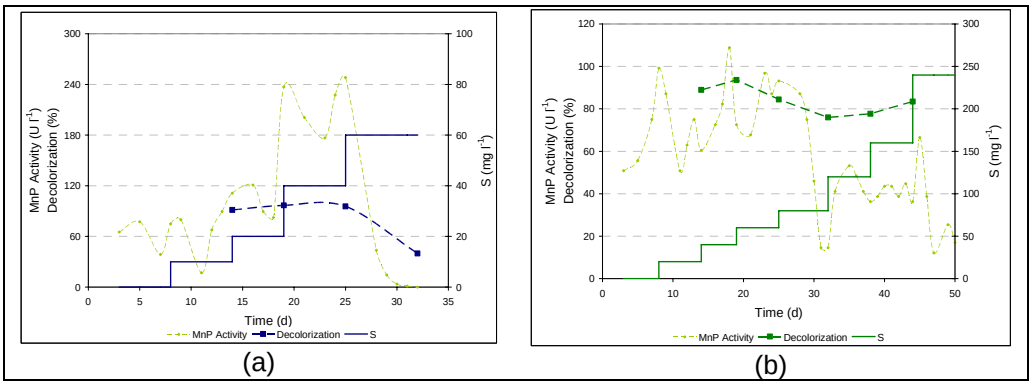

Figure 2. Decolourization of mixture and enzymatic activity in bioreactor of basic (a) and acid (b) dyes.

The Figure 2b shows that during an activity peak (100U·l^{-1}), started to supplement the culture medium with a total concentration of the acid dyes of 20mg·l^{-1}, the addition caused a rapid descent of activity up to 60U·l^{-1}. Later a fluctuating increase is observed up to reaching an activity peak of 110U·l^{-1} in the day 18, period in which the reactor operates with 40mg·l^{-1} of dye. Between the days 20 and 30 the average activity remained in 90U·l^{-1} in circumstances that the dye concentration was increased step by step even 80mg·l^{-1}. Later increases of the concentration to 120 and 160, produces a fluctuating activity level around 40U·l^{-1} until day 48 and after it diminished to 20U·l^{-1}. The monitoring of the decolourization process began on day 12, reaching an absorbance reduction of 90% up to the day 20. Finally this value diminishes up to 80% on day 25, staying constant to the final operation time of the reactor that was of 50 days.

In the Figure 3a is possible to observe that the addition of reactive dyes started when the activity had a value of 70U·l^{-1}. The activity profile shows subsequent increases until the 13' day with a peak of 155U·l^{-1}. Between days 18 and 30, the activity fluctuation was between 90 and 120U·l^{-1}, in this point the concentration was 80mg·l^{-1}. When that concentration was increased to 120mg·l^{-1}, the average activity decreases to the initial value (60U·l^{-1}).

Against continuous increases of concentration values of 160 and 240 mg·l^{-1} it decreased constantly to values around zero on day 50. Decolourization of 80% (on day 14th) augments and then stabilizes on 90% until day 38. Finally it decreases with constant rate to 60% on day 50.

On global terms the system shows a fluctuating behavior on the production of MnP. The maximum levels of activity are 50% of those reached with the basic dyes (120 vs. 240U·l^{-1}, on both cases between 40 and 60mg·l^{-1}), and the expression of activity is more stable. This could indicate that the capacity of the acid dyes to induce the production of MnP is achieved on minor concentrations that those that are observed for the basic dyes, the specific activity values achieved are lower. The reactive dyes induce the synthesis of MnP, showing temporary decreases of activity after each increment of concentration.

The addition of the dyes to the feeding media of the biological units caused a decline of the enzymatic production after each increment of the concentration. In some cases, as can be observed for the basic dyes, low concentrations can be inhibitors (40mg·l^{-1}), unlike the acids and reactive dyes. The generation of coloured compounds sometimes named coloured derivatives, generated through the partial rupture of the dye structures, can be the responsible of the cellular metabolism inhibition. The half-life of the coloured derivatives can affect in this fact.

On the other hand, the generation and/or additional contribution of nitrogen compounds that can be assimilated by the microorganism could result in a reversed secondary metabolic process, favouring growth to the benefit of the expression. Such a hypothesis would have to be proved by quantifying the biomass and/or concentration of total N in the effluent.

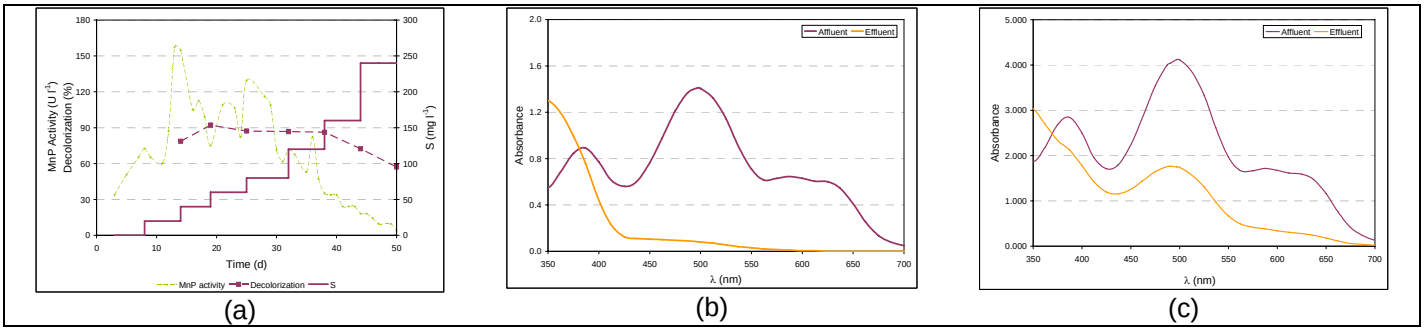

Figure 3. (a) Decolourization of mixture and enzymatic activity in bioreactor of reactive dyes. Bioreactor affluent and effluent absorption spectrum (b) 80mg·l^{-1} and (c) 240mg·l^{-1}, reactive dye.

The Figure 3b shows as an example, the significant reduction obtained for the typical absorbance's peak of the reactive dyes in the mixture when the feed concentration was 80mg·l^{-1}, also was not observed generation of coloured derivatives. Only for the highest concentration of the reactive dyes (240mg·l^{-1}), whose results are presented in the Figure 3c, and basic dyes (60mg·l^{-1}) was not observed the completely reduction of the peaks of maximum absorbance. Under these circumstances the decolourization might be awarded to the adsorption in the mycelium or support, which is concordant with the inhibition observed for the enzymatic system (20).

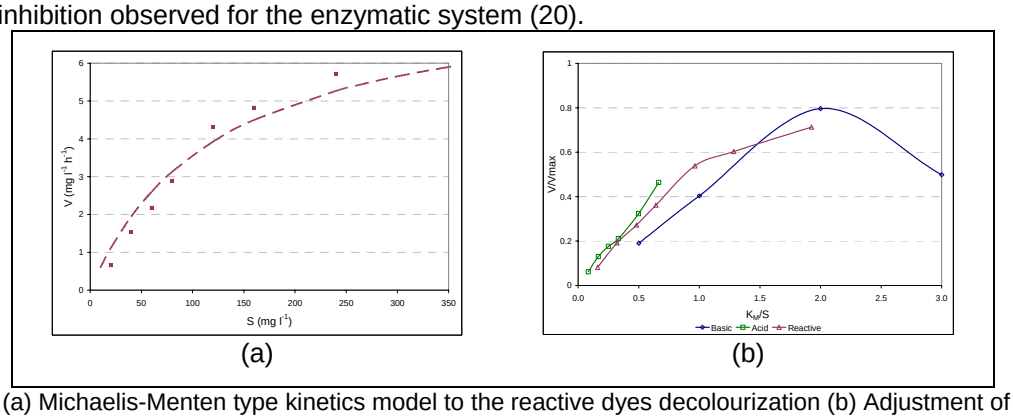

Figure 4. (a) Michaelis-Menten type kinetics model to the reactive dyes decolourization (b) Adjustment of the non-dimensional kinetic model for dye mixtures.

The data decolourization (%) versus substrate concentration was satisfactorily interpreted by the classic Michaelis Menten model (Figure 4a), resulting in a half-saturation constant of 124.6mg·l^{-1}, and a maximum velocity of 8mg·l^{-1}·h^{-1} (R^2=0.949). The mixture of acid dyes had a similar kinetic behaviour, while basic dyes showed an inhibition effect.

Figure 4b shows the dependence of non-dimensional variables V/Vmax versus K_M/S. It also shows that for K_M/S values that are higher than the unit, the system operates with concentrations above K_M.

Both mixtures of acid and reactive dyes show non-saturation regarding these alternative substrata, indicating the feasibility of exploring higher substrate concentrations. Conversely, for basic dyes with a lower K_M value than those referred to above, results imply that a high decolourization level may be reached at low concentrations. However, from a concentration with double K_M value, the system becomes inhibited showing a low affinity of the enzymatic system to these substrates.

Table 2 shows a summary of the kinetic parameters resulting from adjusting a Michaelis-Menten type model.

Table 2. Characteristic parameter of each mixture

	Basic	Acid	Reactive
v_{max} mg·l^{-1}·h^{-1}	2.000	12.000	8.000
K_M mg·l^{-1}	24.610	240.836	124.630
1/ki mg·l^{-1}	0.003	-	-
R^2	0.602	0.935	0.949

Discussion

The present study analyzed a continuous decolourization strategy realized in the fixed bed reactor with immobilized biomass. The purpose to perform the continuous assays with increasing dyes concentration steps is to evaluate the adaptability of the biological system against the different chemical structure of the dyes as alternative substrate. The minimum period for the increasing of the concentration was established in 4 times of the hydraulic retention times (24h). The global decolourization of mixture dyes and MnP activity was considered as response variables which evolution are shown in the Figure 2 for the basic (BV4 - BB24), acid (AB1 – AO6) and reactive (RB19 – RO16) mixtures. On it can be observed that for all assays MnP activity was detected between the days 3-5 before the culture medium was supplemented with dyes reaching 60U·l^{-1}. During decolourization processes MnP activity was only mayor ligninolytic activity detected.

Later to the first addition of dyes the level of MnP activity increased obtaining an activity peak of 240, 150 and 110U·l^{-1} for the 40mg·l^{-1} of basic (Figure 2a), acid (Figure 2b) and reactive (Figure 2c) mixture dyes, respectively. Nevertheless the enzyme production was fluctuating, showing activity descents whenever the dyes concentration increased.

In global terms the activity shown a tendency to increase when the dyes concentration increased which might be explained by the enhancing role of dyes or they by-products on ligninolytic enzyme production, effect reported recently for the laccase production by *P. ostreatus* (21). Wherever the accumulation of intermediates compounds (aromatic amines for example) of degradative processes, it might be a cause to the variable MnP activity levels for the metabolism partial inhibition. Finally it takes place the growth total inhibition to basic (day 30) and reactive (day 50) dyes for 60 and 160mg·l^{-1} respectively. The reactor operated with a mixture acid dye even shows residual MnP activity de 20U·l^{-1} in the day 50.

Higher decolourization was observed for all assays from the 12th-15 day (up to 85%-90%) dropping from the 25th, 38 and 32 day up to 40% (basic dyes), 60% (reactive dyes) and 80% (acid dyes) respectively.

The kinetic analysis of the experimental data obtained during 30-50 days of operation showed the feasibility of operating at higher concentrations than K_M estimated by adjusting a Michaelis-Menten type model for acid and reactive dyes. On the contrary, for basic dyes, a concentration that is double the K_M causes the total inhibition of the fungal system.

By reviewing the values shown in Table 2, it is possible to establish the lower decolourization capacity of the basic dyes as compared to the acid or reactive dyes, as their continued characteristics have a lower value. The determination of the kinetic parameters allows the establishing of the ranges of dye concentration that must be evaluated in order to keep the bioreactor stability (22). It should be mentioned that the treated two-component mixtures had a dye that was labile against the degrading action of the (AB1, RO16, BB24) enzyme, and another dye regarding which the enzyme showed little or zero affinity (AO6, RB19, BV4) (3). Thus the results obtained showed a synergic effect on the decolourization capacity, as it was possible to degrade dyes to which the enzymatic system had not shown affinity at individual level.

Conclusion

The ability of *P. chrysosporium* to survive up to more of 30 days and make a decolourization of a mixture of dyes simultaneously during the sequential step with increasing dyes concentration is an adaptive feature that makes of this strategy a feasible option for an effective removal of synthetic dyes from wastewater.

References

(1) Mielgo, I., Moreira, M.T., Feijoo, G., Lema, J.M. (2002). Biodegradation of a polymeric dye in a pulsed bed bioreactor by immobilized *Phanerochaete chrysosporium*. Water Research, 36, 1896-1901.

(2) Pazarlioglu, N.K., Urek, R.O., Ergun, F. (2005). Biodecolourization of Direct Blue 15 by immobilized *Phanerochaete chrysosporium*. Process Biochemistry, 40, 1923-1929.

(3) Urra, J., Sepúlveda, L., Contreras, E., Palma, C., (2006). Screening of static culture and comparision of batch and continuous culture for the textile dye biological decolorization by *Phanerochaete chrysosporium.* Brazilian Journal of Chemical Engineering, 23, 281-290.

(4) Fu and Viraraghavan T. (2001). Fungal decolorization of dye wastewaters: a review. Bioresource Technology, 79, 251-269.

(5) Tien, M., Kirk, T.K., (1984). Lignin-degrading enzyme from Phanerochaete chrysosporium: Purification, characterization and catalytic properties of a unique H_2O_2-requiring oxygenasa. Proc. Natl. Acad. Sci. USA., 81, 2280-2284.

(6) Kuwahara, M., Glenn, J.K., Morgan, M.A., Gold, M.H. (1984). Separation and characterization of two extracellular H2O2-dependent oxidases from ligninolytic cultures from Phanerochaete chrysosporium. FEBS Lett, 169, 247-250.

(7) Paszczynski, A., Huynh, V.-B., Crawford, R. (1985). Enzymatic activities of an extracellular, manganese-dependent peroxidase from Phanerochaete chrysosporium. FEMS Microbiol. Lett., 29, 37-41.

(8) Bourbonnais, R., Paice, M.G. (1985). Oxidation of nonphenolic substrates—an expanded role for laccase in lignin biodegradation. FEBS Letters, 267, 1,99–102.

(9) Mester, T., Field, J.A., (1998). Characterization of a novel manganese peroxidase-lignin peroxidase hybrid isoenzyme produced by Bjerkandera sp. Strain BOS55 in the absence of manganese. Journal of Biological Chemistry, 273, 15412-15417.

(10) Kariminiaae-Hamedaani, H-R., Sakurai, A., Sakakibara, M. (2007). Decolorization of synthetic dyes by a new manganese peroxidase-producing white rot fungus. Dyes and Pigments,72, 157-162.

(11) Nozaki, K., Beh, C.H., Mizuno, M., Isobe, T., Shiroishi, M., Kanda, T., Amano, Y. (2008). Screening and Investigation of Dye Decolorization Activities of Basidiomycetes. Journal Bioscience and Bioengineering, 105, 69–72.

(12) Novotny, C., Svobodova, K., Kasinath, A., Erbanova, P. (2004). Biodegradation of synthetic dyes by Irpex lacteus under various growth conditions. International Biodeterioration & Biodegradation, 54 215 – 223.

(13) Soares, G.M.B., Amorim, M.T.P., Lageiro, M. and Costa-Ferreira, M. (2006). Pilot-scale Enzymatic Decolorization of Industrial Dyeing Process Wastewater. Textile Research Journal, 76, 4-11.

(14) Moreira, M.T., Palma, C., Mielgo, I., Feijoo, G., Lema, J.M. (2001). In vitro degradation of polymeric dye (Poly R-478) by manganese peroxidase. Biotechnology and Bioengineering, 75, 362-368.

(15) Palma, C., Moreira, M.T., Mielgo, I., Feijoo, G., Lema, J.M. (1999). Use of a fungal bioreactor as a pretreatment or post-treatment step for continuous decolorisation of dyes. Wat. Sci.Tech., 40, 8, 131-136.

(16) Mester, T., Peña, M., Field, J.A. (1996). Nutrient regulation of extracellular peroxidases in the white-rot fungus, *Bjerkandera sp*. Strain BOS55. Applied Microbiology and Biotechnology, 44, 778-784.

(17) Tien, M., Kirk, T,K. (1988). Lignin peroxidase of *Phanerochaete chrysosporium.* Methods in Enzymology, 161, 238-249.

(18) Mielgo, I., Moreira, M.T., Feijoo, G., Lema, J.M. (2001). A packed-bed bioreactor for the continuous decolourisation of azo-dyes (Orange II). Journal of Biotechnology, 89, 99-106.

(19) Field, J.A., De Jong. E,, Feijoo-Costa, G., De Bont, J.A.M. (1992), Biodegradation of polycyclic aromatic hydrocarbons by new isolates of white-rot fungi. Appl. Environ. Microbiol. 58, 2219-2226.

(20) Idbal, M., Saeed, A. (2007). Biosorption of reactive dye by loofa sponge-immobilized fungal biomass of *Phanerochaete chrysosporium*. Process Biochem., 42, 1160-1164.

(21) Casieri, L., Varese, G.C., Anastasi, A., Prigione, V., Svobodová, K., Filippelo Marchisio, V., Novotný, C. (2008). Decolorization and detoxication of reactive industrial dyes by immobilized fungi *Trametes pubescens* and *Pleurotus ostreatus*. Folia Microbiologica, 53, 1, 44-52.

(22) Lopez, C., Moreira, M.T., Feijoo, G., Lema, J.M. (2006). Dynamic modeling of an enzymatic membrane reactor for the treatment of xenobiotic compounds. Biotech. Bioeng., 97, 5, 1128- 1137.

Proceedings of the 10th International Chemical and
Biological Engineering Conference - CHEMPOR 2008
Braga, Portugal, September 4-6, 2008
E.C. Ferreira and M. Mota (Eds.)

Optimization of industrial textile dye colour removal by *Pseudomonas oleovorans*

Edgar Silveira[1,2,3], Petrus P. Marques[2], José L. Lima-Filho[2], Ana L.F. Porto[3], Elias B. Tambourgi[1,*]

[1]School of Chemical Engineering – State University of Campinas, UNICAMP – CP 6066, 13083-970, Campinas – SP, Brazil
[2]LIKA – Pernambuco Federal University, UFPE – Recife – PE, Brazil
[3]DMFA / Cenapesq – Pernambuco Federal Rural University, UFRPE – Recife – PE, Brazil

Keywords: Azo dye; *Pseudomonas*; colour removal; factorial design; optimization
Topic: Integration of life sciences & engineering.

Abstract

This work describes the optimization of industrial textile dye colour removal environmental conditions by Pseudomonas oleovorans. A pre-culture of *Pseudomonas oleovorans* in late exponential phase or early stationary phase was inoculated in tubes containing Nutrient Broth with dye where a factorial experimental design was performed. The variables used in the factorial design (2^{n-2}) were dye concentration (30, 50, 70 mg L^{-1}); agitation (0, 75, 150 RPM); initial pH (6.0, 7.0, 8.0); temperature (27, 32, 37 °C); time (36, 48, 60 hours); tube volume (25, 50, 75%); and initial culture size (0.5, 1.0, 1.5 O.D.). It was observed that decolourization of the industrial dye was negatively influenced by the tube volume and the dye concentration, which should be related with the maximum capacity of the strain to decolourize azo dyes. Time and temperature affected the decolourization positively, although they were not significant. The best conditions to dye decolourization by *Pseudomonas oleovorans* based on the experimental design and also economic factors were agitation 0 RPM, pH 8.0, temperature 32 °C, 25% of tube volume, initial culture size of 0.500 abs, dye concentration of 50 mg L-^{1}.

1 Introduction

There are more than 100,000 commercially available dyes with over than 7 x 10^7 tons of dyestuff produced annually worldwide (Akhtar et al., 2005; Robinson et al., 2001). In Brazil, alone, 26,500 tons are produced (Ulson de Souza et al., 2007).Thus, as result of large production and consumption of dyes, serious environmental problems have been attracted extensive concerns (Wesenberg et al., 2003; Yang et al., 2008).

The elimination of dye containing effluents is mostly based on physic-chemical procedures (e.g. adsorption, concentration, chemical transformation and incineration) (Ramya et al., 2008). These methods are rather costly and sometimes produce hazardous by-products and therefore raise other environmental problems. One attractive strategy is bioremediation, which is becoming an important issue in both developed and developing counties (Wafaa et al., 2003).

It has been observed that some microorganisms can transform azo dyes into colourless products. Bacterial degradation of azo dyes is often initiated by an enzymatic step that involves cleavage of azo linkages with the aid of an azoreductase (Yeh and Chang, 2004). The bacterial ability to decolourize dyes has been reported by several researchers (Barragan et al., 2007; Khalid et al., 2008; Lodato et al., 2007; Mohana et al., 2008; Pandey et al., 2007), although, less attention had been given to conditions optimization for colour removal of contaminated effluents.

Statistical design of experiments is a widely used methodology in upstream and downstream processing (Kammoun et al., 2008; Khosravi-Darani and Zoghi, 2008; Porto et al., 2008), in which differ from the classical optimization methods. The further methods involve single factor variation, keeping the other factors constant. Otherwise, this method is not suitable for multifactor optimization not only because it is time-consuming but also because it is unable of detecting the true optimum due especially to the interactions between the factors (Kammoun et al., 2008; Liu and Tzeng, 1998). To avoid these problems, statistical design of experiments is used. Such designs require a relatively small number of runs per factors allowing the identification of the most important variables and its optimum ranges, as well as the experimental verification of these identified optimum (Weuster-Botz, 2000), the designs can also indicate a promising direction for further experimentation (Lim and Lee, 2008).

This work describes the first step on the optimization of environmental conditions for decolourization of industrial dye by *Pseudomonas oleovorans* in submerse cultures.

2 Materials and Methods

The microorganism was obtained from the collection of the Brazilian Collection of Industrial and Environmental Microorganisms (CBMAI) of the State University of Campinas, previously identified as *Pseudomonas oleovorans* (CBMAI 703).

The strain was preserved in cryotubes containing glass beads and 10% glycerol (v/v). Each crytube was loaded from the same initial culture and had and average of 30 beads. It was thus possible to use the same cell generation for all experiments.

The industrial textile dye was obtained from the kind permission of Clariant of Brazil (Sao Paulo, Brazil). As it is for commercial use, the name, C.I. number and name, and molecular structures will be omitted further in this study. All other reagents are of analytical grade.

For each experiment, an Erlenmeyer flask containing 20 ml of Nutrient Broth (meat extract 3 $g \bullet l^{-1}$ and peptone 5 $g \bullet l^{-1}$) was inoculated with a single glass bead from the same cryotube and incubated at 28 °C for 24 hours when an early stationary phase or final exponential phase was reached.

The influence of variable, namely Temperature (°C), pH, Dye Concentration ($mg \bullet l^{-1}$), Agitation (RPM), Volume (%), Culture Time (hours) and Inoculum Size (O.D.), on the two selected responses, namely Decolourization (%) and Biomass ($g \bullet l^{-1}$), was evaluated from the result obtained from a 2^{7-2}–factorial design plus a central point, which was run in triplicate to allow estimation of pure experimental error. The values selected for these variables are listed in Table 1. All statistical and graphical analysis were carried out with the Statistica 8.0 package (Statsoft Inc., Tulsa, OK, USA).

The decolourization experiments were carried out in screw-topped tubes containing liquid medium as described previously, but also contained the dye concentration, tube volume, inoculum size and pH listed in Table 1. The dyes were filter-sterilised prior to addition to the sterile culture medium. The tubes were incubated under anoxic conditions away from light. Control experiments were performed using the same medium with microorganisms.

The samples from the decolourization cultures were collected and analysed following the methodology described by(Chen, 2002) as follows:

1) OD_{600nm} of the sample mixtures without centrifugation;

2) OD_{600nm} of sample supernatant after centrifugation for 10 minutes at 10,000 g; and,

3) OD_{609nm} of sample supernatant after centrifugation.

The biomass produced was determined by subtracting the value obtained on the first step from the value obtained on second. Colour removal efficiency was determined by the following equation:

$$Decolourization = \frac{A_{\lambda,initial} - A_{\lambda,final}}{A_{\lambda,final}} \quad (1)$$

in which $A_{\lambda,initial}$ is the absorbance before the decolourization process and $A_{\lambda,final}$ is the value obtained on the third step.

3 Results and Discussion

The responses obtained from the 35 runs of the fractional experimental design are listed in Table 1. It was observed that the tube volume was the most influenced variable with a negative response. Negative effects were observed in the volume, dye concentration and inoculum size in the decolourization of the industrial dye. Nevertheless only the inoculum size was not significant to the decolourization. The summarizations of variables' significances are listed in Table 2.

Table 1 – Conditions and Results of the 2^{7-2}–factorial experimental design selected for industrial dye decolourization

Run	temp[a]	pH	dye[b]	agit[c]	vol[d]	time[e]	Inoc[f]	Decolour[g]	Biomass[h]
1	27	8	30	150	25	60	1.5	96.62	0.107
2	27	8	70	0	75	60	1.5	69.65	0.106
3	27	6	70	150	25	60	0.5	90.59	0.168
4	27	6	70	0	25	36	1.5	72.88	0.123
5	27	6	30	150	75	36	1.5	83.88	0.149
6	27	6	70	0	75	36	0.5	54.62	0.181
7	27	8	70	150	25	36	1.5	79.02	0.199
8	27	6	70	150	75	60	1.5	66.80	0.129
9	27	6	30	0	25	60	1.5	89.48	0.240
10	27	6	30	0	75	60	0.5	93.15	0.205
11	27	6	30	150	25	36	0.5	93.24	0.181
12	27	8	30	0	75	36	1.5	84.75	0.246
13	27	8	30	0	25	36	0.5	88.13	0.224
14	27	8	70	0	25	60	0.5	95.34	0.263
15	27	8	30	150	75	60	0.5	94.88	0.327
16	27	8	70	150	75	36	0.5	67.01	0.289
17*	32	7	50	75	50	48	1.0	92.24	0.096
18*	32	7	50	75	50	48	1.0	88.84	0.086
19*	32	7	50	75	50	48	1.0	82.46	0.105
20	37	8	35	150	25	36	0.5	94.31	0.088
21	37	6	35	150	75	60	0.5	90.44	0.100
22	37	8	70	0	25	36	1.5	95.68	0.075
23	37	6	70	150	75	36	0.5	52.85	0.178
24	37	8	35	150	75	36	1.5	89.67	0.088
25	37	8	35	0	25	60	1.5	98.36	0.101
26	37	6	70	150	25	36	1.5	94.39	0.102
27	37	6	70	0	75	60	1.5	62.13	0.091
28	37	8	35	0	75	60	0.5	96.43	0.089
29	37	6	70	0	25	60	0.5	98.10	0.066
30	37	6	35	0	25	36	0.5	95.85	0.085
31	37	8	70	150	25	60	0.5	97.67	0.073
32	37	6	35	150	25	60	1.5	96.14	0.043
33	37	8	70	0	75	36	0.5	79.45	0.089
34	37	6	30	0	75	36	1.5	78.09	0.084
35	37	8	70	150	75	60	1.5	73.79	0.082

[a] – temperature (°C); [b] – dye concentration ($mg \bullet l^{-1}$); [c] – agitation (RPM); [d] – volume (%); [e] – time (hours); [f] – inoculum size (O.D.); [g] – decolourization (%); [h] – biomass ($g \bullet l^{-1}$); * – central point repetitions

The decolourization of the industrial dye was negatively affected by the tube volume and dye concentration; this should be explained by the overall mass of industrial dye in the medium. Industrial dyes generally contains one, or more sulphonic-acid groups on the aromatic rings and may affect the DNA synthesis, since it has been reported that dyes are inhibitors of nucleic acid synthesis, or cell growth (Chen et al., 2003). Furthermore, the biomass production is also negatively effect by the dye concentration.

This also suggests that the medium's dissolved oxygen, as well as the available oxygen within the tube, has a limiting role in the beginning of decolourization process, since it competes with the azo bound as an electron receptor. Once extinct, and when the redox potential is reached, the effective dye decolourization begins (Bromley-Challenor et al., 2000)

Table 2 –Estimated effects of studied parameters (t distribution)

Parameter	Decolourization (%)	Biomass ($g \bullet l^{-1}$)
Temperature (°C)	2.6101	-31.6749[a]
pH	3.1378	5.9704[a]
Dye ($mg \bullet l^{-1}$)	-7.5997[a]	-2.6597
Agitation (RPM)	0.3279	0.6510
Volume (%)	-8.4812[a]	5.4868[a]
Time (hours)	3.7651	-3.5525
Inoculum size (O.D.)	-1.8062	-11.9223[a]
MS Pure Error	24.65213	0.0000903

[a] – $p < 0.05$

Table 2 also shows that, although the agitation has a positive effect on decolourization and biomass production, this effect is little influent over industrial dye decolourization process. Since this study aims an industrial application, the lack of agitation, even in anoxic condition, which deals only with mass transfer rate, is not advantageous.

The industrial dye reduction in anaerobic or anoxic conditions is an extracellular and non-specific process (Kalme et al., 2007), and usually occurs through an enzymatic reaction. This should explain the correlation between biomass production and decolourization as shown in Figure 1.

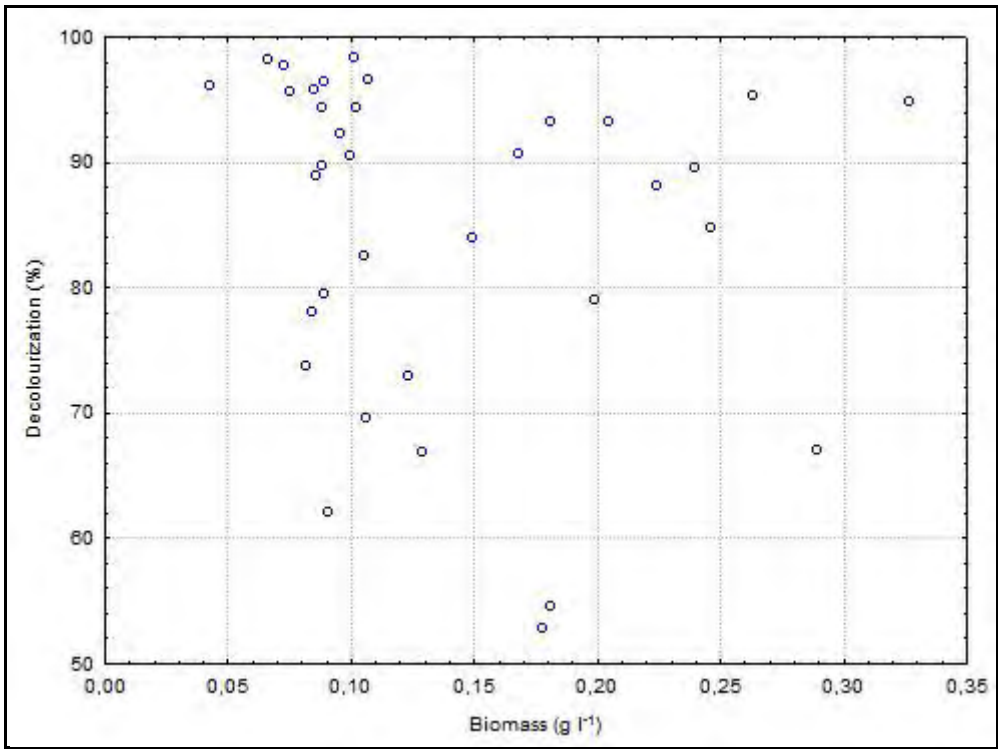

Figure 1 – Decolourization as a function of biomass production

In their studies performed with *Kurthia* sp., Sani and Banerjee (1999) observed that the increased biomass production resulted an increase of triphenylmethane dyes decolourization. They observed that there is a limit to the maximum efficiency of colour removal could be reached. The same was observed with *P. oleovorans*, although its point of best efficiency related on the biomass production and colour removal rate is not the point were there was the major biomass production.

The increase of pH, from an acid pH to a slight basic pH, showed an increase of decolourization, even though it was not significant. Pearce (2003) described that bacterial cultures usually have maximum decolourization rates at neutral pH or low basic. The increase of temperature also showed an increase on decolourization, probably due to enzymatic activity increase, however it is not significant. The culture time showed to affect positively the dye decolourization, with is explained by the longer exposition time of the dye to the enzymatic apparatus of the microorganism.

5 Conclusions

The best conditions to dye decolourization by Pseudomonas oleovorans based on the experimental design and also economic factors were agitation 0 RPM, pH 8.0, temperature 32 °C, 25% of tube volume, initial culture size of 0.500 Optical Density abs, dye concentration of 50 mg L^{-1}.

6 Acknowledjements

The authors would like to acknowledge Fapesp, Capes and CNPq for financial support; and Clariant of Brazil for the dyes provided.

7 References

Akhtar, S., Khan, A. A. and Husain, Q. (2005). Potential of immobilized bitter gourd (Momordica charantia) peroxidases in the decolorization and removal of textile dyes from polluted wastewater and dyeing effluent. *Chemosphere, 60*(3), 291-301.

Barragan, B. E., Costa, C. and Carmen Marquez, M. (2007). Biodegradation of azo dyes by bacteria inoculated on solid media. *Dyes and Pigments, 75*(1), 73-81.

Bromley-Challenor, K. C. A., Knapp, J. S., Zhang, Z., Gray, N. C. C., Hetheridge, M. J. and Evans, M. R. (2000). Decolorization of an azo dye by unacclimated activated sludge under anaerobic conditions. *Water Research, 34*(18), 4410-4418.

Chen, B.-Y. (2002). Understanding decolorization characteristics of reactive azo dyes by *Pseudomonas luteula*: toxicity and kinetics. *Process Biochemistry, 38*, 437-446.

Chen, K.-C., Wu, J.-Y., Liou, D.-J. and Hwang, S.-C. J. (2003). Decolorization of the textile dyes by newly isolated bacterial strains. *Journal of Biotechnology, 101*(1), 57-68.

Kalme, S. D., Parshetti, G. K., Jadhav, S. U. and Govindwar, S. P. (2007). Biodegradation of benzidine based dye Direct Blue-6 by Pseudomonas desmolyticum NCIM 2112. *Bioresource Technology, 98*(7), 1405-1410.

Kammoun, R., Naili, B. and Bejar, S. (2008). Application of a statistical design to the optimization of parameters and culture medium for [alpha]-amylase production by Aspergillus oryzae CBS 819.72 grown on gruel (wheat grinding by-product). *Bioresource Technology, 99*(13), 5602-5609.

Khalid, A., Arshad, M. and Crowley, D. (2008). Accelerated decolorization of structurally different azo dyes by newly isolated bacterial strains. *Applied Microbiology and Biotechnology, 78*(2), 361-369.

Khosravi-Darani, K. and Zoghi, A. (2008). Comparison of pretreatment strategies of sugarcane baggase: Experimental design for citric acid production. *Bioresource Technology, 99*(15), 6986-6993.

Lim, J. H. and Lee, J. S. (2008). A statistical design and analysis illustrating the interactions between key experimental factors for the synthesis of silver nanoparticles. *Colloids and Surfaces A: Physicochemical and Engineering Aspects, 322*(1-3), 155-163.

Liu, B.-L. and Tzeng, Y.-M. (1998). Optimization of growth medium for the production of spores from Bacillus thuringiensis using response surface methodology. *Bioprocess and Biosystems Engineering, 18*(6), 413-418.

Lodato, A., Alfieri, F., Olivieri, G., Di Donato, A., Marzocchella, A. and Salatino, P. (2007). Azo-dye conversion by means of Pseudomonas sp. OX1. *Enzyme and Microbial Technology, 41*(5), 646-652.

Mohana, S., Shrivastava, S., Divecha, J. and Madamwar, D. (2008). Response surface methodology for optimization of medium for decolorization of textile dye Direct Black 22 by a novel bacterial consortium. *Bioresource Technology, 99*(3), 562-569.

Pandey, A., Singh, P. and Iyengar, L. (2007). Bacterial decolorization and degradation of azo dyes. *International Biodeterioration & Biodegradation, 59*(2), 73-84.

Pearce, C. I., Lloyd, J. R. and Guthrie, J. T. (2003). The removal of colour from textile wasterwater using whole bacterial cells: a review. *Dyes and Pigments, 58*, 179-196.

Porto, T. S., Medeiros e Silva, G. M., Porto, C. S., Cavalcanti, M. T. H., Neto, B. B., Lima-Filho, J. L., Converti, A., Porto, A. L. F. and Pessoa Jr, A. (2008). Liquid-liquid extraction of proteases from fermented broth by PEG/citrate aqueous two-phase system. *Chemical Engineering and Processing: Process Intensification, 47*(4), 716-721.

Ramya, M., Anusha, B. and Kalavathy, S. (2008). Decolorization and biodegradation of Indigo carmine by a textile soil isolate Paenibacillus larvae. *Biodegradation, 19*(2), 283-291.

Robinson, T., McMullan, G., Marchant, R. and Nigam, P. (2001). Remediation of dyes in textile effluent: a critical review on current treatment technologies with a proposed alternative. *Bioresource Technology, 77*(3), 247-255.

Sani, R. K. and Banerjee, U. C. (1999). Decolorization of triphenylmethane dyes and textile and dye-stuff effluent by Kurthia sp. *Enzyme and Microbial Technology, 24*(7), 433-437.

Ulson de Souza, S. M. A. G., Forgiarini, E. and Ulson de Souza, A. A. (2007). Toxicity of textile dyes and their degradation by the enzyme horseradish peroxidase (HRP). *Journal of Hazardous Materials, 147*(3), 1073-1078.

Wafaa, M., El-Rahim, A. and Moawad, H. (2003). Enhancing bioremoval of textile dyes by eight fungal strains from media supplemented with gelatine wastes and sucrose. *Journal of Basic Microbiology, 43*(5), 367-375.

Wesenberg, D., Kyriakides, I. and Agathos, S. N. (2003). White-rot fungi and their enzymes for the treatment of industrial dye effluents. *Biotechnology Advances, 22*, 161-187.

Weuster-Botz, D. (2000). Experimental design for fermentation media development: Statistical design or global random search? *Journal of Bioscience and Bioengineering, 90*(5), 473-483.

Yang, Q., Tao, L., Yang, M. and Zhang, H. (2008). Effects of glucose on the decolorization of Reactive Black 5 by yeast isolates. *Journal of Environmental Sciences, 20*(1), 105-108.

Yeh, M.-S. and Chang, J.-S. (2004). Bacterial decolorization of an azo dye with a natural isolate of *Pseudomonas luteola* and genetically modified *Escherichia coli*. *Journal of Chemical Technology & Biotechnology, 79*(12), 1354-1360.

Proceedings of the 10th International Chemical and
Biological Engineering Conference - CHEMPOR 2008
Braga, Portugal, September 4-6, 2008
E.C. Ferreira and M. Mota (Eds.)

Phosphorous removal from water by polyolefins: effect of Al_2O_3 addition

M. Oliveira[1*], J.M. Nobrega[1], A. V. Machado[1], A. G. Brito[2], R. Nogueira[2]
[1]IPC – Institute of Polymers and Composites, Department of Polymers Engineering
University of Minho, Campus de Azurém, 4800–058 Guimarães, Portugal
[2]IBB – Institute for Biotechnology and Bioengineering, Centre of Biological Engineering,
University of Minho, Campus de Gualtar, 4710–057 Braga, Portuga

Keywords: Eutrophication; Phosphorus removal; Polyolefin; Aluminum oxide
Topic: Integration of life sciences & engineering: Improvement of environmental remediation processes.

Abstract

Phosphorus is the main nutrient responsible for eutrophication of aquatic ecosystems, therefore it is important to develop new processes to remove phosphorus that avoid the formation of precipitates. Polyolefins with and without prior activation with aluminum oxide (Al_2O_3), processed as flat plates, were investigated for phosphate removal from an aqueous solution. The maximum amount of phosphorus removal was 0.042 μgP/cm^2 for PE (polyethylene), 0.049 μgP/cm^2 for PE-g-MA (polyethylene grafted with maleic anhydride), and 0.071 μgP/cm^2 for PE-g-MAe (PE-g-MA enriched in MA). Increasing polyolefins' polarity did not result in a significant increase in phosphate removal. Activated polyolefins with Al_2O_3 presented maximum amounts of phosphorus removal of 0.863 μgP/cm^2 for PE, 0.948 μgP/cm^2 for PE-g-MA, and 0.884 μgP/cm^2 for PE-g-MAe. As expected, addition of Al_2O_3 considerably increased phosphate removal. In kinetic experiments carried out with polyolefins activated with Al_2O_3 during 3 months a very high percentage of phosphorus removal was obtained for (> 90 %) as well as a very low remaining phosphorus concentration in solution (< 10 μgP/L).
As a conclusion, polyolefins activated with Al_2O_3 effectively removed phosphorous from aqueous solutions with low concentrations which indicate that this material might be used for in-situ remediation of eutrophic waters. The possibility to recover the material after use to recycle phosphate and the absence of precipitates' formation are two major advantages of this process.

Introduction

Phosphorus (P) is an essential nutrient for plant growth and has been intensively used as a fertilizer in agriculture. This practice contributed to the eutrophication of aquatic ecosystems (e.g. lakes, rivers and marshes), causing algal blooms which ultimately lead to oxygen depletion and generally poor water quality (Ribero et al., 2008). Re-dissolution of phosphate accumulated in the sediments, under certain environmental conditions (temperature, redox potential, pH, dissolved oxygen concentration, bacterial activity), might also be responsible for the occurrence of algae blooms especially when external nutrient sources are controlled (Martins et al., 2008).
P inactivation is a lake restoration technique. Its purpose is to lower the lake's P content by removal of P from the water column (P precipitation) and/or by retarding P release from lake sediments (P inactivation). Remediation solutions have been tested for a long time but with limited success. A literature review on materials used for P removal, classified in appropriate groups, is given in Table 1.

* Corresponding author. Tel + 351-253-510100. E-mail:moliveira@dep.uminho.

Table 1 - Literature review on adsorptive media for phosphorus removal

Aluminum	Calcium	Iron	Industrial by-products	Clay
• *Activated alumina* (7gP/kg)[1] • *Shale* (0.73 gP/kg)[2] • *Bauxite* (0.36 gP/kg)[2] • *Zeolite* (2.15 gP/kg)[3]	• *Wollastonite* (0.85 gP/kg)[4] • *Limestone* (0.68 gP/kg)[2] • *Dolomite* (0.30 gP/kg)[5]	• *Iron oxide* (12.65 gP/kg)[6] • *Iron coated sands* (1.50 gP/kg)[7] • *Red mud* (0.58 gP/kg)[8]	• *Steel slags* (18 gP/kg)[9] • *Blast furnace slags* (8.89 gP/kg)[10] • *Coal fly ash* (8.81 gP/kg)[10]	• *Allophane* ($q= 5.620C^{0.264}$)[11] • *Phoslock™* (11-12 gP/kg)[11] • *Bentonite* (0.42 mgP/kg)[12]

1- Donnert and Salecker, 1999; 2- Drizo et a.l, 1999 ; 3- Sakadevan et al., 1998 ; 4- Hedström, 2006 ; 5- Pant et al., 2001; 6- Zeng et al., 2004 ; 7- Boujelben et al., 2008 ; 8- Huang et al., 2008 ; 9- Zhang et al., 2003 ; 10- Xu et al., 2006 ; 11- Yuan and Wu, 2007 ; 12- Pradas et al., 1992.

From all adsorbents shown in Table 1, activated alumina might be one of the most suitable materials to be used in phosphorus removal from natural waters with eutrophication problems. Activated alumina (aluminum oxide activated at 600 ºC) has a very high surface area (300 m^2/g) and is selective for phosphorus in the presence of nitrate and sulfate ions (Hano et al., 1997; Donnert and Salecker, 1999). The mechanism of phosphate removal by activated alumina is mainly ion exchange associated with chemical reaction, precipitation and formation of complexes (Narkis et al., 1981).

Materials and Methods

Materials

Polyolefins, polyethylene (PE), polyethylene grafted with maleic anhydride (PE-g-MA), and PE-g-MA enriched in maleic anhydride were used as polymeric matrices to remove phosphorus from an aqueous solution. The maleic anhydride increases the polarity of the resulting polymeric matrix thus enhancing the contact between aqueous and solid phases. In addition, the polymeric matrices were loaded with Al_2O_3 (5.0 %) which was dispersed onto their surfaces. Polymeric plates (12 cm × 18 cm × 0.2 cm) were made in a hot plat press (Moore) at a temperature of 453.15 K and using a final pressure of 30 ton. They were divided into sections with variable dimensions. Al_2O_3, provided by Sigma Aldrich in pellets of 3 mm, was crushed and sieved to an effective size in the range of 500 µm to 1 mm.

Stock phosphorus solution

A stock phosphorus solution with a concentration of 40 mg/L was prepared by dissolving 175.75 mg KH_2PO_4 in 1 L of pure water and used to prepare solutions with lower concentrations. Phosphate concentration was determined spectrophotometrically at a wavelength of 882 nm using the Ascorbic Acid method (4500 - PE, in Standard Methods, 17th Edition 1989).

Kinetic experiments

Kinetic experiments were carried out to determine phosphate removal from a solution with an initial P concentration of 100 µg/L. Firstly, experiments were performed in glass beakers where 2.5 g of each material present as granules, PE (3 mm), PE-g-MAe (1 - 3 mm), and Al_2O_3 (0.5 – 1 mm), was placed in contact with 100 mL of a 100 µg/L P solution at 100 rpm and 22 ºC during 7 d. Secondly, polymeric plates with similar areas, 10.5 cm^2 (4.0 cm × 1.0 cm × 0.2 cm), with and without prior activation with Al_2O_3, were placed in glass beakers containing 100 mL of a 100 µg/L P solution at room temperature for 16 d and 90 d without agitation. Samples were taken regularly and the phosphorus content was measured.

Influence of pH on P adsorption onto polymeric plates

Kinetic experiments with polymeric plates activated with Al_2O_3 were carried out as described preciously at pH values of 2, 4, 5, 6, 7, 8 and 9, during 7 d, at 100 rpm and 22ºC. The pH was adjusted by addition of either 2 M NaOH or 2 M HCl.

Determination of phosphorus uptake

The amount of phosphate removed, *q* (µg/cm^2), onto polymeric matrix was calculated by the following equation:

$$q = \frac{(C_i - C_e)}{A} \cdot V \qquad [1]$$

where C_i and C_e are initial and equilibrium phosphorus concentrations in solution (µg/L), V is the solution volume (L), and A is the area of polymeric matrix (cm^2).

Results and Discussion

Kinetic experiments

Figure 1 depicts the concentration of phosphorus in solution obtained in assays carried out with granular polyolefins and Al_2O_3. Phosphorus removal was higher and faster in the presence of Al_2O_3. A decrease of 83 % in phosphorus concentration was observed for Al_2O_3 during the first day as compared to 40 % for PE and 43 % for PE-g-MA.

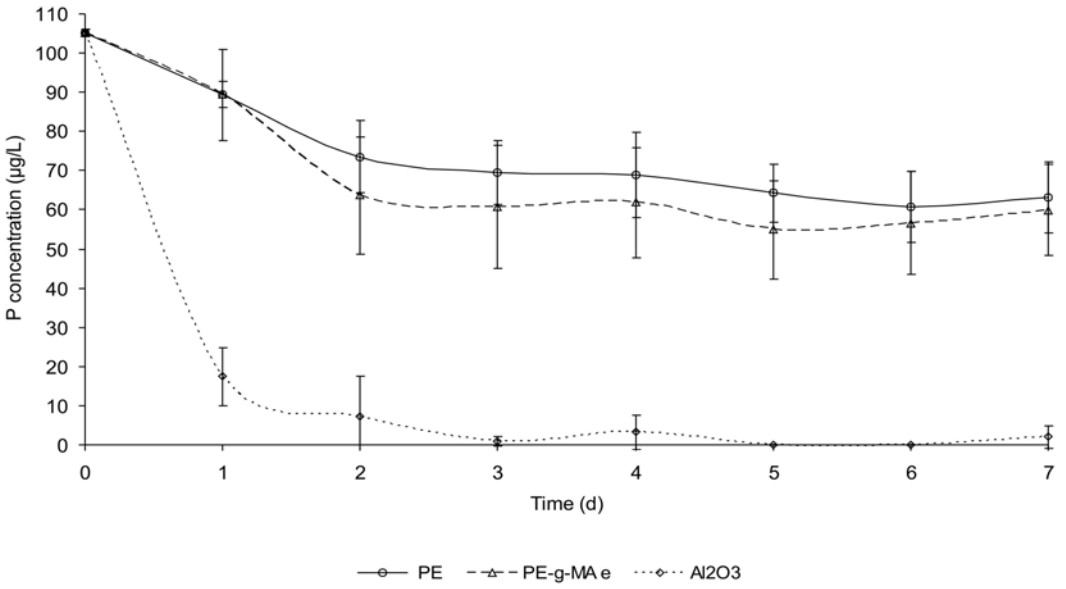

Figure 1 – Phosphorus in solution obtained in assays carried out with granular polyolefins and Al_2O_3.

Figure 2 depicts the concentration of phosphorus in solution obtained in assays carried out with polyolefin plates with and without previous activation with Al_2O_3. A limited affinity between polyolefin plates and phosphorus was observed after 16 d, as indicated by the low amount of P removed, respectively 0.042 µgP/cm^2 for PE, 0.049 µgP/cm^2 for PE-g-MA, and 0.071 µgP/cm^2 for PE-g-MAe. The amount of phosphorus removal was limited by the surface area available. Higher phosphorus removal were obtained for polyolefins activated with Al_2O_3, respectively 0.46 µgP/cm^2 for PE+5% Al_2O_3, 0.56 µgP/cm^2 for PE-g-MA+5% Al_2O_3, and 0.79 µgP/cm^2 for PE-g-MAe+5% Al_2O_3. The highest phosphorus removal was obtained in the case of PE-g-MAe. This result seems to indicate that polymers with higher polarities remove more phosphorus. During the first 19 h of contact phosphorus concentration decreased from 97 µg/L to 72

µg/L and after 16 d a final concentration of 14 µg/L was achieved for PE-g-MAe+5% Al_2O_3. A very high percentage of phosphorus removal was obtained as well as a low remaining phosphorus concentration in solution. By the end of the experiment the equilibrium phosphorus concentration was not yet reached. A new experiment was carried out for 90 d with the most promising materials, as depicted in Figure 3.

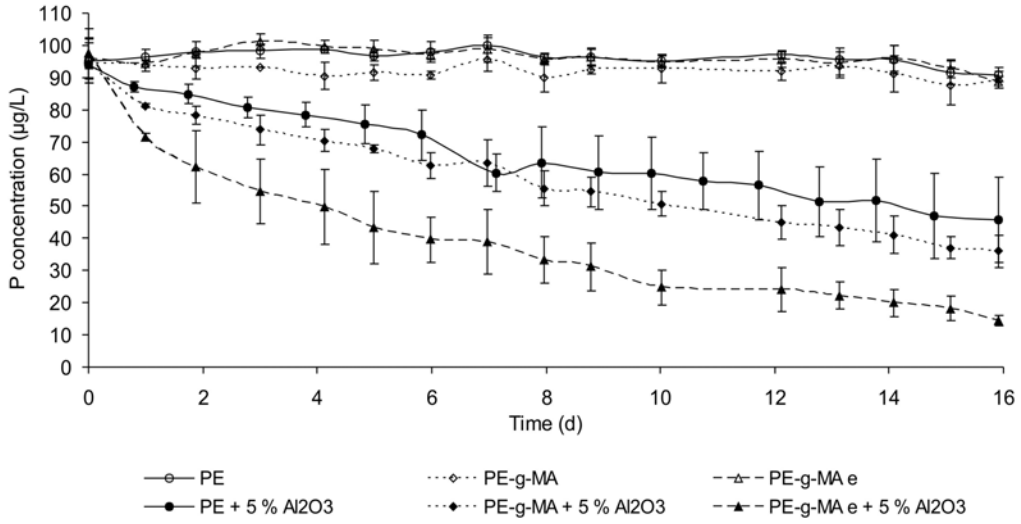

Figure 2 – Phosphorus in solution obtained in assays carried out with polyolefin plates with and without Al_2O_3.

The maximum amount of phosphorus removed by polyolefin plates activated with Al_2O_3 was 0.86 µgP/cm^2 for PE, 0.95 µgP/cm^2 for PE-g-MA, and 0.88 µgP/cm^2 for PE-g-MAe. Although the initially kinetics of phosphorus removal is faster for PE-g-MAe, phosphorus concentration remaining in solution after 90 d was below 10 µg/L in all cases, as depicted in Figure 3.

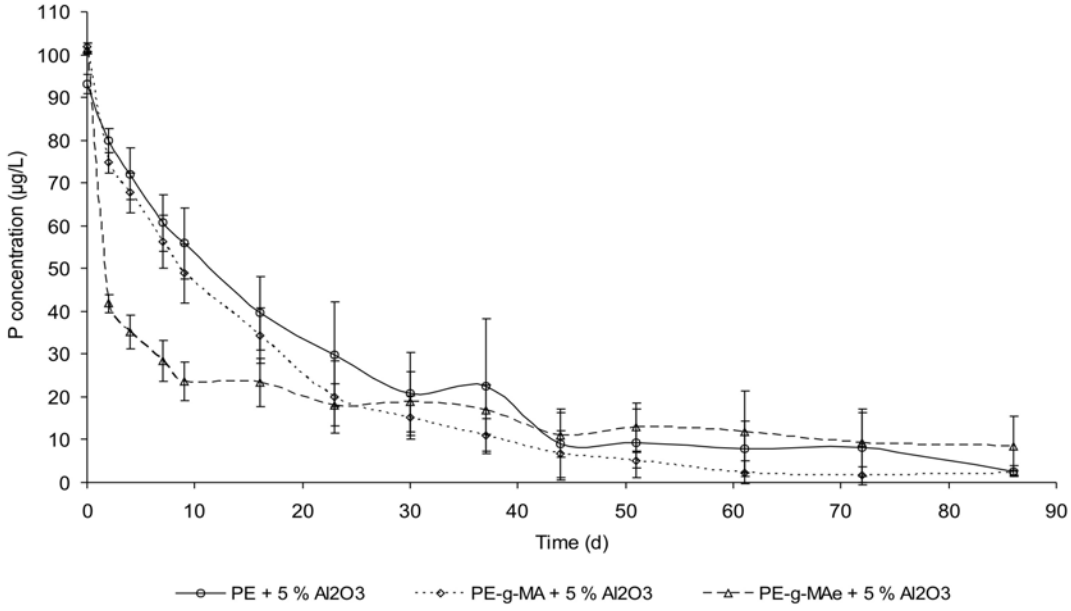

Figure 3 – Phosphorus in solution obtained in assays carried out with polyolefin plates activated with Al_2O_3.

The amount of phosphorus removed by polyolefin plates activated with Al_2O_3 at different pH values is shown in Figure 4. The percentage of phosphorus removal of activated PE and PE-g-MA decreases with an increase of pH while PE-g-MAe presents a stable maximum removal between pH 5 and pH 8 seems to be the most promising one. Increasing PE's polarity shifts maximum phosphorus removal from acidic to neutral/basic pH values. These results seem to indicate that the interaction between pH and polarity is a key factor in phosphorus removal and that the mechanism responsible for phosphorus removal might be ion exchange.

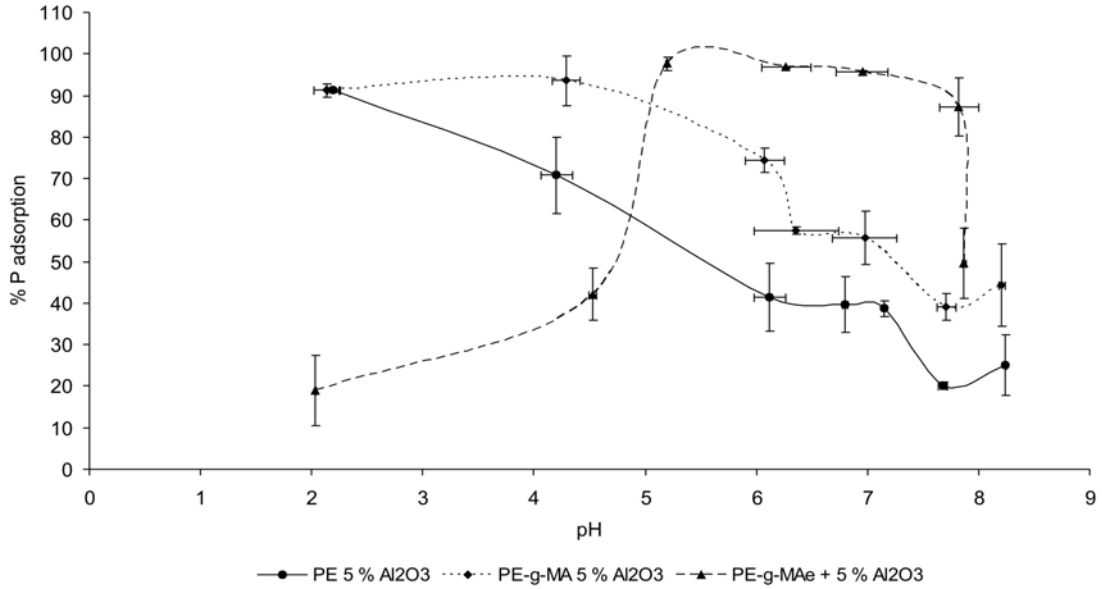

Figure 4 – Percentage of phosphorus removal as a function of pH in assays carried out with polyolefin plates activated with Al_2O_3.

Conclusions

The present study indicates that polyolefins activated with Al_2O_3 remove efficiently phosphorus from low solutions with low concentrations. The maximum removal capacities obtained were 0.86 μgP/cm^2 for PE, 0.95 μgP/cm^2 for PE-g-MA, and 0.88 μgP/cm^2 for PE-g-MAe. Furthermore, it was found that phosphorus removal efficiency depended on pH. The best results were obtained for PE-g-MA enriched in maleic anhydride that presented a maximum phosphorus removal in a pH interval between 5 and 8.

Acknowledgments

This study was financially by Foundation for Science and Technology FCT Project nº SFRH/BD/39085/2007.

References

Boujelben, N., J. Bouzid, Z. Elouear, M. Feki, F. Jamoussi, A. Montiel (2008). Phosphorus removal from aqueous solution using iron coated natural and engineered sorbents, Journal of Hazardous Materials 151: 103-110.

Donnert, D., M. Salecker (1999). Elimination of phosphorus from municipal and industrial waste water, Water Science and Technology 40: 195-202.

Drizo, A., C. A. Frost, J. Grace, K. A. Smith (1999). Physical-chemical screening of phosphate removing substrates for use in constructed wetland systems, Water Research 33: 3595-3602.

Hano, T., H. Takanashi, M. Hirata, K.Urano, S. Eto (1997). Removal of phosphorus from wastewater by activated alumina adsorbent, Water Science and Technology 35: 39-46.

Hedström, A. (2006). Reactive filter materials for ammonium and phosphorus sorption in small scale wastewater treatment, PhD Thesis.

Huang, W., S. Wang, Z. Zhu, L. X. Yao, V. Rudolph, F. Haghseresht (2008). Phosphate removal from wastewater using red mud, Journal of Hazardous Materials, article in press.

Martins G., D. Ribeiro, D. Pacheco, J. V. Cruz, R. Cunha, V. Gonçalves, R. Nogueira, A.G. Brito (2008). Prospective scenarios for water quality and ecological status in Lake Sete Cidades (Portugal): the integration of mathematical modelling in decision processes. *Applied Geochemistry* (in press).

Narkis, N., M. Meiri (1981). Phosphorus removal by activated alumina Environmental Pollution Series B, Chemical and Physical Volume 2, 327-343.

Ribeiro D., G. Martins, R. Nogueira, J. V. Cruz, A.G. Brito (2008). Phosphorus Fractionation in lake volcanic sediments (Azores – Portugal). *Chemeosphere*, 70 7.

Pant, K., K. R. Reddy, E. Lemon (2001). Phosphorus retention capacity of root bed media of sub-surface flow constructed wetlands, Ecological Engineering 17: 345-355.

Pradas, E. G., M. V. Sanches, A. G. Campo (1992). Effects of experimental variables on phosphate adsorption on bentonite, Journal of Chemical Technology & Biotechnology 3: 291-295.

Sakadevan, K., Bavor, H.J. (1998). Phosphate adsorption characteristics of soils, slags and zeolite to be used as substrate in constructed wetland systems. Water Research 32, 393–399.

Xu, D., J. Xu, J. Wu, A. Muhammad (2006). Studies on the phosphorus sorption capacity of substrates used in constructed wetland systems, Chemosphere 63: 344-352.

Yuan, G., L. Wu (2007). Allophane nanoclay for the removal of phosphorus in water and wastewater, Science and Technology of Advanced Materials 8: 60-62.

Zeng, L., X. Li, J. Liu (2004). Adsorptive removal of phosphate from aqueous solutions using iron oxide tailings, Water Research 38: 1318-1326.

Zhang, H.C., Z. H. Cao, Q. R. Shen, M. H. Wong (2003). Effect of phosphate fertilizer application on phosphorus (P) losses from soil in Taihu Lake Region. I. Effect of phosphate fertilizer rate on P losses from paddy soil, Chemosphere 50: 695-701.

Proceedings of the 10th International Chemical and
Biological Engineering Conference - CHEMPOR 2008
Braga, Portugal, September 4-6, 2008
E.C. Ferreira and M. Mota (Eds.)

Application of an *E. coli* biofilm supported on kaolin to the removal of Cd(II), Cr(VI), Fe(III) and Ni(II) from aqueous solutions

Cristina Quintelas[1*], Zélia Rocha[1], Bruna Silva[1], Bruna Fonseca[1], Hugo Figueiredo[1] and TeresaTavares[1]

[1] IBB – Institute for Biotechnology and Bioengineering, Centre of Biological Engineering, University of Minho, Campus de Gualtar, 4710–057 Braga, Portugal.

Keywords: biofilm, biosorption, clay, cadmium, chromium, iron, níquel
Topic: Integration of life sciences & engineering

Abstract

The pollution caused by heavy metals is one the major environmental problems that is imperative to be solved. New technologies, easy to implement and to adapt to any system, deserve special attention and are the focus of this presentation. This paper aims to investigate the biosorption behaviour of a biofilm of *E. coli* supported on kaolin clay for the treatment of cadmium, iron, nickel and chromium aqueous solutions. The effect of metals initial concentrations were studied and the relationship between pH and removal efficiency were analysed. Adsorption characteristics of a biosorbent can be depicted by an adsorption isotherm. Langmuir, Redlich-Peterson and Sips are commonly used for the description of adsorption data and were applied to the experimental results described by this report. The presence of functional groups in the suspended biomass that may have a role in biosorption process was confirmed by FTIR. It was demonstrated that a biofilm of *E. coli* supported on kaolin is able to remove Cr (VI), Cd (II), Ni (II) and Fe (III) from aqueous solutions. The isotherms were fitted and the best fit for chromium and nickel was obtained with the Redlich-Peterson model isotherm and for cadmium the best fit was the obtained with the Sips model. In terms of removal percentage, the results showed 100% of removal for iron for the whole range of concentrations tested. For cadmium, the removal percentage remains around 70% for all the initial concentrations tested (between 67.1% and 78.9%) and is higher than the obtained for nickel and chromium. The analyses by FTIR showed that functional groups on the biomass, such as hydroxyl, carboxyl and phosphate groups, may be the main binding sites for biosorption of the studied heavy metals by *E. coli*. Finally, the metal affinity to the biofilm was found to follow the sequence Fe > Cd > Ni > Cr and the preference of a sorbent for a metal may be explained on the basis of electronegativity of the metal ions and on the basis of the cation/anion state.

Materials and Methods

The bacterium *Escherichia coli* was obtained from the Spanish Type Culture Collection of the University of Valência. Heavy metals solutions were prepared by diluting $K_2Cr_2O_7$, $FeCl_3.(6H_2O)$, $CdSO_4.(8/3H_2O)$ and $NiCl_2(6H_2O)$, in distillated water. Atomic absorption spectrometric standards were prepared from 1000 mg/l metal solutions. The kaolin was obtained from Minas de Barqueiros, S.A. (Apúlia, Portugal).

A medium with 5 g/l of beef extract, 10 g/l of peptone and 5 g/l of NaCl (pH 7.2) was used for the microorganism growth. The medium was sterilized at 121 ºC for 20 min, cooled to room temperature, inoculated with bacteria and kept at 37 ºC for 24 h with

* Corresponding author. Tel + 351-253604400. E-mail:cquintelas@deb.uminho.pt

moderate stirring in a incubator. Then, batch experiments were conducted using 1 g of kaolin clay with 15 ml of *E. coli* culture media and 150 mL of the different metal solutions (10, 25, 50, 70, 80, 100 mg/l) in 250 ml Erlenmeyer flasks. All experimental work was conducted in duplicate. The Erlenmeyer flasks were kept at 37 ºC, with moderate stirring for about 10 days. Samples of 1 ml were taken, centrifuged and analyzed for metals using atomic absorption spectrophotometry, Varian Spectra AA-400.

Infrared spectra of the unloaded biomass and heavy metal loaded biomass, both in suspension, were obtained using a Fourier transform infrared spectrometer (FTIR BOMEM MB 104). For the FTIR study, biomass is centrifuged and dried, followed by weighting. Then 10 mg of finely ground biomass was encapsulated in 100 mg of KBr in order to prepare translucent sample disks. Elemental chemical analyses (Si, Al, Na, Cr, Cd, Fe and Ni) were performed by Inductively Coupled Plasma Atomic Emission Spectrometry (ICP-AES) using a Philips ICP PU 7000 Spectrometer on samples.

Results and Discussion

The results obtained for the batch biosorption studies showed differences on the biosorption performance between the four metals studied (Table 1). Kaolin surface in water has a net negative surface charge (Turan *et al.*, 2007) and the bacteria have also a net negative charge (Tavares *et al.*, 2006). These negative surfaces obviously favour the biosorption of cations. In addition to the valence state, the electronegativity, atomic weight and ionic radius are also characteristics that influence the biosorption capacity.

Table 1- Uptake values (mg/g) and removal percentage values for Cr (VI), Cd (II), Fe (III) and Ni (II), obtained for the highest initial concentration of metal (37 ºC, 150 rpm), for the biofilm of *Escherichia coli* supported on kaolin

Cr (VI)			**Cd (II)**		
C_0 (mg/l)	**Uptake (mg/g)**	**Rp (%)**	**C_0 (mg/l)**	**Uptake (mg/g)**	**Rp (%)**
116	4,6	26,2	97	10,3	71,3
Fe (III)			**Ni (II)**		
C_0 (mg/l)	**Uptake (mg/g)**	**Rp (%)**	**C_0 (mg/l)**	**Uptake (mg/g)**	**Rp (%)**
110	16,5	100	101	6,9	45,3

The sequence in terms of uptake values by the *E. coli* biofilm supported on kaolin was Fe > Cd > Ni > Cr. The worst biosorption behaviour obtained for chromium is justified by the anionic state. Comparing the results obtained for the cationic metals, better results were obtained for iron and can be justified with the higher electronegativity and reduced ionic radius which promote the penetration into the polymeric net of the biofilm. Considering the ions Cd and Ni, this last one has higher electronegativity, lower atomic weight and ionic radius and these characteristics allows good qualities for metal entrapment. However, better results were obtained for cadmium. A possible explanation for these unexpected results might be the xenobiotic effect of the metal, more accentuated in the nickel case, on the biofilm. In a system biofilm-kaolin both materials contribute to the biosorption performance and if the biofilm is affect by the toxic nickel ion, the biosorption performance is affect too.

It is possible to characterize biosorbents under various operational conditions through the modelling of equilibrium data and this point is essential for future industrial applications. Adsorption isotherms were experimentally determined for the biosorbent used (biofilm + kaolin), and results are shown in Figure 1. Three different models - Langmuir, Sips and Redlich-Peterson- were fitted to the experimental data and constants calculated for the best fit are presented in Table 2. For iron and for the range of initial concentrations tested, the whole metal was immediately and totally biosorbed so the concentration at equilibrium was always zero and consequently it is not possible to represent Ce (mg/l) vs Qe (mg/g). The best fit for chromium and for nickel was obtained with the Redlich-Peterson model isotherm and for cadmium the best fit was reached with the Sips model.

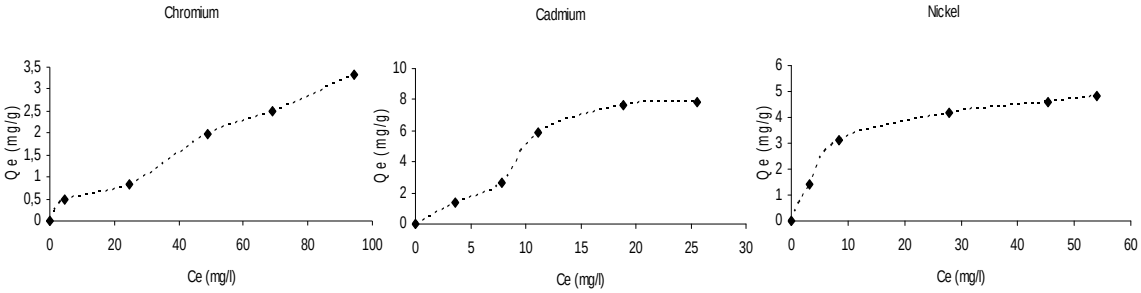

Figure 1- Adsorption isotherms for chromium, cadmium and nickel, at 37 ºC, using a biofilm of *Escherichia coli* supported on Kaolin.

Table 2- Adsorption isotherm constants for the isotherm best fit models, for Cr(VI), Cd(II) and Ni(II) onto a biofilm supported on Kaolin

Chromium				
Best fit model	K_R	a_R	β	R^2
Redlich-Peterson	0,615	8,629	0,143	0,984
Cadmium				
Best fit model	K_s	a_s	b_s	R^2
Sips	0,019	0,002	2,750	0,977
Nickel				
Best fit model	K_R	a_R	β	R^2
Redlich-Peterson	0,733	0,136	1	0,994

The FTIR spectra of unloaded and metal loaded *Escherichia coli* biomass in the range of 500–4000 cm^{-1} were taken to confirm the presence of functional groups that may be responsible for the biosorption process and are presented in Figure 2. As it may be seen, unloaded biomass displays a number of absorption peaks, reflecting the complex nature of the biomass. In the unloaded biomass spectrum, a peak at 3500–3200 cm^{-1} region is due to the stretching of the N–H bond of amino groups and indicative of

bonded hydroxyl group [40]. A change in peak position in the spectrum of the chromium and iron- loaded samples indicates the binding of chromium and iron with amino and hydroxyl groups. The absorption peaks at 2900–3000 cm^{-1} are ascribed to the asymmetric stretching of γC–H bond of the $–CH_2$ groups combined with that of the CH_3 groups [41]. The nickel and cadmium-loaded samples present slight changes in this region. In the unloaded spectrum, the γC=O of amide I and γNH/γC=O combination of the amide II bond were present at 1650 and 1544 cm^{-1}, respectively, indicating the presence of carboxyl groups. Interestingly, the 1544 cm^{-1} peak increased with the presence of chromium and iron suggesting an interaction of Cr and Fe with carboxyl groups. The peaks in the range 1300-1067 cm^{-1} are attributable to the presence of carboxyl and phosphate groups [42] and at 861 cm^{-1}, to the presence of aromatic –CH stretching peak [43]. Studies developed by Pradhan *et al.* [37] and Volesky (2007) [44] conclude that the main functional groups responsible for a biosorption process are the hydroxyl, carbonyl, carboxyl, sulfonate, amide, imidazole, phosphonate and phosphodiester groups, some of them present on the *Escherichia coli* biomass.

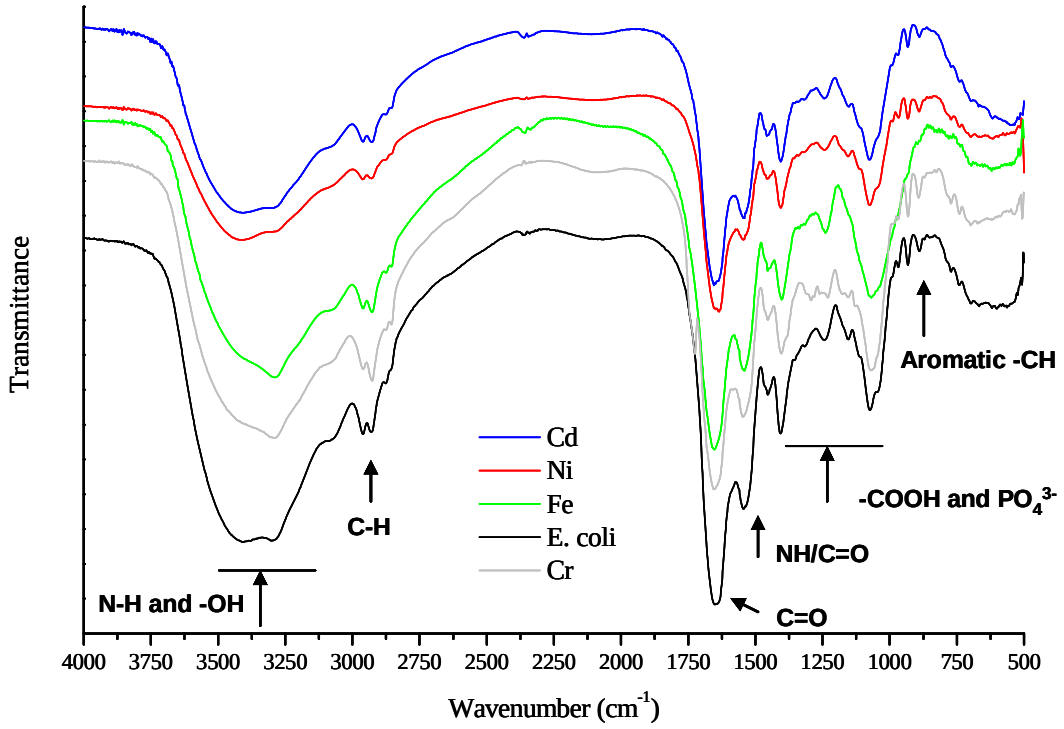

Figure 2- FTIR spectra of *Escherichia coli* before and after metal loading.

Acknowledgements

The authors would like to gratefully acknowledge the financial support of this project by the Fundação para a Ciência e Tecnologia, Ministério da Ciência e Tecnologia, Portugal (POCTI/CTA/44449/2002), financed by FEDER. Bruna Silva, Hugo Figueiredo and Bruna Fonseca thank FCT for a PhD grant and Cristina Quintelas thanks FCT for a Pos-Doc grant. The authors would like also to thank to Minas de Barqueiros, S.A. that gently offered the kaolin.

References

Tavares, M.T., Quintelas, C., Figueiredo, H., Neves, I. (2006). Comparative study

between natural and artificial zeolites as supports for biosorption systems. *Materials Science Forum*, 514-516, 1294-1298.

Turan, P., Dogan, M., Alkan, M. (2007). Uptake of trivalent chromium ions from aqueous solutions using kaolinite. *Journal of Hazardous Materials*, 148, 56-63.

Pradhan, S., Singh, S., Rai, L.C. (2007). Characterization of various functional groups present in the capsule of Microcystis and study of their role in biosorption of Fe, Ni and Cr. *Bioresource Technology*, 98, 595-601.

Park, D., Yun, Y-S., Park, J.M. (2008). XAS and XPS studies on chromium-binding groups of biomaterial during Cr(VI) biosorption. *Journal of Colloid and Interface Science*, 317, 54–61.

Kazy, S., Das, S.K., Sar, P. (2006). Lanthanum biosorption by a Pseudomonas sp.: equilibrium studies and chemical characterization. *Journal of Industrial Microbiology and Biotechnology*, 33, 773-783.

Pistorius, A. (1995). Biochemical applications of FT-IR spectroscopy. *Spectroscopy Europe*, 7, 8-15.

Tunali, S., Çabuk, A., Akar, T. (2006). Removal of lead and copper ions from aqueous solutions by bacterial strain isolated from soil. *Chemical Engineering Journal*, 115, 203-211.

Volesky, B. (2007). Biosorption and me. *Water Resource*, 41, 4017-4029.

Proceedings of the 10th International Chemical and
Biological Engineering Conference - CHEMPOR 2008
Braga, Portugal, September 4-6, 2008
E.C. Ferreira and M. Mota (Eds.)

Reactive dyestuff removal by cork residues

Isabel Torres, Ana Guimarães, Valentina M.F. Domingues*, Cristina M.F. Delerue-Matos
REQUIMTE /*Instituto Superior de Engenharia do Porto,* R. Dr. António Bernardino de Almeida, 431, 4200-072 Porto

Keywords: cork, adsorption, dyestuff
Topic: Suitable Integration of life sciences & engineering

Abstract

The need of treating textile wastewaters is nowadays well known, not only concerning primary and secondary treatments for organic matter and suspended solids removal, but also a tertiary treatment, mostly for residual colour removal.

Considerable work has been carried out on the removal of colour from textile wastes through chemical coagulation, chemical oxidation and biological techniques and by adsorption. Adsorption appears to offer the best prospects over all the other treatment techniques.

Activated carbon is one of the most widely used adsorbents in wastewater treatment. However, this treatment needs a high investment and leads to high operation costs, due to the high price of the activated carbon and to the high wastewater flow rate always involved, which can be greatly increased when there are no regeneration units nearby, as in the case of Portugal. This work intends to explore the adsorption capacity of cork (*Quercus suber L.)* granules to remove dye (Rouge Maxilon), from contaminated waters. The cork adsorption capacity has been studied for other pollutants (Domingues *et al*. 2007).

Adsorption batch assays with dye, using granulated cork with several different sizes, several pH values and different temperatures, were performed, either to determine the equilibrium time or the efficiency of the removal.

The results obtained have demonstrated that the cork is a cheap, efficient natural removing agent for Red Maxilon that may be explored in future to act as a treatment of wastewaters in textile industry.

1 Introduction

Among the different pollutants of aquatic ecosystems, dyes are a large and important group of industrial group in industrial chemicals. Most of this quantity is used in the textile industry and the dyes in use include many different compounds and their environment behaviour is largely unknown. Most dyes and pigments are considered either inert or non-toxic, although some are not totally innocuous. Interest in the environmental behaviour of dyes is prompted primarily by concern over their possible toxicity.

Concern as increased about the long-term toxic effects of water containing these dissolving pollutants. The wastewaters discharged from dyeing processes are highly colored, hot and alkaline, containing high amounts of dissolved solids (Rajeshwarisivaraj et al., 2001). Textiles wastewaters are significantly less biodegradable than many other carbonaceous wastes because the structures of the dye residues are designed to resist environmental conditions. There is a wide range in pH, making conventional biological and chemical treatment processes troublesome. The disposal of colored wastes such as dyes and pigments into receiving water damages the environment as they are toxic to aquatic life. In many cases,

* Corresponding author. Tel + 351-228340500. E-mail:vfd@isep.ipp.pt

the treatment of textile wastewaters takes places at municipal wastewater treatment plants using the activated sludge process.

Sorption is considered to be the primary removal mechanism for most dyes (Basibuyuk and Forster, 2003). A wide range of carbons exist for the possible use as adsorbents. A large number of activated carbons have been prepared from different raw materials, as coconut shells, rice husks, nut shells, peat moss and peat. Each has its own applications and limitations. Commercially available activated carbon is expensive. Taking this in account it is better to find out low-cost adsorbents to be used in this field.

Cork has already been studied to solve environmental issues. Chubar et al (Chubar et al., 2003) used cork biomass as sorbent for copper, zinc and nickel. Carvalho et al (Carvalho et al., 2003) produced activated carbon from cork waste to adsorb gas components. Cork residues has been used to adsorb pesticides from water (Domingues et al., 2005; Domingues et al., 2007). Cork industry creates an enormous volume of waste (specially particles with very small dimensions). The chemical composition of cork is described as suberin, 39%; lignin 22%; polysaccharides 18%; extractives 15% and ash 1% (Pereira, 1988).

In this work, adsorption characteristics of red maxilon in various solutions conditions are investigated. All isotherms were obtained in pH controlled solutions. Some of the experimental isotherms are fitted by Langmuir model.

2 Materials and methods

Materials

Granulated cork from the same geographical area and therefore with similar composition, was supplied by Amorim & Irmãos, S.A., Portugal. The cork fractions with a particle diameter between 1-2 mm (1<d<2) and 3-4 mm (3<d<4) were separated and used. To remove exceeding powder, all the granulated material was washed with deionized water and dried at 105 ± 5ºC for 4 days.

The adsorbate used was the rouge maxilon kindly given by CIBA. All the solutions were prepared with deionised water. A solution of hydrochloric acid and sodium hydroxide was use for pH adjust.

Batch adsorption study

For kinetic studies, a series of Erlenmeyer flasks of 100 mL capacity containing 50 mL of dye solution of known initial concentration was shaken in a rotary shaker (75 rpm) with 0.2 g of cork 1<d<2 or 3<d<4.. Light was excluded to prevent photodegradation. An Erlenmeyer flasks without adsorbent was study simultaneously in each experiment to verify a stability of the dye.

The equilibrium adsorption experiments were conducted to obtain sorption isotherms with a equilibrium time of 1 weak. The adsorption capacities of both granules of cork were determined using batch experiments at 40ºC and 10ºC with a Thermostatcabinet Lovibond. The adsorption study of these adsorbates was achieved by varying the weight of adsorbent. Additionally, flasks with red of maxilon and without cork were used as controls.

At the end of adsorption period, the solution went trough a metal sieve. The filtrate was analyzed on a spectrophotometrically (UV Visible Recording Spectrophotometer 260 – Shimadzu). The adsorption values of dye before and after adsorption were measured at is maximum wavelength (530 nm).

Calibrations curves are obtained with standards of red maxilon solutions in pH 4 and pH 9. The amounts of dye adsorbed were calculated by subtracting final solution concentrations

from the initial concentration of aqueous solution. Blank solutions were used for each series of experiments.

$$q = (C_0 - C_e)\frac{V}{m} \qquad (1)$$

Where q is the red maxilon amount adsorbed per gram of cork, C0 and Ce is the initial and equilibrium concentration of dye in solution (mg/L), V is the volume of red maxilon (L) and m is the mass of adsorbent (g).

3 Results and discussion

Preliminary experiments showed that the effect of the time on the amount of dye in Erlenmeyer flaks without cork was neglible.

At equilibrium the adsorption process is considered to be a dynamic state in which the rate of the adsorption process equals that the desorption process. The studies to determine equilibrium time are represented in Figure 1.

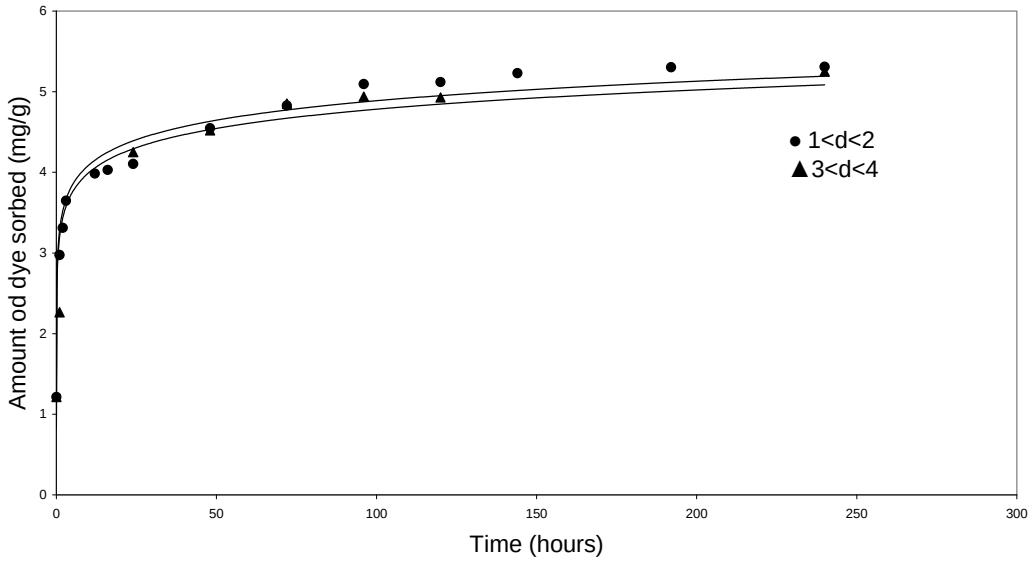

Figure 1. Equilibrium time determination of red maxilon in cork 1<d<2 and cork 3<d<4.

The equilibrium was reached after six days for both sorbents, denoting a slightly faster equilibrium for cork. An incubation period of a weak was adopted for all sorbents to ensure that equilibrium was reached. The sorption kinetics of cork correspond to the L type in the classification proposed by Giles et al (Giles et al., 1960), which means that as the adsorption sites are being occupied, it becomes increasingly more difficult for adsorbate molecules to find vacant sites.

Adsorption equilibrium is governed by several factors such as the nature of adsorbate and adsorbent as well pH and temperature (Dogan et al., 2008).

A plot of red maxilon quantity on the adsorbent against the equilibrium concentration of red maxilon in the solution at a constant temperature is commonly referred as an isotherm. It can

be said that the adsorption isotherm is the equilibrium relationship between the concentration in the fluid phase and the concentration in the adsorbent particle at a given temperature.

The experiment isotherms of red maxilon in cork residues with granule diameter of 3-4 mm and 1-2 mm at 10ºC and 40ºC are shown in Fig 2 and Fig 3 respectively.

It is clearly seen from the experimental results that red maxilon was removed more effective by cork at pH 4 than pH 9.

Although the red maxilon adsorption isotherms reveal adsorption at pH 4 all are non-linear indicating the sorption occurred by a physical adsorption mechanism.

Langmuir model was used to analyze the adsorption behaviour and to determine the red maxilon adsorption capacity on cork with different sizes. For a single solute system, Langmuir isotherm may be expressed as

$$q = \frac{q_m K_L C_{eq}}{1 + K_L C_{eq}} \qquad (2)$$

where *qm* is *q* for a complete monolayer, *KL* is the Langmuir constant and *Ceq* is the concentration of red maxilon in equilibrium.

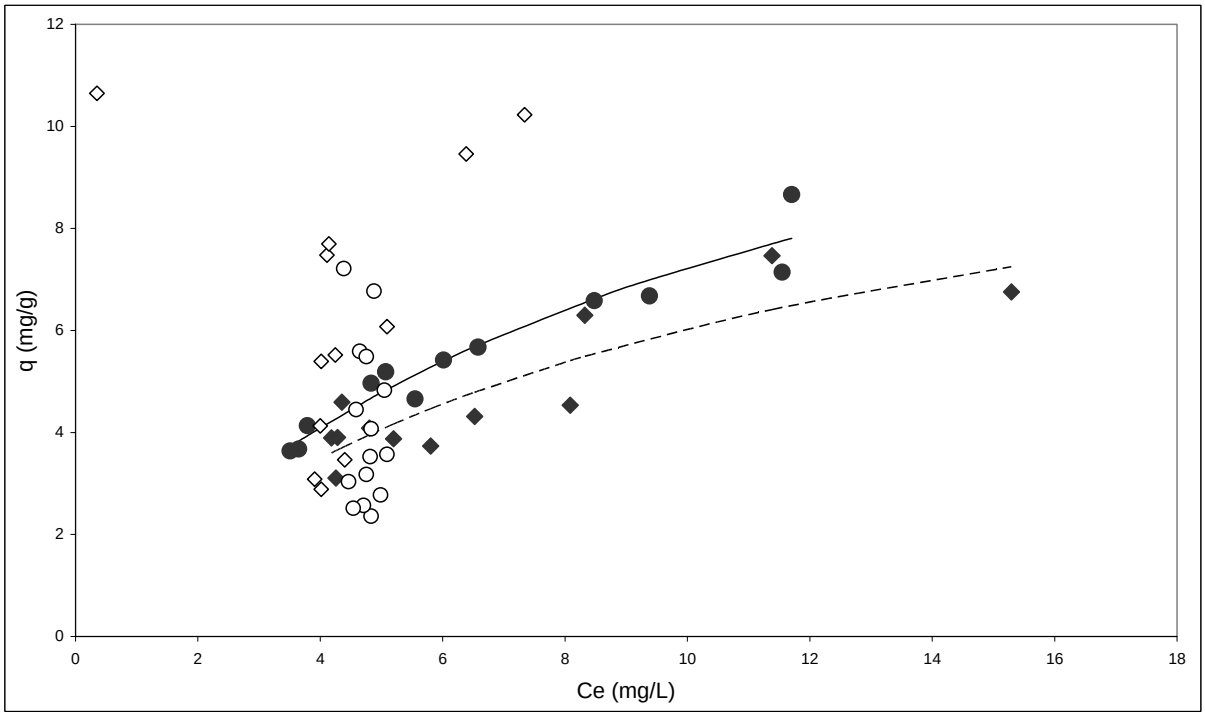

Figure 2. Experimental isotherm at 10ºC of red maxilon on cork with diameter 3-4 (♦) and 1-2 mm (●) at pH 4 fitted by Langmuir model and cork 3-4 (◊) and 1-2 mm (○) at pH 9.

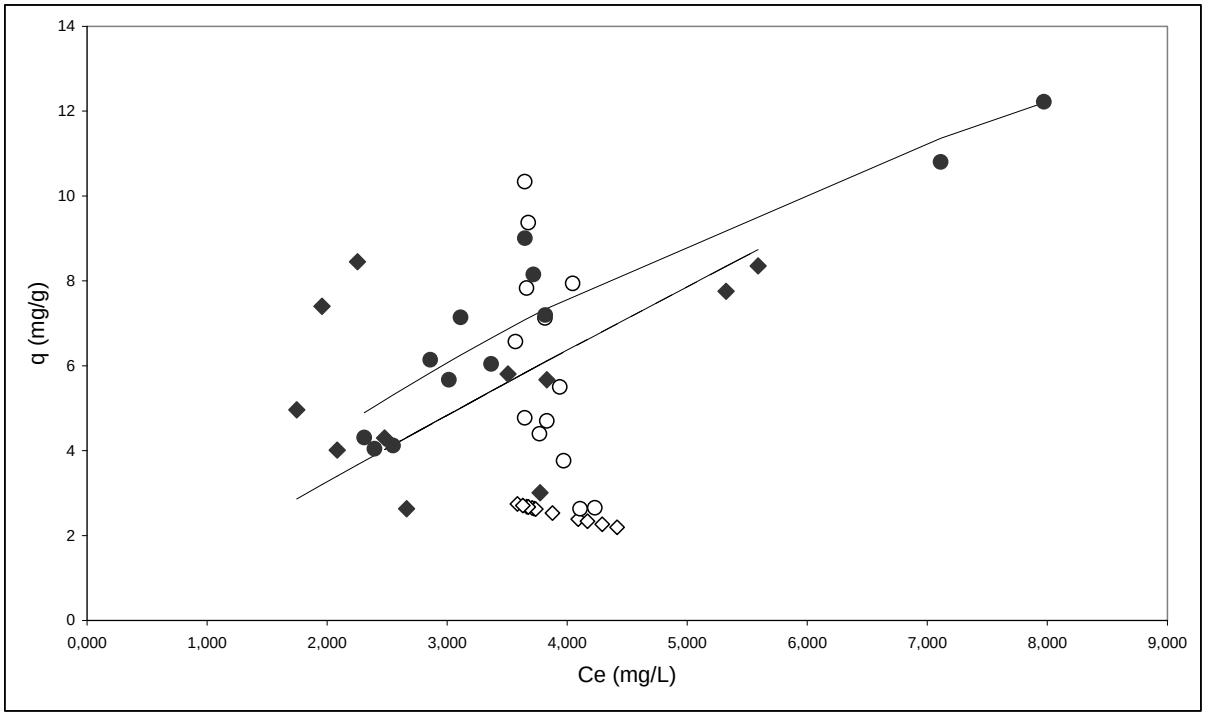

Figure 3. Experimental isotherm at 40ºC of red maxilon on cork with diameter 3-4 (♦) and 1-2 mm (●) at pH 4 fitted by Langmuir model and cork 3-4 (◊) and 1-2 mm (○) at pH 9.

The above equation (2) can be modified to give

$$\frac{1}{q} = \frac{1}{q_m} + \frac{1}{K_L q_m C_{eq}} \quad (3)$$

A plot of *1/q* against *1/Ceq* will give a straight line for the isotherm if the relationship can be applied. Consequently, the *qm* can be found from the intercept of the stright line. It is common to describe the fit of linear regression in term of R^2, which is the square of correlation coefficient. If the R^2=1, then the fit is perfect, but R^2 is always less than unity (Wibulswas, 2004).

Another possibility to achieve *qm* is to use the solver tool from Excel®, with minimization the differences between the *q* experimental and *q* with Langmuir equation.

In Table 1. are represented the *qm* achieved by minimization the differences and by linearization.

Table 1. Red maxilon adsorption capacity by means of Langmuir isotherm

Adsorbent	pH	Temperature (ºC)	Adsorption capacity by minimization of differences (mg/g)	Adsorption capacity by linearization (mg/g)	R^2
Cork 1-2 mm	4	10	14.75	15.53	0.956
Cork 3-4 mm	4		11.73	12.53	0.806
Cork 1-2 mm	9		Not fit	Not fit	
Cork 3-4 mm	9		Not fit	Not fit	
Cork 1-2 mm	4	40	31.20	91.75	0.991
Cork 3-4 mm	4		129,37	33.12	0.291
Cork 1-2 mm	9		Not fit	Not fit	
Cork 3-4 mm	9		Not fit	Not fit	

The *qm* data obtained by linearization and by minimization of the differences are consistent for pH 4, at 10ºC for cork 1-2 mm and cork 3-4 mm. Cork 1-2 with a *qm* higher than cork 3-4, that means the available surface are to adsorption is essential the external one.
The results show that adsorption increases with temperature, nevertheless cork 3-4 obtain a higher *qm* it does not fit so well than the other data (R^2=0.291).

4. Conclusions

The adsorption of red maxilon on cork was endothermic indicating that a higher temperature would be favourable for carrying out the removal of dye, which is especially adequate for textile water treatment.
However the binding of red maxilon to cork residues was poor at pH 9. Only the adsorption isotherm at pH 4 is fitted by Langmuir model. The cork particle 1<d<2 shows a higher adsorption than cork particle 3<d<4.
The results of present investigation show that cork particles, low cost material, have suitable adsorption capacity with regard to the removal of red maxilon from its aqueous solution. The cost and adsorption characteristics favour cork to be used as an effective adsorbent for removal the red maxilon from wastewater in Portugal.

References

Basibuyuk, M., and C.F. Forster. (2003). An examination of the adsorption characteristics of a basic dye (Maxilon Red BL-N) on to live activated sludge system. *Process Biochemistry*. 38, 1311-1316.

Carvalho, A.P., B. Cardoso, J. Pires, and M.B. de Carvalho. (2003). Preparation of activated carbons from cork waste by chemical activation with KOH. *Carbon*. 41, 2873-2876.

Chubar, N., J.R. Carvalho, and M.J.N. Correia. (2003). Cork biomass as biosorbent for Cu(II), Zn(II) and Ni(II). *Colloids and Surfaces a-Physicochemical and Engineering Aspects*. 230, 57-65.

Dogan, M., H. Abak, and M. Alkan. (2008). Biosorption of methylene blue from aqueous solutions by hazelnut shells: Equilibrium, parameters and isotherms. *Water Air and Soil Pollution*. 192, 141-153.

Domingues, V., A. Alves, M. Cabral, and C. Delerue-Matos. (2005). Sorption behaviour of bifenthrin on cork. *Journal of Chromatography A*. 1069, 127-132.

Domingues, V.F., G. Priolo, A.C. Alves, M.E. Cabral, and C. Delerue-Matos. (2007). Adsorption behavior of alpha-cypermethrin on cork and activated carbon. *Journal of Environmental Science and Health Part B-Pesticides Food Contaminants and Agricultural Wastes*. 42, 649-654.

Giles, C.H., T.H. Macewan, S.N. Nakhwa, and D. Smith. (1960). Studies in Adsorption .11. A System of Classification of Solution Adsorption Isotherms, and Its Use in Diagnosis of Adsorption Mechanisms and in Measurement of Specific Surface Areas of Solids. *Journal of the Chemical Society*, 3973-3993.

Pereira, H. (1988). Chemical-Composition and Variability of Cork from Quercus-Suber L. *Wood Science and Technology*. 22, 211-218.

Rajeshwarisivaraj, S. Sivakumar, P. Senthilkumar, and V. Subburam. (2001). Carbon from Cassava peel, an agricultural waste, as an adsorbent in the removal of dyes and metal ions from aqueous solution. *Bioresource Technology*. 80, 233-235.

Wibulswas, R. (2004). Batch and fixed bed sorption of methylene blue on precursor and QACs modified montmorillonite. *Separation and Purification Technology*. 39, 3-12.

Proceedings of the 10th International Chemical and
Biological Engineering Conference - CHEMPOR 2008
Braga, Portugal, September 4-6, 2008
E.C. Ferreira and M. Mota (Eds.)

Influence of airflow rate on soil remediation using Soil Vapour Extraction

J. T. Albergaria[1*], C. M. Delerue-Matos[1], M. C. M. Alvim Ferraz[2]
[1] REQUIMTE, Instituto Superior de Engenharia do Porto, Rua Dr. António Bernardino de Almeida 431, 4200-072 Porto, Portugal
[2] LEPÆ, Faculdade de Engenharia da Universidade do Porto, Rua Dr. Roberto Frias, 4200-465 Porto, Portugal

Keywords: Soil Vapour Extraction, Airflow rate, Soil, Volatile Organic compounds
Topic: Integration of life sciences & engineering

Abstract

The release of contaminants into the soil matrix produces a negative impact on soil quality, creating, in some cases, situations of risk to public health. Halogenated volatile organic compounds and the group constituted by benzene, toluene, ethylbenzene and xylene are common compounds found in contaminated sites. To remediate these sites several techniques can be used: biological processes (such as bioremediation or phytoremediation), thermal processes (such as incineration or thermal desorption) and physico-chemical processes (such as chemical oxidation or soil vapour extraction).

Soil Vapour Extraction (SVE) is one of the most used technologies that can be applied to soils contaminated with volatile or semi-volatile organic compounds in the unsaturated zone. It applies vacuum to the soil matrix, creating an airflow that transports the contaminants to extraction wells. The air circulation through the soil matrix produces mass transfer into the gas phase, due to free pollutant volatilization, desorption from the soil and dissolution from the aqueous phase. Before reaching the atmosphere, these vapours are usually treated to guarantee legal limits and air quality. The success of a soil vapour extraction project depends on several parameters including contaminant characteristics such as vapour pressure and solubility, soil properties such as natural porosity, permeability, organic matter or water contents and operational conditions like temperature or airflow rate.

Experiments previously carried out with two soils contaminated with cyclohexane allowed concluding that for air flow rates lower than 1.5 $cm^3\ s^{-1}$, at Standard Temperature and Pressure (STP), the remediation efficiency did not depend on the volume of gas passed through the soil, because the equilibrium between the pollutant and the different phases present in the soil was reached and the diffusion effects were avoided.

A laboratorial installation was developed and used to simulate soil remediation using SVE. The remediation process was monitored and the contaminant quantification performed by gas chromatography using a flame ionisation detector.

In this work, six typical petroleum contaminants were studied, allowing the establishment of operational SVE conditions for the remediation of frequently found contaminated soils. The influence of airflow rate on soil vapour extractions was evaluated for sandy soils contaminated with benzene, toluene, ethylbenzene, xylene, trichloroethylene and perchloroethylene. The main objective was to select the best airflow rate to remediate soil contaminated with the studied contaminants and under the contaminations range experimented.

The results obtained for SVE performed with airflow rates within 0.50 and 5.3 $cm^3\ s^{-1}$ (STP) in sandy soils contaminated with the selected pollutants allowed concluding that: a) the

* Corresponding author. Tel + 351-228-340500. E-mail:jta@isep.ipp.pt

remediation efficiencies were always higher than 90%, b) depending on the contaminant, the airflow rates should be lower than 1.2 - 1.9 $cm^3 s^{-1}$ (STP).

1 Introduction

Human activities caused in the last decades severe impacts on the environment, namely in soil. Handling and abusive use of petroleum products and pesticides and industrial activity are simple examples of situation that lead to soil remediation. Increasing efforts have been done in order to invert and remediate these situations. For each specific case of soil contamination it is essential to choose the most appropriate remediation technology and to preview the remediation time. From the balance of these two items the most applicable technology may be selected. Soil vapour extraction (SVE) is one of the most used *in situ* technologies that can be applied to soils contaminated with volatile and semi-volatile compounds in the unsaturated zone. It is based on application of vacuum to the soil matrix creating airflow that transports the contaminant to extraction wells and consequently out of the soil for prior treatment before release to the environment.

The success of a soil vapor extraction action is influenced by contaminant characteristics, soil properties and operational conditions. These conditions enhance the volatilization of the contaminant becoming more available and easy to extract (Chai and Miura, 2004). High porosity and high permeability also benefits SVE, mainly, due to their positive impact on the airflow rate through the soil (Poulsen et al, 1999). On the opposite situation contaminants with high solubility and soils with high contents of water or natural organic matter create more difficult conditions for SVE (Albergaria et al, 2006; Yoon et al, 2002), due to dissolution in the soil water or to the adsorption on the organic matter, which decrease the mass transfer between the gas phase and the soil matrix. The induced gas flow towards the extraction wells causes the evaporation of the nonaqueous liquid phase, the volatilization of contaminants dissolved in the pore water and the desorption of chemicals from the porous material, increasing the mobility and availability of the contaminant, consequently increasing the remediation efficiency (Kaleris and Croisé, 1997). The air circulation into the soil matrix is not homogeneous, being influenced by soil heterogeneities. Due to this, the air flows through paths of lower resistance, avoiding regions of lower permeability. These regions will not be crossed by the airflow and consequently will be remediated only through diffusion. Furthermore, these untreated regions can act as sources of contamination to surrounded remediated soils and groundwater (Reddy and Adams, 2001) leading to higher remediation times, lower efficiencies and more expensive processes. The remediation time of soils using soil vapor extraction is inversely proportional to the air flow rate, but to take full advantages of that relation, equilibrium between the pollutants and the different phases present in soil matrix is necessary, and slow diffusion effects should not occur. Even modest non-equilibrium and slightly slow diffusion effects can strongly affect the efficiency and cost of the remediation process (Albergaria et al, 2006). This work reports the study of the influence of the airflow rate on soil vapour extraction remediation time and efficiency in a sandy soil contaminated with benzene, toluene, ethylbenzene, xylene, trichloroethylene and perchloroethylene.

2 Materials and Methods

2.1 Materials

Pro-analysis Benzene and Perchloroethylene were obtained from Riedl-de-Haën; Toluene, Xylene and Ethylbenzene were obtained from Merck; Trichloroethylene was obtained from Fluka.

2.2 Apparatus and chromatography

An Ai Cambridge GC95 gas chromatograph equipped with a flame ionisation detector was used to the quantification of the contaminants. A Chrompack Hayesep Q 80-100 mesh (3m x ¼" x 4 mm) packed column was used. The injector and the detector were set at 230 ºC and the oven worked isothermically at 200ºC. Flame gases were air, at 270 cm^3 min^{-1}, and hydrogen at 30 cm^3 min^{-1}. The carrier gas was nitrogen at 30 cm^3 min^{-1}. The direct calibration method was used.

2.3 Soil preparation and characterization

The sandy soil was collected in different places of a beach of Oporto region in Portugal, being stored in appropriate vessels. This sandy soil was mainly constituted by silica and shell debris, with negligible amounts of clay and natural organic matter. The preparation of soils involved: a) washing till clean water was obtained; b) drying, at room temperature during 5 days and then at 110ºC for 24 hours; c) sieving in a 2 mm sieve to obtain a granulometric fraction of the soil with uniform physical and chemical properties; and d) adding deionised water to induce the 2% water content in the soil. International standard methodologies were used for the characterization of the soil, including the determination of apparent density, particle density, porosity, pH, and the contents of water and natural organic matter (Albergaria, 2003).

2.4 Equilibrium isotherms

Equilibrium isotherms relating the contaminant concentration in the gas phase with the total amount of contaminant in soil were used to calculate remediation efficiencies, only through the experimental determination of contaminant concentration in the gas phase. The equilibrium isotherms were obtained performing experiments in stainless steel columns. These experiments involved: i) introduction of the soil in the column; ii) soil contamination (ranges within 6 up to 200 mg kg^{-1}); iii) equilibrium establishment (at 296K from 24 to 48 hours, depending on the contaminant); and iv) determination of the concentration of the contaminant in the gas phase (C_{gas}) through gas chromatographic analysis. The equilibrium was reached when C_{gas} in different levels of the column was similar (less than 5% deviation).

2.5 Soil vapour experiments

To perform the SVE experiments, columns were prepared in a similar way of the used to the equilibrium isotherms. The only difference was the contamination of the soil that ranged from 250 to 500 mg Kg^{-1}. After the equilibrium establishment a vacuum pump created an airflow rate (ranging from 0.50 cm^3 s^{-1} to 5.4 cm^3 s^{-1} at standard temperature and pressure (STP)) measured with a flow meter. The flow passed through the soil column and then to a sampling system where the contaminated emissions were monitored by gas chromatography. Before reaching the atmosphere and to avoid atmospheric contamination, the contaminant was adsorbed in activated carbon. The remediation process was considered finished when C_{gas} was below 1.0 mg L^{-1}. This time was considered the remediation time.

3. Results

3.1 Soil characteristics

Table 1 shows the results of the characterization of the sandy soil. The clay content was under the detection limit.

Table 1 – Characteristics of the sandy soil (particle size <2mm).

Apparent density ($g\ mL^{-1}$)	Particle density ($g\ mL^{-1}$)	Porosity (%)	pH	Water content (%)	Natural organic matter content (%)
1.3	2.5	49	8.8	2.0	<0.02

3.2 Equilibrium isotherms

Figure 1 shows the equilibrium isotherms obtained for all the contaminants and the respective trend lines. These equilibrium isotherms allowed the prevision of the amount of contaminant in the soil matrix only through the determination of contaminant concentration in the gas phase.

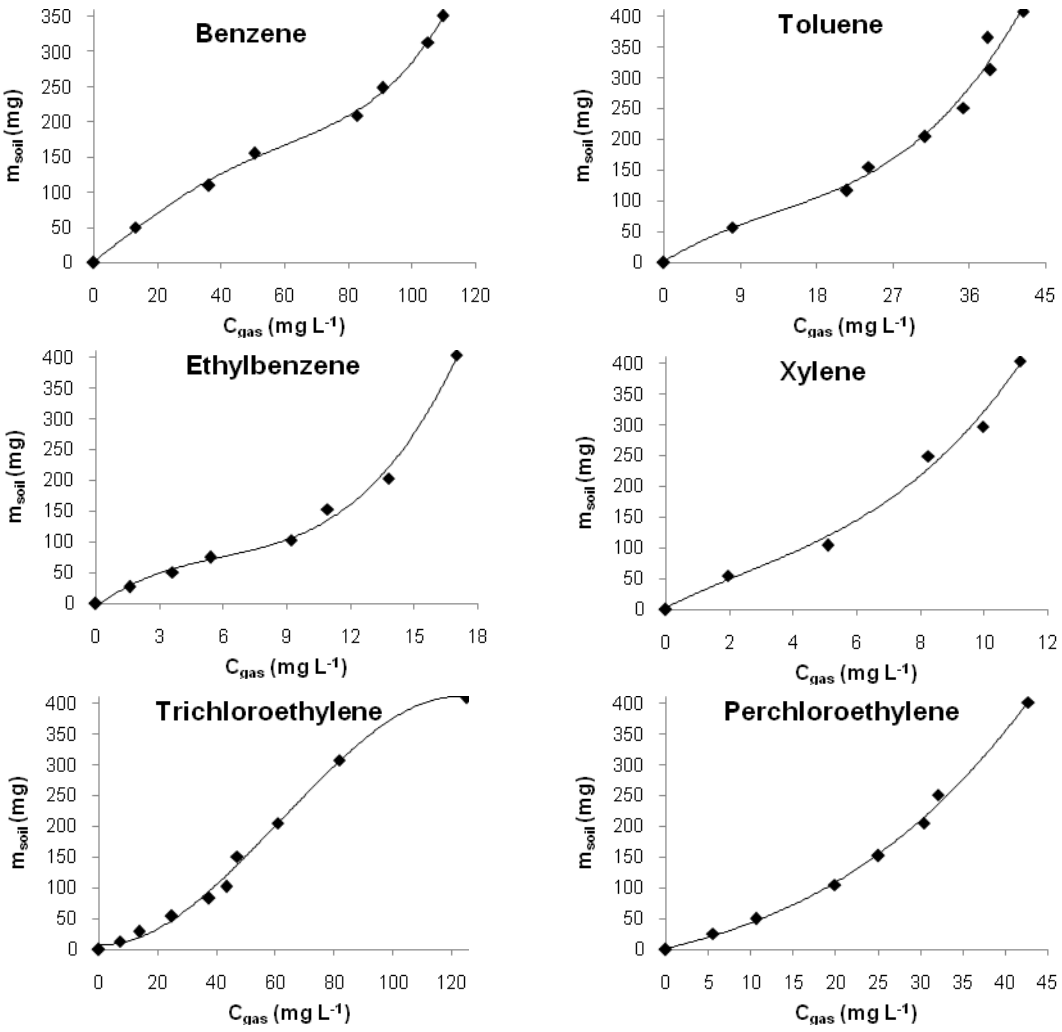

Figure 1 – Equilibrium isotherms for the different contaminants in a dry sandy soil.

3.3 Soil vapor extraction experiments

During the soil vapor extractions experiments the concentration of the contaminant in the emissions was monitored. When the concentration reached 1.0 mg L^{-1} the process was considered finished and the remediation time (tr) registered. The volume of air used (V) and the process efficiency (η) was then calculated, using equations 1 and 2 respectively, where Q is the airflow rate and t the time.

$$V = \int Q \, dt \qquad (1)$$

$$\eta = \frac{(m_{tot} - m_{rem})}{m_{tot}} \times 100 \qquad (2)$$

The results obtained in SVE experiments are presented in Figure 2. The results showed that for the prepared sandy soil the efficiencies were always above 90%, excepting SVE performed with PCE with the two highest airflow rates. These high values could be expected because the soil had undetectable amounts of organic matter, and consequently there were not enough strong bonding between the soil and the contaminants, leaving them more available to be extracted through SVE. Efficiencies increased for lower airflow rates indicating that equilibrium conditions favors contaminant extraction. The remediation time was inversely proportional to the airflow rate, showing that higher airflow rates allowed faster remediations.

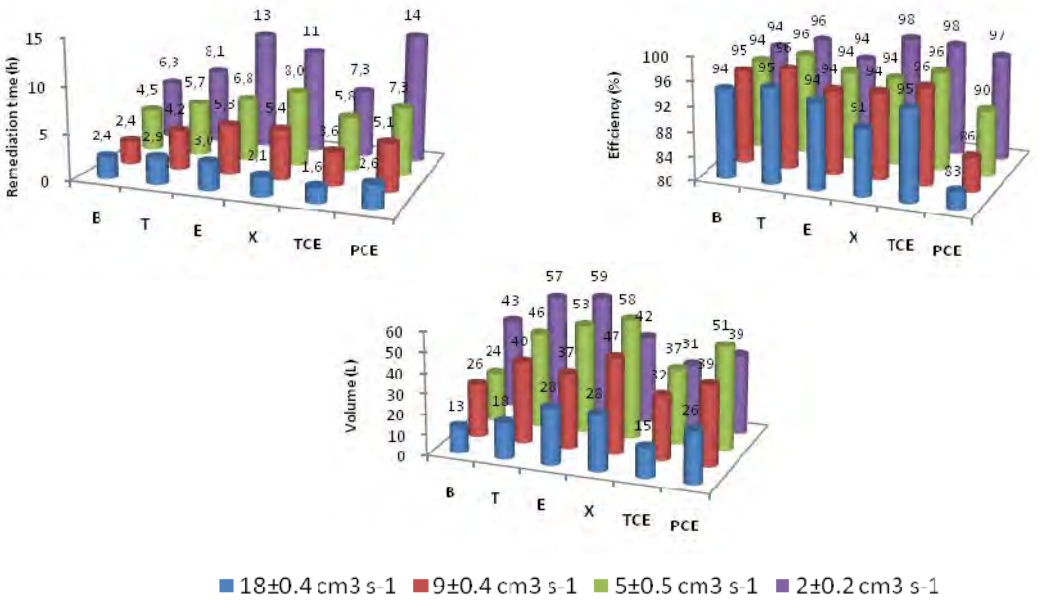

Figure 2 – Results obtained in the SVE experiments with sandy soils.

3.4 Selection of the most efficient airflow rate

All the results showed that the remediation time is inversely proportional to the air flow rate. Nevertheless, to take full advantage of airflow increase, equilibrium between the pollutants in the different phases must be reached and slow diffusion effects must be avoided. In these circumstances the remediation efficiency does not depend on the volume of air passed through the soil. To evaluate if those conditions were obeyed Figure 3 was constructed. It relates the remediation efficiency and the volume of gas passed through the column for the prepared soil. Two types of curves were observed: Trichloroethylene type (similar to xylene) where all curves are overlaid; and Toluene type (similar to benzene, ethylbenzene and perchloroethylene) where the curves tend to an equilibrium behavior.

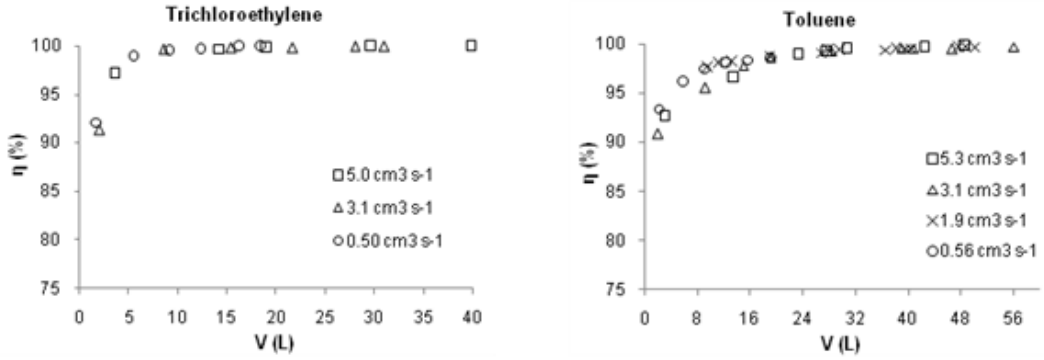

Figure 3 - Influence of airflow rate on the efficiency of SVE on the prepared soils (2% water content).

Attending to the curves obtained for all contaminants it was observed that for xylene and TCE the equilibrium was reached and slow diffusion effects were not observed for all the airflow rates used. For smaller volumes of air (smaller efficiencies) that behavior was reached for the other pollutants using flow rates smaller than 1.2 - 1.9 cm^3 s^{-1} (STP). Nevertheless, for higher efficiencies, flow rates of 5.3 cm^3 s-1 (STP) guarantee equilibrium and negligible diffusion effects.

4. Conclusions

The results obtained for SVE performed with airflow rates within 0.50 and 5.3 cm^3 s^{-1} (STP) in sandy soils contaminated with benzene, toluene, ethylbenzene, xylene, trichloroethylene and perchloroethylene allowed concluding that:

a) The remediation efficiencies were always higher than 90%;
b) For xylene and TCE the equilibrium was reached and slow diffusion effects were not observed for all the airflow rates used. For smaller volumes of air (smaller efficiencies) that behavior was reached for the other pollutants using flow rates smaller than 1.2 - 1.9 cm^3 s^{-1} (STP).

Acknowledgements

The authors are grateful to Fundação para a Ciência e Tecnologia (Projecto POCI/AMB/61315/2004 and PTDC/ECM/68056/2006) for the material support for this work.

References

Alvim-Ferraz, M.C.M., Albergaria, J.T., Delerue-Matos, C. (2006). Soil Remediation Time to Achieve Clean-Up Goals: II: Influence of natural organic matter and water contents. Chemosphere, 64, 817-825.

Chai, J.C., Miura, N. (2004). Field vapor extraction test and long-term monitoring at a PCE contaminated site. Journal of Hazardous Materials, 110, 85-92.

Kaleris, V., Croisé, J. (1997). Estimation of cleanup time for continuous and pulsed soil vapour extraction. Journal of Hydrology, 194, 330-356.

Poulsen, T.G., Moldrup, P., Yamaguchi, T., Schjonning, P., Hansen J.A. (1999). Predicting soil-water and soil – air transport properties and their effects on soil-vapour extraction efficiency. Ground Water Monitoring and Remediation, 19, 61-70.

Reddy, K.R., Adams, J.A. (2001). Effects of soil heterogeneity on airflow patterns and hydrocarbon removal during in situ air sparging. Journal of Geotechnical and Geoenvironmental Engineering, 127, 234-247.

Yoon, H., Kim, J.H., Liljestrand, H.M., Khim J. (2002). Effect of water content on transient nonequilibrium NAPL-gas mass transfer during soil vapour extraction. Journal of Contaminant Hydrology, 54, 1-18.

Proceedings of the 10th International Chemical and
Biological Engineering Conference - CHEMPOR 2008
Braga, Portugal, September 4-6, 2008
E.C. Ferreira and M. Mota (Eds.)

Relative hydrophobicity of (PEG or Ucon)-salt ATPSs

Sara C. Silvério[1,2], Pedro P. Madeira[1,2], Oscar Rodríguez[1], José A. Teixeira[2], Eugénia A. Macedo[1*]

[1] LSRE/LCM – Laboratory of Separation and Reaction Engineering, Faculdade de Engenharia da Universidade do Porto, Rua Dr. Roberto Frias, 4200-465 Porto, Portugal.

[2] IBB – Institute for Biotechnology and Bioengineering, Centre of Biological Engineering, University of Minho, Campus de Gualtar, 4710–057 Braga, Portugal.

Keywords: aqueous two-phase systems, partition coefficient, hydrophobicity, amino acids
Topic: Integration of life sciences & engineering.

Abstract

Aqueous Two-Phase Systems (ATPSs) are biphasic systems composed mainly by water. ATPSs are obtained upon mixing of two aqueous solutions of certain polymers or a polymer and a salt (above certain critical conditions, e.g. concentration, temperature). These systems are commonly indicated for the extraction of biomolecules. In this work, the partition coefficients for a series of five dinitrophenylated amino-acids (ranging from glycine to amino-caprylic acid) were determined experimentally in five different polymer-salt ATPSs (polymers: PEG or Ucon; salts: Na_2SO_4, Li_2SO_4 or $(NH_4)_2SO_4$) at 23ºC. Values of the free energy of transfer of a methylene group, $\Delta G(CH_2)$, for the five ATPSs were obtained from the partition coefficients and compared with $\Delta G(CH_2)$ previously obtained for PEG-Na_2SO_4 (Rodríguez et al., 2007). Ucon-salt ATPSs presented higher values of $\Delta G(CH_2)$ than the corresponding PEG-salt systems, witch indicates that the Ucon-rich phase is more hydrophobic than the PEG-rich phase.

1 Introduction

Aqueous Two-Phase Systems (ATPSs) are biphasic systems composed mainly by water. ATPSs are obtained upon mixing of two aqueous solutions of certain polymers or a polymer and a salt (above certain critical conditions, e.g. concentration, temperature). These systems are regarded as a powerful extraction technique for biotechnology because each phase is predominantly composed of water (> 80%) and provide a gentle environment for the partitioning of sensitive biomaterials. For over 40 years ATPSs have been used for the purification and recovery of biological solutes such as proteins, amino acids, lipids, nucleic acids, viruses, plant and animal cells, etc. In the last 10 years ATPSs formed by thermo-separating polymers have been successfully used for the separation and purification of different types of biomolecules with considerable advantages in the recycling of the polymers (Pereira et al. 2003). Thermo-separating polymers, such as Ucon, are polymers whose solubility in water changes drastically with temperature and thus, can be easily recovered from the aqueous solution (and re-used).

Although the potential of ATPSs is well known, the wide use of this technology is partially limited by the lack of a clear comprehension of the factors and mechanisms that govern the distribution of solutes in ATPSs. Therefore, all attempts to obtain more information that allows understanding and predicting the behaviour of a solute are extremely important.

* Corresponding author. Tel + 351-22-508-1653. E-mail: eamacedo@fe.up.pt

Among the studied solvent properties of ATPSs, the free energy of transfer of a methylene group between the coexisting phases, $\Delta G(CH_2)$, has been shown (Zaslavsky, 1995; Willauer et al., 2002) to be useful for the characterization of ATPSs. $\Delta G(CH_2)$ represents the affinities of the phases for a CH_2 group and is considered as a measure of the relative hydrophobicity of the phases. Hydrophobic interactions are critical for protein stability and thus, may play an important role in the partitioning of proteins in ATPSs.

In this work, $\Delta G(CH_2)$ for five different polymer-salt ATPSs are obtained from the experimental partition coefficients (K) of a series of dinitrophenylated amino-acids (DNP-amino-acids) at 23 ºC.

2 Experimental

Preparation of ATPSs: Biphasic systems were prepared at 23 ºC mixing suitable amounts of water and stock solutions of the polymers (PEG or Ucon) and the salts (Na_2SO_4, Li_2SO_4 or $(NH_4)_2SO_4$) in eppendorf tubes. The total weight of all systems was approximately 1.2 g.

Partition coefficients: The partition coefficients of the five DNP-amino-acids (*N*-(2,4-dinitrophenyl)glycine, *N*-(2,4-dinitrophenyl)-L-alanine, *N*-(2,4-dinitrophenyl)-DL-*n*-valine, *N*-(2,4-dinitrophenyl)-DL-*n*-leucine and *N*-(2,4-dinitrophenyl)-DL-α-amino-*n*-caprylic acid) were obtained adding different amounts of a given DNP-amino-acid stock solution (from 0 to 100 mg) to six replicates of the ATPSs with the same feed composition (table 1). The corresponding amount of water (ranging from 100 to 0 mg) was also added to keep all compositions constant except the solutes. The components were vortex mixed for 2 minutes and then centrifuged at 10^4 r.p.m. for 15 minutes to achieve phase separation. Samples of each phase were withdrawn, conveniently diluted, and their absorbance at 362 nm was measured. Partition coefficients were calculated as the slope of the straight line obtained when comparing the concentration (mg/mL) in the polymer-rich phase against that in the salt-rich phase, corrected with the corresponding dilution factor (DF):

$$K = \frac{Abs(polymer) \times DF_{polymer}}{Abs(salt) \times DF_{salt}} \quad (1)$$

Table 1: Tie-line feed compositions for partitioning experiments, in mass fraction

System	Salt	Polymer
PEG-Na_2SO_4	0.0727	0.1186
PEG-Li_2SO_4	0.1000	0.1400
PEG-$(NH_4)_2SO_4$	0.1100	0.1250
Ucon-Na_2SO_4	0.0413	0.1676
Ucon-Li_2SO_4	0.0570	0.1200
Ucon-$(NH_4)_2SO_4$	0.0650	0.1260

3 Results and Conclusions

The phase diagrams of the biphasic systems used in this work were previously obtained experimentally at 23ºC: PEG- Na_2SO_4 (Rodríguez et al., 2007), PEG-Li_2SO_4, Ucon-Na_2SO_4, Ucon-Li_2SO_4 (Silvério et al., 2008) and Ucon-$(NH_4)_2SO_4$ (Pereira et al., 2004). The phase diagram for the system PEG-$(NH_4)_2SO_4$ was obtained from the literature (Zaslavsky, 1995).

The logarithms of the partition coefficients (ln *K*) as a function of the average number of equivalent methylene groups, $n(CH_2)$, in the aliphatic side-chain of the homologous DNP-amino-acids are shown in figure 1.

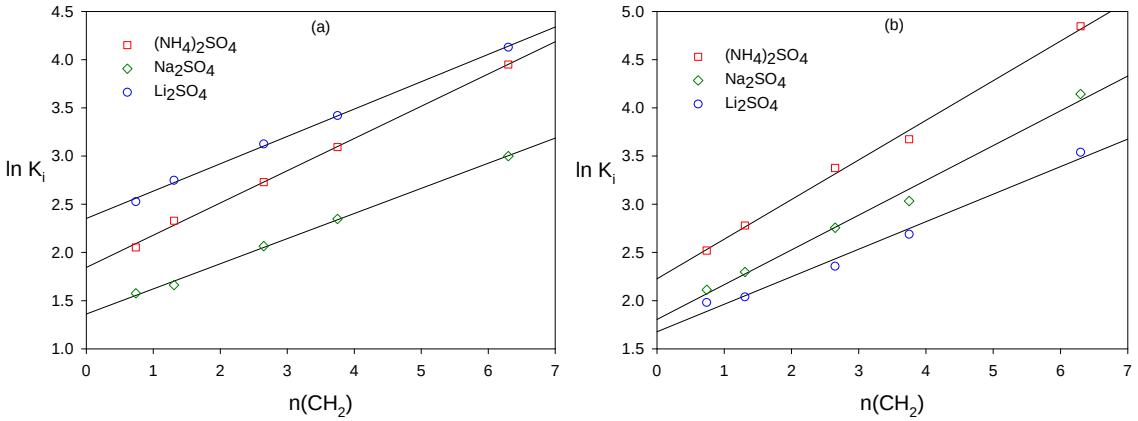

Figure 1: Logarithm of partition coefficients for a series of DNP-amino-acids in (a) PEG-salt and (b) Ucon-salt ATPSs at 23 ºC. Lines are linear regressions of experimental data.

The linearity observed in figure 1 is described as:

$$\ln K = C + E \times n(CH_2) \tag{2}$$

where *C* and *E* are constants which have been previously described in detail (Zaslavsky, 1995). Parameter *E* is a measure of the difference between the different affinities of the two phases for methylene groups, i.e., a measure of the relative hydrophobicity of the phases. Both parameters *C* and *E* were obtained by linear regression. Parameter *E* is related to the free energy of transfer of a methylene group between the phases:

$$\Delta G(CH_2) = -R \times T \times E \tag{3}$$

with *R* being the universal gas constant and *T* the absolute temperature.

$\Delta G(CH_2)$ values calculated from the partition coefficients of the five DNP-amino-acids in the five polymer-salt ATPSs using equations (2) and (3) (Zaslavsky, 1995) are presented in Table 2 together with values from literature (Rodríguez et al., 2007) for comparison purposes.

Table 2: Comparison of $\Delta G(CH_2)$ for six ATPSs at 23ºC

System	**$-\Delta G(CH_2)$, kcal/mol**
PEG-Na_2SO_4	0.153*
PEG-Li_2SO_4	0.167
PEG-$(NH_4)_2SO_4$	0.196
Ucon-Na_2SO_4	0.212
Ucon-Li_2SO_4	0.179
Ucon-$(NH_4)_2SO_4$	0.242

* from Rodríguez et al. (2007).

Ucon-salt ATPSs provide higher values of $\Delta G(CH_2)$ than the corresponding PEG-salt systems. This fact indicates that the Ucon-rich phase is more hydrophobic than the PEG-rich phase. The same conclusion can be obtained from the direct inspection of the PEG and Ucon chemical structure: PEG is an ethylene oxide homopolymer while Ucon is a random copolymer of ethylene oxide and propylene oxide monomers (larger alkyl chain).

The higher relative hydrophobicity of the Ucon-rich ATPSs suggests a more efficient biphasic separation system, with lower cross-contamination between the equilibrium phases. The use of thermo-separating polymers, like Ucon, provides thermal phase separation and simplifies the recycling of polymers. When heated above the critical temperature (about 50ºC) Ucon suffers phase separation into one separate polymer enriched phase and one aqueous solution (Persson et al., 2000). This results in a more suitable ATPSs for use in large scale, continuous processes: Ucon can be recovered and recycled, with a reduction in the production costs.

References

Pereira, M., Wu, Y.-T., Madeira, P.P., Venâncio, A., Macedo, E.A., Teixeira, J.A. (2004). Liquid-liquid equilibrium phase diagrams of new aqueous two-phase systems: Ucon 50-HB5100 + Ammonium sulfate + water, Ucon 50-HB5100 + poly(vinyl alcohol) + water, Ucon 50-HB5100 + hydroxypropyl starch + water, and poly(ethylene glycol) 8000 + poly(vinyl alcohol)+ water. *Journal of Chemical and Engineering Data*, 49, 43-47.

Pereira, M., Wu, Y.-T., Venâncio, A., Teixeira, J.A. (2003). Aqueous two-phase extraction using thermoseparating polymer: a new system for the separation of endo-polygalacturonase, *Biochemical Engineering Journal*, 15, 131–138.

Persson, J., Johanson, H.O., Galaev, I., Mattiasson, B., Tjerneld, F. (2000). Aqueous polymer two-phase systems formed by new thermoseparating polymers, *Bioseparation*, 9, 105–116.

Rodriguez, O., Silvério, S.C., Madeira, P.P., Teixeira, J.A., Macedo, E.A. (2007). Physicochemical characterization of PEG8000-Na2SO4 aqueous two-phase system. *Industrial & Engineering Chemistry Research*, 46, 8199-8204.

Silvério, S.C., Madeira, P.P., Rodriguez, O., Teixeira, J.A., Macedo, E.A. (2008). ΔG(CH2) in PEG-Salt and Ucon-Salt Aqueous Two-Phase Systems. *Journal of Chemical and Engineering Data*, DOI: 10.1021/je800154y.

Willauer, H.D., Huddleston, J.G., Rogers, R.D. (2002). Solvent properties of aqueous biphasic systems composed of polyethylene glycol and salt characterization by free energy of transfer of a methylene group between the phases and by linear solvation energy relationship. *Industrial & Engineering Chemistry Research*, 41, 2591-2601.

Zaslavsky, B.Y. (1995). Aqueous two-phase partitioning, Marcel Dekker Inc., New York.

Proceedings of the 10th International Chemical and
Biological Engineering Conference - CHEMPOR 2008
Braga, Portugal, September 4-6, 2008
E.C. Ferreira and M. Mota (Eds.)

Biofilms Formation and Biocorrosion in Coupons Exposed in Marine Environment

[1]Maria Alice G. de Andrade Lima, [2]Sara H. de Oliveira, [1]Lívia A. Santos, [1]Glória Mª Vinhas, [2]Severino L. Urtiga F., [1]Alice Alexsandra S. Vieira, [1]Mitsue M. Nakazawa, [3]Francisca Pessoa de França.

[1-2]Universidade Federal de Pernambuco – Departamentos de Engenharia Química e Eng. Mecânica; Av. Prof Artur de Sá, S/N - Cidade Universitária, Recife – PE, Brazil. CEP: 50740-521. E-mail: magalufpe@yahoo.com.br

[3]Universidade Federal do Rio de Janeiro – Departamento de Engenharia Bioquímica – Escola de Química, Ilha do Fundão, Rio de Janeiro – RJ, Brazil.
E-mail: fpfranca@eq.ufrj.br

Keywords: biocorrosion, biofilm, carbon steel AISI 1020, stainless steel AISI 304L

Abstract

The biocorrosion study attract numerous investigators due to necessity of developing technologies that aims to increase the lifetime of materials used in industries, or the development of new more resistant materials (VIDELA, 2005). So that such fact occurs is necessary a deeper knowledge regarding the mechanisms that involve the formation of biofilms as well as the involved microorganisms in this process, considering the variety of microorganisms species of different regions (FRANÇA et al. 2000). It is estimate that 90% of the microorganisms of the planet live under the form of biofilms and that almost does not exist no surface that is not or it cannot come to be colonized for bacteria (CHARACKLIS and MARSHALL, 1990). This work had for objective to study the biocorrosion in a static system using sea water from a located Thermoelectric Plant in SUAPE-PE, Brazil.

Introduction

The microbiological corrosion or biocorrosion corresponds to the deterioration of metallic materials in consequence of the activity of a variety of microorganisms. During the microbial metabolism they generate aggressive substances, modifying the interface metal/solution that can induce, speed up or inhibit the anodic or cathodic process that controls the corrosion reaction (NATISHAN et al., 1999)

The biocorrosion mechanism involves the growth of microorganism with formation of biofilm wich promotes an increasing in the corrosive process in metallic surface. Generally biofilms is constituted by immobilized cells on the substratum and extracellular polymers produced by the microorganisms (BEECH et al., 2005)

Some metallic substances tend to reach been of lesser energy, changed into metallic oxide or sulfites, what it justifies the intense research to solve the biocorrosion problem. Amongst metals the stainless steel is nobler than the carbon steel, however, still is considered an ideal substratum for the microorganisms settling. Therefore this is normally susceptive to the corrosion located in way contends chlorides (VIDELA, 2005).

In this work the process of biocorrosion was evaluated in the carbon steel AISI 1020 and stainless steel AISI 304L in static system, having as electrolyte the water of the sea proceeding from the port region of SUAPE-PE-BRAZIL.

Materials and methods

Materials

Two types of coupons had been used: carbon steel AISI 1020 and stainless steel AISI 304L, with dimensions 30x25x 3mm and 50 x 50 x 2,5mm respectively.

Treatment of metallic coupons

The metallic coupons had been previously treated before each experiment, through abrasive cleaner with micron glass spheres for removal of incrustations adhered in the surface, treated with isopropyl alcohol for removal of fats, and later treated with acetone. After drying for 24 hours, the coupons had been weighed to tenth of milligram and used in the experiments (TORRES, 2005).

Process Fluid

The sea water samples had been always collected in the same local (SUAPE-PE-BRAZIL) and analyzed under the microbiological aspect.

Microbiologic analyses

I - Quantification of Aerobic Bacteria - they had been quantified through the technique (MPN) method, using saline solution (35,9g/L NaCl) for the dilutions. The incubation was at 30±1ºC for 48 hours (TORRES, 2005).

II - Quantification of *Pseudomonas aeruginosa* - had been quantified through two techniques; (MPN) method for analysis of the planctonics microorganisms, with presumptive assay in medium Asparagine (96h and 35ºC) and confirmative assay in medium Acetamide (48h and 35ºC). The analysis of the *Pseudomonas* sessile was made through Colony Forming Unit (UFC), using the technique "pour-plate", in plates of Petri contends medium for isolation of *Pseudomonas* (*Pseudomonas* isolation agar). The determination of the cellular growth was made after incubation at 30±1ºC for 48 hours (SILVA et al., 2005).

III – Quantification of the Iron-Reducing Bacteria - had been quantified by the technique (MPN), using medium ammoniac ferric citrate, incubation at 30±1ºC for 14 days, protected from the light. The formation of a red coloration caused for the iron oxide formation, characterized the growth of these microorganisms (TORRES, 2005).

IV - Quantification of Anaerobic Bacteria - had been quantified by the technique (MPN) using bottles 10mL of capacity, contend 9,0mL of fluid thioglycollate medium, purged with nitrogen during 20 minutes and 1,0mL of the reducing solution with the inoculum. The incubation was at 30±1ºC for 28 days (TORRES, 2005).

V - Quantification of Sulfate-Reducing Bacteria (SRB) - had been done by the technique (MPN), in the medium modified Postgate E, with incubation at 30±1ºC in the period of 28 the 45 days. The black coloration is consequence of the formation of deposits of iron sulfite (TORRES, 2005).

VI - Quantification of Filamentous Fungi - These microorganisms also was quantified through the Colony Forming Unit (UFC), using the technique "pour-plate", in medium Sabouraud. The incubation was at 30±1°C for 72 hours (TORRES, 2005).

To evaluate the percentage of the microbiological corrosion in coupons was done sterile test with addition of 0.5% of sodic azide.

Biocorrosion Test

The experiments had been done in open static system in glass reactor with dimensions of 50 x 25 x 30 cm³ and useful volume of 34L.

The metallic coupons had been exposed in the sea water and the monitorament of these was made with the exchange of water, each 15 days. Biocupons had been analyzed through loss of mass, rate of corrosion and sessile microorganisms. Also was determined planctonics microorganisms during the process.

Loss of mass and rate of corrosion

The coupons had been weighed before the treatment, when they had been bathed in acid chloridric (26%) solution for 5 seconds, washed in distilled water, neutralized with solution of NaOH 10% (p/v) during 5 seconds and, washed again in distilled water. Finally, the coupons had been immersed in isopropyl alcohol per 5 seconds and, later, in acetone per more 5 seconds. The coupons treated were dried for 24h and weighted (TORRES, 2005).

Results and Discussion

In carbon steel coupons AISI 1020 it was observed presence of different microbial groups on metal surface in function of exposition time. Important microorganisms responsible for the biocorrosion process were present. The iron-oxidants bacteria had reached the maximum value in 30 days (Figure 1). These bacteria are capable to produce flocs and fouling deposits (inorganic and biological) in the industrial water systems and produce cloggings in the extractive industry of oil (GENTIL, 2003).

The concentrations of anaerobes and SRB had increased with time; this should be certainly because of decrease of oxygen in the system, in consequence of its consumption for the aerobic microorganisms and formation of biopolymers that hinder the access for the biofilm base (Figure 1).

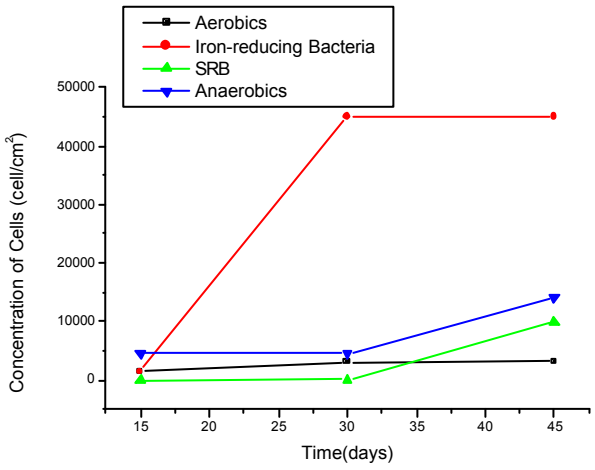

Figure 1 - Populations of aerobic, anaerobic, SRB and iron-reducing bacteria in biofilms formed on steel carbon AISI 1020 coupons, in function of the time of exposition in the system.

The microbial population of *Pseudomonas aeruginosa* and filamentous fungi in carbon steel AISI 1020 remained stable during exposition of coupons at sea water (Table 1).

Table 1 - Concentration of Pseudomonas aeruginosa and filamentous fungi present in immersed coupons in the seawater.

Analysed Coupons	Concentration 15 days	Concentration 30 days	Concentration 45 days
Pseudomonas (UFC/cm^2)	Presence	3x10^2	2x10^2
Filamentous Fungi (UFC/ cm^2)	4	4	6

The formation of not uniform deposits in the surface of carbon steel AISI 1020 after 45 days of exposition in the sea water is presented in Figure 2. It can be observed a thick layer of adhered material in the metal surface probably consisting by microorganisms, extracellular products of corrosion, polymeric substances, organic and inorganic particles that had contributed in the biocorrosion process (WIMPENNEY et al. 2000).

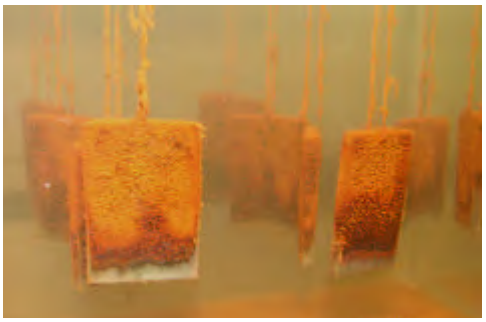

Figure 2 - Formation of biofilm in steel carbon AISI 1020 coupons after 45 days of exposition to the sea water.

The biofilms formed in the surfaces of stainless steel coupons AISI 304L had also shown the presence of different microbial groups. It was observed that sessile bacteria had showed a reduction in its concentration with time, except for SRB and fungi that had presented a small increase (Table 2).

Table 2 - Concentration of microorganisms in the coupons with 90 and 180 days.

Sessile Microorganisms	Aerobics (MPN)	Iron-reducing bacteria (MPN)	Anaerobics (MPN)	SRB (MPN)	*Pseudomonas aeruginosa* (UFC)	Fungi (UFC)
90 days	4,5x10^5	1,4x10^6	1,1x10^5	9	1,9x10^3	1,4x10^1
180 days	4,5x10^4	1,5x10^5	3,0x10^4	1,5x10^1	7,3x10^2	5,7x10^1

Figure 3.1 shows the presence of adhered microbial growth in the coupon surface, inside the reactor. A fungi colony can be observed as the predominant formation of deposits in superior surface of the stainless steel. Figure 3.2 shows the local corrosion after the removal of fungi colony that it was found adhered in the inferior coupon surface. This intense located corrosion was resultant of microorganisms presence that had made it difficult the access of oxygen, probably causing the formation of corrosion for distinguishing aeration. This result showed the tendency of the localized corrosion usually detected in the stainless steel (PANOSSIAN, 1993).

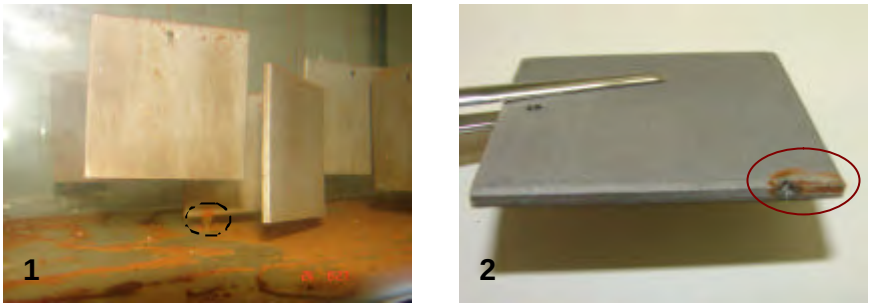

Figure 3 - Presence of microbial growth adhered to the coupon surface (1) and corrosion located in stainless steel coupon 304L after removal of aggregate of microorganisms (2)

Rate of Corrosion

After 45 day of exposition to the sea water, it was observed the presence of all the analyzed microorganisms and a moderate corrosive rate of 0.0882 mm/year in carbon steel coupons AISI 1020 (Figure 4).

The standard analyze, without microorganisms, the corrosion rate was 0.0722mm/year. The proportion of the induced corrosion by microorganisms (MIC) was 18.14%.

Stainless steel AISI 304L revealed itself more resistant, presenting low rate of corrosion (between 0,0007 and 0,0023) in the sea water analyzed (Table 3).

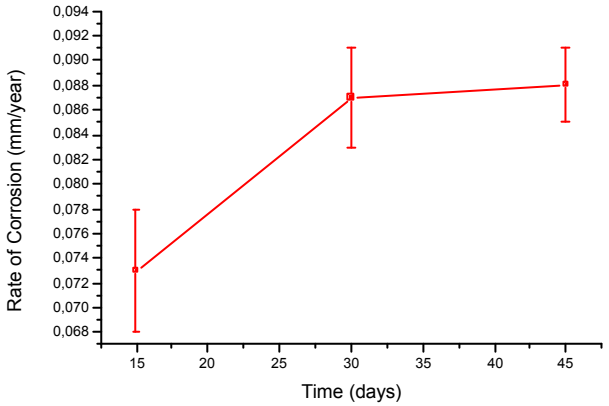

Figure 4 - Rate of corrosion in carbon steel coupons AISI 1020 displayed sea water

The stainless steel coupons 304 L that had been immersed in sea water showed the losses of mass and low rate of corrosion (Table 3). The results shows that the rate of corrosion in the period of 90 days was superior to the one of 180 days. This fact can be justified by the presence of the aggregate of microorganisms in the metal during the period of 90 days.

Table 3 - Rate of Corrosion of the coupons stainless steel AISI 304L

Coupons (days)	Rate (mm/year)	Corrosivity
90	0.0023	Low
180	0.0007	Low

Conclusions

1. The concentrations of anaerobic bacteria and SRB in carbon steel coupons AISI 1020 had increased with time, which is certainly due to decrease of oxygen in the base of biofilm.

2. The filamentous fungi and *Pseudomonas aeruginosa* bacterium had remained steady in the times of exposition of carbon steel coupons AISI 1020 in sea water.

3. The iron-reducing bacteria had presented growth accented in fluids and carbon steel coupons AISI 1020 having actively influenced more in the biocorrosion process.

4. In carbon steel AISI 1020 the biocorrosion percentage was approximately 18.14%.

5. The corrosion rate for the steel carbon AISI 1020 was classified as moderate whereas for the stainless steel AISI 304 L was found as low corrosivity.

6. The presence aggregate of microorganisms in the stainless steel AISI 304L favored an intense corrosion located due to difficulty of the access of the oxygen, causing the formation of the corrosion for differential aeration.

References

Beech, I. B., Sunner, J. A., Hiraoka, K. (2005) Microbe-surface interactions in biofouling and biocorrosion processes. *International Microbiology*, v.8, p.157-168.

Characklis, W.G., Marshall, K.C. (1990) *Biofilms*: A basis for in interdisciplinary approach. In Characklis, W.G., Marshall, K.C. Biofilms. New York: John Wiley & Sons, 796.

França, F. P., Ferreira, C. A., Lutterbach, M. T. S. (2000) Effect of different salinities of a dynamic water system on biofilm formation. *Journal of Industrial Microbiology & Biotecnology*, 25, 45-48.

Gentil, V., (2003), *Corrosão*. Livros Técnicos e Científicos. 4ª ed. Rio de Janeiro: Editora S.A, p. 341.

Natishan, P. M., Jones-Meehan, J., Loeb, G.I., Little, B. J., Ray, R., Beard, M. (1999) Corrosion behavior of some transition metals and 4340 steel metals exposed to sulphate-reducing bacteria. *Corrosion.* v.55, n.1, p.1062-1068.

Panossian, Z. (1993) Corrosão e Proteção contra corrosão em equipamentos e estruturas metálicas. 1ª ed. São Paulo: Instituto de Pesquisas Tecnológicas. 636p.

Silva, N., Neto, R. C, Junqueira, V. C. A., Silveira, N. F. A., (2005), *Manual de métodos de análise microbiológica da água.* São Paulo: Varela Editora e Livraria LTDA, p. 164.

Torres, E. S., (2005), *Potencialidade de PIGs na remoção de biofilmes formados em dutos*. Tese (Doutorado) - Escola de Química, Universidade Federal do Rio de Janeiro, Rio de Janeiro.

Videla, H. A., Herrera, L. K. (2005) Microbiologically influenced corrosion: looking to the future. *International Microbiology*, 8, 169-180.

Wimpenney, J., Allison, D. G., Gilbert, P., Lappin-Scott, H. M., Wilson, M. (2000) Overview of biofilms as functional communities. eds, Communities, Structures and Co-operation in Biofilms. UK: Cambridge University Press, p. 1-24, 2000.

Acknowledgements

The authors are thankful to the CNPq, CAPES, ANEEL and FAPERJ for the financial support.

Proceedings of the 10th International Chemical and
Biological Engineering Conference - CHEMPOR 2008
Braga, Portugal, September 4-6, 2008
E.C. Ferreira and M. Mota (Eds.)

Drinking water biofilm monitoring by Propella™ and Flow Cell bioreactors under different operating conditions

Lúcia C. Simões[1], Manuel Simões[2], Maria J. Vieira[1]
[1]IBB – Institute for Biotechnology and Bioengineering, Centre of Biological Engineering, University of Minho, Campus de Gualtar, 4710-057 Braga, Portugal
[2]CITAB-Departamento de Fitotecnia e Engenharia Rural, Universidade de Trás-os-Montes e Alto Douro (UTAD), Edifício Ciências Agrárias, Apartado 1013, 5001-801 Vila Real, Portugal

Keywords: Drinking water; Biofilm monitoring; Flow rate; Support material
Topic: Integration of life sciences & engineering

Abstract

Monitoring of biofilm subjected to different process conditions was performed using two distinct bioreactors, Propella™ and flow cell system. Biofilms were grown on polyvinyl chloride (PVC) and stainless steel (SS) coupons under laminar (Reynolds number of 2000) and turbulent (Reynolds number of 11000) flow. The parameters analyzed were culturable cells, using R2A, and total bacteria, which were assessed using a DNA-binding stain coupled with epifluorescence microscopy. The impact of the different operating conditions in the studied parameters was established after the biofilms reached the steady-state. It was found that the biofilm steady-state was achieved 3 d after the starting of operating conditions for turbulent flow and for both bioreactors and adhesion surfaces. Under laminar flow it was only achieved 6 d after. The number of total bacteria was invariably higher than the culturable cells. The number of total and culturable bacteria in turbulent flow-generated biofilms were similar in both bioreactors, regardless the adhesion surface tested. Under laminar flow, the Propella™ bioreactor allowed the formation of steady-state biofilms with a higher number of total and culturable bacteria than those from the flow cell system. Comparing the effect of the flow regime on biofilm accumulation, only turbulent flow-generated biofilms formed on the flow cell system had a higher amount of total and culturable bacteria than those formed under laminar flow. In terms of adhesion surface effect on steady-state biofilms, a higher number of total and culturable cells were found on PVC surfaces comparatively to SS when biofilms were formed using the flow cell system. Biofilm formation on PVC and SS was similar in the Propella™ system for both flow regimes.

1-Introduction

The dynamics of the microbial growth in drinking water networks is very complex, as a large number of interacting processes are involved. Many problems in drinking water distribution systems (DWDS) are microbial in nature, including biofilm growth, nitrification, microbial mediated corrosion, and the occurrence and persistence of pathogens (Camper 2004; Emtiazi et al. 2004). Biofilms are suspected to be the primary source of microorganisms in DWDS that are fed with treated water and have no pipeline breaches, and are of particular concern in older DWDS (Simões et al. 2006). By adopting this sessile mode of life, biofilm-embedded microorganisms enjoy a number of advantages over their planktonic counterparts. One advantage is the ability of the extracellular polymeric matrix, they excrete, to capture and concentrate a number of environmental nutrients, such as carbon, nitrogen and phosphate (Simões et al. 2006). Another advantage to the biofilm mode of growth is that it enables resistance to a number of control strategies (Simões et al. 2005). DWDS disinfection with chlorine dioxide and chlorine, for example, can reduce the concentration of planktonic bacteria, but have little to no effect on the concentration of biofilm bacteria (Gagnon et al. 2005). This inherent resistance to antimicrobial factors is mediated through very low metabolic levels and drastically downregulated rates of cell division of the deeply embedded

microorganisms. Biofilms act as a diffusion barrier, slowing down the penetration, to some antimicrobial agents (Simões et al. 2005). Other important advantage of the biofilm mode of growth is the potential for dispersion via detachment. Under the direction of fluid flow, detached microorganisms travel to other regions to attach and promote biofilm formation on clean areas (Codony et al. 2005).

Drinking water pipes inner-surfaces are invariably colonized by biofilms, regardless the presence of a residual disinfectant. In addition to the possibility of causing corrosion, taste and odour problems, biofilms control the microbiological contents of the distributed water and are a potential source of pathogens (Szewzyk et al. 2000). In fact, biofilms formed within potable-water systems contain bacterial pathogens such as *Legionella pneumophila* and coliforms of intestinal and nonintestinal origin (World Health Organization 1993). Furthermore, protozoa are commonly found within water distribution systems and have been associated with the persistence and invasiveness of pathogens (Simões et al. 2007a). Such findings implicate the importance of maintaining a continuous residual disinfectant in DWDS. Moreover, the examination of a DWDS reveals the complexity of such a technical system. There are not only many different materials used for the transportation and regulation of the water flow but also dramatic variations in the flow conditions between different locations. Obviously, microorganisms face a diversity of habitats with distinct physicochemical and nutritional conditions during treatment, storage, and distribution of drinking water.

The purpose of the present study was to evaluate the drinking water biofilm formation by drinking water autochthonous bacteria on stainless steel and polyvinyl chloride, two support materials commonly used on drinking water networks, under different water flow rates, using the Propella™ bioreactor and the flow cell system.

2-Material and Methods

2.1-Bioreactors and biofilm monitoring

In this study, monitoring of drinking water biofilm subjected to different conditions was performed using two distinct bioreactors, flow cell system and Propella™. The configurations of these bioreactors are presented in Figure 1.

The drinking water source was from the public network in Braga (North of Portugal). Briefly, tap water was collected in a reservoir, which was connected to one of two consecutive granular activated carbons (GAC) filter columns. It has been shown elsewhere that the first GAC filter eliminates free chlorine and biodegradable matter contained in the tap water, while the second is a biological activated filter providing a continuous bacterial inoculum to the bioreactor (Morin and Camper 1997). To avoid the presence of large carbon particles released from the columns, two filters (pore sizes 20 µm and 5 µm) were placed between the second GAC filter and the mixing tank. This tank supplied a constant inoculum at a flow rate of approximately 0.02 L h^{-1} into each of the flow cells or 1.12 L h^{-1} into the Propella™, in order to obtain the adequate dilution rate and similar to both bioreactor systems. Absence of free chlorine in the mixing tank was certified by regular sampling, using the free chlorine ion specific meter HI-93701 (Hanna Instruments, USA).

Biofilms were grown on polyvinyl chloride (PVC) and stainless steel ASI 316 2R (SS) coupons. The water flow rate through the bioreactors was controlled by recirculating the water by means of recirculation pumps (flow cells) or by means of motor for water agitation (Propella™). The biofilms were developed under laminar (Reynolds number of 2000) and turbulent (Reynolds number of 11000) flow rate. Temperature in the both bioreactors was maintained at 20 ± 1 ºC by an external refrigeration mechanism (Thermomix® BU, B. Braun – Biotech SA).

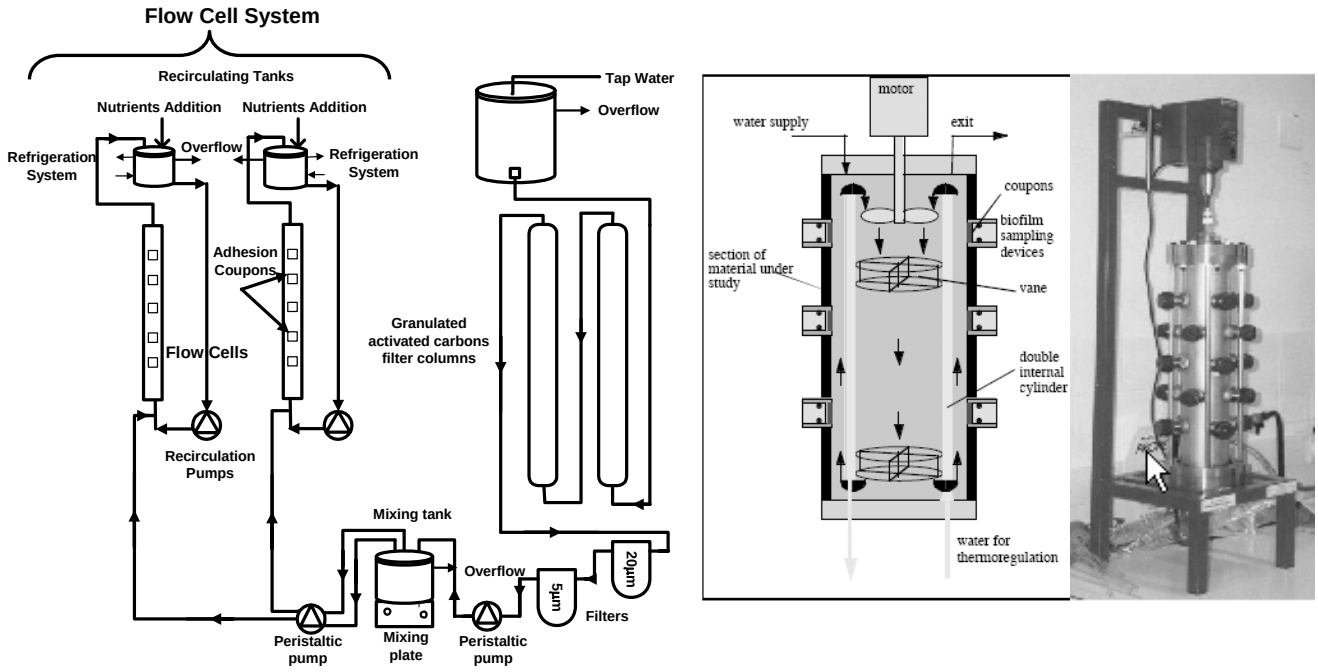

Figure 1 – Experimental set-ups, showing the GAC filter columns and the flow cell system (a); and the Propella^{TM} bioreactor (b).

2.2-Biofilm sampling

Biofilm sampling was made from the top to the bottom of the bioreactors under aseptic conditions and the coupons removed were substituted with new ones that were previously cleaned, immersed in ethanol (70 % v/v) for 30 min, and rinsed in sterile distilled water. The removed coupons were gently washed with sterile saline phosphate buffer (pH=7.0) to remove loosely attached microorganisms and scraped with a scalpel into 15 mL glass tubes containing 10 mL of sterile phosphate buffer. Before serial dilutions, biofilm suspensions in the tubes were vortexed for 2 min and used to assess both colony forming units (CFU) and total cell counts (TB).

2.3-Culturable and total cell counting

CFU`s were evaluated by standard culture methods on R2A (Oxoid, UK) prepared according to manufacturers instructions. Triplicate plates were used for each dilution and for each tested biofilm. CFU's were counted after 15 d of incubation at 20 ± 3 ºC, and the results were expressed as CFU cm^{-2}. TB were obtained by filtering the adequate volume (up to 10 mL as a function of the bacterial concentration) through a 25 mm black Nucleopore® polycarbonate membrane with a pore size of 0.2 µm (Whatman, UK). Before the filtration step, 2 % (v/v) formaldehyde (Merck, Germany) was added to the solution for sample fixation and preservation. After filtration, cells in the membrane were stained with 100 µg mL^{-1} of 4,6-diamino-2-phenylindole (DAPI) (Sigma, Portugal) for 5 min and the preparations were stored at 4 °C for up to 7 d in the dark, before visualization. No significant decay of fluorescence was noticed during this time span. Cells were visualised under an epifluorescence microscope (Carl Zeiss, Germany) equipped with a filter sensitive to DAPI fluorescence (359 nm excitation filter in combination with a 461 nm emission filter). A total of 20 fields were counted and the average of three membranes was used to calculate total cells per cm^2.

2.4.-Statistical analysis

Paired t-test analyses were performed to estimate whether or not there was a significant difference between the results obtained. Statistical calculations were based on confidence level equal or higher than 95%.

3-Results and Discussion

Biofilms constitute a protected mode of growth that allows microorganisms to survival in hostile conditions, being their phenotype significantly different from their planktonic counterparts. Their development, behavior and population characteristics are strongly influenced by many environmental factors and by intrinsic biological properties (Sauer and Camper, 2001; Purevdorj et al. 2002). From the most important environmental factors affecting biofilm structure and behaviour are the velocity field of the fluid in contact with the microbial layer and the support material for bacterial adhesion and further biofilm development (Vieira et al.1993; Stoodley et al.1999; Simões et al. 2006). Hydrodynamic conditions will determine the rate of transport of cells, oxygen and nutrients to the surface, as well as, the magnitude of shear forces acting on a developing biofilm (Vieira et al. 1993). Regarding the effects of the support material, microbial attachment will occur most readily on surfaces that are rougher, more hydrophobic, and coated by surface conditioning films (Donlan, 2002).

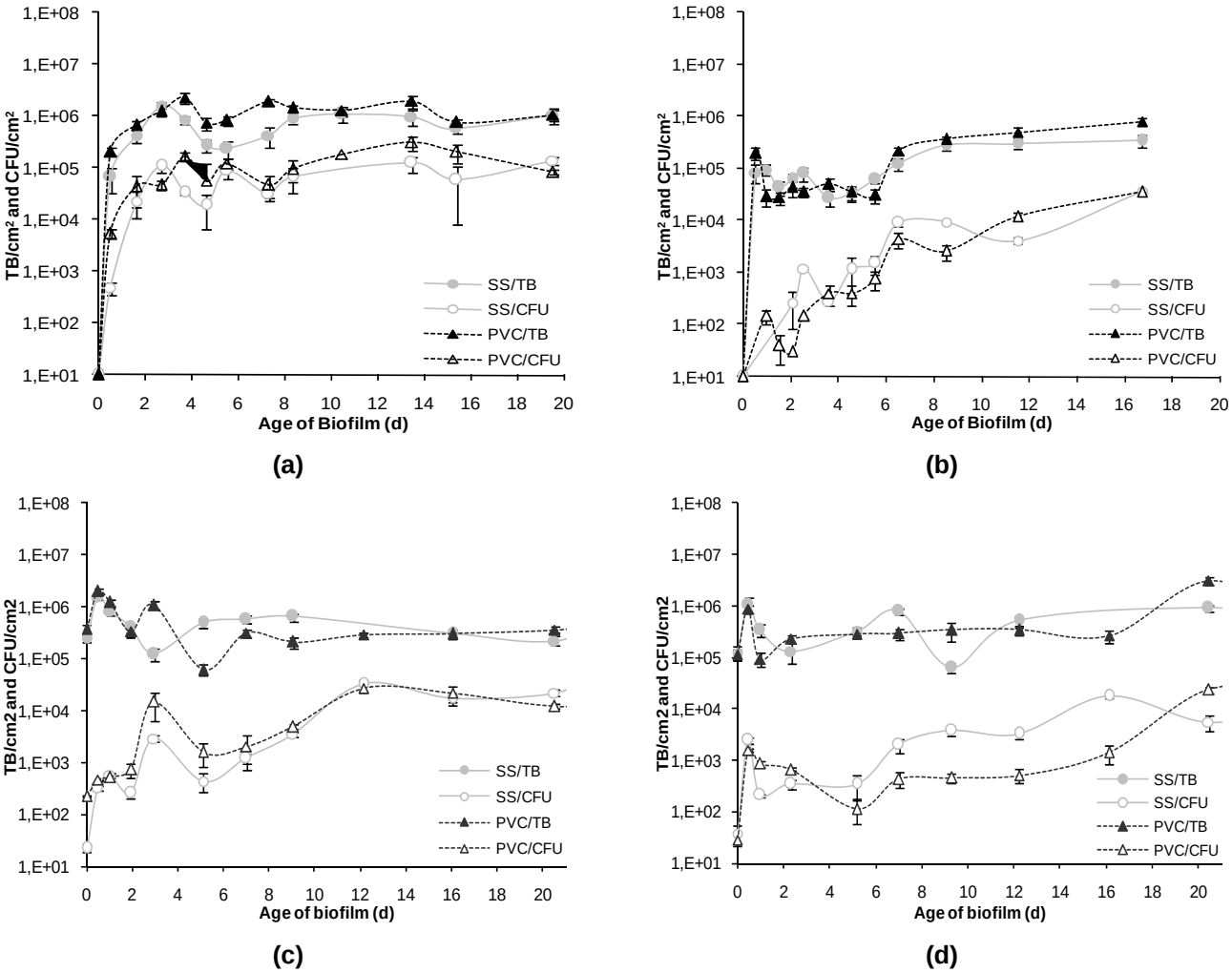

Figure 2 – Kinetics of biofilm growth obtained for the different conditions with the two bioreactors. Biofilm accumulation along time (assessed by TB and CFU) on SS and PVC surfaces. (a) turbulent flow and (b) laminar flow in flow cell bioreactor. (c) turbulent flow and (d) laminar flow in the Propella^{TM} bioreactor.

Biofilm accumulation in all experiments, expressed both in CFU and TB, increased markedly in the first few days, following a sigmoidal curve (Figure 2). Biofilm steady-state was achieved 3 d after the starting of operating conditions for turbulent flow conditions and for both bioreactors and adhesion surfaces. Under laminar flow conditions, it was only achieved 6 d after. For those cases, the number of total bacteria was invariably higher than the culturable cells (differences always higher than 2 log). It has long been recognized that the use of culture-based enumeration techniques may significantly underestimate the numbers of viable cells. Several reasons may account for this difference: the presence of starved or injured cells or potentially viable but nonculturable cells (VBNC) that are not able to initiate cell division at a sufficient rate to form colonies; inadequate culture conditions; aggregation of bacteria that can lead to the formation of one colony from more than one cell, thereby underestimating the total number of cells (Banning et al. 2002). However, total and culturable bacteria in turbulent flow-generated biofilms were similar in both bioreactors, regardless the adhesion surface ($p > 0.05$). This result suggests that increased hydrodynamic stress favours biofilm bacteria culturability. Vieira et al. (1993) found that mass transfer limitations existed in a higher extent in biofilms formed under laminar flow than for turbulent conditions. Consequently, the higher oxygen rate and transport of substrate, even if at very low levels in DWDS, from the fluid to the biofilm (mass transfer effects), should favour microbial metabolism and cell replication. Comparing the effect of the flow regime on biofilm accumulation, it was only found for the flow cell system that turbulent flow-generated biofilms had a higher amount of total and culturable bacteria than those formed under laminar flow ($p < 0.05$). This result is in agreement with previous studies (Stoodley et al. 1999; Simões et al. 2007b), with single and mixed species biofilms formed on flow cell systems, showing that biofilms formed under turbulent flow had a significant higher cell density than the laminar counterparts. Turbulent and laminar flow-generated biofilms formed on the Propella™ bioreactor had comparable cell densities. Moreover, the Propella™ system allowed the formation of steady-state laminar flow-generated biofilms with a higher number of total and culturable bacteria than those formed on the flow cell system ($p < 0.05$). In fact, there are significant differences on the design of the used bioreactor systems that can account for the differences obtained. For example, the hydrodynamic stress is obtained by distinct mechanisms when using Propella™ bioreactor (agitation by means of a rotating device system) and the flow cell system (fluid flow). In terms of adhesion surface effects, in the flow cell system, a higher number of cells formed biofilms on PVC surfaces comparatively to SS ($p < 0.05$), while biofilm formation on PVC and SS was similar ($p > 0.05$) in the Propella™ system, for both flow regimes. In a previous study (Simões et al. 2007c), it was demonstrated that the tested materials had similar physico-chemical characteristics, such as hydrophobicity, and both are prone to colonization by drinking water isolated bacteria. Consequently, it was expected a low biofilm data variability as a consequence of adhesion surface differences.

3-Conclusions

The development and validation of reliable biofilm monitoring techniques is required in order to mimic real environmental situations using laboratorial systems. This work demonstrates that distinct bioreactor configurations provide different biofilm data. In fact, the use of PVC or SS as adhesion surfaces and distinct hydrodynamic conditions lead to biofilm accumulation variability in terms of CFU and TB when using the Propella™ or the flow cell bioreactors. Moreover, this study highlights the need for a deeper understanding of how the large spectrum of conditions interact and affect biofilm formation potential and accumulation with the final purpose of predicting the total and culturable bacteria attached to real drinking water distribution pipes, based on the system characteristics. Although the practical use of these conclusions by drinking water network companies is still limited, the information provided here might be used as a framework for future studies.

Acknowledgments

The authors acknowledge the financial support provided by the Portuguese Foundation for Science and Technology (SFRH/BD/31661/2006 – Lúcia C. Simões and Manuel Simões – Ciência 2007).

References

Banning, N., Toze, S., Mee B.J. (2002). *Escherichia coli* survival in groundwater and effluent measured using a combination of propidium iodide and the green fluorescent protein. Journal of Applied Microbiology, 93, 9-76.

Camper, A.K. (2004). Involvement of humic substances in regrowth. International Journal of Food Microbiology, 92, 355-364.

Codony, F., Morato, J., Mas, J. (2005). Role of discontinuous chlorination on microbial production by drinking water biofilms. Water Research, 39, 1986-1906.

Donlan, R.M. (2002). Biofilms: microbial life on surfaces. Emerging Infectious Diseases, 8, 881-890.

Emtiazi, F., Schwartz, T., Marten, S.M., Krolla-Sidenstein, P., Obst, U. (2004). Investigation of natural biofilms formed during the production of drinking water from surface water embankment filtration. Water Research, 38, 1197-1206.

Gagnon, G.A., Rand, J.L., O`Leary, K.C., Rygel, A.C., Chauret, C., Andrews, R.C. (2005). Disinfectant efficacy of chlorite and chlorine dioxide in drinking water biofilms. Water Research, 39, 1809-1817.

Morin P, Camper AK. (1997). Attachment and fate of carbon fines in simulated drinking water distribution system biofilms. Water Research, 31, 399-410.

Purevdorj, B., Costerton, J.W., Stoodley, P. (2002). Influence of hydrodynamics and cell signalling on the structure and behaviour of *Pseudomonas aeruginosa* biofilms. Applied and Environmental Microbiology, 68, 4457-4464.

Sauer, K., Camper, A.K. (2001). Characterization of phenotypic changes in *Pseudomonas putida* in response to surface-associated growth. Journal of Bacteriology, 183, 6579-6589.

Simões, M., Pereira, M.O., Vieira, M.J. (2005). Effect of mechanical stress on biofilms challenged by different chemicals. Water Research, 39, 5142-5152.

Simões, L.C., Azevedo, N., Pacheco, A., Keevil, C.W., Vieira, M.J. (2006). Drinking water biofilm assessment of total and culturable bacteria under different operating conditions. Biofouling, 22, 91-99.

Simões, L.C., Simões, M., Vieira, M.J. (2007a). The role of microbial interactions in drinking water biofilms. Biofilms: Coming of Age (Gilbert, P., Allison, D., Brading, M., Pratten, J., Spratt, D., Upton, M., eds.), 43-52, The Biofilm Club, Manchester.

Simões, M., Pereira, M.O., Sillankorva, S., Azeredo, S., Vieira, M.J. (2007b). The effect of hydrodynamic conditions on the phenotype of *Pseudomonas fluorescens* biofilms. Biofouling, 23, 249-258.

Simões, L.C., Simões, M., Oliveira, R., Vieira, M. (2007c). Potential of the adhesion of bacteria isolated from drinking water to materials. Journal of Basic Microbiology, 47, 174-183.

Stoodley, P., Lewandowski, Z., Boyle, J.D., Lappin-Scott, H.M. (1999) Influence of hydrodynamic conditions and nutrients on biofilm structure. Journal of Applied Microbiology, 85, 19S-28S.

Szewzyk, U., Szewzyk, R., Manz, W., Schleifer, K.-H. (2000). Microbiological safety of drinking water. Annual Reviews in Microbiology, 54, 81-127.

Vieira, M.J. Melo, L., Pinheiro, M.M. (1993) Biofilm formation: hydrodynamic effects on internal diffusion and structure. Biofouling, 7, 67-80.

World Health Organization (1993). Guidelines for drinking water quality. 2nd ed. Volume 1. World Health Organization, Geneva, Switzerland.

Proceedings of the 10th International Chemical and
Biological Engineering Conference - CHEMPOR 2008
Braga, Portugal, September 4-6, 2008
E.C. Ferreira and M. Mota (Eds.)

Environmental conditions in *Nannochloropsis gaditana* cultivation for effective aquaculture live feed

Marta H.F. Henriques[1,2,*], Ana I.C. Silva[2], Sara H.N. Vicente[2], Jorge M.S. Rocha[2]
[1] Escola Superior Agrária de Coimbra - Department of Food Science and Technology, Polytechnic Institute of Coimbra, Bencanta, 3040-316 Coimbra, Portugal
[2] CIEPQPF, Chemical Engineering Department, Faculty of Science and Technology, University of Coimbra, Rua Sílvio Lima – Pólo II, 3030-790 Coimbra, Portugal

Keywords: *Nannochloropsis gaditana*, culture conditions, fatty acids, pigments, aquaculture
Topic: Integration of life sciences & engineering.

Abstract

The influence of different media composition on the *Nannochloropsis gaditana* growth rate, pigments and fatty acids production, was compared with the goal of selecting the most appropriate conditions for scale-up. The simple use of natural resources, such as sun light radiation without precautions, may not be the best way to achieve high productivities. The synergy (or cross effect) between the light intensity and the daily temperature variation has a stronger effect than both factors dissociated, and it must be the main criterion for the selection of the culture system (either indoor or outdoor). Increased concentrations of $MgSO_4$ (6-9 mM) in the culture medium favoured the cell density and chlorophyll yield but not the fatty acids and chlorophyll cell content. pH control is essential for large scale cultivation, that must use sun light but avoiding large temperature variations, as well as light inhibition. The production of EPA, as a structural fatty acid, was shown to be associated to the cell growth and not directly obtained from reserve lipids.

1 Introduction

Important drawbacks in aquaculture hatcheries are the need of large space facilities and the associated costs to produce microalgae in large quantities. The use of new and versatile photobioreactors, as well as the optimization of culture conditions to produce enriched microalgal biomass, is the preferred way to improve the production yield on-site with reduced costs (Tredici and Materassi, 1992). Simultaneously, microalgae must have particular attributes for aquaculture purposes, such as high growth rates, and must be not very sensitive to fluctuations in temperature, light radiation or nutrient composition, that usually occur in open and outdoor cultivation systems. They must also have a good nutritional composition that might be transferred up the food chain.

Nannochloropsis gaditana is employed in aquaculture hatcheries as the start of the food chain, and it is recognized as a source of pigments and polyunsaturated fatty acids. Its high content in EPA (C20:5n3) is particularly attractive, from a dietary point of view. Rotifers that consume the microalgae carry the fatty acids to the fish larvae. However, the benefits of those compounds must be economical balanced. In fact, the environmental microalgae culture conditions, such as temperature, pH, availability of essential ions in the medium and light radiation intensity are the main factors that strongly affect both the microalgae growth and the pigments and PUFAs production yields. Finding the optima of those factors, in order to maximize the metabolite productivity, is not an easy task, mainly because their crosslinked interferences.

* Corresponding author. Tel + 351-239-802940. E-mail:mhenriques@esac.pt

2 Material and Methods

2.1 Growth conditions

Nannochloropsis gaditana was obtained from Necton (Portugal). It was grown in three culture media: (i) the synthetic seawater medium (Henriques et al. 2007), referred here as industrial medium (IM); (ii) the F/2 medium (Guillard and Ryther 1962) made by filtered sea water, added with a buffer (Tris/HCl) and stock vitamins (biotin and B12); (iii) the so called enriched medium (EM), when the IM medium was reinforced with $MgSO_4$ to evaluate the influence of the magnesium concentration in chlorophyll production.

The growth was autotrophic with CO_2 from the atmosphere as the unique carbon source, reaching the culture through a cotton stopper or by bubbling. The culture systems included Erlenmeyer flasks and tubular bubble reactors. Erlenmeyer flasks were illuminated by direct or indirect sun light, and the cultures were run either at room or outdoor temperatures. Tubular bubble reactors with a volume of 0.7 L (glass tubes with 0.7 m length and 0.05 m diameter) sparged with air at 120 mL min^{-1} flow rate, were operated under two ranges of temperature (18 and 22±1 ºC) and two light regimes with *c. a.* 10/14h light/dark cycles.

2.2 Analytical methods

Cell density was evaluated by measuring the optical density of the culture at 540 nm in a Beckman DU Series 600 spectrophotometer. Absorbance was correlated to the cell number concentration by counting cells with a Neubauer Hemocytometer. The cellular amount of chla and carotenoids was evaluated through the Lichtenthaler (1983) correlation, referred by Welburn (1994), using methanol as extraction solvent for 24 h at 8 ºC. The fatty acids methyl esters (FAME) were obtained by transesterification of lyophilized cells, according to the Sato and Murata (1988) method, and analysed by GC using C19:0 as an internal standard. FAME samples were analyzed by a TREMETRICS 9001 chromatograph with a FID detector and a DB225 J&W SCIENTIFIC capillary silica column.

3 Results and Discussion

3.1 Effect of magnesium concentration

Magnesium is expected to be a potential precursor to chlorophyll production bust not necessary to fatty acids production. To evaluate the effect of Mg concentration in chlorophyll *a* (chla) and fatty acid production in *Nannochloropsis gaditana* an industrial medium (IM) ([$MgSO_4$] = 0.02 mM) and an enriched medium (EM) ([$MgSO_4$] = 1 mM) were used.

The cell density, as well as the chla concentration, increased with Mg concentration in the enriched medium (Fig. 1a). The greater availability of magnesium in the culture medium drove the cell metabolism to the production of a higher content of chlorophyll.

However, a reduction of total fatty acids produced with the use of additional magnesium (EM) was observed. In this last case only 14.6% mg mg^{-1} DW (dry weight) of total fatty acids was achieved compared to 42.5% mg mg^{-1} DW in the IM (Fig. 1b). The larger availability of magnesium induced the cellular metabolism to produce pigments but did not favoured the accumulated of lipids. Also the content of EPA followed the same trend, with 9.1% mg mg^{-1} DW in the IM assay and only 2.2% mg mg^{-1} DW in the EM assay.

The results obtained with higher concentrations of magnesium (1, 3, 6 and 9 mM, data not shown) confirmed the positive influence on the cell density achieved.

However, the chlorophyll content increase in the culture was found to be non linear with the Mg concentration. The highest Mg concentration tested (9 mM) showed the lowest relative increase of chlorophyll in the culture. On the other hand when cell content of chla was evaluated, a significant decrease of chlorophyll per cell was observed with the increase of Mg concentration. These results suggest that Mg may interfere in a deeper way with the

protein formation (resulting in higher cell densities) than with chlorophyll production, corroborating the results achieved by Zielinski and Price (1978) with other species, even for higher Mg concentrations. Therefore, the chla yield increase associated to Mg comes from the greater of cell density, more than from a higher cell content.

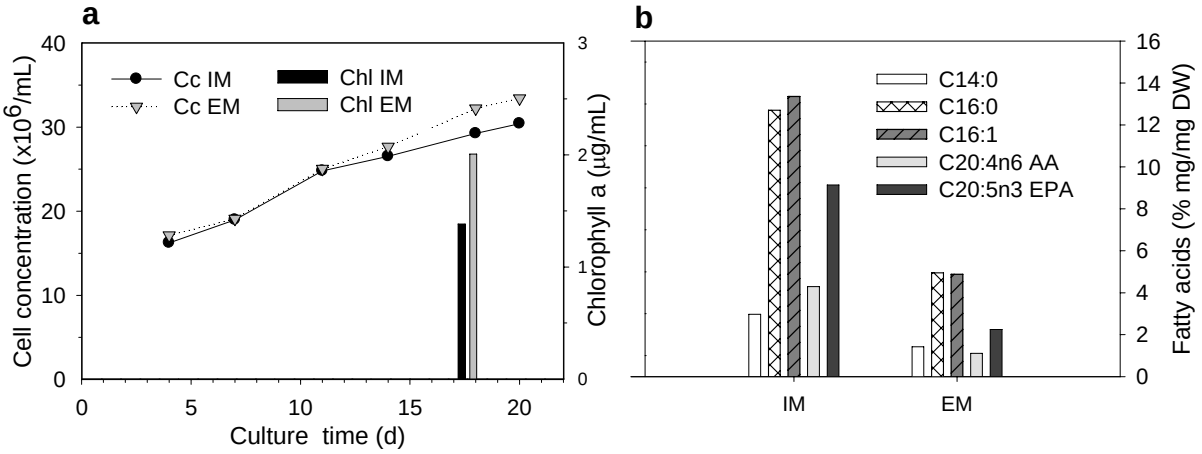

Figure 1. Effect of Mg availability on: (a) cell concentration (Cc) and chlorophyll a content (Chl); (b) fatty acid composition of the cells. IM – Industrial medium ([$MgSO_4$] = 0.02 mM); EM – Enriched medium ([$MgSO_4$] = 1 mM). Natural light illumination at 21 ºC.

3.2 Effect of culture medium composition

In this section some of the control variables were jointly tested by using two different media: the IM and the F/2. The main differences between the IM and the F/2 media were the buffering with Tris/HCl, the use of filtered sea water (instead of artificial sea water) and the increment with additional vitamins, in the second one.

After the two days lag phase for both cultures, cell growth rate was clearly favoured with the F/2 medium (data not shown). The main influence must come from the use of a buffer in the F/2 medium that allows a constant pH. In fact, the pH variations with IM medium (without any pH control) were really strong (from 6 to 9 in 20 days). Most of microalgae cultures are affected by pH variations due to the consumption of carbon dioxide during the photosynthesis and also the metabolites excreted by cells. This variation may be prejudicial both to the culture growth and to the production of pigments. In previous works, Zittelli et al. (1999) and Rocha et al. (2003) concluded that the use of a buffer is beneficial for the cell growth of *Nannochloropsis* strain, with an optimum pH value between 7.8 and 8.2.

Fig. 2 shows that the F/2 medium clearly favours the pigment concentration in the culture (*c.a.* 150% increase in chlorophyll and 155% in carotenoids), which follows the cell growth trend. When the specific content of pigments is evaluated, it is confirmed that F/2 medium is much more favourable compared to the IM medium. A decrease in pigment cell content during the second phase of the culture period that occurs in the F/2 medium, may be related to the fast growth rate promoted by using favorable growth conditions (vitamins and constant pH). In this case, cells do not need to produce a significative amount of pigments to make the photosynthetic process more efficient. Also, the shadow effect created by cells one another may explain the reduction of the specific content of pigments when a large concentration of cells is achieved.

Medium buffering, the use of filtered sea water and the addition of vitamins improve the cell growth and the production of pigments in the cells. However, taking in mind the use of microalgal biomass, the main feature may be the nutritional value in pigments itself, or the overall concentration of live food to be used in hatcheries. When the algal colour attraction is

an important goal to reach, microalgae cells must be harvested sooner (before a plateau in cell density is reached).

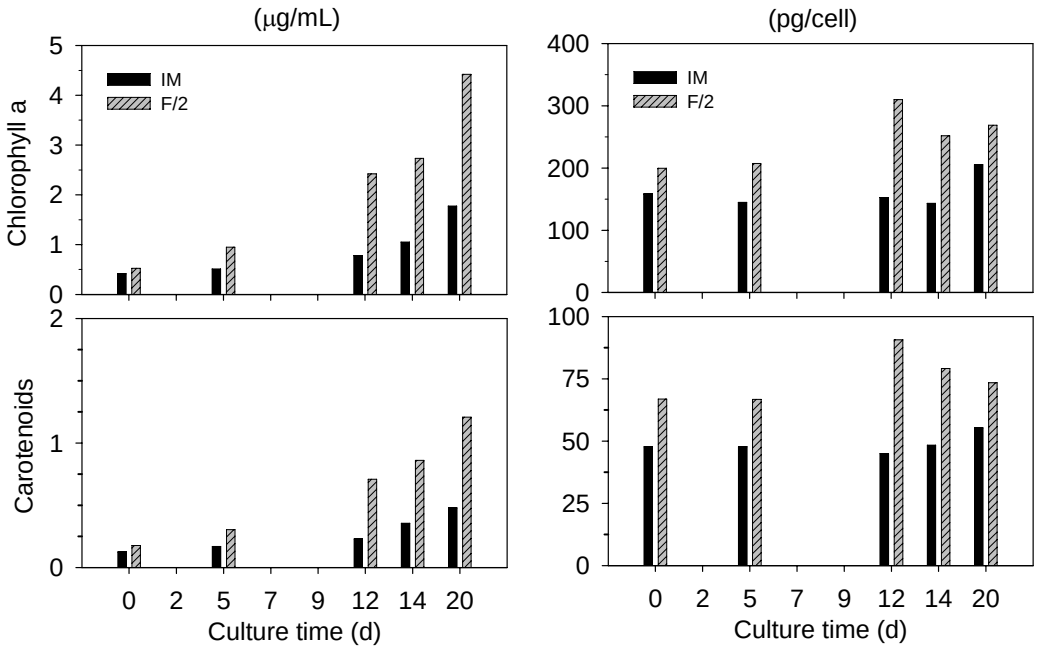

Figure 2. Effect of the culture medium composition on the chla and total carotenoids content (volumetric, left graph and specific, right graph). Cultivation in Erlenmeyer flasks. IM – Industrial medium. F/2 – Buffered medium with filtered sea water and vitamins. Temperature range: 15–20 ºC. Indirect sun light illumination, indoor.

3.3 Effect of daily temperature changes

Temperature and light intensity interactions are strongly linked in the Nature. In order to reduce temperature variations from sun light cycle, two experiments were performed in Erlemmeyer flasks submitted to the same light cycle and intensity, but in outdoor and indoor environments (separated by a glass), during winter time.

Cultures submitted to large temperature variations (outdoor) were not favoured, neither to the growth rate nor to the chla content. Seven days after the inoculation, the outdoor culture was yellow-green and at the 10th day it was completely yellow, showing chlorophyll degradation. A significative growth was visible in the indoor culture, under the same light regimen, but at a more constant temperature around 21 ºC. The observed results confirm that although the abundance of light is a primary need to phototrophic production, the range of daily temperature variations is also very important, mainly because direct light inhibition phenomena are stimulated by temperature (rather than the inconvenience of outdoor low temperatures, during the night, that even reduce the respiration phenomenon activity).

The total amount of fatty acids at the indoor cultivation was higher (42.5% mg/mg DW) than the one obtained in outdoor (26.2% mg mg^{-1} DW). Temperature variation along the daily cycle was not beneficial to the production and accumulation of lipids. Although the biomass cultivated indoors had a larger amount of EPA (9.1% mg mg^{-1} DW), its relative percentage with respect to the total lipid concentration was higher at outdoors. Cell protection from environmental stress can be pointed out as one of the factors that contributed to this behaviour. In fact, EPA is a structural fatty acid associated to the microalga cell wall.

Although the simultaneous temperature and illumination effects are not yet totally understood in outdoor systems, exposed to daily and seasonal variations, our results confirm the ones obtained by Zittelli et al. (1999), that the minimum temperature achieved during the night influences both the quantity and composition of total fatty acids.

3.4 Influence of light intensity and temperature in the fatty acids metabolism

Some bioprocesses are run under sequential two growth phases, first promoting the cell growth rate, and afterwards submitting the cells to some kind of stress to induce the production of interesting metabolites. Previous work (Henriques and Rocha 2006) suggested the increase in EPA content of cells exposed both to low light intensity (1.52 W m^{-2}) and low temperature (*c.a.* 18 ºC).

In order to evaluate the effect of a change in environmental conditions, such as light intensity (constant or variable during the illuminated period), as well as a temperature decrease, on the polyunsaturated fatty acids metabolism, a culture with a bubble column photobioreactor was done. This culture was performed under two distinct growth phases: the first one with natural illumination supplemented with two fluorescent lamps (18 W each); in the second one the photobioreactor was exclusively submitted to artificial illumination. For both phases the light/dark regime was 10/14h. Daily natural oscillations in light intensity occurred in the first part of the culture, while a light intensity of 5.85 W m^{-2} was kept constant during the illuminated period of the second phase (Fig. 3). Temperature decreased from 22 ± 2 ºC in the first phase to 18 ± 1 ºC in the second one.

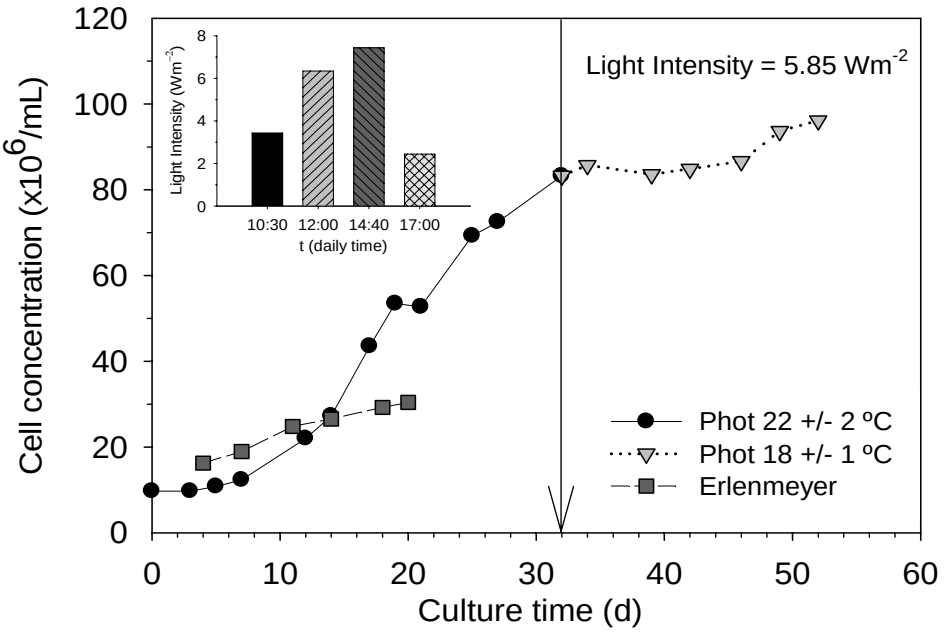

Figure 3. Cell concentration in photobioreactor and Erlenmeyer cultivation (light/dark cycles = 10/14h); IM medium.

Cell growth rate in the photobioreactor was higher than in Erlenmeyer flasks (Fig. 3), and at the 32th day the culture was submitted to a lower temperature. Although the average light intensity was kept constant in both phases of the culture, the light distribution was deficient in the last one because lamps were static and only one side of the photobioreactor was illuminated. Natural illumination decreased the shadow effect of the cells, that surely happened with artificial illumination. Agitation promoted by bubbling in the photobioreactor minimized the light deficiency in the culture; nevertheless it could not totally eliminate this drawback and light limitation was probably the main factor responsible for the lower cell growth in the second phase.

The change of temperatures and light conditions reduced not only the cell growth rate, as expected, but also the total fatty acids and the EPA contents. PUFA's act mainly as structural

fatty acids associated to cell membranes, and their synthesis was not favoured by transformation from saturated or mono-unsaturated fatty acids (which main role is reserve lipids), at the stationary growth phase.

In fact, the consumption of some lipidic reserves must have occurred, because a reduction of total fatty acids from 21 to 17% mg mg^{-1} DW was observed, probably used for cell maintenance. Structural lipids in this microalga are closer to primary metabolites and their production must be stimulated during the exponential growth phase.

These results show that the synergy of environmental factors is important, because their combined effect may lead to opposite results from the ones obtained when each factor is tested individually.

References

Guillard, R.R.L., Ryther, J.H. (1962). Studies on marine planktonic diatoms: I. Cyclotella nana Hustedt, and Detonula confervacea (Cleve) *Gran. Can. J. Microbiol.*, 8, 229–239.

Henriques, M.H.F., Rocha, J.M.S. (2006). The influence of temperature and type of illumination on the biochemical composition and EPA production of Nannochloropsis gaditana. In: Modern Multidisciplinary Applied Microbiology. Exploiting Microbes and Their Interactions (Mendez-Vilas A. ed), pp. 166-170, 1st edition, Wiley-VCH

Henriques, M.H.F., Silva A., Rocha, J.M.S. (2007). Extraction and quantification of pigments from a marine microalga: a simple and reproducible method. In: Communicating Current Research and Educational Topics and Trends in Applied Microbiology (Mendez-Vilas A. ed). 1st edition, Wiley-VCH

Lichtenthaler, H., Wellburn, A. (1983). *Determination of total carotenoids and chlorophylls a and b of leaf extracts in different solvents.* Biochemical Society Transactions, London, 11, 591-592.

Rocha, J.M.S., Garcia, J.E.C., Henriques, M.H.F. (2003). Growth aspects of the marine microalga Nannochloropsis gaditana. *Biomol. Eng.*, 20, 237-242.

Sato, N.S., Murata, N. (1988) *Membrane lipids. In: Methods in Enzymology,* Academic Press, New York.

Tredici, M.R., Materassi, R. (1992). From open ponds to vertical alveolar panels: The Italian experience in the development of reactors for the mass cultivation of phototrophic microorganisms. *J. Appl. Phycol.*, 4, 221–231.

Wellburn, A. (1994). The spectral determination of chlorophylls a and b, as well as total carotenoids using various solvents with spectrophotometers of different resolution. *J. Plant. Physiol.*, 144(3), 307-313.

Zielinski, R.E., Price, C.A. (1978). Relative requirements for magnesium of protein and chlorophyll synthesis in Euglena gracilis. *Plant Physiol.*, 61, 624-625.

Zittelli, G.C., Lavista, F., Bastianini, A., Rodolfi, L., Vincenzini, M., Tredici, M.R. (1999). Production of eicosapentaenoic acid by Nannochloropsis sp. cultures in outdoor tubular photobioreactors, *J. Biotech.*, 70, 299-312.

Proceedings of the 10th International Chemical and
Biological Engineering Conference - CHEMPOR 2008
Braga, Portugal, September 4-6, 2008
E.C. Ferreira and M. Mota (Eds.)

On-line monitoring of penicillin G acylase production using a fuzzy logic algorithm.

Edson R. Nucci, Vanessa R. Souza, Rosineide G. Silva, Raquel L.C. Giordano, Roberto C. Giordano, Antonio J.G. Cruz*

LaDABio – Laboratory for Development and Automation of Bioprocesses,
Department of Chemical Engineering, Federal University of São Carlos, P.O. Box 676,
13565–905, São Carlos – SP, Brazil.

Keywords: Computational intelligence, Bioprocess automation, Fermentation process, Enzyme, *Bacillus megaterium*.
Topic: Systematic methods and tools for managing the complexity.

Abstract

The ability to control bioprocesses at their optimal states is of considerable interest to modern fermentation industries. The aim is to reduce production costs and increase yield while at the same time maintaining the quality of the metabolic products. The objetive of this paper is to apply fuzzy logic to the Penicillin G acylase (PGA) production process. PGA hydrolyzes penicillin G to yield 6-aminopenicilanic acid (6-APA) and phenyl acetic acid. 6-APA is an important raw material, used to produce semi synthetic β-lactam antibiotics. Several experiments were carried out in a bench-scale bioreactor with diferent experimental conditions. The fuzzy algorithm could accurately infer the time for bioreactor harvesting and the output linguistic variable “stop cultivation” was defined between 0 and 100% certainty. The best experimental result was obtained when the dissolved oxygen concentration was maintained close to 0.5% of saturation.

1 Introduction

Penicillin G acylase (E.C.3.5.1.11) is an enzyme of great importance for the pharmaceutical industry, which is used in the production of 6-aminopenicilanic acid (6-APA), a key component for the synthesis of β-lactam antibiotics. There are some microrganisms that produce this enzyme, and recombinant *Escherichia coli* has been used for industrial applications. *Bacillus megaterium* is one of the microorganisms that excretes this enzyme to the medium. As a consequence, separation and purification steps are simplified (Silva et al., 2006; Chandel et al., 2008).

During PGA production, variables such as cell and enzyme concentrations are determined by off-line laboratory analysis, commonly measured only after long delays. Classical inference and control techniques, however, many times are not sufficient to reach reasonable results due to the inherent complexity of these processes. The use of advanced non-conventional techniques is necessary to overcome these difficulties (Shügerl, 2001) and considerable attention has been focused on the development of on-line, software-based state estimators (the so-called software sensors), and the fuzzy logic system presented here is one example (Sousa Jr and Almeida, 2001; Fernandes et al., 2007).

Fuzzy logic refers to a method which tries to embed intuitive and heuristic knowledge of an expert human operator about a particular system into a mathematically justified representation. The essence of this method is a set of IF–THEN rules manipulating the input–output relationship of a system, which is usually represented in linguistic terms, based on the fuzzy set theory (Zadeh, 1965). The promising capability of this method is that it may deal with systems with significant complexity, especially with regard to uncertainties, vagueness and incompleteness (Hisbullah et al., 2003; Nucci et al., 2006).

* Corresponding author. Tel + 55 16 3351-8002. E-mail:ajgcruz@ufscar.br

Various control strategies with fuzzy logic have been developed to control fermentation processes in the literature (Alfafara et al., 1993; Shiba et al., 1994; Sousa Jr and Almeida, 2001; Hisbullah et al., 2003; Karakuzu et al., 2006). The most evident advantage of the fuzzy modeling and control is to organize expert knowledge about the relevant process. Another advantage of this technique is that it does not need detailed mathematical description of the process. It is therefore an adequate intelligent controller.

The aim of the present work is to find the best experimental condition during PGA production process and at the same time to use of a fuzzy logic algorithm (programmed in MatLAB®) to infer the time for bioreactor harvesting. Accurate determination of the moment to begin the harvesting operation is very important for minimizing industrial costs, reducing dead times and avoiding unnecessary degradation of the product during the final stages of a batch or fed-batch cultivation.

2 Material and Methods

The microorganism employed was *B. megaterium* ATCC 14945 from Fundação Tropical (Campinas, SP, Brazil). For inoculum preparation (in $g.L^{-1}$): salt solution (0.2), cheese whey (7.0) and a solution of pool of seven amino acids: alanine (0.71), aspartic acid (2.31), lysine-HCl (0.95), serine (0.83), threonine (0.28), arginine (0.95) and glutamic acid (3.98). For production medium ($g.L^{-1}$): the same solution of amino acids (10.0), salt solution (0.5), cheese whey (19.6), and phenyl acetic acid (2.7) as inductor.

The experiments were carried out in a 2-liters bioreactor (Applikon®) using batch or fed-batch operation. Temperature was kept at 30°C, airflow at 1 vvm and the concentration of dissolved oxygen (DO) was mantained/controled in values between 0 and 20% of the saturation (by the automatic manipulation of stirrer speed via PID control). The bioreactor was coupled to a data acquisition system (National Instruments®) and on-line variables were stored each 10 seconds (pH, temperature, dissolved oxygen concentration, stirrer speed and molar fractions of carbon dioxide in the effluent gas).

Cultivation assays started with the incubation of 15 ml of cell spores in 135 ml of culture medium for 12 h, 300 rpm at 30°C (1,000 ml shake flasks). The inoculum was 10% of the reactor volume. The enzyme activity was determined by colorimetric PDAB-method (Balasinghan *et al.* (1972)) and the cell concentration by optical density (Nucci et al., 2007). Further details about the compostion, procedure and laboratory analyses can be found in Silva et al., 2006 and Nucci et al., 2007.

3 Methodology

Fuzzy set theory, proposed by Zadeh (1965), can deal with the vagueness and uncertainty of human knowledge and with noisy on-line data, and it allows the representation of the system using linguistic terms (*very slow*, *slow*, *fast*, *very fast*, and so on) to develop causal relationships between input and output variables. In general, qualitative information is both imprecise and uncertain. Unlike classical set theory, which crisply classifies the elements of a set (0 or 1 pertinence), a fuzzy set has an ability to classify elements into a continuous realm using the concept of degree of membership. The characteristic function or membership function is not only 0 or 1, but can aasume values in between (Tahera et al., 2008). A membership function is a curve that describes how each point in the input space is mapped to a membership value (or degree of membership).

The first step in designing a fuzzy control is to identify fuzzy input and output monitoring variables. During PGA production process by *B. megaterium* 14945, a strong relationship was observed between experimental enzyme activity and carbon dioxide concentration in the effluent gas. The fuzzy logic algorithm presented here, with 13 rules (Table 1), was written in MatLAB® and implemented in a LabVIEW® environment. Data strings were exchanged in real time between the MatLAB program and the data acquisition software, which was coupled to the bioreactor. The typical architecture of a fuzzy logic algorithm is comprised of four

principal components: *Fuzzifier*, *Fuzzy rule base*, *Inference engine* and *Defuzzifier*. More details about fuzzy logic can be found in Zadeh (1965) and Lee (1990).

Several variables were tested to discovered the best fuzzy inputs (batch time, carbon dioxide concentrations in the effluent gas, stirrer speed, pH and derivates of carbon dioxide concentration and pH) and the results show that batch time, carbon dioxide concentration and its derivate were the best choice. All the rules include all the input variables, each one associated to three fuzzy sets: a) antecedent: input *batch time* – early (ET), excellent (XT) and late (LT); input *carbon dioxide concentration in the effluent gas (molar fraction)* – low (LC), medium (MC) and high (HC) and input *carbon dioxide concentration derivate* – negative (DCN) and zero or positive (DCZP); b) consequent: no-stop cultivation (NS), attention (AT) and stop cultivation (S). The Table 1 shows the fuzzy logic rules implemented in this algorithm.

Table 1 – Fuzzy set rules of input and output variables.

Rules	IF (antecedent)	THEN (consequent)
1	ET **AND** LC **AND** DCN	NS
2	ET **AND** LC **AND** DCZP	NS
3	ET **AND** HC **AND** DCZP	NS
4	ET **AND** HC **AND** DCN	AT
5	XT **AND** HC **AND** DCZP	NS
6	XT **AND** HC **AND** DCZP	AT
7	XT **AND** MC **AND** DCN	S
8	XT **AND** MC **AND** DCZP	AT
9	XT **AND** HC **AND** DCN	S
10	XT **AND** LC **AND** DCN	NS
11	LT **AND** LC **AND** DCZP	NS
12	LT **AND** HC **AND** DCZP	NS
13	LT **AND** MC **AND** DCZP	NS

4 Results and Discussion

During the PGA production process several experimental condition were tested with the aim of obtaining a high enzyme concentration. At the same time, a fuzzy logic algorithm was developed. The data were composed by ten experiments, and this set was split in two: fuzzy parameters tuning (Runs 1-5) and validation of the algorithm (Runs6-10).
The best results were obtained using triangular and trapezoidal membership functions, as illustrate in Figures 1 and 2.

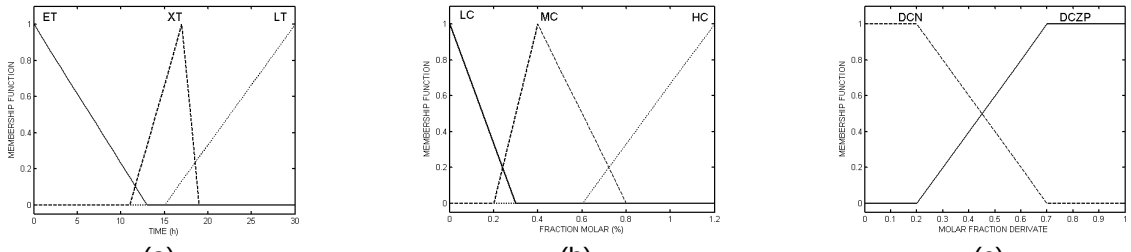

(a) (b) (c)

Figure 1. Final membership functions of antecedent part after parameters tuning: (a) Batch time; (b) molar fraction of CO_2; (c) derivate of CO_2molar fraction.

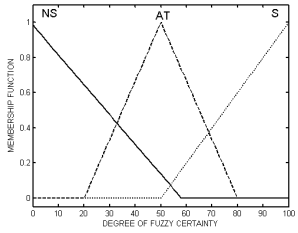

Figure 2. Final membership functions of consequent part (fuzzy certainty) after parameters tuning.

A sumary of the experimental data set used in this work, and the most important experimental results are shown in Table 2 and 3, respectively.

Table 2 – Experimental data set.

Assays	Operation Way	Stirrer speed control	Dissolved oxygen control (% sat.)	Experimental Initial pH	Feed
1	Batch	-	20%	8.0	-
2	Batch	-	20% and 5% after 8 h	8.0	-
3	Batch	-	10%	8.0	-
4	Batch	ISS*	-	8.0	-
5	Batch	-	0.5%	9.0	-
6	Batch	-	0.5%	8.0	-
7	Fed-batch	ISS	-	8.0	F=180 mL.h^{-1}; AA and CW (8h)
8	Batch	-	10%	8.0	-
9	Fed-batch	-	20% and 5% after 12 h	8.0	F = 30 mL.h^{-1} PAA (12 h)
10	Batch	ISS	-	8.0	

*ISS = Increasing stirrer speed (~20% saturação); F = feed flow; AA = mixture of amino acids (10 g.L^{-1}); CW = Cheese whey solution (19.6 g.L^{-1}); PAA = phenyl acetic acid (16.0 g.L^{-1}).

The best result was obtained when the dissolved oxygen concentration was maintained close to 0.5% of saturation between five and eighteen hours of culture (Runs 5-6). De Leon et al. (2003) obtained similar results during PGA producion process by *E. coli* .The dissolved oxygen concentration was maintained at 0.3 % of saturation.

Table 3 - Results of cell concentration, enzyme activity, fuzzy degrees and optimal time interval during penicillin G acylase production process by *Bacills megaterium*.

Assays	Cell Concentration (g.L^{-1})	Enzyme Activity (UI.L^{-1})	Degree of Fuzzy Certainty (%)	Optimal interval to stop the cultivation (h)
1	4.6±0.5	283± 5	81 % (12 h)	12 – 14
2	4.1±0.4	284± 4	82 % (16 h)	15 – 17
3	4.2±0.3	297± 4	80 % (14 h)	14 – 16
4	3.6±0.3	275±13	81 % (15 h)	16 – 18
5	4.5±0.3	532±13	80 % (16 h)	16 – 18
6	4.0±0.4	535±14	80 % (14 h)	15 – 16
7	4.6±0.3	275± 3	85 % (16 h)	18 – 20
8	4.9±0.3	346±10	81 % (12 h)	12 – 13
9	4.5±0.3	143±10	81 % (18 h)	17 – 20
10	4.1±0.2	240± 6	83 % (16 h)	16 – 18

The algorithm identifies one time interval to finish the cultivation, which was compared with the experimental region of maximum enzyme activity. It can be seen (Figure 3) that the fuzzy algorithm could successfully infer the region of maximum enzyme concentrations.

In Run-1 the interval 11.0 and 13.0 hr was determined by the algorithm as the end time with more than 81% degree of Fuzzy certainty (Figure 3a). Laboratory analyses showed that maximum enzyme activity was achieved at 14.0 hr (283± 5 IU.L^{-1}). In Run-2 the end of cultivation was defined by the fuzzy algorithm around 14.5 and 17.0 hr (82% fuzzy certainty), Figure 3b. The experimental maximum activity (284± 4 IU.L^{-1}) occurred in 16.0 hr. For Runs-3 and 4 (Figure 3c-d), the fuzzy algorithm indicated the end of the cultivation in 13.0 and 18.0 hr, respectively (80 and 81% fuzzy certainty). Maximum activity obtained was 297± 4 IU.L^{-1} (Run-3) and 275± 13 (Run-4). The results obtained during the adjust parameters showed that the Fuzzy algorithm was able to indicate the end of the experiments with good precision.

Five validation experiments were used to test the robustness and efficiency of the algorithm. The validation of the algorithm was done after running the inference on-line and identifying the end of cultivation (fuzzy certainty) at the time intervals shown in Figure 4. Nevertheless, the runs continued up to approximately 24 hr to provide extra data that would confirm the adequacy of the fuzzy inference. Of course, an actual industrial reactor should start harvesting when the maximum enzyme activity was reached. The fuzzy algorithm was successful in its predictions, providing time estimations of maximum enzyme activity within the correct experimental time span.

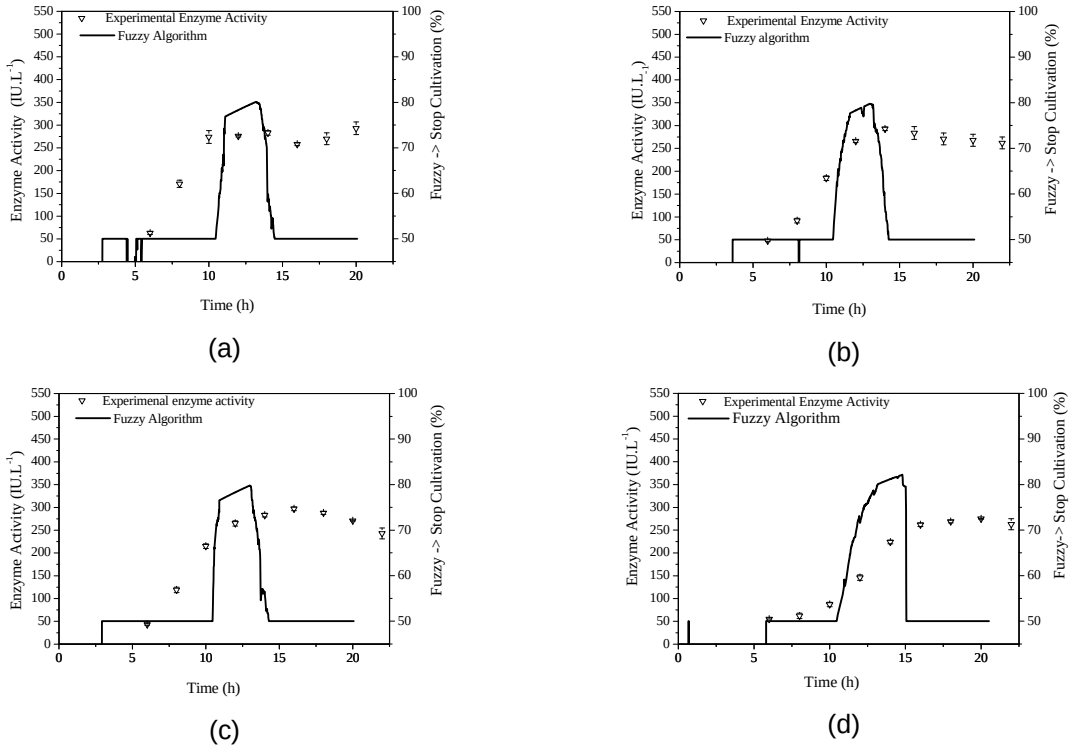

Figure 3. Training data set for tuning the fuzzy algorithm: (a) Run-1; (b) Run-2; (c) Run-3 and (d) Run 4. Bar errors standard deviations of triplicates.

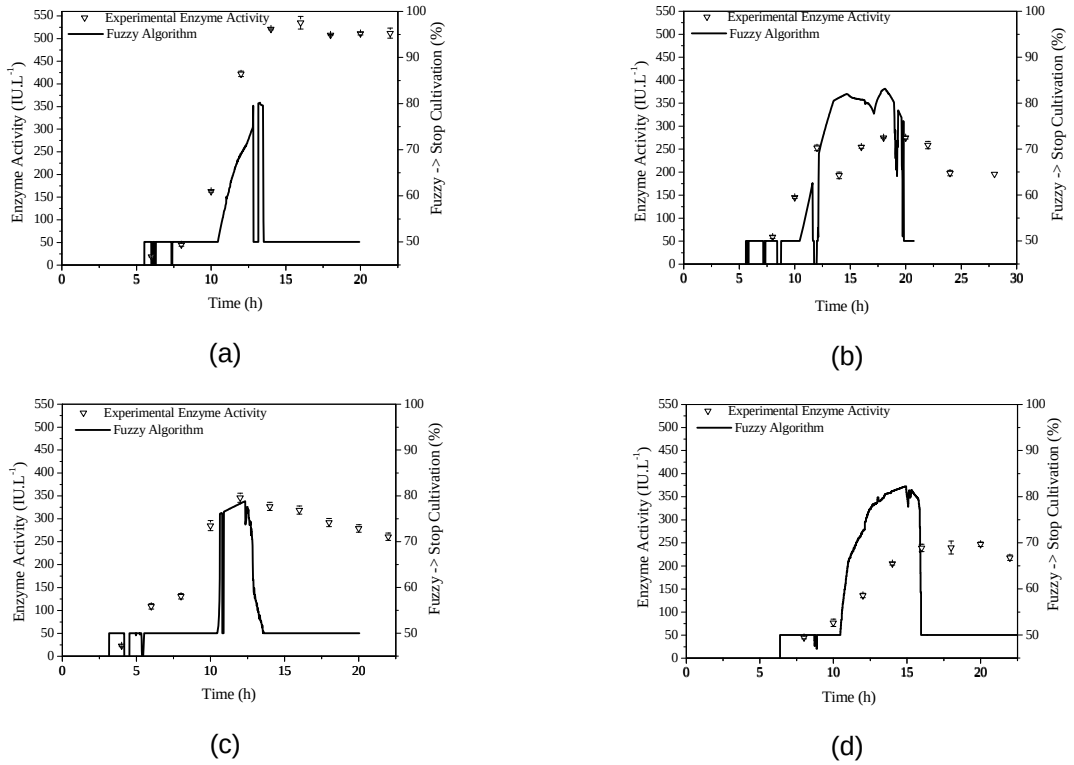

Figure 4. Validation of the fuzzy algorithm: (a) Run-6, estimated stop time with 80% of fuzzy certainty (between 12.8 and 14 hr), maximum experimental enzyme activity 16 hr (535±14 $IU.L^{-1}$); (b) Run-7, estimated stop time with 85% fuzzy certainty between 13 and 18 hr, maximum experimental enzyme activity 18.0 hr (275± 3 $IU.L^{-1}$); (c) Run-8, estimated stop time between 11.0 and 12.5 hr (81% fuzzy certainty), maximum experimental enzyme activity 12.0 hr (346±10 $IU.L^{-1}$) and (d) Run-10, estimated stop time between 11.0 and 16.0 hr (83% fuzzy certainty), maximum experimental enzyme activity 16.0 hr (240± 6 $IU.L^{-1}$). Bar errors: standard deviations of triplicate measurements.

5 Conclusion

The fuzzy logic algorithm developed in this work employs a simple model based on the Mandani inference method. It can be seen that the fuzzy algorithm could succesfully establish the region of maximum enzyme concentration, when harvesting should start, with values above eighty percent in all cases. The best experimental result during the PGA production process was obtained when the dissolved oxygen concentration was maintained close to 0.5% of saturation between five and eighteen hours of culture (Runs 5-6).

Acknowledgments The authors thank FAPESP, CNPq and CAPES for the financial support.

References

Alfafara, C.G., Miura, K., Shimizu, H., Shioya, K.-I.S., Suzuli, K. (1993). Fuzzy control of ethanol concentration and its aplication to maximum glutathione production in yeast-batch culture. *Biotechnology and Bioengineering*, 41, 493 – 501.

Balasingham, K. et al. (1972). The isolation and kinetics of penicillin amidase from *Escherichia coli*. *Biochimica ET Biophysica Acta*, 250-256.

Chandel, A.K., Rao, L.V., Narasu, M.L, Singh, O.V. (2008). The realm of Penicillin G acylase in β-lactam antibiotics. *Enzyme and Microbial Technology*, 42, 199–207.

De Leon, A.R., Garcia, B., Barba de La Rosa, A.P., Villaseñor, F., Estrada, A., Lopez, R. (2003). Periplasmic Penicillin G acylase activity in recombinant *Escherichia coli* cells permeabilized with organic solvents. *Process Biochemistry***,** 39, 301-305.

Fernandes, P.L., Nucci, E.R., Jesus, C.D.F., Giordano, R.L.C., Camargo, H.A., Giordano, R.C. (2007) Controle do início da vazão de meio suplementar e do término da corrida durante o cultivo *Bacillus megaterium* por algoritmo *Fuzzy*. *Proceedings of 16th National Bioprocess Symposium – SINAFERM*, 1, 1 – 6.

Hisbullah, M.A.H., Ramachandran, K.B. (2003). Design a fuzzy logic controller for regulating substrate feed to fed-batch fermentation. *Institution of Chemical Engineering*, 81, 138 – 146.

Karakuzo, C., Turker, M., Ozturk, S. (2006). Modelling, on-line state estimation and fuzzy control of production scale fed-batch baker's yeast fermentation. *Control Engineering Practice*, 14, 959 – 974.

Lee, C.C. (1990). Fuzzy Logic in control systems: *Fuzzy* logic controller - Part I & part II. *IEEE Transactions on Systems, Man and Cybernetics*, 20, 2, 404 - 435.

Nucci, E.R., Silva, R.G., Souza, V.R., Giordano, R.L.C., Giordano, R.C., Cruz, A.J.G. (2006). Neuro-fuzzy system applied during penicillin G acylase (PGA) production process. *Proceedings of 7th Portuguese Conference on Automatic Control*, 1, 1–6.

Nucci, E.R., Silva, R.G., Souza, V.R., Giordano, R.L.C., Giordano, R.C., Cruz, A.J.G. (2007). Comparing the performance of multi layer perceptrons networks and neuro-fuzzy systems for on-line inference of *Bacillus megaterium* cellular concentrations. *Bioprocess and Biosystem Engineering*, 30, 429 - 438.

Shiba, S., Nishida, Y., Parque, Y.S., Ijima, S., Kobayashi, T. (1994). Improvement of cloned α-amilase gene-expression in fed-batch culture of recombinant *Saccharomyces cerevisiae* by regulation both glucose and ethanol concentrations using a *Fuzzy* controller. *Biotechnology and Bioengineering*, 44, 1055 – 1063.

Shügerl, K. (2001). Progress in monitoring, modeling and control of bioprocesses during the last 20 years. *Journal of Biotechnology*, 85, 149–173.

Silva, R.G., Souza, V.R. Nucci, E.R., Pinotti, L.M., Cruz, A.J.G, Giordano, R.C., Giordano, R.L.C. (2006). Using a medium of free amino acids to produce penicillin G acylase in fed-batch cultivations of *Bacillus megaterium* ATCC 14945. *Brazilian Journal of Chemical Engineering*, 23, 37–43.

Sousa Jr, R., Almeida, P.I.F. (2001). Design of *fuzzy* system for the control of a biochemical reator in fed-batch culture. *Process Biochemistry*, 461–469.

Tahera, K., Ibrahin, R.N., Lochert, P.B. (2008). A fuzzy logic approach for dealing with qualitative quality characteristics of a process. *Expert System with Applications*, 34, 2630 – 2638.

Zadeh, L. A. (1965). Fuzzy sets. *Information and Control*, 8, 338–353.

Proceedings of the 10th International Chemical and
Biological Engineering Conference - CHEMPOR 2008
Braga, Portugal, September 4-6, 2008
E.C. Ferreira and M. Mota (Eds.)

Monitoring by HPLC-PDA Impurities Generated by Forced Degradation Conditions on an Active Pharmaceutical Ingredient

Dália M.D.Barbosa[1,2*], Teresa Alves[1], Lara Ribeiro[2], Joaquim P.Queiroga[1], José C. Menezes[2]

[1] Laboratórios CIPAN SA, Rua da Estação, 42, Vala do Carregado, P-2600-726 Castanheira do Ribatejo, Portugal

[2] IBB - Institute for Biotechnology and Bioengineering, Centre for Biological & Chemical Engineering BioSystems Engineering Lab, IST, Technical University of Lisbon; Av. Rovisco Pais, P-1049-001, Lisbon, Portugal

Keywords: Degradation; stress studies; Liquid chromatography; Active Pharmaceutical Ingredient (API); Impurities in drug substances;
Topic: Stability testing of new Drug Substances

Abstract

FDA stability guidance document stipulates that an API should be subjected to a number of forced degradation and stress conditions. The current International Conference on Harmonization (ICH) guidances (Q2A and Q2B) do not specify how degradation studies are to be conducted; this was left to the discretion of the responsible companies.

Forced degradation should be one of the activities performed early in the development process to ensure that the method is discriminating before a lot of time, effort and money have been expended. The guidance documents do not indicate detailed conditions, so the conditions and interpretations are left up to the team who work in the field.

Trial and error are needed to find the proper combination of stress agent concentration and time to effect degradation, preferably in the 20-30% range. Depending on the API, not every stress agent may effect degradation, but each agent has to be evaluated to determine whether degradation results.

Here we described the decomposition of an active pharmaceutical ingredient (API) under hydrolytic (acidic, alkaline), oxidative, dry heat and photolytic conditions.

1 Introduction

In order to achieve a high level of safety and effectiveness of pharmacotherapy the requirements on quality of active substance are growing[1,2]. The Investigation of stability of drugs represents an important issue in drug quality evaluation. Many environmental conditions, for example heat, light, humidity as well as substance ability for hydrolysis or oxidation can play an important role in drug stability. Stress testing[3] of a drug substance can help identify the degradation products and provide important information about the inherent stability of the drug substance under hydrolytic, oxidative and photolytic conditions. Moreover, during a stress study the suitability of the proposed analytical procedure to control the purity of samples may be verified.

* Corresponding author. e-mail:bsel@ist.utl.pt

The HPLC method described in European Pharmacopoeia[4] were used to monitor and identify the degradation products.

2 Experimental

2.1 Chemicals and Reagents

Active pharmaceutical ingredient working standard power was supplied by CIPAN S.A. Sodium hydroxide, hydrochloric acid, hydrogen peroxide, sodium dihydrogen, phosphoric acid and all used solvents of HPLC grade were purchased from Merck (Darmstadt, Germany). Purified HPLC grade water was obtained by reverse osmosis and filtration through a Milli-Q® system (Millipore, Milford, MA, USA) and was used to prepare all solutions.

2.2 HPLC instrumentation and conditions

Chromatographic experiments were performed using a Waters chromatograph 2695 separations module equipped with a Photodiode array detector Model 2996.

The column used was: 100mmx4.6mm I.D. Hypersil ODS with 5µm particle.

The mobile phase was prepared as follows:

mobile phase A: a 7.8g/l solution of sodium dihydrogen phosphate adjusted to pH 4.0 with phosphoric acid.

mobile phase B: a mixture of equal volumes of mobile phase A and methanol HPLC

Time (min)	Mobile phase A (per cent V/V)	Mobile phase B (per cent V/V)
0-4	100	0
4-15	100→50	0→50
15-18	50	50
18-24	50→100	50→0
24-39	100	0

The mobile phases were filtered through a 0.2µm filters and degassed under vacuum prior to use. The flow rate was 1.0ml/min. The column was maintained at 40ºC and an injection volume of 20µl was used.

The HPLC method was employed to study decomposition of API in reaction mixtures. The blank consists in mobile phase A.

For analysis of forced degradation samples, the photodiode array detector was used in scan mode with a scan range of 210-600nm. Peak homogeneity was expressed in terms of peak purity values, and was obtained directly from spectral analysis report obtained using the instrument software.

2.3 Sample preparation

Solutions of API (10mg/ml) were prepared by accurately weighing approximately 100mg of API into 10ml A-grade volumetric flask and making up to volume with mobile phase A. The solution has to be prepared immediately before use.

2.4 Forced degradation studies of API

All stress tests were carried out on a single batch of API. All solutions prepared for use in forced degradation studies were prepared to yield starting concentrations of API of 10mg/ml.

2.4.1 Oxidative studies

Solution for oxidation study was prepared in 3% H_2O_2, protected from light and stored at room temperature for 10 minutes.

2.4.2 Acid degradation studies

Solution for acid degradation study was prepared in 0.01M hydrochloric acid, protected from light and stored at room temperature for 30 minutes.

2.4.3 Alkali degradation studies

Solution for alkali degradation study was prepared in 0.01M sodium hydroxide, protected from light and stored at room temperature for 10 minutes.

2.4.4 Temperature stress studies

Susceptibility of the drug to dry heat was studied by exposing the drug to 60ºC for 5 days.

2.4.5 Photostability studies

API powder was spread on a glass dish and exposed to light for 9 days resulting in overall illumination of 200wh/m^2 with UV radiation at 360nm.

3 Results and discussion

In order to determine whether the analytical method was stability-indicating, API powder was stressed under various conditions to conducted forced degradation studies. Regulatory guidance ICH Q2A, Q3B and FDA 21 CFR section 211 all require the development and validation of stability indicating potency assays. Unfortunately, the current guidance documents do not indicate detailed degradation conditions in stress testing. However, the used forced degradation conditions, stress agent concentration and times of stress, were found to effect degradation, preferably not less than 10% and not complete degradation of active materials. The discovery of such conditions was based on trial and error.

The chromatogram of the starting sample of Bulk API taken to the stress tests is presented in Fig. 1.

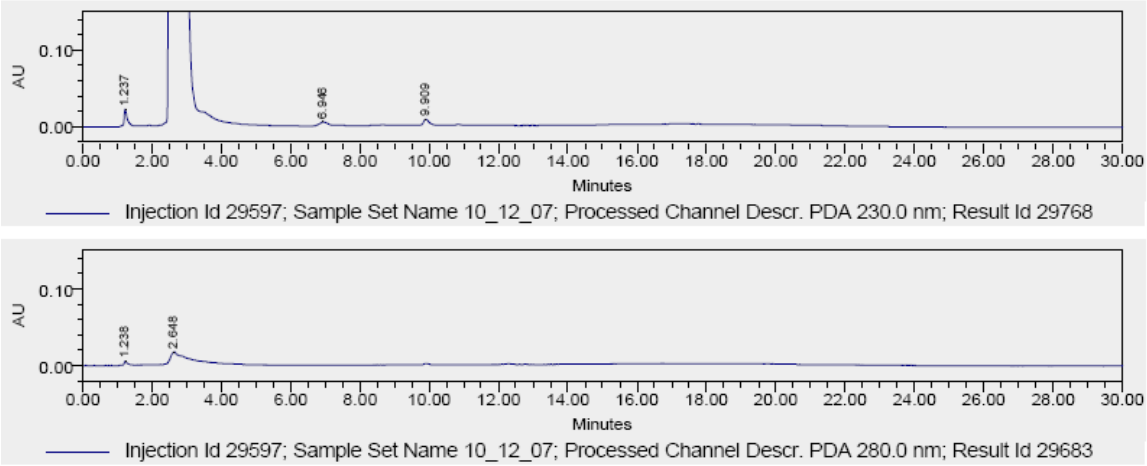

Figure 1- Chromatogram of bulk API before stress test at 230nm and 280nm

Under the dry heat (even after exposure to 60ºC for 5 days) and after 9 days of UV light exposure the samples were found to be stable (fig. 2 and fig.3).

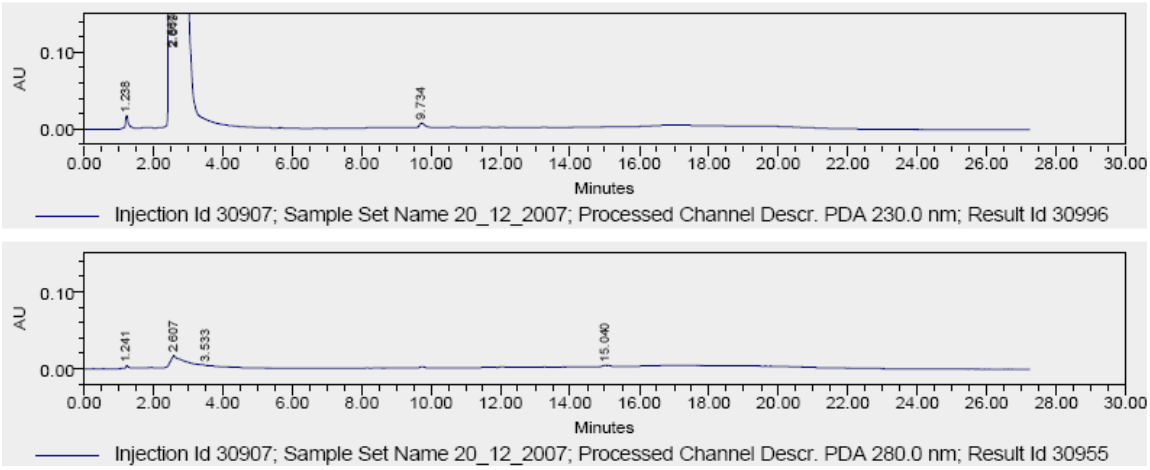

Figure 2- Chromatogram of sample subjected to dry heat (60ºC, 5 days) at 230nm and 280nm

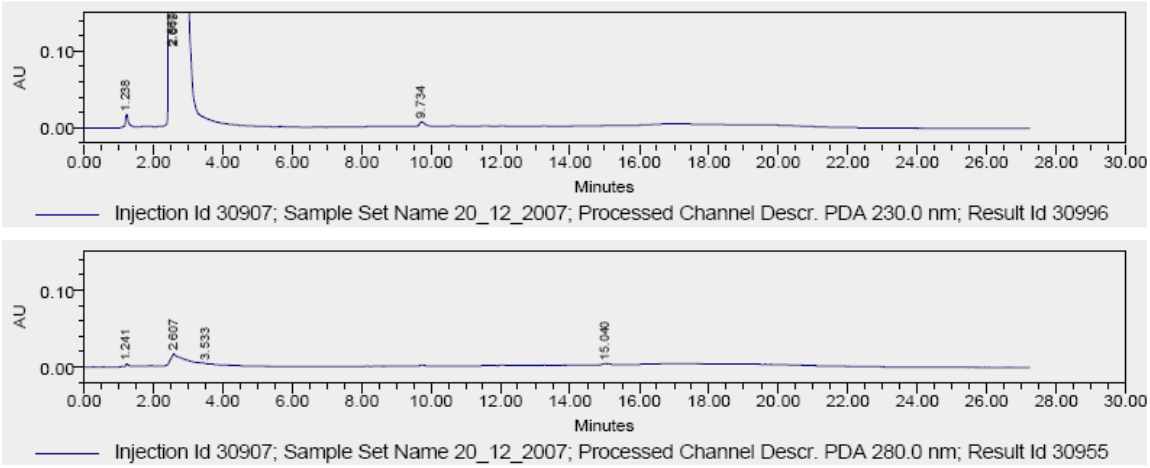

Figure 3- Chromatogram of sample subjected to UV light (9 days) at 230nm and 280nm

The studies under acidic and basic conditions shown that bulk API seemed to be really sensitive to pH variation (fig. 4 and Fig 5).

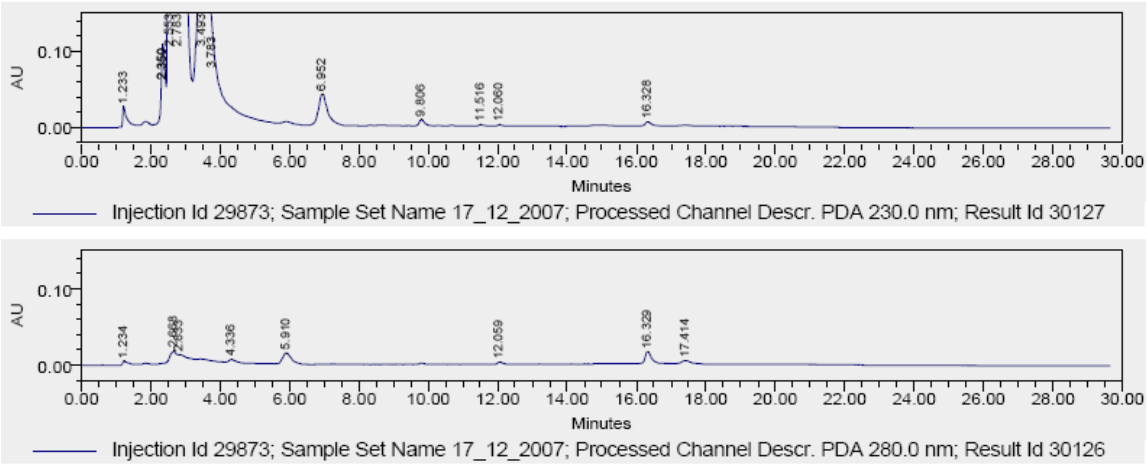

Figure 4- Chromatogram of sample subjected to 0.01M hydrochloric acid (30 min) at 230nm and 280nm

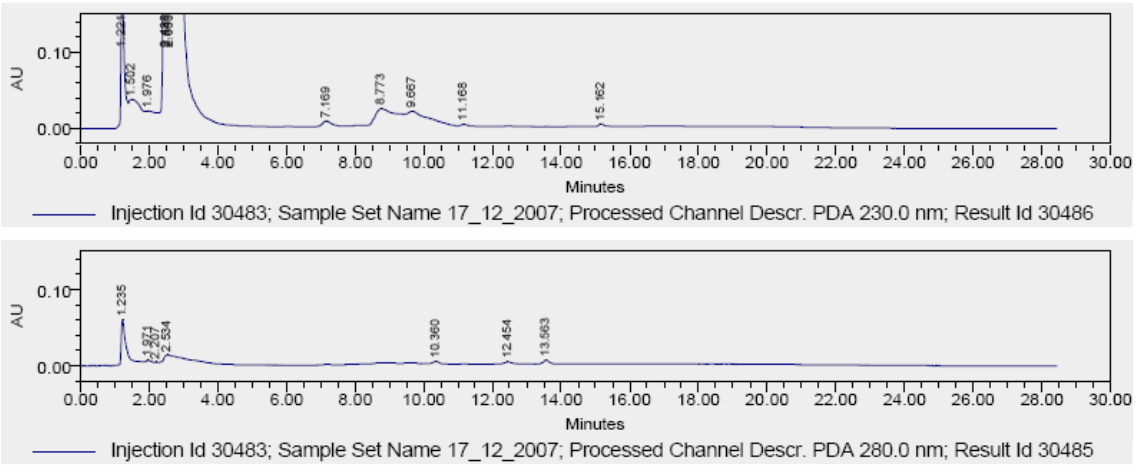

Figure 5- Chromatogram of sample subjected to 0.01M sodium hydroxide (10min) at 230nm and 280nm

Bulk API was very instable in 3% hydrogen peroxide at room temperature after 10minutes almost 50% of API was disappeared (figure 6).

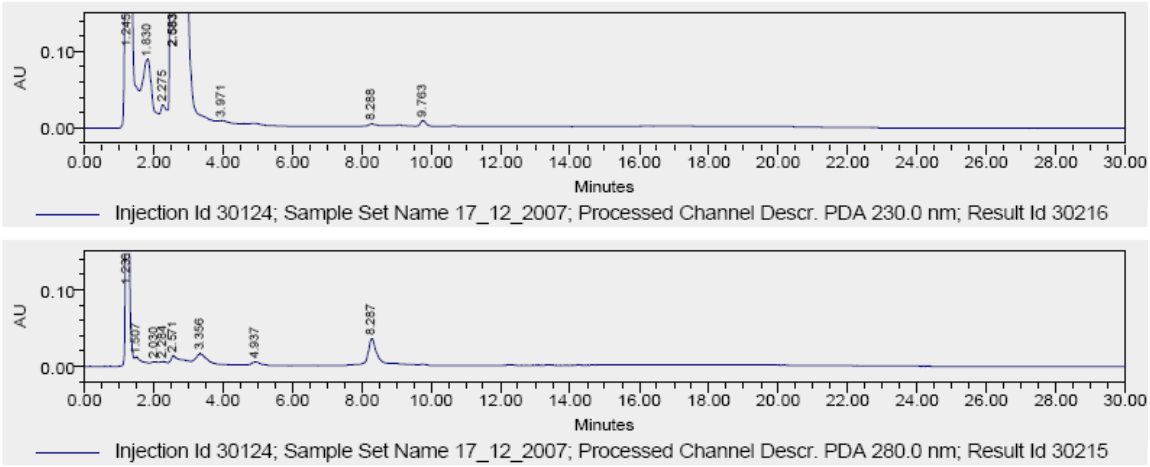

Figure 6- Chromatogram of sample subjected to 3% H_2O_2 (10min) at 230nm and 280nm

4 Conclusions

The results of stress tests undertaken according to the ICH guidelines reveal that the method is selective and stability-indicating. The proposed method is simple and has the ability to separate the drug from degradation products. The method is suitable for the routine analysis of bulk API powder. The simplicity of the method allows for application in laboratories that lack sophisticated analytical instruments, such as LC-MS or GC-MS. These methods are complex, time consuming and more costly than a simple HPLC-UV method. In addition, the HPLC procedure can be applied to the analysis of samples obtained during accelerated stability experiments to predict expiry dates of pharmaceuticals.

References

[1] Stability Testing of new Drug Substances and Products. Q1A (R2), International Conference on Harmonization of Technical Requirements for Registration of Pharmaceuticals for Human Use

[2] Stability Testing: Photostability Testing of New Drug Substances and Products. Q1B, International Conference on Harmonisation of Technical Requirements for Registration of Pharmaceuticals for Human Use

[3] S. Singh, M. Bakshi, Guidance on conduct of stress Tests to determine inherent stability of drugs, Pharmaceutical Technology On-line, April 2000

[4] European Pharmacopoeia fifth ed., Council of Europe, Strasbourg, France 2005

Proceedings of the 10th International Chemical and
Biological Engineering Conference - CHEMPOR 2008
Braga, Portugal, September 4-6, 2008
E.C. Ferreira and M. Mota (Eds.)

FT-IR Spectroscopy and Chemometrics in Clinical Microbiology

O. Preisner[1,*], R. Guiomar[2], J. Machado[2], J. C. Menezes[1], J. A. Lopes[3]

[1] IBB-Institute for Biotechnology and Bioengineering, Centre for Biological and Chemical Engineering, Instituto Superior Técnico, Technical University of Lisbon, Av. Rovisco Pais, P-1049-001 Lisbon, Portugal, Tel. (+351) 218419838, Fax. (+351) 218419197; bsel@ist.utl.pt
[2] Enterobactereaceae Unity, Bacteriology Center, National Health Institute Ricardo Jorge, Av. Padre Cruz, 1649-016 Lisbon, Portugal, Tel. (+351) 217519200, Fax. (+351) 217526400
[3] Requimte, Serviço de Química-Física, Faculdade de Farmácia, Universidade do Porto, Rua Anibal Cunha, 164, 4099-030 Porto, Portugal, Tel. (+351) 222078994, Fax. (+351) 222078961

Keywords: FT-IR Spectroscopy, Multivariate Analysis, Microbiology
Topic: Systematic methods and tools for managing the complexity

Abstract

Clinical microbiology deals with the laboratory diagnosis of infectious diseases trying to elucidate spreading routes of given bacterial strains and further characterise the microbial species and their resistance to antimicrobial agents. Most clinical laboratories rely on the phenotype-based or molecularly oriented methods for straightforward microbial typing at the different taxonomic levels. Although precise, these methods are expensive, time consuming, and they require a highly trained staff, which limits their applicability on the routine basis.

The Fourier transform infrared (FT-IR) spectroscopy has been by now successfully applied for rapid, accurate and cost-effective identification of pathogenic microorganisms. It is considered to be a powerful and versatile technique in microbiology that can assess the overall molecular composition (spectral fingerprints) of microbial cells in a non-destructive manner. Still a major concern in using FT-IR for pathogens discrimination are spectral pre-processing procedures and their impact on the increase of chemometrics models robustness. A hierarchical classification strategy together with unsupervised and supervised (Principal Component Analysis – PCA, Partial Least Squares - PLS) pattern recognition methods was used for the discrimination. Since selection of discriminative spectral regions is a critical step in calibration model development, different variable selection methods (genetic algorithm, PLS-bootstrap) have been tested as well.

Here the general contribution of FT-IR spectroscopy and chemometrics to pathogenic microorganisms' discrimination at different taxonomic levels will be discussed. Analysis of *Acinetobacter baumanni*, *Enterococcus faecium* and *Staphylococcus aureus* isolates showed clear separation within the genus level. Closely related *Salmonella enterica* serotypes (Enteritidis, Typhimurium, Bredeney, Goldcoast, Rissen, Hadar, Derby, Essen, Virchow, Mbandaka, Menden, Agona, Brikama, Saintpaul, Anatum, Infantis, Braenderup, Mikawasima) examined by FT-IR spectroscopy and chemometrics demonstrated the possibility of correct differentiation at the serotype level. Our latest results show as well that there is a considerable potential to effectively fulfil the current requirements for rapid and correct differentiation of *Salmonella* Enteritidis phage types.

* bsel@ist.utl.pt

1 Introduction

Because of the increasing prevalence of infectious diseases, there is a continuing requirement for accurate, rapid, and reliable methods for the discrimination among a wide range of clinically relevant pathogenic microorganisms.

Vibrational spectroscopic techniques, namely Fourier transform infrared (FT-IR) and Raman spectroscopy, have been used since the 1980s as complementary methods for bacteria differentiation owing to their rapid 'fingerprinting' capabilities and the molecular information that they can provide [1–3]. FT-IR spectra comprise the vibrational characters of all cell constituents, that is, DNA/RNA, protein, membrane and cell-wall components. Figure1 depicts typical raw bacterial FT-IR spectra.

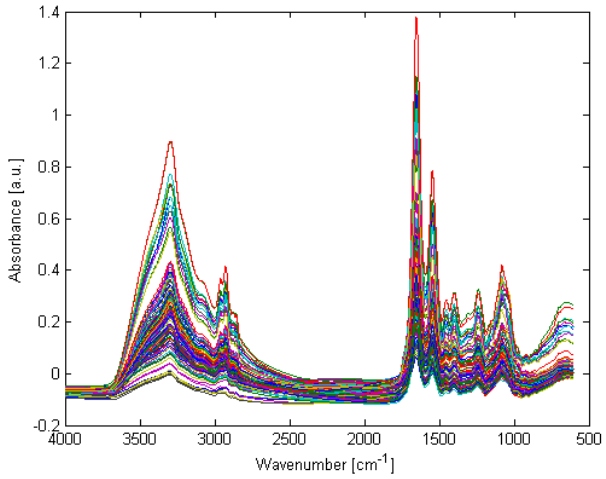

Figure1. Observed FT-IR raw spectra collected for *Acinetobacter baumanni*, vancomicin-teicoplanin resistant *Enterococcus faecium* (VRE), and meticillin resistant *Staphylococcus aureus/epidermidis* (MRSA)

FT-IR spectroscopy generates large amounts of data, hence requiring appropriate multivariate statistical methods depending on the specific objective. We have applied both supervised and unsupervised techniques in order to represent the information from hyper-spectral data, namely Principal component Analysis (PCA), Partial Least Squares regression (PLS), Partial Least Squares Discriminant Analysis (PLSDA) among others. With the purpose of optimizing the discrimination between diverse microbial species and strains on a routine basis, we analyzed different spectra pre-processing methods and assessed their impact on spectral variability, model complexity reduction (e.g., number of latent variables), and influence on model robustness.

2 Experimental

2.1 Phenotypic typing (FT-IR)

The strains were cultured in tryptose soya agar (TSA), 24 h at 37°C. Thirty five microliter aliquots of the bacterial suspensions were evenly applied onto each well in a plate. Prior to analysis the samples were over dried at 44°C for 40 min. Samples were run in replicate and analyzed by FT-IR spectroscopy using a TENSOR spectrometer (Bruker Optik GmbH) in transmittance mode. Spectra were collected over the wavenumber range of 4,000 cm^{-1} to 600 cm^{-1} under the control of a personal computer using OPUS 5.0 software. Spectra (see Figure1) were displayed in terms of absorbance as a function of the wavenumber (cm^{-1}).

2.2 Data analysis and calibration development

The quality of each spectrum was evaluated using a quality test in the OPUS 5.0 software. All calculations were carried out using Matlab version 6.5 release 13 (MathWorks, Natick, MA) and the PLS Toolbox version 3.5 for Matlab (Eigenvector Research, Manson, WA). Savitzky-Golay derivatives, multiplicative scatter correction (MSC), extended multiplicative scatter correction (EMSC), and standard normal variate (SNV) were applied to the spectra and compared.

3 Results and discussion

3.1 Discrimination of pathogenic microorganisms within the genus level

A total of 105 isolates of multiresistant *Acinetobacter baumanni*, vancomicin-teicoplanin resistant *Enterococcus faecium* (VRE), and meticillin resistant *Staphylococcus aureus/epidermidis* (MRSA) from two Portuguese Hospitals during the years 2004 to 2007 were analyzed. Strains were isolated from feces, catheters, perianal swab, urine, respiratory samples, pus, blood and pleural fluid. Isolates were evaluated by infrared spectroscopy. Simultaneous molecular typing was performed with the use of PFGE (Pulse Field Gel Electrophoresis).

By viewing the PCA score plots of the first two latent variables (Figure 2), it is possible to observe three non-overlapping clusters corresponding to known strain types under investigation. Group of *Staphylococcus* shows clear division between *Staphylococcus aureus* (bigger cluster) and *Staphylococcus epidermidis* (smaller cluster). Obtained results demonstrate concordance with simultaneous classification obtained with use of PFGE typing.

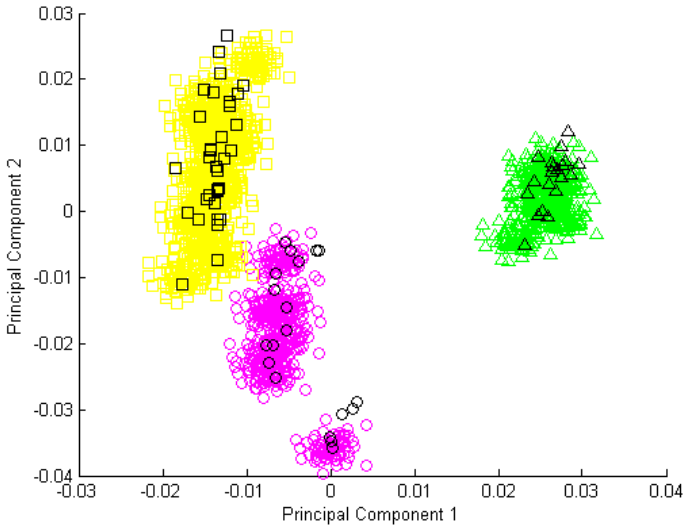

Figure2. Score plot mapping the first against the second principal components of PCA. Scores are represented with markers (□ — *Acinetobacter baumani*, ○ — *Staphylococcus aureus/Staphylococcus epidermidis*, Δ — *Enterococcus faecium*). 95% confidence limits for each group.

3.2 Discrimination of pathogenic microorganisms at the serotype level

A total of 148 isolates of closely related *Salmonella enterica* serotypes (Enteritidis, Typhimurium, Bredeney, Goldcoast, Rissen, Hadar, Derby, Essen, Virchow, Mbandaka, Menden, Agona, Brikama, Saintpaul, Anatum, Infantis, Braenderup, Mikawasima) examined by FT-IR spectroscopy and chemometrics demonstrated the possibility of correct differentiation at the serotype level. The analysed *Salmonella* strains were obtained from the Portuguese Salmonella Reference Laboratory collection and have clinical and food origin. Simultaneous serotyping analysis was performed and classification was deduced from the specific pattern of agglutination reactions using the Kauffmann-White classification scheme that lists antigenic formulas of *Salmonella*.

Figure3 shows a clear distinction of serotypes representing the *Salmonella enterica* serogroup B: *Salmonella* Typhimurium, *Salmonella* Bredeney, *Salmonella* Saintpaul, and *Salmonella* Heidelberg. Obtained results demonstrate concordance with simultaneous classification obtained by serotyping.

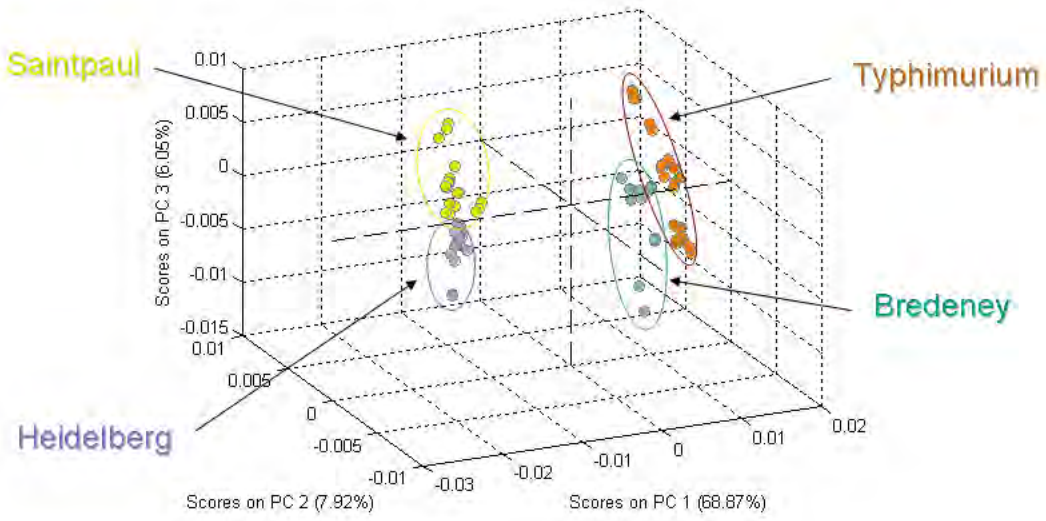

Figure3. Score plot mapping the three first principal components of PCA for analysis of *Salmonella* Typhimurium, *Salmonella* Bredeney, *Salmonella* Saintpaul, and *Salmonella* Heidelberg.

4 Conclusions

The aim of our study was to differentiate selected pathogenic microorganisms at different taxonomic levels. We have analyzed and optimized different spectra pre-processing methods and their impact on the reduction of spectral variability and on the increased robustness of chemometrics models. Fourier Transform Infrared Spectroscopy together with chemometric techniques have shown considerable potential to effectively fulfil the current requirements for fast and correct differentiation of bacteria.

Reference

[1] Maquelin K, Kirschner C, Choo-Smith LP, Van den Braak N, Endtz H, Naumann D, Puppels GJ (2002) J Microbiol Methods 51:255–271.
[2] Naumann D, Helm D, Labischinski H (1991) Nature 351:81–82.
[3] Naumann D, Keller S, Helm D, Schultz Ch, Schrader B (1995) J Mol Struct 347:399–406.

Proceedings of the 10th International Chemical and
Biological Engineering Conference - CHEMPOR 2008
Braga, Portugal, September 4-6, 2008
E.C. Ferreira and M. Mota (Eds.)

Risk Quantification of Microbiological Contamination in Aseptic Processes

Ana M.Quinto[1,2]*; Pedro A. Barata[1]; José M. Martins[1], José C. Menezes[2]

[1] Laboratórios Atral SA; Rua da Estação, 42, Vala do Carregado, P-2600-726 Castanheira do Ribatejo, Portugal

[2] IBB – Institute for Biotechnology and Bioengineering ,Centre for Biological and Chemical Engineering, IST, Technical University of Lisbon; Av. Rovisco Pais, P-1049-001, Lisbon, Portugal

Keywords: Risk quantification, aseptic processes, microbiological contamination, quality by design, pharmaceutical industry.
Topic: Risk quantification tool to perform a rational integration of information regarding Microbiological contamination.

Abstract

Being the sterility assurance of products based on the conformity of all the manufacturing process parameters – Quality by Design, it's essential to have a way of measuring the impact of the different manufacturing scenarios on the global microbiological risk.

Here we report on a risk quantification tool that allows the rational integration of the available information regarding microbiological contamination of aseptic processes.

This tool is based on a mathematical model appropriate to quantify situations involving multiple criteria. The success of its implementation depends on the correct identification of the critical points and the cooperation of people with solid process understanding.

Although the work presented emphasizes the process characterization, like the enhancement of possible worst-case manufacturing scenarios, other applications can be considered, like the support of batch release decisions or as a PAT tool, since it's possible to use in it real time data.

A discussion of all these aspects will be made based on the experience obtained in developing and applying this toll in a sterile production facility.

1 Introduction

The most critical issue when dealing with aseptic processes is the contamination control. Evaluation of the contamination risk involves the analysis of several parameters known to have possible impact on the sterility of products. This means that an investigation of a microbiological contamination event involves a detailed review of all the available information about the process in order to help evaluating the situation and to support decisions (EC GMP, 2008).

Understanding the meaning of the data available is a major concern and not always easy to accomplish since the data is not easy to read or to relate and does not give obvious answers. The location of a contamination detected, the number of colonies forming units (c.f.u.) involved, and the type of microrganisms (m.o.) identified are parameters always considered when evaluating the contamination risk to a sterile product. It is easy to recognize that contamination detected inside a Class A environment, where sterile product is exposed,

* bsel@ist.utl.pt

points to a more critical situation concerning product sterility then a contamination detected in auxiliary areas. Nevertheless there are other facts also important to take into consideration when evaluating contamination risk since they can influence the meaning of the data available. The skills of the operators engaged on the process, the number of people involved, results from risk assessment of the aseptic process, specific conditions of the production line, are important information that even unconsciously is taken into consideration by someone with deep process knowledge when reviewing the data.

Even considering all the factors involved in a certain process it is difficult to make a rational integration of all that information, especially when dealing with larger quantities of factors and factors with different weighs. The case study presented is an approach to do a rational integration of different factors when evaluating risk contamination of aseptic processes. This was achieved using a tool based on a mathematical model – Analytic Hierarchy Process (AHP) – appropriate to quantify situations involving multiple criteria. The use of a quantification method was considered useful in order to allow easily characterizing each situation regarding contamination risk in a comparable way.

The AHP is a decision support method, in which a complex problem is broken into a simple hierarchy structure of constituent elements, where weights are determined by pairwise comparisons (Douligeris et al, 1994; Fogliatto et al, 2003; Vila et al, 1995). The success of its implementation depends on the correct identification of the critical points and the cooperation of people with solid process understanding.

1.1 Analytical Hierarchy Priority - AHP

The Analytic Hierarchy Process is a decision support method, in which a complex problem is broken into a simple hierarchy structure of constituent elements, where weights are determined by pairwise comparisons (Douligeris et al, 1994; Fogliatto et al, 2003; Vila et al, 1995).

The steps to follow while implementing the AHP process are:

1 – Set up a decision hierarchy;
2 – Collect input data by pairwise comparisons of decision elements;
3 – Assessment of the consistency of the decisions taken – consistency ratio;
4 – Determination of the relative weights of the components of decision.

Decision Hierarchy

A decision hierarchy is set up by breaking down the problem into a hierarchy of interrelated decision elements – criteria and alternatives. The overall goal is placed at the top, with the remaining attributes on levels bellow (See Figure 1).

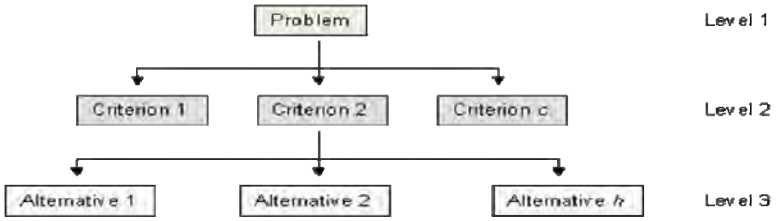

Figure 1 – Hierarchical scheme of a decision problem (Vila et al, 1995).

Pairwise Comparisons of Decision elements

The input data is generated by comparing all pairs of elements in one level with respect to one element in the previous adjacent level. The resulting comparisons are organized in comparison matrices n x n, where n represents the number of alternatives in each level and the order of the matrix (See Table 1). Each entry of the matrix (aij) corresponds to the pairwise comparison, showing the strength of element i in comparison with element j (Vila et al, 1995).

Table 1 – General comparison matrix (Vila et al, 1995).

	1	2	…	N
1	1	A12	…	A1N
2	A21	1	…	A2N
…	…	…	…	…
N	aN1	aN2	…	1

The pairwise comparison is quantified according to its importance for the decision element or team, which is based on a 1 to 9 scale – Saaty's scale (Fogliatto et al, 2003).

An element is equally more important when compared to itself, thus the main diagonal of a comparison matrix must consist of 1's. Comparison of element B with element A is the reciprocal of the comparison between element A and B, i.e. aBA = 1 / aAB (Fogliatto et al, 2003).

To analyze the problem in Figure 1, c+1 comparison matrices must be generated: c matrices comparing the alternatives in Level 3 with respect to each criterion in Level 2, and one matrix comparing the criteria in Level 2 with the problem statement in Level 1 (Fogliatto et al, 2003; Vila et al, 1995).

Assessment of the consistency of the decisions taken

In order to consider the decisions taken by the decision elements valid and consistent, it is necessary that the consistency ratio (CR – ratio between the constancy index (CI) and a random consistency index (RI)) correspondent to each matrix obeys to the following statement (Equation 1):

Equation 1 - Calculation of the CR.

$$CR = \frac{CI}{RI} = \frac{(\lambda_{máx} - n) \diagup (n-1)}{RI} \leq 0{,}10$$

Where n is the order of the matrix, and λmáx is the largest or principal "eigenvalue" of the comparison matrix, which can be shown to satisfy λmáx ≥ n.

The consistency index (CI) gives an indication of the accuracy of the method. The consistency index of a randomly generated reciprocal matrix from the scale 1 to 9, with reciprocal forced, is called the Random Index (RI), and it was proven that it has typical values.

Determination of the relative weights of the components of decision

To estimate the vector of priorities (VP), sum the elements in each row of the comparison matrix and normalize this sum by dividing it by the total of sums. The results of all sums should add up to unity (Fogliatto et al, 2003).

The final purpose of AHP is to aggregate the relative weights of decision elements to arrive to a final score for each option, adjusting the scores reflecting the weight given to the criteria with the score reflecting the weight of each alternative, as it is shown in Equation 2 (Fogliatto et al, 2003).

Equation 2 - Calculation of relative weights.

Problem = [VP(Criteria 1) x VP(Combined alternative)] +

[VP(Criteria 2) x VP(Combined alternative)] +

[VP(Criteria c) x VP(Combined alternative)]

2 Case Study

The key steps were the construction of the decision hierarchy, identifying the problem, the criteria and the alternatives.

2.1 Decision Hierarchy

The main purpose of this case study was to quantify each possible situation regarding contamination risk that could happen in the aseptic processing areas (APA) under study. The first step of the process was to identify the data available and other information that could influence the meaning of the data available even in a minor way, and adapt it to a format that allowed the application of the method. This was a critical part of the process since it was where all the variables we wanted to consider were structured.
The decision hierarchy obtained is represented on Figure 2.

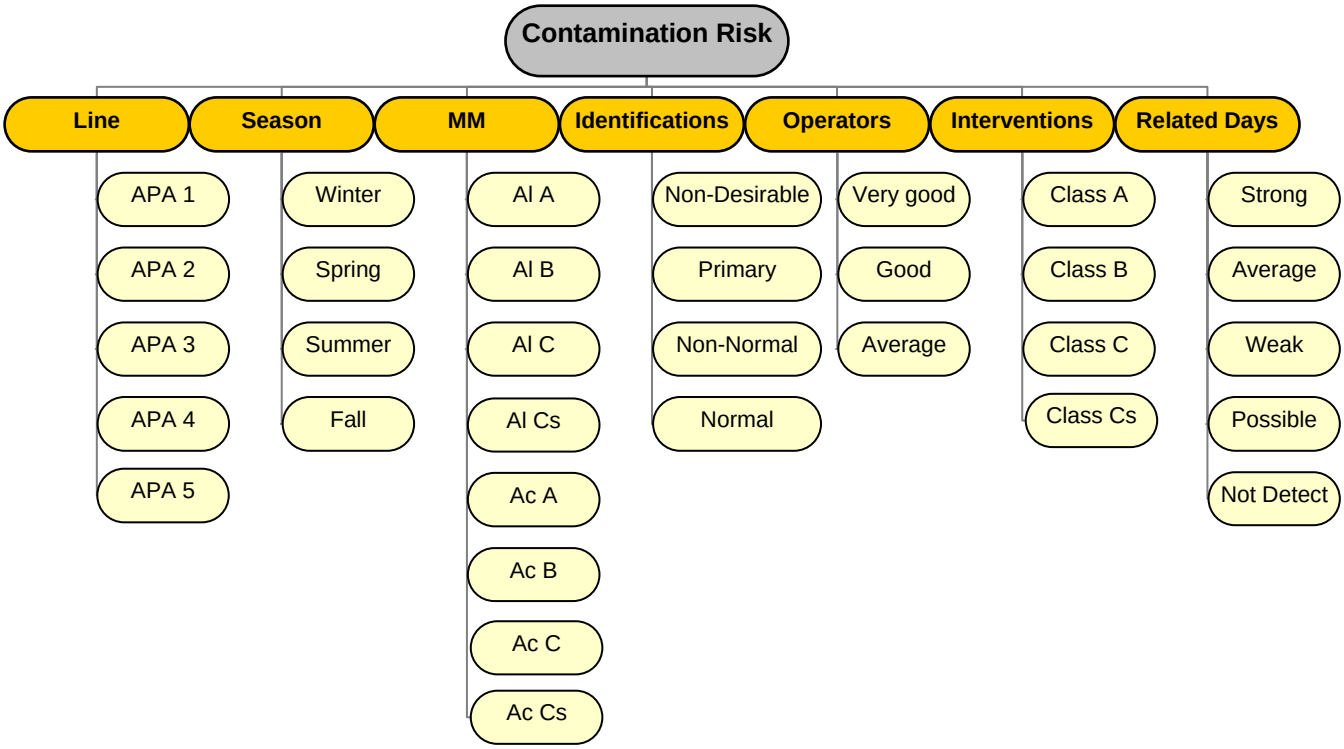

Figure 2 - Hierarchical scheme related to the problem in study - contamination risk of sterile products.

2.2 Pairwise Comparisons of Decision elements

The comparison between the criteria and alternatives was done through the construction of matrices where all the elements were compared with each other in what concerned to their impact on the contamination risk. The comparison between criteria and an example of comparison between alternatives are present next.

Table 2 - Global matrix: comparison between criteria concerning the problem.

	PL	S	MM	ID	OP	IT	RD	PV
Production Line (LP)	1	5	1/5	1/3	1	1/5	1/3	0,077
Season (S)	1/5	1	1/9	1/8	1/5	1/9	1/8	0,018

Microbiological Monitoring (MM)	5	9	1	3	5	1	3	0,256
Identifications (ID)	3	8	1/3	1	3	1/3	1	0,158
Operators (OP)	1	5	1/5	1/3	1	1/5	1/3	0,077
Interventions (IT)	5	9	1	3	5	1	3	0,256
Related Days (RD)	3	8	1/3	1	3	1/3	1	0,158
								1

Table 3 - Comparison matrix of the alternatives concerning identifications.

	ND	**PP**	**NNF**	**NF**	**PV**
Non-Desirable (ND)	1	5	7	9	0,589
Primary Pathogenic (PP)	1/5	1	3	5	0,247
Non-Normal Flora (NNF)	1/7	1/3	1	3	0,120
Normal Flora (NF)	1/9	1/5	1/3	1	0,044
					1

2.3 Assessment of the consistency of the decisions taken

The decision team was responsible for the scores given in all the matrices, using the Saaty's scale. The validation of these decisions was accomplished through the calculation of the consistency ratio (CR) concerning each matrix. All the matrices fulfilled the requisites to consider the decisions valid – $\lambda máx > n$ and $CR < 0,10$, being all the decisions taken by the decision team considered valid.

2.4. Determination of the relative weights of the components of decision

The calculations were made using Equation 2 regarding each combination of factors. Example on

Table 4 shows the combination of factors representing the worst case scenario concerning the contamination risk:

- Production line (0,077) – APA 4 or 5 (0,387)
- Season (0,018)- Winter (0,484)
- Microbiological monitoring (0,256) – Action level Class A (0,307)
- Identifications (0,158) – Non-desirable (0,589)
- Operators (0,077) – Average (0,696)
- Interventions (0,256) – Class A (0,589)
- Related days (0,158) – Strong (0,436)

Table 4 – Example of calculations and results for the worst case scenario.

RESULT	
(0,077 x 0,387) + (0,018 x 0,484) + (0,256 x 0,307) + (0,158 x 0,589) + (0,077 x 0,696) + (0,256 x 0,589) + (0,158 x 0,436) =	0,483

2.5. Results

Using this tool it is possible to characterize each process situation regarding contamination risk in a comparable way. Figure 3 is a chart constructed using data collected during one year from one of the production lines where is possible to view profound differences in the values obtained depending on the circumstances.

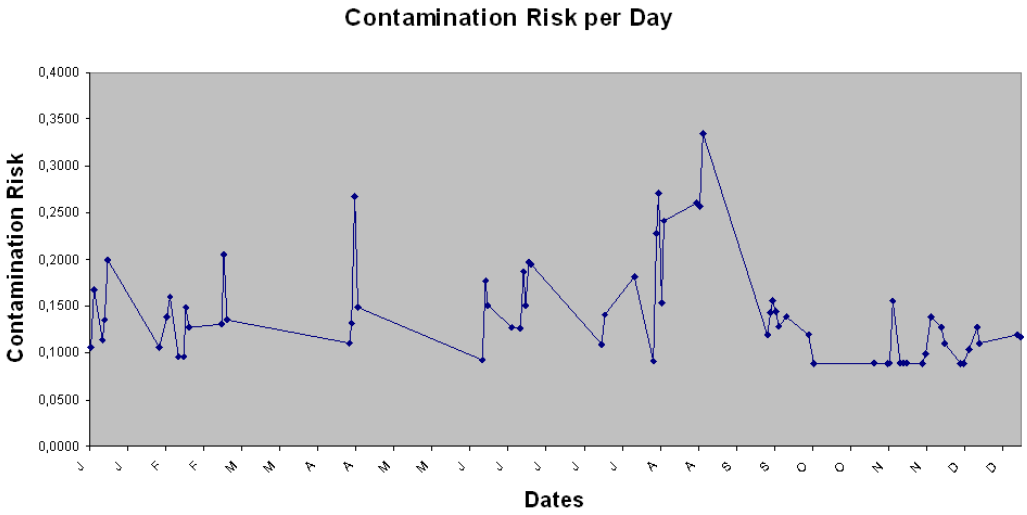

Figure 3 – Results of Contamination Risk per Day.

3. Conclusions

Contamination control is the major issue when dealing with aseptic processing. Evaluation of the contamination risk involves the analysis of several parameters known to have possible impact on the sterility of products. To take into consideration all the factors involved in a certain process it is important to make a rational integration of all that information.

The case study presented is an approach to do this rational integration of different factors that influence risk contamination of aseptic processes. This was achieved using a tool based on a mathematical model – Analytic Hierarchy Process (AHP) – appropriate to quantify situations involving multiple criteria.

Although the work presented emphasizes the process characterization using a specific type of available data, other applications can be considered, like the support of batch release decisions based on the risk level obtained, or as a PAT tool, since it's possible to apply this tool with real time data.

4. References

EC Guide to Good Manufacturing Practice Revision to Annex 1 (2008): Manufacture of Sterile Medicinal Products.

Douligeris, C., Pereira, I. (1994). "A Telecommunications Quality Study Using the Analytic Hierarchy Process", IEEE Journal on Selected Areas in Communications, Volume 12 (2).

Fogliatto, F., Albin, S.,(2003). " An AHP-based procedure for sensory data collection and analysis in quality and reliability applications", Food Quality and Preference, Volume 14.

Vila, J., Beccue, B. (1995). "Effect of Visualization on the Decision Maker When Using Analytic Hierarchy Process", Proceedings of the 28th Annual Hawaii International Conference on System Sciences.

Proceedings of the 10th International Chemical and
Biological Engineering Conference - CHEMPOR 2008
Braga, Portugal, September 4-6, 2008
E.C. Ferreira and M. Mota (Eds.)

Novel method for accelerated analytical control of biological (bacteriological) agents

Valery P. Nesterenko*
Ecology Department, Belarusian National Technical University
65, Nezavisimosty Avenue, 220027, Minsk, Republic of Belarus

Keywords: biological pollution, analytical control, hard nutrient media, solid inorganic material.
Topic: Integration of life sciences & engineering.

The permanently rising biological pollution of the environment including the water objects requires organization of legible and operating scientific grounded control quality system concerning to such pollution in view of maintenance of a principle of epidemic safety. The solution of these problems with the purpose of the water-sources protection from biological pollutions, including the case of biological terrorism, is actual today and will be in future (Rosebury et al., 1947; Rosebury, 1949; Rożniatowski and Żółtowski, 1957).

One of the most important directions of scientific research in the field of studying and hygienic setting of biological pollution is the development of effective monitoring system. In its turn, the basic moment for monitoring implementation of the water-sources is developing and perfecting of indication methods of different kinds of biological contaminants including working out of accelerated methods of microorganism extraction from environment. And the success of antibacteriological protection in many respects depends on as far as the indication can be fast carried out (Rothschild, 1964; Hersh, 1969; Archangelsky et al., 1971).

The present work is devoted to creation of the accelerated microbiological analysis for environment monitoring including the water objects. Mainly, in the practice of modern microbiology at the estimation of environment quality the microbiological analyses are carried out by cultivating microorganisms on different hard nutrient media prepared by dissolution of nutrient materials and special solidifying matter (agar, gelatine, derivatives of cellulose, etc.) in water with the subsequent formation of gel (Meynell and Meynell, 1965). From known ways of preparing of hard nutrient media the way with usage of agar is the best. However, the process of preparing of this nutrient medium to an inoculation is characterized by large duration (3-5 hours) and complexity, including operation of sterilization for which, besides, the special equipment is necessary.

In this work the new approach to preparation of hard nutrient media is proposed, namely, – impregnation by solution of nutrient materials by a special way of the treated plates from solid inorganic materials. Applying such materials as a basis for hard microbiological nutrient media became possible after the capacity of different microorganisms for active growth and formation of colonies on a surface of such nutrient media was detected in which were used as a sealing basis specially prepared solid inorganic materials but not gel-forming matters. The plates prepared by the given way in sterile conditions are sealed in polyethylene packages where they can be stored a long time without loss of exploitative properties. The duration of preparation of such nutrient media directly to an inoculation equals 5-10 min. The specimens of different microorganism groups, actinomyces, streptococci, yeasty and mouldy fungi grow well on such media.

* Tel + 7 (495) 2411456. E-mail: v.nesterenko@mail.ru

Example 1. Round plates with a diameter of 90 mm and thickness 8 mm of a solid inorganic material with open pores of a specific size and hardness on a Moos's scale equal 6 were applied. The plates were impregnated with a liquid Czapek's medium and sterilized in autoclave under 175 kPa during 30 min, then dried up at the temperature of 353-363 K up to constant weight. The prepared plates in sterile conditions were put in packages of polyethylene sterilized by ethanol and packages were sealed.

Test of operation properties of a dry nutrient medium prepared by the given method was made as follows. The packages with plates stored for 72 hours were treated by ethanol and opened by sterile scissors. 20 plates were put by sterile tweezers in sterile Petri dishes by one plate into dish. Sterile distilled water was introduced into dishes and was swallowed by plates. The duration of preparation of a medium to inoculation equals 5-10 min.

In comparison a powder of a dry nutrient medium "Czapek's agar" was kept in distilled water for swelling within 1 hour, was dissolved under heating on boiling water bath, was sterilized in autoclave under 175 kPa during 30 min, poured out in 20 sterile Petri dishes and was kept under room temperature till solidification. The duration of preparation of a medium to inoculation equals 2-3 hours. In addition for a comparison dissolved, cooled sterile Czapek's medium, stored a flask, was melt down, poured out in 20 sterile Petri dishes and kept till solidification. The duration of preparation of a medium to inoculation is in this case is increased for 1-2 hours and equals in general 3-5 hours.

The surface of the prepared in this way media was inoculated by suspensions of spores of *Aspergillus niger* and *Penicillium chrysogenum* mouldy fungi, containing 1 million spores/ml, putting 0.05 ml suspension in three symmetrical points on a surface of a medium in each dish. The dishes were incubated in the thermostat under 301 K during 120 hours. The average diameter of *Aspergillus niger* colonies on a medium prepared according to point 1 equals 15.8 ± 4.7 mm, on agar medium equals 15.6 ± 4.4 mm. The average diameter of *Penicillium chrysogenum* colonies on a medium prepared according to point 1 equals 13.8 ± 3.1 mm, on agar medium equals 14.1 ± 3.3 mm.

As an example, the comparative data of accumulation of yeasty and mouldy fungi biomass on hard nutrient media with a solid porous material and agar are indicated in the Table 1.

Table 1. Sizes of microorganism colonies on hard nutrient media with a solid porous material and agar

Species of microorganisms	Duration of incubation, hours	Solidifying basis	Average diameter of colonies, mm
Aspergillus niger	120	Solid material	16.0 ± 6.1
Aspergillus niger	120	Agar	16.4 ± 6.2
Penicillium chrysogenum	120	Solid material	14.0 ± 2.6
Penicillium chrysogenum	120	Agar	15.0 ± 3.1
Candida utilis	96	Solid material	7.1 ± 0.3
Candida utilis	96	Agar	6.7 ± 0.6

Saccharomyces cerevisiae	96	Solid material	6.8 ± 0.2
Saccharomyces cerevisiae	96	Agar	6.9 ± 0.4

Example 2. Dry hard microbiological nutrient media solidified by specially prepared solid porous materials were applied. These nutrient media were kept in usual room conditions during 1 year. All other operations are the same as in point 1.The average diameter of *Aspergillus niger* colonies on a medium prepared according to point 1 equals 15.8 ± 2.9 mm, on agar medium equals 15.6 ± 5.1mm. The average diameter of *Penicillium chrysogenum* colonies on a medium prepared according to point 1 equals 13.9 ± 4.6 mm, on agar medium equals 13.8 ± 3.1 mm.

Example 3. Hard nutrient Czapek's-Dox's medium, in which agar was replaced by a solid porous material with hardness on a Moos's scale equal 5 was prepared. Disks with a diameter 90 mm and thickness 8 mm, which were put in Petri dishes were made of it. Ingredients of Czapek's-Dox's medium were dissolved in distilled water, then with an received solution disks till saturation were impregnated. Prepared hard nutrient medium was sterilized in autoclave under 175 kPa during 30 min. The surface of prepared nutrient medium was inoculated by suspensions of spores of *Aspergillus niger* and *Penicillium chrysogenum* mouldy fungi, containing 1 million spores/ml, putting on each disk in three symmetrical points 0.05 ml suspension of one of fungi and after this dishes were incubated in the thermostat under 301 K.

In comparison in the same way poured out in Petri dishes sterile agar Czapek's-Dox's medium was inoculated. The dishes with inoculated agar medium were incubated in the same conditions. Each of four indicated variants was tested on 10 Petri dishes.

Example 4. Hard nutrient medium of non-hopped must with strength 7 º on polarimeter, in which agar is replaced by a solid porous material was prepared. A medium was inoculated by suspensions of yeast *Candida utilis* and *Saccharomyces cerevisiae* cells with concentration in 1 mln of cells/ml as is indicated in point 1. In comparison the sterile agar musty medium poured out in Petri dishes was inoculated in the same way. All other operations are the same as in point 1.

The comparative results in cultivation of microorganisms according to examples 3 and 4 (suspension of *Streptococcus* culture cells, taken from the patient with chronic tonsillitis

Table 2. Comparative results in cultivation of microorganisms on nutrient media solidified by a solid material and agar

Species of microorganisms	Duration of incubation, hours	Solidifying basis	Average diameter of colonies, mm
Streptococcus	48	Solid material	1 - 3
Streptococcus	48	Agar	1 - 3
Actinomyces flavus	288	Solid material	4.9 ± 0.6
Actinomyces flavus	288	Agar	5.0 ± 0.8

and suspension of *Actinomyces flavus* spores) on nutrient media, respectively, sterile meat-peptone medium with adding 10 % by volume of sterile serum of the bull blood and starch-ammonia medium of composition, namely, starch soluble (amilose) – 10g, $(NH_4)_2SO_4$ – 2g, 1g each of K_2HPO_4 , $MgSO_4$ and NaCl, water – up to 1.0 l are indicated in the Table 2. Sealing basis is solid porous material and agar.

Example 5. Disks with cultures of microorganisms from points 1 and 2 were autoclaved under 200 kPa during 30 min, were tempered under 873 K during 1.5 hours, cooled in the air, boiled in water 1 hour and dried up under 383 K up to constant weight. Then on the base of these disks hard nutrient media were prepared, which were inoculated and incubated as in points 3 and 4. The average diameter of *Aspergillus niger* colonies equals 16.5 ± 3.3 mm, *Penicillium chrysogenum* colonies equals 14.6 ± 2.5 mm, *Candida utilis* colonies equals 7.2 ± 0.2 mm, *Saccharomyces cerevisiae* colonies equals 6.7 ± 0.3 mm.

Table 3. Results in cultivation of microorganisms after two stages of solid solidifying basis regeneration [1)]

Species of microorganisms	Duration of incubation, hours	Solidifying basis	Average diameter of colonies, mm
Aspergillus niger	120	Solid material *	16.5 ± 3.3
Penicillium chrysogenum	120	Solid material *	14.6 ± 2.5
Candida utilis	96	Solid material *	7.2 ± 0.2
Saccharomyces cerevisiae	96	Solid material *	6.7 ± 0.3
Aspergillus niger	120	Solid material **	16.2 ± 3.4
Penicillium chrysogenum	120	Solid material **	14.2 ± 2.6
Candida utilis	96	Solid material **	7.3 ± 0.3
Saccharomyces cerevisiae	96	Solid material **	6.6 ± 0.4

[1)] Note: * – after the first stage of regeneration; ** – after the second stage of regeneration.

Example 6. Secondary regeneration of a solidifying basis was conducted. For this purpose the disks with cultures of microorganisms from point 5 were treated as in point 5. The average diameter of *Aspergillus niger* colonies equals 16.2 ± 3.4 mm, *Penicillium chrysogenum* colonies equals 14.2 ± 2.6 mm, *Candida utilis* colonies equals 7.3 ± 0.3 mm, *Saccharomyces cerevisiae* colonies equals 6.6 ± 0.4 mm.

The results of four species cultivation of microorganisms after two successive stages of solid solidifying basis regeneration, as in examples 5 and 6, are indicated in the Table 3.

Applying solid porous inorganic materials as a basis for hard microbiological nutrient media has advantage before usage of known solidifying matters, as the nutrient media prepared on the new basis, have higher mechanical strength. The solidifying basis is cheaper and accessible and can be used repeatedly.

The results of tests of hard microbiological nutrient media prepared by developed and known ways have shown that the developed way allows to prepare nutrient media with higher exploitative properties, provides essential reduction of duration and simplification of preparation process of media to an inoculation. It meets the requirements of express extraction pathogenic microorganisms from environment and their cultivating.

References

Rosebury, T., Boldt, Kabat, T. (1947). Bacterial Warfare*, Journ. of Immunology*, 7-96.

Rosebury, T. (1949). *Peace or Pestilence, New* York.

Rożniatowski, T., Żółtowski, Z. (1957). *Wojna Biologiczna, Groźba a Rzeczywistość,* Wydawnictwo Ministerstwa Obrony Narodowej, Warszawa.

Rothschild, J. H. (1964). *Tomorrow's Weapons*, New York.

Hersh, S. (1969). *Chemical and Biological Warfare*, The Bobbs-Merrill Company, Indianapolis - New York.

Archangelsky, A.M., Grigoriev, A.M., Gromozdov, G.G., Kamorsky, N.M., Nujdin, I.N. (1971). *Bacteriological Weapon and Protection against It*, Voyenizdat, Moscow.

Meynell, G., Meynell, E. (1965). *Theory and Practice in Experimental Bacteriology,* At the University Press, Cambridge.

Proceedings of the 10th International Chemical and
Biological Engineering Conference - CHEMPOR 2008
Braga, Portugal, September 4-6, 2008
E.C. Ferreira and M. Mota (Eds.)

Influence of phosphate and maltose concentrations in the dextransucrose production by *Leuconostoc m. B-512-f*

M. Hernández, M. Peña Miranda*, G. González Benito
Department of Chemical Engineering and Environmental Technology
University of Valladolid. Pº Prado de la Magdalena s/n, 47011 Valladolid, Spain

Keywords: dextransucrose, dextran, *Leuconostoc mesenteroides*,

Abstract

In this work the obtention of the enzyme dextransucrose by *Leuconostoc mesenteroides B-512-f* has been made. The influence in the activity of the enzyme of phosphate concentration and the presence of the acceptor maltose was analysed. The technic of capilar electroforesis allowed identify dextransucrose as well as other enzymes in very low concentrations.

1 Introduction

Dextran $(C_6H_{10}O_5)_n$ is a high-molecular-mass polysaccharide of D-glucose, mainly linked by $\alpha(1\rightarrow6)$ glucosidic bonds in their major chains, which also possesses side-chains stemming 1-3, y 1-4 bonds (depending on the specific activity of dextransucrose). Dextran is a high added value product whose main applications are: blood-plasma substitute in the pharmaceutical industry, chromatographic separations, or as a sweetener and thickening agent in the food products.

The enzyme responsible for the synthesis of dextran is known as dextransucrose. These enzymes are synthesized from sucrose by various bacterial species from two genera *Leuconostoc mesenteroides and Streptococcus*. These enzymes are not however the only extracellular enzymes produced by these bacterium. Other enzymes able to produce others polymers are also generated, with the consequent negative influence on dextran production.

This research evaluated the influence of both phosphate and maltose concentration on the production of dextranosucrose by *Leuconostoc mesenteroides* B-512-f using sucrose as substrate, based on the hypothesis that the presence of activators can enhance the production of dextransucrose. Also the presence of other enzymes different to dextransucrose is studied.

2 Material and Methods

Microorganism

Leuconostoc mesenteroides NRRL B512-f from DSMZ (Deutsche Sammlung von Mikroorganismen und Zellkulturen GmbH) was used in the present investigation. The strain was stored at 4º C in Petri dishes of broth MRS (Cultimed) prior to inoculation. The inoculum was prepared by transferring bacterial colonies from Petri dishes to stirred E-flasks supplied with MRS broth and cultivated for 18 h at 30 ºC.

* Corresponding author. Tel + 34 983 423176. e-mail:pena@iq.uva.es

Dextransucrose was produced in a 1 L batch magnetically stirred tank reactor at 200 rpm. The fermentations were conducted at 23ºC and an initial value of pH of 7The composition of the medium was: 40 g/L sucrose, 20 g/L extract yeast; NaCl: 0,01 g/L; MnSO4·H2O: 0,01 g/L; FeSO4·7H2O: 0,01g/L MgSO4·2H2O: 0,20 g/L; CaCl2 : 0,10g/L {[5]. K2HPO4 concentrations ranged from 1 to 40g/L and Maltose concentrations from 2.5 to 10 g/L.

Analytical methods

The pH-value of every taken sample is analysed with a pH-Meter micropH 2002 (Crison). For the measurement of the optical density a spectrophotometer Hitachi U-2000 is used.

The method employed for determine the enzymatic activity of dextransucrose (measured as DSU) was described in a previous paper.

Analysis of carbohydrates was carried out by HPLC with an Aminex HPX-87-N column and a refractive index detector from Waters.

Electrophoresis in polyacrilamide gel with SDS (Bio-Rad MiniProtean III) was the technique used to identify dextransucrose.

3 Results

Influence of the acceptor maltose

Figure 1 show the results corresponding to two different fermentations, without maltose (a) and with a concentration of 5 g/L (b). As it can be seen the enzyme activity is higher when maltose is present in the fermentation medium.

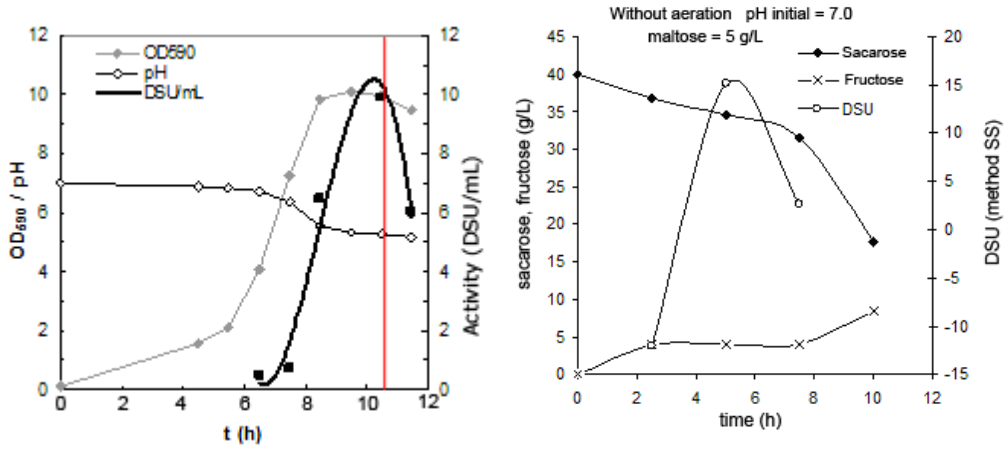

(a) (b)

Figure 1. Enzymatic activity. Influence of maltose concentration: 0 g/L (a) and 5 g/L (b)

Influence of phosphate concentration

The results obtained in the essays with different concentrations of phosphate are depicted in figure 2: 40 g/L (a), 10 g/L (b) and 1 g/L (c). All experiments were carried out with 5 g/L of maltose.

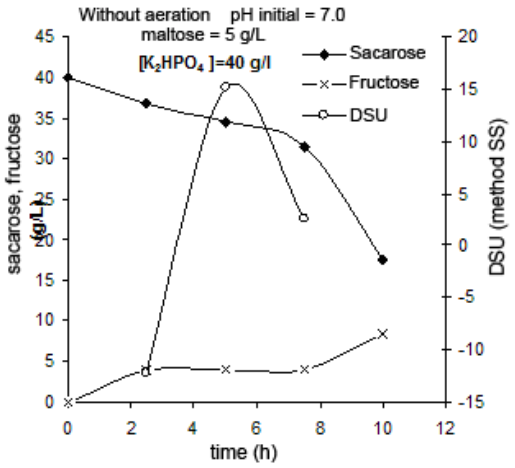

(a)

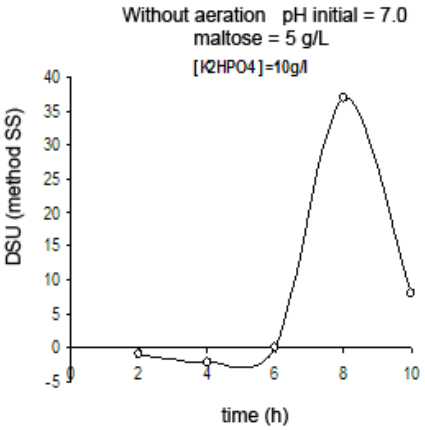

(b)

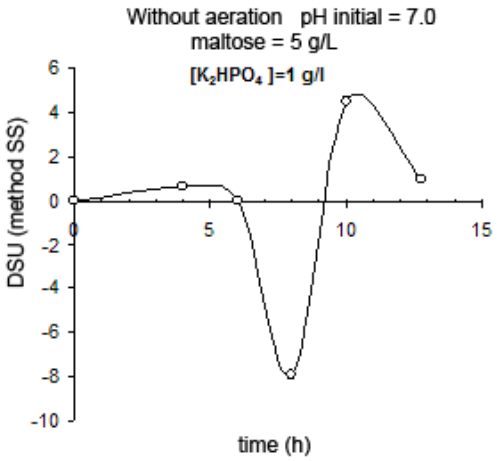

(c)

Figure 2 Enzymatic activity. Influence of K_2HPO_4 concentration: 40 g/L (a), 10 g/L (b), 1 g/L (c)

From the obtained results, it can be established that 10 g/L of phosphate is the best concentration that let the maximal activity of the enzyme, for an operation time of 8 h. Next, new tests were established to determine the most adequate level of maltose for this concentration of 10 g/L of phosphate. The results depicted in figure 3 indicate that dextransucrose exhibited a greater activity in the presence of 5 g/l of maltose (up to 35 DSU).

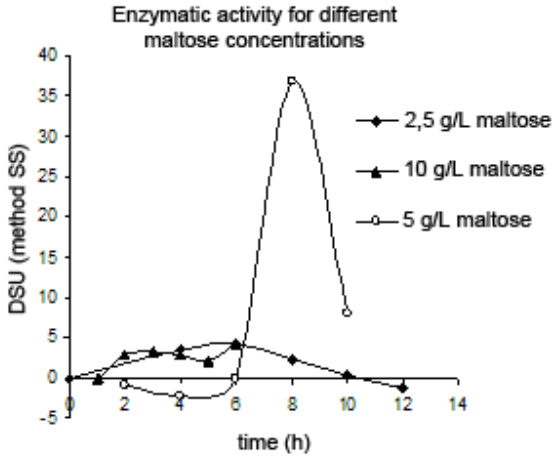

Figure 3 Enzymatic activity. Influence of maltose concentration

Identification of dextransucrose

In order to check the presence of enzymes different from dextransucrose, the gel electrophoresis technique was employed. The results are shown in figure 4. It can be seen a clear lane corresponding to a molecular weight of 190 kDa related to dextransucrose. Also, it appears diffuse lanes, that would indicate the presence of other enzymes in very low concentrations, and that could interfere in the activity of dextransucrose.

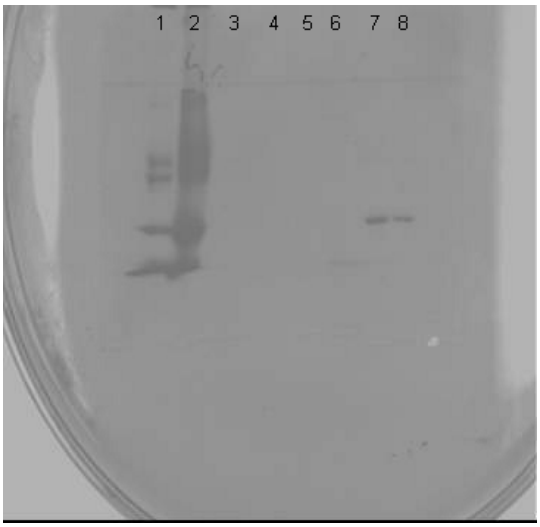

Figure 4 Identification of dextransucrose by electrophoresis

Acknowledgements
The authors acknowledge the financial support of this research to Ministerio de Educación y Ciencia CTQ2004-07312/PPQ.

References

Shah Ali UI-Qader, Lubna Iqbal,Husan Afroz Rizvi and Rabia Zuberi (2001). *Production of dextran from sucrose by a newly isolated strain of Leuconostoc mesenteroides (PCSIR-3) with reference to L.mesenteroides NRRL B-512*. Biotechnol.App.Biochem. 34, 93 - 97.

Rodrigues,S. Lona, L.M.F and Franco T.T (2003). *Effect of phosphate concentration on the production of dextransucrase by Leuconostoc Mesenteroides NRRL B512f*. Bioprocess and Biosystems Engineering, 26, 57 – 62.

Prabhu Arcot Padmanabhan, Dong-Shik Kim (2002). *Production of insoluble dextran using cell-bound dextransucrase of Leuconostoc Mesenteroides NRRL B-523.* Carbohydrate Research, 37, 1529 – 1533.

Lopretti, M.; Martinez, E.; Torres, L.; Perdomo, R.; Santos, M.; Rodrigues, A.E (1999) I*nfluence of nitrogen/carbon ratio and complementary sugars on dextransucrase production by Leuconostoc Mesenteroides NRRL B512f* . Process Biochemistry,.34, 879 – 884.

Rodríguez J., Peña M., García M., González G. *Producción óptima de dextranosacarosa a partir de Leuconostoc Mesenteroides NRRL B-512f.* Proceedings of Biotec'2004 Oviedo (Spain).

Proceedings of the 10th International Chemical and
Biological Engineering Conference - CHEMPOR 2008
Braga, Portugal, September 4-6, 2008
E.C. Ferreira and M. Mota (Eds.)

A Software Tool for Design of Evaporator Systems

Fernando G. Martins[1*], Marta I.M.S. Cruz[1], Domingos Barbosa[2]

[1] LEPAE – Chemical Engineering Department, Faculty of Engineering, University of Porto, Rua Dr Roberto Frias s/n, 4200-465 Porto, Portugal.

[2] CBQF-Pólo FEUP – Chemical Engineering Department, Faculty of Engineering, University of Porto, Rua Dr Roberto Frias s/n, 4200-465 Porto, Portugal.

Keywords: Evaporation, Single and multiple-effect evaporators, Add-in, Spreadsheet.

Topic: Educating chemical and biological engineers for coming challenges.

Abstract

A software tool, in the form of an add-in for Microsoft Excel, was developed for design of single and multiple-effect evaporators. The program uses the Newton-Raphson method to solve the system of equations describing the evaporation unit, and is applicable to forward and backward feed systems, with negligible or significant boiling point raises. This software can be used as an helpful teaching aid, or as a good tool for operator training or for preliminary design of evaporator systems.

1. Introduction

The concentration of a solution of a non-volatile component is usually accomplished by evaporation (McCabe et al., 1993). Evaporators are used in different types of industries, including the food and the chemical industry. Due to the fact that evaporation is one of the most energy intensive separation processes, multiple-effect evaporators are usually used to reduce energy consumption. Indeed, in multiple-effect evaporators the decrease in energy consumption is roughly proportional to the number of effects when the boiling point raise is negligible. However, the corresponding increase in equipment cost limits the maximum number of evaporators to be used in a multiple-effect system for a given separation. The calculation of the optimum number of effects requires an exact design and cost evaluation of the evaporation system.

Evaporator calculations are usually iterative and tedious, a hard task to carry out manually. These calculations require solving a system of non-linear equations, corresponding to the mass and heat balances, the phase equilibrium and the heat transfer. Moreover, the data for enthalpy and boiling point raise (BPR) is usually available in the form of graphics and tables, which makes the calculations tougher and even more tedious. Therefore, the development of a software tool, easily accessible, for the design of single and multiple-effect evaporators will be an especially useful tool for engineers.

This work presents a computer program, developed in Visual Basic for Applications, and available in the form of an add-in for Microsoft Excel, a widespread working tool for engineers. The software is able to perform calculations of single and multiple-effect, forward and backward, evaporator systems with up to ten effects, having either negligible or significant boiling point raises. The model equations are solved by means of the Newton-Raphson method (Holland, 1975), which proved to be fast and reliable for this type of calculations.

* Corresponding author. Tel + 351-22-5081974. E-mail:fgm@fe.up.pt

2. Model equations

To design an evaporator system, the following equations must be solved: mass balances, energy balances, phase equilibrium equations (i.e., the relationships between the saturation temperature of the solution and that of the pure solvent at the same total pressure), and heat transfer equations (i.e., the equations used to calculate the heat transfer areas). To exemplify the type of equations used, the three-effect forward evaporator system, shown in Figure 1, will be considered. The equations that describe this evaporation unit are the following (Holland, 1975):

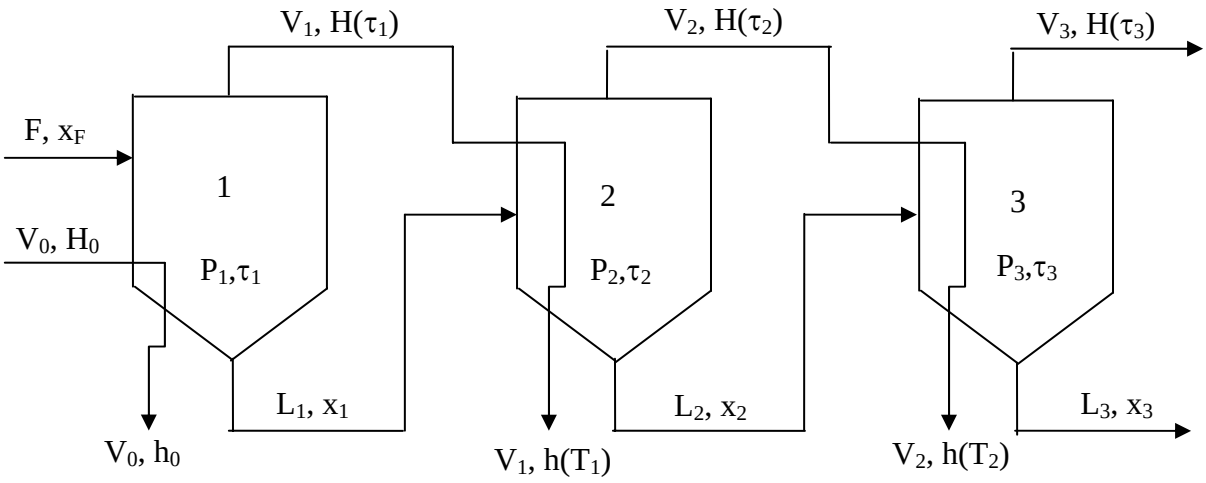

Figure 1 – Three-effect forward evaporator system

First effect:

$$f_1 = F[h(T_F,x_F) - h(\tau_1,x_1)] + V_0\lambda_0 - (F - L_1)[H(\tau_1) - h(\tau_1,x_1)] \quad (1)$$

$$f_2 = U_1A(T_0 - \tau_1) - V_0\lambda_0 \quad (2)$$

$$f_3 = \tau(T_1,x_1) - \tau_1 \quad (3)$$

$$f_4 = Fx_F - L_1x_1 \quad (4)$$

Second effect:

$$f_5 = L_1[h(\tau_1,x_1) - h(\tau_2,x_2)] + (F - L_1)[H(\tau_1) - h(T_1)] - (L_1 - L_2)\,[H(\tau_2) - h(\tau_2,x_2)] \quad (5)$$

$$f_6 = U_2A(T_1 - \tau_2) - (F - L_1)[H(\tau_1) - h(T_1)] \quad (6)$$

$$f_7 = \tau(T_2,x_2) - \tau_2 \quad (7)$$

$$f_8 = Fx_F - L_2x_2 \quad (8)$$

Third effect:

$$f_9 = L_2[h(\tau_2,x_2) - h(\tau_3,x_3)] + (L_1 - L_2)[H(\tau_2) - h(T_2)] - (L_2 - L_3)\,[H(\tau_3) - h(\tau_3,x_3)] \quad (9)$$

$$f_{10} = U_3A(T_2 - \tau_3) - (L_1 - L_2)[H(\tau_2) - h(T_2)] \quad (10)$$

$$f_{11} = \tau(T_3,x_3) - \tau_3 \quad (11)$$

$$f_{12} = Fx_F - L_3x_3 \quad (12)$$

where:

T_j – saturation temperature of pure solvent on effect j, at pressure P_j;

τ_j – boiling point temperature of the liquid solution on effect j, at pressure P_j and composition x_j;

$h(T_j)$ – enthalpy of pure solvent in the liquid state, evaluated at the saturation temperature T_j corresponding to pressure P_j on effect j;

$H(T_j)$ – enthalpy of pure solvent in the vapour state, evaluated at the saturation temperature T_j corresponding to pressure P_j on effect j;

$H(\tau_j)$ – enthalpy of the solvent in the vapour state, evaluated at the temperature of the liquid solution, τ_j, on effect j, corresponding to pressure P_j and composition x_j;

$h(\tau_j,x_j)$ – enthalpy of the liquid solution leaving effect j, evaluated at P_j, τ_j, and x_j;

$h(T_F,x_F)$ – enthalpy of the liquid feed, evaluated at the feed temperature, pressure and composition (T_F,P_F, x_F).

For calculating the solution temperature and enthalpy, the program allows the operator to fit the existing experimental data to Equations (13) to (15). Equation (13) correlates the data for the boiling point raise, BPR = $\tau_j - T_j$, which is usually in the form of a Dühring diagram, that relates the solution temperature to the pure solvent saturation temperature at the same total pressure. Equation (14) is used to correlate the available data for the solution enthalpy, which, alternatively, may be evaluated by means of heat capacity data (equation (15)).

$$BPR = ax^3 + bx^2 + cx + d + e/x + f/x^2 \quad (13)$$

$$H = aT^3 + bT^2 + cT + dx^3 + ex^2 + fx + g/x + h \quad (14)$$

$$C_P = aT^3 + bT^2 + cT + dx^2 + ex + f \quad (15)$$

The system of equations, f_1 through f_{12}, was solved by the Newton-Raphson method,

$$\underline{\underline{J}}_k \, \underline{\Delta X}_k = -\underline{f}_k \quad (16)$$

where $\underline{\underline{J}}_k$ is the system Jacobian, a 12x12 matrix of the partial derivatives of equations f_1 – f_{12} relative to the 12 project variables (i.e., V_0, τ_1, T_1, L_1, x_1, τ_2, T_2, L_2, x_2, τ_3, L_3, A), which is numerically evaluated, $\underline{\Delta X}_k$ is the vector of increments for the 12 unknowns in the k^{th} iteration, and $\underline{f}_k$ is the vector with the values of the 12 functions in the k^{th} iteration, which must be equal to zero when solution is reached. A more detailed discussion of the application of the Newton-Raphson method to solve the non-linear system of equations for multiple-effect evaporators can be found in Holland (1975).

3. Calculation example

The developed add-in for the calculation of the evaporator system allows the user to interact with the program by means of self-explanatory user-forms. The input data and the results are summarized in a spreadsheet.The add-in allows the operator to use this generated spreadsheet to run again the program for other conditions, without needing to type in all the input information. The program also allows the user to choose between giving the first estimates, which can be helpful when dealing with difficult converging problems, or letting the program to calculate them. The operator can also set the convergence tolerance and the maximum number of iterations. In the specification of the problem, besides the feed flowrate and the inlet and outlet solute concentrations, the pressure (or temperature) in the last effect, the pressure (or temperature) of the steam used as heating medium, and the enthalpic feed condition must be specified.

The application of the software will be exemplified by considering the concentration of a stream of 7500 kg/h of a solution of sodium hidroxide (NaHO), from 10-60%, in a 3-effect forward feed evaporation system. The remaining input data can be seen in Figures 2 and 3, which are screenshots of the input form and the spreadsheet generated by the program, respectively. The boiling point and enthalpy data for the NaHO solution was obtained by fiting Equations (13) and (14) to the curves of the Dühring and solution enthalpy diagrams, respectively, available in McCabe et al. (1993). This is a good example of a difficult converging problem, due to the significant boiling point elavation. Nevertheless, the solution was reached after 5 iterations, using first estimates generated by the program.

To further exemplify the potencialities of the developed add-in, the same example was also run assuming backward feed. The results of these calculations are shown in Figure 4.

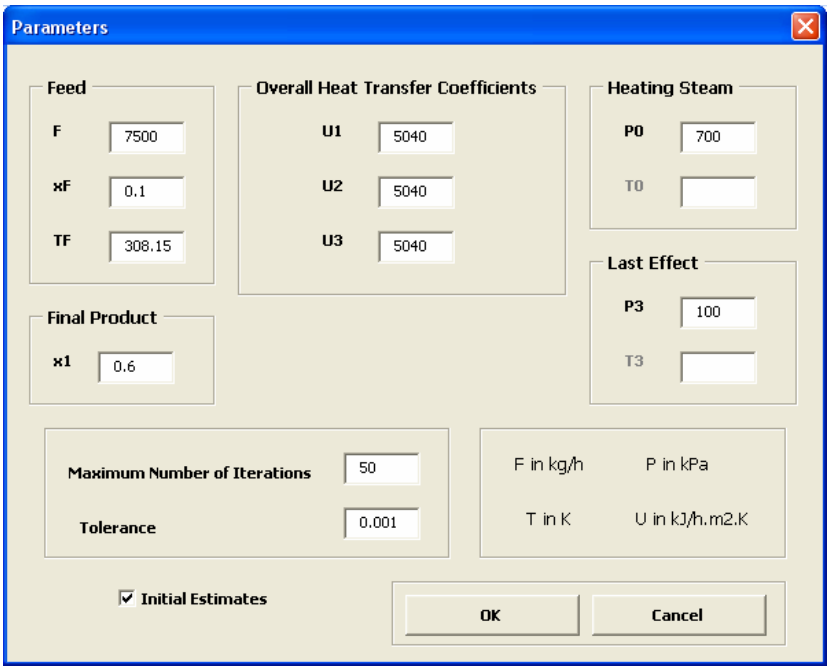

Figure 2 – Screenshot of the input form for a 3 multiple-effect evaporator system

4. Conclusions

An add-in for Microsoft Excel was developed for design of single and multiple-effect evaporators, with forward or backward feed, and having negligible or significant boiling point raises. The interaction with the operator is made by self-explanatory forms, and the physical data input by means of equations (eq. 13-15), whose constants may be obtained by fitting them to available experimental data. The resulting system of equations is solved by means of the Newton-Raphson method, which revealed to be reliable and fast for these types of calculations. The first estimative may be given by the operator, or generated by the program. The results and corresponding input data are summarized in a spreadsheet, which can be used by the program as an input file to run other examples under different initial conditions.

This software can be used as an helpful teaching aid, and as a good tool for operator training or for preliminary design of evaporator systems.

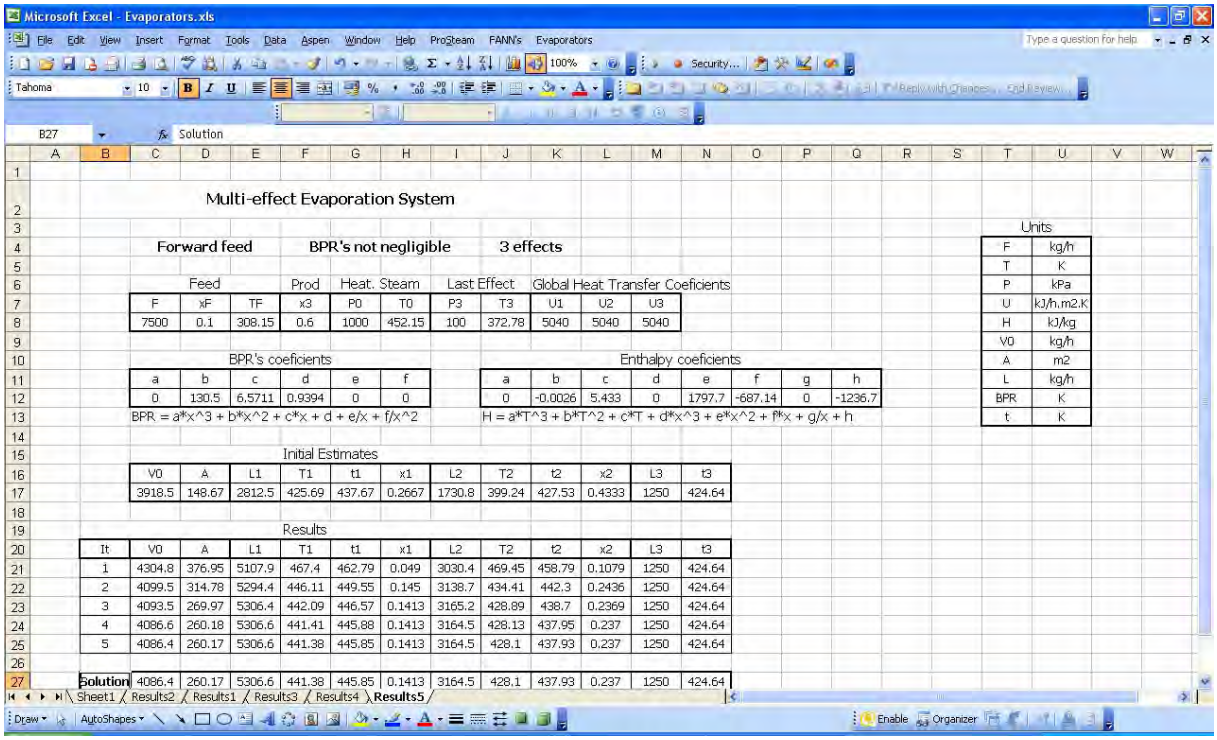

Figure 3 – Screenshot of the spreadsheet generated for the forward feed example.

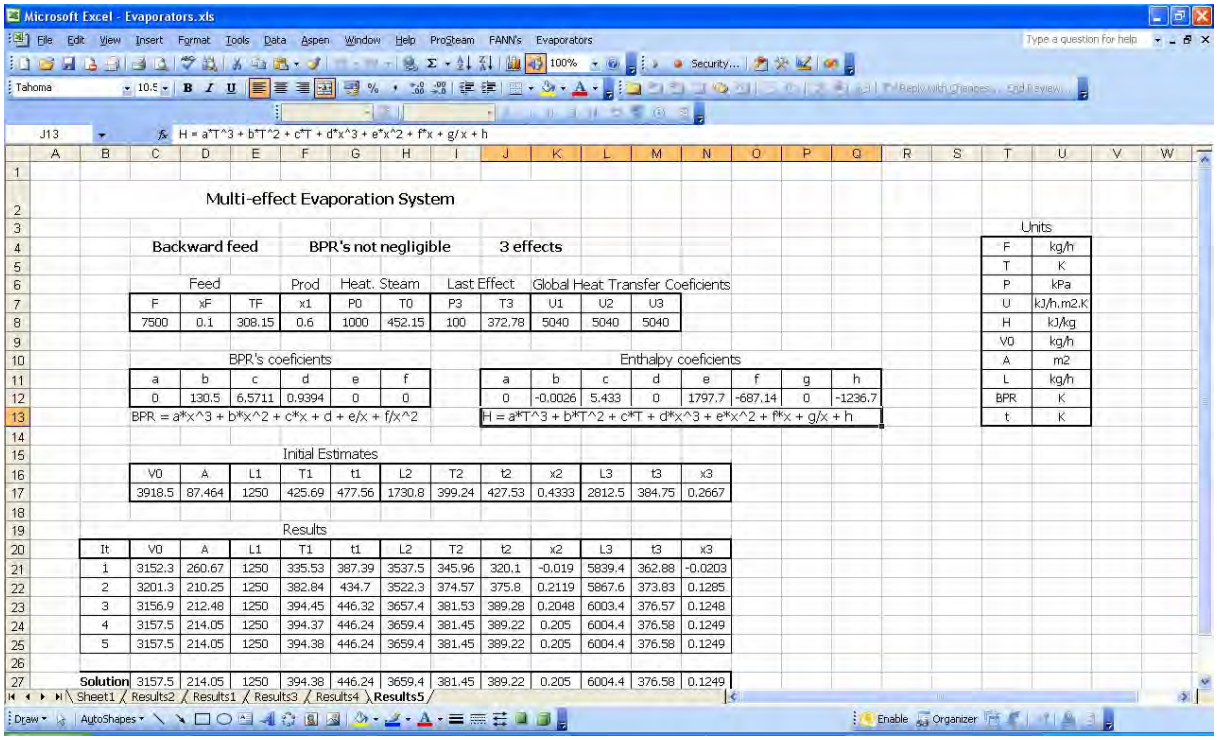

Figure 4 – Screenshot of the spreadsheet generated for the backward feed example.

References

Holland, C.D. (1975). Fundamentals and Modeling of Separation Processes: Absorption, Distillation, Evaporation and Extraction, Prentice-Hall, New Jersey.

McCabe, W.L., Smith, J.C., Harriott, P. (1993). Unit Operations of Chemical Engineering, 5th edition, McGraw-Hill International Editions, Singapore.

Proceedings of the 10th International Chemical and
Biological Engineering Conference - CHEMPOR 2008
Braga, Portugal, September 4-6, 2008
E.C. Ferreira and M. Mota (Eds.)

Process synthesis for hydrogen production from glucose: bioreactor design and scale-up and downstream process

Alice M. de Lima, Adilson J. de Assis[1*]
[1] School of Chemical Engineering, Federal University of Uberlandia
Av. Joao Naves de Avila 2121 Bl. 1K, Campus Santa Monica, 38408–100 Uberlandia MG, Brazil.

Keywords: Reactor scale-up; hydrogen from biomass; separation; process simulation.
Topic: Educating chemical and biological engineers for coming challenges.

Abstract

Recognized as one of the most promising energy carrier of the future hydrogen can be produced using several sources, renewable or not. Amongst the renewable alternatives, some have been distinguished as the most promising, such as: electrolysis of water, electrolysis of steam, thermochemical decomposition of water, photoelectrochemical processes, biophotolysis of water, photodecomposition of organic compounds, ethanol reforming and fermentation of organics. The fermentation of organic compounds is considered one of the most promising sustainable alternatives in the future for hydrogen production from biomass. On this basis, this work aims to discuss the integration of the following subjects in process synthesis and design: experimental data published in literature; bioreactor design and scale-up; synthesis of downstream process; process simulation; technical-economic viability analysis, and sustainability. The authors hope that the integrated methodology presented here can help senior process design course instructors to plan their activities.

1 Introduction

Recognized as one of the most promising energy carrier of the future hydrogen can be produced using several sources, renewable or not. Amongst the renewable alternatives, some have been distinguished as the most promising, such as: electrolysis of water, electrolysis of steam, thermochemical decomposition of water, photoelectrochemical processes, biophotolysis of water, photodecomposition of organic compounds, ethanol reforming and fermentation of organics. The fermentation of organic compounds is considered one of the most promising sustainable alternatives in the future for hydrogen production from biomass (Liu et al., 2008; Vijayaraghavan and Soom., 2008).

On this basis, this work aims to do a technical-economic viability analysis of hydrogen production by fermentation route considering bioreactor design and scale-up as well as downstream process. It will be discussed the integration of the following subjects in process synthesis and design: experimental data published in literature; bioreactor design and scale-up; synthesis of downstream process; process simulation; technical-economic viability analysis, and sustainability.

The authors hope that the integrated methodology presented here can help senior process design course instructors to plan their activities.

2 Reactor design and scale-up

The species from the genus *Clostridium* are known as acid producers and usually they can ferment glucose to butirate, acetate, carbon dioxide and molecular hydrogen. The following reactions show

*Corresponding author. Tel. +55-34-3239-4292. E-mail: ajassis@ufu.br

hydrogen production trough fermentation of glucose:

$$C_6H_{12}O_6 \longrightarrow 2CH_3COOH + 4H_2 + 2CO_2 \quad (1)$$

$$C_6H_{12}O_6 \longrightarrow C_3H_7COOH + 2H_2 + 2CO_2 \quad (2)$$

$$C_6H_{12}O_6 \longrightarrow 2C_2H_5OH + 2CO_2 \quad (3)$$

Lin et al. (2007) carried out a series of experiments with four species of *Clostridium* and proposed a Monod like kinetic model modified by an empirical law that takes into account pH inhibition (I_{pH}). Amongst the studied microorganisms, *C. beijerinckii* presented the greatest productivity, whose parameters of reference had been used in this work.

For the rate of glucose consumption, it was used the expression $r_{glu} = (q_{Glu}^{max} S_{Glu} X)/(K_{Glu}+S_{Glu}).I_{pH}$, where *X* denotes biomass concentration, q_{Glu}^{max} maximum specific glucose consumption rate, S_{Glu} residual glucose concentration, and K_{Glu} Monod half-saturation constant. The empirical lower pH inhibition term, I_{pH}, according to Lin et al. (2007), was defined as being $I_{pH} = exp(-3((pH - pH_{UL})/(pH_{UL} - pH_{LL}))^2)|_{pH<pH_{UL}}$, where pH_{UL} and pH_{LL} represents the upper limit at which bacteria are not inhibited (I_{pH}=1 when pH > pH_{UL}), and the lower limit at which inhibition is complete. Using the experimental and kinetic data presented by Lin et al. (2007), new kinetic parameters model were adjusted in this work, considering only glucose as limiting substrate.

After that, bioreactor scale-up was accomplished (stirred batch reactor), using mathematical unsteady-state mass balances (Bailey and Ollis, 1986) and computer simulation. The glucose consumption was directly calculated, and the changes in biomass (*X*), hydrogen (C_{H_2}), carbon dioxide (C_{CO_2}), butanol ($C_{Butanol}$), lactic acid (C_{HLa}), acetate (C_{HAc}) and butyrate (C_{HBu}) concentrations was calculated using the stoichiometric relations as shown in Table 1.

Table 1: Stoichiometric matrix of glucose fermentation

	S_{glu}	S_{HAc}	S_{HBu}	S_{H_2}	X
Glucose consumption	-1	$(1-Y)f_{HAc}$	$(1-Y)f_{HBu}$	$(1-Y)f_{H_2}$	Y

In order to perform the reactor design and scale-up, a suitable dynamic model was developed through mass balances. The model is a set of ordinary differential equations with initial value problem as showed in the following equations:

$$\frac{dS_{Glu}}{dt} = -r_{Glu} \quad (4)$$

$$\frac{dX}{dt} = -Y.\frac{dS_{Glu}}{dt} \quad (5)$$

$$\frac{dC_{H_2}}{dt} = -(1-Y).f_{H_2}.\frac{dS_{Glu}}{dt} \quad (6)$$

$$\frac{dC_{CO_2}}{dt} = -Y_{CO_2}.\frac{dS_{Glu}}{dt} \quad (7)$$

$$\frac{dC_{Butanol}}{dt} = -Y_{Butanol}.\frac{dS_{Glu}}{dt} \quad (8)$$

$$\frac{dC_{HLa}}{dt} = -Y_{HLa}.\frac{dS_{Glu}}{dt} \quad (9)$$

$$\frac{dC_{HAc}}{dt} = -(1-Y).f_{HAc}.\frac{dS_{Glu}}{dt} \quad (10)$$

$$\frac{dC_{HBu}}{dt} = -(1-Y).f_{HBu}.\frac{dS_{Glu}}{dt} \quad (11)$$

The model was solved using the free software Scilab (www.scilab.org) with **ode** function and **lsoda** integrator. With the new parameters adjusted in this work, it was obtained a good concordance between simulated (this work) and experimental data (Lin et al., 2007), as showed in Figure 1.

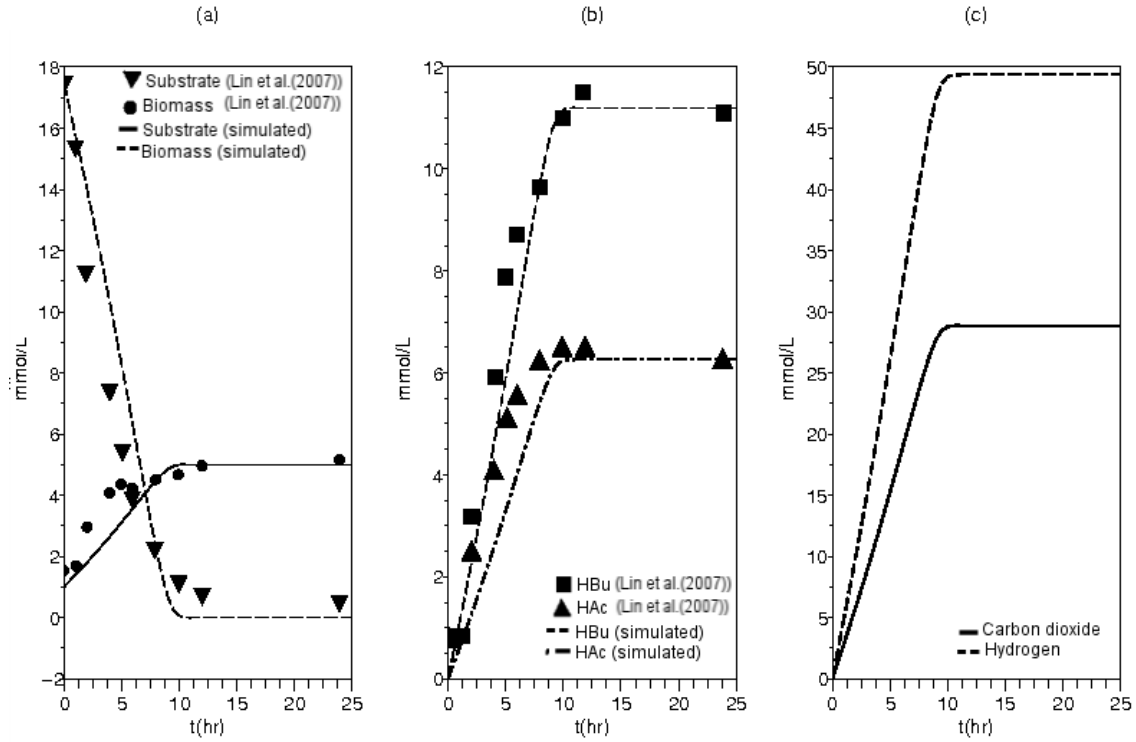

Figure 1: Simulation result for: (a) substrate and biomass concentrations, (b) acids concentrations, (c) gases.

3 Downstream process synthesis

The proposed downstream process is constituted basically by:

1. Gas separation subsystem, with hydrogen recovery and compression; it was also considered the purification and compression of carbon dioxide as valuable byproduct;
2. Liquid separation, namely acetic and butyric acids, by means of liquid-liquid extraction and distillation.

The process flowsheet synthesis was accomplished following the conceptual design methodology proposed by Douglas (1988) at level 4, and it is shown in Figure 2. For CO_2 capture, it was considered absorption with MEA and a 99% of recovery, as reported in the literature. The vapour phase from exit reactor is feed in an absorber tower (T-101) bottom and the solvent solution on the top of it. Inside the absorber, the absorvent solution (MEA) reacts chemically with carbon dioxide from effluent gas. The gas rich in hydrogen follows to the section of recuperation and compression. The solution rich in carbon dioxide follows to the regeneration tower (T-102). In this column, CO_2 is withdrawn from MEA through temperature increase. The solvent (MEA) is colled in heater exchanger (E-101) to increase the solubility of CO_2, making it possible the absorption operation. The CO_2 liberated in stripping column follows to compression (C-101 and C-102) and cooling (E-102 and E-103), allowing gas condensation on technically viables temperatures, what is realized in two stages. The gas is then sent to a flash vessel (V-101) for withdrawn of vapour and solvent. After that, it is compressed (C-103) and colled (E-104), and then sent to an adsorption column (T-103) that uses silica gel as dessicant agent, to remove moisture from gas mixture, avoiding ice formation in the next heater exchanger (E-105). In sequence, CO_2 is sent to be stored (V-102).

To recuperate and compress hydrogen, the gas stream from absorption tower (T-101) is cold in a heater exchanger (E-201), compressed (C-201) and then follows to a flash vessel (V-201), where water and CO_2 are separated. To remove traces of CO_2, the mixture is colled (E-202) and follows to a flash (V-202). The liquid stream from flash is sent to a section that captures CO_2. The vapor phase exiting V-202 follows to another stage of compression (C-202), where it is compressed to 340 atm, the usual pressure to store

liquid hydrogen.

Separation of liquid stream is done by liquid-liquid extraction tower (T-301). The stream rich in butyric acid (extract phase) is heated (E-301) and sent to a flash (V-301) for withdrawn of water and then heated again (E-302). The stream 35 (water, butyric and acetic acids, and solvent – decanol or oleyl alcohol) is sent to a first distillation column (T-302), where the distillate product is a acetic solution, and the bottom product follows to the second distillation column (T-303), where the top product is a butyric acid solution, and the bottom product returns to the extractor column.

The proposed downstream process flowsheet was simulated using the free software and chemical processes simulator Sim42 (Assis and Oliveira-Lopes, 2005; Assis et al., 2006) with VMGSim interface from Virtual Materials (www.virtualmaterials.com). Peng-Robinson and Advanced Peng-Robinson were used as thermodynamic package in all simulations. Simulation shows that it is possible to obtain hydrogen with a high purity (0.999%), which increases the yield of fuel cells using hydrogen and oxygen as reactants for energy generation.

4 Economic evaluation

The costs of the equipments were calculated using the methodology proposed by Peters and Timmerhaus (1991) and Henley and Seader (1981). For reaction and gas separation subsystem, the mainly direct annualized costs are showed on Table 2, using a return rate of 20%. The installed costs were estimated with inflaction factor indices of year 2000 (CEPCI=392.4 and MSI=1089). The costs of utilities, maintenance, start-up, piping, instrumentation and control, were estimated according to Peters and Timmerhaus (1991). All calculations were done using Scilab.

The accuracy of a "preliminary design estimate" is typically -30% to +50% (Peters and Timmerhaus, 1991). At this level of accuracy, the resulting costs of production were 1.17 USD and a profit of 0.66 USD for kilogram of produced hydrogen. Thus, the cost of hydrogen production by fermentation reveals to be economically attractive, and more viable than the gasification of the biomass, that presents a cost of production of 2.2 USD for kilogram of H_2, approximately.

Table 2: Direct and Indirect costs of process.

Equipment	Installed Cost ($)	Annualized Cost ($/year)
Fermentor	2,980,636.00	596,127.00
Stirrer	69,834.00	13,968.00
V-101	134,537.00	26,908.00
T-103	49,443.00	9,889.00
C-101	32,700.00	6,540.00
C-102	21,800.00	4,360.00
C-103	14,170.00	2,834.00
V-201	328,869.00	65,773.00
V-202	127,437.00	25,487.00
C-201	1,417.000.00	283,400.00
C-202	872,000.00	174,400.00
Total	6,048,425.00	1,209,685.00
Annual Profit		6,285,505.00
Utilities		241,937.00
Maintenance		96,775.00
Start-up		120,969.00
Piping		241,937.00
Instrumentation and Control		96,775.00
Annual Profit		5,487,112.00

5 Conclusions

Although in initial steps of development, the technology of hydrogen production by fermentation reveals to have both technical and economical viability. In this work, it was presented a preliminary design flowsheet considering reaction and downstream. The profit showed to be attractive and detailed flowsheet and cost estimates should be done in further investigations. Based on the steps presented here, the student can see how to integrate basic and technical information in sustainable process design and simulation. Furthermore, the authors hope that the integrated methodology presented here can help senior process design course instructors to plan their activities.

Acknowledgement

This work was supported by Brazilian funding agency CNPq (undergraduate scholarship PIBIC/UFU). The authors are grateful for the assistance of Dr. Ubirajara Coutinho Filho in bioreactor design and scale-up.

References

Assis, A. J., Oliveira-Lopes, L. C. (2005). Free software for chemical engineer's educational needs. *ENPROMER 2005 - 2nd. Mercosur Congress on Chemical Engineering, 4th. Mercosur Congress on Process System Engineering*, Rio de Janeiro, Proceedings, v. 1. p. 1-10.

Bailey, J.E., Ollis, D. F. (1986). *Biochemical Engineering Fundamentals*, McGraw-Hill, New York.

Dias, R. S., Silva, L. C., Assis, A. J. (2006). Plant wide simulation using the free chemical process simulator Sim42: natural gas separation and reforming, *17th International Congress of Chemical and Process Engineering*, Prague, v. P5.105, p. 1-14.

Douglas, J. M. (1988). *Conceptual design of chemical processes*, McGraw-Hill.

Henley, E.J., Seader, J.D. (1981). *Equilibrium Stage Separation Operations in Chemical Operations*, John Wiley & Sons, USA.

Lin, P., Whang, L.-M., Wu, Y.-R., Ren, W.-J., Hsiao, C.-J., Li, S.-L., Chang, J.-S. (2007). Biological hydrogen production of the genus *Clostridium*: metabolic study and mathematical model simulation, *International Journal of Hydrogen Energy*, 32, n. 12, 1728-1735.

Liu, X., Ren, N., Song, F., Yang, C., Wang, A. (2008). Recent advances in fermentative biohydrogen production, *Progress in Natural Science*, 18, n. 3, 253-258.

Peters, M. S., Timmerhaus, K. D. (1991). *Plant Design and Economics for Chemical Engineers*, McGraw-Hill, New York.

Vijayaraghavan, K., Soom, M. A. M. (2008). Trends in biological hydrogen production –a review, *International Journal of Hydrogen Energy*, `http://dx.doi.org/10.1016/j.ijhydene.2004.10.007`.

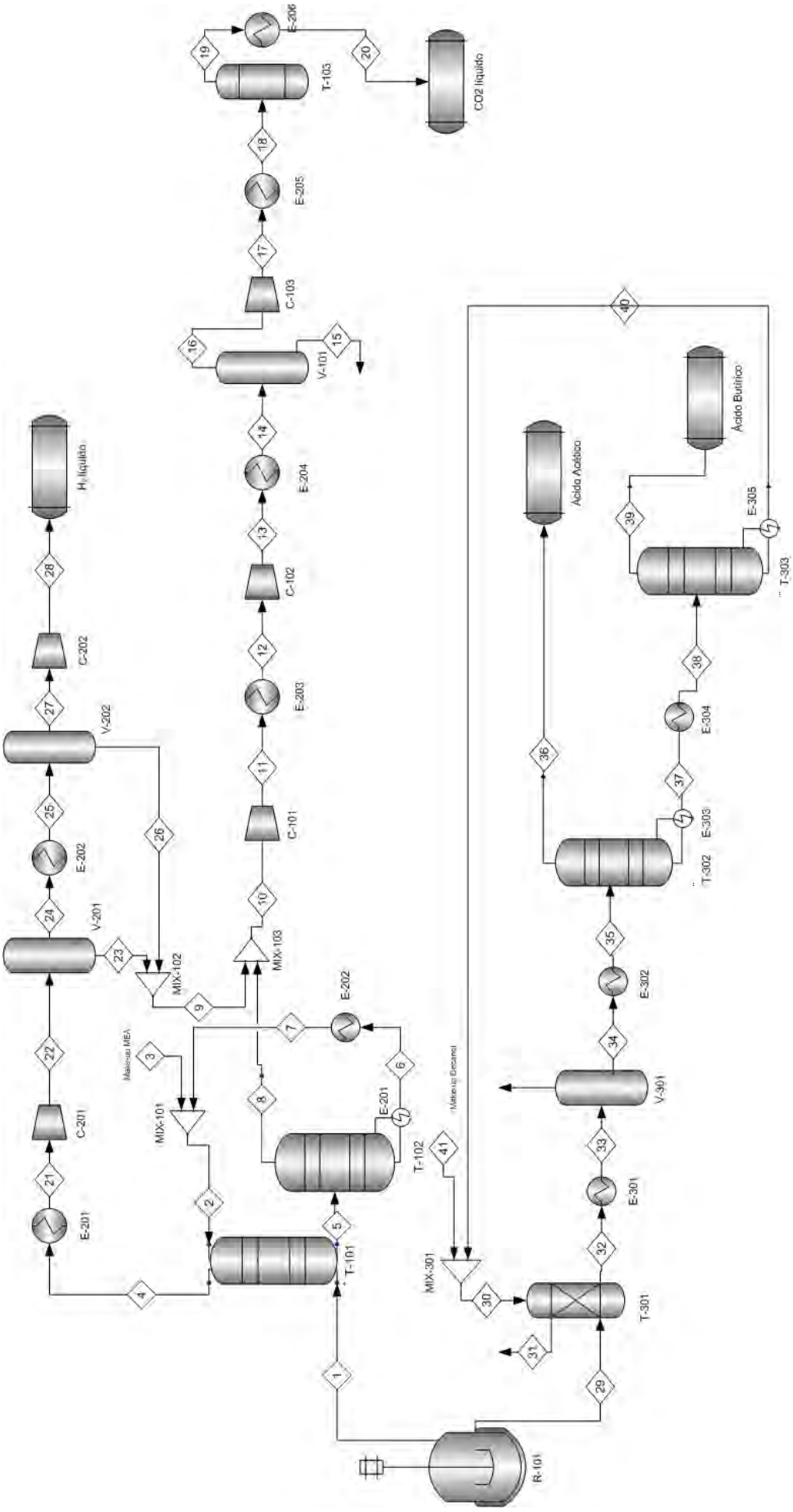

Figure 2: Proposed flowsheet for hydrogen production using fermentation route.

Proceedings of the 10th International Chemical and
Biological Engineering Conference - CHEMPOR 2008
Braga, Portugal, September 4-6, 2008
E.C. Ferreira and M. Mota (Eds.)

Teaching and learning strategies to improve the development of student skills in Chemical Engineering Degree

S. Lucas, M.T. García-Cubero, A. Cartón, S. Bolado, P.A. García-Encina, G. González-Benito, M-A. Urueña
Departamento de Ingeniería Química y Tecnología del Medio Ambiente – Facultad de Ciencias, Universidad de Valladolid, Prado de la Magdalena s/n, 47011 Valladolid, Spain

Keywords: Teaching-learning strategies, Skills, Chemical Engineering
Topic: Educating chemical and biological engineers for coming challenges

Abstract

The new reorganization of university education according to the European Higher Education Area (EHEA) guidelines involves relevant changes in teaching and learning methodologies. In this sense specific strategies will have to be implemented in order to help students to learn more successfully and to develop important skills and competences requested by the professional world. The subjects included in each level of education degree will be design in terms of learning outcomes and competences. Learning outcomes will be defined on basis of specific contents developed in each subject whereas the acquisition of skills requires a parallel programming of them. A summary of the main progress in competence training for chemical engineers of Valladolid University got up to now is presented in this work. Moreover, main transferable skills are identified, the possibilities and resources to develop them within our actual program of studies are analysed, including a detailed description of an educational activity based on a case study methodology, and a reflection of evaluation procedure is done.

1. Introduction

The education of chemical engineers in the frame of Bologna process must be focused not only to develop learning outcomes directly connected with knowledge but also transferable skills. In this sense, the new European Higher Education Space involves an important modification of the actual teaching-learning system, based on the use of new methodologies to help student to acquire the knowledge and the skills and competences requested by the professional world.

The teaching and learning methods should also help to develop students' skills (Molzahn, 2006), to work both independently and in teams. Thus, to learn to function in teams, group work is necessary. To be able to communicate, communication tasks must be given and solved. To learn to learn and to take responsibility for their own learning, students must receive appropriate self-study and problem solving tasks during their study. To understand ethical, societal, environmental and professional issues, suitable examples for illustration or discussion must be included (Felder & Brent, 1999).

Recent studies have revealed that the majority of chemical engineering graduates find employment in a wide range of industries including oil, petrochemicals, pharmaceuticals, biotechnology, food and the environment. Chemical engineers are professionals able to tackling a wide variety of problems: turn laboratory bench-top phenomena into production processes, have an integrated approach to systems, work within and often manage teams of theoretical and experimental chemists, mechanical and civil engineers, accountants and health and safety officials, apply fundamental scientific understanding and engineering principles to industrial, laboratory and molecular processes. The new working positions require the development of general and transferable skills besides chemical engineering knowledge. As a consequence universities should place more emphasis on developing

students' transferable skills (Grant and Dickson, 2006).

In this work the main progress in competence training for chemical engineers of Valladolid University got up to now is presented. The partial objectives to be carried out in order to get this global aim are the followings:

1. Identify the main transferable skills for chemical engineering curricula
2. Adapt the subject programmes to help students to develop these transferable skills
3. Evaluate the student's competence and knowledge acquisition levels

2. Identification of transferable skills

Taking as reference the analysis extracted from numerous studies related to accreditation of engineering programs contributed by leaders of universities, associations or professional bodies (ICheme, ABET, ANECA, WCEC and UVa) have revealed that the most important generic attributes for chemical engineers are connected with the capacity to communicate effectively, including in english, the ability to work in multidisciplinary teams, the capacity to understand the basic principles underlying chemical engineering and be able to use them to set up and to solve problems and the ability to learn on his/her own, and have a recognition of the need for life-long learning (Cartón *et al*., 2007). As an example, the relevance and development degree of transferable skills and abilities to work as chemical engineers in a scale 1 to 5 (1 means very low and 5 very high) are presented in **Figure 1** (WCEC, 2004).

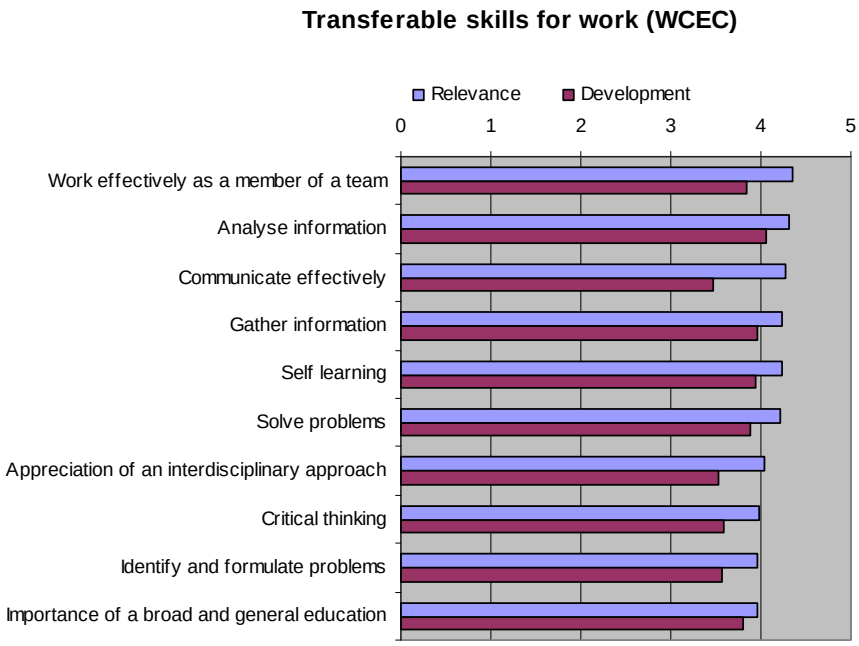

Figure 1. Relevance and development degree of transferable skills to work as chemical engineers.

3. Teaching and learning strategies for transferable skills acquisition

Integrated and global teaching and learning methodologies have been carried out in Chemical Engineering Degree at Valladolid University to help students to develop these transferable skills The learning objectives were established not only for every one of the specific subjects considered but also for the general skills to be acquired for the student. So, these learning methodologies include classical theoretical and practical classes but also propose individual and team works. Different activities such as oral presentations, written reports, discussion sessions, conferences and technical visits have been planned for all the semester subjects (Lucas *et al.*, 2008). Moreover, new methodologies for improving these

transferable skills were applied. In this sense, as an example, Based Problem Learning or appropriate computational tools facilitate the application of basic principles to problem resolution, the preparation of written reports, mini-projects and oral presentations improve the student capacity to communicate effectively or common collaborative techniques such as jigsaw, peer review, brainstorming or case study promote the learning based on work in teams (De Miguel, 2006).

In this paper a common activity based on the ***case study methodology*** applied to a real industrial production process is analyzed. This learning strategy is the main part of the global course activities developed and implemented in the seventh semester of a 5 years Chemical Engineering Degree and allow to integrate the different subjects involve in this course: Chemical reactors, separation processes, environmental technology and process instrumentation. The students, working in teams, study the proposed chemical process initially as a whole and later defined in different blocks. For each subject, different block aspects were detailed: selection of alternatives, operation mode, dimensioned for the equipment selected, system analysis, etc. At the final of the semester, students present the main results in a written report and also in an oral presentation in public session with all the teaching staff involved in the course, invited professionals and the rest of students. After every presentation, a discussion time is programmed in order to establish the main considerations to be made for every problem proposed.

The main objectives of the proposed methodology were to provide to the student with a holistic, integrated and applied vision of the different subjects involved in Chemical Engineering and at the same time to help students to develop transferable skills (team work, communication skills, life long learning).

The partial objectives to be carried out in order to develop and implemented this methodology were:

1. Adapt the programs of the different subjects to the total available workload of the students (ECTU) including the learning outcomes and the general abilities and competences previously established
2. Select and plan the case study. Production of ethanol from sugar beet was the selected industrial process for this course
3. Programme the different activities and elaborate an specific schedule for students that includes oral presentation and written reports, tutorial sessions, conferences, technical visits (student guide)
4. Evaluate the learning strategy as a whole taking into account the academic results (skills and knowledge acquisition) and the global learning process (planning, coordination, workload, etc.)
5. Create effective virtual case study course with Moodle that includes forums, textual resources (general information related to educational methodology, chemical engineers abilities and evaluation criteria; textbooks and exercise books), home-learning resources (video recordings, audio recordings), demonstration resources (laboratory experiments, simulators…), quizzes (partial evaluations), calendar (global, group and user events) and other activities (technical visits, conferences, upcoming events). The global structure of the virtual course is shown in **Figure 2**.

A complete description of case study methodology can be found in previous works (García Cubero *et al.*, 2007 and 2008)

4. Teaching and learning process evaluation: transferable skills and knowledge acquisition levels

Figure 2. Structure of case study virtual course.

Academic results of students during the last three years are collected in **Figure 3**. All students involved in the case study activity pass the evaluation. Most of students (> 70%) are in the range of qualifications 7 – 9 (good/very good) and a 25% of students are in the range of 9-10 (excellent). These results indicate the high motivation and implication level of the students in the activity proposed. Moreover during the last course, when virtual course was implemented in Moodle, no significant differences have been found in the students yield.

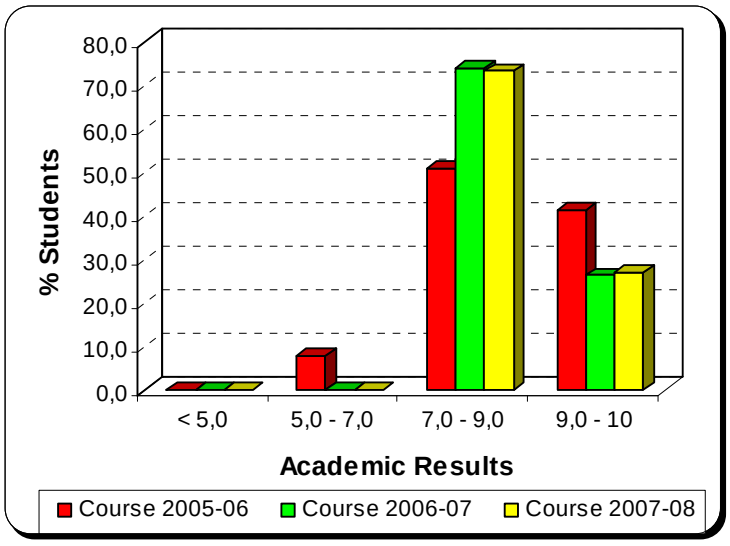

Figure 3. Trend in the academic results of students in the case study activity.

As it has been mentioned previously, one of the main objectives of this activity was to provide the student an integrated vision of the subjects involved in the seventh semester of the degree. Moreover, the acquisition of important transferable skills as team work, communication skills, etc. are intended to promote with the implementation of this learning strategy. A questionnaire with 15 transferable and specific skills was prepared. Both students and teachers evaluate every one of the skills in a 1 to 5 points scale (very low to very high) with a double sense: firstly the relevance that every item had for them and secondly the level of acquisition got with the proposed methodology in the case study activity. Results are summarized in **Figure 4.**

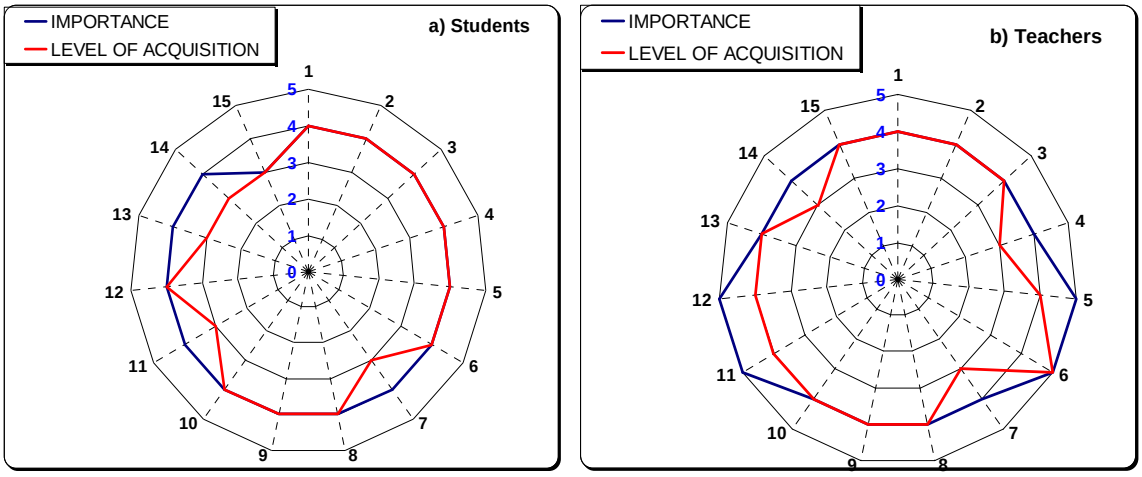

Figure 4. Results of skills evaluation procedure of case study activity.

From the analysis of **Figure 4** it can be concluded that teachers and students consider with a high punctuation (always higher than 3) the majority of transferable and specific skills evaluated. Only the written communication skills obtained a lower importance level. From a point of view of the level of acquisition, students recognize, according to their perception, a good level of acquisition (higher than 4) for most of the items tested, except those involved with oral and written communication skills (items 7 and 15 in Figure 4a) and the integration of operations and processes with the aim to attain global improvements (item 11 in Figure 4a). Teachers appreciate specific skills in a higher extent than transferable ones and assign a higher level of acquisition than students opinion showed, except on oral communication skills (item 7 in Figure 4 b) and leadership and making decision skills (item 4 in Figure 4b).

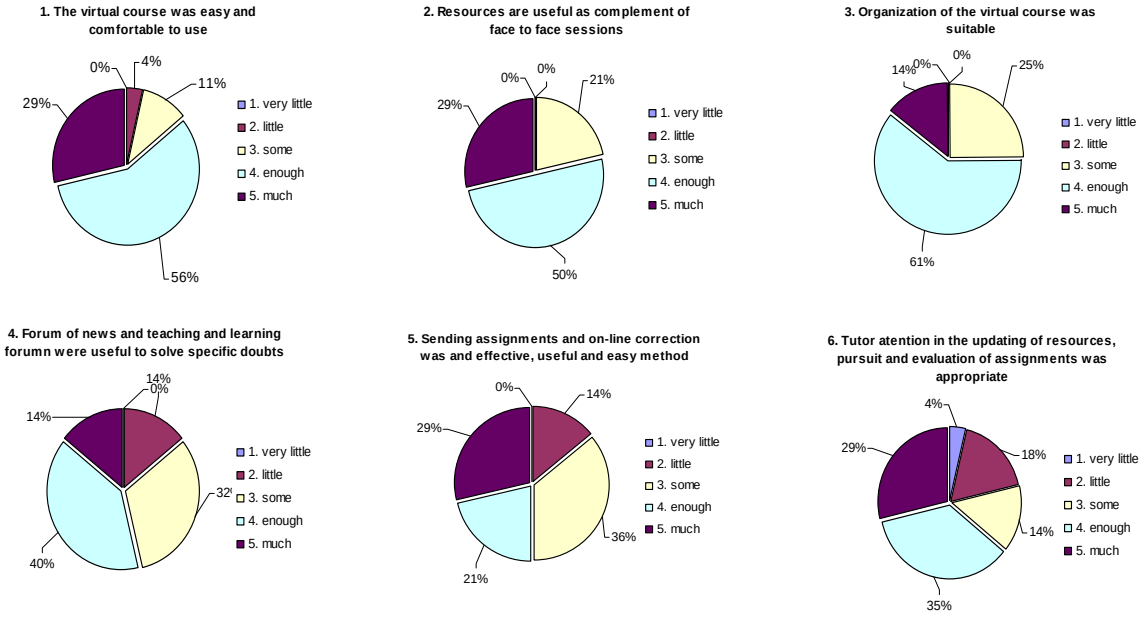

Figure 5. Student's opinion about the virtual case study.

Finally, **Figure 5** shows students opinion about the virtual case study used as a complement during the last course. The tool is easy or very easy to use for more than 80% of students. A 75% consider that resources (power point slides, information resources, web links, etc…) and organization of the virtual course result appropriate. However, teaching and learning forums has not attained a good evaluation: more than 30% of students consider forums useless. The use of Moodle to send the different assignments, to evaluate and to check qualifications is considered very positive for the 50% of students and the tutor attention is adequate or very adequate for more than 60% of students.

5. Conclusions

1. Case study is an effective tool to promote the holistic, integrated and applied vision of the different subjects involved in the seventh semester of the Chemical Engineering degree. At the same time, this new methodology help students to develop transferable skills of importance for their professional future (team work, communication skills, life long learning, etc) without resigning to the theoretical contents of each subject (knowledge acquisition)
2. The use of a virtual course as a complementary tool has allowed maintaining continuously updated resources, activities, etc. Moreover the teaching and learning forums allow the opinions and information exchange among teams and teachers involved in the activity.
3. The combination of technology-based materials and face-to-face sessions, allow developing innovative ways to motivate people to learn, provide greater access to information, help students learn conceptual matters and allow developing interpersonal skills.

References

Cartón López, A., García Cubero, M.T., González Benito, G, Lucas Yagüe, S., Bolado Rodríguez, S., García Encina, P.A., Urueña Alonso, M.A. (2007). Diseño de estrategias de enseñanza-aprendizaje para la adquisición de competencias en el título de Ingeniero Químico. III Jornadas de Intercambio de Experiencias de Innovación Docente de la Universidad de Valladolid (Spain).

De Miguel Díaz, M. (2006). Metodologías de enseñanza y aprendizaje para el desarrollo de competencias. Orientaciones para el profesorado universitario ante el Espacio Europeo de Educación Superior. *Educatio siglo XXI*, 24, 207-210. Editorial Alianza.

Felder, R.M.; Brent, R. (1999). How to Improve Teaching Quality. *Quality management Journal*, 6(2): 9-21

García Cubero, M.T., Lucas Yagüe, S., Bolado Rodríguez, S., García Encina, P.A., González Benito, G., Urueña Alonso, M.A. (2007). Implementación de la metodología del estudio de caso en el título de ingeniero químico. evaluación de competencias. II Jornadas Internacionales de Innovación Educativa, CD "El Espacio Europeo de Educación Superior: Una oportunidad para las enseñanzas técnicas, Zamora.

García Cubero, M.T., Lucas Yagüe, S., Bolado Rodríguez, S., García Encina, P.A., González Benito, G., Urueña Alonso, M.A., Cartón López, A. (2008). Tareas de coordinación en la implementación de una metodología integrada de enseñanza - aprendizaje en 4º curso de ingeniero químico de la universidad de valladolid. V Congreso Internacional de Docencia Universitaria e Innovación, Lleida.

Grant D.C., Dickson, B.R. (2006). Personal skills in Chemical Engineering graduates. The development of skills within degree programmes to meet the needs of employers. *Education for Chemical Engineers*, 1(1), 23-29.

Lucas Yagüe, S.; García Encina, P.A.; Bolado Rodríguez, S.; García Cubero, M.T.; González Benito, G.;Urueña Alonso, M.A. (2008). Teaching and learning strategies and evaluation changes for the adaptation of the Chemical Engineering degree to EHES. *Education for Chemical Engineers,* 3, e33-e39.

Molzahn M. (2006). New curricula for new careers – the EFCE Bologna recommendations. 17th International Congress of Chemical and Process Engineering. I1.1 Presentation, Prague, Czech Republic.

WCEC, World Chemical Engineering Council, How Does Chemical Engineering Education Meet the requirements of Employment? Dechema. Frankfurt (2004). http://www.chemengworld.org [10/07/2008]

Proceedings of the 10th International Chemical and
Biological Engineering Conference - CHEMPOR 2008
Braga, Portugal, September 4-6, 2008
E.C. Ferreira and M. Mota (Eds.)

Another basic segregation mechanism in aerated gravity flows of particulate solids

Dolgunin V.N.*, Kudy A.N., Klimov A.M. and Ivanov O.O.
Department of Technological Equipment and Food Technology,
Tambov State Technical University,
106 Sovetskaya str., 392000, Tambov, Russia

Keywords: granular material, gravity flow, mixing, segregation, migration
Topic: Advancing the chemical engineering fundamentals (Particulate systems)

Introduction

Transversely aerated gravity flows of particulate solids are used widely in particle technology for the processes of heat-mass transfer and dust removal as well as for pneumatic transport in open channel. The results of experimental and analytical investigations presented earlier in [1] have shown that the aeration intensity and aeration direction considerably influence the segregation-mixing process in gravity flows of non uniform particles.

The prediction of segregation effects in aerated gravity flow of particles is of great significance for the industrial application because segregation may considerably upset the mixture uniformity which will influence the character of the subsequent technological processes and the quality of the finished products.

Earlier in the work [1] in order to forecast the segregation-mixing effects in aerated gravity flows of particulate solids differing in size and density the general segregation model [2] was adapted. In our further investigation [3] the general segregation model was developed by means of a closer definition of segregation kinetics and consideration of a quasi-diffusional separation mechanism. In the present paper this model is used in the experimental and analytical research on segregation in aerated gravity flow of particulate solids in order to reveal more accurately physical segregation mechanisms.

Experimental

The technique and the apparatus were analogous to the ones used earlier in the work [1]. The test unit (Fig. 1) consists of an inclined open channel of square cross-section 1 with a rough bottom. The slope of the channel can be adjusted. There is a horizontal tray 3 which used to collect the particles falling down the channel. To determine the particle distribution along the bed depth the tray contains cells 4. The slide–valve 2 is installed at the top of the channel to control the depth and the length of the moving bed.

The bottom of the channel is made of a steel plate 9 with holes 8 mm in diameter. The total holes area equals ≈ 70% of bottom area. The perforated plate 10 below the bottom is installed to distribute the air flow uniformly. The diameter of the plate holes and their total area are much smaller than the diameter and the total area of the holes in the bottom.

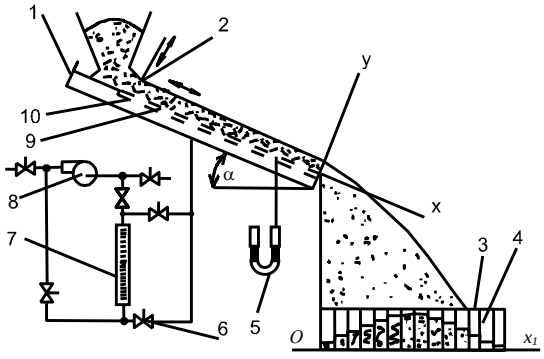

Fig.1 Schematic of test unit:
1 - channel;
2 - slide -valve;
3 - tray;
4 - cell;
5 - differential manometer;
6 - valves;
7 - rotameter;
8 - blower;
9, 10 - perforated plates

* Corresponding author. E-mail: ioo_c4@rambler.ru

Under the perforated plates there is a box connected with the air pipeline. Valves 6 are designed to control the air flow rate and to change the direction of the bed aeration. A rotameter 7 is used to measure the air rate. A differential micro-air-pressure gauge 5 is used to measure the pressure differential in the bed.

The research was carried out in the steady-state sliding flow of particulate solids [1] close to the boundary of the splashing flow. Such a state exists in a non-aerated gravity flow on a rough incline at the slopes approximate to the material angle of repose. During the aeration the above mentioned flow state is achieved by a corresponding variation of the slope. While varying the intensity of aeration the slope of the chute is changed so as to ensure sticking of the particles in the bottom analogous to the sticking taking place in non-aerated particle flow. The adequacy of particle sticking conditions is determined visually after the particles have flown down. Besides the adequacy of the flow state is controlled using the method proposed by Ishida et al [4].

According to the data described in [4] the minimum flow depth of rolling particles is registered at the boundary between the sliding and splashing flows. A similar dependence between the bed depth and the state of the particulate solid flow is registered in the present research both during aeration in the direction to the free surface and during aeration towards the bottom. The material flow depth was the same in both cases. This depth doesn't depend on the intensity of aeration.

The following experimental procedure is used. After setting the required chute slope α as well as the length of the incline and the air rate the material is metered out into the chute at the required feed rate. When the flow stationary state is achieved (which is determined experimentally) the particles go into the receiving tray.

Thus the profiles of velocity, the fraction of void volume and the test particles distributions along the bed depth were defined experimentally. These results were defined on the basis of the experimental data including bed depth in the channel h, channel inclination angle α, particles distribution function along the tray and vertical distance between the tray and the discharge threshold of the channel.

Taking into consideration the problems arising during direct experimental determination of the velocity and concentration profiles and also the void volume distribution along the thin bed depth for a rapid gravity flow of particles the present investigation was carried out by using the previously discussed experimental-analytical method [1]. The method is based on the combined analysis of the above mentioned experimental data using the law of a free falling body and taking into account the function of the interrelationship between the dilatation, shear rate and pressure along the bed depth [2]. This function was defined using the analogy between the particulate medium at a rapid shear flow and a dense gas as follows

$$p_t \bar{\varepsilon} = \psi \vartheta \tag{1}$$

where p_t is the total pressure of the particulate medium, $\bar{\varepsilon}$ is the shear flow dilatation [2], ϑ is the granular material 'temperature', expressed as a function of the shear rate [2], ψ is the coefficient of the physical and mechanical properties of the particles which is determined during modeling.

The total pressure $p_t(y)$ for the aerated gravity flow was defined as the sum of the hydrostatic pressure $p_s(y)$ analogue and the hydrodynamic pressure $p_d(y)$, generated by the aerating flow.

At small values of the air velocity (Re - number) the Kozeni-Karman equation is used for the hydrodynamic pressure determination.

Thus the total granular medium pressure is expressed in the following integral form

$$p_t(y) = p_s(y) + p_d(y) = \int_{h-y}^{h} \rho(1-\varepsilon(y)) g \cdot \cos\alpha \cdot dy + \int_{h-y}^{h} \frac{\lambda}{\varphi d_c(y)} \cdot \frac{\rho_g w^2}{2} \cdot \frac{1-\varepsilon(y)}{\varepsilon(y)^3} dy \tag{2}$$

where λ is the hydraulic resistance coefficient; d_C is the equivalent channel diameter in the bed of particles. This diameter is calculated as a function of the void volume fraction and mean particle diameter

$$d_C(y) = \frac{2\sqrt{3}}{\pi}\left(\sqrt[3]{\frac{1-\varepsilon_0}{1-\varepsilon(y)}}\right)^2 \cdot d - d \qquad (3)$$

The hydraulic resistance coefficient λ is expressed by an iteration procedure as the following function of Re

$$\lambda = A \cdot \mathrm{Re}^{-0.46}, \ \mathrm{Re} = 20 \div 150 \qquad (4)$$

where $A = 5 \div 8$

According to the procedure described in the work [2] and taking into account the above mentioned relations we have investigated the profiles of velocity and the fraction of void volume in the aerated gravity flow of silica gel and supephosfate granules differing in size. The investigation was carried out during the aeration oriented from the bed bottom to its free surface as well as to the reverse direction and without aeration.

As an example Fig.2 shows the profiles of velocity and the fraction of void volume in gravity flows of silica gel granules, which demonstrate the significant aeration effects depending on the aeration intensity and the aeration direction.

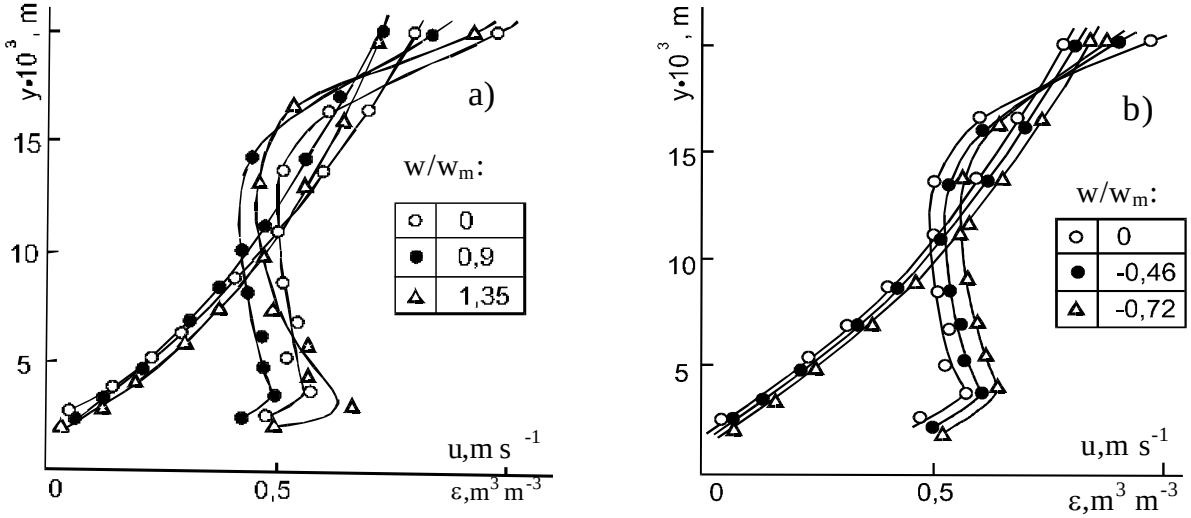

Fig.2. Profiles of velocity $u(y)$ and the void volume fraction $\varepsilon(y)$ in the gravity flow of silica gel granules (-3.75+3.5mm -50%; -4.25+4.0mm -50%) for various aerating air velocity w / w_m towards the free surface of the bed (a) and towards the bottom of the bed (b).

Analytical

In order to reveal more accurately physical mechanisms of aeration influence on particle segregation in gravity flows the mathematical modeling of segregation dynamics is carried out on the basis of the recently developed mathematical model [3]. For steady twodemensional shear flow the general equation of segregation dynamics is formulated as follows

$$\frac{\partial c \cdot \rho_b}{\partial t} = -\frac{\partial(u \cdot c \cdot \rho_b)}{\partial x} + \frac{\partial}{\partial y}\left(\rho_b\left(D_{dif} \cdot \frac{\partial c}{\partial y} - D_m \cdot c \cdot \frac{\partial \ln s}{\partial y} - K \cdot \Delta M \cdot c\right)\right) \qquad (5)$$

It takes into account the fluxes of convection, quasi-diffusional mixing, migration and hydromechanical segregation. In case of rapid shear flows of cohesionless non-elastic spherical particles all the parameters in Eq.(5) excluding coefficient *K* are calculated analytically as functions of traditional physical and mechanical characteristics of particles and flow parameters [3]. Only the kinetic constant *K* is determined experimentally by the method described in Ref [3].

The segregation driving force ΔM in aerated flows is calculated as the excess momentum of forces acting on the test particle [1] in nonuniform particulate media. This momentum is calculated according to the schematic of particle interactions in aerated gravity flows shown in Fig.3.

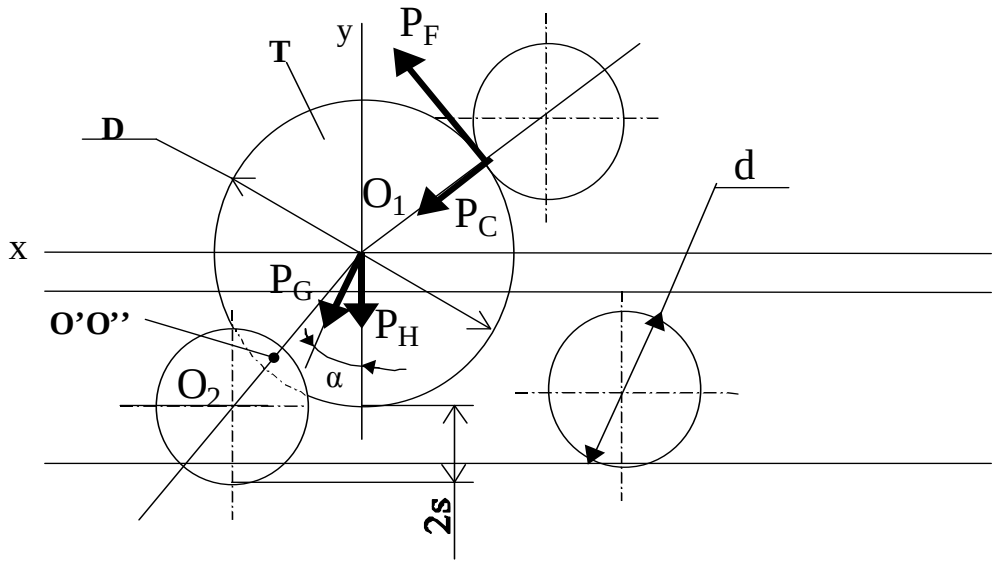

Fig.3. Schematic of particle interactions in aerated gravity flow: T, test particle; O'O'', instantaneous axis of rotation of a test particle.

The calculation scheme allows to determine the momentum of hydrodynamic pressure forces in the following way

$$M_D = \frac{d\left(p_d(y)\right)\cdot D^4}{dy}\cdot\frac{\pi\left((d+D)^2-(d+s)^2\right)^{\frac{1}{2}}}{8(d+D)}\cdot\cos\left(\arcsin\frac{D-d+4s}{\left((d+D)^2-(d+s)^2\right)^{\frac{1}{2}}}\right) \qquad (6)$$

where *pd(y)* is the hydrodynamic pressure, which equals to the second item in the right part of Eq.(2).

Then taking into consideration the additional momentum of forces (6) appearing in aerated gravity flows we can describe the segregation driving force as follows

$\Delta M = M - M_0$ (7)

where $M = M_G + M_F + M_C + M_D$ is the total momentum of gravity, friction, impact and hydrodynamic pressure forces, acting on the test particle relatively to their instantaneous axis of rotation, *M0* is the analogous momentum of forces acting on an average particle in a conventionally uniform medium at the same flow conditions [2].

Equation (5) was integrated numerically for the initial condition

$c(0,x,y) = c_0$

where c_0 is the mean concentration of test particles.

Boundary conditions were formulated in the following way

$$D_{dif}\cdot\frac{\partial c}{\partial y} = D_m\cdot c\cdot\frac{\partial \ln s}{\partial y} = K\cdot\Delta M\cdot c = 0, \qquad \text{if} \quad y = 0, h$$

$c(\tau,0,y) = c_0$

The profiles of velocity and fraction of void volume presented in the previous paper part (Fig.2) were used to obtain *u* and *s* values. The calculated results shown in Figs. 4 and 5 were obtained on the basis of the two different calculation versions. The first version takes

into account all the particle fluxes in accordance with Eq.(5) and the second one ignores the migration flux, i.e. it assumes that *Dm=0*.
It should be pointed out that the adequate modeling results in a case of non-aerated gravity flow of particles differing in size may be obtained often without taking into consideration the migration flux as it shown in Fig.4. However, analyzing the concentration profiles calculated in case of aerated flows (Figs.4,5) we observed the considerable migration effects in the vicinity of the free surface of the bed and the segregation increase in the central part of the bed. These phenomena are explained by the shear rate increase in all the bed depth and expanding the loose zone in the upper part of the bed.

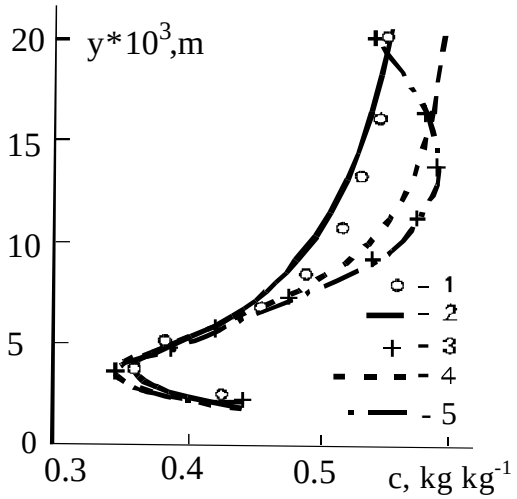

Fig.4. Concentration profiles in the gravity flow of silica gel granules (-3.75+3.5mm - 50%; -4.25+4.0mm -50%) for various aerating air velocity towards the bed bottom: 1 - w/w_m=0 (experimental [1]); 2 - w/w_m=0 calculated at $D_m=0$); 3 - w/w_m=-0.46 (experimental); 4 - w/w_m=-0.46 (calculated at $D_m=0$); 5 - w/w_m=-0.46 (calculated according to (5)).

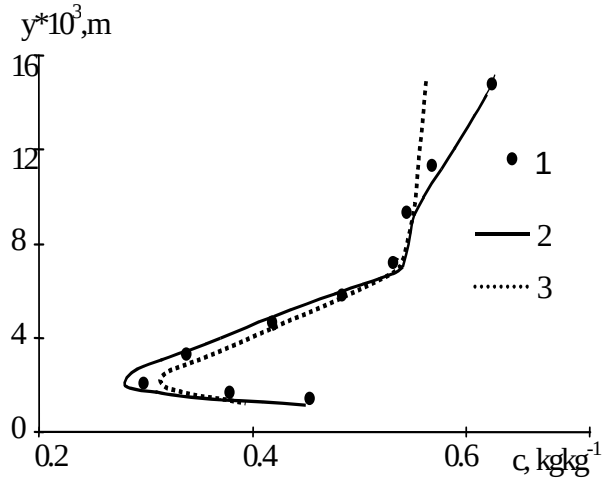

Fig. 5. Concentration profiles in the aerated gravity flow of superphosphate granules (-2.2+2.0mm -50%; -2.8+2.6mm -50%) for aerating air velocity w/w_m=0.405 towards the bed bottom: 1 – experimental [1]; 2 – calculated according to Eq.(5); 3 – calculated without migration flux $(D_m=0)$.

Thereby it is important to note that the same value of segregation coefficient *K* is used for modeling in aerated and non-aerated flows. This fact can be considered as an indirect proof of the relatively high forecasting properties of the mathematical model.
Thus the investigation results allowed us to maintain that the quasidiffusional separation (migration) is one more basic segregation mechanism in aerated gravity flows of granular materials.

Conclusions

In order to reveal more accurately physical mechanisms of aeration influence on particle segregation in gravity flows the mathematical modeling of segregation dynamics was carried out. This modeling has taken into account the fluxes of nonuniform particles in consequence of convection, quasidiffusional mixing, segregation and quasidiffusional separation (migration). The results of the mathematical modeling were comprised with experimental data. The comparison has shown that these results are quite satisfactory. It is found out that the quasidiffusional separation (migration) is one more basic segregation mechanism in aerated gravity flows of granular materials.

List of symbols

c test component concentration ($kg \cdot kg^{-1}$)
d mean particle diameter (m)
D test particle diameter (*m*)
d_c equivalent channel diameter (m)
Ddif quasi-diffusion coefficient ($m^2 \cdot s^{-1}$)
Dm migration coefficient ($m^2 \cdot s^{-1}$)
g gravity acceleration ($m \cdot s^{-2}$)
h bed depth (m)
K segregation coefficient (coefficient of relative rate of segregation) (*N s*)-1
M momentum of forces acting on the test particle (*N m*)
ΔM segregation driving force (non-uniformity parameter of particulate medium) (*N m*)
p_t total pressure ($N \cdot m^{-2}$)
p_s hydrostatic pressure ($N \cdot m^{-2}$)
p_d hydrodynamic pressure ($N \cdot m^{-2}$)
s mean distance between particles (*m*)
u particle velocity ($m \cdot s^{-1}$)
w air velocity ($m \cdot s^{-1}$)
w_m minimum fluidization velocity ($m \cdot s^{-1}$)
x, y Cartesian coordinate, Fig.1

Greek letters
α channel inclination angle (*deg*)
α_0 angle of repose of the material (*deg*)
ε fraction of void volume ($m^3 \cdot m^{-3}$)
$\bar{\varepsilon}$ bed dilatation ($m^3 \cdot m^{-3}$)
ε_0 fraction of the void volume of dense packed particles ($m^3 \cdot m^{-3}$)
λ hydraulic resistance coefficient
ρ_b bulk density of the mixture ($kg \cdot m^{-3}$)
ρ_g gas density ($kg \cdot m^{-3}$)
ψ , φ coefficients

References

[1] Dolgunin V.N., Kudy A.N. and Klimov A.N. (1998). Segregation in aerated gravity flows of particulate solids, World Congress on Particle Technology 3 – Abstracts of papers, Brighton (UK), p. 125.
[2] Dolgunin V.N., Ukolov A.A. (1995). The segregation of particles undergoing rapid granular flow down an inclined chute, *Powder Technol*.,83, 95-103.
[3] Dolgunin V.N., Ukolov A.A. and Ivanov O.O. (2006). Segregation kinetics during rapid gravity flow of granular materials, *Theor. Osn. Khim. Technol*., 40, 423-435.
[4] Ishida M., Hatano H., and Shirai T. (1980). The flow of solid particles in an aerated inclined channel, *Powder Technol.*, 27, 7-12.

Proceedings of the 10th International Chemical and
Biological Engineering Conference - CHEMPOR 2008
Braga, Portugal, September 4-6, 2008
E.C. Ferreira and M. Mota (Eds.)

Biofouling Control in Cooling Water

T. Reg. Bott
Department of Chemical Engineering, University of Birmingham, Birmingham B15 2TT, U.K.

Keywords: Biofouling, Cooling Water, Chemical Control, Physical Control
Topic: Environmental Engineering and Management

Abstract

An important aspect of environmental engineering is the control of greenhouse gas emissions. Fossil fuel fired power stations for instance, represent a substantial contribution to this problem. Unless suitable steps are taken the accumulation of microbial deposits (biofouling) on the cooling water side of the steam condensers, can reduce their efficiency and in consequence, the overall efficiency of power production, with an attendent increase in fuel consumption and hence CO_2 production. Biofouling control therefore, is extremely important and can be exercised by chemical or physical techniques or a combination of the two. The paper gives some examples of the effectiveness of different approaches to biofouling control.

1 Introduction

The importance of good energy management is becoming far more demanding than in the past. The substantial increase in energy costs and the threat of climate change due to greenhouse gas emissions, makes it imperative that all steps are taken to reduce energy usage. Of particular importance is the effectiveness of cooling water, specially in the steam condensers of fossil fuel fired power stations, to maintain electrical energy output per tonne of fuel at its highest possible level.

Despite efforts to provide an effective design of heat exchanger, and careful attention to the maintenance of the design operating conditions, it is likely that fouling on the water-side of the heat exchangers will occur unless suitable precautions are taken. The common practice of taking water from natural sources such as rivers and lakes for cooling purposes, means that it will contain micro organisms, which will colonise the heat transfer surfaces, to the detriment of cooling efficiency, The problem will be aggravated by the fact that the temperature of the water-side surface in the heat exchanger, is usually close to the optimum temperature for maximum microbial growth. In addition water from natural sources will contain nutrients from the breakdown of naturally occurring organic material. Unless this bioactivity is controlled the efficiency of the heat exchanger will be seriously reduced. In fossil fuel fired power stations this will require additional fuel to be burnt to maintain the required electricity output with an attendant increase in the emission of green house gases There are basically two methods of controlling this problem, chemical and physical, that might be used separately or in some sort of combination. Three conferences held in Portugal, Melo et al (1987), Melo et al (1992) and International Water Association and Collaborators (2002) did much to stimulate interest is these techniques and their effective use. In addition conferences organised by EPI have also covered aspects of the associated technology. The most recent conference was held inTomar, Portugal in 2007, organised by Müller-Steinhagen et al (2007).

2 Chemical Control

In essence chemical control generally involves the use of biocides to kill the micro organisms in *the cooling* water, or biostats to reduce their activity. For many years the preferred biocide was chlorine because it was relatively cheap and available. However its use is becoming

severely restricted on account of its detrimental effects on the quality of the water discharged back to the natural environment from where it was abstracted and its effect on other living creatures including humans. In contact with organic material in the natural environment chlorine can form chloromethanes that are carcinogenic. An alternative to the discharge of chlorine-contaminated water is to dechlorinate before disposal. The techniques for dechlorination are likely to add considerably to the operating costs. As a result ther are efforts being made to provide alternatives and to be economical in their application. A wide range of chemicals is used as a basis for biocides. They may be classified as oxidising or non-oxidising. Oxidising agents include; chlorine and chlorine yielding chemicals, ozone and hydrogen peroxide. Amongst the non oxidising compounds are amines, heavy metal compounds, aldehydes, organo-bromine compounds and isothiazolones.

So-called “environmentally friendly” biocides are generally those that have a relatively short life after application, breaking down to innocuous products. Simple examples are ozone which reverts to oxygen on decomposition and hydrogen peroxide that breakdown to water. Alternatives to these inorganic chemicals usually involve complex organic compounds that readily break down after application. It also has to be appreciated that sometimes these breakdown products are nutrients for micro organisms!

Clearly the objective is to remove any biofilm as it forms. In order to be economical and effective the technology of dosing has to be carefully considered. The addition of chemicals to cooling water may be made in three ways;

a) Continuous. The maintenance of a fixed concentration in the circulating water. The dose depending on the concentration and species of the micro organisms present.

b) Shock. An intermittent dose of relatively high concentration, maybe only once in 24 hours.

c) Pulse. Involves dosing on a fixed schedule but more frequently than shock dosing-maybe once per hour for example.

The method of dosing will, in general, depend on the season and the quality of the water involved. Careful choice of dosing regime based on trials, preferably in a pilot plant, will help maximise control and minimise cost. It could be beneficial to employ a side-stream test section on the cooling water system, to optimise the dosing regime, and to make comparisons between alternative biocides.

Some bacteria can develop a potential tolerance to an applied biocide, particularly biocides that affect cell membranes. A change in the dosing regime or a change in the biocide, may be effective in overcoming this drawback. Biocides that actually destroy the cell structure are more likely to be the most effective.

In pilot plant studies (Grant and Bott,2005) using *Pseudomonas fluorescens* as the biofllm forming species in single tubes, bulk water flow velocities of 0.5 and 1.3 m/s and a proprietary biocide, suggested that pulse dosing, based on comprehensive preliminary testing, is likely to be the most effective regime. This observation is not surprising since pulse dosing is the closest to continuous biocide application.

An alternative to the use of environmentally friendly biocides to meet discharge regulations is to have “zero discharge” i.e. to reuse the cooling water, with only “make up” water to replace operating losses. It would allow less costly biocides to be used but such a procedure may be costly in other ways to maintain an acceptable quality of the circulating water.

3 Physical control

In theory at least, it should be possible to control biofouling by passing the water through the exchanger at high velocity to increase the removal forces acting on the biofilm. Although this may be feasible, it it is not really practical because of the high energy requirement to overcome the large pressure drop involved. There are a number of other physical techniques

that may be applied to cooling water systems to reduce the incidence of biofouling, but it has to be said that many are still in the development stage and it remains to be seen if they are practical and economically attractive.

a) Circulation of sponge rubber balls.

The use of circulating sponge rubber balls with the cooling water, through the tubes of steam condensers has been practiced with success, for many years. The balls having a diameter slightly larger than the internal diameter of the tubes, wipe away any biofilm that begins to form. Cleaning is a random process, so that the concentration of balls in the system has to be sufficiently high to ensure that every tube receives balls frequently enough to ensure effective cleaning. In addition there has to be a replacement policy since the balls loose their effectiveness after a time due to reduced diameter through wear, but this can be made automatic through suitable design.

b) The use of inserts

The inclusion of inserts in tubes, originally intended to boost heat transfer, by the destruction of the laminar sublayer on the tube surface, are also capable of reducing the incidence of biofouling at modest water velocities. Two basic types are available; (i) Static inserts such as “Hitran” wire wound inserts that break up the laminar sublayer by creating turbulence and associated removal forces at the heat transfer surface, and (ii) inserts that oscillate in response to the water flow such as “Total “ inserts, that remove the developing biofilm by abrasion.

Both types of device will increase the pressure drop and hence the operating costs, although this may be offset to some extent by suitable design. Some data (Bott, 2001) on the effect of “Hitran” inserts on the accumulation of biofilm consisting of the slime forming species *Pseudomonas Fluorescens* demonstrate that although there is some scatter in the data, it is evident that the presence of the insert reduces the accumulation of biofilm. In one test, after 700 hours operation, the reduction of biofilm accumulation compared to an equivalent test with no insert prsent, was aproximately 33% with a water flow velocity of 0.86 m/s and approximately 64% with a water velocity of 1.27 m/s.

c) The use of ultrasound

Ultrasound has the property of disturbing liquids and the structure of solids. It is employed for instance, to remove hard mineral deposits from heat exchange surfaces exposed to high temperature combustion gases in boiler installations. It has been demonstrated experimentally (Bott, 2000) that biofilm accumulation (*Pseudomonas fluorescence*) on the inside of tubes can be reduced by the modest use of ultrasound of 20 kHz. Depending on the amplitude (20 or 40%), the length (time) and frequency of groups of bursts of ultrasound, the reduction in biofilm accumulation varied between 20 and 93%. The water flow velocity was 1m/s. Some further detail is given in Table1

A major drawback in respect of the use of ultrasound for the control of biofouling is the initial cost of the equipment and its inclusion in heat exchanger design.

Table1. Control of biofilm formation with different ultrasound treatments.

Amplitude of Ultrasound %	Number of 30s bursts	Frequency of bursts each day	Reduction of biofilm growth compared with no treatment %
20	3	1	20.0
20	3	6	65.5
20	1	8	40.3

d) Circulation of polymer fibres.

Some preliminary work (Bott, 2001) on the use of Arimid fibres to control biofouling suggests that the technique could be useful. Again using *Pseudomonas fluorescens* as the biofouling bacterium, it was shown that a concentration of fibres of 100 ppm, with a water velocity of 1.6 m/s is adequate for effective control of biofilm formation. It was noteworthy that if fibre addition was stopped, a biofilm soon began to form. Considerably more work on the technology will be required however, before it could be applied effectively for industrial cooling water. A major difficulty that would have to be faced would be the recovery of the fibres prior to the final discharge of the water. Fibre removal might also be necessary before passing the water through a cooling tower in a recirculating system to avoid potential accumulation and associated blockage problems. Some preliminary work suggests that the fibres do not accelerate the wear on the associated pumps.

4. Combined chemical and physical control

It is possible that a combination of chemical and physical techniques of control could be more effective than either solely applied.

a) Ozone and ultrasound

Experimental work using a combination of ozone and ultrasound over a four week period (Bott and Liu Tianqing, 2003), again using *Pseudomonas fluorescens* as the biofilm former and a water velocity of 1m/s demonstrated that this was a more effective control than ozone alone.. During the first week of a four week period, no treatment was applied to allow a biofilm to develop. The biofilm thickness at the end of that first week ranged from 45-60μm. Table 2 presents some of the data obtained during the subsequent three weeks, demonstrating that the application of the ultrasound (20kHz at 20% amplitude) for three minutes each day made a considerable difference to the retention of biofilm. The ozone concentration in the water during these tests was very low, since water containing an ozone concentration of around 2.2 - 2.8 mg/l was pumped into the system to be mixed with the bulk water for only three hours each day. The data contained in Table indicates that the application of ultrasound made a considerable reduction in the accumulated biofilm.

Table2. Mean biofilm thickness over a period of 28 days with different treatments.

Week	Biofilm thickness for different tubes μm	
	Ozone only	Ozone + ultrasound
2	26, 18, 17, 18	9, 8
3	43, 15, 24, 20	11, 12
4	111, 49, 60, 51	7, 5

b) Propriety biocide and inserts

Limited results (Wills et al, 2002) using Hitran inserts in conjunction with a propriety biocide have demonstrated that whereas a biocide concentration of around 50 mg/l would normally be required to control biofilm formation, but in the presence of inserts the concentration required could be as low as 10 mg/l The conditions of these tests were similar to those quoted elsewhere in this paper.

5. Concluding remarks.

This brief summary of investigations into the factors that influence biofilm formation and perhaps more importantly the opportunities for control of biofilm growth, demonstrate how the application of chemical engineering and associated technologies, can help meet the challenge of climate change and the associated impact on the well-being of humanity.

Conferences such as Chempor, do much “to spread the word” about what is possible through the application of chemical engineering principles. Furthermore the “networking” that is a direct result of conference attendance is extremely valuable in that it facilitates a combined approach to meeting the challenge.

References

Bott T.R, (2000), *Biofilm Control with Ultrasound,* Heat Trans. Eng. 21, 43-49.

Bott T.R. (2001), *Potential Physical Methods for the Control of Biofouling in Water Systems,* Trans. IChemE., 79, Part A, 484-490.

Bott T.R. and Liu Tianqing, (2003), *Ultrasound Enhancement of Biocide Efficiency,* Ultrasonics, 11, 323-326.

Grant D.M. and Bott T.R, (2005), *Biocide Dosing Strategies for Biofilm Control*. Heat. Trans. Eng., 26, 44-50.

International Water Association and Collaborators,(2000). *International Specialised Confrence on Befouling Monitoring.*

Melo L.F., Bott T.R. and Bernardo C.A.(1988), *Fouling Science and Technology,* Kluwer Academic Publishers, Dordrecht.

Melo L.F., Bott T.R., Fletcher M., and Capedeville B.,(1992) *Biofilms Science and Technology,* Kluwer Academic Publishers, Dodrecht.

Müller-Steinhagen H., Watkinson A. P. and Malayeri R.,(2007), *Heat exchanger Fouling and Cleaning VII,* Engineering Conferences International, New York.

Wills A.M., Bott T.R. and Gibbard, I. (2002), *The Effect of Tube Inserts on Biocide Effiecency,* in Müller Steinhagen H., ed. Heat Exchanger Fouling- Fundamental Approaches and Technical Solutions, Publico Publications, Essen.

Proceedings of the 10th International Chemical and
Biological Engineering Conference - CHEMPOR 2008
Braga, Portugal, September 4-6, 2008
E.C. Ferreira and M. Mota (Eds.)

Comparison of Hydrodynamic Parameters between an Internal and an External Airlift Column

M. Teresa M. Sena Esteves[1*], Isabel M.B. Pereira[1], Maria N.M. Coelho Pinheiro[2,3], Alexandra M.F.R. Pinto[3]

[1]CIETI, Departamento de Engenharia Química, Instituto Superior de Engenharia do Instituto Politécnico do Porto, R. Dr. António Bernardino de Almeida, 431, Porto, Portugal.
[2]Departamento de Engenharia Química e Biológica, Instituto Superior de Engenharia do Instituto Politécnico do Coimbra, R. Pedro Nunes, Coimbra, Portugal
[3]Centro de Estudos de Fenómenos de Transporte, Departamento de Engenharia Química, Faculdade de Engenharia da Universidade do Porto, R. Roberto Frias, Porto, Portugal

Keywords: airlift column/reactor, slug flow, gas-liquid systems

Abstract

The present work reports a series of experiments performed in an external loop airlift column (ELARL) with a 2.74 m high riser tube. This column could be operated under the same range of operating conditions used previously by Santos (2004) in an internal loop airlift column (ILARL), using a similar aqueous glycerol solution in columns with different configurations (riser tubes with 22, 32 and 52 mm internal diameter) and injecting different gas flow rates. The objective of the present study was to analyse if similar hydrodynamic parameters could be obtained as in the ILARL column spending approximately 22% of liquid volume.

Several experiments were performed and analysed for riser tubes with 22 and 32 mm internal diameters. A 78% (w/w) aqueous glycerol solution (μ = 0.05 Pa.s) was used, for different air flow rates (15×10^{-6} to 98×10^{-6} m^3/s), and a 0.94 submergence ratio was imposed. Slug flow regime was observed for these conditions.

The experimental data of gas hold-up, velocity of gas slugs (Taylor bubbles) and liquid circulation velocity were compared with the results obtained previously for the ILARL. For the conditions used during experiments performed in the ELARL the solution viscosity was 6% lower than the value measured for the solution used in the ILARL. This discrepancy was mainly due to the impossibility of working at the same temperature as in the ILARL. In general, differences inferior to 3.3% were found in the liquid circulation velocity, 8.1% in the gas hold-up and 17% in the Taylor bubbles rise velocity.

The present study ensures that the two experimental designs lead to similar hydrodynamics parameters.

1 Introduction

In many bubble columns the gas is injected at the bottom and rises through the liquid in the shape of bubbles that induce the circulation of the liquid. When the gas rises oriented by a riser tube the flow patterns become more ordered and the liquid flow rate increases. These are called airlift columns. In the internal loop airlift column, ILARL, the liquid rises along with the gas through an internal riser tube, separates total or partially at its top, and descends between the main column and the riser tube. In the external loop airlift column configuration, ELARL, the gas and liquid rise through an external tube (riser) and the liquid flows down through the main column (downcomer).

* Corresponding author. Tel + 351-22-8340500. E-mail:mte@isep.ipp.pt

Airlift columns are commonly used as gas-liquid reactors, in wastewater and sewage treatment processes, in nuclear, pharmaceutical and biochemical industries. The design of this type of columns involves the knowledge of pressure drop, gas hold-up and liquid recirculation velocity. This last parameter influences the mixture characteristics of these columns and also heat and mass transfer coefficients, when mass transfer between the two phases (gas and liquid) occurs. Each of these factors is conditioned by the physical and chemical properties of the gas and liquid, by the gas and liquid flow rates and configuration (geometry) of the bubble column.

In the literature there are few studies about ILARL and ELARL especially for slug flow regime. In this regime, long bullet-shaped bubbles, usually called Taylor bubbles, occupy most of the tube cross section. Between the gas bubble and the tube wall flows a thin film of liquid and at the bubble rear there is a separated region, the wake, characterized by strong mixing. It is known that the flow pattern in the wake, in the liquid around the bubble and between gas slugs determine the mixing level in gas-liquid slugging columns. In the literature there is also a lack of information for laminar flow in the liquid, obtained when liquids of high viscosities are used

To enlarge the knowledge about the performance of airlift columns/reactors, in the slug flow regime, an ILARL column was designed by Santos (2004) (see also Santos et al., 2005) to ensure high precision and quality of the experimental results, with very simple experiments. This ILARL column can be operated with different submergence ratios of the riser tube and a wide range of operating conditions. In that study several hydrodynamic parameters were studied, namely: gas hold-up and liquid superficial velocity in the internal riser tube, bubbles rise velocity, bubble length and average number of gas slugs in the internal tube.

The disadvantage of this ILARL column was the volume of liquid required to perform the experiments. When the design of an ELARL column was considered the advantage was that the volume of liquid used could be considerably reduced when compared to the ILARL column. The ELARL built, with a 2.74 m high riser tube, could be operated under the same range of operating conditions used previously in the ILARL column, i.e., different viscosities of the liquid solutions in columns with different configurations (riser tube with 22, 32 and 52 mm internal diameter), injection of different gas flow rates and variable submergence ratios. The objective of the present study was to analyse if similar results for the gas hold-up, liquid superficial velocity and bubbles rise velocity in the riser tube could be obtained as in the ILARL column but spending approximately 22% of liquid volume.

2 Experimental set-up and measurements

The experimental set-up built for the hydrodynamic study of an ELARL column is sketched in Fig. 1. This set-up, which has a main column (downcomer) in flexible and transparent PVC, of 50 mm of internal diameter and 2.75 m of height, can be operated for different submergence ratios and a wide range of operating conditions. These conditions correspond to different types of flow regimes in the main liquid between bubbles and in the wake of gas slugs. These regimes can be obtained using different liquid viscosities, in external riser tubes with different internal diameters and injecting different gas flow rates. In the experiments performed transparent acrylic riser tubes with 22 and 32 mm I.D. were used. The riser tubes were 2.74 m high and the liquid free surface in the downcomer was 0.17 m below the top of the risers, which set a submergence ratio of 0.94. The liquid used was a 78% (w/w) aqueous solution of glycerol with ρ = 1203 kg/m^3 and μ = 0.05 Pa.s, for a temperature of 21ºC. The air injected at the bottom of the riser tube, with flow rates ranging from 15×10^{-6} to 98×10^{-6} m^3/s, was provided from a compressed-air line. The experimental values of gas hold-up, ε, rise velocity of the gas slugs, v_s, and liquid circulation velocity in the riser tube, v_L, were determined.

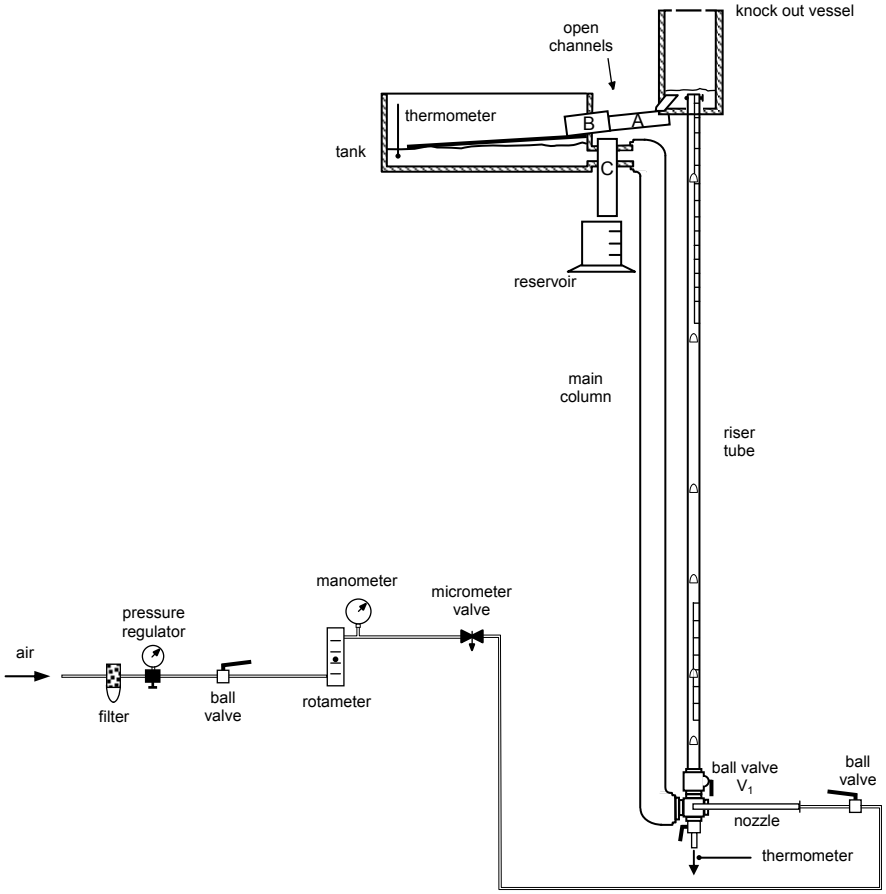

Figure 1 - Sketch of the experimental set-up

The air was continuously injected through a nozzle at the bottom of the riser tube generating the circulation of liquid, upwards in the riser tube and downwards in the main column (downcomer). At the top of the riser, the gas was separated from the liquid in a knock out vessel and the liquid was directed to a tank through a system of two small open channels. In the tank, the liquid was discharged on a wide ramp, with a small inclination, where the velocity of the liquid was greatly reduced in order to obtain the liquid free of small bubbles dispersed. The tank was connected to the main column allowing the liquid to flow downwards along the downcomer. The temperature of the liquid was measured regularly to verify if any change in the viscosity had occurred. The viscosity of the liquid was measured with a rotating Brookfield viscometer.

To measure the gas hold-up, valve V_1 at the bottom of the riser tube was closed. Sometime after the closure of the tube, the level of liquid was measured with a tape measure fixed at the top of the riser. This determination was repeated ten times for each gas flow rate.

The system of two small open channels that connected the knock out vessel to the tank was used to measure the volumetric flow rate of liquid circulating in the airlift. When the flow was steady and the measurement was to be made, the position of channel B (channel closer to the tank) was changed so the flow of liquid was directed to channel C that discharged the liquid into a reservoir. The volume of liquid collected (approximately 10^{-3} m^3), for an interval of time registered with a chronometer, was then weighted on an analytical balance and the mass flow rate was calculated. It was then converted to volumetric flow rate with the density experimentally determined at the temperature of the experiment. Because the tank was designed with large dimensions (0.50 m length and 0.20 m width), the liquid level (and the submergence ratio imposed) maintains essentially constant when the volume of liquid was

removed during flow rate measurements; the liquid level in the tank lowered approximately 8 mm, which is responsible for a decrease of only 3.5% in the volumetric flow rates. The procedure described for the determination of the mass flow rate was repeated six times and until, at least, three values of flow rate with deviations inferior to 5% were obtained.
The rise velocity of the gas slugs in the riser tube was determined by filming a section of the tube with a video camera that recorded 25 frames per second, and was placed 1 m away. The section with 0.25 m of length was marked with two white stripes, 2 m above the injection of gas. The videos were transferred to a computer using a *Pinnacle* video board and its software, and the frames were analysed with the software *Adobe Premiere 6*. The time of rise of a gas slug between the first mark and the second mark was given by the number of frames visualised between the reference positions, which correspond to the nose coincident with each mark. The rise of 8 to 12 consecutive gas slugs was analysed and an average value of the rise velocity was determined. Whenever a gas slug coalesced with the one above it, in the frames in analysis, its rise velocity was not calculated.

3 Results and discussion

The results obtained in the ELARL column are compared with the results presented by Santos et al. (2005) and Santos (2004) for an ILARL column operating with a similar aqueous glycerol solution. The liquid flow regime in the experiments was laminar in the main liquid between Taylor bubbles ($53 < Re_{v_L} < 378$, where Re_{v_L} is the Reynolds number of the flowing liquid) and transitional in their wake ($156 < Re_V < 532$, where Re_V is the Reynolds number of the flowing liquid based on the liquid velocity relative to the bubble) according to Pinto *et al.* (1998).

In Figures 2 and 3 the experimental values of the gas hold-up, ε, obtained in the ILARL and ELARL columns are plotted against the superficial liquid velocity in the riser tube, v_L, for the 22 and 32 mm I.D. riser tubes, respectively. The error bars were also drawn in these figures representing the total uncertainties associated with the average experimental values of gas hold-up. The experimental results obtained in the ELARL with the 22 mm I.D. riser tube are in accordance with the ILARL, with deviations less than 7.2%, as depicted in Figure 2. Exception must be made for the lowest velocity where the difference is 17.8%. For the results of the 32 mm I.D. riser tube, shown in Figure 3, differences are lower than 8.1%. The lower values obtained in the ELARL may be due to the lower viscosity of the liquid used in the present work; the impossibility to control the temperature did not allow the same liquid viscosity as in the ILARL, although a similar aqueous glycerol solution was used in both situations.

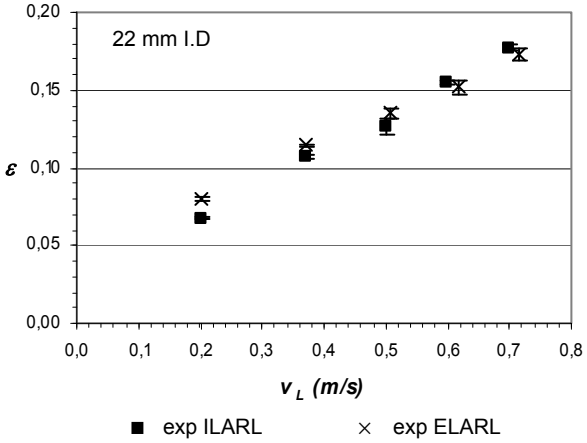

Figure 2 - Experimental values of ε for an ILARL and ELARL column with a riser tube of 22 mm I.D. and laminar regime in the liquid.

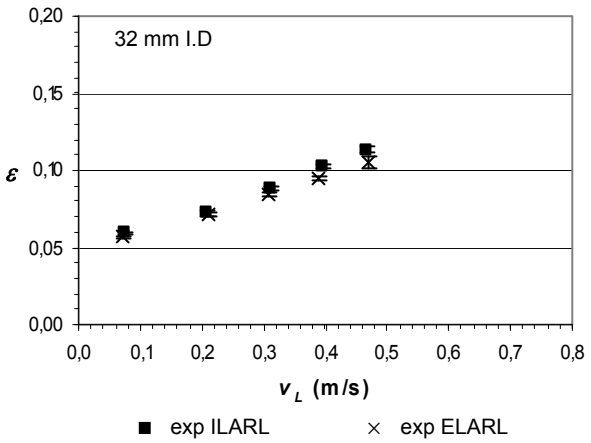

Figure 3 - Experimental values of ε for an ILARL and ELARL column with a riser tube of 32 mm I.D. and laminar regime in the liquid.

As reported by Santos *et al*. (2005) and Santos (2004) for the ILARL column, the results in both riser tubes diameters are well predicted by theory for laminar flow regime in the liquid.

The experimental values of Taylor bubbles rise velocity, v_s, for the ILARL and the ELARL columns are represented in Figures 4 and 5 against v_L, for the 22 and 32 mm I.D. riser tubes, respectively. The error bars associated with the data are also drawn. The experimental results for the 22 mm I.D. riser (Fig. 4) show differences lower than 17% between the ELARL and the ILARL. Again for the lowest liquid velocity the deviation is higher with a value of 23%. It should be emphasized that the differences observed for v_L > 0.3 m/s are within the uncertainties associated with the experimental determinations. Better results can be observed in the 32 mm I.D. riser tube (Fig. 5) where the differences are lower than 10.2%.

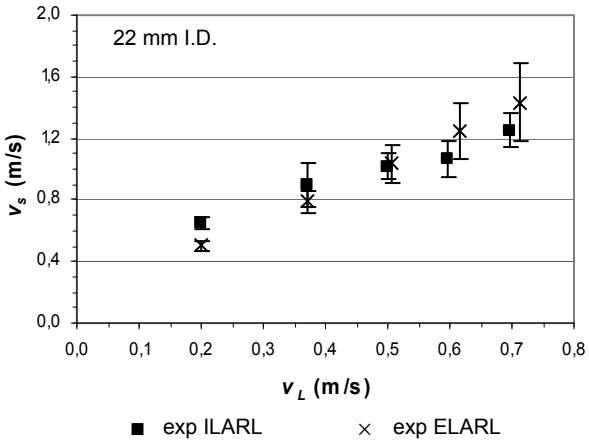

Figure 4 - Experimental values of v_S for an ILARL and ELARL column with a riser tube of 22 mm I.D. and laminar regime in the liquid.

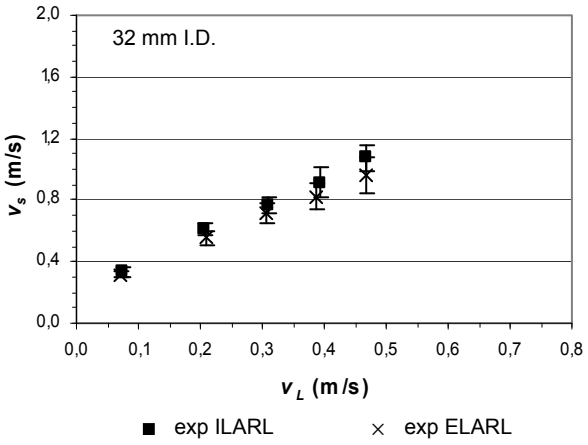

Figure 5 - Experimental values of v_S for an ILARL and ELARL column with a riser tube of 32 mm I.D. and laminar regime in the liquid.

In previous studies Santos *et al*. (2005) and Santos (2004) compared the experimental Taylor bubble velocities obtained in the ILARL with the predictions made by Nicklin *et al.* (1962) for laminar flow regime in the liquid and concluded that they are in reasonable good agreement. They obtained deviations less than 5% for the 32 mm I.D. riser tube and less than 27% for the 22 mm I.D. riser tube.

In Figures 6 and 7 the experimental values (and respective error bars) of v_L are represented against the gas flow rate, Q_G, for the 22 and 32 mm I.D. riser tube, respectively.

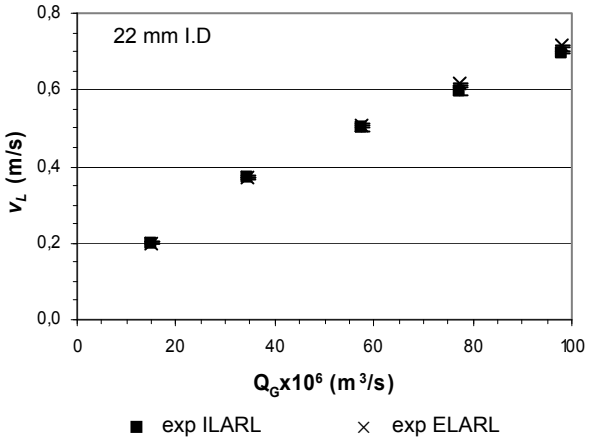

Figure 6 - Experimental values of v_L for an ILARL and ELARL column with a riser tube of 22 mm I.D. and laminar regime in the liquid.

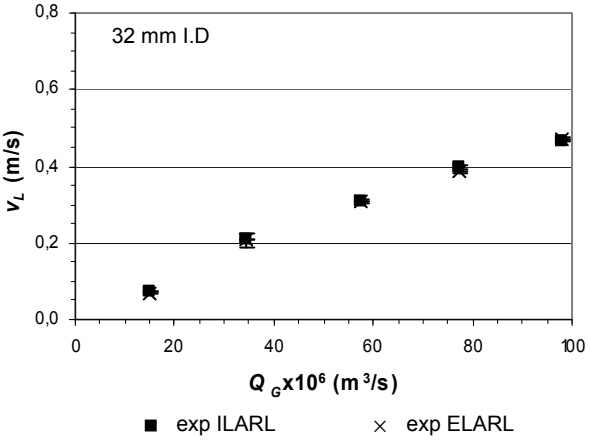

Figure 7 - Experimental values of v_L for an ILARL and ELARL column with a riser tube of 32 mm I.D. and laminar regime in the liquid.

As depicted in these figures good agreement is observed between the results of the ELARL and ILARL columns. In Figure 6 (22 mm I.D riser tube) the deviations are lower than 3.3% and in Figure 7 (32 mm I.D. riser tube) the differences do not exceed 1.8% (except for the lowest air flow rate for which the deviation is 5.1%).

The previous experimental values for v_L in the ILARL were compared by Santos *et al*. (2005) and Santos (2004) with the predictions of a hydrodynamic model (based in mechanical energy balances along the circulation path) developed by Sena Esteves (1998), valid for laminar regime in the main liquid. The model underpredicted the experimental results with deviations lower than 33% in the 22 mm I.D. riser and 17% in the 32 mm I.D. riser.

4 Conclusions

Hydrodynamic parameters, namely gas hold-up, Taylor bubble rise velocity and superficial liquid velocity in the riser tube, obtained in an ELARL column were compared with the results of an ILARL column. In both airlifts aqueous glycerol solutions with similar viscosities (0.05 Pa.s) were used with riser tubes of 22 and 32 mm I.D. The operating conditions selected guaranteed laminar flow regime in the liquid between bubbles and transitional flow regime in the bubble wake.

The experimental values of gas hold-up in the ELARL do not differ more than 8.1% from the ILARL results. The experimental values of Taylor bubble rise velocity show reasonable agreement with the results obtained in the ILARL, with differences lower than 17%. The experimental results of superficial liquid velocity in the riser tube obtained in the ELARL are in accordance (deviations less than 3.3%) with the results obtained in the ILARL.

The present study ensures that the two experimental designs lead to similar hydrodynamic parameters. With the ELARL configuration it is possible to spend approximately 22% of the liquid volume used in the ILARL configuration.

References

Nicklin, D. J., Wilkes, J. O., Davidson, J. F. (1962). *Two-phase flow in vertical tubes*. Trans. Instn Chem. Engrs, vol. 40, 61 - 68.

Pinto, A. M. F. R., Coelho Pinheiro, M. N. and Campos, J. B. M. L. (1998). *Coalescence of two gas slugs rising in a co-current flowing liquid in vertical columns. Chem. Engng. Sci., vol. 53, 16, 2973-2983.*

Santos, M. E. M., Sena Esteves, M. T. M., Coelho Pinheiro, M. N. and Pinto, A. M. F. R. (2005). *Experimental Setup for the Hydrodynamic Study of an Internal Loop Airlift Column*. Proceedings of the 9th International Chemical Engineering Conference Chempor2005, Coimbra, Portugal.

Santos, M. E. M. (2004). *Estudo hidrodinâmico de uma coluna de recirculação de líquido por borbulhamento através de um tubo interior*, M.Sc. Thesis, Faculdade de Engenharia, Universidade do Porto, Portugal.

Sena Esteves, M.T.M. (1998). *Caracterização hidrodinâmica e transferência de massa em sistemas Gás-Líquido com bolhas tubulares*, Ph.D. Thesis, Faculdade de Engenharia, Universidade do Porto, Portugal.

Acknowledgements

The partial support of Fundação para a Ciência e Tecnologia - Portugal through project POCTI/EQU/46880/2002 is gratefully acknowledged.

The research team would like to thank the students Menno van der Zanden and Rui Silva for the experimental work performed.

ORGANIZATION

University of Minho
Dept. Biological Engineering

Ordem dos
Engenheiros

IBB
INSTITUTE FOR BIOTECHNOLOGY AND BIOENGINEERING

SUPPORT

SOCIEDADE
PORTUGUESA
DE QUÍMICA

spbt
sociedade
portuguesa de
biotecnologia

SPONSORS

MEDIA PARTNERS

New Journals IMPACTING Science

Recent Patents on Electrical Engineering

publishes review articles by experts on recent patents in electrical engineering. A selection of important and recent patents on electrical engineering is also included in the journal. The journal is essential reading for all researchers involved in electrical engineering science.

Volume 1, 3 Issues, 2008
Personal Subscription: $ 340.00

Recent Patents on Biomedical Engineering

publishes review articles on recent patents in the field of biomedical engineering e.g. new medical devices and biomaterials. A selection of important and recent patents on biomedical engineering is also included in the journal. The journal is essential reading for all researchers involved in biomedical engineering.

Volume 1, 3 Issues, 2008
Personal Subscription: $ 340.00

Current Molecular Pharmacology

publishes the latest developments in cellular and molecular pharmacology. Each issue contains in-depth reviews written by leaders in the field.

Volume 1, 3 Issues, 2008
Personal Subscription: $ 140.00

Recent Patents on Chemical Engineering

publishes review articles by experts on recent patents in chemical engineering. A selection of important and recent patents on chemical engineering is also included in the journal. The journal is essential reading for all researchers involved in chemical engineering science.

Volume 1, 3 Issues, 2008
Personal Subscription: $ 340.00

Recent Patents on Materials Science

publishes review articles by experts on recent patents in all fields of materials science. A selection of important and recent patents on materials is also included in the journal. The journal is essential reading for all researchers involved in materials sciences.

Volume 1, 3 Issues, 2008
Personal Subscription: $ 340.00

Recent Patents on Mechanical Engineering

publishes review articles by experts on recent patents in mechanical engineering. A selection of important and recent patents on mechanical engineering is also included in the journal. The journal is essential reading for all researchers involved in mechanical engineering science.

Volume 1, 3 Issues, 2008
Personal Subscription: $ 340.00

Current Radiopharmaceuticals

publishes original research articles on all aspects on radiolabelled compound preparations, including radio imaging techniques, therapies, preparation and application of radionuclide compounds.

Volume 1, 3 Issues, 2008
Personal Subscription: $ 140.00

Recent Patents on Computer Science

publishes review articles by experts on recent patents in all areas of computer science. A selection of important and recent patents on computer science is also included in the journal. The journal is essential reading for all researchers involved in computer science.

Volume 1, 3 Issues, 2008
Personal Subscription: $ 340.00

Current Drug Abuse Reviews

publishes reviews and meta-analyses on all the latest advances on alcohol and drug abuse and addiction.

Volume 1, 3 Issues, 2008
Personal Subscription: $ 140.00

Current Aging Science

publishes frontier review and experimental articles in all areas of aging and age-related research that may influence longevity. The journal is essential reading for gerontologists, neuroscientists, clinicians, health science planners, granting agencies and pharmaceutical scientists.

Volume 1, 3 Issues, 2008
Personal Subscription: $ 140.00

20% Discount! ***Valid until November 15th, 2008***

To subscribe, quote your priority code **ICBE08** at:
subscriptions@bentham.org

- *Information*
- *FREE online issues*

www.bentham.org

20% Conference Subscription Discount

BENTHAM SCIENCE